Proceedings of the 7th International Colloquium on Bluff Body Aerodynamics and Applications

Co-editors: Haifan Xiang
Yaojun Ge
Shuyang Cao

人民交通音像电子出版社
China Communications Audio-Visual & Electronic Press

Proceedings of the 7th International Colloquium on Bluff Body Aerodynamics and Applications

Shanghai , China , September 2-6 , 2012

Co-editors

Hai-Fan XIANG

Yao-Jun GE

Shu-Yang CAO

人民交通音像电子出版社

China Communications Audio-Visual & Electronic Press

Brief Introduction

The Seventh International Colloquium on Bluff Body Aerodynamics and Applications (BBAA7) is held in Shanghai, China, on September 2-6, 2012. BBAA7 is co-organized by Tongji University, China Academy of Building Research, Hunan University, Southwest Jiaotong University, State Key Laboratory of Disaster Reduction in Civil Engineering and CCCC Highway Consultants Co., Ltd., and in cooperation with International Association for Wind Engineering, Natural Science Foundation of China, Shijiazhuang Tiedao University, Chang'An University, Key Laboratory of Wind Resistance Technology of Bridges of Ministry of Transport and Tianjin Research Institute for Water Transport Engineering of Ministry of Transport. It follows the sprits set in the previous 6 BBAA Colloquia held in Japan in 1988, Australia in 1992, United States in 1996, Germany in 2000, Canada in 2004 and Italy in 2008. It provides a stimulating and constructive forum to facilitate the exchange of the latest scientific and technical information in the field of flow around fixed and vibrating bluff bodies both in terms of fundamentals as well as applications, particularly to Wind Engineering. The major topics for BBAA7 include experimental, computational and analytical studies of vortex shedding and wakes, fluid-structure interaction and aerodynamics of bridges, cables, buildings and vehicles and so on. A total of 200 papers are collected in the colloquium proceedings, including 5 keynote session papers and 195 parallel session papers.

Title: **Proceedings of the 7th International Colloquium on Bluff Body Aerodynamics and Applications**

Authors: Hai-Fan XIANG Yao-Jun GE Shu-Yang CAO

Responsible Editors: Le QU Zhe LI

Publisher: China Communications Audio-Visual & Electronic Press

Address: NO. 3 Waiguanxie Stress, Chaoyang District, Beijing, 100011

Website: http://www.ccpress.com.cn

Tel: 0086-10-85285984

Edition: First edition, August 2012

ISBN: 978-7-900265-90-6

Total Price: ¥ 185.00

Co-organized by

Tongji University
China Academy of Building Research
Hunan University
Southwest Jiaotong University
State Key Laboratory of Disaster Reduction in Civil Engineering
CCCC Highway Consultants Co., Ltd.

In cooperation with

International Association for Wind Engineering
Natural Science Foundation of China
Shijiazhuang Tiedao University
Chang'An University
Key Laboratory of Wind Resistance Technology of Bridges of Ministry of Transport
Tianjin Research Institute for Water Transport Engineering of Ministry of Transport

Committees

International Advisory Committee

Co-Chairman: Y. Tamura (Japan) and H. F. Xiang (China)
Secretary: S. Y. Cao (China)
Members:

C. Borri (Italy)
L. S. Cochran (USA)
G. Diana (Italy)
Y. J. Ge (China)
C. Geurts (Netherlands)
R. Hoeffer (Germany)
A. Huber (USA)
N. R. Iyer (India)
A. Kane (India)
A. Kareem (USA)
K. Kwok (Australia)
C. Letchford (Australia)
D. Reed (USA)
G. Solari (Italy)
T. Stathopoulos (Canada)
M. Sterling (UK)

International Scientific Committee

Co-Chairman: H. F. Xiang (China) and Y.J. Ge (China)
Secretary: S. Y. Cao (China)
Members:

B. Blocken (Netherlands)
C. Borri (Italy)
Z. Q. Chen (China)
L. S. Cochran (USA)
G. Diana (Italy)
Q. S. Ding (China)
C. Geurts (Netherlands)
M. Gu (China)
Z. S. Guo (China)
H. Hangan (Canada)
R. Hoeffer (Germany)
K. Hourigan (Australia)
P. Huang (China)
X. Y. Jin (China)
A. Kareem (USA)
H. Kawai (Japan)
G. Kopp (Canada)
K. Kwok (Australia)
S. Lee (Korea)
Q. S. Li (Hong Kong, China)
S. G. Liang (China)
H. L. Liao (China)
J. X. Liu (China)
W. J. Lou (China)
M. Matsui (Japan)
M. Matsumoto (Japan)
G. Piccardo (Italy)
Y. Quan (China)
P. Richards (New Zealand)
H. Shirato (Japan)
G. Solari (Italy)
T. Stathopoulos (Canada)
M. Sterling (UK)
D. Sumner (Canada)
T. Tamura (Japan)
Y. Tamura (Japan)
M. Tsubokura (Japan)
J. Xie (Canada)
H. Yamada (Japan)
Y. X. Yang (China)
A. Zasso (Italy)
L. Zhao (China)
D. Zhou (China)
X.Y. Zhou (China)
Z.Y. Zhou (China)
L.D. Zhu (China)

Local Organizing Committee

Chairman: Y. J. Ge (Tongji Univ.)
Vice Chairmen: Z. Q. Chen (Hunan Univ.)
H. L. Liao (Southwest Jiaotong Univ.)
X. Y. Jin (China Academy of Building Research)
X. G. Zhang (CCCC Highway Consultants Co., Ltd.)
Secretary: L.D. Zhu (Tongji Univ.)
Members:

J. F. Bai (TRIWTE)
S. Y. Cao (Tongji Univ.)
K. Chen (CABR)
Q. S. Ding (Tongji Univ.)
Z. S. Guo (Tongji Univ.)
X. H. Hu (Tongji Univ.)
X. G. Hua (Hunan Univ.)
P. Huang (Tongji Univ.)
J. W. Li (Chang'An Univ.)
M. S. Li (Southwest Jiaotong Univ.)
Y. Q. Li (Tongji Univ.)
G. Liu (CCCC Highway Consultants)
Q. K. Liu (Shijiazhuang Tiedao Univ.)
Y. Quan (Tongji Univ.)
J. Y. Xu (Tongji Univ.)
L. Xu (Tongji Univ.)
Y. X. Yang (Tongji Univ.)
L. Zhao (Tongji Univ.)
X.Y. Zhou (Tongji Univ.)
Z.Y. Zhou (Tongji Univ.)

Contents

Session C-1: Prism Aerodynamics - Rectangular

Session D-1(OS1): NSFC-JST Project of New Strategies for Wind Disaster Risk Reduction of Wind Sensitive Infrastructures

Session A-2: Bridge Aerodynamics – Modeling

Session B-2: Building Aerodynamics - Interference

Session C-2: Prism Aerodynamics - Circular

Session D-2: Cable Aerodynamics

Session A-3: Bridge Aerodynamics – Buffeting

Session B-3: Building Aerodynamics - High-rise

Session C-3: Prism Aerodynamics - Square

Session D-3 (OS2): Bluff body aerodynamics: Application to dispersion of pollutants

Session A-4: Bridge Aerodynamics - Vortex Excitation

Session B-4: Aerodynamics of Other Structures (1)

Session C-4: Building Aerodynamics - Low-rise

Session D-4: Aerodynamics of Other Structures (2)

Session A-5: Bridge Aerodynamics - Flutter

Session B-5: Wind energy

Session C-5: Tree/Vegetation

Session D-5: Vehicular Aerodynamics (1)

Session A-6: Bridge Aerodynamics - CFD

Session B-6: Aerodynamics of Other Structures (3)

Session C-6: Wind Environment (1)

Session D-6: Vehicular Aerodynamics (2)

Session A-7: PIV Application

Session B-7: Wind Characteristics

Preface

August 15, 2012

The Seventh International Colloquium on Bluff Body Aerodynamics and Applications (BBAA7) is to be held in Shanghai, China, on September 2-6, 2012. It is co-organized by Tongji University, China Academy of Building Research, Hunan University, Southwest Jiaotong University, State Key Laboratory of Disaster Reduction in Civil Engineering and CCCC Highway Consultants Co., Ltd., and in cooperation with International Association for Wind Engineering, Natural Science Foundation of China, Shijiazhuang Tiedao University,Chang'An University, Key Laboratory of Wind Resistance Technology of Bridges of Ministry of Transport and Tianjin Research Institute for Water Transport Engineering of Ministry of Transport.

BBAA7 follows the spirits set in the previous BBAA Colloquia held in Japan in 1988, Australia in 1992, United States in 1996, Germany in 2000, Canada in 2004 and Italy in 2008. It provides a stimulating and constructive forum to facilitate the exchange of the latest scientific and technical information in the field of flow around fixed and vibrating bluff bodies both in terms of fundamentals as well as applications, particularly to Wind Engineering. The major topics for BBAA7 include experimental, computational and analytical studies of vortex shedding and wakes, fluid-structure interaction and aerodynamics of bridges, cables, buildings and vehicles and so on.

A total of 200 papers are collected in the colloquium proceedings, including 5 keynote papers, 20 organized session papers and 175 general papers. The three organized sessions are NSFC-JST Project of New Strategies for Wind Disaster Risk Reduction of Wind Sensitive Infrastructures - focusing on Typhoon simulation and Universal ESWL, Bluff Body Aerodynamics: Application to Dispersion of Pollutants, and New Technology for CFD Wind-resistant Design of Buildings. The specific topics of general papers cover Wind Environment; Wind Characteristics; Prism Aerodynamics including Rectangular, Circular and Square; Bridge Aerodynamics including General, Modeling, Buffeting, Vortex Excitation, Flutter and CFD; Building Aerodynamics including CFD, Interference, High-rise, and Low-rise; Vehicular Aerodynamics; Cable Aerodynamics; Aerodynamics of Other Structures; Tree/Vegetation; PIV Application; and Wind Energy. All the papers included in this proceedings have received peer reviews under the coordination of the International Scientific Committee of BBAA7.

The editors would like to express sincere gratitude to all contributors for their submissions with high academic quality and to the organizers of three organized sessions for their organization with interesting topics as well as to reviewers for their useful opinions and comments to make this 2000-page proceedings extraordinarily outstanding. We hope this special issue will serve as a milestone in BBAA and provide indications for further research and development in the wind engineering field.

Co-edited by
Hai-Fan Xiang, Chairman of Scientific Committee
Yao-Jun Ge, Vice Chairman of Scientific Committee
Shu-Yang Cao, Secretary of Scientific Committee

Bluff body vorticity generation and wake transitions

Kerry Hourigan[a], Morten Brøns[b], Mark C. Thompson[a], Thomas Leweke[c]

[a]*FLAIR, Department of Mechanical and Aerospace Engineering & Division of Biological Engineering, Monash University, Melbourne, Australia*
[b]*Department of Mathematics, Technical University of Denmark, Lyngby, DK-2800, Denmark*
[c]*Institut de Recherche sur les Phénomènes Hors Équilibre (IRPHÉ), UMR 7342 CNRS / Aix-Marseille Université, Marseille, France*

ABSTRACT: Although vorticity is an essential characteristic of bluff body wakes, its origin, transport and conservation is not always explored or understood. Prior to discussing the evolution of wakes from cylinders, a generalised formulation of vorticity generation at boundaries is presented, ranging from free to no-slip boundary conditions and including fluids ranging from the limits of solid to vacuum. Vorticity is found to be generated by tangential pressure gradients or relative acceleration of fluid at interfaces. Examples of vorticity generation, diffusion and storage are given, including that for a rotating cylinder. The enigma of apparent vorticity disappearance for a submerged cylinder is explained. Alternative descriptions in terms of vorticity and momentum are contrasted; vorticity is shown to be conserved in each case. The wake transitions from two-dimensional vortex sheets to three-dimensional modes for the circular cylinder are shown to change dramatically under the influence of oscillation and geometrical modification.

KEYWORDS: Vorticity, Bluff Bodies, Wakes, Stability

1 INTRODUCTION

Fundamental to some of the major problems - such as vortex induced vibrations - that arise in the flow around stalled airfoils and bluff bodies in aeronautics and wind engineering are the dynamic wake structures and the transitions between different wake modes. In particular, as smaller structures such as micro-aircraft and surface modifications are considered, the question of wake structure and stability in the Reynolds number range of 10-10^3 becomes increasingly important.

Vorticity is one of the most important physical quantities in fluid mechanics. Boundary layers, wakes and turbulence in bluff body flows owe their presence to, and are essentially defined by, vorticity and vortices, whose motions are "the sinews and muscles of fluid motions" (Küchemann[1]) and are associated with fluctuating forces in a flow.

A dynamical formulation for the generation of vorticity has previously been sought (Morton[2]). Considering mainly the flow next to a solid wall, it was concluded:

1. Vorticity is generated at boundaries by the relative acceleration of fluid and wall produced instantaneously:
   i) from the fluid side by tangential pressure gradients;
   ii) from the wall side by acceleration of the boundary, where generation is again partially masked by viscous diffusion when there is continuing generation.
2. For an impulsive change, wall stress does not produce vorticity.
3. The only means of decay or loss of vorticity is by cross-diffusion and annihilation of vorticity of opposite signs.

The case of a free surface has also been studied, and it has been shown that vorticity is conserved (Lundgren and P. Koumoutsakos[3]). That is, vorticity (in terms of total circulation) is not

lost through the free surface but rather is "stored" in the line vortex representing the free surface. This is an important result that needs to be considered in our formulation.

The aims of this paper are:

i) to demonstrate how vorticity is generated at boundaries, redistributed into the flow, and interacts with other boundaries;
ii) to examine the 3D transitions that arise in the vorticity generated at, and shed from, bluff body surfaces.

A generalised description of the generation of vorticity at interfaces between fluids ranging from a vacuum to a solid, and for partial slip conditions at the interface ranging from free to no-slip, is presented. We extend important previous works (Morton[2], Lundgren and P. Koumoutsakos[3]) to cover vorticity generation at interfaces, both flat and curved, between fluids for a range of densities and viscosities, in addition to different degrees of slip. Furthermore, a number of examples are considered to demonstrate the power of this generalised formulation and to provide a physical insight into the generation, redistribution and conservation of vorticity. These include planar Couette flow, a cylinder translating horizontally below a free surface, and a rotating circular cylinder in a fluid with an outer radial boundary. The development of three-dimensional wakes modes from the initial two-dimensional vorticity shed from cylinders is then studied, with emphasis on the difference in the order of appearance and characteristics of the modes.

2 NUMERICAL METHODS

A spectral-element solver using a semi-implicit time-stepping scheme was used to solve the Navier-Stokes and continuity equations (Thompson et al.[4]). The Navier-Stokes equations were discretised with the use of a semi-implicit spectral-element scheme that uses time-splitting for the temporal discretisation. This code has previously been employed to obtain accurate solutions for the flow around cylinders (Thompson et al.[4,5]; Ryan et al[6]), spheres (Thompson et al.[7]; Thompson et al.[8]) and rings (Sheard et al.[9]). The implementation for the time-splitting or fractional step method is given in Karniadakis et al.[10], which is based on a method originally proposed by Chorin[11].

To examine the sensitivity of the flow around the bluff body to three-dimensional perturbations in the spanwise direction, a linear stability analysis is carried out. This involves solving the linearized Navier–Stokes equations based on a pre-computed two-dimensional base flow. The approach has been documented in, for example, Ryan et al.[6]

3 RESULTS

The formation of wakes behind two-dimensional bluff bodies consists initially of the generation of two-dimensional vorticity at the surface, then the shedding of the vorticity into the wake, and finally the development of three-dimensional wake modes. We first examine how vorticity is generated and behaves near interfaces between fluids of varying properties. Then, the results of some previous two-dimensional and axisymmetric studies are examined to understand the generation and apparent disappearance of vorticity. Finally, the appearance of three-dimensional vortex structures originating from unstable two-dimensional bluff body wakes is presented.

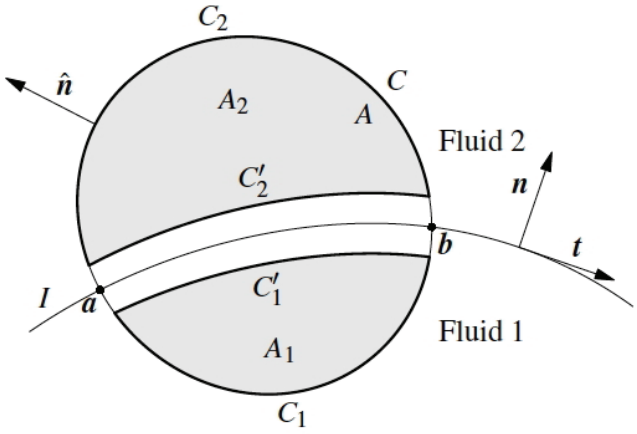

Figure 1. The interface I with normal vector **n** and tangential vector **t**. Shaded sub-regions A_1, A_2 of the region A in each fluid are bounded by the curves C_1,C_1' and C_2,C_2', respectively. The outward normal vector of a region is denoted by $\hat{n}$ and **n** is the outward normal vector to the interface.

3.1 *Vorticity in a two-fluid system*

A generalised formulation of vorticity generation is presented that includes the spectrum of fluids from solid to vacuum. The Helmholtz vorticity equation,

$$\partial\omega/\partial t + (\mathbf{v}.\nabla)\boldsymbol{\omega} = (\boldsymbol{\omega}.\nabla)\mathbf{v} + \nu\nabla^2\omega, \quad (1)$$

where ω is vorticity, **v** is velocity, and ν is the kinematic viscosity, gives little information on how vorticity is generated because it contains no true generation term (Morton[2]). The first term on right is a processing term describing the effects of local amplification (or concentration) of vorticity by stretching and/or local turning of vortex filaments. The second term on right represents viscous diffusion; that is, the spread of vorticity due to viscosity. Therefore, for a homogeneous fluid, vorticity is generated only at boundaries.

Consider a two-dimensional, viscous incompressible fluid in some domain in the plane (see Fig. 1). Let A be a material region in the domain, bounded by the simple curve C. From a standard application of the divergence theorem on the vorticity transport equation, one obtains for the rate of change of vorticity in A:

$$d/dt \int_A \omega \, dA = \oint_C \nu\nabla\boldsymbol{\omega}.\mathbf{n} \, ds, \quad (2)$$

where **n** is the outward unit normal. The equation states that the total vorticity in the region changes only because vorticity diffuses across the boundary. Thus, there are no sources of vorticity in the simple domain A. However, vorticity may arise at the interface, as will be shown.

Assume now that an interface between two fluids passes through A. We assume that all relevant physical quantities and all of their derivatives have limits as the interface is approached in each of the fluids. These limits when approached in fluid 1(2) are denoted by the subscript 1(2). Only if a quantity **q** is continuous across the interface is it well-defined at the interface. Otherwise, only the jump $[[\mathbf{q}]] = \mathbf{q}_2 - \mathbf{q}_1$ is single-valued at the interface.

Restricting attention to interfaces that do not change location in time (i.e., the normal velocity of the fluids at the interface is zero), then after some manipulation, one can show that the time rate of change in total circulation is related to the pressure (p) difference along the interface:

$$d/dt(\int_A \omega \, dA + \int_a^b \gamma \, ds) = \oint_C \nu \nabla \boldsymbol{\omega} . \mathbf{n} \, ds + [[p/\rho]]_a - [[p/\rho]]_b. \quad (3)$$

where ρ is the local density of the fluid and γ is the circulation. The first term on the right side of the equation is not a generation term – rather, it represents the flow of vorticity into or out of the region due to viscous diffusion. The second term on the right represents the generation of vorticity due to tangential pressure gradients along the interface boundary for each fluid. The quantity $\gamma = -[[\mathbf{u}.\mathbf{t}]]$ represents the tangential velocity jump across the interface.

For the case where the interface is infinitely long or the pressure is the same at each end (e.g., bluff body) and for regions where no vorticity is diffusing across the outer boundaries, we have no net source terms (although there may be local ones at the interface), and vorticity is conserved:

$$d/dt \, (\int_A \omega \, dA + \int_a^b \gamma \, ds) = 0. \quad (4)$$

Note that the results of the present section are independent of any boundary conditions on the outer boundary or the interface; only the Navier-Stokes equations and incompressibility constraint are assumed.

3.2 *Vorticity in a single-fluid system*

Many problems in fluid dynamics are formulated as a single fluid region with boundary conditions imposed instead of an interface with another fluid. We now derive the vorticity integrals for single fluid domains by reducing the interface between two fluids to boundary conditions for two common cases: the no-slip condition and the free-surface condition.

3.2.1 *No-slip boundary condition*

Let fluid 2 be replaced by a solid body with a no-slip boundary condition imposed at the interface *I* **(**see Fig. 1**).** If the velocity of the surface of the solid body is denoted by **U**, the vorticity balance now has the form:

$$d/dt \, (\int_{A_1} \boldsymbol{\omega} \, dA \,) = \oint_{C1} \nu \nabla \boldsymbol{\omega} . \mathbf{n} \, ds - d/dt \, (\int_a^b \mathbf{U}.\mathbf{t} \, ds) - (p_1/\rho_1|_b - p_1/\rho_1|_a). \quad (5)$$

Note that no vorticity is stored at the no-slip boundary but a vorticity generation term (second on right) appears as a result of acceleration of the boundary (in addition to the generation term due to fluid pressure gradient along the boundary: the third term on the right), as found by Morton[2]. The boundary condition $\mathbf{u} = \mathbf{U}$ does not produce a simple boundary condition in terms of vorticity $\boldsymbol{\omega}$.

3.2.2 *Free-slip boundary condition*

Now consider the case where the interface has free slip, such as for a free surface of fluid 1. That is, we assume that the shear stress at the interface in fluid 1 is zero. For the mathematical formulation of the flow in fluid 1, no description of fluid 2 is needed. The vorticity balance for the flow region A_1 is:

$$d/dt \, (\int_{A_1} \omega \, dA + \int_a^b \mathbf{u_1}.\mathbf{t} \, ds) = \oint_{C1} \nu \nabla \boldsymbol{\omega} . \mathbf{n} \, ds - (p_1/\rho_1|_b - p_1/\rho_1|_a). \quad (6)$$

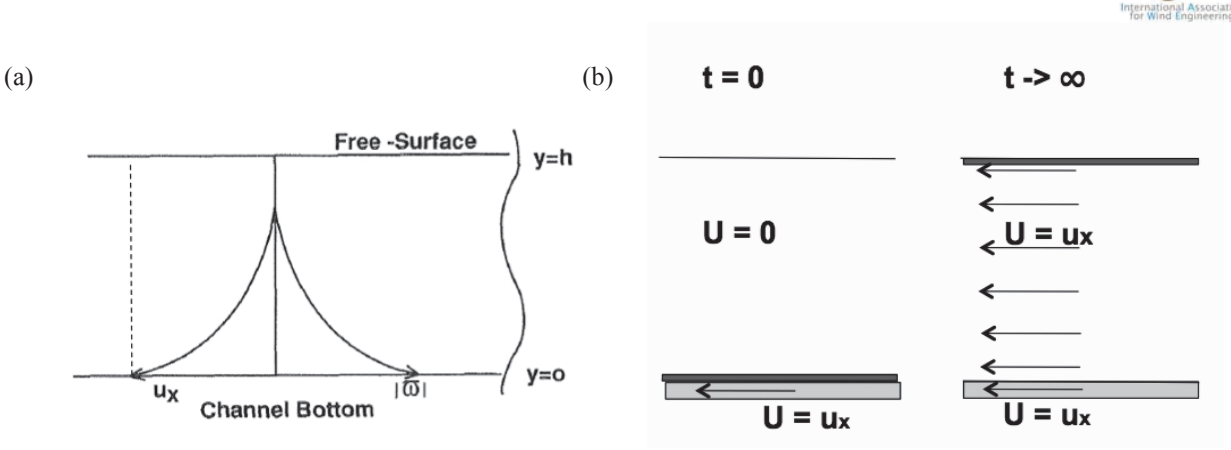

Figure 2. (a) Schematic after Rood[12]. Bottom plate is accelerated impulsively from rest to velocity u_x at $t = 0$. (b) As time approaches infinity, the initially quiescent fluid layer uniformly co-moves with the plate. The thicker dark lines on the bottom plate at $t = 0$ and at the upper free surface at $t \rightarrow \infty$ denote vorticity originally generated by the impuslively accelerated plate and vorticity stored at the interface in a vortex sheet, respectively.

That is, vorticity is generated in this case for a free or slip surface by a pressure gradient in the fluid along the surface, with vorticity being stored at the boundary (second term in brackets on the left). The boundary condition on vorticity (for zero normal velocity) is given by

$$\omega_1 = 2\,\mathbf{u_1}.\mathbf{t}\,\kappa = \kappa V_1. \tag{7}$$

Here, V_1 is the tangential fluid velocity at the interface and κ is the fixed surface curvature. Thus, vorticity can appear at the boundary due to curvature of the interface and tangential velocities induced by pressure gradients. However, this "additional" vorticity is balanced by the amount stored at the interface in the case; where there is no diffusion of vorticity into/out of the system, the total vorticity is conserved.

3.3 *Examples of vorticity generation and diffusion*

3.3.1 *Planar Couette flow with a free surface*

When the plate at the bottom of a finite, initially quiescent, fluid layer is impulsively accelerated, the final flow as time approaches infinity is a horizontal, uniform fluid flow of velocity equal to the plate velocity (see Fig 2). There appears to be no vorticity remaining as no velocity gradients exist in the fluid. Rood[12] concluded: "Vorticity is neither conserved nor is it angular momentum. Therefore it is physically acceptable that vorticity entirely disappears from a flow. The disappearance of the vorticity is unsettling if vorticity is erroneously ascribed the same conservation principle that applies to momentum". Contrary to this, we find that vorticity conservation is common, even for systems where momentum is continually changing.

According to (5), vorticity is generated at $t = 0$ due to the impulsive acceleration of the solid plate, i.e., through the d/dt ($\int_a^b \gamma\, ds$) term with γ (the velocity jump across the interface) = u_x (the plate velocity). Vorticity then diffuses away from the plate towards the free surface above. In the final state, there are no velocity gradients or vorticity diffusion in the flow (uniform horizontal flow) but the velocity at the free surface interface has increased from zero to u_x. If we consider the velocity in the vacuum above to have remained zero then this means that the velocity jump

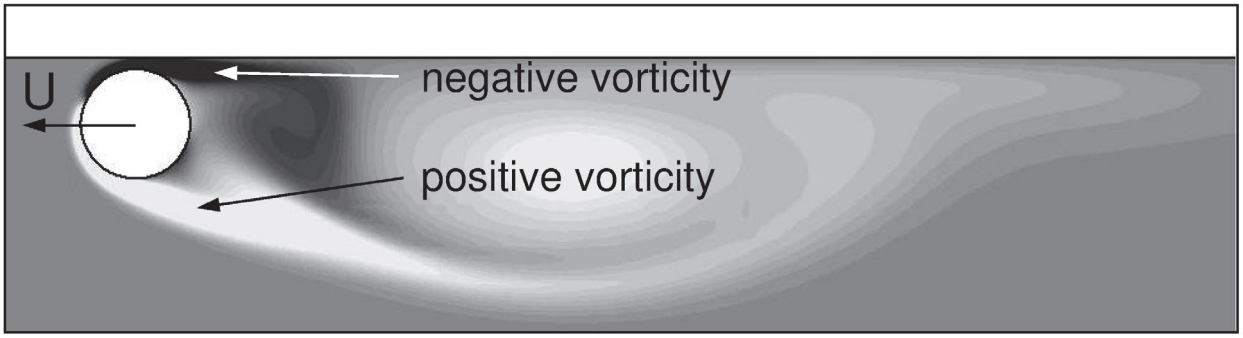

Figure 3. Cylinder translating horizontally, right to left, very close to a free surface. Vorticity layers shed from the upper and lower surfaces of the cylinder are of opposite sign. The net circulation within the fluid and within the vortex sheet at the free surface remains constant.

initially at the bottom interface is now at the top surface. Therefore, vorticity is impulsively introduced and is conserved here; accounting for its balance is simple. Interestingly, to keep the plate moving at constant velocity to overcome frictional resistance, momentum is required to be continuously introduced into the fluid and is therefore more complicated to track.

3.3.2 *Submerged cylinder*

Second, as a cylinder, relatively translating horizontally in a fluid layer, is moved closer towards a free surface, an intriguing phenomenon is observed (Sheridan et al.[13], Reichl et al.[14]). The vorticity shed from the upper cylinder surface rapidly disappears as it advects downstream and a net circulation seems to manifest in the flow (see Fig 3). No net vorticity is shed from the cylinder because its boundary is a closed curve and therefore no net pressure gradient can result (and there is no tangential acceleration of the solid surface). However, a closer examination shows that the deficit in vorticity present in the flow from the disappearing upper shear layer shedding is balanced precisely by the increase in the circulation of the line vortex (or velocity jump) at the free surface. Again, total vorticity in the flow is conserved even though the magnitude of the momentum of the flow is continuously increasing.

3.3.3 *Rotating cylinder*

Third, the case of a spinning cylinder in a flow is considered. When a circular cylinder is impulsively spun-up to angular velocity Ω in an initially quiescent flow, vorticity of sign opposite to that in the solid cylinder ($\omega = -2\Omega$) is generated at the surface of the fluid in contact with the cylinder. That is, instantaneously, a circular vortex sheet is generated in the fluid. This vortex sheet diffuses radially outwards in the fluid and distributes to a larger and larger area such that at any given point, $\omega \to 0$ for $t \to \infty$. At a given point, $|\omega|$ first increases and then tends to zero but never reaches that value. The flow tends to the potential flow around a line vortex having circulation equal that of the cylinder. The total vorticity of the system (cylinder plus fluid) remains zero.

When an outer free slip boundary is placed at a finite radius (see Fig. 4), one may expect the final solution to be analogous to that of example 1, where no vorticity remains in the main body of the fluid but resides in the vortex sheet at the surface. However, for a curved boundary, the boundary condition on vorticity is $\omega = 2\mathbf{u}_1.\mathbf{t} = \kappa V_1$, where V_1 is the tangential fluid velocity at the interface and κ is the fixed surface curvature. In the plane free-surface case, the curvature of the surface is zero and the vorticity is therefore identically zero there. In the curved surface case, non-zero and varying vorticity can be present at the free surface.

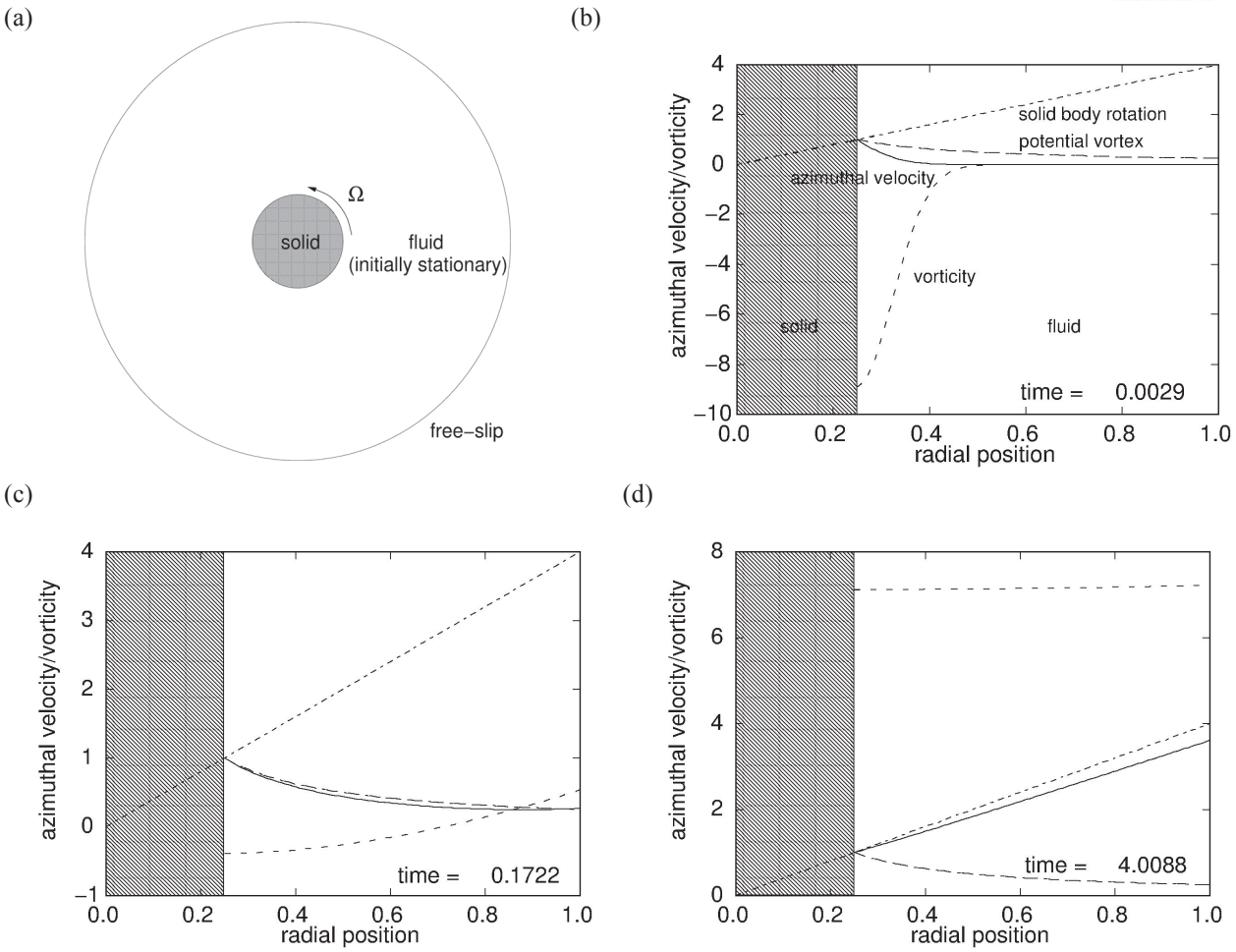

Figure 4 (a) Schematic of rotating cylinder with outer free boundary. (b), (c), (d): solutions for the velocity (solid line) and vorticity (medium dashed line) profiles in fluid at successive normalized times. Also shown for reference are the velocity distributions for the potential flow around a line vortex (long dashed lines) and for solid body rotation (short dashed lines).

When the cylinder is impulsively spun-up, the vorticity generated at the fluid inner boundary diffuses radially outwards, with a velocity profile initially tending to potential flow around a line vortex, as in the unbounded cylinder case. However, this potential flow solution is incompatible with the vorticity boundary condition at the free surface, and vorticity is fed back radially from the interface, leading ultimately to solid body rotation in the fluid. Nonetheless, vorticity is conserved in this problem, with the balance of vorticity stored in the circular vortex sheet at the outer boundary. Note again that no net vorticity is added after the initial spin-up but that angular momentum needs to be continually transferred to the system to keep the cylinder rotating at constant angular velocity.

3.4 *Transition of wakes to three-dimensionality*

Above, we have considered the generation and transport of vorticity in two dimensions or axisymmetry. For many bluff body flows, when the Reynolds number exceeds a threshold, the two-

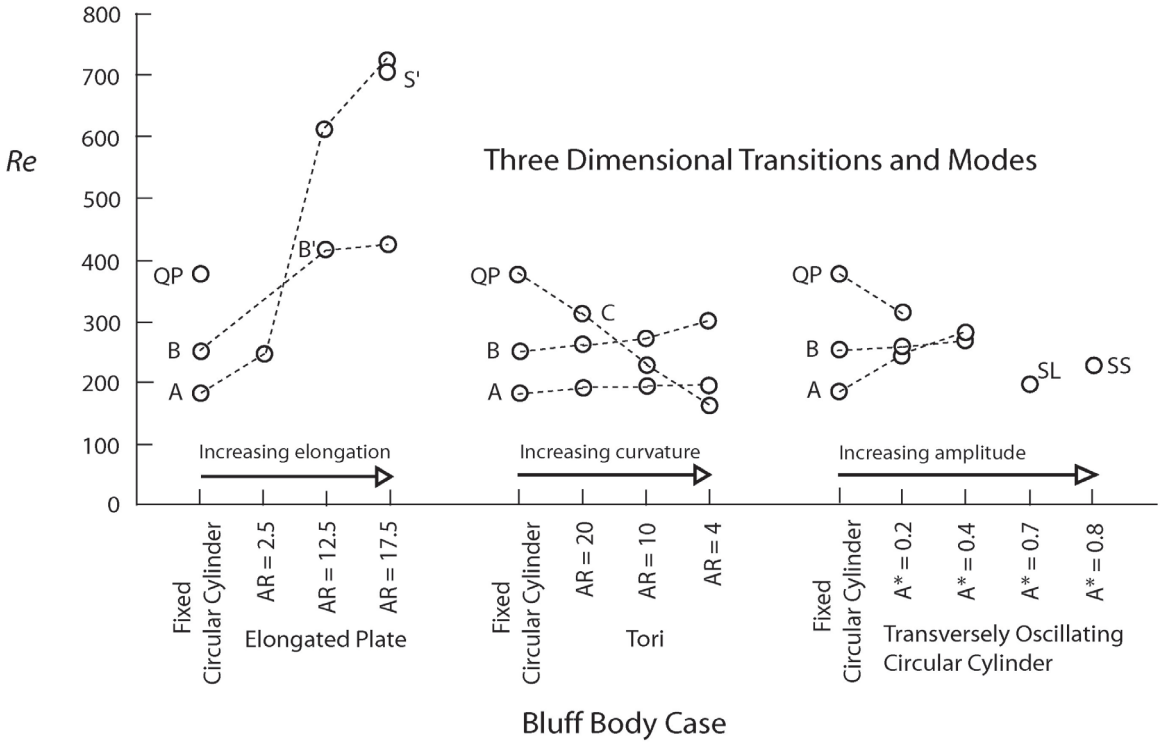

Figure 5. Three-dimensional transitions of different modes for variations of the fixed cylinder flow: elongation in direction of flow; increasing curvature to limit of sphere; increasing oscillation at the natural Strouhal frequency.

dimensional wakes, formed by vorticity shed from the bluff body surface, are found to transition to three-dimensionality. The canonical geometries for bluff bodies are the circular cylinder and the sphere, for which a considerable number of experimental and computational studies have been undertaken. Here, we will consider the basic geometry of a cylinder and examine the change in wake transition as the cylinder geometry is varied, or if the cylinder is oscillated as occurs in vortex-induced vibration.

For the circular cylinder, stability analysis indicates that the two-dimensional periodic wake becomes linearly unstable to mode A at Re ≈ 190, and the base flow undergoes a further bifurcation to mode B at Re ≈ 260. Experiments and direct numerical simulations (DNS) show that mode B becomes unstable at a significantly lower Reynolds number (Re = 230-240). At slightly higher Reynolds numbers, there is a strong nonlinear interaction between the modes and the wake undergoes a rapid transition to spatio-temporal chaos, so that it is effectively turbulent for a Reynolds number of just a few hundred.

In the case of the sphere, the wake undergoes a regular (i.e., time-steady) transition at Re = 212 to the two-threaded wake. This wake then becomes unstable at Re ≈ 270 through a Hopf (steady to periodic) bifurcation. At Re ≈ 350, the vortical wake structures no longer maintain the same strict alignment from one shedding cycle to the next. The overall wake structure is similar at considerably higher Reynolds numbers, although much more chaotic.

Although the wakes of the circular cylinder and the sphere have been well studied, the question is whether they really are generic or universal with respect to wake transitions. Shown in the Figure 5 are the wake transitions to three-dimensionality for a cylinder that is (i) increasingly elongated in the streamwise direction, (ii) increasingly curved and contracted into a torus (and eventually a sphere), and (iii) oscillated with increasing amplitude at the natural Strouhal fre-

quency. As can be observed, the transitions are not universal: not only does the Reynolds number at which transitions occurs change significantly, but the order of appearance of the modes varies, and in fact new modes can appear. For example, with increasing curvature of a torus, mode C appears before both modes A and B. Likewise, as the amplitude of transverse oscillation of a cylinder increases, mode B can appear at a lower Reynolds number than mode A and eventually other modes (SL, SS) appear. This has implications for the route to turbulence in the wakes of different bluff bodies and the difficulty of defining a "canonical" bluff body.

4 CONCLUSIONS

A formulation is presented of vorticity generation and behavior at fluid-fluid interfaces, where the fluid properties are generalised to include the limits of a solid and free surface, and the *fluids* can range in properties from a solid to a vacuum. The two-fluid model can also be reduced to the traditional one-fluid model with boundary conditions. As proposed by Morton[2], vorticity is generated at boundaries due to pressure gradients in the fluid or relative acceleration of the contiguous fluids. Consistent with Lundgren and Koumoutsakos[3], vorticity can be stored as a vortex sheet at a free surface, leading to conservation of vorticity in the system. Examples showing the generation, transport and conservation of vorticity are discussed to demonstrate the power of the formulation. In the second part of the article, the transition to three-dimensionality of initially two-dimensional wakes shed by bluff bodies is examined. In particular, the flow around the circular cylinder, which is considered the generic case for two-dimensional bluff bodies, is examined. It is found that the modes and order of transition can differ dramatically from those of a fixed circular cylinder when the cylinder shape is varied or the cylinder is oscillated.

5 ACKNOWLEDGEMENTS

The support from Australian Research Council Discovery Grants DP0877327 and DP0877517 and computing time from the National Computational Infrastructure (NCI) and the Monash Sungrid are gratefully acknowledged.

6 REFERENCES

1. D. Küchemann, Report on the IUTAM Symposium on Concentrated Vortex Motion in Fluids. J. Fluid Mech. 21 (1965), pp. 1–20.
2. B.R. Morton, The generation and decay of vorticity. Geophys. Astrophys. Fluid Dyn. 28 (1984), pp. 277–308.
3. T. Lundgren and P. Koumoutsakos, On the generation of vorticity at a free surface. J. Fluid Mech. 382 (1999), pp. 351–366.
4. M.C. Thompson, T. Leweke and K. Hourigan, Sphere-wall collision: vortex dynamics and stability. J. Fluid Mech. 575 (2007), pp. 121-148.
5. M.C. Thompson, T. Leweke and C.H.K. Williamson, The physical mechanism of transition in bluff body wakes. J. Fluids and Structures 15 (2001), pp. 607-616.
6. K. Ryan, M.C. Thompson and K. Hourigan, Three-dimensional transition in the wake of bluff elongated cylinders. J. Fluid Mech. 538 (2005), pp. 1-29.
7. M.C. Thompson, T. Leweke and M. Provansal, Kinematics and dynamics of sphere wake transition. J. Fluids and Structures 15 (2001), pp. 575-586.
8. M.C. Thompson, K. Hourigan, K. Ryan and G.J. Sheard, Wake transition of two-dimensional cylinders and axisymmetric bluff bodies. J. Fluids and Structures 22 (2006), pp. 793-806.
9. G.J. Sheard, M.C. Thompson and K. Hourigan, From spheres to circular cylinders: The stability and flow structures of bluff ring wakes. J. Fluid Mech. 492 (2003), pp. 147-180.
10. G.E. Karniadakis, M. Israeli and S.A. Orszag, High-order splitting methods for the incompressible Navier–Stokes equations. J. Comput. Phys. 97 (1991), pp. 414–443.

11. A.J. Chorin, Numerical solution of the Navier–Stokes equations. Math. Comput. 22 (1968), pp.745–762.
12. E.P. Rood, Interpreting vortex interactions with a free surface. Trans. ASME J. Fluids Engng 116 (1994), pp. 91-94.
13. J. Sheridan, J.-C. Lin and D. Rockwell, Flow past a cylinder close to a free surface. J. Fluid Mech. 330 (1997), pp.1-30.
14. P. Reichl, K. Hourigan and M.C. Thompson, Flow past a cylinder close to a free surface. J. Fluid Mech. 533 (2005), pp. 269-296.

Flutter and Its Application - Flutter mode and Ship Navigation

Masaru Matsumoto

Professor Emeritus,Kyoto University, Kyoto, Japan
Visiting Professor,Osaka Electro and Tele-Communication University, Osaka, Japan

1 INTRODUCTION

Galloping, Torsional flutter and coupled flutter, all of these are here classified as flutter, have been widely studied by numerous researchers. Their generation mechanisms have been clarified, through previous studies. These flutter phenomena are summarized from author' view-points. Galloping is classified into unsteady and quasi-steady galloping, and into flow reattachment type galloping and flow non-reattachment type galloping.(Matsumoto and Laneville[2011], Matsumoto[2011])) In these, it is described that inner circulatory flow and separation bubble plays essentially important role for satisfactory of den Hartog Criteria[1956], $dCF/d\alpha<0$. Furthermore, inclined cable aerodynamics, those are rain-wind induced vibration and dry galloping, which have become greatly concerns to cable-stay bridge design0, are briefly explained from their generation point of view. On torsional flutter, pointing out important role of separation bubble, it is explained that the change of flutter of rectangular cylinder with different side ratio, B/D, from torsional flutter to coupled flutter occurs continuously with B/D, bounded approximately with B/D=10.(Matsumoto[1997]) Analogy of aerodynamic derivatives between H-shaped cylinders and rectangular cylinders is introduced (Matsumoto[2004]). Related to Tacoma Narrows Bridge failure, on sudden change of oscillation mode, from 5th symmetrical heaving mode to 1st asymmetrical torsional mode, another possible cause of increasing wind velocity is shown through wind tunnel test (Matsumoto[2004]). On coupled flutter, step-by-step (SBS) flutter analysis is introduced in contrast to conventional complex eigen value flutter analysis(Matsumoto[2010]). Classification of flutter branch and fundamental flutter mode is explained. Furthermore, on similar Selberg formula[1961] to estimate coupled flutter critical velocity for thin plate, is driven basing on simple assumption(Matsumoto[2010]. As application of knowledge of flutter, fundamental flutter mode, that is H-90 mode, definitely important role to produce propulsion force. A primary ship navigation test has been carried out and generation mechanism of propulsion force by flapping plate has been discussed. Navigation system by flapping plate might have significantly advantage of saving power because of intelligent utilization of flutter power generation system in flapping plate(Matsumoto and Ishizaki[2010]).

2 GALLOPING –1DOF HEAVING FLUTTER

2.1 *Non-flow Reattachment Type Galloping*

Galloping can be classified into "Quasi-steady Galloping" and "Unsteady Galloping" (Nakamura and Hirata[1996] and Matsumoto[2008]). "Quasi-steady Galloping" which is 1DOF heaving flutter, has been known to be catastrophic fluid-induced vibration, and negative slope associated with pitching angle of lift force coefficient, that is $dCF/d\alpha<0$, is definite condition for its excitation, as den Hartog Criteria[1956]. A numerous studies on quasi-steady galloping have been carried out to verify its generation mechanism from the point of flow fields

around bluff bodies. As summary, the characteristic flow fields related to appearance of negative lift slope, dCF/dα<0, are classified into two different one, that is inner-circulatory flow appearance on side surface of bluff body, which is originally proposed by Bearman[1972], and separation bubble formation on side surface of body. On former flow field, Nakamura[1981] lately pointed out “flow reattachment type pressure distribution flow”. For 2D rectangular cylinders with pitching angle of 0°, quasi-unsteady galloping caused by this flow field can be observed at the range of side-ratio, B/D (B: along-wind length, D: cross-wind length) between 0.75 and 2.8 in smooth flow (see Fig.1)

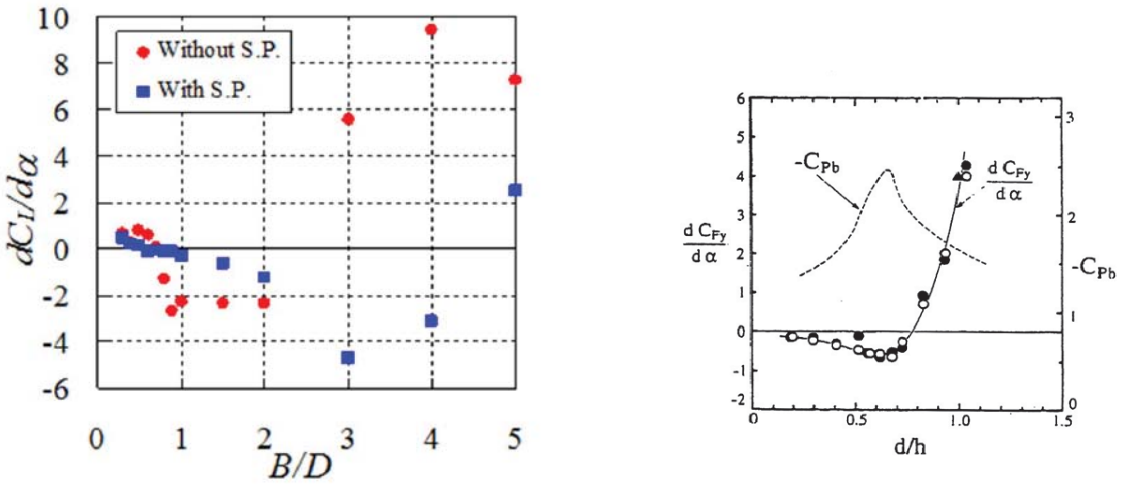

Matsumoto[2006] Nakamura[1996]

Fig.1. dCL/dα-B/D Diagrams of Rectangular Cylinders

2.2 *Flow Reattachment Type Galloping*

On the later flow field, stalling phenomena of airfoil at stalling pitching angle has been well known. McAlister and Carr[1978] has shown clear visualized separated vortex and vortex patch during forced torsional motion of airfoil at stalling angle and Shimizu, Nishihara and Ishihara[2006], and Matsumiya, Nishihara and Shimizu[2010] studied on galloping on transmission line with snow, and indicated that flow reattachment and formation of separation bubble should excite galloping instability at critical pitching angle, as shown in Fig.2.

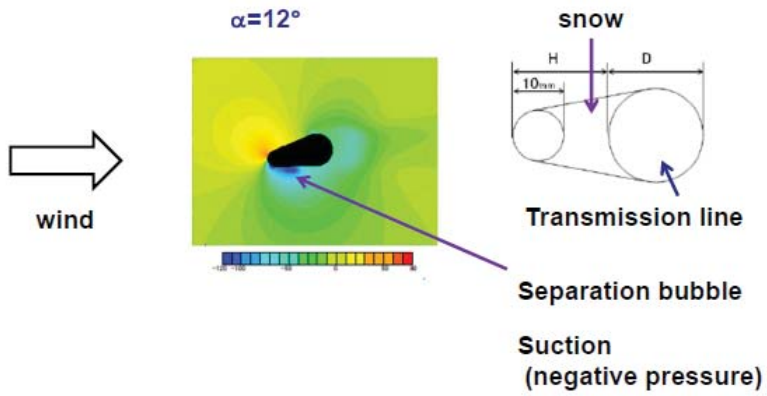

(a) Visualized Flow by CFD (Shimzu, Oka and Ishihara[2006])

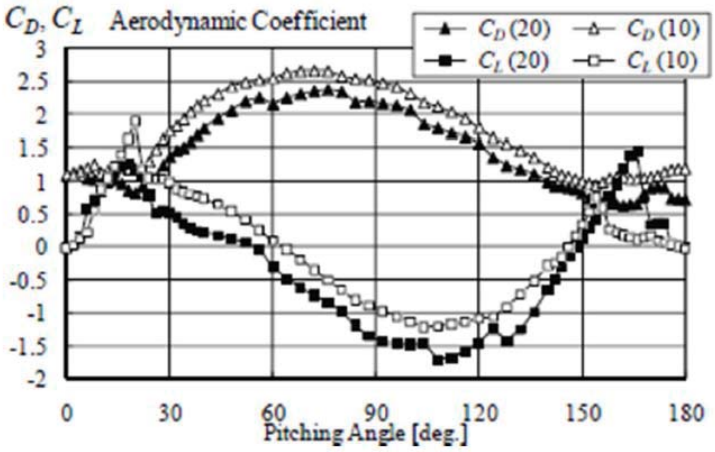

(b) CL-α and CD-α Diadrams

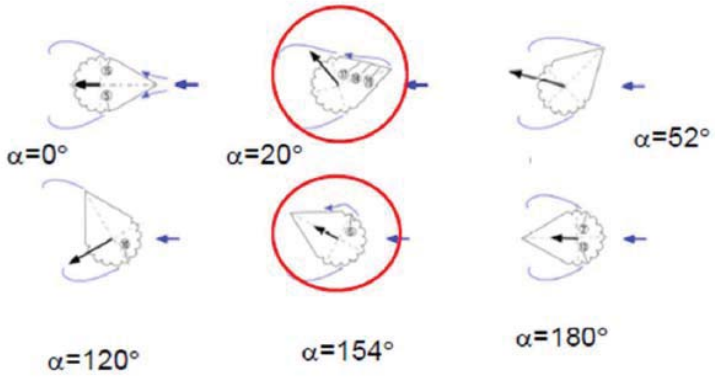

(c) Flow Reattachment and Formation of Separation Bubble at $\alpha=20^0$ and $\alpha=154^0$ corresponding Galloping Appearance(Matsumiya, and Shimizu[2010])

Fig 2. Quasi-Steady Galloping of Transmission Line caused by Flow Reattachment and Formation of Separation Bubble (from Shimizu, Oka, Ishihara[2006] and Matsumiya, Nishihara and Shimizu[2010])

2.3 *Unsteady Galloping*

As far as “unsteady Galloping”, Nakamura and Hirata[1994] reported “Low Speed Galloping (LSG)” for bluffer rectangular cylinders with less than B/D=0.75, which appeared at lower reduced velocity range than Vr=1/St. These bluffer cylinders do not show $dC_L/d\alpha<0$, but $dC_L/d\alpha>0$ as shown in Fig.1. Hirata[1993] precisely measured the unsteady presure on side surface during LSG, and found the appearance of “reattachment type pressure” on side surface. Therefore, LSG must be unsteady galloping, which cannot be excited by den Hartog criteria. Appearance reduced Ranges of conventional quasi-steady galloping(Nakamura[1994] named it as High Speed Galloping(HSG) for contrast to LSG, and LSG of rectangular cylinders are illustrated as show in Fig.3(by Nakamura[1994]).

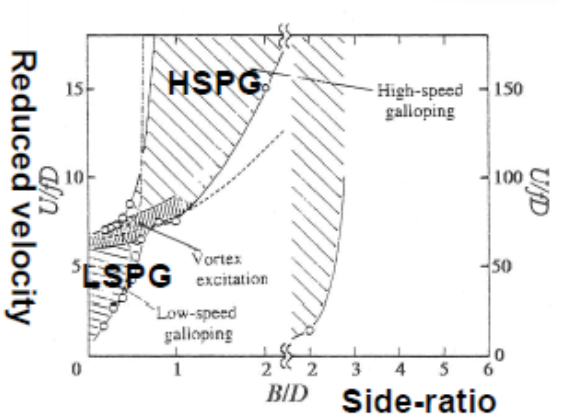

Fig 3. HSG and LSG of Rectangular Cylinders(Nakamura[1994])

As another exmaple of unsteady galloping, yawed circular cylinder with yawing angle of 45°, significant cross-flow response appears when Karman vortex(KV) shedding becomes weak as shown in Fig.4. On Generation of quas-isteady galloping in relation to mitigation/damaged Karman vortex(KV), further investigation might be needed.

(a) Model

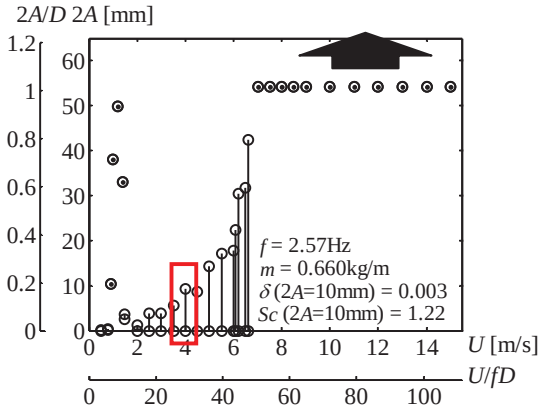

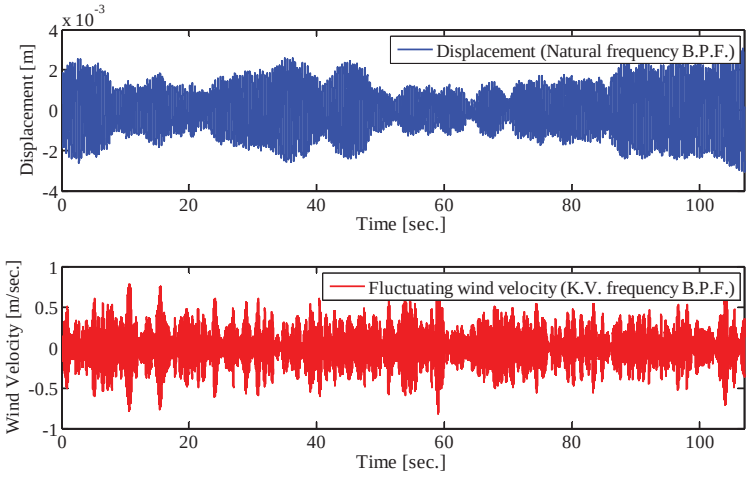

(c)Time-Histories of Cross Flow Response and Flctuating Velocity in a Wake

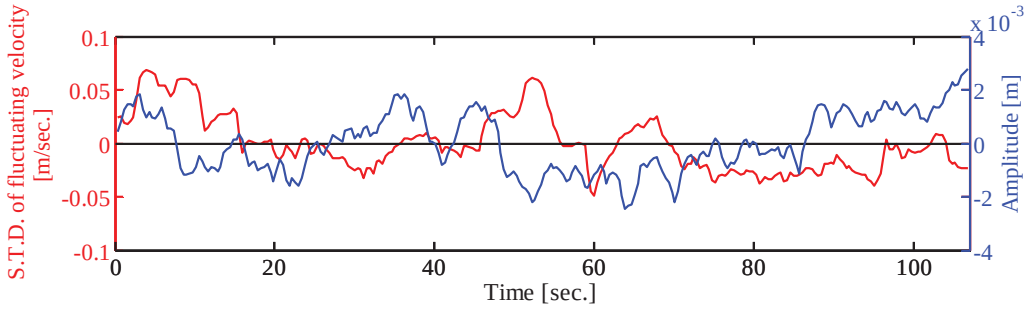

(d) Band-Passed Amplitude of Cross Flow Response and Standard Deviation of Fluctuating Velocity in a Wake
Fig.4 Unsteady Cross-Flow Response of Yawed Circular Cylinder with Yawing Angle of 45°(Matsumoto[2007])

Furthermore, bluff rectangular cylinders , thoseside ratios are B/D=0.3, 0.4,0.5,0.6,0.7, with fixed splitter plate in a wake show unsteady galloping. An example of C_L, C_D, C_L', and Strouhal number v.s. pitching angle, , diagrams as shown in Fig.5 and its H_1*, which is related to aerodynamic damping, defined by Scanlan[1971],shows large positive magnitude. Basing on den Hartog Criteria, galloping is never excited, but violent galloping is observed in free bibration test for this case. (see Fig.5 and Fig.6) This galloping should be caused by "fluid-memory", corresponding the undulation of seaprared flow in near wake generated by body motion,. In another expression the lift force has significant phase lag from body motion. That means typical unsteady effect of lift force. Circular cylinder with a fixed splitter plate would show unsteady galloping.

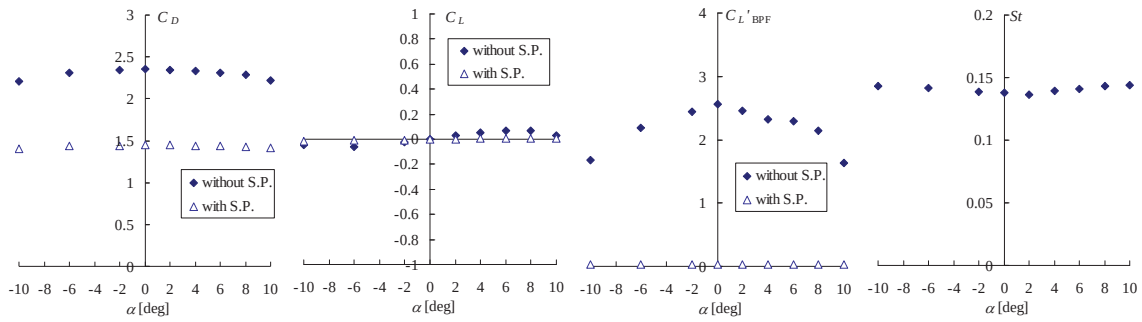

Fig. 5 C_L, C_D. C_L', St v.s. α of rectangular cylinder with B/D=0.5

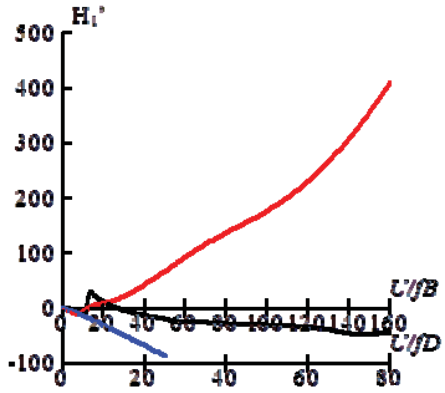

Fig 6. H_1* of rectangular cylinder without a splitter plate (black line) and with a fixed splitter plate (red-line) (blue line is obtained from Teodorsen function)

2.4 *Galloping of Inclined Stay Cables of Cable Stay Bridges*

Aerodynamic vibration of stay cable of cable stay bridge has frequently observed observed in dry state, that is without rain, or in wet state, that is in rainy state. Those are called as Rain Wind induced vibration(RWV) and dry galloping(DG). Recently author has summarized that three major factors play definitely important role for excitation of RWV and DG, independently and individually. Those are formation of water rivulet(WR) on upper cable surface originally pointed out by Hikami[1986], axial flow(AF) in a near wake originally pointed out by author[1989,2008,2010], and critical Reynolds number(Recr) which has originally pointed out by Macdonald[2005]. All of these factors generate particular flow field around cable surface, that is "separation bubble" by local flow-reattachment (Matsumoto[2011]). Taking into account of the appearance of "separation bubble" in "flow reattachment type galloping" in the process from non-flow reattacment state to flow reattachment state, on the other hand, the appearance of "inner circulatory flow" in "flow non-reattachment type galloping" in the process from flow separation state to flow reattachment state, DG at the range where Re number towards to Recr, corresponding to drag crisis, separeted flow tends to closely moves to cable surface, "inner circulatory flow" should be generated. At Recr separated flow reattaches on cable-surface, then "separation bubble" is generated on cable surface(Bass[1985]). Thus, generation mrchanism of inclined RIV and DG is summarized as indicated in Fig.7 and Fig.8.

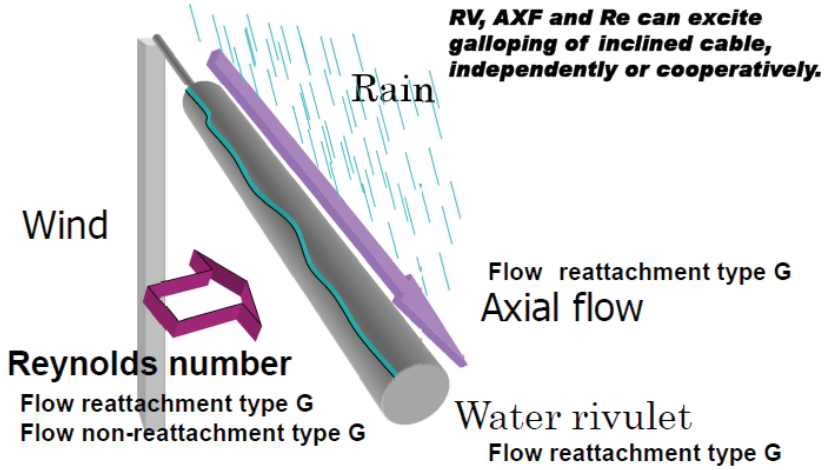

Fig 7. Illustration of Three Major Factors in Relation to RWV an DG of Inclined Stay Cable(Matsumoto[2011])

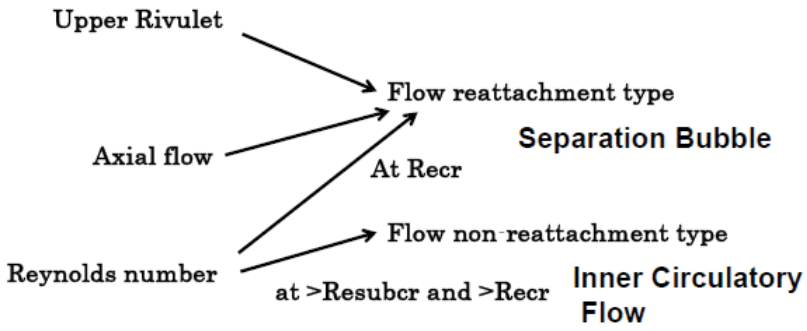

Fig 8. Characteristic Flows for excitation of RWV and DG of Inclined Stay Cable (Matsumoto[2011])

3 TORSIONAL FLUTTER

It has widely known that airfoil shows torsional flutter near stalling angle and its flow field can be characterized by flow separation, flow reattachment and formation separation bubble. Fig.9 is visualized flow pattern during torsional motion of airfoil by Mc-Alister and Carr[1978]. It has been verified that unsteady change of size of sepparation bubble during torsional oscillation should be generation mechanism.

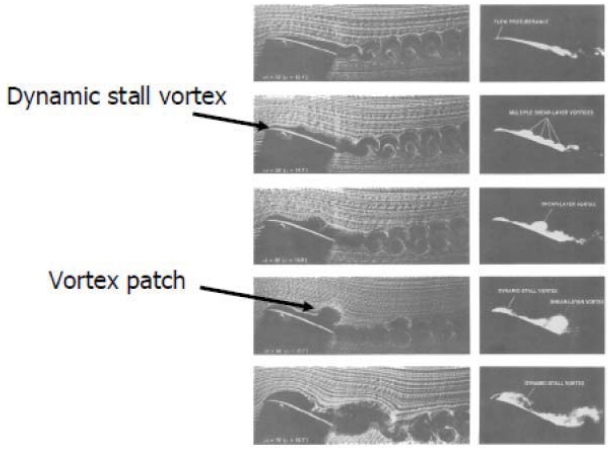

Fig 9. Visualized Flow Field of Airfoil, NACA0012, during Torsional Motion (by Mac-Alister and Carr[1978])

For rectangular cylinders with B/D from 5 to 20, unsteady pressure properties,those are amplitude of pressure coefficient, Cp, and phase, ψ, of negative pressure from the maximum angle of attack (for heaving motion: neutral position during downward motion and for torsional response nose up maximum) are shown in Fig. 6. It can be verified that flow separates from the leading edge of cylinder and flow reattaches on side surface for B/D=8,10,12.5, 15 and 20, and for B/D=5, flow tends to reattaches near at trailing edge. It should be noted that the maxmum peak of Cp appears at almost same positionon side surface for all cylinders and phase,ψ, is almost identical in various side ratios. Furthermore, it should be noted that if relative angle of attack in heaving and torsional motions is identical, Cp and ψ are almost same. Basing on these unsteady characteristics, it is verified that flow field around rectangular cylinders with B/D=5 to 20 might be less affected by the after body-length. Heaving and torsional 2DOF differential equations are expressed as follows:

$$m\ddot{\eta} + c_\eta\dot{\eta} + k_\eta\eta = \rho b^2\omega_F H_1^*\dot{\eta} + \rho b^2\omega_F^2 H_4^*\eta + \rho b^3\omega_F H_2^*\dot{\phi} + \rho b^3\omega_F^2 H_3^*\phi$$

$$I\ddot{\phi} + c_\phi\dot{\phi} + k_\phi\phi = \rho b^3\omega_F A_1^*\dot{\eta} + \rho b^3\omega_F^2 A_4^*\eta + \rho b^4\omega_F A_2^*\dot{\phi} + \rho b^4\omega_F^2 A_3^*\phi$$

where, m and I:mass and mass inertia per unit length, c_η and c_ϕ :heaving and torsional damping coefficient, k_η and k_ϕ :heaving and torsional stiffness, b:half chord length, ρ : air density, ω_F : flutter circular frequency, H_i^* and A_i^* (i=1-4) :aerodynamic derivatives.These 8 aerodynamic derivatives can be obtained from unsteady pressure properties(Scanlan[1971]), those are Cp and ψ , as follows:

$$H_1^* = \frac{-V^2}{2b\omega^2\eta_0}\int_{-1}^{1}\tilde{C}_p\cos\psi_H dx = \frac{V^2}{2b\omega^2\eta_0}\int_{-1}^{1}\tilde{C}_p H_1^* dx$$

$$H_4^* = \frac{-V^2}{2b\omega^2\eta_0}\int_{-1}^{1}\tilde{C}_p\sin\psi_H dx = \frac{V^2}{2b\omega^2\eta_0}\int_{-1}^{1}\tilde{C}_p H_4^* dx$$

$$A_1^* = \frac{-V^2}{2b\omega^2\eta_0}\int_{-1}^{1}\tilde{C}_p x\cos\psi_H dx = \frac{V^2}{2b\omega^2\eta_0}\int_{-1}^{1}\tilde{C}_p A_1^* dx$$

$$A_4^* = \frac{-V^2}{2b\omega^2\eta_0}\int_{-1}^{1}\tilde{C}_p x\sin\psi_H dx = \frac{V^2}{2b\omega^2\eta_0}\int_{-1}^{1}\tilde{C}_p A_4^* dx$$

$$H_2^* = \frac{V^2}{2b^2\omega^2\phi_0}\int_{-1}^{1}\tilde{C}_p \sin\psi_T dx = \frac{V^2}{2b^2\omega^2\phi_0}\int_{-1}^{1}\tilde{C}_p H_2^* dx$$

$$H_3^* = \frac{-V^2}{2b^2\omega^2\phi_0}\int_{-1}^{1}\tilde{C}_p \cos\psi_T dx = \frac{V^2}{2b^2\omega^2\phi_0}\int_{-1}^{1}\tilde{C}_p H_3^* dx$$

$$A_2^* = \frac{V^2}{2b^2\omega^2\phi_0}\int_{-1}^{1}\tilde{C}_p x\sin\psi_T dx = \frac{V^2}{2b^2\omega^2\phi_0}\int_{-1}^{1}\tilde{C}_p A_2^* dx$$

$$A_3^* = \frac{-V^2}{2b^2\omega^2\phi_0}\int_{-1}^{1}\tilde{C}_p x\cos\psi_T dx = \frac{V^2}{2b^2\omega^2\phi_0}\int_{-1}^{1}\tilde{C}_p A_3^* dx$$

In particular, torsional instability can be measured from A_2^*. If $A_2^*>0$, torsional flutter appears, on the contrary if $A_2^*<0$, aerodynamically stable against torsional flutter. Positive or negative of A_2^* can be determined by the position of diagram of $C_pH_2^*$, it means if it locates upstrem side or downstream one from mid-chord point, A_2^* shows negative or positive, respectively. (see Matsumoto[2005])

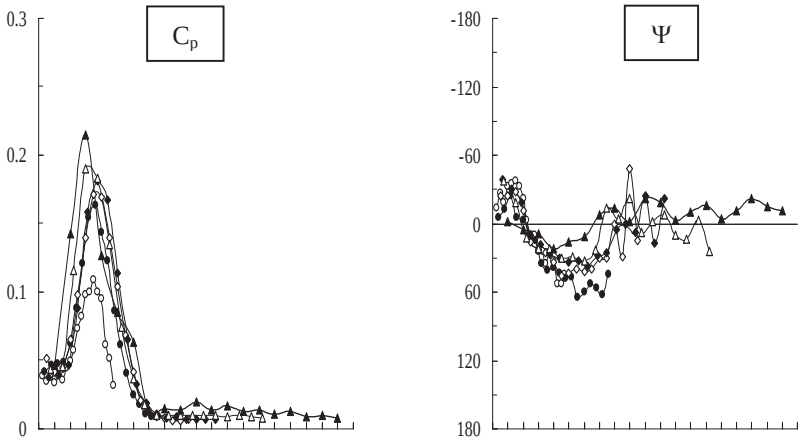

(a) by Forced Heaving Oscillation

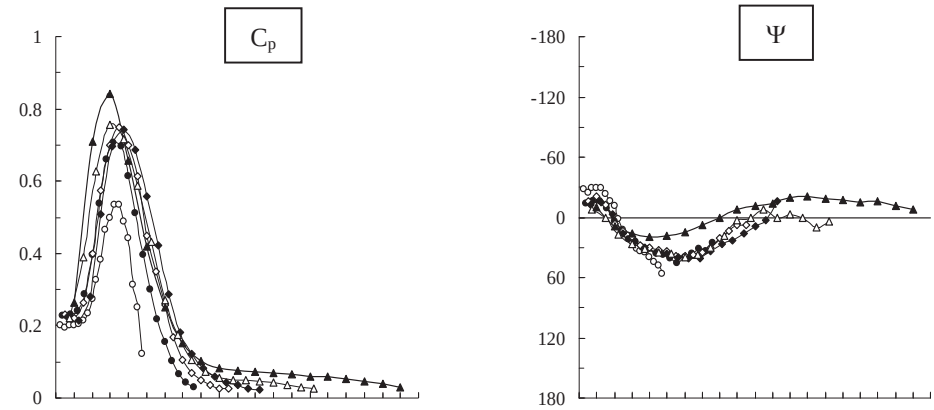

(b) by Forced Torsional Oscillation

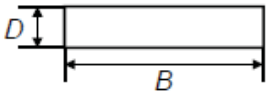

○:B/D=5
●:B/D=8
◇:B/D=10
◆:B/D=12.5
△:B/D=15
▲:B/D=20

Fig 10 .Unsteady Pressure Characteristics, C_p and ψ, of Rectangular Cylinders with Various Side-Ratios from B/D=5 to 20 under Forced Heaving(a) and Torsional vibrations (b)(Matsumoto[2005])

Aerodynamic derivative of A_2^* , in consequence, changes continuously from negative to positive with increase of B/D as shown in Fig.10. The rectangular cylinder with B/D=10 shows almost $A_2^*=0$, and more bluffer cylinders with less than B/D=10 up to B/D=4 studied here, $A_2^*>0$, that means appearance of torsional 1DOF flutter. Rectangular cylinders with more than B/D=10 show coupled flutter instability.

On the aerodynamic derivatives between rectangular cylinders and H-shaped cylinders, there exists similarity as shown in Fig. 10. From this diagram, H-shaped cylinder possesses aerodynamically more bluff than rectangular cylinder, even though their side ratio,B/D, are identical.

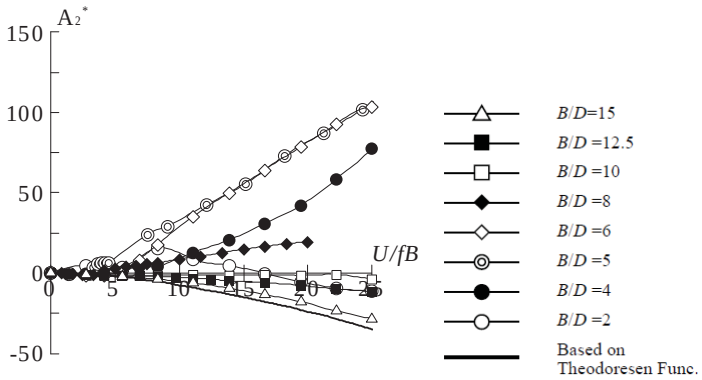

Fig 11. Aerodynamic Derivative of A_2^* of Rectangular Cylinders with Various Side Ratios (Matsumoto[2005])

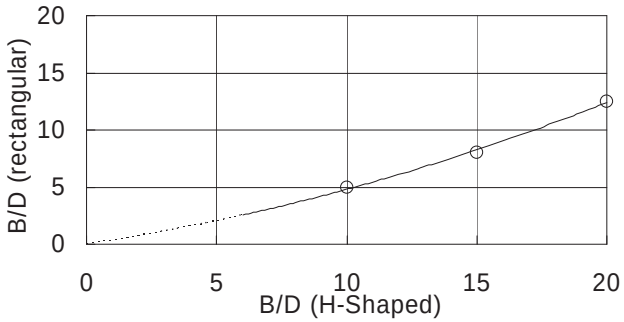

(a) Analogy of Flutter Derivatives of H-Shaped and Rectangular Cylinders

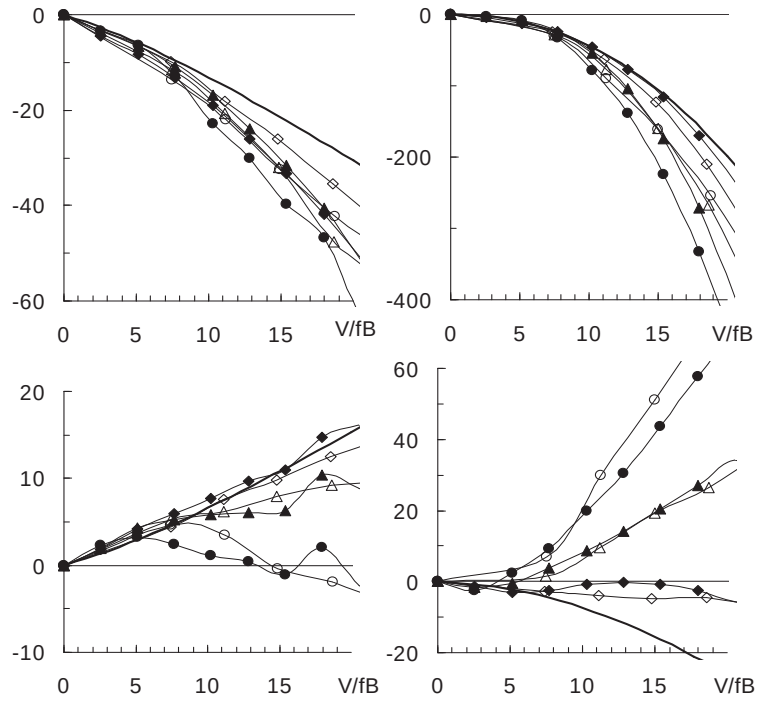

(b) Comparison of Aerodynamic Derivatives, A_1^*, A_2^*, H_1^* and H_3^*, of H-Shaped and Rectangular Cylinders

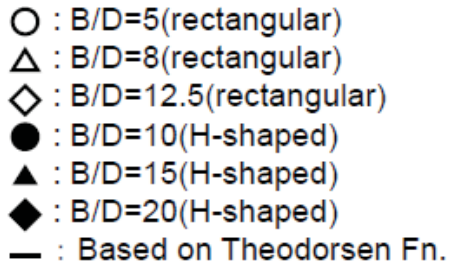

Fig.12 Analogy of Aerodynamic Characteristics between H-Shaped and Rectangular Cylinders (Matsumoto[2004])

For bluff bodies which indicate torsional flutter, including rectangular cylinders, and H-shaped cylinders, aerodynamic interference between vortex-induced vibration(VIV) and torsional flutter becomes significant issues at particular frequency ratio in torsional frequency, $f_{\varphi 0}$, and heaving one, $f_{\eta 0}$. For example, original Tacoma Narrows Bridge had plate-girder with H-shape section with B/D=5. This bridge showed catastrophic torsional oscillation by 1st asymmetrical mode, after showing 5th heaving symmetrical mode under wind velocity less than 20m/s. Its frequency ratio, $f_{\varphi 0}/f_{\eta 0}$. , corresponding these modes, is 2.5.

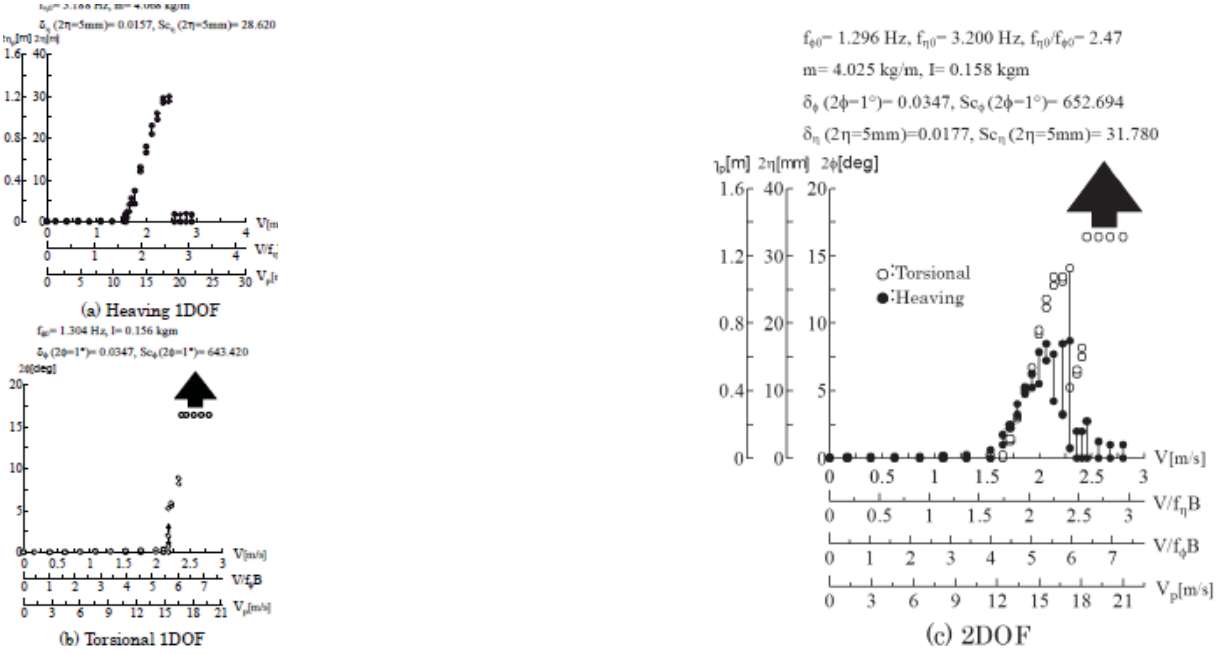

(a) Response of Original Tacoma Narrows Bridge in 1DOF Heaving, 1DOF Torsional and 2DOF 2DOF Heaving and Torsional Vibration Systems

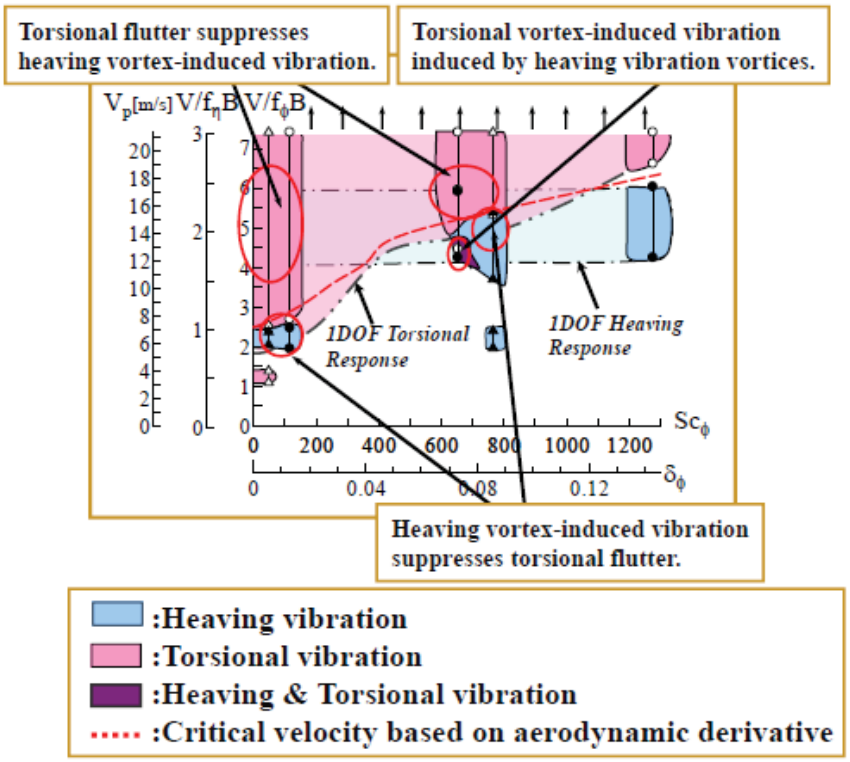

(b) Aerodynamically Unstable Range (Scruton Number-Velocity Diagram)
Fig.13 Response Characteristics of Original Tacoma Bridge (Matsumoto[2004])

The response characteristics investigated by wind tunnel test are shown in Fig.13. The Farquarhsen report [1949] pointed out sudden change of vibration mode, from 5th heaving to 1st torsional might be caused by broken of center diagonal stay cables by heaving VIV. However, the another explanation, basing on these wind tunnel test, might be possible. It might be caused by slight inrcease of wind velocity from 18m/s to 19m/s, which correspond to 16.3m/s to 17.2m/s as effective wind velocity crossing perpendicularly bridge girder, because of skewly crossing to the Tacoma Narrows Chanel by 25^0. Furthermore, Looking at 35mm film taken by Farqursen'group at the bridge site, during 5th mode torsional vibration of main span, vibration of side-span still maintained the frequency of 5th symmetrical heaving mode. Taking into account of velocity mitigation near land than the center part of channel. It should be natural in thinking that these different vibration modes should be caused by the difference of wind velocity. Also many cable strands of the main cable near at the cable band of center-diagonal stay cables had been severly damaged. Cable band does not move,in general, for heaving vibration, because of the role of center diagonal stay cable to prevent the torsional displacement of girder. The fact that many cable strands were severly damage near cable band, cater stay cables must be suvive after appearance of torsional vibration of girder.

4 COUPLED FLUTTER

4.1 *SBS Flutter Analysis*

2DOF Heaving and torsional differential equations are expressed by equation (2.1) and (2.2). Aerodynamic derivatives of thin plate can be expressed by Theodorsen function as follows:

$$H_1^*(k) = -(2\pi / k)F(k)$$
$$A_1^*(k) = (\pi / k)F(k)$$
$$H_2^*(k) = -(2\pi / k)(-(1/2) + F(k)/2 - G(k)/k)$$
$$A_2^*(k) = (\pi / k)(-(1/2) + F(k)/2 - G(k)/k)$$
$$H_3^*(k) = -(2\pi / k)(F(k)/k + G(k)/2)$$
$$A_3^*(k) = (\pi / k)(F(k)/k + G(k)/2)$$
$$H_4^*(k) = -(2\pi / k)G(k)$$
$$A_4^*(k) = (\pi / k)G(k)$$

where C(k)=F(k)-iG(k) (4.1)

2DOF coupled flutter can be characterized by four properties, those are frequency v.s. velocity(ω-V) property, damping v.s. velocity (δ-V) property, amplitude ratio v.s. velocity(η_0/φ_0-V) property and phase difference v.s. velocity (ψ-V)property. These characteristic values are, in general, analyzed by complex eigen value analysis.
On the other hand, author has developed Step-by-Step analysis to get these values. (Matsumoto[2010])Branch switching in these values can be studied by use of SBS flutter analysis. Its procedure is briefly explained in Fig.10. Clarification of flutter branch is definitely important to understand of multi-mode flutter characteristics. Because coupled flutter should be coupled wind-induced vibration between heaving and torsional modes. Therefore, if flutter begins with HB or TB, then the other torsional modes or heaving modes, , except of fundamental pairing mode, must mainly contribute to change flutter onset velocity,V_{cr}, more or less, respectively. Moreover, through wind tunnel test, flutter onset in T0 mode might be milder than in H-90 mode. But on this flutter property, further studies should be needed.

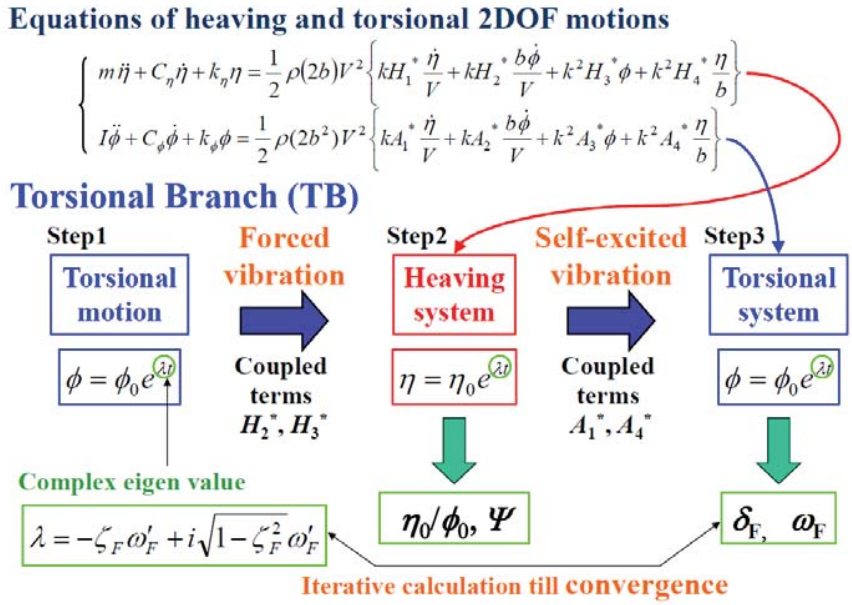

(a) Torsional Branch (TB)

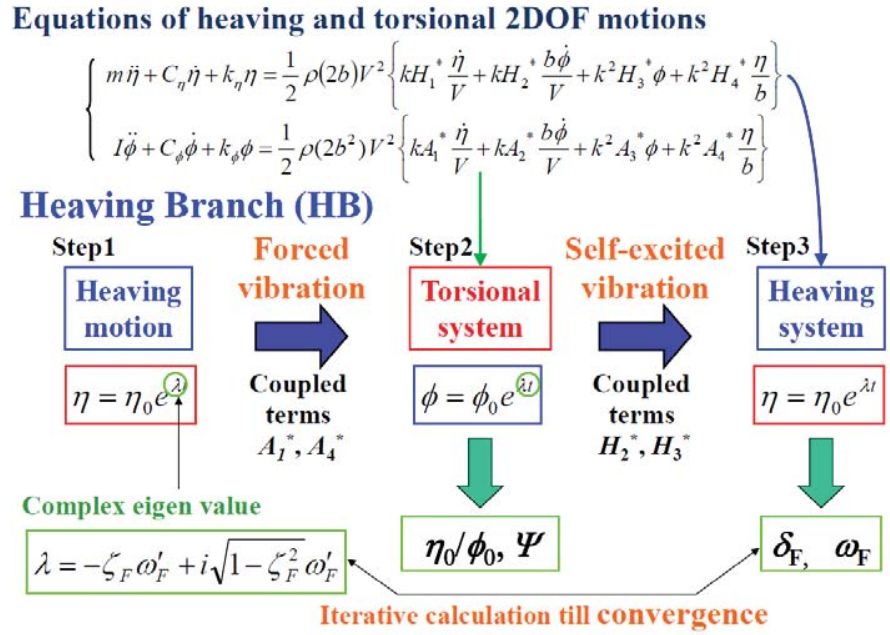

(b) Heaving Branch (HB)
Fig .14. Illustration of SBS Flutter Analysis

Flutter properties analyzed by SBS and conventional Complex Eigen Value flutter analysis(CEV) for thin plate under certain structural dynamics are indicated in Fig.14 Theodorsen function are used for aerodynamic derivative as indicated above.

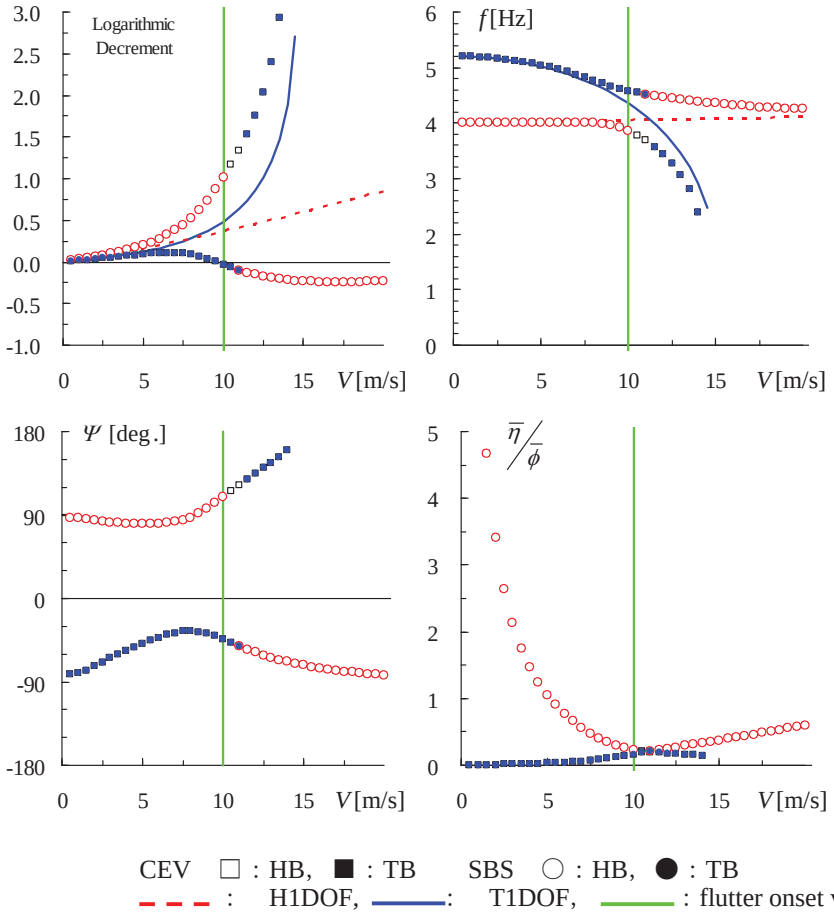

B=0.30 [m], m=2.42 [kg/m], I=0.0181 [kgm2/m], ρ=1.225 [kg/m3], $f_{\eta 0}$=4.0 [Hz] , $f_{\varphi 0}$=5.2 [Hz]
Fig 15. Coupled Flutter Properties of Thin Plate (frequency ratio: $f_{\varphi 0}/f_{\eta 0}$=1.30)

Flutter values characterizing property, ω,δ, (η_0/φ_0) and ψ, are completely identical in the both cases of CEV and SBS, as shown in Fig.1, but flutter branch at higher velocity after V_{cr}(=10m/s)are completely different in CEV analysis and SBS analysis. In SBS analysis, at a little bit higher velocity, 12.5m/s, than V_{cr}=10m/s、flutter branch suddenly changes from heaving branch(HB) to torsional branch (TB) or from TB to HB. At higher velocity range, HB flutter appears in SBS analysis, on the other hand, TB flutter appears in CEV analysis. Looking at ω-V diagram,ω is close to frequency of torsional 1DOF. This apparently indicates that at higher velocity range than flutter onset, this ω must correspond to TB not to HB. Therefore at near V_{cr} branch switching, from HB to TB, should occurs to satisfy this ω-property belonging to TB. Two flutter-values, ω and δ, from four-ones have been spot-lightened, because of determination of reduced velocity Vr=V/bω, which characterizes unsteady lift and pitching moment, and flutter onset velocity, Vcr. However, the another two flutter values, (η_0/φ_0) and ψ, have been less paid attention in discussion of flutter instability. It should be noted that these two flutter-values characterize flutter branches and flutter modes. These are significantly important to precisely verify the flutter coupling mechanism in multi-modes, that is multi-mode flutter, mechanism and generation mechanism of propulsion force during heaving and torsional coupling motion.

4.2 *Flutter Modes*

In coupled flutter, 6 fundamental modes can be defined as follows:

1. H mode: This is pure 1DOF heaving mode without torsional displacement, in another expression, is pure torsional mode around rotational axis fixed at the infinite point from mid-chord point of plate.

2. T mode: This is pure rotational mode around rotational axis fixed at mid-chord point of plate, without heaving displacement at this point.

3. T0 mode: This is pure rotational mode around leading edge. At heaving motion (the lowest is maximum)at mid-chord point has no phase difference against torsional motion(windward nose-up positive) at this point.

4. T180 mode: This is pure rotational mode around trailing edge. In this mode, torsional maximum delays from heaving maximum by -180 degree.

5. H90 mode: In this mode, the heaving maximum delays from the torsional maximum by 90 degree. This mode appears from quasi-steady point if $dC_L<0$.

6. H-90 mode: In this mode, the heaving maximum delays from the torsional maximum by -90 degree, it means the heaving maximum proceeds ahead to the torsional maximum by 90 degree. This mode appears from quasi-steady point if $dC_L>0$.

These four modes, T0, T180, H90 and H-90, are illustrated in Fig.2.

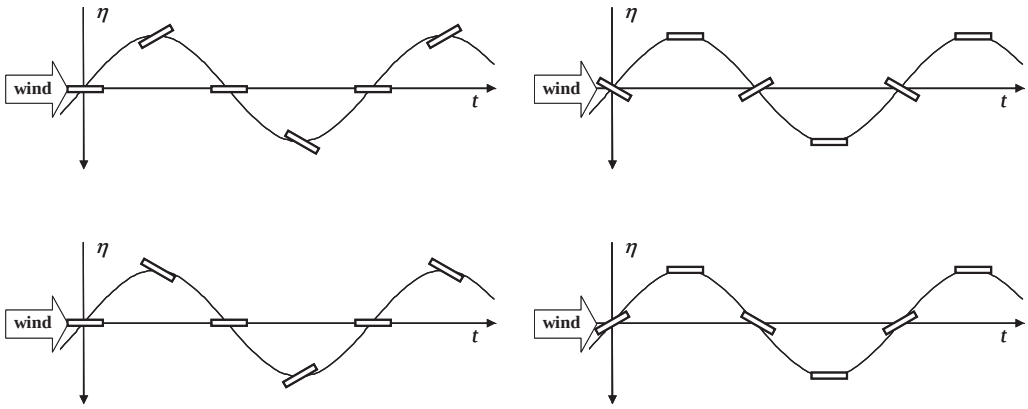

Fig.16 Fundamental flutter modes : T0, T180, H90 and H-90

4.3 *Flutter Branches*

Flutter branches can be defined from Amplitude ratio, η_0/φ_0, as shown in Fig.16. Around flutter onset, amplitude ratio, η_0/φ_0, shows the minimum. At lower velocity than Vcr,η_0/φ_0 for HB tends to infinite with decreasing velocity, it means heaving displacement dominates than torsional one .At V=0,torsional displacement becomes zero, $\varphi_0=0$, it means coupling motion is pure heaving motion or rotational axis at infinite point in upstream- or downstream-ward. On the other hand, for η_0/φ_0 of TB decreases together with decreasing velocity approaching zero at V=0. At V=0, heaving displacement is zero $\eta_0=0$. This means that flutter properties can be defined as TB at lower velocity range than around flutter onset. Similarly at higher velocity than

around flutter onset, HB and TB can be defined as HB and TB respectively basing upon flutter properties obtained by SBS flutter analysis.

At velocity range near V_{cr}, flutter branch would be defined from phase difference,ψ, as following procedure. Taking into account of flutter modes, H mode, T mode, T0 mode, T180 mode, H90 mode and H-90 mode, their torsional motion, φ(t), and heaving motion, η(t) are expressed respectively as follow:

$$H \bmod e : \eta(t) = \eta_0 \sin \omega t \qquad \varphi(t) = 0 \tag{4.2}$$

$$T \bmod e : \varphi(t) = \varphi_0 \sin \omega t \qquad \eta(t) = 0 \tag{4.3}$$

$$T0 \bmod e : \varphi(t) = \varphi_0 \sin \omega t \qquad \eta(t) = \eta_0 \sin \omega t \tag{4.4}$$

$$T180 \bmod e : \varphi(t) = \varphi_0 \sin \omega t \qquad \eta(t) = -\eta_0 \sin \omega t \tag{4.5}$$

$$H90 \bmod e : \varphi(t) = \varphi_0 \sin \omega t \qquad \eta(t) = -\eta_0 \cos \omega t \tag{4.6}$$

$$H-90 \bmod e : \varphi(t) = \varphi_0 \sin \omega t \qquad \eta(t) = \eta_0 \cos \omega t \tag{4.7}$$

When phase difference between torsion and heaving motion is ψ, coupling of heaving and torsional motions can be expressed as follow depending on ψ which varies between -90^0 and 180^0 in flutter property obtained by flutter analysis :

$$180^0 > \psi > 90^0 : \cos\psi < 0 \; and \; \sin\psi > 0 \tag{4.8}$$

$$90^0 > \psi > 0^0 : \cos\psi > 0 \; and \; \sin\psi > 0 \tag{4.9}$$

$$0^0 > \psi > -90^0 : \cos\psi > 0 \; and \; \sin\psi < 0 \tag{4.10}$$

Then,

$$\varphi(t) = \varphi_0 \sin \omega t \tag{4.11}$$

$$\eta(t) = \eta_0 \sin(\omega t - \psi) = \eta_0 \sin \omega t \cos\psi - \eta_0 \cos \omega t \sin\psi \tag{4.12}$$

For all terms on right hand of the upper equation, coupling motions can be resolved as follows:

$$180^0 > \psi > 90^0 : \varphi(t) = \varphi_0 \sin \omega t \qquad \eta(t) = -T180 \cos\psi - H90 \sin\psi \tag{4.13}$$

$$0^0 > \psi > -90^0 : \varphi(t) = \varphi_0 \sin \omega t \qquad \eta(t) = -T0 \cos\psi - H-90 \sin\psi \tag{4.14}$$

$$90^0 > \psi > 0^0 : \varphi(t) = \varphi_0 \sin \omega t$$
$$\eta(t) = T0 \cos\psi + H90 \sin\psi \qquad (4.15)$$

In HB and TB consist in two fundamental flutter modes depending on their amplitude ratio, η_0 / φ_0, and phase, ψ, as indicated in Fig.3. In detail,

for HB, at V=0 : H mode only,
at 0<V<Vcr : T0 mode and H90 mode,
at Vcr<V : T0 mode and H-90 mode,

and for TB,

at V=0 : T mode only,
at 0<V<Vcr : T0 mode and H-90 mode,
Vcr<V : T0 mode and H-90 mode.

At near Vcr, flutter branch, HB or TB, which consists of T0 mode and H-90 mode for amplitude ratio- velocity diagram, can be classified by their magnitude of coefficients, those are sinψ and cosψ. If ψ=-45°, the contribution to flutter of TB and HB are identical. If ψ<-45°, HB plays more significantly for flutter onset than TB, and contrary if ψ>-45°, TB does than HB. Flutter branch when flutter occurs changes not only with different aerodynamic derivatives caused by change of geometrical shape of structures or with angle of attack of wind, but also with structural dynamics. Example of change of flutter branch is shown in Fig.17.

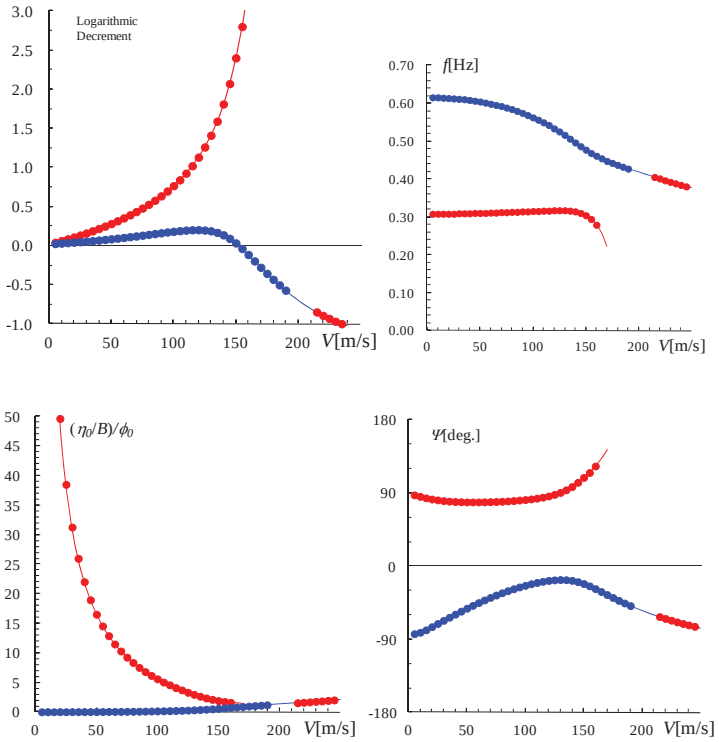

(a) Case1(B=27.8m, M=2.065e04Kb/m, I=1.90e06Kgm2/m, $f_{\eta 0}$=0.31sec-1, $f_{\varphi 0}$=0.62sec-1, $f_{\varphi 0}/f_{\eta 0}$=2.0, $\delta_{\varphi 0}/\delta_{\eta 0}$=0.02), where red plot for HB, blue plot for TB

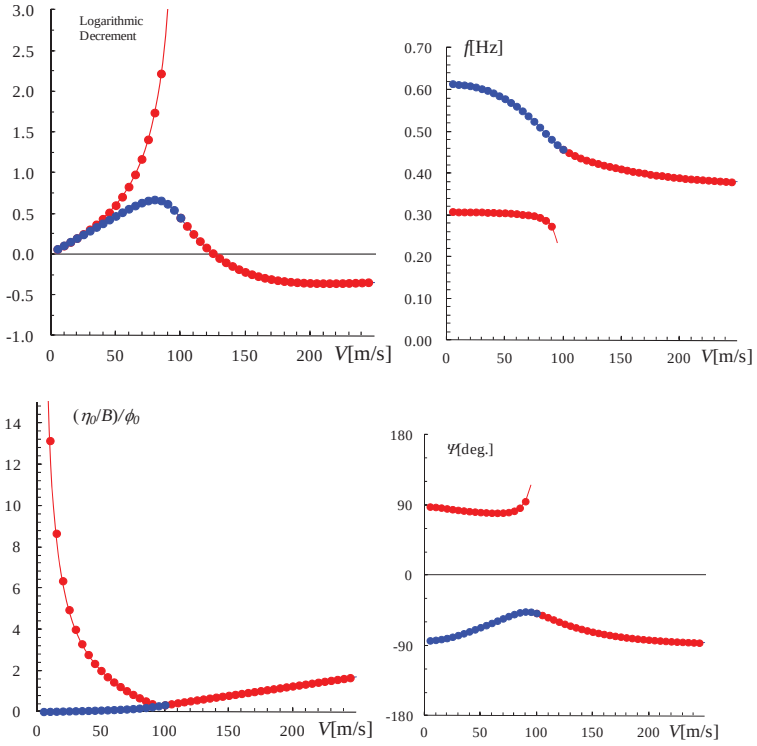

(b) Case2(B=27.8m, M=2.065e04Kg/m, I=1.90e06Kgm2/m, $f_{\eta 0}$=0.31sec-1, $f_{\varphi 0}$=0.465sec-1, $f_{\varphi 0}/f_{\eta 0}$=1.50, $\delta_{\varphi 0}/\delta_{\eta 0}$=0.02)
Fig 17. Flutter Property of Thin Plate (red plot for HB, blue plot for TB)

Fig17 shows that flutter begins with TB(case1) or HB (case2), respectively. It should be noted that flutter branch at flutter onset changes by structural dynamics. On the other hand, Xu[2011] recently reported that flutter of full scale elastic model of the Sutong Bridge in China, the longest cable stayed bridge in the world, begins with To mode under the condition of horizontal wind, but it begins with H-90 mode under up-ward wind with the angle of attack of 3°. In this case, different aerodynamic derivatives change flutter branch at flutter onset.

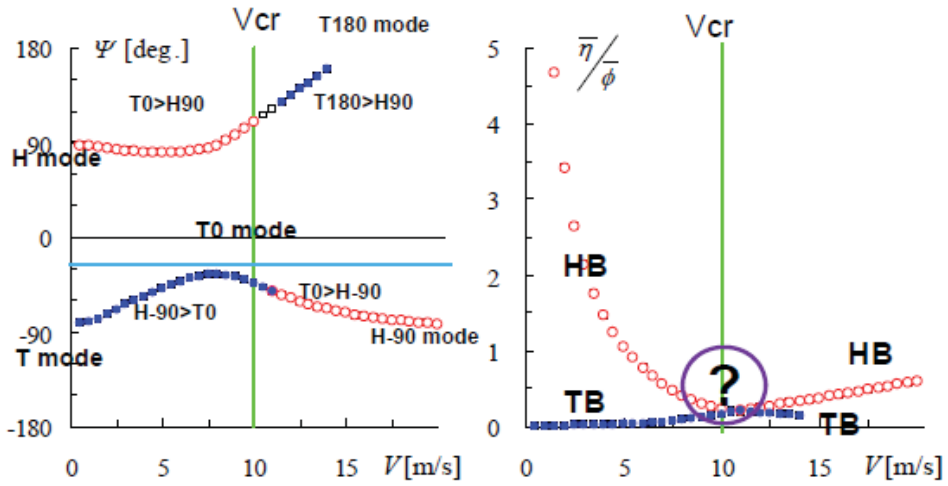

Fig.18 Illustration of Flutter Branch and Flutter Mode in Amplitude Ratio(η0/φ0)-Velocity(V) Diagram and Phase(ψ)–Velocity(V) Diagram (Thin Plate, B=0.3m,m=2.42Kg/m, I=0.081Kgm2/m, fφ=0.5.2sec-1, fη0=4.0sec-1, fφ0/fη=1.3, φ0=δη0=0)

Flutter branches and flutter modes of thin plate explained before are illustrated in ,velocity diagram and ψ -velocity diagram in Fig.18.

4.4 *Selberg Formula*

Selberg formula[1961] has been widely used for estimation of flutter critical velocity, in primary stage of design of long span bridge, as a desk work. Vcr obtained from Selberg Formula is for thin plate section, so the exact Vcr should be investigated by wind tunnel tests using scaled section-model or full scale elastic model, in indirect, measurement of aerodynamic derivatives or direct measurement of Vcr. However, how to be driven this useful Selberg Formula has been not clarified. Under following simple assumptions, significantly similar formula can be obtained (Matsumoto[2010]).

Assumptions:1. When torsional frequency,, decreasing with wind velocity, is identical to heaving frequency,, no-affected by wind velocity, that is , flutter appears.

2.fφis characterized by onlyA_3^*, and $A_3^*$is expressed by. $A_3^*=((\pi/k)(F(k)/k-G(k)/2))^{1/2}$

3.3.Using quasi-steady assumption,:F(k)=1 and G(k)=0, where k is reduced velocity=bω/V.

Then V_{cr} can be expressed similarly with Selberg Formula as follows:

$$V_{cr}=3.71 f_{\varphi_0}(2b)\left((mI)^{1/2}/\left(\rho(2b)^3\right)\left(1-\left(f_{\varphi_0}/f_{\eta_0}\right)^2\right)\right)^{1/2} \tag{4.16}$$

Selberg Formula

$$V_{cr}=3.81 f_{\varphi_0}(2b)\left((mI)^{1/2}/\left(\rho(2b)^3\right)\left(1-\left(f_{\varphi_0}/f_{\eta_0}\right)^2\right)\right)^{1/2} \tag{4.17}$$

obtained from upper assumptions for thin rectangular section

TheV_{cr}-values calculated two formula under some structural dynamics and exact ones analyzed by CEV analysis and SBS analysis are compared in Fig. 15.

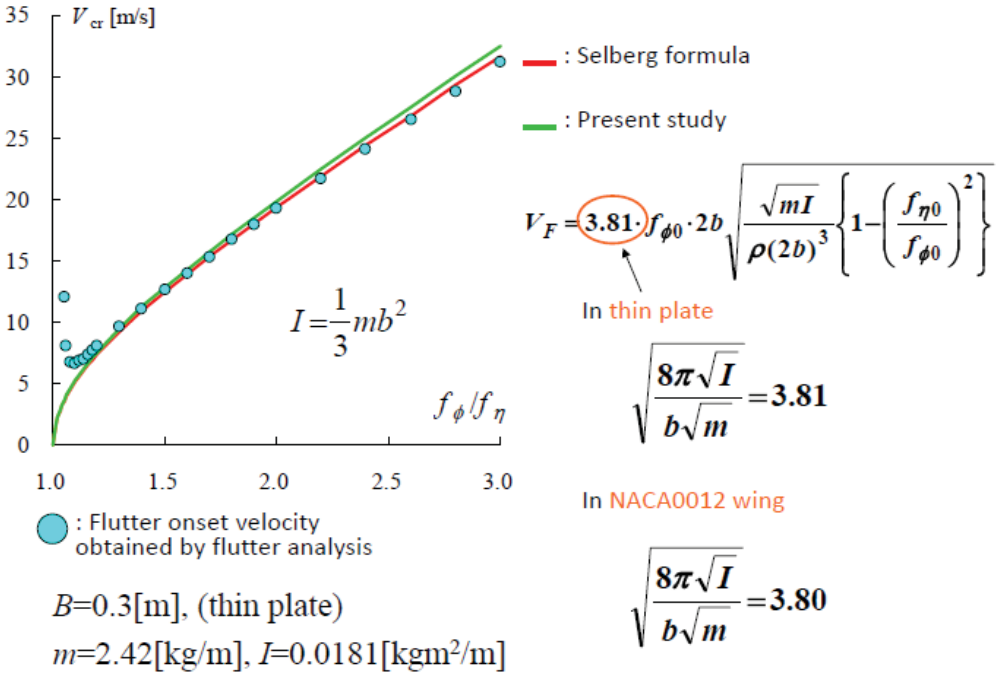

Fig.19 Comparison of Vcr obtained by Selberg Formula(equation(4.16)), Formula(equation (4.17)) and Flutter Analysis (Matsumoto[2010])

5 APPLICATION OF FLUTTER –GENERATION OF PROPULSION FORCE

5.1 *Generation of Propulsion Force*

According to former literatures, instantaneous propulsion force might be generated by coupling motion of heaving and pitching as term related to thin-airfoil theory,$F_{pair\text{-}foil}$, which consists in lift and drag force,$F_{PL\&D}$, and virtual mass effect,F_{pmass}, and jet disgorging term,F_{pjet} . Then, the propulsion force, F_P, can be expressed as follows:

Airfoil Theory term1 :

$$\begin{aligned} F_{P_{L\&D}} &= L(\alpha_{re})\sin\alpha^*_{re} - D(\alpha_{re})\cos\alpha^*_{re} \\ &= (1/2)\rho V_{re}^2 2blC_L(\alpha_{re})\sin\alpha_{re} - (1/2)\rho V_{re}^2 2blC_D(\alpha_{re})\cos\alpha^*_{re} \end{aligned} \tag{5.1}$$

where, L,D, C_L,C_D: unsteady force and coefficients

$$V_{re} = \left\{ V^2 + (d\eta/dt)^2 \right\}^{1/2} \tag{5.2}$$

$$\alpha^*_{re} = \arctan\left\{ (d\eta/dt)/V \right\} \tag{5.3}$$

$$\alpha_{re} = \alpha^*_{re\eta} + \phi \tag{5.4}$$

Airfoil Theory term 2(Karman&Sears[1938]) :(Virtual Mass Effect):

$$L_{mass} = \pi\rho b^2 I\left(d^2\eta/dt^2 + Vd\phi/dt\right)\text{: normal to plate, at } \eta(t)=0 \quad (5.5)$$

$$F_{P_{mass}} = L_{mass}\sin\phi\text{ : propulsive component, at } t=0 \quad (5.6)$$

Jet Disgorging term:

$$F_{P_{jet}} = \rho A_0(V+v)\{(V+v_p)-v\} = \rho A_0 v_p(V+v) \quad (5.7)$$

where, $v_p = v/2$ (5.8)

A_0 effective area at near trailing edge *where* jet passes into wake:,
v_p: disgorging jet velocity through A_0
v: jdisgorging jet velocity in a wake

Propulsion force in term of airfoil theory,$F_{PL\&D}$ and jet disgorging term,F_{pjet} show the maximum at having velocity maximum, that is pitching angle of zero in H-90 flutter mode, on the other hand F_{pmass} shows the maximum at zero heaving velocity, that is maximum pitching displacement.

Propulsion force, , is classified into 6 cases depending combination of torsional and heaving displacement, as follows (Matsumoto and Ishizaki([2010]):

I.Up-ward heaving motion(α_{re}^*<0)

I.1 Positive torsional angle(φ>0)

I.1.1 Absolute value of Torsional angle is larger than the one of relative angle of attack due to heaving velocity: $|\varphi|>|\alpha_{re}^*|$ (case1)

I.1.2 Absolute value of Torsional angle is smaller than the one of relative angle of attack due to heaving velocity: $|\varphi|<|\alpha_{re}^*|$(case2)

I.2 Negative torsional angle (case3)

Ⅱ.Down-ward heaving motion

Ⅱ.1.Positive torsional angle (φ>0)

Ⅱ.2 Negative torsional angle (φ<0)

Ⅱ.2.1 Absolute value of Torsiona gle of attack

ve angle of

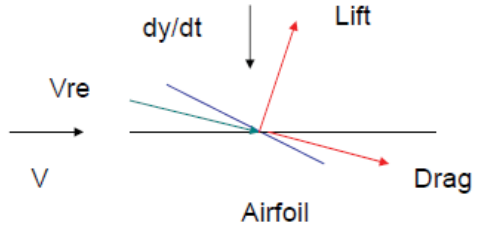

Case1

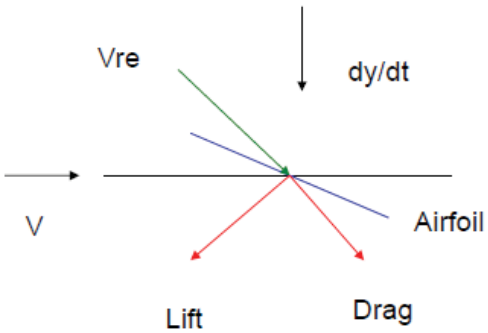

case2

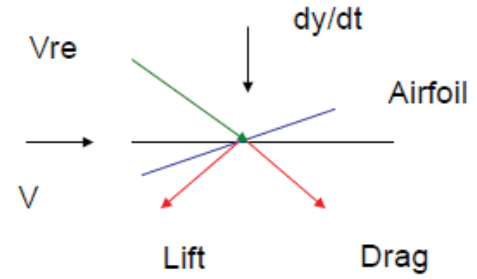

Case3

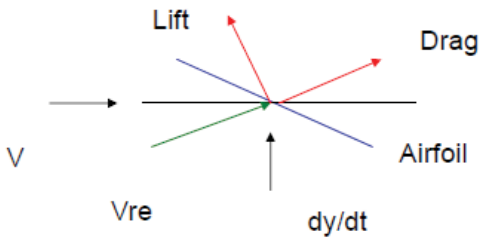

case4

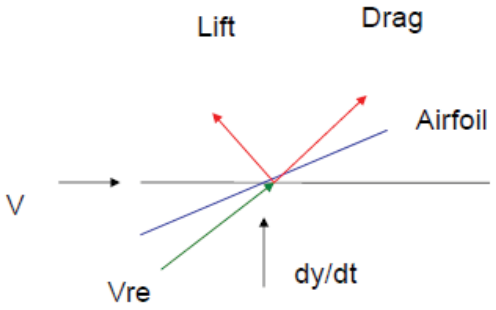

Case5

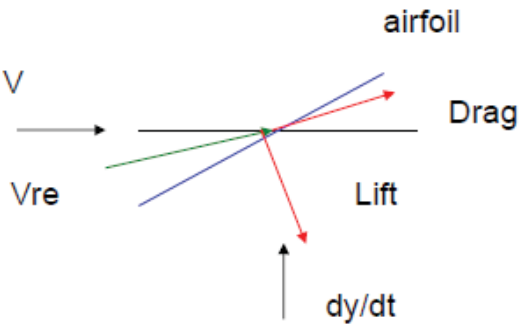

case6

Fig.20 Lift and Drag Induced by Relative velocity Depending on Heaving and Torsional Displacement for 6 cases

From these generation mechanism of Lift and Drag depending torsional and heaving displacement, the following conditions to generate the positive propulsion force, , are definitely required:

For generation of lift force with the up-stream ward force component:

$$(\eta_0 / b)\varphi_0 > V_r = V / b\omega \tag{5.9}$$

For that the propulsive component of lift is larger than the one of drag:

$$\gamma(\alpha_{re})\tan\alpha_{re} - 1 > 0 \tag{5.10}$$

Where,

and : amplitude of heaving and torsional motion of flapping plate, respectively

V: propulsion velocity (or oncoming flow velocity)

: circular frequency of flapping plate

: lift and drag ratio

α_{re}: relative angle of attack ($=\alpha_{re}^{*}+\varphi$)

α_{re}^{*}: angle of attack induced by heaving velocity ($=\arctan(d\eta.dt)/V$)

It is verified that positive propulsion force, $F_{PL\&D}$, can be always generated in H-90 flutter mode, if upper conditions are satisfied, as shown in Fig.17.

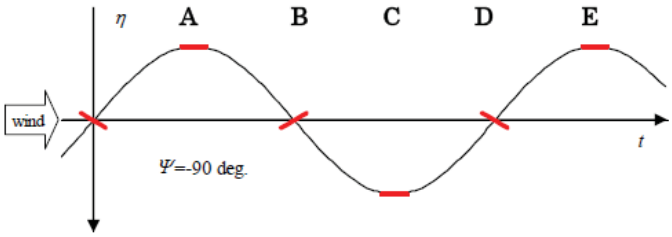

[A-B-C] case5(PF>0) and [C-D-E] case2 (PF>0)
Fig.21 Generation of Positive Propulsion Force during Coupling Motion of H-90 Flutter Mode

Previous studies on navigation mechanism of fish swimming(Tanaka and Nagai[1996]) and ship navigation by flapping plates(Terada, Yamamoto, Nagamatsu and Imaizumi[1998], Barannyk, Buckham and Oshkai[2010]) reported that the coupled motion on tail-fins of fish and flapping plate were controlled by H-90 flutter mode effectively generation of propulsion force. Tail-fin movement in fish swimming is shown in Fig.22 (Tanaka & Nagai[1996])

Fig.22 Tail-fin motion of Fish Swimming(Tanaka and Nagai[1996])

On propulsion force generated by jet disgorging, F_{pjet}, it has not been clarified at present as pointed by Barannyk[2010]. This jet disgorging might generate inverse Karman vortex in a wake, however, its detail mechanism and its effect on propulsion force should be studied more in a future.

5.2 *Ship Navigation Test by Double Flapping Plates controlled Inverse Phase H-90 Modes*

The propulsion force measurement has been conducted by use of ship model with 2.5Kgf in weight, 0.72m in length, 0.33m in width and 0.01m in submerged depth, as shown in Fig. 19. Two rigid, flexible and half-flexible two flapping plates (see Fig.20) were installed at near trailing edge, and they were controlled in inverse phase in order to cancel the sway forces, mutually. Each flapping plate was controlled in H-90 mode, individually. The distance at each neutral position between two plates was 0.22 m. The size of flapping plates were, 0.04m(half chord length for rigid plate), 0.08m(half chord length for flexible plate), 0.06m(height for all plates). The thickness of plates were 1.5mm (for rigid and flexible plate) and 2.0mm(for elastic plate). The pitching axis was fixed at up-stream-ward quarter-point for flexible plate-2 and at mid-chord point for the others. The frequency of flapping plate was mainly 4Hz and flow velocity in water channel for measurement of resistance force was carried out in approximately

0.24m/s, 0.26m/s, 0.30m/s and 0.34m/s. The propulsion forces were measured in still water. The amplitude of heaving and pitching motion was fixed as 0.02m and $19.5^{0,}$ respectively. Besides, navigation velocity of ship model was measured in still water. The maximum navigation speed for flexible flapping plate was observed as over 0.55m/s in the case of f_0=4.35Hz, and the one for rigid plate 0.45m/s at f_0=4.35Hz as well.

An example of time history of propulsion force for rigid plate with f_0=4Hz at V=0m/s is shown in Fig.10. The propulsion force varies with time with showing many local peaks, but mainly fluctuates with the frequency of flapping plate. The maximum propulsive force is roughly evaluated as 170gf. It should be noted that this force fluctuating property, that is one peak appearance in one cycle motion of two flapping plates, This one peak appearance can be explained by effect of enhanced jet disgorging between two flapping plate controlled in inverse phase motion. The enhanced jet flow appears once in one cycle motion of flapping plate.

Ship navigation speed diagrams with various flapping plates and frequency are indicated in Fig.13.

Fig.23 Ship model

Distance for measurement : 400[cm]
Flapping frequency : 2.998[Hz], 3.968[Hz], 4.231[Hz], 4.347[Hz]
Flapping plate:W160[mm]×H60[mm]×t1.5[mm](flexible)
W80[mm]×H60[mm]×t2.0[mm]elastic wing)
W80[mm]×H60[mm]×t1.5[mm](rigid wing/plate)

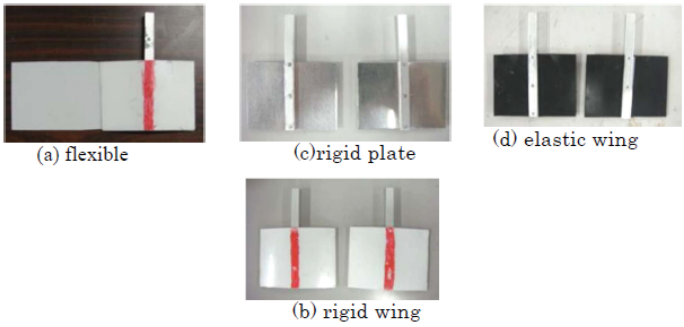

Fig24. Flapping Plates used in the Test

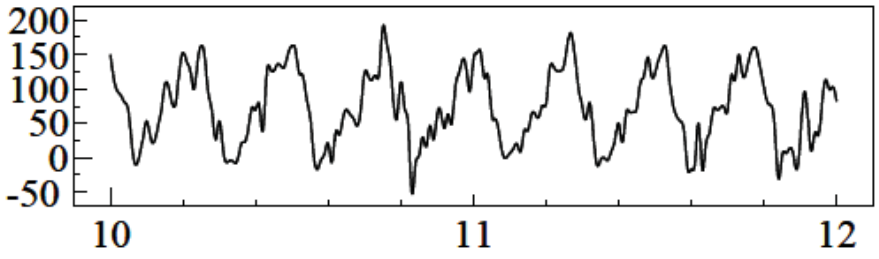

Fig.25 Time-History Propulsion Force (rigid plate, f0=4Hz)

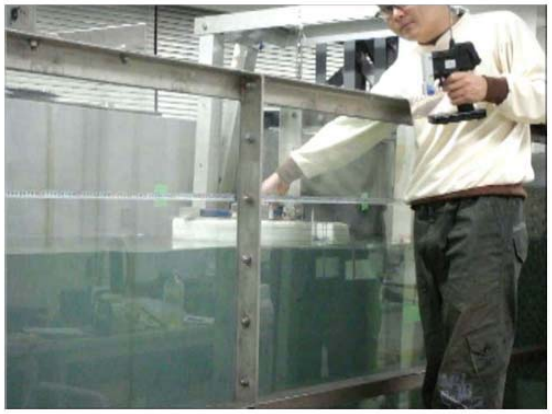

Fig.26 View of Ship Navigation Test

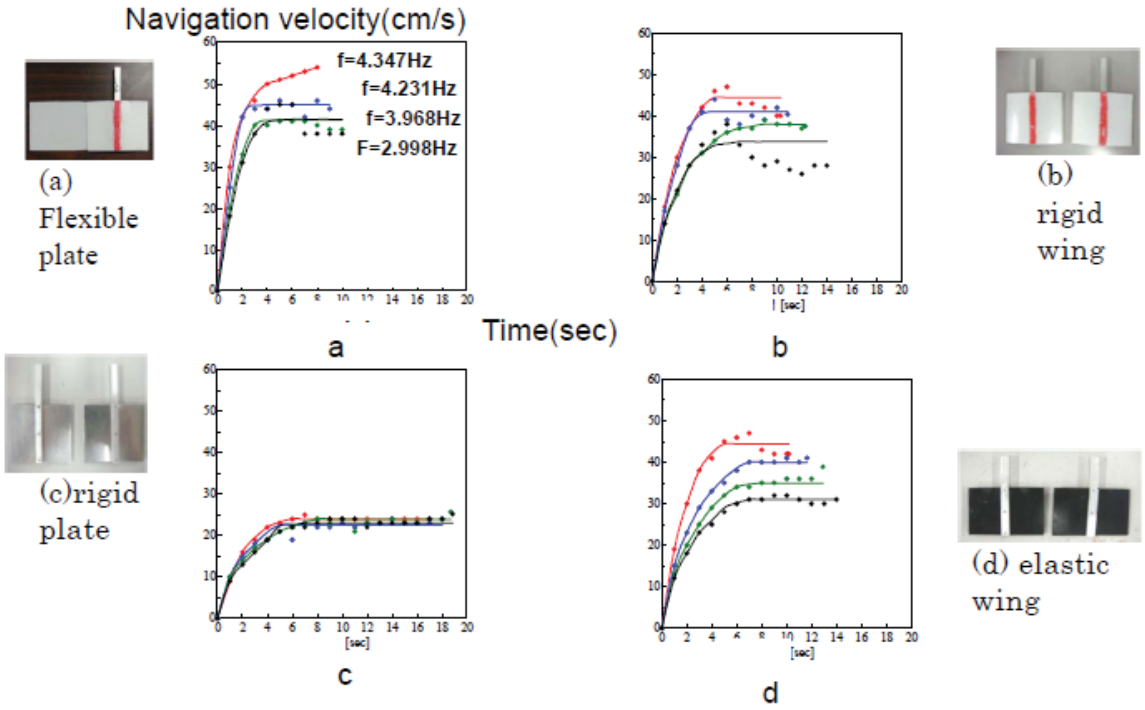

Fig.27 Time History of Navigation Velocity with Various Flapping Plates

As shown in this figure, navigation speed gradually increases after start (t=0). The maximum speed is over 55cm/s in the case of flexible flapping plates. For rigid plate, maximum speed is up to 45 cm/s as shown in Fig.27.Because of uncertainties on unsteady and non-linear force characteristics during coupling motion with large amplitude over stalling angle of attack and taking into account of appearance of quasi-steady behavior of H-90 flutter mode at high reduced velocity, it might be assumed to be quasi-steady force, F_{pquasi}, that is $F_{pairfoil} \cong F_{pquasi}$,at a primary study.

5.3 *Estimation of Propulsion Force induced Jet dDsgorging, Fpjet basing on CFD Analysis by Isogai[2006] for Dolphin Standing Swimming*

Described before on uncertainties on evaluation of propulsion force generated by jet disgorging, F_{pjet}, might be approximately estimated from CFD results for standing swimming of dolphin in still water analyzed by Isogai[2006], under assumption of quasi-steady lift and drag forces. CFD result showed dolphin can generate upward propulsion force to cancel dolphin weight(W=138Kgf) by flapping motion of tail fin (b=0.072m at center, l=0.432m, tail fin area =0.0377m^2, aspect ratio=4.96) with frequency of 4.07Hz. Amplitude of torsional and heaving motions are 58.9^0 and 0.36m, respectively. The tail-fin motion is controlled in almost H-90 flutter mode, where phase is not -90^0degree but -75.8^0. In this case, maximum propulsion force of 2750 N can be generated at the instant of heaving maximum velocity, 9.25m/s. The flow field around tail fin at the moment of $d\eta/dt|_{max}$ is shown in Fig.28.

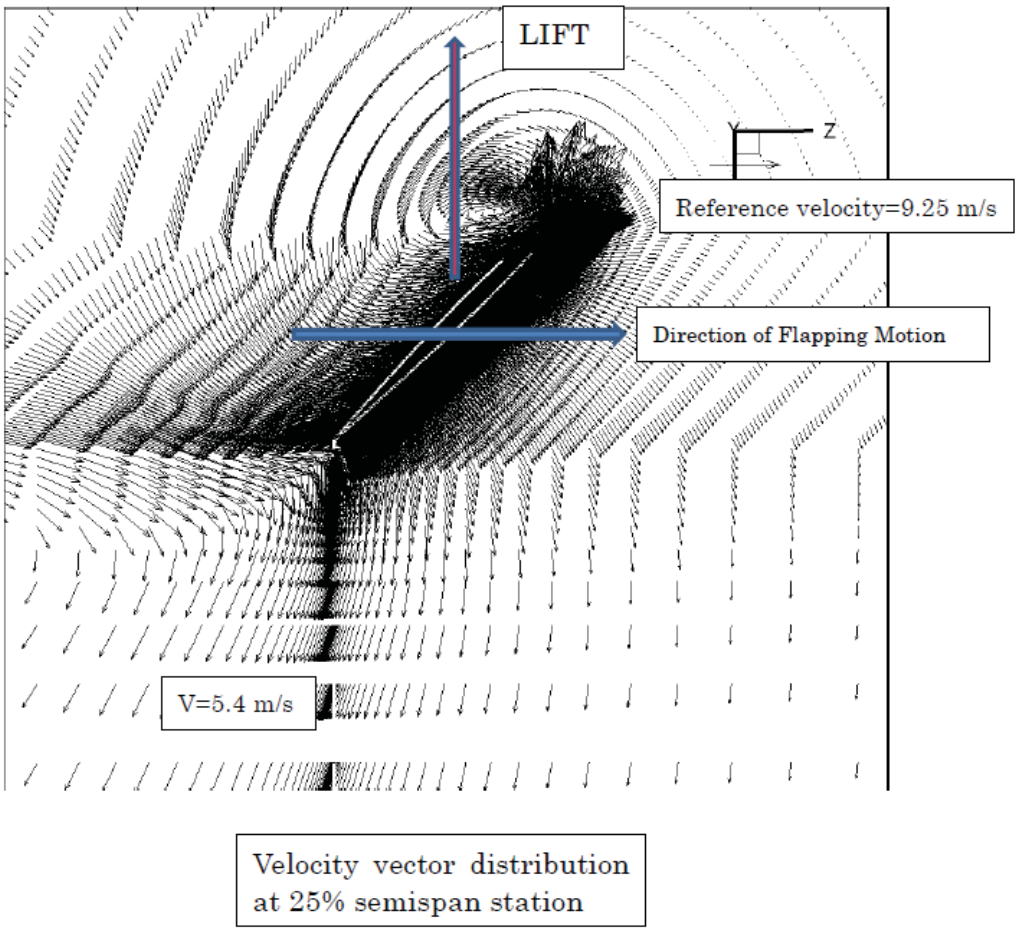

Fig. 28 Flow Field around Tail Fin of Dolphin during Standing Swimming (CFD by Isogai[2010])

It should be noted that jet disgorging velocity in a wake is v=5.4m/s in equation(5.7). Relative angle of attack, $\alpha_{re}=d\eta/dt/\ V+\varphi=90-58.9°=31.1°$, $C_L(\alpha_{re})=1.0$ and $C_D(\alpha_{re})=0.8$, of which values are for 3DOF delta wing measured by Okamoto[2008]. Then, basing on quasi steady lift

and drag forces, F_{Pquasi}, can be calculated as 1595.5N. Furthermore, if effective aera, Ao ,where jet ispassing, near trailing edge of tail-fin can be expressed by A_0=0.1555m2 (=$\eta_0 x_l$=0.36(m)×0.432m), besides jet disgorging up-ward velocity component is approximately 3.82m/s. Then from eq.(), maximum propulsion force at the moment of maximum heaving velocity, $d\eta/dt|_{max}$, generated by jet disgorging into wake, F_{pjet}, is obtained as F_{pjet}=1136N. Therefore, the total maximum propulsion force, $F_p|_{max}$, at the moment of maximum heaving velocity is obtained as 2730.5 N by summation of $F_{pquai}|_{max}$ and $Fp_{jet}|_{max}$ at heaving velocity maximum. This value is similar to the maximum propulsion force obtained by CFD (by Isogai[2006]). Of course, there are many simplified assumption in this calculation, so these agreement might be eventual one. However, contribution ratios of $Fp_{airfoil}|_{max}$ (=$Fp_{L\&D}|_{max}$) and $Fp_{jet}|_{max}$ to total maximum propulsion force, $Fp|_{max}$, in might be roughly evaluated from this result. That means $Fp_{jet}|_{max}$ and $Fp_{airfoil}|_{max}$ contribute to total maximum propulsion force, $Fp|_{max}$ by 42% and 58%, respectively.

5.4 *Flutter Power Generation*

The “concept of Flutter Power Generation(FPG)” has been proposed by Isogai [2003]. This is a practical application of coupled flutter. If forced torsional vibration to the plate or airfoil, then significantly intensive heaving vibration can be excited because of appearance of natural coupled flutter in flutter fundamental H-90 mode in this system. The point of this FPG is that enough small power for forced torsional motion can generate a big power by intensive heaving vibration of plate/airfoil. Isogai pointed that giving power for torsion is less 1% of obtaining power by heaving motion. At present, Abiru[2010]is demonstrating in the field (in small river), to show its efficiency.

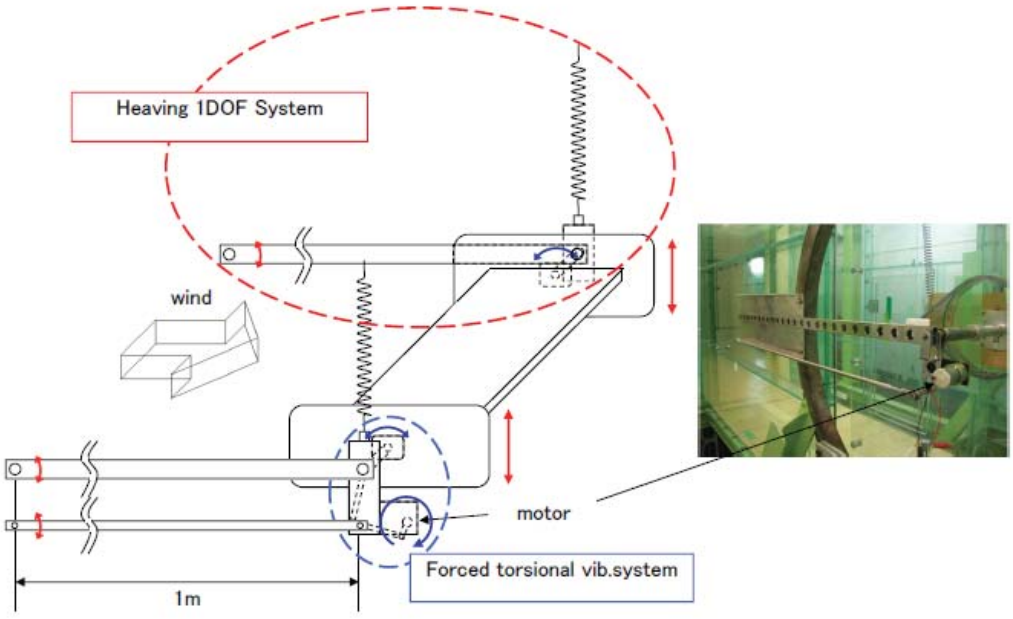

Fig.29 Flutter Power Generation System (Model: Rectangular cylinder with B/D=20 (Matsumoto[2006])

Its system in wind tunnel is shown in Fig.29. The of amplitude ratio between heaving response and forced torsional vibration for rectangular cylinder with B/D=20 measured FPG experiment under forced torsional vibration with p-p amplitude of $10^0$is compared with analytical results in Fig.30.

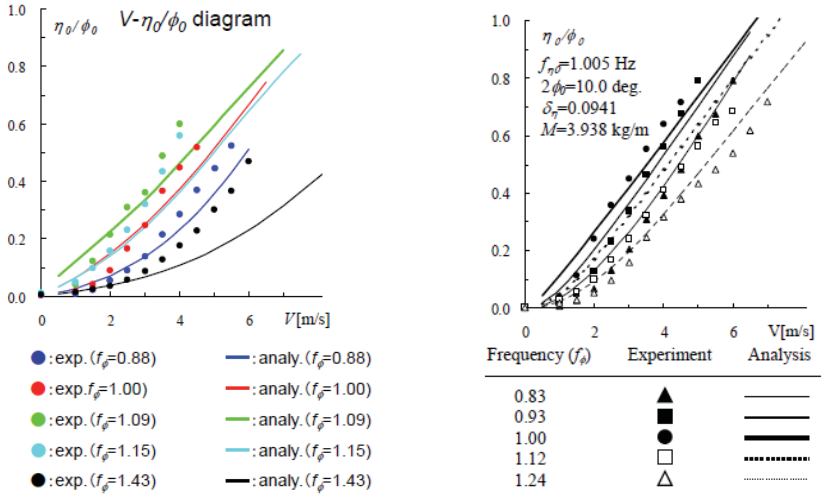

(a) Rectangular Cylinder with B/D=20 (b)Rectangular Cylinder with B/D=5

Fig. 30 Comparison of Amplitude Ratio in FPG of Experimental results and Analytical ones for B/D=20 and 5, under Forced Torsional Vibration with p-p Amplitude of 10^0. (Matsumoto[2006])

It should be noted that FPG system uses naturally appearing coupled flutter in H-90 flutter mode. In Ship navigation system with flapping plate has significant advantage in saving power for driving coupled motion to the flapping plate. The detail is described below.

5.5 *Advantage of Flapping plate System for Ship Navigation*

In order to generate the positive propulsion force by coupled torsional and heaving motion, equations (5.9) and (5.10) are definitely satisfied. Therefore naturally generated coupled flutter of plate-like sections cannot generate positive propulsion force, because in amplitude ratio between heaving and torsional motion, η_0/φ_0 v.s. velocity diagram, equation (5.9) is not satisfied as shown in Fig.27. This η_0/φ_0-velocity diagram is same one in Fig.15 (or Fig18(a)). In another words, natural coupled flutter must generate negative propulsion force, which means generation downstream-ward force fluctuation during coupling motion. In particular, this peak of negative propulsion force appears twice, because of twice appearance of $|d\eta/dt|_{max}$, in one cycle flutter motion, it means f_{Fp}(propulsion force frequency) is twice of f_F(flutter frequency). During heaving and torsional 2DOF coupled flutter with frequency of f_F, windward vibration with $2f_F$ can be excited.

By the way, for ship navigation by the flapping plate, when ship starts from still state, initial power to generate the coupled motion, which satisfied equations (5.9) and (5.19), then ship moves with certain velocity, V. At this moment in getting velocity V, given torsional motion can generate heaving motion by the mechanism of Flutter Power Generation, therefore, to get continuously the positive propulsion force to navigate a ship, the lack heaving amplitude, ηlack, should be added to satisfied equations (5.9) and (5.10). Namely in ship navigation with flapping

plate, once ship starts, rather mount power would be saved aided by the mechanism of flutter power generation as illustrated in Fig.28.

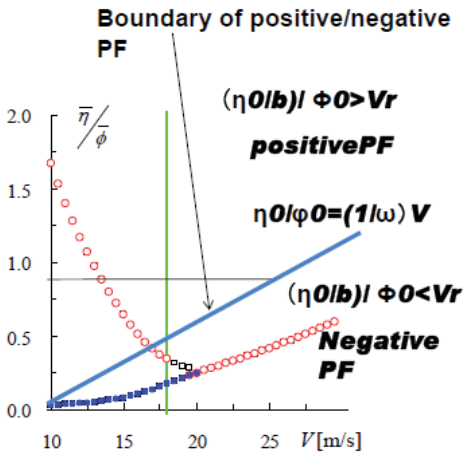

Fig.31 Critical Boundary to get Positive PF

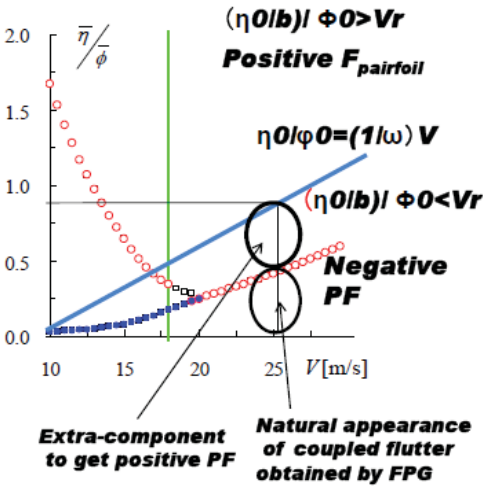

Fig.32 Illustration of Power Saving by use of FPG in Flapping Plate System

A lot of further studies for needed for practical realization of ship navigation with flapping plate, however there must be significant advantage in ship navigation with flapping plate from the point of power saving.

6 CONCLUSIONS

In this paper, fundamental of flutter phenomena, including galloping, torsional flutter and coupled flutter, has been introduced and as application, it is explained that propulsion force can be intelligently produced by use of the fundamental flutter mode, H-90.

Finally, author would like to acknowledge to Dr. Hiroshi Ishizaki(Hanshin Express way Technical and Maintenance Research Institution) for his valuable advises to this study. Furthermore, he should express acknowledge to Dr. Tomomi Yagi (Kyoto University), Mr.Rikuma Shijou(Mitsubishi Heavy Industry), Mr.Kazumasa Ookubo(Kajima corporation), Yoshiaki Ito(Shimizu Corporation), Hisato Matsumiya(Cetral Research Institute of Electric Power Industry), Mr. Michio Hashimoto(Shimizu corporation), Mr.Keisuke Mizuno(JR West Corporation), Dr. Kotaro Hori(Numerical Flow Design Corporation), Miss. Yuki Kawashima (All Nippon Airline) for their contribution on numerous experiments related to flutter fundamentals. Furthermore, on ship navigation test, author should express acknowledge to Prof N.Ishii, Mr. S.Kometani (former graduate student of OTCU) and Mr.T.Tsuji (graduate student of OTCU) and to Dr. Kouji Isogai of Professor Emeritus of Kyushu University, Japan, and Dr. Oleksandr Barannyk and Professor Peter Oshkai of University of Victoria, Canada, for offering various valuable data through personal communications.

7 REFERENCES

1 H.Abiru & A. Yoshitake, Flapping Wing Hydroelectric Power Generation System , Proc. of Advanced in Interaction and Multi-scale Mechanics(AIMM'10), Jeju, Korea, 2010

2 O.Barannyk, B.Buckham and P.Oshkai , Effect of Chord-wise Flexibility and Depth of Submergence on an Oscillating Plate under Water Propulsion System , Proc. of the ASME 2010 3rd Joint US-European Fluid Engineering Summer Seminar

3 R.I.Bass , Aerodynamic forces on structures of circular cross-sections, J of Wind Eng. And Industrial Aerodyn., 1985 , Part I, Vol.21.pp

4 P.M.Bearman & D.M.Trueman, An Investigation of the flow around rectangular cylinders, The Aeronautical Quarterly, 1972, Vol.XXIII, pp1-6,

5 F.B. Farquharson, Aerodynamic Stability of Suspension Bridges, 1949, Part I-IV

6 J.P.Den Hartog, Mechanical Vibration, New York, McGraw-Hill, 1956, pp299-305

7 Y. Hikami, Rain vibrations of cables of cable-stayed bridge, Journal of Wind Engineering, JAWE, 1986, No.27, (in Japanese)

8 K. Hirata , Study on Generation Mechanism of Galloping, Doctor Thesis of Kyushu University, 1993(in Japanese)

9 Isogai, K and et al., Design study of elastically supported flapping wing power generator , Proc. of International Forum on Aero-elasticity and Structural Dynamics,2003

10 K.Isoga and et al. , Propulsive Performance of Dolphin's Tail Fin- Optimum Desigh of Fin Motion and Its Experimental Validation, Proc. of 36th Japan Conference on Fluid Dynamics, 2006, pp293-296

11 K.Isogai: Personal Communication, 2010

12 T.V. Karman & W.R.Sears, Airfoil Theory for Non-Uniform Motion, Journal of The Aeronautical Sciences, 1938, Vol.5, August, No.10, pp379-389

13 J.H.G.Macdonald, Quasi-Steady Analysis of 2DOF Inclined Cable Galloping in the Critical Reynolds Number Range, Proc. of 6th ISCD, 2005, pp435-442

14 H.Matsumiya, T.Nishihara, ZM.Shimizy, Aerodynamic Characteristics of Ice and Snow accreted Conductors of Overhead Transmission Lines, Proc. of 10th ICWE, Amsterdam, Holland, 2010

15 M. Matsumoto and et al., Inclined Cable Aerodynamics , Structural Design, Analysis & Testing, in Proc. of Structural Congress '89, ASCE, 1989

16 M. Matsumoto and et al., Rain-wind induced vibration of cables of cable-stayed bridges , Journal of Wind Engineering and Industrial Aerodynamics, 1992, 41-44, pp.2011-2022

17 M.Matsumoto and et al., Cable Vibration and Its Aerodynamics/Mechanical Control, Proc. of International Conference of Cable Stayed and Suspension Bridges, Deauville, IABSE, 1994

18 M.Matsu,moto and et al., Torsional Flutter of Bluff Bodies , JWEIA, 1997, Vol.69-71, pp871-881

19 M. Matsumoto and et al., Wind-induced Vibration of Cables of Cable-Stayed Bridges , J. Wind Eng. Ind. Aerodyn. 1998, pp317–327

20 M. Matsumoto, Observed behavior of prototype cable vibration and its generation mechanism, Bridge Aerodynamics, in Proceedings of the International Symposium on Advances in Bridge Aerodynamics, Copenhagen, Denmark, May, 1998, pp.189-211

21 M.Matsumoto and et al., Effect of Aerodynamic Interferences between Heaving and Torsional Vibration of Bridge Decks- the Case of Tacoma Narrows Bridge , JWEIA, 2004, Vol.91, No.12-15, pp1547-1557

22 M.Matsumoto and et al., Flutter Characteristics of H-Shaped Cylinders with Various Side-Ratios and Similarity to Rectangular Cylinder Ones, Proc. of the 5th International Colloquium on BBAA, Ottawa, 2004

23 M.Matsumoto and et al., The Flutter Instability Mechanism – Coupled flutter and Torsional Flutter,, 2005

24 M.Matsumoto, Flutter Instability of Structures, Proc.of the4th EAWCE (key note), Prague,,2005

25 M. Matsumoto and et al., Effects of Axial Flow and Karman vortex interference on dry-state galloping of inclined stay-cables, Proceedings of 6th International Symposium on Cable Dynamics, Charleston, South Carolina, USA., 2005, 247-254

26 M.Matsumoto, K., K. Okubo and Y.Ito, Fundamental Study on the Efficiency of Power Generation by Use of the Flutter Instability, Proceedings of PVP 2006-ICPVT-11, 2006 ASME Pressure Vessels and Piping Division Conference、Vancouver, Canada,2006

27 M.Matsumoto, K., K. Okubo and Y.Ito, Fundamental Study on the Efficiency of Power Generation by Use of the Flutter Instability, Proceedings of PVP 2006-ICPVT-11, 2006 ASME Pressure Vessels and Piping Division Conference、Vancouver, Canada, 2006

28 M.Matsumoto and et al., Karman Vortex Effect on the Aerodynamic Forces of Rectangular Cylinders, Proceedings of PVP 2006-ICPVT-11, 2006 ASME Pressure Vessels and Piping Division Conference、Vancouver, Canada, 2006

29 M. Matsumoto, Mechanism of wind & rain/wind induced cable vibrations –role of Karman vortex on inclined cable aerodynamics, Proceedings of Wind Induced Vibration of Cable Stay Bridges Workshop, St. Louis, Missouri, USA, 2006
30 M.Matsumoto, et al., Fundamental Study on the Efficiency of Power Generation System by Use of Flutter Instability , Proc. of PVP 2006-ICPVT 2006 ASME, Vancouver
31 M.Matsumoto et al., Cross Flow Response of Circular Cylinder Influenced by Karman Vortex Mitigation, Proc. of the 7th ISCD, Vienna, 2007, pp323-330
32 M.Matsumoto and et al., Study on the Role of Karman Vortex on galloping of Bluff Bodies, Proc. of the 9th Intl. Conf. on FIV, Prague, 2008
33 M.Matsumoto, The Role of Axial Flow in Near Wake on the Cross-Flow Vibration of the Inclined Cable of Cable-Stayed Bridges, Proceedings of ASME 2010 3rd Joint US-European Fluids Engineering Summer Meeting, FEDSM-ICNMM2010
34 M.Matsumoto and et al. , Dry galloping characteristics and its mechanism of inclined/yawed cables, J of Wind Eng. and Industrial Aerodyn. 2010, 98, pp317-327
35 M.Matsumoto, H.Matsumiya, S.Fujiwara, and Y.Ito, New consideration on flutter properties based on step-by-step analysis, J. of WEIA, 2010, Vol.98, pp429-437
36 M.Matsumoto & H. Ishizaki, Study on Propelling Forces by taking into account of Flutter Modes, Proc. of Advanced in Interaction and Multi-scale Mechanics(AIMM'10), Jeju, Korea, 2010
37 M. Matsumoto & A. Laneville, Generation of Galloping of Bluff Body in Relation to Karman Vortex, Proceedings of the 13th ICWE, 2011
38 M.Matsumoto, On Generation Mechanism of Rain Vibration and Dry Galloping of Inclined stayed-cables of cable-Stayed Bridges, basing on Their Flow Fields, Proc. of 9th ICSD, 2011, pp207-214, Shanghai, China,
39 K.W.McAlister, L.W.Carr, Water Tunnel Visualization of Dynamic Stall , ASME Publication, Symposium on Nonsteady Fluid Dynamics, Winter Meeting, 1978, pp 103-111
40 Y.Nakamura, & Y.Tomonari, The Aerodynamic Characteristics of D-section Prism in a Smooth and in a Turbulent Flow , Aeronautical Qurterly, 1981,Vol.32, pp153-168
41 Y.Nakamura & K.Hirata, The Aerodynamic Mechanism of Galloping, Trans. Japan Soc. Aero. Space Sci., 1994, Vol.36, No.114
42 M.Okamoto & Y.Jinba, (2008), Experimental Study of Aerodynamic Characteristics of Wing Platform at Low Reynolds Number , pp42-50Bullitein of Akita Liberal Engineering High School, No.44,
43 R.H.Scanlan and J.J.Tomko (1971), Airfoil and Bridge Deck Flutter Derivatives, J. of Eng. Mech. Division, 97, EM6, ASCE, pp1717-173
44 A. Selberg, Oscillation and aerodynamic Stability of Suspension Bridges, ACTA, Polytechnica Scannavica, Civil Engineering, Civil Engineering and Construction Series , 1961
45 M.Shimizu, S.Oka, T.Ishihara, Development of Web-Based Ice-Accreted Transmission Line Aerodynamic Analysis System , Proc. of 19th Japan Symposium on Wind Engineering, (in Japanese) , 2006
46 I.Tanaka & M.Nagai, Fluid Mechanics on Resistance and Propulsion-Learning from High Speed Swimming Capability of Fishes, Ship and Ocean Foundation,(in Japanese), 1996
47 I.Terada, I.Yamamoto, T.Nagamatsu and Y.Imaizumi, Development of Oscillating Fin Propulsion System and Its Application, Technical Report of Mitsubishi Heavy Industry, 1998, Vol.35, No.2, (in Japanese)
48 F.Y.Xu and et.al., Aeroelastic divergences research of Sutong Bridge , Proc. of ICWE13, 2011

Wind induced effects on bluff bodies in turbulent flows: nonstationary, non-Gaussian and nonlinear features

Ahsan Kareem [a], Teng Wu [a]

[a] *Nathaz Modeling Laboratory, University of Notre Dame, Notre Dame, IN, USA*

ABSTRACT: Notwithstanding the developments made in recent decades in bluff body aerodynamics and aeroelasticity, which have enhanced our abilities to better understand and capture the effects of turbulenct wind on structures, we are at an appropriate juncture to reflect on these developments, reassess their merits and shortcomings, and identify the need for embarking on different modeling philosophies and paradigms. In this context, there is a need to revisit the current paradigms and to look for improved understanding concerning the nature of wind fields, the associated aerodynamics and the resulting load effects in recognition of the following emerging realities: non-stationarity/non-homogeneity/transient wind events; non-Gaussianity; nonlinearity of structural and aerodynamic origins; unsteady/transient aerodynamics. Also, one needs to take note of recent advances in analysis and identification tools, and modeling frameworks, which promise to offer better understanding of the underlying complexities associated with the preceding themes. This paper discusses these issues and illustrates their significance in bluff body aerodynamics and aeroelasticity from the perspective of wind effects on built infrastructure.

KEYWORDS: Turbulence; Bluff body; Nonstationarity; Non-Gaussianity; Nonlinearity; Modeling

1 INTRODUCTION

The assurance of structural safety and reliability under wind loads requires accurate modeling of wind load effects relying heavily on our understanding of bluff body aerodynamics and aeroelasticity. The intractability of wind-structure interactions amidst complex urban topography has precluded analytical treatment of the subject with rather few exceptions such as buffeting effects (Davenport 1967; Zhou and Kareem 2001; Kwon and Kareem 2009). Therefore, physical modeling of wind effects in boundary layer wind tunnels has served as a most effective tool for ascertaining these load effects (Cermak 1975). Accordingly, the last few decades have witnessed significant advances in wind tunnel technology, full-scale monitoring, sensors/transducers, instrumentation, data acquisition systems, data fusion and mining strategies, laser Doppler-based technologies, geographical information and positioning systems (GIS) & (GPS) and information technologies, which have increased our ability to better monitor and process gathered information for improved understanding of the complexities and nuances of how wind interacts with structures, the attendant load effects and their modeling. On the other hand, in the last few decades, there have been major developments in the computational area to numerically simulate flow fields and their effects on structures. Developments in computational methods, e.g., stochastic computational mechanics, have led to useful tools to further advance the role of numerical analysis. The availability of high-speed computers, individually, in networked clusters, or in the cloud has enhanced the portability and interoperability of computational codes, to most research laboratories and design offices. Rapid advances on all fronts have accordingly led to advances in our understanding of aerodynamics and aeroelasticity and associated load effects and, as a consequence, have improved the prospect of developing the next generation of load simula-

tion facilities and wind tunnels, database enabled design aids, web-based e-technologies and codes and standards.

These developments have undoubtedly enhanced our abilities to better understand and capture the effects of wind on structures. It is appropriate time, however, to reflect on these developments, reassess their merits and shortcomings, and identify the need for embarking on different modeling philosophies and paradigms as called for by the recent observations. In this context, the rest of this paper will identify and discuss a few selected frontiers in bluff body aerodynamics and aeroelasticity with particular reference to wind loads on structures and the challenges these pose to the fluid dynamics and wind engineering communities. These topics include non-stationarity/non-homogeneous/transient wind events; non-Gaussianity; nonlinearity of structural and aerodynamic origins; unsteady/transient aerodynamics and the relevant modeling frameworks and identification tools. Improved understanding of turbulence effects on bluff bodies is stressed.

2 NONSTATIONARY/TRANSIENT WINDS

Most extreme wind events are nonstationary in nature and are often highly transient, e.g., wind fields in hurricanes, tornadoes, downbursts and gust fronts. Therefore, the most critical issue in wind field characteristics concerns the transient wind events, e.g., gust-fronts generated by downdrafts associated with thunderstorms. The significance of these transient wind events and their load effects can be readily surmised from an analysis of thunderstorms databases both in the U.S. and around the world, which suggest that these winds actually represent the design wind speed for many locations (Twisdale and Vickery 1992; Brooks et al. 2001).

The mechanics of gusts associated with convective gust-fronts differs significantly from conventional turbulence (driven by momentum) both in its kinematics and dynamics. A survey of full-scale studies in the meteorological field suggests that winds spawned by thunderstorm, both on the updraft side as tornadoes and on the downdraft side as downburst, fundamentally differ from the synoptic winds in neutrally stable atmospheric boundary layer flows. The key distinguishing attributes are the contrasting velocity profile with height and the statistical nature of the wind field. In gust-fronts, the traditional velocity profile does not exist; rather it bears an inverted velocity profile with maxima near the ground potentially exposing low- to mid-rise structures to higher wind loads (e.g., Wood and Kwok 1998; Letchford and Chay 2002; Butler et al. 2010). This is compounded by the inherent transient nature of energetic convective gusts, raising serious questions regarding the applicability of conventional aerodynamic loading theories. Although the size of gust-fronts may be relatively small and their effects rather local, the fact remains that they can produce significantly damaging winds. The famous Andrews Air force base downburst of 1983 clocked peak gusts of 67 m/s, whereas, ASCE Standard provisions list 50-year recurrence winds of 40-45 m/s in this region (Fujita 1985). Accordingly, one should question the appropriateness of a design based on conventional analysis frameworks in codes and standards, which generically treat these fundamentally different phenomena in the same manner.

The major challenge in this area is at least twofold, i.e., firstly, the nature of flow fields in rain bands, the eye wall of hurricanes, downdrafts and gust fronts needs to be better quantified, and secondly, analysis and modeling tools to capture these features need to be established. Design loads are based on the mean wind speed for a given site and direction and rely on the assumption that the fluctuations in the mean are characterized by a statistically stationary process, which has led to useful and practical simplifications. The gust-fronts generated in thunderstorms/downdrafts differ from the large-scale (extratropical/ depressional) storms as the mean wind speed exhibits sharp changes and in some cases changes in wind direction. This leaves the assumption of stationarity open to serious criticism.

Besides this departure in statistical attributes of the wind field, gust-fronts are likely to be associated with rapid and substantial changes in the local flow around structures and will likely be correlated over a larger area. These changes in the kinematics and dynamics of the flow field would potentially result in higher aerodynamic loads. These attributes further complicate the concept of "gust factors" which in some forms are central to most wind load assessments. The gust factor concept used for extratropical winds must be revisited as the period used to evaluate average wind speed for thunderstorm winds must be shortened to obtain meaningful results. Longer periods, such as an hour, if used for thunderstorm winds may result in gust factor values almost 2-3 times the corresponding values in extratropical winds. Current efforts toward gleaning information regarding the thunderstorm outflow characteristics through modeling non-stationary winds would aid in better capturing the salient features of winds in transient events (Gast et al. 2003; Wang and Kareem 2004a; Chen and Letchford 2005a). In a recent study, Kwon and Kareem (2009) presented a new framework to capture the flow field in a gust front and its attendant load effects.

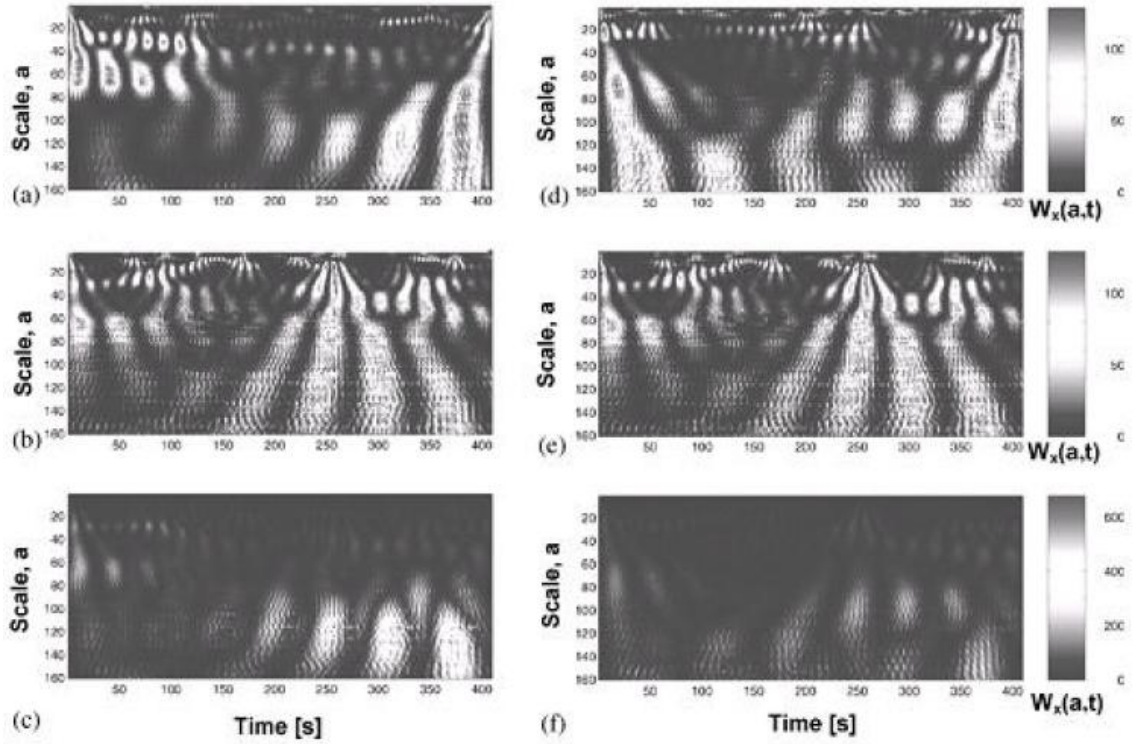

Figure 1: (a) Scalogram of upstream wind velocity 1; (b) scalogram of rooftop pressure; (c) coscalogram of these two correlated processes; (d) scalogram of upstream wind velocity 2; (e) scalogram of rooftop pressure: (f) coscalogram of these two uncorrelated processes (after Gurley and Kareem, 1999)

Simulation of non-stationary events like gust fronts and hurricane wind fields can be accomplished by the generic summation of trigonometric time series approaches, but it is computationally inefficient, since, due to lack of ergodicity, ensemble averaging requires simulation of a large number of time series. The (proper orthogonal decomposition) POD based approach offers computational expediency, but thus far has been explored to only account for the amplitude modulations (Chen and Letchford 2005b). The wavelet-based simulation offers an alternative, which may better capture both time and frequency modulations (Wang and Kareem 2004a; 2004b; 2005). The dual nature of wavelet transforms, being a simultaneous transform in time and frequency, justifies its recent extension to civil engineering applications. The transform can be

adapted to a number of situations where Fourier transforms (for frequency domain analysis) or Hilbert transforms (for time domain system identification) are traditionally used to define quantities of interest. When considering the time and frequency information in tandem, wavelets can be used to determine the times and frequencies at which signal energy content is strongest by examining scalograms and co-scalograms (Gurley et al. 1997; Gurley and Kareem 1999; Kareem and Kijewski 2002). Fig. 1 displays a coscalogram comparison for full-scale pressure measured on a building and the two upstream wind velocity records. The first record is monitored simultaneously with the pressure time history under consideration and the second is from a different wind event. Fig. 1 (a-c) shows the scalogram and coscalograms of wind pressure and the first wind velocity, which is knowingly correlated. Note the pockets of white beyond 250 seconds revealing timevarying pockets of correlation in different frequency bands. This may be compared to a similar analysis for wind pressure and velocity that is known to be uncorrelated, for which no marked white pockets, indicative of correlation, are present. The presence of subtle light pockets, indicative of spurious correlation, present in both the correlated and uncorrelated examples in Fig. 1 is due to a lack of ensemble averaging (Kareem and Kijewski 2002).

3 NON-GAUSSIANITY

The wind velocity could be well represented as a Gaussian process, which is verified by numerous experiments and field observations. As a result, with the assumption of linear relationship between the input (wind velocity) and output (structure response), many of the studies encompassing analysis and modeling of wind effects on structures have assumed that the involved random processes are Gaussian. In general, for large structures the assumption of Gaussianity may be valid as a consequence of the Central Limit Theorem. However, the regions of structures under separated flows experience strong non-Gaussian effects in the pressure distribution characterized by high skewness and kurtosis. Fig. 2 illustrates the nature of pressure fluctuations on the windward and roof regions, where the rooftop region distinctly exhibits non-Gaussian features as noted in the time history of pressure fluctuations. It is also noteworthy that the bending moments (bottom time history) at the supports also exhibit non-Gaussian features despite the fact that the bending moments result from the summation of several force components. The departure from the Central Limit Theorem stems from the fact that the loads over the structures are correlated, which is in contradiction to the premise of the theorem.

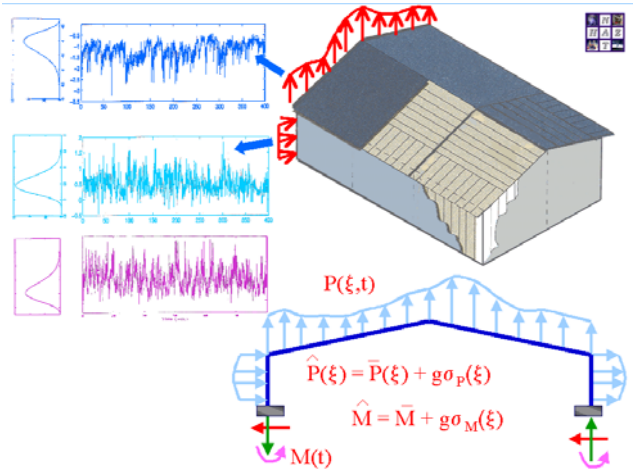

Figure 2: Schematic of pressure fluctuations on a building envelope

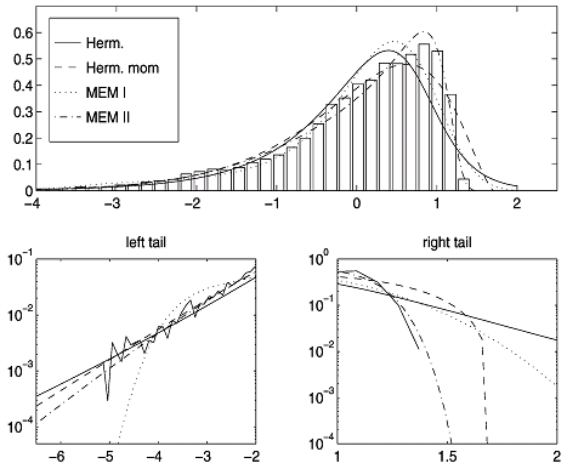

Figure 3: Top - PDF of pressure fluctuations in a separated region; Bottom – Close up of the tail regions (after Gurley et al. 1997)

The probability density function (PDF) of pressure fluctuations with large skewness observed in separated flow regions is critical to the modeling of loads on cladding and components, as well as loads on main load-resisting systems (Fig. 3). Often researchers have attempted to use the lognormal distribution for pressure fluctuations, but this fails to represent the tail region with high fidelity (Gurley et al. 1997). Among different alternatives, including the Maximum Entropy based model, it is noted in Fig. 3 that the Hermite moment-based distribution provides the best match to the data, especially for the negative tails (Gurley et al. 1997). This model also captures the significance of non-Gaussian pressure fluctuations for determining the equivalent constant pressure for glass design (Gurley et al. 1997), while providing a useful format to account for non-Gaussianity in the estimation of wind induced fatigue damage, as characterized by a correction factor (Gurley et al. 1997). The non-Gaussian effects result in enhanced local loads and may lead to increased expected damage in glass panels and higher fatigue effects on other components of cladding (Gurley et al. 1997).

Progress in quantifying and simulating the non-Gaussian effects of wind on structures has been elusive due to the limitations of traditional analytical tools (Gurley et al. 1996; Grigoriu 1998). Earlier work based on correlation distortion has been based on an inverse mapping of the desired PDF, a summary of which may be found in Gurley et al. (1996). In Gurley and Kareem (1997), a simulation approach, which is significantly more robust than the correlation distortion schemes, was presented. The non-Gaussian features and the frequency contents in the form of the first four moments and the target power spectral density (PSD) of the process were used; alternatively analytical expressions or other estimates of the distribution may be employed. The approach is named the spectral correction method relying on a few iterations to match both the spectral and probabilistic features. Fig. 4 shows an example of a simulation run based on a measured time history of a highly skewed full-scale pressure measurement. Also included are the PDF and PSD of the target and the simulated records which show good agreement. Additional follow-up work in this broad framework can be found in Grigoriu (1998), Deodatis and Micaletti (2001) and Masters and Gurley (2003). This approach has been extended to multi-variate processes including conditional simulations and random fields (Gurley and Kareem 1998a; 1998b; Gurley et al. 2001).

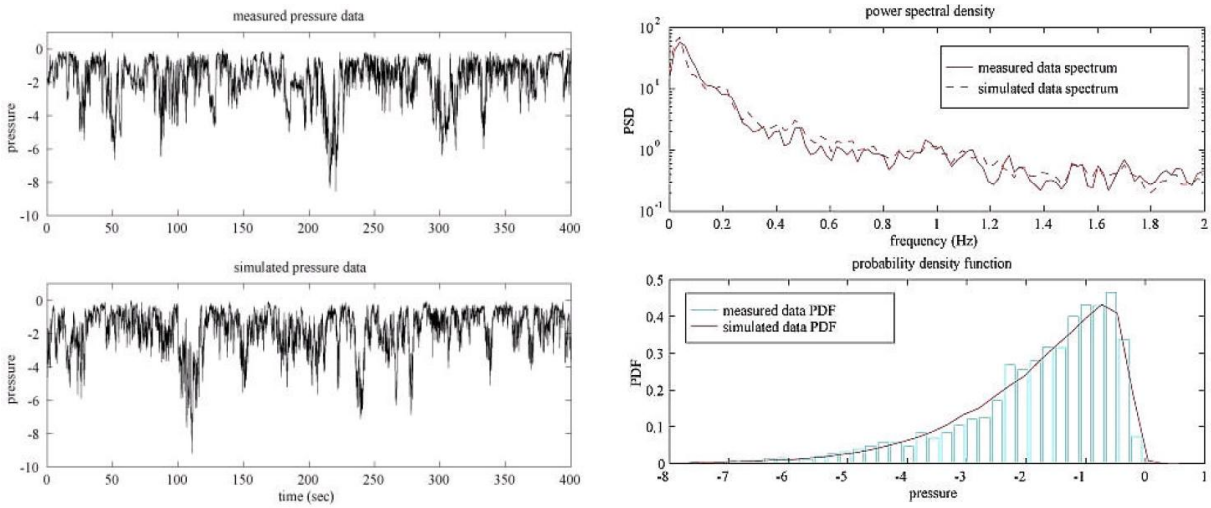

Figure 4: Left - Measured and simulated pressure time histories; Right - Comparison of PSD and PDF of simulated and measured time histories (after Gurley, et al. 1997)

Inasmuch as these techniques are based on static transformations, they may fail to encapsulate any memory that may be present in the target signals. A Volterra series-based scheme offers

an alternative that ensures preservation of memory. However, the Volterra kernels needed for such simulation may not always be available (Gurley and Kareem 1997). A class of single point non-Gaussian processes, e.g., pressure fluctuations at a location, can also be simulated through manipulation of the phase and utilization of neural networks (e.g., Gurley et al. 1996; Seong and Peterka 1998).

4 NONLINEARITY

In the area of wind effects on structures there are three types of nonlinearities that are generally experienced, i.e., geometric, material and aerodynamic. The geometric nonlinearity is most prevalent in cable-suspended and guyed structures, i.e., suspension and cable stayed bridges and guyed towers and masts, and pneumatic structures. The material nonlinearities may arise from materials of construction, e.g., concrete and composites that do not follow linear constitutive relationships. These effects can be adequately modeled for most structures using finite element models.

The nonlinearity of aerodynamic and aeroelastic origins are prevalent in wind effects on structures. Customarily, in these situations, linearized solutions are invoked, e.g., the widely used gust loading factor in codes and standards is based on the Gaussian framework, thus the term containing the square of the velocity fluctuations is dropped from the formulation. Kareem et al. (1998) presented a gust loading factor, which included the square velocity term, using the Hermite moment-based distribution in place of the Gaussian distribution. Earlier attempts to capture this effect using Edgeworth series did not adequately represent the tail regions of the distribution.

A linear assumption is often used to compute the response of structures to buffeting forces when nonlinearity in aerodynamic loading arises from the squared velocity term, as alluded to previously and due to dependence of aerodynamic coefficients on the angle of attack. Currently, reliance on the quasi-steady theory is a method of choice to take into account aerodynamic nonlinearities. According to the quasi-steady (QS) assumption, aerodynamic forces on structures are expressed as a nonlinear memoryless transformation of the flow-structure relative velocity and the angle of attack, which are variable in time due to oscillation of the body and the presence of turbulence in the incoming flow. The projection of the aerodynamic forces on the shape-functions employed in the finite element or Galerkin discretization of the structure requires approximating the nonlinearities by polynomial expressions. This can be carried out through a Taylor series expansion (Denoël and Degée 2005) or by an optimization procedure aimed at minimizing some error measure (Carassale and Kareem 2010).

On the other hand, one of the challenges in aeroelastic analysis remains in the modeling of wind-induced forces that take into consideration nonlinearities in both structural dynamics and aerodynamics in an unsteady analysis framework. As the measured information utilized in the traditional analysis framework, e.g., flutter derivatives, wind spectra, and aerodynamic admittances, are all natural functions of frequency, the aerodynamic issues are conventionally analyzed in frequency-domain (Scanlan and Tomko 1971). These frequency-domain analysis approaches are not suitable for accommodating the computational challenges of the nonlinear considerations.

In order to consider the unsteady effect in time domain, the indicial function approximation (Scanlan et al. 1974) or rational function approximation (Bucher and Lin 1988) is utilized. One of the earliest performance of the bridge aerodynamic/aeroelastic unsteady analysis in time domain is carried out by Beliveau et al. (1977) based on the indicial function approximation. Recently, Chen et al. (2000) and Chen and Kareem (2001) conducted the bridge aerodynamic/aeroelastic unsteady analysis in time domain based on the rational function approximation.

The proposed time domain analysis framework by Chen et al. (2000) and Chen and Kareem (2001) incorporates the frequency-dependent characteristics of aerodynamic forces that have been often neglected in most of the previous studies in time domain aeroelastic analysis, potentially impacting the accuracy of the response estimates.

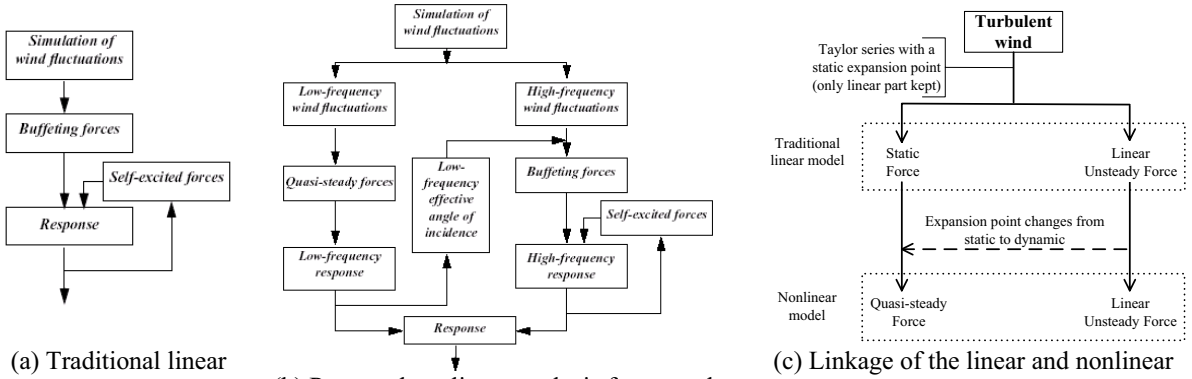

(a) Traditional linear analysis framework (b) Proposed nonlinear analysis framework (c) Linkage of the linear and nonlinear analysis frameworks

Figure 5: Traditional and nonlinear analysis frameworks ((a) and (b)after Chen and Kareem 2003)

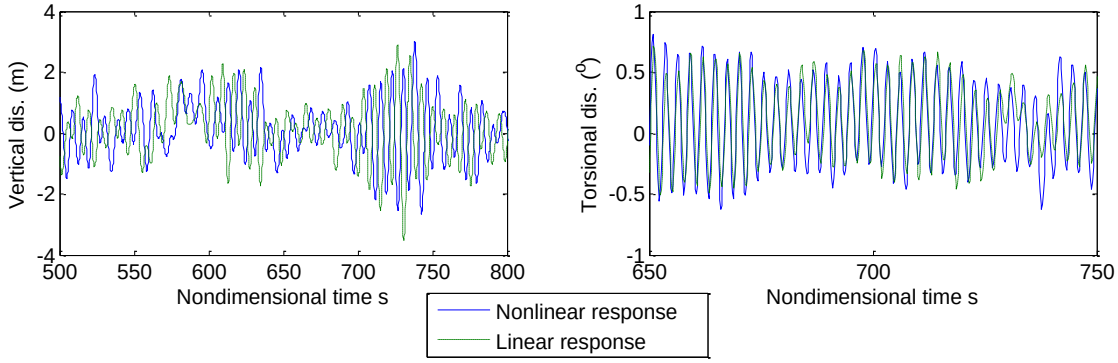

Figure 6: Time history of linear and nonlinear bridge deck responses

Furthermore, an advanced nonlinear aerodynamic force model and attendant analysis framework has been presented by Chen and Kareem (2003) that focused on the needs for modeling of aerodynamic nonlinearity of long span bridges. This nonlinear analysis framework transforms the problem into a full-time-domain formulation by means of a rational-function approximation and solves the equations of motion in the time domain through among others an integrated state-space approach. The aerodynamic forces are separated into the low- and high-frequency components in accordance with the effective angle of incidence corresponding to the frequencies lower than and higher than a critical frequency, e.g., the lowest natural frequency of the bridge. The low-frequency force component can be modeled based on the QS theory due to its high reduced velocity, while the high–frequency force component is separated into self-excited and buffeting components which are modeled in terms of the frequency dependent unsteady aerodynamic characteristics at the low-frequency spatiotemporally varying effective angle of incidence. Beside, this nonlinear scheme, proposed by Chen and Kareem (2003), has a clear connection with the traditional linear analysis framework. The traditional linear and advanced nonlinear analysis frameworks are summarized in Fig. 5 along with the basic relationship between these two analysis schemes. Actually, the advanced nonlinear scheme uses expansion of the aerodynamic force term about a dynamic position of the deck as opposed to a static position,

which represents the mean displaced position of the deck as employed in a traditional linear scheme. In other words, this nonlinear analysis framework represents piecewise linearization in a dynamic scheme as opposed to the static approach (Wu and Kareem 2011). The time histories of the nonlinear aerodynamic responses, namely vertical and torsional displacements for a long span bridge are presented in Fig. 6 compared with the traditional linear results.

5 HYSTERETIC NONLINEAR BEHAVIOR

The hysteretic nonlinear phenomenon is well known in vortex induced vibration of bluff bodies since it was initially observed experimentally by Feng (1968). Recently, the hysteretic phenomenon in the aerodynamic/aeroelastic forces on both the bridge decks and the cables of cable-stayed bridges has been a focus of interest (Diana et al. 2010; Wu and Kareem 2012a). The hysteretic behavior that appears in bridge aerodynamics/aeroelasticity suggests a higher-order memory in the system. Details of the hysteresis phenomenon, common to many fields, may be found in the literature (e.g., Brilliant 1958). The examples carried out by the authors indicate that the wind-induced responses of a typical modern bridge deck and of a stayed cable are significantly increased by introducing the hysteretic behavior in the respective response prediction schemes (Wu and Kareem 2012b; Wu et al. 2012). The hysteretic phenomenon could be modeled through a rheological model (Diana et al. 2010) or through a more generalized higher-order polynomial model based on the Moore-Penrose pseudoinverse identification scheme (Wu and Kareem 2012a). Fig. 7 presents the hysteretic phenomena observed in the lift forces acting on a bridge deck and on a typical stay cable based on wind-tunnel studies together with the numerically fitted model utilizing Moore-Penrose pseudoinverse identification scheme which shows a good agreement (Wu and Kareem 2012a).

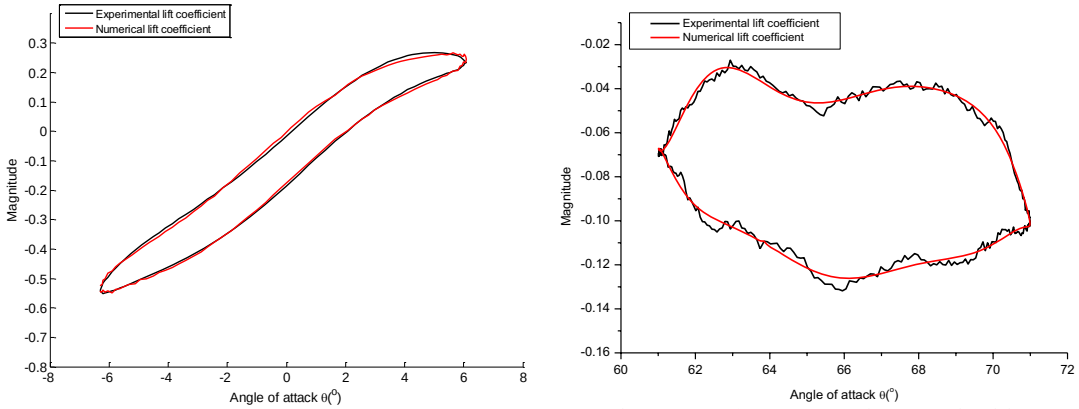

(a)) Hysteretic effect on the bridge deck (b) Hysteretic effect on the stayed cable

Figure 7: Modeling the hysteretic behavior related to the lift coefficient (after Wu and Kareem 2012a)

However, both of these schemes are based on a unique independent variable, namely the effective angle of attack. In other words, these schemes assume that all other interacting components (bridge deck motions and turbulences) that are represented by this unique independent variable have equal weighting on the bridge aerodynamic behavior, which poses an unwarranted constraint in the aerodynamic force description (Wu and Kareem 2011). On the other hand, Wu and Kareem (2011) proposed a neural network model to simulate the hysteretic nonlinear behavior, which can be easily expanded for a single term input parameter to several input parameters through introduction of added weights and neurons as illustrated schematically in Fig. 8.

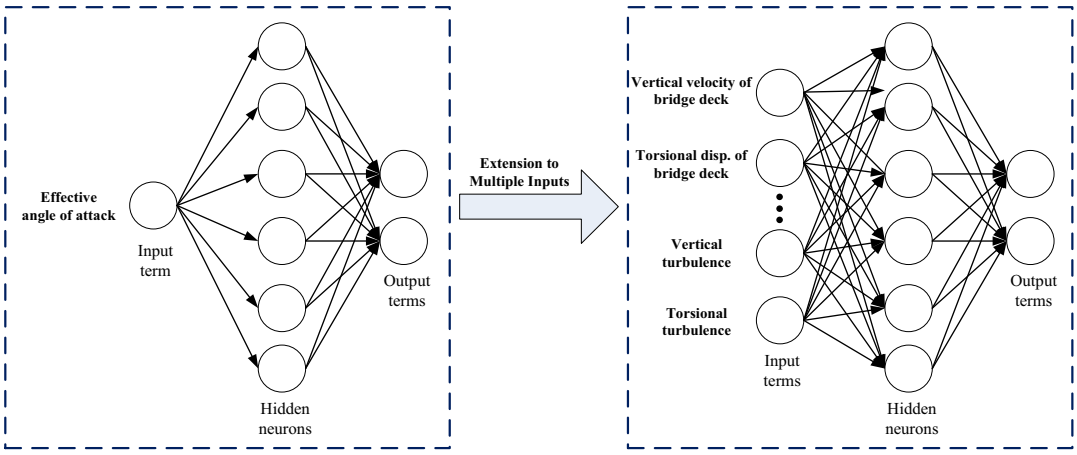

Figure 8: Schematic of the neural network for hysteretic nonlinear phenomenon

This data-driven model is determined by input-output information, which automatically captures intrinsic aerodynamic/aeroelastic nonlinearity and structural nonlinearity of the wind-bridge interaction system, as shown in Figure 9. Besides, the hysteretic nonlinearity modelling capability is enhanced through the higher-order neurons in the hidden layer, which results from the power terms of the first-order terms themselves as well as their cross terms. The cellular automata optimization scheme is applied to determine the configuration of the neural network with the aim of modelling bridge aerodynamics and aeroelasticity (Wu and Kareem 2011).

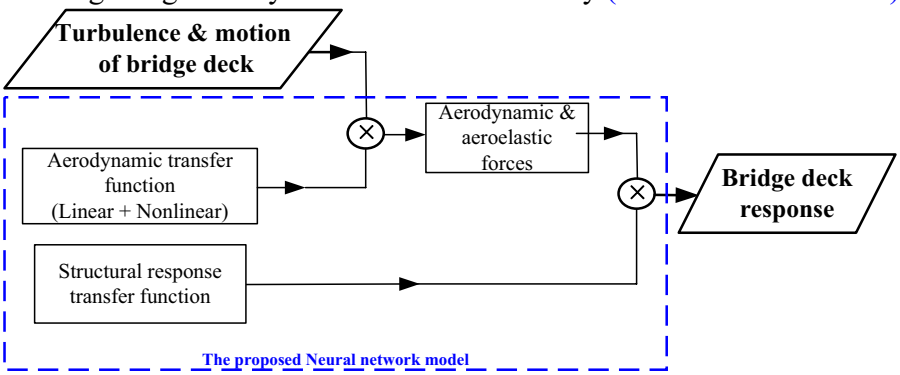

Figure 9: Integration of structural and aerodynamic nonlinearities via neural network model

6 ROLE OF TURBULENCE

The role of turbulence in the aerodynamics of stationary bluff bodies has been extensively documented in the literature (e.g., Gartshore 1973; Lee 1975; Kareem and Cermak, 1979; Saathoff and Melbourne 1989; Nakamura 1993). More recent studies investigating the effects of turbulence on rectangular sections have focused on both stationary and/or oscillating prisms with applications to improved understanding of building and bridge aerodynamics to turbulence (Larose 1993; Haan and Kareem 2009). Studies have shown that the flow around bluff bodies is governed by the separation and reattachment of the shear layers and by vortex shedding. The shear-layer thickness and the body size are length scales associated with these two phenomena, respectively. Turbulent eddies on the order of these scales are most effective at altering flow structure. The main effect of small-scale turbulence is to cause earlier reattachment of the flow through enhanced mixing in the shear layers. Turbulence in the range of the body scale can enhance or weaken vortex shedding depending on the body geometry. A schematic diagram of the multi-

scale fluctuations involved in typical bluff body wind interactions is shown in Fig. 10. Clearly there are three distinct bands of frequency characterized by the incident, shear layer or near wake and the wake fluctuations.

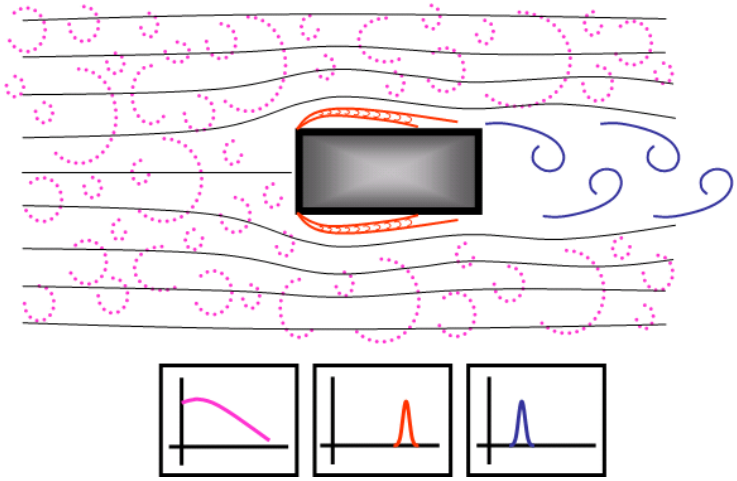

Figure 10: Schematic of flow around a bluff cross-section highlighting three distinct regions of fluctuations

Current fundamental and applicable research in turbulence effects on bluff bodies is summarized in Fig. 11, while only a selected few topics will be discussed in the following sections.

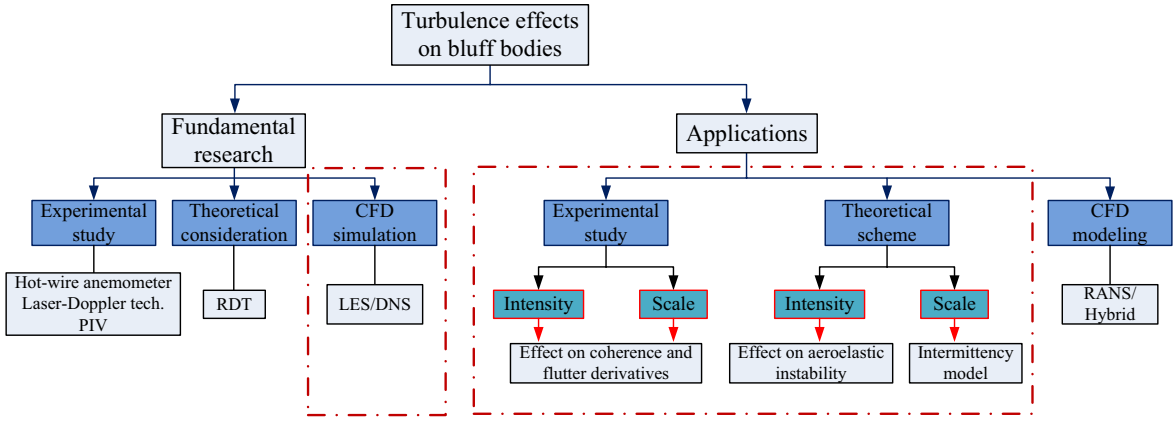

Figure 11: Current studies of turbulence effect on bluff bodies

6.1 *Fundamental research*

Although the "rapid distortion theory" (RDT) presents promising features to simplify the nonlinear nonlocal turbulent flow controlled by Navier-Stokes equation, this linear partial differential equation is still mathematical intractable as applied to the bluff bodies (Hunt et al. 1990). While current fundamental understanding of turbulence effect on bluff bodies mainly relies on the experimental studies involving significant improvement of the data acquisition systems, such as the Hot-wire anemometer, Laser-Doppler based technologies and particle image velocimetry (PIV), there have been remarkable developments in the area of computational wind engineering centered on the flow around bluff bodies involving 2-D and 3-D prisms and the role of turbulence (e.g., Murakami and Mochida 1999; Yu and Kareem 1997; Tamura and Ono 2003). The Large

Eddy Simulation (LES) framework is emerging as a numerical scheme of choice for the solution of Navier-Stokes equations (Murakami and Mochida 1999). For example, recent studies have shown that the simulated pressure field around prisms has convincingly reproduced experimentally-observed characteristics. This is true with respect to variations in the mean and RMS pressure coefficients of the drag force and regions of flow reattachment, even as the aspect ratio of the prism is varied (Murakami 1999; Yu and Kareem 1997). Other computational schemes like detached eddy and hybrid simulation schemes are offering other opportunities for improved simulations (Wei and Kareem). Fig. 12 shows instantaneous contours of vorticity for prisms of aspect ratios: 3:1 and 1:3 based on 3D LES schemes. In Fig. 13 time histories of the drag and lift forces along with their respective PSD and time-frequency scalograms are shown. Examination of the drag and lift force time histories for the selected aspect ratios reveal distinctive features both above and below the critical aspect ratio of 0.62. For aspect ratios below the critical value intermittent behavior (periods of low and high drag force) occurs, while beyond the critical value, the drag force has less intermittence. The corresponding spectral descriptions show a global distribution of energy. The scalograms (Fig. 14) reaffirm the intermittent bursts of energy for aspect ratio 3:1 and relatively more evenly distributed fluctuations for the 1:3 prism.

One of the challenges remaining in this field entails the inclusion of surrounding structures to capture the influence of flow modification, shielding and interference, as well as the simulation of inflow turbulent boundary layer flow conditions. Recently, advances have been made in these areas, including modeling of aeroelastic instabilities, CFD techniques for practical applications, and modeling of urban roughness and terrain effects (Tamura et al. 2002; Tamura and Ono 2003). Coupled with computer aided flow animations, such simulation techniques may in the near future provide “numerical wind tunnels” to analyze the evolution of flow around structures and estimate attendant load effects. More recently, developments in CFD on the cloud are evolving (vortex-winds.org).

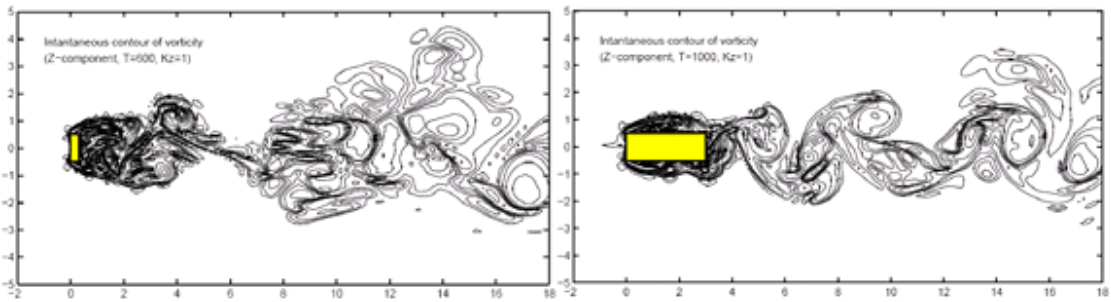

Figure 12: Instantaneous vorticity contours for rectangular prisms with aspect ratio; Left - 0.3 and Right - 3.0 (after Yu et al. 2006)

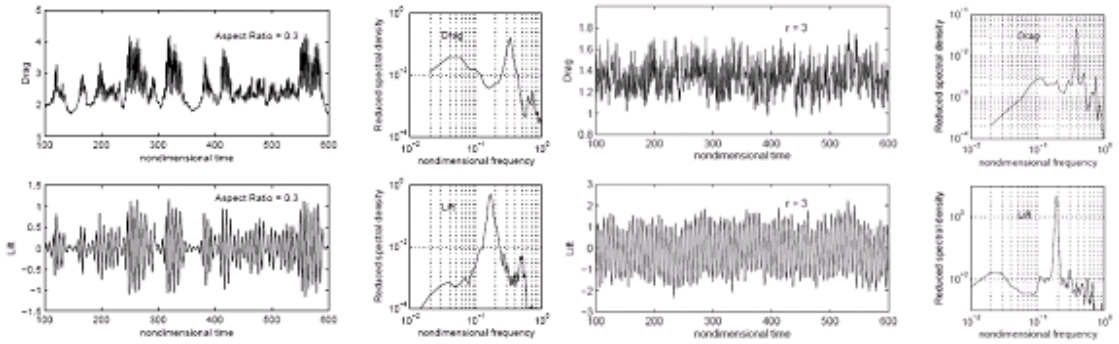

Figure 13: Drag and lift force fluctuations and respective PSD for prisms with aspect ratios: Left 0.3; Right 3.0 (after Yu et al. 2006)

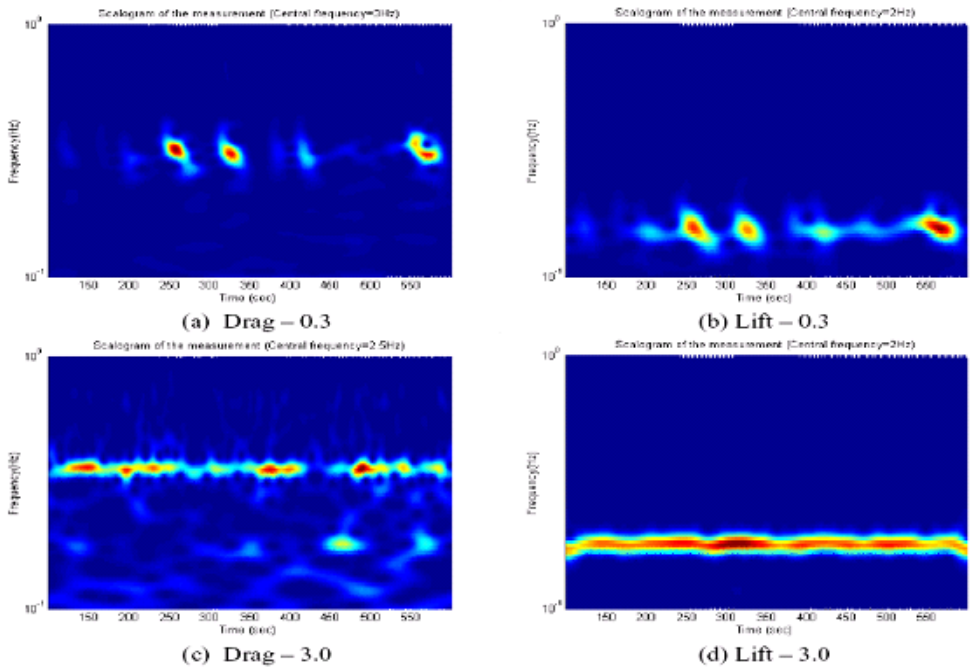

Figure 14: Wavelet based scalogram of drag and lift fluctuations for aspect ratio 0.3 (a, b) and 3.0 (c, d), respectively, (after Yu et al. 2006)

6.2 *Applications*

While the turbulence simulation based on LES or direct numerical simulation (DNS) is limited to a relative low Reynolds number due to the extremely computational consumption together with the intricacies of the inlet turbulence modeling, applications of CFD modeling based on various turbulence models have been developed in bluff body aerodynamics. However, the following sections will focus on the improved understanding of the turbulence effects on bluff bodies based on the experimental studies and on the theoretical schemes.

6.2.1 *Experimental study*

Because bridges and buildings often have rectangular or near rectangular shapes, a notable amount of wind tunnel work has been done studying varieties of rectangular bodies and the shear layers separating from them. Most of this work has been done for stationary bodies, but some has been for prisms in motion. While experimental studies focusing on the effects of turbulence on bridge aerodynamics (e.g., Scanlan and Lin 1978; Huston 1986; Matsumoto et al. 1991; Larose et al. 1993; Haan et al. 1999) have typically noted an increase in critical wind velocity with added turbulence, several studies have reported destabilizing trends associated with turbulence (Matsumoto et al. 1991; Huston 1986). The cause of these disagreements remains to be conclusively determined and signifies the limitations in current understanding of the problem (e.g., Scanlan 1997; Chen et al. 2000; Haan and Kareem 2009).

Recent experimental studies put significant attention on the turbulence effects on the flutter derivatives and on the correlation of the wind-induced forces. Scanlan and Lin (1978) first investigate the turbulence effect on the bridge aeroelasticity experimentally by utilizing the flutter derivatives under turbulence wind condition. Observation indicates there is no distinct difference of flutter derivatives resulting from laminar and turbulent flow conditions. It should be noted that the turbulence in wind tunnel cannot reproduce the natural condition accurately. Specifically, the

turbulence integral scale in wind tunnel will be very small compared with the reasonable one based on the scale law.

It is well known that not only the turbulence intensity but also turbulence scale will contribute the effect on the bluff body. Gartshore (1973) investigate the turbulence scale effects on various prisms by emphasizing the modification of the shear layer. Besides, Nakamura (1993) pointed out the small-scale turbulence could influence torsional flutter through resulting in earlier reattachment of flow on the solid surface. Recently, a detailed investigation of the turbulence effects on the aerodynamics of an oscillating prism in wind tunnel indicates the turbulence intensity and turbulence scale will simultaneously affect the flutter derivatives with different mechanisms (Haan and Kareem 2009). The former mainly changes the flutter derivatives which are sensitive to the pressure phase such as A_2^* (weighting the contribution to the moment from torsional velocity) while the latter mainly changes the flutter derivatives which are sensitive to the pressure amplitude such as A_3^* (weighting the contribution to the moment from torsional displacement) (Haan and Kareem 2009).

Instead of directly dealing with the turbulence effect on the flutter derivatives, Haan and Kareem (2009) investigated the distribution of the pressure field around the prism in both chordwise and spanwise directions, including their correlations and in bridge related studies the correlation of the pressure field in comparison with upstream turbulence. In the following, a summary of some of the findings of this recent study, which has not been widely reported in the literature thus far, is presented. It brings out some useful observations and important ramifications for the current state of the art of aerodynamic analysis of long span bridges (Haan and Kareem 2009). In this study, grid generated turbulence was used to study the effects of both turbulence intensity and turbulence scale on aerodynamic forces. By examining the unsteady pressure distributions over the bridge model rather than the flutter derivatives alone, a clearer understanding of how turbulence affects the unsteady forces was obtained. Both increasing turbulence intensity and turbulence scale decreased the amplitudes of self-excited pressure fluctuations. The basic shape of the chordwise distributions of pressure amplitude—a single hump shape—is shifted upstream with increasing intensity of the free stream turbulence. This shift, however, was only slightly affected by the turbulence scale. Fig. 15 shows a space time portrait of the pressure distribution highlighting this observation.

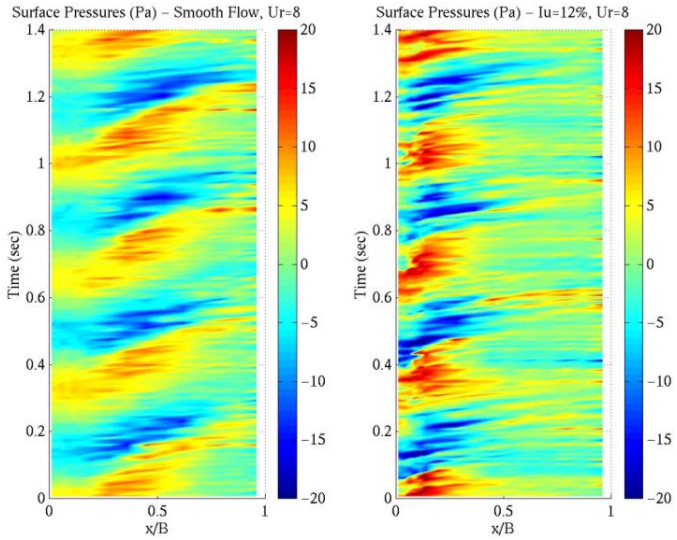

Figure 15: Surface plots of the temporal and spatial evolution of the surface pressure on a rectangular prism undergoing torsional oscillations (X/B - streamwise direction/deck width; left - smooth flow; right - turbulent flow) (after Haan 2009)

Haan and Kareem (2009) also observed that the phase values of the self-excited pressure (with respect to the body motion) had several regimes in the streamwise direction. Near the leading edge, phase was nearly constant. Downstream of this locale was a region where phase increased rapidly. Beyond this rapidly increasing phase zone was a region where the phase values leveled off and even decreased in some cases. While scale had little discernible effect on this phase value, turbulence intensity shifted the region of rapidly increasing phase toward the leading edge. The stabilizing effects of turbulence observed in the flutter derivatives were related to these turbulence-induced shifts in the pressure amplitudes and phase distributions. By tracking the integrands of expressions for lift and moment, specific changes in pressure amplitude and phase were linked to flutter derivative modifications. In addition, this upstream shifting in the unsteady pressure on the oscillating models was found to be similar to the behavior observed for pressure distributions over stationary models. This suggests that the vast amount of research done in bluff body aerodynamics on stationary bodies may aid in the understanding of oscillating body problems as well.

Prior to this study, no experimental study had justified the conventional analysis technique in which the aerodynamic forces are separated into flutter and buffeting components. Pressure measurements made on oscillating models allowed experimental assessment of this assumption. Overall, the assumption is quite close. Examination of the lift and moment spectra showed close agreement throughout the frequency range considered. Where the stationary and oscillating model spectra did not agree, however, the oscillating model values were larger. This oscillation-induced increase in the broadband energy occurred mainly for frequencies above $fD/U = 0.1$ although some differences were observed for lower frequencies as well. Quantitative analysis of these differences showed that oscillating model buffeting forces could have RMS values as much as 10% higher than their stationary model counterparts. This difference decreased for increased turbulence intensity and increased turbulence scale. For the flow with the highest intensity and scale considered, these differences were only around 2-3%. Observation of the streamwise distribution of such differences revealed that the location of oscillation-induced broadband increase was upstream of reattachment—for this case, this meant upstream of the location of the maximum RMS pressure value. This implies that bodies which experience separation over smaller portions of their surface may exhibit less significant differences between stationary and oscillating model buffeting levels.

Through both coherence measurements and correlation calculations of self-excited force components, the self-excited forces were found to have near unity coherence over the entire spanwise separation range considered. It was noted that cases with larger turbulence length scale showed a slightly lower correlation than those of smaller scales, the estimated 95% confidence intervals of ±0.03 puts all results within the statistical spread of the others suggesting no influence of length scale. The conventional assumption of self-excited forces being fully correlated in the spanwise direction was thus supported by the results of this study. Of course, this also means that the often-suggested hypothesis that a decrease in spanwise correlation of the self-excited forces causes the turbulence-induced increase in the critical flutter velocity is not supported by the current results. Although the stabilizing effect of spanwise correlation loss may be apparent for single-mode torsional flutter (Scanlan 1997), it is not obvious that this will apply to multi-mode coupled flutter cases. Correlation loss along the span may stabilize a deck by reducing negative damping effects, and yet it may destabilize a deck by reducing favorable damping (Chen and Kareem 2003). This issue will become even more important as bridge spans grow longer and multi-mode flutter becomes more probable. A conclusive investigation of self-excited force coherence would require much longer span lengths to observe whether appreciable changes occur for longer spanwise separations. Coherence calculations also showed that the broad band

coherence of the oscillating model matched that of the stationary model to within the uncertainty of the experiment.

While spanwise correlation of pressure and buffeting forces on static models in turbulent flows have been measured by a number of researchers, little if any experimental work has been done on the spanwise behavior of the self-excited forces. Full correlation of the self-excited forces is generally assumed in the response analysis, as alluded to earlier by findings in Haan et al. (1999). This suggests, however, that the turbulence-induced behavior of full-bridge models mentioned previously cannot be explained entirely due to a decrease in self-excited force coherence. In view of this, there is a clear need for improved knowledge of the basic physical phenomenon. Analysis framework based on recent developments in bridge aerodynamics may facilitate improved understanding in the subject area (Chen and Kareem 2006a; 2006b; Wu and Kareem 2011)

6.2.2 *Theoretical scheme*

Although both the effects of turbulence in the incoming flow and the signature turbulence should be taken into account, there is no well developed scheme to account for the effect of signature turbulence except utilizing the CFD technique. On the other hand, the incoming turbulence effect can be well represented utilizing the theoretical Küssner function or Sears function for streamlined structures, or employing the measured admittance function for bluff bodies. However, the incoming turbulence effects on aeroelastic instability is not able to be considered based on these schemes. With some ad hoc assumptions, turbulence intensity effect on the aeroelastic instability could be considered either based on randomizing the dynamic pressure and invoking stochastic approaches, or through the incorporation into the effective angle of attack based on the QS concept.

Lin and Ariaratnam (1980) and Bucher and Lin (1988) theoretically demonstrated the turbulent intensity effect on aeroelastic instability by solving the linear stochastic differential equations based on Itô's differential calculus. The second-moment stability is emphasized in this analytical scheme. It is proved that the turbulence with small intensity has uncertain (either "stability" or "destability") effect on the bridge aeroelasticity while the turbulence with larger intensity has "destability" effect on the bridge aeroelasticity. However, this analytical scheme has some obvious limitations, such as the turbulence is assumed to be Gaussian stationary process with small turbulence intensity and the solutions are assumed as Markov processes. More importantly, only the along-wind turbulence component is considered while the vertical turbulence component is neglected which is usually considered as more important role contributing to turbulence effect.

On the other hand, the QS theory based models can also take into account the turbulence intensity effect after integrating the fluctuation into the effective angle of attack. For many innovative bridge sections, even at low levels of turbulence, the effective angle of attack due to structural motion and incoming wind fluctuations may vary to a level such that the nonlinearities in the aerodynamic forces may no longer be neglected. However, the QS assumption based model is a well-known memoryless system, where the unsteady effect is not considered.

The nonlinear analysis framework proposed by Chen and Kareem (2003) could incorporate the effects of turbulence on long span bridges. In this analysis framework, the low frequency force component can be modeled based on the quasi-steady theory, while the high–frequency force component can be modeled by utilizing the traditional unsteady scheme. Actually, the effects of low-frequency turbulent fluctuations are taken into account analytically through the QS concept with the effective angle of attack and the effects of high-frequency turbulent fluctuations could be considered experimentally through the measured flutter derivatives under turbulent wind condition.

Flutter studies utilizing full-bridge models have often shown critical velocity boundaries to be sharply defined in smooth flows and higher or nonexistent in turbulent flows. Under turbulent wind condition, there are some observations that the flutter instability will not happen suddenly with a distinct flutter boundary as the Scanlan's linear analysis predicts. One possible illustration of this phenomenon is the turbulence, not only the oncoming turbulence but also the signature turbulence, build up the exchange of energy between different structural modes with more complicated manners, which leads to the gradual incidence of flutter (Scanlan and Jones 1990). The proposed analysis framework by Chen and Kareem (2003) is able to investigate this behavior quantitively. Within this framework, the effects of turbulence on flutter are modeled through the changes in the effective angle of incidence caused by turbulence and its influence on the self excited forces and the flutter instability. The application of this framework to a long span suspension bridge, with aerodynamic characteristics sensitive to the angle of incidence, revealed a gradual growth in response with increasing wind velocity around the flutter onset velocity, which is similar to the wind tunnel observations of full-bridge, aeroelastic models in turbulent flows (Fig. 16).

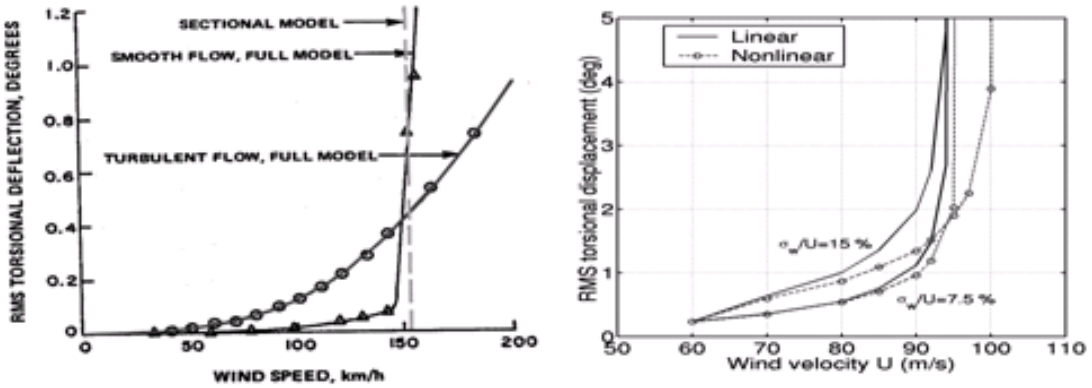

Figure 16: Left - Torsional response of Lions' Gate Bridge (Irwin 1977); Right - Linear and nonlinear predicted response of a bridge (after Chen and Kareem 2003a)

Currently there is no theoretical consideration of the turbulence scale effect on the bluff bodies. However, recently development of the intermittency modeling in turbulent flows may shed some light on this consideration. As a violent discontinuous nature of turbulence, internal intermittency seems only change the velocity statistics slightly (a slightly wider PDF compared with Gaussian distribution), while it has significant effects on the statistics of the velocity difference (a considerably larger PDF tail compared to Gaussian distribution). Conventional simulation scheme such as spectral representation cannot consider the multi-scale property of turbulence while the wavelet based expansion has been applied to simulate the intermittency with promising results (Kitagawa and Nomura 2003; Yin et al. 2012). The simulated PDFs of different scales (represented by the wavelet coefficients) in turbulence are presented in Fig. 17 compared with the measured results. These tails of PDFs can make significant contributions to higher-order moments, which impact the rare events. The simulation with intermittency consideration will directly contribute to the inlet turbulence modeling. Though the small scales contains little energy, it is well known that the intermittency in turbulence has significant effect on the transport and diffusion of material by the turbulence (Ecke 2005), which could be important to the environmental wind engineering community. The QS assumption may describe adequately the effects of large scales, which has high accuracy in galloping modeling. On the other hand, there is no theoretical analysis to investigate the effect of small scales on the bluff bodies. While it is reasonable to ignore the turbulence effects with the scale significantly smaller than the struc-

tural dimensions, there is demand to advance the analysis approach for the turbulence effects with comparative scale sizes. The simulated turbulent flow with intermittency consideration could be utilized in the analysis of aerodynamics and aeroelasticity in time domain, where the turbulence scale effect could be investigated in detail.

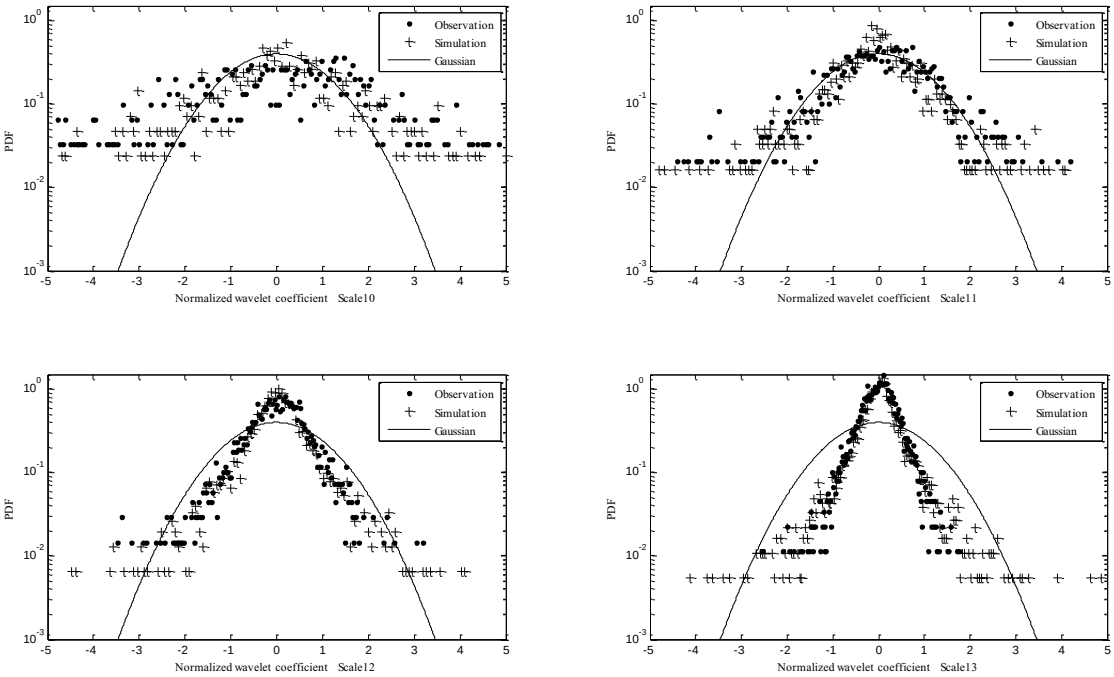

Figure 17: PDFs of wavelet coefficients at typical scales

In closing this section, it is very important to note that the preceding anthology of the role of turbulence on the bluff body aerodynamics of prismatic bodies, with applications to buildings and bridges, excluded a vast amount of literature concerning circular cylinders which is available in a number of review articles. On the other hand, although there is strong correlation between the circular cylinder and the bluff bodies with prismatic shape, the difference between them is unnegligible. For example, bridge deck, which features a significant afterbody, has fixed separation points instead of moving separation points varying as Reynolds number and oscillation frequency and amplitude. Besides, the torsional force induced by the wake vortices may be more important for prismatic bodies since this structural geometry possesses a long afterbody. Hence, wake-vortex-induced effect of prismatic bodies may differs significantly from that of the circular cylinder.

7 CHANGING DYNAMICS OF AERODYNAMICS

The subject of aerodynamics has been treated traditionally by invoking quasi-steady and strip theories and has been extended to unsteady aerodynamic theories for loads originating from wake aeroelastic effects. The current challenges are to address aerodynamics in transient flows. In the following, a brief discussion of these areas is provided with an outlook for their treatment of transient conditions, and lessons one may learn from aerodynamics in nature.

7.1 *Quasi-steady Aerodynamics*

Quasi-steady and strip theories offer reliable estimates of load effects when the dominant mode of loading is attributed to buffeting, e.g., surface pressure responding to large-scale, low frequency turbulence for the alongwind buffeting load effects. The quasi-steady theory fails to relate the approach flow and the ensuing pressure fluctuations on surfaces in separated flow regions. The shortcoming of the theory stems from the fact that it does not account for the wind-structure interactions at several scales, which may introduce additional components, thus highlighting the need for unsteady aerodynamics. The quasi-steady theory has been successfully applied to the analysis of galloping behavior of structures, often observed in structures exposed to winds at high reduced velocity, e.g., ice coated transmission line cables and cables experiencing skewed winds.

An obvious shortcoming of QS theory is that it cannot take into the unsteady effect of fluid-structure interaction. In order to take into account the fluid memory effects based on the static wind-tunnel tests, Steinman (1950) introduced phase correction factors resulting from pressure distribution graphs of stationary titled straight models (for the effects of vertical velocity and wind angle of attack) and horizontal curved models (for the effects of angular velocity). A more familiar approach to consider the fluid memory effects is to modify the steady-state coefficients based on the unsteady effects measured in the wind tunnel and hence to improve the simulation accuracy (Diana et al. 1993). This corrected QS theory could partially include the fluid memory consideration, which indicates that the flow around a structure is not only dependent on the instantaneous relative states (structural motions and flow fluctuations) but also on their previous time history. Actually, it is difficult to select an appropriate frequency to calculate the reduced wind velocity in the corrected QS scheme especially as the bridge aerodynamic effects involved. In order to overcome this shortcoming of the corrected QS theory, a more detailed scheme named "band superposition" was proposed by Diana et al. (1995), where the aerodynamic/aeroelastic forces are linearized about a reference value of the effective angle of attack.

7.2 *Unsteady Aerodynamics*

Notwithstanding the improved knowledge of wind effects on structures over the past few decades, our understanding of the mechanisms that relate the random wind field to the various wind-induced effects on structures has not developed sufficiently for functional relationships to be formulated. Not only is the approach flow field very complex, the flow patterns generated around a structure are complicated by distortion of the wind field, flow separation, vortex formation and wake development. Nonlinear interaction between the body motion and its wake results in the 'locking in' of the wake to the body's oscillation, resulting in vortex-induced vibrations over a range of wind velocities. The stability of aeroelastic interactions is of crucial importance (Matsumoto 1999). In an unstable scenario, the motion-induced loading is further reinforced by the body motion, possibly leading to catastrophic failure. Depending on the phase of the force with respect to the motion, self-excited forces can be associated with displacement, velocity, or acceleration. Furthermore, aeroelastic effects can couple modes that are not coupled structurally, leading to more complex issues in bridge aerodynamics as discussed earlier. The intractability of these unsteady aerodynamic features has led to experimental determination of these effects using scale models in wind tunnels. These measurements have led to loading characterizations in terms of spectral distributions of local and integral load effects and aerodynamic flutter derivatives, which, when combined with structural analysis, yield measures of overall structural behavior.

Concerning building aerodynamics, the most widely used wind tunnel technology involving the high frequency base balance (HFBB) does not include motion induced loads. Kareem (1982) noted in a validation study concerning the crosswind spectra derived from statistical inte-

gration of surface pressure that the response estimates computed by using the measured spectra began to depart from the estimated values based on aeroelastic model test of the same building at reduced velocities above 6. The damping estimates from the aeroelastic model suggested a constant increase in the negative aerodynamic damping. By including the negative aerodynamic damping, the response predictions provided a better comparison with the aeroelastic tests at higher reduced velocities. It is also important not to simply attribute all motion induced effects to aerodynamic damping. Indeed the motion of a structure also modifies the flow field around it. Particularly it tends to enhance the spanwise pressure correlation, which may lead to an increased forcing in comparison with that measured by a force balance. A recent study critically evaluates the role of several modeling parameters needed to accurately model aeroelastic effects for base pivoted models (Zhou and Kareem 2003).

In attempts to relate the incident turbulence to pressure fluctuations in separated regions, higher-order modeling via bispectral approach has been utilized, which has identified some correlation although it has not provided a functional relationship. It is noteworthy that that the intermittent nature of the unsteady aerodynamic relationship is vitiated using Fourier based analysis (Gurley et al. 1997). Higher-order bispectral analysis utilizing a wavelet basis offers promise to capture intermittent relationship between the incident turbulence fluctuations and the attendant pressures under separated flows (Gurley et al. 2003). Thus, challenges remain in establishing transfer functions that could relate, at higher-orders in a localized basis, the complexities inherent to bluff body aerodynamics.

7.3 *Transient Aerodynamics*

Both earlier and more recent studies in fluid dynamics have pointed out an overshoot in aerodynamic/hydrodynamics loads on cylinders in unsteady flows (Sarpakaya 1963). It has also been noted that for the analysis of structures in non-stationary atmospheric turbulence, the traditional stationary analysis fails to account for possible transient overloads, e.g., the sharp changes in gusts were found to cause a transient aerodynamic force on a bridge model, which cannot be explained by a stationary statistical analysis. This clearly points at the need to critically assess the impact of abrupt changes in the wind field magnitudes and associated modifications in aerodynamics of structures and appraises the need for refining the current load descriptions.

7.4 *Aerodynamics in Nature: Some Lessons*

Natural objects with bluff profiles like trees, plants and jellyfish experience forces in a flowing medium like air or water. Often these objects have the ability to minimize drag by shape reconfiguration, e.g., palm trees bend and through their compliant action survive the fury of hurricanes. This is not an option available to most of the built environment as their shapes are fixed In architectural and structural communities tapered, twisted and tilted towers are being built. The fixed shapes used in man-made structures are arrived at on the basis of aerodynamic considerations, but are undertaken a priori and the possibilities of changes in real-time during wind storm are not available. Other possible avenues of managing flow around buildings are possible by using biomematics through introducing scalloped leading edges like whale flippers, which act like vortex generators.

Unfortunately, these fundamental phenomena in nature may not benefit the built environment. As in nature, more flexibility may help survive adverse environmental conditions through excessive bending, however, tall buildings or bridges may not be able to afford this luxury as they may lose their functionality, e.g., occupants of a building experiencing large excursions of motion may get symptoms of sea sickness leading to discomfort and in extreme cases nausea and

vertigo. However, such flexible behavior has been utilized in offshore drilling platforms, where the human comfort considerations are not as stringent.

8 IDENTIFICATION TOOLS

The higher-order spectrum is the Fourier transform of the higher-order correlation. It identifies nonlinear interactions among frequency components and also preserves the phase information, which is generally a more sensitive marker to identify the departure from linearity as compared to information related to amplitude (Ueda and Dowell 1984). For a linear system, the second-order information embedded in a power spectrum represents distribution of energy at different frequencies which fully characterizes a linear system in the frequency domain. The normalized value of the cross-power spectrum captures the phase relation at the same frequency between two different signals. However, for nonlinear system higher-order spectrum is needed because the power spectrum cannot portray the energy transformation between different frequency components which is a typical feature of nonlinear systems. Among these higher-order spectra, the bispectrum, the Fourier transform of triple correlation can capture quadratic nonlinearities. Further higher-order interactions can be tracked by trispectra and beyond, but each additional order adds significantly to the computational demand and need for added length of data sets. (e.g., Kim and Powers 1979; Gurley et al. 1996; Tognarelli 1999; Hajj and Silva 2004). A bispectrum is easy to visualize since it can be displayed as a three-dimensional (3-D) plot, whereas, further higher-order spectra can be only viewed in 3-D by slicing the hyper-dimension at different frequencies.

The auto-/cross-bispectrum and auto-/cross-bicoherence could be applied to both the pressure signal or the force signal obtained in wind-tunnel experiments. Fig. 18 presents the second-order spectrum of an aerodynamic force acting on a typical bridge deck obtain in a wind tunnel. The nontrivial values in the figure indicate nonlinear interactions between the frequency components, suggesting the presence of such interactions in the aerodynamics of bridge decks.

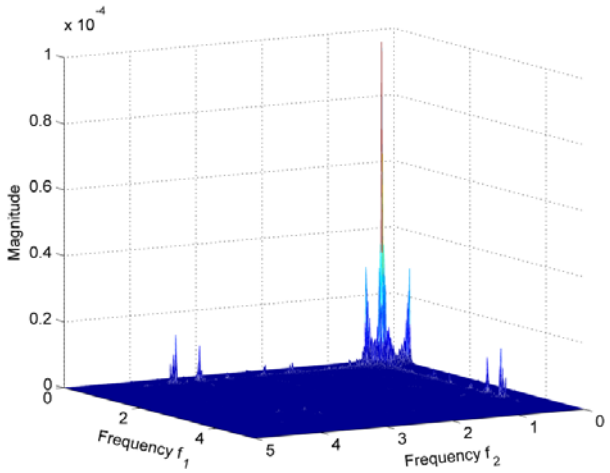

Figure 18: Auto-bispectrum of aerodynamic force on a bridge deck (after Wu and Kareem 2012a)

On the other hand, the evidence of nonlinear input-output relationship could be obtained in time domain through the second-order Volterra kernel, which corresponds to the double inverse Fourier transform of the higher-order transfer functions of the nonlinear system. Fig. 19 presents the linear and nonlinear Volterra kernels of a simulated bridge aerodynamic system, where the nontrivial values of the second-order kernel indicate that nonlinearity exists in the system.

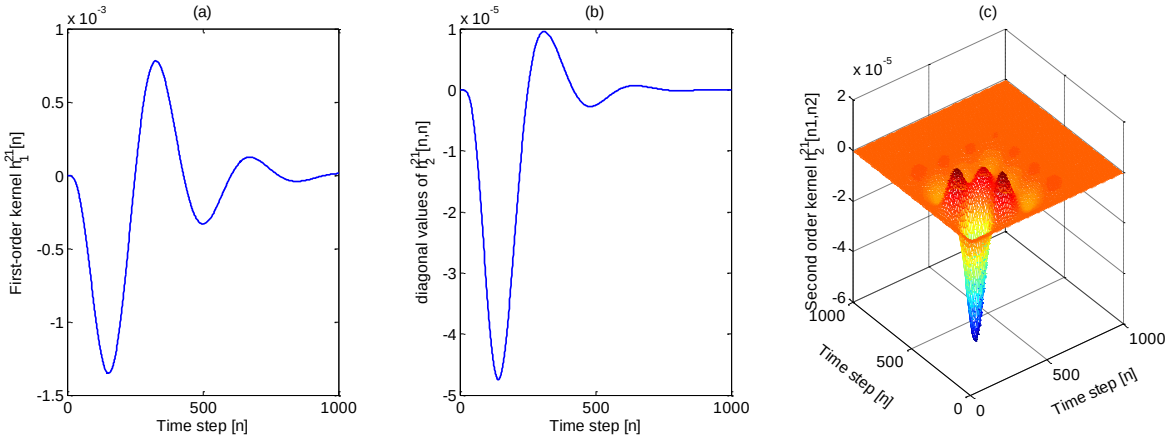

Figure 19: Linear and nonlinear Volterra kernels of a simulated bridge aerodynamic system (after Wu and Kareem 2012c)

More specific insights into the linear and quadratic interplay between two signals in both time and frequency can be gained utilizing wavelet coherence and bicoherence measures (Gurley et al. 2003). However, by exploiting the dual potential of wavelets, other analyses based primarily in either the time or frequency domain can also be performed. By tracking the variation of wavelet transform coefficients in the time domain, system identification can be readily performed (Kijewski and Kareem 2003). Similarly, the distribution of wavelet coefficients with frequency at a window in time provides a familiar spectral representation whose evolutionary properties can be monitored to provide insights into nonlinear behavior (Kareem and Kijewski 2002).

9 CONCLUDING REMARKS

This paper reflected on recent developments in aerodynamics and aeroelasticity of bluff bodies with a viewpoint concerning turbulent wind effects on structures. Some of the overarching issues for the future encompass the modeling and impact of imperfect correlation, transient/nonstationary effects, non-Gaussian and nonlinear features involving recent development of the modeling frameworks and identification tools. Improved understanding of turbulence effects on bluff bodies is stressed. Advances in experimental and theoretical methods with improved sensing capabilities based on wireless sensors, smart sensors, GPS, laser Doppler based technologies and optical and sonic systems would aid in effectively addressing some of the needs highlighted. With foundations steeped in bluff body aerodynamics and aeroelasticity theories and projected research paths imbued in advanced and e-technologies, our abilities will certainly be lifted up to a higher level of understanding, modeling, analysis, design and monitoring of wind effects on structures.

10 ACKNOWLEDGEMENTS

The author gratefully acknowledges the support provided in part by NSF Grant CMMI 0928282. The support in part for the study was also provided by the Global Centre of Excellence at Tokyo Polytechnic University: *New Frontier of Education and Research in Wind Engineering* funded by the Ministry of Education, Culture, Sports, Science and Technology (MEXT), Japan. The author is deeply indebted to the intellectual contributions of his former and present graduate students, post-doctoral and visiting researchers.

11 REFERENCES

1 Brilliant, M. B., 1958. Theory of the analysis of nonlinear systems. M.I.T., Res. Lab. Electron., *Tech. Rep. 345*.

2 Brooks, H.E., Doswell III C.A. and Kay, M.P., 2001. Climatology of tornadoes and severe thunderstorm winds in the United States. *Proceedings of the 1st American Conference on Wind Engineering*, Clemson, June 4-6.

3 Bucher, C. G., and Lin, Y. K., 1988. Stochastic stability of bridges considering coupled modes. *J. Eng. Mech.*, 114(12), 2055–2071.

4 Butler, K., Cao, S., Kareem, A., Tamura, Y. and Ozono, S., 2010. Surface pressures and wind load characteristics on prisms immersed in a transient gust front flow field. *Journal of Wind Engineering and Industrial Aerodynamics*, 98(6-7), 299-316.

5 Béliveau, J. G., Vaicaitis, R. and Shinozuka, M., 1977. Motion of suspension bridge subject to wind loads. *J. Eng. Struct.* Div. ASCE, 103(ST6), 1189-1205.

6 Carassale, L. and Kareem, A., 2010. Modeling Nonlinear Systems by Volterra Series. *J. of Engineering Mechanics*, ASCE 136(6), 801-818.

7 Cermak, J.E., 1975. Application of Fluid Mechanics to Wind Engineering…A Freeman Scholar lecture. J. of Fluids Engrg., ASME 97 9038.

8 Chen, L. and Letchford, C.W., 2005a. Proper orthogonal decomposition of two vertical profiles of full-scale nonstationary downburst wind speed. *J. of Wind Eng. and Ind. Aerodyn.*, Vol. 93, No. 3., 187-216.

9 Chen, L. and Letchford, C.W., 2005b. Simulation of extreme winds from thunderstorm downbursts. Proceedings of the 10th Americas Conference on Wind Engineering, June 2005, Baton Rouge.

10 Chen, X., Matsumoto, M. and Kareem, A., 2000. Time domain flutter and buffeting response analysis of bridges. J. of Engrg. Mech., ASCE, 126, 7-16.

11 Chen, X. and Kareem, A., 2001. Aeroelastic Analysis of Bridges Under Multi-Correlated Winds: Integrated State-Space Approach. *J. Engrg. Mech.*, ASCE, Vol. 127, No. 11.

12 Chen, X., and Kareem, A., 2003. New frontiers in aerodynamic tailoring of long span bridges: an advanced analysis framework. *J. of Wind Eng. and Ind. Aerodyn.*, 91, 1511-1528.

13 Chen, X. and Kareem, A., 2006a. Revisiting multimodal coupled bridge flutter: some new insights. *J. of Engrg. Mech.* ASCE, 132(10), 2006, 1115-1123.

14 Chen, X. and Kareem, A., 2006b. Understanding the underlying physics of multimode coupled bridge flutter based on closed-form solutions. *Proc. Computational Wind Engineering*, Yokohama, Japan, July 2006.

15 Davenport, A.G., 1967. Gust loading factor. ASCE Journal of Structures Division, 93(3), 11-34.

16 Denoël, V. and Degée, H., 2006. Influence of the non-linearity of the aerodynamic coefficients on the skewness of the buffeting drag force. *Wind and Structures*, 9(6), 457-471.

17 Deodatis, G. and Micaletti, R.C., 2001. Simulation of highly skewed non-Gaussian stochastic processes. *J. of Engrg. Mech., ASCE, Vol.* 127, No. 12, 1284-1295.

18 Diana, G., Bruni, S., Cigada, A. and Collina, A., 1993. Turbulence effect on flutter velocity in long span suspended bridges. *Journal of Wind Engineering and Industrial Aerodynamics*, 48 (2-3), 329-342.

19 Diana, G., Falco, M., Bruni, S., Cigada, A., Larose, G. L., Damsgaard, A. and Collina, A., 1995. Comparisons between wind tunnel tests on a full aeroelastic model of the proposed bridge over Stretto di Messina and numerical results. *Journal of Wind Engineering and Industrial Aerodynamics,* 54-55, 101-113.

20 Diana, G., Rocchi, D., Argentini, T. and Muggiasca, S., 2010. Aerodynamic instability of a bridge deck section model: Linear and nonlinear approach to force modeling. *Journal of Wind Engineering and Industrial Aerodynamics*, v 98, n 6-7, 363-374.

21 Ecke, R., 2005. The turbulence problem: an experimentalist perspective. *Los Alamos Science*, 29, 124-141.

22 Feng, C.C., 1968. The measurement of vortex-induced effects in flow past stationary and oscillating circular and D-section cylinders. *MASc thesis*. Univ. Br. Columbia, Vancouver.

23 Fujita, T.T., 1985. The Downburst: Microburst and Macroburst. *Report of Projects NIMROD and JAWS*. Satellite and Mesometeorology Research Project, Research Paper Number 210. University of Chicago.

24 Gartshore, I.S., 1973. The effects of free Stream turbulence on the drag of rectangular two-dimensional prisms. University of Western Ontario, Canada, BLWT-4-73.

25 Gast, K., Schroeder, K. and Spercell, J.L., 2003. Rear-Flank Downdraft as sampled in the 2002 Thunderstorm Outflow Experiment. Proc. 11 ICWE, Lubbock, TX, June.

26 Grigoriu, M., 1998. Simulation of stationary non-Gaussian translation processes. *J. of Engrg. Mech.*, ASCE, Vol 124, No. 2, 121-126.

27 Gurley, K. and Kareem, A., 1997. Analysis, Interpretation, modeling and simulation of unsteady wind and pressure data. *Journal of Wind Engineering and Industrial Aerodynamics*, (67-71), 657-669.

28 Gurley, K. and Kareem, A., 1998a. A conditional simulation of non-normal velocity/pressure fields. *Journal of Wind Engineering and Industrial Aerodynamics*, (67-68), 673-684.

29 Gurley, K. and Kareem, A., 1998b. Simulation of correlated non-Gaussian pressure fields. MECCANICA, 33(3), 309-317.
30 Gurley, K. and Kareem, A., 1999. Applications of wavelet transforms in earthquake, wind and ocean engineering. Engineering Structures, 21, 149-167.
31 Gurley, K., Kareem, A. and Tognarelli, M.A., 1996. Simulation of a class of non-normal random processes. Journal of Nonlinear Mechanics, 31(5), 601-617.
32 Gurley, K., Tognarelli, M.A. and Kareem, A., 1997. Analysis and Simulation Tools for Wind Engineering. Probabilistic Engineering Mechanics, 12(1), 9-31.
33 Gurley, K., Jacobs, J. and Kareem, A., 2001. Simulation of multidimensional non-Gaussian stochastic fields. *Proceedings of the Monte Carlo Simulation*, Schueller and Spanos, eds., Balkema, Rotterdam.
34 Gurley, K., Kijewski, T. and Kareem, A., 2003. First and higher-order correlation detection using wavelet transforms. ASCE *Journal of Engineering Mechanics*, 129(2), 188-201.
35 Haan, Jr. F. L. and Kareem, A., 2009. Anatomy of Turbulence Effects on the Aerodynamics of an Oscillating Prism. *Journal of Engineering Mechanics*, ASCE, 135 (9), 987-999.
36 Haan, F.L., Kareem, A. and Szewczyk, A.A., 1999. Influence of turbulence on the self-excited forces on a rectangular cross section. *Wind Engineering into the 21st Century*, Proceedings of the 10th International Conference on Wind Engineering, Larsen et al. (eds.), Balkema, Rotterdam, p. 1665-1672.
37 Hajj, M. R. and Silva, W. A., 2004. Nonlinear flutter aspects of the flexible high-speed civil transport semispan model. *Journal of Aircraft*, 41 (5), 1202–1208.
38 Hunt, J.C.R. Kawai, H., Ramsey, S.R., Pedrizetti, G. and Perkins, J., 1990. A review of velocity and pressure fluctuations in turbulent flows around bluff bodies. *Journal of Wind Engineering and Industrial Aerodynamics*, 35, 49-85.
39 Huston, D.R., 1986. *The effect of upstream gusting on the aeroelastic behavior of long-span bridges*, Dissertation, Princeton University, Princeton, N.J.
40 Kareem, A., 1982. Acrosswind response of buildings. *J. Struct. Eng.*, ASCE, 108(4), 869-887.
41 Kareem, A. and Cermak, J.E., 1979. Wind-tunnel simulation of wind structures interactions. *ISA Transactions*, 18(4), 23-41.
42 Kareem, A. and Kijewski, T., 2002. Time-frequency analysis of wind effects on structures. *Journal of Wind Engineering and Industrial Aerodynamics*, 90, 1435-1452.
43 Kijewski, T. and Kareem, A., 2003. Wavelet Transforms for System Identification in Civil Engineering. *Computer-Aided Civil and Infrastructure Engineering*, Vol. 18, No. 5, pp. 339-355.
44 Kim, Y. C. and Powers, E. J., 1979. Digital bispectral analysis and its applications to nonlinear wave interactions. *IEEE Transactions on Plasma Science*, PS-7 (2), 120–131.
45 Kitagawa, T. and Nomura, T., 2003. A wavelet-based method to generate artificial wind fluctuation data. *Journal of Wind Engineering and Industrial Aerodynamics*, 91(7), 943-964.
46 Kwon, D. and Kareem, A., 2009. Gust-Front Factor: New Framework for Wind Load Effects on Structures. Journal of Structural Engineering, ASCE, 135(6), 717-732.
47 Larose, G.L., Davenport, A.G. and King, J.P.C., 1993. On the unsteady aerodynamic forces on a bridge deck in turbulent boundary layer flow. *Proc. 7th U.S. National Conference on Wind Engineering*, UCLA.
48 Lee, B.E., 1975. The effect of turbulence on the surface pressure field of a square prism. *Journal of Fluid Mechanics,* v. 69 (2), 263-282.
49 Letchford, C.W. and Chay, M.T., 2002. Pressure distribution on a cube in a simulated thunderstorm downburst. Part B: moving downburst observations. *Journal of Wind Engineering and Industrial Aerodynamics*, 90(7), 733-753.
50 Lin, Y. K. and Ariaratnam, S. T., 1980. Stability of bridge motion in turbulent winds. *J. Struct. Mech.*, 8(1), 1-15.
51 Masters, F.J. and Gurley, K., 2003. Non-Gaussian simulation: Cumulative distribution function map-based spectral correction. J. of Eng. Mech., ASCE, 129(12), 1418-1428.
52 Matsumoto, M., 1999. Recent study on bluff body aerodynamics and its mechanisms. *Wind Engineering into the 21st Century*, Proceedings of the 10th International Conference on Wind Engineering, Larsen et al. (eds.), Balkema, Rotterdam, p. 67-78.
53 Matsumoto, M., Shiraishi, N. and Shirato, H., 1991. Turbulence unstabilization on bridge aerodynamics. *Proc. Int. Conf. Innovation in Cable-Stayed Bridges*, Fukuoka, Japan, p. 175-183.
54 Murakami, S. and Mochida, A., 1999. Past, present, and future of CWE: the view from 1999. *Wind Engineering into the 21st Century*, Proceedings of the Tenth International Conference on Wind Engineering, Larsen et al. (eds.), Balkema, Rotterdam, p. 91-104.
55 Nakamura, Y., 1993. Bluff-body aerodynamics and turbulence. *Journal of Wind Engineering and Industrial Aerodynamics*, v. 49, p. 65-78.

56 Saathoff, P.J. and Melbourne, W.H., 1989. The generation of peak pressure in separated/reattaching flows. *Journal of Wind Engineering and Industrial Aerodynamics*, v. 32(1-2), 121-134.
57 Sarpkaya, T., 1963. Lift, drag, and mass coefficients for a circular cylinder immersed in time dependent flow. *ASME Journal of Applied Mechanics*. 30(1), 16-24.
58 Scanlan, R.H., 1997. Amplitude and turbulence effects on bridge flutter derivatives. ASCE *Journal of Structural Engineering*, 123(2), 232-236.
59 Scanlan, R.H. and Tomko, J.J., 1971. Airfoil and bridge deck flutter derivatives. J. Eng. Mech., 97(EM6), 1717–1737.
60 Scanlan, R.H. and Lin, W.H., 1978. Effects of turbulence on bridge flutter derivatives. *Journal of the Engineering Mechanics Division*, ASCE 104 (EM4), pp. 719–733.
61 Scanlan, R.H. and Jones, N.P., 1990. Aeroelastic analysis of cable-stayed bridges. *Journal of Structural Engineering*, ASCE 116 (2), 279–297.
62 Scanlan, R.H., Béliveau, J.G. and Budlong, K. S., 1974. Indicial aerodynamic functions for bridge decks. *J. Eng. Mech.* Div. ASCE, 100(EM4), 657-672.
63 Seong, S.H. and Peterka, J.A., 1998. Digital generation of surface-pressure fluctuations with spiky features. *Journal of Wind Engineering and Industrial Aerodynamics*, 73, 181-192.
64 Steinman, D. B., 1950. Aerodynamic theory of bridge oscillations. *Transactions of the American Society,* Vol. 115, Paper No. 2420, 1180-1217.
65 Tamura, T. and Ono, Y., 2003. LES Analysis on aeroelastic instability of prisms in turbulent flow. *Journal of Wind Engineering and Industrial Aerodynamics*, 91, 1827-1826.
66 Tamura, T., Okuda, Y. and Okada, H., 2002. LES estimation of wind characteristics in the surface layer over various grounds - urban roughness effects and terrain effects. *Proc. of the UJNR Panel on Wind and Seismic Effects (Task Committee D)*, Seattle.
67 Tognarelli, M., 1999. Non-*Gaussian Response Statistics of Ocean Structures*. Ph.D. Thesis, University of Notre Dame, Notre Dame.
68 Twisdale, L.A. and Vickery, P.J., 1992. Research on thunderstorm wind design parameters. Journal of Wind Engineering and Industrial Aerodynamics, 41(1-3), 545-556.
69 Ueda, T. and Dowell, E. H., 1984. Flutter analysis using nonlinear aerodynamic forces. *Journal of Aircraft*, 21, 101–109.
70 Wei, Z. and Kareem, A., 2011. A benchmark study of flow around a rectangular cylinder with aspect ratio 1:5 at Reynolds number 1.E5. *Proceedings of the 13th International Conference on Wind Engineering*, Amsterdam, July 10-15.
71 Wang, L. and Kareem, A., 2004a. Simulation of earthquake ground motion based on wavelet and Hilbert transforms. *Proceedings of 9th Joint Specialty Conference on Probabilistic Mechanics and structural Reliability*, Albuquerque, July.
72 Wang, L. and Kareem, A., 2004b. Modeling of Non-Stationary Winds in Gust Fronts. *Proceedings of 9th Joint Specialty Conference on Probabilistic Mechanics and structural Reliability,* Albuquerque, July.
73 Wang, L. and Kareem, A., 2005. Modeling and simulation of transient winds: downbursts/hurricanes. *Proc. of the 10th American Conf. on Wind Engineering*, Baton Rouge, LA.
74 Wood, G.S. and Kwok, K.C.S., 1998. A Empirically derived estimate for the mean velocity profile of a thunderstorm downburst. Proc. 7th Australian Wind Engineering Society Workshop, Auckland.
75 Wu, T. and Kareem, A., 2011. Modeling hysteretic nonlinear behavior of bridge aerodynamics via cellular automata nested neural network. *Journal of Wind Engineering and Industrial Aerodynamics*, 99(4), 378-388.
76 Wu, T. and Kareem, A., 2012a. Aerodynamics and Aeroelasticity of Cable-Supported Bridges: Identification of Nonlinear Features. *Journal of Engineering Mechanics*, ASCE. Submitted.
77 Wu, T. and Kareem, A., 2012b. Comparison of various modeling schemes for bridge aerodynamics and aeroelasticity. *Proceedings of the BBAAVII,* Shanghai, China, September.
78 Wu, T. and Kareem, A., 2012c. Modelling of nonlinear bridge aerodynamics and aeroelasticity: a convolution based approach. *International Conference on Structural Nonlinear Dynamics and Diagnosis*, Marrakech, April.
79 Wu, T. and Kareem, A. and Li, S., 2012. Excitation Mechanism of Rain-Wind Induced Vibration of Cables: Unsteady and Nonlinear Aspects. *Proceedings of the BBAAVII,* Shanghai, China, September.
80 Yin. C., Wu, T. and Kareem, A., 2012. Turbulent simulation in wavelet domain based on Log-Poisson model: non-Gaussian and nonstationary wind processes. *Proceedings of the BBAAVII,* Shanghai, China, September.
81 Yu, D. and Kareem, A., 1997. Numerical simulation of flow around rectangular prisms. *J. of Wind Eng. and Ind. Aerodyn*., (67-68), 195-208.
82 Zhou, Y. and Kareem, A., 2003. Aeroelastic Balance. Journal of Engineering Mechanics, ASCE, Vol. 129(3), 283-292.

Wind tunnel tests and numerical approach for long span bridges: the Messina bridge

Giorgio Diana, Giuseppe Fiammenghi

Dipartimento di Meccanica, Politecnico di Milano, Via La Masa, 1 – Milano, Italy
Società Stretto di Messina, Via Marsala, 27 - Rome, ITALY

ABSTRACT: An overview of the wind tunnel activities and methodologies to support the design of long span suspension bridges is proposed. The most important aspects of the wind-bridge interaction are investigated considering the aerodynamic phenomena affecting the different parts of the bridge (mainly deck and towers). The experimental activities and results are proposed in the framework of a synergic approach between numerical and experimental methodologies that represents the common practice in defining the full scale aeroelastic behavior of the bridge starting from scaled reproduction of the wind-bridge interaction. Static and dynamic wind loads, aeroelastic stability, vortex induced vibrations will be investigated.

KEYWORDS: wind tunnel tests, bridge aerodynamics, aeroelasticity, numerical approach

1 INTRODUCTION

The definition ‘long span bridge’ is usually related to bridges with the main span of the order of one thousand meters or longer. For these bridges the flexibility is high and the first natural frequencies are of the order of 0.1 Hz or lower. Increasing the span length over 1 km, the bridges are classified as very long span bridges and the their natural frequencies are decreasing with the inverse proportion of the span length. For the 3.3 km of the Messina bridge main span, the first natural frequency is 0.03 Hz. These bridges are really sensitive to the wind action and for them the wind becomes the major problem affecting the overall design.

The maximum span length of a cable stayed bridge is 1.1 km: all the bridges with longer spans are suspension bridges. Actually the longest bridge is the Akashi in Japan, with its main span of 1990 m. Considering the bridges at the stage of the detailed final design, the longest is the Messina in Italy.

For these very long span bridges, as already said, the wind plays the most important role in the bridge design. In the following, we will make reference mainly to suspension bridges.

Many problems must be faced to guarantee the bridge performance to the wind action: the major are:

1) Static load, due to the average component of the wind blowing on the structure
2) Dynamic load, due to the incoming wind turbulence
3) Instability of the bridge
4) Vortex shedding on the tower, deck and cables.

The handling of these problems required the development of special analytical models. These models need tests in wind tunnel to identify the aerodynamic and aeroelastic behaviour of the different bridge components. Various types of wind tunnel tests are needed:

- on models of the deck, tower and cables
- of the full aeroelastic bridge model: this is the final check.

The analytical methods and the experimental tests in the wind tunnel are strongly correlated and some of the wind tunnel tests are dedicated to the identification of the aerodynamic and aeroelastic parameters used in the computation programs.

The paper is mainly aimed at describing the numerical tools and the type of wind tunnel tests that are used to design a long span bridge in order to guarantee the correct performances.

It is useful to mention that the Specifications used for the design of the Messina Bridge describe in the detail the type of tests to be carried out in the wind tunnel together with the analyses to be performed. These Specifications can be considered as a Standard for long span bridges design.

The present paper is organized in the following paragraphs:

1) Introduction
2) Analytical methods for the analysis of the bridge response to the wind
3) Wind Tunnel tests
4) Numerical results
5) Conclusions.

2 ANALYTICAL METHODS FOR THE ANALYSIS OF THE BRIDGE RESPONSE TO THE WIND

It is common practice to develop finite element schematizations of the bridge (Figure 1) to identify its response to the different actions of interest: wind, earthquake and traffic.

For what concerns the wind action, generally beam elements are used for deck and tower, while taut string or tensioned beam elements are used for the cables. These models are generally used to compute the global behavior of the bridge to the different actions and they can be non linear or linear, as a function of the type of excitation.

A non linear approach is used to identify the static position of the bridge under the permanent load, or static load, like the traffic and the wind loads due to the average wind [1].

For what concerns the dynamic load, a linear approach is generally used, being the linearization performed around the static equilibrium configuration [1], [2], [3], [4].

To compute the stress induced by the dynamic load – or local effect – a more sophisticated schematization of the deck and tower is used, employing plate elements. In Figure 2 the finite element schematization of the Messina deck is reported together with the drawing of the deck section. This FEM has been used to assign the stresses on the boxes welding, in order to verify the fatigue problem.

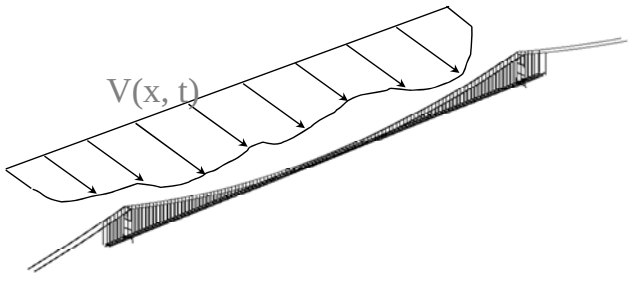

Figure 1. Global FEM schematization of the Messina Bridge and incoming wind.

The global bridge FEM (Figure 1) is used to compute the bridge natural frequencies (Figure 3), which are fundamental for the analysis of the bridge response to the wind action.

The ratio between the torsional and vertical frequencies of the same mode is very important for the flutter instability problem: the greater this ratio, the higher the flutter velocity.

In order to reproduce the bridge response to the turbulent wind, the dynamic load due to the incoming turbulence has to be applied to the FEM schematization.

Knowing the structure of the wind in the site surrounding the bridge, it is possible, by special tools [5][6], to reproduce a space and time wind distribution, as shown in Figure 1.

The forces acting on the bridge are a function of the incoming turbulence.

On the other hand, the bridge motion produces aerodynamic forces which are motion dependent.

As a consequence, the aerodynamic forces acting on the bridge are functions both of the incoming turbulence and of the bridge motion.

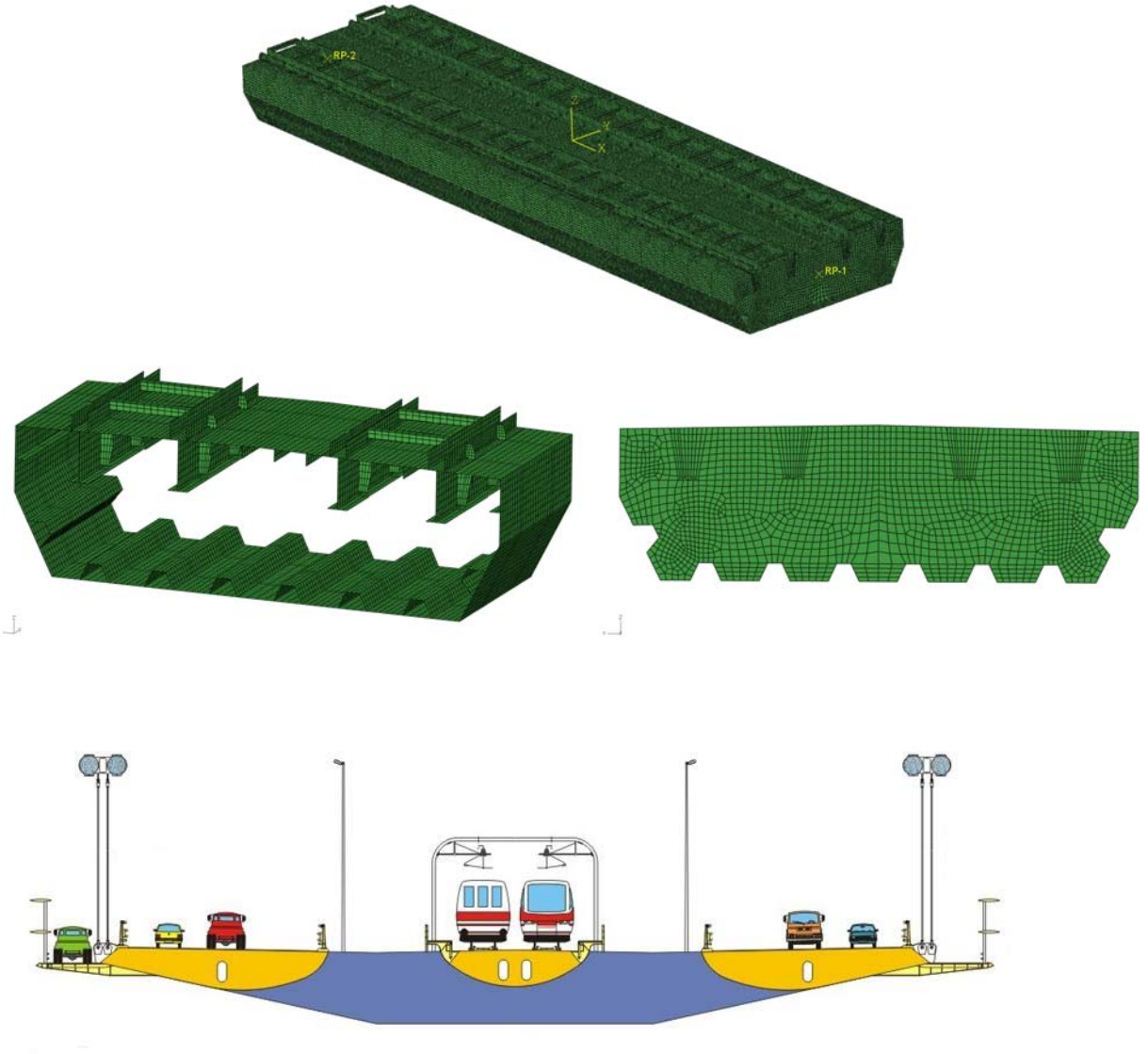

Figure 2. FEM schematization of the Messina deck and deck drawing.

I vertical mode. f = 0.06 Hz

I torsional mode. f = 0.081 Hz

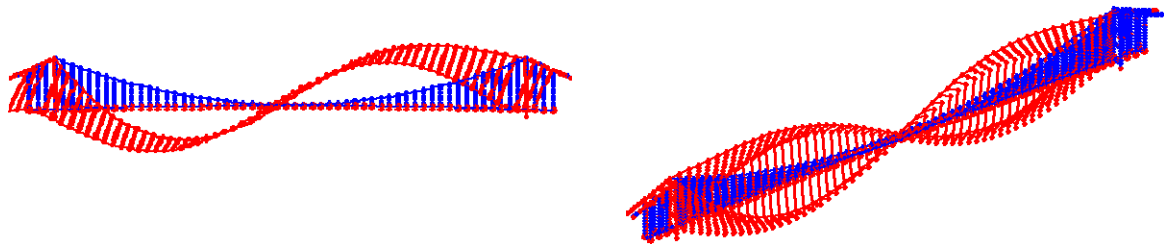

Figure 3. Vertical and torsional mode shapes of the Messina Bridge.

In order to reproduce the over mentioned wind forces in the bridge FEM, the following equation have to be considered:

$$M_s \ddot{X} + R_s \dot{X} + K_s X = F_a\left(X, \dot{X}, s(t)\right) \tag{1}$$

where M_s, R_s, K_s are mass, damping and stiffness matrices of the bridge structure linearized in the neighbourhood of the static equilibrium position, X is a vector containing the bridge degrees of freedom.

The X vector defines the motion of the bridge components: deck, towers, cables.

F_a is the vector defined by the aerodynamic forces acting on the different sections of the bridge deck, towers, cables.

F_a is function, as previously said, of the bridge motion X and of the associated velocity $\dot{X}$, as well as of the incoming turbulence vector s(t).

The identification of this non linear function through wind tunnel tests is a complex matter and it is for sure one of the most advanced topics of the research in this area[7], [8], [9].

2.1 *Linear approach*

The most used approach consists in linearizing the aerodynamic forces in the neighborhood of the static equilibrium position of the bridge X_0, identified by a given average wind V_m. This leads to:

$$\begin{aligned} &M_s \ddot{X} + R_s \dot{X} + K_s (X - X_0) = F_{a0}\left(X_0, 0, V_{m0}\right) \\ &+\left(\frac{\partial F_a}{\partial X}\right)_{X_0,0,V_{m0}} (X - X_0) + \left(\frac{\partial F_a}{\partial \dot{X}}\right)_{X_0,0,V_{m0}} \dot{X} + \left(\frac{\partial F_a}{\partial s}\right)_{X_0,0,V_{m0}} \left(s(t) - V_{m0}\right) \end{aligned} \tag{2}$$

being s(t) a vector containing the incoming wind turbulent velocity in the different sections of the bridge, where F_a is applied.

The aerodynamic forces F_a and the associated derivatives must be identified through suitable wind tunnel tests on the deck, towers and cables, as will be better explained in the next paragraphs. The aerodynamic forces playing the most important role in the bridge motion and stability are those acting on the deck.

The aerodynamic forces acting on a deck section (Figure 4) are as already said function of the vertical (z), the horizontal (y) and the torsional (θ) deck motion, as well as of the incoming wind turbulent velocity.

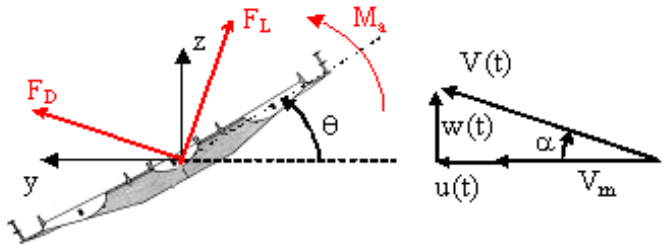

Figure 4. Aerodynamic forces acting on the deck

As usual, the aerodynamic forces due to the incoming turbulence are defined by a lift component normal to the direction of the wind V(t) and a drag component parallel to V(t), both applied at the center of the section, plus a moment of the aerodynamic forces M_a, as in Figure 4.

Coming back to equation (1), the lift, drag and moment on each section of the deck represent a sub-vector of the vector containing all the lift, drag and moment forces applied to all the bridge sections while X is the vector of all the section displacements and $\dot{X}$ of all the section velocities.

If we use a linearised approach as in (2) with the notation:

$$\left(\frac{\partial F_a}{\partial X}\right) = -K_a; \quad \left(\frac{\partial F_a}{\partial \dot{X}}\right) = -R_a; \quad \left(\frac{\partial F_a}{\partial s}\right) = A_m$$

equation (2) can be written in the following way:

$$M_s \ddot{X} + (R_s + R_a)\dot{X} + (K_s + K_a)X = A_m\left(s(t) - V_{m0}\right) \tag{3}$$

where $s(t)-V_m$ is a vector defined by the w,u, v components of the wind turbulence in the different points of the structure.

R_a and K_a are the equivalent damping and stiffness matrices due to the aerodynamic forces.

In other words, the linearization of the aerodynamic forces produces an equivalent elastic and damping system that is added to the structural one, changing the natural frequencies and the overall damping. An aeroelastic system is produced.

The K_a matrix, as well as the R_a matrix, are non symmetric and can give rise to flutter instability.

R_a, if non positive defined, can give rise to the so called one degree of freedom instability according to a torsional or vertical motion when the slope of the lift or moment coefficients is not positive.

A_m is the so called Admittance matrix.

All the parameters needed to define the K_a , R_a and A_m matrices must be identified through wind tunnel tests in order to reproduce the bridge response to the turbulent wind.

Equation (3) can also be solved in the frequency domain [3], [4],[10]: in this case the wind input is the spectrum of the incoming turbulence.

2.2 *Non Linear approach*

Even if linear approaches are the widest adopted method to study the bridge aerodynamic stability and response of the bridge to turbulent wind they are not able to deal with the important non linear effect intrinsically present in the aeroelastic problem. As already presented, the dependence of the aerodynamic forces from the deck motion and from the turbulent wind velocity components is fully non linear (see equation 2).

$$M\,\underline{\ddot{X}} + R\,\underline{\dot{X}} + K\,\underline{X} = \underline{F}_A\left(\underline{X}, \underline{\dot{X}}, V_m, v(t), w(t)\right) \tag{4}$$

The two main causes of non-linearities are the dependence of the aerodynamic forces on the angle of attack and on the reduced velocity. The QST [10] is able to take into account the dependence on the mean angle of attack in a non linear way but it is valid only at high reduced velocities. On the contrary the linear approaches are able to take into account the dependence on the reduced velocity through the flutter derivatives and the admittance function coefficients but they represent a solution around a fixed mean angle of attack. Measurements performed on full scale bridges highlighted that during the common operating condition the relative angle of attack between the bridge deck and the wind direction may reach large values that make the linear hypothesis not applicable. Some non linear approaches have been developed [7] [8] [9] to deal with the fully non linear aeroelastic problem. In this section we can only introduce the basic ideas of the "Band Superposition" approach and of the "rheological model" approach, and refer the reader to the literature for a more exhaustive description.

The "Band Superposition" approach relies on the possibility of separating the low frequency and the high frequency contributions of the wind spectrum. The idea is that the low frequency part of the wind spectrum is responsible for the larger fluctuations of the angle of attack and it acts at high reduced velocity. A correct QST [11] is therefore proposed to account for this part taking into account the non linear dependence on the angle of attack. The part of the wind spectrum at high frequency is characterised by smaller amplitudes and lower reduced velocity. To consider the effects induced by this part of the wind spectrum, the aeroelastic forces are linearized around the angle of attack that is instantaneously computed by solving the low frequency part of the problem. The problem becomes linear in the high frequency range, but with coefficients changing with the time.

An alternative approach is to consider the whole wind spectrum effects in a single time domain model as represented by the "rheological model". This approach is based on a numerical model that is able to consider both the angle of attack and the reduced velocity dependence in a single time domain approach. To identify the numerical model parameters, aerodynamic hysteresis loops are measured on deck sectional models in wind tunnel by changing the instantaneous angle of attack. The variation of the angle if attack is produced by moving the sectional model or by using the active turbulence generator with high amplitudes at different frequencies [7].

3 WIND TUNNEL TESTS

The procedures adopted for the most important long bridges at the design or construction stage will be described. These represent the state of the art on the subject. The tests on deck, towers and cables will be separately considered because the adopted approach is, even if in a small amount, different.

3.1 *Aerodynamic tests on the deck*

The procedure generally adopted for the wind tunnel tests on the deck is herein after described:

1) Static tests on the deck section, in order to measure the lift, drag and moment coefficients as a function of the angle of attack (α). This part is covered in section 3.1.1.
2) Optimization of the deck shape, in order to fulfill the bridge stability requirements, analyzing the slope of the lift and moment coefficients obtained by the static tests (section 3.1.1). This part is described in section 3.1.2.
3) Verification of the vortex shedding excitation, analysing the vibration level as a function of the Scruton number. This will be described in section 3.1.3. If the vibration level fulfils the Specifications at the real bridge Scruton number, the optimization procedure is closed, otherwise the deck shape is changed in order to control vortex shedding and the procedure must be repeated, starting from step 2).
4) Once the deck optimization has been completed, dynamic tests in order to identify the flutter derivatives and the admittance functions should be performed, as reported in detail in section 3.1.4.

The optimization procedure from point 1) to 3) is generally performed with small changes of the deck geometry with respect to the preliminary design, such as modification of the wind barriers, if present, or modification of the traffic barriers or parapet screens, or addition of special devices to control the wind flow.

3.1.1 *Deck static tests*

The most important test for the deck, as well as for the other components, is the definition of the static aerodynamic coefficients as a function of the angle of attack.

This test is made in a wind tunnel on a sectional model of the deck (Figure 5)

The sectional deck model is placed on a dynamometric system (Figure 5) generally placed outside the wind tunnel test section [12],[13].

The model can rotate around a deck longitudinal axis and the lift, drag and moment aerodynamic forces are measured as a function of the wind angle of attack, by changing the deck angle of rotation.

Some laboratory uses a deck sectional model with a dynamometric central part (Figure 6).

This type of device is also very useful to measure the dynamic aerodynamic forces, as it will be better explained in the following.

The output of this type of tests is shown in Figure 7 for different deck types (taken from [14]).

Figure 5. Deck sectional model in wind tunnel (external balance).

Figure 6. Deck sectional model in wind tunnel (internal balance).

The static forces, due to the average wind, on all the bridge components can be derived from Figure 7 and similar ones for towers and cables. The static forces on all the bridge due to the average wind can be computed in order to define, through a FEM simulation, the deflection of the bridge and the related stresses.

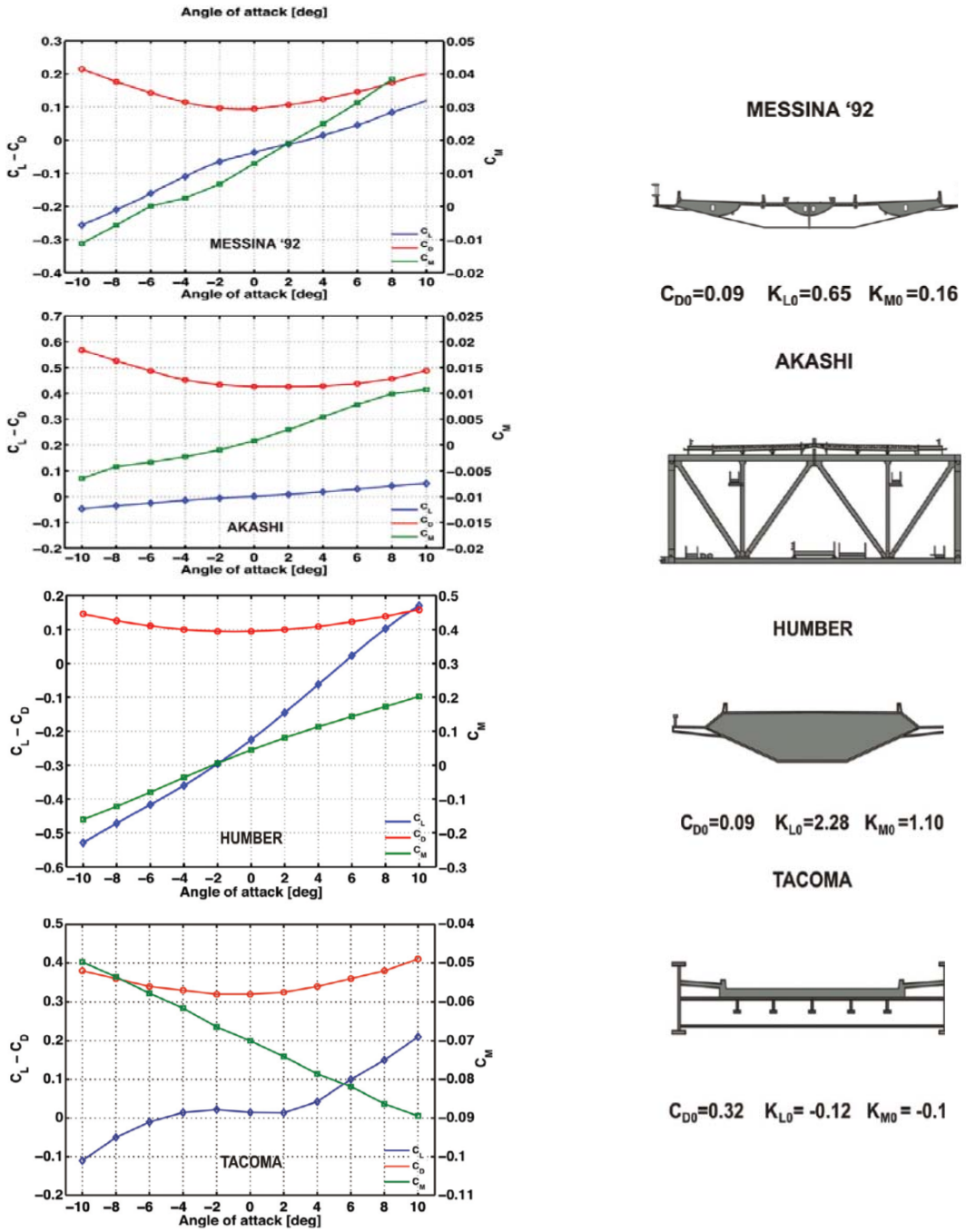

Figure 7. Aerodynamic coefficients of different deck geometry.

3.1.2 *Aerodynamic optimization of the deck*

The lift, drag and moment coefficient figures are very important for the bridge deck optimization.

The moment and lift coefficient slopes are very important for the bridge stability. They must be positive, with the conventions set in Figure 4, to avoid one-degree-of-freedom instability and, in order to have a high flutter velocity, their slopes must be as much as possible lower than the values of a flat plate: 2π for the lift coefficient and $\pi/2$ for the moment coefficient.

The slope value to guarantee stability is a function of the ratio between the bridge torsional and vertical frequencies. This ratio is decreasing with the span length: see Figure 8.

In the Messina Specifications the ratio between the first torsional and the first vertical frequencies is 1.36, leading to a prescription for a value of the moment coefficient derivative comprised between 1/5 $\pi/2$ and 1/10 $\pi/2$ and for a value of the lift coefficient derivative comprised between 1/5 2π and 1/10 2π.

The final reason for this requirement is that the positive slope of the moment coefficient produces a negative torsional stiffness which decreases the torsional frequency, such making it equal to the vertical one and producing the two-degrees-of-freedom flutter instability.

Another important issue is to take the deck drag as low as possible, because the drag forces on the deck are the most important and are transferred to the top of the towers by the hangers and the main cables, producing a moment that affects the overall tower design.

In order to fulfill these requirements, for a very long span bridge – over 2000 m – it is mandatory to use a multi box section.

A long optimization work is needed to obtain positive lift and moment coefficients with small slopes for all the wind angles of attack, or at least for a ± 4 degrees portion.

For the Messina bridge deck, the optimization involved the railway box shape and the wind barriers shape and porosity both for the road and railway box girders.

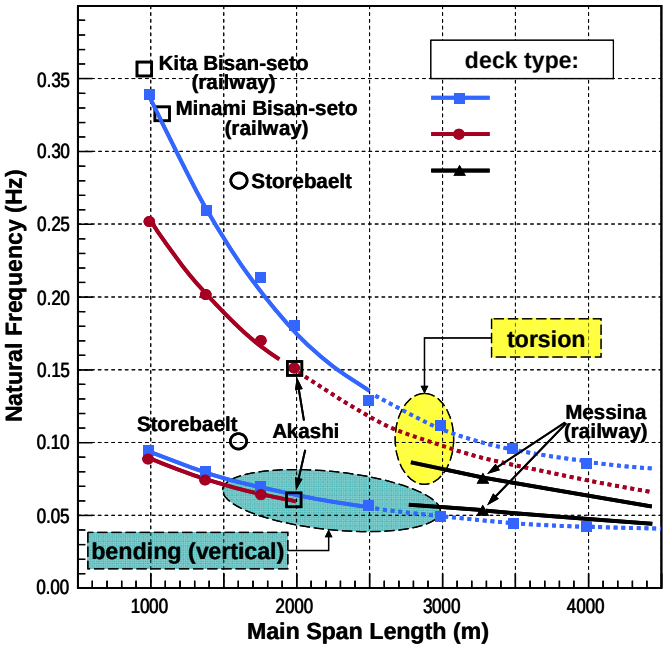

Figure 8. Bridge torsional and vertical frequency as a function of the span length

3.1.3 *Vortex shedding*

Vortex induced vibrations (VIVs) represent one of the most important aspects of the deck shape design. Even though the bridge deck of the last generation have an airfoil like geometry, flow separation occurs in correspondence of the deck sharp corners, in presence of adverse pressure gradients and of wind shields that are usually adopted to protect traffic. VIV is a serious problem that took also a part in the collapse of the Tacoma Narrow Bridge and has to be carefully analyzed. In fact, even if it can be separated from the stability problem for the modern bridges, it can lead the deck to reach very large vibration amplitudes in case of low Scruton numbers

$$Sc = 2\pi \frac{mh_s}{\rho B^2} \tag{5}$$

where m is the mass per unit length, h_S is the structural damping, B is the deck chord and ρ is the air density, also at very low wind speeds having a high probability of occurrence.

Nevertheless the problem is widely known and studied, past and present experiences highlighted that it represents one of the major concerns in the bridge design. In 2010 Russian authorities shut down the Volga River bridge because of the VIV. For the Storebealt bridge, guide vanes were installed close to the bottom plate/lower side panel joints, for mitigation of the vortex-induced oscillations occurred during the final phases of girder erection. The solution was identified after an ad hoc monitoring activity on the bridge at full scale and a specific wind tunnel activity, and its realization required a specially designed gantry/working platform.

Wind tunnel tests are performed on elastically suspended models (Figure 9). Special attention is paid, in wind tunnel tests, to keep the Scruton number as low as possible by using light models with low structural damping, in order to better highlight vortex shedding phenomena.

The model response in the lock-in range is usually measured in order to define:

1) the oscillation amplitudes reached at regime condition throughout the lock-in range
2) the amount of energy that the flow is able to insert in the system, that may be expressed by a negative value of the aerodynamic damping coefficient measured during build-up tests performed by releasing the deck model under mean wind condition and measuring the growing vibration amplitude starting from rest.

Figure 9. Free motion experimental set-up: Suspension system, tensioned steel stays and spring system.

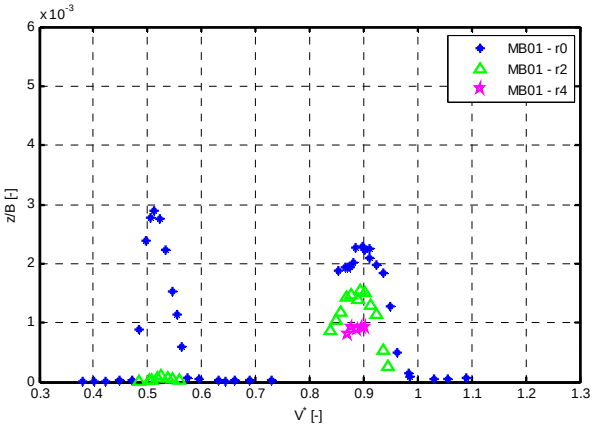

Figure 10. Steady state response: non dimensional oscillation amplitude, flexural motion as function of the reduced velocity varying the Scrouton number (r0=0.007; r2=0.022; r4=0.033).

While single box deck shapes generally shows a single mechanism of vortex shedding, basically related to the vortexes detached in the girder wake, multi box decks may present different vortex shedding phenomena because of the different possibility of flow interactions between the wake of the upwind box and the other boxes.

The different vortex shedding mechanism may excite both the heaving and the torsional motion of the bridge.

As an example Figure 10 presents the two lock-in ranges for the flexural motion of the Messina Bridge multi box deck section for different Scrouton number:

From the maximum values of the amplitudes measured in the lock-in range at different Sc, it is possible to define a figure that reports the non-dimensional amplitudes as a function of Sc.

In Figure 11, the vertical amplitudes of the deck divided by the deck chord B are reported as function of Sc – solution MB02. From this type of figure, it is possible to identify what is the damping of the real structure able to control VIVs. Making reference to Figure 11, the 3 vertical dashed lines represent 3 different values of Sc that for the Messina bridge correspond to 3 different levels of non-dimensional ratios of structural damping equal to: $2\ 10^{-3}$, $3\ 10^{-3}$ and $5\ 10^{-3}$. In order to avoid VIVs the structural damping of the Messina bridge should be greater than $3\ 10^{-3}$.

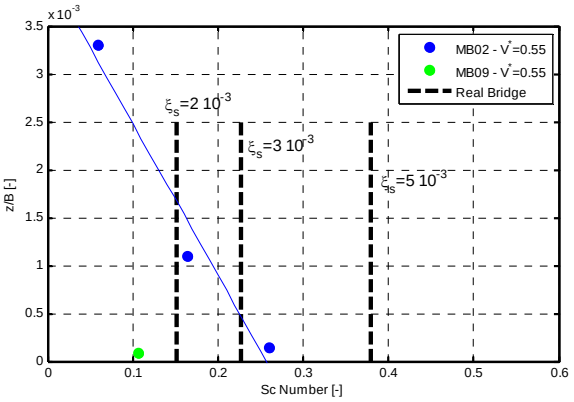

Figure 11. Steady state response: non dimensional oscillation amplitude, MB02 and MB09 configurations, flexural motion as function of Scruton Number.

To avoid VIVs also for lower values of structural damping, that are not expected, the solution is to adopt porous screens between the railway box and the road boxes (solution MB09 reported in Figure 12). In this case no VIVs are produced even for very low damping.

Measurements of the surface pressure distribution on each single box represent a valuable tool to a better understand of the vortex shedding phenomenon.

In Figure 13 the pressure distribution measured on the Messina bridge model when it experiences the largest vibrations (lock-in) is reported in terms of the magnitude of the pressure coefficient C_P fluctuations at the vortex shedding frequency:

$$C_P = \frac{p}{\frac{1}{2}\rho U^2} \tag{6}$$

where p is the pressure and U is the wind speed. The arrows that are pointing outwards the deck profiles are proportional to the value of the pressure coefficient amplitude.

It is possible to appreciate how the vortex shedding is mainly related to the capability of the flow to be attached or separated on the curvilinear profile of the upwind box that is run over

by an undisturbed flow. , It is clear where the vortex are generated and it is clear that there is a strong pressure fluctuation in the gap between the downwind roadway girder and the railway girder. The aerodynamics of the downwind boxes is, in fact, strongly influenced by the disturbances introduced in the flow by the wind interaction with the upwind box and by the gap between the boxes.

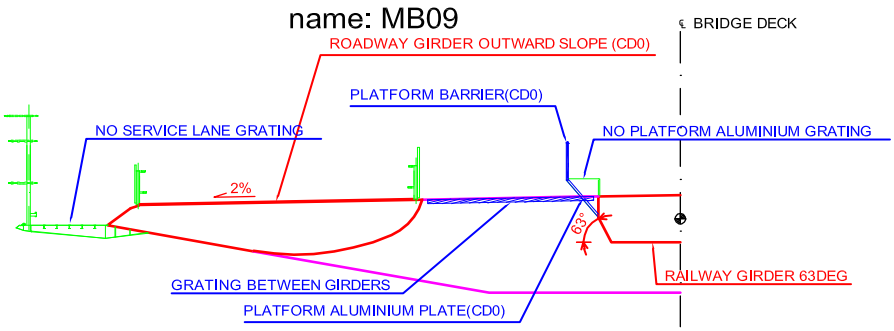

Figure 12. Solution MB09: deck with porous screens between the boxes

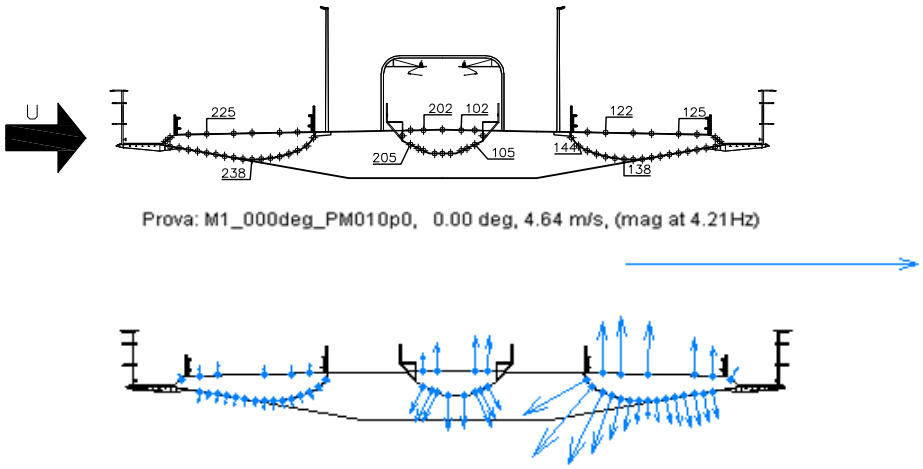

Figure 13. C_p magnitude at f=4.21 Hz.

3.1.4 *Dynamic tests on the deck*

To define the aerodynamic forces as a function of the deck motion and the incoming turbulence, as reported in the previous paragraph, the lift, drag and moment forces have to identified as a function of the y, z and θ coordinates representing the deck motion and of the w an u velocity components defining the incoming wind turbulence.
For what concerns the forces identification as a function of the bridge motion, two methods are available: the free motion method and the forced method.

3.1.4.1 Free motion method

During free motion tests the deck sectional model is let free to vibrate under the mean wind speed action, by means of an elastic supporting system. The response of the system to imposed initial condition is measured and flutter derivatives coefficients are defined by computing the

variation of the structural re response at a given wind velocity compared to the values obtained in still air.

3.1.4.2 Forced motion method

This method is more expensive than the previous, but is much more reliable.

A deck sectional model is forced to vibrate, as in Figure 14, in the three y, z and θ directions and the lift, drag and moment forces are measured for a given constant velocity V_m.

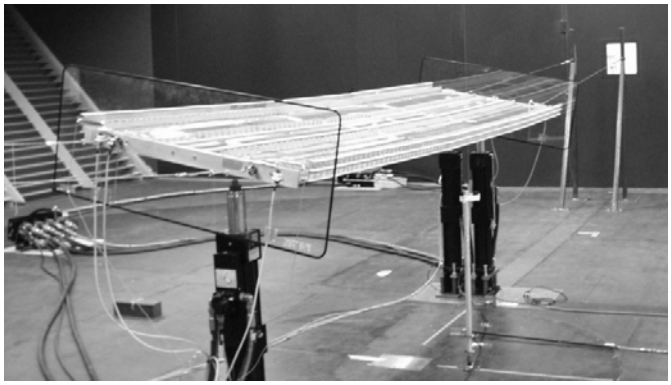

Figure 14. Sectional model on oil dynamic actuators driving its rigid vertical and torsional motion

As already said, the forces are non linear functions of the motion.

More in detail, for the deck (see Figure 4):

$$Lift = F_L = \frac{1}{2}\rho V^2 S C_L(X, \dot{X})$$

$$Drag = F_D = \frac{1}{2}\rho V^2 S C_D(X, \dot{X})$$

$$Moment = F_M = \frac{1}{2}\rho V^2 S B C_M(X, \dot{X}) \qquad (7)$$

being:

$$X = \begin{Bmatrix} y \\ z \\ \vartheta \end{Bmatrix}$$

The identification of the C_L, C_D, C_M coefficients, non linear functions of $X, \dot{X}$, as already said, is not an easy task and represents a research topic.

Methods have been developed by some researchers and are reported in [7] and [8]: for those based on rheological models and in [9] for those based on neural network algorithms.

What is generally done is to linearize the forces around a static equilibrium position of the deck identified by X_0 (equation 2).

$$F = \begin{Bmatrix} F_D \\ F_L \\ F_M \end{Bmatrix} = \frac{1}{2}\rho V^2 S\left(\left[K_a\right]X + \left[R_a\right]\dot{X}\right) \tag{8}$$

The 3x3 K_a and R_a matrices contains the flutter derivatives coefficients:

$$\left[R_a\right] = \frac{1}{2}\rho V^2 S\begin{bmatrix} -p_5^*\frac{1}{V} & -p_1^*\frac{1}{V} & -p_2^*\frac{B}{V} \\ -h_5^*\frac{1}{V} & -h_1^*\frac{1}{V} & -h_2^*\frac{B}{V} \\ -a_5^*\frac{B}{V} & -a_1^*\frac{B}{V} & -a_2^*\frac{B^2}{V} \end{bmatrix} \left[K_a\right] = \frac{1}{2}\rho V^2 S\begin{bmatrix} p_6^*\frac{\pi}{2V_\omega^{*2}}\frac{1}{B} & p_4^*\frac{\pi}{2V_\omega^{*2}}\frac{1}{B} & p_3^* \\ h_6^*\frac{\pi}{2V_\omega^{*2}}\frac{1}{B} & h_4^*\frac{\pi}{2V_\omega^{*2}}\frac{1}{B} & -h_3^* \\ a_6^*\frac{\pi}{2V_\omega^{*2}} & a_4^*\frac{\pi}{2V_\omega^{*2}} & -a_3^* B \end{bmatrix} \tag{9}$$

As a matter of fact, the identification of the flutter derivatives is not an easy task. The best results are obtained, imposing a harmonic motion and measuring the aerodynamic forces on the central part of the sectional model. From these tests the derivatives value as a function of the frequency of the motion, as well as of the static equilibrium position angle θ_0 around which the tests are done, can be derived.

The frequency is generally reproduced by the reduced velocity

$$V_r = \frac{V}{fB} \tag{10}$$

where B is the deck width, f is the frequency of the imposed motion and V is the velocity at which the test is performed.

As an example, the h_3^* value of the expression (9) for the Messina deck are reported in Figure 15.

The reduced velocity is reported in the abscissa and the different curves presented for each one of the coefficients of equation 6 are related to different angles of attack θ_0 around which the harmonic motion is applied.

3.1.4.3 Identification of the Admittance matrix

A method used in our wind tunnel and also by Chinese researcher [12] to identify the aerodynamic forces as a function of the incoming turbulence is to generate a well defined wind turbulence by an active device of the type shown in the Figure 16.

The airfoil can rotate around a fixed axis with a given motion, which is generally harmonic, with different frequencies. This generates a given fluctuation of the incoming wind, that can be measured through suitable anemometers, like the hot-wire or multi hole pressure probes anemometers. The aerodynamic forces are measured on a sectional deck model for a given average angle of attack θ_0 and the coefficients of the admittance matrix are identified, in a similar way as the flutter derivatives.

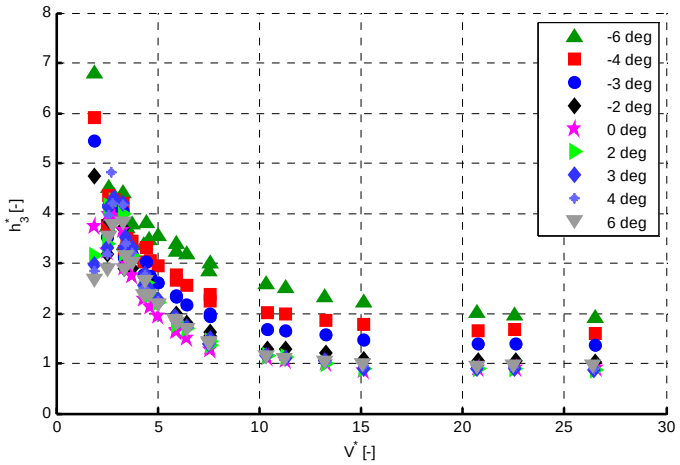

Figure 15. Flutter Derivatives (Messina bridge).

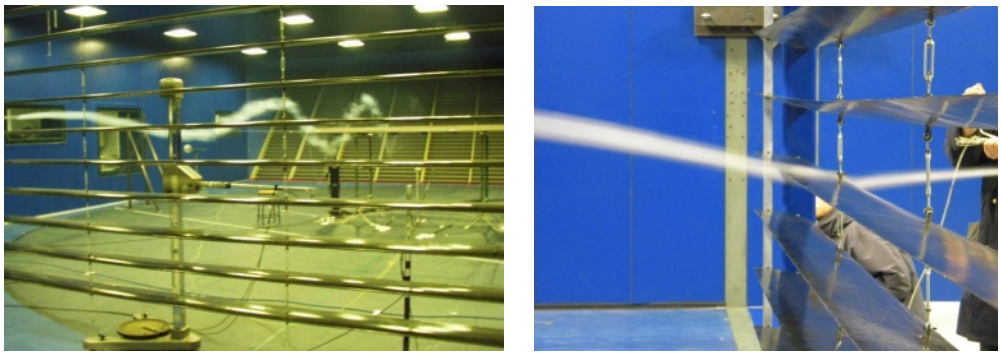

Figure 16. Active turbulence generator.

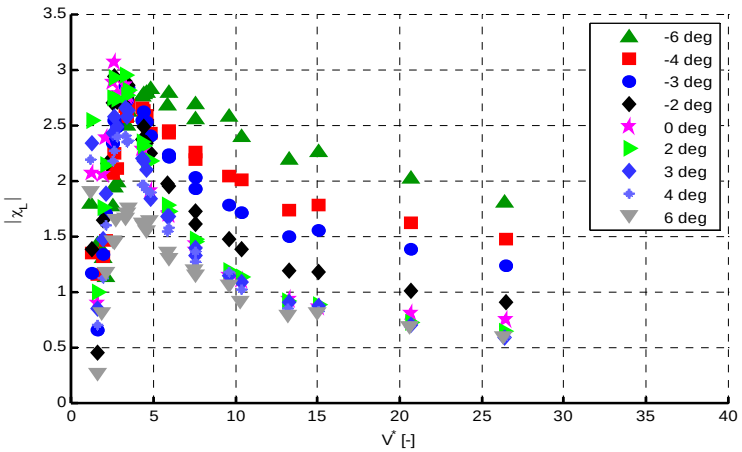

Figure 17. Admittance function (Messina bridge).

The admittances are functions of θ_0 and of the reduced velocity at which the test is performed. As an example, one of the admittance function coefficients is reported in Figure 17.

They are related to the following expressions of the aerodynamic forces:

$$F = \frac{1}{2}\rho V^2 S[\chi_a]w$$

$$\begin{aligned} F_y &= \frac{1}{2}\rho V^2 S\left[\mathrm{Re}\left(\chi_{y,w}\frac{w}{V}\right) + \mathrm{Im}\left(\chi_{y,w}\frac{w}{V}\right)\right] \\ F_z &= \frac{1}{2}\rho V^2 S\left[\mathrm{Re}\left(\chi_{z,w}\frac{w}{V}\right) + \mathrm{Im}\left(\chi_{z,w}\frac{w}{V}\right)\right] \\ F_\vartheta &= \frac{1}{2}\rho V^2 SL\left[\mathrm{Re}\left(\chi_{\vartheta,w}\frac{w}{V}\right) + \mathrm{Im}\left(\chi_{\vartheta,w}\frac{w}{V}\right)\right] \end{aligned} \qquad (11)$$

3.2 *Tower*

The main problem that has to be addressed during the aerodynamic design of bridge towers is VIV both if we consider cable stayed bridges that usually have single leg or reversed Y-shape towers or suspension bridges that have H-shape towers with two legs connected by one or more transverse beams. In both cases specific wind tunnel tests are performed using sectional or aeroelastic models. The usual wind activities on towers are

1) The measurement of the static aerodynamic coefficients on tower sectional model;
2) The measurement of VIV response using elastically suspended tower sectional models
3) The measurement of VIV response using aeroelastic models.

Figure 18. Cable stayed bridge tower sectional model in the wind tunnel test section: measure of static aero-dynamic coefficients.

Figure 19. Free standing tower.

Static coefficients are measured in a similar way of what is done on the deck, adopting sectional models with internal or external dynamometers and measuring the aerodynamic forces at different angles of attack. Figure 18 shows a tower sectional model during the wind tunnel tests.

For towers with two legs and transversal beams, the aerodynamic coefficients are measured separately on each leg by using a model that represents a tandem arrangement of the two legs where transversal beams are not present.

VIV of bridge towers are investigated in the wind tunnel by measuring the dynamic response of sectional models that are elastically suspended in the flow in a similar manner of what already described for the deck or of aeroelastic models.

While the vortex shedding phenomenon is basically two-dimensional on the deck, on the contrary, for the tower, it is affected by the three dimensional end effects at top and by the presence of the transversal beams along the height. Wind tunnel tests performed on aeroelastic models are therefore aimed to represent the full 3D tower geometry and the related aerodynamic effects.

Aeroelastic models are moreover used to investigate the different construction stages (Figure 19) of the tower, since its dynamic characteristics may largely vary from the free standing condition to the bridge completion condition. If wind tunnel test results highlighted that VIV may reach dangerous values, suitable countermeasures have to be implemented and design on the basis of the experimental results that have also to consider the dynamic effects of all the scaffolding and cranes that are connected to the structure and participate to the dynamic response of the system.

It is not easy to optimize the shape of the tower in order to avoid vortex shedding excitation. The final output of the analysis is similar to the deck one and the VIVs are reported as a function of Scrouton number. Tuned mass dampers (TMD) are generally used to control VIV of the towers.

3.3 *Reynolds effect*

The scaled reproduction of the wind-structure interaction must necessarily consider Reynolds number effects. To keep the correct ratio between the inertial and the viscous forces, the Reynolds number parameter:

$$\mathrm{Re} = \frac{VB}{\nu} \tag{12}$$

where B is a reference length for the deck width and ν is the air kinetic viscosity, should be same of the full scale condition. Due the practical limitations in the possibility to manage the single parameters, this request is commonly not satisfied and in the usual wind tunnel practice a sensitivity analysis on the Reynolds number dependency is performed. Reynolds number dependency is tested by comparing results obtained at different wind speed and/or on models with different scaling factor.

As an example, in Figure 20, the static aerodynamic coefficients of the Messina bridge deck are reported for different Reynolds numbers. The deck model is in 1:45 scale, being the model width B equal to 1.33m. Both the drag coefficient and the aerodynamic moment coefficient show, even in a very small amount, a univocal trend of modification increasing the Reynolds number parameter. For the maximum wind speed of 45m/s, the Re number value is $4\ 10^6$.

In some cases, dealing with curvilinear shapes, it is possible to modify the surface finishing by using an increased roughness in order to simulate at lower Re similar fluid dynamic effects of higher Reynolds number conditions (Figure 21).

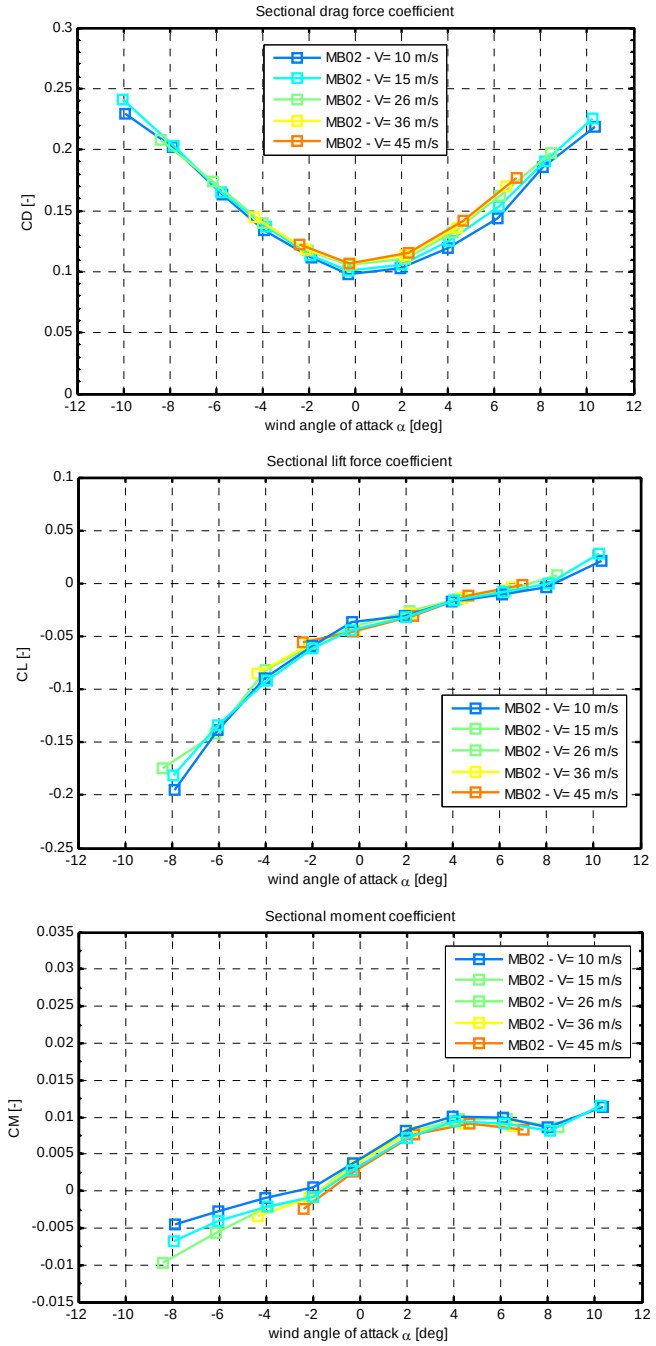

Figure 20. Reynolds number dependency of the deck aerodynamic coefficients varying the wind speed.

This wind tunnel practice allows to develop on a smaller model similar boundary layer conditions to what is produced at higher Reynolds number. Comparing the results of Figure 20 with those reported in

Figure 22, obtained at the same wind speed on the same deck sectional model with increased surface roughness, it is possible to observe how the slope of the lift and of the aerodynamic mo-

ment coefficient tends to increase at higher Reynolds number. The values obtained with smooth surface are very close to those obtained at low speed (10 m/s) with rough surface. In any case, with rough surface, for velocity above 36 m/s, Re=3.2 10^6 and more, these values should represent the value to be considered representative of the real situation. This is mainly due to the different fluid dynamic behavior that is present on the curvilinear part of the upwind box as reported in Figure 23, where the pressure distribution for the nominally smooth and for the rough model are overlapped.

Another parameter that has to be controlled during the wind tunnel tests on scaled models, trying to respect the Reynolds number similitude is the turbulence characteristics of the flow. Different incoming turbulence conditions may lead on the same model to different results in terms of aerodynamic coefficients obtained at the same wind speed. Nominal wind tunnel smooth flow conditions are actually low turbulence conditions that depends on the quality of the flow of the wind tunnel facility (0.2<Iu<2%).

Although the value of turbulence intensity is very small, in some cases, it may play an important role and it could explain the discrepancies that sometimes arise between results obtained in similar conditions in different wind tunnel plants.

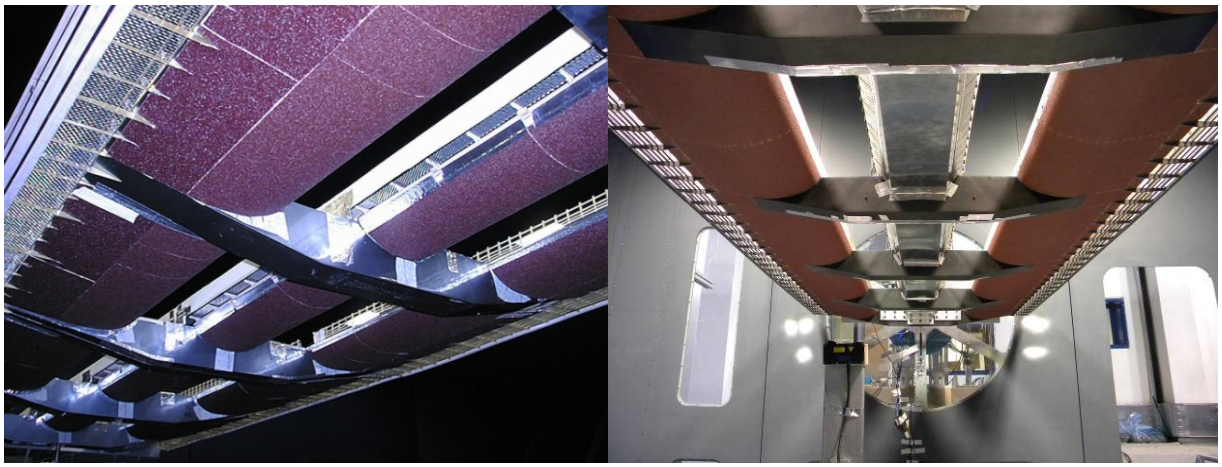

Figure 21. Deck sectional model with increased surface roughness.

4 NUMERICAL RESULTS

Once all the above described aerodynamic tests have been completed, it is possible to compute the bridge response to the turbulent wind.

First of all the static equilibrium position of the bridge under the turbulent wind must be computed as already explained.

For each section of a bridge a time history of the turbulent wind must be generated. The spectrum of the single time history can be identified and the equation (3) can be solved, for instance, in the frequency domain, taking into account that the flutter derivatives and the admittance function are frequency dependent.

Other methods are available to solve this problem in the time domain [15], generally with modal approach [1], and some of these methods, as already mentioned, take into account also the non linear effects of the aerodynamic forces [11], [16].

Some example of output result are reported in the following.

Figure 24 reports the static deflection of the Messina bridge deck under the action of mean wind forces for different mean wind speeds.

Figure 25 reports RMS values of the vertical acceleration of the different deck section along the bridge axis of the Messina bridge deck under the action of turbulent wind.

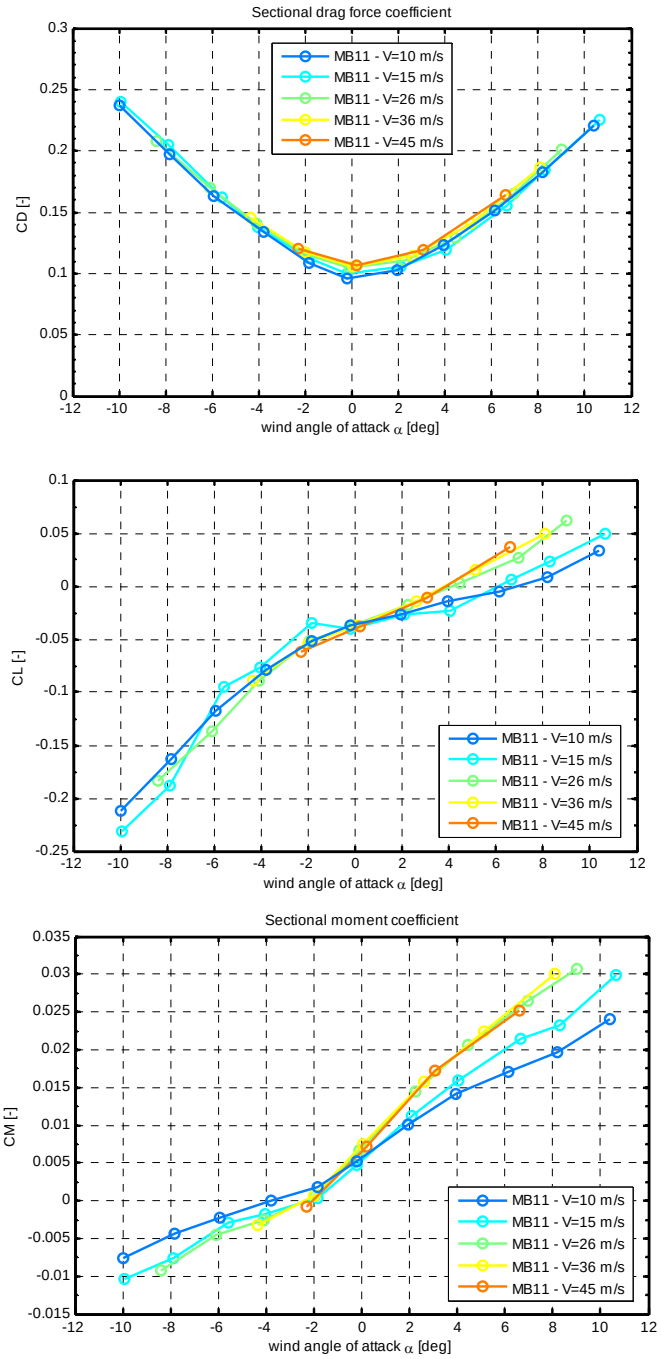

Figure 22. Reynolds number dependency of the deck aerodynamic coefficients varying the wind speed (model with increased surface roughness).

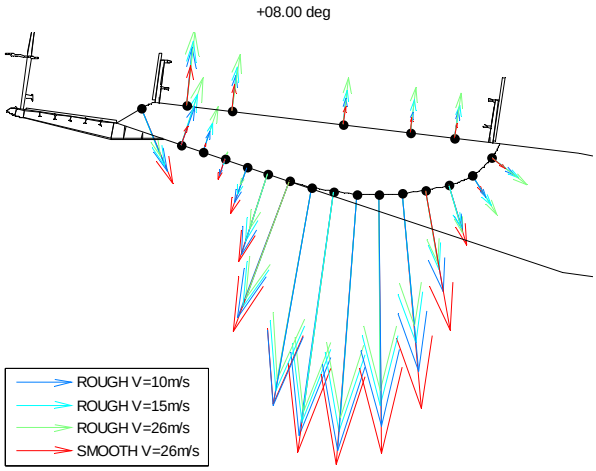

Figure 23. Different boundary layer development (Surface pressure distribution, smooth vs rough model surface, different incoming wing speeds, angle of attack +8deg).

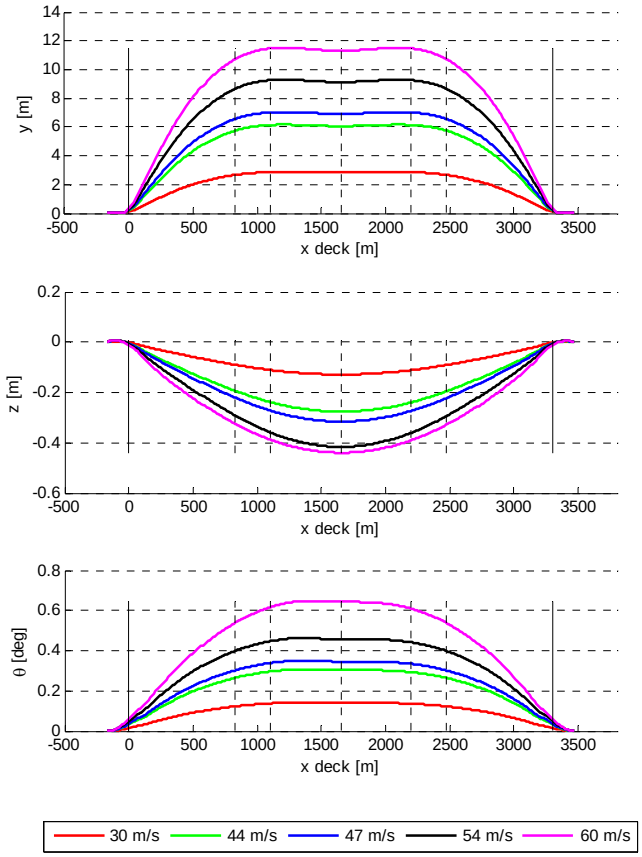

Figure 24. Static deformation under different mean wind speeds.

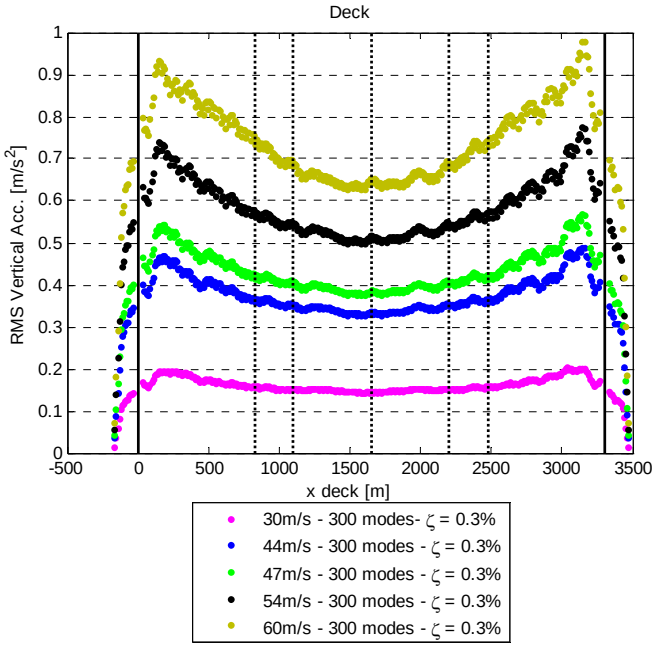

Figure 25. RMS values of the vertical acceleration of the different deck section along the bridge axis.

For the locations reported in Figure 26, The stress in the road boxes for a wind speed 30 m/s and Iu=13.8% are reported in Figure 27 in terms of standard deviation of the normal stresses on the downwind road box (y>0) of the only fluctuating part at point A:

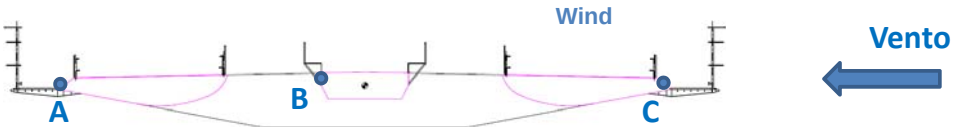

Figure 26. Considered point on the road and railway boxes of the Messina bridge deck section.

5 CONCLUSIONS

The common approach to design very long span bridges is to adopt a combined methodology relying on both wind tunnel tests on scaled models and numerical models of the wind-bridge interaction.

Wind tunnel tests on sectional models allows to measure:

- the aerodynamic static coefficients that are used for the definition of the static wind loads and for the check if one degree of freedom instability conditions may occur
- the aerodynamic coefficients (flutter derivatives) that are used for the definition of the buffeting response and for defining the flutter critical wind speed
- the response of deck and tower to vortex induced vibrations as a function of the Sc number.

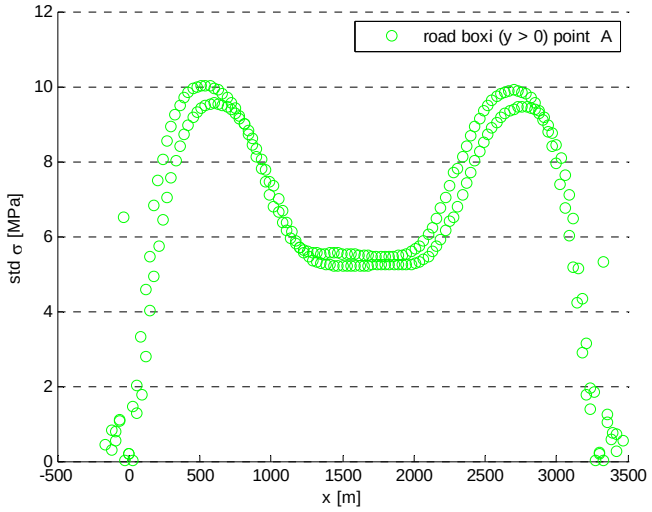

Figure 27. Standard deviation of the stresses at the point A of the different deck sections along the bridge axis.

The same quantity is reported in Figure 28 for the point B located on the railway box in Figure 26:

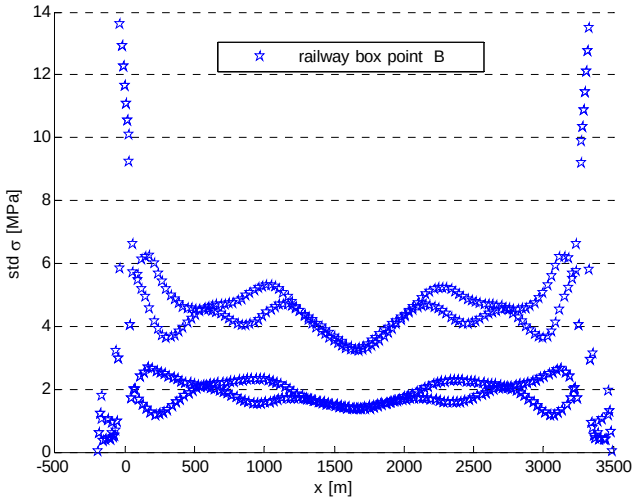

Figure 28. Standard deviation of the stresses at the point B of the different deck sections along the bridge axis.

Wind tunnel results with numerical models are able to drive in the early stage the optimization of the aerodynamic design of the deck and tower geometry the designer choice for the most important aeroelastic problems that are the aerodynamic stability of the bridge and the VIV of the deck, tower and cables.
The most promising solution is therefore analysed most in detail through aeroelastic full bridge models in wind tunnel.
The results of the full aeroelastic model are compared with the numerical simulations in order to control all the design procedure.

6 ACKNOWLEDGEMENTS

I want to express my first acknowledgements to the staff of the wind engineering group of the Mechanical Department of the Politecnico di Milano: Ferruccio Resta, Alberto Zasso, Fabio Fossati, Marco Belloli, Daniele Rocchi, Sara Muggiasca, Tommaso Argentini and to the Wind Tunnel team: Luca Ronchi, Stefano Giappino, Lorenzo Rosa.
Special acknowledgments are also due to Società Stretto di Messina, who promoted relevant investigations on bridge aero elasticity.

7 REFERENCES

[1] Diana, G., Bruni, S., & Rocchi, D. (2005). A numerical and experimental investigation on aerodynamic non linearities in bridge response to turbulent wind. *Proceedings oftheEACWE4.* Prague.

[2] Chen, X., Kareem, A., & Matsumoto, M. (2000). Coupled flutter and buffeting response of bridges. *Journal of Engineering Mechanics*, 17-26.

[3] Jain, A., Jones, N., & Scanlan, R. H. (1996). Coupled flutter and buffeting analysis of long-span bridges. *J. Struct. Engrg*, 716-725.

[4] Katsuchi, H., Jones, N. P., & Scanlan, R. H. (1999). Multimode coupled flutter and buffeting analysis of the Akashi-Kaikyo Bridge. *J. Struct. Engrg*, 60-70.

[5] Chen, X., & Kareem, A. (2001). Aeroelastic Analysis of Bridges under Multicorrelated Winds: Integrated State-Space Approach. *Journal of Engineering Mechanics*, 1124-1134.

[6] Ding, Q., Zhu, L., & Xiang, H. (2006). Simulation of stationary Gaussian stochastic wind velocity field. *Wind and Structures*, 231-243.

[7] Diana, G., Resta, F., & Rocchi, D. (2008, October-November). A new numerical approach to reproduce bridge aerodynamic non-linearities in time domain . *Journal of Wind Engineering and Industrial Aerodynamics, 96*(10-11), 1871-1884.

[8] Diana, G., Rocchi, D., Argentini, T., & Muggiasca, S. (2010, June-July). Aerodynamic instability of a bridge deck section model: Linear and nonlinear approach to force modeling. *Journal of Wind Engineering and Industrial Aerodynamics, 98*(6-7), 363-374.

[9] Wu, T., & Kareem, A. (2011, April). Modeling hysteretic nonlinear behavior of bridge aerodynamics via cellular automata nested neural network. *Journal of Wind Engineering and Industrial Aerodynamics, 99*(4), 378-388.

[10] Minh, N. N., Yamada, H., Miyata, T., & Katsuchi, H. (2000, December). Aeroelastic complex mode analysis for coupled gust response of the Akashi Kaikyo bridge model. *Journal of Wind Engineering and Industrial Aerodynamics, 88*(2-3), 307-324.

[11] Diana, G., Falco, M., Bruni, S., Cigada, A., Larose, G. L., Darnsgaad, A., et al. (1995, February). Comparisons between wind tunnel tests on a full aeroelastic model of the proposed bridge over Stretto di Messina and numerical results. *Journal of Wind Engineering and Industrial Aerodynamics, 54-55*, 101-103.

[12] Niu, H. W., Chen, Z. Q., Liu, M. G., Han, Y., & Hua, X. G. (2011). Development of the 3-DOF Forced Vibration Device to Measure the Aerodynamic Forces on Section Models. *Proc. of ICWE.* Amsterdam.

[13] Cigada, A., Falco, M., & Zasso, A. (2001, June). Development of new systems to measure the aerodynamic forces on section models in wind tunnel testing. *Journal of Wind Engineering and Industrial Aerodynamics, 89*(7-8), 725-746.

[14] Brancaleoni, F., Diana, G., Faccioli, E., Fiammenghi, G., Firth, P. T., Gimsing, N. J., et al. (2009). *The Messina Strait Bridge*. CRC Press.

[15] Caracoglia, L., & Jones, N. P. (2003). Time domain vs. frequency domain characterization of aeroelastic forces for bridge deck sections. *Journal of Wind Engineering and Industrial Aerodynamics, 91*, 371-402.

[16] Chen, X., & Kareem, A. (2001, December). Nonlinear response analysis of long-span bridges under turbulent winds. *Journal of Wind Engineering and Industrial Aerodynamics, 89*(14-15), 1335-1350.

The Seventh International Colloquium on Bluff Body Aerodynamics and its Applications (BBAA7)
Shanghai, China; September 2-6, 2012

Aerodynamic optimization in super-tall building designs

Jiming Xie

RWDI International China Inc. 24D-838 Zhangyang Road, Pudong, Shanghai, China

ABSTRACT: To ensure the structure safety in strong winds and control the wind-induced motion of super-tall buildings, aerodynamic optimization is considered to be the most efficient way, because the aerodynamic optimization is aimed at the source of problems. However, aerodynamic optimization can be at the cost of other design aspects, such as increased construction cost, reduced usable space and/or increased construction difficulties. Therefore, the aerodynamic optimization can only be reached by interdisciplinary collaboration between wind engineers and architects. This paper summarizes the aerodynamic approaches that have been used in building design, and discusses the principles and effectiveness of these approaches. To provide a guideline for building aerodynamic optimizations, this paper proposes an approach of assessing the effects of tapering, twisting and set-back, three common schemes in super-tall building design for wind response reductions with limited wind tunnel tests.

KEYWORDS: building aerodynamics, across-wind response, vortex shedding, wind tunnel tests, wind spectrum, super-tall buildings.

1 INTRODUCTION

Wind effects are the challenges that designers have to deal with in super-tall building design. In association with high slenderness, low natural frequencies, low inherent damping level and high wind speed at upper lever, super-tall buildings are more susceptible to winds, particularly to vortex shedding excitations. Not only wind loads, the wind-induced building motions are also within the scope of design to ensure the building's safety as well as performance, such as comfort level for building occupancy. It is well known that the behavior of wind response is largely determined by building shapes. Considerations on aerodynamic optimization in early architectural design stage is proved to be the most efficient way in wind-resistant design.

Wind-resistant design and aerodynamic optimization are the modern topics in building design community. However, its practice and success projects can be traced back a long time ago.

Figure 1. Three pagodas, Dali, Yunnan Province, China

In ancient China, tall buildings appear to be traditional pagodas. Some of them even meet the modern definition of super-tall shape.

Figure 1 shows one of the tallest ancient pagodas in China. These three pagodas located in Chong-Sheng Temple (崇圣寺), Dali, Yunnan Province, China, were built 1180 years ago (824-859AD). The tallest one is 69.13m in height with the base width of 9.9m (square), the slenderness (height/width ratio) being 7. The two identical shorter pagodas also have a height of 42.19m. Over the long period of extreme climates and natural disasters, the original temple buildings which were built after the pagodas were destroyed but the original pagodas have survived with wonder. In addition of extremely strong earthquakes (in 1514 and 1925), the pagodas also experienced strong winds in history. Dali

is located in the western part of the Yunnan-Guizhou Plateau where the East-Asian monsoon and southwest monsoon alternately affect the region. Due to its special topography, Dali is well-known as "windy city" with occurrence of strong winds being more than 35 days per year. Statistics show that the return period winds are even higher than those in Shanghai, a typhoon prone coastal city of China. Figure 2 shows the comparison of return period basic wind speeds between Dali and Shanghai. These survived ancient structures at least revive two important concepts for modern design practice.

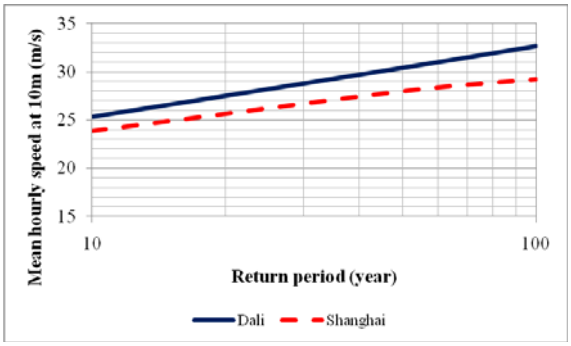

Figure 2. Comparison of wind speed between Dali Shanghai

(1) Being masonry structures, the ancient pagodas cannot compete in strength to modern structures that are built with steel and pre-stressed concrete. However, the shortcoming in strength seems to be largely compensated by increased inherent damping, which is more effective for dynamic loading.

(2) All these pagodas have their width tapered along the height and also have sizeable overhanging eaves. These features significantly reduce the potential across-wind oscillations that are commonly seen in super-tall buildings. Without these important features, these pagodas might have been damaged several times by severe vortex-induced oscillations at critical vortex shedding speed.

One of the major achievements in modern building design practice is to understand the underlying principles that may have been contained in historical wonders by coincidence and explore more creative ways to apply these principles in design.

Many investigations have been conducted on building aerodynamic optimizations. A pioneer work on building aerodynamics was done by Davenport (1971) who investigated the shape effects by using aerodynamic model tests. With super-tall's booming in 1990's, many more investigations have been done, which include building corner modifications and their impact on aerodynamic forces (Kwok 1988, Dutton and Isyumov 1990, Tamura 1998 and Miyagi 1999), effects of openings and slots (Isyumov 1992, Miyashita et al. 1993), and effects of twisting (Xie et al. 2009). The potential impacts of these aerodynamic modifications on economical aspects (cost and usable space) are also investigated (Tse et al. 2009).

Although aerodynamic shape plays important role for super-tall building design, aerodynamic optimization cannot be reached without considering other design aspects. The major challenge in building aerodynamic optimization is not only to find out the best shape for wind response, but also to find out the best balance between all the design aspects, including architectural concept, economical outcomes, etc. Aerodynamic optimization may therefore be classified into two categories:

Aerodynamic modification: an approach that is applicable to buildings which require mitigations for wind response but cannot have significant geometry changes on overall building concepts. Corner treatments, such as chamfering, slotting and roundness are common approaches in this category. The challenge with this category is that given the available/feasible aerodynamic modifications, the level of improvement may not be enough to meet the design objective. Structural measures or supplemental damping devices are still need in many cases.

Aerodynamic design: an approach that is integrated with architectural design in early stage. All the aerodynamic measures are available in this stage and the outcomes can be most efficient. However, the challenge with is category is to have reasonable estimates on the effects of various aerodynamic schemes on wind response reductions, so that an optimized balance between many

design aspects can be achieved. A series of wind tunnel tests are generally required to serve this purpose.

This paper is to summarize various schemes of aerodynamic approaches in super-tall building design and to discuss the principles of these schemes. To serve the needs of aerodynamic design, a method is proposed in this paper. This method is used to assess the effectiveness of aerodynamic optimization schemes, such as tapering, twisting and set-back, the three common schemes in super-tall building design, with limited amount of wind tunnel tests. The proposed method is approximate and comparative. Detailed wind tunnel tests are still needed for super-tall building designs. However, with ability of parametric analysis for aerodynamic effectiveness, the proposed method can provide a reasonable aerodynamic guideline for architectural design.

2 GENERAL APPROCHES OF AERODYNAMIC OPTIMIZATION

2.1 *Along-wind and across-wind responses*

For wind-resistant design of buildings, it's important to identify the type of wind response that governs the design. For most super-tall buildings, it is often found that the across-wind dynamic response dominates the design wind loads and/or cause excessive motions. Figure 3 presents a typical wind loading azimuth plot where the magnitude of the inertial loads caused by building motions in across-wind direction is much higher than the mean wind loads plus dynamic loads along the wind direction.

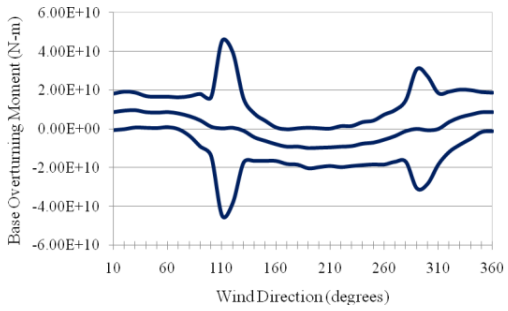

Figure 3. Illustration of across-wind loading at 110°

The main reason that across-wind can dominate the design for super-tall buildings is explained by Figure 4. Figure 4 shows a typical across-wind spectrum in comparison with an along-wind spectrum. While the along-wind spectrum reflects the approaching wind turbulence properties, the across-wind spectrum is determined by flow separation off the building, so called "signature turbulence". The peak of the across-wind spectrum corresponds to the effective Strouhal number of the building. Compared with along-wind response, across-wind response is more sensitive to wind speed. In lower wind speed, the along-wind loads normally dominant but with increase of wind speed the across-wind loads take over. Due to relatively lower building natural frequency of super-tall buildings (or higher building natural period) plus high wind speed at upper level of the boundary layer, the reduced frequency of a super-tall building at design wind speed can be very close to the peak of the across-wind spectrum. For example of a typical super-tall building, the building width is about 60m and the first sway period is around 8 seconds or higher, the vortex-induced resonance can happen at about 60m/s winds at upper level for a rectangular building or 33m/s at standard 10m height.

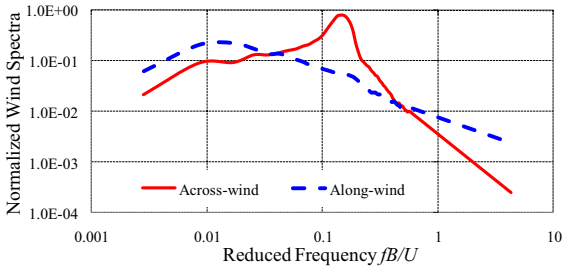

Figure 4. Comparison of along-wind and across-wind spectra

The aerodynamic optimization approaches tend to be different when dealing with along-wind or across-wind response. Although some approaches that can benefit both, many approaches focus on one type or other.

For optimization of along-wind response, a basic approach is to reduce the drag coefficient by modifying building corners, such as round or chamfer. Opening is also an option. Adjustment of building orientation to an optimized position where the direction of highest drag coefficient is far away from the local prevailing wind directions is also an effective approach.

For across-wind response, the aerodynamic optimization can be classified into two basic approaches: (1) to reduce the magnitude of wake excitation by modifying the building's cross-section such as corner recession or opening; and (2) to reduce the synchronization and correlation of fluctuating excitation by varying building's shape along the height such as tapering or twisting.

Since across-wind dynamic response is normally the main source that causes excessive wind loading and discomfort for occupants. The following discussion will focus on the aerodynamic optimizations for across-wind dynamic response.

2.2 *Modification of cross-sections*

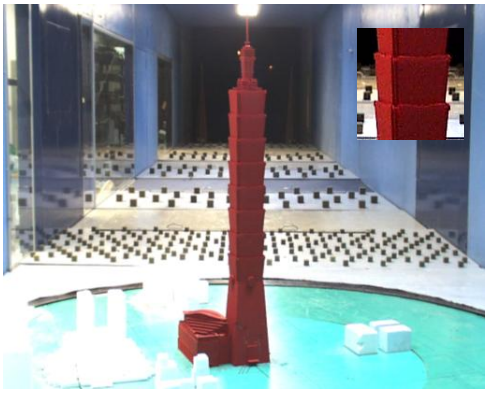

Figure 5. Corner recession

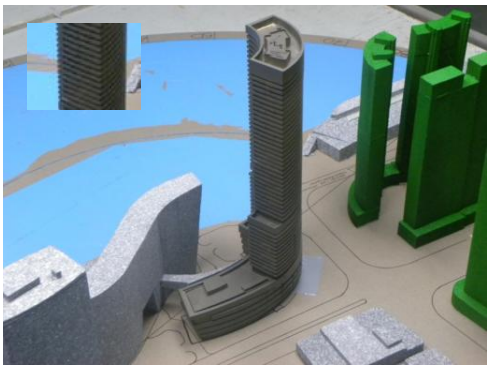

Figure 7. Corner balconies

A few examples of aerodynamic modifications for building cross-sections are shown in Figures 5 through 7. These modifications are proved to be effective for reducing across-wind response. The corner of Taipei 101 Tower, shown in Figure 5, was designed during wind tunnel testing, which effectively reduces the overall design wind loads by about 25% compared with the original design of square section.

During the wind tunnel tests of Taipei 101, other type of corner modifications are also investigated, shown in Figure 6. With the dimension of modifications being about 0.1B (10% of building width), the effects of these modifications are similar. The final selection of the corner modification was basically the choice of architects.

Figure 6. Corner modifications considered in Taipei 101 design

Helical strike is a traditional device to suppress vortex excitation to chimney stacks. However, few of these devices are used for buildings due to aesthetical concern. However, it has been found that commonly designed corner balconies can perform similar roles in suppressing vortex shedding (Brown et al. 2005). The concept was used again in a recent tall building in a very strong typhoon area, shown in Figure 7, and proved to be able to reduce design

wind loads by about 20%. The overhang eaves shown in ancient pagodas, Figure 1, are also the examples

Opening is not commonly used in design practice due to potential impact on useable spaces. However in some cases the corner slot can not only significantly reduce the across-wind excitation, but also make internal space design more logical, shown in Figure 8.

Figure 6. Corner slot

2.3 *Modification of building elevations*

The basic concept of this approach is to increase the variation of building shape alone the height, either in section geometry, or in section dimension, or in section orientation. There are four basic forms of elevation modification:

1) tapering, as shown in Figure 9
2) twisting, as shown in Figure 10
3) Setting back, as shown in Figure 11
4) Sculpture top, as shown in Figure 12

A combination of all these basic forms is shown in Figure 13.

These forms share a common mechanism in reducing wind response. Due to various building geometry along the height, the properties of vortex shedding are also varies with height, leading to much less correlated excitations for across-wind response. The study conducted for twisting effects, shown in Figure 10, indicates that effectiveness increases with the increase of twisting angles within the range of 100^{o} to 180^{o}. However, to balance between the aerodynamic benefits and potential complication on cladding system, the 120^{o} twist from base to top is selected as final version that represents about 15% reduction on wind loading.

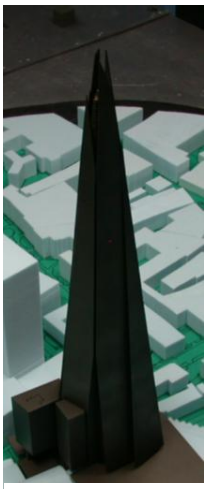

Figure 9. Tapering

Figure 10. Twisting

Figure 11. Set-back

Figure 12. Toping

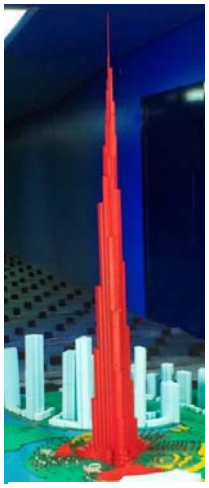

Figure 13. Combination

The effects of tapering in reducing across-wind response can be explained in a similar manner as for the twisting. Since the vortex shedding frequency is inversely proportional to a building width, the tapered width causes the outstanding frequency of wake excitation varies along the building height so that the outstanding frequencies of excitation are spread out to a wide range.

As mentioned before, modifications on building elevations are much more dramatic in visual impacts and can lead to a totally different design. Therefore modifications on building elevation are more suitable during the early stage of architectural design.

While aerodynamic modifications bring in benefits for reduced design wind loads and vibrations, these modifications often create conflicts with other design aspects. A good design is to reach optimized balance among many design aspects. For this reason, it is important to have an approach to estimate the level of effects with different modification schemes, so that the pros and cons of these aerodynamic modifications can be assessed and an overall optimized balance can be reached. A series of wind tunnel tests to examine various modification schemes is technically feasible but financially expensive and time consuming.

The next section is to discuss a method that is based on minor wind tunnel tests and major numerical analysis. This method is especially useful at early stage of architectural design to assess the aerodynamic improvements by tapering, twisting or set-back.

3 DILEMMA AND CHALLENGES IN OPTIMIZATION PRACTICE

3.1 *Expression of sectional wind loads at level z*

Basic parameters that describe sectional wind loads acting at level *z* of a building include:
Reference wind pressure:

$$q_z = \frac{1}{2}\rho U_z^2 = q_0 V_q(z) \tag{1}$$

Reference dimension (building width):

$$B_z = B_0 V_B(z) \tag{2}$$

Building twisting:

$$\theta(z) = \theta_0 V_\theta(z) \tag{3}$$

A common case is considered in the paper that the basic shape of building cross section remains the same along the height, but its dimensions and orientations vary. The varied dimension represents tapered width and varied orientation characterizes twisting. Some special set-back scheme can also be addressed with this typical case. The basic aerodynamic properties at Level *z* are given as follows.
Static drag coefficient:

$$C_D(z) = C_{D0} V_{Cd}(z) = C_{D0} V_{Cd}(\theta(z))$$

Static Lift coefficient:

$$C_L(z) = C_{L0} V_{Cl}(z) = C_{L0} V_{Cl}(\theta(z))$$

Dynamic Lift coefficient:

$$\tilde{C}_L(z) = \tilde{C}_{L0} V_{\tilde{C}l}(z) = \tilde{C}_{L0} V_{\tilde{C}l}(\theta(z))$$

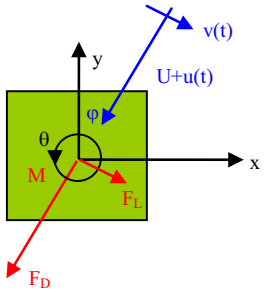

Figure 14. Wind loads on Level *z*

The sectional drag and lift force can be expressed by

$$F_D(z,t) = \frac{1}{2}\rho(U_z + u_z(t))^2 B_z\left(C_D(z) + \frac{dC_D(z)}{d\alpha}\alpha\right) \tag{4}$$

$$F_L(z,t) = \frac{1}{2}\rho(U_z + u_z(t))^2 B_z\left(C_L(z) + \frac{dC_L(z)}{d\alpha}\alpha + \tilde{C}_L(z,t)\right) \tag{5}$$

where

$$\alpha = -\frac{v_z(t)}{U_z} \qquad \frac{dC_D(z)}{d\alpha} = C'_{D0}(z) \qquad \widetilde{C}_L(z,t) = \widetilde{C}_L(z)T(t)$$

The mean loads are given by

$$\overline{F}_D(z) = q_z B_z C_D(z) = \left(q_0 B_0 V_q(z) V_B(z)\right) C_D(\theta_z) \tag{6}$$

$$\overline{F}_L(z) = q_z B_z C_L(z) = \left(q_0 B_0 V_q(z) V_B(z)\right) C_L(\theta_z) \tag{7}$$

The dynamic portion can be expressed in the form of power spectra, i.e.,

$$S_D(f,z) = \left(q_0 B_0 V_q(z) V_B(z)\right)^2 \sigma_D^2(\theta_z) S_D^*(f_z^*, \theta_z) \tag{8}$$

$$S_L(f,z) = \left(q_0 B_0 V_q(z) V_B(z)\right)^2 \sigma_L^2(\theta_z) S_L^*(f_z^*, \theta_z) \tag{9}$$

where $f_z^* = \dfrac{fB_z}{U_z}$

With simultaneous pressure measurements, the above non-dimensional aerodynamic properties can be easily determined, including C_D, C_L, $\sigma_D^2 S_D^*$, and $\sigma_L^2 S_L^*$.

3.2 *Overall wind loads on building structures*

The overall mean loads can be determined by simply integration as follows.

Mean along-wind loads: $$\overline{F}_D = q_0 B_0 \int_h V_q(z) V_B(z) C_D(\theta_z) \cdot dz \tag{10}$$

Mean across-wind loads: $$\overline{F}_L = q_0 B_0 \int_h V_q(z) V_B(z) C_L(\theta_z) \cdot dz \tag{11}$$

The overall dynamic along-wind and across-wind loads are given by

$$S_D(f) = \left(q_0 B_0\right)^2 \iint_H V_q(z_1) V_q(z_2) V_B(z_1) V_B(z_2) \sigma_D(\theta_{z1}) \sigma_D(\theta_{z2}) \sqrt{S_D^*(f_{z1}^*, \theta_{z1}) S_D^*(f_{z2}^*, \theta_{z2})} C_{HD}(f, \Delta z_{12}) \cdot dz_1 dz_2 \tag{12}$$

$$S_L(f) = \left(q_0 B_0\right)^2 \iint_H V_q(z_1) V_q(z_2) V_B(z_1) V_B(z_2) \sigma_L(\theta_{z1}) \sigma_L(\theta_{z2}) \sqrt{S_L^*(f_{z1}^*, \theta_{z1}) S_L^*(f_{z2}^*, \theta_{z2})} C_{HL}(f, \Delta z_{12}) \cdot dz_1 dz_2 \tag{13}$$

Although the expressions for the along-wind and across-wind are similar, they can be very different in properties. The spectrum *S** and cross-coherence C_H are governed by approaching wind turbulence for along-wind, but by signature turbulence for across-wind. Most interesting portion for aerodynamic optimization of super-tall buildings is to examine the generalized forces excited by across-wind excitations, which can be expressed by

$$S_j(f) = \left(q_0 B_0\right)^2 \iint_H V_q(z_1) V_q(z_2) V_B(z_1) V_B(z_2) \sigma_L(\theta_{z1}) \sigma_L(\theta_{z2}) \sqrt{S_L^*(f_{z1}^*, \theta_{z1}) S_L^*(f_{z2}^*, \theta_{z2})} C_{HL}(f, \Delta z_{12}) \Phi_{j,z1} \Phi_{j,z2} \cdot dz_1 dz_2 \tag{14}$$

where Φ_j is the *j*-th mode shape.

The effectiveness of shape variations on across-wind response can thus be assessed by comparing the difference of the spectra as follows:

$$R = \sqrt{\frac{S_j(f_j)}{S_{0j}(f_j)}} \tag{15}$$

where $S_{0j}(f_j)$ is the spectrum for a reference building geometry.

4 CONCLUSION REMARKS

Aerodynamic optimization is an important portion of super-tall building design. Two categories of optimization are discussed in the paper: aerodynamic modifications which are mostly considered as remedial measures with a limitation of not making significant changes on building's overall geometry or visual image; and aerodynamic designs which are feasible only with collaboration with architects in early design stage and can be very effective. While aerodynamic modifications mostly involved building corner treatments, aerodynamic designs have much more freedom in building geometry including overall building elevation optimizations, such as tapering, twisting, opening, set-back, top sculpture, etc. But aerodynamic designs are also limited by other design aspects, such as cladding, internal spacing, etc. The method proposed in this paper can be used to assess the effectiveness of various aerodynamic optimization schemes in order to achieve a balance between aerodynamic satisfaction and fulfillment of other design aspects.

5 REFERENCES

1 Davenport, A.G., The response of six building shapes to turbulent wind, Phil. Trans. Roy. Soc. A, 1971, v.269, A discussion on architectural aerodynamics, 385-394

2 Kowk, K.C.S., Effect of building shape on wind-induced response of tall buildings, J. Wind Eng. Ind. Aerodyn., 1988, vol.28

3 Isyumov, N., R. Dutton, and A.G. Davenport, Aerodynamic methods for mitigating wind-induced building motions, Proc. ASCE Structures Congress, 1989.

4 Dutton, R. and N. Isyumov, Reduction of tall building motion by aerodynamic treatments, J. Wind Eng. Ind. Aerodyn., 1990, 36

5 Hayashida, H and Y. Iwasa, Aerodynamci shape effects of tall building for vortex induced vibration, J. Wind Eng. Ind. Aerodyn., 1990, 33, 237-242

6 Xie, J. et al, Wind engineering studies for Taipei 101 tower, RWDI report, 1997

7 Irwin, P.A., B. Breukelman, C. Williams, and M. Hunter, Shaping and orienting tall buildings for wind, Proc. Str. Eng. World Congress ASCE, 1998

8 Kareem, A. T. Kijewski and Y. Tamura, Mitigation of motion of of tall buildings with recent applications, Wind and structures, 1999, vol.2, 201-2511

9 Kowk, K.C.S. and N. Isyumov, Aerodynamic measures to reduce the wind-induced response of buildings and structures, Proc. Str. Eng. World Congress ASCE, 1998

10 Kim, Y-M, and K-P You, Dynamic responses of a tapered tall building to wind loads, J. Wind Eng. Ind. Aerodyn., 2002, 90, 1771-1782

11 Kim, Y-M, K-P You and N-H Ko, Across-wind responses of an aeroelastic tapered tall buildings, J. Wind Eng. Ind. Aerodyn., 2002, 96, 1307-1319

12 Browne, M. and S. Kumar, Effect of corner balconies on wind-induced response of tall buildings, Proc. 10th Americas Conf. Wind Eng., 2005

13 Xie, J. et al., Wind engineering studies for Shanghai Center Tower, RWDI report, 2009

14 Tse, K.T, P.A. Hitchcock, K.C.S. Kowk, S. Thepmongkorn and C.M. Chan, Economic perspectives of aerodynamic treatments of square tall buildings, J. Wind Eng. Ind. Aerodyn., 2009, 97, 455-467

15 Merrick, R. G. Bitsuamlak, Shape effects on the wind-induced response of high-rise buildings, J. Wind and Engineering. 2009, vol.6, 1-18

The Seventh International Colloquium on Bluff Body Aerodynamics and Applications (BBAA7)
Shanghai, China; September 2-6, 2012

Bluff body aerodynamics of simplified bridge decks for aeroelastic optimization

S. Hernández [a], F. Nieto [a], J. A. Jurado [a], I. Pérez [a]

[a] *School of civil Engineering, University of La Coruña, Campus de Elviña, A Coruña, Spain*

ABSTRACT: Long span bridges need to be designed to accomplish tensional, deformational and aeroelastic constraints. However the geometry of a bridge deck aimed to fulfill adequately conditions on stresses and displacements is very different than the shape that provides good aeroelastic behaviour. The necessity to satisfy all these considerations leads usually to a sequence of intermediate prototypes worked out by trial and error procedures. Then, the performance under wind flow of a given design is tested in wind tunnel laboratories. In this paper a technique that allows to obtain the optimum design of several deck shapes from the structural point of view is presented. Afterwards the flutter speed for each optimum design is obtained. It is demonstrated that a combined optimization procedure that takes in account jointly both structural and aeroelastic constraints will be able to identify the optimum bridge deck shape. An application example of a simplified deck of a cable stayed bridge is used to describe the capabilities of this methodology.

KEYWORDS: Bridge deck, long span bridges, computational fluid dynamics, flutter speed, design optimization.

1 INTRODUCTION

Cable stayed bridges are designed currently with ever longer spans. Therefore these structures are very flexible and the required limits to vertical displacements under static loads must be maintained. This leads to the evaluation of the necessary stiffness that is obtained by providing the proper value of inertia modulus of the cross section. The easiest way to do it is by defining very depth decks because this approach will reduce the amount of material. In that case the design is driven by stiffness.

On the other hand long span bridges are prone to aeroelastic phenomena so their design needs to be aeroelastically sound and instabilities as flutter must be avoided. Hence, decks should be as much aerodynamic efficient as possible and thus prototypes with small depth are preferred. In that regard the design is driven by the aeroelastic behavior. But decks having small depth need more material to maintain the required value of inertia so the solutions for a bridge deck from the stiffness perspective and the aeroelastic approach are contradictory and enhancing the aeroelastic response implies reducing bridge deck and thus increasing the cross section area and deck cost.

Commonly the final design for the configuration of the deck of a long span bridge is a process that requires many intermediate prototypes that represent alternatives evaluated to figure out their capabilities. Along the way they are refined or discarded, until a decision is made and the deck shape is finally fixed. In figure 1 two different alternatives of the deck of two very well known bridges that were considered along the design process are presented.

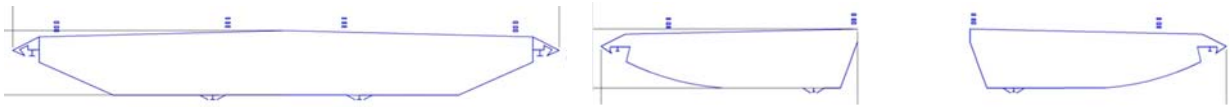

a) Alternatives for the Forth Replacement Crossing

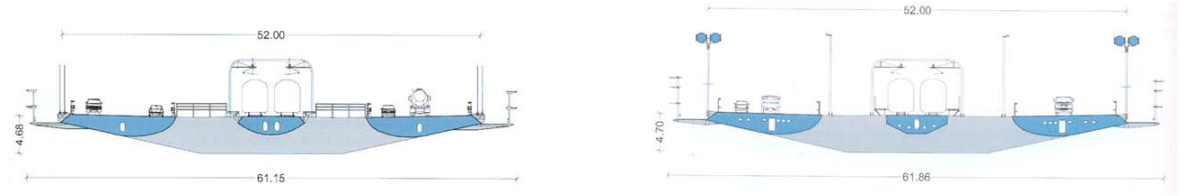

b) Alternatives for the Messina Strait Bridge

Figure 1. Deck design of the Forth Replacement Crossing and Messina Strait bridge

2 DECK DESIGN OF CABLE SUPPORTED BRIDGES

Commonly, in the design process of a bridge deck, after fixing the necessary stiffness (the value of inertia modulus) and the aeroelastic constraint related to flutter (the value of flutter speed) the final solution is carried out by trial and error methods until a good enough prototype is obtained. Nevertheless it should be interesting to identify the shape of a bridge deck that possesses the minimum amount of material possible for accomplishing the previously mentioned requirements.

This can be done by an optimization procedure. This methodology uses numerical optimization algorithms to find out the best solution of a problem. Texts describing this technique have been written by Haftka [1], Vanderplaats [2] or Arora [3] and it has been used extensively in some technological fields as aerospace, mechanical or car engineering. A book by Hernandez and Fontan [4] relates several practical examples in these disciplines. Applications in bridges are scarce but works by Hernandez et alt. [5] or by Baldomir et alt. [6] can be mentioned. A pioneer initiative in aeroelastic design of bridges aimed to optimize the mechanical parameters of the deck in long span suspension bridges considering kinematic and flutter considerations was carried out by Nieto and others [7].

A flowchart of the iterative process carried out in design optimization is presented in figure 2.

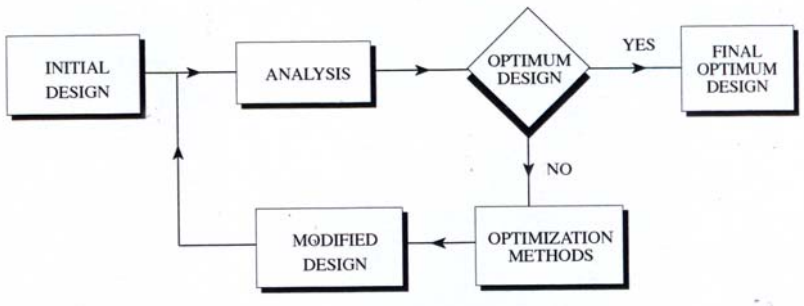

Figure 2. Flowchart of optimization methodology.

3 OPTIMUM DESIGN OF BRIDGE DECK

The goal of the research concluded by the authors is to obtain, for a given bridge geometry, the cable supported bridge that has the minimum weight and fulfills the required stress and kinematic constraints while also accomplishing the requested flutter response.

3.1 *Definition of the cable-stayed bridge and the simplified box girder*

The Miradoiros Cable-Stayed Bridge currently designed in Spain has been chosen as a study case. It is a 658 m main span bridge which is not symmetric as the deck has some slope in elevation (see figure 3).

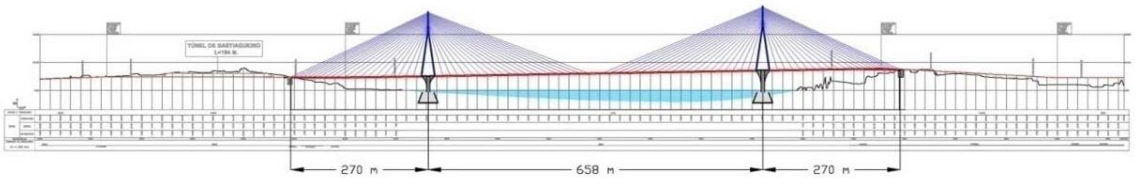

a) Elevation

b) Computer picture

Figure 3. Elevation of the Miradoiros Cable-Stayed Bridge

Due to the academic purpose of the research the cross-section of the aerodynamic box girder of the original design has been substituted by a simplified cross section (see figure 4). Dimension B= 34 m that represents deck width is fixed while corner angle β is allowed to change, thus the deck cross-section shape depends on a single parameter β which is the design variable responsible for the change in the deck cross-section geometry. The corners are not perfectly sharp as a radius of curvature r/B= 0.0075 has been considered for all shapes studied.

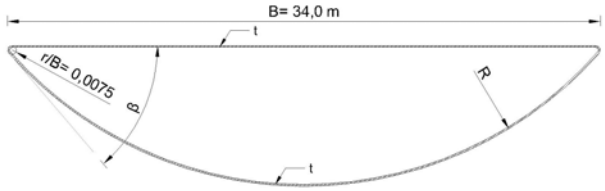

Figure 4. Simplified cross-section of deck

4 STRUCTURAL OPTIMIZATION OF SIMPLIFIED BRIDGE DECK

In this part of the research the goal was to obtain the bridge of minimum weight considering two situations: the bridge during construction at the final stage of the balanced cantilever construction and the bridge fully erected. The structural models of both situations appear in figure 5.

a) Bridge before completion

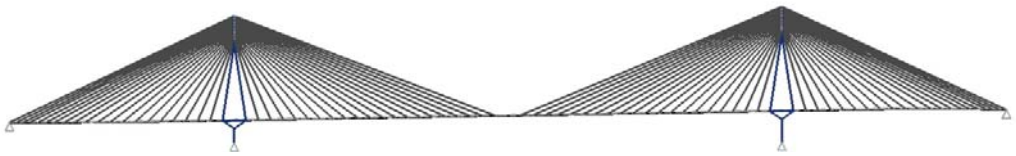

b) Fully erected bridge

Figure 5. Structural models

The bridge under construction is subjected to the self weight and two isolated loads at cantilever tip representing half the weight of the remaining bridge deck. The completed bridge is subjected to self weight and three different load cases representing the service load at right, center or left span.

In this problem the objective is to obtain the minimum weight for the deck and cables, in other words

$$\min F = t_d p_d l_d + 2\sum_{i=1}^{80} A_i l_i \tag{1}$$

being t_d, p_d, l_d deck thickness, perimeter and length, A_i and l_i (i =1,...80) the area and length of each cable. Expression (1) takes in account that the bridge is symmetric with regards to a longitudinal plane.

Design variables are constituted by deck thickness and cross area of cables, namely 81 design variables are considered.

Design constraints were linked to the behavior of the bridge. It was required that the stress value of cables was lower than 800 MPa, deck deflections during construction and horizontal displacement of tower top was null and for the completed bridge was requested that deck deflection was lower than 1/550 of the span length and the horizontal displacement of tower top was also lower than 1/550 of tower altitude.

The numerical results for each value of β appears in table 1. It can observed that as the value of β increases the amount of material of the deck decreases and so the volume of cables does. This trend could be known in advance but the study carried out allows that such common sense feeling had been quantified at the end of the numerical optimization process.

Table 1. Numerical results for optimum design

Deck angle (º)	Deck thickness (m)	Deck area (m2)	Horizontal bending inertia (m4)	Vertical bending inertia (m4)	Torsional (m4)	Mean area of cables (m2)	Deck volume (m3)	Cables Volume (m3)	Total volume (m3)
20	0.02349	1.613	2.238	156.700	6.393	0.04439	1932.4	3127.2	5059.5
25	0.02141	1.479	3.252	144.400	9.223	0.03811	1771.8	2677.5	4449.4
30	0.01861	1.295	4.169	127.200	11.730	0.02298	1551.4	1842.8	3394.2
35	0.01745	1.225	5.466	121.200	15.260	0.02420	1467.6	1891.3	3358.9
40	0.01627	1.154	6.868	115.200	19.000	0.02272	1382.5	1776.3	3158.8
45	0.01496	1.073	8.279	108.200	22.680	0.02186	1285.5	1737.0	3022.4
50	0.01398	1.017	9.949	103.900	26.970	0.02038	1218.4	1666.0	2884.3
55	0.01250	0.923	11.250	95.620	30.160	0.02061	1105.2	1707.6	2812.7
60	0.01183	0.888	13.330	93.640	35.280	0.01938	1064.1	1571.3	2635.3

5 COMPUTATIONAL EVALUATION OF AERODYNAMIC COEFFICIENTS

The flow around the simplified deck cross-section has been modeled considering a 2D unsteady flow (see figure 6 where *B* is the deck width and the cross-section is not scaled). The URANS κ-ω SST turbulence model has been used considering a turbulence intensity of 1% and length scale of 0.1B. Dirichlet conditions have been set at the inlet and outlet boundaries of the flow domain.

With the aim of validating the CFD approach for computing the aerodynamic coefficients of the simplified deck the numerical results at Re= 1E+05 have been compared with the experimental ones published by Novak and Tanaka [8] at Re= 9E+04 for a corner angle β=90º. Two different meshes have been considered: 2.24E+05 cells and 3.35E+05 cells. The results obtained are reported in table 2 and it has been found that the 2.24E+05 mesh with a nondimensional time step of 0.01 for advancement in time provides accurate results with lower computational cost. In figure 7 a general view of that is presented. The definition of the aerodynamic coefficients is as follows and the sign criteria is shown in figure 8.

$$C_D = \frac{D}{\frac{1}{2}\rho U^2 B};\quad C_L = \frac{L}{\frac{1}{2}\rho U^2 B};\quad C_M = \frac{M}{\frac{1}{2}\rho U^2 B^2} \tag{2}$$

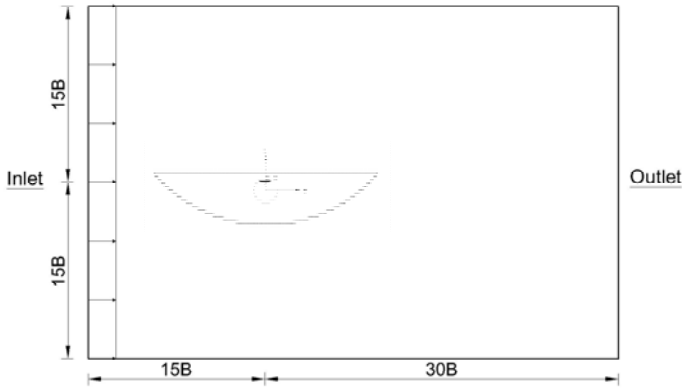

Figure 6. Flow domain (deck not to scale).

Table 2. Aerodynamic coefficients and Strouhal number for β=90º.

Grid cells	Δt*	C_D	C_L	C_M
224.501	0,01	0,43	0,54	0,16
335.615	0,01	0,42	0,54	0,16
Wind Tunnel. (Novak & Tanaka)		0,4	0,5	0,15

For the angles of interest for deck cross-sections 20<β<60, the aerodynamic coefficients and the slopes at 0º angle of attack have been evaluated numerically and appear in table 3.

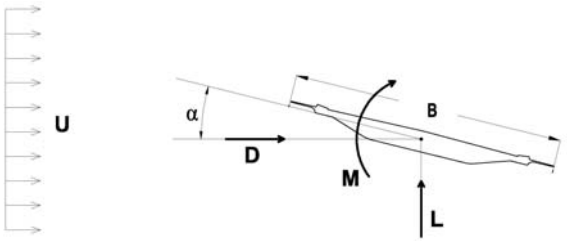

Figure 7. Sign convention for aerodynamic coefficients

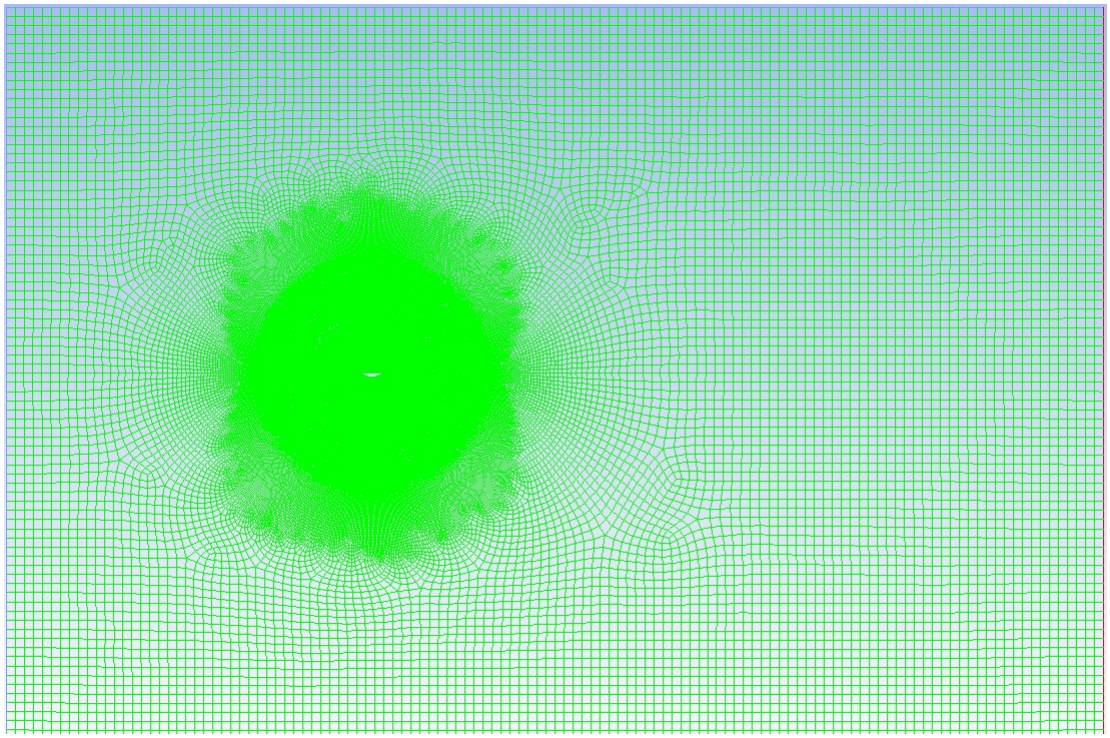
Figure 8. A general view of the mesh with 3.35E+05 cells

Table 3. Aerodynamic coefficients and derivatives at attack angle 0º.

Attack angle (º)	C_{D0}	C'_{D0}	C_{L0}	C'_{L0}	C_{M0}	C'_{M0}
20	0.0178	0.0258	-0.3344	5.0793	0.0070	1.2662
25	0.0226	0.0286	-0.3540	4.9332	0.0141	1.2748
29	0.0271	0.0458	-0.3559	4.6438	0.0220	1.2777
35	0.0396	0.0573	-0.3414	4.7928	0.0368	1.2806
40	0.0527	0.0945	-0.3090	5.3514	0.0527	1.3178
45	0.0711	0.1089	-0.2795	6.8182	0.0691	1.3866
50	0.0946	0.0945	-0.2528	8.8121	0.0856	1.4209
60	0.1381	-0.3352	0.0726	16.2548	0.1273	0.7821
75	0.2360	-0.4240	0.3667	11.7141	0.1403	-0.3982
90	0.4261	-0.5443	0.5413	9.4796	0.1375	-0.2951

6 EVALUATION OF FLUTTER SPEED OF STRUCTURAL OPTIMA

For each optimum design obtained considering exclusively structural constraints the flutter speed can be calculated. It is done by using the Scalan theory [9] defining the aeroelastic forces and establishing the dynamic equilibrium of the structure under such set of forces.

$$\mathbf{M}\ddot{\mathbf{u}} + \mathbf{C}\dot{\mathbf{u}} + \mathbf{K}\mathbf{u} = \mathbf{f}_a = \mathbf{C}_a\dot{\mathbf{u}} + \mathbf{K}_a\mathbf{u} \tag{3}$$

Where $\mathbf{M}$,$\mathbf{C}$,$\mathbf{K}$ are the mass, damping and stiffness matrices of the structure, $\ddot{\mathbf{u}}, \dot{\mathbf{u}}, \mathbf{u}$ the vectors of accelerations, velocities and displacements of the degrees of freedom of the structure and $\mathbf{f}_a$ the vector of aeroelastic forces than depends on the velocities and displacements of the structure according with the following expression and the conventions shown in figure 9.

$$\mathbf{f}_a = \begin{Bmatrix} F_y \\ F_z \\ M_x \end{Bmatrix} = \frac{1}{2}\rho VKB \begin{pmatrix} P_1^* & -P_5^* & -BP_2^* \\ -H_5^* & H_1^* & BH_2^* \\ -BA_5^* & BA_1^* & B^2A_2^* \end{pmatrix} \begin{Bmatrix} \dot{v} \\ \dot{w} \\ \dot{\varphi}_x \end{Bmatrix} + \frac{1}{2}\rho V^2K^2 \begin{pmatrix} P_4^* & -P_6^* & -BP_3^* \\ -H_6^* & H_4^* & BH_3^* \\ -BA_6^* & BA_4^* & B^2A_3^* \end{pmatrix} \begin{Bmatrix} v \\ w \\ \varphi_x \end{Bmatrix} \tag{4}$$

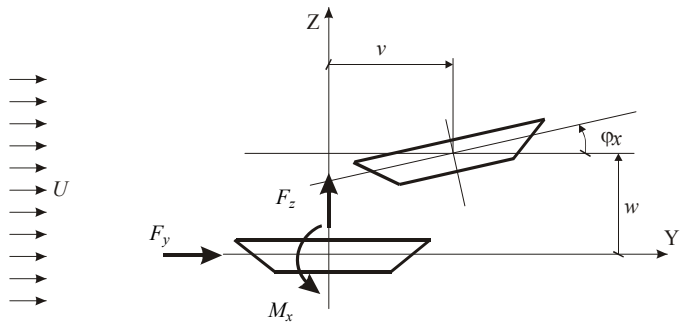

Figure 9. Convention for aeroelastic forces.

Where ρ is air density, V is wind speed, B is bridge width, K is the reduced frequency $K=B\omega/V$, ω is the vibration frequency and $A_i^*, H_i^*, P_i^* \quad (i=1,...,6)$ are the flutter derivatives.
In absence of a proper identification of flutter derivatives the evaluation of flutter speed can be done by using the quasi-steady theory which represents a simplification of the problem. Formulation of the quasi-steady approach can be found in Salvatori and Spinelli [10] or Lazzari [11]. The approximations of the flutter derivatives are presented in equation (5), where μ, that represents the distance between the elastic centre and the geometric centre of the cross section, can be estimated as A_1^*/H_1^* or A_3^*/H_3^* according to Febo and D'Asdia [12].

$$P_1^* = -\frac{2C_{D0}}{K} \qquad P_2^* = \frac{C'_{D0} - C_{L0}}{K}\mu \qquad P_3^* = \frac{C'_{D0}}{K^2} \qquad P_5^* = -\frac{C'_{D0} - C_{L0}}{K}$$
$$H_1^* = -\frac{C'_{L0} + C_{D0}}{K} \qquad H_2^* = -\frac{C'_{L0} + C_{D0}}{K}\mu \qquad H_3^* = -\frac{C'_{L0}}{K^2} \qquad H_5^* = \frac{2C_{L0}}{K} \qquad (5)$$
$$A_1^* = \frac{C'_{M0}}{K} \qquad A_2^* = \frac{C'_{M0}}{K}\mu \qquad A_3^* = \frac{C'_{M0}}{K^2} \qquad A_5^* = \frac{2C_{M0}}{K}$$

The numerical values of μ and the results for the flutter speed corresponding to each optimum design from the structural point of view are presented in table 4 and the latter appear in figure 10.

Table 4. Values of μ and flutter speed

Angle (°)	20	25	30	35	40	45	50	55	60
μ	-0.248	-0.257	-0.272	-0.265	-0.244	-0.201	-0.160	-0.087	-0.048
Flutter speed (m/s)	59.1	83.4	102.5	116.9	124.7	118.6	107.9	82.7	97.3

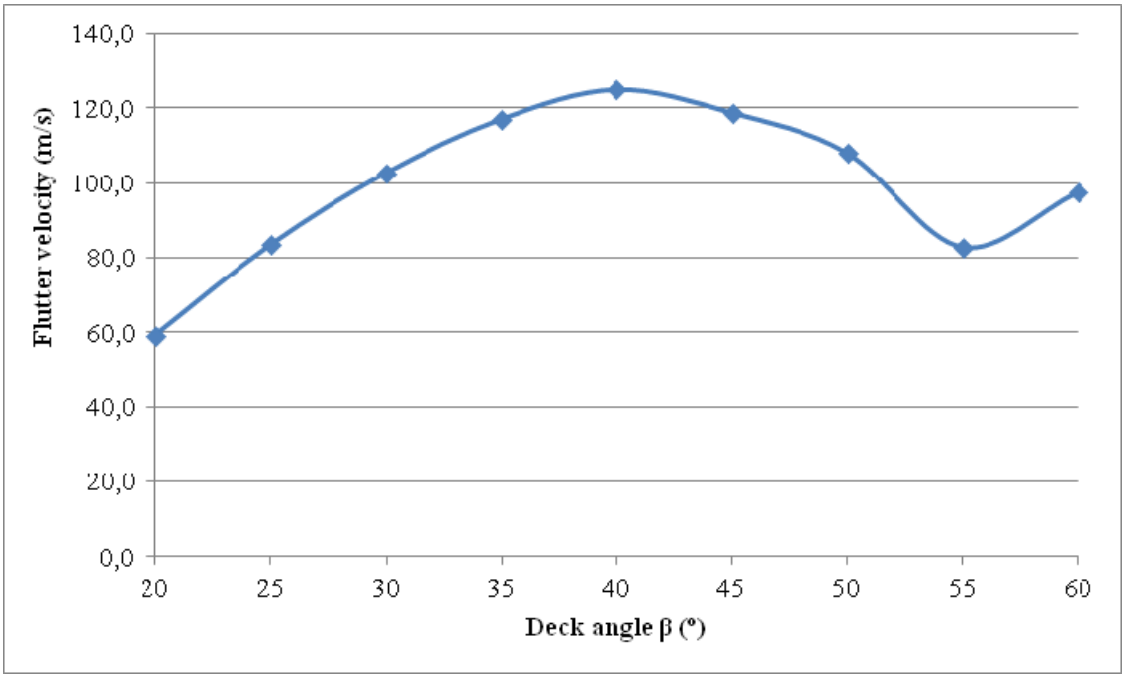

Figure 10. Flutter speed for optimal solutions from the structural point of view.

It can be observed that flutter speed does not evolve monotonically with respect to angle β. For instance for small β values flutter speed increases, then a maximum around $\beta = 40º$ appears. For higher β values the flutter speed decreases and afterwards there is also a local minimum. These numerical results show that if a defined flutter speed is requested, for instance V=100 m/s it can be obtained with two different designs, namely $\beta = 30º$ and $\beta = 52º$; but recalling table 1 it can be concluded that $\beta = 52º$ should be preferred as the amount of material is lower. There is also another conclusion: from the structural perspective, in other words for stresses and displacements considerations, the higher the value of β the better the behavior of the bridge,. But from the aeroelastic point of view the bridge response is different and increasing β, for instance, from $\beta = 35º$ to $\beta = 50º$ the flutter response is worsened. Although this consideration can be known for an experienced designer this research allows to identify such behavior in a quantitative way.

7 COMBINED STRUCTURAL AND AEROELASTIC OPTIMIZATION OF BRIDGE DECK

In the previous paragraphs the design of the bridge deck has been made considering independently structural constraints and aeroelastic constraints. This was done because this is the usual way to do it. Nevertheless in this research the structural part of the design provided the minimum value of the material volume which cannot be obtained by conventional trial and error techniques. Proceeding along this way a value of the flutter speed in obtained by each optimum for a given value of angle β. As mentioned before such value corresponded to two different values of β and the one with less material volume is to be chosen. Therefore this is not the best solution.

The best way to proceed is to consider jointly the constraints related to stresses and displacements and also the value of flutter speed. In other words the limits for the stresses in the material and the displacements of the structure need to be defined and also a value of the flutter speed needs to be established. In that case in the evaluation of the optimum solution the angle β that defines the geometry of the simplified deck needs to be considered as a design variable in addition to the thickness of the deck and the cross area of stays. The output of that optimization problem will lead to a design that is able to have the requested flutter speed with the minimum amount of material. In other words the value of β will be the one producing the maximum flutter speed similarly to the situation shown in the figure 10, in which that maximum will be exactly the required wind velocity.

8 CONCLUSIONS

The following conclusions can be extracted from this research:

1. Design of long span bridges produces a set of intermediate prototypes which usually delays the definition of the final design.
2. Design of long span bridges is a multidisciplinary problem that requires taking advantage of the more cutting edge technologies.
3. In this regards application of numerical optimization techniques can be very helpful for identifying the optimal shape of bridge deck.
4. A procedure working independently with structural constraints and aeroelastic constraints has been formulated.
5. Such procedure has been applied to a cable stayed bridge of 658 m of main span length.

6. Such methodology allows to quantify the relevance of both, the structural and aeroelastic considerations and demonstrate that a joint formulation of the problem is necessary and the optimum design only can be obtained with that combined approach.

9 ACKNOWLEDGEMENTS

This research is funded by the Spanish Ministry of Science and Technology under research project BIA2010-19989.

10 REFERENCES

1 Haftka, R. T. and Gurdal, Z. 1992. Elements of structural optimization. Kluwer Academic Publishers.
2 Vanderplaats, G. N., 2001. Numerical optimization techniques for engineering design. VR & D.
3 Arora, J., 2007. Optimization of structural and mechanical systems. Word Scientific.
4 Hernandez, H. and Fontan A.N., 2002. Practical applications of design optimization. WIT Press.
5 Hernandez, S., Fontan, A. N., Diaz, J. and Marcos, D., 2010. VTOP. An improved software for design optimization of prestressed concrete beams. Advances in Engineering Software, 41 (3), 415-421.
6 Baldomir, A., Hernandez. S., Nieto, F. and Jurado, J. A., 2010. Cable optimization of a long span cable stayed bridge in La Coruña (Spain). Advances in Engineering Software, 41 (7-8), 931-938.
7 Nieto, F., Hernandez, S., and Jurado, J.A., 2009. Optimum design of long span suspension bridges considering aeroelastic and kinematic constraints. International Journal of Structural and Multidisciplinary Optimization, 39, 133-151.
8 Novak, M. and Tanaka, H. 1974 Effect of turbulence on galloping instability. Journal of the Engineering Mechanics Division, ASCE, Vol. 100, No. EM1, 27-47.
9 Scanlan, R.H., 1987. On flutter and buffeting mechanisms in long span bridges. Journal of Engineering Mechanics Division, ASCE, 113, 555-575.
10 Salvatori, L. and Spinelli, P. 2007. A discrete 3D model for bridge aerodynamics and aeroelasticity: nonlinearities and linearizations. Meccanica, 42, 31-46.
11 Lazzari, M., 2005. Time domain modeling of aeroelastic bridge decks: a comparative study and an application. International Journal for Numerical Methods in Engineering, 62, 1064-1104.
12 Febo, S., D'Asdia P., 2010. Aeroelastic pre-design of streamlined multiple-box decks, in: XI Convegno Nazionale di Ingegneria del vento, IN-VENTO 2010, ANIV.

The Seventh International Colloquium on Bluff Body Aerodynamics and Applications (BBAA7)
Shanghai, China; September 2-6, 2012

Reynolds number effects on aerodynamics forces of Kwangyang Bridge girder

Seungho Lee[a], Seung Hee Kang[b], Jah-Geol Yoon[c], Soon-Duck Kwon[a]

[a]*KOCED Wind Tunnel Center, Dept. of Civil Engineering, Chonbuk National University, Chonju, Chunbuk, Korea*
[b]*Dept. of Aerospace Engineering, Chonbuk National University, Chonju, Chunbuk, Korea*
[c]*Daelim Industrial Company, 146-12, Susong, Jongno, Seoul, Korea*

ABSTRACT: In this paper, the experimental results for twin box girder of the Kwnagyang Bridge are presented in order to investigate the sensitivity of the Reynolds numbers on aerostatic force coefficient. High speed wind tunnel testing on 1:30 scale sectional model were carried out at the aeronautical wind tunnel in Korea Air Force Academy. The drag and lift coefficients revealed significant decrease of nearby 23% at supercritical region. The safety rail prevented the Reynolds number dependency of aerostatic force coefficients at negative angles of attack. In similar way, the boundary layer trip strip attached at bottom surface of girder reduced the Reynolds number dependency of aerostatic forces by fixing the location of flow transition. The pressure coefficients at girder surface near the gap significantly changed as the Reynolds number increase because of variation of the locations of flow separation and transition. The unbalanced burden of the drag force and lift forces at each box girder appeared in subcritical region was gradually resolved, and both boxes were almost equally loaded the forces at supercritical region.

KEYWORDS: Reynolds number, wind tunnel, suspension bridge, twin box girder.

1 INTRODUCTION

It is generally known that the flow around bluff and sharp edged bodies is independent of the Reynolds number, and the aerostatic forces measured at low speed wind tunnel testing may be directly applicable to the prototype bridge. The modern bridge girders are no longer sharp bluff body and are more likely streamlined section. The Reynolds number at ordinary wind tunnel tests of bridge girder has been generally 10^2 to 10^3 times smaller than that at actual bridges. Accordingly the aerostatic forces, especially drag force, of streamlined bridge sections seem to be no longer free from the Reynolds number.

Drag coefficients of some bridge girder sections were reported remarkably dependency of Reynolds number [1, 2]. In case of the Stonecutter Bridge girder, the drag force coefficient varied 30% according to wind speeds [3]. Considering the flexibility of long span bridges, those variations may significantly affect on structural and economical aspects of bridge design although the drag coefficients obtained at the low Reynolds number appear generally conservative for bridge design. Consequently there is some possibility of Reynolds number effects on girder of the Kwangyang Bridge that is extremely streamlined.

The Kwangyang Bridge, alternatively called as Yi Sun-sin Bridge, is located in south seashore of Korean peninsula which is frequently exposed to the typhoon at summer. During the Typhoon Maemi in 2003 passing nearby the bridge site, maximum instantaneous wind velocity was recorded 49.2 m/s at Yeosu Weather Station which is about 18km away from bridge site. Moreover the bridge superstructure locates 81m above sea level, and accordingly high wind is expected at the deck. Therefore the aerodynamic stability of the bridge is main concern of the design.

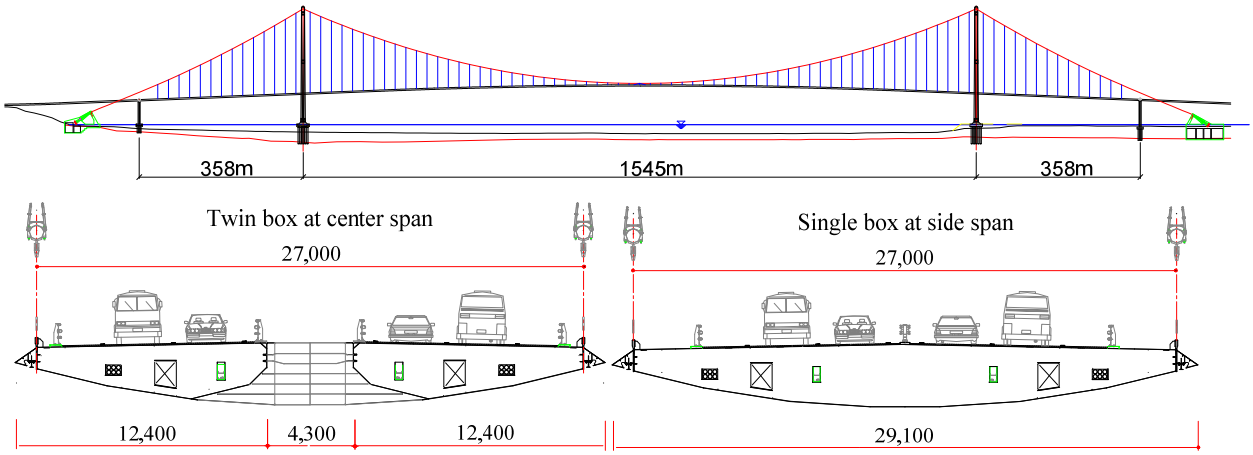

Figure 1. The Kwangyang Bridge.

The objective of present study is to investigate the sensitivity of aerostatic force coefficients of twin box girder of the Kwangyang Bridge according to the Reynolds numbers. This paper presents the 1:30 scale sectional model testing conducted at aeronautical wind tunnel in Korea Air Force Academy. Comparison with the results at low Reynolds number obtained in KOCED Wind Tunnel Center in Chonbuk National University is also provided.

2 TEST SETUP

The ordinary section model tests with scale of 1:70 were performed at the KOCED Wind Tunnel Center in Chonbuk National University during the design of the Kwangyang Bridge. The general results for aerodynamic design of main span girder can be found at Ref [5]. Those were, however, tested at low Reynolds number which was less than 4.8×10^5 (based on total girder width). Moreover smooth ventilation of air flow through narrow gap of 4.3m needs to be confirmed from the high speed wind tunnel tests, because different flow structure around guide vane according to wind speeds was observed at the Stonecutter Bridge.

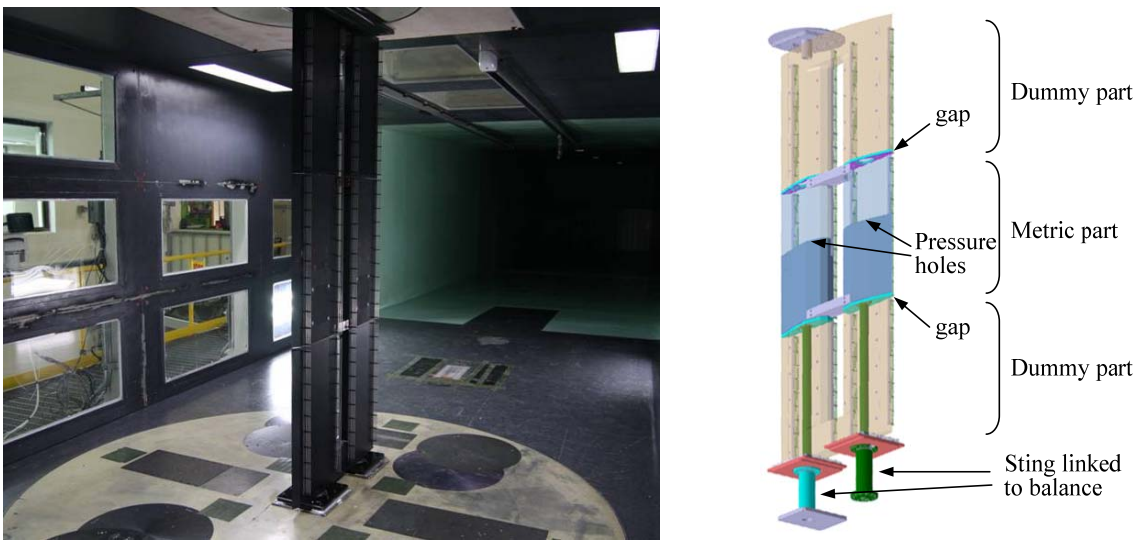

Figure 2. 1/30 scale model at wind tunnel in Korea Air Force Academy

The mid-size aeronautical wind tunnel at Korea Air Force Academy was used in present investigation in order to test at high wind speeds (high Reynolds numbers). Size of the test section was 3.5m(W)×2.45m(H). Contraction ratio was 7.3:1, maximum wind speed was 92m/s, and turbulent intensity was less than 0.038% at 74m/s. This closed circuit wind tunnel equipped boundary layer removal system and external pyramidal balance.

A 1:30 scale section model weighed over 250kg was made by aluminum and steel to resist high wind speed. Length and width of the model were respectively 1.94m and 1.0m which represented 72m of actual bridge girder. As shown in Figure 2, the model consists of three parts, one metric part and two dummy parts. Aerodynamic forces acting on metric part were measured by external pyramidal balance through two stings penetrating dummy part. Electric line sensors were attached at the gaps to warn the contact between metric part and dummy parts. Wind pressures were measured from 92 pressure holes in metric part. The pressure tubes were connected to pressure measurement system (PSI-8400).

Table 1 shows the experimental cases: girder without safety railing (case1), girder with safety railing (case2), girder with safety railing and boundary layer trip strip (case3). Case1 simulated the girder at construction stage where safety rails were generally not installed. Case2 and Case3 represented the girder at completion stage. The boundary layer trip strip is an artificial roughness added to the wind tunnel model in order to fix the location of transition from a laminar to turbulent boundary on the model [6]. The thickness of trip strip used in present investigation was 0.29mm. The trip strip was added on the bottom surface at 1.1m (at prototype) away from leading edge of the girder.

Table 1. Experimental Cases

Test case	Stage	Installation		Wind speed (m/s)	Angle of attack (deg)
		Safety rail	Trip strip		
Case1	Construction	×	×	10~45	+3 ~ -3
Case2	Completion	○	×	10~70	+5 ~ -5
Case3	Completion	○	○	10~45	+5 ~ -5

3 TEST RESULTS

3.1 *Aerostatic force coefficients*

Figure 3 shows the aerostatic force coefficients of the girder normalized by full girder width. As can be seen in the figure, the aerostatic force coefficients obtained from the 1:70 scale model well correspond with those measured from the 1:30 scale model at low Reynolds number. As Reynolds number (Re) increase gradually, the drag and lift coefficients revealed significant decrease of nearby 23%, while pitching moment coefficients were relatively consistent. The drag coefficient at $Re=1.5\times10^5$ (based on full girder width) was 0.083 but dropped to around 0.064 at $Re=7\times10^5$ and kept consistent. The lift coefficient also dropped from -0.096 to -0.347. The critical Reynolds number in present girder was found to be 2×10^5~7×10^5 that is near the range of wind speeds at ordinary section model tests.

It is noticeable that the safety rail significantly influences to the drag and lift coefficients regardless of the Reynolds number. The drag coefficient without safety rail (Case1) was almost half of that with safety rail (Case2 & 3). These represent that any obstacles attached at leading edge of the girder strongly change the drag and lift coefficients.

Higher pressure drag as compared to skin friction drag at low Reynolds number region introduces additional drag. As Reynolds number increases, the transition point has moved forward and drag has reduced accordingly. Two distinct features depending on Reynolds number are the

location of boundary layer transition and the location of separation. A boundary layer trip strip is a tool used for making transition to occur earlier than it is [6]. Unfortunately the girder with the boundary layer trip strip (Case2) was not tested at the critical Reynolds number region. The effect of the trip strip on the Reynolds number independency is not identified in the range of the tested Reynolds number.

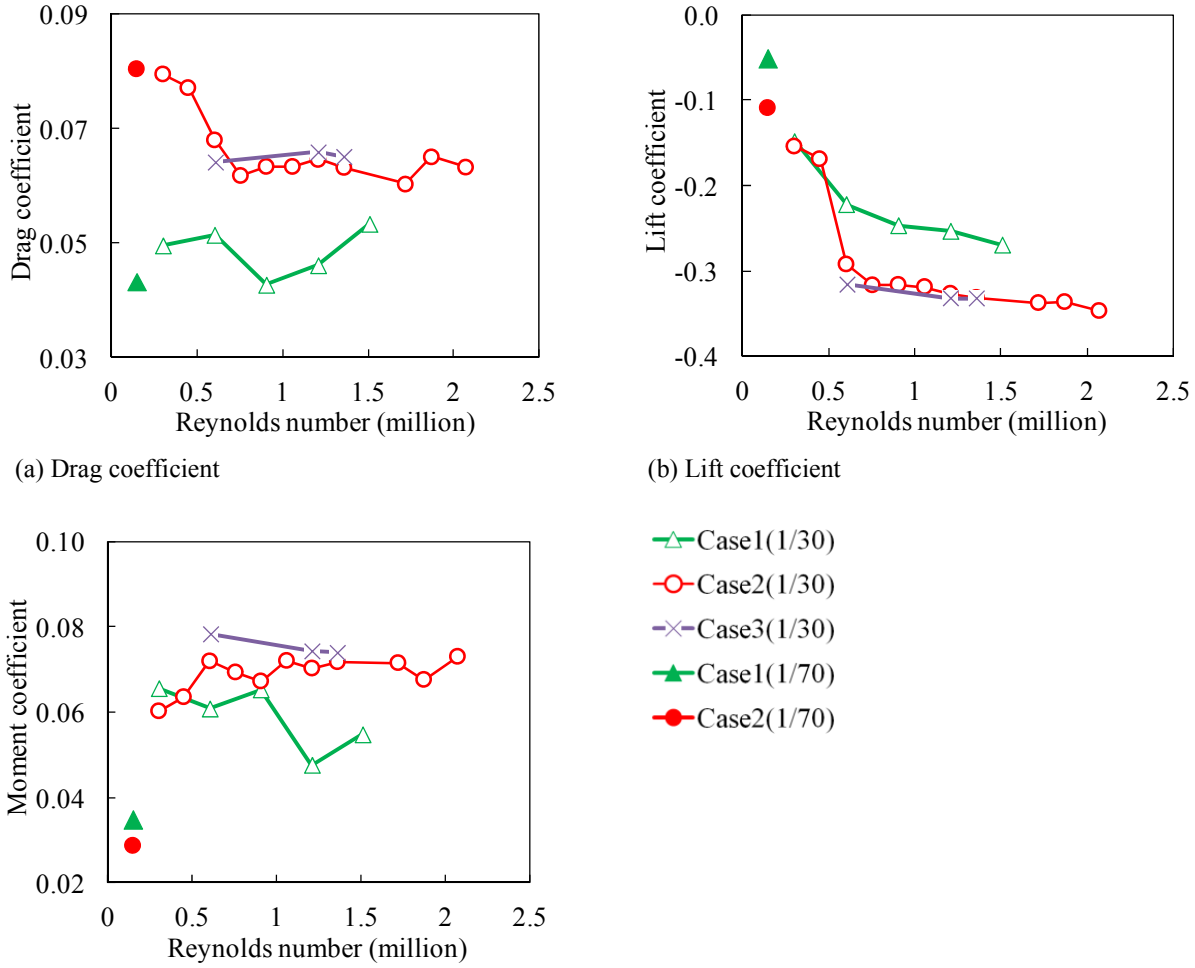

(a) Drag coefficient

(b) Lift coefficient

(c) Pitching moment coefficient

Figure 3. Aerostatic force coefficients at 0º angle of attack

The girder without safety rail definitely revealed the Reynolds number dependency on its aerostatic force coefficients. The tendency is, however, slightly different at the girder with safety rail. Figure 4 shows the aerostatic force coefficients of the girder with safety rail (Case2) according to angle of attack and the Reynolds number. The Reynolds number dependency was observed at zero and positive angles of attack (nose up), yet was not observed at negative angles of attack (nose down). In negative angles of attack, the location of separation on the bottom surface of the girder might be dependent on the Reynolds number. The location of separation did not, however, change because of the safety rail equipped at leading edge when the girder was inclined to negative angles of attack. The safety rail might fix the location of boundary layer transition and the location of separation.

When carefully watching the drag and lift coefficients shown in Figure 4(a) and (b), sudden drops of the coefficients are observed at certain angles of attack, e.g. 2º and 3º. Those drops already occurred at 0º angle of attack moved forward to higher Reynolds number in positive angles of attack. These represent that the critical Reynolds number changes according to angles of attack generally moved to higher value at high positive angle of attack.

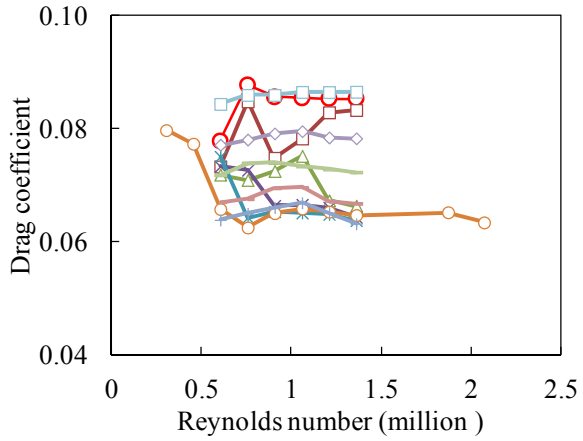

(a) Drag coefficient

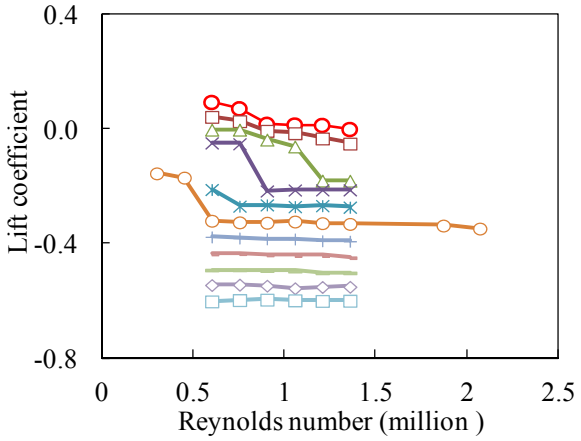

(b) Lift coefficient

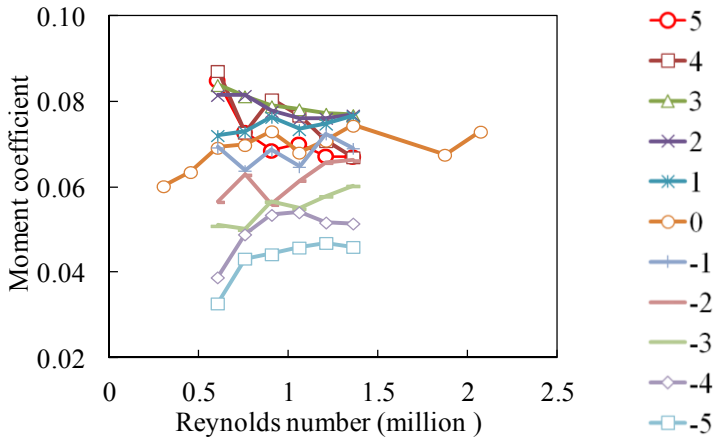

(c) Pitching moment coefficient

Figure 4. Aerostatic force coefficients of girder with safety rail according to angle of attack

As mentioned earlier, the effectiveness of the boundary layer trip strip which was not clearly identified because the tests were carried out at super critical Reynolds number. This effectiveness can be observed in the delayed critical Reynolds number at high positive angle of attack. The sudden drop of the drag and lift coefficients at the critical region occurred at the girder was eliminated at the girder by patching the boundary layer trip strip at its bottom surface. This removal of critical region from the test ranges represent that the trip strip effectively fix the location of transition from a laminar to turbulent boundary on the model, and can be used for simulating the high Reynolds number effect at low wind speed.

3.2 *Pressure distributions*

Figure 5 shows pressure coefficients along girder section. Pressure coefficient heading outside the box represents negative pressure (suction) and inside means positive. As can be seen in Figure 5(a) for girder without safety rail (Case1), the pressure coefficients at front edge of the leeward box change from negative to positive as the Reynolds number increase. This inconsistency of pressure coefficients is probably a result of moved locations of separation and boundary layer transition as wind speed up. These variations of pressure coefficients result in the Reynolds number dependency of the aerostatic force coefficients.

In case of girder with safety rail (Case2) at low Re, the pressure distribution of leeward box did not change much. However, the pressures at rear and mid bottom surface of windward box were changed at critical Re. The uniformly distributed negative pressures were observed at rear bottom surface of windward box in low Re. As wind speed increases, the strong negative pressure peaks were observed at folded edge of bottom surface above the critical Re.

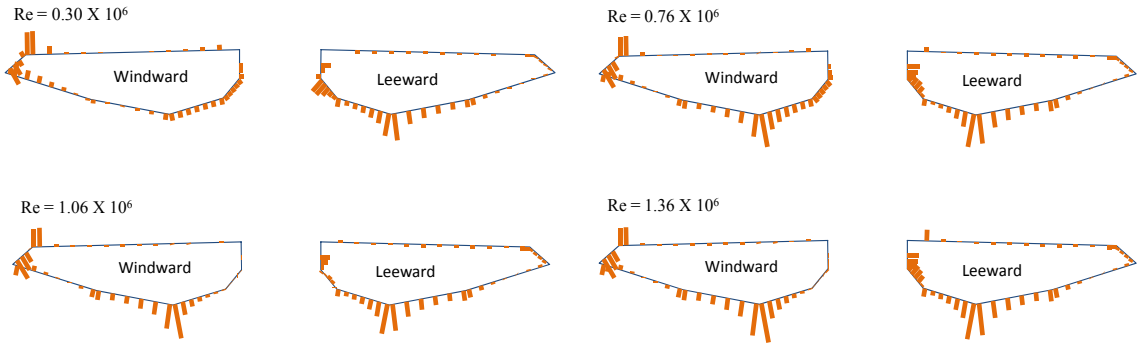

(a) Girder without safety rail (Case1)

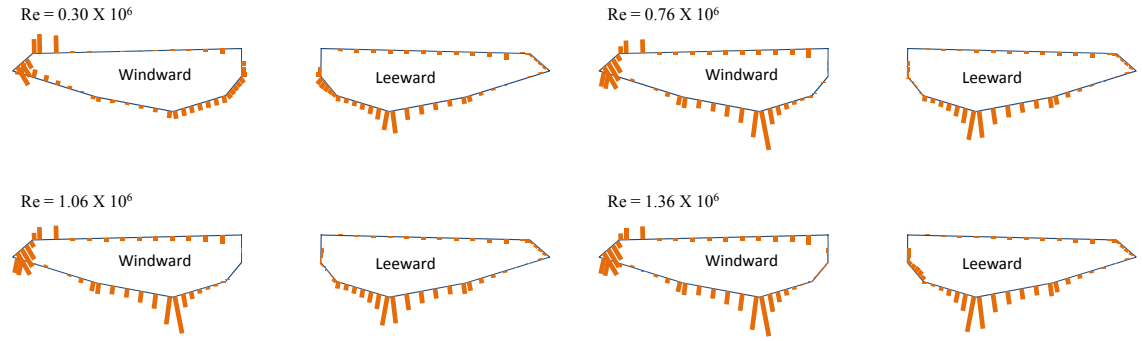

(b) Girder with safety rail (Case2)

Figure 5. Mean pressure coefficients at 0° angle of attack

3.3 *Aerostatic forces acting on each twin boxes*

The aerostatic force sharing ratios between windward box and leeward box are given in Figure 6 as a function of the Reynolds number. The forces were evaluated by integrating the measured pressures along girder sections. At the low Re in subcritical region, the windward box burdened the drag force mostly, yet the leeward box mostly burdened the lift force. It is interesting that the drag force and lift force acting on the leeward box were respectively negative and almost zero at subcritical region.

This unbalanced division of forces was gradually reduced at critical region, and then force ratio was almost equal in both sides of boxes at supercritical region of the Reynolds number. Figure 7 shows the aerostatic force coefficient and division ratio of forces between windward box and leeward box at supercritical region, Re=1.36×10^6. Accordingly it is reasonable to assume in design of twin box girder that the aerostatic forces acting on each boxes can be equally divided into the windward box and leeward box.

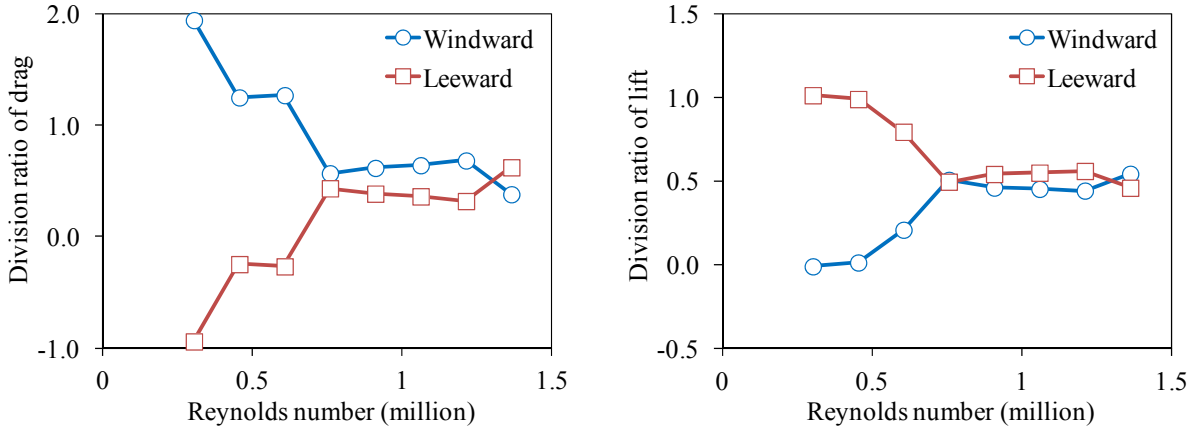

(a) Girder without safety rail (Case1)

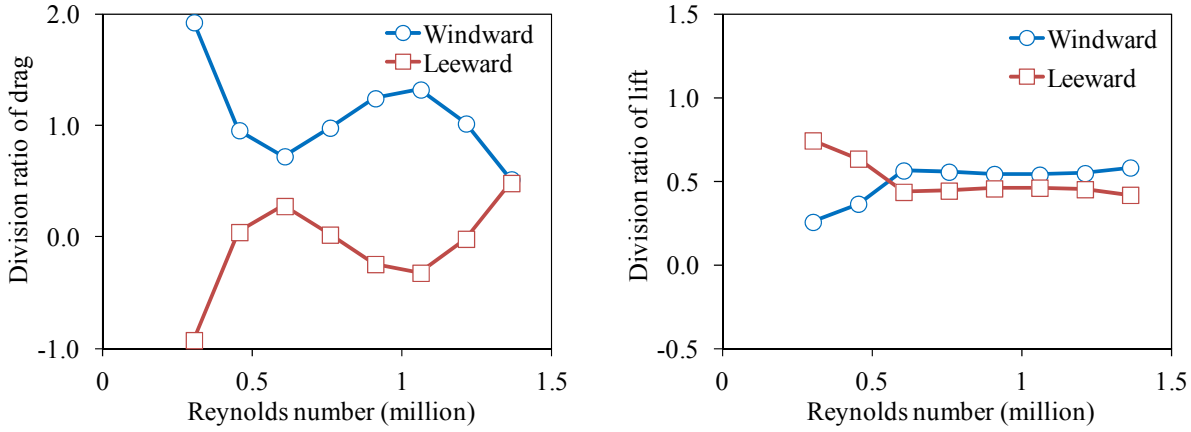

(b) Girder with safety rail (Case2)

Figure 6. Division ratio of aerostatic forces between windward box and leeward box according to Reynolds number

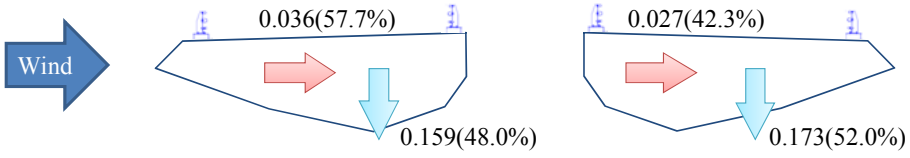

(a) Girder without safety rail (Case1)

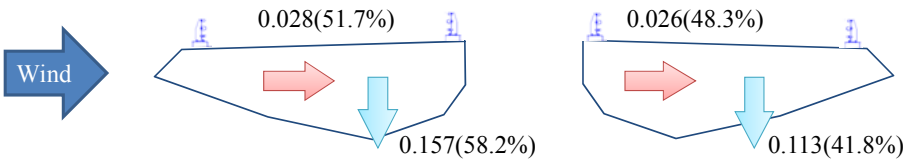

(b) Girder with safety rail (Case2)

Figure 7. Aerostatic force coefficients and division ratio at supercritical region ($Re=1.36\times10^6$)

4 CONCLUSIONS

The sensitivity of the Reynolds numbers on aerostatic force coefficients of twin box girder were investigated through ordinary section model tests and high speed tests at aeronautical wind tunnel. Main finding obtained from the tests are summarized as follows:

- The Reynolds number dependency of aerostatic force coefficients were observed at present streamlined twin box girder. The drag and lift coefficients revealed significant decrease of nearby 23% at supercritical region. This Reynolds number dependency was only observed at positive angles of attack (nose up) because of the safety rail.
- The boundary layer trip strip was found to reduce the Reynolds number dependency of aerostatic forces by fixing the location of flow transition. The trip strip can be used to simulate the flow structure at supercritical region in low wind speed.
- The pressure coefficients at bottom rear surface of windward box girder and at frontal face of the leeward box girder significantly changed as the Reynolds number increase because of variation of the locations of flow separation and transition.
- The windward and leeward box girders respectively burdened most of the drag force and lift force at subcritical region. This unbalanced division of forces at each box girder was gradually resolved, and both boxes almost equally divided the forces at supercritical region.

ACKNOWLEDGEMENT

This research was supported by the grant (11CCTI-A052604-04-000000) from the Ministry of Land, Transport and Maritime of Korean government through the Core Research Institute at Seoul National University for Core Engineering Technology Development of Super Long Span Bridge R&D Center.

REFERENCES

[1] Schewe G. and Larsen A., “Reynolds Number Effects in the Flow around a Bluff Bridge Deck Cross Section”, *Journal of Wind Engineering and Industrial Aerodynamics*, Elsevier, Vols. 74-76, 1998, pp. 829-838.

[2] Larose G., Larsen S.V., Larsen A, Hui M. and Jensen A.G., *Sectional Model Experiments at High Reynolds Number for the Deck of a 1018 m Span Cable-Stayed Bridge*. ICWE11, Lubbock, USA, 2003.

[3] Matsuda k., Cooper K.R., Tanaka H., Tokushige M., and Iwaski T., “An Investigation of Reynolds Number Effects on the Steady and Unsteady Aerodynamic Forces on a 1:10

Scale Bridge Deck Section Model", *Journal of Wind Engineering and Industrial Aerodynamics*, Vol. 89, 2001, pp. 619-632.

[4] Larose G. L. and D'auteuil A., "One the Reynolds Number Sensitivity of the Aerodynamics of Bluff Bodies with Sharp Edges", *Journal of Wind Engineering and Industrial Aerodynamics*, Vol. 94, 2006, pp. 365-376.

[5] Kwon S.D., Lee S.H., Uejima H., Lee M.J., and Kim J.H., "Aerodynamic Design of Kwangyang Suspension Bridge with Main Span 1545m", *BBAA VI*, 2008, pp. 89-92.

[6] Barlow J.B., Rae W.H., and Pope A., *Low-Speed Wind Tunnel Testing*, 3rd ed., John-Wiley & Sons, New York, 1999.

Superposability of the unsteady aerodynamic loads on bridge deck sections

Zhitian Zhang
Wind Engineering Research Center, Hunan University, Changsha, 410082, China.

ABSTRACT: The 2-dimensional unsteady aerodynamic forces are investigated from a point of view of whether these forces conform to the principle of linear superposition. It is shown that the basic preconditions, which lead to the linear superposability in cases of thin airfoil sections, are no longer valid for a bluff section. However, theoretical models in bridge aerodynamics, such as the one of flutter-buffeting analysis and those concerning aerodynamic admittance (AA) functions, always necessitate this superposability. The contradiction revealed in this literature may throw light on the perplexing problem of AA functions pertaining to the wind loads on bridge decks. Some theoretical AA models, which were employed rather extensively and derived from flutter derivatives according to interrelations resulted from thin airfoil theories, are demonstrated to a great extent to be illogical. Finally, with understanding of the linear superposability of the unsteady aerodynamic forces, suggestions in connection with experiment-based AA functions are presented in the last section.
KEYWORDS: bridge; unsteady; aerodynamic; superposition; buffeting; flutter

1 INTRODUCTION

Aerodynamic forces acting on bridge decks have generally been classified into steady and unsteady, according to whether or not the loads are time-varying. Unsteady loads in this context are distinguished from those of quasi-steady in whether they are dependent uniquely on the current state of motions (both structure and wind fluctuation) or on the whole motion histories [1]. Strictly speaking, both the motion-related and the turbulence induced aerodynamic forces are, to some extent, unsteady. The determination of aerodynamic response of a long flexible bridge involves the description of the mean wind loads, the motion induced loads (self-excited), and the turbulence induced loads. These three parts of aerodynamic loads are generally described with aerostatic coefficients, flutter derivatives and aerodynamic admittance (AA) functions respectively, and then, are linearly superposed according to the principle of linear superposition. However, it will be shown in the paper that a question arises as to whether these loads can be linearly superposed or, in other words, as to whether there exist a group of AA functions independent neither on the turbulent gust structure nor on the structural motions. That is the main concern of this literature.

2 FUNDAMENTALS OF BRIDGE AERODYNAMICS

The stochastic response of an elongated and flexible bridge structure to turbulent wind flow can be determined roughly by two classes of dynamic loads: (i) those due to wind-structure interactions, namely aeroelastic effects; (ii) those due to the wind speed fluctuations, including those inherent in the oncoming flow and those initiated by the body section itself.

Scanlan and Tomko [2] put forward a method to describe the self-excited loads for bluff sections put in smooth flow, which necessitates six experiment-based flutter-derivatives, functions of a dimensionless frequency. Later, Scanlan and Jones [3] expanded this method and expressed the lift and torque per unit span with eight flutter-derivatives, allowing for inclusion of the displacement terms, as below:

$$L_{ae} = \frac{1}{2}\rho U^2 B[KH_1^* \frac{\dot{h}}{U} + KH_2^* \frac{B\dot{\alpha}}{U} + K^2 H_3^* \alpha + K^2 H_4^* \frac{h}{B}] \quad (1)$$

$$M_{ae} = \frac{1}{2}\rho U^2 B^2 [KA_1^* \frac{\dot{h}}{U} + KA_2^* \frac{B\dot{\alpha}}{U} + K^2 A_3^* \alpha + K^2 A_4^* \frac{h}{B}] \quad (2)$$

where ρ is the air density, U the steady wind velocity, $K=B\omega/U$ the dimensionless frequency, ω the oscillation frequency, B the reference width of the deck section, $H_i^*(i=1\sim4)$ and $A_i^*(i=1\sim4)$ flutter derivatives, h the vertical motion, α the section rotation, $\dot{h}$ and $\dot{\alpha}$ the derivatives of h and α to real time t, respectively.

Though the part of aerodynamic load due to wind fluctuations is, strictly speaking, unsteady both for well-streamlined and bluff body sections, it is always given in quasi-steady form, as

$$D_b(t) = \frac{1}{2}\rho U^2 B\left(2C_D \chi_{Du} \frac{u(t)}{U} + C_D' \chi_{Dw} \frac{w(t)}{U}\right) \quad (3)$$

$$L_b(t) = \frac{1}{2}\rho U^2 B\left(2C_L \chi_{Lu} \frac{u(t)}{U} + (C_L' + C_D) \chi_{Lw} \frac{w(t)}{U}\right) \quad (4)$$

$$M_b(t) = \frac{1}{2}\rho U^2 B^2\left(2C_M \chi_{Mu} \frac{u(t)}{U} + C_M' \chi_{Mw} \frac{w(t)}{U}\right) \quad (5)$$

Where $u(t)$ and $w(t)$ are horizontal and vertical wind fluctuations, respectively; C_D, C_L, C_M are aerostatic drag, lift and torque coefficients; C_D', C_L', C_M' are the derivatives of C_D, C_L, C_M with respect to wind attack angle α; χ_{Du}, χ_{Dw}, χ_{Lu}, χ_{Lw}, χ_{Mu}, χ_{Mw} are the so-called aerodynamic admittances, functions of dimensionless frequency K, playing the role of connecting the wind fluctuations with the buffeting loads.

The most important assumption implied implicitly in Eqs. (3) to (5) is that the AA functions wherein are dependent uniquely upon the reduced frequency and therefore would not be affected by the turbulent gust structures, or, shapes of the curves of wind spectrum.

3 SUPERPOSABILITY OF WAKE EFFECTS

3.1 *Basic theory*

A general form describing the periodic motion of an airfoil with circular frequency ω is [5, 6]

$$w(\theta) = Ue^{i\omega t}\left\{A_0 + 2\sum_{n=1}^{\infty} A_n \cos n\theta\right\}, \quad (6)$$

where w is the vertical velocity distribution relative to the airflow along the chord of the airfoil, and the relationship between x and θ is $x = \cos\theta$.

The multiplier $e^{i\omega t}$ on the right side of Eq. (6) describes the periodic variation of the velocity with respect to time; the infinite series in the bracket expresses the modes of velocity distribution along the chord. The first five modes (x = -1 to 1) are plotted in figure 1. Especially, the term of A_0 denotes the mode of translatory oscillation where a uniform velocity distributed along the whole chord width; the term of A_1 denotes the mode of rotational oscillation where the velocity is proportional to x, the distance aft of the midpoint. The first two terms describe the rigid motion and the other higher-order terms allow the deformative motions.

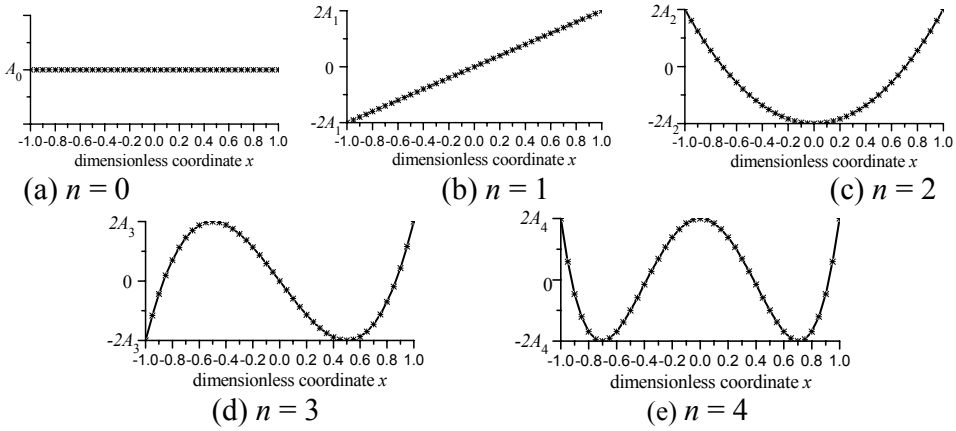

Fig. 1 Fundamental vertical distributions of the first five terms in Eq. (6)

It is worthy of mention that the resulted lift depends only on the first three coefficients in Eq. (6) and the moment on the first four, which means, for any given velocity distributions, the aerodynamic effects are embodied in these four terms. Sears [6] summarized the total lift and moment (about the midpoint) acting on a airfoil with chord length of B, corresponding to the general form of velocity expressed by Eq. (6), as

$$L = \pi\rho BU^2 e^{\mathrm{i}\omega t}\left\{(A_0 + A_1)C(k) + (A_0 - A_2)\cdot \mathrm{i}k/2\right\}, \tag{7}$$

$$M = (\pi/4)\rho B^2 U^2 e^{\mathrm{i}\omega t}\left\{A_0 C(k) - A_1[1 - C(k)] - (A_1 - A_3)\cdot \mathrm{i}k/4 - A_2\right\}. \tag{8}$$

where $k = B\omega/(2U) = K/2$, and $C(k) = K_1(\mathrm{i}k) / [K_0(\mathrm{i}k)+K_1(\mathrm{i}k)]$ is in accord with the Theodorsen circular function that was expressed in the original paper as [10]

$$C(k) = \frac{\displaystyle\int_1^\infty \frac{x_0}{\sqrt{x_0^2 - 1}} e^{-\mathrm{i}kx_0}\,dx_0}{\displaystyle\int_1^\infty \frac{x_0 + 1}{\sqrt{x_0^2 - 1}} e^{-\mathrm{i}kx_0}\,dx_0} = \frac{K_1}{K_0 + K_1}. \tag{9}$$

The Theodorsen circular function is commonly expressed in complex form as

$$C(k) = F_T(k) + \mathrm{i}G_T(k) \tag{10}$$

where $F_T(k)$ and $G_T(k)$ are real functions of the reduced frequency k.

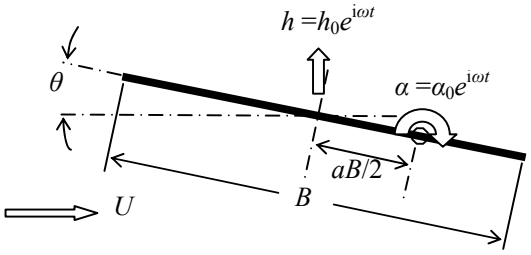

Fig. 2 Diagram show the rigid motion of the airfoil

3.2 *Rigid motion induced loads*

Considering a type of periodic rigid motion shown in figure 2, where the vertical motion is $h = h_0 e^{\mathrm{i}\omega t}$, the torsional motion is $\alpha = \alpha_0 e^{\mathrm{i}\omega t}$, $aB/2$ is the distance from the airfoil mid-chord to the oscillatory rotation point ($a > 0$ denote the location at the right half chord), the relative vertical velocity distribution of the mode shown in Fig. 1(b) in this case is

Reservation of A_0 and A_1 in Eq. (7) and (8) could result in the lift and moment immediately, as

$$L = -\pi\rho UBC(k)\left[U\alpha + \dot{h} + \frac{B}{2}\left(\frac{1}{2} - a\right)\dot{\alpha}\right] - \frac{\pi\rho B^2}{4}\left(U\dot{\alpha} + \ddot{h} - \frac{B}{2}a\ddot{\alpha}\right), \tag{11}$$

$$M_{1/2} = -\frac{\pi\rho UB^2}{4}C(k)\left[U\alpha + \dot{h} + \frac{B}{2}\left(\frac{1}{2} - a\right)\dot{\alpha}\right] + \frac{\pi\rho B^3}{16}\left[\dot{\alpha}U + \frac{B}{8}\ddot{\alpha}\right]. \tag{12}$$

It should be noted that the moment expressed by (12) is about the mid-chord point of the airfoil. The moment about the rotation point may be calculated by

$$\begin{aligned} M_a = M_{1/2} + L\cdot\frac{aB}{2} = &-\frac{\pi\rho UB^2}{2}\left(a + \frac{1}{2}\right)C(k)\left[U\alpha + \dot{h} + \frac{B}{2}\left(\frac{1}{2} - a\right)\dot{\alpha}\right] \\ &-\frac{\pi\rho B^2}{4}\left[\frac{aB}{2}\ddot{h} - \frac{B^2}{4}\left(a^2 + \frac{1}{8}\right)\ddot{\alpha} - \frac{BU}{4}\dot{\alpha} + \frac{BUa}{2}\alpha\right] \end{aligned}. \tag{13}$$

The lift and moment, i.e., Eqs. (11) and (13), are in accord with those reported in other literatures [7,9].

3.3 *Wind gusts induced loads*

A vertical gust that changes harmonically both in time and space could, if the coordinate axes are fixed to the airfoil, be described as a form of relative velocity distribution of the airfoil, as

$$w = We^{\mathrm{i}\omega(t - x/U)} = We^{\mathrm{i}\omega t}e^{-\frac{\mathrm{i}\omega x}{U}}, \tag{14}$$

the expressions of lift and moment can be simplified to

$$L = \pi\rho BUWe^{\mathrm{i}\omega t}\left\{[J_0(k) - \mathrm{i}J_1(k)]C(k) + \mathrm{i}J_1(k)\right\}, \tag{15}$$

$$M_{1/2} = L\cdot\frac{B}{4}, \tag{16}$$

where the Bessel functions $J_0(k)$ and $J_1(k)$ have the forms as bellow

$$J_0(k) = \frac{2}{\pi}\int_1^\infty \frac{\sin kx}{\sqrt{x^2 - 1}}dx, \quad J_1(k) = -\frac{2}{\pi}\int_1^\infty \frac{x\cos kx}{\sqrt{x^2 - 1}}dx. \tag{17}$$

Expression (15) can be rewritten in the notation of complex AA as

$$L = \pi\rho BUWe^{\mathrm{i}\omega t}\chi_s(k), \tag{18}$$

where

$$\chi_s(k) = F_s(k) + \mathrm{i}G_s(k) = [J_0(k) - iJ_1(k)]C(k) + \mathrm{i}J_1(k) \tag{19}$$

is the so-called complex Sears aerodynamic admittance function.

In the case of when the flow turbulence of broad-spectrum and steady stochastic, instead of a gust with a pure circular frequency ω, is encountered, the contributions of each gust component to the unsteady aerodynamic forces could be superposed linearly due to the potential flow around the section induced by gust components fulfill the principle of superposition. Thus, the power spectral density of L in this case can be obtained according to (19), as

$$S_L(k) = \left(\frac{1}{2}\rho UBC_L'\right)^2 |\chi_s|^2 S_w(k), \tag{20}$$

where S_w is the power spectral density of the vertical gust, $C_L' = dC_L/d\alpha = 2\pi$ is the differential of the lift coefficient with respect to wind attack angle α, $|\chi_s|^2 = F_s^2(k) + G_s^2(k)$ is known as the Sears admittance function which serves to link, for an airfoil, the spectrum of vertical gusting

velocity to that of associated lift [4].

In the case of when both the rigid motions and wind fluctuations are involved, the unsteady aerodynamic lift or torque acting on an airfoil section can, theoretically, be determined by the linear superposition of those determined by (11) and (15), or those by (12) and (16), respectively.

3.4 *Applications of superposability via indicial functions*

Another application of the superposability of unsteady aerodynamic loads in 2-D thin airfoil theory is that the resulted aerodynamic forces acting on a section in question due to arbitrary rigid motions or wind gusts could be expressed as convolution integrals over the time histories, resorting to a kind of so-called indicial functions. The general mathematic expression of the indicial function takes the form of

$$\varphi(s) = 1 - \sum_{1}^{i} a_i e^{-d_i s}, \tag{21}$$

Where $s=Ut/(2B)$ is dimensionlesstime, a_i, d_i are constants to be identified and $d_i > 0$.

Applying the following Fourier transform

$$\bar{f}(k) = \int_{-\infty}^{\infty} f(s) e^{-\mathrm{i}ks} ds, \tag{22}$$

to $\varphi'(s)$, the derivative of $\varphi(s)$ with respect to s, and then plus $\varphi(0)$ would yield

$$\varphi(0) + \overline{\varphi}' = 1 - \sum_{1}^{i} a_i + \sum_{1}^{i} \frac{a_i d_i^2}{d_i^2 + k^2} - \mathrm{i}k \sum_{1}^{i} \frac{a_i d_i}{d_i^2 + k^2}, \tag{23}$$

which will be employed for power spectrum analysis later in this paper.

3.4.1 *Wagner function*

One of the typical transient phenomena is, the lift acting on a flat-plate section due to an abrupt step-function change of the attitude of the section relative to the oncoming flow, a_0, would undergo a transient evolution described by

$$L(s) = \frac{1}{2} \rho U^2 B C_L' \alpha_0 \varphi(s), \tag{24}$$

where $C_L' = dC_L / d\alpha$, $\varphi(s)$ is an indicial lift-growth function.

If an arbitrary small rotation $\alpha(s)$ is encountered, the resulted lift would, according to the principle of superposition, be obtained with a convolution integral as

$$L(s) = \frac{1}{2} \rho U^2 B C_L' \int_{-\infty}^{s} \varphi(s-\sigma) \alpha'(\sigma) d\sigma, \tag{25}$$

where $\alpha'(\sigma) = d\alpha / ds$.

A change of variables and integration by parts in Eq. (25) would lead to

$$L(s) = \frac{1}{2} \rho U^2 B C_L' \left[\varphi(0)\alpha(s) + \int_{0}^{\infty} \varphi'(\sigma) \alpha(s-\sigma) d\sigma \right]. \tag{26}$$

3.4.2 *Kössner function*

Another typical transient phenomenon is associated with a flat-plate section entering a sharp-edged vertical gust. The lift evolution in this situation is described by

$$L(s) = \frac{1}{2} \rho U^2 B C_L' \alpha_0 \psi(s) \tag{27}$$

Where $\psi(s)$, different from the Wagner function, is the so-called Küssner function, of which an

excellent approximation was also offered by Jones [8], as

$$\psi(s) = 1 - 0.5e^{-0.13s} - 0.5e^{-s} \tag{28}$$

Now consider the section penetrating a gust of any form $w(s)$ of variable vertical velocity. In a similar way as that leading to equation (26), the lift in this case can be expressed as

$$L(s) = \frac{1}{2}\rho UBC_L'\left[\psi(0)w(s) + \int_0^\infty \psi'(\sigma)w(s-\sigma)d\sigma\right]. \tag{29}$$

4 PRINCIPLES FROM AIRFOIL THEORY TO BRIDGE AERODYNAMICS

4.1 *"Equivalent" indicial function*

Scanlan put forward a method trying to acquire the AA functions for bluff bridge deck sections from tested flutter derivatives [3, 9, 10]. This method is outlined in the following paragraphs.

Taking the lift for an example and considering the part due to vertical motion only, a replacement of α in eq. (26) by $\dot{h}/U$ and φ by φ_{Lh}, may lead to

$$L(s) = \frac{1}{2}\rho U^2 BC_L'\left\{\varphi_{Lh}(0)\frac{h'(s)}{B} + \int_0^\infty \varphi_{Lh}'(\sigma)\frac{h'(s-\sigma)}{B}d\sigma\right\}, \tag{30}$$

where $h' = dh/ds$ and $\varphi' = dh/ds$.

Applying the Fourier transform of (22) to Eq. (1) (Neglecting the terms of α and $\dot{\alpha}$) and to (30) would yield

$$4k(H_1^* - \mathrm{i}H_4^*) = C_L'\,[\varphi_{Lh}(0) + \overline{\varphi}_{Lh}'], \tag{31}$$

Other relations associated with rotation could be obtained in a similar way.

On the other hand, the connection between Küssner function and AA function, for example, the complex Sears AA function, may be resulted from the Fourier transform, as

$$\overline{L}(k) = \frac{1}{2}\rho UBC_L'[\psi(0) + \overline{\psi}']\overline{w} = \frac{1}{2}\rho UBC_L' \cdot \chi_{L'} \cdot \overline{w}, \tag{32}$$

where $\chi_{L'}$ is also a complex aerodynamic admittance function.

Scanlan assumed directly the equivalence between the Küssner function ψ and the Wagner function φ. Thus, according to (31) and (32), one obtain immediately [3]

$$\overline{L}(k) = 2\rho UBk[H_1^* - \mathrm{i}H_4^*]\overline{w} = \frac{1}{2}\rho UBC_L' \cdot \chi_{L'} \cdot \overline{w}. \tag{33}$$

Multiplying (33) by its complex conjugate yields the relation between the auto-PSD of the lift and that of the vertical gust:

$$S_{LL}(k) = (2\rho UBk)^2 \cdot \left[(H_1^*)^2 + (H_4^*)^2\right] \cdot S_{ww} = \left(\frac{1}{2}\rho UBC_L'\right)^2 \cdot |\chi_{L'}|^2 \cdot S_{ww}. \tag{34}$$

This yields immediately a bearing between the aerodynamic admittance and the flutter derivatives, as

$$|\chi_{L'}|^2 = 16k^2\left[(H_1^*)^2 + (H_4^*)^2\right]/(C_L')^2 = 4K^2\left[(H_1^*)^2 + (H_4^*)^2\right]/(C_L')^2. \tag{35}$$

Other AA functions associated with torsional motion or with resulted moment could be derived in a similar way as that of (35).

The vital question in such a methodology is whether or not $\dot{h} = e^{-\mathrm{i}\omega t}$ equals to $w = e^{\mathrm{i}\omega t}e^{-\mathrm{i}\omega x/U}$ as to the resulted aerodynamic effects. The answer is obviously negative.

We can see from what follows that the AA function so obtained would result in incorrect

power spectrum of the associated aerodynamic force component.

Considering only vertical translatory velocity in Eq. (11) and ignoring the apparent mass and quasi-steady terms would result in

$$L = -\pi\rho UBC(k)\dot{h} = -\frac{1}{2}\rho UBC_L' \cdot C(k) \cdot \dot{h} \tag{36}$$

The interrelation between the Theodorsen function and the indicial function can be resulted from a comparison of the Fourier transform of Eq. (36) to that of Eq. (30) for $\alpha = \dot{h}/U$, as [11]

$$C(k) = \varphi(0) + \overline{\varphi'}, \tag{37}$$

Thus, the following relationships could be established according to Eq. (10) and Eq. (23):

$$F_T(k) = 1 - a_1 - a_2 + \frac{a_1 d_1^2}{d_1^2 + k^2} + \frac{a_2 d_2^2}{d_2^2 + k^2} = 0.5 + \frac{0.0003416}{0.00207 + k^2} + \frac{0.03015}{0.09 + k^2}, \tag{38}$$

$$G_T(k) = -k\left[\frac{a_1 d_1}{d_1^2 + k^2} + \frac{a_2 d_2}{d_2^2 + k^2}\right] = -k\left[\frac{0.0075075}{0.00207 + k^2} + \frac{0.1005}{0.09 + k^2}\right], \tag{39}$$

Where $F_T(k)$ and $G_T(k)$ are the real and imaginary parts of the Theodorsen function. These lead immediately to

$$\lim_{k\to\infty}\left|\chi_T\right|^2 = \lim_{k\to\infty}\left[F_T^2(k) + G_T^2(k)\right] = \left(1 - \sum a_i\right)^2 = 0.25. \tag{40}$$

where $\left|\chi_T\right|^2 = F_T^2(k) + G_T^2(k)$ is recognized as Theodorsen aerodynamic admittance function [12].

In a similar way, the limit value of Sears AA function can be obtained as

$$\lim_{k\to\infty}\left|\chi_s\right|^2 = \lim_{k\to\infty}\left[F_s^2(k) + G_s^2(k)\right] = \left(1 - \sum a_i\right)^2 = 0 \tag{41}$$

The comparison of the Theodorsen and Sears AA functions is plotted in figure 3, where it can be seen that the relative discrepancy between the two curves increases rapidly with k.

Thus, the methodology of deriving AA functions by "equivalent" indicial functions would lead to a limit value of the AA functions determined by $(1 - \sum a_i)^2$, which is dependent on the identified parameters and therefore not necessary a zero value.

The essence of this incorrect can be ascribed to the introduction of an assumption that doesn't even hold in aeronautics to bluff sections (the equivalence between Küssner function and Wagner's indicial function). This is logically unacceptable.

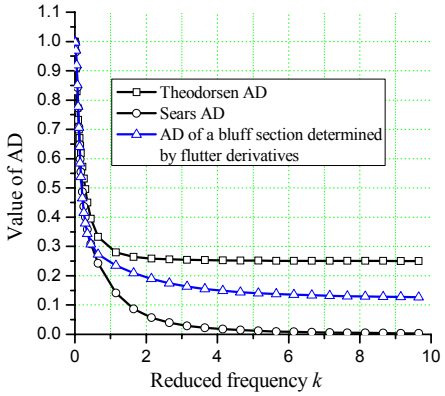

Fig. 3 Thoedorsen and Sears aerodynamic admittance

It is this nonzero limit characteristic of the above AA model that leads to a modification factor

to yield correct limit AA values [9,12], as

$$|\chi_{L'}|^2 = \frac{k^2}{(C_L')^2}\left[\left(H_1^*\right)^2 + \left(H_4^*\right)^2\right]\cdot R(c)\,, \tag{42}$$

Where

$$R(c) = \int_0^B\int_0^B \exp\left[-c_0\frac{\sigma_w}{U}n|x_1 - x_2|\right]dx_1dx_2 \tag{43}$$

is the introduced coefficient determined by the along-wind coherence of vertical gusting over the whole chord width, where B is the chord width, c_0 a constant reflecting the level of coherence, σ_w/U the turbulence intensity and n the frequency of turbulent component. Note that in this situation $R(c) \to 0$ when $n \to \infty$.

While the introduction of $R(c)$ provided the AA function with a correct limit value when k (or n) approaches to an infinite value, there still seems to be no way to provide a quantitative validation for such a model resulted from the combination of an illogical one and a quasi-steady factor based upon the wind coherence.

4.2 *"Equivalent" Theodorsen function*

A number of researchers also tried to determine the AA functions via flutter derivatives, as that proposed by Scanlan but in another point of view of "equivalent" Theodorsen function [13-16]. The main idea of this method is supposing Eq. (19), the bearing between Theodorsen circulation function $C(k)$ and Sears function $\chi_s(k)$, is applicable in bluff deck sections. Thus, according to (31), an "equivalent" indicial function can be identified through the experimentally obtained flutter derivatives, then a "equivalent" $C_{eq}(k)$ may be determined by Garrick's interrelation $C(k) = \varphi(0) + \overline{\varphi'}$, finally the "equivalent" Sears admittance function can be written according to (19) as

$$\chi_{eq,s}(k) = [J_0(k) - \mathrm{i}J_1(k)]C_{eq}(k) + \mathrm{i}J_1(k)\,. \tag{44}$$

This is logically incorrect either. As a matter of fact, according to Theodorsen's original paper [10], one may obtain

$$C(k) = F + \mathrm{i}G = \frac{-J_0(k) + \mathrm{i}Y_1(k)}{-[J_0(k) + Y_0(k)] + \mathrm{i}[Y_1(k) - J_0(k)]}\,, \tag{45}$$

where the integration of J_0 and J_1 are given out in Eq. (17), Y_0 and Y_1 were expressed in the original paper as

$$Y_0(k) = -\frac{2}{\pi}\int_1^\infty \frac{\cos kx}{\sqrt{x^2-1}}dx\,,\quad Y_1(k) = -\frac{2}{\pi}\int_1^\infty \frac{x\sin kx}{\sqrt{x^2-1}}dx\,. \tag{46}$$

Obviously, J_0, J_1, Y_0, Y_1 all are component functions included in the Theodorsen function $C(k)$. Thus, if one tries to use an "equivalent" form of $C(k)$ to describe aerodynamic characteristics of bluff sections, it warrants justification for component functions J_0 and J_1 remaining the original forms applied in aeronautics instead of "equivalent J_{eq0}" and "equivalent J_{eq1}".

5 EXPERIMENT-BASED AA FUNCTIONS

A number of researchers have experienced the method of determining the AA functions of bluff bridge deck sections through model tests in wind tunnel with certain turbulence characteristics [17-20]. This seems to be the only possible approach to date to deal with bluff sections, and the AA functions so-obtained are expected to be applicable to the buffeting assessment of the full

bridge immersed in various turbulent fields, as that of a thin airfoil. Such a methodology entails the AA functions being univariate functions of the reduced frequency k and, particularly being independent on the structural motion and the turbulent gust structure. This is true for an airfoil due to the assumption of potential flow around it always works, and also due to un-stationary aerodynamic forces resulted from rigid translation, rigid rotation, harmonic gusts, or an arbitrary combination of them can be treated separately and superposed linearly.

Thus, for a bluff body section, the critical problem is not whether the linear superposition principle still holds, but, for a given configuration, to what extent this principle can be considered to hold approximately. Some researches indicate that the AA functions of bridge deck do show dependence on the wind field characteristics (Matsuda, et al, 1999; Larose and Mann, 1998). But they failed to provide an explanation. Therefore, if experiments are designed in order to identify AA functions of a bridge deck section, the following two problems should be considered cautiously:

6 CONCLUSIONS

Theoretical investigation presented in this paper indicated that the linear superposability of the unsteady aerodynamic forces acting on a 2-dimensional section, which is applicable for a thin airfoil where wake effects are linear superposable, would not be valid for bluff bridge deck sections due to a series of hypotheses, such as the approximate linear distribution of the wake vortices, incompressible and inviscid flow, as well as potential flow around, etc., are no longer applicable. This directly throws doubt on some basic concepts underlying the current bridge aerodynamics, especially on, for a given deck configuration, the existence of AA functions dependent uniquely on reduced frequency. Some theoretical AA models, which have been obtained in essence according to the linear superposition principle and employed now rather extensively in bridge aerodynamics, are discussed in this literature and turn out to be, to a great extent, illogical. Thus, the superposability of the unsteady aerodynamic forces, or the level of this superposability could arrive at, should probably be a root factor relating to the issue of AA functions as well as to the flutter-buffeting theoretical model in bridge aerodynamics. Future work relating to this subject, the superposability of unsteady aerodynamic forces, will be experiment-based investigations aiming at deck configurations extensively employed in long-span bridges.

7 ACKNOWLEDGEMENTS

The authors would like to acknowledge the support of the National Science Foundation of China (Grant Number 90915002 and 51178182) to the work described in this paper.

8 REFERENCES

1 Dowell EH. A modern course in aeroelasticity, 4th Edition. Boston: Kluwer academic publishers; 2004.
2 Scanlan RH, Tomko JJ. Airfoil and bridge deck flutter derivatives. J Eng Mech, ASCE 1971; 97(EM6):1717-1737.
3 Scanlan RH, Jones NP. A form of aerodynamic admittance for use in bridge aeroelastic analysis. J Fluid Struct 1999; 13(7-8): 1017-1027.
4 Scanlan RH. Problematics in formulation of wind-force models for bridge decks. J Eng Mech, ASCE 1993; 119(7):1353-1375.
5 Karman Th V, Sears WR. Airfoil Theory for Non-Uniform Motion. J Aeronaut Sci 1938; 5(10):5-15.
6 Sears WR. Some aspects of non-stationary airfoil theory and its practical application. J Aeronaut Sci 1941; 8(3): 104-108.

7 Theodorsen T. General theory of aerodynamic instability and the mechanism of flutter. NACA Report 496, US Advisory Committee for Aeronautics, Langley, VA, USA. 1935.
8 Jones RT. The unsteady lift on a wing of finite aspect ratio. NACA report 681, US Advisory Committee for Aeronautics, Langley, VA, USA. 1940.
9 Scanlan RH. Motion-related body force functions in two-dimensional low-speed flow. J Fluid Struct 2000; 14(1): 49-63.
10 Scanlan RH. Bridge deck aeroelastic admittance revisited. J Bridge Eng, ASCE 2000; 5(1):1-7.
11 Garrick IE. On some reciprocal relations in the theory of nonstationary flows. NACA Report 629, US Advisory Committee for Aeronautics, Langley, VA, USA. 1938
12 Scanlan RH. Reexamination of sectional aerodynamic force functions for bridges. J Wind Eng Ind Aerodyn 2001; 89(14-15):1257-1266.
13 Hatanaka A, Tanaka H. New estimation method of aerodynamic admittance function. J Wind Eng Ind Aerodyn 2002; 90(12-15):2073-2086.
14 Hatanaka A, Tanaka H. Aerodynamic admittance functions of rectangular cylinders. J Wind Eng Ind Aerodyn 2008; 96(6-7):945-953.
15 Costa C. Aerodynamic admittance functions and buffeting forces for bridges via indicial functions. J Fluid Struct 2007; 23(3):413-428.
16 Costa C, Borri C, Olivier Flamand, O, Grillaud G. Time-domain buffeting simulations for wind-bridge interaction. J Wind Eng Ind Aerodyn 2007; 95(9-11):991-1006.
17 Larose GL, Tanaka H, Gimsing NJ, Dyrbye C. Direct measurements of buffeting wind forces on bridge decks. J Wind Eng Ind Aerodyn 1998; 74-76:809-818.
18 Larose GL, Mann J. Gust loading on streamlined bridge decks. J Fluid Struct 1998; 12(5):511-536.
19 Diana G, Bruni S, Cigada A, Zappa E. Complex aerodynamic admittance function role in buffeting response of a bridge deck. J Wind Eng Ind Aerodyn 2002; 90(12-15):2057-2072.
20 Matsuda M, Hikami Y, Fujiwara T, Moriyama A. Aerodynamic admittance and the ‘strip theory’ for horizontal buffeting forces on a bridge deck. J Wind Eng Ind Aerodyn 1999; 83(1-3):337-346.

The Seventh International Colloquium on Bluff Body Aerodynamics and Applications (BBAA7)
Shanghai, China; September 2-6, 2012

The influences of sectional parameters to aerodynamic performances of H-section hangers

M.G. Liu [a]; Z.Q. Chen [b]

[a]*State Key Laboratory of Subtropical Building Science, South China University of Technology, Guangzhou, Guangdong, China*
[b]*Wind Engineering Research Center, Hunan University, Changsha, Hunan, China*

ABSTRACT: An in-depth investigation on the H-section hangers' aerodynamic performances in forms of flutter, galloping and vortex shedding has been conducted through a series of wind tunnel tests. A total of 7 H-section models with different flange perforation ratio and depth-to-width ratio are tested to investigate their effects on aerodynamic behaviors of hangers, respectively. It is found that the flange perforation may enhance the aerodynamic capability against galloping and vortex resonance to some extent but have no obvious effects on flutter instability, at least for the shallow H-section with D/B=0.417 (flange depth D to web width B). The aerodynamic performances of H-sections could be significantly influenced by the increase of depth-to-width ratios. The results indicate the increase of depth-to-width is better than the flange perforation in resisting wind-induced vibrations of H-section hangers.

KEYWORDS: Hangers; H-sections; Wind-induced vibration; Flutter; Galloping; Vortex-induced vibration; Wind tunnel test.

1 INTRODUCTION

In recent years, slender hangers with H-sections are widely adopted in arch bridges built in China. In comparison with hangers with circular section, the H-section hanger is prone to variously wind-induced vibrations due to unfavorably aerodynamic shape. From the early 1970's large-amplitude wind-induced vibrations of H-shape have been observed in several arch bridges worldwide. Ulstrup[1] listed 9 episodes of wind-induced vibrations on slender bridge components. In the 1990's, the H-shaped hangers of Jiujiang Yangtze River Bridge built in China, suffered vortex-induced vibration at moderate wind shortly after completion of the bridge[2]. In August 2006, large-amplitude torsional vibrations of H-section hangers were observed in Dongping Bridge, which were characterized as torsional flutter through wind tunnel studies conducted by Chen and co-workers[3].

Many efforts have been made to study aerodynamic characteristics of H-sections in the past decades. Chi *et al*.[4] conducted wind tunnel tests of three typical H-sections with aspect ratios being approximately 1:1, 3:4 and 1:2, and they determined that the Strouhal numbers for these sections are in the neighborhood of 0.125~0.134. Chi & Vossoughi[5] predicted the vortex-induced response of H-section cylinders by a modified Hartlen-Currie model which needs to be calibrated with wind tunnel data. Maher & Wittig[6] investigated the vibration of H-shaped members of the Commodore Barry Bridge and its possible remedy countermeasures including modifying H sections into box sections and the uses of cable ties and perforated web. They concluded that vortex-excited vibration in heaving modes and torsional modes may build up for the H-sections studied and the vibration in the Commodore Barry Bridge is very likely to a kind of traditional Karman vortex shedding. Kubo *et al*.[7] studied the vortex-excited oscillation and galloping of H-section cylinders of Langer bridge, Japan, in both laminar and turbulent flow. They clarified that both vortex-induced vibrations and galloping may develop in the laminar flow, but

in the turbulent flow the former seldom takes place and the oscillation became mainly a galloping one. Ruscheweyh[8-9] developed a mathematical model for predicting the vortex-excited vibration, formulated taking into account the increasing correlation length of the exciting force with increasing vibration amplitude. Using this model, Ruscheweyh predicted the amplitudes of the vortex-excited bending vibration of several steel stacks and bridge hangers. The predicted amplitudes had been verified with full-scale measurements and the agreement is very good. This model had been included into Eurocode ENV 'Wind Action'. Ma *et al.*[10] studied the characteristics of galloping and vortex-induced vibration of H-section hangers, and they pointed that there were apparent effect on the galloping stability by changing the size/shape of web perforation in hangers.

Although H-sections are aerodynamically unstable, they are convenient in manufacture connection and maintenance and are frequently adopted in practice. It is therefore very important to study aerodynamic characteristics of H-sections from the point of view of its wind resistant design. More systematic studies of H-sections, including four section models with different web perforation ratios and 16 section models with different depth-to-width ratios, web and flange perforation ratios, were conducted to studying the performances of flutter, galloping and vortex-excited vibration by Chen & Liu[3, 11]. As a follow-up study, seven section models are conducted to studying the influence of flange perforation ratios and depth-to-width ratios on the aerodynamic performances of H-sections, respectively.

2 EXPERIMENT SETUP

2.1 *Model construction*

A prototype suspender is selected as a basic section for wind tunnel study of aerodynamic characteristics of H sections. The web is 1.2m wide and the flange is 0.5m deep. The depth-to-width ratio of the H-section is D/B=0.5/1.2=0.417, and the model is denoted as M0. On the basis of the model M0, two groups of models are designed and tested in wind tunnel, respectively. The sectional parameters of the models are provided in Table 1. The first group of section models haves the same depth-to-width ratio as the model M0, but with different flange perforation ratios (the flange perforation is a rectangular hole as shown in Figure 1, and perforation ratio is defined as the ratio of perforation area to the whole flange area before openings). The flange perforation ratios of these models are 11%, 20.1% and 28.6%, and these three models are named as A-1, A-2 and A-3, respectively. Another group with models named as B-1, B-2, B-3, respectively, have the same flange perforation ratios as the model M0, with different depth-to-width ratios of 0.625, 1.0 and 1.333, respectively.

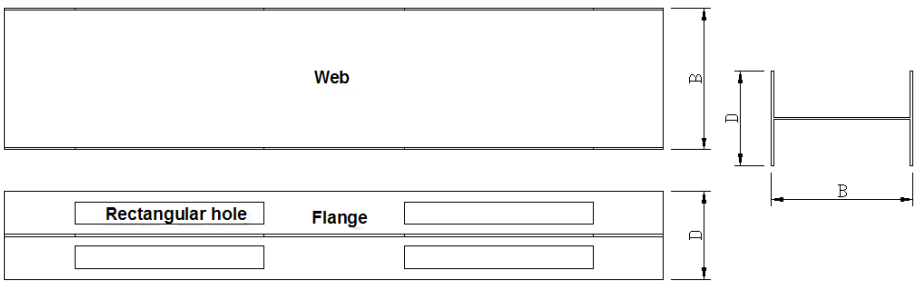

Figure 1 Cross-section parameters for H-section

Table 1 The prototype sectional parameters of the 7 models

Model	Width *B* (cm)	Depth *D* (cm)	Depth-to-width ratio *D*/*B*	Flange perforation ratio (%)
M0	120	50	0.417	0
A-1	120	50	0.417	11
A-2	120	50	0.417	20.1
A-3	120	50	0.417	28.6
B-1	120	75	0.625	0
B-2	120	120	1.0	0
B-3	120	160	1.333	0

2.2 *Experiment procedure*

All the wind tunnel tests are carried out in uniform flow at HD-2 wind tunnel of Hunan University. The section models are manufactured at 1:4 geometrical scale except model B-2 and B-3 with scale of 1:6. The dynamic modes of the hanger are analyzed with a finite element model using shell elements, the axial force applied on the prototype is considered as the initial stress effect, and the axial force for all prototype hangers is the same value. Table 2 summarized the main parameters of the seven prototype H-section hanger. The section models are elastically suspended in wind tunnel with 8 springs in the way that the ratio of torsional frequency to weak-axis-bending frequency is nearly the same ratio of the prototype's, as shown in Figure 2. Each spring is connected to a dynamometer to measure the vibration. The highest prototype wind speed for each section model testing is higher than 70m/, which is calculated as torsional mode. The definition of wind attack angle α is illustrated in Figure 3. The wind direction normal to the flange is defined as α=0°, and the direction perpendicular to the web is defined as α=90°. The tests are carried out for wind attack angles in the range of 0°~90° with an increment of 5°.

Table 2 Parameters of H-section hangers

Prototype parameters		M0	A-1	A-2	A-3	B-1	B-2	B-3
Mass (kg/m)		235.6	219.7	206.4	194.1	307.9	444.6	559.8
Mass moment (kg.m^2/m)		64.0	58.1	53.2	48.6	94.9	149.4	182.8
Frequency (Hz)	Weak-axis bending	1.901	1.891	1.888	1.849	2.462	3.766	5.094
	Torsion	2.175	2.160	2.132	2.033	2.684	3.614	4.063
	Strong-axis bending	6.057	5.943	5.786	5.580	6.174	6.198	6.108
Model parameters								
Wind speed ratio	Weak-axis bending	1:3.24	1:3.10	1:2.97	1:2.91	1:3.48	1:3.99	1:6.02
	Torsion	1:3.30	1:3.05	1:2.91	1:2.97	1:3.44	1:4.04	1:5.94
	Strong-axis bending	1:10.3	1:9.74	1:9.12	1:8.79	1:8.72	1:6.57	1:7.22
Damping ratio (%)	Bending	0.11	0.13	0.16	0.19	0.10	0.13	0.14
	Torsion	0.10	0.14	0.14	0.15	0.13	0.12	0.12

Figure 2 Section model suspended in wind tunnel

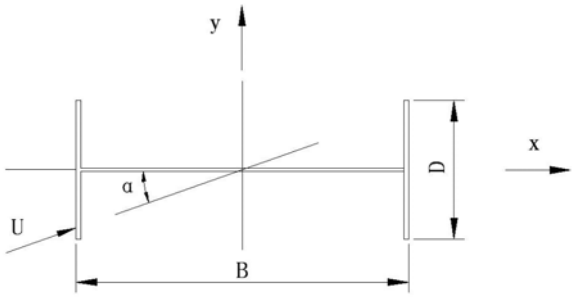

Figure 3 Definition of wind attack angle

3 RESULTS AND DISCUSSIONS

3.1 *Aerodynamic performance of model M0*

The flutter and galloping instabilities develop for the model M0, Figure 4 shows the prototype critical wind velocity of flutter and galloping under different attack angles. It is shown that galloping instability occurs at attack angles close to 0^o and 90^o, the corresponding critical wind speed is around 23.6m/s and 60m/s, respectively. Moreover, the flutter instability develops for wind attack angles from 20^o to 35^o, and the lowest critical wind speed is in the vicinity of 20m/s, a wind velocity being likely to occur in most parts of China. The criterion for flutter instability is taken as the mean square deviation of torsional amplitude being large than 0.5^o; this threshold is based on the Chinese design standard[12].

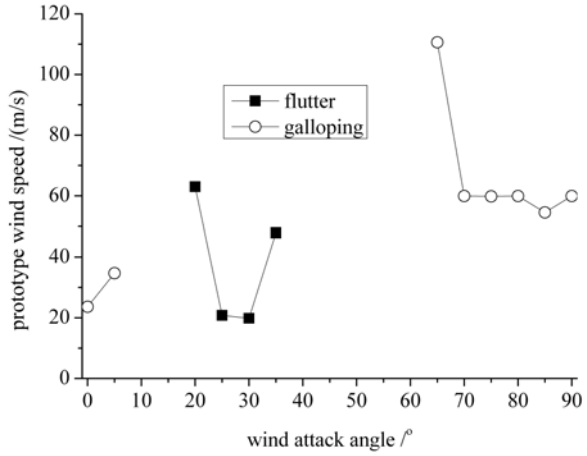

Figure 4 Flutter and galloping characteristics of model M0

Table 3 shows the vortex-induced vibration characteristics for model M0 for the wind attack angles from 0° to 90°. The wind speed and amplitude of vortex shedding response in Table 3 have been converted to full scale values. The permitting amplitude of vortex resonance is determined as[12]:

$$[h_a] = \frac{0.04}{f_b} \tag{1a}$$

$$[\theta_a] = \frac{4.56}{Bf_t} \tag{1b}$$

where $[h_a]$ and $[\theta_a]$ are the permitting amplitude for bending and torsion, respectively; f_b and f_t are the bending frequency and torsion frequency, respectively, and B is the width of H-section. the Strouhal number is calculated as:

$$St = \frac{fL}{V} \tag{2}$$

where f is the frequency of vortex-excited resonance; L is a characteristic dimension of the body projected on a plane normal to the mean flow velocity, defined as $L=D$ for $0^o \le \alpha \le 45^o$ and $L=B$ for $45^o < \alpha \le 90^o$; V is the velocity of the oncoming flow. From table 3, it is shown that: (1) the onset wind speed of vortex resonance at different angels is around 4-10.5m/s for bending and 8.6-21.5m/s for torsion, which is generally low value; (2) the lock-in wind speed of vortex resonance for bending is generally less than 3.3m/s. However, the wind speed of torsional vortex-induced vibration is large and the maximum is around 30m/s observed at attack angle of 20°; (3) the maximum amplitude for bending and torsion at different attack angles is 0.132B and 5.3°, respectively, which are both exceeding the permitting amplitude.

Table 3 Vortex resonance characteristics of model M0

Wind attack angle (°)	Wind speed (m/s)	Vibration type	Maximum amplitude	Permitting amplitude	Strouhal number
0	4.0-6.9	Bending	0.132B	0.018B for weak-axis bending	0.238
	8.6-10.5	Torsion	1.1°		0.126
	19.1-22.2	Torsion	5.1°		0.057
5	4.9-6.9	Bending	0.073B		0.194
	17.5-32.1	Torsion	5.2°	1.8° for torsion	0.062
15	13.4-20.1	Torsion	4.6°		0.081

20	16.8-20.7	Torsion	3.6^{o}	0.065
	21.5-57.4	Torsion	5.3^{o}	0.051
30	10.5-13.8	Bending	0.022*B*	0.091

In order to facilitate comparison the vortex-induced vibration characteristics of H-section with different sectional parameters, a normalized value *R* which is used to evaluate the vortex resonance, considering the influence of onset wind speed, lock-in wind speed and maximum amplitude, is determined using:

$$R = \sum_{i=1}^{n} \frac{\Delta V_i}{V_i} \cdot \frac{A_i}{[\cdot]} \tag{3}$$

where ΔV, A and V are the lock-in wind speed, maximum amplitude and onset wind speed at a certain vortex-induced vibration; [.] is the permitting amplitude calculated using equations (1a) and (1b); n is the total number of the vortex resonance. From the expression (3), it is shown that the greater the index value *R*, the worse the performance of vortex-induced vibration. The normalized *R* for model M0 is 17.5.

3.2 *Effect of flange perforation ratios*

Torsional flutter and galloping instability is observed for all the models under different wind attack angles. Table 4 summarizes the ranges of wind attack angle and the prototype critical wind velocities. Compared with the model M0, the attack angles occurring torsional flutter increase for the three models with flange perforation, and the flange perforation does not visibly promote the flutter critical wind speed of H-sections. These results conclude that flange perforation has little effect on the flutter performance of H-section hangers.

As seen in Table 4, flange perforation has different impact of the galloping instability for weak axis and strong axis. For the model A-1, the galloping instability still appear at 0^{o} and 5^{o} (weak axis) with a little increasing in critical wind speed compared with model M0. For the model A-2 and A-3, no galloping instability occurs at weak axis. It is concluded that the galloping performance for the weak axis of H-sections is much improved by flange perforation. However, the flange perforation only promote the attack angles occurred galloping instability rather than the critical wind speed.

Table 4 Flutter and galloping characteristics of H-section hangers with different flange perforation ratios

Model		Wind attack angle	Lowest prototype wind speed	Reduced wind speed *V/fB*
M0	Flutter	20^{o}-35^{o}	19.8m/s	7.6
	Galloping	0^{o}-5^{o}	23.6m/s	10.3
		65^{o}-90^{o}	54.5m/s	7.5
A-1	Flutter	10^{o}-35^{o}	24.5m/s	9.5
	Galloping	0^{o}-5^{o}	27.0m/s	11.9
		70^{o}-90^{o}	51.7m/s	7.3
A-2	Flutter	0^{o}-25^{o}	14.3m/s	5.6
	Galloping	80^{o}-90^{o}	36.6m/s	5.3
A-3	Flutter	0^{o}-25^{o}	21.0m/s	8.6
	Galloping	80^{o}-90^{o}	46.7m/s	7.0

Table 5 shows the vortex-induced vibration characteristics of the three H-section models for the wind attack angles from 0^{o} to 90^{o}. It is concluded that: (1) for the model A-1 with small flange perforation, the vortex-induced resonance occurs mainly in the weak axis, which is similar to model M0. For the model A-2 and A-3 with large flange perforation, vortex induced vibra-

tion occur both in the weak axis and strong axis; (2) the attack angle interval occurred vortex resonance for model A-3 with flange perforation ratio of 28.6% is less than other models'; (3) the wind velocity of vortex-induced vibrations is less than 10m/s, not improved compared with the model M0; (4) the flange perforation can improve the maximum amplitude in the weak axis, but no effect is found to reducing the amplitude in torsion and strong axis; (4) the normalized *R* is declined with the flange perforation gradually increasing, it is shown that flange perforation play a beneficial role in improving the vortex vibration performance of the H-section hangers.

Table 5 Vortex resonance characteristics of H-section hangers with different flange perforation ratios

Model	Wind attack angle (^{o})	Bending vortex resonance				Torsional vortex resonance				*R*
		Wind speed (*m/s*)	Maximum amplitude	Permitting amplitude	Strouhal number	Wind speed (*m/s*)	Maximum amplitude	Permitting amplitude	Strouhal number	
A-1	0	5.0-5.8	0.088*B*	0.018*B*	0.189	6.5-9.9 10.6-23.2	4.3^o 5.3^o	1.8^o	0.167 0.102	18.5
	5	4.1-5.9	0.072*B*		0.231	7.1-11.5 12.0-23.2	4.1^o 5.2^o		0.154 0.091	
	10	/	/		/	12.9-34.8	4.8^o		0.083	
	15	/	/		/	14.4-24.8	4.8^o		0.074	
	20	12.2-12.3	0.004*B*		0.077	18.2-21.4	2.1^o		0.060	
	25	13.7-14.5	0.003*B*		0.069	/	/		/	
A-2	0	/	/	0.018*B*	/	6.1-12.8	4.2^o	1.8^o	0.174	12.0
	5	4.8-5.5	0.027*B*		0.198	6.2-6.3 7.1-11.3	1.8^o 5.0^o		0.174 0.149	
	10	5.1-5.5	0.005*B*		0.189	7.4-24.9	5.1^o		0.144	
	70	50.9-57.8	0.005*B*		0.137	/	/		/	
	75	48.1-52.7 66.6-76.2	0.006*B* 0.006 *B*	0.006*B*	0.145 0.104	/	/		/	
	85	36.7-48.1	0.007*B*		0.189	/	/		/	
A-3	0	4.5-5.7	0.018*B*	0.018*B*	0.208	6.8-17.8	5.2^o	1.9^o	0.149	10.1
	5	4.5-5.0	0.015*B*		0.208	7.3-19.4	5.4^o		0.139	
	70	51.8-56.2	0.004*B*	0.006*B*	0.130	/	/		/	
	75	51.3-69.4	0.007*B*		0.130	/	/		/	

3.3 *Effect of depth-to-width ratios*

Table 6 summarizes the ranges of wind attack angle, the prototype critical wind velocities and the reduced wind speed for flutter and galloping. Compared with the model M0, the critical wind speed of flutter for the three models B-1, B-2 and B-3 is much improved and about one times higher than M0'. However, as seen in Table 6, the critical wind speed is not varied with the depth-to-width ratios changing from 0.625 to 1.333. Additionally, the ranges of wind attack angle for model B-2 and B-3 is much smaller than the model M0 and B-1. It is concluded that the increase of depth-to-width ratios have positive effect in stabilizing the flutter of H-sections.

Form the Table 6, it is shown that increasing the depth-to-width ratios notably improves the galloping performances in strong axis, namely enhancing the critical wind speed and reducing the attack angle intervals occurred galloping instability. Nevertheless, the increase of depth-to-width ratios can promote the critical wind speed while enlarging the attack angle intervals in the weak axis.

Table 6 Flutter and galloping characteristics of H-section hangers with different depth-to-width ratios

Model		Wind attack angle	Lowest prototype wind speed	Reduced wind speed *V/fB*
M0	Flutter	20^o-35^o	19.8m/s	7.6

	Gallop-	0^o-5^o	23.6m/s	10.3
	ing	65^o-90^o	54.5m/s	7.5
	Flutter	15^o-40^o	39.2m/s	12.2
B-1	Gallop-	0^o-10^o	22.4m/s	7.6
	ing	75^o-90^o	59.5m/s	8.0
	Flutter	15^o; 75^o	38.8m/s	8.9
B-2	Gallop-	0^o-10^o	39.4m/s	8.7
	ing	80^o-90^o	69.6m/s	9.4
	Flutter	75^o-80^o	44.5m/s	9.1
B-3	Gallop-	0^o-20^o	57.6m/s	9.4
	ing	85^o-90^o	80.1m/s	10.9

Table 7 shows the vortex-induced vibration characteristics of the three H-section models for the wind attack angles from 0^o to 90^o. These results concluded that: (1) the ranges of attack angle is significantly more than the model M0. For the model B-1, vortex induced vibration develop for 12 of the 19 wind attack angles; (2) bending motions of vortex-induced vibrations dominate for the models with $H/B \geq 0.625$, and the three models develop torsional motions at a certain wind attack angle; (3) most of the onset wind speed of vortex-induced vibrations for model B-1 is less than 10m/s. For the models B-2 and B-3, the lowest wind velocity is around 30m/s; (4) most of the maximum amplitude of vortex resonance for model B-1 are below the permitting amplitude, which is notably improvement compared with the model M0. However, for the model B-2 and B-3, the maximum amplitude appear to deteriorate with the depth-to-width ratios increasing; (5) the normalized R of model B-1 is only 1.7, but for the model B-2 and B-3, the values are 8.4 and 12.8, respectively. It is concluded that the modest depth-to-width have positive effect in stabilizing the vortex resonance of H-sections.

Table 7 Vortex resonance characteristics of H-section hangers with different depth-to-width ratios

Model	Wind attack angle (^{o})	Bending vortex resonance				Torsional vortex resonance				R
		Wind speed (m/s)	Maximum amplitude	Permitting amplitude	Strouhal number	Wind speed (m/s)	Maximum amplitude	Permitting amplitude	Strouhal number	
	0	5.5-6.3	0.016B		0.336	8.2-11.7	0.5^o		0.250	
	5	5.7-6.4	0.009B		0.324	9.4-13.5	0.2^o		0.216	
	10	4.3-5.2	0.001B		0.429	/	/		/	
	15	4.5-5.1	0.005B		0.410	/	/		/	
	20	5.5-6.4	0.001B		0.336	/	/		/	
	25	6.6-7.6	0.001B	0.014B	0.455	/	/		/	
B-1	30	7.7-8.6	0.001B		0.385	/	/	1.4^o	/	1.7
	35	9.3-10.1	0.001B		0.202	/	/		/	
	40	15.1-17.7	0.004B		0.123	/	/		/	
		25.6-27.4	0.005B		0.192					
	45	27.4-34.6	0.017B		0.067	/	/		/	
	85	41.9-50.7	0.006B	0.005B	0.175	/	/		/	
	90	44.5-50.9	0.012B		0.167	/	/		/	
	10	/	/		/	39.9-50.5	3.1^o		0.109	
	20	35.6-38.7	0.155B		0.126	/	/		/	
	25	40.7-42.7	0.213B	0.009B	0.111	/	/	1.1^o	/	8.4
B-2	40	52.3-55.5	0.347B		0.086	/	/		/	
	45	53.5-59.5	0.175B		0.085	/	/		/	
	80	/	/		/	40.8-45.2	2.9^o		0.106	
B-3	0	38.2-54.0	0.053B	0.007B	0.215	/	/	0.9^o	/	12.8
	5	41.7-54.2	0.051B		0.196	/	/		/	
	10	48.0-54.3	0.040B		0.171	/	/		/	
	15	63.8-66.8	0.056B		0.128	/	/		/	
	35	81.5-93.1	0.150B		0.120	/	/		/	

40	89.5-96.7	0.069*B*		0.109	/	/	/
45	85.2-96.7	0.059*B*		0.115	/	/	/
50	89.5-96.7	0.062*B*		0.082	/	/	/
55	93.1-100.3	0.030*B*		0.079	/	/	/
85	/	/	0.006*B*	/	29.1-74.3	3.1°	0.167
90	/	/		/	29.1-35.1 50.6-60.0	2.4° 3.4°	0.167 0.096

4 CONCLUSIONS

A series of experimental study of wind-induced vibrations of vertical flexible hangers with H-sections for different flange perforation ratios and depth-to-width ratios is carried out using section models. The main conclusions from this study are as follows:

(i) flange perforation can enhance the aerodynamic capability against galloping and vortex induced vibration;

(ii) the increase of depth-to-width ratios significantly improves the aerodynamic performances except the vortex resonance, which gives a best vortex shedding capability with depth-to-width ratio D/B=0.625;

(iii) the increase of depth-to-width is better than the flange perforation in resisting wind-induced vibrations.

5 ACKNOWLEDGEMENTS

This study is supported by the Fundamental Research Funds for the Central Universities, SCUT (No. 2009ZM0110), and is supported by Hunan Province Key Lab of Wind Engineering and Bridge Engineering, Hunan University.

6 REFERENCES

1 C.C. Ulstrup, Aerodynamic lessons learned from individual bridge members, Annals of the New York Academy of Sciences, 288 (1980) 265-281.
2 L. Yu, J.J. Gu and Z.X. Wang, Experimental study of vortex-induced oscillation for the booms on large bridge, Journal of Mechanical Strength, 18 (1996) 16-20 (in Chinese).
3 M.G. Liu and Z.Q. Chen, Experimental Study on Aerodynamic Stability of H-Shaped Hangers with Different Sizes of Web Holes, Journal of Vibration and Shock, 27 (2008) 30-34(in Chinese).
4 M. Chi, E. Neal and B G. Dennis, Determination of Strouhal Characteristics and power Spectrum for Elastically Restrained H-Shape Sections, Federal Highway Administration, Washington, D.C. Office of Research, 1977, 85 pages.
5 M. Chi and J. Vossoughi, Response of slender structural members in self-excited oscillation, Journal of Sound and Vibration, 101 (1985) 75-83.
6 F.J. Maher and L.E. Wittig, Aerodynamic Response of Long H-Sections, Journal of the Structural Division, ASCE, 106 (1980) 183-198.
7 Y. Kubo, K. Sakurai and S. Azuma, Aerodynamic characteristics of H-shaped section cylinder in laminar and turbulent flows, Memoirs of the Kyushu Institute of Technology, Engineering, 10 (1980) 1-14.
8 H. Ruscheweyh, Practical Experiences with wind-induced vibrations, Journal of Wind Engineering and Industrial Aerodynamics, 33 (1990) 211-218.
9 H. Ruscheweyh, Vortex-excited vibrations and galloping of slender elements, Journal of Wind Engineering and Industrial Aerodynamics, 65 (1996) 347-352.

10 C.M. Ma , H.L. Liao, S.X. Zheng and J.S. Li, Wind tunnel experiment on the aerodynamic performances of H-shaped booms, China Railway Science, 36 (2005) 42-46 (in Chinese).
11 Z.Q. Chen, M.G. Liu, G.D. Liu and Z.J. Jin, Wind-induced vibration and wind-resistant design of H-shaped suspenders under large attack angle, China Civil Engineering Journal, 43 (2010) 1-11(in Chinese).
12 JTG/TD60-01-2004 Wind-resistent Design Specification for Highway Briders. Beijing: China Communications Press, 2004. (in Chinese)

Messina strait bridge - confirmatory wind tunnel testing of the bridge towers

S. Stoyanoff, P.O. Dallaire, and J. Garber, RWDI
A. Zasso, G. Diana, Politecnico di Milano
E. Vullo, Stretto di Messina
D. Khazem, K. Serzan, Parsons

1. Introduction: As a part of Messina Strait Bridge design, a confirmatory wind tunnel test was undertaken by RWDI on a 1:100 scale aeroelastic mode. The model was designed based on drawings provided by COWI and structural dynamic information analyzed by Parsons Transportation Group (PTG), the Project Management Consultants for the Stretto di Messina Project. This large model (4 m tall) allowed physical modeling of tuned mass dampers and simulations of a wide range of additional damping. Tested Re range was 1×10^5-3.5×10^5 in smooth flow. The aeroelastic model test was supplemented with a sectional model test in scale 1:100 at Re 2×10^4-2×10^5.

The aeroelastic model test focused on "Free-Standing" and "In-Service" towers configuration. Being confirmatory, the tests were limited in scope compared to the breadth of the original tests carried out by the Project Contractors Eurolink (EIK) The confirmatory tests found various wind induced instabilities that will need to be mitigated both "In-Service" tower configuration and during construction.

2. Aeroelastic Model Tests

The objective of the wind tunnel investigation was to verify the fundamental aerodynamic stability of the structure in smooth flow and to compare against the results obtained by EIK. A 1:100 scale multi-degree-of-freedom (Figure 1) aeroelastic model of the standalone tower was designed and built to simulate the aerodynamically important tower modes as computed by Parsons. The results of the aeroelastic model test were converted to full scale response predictions by application of appropriate scaling factors.

The aeroelastic model was composed of a spine and shell system, to provide the required structural stiffness, the inertial properties, and the geometric shape. For the legs, the spine consisted of a hollow rectangular steel tube over the first 2/3 of height where a splice system connects it to an aluminum rectangular

Figure 1: Tower 1:100 aeroelastic model, In-Service configuration.

tube extending to the tower top. The two lower crossbeam spines consisted of machined steel H-beams whereas the upper crossbeam spine was a machined H-beam made from aluminum. The upper portion of the leg spine was required to be made of aluminum for the selected damping mechanism and due to mass requirements. The exterior geometry of the shell was hand- built using a strong foam core with smooth finish, thin wood diaphragms and robust plywood seats (Figure 2). The top shell of each leg was built utilizing the stereo lithography modeling technique which uses an epoxy resin. The shell was separated into multiple segments, with small air gaps in between of about 2 mm. All gaps were taped with a soft, elastic tape to ensure air tightness of the model without influencing its mechanical properties. The shell segments were painted, sanded and polished to ensure a very smooth finish with the least possible imperfections which possibly could trigger an early transition into critical Re regime.

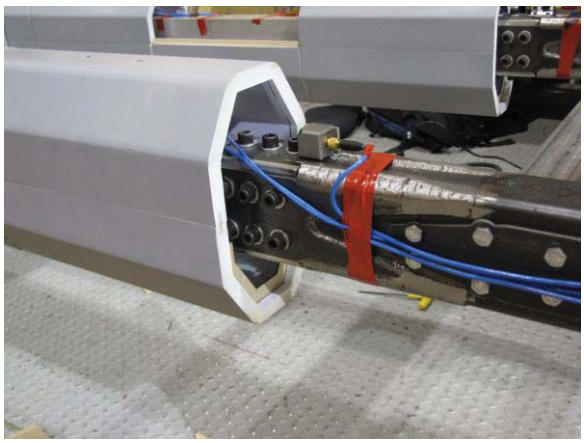

Figure 2: Model details – spine & shell, 3-axial accelerometer

The mass and its distribution on the model were designed to meet the similarity requirements for the generalized mass based on the provided full scale mass information. This was achieved by augmenting the mass of the spine and shell system with lumped masses where required.

To represent the tower in its In-Service condition, a system consisting of an aluminum spine extension and tensioned steel cables mounted at the top of the Free-Standing tower was designed to simulate the first longitudinal and torsional modes. This design was also verified by carrying out a finite element dynamic analysis on the overall structure. The measured mode shapes were in good agreement with the targets (Figures 3). Note that the In-Service model did include the necessary additional stiffness to replicate the targeted mode shapes for the longitudinal direction. The In-Service condition transverse modes were not simulated in terms of generalized mass since they would entail significant additional mass from the main cable and deck motions. The intent of replicating this given configuration was to study the across-wind vortex shedding vibrations (stability) alone, considering the transverse modes not being a problem for the bridge in service.

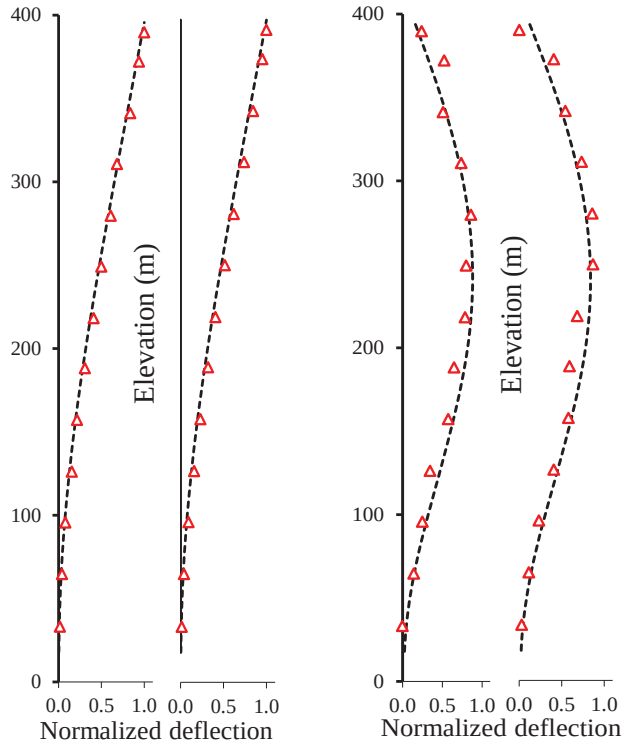

a) Free-Standing tower b) In-Service tower

Figure 3: Mode Shapes - Analytical vs. Model (1st mode comparisons)

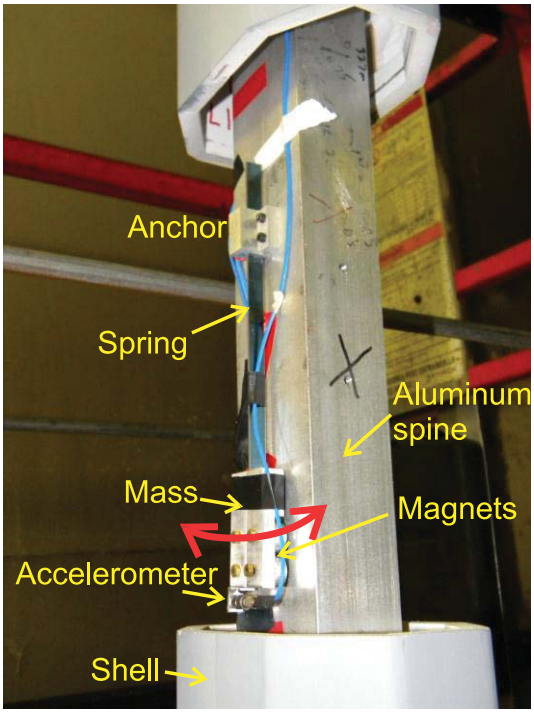

Figure 4: Tune Mass Damper installed on model spine.

To allow for damping variation in the fundamental modes of vibration being studied, tuned-mass dampers (TMD) were designed and built based on the Eddy current mechanism where the relative motion of a magnetic field in a conductor dissipates energy (Figure 4). By introducing an aluminum spine over the upper portion of the tower legs, the spine itself became the conductor able to dissipate energy. Multiple TMDs were attached to the spine representative of the behavior of general inherent structural damping, in the range from about 0.5% to 3.3% of critical. The model without dampers had very low inherited damping in the range of about 0.1% being close to linear over a wide range of amplitudes. Each TMD was made from spring steel flexures supporting an aluminum block where 4 magnets were fixed. Due to internal modeling constraints, the dampers were located at 3 discrete heights, corresponding to full scale elevations of approximately 280m, 310m and 340m. At each of these heights, up to 4 TMDs were installed and tuned to the desired frequencies. The dampers were also constrained by the internal void space in the shells, requiring the selection of an over-damped type system to limit the TMD motions. Based on the above considerations, the dampers were designed with an active mass of 94.5

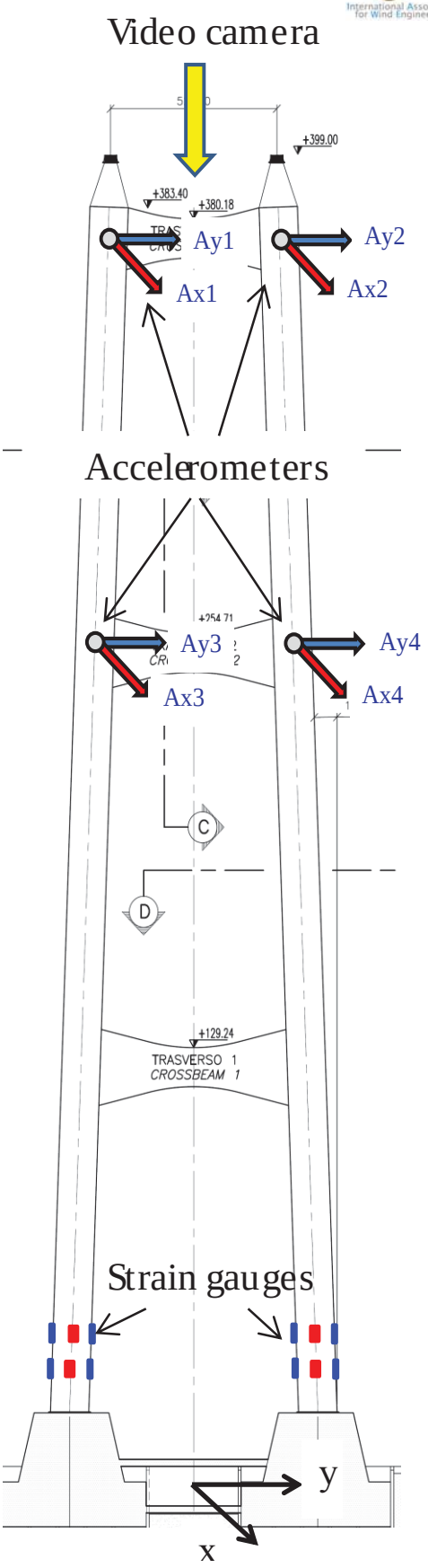

Figure 5: Instrumentation package

grams each. For the Free-Standing tower configuration, the TMD frequency was set to be equal to the fundamental longitudinal model frequency (4.45 Hz), and the TMD damping ratio was set to approximately 17% of critical. By selecting 1 to 4 TMDs located at the available mounting positions, variation in damping levels was achieved. The same devices were applied on the In-Service tower where the TMD damping ratio was approximately 6%. Note that in this case, TMDs were used to increase simultaneously the damping for the longitudinal and torsional modes (16.3 Hz and 19.4 Hz). The damping of the various modes of vibration was measured in off-wind conditions, using the free vibration decay method, and was found to be linear over a wide range of amplitudes for most of the tested cases; slightly un-tuned TMDs resulted in beating effects which were observed in the free decay signals. Even in this case, where both the model and the dampers exhibited damping linear to the amplitude, fitting the response envelope was possible to reliably estimate the actual damping of the system. The model was instrumented with four tri-axial accelerometers mounted on the tower leg spines above the middle cross beam (elevation 259.9 m) and at the top cross beam (elevation 372.2 m), to measure accelerations in the horizontal plane in x and y directions. Strain gauges were installed on the leg spines, at elevations of 33.7 m and 64.2 m, to measure bending moments about axes x and y. Figure 5 shows the selected coordinate system and the instrumentation locations.

The wind tunnel test took place at the 3 m x 6 m Propulsion and Icing Wind Tunnel of the NRC-IAR Aerodynamics Laboratory. This wind-tunnel has an open-circuit layout with a test section of 3.1 m x 6.1 m cross section with a 12.2 m length. The fan is normally driven electrically (750 kW) but high-speed operation (up to 70 m/sec) can be accommodated by a gas turbine drive system (6,000 kW). The minimum wind speed is about 4 m/sec when outside atmospheric winds are calm whereas the maximum speed that can be reached is around 35 m/sec on the electrically driven fan alone.

The model was mounted at the centre of a 25 mm thick steel turning disc to allow variation of the wind direction. For all tested stability runs, uniform and smooth flow was simulated. Under this uniform, smooth-flow like conditions, the background turbulence level in the wind tunnel is approximately 0.5% to 1.0%. The signals from the accelerometers, strain gauges and propeller anemometers, were collected at 250 Hz for 90 seconds at each measurement point and the data was low pass filtered at 80 Hz prior to A/D conversion. The data acquisition system also acquired the ambient temperature, pressure, and relative humidity, as well as the reference pitot-static wind-speed. The primary intent of the study was to identify any fundamental aerodynamic phenomenon in the range from about 10 m/sec up to about 75 to 80 m/sec at full scale. The following scaling principles have been used for this study:

$[\text{Dimension}]_m = [\text{Dimension}]_p \times 100^{-1}$	(geometry)
$[m]_m = [m]_p \times 100^{-3}$	(lumped mass)
$[m_L]_m = [m_L]_p \times 100^{-2}$	(mass per unit length)
$[\zeta]_m = [\zeta]_p$	(structural damping ratio)
$[V]_m = [V]_p \times [f]_m \times [f]_p^{-1} \times 100^{-1}$	(wind speed)
$[\delta]_m = [\delta]_p \times 100^{-1}$	(displacement)
$[A]_m = [A]_p \times [f]_m^2 \times [f]_p^{-2} \times 100^{-1}$	(acceleration)
$[F]_m = [F]_p \times [f]_m^2 \times [f]_p^{-2} \times 100^{-4}$	(force)
$[M]_m = [M]_p \times [f]_m^2 \times [f]_p^{-2} \times 100^{-5}$	(moment)

where "p" designates the prototype (i.e., full scale) and "m" the model. Since it is not critical to follow Froude scaling for vertical structures such as the current stand alone bridge tower (except for the secondary P-Delta effects) the Froude number scaling was not applied for optimal model design. The stiffness of each element (tower legs and crossbeams) was adjusted to achieve target frequencies

and mode shapes which combined with the operational speed range of the wind tunnel, could convert to the required full-scale wind speed range. At the beginning of the test campaign, a speed sweep test was carried out, measuring base moments and forces to ensure the test would remain in the subcritical Re range. In the tested range 1×10^5-3.5×10^5, measured base loads normalized by pressure remained similar without a drop which would be an indication of a transition into the critical Re range. Wind direction 0° designates winds normal to bridge span.

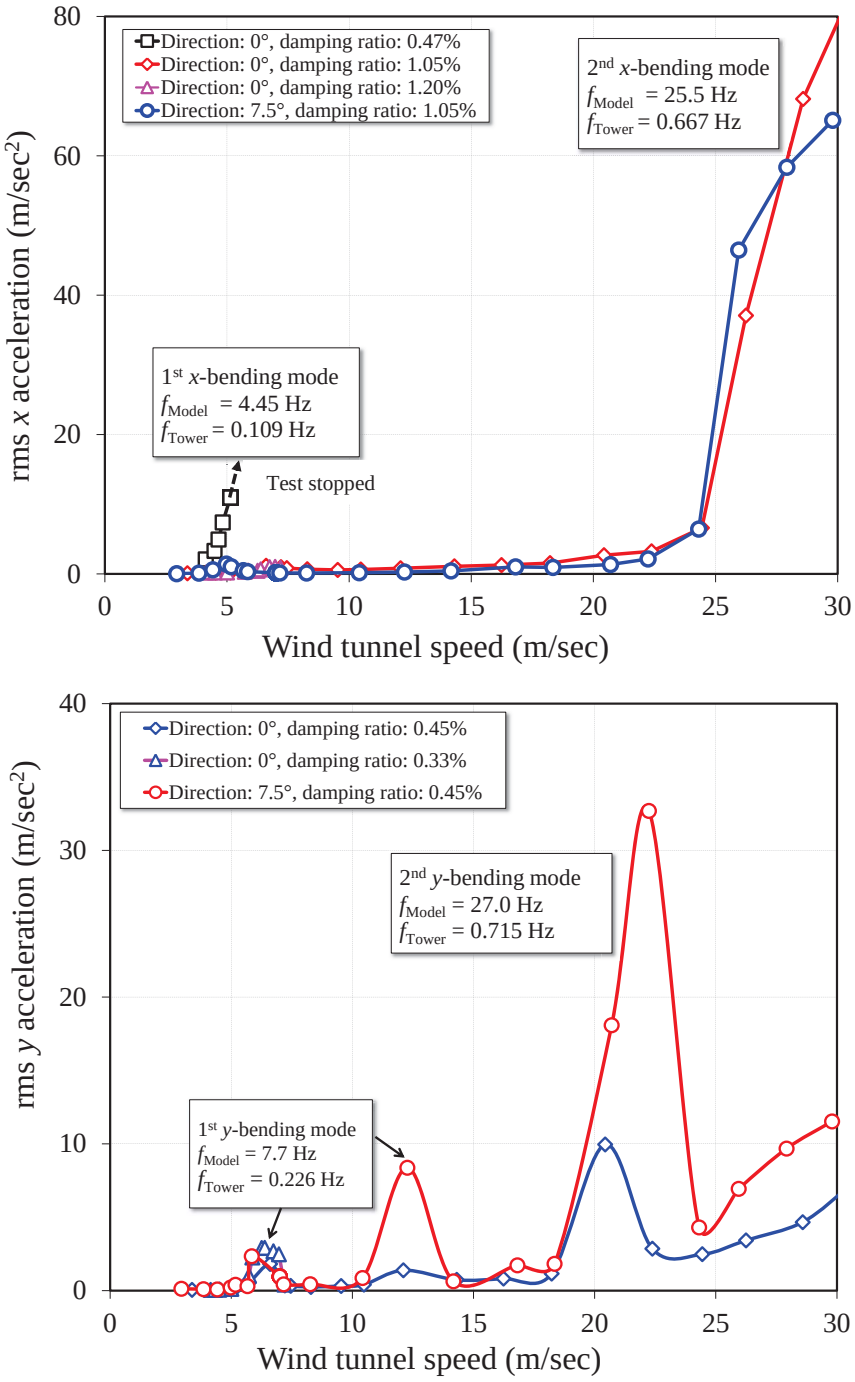

Figure 6: Free-Standing tower response in smooth flow, wind directions 0 & 7.5 deg. rms x/y accelerations vs. wind tunnel speed at top cross-beam

2.1 The Free-Standing Tower

The Free-Standing tower is often identified as a critical stage during bridge construction due to aerodynamic instability problems. In this test multiple vortex shedding excitations were found involving many modes of vibrations. The top of Figure 6 summarizes x longitudinal accelerations at the elevation 3.78 m (upper cross-beam). Vortex shedding responses were observed in the first longitudinal mode for directions 0° and 7.5° and for speeds from 4 to 7 m/sec, corresponding to full scale speeds of 9.5 to 16.7 m/sec. The actual test was stopped during the low damping test to avoid damaging the model when maximum root-mean-square (rms) accelerations of about 11 m/sec^2 (0.62 m/sec^2 full scale) were recorded at speed 5.1 m/sec (12.2 m/sec full scale) for damping ratio 0.47%. Note, the project acceleration limit is 0.5 m/sec^2. All other tests were carried with increased by TMDs damping of at least about 1.0% thus the vortex shedding responses did not reach more than 1.5 m/sec^2 which corresponds to a full scale rms acceleration of 0.09 m/sec^2.

Vortex shedding responses were observed in the 2nd longitudinal mode of vibration at wind directions 0° and 7.5° where the onset speed was about 25 m/sec (full scale speed of 62.3 m/sec). Just before the tests were stopped, the model scale rms accelerations obtained were beyond 60 m/sec^2 (3.7 m/sec^2 full scale). This level of accelerations corresponds to a damping value of about 0.5% of the critical, value which was assumed to be reasonable for second-order modes.

Transvers y-accelerations are also shown in the lower Figure 6. Vortex shedding responses were identified for the first transverse mode of vibration, at directions 0° and 7.5°, for speeds from 5.4 m/sec to 7 m/sec, corresponding to full scale speed from 15.4 m/sec to 20 m/sec. The maximum acceleration was in the range of 3 m/sec^2 (corresponding to a full scale value of 0.24 m/sec^2) where the damping ratio was 0.33% of the critical. A stronger vortex shedding response, again associated with the first transverse mode of vibration, was identified for 7.5° at about 12.3 m/sec (33.5 m/sec full scale). The acceleration was about 8.4 m/sec^2 (corresponding to a full scale value of 0.62 m/sec^2) and for a level of damping 0.45%. For the same wind speed at direction 0°, it seems that the tower was also excited by vortex shedding but at lower amplitudes.

A third vortex shedding response peak was found for 0° at 20.4 m/sec (50.8 m/sec full scale) and for 7.5° at 22.2 m/sec (55.3 m/sec full scale) , where the second transverse mode of vibration was excited. Measured accelerations were in the range of 10 m/sec2 (corresponding to a full scale value of 0.6 m/sec2) and 32.7 m/sec2 (full scale value of 2.0 m/sec2), respectively. These accelerations were measured with damping value of 0.5%. Note all damping levels refer are in off-wind conditions.

The first torsional mode (not shown here) was excited by vortex shedding for both directions 0° and 7.5°, at 20.4 m/sec (53.5 m/sec full scale) and 16.8 m/sec (44.1 m/sec full scale), respectively. At 0°, an acceleration of 17.3 m/sec^2 (corresponding to a full scale value of 1.19 m/sec2) was measured whereas a value of 11.8 m/sec^2 (full scale value of 0.81 m/sec^2) was found for 7.5°. These accelerations were measured with a damping ratio of 0.5%.

2.2 The In-Service Tower

In-Service tower was modeled by tying the top of the tower to the tunnel walls. It should be noted that stiffness effects of the main cable were modeled by offsetting up the attachment point. Added

mass effects were not modeled but these were considered small for most of the x-modes of interest where the tower would pivot about the main cable saddle points.

Figure 7 presents accelerations measured from different runs where the model scale accelerations are shown as a function of the tunnel speed for different wind directions and levels of damping. Presented x-accelerations were measured at the model elevation of 2.60 m corresponding to the middle cross beam elevation, 259.9 m.

The level of damping was varied for the first longitudinal mode of vibration (16.3 Hz) and first torsional (19.4 Hz) mode, and was not adjusted for the first transverse (8.4 Hz). Using again the same set of TMDs tuned to the required frequencies, the obtained damping levels for the first longitudinal mode were from about 0.3% to 3.2% and 0.27% to 2.9% for the first torsional mode. The inherent damping of the first transverse mode was in the range of 0.48% to 0.75% for all test runs. The test results obtained for the In-Service tower showed multiple vortex shedding excitations. Vortex shedding x-responses were observed in the first longitudinal mode of vibration for all directions (0°, 7.5° and 20°), for 15 m/sec to 19 m/sec, corresponding to full scale speed speeds of 40 m/sec to 50.7 m/sec. Before the test was stopped (because the model was damaged), a maximum acceleration of about 20.7 m/sec^2 (1.58 m/sec2 full scale) was recorded at 17.3 m/sec (45.4 m/sec full scale) for to a damping ratio of 0.3%. By increasing the damping ratio to approximately 1.0% of the critical, the vortex shedding responses at direction 0° were suppressed. However, the vortex shedding responses remain significant for directions 7.5° and 20°, even with levels of damping in the range of 1.5% to 1.6%. For instance, the measured acceleration for direction 20° reached 7.8 m/sec^2 (0.58 m/sec^2 at full scale).

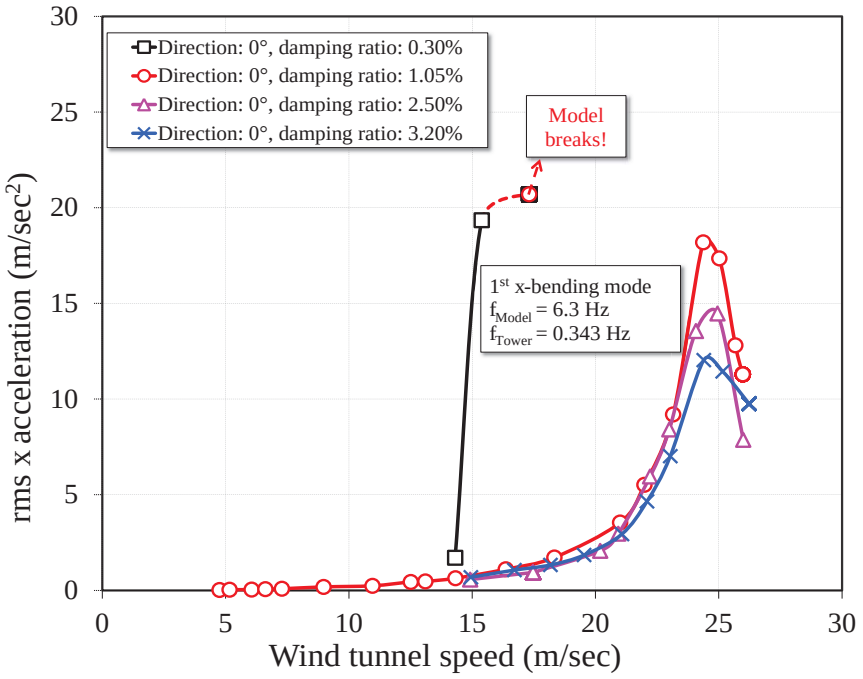

Figure 7: In-Service tower: rms x-accelerations vs. wind tunnel speed at the middle cross-beam

At wind direction 0° only, persistent vibrations were observed in the first longitudinal mode of vibration and for speeds between 22 m/sec (full scale speed of 58.7 m/sec) and 26 m/sec (69.4 m/sec). Peak acceleration of 18.2 m/sec^2 (1.31 m/sec^2 full scale) and 12 m/sec^2 (0.85 m/sec^2 full scale) were measured for damping levels of 1.05% and 3.2%, respectively.

Observed responses in the transverse y-direction (not shown here) cannot be directly applied for full scale predictions due to the expected high added mass and aerodynamic damping by the main cable motions which would likely subdue all tower motions in transverse direction.

The first torsional mode was found to be excited by vortex shedding for direction 0° at 14.3 m/sec (42.7 m/sec full scale) and for the relatively low damping value of 0.27%. The differential peak acceleration estimated was about 14.9 m/sec^2 (corresponding to a full scale value of 1.33 m/sec^2). This instability was suppressed by adjusting the damping level to 1.0%.

As with the along-the-bridge responses, a persistent vortex shedding response was identified at higher wind speeds (> 24 m/sec model scale, corresponding to > 71.9 m/sec at full scale) for directions 0° and 7.5°. The measured accelerations reached 24.2 m/sec^2 (2.17 m/sec^2 full scale) for a damping level of 1.05% of critical at 0°. By increasing the damping to 2.9% of the critical, this value was reduced to 15.0 m/sec^2 (1.35 m/sec^2 full scale). With a level of damping of about 1.9% of the critical and for direction 7.5°, the peak acceleration was in the range of 17.2 m/sec^2 (1.51 m/sec2 full scale) for a speed of 25.4 m/sec (corresponding to a full scale value of 75.2 m/sec).

2.3 Summary of the aeroelastic model test

Free-Standing tower

1. Tests through a range of wind speeds, damping and wind azimuths did capture aerodynamic instabilities where multiple modes of vibration were excited;
2. Some of these excitations exceeded the design criterion of 0.5 m/sec^2;
3. The excitations were identified as: a) vortex shedding at lower speeds and b) wake instabilities at higher speeds in along-, across-flow and torsional motions for directions normal to the bridge span.

In-Service tower

1. The In-Service tower was modeled by installing tensioned cables above the top tower elevation.
2. Tests were carried through a range of wind speeds where the amount of damping was tuned to different quantities for control of vibrating modes involving along the bridge motions only. Vortex shedding instabilities and wake excitation induced motions in several modes.
3. Some results exceed the design criterion at damping levels higher than the design specification.
4. Three excitation mechanisms were identified:
    a) Vortex shedding involving in-phase motions of the tower legs (bending mode) with St=0.2;
    b) Vortex shedding involving out-of-phase motions of the tower legs (torsional mode) characterized by St>0.2;
    c) Vortex shedding and wake induced instability with St=0.135 (combined bending & torsion).

5. Additional verification tests on aeroelastic model in scale 1:200 were also carried out at Politecnico di Milano at similar low Re range which confirmed the main finding of this study.
6. POLIMI & PARSONS tests brought to the conclusion that the wake induced type of excitation (St=0.135) was more difficult to suppress, but also that with 4% non-dimensional damping the design criterion request could be attained. As a final judgment it was recommended that additional tests in the large scale 1:100 should be performed during the Esecutivo Design Phase with TMD devices more closely reflecting the full scale ones, specifically as far as concerns the TMD "stand alone" damping ratio. The correct design of the TMD for Tower Free-Standing conditions was in fact forced to the In-Service conditions (higher frequency and same TMD mass) with a final 6% “stand-alone” TMD damping ratio at the In-Service frequency. So that the TMD Wide-Band design changed in a Narrow-Band design having more critical behavior in terms of tuning.

3. Sectional Mode Tests

The same model shells as of the aeroelastic model were used to produce a sectional model with similar mass & damping properties. This part of the study included: a) measurement of static force and moment coefficients required for wind loads; b) aerodynamic stability; and, c) decay / build-up & limit-cycle data base collection for vortex shedding numerical simulation model parameter identification.

Static force and moment coefficients were measured where one of the two tower legs was mounted on a force and moment balance flexure. An identical "dummy" leg was mounted downwind, initially, from the instrumented model. The entire assembly was installed on a turntable which could be rotated to any angle of interest. The assembly (upper Figure 8) also included large splitter plates to ensure two-dimensional flow. Measured coefficients are shown in Figure 9.

A sectional model test simulating expected mass and damping properties at full scale was carried out. An analytical model was developed to predict the across-wind vortex shedding vibration using the single-degree-of-freedom (Van der Pol oscillator) formulation proposed by Scanlan [1,2,3]. Figure 10 shows a good agreement where the predicted rms amplitudes generated with damping levels 0.85% and 2.0% are in line with the experimental data.

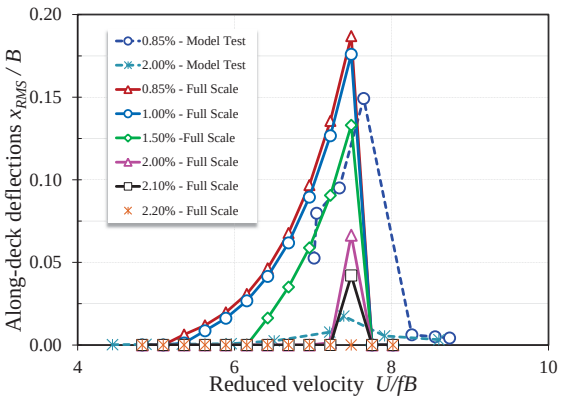

Figure 10: 1:100 sectional model test vs. analytical predictions of x-deflections.

Figure 8: Tower 1:100 sectional model test

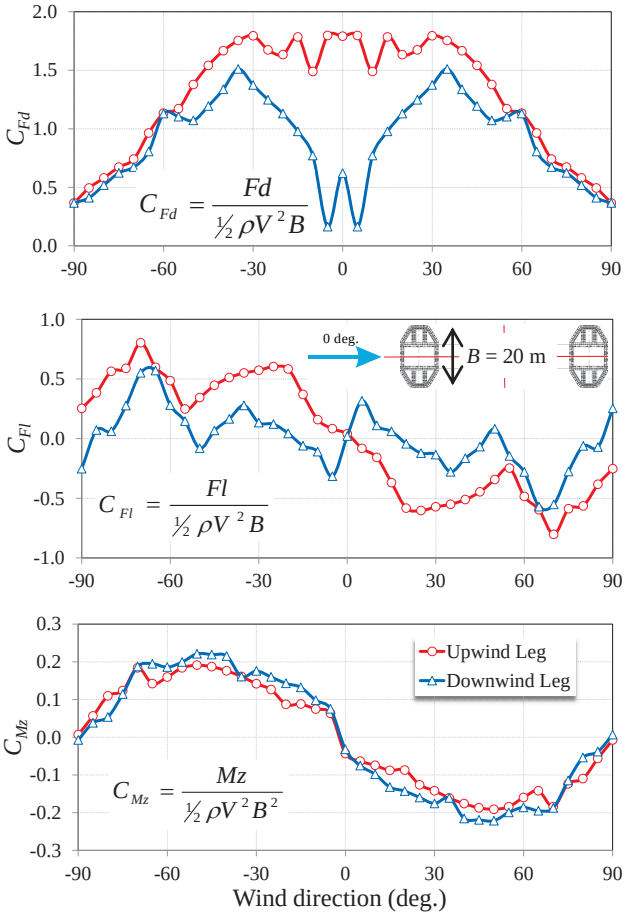

Figure 9: Static force and moment coefficients.

The sectional model test however did not show the St=0.2 mechanism found of the aeroelastic model. It was possible to suppress vortex shedding vibrations in vertical and torsional direction at St=0.12~0.14 with relatively modest level of damping (2~3%). The fact that during the aeroelastic model test, it was not possible to suppress the vibration at St=0.135 even with 3% damping, implies that these are likely different mechanisms where wake and other 3D effects did prevail in the aeroelastic model test. Another torsional motion peak was found at St=0.25, a speed similar to that found in the aeroelastic model test, although at lower lever of excitations.

Compared to the aeroelastic model tests, the observed differences were attributed to: 3D end effects near the tower top; simplifications - inclined legs with variable distance taken as parallel; presence of wide cross-beams at critical locations (tower top, 2/3 elevation); and possible Reynolds number effects. The predictions in terms of amplitudes of the 2D sectional model test were viewed as conservative since they do not include any 3D flow effects which will tend to reduce the uniformity of the vortex wake and the associated fluctuating forces on the tower legs.

4. Conclusions

A unique aeroelastic model test programme was carried out for the Messina Strait Bridge tower. On a comparatively large model in scale of 1:100, damping was controlled by TMD devices which effectively replicated their full scale mechanics in terms of active mass, frequency and viscos damping. Although not fully explored to its capacity, this allowed assessing the effectiveness of the TMD system proposed for the real tower in a manner reflecting the full scale conditions.

The most important result of the test campaign was that the Messina Strait Bridge towers will need auxiliary devices for motions control (dampers) during both construction and In-Service conditions. Whereas the vortex shedding sources of vibrations were relatively straightforward to suppress, requiring likely damping in the order of 2% to control the motions, the wake induced type of excitation proved more difficult, requiring level of damping in the range of over 3 to 4% to attain the required motion criteria.

Acknowledgments

The team of National Research Council of Canada led by Dr. G. Larose who carried out instrumentation, testing and data reduction is highly acknowledged. The authors would like to thank to the specialists of RWDI and Motioneering Inc., for the design and construction of all models and damper system, and wind tunnel testing.

References

[1] E. Simiu and R.H. Scanlan, Wind Effects on Structures : Fundamentals and Applications to Design, Wiley, 3rd edition, 1996.
[2] R.H. Scanlan, Bridge flutter derivatives at vortex lock-in, Journal of Structural Engineering, Vol. 124, pp. 450-458, 1998.
[3] I. Goswami, R.H. Scanlan and N.P. Jones, Vortex-Induced Vibration of Circular Cylinders. II: New Model, Journal of Engineering Mechanics, Vol. 119, No. 11, pp. 2288-2302, 1993.

The Seventh International Colloquium on Bluff Body Aerodynamics and Applications (BBAA7)
Shanghai, China; September 2-6, 2012

Aerodynamic effects on streamline box girder in active wind tunnel with multiple fans and vibrating airfoils

T.T. Ma, L. Zhao, S.Y. Cao, Y.J. Ge

SLDRCE, Tongji University, Shanghai, China, tingtinghorse@126.com

ABSTRACT: The aerodynamic behavior of a streamline box section model is characterized in an active wind tunnel with multiple fans and vibrating airfoils in Miyazaki University, Japan. A series of single harmonic fluctuating wind with discrete frequencies are generated. The aerodynamic admittance components obtained via cross spectral identification method for different oncoming flows present obvious deviation between each other, which implies the limitation of traditional buffeting theory. More attention is emphasized on the relationship between aerodynamic forces and wind turbulence components, along- and cross-wind, in sinusoidal flow conditions. It is found that the cross-wind turbulence has dominant influence on lift and pitching moment forces. With the strengthening of along-wind turbulence, the lift force increases, while the drag and pitching moment forces vary with different trend in different range of frequency. Moreover, it is found that the contribution of along-wind turbulence to lift and pitching moment forces is neglectable compared with that of the cross-wind turbulence, while for the drag force, the two turbulence components present comparative contributions.

KEYWORDS: Active wind tunnel; Two-dimensional harmonic fluctuating flow; Streamline box section; Aerodynamic admittance; Turbulence statistics; Aerodynamic effects

1 INTRODUCTION

Buffeting is a kind of stochastic forced vibration caused by the turbulence existing inherently in natural wind. Buffeting is hence inevitable for any bridges exposed to the natural wind. To ensure the safety of the construction for long-span bridges, the buffeting analysis is necessary to be refined. Many previous studies have made great contribution to the development of buffeting theory [1-4]. For the consideration of the non-stationarity and incompletely spanwise coherence of natural turbulence, the aerodynamic admittance was employed to modify the quasi-steady aerodynamic forces. On buffeting analysis, Sears's function for a vertical wind gust [1] and Devenport's formula for an along wind gust [2] are usually employed. The accuracy of the result depends largely upon the accurate estimation of aerodynamic admittance. Wind tunnel testing is the most popular method to investigate the effects of wind on long-span bridges. Some studies focused on aerodynamic admittance have been conducted in conventional boundary-layer wind tunnels [3-4]. Considering the limits like the adjustment of wind power spectral density and the integral length scale in passive turbulence generation method, a few actively controlled wind tunnels have been proposed [5-8].

Multiple-fan wind tunnel is a relatively fine active generation technique in Japan. In the active wind tunnel in Miyazaki University, 99 fans arranged in a 9 wide by 11 high matrix has been used to generate only along-wind turbulence (*u*-turbulence), which coincide well with the natural turbulent flow [9]. Then in this wind tunnel, a series of single harmonic fluctuating wind were generated to research the relationship between aerodynamic forces induced by sinusoidal fluctuating wind with discrete frequency and broadband turbulence, which verifies the principle of

superposition of aerodynamic forces for sinusoidal flows in some specified frequency range (Fig. 1)[10,11]. However, active wind tunnel with only multiple-fan equipment could not produce sufficient cross-wind turbulence (*w*-turbulence), which may result in significant effects on buffeting forces. In contrast, there is some testing conducted in a wind tunnel equipped with only a series of wings to produce *w*-turbulence, while the *u*-turbulence is neglected [12]. However, the contribution of *u*-turbulence and *w*-turbulence to aerodynamic forces has not been clearly understood. Based on the limits of the existing active wind tunnels, additory active vibrating airfoils are equipped in the wind tunnel of Miyazaki University together with the multiple-fan equipment to produce two-dimensional (*u*- and *w*-) active turbulence. Based on the superposition principle of aerodynamic forces referred above, more attention is emphasized on the relationship between aerodynamic forces and wind turbulence components in sinusoidal flow condition.

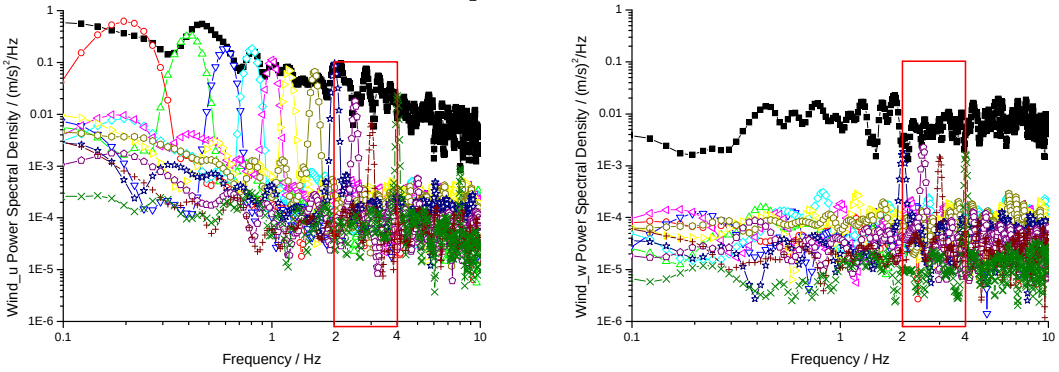

a) PSD of broadband and sinusoidal turbulence

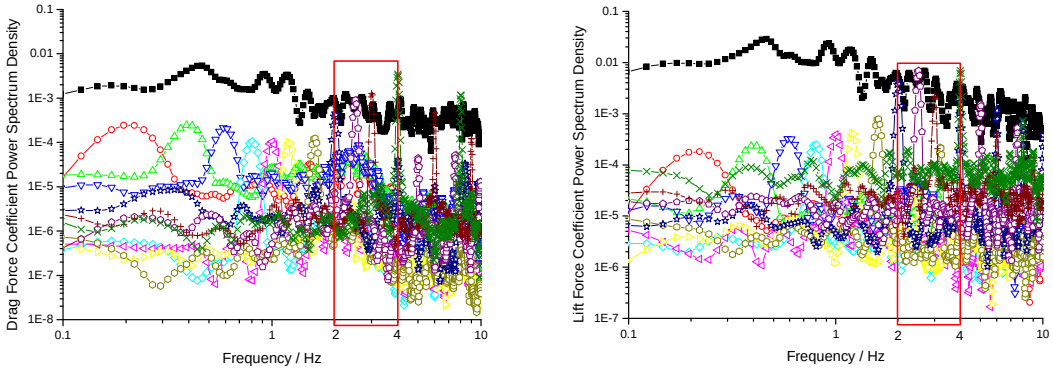

b) PSD of aerodynamic forces of broadband and sinusoidal turbulence

Figure 1 Linear superposition of sinusoidal flow for Streamline Box Girder section

2 EXPERIMENTAL ARRANGEMENT

2.1 *Active turbulence generator*

Fig.1 shows the active wind tunnel with multiple fans and vibrating airfoils in Miyazaki University, Japan. This wind tunnel is an open-circuit one with 99fans of 270mm in diameter at the front. The fans are arranged in a 9 wide by 11 high matrix (Fig. 1(a)). The vibrating airfoils are set to be 1.5m downstream from the honeycomb (Fig. 1(b)). The test section is 15.5m long (maximum), 2.538m wide and 1.804m high. The maximum wind velocity is about 15m/s, while 9m/s for sinusoidal flows with fluctuating amplitude of 3.5m/s. The maximum fluctuating frequency can reach to 5Hz. In this experiment, active fans and vibrating airfoils are combined to produce

sinusoidal turbulent flows of different dominant frequencies and different values of power spectral density (PSD) of *u*- and *w*- turbulence, denoted as S_u and S_w respectively.

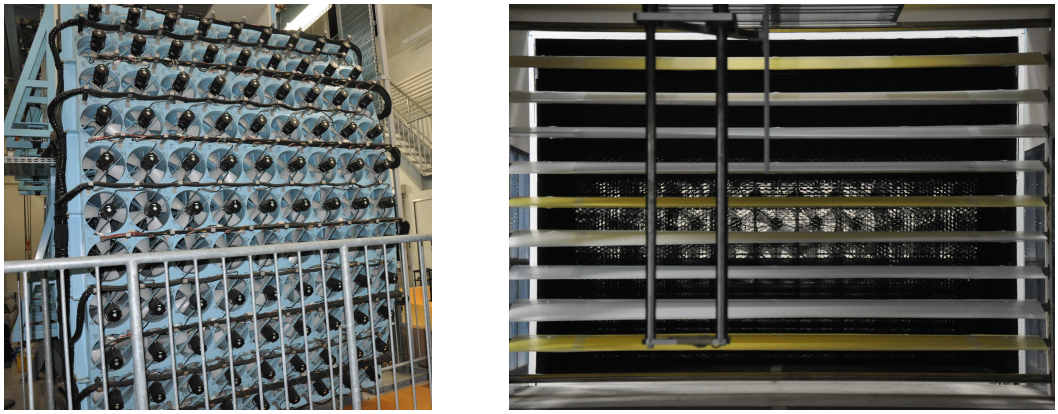

(a) Multiple fans (b) Vibrating airfoils

Fig. 2 Active wind tunnel with multiple fans and vibrating airfoils

2.2 *Fixed model tests*

The deck section adopted for tests is a 1:60 scale section model of a streamline box shape. Fig. 3 shows the cross section of the section model and the model in tests. A pressure measurement system was set up for the measurement of aerodynamic forces. There are 80 points around the section under measurement and for each testing process two sections (section 1 and section 2) are simultaneously measured. The static angle of attack of the bridge section is 0°.

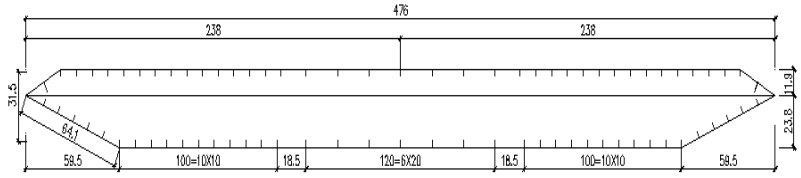

(a) Cross section of the section model

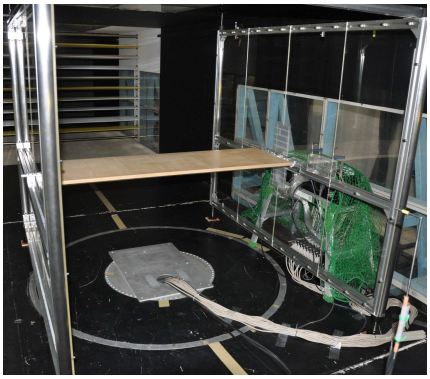

(b) Section model in tests

Fig. 3 Streamline box section model

In this experiment, special study about the turbulence statistics along the test section is conducted to identify the relatively steady section for model tests. Fig. 4 shows the variation of PSD,

integral scale, turbulence intensity and average wind velocity of two measure points. It illustrates that when the distance from the honeycomb ranges between 4.1m and 4.6m, the turbulent flows keep relatively steady. The section model is finally fixed 4.4 meters away from the honeycomb.

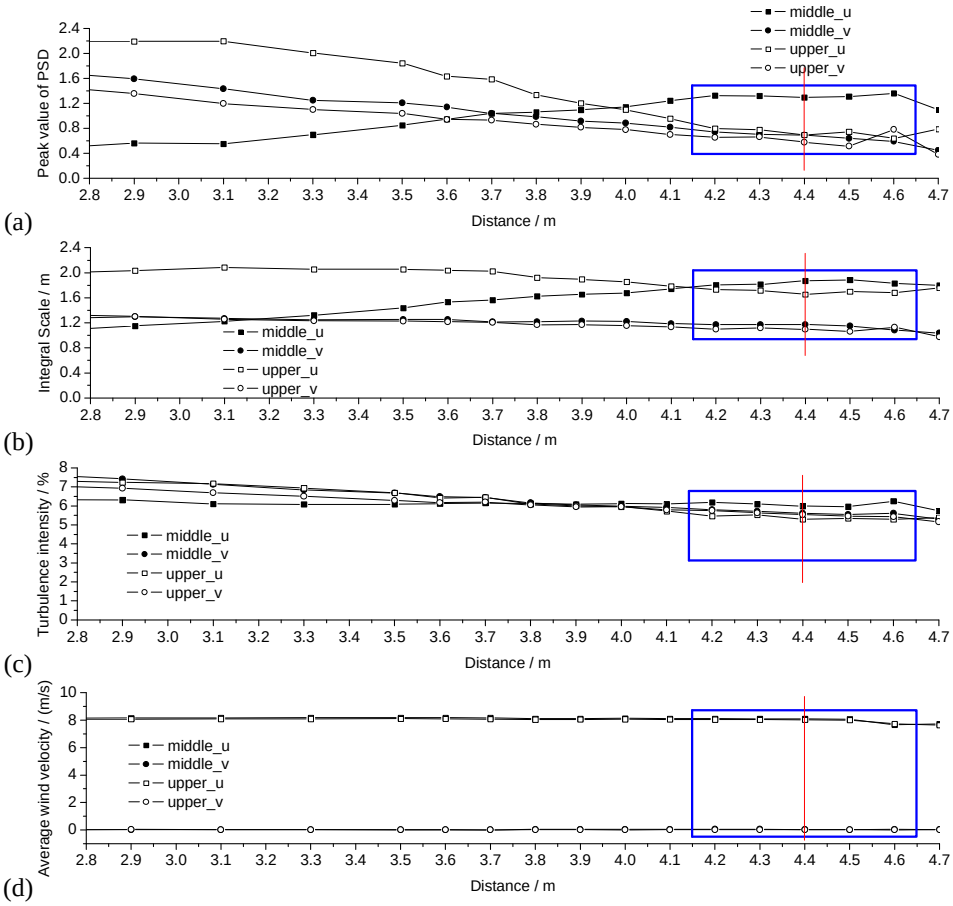

Fig. 4 Variation of (a) PSD, (b) integral scale, (c) turbulence intensity and (d) average wind velocity along test section

In order to study the relationship between aerodynamic forces and wind turbulence components, the active fans and vibrating airfoils are combined to produce a series of sinusoidal fluctuating winds. The detailed testing conditions are listed in Table 1. There are totally three kinds of combination between active fans and vibrating airfoils. In Table 1, f means the dominant frequency of the sinusoidal flow.

Table 1 Different combination of motion for active fans and vibrating airfoils

Testing serial No.	Description of fluctuating flows in entrance section
1	Multiple fans: f=0.2-4.0Hz; $\triangle f$=0.1Hz Average wind velocity U=8m/s ; Amplitude A1=2m/s Airfoils: Vibrating with the same frequency as active fans Amplitude A2=10°
2	Multiple fans: U=8m/s; A1=0 Airfoils: f=0.2-4.0Hz; $\triangle f$=0.2Hz; A2=10°
3	Multiple fans: f=0.2-4.0Hz; $\triangle f$=0.2Hz; U=8m/s; A1=2m/s Airfoils: static

3 EXPERIMENTAL RESULTS

3.1 *Identification of aerodynamic admittance*

Based on the traditional buffeting theory, the aerodynamic admittance functions have been employed to modify the quasi-steady aerodynamic forces. For example, the lift component is expressed as [2]

$$L_b(t) = \rho UB\left(C_L(\alpha)\chi_{Lu} + 1/2\left(C_L'(\alpha) + C_D(\alpha)\right)\chi_{Lw} w(t)\right) \tag{1}$$

where ρ=air density; U=mean wind velocity; B=2b is the bridge deck width; C_L and C_D =mean lift and drag coefficients, respectively; $C_L' = dC_L / d\alpha$;α is the mean static angle of attack of the bridge section; and χ_{Lu}, χ_{Lw} = aerodynamic admittance functions for lift force.

The aerodynamic admittance components here are identified by cross spectral admittance identification method. The aerodynamic admittance for lift force can be expressed by

$$\chi_{Lu}(f) = \frac{S_w(f)S_{Lu}(f) - S_{wu}(f)S_{Lw}(f)}{\rho UBC_L(\alpha)\left[S_u(f)S_w(f) - S_{wu}(f)S_{uw}(f)\right]} \tag{2a}$$

$$\chi_{Lw}(f) = \frac{S_u(f)S_{Lw}(f) - S_{uw}(f)S_{Lu}(f)}{1/2\,\rho UB\left[C_L'(\alpha) + C_D(\alpha)\right]\left[S_u(f)S_w(f) - S_{uw}(f)S_{wu}(f)\right]} \tag{2b}$$

where $S_{Lu}(f)$, $S_{Lw}(f)$ = cross power spectrum between lift force and u- , w- turbulence respectively; $S_{wu}(f)$, $S_{uw}(f)$ = cross power spectrum between u- and w- turbulence; $S_u(f)$, $S_w(f)$ =PSD of u- and w- turbulence.

For the comparison with Sears function, the aerodynamic admittance components shown in Eq. (2) are transformed into equivalent aerodynamic admittance (EAA) with an expression as follows

$$\left|\phi_{LL}(K)\right|^2 = \frac{4C_L^2(\alpha)\left|\chi_{Lu}\right|^2 S_u(K) + \left(C_L'(\alpha) + C_D(\alpha)\right)^2\left|\chi_{Lw}\right|^2 S_w(K)}{\left(4C_L^2(\alpha)S_u(K) + \left(C_L'(\alpha) + C_D(\alpha)\right)^2 S_w(K)\right)} \tag{3}$$

where $\left|\phi_{LL}(K)\right|$ is EAA for lift force; K=2πBf/U. EAA for drag and pitching moment forces, denoted as $\left|\phi_{DD}(K)\right|$ and $\left|\phi_{MM}(K)\right|$, have similar expression as Eq. (3).

3.2 *Aerodynamic admittance of streamline box section*

In this experiment, the time histories of buffeting forces components, i.e. lift, drag, and pitching moment components are obtained by integration of pressure measured around the model section. Three equivalent aerodynamic admittances are identified for each different testing condition listed in Table 1. Fig. 5 shows the comparisons of equivalent aerodynamic admittance (EAA) between different fluctuating flows for section 1. It is clearly shown that the aerodynamic admittance components obtained by cross spectral identification method present obvious deviation between different fluctuating flows. This indicates the limitation of traditional buffeting theory.

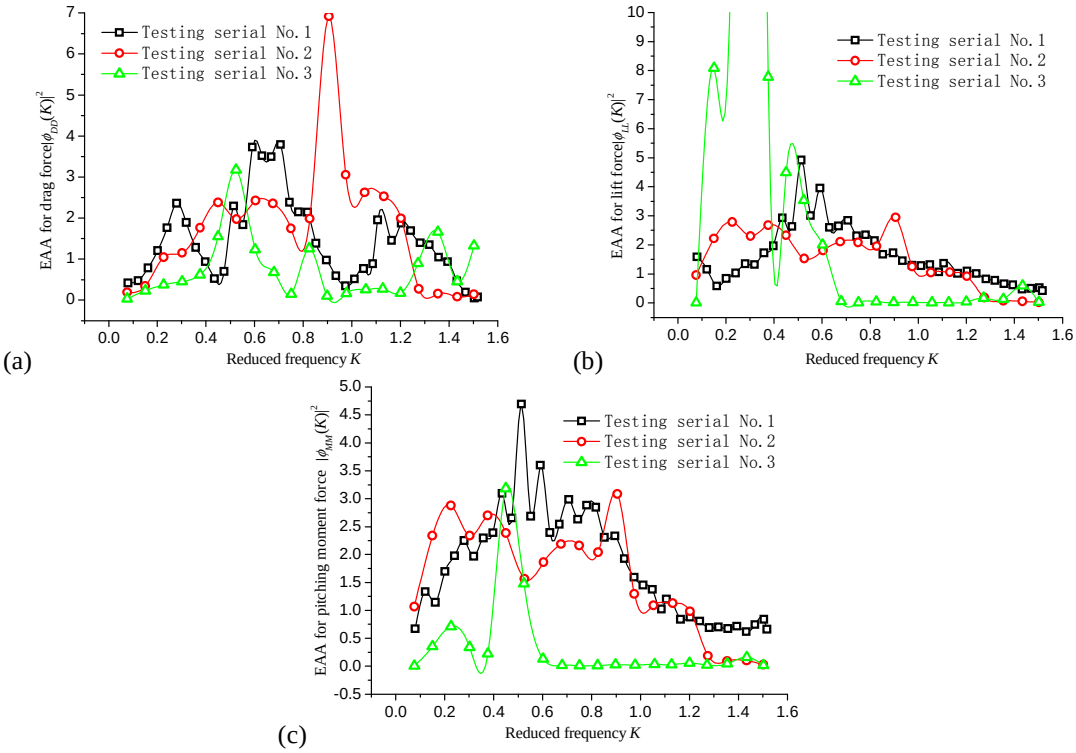

Fig.5 Comparison of equivalent aerodynamic admittance (EAA) for (a) drag force, (b) lift force, and (c) pitching moment force

For further understanding of the effects of turbulence on aerodynamic forces, the testing results for both section 1 and section 2 in a sinusoidal flow with dominant frequency of 2Hz are shown in Fig. 6. Although the PSD of horizontal and vertical turbulence, S_u and S_w, around dominant frequency shows much difference, the aerodynamic forces remain almost the same. This indicates that the aerodynamic admittance is related to the turbulent characteristics, which is different from the traditional buffeting theory.

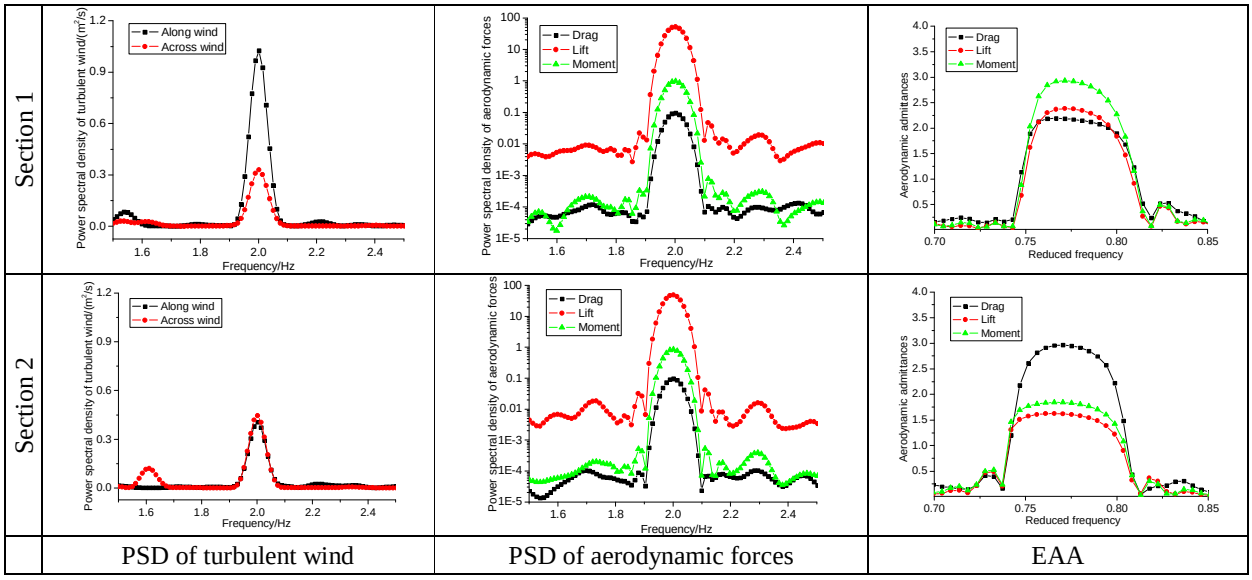

Figure 6 Comparison of the testing results of section 1 and section 2

3.3 *Sensitivity analysis of buffeting forces to turbulence*

For the sake of the limits in traditional buffeting theory, the effects of *u*- and *w*- turbulence (S_u and S_w) on buffeting forces (PSD of buffeting forces: S_L , S_D and S_M) are directly analyzed without the employment of aerodynamic admittance functions. For the purpose of the analysis about the sensitivity of buffeting forces to turbulence, several pairs of results with almost the same values of S_u (or S_w) at the same dominant frequency are selected. In contrast, the values of S_w (or S_u) present relatively obvious differences. The results are listed in Table 2 and Table 3.

Table 2 Sensitivity of buffeting forces to *w*-turbulence

f	S_u	S_w	S_D	S_L	S_M	With the increase of S_w		
						S_D	S_L	S_M
0.8	3.095	0.805	0.155	133.489	2.092	↑	↑	↑
0.8	3.050	0.004	0.030	1.676	0.003			
1	2.377	1.006	0.219	196.360	3.043	↑	↑	↑
1	2.414	0.001	0.029	0.657	0.001			
1.2	1.053	1.478	0.257	254.082	3.995	↑	↑	↑
1.2	1.130	0.004	0.001	0.006	0.001			
1.4	0.301	2.975	0.345	284.919	4.456	↑	↑	↑
1.4	0.314	0.004	0.026	2.231	0.015			
2	0.405	0.445	0.096	49.033	0.856	↑	↑	↑
2	0.404	0.006	0.025	1.824	0.056			
2.2	0.724	0.410	0.055	46.572	0.987	↑	↑	↑
2.2	0.728	0.007	0.030	1.0603	0.014			
3.2	0.520	3.671	0.333	213.520	3.447	↑	↑	↑
3.2	0.505	0.003	0.127	0.553	0.021			

Key: ↑= increase of S_F (F=*D*, *L*, *M*)

Table 2 Sensitivity of buffeting forces to *u*-turbulence

f	S_u	S_w	S_D	S_L	S_M	With the increase of S_u		
						S_D	S_L	S_M
0.2	57.335	0.010	0.222	8.201	0.001	↓	↑	↓
0.2	52.080	0.012	0.286	3.001	0.025			
1.2	0.731	0.001	0.029	0.314	0.001	↑	↑	↑
1.2	0.274	0.001	0.000	0.002	0.000			
2	1.322	0.003	0.042	0.332	0.015	↑	↑	↑
2	0.140	0.003	0.000	0.005	0.001			
2.8	0.117	0.011	0.055	0.579	0.016	↓	↑	↑
2.8	0.070	0.012	0.086	0.296	0.004			

Key: ↑= increase of S_F (F= *D*, *L*, *M*); ↓=decrease of S_F (F=*D*, *L*, *M*)

It is shown in Table 2 that all the three aerodynamic forces present increase with the increase of S_w. The contribution of S_w is predominant especially for lift and pitching moment forces. The results indicate the importance of correct simulation of *w*-turbulence in wind tunnels. From Table

3, we can see that the contribution of S_u to buffeting forces is more complex than that of S_w. With the increase of S_u, the lift force increases, while the drag and pitching moment forces present different trend of variation in different ranges of frequency.

Moreover, comparisons about the effects of *u*-turbulence and *w*-turbulence on buffeting forces are conducted. The results with regard to turbulent flows with dominant frequencies of 1.2Hz and 2.0Hz are selected from both Table 2 and Table 3. Here we define an average effects index k_u (or k_w) expressed as

$$k_u(or k_w) = \frac{\delta S_F}{\delta S_u(or \delta S_w)} \quad (F=D, L, M) \tag{4}$$

where δS_u, δS_w=variation of PSD of *u*-turbulence and *w*-turbulence at the dominant frequency and δS_F is the relative variation of PSD of buffeting forces. Fig. 7 shows the average variation of S_F resulted from the unit change of S_u and S_w.

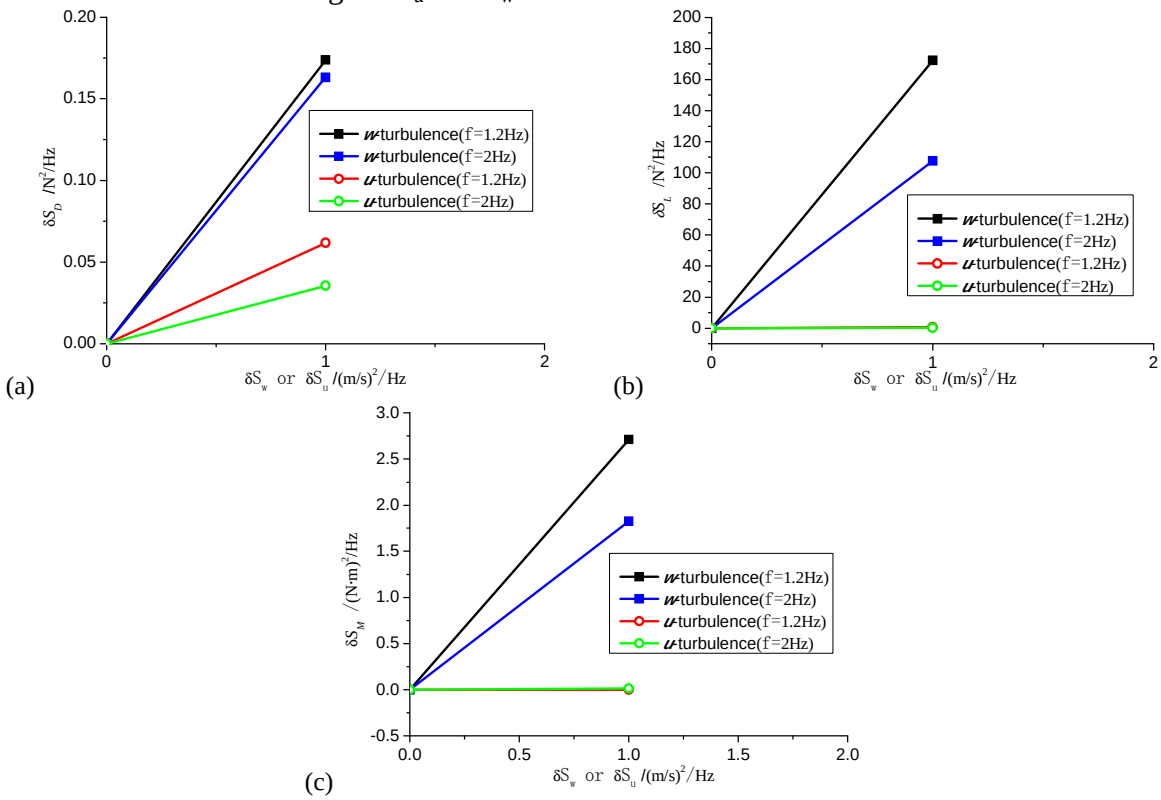

Fig. 7 Average effects of *u*- and *w*- turbulence on (a) drag, (b) lift and (c) pitching moment forces

It is clearly indicated in Fig. 7 that the lift and pitching moment forces are much more sensitive to the *w*- turbulence than *u*- turbulence. It is acceptable to neglect the contribution of *u*- turbulence. For the drag force, the contribution of the *u*- turbulence is less than that of *w*- turbulence. However, they keep the same order of magnitude, i.e. both the *u*- and *w*- turbulence should be corrected simulated for the accurate simulation of drag force.

4 CONCLUSIONS

A series of single harmonic fluctuating winds with different combination of *u*- and *w*- turbulence are generated in an active wind tunnel with multiple fans and vibrating airfoils in Miyazaki University. The experimental results about the relationship between flow turbulence and buffeting forces are analyzed. Conclusions of this study are summarized as follows:

(1) The traditional buffeting theory based on aerodynamic admittances has some limits. The aerodynamic admittance is related to the characteristics of the flow, which is different from the traditional buffeting theory.
(2) The *w*- turbulence has positive contribution to all the three buffeting forces, while the *u*- turbulence presents positive contribution only to lift force. The drag and pitching moment forces present different trend of variation in different ranges of frequency.
(3) The lift and pitching moment forces are much more sensitive to the *w*- turbulence than *u*- turbulence. It is acceptable to neglect the contribution of *u*- turbulence.
(4) Both the *u*- and *w*- turbulence should be corrected simulated for the accurate simulation of drag force, although the contribution of the *u*- turbulence is less than that of *w*- turbulence.

The conclusions above are qualitative ones based on the premise of 0° static angle of attack of the bridge section. More quantitative analyses based on different angle of attack are expected in future.

5 ACKNOWLEDGEMENTS

The authors would like to gratefully acknowledge the supports of the National Science Foundation of China (51021140005, 50978202 and 51178353), and the supports by Kwang-Hua Fund for College of Civil Engineering, Tongji University

6 REFERENCES

[1] T. Von Karman and W.R. Sears, Airfoil theory for non-uniform motion, Journal of Aeronautical Science, 5(1938) 379-390.
[2] A. G. Davenport, Buffeting of a suspension bridge by storm winds, J. Struct. Eng., 88(ST3)(1962)233-268.
[3] P.P. Sarkar, N.P. Jones and R.H. Scanlan, Identification of aeroelastic parameters of flexible bridges，Journal of Engineering Mechanics, 1994, 120(8):1718-1742.
[4] G.L. Larose, H. Tanaka, N.J. Ginsing, et al., Direct measurement of buffeting wind forces on bridge decks, Journal of Wind Engineering and Industrial Aerodynamics, 1997,74-76: 809-818.
[5] B. Bienkiewicz et al., Active modeling of large-scale turbulence, J. Wind Eng. Ind. Aerodyn. 13(1983)465.
[6] H. Kobayashi, A. Hatanaka, Active generation of wind gust in two-dimensional wind tunnel, J. Wind Eng. Ind. Aerodyn. 41/44(1992)959.
[7] A. Nishi, H. Kikugawa, Y. Matsuda, et al., Turbulence control in multiple-fan wind tunnels, Journal of Wind Engineering and Industrial Aerodynamics, 1997, 67:861-872.
[8] A. Nishi, H. Kikugawa, Y. Matsuda, et al., Active control of turbulence for an atmospheric boundary layer model in a wind tunnel, Journal of Wind Engineering and Industrial Aerodynamics, 1999, 83:409-419.
[9] S.Y. Cao, A. Nishi, H. Kikugawac, et al., Reproduction of wind velocity history in a multiple fan wind tunnel, Journal of Wind Engineering and Industrial Aerodynamics. 2002,90: 1719-1729.
[10] L. Zhao, S.Y. Cao, Y.J. Ge, et al., Investigation of aerodynamic loading effects on typical streamline cross-section under active turbulence-generated conditions. 13th ICWE, Amsterdam, Netherlands, July 10-15, 2011.
[11] L. Zhao and Y.J. Ge, Buffeting Response Sensitivity of Multi-component Aerodynamic Admittance Function of Typical Bridge Deck. APCWE-VII, November 8-12, 2009, Taipei, Taiwan 2009.
[12] G. Diana, B. Stefano, C. Alfredo, et al., Complex aerodynamic admittance role in buffeting response of a bridge deck, Journal of Wind Engineering and Industrial Aerodynamics, 2002,90:2057-2072.

Investigation of spatial coherences of aerodynamic loads on a streamlined bridge deck under active-generated flow conditions

K. Xu [a], L. Zhao [b], S.Y. Cao[c], Y. J. Ge [d]

[a] *SLDRCE, Tongji University, Shanghai,China, firework198864@163.com*
[b] *SLDRCE, Tongji University, Shanghai, China, zhaolin@tongji.edu.cn*
[c] *SLDRCE, Tongji University, Shanghai,China, caoshuyang@hotmail.com*
[d] *SLDRCE, Tongji University, Shanghai, China, yaojunge@tongji.edu.cn*

ABSTRACT ： A pressure measuring experiment on a streamlined bridge deck section model was conducted under simultaneous two-dimensional incident flows in an active-controlled wind tunnel. A commendable wind velocity modification approach based on the stable flow features of the active-controlled wind tunnel was adopted. The correlations of both incident winds and aerodynamic forces were studied, and an obvious impact of integral scales can be seen in this study. The decaying trend of root coherence with large ratios of integral scale to section-interval is a far cry from the conventional exponential expression, thus a new empirical expression is proposed to reflect the spatial coherence features in low frequency region.

KEYWORDS: active-controlled turbulences; aerodynamic loads; correlation coefficients; spatial coherences; empirical expression

1 INTRODUCTION

The existing buffeting theory for bluff body is derived from the airfoil aerodynamics, which is based on a “strip” assumption. The aerodynamic loads on a deck cross section, thus, are only due to the incident flows in the same plane with that section, which gives the aerodynamic loads a two dimensional feature. When these 2D (two-dimensional) forces are applied to a 3D (three-dimensional) structure, the spatial distribution and correlation of these forces along the span-wise have to be sufficiently considered. A criterion for assessing the correlation features of aerodynamic loads or incident flows between two cross-sections is correlation coefficient:

$$\mathrm{Cor}(x_1, x_2) = \frac{\overline{v_1(x_1,t)\cdot v_2(x_2,t)}}{\sigma_{v1}\sigma_{v2}} \quad (1)$$

where the over bar denotes time-averaging; v(x,t) is turbulent wind velocity ; σ_v is standard deviation of the turbulent components.

In the frequency domain, the joint acceptance function is used to represent the distribution and correlation features of aerodynamic loads or incident winds along the span-wise and between different modes:

$$|J(K)|^2 = \iint_0^L \frac{S_{R_1R_2}(K,\Delta x)}{\sqrt{S_{R_1}(K)}\sqrt{S_{R_2}(K)}}\Phi_i(x_1)\Phi_i(x_2)dx_1dx_2 \quad (2)$$

where $S_{R1R2}(K,\Delta x)$ denotes the cross-spectrum of buffeting forces or oncoming flows on different cross-sections at a distance of Δx; S_{Ri} (i=1,2) represents the auto-spectrum of buffeting forces or oncoming flows; $\Phi_i(x)$ is the i^{th} modal shape of the deck; $K=B\omega/U$ is reduced frequency; B is deck width; ω is oscillation frequency; U is average wind speed; L is deck length. In the above function the normalized cross-spectrum is defined as the root coherence function:

$$\mathrm{coh}_{R}^{1/2}(K,\Delta x)=\frac{S_{R_1R_2}(K,\Delta x)}{\sqrt{S_{R_1}(K)}\sqrt{S_{R_2}(K)}} \tag{3}$$

Davenport (1961) proposed one of the first heuristic root-coherence expressions for longitudinal turbulence, which is based on field measurements:

$$\mathrm{coh}_{u}^{1/2}(f,\Delta X)=\exp\left(-c*\frac{f\Delta X}{U}\right) \tag{4}$$

where c is decay factor; fΔx/U is reduced frequency, also used as a collapsing parameter. In early studies, the distribution of buffeting forces along span-wise was considered to be the same as the incident flows, however, a lot of experiments conducted in wind tunnels revealed a larger spatial coherence of the aerodynamic forces. And spatial coherence is not only related to the flow frequency and section-intervals but also has a relation with the integral scale, turbulence intensity, section features like the ratio of deck width to deck thickness, etc (*Matsumoto, 1994; Larose, 1998, 2003; Nagaoa, 2003; el at*).

Nevertheless, all those experiments were carried out in passive atmospheric boundary wind tunnels, some of the key fluid features, such as integral scale, oncoming flow coherence, PSD function of fluctuating wind, etc, cannot be easily reproduced in a passive wind tunnel. Integral scale of stochastic fluctuating wind, however, has a considerable influence on the spatial coherences of the aerodynamic loads, but the integral scale of stochastic fluctuating generated by a passive wind tunnel is always too small, comparing with the model scale. Furthermore, because the incident flow features on the central point of section model cannot be measured directly, the flow features at the up-stream or at the lateral of the section model were just adopted as replacements. As is known, the flow energy decays along the longitudinal direction and the wind velocities are not fully correlated along the lateral direction in a passive wind tunnel, thus the measured wind features cannot represent the real features on the central points of pressure measuring cross-sections, which leaves something to be desired. Moreover, the vertical and longitudinal turbulences cannot be well reproduced simultaneously in a passive wind tunnel, thus the spatial coherence features under simultaneous 2D turbulences have never been fully studied before.

In order to study the spatial correlations of aerodynamic loads under effectively simulated wind features and two-dimensional simultaneous incident flows, an experiment involving a stream-lined cross-section model was conducted in the active-controlled atmospheric boundary wind tunnel in Miyazaki University of Japan. The appellation “streamlined” refers to a closed-box deck designed with emphasis put on aerodynamics, but it is a strictly speaking bluff body with separated shear layers.

2 EXPERIMENTAL ARRANGEMENT

2.1 *Wind tunnel and experimental facilities*

Multiple-fans active wind tunnel in Miyazaki University consists of 99 independent blowers. It can effectively simulate the longitudinal average wind speed, turbulence profiles and different integral scales. Moreover, it can reproduce artificial stochastic wind waves under given controlling parameters (*Nishi et al. 1997; Nishi et al.1999; Cao et al. 2002)*. To generate the vertical turbulent components, an active-vibration grids is adopted which can generate the vertical turbulent wind sufficiently. Altogether 390 pressure tapping points were arranged in 5 parallel sections along span-wise, each section consists of 78 tapping points arranged along

chord-wise. Sampling frequency is 200Hz and sampling time is 100s. 3D hot-wire anemometers (KANOMAX model 1008), high precision electronic pressure scanners and simultaneous acquisition facilities (DASBOX model 2800) were adopted. Deviation of the signal caused by the length and diameter of piezometer tubes was modified.

The following figure illustrates the multi-fans and active-vibration grids in the active wind tunnel as well as the arrangement of tapping points:

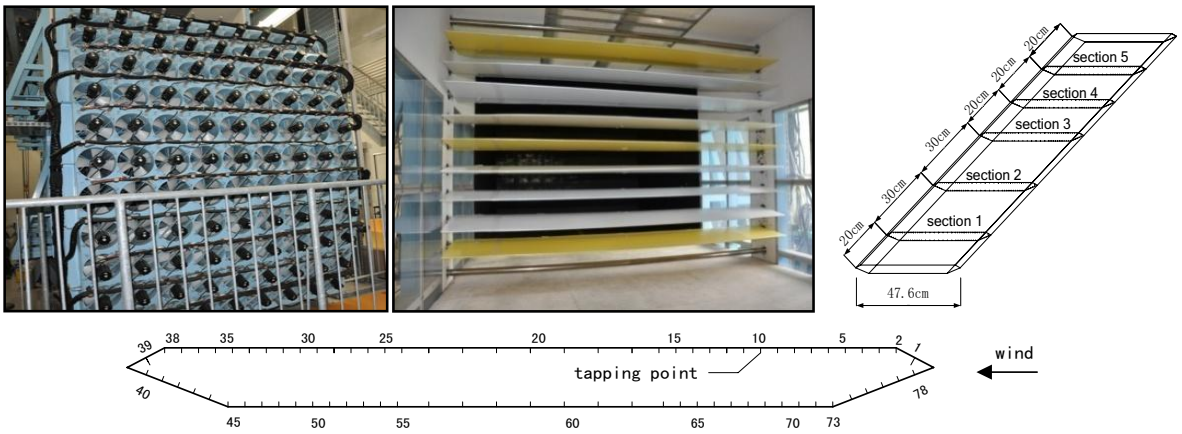

Figure 1. Active wind tunnel facilities and arrangement of tapping points

2.2 *Oncoming flow control and wind velocity modification*

The multiple-fans active wind tunnel can reproduce the target wind features sufficiently under given parameters. The von karman type wind spectrum was chosen as the target longitudinal wind spectrum, which has the following form:

$$S(f) = \frac{4 \cdot I^2 L_x / U}{\left[1+70.8 \cdot \left(\frac{f L_x}{U}\right)^2\right]^{5/6}} \tag{5}$$

where S(f) denotes the wind power spectrum; I, U, Lx and f represent the turbulence intensity, average wind speed, integral scale along the span wise, and wind frequency, respectively. As to the vertical turbulent wind spectrum, the Panofsky spectrum with the following form is adopted:

$$S(f) = \frac{\alpha \cdot u_*^2 / U}{(1+\beta \cdot \frac{f}{U})^2} \tag{6}$$

where α and β are coefficients relating to height. Figure 2 shows the target and measured spectrums of the u and w components:

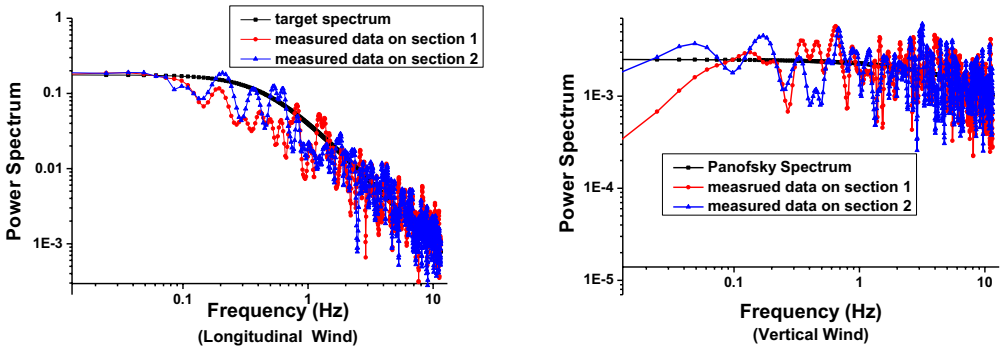

Figure 2. Target and measured power spectrums of longitudinal and vertical components

Aerodynamic forces are caused by the incident flows and are functions of the turbulent wind velocities at the reference point. The 1/4 chord point is often taken as the reference point according to the airfoil theory, and for bridge deck, the central point is always adopted. Because of the existence of section model, wind velocity at the central point of the model cannot be measured directly, thus the flow features are always measured at the up-stream or at the lateral of the deck. The measured wind features, however, are often taken as the flow features at the reference point. Because the wind energy decays along the longitudinal direction, and the wind velocities are not fully correlated between two points along the lateral direction, thus, the measured flow features cannot represent the real flow characters of the reference point.

To reflect the wind features of the reference point, a modification approach was adopted based on the stable flow features in active wind tunnel under given parameters. Firstly, a 3D hot-wire anemometer was fixed at the central point of the pressure-measuring section without installing the section model, then another one was fixed 45cm above it. Secondly, the wind velocities at these two points were measured simultaneously for a while, and the correlations of flow features like magnitude and phase between these two points were studied. A modification algorithm was proposed to reproduce the features of the lower point by using the data measured on the upper point. To examine the efficiency of this algorithm, ten validation tests under different flow conditions were conducted and it came to a commendable result.

Figure 3 illustrates a good modification result. “Target wind velocity” in this figure denotes the measured data by the 3D hot-wire anemometer fixed at the central point of pressure measuring section without the section model being installed, and the “measured data” denotes the wind velocity measured by the 3D hot-wire anemometer 45cm above the former one.

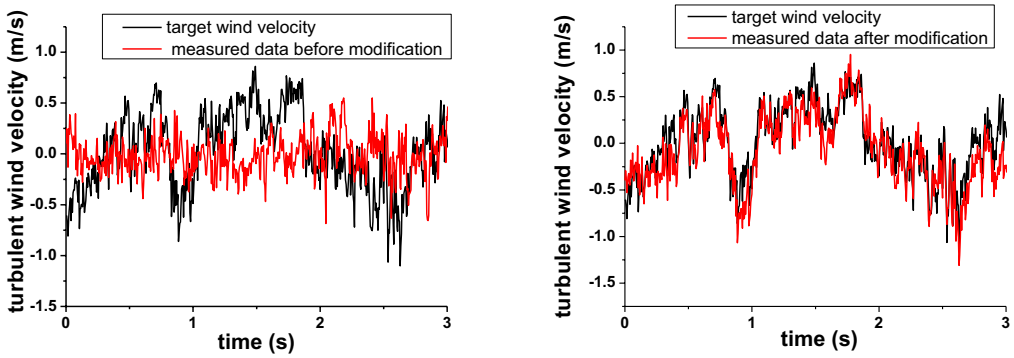

Figure 3. Target wind velocity series and measured data before and after modification

3 EXPERIMENT RESULTS AND DISCUSSION

Altogether 14 oncoming flow conditions with different flow features, like integral scale, turbulence intensity and average wind speed, were reproduced in the multiple-fans wind tunnel. Only the cross-section pressures of section 1, section 2 and section 4 were measured simultaneously with the incident flow velocities, because of the limit on the number of 3D hot-wire anemometers. Thus, the test conditions consist of 3 section-intervals (30cm, 50cm, 80cm) under 14 different flow conditions. The correlation features of aerodynamic forces and incident flows were studies in both time and frequency domains. The schematic diagram of simultaneous measurement of wind velocities and chord-wise pressures is as follows, where the red circles in this figure denote 3D hot-wire anemometers.

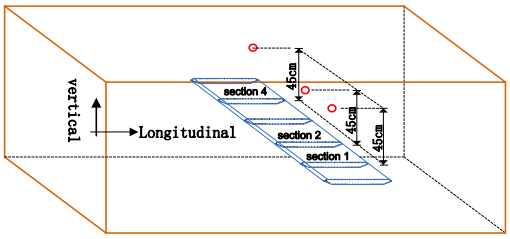

Figure 4. Schematic diagram of simultaneous measurement of wind velocities and chord-wise pressures

3.1 *Correlation coefficients with different section intervals*

In time domain, the correlation coefficients with different section intervals under a given flow condition were calculated, and an obvious phenomenon can be found that the correlation coefficients have a tight relationship with integral scales.

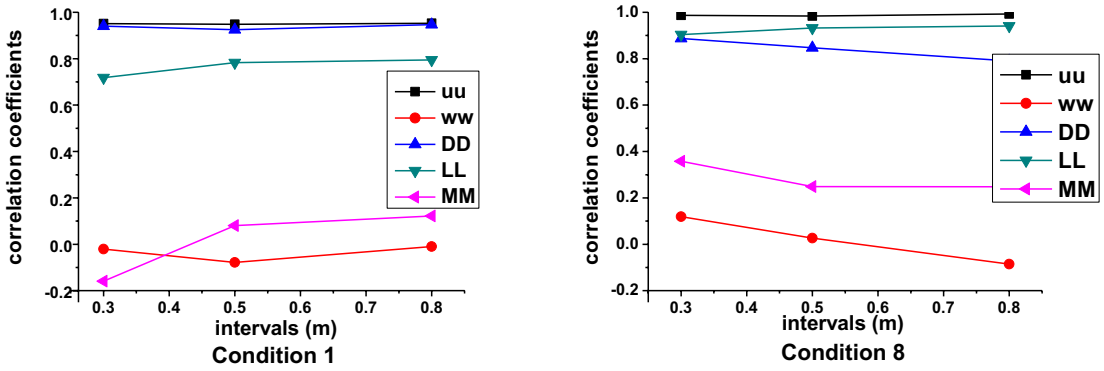

Figure 5. Correlation coefficients of aerodynamic forces and oncoming flows under condition 1 and 8

Figure 5 illustrates the correlation coefficients under condition 1 ($L_u^x = 2.033\text{m}, L_w^x = 0.097\text{m}, U = 4.57\text{m/s}$) and condition 8 ($L_u^x = 3.782\text{m}, L_w^x = 0.166\text{m}, U = 6.54\text{m/s}$). By comparing these two pictures, we can find that the longitudinal turbulent wind and the aerodynamic drag force obey the same trend, and the correlation coefficients primarily dominated by the integral scale of longitudinal turbulent wind. If the integral scale of longitudinal turbulent wind is large enough (much bigger than the section-intervals), the drag forces and longitudinal turbulent winds are almost fully correlated (around 0.95) and do not decay with the increase of section-intervals. Both the aerodynamic lifts and moments show a larger correlation feature than the vertical turbulences.

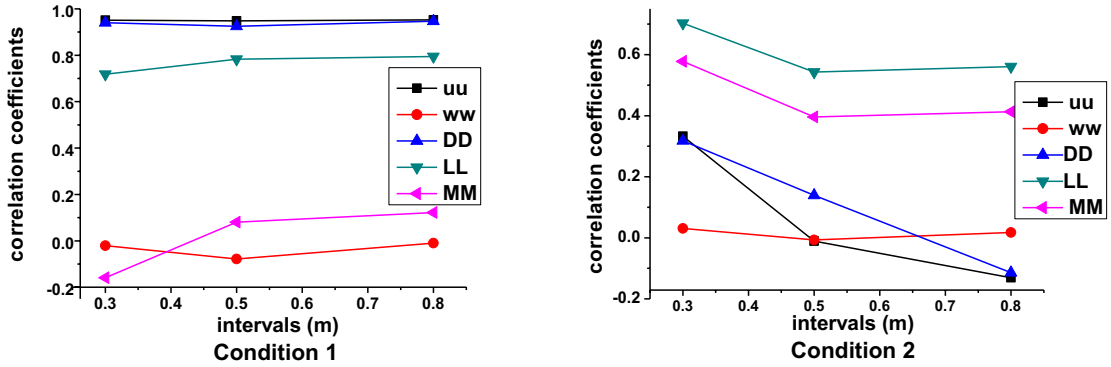

Figure 6. Correlation coefficients of aerodynamic forces and oncoming flows under condition 1 and 2

This figure illustrates the correlation coefficients under condition1 ($L_u^x = 2.033\text{m}, L_w^x = 0.097\text{m}, U = 4.57\text{m/s}$), and condition2 ($L_u^x = 0.562\text{m}, L_w^x = 0.2\text{m}, U = 4.61\text{m/s}$). By comparing these two pictures, we can find that the longitudinal turbulent wind and the aerodynamic drag still obey the same trend, although the integral scale changes a lot. With the integral scale of longitudinal wind changing from 2.033m to 0.562m, an obvious decaying trend of the correlation coefficients for both longitudinal wind and aerodynamic drag occurs. With the integral scale of vertical wind changing from 0.097m to 0.2m, an obvious increase of the correlation coefficients of aerodynamic moments can be seen. Both the lifts and moments show a much higher correlation feature than vertical wind.

3.2 *Spatical coherences and a new empirical function*

The root coherences of the three-direction aerodynamic loads have different decaying trends versus frequency. The root coherence of aerodynamic drag is bigger than that of the longitudinal wind at the higher frequency region, which has been observed by other researchers too. The aerodynamic lift has an inconsistent decaying trend with the vertical wind, and is more correlated in the frequency range of interest. The aerodynamic moment shows a similar decaying trend with the vertical turbulence and has a lower correlation feature than both of the drag and lift forces.

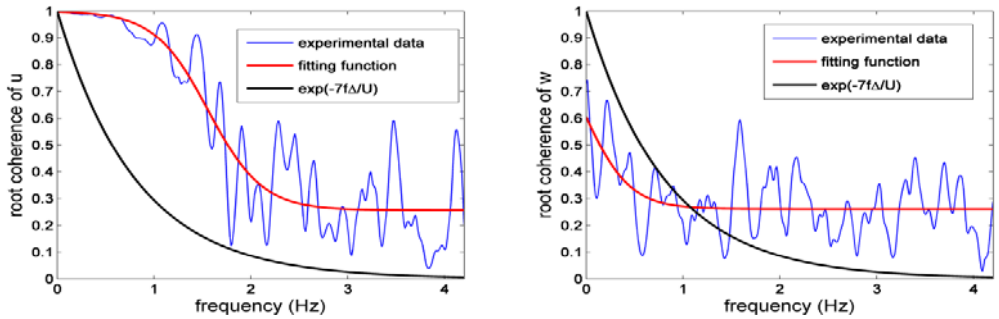

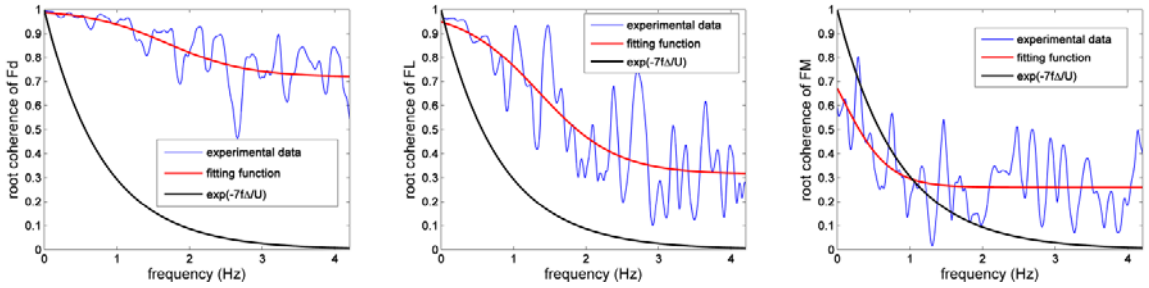

Figure 7. Root coherences of turbulent winds and aerodynamic forces under condition 1

The above figure illustrates the root coherences of the incident flows and aerodynamic forces between two cross sections at an interval of 80cm, under condition 1. The blue solid line in this figure denotes the experimental data, and the red and black solid lines respectively denote the fitting functions using the exponential expression and a new empirical function, which will be discussed later.

In order to detect the impacts of integral scales and turbulence intensities on the coherences of aerodynamic loads, a series of cases with different ratios of integral scale to section-interval were studied.

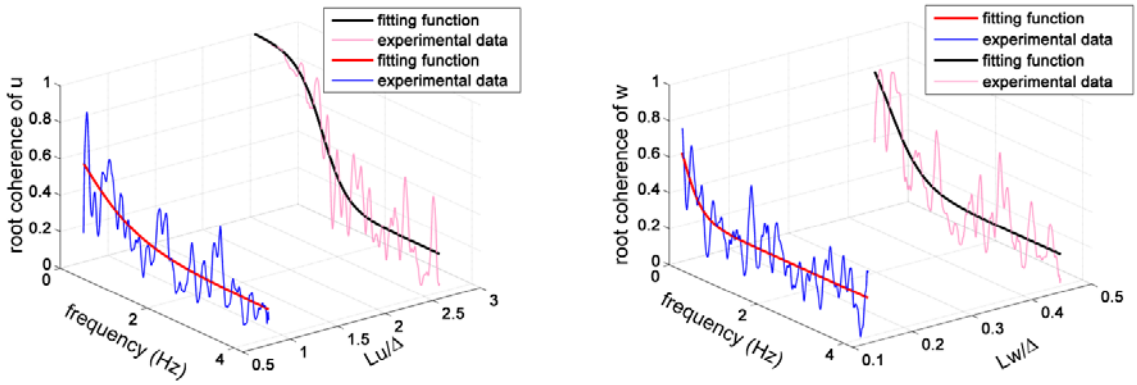

Figure 8. Root coherences of turbulent winds with different integral scales

Figure 8 illustrates that the wind correlation feature improves with the increase of integral scale, which is not difficult to understand. It is worth noting that, under a large integral-scale condition, (e. g $L_u/\Delta = 2.5$), the root coherence shows a different decaying trend versus frequency, especially in the low frequency range, where the exponential expression is no longer applicable.

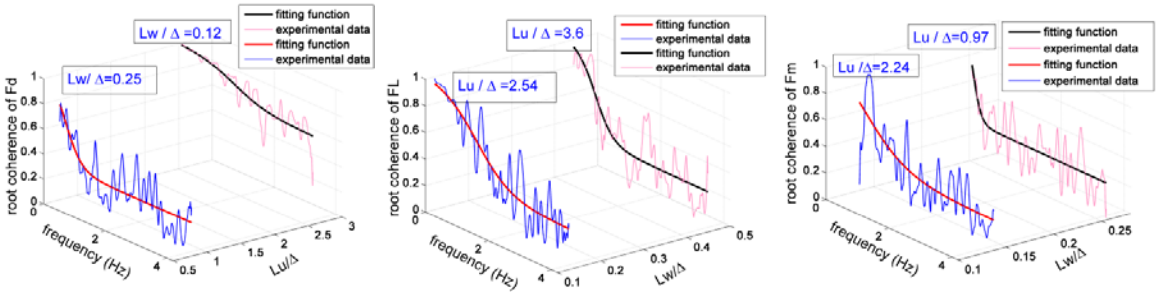

(a) Drag (b) Lift (c) Moment

Figure 9. Root coherences of aerodynamic forces under different flow conditions

Figure 9(a) shows the coherences of aerodynamic drags under different incident flow conditions. As can been seen from that picture, the aerodynamic drag is primarily dominated by the longitudinal wind, since the coherence of the aerodynamic drag decays fiercely with the decrease of longitudinal wind integral scale, though the integral scale of the vertical wind is increased. As to the aerodynamic moment, the coherence is mainly dominated by the vertical wind, on account of the similar decaying trends versus frequency at similar vertical wind integral scales, although the longitudinal components changes violently, which is reflected in Figure 9(c). The aerodynamic lift, however, seems to have a relation with both of the vertical and longitudinal incident flows, as can be seen from Figure 9(b), and its spatial coherence features cannot be simply evaluated by those of the vertical winds. The influence of turbulence intensity was also considered in this approach, and an intuitional sense is that, with the increase of turbulence intensity the value of root coherence trends to become bigger in the higher frequency region. However, because the variation range of turbulence intensities generated in this experiment is small, the detail and respective impacts of I_u and I_w on three aerodynamic forces need further experiments.

As mentioned above, the form of root coherence differs with the changes of integral scale and turbulence intensity, and once the ratio of integral scale to section interval is large enough(>1), the root coherence shows a totally different decaying trend with the exponential expression. Besides, the longitudinal and vertical turbulences have different contributions to different direction aerodynamic forces. In order to reflect the influences of these relevant factors and taking into account the different decaying trend with the exponential expression under large integral scale conditions, a new empirical expression of root coherence is proposed, which is based on the nonlinear least square method and has the following form:

$$\mathrm{Coh}^{1/2}(f,\Delta x)=c_1+\frac{1-c_1}{1+\exp\left(c_2*\left(\frac{f\cdot B}{U}\right)-c_3*\left(\frac{L^x}{\Delta x}\right)^{c4}-c_5*I_t\right)} \tag{7}$$

In this expression, f represents the frequency; Δx denotes the distance between two cross sections; U is average wind speed; B is deck width; $c_1 \sim c_5$ are fitting coefficients. As to L^x and I_t, they denote the integral scale of incident wind along the span-wise and the corresponding turbulence intensity, respectively. For the root coherence of longitudinal or vertical turbulent wind, L^x and I_t signify the flow features of its own. And for the aerodynamic forces, the static coefficients are adopted to measure the contribution ratios of different turbulent winds to different aerodynamic forces. The static coefficients were measured under uniform flow condition in the TJ-1 wind tunnel of Tongji University, Shanghai, China. Table 1 shows the values of static coefficients and their slopes under attack angle of zero:

Table 1. Static Coefficients Measured in TJ-1

C_d	0.039	C_d'	0.115
C_L	-0.012	C_L'	3.678
C_M	0.004	C_M'	1.875

The integral scales and turbulence intensities used in the root coherences of aerodynamic forces can be defined as follows:

$$L^x_{drag}=\frac{C_d*L_u+C_d'*L_w}{C_d} \qquad I_{drag}=\frac{C_d*I_u+C_d'*I_w}{C_d} \tag{8}$$

$$L^x_{lift}=\frac{|C_L|*L_u+C_L'*L_w}{C_L'} \qquad I_{lift}=\frac{|C_L|*I_u+C_L'*I_w}{C_L'} \tag{9}$$

$$L^x_{moment}=\frac{C_M*L_u+C_M'*L_w}{C_M'} \qquad I_{moment}=\frac{C_M*I_u+C_M'*I_w}{C_M'} \tag{10}$$

And the fitting coefficients through the nonlinear least square fit are illustrated below:

Table 2. Fitting Coefficients

C_1	C_2	C_3	C_4	C_5
0.23	15~25	0.85	0.85	3

(The value of C_2 is 20~25 for turbulent winds and 15~20 for aerodynamic forces.)

This expression can reflect the impacts of turbulence intensity and ratio of integral scale to section-interval on spatial coherences, and can account for the different decaying trends between aerodynamic forces and incident winds through their corresponding integral scales and turbulence intensities. But it is worth noting that this expression is derived from the experimental conditions with different integral scales but limited section-intervals. It can reproduce the decaying trend of root coherences of both aerodynamic forces and incident winds in the low frequency region preferably, which is the insufficiency of the exponential expression. However, this expression cannot demonstrate the correlations in high frequency region. The combined use of this expression with the exponential expression or a united expression containing both features of these two expressions needs further experiments and study.

4 CONCLUSION

The root coherences of both incident winds and aerodynamic forces were studied and an obvious impact of integral scale can be seen. The three-direction aerodynamic loads have different correlation features under same incident flow conditions, and the decaying trend of root coherence under large ratios of integral scale to section-interval is a far cry from the exponential expression. A new empirical expression is proposed to reflect the spatial coherence features in low frequency region and taking into account the different contribution ratios of incident winds to different aerodynamic loads. Since it is not applicable for high frequency region, the combined use of this expression with the exponential expression or a united expression containing both features of these two expressions needs further experiments and study.

5 ACKNOWLEDGE

The authors gratefully acknowledge the supports of the National Science Foundation of China (51021140005, 50978202 and 51178353), and the supports by Kwang-Hua Fund for College of Civil Engineering, Tongji University.

6 REFERENCES

[1] Matsumoto M, Chen X, Shiraishi N. Buffeting analysis of long span bridge with aerodynamic coupling (Processing of 13th National Symp on Wind Engineering) [J]. Japan Association for Wing Engineering, 1994, 227-232.

[2] Larose G L, Mann J. Gust loading on streamlined bridge decks [J]. Journal of Fluids and Structures, 1998, 12(5): 511-536.

[3] Larose G L, Tanaka H, Gimsing N J, et al. Direct measurements of buffeting wind forces on bridge decks [J]. Denmark Journal of Wind Engineering and Industrial Aerodynamics, 1998, (74-76): 809-818.

[4] Larose G L. The spatial distribution of unsteady loading due to gusts on bridge decks [J]. Journal of Wind Engineering and Industrial Aerodynamics, 2003, (91): 1431-1443.

[5] Nagaoa F, Utsunomiya H, Noda M, et al. Basic study on spatial correlations of fluctuating lifts acting on plates [J]. Journal of Wind Engineering and Industrial Aerodynamics, 2003, (91): 1349-1361.
[6] Nishi A, Kikugawa H, Matsuda Y, Tashiro D. Turbulence Control in Multiple-fan Wind Tunnels [J]. Journal of Wind Engineering and Industrial Aerodynamics, 1997, (67&68): 861-872.
[7] Cao S Y, Nishib A, Kikugawac H, Matsuda Y. Reproduction of Wind Velocity History in A Multiple-fan Wind Tunnel [J]. Journal of Wind Engineering and Industrial Aerodynamics, 2002, (90): 1719.

The Seventh International Colloquium on Bluff Body Aerodynamics and Applications (BBAA7)
Shanghai, China; September 2-6, 2012

Analytical study on lateral-torsional buckling of long-span suspension bridge

Hiroshi Katsuchi [a], Hitoshi Yamada [b], Kai Hasegawa [c]

[a]*Yokohama National University, Yokohama, Japan*
[b]*Yokohama National University, Yokohama, Japan*
[c]*JFE Engineering Corporation, Yokohama,Japan*

ABSTRACT: Not only aerodynamic instability such as flutter but also aerostatic instability such as lateral-torsional buckling would be concerns of wind-resistant design of super long-span suspension bridges. Authors' past analytical study on lateral-torsional buckling proved the difficulty of distinction of lateral-torsional buckling from divergence, both of which are divergent response phenomena. This study tried to numerically identify lateral-torsional buckling of a long-span suspension bridge with considering geometric and aerodynamic non-linearity under wind loading.

KEYWORDS: Lateral-torsional buckling, suspension bridge, geometric nonlinearity, aerodynamic nonlinearity

1 INTRODUCTION

As the main span length of a suspension bridge becomes much longer, it was pointed out (Nakamura, et al., 1998) that not only aerodynamic instability such as flutter but also aerostatic instability such as lateral-torsional buckling would be concerns of wind-resistant design. Hirai (1942) of the University of Tokyo of those days firstly proposed a calculation formula of the critical wind speed of lateral-torsional buckling of a suspension bridge. This formula included some simplifications such as only consideration of force equilibrium of a wind-loaded girder and exclusion of geometric nonlinearity. Since then, analytical studies (Nazmy, et al., 1990, Boonyapinyo, et al., 1993) on lateral-torsional buckling including aerodynamic, geometric and material nonlinearity have been conducted.

Recently, owing to the availability of powerful advanced FEM analysis softwares, sophisticated structural analysis including nonlinearities and wind-structure interactions can be possible. Authors have tried to analyze lateral-torsional buckling of suspension bridges (Yamada, et al., 2009). However difficulty of distinguishing lateral-torsional buckling from divergence was encountered. Because they are both aerostatic instability accompanying sudden large wind-induced deflections at a certain high wind speed.

In this study, a Mode Tracing Flutter Analysis method (Nguyen, et al., 1998), which was originally developed to trace modal parameters of pre-selected particular vibration modes in flutter analysis, was used to identify and distinguish lateral-torsional buckling from divergence. The paper presents the analytical methodology and demonstration results for lateral-torsional buckling of a long-span suspension bridge.

2 CLOSED-FORM SOLUTION OF AEROSTATIC INSTABILITY

2.1 *Lateral-torsional buckling*

A girder of a suspension bridge deflects largely in an along-wind direction under wind loading. Not only lateral bending moment due to a drag force but also vertical lift and torsional moment are applied to the bridge girder. This may accelerate the occurrence of lateral-torsional buckling of the girder more than only drag force case.

Hirai (1942) firstly proposed a calculation formula of the critical wind speed of lateral-torsional buckling of a suspension bridge girder. A girder is subjected to a drag force laterally about its strong axis, a lift force vertically about its weak axis and a pitching moment about its rotation center, as shown in Figure 1. Equilibriums of all forces for the girder are written in Equation (1).

$$EI\frac{d^4\eta}{dx^4} - 2H_\omega\frac{d^4\eta}{dx^4} - 2h_1\frac{d^2y}{dx^2} + \frac{d^2}{dx^2}(\mathrm{M}\varphi) - (S + C_d)pb\varphi = 0 \tag{1a}$$

$$M\frac{d^2\eta}{dx^2} - EC_\omega\frac{d^4\eta}{dx^4} - \left(GK + \frac{H_\omega b^2}{2}\right)\frac{d^2\eta}{dx^2} - bh_2\frac{d^2y}{dx^2} - S_t pb^2\varphi = 0 \tag{1b}$$

where η and φ are a vertical and torsional displacement, respectively, and EI, GK and EC_w are a bending, torsional and bending-torsion stiffness, respectively. H_w is a cable tension under self weight, M is lateral bending moment of the girder. C_d, S and S_t are a drag coefficient, slopes of lift and pitching moment coefficients, respectively. In addition, h_1 and h_2 are an increment of a cable horizontal tension by η and φ, respectively.

Secondly, Hirai developed an equation of motion with including an inertia term of the girder. He identified the critical wind speed condition by comparing a critical condition of lateral buckling, as shown in Equation (2).

$$V_k^{\,2} = \frac{142.2}{\mu C_D \rho b l^3}\sqrt{EJ\cdot\overline{GK}} \tag{2}$$

where $EJ = EI + \dfrac{l^2}{2\pi^2}H_\omega$, $\overline{GK} = \dfrac{4\pi^2}{l^2}EC_\omega + GK + \dfrac{b^2}{2}H_\omega$ and $\mu = \sqrt{1 + 0.287\dfrac{S + C_D}{C_D}}$

Equation (2) assumes an asymmetric lateral-torsional buckling mode for a mono span suspension bridge. Therefore, some correction is necessary for a multi span suspension bridge or different boundary conditions such as the transmission of wind load to main cables (JSCE, 1967 & Okauchi, et al., 1967).

2.2 *Divergence*

Divergence is another aerostatic instability which is negative feedback of torsional deflection due to pitching moment. A critical wind speed for divergence is given in Equatin (3) by equilibrium of pitching moment and torsional restoring force. Although divergence is clearly different from lateral-torsional buckling from the viewpoint of occurrence mechanism, it is very difficult to distiguish between two aerostatic instabilities by numerical prediction. Because both two phenomena suddenly occur at a certain wind speed.

$$U_C = \sqrt{\frac{2k_\alpha}{\rho B^2 S_t}} \tag{3}$$

where k_a is torsional stiffness.

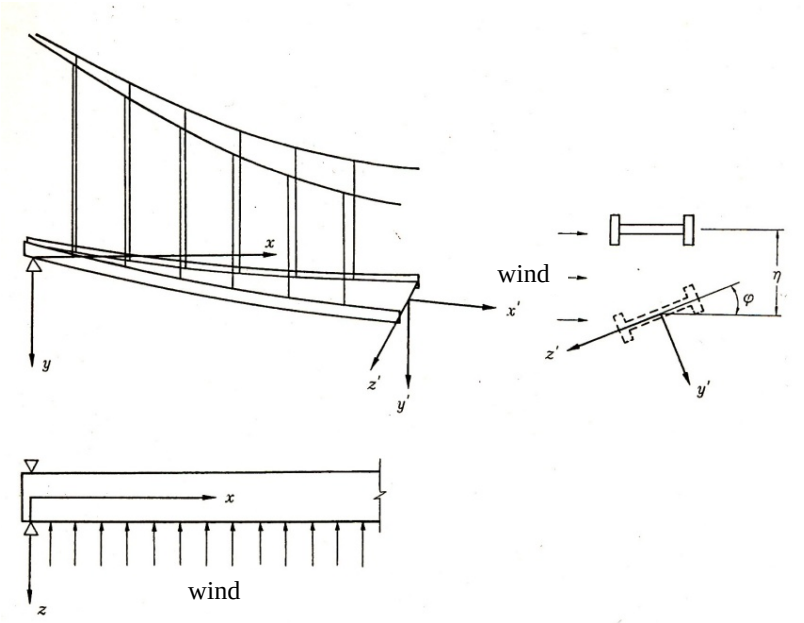

Figure 1. Deflection of suspension bridge girder under wind loading

3 ANALYTICAL FORMULATION OF LATERAL-TORSIONAL BUCKLING

3.1 *Mode-trace Method*

A mode-trace method, which was developed by Dung (1998), et al, is a flutter analysis method with consideration of large wind-induced deflection of a bridge. It consists of two parts: static and dynamic analyses. The static analysis part solves an equilibrium condition of the bridge structure under wind loading and corresponding large deflection at each analytical wind speed step. The dynamic analysis part uses that equilibrium condition and solves an eigenvalue problem with consideration of aeroelastic wind forces. In particular, the mode-trace method can solve only eigenvalues of interest which are selected in advance. Using this method, particular modes only can be sought with the increase of wind speed.

In this study, the static analysis part is used to find the critical condition of lateral-torsional buckling. In case of a suspension bridge, large wind-induced deflection is caused by wind load. Geometric nonlinearity should be considered. In addition, wind load of a suspension bridge girder is dependent on angle of attack (wind-induced torsional deflection). Wind load should also be updated according to wind-induced torsional deflection obtained at each wind speed.

As described in 2, lateral-torsional buckling and divergence are both static instability that torsional deflection suddenly increases at a certain wind speed. It is difficult to distinguish those two phenomena from wind-induced torsional deflection only. In this study, lateral-torsional buckling is identified by searching a condition that any diagonal term in the stiffness matrix is non positive during conducting the static analysis part of the mode-trace method.

3.2 *Benchmark study*

In order to validate the identification method of lateral-torsional buckling by diagonal terms, a benchmark study was conducted with using a simple beam subjected to uniform distributed loads as shown in Figure 3. The beam has a 10 m I shape cross section with 300 mm wide, 500 mm high, 11 mm flange thickness and 18mm web thickness. Lateral load which is equivalent to 0.1% span length imperfection was applied. Increasing the uniform distributed load, a critical condition that any diagonal term in the stiffness matrix is non positive was sought.

Figure 4 shows vertical, lateral and torsional deflections in the middle of span versus uniform distributed load intensity. Lateral and torsional deflections suddenly increase at the load intensity of 84 kN/m while vertical deflection increases linearly. At this step, diagonal terms of the stiffness matrix became no positive. It turned out that identification of lateral-torsional buckling by non positive diagonal terms in the stiffness matrix is valid.

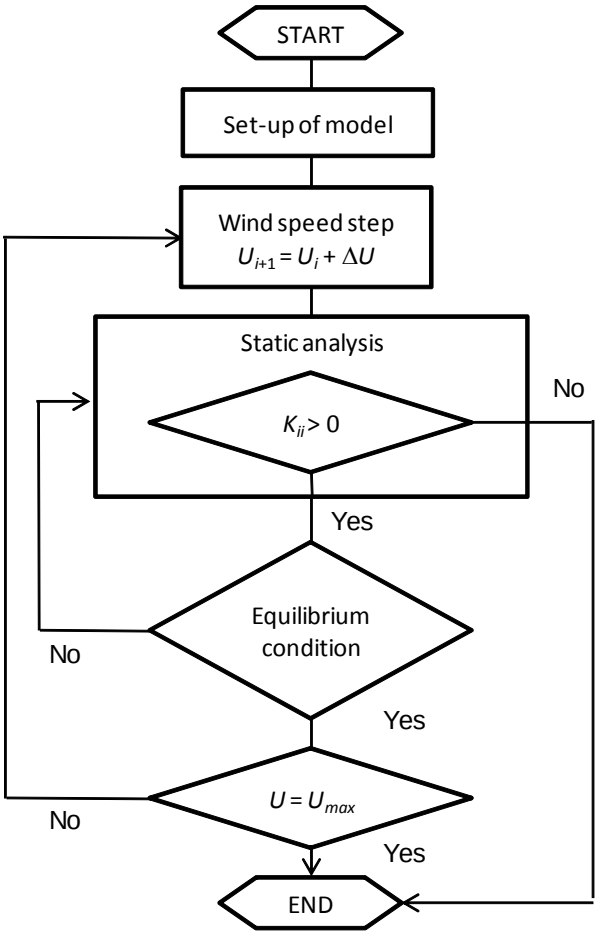

Figure 2. Flowchart of analysis of lateral-torsional buckling

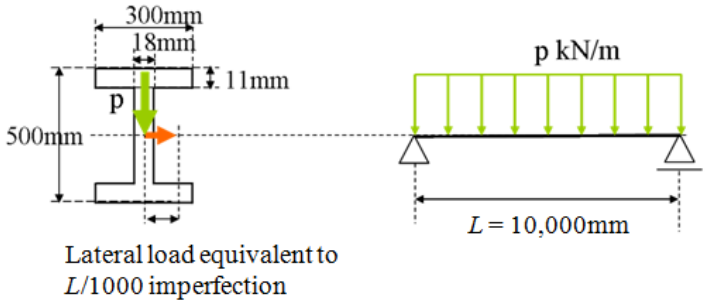

Figure 3. Simple beam for benchmark study

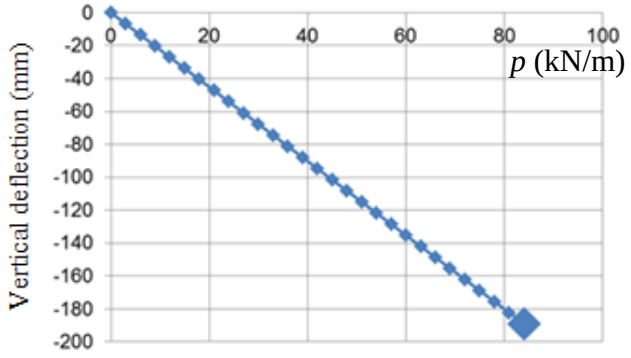

(1) Vertical deflection

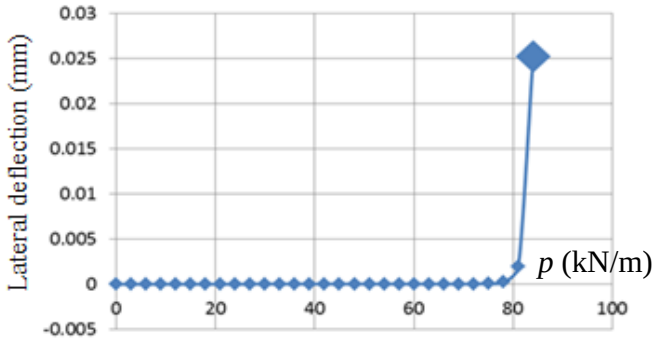

(2) Lateral deflection

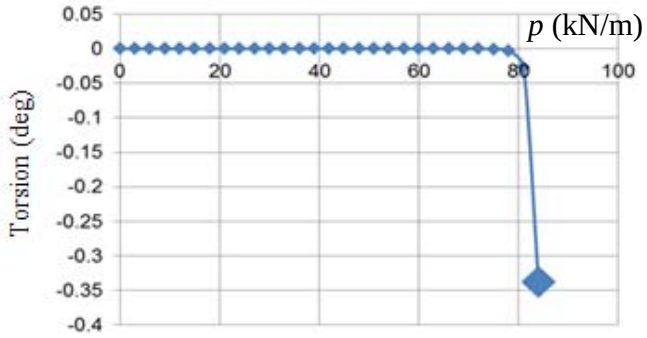

(3) Torsional deflection

Figure 4. Deflection at span center vs. load intensity

4 LATERAL-TORSIONAL BUCKLING OF AKASHI KAIKYO BRIDGE

4.1 *Original analysis*

Using the mode-trace method, lateral-torsional buckling of the Akashi Kaikyo Bridge was analyzed. It has a truss-stiffened girder with the center span of 1,991 m and two side spans of 960 m. It was modeled by a 3D frame model with lumped masses as shown in Figure 5. Figure 6 shows three component force coefficients vs. angle of attack.

According to the three component force coefficients and an angle of attack at each wind speed step, drag, lift and pitching moment were applied at shear centers of the girder. In addition, drag and lift were applied at main cables, and drag was applied at towers.

Figure 7 shows wind-induced deflections in the middle of the center span of (1) vertical, (2) Lateral and (3) torsion versus wind speed. Vertical and torsional deflections suddenly increase at a wind speed of 140 m/s where a diagonal term of the stiffness matrix is non positive. Because a diagonal term of the stiffness matrix is non positive, this sudden increase of vertical and torsional deflections at a wind speed of 140 m/s must result from the onset of lateral-torsonal buckling, which is clearly different from divergence.

4.2 *Parameter analysis*

In order to investigate the contribution of each three component force coefficient to lateral-torsional buckling, parameter studies with different combinations of three component force coefficients were carried out.

Firstly, drag forces were only applied (CD only). Figure 8 and Table 1 show comparisons of wind-induced torsional deflection between drag only case and original case (Figure 7). This case exhibited lateral-torsional buckling at a wind speed of 305 m/s, which is much larger than the original case. This shows that a drag force can cause lateral-torsional buckling due to the structural feature of a suspension bridge that the girder is suspended by hungers. In addition, it can be understood that a lift force and pitching moment can enhance the onset of lateral-torsional buckling because those forces act out of the lateral direction.

Secondly, effects of a lift force were investigated. Figure 9 and Tabale 1show comparisons of wind-induced torsional deflection among different lift force coefficient cases. The case that lift force coefficients were decreased to 1/10 exhibited lateral-torsional buckling at a wind speed of 140 m/s. In addition, the 10 times case yielded 125 m/s. From both results, it can be understood that lateral-torsional buckling is not affected much by lift forces.

Finally, effects of a pitching moment were investigated. Figure 10 and Table 1 show comparisons of wind-induced torsional deflection among different pitching moment coefficient cases. From the cases with 10 times and 1/10 pitching moment coefficients, it can be understood that lateral-torsional buckling is largely affected by a pitching moment. Furthermore, only pitching moment cannot case lateral-torsional buckling easily. It can also be understood that lateral-torsional buckling is an instability phenomenon caused by a multiplication effect of a drag, lift and pitching moment.

Table 1. Analytical conditions of parameter study.

Cases	Critical wind speed (m/s)
Original	140
CD only	305
CL/10	140
10CL	125
CM/10	215
10CM	60
CM only	220
10CM only	70

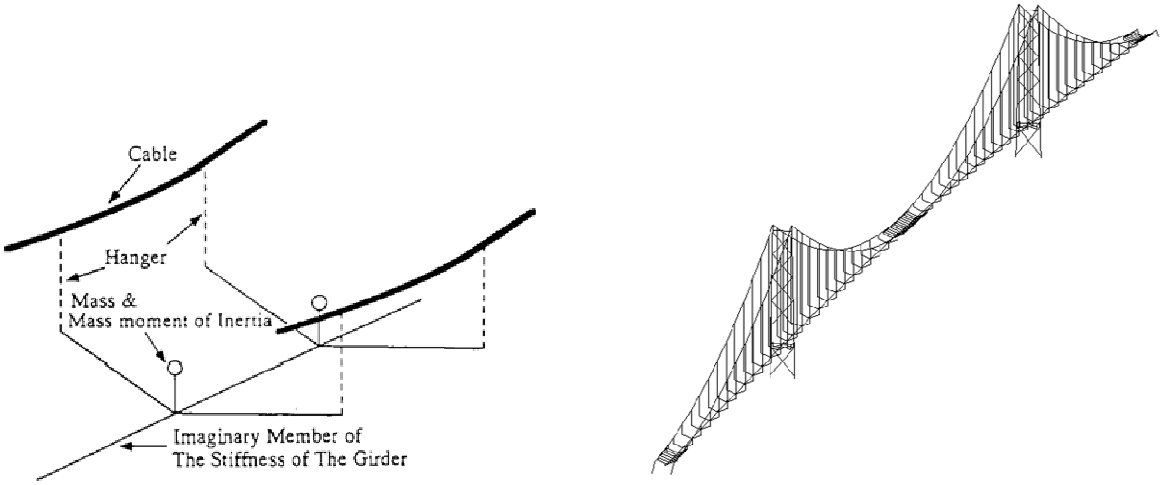

(1) Close-up of truss girder model (2) Skeleton

Figure 5. Analytical model of Akashi Kaikyo Bridge

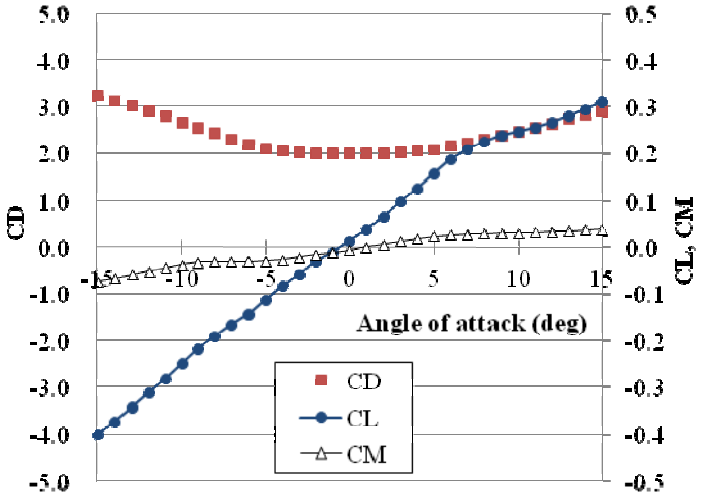

Figure 6. Three component force coefficients

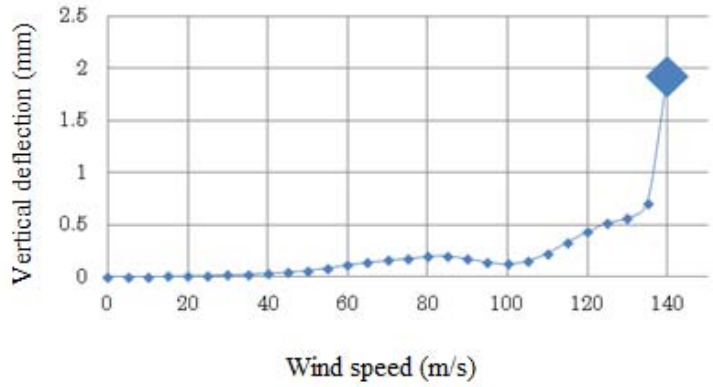

(1) Vertical deflection

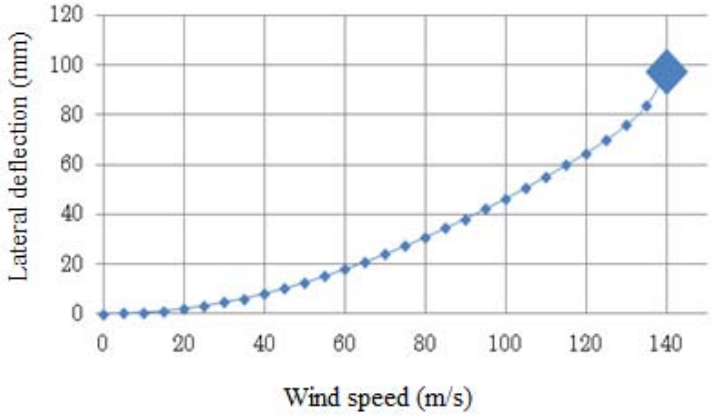

(2) Lateral Deflection

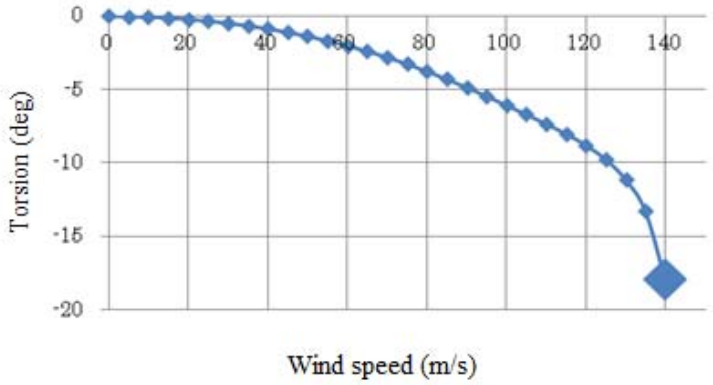

(3) Torsional deflection

Figure 7. Deflection at span center vs. wind speed

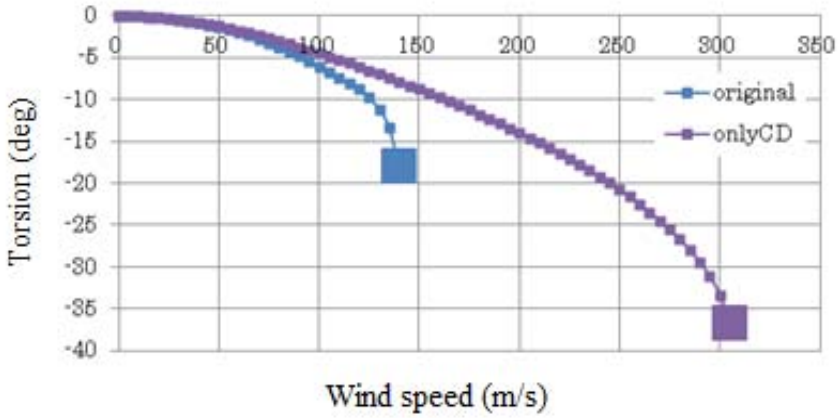

Figure 8. Deflection at span center vs. wind speed for drag only case

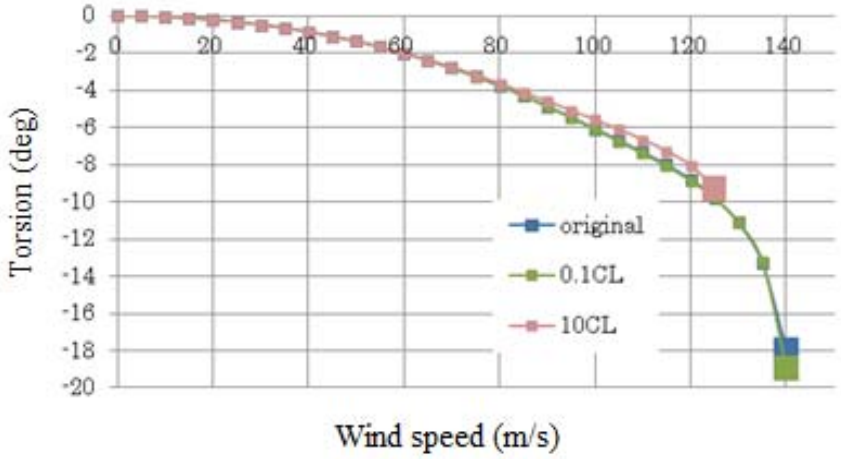

Figure 9. Deflection at span center vs. wind speed for different lift coefficient case

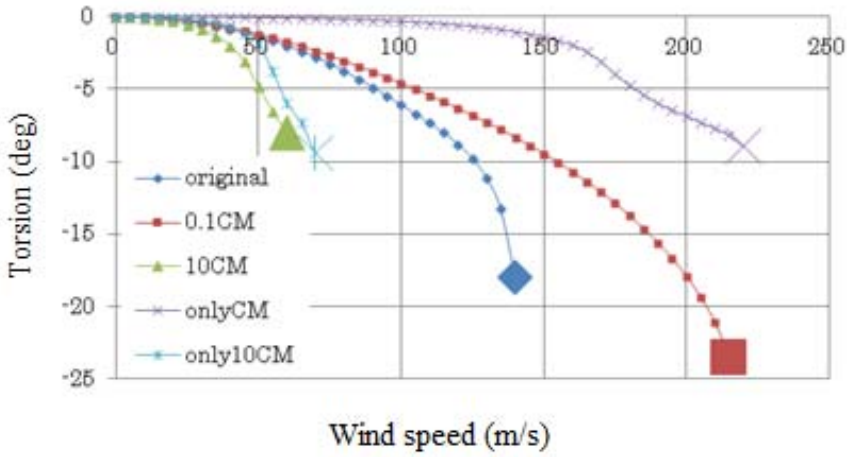

Figure 10. Deflection at span center vs. wind speed for different pitching moment coefficient case

5 CONCLUSIONS

Numerical estimation of lateral-torsional buckling of a long-span suspension bridge with using a Mode Tracing Flutter Analysis method was carried out. Results obtained in this study are as follows:

Onset of lateral-torsional buckling was identified by a non-positive value of diagonal terms in the stiffness matrix incorporating wind-loading effects. A benchmark study for a simple beam and an application for the Akashi Kaikyo Bridge showed that a deflection process with the increase of wind speed well represented a sudden onset of instability where a non-positive value was detected in a diagonal term of the stiffness matrix. However experimental work to validate the estimation method should be done in future.

REFERENCES

Boonyapinyo, V., Yamada, H. and Miyata, T. 1993. Nonlinear buckling instability analysis of long-span cable-stayed bridges under displacement-dependent wind load, J. of Structural Engineering, JSCE, Vol.39A, pp.923-936.

Hirai, A. 1942. On stability of suspension bridges against torsional vibration, *Journal of Japan Society of Civil Engineers*, JSCE, vol.28, No.9, pp.769-786.

Japan Society of Civil Engineers 1967. Feasibility study report on Honshu-shikoku Bridges, Annex 1: Guidelines of wind-resistant design.

Nakamura, T., Miyata, T. and Yamada, H. 1998. Study on wind-induced static instability and its analytical method of long-span suspension bridge, *Proc. of 53rd annual meeting of JSCE*, I-B62, pp.124-125.

Nazmy, A.S. and Abdel-Ghaffar, A.M. 1990. Three-dimensional nonlinear static analysis of cable-stayed bridges, Computers & Structures, Vol.34, No.2, pp.257-271.

Nguyen, N. D., Miyata, T., Yamada, H. and Ngyuen, N. M., 1998. Flutter responses in long span bridges with wind induced displacement by the mode tracing method, *Journal of Wind Engineering and Industrial Aerodynamics*, Vol.77&78, pp.367-379.

Okauchi, I., and Nemoto, K. 1967. On lateral-torsional buckling of suspension bridges under wind pressure, *Proc. of 22nd annual meeting of Japan Society of Civil Engineers*, JSCE, vol.22, pp.136-1, 136-4.

Yamada, H., Katsuchi, H. and Sasaki, E. and Ishihara, D. 2009. Wind-induced lateral-torsional buckling analysis of long-span suspension bridge, *Proc. of 10th International Conference on Structural Safety and Reliability*, Osaka, Japan, pp.818-823.

The Seventh International Colloquium on Bluff Body Aerodynamics and Applications (BBAA7)
Shanghai, China; September 2-6, 2012

A comparison of RANS computations and wind tunnel tests for RMS pressures on a high-rise building model

Ivo Kalkman [a], Jörg Franke [b], Alexander Bronkhorst [a,c] and Carine van Bentum [a]

[a] *TNO, Delft, the Netherlands*
[b] *Universität Siegen, Department of Mechanical Engineering, Siegen, Germany*
[c] *Eindhoven University of Technology, Department of the Built Environment, Eindhoven, the Netherlands*

ABSTRACT: Five root-mean-square (RMS) pressure models are used in combination with different turbulence models to determine whether it is possible to obtain a conservative estimate of RMS pressures on a high-rise building model from a RANS calculation. When a precursor domain is used for the generation of inlet profiles the turbulent kinetic energy is severely underestimated and, as a result, all RMS models are found to be highly non-conservative, irrespective of the turbulence model which is used. Although the prescription of an ABL profile of the desired shape at the inlet or the prescription of more appropriate wall functions on the bottom of the computational domain might lead to more conservative results it is concluded that new models are needed to enable the calculation of RMS values from RANS calculations for engineering purposes.

KEYWORDS: RMS pressure model, high-rise building, RANS

1 INTRODUCTION

Although much progress has been made in recent years, the prediction of local peak wind pressures on building facades with CFD analysis has proven difficult (Stathopoulos, 1997). Time dependent techniques like DES or LES are required to obtain accurate solutions (Lim (2009)). However, these techniques are currently too expensive and complex for everyday use by construction engineers. Combined with the fact that validation of these techniques for this application is still an ongoing effort, it is unlikely that CFD analysis will be a viable alternative for building codes or wind tunnel testing in the near future. However, the application of CFD could be beneficial in the early design phase of a building, where a cheap, quick, rough estimate of wind loads is desired. A Reynolds Averaged Navier-Stokes (RANS) simulation meets these criteria.

Unfortunately, this type of simulation only provides information on the mean wind pressures. For the calculation of peak pressures, some assessment of the pressure fluctuations such as a root-mean-square (RMS) pressure is needed. A turbulence model contains some information on the fluctuating state of the flow. For example, the RMS values of the fluctuating velocity components are directly related to the square-root of the time-averaged turbulent kinetic energy. Paterson and Holmes (1989), Selvam (1992), Paterson (1993) and Richards and Wanigaratne (1993) derived models for estimating the RMS pressure from the mean turbulence characteristics of the flow. Another option, the generation of a synthetic turbulent velocity field using a stochastic model and subsequently solving the Poisson equation that governs the pressure fluctuations field (Senthooran, 2004) is outside the scope of the current paper.

These models were developed with best agreement between calculation and experiment in mind. While this is a logical approach from a scientific point of view, for a construction engineer the most important question is whether the model will result in a safe prediction of the actual wind loads. For a safe prediction, the model needs to produce a conservative estimate. From this point of view the most appropriate model is therefore not necessarily the most accurate one.

This study investigates five RMS pressure models using three turbulence models (Standard k-ε, Realizable k-ε, and RNG k-ε) for an isolated high-rise building in suburban terrain conditions. The goal of this study is to determine for the 15 combinations of turbulence and root-mean-square models whether:

- The combination of turbulence model and RMS model is conservative;
- If not, in which regions of the high-rise building model the combination is not conservative.

2 MODEL DEFINITION

2.1 *Wind tunnel model*

Wind tunnel experiments have been carried out in the open circuit atmospheric boundary layer wind tunnel of TNO in the Netherlands, depicted in figure 1a. It has a working section of approximately 13.5 m in length, 3 m in width and 2 m in height. The boundary layer used in this study was developed over the length of the test section using 50 mm cubic roughness elements and 6 spires located at the beginning of the test section, resulting in a wind tunnel roughness length of z_0 = 0.0032 m. The roughness elements extended onto the turntable to prevent the development of an internal boundary layer.

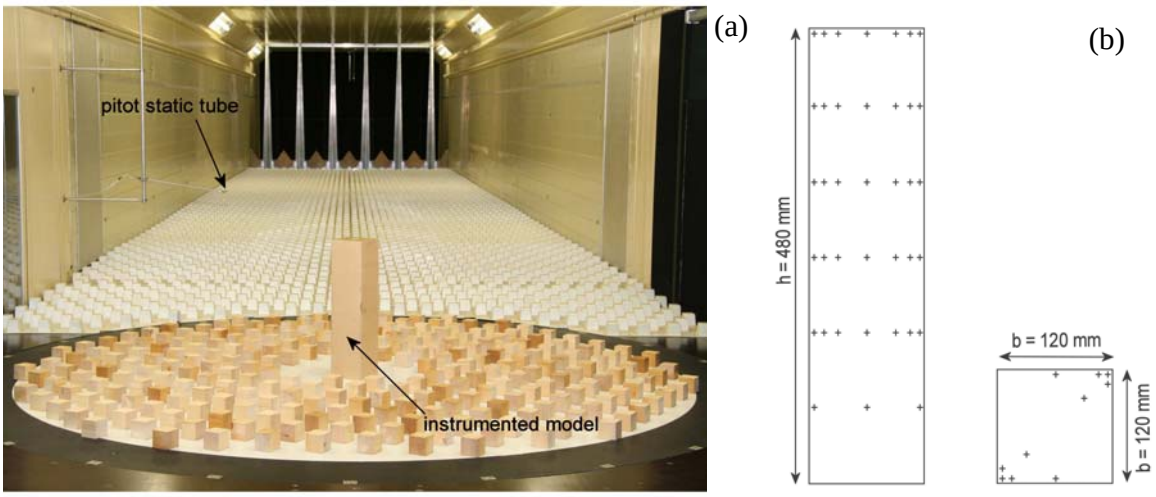

Figure 1. (a) Test configuration in the wind tunnel of TNO, (b) pressure tap distribution on the model faces

Experiments were performed on a geometrical scale of 1:250. The building model was a square cylinder with a height of h = 48 cm and side b = 12 cm. The reference model was instrumented with pressure taps at 86 locations, illustrated in figure 1b, which were sampled simultaneously. After one measurement run the model was rotated 90 degrees and a second run was performed for the same configuration, giving pressure data at 86 new locations. The total number of locations where pressure measurements were performed was therefore 172.

A hot wire anemometer was used to measure both wind speed and turbulence intensity characteristics of the boundary layer flow. Figure 2 illustrates the velocity magnitude and turbulent kinetic energy above the centre of the turntable without model present.

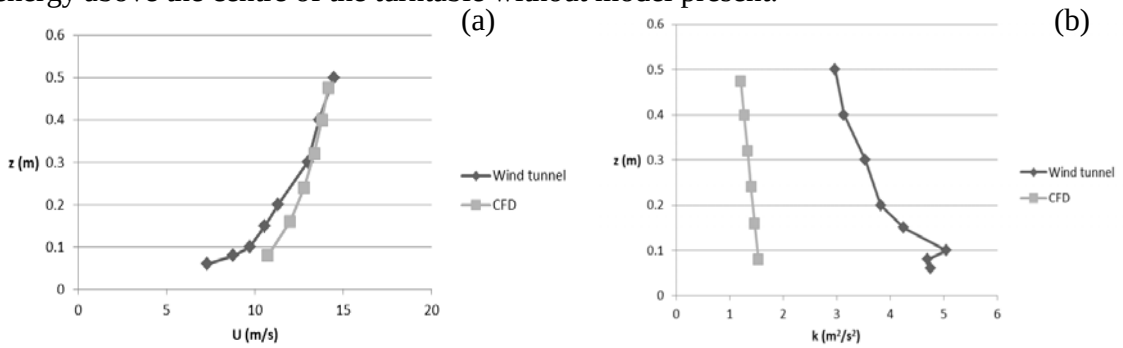

Figure 2 Approach flow profiles of (a) velocity magnitude and (b) turbulent kinetic energy

The wind speed in the wind tunnel in the presence of the model, measured with a pitot static tube, was U_{ref} = 14.2 m/s at model roof height (h_{ref} = 0.48 m). Building pressures were measured with a sampling rate of 400 Hz for a period of approximately 20.5 seconds. The pressures were converted to mean pressure coefficients, defined as

$$C_{\bar{p}} = \frac{\bar{p}}{\frac{1}{2}\rho U_{ref}^2} \tag{2}$$

in which $\bar{p}$ is the time-average of the entire measured pressure signal and ρ the air density.

2.2 *CFD model*

The numerical simulations were performed with the open source flow solver OpenFOAM 2.1.0. The statistically steady flow field was computed by solving the RANS equations using the simpleFoam solver for steady state incompressible flows. Three different turbulence models were employed: the standard *k*-ε model, the realizable *k*-ε model and the RNG *k*-ε model. All calculations were run until the residuals showed no further improvement. For the standard and realizable *k*-ε models residuals of approximately $1.0 \cdot 10^{-6}$ or smaller were achieved. For the RNG *k*-ε model the residuals were much higher, with a maximum of $3.5 \cdot 10^{-3}$ for the lateral velocity component in several calculations. These residuals were much reduced upon mesh refinement (see section 2.3), indicating that this effect is most likely due to a greater mesh sensitivity for this model. Since observed differences in the solution upon refinement were small the results were nevertheless considered adequately converged.

The computational domain corresponded to the wind tunnel model described in the previous paragraph. Velocity, turbulent kinetic energy and turbulent dissipation rate equilibrium profiles were generated by running a precursor computation on a periodic domain and prescribing the resulting profiles at the inlet of the model computational domain. Both the lateral boundaries and top boundaries were modeled as symmetry planes. The building surface was treated as a solid smooth wall. Standard rough wall functions based on the local velocity field (nutURoughWallFunction) were employed at the bottom of the domain.

Gauss linear schemes were used for the calculations of gradients and Gauss linear corrected schemes for the Laplacians. Furthermore linear interpolation and corrected surface normal gradient schemes were selected. For the calculation of divergence the limitedLinear2V scheme was used for the velocity field, in which the calculated face gradient is used to blend in a small amount of the solution in the upwind cell (here a multiplication factor between 0.2 and 0 was used) in order to damp high-frequency oscillations in the solution. Self-filtered central differencing was applied for the calculation of divergences for the k and ε fields. For the last divergence term, involving the effective viscosity, a Gauss linear scheme was applied.

2.3 *Computational grid*

The CFD model of the high-rise building had a length of (L = 10.08 m), a width of (W = 3.00 m) and a height of (H = 2.00 m). The domain measured 4.4 h_{ref} (= 2.1 m) upstream of the building, 16.4 h_{ref} (= 7.86 m) in the downstream direction, 3.0 h_{ref} (= 1.44 m) to each side and 3.2 h_{ref} (= 1.52 m) in the height direction. These values were chosen to enable a fair comparison with the results from the wind tunnel tests and lead to a very low blockage of 0.96 %. They also correspond with most recommendations specified in COST Action 732 (2007).

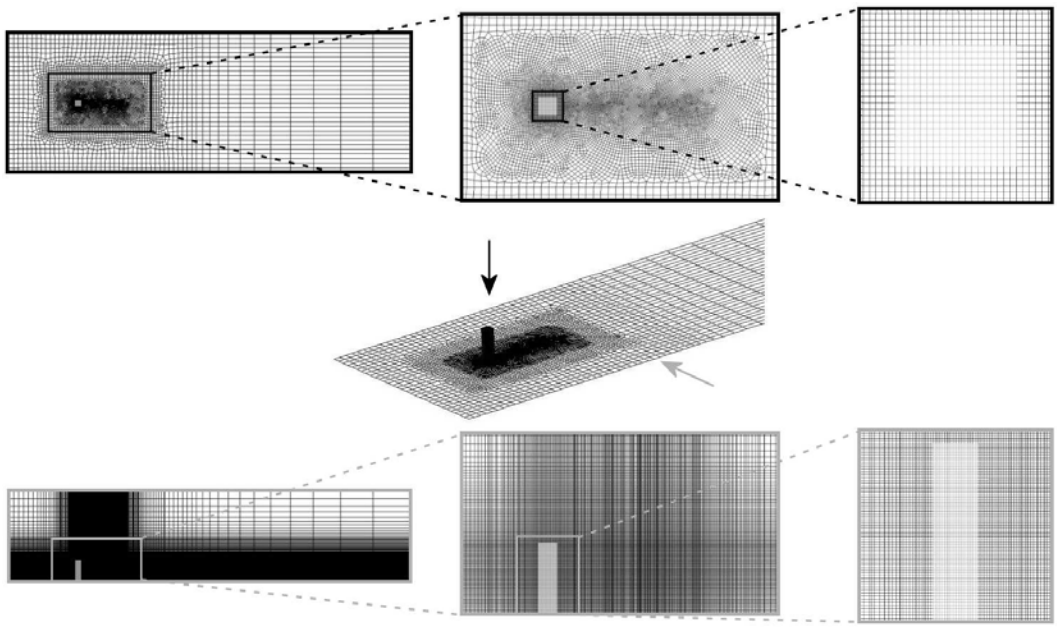

Figure 3 Coarsened mesh (top view in black, side view in grey).

Purely hexahedral meshes were created using Gambit 2.4.6. A coarsened version of the mesh used in the calculation at a zero degree angle of attack is depicted in figure 3. The mesh was successively refined towards the building surfaces and in the wake of the building. This was done by specifying the desired cell size on the building surface and in the wake, meshing the ground plane using a quad pave scheme and extruding the resulting surface mesh in the vertical direction. The smallest cell size at the building surface was approximately 5 mm in each direction, leading to a y^+ range of $1.03 \leq y^+ \leq 310.74$ for all calculations with a mean value of $y^+ = 79.02$. The number of cells over the building surfaces was 24 in the streamwise and spanwise directions and 88 over the building height. The total number of cells used was 2,219,268.

For a mesh refinement study a coarser and a finer mesh with 369,078 and 5,747,816 cells, respectively, were also used. From this study it was concluded that the average difference between $C_{p,mean}$ values calculated for the medium and fine meshes was very small: 0.59 % for the standard k-ε model, 1.14 % for the realizable k-ε model and 0.87 % for the RNG k-ε model. Close to building edges differences up to nearly 100 % were observed owing to the numerical difficulties in modeling sharp corners. Since large near-wall gradients exist for the turbulent kinetic energy the average differences for calculated k values were substantially larger: 6.37 % for the standard k-ε model, 15.41 % for the realizable k-ε model and 23.52 % for the RNG k-ε model. Local differences up to 212 % were observed.

Nine more angles of attack were calculated, ranging from 5 to 45 degrees at 5 degree intervals. Both the resolution near the building as well as the total number of cells in these nine meshes were similar to those for the 0 degree angle of attack medium resolution mesh.

2.4 *RMS pressure models*

Various models have been developed for determining the RMS pressures in a RANS simulation. Paterson and Holmes (1989) published the first formula for prediction of RMS pressure coefficients. Starting from Bernoulli's equation and using experimental results, they obtained:

$$C_{p,RMS} = \frac{2\left[k/3+0.816\cdot\left|C_{p,mean}\right|\cdot U_o\sqrt{k_o}\right]}{{U_h}^2} \tag{2}$$

Here U_o and k_o are the mean velocity and turbulent kinetic energy of the approach flow at the height of interest, $C_{p,mean}$ is the local mean pressure coefficient, k is the local turbulent kinetic energy and U_h is the mean reference velocity at building height. The part proportional to k is associated with small-scale local pressure fluctuations in a flow free of mean velocity gradients, the part containing U_o is a 'quasi-steady' term associated with the amplification of upwind pressure fluctuations by velocity gradients.

Applying a similar procedure as Paterson and Holmes (1989) to derive equation (2), Selvam (1992) deduced an alternate equation for the RMS pressure coefficients:

$$C_{p,RMS} = \frac{2\left|C_{p,mean}\right|\cdot\left[1.414\cdot U_h\sqrt{k_h}+k_h\right]}{{U_h}^2} \tag{3}$$

in which U_h and k_h are the mean velocity and turbulent kinetic energy in the approach flow at building height.

Paterson (1993) derived a second model for large Reynolds numbers from the stream-wise component of the Navier-Stokes equations:

$$C_{p,RMS} = \frac{8{k_o}^2}{{U_o}^4} + \frac{8{C_{p,mean}}^2{U_o}^2 k_o}{\left({U_o}^2+2k_o-2k\right)^2} \tag{4}$$

According to Paterson, results obtained with equation (4) were in better agreement with full-scale and wind tunnel results of the TTU experimental building than results using equation (2). Richards and Wanigaratne (1993) derived a similar equation as Paterson and Holmes' (1989) equation (2), but suggested it should be more of the form

$$C_{p,RMS} = \frac{2\left[Ek_o{}^2 + 0.816^2 \cdot C_{p,mean}{}^2 \cdot U_o{}^2 k_o \right]^{\frac{1}{2}}}{U_h{}^2}, \tag{5}$$

This is a variation on equation (2) where the local turbulent kinetic energy term was replaced with a function of the approach flow turbulence, $Ek_o{}^2$. $E \approx 0.5$, which was determined through investigation of the value of $C_{p,RMS}$ in regions where $C_{p,mean} \approx 0$. Richards and Wanigaratne (1993) developed an additional model through consideration of the flow oriented with respect to the mean stream lines:

$$C_{p,RMS} = 2\left[\begin{array}{l} Ek_o{}^2 + \left(U_o{}^2 \sigma_{uo}{}^2 + Ek_o{}^2 \right) \cdot \left((1-F) + F \dfrac{C_{p,mean} U_h{}^2}{U_o{}^2 + 2k_o} \right)^2 \\ + \left(\dfrac{U_o{}^2 \sigma_{uo}{}^2 + Ek_o{}^2}{\left(U_o{}^2 + 2k_o \right)^2} + 0.25 \right) F^2 \left(\dfrac{\partial C_{p,mean}}{\partial \theta} \right)^2 U_h{}^4 \dfrac{\sigma_{vo}{}^2}{U_o{}^2} \end{array} \right]^{\frac{1}{2}} / U_h{}^2. \tag{6}$$

In which $\sigma_{uo} = \sqrt{\overline{u'_o{}^2}}$, $\sigma_{vo} = \sqrt{\overline{v'_o{}^2}}$. A value $F = 0.64$ was found through investigation of the relationship between $C_{p,RMS}$ and $C_{p,mean}$ for a dataset of wind tunnel measurements.

2.5 *Comparison of wind tunnel measurements and CFD results*

In all locations where a comparison between wind tunnel measurements and CFD results could be made, the five RMS models presented in the previous section were applied to the CFD results for all three turbulence models, leading to a total of 15 combinations. The evaluation of the term $\partial C_{p,mean} / \partial \theta$ in equation 6 was done in a central differencing fashion using the results of the calculations at a ± 5 degree angle of attack with respect to the evaluated angle. In this it was assumed that the units of θ are degrees, as is common in the field of wind engineering, although this was not specified in the original paper. The terms σ_{uo} and σ_{vo} were derived from the calculated Reynolds stresses.

At each pressure tap point the difference between wind tunnel data and the computational result for the mean and RMS pressure coefficients was determined as

$$\Delta C_p = \left| C_{p,CFD} \right| - \left| C_{p,WT} \right| \tag{7}$$

While it is possible to define a quality parameter which is directly related to these difference data, this would lead to a dependence on the choice of measurement locations. In order to overcome this problem the data were interpolated on a regular grid measuring 111 points in the

streamwise and spanwise directions and 396 points in the height. While this approach makes the results dependent on the interpolation method, it reduces the chosen dependence on the pressure tap positions. The interpolation was performed using the Matlab gridfit routine using a triangular interpolation scheme and a smoothness parameter of 1 in the streamwise and spanwise directions and 2 in the height direction. No extrapolation was performed.

To evaluate the performance of different models from a comparison between wind tunnel data and CFD calculations three quality parameters were defined: the fraction of all locations where the evaluated parameter is underpredicted, the average amount of underprediction per underpredicted location and the overall average amount of underprediction. The latter thereby equals the product of the former two.

A comparison of the wind tunnel and computational results is made for four angles of attack (0°, 15°, 30° and 45°). The three quality parameters defined above, derived for each of the wind directions, are averaged to produce an overall quality estimate. Evaluation of the quality parameters is performed on the interpolated grid.

3 RESULTS

In figure 2 the turbulent kinetic energy and velocity magnitude profiles which were measured in the empty wind tunnel are compared with the profiles calculated in the precursor domain of the CFD calculation. The calculated turbulent kinetic energy is lower than the wind tunnel result by a factor of roughly 2.5 to 3. A clear difference between the velocity magnitude profiles can also be observed, especially close to the ground.

The three quality parameters defined in section 2.5, evaluated for every combination of turbulence model and RMS model, are presented in tables 1-3. In these tables the root mean square pressure models are abbreviated as P&H (Paterson and Holmes, equation 2), S (Selvam, equation 3), P (Paterson, equation 4) and R&W 1 and 2 (Richards and Wanigaratne, equations 5 and 6).

Table 1. Fraction of underpredicted locations. For the abbreviations of the RMS pressure models see text.

Turbulence model	$C_{p,mean}$	$C_{p,RMS}$ (P&H)	$C_{p,RMS}$ (S)	$C_{p,RMS}$ (P)	$C_{p,RMS}$ (R&W 1)	$C_{p,RMS}$ (R&W 2)
Standard k-ε	0.3551	0.9880	0.6819	0.9999	0.9987	1.0000
Realizable k-ε	0.4386	0.9988	0.8178	1.0000	0.9995	1.0000
RNG k-ε	0.4251	0.9990	0.8102	1.0000	0.9996	1.0000

Table 2. Average amount of underprediction per underpredicted location. For the abbreviations of the RMS pressure models see text.

Turbulence model	$C_{p,mean}$	$C_{p,RMS}$ (P&H)	$C_{p,RMS}$ (S)	$C_{p,RMS}$ (P)	$C_{p,RMS}$ (R&W 1)	$C_{p,RMS}$ (R&W 2)
Standard k-ε	0.0878	0.0829	0.0732	0.1387	0.0979	0.1226
Realizable k-ε	0.0744	0.0950	0.0686	0.1454	0.1045	0.1259
RNG k-ε	0.0934	0.0970	0.0702	0.1458	0.1046	0.1263

Table 3. Overall average amount of underprediction. For the abbreviations of the RMS pressure models see text.

Turbulence model	$C_{p,mean}$	$C_{p,RMS}$ (P&H)	$C_{p,RMS}$ (S)	$C_{p,RMS}$ (P)	$C_{p,RMS}$ (R&W 1)	$C_{p,RMS}$ (R&W 2)
Standard k-ε	0.0312	0.0819	0.0499	0.1387	0.0978	0.1226
Realizable k-ε	0.0326	0.0949	0.0561	0.1454	0.1045	0.1259
RNG k-ε	0.0397	0.0969	0.0569	0.1458	0.1046	0.1263

As will also be concluded in section 4 it can immediately be seen from table 3 that the best results are obtained when the model of Selvam is used in combination with the standard k-ε model. In order to understand the reason for this, the average amount of underprediction in $C_{p,RMS}$ values for this combination of models is plotted at 0 and 45 degree angles of attack in figure 4 and figure 5, respectively. In these figures bright green represents a conservative estimate (no underprediction).

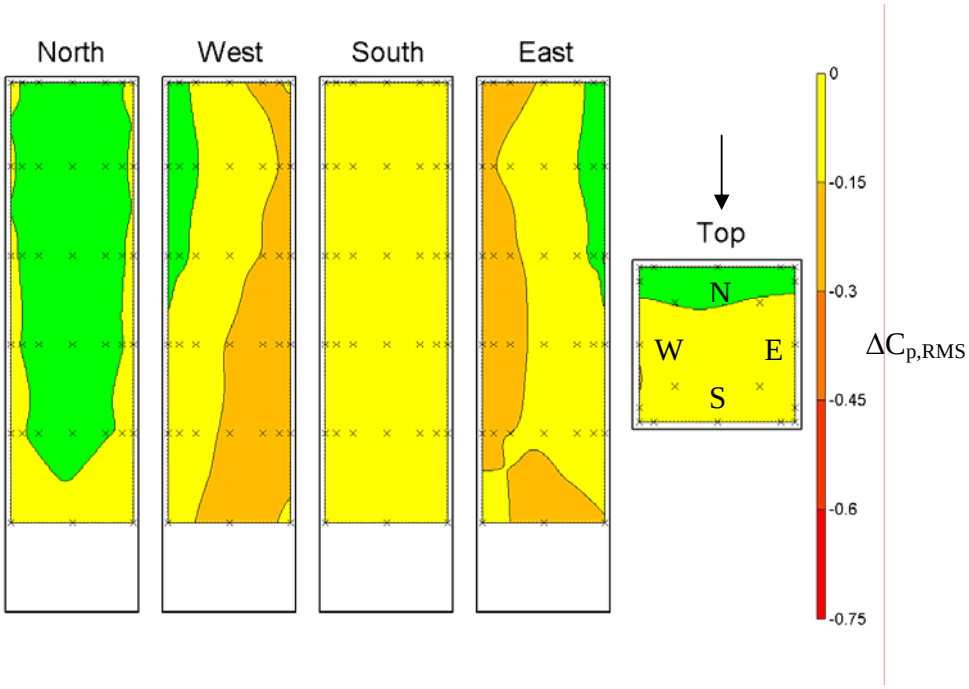

Figure 4 Amount of $C_{p,RMS}$ underprediction as a function of location for the model of Selvam using the standard k-ε turbulence model. 0 Degree angle of attack.

4 DISCUSSION

It can be seen from table 1 that the underprediction fractions for all RMS models are much larger than 0.5, indicating that none of the models are conservative. Both the models of Paterson and Holmes and that of Paterson perform especially poorly in this respect, leading to an underprediction for (almost) every location. Also apparent is the fact that, for the case considered here, the influence of the RMS model which is chosen is much more important than the turbulence model. The differences between the turbulence models show that the standard k-ε model is the most conservative which might be due to the well-known overprediction of turbulent kinetic energy in stagnation areas for this model. All papers where these models were introduced exclusively used the standard k-ε model.

The average amount of underprediction per underpredicted location is given in table 2. Again, although the differences between the results of the three turbulence models are not negligible they are much larger when different RMS models are compared. The least amount of underprediction is found using the model of Selvam whereas that of Paterson again performs poorly.

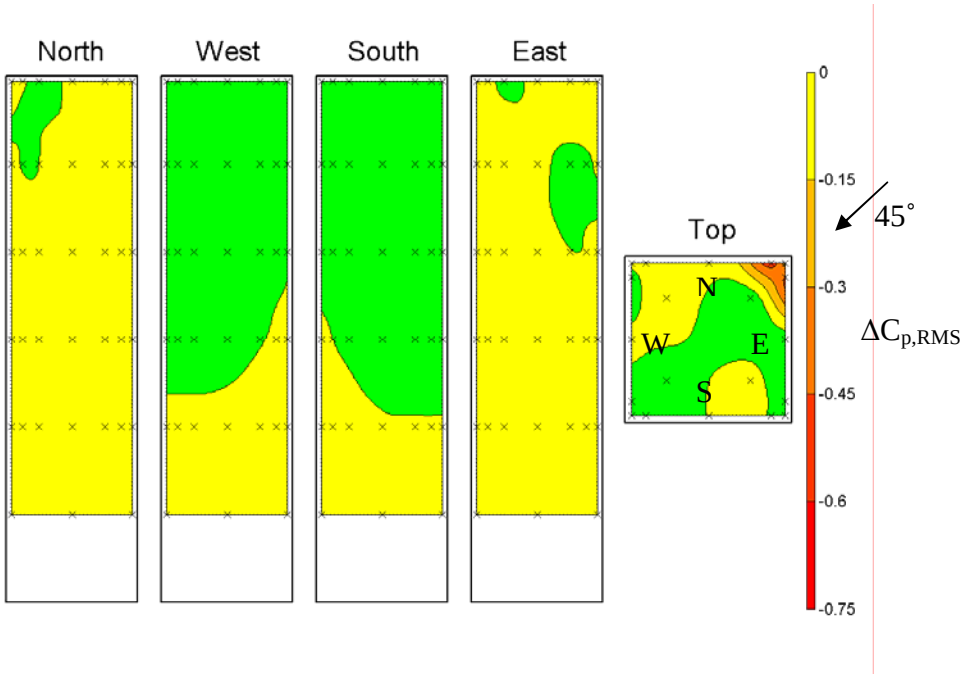

Figure 5 Amount of $C_{p,RMS}$ underprediction as a function of location for the model of Selvam using the standard k-ε turbulence model. 45 Degree angle of attack.

Combining the data in tables 1 and 2 by taking the product of both, the data in table 3 are derived. The values represent an average amount of underprediction for the selected model when overprediction is neglected. The best results are obtained when the model of Selvam is used in combination with the standard k-ε model, leading to an average amount of underprediction of $C_{p,RMS}$ of 0.0499. The worst results are obtained by combining the model of Paterson with the RNG k-ε model in which case the average amount of underprediction is almost three times as high.

The difference between the velocity magnitude and turbulent kinetic energy profiles for the wind tunnel and CFD datasets observed in figure 2 is caused by the wall functions used at the bottom of the CFD computational domain and in the absence of more appropriate wall functions cannot be avoided completely (Blocken, 2007; Kalkman, 2011). The effect of this discrepancy on the quality parameters given in tables 1-3 was therefore estimated through another analysis using the linearly interpolated wind tunnel dataset for the terms U_0, U_h, k_0 and k_h, resulting in a change of 30.5 ± 38.0 %. The most conservative model is again found to be Selvam's. However, although the results of this reanalysis are considerably more conservative even this model still underpredicts RMS pressure values on 32.6 % of the inspected surface area.

5 CONCLUSION

The observation that the RMS pressure models introduced by Paterson and Holmes (1989), Selvam (1992), and Paterson (1993) are generally non-conservative has already been made by the respective authors. Richards and Wanigaratne (1993), however, showed by comparison with data from the Silsoe building that their models performed rather well. In this paper it is shown that

this is no longer the case when they are applied to a high-rise building model. A very likely source of discrepancy is the mismatch between wind tunnel and CFD inflow profiles. As an alternative to the precursor simulation method used in the present investigation one could prescribe an ABL profile of the desired shape, in disregard of the fact that it will not be maintained throughout the computational domain. Another possible explanation for the relatively poor performance of the model derived by Richards and Wanigaratne for the present case is that the factors E and F, which were determined from a fit to the Silsoe building data set, are not universally applicable. Although the mathematical basis for the model introduced by Selvam (1992) is not completely clear it does seem to have a wider range of application. From figure 4 and figure 5 it can be observed that, away from reattachment zones and areas affected by corner vortices, it does not perform too poorly. Nevertheless, it is still non-conservative and therefore not applicable in an engineering context. New models are therefore required.

The effect of the turbulence model on the performance of the RMS model is comparatively minor. Future work should therefore focus on deriving an equation for the RMS pressures from first principles. Closure should be obtained with modelling assumptions also used in the turbulence models. RSM models could be helpful for this.

6 REFERENCES

Bronkhorst, A.J., Geurts, C.P.W., Blocken, B., van Bentum, C.A., 2011. Pressure effects due to wind interference between mid-rise and high-rise buildings, 13th International Conference on Wind Engineering, Amsterdam, the Netherlands.

Blocken, B., Stathopoulos, T., Carmeliet, J., 2007. CFD simulation of the atmospheric boundary layer – wall function problems, Atmospheric Environment 41, 238-252.

Franke, J., Hellsten, A., Schlünzen, H., Carissimo, B., 2007. Best practice guideline for the CFD simulation of flows in the urban environment. COST Action 732, Quality assurance and improvement of microscale meteorological models.

Gibson, M.M., Launder, B.E., 1978. Ground effects on pressure fluctuations in the atmospheric boundary layer. Journal of Fluid Mechanics 68, 537-566.

Kalkman, I.M., Bronkhorst, A.J, van Bentum, C.A., 2011. A comparison of neutral atmospheric boundary layer simulation methods for building pressures, 13th International Conference on Wind Engineering, Amsterdam, the Netherlands.

Lim, H.C., Thomas, T.G., Castro, I.P., 2009. Flow around a cube in a turbulent boundary layer: LES and experiment. Journal of Wind Engineering and Industrial Aerodynamics 97, 96–109.

Paterson, D.A., Holmes J.D., 1989. Computation of wind flow around the Texas Tech Building. Proc. of Workshop on Industrial Fluid Dynamics, Heat Transfer and Wind Engineering, CSIRO Division of Building, Construction and Engineering, Highett, Australia.

Paterson, D.A., 1993. Predicting r.m.s. pressures from computed velocities and mean pressures. Journal of Wind Engineering and Industrial Aerodynamics 46&47, 431-437.

Richards, P.J., Wanigaratne, B.S., 1993. A comparison of computer and wind-tunnel models of turbulence around the Silsoe Structures Building. Journal of Wind Engineering and Industrial Aerodynamics 46&47, 439-447.

Selvam, R.P., 1992. Computation of pressures on Texas Tech Building. Journal of Wind Engineering and Industrial Aerodynamics, 41-44, 1619-1627.

Senthooran, S., Lee, D.-D., Parameswaran, S., 2004. A computational model to calculate the flow-induced pressure fluctuations on buildings. Journal of Wind Engineering and Industrial Aerodynamics 92, 1131–1145.

Stathopoulos, T., 1997. Computational wind engineering: Past achievements and future challenges. Journal of Wind Engineering and Industrial Aerodynamics 67&68, 509-532.

Numerical estimation of added mass for circular membrane vibrating in still air

Y. Zhou[a], Y.Q. Li[a, b], Z.Y. Shen [a, b] and Yukio Tamura [c]

[a]*Department of Building Engineering, Tongji University, Shanghai, China*
[b]*State Key Laboratory for Disaster Reduction in Civil Engineering, Tongji University, Shanghai, China*
[c]*Wind Engineering Research Center, Tokyo Polytechnic University, Kanagawa, Japan*

ABSTRACT: The added mass has significant effect on the vibration of the membrane structures, which depends on the mode shapes and can not be ignored during their vibration analysis. In this paper, the added mass of the circular membrane is investigated by the proposed numerical analysis method. Using the Realizable *k-ε* and RNG *k-ε* model of the FLUENT commercial computational Codes associated with the Dynamic-mesh technique to simulated the air loading on the circular membrane and using FEM to obtain the dynamic matrix equation for the circular membrane, the natural frequencies in consequence of considering the effect of the surrounding air is observed. An existing test result is employed to verify the proposed method. The problem presented herein may be considered as the air-structure coupled problem.

KEYWORDS: added mass, circular membrane, numerical estimation

1 INTRODUCTION

When structures vibrate in a certain kind of fluid, part of the surrounding fluid will be invoked and will vibrate together with structures; this effect is called added mass. Generally, the added mass of building structures vibrating in air, such as steel structures or concrete structures, can be ignored, because their material densities are much greater than that of air. However, the added mass has a significant influence on the vibration of membrane structures due to the light weight of their material.

Actually, the added mass of typical objects, such as cylinders and spheres, moving in fluid with acceleration has been widely investigated. Currently, research on the added mass of membranes is still limited. A study by Minami [1] indicated that the added mass has no relationship to the vibration frequency and amplitude but only to the air density and the dimension of the membrane. The added mass is equivalent to the air uniformly distributed on the membrane with an estimated height equal to 68% of the length of the membrane. Irwin and Wardlaw [2] presented an empirical equation for estimating the added mass of the Montreal Stadium. Li, et al [3] proposed a simplified added mass model which can take into account complicated vibration mode shape of flat membranes, i.e., the added mass above each vibration region is equal to the uniformly distributed air with height of 0.65*l*, in which *l* is the diameter of the inscribed circle of the region. The vibration regions are separated by the boundary lines which are made up of the points at which the displacement in the mode shape is zero.

A numerical method for added masses of the circular membrane vibrating in still air is developed by using the FLUENT commercial computational Codes in this paper with the Realizable k-ε and RNG k-ε model associated with the Dynamic-mesh technique. The vibration of the circular membrane can be simulated and the air loading on the circular membrane can be obtained. Based on the concept of kinetic energy, the added mass of the circular membrane can be derived out. The dynamic matrix equation for the structure is obtained by means of FEM and the natural frequencies in consequence of considering the

effect of the surrounding air is observed. Finally, an existing test result is employed to validate the efficiency of the proposed method.

2 DETERMINATION OF THE ADDED MASS

In the case of an incompressible inviscid stationary fluid, the change rate in time of kinetic energy of any part of the fluid is equal to the work done by the pressures on its surface.

$$\frac{dE}{dt} = -\int_A V_N \Delta p dA \tag{1}$$

where E is the kinetic energy, A is the surface bounding the fluid region and V_N denotes the velocity of the fluid particle in the derection of the normal N. The last integral thus expresses the rate at which the pressure $\triangle p$; exerted from outside an element of the boundary, is doing work. Assuming the fluid-solid interface of the membrane can be expressed as

$$\frac{dE}{dt} = -\int_A \frac{\partial h}{\partial t} \Delta p dA \tag{2}$$

Where $\partial h / \partial t$ is the velocity of the membrane in the normal direction. h is the surface displacement of the circular membrane.

On the other hand, the change rate of kinetic energy in time of the oscillating circular membrane having a mass per unit area equivalent to the added mass, M_a, can be given

$$\frac{dE}{dt} = -M_a \int_A \frac{\partial h}{\partial t} \frac{\partial^2 h}{\partial t^2} dA \tag{3}$$

So an expression for the added mass per unit area can be given in the following form:

$$M_a = \frac{\int_A \frac{\partial h}{\partial t} \Delta p dA}{\int_A \frac{\partial h}{\partial t} \frac{\partial^2 h}{\partial t^2} dA} \tag{4}$$

Eq.(4) indicates the essential dependence of the added mass of the oscillating circular membrane upon the fluid loading, $\triangle p$. The understanding of the properties of added mass will allow the fluid loading to be obtained in the most suitable form.

3 FORMULATIONS OF FLUID STRUCTURE INTERACTION (FSI)

In theoretical considerations, to take into account the fluid effect on the surrounded vibrating structure, the system has to be treated as a fluid structure interaction problem. In that case, the structural dynamics equation has to be coupled with the fluid equations.

It is well known that the discretized structural dynamics equation can be formulated as follows:

$$[K]\{u\} + [C]\{u'\} + [M]\{u''\} = \{P\} \tag{5}$$

In which $[K]$ is the structural stiffness matrix; $[C]$, the structural damping matrix; $[M]$, the structural mass matrix, and $\{u\}$, $\{P\}$ are the displacement and force vector, respectively.

The equation of motion of an undamped dynamic sytem in matrix notation is

$$[K]\{h\} + [\overline{M}]\{\frac{\partial^2 h}{\partial t^2}\} = \{0\} \tag{6}$$

where $[\overline{M}] = [M] + [M_a]$.

The membrane mass matrix is taken as diagonal with the masses corresponding to the collocation points. It can be transformed to the standard eigenvalue problem

$$([K] - \omega^2 [\overline{M}])\{h\} = \{0\} \tag{7}$$

Where ω is the eigenvalue, and the square root of the eigenvalue is the natural frequent considering the effect of the surrounding air.

4 DETERMINATION OF THE FLUID LOADING

4.1 *Mathematical model*

The finite volume method is employed to resolve the fluid governing equations, transforming a continuum domain into a discretized space of small cells where an algebraic system of equations is resolved after linearization and discretization of the original mathematical equations for the mass and momentum conservation. Considering the present vibration of the circular membrane, the following basic characteristics have been implemented in the model:

- Full-scale simulation of the circular membrane over a 3D domain is used segregated solver which solves the equation set sequentially.
- The governing equation of the flow is described by incompressible viscous Navier-Stokes equation.
- Unsteady resolution of the circular membrane using the smoothing techniques and remeshing techniques for dynamic meshes.
- Implementation of a parametric UDF to simulate the vibration of circular membrane can update the position of each node based on the deflection due to fluid-structure interaction.

4.2 *Turbulent model*

Up to know, significant progress in the field of CFD (Computational Fluid Dynamics) has been achieved, and it has been used as an efficient tool for prediction of fluid loads. Generally, the governing equation of the flow is described by incompressible viscous Navier-Stokes equation. Because Reynolds-averaged Navier–Stokes (RANS) modeling can reasonably simulate mean wind characteristics and require less computing time than other CFD methods, it becomes the most widely used method in many industrial applications. For numerical simulation, the governing equations of the incompressible turbulent wind flow around circular membrane are presented by the RANS equations as follows:

$$\frac{\partial}{\partial x_i}(\rho u_i) = 0 \tag{8}$$

$$\frac{\partial}{\partial t}(\rho u_i) + \frac{\partial}{\partial x_j}(\rho u_i u_j) = -\frac{\partial p}{\partial x_i} + \mu \frac{\partial}{\partial x_j}(\frac{\partial u_i}{\partial x_j}) + \frac{\partial}{\partial x_j}(-\rho \overline{u_i' u_j'}) \tag{9}$$

The turbulent kinetic energy, the k equation in Realizable k-ε model is the same as that in the standard k-ε model and the RNG k-ε model. However, the form of the ε equation in Realizable k-ε model is quite different from those in the standard and RNG-based k-ε models. One of the noteworthy features is that the production term in theε equation does not involve the production of k; i.e. It is believed that the present form better represents the spectral energy transfer. It is a mathematical theory which can be used to derive a turbulence model which is similar to the k-ε model. Following improvements compared to standard k-ε model: (1). Additional term in ε equation improves the accuracy when modelling rapidly strained flows. (2). The effect of swirl turbulence is included in the RNG model. (3). The RNG model enables to use Prandtl numbers (turbulent viscosity/turbulent heat conductivity) as variables. (4). Enables to use lower Reynolds numbers than in standard model. The analytical derivation results in a model with constants different from those in the standard k-ε model, and additional terms and functions in the transport equations for k and ε.

4.3 *SIMPLIC algorithm*

The pressure–velocity coupling was resolved using the SIMPLIC algorithm and the under relaxation factors were kept within typical ranges (0.3 for the pressure correction equation and 0.7 for the momentum equation), which helped to speed up the convergence process.

4.4 *Dynamic meshes*

Dynamic and deformable meshes allow the displacement of the domain boundaries in CFD simulations, adjusting the associated mesh to the new locations accordingly. With the dynamic mesh model in FLUENT, it allows an arbitrary motion of fluid boundaries, and the response of the fluid to the prescribed boundary motion can be captured. Meanwhile, the motion control of the circular membrane can be realized by using DEFINE GRID MOTION UDF in FLUENT, and a grid motion UDF can update the position of each node based on the deflection due to fluid-structure interaction.

Different schemes for the mesh reconstruction can be found in the literature, according to the basic characteristics of the moving mesh. In the present study, two fundamental methods have been employed for efficient treatments of the vibration of the circular membrane. One is smoothing techniques: where the initial connectivity of the mesh nodes is remained unchanged. The nodes are repositioned as if they were connected by small springs. Though there is no restriction about the original mesh type, it can be used only in the case of small deformations. The other is remeshing techniques: which is an alternative to the smoothing algorithm when there are excessively large deformations in the model. The mesh has to be locally rebuilt after the changes in the boundaries are completed.

4.5 *Boundary conditions*

It is necessary to impose the boundary condition artificially because the computational domain can not be infinite. The entrance boundary condition is defined by pressure-inlet where the specification of a static (gauge) pressure at the inlet boundary is set to zero. The exit boundary condition is defined by pressure-outlet where the specification of a static (gauge) pressure at the outlet boundary is set to zero. The boundary condition at the top and on both sides of flow field is symmetric boundary which is equivalent to the free-slip wall. The no-slip boundary condition is enforced at wall of the circular membrane surface and the ground.

5 RESULTS AND COMPARISON

Li, et al [3] investigated the vibration of circular membrane vibrating in air and in vacuum. A vacuum chamber was designed to test the vibration of a circular flat membrane in still air with various air pressures. The membrane was clipped by a top circle and a bottom circle. The pressures was imposed uniformly by lifting an inner circle. As Table 1 shown, the vibration of the membrane was measured in 1atm, and 0.6atm. Two membrane materials were used in the tests, including a latex and a rubber membrane, and five prestress levels of the membrane were tested. The natural frequencies of the membrane in 1atm, and 0.6atm were given in Table 2. Using the Realizable k-ε model and the RNG k-ε model of FLUENT commercial computational Codes to derive the aerodynamic pressure, and associating with FEM to derive the natural frequencies in consequence of considering the effect of the surrounding air, the results are shown in Table 3. The fundamental frequency in vacuum was estimated with Finite Element Method (FEM), as listed in Table 4.

Table 1 Test cases

Air pressure	Latex membrane Prestress (MPa)			Rubber membrane Prestress (MPa)	
	σ_1=0.092	σ_2=0.178	σ_3=0.297	σ_4=0.471	σ_5=0.828
1 atm	A1	B1	C1	D1	E1
0.6 atm	A2	B2	C2	D2	E2

Table 2 Natural frequency of the circular membrane vibrating in 1atm, and 0.6atm

mode	case									
	A1	A2	B1	B2	C1	C2	D1	D2	E1	E2
1st mode	11.05	12.25	15.46	18.10	21.22	24.34	35.58	39.95	51.20	53.99
2nd and 3rd mode	23.11	24.51	32.60	35.86	44.63	49.31	67.42	73.04	97.38	102.4
4th and 5th mode	-	-	-	-	-	-	97.38	-	151.1	-
6th mode	33.55	39.74	47.63	57.70	71.47	78.91	-	-	-	-

Table 3 Natural frequency of the circular membrane vibrating in 1atm, and 0.6atm using Realizable k-ε model and RNG k-ε model

Case	The result of using Realizable k-ε model				The result of using RNG k-ε model			
	1st mode f_1 (Hz)	2nd and 3rd mode f_2 (Hz)	4th and 5th mode f_3 (Hz)	6th mode f_4 (Hz)	1st mode f_1 (Hz)	2nd and 3rd mode f_2 (Hz)	4th and 5th mode f_3 (Hz)	6th mode f_4 (Hz)
A1	12.80	23.28	33.94	37.56	12.85	23.39	34.31	37.64
A2	15.14	26.79	38.94	42.55	15.19	27.08	39.07	42.67
B1	17.81	32.38	47.21	52.25	17.88	32.54	47.72	52.35
B2	21.05	37.26	54.17	59.19	21.13	37.66	54.35	59.36
C1	23.00	41.83	60.98	67.49	23.09	42.03	61.64	67.62
C2	27.20	48.13	69.97	76.45	27.29	48.65	70.20	76.67
D1	37.47	65.70	93.26	102.12	37.58	65.62	93.97	102.25
D2	42.23	72.11	101.67	110.31	42.32	72.60	101.86	110.50
E1	49.68	87.01	123.65	135.40	49.83	87.01	123.44	135.58
E2	55.96	95.61	134.80	146.26	56.11	96.26	135.06	146.51

Table 4 Natural frequencies of the circular membrane vibrating in vacuum

Prestress (MPa)	Finite Element Analysis				Fitting result of test			
	1st mode	2nd and 3rd mode	4th and 5th mode	6th mode	1st mode	2nd and 3rd mode	4th and 5th mode	6th mode
σ_1=0.092	24.45	39.08	52.48	56.43	24.45	33.38	-	61.96
σ_2=0.178	34.00	54.36	73.00	78.50	34.00	50.97	-	92.92
σ_3=0.297	43.98	70.02	82.50	101.39	43.98	72.18	-	110.18
σ_4=0.471	55.43	88.42	118.75	127.69	55.43	87.13	114.24	-
σ_5=0.828	73.49	117.24	157.45	169.30	73.51	121.13	-	-

Comparing the result of the natural frequencies in Table 2 and Table 3, the FLUENT results have a good agreement with the experimental results and the result of using the Realizable k-ε model and the RNG k-ε model is almost the same. The proposed numerical method is effective and can be used for the analysis of free vibrations of flat membrane. Comparing the result of the natural frequencies vibrating in 1atm and 0.6atm and the result of the natural frequencies vibrating in vacuum, it can find the effect of the air surrounding the membrane structure on the natural frequencies of the structure is very significant.

6 CONCLUSIONS

The numerical method for obtaining added masses of the circular membrane vibrating in still air is proposed in this paper. The aerodynamic pressure associated with the structure deformations is derived by the FLUENT commercial computational Codes and the natural

frequencies in consequence of considering the effect of the surrounding air is observed by FEM. The result based on this method is verified by comparing with the existing test results. Through the numerical example calculated with the use of the air mass, it can find that the effect of the air surrounding the membrane structure on the natural frequencies of the structure is very significant.

7 ACKNOWLEDGEMENTS

The authors are grateful to the financial support by the national Natural Science Foundation of China (No.50978192), the Research Fund of the State Key Laboratory of Disaster Reduction in Civil Engineering (No.SLDRCE09-B-01), and the Kwang-Hua Fund of College of Civil Engineering, Tongji University, and the Global COE Program of Tokyo Polytechnic University awarded by the Ministry of Education, Culture, Sports, Science and Technology, Japan.

8 REFERENCES

[1] H. Minami. Added mass of a membrane vibrating at finite amplitude, Journal of Fluids and Structures, 1998,Vol.12, pp. 919-932
[2] H.P.A.H. Irwin, R.L. Wardlaw. A wind tunnel investigation of a retractable fabric roof for the Montreal Olympic stadium. Proceedings of the 5th International Conference, Colorado, USA: Cermak J. E., 1979, pp. 925-938.
[3] Y.Q. Li, L. Wang, Z.Y. Shen, Y. Tamura. Added mass estimation of flat membranes vibrating in still air, Journal of Wind Engineering and Industrial Aerodynamics, 2011,Vol. 99, pp.815-824.

The Seventh International Colloquium on Bluff Body Aerodynamics and Applications (BBAA7)
Shanghai, China; September 2-6, 2012

A Numerical Study of the Effects of Moving Tornado-Like Vortex on a Cube

Pham Van PHUC[a], Tsuyoshi NOZU[b], Kojiro NOZAWA[c], Hirotoshi KIKUCHI[d]

[a,b,c,d]*Institute of Technology, Shimizu Corporation, 3-4-17, Etchujima, Koto-ku, Tokyo, Japan*

ABSTRACT: A numerical movable tornado simulator using Large Eddy Simulation has been constructed to generate the tornado-like vortices and used to evaluate the effects of the translational moving of the vortices on the wind pressure distribution around a cube building. The performance of the simulator has been verified in comparison with the previous experimental results. Although, wind pressure on the surface of the cubic was almost constant in time inside the stationary tornado-like vortices, the pressure was changed significantly when the vortices were translated. The significant changing has also clarified from the wind flow around the cubic with strong whirl vortices and vertical wind components.

KEYWORDS: Tornado-like Vortices, Cubic, Wind Pressure, LES Model, Moving Effect

1 INTRODUCTION

Damages caused by tornado are often due to the destroy or damage on the walls or roofs and tiles of building, those things are then scattered and wrap around a new building or structure to create a new damage. In order to reduce the damages, better understanding of flow field and wind pressure acting on building in tornado needs to be clarified.

Because of the sudden and local occurrence of a tornado, it was found that the measurement of a flow field near the ground in a tornado was difficult[1)]. Some meteorological numerical simulations in the meso-scale tried to elucidate the generation mechanism of a tornado that needed to model a giant cumulonimbus cloud, in which dozens of kilometers wide was in two orders of magnitude of the tornado. The scale of the simulation would become too large to evaluate the flow field near the ground as well as the wind pressure acting on building in detail[2)]. On the other hand, several studies[3,4)] to better understand tornado structure used physical models that simulate tornado-like vortices as a flow field of tornado near the ground below a cumulonimbus cloud. Some experiments[4)] indicated the changing in structure of vortex by Reynolds number and swirl ratio. Recently, Yang et al.[5)] showed the appropriateness of the physical model in modeling the flow field of tornado in comparison with field measurement's results. However, most experiments were carried out in 1/1000 to 1/10,000 of real scale. Because of the constraints of the experimental devices, it was difficult to investigate in detail the structure of the vortices as well as the changing in wind pressure of the building. Numerical simulation using computational fluid dynamic is expected as one of effective method to solve the problem[6,7)].

While those studies made an effort to evaluate the flow field and wind loads on building the in tornado-like vortices, most of them ignored the translational movement of the vortices that could be an important reason of damages caused by tornado. In recent years, some researcher[5,8)] tried to design the prototype of the experimental apparatus that could translate a vortex forcibly. Selvam et al.[9)] proposed a numerical simulator using the Rankine-Combined Vortex Model (RCVM) to simulate the effect of translational movement of the tornado on the forces acting on buildings. Although, this model did not include the vertical velocity, which did occur inside the vortex core of actual tornado, it was found that the forces were higher than the results in the

straight boundary layer wind in the vertical direction. Some new model including the vertical velocity needs to be considered for better understanding.

In this study, a numerical movable tornado simulator using Large Eddy Simulation and dynamic mesh generation has been developed. The performance of the simulator has been verified in comparison with the wind velocity profile and wind pressure distribution of previous experiment. The simulator was then used to evaluate the effects of translational moving of the tornado-like vortex on wind flow field and the wind pressure distribution on a cube building.

2 NUMERICAL MOVABLE SIMULATOR

Schematic of the movable tornado simulator is shown in Fig.1. A Ward-type tornado simulator has been modeled basing on the dimensions of the stationary simulator model of Matsui's experiment[4]. Simulator included a convergent zone of h=20cm height with a shear inflow layer of direction θ, a convection zone with an exhaust outlet and was moved with the translational velocity U_{mov}. Table 1 shows the analysis conditions and those conditions in the actual atmosphere[4,10]. The scale is about 1/1000~1/10000. As the same as previous studies, the swirl ratio($S = d/4h \times tan\theta$) was considered to be the main dimensionless quantity. The ratio of translational velocity and maximum velocity obtained inside the vortex (U_{mov}/U_{max}=0.6/12) is in the range of 0~30/90 in the actual phenomena.

Fig.2 illustrates the mesh of convergent zone in the plan view (a), close-up of the stationary mesh area in the convergent zone (b) and mesh of computational domain. Moving meshes with sliding interfaces were adapted to model the moving of tornado from left to right. In order to minimize the effects of the moving meshes, a stationary mesh zone around the building was modeled. Dynamic layering method was also adapted to split or merge mesh cells to maintain the quality of mesh around the building. Computational model had 779 thousand mesh cells.

Navier-Stokes equations for incompressible flow including the continuous equation and momentum equations were solved using Fluent 6.3 software[12]. LES turbulence model was used in which small eddies were modeled using the standard Smagorinsky model. Governing equations were discretized by the finite volume method. A central difference scheme for convective terms and a second-order implicit scheme for unsteady terms were used.

A cube of width B=0.1h was set up at the center of floor of the simulator. Wind speed U_0=6m/s was kept constant at the outlet boundary, whose outflow's volume was 0.3m^3/s, to generate the upward flow in the convection zone. A same volume of inflow with angle θ=60deg was applied to the inlet boundary to generate a tornado-like vortex with a swirl ratio S=0.65. Walls of simulator were modeled as the moving wall boundaries. Walls of cubic were no-slip boundaries.

In order to clarify the effect of translational movement of the tornado-like vortices, two case studies have been simulated with translational moving velocity U_{mov}=0 and 0.6m/s as the stationary condition and the moving condition, respectively. In case 1, the numerical simulator was not moved (U_{mov}=0m/s), hereinafter referred to the case of the stationary condition. The wind flow field was generated from the analysis conditions to obtain the wind pressure acting on a cubic. In case 2, the numerical simulator was firstly set up in the 0.4m left-hand side of the cube. After 7000 steps of an approach run, which was enough to generate a tornado-like vortex, the simulator was moved to the right hand side with a translational velocity of U_{mov}=0.6m/s, hereinafter referred to the case of the moving condition. Wind pressure acting on the cubic was estimated during the vortex's passing. Each simulation was carried out for 16s at time increment of 0.001s.

Because of time-space changing of wind speed and static pressure in the tornado-like vortices, the method using in straight boundary layer to estimate the wind pressure coefficients cannot be applied. In this study, the pressure coefficient was obtained by the following equation[4].

$$C_p = (P - P_s)/0.5\rho V_0^2 \quad (1)$$

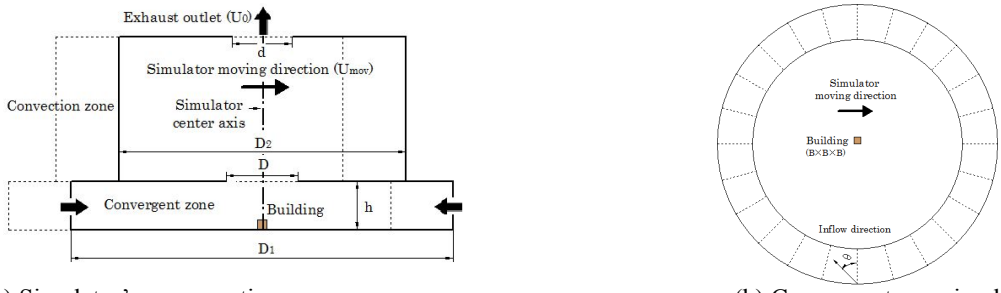

(a) Simulator's cross section (b) Convergent zone in plan view

Figure 1. Schematic of movable tornado simulator

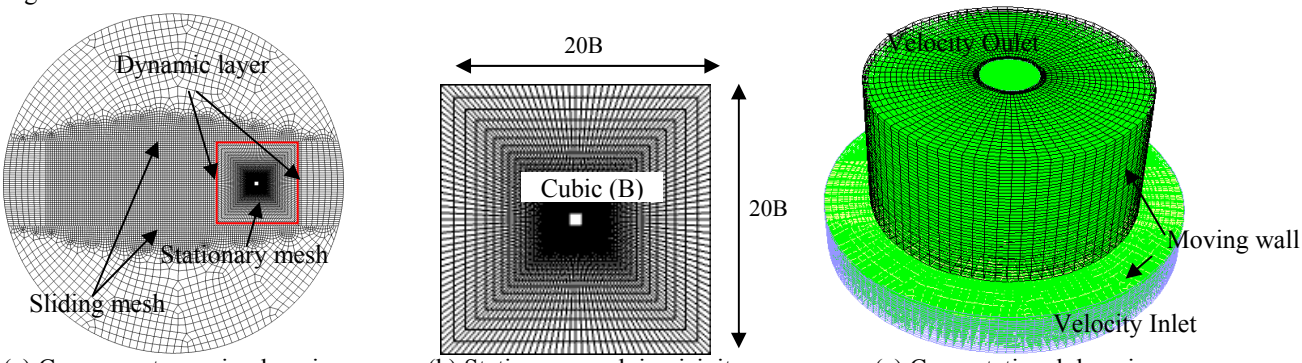

(a) Convergent zone in plan view (b) Stationary mesh in vicinity (c) Computational domain

Figure 2. Meshes of numerical model

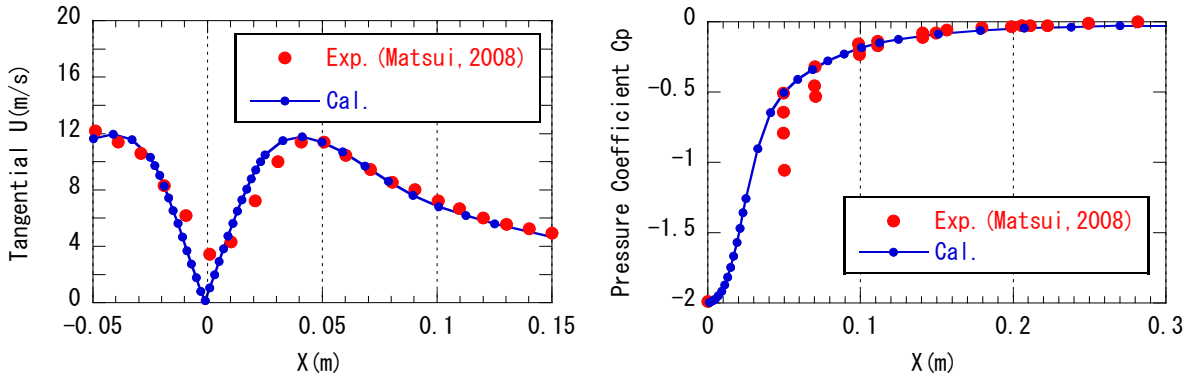

Figure 3. Wind velocity and ground surface pressures in comparison with experimental results

Table 1. Dimensions of the movable simulator and analysis conditions

Parameters	Symbol	Numerical study	Real Scale[4,10]
Upward hole diameter	D	0.3m	1~3km
Convergent zone height	h	0.2m	0.5~2km
Convection zone diameter	D1	1.6m	-
Exhaust outlet diameter	d	0.25m	-
Convection zone diameter	D_2	1.2m	-
Swirl ratio ($d/4h\tan\theta$)	S	0.65	0.05~2
Inflow angle	θ	60deg	-
Outlet volume	Q	0.3m^3/s	10^8~10^9 m^3/s
Outlet velocity	U_0	6m/s	-
Maximum tangential velocity	U_{max}	12m/s	70~90m/s
Translational moving speed	U_{mov}	0, 0.6m/s	0~30m/s
Cubic building width	B	0.02m	20~200m

Where, P is the wind pressure, P_s is the maximum wind pressure far enough away vortex, ρ is the density of air. V_0 is the reference wind speed which was calculated from the difference between the maximum wind pressure of the ground surface and the minimum wind pressure at the center of the vortex that obtained in a stationary condition of the simulator without any cubic. Following the definition, the pressure coefficient at the floor surface is mathematically between -2 to 0 when the vortex is assumed as the Rankine vortex. The pressure coefficient of -1 will also match to the position of the maximum wind speed of the vortex.

Fig.3 illustrates a comparison of tangential velocity and ground surface pressure distributions between experiment and simulation in the stationary condition without any cube. The simulated results showed a good agreement with experimental ones. In addition, the wind pressure coefficient is between -2 to 0, and at the coefficient of 1, the tangential component of wind speed can be seen that nearly becomes the maximum.

3 RESULTS AND DISCUSSIONS

3.1 *Wind Pressure Distributions on a Cube*

Fig. 4 illustrates the wind velocity time series at the 0.75h height, which is on the top of the cube. Comparing to the result in the stationary state, the wind velocity increased in 7.6~8.2s and decreased in 8.2~8.6s as a sudden gust wind occurring when the simulator was passing. Fig. 5 and Fig.6 show the maximum and minimum wind pressure time series acting on each surface of cube in the stationary state and moving state of simulator. A plus (+) mark including A, B, C, D, E letter indicates a developed view of the surfaces of the cube. The rotational direction and translational direction of the tornado-like vortex are also described together. In the stationary condition, wind pressure acting on each surface of the cube becomes almost constant in time. The pressure coefficients on the roof and side surfaces are between 0.0 to -1.0 that is similar to the values obtained by the previous experiment[7]. On the other hand, in the moving condition, a large wind pressure does not occur when the center axis of the simulator is approaching. After the central axis passed the cubic, the pressures change rapidly at 8.2s. The maximum and minimum pressures are up to +3 and -3, simultaneously, whose range is larger than the range of -2 to 0 in assumption of Rankine vortex which has been mentioned above. Incidentally, the position at the time of 8.2 seconds is the same as the position of approximately 0.05m from the vortex center (Fig.3a) that corresponds with the maximum wind speed of the tangential direction of the vortex.

Fig. 7 and 8 shows the vorticity contours and distribution of wind pressure acting on the ground and surfaces of cube at 8.2s. A square in figure (b) is the roof and figure (c) shows the developed view of the surfaces of the cube. In the stationary condition, the vortex axis and minimum pressure distribution are biased in the rotational direction at a position 0.05m away. It can be explained by the effect of the presence of cube. Detail for the effects of cube in dimensions will be discussed in next section. In addition, the wind pressure distribution and vorticity contour in the analysis has been confirmed to be a nearly steady state. On the other hand, in the case of moving, the tornado-like vortex has been almost hit to the cube as shown in Fig-7(a), resulted in a strong negative pressure at the corner ② of the roof as shown in Fig.7(c). A strong positive pressure near the corner① and negative pressures at the other side corners are also found.

In order to clarify the characteristics of wind pressure caused by the translational moving effect of the tornado-like vortex, the flow field in the vicinity of the cube is investigated. Fig.9 (a) and (b) show wind velocity contour and vector in the horizontal plane of z=0.8B at the time of 8.2s. The flow separates and creates one small vortex at the corner ①and one large vortex at the

corner ④ that reattaches to other sides of cubic. The points of separation and reattachment are corresponding with the regions of strong positive and negative pressure in Fig.8(c). Although, these separation vortices are found as similar as the vortices in the boundary layer flow, the generated flow field around the cubic is typically whirled up, as shown in Fig.9(a). Moreover, a sudden changing in wind speed is also found at the separation points, with a strongly rising up flow field at the reattachment points. Fig.9 shows the contour and vector of wind speed in the vertical plane of x=-0.4B. A large upward flow near the corner② has been occurred corresponding to the strong negative pressure obtained in the roof as shown in Fig.8(c). Consequently, it can be found that a complex three-dimensional flow formed by the swirling and strong upward flow caused a strong locally negative pressure in the vicinity of the cube from the tornado-like vortex.

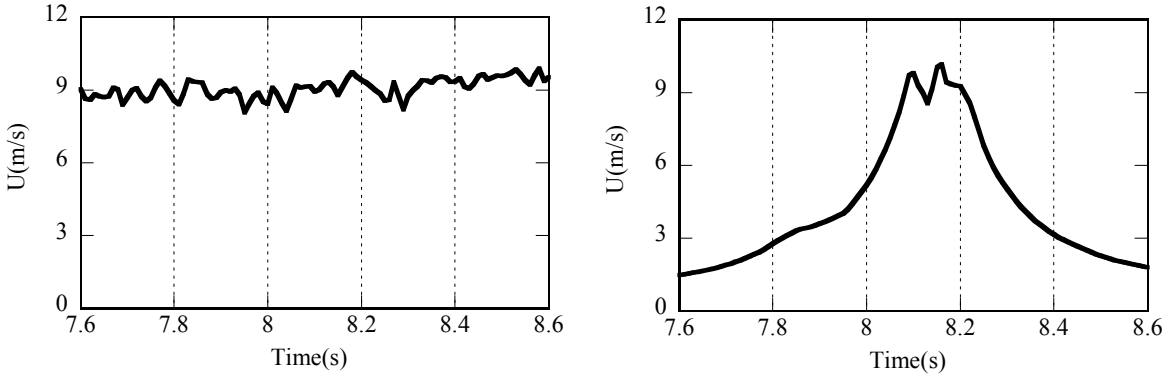

Figure 4. Wind velocity time series at 3/4h height on the top of cube (left: stationary, right: moving)

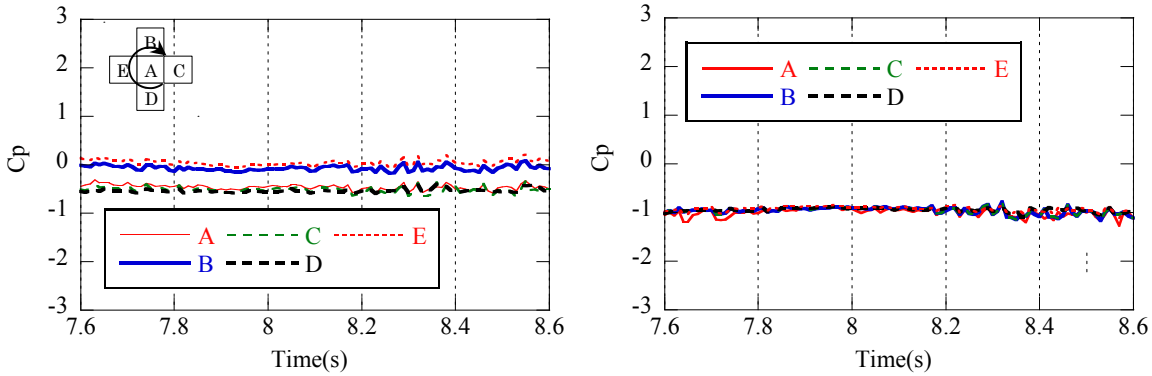

Figure 5. Maximum (left) and minimum (right) wind pressure acting on the cube in stationary condition of simulator

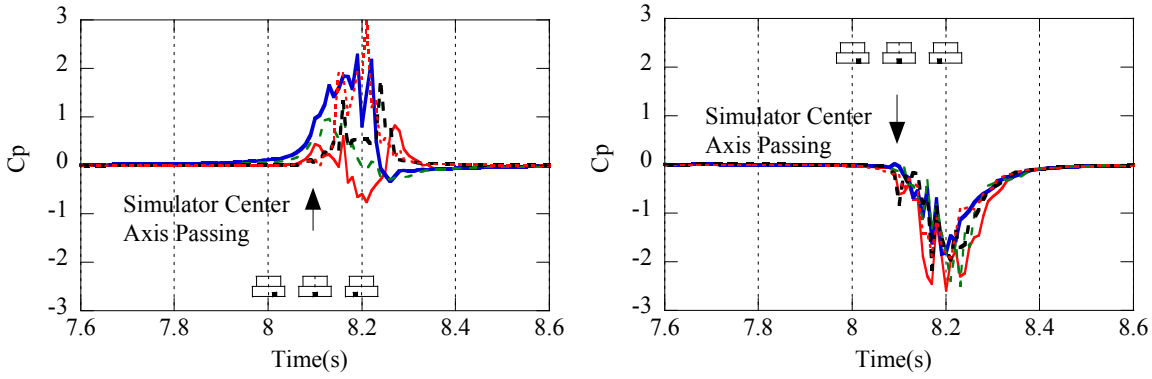

Figure 6. Maximum (left) and minimum (right) wind pressure acting on the cube in moving condition of simulator

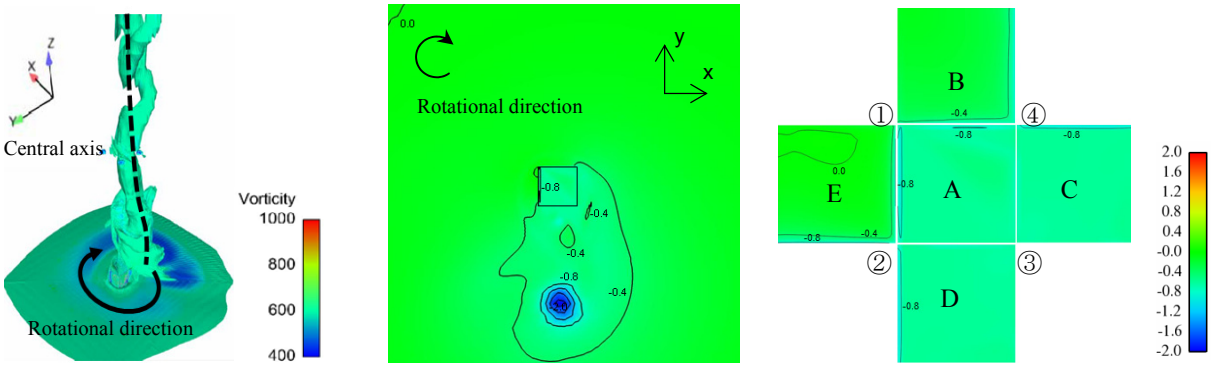

(a) Vorticity countour (b) Pressure distribution on the ground (c) Pressure distribition on surfaces

Figure 7. Voricity countour and pressure distribution in the stationary condition

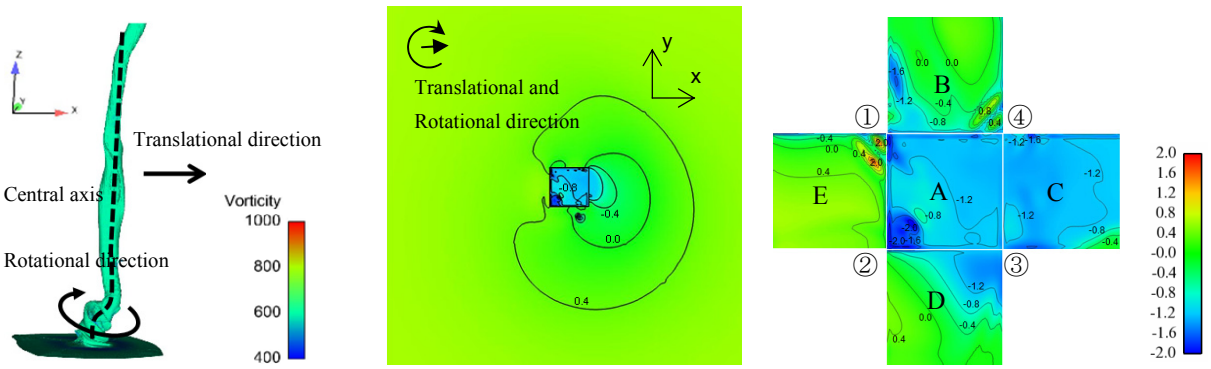

(a) Vorticity countour (b) Pressure distribution on the ground (c) Pressure distribition on surfaces

Figure 8. Voricity countour and pressure distribution in the moving condition at time of 8.2s

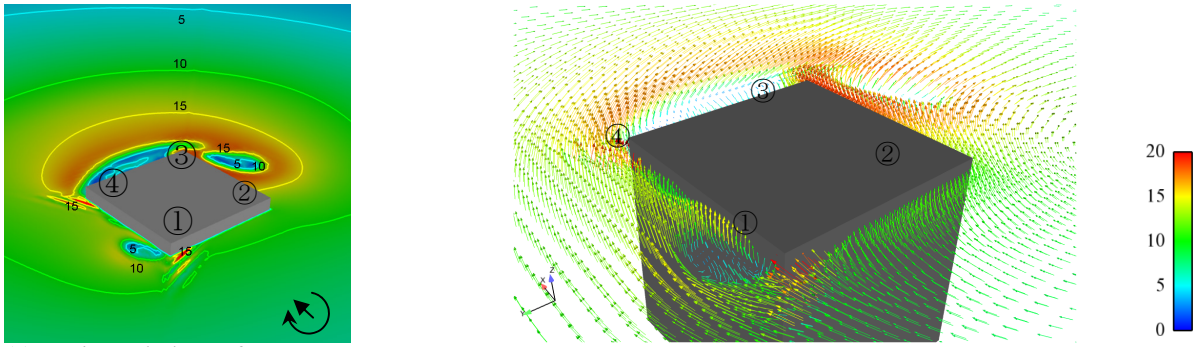

(a) Horizontal plane of z=0.8B

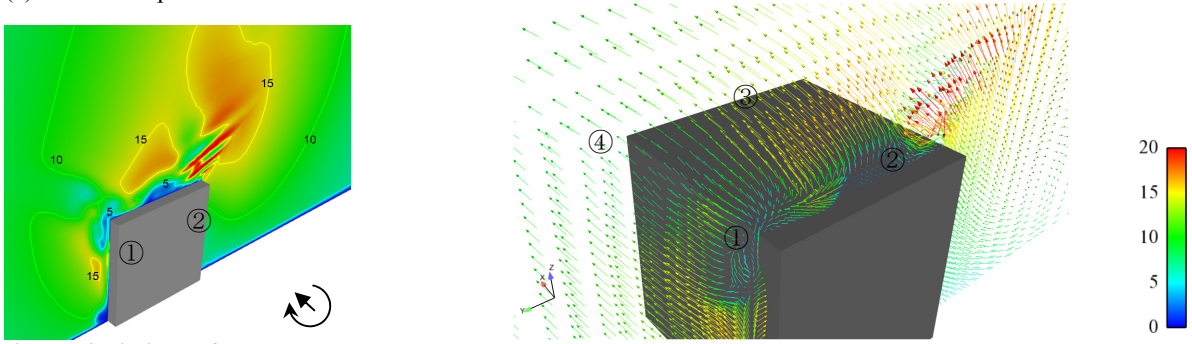

(b) Vertical plane of x=-0.4B

Figure 9. Wind flow field around a cube (left: wind velocity contour, right: vector of wind velocity)

3.2 *Wind vortices around a Cube*

In order to clarify the effect of dimensions of cubic in the tornado-like vortex, a simulation with a cube of *B=0.5h* was also carried in the stationary condition. Vorticity magnitude was estimated from the wind flow of stationary and moving simulators and visualized in 3D volume rendering. Fig.10 illustrates the vortex in the stationary condition with cube of *B=0.1h* and *B=0.5h*. When the width of cube became large, the tornado-like vortex was separated into small vortices. The small vortices were occurred around the corner of the cubic and turn in the tornado direction. In other hand, the moving of the vortex before and after passing the cubic is shown in Fig.10. When the vortex is moving, the core of vortex was bent under effect of ground. Strong vortices are also found around the cubic from the tornado-like vortex.

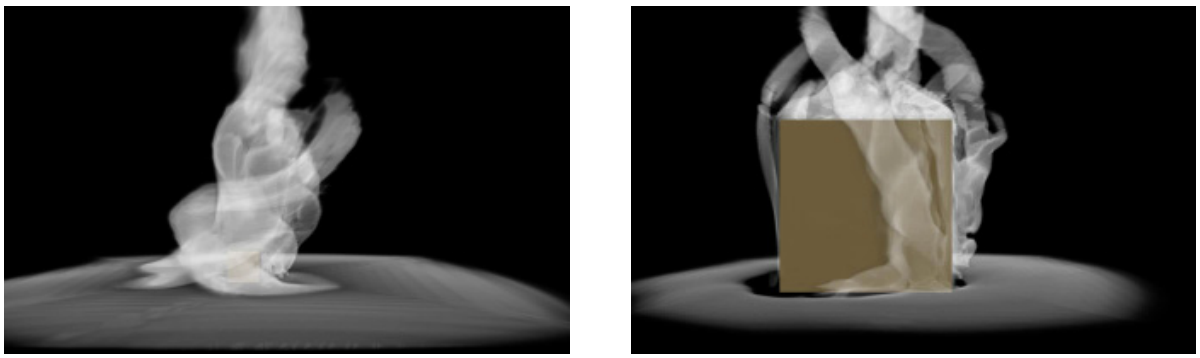

Figure 10. Wind flow around cubes (left: B=0.1h, right: B=0.5h) in stationary condition

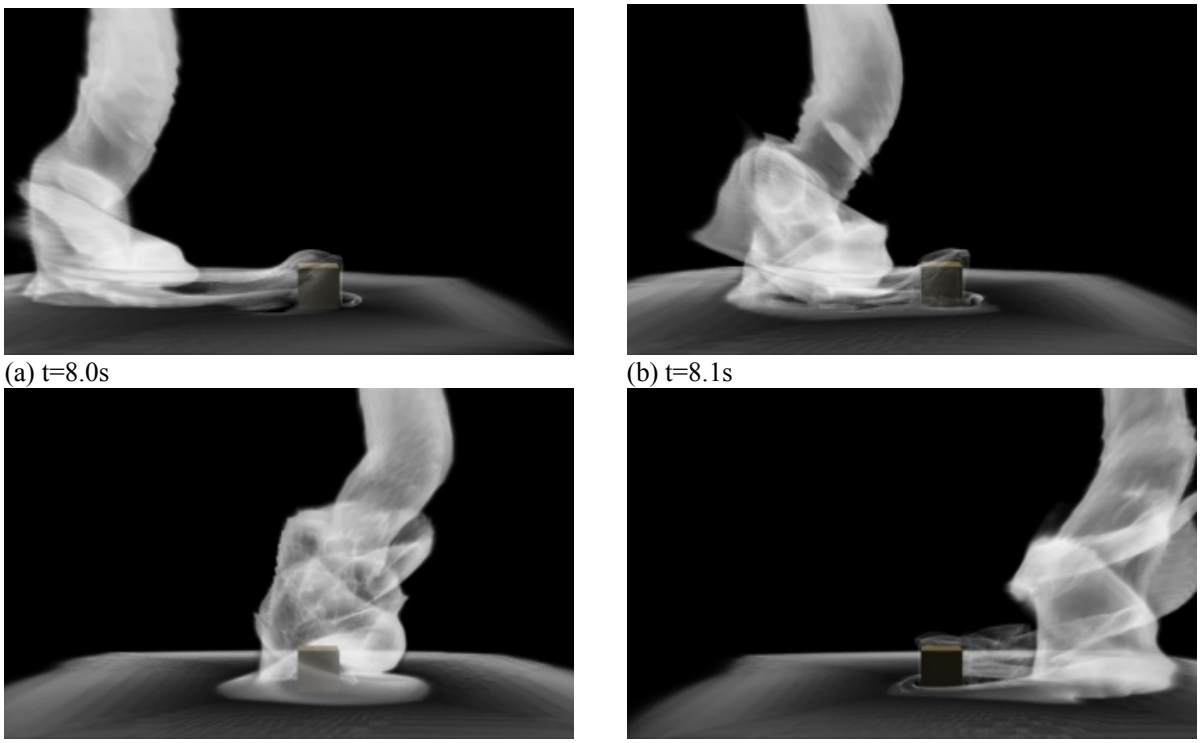

(a) t=8.0s (b) t=8.1s

(c) t=8.2s (d) t=8.3s

Figure 11. Wind flow around a cube (B=0.1h) in moving condition

4 CONCLUSION

A numerical movable tornado simulator using LES has been developed to evaluate the effects of the moving of the tornado-like vortices on the wind pressure distribution and wind flow around a cube. Although, the wind pressure on the surface of the cubic is almost constant in time inside the stationary tornado-like vortices, the pressure is changed significantly under moving of the vortices when the vortices were passing. The significant changing was also clarified from the wind flow around the cubic with strong whirl vortices and vertical wind components.

5 REFERENCES

1 J. Wurman, The DOW mobile multiple-Doppler network, 30th International Conference on Radar Meteorology, American Meteorological Society, Munich, Germany, 2001.
2 H. Niino, A.T. Noda, Numerical Simulation of a Tornado: Current Status and Future Tasks, NCTAM, pp.19-23, 2005 (Japanese).
3 N.B. Ward, The exploration of certain features of tornado dynamics using a laboratory model, Journal of the Atmospheric Sciences, Vol.29, pp.1194-1204, 1972.
4 M. Matsui, Y. Tamura, Experimental study on tornado-like flow as functions of swirl ratio and surface roughness, Proc. 19th National Symposium on Wind Engineering, pp.7-12, 2006 (Japanese).
5 Z.Yang, P. Sarkar, H. Hu, An experimental study of a high-rise building model in tornado-like winds, Journal of Fluid and Structures, Vol.27, pp. 471-486, 2011.
6 T. Maruyama, Numerical simulation of tornado-like vortex, Journal of Wind Engineering, JAWE, No.111, pp. 99-100, 2007 (Japanese).
7 P.V. Phuc, T. Nozu,T., K. Nozawa, H. Kikuchi, A Numerical Study of Tornado-like Vortices using Large Eddy Simulation, Proc. 23th Symposium on Computational Fluid Dynamics, CD-Rom, G1-3, 2009 (Japanese).
8 M. Matsui, Y. Tamura, A. Yoshida, Wind pressure distribution around cube in tornadic flow and moving effects on tornadic flow, Proc. 20th National Symposium on Wind Engineering, pp.319-324, 2008 (Japanese).
9 R.P. Selvam, and P.C. Millett, Large eddy simulation of the tornado-structure interaction to determine structural loadings, Wind and Structures, Vol. 8, pp.49-60, 2005.
10 C.R. Church, T. Snow and E. M. Agee, Characteristics of tornado-like vortices as a function of swirl ratio: Laboratory investigation, Journal of Atmospheric Science, Vol.36, pp.1755-1776, 1979.
11 H. Niino, T. Fujitani, N. Watanabe, A Statistical Study of Tornadoes and Waterspouts in Japan from 1961 to 1993, J. Climate, Vol. 10, pp.1730–1752, 1997.
12 FLUENT 6.3, User's Guide, 2006.

The Seventh International Colloquium on Bluff Body Aerodynamics and Applications (BBAA7)
Shanghai, China; September 2-6, 2012

Application of nonlinear eddy viscosity model in simulations of flows over bluff body

Jian Zhang [a,b], Qingshan Yang [b], Q. S. Li [a]

[a] *Dept of Civil and Architectural Engineering, City University of Hong Kong, Hong Kong*
[b] *School of Civil Engineering, Beijing Jiaotong University, Beijing, 100044, China*

ABSTRACT: Turbulent wind flows around building structures (bluff bodies) are investigated numerically using Reynolds Averaged Navier-Stokes (RANS) turbulence models. A non-linear viscosity assumption model, which can take into account the anisotropy of turbulence with less numerical cost than LES method, is adopted herein as a turbulence treatment method. Model coefficients of the nonlinear terms are adjusted, aiming to model three-dimensional flows over bluff bodies. Compared with the results of the linear eddy viscosity model and experimental measurements, the nonlinear eddy viscosity model yields more reasonable results, especially for the reattachment length and pressure coefficients. It is also noted that the nonlinear eddy viscosity model performs satisfactorily to reproduce complex turbulent flows around bluff bodies.

KEYWORDS: Nonlinear eddy viscosity model, CFD, Bluff body, Wind flow, RANS models

1 INTRODUCTION

Turbulent wind flows around building structures (bluff bodies) have been studied extensively by wind tunnel tests and field measurements. Rapid developments of computer technology in recent years have made it possible to adopt numerical methods, such as Large Eddy Simulation (LES) or Reynolds Averaged Navier-Stokes (RANS) models, to simulate turbulent flows around bluff bodies. Although LES is an effective tool to calculate turbulent flows around civil structures, RANS turbulence models, such as eddy viscosity models or Reynolds Stress Models, are still valid because they require less computer hardware sources than LES. However, it is imperative to overcome the limitations of RANS models. From the viewpoint of computational efficiency and practical application, nonlinear eddy viscosity models are attractive for simulations of flows influenced by anisotropy of turbulence.

The two-equation turbulence models, for instance, the $k-\varepsilon$ and the $k-\omega$ series models, offer significant simplicity and numerical stability in many cases for predictions of flow fields. The Linear Eddy Viscosity Models (LEVMs) construct eddy flow field using solvable turbulence quantities, such as k, ε and ω (Versteeg & Malalasekra, 2007). The Boussinesq hypothesis, together with the standard $k-\varepsilon$ model (Launder & Spalding, 1974), is generally regarded as the conventional linear eddy viscosity concept. It is found that LEVMs can be successfully applied to two-dimensional boundary layers, three-dimensional flow around simple bodies and thin shear flows which can be treated as approximately equilibrium (Hellsten and Bezard, 2005). This is because the LEVM is only able to provide principle stress component correctly in such flows. Therefore, it is not applicable in flows where anisotropic turbulence eddy fluctuations essentially influence the mean flow. Complex phenomena such as strong three-dimension, separations, recirculations and reattachments are common in wind flows over building structures. It is noted

that the standard LEVMs have severe defects for simulations of complicated flow fields. Consequently, it is required to extend the applicability of the linear eddy viscosity models for capturing anisotropic stress fields.

Recent studies have been mainly focused on the nonlinear relationship between the Reynolds stress and mean flow quantities. The aim of adopting the Nonlinear Eddy Viscosity Model (NLEVM) is to introduce mean flow strain rate (or vorticity) into the Reynolds stress expressions to construct nonlinear stress terms. Quadratic, cubic and fifth order models are commonly used in the NLEVM's, which are different from each another with the degrees of nonlinearity. Craft et al. (1997) and Huang & Rajagopal (1996) developed individual quadratic NLEVM models to simulate two-dimensional turbulent flow over a backward-facing step. Their results showed that the two quadratic NLEVMs successfully predicted the reattachment length of flow over the step. Meanwhile, the quadratic models demonstrated great robustness while CPU cost was not significantly increased. Other quadratic models have been proposed by Speziale (1987) based on the strain rate and by Rubinstein (1990) based on renormalisation-group approach. These models yielded satisfactory results for simple cases.

Jongen et al. (1998) observed that the sensitivity of quadratic models to the rotation is inadequate to predict fully developed channel flow subjected to rapid spanwise rotation. Craft et al. (1995) argued that a cubic Reynolds stress expansion is needed for predicting complex flows with large streamline curvature effects. Craft et al. (1995) adopted a third-order term to sensitize the model to curvature effects to overcome the overestimation of turbulence energy in the impingement area. To capture non-equilibrium flows, Craft et al. (1997) developed a more complicated model, in which the second anisotropy invariant is added in Reynolds stress expansions to form a three-equation of NLEVM. This new model was designed especially for low-Reynolds number transitional and turbulent flows. Apsley & Leschziner (1998) derived a cubic model based on successive iterative approximations to an algebraic Reynolds stress model. They validated the model by considering several flows including a high-lift airfoil flow and separating flow in two-dimensional diffuser. However, they just used the original coefficient-formulas as relationships between the coefficients and recalibrated their values to capture the low-Reynolds number near-wall flow.

Applications of these NLEVMs to complex turbulent flows have displayed inspiring results on flow anisotropy, strong streamline curvature, recirculation and adverse pressure gradient. To evaluate the performance of the NLEVMs in predicting complex turbulent flows fields, this paper presents numerical simulations of wind flow over a bluff body with a quadratic NLEVM in comparison with field measurement data. It should be noted that throughout the numerical simulations, realizability conditions are applied to the NLEVM. It will prove that the NLEVM can be applied to the simulations of turbulent flows with strong anisotropy usually encountered in engineering practices.

2 THE NONLINEAR $k-\varepsilon$ TURBULENCE MODEL

2.1 *Basic equations*

The basic equations of continuity and momentum for steady incompressible flows are:

$$\begin{cases} \dfrac{\partial \rho}{\partial t} + div(\rho \mathbf{u}) = \mathbf{0} \\ u_j \dfrac{\partial u_i}{\partial x_j} = -\dfrac{\partial p}{\partial x_i} - \dfrac{\partial u_i' u_j'}{\partial x_j} + \mu \dfrac{\partial^2 u_i}{\partial x_j^2} \end{cases} \tag{1}$$

Realizable $k-\varepsilon$ model is adopted in this study as follows:

$$\begin{cases} \dfrac{\partial(\rho k u_j)}{\partial x_j} = \dfrac{\partial}{\partial x_j}[\alpha_k \mu_{eff} \dfrac{\partial k}{\partial x_j}] + G_k - \rho\varepsilon, \\ \dfrac{\partial(\rho \varepsilon u_j)}{\partial x_j} = \dfrac{\partial}{\partial x_j}[\alpha_\varepsilon \mu_{eff} \dfrac{\partial \varepsilon}{\partial x_j}] + \rho C_1 S \varepsilon - \rho C_{2\varepsilon} \dfrac{\varepsilon^2}{k + \sqrt{\nu\varepsilon}} + \rho C_{1\varepsilon} \dfrac{\varepsilon}{k} C_{3\varepsilon} G_b. \end{cases} \tag{2}$$

where x_i and x_j are the spatial coordinates; u_i and u_j are the averaged wind velocities; $-u_i' u_j'$ is the Reynolds stress; p is the averaged pressure; ρ is the density of fluid; k is the Turbulent Kinetic Energy (TKE); ε is the turbulent energy dissipation rate; ν_t is the turbulent dynamic eddy viscosity, μ is the molecular viscosity and $\sigma_k = 1.0$, $\sigma_\varepsilon = 1.3$, $C_1 = 1.44$, $C_2 = 1.92$ are the model constants.

For two-equation turbulence model, Reynolds stress tensors τ_{ij} are expressed by the linear constitutive equation:

$$\tau_{ij} = -\rho \overline{u_i' u_j'} = \mu_t \left(\frac{\partial \overline{u_i}}{\partial x_j} + \frac{\partial \overline{u_j}}{\partial x_i} \right) - \frac{2}{3} k \delta_{ij} \quad \mu_t = \rho C_\mu \frac{k^2}{\varepsilon} \tag{3}$$

2.2 *The quadratic eddy viscosity assumption*

Since the standard two-equation model does not take into account the anisotropy of the Reynolds stresses. This shortcoming can be overcome to some extent by introducing a nonlinear constitutive expression as follows:

$$\begin{aligned} \rho u_i' u_j' =& -\mu_t S_{ij} + 2/3 \delta_{ij} k + C_1 \mu_t \frac{k}{\varepsilon}(\Omega_{ik} S_{kj} + \Omega_{jk} S_{ki}) \\ &+ C_2 \mu_t \frac{k}{\varepsilon}(S_{ik} S_{kj} - 1/3 S_{kl} S_{lk} \delta_{ij}) + C_3 \mu_t \frac{k}{\varepsilon}(\Omega_{ik} \Omega_{kj} - 1/3 \Omega_{kl} \Omega_{lk} \delta_{ij}) \end{aligned} \tag{4}$$

where $S_{ij} = \partial u_i / \partial x_j + \partial x_j / \partial x_i$ and $\Omega_{ij} = \partial u_i / \partial x_j - \partial x_j / \partial x_i$

For three-dimensional flows around bluff bodies, the coefficients of Reynolds stress terms are needed to be tuned by consideration of the anisotropy (Champagne, 1970). Firstly, Reynolds stress components are extracted and simplified. According to zero-pressure gradient flow over a smooth plate, wind velocity component can be expressed as follows:

$$\begin{cases} u_1 = u_{y_0} \left(\dfrac{y}{y_0} \right)^\alpha \\ u_2 = u_3 = 0 \end{cases} \tag{5}$$

Then, shear deformation invariant $S = \dfrac{k}{\varepsilon} \sqrt{\dfrac{1}{2} \left(\dfrac{\partial u_i}{\partial x_j} + \dfrac{\partial u_j}{\partial x_i} \right)^2}$ and vorticity deformation invariant $\Omega = \dfrac{k}{\varepsilon} \sqrt{\dfrac{1}{2} \left(\dfrac{\partial u_i}{\partial x_j} - \dfrac{\partial u_j}{\partial x_i} \right)^2}$ can be simplified as:

$$S = \Omega = M = \frac{k}{\varepsilon} \frac{\mathrm{d}u_x}{\mathrm{d}y} \tag{6}$$

where $M = \max(S, \Omega)$ is deformation tensor invariant.

The normal Reynolds stress components are expressed as follows:

$$\begin{cases} \dfrac{u_1'u_1'}{k} = \dfrac{2}{3} + C_\mu \dfrac{2C_1 - C_3}{3} M^2 \\ \dfrac{u_2'u_2'}{k} = \dfrac{2}{3} + C_\mu \dfrac{-C_1 + 2C_3}{3} M^2 \\ \dfrac{u_3'u_3'}{k} = \dfrac{2}{3} + C_\mu \dfrac{-C_1 - C_3}{3} M^2 \end{cases} \tag{7}$$

In two-dimensional boundary flows, constants $C_1 = 0.4$, $C_2 = 0$, $C_3 = -0.13$ and $C_\mu = 0.09$ vary with anisotropic flow characteristics. To satisfy the above mathematical constraints, damping function f_M is introduced into C_1~C_3 as:

$$C_1 = 0.4 f_M(M), \quad C_2 = 0, \quad C_3 = -0.13 f_M(M) \tag{8}$$

It is well-known that the tensor τ_{ij} is positive, the following inequalities are thus satisfied:

$$\begin{cases} \tau_{ii} \geq 0 \\ |\tau_{ij}| \leq (\tau_{ii}\tau_{jj})^{0.5} \\ det(\tau_{ij}) \geq 0 \end{cases} \tag{9}$$

We refer to these three properties as realizability conditions. The normal Reynolds stress components can be concluded based on the first realizability condition in equation (9) as follows:

$$\begin{cases} \dfrac{u_1'u_1'}{k} = \dfrac{2}{3} + C_\mu \dfrac{2C_1 - C_3}{3} M^2 \geq 0 \\ \dfrac{u_2'u_2'}{k} = \dfrac{2}{3} + C_\mu \dfrac{-C_1 + 2C_3}{3} M^2 \geq 0 \\ \dfrac{u_3'u_3'}{k} = \dfrac{2}{3} + C_\mu \dfrac{-C_1 - C_3}{3} M^2 \geq 0 \end{cases} \tag{10}$$

From the second expression of equation (10), constant C_μ satisfies:

$$C_\mu \leq \frac{2}{(C_1 - 2C_3)M^2} = \frac{2}{0.66 f_M(M) M^2} \tag{11}$$

Based on the realizable $k-\varepsilon$ model, turbulent kinetic energy generation G_k, Reynolds shear stress $-u_1'u_2'$ and turbulent viscosity μ_t are expressed below:

$$G_k = -u_1'u_2' \frac{\mathrm{d}u_x}{\mathrm{d}y}, \quad -u_1'u_2' = \nu_t \frac{\mathrm{d}u_x}{\mathrm{d}y}, \quad \nu_t = C_\mu \frac{k^2}{\varepsilon} \tag{12}$$

Reynolds shear stress $-u_1'u_2'$ can be derived by equations (11) and (12):

$$\frac{u_1'u_2'}{k} = -C_\mu M \tag{13}$$

Then another C_μ expression is derived as follows:

$$C_\mu \leq \frac{(C_1 + C_3)S + \sqrt{(C_1 + C_3)^2 S^2 + 4[9 + (2C_1^2 + 2C_3^2 - 5C_1C_3)S^2]}}{9S + (2C_1^2 + 2C_3^2 - 5C_1C_3)S^3} \tag{14}$$

To make sure C_μ satisfies the realizability condition, C_μ expression is given as follows:

$$C_\mu = \min(0.09, 0.3 f_M(M)) \tag{15}$$

Based on the above derivation, the three-dimensional quadratic eddy viscosity model can be expressed as:

$$\begin{cases} \rho u_i' u_j' = -\mu_t S_{ij} + 2/3\delta_{ij}k + C_1\mu_t\dfrac{k}{\varepsilon}(\Omega_{ik}S_{kj} + \Omega_{jk}S_{ki}) \\ \qquad\qquad +C_2\mu_t\dfrac{k}{\varepsilon}(S_{ik}S_{kj} - \dfrac{1}{3}S_{kl}S_{lk}\delta_{ij}) + C_3\mu_t\dfrac{k}{\varepsilon}(\Omega_{ik}\Omega_{kj} - \dfrac{1}{3}\Omega_{kl}\Omega_{lk}\delta_{ij}) \\ C_1 = 0.4f_M(M), \quad C_2 = 0, \quad C_3 = -0.13f_M(M), \\ C_\mu = \min\left(0.09, 0.3f_M(M)\right), \quad f_M(M) = \dfrac{1}{1+0.01M^2} \end{cases} \tag{16}$$

Turbulence modeling, aiming to wind engineering applications, should take the anisotropy of turbulent flow into consideration. It is important to maintain the ease of use and computational stable of the two equation models. Therefore, nonlinear expansions of the Boussinesq hypothesis--the quadratic expressions proposed by Craft et al. (1997)--have been extended in an attempt to account for anisotropic turbulence and curvature related strain effects. Numerical tests of the quadratic model will be carried out in the following section.

3 NUMERICAL DISCRETIZATIONS, MESH SCHEMES AND TEST CASE

3.1 *Numerical Discretizations*

The commercial package FLUENT has been used to solve the governing equations for mean wind velocities and turbulent quantities. The equations are discretized by the finite volume method on structure grids. The second-order upwind differencing scheme and SIMPLEC algorithm are used for convective terms and the pressure-velocity terms individually. The modified quadratic model is incorporated in FLUENT. The turbulent viscosity μ_t is also modified based on the new expressions.

3.2 *Boundary Conditions*

For inlet condition, a fully developed velocity profile is adopted, which is expressed by a power law:

$$u_x = u_{y_0}\left(\frac{y}{y_0}\right)^{\alpha} \tag{17}$$

where u_y (m/s) is the mean wind velocity at height y(m), u_{y_0}(m/s) is the reference velocity at height y_0(m). α is the roughness category coefficient.

Turbulence intensity I is defined in AIJ code (Architectural Institute of Japan, 2004):

$$I = \begin{cases} 0.1\left(\dfrac{y}{Y_G}\right)^{-\alpha-0.05} & , Y_b < y <= Y_G; \\ 0.1\left(\dfrac{Y_b}{Y_G}\right)^{-\alpha-0.05} & , y <= Y_b. \end{cases} \tag{18}$$

where y is the height along the fetch; Y_b, Y_G and α are parameters which can be found in AIJ code. The inlet condition of turbulence kinetic energy (TKE) is defined as a function of turbulence intensity I:

$$k = \frac{3}{2}(u_x \cdot I)^2 \tag{19}$$

Dissipation rate ε can be determined by k and turbulence length scale L, and the relationship is:

$$\varepsilon = C_\mu^{3/4}\frac{k^{3/2}}{L} \tag{20}$$

where C_μ is defined as a constant (0.09).

Turbulence length scale L is defined independently of the terrain conditions of the site as:

$$L = \begin{cases} 100\left(\frac{y}{30}\right)^{0.5}, & 30 < y <= Y_G; \\ 100, & y <= 30m. \end{cases} \tag{21}$$

In summary, the inlet boundary conditions of TKE k and dissipation rate (D) ε are listed below:

$$\begin{cases} k(x) = \frac{3}{2}\left(u_0(\frac{y+y_0}{y_0})^\alpha \cdot I\right)^2 \\ \varepsilon(x) = C_\mu^{3/4}\frac{k^{3/2}}{L} \\ I = \begin{cases} 0.1\left(\frac{y}{Y_G}\right)^{-\alpha-0.05}, & Y_b < y <= Y_G; \\ 0.1\left(\frac{Y_b}{Y_G}\right)^{-\alpha-0.05}, & y <= Y_b. \end{cases} \\ L = \begin{cases} 100\left(\frac{y}{30}\right)^{0.5}, & 30 < y <= Y_G; \\ 100, & y <= 30m. \end{cases} \end{cases} \tag{22}$$

The boundary conditions of the top and bilateral boundaries of the fetch are set as slip boundary conditions, which are expressed as:

$$\begin{cases} u_y = 0, \ \frac{\partial}{\partial x}(u_x, u_z, k, \varepsilon) = 0, \\ u_z = 0, \ \frac{\partial}{\partial x}(u_x, u_y, k, \varepsilon) = 0. \end{cases} \tag{23}$$

The outflow face is assumed as fully developed outflow boundary condition, which can be expressed as:

$$\frac{\partial}{\partial x}(u_x, u_y, u_z, k, \varepsilon) = 0 \tag{24}$$

3.3 *Numerical model and mesh schemes*

To examine the performance of the quadratic eddy viscosity model, numerical simulations of wind flow over a 6m cube are carried out based on the standard realizable $k-\varepsilon$ turbulence model and the quadratic eddy viscosity model. The 6m cube is mounted in atmospheric boundary layer (ABL) at a normal orientation to the incident wind with the computational domain shown in Figure 1. Specific representations of the computational domain and mesh arrangements can be seen in Figure 2.

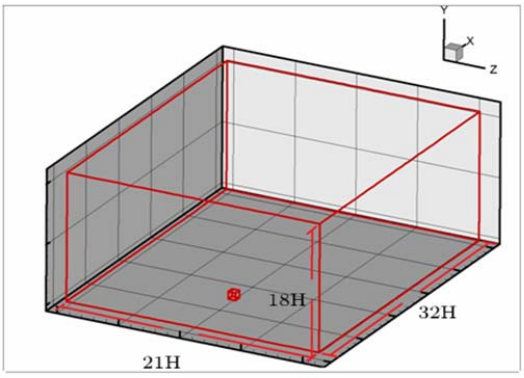

Figure 1. Computational domain around 6m cube.

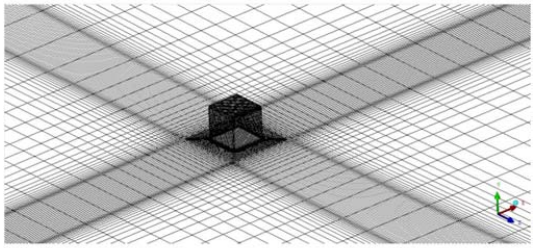

Figure 2. Grids scheme for 6m cube model.

Reynolds number based on the incident wind velocity and the height of the 6m cube model is around 10^7. To resolve the flow field around the bluff body, the first-layer cell near the cube surface is set as $0.015H_c$, which is appropriate for the realizable $k-\varepsilon$ model. The cells are non-uniformly distributed and the stretching ratio is 1.12 along the surfaces. 32 grids are placed on the windward, roof and leeward surfaces of the cube (z-direction). 40 grids are located along the lateral faces of the cube (y-direction). 30 grids with stretching ratio 1.2 are placed in the wake zone of the computational domain.

4 NUMERICAL RESULTS

The computational results are compared with those by the linear eddy viscosity model (the realizable $k-\varepsilon$ model) and the field measurement results (Richards et al., 2001).

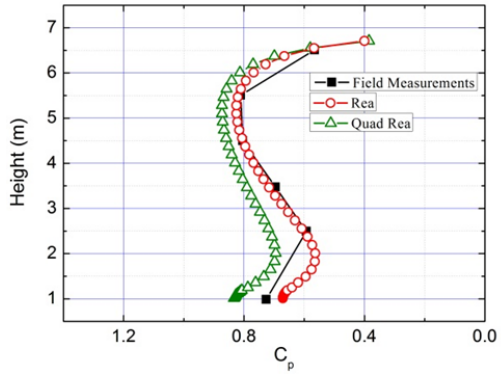

Figure 3. Pressure distributions along the windward face.

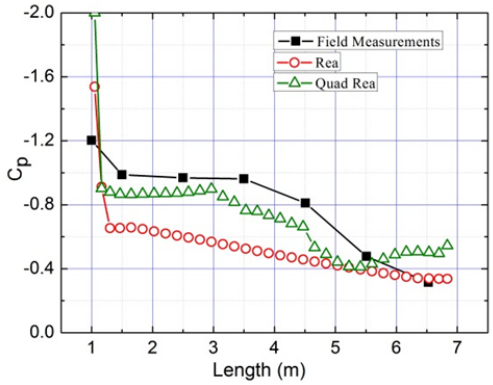

Figure 4. Pressure distributions along the roof face.

Figure 3 shows comparisons of mean pressure coefficient distributions on the windward face. It can be seen that the two turbulence models yield almost same results around the flow stagnation point. The pressure coefficients on the remaining part show relatively similar distribution shapes with differences within approximately 10 percent of the measurement values. It is apparent that the CFD predicted pressure spike position is approximately 0.67m lower than that obtained by measurement results. Figure 4 shows the pressure distributions on the cube roof. The quadratic nonlinear model predicted closer results with the measurements than the linear eddy viscosity model. Both models over predicted the pressure at the front edge of the cube.

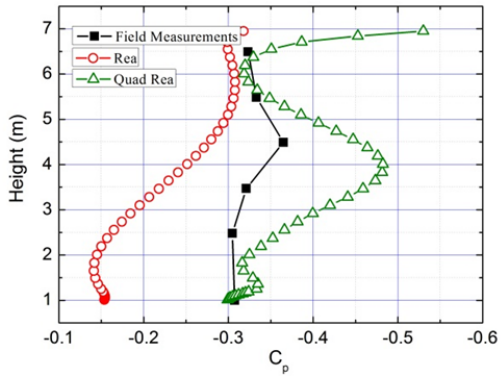

Figure 5. Pressure distributions along the leeward face.

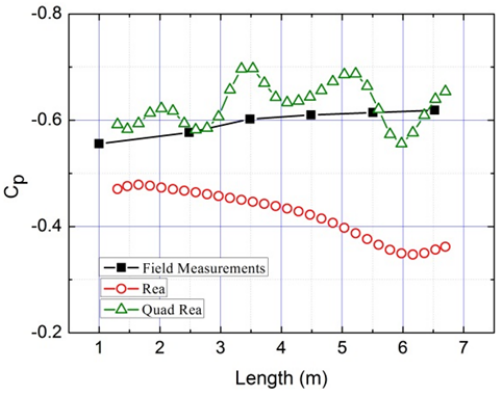

Figure 6. Pressure distributions along the side face.

The pressure distributions on the leeward face are showed in Figure 5. It is apparent that neither of the models could accurately predict the measurement results. The better approximations are obtained by the quadratic model, although the errors are around 45 to 50 percent. The pressure distributions on the side face are displayed in Figures 6. The measurement results on the side face shows a slow increase in negative magnitude as the wind velocity increases with height. The quadratic model predicts more accurate values than the standard linear eddy viscosity model. It has been proved that the size and strength of the roof recirculation zone is reduced as the flow approaching the side walls of the cube. The mass of air flowing over the roof is also reduced. It is therefore clear that the measurement results are affected to a much larger extent by three-dimensional flow phenomenon, due to significant difference between the centre and edge negative pressures. This suggests that the roof recirculation zone in the full-scale measurement contains a much stronger vortex than that predicted by CFD, which causes the pressure difference between the measurements and CFD results.

5 CONCLUSION

The quadratic eddy viscosity model, including new considerations of mathematic constraints, was developed in this paper to predict turbulent flows around bluff bodies. This study shows that adoption of the nonlinear eddy viscosity model yields better results than the standard linear eddy viscosity model, especially for the pressure distributions on the windward, roof and side faces of a 6m cube. Meanwhile, this nonlinear eddy viscosity model has great robustness to calculate turbulence anisotropy and is suitable for numerical simulation of complex flows around building structures. It is indicated that the quadratic NLEVM exhibit its advantages in capturing the pressure variations on a low-rise building, compared with those predicted by the standard two-equation turbulence models.

6 ACKNOWLEDGEMENTS

The work described in this paper is fully supported by grants from National Natural Science Foundation of China (Project No. 90815021 and 50778059) which are gratefully acknowledged.

7 REFERENCES

1 ANSYS Fluent 12.1 User Guide[M]. ANSYS Inc, 2010

2 Apsley, D. and Leschziner, M., A new low-Reynoldsnumber nonlinear two-equation turbulence model for complex flows. International Journal of Heat and Fluid Flow, 1998, 19, 209–222.

3 Architectural Institute of Japan, AIJ Recommendations for Loads on Buildings Tokyo, Japan: Architectural Institute of Japan, 2004.

4 Champagne FH, Harris VG, Corrsin S. Experiments on nearly homogeneous turbulent shear flow. Journal of Fluid Mechanics, 1970; 41:81–139.

5 Craft, T.J., Launder, B.E., Suga, K., A non-linear eddy viscosity model including sensitivity to stress anisotropy. In: Tenth Symposium on Turbulent Shear Flows. Pennsylvania State University, University Park, 1995, 23/19–23/24.

6 Craft, T., Launder, B., and Suga, K., Prediction of turbulent transitional phenomena with a nonlinear eddyviscosity model. International Journal of Heat and Fluid Flow, 1997, 18, 15–28.

7 Hellsten, A. and Be´zard, H., Behaviour of nonlinear two-equation turbulence models at the free-stream edges of turbulent flows. In: W. Rodi and M. Mulas, eds. Engineering Turbulence Modelling and Experiments 6. Elsevier, 2005.

8 Huang, Y.-N., Rajagopal, K.R., On a generalised nonlinear k–e model for turbulence that models relaxation effects. Theor. Comput. Fluid Dynam, 1996, 8, 275–288.

9 Jongen, T., Machiels, L., and Gatski, T., Predicting noninertial effects with linear and nonlinear eddyviscosity, and algebraic stress models. Flow, Turbulence and Combustion, 1998, 60, 215–234.

10 Launder B. E., Spalding D. B. The Numerical Computation of Turbulent Flows, Comput. Methods Appl. Mech. Eng, 1974, 3: 269-289

11 Richards P.J., Hoxey R.P. and Short L.J., Wind pressures on a 6m cube, Journal of Wind Engineering and Industrial Aerodynamics, 2001, 89, 1553-1564

12 Speziale C. G., On nonlinear K-l and K-ε models of turbulence, Journal of Fluid Mechanics, 1987, 178 : pp 459-475.

The Seventh International Colloquium on Bluff Body Aerodynamics and Applications (BBAA7)
Shanghai, China; September 2-6, 2012

Embedded-LES and experiment of turbulent boundary layer flow around a floor-mounted cube.

Nina Gall Jørgensen [a], Holger Koss [a], Jens Chr. Bennetsen[b]

[a]*Technical University of Denmark, Department of Civil Engineering, Kgs. Lyngby, Denmark*
[b]*Rambøll Danmark A/S, Copenhagen S, Denmark*

ABSTRACT: An Embedded LES approach is used to numerically simulate fluctuating surface pressures on a floor-mounted cube in a turbulent boundary layer flow and compared to wind tunnel experiments. The computation were performed with the CFD software ANSYS FLUENT at a Reynolds number at cube height of $Re_h = 1.3x10^5$. The computational mesh exists of 0.77 and 4.7 million hexahedra cells in the RANS and LES domains, respectively. The computed mean values are found to be accurate while the frequency spectrum of the upstream flow is not well captured due to failure of the upstream RANS-LES interface to produce correct velocity scales. However, the body induced turbulence is well captured in the fluctuating pressure coefficients.

KEYWORDS: Embedded LES, Turbulent boundary layer flow, floor-mounted cube.

1 INTRODUCTION

With the advancement in computational performance over the last decade Computational Fluid Dynamics (CFD) has become a powerful and widespread tool and finds increasingly application in the field of Wind Engineering. The here presented study is a part of a research initiative on applying CFD for simulating wind loads on building structures. The reference case is a floor-mounted cube in a turbulent boundary layer (TBL) flow as have been used in numerous other comparative studies. Main focus is on the complex flow field around the cube and the induced surface pressures. Various authors have performed numerical simulations of the flow around a floor-mounted cube. Reynolds-Averaged Navier-Stokes (RANS) models have shown good results when the flow can be described by mean flow quantities, while for predicting unsteady flow patterns and hence peak wind load features Direct Numerical Simulations (DNS) or Large Eddy Simulations (LES) have shown high potential. LES has been used to simulate the flow around floor-mounted cubes in both smooth-walled channels with a high grid resolution (Shah et al., 1997) and with coarser meshes (Krajnovic and Davidson, 2002), and in turbulent boundary layer flows (Nozawa, Tamura, 2002; Lim et al., 2009). Despite the potential of LES shown for the above mentioned studies it is still computationally expensive (in terms of hardware, license and time) to capture the small structures in wall bounded flows. The use is therefore limited for real life wind engineering applications with higher Reynolds number and complex geometries.

The aim of the presented work is to use embedded LES (E-LES) approach trying to combine the advantage of fast time-averaged solution from RANS over the entire domain and apply time resolved solution using LES in the vicinity of the bluff body to get the stochastic loading process. Thus limiting LES to the target flow around the investigated body reducing the overall cost of the simulation compared to a full LES, significantly. For the computations the commercial CFD software ANSYS FLUENT was used. The Shear-Stress Transport (SST) k-ω model (Menter, 1994) and the Wall-Modeled LES (WMLES) SGS model were used in the RANS and LES domains respectively.

2 EXPERIMENTAL AND COMPUTATIONAL TECHNIQUES

2.1 *Simulated Geometry*

The wind tunnel experiments were carried out in the closed-circuit wind tunnel at the department of Civil Engineering at the Technical University of Denmark. Figure 1 shows a longitudinal section of the wind tunnel with the flow processing unit (FPU) and the test section (TS). The wind tunnel test setup is the physical reference in this case and not considered as a scaled model of a building structure in nature. The TBL flow is simulated using spires and roughness elements (Irwin 1981). The cube size, h = 0.1m, leads to a total blockage of 4.5% of the cross section. The roughness elements were restricted to the FPU and not continued into the TS, since they would influence the flow around the cube. They thereby give space for the TBL to develop in front of the cube. The simulations are carried out at a Reynolds number of $Re_h = 1.3x10^5$ based on the velocity, U_h, at cube height. For the numerical simulation the flow is calculated by a RANS domain for the TS (indicated by the dashed line) and in close vicinity to the cube by an embedded LES domain (hatched area) as shown in Figure 1.

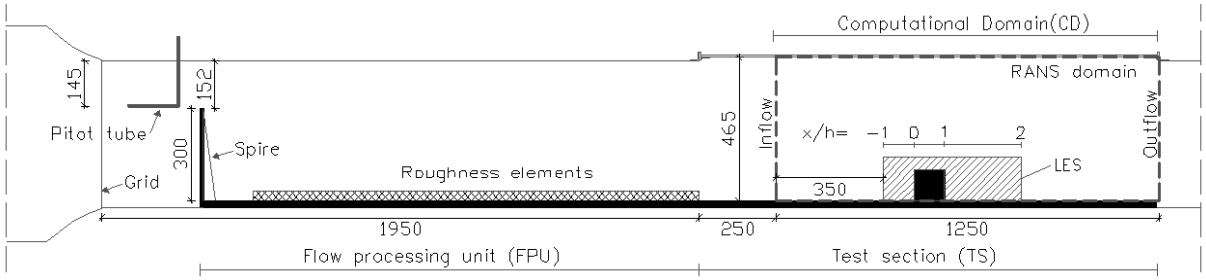

Figure 1. Longitudinal section of the wind tunnel FPU and TS.

2.2 *Velocity and surface pressure measurements*

For the velocity measurements a 4-hole Cobra probe was used providing the fluctuating time series of all three flow components. The surface pressure on the cube was measured using a Kulite piezoresistive pressure transducer (XTL-140M) directly integrated in the cube surface. The sampling frequency for both flow and surface pressure measurements was 2000Hz. Data were acquired by National Instruments LabVIEW software. The reference velocity was sampled with a static Pitot tube upstream of the FPU.

2.3 *Governing equations for LES*

In the LES zone the three-dimensional and unsteady turbulent scales up to a cut-off wave number are directly resolved by the computational mesh, while the effect of the small scale motions is modeled. To separate the time-dependent velocity vector, u_i, into a resolved component, $\overline{u}_i$, and a modeled subgrid-scale (SGS) component, u'_i, the time-dependent basic variables are filtered with a low pass filter in space. Convolution of the velocity field by the filter function $G(x-x')$ is calculated from:

$$\overline{u}_i(x,t) = \int G(x-x')u_i(x',t)dx', \qquad \int G(x')dx' = 1 \tag{1}$$

with the specific box filter function that cuts off values beyond a half filter width, $\Delta = \sqrt[3]{\Delta x \Delta y \Delta z}$:

$$G(x,x') = \begin{cases} 1/\Delta, & |x-x'| \le \Delta/2 \\ 0, & |x-x'| > \Delta/2 \end{cases} \tag{2}$$

Filtering the Navier-Stokes equations for incompressible flow gives the equations used for LES governing the resolved large scales of motion:

$$\frac{\partial \rho}{\partial t} + \frac{\partial}{\partial x_i}(\rho \bar{u}_i) = 0 \tag{3}$$

$$\frac{\partial \bar{u}_i}{\partial t} + \bar{u}_j \frac{\partial \bar{u}_i}{\partial x_j} = -\frac{1}{\rho}\frac{\partial \bar{P}}{\partial x_i} + \frac{\partial}{\partial x_j}\left(\nu \frac{\partial \bar{u}_i}{\partial x_j}\right) - \frac{\partial \tau_{ij}}{\partial x_j} \tag{4}$$

where the SGS stress term, $\tau_{ij} = \overline{u_i u_j} - \bar{u}_i \bar{u}_j$, featuring the effect of the small scales on the resolved ones is unknown and must be modeled. In ANSYS FLUENT the SGS stresses are computed from the SGS turbulent viscosity, μ_t, $\tau_{ij} = -2\mu_t \bar{S}_{ij}$. The modified algebraic WMLES SGS model proposed by Shur et al. (2008) is used to compute the SGS eddy viscosity. The model combines a mixing length model and a modified Smagorinsky model where the eddy viscosity is calculated from:

$$\nu_t = \min\left[(\kappa d_w)^2, (C_{Smag}\Delta)^2\right] \cdot S \cdot \left\{1 - \exp\left[(y^+/25)^3\right]\right\} \tag{5}$$

where d_w is the wall distance, S is the strain rate, $\kappa = 0.41$, $C_{Smag} = 0{,}2$ and y^+ is the normal to the wall inner scaling.

2.4 *Computational configuration*

The computational domain is shown in Figure 1 where a Cartesian coordinate system is placed at the bottom center of the front face of the cube with the x axis aligned with the streamwise, u component, of the flow. The boundaries of the LES domain are chosen quite tight around the cube based on the idea of "economizing" the LES effort to a minimum. LES resolves only the scales larger than 2Δ (twice the mesh elements) and uses the WMLES SGS model to model the influence of the smaller scales on the resolved ones. The high Reynolds number treated in the turbulent boundary layer flow requires high grid resolution near the solid walls and the cube. The WMLES models advantage is that it allows for a coarser near-wall grid resolute than in the classical LES requirements reducing the required near wall mesh density. The WMLES resolution requirements are:

$$\Delta_x = \frac{\delta}{10}, \quad \Delta_y = \frac{\delta}{40} \sim \frac{\delta}{30}, \quad \Delta_z = \frac{\delta}{20}, \tag{6}$$

where δ is the boundary layer thickness. The RANS and the LES domain include 0.77 and 4.7 million structured hexahedra cells respectively. Overall for the entire domain the grid is stretched in normal direction from the domain boundaries and cube walls.

The governing equations were discretised using the cell-centered finite-volume method. A pressure based solver where the governing equations are solved sequentially was used. For deriving the pressure equation from the discrete continuity equation velocity-pressure coupling was

achieved by the SIMPLEC algorithm. The continuity equation (3) and momentum equation (4) were discretised in space using a bounded central difference method and in time using first order implicit time integration.

2.4.1 *Interfaces between RANS and LES domains*

The RANS and LES domains are connected with two dimensional interfaces. As the LES zone requires turbulence quantities at the inlet the upstream modeled turbulent kinetic energy from the RANS domain is converted explicitly to resolved scales at the RANS-LES interface. At the RANS-LES interface a 2D vortex method is used, which generates small-scale turbulent motions by adding random perturbations to the mean flow via a fluctuating vorticity field (Mathey et al. 2006). The method is based on the Lagrangian form of the 2D evolution equation of the vorticity.

$$\frac{\partial \omega}{\partial t} + \left(\vec{u}.\nabla\right)\omega = \nu\nabla^2\omega \tag{7}$$

For solving equation (7) a particle discretisation is used where particles carrying information about the vorticity field represented by the circulation, Γ_i, and the assumed spatial distribution, η, are convected randomly:

$$\Gamma_i(x,y) = 4\sqrt{\frac{\pi A k(x,y)}{3N\left(2\ln(3)-3\ln(2)\right)}} \quad and \quad \eta\left(\vec{x}\right) = \frac{1}{2\pi\sigma^2}\left(2e^{-|x|^2/2\sigma^2}-1\right)2e^{-|x|^2/2\sigma^2} \tag{8}$$

where (x,y) are the coordinates in the plan of the interface, A is the total area of the interface, k the modeled turbulent kinetic energy, N the number of vortex points and σ provides control over the local vortex size. At the LES-RANS interfaces the turbulent quantities from an initial RANS simulation are used.

2.4.2 *Boundary conditions*

At all solid wind tunnel walls and at the cube surface the no-slip boundary conditions for a smooth wall were applied.

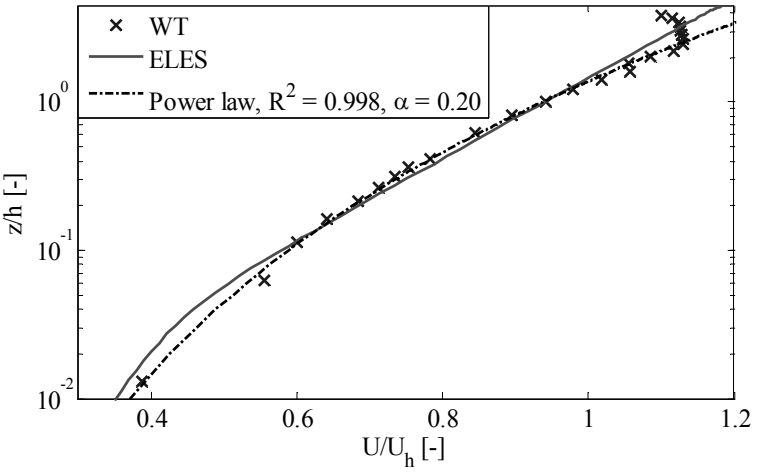

Figure 2. Time-averaged streamwise velocity profiles at the inflow of the computational domain.

At the inflow of the RANS domain a mean wind speed profile comparable to the wind tunnel experiment shown in Figure 2 was imposed. The wind tunnel data follow a power law profile up to z/h = 3:

$$U(z) = U_{10}\left(z/10\right)^{\alpha} \tag{8}$$

with a determination coefficient $R^2 = 0.998$ and a profile exponent $\alpha = 0.20$, which corresponds to terrain class III (Eurocode 1). The turbulence intensity, I_u, at the cube height is around 10%.

3 RESULTS

In the results the computed overall TBL flow around the cube is compared to the experimental data. Furthermore, the cube surface pressure at selected points is compared. Results are presented in form of time-averaged variables, frequency spectra and probability density functions. The numerical data were sampled for 14 flow-through domain times corresponding to 166 large-eddy turnover times (LETOT), $T_b = h/U_h$, which should be sufficient to compute mean field data.

3.1 *Overall flow around the cube*

The mean velocity magnitude vectors around the cube are shown in Figure 3. The center of the horseshoe vortex upstream of the cube is located at around x/h ≈ -0.4, z/h ≈ 0.1. The stagnation point on the cube upstream face is located at z/h ≈ 0.7 and the reattachment point on the cube top surface at around x/h = 0.88. The velocity magnitude plot shows how the flow field is affected by the cube at the position of the RANS-LES inlet interface at x/h = -1. A better choice of the interface placement would therefore be further upstream of the domain in the undisturbed flow field. Thereby allowing the turbulent quantities to get more development before they approaches the cube. Figure 4 shows an instant view of the coherent vortex structure around the cube. The shedding from the front corners of the cube and the body induced turbulence structures are clearly visible. Furthermore the horseshoe vortex in front of the cube can be identified.

3.1.1 *Mean and fluctuating velocities*

Figure 5 (top) shows the mean streamwise and vertical velocity components upstream of the cube at z = h, normalized by the streamwise velocity, U_h. The wind tunnel time histories are filtered with a cut-off high pass frequency corresponding to the maximum frequency resolved in the ELES. The mean flow in the region in front of the cube is well predicted using both RANS and LES models. Figure 5 (bottom) shows that the computed standard deviation for all velocity components is under-predicted in the RANS domain, but increases in the RANS-LES interface to a higher level. The transition between the RANS and LES domain shows some short comings. The streamwise component is captured approximately 0.015m behind the interface; however the spanwise and vertical components are over-predicted. This indicates that the computed turbulent length scale fluctuations are to isotropic compared to the ones found in the wind tunnel.

The computed mean spanwise and vertical flow above the cube shown in Figure 6 (left) and the vertical standard deviation, σ_w, shown in Figure 6 (right) are well predicted. The vortex shedding generated by the front top edge of the cube are generating large part of the turbulence and the transient flow quantities and the influence of the RANS-LES interface are limited in this region. Less agreement is though found in the streamwise standard deviation, σ_u, which can be a result of the horizontal interface above the cube influencing the flow. Further investigations are required to investigate this discrepancy in the streamwise fluctuations.

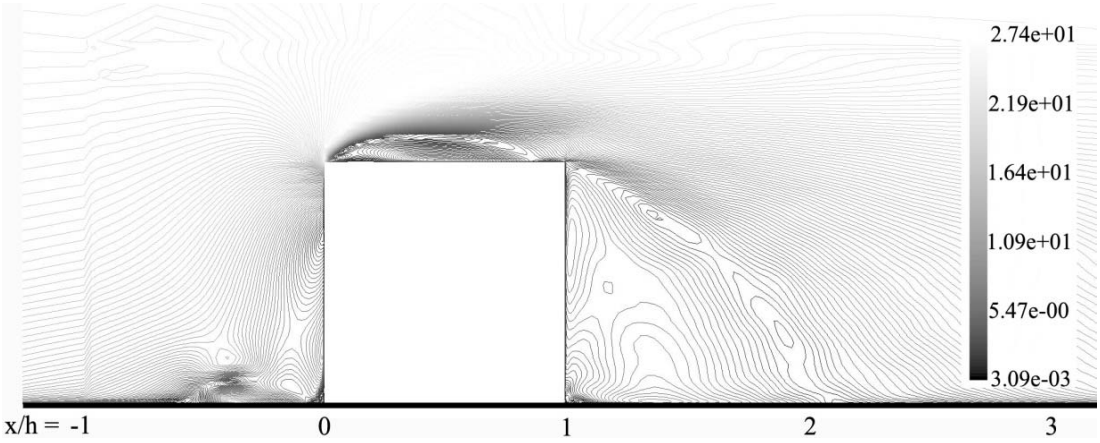

Figure 3. Mean velocity vectors in the x-z plane through the cube.

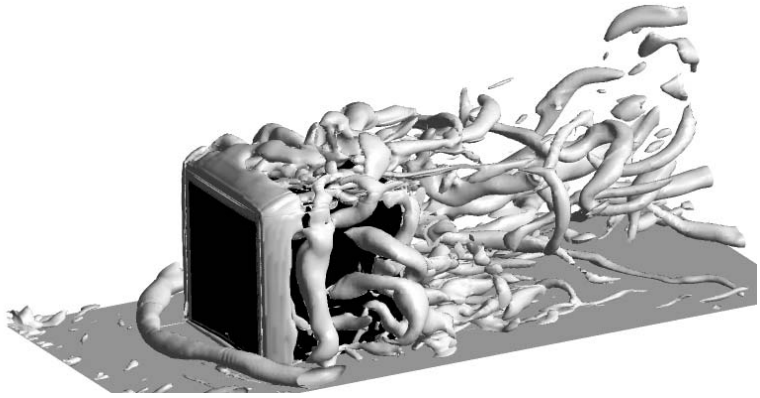

Figure 4. Coherent small scale vortex structure in the LES domain around the cube.

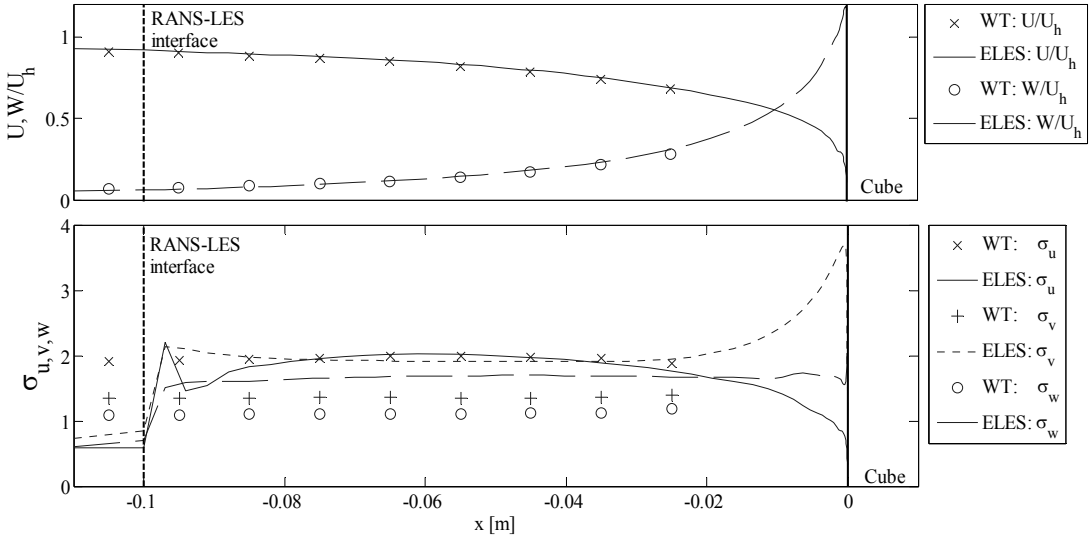

Figure 5. Mean values of u and w (top) and σ of u, v and w (bottom) velocity components in front of the cube.

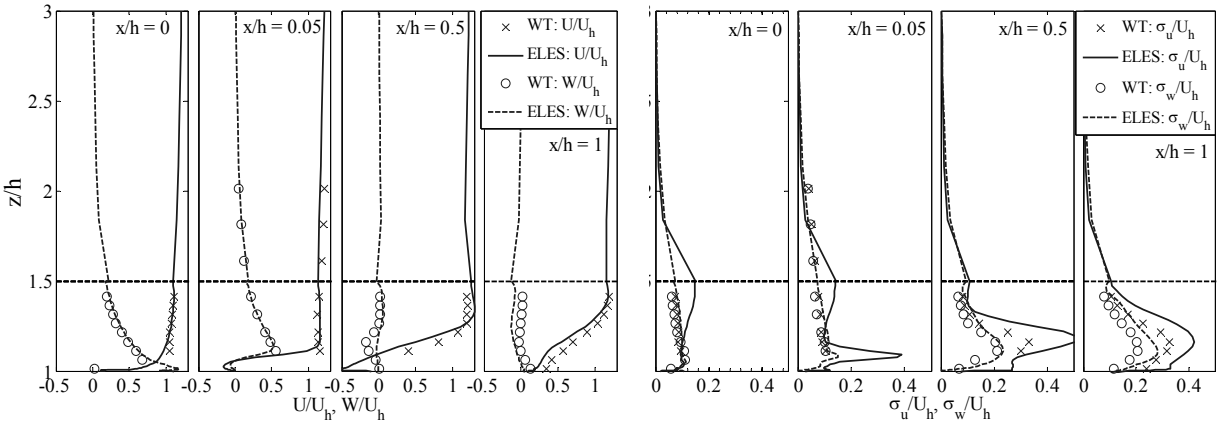

Figure 6. Normalized mean and σ profiles of u and w at four positions at the streamwise centreline on cube top face.

3.1.2 *Spectral density functions*

Figure 7 shows frequency spectra of the streamwise velocity component at z/h = 1 and x/h = -0.75. Even though already in the flow regime affected by the cube this position has been chosen to give the best view on the wind spectrum developed so far in the LES domain. The wind tunnel spectrum was fitted with a von Kármán spectral function which generally can be used to describe the fluctuation of the streamwise component in a free turbulent atmospheric boundary layer flow. The computed spectrum is deformed and does not represent the equilibrium turbulent boundary layer flow in the wind tunnel. The computed time histories do not have the correct stochastic nature resulting in a spectrum consisting of two quite defined peaks. There is no production of large scales and also the small scales supposed to be generated by the interface are missing. This is also apparent from Figure 4 where no small scales are visible in front of the cube. Hence it can be concluded that the RANS-LES interface fails in producing correct scales and is placed too close to the cube for an equilibrium turbulent boundary layer flow to be developed.

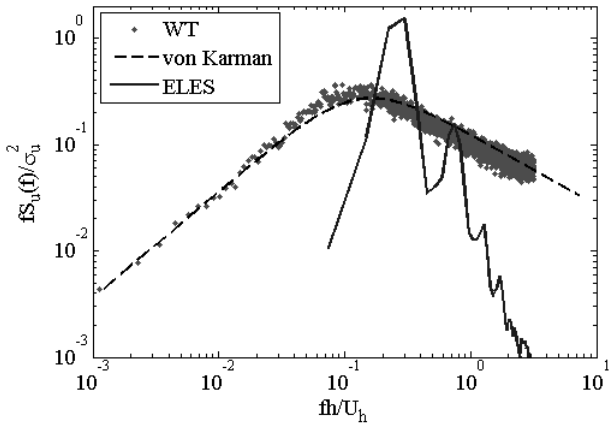

Figure 7. Spectra of the streamwise velocity component at x/h = -0.75 and z = h = 0.1m.

3.2 *Cube surface pressure*

The fluctuating surface pressure was measured in the wind tunnel at five positions along the streamwise centreline of the cube. The measurement points were chosen in the most characteristic body-near flow regions, which are assumed to be equally characteristic for the flow-induced load: 1 - stagnation point on upstream wall (x'/h=0.7). 2 - separation at leading edge on cube top face (x'/h=1.1). 3 - reattachment zone behind separation bubble (x'/h=1.2). 4 - reattached flow on the downstream half of the cube top side (x'/h=1.7). 5 - pressure in wake flow on rear side (x'/h=2.1).

As the energy content of the upstream cube flow is not captured by the ELES deviations in the surface pressure on the cube can be expected. The time-averaged, C_p, and standard deviations, σ_{Cp}, of the fluctuating surface pressure coefficients are shown in Figure 8 where x' denotes the spanwise distance along the centerline of the cube starting at the bottom of the cube upstream face. For further comparison the results from LES computation of turbulent boundary layer flow around a cube at $Re_h = 2x10^4$ by Lim et al. (2009) are also shown in the figure. The experimental and computed values of the mean pressure reflect the characteristic wind load distribution on a floor-mounted bluff body in a turbulent boundary-layer flow: maximum positive mean pressure at the stagnation point on the upstream wall and maximum negative mean pressure inside the separation bubble near the leading edge on the cube top. However, there are deviations in the mean values of up to 30 percent. The experimental and computed σ_{Cp} values are comparable except from a large deviation in point 4 at x'/h = 1.7 at the cube top surface. Furthermore, the distribution of σ_{Cp} is different from what one would expect for a cube in a TBL flow with largest fluctuations at the separation on the top face just after the leading edge. Further research of the cube surface pressure is required to explain the obtained distribution.

Spectra of the pressure coefficients, at points 1, 3, 4 and 5 are shown in Figure 9.The spectra in the stagnation point are most similar to the upstream flow spectrum. Here the computed spectrum is again very deformed. At the other points where the turbulence and length scales generated by the cube are dominant the computed spectra capture well the body-induced turbulence. The lack in fluctuation magnitudes in the computed spectra at the low frequency range is hence largest at the stagnation point but also apparent in points x'/h = 1.7 and 2.1.

3.3 *Probability density functions of Cp*

The variation of C_p is described and compared by using the probability density function (PDF) of the occurring instantaneous values. In Figure 10 PDF's for the fluctuating C_p values at points 1, 3, 4 and 5 are shown and values for the first four moments are given. The short time history for the ELES data results in significant shortage of data point in the computed PDFs.

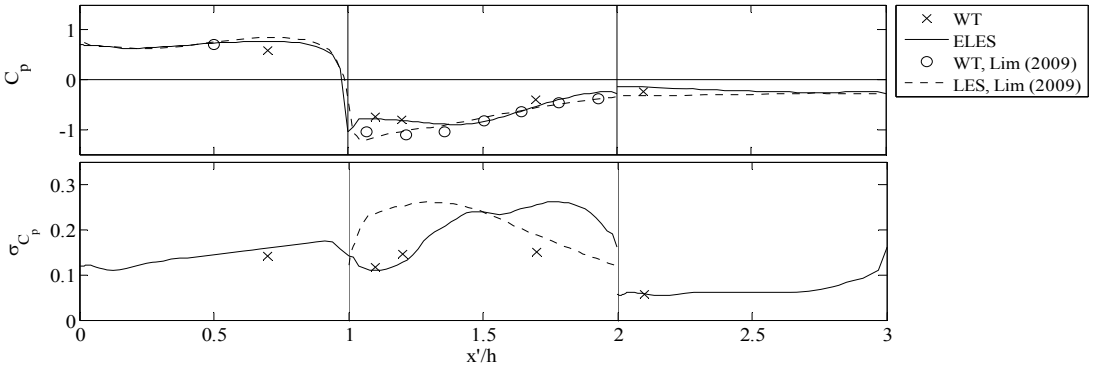

Figure 8. Time-averaged and σ of fluctuating surface pressure coefficients along the axial centerline of the cube.

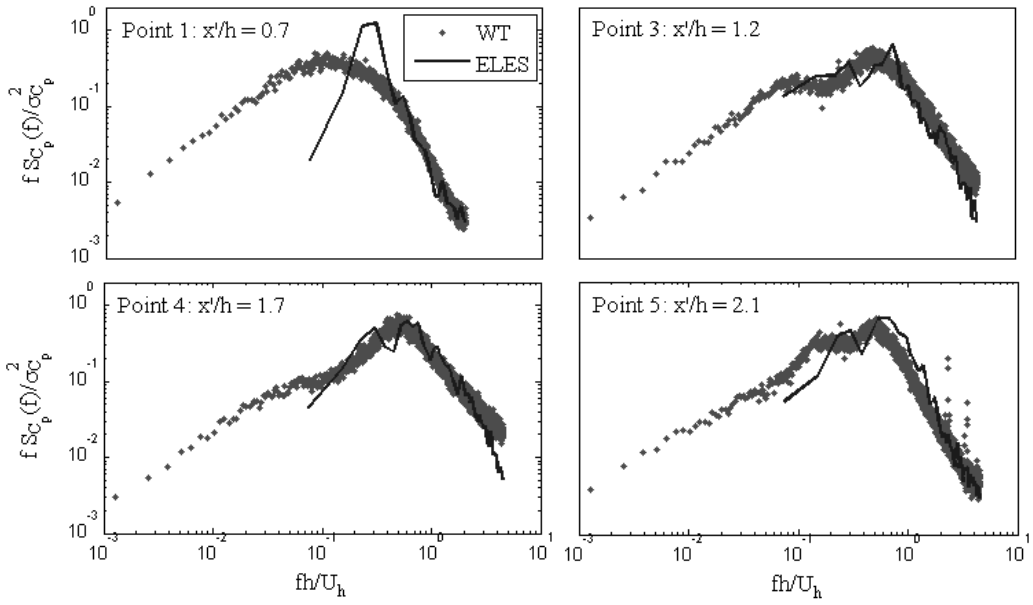

Figure 9. Spectra of the surface pressure coefficients.

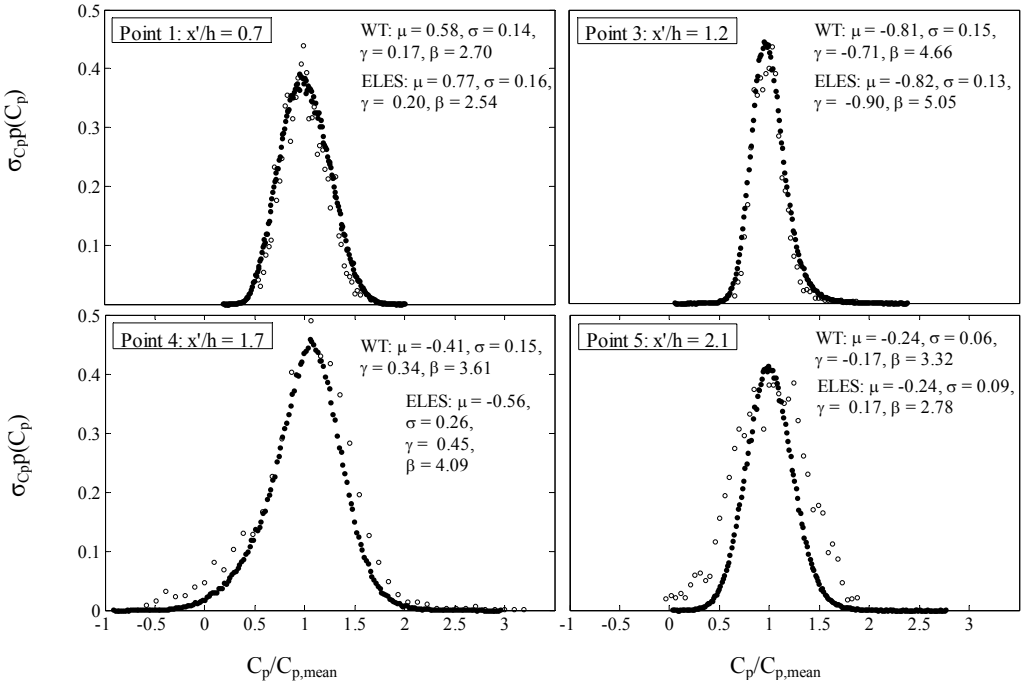

Figure 10. Normalized probability density of the surface pressure coefficients. WT: • and ELES: o.

The PDFs have similar modes and mass distributions. At some positions the outer tail values of the computed data are missing. This can be a result of the peak values not captured due to them not occurring in the limited time computed. Another explanation is the missing low frequency energy magnitude (shown in Figure 9) needed to give the sufficient amplitude for the peak to appear.

4 CONCLUSION

For the purpose of structural design the peak values of the local loading process play a central role and are hence indispensable. As it is known from wind tunnel testing, the flow and load simulation needs to reflect accurately the fluctuation process over the entire frequency range. In case of this study it can be concluded that the development of the upstream turbulent flow within the LES-zone is in this respect insufficient. It is difficult to create correct correlated turbulent inflow boundary conditions by the RANS-LES interface and it is apparent that the interface is not able of producing the correct scales of turbulence. A possible improvement could be achieved by changing the conditions at the interface or achieved by expanding the LES-zone upstream, vertically and horizontally providing longer space for the turbulent flow to develop.

Despite the lower accuracy of the computed turbulent flow the mean and standard deviations of the streamwise flow component are consistent with the experimental data while the vertical and turbulent components are over-predicted. The fluctuating surface pressure coefficients on the cube are also affected by the incorrect upstream flow. However, the body induced turbulence is well captured by the simulation.

5 ACKNOWLEDGEMENTS

The authors wish to thank Alf Lassen Nielsen for his contribution to the presented work as a part of his MSc thesis at the Civil Engineering department at the Technical University of Denmark.

6 REFERENCES

Eurocode 1: Action on structures – Part1-4: Wind actions. EN 1991

Irwin, H.P.A.H. 1981. The design of spires for wind simulation. Journal of Wind Engineering and Industrial Aerodynamics, 7, 361-366.

Krajnovic S. and Davidson, L., 2002. Large-Eddy Simulation of the Flow Around a Bluff Body. AIAA Journal, Vol. 40, No. 5.

Lim, H.C., Thomas, T.G., Castro, I.P., 2009. Flow around a cube in a turbulent boundary layer: LES and experiment. Journal of Wind Engineering and Industrial Aerodynamics, Vol. 97, pp. 96-109.

Martinuzzi, R., Tropea, C., 1993. The Flow Around Surface-Mounted Prismatic Obstacles Placed in a Fully Developed Channel Flow. Journal of Fluids Engineering, Vol. 115, No. 1, pp. 85-91.

Mathey, F., Cokljat, D., Bertoglio, J. P., Sergent, E., 2006. Assessment of the vortex method for Large Eddy Simulation inlet conditions. Progress in Computational Fluid Dynamics, Vol. 6, Nos. 1/2/3, pp.58-67.

Menter F. R., 1994. Two-Equation Eddy-Viscosity Turbulence Models for Engineering Applications. AIAA Journal, 32(8):1598-1604.

Nicoud, F. and Ducros, F. 1999. Subgrid-scale stress modelling based on the square of the velocity gradient tensor. Flow, Turbulence and Combustion. 62, 183-200.

Nozawa, K., Tamura, T., 2002. Large eddy simulation of the flow around a low-rise building immersed in a rough-wall turbulent boundary layer. Journal of Wind Engineering and Industrial Aerodynamics, Vol. 90, pp. 1151-1162.

Shah, K.B., and Ferziger, J. H., 1997. A fluid Mechanicians View of Wind Engineering: Large Eddy Simulation of Flow past a Cubic Obstacle. Journal of Wind Engineering and Industrial Aerodynamics, Vol. 67, pp. 211-244.

Shur M. L., Spalart P. R., Strelets M. K., and Travin A. K., 2008. A hybrid RANS-LES Approach with Delayed-DES and Wall-Modelled LES capabilities. International Journal of Heat and Fluid Flow, 29:6, 1638-1649.

Numerical studies on the behaviors of wind-structure interaction for membrane structures

Xiao-Ying SUN[a], Zhao-Qing CHEN[b], Yue WU[c] and Shi-Zhao SHEN[d]

[a] *School of Civil Engineering, Harbin Instituted of Technology, China, sxy_hit@163.com*
[b] *School of Civil Engineering, Harbin Instituted of Technology, China, chenzhq2004@163.com*
[c] *School of Civil Engineering, Harbin Instituted of Technology, China, wuyue_2000@163.com*
[d] *School of Civil Engineering, Harbin Instituted of Technology, China, szshen@hit.edu.cn*

ABSTRACT: In this paper, a combined numerical approach on the time-dependent fluid-structure interaction for tension structures with large displacements is presented. The general idea of this approach is to divide the structural response under wind actions into three components: mean response, background response and resonant response. The first component is a static interaction process, which is due to the change of structural geometry under mean wind pressure. The second component can be regard as a steady interaction process, which relates to the motion of large scale eddies. The last component can be called as a transient interaction process, in which the dynamic magnification effect should be considered mainly. Due to the different characteristics of each component, different methods should be adopted respectively. For static and steady interaction, the suitable method is CFD simulation, in which the wind pressure change due to structural deformation will be considered mainly; for transient interaction, the suitable method is nonlinear random vibration analysis in time domain. Base upon the combined procedure, some numerical examples include one-way type roofs and saddle-shaped membrane structures are carried out finally. From the comparison with direct numerical method, which can be seen as a accurate method, it can be concluded that the results obtained from the combined procedure are very close to the direct numerical method; moreover, the combined procedure seems easier for application.

KEYWORDS: membrane structures; wind-structure interaction; CFD numerical simulation; aeroelastic effects; aerodynamic response; geometrical nonlinearity

1 INTRODUCTION

Membrane structures are the most widely used long-span tension structures. As being characterized by lightweight and flexible, they are highly susceptible to the wind action. How to determine the aerostatic and aerodynamic response due to the wind action is a major concerned problem for the design of tension structures. Up to now, comprehensive studies have been performed, but the mechanism of wind-induced vibration of membrane structures has not been recognized in enough detail. The main reasons lie in two aspects: one is the strongly geometrical nonlinearity,

which make the dynamic characteristics of tension structures are obviously different from those of bridges and high-rising buildings, so traditional methods of random vibration analysis in frequency domain can not be used directly. The other reason is the weak local rigidity, which can make membrane structures produce rather large vibration under wind excitation. Sometime, these large vibrations can even affect the surrounding fluid field remarkably; that is to say, the wind-structure interaction or the aeroelastic effects can not be neglected. To solve the previous problem, some nonlinear random vibration analysis methods in time domain have been developed successfully [1]. But all those methods are based on the condition that the inlet flow or the wind pressure process has been determined beforehand, so they can not consider the fluid-structure interaction actually. To determine the actual wind loads on tension structures, especially to reveal the mechanism of wind-structure interaction, some semi-empirical methods have been developed [2], also some wind tunnel tests has been carried out [3]. However, some unavoidable errors will occur when using simplified methods, and wind tunnel tests are too expensive to carry out extensive studies, therefore those methods are only limited to certain special structures.

In recent years, with the development of high speed computer and numerical computational methods, it has been available to integrate computational fluid dynamics (CFD) and computational structure dynamics (CSD) technique to simulate structures and surrounding flow simultaneously, which is called as numerical wind tunnel method. Comparing to those simplified methods and wind tunnel tests, numerical wind tunnel method can solve flowing problems of complex geometrical bodies without disturbing the fluid field, construct computational models whose dimension are same as that of original structures so as to avoid the similarity requirements in wind tunnel test, completely control the properties of fluid and provide great flexibility for selecting flowing parameters to carry out parametric analysis. Because of these superior characteristics, numerical wind tunnel method is highly valued by researches and developed quickly. Now this method has been applied to solve some aeroelastic problems, such as for bridges [4] and also for membrane structures [5]. But due to the tremendous calculate work, this method also can not be used in engineering practice.

In this paper, an overview of the studies on wind-structure interaction of tension structures is provided firstly. Then a combined numerical approach based on CFD simulation method and random vibration analysis method is presented. Finally, Base upon the combined procedure, some numerical examples include one-way type roofs and saddle-shaped membrane structures are carried out.

2 METHODOLOGY

Wind-induced response of tension structures can be theoretically described as a problem of unsteady coupling vibration between incompressible viscous fluid and geometrical nonlinear elastic body. Due to the fluid forces and structure displacements on the interface between fluid and structure are unknown, it is impossible to solve the fluid field and structural field separately, so we have to find some methods that can solve these two fields simultaneously. Undoubtedly, the numerical wind tunnel method provides a good platform for solving this problem.

In Ref. [6], the author had developed a FEM program for calculating two-dimension problem. There were three modules included in this program, each for CFD, CSD and CMD (Computational Mesh Dynamics) calculation, respectively. The flowchart is shown in fig.1. The dynamic fluid-structure interaction was performed by a partitioned solution approach, and the time-dependent simulation process was controlled by an iteration procedure between these three modules until convergence was reached in each time-step. Based on this program, the aeroelastic re-

sponse of one-way type pretensioned membrane roofs has been studied. The effects of several factors, such as height-span ratio, roof slope, roof mass and pretension force et al, were investigated. From these studies, some preliminary but very important conclusions about the mechanism of wind-structure interaction were obtained [7].

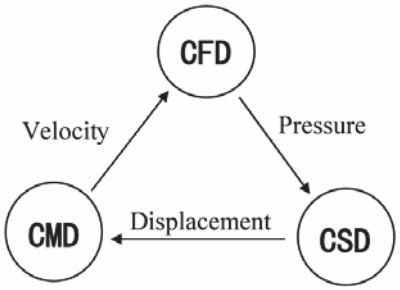

Fig. 1 Flowchart of CFD simulation program

The practical cable/membrane structures are 3-dimensional with complicated surfaces. Using the CFD simulation approach as mentioned above to study the aeroelastic effects of 3-D structures has theoretically possible, but will be very difficult in practice at present. Firstly, the time-consuming of simulating 3-D problem is hundreds times of 2-D problem, which can not be tolerated for systemically studies. Secondly, the increasing computing time will cause lots of numerical dissipation and error cumulation. So if we use the method proposed in Ref. [9] to solve 3-D problem, it means that all the numerical methods in this 2-D program should be improved to get more computing efficiency and precision, however the work is obviously enormous. At the same time, there are two facts: (1) Various CFD commercial software are developing quickly, they have provide more efficient numerical platform to solve fluid problem, however, the problem of fluid-structure interaction can hardly be resolved by these software. (2) From the viewpoint of engineering, engineers usually don't concern about the details of coupling vibration process but some statistic information, such as the mean and peak value, and whether or when will the aeroelastic instability occur. So it is possible to solve the coupling problem by another new method, which is to adopt some simplified analytical methods and numerical methods to get the statistical information of the coupling process, and give up the simulation on wind-structure interaction in detail. The precondition of this method is to give a reasonable explanation about the coupling mechanism of wind-structure interaction.

According to the wind-induced structural vibration theory proposed by Davenport [8], the structural response can be broken into three components: mean response $\bar{r}$, background response $\tilde{r}_B$ and resonant response $\tilde{r}_R$ (Fig.2). The mean response is induced by average wind pressure, and does not change with time. The background responses relates to the motion of large scale eddies, and vary slowly and irregularly with time. It is essentially a quasi-static process and has no dynamic amplificatory effect. The resonant response usually happens at frequencies adjacent with the structural natural frequency, and has obvious dynamic amplificatory effect. If we assume that the wind-induced vibration response of membrane structures has the same characteristics as mentioned above, then different methods can be adopted for different components to get the statistic information separately.

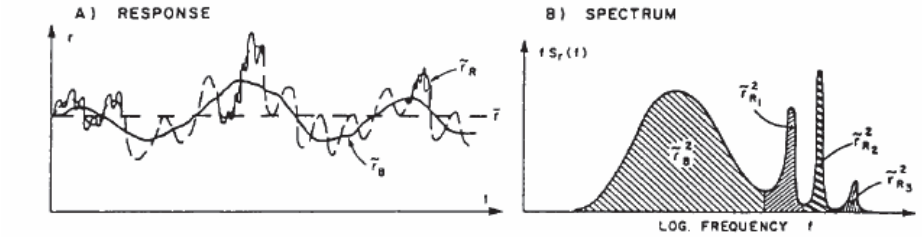

Fig. 2 Response to wind

For the mean response, the coupling effects are mainly induced by the structural average deformation, which will make the mean wind pressure change consequently. It is a static process and can be solved directly by steady CFD numerical simulation with several iterative steps. For the background response, the coupling effects are mainly induced by the effect of the spatial correlation of fluctuating wind, that is to say, we have to find these critical distributions of fluctuating wind pressure which can make structure produce maximum or minimum steady response. It is a quasi-static process in which the dynamic amplificatory effect can be ignored and only some modes of steady deformation are considered. For the resonant responses, dynamic coupling between the higher frequency parts of fluctuating wind and structure is mainly considered, it means that the resonant response of structure is mainly induced by those small-scale eddies. Due to the effect of those small-scale eddies is a random process, the suitable method for solving the resonant responses is nonlinear random vibration analysis methods in time domain. It is worth to explain that the calculation of each component will based on the result of the calculation on the former component.

To sum up, the wind-structure interaction can be divided into three parts (Fig.3): static interaction, steady interaction and transient interaction. Mean response belongs to the static interaction, background response belongs to the steady interaction, and resonant response belongs to transient interaction. The static interaction and the steady interaction should be studied specially by means of CFD numerical simulation. The transient interaction should be studied by means of nonlinear random simulation in time domain.

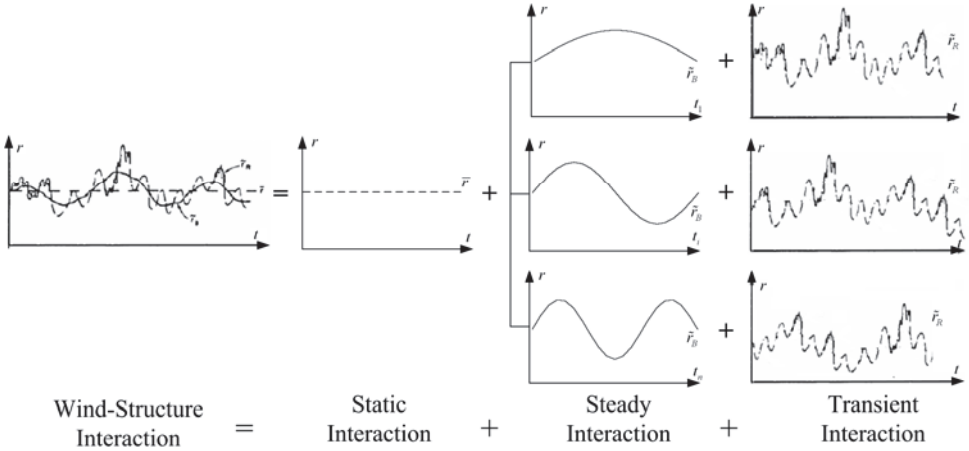

Fig. 3 the sketch of wind-structure interaction

3 GENNERAL FORMULATIONS

3.1 *Static Interaction*

Static interaction is expressed as follow:

$$K_{s0} \cdot \overline{x}_0 = \overline{p} \tag{1}$$

Where $\overline{x}_0$ is the mean response; K_{s0} and $\overline{p}$ are the stiffness and mean wind pressure corresponding to the mean deformation respectively; $\overline{p}$ can be calculated by means of CFD simulation.

3.2 *Steady Interaction*

Steady interaction is expressed as follow:

$$K_{s1} \cdot x_1(t) = p(t) \tag{2}$$

Where $p(t)$ is the fluctuating wind pressure, which can be calculated by CFD simulation.

According to the Proper Orthogonal Decomposition (POD) technique, $p(t)$ can be decomposed as follow:

$$p(x,y,z,t) \approx \sum_{i=1}^{n} \hat{p}_i(x,y,z,t) = \sum_{i=1}^{n} a_i(t)\,\mathrm{G}_i \tag{3}$$

where G_i is the *i*th eigenmode of the wind pressure field, $a_k(t)$ is the corresponding principal coordinate, $\hat{p}_i(t)$ is the wind pressure time history corresponding to the *i*th eigenmode, represents the dominant wind pressure distribution on structural surface.

Substitute Eq.(3) into Eq.(2), Eq.(2)can be rewritten as:

$$K_{s1} \cdot x_1(t) = \sum_{i=1}^{n} \hat{p}_i(t) \tag{4}$$

Assuming the steady deformation is the summation of the effects of each eigenmode

$$K_{s1} \cdot x_{1i}(t) = \hat{p}_i(t), \quad x_1(t) = \sum_{i=1}^{n} x_{1i}(t) \tag{5}$$

where $x_{1i}(t)$ is defined as the time-history of the quasi-static response induced by the *i*th eigenmode. Then the variance of background response σ_1 can be expressed as

$$\sigma_1 = \sqrt{\sum_{i=1}^{n} {\sigma_{1i}}^2} \tag{6}$$

where σ_{1i} is the variance of steady deformation $x_{1i}(t)$ induced by the *i*th eigenmode. So the following formula can be used to estimate the contribution of each eigenmode to the whole steady deformation.

$$\gamma_{1i} = \frac{{\sigma_{1i}}^2}{{\sigma_1}^2} \tag{7}$$

According to the POD technique, Eq. (4) can be expressed as:

$$K_{s1} \cdot x_{1i}(t) = a_i(t)\,\mathrm{G}_i \tag{8}$$

From Eq. (8), it is educed that the vibration mode of $x_{1i}(t)$ is determined by the stiffness K_{s1} and the *i*th eigenmode G_i, and the vibration amplitude of $x_{1i}(t)$ is determined by the principal coordinate $a_i(t)$. So the maximal steady deformation $x_{1i}(t_j)$ of $x_{1i}(t)$ can be determined by finding the moment t_j, which is corresponding to the peak value of $a_i(t)$.

3.3 *Transient Interaction*

Transient interaction is expressed as follow:

$$M_s\ddot{x}_{2i}(t)+C_s\dot{x}_{2i}(t)+K_s x_{2i}(t)=\tilde{p}\left(t,x_{2i}(t),\dot{x}_{2i}(t),\ddot{x}_{2i}(t)\right) \tag{9}$$

$$\tilde{p}\left(t,x_{2i}(t),\dot{x}_{2i}(t),\ddot{x}_{2i}(t)\right)=\tilde{\tilde{p}}(t)+f\left(x_{2i}(t),\dot{x}_{2i}(t),\ddot{x}_{2i}(t)\right) \tag{10}$$

Where $x_{2i}(t)$ is transient deformation relative to the peak steady deformation of the *i*th eigenmode; $\tilde{p}(\cdot)$ represents the high frequency part in fluctuating wind including the motion-induced aerodynamic force; $\tilde{p}(\cdot)$ can be decomposed into $\tilde{\tilde{p}}(t)$ which does not consider the structure vibration and $f(\cdot)$ which is induced by structure vibration. $\tilde{\tilde{p}}(t)$ is gained from the high frequency parts of results of CFD simulation, which based on the form corresponding to each peak steady response; $f(\cdot)$ is added aerodynamic term which can be transformed into added mass M_a and aerodynamic damp C_a by means of simplified aeroelastic model theory[9]. So Eq.(8)can be rewritten as:

$$(M_s+M_a)\ddot{x}_{2i}(t)+(C_s+C_a)\dot{x}_{2i}(t)+K_s x_{2i}(t)=\tilde{\tilde{p}}(t) \tag{11}$$

It is especially emphasized that transient interaction is based on the possible peak steady deformation of the *i*th eigenmode $\left\{\overline{x}+x_{1i}(t_j)\right\}$, i.e. different $\left\{\overline{x}+x_{1i}(t_j)\right\}$ correspond to different transient interaction response.

3.4 *Peak Response*

The peak response of structure is solved by means of superposition theory after getting $\overline{x}$, $x_{1i}(t)$ and $x_{2i}(t)$:

$$x_{\max}=\overline{x}+\sum_{i=1}^{n}\sigma_{1i}^2+\max\left(\sigma_{2i}^2\right) \tag{12}$$

Based on the theory mentioned above, the flowchart of the combined numerical approach is shown as figure 4.

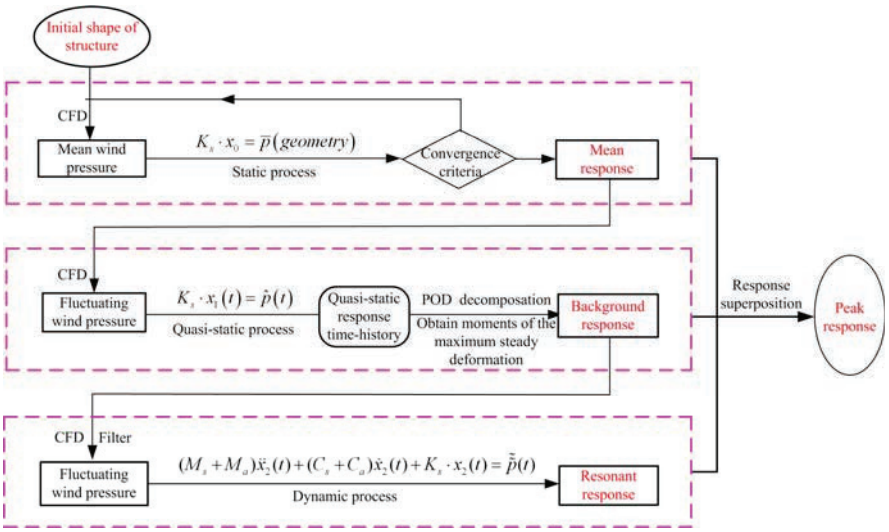

Fig. 4 Flowchart of the combined numerical approach

4 NUMERICAL EXAMPLE

4.1 *Coupling Effects of One-Way type roofs*

The roof span is 40m and 10m high, the computational domain is shown in figure 5. The inflow velocity profile is defined by $V(y) = 30(y/10)^{0.16}$ m/s， leading to a velocity value of 30m/s at roof level. Thus, the Reynolds number becomes $\mathrm{Re} = 2.07 \times 10^7$. The fixed wall is assumed as no-slip flow boundary, local one-way condition is adopted on the boundary of the outlet, and the gradient of flow speed of the outlet is zero; non-dimensional time step $\Delta t = 0.005$. Here we assume the roof is a cable structure, the mass per length g is 5kg/m, the prestressing tension force T is 20kN. According to the results of computation, the first and second frequency of structure is 0.82Hz and 2.34Hz, respectively.

Figure 6 shows the streamline drawing of flow around the fixed roof, it means that the coupling effect does not been considered. Figure 7 shows the streamline drawing of flow around the elastic roof with the consideration of coupling effect. It can be seen that, because the shape of the elastic roof changes with wind action, which directly change the boundary of the fluid field, so the characteristics of flow around a elastic roof is much different from those of rigid roof. For the elastic roof, the separation point of airflow appears at the back of the front of the roof, and the effects of vortex dropping weaken significantly. The whole average wing pressure on the elastic roof is close to that of rigid roof, but the pulse wind pressure decrease significantly, which illustrates that when vortex downstream along the roof, coupling effect induced energy dissipation lead to minor pulse pressure.

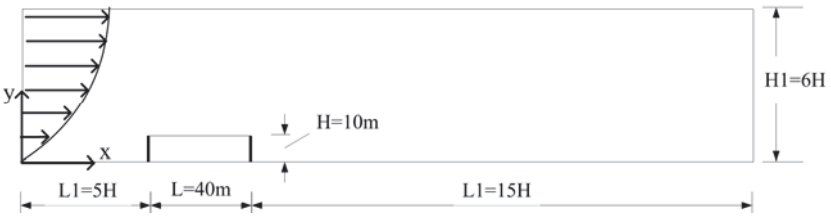

Fig. 5 Computational domain for flow around a one-way type roof

It worth to be explained that the above result was gotten from the method in ref. [6], here we call it as direct numerical method, which can be seen as a accurate method. It can be seen that by the direct numerical method, we can get the entire information of the coupling process. But from the viewpoint of engineering, we usually only concern about those statistic information, such as the mean and peak value, it means that we spend a large amount of time to get those useless information. Next, the combined procedure proposed in this paper will be adopted to calculate that statistic information. The result is shown in figure 8. It can be seen that the result of combined approach seems very close to that of direct numerical method, but quite different to the result of random vibration analysis. It shows that by using the combined approach we can also get fairly accurate result, and the time consuming by this method is quite small compare to the direct numerical method.

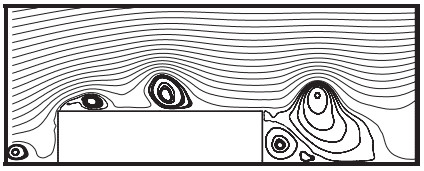

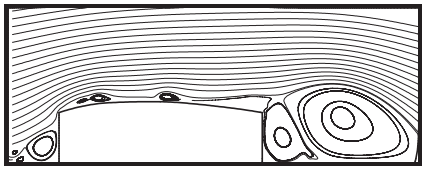

Fig. 6 Streamline around the fixed roof

Fig. 7 Streamline around the elastic roof

We also calculate the one-way type roof with 1/10L sag (as shown in fig. 9) and with 1/10L rise (as shown in fig. 10). It can be seen that for these two different shape roofs, the combined procedure can get very close results to that of accurate method. For the arch-shaped roof, the effect of fluid-structure interaction seams very small, it can be explained that the roof shape plays an important role to the coupling effect. The coupling effect will change the structural shape from bluff body to streamlined body, if the structural shape close to streamline body, then the coupling effect will be small.

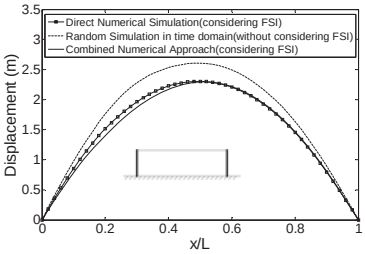

Fig. 8 Maximum response of flat roof

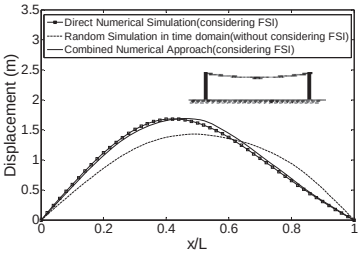

Fig. 9 Maximum response of suspension roof

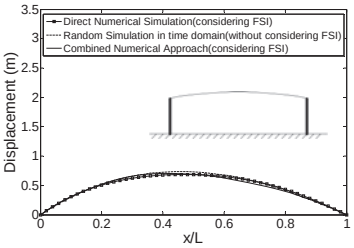

Fig. 10 Maximum response of arch roof

4.2 *Coupling Effects of Shaddle-Shape Membrane Structures*

The roof span L is 28m, the ratio of sag to span (*f*/L) is 1/16, the mass per area is 1.25kg/m^2, the tension force is 2.5kN/m. The first and second frequency of structure is 2.26Hz and 3.03Hz, respectively. The calculate model is shown in figure 10. The other calculate parameters are same as the two-way type roof.

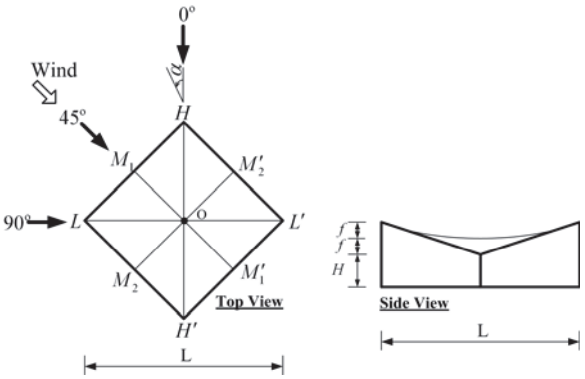

Fig. 10 The calculate model

Figure 11 shows the maximum displacement of membrane structure calculated by these three methods. It can be seen that the coupling effect of 3-D structures seems more complicate than 2-D structures, but if we compare the maximum displacement point between the results of these three methods, it is also show that the result from combined procedure seems fairly close to the direct numerical method, but larger than the result of random vibration analysis.

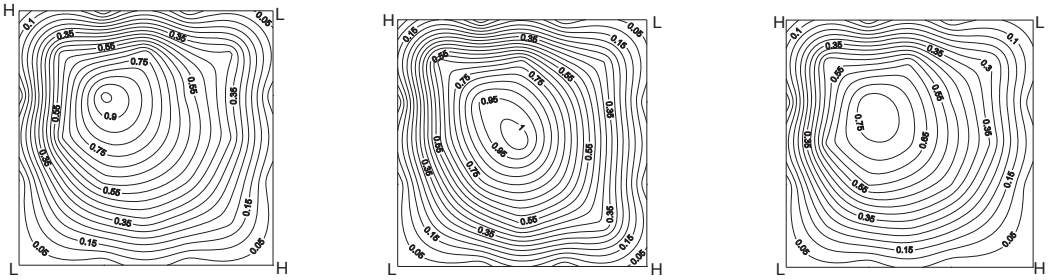

a) Combined Approach b) Direct Numerical Method c) Random vibration analysis

Fig. 11 Maximum displacement on roof by different methods

5 CONCLUSION

In this paper, a combined numerical approach for solving the fluid-structure interaction for tension structures was proposed. With the comparison to the direct numerical method and random vibration method, it can be seen that the combined approach seems more accurate than the random vibration method and more efficient than the direct numerical method.

According to the calculate result of two-way type, it can be conclude that the coupling effect trend to change the structural shape from bluff body to streamlined body, so if the structural shape close to streamline body, then the coupling effect will be small.

ACKNOWLEDGEMENTS

The investigation is supported by the National Science Fund Council of People's Republic of China under Contract No. 50908068 and No. 90815021.

REFERENCE

1、 S.Z. Shen and Q.S. Yang (1999), "Wind-induced Response Analysis and Wind-resistant Design of Hyperbolic Paraboloid Cable Net Structures", Int. J. Space Structures, 14(1), 57-65

2、 T. Matsumoto (1990), "Self-excited Oscillation of a Pretensioned Cable Roof with Single Curvature in Smooth Flow", J. Wind Eng. Ind. Aerodyn., 34 (3), 304-318

3、 H. P. A. H. Irwin and R. L. Wardlaw (1981), "A Wind Tunnel Investigation of a Retractable Fabric Roof for the Montreal Olympic Stadium", Proc. 5th Int. Conf. on Wind Eng., Pergamon, 925-938

4、 A. Larsen (1998), "Computer Simulation of Wind-Structure Interaction in Bridge Aerodynamics", J. Struct. Engrg. IABSE, 8(2), 105-117

5、 M. Glück, M. Breuer, F. Durst, A. Halfmann, E. Rank (2001), "Computation of Fluid-Structure Interaction on Lightweight Structures", J. Wind Eng. Ind. Aerodyn, 89(14-15): 1351-1368

6、 Y. Wu and S. Z. Shen (2005), "Computation of Wind-Structure Interaction on Tension Structures", Proc. 6th Asia-Pacific Conference on Wind Engineering. Seoul, Korea, 1671-1681

7、 Y. Wu and S. Z. Shen (2006). "Numerical studies on the behaviors of wind-structure interaction for one-way type roofs". Proc. 4th Int. Conf. on Computational Wind

Engineering. Yokohama, Japan, 389-392
8、 A. G. Davenport (1967), “Gust Loading Factor”, J. Struct. Div. ASCE., 93(ST3), 11-34
9、 Wu, Y., Yang, Q. S. et al, Studies on Wind-Structure Interaction by Wind Tunnel Tests, Proceedings of the 11th National Conference on Wind Engineering, Sanya, China, 2003. (in Chinese)

The Seventh International Colloquium on Bluff Body Aerodynamics and Applications (BBAA7)
Shanghai, China; September 2-6, 2012

Wind flow around rectangular obstacles and the effects of aspect ratio

Dan Gu[a], Hee-Chang Lim[b]

[a]*Graduated student of school of mechanical engineering, Pusan Nat'l Univ., san 30, Jangjeon-dong, Geumjeong-gu, Pusan, South Korea*
[b]*Assistant professor of school of mechanical engineering, Pusan Nat'l Univ., san 30, Jangjeon-dong, Geumjeong-gu, Pusan, South Korea*

ABSTRACT: It has long been studied about the flow around bluff bodies, but the effect of aspect ratio on the sharp-edged bodies in a thick turbulent boundary layer is still argued. The study is aiming to understand the surface pressure distribution around the bodies such as the suction pressure in the leading edge on the top surface when the aspect ratio of bodies is changed. Therefore, the authors firstly carried out the wind tunnel measurement around a series of rectangular bodies ($40^d \times 80^w \times 80^h$, $80^d \times 80^w \times 80^h$, $160^d \times 80^w \times 80^h$, $80^d \times 40^w \times 80^h$ and $80^d \times 160^w \times 80^h$ in mm) placed in a deep turbulent boundary layer. With modern numerical calculations, the RANS based on the k-ε model and the DES turbulence model were used, and the numerical results were compared with wind-tunnel experiments. The results show that the transverse width has a substantial effect on the surface pressure around the bodies, while the longitudinal length has a little influence on the surface pressure.

KEYWORDS: Rectangular bodies, Wind environment, Aspect ratio, Surface pressure distribution, Wind-tunnel measurement, CFD

1 INTRODUCTION

The flow characteristics on a bluff body immersed in a turbulent flow has long been of fundamental interest in the study of fluid dynamics. Such investigations are critical in the design and development of practical objects such as windmills, buildings and bridges, etc. Above all, the study of flow characteristics around a bluff body is generally considered to be important in academic circles as well as in the engineering applications and now there are still lots of topics left to be studied.

Regarding to the flow around buildings or all kinds, there have been numerous empirical data and comparisons between wind-tunnel and full-scale (field) data. One of the well-cited papers in this area is the wind-tunnel experiments of Castro & Robins (1977)[1] (hereafter denoted by CR), which measured the flow around the surface-mounted cubes. In addition, Tieleman & Atkins (1996)[2] reported that the variation of the base/side surface pressure of surface-mounted rectangular prisms was determined by the interaction of the incident turbulence with the separated shear layers. More recently, Cigada et al. (2006)[3] investigated the fluid-dynamic forces acting on a rectangular cylinder for unbounded flow conditions. Especially, they focused on the effects of a fixed wall placed at various distances from a rectangular cylinder and observed that the force component acting on the cylinder depends on the periodical motion and provides the dynamic characterization of the loading and of the wake shedding. In addition, the aspect ratio of the body governs effects of the wall condition on the force coefficients and the Strouhal number. Then, Larose & Auteuil (2008)[4] made a wind tunnel measurement on rectangular prisms with aspect ratio of 2, 3 and 4 at high Reynolds number.

With regard to the CFD techniques, there have been a substantial change in the numerical modeling as well as the hardware development and it still develops rapidly. There have been a lot of attempt for simulating the precise flow around a various bodies by solving the governing Navier–Stokes equations. Especially, in the early stage, there were a lot of turbulence models to solve the complicate turbulent flow around a body and some of them were compared each other for the systematic efficiency of the models (i.e. Murakami (1993)[5]; Zhang et al. (1996)[6]; Meroney et al. (1999)[7]). What they found is that the accuracy of the numerical calculation was highly dependent of the choice of the turbulence model. However, most previous studies have been focused on the typical Reynolds-Averaged Navier–Stokes (RANS) method, especially the standard k- ε model (see e.g. Iaccarino et al. (2003)[8]; Li and Stathopoulos (1997)[9]; Tominaga and Stathopoulos (2009)[10]) was one of kinds. However, it was reported that the RANS simulation was unsuccessful as usual. In contrast to RANS method, rather the large-eddy simulation(LES) resolved large-scale unsteady motions and it showed a good agreement with wind tunnel experiments (i.e. Krajnovic´ and Davidson (1999)[11], (2001)[12]; Shah and Ferziger (1997)[13]), whereas the LES simulation was a bit costly and spent much more time and had a high request for the CPU time. Therefore, in a very recent time, there has been a trend to use an eclectic approach to balance the computational costs and the precision of calculation, namely Detached Eddy Simulation (DES) method. Due to the limited number of papers, Jochen & Dominic (2008) [14] was one of them describing the usefulness and high potential of the LES/RANS turbulence models for using a practical application.

The immediate emphasis in this paper is on the flow characteristics around the rectangular bodies with various aspect ratio. The aspect ratio is responsible for the type of generated wake and, ultimately, for the structural loading and pressure and especially structure excitation. For example, the drag coefficient of an elongated rectangular-section body in a flow is a function of the width of the body. (see Fig.1) As shown in the figure, the drag is a function mainly of the elongation d/w of the body. Therefore, the paper consists of a carefully designed set of experiments and numerical simulation on a simulated turbulent boundary layer flow, which is tailored in the atmospheric environment condition, over a surface-mounted various rectangular obstacles. In the numerical calculation, the standard k-ε and the DES model were used and finally compared with the experimental data (i.e., the wind tunnel and the field study).

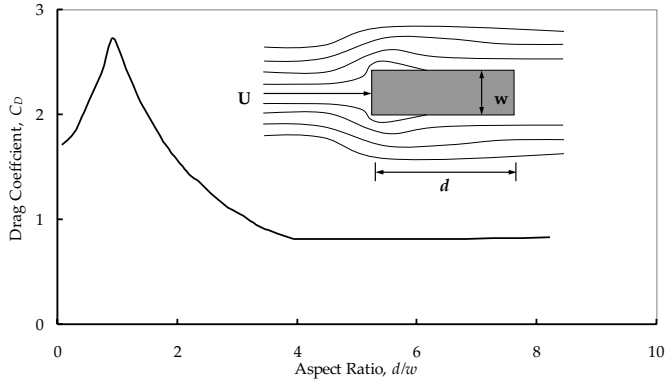

Figure 1. Drag coefficient versus aspect ratio of rectangular body. (Simiu and Scanlan, 1996[15]).

The following section §2 outlines the experimental techniques, §3 describes the computational techniques, §4 summarizes the surface pressure characteristics, as well as some findings and discussions about the major results around the models under a simulated turbulent boundary layer , finally §5 gives the major conclusions.

2 EXPERIMENTAL TECHNIQUES

2.1 *Atmospheric boundary layer wind tunnel*

Figure 2 illustrates the set-up, showing the model location in the wind tunnel. Experiments were conducted in the middle closed-circuit subsonic wind tunnel, whose working section dimension is $0.6m^{wide}\times0.72m^{high}\times6m^{long}$ having a maximum wind speed of about 40m/s at the Pohang University of Science and Technology in South Korea. It is suitable for generating an artificial boundary layer and is also equipped with modern hot-wire anemometry (IFA100) and a PIV system for optical measurements of the airflow. The rectangular models used in the study are made of plexiglass, and they consist of 3 bodies - a cube ($80^{d}\times80^{w}\times80^{h}$ in mm for 1×1) for comparing the existing results in a reference, two rectangular bodies ($40^{d}\times80^{w}\times80^{h}$ for 2×1s and $160^{d}\times80^{w}\times80^{h}$ for 1×2), and especially the flow around rectangular bodies could make two more aspect-ratios rotating it 90^{o} (e.g., $80^{d}\times40^{w}\times80^{h}$ for 1×2s and $80^{d}\times160^{w}\times80^{h}$ for 2×1).

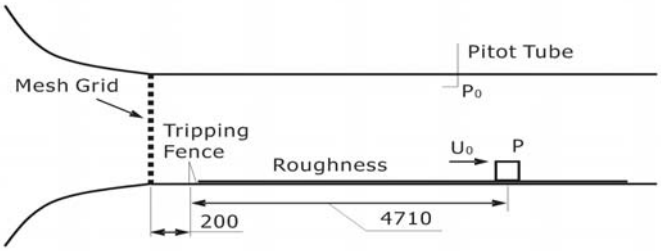

Figure 2. The 0.6m×0.72m×6m wind tunnel test section and model set up.

2.2 *Simulated atmospheric boundary layer*

Thick boundary layers were generated using a technique often employed by wind-engineering practitioners, first devised by Cook (1978)[16]. Toothed barriers spanning the floor of the working section near its entry, followed by a square section, bi-planar mesh across the entire working section and an appropriate rough surface thereafter can together be designed to yield mean-velocity profiles which are closely logarithmic over a significant portion of the working-section height, with turbulence stresses and spectra similar to those found in atmospheric neutrally stable boundary layers. Since it was intended to make comparisons with the existing data such as wind tunnel and field data(e.g. a 6m height cube in Silsoe, UK[17]) - less than one-tenth of the height of the logarithmic region - maximizing the depth of this region was deemed the most important. It is crucial to design the barrier wall and mixing grid geometries in tandem with the intended roughness, since any mismatch will yield unacceptably long fetches before reasonably well-developed flows are attained. In the present case, commercially available artificial plastic artificial grass was used to provide the surface roughness. This gave a roughness length, z_0, of 0.17mm, where z_0 is defined in the usual way via the mean velocity log law expressed as:

$$\frac{U}{u_*}=\frac{1}{\kappa}\ln\frac{(z-d)}{z_0} \tag{1}$$

where u* = the friction velocity; d = 'zero plane displacement'.

Obtaining the three unknowns (u*, d and z_0) from the mean velocity profile alone is, as is well-known, a very ill-conditioned process. In the present study, u* was deduced from an extrapolation of the measured turbulence shear stress to the surface (see Lim et al., 2007[18]), with d and z_0 then following from a best fit of the mean velocity data to eq.(1). In the tunnel, the barrier wall had a height of 50mm, with triangular cut-outs at the top, of pitch 50mm and depth 50mm, and the mixing grid consisted of a biplanar grid of 10mm bars at a pitch of 50mm.

3 COMPUTATIONAL THCHNIQUES

3.1 *Numerical methods*

The schematic diagram of the numerical tunnel with a wall-mounted cube is shown in Fig.3. For an appropriate calculation, the proper domain size is a prerequisite in the beginning state so that the cube (e.g., see $80^d \times 80^w \times 80^h$) has the computational domain size of 14h×4h×7h in Cartesian coordinate system, where h is the cube's height. The origin of the domain is located at the wind-side foot of the cube bottom. The computational grid was made by a preprocess software ICEM CFD, and the boundary conditions are shown in the Fig.3. Then the software FLUENT calculates the governing equation depending on the boundary conditions. Even though the geometry of the flow configuration is rather simple, the flow characteristics are essentially unpredictable, which has multiple separations and large and small-scale vortex regions.

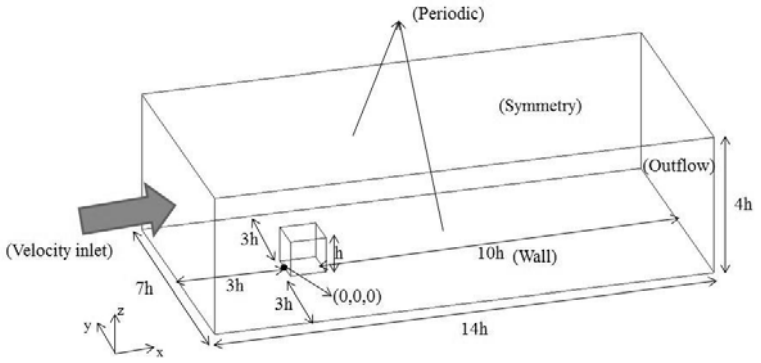

Figure 3. The computational domain and boundary conditions.

In terms of the mesh size to resolve the small-scale turbulent flow, 178×73×115 nodes were used, while the first grid spacing near the wall was 0.025h to ensure the y^+ was acceptable. For example, the inlet surface grid mesh is just like Fig.4, it required such a fine mesh resolution near the (model) wall. When the aspect ratio of the models varies, the computational domain and the number of grid should be reconstructed as listed in Table 1.

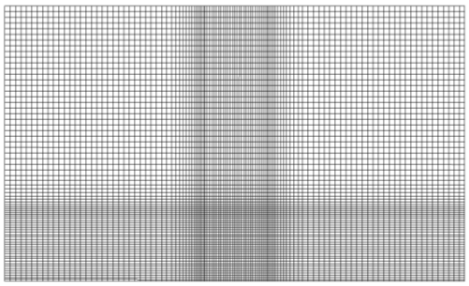

Figure 4. Frontal view of grid mesh in the inlet condition.

Table 1. Calculation domain and grid nodes of all cases

Case	Domain	Grid nodes	Abbrev
1	14h×4h×7h	178×73×115	1×1
2	14h×4h×8h	178×73×145	2×1
3	15h×4h×7h	208×73×115	1×2
4	13.5h×4h×7h	163×73×115	2×1s
5	14h×4h×6.5h	178×73×100	1×2s

3.2 *Turbulence models*

The present numerical simulation has been carried out according to the experiment study. The Reynolds number based on h (model height) and U_h (mean inlet velocity at h) was 4.6×10^4. The inlet mean-velocity profiles were compiled by UDFs, which are shown in Fig.5 (a) compared with the experiment profiles. As shown in the vertical wind profiles, it can be seen that a fully developed shear flow was made in the wind tunnel as well as numerical tunnel, which were specifically designed to be similar to the (rural) atmospheric boundary layer. Two approaching methods (i.e., Reynolds-averaging (RANS model) and filtering methods (LES model)) were employed to render the Navier-Stokes equations tractable so that the small-scale turbulent fluctuations do not have to be directly simulated. Firstly, what we consider in this study is the standard k-ε model. Here, the self-developed code of the turbulence kinetic energy (k) and its dissipation rate (ε) was used to obtain the turbulence intensity, which should be consistent with the experiment, see Fig.5 (b). As the LES simulation takes usually a high computational cost, herein, we select the DES model which is often referred to as the hybrid LES/RANS models. In this case, the DES model is based on the one-equation Spalart-Allmaras model and the transient calculations were carried out with the time step 0.0001s.

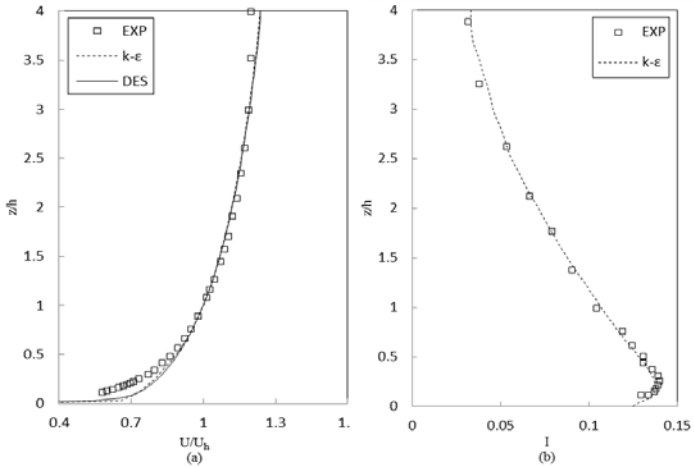

Figure 5. Mean velocity (a) and turbulent intensity (b) profiles.

4 RESULTS AND DISSCUSSION

4.1 *Surface pressure distribution - a cubical model (1×1)*

Firstly, the surface pressure distributions along the centerline around the 1×1 model are shown in Fig.6. The variation of the mean static pressure coefficient C_p ($=(p-p_r)/(0.5\rho U_h^2)$, where p_r is the mean static pressure in the upstream flow) is compared between numerical and experimental results. In addition, the figure also includes the existing results - wind tunnel(WT) and full field scale(FS) measurement, which is as a function of the measurement location *x/h*; *x*=0 corresponds to the foot at the front face of the model body - actually depending on the wind direction (e.g., see the solid line on the right figure). Note that the rest of the subsequent figures are arranged in a similar manner to this figure. It is no doubt that the profiles in the figure has an expected shape, in that the largest negative pressures occur just beyond separation at the leading edge and are followed by a substantial pressure recovery on the top surface, as shown frequently by previous studies. Note that the experiment data agree well with the earlier field data of LCH's (Lim, Castro & Hoxey, 2007[19]) but are significantly different from the wind-tunnel data of CR (Castro &

Robins, 1977). The latter are similar to those of Murakami & Mochida (1988) [20] and, in agreement with CR's discussion, are undoubtedly a result of very much higher upstream turbulence levels, leading to much earlier attachment and pressure recovery on the top surface. In addition, the k-ε model data are nearly similar except the region on the just right corner of the position x/h=1 which has a negative peak. This seems to be caused by the turbulence model itself so that in this regard, the DES model seems to have better performance than the k-ε model when simulating the flow around a sharp-edged bluff body.

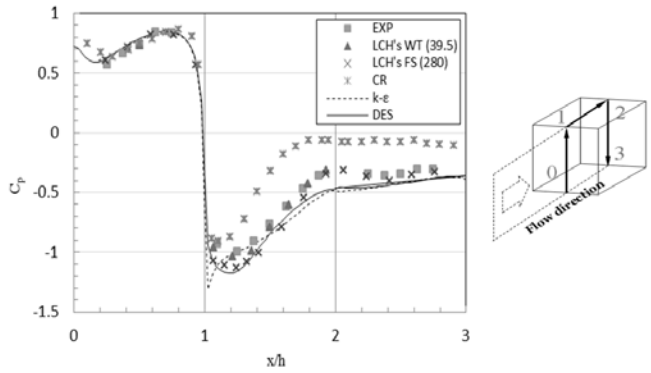

Figure 6. Mean surface static pressure coefficient along the central section with wind normal to face.

Figure 7 shows the mean surface pressure along the mid-height of the cube. As shown in the figure, the experiment data agree well with the field measurement data except the CR's result which has been explained before. The k-ε model data are similar to the experiment data, but still has a significant difference on the just right corner of the position x/h=1, whereas the DES model data seem to improve the accuracy of the prediction in this region - a negative peak. However, the numerical data show relatively low value compared to the other experiment data. Perhaps, this can be explained that the upstream turbulence level in the approaching flow is not high enough so that the attachment and pressure recovering seem to be delayed.

Even though the current experiment and numerical data in this section are showing the simple comparison with the existing results, the immediate implication is that the comparison with the existing results confirms the high accuracy and reliability of the current study, and the identical condition with the field measurement yields the significant reduction of the measurement and calculation errors. Therefore, the current section could be a precursor of the rest of the pressure profiles and the next section will discusses the pressure profiles around the rectangular obstacles with the same boundary layers.

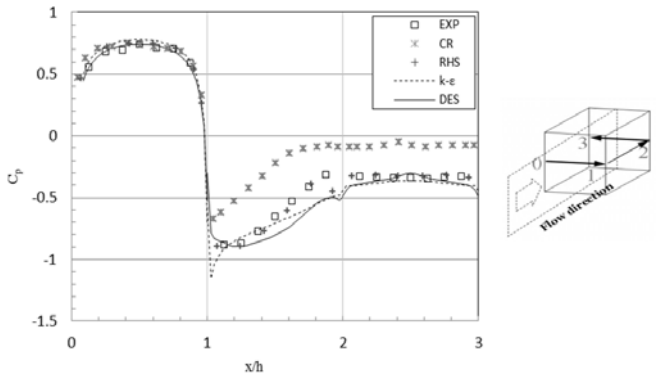

Figure 7. Mean surface static pressure coefficient at the mid-height of the cube.

4.2 *Surface pressure distribution - models with aspect ratio*

Mean surface static pressure profiles along the centerline of the models with the three different aspect ratios are plotted in Fig.8. The figure shows how the surface pressure on the top as well as on the front and rear face changes with changing of the width of the body. Note that several subsequent figures are arranged in a similar manner to Figure 8, i.e. the experiment pressure profiles are shown on the upper-left and the CFD (k- ε model) pressure profiles are shown on the upper-right. In addition, models to compare each other are shown underneath, to easily visualize the measurement locations around the body. The immediate implication of the data in Fig.8 is that the width variation while maintaining the depth makes the surface pressure on the top surface more negative, whereas the front and rear face are almost consistent for the width variation. In addition, as it can be seen, the solid arrow shows the direction of the pressure drop as the width changes.

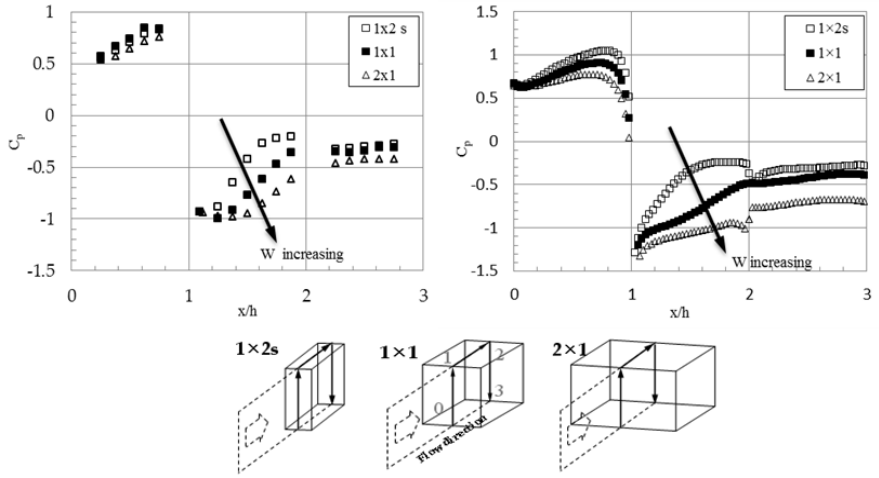

Figure 8. Mean surface static pressure coefficient along the centerline with changing transverse width.

In Figure 9, the mean surface static pressure along the side face at the mid-height of the three different boxes with changing transverse width is presented. The abscissa in the figure is normalized with the body height. As consistent with the previous figure, the pressure drop with increasing width was noticeable to the negative direction. These results demonstrate that with an increase in the horizontal width, i.e. as increasing the aspect ratio, there is a concurrent suction pressure drop on the side face.

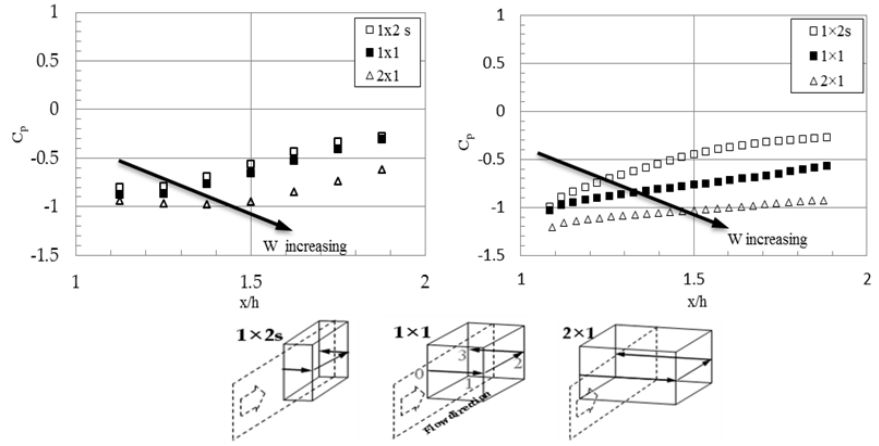

Figure 9. Mean surface static pressure coefficient at the mid height with changing transverse width.

Figures 10 and 11 show the mean surface static pressure profiles along the centerline and the mid-height of the models with changing longitudinal length(i.e. the depth). The different size of the depth maintaining the front face area makes different length of the side face - the ratio of 1:2:4, respectively. The flows around wall-mounted sharp-edged models usually have separation and often attachment around the body so that the pressure profiles in the figure have the similar shape, as shown in the above results. The pressure profiles seem to have a similar trend and it is noted that the overall distribution of the surface pressure makes good agreement and the longitudinal length of the body only affects the recovery region on the top surface, and there appears a little discrepancy in the side face.

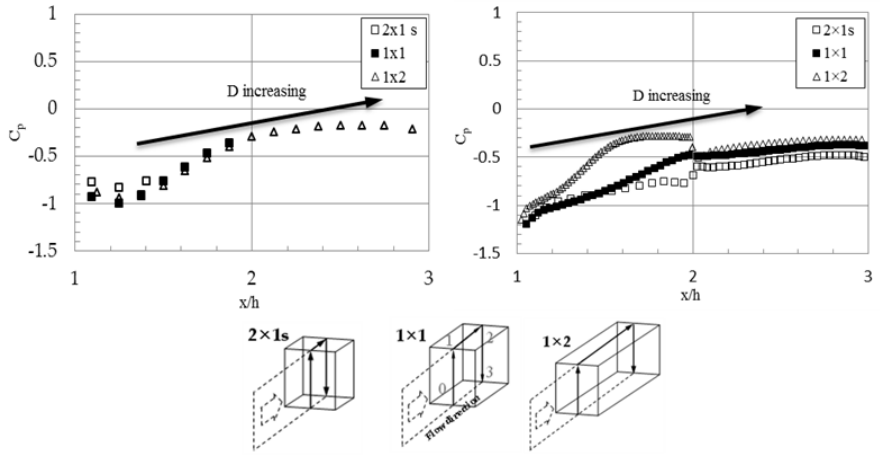

Figure 10. Mean surface static pressure coefficient along the centerline with changing longitudinal length.

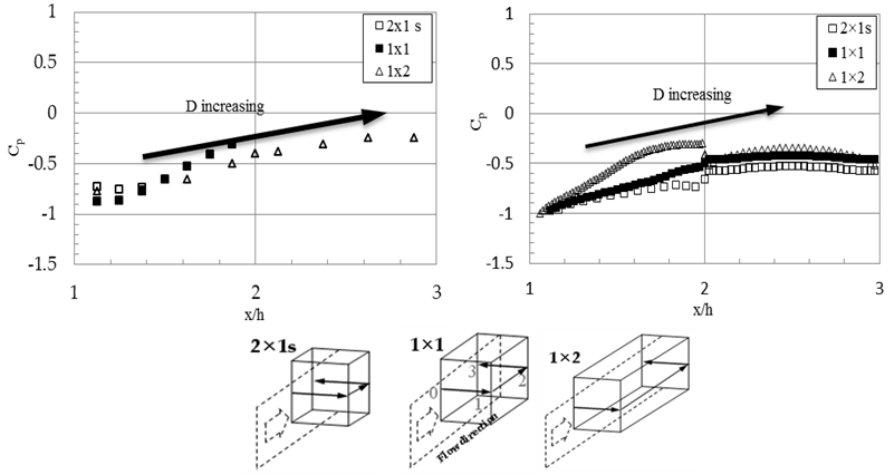

Figure 11. Mean surface static pressure coefficient at the mid height with changing longitudinal length.

Figure 12 presents the variation of the mean static pressure C_p appropriately normalized as making a proper scaling. Note that the above two pictures are the experiment data and the following two pictures are the CFD (k- ε model) data. It is also noted that the abscissa in the previous section was presented as a non-dimensional axis normalised by a body height h, whereas the current axes are normalized along the the axial centerline of the models by the characteristic length - the width(W, width effect) and the depth(D, the depth effect), respectively. In the figure, they are generally in good agreement. Therefore, it can be described that even

though the length and width of the rectangular body are changed, the characteristics of the static surface pressure profiles along at least the centerline itself remains unchanged, if any, it ought to be a litter scatter.

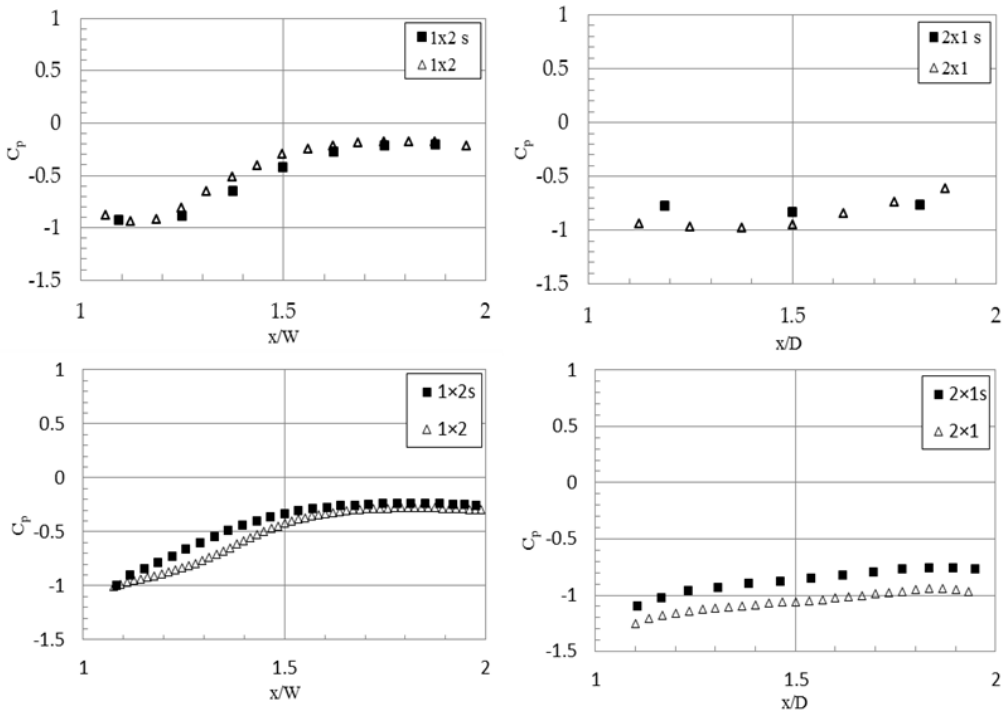

Figure 12. Mean surface static pressure coefficient along the centreline on the various boxes with the normalization of width (W) and the depth (D), respectively.

5 CONCLUDING REMARKS

Although more comparisons are needed to end up with the conclusions, the study has contributed in making the following conclusions:

(1) As a usual, the CFD results agree well with the experiment results, as well as the earlier field results, but there still appears a litter discrepancy, which should be discussed in detail in the next study.

(2) In this comparison, the DES model seems to be better than k-ε model when simulating the wind flow around a variety of bluff body.

(3) When the aspect ratio of a rectangular body changes, the transverse width has a substantial effect on the surface pressure around the bodies, while the longitudinal length shows a little influence on the surface pressure.

6 ACKNOWLEDGEMENTS

This work was supported by the Human Resources Development of the Korea Institute of Energy Technology Evaluation and Planning (KETEP) grant funded by the Korea government Ministry of Knowledge Economy (No. 20114030200070, 20114010203080). In addition, this work was supported by the Ministry of Education, Science and Technology (MEST) in 2011.

7 REFERENCES

1 I.P. Castro and A.G. Robins, The flow around a surface mounted cube in uniform and turbulent streams, J. Fluid Mech., 79 (1977) 307-335.
2 H.W. Tieleman and R.E. Akins, The effect of incident turbulence on the surface pressures of surface-mounted prisms, J. Fluids and Structures, 10 (1996) 367-393.
3 A. Cigada, S. Malavasi and M. Vanali, Effects of an asymmetrical confined flow on a rectangular cylinder, J. Fluids and Structures, 22 (2006) 213-227.
4 G.L. Larose and A.D'Auteuil, Experiments on 2D rectangular prisms at high Reynolds numbers in a pressurised wind tunnel, J. Wind Engng Ind. Aero., 96 (2008) 923-933.
5 S. Murakami, Comparison of various turbulence models applied to a bluff body, J. Wind Eng. Ind. Aerodyn., 46-47 (1993) 21-36.
6 Y.Q. Zhang, S.P. Arya and W.H. Snyder, A comparison of numerical and physical modeling of stable atmospheric flow and dispersion around a cubical building, Atmos. Environ., 30 (1996) 1327-1345.
7 R.N, Meroney, B.M, Leitl, S. Rafailidis and M. Schatzmann, Wind tunnel and numerical modeling of flow and dispersion about several building shapes, J. Wind Eng. Ind. Aerodyn., 81 (1999) 333-345.
8 G. Iaccarino, A. Ooi, P. Durbin and M. Behnia, Reynolds averaged simulation of unsteady separated flow, Int. J. Heat Fluid Flow., 24 (2003) 147-156.
9 Y. Li and T. Stathopoulos, Numerical evaluation of wind-induced dispersion of pollutants around a building, J. Wind Eng. Ind. Aerodyn., 67-68 (1997) 757-766.
10 Y. Tominaga and T. Stathopoulos, Numerical simulation of dispersion around an isolated cubic building: comparison of various types of k-ε models, Atmospheric Environment., 43 (2009) 3200-3210.
11 S. Krajnovic´ and L. Davidson, Large-eddy simulation of the flow around a surface-mounted cube using a dynamic one-equation subgrid model, In S. Banerjee and J. Eaton (Eds.), The First Int. Symp. on Turbulence and Shear Flow Phenomena, Beggel House, Inc, New York, 1999.
12 S. Krajnovic´ and L. Davidson, Large eddy simulation of the flow around a three-dimensional bluff body, AIAA 2001-0432, 39th AIAA Aerospace Sciences Meeting and Exhibit, Reno, Nevada, 8-11 January, 2001.
13 K. Shah and J. Ferziger, A fluid mechanicians view of wind engineering: large eddy simulation of flow past a cubic obstacle, J. Wind Eng. Ind. Aero., 67-68 (1997) 211–224.
14 F. Jochen and V T. Dominic, Hybrid LES/RANS methods for the simulation of turbulent flows, J. Progress in Aerospace Sciences, 44(5) (2008) 349-377.
15 E. Simiu and R.H. Scanlan, Wind effects on Structures, Wiley, New York, 1996
16 N.J. Cook, Wind tunnel simulation of the adiabatic atmospheric boundary layer by roughness, barrier and mixing device methods, J. Wind Engng Ind. Aero., 3 (1978) 157~176.
17 P.J. Richards, P.J. Hoxey, and L.J. Short, Wind pressure on a 6m cube, J. Wind Engng Ind. Aero., 89 (2001) 1553-1564.
18 H.C. Lim, Generation of a turbulent boundary layer using LES, Trans of the KSME (B), 31 (2007) 680-687.
19 H.C. Lim, Ian P. Castro and R.P. Hoxey, Bluff bodies in deep turbulent boundary layers Reynolds-number issues, J. Fluid Mech., 571(2007) 97-118.
20 S. Murakami and A. Mochida. 3D numerical simulation of airflow around a cubic model by means of k- ε model, J. Wind Engng Ind. Aero., 31 (1988) 283-303.

The Seventh International Colloquium on Bluff Body Aerodynamics and Applications (BBAA7)
Shanghai, China; September 2-6, 2012

Flow conditions for aerolastic stability of modular slender structures

Elena Dragomirescu[a], Yarzar Tun [a]

[a]*University of Ottawa, 161 Louis Pasteur, Ottawa, Canada*

ABSTRACT: While the wind flow around conventional shapes was well studied, and its aerodynamic mechanisms were well established, for structures as buildings and bridges with geometric shapes of particular modulations, a distinctive investigation is required. In terms of wind flow-structure interaction and the aerodynamic stability, among all the studied structural shapes, one has distinguished as exceptionally stable for high wind speeds. The structure itself is a post-modernist sculpture entitled "Endless Column", created by C. Brancusi in 1916. The sculpture, which fells under the UNESCO patronage, was the object of several wind tunnel studies, which acknowledged the stability of the Column and the lack of galloping vibrations. However, considering the limitations of the experimental facilities, a clear explanation for these phenomena was difficult to provide. The current research completes the experimental series performed on the Column, through analytical means of CFD (Computational Fluid Dynamics), and provides a better understanding of the flow-structure interaction for this particular modular shape. For wind velocity of 5.45 m/s and, angles of attack of 0° and 10° were found to have certain influence on the formation of three-dimensional vortices on the rear side of the Column; the most stable case with a regular flow pattern behind the Column was identified for 45° angle of attack, where a vertical motion along each module was detected.

KEYWORDS: Endless Column, Wind-structure interaction, Flow pattern, CFD simulation.

1 INTRODUCTION

Constructed in 1916 as a commemorative monument for the victims fallen in the First World War, The Endless Column is situated in the central part of Romania, in the city of Tg. Jiu. Its creator, the famous post-modernist sculpture C. Brancusi has envisioned a slender shape for his masterpiece, composed by a repetition of 15 pyramidal modules of dimensions 45 x 90 x 45 cm, plus two halves-modules at the extremities. The cast iron modules have inside a rectangular steel shaft, which spans the entire height of the column of 30 m (Fig. 1 a). For a structure of such dimensions, taller than most of the surrounding buildings and slenderer than a chimney, the stability to wind would be a main concern; however, the Column has intrigued the aerodynamicists of our times through its stability. Some researchers considered the interaction between wind flow and the Column's modular shape as an explanation for this stability, and they characterized the Column as "aerolastic indifferent" (Safta et al, 2003, Sofronie et al, 2001, Gabbai et al, 2007). In 2000 when the Column was dismantled for rehabilitation, Column's structural characteristics, such as natural periods, distributed mass and damping were determined through in-situ measurements (Lungu et al, 2001), and consequently wind tunnel experiments were performed, for a fixed scaled segment of 4 modules of the Column, under laminar flow conditions (Solari et al, 2002). In 2005 a complete series of wind tunnel experiments were carried out for a scaled segment of 6 modules and for a complete three-dimensional Column model (Fig. 1 b), which preserved the geometric and dynamic properties from its original prototype through aerodynamic scaling (Yamada et al, 2005, Dragomirescu et al, 2009). Tests on a conventional square shape column were also performed for comparison. Both wind tunnel experiments have shown that the Endless Column model is very stable for high wind speeds, where the square model will encounter already galloping vibrations. However, for the lower wind speeds, the resonant phenomenon of lock-in was encountered with similar magnitudes of vibrations for both models, the square and the Endless Column.

Figure 1: Endless Column, Tg. Jiu, Romania (a) Site location (Dragomirescu et al, 2009), (b) Wind Tunnel Experiment (Yamada et al, 2005)

Several countermeasures in the form of dimples, helical spires, etc., exist already for overcoming the resonant lock-in phenomenon for slender structures; for galloping wind induced vibrations however, more complicated measures or control devices, such as dampers, must be considered. Unexpectedly, the "aerolastic indifference" of the Endless Column, manifested through stability for high wind speeds, might be considered as a geometric countermeasure against galloping. Nevertheless, none of the performed wind tunnel experiments have included a three-dimensional visualization of the wind flow around the Endless Column, and a clear explanation of the flow-structure interaction could not be expressed, hence the usage of its modular shape as a countermeasure for galloping could not be attested. Therefore, the current research employs an extensive 3D Computational Fluid Dynamics (CFD) simulation for elucidating the flow formation at different levels of the Endless Column and the induced aerodynamic forces.

2 SIMULATION ALGORITHM

The flow around The Endless Column was simulated in a rectangular domain; the dimensions of the Column were considered as per the aerolastic model described in Yamada et al, 2005 and Dragomirescu et al, 2009, namely 1,467 cm height, 4.5 cm module's big base and 2.25 cm module's small base which corresponds to a scale of 1:20 from the prototype. The grid system had the major axis of 5H, the minor axis and the thickness were 1.33 H, where H = 1.4675 m, is the height of the Column, as schematically represented in Figure 2 a. The Cartesian referential system x, y and z axes were chosen for along stream-wise direction, transverse to the stream-wise direction and the column-span direction respectively. A total number of 1.5 million tetrahedral cells and 250,000 nodes were employed. The non-slip boundary condition was specified on the surfaces of the Column, and the in-flow boundary condition was set to ux = 5.45 m/s uy = uz = 0.

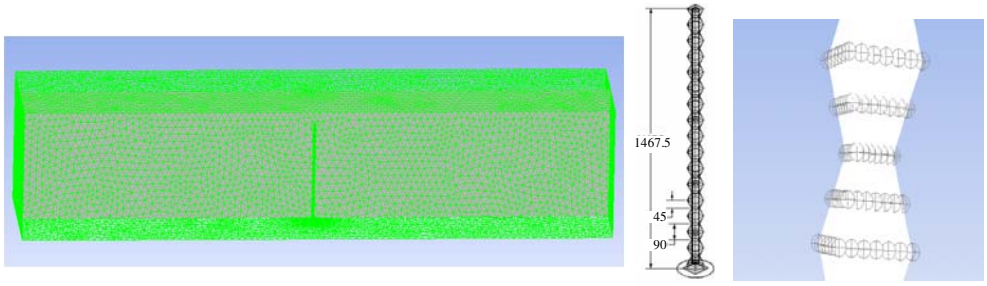

Figure 2: CFD Simulation details (a) Mesh Characteristics, dimensions in mm, (b) Monitored points

Pressure was monitored along an entire pyramidal module by sampling data from 5 rings (Fig. 2 b). This arrangement will help identify the influence of the geometric shape upon the wind induced pressure and the disturbance of the wind flow created by one module. The previous experimental investigations (Yamada et al, 2005) have shown a better response of the column for 45° and a slight vibration for 0° and 10°, starting at a wind speed of 5.45 m/s. Hence, three wind directions were investigated herewith, for angle of attack of $\alpha = 0°$, 10° and 45°.

The large eddy simulation (LES) with the Smagorinsky subgrid-scale model was employed for the CFD simulation. The three dimensional incompressible Navier-Stokes equation and the equation of continuity in non-dimensional form are:

$$\frac{\partial \mathrm{u_i}}{\partial t} + \mathrm{u_j}\frac{\partial \mathrm{u_i}}{\partial t} = -\frac{\partial P}{\partial \mathrm{x_i}} + 2\frac{\partial}{\partial x_\mathrm{i}}\left(\frac{1}{\mathrm{Re}} + v_{sgs}\right)D_{ij} \tag{1}$$

$$\frac{\partial \mathrm{u_i}}{\partial \mathrm{x_i}} = 0 \tag{2}$$

where u_i is the velocity component of grid-scale, and P is the sum of the grid-scale pressure and the residual stress. $D_{i,j}$ in Eq. (1) is the strain-rate tensor on the grid-scale velocity components:

$$D_{ij} = \frac{1}{2}\left(\frac{\partial \mathrm{u_i}}{\partial \mathrm{x_j}} + \frac{\partial \mathrm{u_j}}{\partial \mathrm{x_i}}\right) \tag{3}$$

The subgrid-scale eddy-viscosity, v_{sgs}, in Eq. (1) is expressed as:

$$v_{sgs} = \left(C_s\Delta\right)^2\sqrt{2D_{ij}D_{ij}} \tag{4}$$

where Δ is the filter width and was given as the cubic-root of grid volume and the C_s, Smagorinsky constant, was set to 0.1 in this study. The invicid flux vector was determined by a standard upwind, flux-difference splitting through the low-diffusion Roe approach. For estimation of the secondary diffusion terms and velocity derivatives, the least square cell based spatial discretization was used and Third-Order MUSCL equation was considered for the flow density-based solver. The time step was chosen as t = 0.003 s; pressures along the entire surface of the model was integrated, and lift and drag aerodynamic forces were determined. More convenient, drag and lift coefficients C_D, C_L, were extracted from the definition formulas below (Simiu and Scanlan, 1996):

$$\mathrm{F_D} = \frac{1}{2}\rho \mathrm{U^2 B C_D} \quad \text{and} \quad \mathrm{F_L} = \frac{1}{2}\rho \mathrm{U^2 B C_L} \tag{5}$$

Where F_D, F_L are the drag and lift aerodynamic forces, ρ is density of air, U is wind speed upstream from the model deck and B is the nominal diameter of the Column's model.

3 TWO-DIMENSIONAL FLOW-STRUCTURE INTERACTION

In order to determine the effect of the pyramidal module upon the aerodynamic stability of the Column, localized velocity field distribution were recorded at different heights along the module for 0°, 10° and 45° (Figs. 4 a to f).

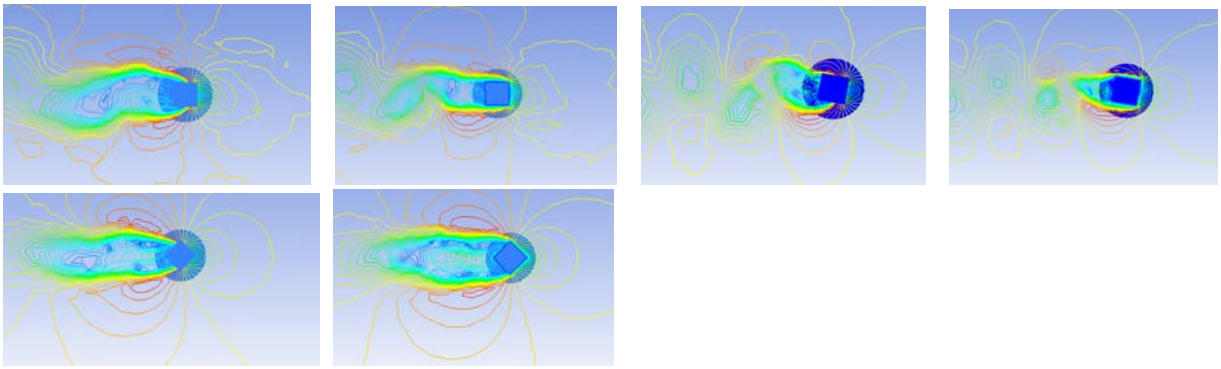

Figure 3. Two-dimensional instantaneous velocity isolines for (a) Small base, $\alpha = 0°$, (b) Large base, $\alpha = 0°$, (c) Small base, $\alpha = 10°$, (d) Large base, $\alpha = 10°$, (e) Small base, $\alpha = 45°$ and (f) Large base, $\alpha = 45°$.

For 0°, around the small base of the module (Fig.3 a), alternation of shear layers is noticed from both edges of the Column which, however, will not interfere with each other downstream the flow. For the large base of the same module (Fig.3 b), the streamlines of the velocity field have a similar evolution; however downstream the Column these shear layers tend to connect generating turbulent flows. Shedding of several vortices downstream the Column was noticed for 10°, generated by the shear layers which detach from the edges of the Column, around both small and large base of the module (Figs. 3 c and d) while for 45° a slight turbulence can be noticed within the shear layers which envelop one major vortex, which varies in intensity and shape with the position along the Column, e.g. smaller vortex behind the small base of the module (Fig. 3 e) and bigger vortex formation behind the larger base of the module (Fig. 3 f).

Pressure monitored around the module at the small and large base location showed that after a dominant positive pressure at the incoming flow, the Column was dominated by suction especially on its rear side. For $\alpha = 0°$, pressure varied between 19 Pa, on the front side of the column, where the incoming flow directly hits the structure, and a suction of up to - 17 Pa downstream the Column was noticed, for the crest of the module where surface exposed to wind is higher (Fig. 4 a). On the small base of the module, an earlier flow detachment is noticed. Also behind the Column after the shear layers detach from the edges, a constant region of negative pressure is noticed, indicating that no vortex formation appeared in the vicinity of the Column surface. For 10° angle of attack, after the sudden drop in pressure from 10 Pa to -20 Pa, indicating the shear layer detachment from both edges of the Column, a variation in the suction monitored on the rear side was noticed, of the as it can be seen in Figure 4 b; this might be due to the alternate vortex formations, which might be a possible cause of unbalanced lift force and appearance of incipient vibrations described during the experiments (Dragomirescu et al, 2009). The maximum induce pressure, was in the same range of 19 Pa, however the suction created on the rear side of the Column and through the vortex formation, was - 27 Pa, much lower than for 0° and 45°. A gradual transition from the strong pressure induced by the incoming flow, towards the negative pressure registered on the rear of the Column could be noticed for 45°, caused by the triangular exposed shape (Fig. 4 d). A constant suction on the rear side of the Column indicated that no vortex or turbulent flow formations will reattach to the module in this area. No significant difference was noticed between the flow acting on the small base and on the large base of the module.

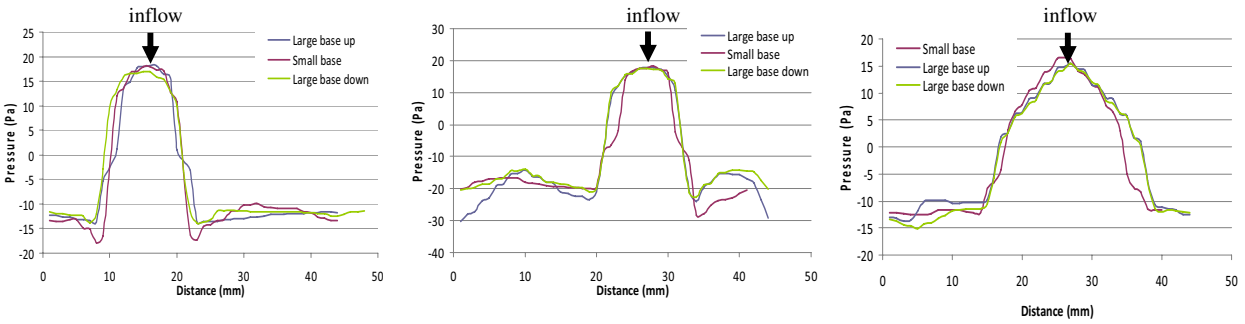

Figure 4. Average pressure on the surface of the Column, for different heights along the module for (a) $\alpha = 0°$, (b) $\alpha = 10°$, and (c) $\alpha = 45°$.

The coefficients C_D and C_L, represented by hollow triangles in Figures 5 a and b, were found to be in good agreement with the experiments performed by Solari et al, 2000, represented by hollow dots, and with those performed by Dragomirescu et al, 2009, represented by full dots in the same figure. The highest lift force is registered for 10°, as also indicated by the previous experiments, while the drag force would be dominant for 45°; when the wind speed is perpendicular to the front face of the Column, ($\alpha = 0°$) both aerodynamic forces were within moderate limits. In spite of the averaged values of the aerodynamic forces, the experiments (Yamada et al, 2005, Dragomirescu et al, 2009) have shown that if the Column is allowed to vibrate in smooth flow, the highest across-wind vibrations for 5.45 m/s are registered for $\alpha = 10°$ followed by $\alpha = 45°$. It should be mentioned that the same experiments have revealed that a square column tested under the same conditions would have four times higher vibration amplitude.

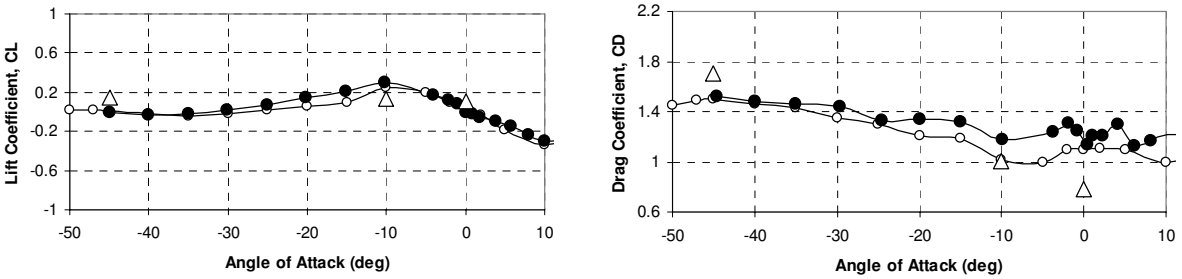

Figure 5. Variation of aerodynamic coefficients with the angle of attack: (a) Lift Coefficient, C_L, (b) Drag Coefficient, C_D

4 THREE-DIMENSIONAL FLOW-STRUCTURE INTERACTION

The particular shape of the Endless Column was considered to provide certain stability against galloping vibrations at high wind speeds and this was certified by several wind tunnel tests (Solari et al, 2000, Yamada et al, 2005). Most of the aerodynamic theories consider the cross section as a reference nominal area; however a two-dimensional cross section in this case would be reduced to a basic square shape, for which aerodynamic characteristics are much below the structural capacities of the Endless Column. Hence a three-dimensional interpretation of the wind flow structure interaction is required for better understanding the aerodynamic stability of this particular structure.

The flow visualization was conducted by sampling instantaneous velocity streamlines, simulation very similar to smoke visualisation practiced in the experiments. The velocity stream-

lines indicated a vertical motion along the Column, initiated by the free-end effect, in spite of the horizontal direction of the incoming wind flow, and sometimes rotational flow formations appeared between the modules behind the Column. At $\alpha = 0°$, when the entire front side of the modules is facing the incoming wind flow of initial velocity 5.45 m/s, the impact with the Column will determine a change in direction of the velocity streamlines, otherwise horizontal, and will produce vertical downwards flow movements, periodically re-attaching to the Column in the module's crest region (Fig. 6 a). For the case of 10°, the modules will accelerate slightly the lateral streamlines of velocity up to 6.0 m/s. Also, due to the trough between the modules and the inclination of the wind direction, the wind velocity was redirected downwards along the Column, which changed their linear pattern into a more irregular one (Fig. 6 b). When the corner of the Column is directly exposed to the wind ($\alpha = 45°$), acting as a wind breaker (Fig. 6 c), the regular velocity streamlines were partially maintained even after encountering the structure, a slight disturbance being observed only downstream the Column, at a distance of 0.2 m.

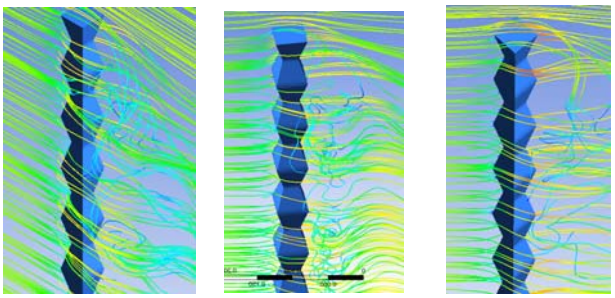

Figure 6. Three-dimensional flow pattern streamlines for (a) $\alpha = 0°$, (b) $\alpha = 10°$ and (c) $\alpha = 45°$,

Whenever the vectors of the velocity curl are extracted, indicating the rotation axis and the sense given by the right-hand rule for each rotational formation appearing around the structure, was noticed that, for all the investigated cases, $\alpha = 0°$, 10° and 45°, often on the edges of the Column, where wind detaches after the impact, the vectors will have opposite senses, hence cancelling out the motion along each of the modules, as represented in Figures 7 a to c. The rotational activity on the vertical direction is not entirely absent, but appears on the rear side of the Column, having very small intensity, of 1.36 s^{-1} and which is more concentrated in the troughs for the case of 0°. For 10°, the velocity curl reaches higher values of 1.04 x 10^3 s^{-1}, and is unevenly distributed along the rear side of the Column and along the edges; dominant direction of the flow will remain the along-wind direction. For 45°, lower intensity of the rotational activity was recorded, and opposite vectors appear clearly on the right side and left side along the edges, where detachment is encountered and more organized patterns and dominant along-wind flow vectors were noticed surrounding the Column.

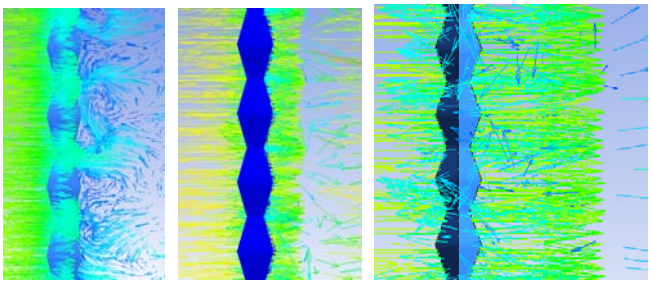

Figure 7: Velocity curl vectors for 5.45 m/s for the Endless Column at (a) $\alpha = 0°$, (b) $\alpha = 10°$ and (c) $\alpha = 45°$,

In Figures 8 three-dimensional flow formation around the entire Column are depicted. For $\alpha = 0°$, well defined three-dimensional turbulent formations are shed from both edges of the structure, and form a series of vertical flow patterns, which travel until 0.4 m downstream the Column. The measurements showed suction on the edges of the Column, of about -20 Pa, in the trough region, while on the crest of the modules, positive pressure of up to 19 Pa is recorded. The three-dimensional turbulent formation is also present downstream the Column at $\alpha = 45°$ (Fig. 8 c) however it seems to be only one single vertical vortex behind the Column instead of several shed vortices as for 10°, and the distance spanned by it is much lower, of 0.52 m. the most critical case of $\alpha = 10°$ showed a complex flow formation behind the Column, with several vertical vortices which travel in their consistent shape on higher distances of up to 0.8 m downstream the Column (Fig. 8 b). The color code indicates suctions of up to -40 Pa were achieved at the detachment surfaces.

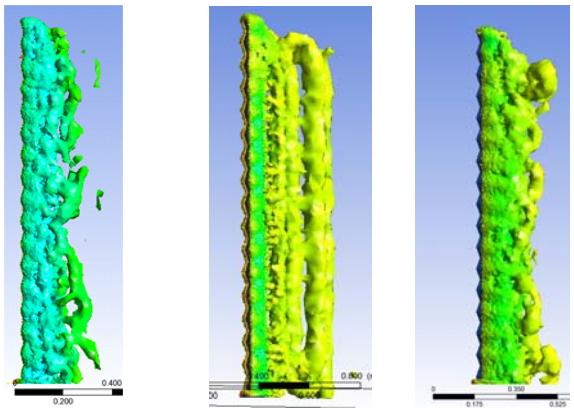

Figure 8: Three-dimensional flow formation around the Endless Column for (a) $\alpha = 0°$, (b) $\alpha = 10°$ and (c) $\alpha = 45°$.

A section through the three-dimensional flow formations revealed the vertical pressure distribution for angles of attack 0°, 10° and 45° (Figs. 9). Clear shedding of turbulent flow can be noticed initiated from the large base of each module towards downstream and local pressures of -10 Pa to -20 Pa alternate for the regions between two consecutive crests for 0° (Fig. 9 a). Several rows of vortices were confirmed along the height of the Column, of different intensities and induced pressures.

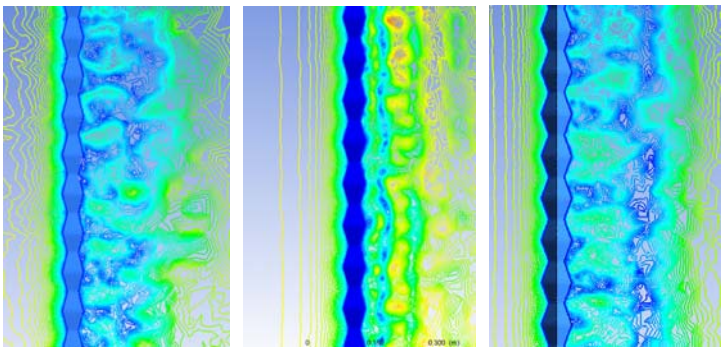

Figure 9: Pressure distribution around the Endless Column for (a) $\alpha = 0°$, (b) $\alpha = 10°$ and (c) $\alpha = 45°$.

The pressure measured on the exterior three-dimensional vortices shed downstream the Column was of 27 Pa; the interior of the vortices however, will exhibit a strong suction of -25 Pa, in the immediate vicinity of the Column and -12 Pa, when departed from it, for the α =10° (Fig. 9 b). The vertical pressure distribution for 45° clearly showed the main vertical vortex formed on the rear side of the Column had a local pressure of -10 Pa and only localized spots of -20 Pa, which dissolved quickly in the flow (Fig. 9. c).

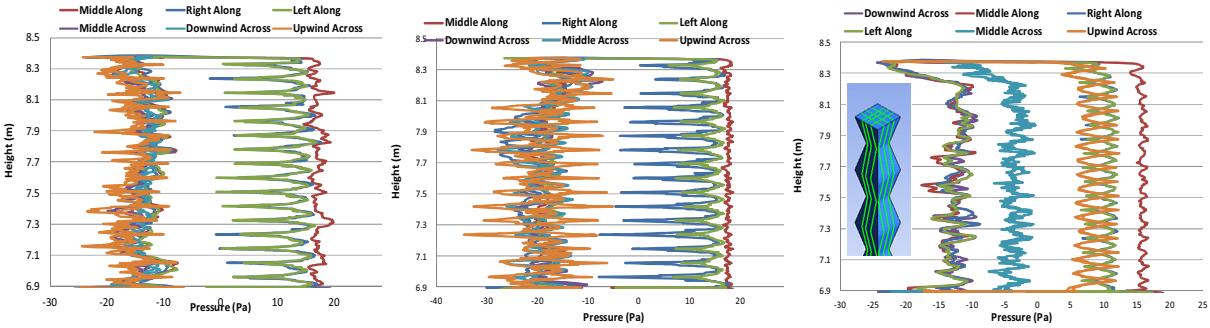

Figure 10. Instantaneous pressure on the height of the Endless Column, for (a) α = 0°, (b) α = 10°, and (c) α = 45°.

Figures 10 a, b and c show the pressure distribution at the surface of the Column for the incoming wind direction considered as the middle position and at 0.1 m left and right from the middle position. Also on the across-wind direction the middle line was monitored and the two lines at 0.1 m towards the incoming flow (upstream) and towards the downstream of the Column, as it can be seen in the detail of Figure 10 c.

For the α = 0°, mainly suction (-15 Pa to -20 Pa) was registered on the middle line in the across-wind direction indicating the shear layer detachments showed also in Figures 3 a and b, while the middle line in the along-wind direction, as expected high pressure of almost 20 Pa was registered on one side and suctions of -10 Pa were registered on the other side of the structure. Little fluctuation was noticed for both middle lines. For the other two lines in the along-wind direction (left and right) however, high fluctuations were noticed at the incoming flow along the modules, reaching 19 Pa at the large bases and almost 0 Pa at the small base of the modules, while limited fluctuation is shown on the rear side of the Column the right along- and left along-wind lines. For the across-wind direction, the upwind line showed the highest pressure fluctuations of -10 Pa to -20 Pa, which indicates that turbulent flow around the Column is already formed before the shear layers detach from it. The pressure on the downwind across-wind line had similar values and variations as for the middle across-wind line.

Consistent positive pressures of around 19 Pa were registered for the incoming wind surface of the Column on the middle line for α = 10°, as it can be seen in Figure 10 b, while the left and right lines for the same along-wind direction had similar pressure patterns as for the α = 0°. On the across-wind direction the upwind line had extreme variations along the modules spanning from -10 Pa to -30 Pa which is consistent with the pressure distribution and the vertical vortices formations reported in Figures 8 b and 9 b. The downwind line will also register fluctuations along the module's height however the pressures are not very high, being in the region immediate after detachment.

The case of α = 45°, was the most stable in terms of pressure distribution on the across- and along-wind directions as follows (Fig. 10 c): the middle line for the along-wind direction registered smaller pressures of around 16 Pa due to the minimum nominal area exposed to wind and had a very limited fluctuation along the modules. The across-wind middle line registered the smaller suction of -5 Pa which confirms the absence of any turbulent or vortex formation down-

stream, in the immediate vicinity of the Column. The left and right lines on the along-wind direction will have similar patterns as for the 0° and 10°, however the values of the recorded pressure are much lower of around 5 Pa to 10 Pa on the incoming wind face and -10 Pa to -15 Pa for the rear side of the Column. The main difference for the $\alpha = 45°$ is that the upwind across-wind line will yield only positive pressures which indicates a flow attached to the outside edges of the Column, which does not appear in any of the above figures. The downwind across line will register only negative pressures as for the other two cases of 0° and 10°.

5 CONCLUSIONS

The three-dimensional flow visualization was conducted through CFD simulations for the Endless Column, in order to clarify the effect of the modular shape upon the stability to galloping vibrations and to determine the detailed flow-structure interaction. The dimensions of the model, the wind speed and angle of attack were chosen so that it followed the wind tunnel experiments reported by Dragomirescu et al, 2009.

The effect of the geometric shape of one pyramidal module was investigated and was determined that the crest regions of the module would have less influence upon the aerodynamic activity, while the crest regions would establish a continuous accumulation of suction on the rear side of the Column, which indicates the existence of a vortex formation. The velocity streamlines, pressure contours and vertical flow formations re-attested the fact that the Column facing the wind at an attack angle of 10° would be the most inconvenient arrangement; these wind directions would produce an earlier detachment of the incoming wind flow, after the impact with the structure, and would determine the creation of several three-dimensional vertical vortices of high suction behind the Column, in its immediate vicinity and up to 0.8 m downstream. The negative pressure will determine an unbalanced lift force which might explain the incipient vibrations reported by the wind tunnel experiments (Yamada et al, 2005, Dragomirescu et al, 2009).

The angle of attack of 45°, when the corners of the aligned pyramidal modules are facing the incoming flow acting as a wind breaker, would ensure a smoother flow detachment, hence the vertical vortices behind the Column will register a weaker suction on the rear side which would confer a higher aerodynamic stability for the entire Column. Also was noticed that the vertical fluid motion was cancelled for trough regions along the modules, indicated by the opposite sense of the curl vectors. However, for completely understanding the lack of galloping for the “Endless Column” and the effect of its particular shape composed of a repetition of pyramidal modules, numerical CFD simulations should be conducted for a broader range of wind speeds, of up to 15 m/s, where the experiments were stopped due to limitations of the instrumentation.

6 REFERENCES

1 R.D., Blevins, Flow-induced vibrations (2nd edition), Van Nostrand Reinhold, New York, 1990.
2 P.W., Berman, S.C., Luo, Investigation of the aerodynamic instability of a square-section cylinder by forced oscillation. Journal of Fluids and Structures, 2 (1988) 161-176.
3 E., Dragomirescu, H., Yamada and H., Katsuchi, Experimental investigation of the aerodynamic stability of the ‘‘Endless Column’’, Romania, J. Ind. Aerodyn., 97 (2009) 475–484.
4 R.D., Gabbai, On the aerolastic indifference of Brancusi’s Endless Column, Proceedings of 12th International Conference on Wind Engineering, Cairns Australia, 2007, pp.1111-1118.
5 H., Kawai, Vortex induced vibration of tall buildings. J. Ind. Aerodyn., 41-44 (1992) 17-128.
6 J.T., Klamo, A., Leonard, A., Roshko, The effects of damping on the amplitude and frequency response of a freely vibrating cylinder in cross-flow. Journal of Fluids and Structures 22 (2006) 845-856.
7 D., Lungu, G., Solari, G., Bartoli, M., Righi, R., Vacareanu, A., Aldea, Reliability under wind loads of the Brancusi Endless Column, Romania. International Journal of Fluid Mechanics Research 29 (2002) 323-328.

8 C.A., Safta, Aerolastic Indifference of the Endless Column, in: Proceedings of 28th Congress of American – Romanian Academy, Targul Jiu, Romania, 2003, pp.42-49.
9 E., Simiu R.H, Scanlan, Wind effects on structures: An introduction to wind engineering, John Wiley & Sons, New York, 1996.
10 R., Sofronie, Brancusi and the obsession of gravity in: Proceedings of International Congress of ICOMOS and UNESCO, Paris, France, 2001, pp.4 – 14.
11 G., Solari, D., Lungu, G., Bartoli, M., Righi, R.,Vacareanu, A., Villa, Brancusi Endless Column, Romania: Dynamic response and reliability under wind loading, in: Proceedings of the 2nd International Symposium on Wind and Structures, Pusan, Korea, 2002, pp.79-86.
12 C., Scruton, On the wind exited oscillations of stacks, towers and masts. International Conference of Wind Effects on Buildings and Structures Proceedings 2, Teddington, U.K., 1963, p.798-836.
13 H., Yamada, H., Katsuchi, E., Dragomirescu, Y., Takaoka, Wind-tunnel study on aerodynamics of Endless-Column, Proceedings of National Conference of Wind Engineering, Tokyo, Japan, 2005, pp. 45 – 48.

The Seventh International Colloquium on Bluff Body Aerodynamics and Applications (BBAA7)
Shanghai, China; September 2-6, 2012

Study on turbulence effects on flow patterns around rectangular cylinders

Panpipat Sangchuwong [a], Hitoshi Yamada [b], Hiroshi Katsuchi [c]

[a,b,c]*Dept. of Civil Engineering, Yokohama National University, 79-5 Tokiwadai, Hodogaya-ku, Yokohama, Kanagawa, JAPAN*

ABSTRACT: Wind tunnel experiments were performed to study the flow pattern around bluff bodies. Flows around square and rectangular cylinders with various slenderness ratios were studied. Flows with turbulence intensity ranging between 5.66% to 11.43% were generated by installing a grid in the wind tunnel. The study concentrated on the effect of turbulence properties on the flow structures around bluff bodies.

KEYWORDS: small-scale turbulence, turbulence partial simulation, reduced turbulence intensity, bluff-body, rectangular cylinder, wind tunnel.

1 INTRODUCTION

Flow patterns around bluff bodies have long been interesting topics among researchers but the relationships between flow patterns and flow parameters such as turbulence intensity are still vague.

Nakamura and Ohya [1] showed that flow structures strongly depend on small-scale turbulence in the incoming flow. It increases negative base pressures of a long rectangular cylinder (a rectangular cylinder which has slenderness ratio more than 0.6). Nakamura and Ozono [2] stated in their research that if the turbulence scale has more magnitude than twice the frontal dimension (or depth of a cylinder; D), the effect of the turbulence scale will approach to that of smooth flow. Then, large turbulence scale will have no significant effect on the mean pressures on the side surfaces.

However, Cherry et al.[3] and Kiya and Sasaki [4] argued that explaining by using only the magnitude of mean pressures is inadequate to describe the behavior of complicated natural flow fields. Haan et al. [5] defined that turbulence intensity or turbulence scale alone cannot fully explain changes of aerodynamic behavior of bridge decks.

Irwin et al. [6] stated that because past studies discovered that small-scale turbulence affects flow pattern and aerodynamic parameters, then it is reasonable to match the power spectrum of turbulence only at high frequencies which is the range that small-scale turbulence dominates the flow. This approach is called “turbulence partial simulation”.

Matching between the power spectrum of a wind tunnel model and that of the prototype (full-scale) can be formulated as shown in Equation 1.

$$\left(f\frac{S_u}{U^2}\right)_m = \left(f\frac{S_u}{U^2}\right)_p \tag{1}$$

where f = frequency; S_u = power spectrum of the longitudinal component of turbulence; and U = mean wind speed.

Irwin et al. also recommended that turbulence partial simulation would be more reasonable to compare wind-induced vibration of bridge decks between wind-tunnel test and full scale observation.

Katsuchi and Yamada [7] initiated to use new parameter "reduced turbulence intensity" combining turbulence intensity and turbulence scale together. Formulation of reduced turbulence intensity begins with assuming the Karman type PSD in Equation 2.

$$f\frac{S_u}{\sigma_u^2}=\frac{4\left(fL_u^x/U\right)}{\left(1+70.8\left(fL_u^x/U\right)^2\right)^{5/6}} \tag{2}$$

where σ_u = fluctuating part of wind speed; L_u^x = length scale of turbulence (or turbulence scale).

Equation 2 can be transformed to Equation 3 by determining the simulation of a high frequency part of the power spectrum.

$$f\frac{S_u}{\sigma_u^2}=\left(\frac{fL_u^x}{U}\right)^{-2/3} \tag{3}$$

Multiplying (U^2/U^2) in the left hand side of Equation 3 leads to

$$f\frac{S_u}{U^2}=I_u^2\left(\frac{fL_u^x}{U}\right)^{-2/3} \tag{4}$$

where I_u = turbulence intensity = σ_u/U

The dimension of *f/U* is inverse dimension of length, then *f/U* can be transformed to *1/D* (where *D* = representative length). Equation 4 can be rewritten in the term of *1/D*.

$$f\frac{S_u}{U^2}=\left(\frac{I_u}{\left(L_u^x/D\right)^{1/3}}\right)^2 \tag{5}$$

After that, substituting Equation 5 into Equation 1 leads to Equation 6.

$$\left(\frac{I_u}{\left(L_u^x/D\right)^{1/3}}\right)_m=\left(\frac{I_u}{\left(L_u^x/D\right)^{1/3}}\right)_p \tag{6}$$

Katsuchi and Yamada named the new parameter obtained from Equation 6 as "reduced turbulence intensity" which is equal to turbulence intensity divided by cubic root of the ratio between turbulence scale and the representative length (L_u/D, this parameter will be called length scale ratio hereafter).

$$I_r=\frac{I_u}{\left(L_u^x/D\right)^{1/3}} \tag{7}$$

It can be seen from Equation 6 that reduced turbulence intensity of the prototype is equal to that of the wind-tunnel model. Moreover, this parameter also represents the effect of small scale turbulence as explained above. Then, it is expected that using reduced turbulence intensity as a new representative will be more reasonable and give us better understanding than using only turbulence intensity or length scale ratio alone.

The aim of this study is to understand more clearly the effects of the turbulence parameters of flow fields on the flow structures around bluff bodies by focusing on the reduced turbulence intensity.

2 EXPERIMENTAL SETUP

Experiments were carried out in a closed-circuit wind tunnel located at Yokohama National University. Its working section is 1.3 m. (width) x1.8 m. (height). Three square cylinders with breadth (B) and depth (D) of 100 mm. were used in this experiment. Each cylinder had four pressure probes installed in each side, giving a total of 16 pressure probes per section in a cylinder. In order to study the effect of slenderness ratio (B/D), we adjoined 2 or 3 square cylinders to be a rectangular cylinder with a slenderness ratio of 2.0 or 3.0 respectively. The cylinder was mounted between two acrylic end plates in the center of the working section. It could also be rotated in order to study the effect of angle of attack.

Representative wind speeds in this experiment were 6 m/s and 9 m/s, giving the corresponding Reynolds number of 40,000 and 60,000 respectively.

Turbulent flow fields were generated by using a wooden grid with bar size of 60 mm. and bar spacing of 240 mm. The grid was installed at 3 different locations upstream of the cylinder. Turbulent flow properties such as turbulence intensity and turbulence scale were measured by using a hot-wire anemometer. There were four types of flow fields studied in this experiment. They were smooth flow and turbulent flow with turbulence intensity of 5.66%, 7.40%, and 11.43%.

Pressure data measured from the pressure probes were sent to an A/D converter to transform from analog signal to digital signal. After that the data were sent to a personal computer for recording.

Turbulence scales were calculated by using the peak frequency method which was suggested by Fichtl and McVehil [8]. The frequency that the power spectrum reaches to the maximum value will be brought to calculate the turbulence scale as shown in Equation 8.

$$L_u^x = \frac{1}{2\pi}\left(\frac{U}{f_{peak}}\right) \tag{8}$$

Reliability of the turbulence scale obtained from this method has been proved by comparing an experimental power spectrum with that obtained by substituting the turbulence scale into Equation 1. An example of the comparing results can be seen in Figure 1.

It can be seen from Figure 1 that calculated power spectrum matches the experimental power spectrum very well. Thus, the turbulence scales calculated from the peak frequency method are reasonable.

Turbulence parameters in this study such as turbulence intensity, turbulence scale and reduced turbulence intensity are shown in Table 1. Figure 2 shows the power spectrums of all cases corresponding to the data in Table 1.

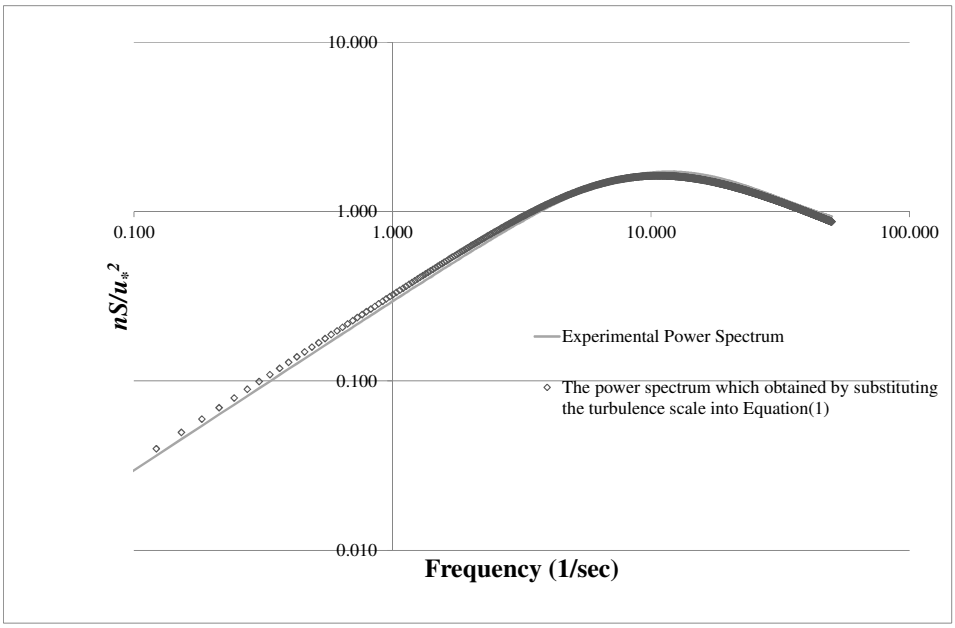

Figure 1. An example of the comparing results of power spectrum.

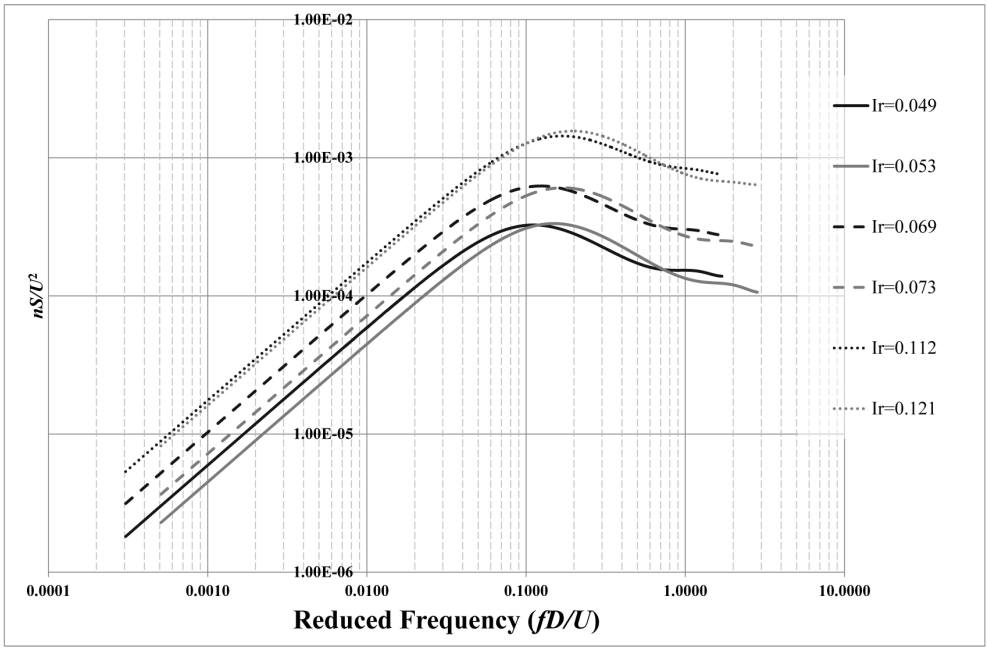

Figure 2. Power spectrums obtained from the experiment.

Table 1. Turbulence parameters.

Wind speed :U (m/s)	Reynold No.	I_u	L_u (cm)	L_u/d	$I_r = I_u/(L_u/d)^{1/3}$
6.0	40,000	0.0537	0.11	1.06	0.0526
		0.0715	0.09	0.93	0.0732
		0.1125	0.08	0.81	0.1206
9.0	60,000	0.0552	0.14	1.38	0.0496
		0.0728	0.12	1.17	0.0692
		0.1102	0.09	0.92	0.1134

3 EXPERIMENTAL RESULTS

Some results obtained from the experiment can be seen in Figure 3 which illustrates mean surface pressure coefficients (C_p) for every cases of reduced turbulence intensity around a square cylinder and a rectangular cylinder with a slenderness ratio of 2.0 and 3.0. The figure shows that increasing reduced turbulence intensity clearly makes the side surface pressures on the after-body decrease especially in a long rectangular cylinder. The peaks of the mean pressures can be also seen more obviously and shift closer to the leading edge. This means that re-attachment of the flow around bluff bodies is induced by increasing reduced turbulence intensity. Negative pressures on leeward surface were also reduced due to growth of turbulence level.

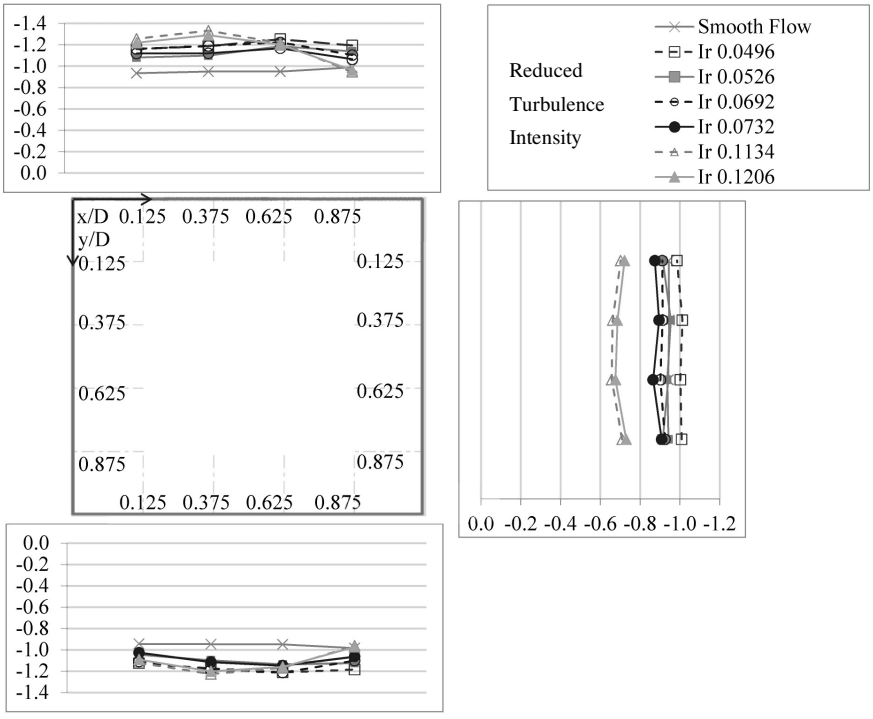

Figure 3a. Mean surface pressure coefficients (C_p) around a square cylinder

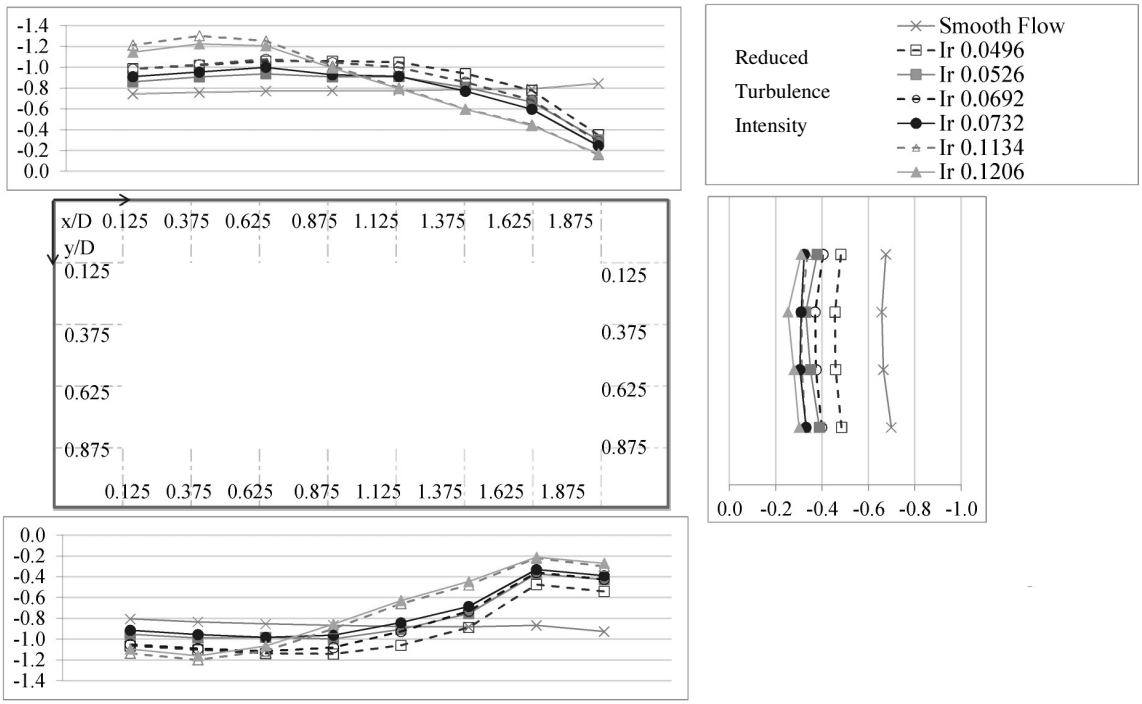

Figure 3b. Mean surface pressure coefficients (C_p) around a rectangular cylinder with a slenderness ratio (B/D) of 2.0

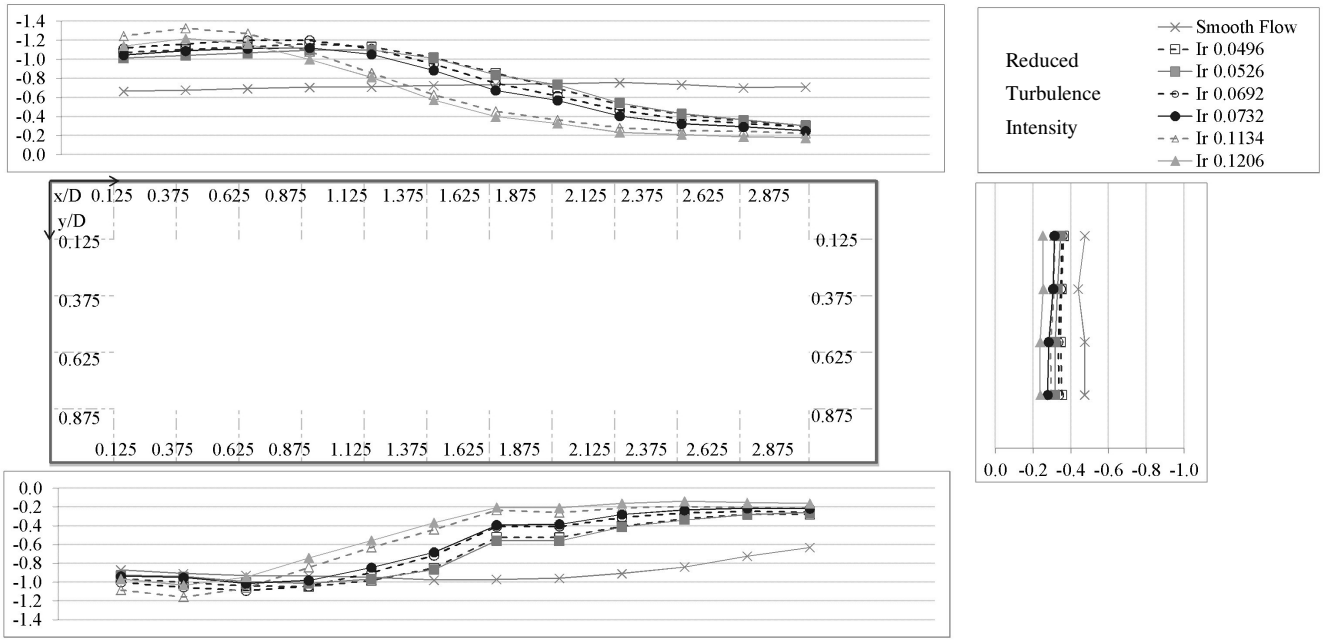

Figure 3c. Mean surface pressure coefficients (C_p) around a rectangular cylinder with a slenderness ratio (B/D) of 3.0

The capability to be a representative for turbulence level of reduced turbulence intensity will be pointed out in this section. In the case of 0.0496 and 0.0526 reduced turbulence intensity, the surface pressures of the rectangular cylinder with a slenderness ratio of 2.0 decrease obviously against increasing reduced turbulence intensity. On the contrary, the surface pressures decrease with reduction of turbulence intensity from 0.0552 (corresponding to 0.0496 of I_r) to 0.0537 (corresponding to 0.0526 of I_r). It might be because turbulence intensity in this case almost does not change (from 0.0552 to 0.0537) but turbulence scale ratio decreases from 1.38 to 1.06 , then corresponding reduced turbulence intensity calculated from the first two parameters also decreases. This means that reduced turbulence intensity might be the better representative than turbulence intensity because it can capture change of the flow while turbulence intensity cannot in this case.

Locations of the peak of mean surface pressures were identified by fitting mean surface pressure curves with sixth order parabola equations. The locations of the peak pressures of the rectangular cylinder with a slenderness ratio of 2.0 and 3.0 are shown in Table 2. It can be seen that the locations of the peak pressures on both top and bottom surface shift to the leading edge when reduced turbulence intensity increases. The locations of the peak pressures on the top surface are not identical to that of the bottom surface. It can be noticed from the locations of the peak pressures or from the pressure graphs in Figure 3 that the flows are not symmetric as they should be. The reason of this behavior is still obscure but it might be because two-dimensional flow behaviors were not fully developed due to the grid or other reasons.

Table 2. Locations of the peaks of mean surface pressures.

Locations of the peak of mean surface pressures (x/D)				
I_r	Cylinder with a slenderness ratio of 2.0		Cylinder with a slenderness ratio of 3.0	
	Top	Bottom	Top	Bottom
0.0496	0.87	0.63	0.85	0.75
0.0526	0.75	0.55	0.92	0.80
0.0692	0.71	0.58	0.72	0.66
0.0732	0.60	0.58	0.73	0.69
0.1134	0.42	0.42	0.38	0.33
0.1206	0.47	0.40	0.40	0.34

Therefore, this phenomenon leads a net mean lift force not to be zero. Table 3 summarizes the net mean lift coefficients (C_L). It can be noticed that in the case of the rectangular cylinder with a slenderness ratio of 2.0, the net mean lift coefficient decreases to be negative value (or downward direction) against increasing reduced turbulence intensity. On the other hands, the net mean lift coefficient of the rectangular cylinder with a slenderness ratio of 3.0 does not change significantly and the magnitude of the coefficient is negative in every cases. The cause of this inconsistency is still unclear but it might be because of some effects of complicated three-dimensional flow fields as stated before.

Table 3. Net mean lift coefficient (C_L).

I_r	Net mean lift coefficient (C_L)	
	Cylinder with B/D of 2.0	Cylinder with B/D of 3.0
0.0496	0.019	-0.134
0.0526	0.008	-0.121
0.0692	-0.026	-0.158
0.0732	-0.035	-0.144
0.1134	-0.101	-0.146
0.1206	-0.107	-0.153

4 CONCLUSION

The results from this experiment emphasized that increasing turbulence level will enhance the re-attachment of the flow on sharp-edged bluff bodies. Therefore, there will be pressure recovery occurring on the after-body. The size of recirculation bubbles become smaller and shift closer to the leading edge due to the effect of turbulence. Reduced turbulence intensity can be efficiently used as a representative for turbulence level of the flow. The results also showed that the flow was not symmetric as it should be. Therefore, a net lift force was not zero due to asymmetric flow. The reason of asymmetric flow is still unclear but it was predicted that might be because three-dimensional flow effects.

Flow visualization around bluff bodies will be studied in the future for observation of the mechanisms of the flow fields around these bodies. The authors believe that studying flow visualization could make effects and mechanisms of turbulence on flow structures more understandable.

5 REFERENCES

1 Y. Nakamura and Y. Ohya, The effects of turbulence on the mean flow past two-dimensional rectangular cylinders, J. Fluid Mech., 149 (1984) 255-273.
2 Y. Nakamura and S. Ozono, The effects of turbulence on a seperated and reattaching flow, J. Fluid Mech., 178 (1987) 477-490.
3 N.J. Cherry , R. Hillier and M.E.M.P. Latour, Unsteady measurements in a seperated and reattaching flow, J. Fluid Mech., 144 (1984) 13-46.
4 M. Kiya and K. Sasaki, Free-stream turbulence effects on a separation bubble, J. Wind Eng. Ind. Aerodyn., 14 (1983) 375-386.
5 F.L. Haan Jr., A. Kareem and A.A.Szewczyk, The effects of turbulence on the pressure distribution around a rectangular prism, J. Wind Eng. Ind. Aerodyn., 77&78 (1998) 381-392.
6 P.A. Irwin, Bluff body aerodynamics in wind engineering, J. Wind Eng. Ind. Aerodyn., 96 (2008) 701-712.
7 H. Katsuchi and H. Yamada, Study on turbulence partial simulation for wind-tunnel testing of bridge deck, Proc. of ICWE 13, Amsterdam, Netherlands, (2011)
8 G. H. Fichtl and G. E. McVehil, Longitudinal and lateral spectra of turbulence in the atmospheric boundary layer, AGARD-CP-48, (1969)

The Seventh International Colloquium on Bluff Body Aerodynamics and Applications (BBAA7)
Shanghai, China; September 2-6, 2012

Numerical simulation and visualization of flow around rectangular bluff bodies

Xuyong Ying[a], Fuyou Xu[b], Zhe Zhang[c]

Faculty of Infrastructure Engineering, Dalian University of Technology, China
[a]yingxuyong@hotmail.com, [b]fuyouxu@hotmail.com, [c]zhangzhe@dlut.edu.cn

ABSTRACT: A comprehensive study of unsteady flow around rectangular cylinders at Reynolds number of 21400 is presented in this paper. The influence of different simulation parameters, such as grid quality, turbulence model etc., are investigated in detail. Unsteady computations are performed using 2D Reynolds averaged Navier-Stokes (RANS) models and 3D large eddy simulation (LES). Time-averaged global quantities such as the mean drag coefficient, the *rms* value of lift coefficient, the Strouhal number, the recirculation length, and the surface pressure coefficient are calculated and compared with the available wind tunnel test results proposed in the literature. A series of instantaneous and time- and spanwise-average velocity, streamlines and vorticity magnitude iso-surface are also presented.

KEYWORDS: Unsteady flow; Square cylinder; Rectangular cylinder; Computational Fluid Dynamics (CFD); Large eddy simulation; Reynolds averaged Navier-Stokes;

1. INTRODUCTION

As modern long-span bridges and buildings become more flexible, the dynamic response under unsteady wind load has a greater impact on the design of these structures. Accurate prediction of wind effects on these structures is becoming increasing significant. In this respect, aerodynamic characteristics of rectangular cylinders, because of their common use in bridge and building industry, have received particular interest from both practical and academic standpoints. Bodies with a rectangular cross-section are termed as bluff bodies, in which the shear layer separated from windward corner, reattachment characteristics of the flow and vortices shedding into the wake are dependent on the cylinder's aspect ratio (width to height, *B/D*). Thus, it is important to study their aerodynamic characteristics and flow structures in details.

Okajima [1] and Tamura et al. [2] conducted detailed experimental studies to understand the aerodynamic characteristics of square cylinder and rectangular cylinders with different aspect ratios. As a consequence of the rapid growth of computation power and improvement of Computational Fluid Dynamics (CFD) technology, the numerical approach based on CFD provides a new approach for investigating aerodynamic characteristics of structures. The main purpose of the current study is to investigate to which extent a numerical simulation based on CFD can be employed to reasonably predict aerodynamic characteristics and flow structures of such a bluff body. Since the numerical approach is relatively affordable and easy to use, it is especially interesting for industrial and civil applications. Iaccarino et al. [3] examined the accuracy of RANS turbulence model in predicting complex flow with separation. The unsteady flow around square cylinder and over a wall-mounted cube were simulated and compared with experimental data. Their study demonstrated that the unsteady RANS does indeed predict periodic shedding, and leading to good concurrence with available experimental data. Shimada

and Ishihara [4] numerically predicted flow features around rectangular cylinders with various aspect ratio ranging from B/D=0.6 to 8.0 by a two-layer modified $k-\varepsilon$ model. Recently, Sohankar [5] successfully reproduced the turbulent statistics of flow around rectangular cylinders with B/D=0.4~4.0 as well as the aerodynamic forces by employing unsteady and 3D large eddy simulation (LES).

In present paper, we identify a reliable CFD approach for evaluation of bluff-body flows through the simulation of flow around a square cylinder. The influence of different simulation parameters, such as grid quality, turbulence model etc., is analyzed. The numerical results are compared with the available wind tunnel test results proposed in the literature. In all the computations presented in this paper the body geometry is kept fixed and the Mach number is very low, so that compressibility effects are negligible. Furthermore, unsteady flows with zero incidence attack angle over rectangular cylinders with B/D=2.0~10.0 are numerically simulated. Also, the flow field around rectangular cylinders are analyzed in 2D and 3D space.

2. NUMERICAL METHODS

A commercial computational fluid dynamics (CFD) code, ANSYS FLUENT, was used to perform present numerical simulations. The turbulent models used in this study are the standard $k-\varepsilon$ model, RNG $k-\varepsilon$ model, realizable $k-\varepsilon$ model, standard $k-w$ model, SST $k-w$ model, RSM model, and LES model. The more detailed descriptions for all turbulent models may be found in ANSYS FLUENT Theory's Guide [6].

The ANSYS FLUENT uses the finite-volume method (FVM) to solve the governing equations for a fluid. The second order implicit scheme is used for time discretization and the second order upwind scheme is used for spatial discretization. SIMPLE (semi-implicit pressure linked equations) algorithm is employed for solving the discretized equations.

In order to obtain reliable and accurate results, it is important to choose carefully the length and width of the computational domain and boundary conditions. The computational domain and boundary conditions used in the present study are given in Figure 1. The dimensions of x_1, x_2, x_3, y_1, and y_2 adopted in the present work are summarized in Table 1. As can be seen in Table 1, for rectangular cylinders, the computational domain covers $50D$~$105D$ in streamwise direction and $30D$ in normal direction, which is larger than that adopted by Sohankar [5] or Sun et al. [7]. The reason for such a choice is to estimate the flow obstacle effect on the inflow and outflow boundary condition, as discussed by Murakami [8].

Considering the mesh number must be as low as possible as we could accept for efficient computation, the hybrid grids are used in the whole computational domain. The traditional finite difference method uses a structured grid, which requires a body-fitted grid transformation from physical domain to computational domain. The mesh near and aligned with the wall surfaces must be refined and stretched with the viscous boundary layer grid. The finite volume method is adopted in the present study, which makes the mesh generation flexible since it has the capacity of deal with both structured grid and unstructured grid. Figure 2 shows the grid arrangement for the rectangular cylinders. The primary characteristic of this mesh style is that the section model is nested in a rectangular area about three times larger than itself. For zone in the nesting rectangular area, the structured quadrangular grid is generated while for zones outside the nesting rectangular area, the unstructured triangular grid is applied. The height of the first layer Δy near the surface of rectangular cylinders is chosen to be $0.005D$. This treatment makes it easier to generate a mesh fine enough in the vicinity of the cylinder surface while keeping the mesh in zones far away from the cylinder surface unchanged or in a proper coarser state. Details of

various mesh system can be seen in Table 1. As LES simulation requires three-dimensional domain, we select the spanwise dimension to be 4D which is a typical spanwise length widely chosen in the other 3D simulations. The 3D grid is obtained by the structured projection of the 2D hybrid grid along the spanwise direction z. As the mean flow is two-dimensional, the spanwise grid spacing, normally taken to be uniform, is usually larger than the grid spacing in the other directions [9]. For LES simulation, we select the number of grid points N_z from 5 to 40 for discretising the spanwise length, as can be seen in Table 2.

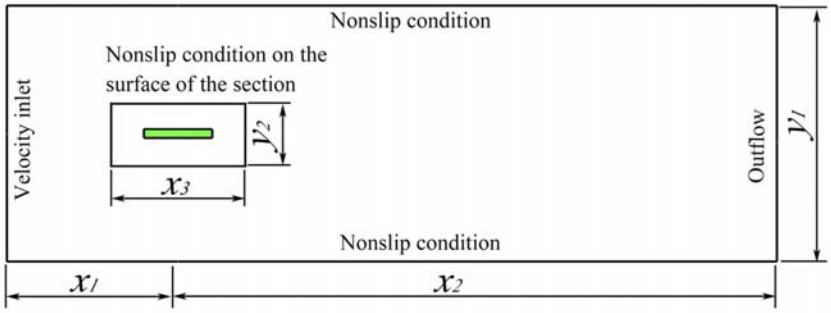

Figure 1. Computational domain and boundary conditions.

Table 1. Mesh system for present simulations.

Aspect ratio	x_1	x_2	x_3	y_1	y_2	Resolution of inner rectangular area ($N_x \times N_y$)	Grid size of computational domain ($N_x \times N_y$)
B/D=1	10D	40D	3D	20D	3D	50×50	50×20
B/D=2	10D	40D	4D	20D	3D	70×50	50×20
B/D=3	15D	50D	5D	20D	3D	90×50	65×20
B/D=4	15D	60D	6D	20D	3D	100×50	75×20
B/D=5	20D	65D	7D	30D	3D	120×50	85×30
B/D=6	20D	65D	8D	30D	3D	135×50	85×30
B/D=7	20D	70D	9D	30D	3D	150×50	90×30
B/D=8	20D	70D	10D	30D	3D	150×50	90×30
B/D=9	25D	75D	11D	30D	3D	150×50	100×30
B/D=10	25D	80D	12D	30D	3D	150×50	105×30

Table 2. 3D computational mesh parameters

Cases	Spanwise grid resolution	Grid scale
Case 1	N_z=5	0.5D
Case 2	N_z=10	0.25D
Case 3	N_z=20	0.2D
Case 4	N_z=30	0.133D
Case 5	N_z=40	0.1D

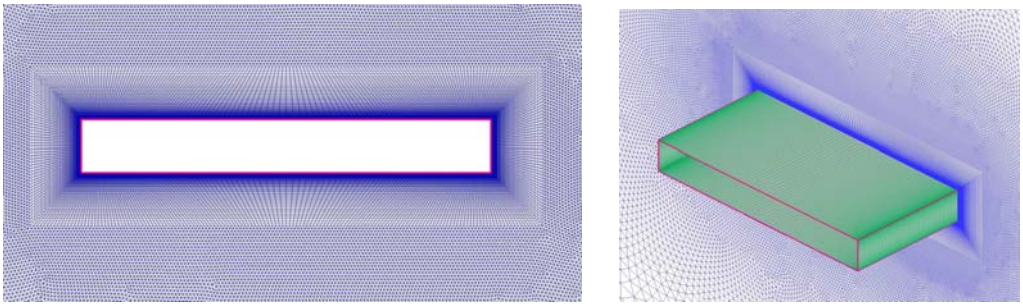

Figure 2. Grid near the surface of B/D=8 rectangular cylinder (Case 4).

The flow calculations are advanced by using a short time step (dt) to get the time dependent flow characteristics. In the present study, the time step is taken to be 0.001s. The use of smaller values of time-step did not produce any significant change in the root mean square (*rms*) and average value of the drag and lift coefficients. The time-averaged quantities for all cases have been obtained by integrating the instantaneous field over a long period of not less than 40 shedding cycles, but without including the initial transients. It is found that this period is sufficient to get a converged time-averaged flow field.

3. INFLUENCE OF MODELING PARAMETERS

3.1 *Spatial discretization*

A spanwise grid-refinement study is performed for the unsteady flow around 3D square cylinder at Reynolds number of 21400 in this section. The LES with standard Smagorinsky sub-grid model is employed. Table 3 and Figure 3 summarize typical flow parameters from the present simulation include the mean drag coefficient (C_d), the rms value of lift coefficient (*rms* C_l), the Strouhal number ($S_t=fD/U$) of the vortex shedding, and the recirculation length (l_R/D). All flow parameters are referred to the body width D. Spectral analysis was performed on the lift coefficient time history, to obtain the Strouhal number (S_t). The recirculation length (l_R/D) is the distance over which the time-averaged streamwise velocity on the rear side of the cylinder is negative. Comparisons are made with the experimental data and other numerical results in the literatures.

Table 3. Result Comparison of flow past square cylinder

Authors	Method	C_d	*rms* C_l	S_t	l_R/D
Present 2D-RANS	SKE	1.611	0.326	0.128	2.05
	RNG	1.896	1.068	0.140	0.91
	RKE	1.954	1.087	0.145	0.87
	SKW	1.956	1.502	0.131	0.80
	SST	2.130	1.435	0.126	0.91
	RSM	2.018	1.115	0.139	1.12
Present 3D-LES	Case 1	2.587	1.208	0.118	0.40
	Case 2	2.589	0.990	0.121	0.41
	Case 3	2.393	1.410	0.125	0.60
	Case 4	2.298	1.450	0.125	0.60
	Case 5	2.281	1.388	0.125	0.62
Rodi [10]	SKE	1.637	0.305	0.134	2.8
Lee [11]	SKE	1.75	–	0.138	–
	RNG	2.12	–	0.133	–
Franke and Rodi [12]	RSM	2.15	1.49	0.136	0.98
Rodi et al. [10]	LES	2.3	1.15	0.13	0.96
Lubcke et al. [13]		2.178	1.47	0.13	0.56
Bearman et al. [14]	EXP.	2.19	–	0.126	–
Lyn et al. [15]		2.10	–	0.132	0.88
Van Oudheusden et al. [16]		2.18	–	–	0.58

As can be seen in Table 3 and Figure 3, C_d is overestimated, while *rms* C_l, S_t and l_R/D are underestimated with the coarse grid. Passing to the fine grid, the accuracy of the calculated results is enhanced and a non-negligible jump is observed in C_d, *rms* C_l, S_t and l_R/D. In contrast, the results change very little passing from the fine to the finest grid. It seems possible to affirm that a reasonable convergence is reached with the fine grid, which is adopted hereafter for all the computations.

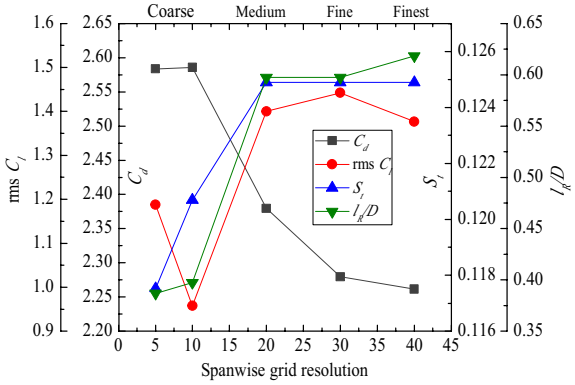

Figure 3. Grid-convergence study results

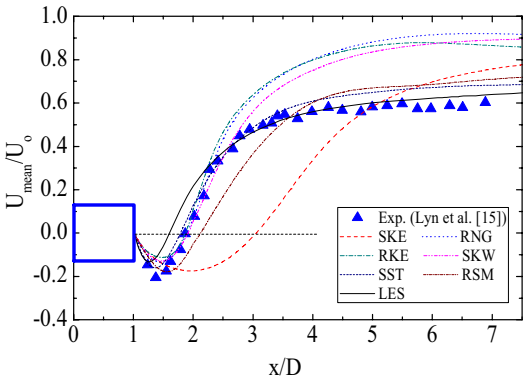

Figure 4. Averaged streamwise velocity along the centerline

3.2 *Turbulence modelling*

The influence of the turbulence model on the results is investigated in this section, and the simulated flow parameters by various turbulence models are also summarized in Table 3. From Table 3, we find that C_d and *rms* C_l predicted by all 2D RANS and 3D LES turbulence models agree well with the experiments and also with the other numerical results. Comparatively speaking, the standard $k-\varepsilon$ model underestimate C_d and *rms* C_l considerably. Most RANS calculations and LES with fine grid yield the correct value of S_t=0.125-0.140, and it appears that St is not very sensitive to the choices of turbulence model. The recirculation length varies most widely with different choices of turbulence model. The experiment and most numerical simulations yield the value of l_R/D≈0.56-0.96. The RSM model overestimates the value of l_R/D slightly while the standard $k-\varepsilon$ model gives the incorrect quantity of l_R/D. These similar results was also found in the calculations of Rodi [10] and Lee [11] in simulating the flow around the square cylinder. It indicates that the standard $k-\varepsilon$ model is not capable of simulating complex unsteady turbulent flow around a bluff body.

The distributions of the time-averaged streamwise velocity U_{mean} along the centerline are displayed in Figure 4. There the results reflect the recirculation length l_R/D behavior discussed already. The standard $k-\varepsilon$ model overpredicts the length of the recirculation zone considerably; introducing the RNG and Realizable modifications improves the calculations. The approach to the free-stream velocity is however faster than the measurement by Lyn et al. [15]. Turning to the $k-\omega$ calculations, it can be seen from Figure 4 that the standard $k-\omega$ model show an unrealistically distributions of U_{mean} along the centerline while the SST model show better behavior. In the near-wake region, the SST calculations show very good agreement with experiments. The SST results are even superior to those obtained by much more complex RSM model which overestimates slightly the recirculation region. Although the LES model underestimates the recirculation region, it approach the exact free-stream velocity compared with Lyn's measurement.

The distribution of the *rms* value of velocity along the centerline, shown in Figure 5, is determined to be too low if the standard $k-\varepsilon$ model is used. This is due to the overproduction of turbulent kinetic energy in front of the cylinder, resulting in a too strong damping of the periodic shedding motion in the wake of cylinder. It should mentioned that there are considerable differences to the calculations of Rodi [10], who with the same model, obtain a much higher lever of fluctuations. This indicates that the results are sensitive to the details of the simulation parameters. The peak values of fluctuations due to the revised $k-\varepsilon$ models, RNG and Realizable, show slight closing to the experiments. The standard $k-\omega$ model underpredicts the

rms streamwise velocity, while the SST and RSM models overpredicts this quantity. The LES computation gives approximately the correct level and distribution of *rms* streamwise velocity. Turning to the *rms* lateral velocity, the standard $k-\omega$ and RSM models also give an unrealistic level and distribution of this quantity, while the SST and LES models improve the calculations. Due to the underestimation of recirculation region, the LES model yields the pick value of *rms* lateral velocity a little to the left.

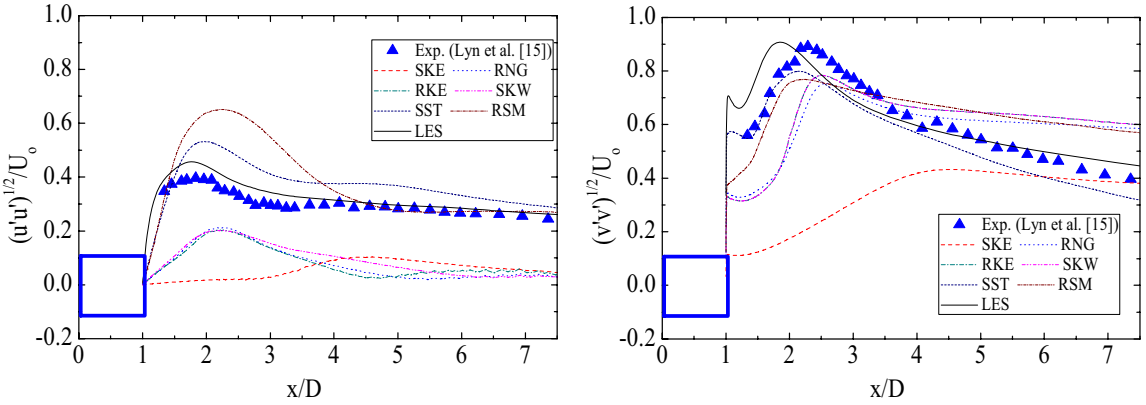

Figure 5. *rms* streamwise velocity and *rms* lateral velocity along the centerline

4. EFFECT OF ASPECT RATIO

The turbulent flow around rectangular cylinders with different aspect ratios ranging from *B/D*=2.0 to *B/D*=10.0 are simulated using SST $k-w$ and LES model in this section. A Reynolds number of 21400 is again performed. Mean drag coefficients, Strouhal number, and *rms* value of lift coefficients of present work are compared in Figure 7 with the wind tunnel experimental results and results of other 3D LES simulations.

In general, the present SST and LES results are almost consistent with both the experimental results and other numerical analysis. The mean drag coefficients and the fluctuating lift coefficients decrease monotonically with increasing aspect ratio. According to the experiments conducted by Okajima (1983), the Strouhal number has a minimum value around *B/D*=2.0, and a maximum around *B/D*=3.0. This fact is well reproduced in the present simulation. Figure 8 shows the streamlines of sections with typical aspect ratios of 2.0, 3.0, 5.0 and 8.0 predicted by SST model. As can be seen in Figure 8, the recirculation vortices are generated near the upper and lower face of the *B/D*=2.0 rectangular cylinder, and the flow separated at the leading edge is not reattached to the wall. In addition, the location of the generated of the vortex behind the cross-section is far away from the surface, and result in the relatively small of Strouhal number. For *B/D*=3.0 and *B/D*=5.0 rectangular cylinder, the flow separation at the leading edge is developed and the separated flow cannot detach themselves fully from the surface but reattach above or below the section during a period of vortex shedding. Also, as can be observed in Figure 8(b) and Figure 8(c), the intermittently reattachment, which results in a narrowing of the wake, accompanied by the discontinuity in Strouhal number between *B/D*=2.0 and *B/D*=3.0. Another discontinuity in Strouhal number can be recognized between *B/D*=6.0 and *B/D*=8.0. From the streamlines plot in Figure 8(d), there is a steady reattachment just behind the leading edge of *B/D*=8.0 rectangular cylinder, and flow finally separates at the trailing edge. The transition of the separated flow from a periodical reattachment type to a steady reattachment type, which leads to a increase in Strouhal number, is predicted well in present calculations. As the aerodynamic behavior of rectangular cylinders with different aspect ratios is characterized by

the absence or presence of reattachment of the shear layer, the rectangular cylinders considered in present simulation is divided into three categories: separated type (B/D=1.0 and B/D=2.0), intermittently reattached type (3.0≤B/D≤6.0), and fully reattached type (7.0≤B/D≤10.0).

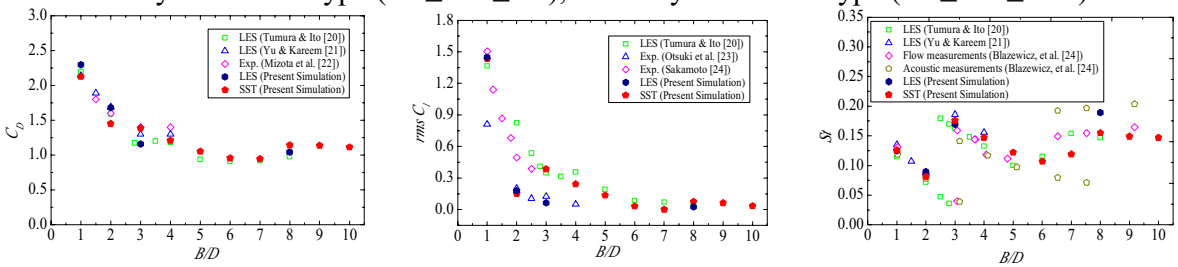

Figure 7. Variation of mean drag coefficients (C_d), Strouhal number (S_t) and *rms* lift coefficients (*rms* C_l) with aspect ratio (B/D), Re=21400

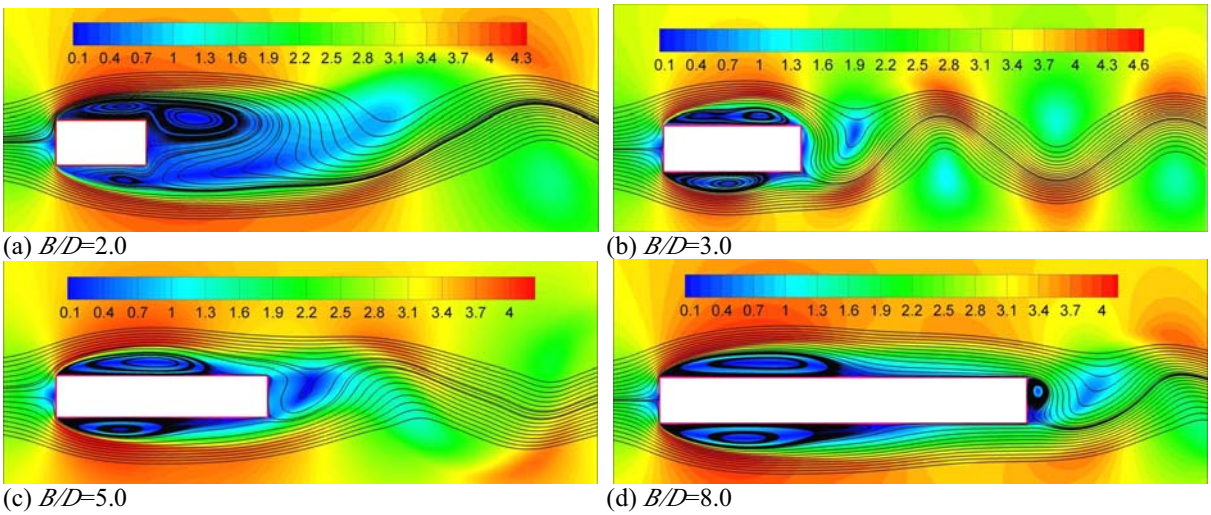

(a) B/D=2.0 (b) B/D=3.0

(c) B/D=5.0 (d) B/D=8.0

Figure 8. Instantaneous velocity contours with streamlines

In Figure 9(a), 10(a) and 11(a), the mean pressure distribution on the side of rectangular cylinders with different aspect ratios is presented. The x-axis in the figure is normalized with the cylinder width. For separated-type rectangular cylinders, the mean pressure remains almost constant along the cylinder surface. The pressure on the side face of B/D=2.0 rectangular cylinder are higher (less negative) than those of a square cylinder, due to the influence of the afterbody on the separated flow. With an increase in the streamwise body width, i.e., aspect ratio, there is a concomitant pressure recovery on the side face due to the reattachment of the flow. Furthermore, the present LES and SST simulations are in good agreement with the experimental data and other LES results.

In Figure 8(b), 10(b) and 11(b), the *rms* pressure fluctuations on the side of rectangular cylinders with different aspect ratios are compared, revealing that for square cylinder and B/D=2.0 rectangular cylinder, a local minimum on the side surface does not exist, but for 3.0≤B/D≤10.0 rectangular cylinders minima are observed. This is also due to the reattachment of the flow. In general, the present simulated *rms* pressure fluctuations are in good agreement with the experimental data and other LES results. However, the present SST simulations slightly underestimate the *rms* pressure fluctuations compared to LES data and experimental results. It should be noted that the total pressure fluctuation includes periodic fluctuation component and stochastic fluctuation component of the pressure, and the stochastic fluctuation component is not

modelled explicitly in any current RANS models. Thus, its value is always underestimated compared to the exact value of its fluctuation.

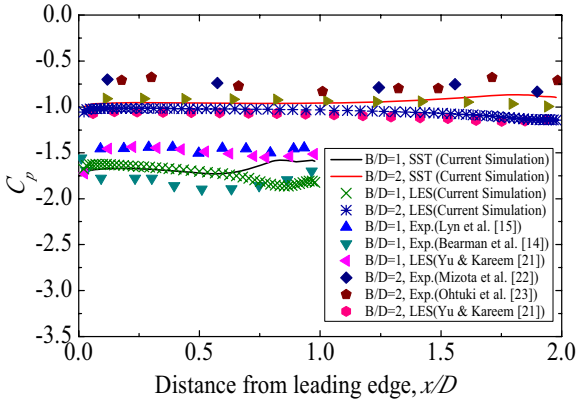

(a) Mean pressure distribution

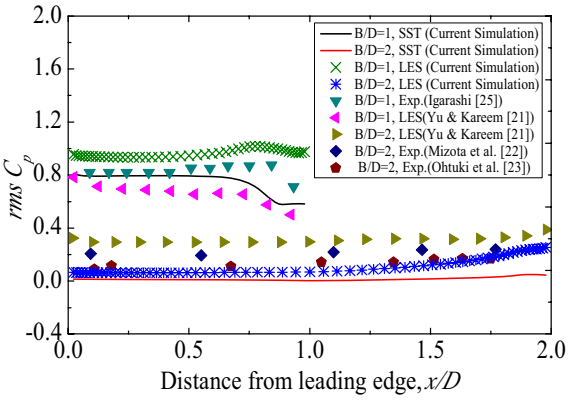

(b) *rms* pressure fluctuations distribution

Figure 9. Comparison of pressure distribution on the side of separated type rectangular cylinders

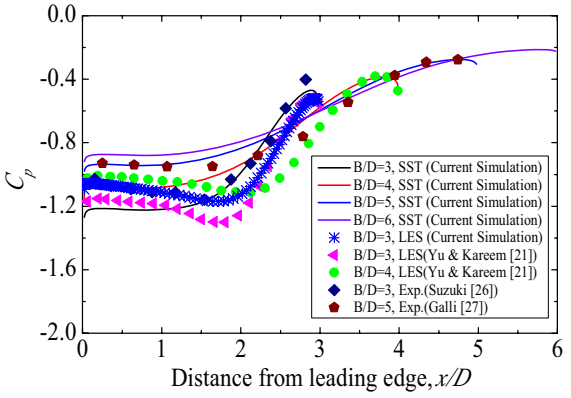

(a) Mean pressure distribution

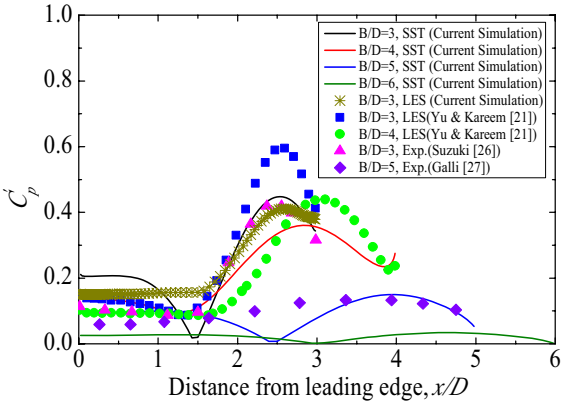

(b) *rms* pressure fluctuations distribution

Figure 10. Comparison of pressure distribution on the side of intermittently reattached type rectangular cylinders

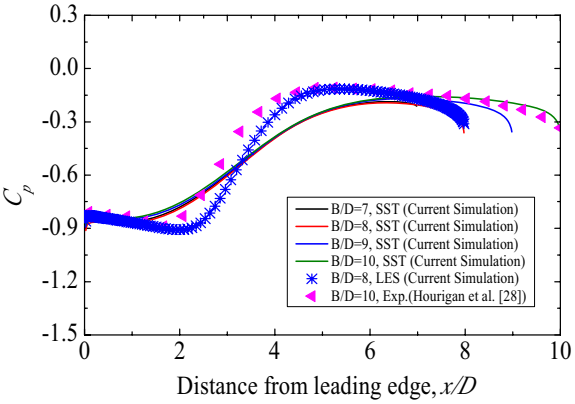

(a) Mean pressure distribution

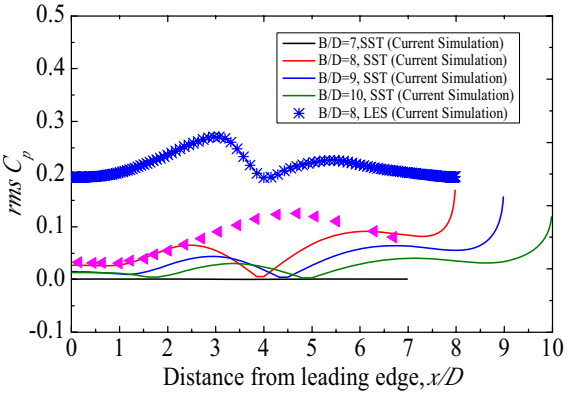

(b) *rms* pressure fluctuations distribution

Figure 11. Comparison of pressure distribution on the side of fully reattached type rectangular cylinders

The 3D flow field around various rectangular cylinders are obtained by LES simulations and the instantaneous vorticity magnitude iso-surface of square cylinder and *B/D*=8.0 rectangular

cylinder are shown in Figure 12. From a qualitative point of view, 3D flow structures clearly appear even though the flow field 2D main features. Generally speaking, the further the location from the separation point at the leading edge, the more significant the 3D features of the flow structures. The wake structure of square cylinder and *B/D*=8.0 rectangular cylinder is irregular and 3D, as clearly seen in Figure 12.

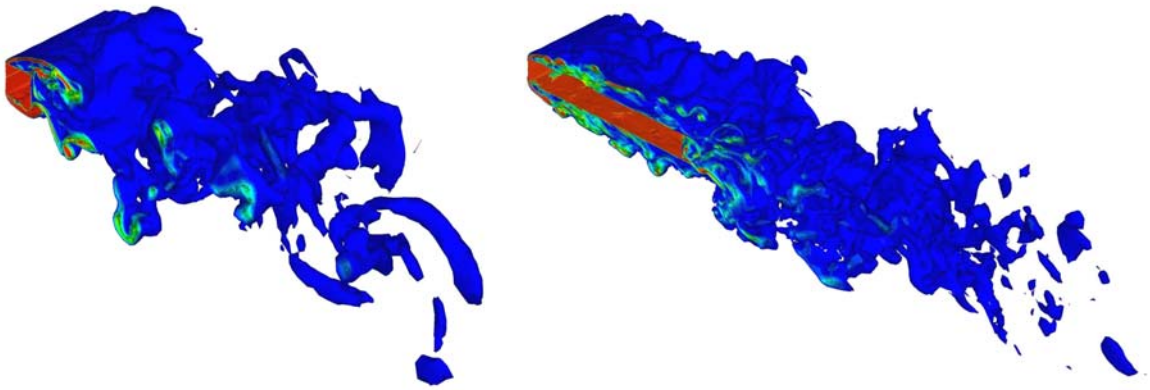

(a) Square cylinder (b) *B/D*=8.0 rectangular cylinder
Figure 12. 3D instantaneous vorticity magnitude

4. CONCLUSIONS

Numerical simulation results of unsteady flows with zero incidence attack angle over rectangular cylinders at Reynolds number of 21400 has been presented in this paper. Despite the simple geometry of the obstacle, the flow develop in its vicinity is very complex with multiple, unsteady flow, various kinds of vortices and strong curvature. The effectiveness of the turbulence models and numerical treatment for simulating the bluff-body flows are investigated in detail. Some partial conclusions can be made:

(1) The spanwise grid dependent results give an idea of the degree of grid refinement necessary to correctly simulate the 3D flows around bluff bodies.

(2) Seven turbulence models have been tested: the 3D LES model can provide satisfactory prediction for the unsteady flow field features of a square cylinder. 2D RANS approach is able to predict the main features of this complex flow reasonably well, while at the same time not being very CPU demanding. The SST $k-\omega$ model is found to be the best choice among RANS models and has accuracy enough to be suitable for practical problems.

(3) Based on the simulated results of the flow around rectangular cylinders with aspect ratio ranging from *B/D*=2.0 to 10.0, it is found that the mean drag coefficients and the fluctuating lift coefficients decrease with increasing aspect ratio. Between *B/D*=2.0 and 3.0, a discontinuity in Strouhal number occurs duo to intermittently reattachment of separated flow. When the aspect ratio *B/D* reaches to about 7.0, a steady reattachment behind the leading edge occurs, which leads to a increase in Strouhal number. The pressure coefficients distribution of rectangular cylinders, simulated by present 2D SST model and 3D LES model, are found to be almost consistent with both the experimental results.

REFERENCES

1 A. Okajima, Strouhal number of rectangular cylinders, J. Fluid Mech., 123 (1982) 379-398.

2 T. Tamura and Y. Ito, Aerodynamic characteristics and flow structures around a rectangular cylinder with a section of various depth/height ratios. Journal of Structural and Construction of Engineering (Transactions of Architectural Institute of Japan), 486 (1996) 153-162.
3 G. Iaccarino, A. Ooi, P.A. Durbin, et al., Reynolds averaged simulation of unsteady separated flow, International Journal of Heat and Fluid Flow, 24 (2003) 147-156.
4 K. Shinada and T. Ishihara, Application of a modified $k-\varepsilon$ model to the prediction of aerodynamic characteristics of rectangular cross-section cylinders. J. Fluid Struct., 16 (2002) 465-485.
5 A. Sohankar, Large eddy simulation of flow past rectangular-section cylinder: Side ratio effects, J. Ind. Aerodyn., 96 (2008) 640-655.
6 FLUENT, Inc., ANSYS FLUENT 12.0 Theory Guide, 2009.
7 D. Sun, J.S. Owen and N.G. Wright, Application of the $k-w$ turbulence model for a wind-induced vibration study of 2D bluff bodies, J. Ind. Aerodyn., 97 (2009), 77-87.
8 S. Murakami, Overview of turbulence models applied in CWE-1997, J. Ind. Aerodyn., 74-76 (1998) 1-24.
9 C.S. Song, S.O. Park, Numerical simulation of flow past a square cylinder using Patially-Averaged Navier-Stokes model, J. Ind. Aerodyn., 97 (2009) 37-47.
10 W. Rodi, Comparison of LES and RANS calculations of the flow around bluff bodies, J. Ind. Aerodyn., 69-71 (1997) 55-75.
11 S. Lee, Unsteady aerodynamic force prediction on a square cylinder using $k-\varepsilon$ turbulent models, J. Ind. Aerodyn., 67&68 (1997) 79-90.
12 R. Franke, W. Rodi, Calculation of vortex shedding past a square cylinder with various turbulence modelling, in: U. Schuman et al. (Eds.), Turbulent Shear Flows, vol. 8, Springer, Berlin, 1998.
13 H. Lubcke, S.T. Schmidt, T. Rung, et al, Comparison of LES and RANS in bluff-body flow, J. Ind. Aerodyn., 89 (2001) 1471-1485.
14 P.W. Bearman, E. D. Obasaju, An experimental study of pressure fluctuations on fixed and oscillating square-section cylinders, J. Fluid Mech., 119 (1982) 297-321.
15 D.A. Lyn, S. Einav, W. Rodi et al, A laser Doppler velocimetry study of ensemble-averaged characteristics of the turbulent near wake of a square cylinder, J. Fluid Mech., 304 (1995) 1471-1485.
16 B.W. van Oudheusden, F. Scarano, N.P. van Hinsberg, et al., Quantitative visualization of the flow around a square-section cylinder at incidence, J. Ind. Aerodyn., 96 (2008) 913-922.
17 S. Sen, S. Mittal and G. Biswas, Flow past a square cylinder at low Reynolds numbers, Int. J. Numer. Meth. Fluids, 67 (2011) 1160–1174.
18 A.K. Saha, K. Muralidhar and G. Biswas, Experimental study of flow past a square cylinder at high Reynolds numbers, Experiments in Fluid, 29 (2000) 553-563.
19 B.E. Lee, The effect of turbulence on the surface pressure field of a square peism, J. Fluid Mech, 69 (Part 2) (1975) 263-282.
20 T. Tumura and Y. Ito, Aerodynamic characteristics and flow structures around a rectangular cylinder with a section of various depth/breadth ratios. Journal of Structure and Construction Engineering (Transactions of Architectural Institute of Japan), 486 (1996) 153-162.
21 D. Yu and A. Kareem, Parametric study of flow around rectangular prisms using LES, J. Ind. Aerodyn., 77&78 (1998) 653-662.
22 T. Mizota, H. Yamada, Y. Kubo, et al., Aerodynamic characteristics of fundamental structures, Part 1, Section 2, J. Ind. Aerodyn., 36 (1988) 50-52 (in Japanese).
23 Y. Otsuki, K. Fuju, K. Washizu, et al., Wind tunnel experiments on aerodynamic forces and pressure distributions of rectangular cylinders in a uniform flow, Proceedings of the Fifth Symposium on Wind Effects on Structures, pp. 169-176.
24 A.M. Blazewicz, M.K. Bull and R.M. Kelso, Characteristics of flow regimes for single plates of rectangular cross-section, Proceedings of the 16th Australasian Fluid Mechanics Conference, Crown Plaza, Gold Coast, Australia, 2007, pp. 935-938.
25 T. Igarashi, Characteristics of flow around a square prism, Bull, JEME 27 (231) (1984) 1858-1865.
26 M. Suzuki, T. Tamura, T. Asajina, et al., A study on aerodynamic sound generated from 2D rectangular cylinder-examination of separation and reattachment flow pattern, Proceedings of the 17th National Symposium on Wind Engineering, Tokyo, Japan, pp. 95-100.
27 F. Galli, Comportamento aerodinamico di strutture snelle non profilate: approccio sperimentale e computazionale. Master's thesis, Politecnico di Torino, Turin, Italy, 2005 (in Italian).
28 K. Hourigan, R. Mills, M.C. Thompson, et al., Base pressure coefficients for flows around rectangular plates, J. Ind. Aerodyn., 49 (1993) 311-318.

The Seventh International Colloquium on Bluff Body Aerodynamics and Applications (BBAA7)
Shanghai, China; September 2-6, 2012

Surface pressures on rectangular cylinders – the dependence on aspect ratio, wind structure and angle of wind attack

Tomasz Lipecki [a], Jarosław Bęc [b], Ewa Błazik-Borowa [c]

[a]*Lublin University of Technology, Lublin, Poland, t.lipecki@pollub.pl*
[b]*Lublin University of Technology, Lublin, Poland, j.bec@pollub.pl*
[c]*Lublin University of Technology, Lublin, Poland, e.blazik@pollub.pl*

ABSTRACT: The paper deals with the results obtained in measurements of vertically placed rectangular cylinders in the wind tunnel. The distributions of mean wind pressure coefficients C_p on the cylinders surfaces were analyzed. The influence of the following aspects was taken into account: 1. wind structure (described by the mean wind speed profile, the turbulence intensity profile, the power spectral density functions), 2. the angle of wind attack, 3. aspect ratio of models, 4. side ratio of the cross-sections of models. The results presented during the 13th ICWE, 2011 are developed here in this paper.

KEYWORDS: rectangular cylinder, wind tunnel, pressure coefficient, surface distribution, aspect ratio, side ratio, wind structure, angle of wind attack.

1 INTRODUCTION

Wind load acting on tall buildings of square or rectangular cross-sections was reported by many researchers who carried out model or full-scale studies as well as numerical simulations. In general investigations performed in wind tunnels considered 2D or 3D models more often of square than of rectangular cross-sections.

Wind action on 3D models were investigated by: Kareem and Cermak (1984) (square, the influence of turbulence), Kareem (1990) (rectangle with side ratio of 1:1.5, the influence of turbulence), Surry and Djakovich (1995) (square and the modified cross-section – diamond or with cut edges, the influence of boundary layer), Sitheeq et al. (1997) (square, the influence of boundary layers), Huang and Chen (2007) (square, different heights), Kim and Kanda (2010) (square and modified cross-sections – with a step changing and tapered), Butler et al. (2010) (square with different aspect ratio, the case of gust front profile which occurs before the storms), Wacker (1994) (rectangles with side ratios of 3:1, 2:1, 1.5:1, 1:1, 1:1.5, 1:2, 1:3, and different heights), Liang et al. (2002) and Liang et al. (2004) (rectangles with side ratios of 1, 2, 3, 4 and different heights), Lin et al (2005) (square and rectangles with side ratios of 0.34, 0.5, 0.63, 1.0, 1.59, 2.0, 2.98, the influence of elevation, aspect ratio and side ratio), Butler and Kareem (2007) (rectangles with side ratios of 1:1.5 (0.67) and 1.5:1 (1.5) different boundary layer), Tamura et al. (2008) (square and rectangles with side ratios of 0.34, 0.4, 0.5, 1 and different heights, the angle of wind attack), Zasso et al. (2008) (rectangle with side ratio of 1:2.56, the influence of turbulence and the angle of wind attack (±90°), Cheng and Tsai (2009) (square and rectangles with side ratios of 1:5, 1:4, 1:3, 1:2, 1:1, 2:1, 3:1, 4:1, 5:1 and aspect ratios of 3, 4, 5, 6 and 7, different boundary layers), Zhang and Gu (2009) (rectangles with side ratios of 1:1, 1:1.5, 1:2, 1:3, 1.5:1, 2:1, and 3:1, two cases of boundary layer), Bartoli and Riciardelli (2010) (rectangle with side ratio of 1:1.5, two different heights, two cases of boundary layer).

Wind load changes associated with the angle of wind attack, with the side ratio of the cross-section and with aspect ratio of the model as well as with the influence of approaching flow characteristics are examined here in this paper.

2 RESEARCH DESCRIPTION

2.1 *Models*

The experiments were carried out in the boundary layer wind tunnel of the Wind Engineering Laboratory in Cracow, Poland. The rectangular cylinders were placed vertically on the rotational table in the working section of the wind tunnel (Fig. 1c). Pressures in points located on surfaces of five models of dimensions collected in Table 1 were measured.

The influence of the slenderness ratio (aspect ratio) of the model (H/B, H = height of the model, B = longer side of cross-section) as well as the slenderness ratio (side ratio) of the cross-section (B/D, D = shorter side of the cross-section) on pressure patterns was investigated. So, three models with side ratio of 2:1 (1:2) and two models with side ratio of 1:4 (4:1) and different aspect ratios were considered.

All measurements were performed for the angle of wind attack, which was changing from 0˚ (the flow is parallel to longer side of the cross-section) to 90° with the step of 15°.

Table 1. Models used in wind tunnel tests.

Model	*H*	*B*	*D*	*H*/*B*	*B*/*D*
	[cm]	[cm]	[cm]	[-]	[-]
R1	100	40	20	2.5	2
R2	100	40	10	2.5	4
R3	100	20	10	5	2
R4	100	20	5	5	4
R5	100	10	5	10	2

2.2 *Wind conditions*

The influence of wind characteristics – wind mean speed profiles, turbulence intensity profiles and PSD functions – on the mean pressure coefficient distributions were examined. Over 40 cases of flows were analysed in details, and for further measurements six of them were selected. Information about wind field can be found in by: Bęc et al. (2011), Lipecki et al. (2011, 2012).

2.3 *Experiment set-up*

Pressure taps were installed on the circumference of each cylinder at 16 level distributed along the height as it is presented in Figure 1a, b. The top covers of models were also equipped with pressure taps in order to discover the influence of 3-D flow.

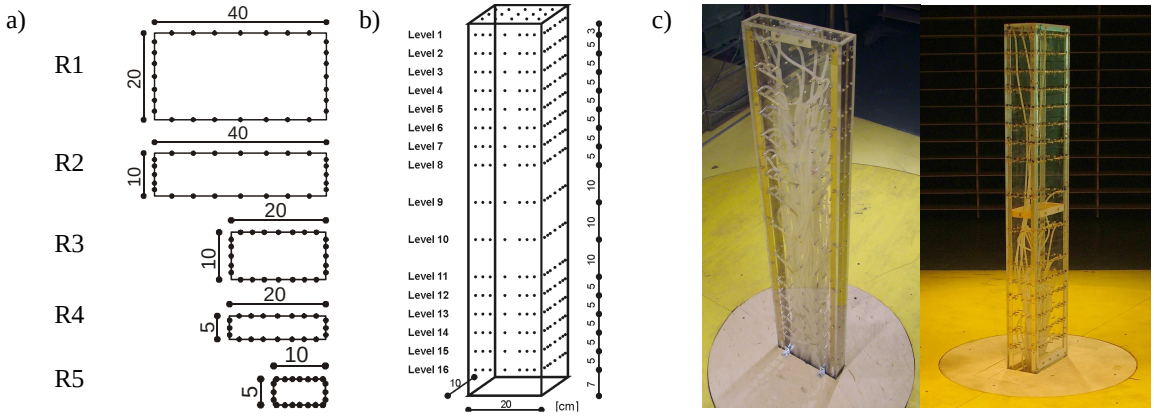

Figure 1. Models: a) pressure taps around circumference, c) pressure taps along height, c) views in the wind tunnel.

Mean pressure coefficients were calculated according to the rule:

$$C_p = p / p_0 \quad (1)$$

where: p = mean dynamic pressure measured at the given location on the cylinder surface, p_0 = reference mean dynamic pressure calculated from: $p_0 = 0.5\rho v_0^2$, where: ρ = 1.25 kg/m^3 = air density, v_o = wind velocity measured in the right front of the model in undisturbed flow at the height of h = 70 cm. Values of mean pressure coefficients were calculated from 6000 steps, with sample frequency 500 Hz which gave time of averaging t equal to 30 sec.

3 RESULTS

3.1 *Surface pressure distribution*

Chosen results concerning: spatial distributions of C_p on windward, leeward and side walls; circumferential distributions at different horizontal levels; vertical distributions of C_p in different vertical cross-sections are presented below with respect to different cases of the approaching flow and changes in the angle of wind attack.

Surface distributions of C_p for the model R2 are presented in Figures 2-6. Results concern changes of C_p in dependence on the angle of wind attack in case of profile 1 (Fig. 2) and in dependence on wind structure for angles 0° and 90° (Figs 3 and 4). The angle of wind attack equal to 0° was established at the position in which the longer side is perpendicular to the mean wind direction. In such position A is a windward wall, B and D – side walls, C – leeward wall. Figures 5-6 are focused on differences in C_p values between models in two cases of wind attack angles – 0° and 90° and for profile 1. For symmetric orientations (0° and 90°) the distributions on walls B and D (angle 0°) and on A and C (angle 90°) are similar, so, only one wall is presented. Limits of C_p values are the same in each figure according to the legend (C_{pmax} = 1.6, C_{pmin} = -1.8).

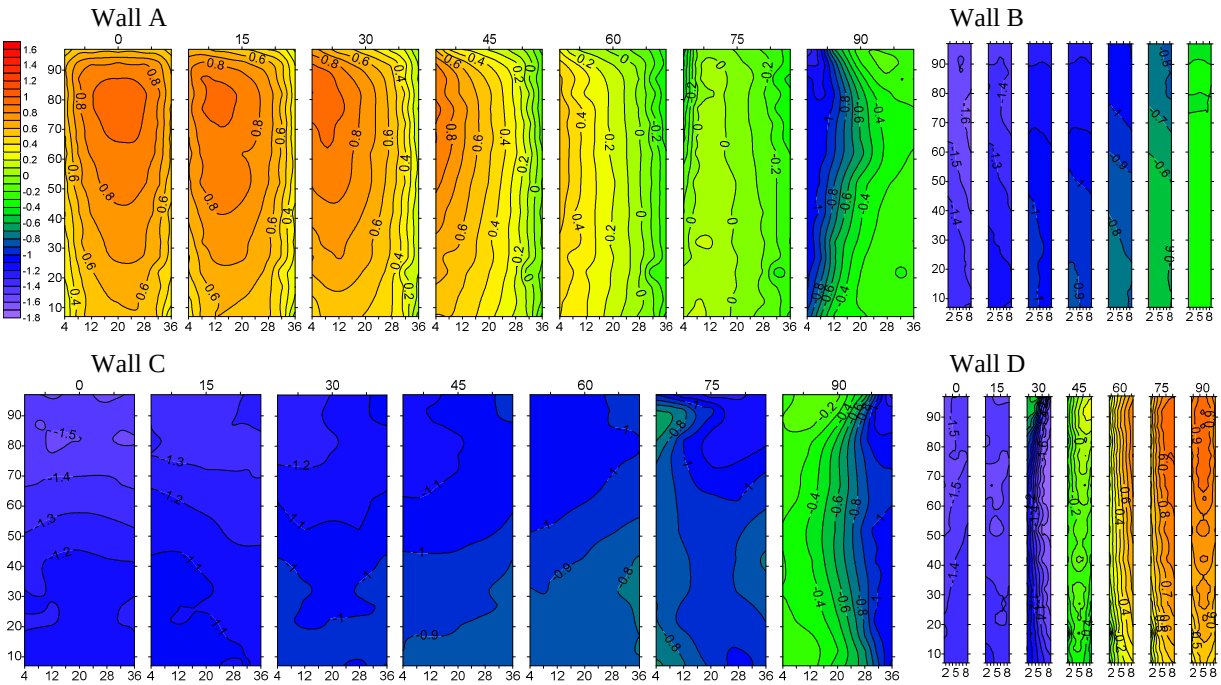

Figure 2. Pressure coefficient C_p, model R2, profile 1, the dependence on the angle of wind attack.

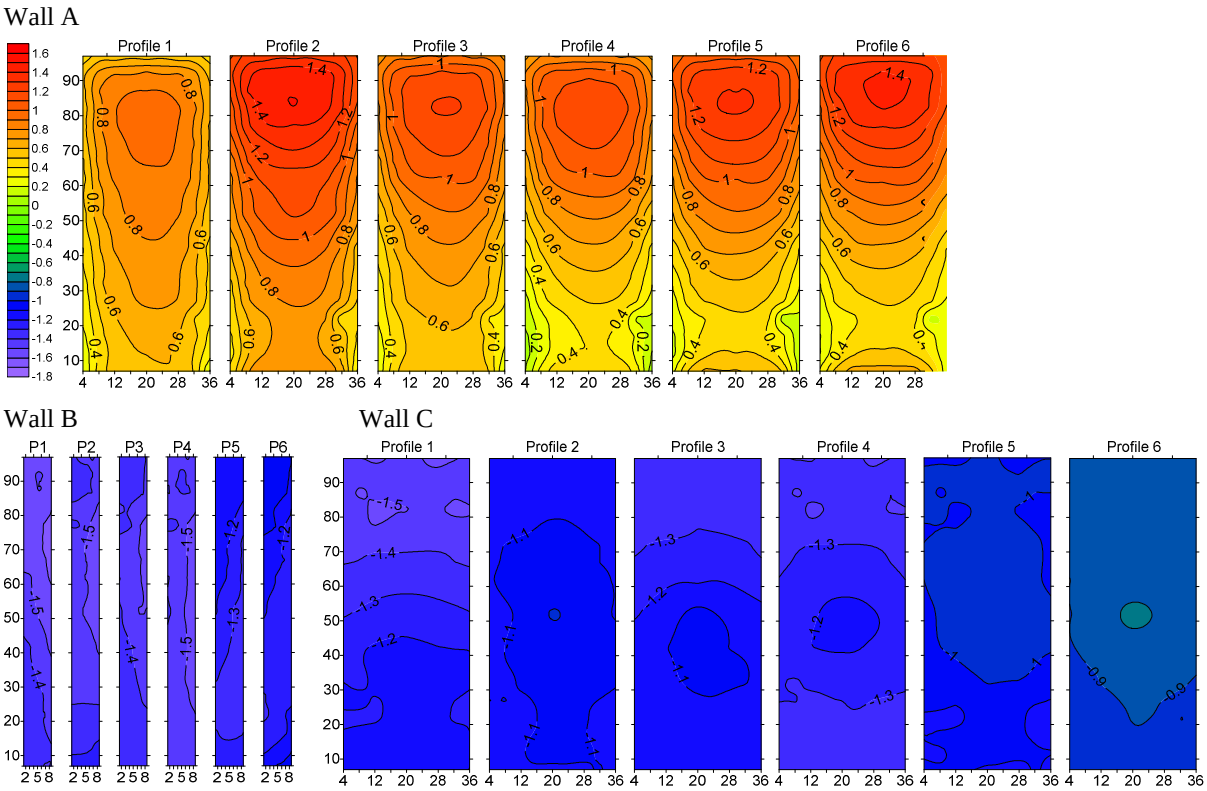

Figure 3. Pressure coefficient C_p, model R2, the angle of wind attack 0°, the dependence on wind structure.

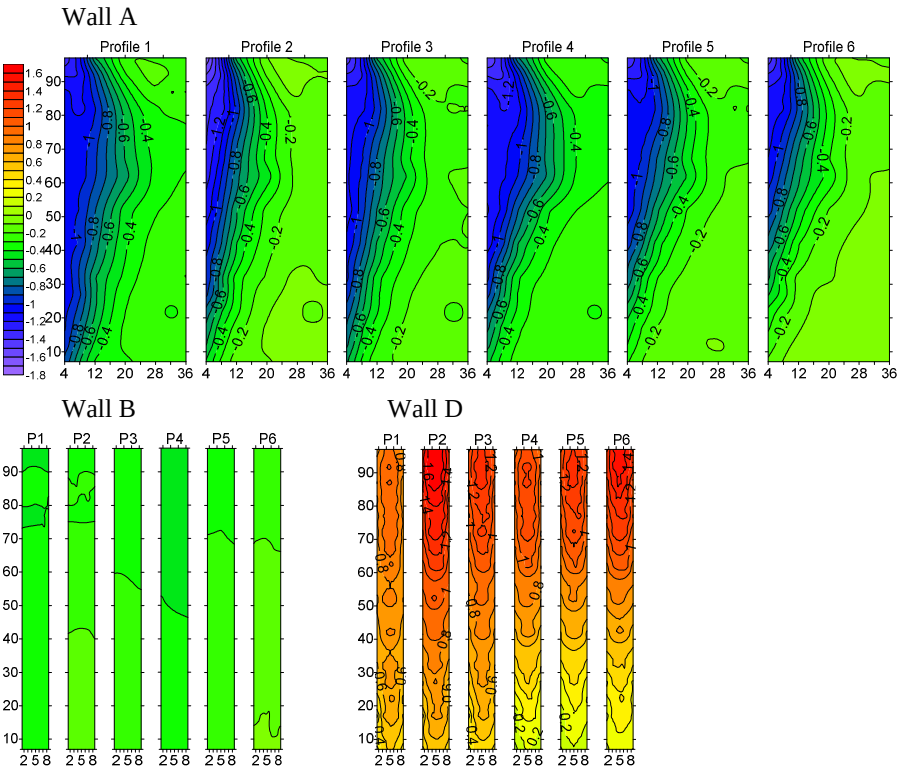

Figure 4. Pressure coefficient C_p, model R2, the angle of wind attack 90°, the dependence on wind structure.

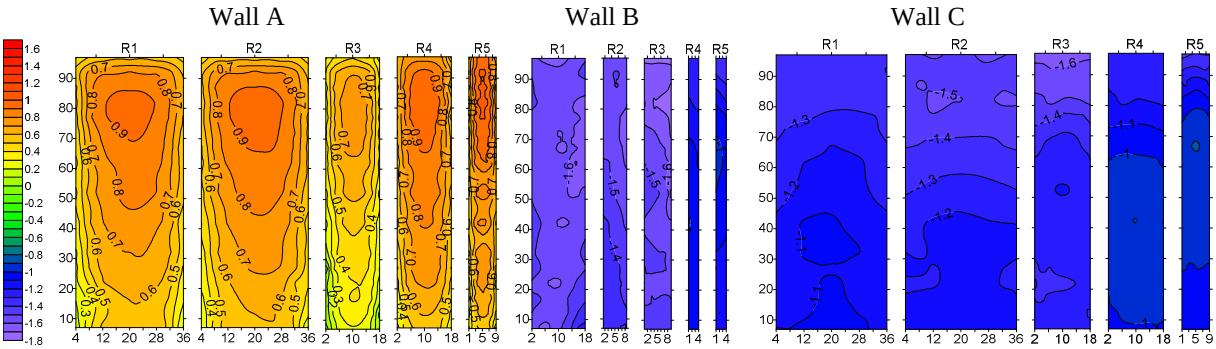

Figure 5. Pressure coefficient C_p, all models, the angle of wind attack 0°, profile 1.

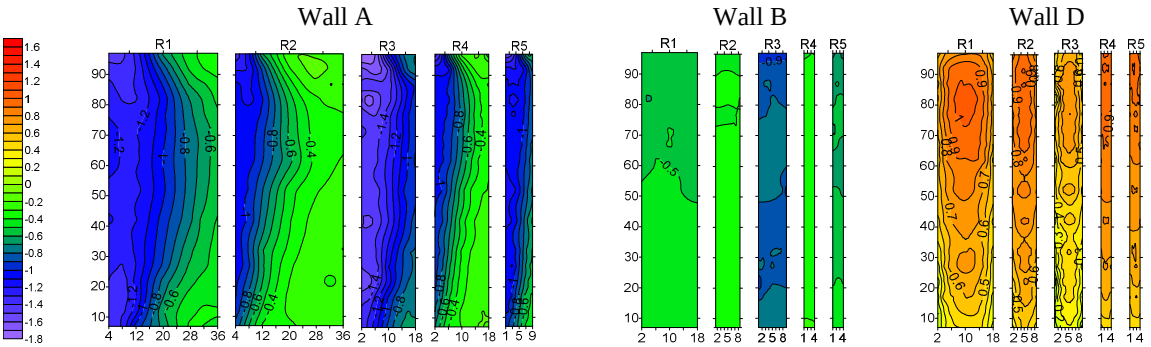

Figure 6. Pressure coefficient C_p, all models, the angle of wind attack 90°, profile 1.

3.2 *Circumferential distributions*

Difference in the value of C_p with respect to the case of the boundary layer can be better noticed at circumferential distribution plots. Three levels (2 – 12 cm, 3D effect associated with the free-end is almost reduced; 9 – 52 cm, the centre of the model; 15 – 12 cm, near the base where the influence of terrain roughness is visible) for two models R1 and R2 are presented in Figures 7-8.

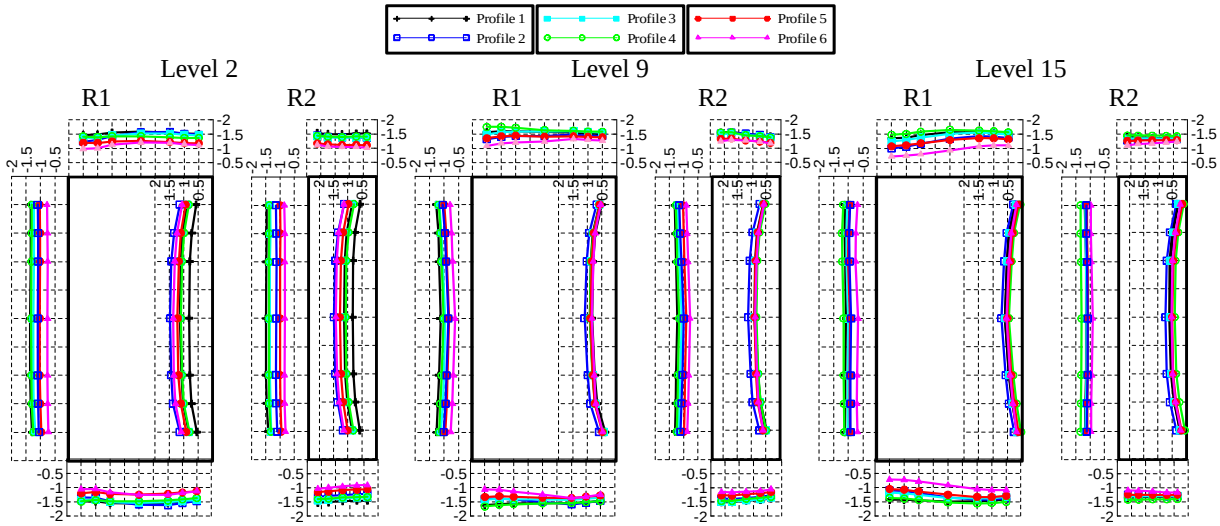

Figure 7. Circumferential distributions of C_p, models R1 and R2, the angle of wind attack 0°, levels 2, 9, 15, the dependence on wind structure.

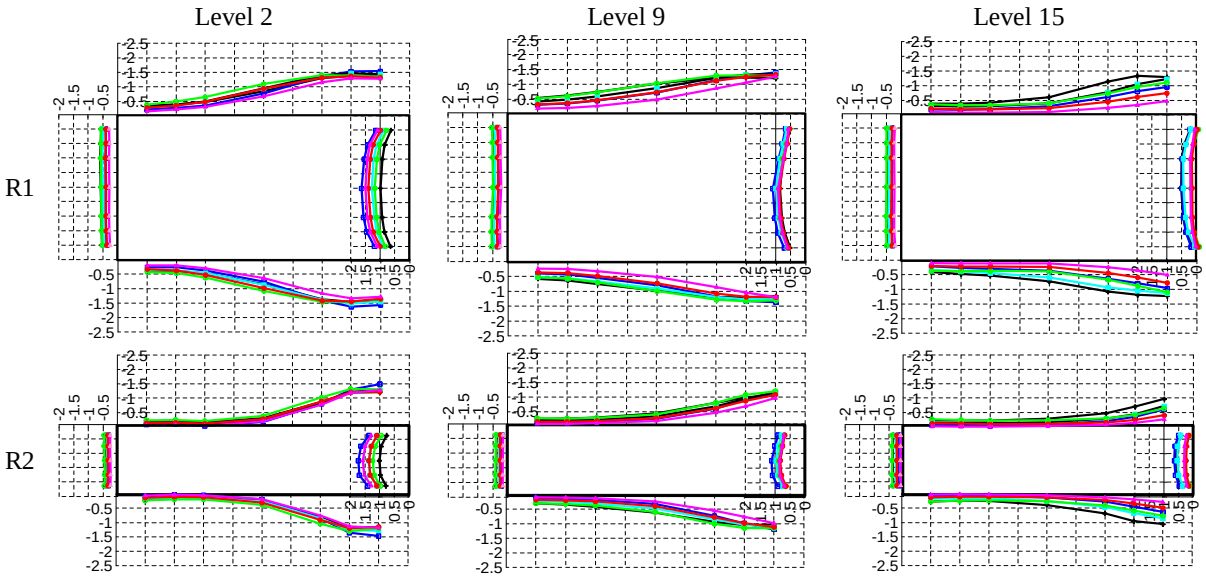

Figure 8. Circumferential distributions of C_p, models R1 and R2, the angle of wind attack 90°, levels 2, 9, 15, the dependence on wind structure.

3.3 *Vertical distributions*

Fluctuation of C_p in different cases of boundary layers along the height of the model for the angle of wind attack 0° together with an explanation of points numbers are presented in Figure 9.

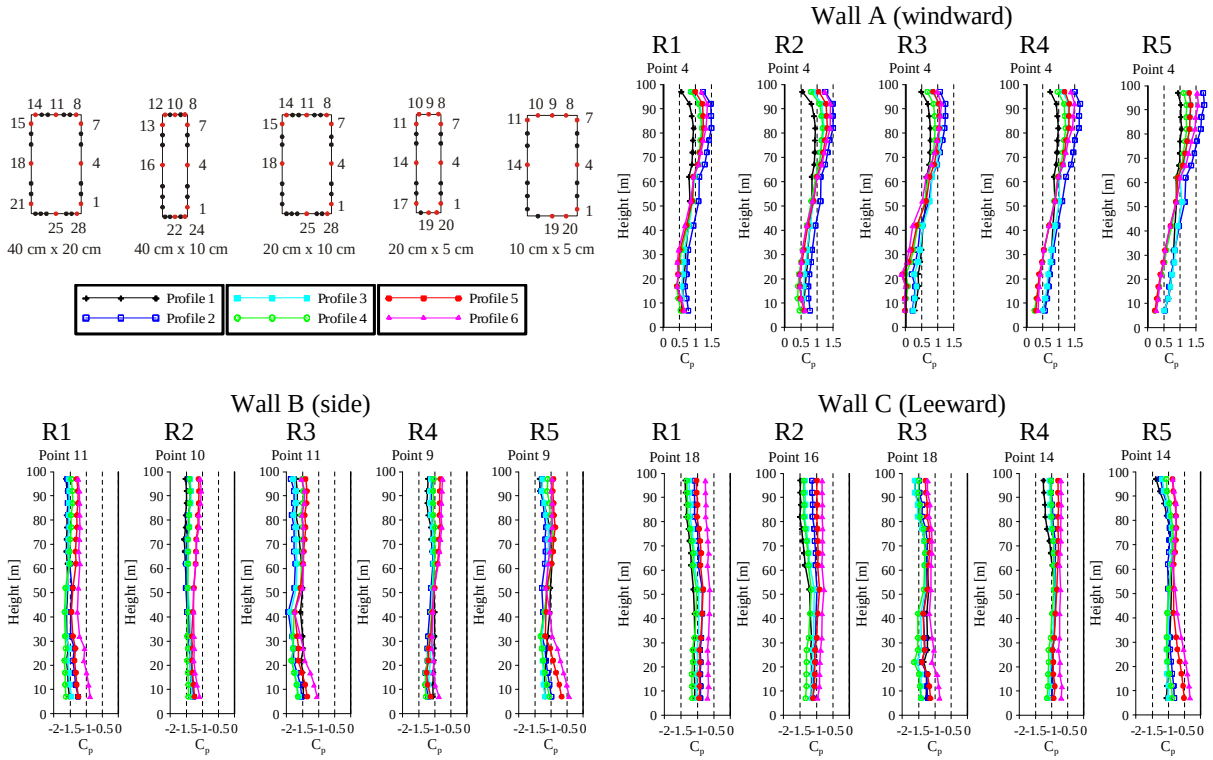

Figure 9. Vertical distributions of C_p, the angle of wind attack 0°, central points of walls, the dependence on wind structure.

4 ANALYSIS OF RESULTS

All three sets of plots illustrate changes of pressure coefficient distribution C_p along the height and around circumference of the model. For angles of wind attack equal to 0° and 90° (Figs 3-4) pressure distributions are symmetrical, pressure occurs on the windward wall, and suction occurs on the side and the leeward walls. The highest values of pressure occur in the middle of windward wall at the height of about 80 - 90% of the model independently from the wind structure. The decrease of pressure appears above this level due to the 3D character of flow around the free-end of the model. On levels lying closer to the base roughness of the terrain increases, and thus the flow turbulence and friction in the boundary layer also increase causing a decrease in wind velocity and then surface pressures. Suction may occur on the windward wall near the edges at the lowest levels. Values of C_p on the windward wall also change along the circumference and reduce close to the edges of the wall. Vortex detachment appears at the edges as a result of friction in the boundary layer and so pressure changes to suction on the side and the leeward walls. The highest values of suction on the side walls are close to the edges with the windward wall.

Analysing changes in the angle of wind attack (Fig. 2) it can be noticed that the lines connecting points of equal values of C_p for angles 15°-75° are arranged in parallel to the vertical edges of the model, with a distinct drop near the top due to 3D flow around the free-end.

Taking into account the surface changes of C_p with respect to models (Figs 5-6) it can be observed that for all cases of flow pressure distributions for all angles are similar, however, there are significant differences in the values. The exemplary percentage differences of C_p values in the case of the model R1 is collected in Table 2 (maximum pressure and suction for all rotations), Tables 3 and 4 (maximum pressure and suction, for angles of wind attack 0° and 90° on particular walls). Comparing C_p distributions by models it appears that higher values of pressure on the windward wall are for smaller models R5 and R4. Almost uniform suction occurs on the side walls and its value is lower for smaller models R5 and R4 for the angle of wind attack 0°. On the other hand, for the angle of 90°, there is the significant decrease in suction on the side walls in direction from the edge with the windward to the leeward wall, and is greater for models R1 and R2, so models with walls of the length of 40 cm. Suction is relatively uniform at particular levels on the leeward wall and increases with the height of the model.

Table 2. Extreme values of C_p, model R1.

	Max pressure	%	location*	Max suction	%	location*
Profile 1	1.044	1	D/90/4	-2.422	1	D/15/1
Profile 2	1.637	56.8	D/90/2	-2.676	10.5	D/15/1
Profile 3	1.294	23.9	D/90/4	-2.64	9.0	D/15/1
Profile 4	1.239	18.7	D/60/4	-2.838	17.2	D/15/1
Profile 5	1.404	34.5	D/90/4	-2.773	14.5	D/15/1
Profile 6	1.505	44.2	D/90/2	-2.325	-4.0	D/15/1

* the location of measuring point: wall/angle/level.

Table 3. Extreme values of C_p, model R1, particular walls, the angle of wind attack 0°.

	Wall A (windward)			Wall B/D (side)			Wall C (leeward)		
	max	%	location*	max	%	location*	max	%	location*
Profile 1	0.934	1	A/4	-1.699	1	B/8	-1.39	1	C/2
Profile 2	1.498	60.4	A/4	-1.695	-0.2	D/1	-1.17	-15.8	C/5
Profile 3	1.21	29.6	A/4	-1.65	-2.9	B/13	-1.274	-8.3	C/3
Profile 4	1.195	27.9	A/4	-1.763	3.8	B/9	-1.358	-2.3	C/3
Profile 5	1.252	34.0	A/4	-1.468	-13.6	B/11	-1.079	-22.4	C/5
Profile 6	1.361	45.7	A/2	-1.371	-19.3	D/10	-0.827	-40.5	C/5

* the location of measuring point: wall/level.

Table 4. Extreme values of C_p, model R1, particular walls, the angle of wind attack 90°.

	Wall D (windward)			Wall A/C (side)			Wall B (leeward)		
	max	%	location*	max	%	location*	max	%	location*
Profile 1	1.044	1	D/4	-1.508	1	c/7/1	-0.631	1	B/4
Profile 2	1.637	56.1	D/2	-1.771	17.4	c/7/1	-0.486	-23.0	B/4
Profile 3	1.294	23.9	D/4	-1.589	5.4	c/7/1	-0.587	-7.0	B/4
Profile 4	1.228	17.6	D/4	-1.526	1.2	c/6/1	-0.622	-1.4	B/4
Profile 5	1.404	34.5	D/4	-1.513	0.3	c/6/1	-0.463	-26.6	B/4
Profile 6	1.505	44.2	D/2	-1.441	-4.4	c/7/1	-0.363	-42.5	B/4

* the location of measuring point: wall/level.

Considering the circumferential distributions of C_p (Figs 7-8) it can be noticed that the order of C_p plots at a given level is similar for different models. The order changes with levels altitude and along side walls for longer walls. For higher cross-sections (level 1), and the angle 0° the lowest pressure is for the profile 1, then 4, 3, 5, 6 and 2. The differences are more apparent in the middle of the cross-section and are better marked for models with aspect ratio of 1:4. On the side walls significantly lower suction is for profiles 5 and 6, higher and similar is for 4, 3, 2, 1. On the leeward wall the lowest suction is for profile 6 then 5 4 3 2 and the highest for 1. Differences on the windward and the leeward walls between profiles are decreasing when the level is getting lower (level 9). At the lowest levels (level 15), these differences increase slightly again and change the sequence of graphs. On the windward wall lower pressure occurs for cases: 6, 5, 4, and higher for 3, 2, 1. At side walls the lowest suction is for 6, the other cases are similar and slightly larger. The difference between the value of C_p close to the windward edge (higher suction) and the leeward edge (lower suction) is larger. On the leeward wall the smallest suction is for profile 6, whereas the highest for 4. In case of the angle equal to 90° observations are generally similar but differences between plots are smaller than for the angle 0°, though they are still significant on the windward wall. The decrease in the suction from the windward to the leeward edge on the side walls is better marked. These differences are lower at levels close to the base. In addition, the sequence of graphs along the wall is changing. For example, the highest suction on the side wall is for the case 2 close to the windward edge, decreases along the wall and becomes one of the smallest at the leeward edge. Values of C_p are nearly constant along the wall and differ slightly between profiles on the leeward wall. The exemplary comparison of percentage changes of C_p around circumference is presented in Tables 5-6 for the model R1, at level 4.

Table 5. Circumferential changes of C_p, model R1, the angle of wind attack 0°, level 4.

	Wall A (windward)			Wall B (side)			Wall C (leeward)		
	max	min	%	max	min	%	max	min	%
Profile 1	0.934	0.47	98.7	-1.64	-1.47	11.6	-1.363	-1.329	2.6
Profile 2	1.498	0.94	59.4	-1.579	-1.378	14.6	-1.135	-1.087	4.4
Profile 3	1.21	0.671	80.3	-1.574	-1.401	12.3	-1.271	-1.221	4.1
Profile 4	1.195	0.697	71.4	-1.59	-1.342	18.5	-1.322	-1.293	2.2
Profile 5	1.252	0.76	64.7	-1.379	-1.143	20.6	-1.052	-1.011	4.1
Profile 6	1.331	0.872	52.6	-1.214	-1.038	17.0	-0.8	-0.746	7.2

Table 6. Circumferential changes of C_p, model R1, the angle of wind attack 90°, level 4.

	Wall A (side)			Wall B (leeward)			Wall D (windward)		
	max	min	%	max	min	%	max	min	%
Profile 1	-1.353	-0.472	186.7	-0.631	-0.529	19.3	1.044	0.576	81.3
Profile 2	-1.521	-0.301	405.3	-0.486	-0.388	25.3	1.575	0.974	61.7
Profile 3	-1.435	-0.452	217.5	-0.587	-0.474	23.8	1.294	0.744	73.9
Profile 4	-1.376	-0.548	151.1	-0.622	-0.53	17.4	1.228	0.724	69.6
Profile 5	-1.372	-0.398	244.7	-0.463	-0.38	21.8	1.404	0.837	67.7
Profile 6	-1.282	-0.238	438.7	-0.363	-0.267	36.0	1.442	0.884	63.1

Considering vertical distributions (Fig. 9) it can be seen that for the windward wall, for higher levels the order of C_p plots is as follows: the highest values are for case 2, then 6, 5, 3, 4, 1. The coefficient obtained for the profile 2 at the bottom levels is almost equal to coefficients for cases 3 and 1, which give the highest values. The lowest values at the bottom are for profiles 6, 5, 4. The vertical distributions clearly show the dependence of the mean wind pressure coefficient on the mean wind speed profile. Above 70 cm (reference point) the sequences of C_p plots and profiles is the same. At bottom levels, this relationship is not unique due to the strong influence of turbulence. Changes of C_p along the height of the model are insignificant in the case of profile 1, while for the other profiles, these fluctuations are relatively high. The lowest suction on the side walls occurs for cases 6 and 5 almost along the whole height. The profile 1 produces the highest values of C_p at the top and one of the lowest at the base whereas highest suction at base is for profiles 3 and 4. Quite similar sequence of plots appears at the leeward wall and differences between profiles along the height seem to be smaller. An example of percentage changes of C_p value along the height is presented in Tables 7-8 in case of the model R1, for central points of walls (Fig .9)

Table 7. Vertical changes of C_p, model R1, the angle of wind attack 0°, points 4, 11, 18 (centre lines of walls).

	Wall A, point 4			Wall B, point 11			Wall C, point 18		
	max	min	%	max	min	%	max	min	%
Profile 1	0.934	0.556	68.0	-1.627	-1.52	7.0	-1.37	-1.077	27.2
Profile 2	1.498	0.67	123.6	-1.586	-1.251	26.8	-1.092	-0.853	28.0
Profile 3	1.21	0.568	113.0	-1.646	-1.455	13.1	-1.247	-0.95	31.3
Profile 4	1.195	0.417	186.6	-1.672	-1.422	17.6	-1.324	-1.021	29.7
Profile 5	1.252	0.423	196.0	-1.457	-1.247	16.8	-1.031	-0.827	24.7
Profile 6	1.361	0.429	217.2	-1.273	-0.876	45.3	-0.759	-0.626	21.2

Table 8. Vertical changes of C_p, model R1, the angle of wind attack 90°, points 4, 11, 25 (centre lines of walls).

	Wall A, point 4			Wall B, point 11			Wall C, point 25		
	max	min	%	max	min	%	max	min	%
Profile 1	-1.067	-0.611	74.6	-0.58	-0.462	25.5	1.044	0.403	159.1
Profile 2	-0.918	-0.291	215.5	-0.404	-0.292	38.4	1.63	0.44	270.5
Profile 3	-1.086	-0.4	171.5	-0.5	-0.4	25.0	1.294	0.369	250.7
Profile 4	-1.205	-0.402	199.8	-0.559	-0.489	14.3	1.228	0.161	662.7
Profile 5	-1.041	-0.226	360.6	-0.392	-0.31	26.5	1.404	0.135	940.0
Profile 6	-0.76	-0.095	700.0	-0.281	-0.211	33.2	1.505	0.188	700.5

Connection between C_p and PSD functions of the flow is not unique. It can be found that for profile 2 the highest values of the coefficient were obtained at a height above 70 cm in each case of the model. The maximum of PSD function reaches one of the greatest values at levels above 70 cm for that profile. Similar remarks can be formulated for profile 6, for which the maximum of PSD function is even higher, but the pressure coefficient values are slightly lower. Comparison of spectra for profiles 2 and 6 shows that for low frequencies the higher values of the spectrum were obtained for profile 2, which probably results in higher values of pressure although wind speed is greater for profile 6.

5 CONCLUSIONS

Distribution of pressure coefficient is strongly affected by the wind structure characteristics. The influence of the mean wind speed profile is clear whereas the effect of PSD function and turbulence is not unique and needs to be investigated in details. It can be expected that further

considerations focused on estimation of local and global drag and lift forces will clarify that dependence.

Patterns of C_p for various angles of wind attack are similar for all cases of flows and between models.

Differences in values of C_p appear between various cases of the approaching flow as well as along the height of the model and around the circumference of the cross-section within single profile. Such differences as shown in Tables 2-8 can be significant. Moreover, the change of the sequence of C_p plots for particular flows is possible along the height and the circumference.

The aspect ratio of the models has the influence on values of C_p but the sequences of plots remains the same.

The free-end effect is distinctly marked in each case of the flow and models.

6 REFERENCES

1 A. Kareem, J.E. Cermak, Pressure fluctuations on a square building model in boundary-layer flows, J. Ind. Aerodyn., 16 (1984) 17-41.

2 A. Kareem, Measurements of pressure and force fields on building models in simulated atmospheric flows, J. Ind. Aerodyn., 36 (1990) 589-599.

3 M.M. Sitheeq, A.K.S. Iyengar, C. Farell, Effect of turbulence and its scales on the pressure field on the surface of a three-dimensional square prism, J. Ind. Aerodyn., 69 71 (1997) 461 47l.

4 G., Huang, X. Chen, Wind load effects and equivalent static wind loads of tall buildings based on synchronous pressure measurements, Eng. Struct., 29 (2007) 2641–2653.

5 K. Butler, S. Cao, A. Kareem, Y. Tamura, S. Ozono, Surface pressure and wind load characteristics on prisms immersed in a simulated transient gust front flow field, J. Ind. Aerodyn., 98 (2010) 299–316.

6 D. Surry, D. Djakovich, Fluctuating pressures on models of tall buildings, J. Ind. Aerodyn., 58 (1995) 81-112.

7 Y. Kim, J. Kanda, Characteristics of aerodynamic forces and pressures on square plan buildings with height variations, J. Ind. Aerodyn., 98 (2010) 449–465.

8 J. Wacker, Towards reliability-based local design wind pressures for simple rectangular-shaped buildings, J. Ind. Aerodyn., 53 (1994) 157-175.

9 S. Liang, S. Liu, Q.S. Li, L. Zhang, M. Gu, Mathematical model of acrosswind dynamic loads on rectangular tall buildings, J. Ind. Aerodyn., 90 (2002) 1757–1770.

10 S. Liang, Q.S. Li, S. Liu, L. Zhang, M. Gu, Torsional dynamic wind loads on rectangular tall buildings, Eng. Struct. 26 (2004) 129–137.

11 N. Lin, C. Letchford, Y. Tamura, B. Liang, O. Nakamura, Characteristics of wind forces acting on tall buildings, J. Ind. Aerodyn., 93 (2005) 217–242.

12 K. Butler, A. Kareem, Characteristics of pressure and integral loads on prisms in boundary layer flows, Proc. 12th Int. Conf. on Wind Engineering, Cairns, Australia, 2007.

13 Y. Tamura, H. Kikuchi, K. Hibi, Peak normal stresses and effects of wind direction on wind load combinations for medium-rise buildings, J. Ind. Aerodyn., 96 (2008) 1043–1057.

A. Zasso, A.M. Aly, L. Rosa, G. Tomasini, Wind induced dynamics of a prismatic slender building with 1:3 rectangular section, Proc of the 6th Int. Coll. on Bluff Bodies Aerodynamics & Applications, Milano, Italy, 2008.

C.M. Cheng, M.S. Tsai, Along wind design wind load for tall buildings (I) Results of wind tunnel tests, Proc of the 5th Int. Advanced School on Wind Engineering, The GCOE Program at Tokyo Polytechnic University. Opole, Poland, 2009.

J. Zhang, M. Gu, Distribution of background equivalent static wind load on high-rise buildings, Front. Archit. Civ. Eng. China 3(3) (2009) 241–248.

G. Bartoli, F. Riciardelli, Characterisation of pressure fluctuations on the leeward and side faces of rectangular buildings and accuracy of the quasi-steady loads, J. Ind. Aerodyn., 98 (2010) 512–519

J. Bęc, T. Lipecki, E. Błazik-Borowa, Research on wind structure in the wind tunnel of Wind Engineering Laboratory of Cracow University of Technology, J. of Physics: Conference Series 318, 072003 (2011), doi: 10.1088/1742-6596/318/7/072003.

T. Lipecki, E. Błazik-Borowa, J. Bęc, (2011): Wind structure influence on surface pressures of rectangular cylinders at various angles of wind attack, Proc of the 13th Int. Conf. on Wind Engineering, Amsterdam, Holland.

T. Lipecki, J. Bęc, E. Błazik-Borowa, The response of aeroelastic models of circular cross-sections to wind action, Proc. of the 7th Int. Coll. on Bluff Bodies Aerodynamics & Applications, Shanghai, China, 2012.

The Seventh International Colloquium on Bluff Body Aerodynamics and Applications (BBAA7)
Shanghai, China; September 2-6, 2012

Coupling investigation on Vortex-induced vibration and Galloping of rectangular cylinders

Claudio Borri [a], Shuai Zhou [*,a, b], Zhengqing Chen [b]

[a] *CRIACIV/Department of Civil and Environmental Engineering, University of Florence, Via S. Marta, 3, Firenze, Italy*
[b] *Wind Engineering Research Center of Hunan University, Changsha, Hunan, China*
* *First and corresponding author*

ABSTRACT: Vortex induced vibration (VIV) is caused by regular alternatively shedding vortices from structure surface; the critical wind velocity where vibration onset can be approximately calculated by Strouhal relation. While, according to quasi-steady galloping theory, the galloping occurrence is originated from aerodynamic instability of specific structure cross sections. The negative slope of lift force coefficient of cross sections is an essential condition to predict the onset velocity of galloping. For those structures, where critical wind velocity by VIV and galloping are very close, the actual structural vibration type is unknown. With the aim of knowing more about the mechanism of this new type vibration, several comparable experiments of rectangular cylinders were conducted; the main results are reported in the present paper. The different experimental cylinders varied in aspect ratios and Scruton numbers. When the predicted critical wind velocity of VIV and galloping were very close to each other, the test results indicated that the cylinders tended to undergo a very different vibration type. There was neither VIV lock-in phenomenon nor galloping divergent type vibration, but consistently increasing vibration amplitude with increased wind velocity. While, for the cases of predicted VIV and galloping critical velocities were deviated largely, the VIV lock-in and divergent type galloping were observed separately. And it is seems that the interaction of VIV and galloping brought relatively large VIV amplitude during lock-in range.

KEYWORDS: Interaction; VIV; Galloping; Amplitude; Rectangular cylinders; Onset velocity

1 INTRODUCTION

Slender structures such as the hangers of large span arch bridges, lateral beams of electricity transmission towers .etc, are inclining to wind induced vibrations. In particular, for the rectangular cross section hangers, the VIV and galloping are the two most frequently occurred vibrations. (Chapin and Bearman, 2005a; Ge, 2008).

To predict the critical wind velocity at which VIV onset in engineering practices, Strouhal relation was used as the most efficient method. The Strouhal number was determined by the structural cross section, Reynolds number, surface roughness, turbulence intensity .etc. Over the past decades' research concerning VIV, mathematical models were developed to describe the vortex excited force and predict the VIV lock-in range; well known reviews about these topics were given by Bearman (1984), Sarpkaya (2004) and Williamson and Govardhan (2004). These models can be basically classified into single Degree of Freedom (SDOF) and two DOF two types in total. Moreover, the SDOF model subdivided into force coefficient based model and negative aerodynamic damping based model. With the beforehand identified aerodynamic parameters, the prevailing Van der Pol-type nonlinear model was verified to reflect the VIV lock-in very well.

Similarly, in order to determine the galloping instability critical point, a relation derived from quasi-steady galloping theory is also available. It takes the consistently changed static force which was caused by relative motions between structure and flow as the original force for galloping instability. The negative slope of lift force coefficient of cross section is an essential requirement for the galloping occurrence, and the onset velocity is positively proportional to the Scruton number and natural frequency. The vibration is considered to divergent after the critical wind velocity threshold which calculated from quasi-steady galloping theory. Nevertheless, Ziller and Ruscheweyh (1997) suggested a new approach to determine the onset velocity of galloping instability, taking into account the nonlinearity of the aerodynamic damping characteristic. Hortmanns and Ruscheweyh (1997) even developed a method to calculate galloping amplitudes considering nonlinear aerodynamic coefficients measured with the forced oscillation method.

To the authors' knowledge, the mechanisms of VIV and galloping are very different, so that the critical wind velocities of these two kinds of vibration can be obtained separately. Therefore, for certain structures, if the critical wind velocity of VIV and galloping are very close, the vibration mechanism is hard to be predicted. More importantly, the better understanding of the mechanism is pretty helpful for the following design of vibration suppressions measures, like the design of tuned mass damper.

2 THEORETICAL ANALYSES

2.1 VIV

The nonlinear vortex induced excitation force model suggested by Scanlan and Ehsan (1990), which was characterized by Van der Pol-type oscillator, the vortex induced excitation force was expressed as follow:

$$P(t)=\frac{1}{2}\cdot\rho\cdot U^2\cdot D\cdot[Y_1(K)\cdot(1-\varepsilon\cdot\frac{v(x,t)^2}{D^2})\frac{\dot{v}(x,t)}{U} + Y_2(K)\cdot\frac{v(x,t)}{D}+\frac{1}{2}\cdot\tilde{C}_L(K)\cdot\sin(\omega\cdot t+\phi)] \tag{1}$$

Where, $v(x,t)$ = the structural displacement response; $Y_1(K)$, $Y_2(K)$, ε, $\tilde{C}_L(K)$, ϕ =the aerodynamic coefficients; ρ = the air density; U =mean wind velocity; D =cross flow dimension; ω = vortex shedding frequency.

For structures undergoing VIV by wind action, the vibration frequency was almost identical to the natural frequency, hence, the aerodynamic stiffness term was negligible (Zhu, 2005); then Eq.(1) became:

$$P(t)=\frac{1}{2}\cdot\rho\cdot U^2\cdot D\cdot[Y_1(K)\cdot(1-\varepsilon\cdot\frac{v(x,t)^2}{D^2})\frac{\dot{v}(x,t)}{U}+\frac{1}{2}\cdot\tilde{C}_L(K)\cdot\sin(\omega\cdot t+\phi)] \tag{2}$$

Moreover, during the large amplitude vibration period of lock-in range, the vortex shedding force can also be neglected compared to the motion induced one, then the final vortex induced excitation force formula was simplified as:

$$P(t)=\frac{1}{2}\cdot\rho\cdot U^2\cdot D\cdot[Y_1(K)\cdot(1-\varepsilon\cdot\frac{v(x,t)^2}{D^2})\frac{\dot{v}(x,t)}{U}] \tag{3}$$

Marra et al. (2011) had proved its accuracy to describe the VIV by the beforehand identified aerodynamic coefficients $Y_1(K)$, ε.

The critical wind velocity at which vibration starts off is set by Strouhal relation, defined as following:

$$St = \frac{f \cdot D}{U} \tag{4}$$

Where, f = natural frequency; St = Strouhal number which is associated with cross section, Reynolds number, surface roughness, turbulence intensity .etc; D = cross flow dimension; U = mean wind velocity.

2.2 Galloping

The aerodynamic force of galloping was originated from continuously changed static force, which was caused by continuously changed relative wind attack angle between structure and approaching flow. (Chen, 2005; Borri et al, 2002).Ignoring the unsteady flow around the structure, the quasi-steady galloping theory was employed. Uniform flow passed through the bluff body, the 2D flow condition was shown in Fig.1.

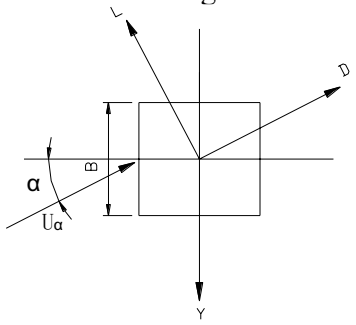

Fig.1. Plane of 2D flow condition

Under the coordinate system of wind direction, the static drag force and lift force assume following form:

$$D(\alpha) = \frac{1}{2}\rho U_\alpha^2 B C_D(\alpha) \tag{5}$$

$$L(\alpha) = \frac{1}{2}\rho U_\alpha^2 B C_L(\alpha) \tag{6}$$

Where, $C_D(\alpha)$ = drag force coefficient; $C_L(\alpha)$ = lift force coefficient; α = relative wind attack angle; B = cross flow dimension; U_α = mean wind velocity.

The combined vertical force F_y obtained:

$$
\begin{aligned}
F_y &= \frac{1}{2}\rho U_\alpha^2 B\left(-C_D(\alpha)\cdot\sin\alpha - C_L\cdot\cos\alpha\right) \\
&= \frac{1}{2}\rho U^2 B\left(-C_D(\alpha)\cdot\sin\alpha - C_L\cos\alpha\right)\cdot\frac{1}{\cos^2\alpha} \\
&= \frac{1}{2}\rho U^2 B\left(-C_D\cdot\tan\alpha - C_L\right)\cdot\sec\alpha
\end{aligned}
\tag{7}
$$

Where:

$$
\begin{aligned}
U_\alpha &= \sqrt{U^2+\dot{y}^2} \\
\alpha &= \arctan\frac{\dot{y}}{U}
\end{aligned}
\tag{8}
$$

While, $\dot{y}=\frac{dy}{dt}$ = structural vibration velocity. Spreading the Eq. (7) as Taylor's series at $\alpha=0$, then Eq. (7) became:

$$
F_y = -\frac{1}{2}\rho U^2 B\cdot[(\frac{dC_L}{d\alpha}+C_D)\cdot\alpha+\frac{1}{2}\cdot(C_L+\frac{d^2C_L}{d\alpha^2}+2\cdot\frac{dC_D}{d\alpha})\cdot\alpha^2+\triangle(\alpha^n)] \tag{9}
$$

Before the large amplitude galloping occurs, the tiny vibration velocity $\dot{y}$ is negligible compared to the approaching wind velocity U, and one can assume that:

$$
\alpha = \arctan\frac{\dot{y}}{U} \doteq \frac{\dot{y}}{U} \tag{10}
$$

The relations between $\alpha=\arctan\frac{\dot{y}}{U}$ and $\alpha=\frac{\dot{y}}{U}$ was plotted in Fig.2, from which can be clearly observed that $\alpha=\arctan\frac{\dot{y}}{U}\doteq\frac{\dot{y}}{U}$ when $\frac{\dot{y}}{U}<0.2$. Actually, at the very tiny vibration period, the high order terms of formula (9) are negligible with respect to the fundamental ones, hence, the formula can be simplified as following:

$$
\begin{aligned}
F_y &= -\frac{1}{2}\rho U^2 B\cdot(\frac{dC_L}{d\alpha}+C_D)\cdot\alpha \\
&= -\frac{1}{2}\rho U^2 B\cdot(\frac{dC_L}{d\alpha}+C_D)\cdot\frac{\dot{y}}{U}
\end{aligned}
\tag{11}
$$

The galloping instability onset velocity U_{cri} obtained by the simplified aerodynamic force of formula (11):

$$
U_{cri} = \frac{-4m\xi\omega}{\rho B\left(\frac{dC_L}{d\alpha}+C_D\right)} \tag{12}
$$

Where, m = equivalent mass; ξ = damping ratio; ω = circular natural frequency; the meaning of other symbols just as mention above.

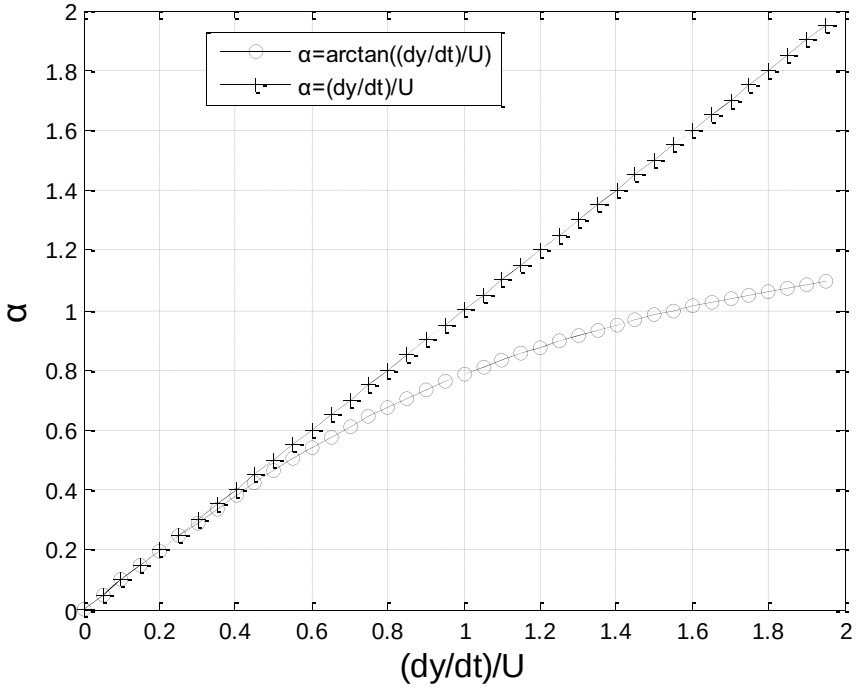

Fig.2. Comparison of $\alpha = \arctan\frac{\dot{y}}{U}$ and $\alpha = \frac{\dot{y}}{U}$

The quasi-steady galloping theory can interpret the galloping onset threshold very clear, and it can be considered that a divergent type vibration after the critical point will appear which is due to the negative damping. However, for the vibration regime after the starting point, the theory cannot help in predicting it. Because, the high order terms of formula (9) cannot be ignored anymore, on the contrary, they played a very important role to the aerodynamic force.

3 EXPERIMENTAL DETAILS

Taking into account the practical engineering background of arch bridge hangers, four groups of rectangular cylinders were selected as section model wind tunnel tests objects. The four groups of cylinders had different cross section aspect ratios, Scruton number and natural frequencies. Static forces tests and flexibly mounted section model tests were performed for each group separately. The section model wind tunnel tests installation set up are shown in Fig.3. Regarding the flexibly mounted section model tests, as shown in the second column of Fig.3, were the flexibly mounted rigid section models. Eight springs supported the model as stiffness system; the physical mass of section model, participating mass of springs and the supporting system mass formed the total mass system. Four force transducers were equipped at the bottom of the model system, connecting the lower four springs with fixed boundary. Vibration signals of heaving, pitching, rolling mode can be easily extracted from the recorded data of the four force transducers.

With respect to the static force tests, just as shown in the third column of Fig.3, rigid section models with end plates were vertically installed in the wind tunnel, the static force measurement scale equipped at the bottom of model.

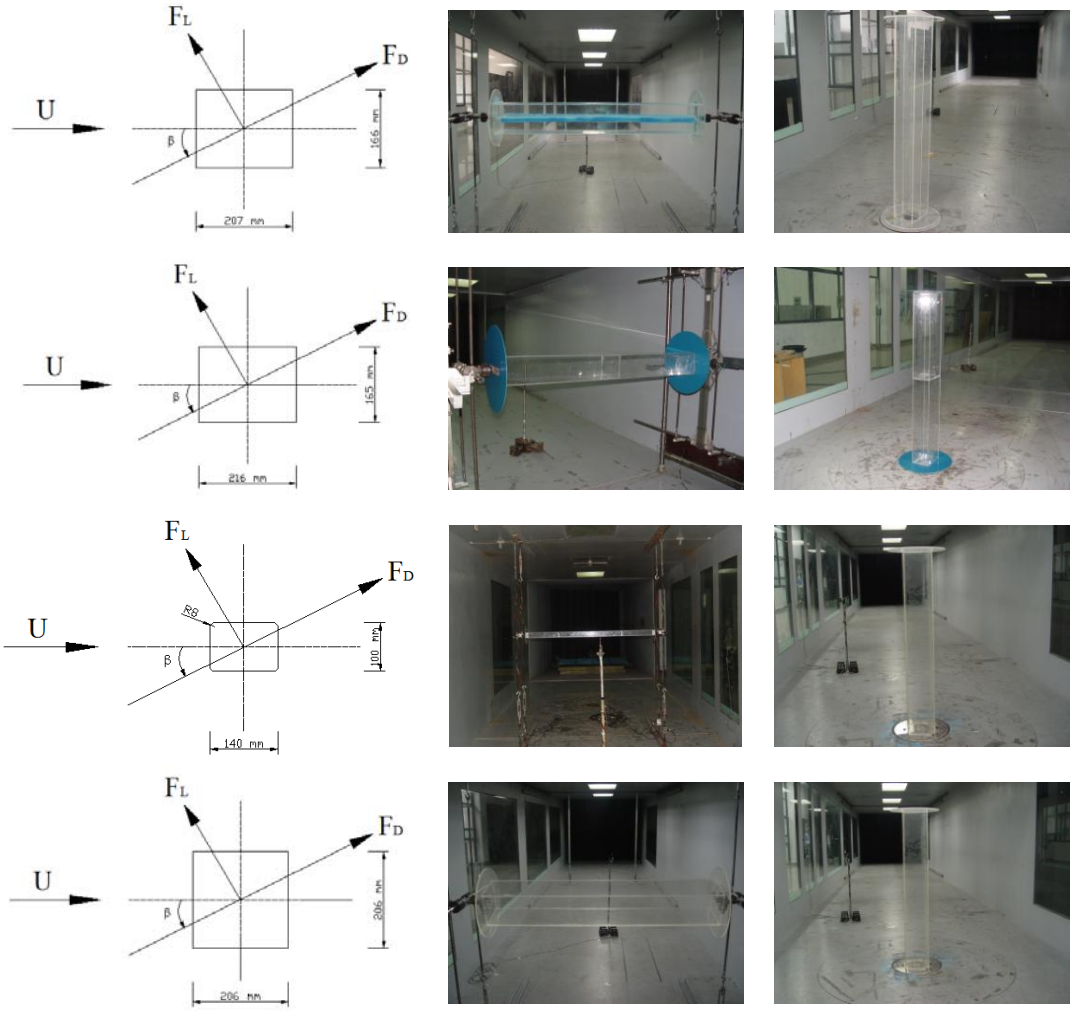

Fig.3 Overview of the four test groups. The consecutively first row to the fourth row indicates the details of Group 1to Group 4, separately. And the first column is the 2D cross section dimensions of each group; flexibly mounted section model rests setup photos are shown in the second column; while the last column is the static force tests photos.

Table.1~Table.4 shows the details of each group Damping ratio identification tests using the best decay estimation method, data analysis was conducted by the recorded decaying signals after the imposed initial displacement. The natural frequencies could also be obtained by FFT of the recorded decaying time series. Strouhal number identification tests were conducted with the same section model; the final values were determined by the Strouhal relation. The galloping instability coefficient was calculated from the static force coefficient curves according to the quasi-steady theory. It was definitely noted that the identical model is characterized by different galloping instability coefficients ($C_L'+C_D$) and Strouhal numbers (St) when the width and height of the cross section weren't identical. Finally, with the previously obtained Strouhal number and the natural frequencies of section model, the critical wind velocity of VIV can be predicted by Strouhal relation. Meanwhile, the galloping instability onset velocity can also be calculated based on quasi-steady galloping theory.

Table.1 Main parameters of Group 1

Parameters			
Length	L	mm	1530
Width	B	mm	207
Height	D	mm	166
Aspect ratio	B/D	-	1.25
Mass	m	Kg/m	16.60
Damping ratio	ξ_v	-	0.00263
Scruton number	Scr	-	12.38
Natural frequency	f_v	HZ	4.49
Strouhal number of short egde	St_1	-	0.11
Strouhal number of long egde	St_2	-	0.12
$C_L'+C_D$ of short edge	$(C_L'+C_D)_1$	-	-1.263
$C_L'+C_D$ of long edge	$(C_L'+C_D)_2$	-	-0.897
Estimated critical wind velocity of VIV of short edge	V_{v1}	m/s	7.06
Estimated critical wind velocity of galloping of short edge	V_{g1}	m/s	14.61
Estimated critical wind velocity of VIV of long edge	V_{v2}	m/s	7.62
Estimated critical wind velocity of galloping of long edge	V_{g2}	m/s	20.57

Table.2 Main parameters of Group2

Parameters			
Length	L	mm	1530
Width	B	mm	216
Height	D	mm	165
Aspect ratio	B/D	-	1.31
Mass	m	Kg/m	16.26
Damping ratio	ξ_v	-	0.00197
Scruton number	Scr	-	8.76
Natural frequency	f_v	HZ	4.20
Strouhal number of short egde	St_1	-	0.10
Strouhal number of long egde	St_2	-	0.12
$C_L'+C_D$ of short edge	$(C_L'+C_D)_1$	-	-1.993
$C_L'+C_D$ of long edge	$(C_L'+C_D)_2$	-	-0.894
Estimated critical wind velocity of VIV of short edge	V_{v1}	m/s	6.85
Estimated critical wind velocity of galloping of short edge	V_{g1}	m/s	6.09
Estimated critical wind velocity of VIV of long edge	V_{v2}	m/s	7.44
Estimated critical wind velocity of galloping of long edge	V_{g2}	m/s	13.57

Table.3 Main parameters of Group3

Parameters			
Length	L	mm	1530
Width	B	mm	140
Height	D	mm	100
Aspect ratio	B/D	-	1.40
Mass	m	Kg/m	14.04
Damping ratio	ξ_v	-	0.00203
Scruton number	Scr	-	19.83
Natural frequency	f_v	HZ	1.51
Strouhal number of short egde	St_1	-	0.11
Strouhal number of long egde	St_2	-	0.15
$C_L'+C_D$ of short edge	$(C_L'+C_D)_1$	-	-3.066
$C_L'+C_D$ of long edge	$(C_L'+C_D)_2$	-	-1.160
Estimated critical wind velocity of VIV of short edge	V_{v1}	m/s	1.37
Estimated critical wind velocity of galloping of short edge	V_{g1}	m/s	1.95
Estimated critical wind velocity of VIV of long edge	V_{v2}	m/s	1.47
Estimated critical wind velocity of galloping of long edge	V_{g2}	m/s	5.16

Table.4 Main parameters of Group4

Parameters			
Length	L	mm	1530
Width	B	mm	206
Height	D	mm	206
Aspect ratio	B/D	-	1.00
Mass	m	Kg/m	18.88
Damping ratio	ξ_v	-	0.00261
Scruton number	Scr	-	11.31
Natural frequency	f_v	HZ	4.30
Strouhal number of short egde	St_1	-	0.12
Strouhal number of long egde	St_2	-	0.12
$C_L'+C_D$ of short edge	$(C_L'+C_D)_1$	-	-1.128
Estimated critical wind velocity of VIV of short edge	V_{v1}	m/s	7.32
Estimated critical wind velocity of galloping of short edge	V_{g1}	m/s	17.77

The static force coefficient and galloping instability result curves are shown in Fig.4. The wind attack angles were defined as 0° when the section model anti-wind with their short edges, therefore, the wind attack angles must be 90° when the model anti-wind with their long edges. The static force coefficient results were shown in the first column of Fig.4. And the galloping

instability coefficients were calculated exclusively through the static force coefficient curves according to the quasi-steady galloping theory.

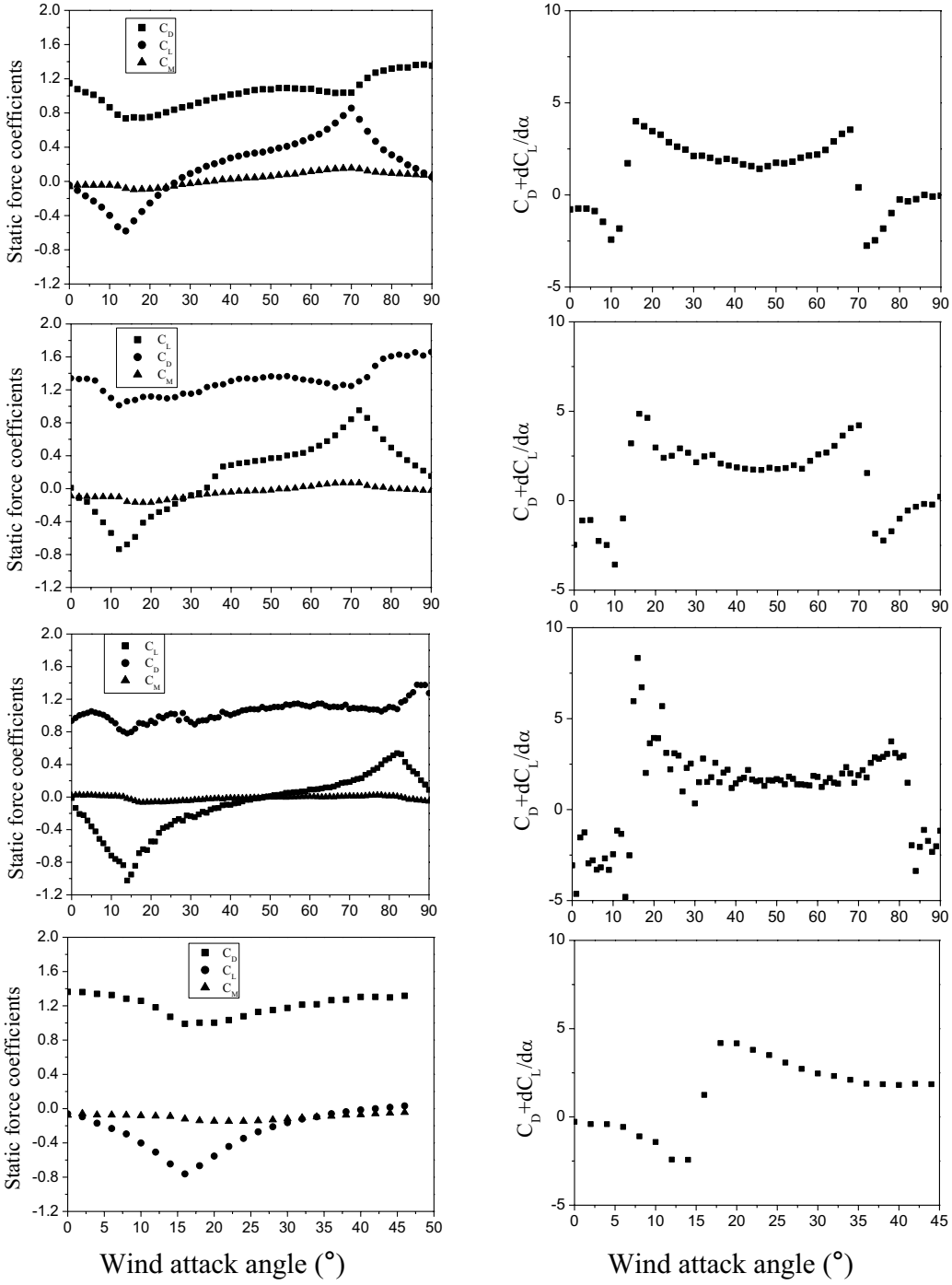

Fig.4. Static force coefficients and galloping instability coefficients curves vs. wind attack angles for the four experimental groups. The 1st to the 4th rows are representing the results of the Group 1to Group 4, separately. While, the first column are the static force coefficient curves and the second column are the galloping instability coefficient curves.

4 RESULTS AND DISCUSSIONS

In this section, the aerodynamic responses were reported by comparing the time series and vibration frequencies of heaving, pitching and rolling modes. The final response curves of each group were also shown together with the corresponding estimated critical normalized wind velocity of VIV and galloping. In particular, for each run of every case, enough time was allowed for the vibration to stabilize before collecting the test data.

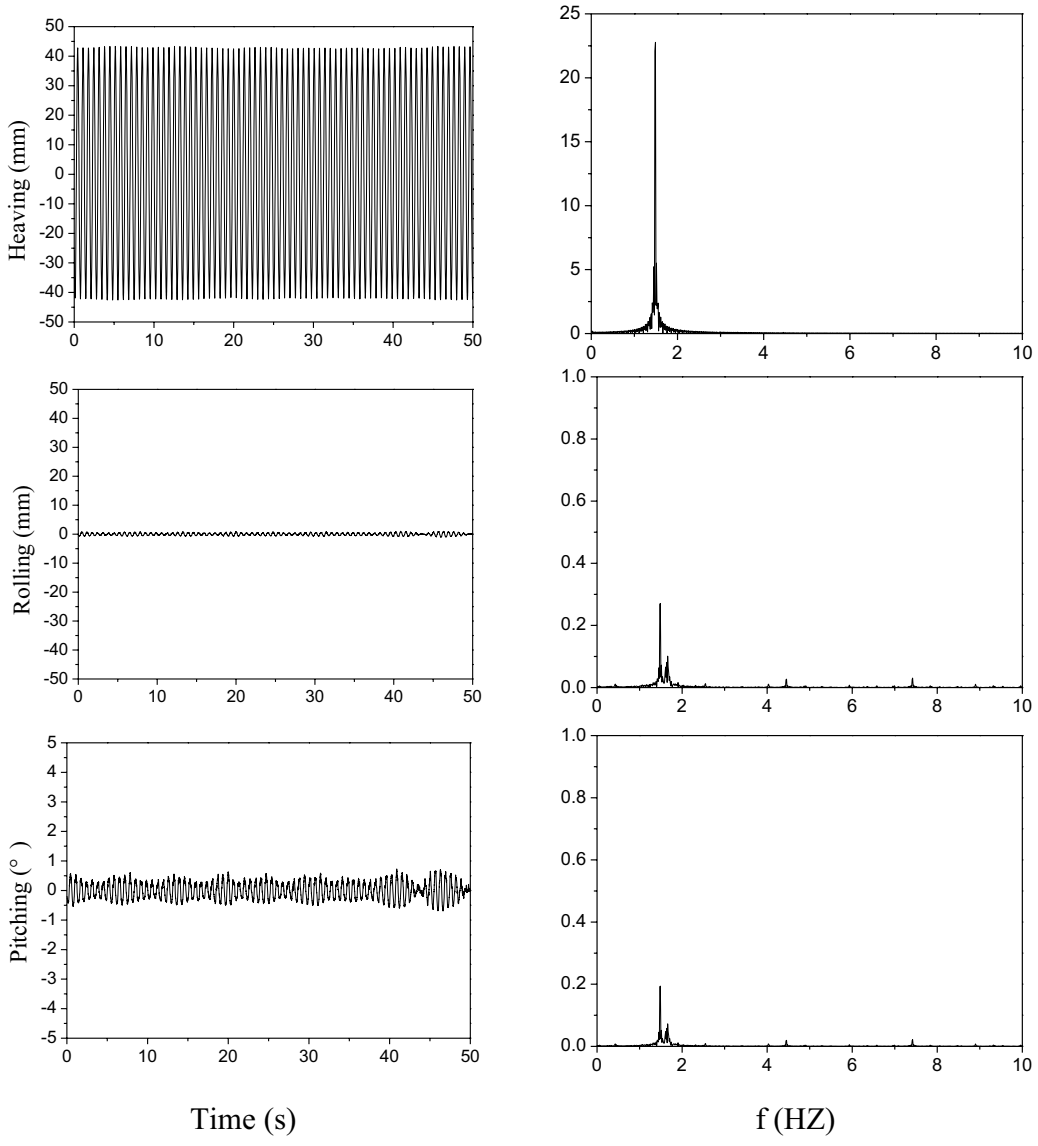

Fig.5. Tests example of Group 3: the section model anti-wind with short edge, at U/fD=23.97, which is related to the measured maximum point of galloping instability .The first row is the time series and corresponding frequency spectrum by FFT of heaving mode; the second row is for rolling mode and the third row is for pitching mode.

Let's take the group 3 as an example to illustrate the data analysis. Just as shown in Fig.5, these are vibration details of group 3 (short edge facing the flow), at the normalized wind velocity of U/fD=23.97. It can be clearly observed from the comparison of three different modes that the

pitching and rolling modes are about 10 times smaller (and therefore negligible) with respect to the heaving mode. Despite the vibration amplitude up to A/D=0.5, the heaving mode still vibrates at the identical frequency to the natural frequency f=1.51HZ and maintains the continuously steady amplitude.

While, for the cases of model anti-wind with long edge of group 3, normalized wind velocity at U/fD=8.89, the vibration details are shown in Fig.6. The peak amplitude of VIV lock-in range was selected. Very similar to Fig.5, in this case, the mode vibrates dominantly at the heaving mode and at the single natural frequency; more importantly, time series also show the steady amplitude vibration.

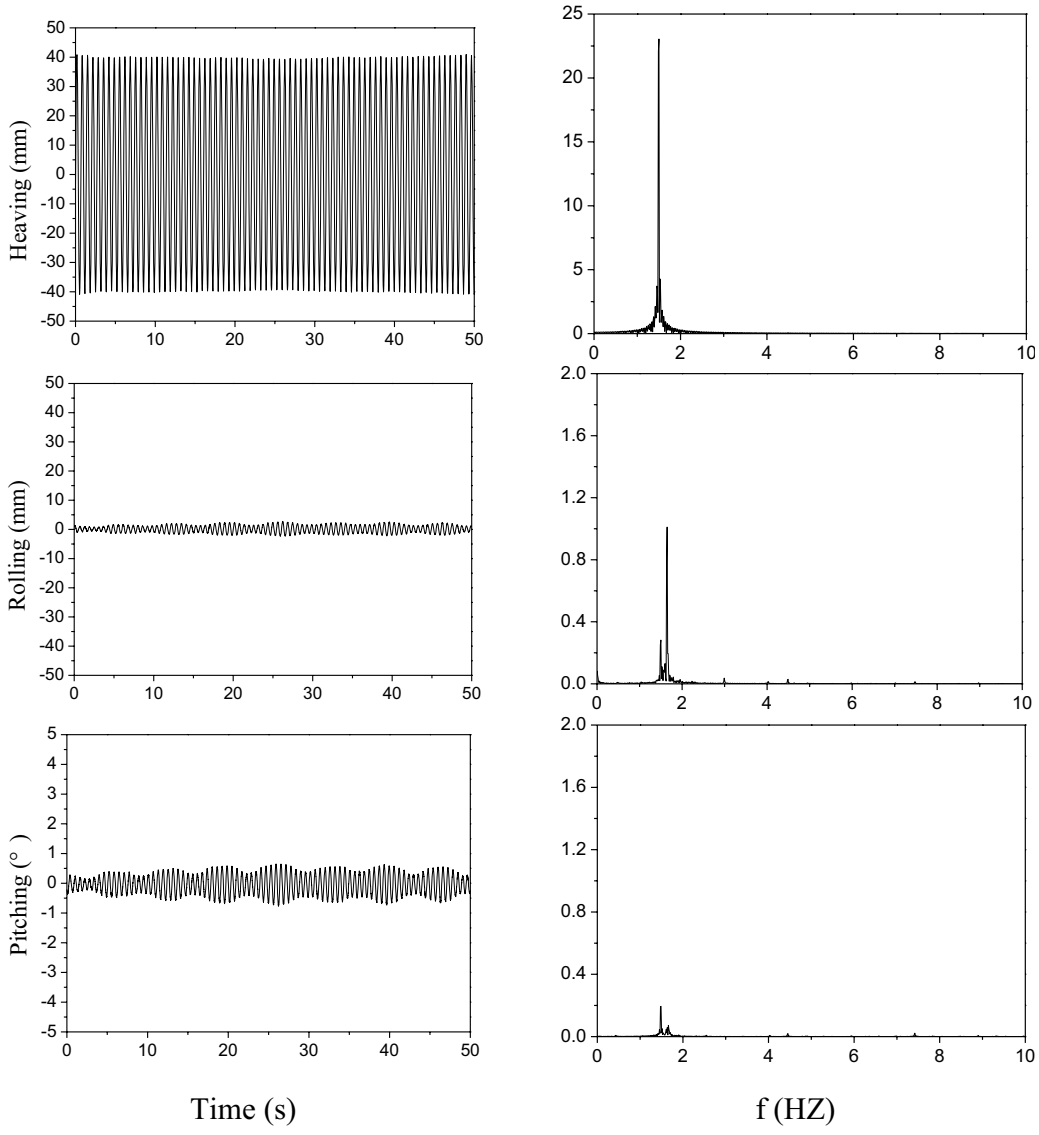

Fig.6. Tests example of Group 3: the section model anti-wind with long edge, at U/fD=8.89, which is related to the maximum point of VIV lock-in range .The first row is the time series and corresponding frequency spectrum of heaving mode; the second row is for rolling mode and the third row is for pitching mode.

The conclusive experimental measured vibration curves of group 1~group 4 are shown in Fig.7, together with the predicted critical wind velocity of VIV and galloping. Unfortunately, the experimental data of group 1and group 4 were not enough when the vibration curves were straightly increasing with the increased wind velocity. Nevertheless, it can be clearly seen from other curves that the measured maximum normalized amplitudes are very large although the Scruton number of each model are over 10.

For the cases of group 2 and group 3, which the estimated critical wind velocity of VIV and galloping are within the range of 1.5 times, an interesting vibration phenomenon occurred. There is neither self-limited VIV lock-in nor divergent type galloping appearing, whereas the vibration amplitude consistently increases with the increasing wind velocity. It can be obviously observed that there with still no indications of trend of the response amplitude to stop increasing even the normalized amplitude A/D rising up to 0.7. Moreover, the vibration time series of each wind velocity component, especially for the large amplitude ones, were very similar to the form of Fig.5. Recorded vibration time series always maintain the astonishing steady amplitude, and vibrated at the natural frequencies. In particular, the factor of 1.5 times between predicted critical wind velocity of VIV and galloping is also recommended by the Eurocode at which the specific research should be undertaken.

However, for the cases of group 1 and group 3, the section models facing wind with their long edges, the estimated critical wind velocity of VIV and galloping were deviated significantly. The separated VIV lock-in range and divergent type galloping phenomenon were observed separately. Meanwhile, it is worth noting that the measured peak amplitudes of VIV lock-in are extraordinary large. The Scruton numbers of these two groups are 12.83, 19.83 respectively, and the experimental measured non dimensional amplitude reach 0.15, 0.29 respectively. In contrast to wind induced vibrations of circular section structures, it is very uncommon for these rectangular section models to oscillate up to such large amplitudes with the relatively large Scruton number. Therefore, one can reasonably assume that the negative aerodynamic damping of galloping instability contributes to the large amplitude VIV to some degree.

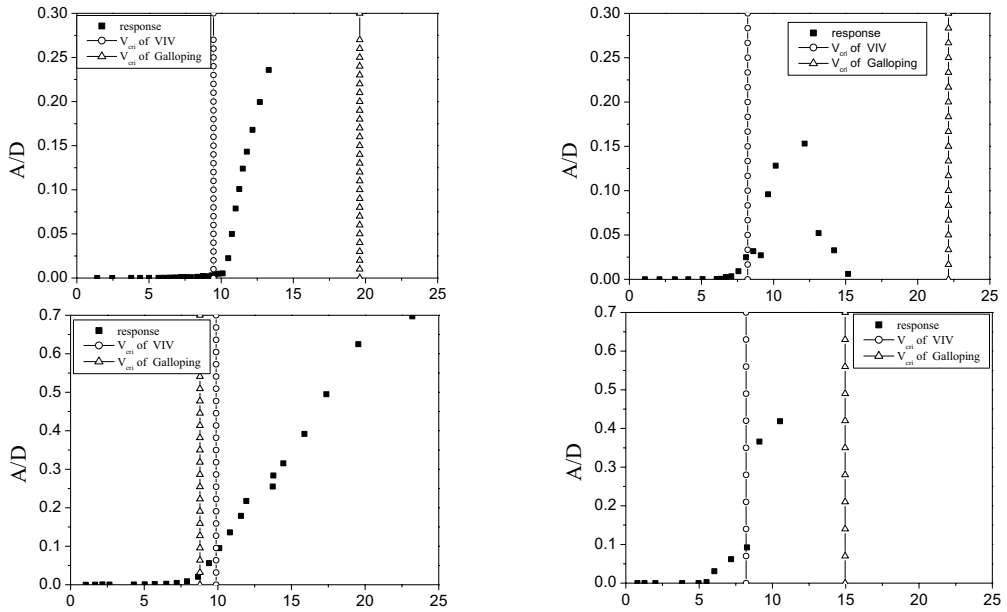

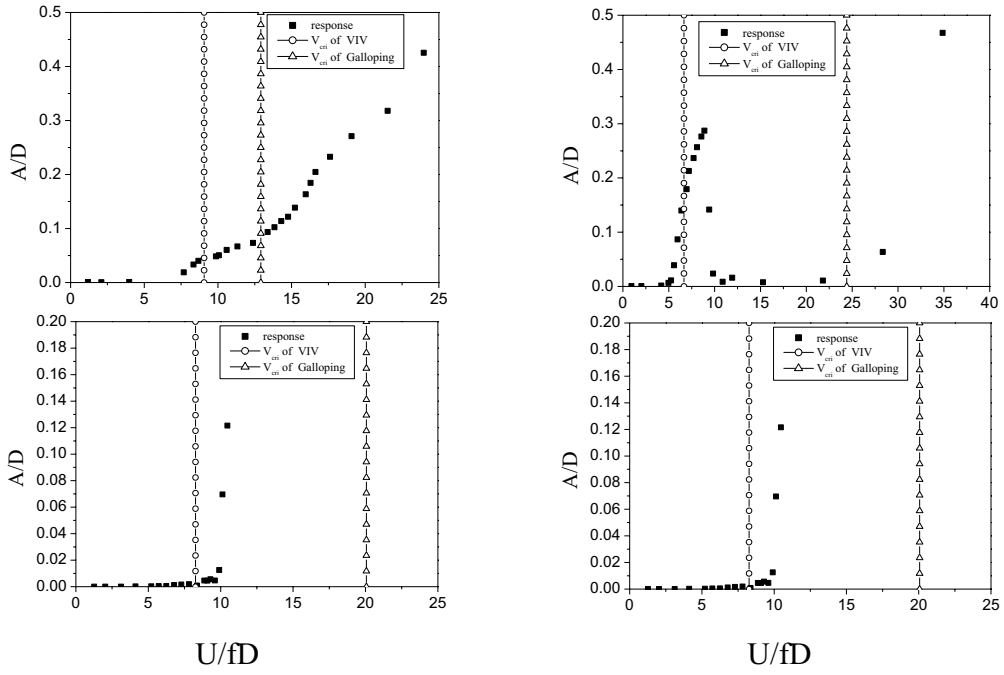

Fig.7. Conclusive test results: non dimensional vibration displacement A/D vs. normalized wind velocity. The first row to the fourth row represent the wind induced vibration curves of group 1~ group 4 respectively. And the entire first column is with respect to the condition of section model of each group anti-wind with short edge, while the whole second column is for the conditions of section models anti-wind with long edge.

5 CONCLUDING REMARKS

Four groups of tests on rectangular section model were performed in wind tunnel, each group of models are varied in aspect ratio and Scruton number. The critical wind velocity of VIV and galloping were also predicted with the beforehand identified aerodynamic coefficients. Main characteristics of result curves allow following remarks.

With respect to the circumstance that estimated critical wind velocity of VIV and galloping are very close, e.g. within the range of 1.5 times, an interesting experimental phenomenon occurs. The interaction of VIV and galloping aerodynamic forces creates a new oscillation type: it shows neither lock-in VIV nor divergent type galloping characteristics. The cross flow vibration amplitudes consistently increases with the increased wind velocity, moreover, the vibration time series of each steady wind velocity always maintains constant amplitude. The VIV aerodynamic force seemed to suppress the occurrence of divergent type galloping.

When the predicted critical wind velocity of VIV and galloping diverge significantly to each other, the fully measured VIV lock-in range demonstrates the relatively large non dimensional amplitude which the circular section structures cannot achieve at the same Scruton number. According to the quasi-steady galloping theory, the circular section will never attain the galloping instability negative damping; whereas the rectangular models investigated in the present work always being the models differentiated in aspect ratio and Scruton number (B/D, Scr, Table 1~4). Hence, it is reasonable to assume that the interaction of VIV and galloping contribute to the distinctively large VIV amplitude.

6 ACKNOWLEDGEMENTS

The Authors are grateful to the Natural Science Foundation of China under the Grant 50738002, 50908085 and graduate students innovation fund of Hunan province; furthermore, the partial support of CRIACIV for his research stay in Germany is also acknowledged.

7 REFERENCES

[1] Chaplin, J.R., Bearman, P.W., Cheng, Y., Fontaine, E., Graham, J.M.R., Herfjord, K., Huera-Huarte, F.J., Isherwood, M., Lambrakos, K., Larsen, C.M., Meneghini, J.R., Moe, G., Pattenden, R.J., Triantafyllou, M.S., Willden, R.H.J., 2005a. Blind predictions of laboratory measurements of vortex induced vibrations of a tension riser. Journal of Fluids and Structures 21, 25–40.

[2] Ge, Y.J., Xiang H.F., 2008. Recent development of bridge aerodynamics in China. Journal of Wind Engineering and Industrial Aerodynamics 96,736-768.

[3] Bearman, P. W., 1984. Vortex shedding from oscillating bluff bodies. Annual Review of Fluid Mechanics, 16(1), 195-222.

[4] Sarpkaya, T., 2004. A critical review of the intrinsic nature of vortex-induced vibrations. Journal of Fluids and Structures 19, 389–447.

[5] Williamson, C. and Govardhan, R. (2004). Vortex-induced vibrations. Annual Review of Fluid Mechanics, 36(1), 413-455.

[6] Ziller, C., Ruscheweyh, H., 1997. A new approach for determining the onset velocity of galloping instability taking into account the nonlinearity of the aerodynamic damping characteristic. Journal of Wind Engineering and Industrial Aerodynamics 69-71, 303-314.

[7] Hortmanns, M., Ruscheweyh, H., 1997. Development of a method for calculating galloping amplitudes considering nonlinear aerodynamic coefficients measured with the forced oscillation method. Journal of Wind Engineering and Industrial Aerodynamics 69-71, 251-261.

[8] Simiu, E., Scanlan R.H., 1996.Wind effects on structures:fundamentals and applications to design, 3rd Edition. John Wiley& Sons, New York.

[9] Zhu L.D.,2005. The quality of system simulation and amplitude correction method of bridge Vortex-induced resonance section model tests. Engineering Mechanics, 22(5), 204-208. (in Chinese)

[10] Marra, A.M., Mannini, C., Bartoli, G., 2011. Van der Pol-type equation for modeling vortex-induced oscillations of bridge decks. Journal of Wind Engineering and Industrial Aerodynamics 99,776-785.

[11] Chen, Z.Q., 2005. Wind Engineering of Bridge. People's Communications Press,BeiJing,China,64-67.(in Chinese)

[12] Borri, C., Costa, C., Zahlten, W., 2002. Non-stationary flow forces for the numerical simulation of aeroelastic instability of bridge decks. Computers and Structures, 1071-1079.

The Seventh International Colloquium on Bluff Body Aerodynamics and Applications (BBAA7)
Shanghai, China; September 2-6, 2012

Numerical Simulation with PCA analysis of flow around 1:5 rectangular cylinder

Shining Zhang[a], Zhiwen Zhu[a]

([a]*Center of Wind Engineering, Hunan University, Changsha, China*)

ABSTRACT: The unsteady flow field around a two-dimensional rectangular prism with aspect ratio of 5 is studied by using Unsteady Reynolds-Averaged Navier-Stokes (URNS) equations. Fundamental flow characteristics are provided with numerical simulation and compared with the experiment, satisfactory agreement is obtained consequently. The aim of this paper is to find the nature of the fluctuating pressure on the surface of the rectangular cylinder indicated by the Principal Component Analysis. To better understand the vortex shedding phenomenon, flow visualization is provided. At last, effects of Reynolds number ranged from 1.03×10^4 to 1.03×10^6 on the flow characteristics are discussed.

KEYWORDS: Rectangular cylinder, CFD, PCA, vortex shedding, Reynolds number effects.

1 INTRODUCTION

In bridge engineering, rectangular shape are commonly employed as the cross section of bridge components, such as the plate girder, tower, pier, etc. The infamous bridge destroyed by the wind-induced vibration and shocking the civil engineers is old Tacoma Narrows Crossing, with its H-shaped stiffening girder at chord-to-thickness ratio very close to 5. Therefore investigation of the flow past such kind of cross section is of great concern. As a benchmark problem, rectangular cylinder had been studied by many researchers over the years through wind tunnel test, numerical simulation method and site measurement.

The aerodynamics of a rectangular cylinder with the aspect ratio of 5 as a benchmark problem has been studied for many years. Both the two-dimensional (2-D) and three-dimensional (3-D) features of the flow characteristics around rectangular cylinders have been clarified in several studies, e.g. in Claudio Mannini(2010), Luca Bruno(2009), Gunter Schewe(2009). Most of what they explored was the mean pressure coefficient distributions, nevertheless, usually it is the fluctuating pressure that mainly affects the variation of aerodynamic forces, therefore fluctuating pressure should be well considered and analyzed when dealing with aerodynamics.

This paper deals with the two-dimensional (2-D) numerical simulation of flow past a rectangular cylinder with a chord-to-thickness ratio B/D=5 at zero flow incidence. The reattachment which significantly relates to the pressure recovery is calculated, some other natures of flow characteristics is analyzed, mainly including principal component of pressure distribution around the upper surface and periodic vortex shedding. The Principal Component Analysis which is recognized an effective method to represent the unsteady flow is employed to deal with the fluctuating pressure. Finally, the effects of Reynolds number on those flow characteristics have been investigated. Through those flow characteristics, we can better understand the fluctuation of aerodynamic forces and find the main factors leading to those variations.

Although the resulting flow field is known to be three dimensional, the current two-dimensional calculation is able to predict important flow properties (D. K. Tafti and S. P. Vanka,

1991). The current 2-D numerical simulation is adopted to explore its capacity and advantages through comparison with the experimental results and three-dimensional (3-D) calculations. Also, this paper will definitely lay a foundation for 3-D research and the results analyzed from 2-D are used to compare with latter 3-D study in order to find the indispensable role and improvement of 3-D effects.

2 FLOW MODEL AND PCA THEORY

2.1 Governing equation and turbulent model

The unsteady, incompressible, 2D viscous fluid flow around the rectangular cylinder is modeled by means of the time-averaged Navier-Stokes equations as follows:

$$\frac{\partial \overline{u_i}}{\partial x_i} = 0 \tag{1}$$

$$\frac{\partial}{\partial t}\left(\rho \overline{u_i}\right) + \frac{\partial}{\partial x_j}\left(\rho \overline{u_i}\,\overline{u_j}\right) = -\frac{\partial \overline{p}}{\partial x_i} + \frac{\partial}{\partial x_j}\left(\mu \frac{\partial \overline{u_i}}{\partial x_j} - \rho \overline{u_i' u_j'}\right) \tag{2}$$

Where x and t are the space and time coordinates, $\overline{u}$ and $\overline{p}$ are the time-averaged velocity and pressure, μ is the turbulent viscosity and ρ is the fluid density. $\rho u_i' u_j'$ is the Reynolds stress.

The Boussinesq hypothesis to relate the Reynolds stresses to the mean velocity gradients:

$$-\rho \overline{u_i' u_j'} = \mu_t \left(\frac{\partial \overline{u_i}}{\partial x_j} + \frac{\partial \overline{u_j}}{\partial x_i}\right) - \frac{2}{3}\left(\rho k + \frac{\partial \overline{u_i}}{\partial x_i}\right)\delta_{ij} \tag{3}$$

In consideration of complex flow near the wall of rectangular cylinder, the shear-stress transport (SST) $k-\omega$ model is employed in present simulation, since $k-\omega$ model effectively blend the robust and accurate formulation of the $k-\varepsilon$ model in the near-wall region with the free-stream independence of the $k-\varepsilon$ model in the far field.

2.2 Principal Component Analysis (PCA) theory

In the study of the pressure fluctuation around bluff bodies using PCA, Holmes(1990) pointed out that the covariance matrix of the pressure fluctuation contains information on the magnitude and distribution of the underlying fundamental modes of the pressure distribution around a body. Studies show that these modes are represented by the eigenvectors of the corresponding covariance matrix of the pressure distribution on the body's surface.

Mathematically, to perform PCA on a data set x, the eigenvalues, λ_i and the eigenvector, e_i of a covariance matrix C_x can be evaluated from the solution of :

$$C_x e_i = \lambda_i e_i \tag{4}$$

The eigenvalues is calculated as the roots of ,

$$\left|C_x - \lambda_i I\right| = 0 \tag{5}$$

Where $i = 1,2,\ldots,n$, n is the total number of the input data and I is the identity matrix.

The eigenvalues are associated with the variance of each of the components. Each eigenvalue is accompanied by an eigenvector, the nonzero vector e_i that satisfies Eq. 4.

The principal components of PCA are made up of columns of eigenvectors of the covariance matrix C_x. By arranging the eigenvectors in the order of descending eigenvalue($\lambda_i > \lambda_{i+1...}$), one gets the most significant changes of the variables in the data in the first principal component.

In PCA, the variables x are decomposed in the process of the eigenanalysis. It is possible to regenerate the variables x using the PCA results as follows:

$$x = A^T Y + \mu_x \tag{6}$$

Where A^T is the transpose matrix whose columns are given by the eigenvector of the covariance matrix and Y is the coefficients of the principal components. μ_x is the mean value of the data set x.

From Eq. 6, the original data can be reconstructed from the terms on the right hand side of the equation to see how well the original data can be represented from the few principal components in the analysis.

3 COMPUTATIONAL MESHES

As we all know that the quality of the computation mesh plays a crucial role in the reliability of numerical simulation. For this reason, a simple grid-convergence study is outlined in order to choose a reasonable grid for the following computations. In this paper the stationary rectangular cylinder at zero-degree angle of attack ($\alpha = 0^\circ$) and Reynolds number Re=$U_\infty B / \nu = 3.42 \times 10^5$ (B is the width of the cylinder and ν the air kinematic viscosity) is chosen as test case.

Three 2-D hybrid grids were investigated, whose main characteristics are listed in Table 1. The fine grid is display in Fig.1 (left). In order to guarantee the accuracy of numerical simulation, the grid along the surface is generated by structured grid. Additionally, the only difference among those three grids is the level of grid refinement in structured grid zone close to the body surface.

The Dirichlet condition on the velocity field and sub-grid kinetic energy is imposed on the inlet boundary. Neumann conditions on the normal component of the stress tensor $\boldsymbol{T}$, as well as the same Dirichlet conditions on turbulence kinetic energy k, are imposed at the outlet boundary. Symmetry conditions are imposed on the both upper and lower boundary of the computational domain, while the no-slip boundary condition is imposed on the body surface, as indicated in Fig.1 (right). In order to represent the imposed physical boundary and reduce the influence from outside boundary, the distance between outside boundaries of the computational domain and the center of the body has also been meticulously selected, as shown in Fig.1 (right).

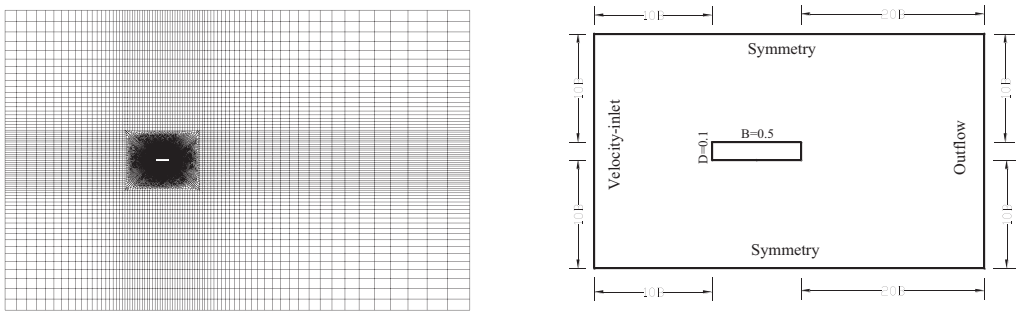

Fig.1. Fine grid and whole computational zone.(units: m)

Table 1. Main properties of grid system. The parameter δ and $\Delta y_{j+1} / \Delta y_j$ is the height and stretching factor of the first structured layer closest to the body surface respectively.

Grid	δ / B	$\Delta y_{j+1} / \Delta y_j$	Total cells	Structured cells	Unstructured cells	Good mesh
Coarse	2.5E-6	1.1	60,883	38,300	22,583	91.7%
Fine	6.0E-6	1.1	94,483	71,900	22,583	89.3%
Finest	6.0E-6	1.03	139,283	116,335	22,948	88.0%

Table 2. Present results of different grid arrangement in comparison with other literature (α =0°)

Grid	Reynolds number	max y^+	St	C_D	$C_L^{'}$	$C_D^{'}$
Coarse	3.42×10^5	4	0.114	1.05	0.1	0.006
Fine	3.42×10^5	0.1	0.113	1.09	0.16	0.009
Finest	3.42×10^5	0.1	0.116	1.08	0.1	0.004
Experiments(Schewe,2009)	2.64×10^5	-	0.111	1.029	0.4	-
Okajima(1983) I=0.4%	0.42×10^5	-	0.110	-	0.15	-
K. Snimada and T. Ishihara ($k-\varepsilon$ model)	-	-	0.118	1.0	0.05	-

After a series of trial calculation with several time-step size (dt), dt=0.0005s is eventually verified small enough, even conservative to resolve the dominant unsteady flow phenomena. Table 2 shows the computed St, the mean drag coefficient C_D and the standard deviation of lift and drag coefficients, $C_L^{'}$ and $C_D^{'}$. The table also reports the maximum value of the maximum value of the computed first-layer non-dimensional distance from the wall, defined as Yplus, y^+, which is recommended around 1 for the higher Reynolds number when utilizing the SST $k-\omega$ turbulent model. Considering the results obtained, the fine grid is found to be a reasonable compromise between accuracy and computational time cost. Therefore this grid will be employed in the following simulations.

4 FLOW RESULTS

4.1 Fundamental flow characteristics

Fig.2 displays the mean and standard-deviation values of the pressure coefficient on the body surface with several wind tunnel results reported for comparison. Usually, since the pressure fluctuation at some points (x/D=0 and 5) is thought to be sensitively affected by the approaching flow, those points have been excluded from the following discussion. The mean pressure coefficient C_P is defined as

$$C_P = (p - p_\infty) / 0.5\rho U^2 \tag{7}$$

Obviously, the mean C_P computed with 2-D SST $k-\omega$ model agrees well with the numerical simulation conducted by T. Ishihara (2001) and the experiment performed by Matsumoto (2005) at higher Reynolds number of 200,000, while a small discrepancy exists near leading edge at Re=100,000. The mean pressure coefficient distribution on the upper surface of rectangular cylinder exhibits a pressure increase toward the rear end. This is the inclination of reattachment of the flow which leads to pressure recovery toward the trailing edge, and this reattachment can be confirmed by streamlines in flow visualization. As for the standard deviation of the pressure coefficient, $C_P^{'}$, the wind tunnel data present a significant dispersion. This is probably due to the fact that the distribution of $C_P^{'}$ is more sensitive to the experimental boundary conditions than the mean values of pressures. Also, from the experiment results (Matsumoto,2005) we can con-

clude that $C_P^{'}$ is relevant to the Reynolds number to some extent. Although the present result of $C_P^{'}$ also distinct from the experiment, it predicts nearly the same position of the peak of $C_P^{'}$, which is a crucial parameter indicating the existence of vortex in this region. As a result, the experimental data provided the position at about x/D=3.7, while this present simulation give the location at x/D=3.85. From the mean friction coefficient distribution on the upper surface of the rectangular cylinder, the present calculation gives a value of x_R/B=0.903, which is slightly larger (3.2%) than the experiment estimated by Matsumoto et al. (2002) based on the distribution of the time-averaged pressure coefficient C_P and RMS value $C_P^{'}$ (x_R/B=7/8).

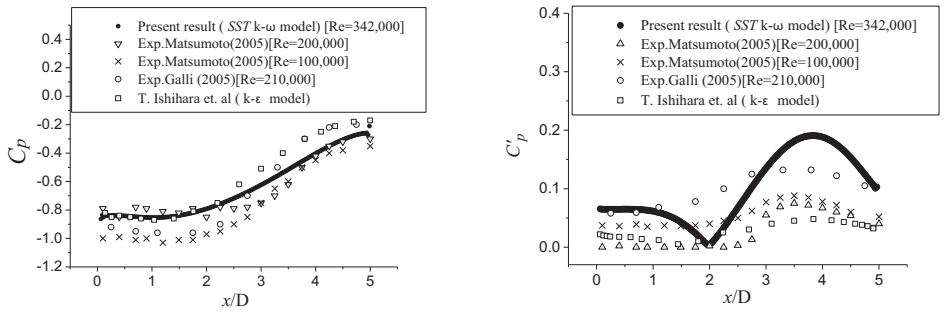

Fig.2. Comparison of pressure coefficient distribution with experiments (Matsumoto,2005 and Galli,2005), left: mean, right: standard deviation.

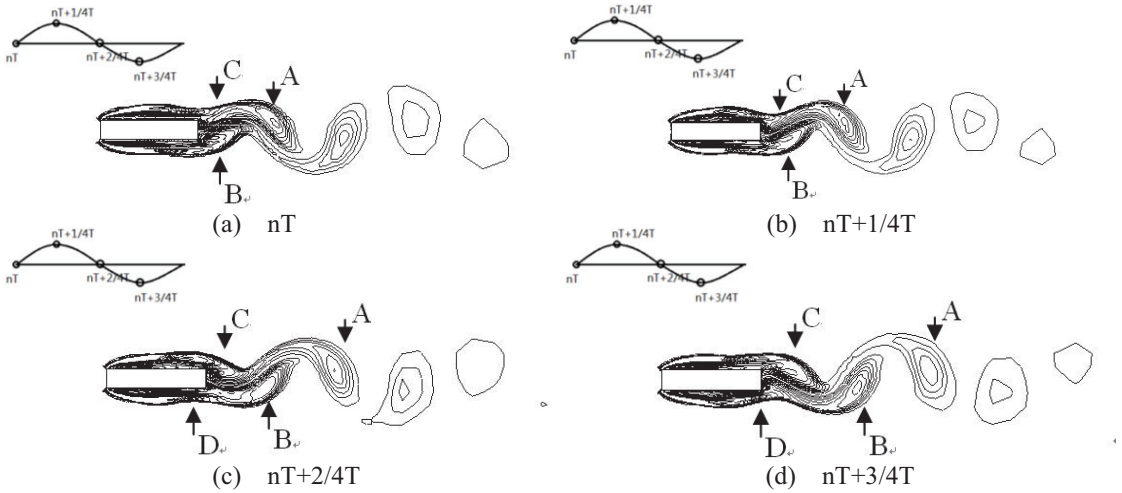

Fig.3. Snapshots of vorticity magnitude in flow field.

Fig.3 clearly describes the shedding of vortices from the rectangular cylinder. In (a), the total lift force on the bluff body is zero, and three vortices are labeled by A, B and C behind the cylinder. A is already shed, preparing to exit into the wake. B was originally from the lower side of the cylinder and is still attached to the rear side of the cylinder. In (b), A moves further towards the wake, while C moves to the center of the rear side surface. In (c), half a cycle of the lift force is completed, and it may be concluded that the vorticity close to the cylinder in (c) is similar to those in (a), but only reversed. In (c), B is completely shed off the rear side surface while a new vortex D is formed at the lower side behind the cylinder.

4.2 Principal Component Analysis results

In this section, the PCA theory is utilized to identify the fluctuating pressure. The analysis is carried out based on the procedures outlined in the previous section (section 2.2). As mentioned

above, the first principal component corresponds to the eigenvalues with the highest values, which quantifies the largest variation of pressure with respect to the total pressure changes in the flow within the time series considered in the analysis.

The principal components represent the fluctuating nature of the flow. Fig.4 depicts the first and second principal component of the pressure distribution on upper surface of the cylinder. It is found that the largest pressure fluctuation is appeared near the trailing edge of the section (upper surface). This indicates the presence of vortex structures at these regions and the peak of the first principal is located at x/D=3.85, which agrees well with the RMS values of C_P' distribution shown in Fig.2. Compared to the first principal component, the second one owns a more even pressure distribution (comparing total area on both sides of the *x*-axis in the graphs).

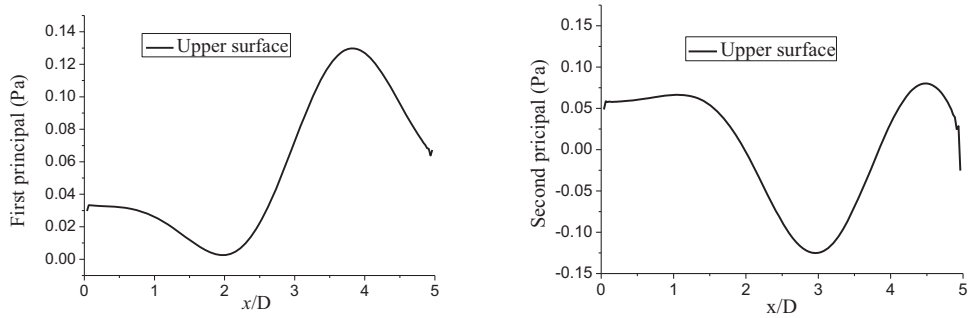

Fig.4. First and second principal component of pressure distribution on upper surface.

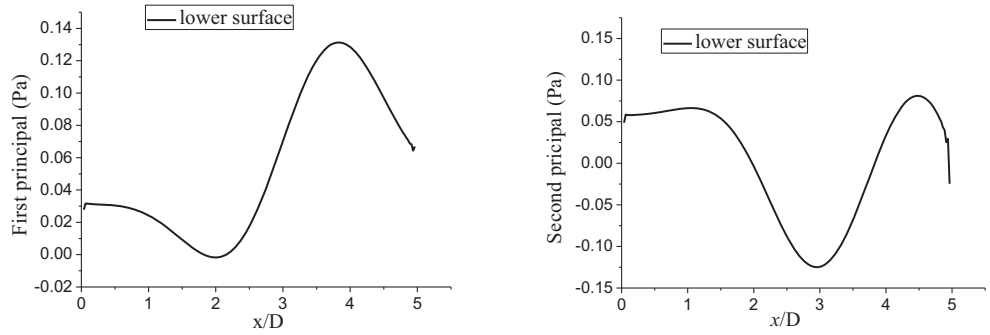

Fig.5. First and second principal component of pressure distribution on lower surface.

Fig.5 displays the first and second principal component of the pressure distribution around lower surface of the cylinder. Notice that the pressure distribution on the upper and lower surfaces of the cylinder shows different trends in the first principal component compared to the second principal component. A large amplitude pressure distribution appears near the trailing edge of the cylinder in the first principal component, while it happens at the middle part of the cylinder in the second principal component (Fig.4-Fig.5). Physically, this indicates the movement of the vortex along the cylinder surface.

When discussing the principal component, the contribution rate reflects energy percentage of one principal component in all components. The contribution rate of *i*th principal component can be defined as

$$CR_i = \frac{\lambda_i}{\sum_1^n \lambda_i} \tag{8}$$

Where λ_i is the value of the *i*th eigenvalue mentioned in section 2.2 and $\sum_1^n \lambda_i$ is the sum of all the eigenvalues.

Fig.6 depicts the contribution rate of the first fifteen eigenvalues. The first and second principal components of the pressure changes account for more than 99.8% of the total changes on the cylinder surface, which suggests that the first and second principal components of the pressure distribution around the cylinder account for most of the total variance of the pressure field without losing much information.

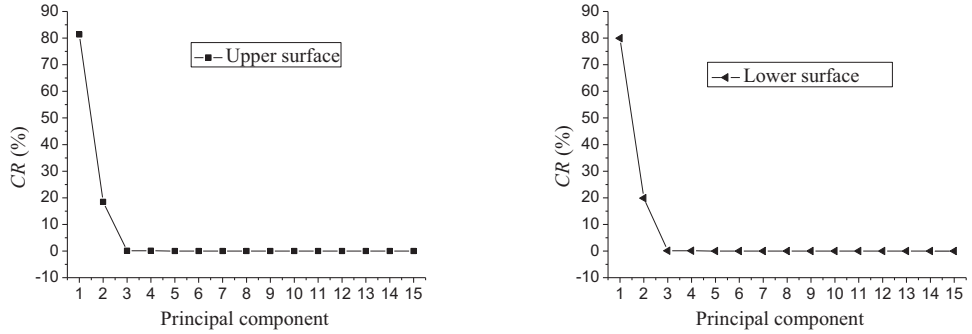

Fig.6. Contribution rate of the principal component on upper and lower surface.

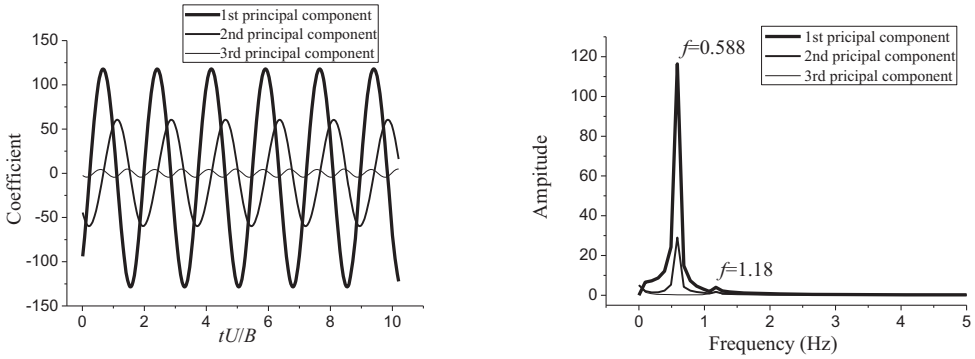

Fig.7. Coefficients and FFT analysis of first 3 principal components on upper surface.

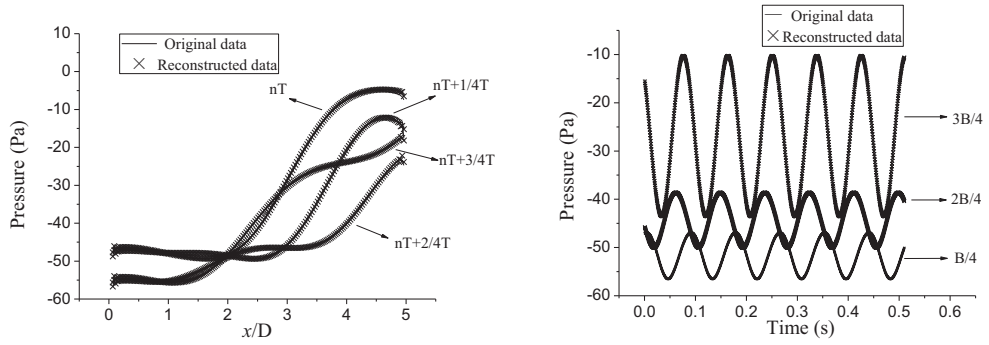

Fig.8. Reconstruction of fluctuating pressure on upper surface (B is width of cylinder).

As mentioned in section 2.2, the coefficients fluctuation of the principal component can be calculated, as shown in Fig.7. From the FFT analysis of the coefficients, one can find that a dominant frequency has been observed from both of the coefficients, with the first and second principal components showing the same frequency. Comparison shows that this frequency agrees well with the Strouhal number. Thus, the frequency feature of the coefficients can be related to the vortex shedding of the flow. A small peak also appears on the spectrum of the third principal component (right in Fig.7). Physically, this is related to smaller eddies and scales in the flow accompanying the main vortex mentioned above. Fig.7 also verifies that the first and second principal component contain most of the variable information, corresponding to the main vortex shedding.

Now that the first two principal components are responsible for the main fluctuation of pressure fluctuation along the surfaces, then we can reconstruct the time-dependent pressure on the surface of cylinder based on the Eq.6. Fig.8 shows the original and reconstructed transient pressure data (left) and time history of pressure at prescribed positions (right) on upper surface. Obviously, the reconstructed data agrees well with the computed data which indicates that the first principal component is enough to reconstruct the fluctuating pressure data along the surface. From Fig.8 (right) we can find that maximum pressure fluctuation occurs at x/D=3B/4, which can also be seen from RMS values of pressure in Fig.2.

From all mentioned above, PCA is proved to be useful and efficient for dealing with the nature of pressure distribution along the surface and original data can be easily reconstructed with few principal components without losing much information.

4.3 Effects of Reynolds number

In this section, effects of Reynolds number on flow characteristics are simulated and discussed. Table.3 lists the several cases performed in this paper, Reynolds number ranges from 1.03×10^4 to 1.03×10^6.

Fig.9 shows the Strouhal number and drag coefficient is insensitive to the variation of the Reynolds number in the range investigated, which has been verified in wind tunnel test. The tendency of 2-D $SST\ \ k-\omega$ model to underestimate the base pressure may be responsible for the overestimation of drag coefficient. From Table.3 one can find the standard deviation of lift and drag coefficient $C_L^{'}$ and $C_D^{'}$ decrease intensely with the increase of Reynolds number.

Table.3. Effects of Re number on aerodynamic parameters

Case	Reynolds number	Velocity (m/s)	max y^+	Time step	St	C_D	$C_L^{'}$	$C_D^{'}$
1	1.03×10^4	0.3	6.0E-03	0.010	0.117	1.14	0.22	0.035
2	3.42×10^4	1.0	1.5E-02	0.001	0.120	1.14	0.20	0.022
3	5.13×10^4	1.5	2.0E-02	0.002	0.119	1.13	0.19	0.017
4	1.03×10^5	3.0	3.5E-02	0.0015	0.113	1.11	0.18	0.013
5	3.42×10^5	10	0.8E-01	0.0005	0.113	1.09	0.16	0.009
6	6.84×10^5	20	1.5E-01	0.0002	0.112	1.10	0.15	0.008
7	1.03×10^6	30	2.3E-01	0.0001	0.113	1.11	0.16	0.009

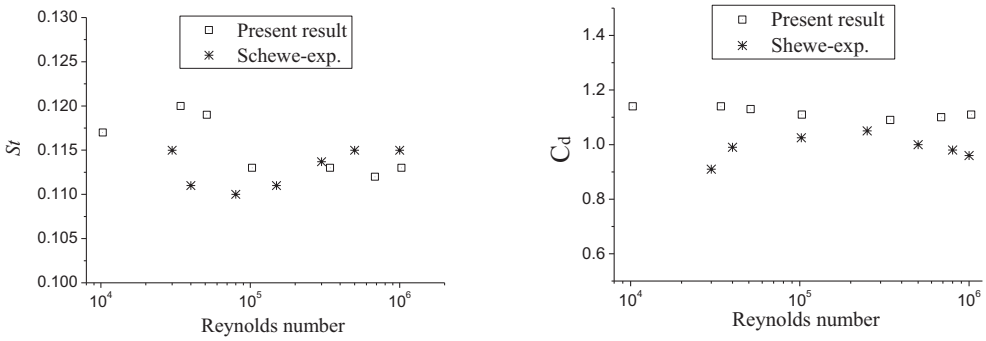

Fig.9. Strouhal number and drag coefficient as function of varying Reynolds number: comparison of current numerical results and experimental result from Schewe (2009).

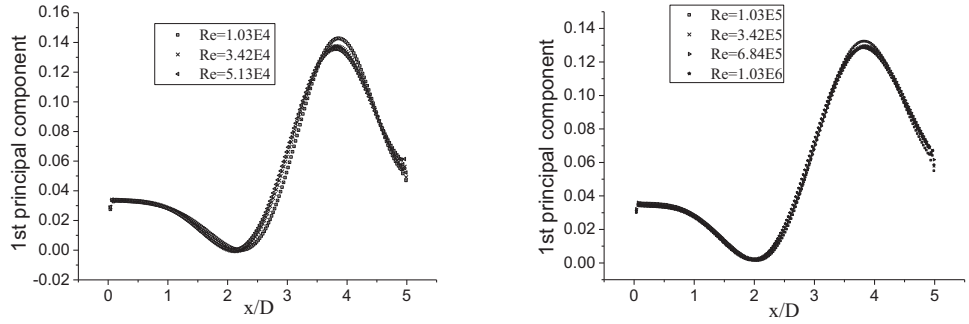

Fig.10. First principal component on the upper surface as functions of varying Reynolds number.

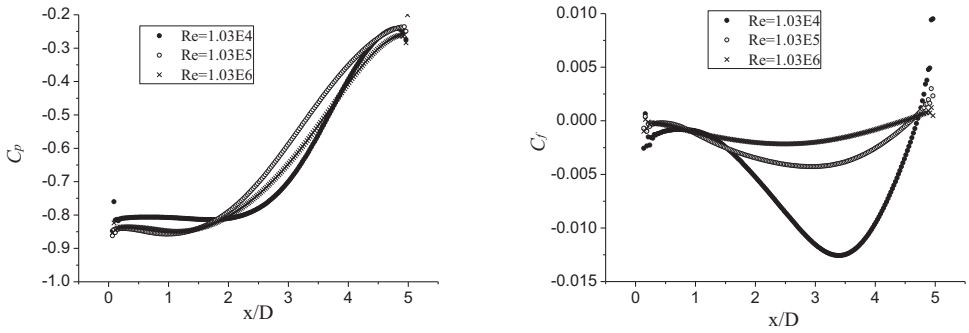

Fig.11. The mean pressure and friction coefficient on the upper surface as functions of varying Reynolds number.

The distribution of the first principal component on upper surface with the varying Reynolds number is depicted in Fig.10. It is found that similar mode is found when the Reynolds number exceeds 1.03×10^5, while less than it the peak of the first principal component will close to the trailing edge as the Reynolds number decreases. Fig.18 displays the mean pressure and friction coefficient on the upper surface as functions of Reynolds number. Similarly, mean pressure coefficient exhibit the same tendency at Re number larger than 1.03×10^5, while Re number is under 1.03×10^4 the position of pressure recovery lag behind the location in case of Re number larger than 1.03×10^5 on the upper surface. This phenomenon can be analyzed from the position of bubble vortices on the surface as shown in Fig.11 (right). The local valley in mean friction coefficient distribution is considered to be the position of the centre of the time-averaged bubble vortices. It is clear that when Re is smaller than 1.03×10^5 the position is closer to trailing edge which impedes the flow reattachment on former portion.

5 CONCLUSIONS

This paper provides the fundamental flow characteristics around the 1:5 rectangle cylinder, and compares the resuts with the experiments.

Main conclusions are included as following:

(1) Consequently, good agreement with the experiment is obtained. According to the numerical result of *St* and force coefficient, 2-D numerical simulation is proved efficient and reliable, which indicates that 2-D numerical simulation can satisfy the engineering requirement.

(2) Based on the distribution of the RMS values of pressure fluctuation, mean vortex shedding position is considered at x/D=3.85 and the fluctuating pressure distribution is considered to 3-D effects. Moreover the numerical flow visualization is provided to better understand the change of aerodynamic force on the side surface of the rectangular cylinder.

(3) Based on the PCA method, the nature of the pressure fluctuation is analyzed in this paper. It is found that the first two principal components are enough to contain the pressure fluctuation information. Furthermore, the pressure is reconstructed with few principal components, verifying the reliability of PCA and providing a feasible method to save the countless data extracted from experiment or numerical simulation. Analysis from the PCA also indicates that the first two modes are mainly responsible for the variations of the pressure on the side surface of this bluff body.

(4) At last, effects of Reynolds number on those flow characteristics are discussed. Changes of *St*, C_D, C_L', C_D', C_P, C_f and principal components varying as the function of Reynolds number are included. Generally, the *St* and C_D are insensitive to the changes of Reynolds number in present Re number range research while C_L' and C_D' both exhibit intensive decline as the Reynolds number increases. As for the C_P, C_f and the principal components, Re=1.03×10^5 is considered to be a critical values for the remarkable changes of those flow characteristics.

Further studies are required to explore the nature of the pressure distribution on the surface of the bluff body based on 3-D numerical simulation and to confirm the present assertion about the effects of Re number on C_P, C_f.

REFERENCES

D. K. Tafti and S. P. Vanka. A numerical study of flow separation and reattachment on a blunt plate. Phys. Fluids July 1991A 3(7) 1749-1759.

Caludio Mannini, Numerical investigation on the three-dimensional unsteady flow past a 5:1 rectangular cylinder, J. Wind Eng. Ind. Aerodyn.99(2011)469-482.

Claudio Mannini,Unsteady RANS modeling of flow past a rectangular cylinder: Investigation of Reynolds number effects, Computers & Fluid 39(2010) 1609-1624

Luca Bruno, 3D flow around a rectangular cylinder: A computational study, J. Wind Eng. Ind. Aerodyn. 98(2010) 263-276

Holmes J D, Analysis and synthesis of pressure fluctuations on bluff bodies using eigenvetors, Journal of Wind Engineering and Industrial Aerodynamics, 1990, Vol.33, p. 219-230.

Schewe G. Reynolds-numer-effects in flow around a rectangular cylinder with aspect ratio 1:5. In: Borri C, Augusti G, Bartoli G, Facchini L, editors. Proc 5th European and African conference on wind engineering, Florence, Italy. Florence: Firenze University Press; 2009

Matsumoto, M., Shirato,H., Aaraki, k., Haramura,T., Hashimoto, T. Spanwise coherence characteristic of surface pressure field on 2D bluff bodies. Journal of Wind Engineering and Industrial Aerodynamics 2002 91, 155-163

Shimada K, Ishihara T. Application of a k-ε model to the prediction of aerodynamic characteristics of rectangular cross-section cylinders. J fluids Struct 2002; 16(4): 465-85.

D. Yu, A. Kareem. Two=dimensional simulation of flow around rectangular prisms. Journal of Wind Engineering and Industrial Aerodynamics 62 (1996) 131-161.

The Seventh International Colloquium on Bluff Body Aerodynamics and Applications (BBAA7)
Shanghai, China; September 2-6, 2012

Shear effects on flow past a rectangular cylinder with side ratio B/D=5

Qiang Zhou, Shuyang Cao*, Zhiyong Zhou

State Key Laboratory of Disaster Reduction in Civil Engineering, Tongji University, Shanghai 200092, P. R. China

ABSTRACT: Large Eddy Simulation (LES) is carried out to investigate shear effects on flow past a rectangular cylinder with side ratio *B/D*=5 at Reynolds number Re=22,000 (based on the thickness of the cylinder). Simulation results showed that the Strouhal number has no significant variation with oncoming velocity shear, while the peak fluctuation frequency of the drag coefficient becomes identical to that of the lift coefficient with increase in velocity shear. The intermittently-reattached flow that features the aerodynamics of the 5:1 rectangular cylinder in non-shear flow becomes more stably-reattached on the high-velocity side and more stably-separated on the low-velocity side. The mean of the drag force was found to have little variation while its standard-deviation increases with increase in velocity shear. The mean and standard-deviation of the lift and moment forces vary almost linearly with the velocity shear. The lift force acts from the high-velocity side to low-velocity side, which is similar to that of a circular cylinder but opposite to that of a square cylinder under the same oncoming shear flow condition.

KEYWORDS: A Rectangular cylinder, Shear parameter, Large eddy simulation, Aerodynamic forces, Vortex shedding, Flow reattachment

1 INTRODUCTION

Rectangular cylinders are common configurations in many structures, such as bridges, tall buildings and so on, thus the flow past a bluff body with a rectangular cross section is of direct relevance to the structural problems in which wind-induced vibration is one of the most important issues to consider. So far, the majority of studies on this issue have been conducted under uniform oncoming flow conditions in which vortices with equal strength alternately shed from each side of the cylinder. However, in many practical applications, a cylindrical structure is immersed in a non-uniform flow. A bridge deck in the atmospheric boundary layer is an example, in which the vertical mean wind profile is one factor to determine the wind load on bridge deck. The influence of velocity profile or velocity shear in the oncoming flow becomes more significant at the situation of non-synoptic wind like a downburst, where the wind speed increases rapidly near the ground and reaches its maximum at the height about 80-100m, and then decreases with increase in height resulting in a stronger velocity shear than in synoptic winds. Strong velocity shear may also be created in complex topography. Therefore, the variation of aerodynamic behaviors of a rectangular cylinder with the velocity shear needs to be studied in detail. In this study, a dimensionless shear parameter $\beta = G \times D / Uc = (dU / dy) \times (D / Uc)$ is defined to express the extent of velocity shear, where U_C is the mean velocity at the center plane, and D is the thickness of the rectangular cylinder and G is the velocity gradient, as illustrated in Fig. 1. The magnitude of the shear parameter implies the velocity difference between the up and down surfaces of the rectangular cylinder.

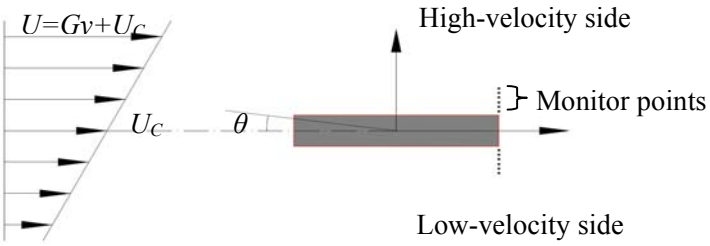

Fig.1. Schematic of shear flow configuration

Although the number of published papers is few, we are still able to find some studies about the shear flow past bluff bodies. Kiya et al. (1980) investigated the vortex shedding from a circular cylinder in shear flow and reported that the critical Reynolds number for the occurrence of vortex shedding becomes larger than in non-shear flow. Kiya's work was followed by many studies on the circular cylinder (e.g. Sumner and Akosile, 2003; Cao et al., 2010), and on the square cylinder (e.g. Cao et al., 2012). However, the common points of interest of these investigations were focused on how the Strouhal number varies with shear parameter and Reynolds number. Little attention was devoted to the shear effects on the aerodynamic forces and underlying background. In addition, there is no other reported study on the shear effects on a rectangular cylinder, expect for the experimental study of Onirsuka et al. (2000). The insufficient study on the shear effect over a rectangular cylinder partly motivates present study.

In this paper, aerodynamic characteristics of a rectangular cylinder with side ratio B/D=5 in shear flows are investigated at Re=22,000, where the Reynolds number Re is based on the thickness of the rectangular cylinder D and the centerline velocity U_C. The side ratio 5:1 is chosen as the study objective because this kind of rectangular cylinder has often been adopted as a reference for investigations of the aerodynamics and aeroelasticity of a bridge deck and other structural members (Matsumoto, 1996; Bartoli and Righi, 2006). In addition, a B/D=5 rectangular cylinder has very delicate dynamic behaviors of vortex shedding that is characterized by massive flow separation due to the sharp leading edges and intermittent-reattachment on side surfaces forming unsteady separating bubbles, and deserves to be studied from the view points of fundamental study of bluff body aerodynamics.

With the occurrence of shear parameter, i.e. an asymmetry in the oncoming flow, the separated flow must differ on the two sides of the rectangular cylinder, resulting in different aerodynamic behaviors with those in non-shear flow. Non-zero-mean lift and moment forces, which are important factors in determining the behavior of flow-structure coupling, must appear. However, there is no reported research on the flow around 5:1 rectangular cylinder in shear flows. Onirsuka et al. (2000) studied experimentally the Strouhal number of rectangular cylinders in linear shear flows at Re=3.2-9.7×10^4 at B/D=0.2-3. But the separated shear layer did not reattach on the side surface when B/D=0.2-3. The side ratio B/D=5 considered in this study involves intermittent flow reattachment, which makes the flow more sensitive to the oncoming velocity shear that brings separated shear layers with different strength and depth at the high and low velocity sides.

In this study, we investigated the vortex shedding and the aerodynamic forces on a rectangular cylinder in shear flows by Large Eddy Simulation (LES). We employed a structured grid mesh system for finite volume approximation of incompressible Navier-Stokes equations. The Fluent© package is used as a solver of the governing equations, but the options offered by Fluent© for simulation were carefully selected in order to achieve a good simulation. The numerical method and details applied in this study are described and validated by presenting the aerodynamic behaviors of a circular cylinder at Re=3,900. The aerodynamic characteristics of the 5:1 rectangular cylinder in shear flows at Re=22,000 are presented by comparison with available experimental and numerical results. Time-mean and unsteady flow patterns around the cylinder are

studied to enhance the understanding of the effects of velocity shear. In addition, the obtained results are compared with those of a circular cylinder (Cao et al. 2010) and a square cylinder (Cao et al. 2012) to achieve a comprehensive understanding of the shear flow around bluff bodies.

2 PROBLEM FORMATION AND NUMERICAL DETAILS

2.1 *Problem formulation*

The numerical model for the flow around a 5:1 rectangular cylinder is formulated using the Cartesian coordinate system. Eqs. (1) and (2) show the filtered continuity and Navier-Stokes equations for Large Eddy Simulation, in which the grid-scale turbulence is solved while the sub-grid-scale turbulence is modeled.

$$\frac{\partial \overline{u_i}}{\partial x_i} = 0 \tag{1}$$

$$\frac{\partial(\overline{u_i})}{\partial t} + \frac{\partial(\overline{u_i u_j})}{\partial x_j} = -\frac{1}{\rho}\frac{\partial \overline{P}}{\partial x_i} + \frac{\partial}{\partial x_j}\left(\nu \frac{\partial \overline{u_i}}{\partial x_j}\right) - \frac{1}{\rho}\frac{\partial \tau_{ij}}{\partial x_j} \tag{2}$$

where all the variables with the upper-marking are filtered components. The subgrid scale stresses (SGS stress), $\tau_{ij} = \overline{u_i u_j} - \overline{u}_i \overline{u}_j$, are expressed as $\tau_{ij} = -\frac{1}{3}\delta_{ij}\tau_{kk} + 2\nu_\tau \overline{S}_{ij}$

$\overline{S}_{ij} = \frac{1}{2}(\frac{\partial \overline{u}_i}{\partial x_j} + \frac{\partial \overline{u}_j}{\partial x_i})$, and $\nu_\tau = l^2 \left|\overline{S}\right|$ where $l = C_s \overline{\Delta}$ ($\overline{\Delta}$ is the size of grid filter).

We studied the flow around the 5:1 rectangular cylinder by performing three-dimensional unsteady simulation of the incompressible governing equations shown above with the aid of Fluent package. The options offered by Fluent© for simulation were carefully selected under the following considerations.

The velocity and the pressure are defined at the center of a control volume, while the volume fluxes are defined at the midpoint of their corresponding cell surfaces. In order to avoid the oscillating problems, the momentum Interpolation Method (MIM) developed by Rhie and Chow (1983) is used. The SIMPLE (Semi-Implicit Method for Pressure-Linked Equations) algorithm proposed by Patankar and Spalding (1972) is utilized, in which governing equations are solved sequentially because of their non-linearity and coupling characteristics and the solution loop is carried out iteratively in order to obtain a converged numerical solution. The pressure field is extracted by solving a pressure correction equation that is obtained by manipulating continuity and momentum equations, while the velocity field is obtained from the momentum equations. In addition, the convergence criterion of the iterative calculation is set to be 10^{-6}, and it takes about 30 iterations to satisfy this criterion in the simulation.

In order to avoid instability caused by central-differencing schemes and non-physical wiggles, the bounded central differencing scheme is applied to spatial differencing of convection term, which is a composite normalized variable diagram (NVD, Leonard, 1991) scheme that consists of a pure central differencing, a blended scheme of the central differencing and the second-order upwind scheme, and the first-order upwind scheme. Meanwhile, a fully-implicit second-

order time-advancement scheme is chosen for temporal discretization to obtain stable and accurate simulation.

2.2 *Numerical model and boundary conditions*

As shown in Fig. 2 (a), the computational domain is 52.5*D* in *x*-direction, 18*D* in *y*-direction and 5*D* in *z*-direction. The blockage ratio is 5.55% that is smaller than the suggestion (6.4%) of Sohankar et al. (2000). The ratio of spanwise length *L* to chord length *B* is set to be *L/B*=1 in order to achieve a good simulation of the mean and RMS of aerodynamic forces (Tamura et al. , 1998). *L/B* was utility also in the simulation of Mannini et al. (2010) and Bruno et al. (2010) . A structured grid system with the number of 325(*x*)×164(*y*)×24(*z*) is used to adequately resolve the flow (see Fig.2) with the first grid Δd near the body surface given empirically as $0.1/\sqrt{\mathrm{Re}}$ ($\Delta d / D = 6.5\times10^{-4}$). For the spatial discretization in spanwise direction, 24 cells are uniformly distributed with a grid length $\Delta z / B = 0.042$ that is smaller than the minimum requirement $\Delta z / B = 0.1$ recommended by Tamura et al. (1998). The non-dimensional time-step, Δt^* is $\Delta t^* = \Delta t U / D = 5\times10^{-3}$ which maintained the Courant number *CL*<1.

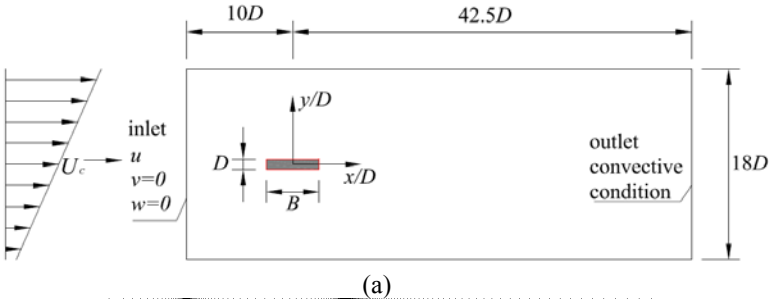

(a)

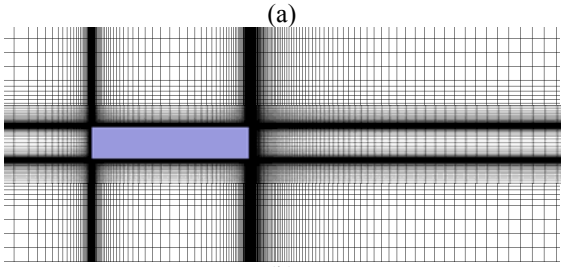

(b)

Fig.2 (a) Computational domain in x-y plane and boundary conditions, (b) Grid example near the cylinder

The boundary conditions for simulation are as follows:

Cylinder body surface: A no-slip condition for u_i=0 and a Neumann condition for pseudo-pressure ϕ are imposed.

Inlet: An UDF (User-Defined Function) condition, i.e., $U = 1 + Gy$, v=0 and w=0, and a Neumann condition of pseudo-pressure ϕ are imposed at the inlet boundary.

Outflow boundary: A convective boundary condition ($\partial\phi/\partial t + \bar{u}\cdot\partial\phi/\partial x = 0$) is applied for pseudo-pressure.

Spanwise: A periodic condition for velocity and pseudo-pressure are applied.

3 NUMERICAL VALIDATION

The flow over a circular cylinder at Re=3900 is often considered as a benchmark test model to check or confirm the accuracy of numerical simulation because there is plenty of reliable experimental and numerical data. Thus, in this study the numerical method is validated by comparing the mean and turbulence statistics of the flow around a circular cylinder at Re=3,900. Fig. 3(a) shows that the mean pressure coefficient distribution obtained by present numerical

shows that the mean pressure coefficient distribution obtained by present numerical method agrees well with other studies, while Fig. 3(b) shows that the streamwise mean velocity on the center line exhibits reasonable agreement also, especially at the near wake. Fig. 4 compares the turbulence statistics obtained at several downstream locations. Although the values deviate somewhat at several points, similar trendy of the variation of $u'u'$ and $u'v'$ in y direction is obtained. In short, the numerical method of present simulation produced reasonably good results, so it may be considered appropriate to simulation the flow over a bluff body with large scale vortex shedding.

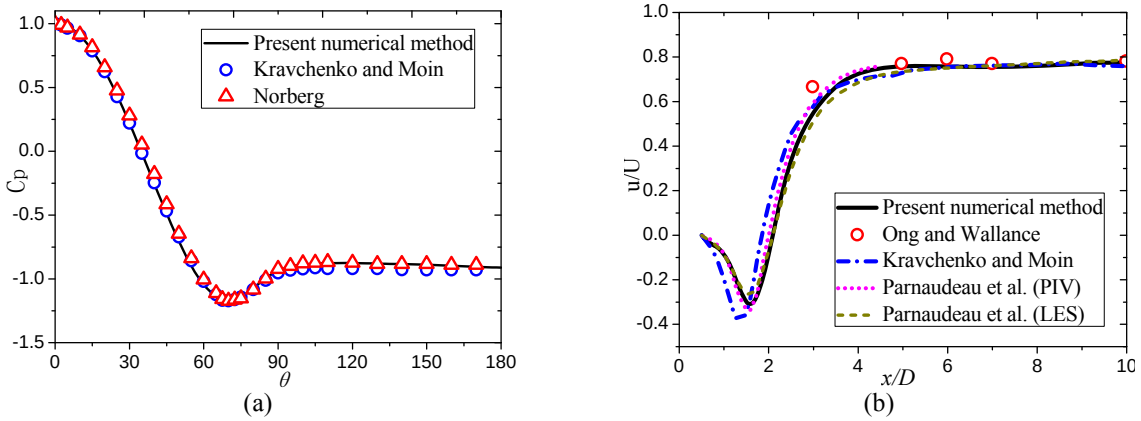

Fig. 3(a) Pressure coefficient distribution on the circular cylinder surface in non-shear flow (Re=4,200 in Norberg's experiment), (b) Mean streamwise velocity on the center line in the wake for the circular cylinder in non-shear flow

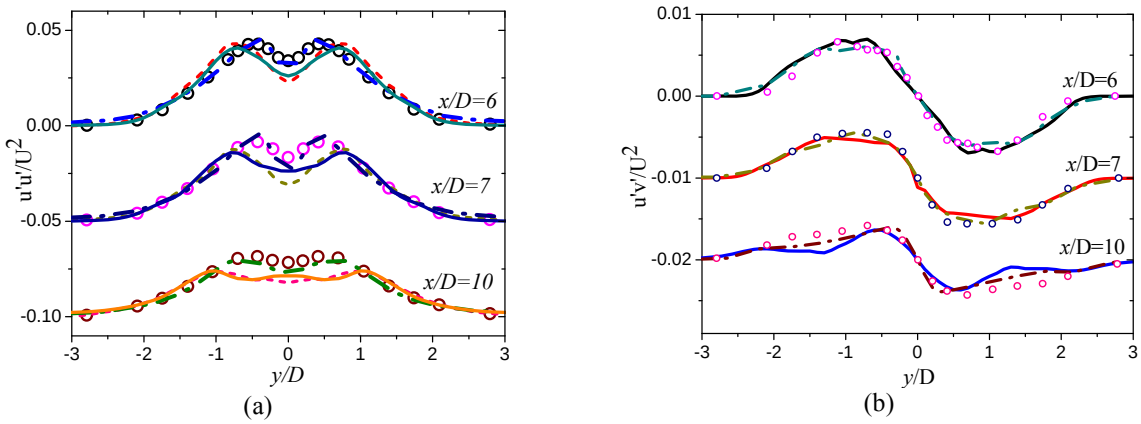

Fig.4 Comparison of the turbulence statistics in the wake of a circular cylinder at Re=3900, (a)Streamwise velocity fluctuations at three locations; (b) Reynolds shear stress at three locations. (—, Present LES; -· -, LES of Kravchenko and Moin, 2000; - - -, LES of Mittal and Moin, 1997; ○, experiment of Ong and Wallace, 1996)

4 NUMERICAL RESULTS AND DISCUSSIONS

4.1 *Vortex shedding*

The Strouhal number $St=fD/U$ is calculated from the FFT analysis of the lift coefficient for the flow around the 5:1 rectangular cylinder at non-shear and shear flows at Re=22,000, where f is the dominant vortex shedding frequency. The result obtained in present study are St=0.118 at β=0, St=0.117 at β=0.05 and St=0.118 at β=0.1, which is almost unchanged with shear parame-

ter. In addition, the Strouhal number obtained in non-shear flow is compared with other studies at Fig. 5, which exhibits the variation of the Strouhal number with side ratio. The present result St=0.118 at non-shear flow is very close to the numerical results of Yu and Kareem (1996) with St=0.114, Bruno et al. (2010) with St=0.115, and the experimental result of Schewe (2009) with St=0.111. In addition, the result that Strouhal number does not vary significantly with shear parameter were also observed at other studies of Cao et al. (2010) on a circular cylinder and Cao et al. (2012) on a square cylinder. It seems reasonably to conclude that the shear parameter does not bring significant change to the Strouhal number although it creates asymmetry into the wake structure as shown later.

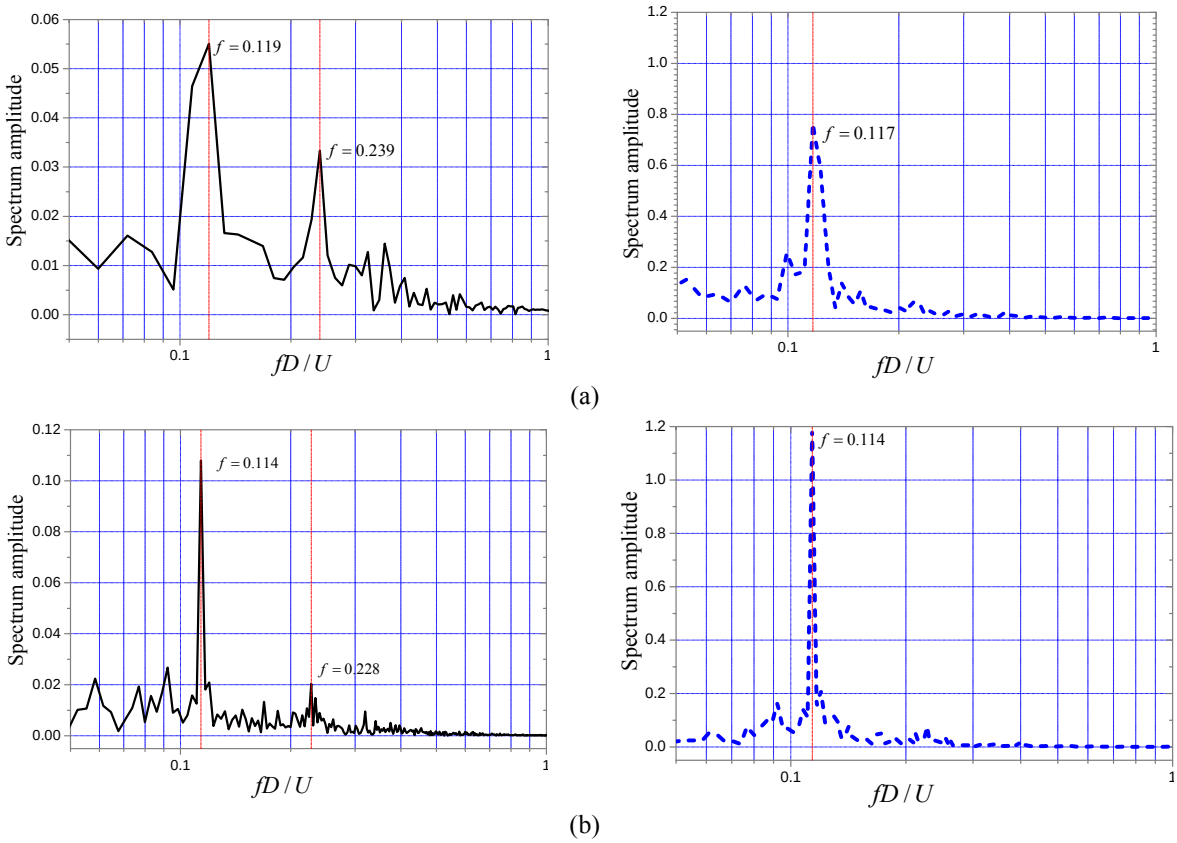

Fig. 6 Spectra of drag and lift coefficients at (a): β=0.05 and (b): β=0.1 (left: drag; right:lift)

Fig. 6 compares the power spectra of the instantaneous drag and lift coefficients at different shear parameters, β=0.05 and 0.1 at Re=22,000 for the 5:1 rectangular cylinder. The solid line shows the spectrum of drag coefficient C_D and the broken line shows that of lift coefficient C_L. Although the fluctuating lift coefficient still has one harmonic, a subharmonic has entered into the fluctuation of C_D. The strength of the subharmonic increases as the shear rate increases and it becomes dominant, resulting in the peak fluctuation frequencies of C_L and C_D becoming identical at β=0.1. A similar phenomenon was also reported in the case of a square cylinder (Cao et al. 2012).

Fig. 7 compares the instantaneous iso-vorticity surface of primary Karman vortex between no-shear and shear flows, where dashed and solid lines represents clockwise and counterclockwise vortices respectively. All the figures correspond to the moment when the lift coefficient is maximum. The vortices appears alternatively in the wake when β=0. However, with an increase in shear parameter, the counterclockwise vortices on the low-velocity side become weaker, and disappear in the far wake at β=0.1. The Karman Vortex Street is broken as result of the shear ef-

fect, but the counterclockwise vortex on the low-velocity still exists at the near wake and vortex shedding never disappears. This complicated phenomenon is also noticed by Saha et al (1999) from their two dimensional simulations on a square cylinder and Cao et al (2010, 2012) on a circular cylinder and a square cylinder. Therefore, it can be concluded that similar wake flow pattern exists for circular, square and rectangular cylinders in shear flows.

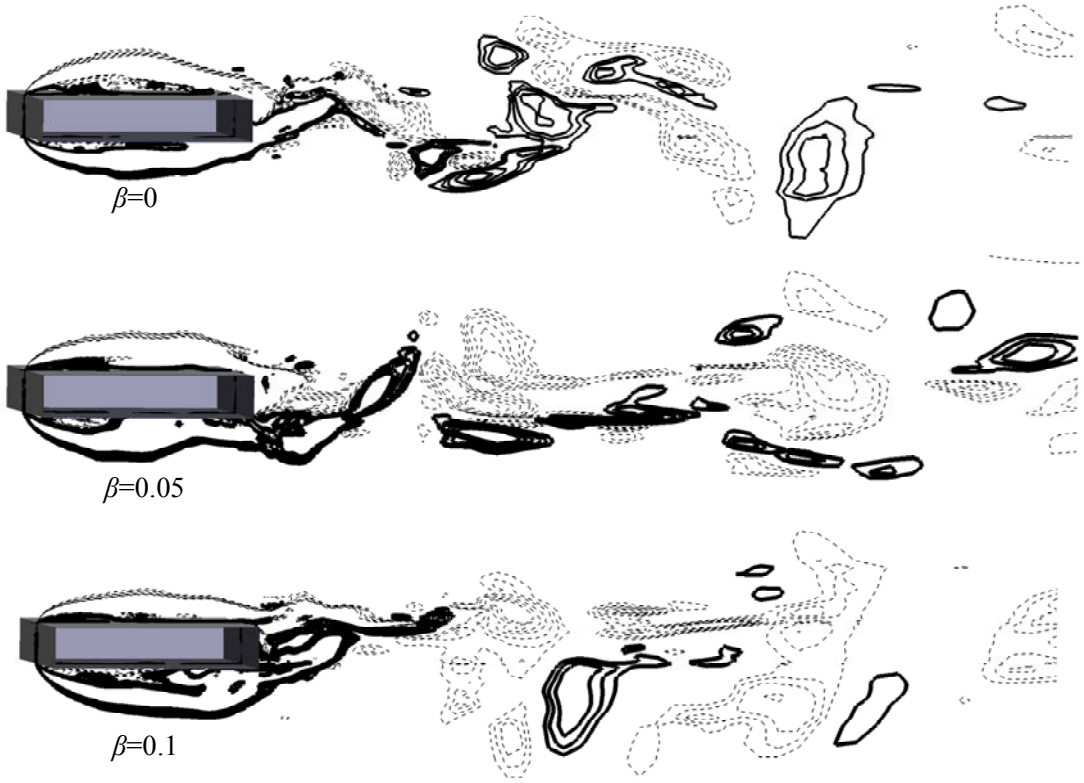

Fig. 7 Instantaneous wake structure with different shear parameters, $\omega_Z=\pm 2$

4.2 *Flow structures and Aerodynamic Forces*

The time-averaged streamlines of flow field around the rectangular cylinder with different shear parameters are compared in Fig. 8. As in the non-shear flow, the first vortex (the main vortex) and the second vortex (the bubble) can be observed both on the upper and lower sides of the rectangular cylinder in shear flow. However, they are no longer symmetric as in non-shear flow. With increase of shear parameter, the center position of the first vortex moves upstream on high-velocity side and downstream on low-velocity side respectively. Meanwhile, the first vortex on the high-velocity side becomes thinner while its counterpart on the low-velocity side becomes thicker. The mean recirculation region was not formed after the trailing edge of the cylinder at β=0.1. These complicated flow phenomena influence the aerodynamic forces on the 5:1 rectangular cylinder directly.

Fig. 9 compares the mean friction coefficient distribution around the rectangular cylinder between in shear and non-shear flows. The distribution of mean friction coefficient distribution becomes asymmetrical in the shear flow. With the increase in shear parameter, the mean reattachment length L_r on the low-velocity side increases from $L_r / D = 4.632$ （β=0） to $L_r / D = 4.850$（β=0.05）and $L_r / D = 4.868$（β=0.1），while it decreases from $L_r / D = 4.632$ （β=0）to $L_r / D = 4.469$（β=0.05）and $L_r / D = 4.073$ (β=0.1), which implies that the flow

will reattach more steadily on the high-velocity side and separate more steadily on the low-velocity side when the shear parameter is large enough.

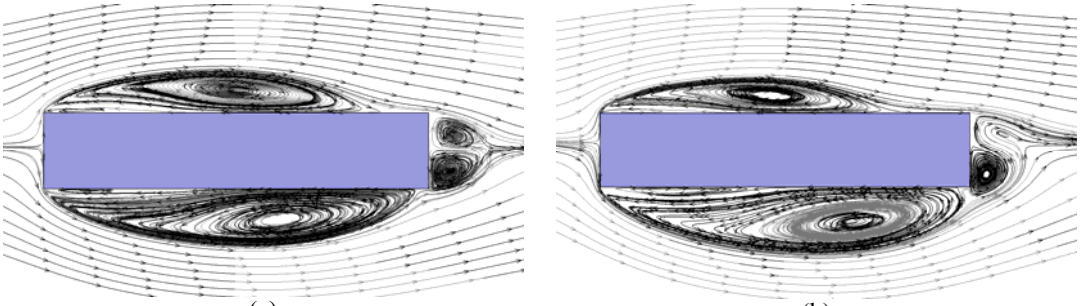

(a) (b)

Fig. 8 Streamlines of the time-averaged flow field around the cylinder, (a) β=0.05; (b) β=0.1

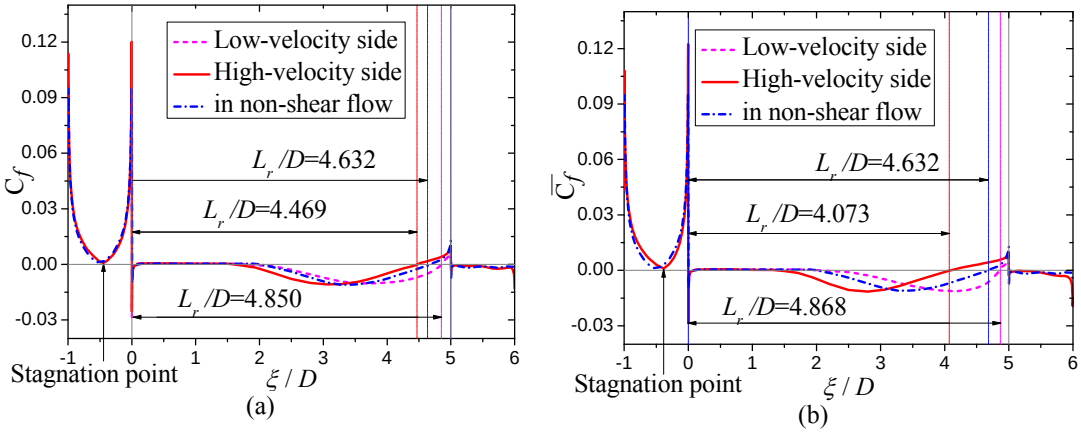

Fig. 9 Comparison on the distribution of the mean friction coefficient in shear flow and non-shear flow; (a) β=0.05; (b) β=0.1

Fig. 10 compares the mean pressure coefficient distribution around the rectangular cylinder surface in non-shear and shear flows. By the comparison in the region of $-1<\xi/D<0$ (the leading surface), it can be evidently observed that the stagnation point moves to the high-velocity side in shear flows.

As shown in Fig. 10, the value of mean pressure coefficients on the upper and lower sides in shear flows is almost the same in the region of $0<\xi/D<2.5$, in which the second vortex (the separate bubble) is formed. Thus it implies that the shear effects have little influence on determining the strength of separate bubble. However, for the region of $2.5<\xi/D<5$ where the first vortex (the main vortex) was formed, a significant deviation exists in the mean pressure distributions on high- and low-velocity sides as a result of the shear effects. Moreover, this deviation increases with the increase in shear parameter. The reason for this deviation is that the main vortex is quite different on the high- and low-velocity sides in shear flows as mentioned previously, and it suggests that the main role of shear effect plays on the large scale vortex.

For the region of $5<\xi/D<6$ (the trailing side), the mean base pressure coefficient increases with increase in shear parameter. This is similar to the finding of Onitsuka et al. (2000) in experimental study of the shear flow around rectangular cylinders with side ratio from 0.1 to 3.0.

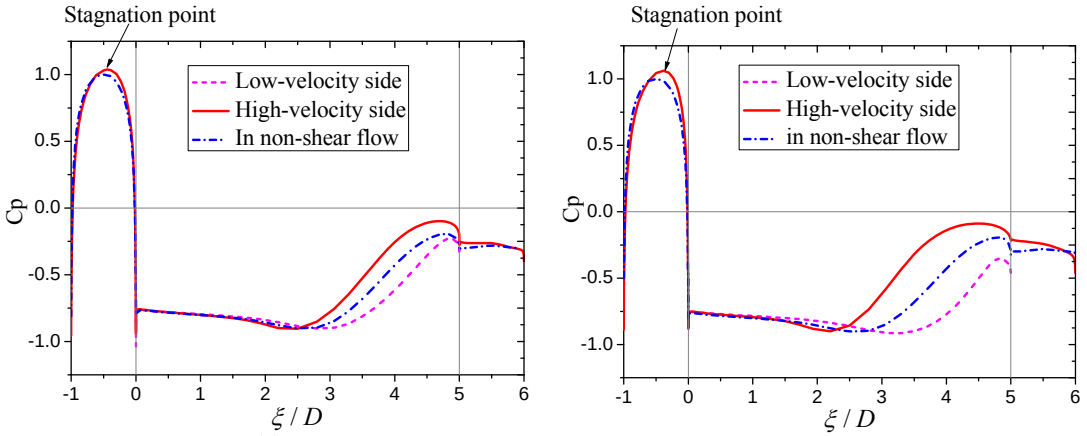

Fig. 10 Comparison of mean pressure coefficient over the rectangular cylinder surface in non-shear and shear flows, (a) β=0.05; (b) β=0.1.

Table 1 Comparison of mean and standard deviation values of aerodynamic force coefficients (normalized with respect to the body thickness D) with different shear parameters.

β	C_D	C_D'	C_L	C_L'	C_M	C_M'	T^*
0	1.100	0.082	--	0.890	--	0.773	279.5
0.05	1.128	0.090	-0.480	0.927	-0.717	0.817	213.4
0.1	1.142	0.111	-1.119	1.011	-1.405	0.867	262.1

As shown in Table 1, the direction of the lift force on a rectangular cylinder is the same to that on a circular cylinder, but opposite to that on a square cylinder. In the case of a circular cylinder, the movement of stagnation point generates a lift force from the high-velocity side to low-velocity side, while the velocity difference of the two sides has a contrary effect. The studies of Cao et al. (2007, 2010) showed that the contribution of the movement of stagnation point is dominant, and thus the lift force on a circular cylinder acts from the high-velocity side to low-velocity side. For the case of a square cylinder, the flow separates completely from leading side without flow reattachment, and the movement of stagnation point does not contribute to the lift force as shown in the simulation of Cao et al. (2012). Thus lift force direction is determined by the velocity difference and accompanying vortices with different strengths on two sides. For a rectangular cylinder with a side ratio B/D=5, the movement of stagnation point still has little influence on determining the direction of lift force. However for this kind of rectangular cylinder, the different movements of mean reattachment points on high- and low-velocity sides result in mean pressure distributions differing on two sides as shown in Fig. 15. Thus the lift force of a 5:1 rectangular cylinder acts from the high-velocity side to low-velocity side in shear flow.

5 CONCLUSIONS

In this paper, we carried out numerical simulations to investigate the aerodynamic characteristics of a 5:1 rectangular cylinder in shear flows at Reynolds numbers Re=22,000. The vortex shedding and aerodynamic forces accompanying with the complicated flow structures are studied.

The Strouhal number was found to have no significant variation in the shear parameter range of 0-0.1 at Re=22,000, which is similar to that in the case of a square cylinder and a circular cylinder. With increasing of shear parameter, the peak frequency of the drag coefficient becomes more identical to that of the lift coefficient due to the change of vortices forming behind

the back side. Although the Karmen vortex is not completely suppressed in the investigated ranges of shear parameter at Re=22,000, the Karmen vortex street in the wake is broken as a result of shear effects.

The intermittently-reattached flow becomes more stably-reattached and results in that the mean reattachment point moves upstream on the high-velocity side in shear flow, whereas it becomes more stably-separated on the low-velocity side. The stagnation point moves to the high-velocity side in shear flow, and the stagnation angle increases almost linearly with increasing of shear parameter.

Due to the movements of mean reattachment point, the mean pressure coefficient distribution over the rectangular cylinder surface is no longer symmetric. In the investigated range of shear parameter at Re=22,000, the mean value of drag force was observed to have unchanged while its standard-deviation increases with an increase in shear parameter. The mean lift force is no longer closing to zero resulting from the difference of the strength and location of the main vortices on two sides. Unlike the case of a square cylinder in a shear flow, the lift acts from high-velocity side to the low-velocity side for a 5:1 rectangular cylinder which is similar to that of a circular cylinder. However, the physical mechanism of the lift force direction of the rectangular cylinder, in which the movement of the mean reattachment point plays a dominating role to the lift force and the separation point is fixed, differs from that of the circular cylinder.

6 ACKNOWLEDGMENTS

This research was funded in part by Natural Science Foundation of China (NSFC) Grant No. 50978202 and Shanghai Pujiang Program number10PJ1409700.

7 REFERENCES

1 G. Bartoli, and M. Righi, Flutter Mechanism for Rectangular Prisms in Smooth and Turbulent Flow, *Journal of Wind Engineering and Industrial Aerodynamics,* **94** (2006), 275-91.

2 L. Bruno, D. Fransos, N. Coste, and A. Bosco, 3d Flow around a Rectangular Cylinder: A Computational Study, *Journal of Wind Engineering and Industrial Aerodynamics,* **98** (2010), 263-76.

3 S. Cao, S. Ozono, K. Hirano, and Y. Tamura, Vortex Shedding and Aerodynamic Forces on a Circular Cylinder in Linear Shear Flow at Subcritical Reynolds Number, *Journal of Fluids and Structures,* **23** (2007), 703-14.

4 S. Y. Cao, Y. J. Ge, and Y. Tamura, Shear Effects on Flow Past a Square Cylinder at Moderate Reynolds Numbers, *Journal of Engineering Mechanics-Asce,* **138** (2012), 116-23.

5 M. Kiya, H. Tamura, and M. Arie, Vortex Shedding from a Circular Cylinder in Moderate Reynolds Number Shear Flow, *Journal of Fluid Mechanics,* **101** (1980), 721-35.

6 A. G. Kravchenko, and P. Moin, Numerical Studies of Flow over a Circular Cylinder at Re-D=3900, *Physics of Fluids,* **12** (2000), 403-17.

7 B.P. Leonard, The Ultimate Conservative Difference Scheme Applied to Unsteady One-Dimensional Advection, *Computer Methods in Applied Mechanics and Engineering,* **88** (1991), 17-74.

8 C. Mannini, A. Soda, and G. Schewe, Numerical Investigation on the Three-Dimensional Unsteady Flow Past a 5:1 Rectangular Cylinder, *Journal of Wind Engineering and Industrial Aerodynamics,* **99** (2011), 469-82.

9 C. Mannini, Unsteady Rans Modelling of Flow Past a Rectangular Cylinder: Investigation of Reynolds Number Effects, *Computers & Fluids,* **39** (2010), 1609-24.

10 M. Matsumoto, Aerodynamic Damping of Prisms, *Journal of Wind Engineering and Industrial Aerodynamics,* **59** (1996), 159-75.

11 M. Matsumoto, H. Shirato, K. Araki, T. Haramura, and T. Hashimoto, Spanwise Coherence Characteristics of Surface Pressure Field on 2-D Bluff Bodies, *Journal of Wind Engineering and Industrial Aerodynamics,* **91** (2003), 155-63.

12 R. Mittal, and Moin P., Suitability of Upwind-Biased Finite Difference Schemes for Large-Eddy Simulation of Turbulent Flows, *AIAA Journal,* **35** (1997), 1415-17.

13 C. Norberg, An Experimental Investigation of the Flow around a Circular-Cylinder - Influence of Aspect Ratio, *Journal of Fluid Mechanics,* **258** (1994), 287-316.
14 C. Norberg, Flow around Rectangular Cylinders: Pressure Forces and Wake Frequencies, *Journal of Wind Engineering and Industrial Aerodynamics,* **49** (1993), 187-96.
15 A. Okajima, Strouhal Numbers of Rectangular Cylinders, *Journal of Fluid Mechanics* **123** (1980), 379-98.
16 L. Ong, and J. Wallace, The Velocity Field of the Turbulent Very near Wake of a Circular Cylinder, *Experiments in fluids,* **20** (1996), 441-53.
17 S. Onitsuka, Ozono, S., Cao, S., Wakasugi, Y., Flow around Rectangular Cylinders in Linear Shear Flow, in *The 16th Japanese National Wind Engineering Symp.* (Tokyo, 2000), pp. 279-84.
18 P. Parnaudeau, J. Carlier, D. Heitz, and E. Lamballais, Experimental and Numerical Studies of the Flow over a Circular Cylinder at Reynolds Number 3900, *Physics of Fluids,* **20** (2008).
19 S.V. Patankar, and D.B. Spalding, A Calculation Procedure for Heat, Mass and Momentum Transfer in Three-Dimensional Parabolic Flows, *Journal of Heat and Mass Transfer,* **15** (1972), 1787-806.
20 G. Schewe, Reynolds-Number-Effects in Flow around a Rectangular Cylinder with Aspect Ratio 1:5, in *Proceedings of the Fifth European and African Conference on Wind Engineering*, ed. by C. Borri, Augusti, G., Bartoli, G., Facchini, L. (Florence, Italy.: Firenze University Press, 2009).
21 K. Shimada, and T. Ishihara, Application of a Modified K-Epsilon Model to the Prediction of Aerodynamic Characteristics of Rectangular Cross-Section Cylinders, *Journal of Fluids and Structures,* **16** (2002), 465-85.
22 J. Smagorinsky, General Circulation Experiments with the Primitive Equations, *Monthly Weather Review,* **91** (1963), 99-164.
23 A. Sohankar, L. Davidson, and C. Norberg, Large Eddy Simulation of Flow Past a Square Cylinder: Comparison of Different Subgrid Scale Models, *Journal of Fluids Engineering-Transactions of the Asme,* **122** (2000), 39-47.
24 D. Sumner, and O. O. Akosile, On Uniform Planar Shear Flow around a Circular Cylinder at Subcritical Reynolds Number, *Journal of Fluids and Structures,* **18** (2003), 441-54.
25 T. Tamura, and Y. Ito, Aerodynamic Characteristics and Flow Structures around a Rectangular Cylinder with a Section of Various Depth/Breadth Ratios, *Journal of Structural and Construction Engineering* **486** (1996), 153-62.
26 T. Tamura, T. Miyagi, and T. Kitagishi, Numerical Prediction of Unsteady Pressures on a Square Cylinder with Various Corner Shapes, *Journal of Wind Engineering and Industrial Aerodynamics,* **74-76** (1998), 531-42.
27 D. Yu, and A. Kareem, Two-Dimensional Simulation of Flow around Rectangular Prism, *Journal of Wind Engineering and Industrial Aerodynamics,* **62** (1996), 131-61.

Turbulence intensity effect on the bluff bodies aerodynamic behavior

M. Belloli [a] , F. Fossati[a], S. Giappino [a], S. Muggiasca [a], F. Robustelli [a]

[a]*Politecnico di Milano, Dipartimento di Meccanica, Milano, Italy*

1 INTRODUCTION

Slender high rise structures are exposed to aerodynamic problems connected to the wind-structure interaction, for example vortex shedding or dynamic instability (e.g. galloping). Generally the design of these structures requires the aid of wind tunnel tests on scaled models. The paper investigates the aerodynamic behavior of a bluff body and the shape is adopted for section of the tower of a cable-stayed bridge (Fossati et al. 2011). The problem is investigated by wind tunnel tests using a rigid sectional model with particular attention on the effects related to the turbulence intensity of the incoming flow. The present paper shows the results obtained in terms of aerodynamic forces and pressure distributions for two level of turbulence, I_u=0.2 % and I_u=2 %. Vortex shedding phenomenon in these two conditions will be also discussed.

2 EXPERIMENTAL SET-UP

The sectional model has been realized scaling the reference section of the real bridge tower (1:18 scaled model). Figure 1 shows the section geometry that is characterized by two curved surfaces and cut edges. The distance D between the two plane sides represents the characteristic dimension of the model and it is equal to 0.446 m. The model has an aspect-ratio L/D equal to 8. It is manufactured using an internal structural beam covered by an external shell that reproduces the required geometry.

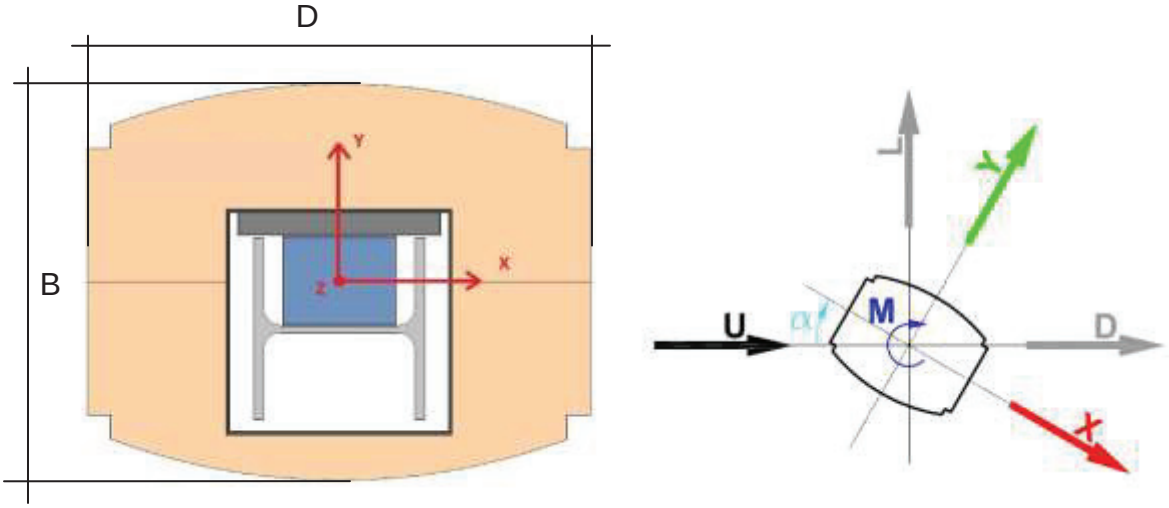

Figure 1 Section geometry: wind exposures and reference system

The external is divided in a dynamometric part, connected to the beam through a six component balance and a non-dynamometric part rigidly connected to the beam to correctly reproduce the boundary conditions for the aerodynamic forces measurements. In particular, drag

and lift forces have been considered, defined in agreement with the sketch reported in Figure 1.
Pressure taps have been placed on different sections of the non-dynamometric part in order to define surface pressure distribution. The taps were connected to high sample-rate scanners allowing high-resolution measurements of the pressure field distribution in time domain. The pressure scanners have been installed inside the model with short pneumatic connections to the pressure taps. This solution guarantees a high frequency response of the tubing system.
A total number of 96 pressure taps distributed on three different sections has been placed on the model: this configuration permit to define pressure distributions in three positions of the sectional model in order to control how the flow evolves in the axial direction. Aerodynamic forces have been obtained integrating pressure distribution along one section, and compared with the forces measured by the balance.
Experimental tests were performed in the Politecnico di Milano wind tunnel, using two different tests sections to obtain the different turbulence intensity conditions.

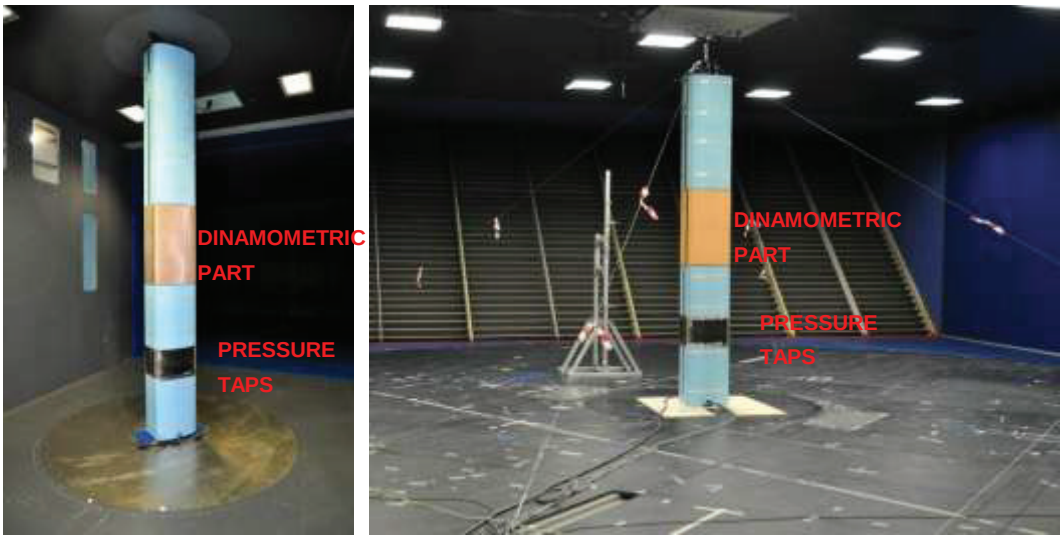

Figure 2. Wind tunnel model setup. (left) 0.2% turbulence condition (right) 2% turbulence condition

Figure 2 shows the model placed in the low turbulence tests section (left) and in the boundary layer tests section (right). Each test section is characterized by a natural value of turbulence intensity, 0.2 % and of the integral length scale L_u^x=0.01 m for the first one and 2 %, L_u^x=0.2 m for the second one. In both cases the model has been fixed on the ground obtaining a stiff structure with high structural frequencies (the lowest natural frequencies of the model are equal to 20 Hz in the low turbulence tests section and 7 Hz in the boundary layer tests section). The dynamic behavior of the model has been checked by means of two accelerometers. The model has been tested for different angles of attack as showed in Figure 1.

3 EXPERIMENTAL RESULTS

Tower sectional model has been tested for different wind exposure (0°–90°) and for different wind velocity (up to 50 m/s in the high speed/low turbulence tests section and up to 15 m/s in the boundary layer tests section). The tests highlight that no significant dependence to the wind velocity can be observed in the tower aerodynamic behavior for the studied velocity range: for this reason the results will be presented only for one wind velocity (V=15 m/s, Re=4.5 10^5). The forces have been obtained from the balance signals and they are in good agreement with the forces obtained integrating pressure distributions. Figure 3 shows the mean drag coefficient as a function of the wind exposure, measured both by the balance and by the pressure system.

Figure 4 compares the drag force coefficient measured in different turbulence intensity conditions as a function of the exposure angle. It is possible to notice that the aerodynamic behavior of the model is very sensitive to this parameter: a small increase in turbulence intensity completely changes the forces. In particular at I_u=0.2 % the drag coefficient is quite high and it become smaller increasing the turbulence intensity. A spectral analysis of the aerodynamic forces points out that the high drag condition is characterized by a well defined vortex shedding, on the other hand the low drag condition do not highlight vortex shedding phenomenon.

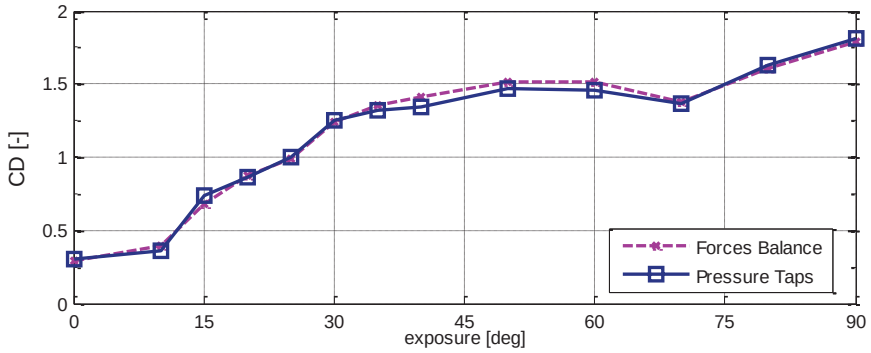

Figure 3. Comparison between drag coefficient measured by balance and pressure systems: I_u=0.2 %, Re=4.5 10^5

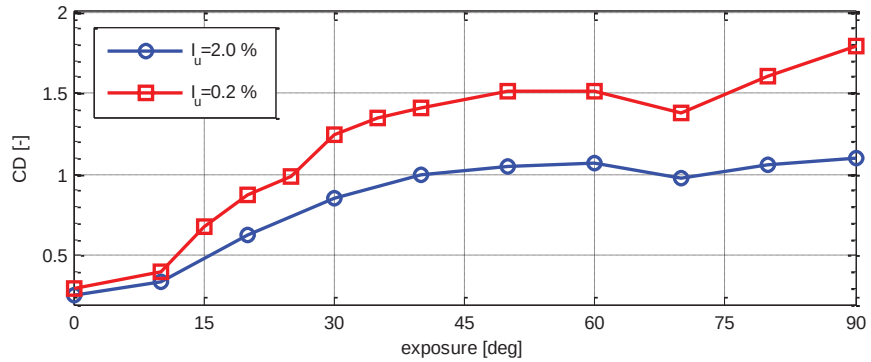

Figure 4. Drag force coefficient at Re=4.5 10^5 as a function of the angle of attack and for the two tested turbulence intensity conditions

Vortex shedding is clearly identified for exposure angles higher than 20° in I_u=2% condition, while for lower angles and lower level of turbulence no significant periodic vortex shedding can be observed.

In order to better understand the phenomenon a deeper analysis has been made for each exposure angle and in particular pressure distributions and harmonic content of aerodynamic forces have been considered. In the following the results relative to 0° and 90° of angle of attack will be presented: these two cases can be considered representative of the different phenomena observed during the tests. Moreover they can also easily related to literature data concerning the aerodynamics of rectangular prisms with different aspect ratio (Holmes. 2007). In particular at 0° the tower section is characterized by an aspect ratio B/D=1.27, while at 90° the ratio is equal to B/D=0.78. Only the case at Re=4.5 10^5 will be reported: similar results have been obtained also for different wind velocities. Only the pressure distributions measured along one section will be presented, others sections show similar results.

3.1 *Exposure angle: 0°*

The tower section at 0° does not show significant vortex shedding in both the wind turbulence conditions. Figure 5, Figure 6 and Figure 7 concern the test performed in low turbulence condition (I_u=0.2%) and they report respectively the aerodynamic coefficients time histories, the

pressure distributions at four different times and the PSD of the aerodynamic coefficients. It is possible to notice that the typical narrow band related to vortex shedding phenomenon is not visible in the time histories and in the PSD of drag and lift coefficients. The absence of a periodic vortex shedding is confirmed by the pressure distributions shown in Figure 6 in terms of pressure coefficients: four different instants have been reported in order to observe how the distribution evolves in the time. The pressure distribution does not change and especially downstream large oscillations in pressure signals have not been found.

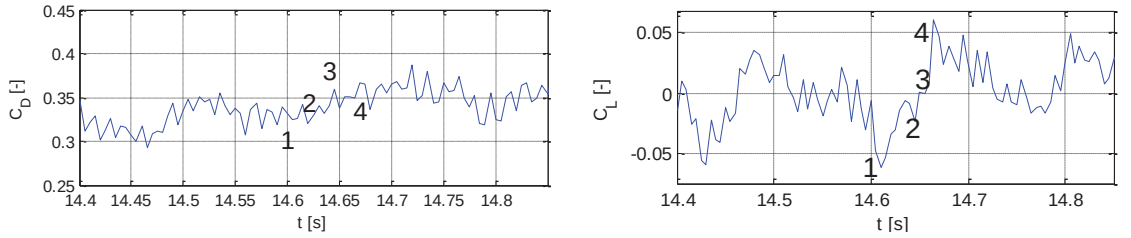

Figure 5. Drag and lift coefficients time histories zoom (I_u=0.2%, Re=4.5 10^5, exposure 0°)

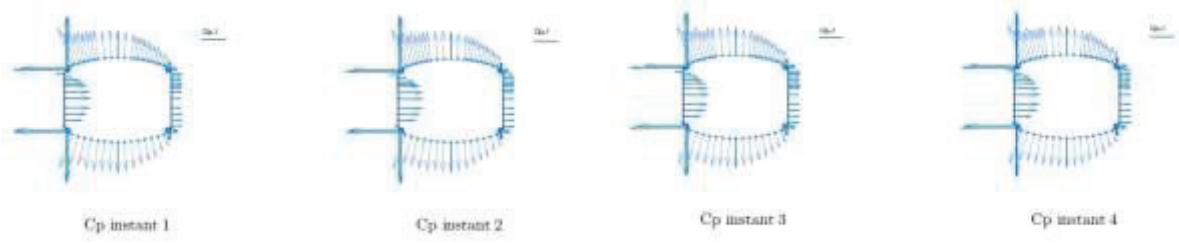

Figure 6. Instantaneous pressure coefficient on the section for the four instants identified in Figure 5 (I_u=0.2%, Re=4.5 10^5, exposure 0°)

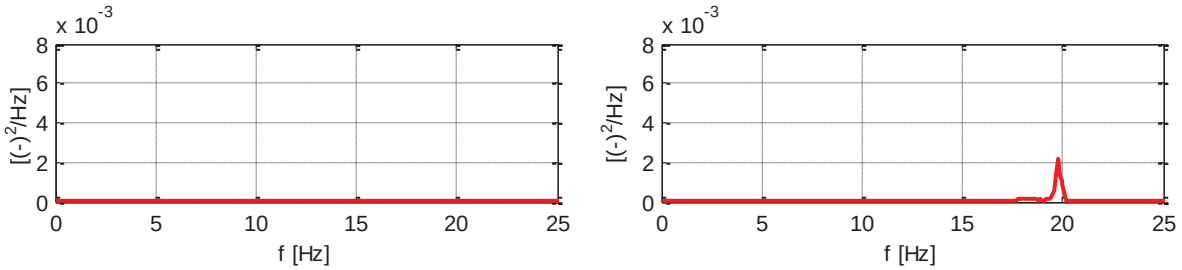

Figure 7. PSD of drag and lift coefficients (I_u=0.2%, Re=4.5 10^5, exposure 0°)

The tower section in higher wind turbulence condition shows a similar behavior compared to the one observed at I_u=0.2 % without a clear vortex shedding. In particular the pressure distributions reported in Figure 9 are comparable with the distributions reported in Figure 6 and they do not change significantly with the time. The small peaks identified in the PSD of the aerodynamic coefficients (Figure 8) and the sinusoidal shape of the drag time history (Figure 10) can be related to a buffeting excitation in correspondence of the two first natural frequencies of the model. This excitation produces small inertial forces on the dynamometric part that were measured by the balance. These peaks are not present in the forces obtained from the pressure system and they are fixed by changing wind velocity, for these reasons they cannot be considered related to vortex shedding phenomenon.

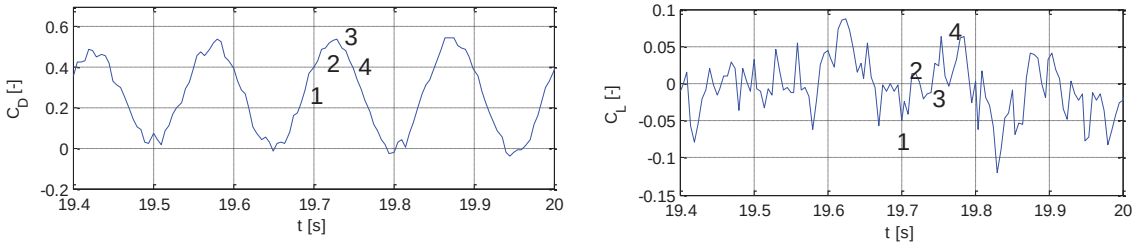

Figure 8. Drag and lift coefficients time histories zoom (I_u=2%, Re=4.5 10^5, exposure 0°)

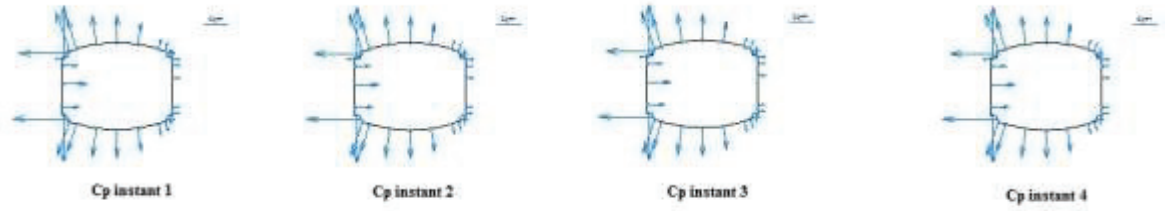

Figure 9. Instantaneous pressure coefficient on the section for the four instants identified in Figure 8(Iu=0.2%, Re=4.5 105, exposure 0°)

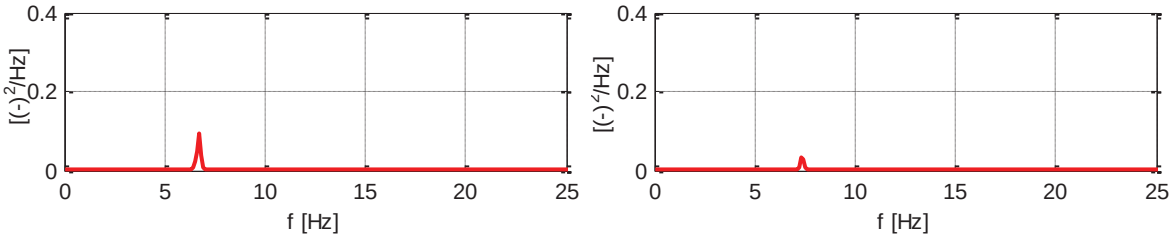

Figure 10. PSD of drag and lift coefficients (I_u=0.2%, Re=4.5 10^5, exposure 0°)

It is possible to note that there are small differences in the standard deviation of the pressure coefficients. The pressure coefficients have been represented as a function of the position along the section for the two wind turbulence conditions in Figure 11. In particular, the turbulence of the incoming wind increases the level of the fluctuating part of the pressures. Similar results have been found also in literature data (Nakamura & Ozono, 1987; Li & Melbourne, 1999; Albin wt al., 1998) considering rectangular prism: an increase in the wind turbulence move downstream the separation point reducing the wake dimension and the drag coefficient (in the presented case C_D=0.25 for I_u=0.2% and C_D=0.29 for I_u=2%).

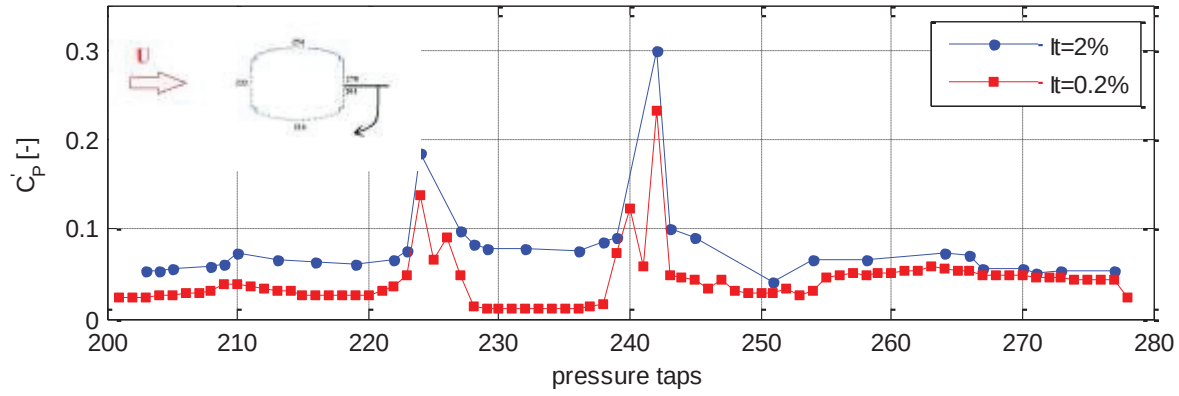

Figure 11.Pressure coefficients standard deviation Re=4.5 10^5 as a function the pressure taps for the two tested turbulence intensity conditions (exposure 0°)

3.2 *Exposure angle: 90°*

Exposure 90° is representative of the behavior experienced by the tower with and without turbulence. The tests performed in the low turbulence test section highlight a clear vortex shedding (Figure 12, Figure 13, Figure 14) while a small increase in the wind turbulence intensity completely suppress vortex shedding (Figure 15, Figure 16, Figure 17)
In particular, in low turbulence condition the lift force coefficient is characterized by a sinusoidal trend observable both in the time history (Figure 12) and in the spectrum (Figure 14). The peak is in correspondence of a frequency equal to 5.4 Hz resulting in a Strouhal number of 0.17 and the peak moves with the velocity. Also the pressure distributions (Figure 13), relative to different points of the lift coefficient cycle, are characterized by strong oscillations: the oscillation in the pressures measured along the horizontal edges are related to the oscillation of the lift force; whereas pressures measured on the downwind curved surface change in the time due to the vortex shedding.

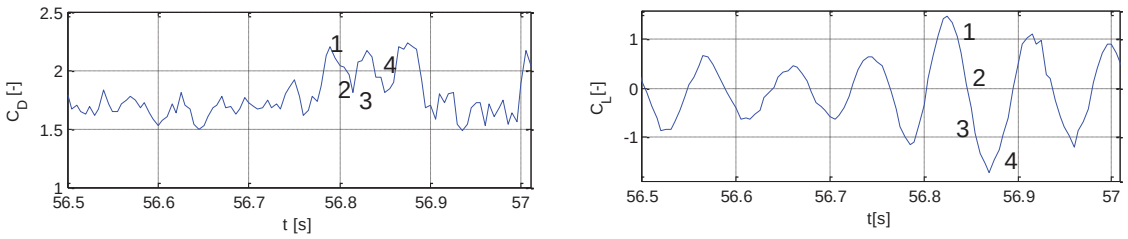

Figure 12. Drag and lift coefficients time histories zoom (I_u=0.2%, Re=4.5 10^5, exposure 90°)

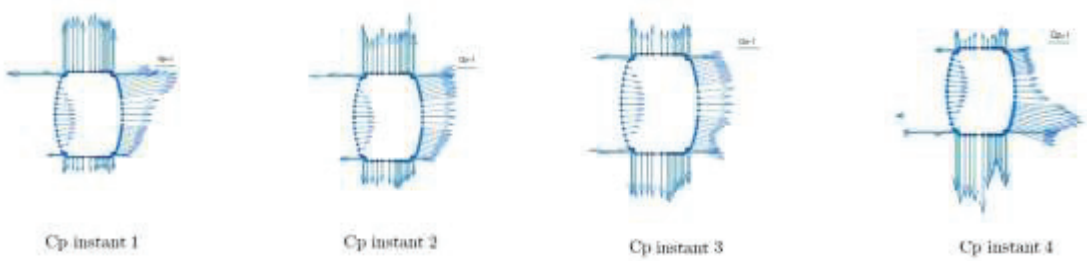

Figure 13. Ins Instantaneous pressure coefficient on the section for the four instants identified in Figure 8(Iu=0.2%, Re=4.5 105, exposure 90°)

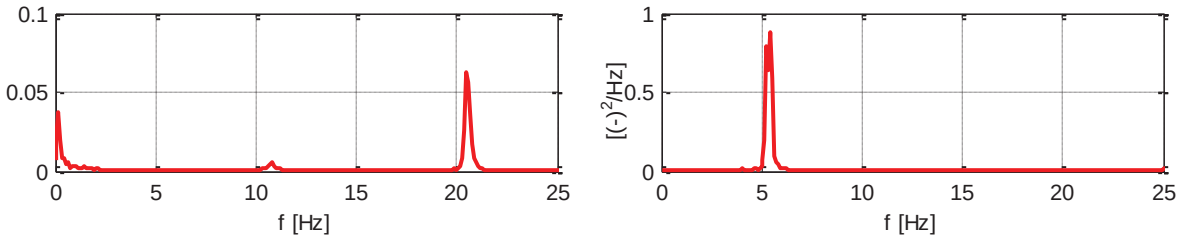

Figure 14. PSD of drag and lift coefficients (I_u=0.2%, Re=4.5 10^5, exposure 90°)

In the higher turbulence condition vortex shedding cannot be observed. The only oscillations observable are in drag and lift coefficients and they are referable to the forcing excitation that excites the first two natural frequencies of the model itself (Figure 15, Figure 17). In fact the pressure distributions do not highlight any vortex shedding phenomena with a constant trend with the time. The absence of vortex shedding also affects the wake dimension resulting in a lower drag compared to the one measured at I_u=0.2%. However, in both the turbulence condi-

tions the mean drag coefficient is higher than the one measured at 0°: this is in agreement with the trend found for rectangular prism as a function of the aspect ratio (Holmes. 2007).

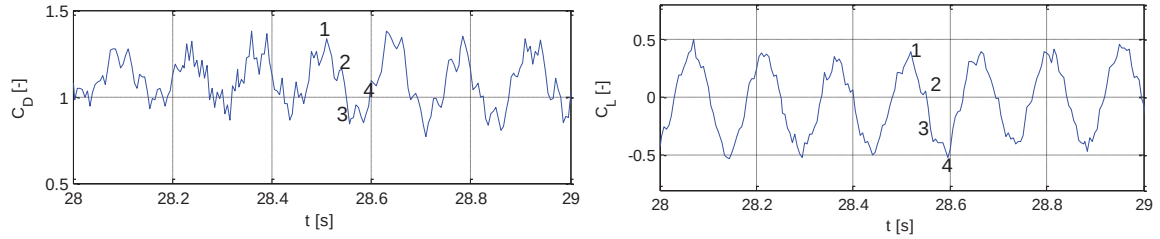

Figure 15. Drag and lift coefficients time histories zoom (I_u=2%, Re=4.5 10^5, exposure 90°)

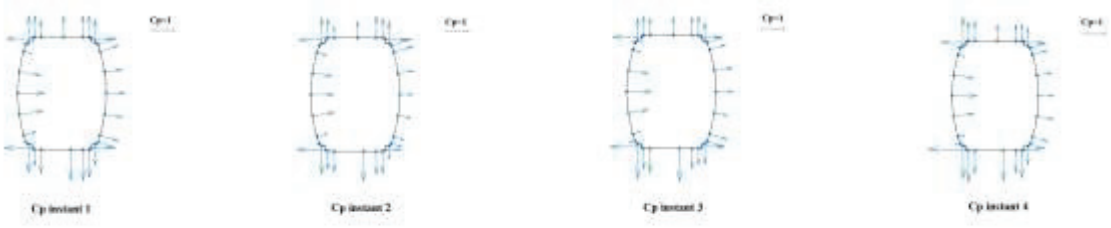

Figure 16. Instantaneous pressure coefficient on the section for the four instants identified in Figure 8(Iu=2%, Re=4.5 105, exposure 90°)

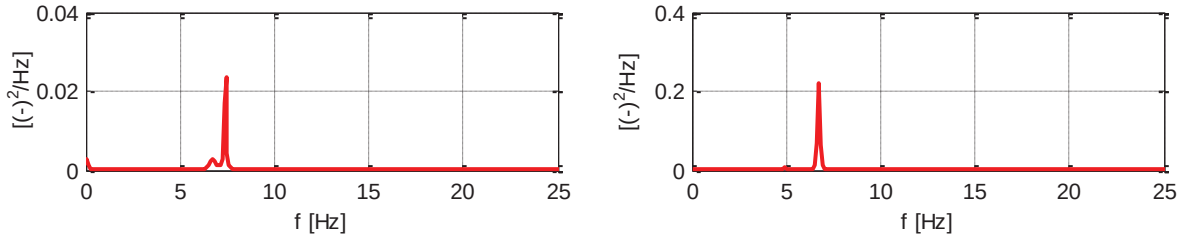

Figure 17. PSD of drag and lift coefficients (I_u=2%, Re=4.5 10^5, exposure 90°)

4 CONCLUSION

Traditionally studying bluff bodies, a dependence of the drag coefficient from Reynolds number is observed. During the experimental campaign performed on a section of a cable stayed bridge tower a wide wind velocity range has been investigated but no significant Reynolds number effects have been observed. On the other hand a strong dependence on the small scale turbulence of the incoming flow has been highlighted. In particular for some tested exposure angles it has been observed that a small increase in the turbulence intensity can completely suppress vortex shedding phenomenon.
Moreover it is author's opinion that not only the turbulence intensity influences the aerodynamic behavior of the model but also the length scale of the turbulence referred to the characteristic dimension of the considered section.

5 REFERENCES

Fossati, F., Belloli, M., Giappino, S., Muggiasca, S., Villani, M., 2011. On the aerodynamic and aeroelastic response of a bridge tower, submitted to the Journal of wind Engineering and Industrial Aerodynamics. 99 (6-7) , pp. 729-733

Holmes J.D.. 2007 Wind loading of structures. Taylor & Francis,.

Nakamura Y. and Ozono S., 1987. The effects of turbulence on a separated and reattaching flow. Journal of Fluid Mechanics, 178:477–490

Li Q.S and Melbourne W.H. 1999. The effect of large-scale turbulence on pressure fluctuations in separated and reattaching flows. Journal of Wind Engineering and Industrial Aerodynamics, 83(1-3):159

Albin A., Szewczyk F. Haan L., Ahsan Kareem, 1998. The effects of turbulence on the pressure distribution around a rectangular prism. Journal of Wind Engineering and Industrial Aerodynamics, 77 - 78:381 – 382,.

The Seventh International Colloquium on Bluff Body Aerodynamics and Applications (BBAA7)
Shanghai, China; September 2-6, 2012

The pressure distribution characteristics of a typical bluff-section model

Banghu Qian [a], Xiaohong Hu [a], Chuanxin Hu[a]

[a]*Department of Bridge Engineering, Tongji University, Shanghai, China*

ABSTRACT: Typical bluff-section model pressure distributions are measured in the condition of fixed model as well as fluttering model with and without stabilizer in this paper. Firstly, surface pressure fluctuation characteristics of the bluff-section model during flutter are analyzed. Then, surface pressure distribution characteristics are analyzed based on proper orthogonal decomposition (POD). In the end, pressure distributions are compared between fixed model and fluttering model with and without stabilizer.

KEYWORDS: Pressure distribution, POD analysis , intrinsic mode , principal coordinate, amplitude spectrums, stabilizer

1 INTRODUCTION

Bridge flutter is one of diverging self-excited vibration. During flutter, vibrating decks are constantly absorbing energy from flowing air, which is greater than that dissipated by structural damping [1]. At present, three main methods are used in researching bridge flutter mechanism. They are flutter driving mechanism analysis method based on aerodynamic derivatives [2], flutter analysis method based on computational fluid dynamics (CFD) [3] and particle image velocimetry (PIV) analysis method[4].

In the process of long-span bridge design, it has to be ensured that structural flutter critical velocity is higher than the flutter checking velocity in order to avoid the occurrence of fatal flutter instability phenomena. Three main measures are used to improve bridge flutter critical velocity, which are: structural measures[5], mechanical measures [6] and aerodynamic measures[7] .

Aerodynamic measures improve bridge flutter critical velocity by changing aerodynamic shape. Central stabilizer is one of the common used aerodynamic measures. The control effects of central stabilizer to flutter have a great relationship with its position. For example, stabilizer control located in upstream has better effect than the downstream one. Meanwhile, control effects of the central stabilizer are strongly affected by the wind attack angle. The most unfavorable attack angles of the stabilizers with different heights are not the same. As the most unfavorable flutter critical velocity first increases and then decreases with the increasing of stabilizer height, there exists a “optimal height”[8].

After the old Tacoma Narrow Bridge was destroyed under wind in November 7th 1940, researches on structural vibration has been carried out from the aspect of the driving effect of vortex. Allan[9] and Green[10] explained the wind-damage reason from the aspect of vortex distribution and the effect on structure in the form of physical model and numerical simulation respectively. In China, Wei Zhang[4] described the vortex driving effect more clearly by obtaining vortex and its moving law around the bridge section by PIV equipments.

POD (Proper Orthogonal Decomposition) technology provides a statistical method of describing structural surface wind pressure field. It decomposes wind pressure field into intrinsic mode only relying on space covariance and principle coordinates only relying on time. POD method can find the hidden characteristics behind the known data of a series of random processes. The most advantage of this method is that it can describe a process only using a few intrinsic mod-

es, while a strong relevance lies in main mode and phenomena's mechanism[11]. Armitt[12] firstly applied POD technology to wind engineering. Zhiyong Zhou [13]applied POD technology to analyze flutter pressure distribution characteristics of box-section with inclined web. He find that one of intrinsic modes obtained from POD method has strong relevance with flutter torsional divergent motion. Its principle coordinate has the same detergency with the irrational displacement and has a predominate frequency as the flutter divergence's frequency.

In this paper typical bluff-section model pressure distributions are measured in the condition of fixed model as well as fluttering model with and without stabilizer. Firstly, analyzing primary model fluttering pressure distribution and comparing model fluttering pressure distribution's intrinsic modes with fixed model's intrinsic modes, the intrinsic modes correlated with fluttering divergent motion can be found. Then, comparing the primary model fluttering pressure distribution's intrinsic modes with barrier model fluttering pressure distribution's intrinsic modes, fluttering pressure distribution's common points and differences can be found.
rief reference to previous work on the subject.

2 BASIC MATHEMATICAL FORMAT OF POD METHOD

$p(x,y,t)$ is assumed as the function of random fluctuation wind pressure ,then, the covariance function $C(x_i,y_i,x_j,y_j)$ can be written as

$$C(x_i,y_i,x_j,y_j)=\overline{p(x_i,y_i,t)\,p(x_j,y_j,t)} \tag{1}$$

The eigenvalue problem of wind pressure covariance matrix is expressed as follows:

$$\int C(x_i,y_i,x_j,y_j)\phi_n(x_j,y_j)dx_jdy_j=\lambda_n\phi_n(x_i,y_i) \tag{2}$$

Calculated in the form of rectangular integration rule, the discrete expression of Eq.(2) can be shown as,

$$\sum_{j=1}^{N}C(x_i,y_i,x_j,y_j)\phi_n(x_j,y_j)\Delta A_j=\lambda_n\phi_n(x_i,y_i) \tag{3}$$

where ΔA_j indicates area of the jth pressure tap, Eq.(3) can be replaced by a matrix equation:

$$[C][\Delta A][\Phi]=[\Lambda][\Phi] \tag{4}$$

where $[\Delta A]=diag(\Delta A_1,\Delta A_2,\ldots\Delta A_N)$, $[\Phi]=[\phi_1,\phi_2,\ldots,\phi_N]$, $[\Lambda]=diag(\lambda_1,\lambda_2,\ldots\lambda_N)$.

As every principal minor of area matrix $[\Delta A]$ is greater than zero, $[\Delta A]$ is a positive definite matrix [14].Therefore there must be a nonsingular matrix $[T]$ meeting the following equation

$$[\Delta A]=[T]^T[T] \tag{5}$$

where $[T]=[\Delta A]^{1/2}=diag[(\Delta A_1)^{1/2},(\Delta A_2)^{1/2},\ldots,(\Delta A_N)^{1/2}]$.

Eq.(4) is substituted into Eq.(5), then Eq.(5) is left multiplied by matrix $[T]$, we can get,

$$[T][C][T]^T[T][\Phi]=[T][\Lambda][\Phi] \tag{6}$$

If assumed that

$$[D]=[T][C][T]^T,[\Phi]_D=[T][\Phi] \tag{7}$$

Eq.(6) can be reformed into

$$[D][\Phi]_D=[\Lambda][\Phi]_D \tag{8}$$

Matrix $[D]$ is a symmetric matrix, because matrix $[D]$ and $[C]$ are congruent transformation and matrix $[C]$ is symmetric

$$[D]=[T][C][T]^T=[T][C][T]^T[T][T]^{-1}=[T]([C][\Delta A])[T]^{-1} \tag{9}$$

From the deduction above, it can be seen that matrix $[D]$ and $[C][\Delta A]$ have the same eigenvalue $[\Lambda]$. The eigenvector of matrix $[C][\Delta A]$ can be represented as $[\Phi] = [T]^{-1}[\Phi]_D$.

The normalized eigenvalue can be obtained by normalizing every eigenvalue

$$\phi_n = \frac{\phi_n}{(\phi_n{}^T \phi_n)^{1/2}} \tag{10}$$

The principal coordinate corresponding relevant eigenvector can be expressed as follow

$$a_n(t) = \int \mathrm{p}(x,y,t)\phi_n(x,y)dxdy = \sum_{n=1}^{N} p(x,y,t)\phi_n(x,y)\Delta A_n \tag{11}$$

3 PRESSURE FLUCTUATION CHARACTERISTICS OF TYPICAL BLUFF-SECTION MODEL WHEN FLUTTERING

Surface pressure distributions of typical bluff-section model with and without stabilizer are measured in this paper. The cross section and pressure taps location are shown in Fig.1. The experimental study is carried out in uniform flow. The sampling rate of surface pressures is 312.5Hz, while the recorded time length is 38.4s.

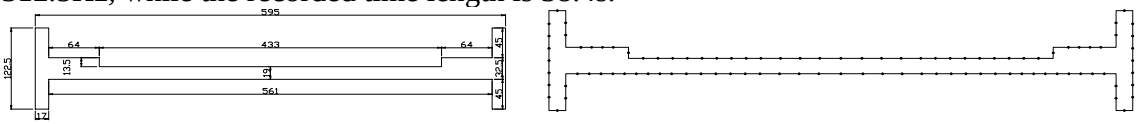

Fig.1 the cross section and pressure taps location of typical bluff-section

The structural bending and torsional frequencies of the bluff-section model are tested at zero wind speed, which are 1.332Hz and 2.339Hz. The flutter critical velocities of primary model with and without stabilizer are 7m/s and 8.5m/s, while the flutter frequencies are 2.308Hz and 2.310Hz correspondingly. The flutter frequency is very close to structural torsional frequency which is the typical feature of separated flow flutter.

In order to make clear pressure fluctuation characteristics of each part of fluttering model, model's surface contour is divided into six part, which are upperside-left, upperside-right,downside-left,downside-right , left -web and right-web. When bluff-section model is fluttering, the contributions to torque of each part are shown in Tab.1. The amplitude spectrums of torques in each part are shown in Fig.2. It clearly shows in Tab.1 and Fig.2 that: upperside-right and downside-left contribute most to torque. The percentage is about 90%.

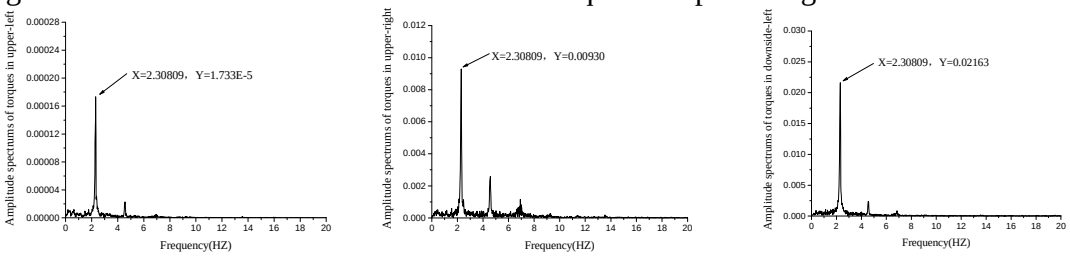

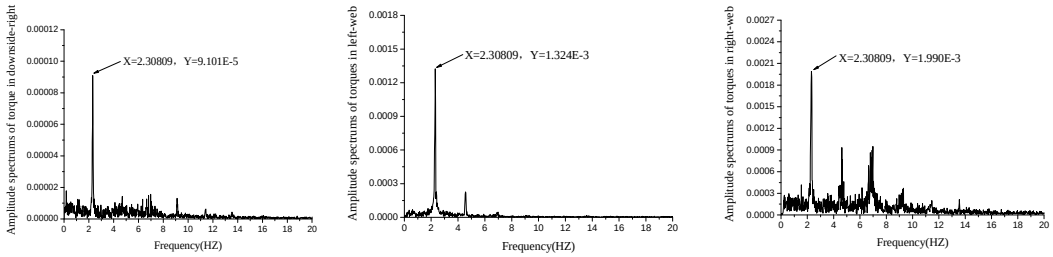

Fig.2 the bluff-section model amplitude spectrums of torques in each part

Table.1 the bluff-section model contribution to the torque of each part

Position	Contribution to torque （%）	Position	Contribution to torque （%）
Upperside-left	0.05	Downside-right	0.26
Upperside-right	27.07	Left -web	3.85
Downside-left	62.97	Right-web	5.79

4 ANALYSIS ON BLUFF-SECTION MODEL SURFACE PRESSURE BY POD

4.1 *Analysis on primary fluttering model surface pressure POD*

As 98 pressure taps are located on the cross section of the section model, covariance matrix is real symmetric matrix of 98 by 98. 98 intrinsic modes can be obtained. Flutter mechanism can be investigated by studying pressure distribution from the aspect of space and time. Because intrinsic mode represents spatial characteristics of pressure distribution and principal coordinate represents time characteristics of pressure distribution. As flutter is the movement of a single frequency, there is only one or a few surface pressure intrinsic modes which have close correlation with fluttering movement when performing POD. Considering that higher modes contain a little energy and have little effect on fluttering motion, the first 8 intrinsic modes are chosen to be analyzed.

The first 8 intrinsic modes $\phi_n(x_i, y_i)$ with their principal coordinates $a_n(t)$ and amplitude spectrums are shown in Fig.3. It can be found that principal coordinates of the 2rd to 7th surface pressure intrinsic modes from POD method have the trend of divergence. But principal coordinate which is after the 3th one have a small amplitude spectrums and have no obvious predominant frequency. The 2rd principal coordinate have an obviously divergent trend, and its amplitude spectrum has an obvious predominant frequency and great amplitude. If eigenvector can be seen as a kind of force distribution, from the 2rd intrinsic mode it can easily figure out that: resultant force is great force but little torque, which causes separated-flow-flutter. Through the 3rd section analysis it can be found: upperside-right and downside-left pressure fluctuation contributes most to torque, a great eigenvector at those parts in the 2rd intrinsic mode. From above discussion, we can reasonably infer that the 2rd intrinsic mode has strong relevance with fluttering motion.

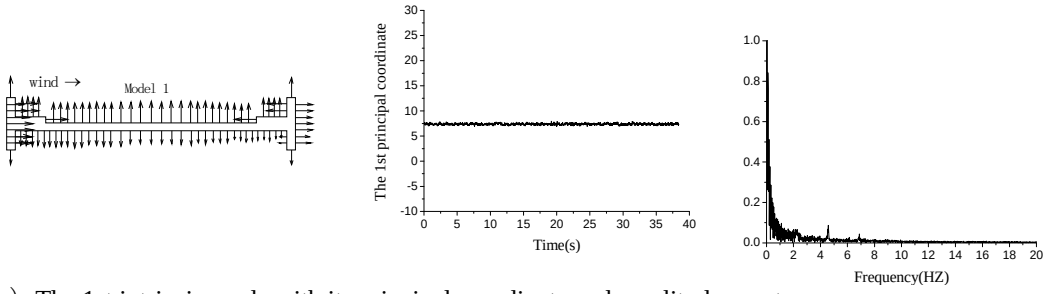

(a) The 1st intrinsic mode with its principal coordinate and amplitude spectrums

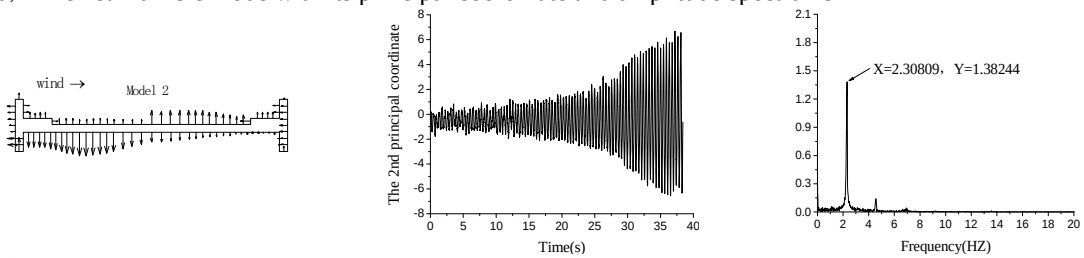

(b) The 2nd intrinsic mode with its principal coordinate and amplitude spectrums

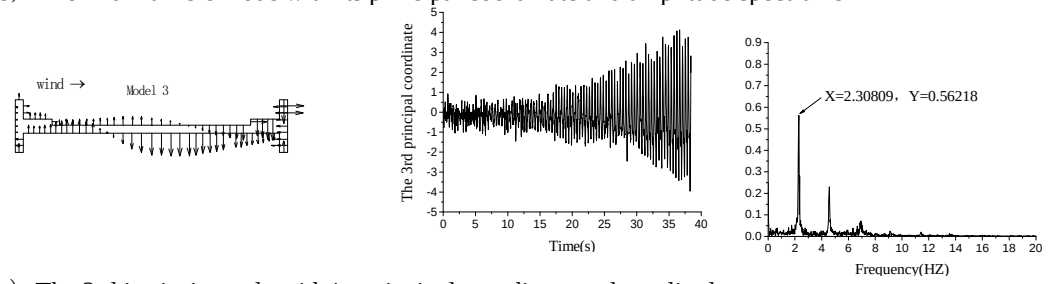

(c) The 3rd intrinsic mode with its principal coordinate and amplitude spectrums

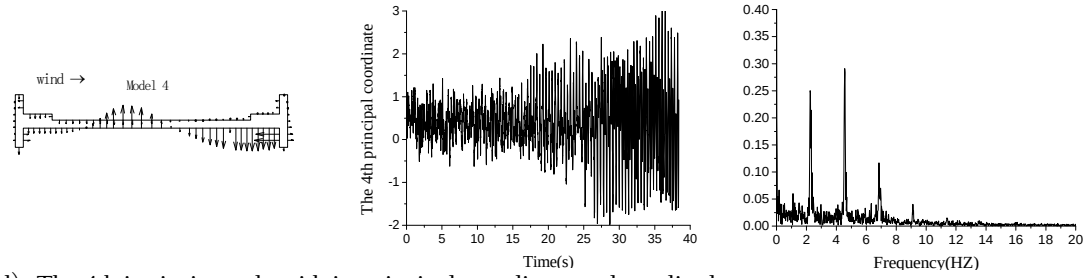

(d) The 4th intrinsic mode with its principal coordinate and amplitude spectrums

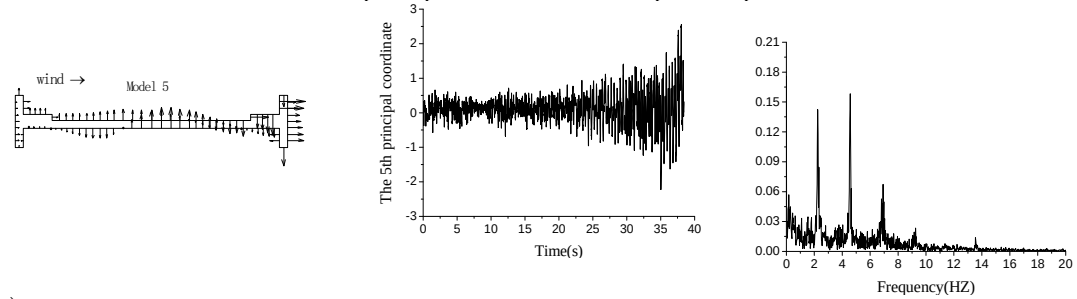

(e) The5th intrinsic mode with its principal coordinate and amplitude spectrums

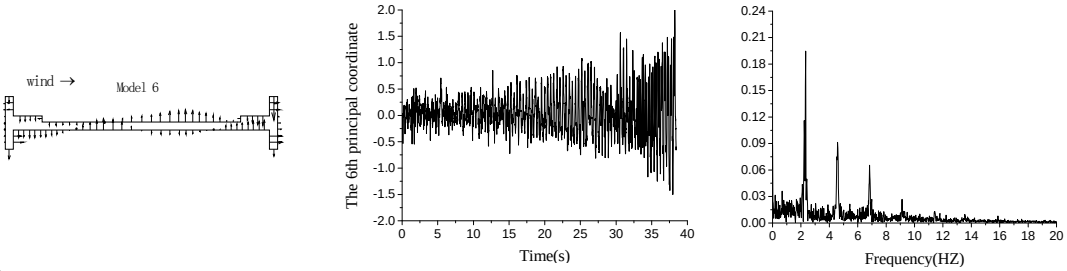

(f) The 6th intrinsic mode with its principal coordinate and amplitude spectrums

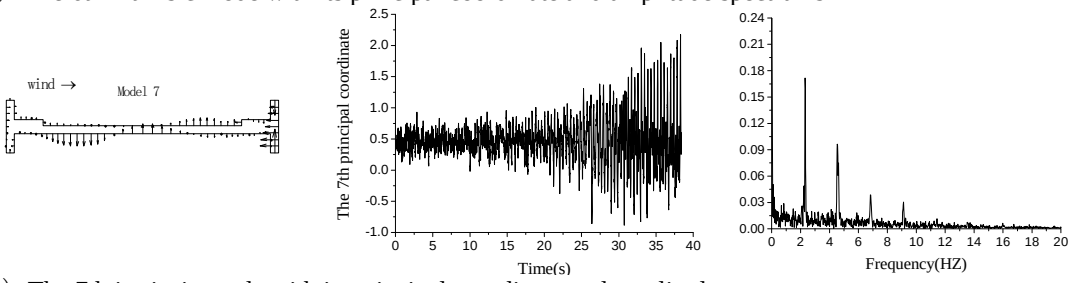

(g) The 7th intrinsic mode with its principal coordinate and amplitude spectrums

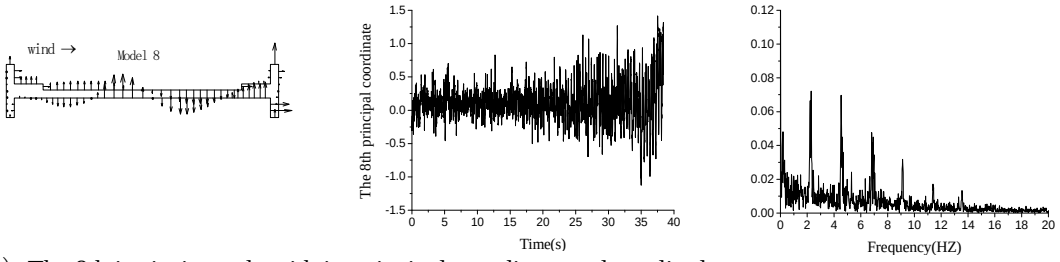

(h) The 8th intrinsic mode with its principal coordinate and amplitude spectrums

Fig.3 the first 8 intrinsic modes of primary fluttering model with them principal coordinates and amplitude spectrums

4.2 *Contrast analysis of surface pressure of fluttering and static primary model*

Fig.4 is a contrast figure of fluttering and fixed primary model surface pressure intrinsic modes. It can be seen in Fig.4 that: the 1st mode of fluttering model is close to the 1st mode of fixed model, the 4th mode of fluttering model is close to the 3rd mode of fixed model, the 5th mode of fluttering model is close to the 6th mode of fixed model, the 6th mode of fluttering model is close to the5th mode of fixed model, the 7th mode of fluttering model is close to the 4th mode of fixed model, the 8th mode of fluttering model is close to the 2nd mode of fixed model, the 2nd and 3rd intrinsic modes of fluttering primary model have not a close one in fixed model, and the other intrinsic modes all have a close one.

(a)The 1st mode of fluttering model (left) and the 1st mode of fixed model (right)

(b) The 4th mode of fluttering model (left) and the 3rd mode of fixed model (right)

(c) The 5th mode of fluttering model (left) and the 6th mode of fixed model (right)

(d) The 6th mode of fluttering model (left) and the 5th mode of fixed model (right)

(e) The 7th mode of fluttering model (left) and the 4th mode of fixed model (right)

(f) The 8th mode of fluttering model (left) and the 2nd mode of fixed model (right)
Fig.4 contrast figure of fluttering and fixed primary model surface pressure intrinsic modes

4.3 *Contrast analysis of surface pressure of fluttering primary model with and without stabilizer*

Flutter critical velocity increases from 7m/s to 8.5m/s as 2.6cm (0.52m in actual bridge) height stabilizer is added to model's upper-middle. Fig.5 is a contrast figure of surface pressure intrinsic modes of fluttering primary model with and without stabilizer. It is shown in Fig.5 that, there is faint difference between two model's the 1st intrinsic mode, with the influence of stabilizer, the eigenvector before stabilizer is greater and after stabilizer is smaller. The 2nd to 8th intrinsic modes of both models are close to each other. Reference[13] shows that the 1st intrinsic mode represents normalized mean pressure distribution, so we can reasonably infer that stabilizer changes the mean pressure distribution as it changes model's outside shape, that is to say stabilizer have some effect on the 1st intrinsic mode while it have no effect on the other intrinsic modes.

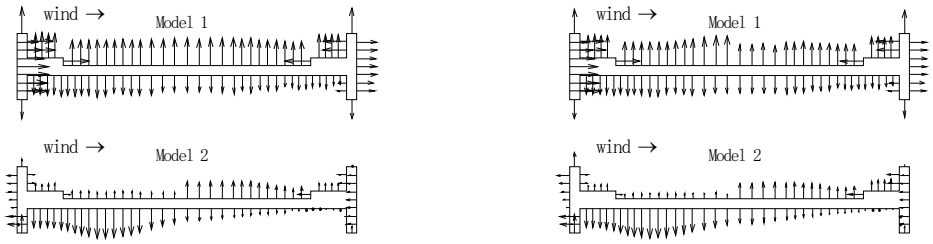

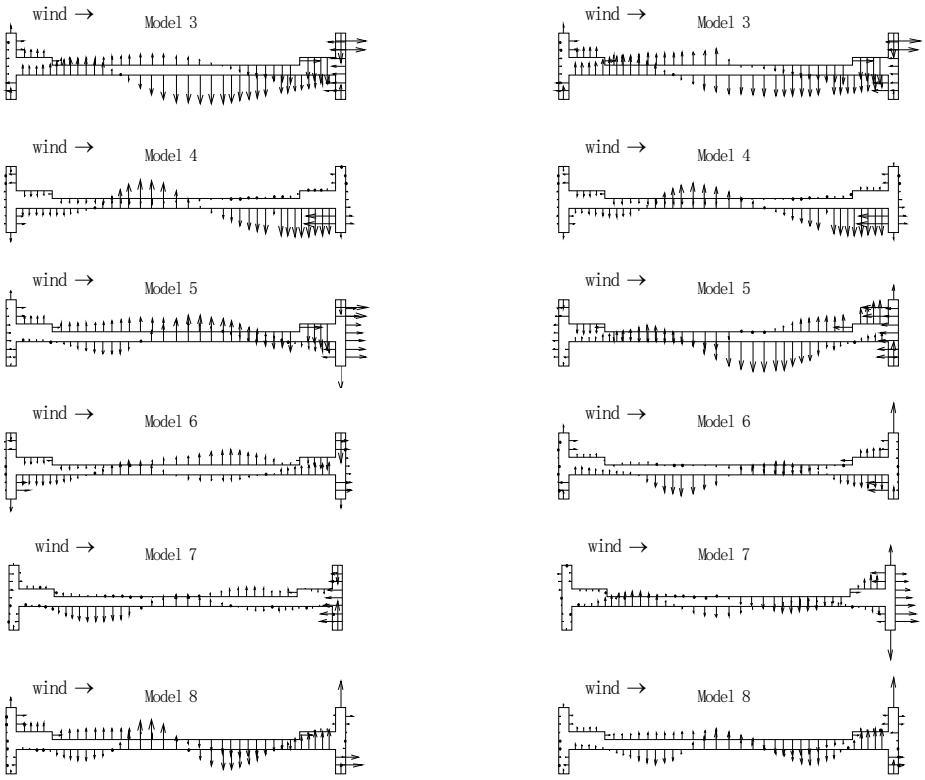

First 8 intrinsic modes of fluttering model without stabilizer First 8 intrinsic modes of fluttering model with stabilizer

Fig.5 contrast figure of surface pressure intrinsic modes of fluttering primary model with and without stabilizer

5 CONCLUSIONS

Through surface pressure acquisition and POD analysis of typical bluff-section model with and without stabilizer, the mechanism of fluttering divergence is investigated from the aspect of pressure distribution. Some conclusions can be made, which are,

(1) Upperside-right and downside-left pressure fluctuations of bluff-section fluttering model contribute most to torque.

(2) The 2rd principal coordinate of fluttering primary model have an obviously divergent trend, and its amplitude spectrum have an obvious predominant frequency and great amplitude.

(3) The 2nd and 3rd intrinsic modes of fluttering primary model have no close ones in fixed model, the other intrinsic modes all have a close similar ones.

(4) Stabilizer only changes the mean pressure distribution by altering model's aerodynamic configuration. That is to say stabilizer has a effect on the 1st intrinsic mode while it has no effect on the other intrinsic modes.

6 REFERENCES

[1] Haifan Xiang etc. Modern theory and practice on bridge wind resistance. Beijing :China Communications Press.2005

[2] Yong xi Yang. Two-dimensional flutter mechanism and its application for long-span bridges.Shanghai :Doctoral Dissertation of Tongji University ,1998
[3] Zhiyong Zhou. Numerical calculation of aeroelastic problems in bridges by discrete vortex thod .Shanghai:Tongji University Postdoctoral Research Report,2001
[4] Wei Zhang,Yaojun Ge. Flow-map mechanism of wind induced vibrations of H-shape bridge decks. China Civil Engineering Journal, 2009,42（5）
[5] M.Miyazaki. Wind resistant design of long span suspension bridges with stay cable system.Wind engineering into 21th century ,1999,2
[6] Saeid Pourzeynali,T.K.Datta. Control of flutter of suspension bridge deck using TMD.Wind and Structure,2002,5(5)
[7] Zhiyong Zhou,Airong Chen. The stabilizing plate to improve the flutter critical wind speed and its mechanism analysis. The 11th National Conference on structural wind engineering ,2003
[8] Xiaojie Zou. Flutter control measures and mechanism of super-long span suspension bridges.Shanghai: Master Dissertation of Tongji University,2005
[9] Allan Larsen, Aerodynamics of the Tamoca Narrows Bridge-60 years later. Structural Engineering International,2000,10(4)
[10] Green,D.,W.G.Unruh.The failure of the Tacoma Bridge:a physical model.American Journal of Physics,2006,74(8)
[11] Bienkiewicz B, Tamura Y, Ham H J, Ueda H, HibiK.Proper orthogonal decomposition and reconstruction of multi-channel roof pressure. J. Wind Eng.Ind.Aerodyn, 1995, 54/55: 369~381
[12] Armitt J. Eigenvector analysis of pressure fluctuations on the West Burton instrumented cooling tower [R]. Central Electricity Research Laboratories (U K),Internal Report RD/L/N 114/68, 1968
[13] Zhiyong Zhou,Likun Yang . Anlysis on the flutter mechanism and the characteristic of the surface pressure for the flexible suspension rigid model.Acta Aerodynamica Sinica.2010
[14] Tongji University Department of Computational Mathematics.Modern numerical mathematics and computing.Shanghai:Tongji University press,2004

The Seventh International Colloquium on Bluff Body Aerodynamics and Applications (BBAA7)
Shanghai, China; September 2-6, 2012

Radial distribution of typhoon pressure fields measured by ground multi-point pressure distribution

L. Zhao, A.P. Lu, L.D. Zhu, S.Y. Cao, Y.J. Ge

SLDRCE, Tongji University, Shanghai, China, zhaolin@tongji.edu.cn

ABSTRACT: It is common at international level to predict the extreme wind speed with mature typhoon numerical model. And it is necessary to analyze the radial wind-pressure field and radial wind-speed field of typhoon in numerical simulation before the prediction. The paper analyzes the analytic model, proposed by Holland, for the radial wind-pressure field and radial wind-speed field of typhoon and discusses what influence the different values of β , distribution coefficient of radial typhoon pressure (also referred to as Holland parameter β), introduced by Holland, will produce on radial distribution of typhoon pressure and speed and it also reviews and concludes existing formulas, which have been proposed by numerous scholars, for calculating wind-pressure distribution coefficient β. We have studied and compared the values of β, which had been computed by various formulas, and their impacts on calculating results of radial typhoon pressure distribution and also compared it with the data fitting conclusions of measured pressure from ground stations, according to the Holland empirical analytic model for wind-pressure field and wind-speed field of typhoon and by using the actual air pressure data from hundreds of ground stations in Zhejiang province, China. Since the maximum wind-speed radius, central pressure differential, latitude of typhoon center and surface temperature of the ocean, all of these can affect the value of wind-pressure distribution coefficient β, further study and verification are needed to figure out which method to calculate β will work out best fitting precision for radial wind-pressure distribution of typhoon.

KEYWORDS: Typhoon; Wind-pressure field; Maximum wind-speed radius; Central pressure differential

1 INTRODUCTION

Long-span and towering structures have sprung up in coastal areas in the past few years. All of these structures are sensitive to extreme wind speed within their service life. Therefore, it is really necessary to predict the extreme typhoon speed reasonably during the reoccurrence life of target structures and thus figure out reasonable basis for safety design and risk assessment of building structures. In addition, mature prediction for extreme typhoon speed with numerical modeling is commonly used at international level. In the numerical simulation process of typhoon, it is critically important to simulate and calculate the wind field of typhoon or the radial speed distribution of typhoon (also referred to as radial wind profile of typhoon). Research results [1, 2], which are based on the sensitivity analysis method, suggest that the typhoon pressure distribution coefficient β impacts the determination of the design wind speed during the recurrence interval at the engineering site. Therefore, we make use of the actual pressure data from the hundreds of ground stations in Zhejiang province, China, study and compare the values of the coefficient β, which have been figured out by different formulas, as well as their influence on the calculated results of radial typhoon pressure distribution, and we also compare it with the fitting results of measured data from ground stations.

An accurate calculation of the radial wind profile of typhoon plays a very important part in the prediction of the extreme typhoon speed and the evaluation of typhoon disasters. Thus, a

great number of scholars have proposed their models to calculate the radial typhoon profile. However, most of the previous scholars have based the statistical fitting on measured data. They usually present the empirical formulas, such as Schloemer [3] and Atkinson [4], to calculate the radial wind profile. In 1980, Holland [5] innovatively combined the empirical function for typhoon pressure distribution, which had been obtained by Atkinsonand, Holliday and Dvorak [6], with the equilibrium equation of radial pressure gradient of typhoon cyclone, and thus figured out the analytic function model of radial typhoon speed distribution. The analytic model is better by having only one parameter, namely the typhoon radial wind pressure distribution coefficient β. But it also relies on measured data to estimate the value of β. In conclusion, the fitting results, from the numerical simulation calculation of typhoon in the Atlantic and Australia by Holland analytic model, are more accurate than those of empirical function models.

2 HOLLAND ANALYTIC MODEL

A great deal of actual measurement for radial wind pressure distribution of typhoon has been made and many measured data and information have been obtained in early years. The measured data of typhoon pressure is standardized, to remove the influence from different typhoon centers and different air pressures on the variability of measured results, shown as below:

$$\mathrm{P_{st}} = \left(P_r - P_c\right)/\left(P_a - P_c\right) \tag{1}$$

In which, P_r means wind pressure at the distance of r away from the typhoon center; P_c is central pressure of typhoon; P_a is natural air pressure, it is theoretically the pressure where r is infinitely great.

On the basis of measured data, many scholars, such as Depperman [7] and Schloemer [3], have used researches to suggest that the radial wind pressure distribution of typhoon complies with the negative exponent relationship. Holland presents them all in the following functional expression:

$$\mathrm{P_{st}} = \frac{\left(P_r - P_c\right)}{\left(P_a - P_c\right)} = \exp\left[-\left(\frac{R_{\max}}{r}\right)^{\beta}\right] \tag{2}$$

In the above formula, P_a-P_c is low pressure differential ΔP; R_{max} is maximum radius of wind speed; β wind pressure distribution coefficient, also named as Holland parameter. Eq. (2) can be transferred to Schloemer equation when $\beta = 1$.

Equilibrium equation of radial pressure gradient of typhoon cyclone:

$$\frac{1}{\rho_A}\cdot\frac{\partial P_r}{\partial r} = \frac{V^2}{r} + fV \tag{3}$$

In the equation, ρ_A = air density, kg/m^3; P_r = wind field pressure distribution function, hPa; r = radius from typhoon center, km; V = average tangential wind speed of air micelle, r away from typhoon center, m/s; f is Coriolis coefficient, $f = 2\Omega\sin\Psi$, in which Ω (radian/ s) represents the revolving speed of the earth and Ψ is the latitude of the air micelle.

It can be learned from equation (3):

$$V = \sqrt{\frac{r}{\rho_A}\cdot\frac{\partial P_r}{\partial r} + \frac{1}{4}f^2r^2} - \frac{1}{2}fr \tag{4}$$

$$V = \sqrt{\frac{\beta}{\rho_A} \cdot (\frac{R_{\max}}{r})^B \cdot [100] \cdot (P_r - P_c)} \quad (5)$$

$$V_{\max} = \sqrt{\frac{\beta \Delta P}{e \rho_A}} \quad (6)$$

Coriolis strength is much smaller than the gradient pressure of cyclone and its centrifugal force in the maximum speed region of typhoon, so the Coriolis strength is ignored. The functional expression for average tangential wind speed V at r away from typhoon center is worked out from equation (2) and (4). When r=R_{max} is obtained from $\partial V / \partial r = 0$, the average tangential wind speed reaches the maximum value.

In the equation, e = 2.71828, it is the base number of natural logarithm. [100] = hPa is converted into Pa.

Thus it can be seen that if typhoon central pressure P_c = 950 hPa, natural air pressure P_a = 1010 hPa, maximum wind speed radius R_{max} = 20 km, radial air pressure distribution and radial wind speed distribution of typhoon vary to the coefficient β, as is shown in Fig. 1 a) and b). According to Fig. 1 a), when the value of β is enlarged, the eye of typhoon becomes bigger and the wind distribution curves intersect at the maximum wind speed radius. According to Fig. 1 b), as the value of β is enlarged, horrizontal wind profile changes a lot and the wind speed becomes larger within the maximum wind speed radius but smaller beyond it. On the basis of measured data and the upper limit of the air boundary layer, Holland determined that the wind pressure distribution coefficient β be between 1.0 and 2.5. Since the wind pressure distribution coefficient β introduced by Holland numerical model takes many values, Holland numerical model applies to a larger field. It can simulate different typhoons to such a good degree that most scholars accept it.

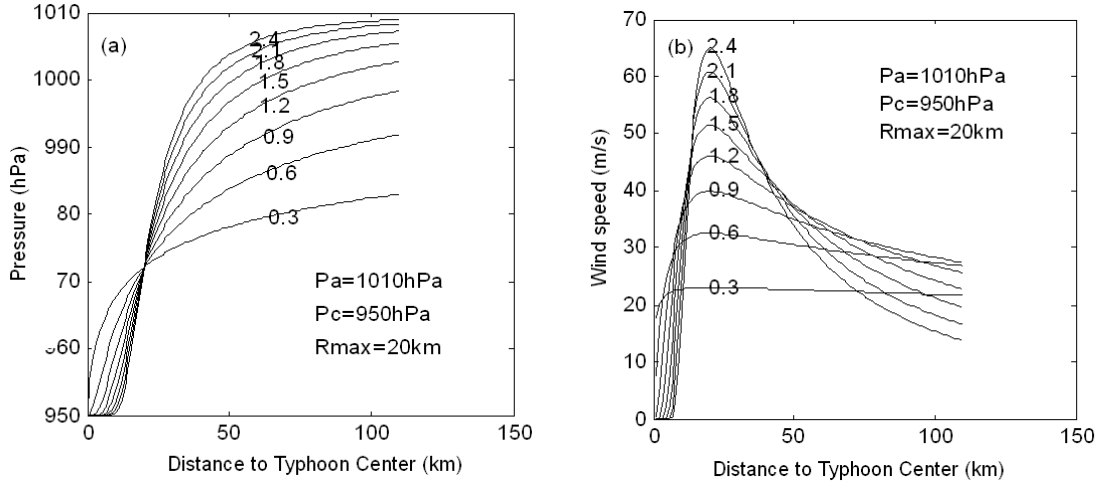

a) Radial pressure distribution b) Radial wind speed distribution

Figure 1. The variation of radial pressure and wind speed distribution with various value of β.

3 COMPUTING METHOD OF WIND PRESSURE DISTRIBUTION COEFFICIENT

The value of wind pressure distribution coefficient β influences the computing accuracy of numerical simulation of typhoon, so scholars have made a lot of researches on it. But such researches are still few in China. There are mainly two methods to estimate the wind pressure distribution coefficient β: one is to make regression analysis on the data of ground air pressure and then to estimate the values of parameters; the other is to get the gradient velocity from the equilibrium equation of barometric gradient and then to compare it with the data of wind speed of the upper frictional layer. Vickery and others [8] compared the two methods. In the first method, the parameter β changes in different phases of typhoon and at different sites of wind field. Thus the value of Holland parameter β is hard to determine. However, this method demonstrates the varying pattern of Holland parameter β to some degree. And in the other method, Holland parameter β can be expressed by the function of central air pressure differential and maximum wind speed radius. The formulas to calculate typhoon pressure distribution coefficient β, suggested by various scholars, are introduced briefly as follows.

3.1 *Love & Murphy*

Love & Murphy [9], according to measured data of typhoon pressure from northern Australia, suggested:

$$\beta = 0.25 + 0.3\ln(\Delta P) \tag{7}$$

In the formula, $\triangle P$ is the central pressure differential.

3.2 *Hubbert and etc.*

When they analyzed the typhoon that attacked Australian coasts, Hubbert and others [10] proposed that wind pressure distribution coefficient parameter β and the smallest central pressure of typhoon P_c comply with linear relation. The expression is shown below:

$$\beta = 1.5 + (980 - P_c)/120 \tag{8}$$

3.3 *Holland & Harper*

Holland & Harper [11] suggested that, as to Australian tropical cyclone, parameter β is a liner function of central pressure differential. They also proposed an empirical equation:

$$\beta = 2.0 - (P_c - 900)/160 \tag{9}$$

3.4 *Jakobsen*

By using the empirical relationship between the maximum wind speed and the central pressure differential as well as the equation of motion, Jakobsen [12] considered the function of Coriolis force and thus put forward a formula to calculate the Holland parameter β:

$$\beta = \frac{e}{r_2^2}\frac{\rho_A}{[100]\Delta P}\left(V_{\max}\right)^2 \quad (10)$$

$$V_{\max} = [\frac{1}{3.6}]K_p(\Delta P)^{\gamma} \quad (11)$$

In the formula, e = 2.71828, it is the base number of natural logarithm; r_2 = 1.05; ρ_A = 1.15 kg/m^3; $\triangle P$ = central pressure differential, hPa; [100] = the value of central pressure differential when it is changed from hPa to Pa; V_{max} = the maximum wind speed within one minute at 500 m above sea level; K_p and γ are regression parameters, K_p = 12.36, γ = 0.73.

3.5 *FEMA*

The technical manual, in the Hazus typhoon disaster analysis software of the American Federal Emergency Management Agency (FEMA), also suggested a computing method of parameter β. This is a linear relational expression of central pressure differential and maximum wind speed radius.

$$\beta = 1.38 + 0.00184\Delta P - 0.00309R_{\max} \quad (12)$$

3.6 *Holland*

In 2008, Holland [14] proposed a new formula to calculate the wind pressure distribution coefficient β. He said that many factors, such as central pressure of typhoon and its variation to time, its moving speed, its wind speed profile and the longitude and latitude of typhoon center. The computing expression is as follows:

$$\beta = b_s(v_{mg}/v_m)^2 \rightarrow 1.6b_s \quad (13)$$

$$b_s = -4.4\times10^{-5}(\Delta P)^2 + 0.01\Delta P + 0.03\partial p_c/\partial t - 0.014\psi + 0.15V_T^{\,x} + 1.0 \quad (14)$$

$$x = 0.6(1 - \Delta P/215) \quad (15)$$

In the formula, $\partial p_c/\partial t$ = variation of central pressure strength, hPa/ h; ψ = absolute value of the central latitude of typhoon; V_T = moving speed of cyclone, m/s; V_{mg}/V_m = conversion factor from gradient wind to surface wind.

4 COMPARISON OF METHODS BASED ON AIR PRESSURE OBSERVATION

4.1 *Introduction to Air Pressure Data from Observation Stations in Zhejiang Province*

To study and verify the analytic model for radial typhoon pressure and speed distribution proposed by Holland, we compare the mentioned functional expressions for computing the typhoon

pressure distribution coefficient β, study the influence from different methods on computing results of radial typhoon pressure distribution and compare them with the fitting results of air pressure data from ground stations. A good deal of data on typhoon pressure is needed. Now we have collected a lot of measured data on wind pressure of the No.8 tropical storm Morakot from ground stations in 2009. It is demonstrated briefly as follows.

The No. 8 tropical storm Morakot was born at approximately 1,000 km away from the eastern Philippines on August 2, 2009. Its minimum central pressure was 945 hPa and the maximum average speed was 43.1 m/ s (in 10 minutes). And few typhoons in the history had had such strength. Typhoon Morakot pass through Zhejiang province from south to north. It is tracked in Graph 2. The abundant air pressure data, which has been measured by observation stations, is typical. Additionally, there are 1,000 and more ground observation stations in Zhejiang province and 270 and more stations at most recorded the landing process of Typhoon Morakot completely. Graph 3 shows the locations of these stations. Each station recorded from 21:00 on August 8 to 20:00 on August 11 and produced every hour a group of data, which includes: date, time, serial number of station, name of station, latitude (°), longitude (°), altitude (0.1 m, -9,999 means the altitude has not been measured.), average wind direction in 10 minutes (0 ~ 359), average wind speed (m/ s) within 10 minutes, maximum wind speed (m/ s) in one hour, extreme wind speed (m/s) in one hour, and air pressure of this station (-9,999 means the altitude has not been measured). The yearbooks [15] of tropical cyclones present the longitude and latitude and pressure of the center of Typhoon Morakot in every hour from 11:00 on August 6 to 20:00 on August 11.

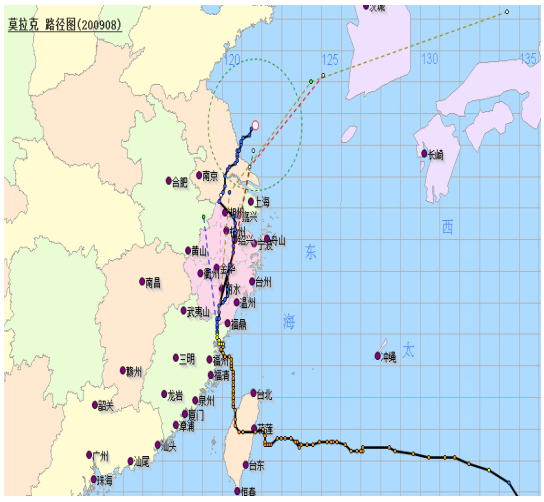

Figure 2. Path of typhoon Morakot.

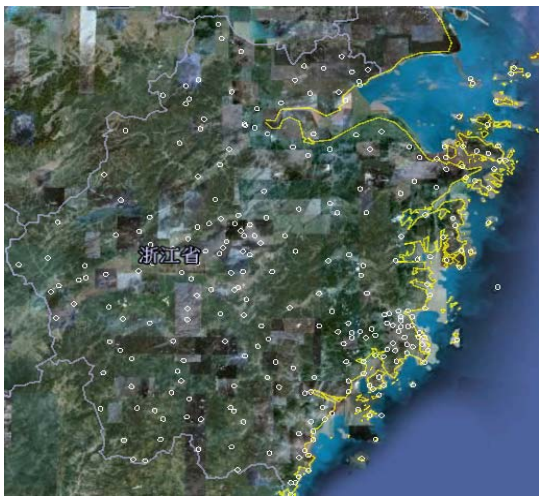

Figure 3. Locations of observation stations in Zhejiang.

4.2 *Values of Coefficient β Calculated by Various Methods and Their Comparison*

As is known, the maximum wind speed radius Rmax is needed when we calculate the typhoon pressure distribution coefficient β with different methods and study their influence on the computing results of radial wind pressure distribution of typhoon. But measured data and yearbooks for tropical cyclones do not record the measured value of the maximum wind speed radius Rmax. Therefore, the value of Rmax can be determined by the empirical functional relation, which has been obtained by Yasui [16] through fitting of measured records, between central pressure differential and maximum wind speed radius of typhoon. The following is the conditions for this relation:

(1) Central pressure of typhoon shall be smaller than 980 hPa;
(2) Distance from the center of typhoon to the engineering site shall be between 100 km and 500 km;
(3) Ground air pressure in the engineering site shall be smaller than 1,000 hPa.

$$E(R_{\max}) = 2.06\times10^{4}\,\Delta P^{-1.27} \tag{16}$$

$$\sigma(R_{\max}) = 4.4\times10^{4}\,\Delta P^{-1.76} \tag{17}$$

In the formula, E() represents the average value of R_{max} and σ() the variance.

On the basis of Holland distribution function for typhoon speed and pressure, the empirical function for Rmax determined by Yasui and yearbooks of tropical cyclones, we use calculate the value of the typhoon pressure distribution coefficient β by various functional expressions and compare the values of β. Fig. 4 shows the values of the wind pressure distribution coefficient β, which have been computed by various methods, throughout the process of Typhoon Morakot. As is seen is the graph, the values of β computed by two methods of Jakobsen and Holland change intensely while those computed by the four methods of Love & Murphy, Hubbert and etc., Holland & Harper and FEMA are relatively stable; the central pressure differentials differ a lot before 3:00 on August 10. The value of β computed by Jakobsen's method is largest and that computed by FEMA's method is smallest and the former is almost twice the value of the latter; as strength of typhoon and central differential reduces in the process, all of the values of β computed by the six methods tend to decrease.

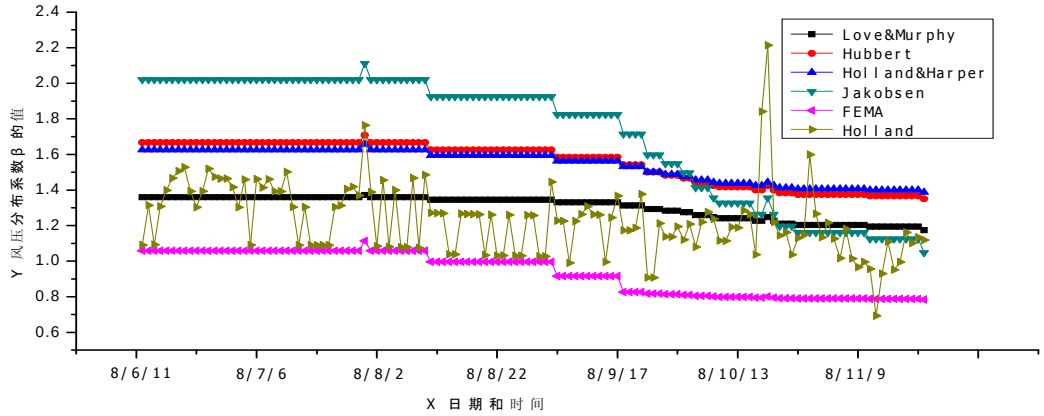

Figure 4. Values of wind pressure distribution calculated by various methods throughout typhoon Morakot.

4.3 *Influence from Different Computing Methods on Radial Typhoon Pressure Distribution*

Radial wind pressure and speed distributions of typhoon refer to the functional relationship between the wind pressure and wind speed on some profile in the center of typhoon and their distance to the center of typhoon. Fig. 5 presents the two-dimensional wind field and the radial wind speed profile of typhoon. Actually, ground observation stations cannot distribute or gather on a radial profile in the special structure of typhoon and the radius of the round vortex is usually from 500 km to 1,000 km. Typhoon can usually reach the lapse limit (15 ~ 20 km) vertically at most. The ration between the vertical and horizontal dimensions is around 1:50. Typhoon is a flat, cyclone and vertical air mass. Therefore it is considered that the wind pressure data of observation stations in two close plane regions is as same as that on a radial profile. On Fig. 6, a real point is a ground observation station; the two dotted oblique lines refer to two special planes;

the full oblique lie between the two dotted lines mean the radial wind profile of typhoon; the dots between the two oblique lines are selected ground observation stations; the quadrant box in the center refers to the center of typhoon; the wind pressure data from ground stations corresponding to these dots is exactly that of the radial wind profile; the two dotted curves represent stations furthest away from the center of typhoon and also the circle that takes the distance as its radius. In the disposal and calculation of wind pressure data from ground observation stations, we take 15 km as the distance between two planes and also between two straight lines. In consideration of landing of typhoon, its central pressure and its intense, we study the radial wind pressure distribution of typhoon at 00:00 on August 9 (before landing), 16:00 on August 9 (landing) and 16:00 on August 10 (after landing). And we reject abnormal wind pressure data from ground stations, in consideration that typhoon pressure shall be not smaller than central pressure and not bigger than barometric pressure.

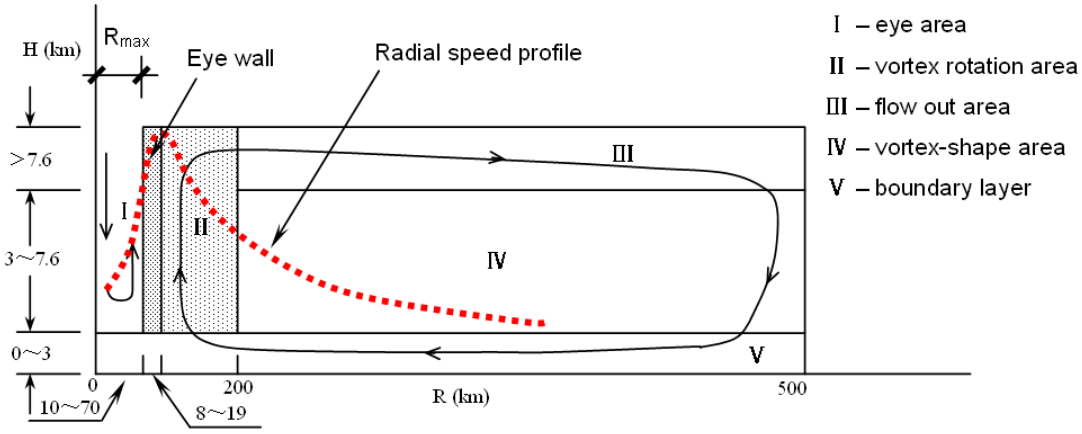

Figure 5. Wind Field Profile of Typhoon.

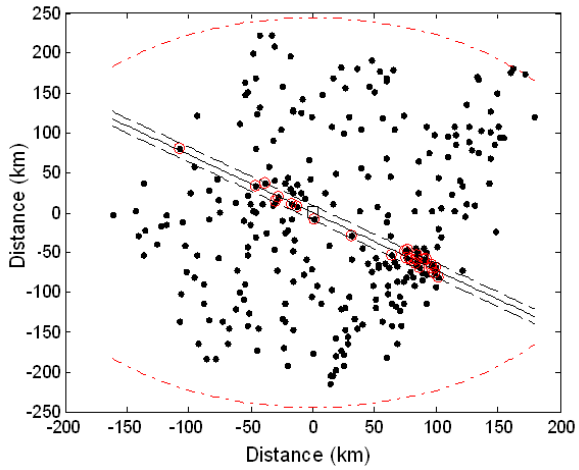

Figure 6. Selection and Disposal of Station Locations.

At 00:00, August 9, Typhoon Morakot did not land. Its center was 25.5° at northern latitude and 120.5° at eastern longitude. Its central pressure P_c was 965 hPa. At that time, 278 stations recorded it completely. Natural air pressure P_a was 1,010 hPa. Therefore, computing results are shown by Fig. 7a) and 7b). At the same time, the distance between two planes is considered

to be 15 km, covering 26 ground stations at most. Abnormal data is removed. And the wind pressure coefficient β is computed as 0.72 through fitting. It can be seen in Fig. 7b) that the wind pressure distribution curve, which is calculated according to Holland typhoon pressure distribution function and Yasui's empirical function of R_{max} and functional expressions of wind pressure distribution coefficient β of various scholars, differs a lot from that obtained through removal of abnormal points and fitting of measured wind pressure data. The wind pressure distribution coefficient of typhoon β=1.93, which is calculated by Jakobsen's method, is the largest one. In this method, the radius of typhoon's eye is biggest and the typhoon pressure is smallest within the region of the biggest speed but it is largest beyond this region; in FEMA method, coefficient β = 1.0, is the smallest one; radius of typhoon eye is smallest; the pressure is biggest in the region of the largest speed but smallest beyond the region. These are more similar to the measured data.

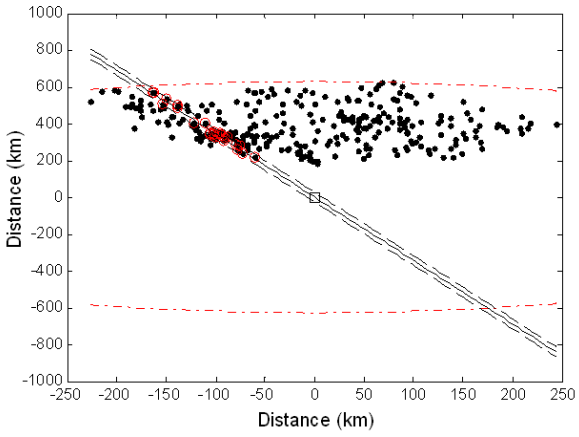

a) Selection of Station Locations

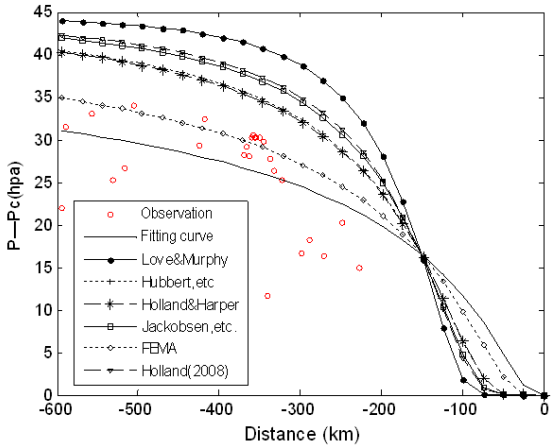

b) Radial Wind Pressure Distribution from Different Calculating Methods

Figure 7. The selection of stations and fitting process of pressure distribution (Before landfall)

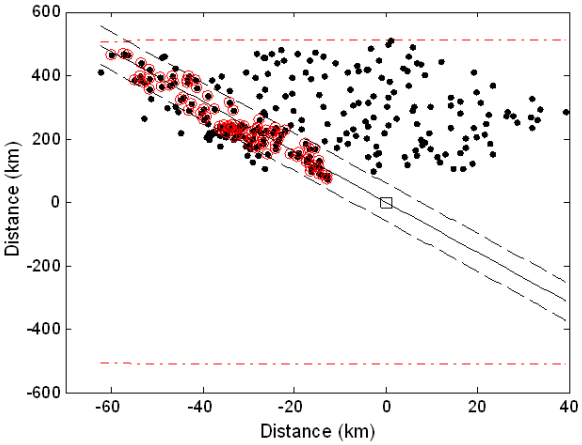

a) Selection of Station Locations.

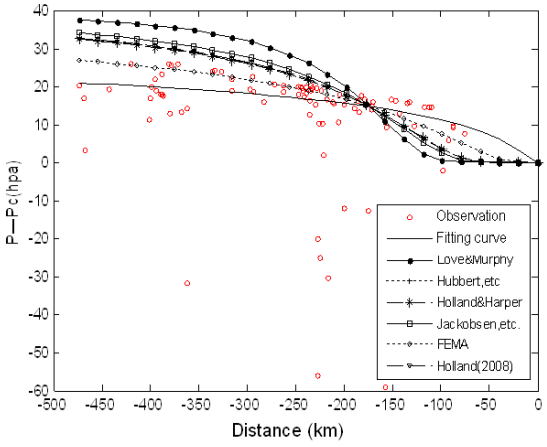

b) Radial Wind Pressure Distribution from Different Calculating Methods.

Figure 8. The selection of stations and fitting process of pressure distribution (While Landing)

When Typhoon Morakot was landing at 16:00 on August 9, the center was 26.5° at northern latitude, 119.9° eastern longitude. The central pressure P_c = 970 hPa. At that time, 252 ground stations recorded it completely. And the natural air pressure Pa was considered as 1,010

hPa. As a result, the computing results are shown by Fig. 8a) and 8b). At the same time, the distance between two planes is considered to be 15 km, covering 90 measuring stations at most. Abnormal points are disposed and the wind pressure distribution coefficient β is calculated as 0.43 through fitting. Fig. 8b) shows that the wind pressure distribution curve, which is calculated according to Holland typhoon pressure distribution function and Yasui's empirical function of R_{max} and functional expressions of wind pressure distribution coefficient β of various scholars, differs a lot from that obtained through removal of abnormal points and fitting of measured wind pressure data, similar to the situation before landing. The wind pressure distribution coefficient of typhoon β=1.82, which is calculated by Jakobsen's method, is the largest one. In this method, the radius of typhoon's eye is biggest and the typhoon pressure is smallest within the region of the biggest speed but it is largest beyond this region; in FEMA method, coefficient β = 0.87, is the smallest one; radius of typhoon eye is smallest; the pressure is biggest in the region of the largest speed but smallest beyond the region. These are more similar to the measured data. However, it is still more than twice the value of the typhoon pressure distribution coefficient β computed by fitting measured data.

Typhoon Morakot has landed at 16:00 on August 10. Its center was 29.1° at northern latitude, 120.3° at eastern longitude, close to the center of Zhejiang province. Central pressure P_c was 992 hPa. At that time, Typhoon Morakot has decreased and become a tropical storm. 275 ground stations recorded it completely. The natural air pressure P_a was considered as 1,010 hPa. Thus the computing results are shown by Fig. 9a) and 9b). At the same time, the distance between two planes is considered to be 15 km, covering 25 measuring stations at most. Abnormal data is removed and the wind pressure distribution coefficient β is computed as 1.33. Among all the methods to calculate the wind pressure distribution coefficient β, Holland's method considered it as 1.66 and it is the largest one; while FEMA considered it as 0.80, the smallest one.

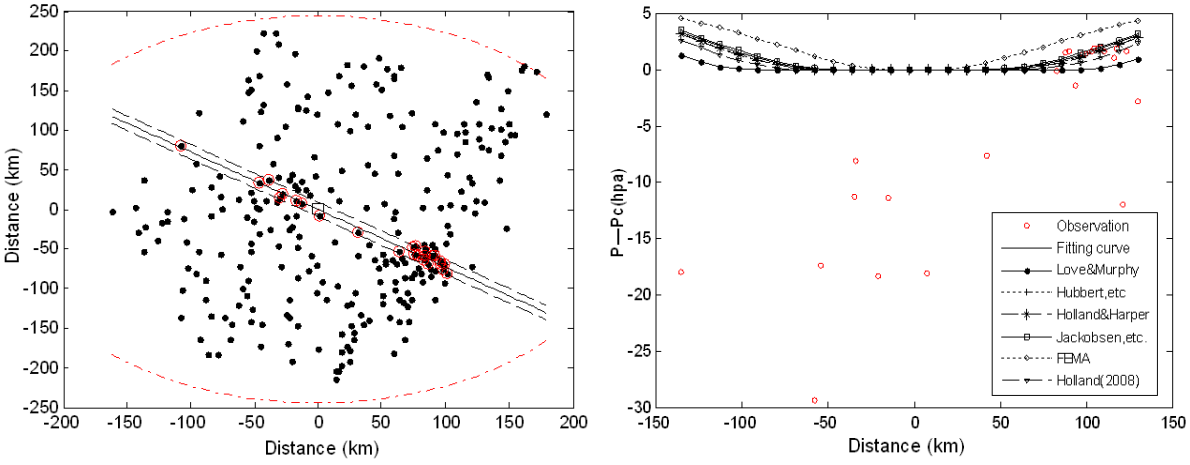

a) Selection of Station Locations

b) Radial Wind Pressure Distribution from Different Calculating Methods

Figure 9. The selection of stations and fitting process of pressure distribution (After landfall)

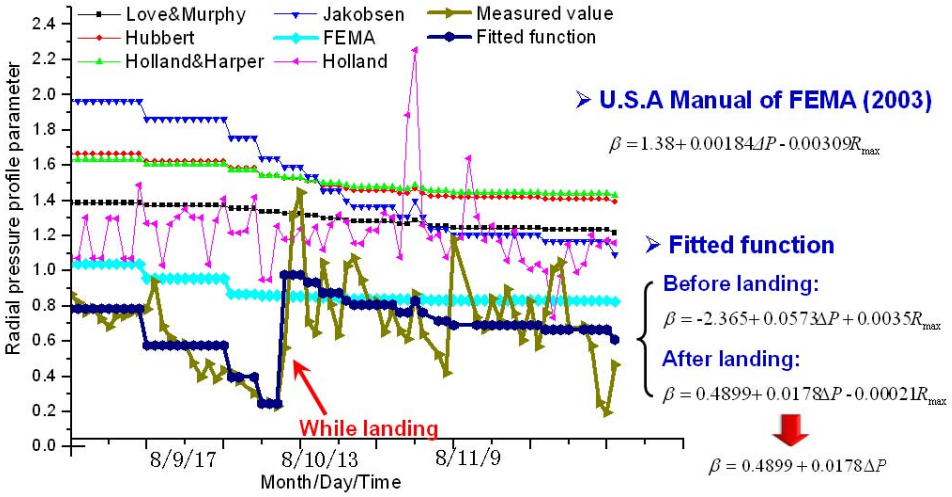

Figure 10. The variation of β with the state of typhoon landfall.

In Fig. 10, the general variation of β with the state of typhoon landfall are illustrated and compared with the other empirical results. Totally, the suggested curve from U.S.A. Manual of FEMA has the similar tendency with the observed curve, the fitted expressions of Eqs. (16) and (17) from the on-spot measurement can refinedly show the detailed change related to the state of typhoon landfall.

$$\beta = -2.365 + 0.0573\Delta P + 0.0035R_{max} \quad \text{(Before landfall)} \quad (16)$$

$$\beta = 0.4899 + 0.0178\Delta P \quad \text{(After landfall)} \quad (17)$$

5 CONLUCSIONS

For the reasons given above, by the analysis of Holland's functional model of radial wind speed and pressure distribution and on the basis of Holland's function of typhoon speed and pressure as well as Yasui's empirical function and measured data of R_{max} and through the comparison of the influence from various computing functional expressions for typhoon pressure distribution coefficient β, the following conclusions can be drawn:

1) The value of the typhoon pressure distribution coefficient β, which is introduced by Holland's functional model, influences the computing result to a large degree. It is necessary to analyze and determine the value of wind pressure distribution coefficient β at the engineering site on the basis of measured data.

2) The values of the coefficient β computed with different functional expressions differ a lot from each other. And the largest is likely to be twice the smallest one.

3) The wind pressure distribution curve, which is calculated according to Holland typhoon pressure distribution function and Yasui's empirical function of Rmax and functional expressions of wind pressure distribution coefficient β of various scholars, differs a lot from that obtained through removal of abnormal points and fitting of measured wind pressure data. It is necessary to work out a functional expression, which suits China's coast situation, to compute wind pressure distribution coefficient β.

4) Comparison between computing results and measured data shows that the computing method for the coefficient β, which is proposed by the technical manual of the Hazus typhoon disaster analysis software of the FEMA, can be used if the data of radial profile of air pressure is out of access. The wind pressure distribution curve obtained by this method is very similar to that obtained through fitting of measured data. But this conclusion needs studying and verifying further.

6 ACKNOWLEDGEMENTS

The authors would like to gratefully acknowledge the supports of the National Science Foundation of China (51021140005, 90815028 and 50978203), and the supports by Kwang-Hua Fund for College of Civil Engineering, Tongji University.

7 REFERENCES

1 L. Zhao, L.D. Zhu, Y.J. Ge, Research on monte-carlo stochastic simulation of wind characteristics of typhoon in Shanghai, Acta Aerodynamica Sinica, 2009, Vol. 27, No. 1, pp 25-31.
2 L. Zhao, Y.J. Ge, L.L. Song, H.Q. Mao, Research on monte-carlo stochastic simulation of features of extreme typhoon in Guangzhou, Journal of Tongji University, 2007, Vol. 35, No. 8, pp 1034-1038.
3 R.W. Schloemer, Analysis and synthesis of hurricane wind patterns over lake Okeechobee, Florida. Hydromet. Rep., 31, Dept of Commerce, Washington D.C., 1954, pp 49.
4 G.D. Atkinson, C.R. Holliday, Tropical cyclone minimum sea level pressures/maximum sustained wind relationship for the North Pacific, Mon. Wea. Rev., 1977, pp 421-427.
5 G.J. Holland, An analytic model of the wind and pressure profiles in hurricanes, Mon. Wea. Rev., 1980, Vol. 108, No. 8, pp 1212-1218.
6 V.F. Dvorak, Tropical cyclone intensity analysis and forecasting from satellite imagery, Mon. Wea. Rev., 1975, Vol. 103, 420-430.
7 C.E. Depperman, Notes on the origin and structure of Philippine typhoons, Bull. Amer. Meteor. Soc., 1947, Vol. 28, 399-404.
8 P.J. Vickery, L.A. Twisdale, Wind-field and filling models for hurricane wind-speed predictions, Journal of Structural Engineering, 1995, Vol. 12, No. 1, pp 1700-1709.
9 G. Love, K. Murphy, The operational analysis of tropical cyclone wind fields in the Australian northern region, Bureau of Meteorology, 1985, pp 44-51.
10 G.D. Hubbert, G.J. Holland, L.M. Leslie, M.J. Manton, A real-time system for forecasting tropical cyclone storm surges, Weather Forecast, 1991, Vol 6, pp 86-97.
11 G.J. Holland, B.A. Harper, An updated parametric model of the tropical cyclone, Hurricanes and Tropical Meteorology, American Meteorological Society, 1999, pp 10-15.
12 F. Jakobsen, H. Madsen, Comparison and further development of parametric tropical cyclone models for storm surge modeling. J. Ind. Aerodyn., 2004, Vol. 92, No. 5, pp 375-391.
13 FEMA, 2003, HAZUS-MH MR1: Technical Manual.
14 G.J. Holland, A revised hurricane pressure–wind model, Mon. Wea. Rev., 2008, pp 3432-3445.
15 Almanac of Tropical Cyclone, 1949~2009, China Meteorological Bureau, China Meteorological Press.
16 H. Yasui, T. Ohkuma, H. Marukawa, J. Katagiri, Study on evaluation time in typhoon simulation based on monte carlo method, J. Ind. Aerodyn., 2002, Vol. 90, pp 1529-1540.

The Seventh International Colloquium on Bluff Body Aerodynamics and Applications (BBAA7)
Shanghai, China; September 2-6, 2012

Evaluation of time history of design wind speeds and directions using typhoon model and empirical wind speed ratio

Masahiro MATSUI [a], Takeshi OHKUMA [b], Yukio TAMURA [a]

[a] *Tokyo Polytechnic University, 1583 Iiyama, Atsugi, Kanagawa, JAPAN*
[b] *Kanagawa University, 3-27-1 Rokkakubashi, Kanagawa-ku, Yokohama, JAPAN*

ABSTRACT: A modified method is proposed for calculating the temporal variation of wind speeds and directions during a typhoon to estimate wind load effects on energy-consuming structural devices and cumulative fatigue damage under an extreme typhoon event. This method is based on the concept of scenario-based design wind speed. It utilizes parameter scaling, and consists of selecting a seed typhoon that has affected the target site, identifying its parameters, modifying them and calculating the temporal change of wind speeds and directions of a virtual typhoon. A calculation example is shown. The calculated temporal wind speeds give the same maximum wind speed as the design wind speed and realistic temporal variations based on meteorological considerations. This method is an extension of what proposed by Matsui et. al. (2010).

KEYWORDS: scenario-based design wind, typhoon model, empirical wind characteristics

1 INTRODUCTION

Conventional wind resistant design consists of setting the design wind speed, calculating the maximum response under that wind speed, evaluating the wind load effects, and checking that they are within required criteria or allowable limits. The design wind speeds are prescribed in regulations or recommendations, and have been estimated from extreme value statistics obtained from historical observed records and special considerations of local wind climates. For example, in Japan, the recommendations for loadings on buildings take typhoon effects into account (AIJ, 2004). The estimated design wind speeds are annual maximum wind speeds under standard observed conditions. The standard conditions are 10-minute mean at 10m above flat and open terrain.

Maximum load effects, e.g. maximum stresses, maximum deformations and maximum accelerations, can be evaluated from maximum wind speeds only. However, for some structural devices these effects need to be evaluated from the viewpoint of energy consumption or cumulative damage. To evaluate these types of devices, the total wind application time or temporal variation of one extreme wind event is required. Existing references, recommendations and regulations do not provide this kind of information.

Matsui et. al. (2010) discussed the problem and proposed the method of how to estimate temporal variations of wind speeds whose maximum values are the same as the design wind speeds under extreme wind events by applying a typhoon model and scaling parameters. This is especially important because typhoons are the most predominant events in the north-west pacific area. The proposed method was based on the concept of a scenario-based design wind speed, so to speak. In this paper, calculation of wind directions is extended to the previous method. Estimations of used values of parameters were shown by comparing with the historical statistics of parameter distributions.

2 EVALUATION OF METHODOLOGY

2.1 *Outline of Procedure*

The proposed method follows a set procedure: selecting a seed typhoon that has affected the target site, identifying its parameters, modifying them, and calculating the temporal change of wind speeds of a virtual typhoon. The calculation utilizes parameter scaling.

2.2 *Original Typhoon Records and Identification of Pressure Parameters*

The first step of the procedure is to select as a seed a remarkable typhoon that has affected the site and to collect its observed records. This typhoon and its observed wind speeds are referred to as a seed typhoon (or an original typhoon) and seed wind records (or original records) hereafter.
The second step is to identify the typhoon's parameters: central pressure depth D_P, radius of maximum wind R_M, translation speed C, etc. These parameters are identified using observed atmospheric pressures around the typhoon's path and applying Schloemer's empirical formula (Schloemer, 1954),

$$P(r) = P_C + D_P \exp(-\frac{R_M}{r}) \tag{1}$$

to fit the distributed atmospheric pressure records.

2.3 *Calculating Temporal Variation of Virtual Typhoon Wind Speeds*

The virtual typhoon is assumed to move along the same path as the seed typhoon. The virtual typhoon's parameters are changed from their original values so that it shows the same maximum wind speed as the design wind speed.

Let $U_{s\text{-}obs}$ and U_{syn} be the wind speeds under the seed and virtual typhoons. These wind speeds are assumed to be those under concentric circle typhoon pressure fields (for seed and virtual typhoon winds, $U_{s\text{-}typ}$, and U_{typ}, respectively), large scale topographical effects and aerodynamic roughness effects of the ground surfaces. The large scale topographical effects and aerodynamic roughness effects of the ground surfaces on the wind speeds are assumed to be linear, and are indicated by E_{env}. These conditions are expressed as,

$$U_{s-obs} = U_{s-typ} \cdot E_{env} \quad , \tag{2}$$

$$U_{syn} = U_{typ} \cdot E_{env} \quad . \tag{3}$$

The wind speeds under concentric circle typhoon pressure fields are calculated from the typhoon model.

If the large scale topographical effects and aerodynamic roughness effects of the ground surfaces are assumed to be identical in equations (2) and (3), equation (2) is expressed as

$$U_{syn} = \left(U_{typ} / U_{s-typ}\right) \cdot U_{s-obs} \quad . \tag{4}$$

Assuming that the temporal variation, whose period is longer than that of the spectral gap pointed out by Van der Hoven (1957), is organized according to the pressure field's movement, the time scale of the seed record is transferred into the value of the virtual typhoon through the non-dimensional time τ.

$$\tau = T/(L/U) \quad , \tag{5}$$

where T, L and U are the reference values of time, length and velocity scales relevant to the typhoon pressure field.

In order to decide the combination of parameters, effects of parameters' perturbations give good references.

$$\begin{aligned} U_{syn} &= U_{typ}/U_{e-typ} \cdot U_{e-obs} \\ &\approx U_{e-obs} + \frac{\partial U_{e-typ}}{\partial D_P}(D_{P-typ} - D_{P-e}) + \frac{\partial U_{e-typ}}{\partial R_M}(R_{M-typ} - R_{M-e}) + \frac{\partial U_{e-typ}}{\partial C}(C_{typ} - C_e) \end{aligned} \tag{6}$$

2.4 *Evaluation of wind direction*

In the previous procedure, wind speed field $\boldsymbol{U}=(u, v)$ on the horizontal plane can be expressed as complex number $\boldsymbol{U}=u+v\mathrm{i}$, where $\mathrm{i}^2=-1$, the wind speed U in equations (1) to (4) is described as the following polar expressions, equation (7), and Φ in the same equation corresponds the wind direction.

$$\boldsymbol{U}=u+v\mathrm{i} = U\exp(\mathrm{i}\Phi), \tag{7}$$

where, $U = (u^2+v^2)^{1/2}$, $\Phi = \tan^{-1}v/u$.

Not only wind speeds (u, v), but also the factor E_{env} should be treated as complex number. The wind speeds and directions can be treated at once in equations (1) to (4) by this extension.

2.5 *Effect of averaging time*

As the averaging time of wind speed is fixed, e.g. 10 minutes, generally, the transformation of the temporal scale by equation (5) requires consideration on the averaging time of the synthesized wind speeds. In this study, the averaging time, 10 minutes, is assumed ranged in the "spectral gap", after Van der Hoven (1957).

If the averaging time of the original wind speed records is 10 minutes, in case that the temporal scale is prolonged, the temporal scale of the synthesized wind speed is more than 10 minutes. In this case, as the maximum wind speed is ensured by the given condition, the entire wind speeds tend to be estimated slightly higher values. In case that the temporal scale is shortened, on the other hand, the averaging time of the synthesized wind speed is less than 10 minutes. The wind speeds should be averaged by 10 minutes and the maximum would be reduced. It requires re-estimation of combination of parameters for higher wind speeds.

2.6 *Model of Typhoon Wind Field*

The typhoon wind field model employed here is Meng's model (Meng et.a al., 1997).

In a typhoon's boundary layer, the vertical wind speed and directional profiles (wind speed and direction, $u(z)$, $\theta(z)$) are given as

$$u(z) = u_G(z/z_G)^{\alpha_u} , \tag{8}$$

$$\theta(z) = \theta_G + \theta_S(1.0 - 0.4z/z_G)^{1.1}, \tag{9}$$

where u_G, θ_G are gradient wind speed and direction; α_u is the power law index; and z_G is the gradient height. The power law index α_u and the gradient height z_G are expressed as functions of the absolute vorticity f_λ and the surface Rosby number $\mathrm{Ro}_\lambda(=u_G/f_\lambda z_0)$. Inflow angle θ_S is a function of the homogeneity of vorticity ξ and the surface Rosby number.

$$\alpha_u = 0.27 + 0.09\log z_0 + 0.018\log^2 z_0 + 0.0016\log^3 z_0, \tag{10}$$

$$z_G = 0.06\frac{u_G}{f_\lambda}(\log R_{O_\lambda})^{-1.45}, \tag{11}$$

$$\theta_S = (69 + 100\,\xi)(\log R_{O_\lambda})^{-1.13}, \tag{12}$$

$$f_\lambda = \left(\frac{\partial u_G}{\partial r} + \frac{u_G}{r} + f\right)^{1/2}\left(\frac{2u_G}{r} + f\right)^{1/2}, \tag{13}$$

$$\xi = \left(\frac{2u_G}{r} + f\right)^{1/2} \Big/ \left(\frac{\partial u_G}{\partial r} + \frac{u_G}{r} + f\right)^{1/2}, \tag{14}$$

The gradient wind direction θ_G is assumed to be parallel to the isobar. The gradient wind speed u_G is evaluated by Meyers and Markin's formula (1961) as

$$u_G = \frac{C\sin\theta_r - fr}{2} + \sqrt{\left(\frac{C\sin\theta_r - fr}{2}\right)^2 + \frac{r}{\rho}\frac{\partial P(r)}{\partial r}}, \tag{15}$$

where C and θ_r are translation speed and direction of a typhoon and f is the Coriolis parameter.

3 EXAMPLE OF CALCULATION

3.1 *Calculation of Temporal Variation of Design Wind Speeds due to Virtual Typhoon at Haneda AMeDAS (Automated Meteorological Data Acquisition System) Site*

The historical records of maximum wind speeds at the site are listed in Table-1. Typhoon MA-ON(T0422) was selected as a seed typhoon, during which the highest wind speed was recorded at Haneda AMeDAS. The typhoon's path is shown in Figure-1.

Since the observation conditions at Haneda AMeDAS were the same as the standard conditions, i.e. observation height 10m and open terrain exposure (terrain category II in the AIJ recommendations), the target wind speed was the right value of the design wind speed 42.5 m/s. After repeated tunings of parameters, following conditions were found in which the maximum wind speed was identical to the design wind speed. The central pressure depth was 1.83 times and translation speed was 0.5 times the original typhoon's values.

The time histories of wind speeds and directions under these conditions are shown in Figure-2 a) and b). To decide the combination of parameters, the sensitivity maps shown in Figures-2 to 3 (Matsui et. al., 2010), are utilized.

Table-1 Historical daily maximum wind speed at Haneda AMeDAS (Automated Meteorological Data Acquisition System)

order	daily maximum wind speed (m/s)	wind direction	date	affecting typhoon
1	29	NNE	Oct. 09, 2004	T0422
2	27	SSE	Sept. 07, 2007	T0709
3	24	SW	Dec. 05, 2004	
4	24	W	Oct. 01, 2002	T0221
5	23	NE	April 18, 2008	
6	23	SSW	June 20, 1997	T9707
7	23	S	Dec. 05, 1996	
8	23	NNW	Sept. 22, 1996	T9617
9	22	SSW	March 31, 2007	
10	22	SSW	March 30, 1996	

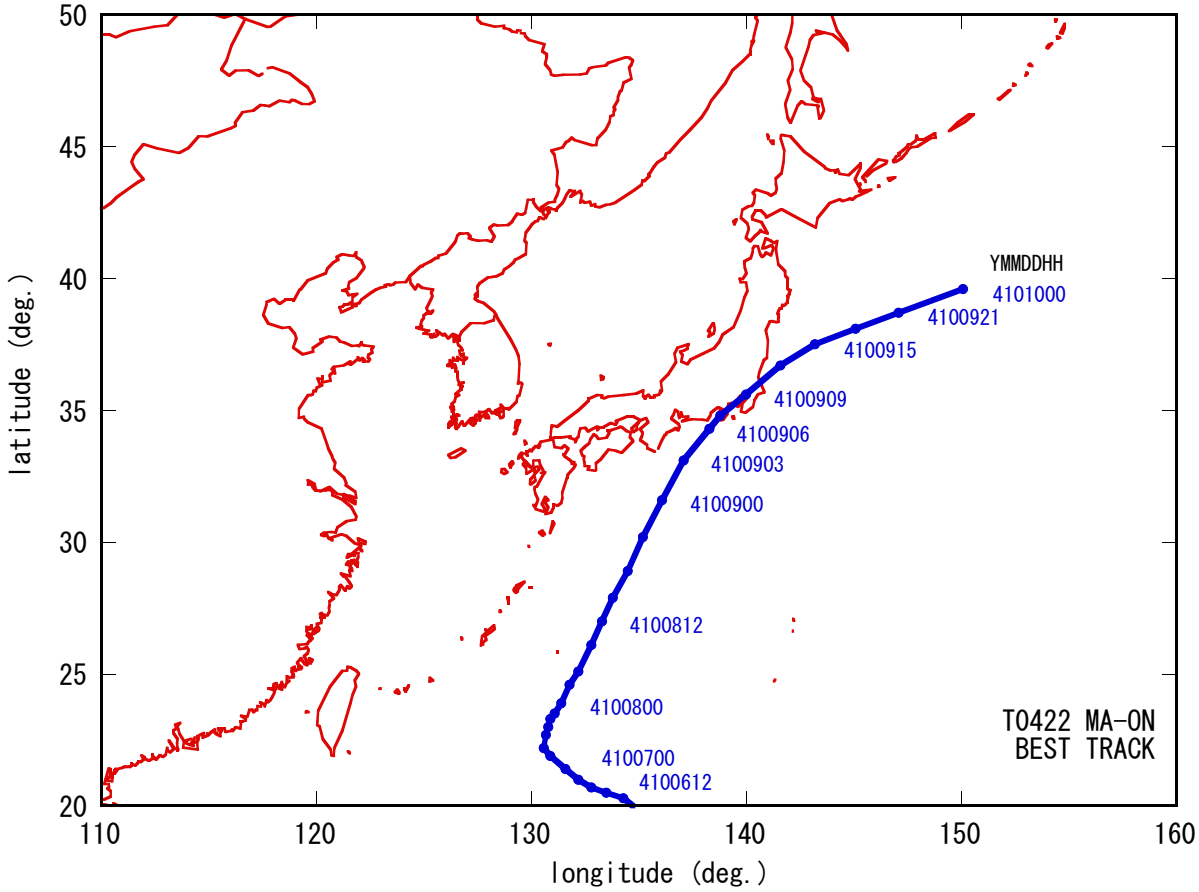

Figure-1: Path of Typhoon MA-ON (T0422) (best track, RSMC Tokyo)

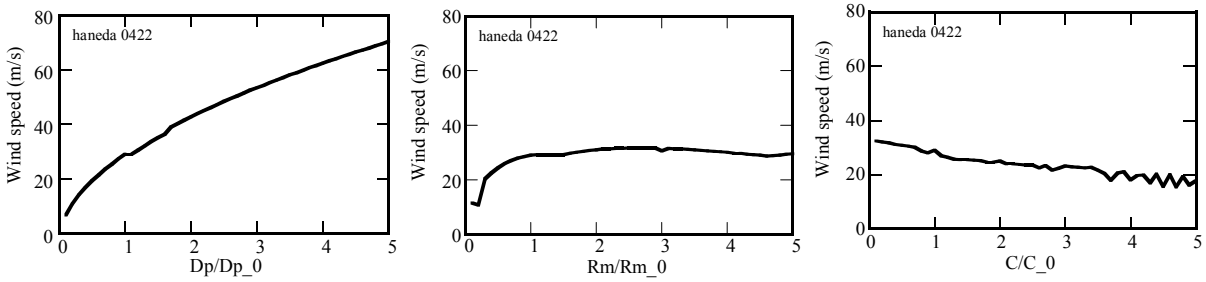

(a) Pressure depth, D_P *(b) Radius of maximum winds, R_M* *(c) Moving speed, C*

Figure-2: Variations of maximum wind speed for a single parameter change, D_P, R_M or C.

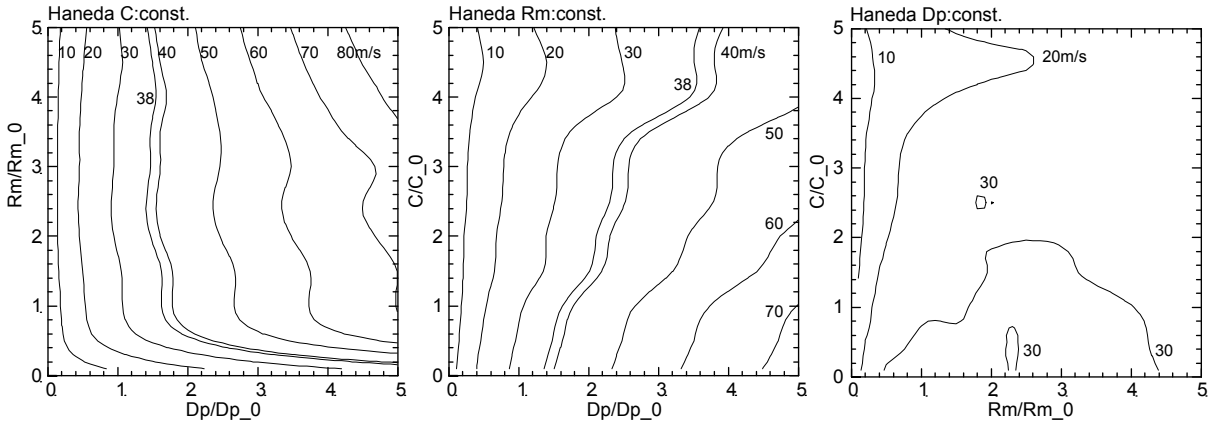

(a) D_P and R_M (b) D_P and C (c) R_M and C

Figure-3: Variations of maximum wind speed for two of three parameters change, between D_P, R_M and C.

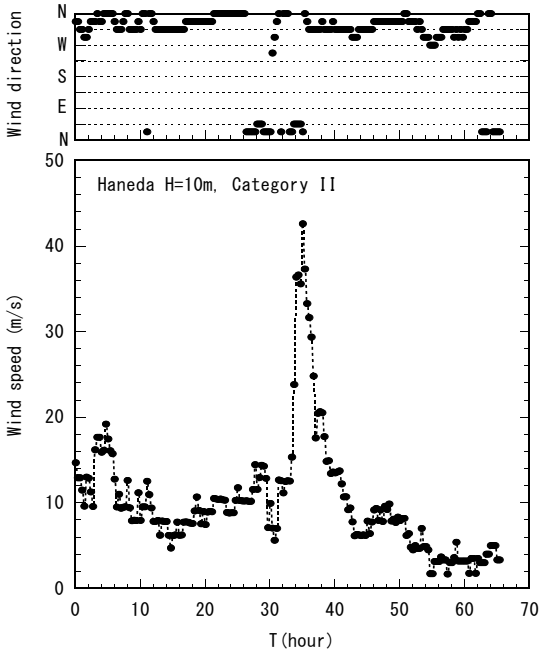

Figure-4: Synthesized temporal wind speed and direction
Site: Haneda AMeDAS, original typhoon: T0422, MA-ON

3.2 *Estimation of typhoon pressure parameters in the calculation*

The typhoon pressure parameters used in the previous sections are estimated from the historical statistics of the parameters around observation site.

For historical typhoons passed inside 500 km from Tokyo for 40 years, their parameters, central pressure depth D_P, radius of maximum winds R_M and translation speed C were estimated and their distributions and correlations are shown in Fig.5. Their probability distributions can be fitted well by log-normal distributions. The correlations of them are not so high.

The values of parameters used in the calculations are also shown in Figure-5. The central depth is around 98% probability of non-exceedance and almost the maximum of all records. The used value of radius of maximum winds is smaller values in the distributions. The used value of translation speed is relatively low value among the distribution. As shown here, the procedure can show the estimation of the virtual typhoon for design wind speed.

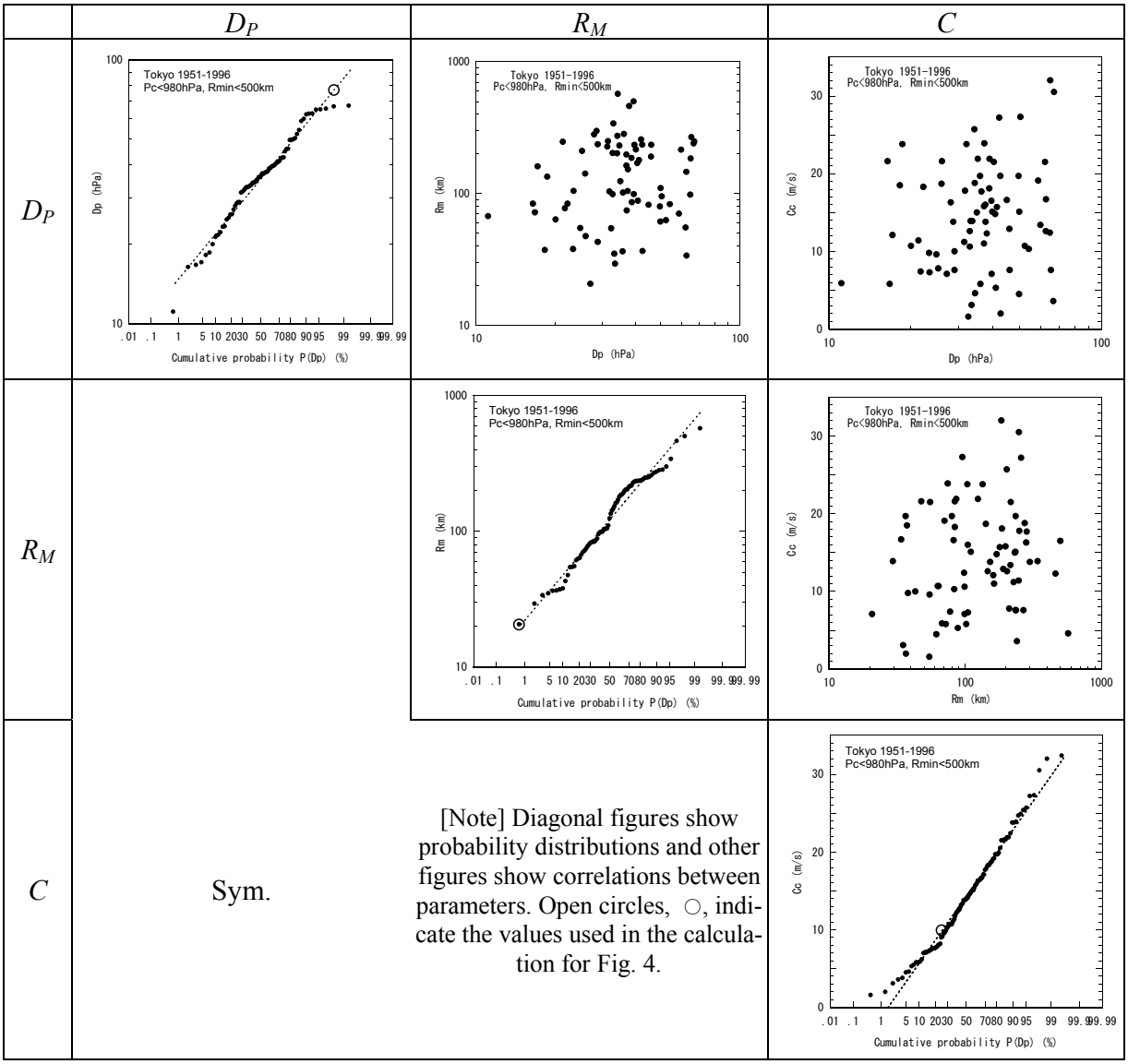

Figure-5: Statistical characteristics of historical typhoon pressure parameters, D_P, R_M and C for typhoons passing inside 500 km from Tokyo for 40 years.

4 CONCLUDING REMARKS

A method has been proposed for estimating the temporal variation of design wind speed and direction under typhoon conditions based on the concept of scenario-based design wind speed. This method utilizes parameter scaling, and consists of selecting a seed typhoon that has affected the target site, identifying its parameters, modifying its parameters and calculating the temporal change of wind speed of a virtual typhoon.

A calculation example has been shown and the effects of modifying the typhoon's pressure parameters have been studied. The calculated temporal wind speeds gave the same wind speeds as the design wind speeds and realistic temporal variations based on meteorological considerations.

The relationship between calculated maximum wind speeds and modification ratios of typhoon pressure parameters can be a useful guide for selection of parameter combinations.

The selected typhoon pressure parameters were estimated based on the statistical distributions of the historical typhoon parameters.

The proposed method can provide time histories of design wind speeds and directions with clear background on the physical image of the design typhoon models.

5 ACKNOWLEDGEMENTS

The authors thank the members of the wind resistant design committee (Chaired by Takeshi Ohkuma) of the Japan Society of Seismic Isolation for their fruitful comments and discussions.

6 REFERENCES

1 Architectural Institute of Japan (2004) "AIJ recommendations for loads on buildings", Architectural Institute of Japan.
2 Matsui, M., Ohkuma, T. and Tamura Y. (2010), "Evaluation of time history of design wind speeds using typhoon model and empirical wind characteristics", 34th IABSE Symposium, Venice, 2010
3 Meng, Y., Matsui, M. and Hibi, K. (1997) "A numerical study of the wind field in a typhoon boundary layer", Journal of Wind Engineering and Industrial Aerodynamics 67&68, 437-448
4 Meyers, V.A. and Malkin,W. (1961), "Some properties of hurricane wind fields as deduced from trajectories", National Hurricane Research Project Report No. 49, US Department of Commerce, Weather Bureau, Washington, DC, 1961.
5 The Regional Specialized Meteorological Center (RSMC) Tokyo, "Best Track Data", Japan Meteorological Agency, http://www.jma.go.jp/jma/jma-eng/jma-center/rsmc-hp-pub-eg/RSMC_HP.htm
6 Schloemer, R.W. (1954) "Analysis and synthesis of hurricane wind patterns over Lake Okeechobee, Florida", Hydrometeorological Report, No. 31, 49pp.
7 Van der Hoven, Isaac (1957) "Power Spectrum of Horizontal Wind Speed in the Frequency Range From 0.0007 to 900 Cycles Per Hour", Journal of Meteorology, Vol. 14, No. 2, pp. 160- 164

The Seventh International Colloquium on Bluff Body Aerodynamics and Applications (BBAA7)
Shanghai, China; September 2-6, 2012

Statistics-based investigation on typhoon transition modeling

Shuoyun Zhang [a], Kazuyoshi Nishijima [b]

[a] *IBK, ETH Zurich, Zurich, Switzerland*
[b] *Department of Civil Engineering, Technical University of Denmark, Lyngby, Denmark*

ABSTRACT: The present study revisits the statistical modeling of typhoon transition. The objective of the study is to provide insights on plausible statistical typhoon transition models based on extensive statistical analysis. First, the correlation structures of the typhoon transition are estimated in terms of autocorrelation function (ACF) and partial autocorrelation function (PACF). This facilitates to specify a set of plausible models for further investigation. Then, the corrected Akaike Information Criterion (cAIC) is applied to investigate the relative goodness of fit of these models. The spatial inhomogeneity and the seasonality are taken into account by developing the models for different spatial grids and seasons separately. An appropriate size of spatial grids is investigated. The statistical characteristics of the random residual terms in the models are also examined. Finally, Monte Carlo simulations are performed to investigate the overall performance of the proposed model.

KEYWORDS: Typhoon transition, statistical analysis, spatial inhomogeneity, seasonality, non-normality, model selection.

1 INTRODUCTION

The methodology for probabilistic modeling of typhoon hazard and risks has experienced significant progress in the last few decades. Based on the methodology, probabilistic models have been developed. Presently, a spectrum of probabilistic models are available and widely utilized as a tool to quantify and manage typhoon risks in different contexts. Successful applications include the determination of design wind loads on structures and the pricing of re/insurance portfolio policies. More recently, the methodology and the probabilistic models have been applied beyond these classical applications: The methodology has been applied for quantifying the impact of the global climate change on wind risks due to typhoons, see e.g. Nishijima et al.[1]; a probabilistic model has been applied for real-time operational decision optimization in the face of an approaching typhoon, see Anders & Nishijima[2]. In these applications, among others, the modeling of typhoon transition plays the key role.

The modeling of typhoon transition from its genesis to dissipation, i.e. its whole life, has become the state-of-the-art in the modeling of the typhoon hazard and risks. This approach has several advantages over classical approaches. For example, a classical statistical approach for modeling the typhoon-induced wind hazard often encounters a lack of sufficient number of observations in reliably estimating the wind speeds of large return periods, whereas this approach alleviates the statistical problem by best utilizing the observations of historical typhoon tracks and by simulating sufficient number of typhoons by Monte Carlo techniques. It also facilitates to consider the spatial correlations of the hazard and risks, which are relevant for the estimation of the portfolio risks, while one of the classical approaches starts Monte Carlo simulations of typhoon events only at neighboring areas or at coastal lines of interest.

Vickery et al.[3] propose the first approach for modeling the transition of typhoon during its whole life, focusing on the Atlantic basin. They employ higher-order of Markov chains for modeling the changes of translation speed and angle as well as intensity of typhoons. Other modeling approaches are also proposed taking basis in different expressions for typhoon transition; see Powell et al.[4], James & Mason[5], Emanuel et al.[6], Rumpf et al.[7], Hall & Jewson[8], [9], Graf et al.[10], Yin et al.[11] and Yasuda et al.[12]. However, in spite of the proposals and their wide applications little attention has been paid on the relative performances of different transition models. Motivated by this and focusing on the Markov chain-based modeling, Graf & Nishijima[13] perform a systematic comparison of the performances of the different models; it is found that the performances are not too sensitive to the choices of the functional forms for the Markov chains and the way to deal with the spatial inhomogeneity (in terms of grid size) and seasonality, as long as the statistics on annual maximum wind speed is concerned. However, they do not investigate the plausibility of different models by extensive statistical analysis.

The present study aims at identifying plausible models by extensive statistical analysis; focusing on the translation speed and angle and the central pressure of typhoons, and restricting to the Markov-chain representation. First, by the statistical analysis, the order of Markov chains and the explanatory variables required in the modeling are investigated. Second, the appropriate size of the spatial grid in which the probabilistic characteristics of typhoons can be assumed to be stationary is examined. Third, the statistical characteristics of the residual terms in the Markov chain models are estimated. Thereby, a set of plausible typhoon transition models is identified. Selecting a proposed typhoon transition model, the performance of the model is compared to other competing models and the historical typhoons with respect to the statistics on the translation speed and angle and the central pressure of typhoons at several latitudes. For the statistical analysis and the modeling of the typhoon transition, the best track data provided by the Japan Meteorological Agency (JMA) in the period between 1951 and 2006 is utilized. In present paper, the term typhoon is employed for referring to tropical cyclones in general.

2 MODELING APPROACH

2.1 *Auto regression*

For the purpose to understand the basic statistical characteristics of the transition of historical typhoons, the successive translation speeds, successive translation angles and successive central pressures of the typhoons are plotted, see Figure 1. V_i, Γ_i and P_i represent the translation speed, translation angle, central pressure at time step i, respectively. These three variables are hereafter called the state variables of typhoons. Note the translation angle of a typhoon is 0^o when traveling north and positive clockwise. It is found that there are linear relationships with moderate randomness between successive translation speeds and translation angles, respectively. This is consistent with the observation made in Emanuel et al.[6], where the historical typhoons in the north Atlantic basin are examined. The similar relationship is observed between the successive central pressures. Furthermore, by developing these scatter plots for different areas and seasons, it is observed that the statistical characteristics of the state variables are different; implying the existence of the spatial inhomogeneity and the seasonality.

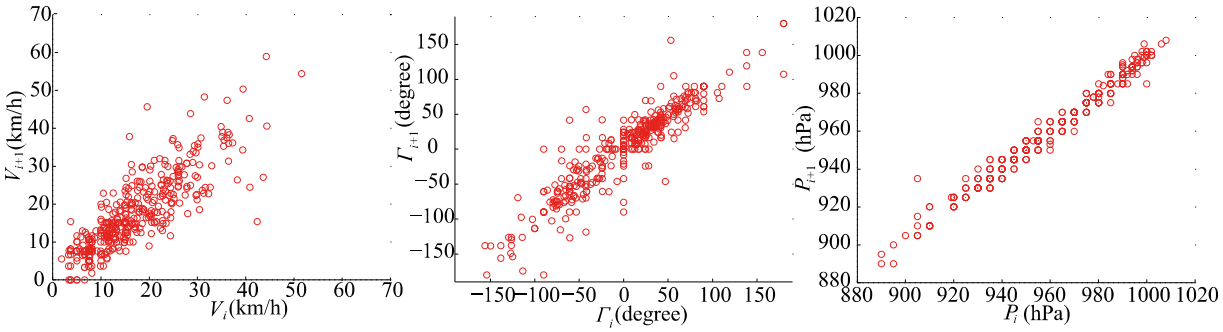

Figure 1. Scatter plots showing relationships between successive translation speeds, successive translation angles and successive central pressures. Track data utilized here to create the plots are on the typhoons travelling within the area bounded by the longitudes [124°E, 132°E] and the latitudes [24°N, 28°N] in September.

2.2 *Exploration of the regression form*

The relationships drawn in the scatter plots suggest that the autoregressive (AR) model can be appropriate to represent the transition of typhoons. Therefore, the autocorrelation coefficient function (ACF) and the partial autocorrelation coefficient function (PACF) are estimated in order to identify the necessary and sufficient orders of the AR models. Taking basis in the area bounded by the longitudes [124°E, 132°E] and the latitudes [24°N, 28°N] and the area bounded by the longitude [140°E, 148°E] and the latitude [28°N, 32°N] in September, and assuming the typhoon transition is stationary therein, ACF's and PACF's are estimated for the state variables as a function of the time lag, see Figure 2. Here, the unit of the time lag is 6 hours, at which interval the JMA best track data is available. Since the ACF's decay as a function of time lag and the PACF's show the cut off at around time lags of 2, it suggests the autoregressive models of the second orders, AR(2), can be plausible. Similar observations are made for other seasons and areas. Therefore, the first plausible transition models for the state variables are:

$$V_{i+1} = a_1 + a_2 V_i + a_3 V_{i-1} + \varepsilon_{V,i} \tag{1}$$

$$\Gamma_{i+1} = b_1 + b_2 \Gamma_i + b_3 \Gamma_{i-1} + \varepsilon_{\Gamma,i} \tag{2}$$

$$P_{i+1} = c_1 + c_2 P_i + c_3 P_{i-1} + \varepsilon_{P,i}\,. \tag{3}$$

Here, $\varepsilon_{V,i}$, $\varepsilon_{\Gamma,i}$ and $\varepsilon_{P,i}$ are the random residual terms for the state variables. Each of the residual term for different time steps is assumed to independently follow an identical distribution. For some seasons and areas the estimated PACF is significantly different from zero only at time lag of 1 for the translation speed and angle; hence, the autoregressive models of the first order, AR(1), are also plausible;

$$V_{i+1} = a_1 + a_2 V_i + \varepsilon_{V,i} \tag{4}$$

$$\Gamma_{i+1} = b_1 + b_2 \Gamma_i + \varepsilon_{\Gamma,i}\,. \tag{5}$$

As the third plausible models, regression models including the possible interrelations between the translation speed and the translation angle are assumed:

$$V_{i+1} = a_1 + a_2 V_i + a_3 V_{i-1} + a_4 \Gamma_i + \varepsilon_{V,i} \tag{6}$$

$$\Gamma_{i+1} = b_1 + b_2 \Gamma_i + b_3 \Gamma_{i-1} + b_4 V_i + \varepsilon_{\Gamma,i}\,. \tag{7}$$

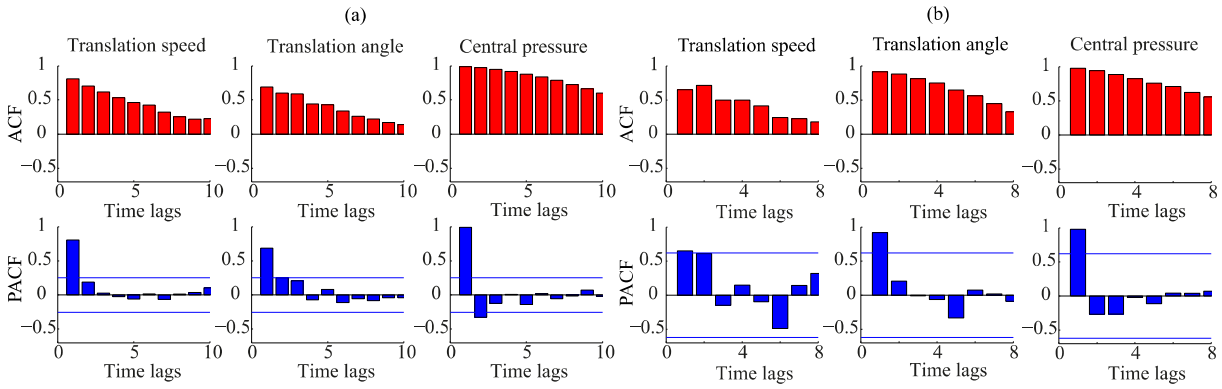

Figure 2. Illustration of the estimated ACF and PACF of the translation speed, the translation angle and central pressure as the function of lags. (a) is for the longitudes [124°E, 132°E] and the latitudes [24°N, 28°N] in September, and (b) is for the longitude [140°E,148°E] and the latitude [28°N,32°N] in September. The two lines in the figures of PACF's correspond to the 5%-significance level at which the PACF is considered to be different from zero.

Vickery et al.[3] indicate that the intensity of typhoon is subject to sea surface temperature (SST). Here, the following functional form is assumed as one of possible plausible models:

$$P_{i+1} = c_1 + c_2 P_i + c_3 P_{i-1} + c_4 T_i + \varepsilon_{P,i} \tag{8}$$

where T_i represents the SST at step i.

The goodness-of-fits of these plausible models is explored. The exploration is performed with respect to: AR(1) model vs. AR(2) model; whether or not the interrelation needs to be considered between the translation speed and the translation angle; whether the SST is necessarily included in the regression model. For this purpose, the corrected Akaike information criterion (cAIC) is employed. Note that the cAIC is capable of accounting for the non-normality of the residual terms, see e.g. Yanagihara[14]. It favors the model with a smaller value of cAIC. The cAIC is calculated for the model for each grid (latitude 4° × longitude 8°) for each month that contains at least 20 samples of the historical typhoon track record. Besides this, typhoons heading westward and eastward are separately treated in calculating the cAIC.

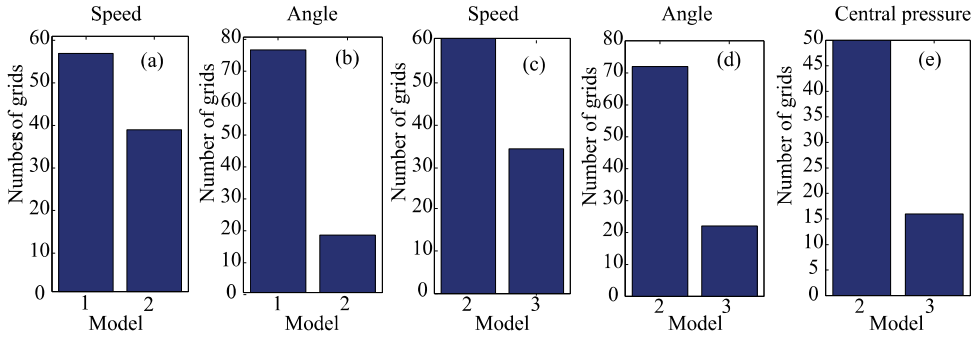

Figure 3. Histograms of the numbers of grids (and directions) with smaller cAIC values. The comparisons of these numbers are with respect to: (a) AR(1) vs. AR(2) for translation speed; (b) AR(1) vs. AR(2) for translation angle; (c) AR(2) for translation speed vs. interrelation model (Eq. (6)); (d) AR(2) for translation angle and interrelation model (Eq. (7)); (e) AR(2) for central pressure vs. model including SST (Eq. (8)). In the horizontal axis, AR(1) and AR(2) are indicated by 1 and 2, respectively, and 3 indicates the interrelation models for translation speed and translation angle and the model including SST for central pressure.

The numbers of the grids (and directions in case of the translation) with less cAIC are counted. In Figure 3, the histograms for these numbers are shown for the comparisons in those respects listed above, for September as an example. The results are: for all the months more grids favor AR(1) than AR(2), see (a) and (b) in the figure; more grids favor non-interrelation translation models, see (c) and (d) in the figure; more grids are in favor of not including SST in the model, see (e) in the figure.

2.3 *Estimation of the coefficients*

In order to reflect the spatial inhomogeneity and seasonality the regression models (Equations (1)-(8)) are developed separately for predefined spatial grids and time frames. The size of the grids must be determined by considering the balance between the numbers of samples available and the homogeneity of the characteristics of the samples in the grids. The average movements of the historical typhoons are approximately 0.4° in latitude and 0.8° in longitude in one time step (i.e. 6 hours). Considering that the set of the plausible models includes the second order of the (auto-) regression models, a grid size that can include two steps of typhoon transitions is required; hence, 0.8° in latitude and 1.6° in longitude at minimum. For the seasonality, it is postulated that the characteristics of typhoons do not significantly differ within one month period; hence, one month for the time frame. Furthermore, in order to taken into account the difference in the characteristics of the typhoon translation (speed and angle) eastward and westward, the models for the translation are developed separately for the two directions. These are the base line for estimating the coefficients of the regression models. However, in cases where sufficient number of samples is not available, the size of the spatial grid is expanded until the sufficient number of sample becomes available. The criteria for this are determined in accordance with the criteria on the validity of the regression analysis such as statistical power level and significance level, see Cohen[15], Cohen et al.[16].

2.4 *Modeling of residual terms*

Based on the functional forms of the plausible models, statistical characteristics of the residual terms are investigated. As shown in Figure 4, it is found that the residual terms for the state variables generally do not follow the normal distributions. This is consistent with the observation in Hall & Jewson[8]. In the figure, the normalized histograms of the frequencies of the residuals are shown together with the probability density functions of the two normal distributions that are fit to the histograms in two ways. One of the two normal distributions is obtained by considering all the data; the other normal distribution is obtained by neglecting both tails at quantiles larger than 1.5 times of the standard deviations. It either exaggerates the randomness if it is modeled by considering all the data (e.g. Graf et al.[10]) or underestimates the randomness if it is modeled by neglecting the tails (e.g. Emanuel et al.[6]).

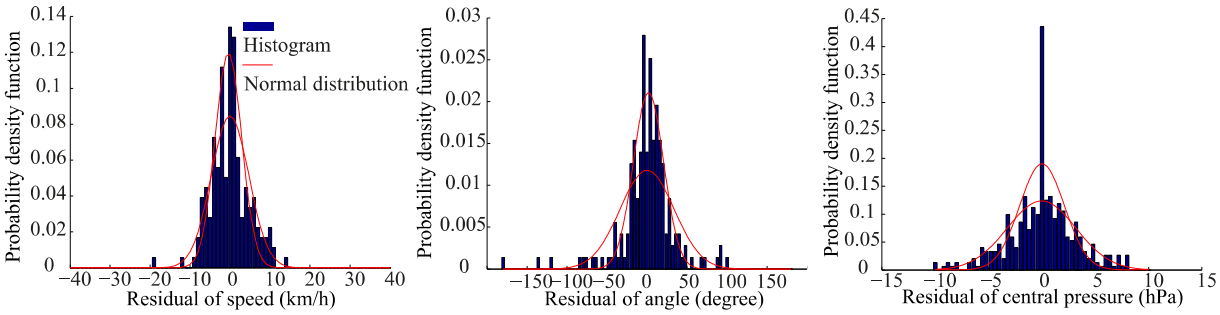

Figure 4. The normalized histograms of the frequencies of residuals for: (a) translation speed with model in Eq. (6); (b) translation angle with model in Eq. (7); (c) central pressure with model in Eq. (8). (a) and (b) are obtained by examining for typhoons in September travelling westward within the area bounded by the longitudes [124°E, 132°E] and the latitudes [24°N, 28°N].

The modeling of the residual terms becomes critical especially e.g. for the case when the typhoon transition model is utilized to predict the future transition of emerging typhoons. The consequences of the two ways of the approximations by the normal distributions on the simulated typhoon tracks are shown in the next section. It is not generally suggested to model the residual terms by the normal distributions; the empirical modeling of the residual terms, similar to the way by James & Mason[5], yet accounting for the spatial inhomogeneity and seasonality, or more flexible modeling such as mixture models are suggested.

3 PERFORMANCE OF MODELS

Based on the statistical investigation in the previous section, the following transition modeling is proposed: Eq. (6), (7) and (8) for modeling the state variables; the coefficients in the model are estimated by the method described in Section 2.3; the empirical distributions of the residual terms are employed. The performance of the proposed model is investigated by simulating typhoons by Monte Carlo techniques and then comparing several statistics of the typhoon transition with those of the historical typhoons. In the Monte Carlo simulation, the initial states of the typhoons are re-sampled from the initial states of the historical typhoons. Then, the transition of the typhoons is simulated using the transition model. Note that evolution of the typhoon intensity after landfall is simulated using a filling model, which takes basis in the modeling by Vickery et al.[17].

Figure 5a shows the tracks of the historical typhoons for the month September in the period between 1951 and 2006. Note that the other plots show the tracks of the simulated typhoons for September in the same period. Figure 5b illustrates the simulated typhoon tracks with the proposed model; Figure 5c with the modeling of the residual terms by the normal distribution considering all the data; Figure 5d with the modeling of the residual terms by the normal distribution considering the data only within the 1.5 times of the standard deviations. As can be clearly seen, two ways to model the residual terms by the normal distributions result in that the tracks are either overly fluctuated or overly smoothed. In contrast, it seems that the modeling of the residual terms by empirical distributions succeeds in reproducing the randomness in the historical typhoon tracks.

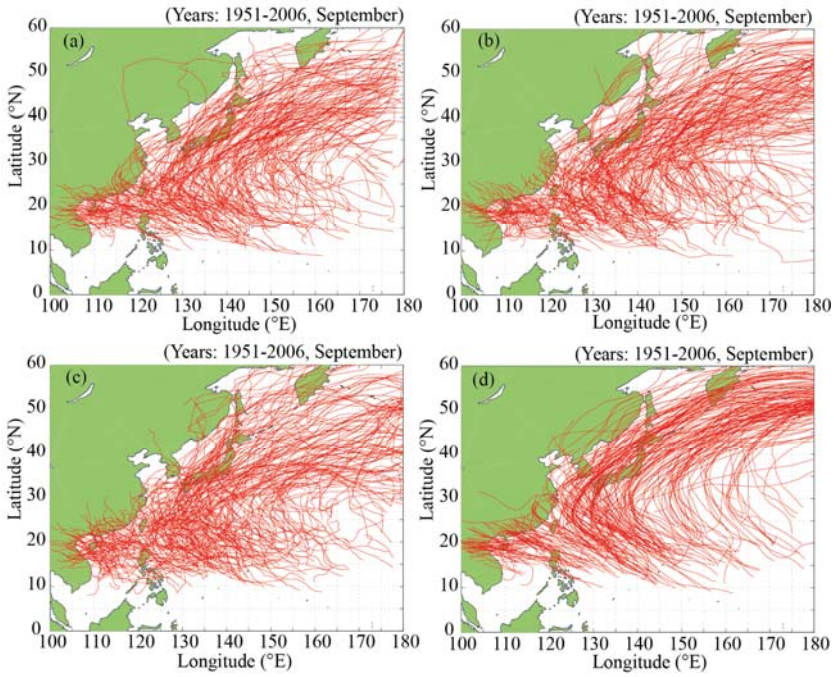

Figure 5. (a) Historical tracks occurred in September during 1951-2006; (b), (c) and (d) are the simulated tracks for the typhoon occurred in September over the same period. (b) is the result of proposed model; (c) is the result by modeling all the residual terms with normal distribution; (d) is the result by modeling the residual term with normal distribution disregarding both tails at quantiles larger than 1.5 times of standard deviation.

The statistics of the transitions of the typhoons simulated with the proposed model are calculated. These are compared to the statistics of the historical typhoons. Moreover, for comparison two competing (not recommended) models are developed and the statistics of the typhoons simulated by these models are also calculated. These competing models are, based on the proposed modeling, yet the ones whose coefficients of the regression models are estimated either by assuming the spatial homogeneity or by assuming no seasonality.

In Figure 6, cumulative annual average numbers (CAAN's) of typhoons are shown as the function of the translation speed, translation angle, and central pressure, respectively. These statistics are obtained by counting the typhoons traveling at the latitude 20°N or 35°N at the longitudes between 120°E and 160°E. CAAN's for translation angle and speed are the measures of the movements of the typhoons and CAAN's for central pressure is the measure of the intensity of the typhoons. The figure shows that the proposed model, as well as the second competing model (no seasonality), performs well in the sense that these agree with the statistics obtained by historical records at both latitudes. On the other hand, the simulations with the first competing model (spatial homogeneity) fail to generally reproduce the statistics obtained from the historical record.

In Figure 7, the statistics are shown for the month September only. It is seen that the simulated results from the proposed model fit the historical statistics for all three state variables at both latitudes. On the other hand, the first competing model fails to reproduce the statistics obtained from the historical record especially at 35°N, which may be accounted by the accumulation of errors in the simulations starting from lower latitudes. The second competing model also fails notably at 35°N, where the seasonality is more dominant.

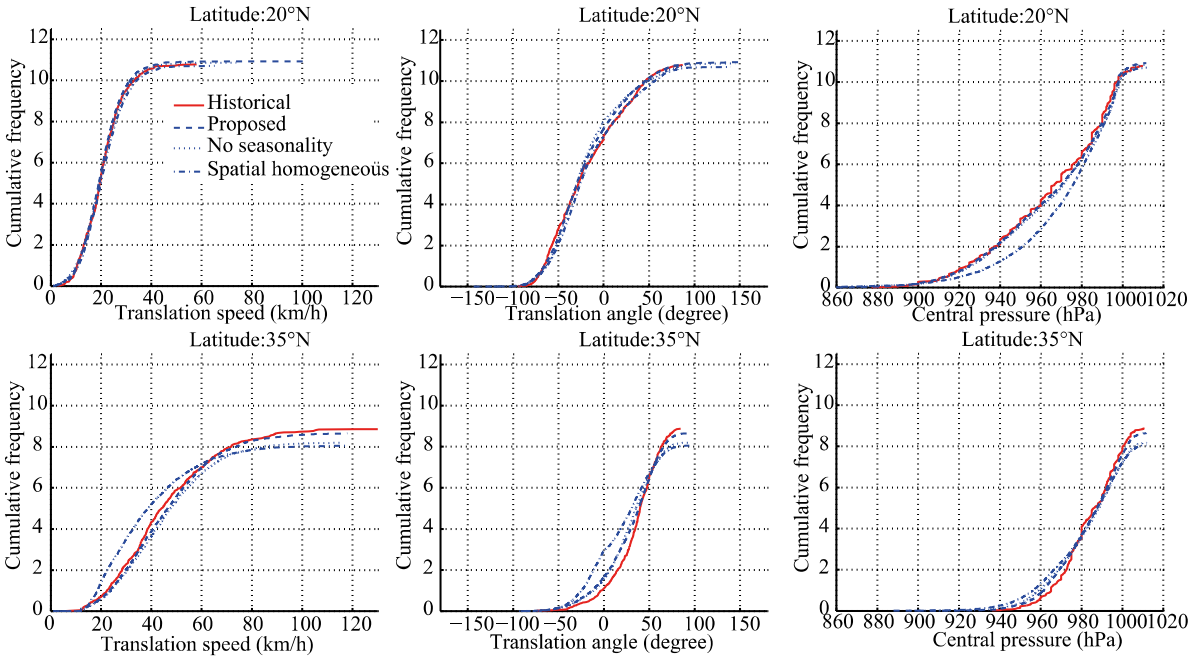

Figure 6. CAAN's calculated with the historical records and the Monte Carlo simulations as a function of the translation speed, translation angle and central pressure at latitudes 20°N and 35°N. By Monte Carlo techniques, 10000 times one- year typhoon events are simulated.

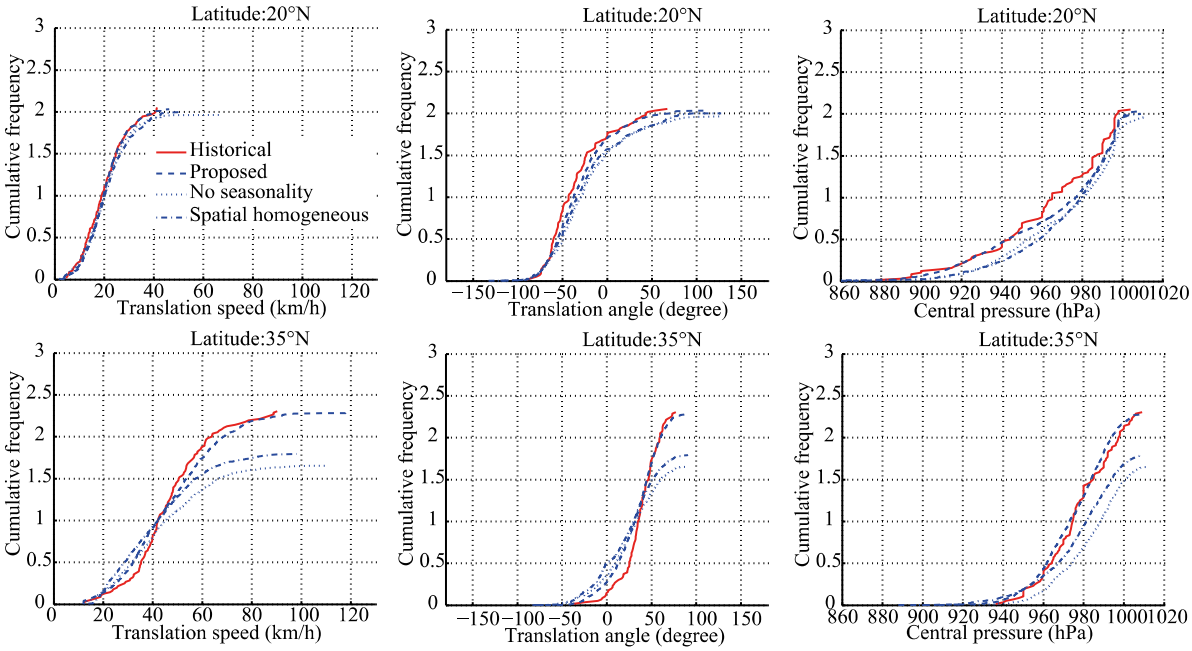

Figure 7. Cumulative average numbers of typhoons in September calculated with the historical records and the Monte Carlo simulations as a function of the translation speed, translation angle and central pressure at latitudes 20°N and 35°N. By Monte Carlo techniques, 10000 times one- year typhoon events are simulated.

4 DISCUSSIONS

The simulation results imply that the spatial inhomogeneity has to be appropriately taken into account in the modeling of the typhoon transition, reflecting the observation that the statistical characteristics show spatial inhomogeneity. The simulated results illustrated in Figure 6 and Figure 7 also show the importance of modeling of seasonality in the case that the typhoon transition of a specific season is of interest. However, the seasonality has not attracted sufficient attention in the statistical modeling of typhoon transition, except for the two of the models mentioned in Section 1; i.e. Emanuel et al.[6] and Graf et al.[10]. The consideration of the seasonality may become relevant for better understating and modeling of the typhoon transition under future climate change. Therefore, it is suggested to develop the transition models for different spatial grids and seasons separately where applicable; yet the optimal size of the grids is to be further investigated.

Although not illustrated in the present paper, it is found that the choice of the functional forms among the plausible models does not play significant roles in the statistical characteristics of the typhoon transition. Since the functional forms with less number of explanatory variables require less amounts of historical records to estimate the coefficients at same levels of confidence, it is suggested to employ simpler functional forms in the case where the numbers of the historical records are limited. On the other hand, if the forecasting of emerging typhoons is of interest, models with more numbers of explanatory variables have the advantage since they facilitate the use of more information.

5 CONCLUSIONS

The modeling of the typhoon transition is investigated by the extensive statistical analysis. First, the estimated ACF's and PACF's for the state variables of typhoon indicate that the second orders of the autoregressive models are sufficient. Second, by the cAIC, it is found that for many of the grids and months simpler functional forms for the modeling of the typhoon transition are in favor. Third, the choice of the functional forms is generally not relevant in the transition modeling; however, modeling of the residual terms has significant impact on the fluctuation of the simulated typhoon tracks. Fourth, the consideration of the spatial inhomogeneity is important in general and the consideration of the seasonality is also important in case the transition of the typhoon in a specific season is of interest. Based on these statistical analyses, the modeling of typhoon transition is proposed.

6 ACKNOWLEDGEMENTS

This study has been conducted during the research stay of the first author at Technical University of Denmark. The first author thanks for the financial support by China Council Scholarship (CSC) for conducting this study.

REFERENCES

1 Nishijima K, Maruyama T, Graf M (2012) A preliminary impact assessment of typhoon wind risk of residential buildings in Japan under future climate change. Hydrological Research Letters 6:23-28. doi:10.3178/HRL.6.23

2 Anders A, Nishijima K (2011) Adaptation of option pricing algorithm to real time decision optimization in the face of emerging natural hazards. Paper presented at the 11th International Conference on Applications of Statistics and Probability in Civil Engineering, Zurich, Switzerland

3 Vickery PJ, Skerlj PF, Twisdale LA (2000) Simulation of Hurricane Risk in the U.S. Using Empirical Track Model. Journal of Structural Engineering 126 (10):1222-1237

4 Powell M, Soukup G, Cocke S, Gulati S, Morisseau-Leroy N, Hamid S, Dorst N, Axe L (2005) State of Florida Hurricane Loss Projection Model: Atmospheric Science Component. Journal of Wind Engineering and Industrial Aerodynamics 93:651-674

5 James MK, Mason LB (2005) Synthetic tropical cyclone database. Journal of Waterway, Port, Coastal, and Ocean Engineering 131:181-192

6 Emanuel K, Ravela S, Vivant E, Ris C (2006) A statistical-deterministic approach to hurricane risk assessment. Bulletin of the American Meteorological Society 87 (3):299-314. doi:10.1175/BAMS-87-3-299

7 Rumpf J, Weindl H, Hoppe P, Rauch E, Schmidt V (2007) Stochastic modelling of tropical cyclone tracks. Mathematical Methods of Operations Research 66 (3):475-490. doi:10.1007/s00186-007-0168-7

8 Hall TM, Jewson S (2007) Statistical modelling of North Atlantic tropical cyclone tracks. Tellus 59A:486-498. doi:10.1111/j.1600-0870.2007.00240.x

9 Hall TM, Jewson S (2008) Comparison of local and basin-wide methods for risk assessment of tropical cyclone landfall. Journal of Applied Meteorology and Climatology 47:361-367

10 Graf M, Nishijima K, Faber MH (2009) A probabilistic typhoon model for the northwest Pacific region. Paper presented at the The seventh Asia-pacific conference on wind engineering, APCWE7, Taipei, Taiwan

11 Yin J, Welch MB, Yashiro H, Shinohara M (2009) Basinwide typhoon risk modelling and simulation for Western North Pacific basin. Paper presented at the The seventh Asia-pacific conference on wind engineering, APCWE7, Taipei, Taiwan

12 Yasuda T, Mase H, Kunitomi S, Mori N, Hayashi Y (2010) Stochastic typhoon model and its application to future typhoon projection. Proceedings of the 32nd International Conference on Coastal Engineering. ASCE,

13 Graf M, Nishijima K (2011) Issues of epistemic uncertainty treatment in decision analysis for tropical cyclone risk management. Paper presented at the The 11th International Conference on Applications of Statistics and Probability in Civil Engineering, Zurich, Switzerland

14 Yanagihara H (2005) Corrected version of AIC for selecting multivariate normal linear regression models in a general nonnormal case. Journal of Multivariate Analysis 97 (2006):1070-1089. doi:10.1016/j.jmva.2005.06.005

15 Cohen J (1988) Statistical Power Analysis for the Behavioral Sciences (2nd Edition). Lawrence Earlbaum Associates

16 Cohen J, Cohen P, West SG, Aiken LS (2003) Applied Multiple Regression/Correlation Analysis for the Behavioral Sciences (3rd edition). Lawrence Earlbaum Associates

17 Vickery PJ, Skerlj PF, Twisdale LA (2005) Simple Empirical Models for Estimating the Increase in the Central Pressure of Tropical Cyclones after Landfall along the Coastline of the United States. Journal of Applied Meteorology 44 (12):1807-1826

The Seventh International Colloquium on Bluff Body Aerodynamics and Applications (BBAA7)
Shanghai, China; September 2-6, 2012

Statistical representation of typhoons in northwest pacific basin

Sungsu Lee[a], Ga Young Kim[b]

[a]Corresponding Author, Faculty of School of Civil Engineering, Chungbuk National University,
410 Seongbong-ro, Cheongju, South Korea, joshua@cbnu.ac.kr

[b]Graduate Student of School of Civil Engineering, Chungbuk National University,
410 Seongbong-ro, Cheongju, South Korea

Abstract

Determination of design wind speed or wind hazard analysis for structure in general requires statistically modeled typhoon information consisting of models genesis, intensity, track and wind field. However, the current typhoon intensity and track models used to simulate the typhoons around Korean peninsula statistically have difficulties in simulating randomness and dynamics of typhoons in the study region. In this paper, more realistic typhoon intensity model and track model for the typhoons around Korean peninsula are proposed. First, defining the central pressure depth (CPD), the deficit between the central and periphery pressures as the representative of a typhoon intensity, the intensity model includes SST (Sea Surface Temperature), relative change of SST, OOR (Oceanic Occupation Ratio), relative change of OOR, latitude and traveling time. An empirical typhoon intensity model is developed by multi-variate regression. The correlation coefficients of CPDs from the present model and the RSMC best tracks for the strong and weak typhoons show 0.93 and 0.76 respectively, which shows a good agreement with the historic intensity. Secondly, a tracking model to describe dynamical typhoon tracks for the typhoons around Korean peninsula was developed. The displacements of typhoon center is determined by the mean displacement and the anomaly from the autoregression (1) model, which are estimated from the historical typhoon displacements collected on the circle with the radius of pre-assigned length scale. Classifying typhoon into the Southern Boundary (SB), the Eastern Boundary (EB) and the Western Boundary (WB) typhoons according to which boundary a typhoon enters into the domain, the spatial density correlation coefficients of the present results and the historical tracks for SB, EB, WB show 0.87, 0.6, and 0.5 respectively. The intensity and the tracking models proposed in this paper are able to reasonably simulate realistic synthetic typhoon in the point of statistical view.

key words : typhoon intensity, oceanic occupation ratio, central pressure depth, sea surface temperature, typhoon track

1. Introduction

Recent disaster records in Korea have shown that natural disasters induced by typhoon are on the rise, and the estimation of typhoon wind speed both for risk assessment and structural design becomes more important. Generally, A Monte Carlo simulation is widely used to estimate the design wind speeds in typhoon-prone regions. The simulation includes statistical models for climatological characteristics of typhoon and physical models consisting mainly of a wind field model, a tracking model and a typhoon intensity model (Russell, 1971; Batts et al., 1980; Vickery et al., 2000). The typhoon intensity is defined by either maximum sustained wind speed or central pressure of a typhoon. Atkinson (1977) showed that the maximum sustained winds speed and the central pressure are highly

correlated. The reliability of the simulation is determined by how well an evolution of the central pressure is represented. Batts et al. (1980) proposed a model of the central pressure which varies on the land and stays constant on the water. Vickery et al. (2000) developed an empirical hurricane intensity model including the effects of the sea surface temperatures (SSTs) by adopting a concept of the relative intensity proposed by Darling (1991). In this paper, similar approach is taken to develop the typhoon intensity model around Korean peninsula. The developed intensity model was for the region covering the area of 30°N ~ 40°N and 120°E ~ 130°E and modeled as a function of SST, relative SST, OOR (Ocean Occupation Ratio), relative OOR, latitude and travelling time.

In the past studies of the tracking model, the typhoon tracking is postulated as moving at constant direction and speed once the typhoon reaches the region of interest. Recent statistical tracking model to describe a dynamic characteristic of typhoon has been developed and a research on simulation modeling the overall track of the typhoon is also in the progress. Vickery et al.(2000) use an autoregressive model for increments in track speed and direction, with a random error term acting as the innovation. Hall, T.M. and Stephen Jewson(2007) simply draw from the set of complete historical tracks, translating the tracks by small random displacements. In this study, an empirical tracking model was developed to simulate dynamic tracking of typhoons around Korean peninsula for the area of 28°N ~ 40°N and 120°E ~ 132°E.

2. Typhoon Intensity Model

SST used in this study is acquired from the data of NOAA Optimum Interpolation 1/4 Degree Daily Sea Surface Temperature Analysis of 1982 ~ 2009, provided by National Climate Data Center (NCDC). And climatological typhoon data are obtained from Regional Specialized Meteorological Center (RSMC) best tracks of 1982 ~ 2009. Total number of 129 typhoons was found to have passed through the study domain of 28°N ~ 40°N and 120°E ~ 132°E in 1982 ~ 2009. In the study, the typhoon intensity is represented CPD or CPD/CPD0 where the central pressure depth (CPD) and CPD0 are defined as deficits between central pressures (P_c) and periphery pressures (P_n) and CPD when a typhoon enters the designated domain, respectively. The maximum of CPD0 of sample typhoons is 88hPa during typhoon YANCY (1993) and MAEMI (2003) follow with CPD0 of 81hPa where P_n is assumed as the standard atmospheric pressure of 1,013hPa.

We also classify typhoon into the Southern Boundary (SB), the Eastern Boundary (EB), the Western Boundary (WB) and, the Northern Boundary (NB) typhoons according to which boundary a typhoon enters into the domain. SB occupies 78%, EB 12%, WB 10% and the NB does not appear. The entire WBs consist weak typhoons which enter the domain after passing the main land of China. EBs consist of 6 weak and 7 strong ones while SBs are 45 weak and 56 strong ones.

In this paper, we have an important non-dimensional dependent variable, CPD/CPD0, to analyze an effect of CPD0 based on the parameters of SST, relative SST, OOR, relative OOR, latitude and travelling time. Initial values of OOR and SST (i.e. OOR0 and SST0, respectively) are given at when a typhoon is entering into research areas. In the intensity model, to exam its dependency on the CPD0, we analyze the correlation of CPD/CPD0 with the independent variables as shown in Figure 3. The CPD0s of the typhoons of interest ranges from 0mb to 109mb, which are divided into two groups; typhoons with CPD0 greater than a certain criteria and ones smaller than the criteria (henceforth, the first group is strong typhoon and the other one is weak typhoon). Figure 2 shows a result of correlation analysis between CPD/CPD0 and other six parameters for strong and weak typhoons, respectively.

The correlation coefficient between CPD/CPD0 and 6 parameters on the all of typhoons is 0.6 which is relatively low, which shows that a single model for various CDP0s seems inappropriate. As shown in Figure 1, the correlation of the strong typhoons is relatively low where the criterion of CPD0 is less than 30mb while the correlation of weak typhoons is nearly constant.

As the results, this study set the value of 30mb as a criterion to classify the sample typhoons into weak and strong typhoons. The numbers of the strong and the weak are 63 and 66, respectively.

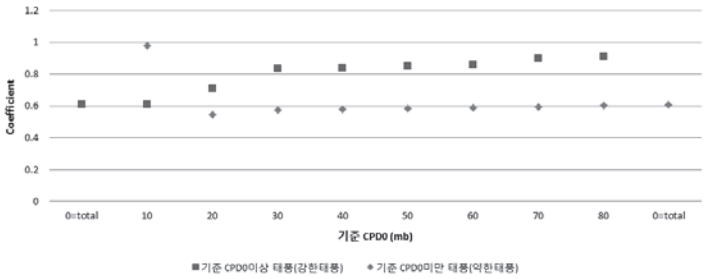

Figure 1. Correlation of model and observation for various CPD0 ranges

Typhoons gain their thermodynamic energy mainly from sea surface and experience the filling when they move over the land. In this paper, OOR (Ocean Occupation Ratio) is defined as the ration of the sea surface area which the typhoon covers to the total area which it covers. In this section we analyze the effect of OOR on the intensity.

We, first determine a representative SST&OOR, which is used to analyze the correlation with the typhoon intensity. The representative grid size for SST and OOR is, first, determined so that SST & OOR on that grid has the maximum correlation with typhoon intensity. We examine SSTs & OORs on G01×01, G03×03 and so on to G59×59, which mean average SSTs & OORs on the grids of Gnn×nn, where nn indicates the number of cells both the zonal and meridian direction in the study domain. Each grid has 1/4 degree distance both in latitude and longitude as given in NCDC data sets. Employing CPD and CPD/CPD0 as parameters, CPD/CPD0 correlates with SSTs higher than CPD for the strong typhoons (see Figure4,5). CPD/CPD0 has the highest correlation coefficient of 0.5041 with SST on the grid of G15×15 while CPD has the coefficient of 0.4863 on the grid of G13×13 for the strong typhoons. Similarly, CPD/CPD0 has a higher correlation with SST/SST0 than CPD does, where SST0 is SST when a typhoon enters into the domain. CPD/CPD0 has the highest correlation coefficient of 0.7335 with SST/SST0 on the grid of G51×G51 while CPD has the coefficient of 0.4528 on the grid of G55×55. For the weak typhoons, values of SST, SST/SST0, OOR, and OOR/OOR0 are analyzed in the same away as the strong typhoons.

We analyze a correlation between the typhoon intensity and the latitude of the center and the travelling time over the domain. For the strong typhoon the intensity has a close correlation with the latitude and travelling time. CPD/CPD0 has a correlation coefficient of -0.8406 with the travelling time while CPD has the coefficient of -0.6455 for the strong typhoon. The latitude also is correlated closely with the intensity because most typhoons move from low to high latitudes as the corresponding travelling times increase. CPD/CPD0 has a correlation coefficient of -0.7701 while CPD has the coefficient of -0.5724 for the strong typhoon.

For the weak typhoon the travelling time has the correlation coefficients of -0.4871 for CPD/CPD0 and 0.0064 for CPD, which seems to be uncorrelated with it. The latitude has correlation coefficients of -0.1365 for CPD and -0.3931 for CPD/CPD0.

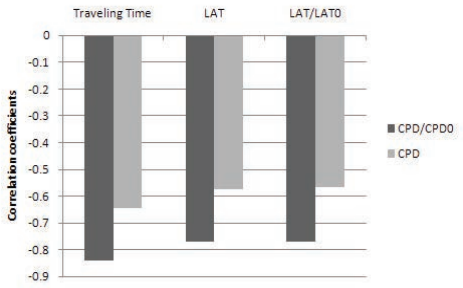

Figure 2. Correlation of typhoon intensity and latitude, traveling time about strong typhoon

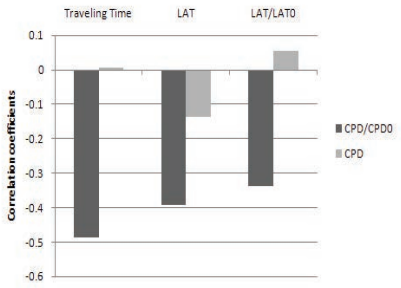

Figure 3. Correlation of typhoon intensity and latitude, traveling time about weak typhoon

In the study we consider CPD and CPD/CPD0 as the typhoon intensity and analyze correlations with SST, SST/SST0, OOR, OOR/OOR0, the latitude of the center (LAT), and, the travelling time (TT). Table 1 lists correlation and contribution coefficients of the 6 parameters. The contribution coefficient is defined as the correlation of a parameter relative to that of TT so that TT has the coefficient of 1. For the strong typhoons, SST shows lower contribution than others while for the weak typhoons, contributions of SST and SST/SST0 are dominant.

Table 1. Correlation and contribution coefficients of parameters affecting CPD/CPD0

Parameters	Strong typhoons			Weak typhoons		
	Correlation	Contribution	Grid	Correlation	Contribution	Grid
TT	-0.84	1.00		-0.49	1.00	
LAT	-0.77	0.92		-0.39	0.81	
OOR	0.73	0.86	G35×35	0.20	0.42	G55×55
OOR/OOR0	0.70	0.83	G39×39	0.09	0.18	G59×59
SST	0.50	0.60	G15×15	0.28	0.57	G15×15
SST/SST0	0.73	0.87	G51×51	0.33	0.68	G11×11

Final form of the proposed empirical typhoon intensity model is as the following

$$\frac{CPD}{CPD0} = \alpha TT + \beta LAT + \gamma OOR + \delta \frac{OOR}{OOR0} + \varepsilon SST + \xi \frac{SST}{SST0} + \eta \quad (1)$$

where the coefficients, α, β, γ, δ, ε, ζ, and η, estimated by a multi-variate regression for strong and weak typhoons.

In this study, the population of typhoon data consists of 81 strong and 50 weak typhoons. To validate this method, we build model using 40 and 25 samples from the strong and weak typhoons, respectively, which is applied to estimate CPDs for the other typhoons excluded from the samples. Figure 4 shows the application for a weak typhoon PABUK(0706) in 2007 and the mean error of CPD is 10.17%.

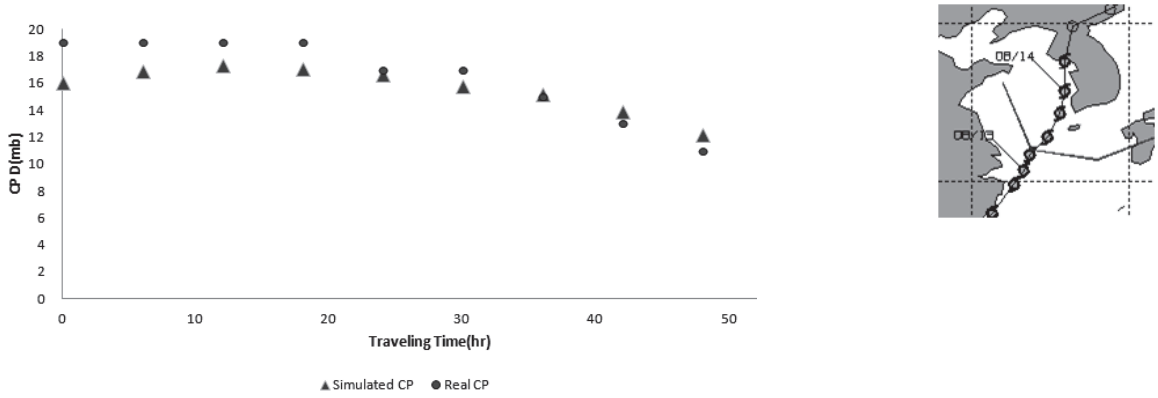

Figure 4. A comparison empirical intensity model(present) and RSMC best track for PABUK(0706)

3. Typhoon Tracking model

According to Hall & Jewson(2007), the *x* (zonal) and *y* (meridional) components of the mean 6-h displacement vector are computed by averaging historical displacements as follows.

$$\bar{x}(r) = \left(\sum_{i=1}^{N_L} x_i exp(-d_i^2/L^2)\right)/\left(\sum_{i=1}^{N_L} exp(-d_i^2/L^2)\right) \quad (2)$$

The d_i is the great-circle distance between the location **r** of the current point and the location $\mathbf{r}_i$ of the *i*-th historical center where the length scale *L* is optimized using an out of sample jackknife procedure. Following Eq. (2), $\bar{x}_{rms}$ is obtained using weighted averages of deviations of center displacements about the optimal mean displacement.

$$\bar{x}_{rms} = \sqrt{\left(\left(\sum_{i=1}^{N_L} x_i^2 exp(-d_i^2/L^2)\right)/\left(\sum_{i=1}^{N_L} exp(-d_i^2/L^2)\right)\right)} \quad (3)$$

Eqs. (2) and (3) can also be applied to y direction. Figure 5 shows the RMS on the forecast error while the length scale is increasing by 20 km from *L*=100 km. As the length scale is growing, the RMS of the forecast error is decreasing where 100 km <= *L* <= 520 km. At the length scale of *L* = 520 km, there is minimum RMS resulting in computational times that are prohibitively expensive. There is a scenario with length scale of *L* = 300 km that has 0.4 km larger RMS on the forecast error than case with minimum RMS. In this case, however the samples are a third of the case, *L*=520 km, resulting in less expensive cost on the simulation times. In this research, the length scale, *L*, is set to 350 km.

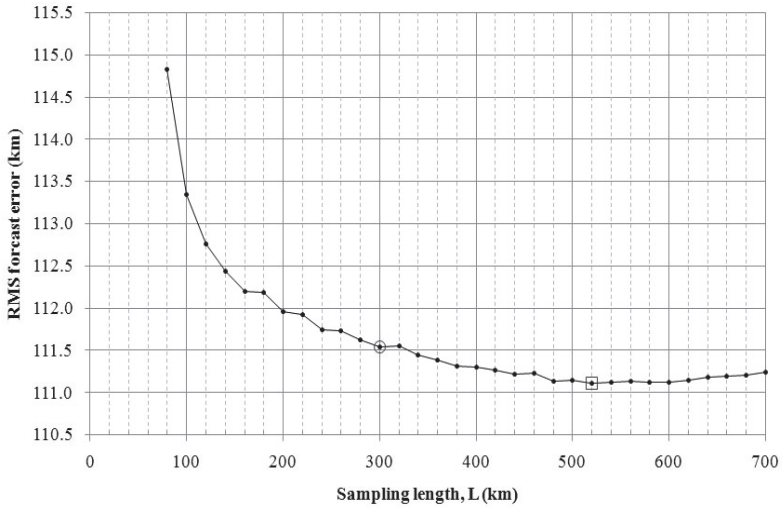

Figure 5. Mean-track average forecast error versus averaging length-scale

According to Hall and Jewson (2007), an anomaly between the previous and current points on the typhoon track determines next displacement. An anomaly at initial location of typhoon is computed from the mean displacement randomly obtained in the normal distribution and RMS given by

$$u = \bar{u} + \epsilon_u u_{rms}, \qquad v = \epsilon_v v_{rms} \quad (4)$$

where *u, v* are normalized Cartesian directions of *x, y* in latitude and longitude, respectively, u is normalized $\bar{x}$. ϵ is a random number on the Gaussian distribution that has 0 mean and 1 variance. In this model, the next travel point of typhoon center is defined so that it moves toward the average travel direction $\bar{u}$, and then moves that point toward horizontal *u* and vertical *v*, and then connect the starting point with the new point. Figure 6 shows the anomalies of record data in scatter plot. These anomalies $\bar{u}, \bar{v}$ represent correlation between their values at the previous step. $\overline{u_n}$ and $\overline{v_n}$ are computed from $(u - \bar{u})/u_{rms}$ and v/v_{rms} by employing the RMS, respectively. These panels show the high correlation at that lag-1.

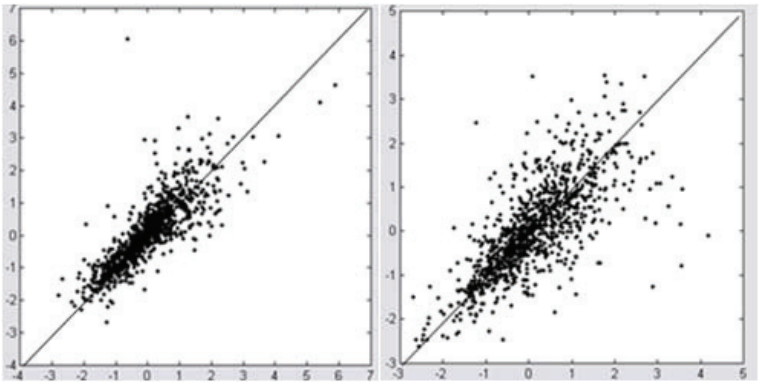

Figure 6. Correlation between present (n) and previous (n+1) at u, v direction

After comparing regression coefficients via auto regressive process (henceforth AR) of $\bar{u}, \bar{v}$ from lag-1 to lag-8, AR with 6 hours step is used. In the directions of *u* and *v*, coefficients on lag-1 are 0.836 and 0.693, respectively, which are relatively larger than other coefficients less than 0.1.

From second point, the anomaly is obtained based on the previous data and the regression coefficient $\emptyset$ given by

$$\overline{u_{n+1}} = \emptyset_u \overline{u_n} + s_u \varepsilon_{u'} \quad \overline{v_{n+1}} = \emptyset_v \overline{v_n} + s_v \varepsilon_v \quad (s = 1 - \emptyset^2) \tag{5}$$

The Eq. (5) represents anomalies from the second point. Based on Eq. (5), the path of the typhoon is estimated by employing Eq. (6) while Eq. (4) initialize the typhoon location.

$$u = \bar{u} + \bar{u} u_{rms}, \qquad v = \bar{v} v_{rms} \tag{6}$$

In this section, we represent verification of the empirical tracking model. To this end, a spatial frequencies of typhoon paths obtained from the empirical model are compared with those of RSMC data. The study area of 30°N ~40°N in latitude and 120°E ~130°E in longitude is divided in 10-by-10 matrix. The comparisons are made respectively for typhoons in different entering directions and each matrix is normalized by the maximum value. Figure 7 shows the entry to south direction into our domain and the spatial correlation between synthetic tracks and historical tracks shows a coefficient of 0.87. Other entry directions show less correlations of 0.62 for WB and 0.5 for EB.

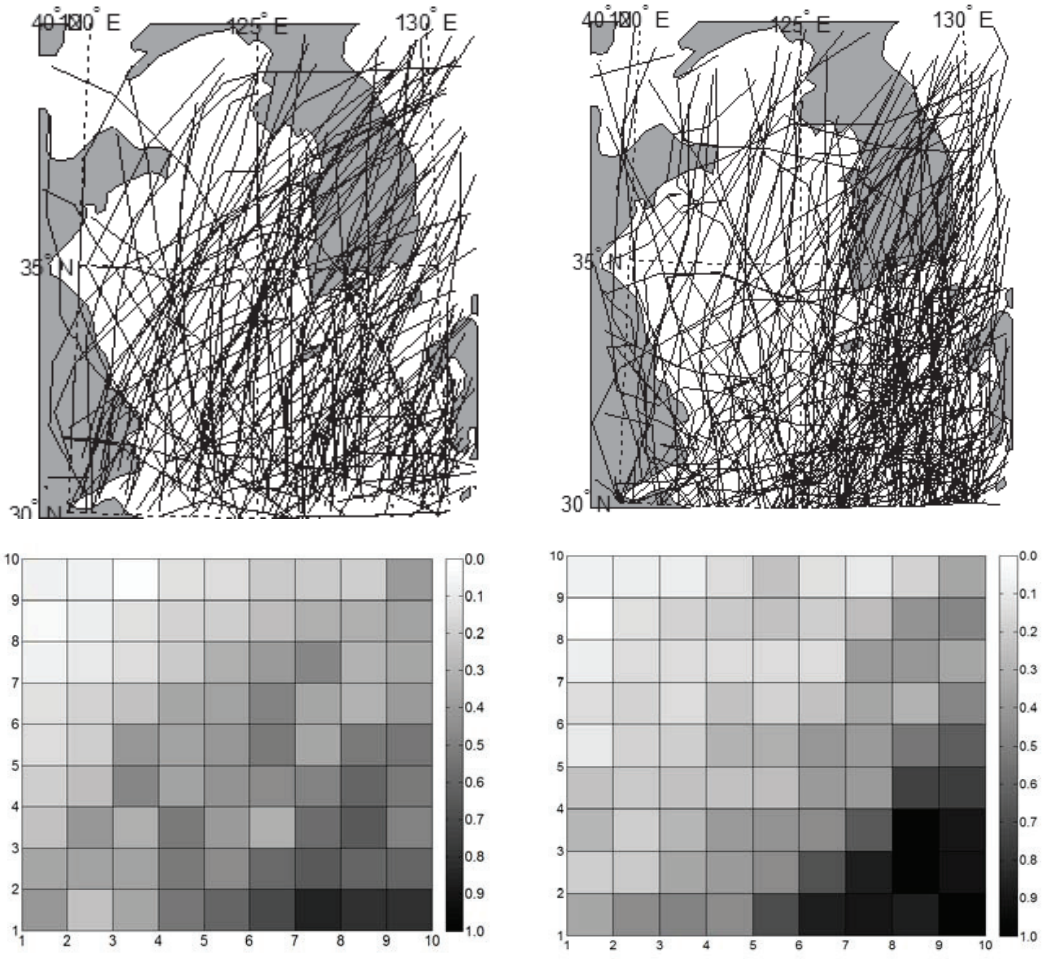

Figure 7. Tracks and spatial frequencies of typhoons from RSMC and present method for SB entry

4. Conclusions

In the study we develop empirical typhoon intensity and tracking models for the regions around Korean peninsula. The typhoon intensity, represented by CPD/CPD0 is modeled as a function of the travelling time, the latitude of the center, SST, SST/SST0, OOR, OOR/OOR0 using a multi-variate regression for the strong and weak typhoons, which were categorized by a criteria of CPD0 at 30mb. In strong typhoons, SST showed small correlation with CPD/CPD0 but other parameters have high correlation. But in weak typhoons, OOR and OOR0 has small correlation and SST, SST/SST0 has high correlation.

The simulated CPDs using the model show a good agreement with the recorded CPDs on the RSMC best tracks, and improvement over existing methods based on the constant CPD and filling rate models.

In this paper, an empirical tracking model to describe dynamical typhoon tracks for the typhoons around Korean peninsula was also presented. The displacements of typhoon center is determined by the mean displacement and the anomaly from the autoregression (1) model, which are estimated from the historical typhoon displacements collected on the circle with the radius of pre-assigned length

scale. Classifying typhoon into the Southern Boundary (SB), the Eastern Boundary (EB) and the Western Boundary (WB) typhoons according to which boundary a typhoon enters into the domain, the spatial density correlation coefficients of the present results and the historical tracks for SB, EB, WB show 0.87, 0.62, and 0.5, respectively. The empirical intensity and the tracking models proposed in this paper are able to simulate realistic synthetic typhoon in the point of statistical view in applications to estimate wind speeds for the structural design and the wind risk assessment.

Acknowledgement

This research was supported by the grant (11CCTI-A052605-04-000000) from the Ministry of Land, Transport and Maritime of Korean government through the Core Research Institute at Seoul National University for Core Engineering Technology Development of Super Long Span Bridge R&D Center.

References

Russell, L. R. (1971), Probability Distributions for Hurricane Effects, Journal of the Waterways, Harbors and Coastal Engineering Division, ASCE, 97(1), pp. 139-154.

Batts, M.E., M.R. Cordes, C.R. Russell, J.R. Shaver, and E. Simiu (1980), Hurricane Windspeeds in the United States, National Bureau of Standards Report Number BSS-124, U.S. Dept. of Commerce, Washington, DC.

Vickery, P. J., P. F. Skerlj, and L. A. Twinsdale (2000), Simulation of Hurricane Risk in the United States Using Empirical Track Model, Journal of Structural Engineering, Volume 126, Number 10, pp. 1222-1237

Atkinson, G.D and C.R. Holliday (1977), Tropical Cyclone Minimum Sea Level Pressure/Maximum Sustained Wind Relationship for the Western North Pacific, Monthly Weather Review, Volume 105, Number 4, pp. 421-427.

Darling, R.(1991), Estimating probabilities of hurricane wind speeds using a large-scale empirical model.J.Clim.4,1035-1046

The Seventh International Colloquium on Bluff Body Aerodynamics and Applications (BBAA7)
Shanghai, China; September 2-6, 2012

Universal equivalent static wind load for structures

Yukio Tamura [a], Akira Katsumura [b]

[a] *Professor, Tokyo Polytechnic University, Iiyama 1583, Atsugi, Kanagawa, Japan*
[b] *Vice-President, Wind Engineering Institute, Kawaguchi 395, Fuji Kawaguchiko-cho, Minami-tsuru, Yamanashi, Japan*

ABSTRACT: Studies on equivalent static wind load (ESWL) distributions are reviewed, and essential matters and necessary conditions of the ESWL are discussed. Then, the efficiency and advantages of multiple-target ESWLs are demonstrated. As an example of a multiple-target ESWL, the universal ESWL (U-ESWL) proposed by Katsumura, Tamura et al. (2004, 2007) is explained in detail. Reproduced largest load effects by GLF-ESWL, LRC-ESWL and U-ESWL are compared with the real largest load effects obtained by time-domain response analysis for some different types of roof systems including an actual airport terminal roof structure. The results demonstrate the feasibility and usefulness of the U-ESWL.

KEYWORDS: Universal Equivalent Static Wind Load, Gust Loading Factor (GLF), Load-Response Correlation (LRC) method, Wind Resistant Design, Long-span Roof, Load Effect

1 INTRODUCTION

Structural design of a building is generally based on largest "load effects", such as internal forces (bending moments, shear forces, axial forces) and stresses in structural members, and in some cases on the largest story deformation or displacement of a particular part of the building. In structural design of buildings, wind load is not applied separately. We have to consider the combined effects of wind load and many other loads such as dead load, snow load, live load and so on. Therefore, it is convenient and necessary to determine a so-called Equivalent Static Wind Load (ESWL) for combinations with other loads. The ESWL is the static load providing the largest "load effects" due to dynamic wind excitations.

Many studies have been made on ESWL. The ESWL reproducing the largest response of a structure was first introduced by Davenport [1] as that produced by the Gust Loading Factor (GLF) method. Accurate evaluation of the maximum load effect is very important in the structural design of a building, and many studies on the ESWL followed Davenport [1], e.g. Simiu [2], Solari [3], Holmes [4], Kasperski [5], Davenport [6], Piccardo & Solari [7], [8], Zhou & Kareem [9], Chen & Kareem [10], [11], Tamura et al. [12], Repetto & Solari [13], and Kwon & Kareem [14].

The GLF method proposed by Davenport [1] was a milestone in the history of wind resistant design of buildings and structures. It has been widely adopted in many modern wind load codes and standards, including some major codes. The ESWL distribution given by the GLF method is proportional to the mean wind pressure/force distribution. The mean wind pressure/force distribution is a temporarily averaged distribution and such a distribution never happens in any instance. Therefore, the ESWL given by the GLF is an unrealistic distribution.

The Load-Response Correlation (LRC) method proposed by Kasperski [5] should be raised as another milestone. The LRC approach is based on a very sophisticated idea with an insight into the physical mechanism of the wind force and response relation. LRC can reproduce the most probable wind load distribution causing a particular maximum (minimum) wind load effect, as Tamura et al. [12] reported by comparing the LRC-ESWLs and ensemble averaged actual pres-

sure distributions causing largest load effects obtained by a conditional sampling (CS) technique. Thus, LRC gives a realistic ESWL distribution.

By the way, when we combine the wind load with dead load or snow load in order to estimate the maximum resultant load effects in a roof beam as an example, not only the up-lift wind effect but also the down-lift wind effect should be considered in determining the critical situation for the targeted beam. Therefore, we should consider both of the largest positive side wind load effect (maximum wind load effect) and the largest negative side wind load effect (minimum wind load effect), and two ESWLs reproducing both the maximum and minimum load effects should be determined (Tamura et al. [12], Kasperski [15], Katsumura, Tamura et al. [16]). In this paper, the term "largest load effect" is used for either the maximum or minimum load effect when it is not necessary to clearly indicate one or the other, or when it is intended to mean both of them.

2 EQUIVALENT STATIC WIND LOAD (ESWL) REPRODUCING LARGEST LOAD EFFECTS

There are various wind load distributions that can reproduce the largest load effect targeted in structural design, if the target is only one load effect. For example, if the target load effect is the maximum tip displacement (Load Effect 1 in Fig.1), any ESWL distribution can be set to reproduce the same tip displacement as shown in Fig.1, i.e. the GLF method, the LRC method, the CS technique, and even a concentrated force at any particular point. They can all reproduce the same maximum tip displacement if the value of each ESWL is appropriately set. In this context, any wind load distribution will work for the ESWL, if there is only one target load effect.

2.1 *Wind-induced response of long-span roof structures*

Time domain dynamic response analyses using fluctuating pressure data obtained by a simultaneous multi-channel pressure measuring system (SMPMS) have been conducted in the practical design of buildings and structures such as long-span roof structures, structures with non-linear dynamic characteristics, and buildings adopting non-linear damping devices since the 1980's in Japan (Tamura, [17]). For tall buildings with complicated sectional shapes changing along the vertical axis, as for many recent tall buildings, eccentricity causes complicated coupled motions of translational and torsional vibration components, and three-dimensional time-domain dynamic response analysis using those resultant fluctuating wind force components or by directly applying pressures obtained by the SMPMS is required to appropriately estimate the combined effects of the various wind force components and the resultant three-dimensional motions. For other buildings, a simpler but sufficiently accurate method is required for wind resistant design. ESWLs reproducing largest load effects have been examined for this purpose.

The wind-induced response behavior of long-span roof structures is very complicated, showing significant contributions of multiple vibration modes of up to 100 or more. The largest load effects such as bending moments, shear forces, and axial forces in a huge number of members, e.g. 10,000 or more, should be considered and their largest values should never happen simultaneously. It is also necessary to consider the effects of wind directions. Different members reach their largest load effects for different wind directions. The structural designer should design all structural members based on the largest load effects found in each member under such complicated conditions. Thus, it is obviously difficult to design such structures using traditional building codes or standards based on the GLF or LRC method, which basically reproduce one particular load effect for a specifically targeted member.

As mentioned before, if there is only one target load effect , say Load Effect 1 in Fig.1, any one of the ESWL distributions shown in Fig.1 would do to reproduce the target load effect. However, if there are two target load effects, say Load Effect 1 and Load Effect 2 in Fig.1, all of the ESWLs except for the U-ESWL would be needed to determine another ESWL distribution to reproduce Load Effect 2 as shown in Fig.1. Thus, if there are *N* target load effects, we need to determine *N* different ESWL distributions to reproduce them. The only exception is the U-ESWL, which can reproduce any number of multiple largest load effects for all the targeted members.

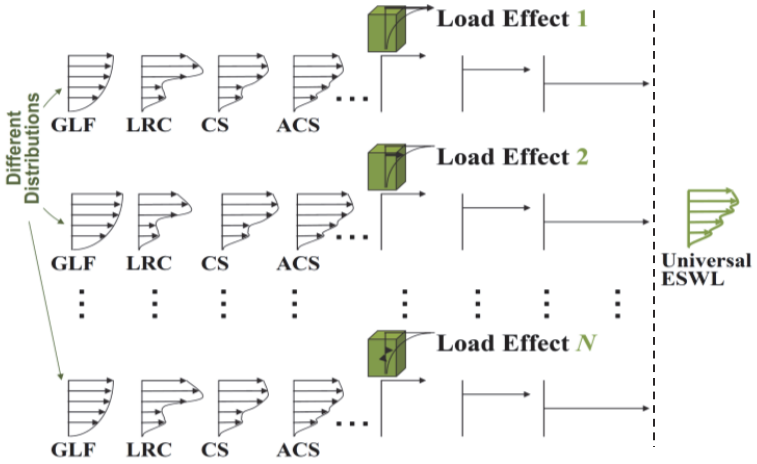

Figure 1. Various ESWL distributions reproducing target load effects

2.2 *Largest load effects and single-target ESWL distributions and multiple-target ESWL distributions*

As an example of single-target ESWLs like those produced by the GLF and LRC methods, let's assume the target largest load effect, $\hat{r}$, is an internal force at a particular point of a beam excited by dynamic wind load. The target load effect is expressed as a scalar value.

$$\hat{r} = \sum_i I_{ri}\hat{F}_i = \{I_r\}^T\{\hat{F}\} \qquad (1)$$

Here, the ESWL distribution $\{\hat{F}\}$ reproducing the largest load effect $\hat{r}$ is given in a vector expression, and $\{I_r\}^T$ is an influence function vector. Once the ESWL $\{\hat{F}\}$ is obtained, the single target largest load effect $\hat{r}$ can be given as the product of the influence function vector $\{I_r\}^T$ and the ESWL vector $\{\hat{F}\}$. Thus, a static analysis can reproduce the load effect equivalent to the largest dynamic load effect.

As an example of the multiple-target U-ESWLs, let's assume target largest load effects at various points of the same beam. The largest load effects should be expressed in a vector form as:

$$\{\hat{R}\} = [I_R]\{\hat{F}\} \qquad (2)$$

Here, $\{\hat{R}\}$ is the largest load effect vector, in which elements are the target load effects at various points, and $[I_R]$ is the influence function matrix. The target largest load effects are given as the product of the influence function matrix $[I_R]$ and the ESWL vector $\{\hat{F}\}$. A scalar value of the target load effect $\hat{r}$ on the left hand side of Eq.(1) is replaced by a target load effect vector $\{\hat{R}\}$ in Eq.(2), and the influence function vector $\{I_r\}^T$ in Eq.(1) is replaced by the influence function matrix $[I_R]$ in Eq.(2). These are differences between mathematical expressions of a single-target ESWL and a multiple-target ESWL.

2.3 *U-ESWL reproducing multiple load effects*

As a multiple-target ESWL distribution, Katsumura, Tamura et al. [16], [18], [19] proposed a U-ESWL method to reproduce all targeted largest load effects $\{\hat{R}\}$ based on Eq.(2).

For the U-ESWL, the targeted largest load effects can theoretically be any load effects, and the number of targeted load effects is not necessarily the same as the number of structural members. An U-ESWL distribution $\{\hat{F}\}$ estimated for the target largest load effects $\{\hat{R}\}$ is assumed to be expressed by a linear combination of a set of basic wind load distributions (BWLD) $\{f_i\}$ as:

$$\{\hat{F}\} = c_1\{f_1\} + c_2\{f_2\} + \cdots\cdot c_M\{f_M\} = [F_0]\{C\} \qquad (3)$$

Here, $[F_0]$ is the BWLD matrix consisting of the BWLD vectors $\{f_i\}$, and $\{C\}$ is the combination factor vector. It is also very important that any wind load distributions, even a set of concentrated forces, are theoretically available for the BWLDs, $\{f_i\}$. It is of course better to use the most efficient distributions for the BWLDs. In Katsumura, Tamura et al. [16], [18], [19], the POD eigenvectors of the wind pressure field acting on the building/structure model obtained by SMPMS are used, but it should be emphasized again that the POD eigenvectors are not necessarily required for the BWLDs in Eq.(3).

Combining Eqs.(2) and (3), the target largest load effect vector $\{\hat{R}\}$ is given as:

$$\{\hat{R}\} = [I_R]\{\hat{F}\} = [I_R][F_0]\{C\} = [R_0]\{C\} \qquad (4)$$

Once the BWLD matrix $[F_0]$ is given, as the influence function matrix $[I_R]$ can be obtained accordingly for the structural system, the product matrix $[R_0] = [I_R][F_0]$ can be a known matrix. Then, the problem is only to solve the combination factor vector $\{C\}$ based on the target largest load effect vector $\{\hat{R}\}$. The target largest load effects $\{\hat{R}\}$ can be obtained by any response analysis, but the time-domain response analysis applying the SMPMS pressure field to an FEM model may be generally made.

If the number of target largest load effects, N_t, is equal to the number of BWLD terms, M, in Eq.(3), i.e., $N_t = M$, Eq.(4) can be solved uniquely. If the number of target largest load effects N_t is less than M, i.e., $N_t < M$, the number of BWLD terms, M, can be appropriately reduced to N_t; thus Eq.(4) can also be solved uniquely.

However, in many cases, the number of target largest load effects, N_t, is more than the number of BWLD terms M, i.e., $N_t > M$, because of the huge number of structural members. Of course, you can increase the number of BWLD terms, M, by increasing the number of loading points for the FEM model or by any other way to equalize N_t and M. In Katsumura, Tamura, et al. [16], [18], [19], the Singular Value Decomposition (SVD) technique has been used to find the most appropriate solutions approximating the simultaneous equations given by Eq.(4). It is a matter of course that any mathematical technique can be used to obtain appropriate solutions.

2.4 *Simple cantilever roof model*

The simple cantilever roof model shown in Fig.3 was discussed in Katsumura, Tamura et al. [16], [19]. Here, the number of structural members N_m is 90, and the number of loading points is set at 48. The loading points are set on the nodes of the grid members, and the number of BWLD terms M is also set at 48. All structural members are targeted, and one largest load effect is considered for each member. Then, the number of target largest load effects is set at $N_t = N_m = 90$. In this case, $N_t > M$. As unique solutions cannot be obtained for Eq.(4), the SVD technique is applied. A wind tunnel experiment was performed to obtain fluctuating pressures acting on the upper and lower roof surfaces at the same 48 positions on the cantilever model. The net wind forces acting at these positions were applied in the FEM model for time domain dynamic response analysis.

Then, a set of largest bending moments and largest shear forces in all 90 members were extracted. Targeting these largest load effects, U-ESWL distributions were obtained. In this case, the POD eigenvectors $\{\phi_i\}$ were adopted for the BWLD vectors $\{f_i\}$. Figures 4(a) and 4(b) show the up-lift side U-ESWLs for the largest bending moments and the largest shear forces.

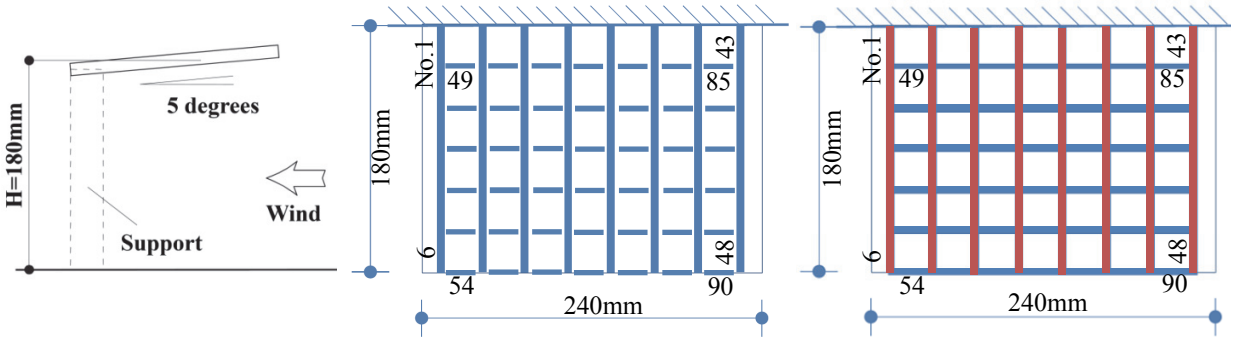

(a) Elevation (b) One-way type frame model (c) Two-way type frame model

Figure 3. Simple cantilever model

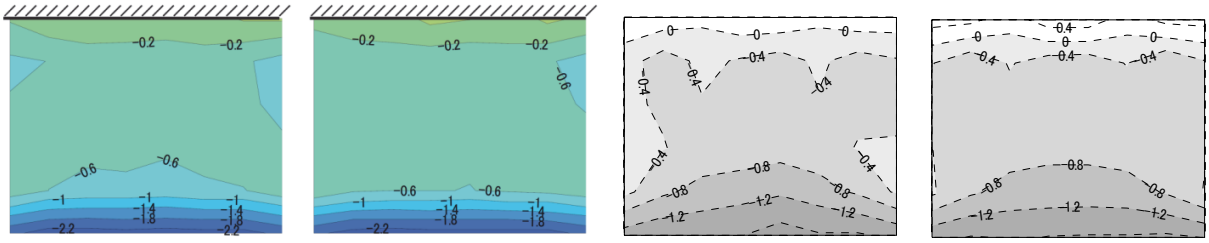

(a) U-ESWL (Shear Fs.) (b) U-ESWL (Bending Ms.) (c) GLF (Shear F., GLF=2.04) (d) LRC (Shear F., g_Q=4.3)

Figure 4. Up-lift side ESWLs for largest load effects on all 90 members ((a) and (b)) and for a single (maximum) largest shear force ((c) and (d)) for a one-way type model shown in Fig.3(b)

Two U-ESWLs for the largest shear forces and the largest bending moments are similar. This suggests that either Fig.4(a) or 4(b) is enough for both load effects in this case. Figures 4(c) and 4(d) show ESWLs obtained by the GLF and LRC methods, respectively, for the largest shear forces. The GLF-ESWL distribution shown in Fig.4(c) is proportional to the mean wind force distribution, which is an unrealistic distribution never happening at any instance as are the U-ESWLs shown in Figs.4(a) and 4(b). However, the LRC-ESWL shown in Fig.4(d) is a realistic distribution, which most probably generates the quasi-static component of the largest shear force of a target member.

Figure 5 compares the largest shear forces in members obtained by the time domain response analysis and those reproduced by the ESWLs (Katsumura, Tamura et al., [16]). The abscissa indicates 48 main members numbered 1 to 48. The maximum shear force in Member No.1 obtained by time-domain dynamic response analysis showed the largest value of all members, and it was selected as the target largest load effect in the calculations of ESWLs for both the GLF and LRC methods. Therefore, the largest shear forces in Member No.1 reproduced by GLF-ESWL and LRC-ESWL are exactly the same as the actual largest shear force obtained by the time-domain dynamic response analysis as indicated in the figure. However, the reproduced largest shear forces in the other members are underestimated by both GLF-ESWL and LRC-ESWL as shown in Figs.5(a) and 5(b), respectively. It is interesting that GLF-ESWL, propor-

tional to the 'unrealistic' mean wind force distribution, gives better estimation than LRC-ESWL, based on the 'realistic' instantaneous wind force distribution. This is understandable because the internal forces in the other members do not necessarily reach their maximum values at the same time that the maximum internal force in the targeted Member No.1 appears.

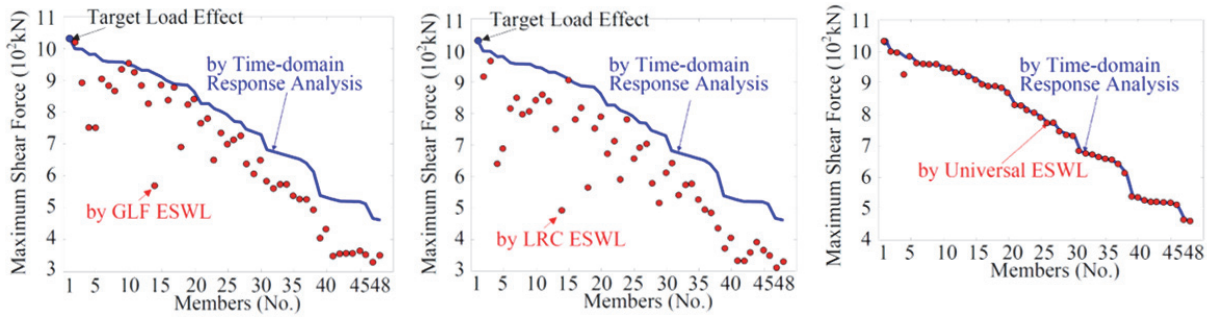

(a) GLF method (G_f=2.04) (b) LRC method (g_Q=4.3) (c) U-ESWL

Figure 5. Comparisons of largest load effects obtained by time domain response analysis and ESWLs

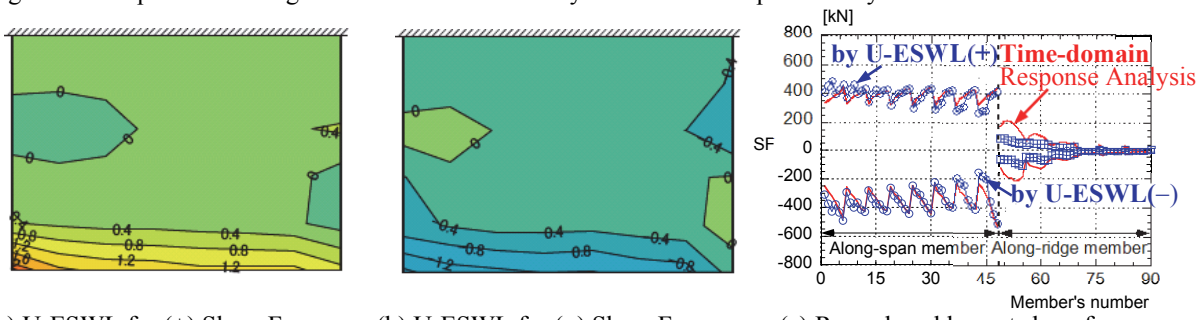

(a) U-ESWL for (+) Shear Fs. (b) U-ESWL for (–) Shear Fs. (c) Reproduced largest shear forces

Figure 7. U-ESWLs for positive side (a) and negative side (b) largest shear forces (without mean components) for a two-way type model (see Fig.3(c)), and (c) comparisons of largest shear forces obtained by time domain response analysis and U-ESWLs

3 REQUIREMENTS FOR ESWL

As seen in Fig.5, the 'realistic' LRC-ESWL distribution is not necessarily better than an 'unrealistic' GLF-ESWL or U-ESWL distribution in terms of reproduction of maximum load effects for "non-targeted" members. The LRC approach can catch the typical load distribution condition causing the largest load effect in a target member (or at a target position). However, this is too typical (or too good) for the target load effect. For example, a typical LRC-ESWL distribution causing the largest bending moment at the end of a roof beam and that causing the largest bending moment at the center of a roof beam are quite different (Tamura et al., [12]). The LRC-ESWL for the beam end bending moment is obviously inappropriate for reproducing the largest beam center bending moment. Superimposition of the two ESWL distributions for these two different targets is of course also inappropriate. For such a multiple-target estimation, an U-ESWL-like approach is required. Anyway, it is strongly suggested that the LRC-ESWL is good only for the target load effect, but not for other load effects. Of course, a realistic LRC-like approach is useful for some particular purposes and has other advantages.

In order to clarify the essential matters in ESWLs, let's go back to the GLF by Davenport [1]. He assumed the following conditions for estimating the ESWL for a structure:

(1) Mean displacement caused by mean wind load is almost proportional to the 1st vibration mode.
(2) The contribution of the 1st vibration mode is predominant in the dynamic response and the contributions of other higher modes are negligible.

Under the above conditions, the distribution of the maximum displacement along the vertical axis of a tall building can be proportional to that of the mean displacement caused by the mean wind load. Therefore, even if the targeted load effect of the GLF is only the maximum tip displacement, the ESWL can also reproduce the maximum displacement at any other story. The temporary and spatially fluctuating pressure field acting on a building never shows the temporary averaged (mean) pressure distribution at any instance. Thus, the mean wind force distribution is a completely 'unrealistic' distribution, and in this regard, there is no difference from a single unrealistic concentrated load.

Thus, the original ESWL proposed by Davenport [1] was intended to reproduce not only the target largest load effect, i.e. the largest tip displacement, but also the other largest load effects simultaneously, i.e. the largest displacements of all other stories. By the way, the reason why Zhou & Kareem [9] adopted the largest base-bending moment rather than the largest tip displacement was to reproduce the largest 'internal forces', which are more important than the largest displacement in the design of tall buildings.

In general, the 1st-mode contribution is predominant for the resonant component of the wind-induced building response, but the dynamic response consists not only of the resonant component but also of the background component. The latter is not necessarily proportional to the 1st vibration mode, and the 2nd condition is not acceptable in some cases. Especially in the case of long-span roof structures, the higher mode contributions are very significant for the maximum internal forces in the structural members, and they never appear simultaneously. Thus, in general, the largest internal forces appear at different instances, and the LRC-ESWL by Kasperski [5] does not guarantee the largest internal forces in other non-targeted members.

Anyway, it is obvious that the main purpose of the ESWL is to reproduce the targeted largest load effect, and it is also essential to reproduce other non-targeted largest load effects. These two are very important requirements for ESWLs in practical applications, and it is also true that a 'realistic' wind force distribution essentially does not satisfy the latter requirement except in some special cases and only 'unrealistic' wind force distributions are possible.

Then, if these two requirements are the most important, it is very natural to directly seek an 'unrealistic' wind force distribution reproducing the largest internal forces simultaneously in all structural members. In answer to this question, Katsumura and Tamura et al. [16], [18], [19] proposed the U-ESWL to reproduce the largest load effects in all structural members.

4 REQUIRED POSITIVE-SIDE AND NEGATIVE-SIDE U-ESWL DISTRIBUTIONS

The U-ESWL distributions are derived by an inverse analysis based on the actual largest load effects in all or some important targeted members obtained by dynamic time domain response analyses applying fluctuating pressure fields. Figure 5(c) compares the actual largest shear forces reproduced by the U-ESWL shown in Fig.4(a) and the actual largest shear forces obtained by the dynamic time domain response analysis in 48 targeted members. By applying the simple U-ESWL distribution shown in Fig.4(a), all largest load effects were almost perfectly reproduced. This is quite different from the results shown in Figs.5(a) and 5(b) for GLF-ESWL and LRC-ESWL. The efficiency of the U-ESWL might be understood from Fig.5(c).

It should be noted that "two" U-ESWL distributions reproducing positive-side and negative-side largest load effects are necessary in building design, considering the combined load effects

with other loads such as dead load, snow load and so on. If we include the mean component of the pressure field, both the obtained maximum and the minimum "wind-induced" load effects in all members can be all positive, all negative, or a mixture of positive and negative. However, if the mean components of pressures are subtracted and only fluctuating components are applied, the maximum load effects can be all positive and the minimum load effects can be all negative.

For simplicity but not losing generality, we only apply the fluctuating components of pressures in the time domain analyses. The effects of the mean components can be taken into account separately or superimposed finally. Figures 7(a) - 7(c) show positive-side and negative-side U-ESWLs and the largest load effects reproduced by these two U-ESWL distributions for the two-way type cantilever frame model shown in Fig.3(c). Here, the red solid lines shown in Fig.7(c) indicate the maximum and the minimum shear forces in all 90 members obtained by time-domain response analysis. If the target load effects are the maximum and minimum shear forces in these 90 (= N_t) members, we should consider N_t positive shear forces Q_j^+ (j = 1, 2, ... N_t) and N_t negative shear forces Q_j^- (j = 1, 2, ... N_t) as the target load effects. In this case, two sets of largest shear forces should be considered for two U-ESWLs, but elements of the two sets are arbitrarily selected. It is not necessary that one set should consist of all positive shear forces and the other should consist of all negative shear forces. Any combination of the largest positive and negative shear forces is theoretically fine, if Q_j^+ and Q_j^- appear in either of the two sets as follows:

Set A: $Q_1^+, Q_2^-, Q_3^+, Q_4^+, Q_5^-, \quad \ldots \quad , Q_{Nt-1}^+, Q_{Nt}^-$
Set B: $Q_1^-, Q_2^+, Q_3^-, Q_4^-, Q_5^+, \quad \ldots \quad , Q_{Nt-1}^-, Q_{Nt}^+$

However, for general use of U-ESWL distributions and its desired robustness with various structural systems, a moderate wind load distribution like those shown in Figs.4(a) or 4(b) is better. If the combination of the signs of the largest load effects in a set was not adequate, even an obtained U-ESWL can reproduce all targeted largest load effects appropriately; the obtained ESWL distribution is too specific for the given structural system and cannot show robustness for different structural systems.

In order to overcome this difficulty, Katsumura, Tamura et al. [16] proposed to use some POD eigenvectors of fluctuating load effects in all members to decide the combination of signs of load effects for the two sets, Set A and Set B. It should be noted that the POD eigenvectors are different from those of the fluctuating pressure field used for the BWLD in Eq.(3). The POD technique is applied for a time series of internal forces in all members obtained by the time-domain response analysis.

4.1 *Two-way type cantilever roof model*

Katsumura, Tamura et al. [16] discussed the contributions of the 1st and 2nd POD modes to the fluctuating shear forces in the 90 members of the two-way frame shown in Fig.3(c). The 1st mode contribution was very significant for the along-span members, while the 2nd mode contribution was very significant for the along-ridge members. Based on these, the signs of the largest shear forces in the along-span members are set the same as the 1st POD eigenvector of the fluctuating shear forces in all members, and those of the largest shear forces in along-ridge members are set the same as the 2nd POD eigenvector. In this way, the two U-ESWL distributions are obtained as shown in Figs.7(a) and 7(b). By applying these two U-ESWL distributions, positive-side and negative-side largest wind load effects can be obtained for all members as shown in Fig.7(c).

4.2 *Flat roof models*

Following the procedure explained before, two sets of U-ESWL distributions are obtained for a truss-beam flat-roof model, as shown in Figs.10(a) and 10(b).

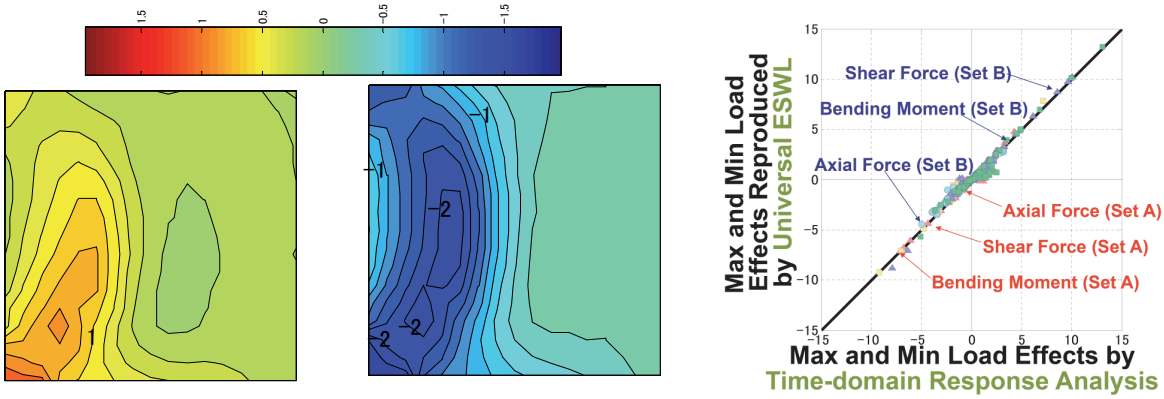

(a) U-ESWL for Set A (b) . U-ESWL for Set B (c) Reproduced largest shear forces

Figure 10. U-ESWL distributions for a flat-roof model and comparison of largest load effects obtained by time-domain response analysis and U-ESWLs

Figure 10(c) compares the largest axial forces, bending moments and shear forces in all members of the truss-beam model obtained by the time domain response analysis and those reproduced by the U-ESWLs. In this case, various different kinds of internal forces are simultaneously targeted, and all of them are appropriately reproduced by only two U-ESWL distributions, as shown in Figs.10(a) and 10(b). Here, the efficiency and the feasibility of the U-ESWL are clearly demonstrated.

5 CONCLUDING REMARKS

The essential matters required for ESWLs are discussed and some advantages of the multiple-target ESWL, especially U-ESWL, are demonstrated for long-span roof structures. There is no significant difference between the procedures for obtaining ESWL by the various approaches. GLF-ESWL, LRC-ESWL, U-ESWL and so on all require the following procedures:

- Getting largest load effects to be targeted, probably by time-domain response analysis
- Conducting inverse analysis to get ESWL based on given target load effect(s)
- Accumulation of ESWL distributions to create database for codification

The GLF method has been widely adopted in many wind load codes and standards, and the aerodynamic database for the GLF methods. The advantage of the simplicity of GLF is also obvious, and can be reasonably applied for tall buildings. It is also well known that many novel ideas on ESWL have been proposed and recent improvement of the GLF method is significant. The Gust Front Factor has been proposed by Kwon & Kareem [14] to envelope the GLF method and to reflect the effects of an unsteady flow field.

However, it is also true that a traditional single-target approach such as GLF or LRC has a limitation for roof structures, and the multiple-target approach such as U-ESWL is required and has the possibility of further development in its application. More studies on U-ESWL are desirable.

6 ACKNOWLEDGEMENTS

This study has been partially supported by TPU Global COE program, MEXT Japanese Government (2008-2013), and NSFC-JST Strategic China-Japan Joint Research Program on "S&T for Environmental Conservation and Construction of a Society with Less Environmental Burden" (2010-2012).

7 REFERENCES

1 A.G. Davenport, Gust loading factors, Journal of Structural Division, ASCE, 93 (1967) 11-34.
2 E. Simiu, Equivalent static wind loads for tall buildings design, J. Struc. Div., ASCE, 102 (1976) 719-737.
3 G. Solari, Alongwind response estimation: closed form solution, J. Struc. Div., ASCE, 108 (1982) 225-244.
4 J.D. Holmes, Effective static load distributions in wind engineering, J. Wind Eng. Ind. Aerodyn., 90 (2002) 91-109.
5 M. Kasperski, Extreme wind load distributions for linear and nonlinear design, Eng. Struc., 14 (1) (1992) 27-34
6 A.G. Davenport, How can we simplify and generalize wind loads, J. Wind Eng. Ind. Aerodyn., 54-55 (1995) 657-669.
7 G. Piccardo and G. Solari, 3-D wind-excited response of slender structures: Closed form solution, J. Struc. Eng., ASCE, 126 (2000) 936-943.
8 G. Piccardo and G. Solari, 3-D gust effect factor for slender vertical structures, Prob. Eng. Mech., 17 (2002) 143-155.
9 Y. Zhou. and A. Kareem, Gust loading factor: new model, J. Struc. Eng., ASCE, 127(2) (2001) 168-175.
10 X. Chen and A. Kareem, Equivalent static wind loads for buffeting response of bridges, J. Struc. Eng., ASCE, 127(12) (2001) 1467-1475.
11 X. Chen and A. Kareem, Equivalent static wind loads on buildings: New model, J. Struc. Eng., ASCE, 130(10) (2004) 1425-1435.
12 Y. Tamura, H. Kikuchi and K. Hibi, Actual extreme pressure distributions and LRC formula, J. Wind Eng. Ind. Aerodyn., 90 (2002) 1959-1971
13 M.P. Repetto and G. Solari, Equivalent static wind actions on vertical structures, J. Wind Eng. Ind. Aerodyn., 92 (2004) 335-357.
14 D.K. Kwon and A. Kareem, Gust-front factor: A new framework for the analysis of wind load effects in gust-fronts, Proc. 12th Int. Conf. on Wind Engineering, Cairns, Australia, 2007
15 M. Kasperski, Design wind loads for low-rise buildings: a critical review of wind load specifications for industrial buildings, J. Wind Eng. Ind. Aerodyn. 61 (1996) 169-179
16 A. Katsumura, Y. Tamura and O. Nakamura, Universal wind load distribution simultaneously reproducing largest load effects in all subject members on large-span cantilevered roof", J. Wind Eng. Ind. Aerodyn., 95 (2007) 1145-1165.
17 Y. Tamura, Design issues for tall buildings from accelerations to damping -- Tribute to Hatsuo Ishizaki and Vinod Modi --, Conference Preprints, The 11th Int. Conf. on Wind Engineering, Vol.1, Lubbock, Texas, 2003, 81-114.
18 A. Katsumura, Y. Tamura and O. Nakamura, Universal equivalent wind load distribution reproducing maximum load effects on structural members, Proc. 5th Int. Coll. on Bluff Body Aerodynamics and Applications (BBAA V), Ottawa, Canada, 2004, 351-354.
19 A. Katsumura, Y. Tamura and O. Nakamura, Maximum wind load effects on a large-span cantilevered roof, Struc. Eng. Int., IABSE, 15, 4 (2005) 248-251.

The Seventh International Colloquium on Bluff Body Aerodynamics and Applications (BBAA7)
Shanghai, China; September 2-6, 2012

For practical use of universal equivalent static wind load

Akira Katsumura[a], Yukio Tamura[b], Osamu Nakamura[c]

[a]*Wind Engineering Institute, 395 Kawaguchi, Fuji-Kawaguchiko-match, Yanamashi, Japan*
[b]*Tokyo Polytechnic University, 1583 Iiyama, Atsugi, Kanagawa, Japan*
[c]*Wind Engineering Institute, 3-29 Kanda-Jimbo-cho, Chiyoda-ku, Tokyo, Japan*

ABSTRACT: This paper describes a method for determining the universal wind load distribution that reproduces the largest load effect on structural members. The method is then applied to a low-rise building and a high-rise building. Quasi-static load effects are investigated for the low-rise building. The largest load effects estimated by the time history response analyses are compared with those reproduced by the GLF method, the LRC method and the universal ESWL. The goal is to provide a database of the universal equivalent static wind load distribution and to develop a wind resistant design method.

KEYWORDS: Largest load effect, Equivalent static wind load, GLF method, LRC method

1 INTRODUCTION

Increasingly complicated building shapes and structural systems have increased the importance of structural design. The safety of all of structural members needs to be confirmed in the structural design stage. Conventional methods of estimating equivalent static wind loads (ESWL) are based on a certain load effect. However, in practice, it is necessary to consider several ESWLs assuming many loading patterns. The authors have proposed a Universal ESWL that simultaneously reproduces the largest load effects on all structural members, and confirmed its effectiveness and rationality by applying it to several structures[1,2]. The technical procedure of this Universal ESWL has been discussed and established. The Universal ESWL makes it possible to reproduce all largest load effects in a unique distribution. Positive and negative load effects are reproduced by a set of the Universal ESWLs. The advantages of this unique method may not yet be sufficiently recognized by many researchers and structural designers. In this study, conventional methods for estimating an ESWL and the method for estimating the Universal ESWL are applied to several structures and the usefulness of the Universal ESWL is verified.

2 EQUIVALENT STATIC WIND LOAD FOR LOW-RISE BUILDING

In standards and laws of many countries the gust loading factor (GLF) method is adapted for estimating an ESWL for low rise buildings. However, the effects of loads acting on members of a low rise building imposed by wind forces on roofs and walls are very complicated. The GLF method is basically aimed at a certain load effect, so it cannot be guaranteed that the resulting ESWL reproduces all of the largest effects. This section investigates ESWLs for a low rise building with a gable roof.

Fluctuating wind pressure data of a low-rise building and its experimental information were down-loaded from the database of the Global COE Wind Engineering Information Center at To-

kyo Polytechnic University[3]. The experimental model was 160mm wide, 240mm deep and 160mm high, and its roof pitch was 9.4 degrees. Its mean wind pressure coefficients and fluctuating wind pressure coefficients are shown in Fig.1 and Fig.2. The maximum mean wind pressure coefficient was 0.8 on the front wall and the corresponding fluctuating wind pressure coefficient was 0.4. The minimum mean wind pressure coefficient was –1.2 on the roof's windward edge and the corresponding fluctuating wind pressure coefficient was 0.4. The mean wind pressure coefficients and the fluctuating wind pressure coefficients on the leeward side of the roof and the leeward wall were small.

Low rise buildings have rigid frames and a background component of load effects would be dominant in members. A simple structural model of a low-rise building was used in this study, as shown in Fig.3. It was constructed of steel frames in the span direction and each all frames were connected by beams and braces in the cross-span direction. The background components of load effects were calculated from the structural model from a time history of fluctuating wind pressure data. Design wind speed was assumed as 30m/s at the building height. The largest load effects on members were estimated from the time history analysis (hereafter referred to as actual largest load effect). The maximum largest axial force occurred at the upper part of the windward column of the 1st floor and the maximum largest shear force and bending moment occurred at the beam's end of the middle frame as shown in Fig.3. ESWLs based on these target largest load effects were calculated by the GLF method and the LRC method. The Universal ESWL that simultaneously reproduces actual largest axial forces, shear forces and bending moments in major members was also calculated.

The ESWL estimated by the GLF method focused on a largest axial force is shown in Fig.4. It is normalized by velocity pressure at the eaves height and the mean component of the wind force coefficient is excluded from it. Although positive and negative largest load effects were estimated, an ESWL that reproduces the same sign of the mean component of load effect is shown in this figure. The gust loading factor of the largest axial force was 3.5. The mean shear force and the mean bending moment in the frame in which the target largest load effects occurred in a member transverse to the wind direction was almost zero, so the GLF method cannot be adopted for both the largest shear force and the largest bending moment.

The ESWL estimated by the LRC method is shown in Fig.5. Although two ESWLs can be estimated from the LRC method, an ESWL that produces negative values on the roof is shown in this figure. The peak factor of the largest axial force, shear force and bending moment were 6.7, 7.1 and 4.3 respectively. The ESWLs are asymmetric to the wind direction and show quite different distributions from the axial force, shear force and bending moment.

The Universal ESWL that simultaneously reproduces largest axial force, shear force and bending moment in main structural members is shown in Fig.6. In the previous study, it was confirmed using a POD eigen vector of fluctuating wind pressure that the Universal ESWL would show a natural and realistic distribution. In this Universal ESWL for low rise buildings, the 1st to 10th POD eigen modes were superimposed. Two Universal ESWLs were estimated for combination of positive and negative largest load effects. Target largest load effects on members were selected by using the same sign as the POD 1st eigen mode of load effect[1]. The Universal ESWL shows asymmetric distribution and is different from the ESWLs estimated by either the GLF method or the LRC method.

Figures 7-9 compare actual largest load effects and those reproduced by all ESWLs. The abscissa shows actual largest load effects for all members and the ordinate shows that reproduced by all ESWLs. The largest load effects are normalized by the maximum actual largest load effects. Comparatively high correlation can be seen in the comparison of largest axial forces estimated by the GLF method and the LRC method and the largest bending moments estimated by the LRC method. However, the correlations of largest shear forces decrease in the LRC method.

Comparison of largest axial force, shear force and bending moment reproduced by the Universal ESWL are shown in Fig.9. The largest load effects reproduced by the Universal ESWL shows comparatively high correlation with the actual largest load effects by the unique distribution.

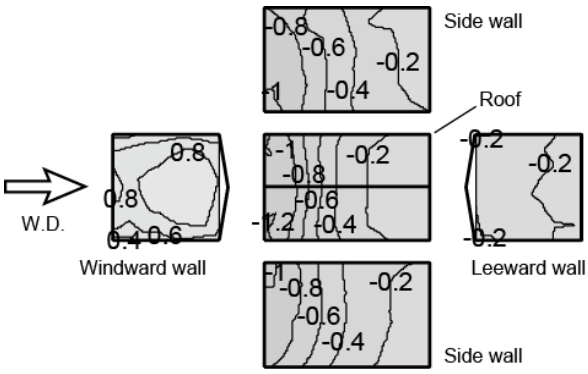

Figure 1. Mean wind pressure coefficient.

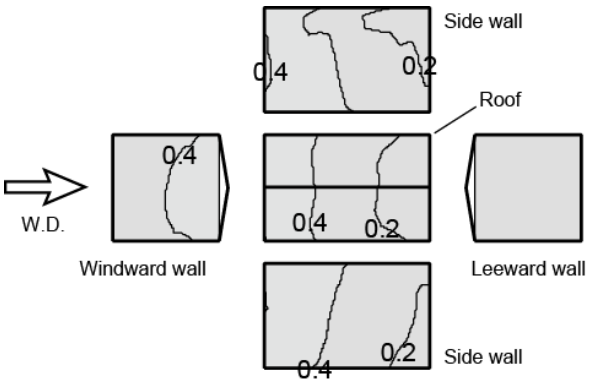

Figure 2. Fluctuating wind pressure coefficient.

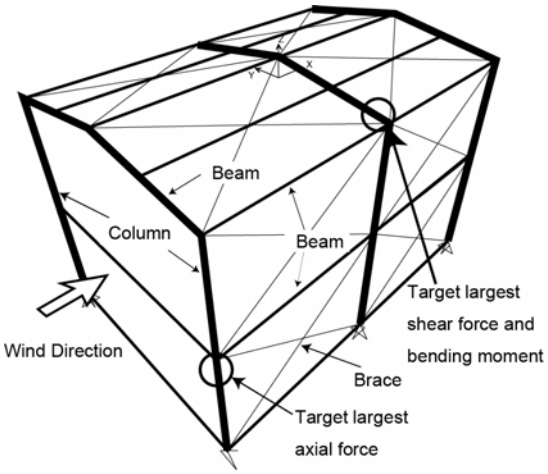

Figure 3

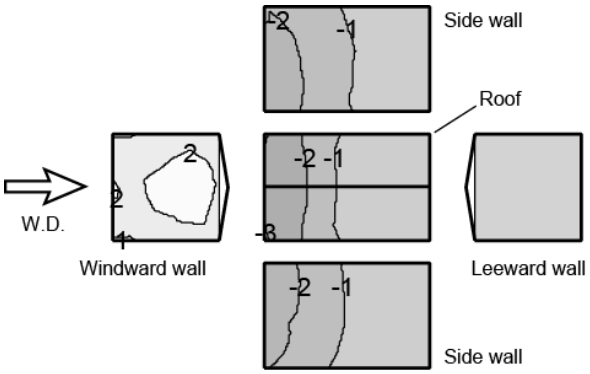

Figure 4

Figure 3. Structural model of low-rise building.
Figure 4. ESWL estimated by GLF method focused on target largest axial force.

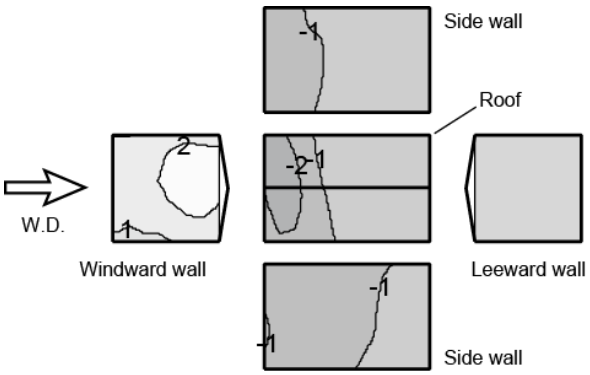

(a) Focused on target largest axial force

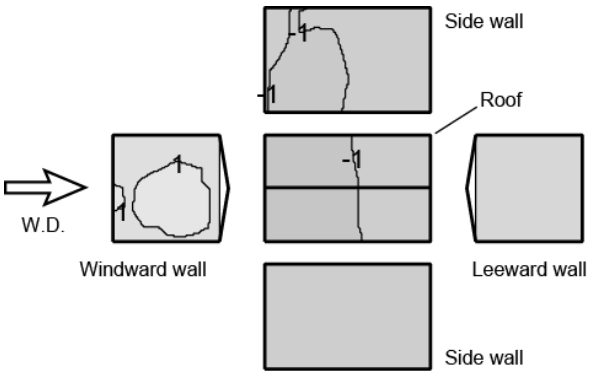

(b) Focused on target largest shear force

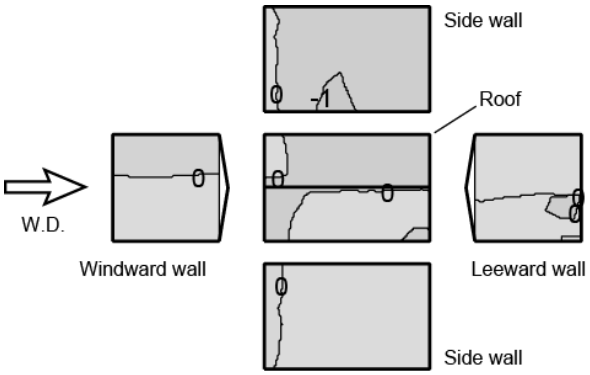

(c) Focused on target largest bending moment

Figure 5. ESWL estimated by LRC method.

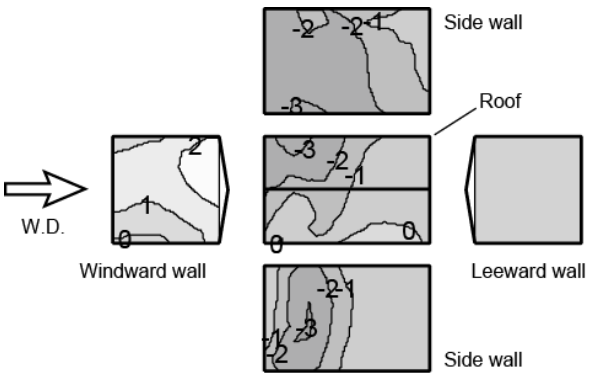

Figure 6

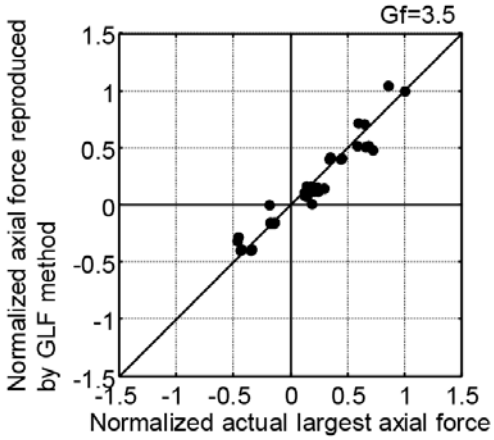

Figure 7

Figure 6. Universal equivalent static wind load.
Figure 7. Comparison of largest axial force reproduced by GLF method.

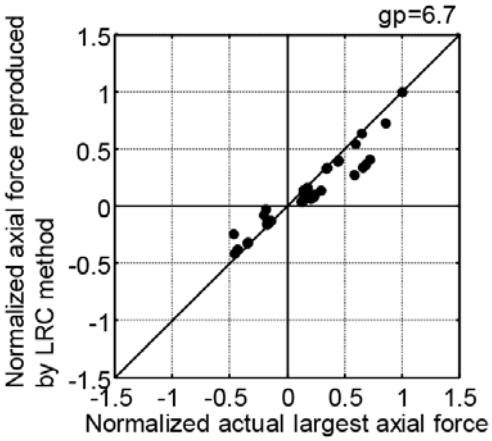

(a) Focused on a largest axial force

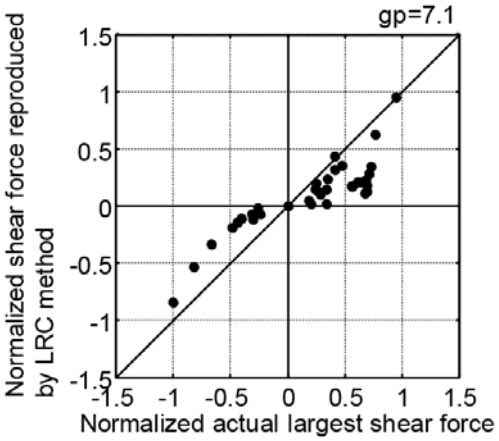

(b) Focused on a largest shear force

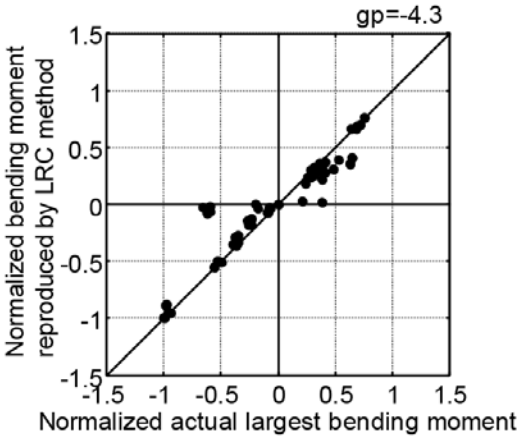

(c) Focused on a bending moment

Figure 8. Comparison of largest load effect reproduced by LRC method.

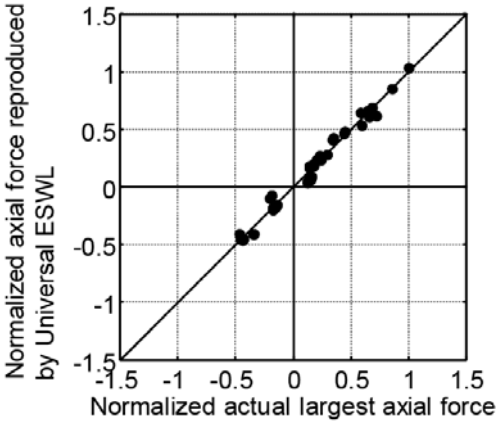

(a)

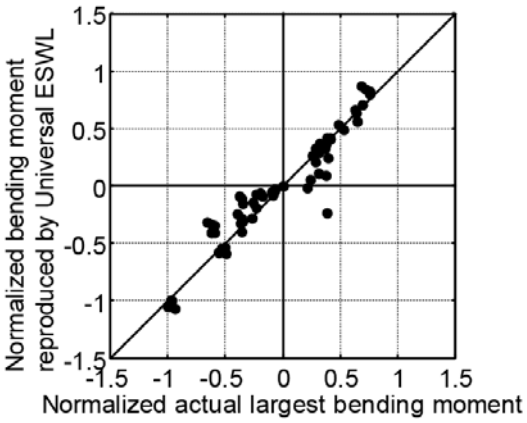

(b)

Figure 9. Comparison of largest load effect reproduced by Universal ESWL.

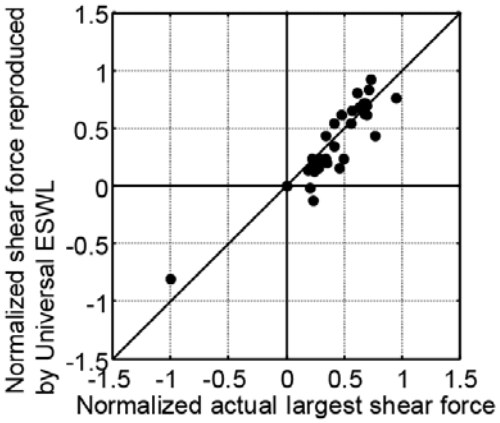

(c)

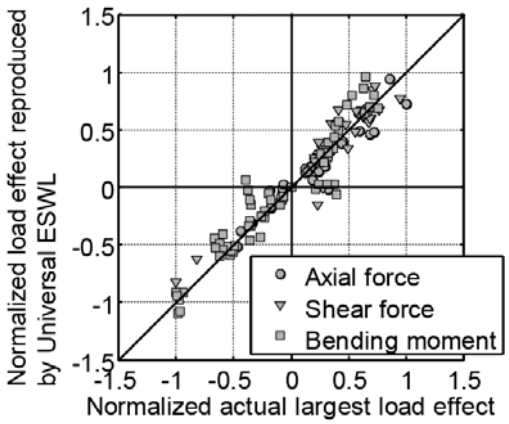

(d)

Figure 9(cont.). Comparison of largest load effect reproduced by Universal ESWL.
(a) Focused on largest axial force, (b) Focused on largest bending moment, (c) Focused on largest shear force, (d) Focused on largest axial force, shear force and bending moment

3 CONCLUSION

In the conventional GLF method and the LRC method, the ESWLs are estimated from a certain target load effect. From a physical point of view, mean or fluctuating wind pressure distributions have been used for the ESWLs that are expected to reproduce the largest load effects in all structural members. The more complicated the structure becomes, for example a low-rise building, the more the target largest load effects increase. A reasonable ESWL would be a complicated distribution apart from the mean or the fluctuating wind pressure distribution. The Universal ESWL automatically provides a reasonable distribution for any building structure and any combination of load effects. It may have been possible to realize a more reasonable ESWL distribution after accumulation of many structural types and designs. We have been developing the database of the Universal ESWL.

4 ACKNOWLEDGEMENTS

This study has been supported by NSFC-JST Strategic China-Japan Joint Research Program on "S&T for Environmental Conservation and Construction of a Society with Less Environmental Bur-den" (2010-2012), which are gratefully acknowledged.

5 REFERENCES

1 KATSUMURA, A., TAMURA, Y., NAKAMURA, O., Universal wind load distribution simultaneously reproducing largest load effects in all subject members on large-span cantilevered roof, Journal of Wind Engineering and Industrial Aerodynamics 95, pp.1145-1165, 2007
2 KATSUMURA, A., TAMURA, Y., NAKAMURA, O., Universal equivalent static wind load distribution on a large-span cantilevered truss roof, Proc. 12th International Conference on Wind Engineering, Cairns, Australia, pp.399-406, 2007
3 Global COE Wind Engineering Information Center at Tokyo Polytechnic University, http://www.wind.arch.t-kougei.ac.jp/system/eng/

The Seventh International Colloquium on Bluff Body Aerodynamics and Applications (BBAA7)
Shanghai, China; September 2-6, 2012

Wind-induced vibrations and equivalent static wind loading for cable-stayed bridges

Yong-Xin YANG, Yao-Jun GE

State Key Laboratory for Disaster Reduction in Civil Engineering
Department of Bridge Engineering at Tongji University, Shanghai 200092, China

ABSTRACT: Although cable-stayed bridges generally have higher rigidity and natural frequencies, flutter instability still can pose threats to some aerodynamic bluff girder sections, such as box girder section with cantilevered slab and two-isolated-girder section. Experimental researches on the flutter instability of these girder sections were carried out to find effective ways to improve their flutter performance. While the adoption of twin box girder can be an effective solution to improve the flutter stability of cable-stayed bridges, more attention should be paid to its vortex-induced vibration performance. Based on a long-span cable-stayed bridge, the vortex-induced vibration performance of twin box girder section was evaluated and aerodynamic control measure was proposed to mitigate the vibration response. Since it is more convenient for a bridge engineer to evaluate buffeting responses of a bridge structure by some kind of equivalent static wind loading than comprehensive buffeting analysis, the method to calculate equivalent wind load of cable-stayed bridges caused by buffeting response, which is recommended by the China Code for wind-resistant design of highway bridges, was demonstrated.

KEYWORDS: vortex-induced vibration; flutter; vortex-induced vibration; vibration control measure; wind tunnel test; equivalent static wind load

1 INTRODUCTION

With the rapid increase of span length, bridge structures are becoming more flexible and more vulnerable to wind-induced vibrations. Compared with suspension bridges with similar main span, cable-stayed bridges usually have higher rigidity and natural frequencies, which implies better aerodynamic stability. However, if the shape of a main girder hasn't been optimized enough to obtain good aerodynamic performance, there still will exist flutter instability problems even when the main span of a cable-stayed bridge isn't very large. For those girder sections which has been optimized to have better flutter performance, another possible self-excited vibration, vortex-induced vibration, may affect the operating performance of a bridge if happens. Furthermore, buffeting always exists when a bridge is exposed to turbulent flow, which is very common in the Atmospheric Boundary Layer. Different from the way flutter and vortex-induced vibration are dealt with, it is more convenient for a bridge engineer to evaluate the buffeting responses of a bridge structure by some kind of equivalent static wind loading, than comprehensive three-dimensional frequency domain or time domain buffeting analysis. In this paper, problems related to flutter and vortex-induced vibration of cable-stayed bridges and their countermeasures are introduced based on some engineering projects in China, and the method to calculate equivalent wind load caused mainly by buffeting response, which is recommended by the China Code for wind-resistant design of highway bridges (cable-stayed bridges and suspension bridges), will be demonstrated.

2 FLUTTER INSTABILITY

Generally speaking, cable-stayed bridges have better flutter performance than suspension bridges for higher rigidity resulted from their unique structural system. Even for a super long-span cable-stayed bridge which have a main span over 1 kilometer, flutter instability never posed a real threat after a spatial cable system and a reasonable girder section were adopted. However, the span length isn't the only key factor which determines the flutter performance of a long-span bridge, as the infamous original Tacoma Narrows Bridge, which suffered from flutter-induced collapse, was not the longest bridge at that time. The dynamic performance of the structural system composed of girder, stay-cables and pylon also matters, as well as the aerodynamic configuration of the girder section. For cable-stayed bridges with middle-range main spans, aerodynamically blunter composite main girders are more preferred by designers in most cases to traditional flat single box steel girders for economical reasons.

2.1 STRUCTURAL INFORMATION

The two girder sections (Figure 1) investigated in this research have been widely used as the main girder section of cable-stayed bridges, especially when the bridge span is not very large. Section A, box girder section with cantilevered slab, and Section B, two isolated rectangular box girder, are main girders of the Main Bridge and the Kezhushan Bridge respectively, which are two major crossings of East Sea Bridge over two main navigational channels between the Yangshan International Deep Water Harbor and Shanghai city.

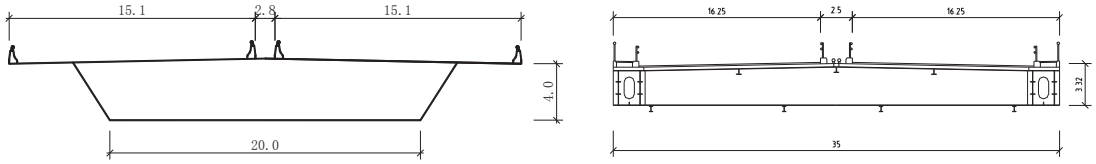

a) Section A b) Section B

Figure 1 Two girder sections of cable-stayed bridges

Although the main spans of these two bridge are not very large, the torsional fundamental frequency are lower than 0.6 Hz and the ratios between the torsional and bending fundamental frequencies are no more than 1.65, due to their general structural layout (single cable plane or parallel cable plane) and composite girder sections.

2.2 FLUTTER PERFORMANCE

Sectional model tests and aeroelastic mode tests were carried out to examine the flutter performance of these two cable-stayed bridges in TJ-1 and TJ-3 Boundary Layer Wind Tunnel in the State Key Laboratory for Disaster Reduction in Civil Engineering (SKLDRCE) of Tongji University as shown in Figure 2.

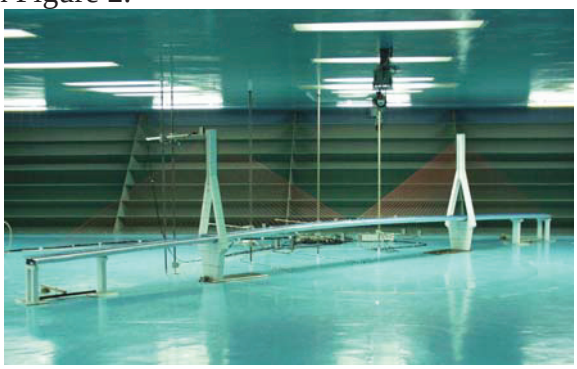


Figure 2 Sectional model and aeroelastic model wind tunnel test for flutter performance

The measured flutter critical speeds for both girder sections of these two cable-stayed bridges are listed in table 1. For Section A, the structure is very aerodynamically stable even after wind speed exceeds 100 m/s when the wind angle of attack is zero or negative. However, when the wind angle of attack turns positive, the flutter onset speed decreases dramatically and is below the flutter checking wind speed. This is the characteristics of the aerodynamic performance for this type of girder section. The flutter performance of Section B is worse than Section A since this is a blunter girder section. The results of aeroelastic model tests generally have good agreement with sectional model tests.

Table 1 Flutter critical speed of the original section（m/s）

Girder	Test	–3°	0°	+3°	[U_{cr}]
Section A	Sectional model	>176	145.0	81.4	84.6
	Aeroelastic model		>100	82.6	
Section B	Sectional model	96.2	74.8	69.0	79.9
	Aeroelastic model		72.5		

Based on the testing results, the flutter critical speeds for both original structures cannot meet the requirement of flutter checking speeds of 84.6 m/s for the main navigational channel bridge and 79.9 m/s for Kezhushan Bridge, so effective preventive measures had to be considered to stabilize the original bridges.

2.3 FLUTTER CONTROL

In order to improve the aerodynamic stability of the main navigational bridge, central barrier was installed on the bridge deck (Section A) as shown in Figure 3. Three different heights of central barrier were chosen to investigate the controlling effect of this aerodynamic measure, which are 0.8m, 1.0m and 1.2m respectively, or 20%, 25% and 30% of the girder depth respectively.

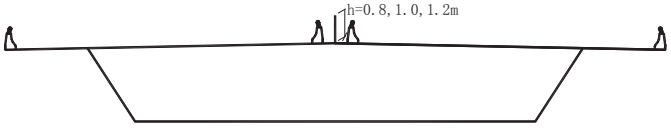

Figure 3 Girder section A with central barrier

The measured flutter critical speeds are listed in table 2. As the results shown, the flutter controlling effect of central barrier is excellent. For three types of central barrier the flutter onset speeds are all exceed the wind speed requirement, and the section with 1.2 m high central barrier has the best aerodynamic performance which increases the flutter onset speed by approximately 11%.

Table 2 Flutter critical speed of Section A with central barriers（m/s）

Angle of attack	–3°	0°	+3°
Original section	>176	145.0	81.4
0.8m central barrier	>176	151.8	85.8

1.0m central barrier	>176	151.8	85.8
1.2m central barrier	>176	154.0	90.2

As mentioned previously, when at positive angle of attack the aerodynamic stability of the original girder section A is rather low and different from those at negative and zero angle of attack. It can be inferred that adjusting aerodynamic configuration of the windward inclined web and the bottom slab will affect the aerodynamic stability of the girder section dramatically. So several measures concerning various positions of the inspection rails were investigated in wind tunnel tests. These testing sections are shown in Figure 4.

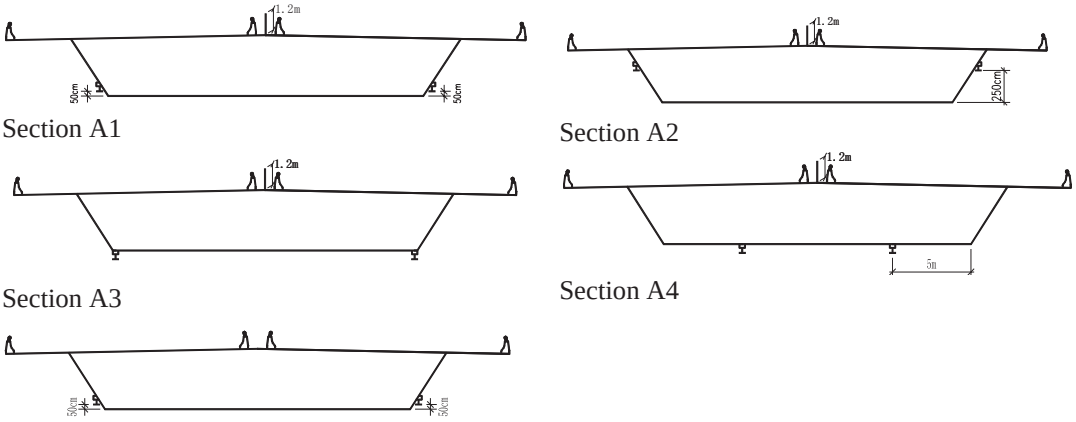

Figure 4 Girder section A with different locations of inspection rails

Section A1 has inspection rails on the bottom of the inclined web, while section A2 has inspection rails on the upper side of the inclined web. In section A3 and section A4 the inspection rails are on the bottom slab. These four sections all have 1.2m high central barrier on the bridge deck. In section A5 the position of inspection rails is the same as in section a, but has no central barrier on the bridge deck. The wind tunnel testing results for these sections with inspection rails are listed in table 3.

Table 3 Flutter critical speed of sections A with different locations of inspection rails (m/s)

Angle of attack	–3°	0°	+3°
Original section	>176	145.0	81.4
Section A1	>176	162.8	94.6
Section A2	>176	151.8	88.0
Section A3	>176	121.0	79.2
Section A4	>176	154.0	90.2
Section A5	>176	154.0	90.2

From the testing results we can see that the aerodynamic stabilities of sections with central barrier and inspection rails being appropriately positioned have been improved remarkably except section A3. Section A1 which has 1.2m central barrier and inspection rails at the bottom of the inclined web has the best aerodynamic performance considering flutter instability. For section A5 which has inspection rails at the same position as section a and no central barrier, the aerodynamic stability also has been improved by 11% and exceeds the flutter verification speed. As section A5 also has economic advantage, this flutter control measure is finally recommended to bridge designer.

The girder section B of the Kezhunshan bridge is a more bluff body compared to the original girder section A of the main navigational bridge. So the first flutter control measure taken into account is the installation of fairings. The girder section with fairings is shown in Figure 5 a).

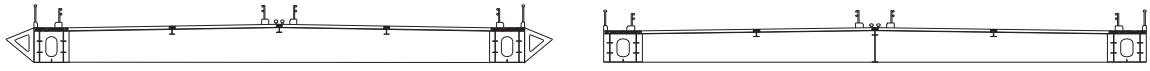

a) Fairing b) Central stabilizer

Figure 5 Girder section B with fairings

The flutter performance of girder section B with fairings was tested in aeroelastic model wind tunnel test, and the results are listed in table 4. For each angle of attack the flutter onset speed is over the flutter verification speed 79.9 m/s, which means it is a very effective measure to improve the aerodynamic stability for such a two-isolated-girder section.

Table 4 Flutter critical speed of section B with fairings and central barrier（m/s）

Angle of attack	–3°	0°	+3°
Original section B		72.5	
Section with fairings	95.0	>100	95.0
Section with central barrier	87.5	82.5	>100

For the interest of research on the effectiveness of flutter control measures, an alternative control measure which has a central barrier installed under the bridge deck and with the same height as the girder section is investigated in this research. The girder section B with central barrier is shown in Figure 5 b). Aeroelastic model tests were carried out to verify the effectiveness of the installation of central barrier. The corresponding testing results are also shown in table 4. Although the flutter controlling effectiveness of the central barrier on this type of girder section is not as remarkable as that of the application of fairings, this measure does improve the aerodynamic stability of the original section to meet the design requirement.

3 VORTEX-INDUCED VIBRATION

Even for aerodynamic stable girder sections which have been optimized to obtain better flutter performance, another kind of self-excited vibration, vortex-induced vibration, may happen at lower wind speed range. Section C is a typical twin box girder with a central vent (Figure 6), which is the main girder of Shanghai Yangtze Bridge, a three-span cable-stayed bridge with a main span of 730m.

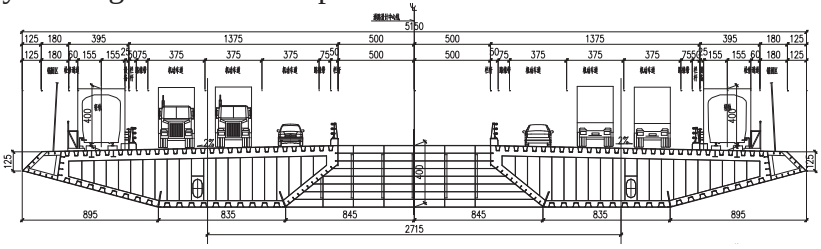

Figure 6 Girder section C

Although twin box girder has been proven to be very effective to enhance the flutter performance of super-long span bridges, more attention should be paid to the vortex-induced vibration performance of this innovative girder section, since the existence of central vent will make the vortex shedding process and its interaction with the movement of the bridge girder more complicated.

3.1 VIV PERFORMANCE

For detailed investigation on VIV responses, a combination of geometrical, mass, stiffness and Reynolds number considerations resulted in the selection of a 1:25 scale for the sectional model. These large-scale sectional models have the total length of about 3.6 m and the width of about 2.06m. The wind tunnel tests were conducted in smooth flow at Tongji University's TJ-3 Boundary Layer Wind Tunnel with the working section of the 15m width, the 2m height and the 14m length. Two rigid and streamlined temporary end walls were designed and built in the working section to accommodate the large sectional model (Figure 7), and the suspension system including eight springs and supporting frames was built in these two end walls together with four laser displacement transducers for the measurement of the response of the sectional model to vortex-shedding excitation.

Figure 7 Large-scale sectional model and supporting system

Both heaving and torsional VIV responses were observed in the testing, and the Strouhal Number and Reynolds Number at the VIV condition are 0.1230 and 90, 768 respectively. Table 1 list the maximum VIV amplitudes and some important parameters in VIV conditions.

Table 5 Maximum VIV amplitudes and important parameters

VIV in heaving (h/D)			VIV in torsion		
Amplitude	S_t	R_e	Amplitude	S_t	R_e
0.054	0.1620	29, 264	0.134	0.1230	90, 768

3.2 VIV CONTROL

Guide vane is a possible VIV control solution, which can smooth air flow around the corner of girder section. After comparisons of the VIV mitigating effects between different locations of guide vanes, the optimum location for Section C was found to be under the bottom slab near central vent, which is shown in Figure 8. The responses of the model with and without guide vanes at -3˚ wind angle of attack are shown in Figure 9. It can be seen that the torsional VIV of the original twin box girder can be mitigated effectively by the installation of guide vanes. No significant heaving VIV of the girder with guide vanes was observed except for the case at -3˚ wind angle of attack. In this case the peak amplitude of heaving VIV was reduced from 21.7 cm to 13.6 cm for the prototype bridge structure with 0.3% structural damping ratio. Guide vane seems to have better mitigating effect on torsional VIV than heaving VIV for twin box girder sections. Comparisons of maximum VIV amplitudes among +3˚, 0˚, and -3˚ wind angles of attack for girder section C and another two long-span bridges having twin-box girders with and without guide vanes at the condition of 0.3% structural damping ratio are listed in Table 6. The results also imply that the VIV control effect of guide vane is rather sensitive to the outboard and inboard shape of a twin box girder section.

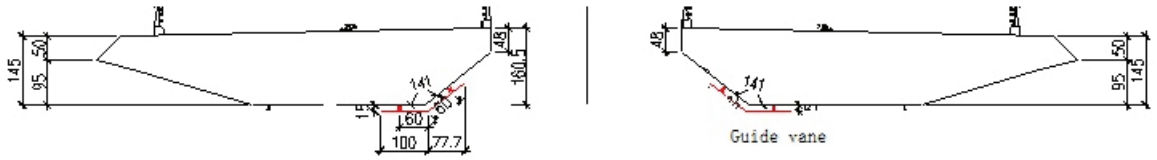

Figure 8 Section C with guide vanes

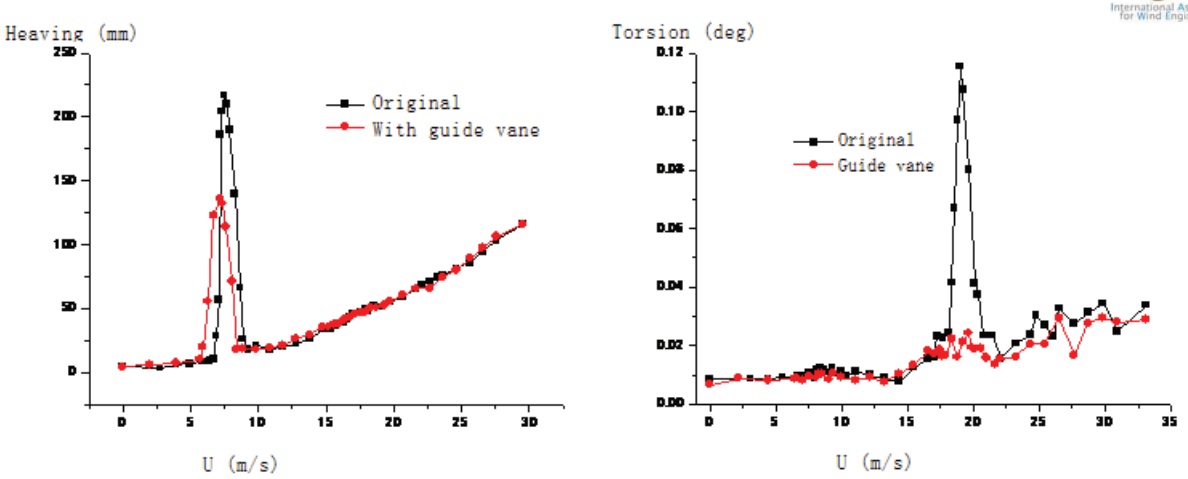

Figure 9 VIV control effect of guide vane on Section C

Table 6 VIV mitigation effects of guide vane on Section C

Bridge	VIV in heaving (h/D)			VIV in torsion		
	Original section	Guide vane	Mitigation	Original section	Guide vane	Mitigation
Xihoumen	0.050	0.039	23%	0.500	0.171	66%
Shanghai Yangtze	0.054	0.034	37%	0.134	0.024	82%
Qingdao Bay	0.077	0.024	69%	0.038	-	-

4 EQUIVALENT WIND LOAD

Buffeting always exists when a bridge is exposed to turbulent flow, which is very common in the Atmospheric Boundary Layer. For a bridge engineer, it is more convenient to evaluate the buffeting responses of a bridge by some kind of equivalent static wind load. Based on the China Code, the total wind load on a bridge structure can be calculated by the following formula:

$$L_{Total} = L_{SG} + L_R$$

Where L_{Total} is the total wind load, L_{SG} is called static gust wind load, which is actually the summation of the static wind load and the equivalent static wind load related to background buffeting responses, and L_R is the equivalent static wind load related to resonant buffeting responses, which can be calculated through Inertia Wind Loading Method.

4.1 STATIC GUST WIND LOAD

According to the China Code for the wind-resistant design of highway bridges, the method to calculate the static gust wind load is the same as static wind load. The only difference is to replace design wind speed with static gust wind speed in static gust wind load evaluation. The conversion factor from design wind speed to static gust wind speed is called static gust wind coefficient, which varies with terrain types at bridge site and horizontal wind-load-bearing length. For the Main Bridge of East Sea Bridge, this coefficient is 1.22 at the service state.

In order to get the static gust wind load, the aerodynamic force coefficients of the girder section were measured through sectional model wind tunnel tests and listed in Table 7. Coefficients of the main pylon were suggested by the code.

Table 7 Aerodynamic force coefficients

Components	Drag force (C_x)		Lift force (C_y)		Pitch moment (C_M)	
	Service	Construction	Service	Construction	Service	Construction
Girder	0.931	0.661	-0.043	0.006	0.054	0.076
Pylon	1.5	2.0	1.5	2.0	0	0

Then the static gust wind load for the main girder at the service stage can be calculated as follows.

$$\bar{W}_y^d(x) = \bar{W}_{y0}^d \alpha_{y0}^d(x) = \frac{1}{2}\rho U_c^2 B C_y = -2.814\ kN/m \tag{1a}$$

$$\bar{W}_z^d(x) = \bar{W}_{z0}^d \alpha_{z0}^d(x) = \frac{1}{2}\rho U_c^2 H C_z = 7.385\ kN/m \tag{1b}$$

$$\bar{W}_\theta^d(x) = W_{\theta 0}^d \alpha_{\theta 0}^d(x) = \frac{1}{2}\rho U_c^2 B^2 C_M = 116.614\ kN\cdot m/m \tag{1c}$$

Where, $\bar{W}_{y0}^d$、$\bar{W}_{z0}^d$、$\bar{W}_{\theta 0}^d$ are maximum values of the vertical, horizontal and torsional components of the static gust wind load for the main girder, α_{y0}^d、α_{z0}^d、$\alpha_{\theta 0}^d$ are distribution function for the three components of the static gust wind load for the main girder, and $\alpha_{y0}^d \equiv \alpha_{z0}^d \equiv \alpha_{\theta 0}^d \equiv 1$.

The static gust wind load for the main pylon at the service stage can be calculated in the similar way.

$$\bar{W}_z^p(z) = \bar{W}_{z0}^p \alpha_{z0}^p(z) = \frac{1}{2}\rho U_t^2 B_D C_D \left(\frac{z}{z_t}\right)^{2\alpha} \frac{B_D(z)}{B_D} = 29.45\left(\frac{z}{z_t}\right)^{0.2} \frac{B_D(z)}{B_D}(kN/m) \tag{2a}$$

$$\bar{W}_x^p(z) = \bar{W}_{x0}^p \alpha_{x0}^p(z) = \frac{1}{2}\rho U_t^2 B_L C_L \left(\frac{z}{z_t}\right)^{2\alpha} \frac{B_L(z)}{B_L} = 25.77\left(\frac{z}{z_t}\right)^{0.2} \frac{B_L(z)}{B_L}(kN/m) \tag{2b}$$

Where, $\bar{W}_{z0}^p$ and $\bar{W}_{x0}^p$ are in-plane and out-of-plane static gust wind load for the main pylon at the top of the pylon, while α_{z0}^p and α_{x0}^p are distribution function for the static gust wind load for the main pylon

$$\alpha_{z0}^p(z) = \left(\frac{z}{z_t}\right)^{0.2} \frac{B_D(z)}{B_D},\quad \alpha_{x0}^p(z) = \left(\frac{z}{z_t}\right)^{0.2} \frac{B_L(z)}{B_L} \tag{3}$$

C_D and C_L are in-plane and out-of-plane aerodynamic force coefficients of the main pylon.

The results of the static gust wind load for the main girder and main pylon of the Main Bridge of the East Sea Bridge is shown in Figure 10.

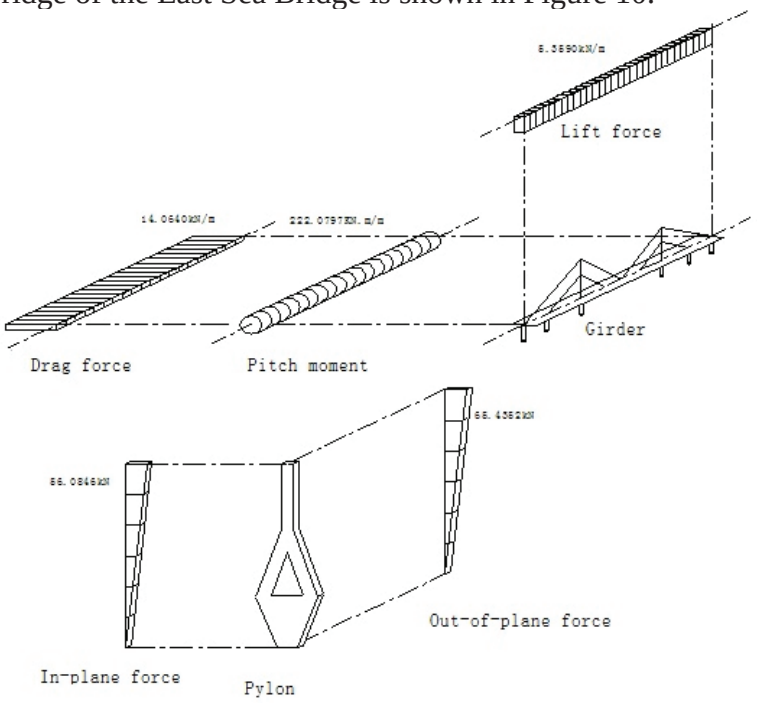

Figure 10 Static gust wind load

4.2 EQUIVALENT STATIC WIND LOAD

The equivalent static wind load related to resonant buffeting responses can be calculated through Inertia Wind Loading Method. So the equivalent wind load can be evaluated by the following formulas.

$$W_y(s)=\bar{W}_y(s)+\tilde{W}_y(s)\approx\bar{W}_{y0}\alpha_{y0}(s)+\tilde{W}_{y1}\alpha_{y1}(s)+\tilde{W}_{y2}\alpha_{y2}(s) \quad (4a)$$

$$W_z(s)=\bar{W}_z(s)+\tilde{W}_z(s)\approx\bar{W}_{z0}\alpha_{z0}(s)+\tilde{W}_{z1}\alpha_{z1}(s)+\tilde{W}_{z2}\alpha_{z2}(s) \quad (4b)$$

$$W_\theta(s)=\bar{W}_\theta(s)+\tilde{W}_\theta(s)\approx\bar{W}_{\theta0}\alpha_{\theta0}(s)+\tilde{W}_{\theta1}\alpha_{\theta1}(s)+\tilde{W}_{\theta2}\alpha_{\theta2}(s) \quad (4c)$$

Where, $\bar{W}_y$、$\bar{W}_z$、$\bar{W}_\theta$ are static gust wind load which can be calculated through equation (1) and (2), $\tilde{W}_y$、$\tilde{W}_z$、$\tilde{W}_\theta$ are vertical, horizontal and torsional components of buffeting inertial forces, $\tilde{W}_{y1}$、$\tilde{W}_{z1}$、$\tilde{W}_{\theta1}$ are peak values of three components of buffeting inertial forces for the first natural vibration mode, $\tilde{W}_{y2}$、$\tilde{W}_{z2}$、$\tilde{W}_{\theta2}$ are peak values of three components of buffeting inertial forces for the second natural vibration mode, $\alpha_{y1}(s)$、$\alpha_{z1}(s)$、$\alpha_{\theta1}(s)$ are distribution functions for the three components of buffeting inertial forces for the first natural vibration mode, $\alpha_{y2}(s)$、$\alpha_{z2}(s)$、$\alpha_{\theta2}(s)$ are distribution functions for the three components of buffeting inertial forces for the second natural vibration mode.

Based on the buffeting responses measured in aeroelastic model wind tunnel tests, the buffeting inertial forces at any measuring points on the main girder or the main pylon can be calculated through the following formula.

$$\tilde{W}_{ri}\alpha_{ri}(s_k)=(2\pi f_i)^2 g_{\sigma i}\sigma_{ri}(s_k)m_r(s_k) \qquad (r=y,z,\theta;\ i=1,2) \quad (5)$$

Where, f_i is the frequency of the ith mode, $g_{\sigma i}$ is the peak factor of the buffeting response of the ith mode, $\sigma_{ri}(s_k)$ is the root-mean-square (RMS) value of the buffeting response at measuring point s_k for the ith mode, $m_r(s_k)$—is the mass or mass moment of inertia at measuring point s_k.

For locations other than those measuring points, the buffeting inertial forces can be evaluated by

$$\tilde{W}_{ri}\alpha_{ri}(s_l)=(2\pi f_i)^2 g_{\sigma i}\sigma_{rim}m_r(s_l)\varphi_{ri}(s_l) \qquad (r=y,z,\theta;\ i=1,2) \quad (6)$$

Where, σ_{rim} is the RMS value of the buffeting response at the location corresponding to the maximum value of the modal function for the ith mode, $m_r(s_l)$ is the mass or mass moment of inertia at any location s_l on the main girder or the main pylon, $\varphi_{ri}(s_l)$—is the value of the normalized ith modal function at the location s_l.

The results of the equivalent static wind load for the main girder and main pylon of the Main Bridge of the East Sea Bridge at the design wind speed is shown in Figure 11.

5 CONCLUSIONS

Experimental researches on the flutter instability of two aerodynamically bluff girder sections, box girder section with cantilevered slab and two-isolated-girder section, which have been widely adopted in the constructions of cable-stayed bridges, were carried out to find effective ways to improve their flutter performance. For single box girder section, the aerodynamic stability under positive wind angle of attack is critical, and adding central barrier on the deck and position adjustment of inspection rails to the bottom of the inclined web are effective aerodynamic measures to improve flutter performance. For two-

isolated-girder section, installing central barrier under the bridge deck and adding fairing can both increase flutter onset speed significantly.
Based on the results of large scaled model wind tunnel tests for a long-span cable-stayed bridge, twin box girders are prone to have vortex-induced vibrations with large amplitude. Installing guide vanes at the bottom of the girder section near central vent can mitigate vortex-induced vibrations, especially in torsional motion.
According to the China Code for wind-resistant design of highway bridges, the equivalent wind load for a cable-stayed bridge is expressed by the summation of static gust wind load and equivalent static wind load. The static gust wind load can be calculated in the similar way as static wind load, and the equivalent static wind load related to resonant buffeting responses can be evaluated by Inertia Wind Loading Method.

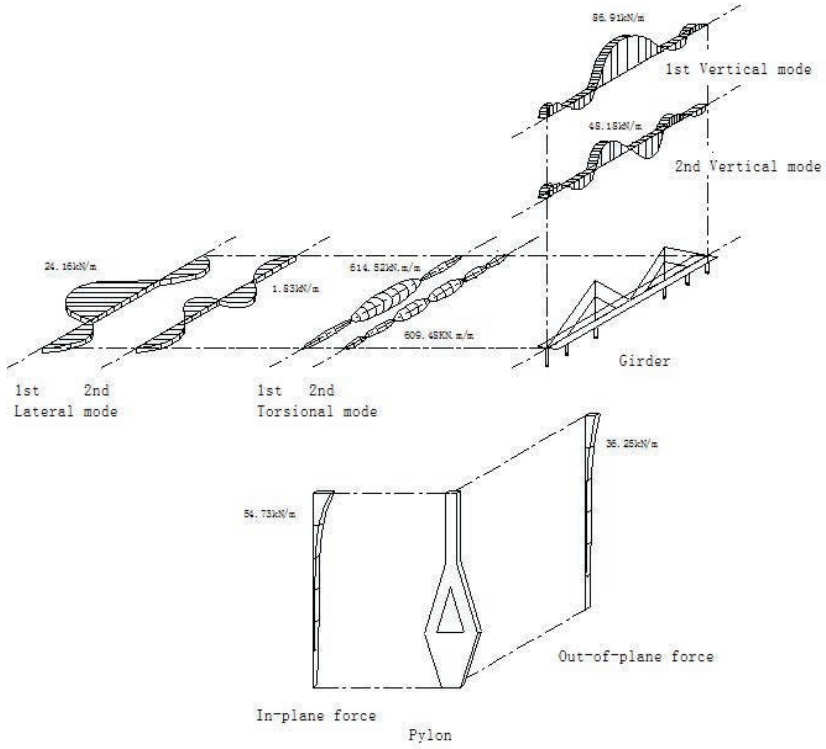

Figure 11 Equivalent static wind load

6 ACKNOWLEDGEMENT

The work described in this paper is partially supported by the Natural Science Foundation of China under the Grants 51078276 and 51021140005, the Ministry of Science and Technology of China under the Grants SLDRCE10-B-05, and the Ministry of Transport of China under the Grants KLWRBMT-04.

7 REFERENCES

Yongxin Yang, Yaojun Ge and Lin Zhao. Aerodynamic Investigation on Flutter Instability of the First Sea-Crossing Bridge in China–The East Sea Bridge, Proceeding of the 4th European and African Conference on Wind Engineering, Czech, 2005

Yongxin Yang, Yaojun Ge and Haifan Xiang. Aerodynamic Flutter Control for Typical Girder Sections of Long-Span Cable-Supported Bridges, Journal of Wind and Structures, Vol.12, No.3, 2009

Yongxin Yang and Yaojun Ge. Equivalent Static Wind Loading For Long-span Bridges, Proceeding of the 3rd Symposium on New Strategy for Wind Disaster Risk Reduction of Wind Sensitive Infrastructures, China, 2010

Yongxin Yang and Yaojun Ge. Equivalent Static Wind Loading for Long-span Arch Bridges, Proceeding of the 4th Symposium on New Strategy for Wind Disaster Risk Reduction of Wind Sensitive Infrastructures, Japan, 2011

The Seventh International Colloquium on Bluff Body Aerodynamics and Applications (BBAA7)
Shanghai, China; September 2-6, 2012

Coupling effects of resonant components of aerodynamic loads acted on hyperbolic spacial structures

S.T. Ke, L. Zhao, Y.J. Ge

SLDRCE, Tongji University, Shanghai, China, zhaolin@tongji.edu.cn

ABSTRACT: An alternative method to account for resonant response coupling effects is proposed in this paper, in consideration that the traditional Inertial Wind Loads (IWL) method and Gust Load Factor (GLF) method are not good at the accurate analysis on resonant loading components of resonant response coupling effects between Equivalent Static Wind Loads (ESWL) and natural mode of large-span roofs and large hyperbolic cooling towers; Firstly, the generalized resonant modal displacement covariance matrix is derived from structural equation of motion; then based on IWL method, covariance matrix of elastic restoring force containing the resonant components is obtained; finally, the resonant response and equivalent static wind loads are calculated with Loads Response Correlation (LRC) method. The proposed procedure avoids the integration process of calculating elastic restoring force and fully considers the modal coupling effects, which can be used to estimate and analyze the Equivalent Static Wind Loads (ESWL) for any complex spacial structures. The calculation of ESWL of super large cooling tower demonstrates and verifies the effectiveness of the present approach.

KEYWORDS: Equivalent static wind loads; resonant components; modal coupling; covariance matrix

1 INTRODUCTION

The three-dimensional structure such as large-span roofs [1] and large hyperbolic cooling towers is usually characterized by light weight, high flexibility, low damping, low natural frequency and small interval, as a typical wind sensitive structures, wind load control should be fully considered in such structural design [2], and therefore it is greatly significant to determine the ESWL in such the structures.

The response of the structure under the effects of fluctuating wind is divided into background response and resonant response based on random vibration theory, the combination of two kinds of responses can be sued to reflect the wind load mechanism; then many scholars adopted the three-component method successfully to calculate ESWL, and made continuous improvement and development on such the method [3]. however, the method hasn't effectively dealt with the selection of resonance model and coupling effect between various components [4].

Many scholars at home and abroad have studied this issue, such as: Zhou and Gu firstly adopted the three-component method to analyze Shanghai Jinmao Tower in 1998, and compared the results with that under the GLF method, and found that the results by the three-component method was more accurate [5]; Holmes proposed to adopt the LRC method in conjunction with the IWL method to calculate ESWL of large span roofs in 2002, and also developed an expression form integrating mean wind loads, background wind loads, and inertia wind load representing multiple resonant components, but this method must be based on a smooth separation between various vibration modes [6]. Chen and Kareem by learning from the seismic analysis method, express the effect of modal resonance response coupling component as a form of the independent modal contribution rate multiplied by the correlation coefficient, think that when the

correlation coefficient is relatively greater, the modal coupling is stronger, thus CQC modal response is recommended, otherwise, SRSS combination is recommended [7]; Chen and Shen by targeting POD and Ritz , made researches on the selection of main resonance mode of long-span roofs , however, they failed to make a effective solution to the coupling effect problem between different modes [8]; Xie and Ni adopted the modal wind vibration force of full CQC combination structures based on LRC, which doesn't distinguish between resonance and background components, the ESWL calculated by such a method contains any modal background, resonance and coupling components, its accuracy is compliance with the requirements, the physical significance of the calculating result by the method is not very clear because it fails to distinguish between background and resonance components[9].

In view of the above research results, in the paper, the generalized resonant modal displacement covariance matrix is derived from the structural equation of motion, then based on the IWL theory, the covariance matrix of the elastic restoring force, which only contains the resonance component is derived , on the basis of the above, it s available to calculate resonant response and ESWL by the LRC via quasi-static force method. This method proposed in the paper avoids the integral process for solving the elastic restoring force, fully considers the coupling between various resonant components, with a clear physical significance and theoretically, it applies to resonant component calculation of ESWL of any complex structure, and finally , the method is applied to wind-induced response and ESWL calculation of a typical three-dimensional structure: super large cooling towers in Ninghai Power Plant [10], the results verify its effectiveness.

2 IMPROVED CALCULATING METHOD

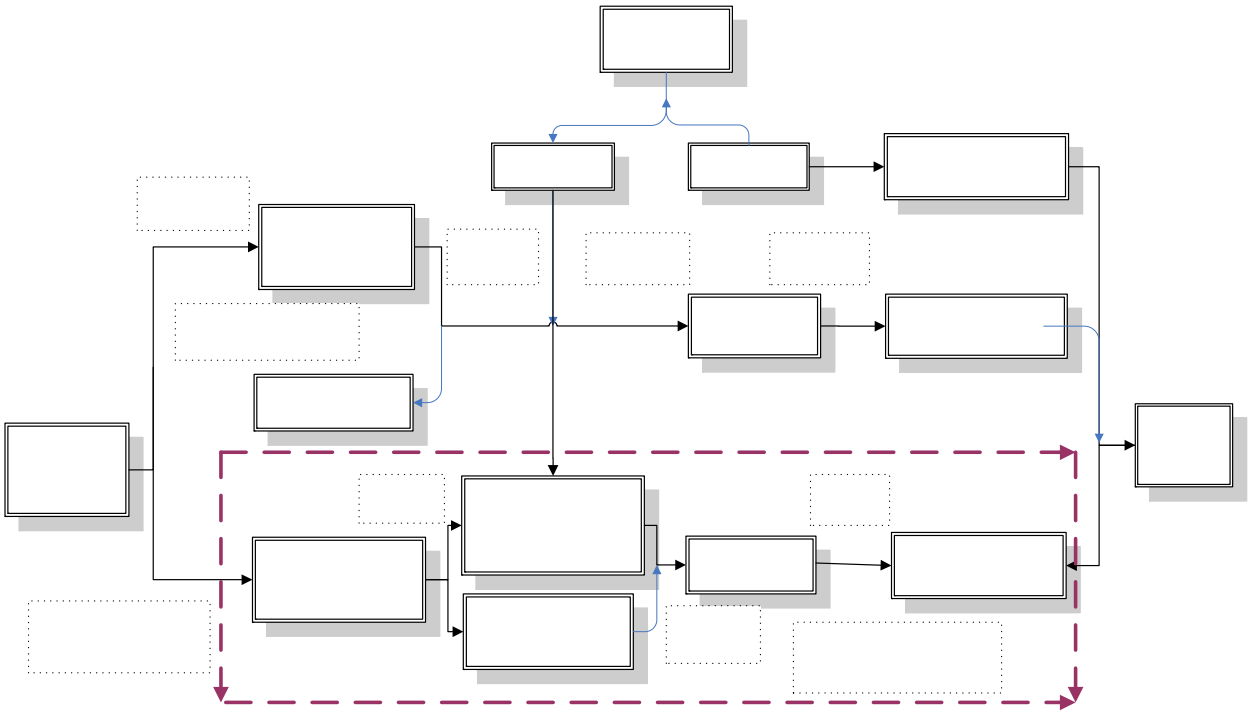

Figure 1. Theoretical framework of calculation of structural equivalent static wind load by the method proposed in the paper.

Figure 1 shows the theoretical framework of the equivalent static wind load, it is shown from the figure that the theoretical basis of the average component and background component is more clear and comprehensible, it is available to calculate it by quasi-static method, the critical step is how to extract influencing coefficient matrix, which can be obtained by the secondary development of static force via finite element software [11]. The calculation of the resonant component is mainly based on modal selection and considerations of the coupling effect between them , which is also the main problem to be solved in the paper, the calculation method of the resonance components is theoretically deduced via the following three steps.

2.1 *Generalized Resonant Modal Response Covariance Matrix*

Firstly, the parameters involved in the derivation process of the present theory are as follows: n is the number of degrees of structural freedom, m is the modal number used in the calculation, p is the number of points of excitation vector, s is the load order after POD reconstruction, ω is the circular frequency of the structure, M, C and K are respectively the quality, damping and stiffness matrix of order n, R is an n × p matrix consisting of 0 and 1, i.e., power indicator matrix, Λ = diag (ω^2_1 … ω^2_m), q is the generalized structural displacement vector, Φ is the characteristic matrix of the structure, A and D are respectively the coordinate function vector and the intrinsic modal matrix of the s and less orders before POD decomposition, I is the structural influence coefficient matrix.

Under the random excitation, the response of the structure is described by the following equation:

$$[M]\{\ddot{y}\}+[C]\{\dot{y}\}+[K]\{y\}=[R]\{p(t)\} \tag{1}$$

The response can be furthered derived via complete mode of vibration:

$$\{y(t)\}=\Phi\{q(t)\}=\sum_{i=1}^{n}\phi_i q_i(t)=\sum_{i=1}^{m}\phi_i q_i(t)+\sum_{i=m+1}^{n}\phi_i q_i(t)=\{y\}_d+\{y\}_s \tag{2}$$

In which, $\{y\ (t)\}_d$ modal contribution response of m and less orders where the resonance effect needs to be considered; $\{y\ (t)\}_s$ means only the residual modal contribution response of quasi-static effect needs to be considered.

Under $\{P\ (t)\}$ loads, its static force response is $[K]^{-1}\{P\ (t)\}$, and also can be expressed by the following equation complete vibration mode, which doesn't consider the power amplification of each vibration mode

$$[K]^{-1}\{p(t)\}=\sum_{i=1}^{n}[F]_i\{p(t)\}=\sum_{i=1}^{m}[F]_i\{p(t)\}+\sum_{i=m+1}^{n}[F]_i\{p(t)\} \tag{3}$$

In which, $[F]$ is the flexibility matrix of the i-th order vibration mode, $\{y\ (t)\}_s$ can be expressed as:

$$\{y\}_s=\sum_{i=m+1}^{n}[F]_i\{p(t)\}=[K]^{-1}\{p(t)\}-\sum_{i=1}^{m}[F]_i\{p(t)\} \tag{4}$$

Based on the equation (2), $\{y\ (t)\}$ is described with the following equation:

$$\{y(t)\} = \{y\}_d + \{y\}_s = \sum_{i=1}^{m} \phi_i q_i(t) + [K]^{-1}\{p(t)\} - \sum_{i=1}^{m} [F]_i \{p(t)\}$$

$$= \sum_{i=1}^{m} (\phi_i q_i(t) - [F]_i \{p(t)\}) + [K]^{-1}\{p(t)\}$$

(5)

Thus it's available to define resonance response with the following equation:

$$\{y(t)\}_r = \sum_{i=1}^{m} (\phi_i q_i(t) - [F]_i \{p(t)\}) \tag{6}$$

Then it is available to derive the i-th order generalized modal response that only contains the resonance component as following:

$$q_{r,i}(t) = q_i(t) - \frac{\phi_i^T \{p(t)\}}{\phi_i^T [K] \phi_i} = q_i(t) - \frac{F_i(t)}{K_i} \tag{7}$$

The cross-power spectrum of the first i-th and j-th generalized resonant modal response is:

$$S_{q_{r,i},q_{r,j}}(\omega) = \int_{-\infty}^{\infty} R_{q_{r,i},q_{r,j}}(\tau) e^{-i2\pi\omega\tau} d\tau = \int_{-\infty}^{\infty} E[q_{r,i}(t), q_{r,j}(t+\tau)] e^{-i2\pi\omega\tau} d\tau$$

$$= (H_i^*(\omega) H_j(\omega) - \frac{1}{K_i} H_j(\omega) - \frac{1}{K_j} H_i(\omega) + \frac{1}{K_i K_j}) S_{F_i,F_j}(\omega)$$

$$= (H_i^*(\omega) - \frac{1}{K_i})(H_j(\omega) - \frac{1}{K_j}) S_{F_i,F_j}(\omega) = \dot{H}_i^*(\omega) \dot{H}_j(\omega) S_{F_i,F_j}(\omega)$$

(8)

It is found from the equation (8) that the calculation of generalized resonance modal response is mainly based on how to determine the transfer function of the generalized resonance frequency response , denoted by.

Based on the above equations, the covariance matrix of generalized resonance modal response can be expressed as:

$$[C_{qq}] = \int_{-\infty}^{\infty} \dot{H}^* S_{FF} \dot{H} \, d\omega = \int_{-\infty}^{\infty} \dot{H}^* \Phi^T R D S_{AA} D^T R^T \Phi \dot{H} \, d\omega \tag{9}$$

In which, S_{AA} is the cross-power spectrum matrix of time coordinate function $A(t)$of the s and less order before POD decomposition, and is used for a reduced-order processing.

2.2 *Covariance Matrix of Elastic Restoring Force (only Containing the Resonance Component)*

By application of modal expansion theory, the elastic restoring force (only containing the resonance component) can be expressed as:

$$\{P_{eqq}\}_r = [K]\{y(t)_r\} = [K][\Phi]\{q(t)\}_r = [M][\Phi][\Lambda]\{q(t)\}_r \tag{10}$$

In combination of equation (9) and (10), the cross-covariance matrix of $\{P_{eqq}\}_r$ can be calculated as:

$$\left[C_{pp}\right]=\overline{\{P_{eqq}\}_r\{P_{eqq}\}_r}=[M][\Phi][\Lambda]\overline{\{q(t)\}_r\{q(t)\}_r}[\Lambda]^T[\Phi]^T[M]^T$$
$$=[M][\Phi][\Lambda]\left[C_{qq}\right][\Lambda]^T[\Phi]^T[M]^T$$

(11)

2.3 *LRC- Based Resonant Response and Equivalent Static Wind Load*

It is shown from the above derivation, $\{P_{eqq}\}_r$ is the elastic restoring force vector only containing the resonance component, and its precision depends on the dynamic characteristics of modal order and system adopted in the calculation of $\{q(t)\}_r$. how to solve the resonant response and equivalent static wind load is converted to how to calculate quasi-static response under $\{P_{eqq}\}_r$ effects , by the LRC principle, it is shown as:

$$\left\{r(t)\right\}_r=[I]\left\{P_{eqq}\right\}_r \tag{12}$$

When I is the flexibility matrix, $r(t)$ is the resonance response, the response covariance matrix is as following

$$\left[C_{rr}\right]=\overline{\left\{r(t)\right\}_r\left\{r(t)\right\}_r}=[I]\left[C_{pp}\right][I]^T=[I][M][\Phi][\Lambda]\left[C_{qq}\right][\Lambda]^T[\Phi]^T[M]^T[I]^T$$
$$=[I][M][\Phi][\Lambda]\int_{-\infty}^{\infty}\dot{H}^*\Phi^T RDS_{AA}D^T R^T\Phi\dot{H}\,d\omega[\Lambda]^T[\Phi]^T[M]^T[I]^T \tag{13}$$

The resonance response of the structure is

$$\boldsymbol{\sigma}_{R,r}=\sqrt{diag\left([C_{rr}]\right)}$$

(14)

In the equation, *diag(.)* is the column vector composed of diagonal elements of matrix.

The resonance ESWL responding to R_i is:

$$\boldsymbol{P}_{eBi}=\left[C_{pp}\right]\boldsymbol{I}_i^T\Big/\sigma_{Ri,r} \tag{15}$$

3 ENGINEERING APPLICATION CASES

In accordance with method proposed in the paper, the corresponding computer program DACM is built by MATLAB language, Ninghai Power Plant super large hyperbolic cooling towers, which are the highest completed towers in Asia [10], are taken as an example, the unsteady surface pressure time-histories obtained via non-rigid wind tunnel experiment are taken as incentives, POD can be adopted for reduced-order processing in the calculation of the generalized resonance modal displacement matrix.

The tower height is 177.15m, the top outer radius is 41.13m, the throat mid-surface radius is 39.11m, the air inlet mid-surface radius is 67.35m, and the diameter of 48 Y-type pillars is 1.30m. the structural modeling adopts the finite element method of the discrete structure, to discrete cooling tower wall to shell elements; the 48 pairs of Y-type pillars connecting top rigid ring and ring base are simulated by space beam elements, the Y-type pillars are fixed on bottom (see Figure 2a). all the modal information was extracted by modal analysis, the structural influencing coefficient matrix was obtained via the secondary static development. The wind tunnel test was made in the TJ-3 wind tunnel of Tongji University, the scale ratio of rigid pressure measurement

model is 1/200 (see Figure 2b), total (12 × 36 = 432) measurement points were laid out on the outside surface of tested cooling tower along the meridian and circumference (see Figure 2c) and the sampling frequency is 312.5Hz, the sampling time is 19.2s.

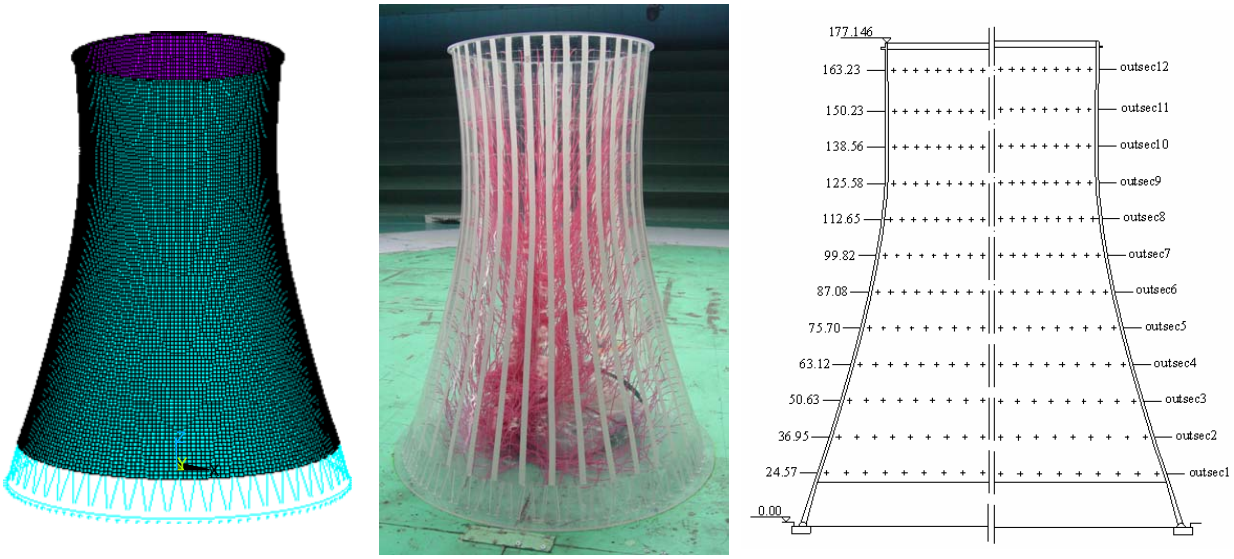

a) Finite element model b) wind tunnel model c) measurement model layout (unit: m)

Figure 2. Calculation and experimental model of cooling tower.

3.1 *Discussion on Cut-Off Modal and Coupling Effect*

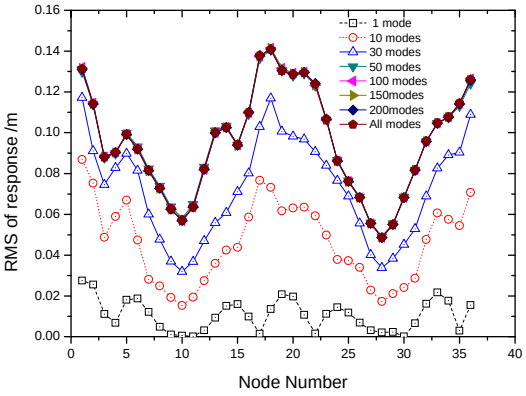

a) CQC calculation results based on different cut-off modal number

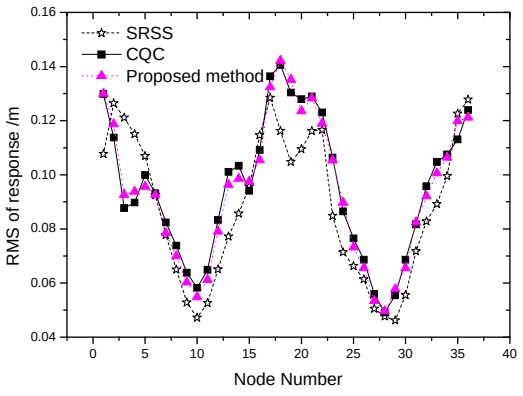

b) Comparison chart of calculation results based on SRSS, the method proposed in the paper and full-modal CQC

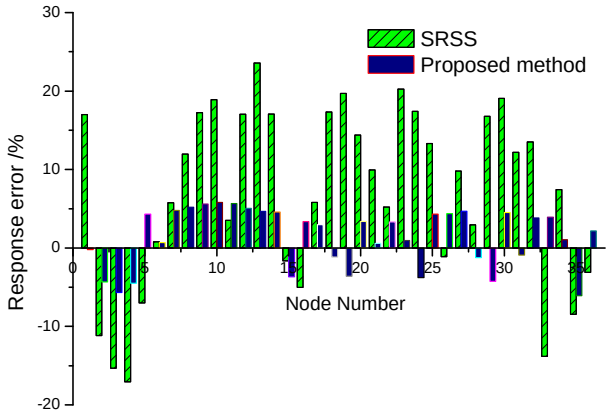

c) Comparison chart of calculation error of SRSS and the method proposed in the paper

Figure 3. Comparison chart of structural displacement response based on different calculation methods.

The wind-induced response can be calculated by adopting different orders of CQC method, and SRSS and the proposed method, and evaluated in accordance with the standard of gull-modal CQC calculated results. Figure 3a shows the CQC calculated results of different orders of tower throat circumferential section (see Figure 2c Section 10), and it is found: the first order of calculated results by GLF and IWL is far lower than actual response value, and there is no predictable pattern in the changes a pattern; as the order increases, the structural response value becomes larger, when it increases to the 50th order, the response value is stabilized and basically consistent with the result from the full modal calculations. Figure 3b and 3c shows the calculation results by the SRSS method ignoring modal coupling effects and the method proposed in this paper, as well as calculation error by the CQC method ,the ignored coupling effect makes a great influence on such a structure, the average error is about 15%, by this method, the average error is only 2%, thus the proposed method is better at considering the coupling effects between the different modes.

3.2 *Power Spectrum of Typical Node Response*

The structural wind-induced response is calculated by different orders of CQC method, the SRSS method and the method proposed in the paper, and the related calculated results are evaluated based on full- modal CQC standards. Figure 3a shows the CQC calculated results of tower throat circumferential section at different orders (see Figure 2c section 10) .

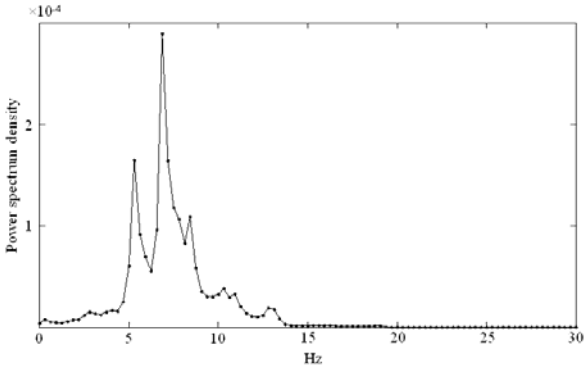

Figure 4. Functional chart of displacement power spectral density.

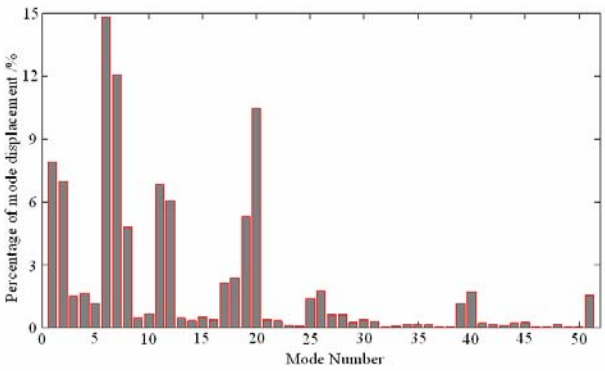

Figure 5. Proportion chart of generalized modal response value at different orders.

Figure 4 shows functional chart of displacement power spectral density of a typical node on the windward face, and it is found that the structural response is mainly resonance response the maximum resonance response is at 7Hz (corresponding to the actual frequency of 1.1Hz, corresponding with the sixth frequency). It is shown from Figure 5, the proportion chart of generalized modal response value at different orders, that the proportion of generalized modal displacement at the sixth-order accounts for the largest proportion, which is fully different with the rule for high-rise buildings and towers: the proportion of generalized modal displacement at the first-order accounts for the largest proportion; and also makes the GLF and IWL methods are no longer applicable to the wind-induced response and equivalent static wind load analysis for such this type of structures.

3.3 *Equivalent Static Wind Load*

Figure 6 compares the accurate calculated results of maximum displacement response at the tower throat circumferential section node and the corresponding displacement calculated by the static force equation under equivalent static wind loads calculated by this method applied; the results shows both two sets of displacement response are entirely consistent, and thus to further prove the effectiveness and correctness of the method proposed in the paper.

By the method proposed in the paper, it's available to calculate the ESWL corresponding to displacement response on the top of the tower, then compare the results calculated with the GBJ (IWL method) in national specification for building structure loads [12](see Figure 7), it is shown that to ignore higher order of modal contribution and coupling effect makes the calculated ESWL far less than the actual value; and on some rigid region of tower shell, the average respond is smaller or even close to zero, under this case, it is inappropriate to adopt the wind-induced vibration coefficient in the IWL method to describe the design load of the structure.

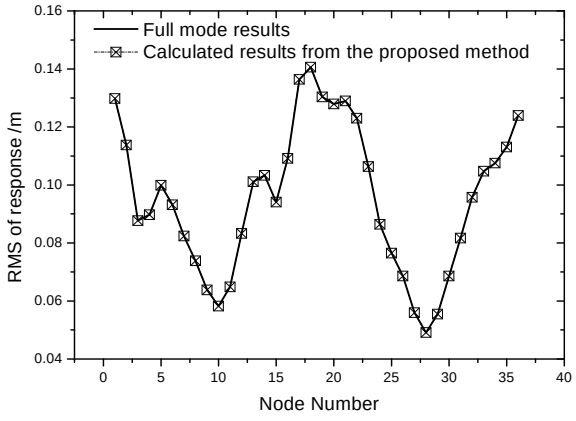

Figure 6. RMS of displacement response on throat circumferential section.

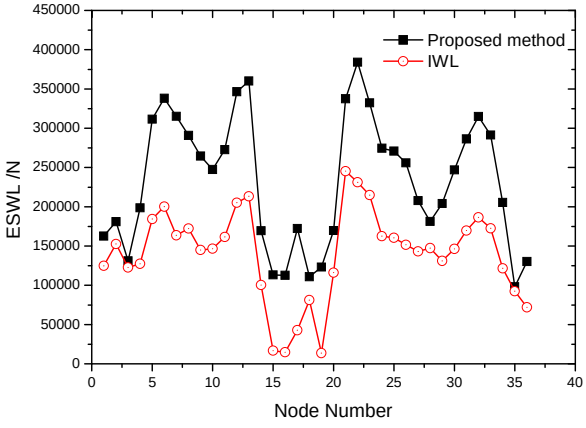

Figure 7. Profile of ESWL on throat circumferential section.

4 CONCLUSIONS

The paper focuses on the calculation of the coupling components between the resonant modes in the research on ESWL under apparent coupling effects. It derives the generalized resonant modal displacement covariance matrix and covariance matrix of elastic restoring force from structural

equation of motion, based on the multi-point simultaneous pressure test in wind tunnel, in combination with the decomposition and reduced-order of surface wind pressure by POD approach, thus integrating and expanding the LRC method again; it proposes an alternative method to account for resonant response coup ling effects; and calculates wind-induced response and ESWL based on the data of Asia's largest cooling tower, and compares calculated results between the full-modal CQC and IWL methods, thus verifies the effectiveness of the method.

It is noted that the case for calculation in the paper is equalized based on the maximum displacement, it only ensures thee accuracy of the calculation of the maximum displacement, may generate errors in calculation of the maximum internal forces. Therefore, the future research should focus on how to improve the accuracy and rationality of such consistent ESWL.

5 ACKNOWLEDGEMENTS

The authors would like to gratefully acknowledge the supports of the National Science Foundation of China (51021140005, 90815028 and 50978203), and the supports by Kwang-Hua Fund for College of Civil Engineering, Tongji University.

6 REFERENCES

1 A. Katsumura, Y. Tamura, O. Nakamura, Universal wind load distribution simultaneously reproducing largest load effects in all subject members on large-span cantilevered roof, J. Wind Eng. Ind. Aerodyn., 2007, Vol. 95, 1145-1165.
2 L. Zhao, Y.J. Ge, Wind loading characteristics of super-large cooling towers, Wind and Structures, An International Journal, 2010, Vol. 13, No. 4, pp 257-274.
3 A. G. Davenport, Gust loading factor, Journal of the Structural Division, 1967, Vol. 93, pp 11-34.
4 M. P. Repetto, G. Solari. Equivalent static wind actions on vertical structures, J. Wind Eng. Ind. Aerodyn., 2004, Vol. 92, No. 5, pp 335-357.
5 Y. Zhou, M. Gu, H. Xiang, Along wind static equivalent wind loads and responses of tall buildings, Part II: Effects of mode shapes, J. Wind Eng. Ind. Aerodyn., 1999, Vol. 79, pp 151-158.
6 J. D. Holmes. Effective static load distributions in wind engineering, J. Wind Eng. Ind. Aerodyn., 2002, Vol. 90, No. 2, pp 91-109.
7 X. Chen, A. Kareem, Equivalent static wind loads on buildings: new model, J. Struct. Eng., 2004, Vol. 130, No. 10, pp 1425-1435.
8 B. Chen, Y. Wu, S.Z. Shen, Research on determination methods for resonance component in equivalent static wind load of span roof structure, Engineering Mechanics, 2007, Vol. 24, No. 1, pp 51-55+66.
9 Z.N. Xie, Z.H. Ni, B.Q. Shi, Equivalent static wind load of span roof structure, Building Structures, 2007, Vol. 28, No. 1, pp 113-118.
10 S. T. Ke, L. Zhao, Y.J. Ge, Wind tunnel test and the response characteristics of large-sized hyperbolic cooling tower aeroelastic model, Journal of Building Structures, 2010, Vol. 31, No. 2, pp31-37.
11 M. Kasperski, H. J. Niemann. The L.R.C. (load-response-correlation) - method a general method of estimating unfavourable wind load distributions for linear and non-linear structural behaviour, J. Wind Eng. Ind. Aerodyn., 1992, pp 1753-1763.
12 GB 50009-2001. Load code for the design of building structures, Ministry of Construction of the People's Republic of China, Beijing, 2001.

The Seventh International Colloquium on Bluff Body Aerodynamics and Applications (BBAA7)
Shanghai, China; September 2-6, 2012

Study on the empirical mathematical model of nonlinear motion-induced aerodynamic force of bridge girder

Liao Haili [a], Suo Qifeng [a], Wang Qi [a]

[a] *Research Centre for Wind Engineering, Southwest Jiaotong University, Chengdu, China*

ABSTRACT: Based on Scanlan's linear model of motion-induced aerodynamic force (MIAF) on bridge deck section, a nonlinear MIAF model with independent variables of amplitude and reduced frequency is proposed by using Taylor expanding method. The model is composed of different harmonic components. For one freedom motion, there are only frequency multiplications in the expression, and for coupled motion, both also frequency multiplications and superposed frequency components are presented in the model. A special wind tunnel tests results verified the existence of high harmonic components in the MIAF of bridge girder under large amplitude of vertical or torsional motion, and the error between reconstructed curve and original curve of nonlinear MIAF history data indicated that the model can describe the nonlinear MIAF accurately. Combining with the free vibration equation of dynamic system, the nonlinear differential equation can describe the aerodynamic stability of girder under different amplitudes and reduced frequencies.

KEYWORDS: Streamline Box Girder; Nonlinear MIAF; Mathematic Model; Wind Tunnel Test

1 INTRODUCTION

The empirical model of motion-induced aerodynamic force (MIAF) on bridge girder proposed by Scanlan[1-4] has been used in flutter and buffeting analysis of long span bridges over 40 years. The model is based on the hypothesis of small displacement, the MIAF is only function of reduced frequency, and is independent of the amplitude of bridge girder. In recent years, because of the motive to understand aerodynamic behavior of long-span bridges under large displacement such as Tacoma's girder, the aerodynamic force of bridge girder under large amplitude oscillation has been concerned.

MIAF of bridge girder is nonlinear essentially. It has been found and verified in wind tunnel tests by many researchers. Noda[5] validated the effects of large amplitudes on aerodynamic derivatives of the flat plates with different thickness. Chen [6] found the high harmonic components in the spectrum of MIAF of π-section girder, and gave a preliminary quantification of nonlinear components. Falco[7] reported the clear nonlinear components in the MIAF of test section of early Messina Bridge. Based on the study of unsteady aerodynamic force of the Messina Bridge sectional model, the aerodynamic hysteresis phenomenon of bridge girder section was first observed by Diana [8-10], and indicated that the neglect of nonlinear component of aerodynamic force could lead to unsafely results in the analysis of aerodynamic stability. Liao[11] observed the aerodynamic hysteresis and the clear nonlinear components of MIAF of streamlined box girder, and found the distinct 8-shape hysteresis loops under the larger pitching amplitude up to 16 degree, which means that the aerodynamic forces can provide both the positive and negative works within one vibration period.

The study on the mathematic model of nonlinear MIAF of bridge girder could trace back to 1950s, after the collapse of Tacoma Bridge. Steinmann[12], proposed a polynomial expression to describe the nonlinear MIAF of H-shape girder of Tacoma Bridge based on the wind tunnel test result, with independent variable of torsional angle and angular velocity. Xu[13] gave a unsteady expression of nonlinear aerodynamic force of flexible and long-span structure by defining the instantaneous incident angle. Based on the instantaneous incident angle and its velocity, Diana [10,14,15] gave an empirical polynomial expression to describe the nonlinear aerodynamic force of bridge girder. Chen[16] based on the soft flutter phenomenon of long-span bridge, used Von Del Pol oscillator to describe the nonlinear MIAF of bridge girder. Wu[17] based on the nonlinear response of bridge, put forward an nonlinear aerodynamic force model using Volterra Series. In these nonlinear aerodynamic force models of bridge girder, Steinmann's expression is too simple to describe the aerodynamic exactly. Xu's model is too complex to be applicable in analysis, and didn't give the identification method of nonlinear variable. Diana's rheological model could describe the nonlinear aerodynamic force from test data exactly, but can't interpret the large amplitude oscillation in the post flutter of Tacoma Bridge. Chen's model ignored the unsteady of nonlinear MIAF, and also implied that there is only the third harmonic in the MIAF.

In this paper, a nonlinear MIAF expressions with independent variables of amplitude and reduced frequency were deduced by using Taylor expanding method. The empirical mathematic model of nonlinear MIAF is composed with different harmonic components. For one freedom motion, there are only frequency multiplications in the model, and for coupled motion, both also frequency multiplications and superposed frequency components are presented in the model. A special wind tunnel tests were conducted, with a 1:50 scale section model of the streamline box girder and more than 150 test cases, and MIAF of the model under different amplitudes and reduced frequencies conditions were obtained. The test results verified the existence of high harmonic components in the MIAF of bridge girder under large amplitude of vertical or torsional motion, and the high harmonic components were more remarkable spatially in a large incidence angle condition. The error between fitting curve and original curve of nonlinear MIAF history data indicated that this empirical mathematical model can describe the nonlinear MIAF accurately. Combining with the free vibration equation of dynamic system, the nonlinear differential equation can describe the aerodynamic stability of girder under different amplitudes and reduced frequencies.

2 EMPIRICAL MATHEMATIC MODEL OF NONLINEAR MIAF

2.1 *Taylor expanding expression*

Aerodynamic force on bridge section in smooth flow is the function of motion state variables, which is defined as a sum of the mean static force, and MIAF. The aerodynamic force, i.e., lift and pitching moment (upward and nose up) components per unit length are expressed as follows:

Lift: $$L = \frac{1}{2}\rho U^2 B C_L(\dot{h}, h, \dot{\alpha}, \alpha) \tag{1a}$$

Pitching Moment: $$M = \frac{1}{2}\rho U^2 B^2 C_M(\dot{h}, h, \dot{\alpha}, \alpha) \tag{1b}$$

Where ρ= air density; U= mean wind velocity; B= the bridge deck width; C_L and C_M = lift and pitching moment coefficients of one moment, respectively, which are the function of motion state variables as displacement h,α, and velocity $\dot{h},\dot{\alpha}$ in vertical and torsional freedom.

If the nonlinear aerodynamic force exists n+1 order derivative, the n order Taylor Series could be obtained at equilibrium position by expanding. Because the aerodynamic coefficients are dominant variables in the expressions, its Taylor expanding expression can represent the main characteristics aerodynamic force. Taking an example of lift coefficient, its Taylor expanding is as follow:

$$\begin{aligned} C_L &= C_L(\dot{h}_0,h_0,\dot{\alpha}_0,\alpha_0)+(\frac{\partial}{\partial\dot{h}}\dot{h}+\frac{\partial}{\partial\dot{\alpha}}\dot{\alpha}+\frac{\partial}{\partial h}h+\frac{\partial}{\partial\alpha}\alpha)C_L(\dot{h}_0,h_0,\dot{\alpha}_0,\alpha_0) \\ &+\frac{1}{2!}(\frac{\partial}{\partial\dot{h}}\dot{h}+\frac{\partial}{\partial\dot{\alpha}}\dot{\alpha}+\frac{\partial}{\partial h}h+\frac{\partial}{\partial\alpha}\alpha)^2 C_L(\dot{h}_0,h_0,\dot{\alpha}_0,\alpha_0) \\ &+\cdots+\frac{1}{n!}(\frac{\partial}{\partial\dot{h}}\dot{h}+\frac{\partial}{\partial\dot{\alpha}}\dot{\alpha}+\frac{\partial}{\partial h}h+\frac{\partial}{\partial\alpha}\alpha)^n C_L(\dot{h}_0,h_0,\dot{\alpha}_0,\alpha_0)+R_n \end{aligned} \tag{2}$$

Where the 1st term $C_L(\dot{h}_0,h_0,\dot{\alpha}_0,\alpha_0)$ = mean static, the 2nd term = the linear term of MIAF, and the 3rd term and above ones, are the nonlinear terms of MIAF, R_n= residual term.

For single freedom motion of the girder, for example vertical motion, lift coefficient could be written as the following if keeping the first three terms only,

$$\begin{aligned} C_L &= \frac{\partial C_L}{\partial\dot{h}}\dot{h}+\frac{\partial C_L}{\partial h}h+\frac{1}{2}\frac{\partial^2 C_L}{\partial\dot{h}^2}\dot{h}^2+\frac{\partial^2 C_L}{\partial\dot{h}\partial h}\dot{h}h+\frac{1}{2}\frac{\partial^2 C_L}{\partial h^2}h^2+\frac{1}{6}\frac{\partial^3 C_L}{\partial\dot{h}^3}\dot{h}^3+\frac{1}{2}\frac{\partial^3 C_L}{\partial\dot{h}^2\partial h}\dot{h}^2h+\frac{1}{2}\frac{\partial^3 C_L}{\partial\dot{h}\partial h^2}\dot{h}h^2+\frac{1}{6}\frac{\partial^3 C_L}{\partial h^3}h^3 \\ &= C^1_{\dot{h}}\dot{h}+C^1_h h+C^2_{\dot{h}^2}\dot{h}^2+C^2_{\dot{h}h}\dot{h}h+C^2_{h^2}h^2+C^3_{\dot{h}^3}\dot{h}^3+C^3_{\dot{h}h^2}\dot{h}^2h+C^3_{h^2\dot{h}}\dot{h}h^2+C^3_{h^3}h^3 \end{aligned} \tag{3}$$

Where C^n_m = nonlinear coefficients, and n=1~3, m= $h^k\dot{h}^l$, and k=0~3, l=0~3. C^n_m is the function of amplitude and reduced frequency K.

For the vertical and pitching coupled motion, the lift coefficient, if keeping the first two terms only, can be written as:

$$\begin{aligned} C_L &= \frac{\partial C_L}{\partial\dot{h}}\dot{h}+\frac{\partial C_L}{\partial h}h+\frac{\partial C_L}{\partial\dot{\alpha}}\dot{\alpha}+\frac{\partial C_L}{\partial\alpha}\alpha \\ &+\frac{1}{2}\frac{\partial^2 C_L}{\partial\dot{h}^2}\dot{h}^2+\frac{1}{2}\frac{\partial^2 C_L}{\partial h^2}h^2+\frac{1}{2}\frac{\partial^2 C_L}{\partial\dot{\alpha}^2}\dot{\alpha}^2+\frac{1}{2}\frac{\partial^2 C_L}{\partial\alpha^2}\alpha^2 \\ &+\frac{\partial^2 C_L}{\partial\dot{h}\partial h}\dot{h}h+\frac{\partial^2 C_L}{\partial\dot{\alpha}\partial\alpha}\dot{\alpha}\alpha+\frac{\partial^2 C_L}{\partial\alpha\partial\dot{h}}\alpha\dot{h}+\frac{\partial^2 C_L}{\partial\dot{\alpha}\partial h}\dot{\alpha}h+\frac{\partial^2 C_L}{\partial\alpha\partial h}\alpha h+\frac{\partial^2 C_L}{\partial\dot{\alpha}\partial\dot{h}}\dot{\alpha}\dot{h} \\ &= C^1_{\dot{h}}\dot{h}+C^1_h h+C^1_{\dot{\alpha}}\dot{\alpha}+C^1_\alpha\alpha+C^2_{\dot{h}^2}\dot{h}^2+C^2_{h^2}h^2+C^2_{\dot{\alpha}^2}\dot{\alpha}^2+C^2_{\alpha^2}\alpha^2 \\ &\quad+C^2_{\dot{h}h}\dot{h}h+C^2_{\dot{\alpha}\alpha}\dot{\alpha}\alpha+C^2_{\alpha\dot{h}}\alpha\dot{h}+C^2_{\dot{\alpha}h}\dot{\alpha}h+C^2_{\alpha h}\alpha h+C^2_{\dot{\alpha}\dot{h}}\dot{\alpha}\dot{h} \end{aligned} \tag{4}$$

Where C^n_m = nonlinear coefficients, and comparing with the Eq.3, the C^n_m adds more terms, here m= $h^k\dot{h}^l$ and $\alpha^k\dot{\alpha}^l$, and the coupled terms $h^k\dot{\alpha}^l$ and $\alpha^k\dot{h}^l$ imply the frequency superposition of aerodynamic force in different motions. One in particular is that the nonlinear coefficients are obtained only in the steady harmonic vibration, not in the arbitrary motion.

2.2 *Plural expression*

For harmonic oscillation with frequency ω at a given wind speed (taking an example of vertical motion)

$$h = h_0 e^{i\omega t},\quad \dot{h} = i\omega h,\quad i = \sqrt{-1} \tag{5a}$$

The 2nd order variables in Eq.3 are:

$$h^2 = h_0^2 e^{i2\omega t},\quad \dot{h}h = i\omega h_0^2 e^{i2\omega t},\quad \dot{h}^2 = -\omega^2 h_0^2 e^{i2\omega t} \tag{5b}$$

The 3rd order variables in Eq.3 are:

$$h^3 = h_0^3 e^{i3\omega t},\quad \dot{h}h^2 = i\omega h_0^3 e^{i3\omega t},\quad \dot{h}^2 h = -\omega^2 h_0^3 e^{i3\omega t},\quad \dot{h}^3 = -i\omega h_0^3 e^{i3\omega t} \tag{5c}$$

The above motion variables can be replaced with $\alpha = \alpha_0 e^{i\omega t}$ for torsional motion.

Replacing the motion variables in Eq.3 by the Eq.5a-5c, the first term in the new equation is as follows:

$$C_L^1 = \frac{\partial C_L}{\partial \dot{h}} i\omega h + \frac{\partial C_L}{\partial h} h = 2K^2 (iH_1^* + H_4^*)\frac{h}{B} = (iH_1^{1\#} + H_4^{1\#}) h_{r0} e^{i\omega t} \tag{6a}$$

Where $H_1^{1\#} = 2K^2 H_1^*$, $H_4^{1\#} = 2K^2 H_4^*$ are defined as the 1st order harmonic component aerodynamic derivatives of lift coefficient; $h_{r0} = h_0 / B$, is the reduced amplitude in vertical; H_1^* and H_4^* are aerodynamic derivatives.

Similarly, the second term is:

$$C_L^2 = (iH_1^{2\#} + H_4^{2\#})(h/B)^2 = (iH_1^{2\#} + H_4^{2\#})(h_{r0})^2 e^{i2\omega t} \tag{6b}$$

Where $H_1^{2\#} = \omega B^2 \frac{\partial^2 C_L}{\partial \dot{h} \partial h}$, $H_4^{2\#} = \frac{1}{2} B^2 (\frac{\partial^2 C_L}{\partial h^2} - \omega^2 \frac{\partial^2 C_L}{\partial \dot{h}^2})$, are defined as the 2nd order harmonic component aerodynamic derivatives of lift coefficient.

The third term is:

$$C_L^3 = (iH_1^{3\#} + H_4^{3\#})(h/B)^3 = (iH_1^{3\#} + H_4^{3\#})(h_{r0})^3 e^{i3\omega t} \tag{6c}$$

Where $H_1^{3\#} = \frac{1}{6} B^3 (3\omega \frac{\partial^3 C_L}{\partial \dot{h} \partial h^2} - \omega^3 \frac{\partial^3 C_L}{\partial \dot{h}^3})$, $H_4^{3\#} = \frac{1}{6} B^3 (\frac{\partial^3 C_L}{\partial h^3} - 3\omega^2 \frac{\partial^3 C_L}{\partial \dot{h}^2 \partial h})$, are defined as the 3rd order harmonic component aerodynamic derivatives of lift coefficient.

For a given amplitude and reduced frequency *K*, the lift coefficient in Eq.3 can be expressed as,

$$C_L^V = (iH_1^{1\#} + H_4^{1\#}) h_{r0} e^{i\omega t} + (iH_1^{2\#} + H_4^{2\#}) h_{r0}^2 e^{i2\omega t} + (iH_1^{3\#} + H_4^{3\#}) h_{r0}^3 e^{i3\omega t} \tag{7a}$$

In which superscript *V* indicates the vertical motion condition.

Similarly, the pitching moment due to vertical motion can be expressed as:

$$C_M^V = (iA_1^{1\#} + A_4^{1\#}) h_{r0} e^{i\omega t} + (iA_1^{2\#} + A_4^{2\#}) h_{r0}^2 e^{i2\omega t} + (iA_1^{3\#} + A_4^{3\#}) h_{r0}^3 e^{i3\omega t} \tag{7b}$$

Where $A_1^{j\#}$ and $A_4^{j\#}$ are the pitching moment coefficient aerodynamic derivatives corresponding to the j^{th} order harmonic component.

If the girder's motion is only in torsional, the aerodynamic lift coefficient and pitching moment coefficient can be similarly deduced as follows:

$$C_L^T = (iH_2^{1\#} + H_3^{1\#}) \alpha_0 e^{i\omega t} + (iH_2^{2\#} + H_3^{2\#}) \alpha_0^2 e^{i2\omega t} + (iH_2^{3\#} + H_3^{3\#}) \alpha_0^3 e^{i3\omega t} \tag{7c}$$

$$C_M^T = (iA_2^{1\#} + A_3^{1\#}) \alpha_0 e^{i\omega t} + (iA_2^{2\#} + A_3^{2\#}) \alpha_0^2 e^{i2\omega t} + (iA_2^{3\#} + A_3^{3\#}) \alpha_0^3 e^{i3\omega t} \tag{7d}$$

Where $H_2^{j\#}$ and $H_3^{j\#}$, $A_2^{j\#}$ and $A_3^{j\#}$, are the lift and pitching moment coefficient aerodynamic derivatives corresponding to the j^{th} order harmonic component. The superscript T indicates the pitching motion condition. The real parts indicate the nonlinear aerodynamic stiffness terms, and the imaginary parts indicate the nonlinear aerodynamic damping terms.

Comparing with the conventional linear model, the 1st order harmonic aerodynamic derivatives $H_k^{1\#}, A_k^{1\#}(k=1\sim 4)$ in Eq.7a-7d , can be written as

$$H_1^{1\#}=2K^2H_1^*,\quad H_4^{1\#}=2K^2H_4^*,\quad A_1^{1\#}=2K^2A_1^*,\quad A_4^{1\#}=2K^2A_4^* \tag{8a}$$

$$H_2^{1\#}=2K^2H_2^*,\quad H_3^{1\#}=2K^2H_3^*,\quad A_2^{1\#}=2K^2A_2^*,\quad A_3^{1\#}=2K^2A_3^* \tag{8b}$$

Where, $H_k^*, A_k^*(k=1\sim 4)$ are the usual aerodynamic derivatives defined by Scanlan.

According to the Taylor expanding, the complex expressions of lift and pitching moment under coupled motion (only keeping the 2nd order harmonic components)

$$\begin{aligned}C_L=&(iH_1^{1\#}+H_4^{1\#})h_{r0}e^{i\omega_1 t}+(iH_1^{2\#}+H_4^{2\#})h_{r0}^2e^{i2\omega_1 t}+(iH_2^{1\#}+H_3^{1\#})\alpha_0e^{i\omega_2 t}+(iH_2^{2\#}+H_3^{2\#})\alpha_0^2e^{i2\omega_2 t}\\&+(iH_{12}^{2\#}+H_{34}^{2\#})h_{r0}\alpha_0e^{i(\omega_1+\omega_2)t}\end{aligned} \tag{9a}$$

$$\begin{aligned}C_M=&(iA_1^{1\#}+A_4^{1\#})h_{r0}e^{i\omega_1 t}+(iA_1^{2\#}+A_4^{2\#})h_{r0}^2e^{i2\omega_1 t}+(iA_2^{1\#}+A_3^{1\#})\alpha_0e^{i\omega_2 t}+(iA_2^{2\#}+A_3^{2\#})\alpha_0^2e^{i2\omega_2 t}\\&+(iA_{12}^{2\#}+A_{34}^{2\#})h_{r0}\alpha_0e^{i(\omega_1+\omega_2)t}\end{aligned} \tag{9b}$$

Where, $H_{12}^{2\#}$ and $H_{34}^{2\#}$ had been defined as the velocity coupling aerodynamic derivative and the displacement coupling aerodynamic derivative, corresponding with the 2nd order harmonic component; ω_1 and ω_2 are the vertical and torsional circle frequency respectively.

Comparing to the 2nd order expression of single freedom motion, there are not only frequency multiplication of independent freedom motion, but also frequency superposition of coupled freedom motion in MIAF. Because of the difference between the amplitude and frequency of the two different motions, the MIAF becomes more complicated due to the non-multiplications.

2.3 *Harmonic expression*

Considering the application of the nonlinear MIAF expressions, the plural expressions need to be transfer to the real expression using Euler's formula. Taking lift coefficient in vertical motion as an example, Eq.6a could be written as:

$$(iH_1^{1\#}+H_4^{1\#})h_{r0}e^{i\omega t}=X_{LV}^1h_{r0}\cos(\omega t+\theta)+iX_{LV}^1h_{r0}\sin(\omega t+\theta)\,. \tag{10}$$

where: $X_{LV}^1=\left|iH_1^{1\#}+H_4^{1\#}\right|$, $\theta_{LV}^1=\tan^{-1}(\dfrac{H_1^{1\#}}{H_4^{1\#}})$

The real part and imaginary part can be chosen according to the application. In this paper the imaginary part had been chosen i.e. the sinusoidal motion is assumed, and the transfer expressions of Eq.7a-7d are as follows,

$$C_L^V=X_{LV}^1h_{r0}\sin(\omega t+\theta_{LV}^1)+X_{LV}^2h_{r0}^2\sin(2\omega t+\theta_{LV}^2)+X_{LV}^3h_{r0}^3\sin(3\omega t+\theta_{LV}^3) \tag{11a}$$

Where, $X_{LV}^j=\left|iH_1^{j\#}+H_4^{j\#}\right|$, $\theta_{LV}^j=\tan^{-1}(\dfrac{H_1^{j\#}}{H_4^{j\#}})$, j=1~3

$$C_M^V=X_{MV}^1h_{r0}\sin(\omega t+\theta_{MV}^1)+X_{MV}^2h_{r0}^2\sin(2\omega t+\theta_{MV}^2)+X_{MV}^3h_{r0}^3\sin(3\omega t+\theta_{MV}^3). \tag{11b}$$

Where, $X_{MV}^{j}=\left|iA_1^{j\#}+A_4^{j\#}\right|$, $\theta_{MV}^{j}=\tan^{-1}(\frac{A_1^{j\#}}{A_4^{j\#}})$, j=1~3

$$C_L^T=X_{LT}^1\alpha_0\sin(\omega t+\theta_{LT}^1)+X_{LT}^2\alpha_0^2\sin(2\omega t+\theta_{LT}^2)+X_{LT}^3\alpha_0^3\sin(3\omega t+\theta_{LT}^3) \quad (11c)$$

Where, $X_{LT}^{j}=\left|iH_2^{j\#}+H_3^{j\#}\right|$, $\theta_{LT}^{j}=\tan^{-1}(\frac{H_2^{j\#}}{H_3^{j\#}})$, j=1~3

$$C_M^T=X_{MT}^1\alpha_0\sin(\omega t+\theta_{MT}^1)+X_{MT}^2\alpha_0^2\sin(2\omega t+\theta_{MT}^2)+X_{MT}^3\alpha_0^3\sin(3\omega t+\theta_{MT}^3) \quad (11d)$$

Where, $X_{MT}^{j}=\left|iA_2^{j\#}+A_3^{j\#}\right|$, $\theta_{MT}^{j}=\tan^{-1}(\frac{A_2^{j\#}}{A_3^{j\#}})$, j=1~3

For the coupled motion, assume the following relation of two motions,

$h_{r0}=\lambda\alpha_0$, $\omega_1=\gamma\omega_2$

The lift can be written as:

$$\begin{aligned}C_L&=X_{LV}^1\lambda\alpha_0\sin(\gamma\omega_2 t+\theta_{LV}^1)+X_{LV}^2\lambda^2\alpha_0^2\sin(2\gamma\omega_2 t+\theta_{LV}^2)+X_{LT}^1\alpha_0\sin(\omega_2 t+\theta_{LT}^1)\\&+X_{LT}^2\alpha_0^2\sin(2\omega_2 t+\theta_{LT}^2)+X_{LVT}^2\lambda\alpha_0^2\sin[(1+\gamma)\omega_2 t+\theta_{LVT}^2]\end{aligned} \quad (12a)$$

Where, $X_{LV}^{j}=\left|iH_1^{j\#}+H_4^{j\#}\right|$, $\theta_{LV}^{j}=\tan^{-1}(\frac{H_1^{j\#}}{H_4^{j\#}})$; $X_{LT}^{j}=\left|iH_2^{j\#}+H_3^{j\#}\right|$, $\theta_{LT}^{j}=\tan^{-1}(\frac{H_2^{j\#}}{H_3^{j\#}})$, j=1~2;

$X_{LVT}^{2}=\left|iH_{12}^{2\#}+H_{34}^{2\#}\right|$, $\theta_{LVT}^{2}=\tan^{-1}(\frac{H_{12}^{2\#}}{H_{34}^{2\#}})$

And the pitching moment can be written as

$$\begin{aligned}C_M&=X_{MV}^1\lambda\alpha_0\sin(\gamma\omega_2 t+\theta_{MV}^1)+X_{MV}^2\lambda^2\alpha_0^2\sin(2\gamma\omega_2 t+\theta_{MV}^2)\\&+X_{MT}^1\alpha_0\sin(\omega_2 t+\theta_{MT}^1)+X_{MT}^2\alpha_0^2\sin(2\omega_2 t+\theta_{MT}^2)\\&+X_{MVT}^2\lambda\alpha_0^2\sin[(1+\gamma)\omega_2 t+\theta_{MVT}^2]\end{aligned} \quad (12b)$$

Where, $X_{MV}^{j}=\left|iA_1^{j\#}+A_4^{j\#}\right|$, $\theta_{MV}^{j}=\tan^{-1}(\frac{A_1^{j\#}}{A_4^{j\#}})$; $X_{MT}^{j}=\left|iA_2^{j\#}+A_3^{j\#}\right|$, $\theta_{MT}^{j}=\tan^{-1}(\frac{A_2^{j\#}}{A_3^{j\#}})$, j=1~2;

$X_{MVT}^{2}=\left|iA_{12}^{2\#}+A_{34}^{2\#}\right|$, $\theta_{MVT}^{2}=\tan^{-1}(\frac{A_{12}^{2\#}}{A_{34}^{2\#}})$

Eqs.11a-11d and Eqs. 12a-12b show clearly that, if the motion of bridge girder is the sinusoidal or cosine, the nonlinear MIAF is composed of different frequency multiplication components for single freedom motion, and is composed of different multiplication and non-multiplication components under coupled motion. The amplitude indicates the value of different harmonic components, and the initial phase indicates the lag. These equations also indicate that, if amplitude and the initial phase of different harmonic components are known, the nonlinear coefficients can be calculated.

2.4 *Discussion*

The configuration of bridge girder determines its aerodynamic property, and the proportions of harmonic components in nonlinear MIAF are different while the girder sections are different. As to the same bridge girder section, the proportions of harmonic components in nonlinear MIAF are different while the amplitudes are different, because of the distinct change of aerodynamic

configuration during oscillation. Even for the same bridge girder section and the same amplitude, the proportions of harmonic components in nonlinear MIAF are also different while the reduced frequencies are different, because of the distinct difference in flow fields under different *K*. Thus the nonlinear aerodynamic parameters in the expression are sensitive to motion and flow conditions. The selection of order in MIAF model should base on the wind tunnel tests. For example if there is only the 3rd order harmonic in the nonlinear MIAF signal derived from testing, the 3rd order components can be kept.

3 IDENTIFICATION OF NONLINEAR AERODYNAMIC COEFFICIENTS

3.1 *Expression of nonlinear aerodynamic coefficients*

Under the condition of the given amplitude and reduced frequency, Eq.3 and Eq.11a describe the same MIAF, so the nonlinear aerodynamic coefficient in Eq.3 can be expressed by using the amplitude and initial phase. Based on the nonlinear MIAF obained from the wind tunnel tests under a given condition, the nonlinear aerodynamic coefficients $C^k_{\dot{h}^m h^n}$ (k=1~3,m,n=0~3) in Eq.3 can be described as

$$C^k_{\dot{h}^m h^n} = \frac{X^k_{VL} k!}{\omega^m} \sin(\theta^k_{VL} + \frac{n\pi}{2}) \tag{13}$$

Where, k=1,2……n, is the order of nonlinear harmonic components; m and n is the nonlinear aerodynamic coefficient order which represents the derivative order of velocity and displacement. X^k_{VL} is the amplitude of the K^{th} order vertical lift harmonic component and the θ^k_{VL} is the initial phase.

3.2 *Identification method*

The nonlinear coefficients in Eq.3 can be identified by least-square method. Based on the original signal obtained from test, one can identify the amplitude X^k_{VL} and initial phase θ^k_{VL} of different harmonic components by using FFT method, but these coefficients can't reconstruct the nonlinear MIAF due to the unacceptable errors. If taking those X^k_{VL} and θ^k_{VL} as the initial values and then applying the least-square method, the exact amplitude X^k_{VL} and initial phase θ^k_{VL} of different harmonic components can be found. It is noted that if the original signal was contaminated by noise, a signal process is definitely required to minimize or eliminate the influence.

3.3 *Examples*

To demonstrate the identification method and verify its accuracy, a sinusoidal signal composed of five order harmonic components with different amplitude and initial phase are constructed.

$$\begin{aligned} X = {} & A_1 \sin(\omega t + P_1) \\ & + A_2 \sin(2\omega t + P_2) + A_3 \sin(3\omega t + P_3) \\ & + A_4 \sin(4\omega t + P_4) + A_5 \sin(5\omega t + P_5) \end{aligned} \tag{14}$$

Where ω= 11.3097 rad/s, A_j= amplitude, P_j= initial phase, j=1~5, the values are shown in Table 1. Table 2 gives the results of identified parameters in Eq.14. The results show that the identification method can minimize the error between identification value and given value, and also can reconstruct the original signal.

Table 1 The amplitude and initial values in Eq.14

amplitude	A_1	A_2	A_3	A_4	A_5
values	2	0.4	0.3	0.2	0.1
Initail phase	P_1	P_2	P_3	P_4	P_5
values	π/4	π/5	π/6	π/7	π/8

Table 2 The identified parameters of Eq.14

Amplitude	*A1*	*A2*	*A3*	*A4*	*A5*
Given values	2	0.4	0.3	0.2	0.1
Identified values	2.0021	0.3982	0.2975	0.1961	0.0954
Error	0.11%	–0.45%	–0.83%	–1.95%	–4.60%
Identified values (LSM)	2.0004	0.3993	0.2983	0.1978	0.0972
Error	0.02%	–0.18%	–0.57%	–1.10%	–2.80%
Initial phase	*P1*	*P2*	*P3*	*P4*	*P5*
Given values	π/4	π/5	π/6	π/7	π/8
Identified values	0.7886	0.6618	0.8199	–0.2035	–0.0266
Error	0.41%	5.33%	56.59%	–145.34%	–106.77%
Identified values (LSM)	0.7854	0.6284	0.5237	0.4489	0.3929
Error	0.00%	0.01%	0.02%	0.02%	0.05%

4 WIND TUNNEL TEST

To obtain nonlinear MIAF and assess its characteristic, tests were conducted in Φ3.2m wind tunnel of Low speed Aerodynamics Institute, China Aerodynamics Research and Development Center (CARDC).A model with streamline box girder section (0.776m wide, 1.2m long) was tested in this study, which was made of glass fiber reinforced plastics to ensure the adequate stiffness and minimal mass and mass moment of inertia. The test model was fixed on the rigid holder and drive by the actuating motor. The drawing of the model is shown in Fig.1. The inertia force , static force and MIAF were acquired through a strain balance directly, and the pure MIAF was obtained by subtracting the inertial force(acquired at the same motion state under windless condition) and static force (mean value of the aerodynamic force).

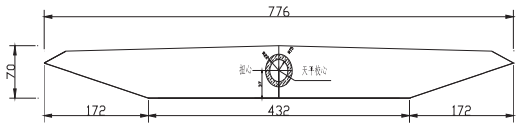

Fig 1 The cross-section of test model

Fig. 2 shows the aerodynamic coefficients in time domain and frequency domain, for the motion condition torsional n with amplitude 20°and at reduced frequency 0.35. In time domain, the pitching motion of models can be described by $\alpha = \alpha_0 \cos(2\pi ft)$, and for the pitching motion $h = h_0 \cos(2\pi ft)$. When the pitching angle is up to 20deg, the coefficient of aerodynamic moment is a distortional wave with high order harmonics, which can be seen clearly on spectrum (Fig. 2). The 2nd and the 3rd order components are so clear that have become the dominant components in high harmonics. On the other hand, with increasing of oscillation amplitude, the high-order har-

monics plays a more and more important role. The similar results had been obtained in the vertical motion tests. The error between original signal and reproduced signal is shown in Fig. 3.

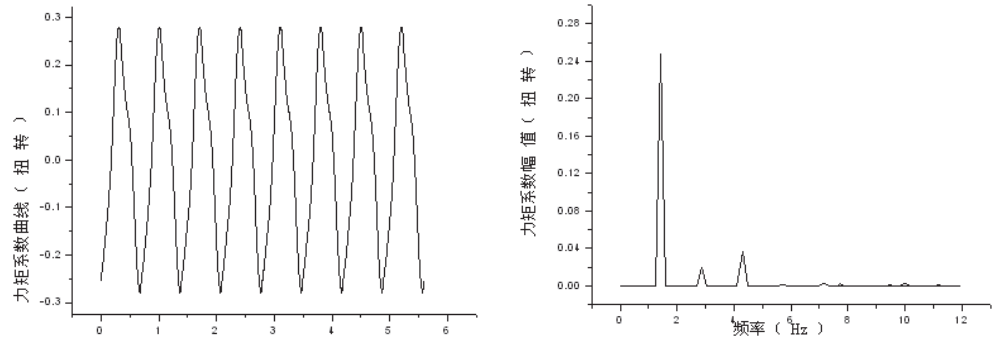

Fig 2. The aerodynamic moment coefficient history curve and spectrum under torsional motion（α_0=20°, K=0.35）

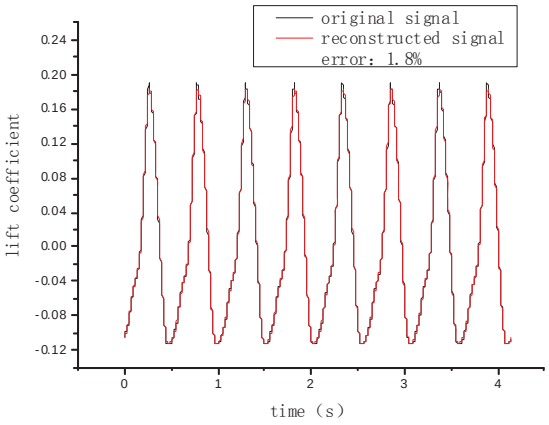

Fig.3 The original and reconstructed lift time history of streamline box girder（α_0=10°, K=0.628）

5 CONCLUSIONS

The nonlinear MIAF expressions with independent variables of amplitude and reduced frequency are deduced by using Taylor expanding method, which is composed of different harmonic components. Wind tunnel tests results verified the existence of high harmonic components in the MIAF of bridge girder, and the error between reconstructed curve and original curve indicated that the model can describe the nonlinear MIAF accurately.

6 ACKNOWLEDGEMENTS

The paper is based on the project, *The study on nonlinear motion-induced aerodynamic force and nonlinear aerodynamic stability of long-span bridge*, which supported by the Major Research plan of the National Natural Science Foundation of China (Grant No. 90815016).

7 REFERENCES

[1] Scanlan R H, Tomko J. 1971. Airfoil and bridge deck flutter derivatives. J. Engrg.Mech.Div., ASCE, 97(6): 1717～1737.
[2] Scanlan R H, Gade, R H. 1977.Motion of suspended bridge spans under gusty wind. J. Struct. Div., ASCE., 103ST9: 1867-1883
[3] Scanlan R H. 1978a. The action of flexible bridges under wind I: Flutter theory. J. Sound and Vibration. 60(2): 187-199
[4] Scanlan R H. 1978b. The action of flexible bridges under wind II: buffeting theory. J. Sound and Vibration, 60(2): 201-211
[5] Noda M. et al.2003. Effects of oscillation amplitude on aerodynamic derivatives. Journal of Wind Engineering and Industrial Aerodynamics 91, 101-111.
[6] Chen Z. et al. 2002. A New Method for Measuring Flutter Self-Exited Forces of Long-span Bridges[J]. China Civil Engineering Journal. 35(5):34-41.
[7] Falco M; Curami A; Zasso A. Nonlinear effects in sectional model aeroelastic parameter identification[J]. J. Wind Eng. & Ind. Aerodynamics, 41-44:1321－1332, 1992.
[8] Diana G., Bruni, S., Rocchi, D., A numerical and experimental investigation on aerodynamic nonlinearity in bridge response to turbulent wind[C]. In: Proceedings of the EACWE 4, Prague CR. 2005.
[9] Diana G, et al. A new approach to model the aeroelastic response of bridges in time domain by means of a rheological model[C], Proceedings of the 12th ICWE. Cairns, Australia, 2007.
[10] Diana G, et al.. Aerodynamic hysteresis: wind tunnel tests and numerical implementation of a fully nonlinear model for the bridge aeroelastic forces[C]. Proceedings of the 4th International Conference on Advance in Wind and Structural-08, 944-960. Jeju, Korea.2008
[11] Liao H., Wang Q.. Aerodynamic hysteresis effects of thin airfoil and streamline box girder under large amplitude oscillation[C]. In: Proceedings of the ICWE 13, Amsterdam NL., 2011
[12] Steinmann D. G., Hangebrücken-Das aerodynamicsche problem und seine lösung[J]. Acier-Steel-Stahl, 19(10-11):495-542.1954.
[13] Xu X., Cao Z.. Linear and nonlinear aerodynamic theory of interaction between flexible structure and wind[J], Applied Mathematics and Mechanics, 22(12): 57-65
[14] Diana G, et al. A new numerical approach to reproduce bridge aerodynamic non-linearities in time domain[J]. Journal of Wind Engineering and Industrial Aerodynamics 96, 1871-1884. 2008.
[15] Diana G, et al. Aerodynamic instability of a bridge deck section model Linear and nonlinear approach to force modeling[J]. Journal of Wind Engineering and Industrial Aerodynamics 98, 363-374.2010
[16] Chen A., Ma R.. Self-excited force model and parameter identification for soft flutter[C]. In: Proceedings of the ICWE 13, Amsterdam NL., 2011
[17] Wu T., Kareem A.. Nonlinear modeling of bridge aerodynamics[C]. In: Proceedings of the ICWE 13, Amsterdam NL., 2011

A novel empirical non-linear model for vortex-induced force on a closed box bridge deck

Le-Dong Zhu [a,b,c], Xiao-Liang Meng [a,b], Zhen-Shan Guo [b,c]

[a] *State Key Laboratory for Disaster Reduction in Civil Engineering, Tongji University, Shanghai, China*
[b] *Department of Bridge Engineering, Tongji University, Shanghai, China*
[c] *Key Laboratory for Wind Resistance Technology of Bridges of Ministry of Transport, Tongji University, Shanghai, China*

ABSTRACT: By taking a cable-stayed bridge as background, the non-linear vortex-induced force on its flat fully-closed box girder was investigated via a series of wind tunnel tests of spring-suspended sectional model at a large scale of 1/25, in which the dynamic displacements of the model and the dynamic forces acting on the outer cladding of the model were simultaneously measured. A non-linear least square fitting method based on the measured history of vortex-induced force was established at first to identify the relevant parameters of various empirical models of vortex-induced force. The well known Scanlan's nonlinear empirical model for the vortex-induced force was then examined by comparing the calculated displacement response with the measured one, and was demonstrated to be not suitable for the vortex-induced force of the flat box girder. A novel empirical model was finally proposed and proved to be proper to the vortex-induced force of the flat box girder. By using this novel model, not only the measured history of vortex-induced force can be well fitted, but also the measured history of dynamic displacement of the sectional model can be well reproduced via numerical calculation.

KEYWORDS: Closed box girder; vortex-induced vibration; nonlinear vortex-induced force; parameter identification; nonlinear least square fitting.

1 INTRODUCTION

The flexible steel bridges with low damping often suffer vortex-induced vibrations (VIV) at relatively low wind speeds. However, the VIV with small amplitude is sometimes allowable, unless it could possibly cause fatigue problems to the structure or discomfort problems to its users. Therefore, a careful prediction of the VIV performance via wind tunnel test or theoretical analysis is very necessary for a bridge suspected of VIV problems. In this connection, a reliable model of vortex-induced force (VIF) should be firstly established to describe the strongly-nonlinear interaction between fluid and structure. Nevertheless, no completely successful analytical method has yet been developed, starting from basic flow principles, to represent the response behavior of an elastic bluff body under the action of vortex shedding (Scanlan, 1986). Instead, it has been relatively fruitful in building empirical models of uncoupled VIF based on wind tunnel tests, such as proposed by Vickery & Basu(1983), Staubli(1983) , Scanlan(1986) and Larsen(1995), and the fluid oscillator models by Hartlen & Currie(1970), Landl(1975), Tamura & Matsui(1979), Berger(1987) and Diana & Cheli(1995). Among these proposed VIF models, only a few, such like the nonlinear model proposed by Scanlan(1986), as well as its generalized model proposed by Larsen(1995), are applicable to bridge VIV because of the special characteristic of vortex shedding mechanism of bluff bridge decks.

Secondly, the identification of the parameters in the empirical models is to some extent decided whether a model is applicable or not. Since the difficulty on the technique of measuring

pure VIF on bluff bodies, almost all the existing parameter identification processes have based on the displacement responses of VIV, instead of the force history excited by vortex shedding. Several assumptions have been induced to deduce the approximate solution of the nonlinear differential equation of motion (Ehsan *et al*. 1990; Larsen 1995). In spite of that, it is still unknown how these assumptions will affect the analysis result.

In this study, a new technique of sectional model wind tunnel test was developed to investigate the VIF directly. The special technique could simultaneously measure the total force (consisting of vortex-induced force and the inertial force), the VIV displacement and acceleration of an oscillating deck model, in free vibration tests, via force balances along with laser displacement sensors and acceleration sensors respectively. The reliability of existing Scanlan and Larsen's models and their parameter identification methods were judged by the vortex-induced force history. Moreover, a novel promising empirical model for VIF on a closed box bridge girder is proposed and its parameters are identified using nonlinear least square method.

2 MODEL, WIND TUNNEL AND MEASUREMENT SYSTEM

2.1 *Sectional model design*

The Xiangshan Harbor Bridge, a typical long span highway bridge in China, was taken as an example to investigate the vortex-induced force on closed box bridge deck. The Xiangshan Harbor Bridge is a cable-stayed bridge with a main span of 688m over the Xiangshan Harbor in Ningbo of China. The deck of the bridge is of flat steel trapezoidal box girder, which is 32.0m wide, 3.5m high and with two sets of side fairing of about 56 degrees.

Considering that the VIV performance is always sensitive to the aerodynamic configuration of bluff bodies, the deck exterior appearance, including the side fairings, hand rails, protection rails and maintenance traces, were modeled in the light of the principle of geometric similarity seriously. The geometric scale of the sectional model was set to be 1:20 while its length is 3.600m after a careful consideration of many factors. These factors include the size of working section of the wind tunnel, the sufficiently large aspect ratio (length-over-width) requirement for the model, the lock-in wind speeds, the frequency of the mass-spring system, and the sensitivity and capacity of the force balance. After scaled, the cross section of the model is 1.600m wide (noted as *B*) and 0.175m high (noted as *D*). The configuration of the model cross section is illustrated in Fig. 1.

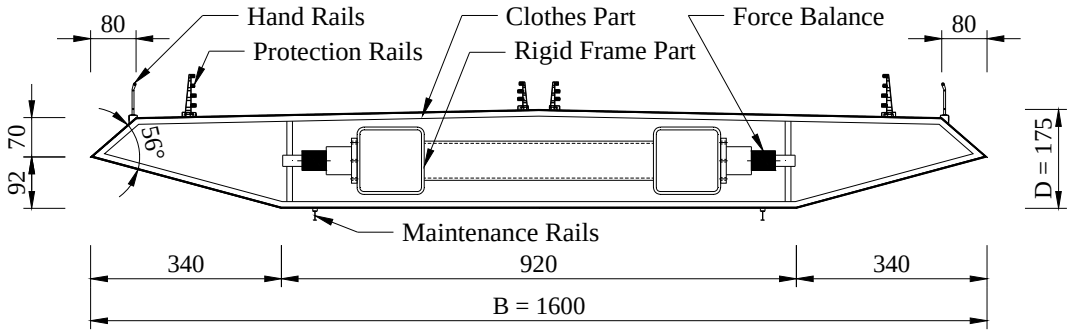

Figure 1. Cross Section of the sectional model (Unit: mm).

The force balance technique was adopted in this study for it is the most reliable way of measuring fluctuating lift in wind engineering. To get the pure vortex-induced force acting on an oscillating bridge deck, the inertial force, which could obtained from the product of acceleration

and mass, along with the aerodynamic force in still air, should be subtracted from the total force measured by the force balance. In factor, the aerodynamic force is always very small regarding to the inertial force caused by the motion of the model. The numerical error will be inevitably induced in this subtraction when the mass connected to the balances is too large. While, low mass of sectional model will result in wake of stiffness and large deformation of the elastically supported "rigid body". To avoid this confliction, an innovative improvement was made in this study. The model was designed into two parts. One of which was the "clothes part" made of wood plates and thin-walled stainless steel tube stiffeners to shape the bridge deck as light as possible, while the other was the "frame part" made of steel tubes to provide the stiffness of the model (See Fig. 1). The force balances were set interiorly between the clothes part and the rigid frame part while the frame part was elastically mounted on an eight spring system (See Fig. 2). Thus, the sampled force signal could contain less inertial components rather than the whole inertial force of the cumbersome sectional model. In other words, the demand of the precision on force balance could not be too rigorous any more. Furthermore, in order to promote the veracity of the aerodynamic force obtained, the clothes part was divided into three segments. The main segment set in middle of the model is 2.400m long, and the two side ones are 0.598m long each, with 2mm wide gaps between the main segment. With the force balances measuring only the forces come from the mid segment, the effects caused by the three dimensional flow around the ends of the model could be significantly eliminated.

2.2 *TJ-3 wind tunnel and measurement system*

Wind tunnel tests were carried out in TJ-3 boundary layer wind tunnel of the State Key Laboratory for Disaster Reduction in Civil Engineering at Tongji University, Shanghai, China. The facility is a closed-circuit wind tunnel which has a test section of 15m wide, 2m high and 14m long. The achievable mean wind speed in the tunnel ranged from 1.0 to 17.6m/s. The whole spring-mass system of the bridge deck model was fixed on two temporarily streamline walls built in the interior of TJ-3 wind tunnel (See Fig. 3). All the tests were carried out in smooth flow. The flow field between the walls was verified by hot wires at the cross section parallel to the central axes of the deck. The maximum non-uniformity of mean wind within the cross section is less than 2% and the turbulence intensity within the same cross section is less than 2.5%.

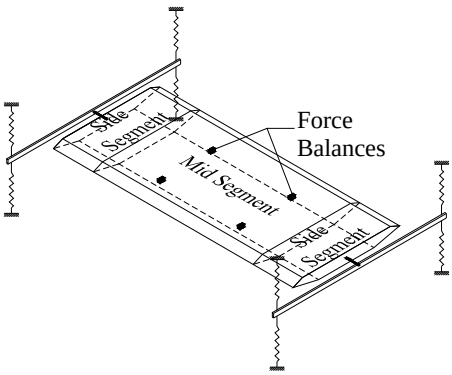

Figure 2. Set up of the sectional model

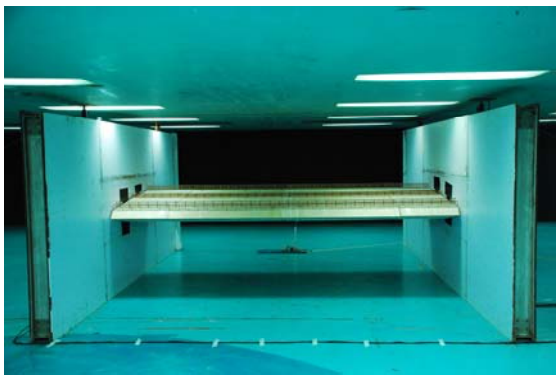

Figure 3. Sectional model in TJ-3 wind tunnel

To obtain the time-histories of oscillation curves of the model at a given position and a given wind speed, four accelerometers along with four laser displacement sensors were mounted on each end of the two support arms. Four electric bridge of the strain force balances were powered by a high-accuracy potentionstatic DC power supply and connected to an eight channels DC

voltage amplifier. A 16-channel data acquisition unit and a computer were used to digitize and record the measurement data. Calibration of the force measurement system was performed before the test to obtain the calibration factor of each force balance, reflecting the relationship between the applied forces and the normalized output voltages. In factor, there were non-neglectable phase delays between the different types of sensors, for the electrical impedances are not the same in each electric circuit. A simple mass-spring oscillator was designed to modify the sampled time histories of force, displacement and acceleration (See Fig. 4). Fig. 5 and Fig. 6 illustrated the normalized time histories before and after modification respectively.

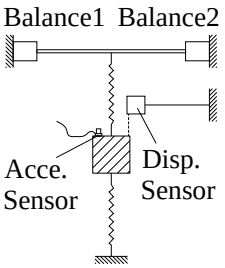

Figure 4. Phase calibration system

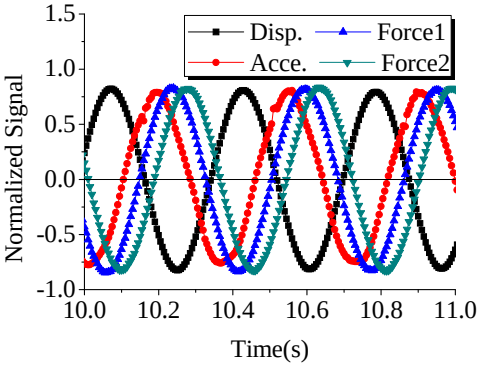

Figure 5. Signals before modified

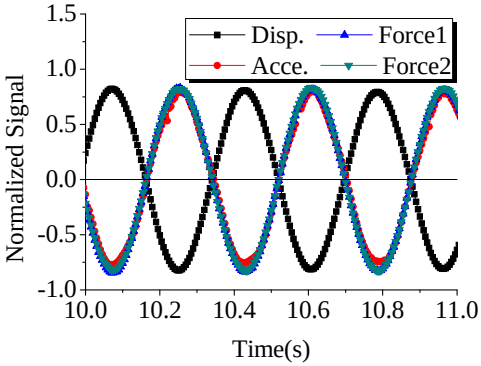

Figure 6. Signals after modified

3 WIND TUNNEL TEST RESULTS AND DISCUSSIONS

3.1 *The added mass parameter m_0 and added damping parameter c_0 in still air*

Air will certainly result in forces on oscillating deck model regardless of whether the air is flowing or not. But, in the differential equation of motion, the aerodynamic force acting on the model in still air is used to be idealized to zero. This idealization will cause problems when the system parameters are identified through free vibration responses in still air while the aerodynamic force is measured by experiment. Because the system parameters used in the equation of motion are identified in still air. That has automatically taken into account the still air force effect. But the special force measured in flowing air still contains the component represent the force effect in static air. In this study, this still air aerodynamic force effect mentioned above is considered by introducing added mass parameter m_0 and added damping parameter c_0. Therefore, the total air force in "lock-in" was the summation of inertial force caused by added mass, damping force caused by added damping, and the pure aeroelastic force regarded as the special vortex-induced force caused by the flowing air. The referred parameters m_0 and c_0 can be identified via the free decay responses and the force history by the force sensors.

The total force measured by the force balances can be regard as the forces come from equivalent mass m_e and damping c_e, as described by Equation 1:

$$f_{measured} = m_e y'' + c_e y' = (m_s + m_0) y'' + c_0 y' = f_{inertial} + f_{static} \tag{1}$$

where $f_{measured}$ = total force measured per unit length; m_s = mass of the measured mid segment per unit length; m_0 = added mass per unit length; and c_0 = added damping per unit length;

$f_{inertial}$ is inertial force caused by the mass of the mid segment per unit length, which could be express as:

$$f_{static} = m_s y'' \tag{2}$$

f_{static} is the still air force per unit length:

$$f_{static} = m_0 y'' + c_0 y' \tag{3}$$

The velocity response can be indirectly obtained from displacement signal by central difference method in time domain. Fig. 7a to Fig. 7d shows the sampled displacement, acceleration, total measured force along with the computed velocity histories of free decay vibration response in still air. With the measured total force history along with the response history of acceleration and velocity, the identification of the parameters of equivalent mass m_e and damping c_e was operated by time domain least square fitting method (See Fig. 7e). The added mass m_0 and added damping c_0 can be obtained by Equation 1, for the mass of the mid segment m_e could directly weighted by the force balances. Then the still aerodynamic force history could be reproduced by the parameters m_0 and c_0 (See Fig. 7f).

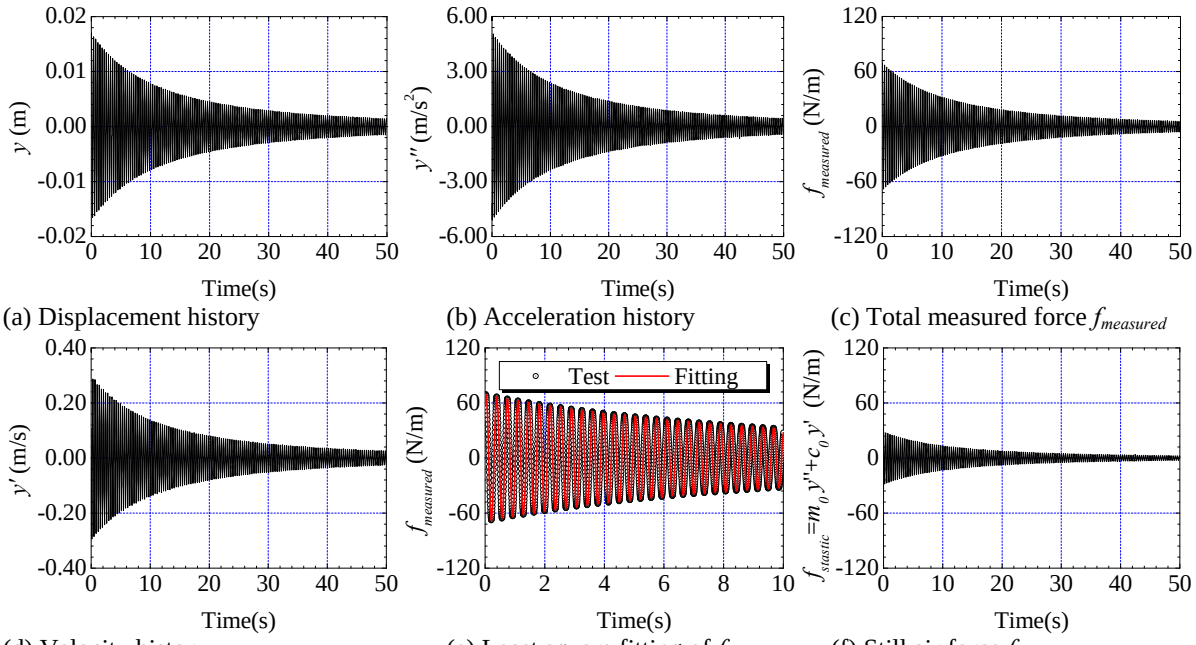

(a) Displacement history (b) Acceleration history (c) Total measured force $f_{measured}$

(d) Velocity history (e) Least square fitting of $f_{measured}$ (f) Still air force $f_{stastic}$

Figure 7. Force and response history of free decay vibration of sectional model in still air

3.2 *The pure vortex-induced force at "lock-in"*

With the estimated parameters m_0 and c_0 (or m_e and c_e), it is easy to obtain the pure vortex-induced force at "lock-in". Just as the operation conducted in the still air, the total force along with the VIV response histories were recorded via the sensors equipped on the model. Then the pure vortex-induced force could be achieved by subtract the inertial force of the mid segment and the still air force caused by the added mass and damping from the measured force. Taking the VIV performance at the wind speed of 9.10m/s as example, the time histories of responses and forces were illustrated in Fig. 8. To verify the reliability of the indirectly measured vortex-

induced force, a time domain analysis on the response of the sectional model was conducted by Newmark-β method, inputting the special vortex-induced force history obtained above.

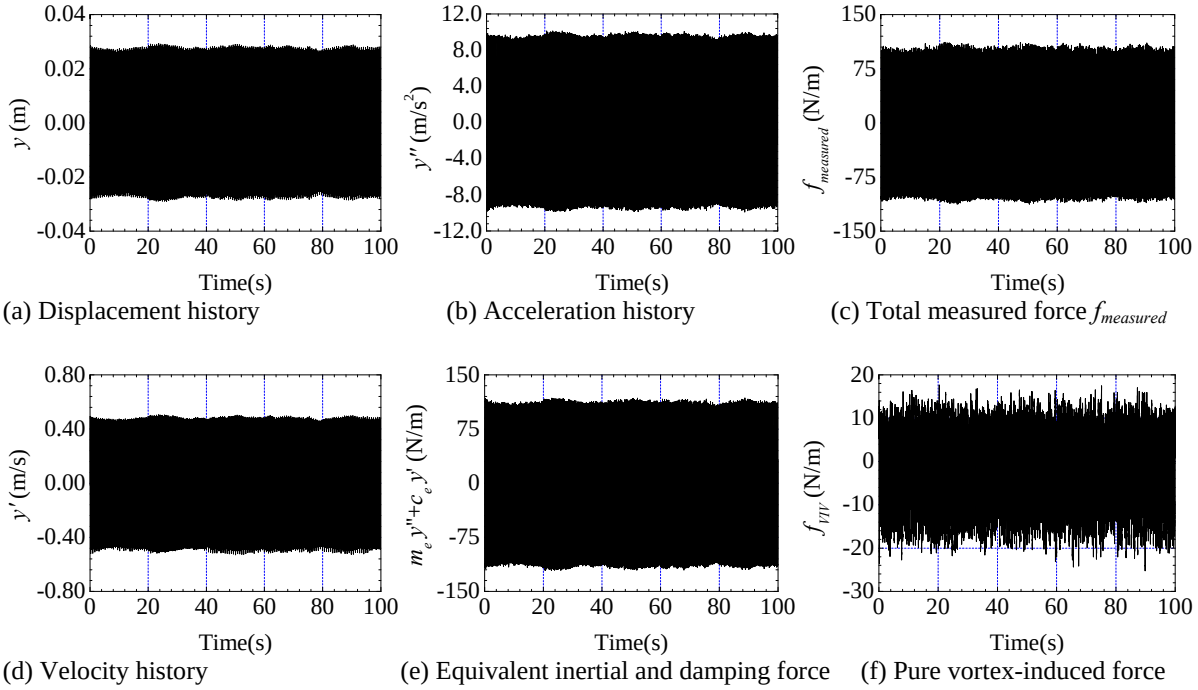

(a) Displacement history (b) Acceleration history (c) Total measured force $f_{measured}$

(d) Velocity history (e) Equivalent inertial and damping force (f) Pure vortex-induced force

Figure 8. Force and response history of vortex-induced vibration at "lock-in"

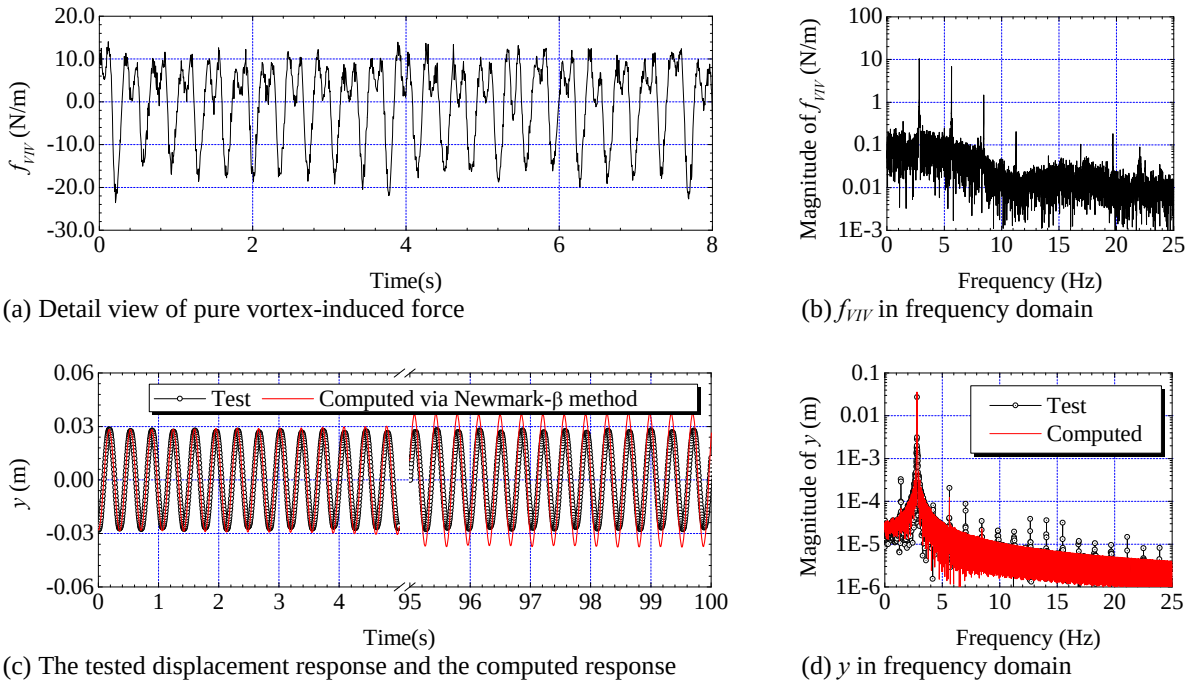

(a) Detail view of pure vortex-induced force (b) f_{VIV} in frequency domain

(c) The tested displacement response and the computed response (d) y in frequency domain

Figure 9. The vortex-induced force and response in time and frequency domain

Fig. 9a shows the vortex-induced force time history in detail and Fig. 9b shows the amplitude spectrum of the vortex-induced force. Fig. 9c and Fig. 9d illustrate the response and force signals in frequency domain, with the ordinate to be the magnitudes of the signal. It can be observed that while the response histories. It can be observed form the figures that, while the motion responses are harmonic-like signals, the vortex-induced force history is much complicate. The vortex-induced force history has two negative peaks and two positive peaks during one period. It results in the significant double and triple frequency components, which could be the main reason for the nonlinear phenomena in VIV. As the computed response is very close to the tested, both in time and frequency domain, it could be concluded that the tested force is reliable and with high precision.

4 SCANLAN'S NONLINEAR MODEL AND PARAMETER IDENTIFICATION METHOD

4.1 *Scanlan's nonlinear model*

Empirical models describing the across-flow response of a rigid bluff body mounting on linear springs submerged in a fluid stream with uniform velocity can be written as following

$$m(y'' + 2\xi\omega_1 y' + \omega_1^2 y) = f_{VIV}(y, y', y'', U, t) \tag{4}$$

where m = mass per unit length; ω_1 = mechanical structure circular frequency; ξ = mechanical structure damping ratio; y = displacement response in across-flow direction; U = the mean follow speed.

Scanlan (1986) proposed a semi-empirical nonlinear model yield the general form mentioned above. In which, the vortex-induced forcing function was defined as

$$f_{VIV}(y, y', y'', U, t) = \frac{1}{2}\rho U^2 (2D)\left[Y_1(K)\left(1 - \varepsilon\frac{y^2}{D^2}\right)\frac{y'}{U} + Y_2(K)\frac{y}{D} + \frac{1}{2}\tilde{C}_L \sin(\omega t + \varphi)\right] \tag{5}$$

where D = characteristic length of the bluff body, in this study, it is the depth of the bridge deck; ρ = air density; the reduced frequency $K = \omega D/U$, where ω is the vortex frequency; and the phase φ.

The non-dimensional form of Equation 4 with the substitution of f_{VIV} in Equation 5 is

$$\begin{aligned} &\eta''(s) + 2\xi K_1 \eta'(s) + K_1^2 \eta(s) = \\ &m_r Y_1(K)[1 - \varepsilon\eta^2(s)]\eta'(s) + m_r Y_2(K)\eta(s) + \frac{1}{2} m_r C_{LV} \sin(Ks + \theta) \end{aligned} \tag{6}$$

where $\eta(s) = y(t)/D$; the mass ratio $m_r = \rho D^2/m$.

4.2 *Parameter identification method via GTR or DTR method*

Ehsan and Scanlan (1990) has developed a parameter identification procedure via the "Decay to Resonance (DTR)" or "Grow to Resonance (GTR)" response of the sectional model in wind tun-

nel tests. The approximate analysis solution of the Van der Pol type function described by Equation 6 was firstly deduced by introducing the slow variation and Van der Pol assumption. The last term of the direct forcing was dropped for the value of C_{LV} was thought to be very small. Then the approximate solution could be described like following

$$\eta(s)=\frac{\beta}{\sqrt{1-\left(\frac{A_0^2-\beta^2}{A_0^2}\right)e^{-(\alpha\beta^2/4)s}}}\cos\left\{Ks-\frac{1}{2K}\left[m_r Y_2(K)+\left(K^2-K_1^2\right)\right]s-\psi_0\right\} \tag{7}$$

where A_0 and ψ_0 are the initial amplitude and phase of the "Decay to Resonance (DTR)" or "Grow to Resonance (GTR)", respectively. α and β are variables containing parameters ε and Y_1

$$\alpha = m_r Y_1(K)\varepsilon \tag{8}$$

$$\beta=\frac{2}{\sqrt{\varepsilon}}\left(1-\frac{2\xi K_1}{m_r Y_1(K)}\right)^{1/2} \tag{9}$$

The variable α and β could be obtained from the resonance amplitude and the envelope of the decay or grow stage of the response. Thus, the parameters ε and Y_1 could be obtained by equation (8) and (9). Furthermore, the parameter Y_2, which was thought to be very small, could also be obtained from the difference between the mechanical frequency and the total frequency during VIV.

When the parameters were identified, not only the vortex-induced oscillating response, but also the vortex-induced fore can be numerically achieved. In this section, the GTR method was adopted to identify the parameters. The estimated parameters are shown in Table 1. Fig. 10 shows the non-dimensional vortex-induced forcing f_{nonVIV} histories achieved by wind tunnel tests and computation. Fig. 11 shows the tested and computed grow to resonance non-dimensional histories. It can be observed from the figures that, although the response of the sectional model calculated from Scanlan's nonlinear empirical model, which parameters are identified via the motion response, is quite close to the test response history, the parameter described vortex-induced force history is remarkably dissimilar to the tested force. The parameter described force has three negative peaks as well as three positive peaks in one period, while, the tested force history has only two negative peaks and two positive peaks.

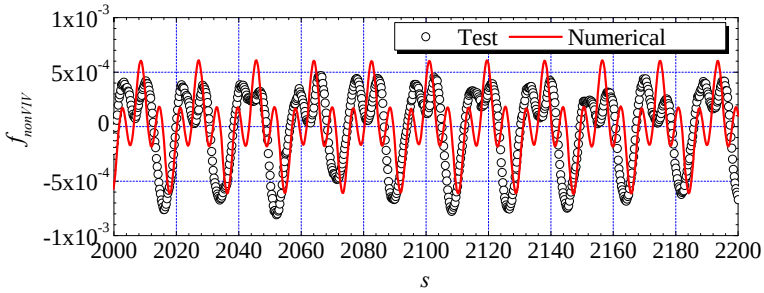

Figure 10. Non-dimensional vortex-induced force history (Scanlan's model, parameters identified via GTR method)

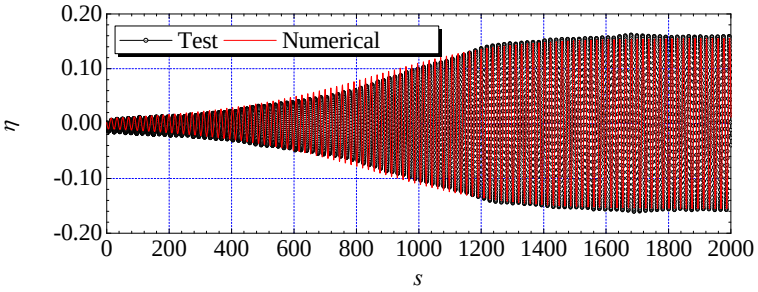

Figure 11. Non-dimensional displacement response (Scanlan's model, parameters identified via GTR method)

4.3 *Parameter identification method via LSQ method*

Just as described above, with the parameters identification method proposed by Ehsan and Scanlan, the Scanlan's nonlinear empirical model could not perfectly rebuild the tested vortex-induced force. That could result from two possible reasons, first, the parameter identification procedure is not suitable for its improper assumptions induced in the approximate solution, and second, the model itself is not able to describe the vortex-induced force.

In this section, a direct curve fitting method based on the nonlinear least square (LSQ) technique was developed to identify the parameters in Scanlan's nonlinear empirical model. The sum squared error was regarded as the objective function, and the numerical optimization function can be defined as

$$R(Y_1, Y_2, \varepsilon, C_L, K, \varphi) = \sum \left(f_{nonVIV}(s_i) - \hat{f}_{nonVIV}(s_i) \right)^2 \tag{10}$$

where $\hat{f}_{nonVIV}(s_i)$ is the estimated non-dimensional vortex-induced force described by Scanlan's model at time s_i, and f_{nonVIV} is the tested value at the same time. The objective is to find Y_1, Y_2, ε, C_L, K and φ to make the value of function $R(Y_1, Y_2, \varepsilon, C_L, K, \varphi)$ to be minimum. The Levenberg-Marquardt method was adopted to solve the nonlinear Equations 11.

$$\begin{cases} \sum_{i=1}^{n} (f_{nonVIV}(s_i) - \hat{f}_{nonVIV}(s_i))(1 - \varepsilon \frac{\eta_i^2}{D^2})\eta_i' = 0 \\ \sum_{i=1}^{n} (f_{nonVIV}(s_i) - \hat{f}_{nonVIV}(s_i))\eta_i^2 \eta_i' = 0 \\ \sum_{i=1}^{n} (f_{nonVIV}(s_i) - \hat{f}_{nonVIV}(s_i))\eta_i = 0 \\ \sum_{i=1}^{n} (f_{nonVIV}(s_i) - \hat{f}_{nonVIV}(s_i))\sin(Ks_i + \varphi) = 0 \\ \sum_{i=1}^{n} (f_{nonVIV}(s_i) - \hat{f}_{nonVIV}(s_i))s_i \cos(Ks_i + \varphi) = 0 \\ \sum_{i=1}^{n} (f_{nonVIV}(s_i) - \hat{f}_{nonVIV}(s_i))\cos(Ks_i + \varphi) = 0 \end{cases} \tag{11}$$

Table 1. The parameters identified in the empirical models

Model	Method	Y_1	Y_2	Y_3	ε	ε_N	C_{LV}	K	θ
Scanlan's	GTR	16.397	0	—	81.199	—	—	—	—
Scanlan's	LSQ	8.406	-2.179	—	-18.671	—	0.792	0.680	-1.997
New model	LSQ	11.966	-2.194	89.408	—	103.361	-0.022	0.4477	-0.0128

The identified parameters for Scanlan's nonlinear model by LSQ method was given in Table 1. Fig. 12 and Fig. 13 shows the rebuilt force and the numerical solution of the differential equation of motion, with the vortex-induced force described by Scanlan's model and the parameters by LSQ method. The results show that, the coefficient of the nonlinear aerodynamic term, ε, was a negative value. That will certainly result in nonlinear negative aerodynamic damping in the numerical system. In other words, the negative aerodynamic damping will grow if the oscillation amplitude grows, and the system will show divergence finally, just as the response history illustrated in Fig. 13.

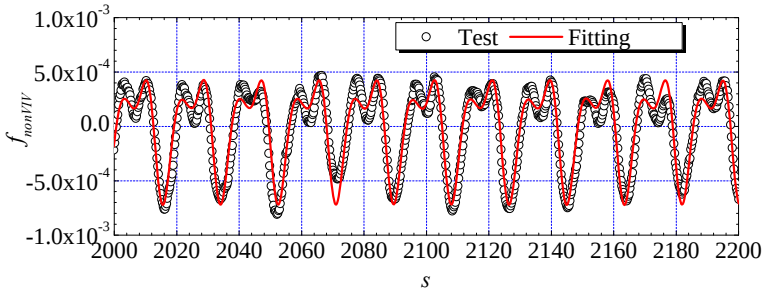

Figure 12. Non-dimensional vortex-induced force history (Scanlan's model, parameters identified via LSQ method)

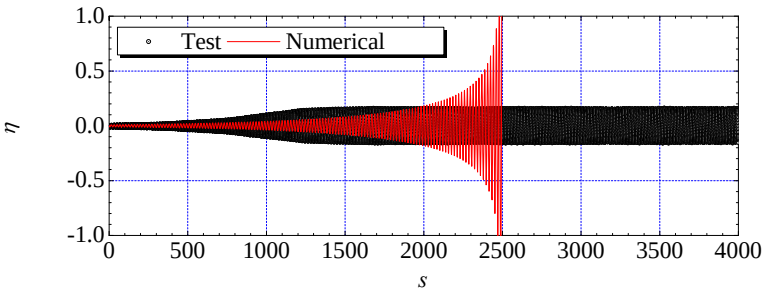

Figure 13. Non-dimensional displacement response (Scanlan's model, parameters identified via LSQ method)

5 NEW VORTEX-INDUCED FORCE MODEL

The evidences above show overwhelmingly that the Scanlan's nonlinear empirical model is not proper to predict the vortex-induced force on closed bridge deck. A new empirical model was suggested, after a really hard try of possible models with the general form of Equation 4, to properly describe the vortex-induced force on the bridge deck. The new model can be defined as

$$f_{VIV}(y,y',y'',U,t)=\frac{1}{2}\rho U^2(2D)\left[Y_1(K)\left(1-\varepsilon_N\frac{y'^2}{D^2}\right)\frac{y'}{U}+Y_2(K)\frac{y}{D}+Y_3\frac{y'y}{UD}+\frac{1}{2}\tilde{C}_L\sin(\omega t+\varphi)\right] \quad (12)$$

This new model also induced a cubical term to ensure that the oscillation is self-limiting, but the special nonlinear aerodynamic damping term was in phase with the cube of velocity, instead of with the product of square displacement and velocity used in Scanlan's model. Furthermore, a second order nonlinear term, which was in phase the product of displacement and velocity, was induced to the model as well, for the remarkable force component of double frequency observed in Fig. 9b. The LSQ method was also adopted to identify the parameters in the new model. The values of the parameters in the new model are given in Table 1. Fig. 14 and Fig. 15 show the vortex-induced force and the response calculated by the new model. The results show that, with the parameters estimated by LSQ method, the new model could not only perfectly rebuild the vortex-induced force, but also reliably predict the vortex response by numerically solving the nonlinear differential equation of motion. However, the computed response is a little larger than the tested response. It could be result from the lack of spanwise correlation on the vortex-induced force and the incoming flow, for the force tested was only the aerodynamic force acting on the mid segment of the model, while the oscillation system was driven by the force acting on the whole model.

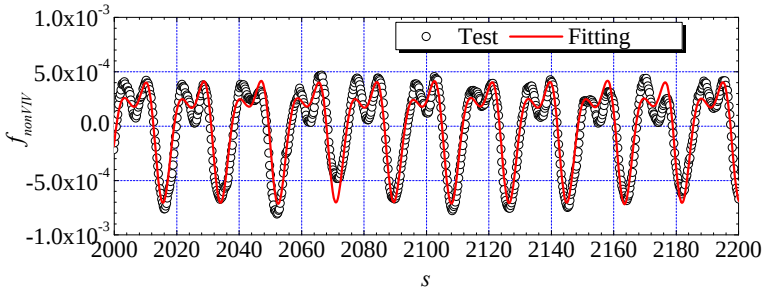

Figure 14. Non-dimensional vortex-induced force history (New model, parameters identified via LSQ method)

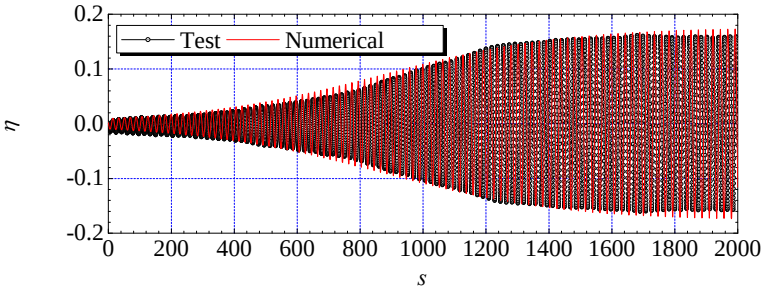

Figure 14. Non-dimensional displacement response (New model, parameters identified via LSQ method)

6 CONCLUSIONS

By taking a closed box bridge deck as an example, the vortex-induced force was tested by sectional wind tunnel tests. The test results has shown that the vortex-induced force is evidently nonlinear, for the significant double and triple frequency components observed in the amplitude spectrum of the tested force.

The reliability of the well known Scanlan's nonlinear empirical model and the parameter identification procedure suggested by Ehsan and Scanlan was discussed. A new parameter estimate procedure, which was based on least square technique to directly fitting the vortex-induced force history, was also developed. By comparing the vortex-induced force and structure response rebuilt by Scanlan's model with the measured results, it can be concluded that the Scanlan's

nonlinear empirical model could not properly describe the special vortex-induced vibration phenomenon.

A new promising nonlinear model was proposed. The model still introduced a three order term to ensure the self-limiting property as well as a second order term to adapt the double frequency component of the vortex-induced force. Aided with the parameters identified by the nonlinear least square fitting method, the new model could either perfectly fit the tested force history, or exactly reproduce the response of VIV.

7 ACKNOWLEDGEMENTS

The work described in this paper was jointly supported by the National Nature Science Foundation of China (Grant 50978204), and the Fundamental Research Fund for State Key Laboratories from the Ministry of Science and Technology of China (Grant No. SLDRCE08-A-02). Any opinions and concluding remarks presented in this paper are entirely those of the writers.

8 REFERENCES

1 A. Larsen, A generalized model for assessment of vortex-induced vibrations of flexible structures, Journal of Wind Engineering and Industrial Aerodynamics, 57(1995) 281-294.
2 B. Vickery, R. Basu, Across-wind vibrations of structures of circular cross-section, Part I. Development of a mathematical model for two-dimensional conditions, Journal of Wind Engineering and Industrial Aerodynamics, 12(1983) 49-73.
3 E. Berger, On a mechanism of vortex excited oscillations of a cylinder, Journal of Wind Engineering and Industrial Aerodynamics, 28(1988) 301-310.
4 E. Simiu and R. H. Scanlan, Wind effects on structures: Fundamentals and applications to Design, 2nd edition, New York, 1986.
5 F. Ehsan, R. H. Scanlan, Vortex-induced vibrations of flexible bridges, Journal of Engineering Mechanics, 116(1990) 1392-1411.
6 G. Diana, F. Cheli and F. Resta, Time domain aeroelastic force identification on bridge decks, Proc. 9th International Conference on Wind Engineering, New Delhi, India, 1995, pp. 938-949.
7 R.T. Hartlen, I.G. Currie, Lift-oscillator model of vortex-induced vibration, Journal of Engineering Mechanics Division, ASCE, 96(1970) 577-591.
8 R. Landl, A mathematical model for vortex-excited vibrations of bluff bodies, Journal of Sound and Vibration, 42(1975) 219-234.
9 T. Staubli, Calculation of vibration of an elastically mounted cylinder using experimental data from a forced oscillation, Journal of Fluids Engineering, 105(1983) 225–229.
10 Y. Tamura, G. Matsui, Wake-oscillator model of vortex-induced oscillation of circular cylinder, Proc. 5th International Conference on Wind Engineering, Fort Collins, Colorado, USA, 1979, pp. 1085-1094.

A new unsteady aerodynamic model with unique parameters

Shiyi Liu[a], Yaojun Ge[b]

[a]*SLDRCE, Tongji University, Shanghai, China, liushiyi_ha@163.com*
[b]*SLDRCE, Tongji University, Shanghai, China, yaojunge@tongji.edu.cn*

ABSTRACT: Unsteady aerodynamic forces can be computed efficiently in time domain by Rational Function Approximation (RFA) method. However, parameter values of existing RFA models are not unique for given input-output characteristics. This property will cause difficulties in nonlinear aerodynamic analysis where interpolations among parameter values may be required. When parameters cannot be uniquely determined, such interpolations may be erroneous. This paper firstly discusses the general form of differential equations for unsteady aerodynamic forces. Then, a new time domain aerodynamic model, namely the Cascade model, is suggested. It can be found that the new model has unique parameters. Finally, the new model is used to fit flutter derivatives and static coefficients of a bridge deck obtained from wind tunnel tests. The unsteady transfer matrix and Quasi-Static limit matrices of the new model are fitted simultaneously. The output time history of the new model under given input is compared with results of frequency-response analysis.

KEYWORDS: Unsteady aerodynamics; Time domain model; Nonlinear least square; General model; Rational function approximation;

1 INTRODUCTION

A reliable aerodynamic force model is core to the prediction of bridge response in wind. Bridge deck sections are generally irregular bluff bodies, which features complicated unsteady characteristics. Although being widely used, traditional frequency domain approaches[1] show significant drawbacks. Firstly, frequency-dependent coefficients, such as flutter derivatives and aerodynamic admittance functions, are difficult to be integrated into structure analysis which is often conducted in time domain. Secondly, superposition based frequency domain methods cannot reasonably consider aerodynamic nonlinearity. Researchers have re-formulated unsteady aerodynamics in time domain by using aerodynamic indicial functions or Rational Function Approximation (RFA) techniques[2][3]. These methods successfully modeled the frequency-dependent characteristics or memory effects of aerodynamics and can be readily used in structural analysis[4]. Aerodynamic nonlinearity has been widely observed[5] in wind tunnel tests. When simulating nonlinear aerodynamic forces, model parameters need to be switched among different values for different wind velocities or angle of attacks. This usually requires interpolation among parameter values. However, traditional RFA models do not have unique parameters. This means that two models with identical transfer characteristics may have totally different parameter values. Therefore, interpolations among different parameter values may be erroneous. To overcome this difficulty, a new unsteady model with unique parameters is required.

2 EXISTING METHODS

In time domain, unsteady aerodynamic forces can be computed by convolution of indicial functions[6]

$$\boldsymbol{f}(t) = \boldsymbol{A}_0\boldsymbol{x}(t) + \boldsymbol{A}_1\dot{\boldsymbol{x}}(t) + \boldsymbol{A}_2\ddot{\boldsymbol{x}}(t) + \int_{-\infty}^{t} \boldsymbol{I}_{fx}(t-\tau)\dot{\boldsymbol{x}}(\tau)\, d\tau \tag{1}$$

where $\boldsymbol{A}_0$, $\boldsymbol{A}_1$and $\boldsymbol{A}_2$ = aerodynamic stiffness, damping and mass matrices, respectively; $\boldsymbol{I}_{fx}(t)$ = indicial function matrix; $\boldsymbol{f}$ = aerodynamic forces; $\boldsymbol{x}$ = structural displacements. Computation of eq.(1) is not efficient due to existence of convolution term. Therefore, researchers have proposed some computationally more efficient alternatives, such as the Roger's RFA method[2] and the Minimum-State RFA method[3].

Using the Leibniz integration formula, the following equation for the convolution term can be obtained:

$$\left[\int_{-\infty}^{t} \boldsymbol{I}_{fx}(t-\tau)\dot{\boldsymbol{x}}(\tau)d\tau\right]' = \boldsymbol{I}_{fx}(0)\dot{\boldsymbol{x}}(t) + \int_{-\infty}^{t} \boldsymbol{I}'_{fx}(t-\tau)\dot{\boldsymbol{x}}(\tau)d\tau \tag{2}$$

By assuming that indicial functions $\boldsymbol{I}_{fx}(t)$ are power series of e, that

$$\boldsymbol{I}_{fx}(t) \approx \sum_{i=1}^{n_l} \boldsymbol{A}_{2+i} e^{-\lambda_i t} \tag{3}$$

the following differential equations can be derived.

$$\begin{cases} \boldsymbol{f} = \boldsymbol{A}_0\boldsymbol{x} + \boldsymbol{A}_1\dot{\boldsymbol{x}} + \boldsymbol{A}_2\ddot{\boldsymbol{x}} + \sum_{i=1}^{n_l} \boldsymbol{\phi}_i \\ \dot{\boldsymbol{\phi}}_i = \boldsymbol{A}_{2+i}\dot{\boldsymbol{x}} - \lambda_i\boldsymbol{\phi}_i, \qquad (i = 1, \dots n_l) \end{cases} \tag{4}$$

where

$$\boldsymbol{\phi}_i = \int_{-\infty}^{t} \boldsymbol{A}_{2+i} e^{-\lambda_i(t-\tau)}\dot{\boldsymbol{x}}(\tau)\, d\tau\,, \qquad (i = 1, \dots n_l) \tag{5}$$

are aerodynamic state variables. It is noteworthy that Eqs. (4) can be solved in time domain efficiently without convolution.

Laplace transform of eqs.(4) can be written as

$$\begin{Bmatrix} \hat{\boldsymbol{f}} \\ \boldsymbol{0} \\ \boldsymbol{0} \\ \boldsymbol{0} \end{Bmatrix} = \begin{bmatrix} \boldsymbol{A}_0 + \boldsymbol{A}_1 s + \boldsymbol{A}_2 s^2 & \boldsymbol{I} & \dots & \boldsymbol{I} \\ -\boldsymbol{A}_3 s & (\lambda_1 + s)\boldsymbol{I} & & \\ \vdots & & \ddots & \\ -\boldsymbol{A}_{2+n_l} s & & & (\lambda_{n_l} + s)\boldsymbol{I} \end{bmatrix} \begin{Bmatrix} \hat{\boldsymbol{x}} \\ \hat{\boldsymbol{\phi}}_1 \\ \vdots \\ \hat{\boldsymbol{\phi}}_{n_l} \end{Bmatrix} \tag{6}$$

where s = complex frequency; hat symbol ˆ represents Laplace transform of a variable. After eliminating states $\hat{\boldsymbol{\phi}}_i$ from eqs.(6), the well-known Roger's Rational Function Approximation of aerodynamic transfer matrix can be obtained:

$$\boldsymbol{T}(s) = (\boldsymbol{A}_0 + \boldsymbol{A}_1 s + \boldsymbol{A}_2 s^2) + \sum_{i=1}^{n_l} \frac{\boldsymbol{A}_{2+i} s}{(\lambda_i + s)} \tag{7}$$

The above expression can be used to fit parameters $\boldsymbol{A}_0$, $\boldsymbol{A}_1$, $\boldsymbol{A}_2$, $\boldsymbol{A}_{2+i}$ and λ_i with experimentally identified flutter derivatives.

Karpel suggested another RFA model, namely the Minimum-State model, as follows:

$$\begin{Bmatrix} \hat{\boldsymbol{f}} \\ \boldsymbol{0} \end{Bmatrix} = \begin{bmatrix} \boldsymbol{A}_0 + \boldsymbol{A}_1 s + \boldsymbol{A}_2 s^2 & \boldsymbol{D} \\ -\boldsymbol{E}s & \boldsymbol{R} + \boldsymbol{I}s \end{bmatrix} \begin{Bmatrix} \hat{\boldsymbol{x}} \\ \hat{\boldsymbol{\phi}} \end{Bmatrix} \tag{8}$$

where $\boldsymbol{A}_0$, $\boldsymbol{A}_1$, $\boldsymbol{A}_2$, $\boldsymbol{D}$, $\boldsymbol{E}$ are full parameter matrices; $\boldsymbol{R}$ is a diagonal parameter matrix:

$$\boldsymbol{R} = \begin{bmatrix} \lambda_1 & & \\ & \ddots & \\ & & \lambda_{n_l} \end{bmatrix} \tag{9}$$

By eliminating state variables $\hat{\boldsymbol{\phi}}$ from eqs.(8), transfer matrix of the Minimum-State

model can be obtained:

$$\boldsymbol{T}(s) = \boldsymbol{A}_0 + \boldsymbol{A}_1 s + \boldsymbol{A}_2 s^2 + \boldsymbol{D}(\boldsymbol{R} + \boldsymbol{I}s)^{-1}\boldsymbol{E}s \tag{10}$$

Expression above can be used to determine parameters by nonlinear Least Square.

In time domain, the Minimum-State model can be written as

$$\begin{cases} \boldsymbol{f} = \boldsymbol{A}_0\boldsymbol{x} + \boldsymbol{A}_1\dot{\boldsymbol{x}} + \boldsymbol{A}_2\ddot{\boldsymbol{x}} + \boldsymbol{D}\boldsymbol{\phi} \\ \dot{\boldsymbol{\phi}} = \boldsymbol{E}\dot{\boldsymbol{x}} - \boldsymbol{R}\boldsymbol{\phi} \end{cases} \tag{11}$$

Both of the Roger's model and the Minimum-State model can reproduce aerodynamic memory effect without convolution. As mentioned previously, the Roger's model is based on the assumption that aerodynamic indicial functions can be expressed as power series of e, indicating that indicial functions are monotonically decreasing. However, there is no evidence supporting this assumption for bluff bodies. Our experience shows that, in many cases, the Roger's expression (7) cannot fit bridge deck flutter derivatives very well. The Minimum-State model is superior to the Roger's model since the Minimum-State model has more adjustable parameters than the Roger's model, and therefore can achieve similar fitting precision with less state variables.

It should be noticed that the coefficient matrices of state variables $\widehat{\boldsymbol{\phi}}$ in the augmented equations of both of the two models (see eqs.(6) and (8)) are diagonal, which mean that the coupling effects among state variables cannot be considered. It can also be observed from eqs.(6) and (8) that state variables (or variable groups) of both two models are arranged in parallel. This means that positions of different state variables and corresponding matrices can be exchanged mutually without modifying the input-output behavior of the system. Models with identical transfer matrix can have multiple sets of parameters, making it difficult to compare and interpolate among different models.

3 DISCUSSION ON THE GENERAL FORM OF UNSTEADY AERODYNAMICS

3.1 General equations

The unsteady characteristics of aerodynamic forces are caused by the movement of the surrounding air, which is relatively independent of structure oscillations and cannot be fully observed from the resulting aerodynamic forces. To correctly reproduce unsteady aerodynamic forces, the air movement must be considered simultaneously. The state variables in the Roger's and the Minimum-State RFA can be viewed as some descriptions of the air movement. These variables are governed by additional differential equations and are coupled with structure displacements. It is reasonable to assume a more general aerodynamic system that consists of two sets of differential equations: one to govern the air movement described by state variables, the other to generate output forces, as shown in eqs.(12).

$$\begin{cases} \boldsymbol{f} = \boldsymbol{g}_x(\boldsymbol{x}, \dot{\boldsymbol{x}}, \ddot{\boldsymbol{x}}, \boldsymbol{\phi}, \dot{\boldsymbol{\phi}}) \\ \dot{\boldsymbol{\phi}} = \boldsymbol{g}_\phi(\boldsymbol{x}, \dot{\boldsymbol{x}}, \ddot{\boldsymbol{x}}, \boldsymbol{\phi}) \end{cases} \tag{12}$$

where $\boldsymbol{x}$ = structure displacements; $\boldsymbol{\phi}$ = aerodynamic state variables; $\boldsymbol{f}$ = output forces; $\boldsymbol{g}_\phi$ and $\boldsymbol{g}_x$ = differential expressions. Any linear or nonlinear expressions of $\boldsymbol{g}_\phi$ and $\boldsymbol{g}_x$ that match experimental or CFD observations can be used.

Our discussion will focus on the following linear version of eqs. (12).

$$\begin{cases} \boldsymbol{f} = \boldsymbol{A}_0\boldsymbol{x} + \boldsymbol{A}_1\dot{\boldsymbol{x}} + \boldsymbol{A}_2\ddot{\boldsymbol{x}} + \boldsymbol{R}_0\boldsymbol{\phi} + \boldsymbol{R}_1\dot{\boldsymbol{\phi}} \\ \dot{\boldsymbol{\phi}} = -(\boldsymbol{T}_0\boldsymbol{x} + \boldsymbol{T}_1\dot{\boldsymbol{x}} + \boldsymbol{P}\boldsymbol{\phi}) \end{cases} \tag{13}$$

where $\boldsymbol{A}_0, \boldsymbol{A}_1, \boldsymbol{A}_2, \boldsymbol{R}_0, \boldsymbol{R}_1, \boldsymbol{T}_0, \boldsymbol{T}_1$ and $\boldsymbol{P}$ are frequency-independent parameters matrices.

Laplace transform of eqs.(13) reads

$$\begin{cases} \hat{\boldsymbol{f}} = (\boldsymbol{A}_0 + \boldsymbol{A}_1 s + \boldsymbol{A}_2 s^2)\hat{\boldsymbol{x}} + (\boldsymbol{R}_0 + \boldsymbol{R}_1 s)\hat{\boldsymbol{\phi}} \\ \quad (\boldsymbol{T}_0 + \boldsymbol{T}_1 s)\hat{\boldsymbol{x}} + (\boldsymbol{P} + \boldsymbol{I}s)\hat{\boldsymbol{\phi}} = \boldsymbol{0} \end{cases} \tag{14}$$

From the second equation of (14), we have

$$\hat{\boldsymbol{\phi}} = -(\boldsymbol{P} + \boldsymbol{I}s)^{-1}(\boldsymbol{T}_0 + \boldsymbol{T}_1 s)\hat{\boldsymbol{x}} \tag{15}$$

Substituting eq.(15) into the first equation of (14), one obtains the transfer matrix of (13):

$$\boldsymbol{T}(s) = \boldsymbol{A}_0 + \boldsymbol{A}_1 s + \boldsymbol{A}_2 s^2 - (\boldsymbol{R}_0 + \boldsymbol{R}_1 s)(\boldsymbol{P} + \boldsymbol{I}s)^{-1}(\boldsymbol{T}_0 + \boldsymbol{T}_1 s) \tag{16}$$

Similar to traditional RFA methods, parameters in model (13) can be determined by comparing the transfer matrix (16) to aerodynamic derivatives obtained by wind tunnel tests.

When fitting transfer matrix to frequency-dependent stiffness and damping matrices obtained through experiments, the nominal aerodynamic stiffness matrix $\boldsymbol{K}(s)$ and damping matrix $\boldsymbol{C}(s)$ can be obtained as follows:

$$\boldsymbol{C}(s) = \mathrm{Im}\big(\boldsymbol{T}(s)\big)/\mathrm{Im}(s)\,, \qquad \boldsymbol{K}(s) = \mathrm{Re}\big(\boldsymbol{T}(s)\big) - \mathrm{Re}(s)\boldsymbol{C}(s) \tag{17}$$

where Re(*) and Im(*) = real and imaginary parts of complex quantities, respectively. $\boldsymbol{T}(s)$ can be expressed in nominal stiffness and damping matrices as

$$\boldsymbol{T}(s) = \boldsymbol{K}(s) + \boldsymbol{C}(s)s \tag{18}$$

3.2 Stability Condition

Since state variables $\boldsymbol{\phi}$ are internal Degree of Freedoms (DoFs), the stability of $\boldsymbol{\phi}$ must be studied. Free oscillations of $\boldsymbol{\phi}$ are determined by

$$\boldsymbol{P}\boldsymbol{\phi} + \dot{\boldsymbol{\phi}} = \boldsymbol{0} \tag{19}$$

The complex frequency of free oscillation can be solved from

$$|\boldsymbol{P} + \boldsymbol{I}s| = 0 \tag{20}$$

where

$$s = -\lambda_i^p, \qquad \big(i = 0,1, \ldots n_\phi - 1\big) \tag{21}$$

is the complex frequency; $\boldsymbol{\lambda}^p$ = Eigenvalues of $\boldsymbol{P}$; n_ϕ = number of state variables. To make $\boldsymbol{\phi}$ stable, the real part of s must be negative. Therefore, the following stability condition can be imposed:

$$\mathrm{Re}(\boldsymbol{\lambda}^p) > 0 \tag{22}$$

It can be inferred that the Roger's and Minimum-State models are stable as long as λ_is in (6) and (9) are positive.

3.3 Limit characteristics

When reduced wind velocity approaches infinity, the complex frequency s approaches zero. In such cases, unsteady aerodynamic forces degenerate into Quasi-Static wind forces. This indicates that the unsteady transfer matrix (16) should equal transfer matrix of Quasi-Static model when s approaches zero. This limit characteristic is especially important for super long span bridges whose reduced wind velocities can be very high.

The term $(\boldsymbol{P} + \boldsymbol{I}s)^{-1}$ can be linearized at $s = 0$ through Taylor expansion:

$$(\boldsymbol{P} + \boldsymbol{I}s)^{-1} \approx \boldsymbol{P}^{-1} + \left[\frac{\mathrm{d}(\boldsymbol{P} + \boldsymbol{I}s)^{-1}}{\mathrm{d}s}\right]_{s=0} s = \boldsymbol{P}^{-1} - \boldsymbol{P}^{-1}\boldsymbol{P}^{-1}s \tag{23}$$

where

$$\frac{\mathrm{d}(\boldsymbol{P}+\boldsymbol{I}s)^{-1}}{\mathrm{d}s} = -(\boldsymbol{P}+\boldsymbol{I}s)^{-1}\boldsymbol{I}(\boldsymbol{P}+\boldsymbol{I}s)^{-1} \tag{24}$$

Substitute $(\boldsymbol{P}+\boldsymbol{I}s)^{-1}$ in (23) into (16) and linearize $\boldsymbol{T}(s)$ at $s=0$, the approximated expression of $\boldsymbol{T}(s)$ can be obtained:

$$[\boldsymbol{T}(s)]_{s=0} \approx (\boldsymbol{A}_0 - \boldsymbol{R}_0\boldsymbol{P}^{-1}\boldsymbol{T}_0) + (\boldsymbol{A}_1 - \boldsymbol{R}_1\boldsymbol{P}^{-1}\boldsymbol{T}_0 + \boldsymbol{R}_0\boldsymbol{P}^{-1}\boldsymbol{P}^{-1}\boldsymbol{T}_0 - \boldsymbol{R}_0\boldsymbol{P}^{-1}\boldsymbol{T}_1)s \tag{25}$$

Expressions of nominal aerodynamic stiffness and damping matrices when s approaches zero can be obtained:

$$\boldsymbol{K}_{s0} = \lim_{s\to 0}\boldsymbol{T}(s) = \boldsymbol{A}_0 - \boldsymbol{R}_0\boldsymbol{P}^{-1}\boldsymbol{T}_0 \tag{26}$$

$$\boldsymbol{C}_{s0} = \lim_{s\to 0}\frac{\mathrm{d}\boldsymbol{T}(s)}{\mathrm{d}s} = \boldsymbol{A}_1 - \boldsymbol{R}_1\boldsymbol{P}^{-1}\boldsymbol{T}_0 + \boldsymbol{R}_0\boldsymbol{P}^{-1}(\boldsymbol{P}^{-1}\boldsymbol{T}_0 - \boldsymbol{T}_1) \tag{27}$$

where $\boldsymbol{K}_{s0}$ and $\boldsymbol{C}_{s0}$ = Quasi-Static limit aerodynamic stiffness and damping matrices, respectively. To ensure model correctness in both ordinary and high reduced wind velocity ranges, the transfer matrix $\boldsymbol{T}(s)$ and the limit stiffness and damping matrices $\boldsymbol{K}_{s0}$ and $\boldsymbol{C}_{s0}$ should be fitted simultaneously.

4 A NEW AERODYNAMIC MODEL: THE CASCADE MODEL

Here, we propose a new unsteady aerodynamic model which has unique parameters theoretically. The new model also considers interactions among different aerodynamic state variables by adding off-diagonal entries to matrix $\boldsymbol{P}$; thus, it can model more complicated aerodynamic behaviors of bluff bodies.

4.1 Differential equations

In the new model, the unsteady part of an aerodynamic force component is represented by a state variable:

$$\boldsymbol{f} = \boldsymbol{A}_0\boldsymbol{x} + \boldsymbol{A}_1\dot{\boldsymbol{x}} + \boldsymbol{A}_2\ddot{\boldsymbol{x}} + \boldsymbol{\phi}_0 \tag{28}$$

where $\boldsymbol{x}$ = input displacements (or wind fluctuations for buffeting forces); $\boldsymbol{f}$ = output aerodynamic forces; $\boldsymbol{\phi}_0$ = state variables representing unsteady components of $\boldsymbol{f}$; $\boldsymbol{A}_0$, $\boldsymbol{A}_1$and $\boldsymbol{A}_2$ = aerodynamic stiffness, damping and mass matrices which generate steady parts of $\boldsymbol{f}$. We assume that the evolution of $\boldsymbol{\phi}_0$ does not only depend on inputs $\boldsymbol{x}$, but also depend on another set of state variables, namely $\boldsymbol{\phi}_1$. So the governing differential equations of $\boldsymbol{\phi}_0$ can be written as

$$\dot{\boldsymbol{\phi}}_0 = -(\boldsymbol{C}_0\dot{\boldsymbol{x}} + \boldsymbol{B}_0\boldsymbol{\phi}_0 + \boldsymbol{\phi}_1) \tag{29}$$

where $\boldsymbol{C}_0, \boldsymbol{B}_0$ = parameters matrices to be determined.

Analogously, the governing differential equations of $\boldsymbol{\phi}_1$ can be written as

$$\dot{\boldsymbol{\phi}}_1 = -(\boldsymbol{C}_1\dot{\boldsymbol{x}} + \boldsymbol{B}_1\boldsymbol{\phi}_1 + \boldsymbol{\phi}_2) \tag{30}$$

…

The above procedure will eventually lead to the following differential equations:

$$\begin{cases} \boldsymbol{f} = \boldsymbol{A}_0\boldsymbol{x} + \boldsymbol{A}_1\dot{\boldsymbol{x}} + \boldsymbol{A}_2\ddot{\boldsymbol{x}} + \boldsymbol{\phi}_0 \\ \dot{\boldsymbol{\phi}}_0 = -(\boldsymbol{C}_0\dot{\boldsymbol{x}} + \boldsymbol{B}_0\boldsymbol{\phi}_0 + \boldsymbol{\phi}_1) \\ \vdots \\ \dot{\boldsymbol{\phi}}_{n-2} = -(\boldsymbol{C}_{n-2}\dot{\boldsymbol{x}} + \boldsymbol{B}_{n-2}\boldsymbol{\phi}_{n-2} + \boldsymbol{\phi}_{n-1}) \\ \dot{\boldsymbol{\phi}}_{n-1} = -(\boldsymbol{C}_{n-1}\dot{\boldsymbol{x}} + \boldsymbol{B}_{n-1}\boldsymbol{\phi}_{n-1}) \end{cases} \tag{31}$$

where n = number of rational terms; $\boldsymbol{A}_j, \boldsymbol{C}_i, \boldsymbol{B}_i (j = 0,1,2;\ i = 0,1,\dots n-1)$ are parameter matrices which can be determined by model fitting. It can be observed from eq.(31) that the

evolution of $\boldsymbol{\phi}_{n-1}$ depends on inputs $\boldsymbol{x}$, and the evolution of $\boldsymbol{\phi}_i$(i=0,2,…n-2) depends on both $\boldsymbol{x}$ and $\boldsymbol{\phi}_{i+1}$. Each set of state variables $\boldsymbol{\phi}_i$ can be understood as an unsteady correction term to the governing differential equations of *parent variables*. Here, the *parent variables* refer to the lower set of state variables, i.e. $\boldsymbol{\phi}_{i-1}$,or the outputs $\boldsymbol{f}$. Because state variable sets are arranged in series, we call new model the Cascade model.

4.2 Transfer matrix

Laplace transform of eqs.(31) can be written as

$$\begin{Bmatrix} \hat{\boldsymbol{f}} \\ \boldsymbol{0} \\ \boldsymbol{0} \\ \vdots \\ \boldsymbol{0} \\ \boldsymbol{0} \end{Bmatrix} = \begin{bmatrix} \boldsymbol{A}_0 + \boldsymbol{A}_1 s + \boldsymbol{A}_2 s^2 & \boldsymbol{I} & \boldsymbol{0} & \boldsymbol{0} & \dots & \boldsymbol{0} \\ \boldsymbol{C}_0 s & \boldsymbol{B}_0 + \boldsymbol{I}s & \boldsymbol{I} & \boldsymbol{0} & \dots & \boldsymbol{0} \\ \boldsymbol{C}_1 s & \boldsymbol{0} & \boldsymbol{B}_1 + \boldsymbol{I}s & \boldsymbol{I} & \dots & \boldsymbol{0} \\ \vdots & \vdots & \vdots & \vdots & \ddots & \vdots \\ \boldsymbol{C}_{n-2} s & \boldsymbol{0} & \boldsymbol{0} & \boldsymbol{0} & \dots & \boldsymbol{I} \\ \boldsymbol{C}_{n-1} s & \boldsymbol{0} & \boldsymbol{0} & \boldsymbol{0} & \dots & \boldsymbol{B}_{n-1} + \boldsymbol{I}s \end{bmatrix} \begin{Bmatrix} \hat{\boldsymbol{x}} \\ \hat{\boldsymbol{\phi}}_0 \\ \hat{\boldsymbol{\phi}}_1 \\ \hat{\boldsymbol{\phi}}_2 \\ \vdots \\ \hat{\boldsymbol{\phi}}_{n-1} \end{Bmatrix} \tag{32}$$

The expression of $\hat{\boldsymbol{\phi}}_{n-1}$ can be obtained from the nth equation of eqs.(32):

$$\hat{\boldsymbol{\phi}}_{n-1} = -(\boldsymbol{B}_{n-1} + \boldsymbol{I}s)^{-1} \boldsymbol{C}_{n-1} s \hat{\boldsymbol{x}} \tag{33}$$

The recursive equation of $\hat{\boldsymbol{\phi}}_i$(i=0,1,…n-2) can be obtained from the $(i+1)$th equation of eqs. (32):

$$\hat{\boldsymbol{\phi}}_i = (\boldsymbol{B}_i + \boldsymbol{I}s)^{-1} \left(-\boldsymbol{C}_i s \hat{\boldsymbol{x}} - \hat{\boldsymbol{\phi}}_{i+1} \right) \tag{34}$$

Based on eq.(33) and the recurrence relation (34), $\hat{\boldsymbol{\phi}}_k$ can be written as follows:

$$\hat{\boldsymbol{\phi}}_k = \sum_{i=k}^{n-1} \left((-1)^{k-i-1} \left[\prod_{j=i}^{k} \left(\boldsymbol{B}_j + \boldsymbol{I}s \right) \right]^{-1} \boldsymbol{C}_i s \right) \hat{\boldsymbol{x}}, \qquad (k = 0,1, \dots, n-1) \tag{35}$$

Notice that eq.(35) is computationally inefficient since each summation term contains a matrix inversion, which can be extracted outside of the summation symbol as follows:

$$\hat{\boldsymbol{\phi}}_k = \boldsymbol{\Omega}_k^{-1} \left[\sum_{i=k}^{n-2} \left((-1)^{k-i-1} \boldsymbol{\Omega}_{i+1} \boldsymbol{C}_i s \right) + (-1)^{n-k} \boldsymbol{C}_{n-1} s \right] \hat{\boldsymbol{x}}, \qquad (k = 0,1, \dots, n-1) \tag{36}$$

where

$$\boldsymbol{\Omega}_i = \prod_{j=n-1}^{i} \left(\boldsymbol{B}_j + \boldsymbol{I}s \right), \qquad (i = 0,1, \dots, n-1) \tag{37}$$

Substitute the expression of $\hat{\boldsymbol{\phi}}_0$ in (36) into the first equation of (32), one obtains the transfer matrix of the Cascade model:

$$\boldsymbol{T}(s) = \boldsymbol{A}_0 + \boldsymbol{A}_1 s + \boldsymbol{A}_2 s^2 + \boldsymbol{\Omega}_0^{-1} \left[\sum_{i=0}^{n-2} \left((-1)^{i+1} \boldsymbol{\Omega}_{i+1} \boldsymbol{C}_i s \right) + (-1)^n \boldsymbol{C}_{n-1} s \right] \tag{38}$$

It should be noted that transfer matrix $\boldsymbol{T}(s)$ can also be computed by eq.(16); however, eq.(38) is computationally more efficient.

4.3 Quasi-Static limit characteristics

According to eqs. (26) and (27), the Quasi-Static limit stiffness and damping matrices of the Cascade model can be written as

$$\boldsymbol{K}_{s0} = \lim_{s\to 0} \boldsymbol{T}(s) = \boldsymbol{A}_0, \qquad \boldsymbol{C}_{s0} = \lim_{s\to 0} \frac{\mathrm{d}\boldsymbol{T}(s)}{\mathrm{d}s} = \boldsymbol{A}_1 - \boldsymbol{R}_0\boldsymbol{P}^{-1}\boldsymbol{T}_1 \tag{39}$$

where

$$\boldsymbol{T}_1 = \begin{bmatrix} \boldsymbol{C}_0 s \\ \vdots \\ \boldsymbol{C}_{n-1} s \end{bmatrix}, \qquad \boldsymbol{P} = \begin{bmatrix} \boldsymbol{B}_0 & \boldsymbol{I} & \boldsymbol{0} & \dots & \boldsymbol{0} \\ \boldsymbol{0} & \boldsymbol{B}_1 & \boldsymbol{I} & \dots & \boldsymbol{0} \\ \vdots & \vdots & \vdots & \ddots & \vdots \\ \boldsymbol{0} & \boldsymbol{0} & \boldsymbol{0} & \dots & \boldsymbol{I} \\ \boldsymbol{0} & \boldsymbol{0} & \boldsymbol{0} & \dots & \boldsymbol{B}_{n-1} \end{bmatrix}, \qquad \boldsymbol{R}_0 = \left[\underbrace{\boldsymbol{I} \quad \boldsymbol{0} \quad \dots \quad \boldsymbol{0}}_{n}\right] \tag{40}$$

By using the blockwise inversion technique, $\boldsymbol{P}^{-1}$ can be divided into $n \times n$ blocks, each of which can be computed as follows:

$$\boldsymbol{P}^{-1}[i,j] = \begin{cases} (-1)^{j-i} \prod_{r=i}^{j} \boldsymbol{B}_{n-r}^{-1} & (i \le j) \\ \boldsymbol{0} & (i > j) \end{cases}, \qquad (i,j = 0,1,\dots,n-1) \tag{41}$$

4.4 Stability

According to stability condition (22), all real parts of Eigenvalues of $\boldsymbol{P}$ must be positive to make the Cascade model stable. For $\boldsymbol{P}$ shown in (40), this condition can be converted into more efficient ones as follows:

$$\mathrm{Re}(\boldsymbol{\lambda}^{\boldsymbol{B}_i}) > 0, \qquad (i = 0,1,\dots,n-1) \tag{42}$$

where $\boldsymbol{\lambda}^{\boldsymbol{B}_i}$ are Eigenvalues of $\boldsymbol{B}_i$.

4.5 Parameter uniqueness

With transfer matrix expression (38), the Laplace transform of outputs $\boldsymbol{f}$ can be expressed as:

$$\hat{\boldsymbol{f}} = \left\{\boldsymbol{A}_0 + \boldsymbol{A}_1 s + \boldsymbol{A}_2 s^2 + \boldsymbol{\Omega}_0^{-1}\left[\sum_{i=0}^{n-2}\left((-1)^{i+1}\boldsymbol{\Omega}_{i+1}\boldsymbol{C}_i s\right) + (-1)^n \boldsymbol{C}_{n-1} s\right]\right\}\hat{\boldsymbol{x}} \tag{43}$$

Left multiplying $\boldsymbol{\Omega}_0$ on both sides of eq.(43), one obtains

$$\boldsymbol{\Omega}_0\hat{\boldsymbol{f}} = \left\{\boldsymbol{\Omega}_0(\boldsymbol{A}_0 + \boldsymbol{A}_1 s + \boldsymbol{A}_2 s^2) + \sum_{i=0}^{n-2}\left((-1)^{i+1}\boldsymbol{\Omega}_{i+1}\boldsymbol{C}_i s\right) + (-1)^n \boldsymbol{C}_{n-1} s\right\}\hat{\boldsymbol{x}} \tag{44}$$

Notice that $\boldsymbol{\Omega}_0$ defined in eq.(37) can be expanded into a matrix polynomial which has the following form:

$$\boldsymbol{\Omega}_0 = \boldsymbol{H}_0 + \boldsymbol{H}_1 s + \cdots + \boldsymbol{H}_{n-1} s^{n-1} + \boldsymbol{I} s^n \tag{45}$$

Also notice that the coefficient matrix of $\hat{\boldsymbol{x}}$ on the right side of eq.(44) can be expanded into a $n+2$ degree polynomial. Therefore, eq. (44) can be expanded into the following form:

$$(\boldsymbol{H}_0 + \boldsymbol{H}_1 s + \cdots + \boldsymbol{H}_{n-1} s^{n-1} + \boldsymbol{I} s^n)\hat{\boldsymbol{f}} = (\boldsymbol{G}_0 + \boldsymbol{G}_1 s + \cdots + \boldsymbol{G}_{n+2} s^{n+2})\hat{\boldsymbol{x}} \tag{46}$$

where $\boldsymbol{H}_i$ and $\boldsymbol{G}_i$ = matrices resulting from polynomial expansion; $\boldsymbol{H}_i$ = $n_f \times n_f$ matrix; $\boldsymbol{G}_i$ = $n_f \times n_x$ matrix; n_f and n_x = sizes of $\boldsymbol{f}$ and $\boldsymbol{x}$, respectively.

Eq. (46) can be written in time domain as

$$\boldsymbol{f}^{(n)} = \boldsymbol{G}_0\boldsymbol{x} + \boldsymbol{G}_1\dot{\boldsymbol{x}} + \cdots + \boldsymbol{G}_{n+2}\boldsymbol{x}^{(n+2)} - \boldsymbol{H}_0\boldsymbol{f} - \boldsymbol{H}_1\dot{\boldsymbol{f}} - \cdots - \boldsymbol{H}_{n-1}\boldsymbol{f}^{(n-1)} \tag{47}$$

It should be noticed that both eq.(47) and eq.(43) contain $n_f n_f n + n_f n_x(n+3)$ entries in all matrices, indicating that the conversion from eq.(43) to eq. (47) are reversible. It is obvious that different parameters of eq. (47) or (46) will lead to different input-output (or transfer) characteristics. Thus, it can also be concluded that parameters of the Cascade model

are unique.

5 FITTING THE CASCADE MODEL

Matrices $\boldsymbol{A}_0, \boldsymbol{A}_1, \boldsymbol{A}_2, \boldsymbol{C}_0, \boldsymbol{C}_1, \ldots \boldsymbol{C}_{n-1}, \boldsymbol{B}_0, \boldsymbol{B}_1, \ldots, \boldsymbol{B}_{n-1}$ in the Cascade Model can be determined by fitting the transfer matrix (38) and Quasi-Static limit stiffness and damping matrices (39) under the stability constraint (42) by nonlinear Least-Square (LS). We used the Levenberg-Marquardt (LM) algorithm[7] to solve the nonlinear LS problem. LM algorithm requires derivative of each fitting function with respect to each parameter. To obtain these derivatives, we developed a symbolic computation program to deduce derivatives automatically based on the Automatic Differentiation (AD) technique[8]. The AD technique is based on the fact that any algebraic expressions is composed of elementary operations and can be differentiated by successively application of Chain Rule. LM algorithm only searches local-optimal parameters. To ensure a reasonable global-optimal solution, we recommend that several sets of randomly generated initial values should be used.

To examine the model fitting procedure, we fitted the Cascade model against the dimensionless Theodorsen aerodynamic model[9] , which is shown in eq.(48).

$$\begin{Bmatrix} \frac{L}{\rho U^2 B} \\ \frac{M}{\rho U^2 B^2} \end{Bmatrix} = \begin{bmatrix} \pi\left(Gk + \frac{k^2}{4}\right) & \pi\left(\frac{Gk}{4} - F\right) \\ -\frac{\pi}{4}Gk & -\frac{\pi}{4}\left(\frac{Gk}{4} - \frac{k^2}{32} - F\right) \end{bmatrix} \begin{Bmatrix} \frac{h}{B} \\ \alpha \end{Bmatrix} + \begin{bmatrix} -\pi F & -\pi\left(\frac{G}{k} + \frac{1}{4} + \frac{F}{4}\right) \\ \frac{\pi}{4}F & \frac{\pi}{4}\left(\frac{G}{k} - \frac{1}{4} + \frac{F}{4}\right) \end{bmatrix} \begin{Bmatrix} \frac{\dot{h}}{U} \\ \frac{B\dot{\alpha}}{U} \end{Bmatrix} \tag{48}$$

where $k = \omega B/U$ is the dimensionless circular frequency; B = chord length; L = lift force; M = moment force; h = vertical displacement; α = torsional angle; ρ = air density; U = wind velocity; $C(k) = F(k) + iG(k)$ is the frequency-dependent Theodorsen circulation function.

The Cascade model can fit Theodorsen equations accurately with only one rational term, which has 2 state variables. The results are shown in Figure 1. In comparison, the Roger's RFA requires 2 rational terms, which has 4 state variables.

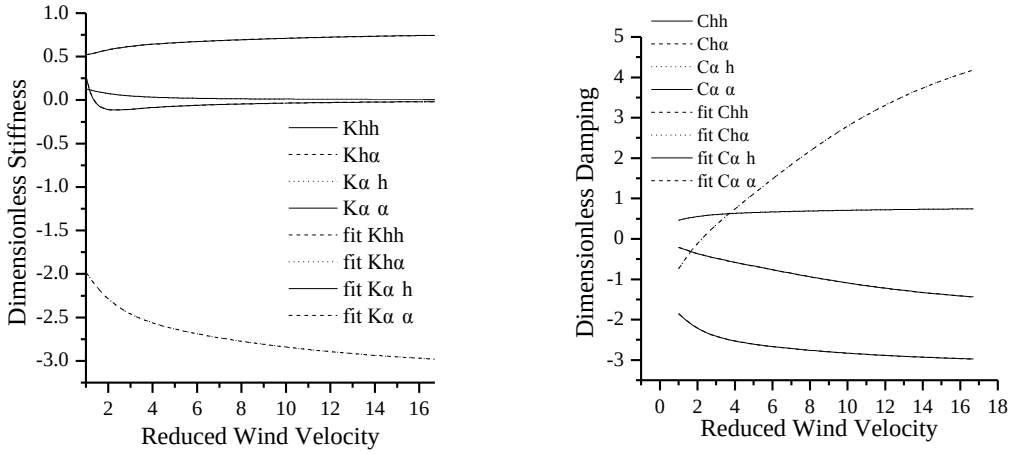

(a) Dimensionless stiffness matrix (b) Dimensionless damping matrix

Figure 1. Fitting dimensionless Theodorsen aerodynamics using the Cascade model

6 BRIDGE DECK SELF-EXCITED FORCES

6.1 Model fitting

In this section, both of flutter derivatives and static coefficients of a bridge deck obtained from section model wind tunnel tests are used to fit the suggested Cascade model. Transfer

matrix of the Cascade model is fitted against following dimensionless unsteady self-excited model expressed in flutter derivatives:

$$\begin{Bmatrix} \frac{L_{se}}{\rho U^2 B} \\ \frac{M_{se}}{\rho U^2 B^2} \end{Bmatrix} = \underbrace{\begin{bmatrix} k^2 H_4^* & k^2 H_3^* \\ k^2 A_4^* & k^2 A_3^* \end{bmatrix}}_{\text{stiffness matrix}} \begin{Bmatrix} \frac{h}{B} \\ \alpha \end{Bmatrix} + \underbrace{\begin{bmatrix} kH_1^* & kH_2^* \\ kA_1^* & kA_2^* \end{bmatrix}}_{\text{damping matrix}} \begin{Bmatrix} \frac{\dot{h}}{U} \\ \frac{B\dot{\alpha}}{U} \end{Bmatrix} \tag{49}$$

where $k = \omega B/U$. flutter derivatives A_i^* and H_i^* are obtained by free vibration tests at 0° Angle of Attack (AoA). They are displayed in Figure 2. In order to increase the number of available flutter derivatives data points, experimentally obtained flutter derivatives are interpolated by Akima interpolation, the interpolation results are shown in Figure 2. Expressions of unsteady nominal stiffness and damping matrices of the Cascade model are obtained using eqs. (17) based on transfer matrix expression (38).

Quasi-Static limit stiffness and damping matrices of the Cascade model are fitted by the following Quasi-Static model which is expressed in static coefficients and their derivatives:

$$\begin{Bmatrix} \frac{L}{\rho U^2 B} \\ \frac{M}{\rho U^2 B^2} \end{Bmatrix} = \underbrace{\frac{1}{2}\begin{bmatrix} 0 & -C_L'(\theta) \\ 0 & C_M'(\theta) \end{bmatrix}}_{\text{stiffness matrix}} \begin{Bmatrix} \frac{h}{B} \\ \alpha \end{Bmatrix} + \underbrace{\frac{1}{2}\begin{bmatrix} -\frac{\mathrm{H}}{\mathrm{B}} C_D(\theta) - C_L'(\theta) & m\frac{\mathrm{H}}{\mathrm{B}} C_D(\theta) + mC_L'(\theta) \\ C_M'(\theta) & -mC_M'(\theta) \end{bmatrix}}_{\text{damping matrix}} \begin{Bmatrix} \frac{\dot{h}}{U} \\ \frac{B\dot{\alpha}}{U} \end{Bmatrix} \tag{50}$$

where C_D, C_L and C_M = drag, lift and moment coefficients, respectively; m = adjustable parameter related to torsional damping coefficients, here $\mathrm{m} = 2$ is used; H/B = height-width ratio of bridge deck, for the tested deck $H/B = 0.1197$. Static coefficients of the tested bridge deck are shown in Figure 3. Only coefficients' values and derivatives at 0° angle of incidence were used.

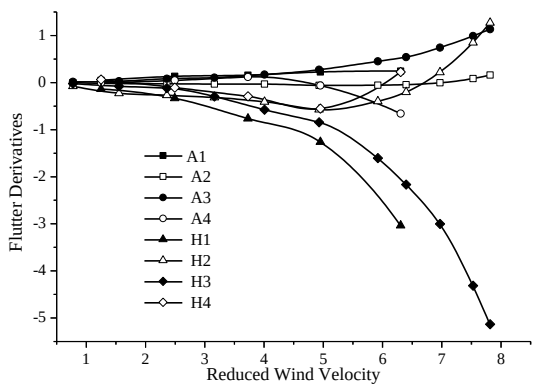

Figure 2. Bridge deck flutter derivatives

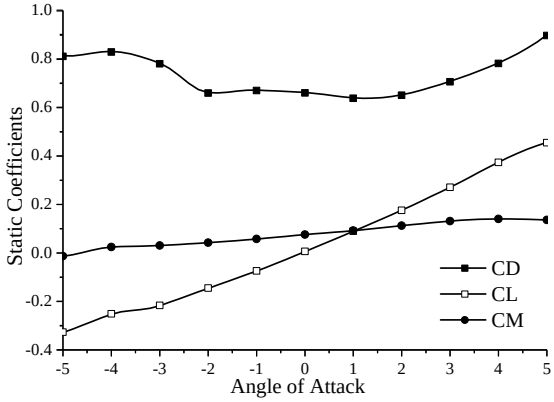

Figure 3. Bridge deck static coefficients

A Cascade model with 4 rational terms is used in fitting. For the 2 DoFs bridge deck system, there are total 8 state variables. Unsteady aerodynamic stiffness and damping matrices and Quasi-Static limit stiffness and damping matrices are fitted simultaneously under the constraint (42). Fitted and target frequency-dependent nominal stiffness and damping matrices are shown in Figure 4. Fitted and target stiffness and damping matrices when reduced wind velocity approaches infinity are shown in Table 1.

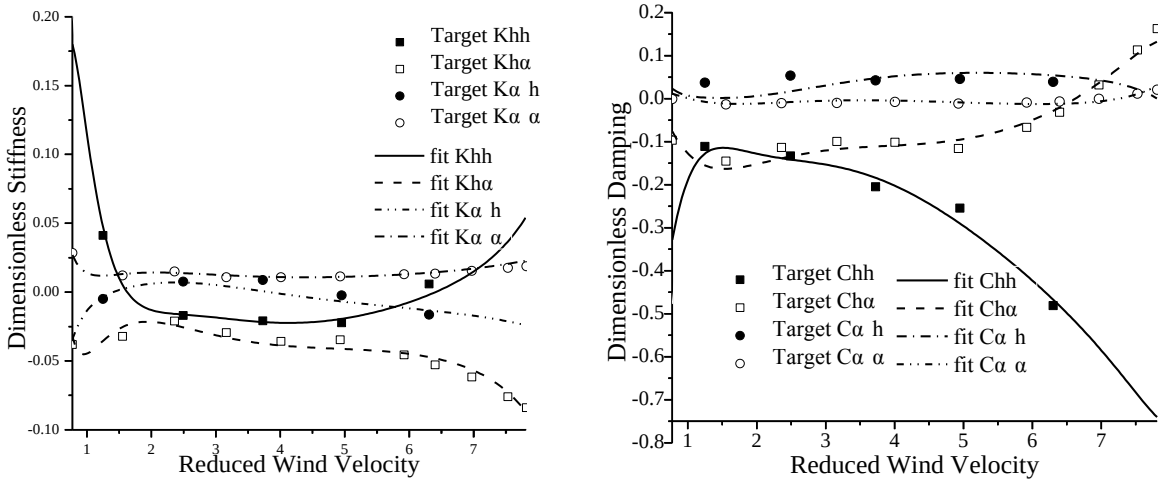

(a) Dimensionless stiffness matrix (b) Dimensionless damping matrix

Figure 4. Fitting results of unsteady nominal stiffness and damping matrices. Target points are computed using flutter derivatives.

Table 1. Fitting results of Quasi-Static limit stiffness and damping matrices.

Quasi-Static limit stiffness matrix				
	K_{hh}	$K_{h\alpha}$	$K_{\alpha\alpha}$	$K_{\alpha h}$
Target	0	-0.0412556	0	0.00869667
Fitted	0.00150069	-0.0416480	-0.000805180	0.00688356
Quasi-Static limit damping matrix				
	C_{hh}	$C_{h\alpha}$	$C_{\alpha\alpha}$	$C_{\alpha h}$
Target	-0.0808154	0.161631	0.00869667	-0.0173933
Fitted	-0.0810962	0.161729	0.00661546	-0.0187633

6.2 Input-output test

A time history containing dimensionless vertical and torsional displacements is used as the input of the fitted Cascade model. The output of the fitted model is compared with the result of traditional frequency-domain analysis which uses flutter derivatives directly.

The input time history consists of a single frequency vibration segment and two zero segments on double ends, as shown in Figure 5. The dimensionless circular frequency of input is 0.3. The phase angle between torsional and vertical displacements is $\mathrm{PI}/2$. To make transitions between zero and non-zero segment smooth, a Turkey window is added to the non-zero segment of the input time history.

Dimensionless self-excited forces caused by the input oscillations are computed in time domain using the fitted Cascade model, and in frequency domain using flutter derivatives for comparison. The 4th order Runge-Kunta method is used in time domain analysis, results of which are shown in Figure 6. The frequency domain analysis is conducted using frequency-response method based on FFT and frequency-response matrix computed from flutter derivatives. Results of frequency-domain analysis are displayed in Figure 7. It can be seem that the output self-excited forces obtained by two approaches are similar.

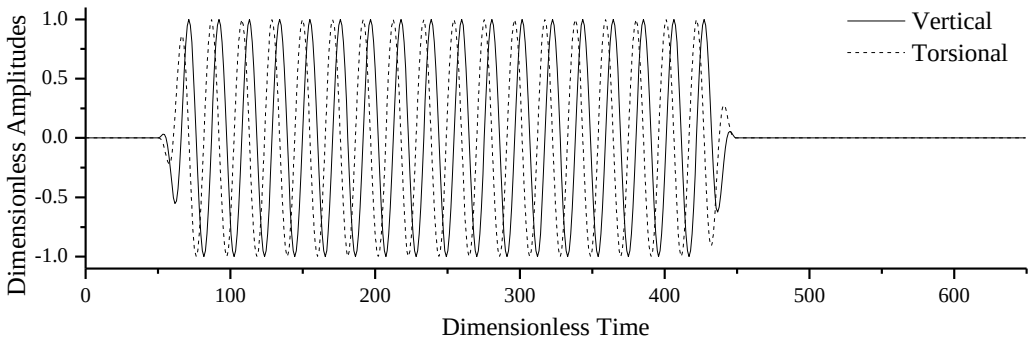

Figure 5. Input time history of vertical and torsional displacements.

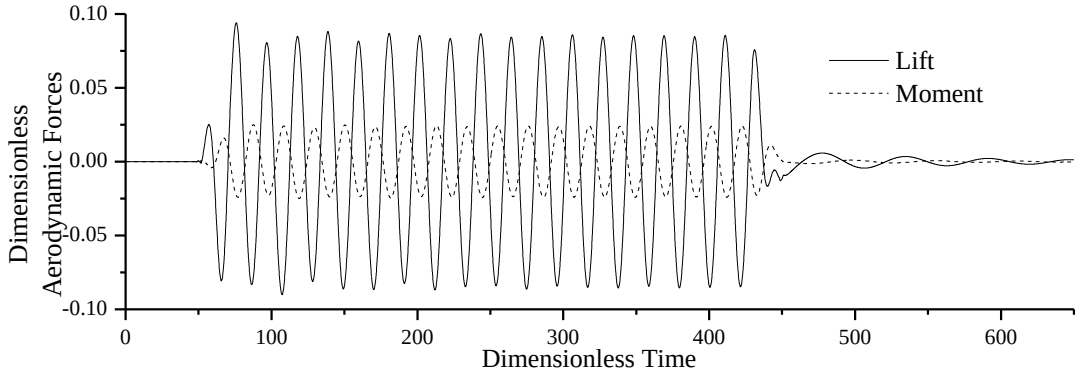

Figure 6. Self-excited forces computed by the fitted Cascade model in time domain

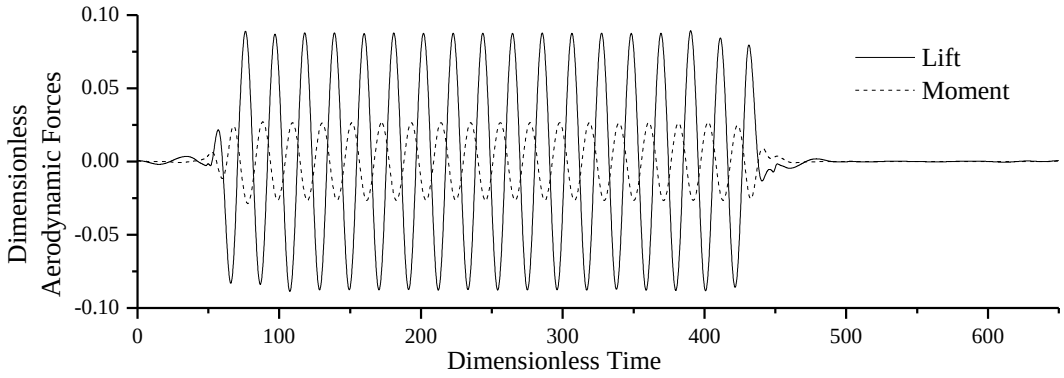

Figure 7. Self-excited forces computed by frequency-domain analysis using flutter derivatives

6.3 Conslusions

It can be seen from Figure 4 that the suggested Cascade model can well fit frequency-dependent aerodynamic stiffness and damping matrices of the tested bridge deck. At the same time, the fitted model approaches the Quasi-Static model when reduced wind velocity approaches infinity, as shown in Table 1. The input-output test showed that there are some differences between the outputs of the fitted model and outputs of frequency analysis based on flutter derivatives. This can be explained as follows: since the model fitting is conducted in a finite frequency range, transfer matrix of the fitted model outside of the frequency range cannot be constrained. The differences are caused by the unconstrained region of the transfer matrix.

7 REFERENCES

[1] Anurag Jain, Nicholas P. Jones, Robert H. Scanlan, Coupled aeroelastic and aerodynamic response analysis of long-span bridges, J. Wind Eng. Ind. Aerodyn., 60(1996) 69-80.

[2] Xinzhong Chen, Masaru Matsumoto, Ahsan Kareem, Time domain flutter and buffeting response analysis of bridges, Journal of Engineering Mechanics, 126(2000) 7-16.

[3] S. Phongkumsinga, K. Wildeb, Y. Fujino, Analytical study on flutter suppression by eccentric mass method on FEM model of long-span suspension bridge, J. Wind Eng. Ind. Aerodyn., 89(2001) 515-534

[4] Zhitian Zhang, Zhengqing Chen, Yiyong Cai, Yaojun Ge, Indicial Functions for Bridge Aeroelastic Forces and Time-Domain Flutter Analysis, Journal of Bridge Engineering, 16(2011) 546-557

[5] G. Diana, D. Rocchi, T. Argentini, S. Muggiasca, Aerodynamic instability of a bridge deck section model: Linear and nonlinear approach to force modeling, J. Wind Eng. Ind. Aerodyn., 98(2010) 363-374.

[6] C. Costa , C. Borri, Application of indicial functions in bridge deck aeroelasticity, J. Wind Eng. Ind. Aerodyn., 94(2006), 859–881.

[7] Jose Pujol, The solution of nonlinear inverse problems and the Levenberg-Marquardt method, Geophysics, 72(2007) W1–W16

[8] A. Griewank, A mathematical view of automatic differentiation. Acta Numerica , 12(2003), 321–398.

[9] R. H. Scanlan, Problematics in formulation of wind-force models for bridge decks, Journal of Engineering Mechanics, 119(1993) 1353-1375

The Seventh International Colloquium on Bluff Body Aerodynamics and Applications (BBAA7)
Shanghai, China; September 2-6, 2012

Non-linear buffeting and flutter analysis of bridges: a frequency domain approach

Luigi Carassale [a], Teng Wu [b], Ahsan Kareem [b]

[a] *University of Genova, via Montallegro 1 Genova, Italy*
[b] *University of Notre Dame, 156 Fitzpatrick Hall, Notre Dame, USA*

ABSTRACT: A frequency domain approach, which is based on the Volterra series expansion, for non-linear bridge aerodynamics is proposed in this paper. The Volterra frequency-response functions (VFRFs) are constructed utilizing the topological assemblage scheme and identified through a full-time-domain non-linear bridge aerodynamic analysis framework. A two-dimensional numerical example of a long-span bridge is presented. The results show good comparison between the time domain simulations and the proposed frequency-domain model for non-linear bridge aerodynamics.

KEYWORDS: Non-linearity; Bridge; Buffeting; Flutter; Volterra series

1 INTRODUCTION

Wind-induced forces on bridges are traditionally represented as the sum of buffeting forces, related to the incoming wind velocity fluctuation, and the self-excited forces, generated by the bridge motion. Both these forces are modelled by linear operators (with memory) whose Frequency Response Functions (FRF) are estimated through specific wind-tunnel tests. On the other hand, when a fluid-structure interaction problem is characterized by high reduced velocity (i.e. the structure time scale is much slower than the fluid time scale) the quasi-steady assumption is invoked and the wind action is represented as a non-linear memory-less transformation of the incoming wind velocity and structural motion, which are often combined in the so-called effective angle of attack. Several experimental experiences suggest that, in some cases, both the mentioned approaches may be inadequate due to the simultaneous presence of both significant nonlinearities and memory effects.

With a specific reference to the case of long-span bridges, some attempts to fill this gap have been made adopting a band-superposition approach in which the quasi-steady model is used to represent the low-frequency part of the forces, while the high-frequency part (both buffeting and self-excited) is modelled through the usual linear models with memory, whose parameters are updated according to the instantaneous low-frequency effective angle of attack [1]. Following this formulation, the high-frequency response is provided by a differential equation whose parameters depend on both time and frequency.

To solve this problem with more efficient computational procedures, Chen & Kareem [2] transformed the problem into a full-time-domain formulation by means of a rational-function approximation and solved the equations of motion in the time domain through an integrate state-space approach. This solution, though mathematically rigorous, consists essentially of a calculation procedure and not a model, thus does not assist in the qualitative assessment of the problem.

In order to circumvent the limitations of the two above approaches, the concept of harmonic-band superposition is revised proposing a full-frequency-domain approach based on the Volterra series expansion of the dynamical systems representing both buffeting and self-excited forces. To this purpose, the governing equations (e.g. [2]) are re-casted into a block-diagram format (Fig. 2) invoking, whenever necessary, polynomial approximations. The synthesis of the result-

ing Volterra system (up to the 3rd order) is carried out adopting the topological assemblage scheme proposed in [3] for scalar systems and generalized in [4] to the case of multi-variate systems.

Section 2 provides some background on Volterra series, with particular reference to its multi-variate form [4]; Section 3 describes the non-linear aeroelastic bridge model assumed as reference; Section 4 shows the synthesis of its Volterra series approximation; Section 5 shows its numerical application for the dynamic analysis of a long-span bridge.

2 VOLTERRA SERIES: THEORETICAL BACKGROUND

Let us consider the nonlinear system represented by the following equation:

$$\mathbf{x}(t) = \mathscr{H}\left[\mathbf{u}(t)\right] \tag{1}$$

$\mathbf{u}(t)$ and $\mathbf{x}(t)$ being vectors with size n and m, respectively, representing the input and the output; t is the time. If the operator $\mathscr{H}[\bullet]$ is time-invariant and has finite-memory, its output $\mathbf{x}(t)$ can be expressed, far enough from the initial conditions, through the Volterra series expansion [e.g. 3, 4]:

$$\mathbf{x}(t) = \sum_{j=0}^{\infty} \int_{\boldsymbol{\tau}_j \in \mathbb{R}^j} \mathbf{h}_j\left(\boldsymbol{\tau}_j\right) \prod_{r=1}^{j} \mathbf{u}\left(t-\tau_r\right) \mathrm{d}\boldsymbol{\tau}_j \tag{2}$$

where $\boldsymbol{\tau}_j = [\tau_1 \ldots \tau_j]^{\mathrm{T}}$ is a vector containing the j integration variables; the functions $\mathbf{h}_j$ have values in $\mathbb{R}^{m \times n^j}$ and are called Volterra kernels. The product operator is interpreted as a sequence of Kronecker products, i.e.:

$$\prod_{r=1}^{j} \mathbf{u}\left(t-\tau_r\right) = \mathbf{u}\left(t-\tau_1\right) \otimes \cdots \otimes \mathbf{u}\left(t-\tau_j\right) \tag{3}$$

The 0th-order term of the Volterra series, $\mathbf{h}_0$, is a constant independent of the input; the 1st-order term is the convolution integral typical of the linear dynamical systems, with $\mathbf{h}_1$ being the impulse response function. The higher-order terms are multiple convolutions involving products of the input values for different time delays.

A Volterra system is entirely determined by its constant output and its Volterra kernels. An alternative representation is provided, in the frequency domain, by the Volterra frequency-response functions (VFRF), the multi-dimensional Fourier transforms of the Volterra kernels:

$$\mathbf{H}_j\left(\boldsymbol{\Omega}_j\right) = \int_{\boldsymbol{\tau}_j \in \mathbb{R}^j} \mathrm{e}^{-\mathrm{i}\boldsymbol{\Omega}_j^{\mathrm{T}}\boldsymbol{\tau}_j} \mathbf{h}_j\left(\boldsymbol{\tau}_j\right) \mathrm{d}\boldsymbol{\tau}_j \tag{4}$$

where $\boldsymbol{\Omega}_j = [\omega_1 \ldots \omega_j]^{\mathrm{T}}$ is a vector containing the j circular frequency values corresponding to $\tau_1, \ldots, \tau_j$ in the Fourier transform pair. The VFRFs are functions with values in $\mathbb{C}^{m \times n^j}$.

3 NON-LINEAR AEROELASTIC BRIDGE MODEL

In this section the non-linear model for the calculation of the aeroelastic response of bridges described in [2] is briefly recalled. For simplicity, the original model is reduced disregarding the effect of the longitudinal turbulence and of the sway degree of freedom; besides, the aerodynamic load is applied to the bridge deck according to the strip theory. These quite strict hypotheses

could be easily relaxed and are here adopted only because the added formal complexity introduced by a more sophisticated bridge model may hide the conceptual structure of the proposed technique. According to this formulation, the dynamic response of the bridge is provided by the differential equation:

$$\mathbf{M}\ddot{\mathbf{x}}+\mathbf{C}\dot{\mathbf{x}}+\mathbf{K}\mathbf{x}=\mathbf{f}_L+\mathbf{f}_H+\mathbf{f}_{se} \tag{5}$$

where $\mathbf{x} = [h, \alpha]^T$ is the displacement vector containing the heave displacement h (positive downwards) and the torsional rotation α (positive nose up), as shown in Fig. 1; the response $\mathbf{x}$ is divided into a low-frequency component $\mathbf{x}_L = [h_L, \alpha_L]^T$ and a high-frequency component $\mathbf{x}_H = [h_H, \alpha_H]^T$, separated by the frequency n_c. $\mathbf{M}$, $\mathbf{C}$ and $\mathbf{K}$ are the mass, viscous damping and stiffness matrixes, respectively; $\mathbf{f}_L$, $\mathbf{f}_H$ and $\mathbf{f}_{se}$ are, respectively, the low-frequency force modeled through a quasi-steady non-linear approach, the high-frequency buffeting force and the self-excited force.

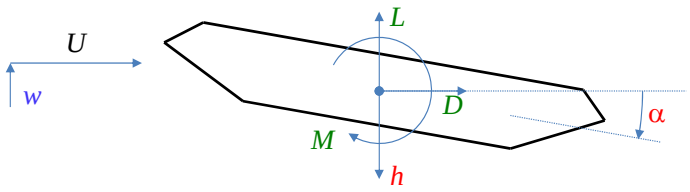

Figure 1. Bridge deck, incoming wind velocity, generalized forces and displacements.

The low-frequency force is defined as:

$$\mathbf{f}_L=\begin{bmatrix}-L\\ M\end{bmatrix}=\frac{1}{2}\rho B l V_r^2\mathbf{R}(\phi)\mathbf{C}(\alpha_e) \tag{6}$$

where ρ is the air density, B the deck width, l the length of the strip on which the load is applied, V_r is the wind-structure relative velocity expressed as:

$$V_r^2=U^2+\left(w_L+\dot{h}_L+m_1 B\dot{\alpha}_L\right)^2 \tag{7}$$

where U is the mean wind velocity, w_L is the low-frequency vertical turbulence (i.e. the vertical turbulence, w, low-pass filtered at the frequency $n = n_c$); $m_1 B$ is the leg for the reduction of the apparent velocity field generated by the torsional velocity; $\mathbf{R}$ is a rotation matrix defined as

$$\mathbf{R}(\phi)=\begin{bmatrix}-\sin\phi & \cos\phi & 0\\ 0 & 0 & 1\end{bmatrix} \tag{8}$$

where ϕ is the apparent (low-frequency) wind angle

$$\phi=\arctan\left(\frac{w_L+\dot{h}_L+m_1 B\dot{\alpha}_L}{U}\right) \tag{9}$$

The vector $\mathbf{C} = [C_D, -C_L, BC_M]^T$ contains the aerodynamic static coefficients, estimated for the effective angle of attack $\alpha_e = \phi + \alpha_L$ through static wind tunnel tests.

The high-frequency buffeting force is modeled as:

$$\mathbf{f}_H = \frac{1}{2}\rho U B l \mathcal{B}\left[w_H;\alpha_e\right] \tag{10}$$

Where w_H is the high-frequency vertical turbulence (i.e. w high-pass filtered at $n = n_c$) and $\mathcal{B}$ is a linear operator whose Frequency-Response Function (FRF) depends of the low-frequency response through the effective angle of attack α_e and is expressed as

$$\mathbf{B}(\omega;\alpha_e) = \begin{bmatrix} -C_D(\alpha_e) - C_L'(\alpha_e) & 0 \\ 0 & C_M'(\alpha_e) \end{bmatrix} \begin{bmatrix} \chi_{wL}(\omega;\alpha_e) \\ \chi_{wM}(\omega;\alpha_e) \end{bmatrix} \tag{11}$$

where C_L' and C_M' are the prime derivatives of C_L and C_M, respectively; χ_{wL} and χ_{wM} are the admittance functions weighting the effect of the vertical turbulence on the lift force and torsional moment, respectively; $\omega = 2\pi n$ is the circular frequency. Since α_e is variable in time due to w_L and $\mathbf{x}_L$, the operator $\mathcal{B}$ may be interpreted as a time-variant linear operator.

The self-excited forces are defined through the model:

$$\mathbf{f}_{se} = \frac{1}{2}\rho B^2 l \mathcal{A}\left[\mathbf{x}_H;\alpha_e\right] \tag{12}$$

where $\mathcal{A}$ is a linear operator whose FRF depends on α_e and is defined as

$$\mathbf{A}(\omega;\alpha_e) = \omega^2 \begin{bmatrix} H_4^*(k;\alpha_e) + \mathrm{i}\,\omega H_1^*(k;\alpha_e) & B\left(H_3^*(k;\alpha_e) + \mathrm{i}\,\omega H_2^*(k;\alpha_e)\right) \\ B\left(A_4^*(k;\alpha_e) + \mathrm{i}\,\omega A_1^*(k;\alpha_e)\right) & B^2\left(A_3^*(k;\alpha_e) + \mathrm{i}\,\omega A_2^*(k;\alpha_e)\right) \end{bmatrix} \tag{13}$$

where $H_j^*(k, \alpha)$ and $A_j^*(k, \alpha)$ are the flutter derivatives estimated at the reduced frequency $k = \omega B/U$ and for a mean angle of attack corresponding to α_e. Likewise the operator $\mathcal{B}$, also $\mathcal{A}$ is linear, but is time-variant because of the dependency on α_e.

4 SYNTHESIS OF A 3RD-ORDER VOLTERRA SYSTEM

In this section, the model described above is synthesized into a 3rd-order Volterra system whose FRFs are calculated adopting the topological assemblage scheme described in [3, 4]. Figure 2 shows a block diagram of the whole system. The input w is separated into w_L and w_H through the low-pass filter $\mathcal{P}_L$ and the high-pass filters $\mathcal{P}_H$, whose FRFs are $P_L(\omega)$ and $P_H(\omega)$, respectively. The output $\mathbf{x}$ is generated by the sum $\mathbf{x}_L$ and $\mathbf{x}_H$ obtained, respectively, as the outputs of the low-frequency and high-frequency stages of the system. A channel delivers the effective angle of attack α_e from the low-frequency stage of the system to its high-frequency stage. The rectangular boxes represent operators defined through a constitutive equation; the boxes with rounded corners are operators defined through experimental data; the triangles are gain blocks; $\mathbf{b}_1 = [1\ 0]$; $\mathbf{b}_2 = [1\ m_1 B]$. The operator $\mathcal{D}$ represents the left-hand side of Eq. (5) and its FRF is $\mathbf{D}(\omega) = -\omega^2\mathbf{M} + \mathrm{i}\omega\mathbf{C} + \mathbf{K}$. The operators $\mathcal{A}_j$ and $\mathcal{B}_j$ (j= 0,…,2) are linear operators whose FRFs, $\mathbf{A}_j$ and $\mathbf{B}_j$, are obtained by a polynomial approximation of $\mathbf{A}$ and $\mathbf{B}$ given by Eq. (11) and (13)

$$\mathbf{A}(\omega;\alpha_e) = \sum_{j=0}^{2} \mathbf{A}_j(\omega)\alpha_e^j; \qquad \mathbf{B}(\omega;\alpha_e) = \sum_{j=0}^{2} \mathbf{B}_j(\omega)\alpha_e^j \tag{14}$$

$\mathbf{A}_j$ and $\mathbf{B}_j$ (j = 0,..,2) are the FRFs of the time-invariant linear operators $\mathcal{A}_j$ and $\mathcal{B}_j$ and represented in Figure 2. Let us assume that the low-frequency and the high-frequency stages of the system can be represented by the operators

$$\mathbf{x}_L = \mathscr{L}[w]; \qquad \mathbf{x}_H = \mathscr{H}[w] \tag{15}$$

and assume that they can be expanded into convergent Volterra series, at least for the range of input amplitude relevant for the application.

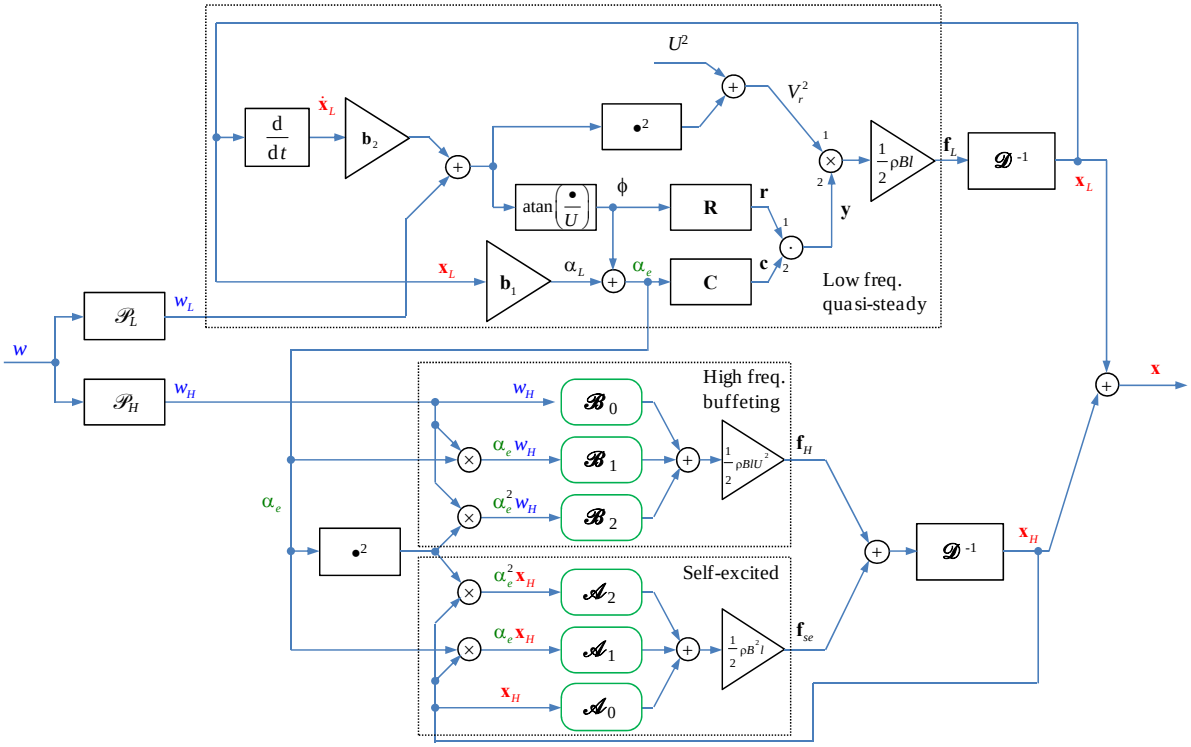

Figure 2. Block diagram of the nonlinear aeroelastic bridge model.

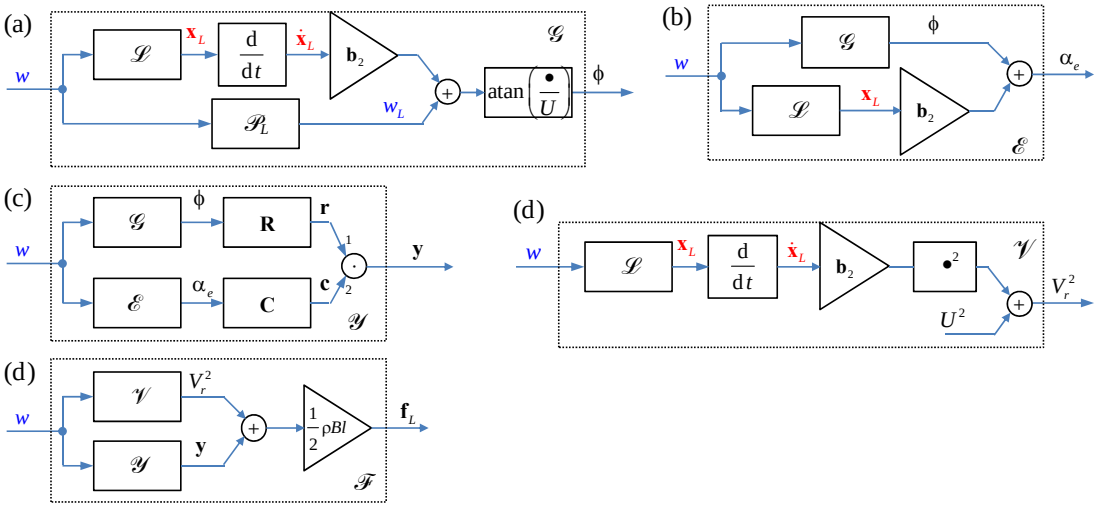

Figure 3. Block diagram of the sub-systems composing the low-frequency stage.

4.1 *Low-frequency stage*

Due to its topology, the identification of the system must start from the synthesis of the components of $\mathscr{L}$. Let $\mathscr{G}$ be the operator providing ϕ given w, described by the block diagram reported in Figure 3a. Its VFRFs G_j can be expressed as the sum of a direct term $G_j^{(d)}$ that does not depends on $\mathbf{L}_j$ and a feedback term $G_j^{(f)}$ that is linear in $\mathbf{L}_j$ [3, 4].

$$
\begin{aligned}
&G_0 = G_2^{(d)} = 0 \\
&G_1^{(d)}(\omega) = \frac{1}{U} P_L(\omega) \\
&G_3^{(d)}(\boldsymbol{\Omega}_3) = -\frac{1}{3U^3}\left[\prod_{r=1}^{3} P_L(\omega_r) + \prod_{r=1}^{3} \mathrm{i}\,\omega_r \mathbf{b}_2 \mathbf{L}(\omega_r)\right] \\
&G_j^{(f)}(\boldsymbol{\Omega}_j) = \frac{1}{U}\mathrm{i}\,\Sigma\boldsymbol{\Omega}_j \mathbf{b}_2 \mathbf{L}_j(\boldsymbol{\Omega}_j) \qquad (j = 1,2,3)
\end{aligned}
\tag{16}
$$

where $\Sigma\boldsymbol{\Omega}_j = \omega_1 + \ldots + \omega_j$. Figure 3b shows the block diagram of the operator $\mathscr{E}$ providing the effective angle of attack α_e. Its VFRFs $E_j = E_j^{(d)} + E_j^{(f)}$ are given as:

$$
\begin{aligned}
&E_0 = \mathbf{b}_1 \mathbf{L}_0 = \alpha_0 \\
&E_j^{(d)}(\boldsymbol{\Omega}_j) = G_j^{(d)}(\boldsymbol{\Omega}_j) \\
&E_j^{(f)}(\boldsymbol{\Omega}_j) = G_j^{(f)}(\boldsymbol{\Omega}_j) + \mathbf{b}_1 \mathbf{L}_j(\boldsymbol{\Omega}_j)
\end{aligned}
\qquad (j = 1,2,3)
\tag{17}
$$

where α_0 is the angle of attack obtained for $w = 0$. Figure 3c shows the block diagram of the operator $\mathscr{Y}$ providing the vector $\mathbf{y} = \mathbf{R}(\phi)\mathbf{C}(\alpha_e)$. The matrix $\mathbf{R}$ and the vector $\mathbf{C}$ are approximated by 3rd-order polynomials of ϕ and α_e, respectively.

$$
\mathbf{R}(\phi) = \sum_{j=1}^{3} \mathbf{R}_j \phi^j; \qquad \mathbf{C}(\alpha_e - \alpha_0) = \sum_{j=1}^{3} \mathbf{C}_j (\alpha_e - \alpha_0)^j
\tag{18}
$$

The VFRFs of $\mathscr{Y}$ are then in the form:

$$
\begin{aligned}
&\mathbf{Y}_0 = \mathbf{R}_0 \mathbf{C}_0 \\
&\mathbf{Y}_1^{(d)}(\omega) = \mathbf{R}_0 \bar{\mathbf{C}}_1^{(d)}(\omega) + \bar{\mathbf{R}}_1^{(d)}(\omega)\mathbf{C}_0 \\
&\mathbf{Y}_2^{(d)}(\boldsymbol{\Omega}_2) = \mathbf{R}_0 \bar{\mathbf{C}}_2^{(d)}(\boldsymbol{\Omega}_2) + \bar{\mathbf{R}}_1(\omega_1)\bar{\mathbf{C}}_1(\omega_2) + \bar{\mathbf{R}}_2^{(d)}(\boldsymbol{\Omega}_2)\mathbf{C}_0 \\
&\mathbf{Y}_3^{(d)}(\boldsymbol{\Omega}_3) = \mathbf{R}_0 \bar{\mathbf{C}}_3^{(d)}(\boldsymbol{\Omega}_3) + \bar{\mathbf{R}}_2(\omega_1,\omega_2)\bar{\mathbf{C}}_1(\omega_3) + \bar{\mathbf{R}}_1(\omega_1)\bar{\mathbf{C}}_2(\omega_2,\omega_3) + \bar{\mathbf{R}}_3^{(d)}(\boldsymbol{\Omega}_3)\mathbf{C}_0 \\
&\mathbf{Y}_j^{(f)}(\boldsymbol{\Omega}_j) = \mathbf{R}_0 \bar{\mathbf{C}}_j^{(f)}(\boldsymbol{\Omega}_j) + \bar{\mathbf{R}}_j^{(f)}(\boldsymbol{\Omega}_j)\mathbf{C}_0 \qquad (j = 1,2,3)
\end{aligned}
\tag{19}
$$

where $\bar{\mathbf{R}}_j = \bar{\mathbf{R}}_j^{(d)} + \bar{\mathbf{R}}_j^{(f)}$ are given as

$$
\begin{aligned}
&\bar{\mathbf{R}}_0 = \mathbf{R}_0 \\
&\bar{\mathbf{R}}_1^{(d)}(\omega) = \mathbf{R}_1 G_1^{(d)}(\omega) \\
&\bar{\mathbf{R}}_2^{(d)}(\boldsymbol{\Omega}_2) = \mathbf{R}_2 G_1(\omega_1) G_1(\omega_2) \\
&\bar{\mathbf{R}}_3^{(d)}(\boldsymbol{\Omega}_3) = \mathbf{R}_1 G_3^{(d)}(\boldsymbol{\Omega}_3) + 2\mathbf{R}_2 G_1(\omega_1) G_2(\omega_2, \omega_3) + \mathbf{R}_3 G_1(\omega_1) G_1(\omega_2) G_1(\omega_3) \\
&\bar{\mathbf{R}}_j^{(f)}(\boldsymbol{\Omega}_j) = \mathbf{R}_1 G_j^{(f)}(\boldsymbol{\Omega}_j) \qquad (j = 1,2,3)
\end{aligned}
\tag{20}
$$

The VFRFs $\bar{\mathbf{C}}_j = \bar{\mathbf{C}}_j^{(d)} + \bar{\mathbf{C}}_j^{(f)}$ can be obtained through Eq. (20) by replacing $\mathbf{R}_j$ with $\mathbf{C}_j$ and G_j with E_j. Figure 3d shows the block diagram of the operator $\mathscr{V}$ providing V_r^2. Its VFRFs are given as

$$
\begin{aligned}
&V_0 = U^2 \\
&V_1 = 0 \\
&V_2(\boldsymbol{\Omega}_2) = P_L(\omega_1) P_L(\omega_2) - \omega_1\omega_2 \mathbf{b}_2 \mathbf{L}_1(\omega_1) \mathbf{b}_2 \mathbf{L}_1(\omega_2) + 2P_L(\omega_1) \mathbf{b}_2 \mathbf{L}_1(\omega_2) \\
&V_3(\boldsymbol{\Omega}_3) = 2\mathrm{i} P_L(\omega_1)(\omega_2 + \omega_3) \mathbf{b}_2 \mathbf{L}_2(\omega_2, \omega_3) - 2\omega_1(\omega_2 + \omega_3) \mathbf{b}_2 \mathbf{L}_1(\omega_1) \mathbf{b}_2 \mathbf{L}_2(\omega_2, \omega_3)
\end{aligned}
\tag{21}
$$

Figure 3e shows the operator $\mathscr{F}$ providing the low-frequency force $\mathbf{f}_L$. Its VFRFs $\mathbf{F}_j = \mathbf{F}_j^{(d)} + \mathbf{F}_j^{(f)}$ are given as:

$$
\begin{aligned}
&\mathbf{F}_0 = \frac{1}{2}\rho B l V_0 \mathbf{Y}_0 \\
&\mathbf{F}_1^{(d)}(\omega) = \frac{1}{2}\rho B l V_0 \mathbf{Y}_1^{(d)}(\omega) \\
&\mathbf{F}_2^{(d)}(\boldsymbol{\Omega}_2) = \frac{1}{2}\rho B l \left(V_0 \mathbf{Y}_2^{(d)}(\boldsymbol{\Omega}_2) + V_2(\boldsymbol{\Omega}_2) \mathbf{Y}_0 \right) \\
&\mathbf{F}_3^{(d)}(\boldsymbol{\Omega}_3) = \frac{1}{2}\rho B l \left(V_0 \mathbf{Y}_3^{(d)}(\boldsymbol{\Omega}_3) + V_2(\omega_1, \omega_2) \mathbf{Y}_1(\omega_3) + V_3(\boldsymbol{\Omega}_3) \mathbf{Y}_0 \right) \\
&\mathbf{F}_j^{(f)}(\boldsymbol{\Omega}_j) = \frac{1}{2}\rho B l V_0 \mathbf{Y}_j^{(f)}(\boldsymbol{\Omega}_j) \qquad (j = 1,2,3)
\end{aligned}
\tag{22}
$$

The VFRFs of the operator $\mathscr{S}$ providing the low-frequency response can be obtained by equating the VFRFs of the operators $\mathscr{D}[\mathscr{D}[\bullet]]$ and $\mathscr{F}$, leading to the equations:

$$
\begin{aligned}
&\mathbf{L}_0 = \mathbf{D}(0)^{-1} \mathbf{F}_0 \\
&\mathbf{D}(\Sigma\boldsymbol{\Omega}_j) \mathbf{L}_j(\boldsymbol{\Omega}_j) - \mathbf{F}_j^{(f)}(\boldsymbol{\Omega}_j) = \mathbf{F}_j^{(d)}(\boldsymbol{\Omega}_j) \qquad (j = 1,2,3)
\end{aligned}
\tag{23}
$$

The 0^{th}-order equation is non-linear due to the dependency of the polynomial approximation of the aerodynamic coefficients from the α_0 (Eq. (18)). The other equations are linear in $\mathbf{L}_j$ ($\mathbf{F}_j^{(f)}$ is linear in $\mathbf{L}_j$) and contain lower-order solutions ($\mathbf{L}_k$ with $k < j$) in the term $\mathbf{F}_j^{(d)}$.

4.2 *High-frequency stage*

The synthesis of the high-frequency stage of the system requires the identification of the operators $\bar{\mathscr{A}}$ and $\bar{\mathscr{B}}$ providing, respectively the high-frequency buffeting force $\mathbf{f}_H$ and the self-excited force $\mathbf{f}_{se}$ (Figure 4). Their VFRFs, respectively, $\bar{\mathbf{A}}_j = \bar{\mathbf{A}}_j^{(d)} + \bar{\mathbf{A}}_j^{(f)}$ and $\bar{\mathbf{B}}_j$ are given as

$$
\begin{aligned}
&\bar{\mathbf{A}}_0 = \mathbf{0} \\
&\bar{\mathbf{A}}_1^{(d)}(\omega) = \mathbf{0} \\
&\bar{\mathbf{A}}_2^{(d)}(\boldsymbol{\Omega}_2) = \mathbf{A}_1(\Sigma\boldsymbol{\Omega}_2)\,\mathbf{H}_1(\omega_1)\,E_1(\omega_2) \\
&\bar{\mathbf{A}}_3^{(d)}(\boldsymbol{\Omega}_3) = \mathbf{A}_1(\Sigma\boldsymbol{\Omega}_3)\left[\mathbf{H}_1(\omega_1)\,E_2(\omega_2,\omega_3) + \mathbf{H}_2(\omega_1,\omega_2)\,E_1(\omega_3)\right] + \mathbf{A}_2(\Sigma\boldsymbol{\Omega}_3)\,\mathbf{H}_1(\omega_1)\,E_1(\omega_2)\,E_1(\omega_3) \\
&\bar{\mathbf{A}}_j^{(f)}(\boldsymbol{\Omega}_j) = \mathbf{A}_0(\Sigma\boldsymbol{\Omega}_j)\,\mathbf{H}_j(\boldsymbol{\Omega}_j) \qquad (j = 1,2,3)
\end{aligned}
\tag{24}
$$

$$
\begin{aligned}
&\bar{\mathbf{B}}_0 = \mathbf{0} \\
&\bar{\mathbf{B}}_1(\omega) = \mathbf{B}_0(\omega)\,P_H(\omega) \\
&\bar{\mathbf{B}}_2(\boldsymbol{\Omega}_2) = \mathbf{B}_1(\Sigma\boldsymbol{\Omega}_2)\,P_H(\omega_1)\,E_1(\omega_2) \\
&\bar{\mathbf{B}}_3(\boldsymbol{\Omega}_3) = \mathbf{B}_1(\Sigma\boldsymbol{\Omega}_3)\,P_H(\omega_1)\,E_2(\omega_2,\omega_3) + \mathbf{B}_2(\Sigma\boldsymbol{\Omega}_3)\,P_H(\omega_1)\,E_1(\omega_2)\,E_1(\omega_3)
\end{aligned}
\tag{25}
$$

The FRFs $\mathbf{H}_j$ of $\mathscr{H}$ can be obtained by equating, order by order, the VFRFs of the systems $\mathscr{D}[\mathscr{H}[\bullet]]$ and $\bar{\mathscr{A}} + \bar{\mathscr{B}}$, leading to the equations:

$$
\mathbf{D}(\Sigma\boldsymbol{\Omega}_j)\,\mathbf{H}_j(\boldsymbol{\Omega}_j) - \bar{\mathbf{A}}_j^{(f)}(\boldsymbol{\Omega}_j) = \bar{\mathbf{A}}_j^{(d)}(\boldsymbol{\Omega}_j) + \bar{\mathbf{B}}_j(\boldsymbol{\Omega}_j) \qquad (j = 1,2,3) \tag{26}
$$

which can be solved with respect to $\mathbf{H}_j$ since $\bar{\mathbf{A}}_j^{(f)}$ is linear in $\mathbf{H}_j$. It can be observed that the j^{th}-order high-frequency response is influenced by the low-frequency response up to the order j-1 through the VFRFs E_k (k = 1,..,j-1).

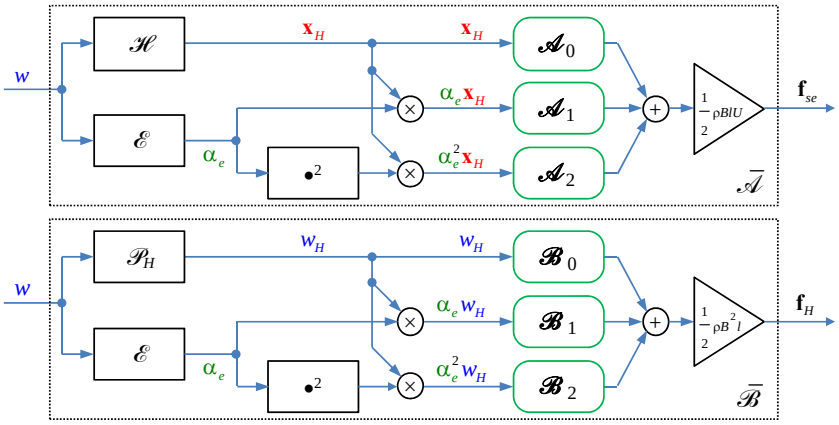

Figure 4. High-frequency stage.

5 NUMERICAL APPLICATION

The accuracy of the Volterra series representation of the non-linear aeroelastic bridge model described in Section 3 is demonstrated through the calculation of the response of a long-span bridge. The static coefficients of the cross section are measured for angle of attack between -10° and 10° with step 1°. These data are approximated through 3$^{\text{rd}}$-order polynomials through a mean-square error minimization procedure [3] (Figure 5a). The admittance function is modeled

through the Sears function and is independent of the angle of attack. The flutter derivatives are estimated for α = -3°, 0°, 3° and are interpolated, for each reduced velocity value, through a 2nd-order polynomial (Figure 5b). The natural frequency of the two considered modes is n_1 = 0.19 Hz and n_2 = 0.53 Hz. The frequency value dividing low and high-frequency components is n_c = 0.10 Hz.

Figure 6 shows the low-frequency response calculated through a Volterra model with order from 1 to 3, compared with the exact non-linear response calculated by a standard ODE solver. The result of the 3rd-order Volterra series appears quite accurate, in particular if compared to the linear model (1st-order Volterra series) which fails in reproducing the torsional response mainly due to its implicit symmetry.

Figure 7 shows the high-frequency response calculated through a Volterra model with order from 1 to 3, compared with the solution obtained by the time-domain procedure proposed in [2]. Also for this response component the 3rd-order Volterra series approximation provides a response very close to the time-domain solution.

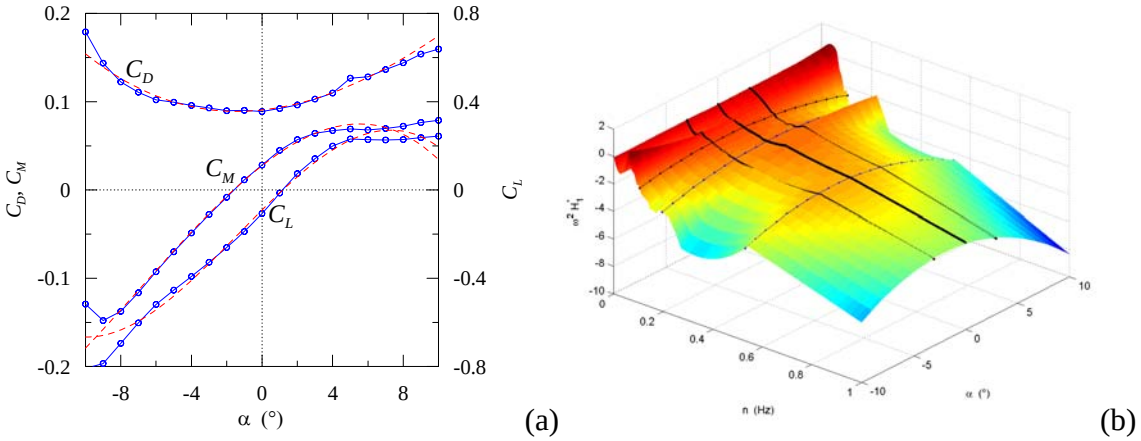

Figure 5. Static aerodynamic coefficients (a); flutter derivative H_1^* function of the mean angle of attack.

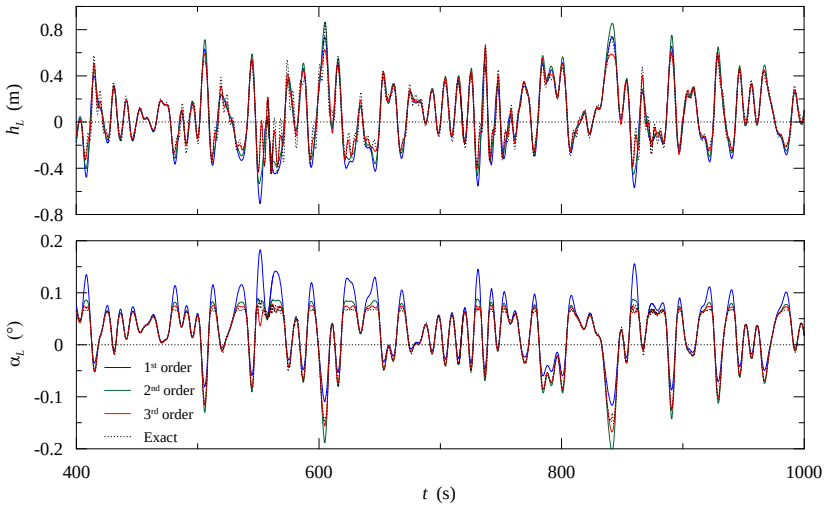

Figure 6. Low-frequency response.

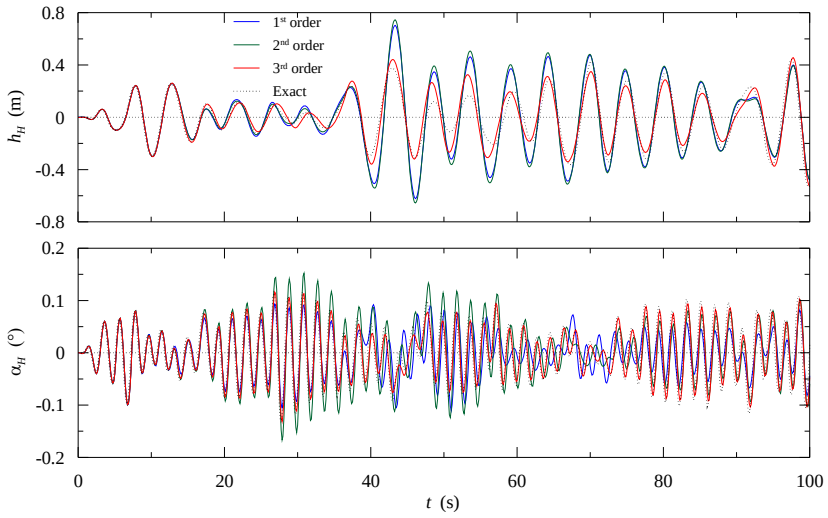

Figure 7. High-frequency response.

6 CONCLUSIONS

The proposed model is essentially the translation of an existing analysis procedure to the frequency domain, and therefore it inherits all its conceptual advantages and limitations (in particular, it is based on the hypothesis of small high-frequency oscillation of the bridge around a slow, possibly large, variation of the effective angle of attack). The added value of this new formulation is mostly related to its potential for deriving qualitative interpretations through this model. Besides, the functional structure of the proposed model may serve as a scaffolding to construct a fully-nonlinear model based on the Volterra series representation, to be identified from ad-hoc experimental procedures.

From a computational point of view, the implementation of the model in the framework of the Volterra series enables the formulation of a very efficient frequency-domain solution based on the concept of Associated Linear Equations (ALE). Accordingly, the model defined herein can be implemented through six linear frequency-domain equations that can be conveniently solvedin a cascade manner.

ACKNOWEDGEMENT

The support of this project was made possible by NSF Grant # CMMI 09 28282

REFERENCES

1 G.Diana, M. Falco, S. Bruni, A. Cigada, G.L. Larose, A. Damsgaard, A. Collina, Comparisons between wind tunnel tests on a full aeroelastic model of the proposed bridge over Stretto di Messina and numerical results. J. Ind. Aerodyn., 54-55 (1995), 101-113.
2 X. Chen, A. Kareem, Aeroelastic analysis of bridges: effects of turbulence and aerodynamic nonlinearities, J. Engrg. Mech. ASCE, 129 (2003), 8.
3 L. Carassale, A. Kareem, Modeling nonlinear systems by Volterra Series, J. Engrg. Mech. ASCE, 136 (2010), 6.
4 L. Carassale, A. Kareem, Synthesis of multi-input Volterra systems by a topological assemblage scheme, In Proc. Conf. on Non-linear Dynamics and Diagnosis, Marrakech, Morrocco, 2012.

The Seventh International Colloquium on Bluff Body Aerodynamics and Applications (BBAA7)
Shanghai, China; September 2-6, 2012

Frequency- and Time-domain Aeroelastic Analysis of Cable-Supported Bridges using Approximated Aerodynamic Transfer Functions

Kilje Jung [a], Hae Sung Lee [b], Ho-Kyung Kim [c]

[a]*Department of Civil and Environmental Engineering, Seoul National University, Seoul, Korea*
[b]*Department of Civil and Environmental Engineering, Seoul National University, Seoul, Korea*
[c]*Department of Civil and Environmental Engineering, Seoul National University, Seoul, Korea*

ABSTRACT: An approximate approach for the frequency- and time-domain aeroelastic analysis of bridge decks is presented. The aerodynamic transfer functions are approximated as a linear function with the coefficients determined through minimization of the weighted error between the exact and approximated transfer function. The weighting function in optimization is introduced for the improved approximation. Using the proposed method, the frequency dependence of the aerodynamic transfer function is eliminated, and a popular time marching algorithm is adopted for the aeroelastic analysis in the time domain. For the frequency domain analysis, a complete set of modal frequencies and modal shapes can be evaluated in a single eigenvalue analysis.

KEYWORDS: *Aeroelasticity; Weighted least square method; Cable-supported bridge; Self-excited force; Flutter analysis; Buffeting analysis*.

1 INTRODUCTION

For aeroelastic analyses of bridge decks under wind action, numerous approaches have been proposed since Scanlan and Tomko[1] defined self-excited forces using flutter derivatives. The difficulty in aeroelastic analysis basically arises from the frequency dependence of self-excited forces. For the frequency-domain aeroelastic analysis, an iterative procedure is required to solve the nonlinear eigenvalue problem, which is referred to as branch method[2]. The critical issue in the time-domain approach is the elimination of the frequency-dependent characteristics of the aerodynamic forces, for which the convolution integral is usually utilized. The impulse response functions are formed with the identified flutter derivatives through optimization in the frequency domain, and the aerodynamic forces are expressed as convolutions between the impulse response functions and the deck motion. The rational function approximation (RFA) has been the most popular approach for forming impulse response functions for the convolution integral[3]. Despite its popularity, however, Caracoglia and Jones[4] reported on the potential limitations of the RFA method on its applicability to bluff sections. Recently, Jung et al. [5] proposed a new algorithm for evaluating impulse response functions through a domain-discretization approximation to overcome the shortcomings of the RFA.

Although the convolution integral approach and the branch method can be successfully applied to time-domain and frequency-domain analyses, respectively, for various

types of sections, they are based on different approximations. The impulse response functions used for the convolution integral become inconsistent with the given flutter derivatives of a section through optimization, while the aerodynamic forces are evaluated at only one assumed frequency in the branch method. Therefore, the consistency between results of a time-domain analysis and a frequency-domain analysis cannot be generally guaranteed.

This paper presents a new unified approach for the aeroelastic analysis of a bridge structure by approximating each component of the aerodynamic transfer functions in frequency domain. Using this approximation, the equation of motion for an aeroelastic system becomes a set of simple second-order differential equations in the time domain. The coefficients of the second-order polynomial are determined through minimization of weighted errors between the exact and approximated aerodynamic transfer function in the frequency domain. The validity of the proposed method is demonstrated by applying to an idealized cable-supported structure.

2 AN APPROXIMATED APPROACH FOR THE AEROELASTIC ANALYSIS

2.1 *Equation of motion of a cable bridge under wind action*

The dynamic virtual work expression of a discretized structure under the action of wind is given as follows:

$$\delta\mathbf{U}^T\mathbf{M}\ddot{\mathbf{U}} + \delta\mathbf{U}^T\mathbf{C}\dot{\mathbf{U}} + \delta\mathbf{U}^T\mathbf{K}\mathbf{U} = \delta\Pi_{ad} + \delta\mathbf{U}^T\mathbf{P}_{ex} \tag{1}$$

where **M**, **C**, **K**, $\mathbf{P}_{ex}$ and **U** are the mass, damping, stiffness matrix of the discretized structural system, the equivalent nodal force vector and the nodal displacements vector, respectively, and δ, when placed in front of a variable, indicates a virtual quantity. The external virtual work done by wind-induced aerodynamic forces is denoted as $\delta\Pi_{ad}$ in Eq. (1), and defined as the summation of the contribution from each element.

$$\delta\Pi_{ad} = \sum_e \delta\Pi_{ad}^e = \sum_e \int_{l^e} (\delta h^e \cdot L_{ad}^e + \delta\alpha^e \cdot M_{ad}^e)dx \tag{2}$$

where and are the aerodynamic lift force and torsional moment per unit length in the local coordinate system for element e, respectively, while h^e and α^e are the vertical and torsional displacement defined also in the local coordinate system, respectively.

In accordance with the Scanlan and Tomko's formulation[1], the self-excited forces acting on a sinusoidally oscillating section in a single frequency are defined as:

$$L_{ae} = \frac{1}{2}\rho U^2 B[KH_1^*\frac{\dot{h}}{U} + KH_2^*\frac{B\dot{\alpha}}{U} + K^2H_3^*\alpha + K^2H_4^*\frac{h}{B}]$$
$$M_{ae} = \frac{1}{2}\rho U^2 B^2[KA_1^*\frac{B\dot{h}}{U} + KA_2^*\frac{B\dot{\alpha}}{U} + K^2A_3^*\alpha + K^2A_4^*\frac{h}{B}] \tag{3}$$

where ρ is the air density, U is the mean wind velocity, B is the width of the section model. $K=B\omega/U$ is the reduced frequency where ω is the angular frequency of the oscillation. The flutter derivatives are denoted as H_m^* and A_m^* (m=1,2,3,4), and are functions of the angular frequency. Because of this frequency dependence, the self-excited forces are usually defined in the frequency domain as follows [5]:

$$\begin{aligned}\begin{pmatrix} F(L_{ad}) \\ F(M_{ad}) \end{pmatrix} &= \frac{1}{2}\rho U^2 \begin{bmatrix} iK^2H_1^* + K^2H_4^* & B(iK^2H_2^* + K^2H_3^*) \\ B(iK^2A_1^* + K^2A_4^*) & B^2(iK^2A_2^* + K^2A_3^*) \end{bmatrix} \begin{pmatrix} F(h) \\ F(\alpha) \end{pmatrix} \\ &= \begin{bmatrix} \Psi_{hh} & \Psi_{h\alpha} \\ \Psi_{\alpha h} & \Psi_{\alpha\alpha} \end{bmatrix} \begin{pmatrix} F(h) \\ F(\alpha) \end{pmatrix} = \mathbf{\Psi}(\omega) F(\mathbf{u}^e) \end{aligned} \tag{4}$$

where F denotes the Fourier transform, and $\mathbf{u}^e$ is the displacement vector containing local displacement components h^e and α^e. Ψ_{mn} is the transfer function between the aeroelastic forces in the m direction and the motion in the n direction, and i is the imaginary unit. Using a standard finite element procedure for the interpolation and the coordinate rotation procedure, the displacement vector in Eq. (4) is expressed in terms of the nodal displacement vector of the discretized structure, **U**, defined in the structural coordinate system.

$$\mathbf{u}^e = \mathbf{N}^e \mathbf{\Gamma}^e \mathbf{T}^e \mathbf{U}$$

(5) $\mathbf{N}^e$ $\mathbf{\Gamma}^e$ $\mathbf{T}^e$

where , and are the shape function matrix for the local displacement vector, the transformation matrix between the local and structural coordinate system and the compatibility matrix that relates h^e and α^e to the structural displacement vector, respectively. The virtual work done by the aerodynamic forces in the frequency domain can easily be obtained using Eq. (4) and Eq. (5).

$$\begin{aligned} F(\delta\Pi_{ad}) &= F(\sum_e \delta\Pi_{ad}^e) = \sum_e \int_{l^e} (\delta h^e \cdot F(L_{ad}^e) + \delta\alpha^e \cdot F(M_{ad}^e)) dx \\ &= \sum_e \int_{l^e} (\delta\mathbf{u}^e)^T \mathbf{\Psi}^e F(\mathbf{u}^e)) dx = \delta\mathbf{U}^T \sum_e (\mathbf{\Gamma}^e\mathbf{T}^e)^T \int_{l^e} (\mathbf{N}^e)^T \mathbf{\Psi}^e \mathbf{N}^e dx \mathbf{\Gamma}^e \mathbf{T}^e F(\mathbf{U}) \\ &= \delta\mathbf{U}^T \mathbf{\Psi}(\omega) F(\mathbf{U}) \end{aligned} \tag{6}$$

where $\mathbf{\Psi}$ is referred to as the aerodynamic transfer function defining the aerodynamic force in terms of the displacement in the frequency domain.

The Fourier transform of Eq. (1) yields the dynamic virtual work expression of an aeroelastic system in the frequency domain.

$$F(\delta\Pi) = \delta\mathbf{U}^T([-\omega^2\mathbf{M} + i\omega\mathbf{C} + \mathbf{K} - \mathbf{\Psi}(\omega)]F(\mathbf{U}) - F(\mathbf{P}_{ex})) = 0$$

(7)

As Eq. (7) should hold for all admissible $\delta\mathbf{U}$, the equation of motion for a structure that is subject to the action of wind is derived in the frequency domain.

$$[-\omega^2\mathbf{M} + i\omega\mathbf{C} + \mathbf{K} - \boldsymbol{\Psi}(\omega)]F(\mathbf{U}) = F(\mathbf{P}_{ex})$$

(8)

The inverse Fourier transform of Eq. (9) yields the equation of motion in the time domain, which contains the well-known convolution expression for the aerodynamic force.

$$\mathbf{M}\ddot{\mathbf{U}} + \mathbf{C}\dot{\mathbf{U}} + \mathbf{K}\mathbf{U} = \mathbf{P}_{ex} + \int_0^t \boldsymbol{\Phi}(t-\tau)\mathbf{U}(\tau)d\tau \qquad (9)$$

Here, $\boldsymbol{\Phi}$ is the aerodynamic impulse response function matrix of the structural system, which is the inverse Fourier transform of the aerodynamic transfer function matrix, $\boldsymbol{\Psi}$. The convolution integral in Eq. (9) is valid if and only if the aerodynamic impulse response function vanishes for $t < 0$, which is referred to as the causality condition[5]. Several approaches have been proposed for forming approximated transfer functions that satisfy the casualty condition using the measured flutter derivatives[3,5].

The aerodynamic transfer functions used for the convolution integral approach and the branch method become different from those formed by the given flutter derivatives. The transfer functions of a section in Eq. (4) are modified in the optimization to enforce the causality condition in the convolution integral approach in Eq. (9). Meanwhile, the aerodynamic transfer functions of Eq. (6) in the branch method represent aerodynamic information related to only one assumed frequency rather than on the whole frequency range. Therefore, the results of an aerodynamic analysis in one analysis domain are generally inconsistent with those for the other analysis domain, which is a crucial drawback of methodologies that are currently used in aeroelastic analyses.

A new unified approach for the aeroelastic analysis can be formulated in case the aerodynamic transfer function matrix can be reasonably approximated by a linear function with respect to frequency as follows:

$$\boldsymbol{\Psi}(\omega) \approx \widetilde{\boldsymbol{\Psi}}(\omega) = i\omega\widetilde{\mathbf{C}} + \widetilde{\mathbf{K}}$$

$\widetilde{\boldsymbol{\Psi}}(\omega)$ (10) $\widetilde{\mathbf{C}}$ $\widetilde{\mathbf{K}}$

where is the approximated aerodynamic transfer function while and are unknown coefficient matrices. By use of Eq. (10) and the inverse Fourier transform of Eq. (8), the approximated equation of motion is defined as a usual second order differential equation in the time domain.

$$\mathbf{M}\ddot{\mathbf{U}} + \widetilde{\mathbf{C}}_{ae}\dot{\mathbf{U}} + \widetilde{\mathbf{K}}_{ae}\mathbf{U} = \mathbf{P}_{ex}$$

$\widetilde{\mathbf{C}}_{ae} = \mathbf{C} - \widetilde{\mathbf{C}}$ $\widetilde{\mathbf{K}}$ (11) $\mathbf{K} - \widetilde{\mathbf{K}}$

where and . The unknown coefficient matrices in Eq. (11) are determined through minimization in the frequency domain.

2.2 *Minimization of the weighted least square error*

The weighted error matrix of the approximation in Eq. (10) is defined by the modulus of a complex number of each component.

$$E_{kl} = \left|\Psi_{kl} - \widetilde{\Psi}_{kl}\right| w_{kl} = ((\Psi_{kl}^R - \widetilde{K}_{kl})^2 + (\Psi_{kl}^I - \omega\widetilde{C}_{kl})^2)^{0.5} w_{kl}$$

Ψ_{kl}^R Ψ_{kl}^I Ψ_{kl}

(12)

where w_{kl}, and are predefined weighting functions, the real and imaginary part of , respectively, while $|\cdot|$ denotes the modulus of a complex number. $\widetilde{K}_{kl}^{r}$ and are the *kl*-components of the corresponding coefficient matrices. The unknown coefficient matrices are determined by minimizing the norm of the weighted errors in Eq. (12).

$$\underset{\widetilde{C}_{kl},\widetilde{K}_{kl}}{\text{Min}}\,\Pi=\frac{1}{2}\int_0^{\omega_{\max}}E_{kl}^2 d\omega=\frac{1}{2}\int_0^{\omega_{\max}}(\Psi_{kl}^R-\widetilde{K}_{kl})^2 w_{kl}^2 d\omega+\frac{1}{2}\int_0^{\omega_{\max}}(\Psi_{kl}^I-\omega\widetilde{C}_{kl})^2 w_{kl}^2 d\omega \tag{13}$$

where $\omega_{\max}$ is the maximum frequency that defines the maximum frequency range of the aerodynamic transfer function. The first-order optimality condition yields the following linear algebraic equations:

$$\widetilde{C}_{kl}=\int_0^{\omega_{\max}}\omega\Psi_{kl}^I w_{kl}^2 d\omega\Big/\int_0^{\omega_{\max}}\omega^2 w_{kl}^2 d\omega,\quad \widetilde{K}_{kl}=\int_0^{\omega_{\max}}\Psi_{kl}^R w_{kl}^2 d\omega\Big/\int_0^{\omega_{\max}}w_{kl}^2 d\omega \tag{14}$$

The weighting functions in the error matrix are introduced to consider the responses of an aeroelastic system in the approximated transfer function of the aerodynamic forces. The approximation errors at frequencies where the responses of an aeroelastic system become small have little effect on the final solution of the aeroelastic analysis, regardless of their magnitude, and thus may be safely neglected in the minimization. Once the weighting functions are properly defined, the frequency-domain integrals in Eq. (14) can be evaluated by means of a numerical integration scheme such as the trapezoidal rule, and the *kl*-components of the coefficient matrices are easily obtained by solving the numerically integrated form of Eq. (14).

3 NUMERICAL EXAMPLES OF THE BRIDGE MODEL

The validity of the proposed method is demonstrated for an idealized model bridge with 8 stay cables, which simulates the center span of a cable-stayed bridge. The span length of the model bridge is assumed to be 200 m. Since the aeroelastic behaviors of a bridge are mainly dependent on the cross-sectional shape of the bridge deck, two extreme types of deck sections are considered. One is a thin rectangular section with a width-to-depth (B/D) ratio of 20 representing a streamlined box section, and the other is a bluff H-type section simulating a slab-on-stringer type girder.

3.1 *A thin rectangular section of B/D=20*

The proposed method is applied to the aeroelastic analysis of a bridge model with a thin rectangular section. Fig. 1 shows the damping ratios of the aeroelastic system obtained by the proposed method and by the branch method. The results obtained by the proposed method are in good agreement with the values obtained by the branch method. The time-domain aeroelastic analysis is performed for the forced vibration at a wind velocity of 55 m/s. Although the aeroelastic analysis is performed near the flutter onset velocity, the proposed method accurately yields displacements compared with those by the convolution integral.

3.2 *A bluff H-type section*

The aeroelastic analysis of the section model with a bluff H-type section is performed. Fig. 3 shows the damping ratios of the aeroelastic system, and Fig. 4 illustrates the free vibration responses at the wind velocity of 8 m/s. Even in the case of the bluff H-type section, the results obtained by the proposed method are also in good agreement with the values obtained by the branch method as well as the convolution integral.

4 CONCLUSIONS

A unified approach for the aeroelastic analysis is proposed. The aerodynamic transfer functions are approximated as a linear function with coefficients determined through the minimization of the weighted error between exact and approximated transfer functions.

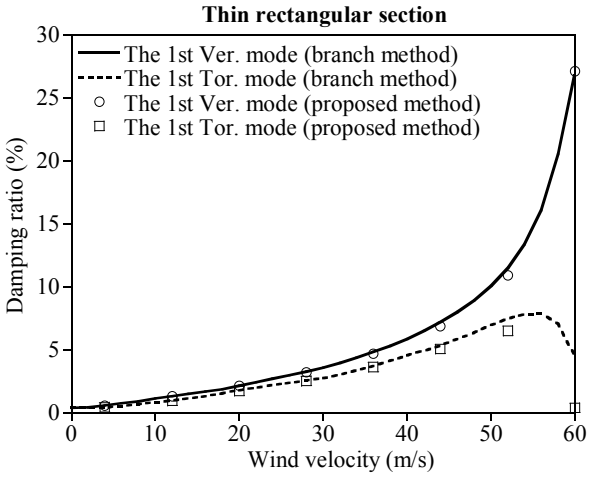

Fig. 1: Predicted damping ratio by the frequency-domain analysis of the bridge model

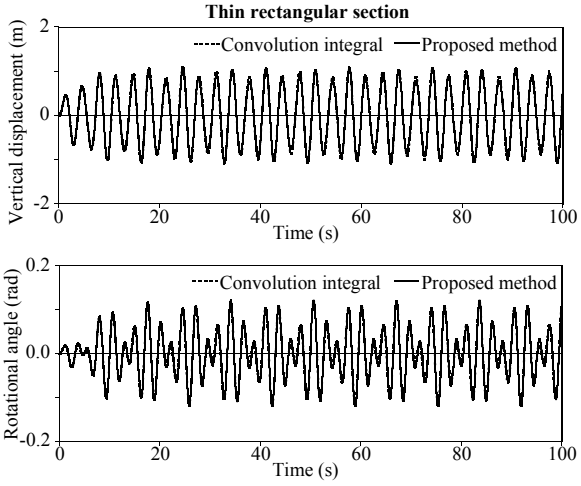

Fig. 2: Forced vibration responses for the wind velocity of 55m/s of the bridge model

With the proposed approximation, the frequency dependence of the aerodynamic transfer function is eliminated, and, as a result, the equation of motion for an aeroelastic system can be simply expressed as the same type of second-order differential equation in the time domain as that for a structural system. The validity of the proposed method is demonstrated for an section model with two extreme types of deck sections. Based on the results of the numerical simulations presented in this study, it can be concluded that the proposed approximation of the aerodynamic transfer function works well, even for the case of a bluff H-type section.

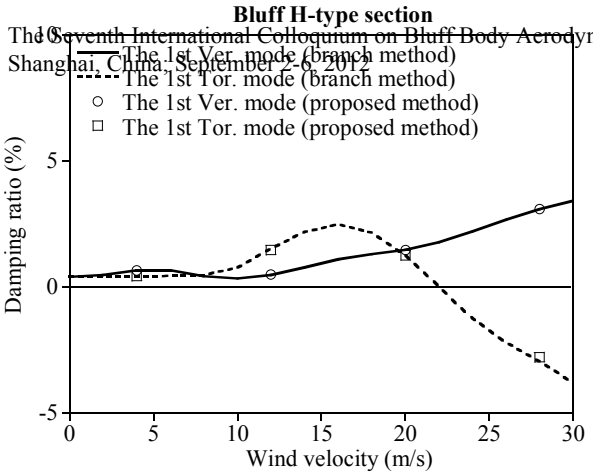

Fig. 3: Predicted damping ratio by the frequency-domain analysis of the bridge model

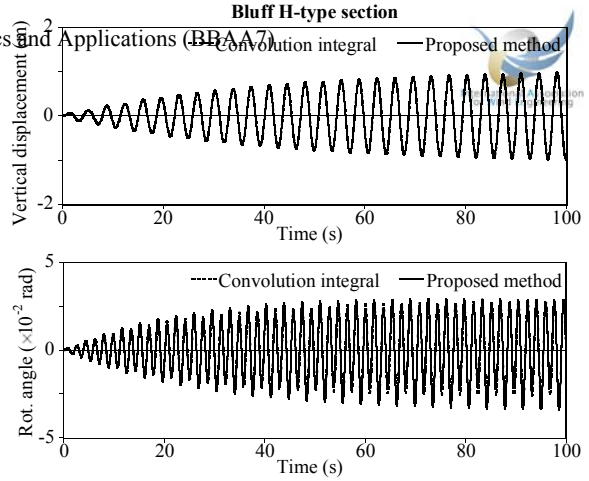

Fig. 4: Forced vibration responses for the wind velocity of 20m/s of the bridge model

5 ACKNOWLEDGEMENTS

This research was supported by the grant (09CCTI-A052531-05-000000) from the Ministry of Land, Transport and Maritime of Korean government through the Core Research Institute at Seoul National University for Core Engineering Technology Development of Super Long Span Bridge R&D Center.

6 REFERENCES

1 SCANLAN, R. H., and TOMKO, J. J., "Airfoil and bridge deck flutter derivatives." *ASCE Journal of Engineering Mechanics Division,* Vol. 97, No. 6, 1971, 1717-1737.
2 AGAR, T. J. A., "Aerodynamic flutter analysis of suspension bridges by a modal technique." *Engineering Structures*, Vol. 11, 1989, 75-82.
3 CHEN X., MATSUMOTO M., and KAREEM A., "Aerodynamic coupling effects on flutter and buffeting of bridges." *ASCE Journal of Engineering Mechanics*, Vol. 126, No. 1, 2000, 17-26.
4 CARACOGLIA, L., and JONES, N.P., "Time domain vs. frequency domain characterization of aeroelastic forces for bridge deck sections." *Journal of Wind Engineering and Industrial Aerodynamics*, Vol. 91, No. 3, 2003, 371-402.
5 JUNG, K., KIM, H. K., and LEE, H. S., "Evaluation of impulse response functions for convolution integrals of aerodynamic forces by optimization with a penalty function." *ASCE Journal of Engineering Mechanics*, 138(5), 519-529.

The Seventh International Colloquium on Bluff Body Aerodynamics and Applications (BBAA7)
Shanghai, China; September 2-6, 2012

Comparison of various modeling schemes for bridge aerodynamics and aeroelasticity

Teng Wu [a], Ahsan Kareem [a]

[a] *Nathaz Modeling Laboratory, University of Notre Dame, Notre Dame, IN, USA*

ABSTRACT: This paper compares five analytical models available in the literature systematically together with a new developed model for bridge aerodynamic/aeroelastic analysis. The models under consideration are quasi-steady (QS) theory based model, corrected QS theory based model, linearized QS theory based model, semi-empirical linear model, hybrid model and the proposed modified hybrid model. Physical significances of each approach in capturing the bridge behavior are highlighted. The interaction between the turbulence and the bridge deck motions is investigated. All these models are utilized in the time domain for consistency.

KEYWORDS: Comparison; Model; Bridge; Aerodynamics; Aeroelasticity

1 INTRODUCTION

The catastrophic failure of the original Tacoma Narrows Bridge has been pivotal in drawing attention to research in the aerodynamic/aeroelastic behavior of long-span bridges. The intense oscillation of the deck of the original Tacoma Narrows Bridge is actually the galloping in torsional degree of freedom (usually refers to torsional flutter). As a result, it is convenient to illustrate this phenomenon based on the QS theory. However, an obvious shortcoming of the QS theory is that it cannot take into the unsteady effect of fluid-structure interaction.

A familiar approach to consider the fluid memory effects is to modify the steady-state coefficients based on the unsteady effects measured in the wind tunnel and hence to improve the simulation accuracy (Diana et al. 1993). On the other hand, in order to circumvent dealing with nonlinear differential equations, QS theory based formula is usually linearized to qualitatively evaluate the wind-induced aerodynamic/aeroelastic forces. The parameters (consists of steady-state coefficients and their first-order derivatives) of this linearized QS theory based formula has their corresponding unsteady analytical expressions for the structure with streamlined cross-section, such as Theodorsen function (Theodorsen 1935).

However, for the cross-sections of bluff body, it is questionable to obtain the analytical expressions for the parameters based on some basic, simplified mechanism (such as potential theory and Kutta condition) due to the flow separation and other bluff-body aerodynamic issues. As a result, the parameters based on the wind-tunnel tests (e.g., aerodynamic admittances and flutter derivatives) is commonly utilized (Scanlan and Tomko 1971). This semi-empirical, linear, unsteady scheme has been applied extensively to simulate bridge aerodynamic and aeroelastic behaviors since its invention. It is emphasized that the QS theory based model could take into account the nonlinearity but no fluid memory while the conventional semi-empirical model could account for the fluid memory but no nonlinearity. Hence, a hybrid scheme has been proposed to simulate both the unsteady and nonlinear effects in wind-bridge interaction (Chen and Kareem 2003). Though the hybrid model could reasonably account for the nonlinear effect, it compromises the consideration of unsteady effect in the low frequency part. A modified hybrid model is proposed in this research, where the steady-state coefficients are modified based on their hysteretic features observed in wind tunnel. As a result, this new model could involve the higher-order memory effect (represented by hysteretic loop) when QS theory (nonlinear effect) is utilized.

2 IMPLEMENT OF VARIOUS MODELS

The coordinate system of the wind-bridge interaction system for analysis in all these models is shown in Fig. 1. A unit-length section of a modern bridge deck subjected to a turbulent wind flow is considered here and the aerodynamic/aeroelastic loads are established based on "strip theory". The incident turbulent wind consists of mean wind velocity U and W and fluctuations u and w in horizontal and vertical direction, respectively. The bridge cross-section has horizontal motion p, vertical motion h, and torsional motion α under the turbulent wind. The wind-induced effects considered are lift force L, drag force D and moment M.

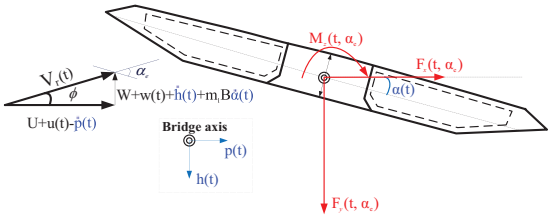

Figure 1: Coordinate system of the wind-bridge interaction system.

Suppose vertical translation and rotational motion are considered, the governing equations of the motion of bridge deck cross-section are modeled by a two-degree-of-freedom oscillator as

$$m\left(\ddot{h}+2\zeta_h\omega_h\dot{h}+\omega_h^2 h\right)=F_y\,;\quad I\left(\ddot{\alpha}+2\zeta_\alpha\omega_\alpha\dot{\alpha}+\omega_\alpha^2\alpha\right)=M_z \tag{1a; b}$$

where the over dot indicates the derivative with respect to time; ζ and ω represent the damping ratio and natural frequency, respectively; m is the effective mass and I the effective mass moment of inertia; F_y and M_z are wind-induced effects (aerodynamic/aeroelastic forces or moments) and the simulation of these effects is emphasized in this research.

2.1 *Quasi-steady (QS) theory based model*

QS theory based model describes the flow-structure interaction with a static nonlinear relationship between the status of the system (e.g., incident flow and structure) and the flow-induced forces exerted on the structure. Based on the QS theory, the lift force and torsional moment per unit span in the global bridge axes are expressed as (Miyata et al. 1995)

$$F_y=F_L\cos(\phi)-F_D\sin(\phi)\,;\quad M_z=M \tag{2a; b}$$

$$F_L=-\frac{1}{2}\rho V_r^2 BC_L(\alpha_e)\,;\quad F_D=\frac{1}{2}\rho V_r^2 BC_D(\alpha_e)\,;\quad M=\frac{1}{2}\rho V_r^2 B^2 C_M(\alpha_e) \tag{3a; b; c}$$

where ρ is air density; B is the bridge deck width; C_L, C_D and C_M are nondimensioanl steady-state coefficients which are conveniently obtained with static wind-tunnel tests, where C_M is respect to the center of the cross-section; V_r is the relative wind velocity calculated as

$$V_r=\sqrt{(U+u)^2+(W+w+\dot{h}+m_l B\dot{\alpha})^2} \tag{4}$$

and α_e is the dynamic angle of attack calculated as

$$\alpha_e=\alpha_s+\alpha+\phi \tag{5}$$

where α_s is the wind angle of attack when bridge deck is at the equilibrium position (also involving potential incident wind angle); α is the torsional displacement of the bridge deck under turbu-

lent wind; and ϕ is the "dynamic" angle of attack induced by the bridge deck motions and wind fluctuations (here the terminology "effective angle of attack" refers the situation that only deck motions contributes the angle of attack) and could be calculated as

$$\phi = \arctan\left(\frac{W + w + \dot{h} + m_1 B\dot{\alpha}}{(U+u)}\right) \tag{6}$$

The parameter m_1 value is selected to appropriately define a equivalent stationary state for the rotational motion.

2.2 *Corrected QS theory based model*

An obvious shortcoming of the quasi-steady theory based model is that it cannot take into account the unsteady effect. In order to improve this model, a corrected QS theory based model has been advanced where a coefficient is introduced to account for the unsteady effects (Diana et al. 1993). Based on the corrected QS theory, the lift force and torsional moment per unit span in the global bridge axes should be revised as

$$F_y = F_L\cos(\phi) - F_D\sin(\phi);\quad M_z = M \tag{2a; b}$$

$$F_L = -\frac{1}{2}\rho V_r^2 B\left\{C_L(\alpha_s) + \int_{\alpha_s}^{\alpha_e} k_{1L}\frac{d[C_L(\tilde{\alpha})]}{d[\tilde{\alpha}]}d\tilde{\alpha}\right\};\ F_D = \frac{1}{2}\rho V_r^2 B\left\{C_D(\alpha_s) + \int_{\alpha_s}^{\alpha_e} k_{1D}\frac{d[C_D(\tilde{\alpha})]}{d[\tilde{\alpha}]}d\tilde{\alpha}\right\};\ M = \frac{1}{2}\rho V_r^2 B^2\left\{C_M(\alpha_s) + \int_{\alpha_s}^{\alpha_e} k_{1M}\frac{d[C_M(\tilde{\alpha})]}{d[\tilde{\alpha}]}d\tilde{\alpha}\right\} \tag{7a; b; c}$$

The parameter k_1 is determined by the unsteady effect of the wind-bridge interaction.

2.3 *Linearized QS theory based model*

Both QS and corrected QS theory based model need to deal with nonlinear differential equations when implemented to calculate the bridge deck responses. In order to circumvent this complexity, QS theory based formula is usually linearized at the static equilibrium position to qualitatively evaluate the wind-induced aerodynamic/aeroelastic forces. Based on the linearized QS theory, the lift, drag and torsional coefficients should be approximated as

$$C_L(\alpha_e) \cong C_L(\alpha_s) + (\alpha+\phi)C_L'\big|_{\alpha_s};\quad C_D(\alpha_e) \cong C_D(\alpha_s) + (\alpha+\phi)C_D'\big|_{\alpha_s};\quad C_M(\alpha_e) \cong C_M(\alpha_s) + (\alpha+\phi)C_M'\big|_{\alpha_s} \tag{8a; b; c}$$

where prime indicates the derivative with respect to angle of attack. With some manipulations, the lift force and torsional moment per unit span based on the linearized QS theory in the global bridge axes could be expressed as

$$F_y = -\frac{1}{2}\rho U^2 B\left\{[C_L] + \left[(C_L' + C_D)\frac{w}{U} + 2C_L\frac{u}{U}\right] + \left[(C_L' + C_D)\frac{\dot{h} + m_1 B\dot{\alpha}}{U} + C_L'\alpha\right]\right\}\Big|_{\alpha_s};\quad M_z = \frac{1}{2}\rho U^2 B^2\left\{[C_M] + \left[C_M'\frac{w}{U} + 2C_M\frac{u}{U}\right] + \left[C_M'\frac{\dot{h} + m_1 B\dot{\alpha}}{U} + C_M'\alpha\right]\right\}\Big|_{\alpha_s} \tag{9a; b}$$

where the first term in the bracket represents static effect; the second term aerodynamic effect and the third term aeroelastic effect.

2.4 *Semi-empirical linear model*

In order to take into account the unsteady effect within a linear framework, the so-called semi-empirical scheme was developed by Scanlan (e.g., Scanlan and Tomko 1971) using wind tunnel tests of a sectional bridge model to account for the aeroelastic effects. On the other hand, the spectral analysis in this linear framework is developed by Davenport (e.g., Davenport 1962) to account for the aerodynamic effects, in which the coefficients of the corresponding linearized terms are also measured based on wind-tunnel test (or based on linearized QS theory). The lift force and torsional moment of frequency domain per unit span based on the semi-empirical linear model in the global bridge axes could be expressed as

$$F_y = -\frac{1}{2}\rho U^2 B\left\{\left[C_L\right]+\left[F_{L_b}\right]+\left[-F_{L_s}\right]\right\}\Big|_{\alpha_s};\quad M_z = \frac{1}{2}\rho U^2 B^2\left\{\left[C_M\right]+\left[M_b\right]+\left[M_s\right]\right\}\Big|_{\alpha_s} \tag{10a; b}$$

where the subscript "b" indicates the buffeting forces (or moment) while "s" indicates the self-excited forces (or moment). The buffeting forces (or moment) induced by turbulent wind are expressed as

$$F_{L_b} = (C_L^{'} + C_D)\chi_{Lw}\frac{w(t)}{U} + 2C_L\chi_{Lu}\frac{u(t)}{U};\quad M_b = C_M^{'}\chi_{Mw}\frac{w}{U} + 2C_M\chi_{Mu}\frac{u}{U} \tag{11a; b}$$

and the self-excited forces (or moment) induced by the bridge deck motions are expressed as

$$F_{L_s} = KH_1^*(K)\frac{\dot{h}}{U} + KH_2^*(K)\frac{B\dot{\alpha}}{U} + K^2H_3^*(K)\alpha + K^2H_4^*(K)\frac{h}{B};\quad M_s = KA_1^*(K)\frac{\dot{h}}{U} + KA_2^*(K)\frac{B\dot{\alpha}}{U} + K^2A_3^*(K)\alpha + K^2A_4^*(K)\frac{h}{B} \tag{12a; b}$$

where χ_{Lw}, χ_{Lu}, χ_{Mw} and χ_{Mu} are aerodynamic transfer functions (modulus is referred as aerodynamic admittance function) between wind fluctuations and buffeting forces (or moment), which are functions of K, wind angle of attack and deck shape; K=Bω/U is dimensionless reduced frequency with ω as circular frequency of bridge deck vibration; the coefficients $H_i^*(K)$ and $A_i^*(K)$ (i=1…4) are aeroelastic transfer function (flutter derivatives), which are also functions of K, wind angle of attack and deck shape.

2.5 *Hybrid model*

It should be noticed that it is intractable to determine the proper reduced wind velocity in the "corrected" quasi-steady theory. Therefore, usually only an unique value of the reduced velocity is utilized. In order to overcome this shortcoming of the corrected quasi-steady theory based model, band superposition model has been developed (Diana et al. 1995). However, this band superposition scheme is not easy to implement for the time-frequency mixed characteristics of the equations of motion and the measurement of the flutter derivatives under the incident wind condition with narrow-band turbulent fluctuations is not feasible. Besides, the interaction between each subrange cannot be considered. In order to further improve the "band superposition" scheme, a numerical analysis framework, which utilizes the rational function approximation scheme to obtain more efficient computational procedures, is proposed (Chen and Kareem 2003). Beside, this proposed scheme has a clear connection with the conventional linear analysis framework (here referred as semi-empirical linear model). This hybrid model simply combines "QS theory based model" and "semi-empirical linear model". Basically, the hybrid model linearizes the wind-induced force around a dynamic equilibrium angle of attack (or instantaneous angle of attack with low-frequency components) instead of a static angle of attack. Based on the hybrid model, the lift force and torsional moment per unit span in the global bridge axes are calculated by combining the forms of Eqs. (2) and Eqs. (10) and could be expressed as

$$F_y = -\frac{1}{2}\rho B\begin{Bmatrix} V_r^{l2}\left\{C_L(\alpha_e^l)\cos(\phi^l) + C_D(\alpha_e^l)\sin(\phi^l)\right\} \\ +U^2\left\{\left[C_L\right]+\left[F_{L_b}\right]+\left[-F_{L_s}\right]\right\}\Big|_{\alpha_e^l} \end{Bmatrix};\quad M_z = \frac{1}{2}\rho B^2\begin{Bmatrix} V_r^{l2}\left\{C_M(\alpha_e^l)\right\} \\ +U^2\left\{\left[C_M\right]+\left[M_b\right]+\left[M_s\right]\right\}\Big|_{\alpha_e^l} \end{Bmatrix} \tag{15a; b}$$

where superscript "l" indicate the low frequency part based on a pinpoint presupposed and

$$V_r^l = \sqrt{(U+u^l)^2 + (W+w^l+\dot{h}^l+m_1B\dot{\alpha}^l)^2};\quad \alpha_e^l = \alpha_s + \alpha^l + \phi^l;\quad \phi^l = \arctan\left(\frac{W+w^l+\dot{h}^l+m_1B\dot{\alpha}^l}{(U+u^l)}\right) \tag{17; 18; 19}$$

Theoretically, the parameters in high frequency part should be measured in the dynamic wind-tunnel tests with turbulent incident wind condition.

2.6 *Modified hybrid model (new)*

Typically, the "static" wind-tunnel tests are featured with the identification of steady-state coefficients while the "dynamic" wind-tunnel tests are featured with the identification of aerodynamic transfer functions or aeroelastic transfer functions in bridge aerodynamics/aeroelasticity. A convenient approach to describe the results from "static" and "dynamic" wind-tunnel tests is to utilize the similar parameters, namely, steady-state coefficients and dynamic-state coefficients, respectively. Both steady- and dynamic-state coefficients are nonlinear with respect to angle of attack, while the dynamic-state coefficients also presents the hysteretic loop feature. As the flutter derivatives (or aerodynamic admittances), the dynamic-state coefficients with hysteresis are dependent on the angle of attack of the equilibrium position and reduced wind velocity. Assume all the components of bridge deck motions and wind fluctuations have the equal weighting on the wind-bridge interaction behavior, as applied in QS theory based model, the bridge aerodynamic/aeroelastic behavior could be described utilizing the dynamic-state coefficients with hysteresis (Diana et al. 2010). However, this assumption is questionable and the error introduced by this assumption is not always acceptable. Some attempts of accounting for different weights for various components of the dynamic angle of attack is to use higher-order artificial neural network (ANN) (Wu and Kareem 2011a). However, as a nonparametric model it is difficult to elucidate the physical meaning of the various weighting functions employed in the ANN model. A critical issue when utilizing the dynamic-state coefficients in bridge aerodynamics/aeroelasticity is that it is very difficult to find a proper frequency to define the reduced wind velocity, especially when wind fluctuations involved. A feasible approach to deal with this issue is to determine an averaged frequency for defining the reduced wind velocity under each mean wind velocity. Another feasible way is to utilize the concept of "band superposition". Different reduced wind velocities could be defined at each subrange to apply the appropriate dynamic-state coefficients measured in wind tunnel. Besides, this approach could improve the hybrid model which compromises the consideration of unsteady effect in the low frequency part to account for the nonlinear turbulence effect on the aeroelastic instability. Based on the modified hybrid model, the lift force and torsional moment per unit span in the global bridge axes should be revised as

$$F_y=-\frac{1}{2}\rho B\begin{Bmatrix}U^2[C_L]+V_r^{I2}\left\{C_L^{hys}(\alpha_e^I)\cos(\phi^I)+C_D^{hys}(\alpha_e^I)\sin(\phi^I)\right\}\\ +V_r^{h_1\,2}\left\{C_L^{hys}(\alpha_e^{h_1})\cos(\phi^{h_1})+C_D^{hys}(\alpha_e^{h_1})\sin(\phi^{h_1})\right\}\Big|_{\alpha_e^I}\\ +\cdots\\ +V_r^{h_n\,2}\left\{C_L^{hys}(\alpha_e^{h_n})\cos(\phi^{h_n})+C_D^{hys}(\alpha_e^{h_n})\sin(\phi^{h_n})\right\}\Big|_{\alpha_e^I}\end{Bmatrix};\quad M_z=\frac{1}{2}\rho B^2\begin{Bmatrix}U^2[C_M]+V_r^{I2}\left\{C_M^{hys}(\alpha_e^I)\right\}\\ +V_r^{h_1\,2}\left\{C_M^{hys}(\alpha_e^{h_1})\right\}\Big|_{\alpha_e^I}\\ +\cdots\\ +V_r^{h_n\,2}\left\{C_M^{hys}(\alpha_e^{h_n})\right\}\Big|_{\alpha_e^I}\end{Bmatrix}\qquad (19a;\ b)$$

where superscript "hys" indicates the dynamic-state coefficients with hysteresis; "h_n" indicate the wind fluctuations of high frequency part are divided into n subranges, and

$$V_r^{h_n}=\sqrt{(U+u^{h_n})^2+(W+w^{h_n}+\dot{h}^{h_n}+m_1B\dot{\alpha}^{h_n})^2}\ ;\quad \alpha_e^{h_n}=\alpha_s+\alpha^{h_n}+\phi^{h_n}\ ;\quad \phi^{h_n}=\arctan\left(\frac{W+w^{h_n}+\dot{h}^{h_n}+m_1^{h_n}B\dot{\alpha}^{h_n}}{(U+u^{h_n})}\right)(20;\ 21;\ 22)$$

Due to a lack of the experimental data, only the dynamic-state coefficients with hysteresis in the subrange with low-frequency fluctuation components is utilized in this research.

3 RESPONSE ANALYSIS

In this section, the aeroelastic and aerodynamic responses of a long-span cable supported bridge have been calculated with the six models discussed in the preceding content. The time histories of wind fluctuations is simulated utilizing the spectral representation scheme with prescribed power spectral density (PSD) function and turbulence integral scales and intensities. Low-pass and high-pass elliptic filter are utilized to separate the wind fluctuation into low- and high- fre-

quency parts. The steady- and dynamic-state coefficients with angle of incidence are measured in wind tunnel and simulated based on the nonlinear least square and the Moore-Penrose pseudoinverse techniques, respectively. All the aerodynamic parameters in frequency domain are transferred into time domain based on the indicial function approximation.

3.1 *Aerodynamic analysis*

3.1.1 *Comparison of aerodynamic responses based on various models*

The aerodynamic responses of this bridge deck under turbulent wind condition are investigated based on the various models previously discussed. Fig. 2 presents the comparison of time histories of the calculated aerodynamic responses based on each model under the mean wind velocity 60 m/s with I_u=15% and I_w=8%.

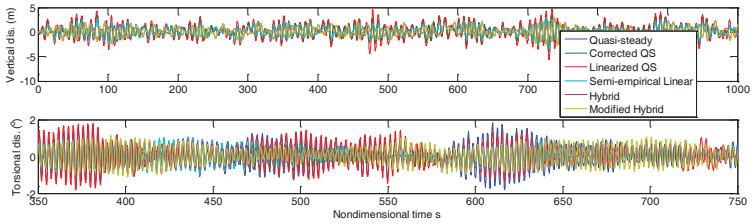

Figure 2. Time histories of the calculated responses based on each model.

Fig. 3 presents the root-mean-square (RMS) values of the vertical and torsional displacements. Since the semi-empirical linear model is the conventional model utilized for bridge aerodynmaics/aeroelasticity, it is treated as a reference model in this research. As discussed in the preceding section, for bridge aerodynamics/aeroelasticity, QS theory based model takes into account nonlinear effect but no fluid memory; corrected QS theory based model considers nonlinear effect with linear fluid memory at a fixed reduced frequency; linearized QS theory based model accounts for linear effect but no fluid memory; semi-empirical linear model considers linear effect with linear fluid memory; hybrid model considers nonlinear effect with linear fluid memory and modified hybrid model accounts for nonlinear effect with nonlinear memory (or higher-order memory featured by hysteresis).

Based on the results calculated by each model, in general it could be concluded that: (1) the aerodynamic responses based on the hybrid or modified hybrid models are close to the semi-empirical linear model, which indicates the nonlinearity or higher-order fluid memory effects captured by these two models in this case is small; (2) the aerodynamic responses based on the corrected QS model are closer to the semi-empirical linear model (larger for the vertical responses and smaller for the torsional responses in this case) compared to those based on the QS model, which indicates the corrected QS model could uncertainly improve the calculated responses by take into account the fluid memory at a fixed reduced frequency; (3) the fluid memory consideration has more significant effects on the torsional degree of freedom rather than the vertical degree of freedom as the relative difference between the torsional responses calculated by the linearized QS model and semi-empirical linear model is larger compared with the relative difference between the vertical responses; (4) the static nonlinearity consideration has more significant effects on the vertical degree of freedom rather than the torsional degree of freedom as the relative difference between the vertical responses calculated by the linearized QS model and QS theory based model is larger compared with the relative difference between the torsional responses. In a sense, the contribution to the aerodynamic responses from fluid memory effects is larger than that from nonlinear consideration based on this comparison. It should be noticed that the relative large torsional response based on the modified hybrid model is due in part to the contribution of

the limit cycle oscillation (LCO) response resulting from subcritical behavior, which indicates the aeroelastic instability resulting from the low-frequency part in the hybrid and modified hybrid models.

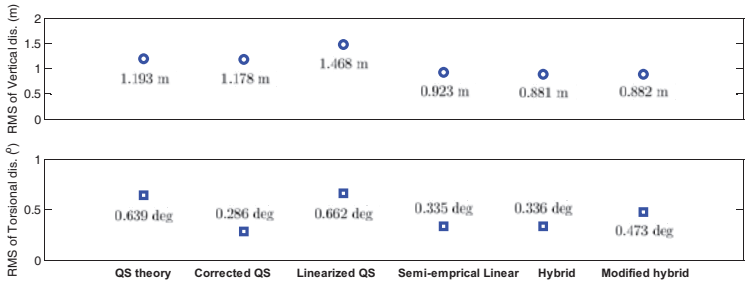

Figure 3. Aerodynamic responses under turbulent flow.

3.1.2 *Comparison of aerodynamic responses under various turbulent wind conditions*

Fig. 4 presents the RMS values of aerodynamics responses based on various models under different mean wind velocities with the turbulence intensity I_u=15% and I_w=8%.

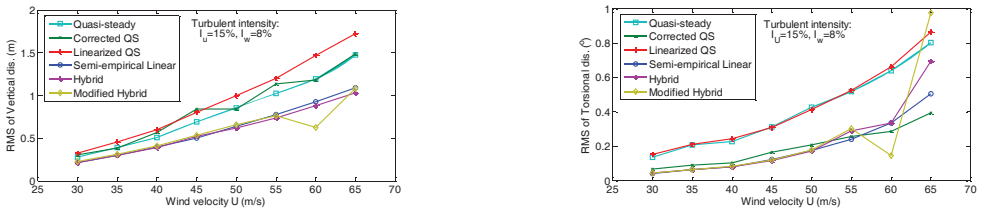

(a) RMS of vertical displacements (b) RMS of torsional displacements

Figure 4. RMS of various models under different wind velocity (I_w=8%).

As shown in this figure, it is obvious that these six model could be divided into two groups based on the calculated aerodynamic responses. One group cannot take into account the fluid memory effects (including QS theory based and linearized QS models) and the other group could account for the fluid memory effects (including semi-empirical linear, hybrid and modified hybrid models), while capability of the reasonable consideration for the fluid memory based on the corrected QS model is uncertain. The results based on no memory consideration group are obviously larger than those based on memory consideration group, which indicates the fluid memory effect consideration reduces the aerodynamic responses at various wind velocities. On the other hand, the hybrid model based results are close to those calculated from the semi-empirical linear model, which indicates that the hybrid model may not fully characterize the nonlinear effects at various wind velocities. Besides, the comparison of the responses based on QS theory and linearized QS theory at various wind velocities indicates that the static nonlinearity (without coupling fluid memory effect) has significant effects on the vertical aerodynamic responses at various wind velocity while it has less effects on the torsional responses in this case. However, it is not necessary that this observation is also applicable for the dynamic nonlinearity effects (with coupling fluid memory effect). The differences of the results based on various models are more significant at higher wind velocity. The ripples in the corrected QS theory based result at some wind velocities are due to the relatively intense change of the correct coefficient k_1 while the large oscillations of the modified hybrid based results at wind velocity 60 m/s and 65 m/s is due to the subcritical behaviors. It should be noted that the observations discussed in the preceding content is based on that all other models are compared with the selected reference model, i.e., the semi-empirical model, which may not provide the "true" answer for the bridge aerodynamics/aeroelasticity.

Fig. 5 presents the RMS values of aerodynamic responses based on various models under different turbulence intensities with the mean wind velocity 40 m/s. As indicated in this figure, in general the incremental values of the aerodynamic responses based on the models which can consider the fluid memory effect are less than those based on the models which cannot account for the fluid memory effect. Besides, as the turbulence intensity is larger than 15%, there is intense nonlinear increases of the aerodynamic responses for most of models.

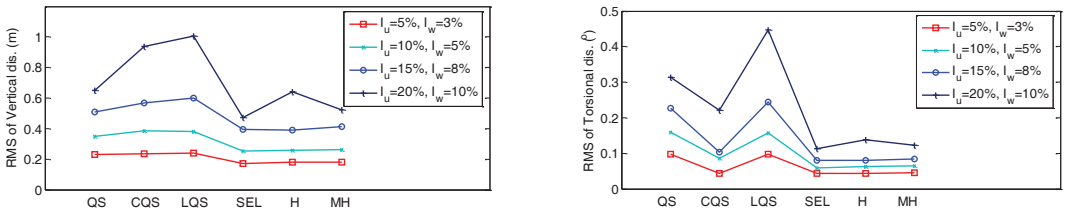

(a) RMS of vertical displacements (b) RMS of torsional displacements

Figure 5. RMS of various models under different turbulent conditions (U=40 m/s).

3.1.3 *Motion induced effects on the aerodynamic responses*

It is well known that the motion induced effects will change the effective structural dynamic parameters (mass, stiffness and damping ratio) and hence affect the aerodynamic responses. The aerodynamic responses discussed in the preceding content actually involves the aeroelastic effects. In order to investigate the motion induced effects on the aerodynamic responses for various models, the aerodynamic responses coupled with the aeroelastic responses are compared with the aerodynamic responses neglecting the motion induced effects as shown in the Fig. 6.

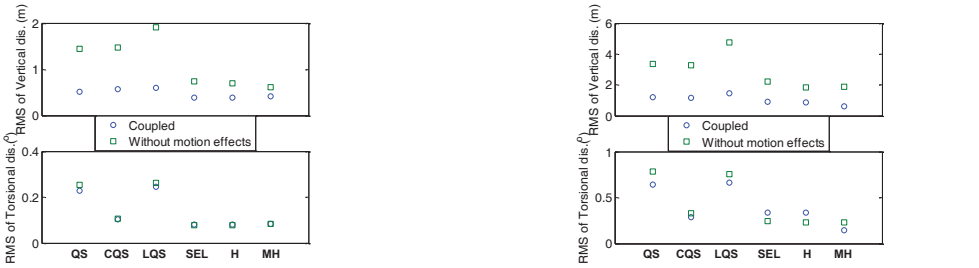

(a) RMS of vertical displacements (U=40 m/s) (b) RMS of torsional displacements (U=60 m/s)

Figure 6. RMS of aerodynamic responses (I_u=15%, I_w=8%) neglecting motion induced effects.

It is obvious that the motion induced effects are larger when the wind velocity increases. It seems there are more significant motion induced effects in the vertical degree of freedom in this case. In general, the motion induced effects will reduce the aerodynamic responses. However, for the torsional responses based on the semi-empirical linear and hybrid models the motion induced effects increase the aerodynamic responses. The errors of neglecting the motion induced effect for the aerodynamic responses based on the no memory consideration models are larger than those for the aerodynamic responses based on the memory consideration models.

3.2 *Aeroelastic analysis*

3.2.1 *Critical flutter wind velocities*

The stability issue is critical in bridge aeroelasticity as most researchers have attribute the catastrophic failure of the Tacoma Narrows Bridge to flutter behavior, which is a typical phenomenon of the bridge aeroelastic instability. Fig. 7 presents the critical flutter wind velocities U_{cr} cal-

culated utilizing these six models under the uniform wind condition. Based on the calculated U_{cr} of various models, in general it could be concluded that: (1) the linear memory effect consideration could increase the aeroelastic response (reduce the critical wind velocity of instability) since the U_{cr} calculated by linearized QS theory based model (no memory) is larger than semi-empirical linear model (linear memory); (2) the nonlinear memory effect consideration could reduce the aeroelastic response (increase the critical wind velocity of instability) since the U_{cr} calculated by modified hybrid model (nonlinear memory) is larger than hybrid model (linear memory); (3) the nonlinear effect consideration involved in the hybrid scheme could reduce the aeroelastic response (increase the critical wind velocity of instability) since the U_{cr} calculated by hybrid model (nonlinear) is larger than semi-empirical linear model (linear). In a sense, the contribution to the aeroelastic response from fluid memory effect is larger than that from nonlinear consideration based on the comparison of the results of these models. However, it should be noticed that while the fluid memory effect (especially linear) is considered well through the unsteady parameters (e.g., flutter derivatives) the nonlinear effects are not fully characterized with an appropriate approach.

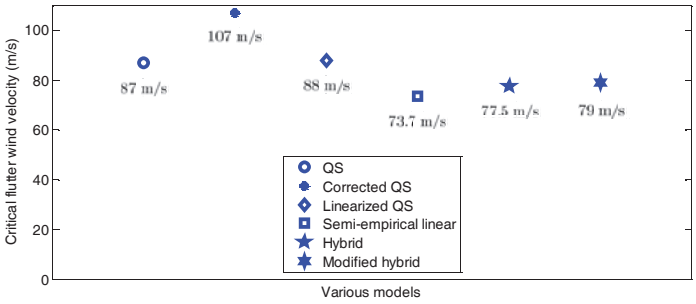

Figure 7. Critical flutter wind velocity under uniform flow.

3.2.2 *Turbulence effects on the instability*

Suppose the turbulence effects on instability are considered in two aspects: the effect on the nonlinearity and the effect on the fluid memory. As the linearized QS model cannot take into account either nonlinearity or fluid memory, the turbulence will not affect the instability based on the linearized QS model. However, though the semi-empirical linear model could take into account the fluid memory effect, the turbulence effects will not significantly change the instability based on this model since the aerodynamic and aeroelastic responses are simply summed based on the superposition theory. Generally, the turbulence consideration will increase the critical flutter wind velocities as its effects on the nonlinearity have more significant contribution on the aeroelastic responses, which is demostrated in the results based on the QS and corrected QS models as shown in Fig. 8. This observation indicates the turbulence effects reduce the aeroelastic responses due to static nonlinearity. On the other hand, if the turbulence effects on the fluid memory have more significant contribution on the aeroelastic responses, the situation becomes more complicated. In this situation, the turbulent fluctuations will reduce the critical flutter wind velocities generally. However, as the turbulence intensity increases, the critical flutter wind velocities slightly increase, as demostrated in the results based on the hybrid and modified hybrid models. This observation indicates the turbulence effects increases the aeroelastic responses due to fluid memory, and this effect is larger for the smaller turbulence intensity. Another possible mechanism for this complicated situation in the hybrid and modified hybrid models is that the turbulence effect on the nonlinearity involved in these model increase significantly as the turbulence intensity becomes larger, which results in the slight increase of the critical flutter wind velocities compared to those with smaller turbulence intensity. Besides, the higher-order fluid memory consideration will significantly reduce the instability based on QS

theory as the subcritical wind velocity in the modified hybrid model is 53 m/s under the uniform inflow condition while that in the hybrid model is 87 m/s. On the other hand, the low-frequency components of the wind fluctuations with small turbulence intensity (e.g., I_u=5%) will slightly change (either reduce or increase) the subcritical wind velocity (from 53 m/s to 52 m/s in the modified hybrid model and from 87 m/s to 88 m/s in the hybrid model) while the low frequency components of the wind fluctuations with larger turbulence intensity (e.g., I_u=15%) will increase the subcritical wind velocity (from 53 m/s to 59 m/s in the modified hybrid model and from 87 m/s to 91 m/s in the hybrid model).

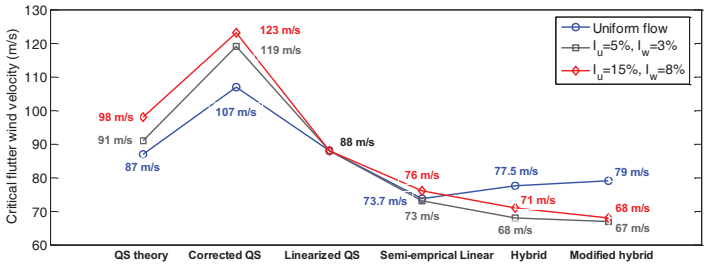

Figure 8. Critical wind velocity under various inflow conditions.

4 CONCLUDING REMARKS

Six models for bridge aerodynamics/aeroelasticity, namely the QS theory based model (nonlinear effect but no fluid memory), the corrected QS theory based model (nonlinear effect with linear fluid memory at a fixed reduced wind velocity), the linearized QS theory based model (linear effect but no fluid memory), the semi-empirical linear model (linear effect with linear fluid memory), the hybrid model (nonlinear effect with linear fluid memory) and the modified hybrid model (nonlinear effect with nonlinear fluid memory), are investigated in detail. It is noted that the consideration of the linear and nonlinear unsteadiness (fluid memory) and the nonlinearity in the wind-bridge interaction significantly changes the bridge aerodynamic/aeroelastic responses.

5 ACKNOWLEDGEMENTS

The support for this project provided by the NSF Grant # CMMI 09-28282 which is gratefully acknowledged.

6 REFERENCES

1 Chen, X. and Kareem, A., 2003. Aeroelastic analysis of bridges: effects of turbulence and aerodynamic nonlinearities. *J. Eng. Mech.*, 129 (8), 885–895.
2 Davenport, A. G., 1962. Buffeting of a suspension bridge by storm winds. *J. Struct. Div., ASCE,* 88(3), 233-268.
3 Diana, G., Bruni, S., Cigada, A. and Collina, A., 1993. Turbulence effect on flutter velocity in long span suspended bridges. *Journal of Wind Engineering and Industrial Aerodynamics*, 48 (2-3), 329-342.
4 Diana, G., Falco, M., Bruni, S., Cigada, A., Larose, G. L., Damsgaard, A. and Collina, A., 1995. Comparisons between wind tunnel tests on a full aeroelastic model of the proposed bridge over Stretto di Messina and numerical results. *Journal of Wind Engineering and Industrial Aerodynamics,* 54-55, 101-113.
5 Diana, G., Rocchi, D., Argentini, T. and Muggiasca, S., 2010. Aerodynamic instability of a bridge deck section model: Linear and nonlinear approach to force modeling. *Journal of Wind Engineering and Industrial Aerodynamics*, v 98, n 6-7, 363-374.
6 Miyata, T., Yamada, H., Boonyapinyo, V. and Santos, J. C., 1995. Analytical inverstigation on the response of a very long suspension bridge under gusty wind. *Proceedings of Ninth ICWE, New Delhi,* Vol. 2, 1006–1017.
7 Scanlan, R. H. and Tomko, J. J., 1971. Airfoil and bridge deck flutter derivatives. *J. Eng. Mech.*, 97(EM6), 1717–1737.
8 Theodorsen, T., 1935. *General theory of aerodynamic instability and the mechanism of flutter.* NACA Technical Report 496.
9 Wu, T. and Kareem, A., 2011. Modeling hysteretic nonlinear behavior of bridge aerodynamics via cellular automata nested neural network. *J. Wind Eng. Ind. Aerodyn.,* 99 (4), 378-388.

The Seventh International Colloquium on Bluff Body Aerodynamics and Applications (BBAA7)
Shanghai, China; September 2-6, 2012

A new state-space model for self-exited forces and straight forward analysis of bridge deck flutter

Zeng-wei Guo [a], Yao-jun Ge [a]

[a] *State Key Laboratory of Disaster Reduction in Civil Engineering, Tongji Univercity, Shanghai, China*

ABSTRACT: Self-exited forces of bridge can be expressed in state space domain according to the state space description of dynamic system in modern control theory, and its formulation is depended on rational functions for approximating aerodynamic transfer function. In order to discuss time and frequency-domain response characteristics of state space formulation of self-exited force, flutter analysis of a simple supported beam with idealized thin plane section is conducted in frequency and time domain simultaneous, using the Roger's and Karpel's rational function approximations for aerodynamic transfer function. It is observed that frequency-response characteristics of the two formulations are both favorable, although flutter results based on Karpel's rational function approximations are more sensitive to residual of flutter derivatives. Besides, time-response characteristics of the two formulations are similar. As a result of unknown initial conditions of the aerodynamic state, structural response may be erroneous in first time period, which can be solved by restricting the lower limit of the aerodynamic parameters associated with aerodynamic states.

KEYWORDS: bridge, flutter, state-space, self-excited force, time and frequency characteristic.

1 INTRODUCTION

Flutter instability is one of the critical concerns for design and construction of long span bridges since it may lead bridge deck to oscillate divergently at some critical wind speed, and eventually result in a total collapse of structure. Since the collapse of Tacoma Narrow Bridge in 1940, great effort has been made to clarify the generation mechanism of this catastrophic aerodynamic behavior of bridge deck. Scanlan primarily proposed a formulation of self-excited force in terms of structural motions and introduced flutter derivatives to describe its unsteady fluid memory effect(Scanlan and Tomko, 1971). Subsequently, massive flutter analysis procedures through multimode or full mode technique have been developed based on this formulation (Ding et al, 2002b; Dung et al, 1998; Ge and Tanaka, 2000; Jain et al, 1996). These procedures must be conducted in frequency domain, since flutter derivatives obtained from sectional model wind tunnel tests are frequency dependent. However, Structural nonlinearities and turbulence effects, which may be prominent for long span bridges, cannot be considered in the frequency-domain analysis. It is necessary to cast the self-excited forces and governing equations of motion in the time domain to take account for structural nonlinearities and turbulence effects in flutter analysis. Corresponding to flutter derivatives, time-domain self-excited forces were expressed in terms of convolution integrals of impulse functions or indicial functions to take into account the effect that self-excited force variation lags behind structural motions. Most researchers (Caracoglia and Jones, 2003; Chen and Kareem, 2002; Costa and Borri, 2006; Wilde and Fujino, 1998) have dealt with convolution integrals of impulse or indicial functions using the following two methods: (1) adopting recursive algorithm similar to the famous Newmark-β method, (2) introducing additional aerodynamic state to represent this convolution integral and proposing state-space formulations.

The assessment of self-excited force in the time domain requires identification of aerodynamic impulse or indicial response functions. However, there are no theoretical solutions of the-

se functions for bluff bridge decks and it is also difficult to determinate these functions directly in wind tunnel tests. In aerospace engineering, Roger approximated the frequency-dependent Theodorsen function in terms of rational functions, and transformed the frequency-dependent aeroealstic forces of airplane into time domain based on the inverse Laplace transform. Analogously, these aerodynamic impulse or indicial response functions for bluff bridge sections can be determined by means of the inverse Laplace transform of Scanlan's formulation, if flutter derivatives can be approximated with continuous functions. Lin introduced rational functions for approximating flutter derivatives in bridge engineering(Lin and Yang, 1983), and there were mainly two formulations for these rational functions, which were noted as Roger's formulation and Karpel's formulation. However, time and frequency response characteristics of self-excited force state space model, which may influence the flutter analysis result both in frequency and time domain, have never been discussed in literatures.

The present paper derives the governing equations of flutter in state space domain based Roger's and Karpel's rational function approximations, and discusses their differences. Taking a simple supported beam with idealized thin plane section as example, we clarify the time and frequency response characteristics of these two state space model of self-excited force.

2 STATE-SPACE FORMULATIONS OF SELF-EXCITED FORCE

For complex sinusoidal motions with circular frequency ω, the self-excited forces per unit length are commonly expressed in terms of flutter derivatives as (Scanlan, 2001):

$$L = \frac{1}{2}\rho U^2 B\left(KH_1^* \frac{\dot{h}}{U} + KH_2^* \frac{B\dot{\alpha}}{U} + K^2 H_3^* \alpha + K^2 H_4^* \frac{h}{B} + KH_5^* \frac{\dot{p}}{U} + K^2 H_6^* \frac{p}{B} \right) \tag{1a}$$

$$D = \frac{1}{2}\rho U^2 B\left(KP_1^* \frac{\dot{p}}{U} + KP_2^* \frac{B\dot{\alpha}}{U} + K^2 P_3^* \alpha + K^2 P_4^* \frac{p}{B} + KP_5^* \frac{\dot{h}}{U} + K^2 P_6^* \frac{h}{B} \right) \tag{1b}$$

$$M = \frac{1}{2}\rho U^2 B^2\left(KA_1^* \frac{\dot{h}}{U} + KA_2^* \frac{B\dot{\alpha}}{U} + K^2 A_3^* \alpha + K^2 A_4^* \frac{h}{B} + KA_5^* \frac{\dot{p}}{U} + K^2 A_6^* \frac{p}{B} \right) \tag{1c}$$

where ρ=air mass density; U=wind velocity; B= bridge deck width; $K=\omega B/U$=reduced frequency; H^*i, A^*i, P^*i(i=1,2,⋯6)=frequency dependent flutter derivative; h, p, α=vertical, lateral and pitching displacement respectively, and the head dot denotes partial differentiation with respect to time t.

By taking the Laplace transform of Eq. (1), the self-excited force formulated utilizing flutter derivatives can be given in a matrix form by

$$\tilde{\mathbf{F}}_{se} = \frac{1}{2}\rho U^2 \mathbf{b}^T \mathbf{Q} \mathbf{b} \tilde{\mathbf{\Delta}} \tag{2}$$

where $\tilde{\mathbf{F}}_{se} = \begin{Bmatrix} \tilde{L} \\ \tilde{D} \\ \tilde{M} \end{Bmatrix}$; $\mathbf{b} = \begin{bmatrix} 1 & & \\ & 1 & \\ & & B \end{bmatrix}$; $\tilde{\mathbf{\Delta}} = \begin{Bmatrix} \tilde{h} \\ \tilde{p} \\ \tilde{\alpha} \end{Bmatrix}$; $\mathbf{Q} = \begin{bmatrix} K^2 H_4^* + pKH_1^* & K^2 H_6^* + pKH_5^* & K^2 H_3^* + pKH_2^* \\ K^2 P_6^* + pKP_5^* & K^2 P_4^* + pKP_1^* & K^2 P_3^* + pKP_2^* \\ K^2 A_4^* + pKA_1^* & K^2 A_6^* + pKA_5^* & K^2 A_3^* + pKA_2^* \end{bmatrix}$

=aerodynamic transfer function; $p=sB/U$, $s=(\xi+i)\omega$, ξ=damping ratio; the superscript indicates the Laplace transformation superscripts.

Approximation of unsteady aerodynamics forces as continuous rational functions allows self-excited forces to be cast in state space realization. The most common forms of these approximating functions used currently in bridge engineering for aerodynamic transfer matrix Q are(Chen and Kareem, 2002; Wilde and Fujino, 1998):

$$\hat{\mathbf{Q}} = \mathbf{A}_1 + \mathbf{A}_2 p + \mathbf{A}_3 p^2 + \sum_{l=1}^{m} \frac{\mathbf{A}_{l+3} p}{p + \lambda_l} \quad \text{(Roger's formulation)} \tag{3a}$$

$$\hat{\mathbf{Q}} = \mathbf{A}_1 + \mathbf{A}_2 p + \mathbf{A}_3 p^2 + \mathbf{D}\left(p\mathbf{I} + \mathbf{\Lambda}\right)^{-1}\mathbf{E}p \quad \text{(Karpel's formulation)} \tag{3b}$$

Where $\mathbf{Q}$ =rational function approximation of aerodynamic transfer function $\mathbf{Q}$; $\mathbf{A}_1,\ldots\mathbf{A}_{l+3}$, $\mathbf{D}$, $\mathbf{E}$, $\mathbf{\Lambda}$, $\lambda_1,\ldots\lambda_m$=frequency-independent ration function coefficients; m indicates the number of the partial fractions.

By defining the partial fractions as follows:

$$\tilde{\mathbf{\Phi}}_{se,l} = \frac{\mathbf{b}^T\mathbf{A}_{l+3}\mathbf{b}}{p+\lambda_l}\left(p\tilde{\mathbf{\Delta}}\right) \quad \text{(Roger's formulation)} \tag{4a}$$

$$\tilde{\mathbf{\Phi}}_{se} = \left(p\mathbf{I} + \mathbf{\Lambda}\right)^{-1}\mathbf{E}\mathbf{b}\left(p\tilde{\mathbf{\Delta}}\right) \quad \text{(Karpel's formulation)} \tag{4b}$$

and substituting Eq. (3) and (4) into Eq. (2), subsequently inverse Laplace transform of Eq. (4), the following state space formulation of self-excited forces can be obtained:

$$\begin{Bmatrix}\mathbf{F}_{se}\\ \mathbf{0}\\ \mathbf{0}\\ \mathbf{0}\end{Bmatrix} = \frac{1}{2}\rho U^2\left(\begin{bmatrix}\mathbf{b}^T\mathbf{A}_1\mathbf{b} & \frac{B}{U}\mathbf{b}^T\mathbf{A}_2\mathbf{b} & \mathbf{I} & \mathbf{I} & \mathbf{I}\\ & & \frac{\lambda_1 U}{B}\mathbf{I} & & \\ & & & \ddots & \\ & & & & \frac{\lambda_l U}{B}\mathbf{I}\end{bmatrix}\mathbf{X}_R + \begin{bmatrix}\mathbf{0} & \left(\frac{B}{U}\right)^2\mathbf{b}^T\mathbf{A}_3\mathbf{b} & \mathbf{0} & \mathbf{0} & \mathbf{0}\\ -\mathbf{b}^T\mathbf{A}_4\mathbf{b} & & \mathbf{I} & & \\ \vdots & & & \ddots & \\ -\mathbf{b}^T\mathbf{A}_{l+3}\mathbf{b} & & & & \mathbf{I}\end{bmatrix}\dot{\mathbf{X}}_R\right)$$

(Roger's formulation) (5a)

$$\begin{Bmatrix}\mathbf{F}_{se}\\ \mathbf{0}\end{Bmatrix} = \frac{1}{2}\rho U^2\left(\begin{bmatrix}\mathbf{b}^T\mathbf{A}_1\mathbf{b} & \frac{B}{U}\mathbf{b}^T\mathbf{A}_2\mathbf{b} & \mathbf{b}^T\mathbf{D}\\ \mathbf{0} & \mathbf{0} & \frac{U}{B}\mathbf{\Lambda}\end{bmatrix}\mathbf{X}_K + \begin{bmatrix}\mathbf{0} & \left(\frac{B}{U}\right)^2\mathbf{b}^T\mathbf{A}_3\mathbf{b} & \mathbf{0}\\ -\mathbf{E}\mathbf{b} & \mathbf{0} & \mathbf{I}\end{bmatrix}\dot{\mathbf{X}}_K\right) \text{(Karpel's formulation)} \tag{5b}$$

Additional aerodynamic states are introduced to express the aerodynamic phase lag behind structural motions. Obviously, addition of each partial fraction for approximating flutter derivatives may result in an additional new aerodynamic state in the state space equations of bridge deck flutter. Since there are three nonzero components of each nodal self-excited force vector, the number of additional aerodynamic state may be 3m and m for Roger's formulation and Karpel's formulation respectively. For Roger's formulation, variance of each aerodynamic state influences only one self-excited force component, and each self-excited force component is determined by only m independent aerodynamic states. However, for Karpel's formulation, variance of each aerodynamic state may influence all self-excited force components, and each self-excited force component may be influenced by all aerodynamic states.

3 FLUTTER ANALYSIS BY STATE SPACE APPROACH

The governing equations of flutter of a bridge deck in the smooth flow are given in matrix form as:

$$\mathbf{M}\ddot{\mathbf{Y}} + \mathbf{C}\dot{\mathbf{Y}} + \mathbf{K}\mathbf{Y} = \mathbf{F}_{se} \tag{6}$$

where $\mathbf{M}$, $\mathbf{C}$, and $\mathbf{K}$=mass, damping, stiffness matrices, respectively; $\mathbf{Y}$=nodal displacement vector; $\mathbf{F}_{se}$= nodal self-excited force vector.

Substituting Eq. (5) into Eq. (6) yields the following state space equations in flutter analysis

$$\dot{\mathbf{X}} = \mathbf{A}\mathbf{X} \tag{7}$$

where A=system matrix, for Roger's formulation, $\mathbf{A} = \begin{bmatrix}\mathbf{0} & \mathbf{I} & \mathbf{0} & \cdots & \mathbf{0}\\ -\bar{\mathbf{M}}^{-1}\bar{\mathbf{K}} & -\bar{\mathbf{M}}^{-1}\bar{\mathbf{C}} & \frac{1}{2}\rho U^2\bar{\mathbf{M}}^{-1} & \cdots & \frac{1}{2}\rho U^2\bar{\mathbf{M}}^{-1}\\ \mathbf{0} & \mathbf{b}^T\mathbf{A}_4\mathbf{b} & \frac{\lambda_1 U}{B}\mathbf{I} & \cdots & \mathbf{0}\\ \vdots & \vdots & \vdots & \ddots & \vdots\\ \mathbf{0} & \mathbf{b}^T\mathbf{A}_{m+3}\mathbf{b} & \mathbf{0} & \cdots & \frac{\lambda_m U}{B}\mathbf{I}\end{bmatrix}$,

and for Karpel's formulation of approximating flutter derivatives $\mathbf{A}=\begin{bmatrix} \mathbf{0} & \mathbf{I} & \mathbf{0} \\ -\bar{\mathbf{M}}^{-1}\bar{\mathbf{K}} & -\bar{\mathbf{M}}^{-1}\bar{\mathbf{C}} & \frac{1}{2}\rho U^2\bar{\mathbf{M}}^{-1}\mathbf{b}^T\mathbf{D} \\ \mathbf{0} & \mathbf{Eb} & -\frac{U}{B}\mathbf{\Lambda} \end{bmatrix}$;

$\mathbf{X}=\begin{Bmatrix}\mathbf{Y} & \dot{\mathbf{Y}} & \mathbf{X}_{se}\end{Bmatrix}^T$; $\bar{\mathbf{K}}=\mathbf{K}-\frac{1}{2}\rho U^2\mathbf{b}^T\mathbf{A}_1\mathbf{b}$; $\bar{\mathbf{C}}=\mathbf{C}-\frac{1}{2}\rho UB\mathbf{b}^T\mathbf{A}_2\mathbf{b}$; $\bar{\mathbf{M}}=\mathbf{M}-\frac{1}{2}\rho B^2\mathbf{b}^T\mathbf{A}_3\mathbf{b}$.

Flutter analysis can be conducted in both frequency and time domain using this preceding frequency independent state space equation.

3.1 *Flutter analysis in frequency domain*

Flutter analysis in frequency domain can be converted to be an algebraic eigenvalue problem, since real part of each complex eigenvalues of system matrix **A** indicates the logarithm decay rates of corresponding modal of structure, which represents its dynamic stability. As the system matrix **A** is frequency independent and parameterized only by wind velocity, complex analysis can be carried out straightforward without frequency iterative to determine the critical flutter wind speed.

The diagonal elements of system matrix **A** determine the behavior of structural states and aerodynamic states, and the non-diagonal elements represent coupling effects between structural states and aerodynamic states. If wind speed is not so high, the coupling effects between structure and fluid may be not significant, the non-diagonal terms of system matrix A are close to zero and A can be appropriately considered to a diagonal matrix. Therefore, eigenvalues of **A** generally consist of 2*n* complex-conjugate pairs of eigenvalues corresponding to structure itself and *m* real values corresponding to aerodynamic states, since structural governing equations are second order differential equations, while governing equations of aerodynamic states are of first order. However, if wind speed is close to critical flutter wind velocity, aeroelastic effects may be significant and the non-diagonal elements are far from zero, so some eigenvalues corresponding to aerodynamic states may become complex, which may be mixed up with structural eigenvalues. Therefore, the inherent eigenvalues corresponding to structure should be sorted out in flutter analysis in frequency domain (Xie and Xiang, 1985).

We identify structural inherent eigenvalues based on the fact that natural mode shape of structures may not change a lot at different wind velocities, especially at two adjacent wind speeds. The procedures of identification of structural inherent eigenvalues at a certain wind speed can be summarized as follows:

(1) Conduct structural damped eigenvalue analysis at zero wind speed, and sort the eigenvalues and their corresponding eigenvectors according to the image part of eigenvalues in descending order, and then store the first *n* complex eigenvalues $\mathbf{\Lambda}_0$ and their corresponding eigenvectors $\mathbf{\Phi}_0$ as structural inherent eigenvalues and eigenvectors.

(2) Assume a wind speed increment ΔU, and set current wind speed $U_i=i*\Delta U$ (i=1,⋯n).

(3) Carry out damped eigenvalue analysis at current wind speed U_i, and hunt for the first *n* natural eigenvectors of structure in sequence according to the sorted structural eigenvectors $\mathbf{\Phi}_{i-1}$ using an evaluating indicator of mode similarity *MSI*, which is defined as

$$MSI=\frac{\left(\mathbf{\Theta}_{j,i}^T\mathbf{\Phi}_{j,i-1}\right)^2}{\left(\mathbf{\Theta}_{j,i}^T\mathbf{\Theta}_{j,i}\right)\left(\mathbf{\Phi}_{j,i-1}^T\mathbf{\Phi}_{j,i-1}\right)} \tag{8}$$

Where $\mathbf{\Phi}_{j,i-1}$=the *j*th column of sorted eigenvectors $\mathbf{\Phi}_{i-1}$ at wind speed U_{i-1}, $\mathbf{\Theta}_{j,i}$=the *j*th column of unsorted eigenvectors $\mathbf{\Phi}_{i-1}$ at wind speed U_i, and the superscript ^{T} indicates vectors or matrix transpose.

(4) Sort the identified structural eigenvalues and their corresponding vectors according to $\mathbf{\Phi}_{i-1}$ at wind speed U_{i-1}, and store the structural eigenvalues $\mathbf{\Lambda}_i$ and eigenvectors $\mathbf{\Phi}_i$ at current wind speed.

If real parts of structural eigenvalues are all negative bridge will be dynamically stable, and if real part of any structural eigenvalue is positive bridge will be dynamically unstable. So the critical flutter wind speed can be defined as the wind velocity at which bridge system has only one eigenvalue λ with zero real part, and the imaginary part of this complex eigenvalue λ is flutter circular frequency.

3.2 *Flutter analysis in time domain*

Flutter analysis can also be conducted in time domain, in which structural and aerodynamic nonlinearities may be incorporated. In the present paper, buffeting force caused by the turbulence existing inherently in natural wind in conjunction with the structural-induced signature turbulence is not considered, and it is taken for granted that governing equation of bridge deck flutter (Eq. (6)) is homogeneous. Free vibration response to a certain initial condition of structure can be readily obtained by any time integration scheme, and subsequently damping ratio can be determined. Flutter instability of bridge deck will be happened when free vibration amplitude is constant or even increasing with time. The initial condition of structure should be given according to its flutter mode shape in order to seek out the critical flutter wind speed more precisely, with the reason that free vibration amplitude might be still decay with time at some wind speed a little larger than critical flutter wind speed with improper initial condition.

4 CASE STUDY

In this section, a simply supported line-like bridge with thin-airfoil cross section is taken as a case study. Since theoretical solution of flutter frequency and flutter wind velocity for this structure is available, this example can be used to verify the state space approach of flutter analysis and investigate the time and frequency domain response characteristics of two state-space formulations of self-excited force. The structural parameters are as follows: span l=300m; width of the bridge deck B=40m; vertically bending rigidity EI_z=2.1×10^{6}MPam^4; laterally bending rigidity EI_y=1.8×10^{7}MPam^4; torsional rigidity GI_t=4.1×10^{5}MPam^4; mass m=20,000kg/m; mass moment of inertia I_m=4.5×10^{6}kgm^2/m and air mass density ρ=1.248kg/m^3. The structural damping is not considered in this example to make a theoretical comparison.

Theodorson functions have been adopted for expressing self-excited forces acting on this simply supported bridge with thin-airfoil cross section, and it should be approximated by rational function firstly before flutter analysis with state space approach. The aerodynamic coefficients in rational function approximation are obtained by minimizing the optimization target J, which is defined as:

$$J\left(A_l,\lambda_l\right)=\sum_{i=1}^{N}w_i\left\|\mathbf{Q}_{\mathrm{Re}}\left(\nu_i\right)-\hat{\mathbf{Q}}_{\mathrm{Re}}\left(\nu_i\right)\right\|_F+\sum_{i=1}^{N}w_i\left\|\mathbf{Q}_{\mathrm{Im}}\left(\nu_i\right)-\hat{\mathbf{Q}}_{\mathrm{Im}}\left(\nu_i\right)\right\|_F \tag{9}$$

where $\mathbf{Q}_{\mathrm{Re}}=\begin{bmatrix}H_4^* & H_3^*\\ A_4^* & A_3^*\end{bmatrix}$, $\mathbf{Q}_{\mathrm{Im}}=\begin{bmatrix}H_1^* & H_2^*\\ A_1^* & A_2^*\end{bmatrix}$ = real and image part of aerodynamic transfer function, respectively ; $\hat{\mathbf{Q}}_{\mathrm{Re}}=\left(\frac{\nu}{2\pi}\right)^2\mathbf{A}_1-\mathbf{A}_3+\sum_{l=1}^{m}\mathbf{A}_{l+3}\frac{\nu^2}{\lambda_l^2\nu^2+4\pi^2}$, $\hat{\mathbf{Q}}_{\mathrm{Im}}=\frac{\nu}{2\pi}\mathbf{A}_2+\sum_{l=1}^{m}\mathbf{A}_{l+3}\frac{\lambda_l\nu^3}{2\pi\lambda_l^2\nu^2+8\pi^3}$ = real and image part of Roger's rational function approximation of aerodynamic transfer function, respectively; $\hat{\mathbf{Q}}_{\mathrm{Re}}=\left(\frac{\nu}{2\pi}\right)^2\mathbf{A}_1-\mathbf{A}_3+\nu^2\mathbf{D}\left(4\pi^2\mathbf{I}+\mathbf{\Lambda}^2\nu^2\right)^{-1}\mathbf{E}$, $\hat{\mathbf{Q}}_{\mathrm{Im}}=\frac{\nu}{2\pi}\mathbf{A}_2+\nu^3\mathbf{D}\left(8\pi^3\mathbf{I}+2\pi\nu^2\mathbf{\Lambda}^2\right)^{-1}\mathbf{\Lambda E}$ = real and

ly; $\hat{\mathbf{Q}}_{\mathrm{Re}} = \left(\frac{\nu}{2\pi}\right)^2 \mathbf{A}_1 - \mathbf{A}_3 + \nu^2 \mathbf{D}\left(4\pi^2\mathbf{I} + \mathbf{\Lambda}^2\nu^2\right)^{-1}\mathbf{E}$, $\hat{\mathbf{Q}}_{\mathrm{Im}} = \frac{\nu}{2\pi}\mathbf{A}_2 + \nu^3\mathbf{D}\left(8\pi^3\mathbf{I} + 2\pi\nu^2\mathbf{\Lambda}^2\right)^{-1}\mathbf{\Lambda E}$ = real and image part of Karpel's rational function approximation of aerodynamic transfer function, respectively; M = the number of elements in aerodynamic matrix Q; n = the number of reduced wind velocity; w_i= weight factor; $\|\cdot\|_F$=F norm of matrix.

Simulated annealing algorithm is applied to solve this optimization problem, and the rational function coefficients of two formulations extracted by approximating Theodorson functions with reduced wind velocity ranging from 0 to 20 are listed in Table 1.

Table 1 Rational function coefficients extracted by approximating Theodorson functions

	Roger's formulation				Karple's formulation			
	Group I		Group II		Group I		Group II	
Residual J	1.51×10^{-4}		6.1×10^{-3}		9.44×10^{-4}		7.9×10^{-3}	
$\mathbf{A}_1$	-3.54×10^{-9}	-6.2832	0.0228	-8.6669	-0.0033	-6.3451	0.0175	-8.6613
	7.12×10^{-10}	1.5708	-0.0057	2.1667	-1.67×10^{-5}	1.5756	-0.0045	2.1539
$\mathbf{A}_2$	-3.1416	-2.3562	-3.1783	-2.3563	-3.1516	-2.3498	-3.1797	-2.3545
	0.7854	-0.1963	0.7946	-0.1963	0.7789	-0.1915	0.7930	-0.1953
$\mathbf{A}_3$	-1.5708	-6.04×10^{-9}	-1.5625	-0.0085	-1.5682	-0.0030	-1.5621	-0.0090
	-1.23×10^{-9}	-0.0491	-0.0021	-0.0470	0.0031	-0.0530	-0.0014	-0.0480
$\mathbf{A}_4$ (Roger) $\mathbf{D}$ (Karpel)	-1.2629	1.7891	-1.2390	1.8730	-5.0253	2.5375	-4.9185	2.5645
	0.3157	-0.4473	0.3098	-0.4683	1.2911	-0.6000	1.2368	-0.6316
$\mathbf{A}_5$ (Roger) $\mathbf{E}$ (Karpel)	-0.0943	1.0131	-0.0863	3.2749	0.2499	-0.3571	0.2517	-0.3805
	0.0236	-0.2533	0.0216	-0.8187	-0.0333	0.4162	-0.0314	1.2746
$\mathbf{\Lambda}$	0.6	0.091	0.5638	0.0200	0.5920	0.0830	0.5630	0.0200

Figure 1 gives the comparison of flutter derivatives based on Theodorson function and its rational function approximation results. It is shown that four groups of aerodynamic coefficients in table 1 can all accord well with flutter derivatives.

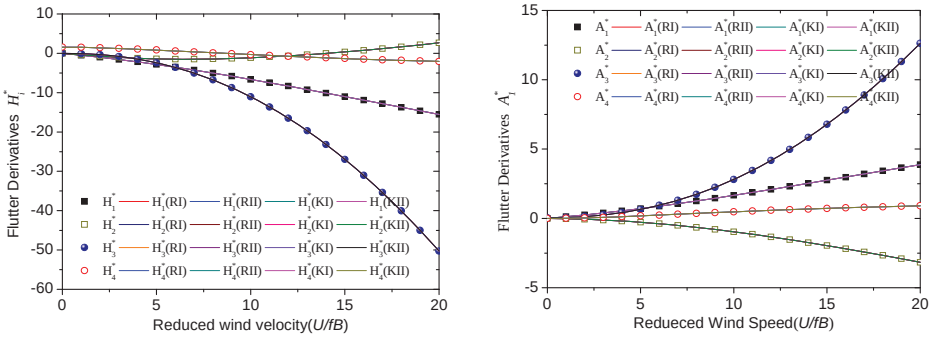

Figure 1 Rational function approximation of flutter derivatives

Applying the aerodynamic coefficients listed in Table 1 and following the identification procedures of structural inherent eigenvalues described in section 3.1, damped complex eigenvalue analysis is conducted under wind velocities from 0 to 150m/s. The critical flutter wind speed and flutter frequencies of this simple supported beam with four groups of rational function coefficients are given in Table 2.

Table 2 Flutter analysis results of the simply supported beam with four groups of rational function coefficients

	Theoretical solutio	Flutter derivatives	Roger I	Roger II	Karpel I	Karpel II
Critical flutter speed(m/s)	139.90	139.79	139.79	139.72	139.86	139.75
Flutter frequency (Hz)	0.3801	0.3800	0.3800	0.3802	0.3799	0.3802

Apparently, critical flutter wind speed and flutter frequency using state space approach with four groups of coefficients are almost the same as the theoretical solution and full order solution (Ding et al, 2002a)directly using flutter derivatives. Choosing group I coefficients of Roger's formulation as an example, the first 10 conjugate pairs of structural complex eigenvalues and complex eigenvectors are also obtained, and the variation of these complex eigenvalues versus wind velocity is plotted in Fig. 1. It is observed that (i) the vibration frequencies of modes except for the first torsional and vertical modes all alert little or even remain unchanged with the increase in wind velocity; (ii) for the first vertical and torsional mode, the frequency increases and decreases in the wind velocity range, respectively; (iii) the vibration damping of first torsional mode firstly increases and then decreases with increasing wind velocities, while damping of the other modes with increasing wind velocities. As shown in Fig. 1(b), the damping of first torsional mode becomes zero at a wind velocity of 139.79 m/s, and the corresponding torsional frequency becomes 0.3940 Hz, namely flutter frequency.

4.1 *Frequency-domain response characteristics of two formulations*

As it is still difficult to identify aerodynamic coefficients in rational function approximation of aerodynamic transfer function of self-excited forces directly in wind tunnel test, these aerodynamic coefficients are usually obtained by fitting flutter derivatives. However, this rational function approximation of aerodynamic transfer function cannot fit flutter derivatives without residual. Precision of flutter analysis results may be determined by frequency response characteristics of two formulations and fitting residual. In order to investigate frequency response characteristics of two formulations, we chose 22 groups of aerodynamic coefficients for two formulations with fitting residual ranging from 1.0×10^{-3} to 10.0 to conduct flutter analysis in frequency domain by state-space approach. For each group of aerodynamic coefficients, the initial iterative values and stopping criteria are identical and ultimate residual is in the same level for both two state-space formulations to confirm that the difference between flutter analyses results based on two formulations is not induced by self-difference of aerodynamic coefficients. Fig. 3 gives the variation of flutter analysis results to approximation residual of flutter derivatives, in which the relative errors of critical flutter wind speed and flutter frequencies are compared with that of full order solution directly using flutter derivatives, not with theoretical solution. It is observed that (i) relative errors of critical flutter wind speed and flutter frequency for both two formulations are no larger than 10% even for approximation residual larger than 10.0; (ii) the flutter analysis results based on Karpel's formulation are more sensitive to approximation errors than that of Roger's formulation although the number of additional aerodynamic states introduced in Karpel's formulation is half of Roger's formulation.

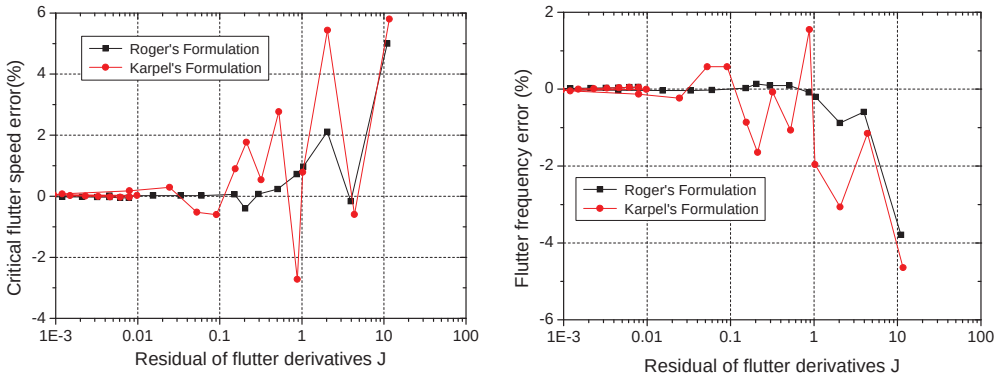

(a) critical flutter wind speed (b) flutter frequency

Figure 3 Variation of flutter analysis results to approximation residual of flutter derivatives

4.2 *Time-domain response characteristics of two formulations*

It is necessary to assume an initial condition of flutter governing equation in smooth wind flow before conducting flutter analysis in time domain. However, it is difficult to determine initial condition of aerodynamic states corresponding to the given initial condition of structural states. With these factitious initial conditions, structural responses may be erroneous in the first time period, although this incorrect response will gradually converge to physical solution with the prolonging of calculating time. Hence, it is essential to investigate the time response characteristic of two state-space formulations of self-excited forces.

In order to study time response characteristics of two self-excited force formulations, time-domain analyses of this simple supported beam have been carried out using the four groups of aerodynamic coefficients listed in table 1, respectively. For a given velocity, the time-domain structural response subjected to an initial excitation can be readily computed using a high precision direct integration time integration scheme. For convenience of comparison, time step size is assumed as 0.1s, while torsional and vertical displacement with value of 1deg and 0.01m respectively are employed as the initial conditions and applied to every node on the beam, and initial conditions of aerodynamic states are set as zero.

Under respective critical wind velocity of four groups of aerodynamic coefficients, the response time histories of mid-point of this simple supported beam are shown in Fig. 4. It is observed that time-domain response characteristics of two state-space formulations of self-excited force are almost identical and structural responses are incorrect in a long period time corresponding to the second group of coefficients for both state-space formulations. It can be noticed that the two groups of aerodynamic coefficients are basically the same except for those related to aerodynamic states no matter for Roger's formulation and Karple's formulation. Therefore, those coefficients related to aerodynamic states may determine the time-domain response characteristics of state-space formulations of self-excited forces.

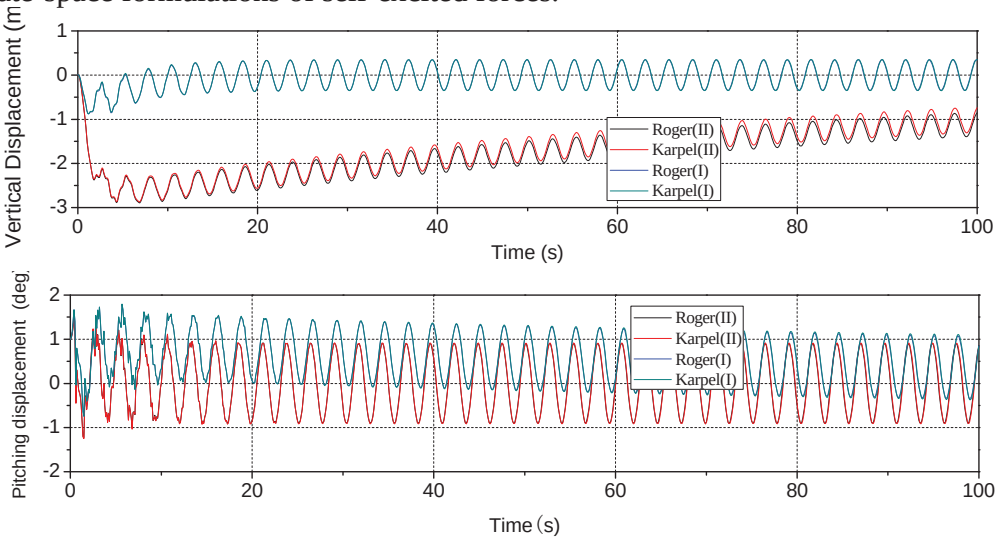

Figure 4 Time history of displacements at center span of simple supported beam

This incorrect response in first time period is mainly caused by improper initial conditions of aerodynamic states. Since these initial conditions of aerodynamic states cannot be determined in advance, it is alternative to make this incorrect response converge to physical solution as soon as possible. As the time-domain response characteristics of these two state-space formulations of self-excited force are almost identical and mainly determined by the characteristic of aerodynamic states, we choose aerodynamic states in Roger's formulation to cast around for solutions to make this initial incorrect response attenuate as soon as possible.

In the critical state of flutter, the motion of bridge deck can be viewed as a simple harmonic motion. Based on this assumption and by taking inverse Laplace transform of Eq. (4a), the aerodynamic state related to self-excited force component F caused by bridge deck motion Δ can be expressed as:

$$X_{sel}^{F\Delta}=A_{l+3}^{F\Delta}\int_{-\infty}^{t}e^{-\frac{\lambda_l U}{B}(t-\tau)}\omega\cos(\omega\tau)\,d\tau=\frac{A_{l+3}^{F\Delta}\omega e^{-\frac{\lambda_l U}{B}t}}{\left(\frac{\lambda_l U}{B}\right)^2+\omega^2}\left[e^{\frac{\lambda_l U}{B}\tau}\left(\omega\sin\omega\tau+\frac{\lambda_l U}{B}\cos\omega\tau\right)\Big|_{-\infty}^{t}\right]=\frac{A_{l+3}^{F\Delta}}{\sqrt{(\lambda_l/K)^2+1}}\sin(\omega t+\theta) \tag{10}$$

where $\theta=\arctan(\lambda_l/K)$. However, the lower limit of this convolution integral must be larger than zero in calculation, namely convolution integral in Eq. (10) is forced to be expressed as:

$$\begin{aligned}X_{sel,0}^{F\Delta}&=A_{l+3}^{F\Delta}\frac{\omega e^{-\frac{\lambda_l U}{B}t}}{\left(\frac{\lambda_l U}{B}\right)^2+\omega^2}\left[e^{\frac{\lambda_l U}{B}\tau}\left(\omega\sin\omega\tau+\frac{\lambda_l U}{B}\cos\omega\tau\right)\Big|_{0}^{t}\right]\\&=A_{l+3}^{F\Delta}\frac{1}{\sqrt{(\lambda_l/K)^2+1}}\sin(\omega t+\theta)-A_{l+3}^{F\Delta}\frac{\lambda_l/K}{(\lambda_l/K)^2+1}e^{-\frac{\lambda_l}{K}\frac{2\pi t}{T}}=X_{sel}^{F\Delta}+X_{sel,a}^{F\Delta}\end{aligned} \tag{11}$$

where $T=1/2\pi\omega$. Obviously, an additional term is introduced if this convolution integral is calculated from zero, and it can be viewed as the initial conditions of aerodynamic states. In flutter analysis, this additional term of aerodynamic state is usually unknown in advance, and it will cause the incorrect structural response. Fortunately, if λ_l is larger than zero this additional term will decay exponentially with time at a rate depending on λ_l/K and ω. The incorrect response may attenuate more quickly by increasing λ_l/K and ω. When this addition term is smaller than five percent of aerodynamic state response, the effect can be neglected. Therefore, the influence of additional term on aerodynamic state response will be smaller than 5% if Eq. (13) is satisfied,

$$\frac{X_{sel,a}^{F\Delta}}{X_{sel}^{F\Delta}}=\frac{\frac{\lambda_l/K}{(\lambda_l/K)^2+1}e^{-\frac{\lambda_l}{K}\frac{2\pi t}{T}}}{\frac{1}{\sqrt{(\lambda_l/K)^2+1}}}<\frac{\lambda_l/K}{(\lambda_l/K)^2+1}e^{-\frac{\lambda_l}{K}\frac{2\pi t}{T}}<\frac{1}{2}e^{-\frac{\lambda_l}{K}\frac{2\pi t}{T}}<5\% \tag{12}$$

which demands that λ_l is larger than $0.366K/n$,and n indicates the number cycles.

5 CONCLUSION

The self-excited force of bridge deck can be descripted in state space domain by using rational function approximations of unsteady aerodynamic forces. This state space equation of bridge deck motion makes flutter analysis straightforward and simplifies the design of efficient vibration suppression systems. The present paper mainly focuses on the time and frequency-domain response characteristics of Roger's and Karpel's state-space formulations of self-excited force and discusses detailed operation techniques of flutter analysis by state-space approach in frequency and time domain. Flutter analysis of a simple supported beam bridge with idealized thin plane section has been conducted as a case study. The concluding remarks can be summarized as follows:

(1) The additional aerodynamic states introduced in Roger's state-space formulation are twice than that of Karpel's formulation.

(2) Frequency-domain response characteristics of two state-space formulations are both favorable, although flutter results based on Karpel's formulation are more sensitive to residual of flutter derivatives than Roger's formulation.

(3) Time-domain response characteristics of two state-space formulations are almost identical; with restricting the lower limit of the coefficients related to aerodynamic states, the time period of incorrect transient response of structure can be shorten.

6 ACKNOWLEDGEMENTS

The work described in this paper is partially supported by the Natural Science Foundation of China under the Grants 90715039 and 51021140005, which are gratefully acknowledged.

7 REFERENCES

L. Caracoglia, N.P. Jones, Time domain vs. frequency domain characterization of aeroelastic forces for bridge deck sections. Journal of Wind Engineering and Industrial Aerodynamics, 91 (2003) 371-402.

X.Z. Chen, A. Kareem, Advances in modeling of aerodynamic forces on bridge decks. Journal of Engineering Mechanics, 128 (2002) 1193-1205.

C. Costa, C. Borri, Application of indicial functions in bridge deck aeroelasticity. Journal of Wind Engineering and Industrial Aerodynamics, 94 (2006) 859-881.

Q.S. Ding, A.R. Chen, H.F. Xiang, A state space method for coupled flutter analysis of long-span bridges. Journal of Structural Engineering and Mechanics, 14 (2002a) 491-504.

Q.S. Ding, A.R. Chen, H.F. Xiang, Coupled flutter analysis of long-span bridges by multimode and full-order approaches. Journal of Wind Engineering and Industrial Aerodynamics, 90 (2002b) 1981-1993.

N.N. Dung, T. Miyata, H. Yamada, N.N. Minh, Flutter responses in long span bridges with wind induced displacement by the mode tracing method. Journal of Wind Engineering and Industrial Aerodynamics, 77-78 (1998) 367-379.

Y.J. Ge, H. Tanaka, Aerodynamic stability of long-span suspension bridges under erection. Journal of Structural Engineering, 126 (2000) 1404-1412.

A. Jain, N.P. Jones, R.H. Scanlan, Coupled flutter and buffeting analysis of long-span bridges. Journal of Structural Engineering, 122 (1996) 716-725.

Y.K. Lin, J.N. Yang, Multimode bridge response to wind excitations. Journal of Engineering Mechanics, 109 (1983) 586-603.

R.H. Scanlan, Reexamination of sectional aerodynamic force functions for bridges. Journal of Wind Engineering and Industrial Aerodynamics, 89 (2001) 1257-1266.

R.H. Scanlan, J.J. Tomko, Airfoil and bridge deck flutter derivatives. Journal of the Engineering Mechanics, 97 (1971) 1717-1737.

K. Wilde, Y. Fujino, Aerodynamic control of bridge deck flutter by active surfaces. Journal of Engineering Mechanics, 124 (1998) 718-727.

J.M. Xie, H.F. Xiang, State-space method for 3D flutter analysis of bridge structures, Proc. Asia-Pacific Symposium on Wind Engineering,1985, New Delhi, India, pp. 269-276.

The Seventh International Colloquium on Bluff Body Aerodynamics and Applications (BBAA7)
Shanghai, China; September 2-6, 2012

Hybrid models for assessing the flutter stability of suspension bridges

Tajammal Abbas[a], Guido Morgenthal[b]

[a]*PhD candidate, Graduate College 1462, Department of Civil Engineering, Bauhaus University Weimar, Berkaer Straße 9, 99423 Weimar, Germany*
[b]*Prof, Modelling and Simulation of Structures, Department of Civil Engineering, Bauhaus University Weimar, Marienstraße 13A, 99423 Weimar, Germany*

ABSTRACT: Long-span cable supported bridges are prone to aerodynamic instabilities caused by wind and this phenomenon is usually a major design criterion. If the wind speed exceeds the critical flutter speed of the bridge, this constitutes an Ultimate Limit State. The prediction of the flutter boundary therefore requires accurate and robust models. This paper aims at studying various combinations of models to predict the flutter phenomenon. Since flutter is a coupling of aerodynamic forcing with a structural dynamics problem, different types and classes of models can be combined to study the interaction. Here, both numerical approaches and analytical models are utilised and coupled in different ways to assess the prediction quality of the hybrid model. Models for aerodynamic forces employed are the analytical Theodorsen expressions for the motion-induced aerodynamic forces of a flat plate and Scanlan derivatives as a Meta model. Further, Computational Fluid Dynamics (CFD) simulations using the Vortex Particle Method (VPM) were used to cover numerical models.

KEYWORDS: Suspension bridge, flutter, CFD, aerodynamic derivatives, numerical simulation

1 INTRODUCTION

Long-span bridges are highly flexible, light weight and have low structural damping. They can be subjected to large dynamic motion due to wind actions. The assessment of aerodynamic behaviour, therefore, plays very important role in the design of long-span bridges. For this reason, flutter is also viewed as essential aeroelastic phenomenon to be studied for these structures. The aeroelastic stability of long-span bridges against flutter is checked by calculating a wind speed at which flutter occurs which is known as the flutter limit. The required aeroelastic properties of the bridge deck section are usually determined in wind tunnel tests.

Scanlan introduced mathematical treatment of flutter in 1960s whereas for the last couple of decades, numerical methods are becoming more popular due to the increasing use of computers in the field of Structural Engineering. In this paper, the study is made on the aerodynamic phenomena, the methods available for flutter analysis for bridges, and to apply the analytical and numerical based analysis on the Lillebælt suspension bridge to calculate ultimately its flutter limit.

2 METHODS OF AERODYNAMIC ANALYSIS

Analytical approaches play very important role in Wind Engineering whereas numerical methods are gaining importance. All methods apply simplifications to a certain extent such as assuming two-dimensionality of the flow or the shedding process like the wake oscillator model for the

case of vortex induced vibration [1]. There are three main types of analysis to for aerodynamic problems:

- Experimental methods
- Analytical methods
- Numerical methods

The last two methods have been used in this study. Analytical solution based on potential flow theory for the motion induced forces on a flat plate exerting sinusoidal heave and pitch motion was given by Theodorsen [2]. In most cases, the empirical models are available which are based on the results of experimental studies. These models are mostly based on 2D situations but in reality the 3D effects are present. Also in analytical models, the basic physical causes are attended but the Fluid-structure Interaction is not addressed. The experimental methods are considered relatively accurate compared to the other methods. Wind tunnel testing and full scale models are the examples of experimental methods.

The wind tunnel testing is very expensive for parametric studies but the numerical approach makes it relatively cheaper. With the advancement in the computer modelling and the processing power and by using the principles of CFD, it is now possible to study wind effects on structures in relatively less time. These methods are also efficient, repeatable and economical. Numerical simulations can be used in place of wind tunnel investigation for the fundamental studies. The accuracy of results from these methods not only depends on the quality of the solver but also on the modelling itself. Therefore, the numerical method must be reliable and robust to be used in place of wind tunnel tests.

3 REFERENCE OBJECT

The Lillebælt suspension bridge, Denmark, has been used as a reference object to employ the various model combinations. The data about the bridge is available in [3] and the structural parameters used for this reference object are given in Table 1. For simplicity in the calculation, the railing and other attachments on the deck are not considered in this study.

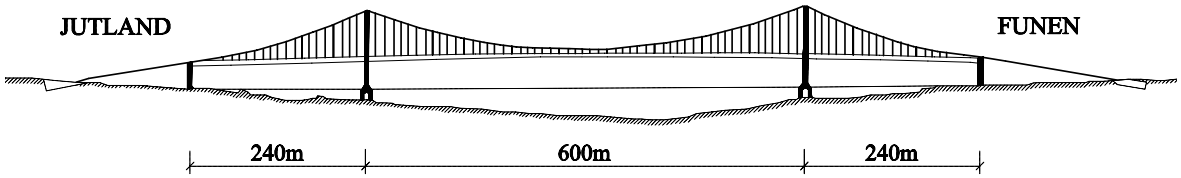

Figure 1. Elevation of the Lillebælt suspension bridge, Denmark used as a reference object in this study.

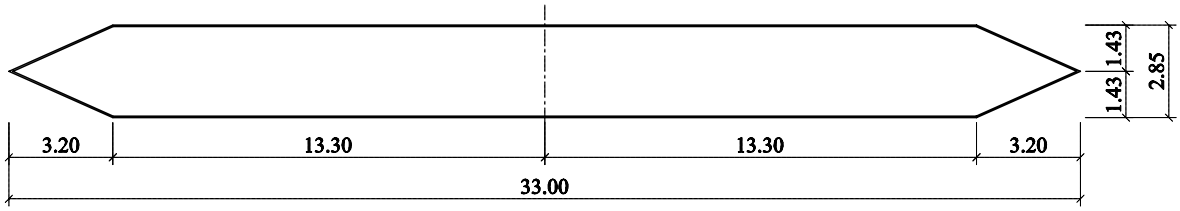

Figure 2. Simplified Lillebælt suspension bridge deck section geometry used in this study (Dimensions: [m]).

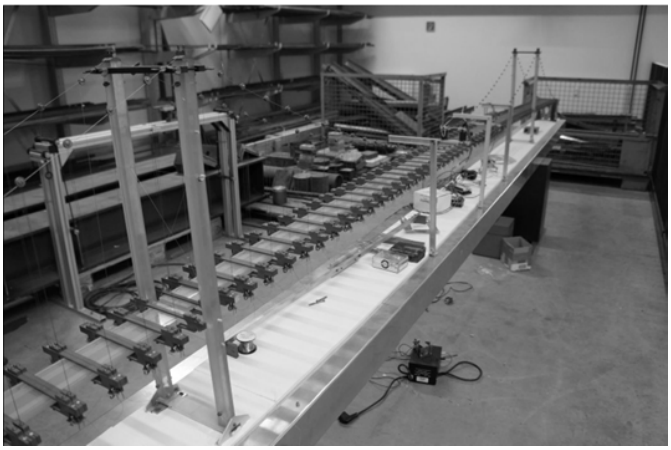

Figure 3. Physical model of the Lillebælt suspension bridge.

Table 1. Basic data and structural properties of the Lillebælt suspension bridge section used in this study.

Section width B [m]	Mass m [kg/m]	Inertial mass I [kg/m^2/m]	Bending frequency f_h [Hz]	Torsional frequency f_α [Hz]	Damping ratio ξ_h, ξ_α [-]
33	11667	1017778	0.156	0.500	0.01

4 COUPLING OF MODELS

Flutter is a coupling of aerodynamic forcing with a structural dynamics problem. Therefore, different types and classes of models can be combined to study the interaction. In this study, both numerical approaches and analytical models are utilised and coupled in different ways to assess the prediction quality of the hybrid model.

The structural representations were dimensionally reduced to two degree of freedom section models calibrated from global models as well as a fully three-dimensional Finite Element (FE) model. A two degree of freedom system was analysed analytically as well as numerically. The following models were thus derived and analysed: Fully analytical, CFD Derivatives-Analytical and Numerical 2D Structural, CFD Derivatives-Numerical 3D Structural, Fully coupled CFD Numerical 2D Structural. This has allowed to investigate a very broad range of model combinations and to study their merits and drawbacks.

Table 2. Model coupling for the flutter analysis used in this study

Structural \ Aerodynamic			Analytical		Numerical	
			Flat Plate		Flat Plate	Lillebælt Section
Analytical		2D	○	●	●	●
Numerical	VPM (CFD)	2D	-		○	○
	FE Software	2D	-		●	●
		3D	-		●	●

○ Simple/ Regular model ● Meta model

4.1 *Analytical Approach (Theodorsen Theory)*

Theodorsen investigated the flutter phenomenon for aircraft wings and gave a very popular approach for the flutter analysis. This approach is independent of the shape of the body but on the other hand it neglects the effect originating from the simplification to the flat plate. From the basic principle of potential flow theory, Theodorsen showed that for thin airfoils in incompressible flow, the expressions for F_L and F_M are linear in displacement h and α and their first and second derivatives [2].

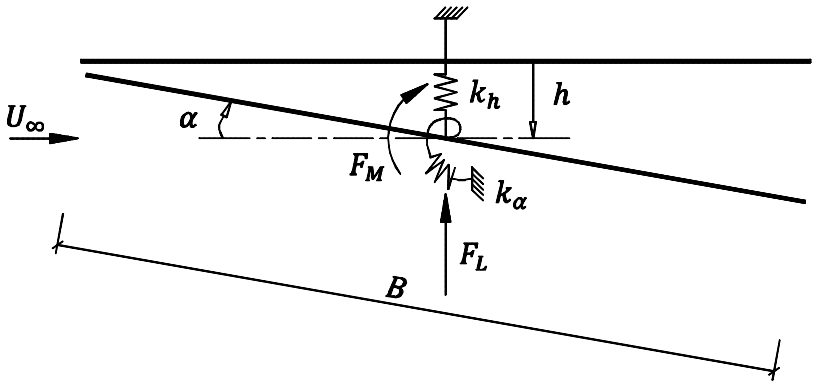

Figure 4. Definition of degrees of freedom (heave h and pitch α) for flutter analysis.

where F_L and F_M are the lift and moment, k_h and k_α are the vertical and rotational spring stiffness and h and α are the vertical displacement and rotation respectively. U_∞ is the oncoming wind speed. The equations of motion can be written

$$F_L = m\ddot{h} + 2m\xi_h\omega_h\dot{h} + m\omega_h^2 h \tag{1}$$

$$F_M = I\ddot{\alpha} + 2I\xi_\alpha\omega_\alpha\dot{\alpha} + I\omega_\alpha^2\alpha \tag{2}$$

where ω_h and ω_α are the natural circular frequencies in heave and pitch degree of freedom respectively. The theoretical expressions on a flat plate airfoil for sinusoidal oscillating lift F_L and moment F_M are

$$F_L = -\rho b^2 U_\infty \pi\dot{\alpha} - \rho b^2\pi\ddot{h} - 2\pi\rho C U_\infty^2 b\alpha - 2\pi\rho C U_\infty b\dot{h} - 2\pi\rho C U_\infty b^2 \tfrac{1}{2}\dot{\alpha} \tag{3}$$

$$F_M = -\rho b^2\pi\tfrac{1}{2}U_\infty b\dot{\alpha} - \rho b^4\pi\tfrac{1}{8}\ddot{\alpha} + 2\rho U_\infty b^2\pi\tfrac{1}{2}CU_\infty\alpha + 2\rho U_\infty b^2\pi C\dot{h} + 2\rho\tfrac{1}{2}U_\infty b^3\pi C\dot{\alpha} \tag{4}$$

where ρ is the air density, C is the Theodorsen's circulation function and $b = B/2$. The system of differential equations (1), (2), (3) and (4) can be written as

$$\begin{bmatrix}\dot{h}\\ \ddot{h}\\ \dot{\alpha}\\ \ddot{\alpha}\end{bmatrix} = \begin{bmatrix}0 & 1 & 0 & 0\\ a_{21} & a_{22} & a_{23} & a_{24}\\ 0 & 0 & 0 & 1\\ a_{41} & a_{42} & a_{43} & a_{44}\end{bmatrix}\begin{bmatrix}h\\ \dot{h}\\ \alpha\\ \dot{\alpha}\end{bmatrix} \tag{5}$$

This is of the form

$$\dot{X} = AX \tag{6}$$

and assuming the response X is of the form

$$X = \boldsymbol{R}.e^{\lambda t} \tag{7}$$

where $\boldsymbol{R}$ is real. This simplifies to Eigenvalue problem as follows:

$$[\boldsymbol{A} - \lambda \boldsymbol{I}]\boldsymbol{R}.e^{\lambda t} = 0 \tag{8}$$

The solution for $h(t)$ and $\alpha(t)$ is of an exponential form. The Eigenvalues of λ_i of the matrix $\boldsymbol{A}$ characterize the response of the system as follows:

- Positive real part: Increasing response
- Negative real part: Decaying response
- Imaginary part: Oscillating response

The system will become unstable when an Eigenvalue has a positive real part. When the imaginary part goes towards zero, the oscillatory part vanishes and the phenomenon of static divergence is observed. In this situation, there will be pure heave or pitch motion which can be interpreted as loss of vertical stiffness. The system is solved successively for increasing U_∞ until at least one Eigenvalue becomes positive real. The code for solving the Theodorsen's equations was written in Matlab. Using the structural parameters for the Lillebælt bridge (see Table 1), the flutter limit was found 93.8m/s.

4.2 *Meta Model (Scanlan Representation)*

Scanlan proposed a set of expressions for the aerodynamic forces on a bridge cross section. It assumes that the self-excited lift F_L and moment F_M for a bluff body may be treated as linear in displacement h and rotation α and their first derivatives [4]. Below is commonly used linearized form.

$$F_L = \frac{1}{2}\rho U_\infty^2 B\left[KH_1^*\frac{\dot{h}}{U_\infty} + KH_2^*\frac{B\dot{\alpha}}{U_\infty} + K^2H_3^*\alpha + K^2H_4^*\frac{h}{B}\right] \tag{9}$$

$$F_M = \frac{1}{2}\rho U_\infty^2 B^2\left[KA_1^*\frac{\dot{h}}{U_\infty} + KA_2^*\frac{B\dot{\alpha}}{U_\infty} + K^2A_3^*\alpha + K^2A_4^*\frac{h}{B}\right] \tag{10}$$

$$K = \frac{B\omega}{U_\infty} \tag{11}$$

where the non-dimensional coefficients H_i^* and A_i^* are known as aerodynamic or flutter derivatives. The frequency of the bridge oscillation under aerodynamic forcing is known as reduced frequency. As the aerodynamic derivatives are the function of this frequency therefore they can only be measured when the bridge is in the oscillatory state. Normally these are measured in special wind tunnel tests.

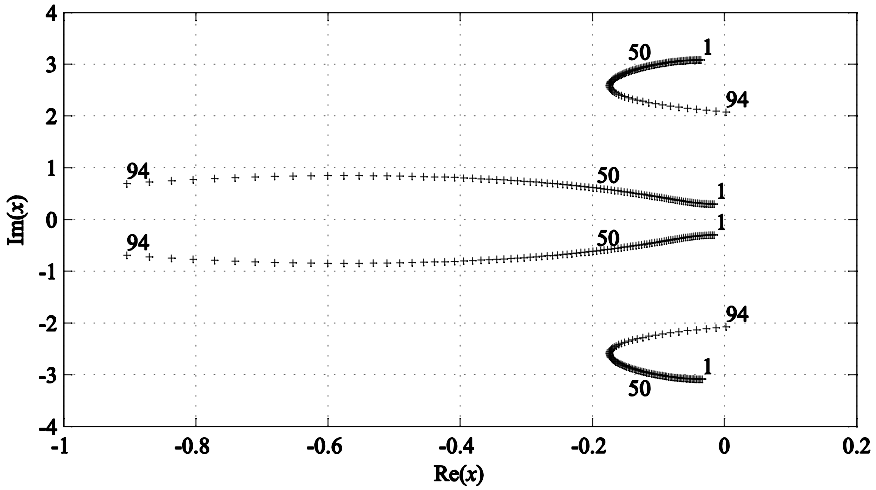

Figure 5. Eigenvalue paths for increasing wind speed U_∞.

The formulation to the Eigenvalue problem in this case is similar as described in Section 4.1. The flutter limit is determined when the real part of at least one Eigenvalue becomes positive as shown in Figure 6. The flutter limit was determined as 93.8m/s using the structural parameters of the Lillebælt bridge given in Table1.

4.3 *Forced Vibration Simulation*

Forced vibration simulations are used to determine motion-induced forces. The resulting lift and moment time histories are used to compute the aerodynamic derivatives. A computer code, VXFlow, based on VPM has been used here to compute these derivatives. Forced vibration simulations were performed on the Lillebælt section and the flat plate (aspect ratio 1:100) in sinusoidal heave and pitch motion over a range of reduced frequencies. The reduced frequency is controlled by changing the period of heave and pitch forcing motion.

$$v_r = \frac{2\pi U_\infty}{b\omega} \tag{12}$$

where v_r is reduced frequency. These simulations are performed in heave and pitch motion separately and the aerodynamic derivatives are computed from the resulting force time histories. The simulation gives time histories for $\overline{\boldsymbol{F}}_{\boldsymbol{L}}$ and $\overline{\boldsymbol{F}}_{\boldsymbol{M}}$ corresponding to known displacement traces $\boldsymbol{h}$. Equations (9) and (10) (with $\alpha = 0$) thus constitutes a system of equations as

$$\overline{\boldsymbol{F}}_{\boldsymbol{L}} = \boldsymbol{C}_h^L \boldsymbol{H}_h^* \tag{13}$$

$$\overline{\boldsymbol{F}}_{\boldsymbol{M}} = \boldsymbol{C}_h^M \boldsymbol{A}_h^* \tag{14}$$

where

$$\boldsymbol{C}_h^L = \frac{1}{2}\rho U_\infty^2 BK \begin{bmatrix} \frac{\dot{\boldsymbol{h}}}{U_\infty} & K\frac{\boldsymbol{h}}{B} \end{bmatrix} \text{ and } \boldsymbol{C}_h^M = B\boldsymbol{C}_h^L \tag{15}$$

$$\boldsymbol{H}_h^* = \begin{bmatrix} H_1^* \\ H_4^* \end{bmatrix}, \ \boldsymbol{A}_h^* = \begin{bmatrix} A_1^* \\ A_4^* \end{bmatrix} \tag{16}$$

System (13) can be solved in the least-squares sense by left-multiplying with the $\boldsymbol{C}$ matrix:

$$\boldsymbol{C}_h^{L^T} \bar{F}_L = \boldsymbol{C}_h^{L^T} \boldsymbol{C}_h^L \boldsymbol{H}_h^* \tag{17}$$

$$\boldsymbol{C}_h^{M^T} \bar{F}_M = \boldsymbol{C}_h^{M^T} \boldsymbol{C}_h^M \boldsymbol{A}_h^* \tag{18}$$

This gives two sets of derivatives in lease-square sense. The procedure to calculate these aerodynamic derivatives can be found in [5] and is summarized as follows:

- perform forced vibration tests in either heave or pitch motion
- calculate a best-fit harmonic of the same forcing frequency to obtain lift coefficient and phase shift
- calculate derivatives

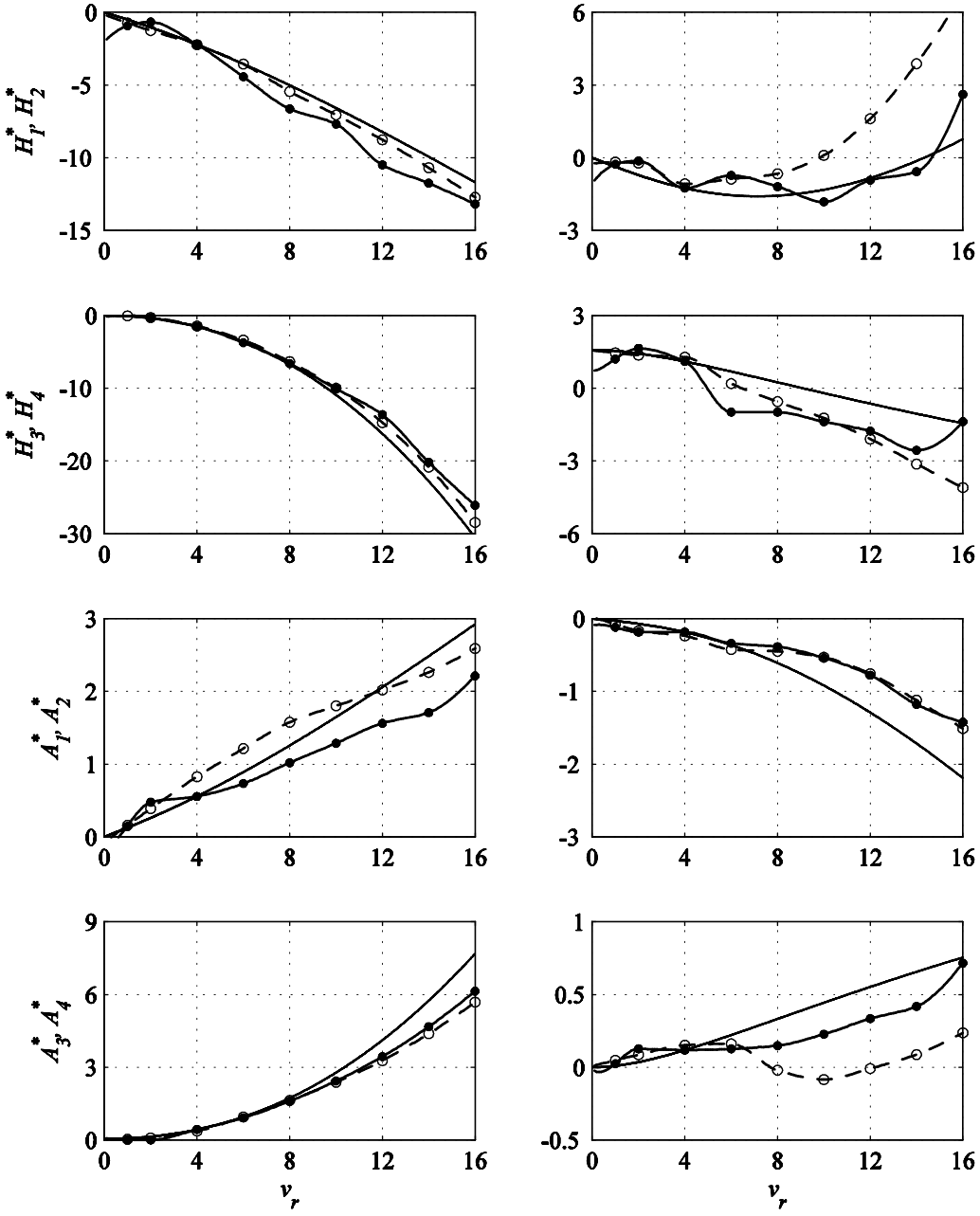

Figure 6. Aerodynamic derivatives (H_i^* and A_i^* where i =1, 2, 3, 4) w.r.t. the reduced speed (v_r): flat plate by Theodorsen theory (——), interpolated values from forced vibration analysis on the Lillebælt section (—•—) and the flat plate (- -o- -).

The resulting aerodynamic derivatives can be used to calculate flutter limit of the bridge. The forced vibration simulation was performed for the Lillebælt section shown in Figure 2 and the flat plate of the same width with aspect ratio of 100. For both these cases, structural parameters given in Table 1 were used. The flutter limit for the Lillebælt section was calculated as 94.2m/s and for flat plate as 88.7m/s.

4.4 *Fluid-structure Interaction Simulation*

VXFlow has been used here for the coupled analysis of the vertical motion and rotation of a 2 degree of freedom spring supported section model. The coupling of fluid dynamics solution and the structural dynamics is done at every time step. The pressure on the surface of the body is integrated to get the resultant force in terms of lift and twisting moment. These are associated with the two degrees of freedom of the structural system. The equations of motion for the system are solved by time marching structural dynamics solution. A stiffness matrix is then created and solution is performed. Rayleigh damping is used to model structural damping, for which the damping matrix is proportional to the combination of mass and stiffness matrices.

Structural parameters, given in Table 1 for the Lillebælt suspension bridge, were used for the bridge section (see Figure 2) and the flat plate of aspect ratio 100. The simulations were performed at various wind speed to identify the flutter instability. It was observed that just before the flutter limit, the section goes in the loss of vertical stiffness stage having extreme heave condition. At 95m/s the bridge section becomes unstable after a few hundred time steps. The flutter limit for the plate section was found as 98m/s.

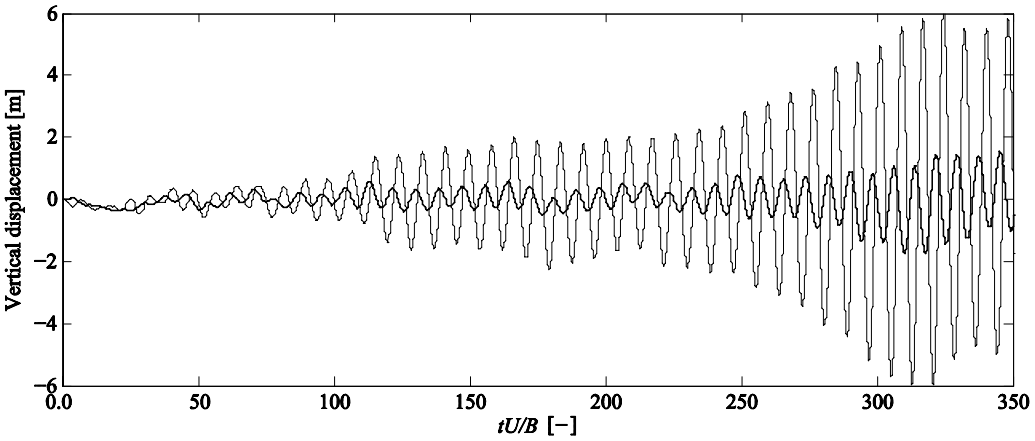

Figure 7. Lillebælt section in Fluid-structure Interaction, displacement time histories at U_∞= 95m/s: leading edge (—), trailing edge (—).

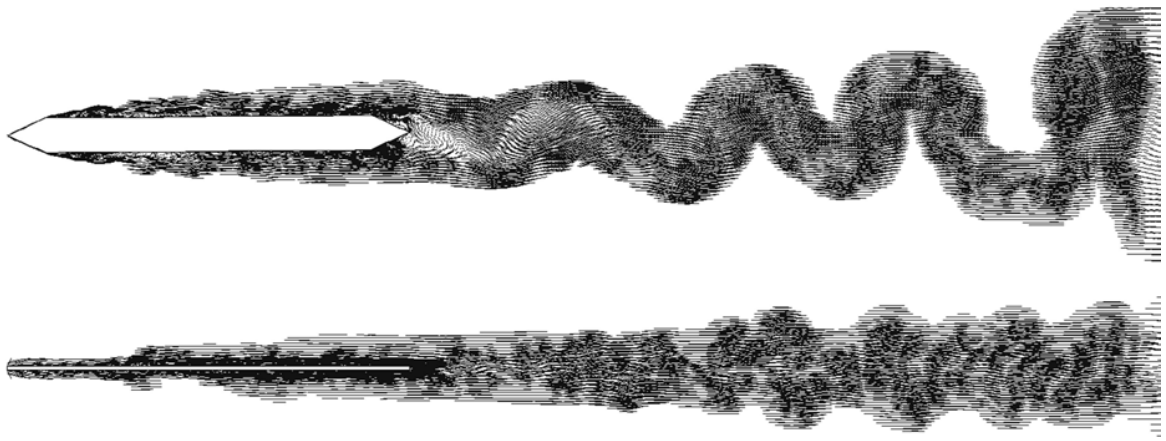

Figure 8. Instantaneous vortex pattern with streak lines for the Lillebælt section (Top) and the flat plate (Bottom).

4.5 *Finite Element Model*

The section of the Lillebælt suspension bridge deck was modelled as a two degree of freedom beam element of unit length in a Finite Element software. The system was supported on springs with vertical and rotational degrees of freedom. The reduced model was calibrated to represent the first bending and first torsional mode of the full bridge model. The dimensional reduction to a 2 degree of freedom system is a simplification but on the other hand it neglects the effects coming from the higher modes. The aerodynamic derivatives obtained through forced vibration analysis (see Section 4.3), for the Lillebælt section and the flat plate, were used to calculate the aerodynamic forces. Dynamic wind history analysis was performed on the system. The flutter limit both for the Lillebælt section and the flat plate was found to be 58.5m/s.

A 3D Finite Element model of the Lillebælt suspension bridge was made and calibrated to represent the structural properties of the bridge given in Table 1. In the calibration process some discrepancies were found and the target frequencies were not achieved exactly. The mode shapes of first bending and first torsional mode with their achieved frequencies are shown in Figure 10. The approach from the two degree of freedom model was implemented to the full 3D model of the bridge and the resulting flutter limits were calculated. The effect of higher modes was observed in the deformed model of the bridge at flutter limit. The flutter limit calculated was 49.0m/s both for the Lillebælt section and the flat plate.

Figure 9. View of full 3D Finite Element bridge model.

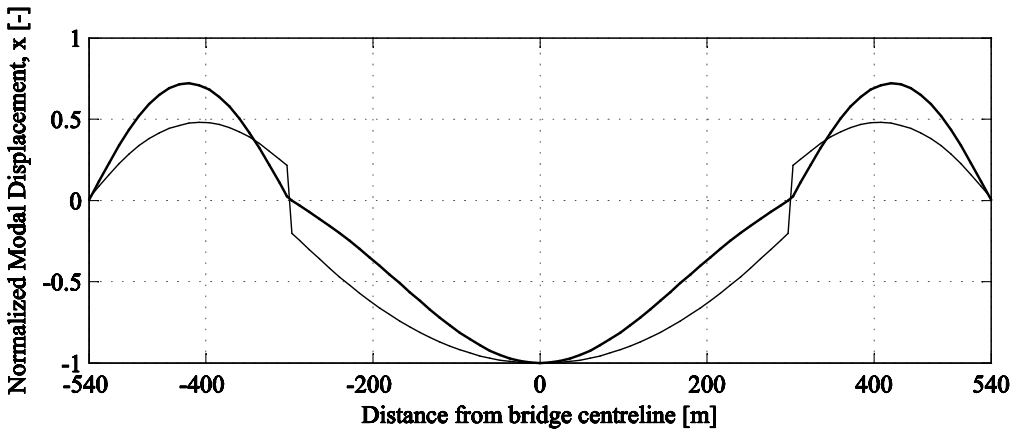

Figure 10. First bending mode (—) (achieved frequency = 0.151 Hz) and first torsional mode (—) (achieved frequency = 0.502 Hz) of full 3D Finite Element bridge model.

5 CONCLUSIONS

The flutter phenomenon was studied employing various combinations of analytical and numerical prediction models. Lillebælt suspension bridge was used as a study object. Generally, all models were able to predict the flutter phenomenon and relatively close agreement was found for the particular bridge. Fully coupled CFD analyses have the advantage that no prior knowledge as to the phenomenon needs to be inserted into the model. Three-dimensional structural representations are superior over dimensionally reduced models in that no prior knowledge as to the modes participating in the flutter coupling is required. Fully analytical models are more direct models and allow a better insight into the force coupling. Simplified aerodynamic models need to be critically assessed with respect to their ability to predict the aerodynamic behaviour of the real cross section. The paper presents in detail all the models used and shows the analysis results.

Table 3. Summary of flutter limits from different model coupling (see Table 2).

Structural \ Aerodynamic			Analytical		Numerical	
			Flat Plate		Flat Plate	Lillebælt Section
Analytical		2D	93.8	93.8	88.7	94.2
Numerical	VPM (CFD)	2D	-		98.0	95.0
	FE Software	2D	-		58.5	58.5
		3D	-		49.0	49.0

6 REFERENCES

1 G. Morgenthal, Comparison of Numerical Methods for Bridge-Deck Aerodynamics, MPhil Thesis, 2000
2 T. Theodorsen, General theory of aerodynamic instability and the mechanism of flutter, TR 496, NACA, 1935.
3 Chr. Ostenfeld, A. G. Frandsen, J. J. Jessen and G. Hass, Motorway Bridge Across Lillebælt, Publication III: Design and Construction of the Bridge, Report, 1970
4 R. H. Scanlan and J. J. Tomko, Airfoil and bridge deck flutter derivatives, ASCE J. of Eng. Mech. 97 (1971), 1717–1737.
5 G. Morgenthal, Aerodynamic Analysis of Structures Using High-resolution Vortex Particle Methods, PhD Thesis, 2002

The Seventh International Colloquium on Bluff Body Aerodynamics and Applications (BBAA7)
Shanghai, China; September 2-6, 2012

Interference effect on local peak pressure between two high-rise buildings with rectangular shape

Yi Hui [a], Akihito Yoshida [a], Yukio Tamura [a]

[a]*Department of Architectural Engineering, Tokyo Polytechnic University, Atsugi, Kanagawa, Japan*

ABSTRACT: This study investigates the interference effects between two rectangular-section high-rise buildings by wind tunnel experiments, focusing on local peak pressure coefficients. Wind tunnel experiments were carried out under all possible wind incidence angles for many configurations. The parallel building arrangements were considered. To evaluate the interference effects for local peak pressures in detail, interference factors for maximum positive and minimum negative peak pressures are presented and discussed. The results show that interference effects greatly depend on the configurations. The interfering building has stronger effects on the smallest minimum negative peak pressure of the principal building than the largest maximum positive peak pressure. The wind direction that causes the largest peak pressure varies with the changing of interfering building's location.

KEYWORDS: high-rise building; interference effects; wind tunnel experiment; Local peak pressure.

1 INTRODUCTION

Modern tall buildings are often built in groups in urban areas. This results in flow interference and wind loads on buildings are modified from the isolated building situation. Catastrophic incidents may result if the interference effect on load has is not considered in design. An investigation of interference effect is complicated by the large number of variables needed to describe the broad set of possible situations – sizes and shapes of buildings, relative locations of adjacent building(s), wind directions, upstream terrain conditions and so on.

Tang and Kwok (2004) investigated interference excitation mechanisms of translational and torsional responses of a pair of identical tall buildings. They found that amplified along-wind, cross-wind and torsional responses were largely induced by the wake of an upstream interfering building. Lam et al. (2011) studied wind-induced interference effects on a row of five square-plan tall buildings arranged in close proximity, and clarified that the design values of peak dynamic responses of a tall building are not significantly magnified when placed in a row. Kim, et al., (2009) discussed interference effect on local peak pressures between two identical square-section tall buildings from the viewpoint of cladding design. They found that the local peak pressure coefficients on the walls of a principal building largely depended on the location of an interfering building.

However, investigating only buildings with the same cross section is not enough for a comprehensive understanding of interference effect. It is apparent that the flow pattern surrounding two buildings will change with building shapes, and this will lead to a change in local peak pressures on buildings. In the present study, in order to obtain more information about the interference effects between two high-rise buildings on the local peak pressure, two rectangular-section building were used to conducted wind tunnel experiments. The experimental results are presented and discussed in this paper.

2 WIND TUNNEL EXPERIMENTS

Wind tunnel experiments were carried out in a Boundary Layer Wind Tunnel located at Tokyo Polytechnic University, Japan. The test section of the wind tunnel was 2.2m wide and 1.8m high. The approaching flow represented an urban wind exposure using the spire-roughness technique with a power law exponent of 0.27. The wind speed and turbulence intensity at the roof height of the model were 8m/s and 17%, respectively. The velocity scale was set to 1/5. Measured longitudinal mean wind velocities and turbulence intensity profiles are shown in Fig. 1. Fig. 1 also shows the power spectrum of longitudinal wind speed at the roof height.

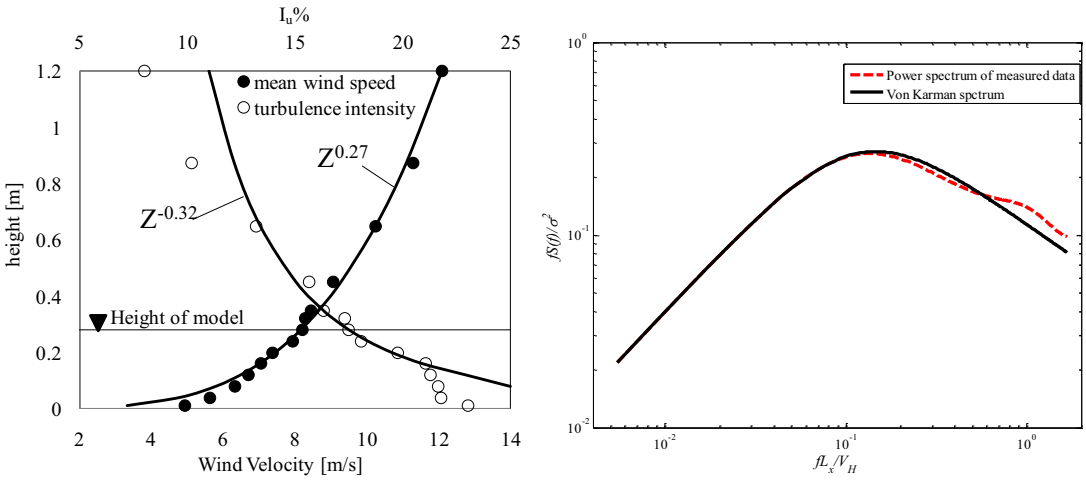

(a) wind profiles of experiment (b) wind power spectrum

Fig. 1. Characteristics of longitudinal wind in experiment.

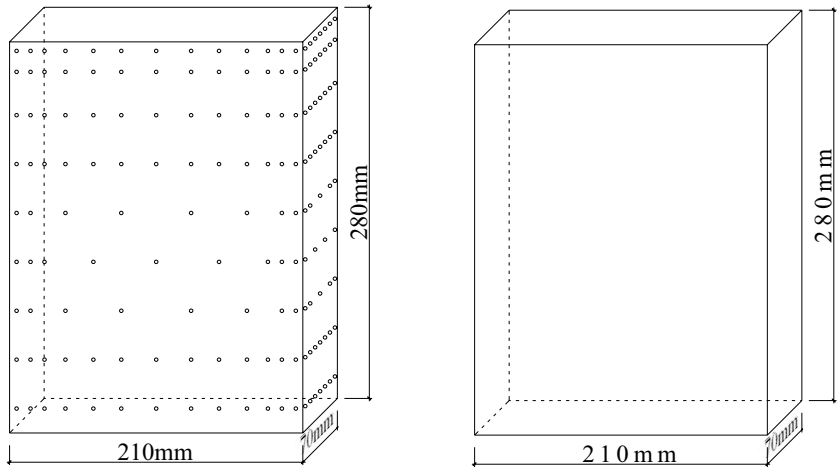

(a) Principal building models (b) Interfering building models

Fig. 2. Building models for pressure measurement.

The model size was 210mm wide, 70mm deep and 280mm high. Two models of the same shape were used (Fig. 2). The one with pressure taps was used as the principal building, the one without pressure taps was used as the interfering building. A total of 318 pressure taps were installed on the walls of the principal building: 103 on each wide face and 56 on each narrow face. The target geometric scale was set to 1:400, so that the models represented full-scale buildings 112m high and 84m×28m in plan.

The parallel and perpendicular arrangements were considered, as shown in Fig. 3. Both models were rigidly mounted on a turn-table. The distance between the two models was varied longitudinally, Y/*b*, and laterally, X/*b*, on the Cartesian coordinates shown in Fig. 3, where "*b*" indicates the depth of the model. Wind tunnel tests were carried out on 54 different configurations by moving the interfering building's location from one spot to another shown in Fig. 3. For each configuration, the angle of incidence wind was varied from 0° to 360° at 5° intervals and the fluctuating wind pressures on the building faces were simultaneously measured at all taps using a multi-channel simultaneous fluctuating pressure measurement system for each wind direction.

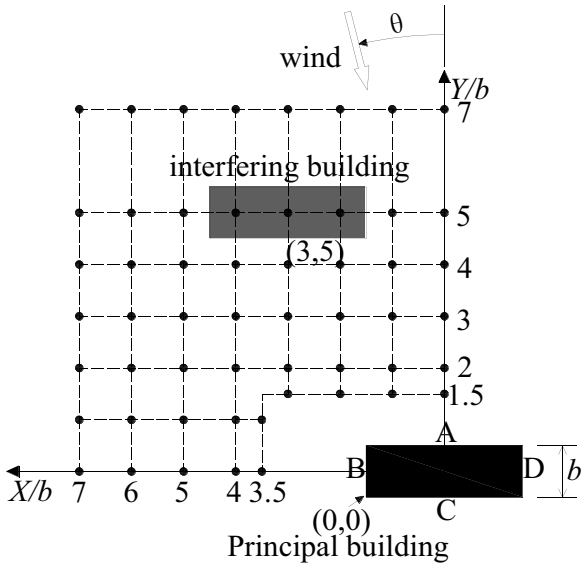

Fig. 3. Experimental arrangements

The sampling frequency for the pressure data was 781Hz. For each wind direction, fifteen 7.5s-long samples were collected, which corresponded to fifteen 10min-long samples in full scale. The time histories of fluctuating pressure were filtered by means of a moving average filter (Holmes 1997) as follows:

$$\tau = 1.0 \times L / \overline{U}_H \tag{1}$$

where τ is the averaging time corresponding to 0.2s in full scale, L is the length of the cladding diagonal in full scale (6m in this study) and $\overline{U}_H$ is the mean wind speed at the roof height of the principal building.

The Cook-Mayne method (Cook and Mayne, 1979) was adopted to obtain the extreme pressure coefficient. The extreme pressure coefficient representing the 50-year return period was calculated using Eq. (2).

$$\hat{C}_p = C_p + 1.4 / a_c \tag{2}$$

where C_p and $1/a_c$ are the mode and scale parameter of the extreme pressure coefficient.

3 RESULTS AND DISCUSSION

3.1 *Interference factor for local peak pressures and unfavorable regions*

As mentioned, the interference effects on the local peak pressures were studied. And it's known that an interfering building might cause different effects on different faces of a principal building. Thus, in order to check in detail and find the difference among them, the interference effects on different faces were checked individually in terms of the largest maximum peak pressure coefficient of Wall-X— $\hat{C}_p^{\mathrm{X}}$ and smallest minimum peak pressure coefficient of Wall-X— $\check{C}_p^{\mathrm{X}}$, where X∈(A, B, C, D). Interference Factor (IF) was introduced into this study as follows:

$$\hat{IF}(\mathrm{X}) = \frac{\hat{C}_p^{\mathrm{X}} \text{ with interferin g building}}{\hat{C}_p^{\mathrm{X}} \text{ without interferin g building}} \tag{3}$$

$$\check{IF}(\mathrm{X}) = \frac{\check{C}_p^{\mathrm{X}} \text{ with interferin g building}}{\check{C}_p^{\mathrm{X}} \text{ without interferin g building}} \tag{4}$$

Based on our experiment, the value $\hat{C}_p^{\mathrm{X}}$ of isolated condition was 2.6. $\check{C}_p^{\mathrm{X}}$ of isolated condition was -4.6 for Wall-A and Wall-C (the narrow faces), and it was -5.7 for Wall-B and Wall-D (the wide faces). These results were used as the basic reference values for evaluating the interference factor.

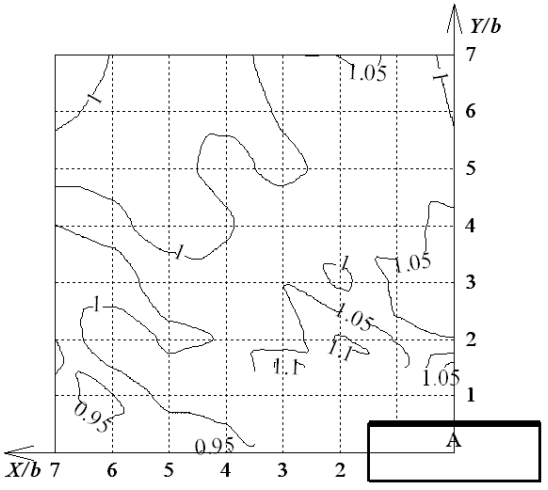

(a) Contour of $\hat{IF}(\mathrm{A})$

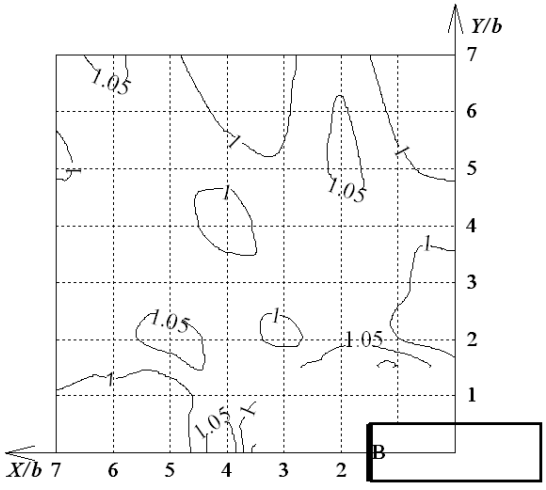

(b) Contour of $\hat{IF}(\mathrm{B})$

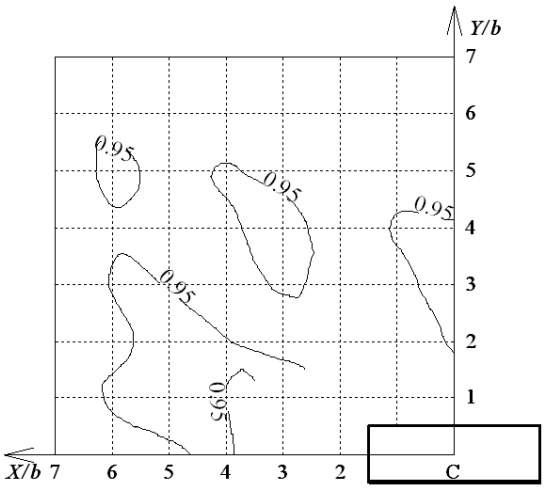

(c) Contour of $\hat{IF}(\mathrm{C})$

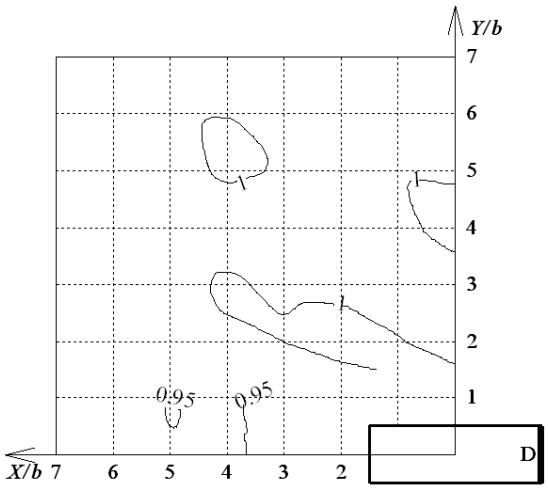

(d) Contour of $\hat{IF}(\mathrm{D})$

Fig. 4. $\hat{IF}(\mathrm{X})$ results of experiment.

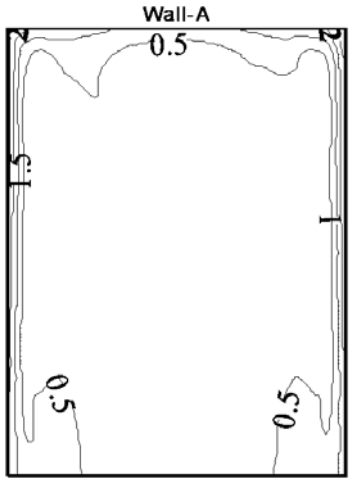

(a) $\hat{C}_p^{\mathrm{A}}(i)$ of case (0, 1.5b)

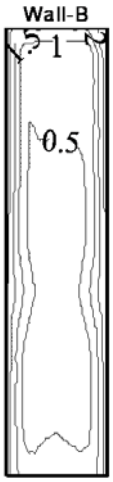

(b) $\hat{C}_p^{\mathrm{B}}(i)$ of case (3.5b, 0)

Fig. 5. $\hat{C}_p^{\mathrm{X}}(i)$ distributions of some configurations in parallel arrangement.

3.1.1 *Interference effects for positive peak pressure*

Fig. 4 clearly shows that the interfering building only slightly affects the $\hat{C}_p^{\mathrm{X}}$ value on the principal building. Most of the $\hat{IF}(\mathrm{X})$ values are in the range of 0.9 to 1.1. Even when the interfering building is located just in front of the principal building with small separation, there is no dramatic decrease in $\hat{C}_p^{\mathrm{A}}$, which was assumed to appear due to the shielding effects. The $\hat{C}_p^{\mathrm{A}}(i)$ distribution shown in Fig. 5(a) shows that the $\hat{C}_p^{\mathrm{A}}(i)$ values are very low, around 0.5, except in

small regions near the edges and corners when the interfering building was at (0, 1.5*b*). Similar results are also obtained for Wall-B when the interfering building was located at (3.5*b*, 0) which was just beside the principal building (Fig. 5(b)). Fig. 5 indicates that the interfering building decreases most of the $\hat{C}_p^{\mathrm{X}}(i)$ values on the face facing it when the two buildings are placed in a row with the same orientation. However, the principal building's edges and corners cannot be totally under the shielding offered of the upstream building at all wind angles.

3.1.2 *Interference effects for negative peak pressure*

The results of the interference factor of each face are shown in Fig. 6. It can seen that the interfering building had significant interference effects on the $\check{C}_p^{\mathrm{X}}$ of the principal building, especially on Wall-A and Wall-B, which faced the interfering building. The maximum value of $\check{IF}(\mathrm{A})$ can be larger than 1.5 when the interfering building is located at (3*b*, 2*b*), and the maximum value of $\check{IF}(\mathrm{B})$ can also be larger than 1.3 when the interfering building is at (3*b*, 2*b*) and (5*b*, 5*b*). However, the $\check{IF}(\mathrm{C})$ and $\check{IF}(\mathrm{D})$ values are all between 0.9 and 1.1, which means that the effects on Wall-C and Wall-D are weaker than on the other two faces.

In this study, the region where $\hat{IF}(\mathrm{X})$ or $\check{IF}(\mathrm{X})$ is greater than 1.1 is nominated as the unfavorable region of Wall-X. If the interfering building is located in an unfavorable region for Wall-X, that means the tested largest maximum peak pressure or smallest minimum peak pressure of Wall-X is more than 10% larger than the design value which is obtained based on the isolated condition, and the design value of the pressure coefficients on Wall-X of the principal building should be modified for safety. The unfavorable regions of Wall-A and Wall-B can also be much larger than those of the other two faces for the parallel arrangement.

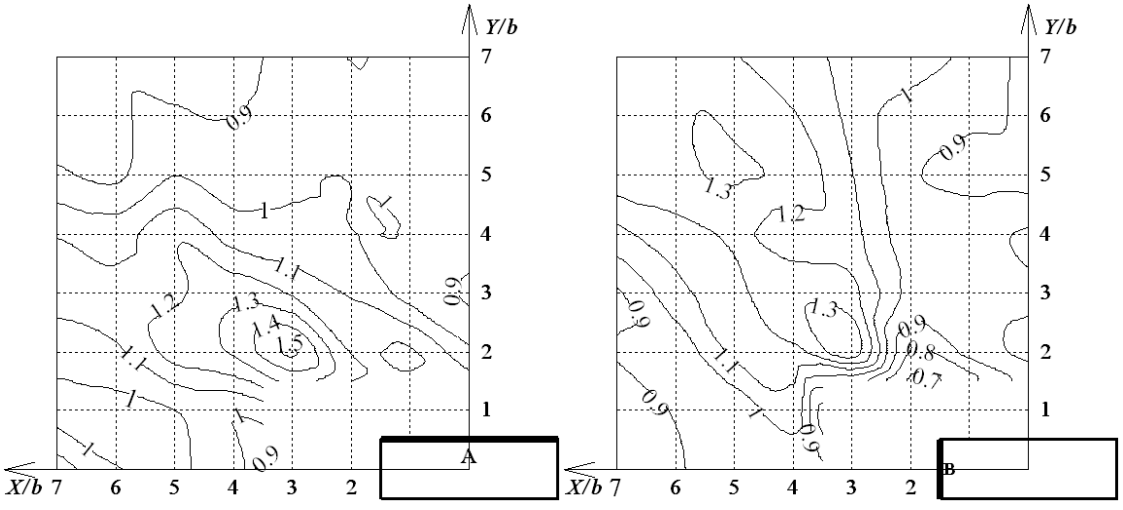

(a) Contour of $\check{IF}(\mathrm{A})$ (b) Contour of $\check{IF}(\mathrm{B})$

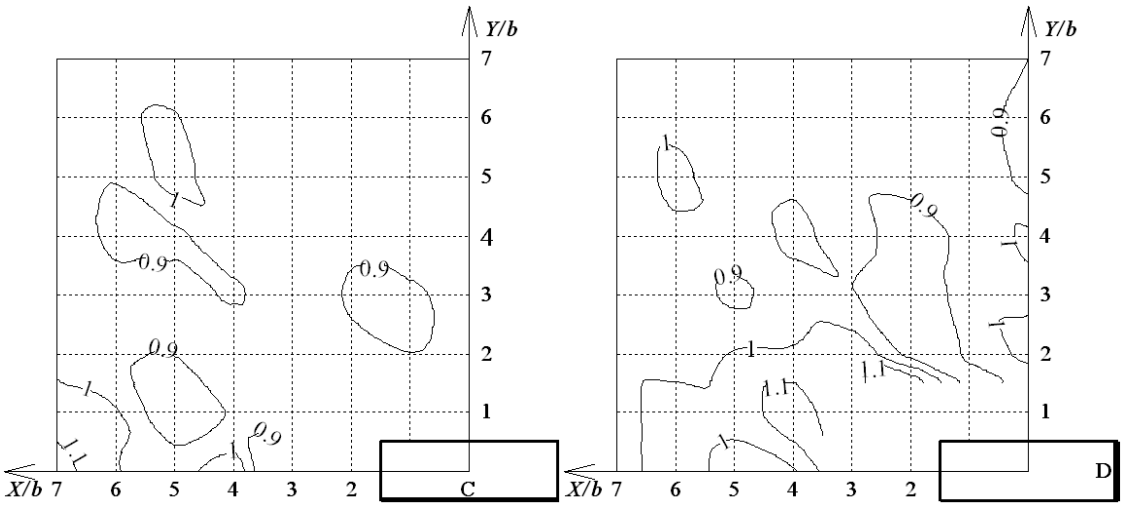

(c) Contour of $\overset{\vee}{IF}(\mathrm{C})$ (d) Contour of $\overset{\vee}{IF}(\mathrm{D})$

Fig. 6. $\overset{\vee}{IF}(\mathrm{X})$ results of experiment.

3.2 *Effect of wind direction*

Wind direction is a very important parameter as well. Engineers are not only interested in $\hat{C}_p^{\mathrm{X}}$ and $\check{C}_p^{\mathrm{X}}$, but also want to know what wind directions cause these $\hat{C}_p^{\mathrm{X}}$ and $\check{C}_p^{\mathrm{X}}$ values. In this study, the wind direction under which the $\hat{C}_p^{\mathrm{X}}$ or $\check{C}_p^{\mathrm{X}}$ of Wall-X is observed is defined as the Unfavorable Wind Direction (UWD) of Wall-X, where $\mathrm{X} \in (\mathrm{A,B,C,D})$.

3.2.1 *Unfavorable wind direction for positive peak pressure*

Fig. 7 gives the positive UWD of four faces of parallel arrangement. The arrow at each position indicates the unfavorable wind direction of the target wall when the interfering building is located there. For Wall-A and Wall-B, the UWD varies with change of the interfering building's position. For most cases of the two faces, the unfavorable winds tilts towards the interfering building from the direction normal to the target face, that means the wind causing high positive pressure attacks the principal building after passing the interfering building. But for the other two faces (Wall-C and Wall-D), it can be seen that although the unfavorable winds also shift a little from the direction normal to the target face, the direction of shifting are random and doesn't depend on the location of the interfering building. This is because when the wind blows directly to the Wall-C and Wall-D, the interfering building is mainly at the downstream direction of the principal building in this experimental setup. Thus the interfering building couldn't affect the coming wind of the principal building.

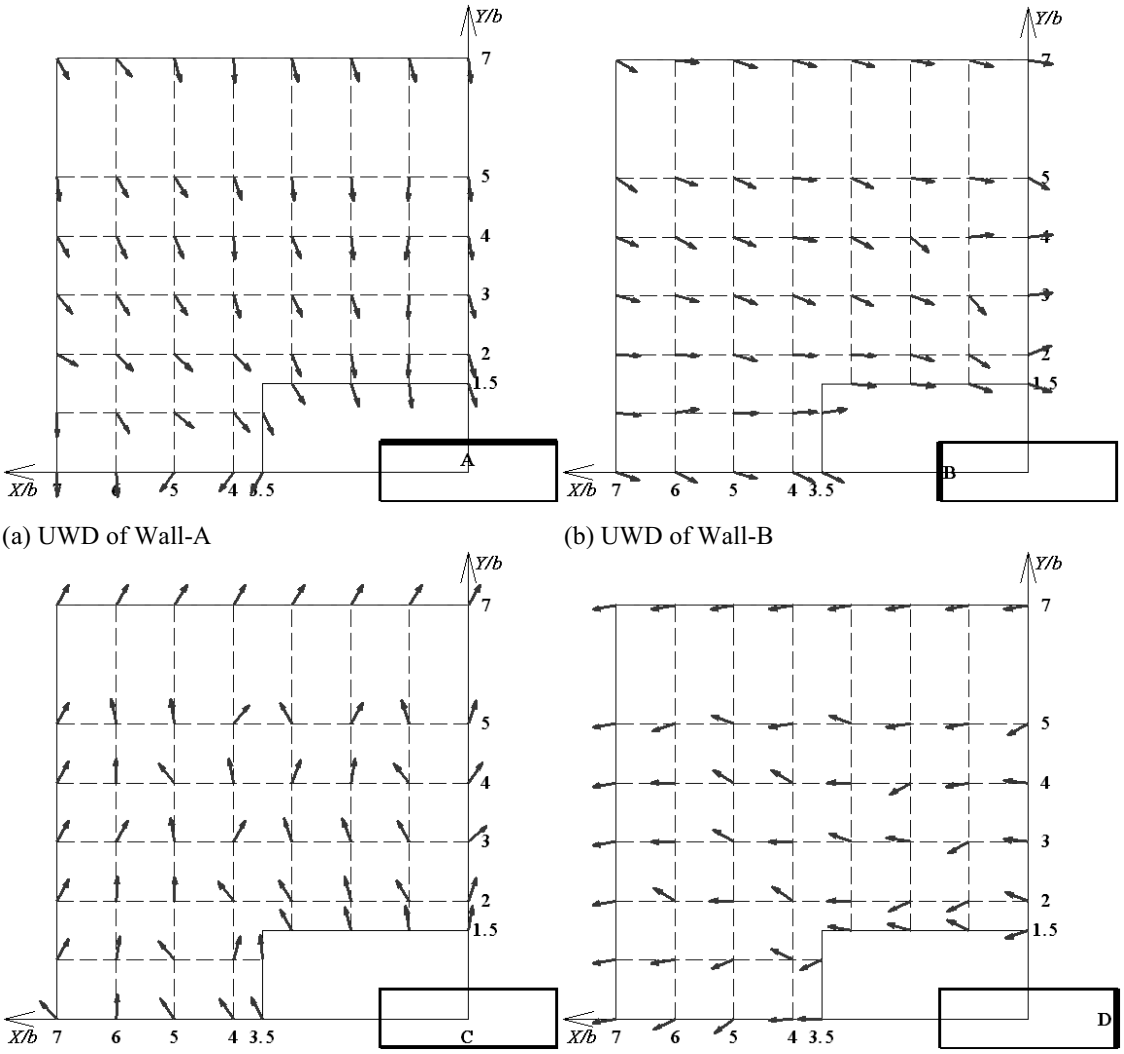

(a) UWD of Wall-A

(b) UWD of Wall-B

(c) UWD of Wall-C

(d) UWD of Wall-D

Fig. 7. Positive UWD of four faces.

3.2.2 *Unfavorable wind direction for positive peak pressure*

Fig. 8 shows the UWD of the parallel arrangement. According to these figures, for Wall-A and Wall-B, the unfavorable wind mostly attacks the principal building from the direction approximately along with the target face after passing the upstream interfering building. The UWD also changes with changing position of the interfering building. But for the other two faces the dependence of unfavorable wind direction on the location of interfering building cannot be clearly found.

Some results in Fig. 8(b) show that in the parallel arrangement when the interfering building is located in the area along the Y-axis where $X \in (0, 2b)$ the unfavorable wind always comes from the back side of Wall-A. But when it is out of the range where $X>2b$, the unfavorable wind changes almost 180º which comes from the front side of Wall-A. This is because when the interfering building is located in the range where $X \in (0, 2b)$, Wall-B is just in the wake of interfering building if wind comes from the front side of Wall-A and consequently the negative pressure on

it is low. If the wind comes from the back side of Wall-A, there is no shielding from the interfering building to protect Wall-B, so the negative peak pressure on Wall-B becomes higher. From Fig. 6(b), it can be checked that the $\overset{\vee}{IF}(\mathrm{B})$ values are all lower than 1 when X$\in$(0, 2*b*). The smallest value among them is only 0.7 when the interfering building is at (2*b*, 1.5*b*). These results imply that even when the interfering building is located in the downstream direction it also affects the $\overset{\vee}{C}_p^{\mathrm{B}}$ value by changing the flow field around the principal building.

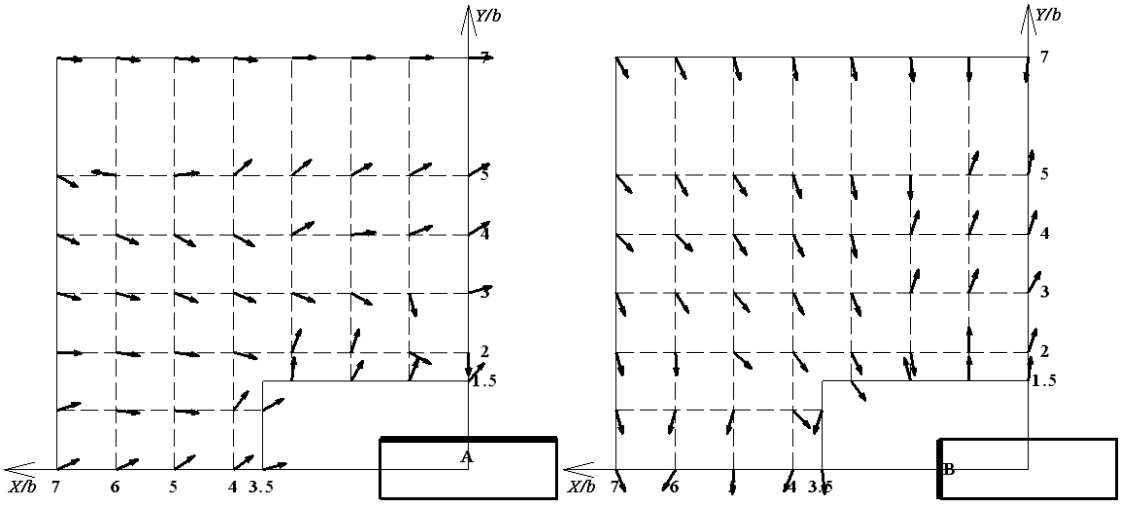

(a) UWD of Wall-A

(b) UWD of Wall-B

(c) UWD of Wall-C

(d) UWD of Wall-D

Fig. 8. Negative UWD of four faces.

4 CONCLUDING REMARKS

Experiments were carried out to investigate the interference effect on local peak pressures between two identical rectangular-cross-section high-rise buildings. The aspect ratio of the build-

ings was Width: Depth: Height=3:1:4. Parallel arrangement of the two buildings was checked. The interference effects on the external local peak pressures were evaluated and analyzed.

Based on the study, on one hand, the interfering building doesn't have a significant effect on maximum positive peak pressure. For most configurations of the interfering building, the interference factors for the largest maximum positive peak pressure were in the range of 0.9-1.1. On the other hand, the interfering building has a strong effect on the smallest minimum negative peak pressure. The unfavorable regions on Wall-A and Wall-B of the two arrangements were very large. The largest interference factor was greater than 1.5, which means the absolute value of the smallest minimum negative peak pressure coefficient is 50% higher than the design value of the isolated building situation.

Wind direction is one of the most crucial parameters. For most cases, the interference effect was stronger when the interfering building was located upstream of the principal building. The unfavorable wind directions depend strongly on the configurations of the two buildings.

5 ACKNOWLEDGEMENTS

This study was funded by the Ministry of Education, Culture, Sports, Science and Technology, Japan, through the Global Center of Excellence Program, 2008-2012. The authors gratefully acknowledge their support.

6 REFERENCES

1 U.F. Tang, K.C.S. Kwok, Interference excitation mechanisms on a 3DOF aeroelastic CAARC building model, J. Wind Eng. Ind. Aerodyn., 92 (2004), 1299-1314.
2 K.M. Lam, J.G. Zhao, M.Y.H. Leung, Wind-induced loading and dynamic responses of a row of tall buildings under strong interference. J. Wind Eng. Ind. Aerodyn. 99 (2011), 573-583.
3 W. Kim, Y. Tamura and A. Yoshida, Interference effects on local peak pressures between two buildings, J. Wind Eng. Ind. Aerodyn., 99 (2011), 584-600.
4 J.D. Holmes, Equivalent time averaging in wind engineering. J. Wind Eng. Ind. Aerodyn. 72 (1997), 411-419.
5 N.J. Cook, J.R. Mayne, A refined working approach to the assessment of wind loads for equivalent static design. J. Wind Eng. Ind. Aerodyn. 6 (1979), 125-137.

The Seventh International Colloquium on Bluff Body Aerodynamics and Applications (BBAA7)
Shanghai, China; September 2-6, 2012

Interference effect on wind pressure of two buildings

Ning Han [a], Ming Gu [a], Peng Huang [a]

[a] *State Key Laboratory of Disaster Reduction in Civil Engineering, Tongji University, Shanghai, China*

ABSTRACT: The interference effect on wind pressure between two identical buildings was analyzed by wind tunnel tests for different locations of the interfering building .The results show that for the tandem configurations, mean pressure on windward face of the principal building is suction when spacing ratio is less than 3.0, otherwise it is positive. The magnitude of mean negative pressure on the side and leeward faces and fluctuating pressure on all faces get maximums when spacing ratio is 3.0.With an increase in spacing ratio for the side-by-side arrangements, the maximum value of mean and fluctuating pressure coefficient interference factor decreases on the inner and outer face while slightly increases on the front and rear face. Notably, the fluctuating pressure coefficient interference factor on the inner face grows visibly and the maximum value is 2.2 on the top leading corner when the spacing ratio is 2.0.

KEYWORDS: Tandem; side-by-side; interference factor; spacing ratio; square building

1 INTRODUCTION

The wind pressure on isolated building has significant change or even becomes quite complex due to the surrounding tall buildings. Interference effect among tall buildings has been studied by many researchers over the past several decades. Khanduri et al. [1] gave a review of interference effect before 1998.After this; Xie & Gu [2-5] reported interference effect on dynamic response and correlation among three tall buildings. For the side-by-side arrangements, Kumar et al. [6] studied wind-induced responses of the principal building caused by interfering building which was located in different positions and had 4 different size ratios such as 0.5, 1.0,1.5 , 2.0.Then they reported that the critical size ratio is 1.0, the response amplitude has no significant differences when size ratio is smaller than 1.0, but it will increase remarkably when the size ratio is greater than 1.0 and reduced velocity is larger than 12. Interference effect on wind pressure of two buildings placed in staggered arrangements has been studied numerically and experimentally by Zhang et al. [7], but only certain points on certain heights were focused on. Wong et al. [8] reported aerodynamic distribution and flow around two side-by-side square buildings with different cross–section, the spacing ratio is between 1.12 and 2.5. Analogously, Chen et al. [9] found that the spacing ratio has a threshold value; a biased gap flow pattern appears when spacing ratio is smaller than this value. But three dimensional effects of interference between two high-rise buildings haven't been considered in this paper. Sakamoto et al. [10] reported changes on fluctuating pressure of two tandem buildings. They found that fluctuating pressure on principal building increases when the spacing ratio is larger than 3.0. Lam et al. [11] investigated interference effects on three closely arranged buildings in oblique wind direction. Mean pressure contours of the principal building in certain spacing ration and wind direction were given. They pointed out that high suction appears on leeward side, but they didn't analyze the effect of changing spacing ratio.

This paper focuses on local wind pressure on walls of the principal building with wind pressure coefficient interference factor. Various locations of an identical interfering building are considered.

2 EXPERIMENTAL SETUP AND DATA ANALYSIS

2.1 *Wind tunnel tests*

Wind tunnel tests were conducted in TJ-2 Boundary Layer Wind Tunnel at Tongji University. Its working section is 3.0m in width, 2.5m in height and15.0m in length. Wind field of Type C at a length scale of 1/400 which is in accordance with the Chinese code [12] was simulated by passive simulation method. The exponents of the mean wind profile for the terrain category C is 0.22, and the corresponding gradient height is 400m. Figure 1 shows the simulated mean wind speed profile and the longitudinal component profile of turbulence intensities. The figures show that both the experimental mean velocity and turbulence intensity are in agreement with the target profiles from Chinese code and A.I.J. [13], respectively. Figure 2 shows the power spectra of longitudinal fluctuating wind speeds.

The experimental models were a pair of identical square buildings. One was referred as the test building and another was referred as the interfering building which was located at various positions. The test building, at a length scale of 1:400, was B×D×H=150mm × 150mm × 900mm. A total of 496 pressure taps, 124 on each face were installed, especially the top and leading edges of the test building as shown in Figure 3.

Figure 4 shows the detailed experimental plan indicating the different locations of the interfering building and wind directions in wind tunnel. The interfering building was orientated with its face normal to the test building and was placed in 16 different arrangements with respect to the test building at origin of coordinates (0, 0). The center-to-center spacing between them was varied by spacing ratio Sx=x/B longitudinally and Sy=y/B laterally. The wind direction was varied in 15° steps in the range from 0° to 345°.

In this paper, only tandem and side-by-side arrangements at wind direction 0° were investigated. The sampling frequency and sampling time of the wind pressure were 312.5 Hz and 48s.

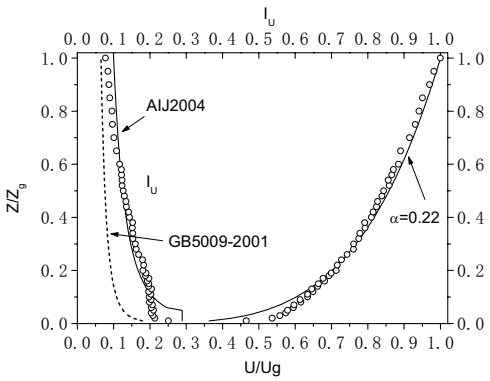

Figure 1. Mean velocity and longitudinal turbulence intensity profile.

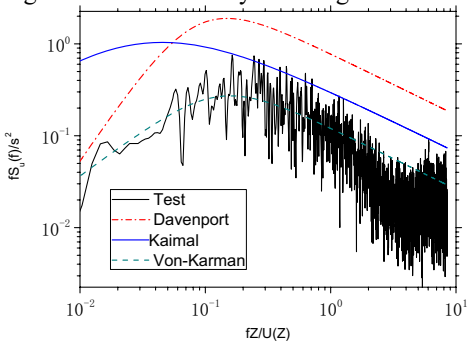

Figure 2. Longitudinal fluctuating velocity spectrum.

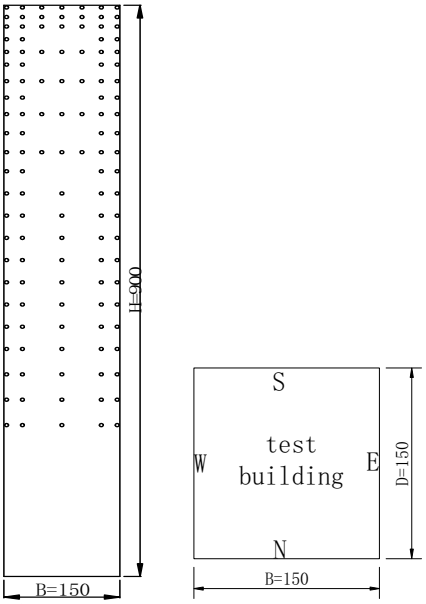

Figure 3. Locations of pressure taps on the test building.

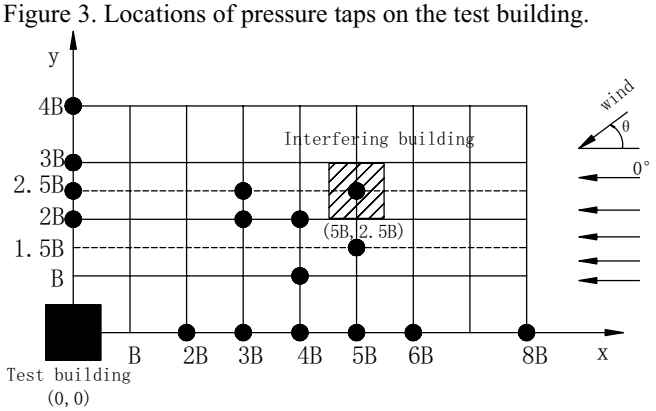

Figure 4. Configurations of interfering building and wind directions.

2.2 *Test data processing*

The pressure coefficient is defined as [14]

$$\overline{C}_p = \left(\overline{p} - p_0\right) \Big/ 0.5\rho\overline{u_r}^2 \tag{1}$$

$$C'_p = \sqrt{\overline{p'^2}} \Big/ 0.5\rho\overline{u_r}^2 \tag{2}$$

Where $\overline{C}_p$ is mean pressure coefficient, $\overline{p}$ is mean pressure, C'_p is r.m.s. fluctuating pressure coefficient, $\sqrt{\overline{p'^2}}$ is r.m.s. fluctuating pressure, p_0 is static pressure, ρ is the density of air, $\overline{u_r}$ is mean longitudinal velocity at the reference point . The reference height is selected at the top of the building.

Interference effect is presented in the form of non-dimensional Interference Factor (IF). IF can be expressed as

$$IF = \frac{C_{p\_\mathrm{inf}er}}{C_{p\_iso}} \tag{3}$$

Where $C_{p\_\inf er}$ represents the mean or R.M.S. pressure coefficients on the building with interference, C_{p_iso} is relative to the mean or R.M.S. pressure coefficients on the isolated building.

$|IF|>1$ represents the increase and $|IF|<1$ represents decrease on the test building due to interference. $IF=1$ suggests that interfering building has no effect on the test building. $IF=-1$ suggests that the sign of wind pressure on the test building changes, but the value doesn't change.

3 RESULTS AND DISCUSSION

3.1 *Mean pressure in tandem configurations*

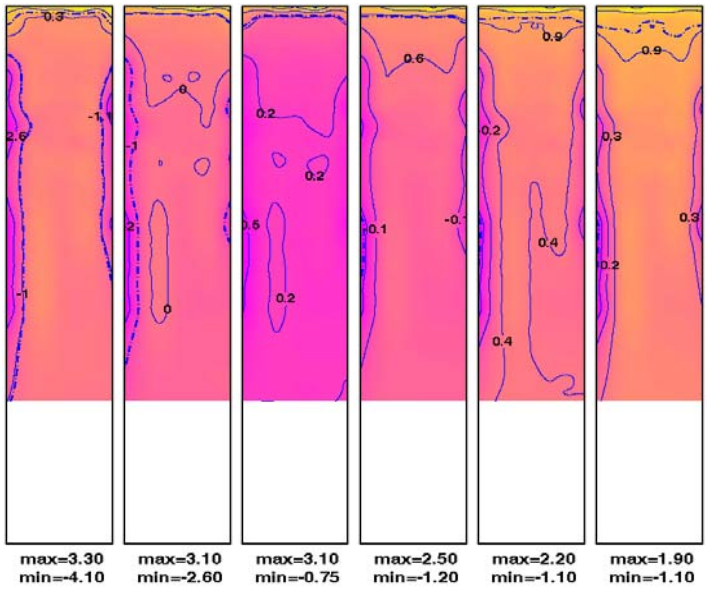

(a)Sx=2.0 (b)Sx=3.0 (c) Sx=4.0 (d)Sx=5.0 (e)Sx=6.0 (f)Sx=8

Figure 5. IF contours of mean pressure coefficient on face N for the test building (θ =0°, Sy=0).

Figure 5 shows IF contours for mean pressure coefficient on face N for the test building at different spacing ratio Sx at 0° wind angle. From the figure we can see that the critical Sx is 3.0, when Sx is smaller than3.0, IF on most part of face N is negative, otherwise negative IF only appears on leading edges. Therefore, there are two different flow patterns when spacing ratio changes in tandem arrangements. When spacing ratio is smaller than the critical value, vortex streets behind the upstream building are inhibited, otherwise vortex streets are formed behind each building and lead to complex vortex street interactions. This is in accordance with the results of Chen et al.[15] and Hasebe et al.[16].As spacing ratio Sx is smaller than3.0, negative pressure appears on face N and IF for mean pressure coefficient lies between -1.0 and 0 on most parts of the face. When spacing ratio Sx is beyond 3.0, the range of 0<IF<1.0 appears on face N and increases with Sx. IF lies between0.3 and 1.0 when Sx is equal to8.0. It is noteworthy that extrema of IF appear mainly on top and leading edges of face N, respectively. The extremum is beyond 1.0 and becomes smaller with the larger Sx. In a word, mean pressure on most zones of front face of the test building decreases due to the upstream building. Khanduri et al. [17] reported similar results. Differently, in this paper the mean pressure is amplified significantly on certain local zones on front face, for example, the top and leading edges.

As against front face N, interference effect on mean pressure of face E follows a regular trend when spacing ratio changes. IF is positive for all tandem configurations as shown in Figure 6. This indicates that mean pressure on face E is still negative when the interfering building is around. It is worth noting that the IF on top leading corner of face E has greater values which are larger than 1. An increase in mean pressure coefficient of 40% is obtained when Sx is equal to5.0. The reason of this situation is that with spacing ratio increasing, the separated flow from upstream building impinges on top of face N which leads to re-separation of the separated flow from the leading top corner of face E. As a result, velocity of the separated flow from the leading edge of face E increases and suction on face E becomes larger.

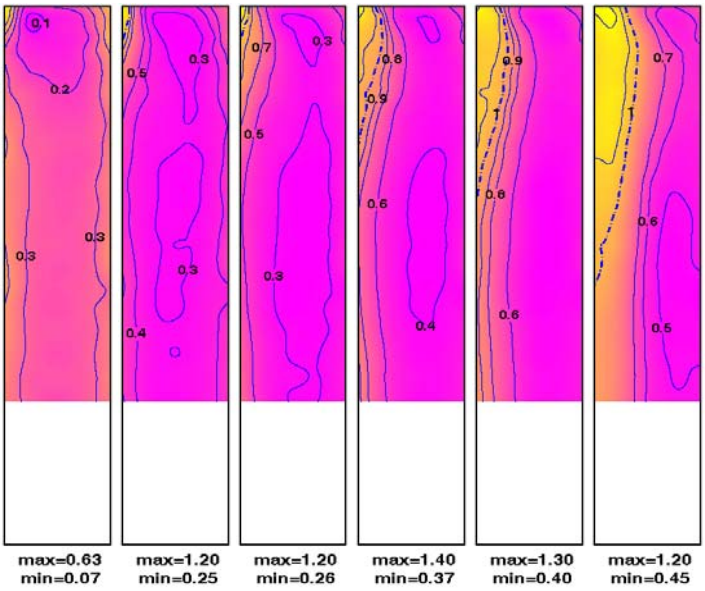

(a)Sx=2.0 (b)Sx=3.0 (c) Sx=4.0 (d)Sx=5.0 (e)Sx=6.0 (f)Sx=8

Figure 6. IF contours of mean pressure coefficient on face E for the test building (θ =0°, Sy=0).

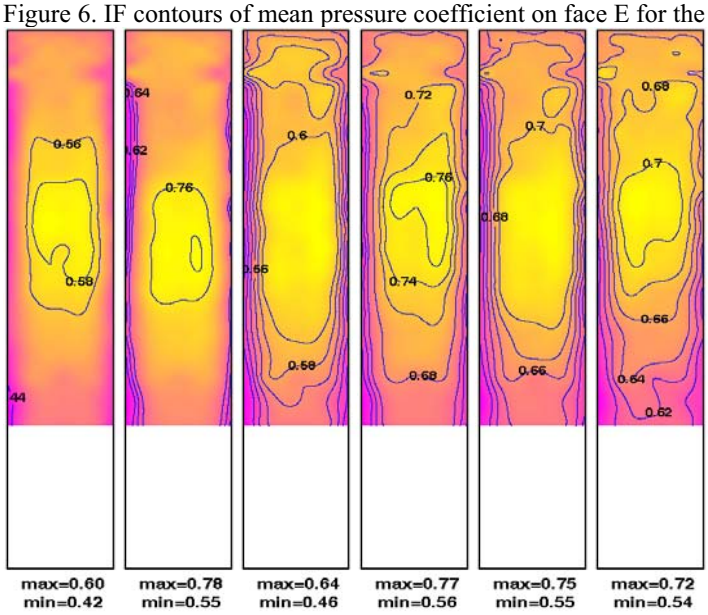

(a)Sx=2.0 (b)Sx=3.0 (c) Sx=4.0 (d)Sx=5.0 (e)Sx=6.0 (f)Sx=8

Figure 7. IF contours of mean pressure coefficient on face S for the test building (θ =0°, Sy=0).

Figure 7 shows IF contours for mean pressure coefficient on face S for the test building at different Sx at 0° wind angle. From the figure we can see that IF is positive and smaller than 1 at any spacing ratio. This indicates that mean pressure on face S is still negative, but it shows a reduction compared with that of the isolated building. This maybe ascribe to the presence of interfering building which leads to decrease in wake velocity from the test building.

3.2 *Mean pressure in side-by-side configurations*

Figure 8 shows IF contours for mean pressure coefficient of the test building at different Sy at 0° wind angle. In Figure8a, IF on face E decreases gradually from leading edge towards trailing edge and the intensity of decrease is mild with an increase of spacing ratio. This is because gap flow forms between the two buildings. The smaller the spacing ratio, the faster the gap flow passes through the channel which leads to larger suction. The extremum of IF becomes smaller with the larger Sy and it gets maximal value 1.9 which locates on the (2/3) H of face E when Sy=2.0. Figure8b shows IF of face W. From the figure we can see that IF gets extremum on trailing top corner. This maybe ascribe to presence of the interfering building which changes the flow pattern of the test building that aggravates the vortex shedding from trailing top corner on face W. Chen et al. [9] reported similar results.

As against the side faces, changes on spacing ratio have little influence on IF on face N. The value of IF has a little increase on most zones of face N. Mean pressure coefficients increase by about 10%~20% compared with those of the isolated building, as shown in Figure8c. In Figure8d, values of IF on face S are larger than 1.0 at any spacing ratio. This indicates that suction on face S increases due to the interfering building. Changes on spacing ratio have little influence on IF on face S as that on face N. It shows that flow pattern behind the test building doesn't change qualitatively. This is in accordance with the results of literatures [8-9].There is a critical spacing ratio less than 2.0 for two buildings placed side-by-side. As spacing ratio is larger than the threshold, flow patterns have transition from asymmetric flow to symmetrical flow and binary vortices behind buildings are formed.

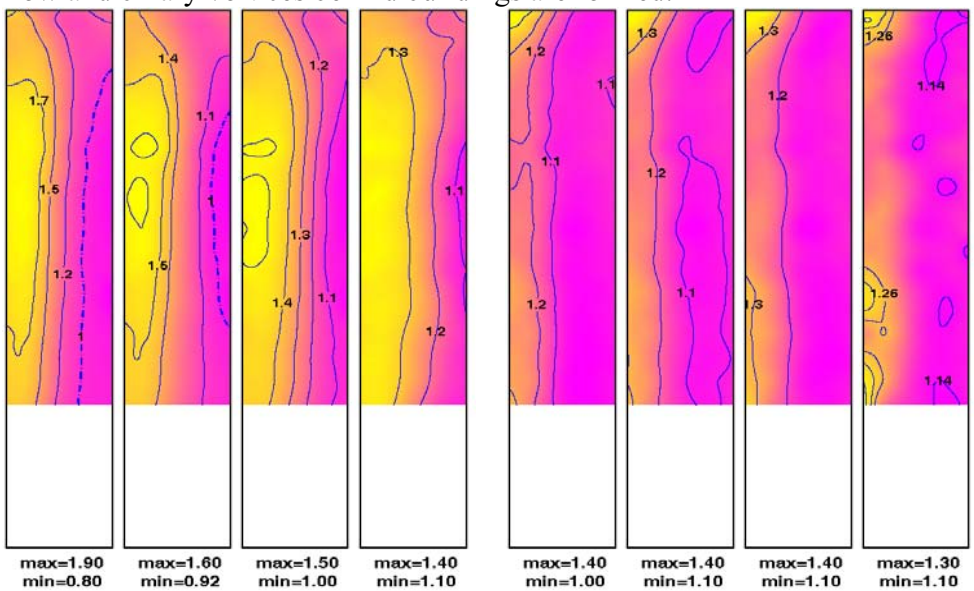

(a) Face E Sy=2.0, 2.5, 3.0, 4.0 (b) Face W Sy=2.0, 2.5, 3.0, 4.0

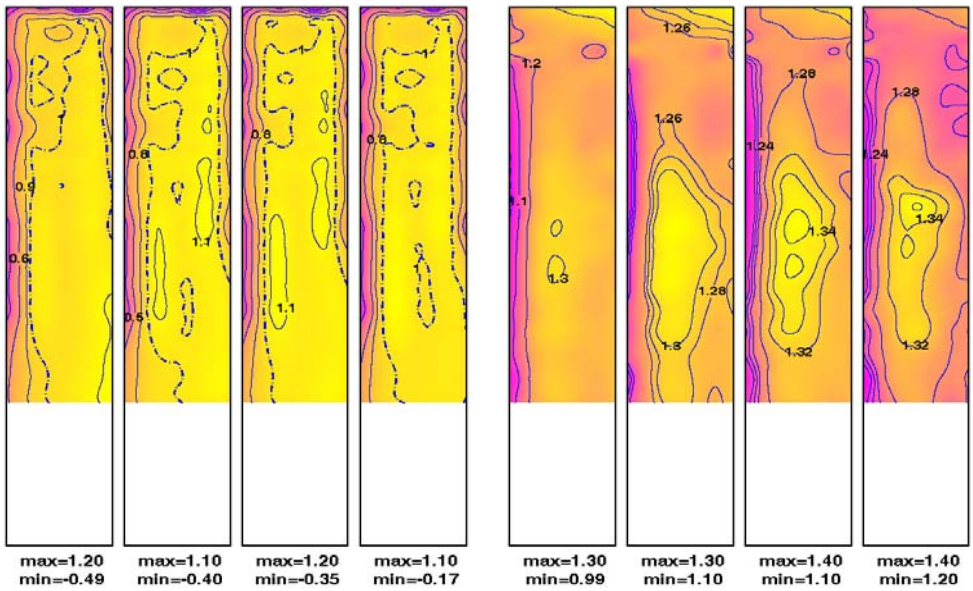

(c) Face N Sy=2.0, 2.5, 3.0, 4.0 (d) Face S Sy=2.0, 2.5, 3.0, 4.0

Figure 8. IF contours of mean pressure coefficient for the test building (θ =0°, Sx=0).

3.3 *Fluctuating pressure in tandem configurations*

Figure 9 shows IF contours for fluctuating pressure coefficient on face N for the test building at different Sx at 0° wind angle. From the figure we can see that the zone of IF>1.0 increases with Sx. It is noteworthy that extremum of IF decreases with Sx and it gets maximal value3.8 which locates on top leading edges of face N when Sx is equal to3.0. The reason for this situation is that when spacing ratio Sx is smaller than3.0, steady vortex zones form between the two buildings. Shear layers separated from the leading edges of the interfering building reattach fast to the side faces of the test building due to the closely spacing, then re-separation happens at the trailing edge of the test building which forms quasi-periodic vortex shedding behind it. This can be observed in Figures10a-10b, the value of IF is larger than 1.0 on the leading edge of face E due to reattachment of shear layers. Vortex shedding forms behind upstream and downstream building respectively when spacing ratio Sx is beyond3.0, fluctuating pressure on face N increases compared with that of the isolated building due to the turbulent of the incoming flow increases. So the zone of IF>1.0 expands as shown in Figures 9c-9f. Fluctuating pressure on face E increases correspondingly. The reason is, vortices in the wake of the upstream interfering building impinge directly on the front face N of the downstream test building which increases the velocity of shear layer separation and leads to intense turbulences as shown in Figures 10c-10f. The zone of IF>1.0 on face E expands when the spacing ratio increases. The extremum of IF becomes smaller with the larger Sx and gets maximal value 2.7 when Sx is equal to3.0.

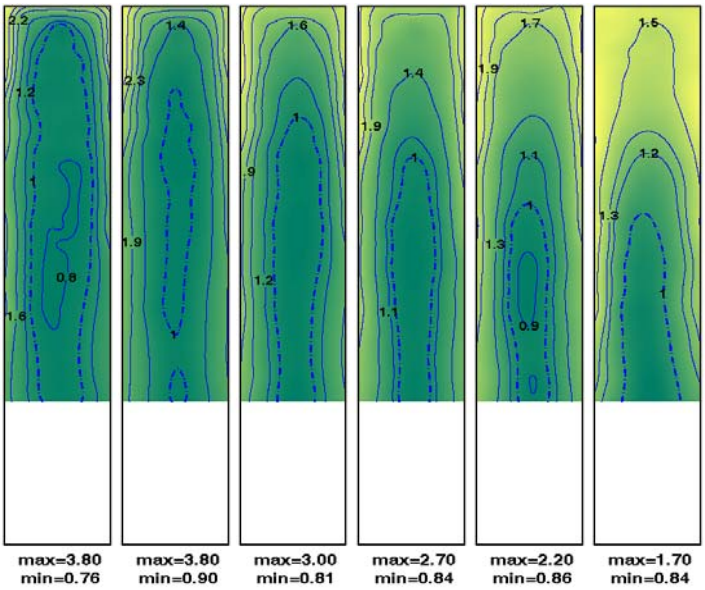

(a)Sx=2.0 (b)Sx=3.0 (c) Sx=4.0 (d)Sx=5.0 (e)Sx=6.0 (f)Sx=8

Figure 9. IF contours of fluctuating pressure coefficient on face N for the test building (θ =0°, Sy=0).

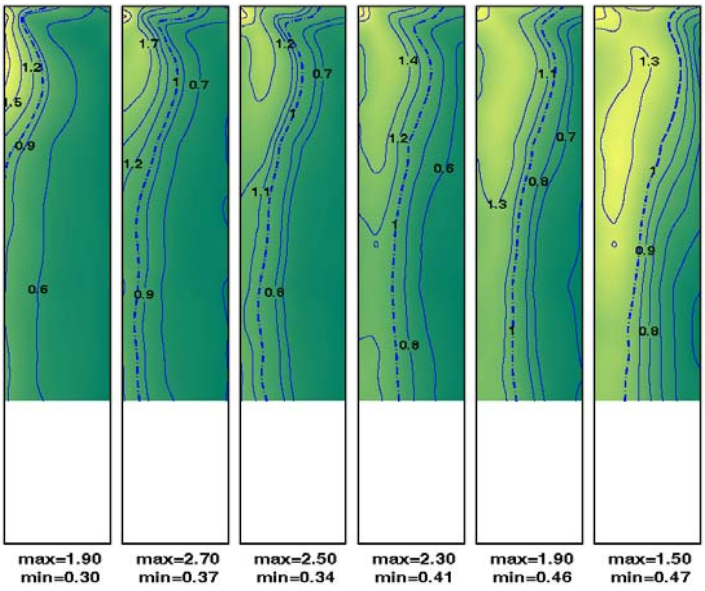

(a)Sx=2.0 (b)Sx=3.0 (c) Sx=4.0 (d)Sx=5.0 (e)Sx=6.0 (f)Sx=8

Figure 10. IF contours of fluctuating pressure coefficient on face E for the test building (θ =0°, Sy=0).

Figure 11 shows IF contours for fluctuating pressure coefficient on face S of the test building at different Sx at 0° wind angle. From the figure we can see that the value of IF which is larger than 1.0 only appear on the middle part of face S when Sx is equal to 3.0. The value of IF is less than 1.0 on other cases. The results illustrate that the vortex shedding intensity behind the test building becomes smaller compared with that of the isolated building due to the upstream building. As a result, the fluctuating pressure on face S reduces.

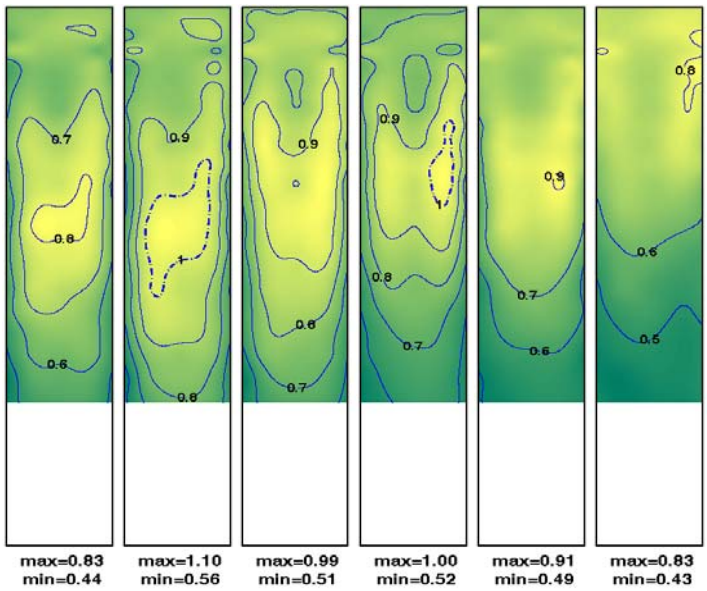

(a)Sx=2.0 (b)Sx=3.0 (c) Sx=4.0 (d)Sx=5.0 (e)Sx=6.0 (f)Sx=8

Figure 11. IF contours of fluctuating pressure coefficient on face S for the test building (θ =0°, Sy=0).

3.4 *Fluctuating pressure in side-by-side configurations*

Figure 12 shows IF contours for fluctuating pressure coefficient on walls of the test building at different Sy at 0° wind angle. In Figure12a, IF on face E is the same as that for mean pressure coefficient on face E which decreases gradually from leading edge towards trailing edge. The extremum of IF becomes smaller with the larger Sy and locates mainly on leading top corner and (0.6~0.8) H on face E. Interference effect tends to average overall as spacing ratio increases. IF on face E gets maximal value 2.2 which locates on leading top corner of face E when Sy=2.0. This is because the position lies in the high-velocity region due to fast separation which leads to the turbulent increases. So these positions are dangerous zones and should be paid much attention to. As against face E, in Figure12b, changes on spacing ratio have little influence on the extremum of IF which mainly lies in the trailing top corner on face W. It is around 1.2. In addition, the flow separated from the leading edges of face N tends to symmetry, as a result, the zone of IF>1.0 increases slightly with Sy increases.

Changes on spacing ratio have little influence on IF for fluctuating pressure coefficient on face N, as shown in Figure12c. The value of IF mostly lies between 0.9 and 1.1, which are very uniform distribution when spacing ratio is equal to4.0. It illustrates that the interference effect decrease with spacing ratio increases. In Figure12d, the zone of IF>1.0 expands slightly with spacing ratio increases and the location on which IF gets extremum gradually approaches the (2/3) H on face S. The value of IF on most part of face S is still larger than 1.0 when Sy is equal to 4.0. This is because the three-dimensional interference leads to turbulences around the test building increase, that is to say interference effect is still significant when spacing ratio is 4.0.

4 CONCLUSIONS

The interference effect for mean and fluctuating pressure on the test building for various locations of an identical interfering building at 0° wind direction has been studied by interference factor contours. The following results were obtained:

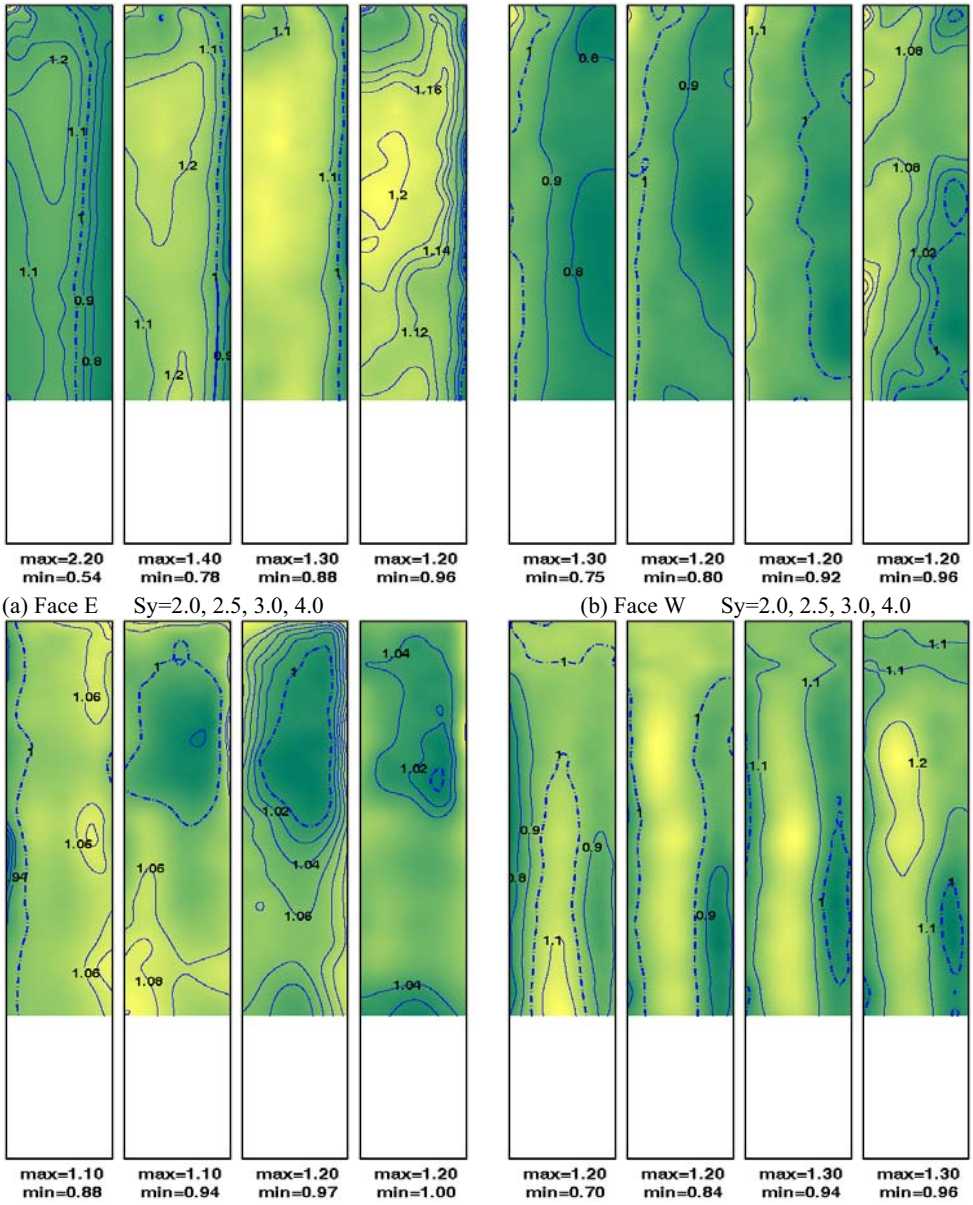

(a) Face E Sy=2.0, 2.5, 3.0, 4.0 (b) Face W Sy=2.0, 2.5, 3.0, 4.0

(c) Face N Sy=2.0, 2.5, 3.0, 4.0 (d) Face S Sy=2.0, 2.5, 3.0, 4.0

Figure 12. IF contours of fluctuating pressure coefficient for the test building (θ =0°, Sx=0).

1 In tandem configurations, mean pressure on front face of the test building is negative as spacing ratio is smaller than 3 and positive when spacing ratio is larger than3.0. The test building experiences considerable shielding due to an upstream interfering building and the extent of shielding is obviously weakened with spacing ratio increases. IF for mean pressure coefficient on front and leeward face is positive, in addition, it gets maximal value when spacing ratio Sx is 3.0. Fluctuating pressure has moderate change with spacing ratio compared with that of mean pressure.Variations of IF for fluctuating pressure coefficient on all faces are similar,they all get maximal value as spacing ratio Sx is 3.0.

2 In tandem configurations, the leading top corner on side faces of the test building should be pay special attention to, especially when spacing ratio Sx is 3.0.

3 In side-by-side configurations, the extrema of IF for mean and fluctuating pressure coefficient on outer and inner face of the test building decrease with spacing ratio increase. However, the extremum of IF for fluctuating pressure coefficient was influenced significantly by the interfering building and gets maximal value 2.2 on inner face when spacing ratio Sy is 2.0. Changes on spacing ratio have little influence on the extrema of IF on front and leeward faces , but IF on leeward face which gets maximal value 1.4 is greater than that on front face.
4 In side-by-side configurations, pressure on inner face of the test building changes significantly, especially on leading top corner of the inner face. So, envelops of these positions in which mean and fluctuating pressure is obviously enlarged should be strengthened when there are adjacent buildings.

5 ACKNOWLEDGEMENTS

This research is jointly supported by the National Natural Science Foundation of China (90715040, 51178352) and Support Project by the Ministry of Science and Technology of China (2006BAJ03B04). Their support is gratefully acknowledged.

6 REFERENCES

[1] Khanduri A.C., Stathopoulos T., Bedard C., Wind-induced interference effects on buildings-a review of the state-of-the-art. Eng. Struct.1998, Vol.20, pp. 617-630.
[2] Xie Z N, Gu M., Mean interference effects among tall buildings. Eng. Struct. 2004, Vol.26, pp. 1173-1183.
[3] Gu M., Xie Z.N. Along-wind dynamic interference effects of tall buildings. Adv. Struct. Eng., 2005, Vol.1, pp. 163-178
[4] Xie Z N, Gu M., Simplified formulas for evaluation of wind-induced interference effects among three tall buildings. J. Wind Eng. Ind. Aerodyn. , 2007, Vol.95, pp. 31-52.
[5] Xie Z N, Gu M., Across-wind dynamic response of high-rise building under wind action with interference effects from one and two tall buildings. The Structural Design of Tall and Special Buildings, 2009, Vol.18, pp. 37-57.
[6] Ajith Kumar R, Gowda B, Sohn C., Interference excitation of a square section cylinder. Journal of Mechanical Science and Technology, 2008, Vol.22, pp. 599-607.
[7] Zhang A, Gu M., Wind tunnel tests and numerical simulations of wind pressures on buildings in staggered arrangement. J. Wind Eng. Ind. Aerodyn. 2008, Vol.96, pp. 2067-2079.
[8] Wong P T Y, Ko N W M, Chiu A Y W., Flow characteristics around two parallel adjacent square cylinders of different sizes . J. Wind Eng. Ind. Aerodyn. 1995, Vol.1, pp. 263-275.
[9] Chen Suqin, Gu Ming, Huang Ziping , Numerical Computation of the Flow Around Two Square Cylinders Arranged Side by Side. Applied Mathematics and Mechanics, 2000, Vol.21, pp. 131-147
[10] Sakamoto H, Hainu H, Obata Y., Fluctuating forces acting on two square prisms in a tandem arrangement. Journal of Wind Engineering and Industrial Aerodynamics, 1987, Vol.26, pp. 85-103.
[11] Lam K M, Leung M Y H, Zhao J G., Interference effects on wind loading of a row of closely spaced tall buildings. J. Wind Eng. Ind. Aerodyn, 2008, Vol.96, pp. 562-583.
[12]Load code for the design of building structures (GB 50009-2001)(2006 edition). China Architecture and Building Press, 2006
[13] Architectural Institute of Japan, AIJ 2004. Recommendations for loads on buildings, Tokyo: Architecture Institute of Japan, 2004.
[14] Holmes John D., Wind loading of structures (second edition) . London: Taylor and Francis, 2007, pp.199-200.
[15] S.Q. CHEN, Z.P. HUANG, J.H. SHEN, Numerical Computation of the Flow around Two Square Cylinders in Tandem Arrangement. Journal of Tongji University (Natural Science).2001, Vol.29, pp. 320-326
[16] Hasebe, H., Watanabe, K., Watanabe, Y. and Nomura, T., Experimental study on the flow field between two square cylinders in tandem arrangement, in: Proceedings of Seventh Asia-Pacific Conference on Wind Engineering (APCWE VII), Taipei, 2009, Paper No.T1-C-4.
[17]A. C. Khanduri, T. Stathopoulos and C. Bedard, Generalization of wind-induced interference effects for two buildings. Wind and Structures, 2000, Vol.3, pp. 255-266

The Seventh International Colloquium on Bluff Body Aerodynamics and Applications (BBAA7)
Shanghai, China; September 2-6, 2012

Numerical study on wind-pressure characteristics of a high-rise building in group of buildings

Wang Dayang[a], Zhou Yun[a], Li Qingxiang[b], Deng Xuesong[a], Zhu Yong[a]

[a]*School of Civil Engineering of Guangzhou University, Guangdong Guangzhou, China*
[b]*Guangdong Provincial Academy of Building Research, Guangdong Guangzhou, China*

ABSTRACT: Wind pressure characteristics of a twin-tower high-rise structure disturbed by surrounding buildings were investigated using large eddy simulation (LES). The computational simulation technique were described initially. Studies have been performed in detail for the mean and fluctuating pressure coefficients. Detail explanations of each analysis results were given in the paper. To study further on the pressure coefficients on the building surfaces, parameter studies on shape coefficient and spatial correlation were performed and investigated subsequently. The numerical obtained in this study are expected to provide practicing engineers a better understanding of wind field around buildings.

KEYWORDS: Numerical prediction; CFD; Pressure coefficient; Disturbance effect; Spatial correlation, High-rise building

1 INTRODUCTION

Computational fluid dynamics has been a widely-used method of wind flow simulation around buildings for more than 20 years. Rapid development is observed especially in recent studies. Traditional standard turbulence models, such as eddy viscosity-based models and various second-order stress models, were found to be inadequate in predicting unsteady flows around bluff bodies (Castro and Graham, 1999; Cowan, 1997; Lim et al, 2009; Leschziner, 1993). Unsteady techniques such as discrete vortex methods and, particularly, large eddy simulation (LES) are found to be much more appropriate for simulating unsteady flow features (Murakami and Mochida, 1995; Shah and Ferziger, 1997; Murakami, 1998; Fasel et al, 2002; Nozawa and Tamura, 2002; Fureby, 2007; Tominaga, 2008). Rodi (1997) compared the performance of LES and Reynolds-Averaged Navier-Stokes (RANS) calculations of vortex-shedding flow passing a square cylinder at Reynolds number, Re=22,000 and that of the 3D flow passing a surface-mounted cube at Re=40,000. Results showed that turbulence fluctuations were severely under-estimated by RANS, while LES was found more suitable and had great potential for complex flow calculations. Validation of LES in predicting flow around an obstacle under turbulent flow condition was also confirmed by Nozawa and Tamura (2002). Breuer et al (2003) investigated the variations of the predicted results among RANS, DES (detached-eddy simulation) and LES for the separated flow around a flat plate at high incidence. The RANS computations were not able to capture the unsteady vortex shedding behaviour and both two- and three-dimensional RANS predictions led to the same steady-state results. The asymmetric vortex shedding motion was well reproduced by DES and LES. But the free shear layer originating from the leading edge of the plate was not well reproduced by DES. Kose and Dick (2010) presented a numerical study of the flow around a cubical building by RANS, hybrid RANS/LES and LES in Re=4×106. Results obtained by LES were the most accurate for coarse grid simulations. Detailed comparison between LES and experiment of both the inflow boundary layer and the flow field around a cube

was performed by Lim et al (2009). Results confirmed that LES is a viable tool for use in wind engineering problems concerning flow over isolated bodies.

It is well-known that there is rarely a case that only one single high-rise building is built in a city district. Many more regional groups of high-rise buildings are built in major cities, which cause structural wind characteristics become much more complex because of interaction and obstruction effects among buildings. Moreover, existing study results on wind characteristics of flow around single building and also some design parameters stipulated in international design codes may not be applicable to buildings under such wind condition. So, the structural wind characteristics influenced by surrounding buildings have been a subject of interest to researchers and engineers because of its significance for the evaluation of building designs. Zhou (2011) studied wind characteristics around a tall structure, which is disturbed by surrounding buildings, using experimental and numerical methods. Results showed that pressure coefficients were greatly disturbed by surrounding buildings. Cheng et al (2003) discussed the predictive performance of LES with various dynamic subgrid-scale models for a fully developed turbulent flow around a matrix of cubes. Su and Chen (2006) predicted the wind-induced surface pressures and wind environment around a complex-shaped high-rise building with annex by the standard k-ε model and the RNG k-ε model. Ma et al. (2007) investigated the wind environment around a single building and a building complex based on and the Reynolds averaged N-S equations and the RNG k-ε turbulence model. Wang et al. (2003) predicted wind-induced pressures on a low-rise single house with gable roofs and a building complex consisting of six low-rise houses with gable roofs by numerical simulation.

This paper aims to assess the wind pressure characteristics of a twin-tower high-rise structure under the interaction and obstruction effects of surrounding buildings. The study results will assist engineers and researchers having a better understanding of the risks involved, such as extreme pressure and unfavorable wind direction, when designing a similar twin-tower. To achieve this, the present paper contains CFD. The CFD simulations were performed using LES method. Studies on LES predictions were made in terms of the mean pressure coefficients for a number of pressure analysis around the outer and inner surfaces of the twin-tower building. Studies were also carried out for disturbance effect and spatial correlation of the fluctuating pressure and interaction and obstruction effect. In addition, the reliability of LES method in simulating flow around group of buildings was also revealed. So, the CFD analyses were investigated to assess the capability and accuracy of the LES method in simulating the wind flow in a group of building complex.

2 COMPUTATIONAL SIMULATION TECHNIQUE

2.1 *Computational model*

In this study, a 1:300 scaled numerical model was designed. In order to eliminate flow obstacle effect on the inflow and outflow boundary conditions (Murakami, 1998), the length of inflow, outflow and side-flow of the computational domain are 5*H*, 12*H* and 5*H*, respectively, as shown in Fig.1 (*H* is the maximum height of the bluff bodies, *H*=0.75m). The total height of the computational domain is 3*H*. The reason for such a choice is to eliminate the flow obstacle effect on the inflow and outflow boundary conditions, and keep the blockage ratio less than 3% as discussed by Murakami (1998). The Reynolds number based on the width *L* and *U(z)* (Inflow velocity at $z=H$) is about 5.4×10^5. Both structured and unstructured grids were used for mesh generation, as shown in Fig. 1. For zones near the bluff body, an unstructured mesh was generated while for zones outside the unstructured mesh, the structured mesh was applied. One

important advantage of this arrangement is that it is convenient to generate a mesh fine enough in the neighborhood of the building surfaces while keeping the mesh in far field zones from the building surfaces unchanged or in a proper coarser mesh. ADINA (2005) platform was adopted in this study, which has the capacity of manage both structured and unstructured grids in its solver. The average distance of the first layer of nodes from the surface is about *L*/5000 in X direction and *B*/5000 (value of *L* and *B* can be found in Fig. 1(a)) in Y direction with same growth factor of 1.2, which are smaller than the values suggested by Murakami (1998) (i.e. *D*/1000) and Huang (2006) (i.e. *D*/4000), so as to ensure that the wall unit $y^+<5$ is satisfied. The maximum grid size used far away from the building is about *H*. Slip boundary conditions are imposed on the velocity near the solid boundaries. The Reichardt wall-law is then used to derive the shear stresses caused by the presence of the wall (Hinze, 1959; Camarri *et al*, 2002). Advantage of this wall law is that it can describe the velocity profile not only in the laminar sub-layer ($y^+<5$) but also in the logarithmic region of a turbulent boundary layer ($y^+ \geqq 40$) and in the intermediate region, which will guarantee correct asymptotic behaviour at the wall of the SGS terms in the Smagorinsky model. Totally, about 800,000 3D grid elements were generated in the present simulation. Computations are carried out on 16 Xeon E5580 3.2GHz CPUs and require about 16GB of Infineon memory and about 8 days of CPU time for the whole simulation. The numerical time step for the transient simulation is 5×10^{-4} sec and 8000 steps, which is equivalent to 4 seconds, are needed to collect data for computational stability purposes. The statistical average of flow field was taken for the last 4000 steps (i.e. 2 sec).

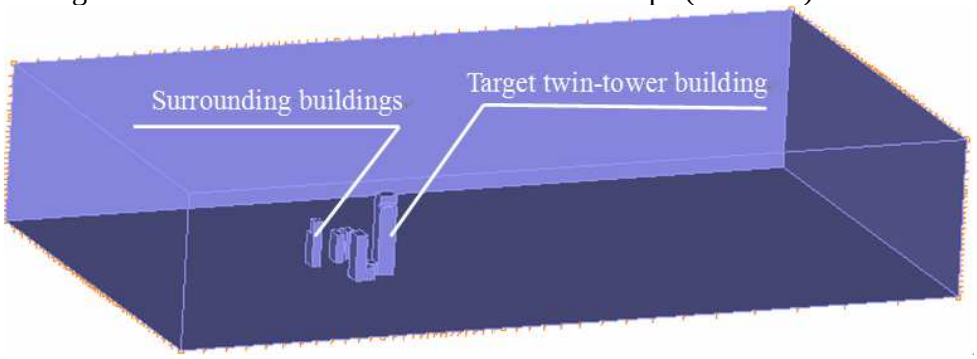

(a) Computational domain (Unit: m)

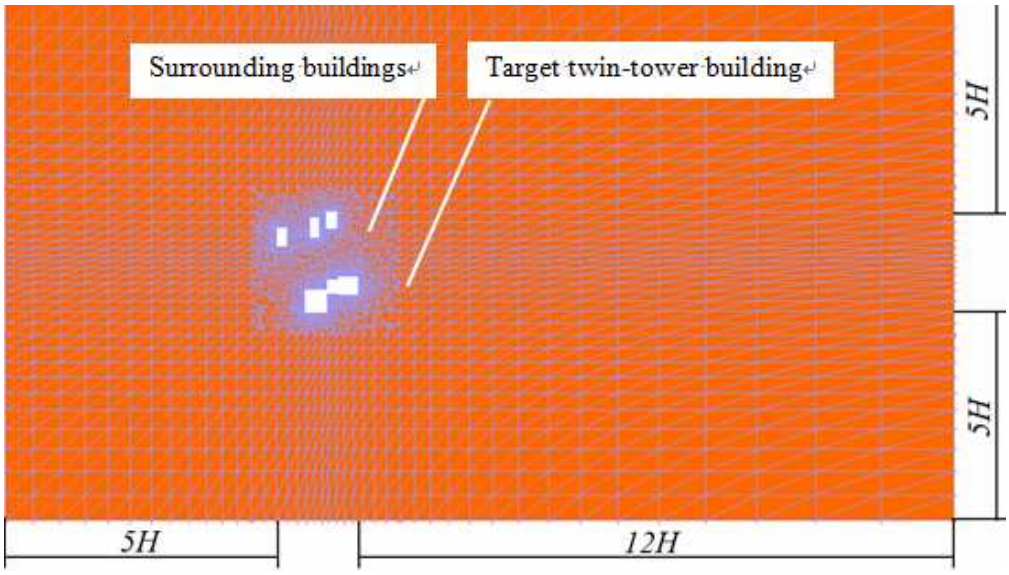

(b) Grid distribution

Figure 1. Computational domain and grid distribution

2.2 *Boundary conditions*

Reasonable boundary conditions will be helpful of saving computational time. For the inflow boundary condition, both the mean and fluctuating wind velocity were considered. The mean wind velocity can be achieved by matching a log-law profile (Obasaju, 1992):

$$\begin{cases} v(z) = 2.5v^* \log_e(40)\left(\dfrac{z}{40Z_0 + D}\right)^{0.25} & \left(\dfrac{z-D}{Z_0}\right) < 40 \\ v(z) = 2.5v^* \log_e\left(\dfrac{z-D}{Z_0}\right) & 40 \le \left(\dfrac{z-D}{Z_0}\right) \le 1000 \end{cases} \tag{1}$$

where, $v(z)$ is the horizontal wind speed at z, v^* is the surface friction velocity defined as $(\tau_\circ / \rho)^{0.5}$ ($\tau_\circ$ being the surface shear stress), D is the height of the zero plane above ground, Z_0 is the surface roughness length parameter. Height of the gradient wind is 450m.

Based on a procedure by Kraichnan (1970) for generation of an isotropic continuous flow field satisfying a spectrum of Dirac function, a new general inflow turbulence generation method for large eddy simulation, also called the discretizing and synthesizing random flow field generation (DSRFG) technique, is proposed by Huang *et al* (2010) and Li *et al* (2007). The isotropic fluctuating velocity in $\mathbf{x}$ space was synthesized by the following superposition of harmonic functions (Huang *et al*, 2010):

$$u_i(\mathbf{X}, t) = \sum_{n=1}^{N}\left[p_i^n \cos\left(k_j^n x_j + \omega_n t\right) + q_i^n \sin\left(k_j^n x_j + \omega_n t\right)\right] \tag{2}$$

$$p_i^n = \varepsilon_{ijm}\zeta_j^n k_m^n, \quad q_i^n = \varepsilon_{ijm}\xi_j^n k_m^n, \quad \zeta_j^n, \xi_j^n, \omega_n \in N(0,1), \quad k_j^n \in N(0, 1/2)$$

Where k and ε are the turbulence kinetic energy and the turbulence dissipation rate, respectively, ε_{ijm} is the permutation tensor used in vector product operation, k_j^n and ω_n, respectively, represent a sample of n wave-number vectors and frequencies of the modeled turbulence spectrum. Detailed calculation about the Eq. (2) can be found in Huang *et al* (2010). The first superiority of the DSRFG is that continuity condition, $div(\mathbf{u}) = 0$, can be ensured strictly. The second is that fluctuating velocity generated in inflow condition satisfies specified power spectrum density function. And the last one is that spatial correlation of inflow condition can be adjusted by scaling factor.

At the outflow, convective boundary condition is applied for velocity and pressure:

$$\partial/\partial t + c\left(\partial/\partial x\right) = 0 \tag{3}$$

where c is taken to be the bulk velocity so as to ensure global mass conservation. Slip condition was assumed for velocity on the two sides and top surfaces of the computation domain. With this kind of boundary condition, one has $\partial U/\partial y = \partial U/\partial w = V = W = 0$. And non-slip condition was used for velocity on the ground surface, that is u_n=0. Neumann condition for pressure was employed on surfaces of building and the computation domain as pressure gradient orthogonal to the surfaces equals to zero.

3 DATA PROCESSING

Pressure data obtained from computational simulation is processed using equations as shown in Table 1. External pressures were normalized with respect to the mean wind pressure at the reference height of *H*. Instantaneous pressure coefficients were determined at each pressure tap location and subsequently analyzed to determine maximum, minimum, mean, and standard deviation of pressure coefficients. Shape coefficient describes distribution status of static pressure on a building surface in wind action, which is influenced mainly by the shape and size of a building. Spatial correlation of fluctuating wind represents pressure dependency of two pressure taps, which is an important index of studying spatial flow status and corresponding transmission pattern.

Table 1 Data processing equations

Wind pressure coefficient	$C_{pi}(n)=\dfrac{p_i(n)}{\rho U_{ref}^2/2} \quad (n=1\cdots N)$
Mean wind pressure coefficient	$\bar{C}_{pi}=\sum_{n=1}^{N}\dfrac{C_{pi}(n)}{N}$
Fluctuating wind pressure coefficient	$C_{pi,rms}=\sqrt{\sum_{n=1}^{N}\dfrac{\left(C_{pi}(n)-\bar{C}_{pi}\right)^2}{N-1}}$
Shape coefficient	$\mu_s=\dfrac{\sum_i \bar{C}_{pi}A_i}{A}$
Correlation coefficient of fluctuating wind	$\rho_{ij}=\dfrac{E\left[\left(C_{pi}(n)-\bar{C}_{pi}\right)\left(C_{pj}(n)-\bar{C}_{pj}\right)\right]}{C_{pi,rms}C_{pj,rms}}$

As shown in Table 1, i is the number of pressure tap; N is the sample length of the wind pressure time series, N =4096; ρ is air density, ρ=1.2kg/m^3; V_{ref} is wind velocity of the reference height; z_i is the height of the i^{th} pressure taps; μ_{zr} is wind pressure coefficient of reference height; μ_{zi} is wind pressure coefficient of the i^{th} pressure taps; μ_{si} is the shape coefficient of the i^{th} pressure taps; A_i is the covered surface area of the i^{th} pressure taps; A is the total surface area.

4 RESULTS AND DISCUSSION

4.1 *Mean pressure coefficient*

The mean pressure coefficient contours obtained from numerical simulations results are shown in Fig. 2. It is well-known that the mean pressure coefficients on the windward face are largely positive for isolated building (Huang et al., 2006; Gomes et al., 2005). However, in this study the mean pressure coefficients were greatly affected by the interaction and obstruction effects between the main and sub-main towers and that of the upstream buildings. For example, the mean pressure coefficients of the main tower on the front face were negative on the lower level for 0^{O}wind incident direction, attributing to the influence of the sub-main tower. The mean pressure on the side and back faces were also greatly disturbed, which are discussed in detail in the next sections.

4.2 *Fluctuating pressure coefficient*

Fluctuating pressure coefficients of the different taps on front faces are largely of similar values, except those at the corner, as shown in Fig.3, which means that flow status on the front faces is relatively stable. At the corner, the fluctuating pressure coefficients increase as stronger vortex motion generates. On the side faces, larger fluctuating pressure coefficients relative to those on the front faces can be observed, especially for the region at the corner, due to the flow separation. The reason is that strong and orderly vortex motion appears on the side faces and greater vortex energy is then aroused, which causes the increase of the fluctuating pressure. On the back faces, the variation of the fluctuating pressure coefficients are complex relatively. The reason is that irregular and disorder vortex is generated in wake flow, which causes the pressure on back faces variable and no precise laws can be used to describe the pressure status.

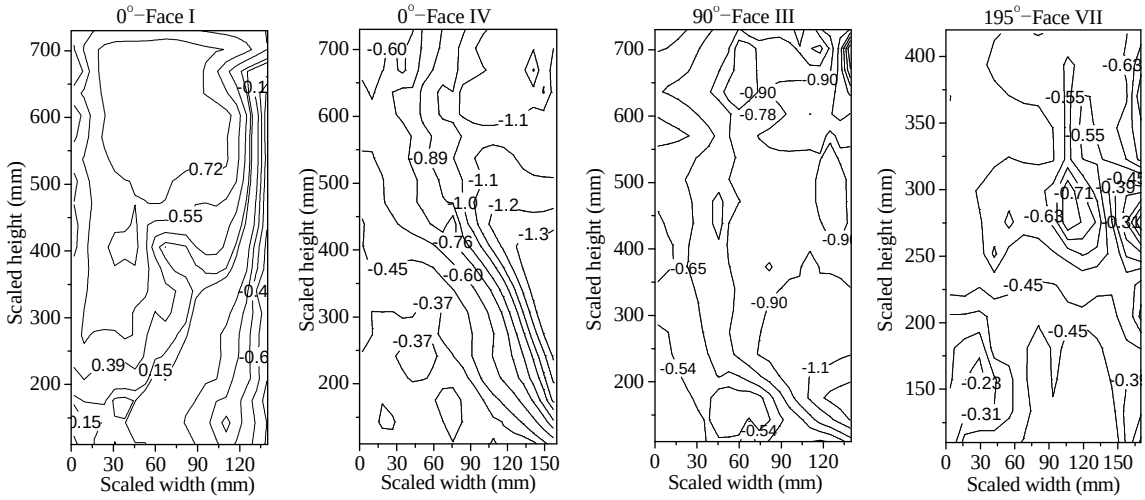

Figure 2. Mean pressure coefficient contours

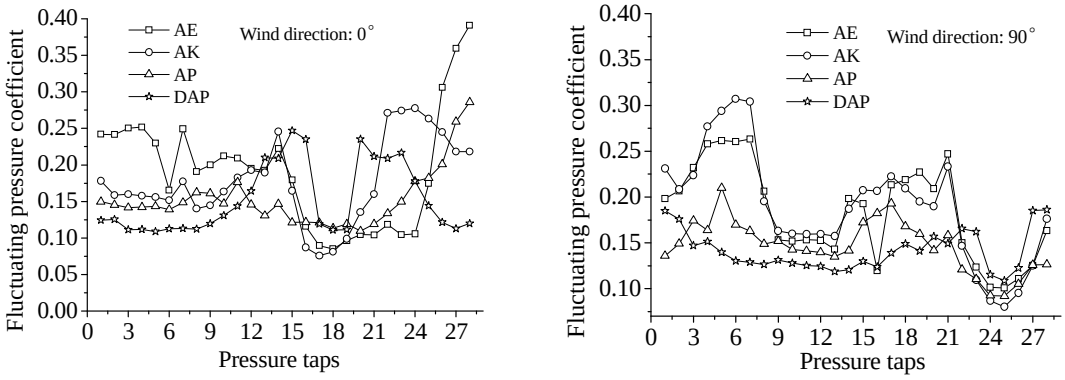

(a) 0° (b) 90°

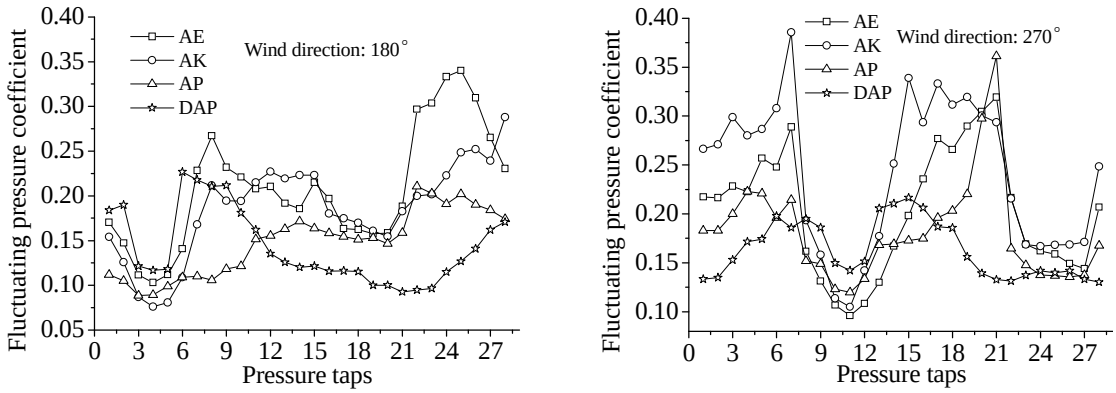

(c) 180° (d) 270°

Figure 3. Fluctuating pressure coefficients in different wind direction

4.3 *Interaction and obstruction effect*

To research the interaction and obstruction effect of among buildings, interaction and obstruction factor γ is defined as:

$$\gamma=\mu_s/\mu_{sn} \tag{4}$$

Where: μ_s is shape coefficient with the interaction and obstruction effect, μ_{sn} is shape coefficient without the interaction and obstruction effect.

Variation of the interaction and obstruction factor along the height of both the main and sub-main towers in different wind directions is shown in Fig. 4. It can be easily found in Fig. 5 that the maximum shape coefficients of the front faces of the twin-tower building is 0.77, which is close to the value of 0.8 stipulated in the Chinese code (2002). However, greater discrepancy have been noticed for the shape coefficients of back and side faces when comparing to the Chinese wind code (2002). The maximum shape coefficients were -1.25 and -0.83 for the side and back faces respectively, which were higher than the values of the Chinese code (i.e. -0.7 and -0.5, respectively). So, it can be deduced that noticeable difference of pressure distribution on building faces exist relative to signal building (no interaction and obstruction effect exist in signal building).

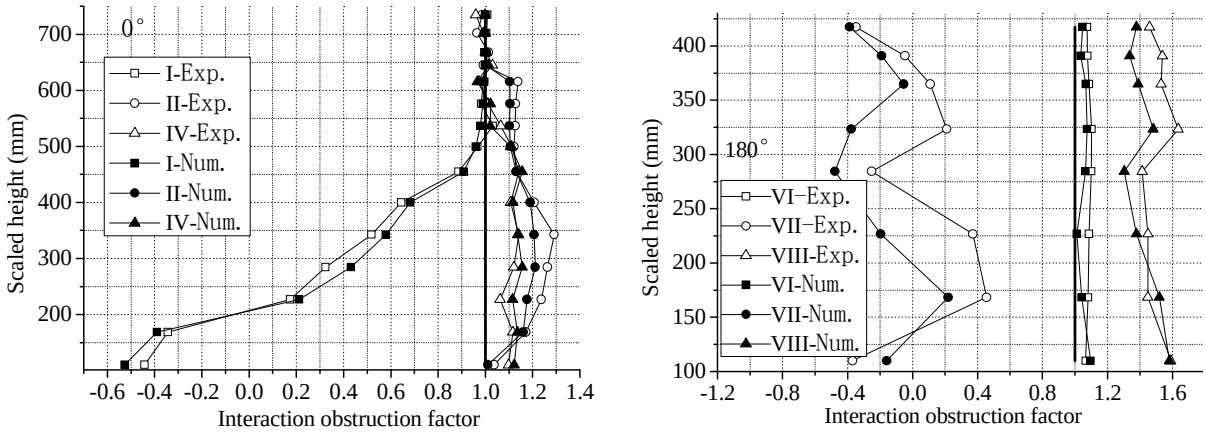

(a) 0°-The main tower (b) 180°-The sub-main tower

Figure 4. Distribution of interaction and obstruction factor along structural height

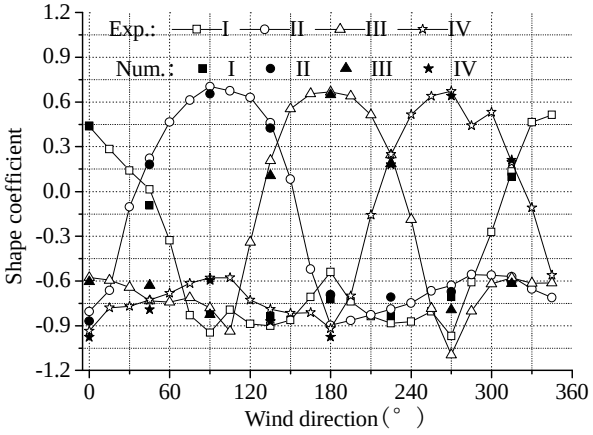

(a) The main tower

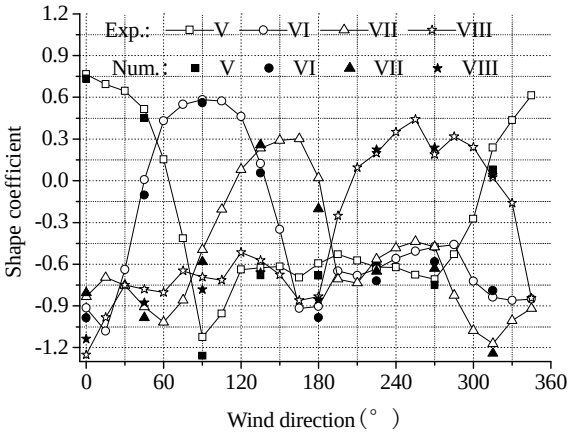

(b) The sub-main tower

Figure 5. Shape coefficients

4.4 *Spatial correlation of fluctuating pressure*

Spatial correlation of fluctuating wind represents pressure dependency of two pressure taps, which is an important index of studying fluctuating pressure characteristic and also spatial flow status. The lateral correlation coefficient contours of fluctuating wind pressure are given in Fig.6. As revealed in these figures, the correlation coefficients decrease gradually as the distance of two pressure points increases. The correlation coefficient is influenced by vortex structure and its motion status of the surrounding flow field. Regular vortex structure (such as vortex shape and dimension) and similar motion status will contribute to enlarge the correlation coefficient in condition of the same distance of two points. E.g., two-point correlation in the middle region is relatively larger than that of the side region of the front faces in same distance.

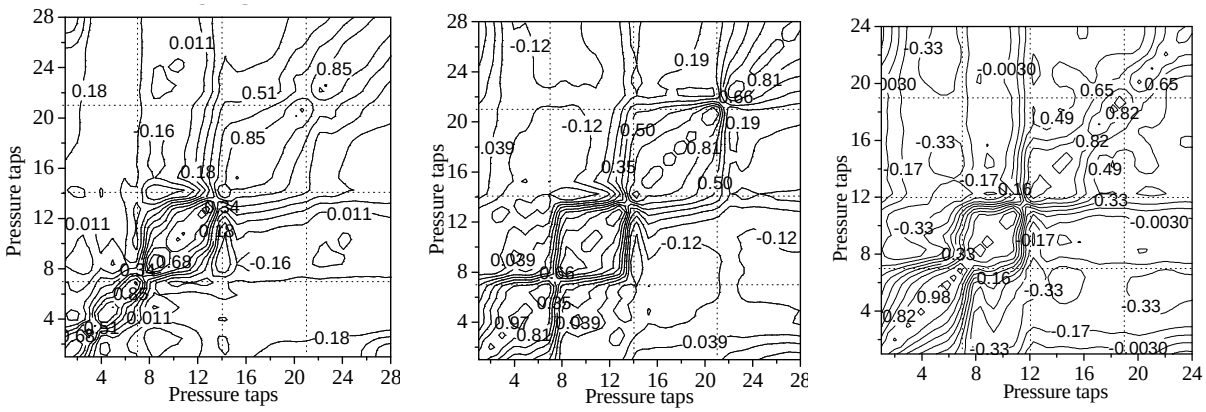

(a) Level AC (b) Level AI (c) Level BG

Figure 6. Lateral correlation coefficient contours for incident wind angles of 45°

5 CONCLUSIONS

The maximum mean pressure coefficients are found to be at the middle of windward surface with height of about 0.8*H*-0.9*H* in 24 wind directions, and the minimum pressure generates at the corner of flow separation. Flow with strong and orderly vortex motion yields large fluctuating pressure, such as the fluctuating pressure on side faces and especially at the corner of flow

separation. On the contrary, smaller fluctuating pressure yields if irregular and disorder vortex motion exist, such as the pressure on back faces.

Interaction obstruction effect of shape coefficients of the twin-tower building is mainly from the interference disturbance between the main and sub-main towers, and the disturbance effect of surrounding buildings. In this study, the disturbance effect of surrounding buildings on the fluctuating pressure of the twin-tower building is smaller than that of the interference disturbance between the main and sub-main towers.

The lateral spatial correlation of fluctuating pressure among pressure taps on the front and side faces are relatively larger than that of the back faces. As for the spatial correlation between two faces, larger correlation can only be found at the corner between the front and side faces. The vertical correlation decreases with increasing of distance between two pressure taps.

6 ACKNOWLEDGEMENTS

This project is supported by the Doctor Special Fund of Higher School (200810780001), Natural Science Foundation of Guangdong Province (8351009101000001), Production and Research Project of Ministry of Education of Guangdong Province (20090912) and Innovation Team Project of Education System of Guangzhou City (09T003).

7 REFERENCES

ADINA R&D, Inc. Theory and Modeling Guide, Volume I, II and III. Watertown, USA, 2005. (www.adina.com)

M. Breuer, N. Jovičić and K. Mazaev, Comparison of DES, RANS and LES for the separated flow around a flat plate at high incidence. Int. J. Numer. Meth. Fl., 41(2003) 357-388.

S. Camarri, M.V. Salvetti, B. Koobus and A. Dervieux, Large-eddy simulation of a bluff-body flow on unstructured grids, Int. J. Numer. Meth. Fl., 40(2002) 1431-1460.

I.P. Castro, J.G.R. Graham, Numerical wind engineering: the way ahead? Proceedings Of The Institution Of Civil Engineers Structures And Buildings, 3 (1999) 275-277.

Y.Cheng, F.S.Lien, E.Yee, R. Sinclair, A comparison of large Eddy simulations with a standard k–e Reynolds-averaged Navier–Stokes model for the prediction of a fully developed turbulent flow over a matrix of cubes, J. Wind Eng. Ind. Aerod., 91(2003) 1301-1328.

R. Clark, J. Ferziger, W. Reynolds, Evaluation of subgrid-scale models using an accurately simulated turbulent flow, J. Fluid Mech., 91(1979) 1-16.

I.R. Cowan, I.P. Castro, A.G. Rorns, Numerical considerations for simulations of flow and dispersion around buildings, J. Wind Eng. Ind. Aerod., 67 & 68(1997) 535-545.

Chinese code, Load code for the design of building structures. China architecture &building press, Beiiing, 2002.

J. Deardorff, A numerical study of three-dimensional turbulent channel flow at large Reynolds numbers, J. Fluid Mech., 2(1970) 453-480.

H. F. Fasel, J. Seidel, and S. Wernz, A Methodology for Simulations of Complex Turbulent Flows, J. Fluid Eng., 124(2002) 933-943.

C. Fureby, ILES and LES of Complex Engineering Turbulent Flows, J. Fluid Eng., 12(2007) 1514-1524.

GPABR. http://www.gdjky.com/jzwl/jzfgcyjs/index.html

M.G. Gomes, R.A. Moret, Pedro Mendes. Experimental and numerical study of wind pressures on irregular-plan shapes, J. Wind Eng. Ind. Aerod., 93(2005) 741-756.

M. Gu, P. Huang, Research History and State of art of Interference Effects of Wind Loads of a Cluster of Tall Buildings, J. Tongji Univ., 7(2003) 762-766

J.O. Hinze, Turbulence, McGraw-Hill: New York, 1959.

S.H. Huang, Q.S. Li and S.L. Xu. Numerical evaluation of wind effects on a tall steel building by CFD, J. Constr. Steel Res., 18(2006) 1-16.

S.H. Huang, Q.S. Li and J.R. Wu, A general inflow turbulence generator for large eddy simulation, J. Wind Eng. Ind. Aerod., 98(2010) 600-617.

D.A. Kose, E. Dick, Prediction of the pressure distribution on a cubical building with implicit LES, J. Wind Eng. Ind. Aerod., 98(2010) 628-649.
R.H. Kraichnan, Diffusion by a random velocity field, Ph. of Fl., 13(1970) 22–31.
H.C. Lim, T.G. Thomas, I.P. Castro, Flow around a cube in a turbulent boundary layer: LES and experiment, J. Wind Eng. Ind. Aerod., 97(2009) 96-109.
A. Leonard, Energy cascade in large-eddy simulations of turbulent fluid flows, Adv. Geophys. A, 18(1974) 237-248.
M.A. Leschziner, Computational modeling of complex turbulent flows, In Computational Wind Engineering 1 (ed. S. Murakami). Elsevier, Amsterdam, 1993, pp. 37-52.
C. Li, Q.S. Li, S.H. Huang, et al, Large eddy simulation on wind load of a complex large-span structure, Proceeding of the 13th Structural Wind Engineering in China, 2007, pp. 995-1005.
S. Murakami, Overview of turbulence models applied in CWE-1997, J. Wind Eng. Ind. Aerod., 74-76(1998) 1-24.
S. Murakami, A. Mochida, On turbulent vortex shedding flow past 2D square cylinder predicted by CFD, J. Wind Eng. Ind. Aerod., 54(1995) 191-211.
J. Ma, G.B. Chen, Y.L. Mao, Study of wind environment around building complex based on CFD, J. Zhejiang Univ. Tech., 3(2007) 351-354.
K. Nozawa, T. Tamura, Large eddy simulation of the flow round a low-rise building immersed in a rough-wall turbulent boundary layer, J. Wind Eng. Ind. Aerod., 90(2002) 1151-1162.
E.D. Obasaju, Measurement of forces and base overturning moments on the CAARC tall building model in a simulated atmospheric boundary layer, J. Wind Eng. Ind. Aerod., 40(1992) 103–26.
H. Pitsch, Large-Eddy Simulation of Turbulent Combustion, Ann. Rev. Fluid Mech., 38(2006) 453-482.
W. Rodi, Comparison of LES and RANS calculation of the flowaround bluff bodies, J. Wind Eng. Ind. Aerod., 69–71(1997) 55–75.
K.B. Shah, J.H. Ferziger, A fluid mechanician's view of wind engineering: large-eddy simulation of flow past a cubical obstacle, J. Wind Eng. Ind. Aerod., 67(1997) 211–224.
G. Su, S.H. Chen, Numerical of simulation of wind pressures and wind environment around complex-shaped high-rise building, Eng. Mech., 8(2006) 144-149.
J. Smagorinsky, General Circulation Experiments with the Primitive Equations, Mon. Weather Rev., 3(1963) 99-164.
R. Stoll, F. Porté-Agel, Large-Eddy Simulation of the Stable Atmospheric Boundary Layer using Dynamic Models with Different Averaging Schemes, Boundary-Layer Meterology, 1(2008) 1-28.
S. Sarkar, and S. Sarkar, Large-Eddy Simulation of Wake and Boundary Layer Interactions Behind a Circular Cylinder, J. Fluid Eng., 9(2009) 091201-14
Y. Sun, Y. Wu, Z.X. Lin, S.Z. Shen, Non-Gaussian features of fluctuating wind pressures on long span roofs, China Civil Engineering Journal, 4(2007) l-5.
T. Tamura, A. Okuno, Y. Sugio, LES analysis of turbulent boundary layer over 3D steep hill covered with vegetation, J. Wind Eng. Ind. Aerod., 95(2007) 1463- 1475.
Y. Tominaga, A, Mochida, S, Murakami, S. Sawaki, Comparison of various revised k–e models and LES applied to flow around a high-rise building model with 1:1:2 shape placed within the surface boundary layer, J. Wind Eng. Ind. Aerod., 96(2008) 389-411.
H. Wang, S.H. Chen, J.C. Tang, Numerical simulation of wind pressures on a low-rise building complex with gable roofs, Eng. Mech., 6(2003) 135-140.
C. Wagner, T. Hüttl, and P. Sagaut, Large-Eddy Simulation for Acoustics, Cambridge University Press, 2007.
D.Y. Wang, Performance-Based Wind Design Method and Wind-Induced Vibration Control of High-Rise Building, Guangzhou University: Ph.D thesis, Guangzhou City, China, 2011.
Y. Zhou, D.Y. Wang, Q.X. Li, Numerical and experimental study on wind characteristics of tall structure disturbed by surrounding buildings, 13th International Conference on Wind Engineering, Amsterdam, the Netherlands, July, 2011.
X.D. Zhang, Modern signal processing (the second edition), Beijing: Tsinghua University Press, 2002.

The Seventh International Colloquium on Bluff Body Aerodynamics and Applications (BBAA7)
Shanghai, China; September 2-6, 2012

Peak pressure effects on a high-rise building influenced by a mid-rise building

Alexander Bronkhorst [a,b], Chris Geurts [a,b], Bert Blocken [a] and Carine van Bentum [b]

[a] *Eindhoven University of Technology, Department of the Built Environment, Eindhoven, the Netherlands*
[b] *TNO, Delft, the Netherlands*

ABSTRACT: Pressure measurements on the surfaces of a high-rise building model with height $h = 0.48$ m and width $b = 0.12$ m were performed in a boundary layer wind tunnel. Experiments were carried out for an isolated model and for three configurations with an interfering half-height building model. The effects of the interfering building to the minimum peak pressures on the reference model were determined. The influence of the separation distance and the shape of the interfering building (square and circular plan form) were investigated. For the smallest separation distance, $S = 0.5b$, the composition of the minimum peak pressures was studied in more detail by assessment of the mean and standard deviation pressure coefficient. This study shows that the magnitude of local minimum peak pressure increases with approximately 25-35% on two facades of the high-rise model. In the top corner of the façade on the side a reduction is observed of 20-40%, depending on the shape of the interfering model.

KEYWORDS: Wind interference, peak pressures, high-rise, mid-rise

1 INTRODUCTION

Wind loads on buildings can be influenced by the presence of nearby buildings. This influence can change the global loads on the interfering buildings, as well as the local loads on their building envelopes. Research on the influence of interference can be grouped in (1) studies on global loads and (2) studies on local loads. According to this categorization, Table 1 provides an overview of previously performed parametric wind tunnel studies on interference between high-rise buildings.

Studies on static global wind loads, performed by e.g. Taniike (1992) and Khanduri (1997), found that the influence of an interfering model with similar or larger height than the reference model can lead to an increase of 70-80%. Khanduri (1997) determined that the influence on the static wind load can be neglected if the interfering building is smaller than ¾ of the reference building height.

Even larger effects were found for dynamic global wind loads. Bailey and Kwok (1985) and Taniike and Inaoka (1988) found an increase in the dynamic base bending moment of respectively 440%, and 2000% for the case of a slender interfering model. Xie and Gu (2004, 2005 and 2007) performed an extensive wind tunnel study on two and three high-rise configurations. They derived a set of simplified guidelines and formulae to provide designers with tools to obtain an estimate for the influence of interference on the static and dynamic base-bending moment. According to these guidelines, an interfering building smaller than half the height of the reference building has no significant influence on the dynamic base-bending moment.

Table 1. Overview of previously performed parametric wind tunnel studies on wind load effects due to interference between high-rise buildings.

Literature source	**Reference model dimensions**	**Flow properties at reference model height**		**Type of load**	**Type of statistic**	**Studied influence parameters**
	bxdxh [m]	***I_u [-]***	***U_{ref} [m/s]***	***[-]***	***[-]***	***[-]***
Bailey and Kwok (1985)	0.06x0.06x0.54	Not reported	Not reported	Global dynamic base moment	Std	• Interfering model shape • Terrain roughness
Taniike and Inaoka (1988); Taniike (1991)	0.07x0.07x0.32	0, 0.12	1.6 – 10	Global dynamic base moment	Std	• Interfering model width and depth • Terrain roughness
Xie and Gu (2004, 2005, 2007)	0.1x0.1x0.6	0.05, 0.08	Not reported	Global static & dynamic base moment	Std	• Interfering model width, depth and height • Number of buildings • Terrain roughness
Taniike (1992)	0.07x0.07x0.32	0	6	Global static force	Mean/Std	• Interfering model width and depth
Khanduri (1997)	0.05x0.05x0.20	0.07, 0.13, 0.25	Not reported	Global static force	Mean/Std	• Interfering model width and depth • Terrain roughness • Angle of incidence
Kim et al (2011)	0.07x0.07x0.28	0.2	8.2	Local static pressure	Peak	• Interfering model height • Angle of incidence

Few comprehensive studies were performed on the interference effects between tall buildings with a focus on local loads. Kim et al (2011) did perform such an extensive parametric wind tunnel study. One of the configurations they tested was a high-rise reference model under influence of a half-height model. Kim et al (2011) concluded that, in urban terrain conditions ($z_0 \approx 1.4$ m), an interfering model with half the height of the reference model has limited influence on the peak pressure coefficients. Bronkhorst et al (2011) performed an analysis on the mean and standard deviation pressure distribution for the same case in suburban terrain conditions ($z_0 \approx 0.8$ m). Three pressure effects resulting from interference were determined:

1. An increase on the faces in the passage for wind parallel to the passage.
2. An increase on the side faces of the reference model at roof height of the half-height interfering model for wind parallel to the configuration.
3. A reduction in the top corner of both side faces for wind parallel to the configuration.

This study investigates the magnitude of these effects when minimum peak pressures are considered. The goals of the study presented in this paper are:

- To determine local peak pressure effects resulting from interference between a high-rise building model and a half-height interfering model.
- To investigate the influence of the separation distance, the shape of the interfering model and the angle of incidence on the peak pressure effects.
- To gain understanding on the composition of these peak pressure effects by assessment of the mean and standard deviation pressure coefficient.

2 MATERIALS AND METHODS

Wind tunnel experiments were carried out in the open circuit atmospheric boundary layer (ABL) wind tunnel of TNO in the Netherlands. Measurements were performed on the isolated configuration and on three tandem configurations as illustrated in Figure 1(a). A detailed description of the experimental set-up can be found in Bronkhorst et al (2011). Both the influence of an interfering half-height model with square and with a half-height model with circular ground plan were investigated. Measurements were performed for twenty-four angles of incidence in 15° increments, for each configuration. The reference model pressure taps were distributed as illustrated in Figure 1(b), with 38 pressure taps on each face. Taps are designated by face F (which can be A, B or C), row (i) and column (j). For example, the pressure tap on face A, in the second row and the fifth column is specified as $A25$; the minimum peak pressure coefficient determined at this position is specified as $C_{p,min}(A25,\theta)$.

The fluctuating pressures acting at the pressure taps were measured with a sampling rate of 400 Hz for a period of approximately 20.5 seconds. The undisturbed static and dynamic pressure were measured with a pitot-static tube positioned at model roof height ($h = 0.48$ m), 2.6 m in front of the model and 0.7 m to the side. The mean velocity at this height (U_{ref}) for all tests was approximately 14.1 m/s, which corresponds with a width-based Reynolds number of $Re_b = U_{ref}b/\nu \approx 1.1 \times 10^5$. The instantaneous static reference pressure, $p_{ref}(t)$, was measured at a pressure tap in the left side wall at 1.2 m height, at the same longitudinal position as the instrumented reference model.

The measured pressure time series were converted to pressure coefficients with:

$$C_p(t) = \frac{p_s(t) - p_{ref}(t)}{q_{ref}} = \frac{p_s(t) - p_{ref}(t)}{\frac{1}{2}\rho U_{ref}^2} \qquad [1]$$

In which $p_s(t)$ is the instantaneous static pressure measured at the pressure taps, q_{ref} is the mean dynamic pressure measured at the pitot-static tube, and ρ is the air density.

The pressure coefficient time series were divided in thirty-two intervals of t = 0.64 s. For each interval, the mean, the standard deviation, and the minimum negative peak pressure coefficient were determined. The averages of each of these statistics over the thirty-two intervals are presented in the next paragraph.

Pressure coefficients have a magnitude and a sign. The magnitude (i.e. the absolute value) of the pressure coefficient is specified as large or small or showing an increase or decrease; the sign is negative or positive.

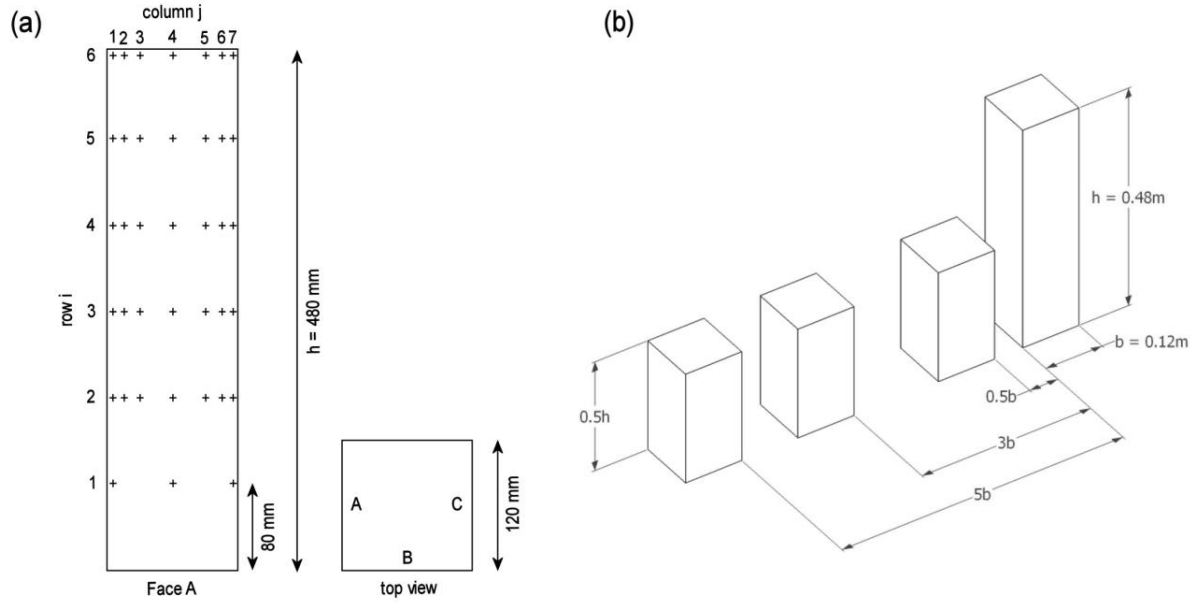

Figure 1. (a) Pressure tap distribution on the faces *A*, *B* and *C* of the instrumented building model, (b) the tandem configurations measured in the wind tunnel illustrated with the square half-height interfering model.

3 RESULTS AND DISCUSSION

This chapter gives results for the minimum peak pressure coefficient, and the mean and standard deviation pressure coefficient. First the overall effects are determined through investigation of the minimum peak pressure coefficients over all angles of incidence, the largest effects are investigated in more detail.

At each tap position, the minimum of the negative peak pressure coefficients over all angles of incidence $C_{p,min}(Fij,all)$ was determined. Figure 2 shows contour plots of the minimum peak pressure coefficient over all angles of incidence. The contour plots provide information on the location and the magnitude of the peak pressure effects which are a result of interference. The influence of the interfering half-height square cylinder is illustrated on the left-hand side; the influence of the circular cylinder is illustrated on the right. The pressure distributions on the model faces in the isolated case are plotted in the centre of the figure. The smallest minimum peak pressure coefficient for the isolated case, $C_{p,min}(F14,all) \approx$ -1.5, is found in the middle of the model face, near the ground. The largest minimum peak pressure coefficients $C_{p,min}(F61,all) \approx C_{p,min}(F67,all) \approx$ -2.4 are observed in the top corners.

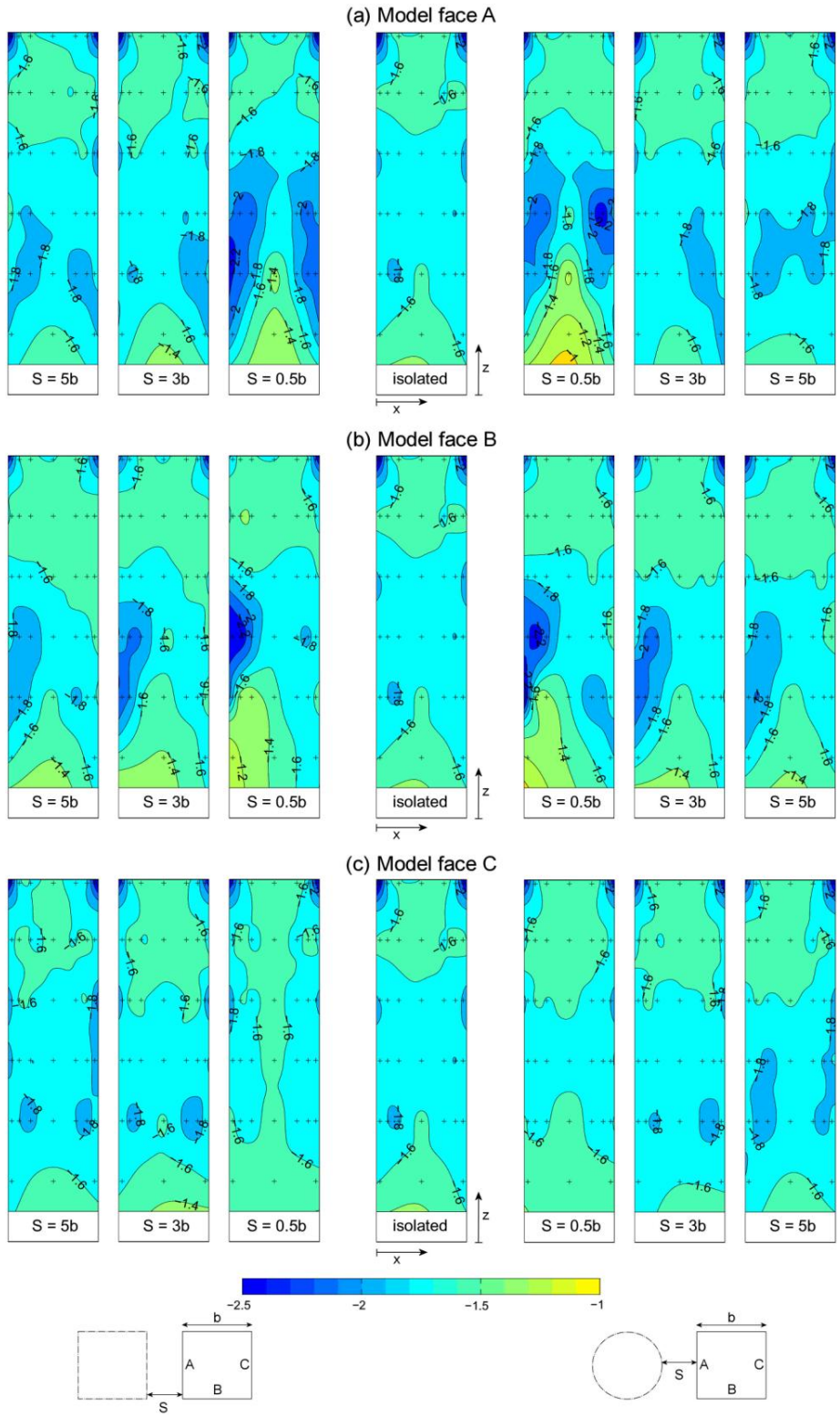

Figure 2. Contours of the minimum peak pressure coefficients over all angles of incidence, $C_{p,min}(Fij,all)$, on (a) face A, (b) face B and (c) face C of the reference model under influence of a square (left) and circular (right) mid-rise building. The contours of the isolated case are illustrated in the centre.

Table 2. Pressure coefficient values for the specified taps in Figure 2. For each position the minimum peak pressure coefficient over all wind directions are provided.

	isolated	***S = 0.5b***		***S = 3b***		***S = 5b***	
		square	***circle***	***square***	***circle***	***square***	***circle***
$C_{p,min}$*(A32,all)*	-1.7	-2.1	-2.1	-1.7	-1.8	-1.8	-1.8
$C_{p,min}$*(A21,all)*	-1.8	-2.2	-1.9	-1.7	-1.7	-1.8	-1.8
$C_{p,min}$*(B61,all)*	-2.4	-1.7	-2.0	-1.9	-2.1	-2.1	-2.2
$C_{p,min}$*(B32,all)*	-1.7	-2.3	-2.3	-2.0	-2.0	-1.9	-1.9

Figure 2(a) shows the influence of the half-height models on the minimum peak pressure distribution of face *A* with increasing separation distance (*S*). The largest interference effects on the minimum peak pressure are observed at taps *A32*, *A36*, *A21* and *A27*. At tap *A32* for a separation distance $S = 0.5b$, both square and circular interfering model increase the magnitude of the minimum peak pressure with approximately 25%. Table 2 shows that the square interfering model has a similar effect at tap *A21*. For $S = 3b$ and $5b$, these effects have disappeared, suggesting that the influence of the half-height interfering models on face *A* is only present for a separation distance smaller than at most three times the model width ($S < 3b$).

Figure 2(b) shows the influence of the interfering models on face B; the largest adverse effects are observed on the side of face B nearest to the interfering model (tap *B32*). At half the height of the reference model, the square and circular interfering models increase the minimum peak pressure coefficient with 25% and 35%. At a separation distance of $3b$ these effects have reduced to approximately 10%; at $S = 5b$ the influence has become negligible. Besides adverse pressure effects, the interfering models also have a positive effect on the local peak pressures. At the top corner near the front edge, tap *B61*, both square and circular interfering model increase the minimum peak pressure coefficient. The square interfering model increases the coefficient with 30%; the circular model results in a 15% increase.

The minimum peak pressure coefficient distributions on model face *C*, illustrated in figure 2(c), show little variation. Both square and circular interfering models have maximum effects which differ only 5% from the minimum peak pressures encountered in the isolated case. These effects are not nearly as large as the effects found on face *A* and *B*. Figure 2 and Table 2 show that the largest pressure effects are found at a separation distance $S = 0.5b$. Further discussion of the results focuses on the pressure effects observed on face *A* and *B* at $S = 0.5b$.

Figure 3 shows graphs of the mean (top graph), standard deviation (middle graph) and minimum peak pressure coefficient (bottom graph) versus angle of incidence for taps *A32*, *A21*, *B61* and *B32*. The graphs in Figure 3(a) show the influence of both a square and circular model ($S = 0.5b$) at pressure tap *A32*. For the isolated case, the largest value is -1.7, which is observed at $\theta = 75°$ and $\theta = 90°$. Both square and circular interfering models increase this minimum peak pressure coefficient to $C_{p,min}(A32,90°) = -2.1$. At this angle of incidence ($\theta = 90°$), the mean and standard deviation pressure coefficient show an increase of approximately 30% and 20%. Therefore, the amplification of the minimum peak pressure coefficient results from an increase in mean suction as well as an intensification of the fluctuations in the pressure signal. At pressure tap *A21*, illustrated in Figure 3(b), the square interfering model has a larger influence than the circular model over a large range of angle of incidence ($\theta = 45°$-$135°$). The largest effect caused by the square interfering model is observed at $\theta = 90°$ ($C_{p,min}(A21,90°) = -2.2$). The circular interfering model has no large influence on the minimum peak pressure coefficient at this location, which indicates the square interfering model has a larger area of influence than the circular model on face *A* of the reference model.

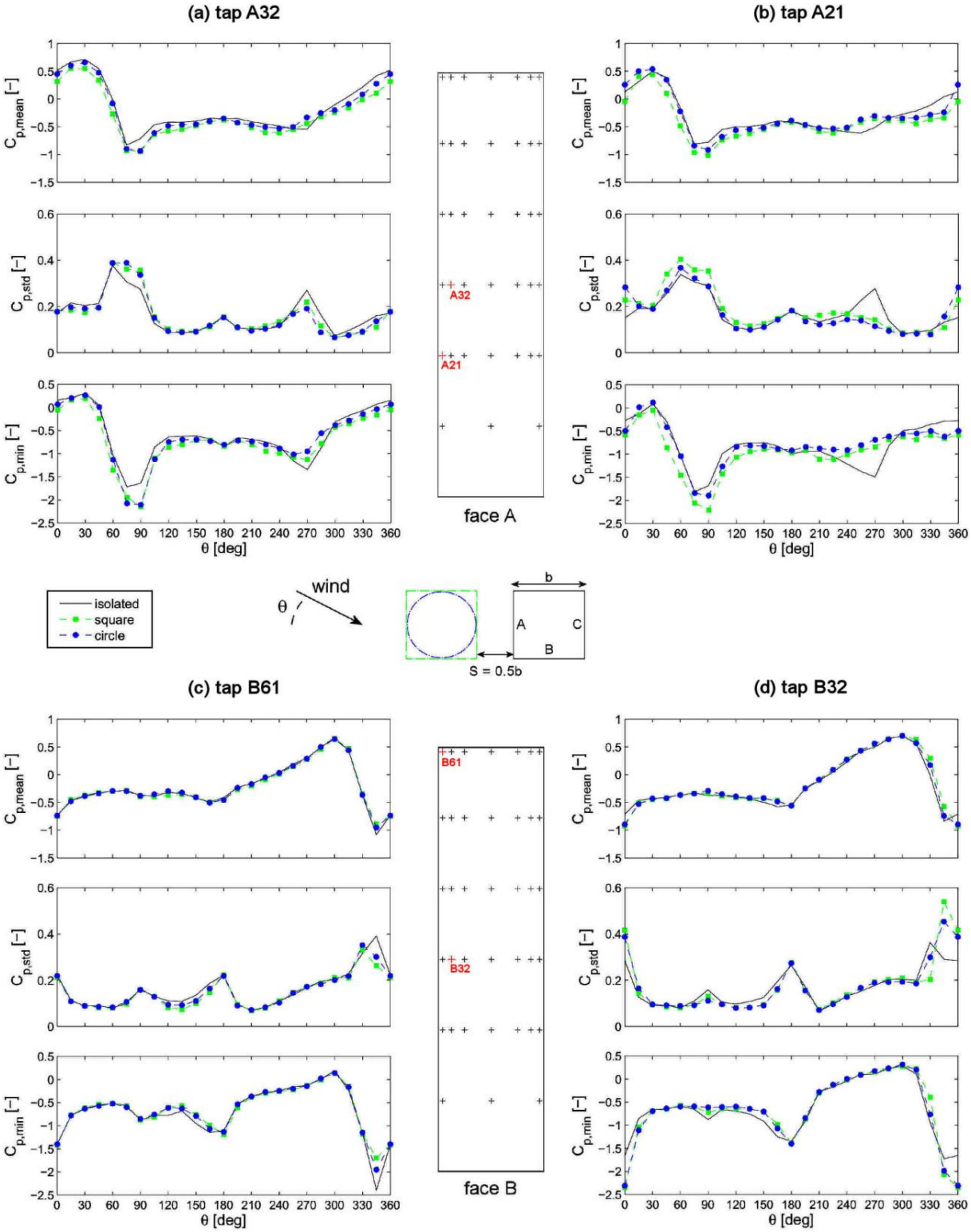

Figure 3. Variation of mean, standard deviation and minimum peak pressure coefficient with angle of incidence at the indicated taps on face A (a) tap *A32* and (b) tap *A21* and on face B (c) tap *B61* and (d) tap *B32*.

The variation of the pressure coefficient with angle of incidence on face *B* at tap *B61* and *B32* is illustrated in Figure 3(c) and (d). Figure 3(c) shows that the decrease in minimum peak pressure observed in Figure 2(b) at tap *B61* is found at $\theta = 345°$. In the isolated case, the peak pressure coefficient at this angle of incidence is $C_{p,min}(B61,345°) = -2.4$. The interfering models reduce this coefficient with 15% (circular cylinder) or 30% (square cylinder). This alleviation effect is mainly caused by a reduction in pressure fluctuations; the interfering model reduces the standard deviation pressure coefficient with 30%, whereas the drop in mean coefficient is 10%.

The results determined for tap *B32* are illustrated in Figure 3(d); they show an increase in minimum peak suction coefficient of 25% and 30% at an angle of incidence of 0° for the square and the circular interfering model. The largest intensities in pressure fluctuations are observed at an angle of incidence of 345°; the square interfering model causes an increase of 90% ($C_{p,std}(B32,345°) = 0.55$) and the circular model an increase of 60% ($C_{p,std}(B32,345°) = 0.47$). The reduction in mean pressure coefficient is responsible for the smaller minimum peak pressure coefficient at this angle in comparison with the coefficient observed at 0°.

Table 3 gives a summary of the largest minimum peak pressure effects encountered on face A and B, and specifies in which ranges of the investigated influence parameters (S and θ) these effects are most severe. The grey areas specified in the figures are indicative for the region of influence. The pressure effect on face A, illustrated in Table 3(a), was also described by Kim et al (2011) and Lam et al (2008). According to these studies, this pressure effect is the result of an increase in velocity through the passage, which is known as channeling. The adverse pressure effect on face B, illustrated in Table 3(b), is most likely caused by the shear layer separating from the roof of the interfering model. Although the largest peak value is observed at $\theta = 0°$, the largest intensity in pressure fluctuations is observed at $\theta = 345°$. At the same angle of incidence, a reduction is observed in the top corner of face B, illustrated in Table 3(c). The pressure effects illustrated in Table 3(b) and (c) appear to be related. Future spectral analysis of the pressure signals and analysis of the velocity field can provide more support for this observation.

Table 3. Summary of the investigated influence parameters and the pressure effects described on face A and face B.

	(a)	(b)	(c)
	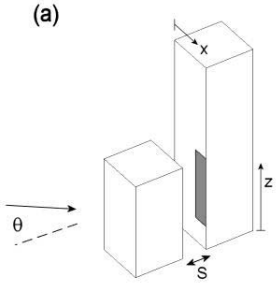	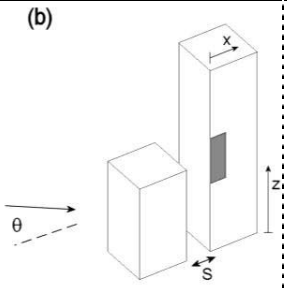	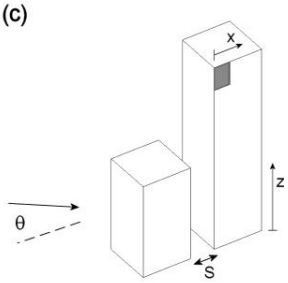
Separation distance (S) [1]	$S < 3b$	$S < 5b$	$S < 5b$
Angle of incidence (θ) [2]	75°-90° and 270°-285° [*]	0°-15° and 345°-0° [*]	15° and 345° [*]
Location largest peak effect			
Square cylinder	$(x, z) = (0.04b; 0.3h)$	$(x, z) = (0.12b; 0.5h)$	$(x, z) = (0.04b; h)$
Circular cylinder	$(x, z) = (0.12b; 0.5h)$	$(x, z) = (0.12b; 0.5h)$	$(x, z) = (0.04b; h)$
Largest minimum peak pressure			
Square cylinder (isolated)	-2.2 (-1.8)	-2.3 (-1.7)	-1.7 (-2.4)
Circular cylinder (isolated)	-2.1 (-1.7)	-2.3 (-1.7)	-2.0 (-2.4)

[1] The specified range in separation distance indicates a region of influence on the reference building in which the influence of the interfering model on the minimum peak pressure is larger than 10% when all angles of incidence are considered.

[2] The specified value gives the angle of incidence at which the largest peak suction was determined.

[*] The region of influence at this angle of incidence is illustrated; the same effect occurs on the opposite side or face at the other specified angle.

4 CONCLUSION

Wind tunnel experiments were performed to determine the interference effects of a half high model on the pressure distribution of a nearby high-rise building model. Mean, standard deviation and peak pressure coefficients were analysed. The main findings are the following:

- For a half high interfering model, local increases in the magnitude of the minimum peak pressure were found on face *A* and face *B* (for definitions, see figure 3).
- Both square and circular interfering model cause a maximum increase of the minimum peak pressure $C_{p,min}(Fij,all)$ (i.e. the minimum over all angles of incidence) of 25% on face *A* and 35% on face *B*, for the investigated configurations.
- The pressure effects on face *A* and face *B* were most pronounced for a separation distance $S = 0.5b$. For $S = 3b$, the interfering model has no significant influence on the pressure distribution of face *A*; the effects on face *B*, although less severe, are still significant for $S = 5b$.
- The effects on face *A* occurred at an angle of incidence of 75° and 90°, i.e. for a wind approximately parallel to the building passage. The interference effects observed in the pressure distribution of face *B* were encountered at an angle of incidence of 345° and 0°.

This work has analyzed the influence of a half high model on the wind-induced local pressures on a high-rise model in terms of three main interference effects and it has established two model configurations in which large adverse pressure effects occur.

The study presented in this paper did not yet define cause-effect relationships between flow phenomena and pressure effects. The definition of such relationships requires more detailed analysis of the measured pressures (e.g. spectral analysis) and further investigation of the flow surrounding the models. Future research will entail more detailed analysis of the measured pressures in the critical configurations; additional experimental and numerical work will be carried out.

5 UNITS

b	Width of the reference model (m)
$C_{p,mean}(Fij,\theta)$	Mean pressure coefficient on face F (*A*, *B* or *C*) at pressure tap *i*, *j* for angle of incidence θ (-)
$C_{p,std}(Fij,\theta)$	Standard deviation pressure coefficient on face F (*A*, *B* or *C*) at pressure tap *i*, *j* for angle of incidence θ (-)
$C_{p,min}(Fij,\theta)$	Minimum peak pressure coefficient on face F (*A*, *B* or *C*) at pressure tap *i*, *j* for angle of incidence θ (-)
h	Height of the reference model (m)
S	Separation distance between the wind tunnel models (m)
U_{ref}	Mean velocity at reference model height (m/s)
θ	Angle of incidence
ρ	Air density (kg/m^3)

6 REFERENCES

Bailey, P.A., Kwok, K.C.S., 1985, Interference excitation of twin tall buildings, J. Wind Eng. Ind. Aerodyn., 21, 323-338.

Cook N.J., Mayne J.R., A refined working approach to the assessment of wind loads for equivalent static design, J. Wind Eng. Ind. Aerodyn., 6, 125-137.

Kim, W., Tamura, Y., Yoshida, A., 2011. Interference effects on local peak pressures between two buildings, J. Wind Eng. Ind. Aerodyn, 99, 584-600.

Khanduri, A.C., 1997. Wind-induced interference effects on buildings: integrating experimental and computerized approaches, PhD thesis, Concordia University.

Lam K.M., Leung, M.Y.H., Zhao, J.G., 2008, Interference effects on wind loading of a row of closely spaced tall buildings, J. Wind Eng. Ind. Aerodyn. 96, 562-583.

Taniike, Y., Inaoka, H., 1988, Aeroelastic behaviour of tall buildings in wakes, J. Wind Eng. Ind. Aerodyn., 28, 317-327.

Taniike, Y., 1991, Turbulence effect on mutual interference of tall buildings, J. Eng. Mech., 117, No. 3, 443-456.

Taniike, Y., 1992, Interference mechanism for enhanced wind forces on neighbouring tall buildings, J. Wind Eng. Ind. Aerodyn., 41-44, 1073-1083.

Xie, Z.N., Gu, M., 2004, Mean interference effects among tall buildings, Eng. Struct., 26, 1173-1183.

Xie, Z.N., Gu, M., 2005, A correlation-based analysis on wind-induced interference effects between two tall buildings, Wind and Struct., Vol. 8, No. 3, 163-178.

Xie, Z.N., Gu, M., 2007, Simplified formulas for evaluation of wind-induced interference effects among three tall buildings, 95, 31-52.

The Seventh International Colloquium on Bluff Body Aerodynamics and Applications (BBAA7)
Shanghai, China; September 2-6, 2012

Research on interference effects of wind loads on tall buildings in staggered arrangement

Tang Yi[a] Jin Xinyang[a] Yang Liguo[a]

(a. China Academy of Building Research, Beijing100013, China)

ABSTRACT: To research the interference effects of wind loads on a real project with three similar-shaped staggered arranged tall buildings, wind tunnel tests about the three tall buildings and one isolated tower were conducted respectively. By comparison of the measured results, effects of wind directions and building positions on the design wind forces for main wind-force resisting system, i.e., along-wind, cross-wind and torsion wind loads, were discussed. Interference mechanisms were analyzed by integrating CFD simulated results and experiment measured data. It indicates that wind loads of the middle tower, named tower 2, are greatly increased compared to isolated cases and in the unfavorable wind direction of 110 degree, the static interference factor of torsion load, dynamic interference factor of wind load in Y and torsion directions are 1.53, 1.32 and 1.37 respectively.

Keywords：tall buildings, synchronization pressure wind tunnel test,staggered arrangement, static interference, dynamic interference

1 INTRODUCTION

Research shows that, wind loads of the tall buildings in the real environment and that of the isolated buildings are not same. In the early 1930s, people have realized the interference effects for a cluster of high-rise building [1]. In 1965, cooling tower collapse in the ferry bridge power plant aroused great research interest in wind interference [2], which marked the beginning of the wind-induced interference effects research. Hereafter, more and more wind tunnel tests were conducted in order to obtain general results[3-6]. In the late 1980s, some research results were applied to the wind load codes, such as the Australian standard. In China, interference research began at the end of 1980s [7]. Recently, interference effects of two and three tandem rectangular buildings models were tested in literature [8, 9] and [10] respectively. These research were mainly about tandem rectangular buildings and focused on the along and across wind results. But in realities, most unfavorable wind direction are not necessarily perpendicular to the facade, and under interfered conditions torsion wind loads are often not negligible [11,12]. In this paper, wind pressure of a real project including three staggered high-rise buildings was test in wind tunnel. A CFD numerical calculation was conducted to figure out the mechanism of interference. Comparison between three grouped buildings and one isolated building indicates the wind direction have great effects on the interfered wind loads.

2 WIND TUNNEL TEST

The project consists of three high-rise buildings, named tower 1, 2 and 3. These buildings are approximately 190m height and have consistent section size. To investigate the interference effect, wind pressure of additional isolated tower was measured after three tower group test. Both experiments were conducted in the 4m×3m test section of the China Academy of Building Research wind tunnel. Wind field of type A was simulated according to the Chinese load code. Rigid pres-

sure model scale ratio is 1:250. In each model, 162 ports are measured using Scanivalve electronic scanning pressure measurement system. Test wind speed is 14m / s at 1m height in wind tunnel. For each port, 4200 pressure signals were recorded in time domain with sampling frequency 312.5Hz.

3 RESULTS AND ANALYSIS

In this paper, maximum bending moments or torque are selected to evaluate the interference effects. Static interference factor can be calculated by

$$\overline{IF} = \frac{\mathrm{SIGN}\left(\overline{M}_s(\alpha_M)\right) \times \mathrm{MAX}\left(\left|\overline{M}_s(\alpha)\right|\right)}{\mathrm{SIGN}\left(\overline{M}_0(\alpha_M)\right) \times \mathrm{MAX}\left(\left|\overline{M}_0(\alpha)\right|\right)} \qquad (1)$$

where $\overline{\mathrm{M}}_s(\alpha)$ and $\overline{\mathrm{M}}_0(\alpha)$ is mean values of base moment or torque in α wind direction for interfered and isolated building respectively; '| |' denotes absolute value calculation; 'MAX' denotes maximum value calculation; 'SIGN' is to obtain number sign; α_M is wind angle where the maximum value occurs.

Dynamic interference factor can be evaluated as

$$IF = \frac{\mathrm{MAX}\left(\sigma_M^s(\alpha)\right)}{\mathrm{MAX}\left(\sigma_M^0(\alpha)\right)} \qquad (2)$$

Where $\sigma_M^s(\alpha)$ *and* $\sigma_M^0(\alpha)$ is RMS value of base moment or torque for interfered and isolated building respectively.

3.1 *Static interference effects*

Fig. 3 (a) ~ (c) show mean base moment and torque in different wind direction. Table 1 gives the static interference factor. It's notable that mean base torque of tower 2 reaches a maximum value in the direction of 110 degree, where the corresponding static interference factor is 1.53, which means that interfered by tower 1 and 3 the maximum static torsion of tower 2 increase by more than 50%. From the CFD simulation results shown in Fig.5, it can be seen that, unlike isolated buildings, wind pressure in the windward face of tower 2 is partially negative, which may result in large unsymmetrical torsional force.

3.2 *Dynamic interference effects*

Dynamic base moments are calculated by stochastic method. It can be seen from Figure 6 although the geometric and structural parameters are exactly the same, maximum responses of tower 2 are larger than that of tower 3.

Table 2 gives the dynamic interference factors. It can be seen from the table that all dynamic interference factors are greater than 1. It indicates that the interfered dynamic responses are to some extent amplified. Especially, in the wind direction of 110 degree, the dynamic interference factor of tower 2 in Y and torsion direction is 1.32 and 1.37 respectively. The pressure power spectra on each facade of tower 2 show obvious vortex peaks. Vortex excitation may result in larger dynamic interference factor as compared with tower 3.

Figure 7 shows the power spectrum of wind pressure in 110 degrees. It's evident that for the tower 2 wind pressure spectrum on each facade show distinguished spectral peak corresponding to votex shedding and for tower 3 and isolated building the votex shedding efftcs are weaken and spectrum peak are relatively not obvious.

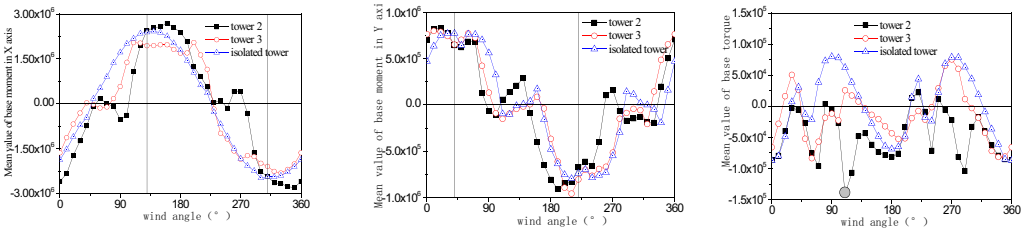

(a) (b) (c)

Fig.3 Mean value of base moments and torque

Tab.1 Static interference factor

Base moments or torque	Isolated building		Tower 3			Tower 2		
	Maximum value(KN.m)	Azimuth	Maximum value(KN.m)	Azimuth	$\overline{IF}$	Maximum value(KN.m)	Azimuth	$\overline{IF}$
$\overline{M_x}$	-2.5×10^6	300°	-2.32×10^6	330°	0.93	-2.82×10^6	350°	1.13
$\overline{M_y}$	-8.0×10^5	210°	-9.6×10^5	210°	1.2	-9.2×10^5	190°	1.15
$\overline{M_T}$	-8.8×10^4	0°	-8.36×10^4	60°	0.95	-1.35×10^5	110°	1.53

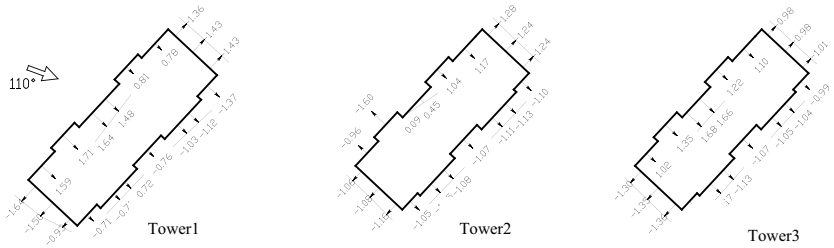

Fig.4 Mean value of wind pressure coefficient on typical floor (110° wind degree)

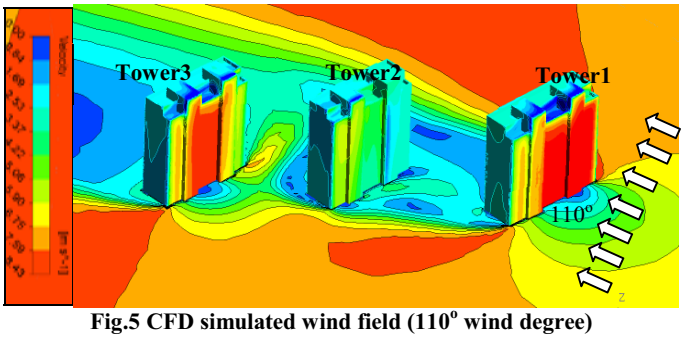

Fig.5 CFD simulated wind field (110° wind degree)

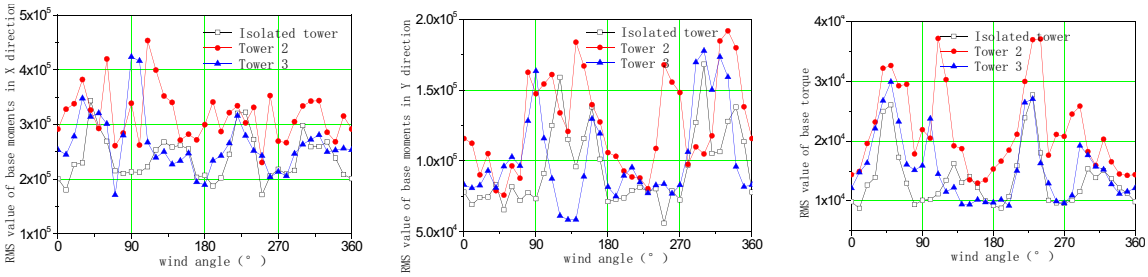

(a) (b) (c)

Fig.6 RMS value of base moments and torque

Tab.2 Dynamic interference factor

Base mo-ments or torque	Isolated building Maximum value(KN.m)	Azimuth	Tower 3 Maximum value(KN.m)	Azimuth	$\widetilde{IF}$	Tower 2 Maximum value(KN.m)	Azimuth	$\widetilde{IF}$
σ_{M_x}	3.4×10^5	40°	4.2×10^5	90°	1.24	4.5×10^5	110°	1.32
σ_{M_y}	1.68×10^5	300°	1.7×10^5	300°	1.01	1.9×10^5	330°	1.13
σ_T	2.7×10^4	230 °	2.9×10^4	50 °	1.07	3.7×10^4	110°	1.37

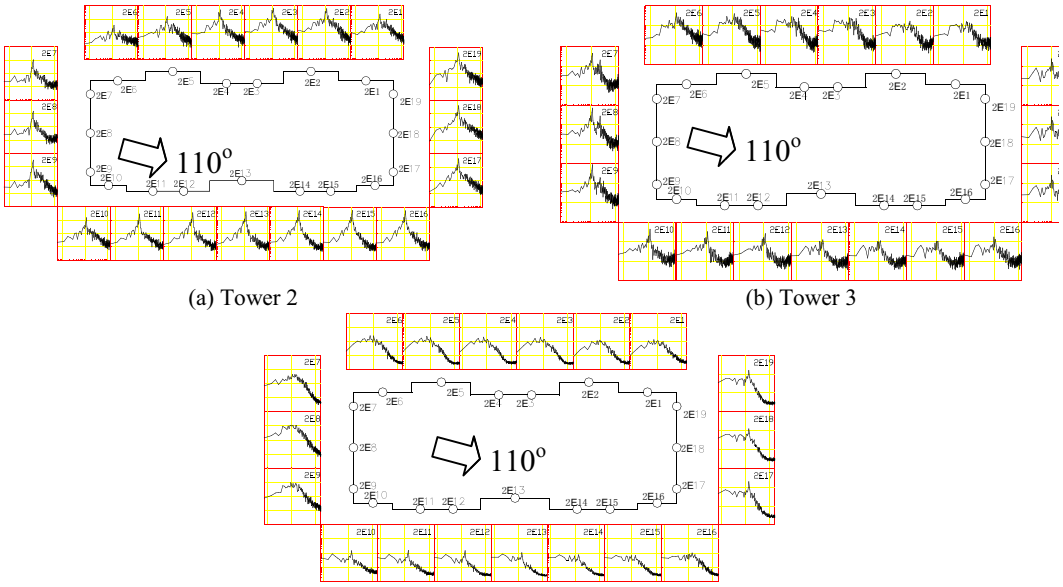

(a) Tower 2 (b) Tower 3

(c) Isolated tower

Fig.7 Comparison of pressure spectral between isolated and interfered buildings (110° wind degree)

4 CONCLUSION

Based on wind tunnel experiment, along-wind, across-wind and torsional load interference effects are discussed in this paper. CFD analysis method is used to figure out interference mechanism. The results show that wind direction and tower location are important factors that influence the interference effect. Tower 2, located in the middle of the staggered group, have much larger interference factor than that of tower 3. In the most unfavorable interference angle of 110 degree, the torsion static interference factor reached 1.53, the dynamic interference factor in weak lateral axis and torsional direction is 1.32 and 1.37 respectively.

5 ACKNOWLEDGEMENTS

The author would like to gratefully acknowledge the support of the National Natural Science Foundation of China (90815015).

6 REFERENCES

1 Khanduri, A.C., T. Stathopoulos, and C. Bedard, Wind-induced interference effects on buildings - a review of the state-of-the-art[J]. Engineering Structures, 1998. 20(7): p. 617-630.
2 Armitt, J., Wind loading on cooling towers[J]. J. Struct. Div. ASCE, 1980. 106(ST3): p. 623-641.
3 Taniike, Y., Turbulence effect on mutual interference on tall buildings[J]. Journal of Engineering Mechanics , ASCE, 1991 117(3): p. 443-456.
4 Taniike, Y., Interference mechanism for enhanced wind forces on neighboring tall buildings[J]. J. Wind Engng Indust. Aerodynam., 1992 41-44: p. 1073-1083.
5 Kwok, K.C.S. Interference effects on tall buildings[C]. in Proceedings of 2nd asia-pacific symposium on wind engineering. 1989. Beijing.
6 Bailey, P.A. and K.C.S. Kwok, interference excitation of twin tall buildings[J]. J. Wind Engng Indust. Aerodynam., 1985. 21: p. 323-338
7 LOU Wenjuan etc., Distribution of wind load on surface of tall buildings with complex shapes[J]. Journal of Building Structures,1995, 21:323-338(in Chinese)
8 HUANG Peng, Wind induced interference effects on tall buildings[D]. Tongji University, Shanghai, 2001(in Chinese)
9 HUANG Peng and GU Ming, Experimental Study of interference effects on wind-induced torisonal responses between tall buildings[J]. Journal of Building Structures,2005, 26(4):86-91(in Chinese)
10 XIE zhuangning,Wind induced interference effects on typical tall buildings[D]. Tongji University, Shanghai, 2003(in Chinese)
11 Boggs, D.W., N. Hosoya, and L. Cochran. Sources of Torsional Wind Loading on Tall Buildings: Lessons From the Wind Tunnel in Advanced Technology in Structural Engineering[C] //Proceedings of the 2000 Structure Congress & Exposition, Philadelphia, 2000.
12 YANG Liguo, TANG Yi, JIN Xinyang, Numerical study and test on wind-induced static interference effects of staggered tall buildings[J].Building Structures,2011, 41(11):126-130(in Chinese)

The Seventh International Colloquium on Bluff Body Aerodynamics and Applications (BBAA7)
Shanghai, China; September 2-6, 2012

Flow past two tandem circular cylinders using Spectral element method

Zhaolong HAN[a], Dai ZHOU[b] , Xiaolan GUI[c]

[a]*School of Naval Architecture, Ocean and Civil Engineering, Shanghai Jiaotong University, Shanghai,China*
[b]*School of Naval Architecture, Ocean and Civil Engineering, Shanghai Jiaotong University, Shanghai,China*
[c]*School of Naval Architecture, Ocean and Civil Engineering, Shanghai Jiaotong University, Shanghai,China*

ABSTRACT: In this paper, flow past around two circular cylinders which are tandem arranged at a Reynolds number of 200 is numerically investigated by spectral element method. To validate the numerical method for incompressible Navier–Stokes equations, the benchmark problem of flow over a single circular cylinder is employed, with the numerical results in a good agreement with the available literatures. Then, by changing the spacing ratios L/D from 1.2 to 10.0, the flow characteristics, including the flow patterns, force statistical parameters such as the drag and lift coefficients as well as wake oscillation frequencies (Strouhal numbers) are investigated. Numerical results show that there are around three wake flow patterns which are determined by the spacing ratio. In addition, the force parameters are highly affected by the flow patterns.

KEYWORDS: spectral element method; laminar flow; spacing ratio; Navier–Stokes equations; two tandem cylinders.

1 INTRODUCTION

The problem of flows past cylinders is very common in the fields of civil engineering, ocean engineering and hydraulic engineering, such as in high-rise buildings, long span cable-stayed or suspension bridges and chimneys experiencing wind loadings, as well as oil pipelines immersed in ocean current. Thus it has attracted, as an important aspect of computational fluid dynamics, much attention in scientific research. Among these problems, the flow past a circular cylinder plays an important part for its broad engineering applications and for being the foundation of flows past other bluff bodies. So far, wind tunnel experiments are still regarded as the most reliable means of studying this flow. In the last decades, however, the numerical simulation has been developed as the potential technique for its low cost, short time period, high efficiency and parameter adjustability.

Concerning the case of flow over two tandem circular cylinders, many important phenomna of fluid flow have been found through both experimental investigation and numerical simulation. For example, there is a critical spacing ratio, $L/D \approx 3.6$ (L is the center-to-center distance between the two cylinders, D is the cylinder diameter), at Reynolds number (Re) of 200, and the vortex shedding behind the upstream cylinder actually disappears when the spacing ratio is smaller than the critical one. Also, if the spacing ratio is over 3.6, the periodic vortex shedding will occur from both cylinders, which significantly changes the fluctuating lift force, drag force and Strouhal number (St).

More recently, some research studies have provided important insights into the numerical analysis of flow past two tandem circular cylinders. Using the Collocated Unstructured Computational Fluid Dynamic Code (CUCFDC), Sharman *et al.*[1] studied this problem when *Re*=100, and found that the critical spacing ratio is identified between 3.75 and 4.0, higher than the typical critical spacing ratio of 3.6, and that a unique reattachment point and a separation point appear at the downstream cylinder. Wu and Hu[2] investigated this problem at Reynolds numbers of 200 and 500 by employing the finite volume method and adaptive triangle meshing technology, and drew the conclusions that the lift and drag forces curves change at different space distance. Carmo and Meneghini[3] also studied this problem at the Reynolds numbers from 160 to 320. They found that, when the Reynolds number is greater than 190, three-dimensional effects occur, thus two-dimensional numerical simulations can not accurately satisfy the requirement of determining the critical spacing ratio.

Spectral element method (SEM) was first proposed by Patera[4], who applied this approach to Naver-Stokes equations under one- and two-dimensions. Spectral element is a high-order element combining the geometrical facility of the finite element method and the high accuracy of the spectral method, by increasing the order of the polynomial *p*. It can achieve a high convergence ability and computing efficiency even though the mesh is coarse. Blackburn and Karniadakis[5] studied the problem of vortex-induced vibration (VIV) of a single cylinder in two- and three-dimensions, and verified the efficiency of the SEM.

The current work pays attention to the problem of flow around two circular cylinders which are particularly arrayed as a tandem configuration at Reynolds number *Re*=200 using the SEM. But to start with, the problem of flows past one circular cylinder is simulated as a validation to examine the SEM computational code. Then using this method, the effects of gap spacing ratio of the two cylinders on the flow characteristics are investigated. In the current case, the numerical simulations are carried out associated with the center-to-center space ratios of *L/D* = 1.2, 1.5, 2.0, 3.6, 4.0, 6.0, 8.0 and 10.0. To show the flow pattern near the wake region, flow vorticity contours are clearly presented. The corresponding flow indexes such as the mean-averaged force coefficients and the frequencies of lift fluctuation are also obtained for all the cylinders.

The framework of this paper is organized as follow: In Section 2 we introduces the governing equations for incompressible viscous flow and provides the detailed processes of the SEM. The verifications of the computer code are achieved through the benchmark problem of flow over a single cylinder in Section 3. Section 4 presents and discusses the descriptions and results for the two tandem cylinders array with various spacing ratios. Main conclusions of the current work are finally summarized in Section 5.

2 GOVERNING EQUATIONS

In Cartesian coordinates, the non-dimensional tensorial forms of the Navier-Stokes governing equations for the incompressible viscous fluid flow in a domain Ω and a time interval [0, T] are written as:

$$\frac{\partial u_i}{\partial t} + u_j \frac{\partial u_i}{\partial x_j} = -\frac{\partial p}{\partial x_i} + \frac{1}{\mathrm{Re}} \frac{\partial^2 u_i}{\partial x_j \partial x_j} \tag{1}$$

$$\frac{\partial u_i}{\partial x_i} = 0 \tag{2}$$

The above equations are solved by employing the *Semtex* code. Released by Prof. H.M. Blackburn (Monash University, Australia), the *Semtex* is a quadrilateral spectral element DNS code that combines the standard nodal Gauss–Lobatto–Legendre (GLL) basis functions and Fourier expansions in a homogeneous direction[6]. More literatures related with *Semtex* include references[7-10]. In the current study, it should be noted that we choose 7 order GLL basis functions and incremental time step of 0.005 for all the computations.

Some definitions of the flow parameters required in the computations are given:

$$C_D = \frac{2F_D}{\rho U_\infty^2 D},\quad C_L = \frac{2F_L}{\rho U_\infty^2 d},\quad St = \frac{f_s D}{U_\infty},\quad C_p = \frac{2(p - p_\infty)}{\rho U_\infty^2}, \tag{3}$$

with the corresponding explanations as: C_D, drag coefficient; C_L, lift coefficient; St, Strouhal number; C_p, pressure coefficient; F_D, force in the stream-wise direction; F_L force in the transverse direction; f_s, vortex shedding frequency; ρ, the fluid density; U_∞, characteristic velocity, p_∞, characteristic pressure; and D, the characteristic length scale (Here it is treated as the cylinder diameter).

3 VALIDATION STUDIE

The problem of unsteady flow over a single cylinder is chosen as a workbench reference to validate the numerical code for further investigations. As shown in Figure 1, a computational domain $50D \times 40D$ is presented, where D is the diameter of the cylinder with the center position (0, 0). The inlet boundary is positioned 20D upstream from the cylinder center with the velocity boundary condition: u=1, v=0. And the boundary conditions of the outlet 30D downstream from the cylinder center point is prescribed as $\partial u/\partial x$=0, $\partial v/\partial x$=0, p=0. Concerning the upper and lower boundaries, they are both 20D away from the horizontal centerline, with a slip boundary condition as: $\partial u/\partial y$=0 and v=0. On the cylinder surface, no-slip conditions are applied as u=0, v=0.

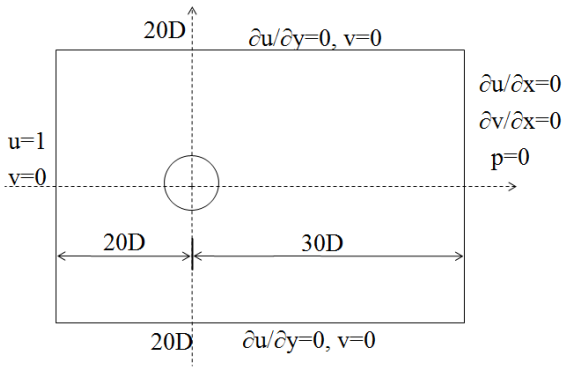

Figure 1.Schematic diagram of the computational domain and boundary conditions.

There are totally 354 spectral elements in the computational domain, as illustrated in Figure 2(a). In the region around the cylinder, the mesh grids are assigned as thin as 0.1D in order to obtain more accurate results (Figure 2(b)).

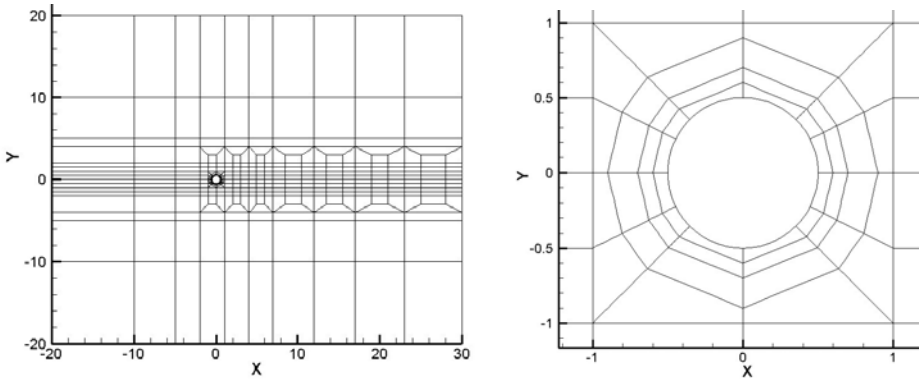

(a) (b)

Figure 2.(a) Spectral element meshes of the computational domain, 354 elements (b) zoomed-in view of the mesh around the cylinder.

We compare the computed mean drag coefficient C_D and Strouhal number St at Re=200 with the data from literatures[11-14] as shown in Table 1. The mean drag coefficient C_D is 1.346 while others range from 1.31 to 1.35. And the St=0.195 varies little to the exited results by Meneghini *et al*.[12] and Franke *et al*.[13]. Moreover, the current curve of St and Re, which is also chosen as a reference, is explored and plotted in Figure 3 with the corresponding data from references[15-17]. With the increase of Re ranging from 60 to 120, the obtained St is found to become larger. Meanwhile, our computed curve is quite close to the results provided by Young and Ni[17]. These evidences mentioned above can be good illustrations for the effectiveness of the *Semtex* computational code for the solutions of laminar flow.

Table 1.Comparisons of the mean drag coefficients C_D and Strouhal numbers St at Re=200

Parameters	C_D	St
Franke *et al*.[13]	1.31	0.194
Farrant *et al*.[14]	1.37	0.196
Meneghini *et al*.[12]	1.30	0.196
Braza *et al*.[11]	1.35	0.200
Present	1.346	0.195

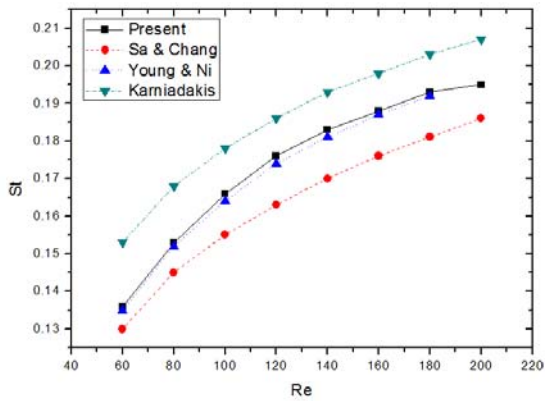

Figure 3.The relationship between the Strouhal number St and Reynolds number Re from 60 to 200 for the problem of flow past a single cylinder. Comparisons are made between the present results and collected data from references[15-17].

4 FLOW AROUND TWO TANDEM CIRCULAR CYLINDERS

4.1 *Problem descriptions*

In this subsection, we present the problem of flow past two tandem cylinders (*Re*=200). Details of the computational models and one sample of the mesh grids are respectively shown in Figure 4(a) and (b). The width and length of the domain and boundary conditions are of the same as those in the above single cylinder case. Two cylinders are marked as "1" and "2" with the distance L between their circular centers. The inlet boundary is 20*D* upstream from the center of the cylinder "1" while the outlet is 30*D* downstream. In the following, different value is relatively set for the distance *L/D* as 1.2, 1.5, 2.0, 3.6, 4.0, 6.0, 8.0 and 10.0. In the example of *L*/*D*=2.5, there are totally 432 mesh grids while there are around 400~500 grids in the cases with other spacing ratios. Meanwhile, high resolutions of grid refinement are adopted around the cylinders and in the wake flow regions.

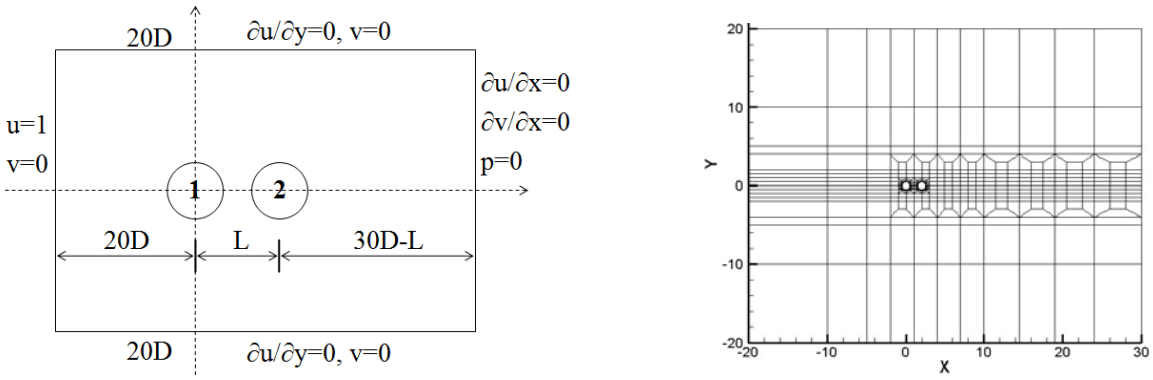

Figure 4.(a) Schematic of the computational model (b) the mesh grids of the spectral element for the case of flow past two tandem cylinders with *L/D*=2.

4.2 *Flow patterns*

The computational vorticity patterns at various spacing ratios are shown in Figure 5(a)-(h). It can be observed that there is a spacing ratio, smaller than which there is no vortex shedding from the upstream cylinder while larger than which periodical vortex shedding occurs. From there figures the critical spacing ratio is estimated at around *L/D*≈3.6. As *L/D*<3.6, the shear layers generated from the upside and downside of the front cylinder also attach on the upper and lower sides of the rear cylinder. In the far region behind the rear cylinder, an obvious Kármán vortex street can be observed. At the critical spacing ratio *L/D*＝3.6, the vortex begins to shed from the upstream cylinder. When the spacing ratio is higher, for example, *L/D*＝4, there is observed Kármán vortex in the gap region between the two cylinders. The vortex from the cylinder "1" periodically impinges on the front surface of the rear cylinder, affecting the flow pattern in the wake region. As the spacing ratio increases, the vortex from the front cylinder seems to have a higher influence on the wake flow. At *Re*=200 in which slight three-dimensional effect has occurred, the wake flow begins to show more complexity in the far region.

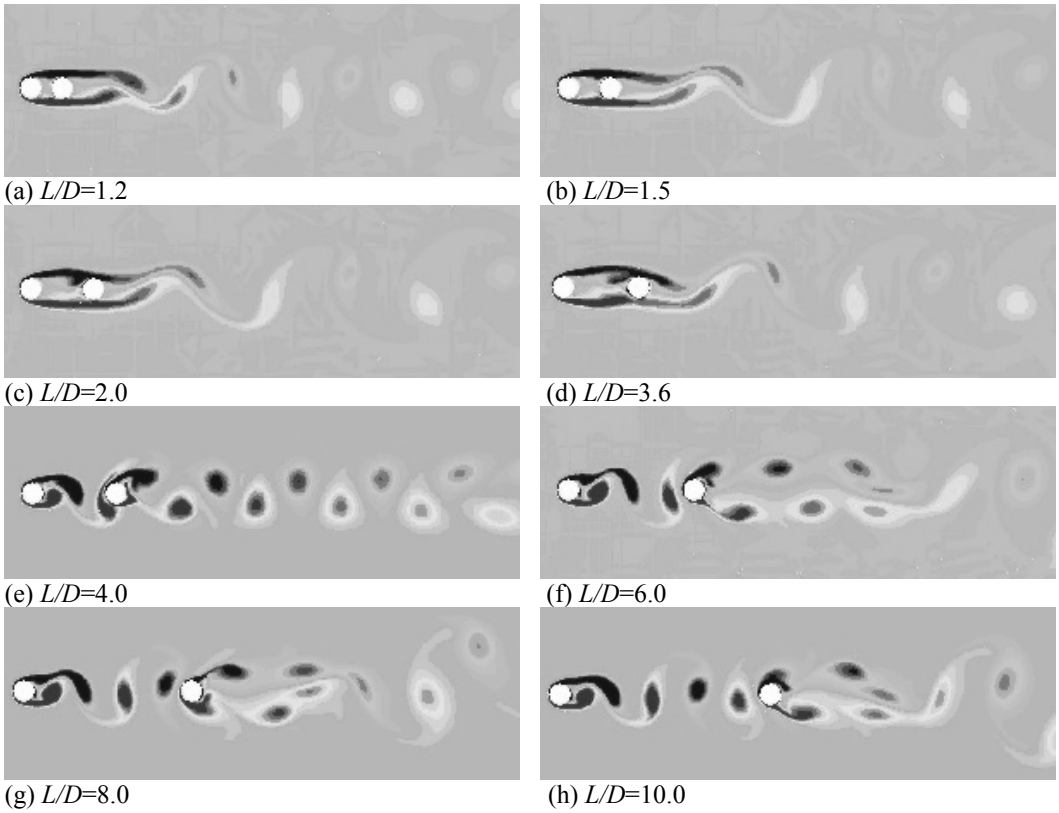

(a) L/D=1.2 (b) L/D=1.5

(c) L/D=2.0 (d) L/D=3.6

(e) L/D=4.0 (f) L/D=6.0

(g) L/D=8.0 (h) L/D=10.0

Figure 5.Vorticity contours with different spacing ratios: (a) L/D=1.2; (b) L/D=1.5; (c) L/D=2.0; (d) L/D=3.6; (e) L/D=4.0; (f) L/D=6.0; (g) L/D=8.0 and (h) L/D=10.0.

4.3 *Lift and drag coefficients*

Figure 6 shows the mean drag coefficients C_D for both cylinders as function of the spacing ratio between two cylinders in tandem. As can be seen, the mean drag coefficients C_D for both cylinders are smaller than that for the single one, while the one for the upstream cylinder is larger than that for the downstream one. The value of C_{D1} for the upstream cylinder decreases gradually with the increasing spacing ratio, and reaches its minimum value at L/D=3.6. At larger spacing ratio L/D=3.6~4.0, C_{D1} increases sharply, reaching the peak at L/D =4.0. Subsequently, it increases to a asymptotic value respectively, which should presumably be that of a single cylinder. For the downstream cylinder, the value of C_{D2} is much smaller than that of the upstream one. Also, at 3.6<L/D<4, the C_{D2} sharply increases like the behavior of C_{D1}. As discussed above, this is because of the transition of the flow patterns. In this spacing ratio region, obvious vortex shedding takes place on the first cylinder and strikes on the rear cylinder. These changes are believed as the main reason of the sharp changes in the drag coefficients. At higher spacing ratio as L/D>4, the vortex shedding modes become stable which is associated with the plat curves of C_{D1} and C_{D2}. Similar performances can also be seen from the relationships of RMS of drag and lift coefficients vs spacing ratios, as shown in Figure 7(a) and (b). There is an obvious changes in the region of 3.6<L/D<4, in which the flow patterns transform. These results are other evidences that vortices patterns determine the flow characteristic parameters.

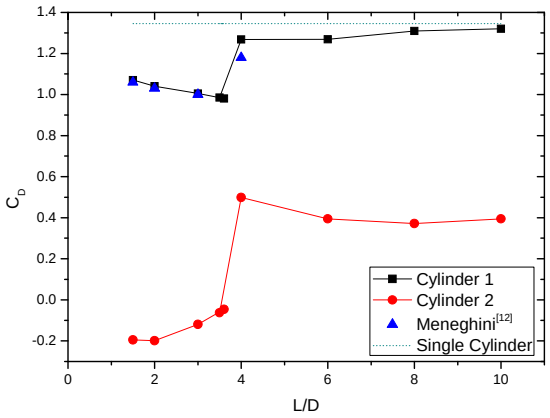

Figure 6.Variation of mean drag coefficients with different spacing ratios.

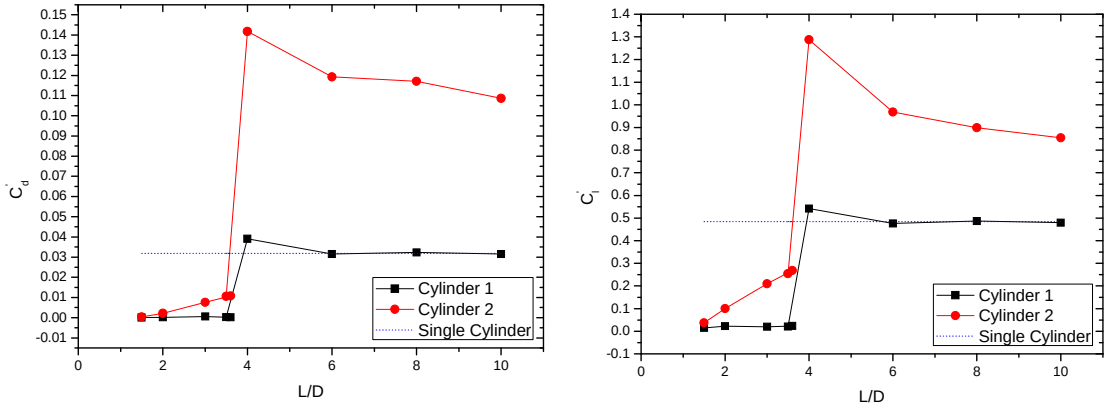

(a) (b)

Figure 7.Variation of (a) the RMS. drag coeffients (b) the RMS. lift coeffients with different spacing ratios

4.4 *Strouhal number*

Since all the parameters have been non-dimensionalized, the Strouhal number, *St*, is equal to the vortex shedding frequency which is obtained through the Fourier transform on the time dependent curve of lift coefficient.

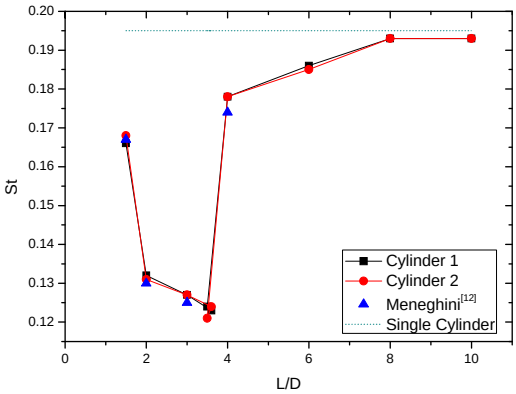

Figure 8. Variation of the Strouhal numbers, *St*, with different spacing ratios, *L*/*D*

The curves of *S*t and *L/D* for the two cylinders are demonstrated in Figure 8 and they are found to be much closed to the corresponding data from Meneghini *et al*.[12]. The Strouhal number shows a decreasing trend as $L/D < 3.6$, and it begins to rapidly increase with higher *L/D* value, especially at $3.6<L/D<4.0$. It is believed that this strong change is mainly caused by the transformation of flow patterns. When $L/D>8$, the Strouhal number becomes an almost constant value around 0.195, approaching the one of the single cylinder case.

5 CONCLUSIONS

In this current study, spectral element method is employed to investigate the flow around two tandem circular cylinders at a Reynolds number of 200. The spacing ratios are found to have a great impact on the flow characteristics and flow patterns. A critical spacing ratio of around 3.6 is observed. At smaller spacing ratio as $L/D<3.6$, no obvious vortex shedding is observed around the upstream cylinder and it only occurs on the downstream cylinder. As $L/D>4.0$, vortices are generated around both the front and rear cylinders. Meanwhile, the vortex from the front cylinder strikes on the surface of the rear cylinder, giving rise to higher drag coefficients and larger vortex shedding frequencies. Good agreements are found between the current study and data from existed literatures. The SEM is tested as an effective and reliable approach to cope with the fluid flow problems at low Reynolds numbers.

6 ACKNOWLEDGEMENTS

Supports from the National Natural Science Foundation of China (Project No. 51078230, 11172174) and the Key Project of Fund of Science and Technology Development of Shanghai (No.10JC1407900) are acknowledged.

7 REFERENCES

1 B. Sharman, F.S. Lien, L. Davidson and C. Norberg, Numerical predictions of low Reynolds number flows over two tandem circular cylinders, International Journal for Numerical Methods in Fluids, 47 (2005) 423-447.
2 G.X. WU and Z.Z. Hu, Numerical simulation of viscous flow around unrestrained cylinders, Journal of Fluids and Structures, 22 (2006) 371-390.
3 B.S. Carmo and J.R. Meneghini, Numerical investigation of the flow around two circular cylinders in tandem, Journal of Fluids and Structures, 22 (2006) 979-988.
4 A.T. Patera, A spectral element method for fluid dynamics: laminar flow in a channel expansion, Journal of Computational Physics, 54 (1984) 468-488.
5 H.M. Blackburn and G.E. Karniadakis, Two- and three-dimensional simulations of vortex-induced vibrations of a circular cylinder, 3rd International Offshore and Polar Engineering Conference, Singapore, 1993, June, 715–720.
6 H.M. Blackburn and S.J. Sherwin, Formulation of a Galerkin spectral element-Fourier method for three-dimensional incompressible flows in cylindrical geometries, Journal of Computational Physics, 197 (2004) 759-778.
7 H.M. Blackburn, D. Barkley and S.J. Sherwin, Convective instability and transient growth in flow over a backward-facing step, Journal of Fluid Mechanics, 603 (2008) 271–304.
8 H.M. Blackburn, S.J. Sherwin and D. Barkley, Convective instability and transient growth in steady and pulsatile stenotic flows, Journal of Fluid Mechanics, 607 (2008) 267–277.
9 H.M. Blackburn and S.J. Sherwin, On quasi-periodic and subharmonic Floquet wake instabilities, Physics of Fluids, 22 (2010) 031701-1–4.
10 H.M. Blackburn and J.M. Lopez, Modulated waves in a periodically driven annular cavity, Journal of Fluid Mechanics, 667 (2011) 336–357.

11 M. Braza, P. Chassaing and H. Ha Minh, Numerical study and physical analysis of the pressure and velocity fields in the near wake of a circular cylinder, Journal of Fluid Mechanics, 165 (1986), 79-130.
12 J.R. Meneghini, F. Saltara, C.L.R. Siqueira and J.A. Ferrar, Numerical simulation of flow interference between two circular cylinders in tandem and side-by-side arrangements, Journal of Fluids and Structures, 15 (2001) 327-350.
13 R. Franke, W. Rodi and B. Schonung. Numerical calculation of laminar vortex shedding flow past cylinders, Journal of Wind Engineering and Industrial Aerodynamics, 35 (1990) 237-257.
14 T. Farrant, M. Tan and W.G. Price, A cell boundary element method applied to laminar vortex-shedding from arrays of cylinders in various arrangements, Journal of Fluids and Structures, 14 (2000) 375-402.
15 G.E. Karniadakis and G. Triantafyllou, Frequency selection and asymptotic states in laminar wake, Journal of Fluid Mechanics, 199 (1989) 441-469.
16 J.Y. Sa and K.S. Chang, Shedding patterns of the near-wake vortices behind a circular cylinder, International Journal for Numerical Methods in Fluids, 12 (1991) 464-474.
17 D.L. Young and W.B. Ni, Penalty finite element applications to flow problems, Recent advance in computational fluid dynamics, Proceedings of the US/ROC (Taiwan) Joint Workshop, 1989, 484-507.

The Seventh International Colloquium on Bluff Body Aerodynamics and Applications (BBAA7)
Shanghai, China; September 2-6, 2012

Properties of wake excitation in tandem circular cylinders with several kinds of surface roughness

Fumiaki Nagao [a], Minoru Noda [a], Masahiro Inoue [b], Shota Matsukawa [b]

[a] *Department of Civil and Environmental Engineering, Institute of Technology and Science The University of Tokushima, Minamijosanjima, Tokushima, 770-8506, Japan*
[b] *Graduate School of Engineering, The University of Tokushima, Minamijosanjima, Tokushima, 770-8506, Japan*

ABSTRACT: Properties of wake excitation of circular cylinders in the tandem arrangement of central distance of three diameters were experimentally investigated. In order to investigate the influence of Reynolds number on the wake excitation, the effects of surface roughness of circular cylinders on it were examined. For circular cylinders with smooth surface, two types of stable limit cycles in transverse responses were measured. Effects of surface roughness on the wake excitation were quite large and the complicated interaction between the separated shear flow from the windward cylinder and the leeward cylinder were observed by flow visualization tests.

KEYWORDS: Wake excitation, Surface roughness of circular cylinder, Tandem arrangement, Vibration of leeward circular cylinder.

1 INTRODUCTION

Properties of wake excitation for tandem and staggered circular cylinders have been studied by lots of researchers, for example, Cooper & Wardlaw [1], Simpson [2], and so on. It is well known that the wake excitation vibrations of circular cylinders are deeply depended on the arrangement of the circular cylinders and Reynolds number, *Re*. Furthermore, for the wake excitation of tandem and staggered circular cylinders, the interaction between the leeward circular cylinder and the wake flow of the windward circular cylinder plays an important role.

Authors also investigated the instability of closely spaced triple circular cylinders [3], where the effect of Reynolds number, *Re*, was found in the onset velocity of wake galloping. In order to reduce the effects of the *Re*, the wake excitation of a circular cylinder in the wake of several shapes of rectangular cylinders was also tested and some interesting results were reported [4, 5].

In the paper, the effects of surface roughness of the circular cylinder on the wake excitation were experimentally investigated and a part of the results achieved here has already been reported in References [6, 7].

2 EXPERIMENTAL SETTING

A wind tunnel with a semi-closed circuit was used and its working section was 1m wide, 1.5m high and 4m long. Two stainless steel circular cylinders were used. Their diameter, *D*, was 42mm and their length was 900mm, respectively. The central distance between both circular cylinders in tandem arrangement was three times of their diameter, 3*D*, where the windward cylinder was fixed to side walls. The responses of the leeward circular cylinder were measured under longitudinal and transverse freedoms (2DOF). The Scruton number, $Sc=2m\delta/\rho D^2$, in which m is the mass, δ is the logarithmic damping and ρ is the air density, was changed from 6.8 to 35.1. Natural frequencies for longitudinal direction, f_x and transverse direction, f_y of the leeward cylinder were almost the same and also changed from 1.7 Hz to 2.7Hz. However, the results obtained un-

der the conditions of Sc=16.4 and f=2.2Hz were only focused on the paper for the lack of space. Properties of the wake of the windward circular cylinder were investigated by I-type hot wire anemometer. Flow visualizing tests were carried out by using the high speed camcorder, where five hundred flames were recorder in a second. The experimental conditions examined here were summarized in Table 1.

The surface roughness of the cylinders was changed by rough plastic meshes, parallel and helical wires whose diameter, d, was 2mm. The interval of helical wires set $2\pi/3$ (three wires were installed), $\pi/3$ (six wires) and $\pi/6$ (twelve wires), respectively. For twelve wires, the inclination from cylinder axis, θ, was changed from 0 to 30 degrees at ten-degree intervals. Moreover, the roughness lengths of surface roughness materials were also measured by I-type hot wire anemometer and summarized in Table 2.

Table 1 Experimental conditions

Diameter, D (mm)	42
Mass, m (kg/m)	2.58
Scruton numbers, $Sc=2m\delta/\rho D^2$	6.8, 16.4, 35.1
Degrees of freedom	Two(Longitudinal and Transverse directions)
Natural Frequency, f (Hz)	1.7, 2.2, 2.7
Surface roughness of cylinders	Plain (smooth), Rough plastic meshes (Mesh A; width, b=1mm, thickness, t=1mm, central distance, B=4mm, Mesh B; b=2mm, t=1.85mm, B=10mm), Parallel wires (diameter, d=2mm, interval of wires, $\pi/6$) Helical wires (inclination from cylinder axis, $\theta=\pi/18$, $\pi/9$, $\pi/6$, d=2mm, interval of wires, $2\pi/3$, $\pi/3$, $\pi/6$)

3 RESULTS AND DISCUSSION

3.1 *Responses of Smooth Surface Cylinders*

Figures 1(a) and (b) show the typical longitudinal and transverse responses and the static displacements, l/D, of leeward circular cylinder in tandem arrangement, Sc=16.4 and f=2.2Hz, in 2DOF. From Figure 1(a), two different transverse responses were measured; the first stable limit cycle (1-SLC) had almost the same amplitude, $2Y/D\approx1.2$, which closely related to the formation of wake of the windward circular cylinder. On the contrary, the second one (2-SLC) vibrated beyond the separated shear flow of windward cylinder and also developed from $2Y/D$=2.25 to 3.0 with the increase of wind speed. Furthermore, two unstable limit cycles were also measured. Longitudinal responses were quite small.

From Figure 1(b), under the same wind speed, the static displacements, l/D, of 2-SLC were much larger than those of 1-SLC and at rest. However, somewhat large l/D of the rest condition for the higher V/fD, larger than 75, was introduced by the longitudinal vibration. Furthermore, the longitudinal vibration in the wake of a square cylinder was not generated at all [4]. Therefore, properties of the wake of the square cylinder and those of the circular cylinder were much different each other.

Effects of damping and natural frequencies on the responses of the wake excitation were reported in References [6, 7]

3.2 *Wind speeds distribution behind a smooth cylinder*

The distribution of the mean wind speed and the turbulence intensity of the wake at the distance of 3D from the center of the windward circular cylinder were given in Figures 2 (a) and (b), re-

spectively. The amplitudes of second stable limit cycle (2-SLC) correspond to the just outside of separated shear flow where wind speeds return to the approaching mean wind speed, V_0. On the contrary, around the amplitude of the first one (1-SLC), the largest turbulence intensity induced by Kármán Vortex was measured, where the mean wind speeds recovered to 80% of the approaching wind speed. Therefore, 1-SLC and 2-SLC occurred inside and outside of the wake of the windward circular cylinder, respectively.

Table 2 Roughness length and appearance of surface materials

Surface material	Roughness length (mm)	Solidity ratio (%)	Appearance
Plain (smooth)	0.0025		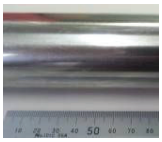
Rough plastic mesh A (Mesh A)	0.20	43.8	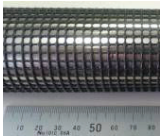
Rough plastic mesh B (Mesh B)	0.52	36	
Twelve parallel wires	0.51	18.1	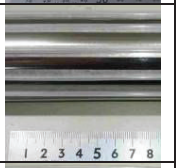
Twelve helical wires $\theta=\pi/18$	0.43	18.5	
Twelve helical wires $\theta=\pi/12$	0.40	19.3	
Twelve helical wires $\theta=\pi/6$	0.25	20.9	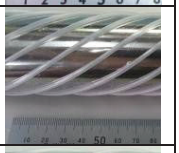
Six helical wires $\theta=\pi/6$	0.19	9.2	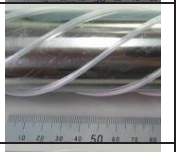
Three helical wires $\theta=\pi/6$	0.06	4.6	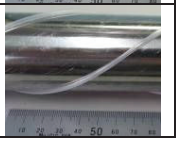

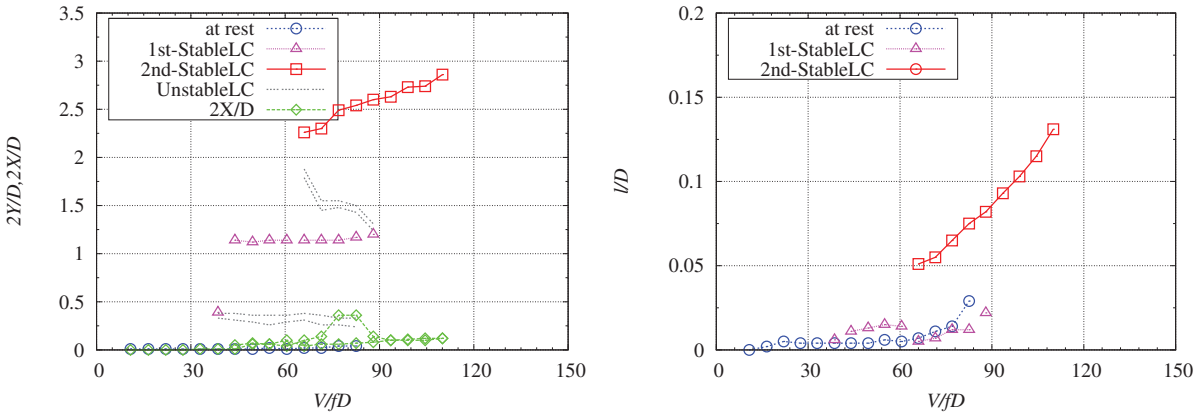

(a) 2DOF responses (transverse and longitudinal modes) (b) Static displacements (*l*/*D*)

Figure 1 Responses and static displacements of the leeward circular cylinder in tandem arrangement, for the central distance of 3*D* , *Sc*=16.4, *f*=2.2Hz.

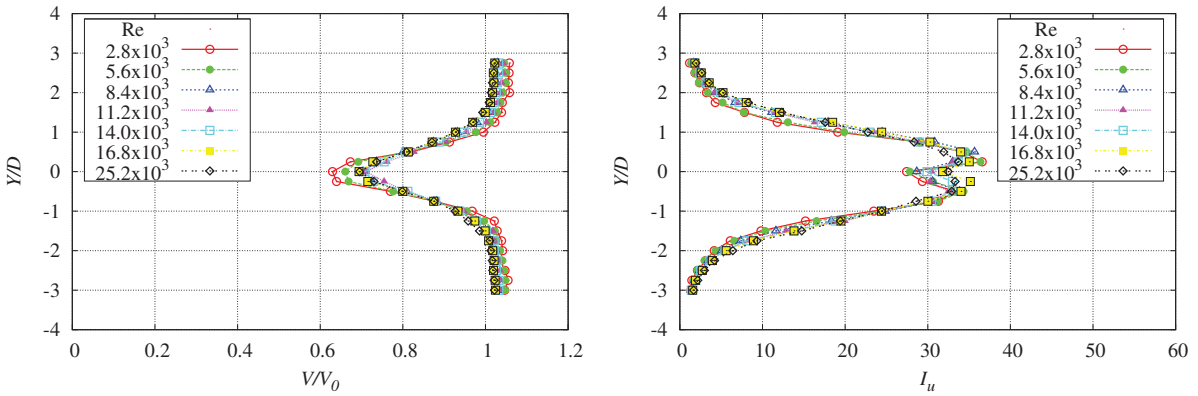

(a). Mean wind speed ratio to approaching wind speed (b). Turbulence intensity (%)

Figure 2 Wind profiles at 3*D* downstream from the center of the windward circular cylinder.

3.3 *Responses with Surface Roughness*

3.3.1 *Rough plastic mesh*

Figure 3 shows the effects of the installation of meshes to circular cylinders on the wake excitation, where amplitudes and wind speeds were normalized by the relative diameter of circular cylinder taking into account of the thickness, *t*, of meshes, *D'=D+2t.* Effects of meshes only installed on the windward circular cylinder were summarized in Figure (a), inversely, Figure (b) showed responses with meshes only attached to the leeward circular cylinder; furthermore, Figure (c) gave the results with meshes on both circular cylinders. From Figure (a), due to the installation of meshes on the windward cylinder, the larger transverse responses, 2-SLC, developed in the lower wind speeds in comparison with those of the smooth surface circular cylinder, where the installation of rougher mesh started the vibration in the lower wind speed. From Figure (b), due to the installation of meshes only on the leeward cylinder, the larger transverse responses of 2-SLC were only measured in the lower wind speeds, on the contrary, in the higher wind speeds, more than 60 for Mesh B, more than 70 for Mesh A, the smaller amplitudes of the 1-SLC were only measured and the larger responses of the 2-SLC were disappeared. For the installation of

meshes on the both circular cylinders as shown in Figure (c), the responses closed to those of the installation of meshes only on the leeward cylinder.

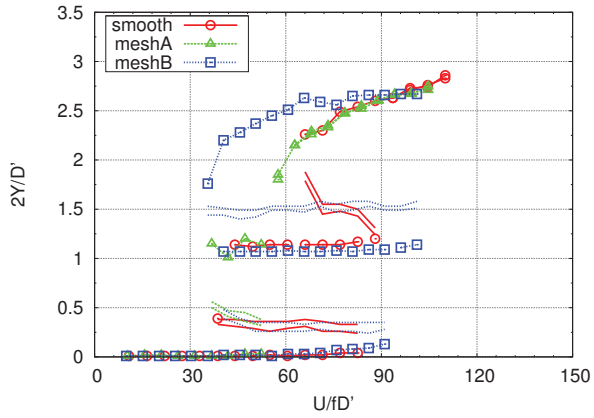

(a) Meshes attached to only the windward cylinder

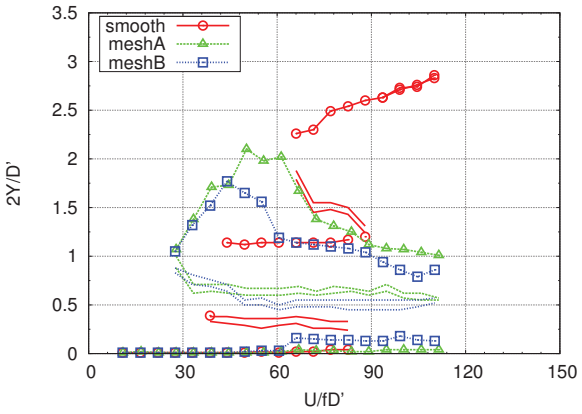

(b) Meshes attached to only the leeward cylinder

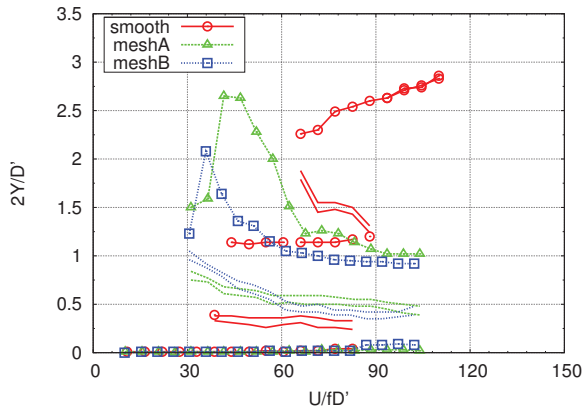

(c) Responses with meshes attached to both cylinders

Figure 3 Effects of the installation of meshes on the wake excitations.

3.3.2 *Helical wires*

Figure 4 shows transverse responses of the leeward circular cylinder with zero, three, six and twelve helical wires, whose diameter, d, was $0.048D$, and the inclination from cylinder axis, θ, was $\pi/6$, in the condition of Sc=16.4, f=2.2Hz, 2DOF, where the helical wires were installed on both cylinders. Due to the installation of three helical wires, the large amplitudes of 2-SLC were completely disappeared. For the installation of six helical wires, 1-SLC was moved toward the higher wind speed and unstable limit cycle was also enlarged in comparison with the results of the installation of three helical wires. In the case of twelve helical wires, the wake excitation was completely disappeared. Therefore, even though the roughness length of twelve helical wires was shorter than that of the rough plastic mesh, Mesh B, the increase of helical wires attached to the cylinders improved the wake excitation efficiently. The efficiency of helical wire on the wake galloping was also reported by Fujino et al. [8] by using the full-size models for parallel cables.

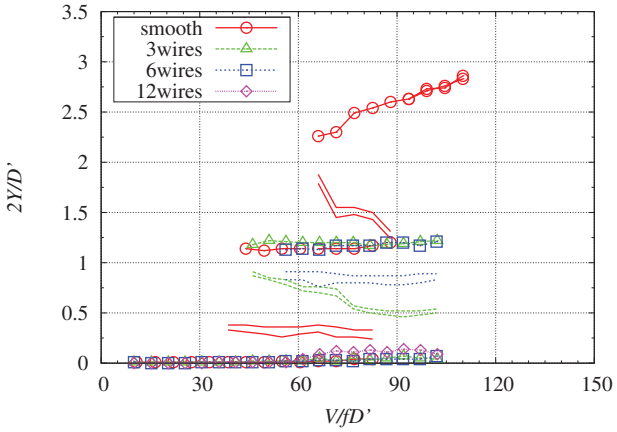

Figure 4 Transverse responses of the leeward cylinder with and without the helical wires, *Sc*=16.4, *f*=2.2Hz.

The effects of the inclination of wires, θ, on transverse responses of the leeward cylinder in the condition of *Sc*=16.4, *f*=2.2Hz, 2DOF were summarized in Figure 5, where twelve wires were installed on both cylinders. For the installation of parallel wires to the cylinder axis, θ=0, the larger amplitudes of 2-SLC were observed in the lower wind speeds, around *V/fD*'= 30, as same as the responses with meshes installed on both cylinders. Due to the installation of helical wires, the large amplitudes of 2-SLC were completely disappeared even if the small inclination of wires such as θ=10 degrees. Furthermore, for the case of the smallest inclination of wires, θ=10 degrees, 1-SLC was moved toward the higher wind speed. The larger inclination of the helical wires removed the wake excitation completely. Therefore it is clear that the increase of the inclination of wires reduced the transverse responses of the leeward cylinder.

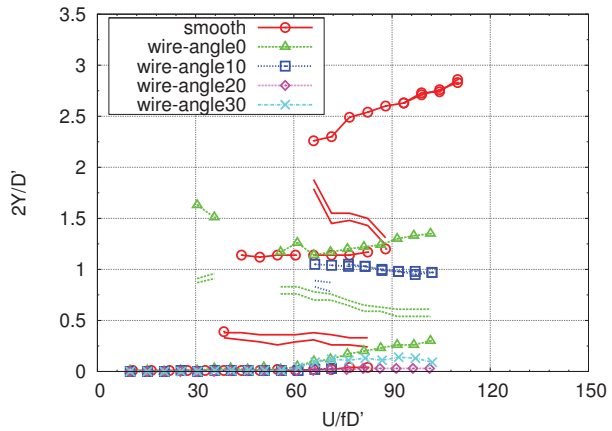

Figure 5 Effects of the inclination of wires from cylinder axis, θ, on the transverse responses, *Sc*=16.4, *f*=2.2Hz.

Figure 6 shows the transverse responses with twelve helical wires attached to the windward cylinder or the leeward cylinder or both cylinders, in the condition of *Sc*=16.4, *f*=2.2Hz, 2DOF. For the installation of twelve wires on only the leeward cylinder, the amplitudes of 1-SLC were

decreased. However, the occurrence of 1-SLC moved toward the lower wind speed and 1-SLC developed from the rest condition without 1-USLC. On the other hand, the amplitudes of 1-USLC were increased by the installation of wires on only the windward cylinder; furthermore, the amplitudes of 1-USLC due to the installation of the windward cylinder were almost the same as that of the 1-SLC of the installation of them on only the leeward cylinder. For the installation of wires on both cylinders, the stabilizing effects for the windward cylinder and the leeward cylinder should act together.

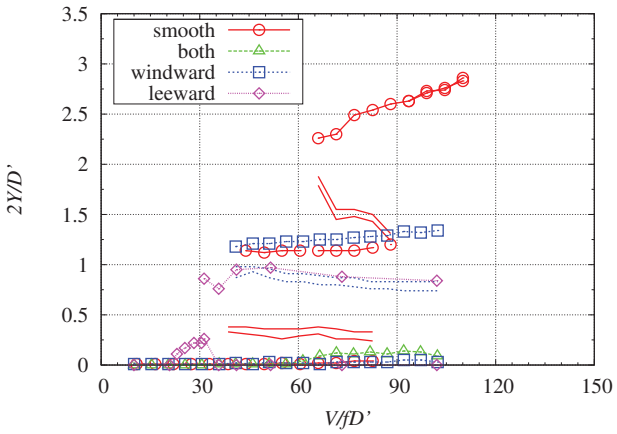

Figure 6 Responses of the leeward circular cylinder with and without the twelve helical wires, *Sc*=16.4, *f*=2.2Hz

3.4 *Flow visualization*

Figures 7 and 8 show the results of flow visualization tests for smooth surface circular cylinders during free vibrations in 1-SLC and 2-SLC under the same reduced wind speed, *V/fD*=65, respectively, where phase angles of the sinusoidal vibration of leeward circular cylinder were changed from the neutral position of 0 (Figure (a)) to 11π/6 (Figure (l)) with the interval of π/6. In the figures, representative streak lines were also shown by solid arrows. As shown in Figure 7, the smaller amplitude of vibration of 1-SLC was restricted by the separated shear flow formed by the windward circular cylinder, where the leeward cylinder was completely included in it. As shown in Figures 6 (d), (e), (j), (k), the wake excitation of 1-SLC was induced by the gap flow into the wake region as detected in previous papaers [8, 9]. On the contrary, under the larger amplitude of 2-SLC, Karman vortices were developed behind the windward circular cylinder during all vibration phases as shown in Figure 8. As given in Figure 2 (a), the amplitudes of second stable limit cycle (2-SLC) almost correspond to the separated shear flow formed behind the single circular cylinder, on the other hand, the amplitudes of first stable limit cycle (1-SLC) restricted by the separated shear flow formed behind the windward cylinder in tandem arrangement of circular cylinders. Therefore, taking into an account of the time integrated mean flow situation, the larger amplitude of 2-SLC could be excited by the similar flow properties for the smaller amplitude of 1-SLC.

As shown in Figures 3 (b) and (c), due to the installation of meshes only on the leeward cylinder or both cylinders, the larger transverse responses of 2-SLC were measured in the restricted lower wind speeds, where flow patterns around cylinders were also similar to those under the larger amplitude of 2-SLC for smooth surface circular cylinders as given in Figure 8. Furthermore, during smaller responses for the installation of meshes or helical wires to the cylinder, flow pat-

terns around cylinders were almost the same to those for smooth surface circular cylinders under the smaller amplitude of 1-SLC as given in Figure 7.

4 CONCLUSIONS

From the experimental investigation of the tandem circular cylinders of central distance of three diameters with several kinds of surface roughness, following results were obtained:

In the range of tested Scruton number, *Sc*, two types of stable limit cycles were occurred in transverse responses. The amplitude of larger responses (2-SLC) almost correspond to the separated shear flow formed behind the single circular cylinder, on the other hand, the smaller amplitudes of first stable limit cycle (1-SLC) restricted by the separated shear flow formed behind the windward cylinder in tandem arrangement of circular cylinders.

Effects of Reynolds number on the wake galloping were quite large. The surface roughness installed on the leeward circular cylinder played a more important role in the wake galloping in comparison with that installed on the windward circular cylinder, however, the stabilizing effects of the installation of helical wires on both cylinders have been accomplished by the mutual effect achieved with the windward cylinder and the leeward cylinder.

The interaction of wake properties and the responses of the leeward circular cylinder should be investigated in detail.

5 ACKNOWLEDGEMENTS

The authors wish to thank for the support by Grants-in-Aid for Scientific Research No.22560480 of Japan Society for the Promotion of Science.

6 REFERENCES

1 K.R. Cooper and R.L. Wardlaw, Aeroelastic Instabilities in wakes, Proceedings of 3rd International Conference on Wind Effects on Buildings and Structures, Tokyo, Japan, 1971,pp. 647-655.
2 A. Simpson, On the flutter of a smooth circular cylinder in a wake, Aeronautical Quarterly, 1971, pp. 25-41.
3 F. Nagao, H. Utsunomiya, M. Noda, M. Imoto, R. Sato, Aerodynamic properties for closely spaced triple circular cylinders, Journal of Wind Engineering and Industrial Aerodynamics, 2003, 91, pp. 75-82.
4 F. Nagao, H. Utsunomiya, M. Noda, M. Katayama, Properties of aerodynamic vibrations of a circular cylinder in the wake of several kinds of rectangular cylinders, Proceedings of 11th International Conference on Wind Engineering, 2003, Vol.2, pp. 2469-2476.
5 F. Nagao, M. Noda, T. Koori, K. Wada, H. Utsunomiya, Wake-excitation mechanism for a circular cylinder in the wake of a square cylinder, Proceedings of 12th International Conference on Wind Engineering, 2007, Vol.2, pp. 1711-1718.
6 F. Nagao, M. Noda, M. Inoue, Effects of surface roughness of circular cylinders on wake galloping, Proceedings of 13th International Conference on Wind Engineering, 2011.
7 F. Nagao, M. Noda, M. Inoue, Basic study on wake excitation of tandem circular cylinders under central distance of three diameters, Proceedings of 9th International Symposium on Cable Dynamics, 2011.
8 Y. Fujino, T. Ishihara; Y. Kubo, Y. Yuki, Experimental study of wake galloping using full-scale parallel models for Higashi Kanjo Bridge, Proceedings of 9th International Symposium on Cable Dynamics, 2011.
9 M. M. Zdravkovich and D. L. Pridden, Interference between two circular cylinders; Series of unexpected discontinuities, Journal of Industrial Aerodynamics, 1977, Vol. 2, pp. 255-270.
10 N. Shiraishi, M. Matsumoto, H. Shirato, On aerodynamic instabilities of tandem structures, Journal of Wind Engineering and Industrial Aerodynamics, 1986, 23, pp. 437-447.

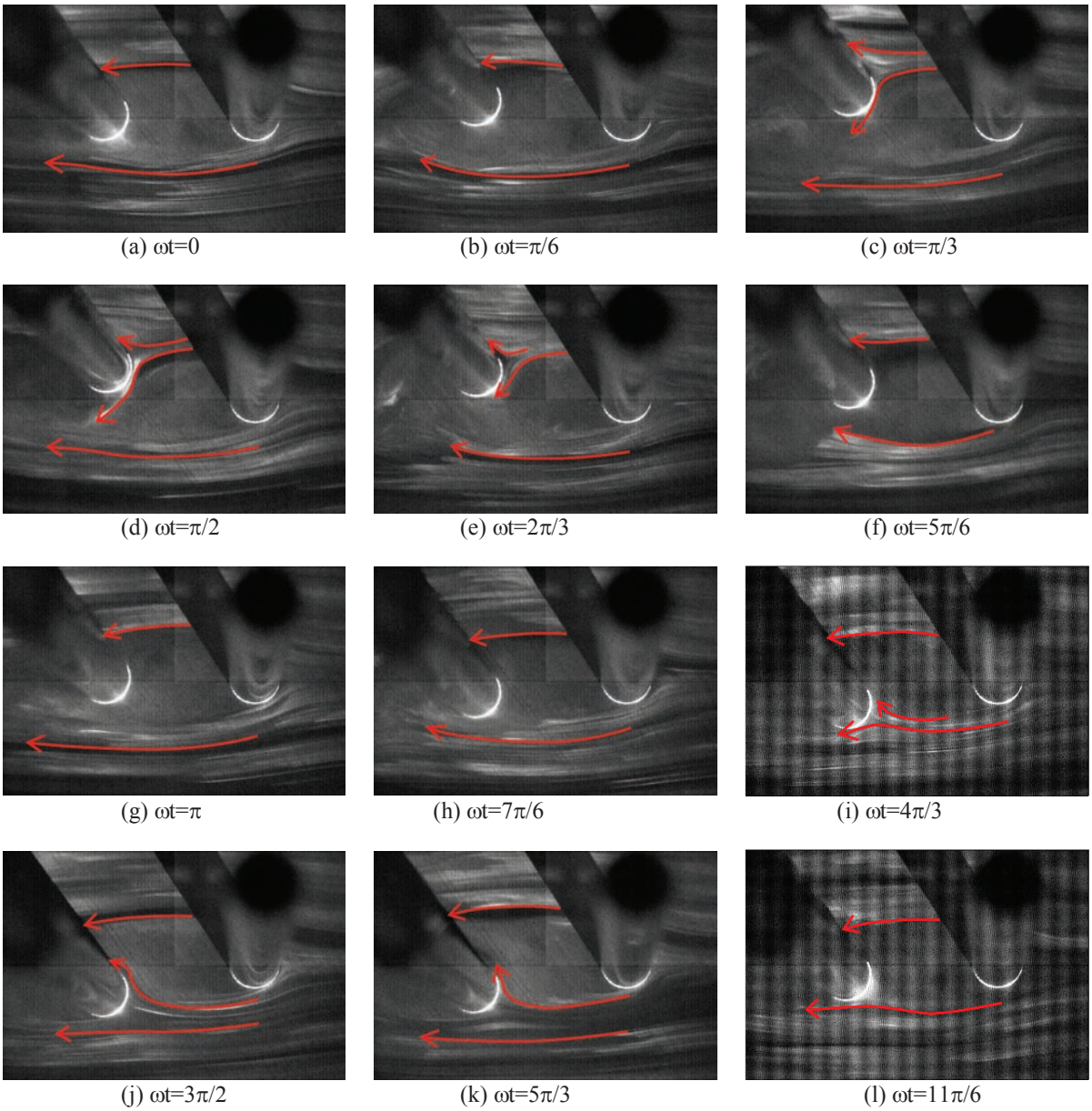

(a) ωt=0 (b) ωt=π/6 (c) ωt=π/3

(d) ωt=π/2 (e) ωt=2π/3 (f) ωt=5π/6

(g) ωt=π (h) ωt=7π/6 (i) ωt=4π/3

(j) ωt=3π/2 (k) ωt=5π/3 (l) ωt=11π/6

Figure 7 Flow around cylinders in free vibration of 1-SLC at V/fD=65.

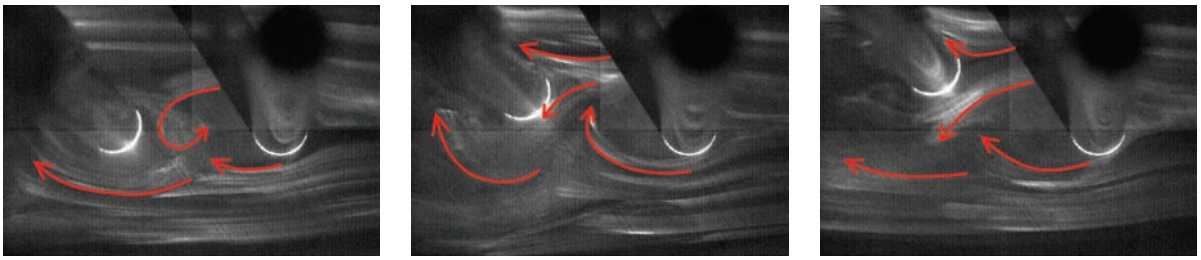

(a) ωt=0 (b) ωt=π/6 (c) ωt=π/3

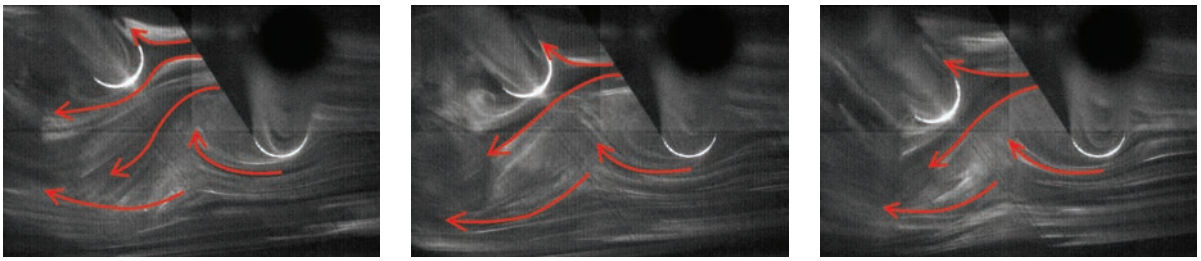

(d) ωt=π/2 (e) ωt=2π/3 (f) ωt=5π/6

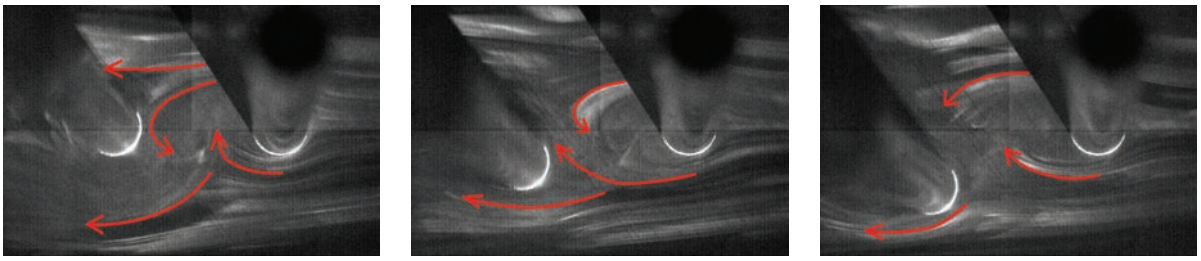

(g) ωt=π (h) ωt=7π/6 (i) ωt=4π/3

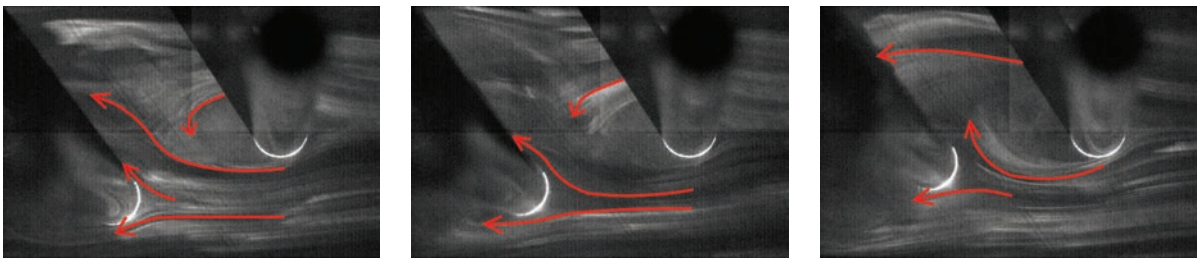

(j) ωt=3π/2 (k) ωt=5π/3 (l) ωt=11π/6

Figure 8 Flow around cylinders in free vibration of 2-SLC at *V/fD*=65.

Investigation on wind tunnel blockage effect of super high-rise building

WANG Lei LIANG Shu-guo TANG huai-qiang SONG Wei-wei

School of Civil & Building Eng., Wuhan University, Wuhan,China

ABSTRACT: As the significant difference in wind tunnel data between two scaled models of a practical engineering, the cause of this difference ,which was regarded as blockage effect，was analyzed in this paper. Research shows that, for wind tunnel test with more surrounding buildings, blockage effect may result in serious data distortion, especially for lateral wind pressure，and existing correction method does not possess universality. Moreover, blockage ratio, as a global concept, is not appropriate to evaluate blockage effect of wind tunnel pressure data at different parts of building models. This study has reference value for blockage effect of wind tunnel pressure date in practical engineering.

KEYWORDS: blockage effect rectangular high-rise building wind pressure coefficient wind tunnel test

1 INTRODUCTION

Wind field of models in wind tunnel has wall boundary, while the wind field of actual structure in the atmosphere is unbounded. Simulation of unbounded atmospheric flow field in the bounded wind tunnel will bring the wall interference. Lateral constraint of flow field around the model by the wind tunnel boundary is known as the body obstruction, and the lateral constraint of the wake flow field is known as the wake blocking, namely, which are blocking effect.

Blocking effect seriously affected the accuracy of test data in some cases. Taking an example that blocking ratio is 15% in the wing - body combination model wind tunnel test, when the attack angle is 90^{o}, the correction value of the drag coefficient reaches 88% of the measured values [1]. Saathoff and Melbourne found through the study on rectangular building blocking effect that when the blocking ratio is 5%, the mean lateral wind pressure near the corner increased by 15%, the root variance of wind pressure increased by 20% [2], which shows the blocking effect of test data cannot be ignored. However, building wind tunnel tests, even when the obstruction is relatively large, its effects are often ignored [3].

The blocking effects correction of aviation and automotive wind tunnel tests have been effectively developed. The correction methods used commonly are mirror method, the vortex lattice method, the wall pressure of Information Act [4] and the Mercker semi-empirical method[5]. However, due to the differences between the shape of the rectangular buildings and aircraft, as well as cars, the above methods cannot be applied to wind tunnel blocking effect correction of rectangular building models.

Wind engineering researchers have investigated on wind tunnel blocking effects of rectangular building models for several decades. As early as 1978, Awbi proposed blocking effect correction method for two-dimensional rectangular section [6] on the basis of the Maskell theory, he believed that the difference of the aspect ratio of rectangular cross section should be taken into account for the blocking effect correction, the blocking effect of the long side windward without reattachment, is more obvious than the shorter side windward [7]. Cherry, Melbourne, et al also pointed out that the

average length of the bluff body surface reattachment will decrease with blockage ratio increasing. Cherry's test results showed that 5% of the blockage ratio makes reattachment length reduce by 20% [8]. According to these theory results, blocking will not only affect the size of the surface pressure, but also affect the pressure distribution. Therefore, the blocking effect mechanism and correction formula based on the Maskell assumption, that the blocking effect affects only the size of wind speed and doesn't affect the pressure distribution, has not been widely accepted. After that, Saathoff [2], Hunt [9], Noda, [10], Atsushi Okajima [11] et researchers also researched on the blocking effect with special wind tunnel tests or numerical simulation. While a large number of scholars are concerned about and studied on the blocking effect of the rectangular cylinder, but so far there is still no generally accepted blocking effect theory and correction method of wind tunnel test for practical rectangular tall building models.

The research objects of above-mentioned studies are single rectangular buildings, the results of these studies can be summarized as follows: 1、blocking effect of the along wind pressure on a rectangular cylinder is very small, makes the lateral pressure increase, change the lateral pressure distribution as the result. 2、most of the blocking effect correction methods focus on the correction of dynamic pressure, however these methods did not jump out of the stereotype of Maskell assumptions. This study found that the above conclusion cannot be applied to the wind tunnel test of an actual building project with group effects.

2. WIND TUNNEL TEST

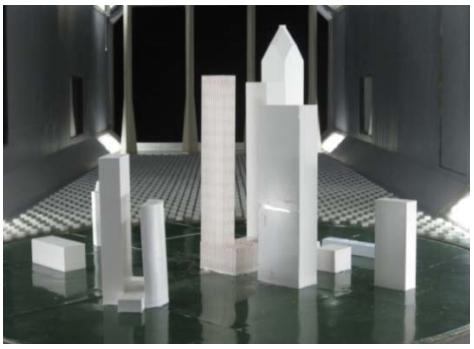

Fig. 1 1/300 model

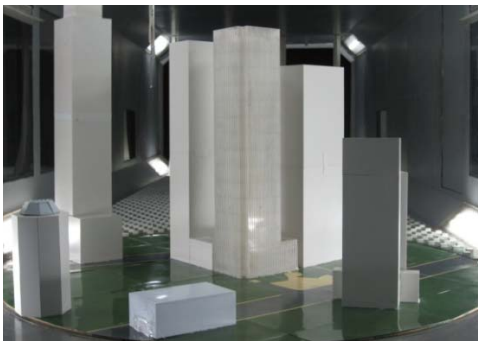

Fig. 2 1/200 model

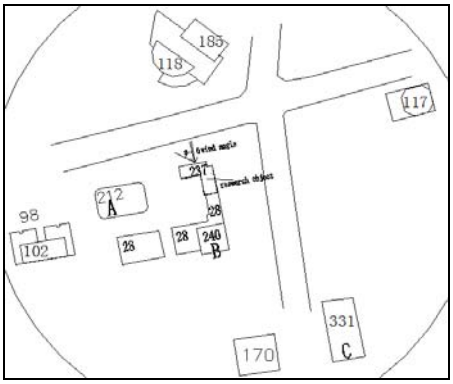

Fig. 3 layout of surrounings

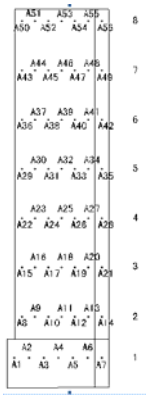

Fig. 3 layout of test points

The layout of manometrical model and surrounding buildings with 1/300 geometrical scale in wind tunnel is shown in Figure 1, the layout of those with 1/200 geometrical scale in wind tunnel is in Figure 2, and two sets of models are same except the geometry sizes. The general layout of the

building surrounding is shown in Figure 3. Among the models, the manometrical model is simulating a 237m-highrise building with rectangular cross section. In actual wind field, there are 9 surrounding buildings whose heights are above one hundred meters, where Building A is 212m, Building B is 240m, and Building C is 331m. The wind tunnel test was carried out in low-speed test section (3m x 2m) of the CGB-1 wind tunnel in Guangdong Provincial Academy of Building Research, and the test wind field is the C category, according to China's code. Under the wind azimuths of 0°, the blocking ratio , the ratio of effective frontal area S to wind tunnel cross-sectional area , reaches the maximum，which were 8.9% for the 1/200 models and 4.1% for 1/300 models, respectively.

3. ANALYSIS OF EXPERIMENTAL DATA

3.1 mean wind pressure coefficients

The mean wind pressure coefficients of the test points on the along wind side, leeward side and the lateral side are illustrated in Figure 5, 6 and 7 respectively, where the abscissa is the point number. The pressure coefficients of 1/300 model are relatively close to those of National Building Codes, To facilitate the analysis here, the difference between the pressure coefficient of 1/200 and 1/300 models is called the absolute difference, the ratio of absolute difference to the pressure coefficient 1/300 model is called the relative difference (seen in Equ. 1 to 4). Figure 8 illustrate the pressure coefficient relative difference on the along wind side, leeward side and the lateral side.

Mean pressure of test points:

$$\overline{w} = (\sum_{i=1}^{N} w_i) / N \qquad (1)$$

Mean wind pressure coefficient:

$$\mu_s = \frac{\overline{w}}{\overline{w}_{h_{ref}}} (\frac{h_{ref}}{h})^{2\alpha} \qquad (2)$$

Absolute difference between the mean wind pressure coefficients:

$$\Delta_1 = \left|\mu_{s200} - \mu_{s300}\right| \qquad (3)$$

Relative difference between the mean wind pressure coefficients:

$$\Delta_2 = \left|\mu_{s200} - \mu_{s300}\right| / \left|\mu_{s300}\right| \qquad (4)$$

Where the mean wind pressure $\overline{w}$ of 1/200 model is corresponding to the pressure coefficient μ_{s200} of 1/200 model and the mean wind pressure $\overline{w}$ of 1/300 model is corresponding to the pressure coefficient μ_{s300} of 1/300 model. h_{ref} is the height of the reference point, and $\overline{w}_{h_{ref}}$ is the wind pressure of the reference point. N is the number of the wind pressure time history sample data, and w_i is the wind pressure at ith time.

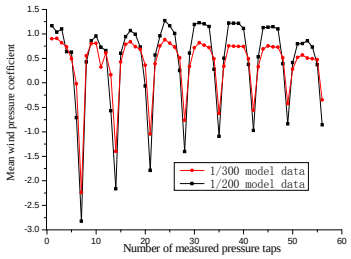

Fig. 5 mean along wind pressure coefficient

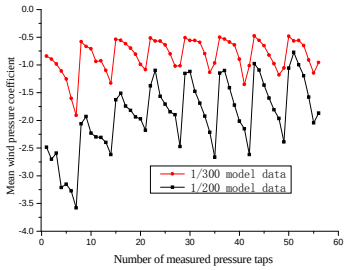

Fig. 6 mean lateral wind pressure coefficient

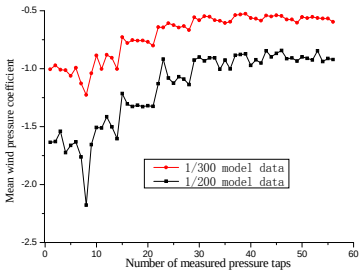

Fig. 7 mean leeward wind pressure coefficient

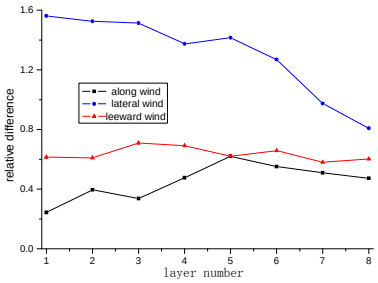

Fig. 8 relative difference of mean wind pressure coefficient

It can be seen from the figures:

a. The absolute value of mean wind pressure coefficients of 1/200 model is much larger than those of 1/300 of load cell model. b. In Figure 5, the mean wind pressure coefficient curves of two model change consistent, along wind pressure distribution doesn't change much with different blocking ratios. In Figure 6, the trend of the two curves is very different, and the peak position is not the same. c. As the height increases, the difference between the two curves is decreasing. It should be noted that the along wind pressure of some points is negative, due to the edges of the building and the surroundings. In fact, the blocking ratio of 1/300 model is still 6.7%, blocking effect exists, thus, the difference between the test data of 1/200 model test data and the correct values should be greater.

It can be seen in Figure 8, the relative difference on the lateral side is more significant than those on the along wind side and leeward side; furthermore, the relative difference of lateral side decreases along the height and the along wind relative differences increase at the beginning, and then decrease along the height. The reason can be explained as follow: the lateral wind pressure is influenced by the blocking effects caused by the manometrical model itself and the surrounding model, and the accelerated air would inevitably lead to the increased pressure coefficient. On the along wind side, in a certain height range from the bottom the blocking effect is the most serious, according to the basic characteristics of the boundary layer of fluid motion, the bottom blockage which has a most serious blockage ratio， will not significantly cause flow velocity changes, but it will only affect on the stream lines high away badly. In the middle of the pressure measurement model, the wind velocity changes most serious; the relative difference near the tor of the mean wind pressure coefficients is small because this effect there is weak, together with the blocking effect of the height decreasing. It is made that the along wind relative differences increase at the beginning, and then decrease along the height. Ultimately that makes the relative difference on the along wind side trend with height first increases and then decreases. Generally, the blocking ratio is definite as an overall concept, but in fact, the degree of blockage along the high greatly affects the quantitative analysis of the blocking effect in wind tunnel tests with surrounding buildings, which is one reason why correction method is not applied to the actual engineering of wind tunnel test.

3.2 RMS wind pressure coefficients

RMS pressure coefficients and differences can be obtained as follow:
RMS wind pressure of test points:

$$w_\sigma = \left(\frac{\sum_{i=1}^{N} w_i^{\,2} - N\overline{w}_i^{\,2}}{N}\right)^{0.5} \quad (5)$$

RMS pressure coefficients:

$$\mu_\sigma = \frac{w_\sigma}{w_{h_{ref}}}\left(\frac{h_{ref}}{h}\right)^{2\alpha} \quad (6)$$

Absolute difference between the RMS wind pressure coefficients:

$$\Delta_{\sigma 1} = \left|\mu_{s\sigma 200} - \mu_{s\sigma 300}\right| \quad (7)$$

Relative difference between the mean wind pressure coefficients:

$$\Delta_{\sigma 2} = \left|\mu_{s\sigma 200} - \mu_{s\sigma 300}\right| \Big/ \left|\mu_{s\sigma 300}\right| \quad (8)$$

Where the RMS wind pressure w_σ of 1/200 model is corresponding to the pressure coefficient $\mu_{s\sigma 200}$ of 1/200 model and the RMS wind pressure w_σ of 1/300 model is corresponding to the pressure coefficient $\mu_{s\sigma 300}$ of 1/300 model.

The comparison charts of the RMS coefficients of the points on the along wind side, leeward side are illustrated respectively in Figure 9, 10 and 11, and in Figure 12 is for the pressure coefficient relative difference on the along wind side, leeward side. It can be seen: the lateral and the along wind and leeward relative differences are small, the lateral relative difference is significant. The RMS wind pressure of 1/200 has been severely distorted, thus, extreme pressure cannot be for engineering wind assessment. It can also be seen from Figure 12, the relative difference of the RMS coefficients on three sides significantly changes along the height, the curve trends are consistent with those of the mean pressure coefficients.

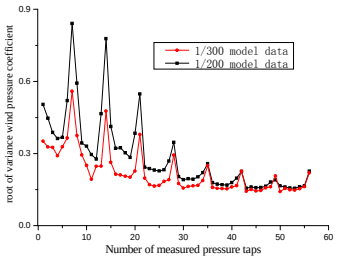

Fig. 9 RMS along wind pressure coefficient

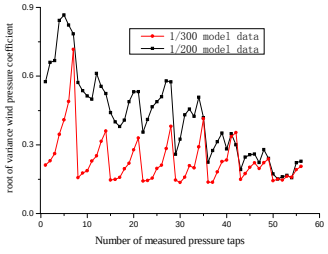

Fig. 10 RMS lateral wind pressure coefficient

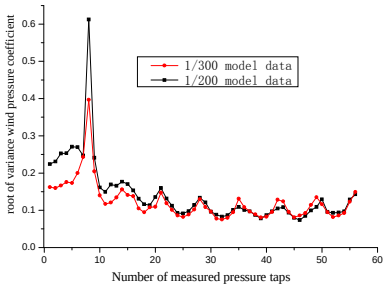

Fig. 11RMS leeward wind pressure coefficient

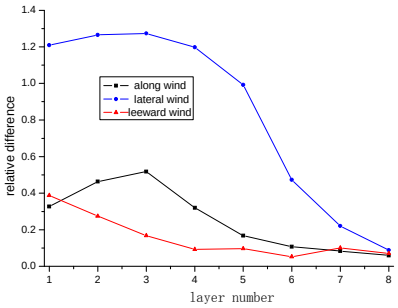

Fig. 12 relative difference of RMS wind pressure coefficient

3.3 data results with correction of reference pressure

There are many blocking effect correction methods, but the pressure data are corrected on the overall proportion according to them. Literature 14 considered that the model blockage makes the wind through the model at wind speed slightly higher than the calibration of no-load wind tunnel, when the air flows through the model, the dynamic pressure at the place in the calculation of the pressure coefficient correction method: $q = q_0(1+1.25\varepsilon)$ .where, when the air flows through the empty wind tunnel model, q_0 is dynamic pressure, ε is blockage ratio. In fact, this correction method is actually that the pressure coefficient is multiplied by the adjustment factor which is less than 1. This correction method extends to be applied to the wind tunnel tests of the building structures. In fact, it is equivalent to the correction of wind speed of the reference point. In this paper, the experimental data were corrected by the correction method in the literature 14.

Figure 13 and Figure 14 shows after the correction of the pressure at the reference point the relative differences of the mean wind pressure coefficient and RMS wind pressure coefficient difference. It can be seen that the relative difference has increased after the correction, but the reduction is only about 10%. And correction of the reference point wind speed is just changing the whole pressure measurement data on the scale, regardless of the differences and other factors among the three sides. This means that the pressure errors of the reference point affect of on the data distortion only a little, or the impact of the blocking effect cannot be eliminated fundamentally, solely by the amendment of the reference point pressure.

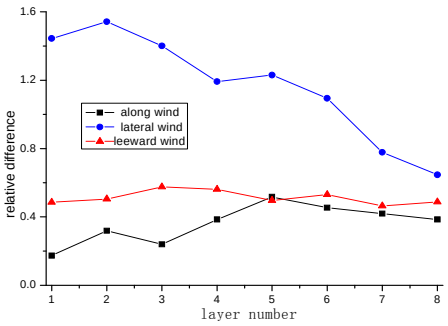

Fig.13 relative difference of the mean wind pressure correcting reference pressure

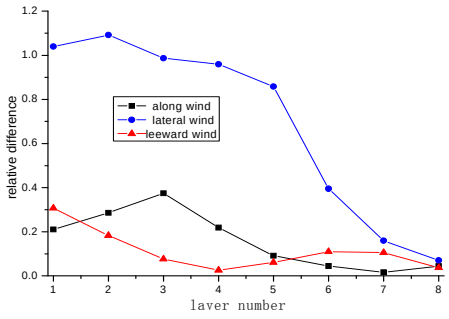

Fig.14 relative difference of the RMS wind pressure coefficient with coefficient with correcting reference pressure

4. CONCLUSIONS

In this paper, the blocking effect on rectangular high-rise buildings with surroundings is studied; the conclusion can be summarized as follows:

(1) Blocking effect on the pressure data cannot be ignored. When the blocking ratio is big, the change of pressure coefficient caused by obstruction is even more than double of the due pressure value without interference

(2) Blocking effect influences the lateral wind pressure greatly, and also changes the lateral wind pressure distribution to some extent; the change on pressure data of windward and leeward caused by blocking effect is relatively small.

(3) For wind tunnel data of high-rise building model with many low surrounding buildings, the influences of blocking effect on its pressure coefficient change along the height significant. In the amendment to blocking effects, blocking effect influenced by the degree of obstruction at different heights should be considered.

(4) For wind tunnel data of rectangular building model with surroundings, blocking mechanism is very complex, so far, there is no universal theory and proper correction method to solve this problem, thus reasonable proportion of the model to control the blocking effect is particularly important.

5 REFERENCE

1 Yun Qilin, Error Analysis and Correction for Wind Tunnel Testing Data [M], Beijing: National Defence Industry Press, 1996.

2 P.J.SAATHOFF and W.H.MELBOURNE, FREESTREAM TURBULENCE AND WIND TUNNEL BLOCKAGE EFFECTS ON STREAMWISE SURFACE PRESSURES [J], Journal of Wind Engineering and Industrial Aerodynamics, 26 (1987) 353-370

3 J.M. Robertson, J.B. Wedding, J.A. Peterka and J.E. Cermak, Wall pressures of separation-reattachment flow on a square prism in uniform flow[J], J. Ind. Aerodyn., 2 (1977) 345-359.

4 Allen. Pope, John, J. Harper, 1978, Low-speed Wind Tunnel Test, trans, Peng Ximing,Yan Junren, Shi Youlun,et, Beijing: National Defence Industry Press

5 E.Merker, A Blockage Correction For Automotive Testing in a Wind Tunnel with Close Test Section[J]. Journal of Wind Engineering and Industrial Aerodynamics,1986,22.

6 E.C. Maskell, A theory of the blockage effects on bluffbodies and stalled wings in a closed wind tunnel,A.R.C.R.M. 3400 (1963).

7 H.B. Awbi, Wind-tunnel-wall constraint on two-dimensional rectangular-section prisms, Journal of Wind Engineering and Industrial Aerodynamics[J], Volume 3, Issue 4, 1978, Pages 285-306.

8 N.J. Cherry, The effects of stream turbulence on a separated flow with reattachment[J], Ph.D. Thesis, Imperial College, University of London, 1982.

9 A. Hunt, Wind-tunnel measurements of surface pressures on cubic building models at several scales[J], Journal of Wind Engineering and Industrial Aerodynamics, 10 (1982) 137-163.

10 M. Noda, H. Utsunomiya, F. Nagao, Basic study on blockage effects in turbulent boundary layer flows[J], Journal of Wind Engineering and Industrial Aerodynamics 54/ELSEVIER 55 (1995) 645-656.

11 Atsushi Okajima, Donglai Yi, Atsushi Sakuda, Tomohito Nakano. Numerical study of blockage effects on aerodynamic characteristics of an oscillating rectangular cylinder[J]. Journal of Wind Engineering and Industrial Aerodynamics 67&ELSEVIER 68 (1997) 91-102.

[12] Wu Delun Wang Jinhai Fing Yiran et, AN EXPERIMENTAL RESEARCH FOR THE WIND BEHAVIOR OF A HIGH-RISE WOODEN PAGODA IN CHINA, Journal of Chongqing Institute of Architecture and Engineering[J],

The Seventh International Colloquium on Bluff Body Aerodynamics and Applications (BBAA7)
Shanghai, China; September 2-6, 2012

The response of aeroelastic models of circular cross-sections to wind action

Tomasz Lipecki [a], Jarosław Bęc [b], Ewa Błazik-Borowa [c]

[a]*Lublin University of Technology, Lublin, Poland, t.lipecki@pollub.pl*
[b]*Lublin University of Technology, Lublin, Poland, j.bec@pollub.pl*
[c]*Lublin University of Technology, Lublin, Poland, e.blazik@pollub.pl*

ABSTRACT: This paper presents results obtained for vertically placed cylinders of circular cross-sections during wind tunnel tests. All models are considered as aeroelastic ones and can represent real chimneys. Accelerations in two perpendicular directions in horizontal plane (along and across wind tunnel) were measured at the tops of 27 cylinders. An attempt to research along-wind as well as across-wind responses with respect to different approaching flows was taken up.

KEYWORDS: circular cylinder, wind tunnel, aspect ratio, wind structure, along-wind response, across-wind response, vortex excitation.

1 INTRODUCTION

Cylinders of circular cross-sections were investigated in wind tunnels by many researches, who carried out experiments in order to obtain pressure distributions on the surface, the lift force and the drag force coefficients, Strouhal number, the correlation coefficient of the load, etc. In general research tasks can be gathered in specific groups: the study on motionless cylinders (measurement of forces and pressures), aeroelastic models (study of dynamic behaviour), vibrating cylinders (f.e.: lock-in). Experiments were performed mainly on stationary cylinders.

Pantazopoulos (1994) collected and characterized the majority of wind and water tunnel studies carried until 1992, which were focused on measurements on fixed cylinders in connection with: rms of lateral force coefficient, the dependence of Strouhal number (St) on Reynolds number (Re), load correlation length coefficient. Changes of St values with Re were presented by Schewe (1983) (smooth cylinder, H/D = 10, H = height, D = diameter), who also studied the change of lateral force based on direct measurements of forces and by Leung et al. (1997) (smooth and rough cylinders). Ribeiro (1991, 1992), for steady and unsteady flow, suggested an empirical relationship for estimating the standard deviation of the local fluctuating lateral force caused by vortices, and based on the knowledge of the distribution of the pressure fluctuations and the correlation coefficient of fluctuating lateral force.

Recently circular cylinders were investigated by: Sumner and Heseltine (2004) and Sumner et al. (2004) who investigated the vortices forming near the free-end of the cylinder (H/D = 3, 5, 7, 9), at Re = $6 \cdot 10^4$. Velocity fields were measured in the excitation area and averaged in time, and then strength of vortices in every measuring point was estimated. General conclusion was that the vortex excitation for the model with the free-end occurs only in certain areas along the height of the model. In the next paper by Sumner and Heseltine (2008) detailed information about the tip vortex structures and their streamwise development were provided. The turbulent wake of cylinders was investigated at Re = $6 \cdot 10^4$ by Adaramola et al. (2006) and was similar for cylinders of aspect ratios of 5, 7, 9 whereas distinctly different was for the cylinder of aspect ratio of 3. More details about the flow around the model of aspect ratio of 9 are presented in the paper by Adaramola et al. (2010). Cao et al. (2007) studied experimentally and Cao and Tamura (2008) studied experimentally and numerically the flow around cylinders (H/D =2.22, 4, 8) in linear

shear flows, at Re = $1.7 \cdot 10^4$-$3.6 \cdot 10^4$. Vortex shedding was investigated by examination of Strouhal number and base pressure variations with respect to shear parameter. Also the mean pressure distributions around cylinder as well as drag and lift forces were studied. The 3D effect of the flow passing over the free-end on vortex shedding in the case of cylinder of small aspect ratio of 3, at Re = $6 \cdot 10^4$-$11 \cdot 10^4$ was investigated by Iungo et al. (2012). Pressures, forces and velocities measurements were conducted during tests. Pressure measurements on the surface of the cylinder at Re = $4.0 \cdot 10^4$-$1.64 \cdot 10^5$ were conducted by Lee et al. (2011) in order to investigate the difference of aerodynamic characteristics between non-accelerated and accelerated flow. Pressure and hot-wire measurements for two cylinders of aspect ratios of 8 and 8.6 and different surface roughness at Re = $1.73 \cdot 10^5$-$5.86 \cdot 10^5$ were conducted by Miau et al. (2011). Particular attention was paid to the flow behavior in the near wake region.

Many papers are devoted to the vibrating cylinders. The results of studies on the relation between St and Re numbers at various intensities of turbulence of the approaching flow in the case elastically mounted model were described by Cheung and Melbourne (1983). The standard deviation of local lift caused by vortex excitation, obtained in studies in turbulent flow in dependence on Re number and turbulence intensity were also examined in that research. Novak and Tanaka (1975) found that the correlation length of the load increases rapidly with the amplitude of vibrations, and the increase is higher for steady flow than for turbulent flow. Howell and Novak (1980) studied the global force acting on cantilever, rigid cylinder, mounted elastically. The authors measured correlation coefficient of pressures as the function of the distance between the reference point and the location of the second point moving along the height. The experiment was performed in steady and turbulent flows, with the model oscillating transversely, at Re number $7.5 \cdot 10^4$. The study showed an increase in lateral force coefficient with increase of the vibration amplitude to 0.1D.

More recent researches on vibrating cylinders were made by Gupta and Arun (2003) who performed measurements of the wind velocity fields around cylinders of different cross-sections, in which oscillations caused by vortices were observed. The dependence of Strouhal number on Reynolds number was formulated. Pastò (2008) analysed the behavior of freely vibrating model in laminar and turbulent flows. Studies were focused on the influence of mass-damping parameter of circular models and Reynolds number on lock-in phenomenon, on the response amplitude and on wake correlation. Measurements of unsteady pressure distributions on the surface of oscillating cylinder were presented by Zasso et al. (2008). Studies were focused on vortex shedding and on integral forces on the cylinder and their correlations with motion. The effect of free-stream turbulence on vortex-induced vibrations of an elastic cylinder (H/D =20) in a cross-flow and the associated fluid forces were investigated experimentally at Re number $5 \cdot 10^3$-$4.1 \cdot 10^4$ by So et al. (2008). Belloli et al. (2012) investigated vortex induced vibrations of the cylinder (H/D = 10) of low structural damping and high mass ratio at Re = $5.4 \cdot 10^4$. Tests showed the clear correlation between wake and force changes during cylinder vibrations.

2 RESEARCH DESCRIPTION

2.1 *Models*

The experiments were carried out in the boundary layer wind tunnel in Wind Engineering Laboratory in Cracow, Poland. Circular cylinders were placed vertically in the working section of the wind tunnel (Fig. 1). The basic geometrical characteristics of the 27 models are collected in Table 1 together with measured frequencies. All models were made of carbon fiber in order to assure particular stiffness, which was necessary to fulfil similarity criteria. The applied material has got the following characteristics: elastic modulus E = 105 GPa, density: ρ = 1455 kg/m^3.

The following parameters are settled in Table 1: geometrical characteristics of the models (D – diameter, H – height, λ – aspect ratio), f = natural frequencies of vibrations calculated from power spectral density functions of top accelerations. There are distribution of natural frequencies with respect to case number and aspect ratio in Figure 2.

Figure 1. View of the wind tunnel with the model place on rotational table and one of the models.

Table 1. Geometric and dynamic characteristics of models.

No	D	H	λ	f	No	D	H	λ	f	No	D	H	λ	f	V_{crit}
	[mm]	[cm]	[-]	[Hz]		[mm]	[cm]	[-]	[Hz]		[mm]	[cm]	[-]	[Hz]	[m/s]
1	16	50	31.25	50.66	10	20	30	15.00	193.12	19	34	80	23.53	54.50	10.295
2	16	40	25.00	73.67	11	24	60	25.00	54.32	20	34	70	20.59	66.17	12.499
3	16	30	18.75	110.72	12	24	50	20.83	77.40	21	34	60	17.65	85.50	16.150
4	18	50	27.78	63.51	13	24	40	16.67	105.04	22	34	50	14.71	107.65	20.334
5	18	40	22.22	89.18	14	24	30	12.50	235.96	23	50	90	18.00	54.77	15.214
6	18	30	16.67	132.10	15	27	70	25.93	50.07	24	50	80	16.00	67.00	18.610
7	20	60	30.00	51.16	16	27	60	22.22	65.07	25	50	70	14.00	82.03	22.785
8	20	50	25.00	65.94	17	27	50	18.52	81.43	26	50	60	12.00	100.73	27.981
9	20	40	20.00	89.89	18	27	40	14.82	136.03	27	50	50	10.00	121.68	33.799

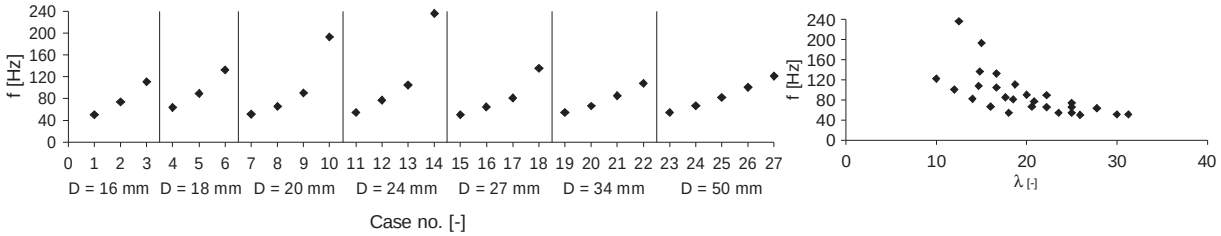

Figure 2. Distribution of natural frequencies against case number and aspect ratio.

2.2 *Wind conditions*

The influence of wind characteristics – wind mean speed profiles, turbulence intensity profiles and PSD functions – on the mean pressure coefficient distributions were examined. Over 40 configurations of barriers, spires and blocks generating boundary layer were taken into account Three (six in case of pipes of the diameter D =16 mm) flows were chosen for further measurements. The mean wind speed profile (power-law formula), intensity of turbulence, and PSD function (similar to Davenport's function) were described by respective equations:

$$v(z) = k \cdot z^{\alpha} \quad \text{for } z > z_{min} \qquad I_v(z) = \frac{\sigma(z)}{\bar{v}(z)} \qquad G(f) = \frac{bf^2}{\left(1 + cf^2\right)^d} \tag{1}$$

where: z = height [cm], z_{min} = minimum height [cm] for which all profiles have the same value at 70 cm, k and α = values selected by the least squares method, $\bar{v}(z)$ = mean wind speed, $\sigma(z)$ = standard deviation of wind speed, b, c, d = coefficients selected by the least squares method. Respective plots are collected in Figure 3.

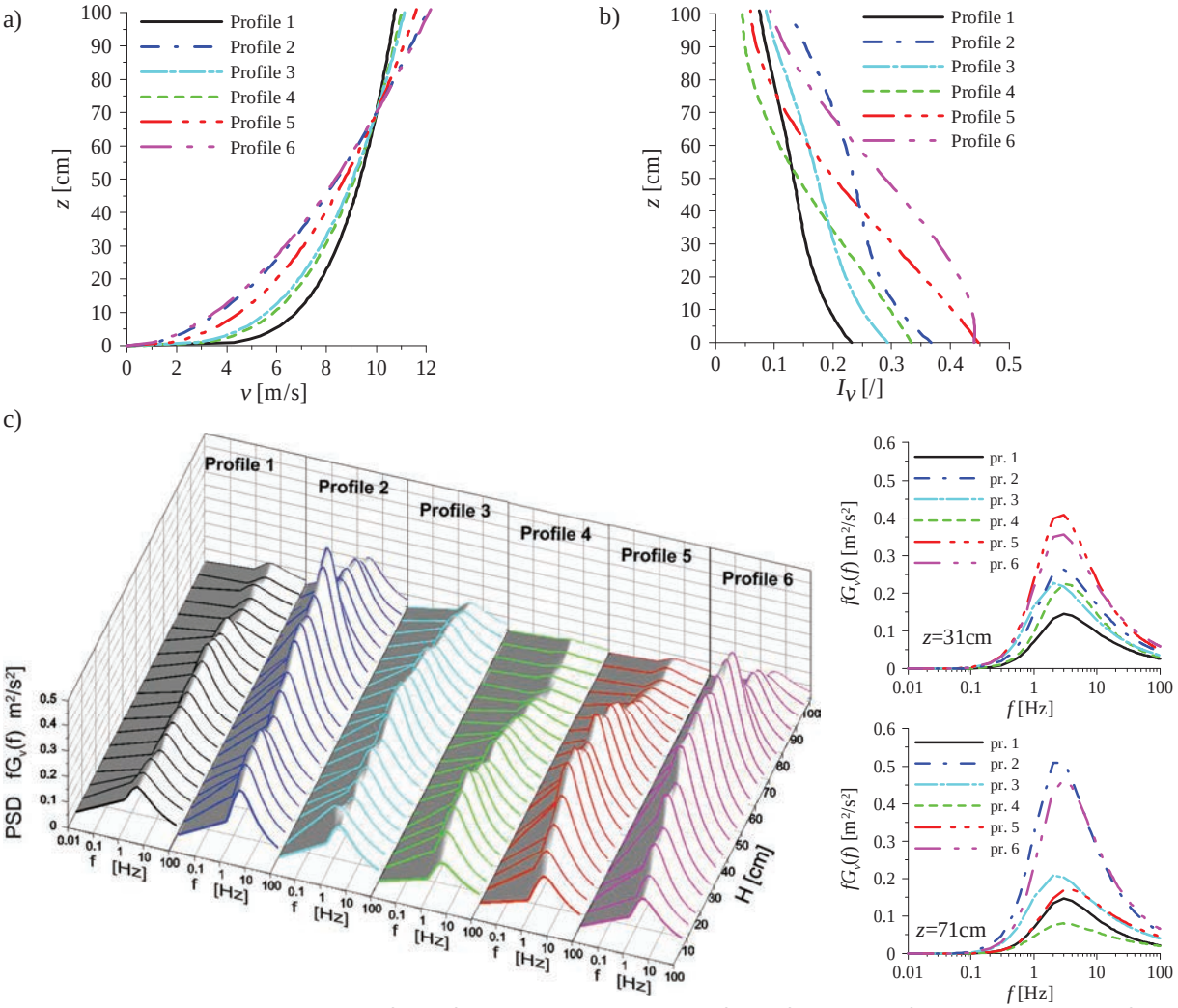

Figure 3. Wind characteristics: a) profiles of mean wind speed, b) profiles of intensity of turbulence, c) PSD functions: spatial distributions and examples at two levels.

2.3 *Experiment*

Two Brüel&Kjær accelerometers were installed at the top of each model. The data was gathered with PULSE system. Time series of accelerations in two perpendicular direction: along and across wind tunnel were measured. The view of a model with installed accelerometers in wind tunnel is presented in Figure 1. The wind speed was changing from 0 m/sec to about 20 m/sec during measurements.

3 RESULTS AND ANALYSIS

Statistical data handling has allowed to define wind speeds at which vortex excitation could take place. Top accelerations in two perpendicular directions and PSD functions of time series with respect to increasing wind speed are presented in Figure 4 in the case of the model No. 8 (D = 20 mm, H = 40 cm) and profile 1. Amplitudes of top accelerations for wind speeds at which vortex shedding occur in cases of the same pipe and profiles 3 and 6 are presented in Figure 5 in order to compare results. The same analysis was carried out for all cases of models and wind structures.

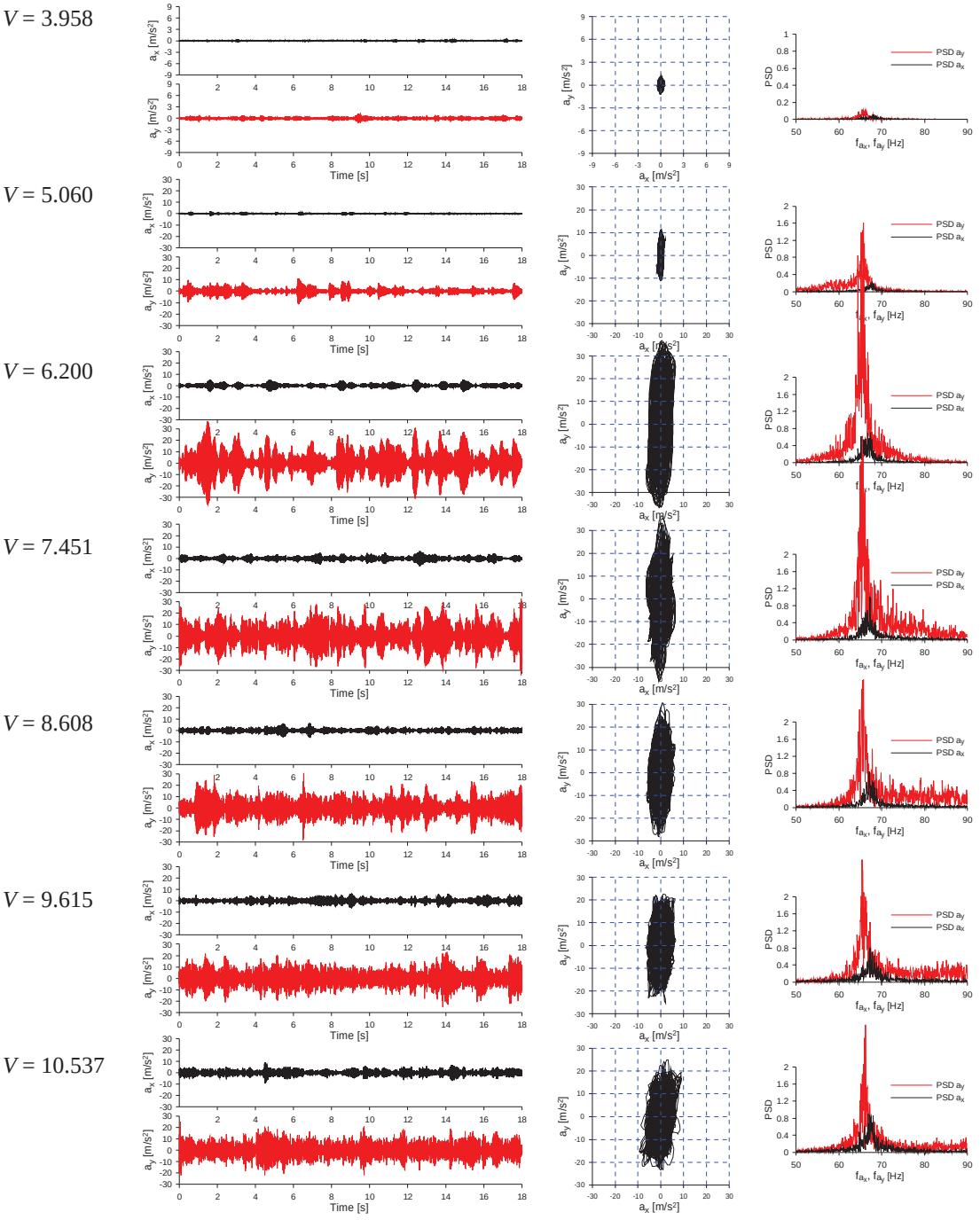

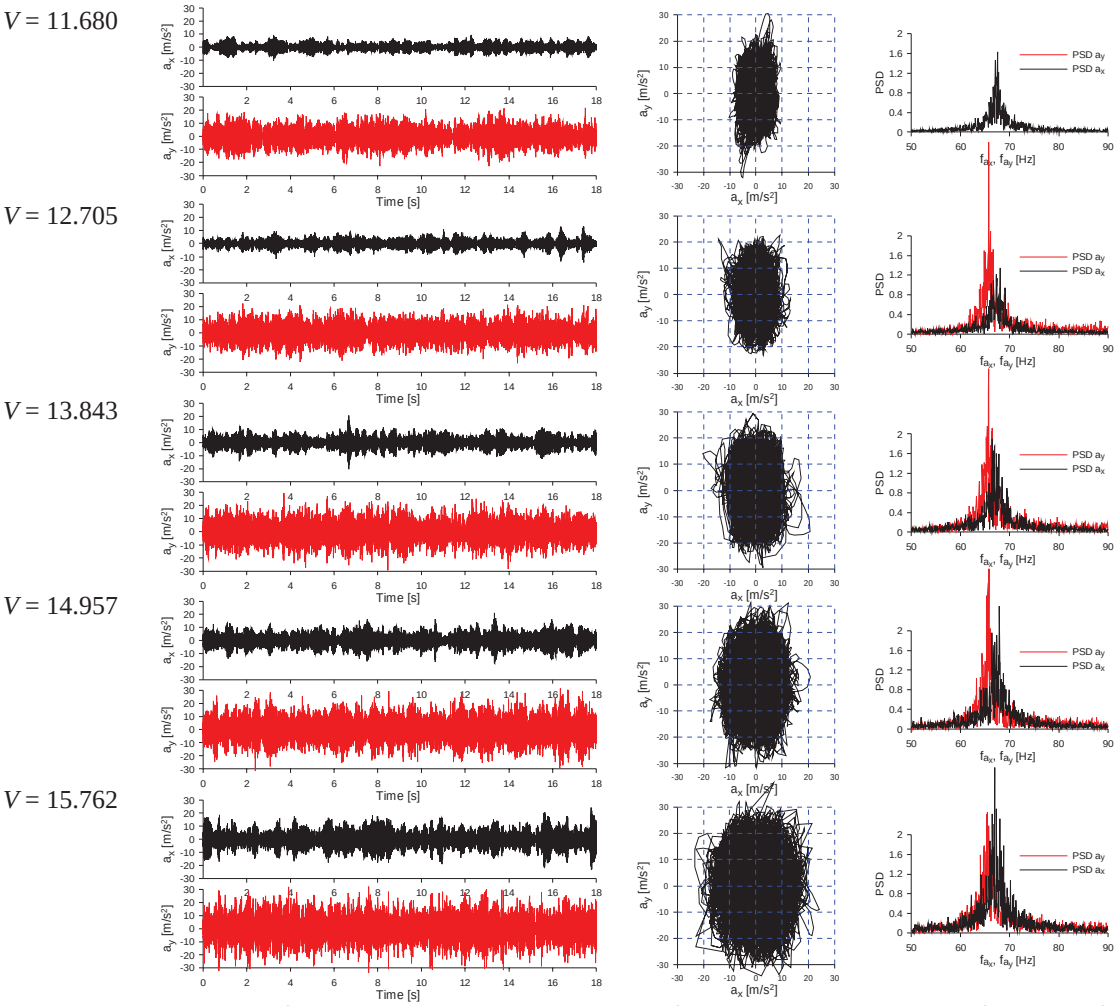

Figure 4. Time histories of accelerations (a_x, a_y), trajectories of top accelerations and PSD functions of along and across- wind components for consecutive wind speeds, for wind profile no. 1, for pipe no 8.

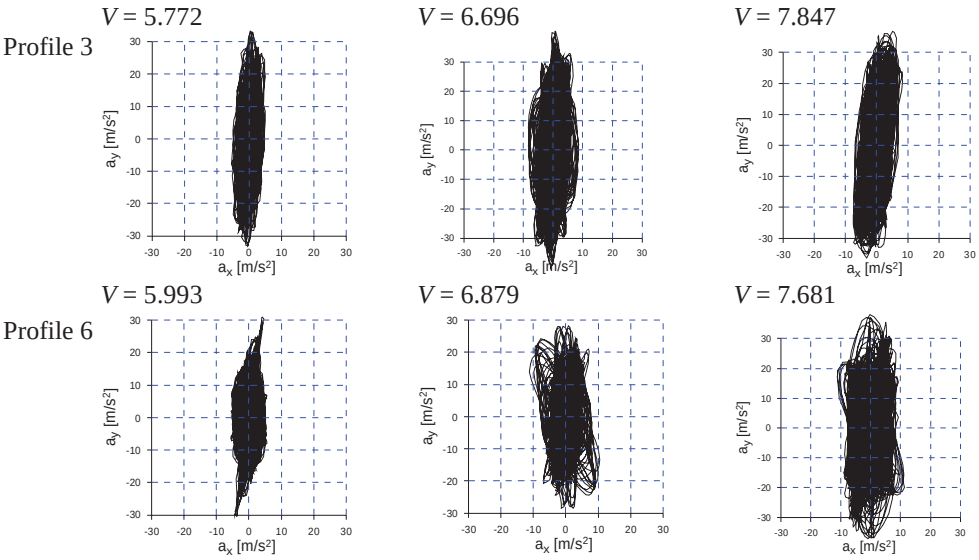

Figure 5. Top trajectories of accelerations at the range of wind speeds at which vortex shedding occur.

Vortex excitation is clearly visible on time histories of accelerations (higher amplitude of the acceleration in direction perpendicular to the flow) as well as on power spectral density functions (higher peak value). Increasing amplitude of the accelerations in both directions are caused by the increasing wind speed.

The reduced standard deviations of top accelerations respectively along and across mean wind speed (σ_{ax}, σ_{ay}) were assumed as results, which allow to compare two components of the cylinder response to the wind action. Examples of normalized standard deviations (σ_{ax}/V^2, σ_{ax}/V^2) and their ratio (σ_{ax}/σ_{ay}) are presented in Figures 6 and 7. As it can be seen in these figures – the range of wind speeds in which vortex excitation appears could be recognized with a good approximation. Some more cases of the ratio σ_{ax}/σ_{ay} are enclosed in Figure 8 and 9 for pipes of the smallest and the largest diameter equal respectively to 16 mm and 50 mm.

Critical wind speed values obtained in the research were evaluated from maxima at plots of standard deviations or their ratio as shown in Figures 6-9. It should be emphasized that values obtained in the studies are approximated and only shows the range of wind speeds close to which vortex excitation can appear. The way of attaching accelerometers at the top of the model pipe causes flow disturbances and then differences in values of measured and calculated critical wind speeds. Vortex exciatation appears in the range of wind speeds different in particular cases of flow. There was no excitation for pipes 18, 22, 26, 27 in considered wind speed range. From the other hand an exact critical wind speed could not be estimated (there are no maxima on plots) but only the beginning of vortex excitation was determined in some cases of pipes. Evaluated and calculated critical wind speeds are collected in Table 2 with respect to case of wind structure. Theoretical value was calculated from $V_{cr} = fD/St$, where St = 0.18

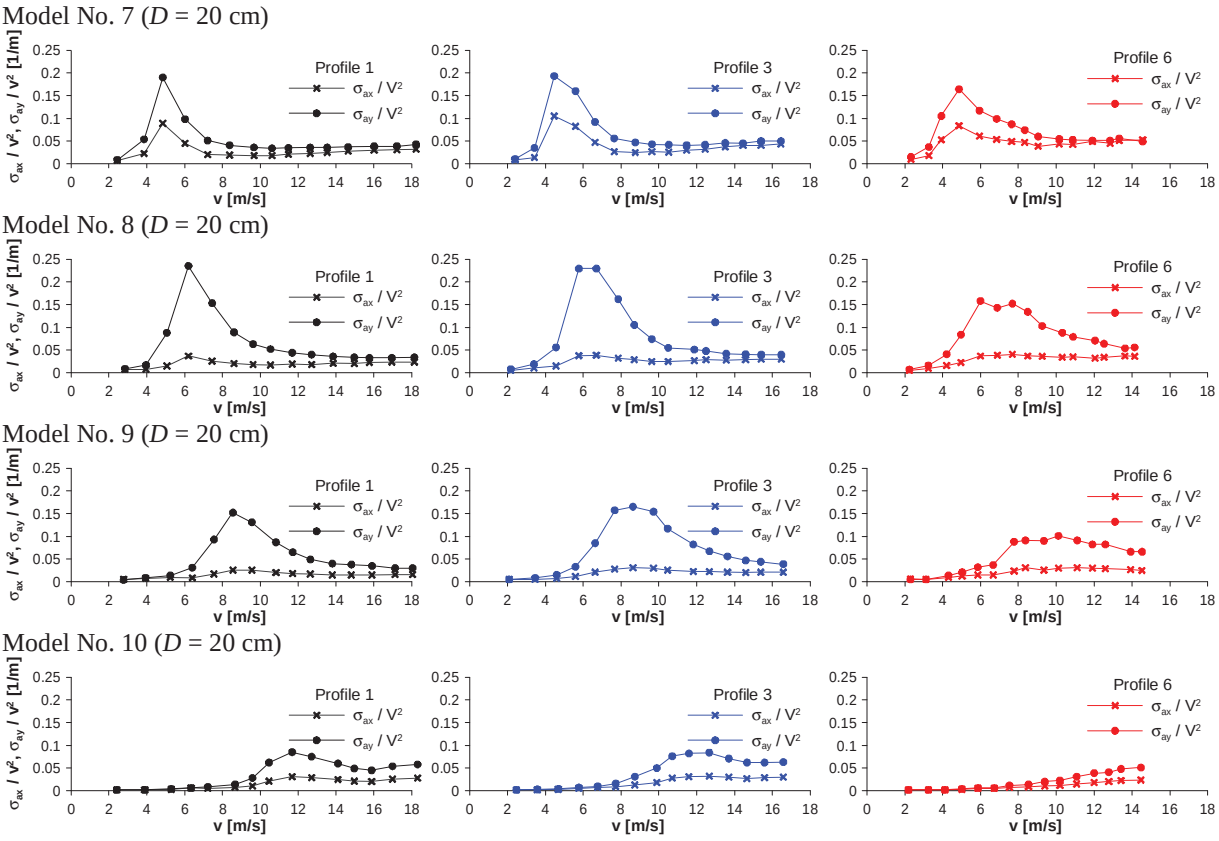

Figure 6. Normalized standard deviations of accelerations (σ_{ay} and σ_{ax}) for three different wind speed profiles against increasing wind speed for four models of the diameter D = 20 m (No. 7-10).

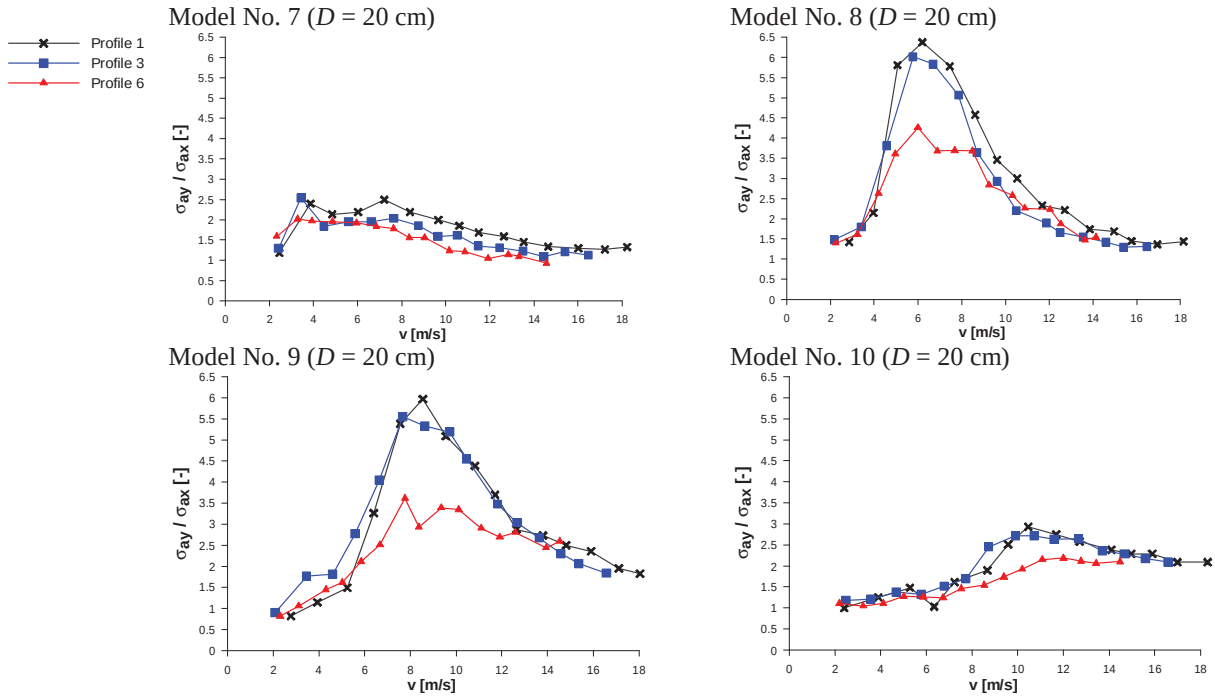

Figure 7. The ratio of standard deviations (showed in Fig. 6) against wind speed for models of the diameter D = 20 m (No. 7-10).

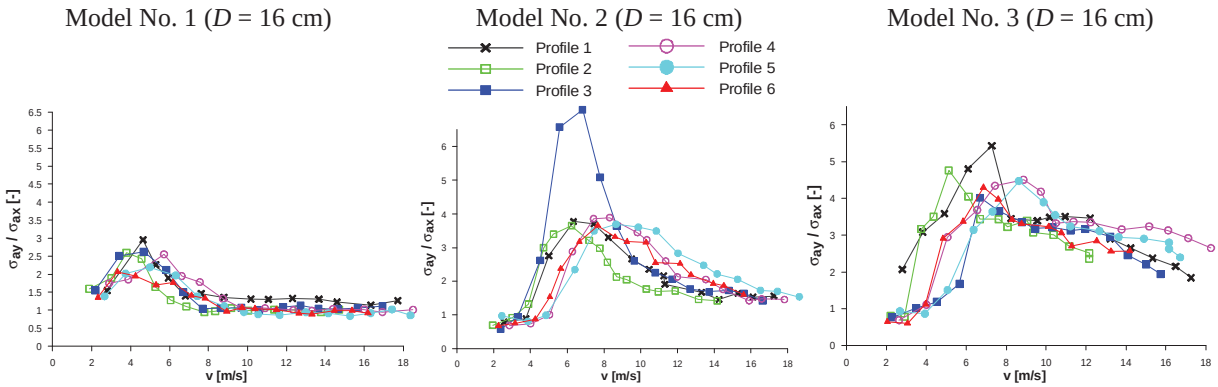

Figure 8. The ratio of standard deviations against wind speed for models of the diameter D = 16 m (No. 1-3).

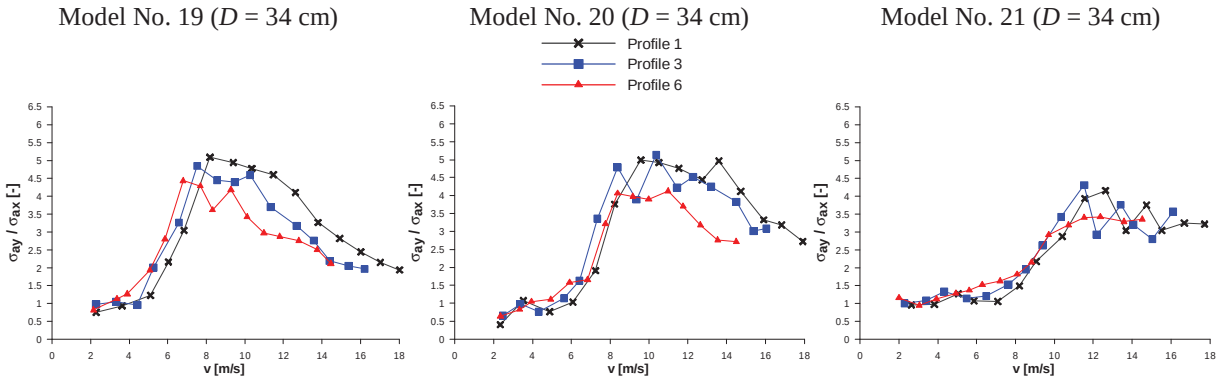

Figure 9. The ratio of standard deviations against wind speed for models of diameter D = 34 mm (No. 19-21).

Table 2. Calculated and measured wind speeds.

No.	V_{cr} (theoretical)	V_{cr} (wind tunnel)					
	[m/s]	[m/s]					
		Profile 1	Profile 2	Profile 3	Profile 4	Profile 5	Profile 6
1	4.501	4.643	3.784	4.675	5.717	4.989	3.338
2	6.549	6.345	6.230	6.836	6.278	8.659	7.655
3	9.842	7.278	5.123	6.696	8.866	8.630	6.857
4	6.351	7.545		5.534			7.652
5	8.918	9.528		8.584			10.818
6	13.210	12.255		13.470			12.342
7	5.684	3.853		3.425			3.269
8	7.327	6.200		5.772			5.993
9	9.988	8.547		7.666			7.769
10	21.458	10.459∗		12.659∗			12.002∗
11	7.243	6.267		6.543			6.620
12	10.320	11.743		8.231			7.786
13	14.005	11.463		11.512			11.971
14	31.462	14.259∗		12.639∗			13.923∗
15	7.510	6.091		6.444			6.527
16	9.760	8.701		8.519			7.653
17	12.214	12.904		12.367			12.563
18	20.404	-		-			-
19	10.295	8.189		7.521			6.797
20	12.499	9.584		10.372			10.977
21	16.150	12.630∗		11.523∗			12.365∗
22	20.334	-		-			-
23	15.214	11.420		10.356			11.145
24	18.610	13.622		12.308			11.792
25	22.785	16.755∗		15.145∗			14.272∗
26	27.981	-		-			-
27	33.799	-		-			-

∗ the beginning of vortex excitation.

4 CONCLUSIONS

Based on the analysis of results it can be stated that the response of aeroelastic models of circular cross-sections depends strongly on the structure of the approaching flow. The response of such models is highly influenced by buffeting load resulting from the turbulence (fluctuations of wind speed and direction) as well as by the vortex excitation load.

It seems that the wind structure have the higher influence on critical speed for models with larger aspect ratios. Perhaps this is related to a combination of wind gusts and vortex excitation. On the other hand, the wind strucutre has less effect on the critical speeds for smaller aspect ratios (lower differences between calculated and measured values – Table 2).

The standard deviations obtained for the profile 6 are in most cases lower than those obtained for other cases. For most of models, the largest standard deviations and their ratios were obtained in case of profile 1 (the lowest turbulence of the flow), the smallest in case 6 (the largest turbulence of the flow).

The studies provided a range of critical wind speeds (different for various cases of flow), which in general is close to the theoretical values obtained for St = 0.18. Differences are caused by the way of accelerometers attachment on the top (disturbance of the flow around). Also the approximated estimation of maxima values on plots in Figures 6-9 causes the difference between

calculated and theoretical values. But it can be clearly noticed that vortex excitation appears in the range of wind speeds almost for each case of the pipe.

It seems that further analyses are necessary to better understand the influence of wind structure on the response of pipes. Numerical simulations of dynamic response taking into account buffeting load as well as vortex excitation is also planned

5 REFERENCES

1 M.S. Pantazopoulos, Vortex-induced vibration parameters: critical review, OMAE, vol. 1, Offshore Technology, The American Society of Mech. Eng. 1994 p.: 199-255.
2 G. Schewe, On the force fluctuations acting on a circular cylinder in cross-flow from subcritical up to postcritical Reynolds numbers, J. Fluid Mech., 133 (1983) 265-285.
3 Y.C. Leung, C.H. Wong, N.W.M. Ko, Characteristics of flows over an asymmetrically grooved circular cylinder in transitional regimes, J. Wind Eng. Ind. Aerodyn., 69-71 (1997) 167-178.
4 J.L.D. Ribeiro, Effects of surface roughness on the two-dimensional flow past circular cylinders, part II: fluctuating forces and pressures, J. Wind Eng. Ind. Aerodyn., 37 (1991) 311-326.
5 J.L.D. Ribeiro, Fluctuating lift and its spanwise correlation on a circular cylinder in a smooth and in a turbulent flow: a critical review, J. Wind Eng. Ind. Aerodyn., 40 (1992) 179-198.
6 D. Sumner, J.L. Heseltine, Tip vortex structure for a circular cylinder wit free ends, Proc. of the 5th Coll. on Bluff Body Aerodynamics & Applications, 2004, 423-426.
7 D. Sumner, J.L. Heseltine, O.J.P. Dansereau, Wake structure of a finite circular cylinder of small aspect ratio, Exp. Fluids, 37 (2004) 720-730.
8 D. Sumner, J.L. Heseltine, Tip vortex structure for a circular cylinder with a free end, J. Wind Eng. Ind. Aerodyn., 96 (2008) 1185–1196.
9 M.S. Adaramola, O.G. Akinlade, D. Sumner, D.J. Bergstrom, A.J. Schenstead, Turbulent wake of a finite circular cylinder of small aspect ratio, J. Fluids Struct., 22 (2006) 919–928.
10 M.S. Adaramola, D. Sumner, D.J. Bergstrom, Effect of velocity ratio on the streamwise vortex structures in the wake of a stack, J. Fluids Struct., 26 (2010) 1–18.
11 S. Cao, S. Ozono, K. Hirano, Y. Tamura, Vortex shedding and aerodynamic forces on a circular cylinder in linear shear flow at subcritical Reynolds number, J. Fluids Struct., 23 (2007) 703–714.
12 S. Cao, Y. Tamura, Flow around a circular cylinder in linear shear flows at subcritical Reynolds number, J. Wind Eng. Ind. Aerodyn., 96 (2008) 1961–1973.
13 G.V. Iungo, L.M. Pii, G. Buresti, Experimental investigation on the aerodynamic loads and wake flow features of a low aspect-ratio circular cylinder, J. Fluids Struct., 28 (2012) 279–291.
14 Y. Lee, J. Rho, K.H. Kim, D.H. Lee, Fundamental studies on free stream acceleration effect on drag force in bluff bodies, J. Mech. Science and Technology, 25 (3) (2011) 695–701.
15 J.J. Miau, H.W. Tsai, Y.J. Lin, J.K. Tu, C.H. Fang, M.C. Chen, Experiment on smooth, circular cylinders in cross-flow in the critical Reynolds number regime. Exp Fluids, 51 (2011) 949–967.
16 J.C.K. Cheung, W.H. Melbourne, Turbulence effects on some aerodynamic parameters of the circular cylinder at supercritical Reynolds number, J. Wind Eng. Ind. Aerodyn. 14 (1983) 399-410, 413-415.
17 M. Novak, H. Tanaka, Pressure correlations on a vibrating cylinder, Proc. of the 4th Int. Conf. on Wind Effects on Buildings and Structures, Heathrow, England, 1975, 227-232.
18 J.F. Howell, M. Novak, Vortex shedding from circular cylinders in turbulent flow, Wind Eng. 1 (1989), Pergamon, Oxford.
19 A.K. Gupta, K. Arun, Vortex shedding induced oscillations around bluff bodies, Proc. of the 11th Int. Conf. on Wind Engineering, Lubbock, USA, 2003, 1937-1944.
20 S. Pastò, Vortex-induced vibrations of a circular cylinder in laminar and turbulent flows, J. Fluids Struct., 24 (2008) 977–993.
21 A. Zasso, M. Belloli, S. Giappino, S. Muggiasca, Pressure field analysis on oscillating circular cylinder, J. Fluids Struct., 24 (2008) 628–650.
22 R.M.C. So, X.Q. Wang, W.C. Xie, J. Zhu, Free-stream turbulence effects on vortex-induced vibration and flow-induced force of an elastic cylinder, J. Fluids Struct., 24 (2008) 481–495.
23 M. Belloli, S. Giappino, S. Muggiasca, A. Zasso, Force and wake analysis on a single circular cylinder subjected to vortex induced vibrations at high mass ratio and high Reynolds number, J. Wind Eng. Ind. Aerodyn. 103 (2012) 96–106.

The Seventh International Colloquium on Bluff Body Aerodynamics and Applications (BBAA7)
Shanghai, China; September 2-6, 2012

Aeroelastic response of an inclined circular cylinder in smooth and turbulent flow

Kichiro Kimura [a], Kusuo Kato [b], Yoshinobu Kubo [b]

[a]*Department of Civil Engineering, Tokyo University of Science, 2641 Yamazaki, Noda-shi, Japan*
[b]*Department of Civil Engineering, Kyushu Institute of Technology, 1-1 Sensuicho, Tobata-ku, Kitakyushu-shi, Japan*

ABSTRACT: In order to clarify the characteristics of large amplitude wind-induced response of cables in cable-stayed bridges, a series of wind tunnel tests was conducted in smooth and grid-generated turbulent flow. Tests were conducted at up to around 50 m/s, using circular cylinder models with inclined angle of 30°, 40° and 45°. *Sc* of the models was somewhat smaller than the prototype. Large responses with amplitude more than 2*D* were observed. The response in more turbulent flow had less intense negative aerodynamic damping, but large nondimensional response, σ/D, around 1.3 was still observed with structural damping in logarithmic decrement δ = 0.027-0.034 for β = 30° and I_u = 4.6% case. For β = 30° case, the order of onset wind speeds in different turbulence intensities seemed to correspond to that of the critical *Re* numbers. However, for the other two cases, the order was opposite. Therefore, the cause of the intense response still needs to be studied for clear understanding. In limited cases, effects of model mass or natural frequency were also studied.

KEYWORDS: Inclined cable, Dry cable galloping, Wind-induced vibration, Wind tunnel test

1 INTRODUCTION

Wind-induced vibrations of stay cables of long-span cable-stayed bridges need to be considered in the design, because they are very flexible with low damping (Tanaka & Yagi[1]). Phenomena such as the rain-wind induced vibration have been drawing attention for decades and their characteristics as well as countermeasures have been clarified so that their harmful effects can be reduced to some extent.

On the other hand, the possibility of dry inclined cable galloping was pointed out relatively recently. There are some theoretical (Macdonald & Larose[2,3]) and computational (Yeo & Jones[4]) studies as well as experimental (Cheng *et al.*[5,6], Matsumoto *et al.*[7]) and field measurement (Zuo and Jones[8]) ones on the dry inclined cable galloping, but its characteristics and mechanism are still not clear. One reason seems to come from that the vibration is difficult to be reproduced even among laboratory experiments.

The authors conducted a series of aeroelastic wind tunnel tests of inclined circular models in smooth flow (Kimura *et al.*[9]). By adjusting the inclination of a fairing plate installed at the windward of the model top end, reasonably good reproducibility was obtained among the test results. This study is to extend the test cases also in grid generated turbulence with heavier models, in order to clarify the response characteristics with conditions more close to the prototype cables.

2 EXPERIMENTAL SETUP

A circular cylinder model with an inclined angle was elastically supported in a closed section of a wind tunnel and its responses were measured.

2.1 *Wind tunnel and flow condition*

The wind tunnel at Sumitomo Heavy Industries Ltd. was used (Fig. 1). The closed test section has the width of 2.0 m, height of 3.0 m, and length of 15 m. The wind speed can be varied between 0.3 and 60 m/s.

Tests were conducted in smooth flow with turbulence intensity less than 0.5 %, and grid-generated turbulent flow. The turbulence generating grid had mesh size of 800 mm and bar size of 100 mm and it was located at 9.05 or 3.66 m upstream of the model. The turbulence intensities of *u*-component (mean wind direction), I_u at the model location were 4.6 % and 10.4 %, respectively. I_v (lateral wind direction component) were 4.8 % and 10.5 %, and I_w (vertical wind direction component) were 5.1 % and 11.9 %.

2.2 *Circular cylinder models and model supporting system*

The circular cylinder models had a diameter D = 114 mm and were made of a standardized polyvinyl chloride pipe. Three types of inclined angles β were tested using different models, i.e., β = 30°, 40°,and 45° (Fig. 2). The circular cylinder model was supported in the vertical plane that includes the wind direction. Only inclined angle β was given without any yaw angle. The height between top and bottom of the models was 1.18 m.

In order to avoid the complicated effects caused by the leakage flow through the gap between the hole of the wind tunnel wall and the circular cylinder model, whole model supporting system was installed in the wind tunnel (Figs. 1 and 2). Model supporting systems as shown in Figure 3 supported the top and bottom of the model which allowed along-wind and across-wind motion of the model. For each supporting system, four bars with air bearings were used, and two sets and one set of coil springs for along-wind and across-wind motion, respectively, were installed to provide the restoring force. The air bearings were used for the small structural damping. The supporting system was designed by taking reference to the study by Sarkar *et al.*[10], but

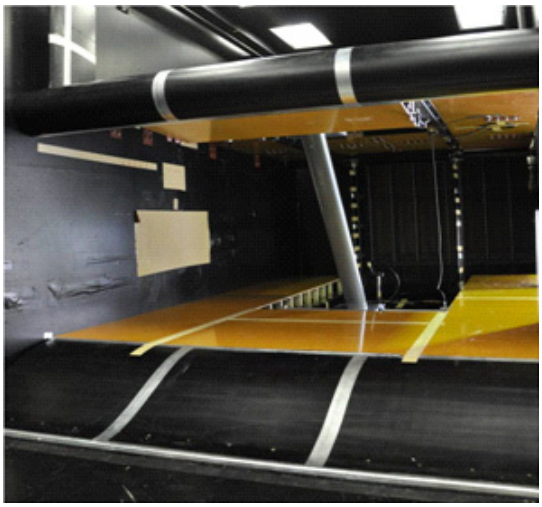

Figure 1. Model set in the wind tunnel

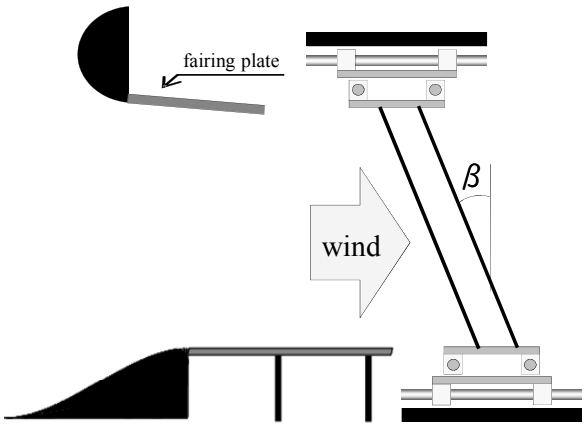

Figure 2. Model side view and definition of inclined angle β

Table 1. Test cases and dynamic characteristics of the models

Skew angle β	Flow	Natural frequency f_0 (Hz)	Logarithmic decrement δ	Mass per unit span m (kg/m)
30°	Smooth	0.990	0.0035	26.32
		0.784	0.0034	
	I_u=4.6%	0.991	0.0029	
		0.995	0.014 - 0.018	
		0.999	0.027 - 0.034	
	I_u=10.4%	0.990	0.0035	
40°	Smooth	0.929	0.0030	26.42
	I_u=4.6%	0.930	0.0028	
	I_u=10.4%	0.929	0.0034	
45°	Smooth	0.892	0.0031	25.65
	I_u=4.6%	0.892	0.0035	
	I_u=10.4%	0.892	0.0030	
	Smooth	1.012	0.0031	12.66

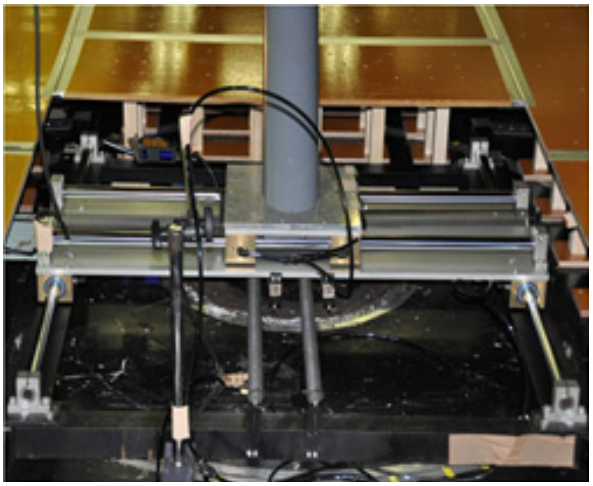

Figure 3. Model supporting system (at the bottom of the model, viewed from leeward)

the system in this study support the model's upper and lower sides instead of its right and left sides in their study. It allowed the response as large as 2D with simple restoring force provided by the coil springs without any secondary stiffness. Although the supporting system allowed 2DOF motion, there were considerable difference between the masses corresponding to the along-wind and across-wind motion; the mass in the along-wind motion was larger by about 40 kg in total than the across-wind motion. Therefore, the along-wind response was used simply to calculate the mean wind force, and only the across-wind motion is considered to be significant and its characteristics are discussed in this study.

The test cases and dynamic characteristics of the model are shown in Table 1. Their Scrouton numbers of the models, Sc, defined as $Sc = 2\ m\delta / (\rho\ D^2)$, were 9.6-11.6 for most of them, which is about half of the prototype stay cables. The logarithmic decrement was close to the prototype value but the model mass could not be increased due to the supporting system's limitation. In the definition of Sc, ρ is the air density. The cases with larger damping for $\beta = 30°$ or lighter mass for $\beta = 45°$ were also conducted to clarify the effects of them.

2.3 *Response measurement*

The along-wind and across-wind motions were measured by laser displacement sensors. The output of the sensors was low pass filtered at 30 Hz, and sampled with 500Hz for 60 sec. Because some of the responses were non-stationary, the standard deviation of the across-wind displacement data for 60sec, σ, was normalized by D, and it was plotted as the response amplitude in the wind speed-amplitude figures. In some cases, time histories of developing response from at rest condition or decaying response from larger initial displacement were measured to obtain the aerodynamic damping data.

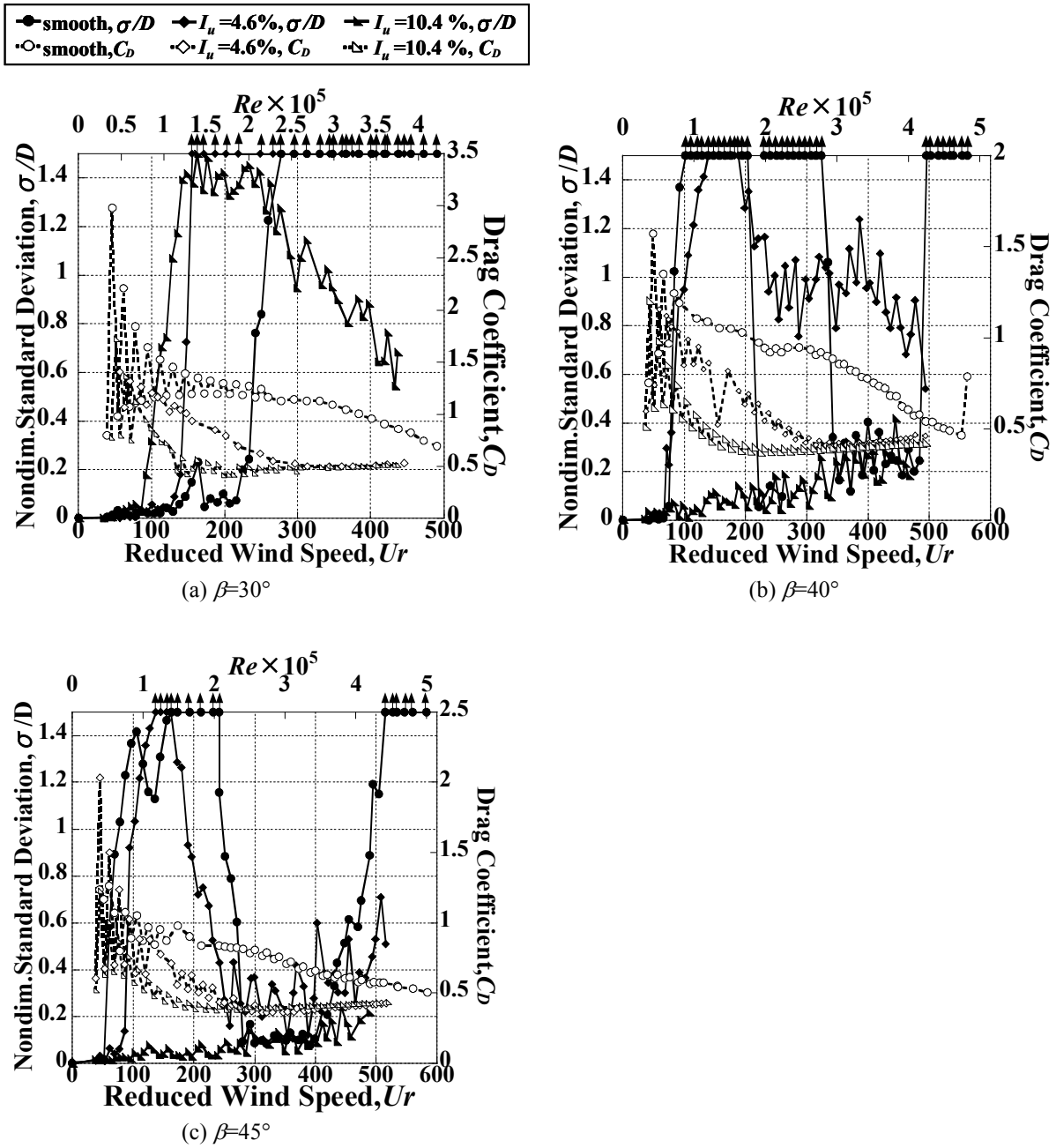

(a) β=30°

(b) β=40°

(c) β=45°

Figure 4. Model responses and drag coefficients

3 EXPERIMENTAL RESULTS

3.1 *Model responses and drag coefficients*

The nondimensional standard deviation across-wind response amplitudes of the models are shown in Figures 4. The horizontal axis is the reduced wind speed $U_r = U / (f_0 D)$ and *Re*. In the figures, drag force coefficients are also plotted that were simply estimated from mean along-wind displacement of the model. The C_D data at particularly lower wind speed seem to change alternately. This is because a half of the data were taken by increasing the wind speed and the rest were taken by decreasing the wind speed between the measurements, so that the wind speed of each measurement was arranged alternately. It should be judged that this simple C_D measurement was not very accurate including the error as much as the amplitude of the alternate change. Nevertheless, a clear tendency can be seen that the critical *Re* decreases with increased turbulence.

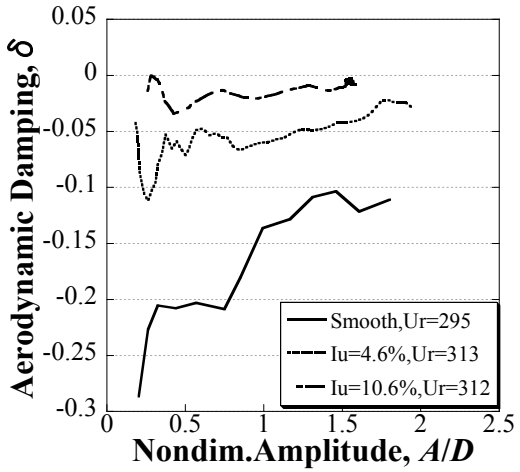

(a) β=30°

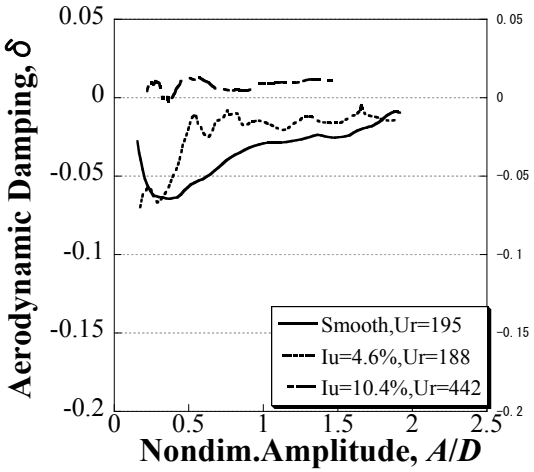

(b) β=40°

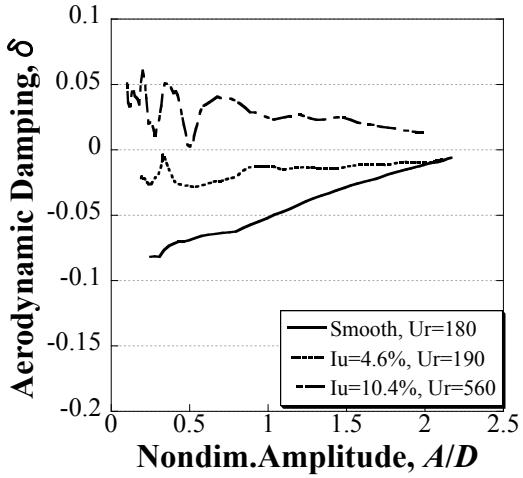

(c) β=45°

Figure 5. Aerodynamic damping in log decrement

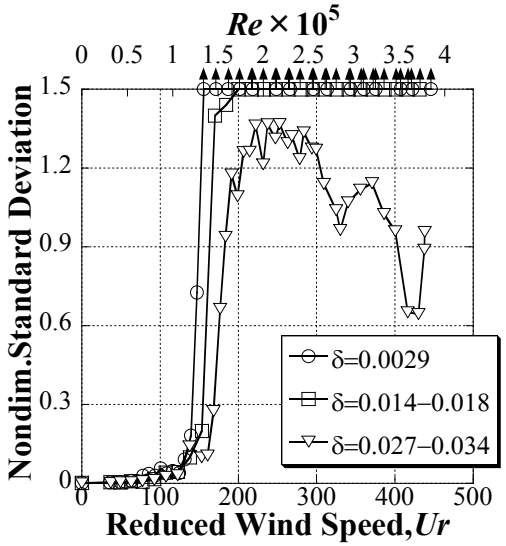

Figure 6. Response with various damping (β=30°, I_u=4.6%)

Large responses with amplitude more than 2*D* were observed in less turbulent flow for all β cases. The response became less intense in more turbulent flow. For $\beta = 30°$ case, the order and value of onset wind speeds in different turbulence intensities seem to correspond to those of the critical *Re*. However, for the $\beta = 40°$ and 45° cases, the order was opposite, and the onset wind speed and critical *Re* do not correspond to each other. Therefore, it is still difficult to identify the possible cause of the intense response.

3.2 *Aerodynamic damping*

Some of the measured aerodynamic damping are shown in Figures 5. The horizontal axis of the figure is A/D, where, A is the model response amplitude in across-wind direction. The exciting force of the large response vibration was strong and the absolute value of negative aerodynamic damping exceeded $|\delta| = 0.2$ for $\beta = 30°$ case in smooth flow at the amplitude less than $A/D = 0.8$. The exciting force was less intense for the response in stronger turbulence. In order to confirm the intense negative aerodynamic damping of the response, a few cases were conducted with added structural damping by attaching adhesive tape to the model supporting springs. It can be seen that large nondimensional standard deviation response around 1.3 was still observed with much larger damping ($\delta = 0.027$-0.034) for $\beta = 30°$ and $I_u = 4.6\%$ case (Fig. 6).

3.3 *Effects of the masses and natural frequencies*

In this study, heavier models were used than the previous study (Kimura *et al.*[9]) as stated in the introduction. The effects of the mass were studied in one set of cases and the responses are shown in Figure 7. It should be noted that the natural frequencies of the models were also different by 13%. The responses were somewhat different, and the effects of the model mass seem to be complex.

The effects of the natural frequency were also studied in one set of cases (Fig. 8). When the horizontal axis is taken as reduced wind speed as in the figure, the onset wind speeds seem to coincide. On the other hand, in the previous study (Kimura *et al.*[9]) where the similar comparison was made with $\beta = 45°$ model, the onset wind speeds were more closely matched when the wind speeds were expressed in terms of *Re*. These different characteristics with respect to the natural

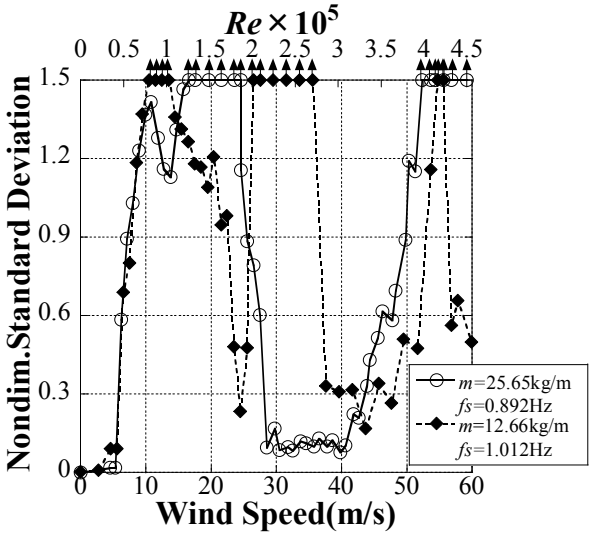

Figure 7. Effects of different masses
($\beta = 45°$, smooth flow)

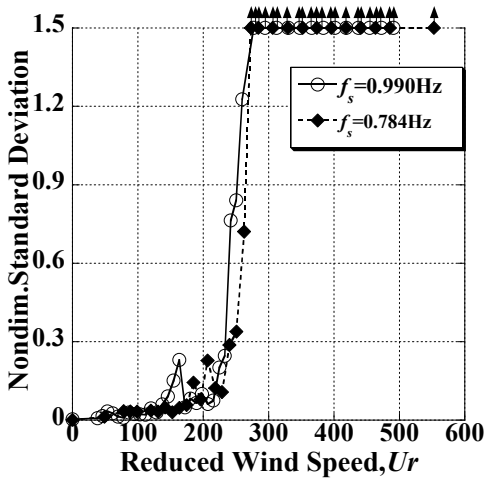

Figure 8. Effects of different natural frequency
(β=30°, smooth flow)

frequency may be due to different β of the models. However, still further studies seem to be necessary for clear understanding.

4 EXCITING FORCE CHARACTERISTICS

In order to understand the response characteristics in more detail, the excitation forces were tried to be computed by numerically integrating the equation of motion. Some examples of the phase difference of the force from the response is plotted with open triangle symbols in Figures 9. The response is also shown in the figures for reference. This way of the force estimation may result in some error, but from the figures, the computed phase lag seems to be more or less consistent.

For $\beta = 30°$ case, positive phase lag up to more than $\pi/2$ was observed during large response in smooth flow (Fig. 9(a)). The phase lag became much smaller in turbulent flow (Fig. 9(b)). The phase lag for $\beta = 40°$ and $45°$ cases were even smaller and nearly zero in turbulent flow with $I_u = 4.6\%$.

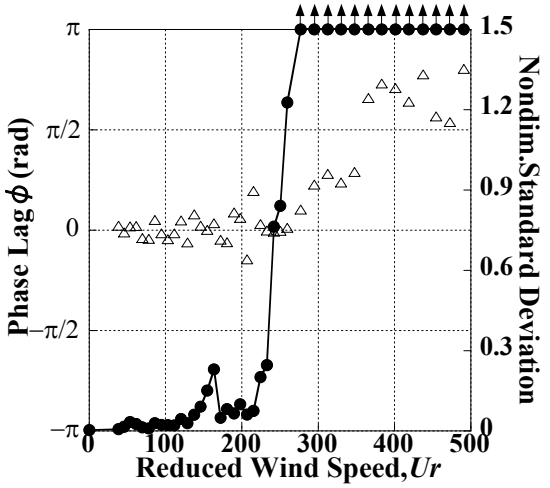

(a) β=30°, smooth flow

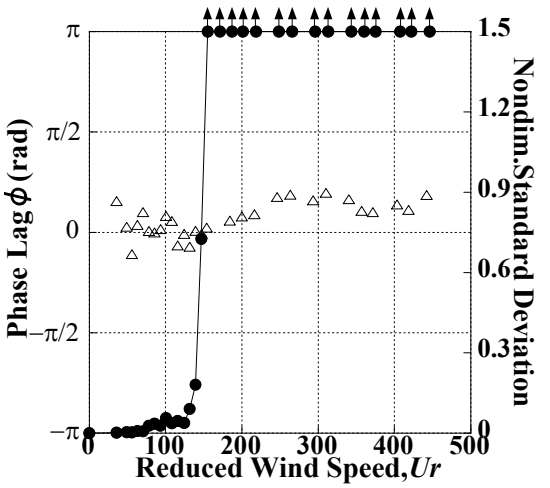

(b) β=30°, I_u = 4.6%

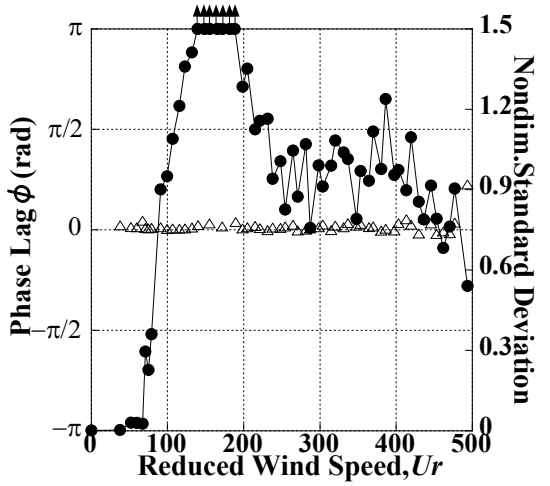

(c) β=40°, I_u = 4.6%

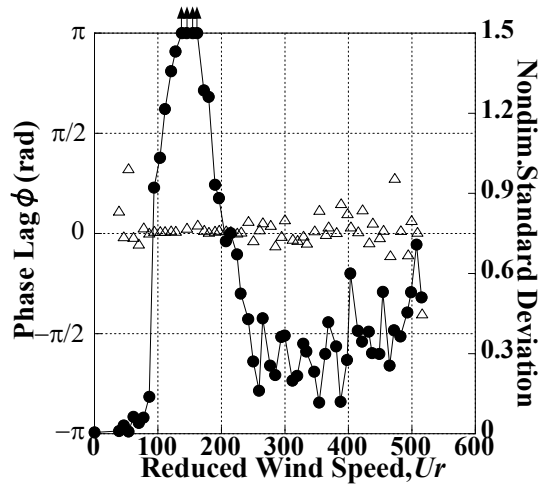

(d) β=45°, I_u = 4.6%

Figure 9. Phase lag of the exciting force from the response

5 CONCLUDING REMARKS

Wind tunnel tests were conducted to clarify the characteristics of large amplitude response of stay cables. The response generally became less intense with increase of turbulence, but large response of $\sigma/D = 1.3$ was still observed with $\delta = 0.027$-0.034 for $\beta = 30°$ and $I_u = 4.6\%$. It is necessary to confirm that the flow condition around the model in this study actually corresponds to the stay-cables with very large aspect ratio. However if it is the case, the large amplitude response in high wind speed may have been reproduced in this study. The characteristics and cause of the response still needs to be studied for clearer understanding.

6 ACKNOWLEDGEMENTS

The authors would like to thank Dr. Masao Miyazaki at Sumitomo Heavy Industries Ltd. and Mr. Kazuhiro Asai at Sumitomo Heavy Industries Engineering & Services Co., Ltd. for their kind arrangements to make the wind tunnel tests possible. Also the help by Mr. Yoshihiro Ohhashi at COA Co., Ltd. and Mr. Yusuke Ogawa and Rokhamsay Chinda at Graduate School of Engineering, Kyushu Institute of Technology are acknowledged with the authors' sincere thanks.

REFERENCES

1 H. Tanaka and T. Yagi, Cable vibrations and control methods, In Y. Fujino, K. Kimura, H. Tanaka, Wind Resistant Design of Bridges in Japan – Developments and Practices, Springer, Tokyo, 2012, pp. 197-229.
2 J.H.G. Macdonald and G.L. Larose, A unified approach to aerodynamic damping and drag/lift instabilities, and its application to dry inclined cable galloping, J. Fluids Struct., 22 (2006) 229-252.
3 J.H.G Macdonald and G.L. Larose, Two-degree-of-freedom inclined cable galloping, J. Wind Eng. Ind. Aerodyn., 96 (2008) 291-326.
4 D.H. Yeo and N.P. Jones, Characterization of flow oblique to a circular cylinder with low aspect ratio using 3-D detached eddy simulation, J. Wind Eng. Ind. Aerodyn., 99 (2011) 1117-1125.
5 S. Cheng, G.L. Larose, M.G. Savage, H. Tanaka and P.A. Irwin, Experimental study on the wind-induced vibration of a dry inclined cable—Part I: Phenomena, J. Wind Eng. Ind. Aerodyn., 96 (2008) 2231-2253.
6 S. Cheng, P.A. Irwin and H. Tanaka, Experimental study on the wind-induced vibration of a dry inclined cable—Part II: Proposed mechanisms, J. Wind Eng. Ind. Aerodyn., 96 (2008) 2254-2272.
7 M. Matsumoto, T. Yagi, H. Hatsuda, T. Shima, M. Tanaka and H. Naito, Dry galloping characteristics and its mechanism of inclined/yawed cables, J. Wind Eng. Ind. Aerodyn., 98 (2010) 317-327.
8 D. Zuo and N.P. Jones, Interpretation of field observations of wind- and rain-wind-induced stay cable vibrations, J. Wind Eng. Ind. Aerodyn., 98 (2010) 73-87.
9 K. Kimura, K. Kato, Y. Kubo and Y. Oh-hashi, An aeroelastic wind tunnel test of an inclined circular cylinder, In Proc. 8th Int. Symp. Cable Dynamics, Paris, 2009, pp.143-148.
10 P.P.Sarkar, A.G.Chowdhury and T.B.Gardner, A novel elastic suspension system for wind tunnel section model studies, J. Wind Eng. Ind. Aerodyn., 92(2004) 23-40.

The Seventh International Colloquium on Bluff Body Aerodynamics and Applications (BBAA7)
Shanghai, China; September 2-6, 2012

Two degrees of freedom flow-induced vibrations on a cylinder

Dai ZHOU [a], Jiahuang TU [a], Yan BAO [a]

[a] *School of Naval Architecture, Ocean and Civil Engineering, Shanghai Jiaotong University, Shanghai,China.*

ABSTRACT: A numerical study is performed on the flow-induced vibrations of isolated cylinder that is elastically mounted in two degrees of freedom with varying in-line to transverse natural frequency ratios, f_{nx}/f_{ny}. A characteristic-based-split finite element method is utilized for obtaining the solution of the incompressible flow equations in primitive variables. The Reynolds number based on upstream flow velocity and cylinder diameter, D, is fixed at Re=150. The computation is carried out for lower reduced mass of M_r=2.0 and for reduced velocities in the range of U_r=3.0-12.0, with increment of one; the structural damping ratio is set to zero to maximize the vortex-induced response of the bodies. We mainly focused on the effect of natural frequency ratios on the characteristics of vortex-induced vibration (VIV) responses, including wake frequencies, orbital trajectories, response amplitudes, aerodynamic forces and wake mode patterns.

KEYWORDS: isolated cylinder; two degrees of freedom (2-dof); vortex-induced vibration(VIV); natural frequency ratio; Arbitrary Lagrangian-Eulerian (ALE) formulation; finite element method.

1 INTRODUCTION

Vortex-induced-vibration (VIV) of cylindrical structures is of practical interest to many engineering fields (such as long span cable-stayed building structures, suspension bridges, heat exchangers *etc.*), and has led to extensive fundamental studies in the past decades.

For flexibly mounted circular cylinders immersed in uniform cross-flows, large amplitude transverse motions are excited, when the vortex shedding frequency of the stationary cylinder is sufficiently close to the natural frequency of cylinder vibration. This well-known condition is called ‘lock-in’ or ‘frequency synchronization’, at which the vortex shedding frequency shifts on the natural frequency of vibration. Dynamic interaction between vortex shedding and cylinder body can also lead to significant oscillation in in-line direction at a double-frequencies of the vortex shedding, due to oscillating drag component exerted on the cylinder. In-line amplitude is typically one-order smaller compared to the values of transverse counterpart, and hence, the in-line response has surprisingly little effect on the transverse response in a regime where the mass ratios are greater than 6. However, Jauvtis and Williamson [1] showed that, as the mass ratios are reduced to below 6, stream-wise response makes dramatic changes in the fluid-structure interaction, yielding massive vibration with three times diameters of peak-to-peak amplitudes. The response branch characterized by this massive oscillation was called by Jauvtis and Williamson [1]as a ‘super-upper’ branch, and the associated periodic vortex mode, in which a triplet of vortices are formed in each half cycle, was defined as a ‘2T’ mode. More recently, a number of research studies have provided important insights into the 2-dof responses [2, 3].

The previous studies of 2-dof VIV response of cylinder with varying natural frequency ratios have been limited to relatively larger Reynolds numbers [4-6]. In the laminar flow regime, the combined in-line and transverse VIV may show quite different response characteristics; this

expectation is derived from the numerical work by Lucor and Triantafyllou [7], since they showed that the two distinct response peaks, which originally appeared in the experiment as the frequency ratio close to 2.0, do not appear in the 2-D numerical simulations, although they explained that the coarse resolution in the frequency ratios does not allow to verify the presence of this double peak. It is, therefore, more desirable to explore the response characteristics of VIV for varying natural frequency ratios in the laminar flow regime.

In this work, we present computational results for VIV response of single cylinder, which is free to vibrate in 2-dof with varying in-line to transverse natural frequencies, corresponding ratio values varies between 1.0 and 2.0. The Reynolds number, based on the diameter of cylinder, is fixed to be 150; therefore, laminar 2-D flow assumption is expected to be valid in this investigation. The main objective of the present work is to systematically study the effects of natural frequencies on 2-dof VIV responses of single cylinder at laminar flow regime. The VIV response is characterized in terms of vortex shedding frequencies, motion trajectories, amplitudes and aerodynamic forces exerting on cylinder. Vortex shedding modes are also scrutinized to reveal the effects of natural frequencies on the unsteady wake patterns behind the cylinder.

2 GOVERNING EQUATIONS AND NUMERICAL METHODS

2.1 *Governing equations*

The fluid flow is governed by the two-dimensional, incompressible, Navier-Stokes equations, which is expressed in terms of the primary variables in Cartesian coordinate system as follows:

$$\frac{\partial u_i}{\partial t} + u_j \frac{\partial u_i}{\partial x_j} = -\frac{\partial p}{\partial x_i} + \frac{1}{\mathrm{Re}} \frac{\partial^2 u_i}{\partial x_j \partial x_j} \tag{1}$$

$$\frac{\partial u_i}{\partial x_i} = 0 \tag{2}$$

where u_i (or u_j) is the velocity component in the x_i (or x_j) coordinate direction and p is the pressure divided by the fluid density, ρ. The dimensionless parameter of Reynolds number, Re, is based on the cylinder diameter, D, the free-stream velocity, U_∞, and the kinematic viscosity of the fluid, υ; i.e., $Re=U_\infty D/\upsilon$.

As the flexible body is under the action of flow-induced forces, it may exhibit oscillatory motions in both in-line and cross-flow directions. The motion of the body can be modeled via a mass-spring system, and is governed by the motion equations, respectively, in in-line and transverse directions as follows:

$$\ddot{X} + 4\pi\xi_x f_{nx} \dot{X} + 4\pi^2 f_{nx}^2 X = \frac{C_D}{2M_{rx}} \tag{3}$$

$$\ddot{Y} + 4\pi\xi_y f_{ny} \dot{Y} + 4\pi^2 f_{ny}^2 Y = \frac{C_L}{2M_{ry}} \tag{4}$$

Here, $\ddot{X}$, $\dot{X}$ and X denote the in-line acceleration, velocity and displacement of the cylinder, respectively; while $\ddot{Y}$, $\dot{Y}$ and Y represent the same quantities corresponding to the transverse motion. f_{nx} and f_{ny} represent the natural frequencies of the cylinder respectively along

in-line and cross-flow directions; $\xi_x=\xi_y=\xi$ are the structural damping ratios; $M_{rx}=M_{ry}=M_r=m/\rho D^2$ are the reduced masses of the body, where m is the mass of the cylinder per unit length. C_D and C_L are the instantaneous drag and lift coefficients, respectively, and calculated as $C_D=2F_D/\rho U_\infty{}^2 D$, $C_L=2F_L/\rho U_\infty{}^2 D$, where F_D, F_L are the forces acting upon the cylinder in the in-line and cross-flow directions. The fluid forces are computed by performing an integration, involving both the pressure and viscous stresses, around the surface of the cylinder. The reduced velocity of the cylinder is based on the natural frequency in transverse direction; i.e., $U_r=U_\infty/f_{ny}D$.

2.2 *Numerical formulations*

To account for the cylinder motions, an Arbitrary Lagrangian-Eulerian (ALE) formulation of the incompressible Navier-Stokes equations is employed for the solution of fluid flows with moving boundaries [8, 9]. The ALE formulation is easily implemented by modifying convective velocity in equation (1) into $c_i=u_i-w_i$, where w_i is the ith component of the grid velocity vector.

A stabilized second-order characteristic-based-split method, as explained in Bao et al. [10], is employed for the discretization of governing equations in ALE form.

Dynamic equations of cylinder motions are solved using an explicit time integration method that was presented in Placzek et al. [11]. They reported that the numerical damping in this algorithm was dramatically reduced by combining a centered upwind and downwind scheme for the prediction of the displacement. The integration step is described as follows:

(i) The cylinder acceleration is explicitly predicted from the previous time step,

$$\ddot{X}^{n+1}=\frac{C_D^n}{2M_{rx}}-4\pi\xi_x f_{nx}\dot{X}^n-4\pi^2 f_{nx}^2 X^n \tag{5}$$

$$\ddot{Y}^{n+1}=\frac{C_L^n}{2M_{ry}}-4\pi\xi_y f_{ny}\dot{Y}^n-4\pi^2 f_{ny}^2 Y^n \tag{6}$$

(ii) The cylinder velocities and displacements at n+1 time step are evaluated using linear approximation:

$$\dot{X}^{n+1}=\dot{X}^n+\Delta t\ddot{X}^{n+1} \tag{7}$$

$$X^{n+1}=X^n+\Delta t[(1-\theta)\dot{X}^n+\theta\dot{X}^{n+1}] \tag{8}$$

$$\dot{Y}^{n+1}=\dot{Y}^n+\Delta t\ddot{Y}^{n+1} \tag{9}$$

$$Y^{n+1}=Y^n+\Delta t[(1-\theta)\dot{Y}^n+\theta\dot{Y}^{n+1}] \tag{10}$$

where, θ is the blending factor, Placzek et al. [11] suggested that θ=0.5 can produce the smallest numerical damping; hence, in the present simulation, we also take the same value.

3 DESCRIPTION OF THE PROBLEM

3.1 *Simulation parameters*

In the present study of 2-dof vortex-induced vibration are conducted. The cylinder has equal diameter of D, and immersed in steady cross-flow of velocity U_∞, yielding the Reynolds number to Re=150. The cylinder is free to vibrate both in the streamline and transverse directions, and take very low value: M_r=2.0. To encourage high amplitude oscillations, the structural damping coefficients in both directions are set to zero; i.e., ξ=0.0. The reduced velocity, U_r (based on the natural frequency in transverse direction), is systematically increased within the range U_r=3.0-12.0 in increments of one. For each reduced velocity, five frequency ratios are considered; i.e., f_{nx}/f_{ny}=1.0, 1.25, 1.5, 1.75 and 2.0.

3.2 *Flow domains and boundary conditions*

The flow configuration and boundary conditions for a single cylinder case are shown in Figure 1. The entire computational domain was defined as Ω = [-25D, 50D] × [-30D, 30D]. A no-slip condition was applied on the surface of the cylinders: $u_x=\dot{X}$, $u_y=\dot{Y}$; a Dirichlet boundary condition was used on the inlet boundary as $u_x=U_\infty$=1. 0 and u_y=0, while at the outlet of the computational domain, it was $\partial u_x/\partial x$=0, $\partial u_y/\partial x$=0. A slip boundary condition was imposed upon the lateral boundaries: $\partial u_x/\partial y$=0 and u_y=0. For each set of numerical simulations, the solution of the stationary counterpart configurations was used as the initial conditions.

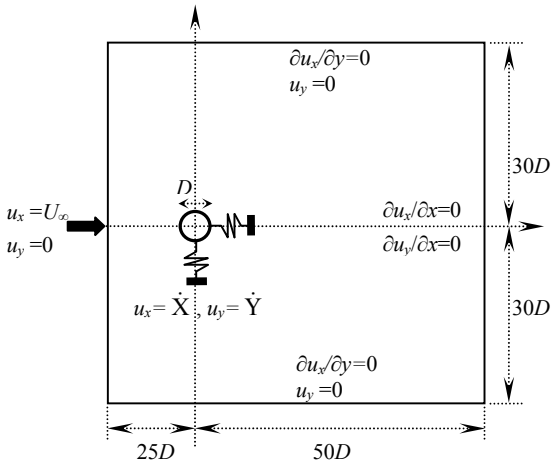

Figure 1. Schematic of the computational domain and boundary conditions for vortex-induced vibration of two-degree-of-freedom single cylinder system.

4 RESULTS AND DISCUSSION

4.1 *Vortex shedding frequency*

In Figure 2, we show the variations of Strouhal frequencies as a function of reduced velocity, corresponding to the motions in the transverse and inline directions. It is noted that, in Figure 2, we only plot the fundamental frequency components of lift and drag signals, and hence only a single value corresponds with a given reduced velocity. The variation curves of the natural fre-

quencies (f_{nx}, f_{ny}) with the reduced velocity are also shown in this figure. In the f_{nx}/f_{ny} range 1.0-1.75, the St_y curves coincide with each other, indicating that the in-line motions have insignificant effect on the frequency synchronization features (U_r=3.0-7.0). At f_{nx}/f_{ny}=2.0, the U_r range associated with the resonant response is equal to that for the lower f_{nx}/f_{ny}, however at U_r=4.0, the corresponding value of St_y is closer to the f_{ny} curve of the cylinder. A similar curve trend in the St_x is observed in Figure 2(b); the St_x curves for the range f_{nx}/f_{ny}=1.0-1.75 also nearly collapse into a single variation curve, whereas a slight difference for f_{nx}/f_{ny}=2.0 is noticed at the lower reduced velocity range. An important frequency feature associated to the dual resonant response can be identified in Figure 2, that is, at f_{nx}/f_{ny}=1.0, the St_x curve is located upper side of the f_{nx}, indicative of the non-occurrence of dual resonant response. At f_{nx}/f_{ny}=1.25-1.75, an intersection of the St_x curve and corresponding f_{nx} curve is evidenced in the plot, showing that frequency synchronization never occurs at this range. A striking frequency behavior is observed at f_{nx}/f_{ny}=2.0, where the St_x goes up along the f_{nx} curve in the U_r range from 4.0-7.0, giving a powerful evidence for the occurrence of frequency synchronization in the in-line direction. From the above observation, it may be inferred that, in contrast to the higher Reynolds number flow, the condition for the occurrence of dual resonant response in the laminar flow regime is strictly restricted, and the associated f_{nx}/f_{ny} is about the value of 2 in a very narrow range.

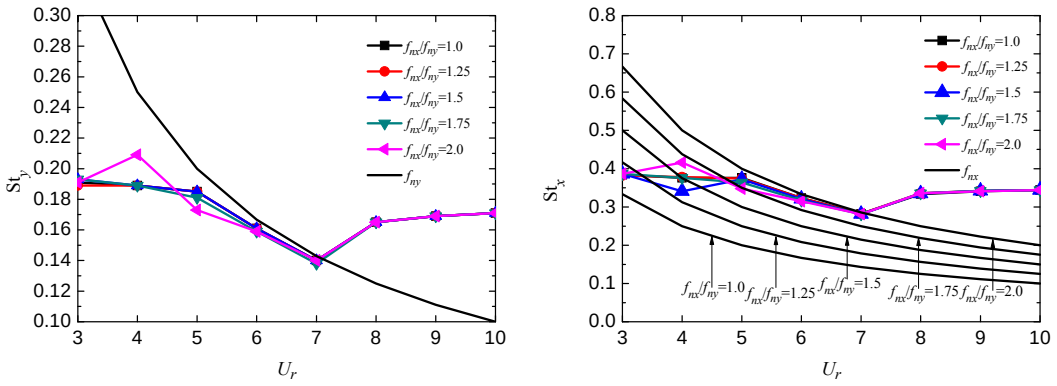

(a) vertical direction (b) in-line direction

Figure 2. Variation of Strouhal numbers of two-degree-of-freedom as a function of reduced velocity at different natural frequency ratios

4.2 *Cylinder orbital trajectories*

In general, the combined in-line and cross-flow vibrations of a single cylinder typically show a Figure-eight motion, due to the fact that the dominant frequency in the drag oscillation is twice that for the lift. The same response in terms of cylinder orbit is also noticed in the current simulations. We select the two cases of f_{nx}/f_{ny}=1.0, 2.0 to display the cylinder orbital trajectories versus the reduced velocity in Figure 3, in which (a) represents the result associated to the 'single-resonant' only in the transverse direction, while (b) corresponds to the dual-resonant response in two degrees of freedom. It can be observed that, except the case of U_r=4.0 at f_{nx}/f_{ny}=1.0, which shows a fairly messy unrepeatable orbit, most of the cylinder motion appears to be a regular periodic Figure-eight trajectories. However, it is not the case in higher Reynolds number flows. Dahl et al. [6] reported that, as the nominal natural-frequency ratio is near 1, many of the orbital shapes appear irregular, due to the fact that in-line motion does not settle into a regular trajectory. In Figure 3, the path direction in the orbital motion is also marked by a letter 'C' or 'CC', which represent the direction of the cylinder motion at the top position of the figure-eight path;

i.e., ‘C’ means clockwise , while ‘CC’ denotes counterclockwise direction. It is found that at f_{nx}/f_{ny}=1.0, the path direction appears to be either clockwise or counterclockwise trajectories; however, at f_{nx}/f_{ny}=2.0, where dual-resonant response could occur, only counterclockwise trajectory accompanies the cylinder motion. This observation is similar with that reported in Dahl et al. [5]. They also argued that the path direction and the orbital shape are important indicators of the appearance of higher harmonic forcing, and show that the counterclockwise path direction is highly repeatable.

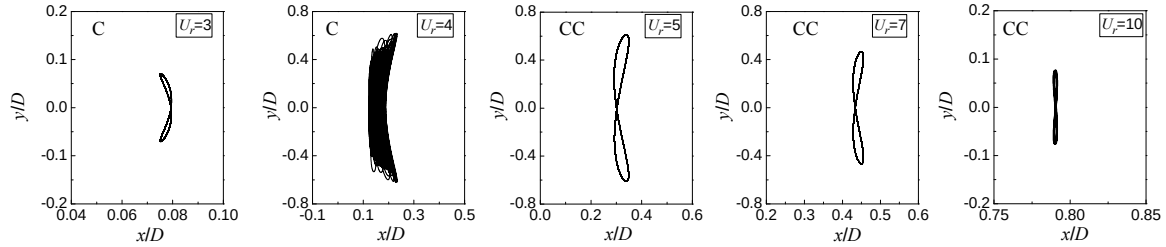

(a) f_{nx}/f_{ny}=1.0

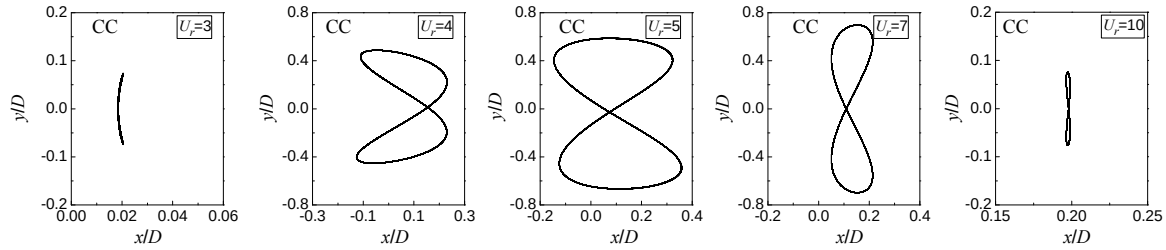

(b) f_{nx}/f_{ny}=2.0

Figure 3. Comparison of Lissajous figures of the trajectory for a single cylinder at different natural frequency ratios; CC (Counterclockwise): trajectory moves upstream at the top of the figure-eight; C (Clockwise): trajectory moves downstream at the top of the figure-eight.

4.3 *Cylinder response amplitudes*

When the mass ratios are less than 6.0, a dramatic change occurs in the fluid-structure interactions and hence, the freedom to oscillate in line greatly affects the transverse vibrations [1]. In this subsection, the effects of the combined 2-dof vibrations on the amplitudes of the cylinder motions are studied at different natural frequency ratios. Figure 4 shows the variation of the non-dimensional maximum vibration amplitudes with U_r for both transverse and inline directions; i.e., Y_{max}/D, X_{max}/D. As observed in Figure 4(a), in the f_{nx}/f_{ny} range from 1.0 to 1.5, the resonant response curves collapse together and exhibit similar variation trend against the reduced velocity. The maximum amplitudes reach a peak value at a reduced velocity, to which the resonant response begins, with the values around Y_{max}/D=0.615. At f_{nx}/f_{ny}=1.75, the response curve shifts slightly, with an increased peak value of Y_{max}/D=0.722. A dramatic change is observed as the frequency ratio increases up to 2.0, where the peak amplitude shifts to occur at a larger reduced velocity of U_r=6.0, with the value rapidly increased to as large as Y_{max}/D=0.86. It is worth noting that, in contrast to the earlier experiments, two distinct response peaks could appear when the frequency ratio is near the value of 2.0 [4,12], however, in the present simulations, we does not observed the presence of the double-peak response. The same numerical results are also reported

recently by Lucor and Triantafyllou [7]; they also ascribed this to the lower level of the resolution of the simulation parameters.

Corresponding to the response curve of the transverse amplitude, a distinct response in the in-line amplitude of the cylinder motion is excited at f_{nx}/f_{ny}=2.0, on which the cylinder undergoes dual-resonant vibrations. The peak value of the non-dimensional amplitude, X_{max}/D, shifts to a larger reduced velocity as that in the transverse direction, and it reaches a value as high as X_{max}/D=0.256; this value is at the same level as reported in the experiment of Dahl et al. [6].

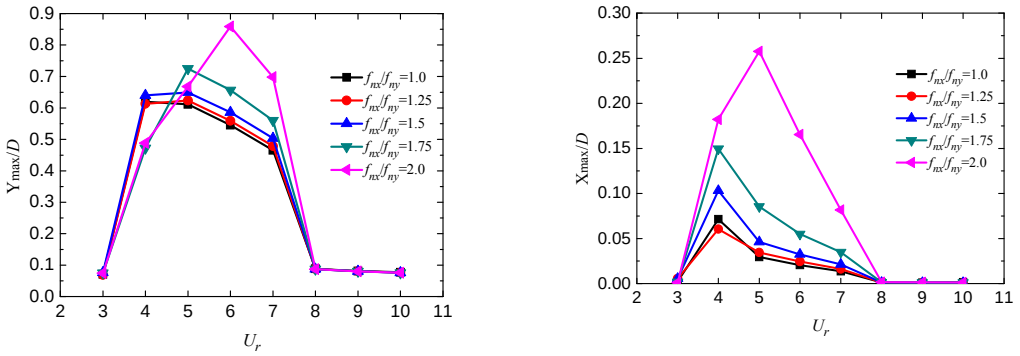

(a) vertical direction (b) in-line direction

Figure 4. The non-dimensionalized maximum vibration amplitudes in two-degree-of-freedom as a function of reduced velocity at different natural frequency ratios.

4.4 *Aerodynamic forces*

In the following, we further investigate the statistical characteristics of the forces exerted on the cylinder. Figure 5 shows the variation of the drag and lift coefficients against the reduced velocity, including mean drag coefficient ($\overline{C}_D$) and lift (C'_L) coefficients. As seen in Figure 5(a), the force curves of mean drag are nearly coincided in the range of f_{nx}/f_{ny}=1.0-1.75, while a marked increase is evidenced as the natural frequency increases to f_{nx}/f_{ny}=2.0. The lift oscillation appears to be less sensitive to the variation of f_{nx}/f_{ny}; the peak response is reduced from C'_L=1.419 to 0.992 at the same reduced velocity as the f_{nx}/f_{ny} increases to 2.0, in Figure 5(b).

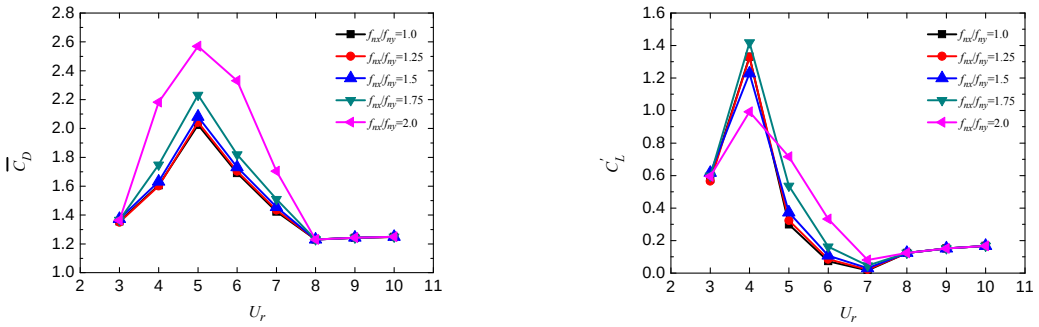

(a) mean drag coefficient (b) r.m.s. of lift coefficient

Figure 5. Variations of drag and lift force coefficients with the reduced velocities at different natural frequency ratios.

4.5 *Vortex shedding modes*

Figure 6 provides the instantaneous wake structure in terms of fully developed vorticity fields for selected natural frequency ratios of f_{nx}/f_{ny}=1.0 and 2.0. As seen in Figure 6(a), a classical 2S mode (two single vortices of opposite sign are shed per cycle) becomes the predominant vortex shedding pattern for the f_{nx}/f_{ny}=1.0. Even so, there exist some differences in the wake structures associated with the different reduced velocities. For example, an irregular unstable vortex street is observed at U_r=4.0, which is consistent with the unrepeatable cylinder motions as shown in Figure 3(a). In addition, the vertical or horizontal spacing between the successive vortices may be different for the different reduced velocities. For example, at U_r=5.0, a two-row vortex structure is formed in the wake, in which the vertical spacing is relatively large. When compared to the results from the case of transverse-only motions [13], the wake pattern for the 2-dof VIV at f_{nx}/f_{ny}=1.0 is basically consistent with the former situations. It is not surprising, because under this condition, the limited oscillation in the in-line direction has only very restricted impact on the wake.

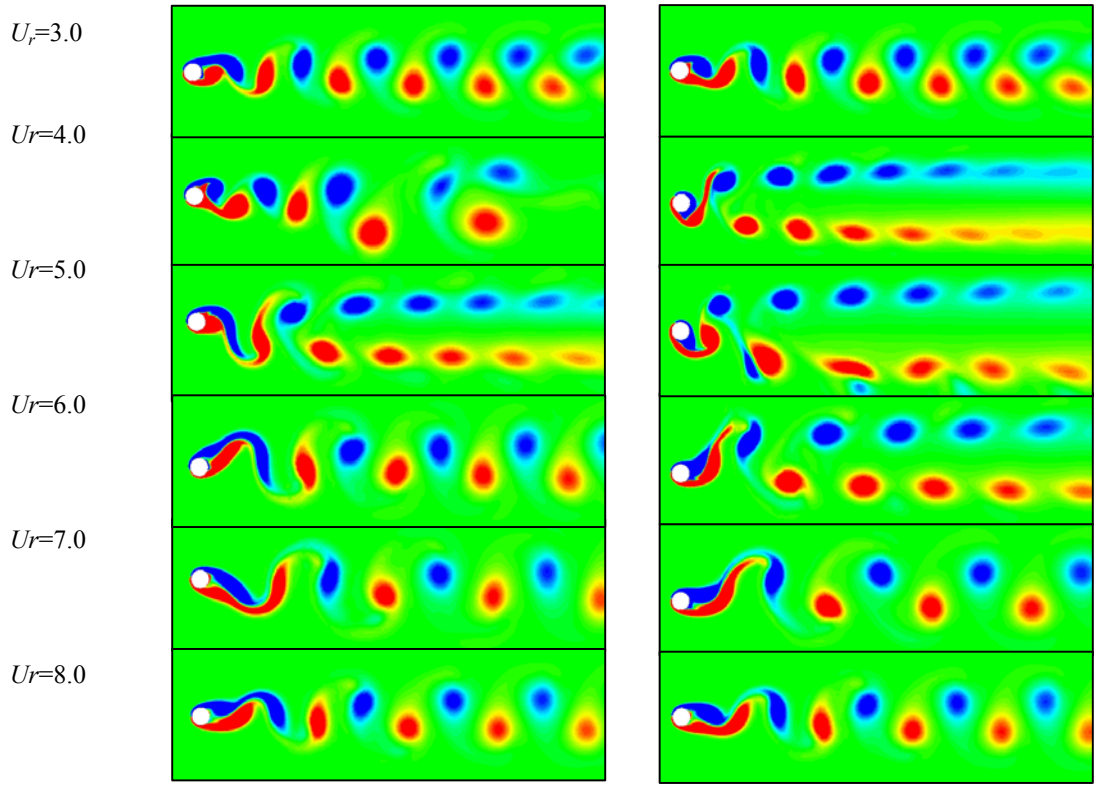

(a) f_{nx}/f_{ny}=1.0 (b) f_{nx}/f_{ny}=2.0

Figure 6. Variation of instantaneous vorticity fields for the fully developed, unsteady flow past a freely vibrating cylinder as a function of reduced velocity at different natural frequency ratios.

A dramatic change in the wake structure is found at f_{nx}/f_{ny}=2.0, as in Figure 6(b). From the in-line amplitude curve in Figure 4(b), we have observed that the X_{max}/D increases with increases in reduced velocity, and reaches its peak at U_r=5.0, after then, it drops down with the further increase of the reduced velocity. Correspondingly, the wake pattern varies with the variation in the amplitude of the cylinder motions. As the reduced velocity changes from 3.0 to 4.0, the wake re-

tains the 2S mode; however, it becomes significantly wider and leads a two-row configuration behind the cylinder. As the reduced velocity further increases to reach U_r=5.0, the in-line amplitude reaches its peak value; correspondingly, the wake pattern transforms from 2S mode to P+S mode (a single vortex and a pair of opposite signed vortices are released per cycle of shedding). After the in-line motion reaches the peak, with the decrease in the X_{max}/D, the wake is appeared as two-row vortex streets firstly, and then it changes into a classical 2S mode in a single vortex street.

5 CONCLUSION

In the present study of 2-dof vortex-induced vibration: the cylinder is immersed in steady cross-flow of velocity U_∞ and is free to vibrate both in the streamline and transverse directions, and the associated reduced masses of the structures are equal to each other and take very low value: M_r=2.0. To encourage high amplitude oscillations, the structural damping coefficients in both directions are set to zero; i.e., ξ=0.0. The reduced velocity, U_r (based on the natural frequency in transverse direction), is systematically increased within the range U_r=3.0-12.0 in increments of one. For each reduced velocity, five frequency ratios are considered; i.e., f_{nx}/f_{ny}=1.0, 1.25, 1.5, 1.75 and 2.0.

Based on the comprehensive analysis of the results, we could draw following findings:

It is found that interaction of the 2-dof dominant force frequencies is significant in the dual-resonant response regime, where the peak frequencies of the drag and lift signals can appear at the same value. In the laminar flow regime, the condition for the occurrence of dual-resonant response is strictly limited around f_{nx}/f_{ny}=2.0.

The cylinder orbital trajectory shows that at f_{nx}/f_{ny}=1.0, the path direction can appear to be either clockwise or counterclockwise; however, at f_{nx}/f_{ny}=1.0, where dual-resonant response could occur, the cylinder orbit is only in counterclockwise patterns. The combined 2-dof vibrations significantly amplify the transverse response of the cylinder, and the peak response delays to appear at a higher reduced velocity. Double-peak response, which occurs at higher Reynolds number flow, is not observed in the present simulation; this difference may be ascribed to the Reynolds number effect. The oscillating drag component is most sensitive to the variation of the natural frequency ratios, and maximized within the dual-resonant regime.

A 2S wake pattern is accompanied to the VIV of single cylinder in the transverse-only resonant response state, however, the vortex distance in both in-line and transverse directions varies with the reduced velocity. As the cylinder experiences dual-resonant response, the wake may convert from 2S to P+S pattern, which would associate to the state where the in-line response reaches its maximum amplitude.

6 ACKNOWLEDGEMENTS

Support from the National Natural Science Foundation of China (Project No. 51078230, 11172071) and the Key Project of Fund of Science and Technology Development of Shanghai (No.10JC1407900) are acknowledged.

7 REFERENCES

1 N. Jauvtis and C.H.K. Williamson, The effects of two degrees of freedom on vortex-induced vibration at low mass and damping, Journal of Fluid Mechanics, 509 (2004) 23-62.

2 F.J. Huera-Huarte and P.W. Bearman, Wake structures and vortex-induced vibrations of a long flexible cylinder-Part 1: Dynamic response, Journal of Fluids and Structures, 25 (2009) 969-990.

3 F.J. Huera-Huarte and P.W. Bearman, Wake structures and vortex-induced vibrations of a long flexible cylinder-Part 2: Drag coefficients and vortex modes, Journal of Fluids and Structures, 25 (2009) 991-1006.

4 J.M. Dahl, F.S. Hover and M.S. Triantafyllou, Two-degree-of-freedom vortex-induced vibrations using a force assisted apparatus, Journal of Fluids and Structures, 22 (2006) 807-818.

5 J.M. Dahl, F.S. Hover and M.S. Triantafyllou, Resonant vibrations of bluff bodies cause multivortex shedding and high frequency forces, Physical review letters, 99 (2007) 144503.

6 J.M. Dahl, F.S. Hover, M.S. Triantafyllou and O.H. Oakley, Dual resonance in vortex-induced vibrations at subcritical and supercritical Reynolds numbers, Journal of Fluid Mechanics, 643 (2010) 395-424.

7 D. Lucor and M.S. Triantafyllou, Parametric study of a two degree-of-freedom cylinder subject to vortex-induced vibrations, Journal of Fluids and Structures, 24 (2008) 1284-1293.

8 T. Hughes, W. Liu and T. Zimmermann, Lagrangian-Eulerian finite element formulation for incompressible viscous flows, Computer Methods in Applied Mechanics and Engineering, 29 (1981) 329-349.

9 J. Donea, S. Giuliani and J. Halleux, An arbitrary Lagrangian-Eulerian finite element method for transient dynamic fluid-structure interactions, Computer Methods in Applied Mechanics and Engineering, 33 (1982) 689-723.

10 Y. Bao, D. Zhou and C. Huang, Numerical simulation of flow over three circular cylinders in equilateral arrangements at low Reynolds number by a second-order characteristic-based split finite element method, Computers and Fluids, 39 (2010) 882-899.

11 A. Placzek, J.F. Sigrist and A. Hamdouni, Numerical simulation of an oscillating cylinder in a cross-flow at low Reynolds number: Forced and free oscillations, Computers and Fluids, 38 (2009) 80-100.

12 T. Sarpkaya, Hydrodynamic damping, flow-induced oscillations, and biharmonic response, Journal of Offshore Mechanics and Arctic Engineering, 117 (1995) 232-238.

13 Y. Bao, D. Zhou and J.H. Tu, Flow interference between a stationary cylinder and an elastically mounted cylinder arranged in proximity, Journal of fluids and structures, 27 (2011) 1425-1446.

Vortex-induced vibrations of a flexible circular cylinder based on the CIBC method

Tao HE[a], Dai ZHOU[b]

[a]*School of Naval Architecture, Ocean and Civil Engineering, Shanghai Jiaotong University, Shanghai,China*
[b]*School of Naval Architecture, Ocean and Civil Engineering, Shanghai Jiaotong University, Shanghai,China*

ABSTRACT: The loosely-coupled partitioned algorithm is intrinsically exposed to the notorious time lag effect whose remedy promotes the combined interface boundary condition (CIBC) method. CIBC correction terms for velocity and traction are introduced at two sequential time steps with a coupling parameter ω. The structural traction ratio that appears explicitly in the traction correction is estimated based on the solution of the structural subsystem. This handling asks for the structural traction before it is corrected by the CIBC method. In this paper, a new formulation for the CIBC method is developed to repair the aforementioned inconvenience. After simple manipulation, the structural traction ratio is removed in constructing the traction correction. Therefore the structural traction is no more needed in CIBC correction terms. A flexible cylinder ar Re = 200 is tested to validate the proposed methodology and some famous features of flow phenomena have been detected successfully.

KEYWORDS: Arbitrary Lagrangian-Eulerian; Finite element method; CBS; Combined interface boundary condition.

1 INTRODUCTION

The vortex-induced vibrations (VIV) of bluff body under wind flow or other fluid flows are of great practical interest and crucial importance in many areas of civil engineering. In the cable-stayed building structures, for instance, the cable is always subjected to the vibration caused by coming wind. The design of the structures experienced VIVs is depended heavily on accurate prediction of structural aerodynamic responses and fluid flow dynamics, where the generation mechanism must also be recognized scientifically.

2 GOVERNING EQUATIONS

2.1 *Incompressible fluid flows*

The incompressible Navier-Stokes equations in the arbitrary Lagrangian-Eulerian (ALE) description read as:

$$\frac{\partial \mathbf{u}}{\partial t} + \mathbf{c} \cdot \nabla \mathbf{u} + \nabla p - \frac{1}{Re} \nabla^2 \mathbf{u} - \mathbf{f} = \mathbf{0} \tag{1}$$

$$\nabla \cdot \mathbf{u} = 0 \tag{2}$$

where **u** represents the fluid velocity, **c** = **u** – **w** the convective velocity, **w** the mesh velocity, ∇ the gradient operator, **f** the body force, p the pressure, Re = $\rho U_\infty D/\mu$ the Reynolds number, U_∞ the free stream velocity, μ the dynamic viscosity. The problem is complete with the proper boundary conditions together with the initial condition.

2.2 *Characteristic-based split (CBS) scheme*

The CBS scheme, which was originally introduced by the trilogy of Zienkiewicz and his co-workers [1-3] since 1995, is employed to solve Eqs. (1) and (2). The procedure of the semi-implicit CBS scheme can be actualized by the following steps:

Step 1: Calculate the intermediate velocity field

$$\tilde{\mathbf{u}} - \mathbf{u}^n = \Delta t\left(-\mathbf{c}\cdot\nabla\mathbf{u} + \frac{1}{Re}\nabla^2\mathbf{u} \right)^n + \frac{(\Delta t)^2}{2}\left(\mathbf{c}\cdot\nabla\left(\mathbf{c}\cdot\nabla\mathbf{u}\right)\right) \tag{3}$$

Step 2: Update the pressure field

$$\nabla^2 p^{n+1} = \frac{1}{\Delta t}\nabla\cdot\tilde{\mathbf{u}} \tag{4}$$

Step 3: Correct the velocity field

$$\mathbf{u}^{n+1} - \tilde{\mathbf{u}} = -\Delta t\nabla p^{n+1} + \frac{(\Delta t)^2}{2}\left(\mathbf{c}\cdot\nabla\left(\nabla p\right)\right)^n \tag{5}$$

In the above algorithm, the body force **f** and third-order term are neglected. The stabilization parameter $(\Delta t)^2/2$ is independent on a local element size, thus leads to some computational savings. The finite element method (FEM) is used for the spatial discretization. A T3 element is considered as it is very convenient to use a low- and equal-order interpolation for velocity and pressure in the CBS scheme. For a compromise between accuracy and efficiency, the lumped mass matrix is used. Imposing boundary conditions follows the suggestion of Ref. [4].

2.3 *Equation of the structual motion*

A rigid structure immersed in a fluid undergoes unsteady forces and its motion is governed by the following equation:

$$\ddot{\mathbf{x}} + 4\pi f_{\mathrm{r}}\zeta\dot{\mathbf{x}} + \left(2\pi f_{\mathrm{r}}\right)^2\mathbf{x} = \frac{\mathbf{C}_{\mathrm{f}}}{2m^*} \tag{6}$$

where m, c and k represent the mass, damping and stiffness of the structure, **x** the structural displacement, $\mathbf{C}_{\mathrm{f}} = [C_{\mathrm{D}}, C_{\mathrm{L}}]^{\mathrm{T}}$ the force coefficient vector, $F_{\mathrm{r}} = f_{\mathrm{n}}D/U_\infty$ the reduced natural frequency, $\zeta = 0.5c/(mk)^{0.5}$ the damping ratio, $m^* = \mathrm{m}/(\rho \mathrm{D}^2)$ the mass ratio, $f_{\mathrm{n}} = (km)^{0.5}/(2\pi\mathrm{m})$ the natural frequency of the oscillator. Eq. (6) is solved by way of Newmark-β method with $\alpha = 0.25$ and $\beta = 0.5$.

3 MESH MOTION

Moving submesh approach (MSA) [5] is employed for re-arranging the deformable fluid mesh in this paper. The main steps of MSA are summarized as follows:

Step 1: Extract the information of the fluid and MSA meshes;
Step 2: Find out which zone a point belongs to;
Step 3: Calculate the interpolation formulae of each point;
Step 4: Gain the motion of the zones adhering to the moving boundaries;
Step 5: Update the fluid mesh using the associated interpolation formulae.

A submesh without interior nodes permits a direct application of MSA. When interior nodes arise, MSA works in conjunction with the ortho-semi-torsional spring analogy method [6] that is solved by a successive over relaxation technique [7].

In this research, a mass source term (MST) [8] is adopted for obeying geometric conservation law. As a result, Eq. (4) can be recast as:

$$\nabla^2 p^{n+1} = \frac{1}{\Delta t}\nabla\cdot\tilde{\mathbf{u}} + S_{\mathrm{MST}} \tag{7}$$

where MST $S_{\mathrm{MST}} = \dfrac{1}{2A_e}\begin{vmatrix} w_1^2 - w_1^1 & w_2^2 - w_2^1 \\ w_1^3 - w_1^1 & w_2^3 - w_2^1 \end{vmatrix}$, A_e is the area of element e, superscript i (i = 1, 2 and 3) means point i of element e and subscript j component j (j = 1 and 2) of coordinates.

4 COMBINE INTERFACE BOUNDARY CONDITION (CIBC) METHOD

As derivated in [9], the new CIBC formulation is expressed as:

$$\delta\mathbf{u}_*^n = \frac{\Delta t}{\rho_{\mathrm{f}}}\left(\frac{\partial\boldsymbol{\sigma}_{\mathrm{f}}^n}{\partial n_{\mathrm{f}}} + \omega\frac{\partial\left(\delta\boldsymbol{\sigma}_*^n\right)}{\partial t}\right) \tag{8}$$

$$\delta\boldsymbol{\sigma}_*^{n+1} = \frac{\Delta t}{2\omega}\left(\rho_{\mathrm{f}}\frac{\partial\mathbf{u}_{\mathrm{s}}^{n+1}}{\partial t} - \frac{\partial\boldsymbol{\sigma}_{\mathrm{f}}^{n+1}}{\partial n_{\mathrm{f}}}\right) \tag{9}$$

with a positive constant ω which should be small enough to make sure the interfacial energy is always stable [10]. Then the velocity and traction along Γ_{fs} are severally corrected by

$$\mathbf{u}_{\mathrm{f}}^{n+1} = \mathbf{u}_{\mathrm{s}}^{n+1} + \delta\mathbf{u}_*^n \tag{10}$$

$$\boldsymbol{\sigma}_{\mathrm{s}}^{n+1} = \boldsymbol{\sigma}_{\mathrm{f}}^{n+1} + \delta\boldsymbol{\sigma}_*^{n+1} \tag{11}$$

Because of our measure for updating the fluid mesh, the interfacial displacement continuity due to Eq. (10) must be corrected as follow:

$$\mathrm{d}\mathbf{x}_{\mathrm{f}}^{n+1} = \mathrm{d}\mathbf{x}_{\mathrm{s}}^{n+1} + \Delta\mathbf{x}_{\mathrm{c}} = \mathrm{d}\mathbf{x}_{\mathrm{s}}^{n+1} + \left(\delta\mathbf{u}_{\mathrm{f}}^n - \delta\mathbf{u}_{\mathrm{f}}^{n-1}\right)\Delta t \tag{12}$$

The loosely-couple partitioned procedure equipped with the CIBC method is summarized as follow:

Step 1: Fluid and structural variables at time n are given;

Step 2: Loop over an FSI cycle in each time interval $t = t_{n+1} - t_n$:

(a) The structural equation (6) is calculated for the new structural variables;

(b) The velocity increment along the interface is obtained by solving Eq. (8) and the fluid velocity is corrected according to Eq. (10);

(c) The coordinates of the fluid-structure interface are updated due to Eq. (12);

(d) MSA is employed to renew the dynamic mesh based on (c);

(e) Eqs. (3), (7) and (5) are solved for the fluid velocity and pressure at time $n + 1$;

(f) The traction increment along the interface is obtained by solving Eq. (9) and the structural traction is corrected according to Eq. (11);

Step 3: Return Step 2 until the computational time is over.

The schematic diagram of the loosely-coupled partitioned procedure is sketched in Figure 1 where S stands for a structural variable while F a fluid variable.

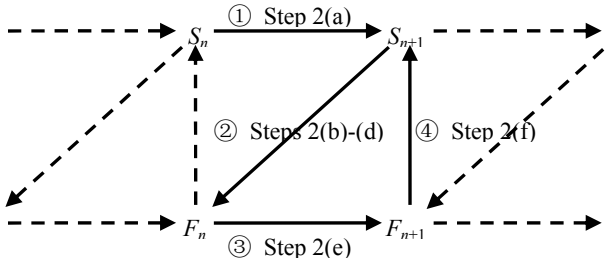

Figure 1. Loosely-coupled partitioned algorithm

5 NUMERICAL EXAMPLE

A free oscillating circular cylinder is simulated numerically to reproduce the numerical analysis of Zhou et al. [11] in this section. The definition of this problem is plotted in Figure 2 while its MSA mesh is viewed in Figure 3.

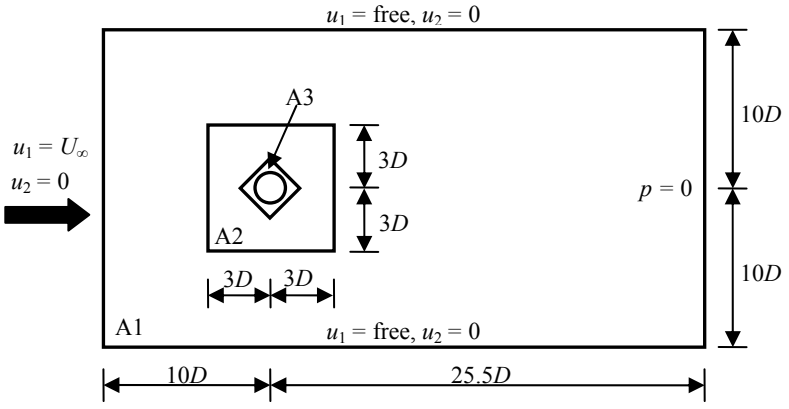

Figure 2. Sketch of the geometry and boundary conditions for a transversely oscillating circular cylinder

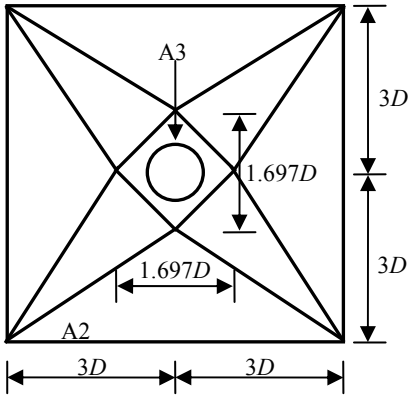

Figure 3. MSA mesh for a circular cylinder

The mesh and time step are considered based on the researches of Prasanth and Mittal [12] and Zhou et al. [11]. The entire computational domain is meshed into 7040 points and 13870 T3 elements. The time step is set to 2.5×10^{-3}. The mass ratio is set to $m^* = 1$, the reduced damping parameter $Sg = 0.01$, the damping ratio $\zeta = Sg/(0.29553\ m^*\pi^2)$ and $Re = 200$. The frequency ratio f_n/f_0 varies from 0.65 to 5.20, where f_0 is the vortex-shedding frequency of a stationary circular cylinder. $\omega/\Delta t = 100$ is selected to implement our computations.

Three mass ratios are considered to research their influence on $2Y_{rms}$, $C_{d,mean}$, $C_{l,rms}$ and f_v/f_0 versus f_n/f_0, as plotted in Figures 4-7. From Figure 4, a smaller m^* brings about a lower value of $2Y_{rms}$ in short. For the case $m^* = 10$ and $Sg = 0.01$, the present data are larger than those of Zhou et al. [11], and comparative with the results of Zhou et al. [11] who consider $m^* = 1$ when $0.87 \le f_n/f_0 \le 1.16$. Unlike Zhou et al. [11], the present $C_{d,mean}$ is less affected by the mass ratio, seen from Figure 5. For $m^* = 1$, the present peak of $C_{d,mean}$ occurs at a higher frequency ratio and significant large values are obtained when $f_n/f_0 = 1.49$ and 1.73. As shown in Figure 6, $C_{l,rms}$ for the smallest m^* is much lower at $f_n/f_0 = 0.65$ but higher when f_n/f_0 is larger than 1.30. The variation trends for $m^* = 5$ and 10 are almost the same. In Figure 7, the f_v/f_0 curve is very smooth for the heavy cylinder with $Sg = 0.01$ studied by Zhou et al. [11], but visible fluctuations are spied under the same conditions in this study. The corresponding peak value of f_n/f_0 appears at $f_n/f_0 = 1.30$. However, the variation trends of f_v/f_0 for all cases are the same.

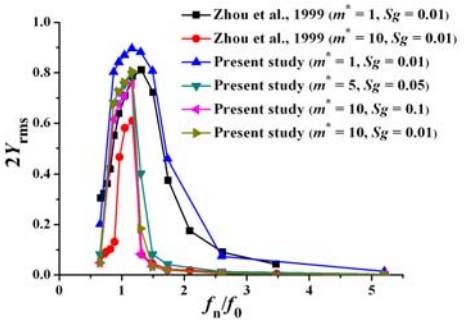

Figure 4. Variation of $2Y_{rms}$ for different mass ratios

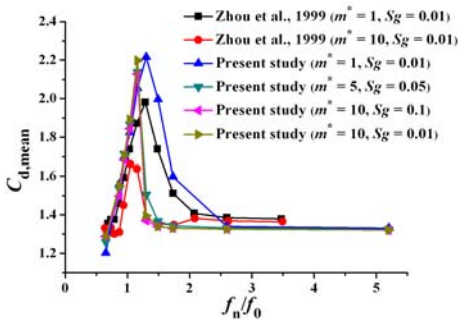

Figure 5. Variation of $C_{d,mean}$ for different mass ratios

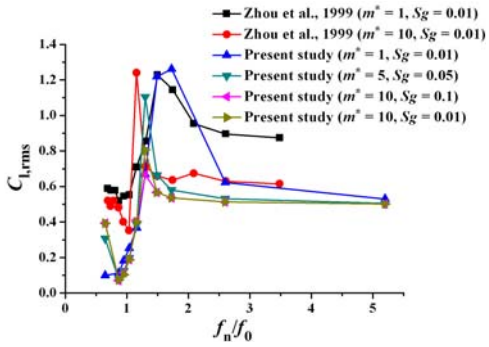

Figure 6. Variation of $C_{l,rms}$ for different mass ratios

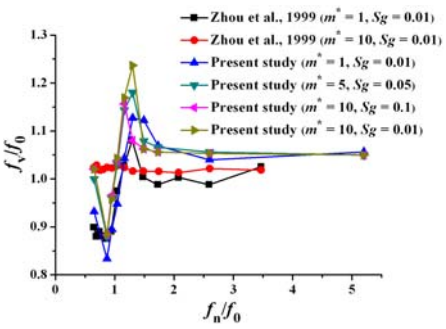

Figure 7. Variation of f_v / f_0 for different mass ratios

Figure 8 illustrates the cylinder trajectories at f_n/f_0 = 1.30 for different mass ratios, displaying the classical *Lissajous* figure of 8. Figure 8(a) shows the clearest figure of 8 shape, similar to that of Zhou et al. [11]. The mass ratio alters the cylinder displacements notably. A lighter circular cylinder gets the larger displacement, thus the amplitudes in X and Y remarkably decrease for m^* = 5 and 10. In addition, the equilibrium position of the cylinder due to the mean drag changes with m^*.

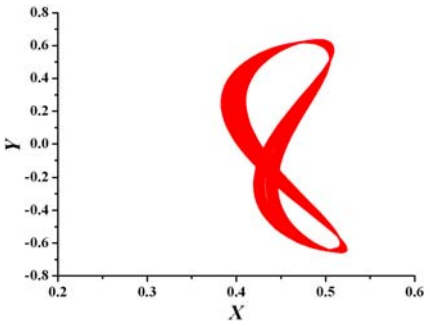

(a) m^* = 1, Sg = 0.01

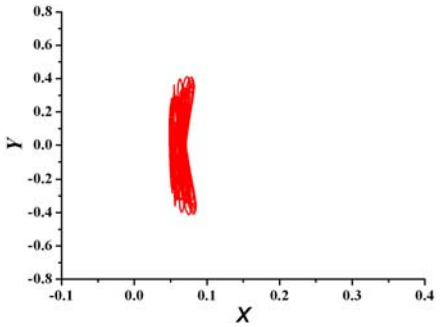

(b) m^* = 5, Sg = 0.05

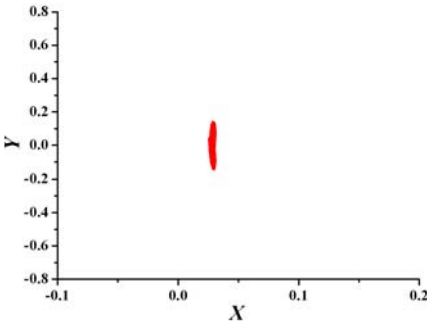

(c) m^* = 10, Sg = 0.01

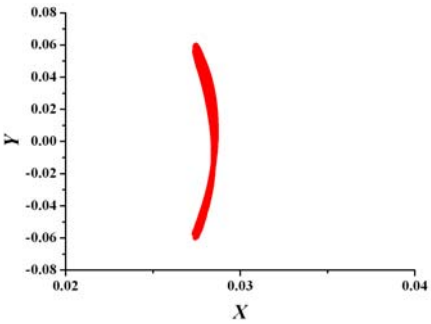

(d) m^* = 10, Sg = 0.1

Figure 8. Vibration trajectory of the circular cylinder at f_n / f_0 = 1.30

Our attention is drawn to the given case $m^* = 1$ and $Sg = 0.01$. Time histories of the drag and lift coefficients, as well as the transverse displacement, are exhibited in Figure 9. The basic characteristics of the present time histories are similar to those of Zhou et al. [11]. When $f_n/f_0 =$ 0.65, 2.60 and 5.20, the transverse vibrations are feeble. The fact that beating is visualized at f_n/f_0 = 1.73 coincides with that of Zhou et al. [11] at the same frequency ratio. The beating phenomenon can be perceived by time histories of the transverse vibrations and drag coefficient. The variation of C_d bears an analogy to that of Y. The amplitudes of C_l become evidently larger when $f_n/f_0 =$ 1.49 and 1.73. The oscillations of C_l and Y become out-of-phase while $f_n/f_0 =$ 0.65 and 0.87. As f_n/f_0 grows up, the transition from in-phase to out-of-phase appears at $f_n/f_0 =$ 0.95. But this transition is less evident than that of Zhou et al. [11].

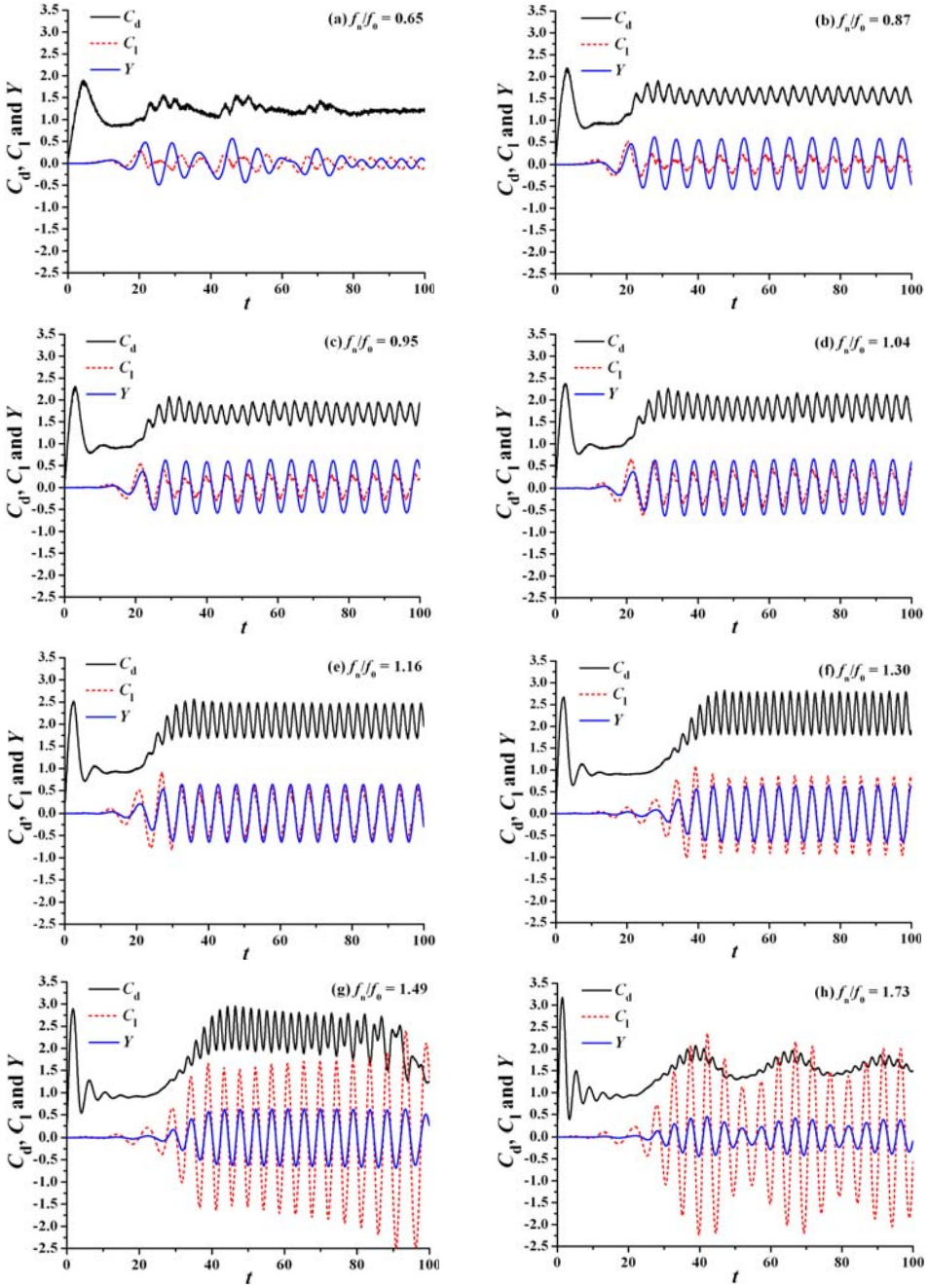

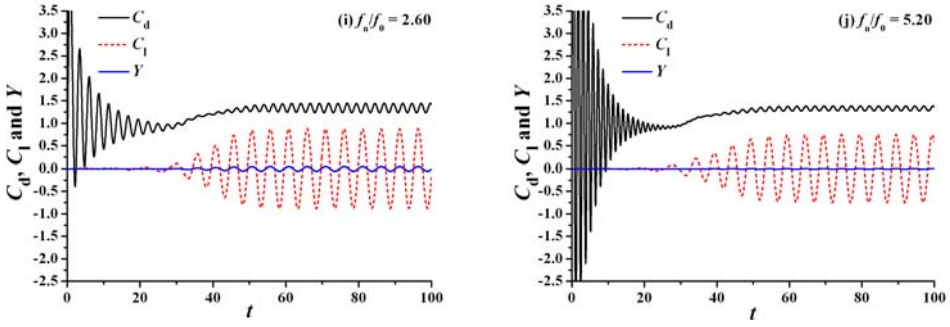

Figure 9. Force coefficients and the transverse displacement of the cylinder at various f_n / f_0

Figure 10 displays the different vortex patterns shedding from the wake of the freely oscillating cylinder. The present vortex-shedding patterns and their transition declare an analogue of those of Zhou et al. [11]. But some scatter is still aware of. Although the classical 2S vortex-shedding mode is watched for all frequency ratios, the region of frequency ratios is split into two parts based on the longitudinal spacings between shedding vortices. The longitudinal spacing for $f_n/f_0 \leq 1.49$ is larger than the one for $1.73 \leq f_n/f_0 \leq 5.20$. The circular cylinder experiences the low-amplitude vibrations at $f_n/f_0 = 2.60$ and 5.20 which imply the vortex-shedding frequencies are far away from the natural frequency, and the regular 2S mode is viewed. When $f_n/f_0 = 1.49$ and 1.73, the vortices apart from the cylinder wake seem to coalesce. This sign indicates that the C(2S) mode [13], a variation of the 2S mode, may occur if the present domain is expansive enough. As the frequency ratio stays at 1.49, the 2S vortices travels a distance, then translates into two batches of the shedding vortices, as the same as the figure shown by Zhou et al. [11]. This change of the vortex shedding consists with the time histories of force coefficients, implying that two different vortex-shedding frequencies exist. The vortices for $f_n/f_0 = 1.16$ and 1.30 are parallel, having large longitudinal spacings. Especially, Zhou et al. [11] analyze that at $f_n/f_0 = 1.16$ the 2S vortices can pass a distance of approximate $20D$, then transform the P + S mode [13]. This conversion can't be realized because of a much shorter downstream scope in the present study. The other explanation is that the P + S mode won't be observed unless *Re* is greater than 300, according to Singh and Mittal [14]. At $f_n/f_0 = 0.95$, 1.04, 1.16 and 1.30, the longitudinal spacings between shedding vortices are larger than those of Zhou et al. [11] apparently. The jack-up of the longitudinal spacings between shedding vortices may explain why a more violently transverse vibration has been received in this study. The transverse peak-to-peak amplitude $2Y_{max}$ is about 1.0 in the analysis of Zhou et al. [11] and 1.504 in this study. The present $2Y_{rms}$ is also roughly larger 10.8% than that of Zhou et al. [11]. Besides, the present lock-in range is a bit wider than that of Zhou et al. [11]. The similarity of the vortex shedding between the present study and work of Zhou et al. [11] emerges once more as the frequency ratio f_n/f_0 goes down to 0.87 and 0.65.

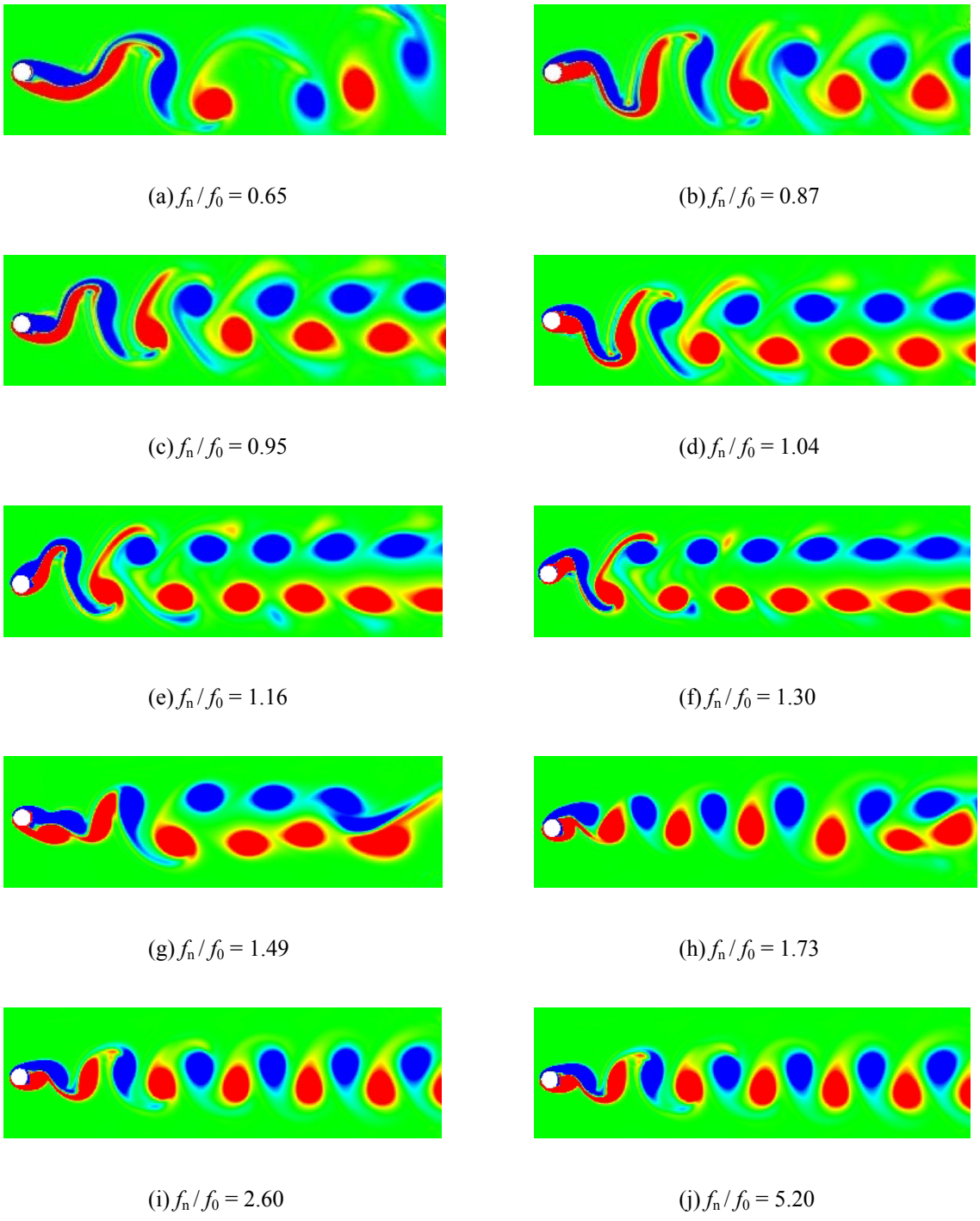

(a) $f_n / f_0 = 0.65$ (b) $f_n / f_0 = 0.87$

(c) $f_n / f_0 = 0.95$ (d) $f_n / f_0 = 1.04$

(e) $f_n / f_0 = 1.16$ (f) $f_n / f_0 = 1.30$

(g) $f_n / f_0 = 1.49$ (h) $f_n / f_0 = 1.73$

(i) $f_n / f_0 = 2.60$ (j) $f_n / f_0 = 5.20$

Figure 10. Vorticity fields of the cylinder at various f_n / f_0

6 CONCLUSION

In this study a new formulation for the CIBC method has been developed. The main contribution of the proposed methodology lies in overcoming the inconvenience due to the employment of the structural traction uncorrected in the original CIBC method. The developed strategy has been tested on the vortex-induced vibrations of a flexible cylinder at $Re = 200$. The obtained results are in

good agreement with the existing data. Some well-known flow phenomena have also been exposed successfully.

7 ACKNOWLEDGEMENTS

Support from the Key Project of Fund of Science and Technology Development of Shanghai (Project No. 10JC1407900) and the National Natural Science Foundation of China (Project Nos. 51078230 and 11172174) are acknowledged.

8 REFERENCES

1 O.C. Zienkiewicz, R. Codina, A general algorithm for compressible and incompressible flow—Part I. the split, characteristic-based scheme, International Journal for Numerical Methods in Fluids, 20 (1995) 869-885.

2 O.C. Zienkiewicz, K. Morgan, B.V.K.S. Sai, R. Codina, M. Vasquez, A general algorithm for compressible and incompressible flow—Part II. tests on the explicit form, International Journal for Numerical Methods in Fluids, 20 (1995) 887-913.

3 R. Codina, M. Vázquez, O.C. Zienkiewicz, A general algorithm for compressible and incompressible flows. Part III: The semi-implicit form, International Journal for Numerical Methods in Fluids, 27 (1998) 13-32.

4 P. Nithiarasu, On boundary conditions of the characteristic based split (CBS) algorithm for fluid dynamics, International Journal for Numerical Methods in Engineering, 54 (2002) 523-536.

5 E. Lefrançois, A simple mesh deformation technique for fluid–structure interaction based on a submesh approach, International Journal for Numerical Methods in Engineering, 75 (2008) 1085-1101.

6 G.A. Markou, Z.S. Mouroutis, D.C. Charmpis, M. Papadrakakis, The ortho-semi-torsional (OST) spring analogy method for 3D mesh moving boundary problems, Computer Methods in Applied Mechanics and Engineering, 196 (2007) 747-765.

7 D.H. Zeng, C.R. Ethier, A semi-torsional spring analogy model for updating unstructured meshes in 3D moving domains, Finite Elements in Analysis and Design, 41 (2005) 1118-1139.

8 Y.J. Jan, T.W.H. Sheu, Finite element analysis of vortex shedding oscillations from cylinders in the straight channel, Computational Mechanics, 33 (2004) 81-94.

9 T. He, D. Zhou, Y. Bao, Combined interface boundary condition method for fluid-rigid body interaction, Computer Methods in Applied Mechanics and Engineering, 223-224 (2012) 81-102.

10 R. Jaiman, P. Geubelle, E. Loth, X. Jiao, Combined interface boundary condition method for unsteady fluid-structure interaction, Computer Methods in Applied Mechanics and Engineering, 200 (2011) 27-39.

11 C.Y. Zhou, R.M.C. So, K. Lam, Vortex-induced vibrations of an elastic circular cylinder, Journal of Fluids and Structures, 13 (1999) 165-189.

12 T.K. Prasanth, S. Mittal, Vortex-induced vibrations of a circular cylinder at low Reynolds numbers, Journal of Fluid Mechanics, 594 (2008) 463-491.

13 C.H.K. Williamson, A. Roshko, Vortex formation in the wake of an oscillating cylinder, Journal of Fluids and Structures, 2 (1988) 355-381.

14 S.P. Singh, S. Mittal, Vortex-induced oscillations at low Reynolds numbers: Hysteresis and vortex-shedding modes, Journal of Fluids and Structures, 20 (2005) 1085-1104.

The Seventh International Colloquium on Bluff Body Aerodynamics and Applications (BBAA7)
Shanghai, China; September 2-6, 2012

Full-scale measurement of wind pressure on the surface of a circular cylinder

Delong Zuo, Jieying Hua

Department of Civil and Environmental Engineering, Texas The University, Mail Box 1023, Lubbock, TX, USA

ABSTRACT: An experimental campaign was conducted to measure wind pressure acting on the surface of a full-scale circular cylinder. The pressure measurements were used with measurements of cylinder acceleration to investigate the interaction between the cylinder and turbulent wind. Different characteristics of this interaction were revealed for different wind regimes.

KEYWORDS: Circular cylinder, wind-induced vibration, full-scale pressure measurement.

1 INTRODUCTION

Slender structural members with circular cross-sections are often susceptible to wind excitation. For example, cables of cable-stayed bridges are known to vibrate at large amplitudes under the excitation of wind with simultaneous occurrence of rainfall and, in certain situations, only wind (e.g., [1]). Also, traffic signal support structures having mast arms with circular cross-sections have exhibit problematic vibration (e.g., [2]). A number of full-scale studies (e.g., [1-4]) have been conducted to understand the characteristics of the vibrations and their correlation with wind and, in the case of cable vibration, with wind and rain. These studies revealed that large amplitude vibrations can be induced both by vortex-shedding and by wind oblique to the cylinder with reduced velocity that are much higher than those associated with classical vortex-induced circular cylinder vibration. As complements to full-scale studies, circular cylinders have been tested in wind tunnels (e.g., [5-7]). In particular, a number of experiments were conducted to expressly explore the potential inherent susceptibility of yawed or inclined dry circular cylinders to wind excitation. The findings from these studies have varied, with some suggesting the importance of an axial flow component in the wake of the cylinder in generating three-dimensional flow around the cylinder and initiating large-amplitude vibration at high reduced velocity ([7, 8]), and the others focusing on the potential of instability in the critical Reynolds number range (e.g., [6, 9]). In addition to the experimental studies, numerical investigations based on computational fluid dynamics (e.g., [10]) suggested that the three-dimensional nature of the flow can play a key role in the excitation mechanism. This paper presents the outcome of a full-scale study conducted to measure wind pressure on the surface of a circular cylinder. It facilitates a characterization of the mean and fluctuating wind loading on an oscillating slender circular cylinder when it is subjected to wind of various mean and turbulent characteristics.

2 EXPERIMENTAL CONFIGURATION

The specimen was a 7.62 m long circular pipe of 22.4 cm in diameter and 0.8 cm in wall thickness. It consisted of a 6.40 m long steel pipe and a 1.22 m long PVC pipe. As shown in Figure 1,

the steel portion was rigidly mounted horizontally near the top of a tapered circular aluminum pole, which was 30.5 and 36.8 cm in diameter at the top and the base, respectively, and had a wall thickness of 1 cm. A ring of 32 pressure taps evenly spaced at 11.25° intervals, as depicted in Figure 2, was installed at a cross-section that is 2.1 m from the free end of the cylinder; four additional taps were installed on the sides of this ring at locations indicated in Figure 2. The taps were connected to pressure transducers with a range of ±1.245 kPa through tubings of 0.91 m in length and 0.6 cm in diameter. With this configuration, the pressure taps were at least 8 diameters and 23 diameters of the cylinder, respectively, from the free and fixed ends. To minimize undesirable end effects on the flow near the pressure taps, a spherical cap was installed at the free end. Besides pressure measurement, a tri-axial accelerometer with a range of ±4 g was installed adjacent to the pressure tap ring to monitor vibration; an ultrasonic anemometer was installed at a height of 1.5 m above the centerline of the cylinder to monitor the wind, and temperature, relative humidity, and barometric pressure sensors were used to provide measurements for calculation of air density. The data acquisition system recorded 10-minute records at 32 Hz. Two additional 10-second records were sampled before and after each 10-minute record for calibration of the pressure transducers. Due to the inability of the pressure measurement system to function properly in rain, the taps were covered in advance when rainfall was anticipated.

Figure 1 Circular cylinder subjected to study

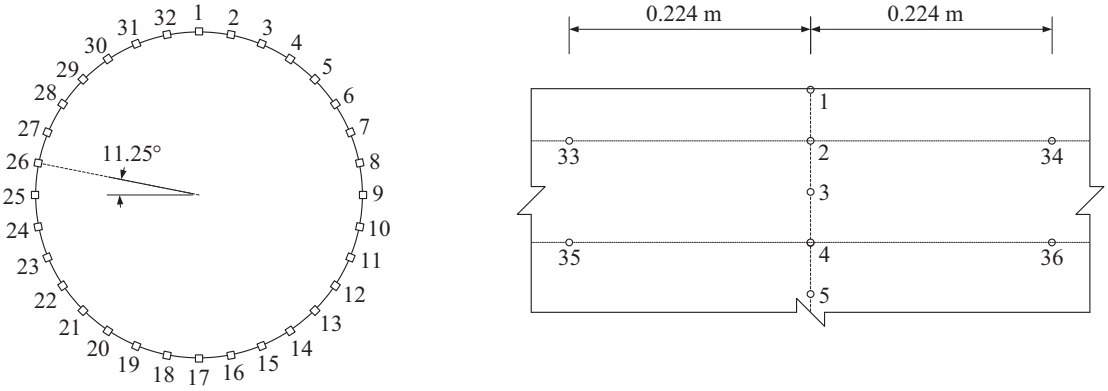

Figure 2 Configuration of pressure taps (not to scale)

3 CHARACTERISTICS OF CYLINDER RESPONSE

To characterize the vibration of the cylinder, the acceleration measurements are numerically integrated to estimate the displacement at the location of the accelerometer. After each integration process, a 5th order high-pass Butterworth filter with a cut-off frequency of 0.2 Hz is applied to

eliminate the spurious effect of low frequency noise. The displacement are then band-pass filtered using a 5th order Butterworth filter to estimate the response in the first two modes of the structure in the in-plane and out-of-plane directions, whose frequencies are identified based on the estimated power spectral density functions of acceleration records. The pass bands of the filter are 0.5 Hz frequency bands centered at the natural frequencies. Finally, the Hilbert transform is applied to the modal displacement to assess the evolution of the amplitude and frequency. The data suggested that during the measurement, the vibration of the cylinder is predominantly in the first in-plane and out-of-plane modes at 2.44 Hz and 2.17 Hz, respectively.

Figure 3 shows the 10-minute mean displacement amplitudes in the first in-plane (A_z) and out-of-plane (A_x) modes against mean speed of the wind component normal to the cylinder axis (V_n). It is seen that the cylinder exhibited significant vibration in the cross-wind direction over a restricted range of wind speeds. This is a clear characteristic of classical vortex-induced vibration. The figure also suggests that at higher wind speeds, the vibration amplitudes increased in both directions with wind speed. This is typical for vibration due to buffeting. Figure 4 shows the mean in-plane vibration amplitude against the reduced velocity (V_r) and the longitudinal turbulence intensity (I_u). The reduced velocity is computed as $V_r=V_n/(fD)$, where f is the mean vibration frequency, and D is the cylinder diameter. It can be seen that vortex-induced vibration occurred over a reduced velocity range centered at a value greater than 5, which is equivalent to the nominal Strouhal number of 0.2 for circular cylinders normal to smooth flow. This can be primarily attributed to two facts. Firstly, according to measurements by an adjacent meteorological tower, the wind speed measured by the anemometer can be 1% to 10% higher than that at the height of the cylinder, depending on the stability of the atmospheric boundary layer. Secondly, according to previous wind tunnel tests [11], organized vortex shedding over circular cylinders can occur over a broad range of Strouhal number, depending on the turbulence intensity of the free stream wind. According to Figure 4, significant vortex-induced vibration did occur over a broad range of longitudinal turbulence intensity.

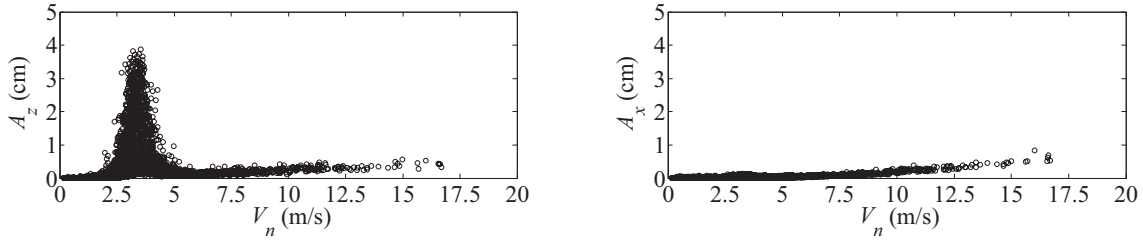

Figure 3 Mean displacement amplitudes in the first in-plane and out-of-plane modes vs. mean wind speed

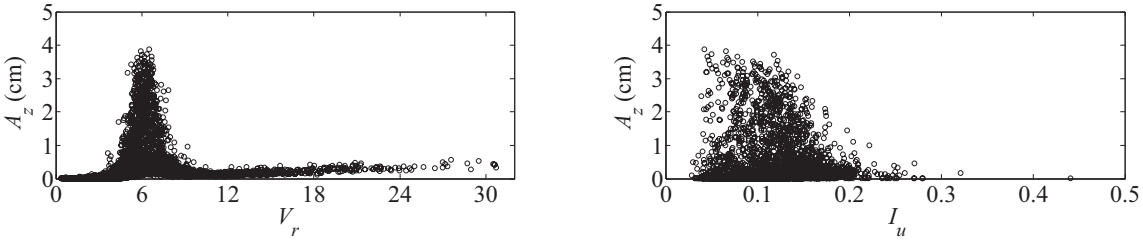

Figure 4 Mean in-plane displacement amplitude vs. reduced velocity and along-wind turbulence intensity

4 INTERPRETATION OF PRESSURE MEASUREMETNS

Incorporation of the measurements by the pressure transducers and the accelerometer have revealed some distinct characteristics of wind loading on the circular cylinder in different wind regimes and different types of wind-structure interaction.

Figure 5 shows the estimated mean drag (C_D) and lift (C_L) coefficients of the cylinder against mean wind speed (V) and the corresponding Reynolds number (Re) for a mean wind direction range of 85° to 95° relative to the cylinder axis. Only records with wind direction variation not exceeding 60° are used here. The Reynolds number is computed based on the mean wind speed, an assumed kinematic viscosity value of 1.5×10^{-5} m^2/s and the cylinder diameter as the reference dimension. It can be seen that when wind is almost normal to the cylinder, the transition from the subcritical to the critical Reynolds number range starts at mean wind speeds between 5 m/s and 7.5 m/s, corresponding to a Reynolds number range of 0.75×10^5 to 1.12×10^5, which is much lower than the Reynolds number (about 2×10^5) at which the transition occurs in smooth flow. Such shifting of critical Reynolds number range is due to the presence of turbulence in the free stream flow, which has been well documented by previous wind tunnel studies (e.g., [11, 12]), although the integral length scale of the wind in these studies were often much smaller than what proper scaling requires for full-scale cylinders such as the one subjected to study herein. Figure 5 also suggests that when the flow is in the subcritical Reynolds number range, the mean lift coefficients are close to zero and that in the critical Reynolds number range, the mean lift coefficients as a trend deviate more from zero. This is also consistent with previous reports (e.g., [9]).

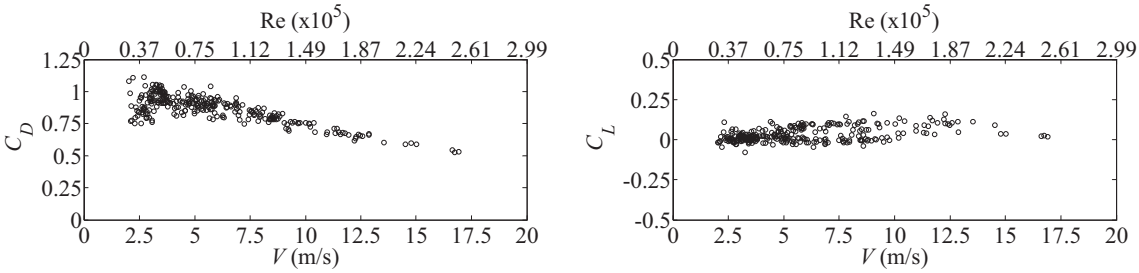

Figure 5 Mean drag and lift coefficients associated winds approximately normal to cylinder axis

It is noteworthy that the mean force coefficients exhibit considerable scatter for low wind speeds. This is partly due to the fact that at these wind speeds, the flow in the lower atmospheric boundary layer is significantly affected by atmospheric stability. The stability state affects not only the ratio of the mean measured wind speed to that at the height of the cylinder, therefore the reference mean dynamic pressure of the wind used for computation of the pressure coefficients, but also the level of shear in the free stream wind, hence the flow-cylinder interaction.

In the following, three representative records with 10-minute mean wind speed and direction (β) as well as turbulence intensity (I_u) listed in Table 1 will be used to illustrate the interaction between the wind and the cylinder when the wind is close to normal to the cylinder.

Table 1 Characteristics of wind of example records with wind approximately normal to cylinder axis

Record Number	V (m/s)	β (°)	I_u
1	3.70	93.40	0.055
2	5.00	89.42	0.140
3	12.22	93.06	0.148

Figure 6 shows the drag and lift coefficients of the cylinder estimated based on the wind and pressure measurements in record 1 and the corresponding spectra. It is evident that the lift coefficient is of narrow band and dominated by a frequency component at 2.43 Hz, indicating organized vortex shedding off the cylinder at this frequency. It also can be seen that the drag coefficient has a significant frequency component at 4.86 Hz, which is twice the dominant frequency of the lift coefficient. This is expected for wind loading of circular cylinders in the along-wind direction due to alternating shedding of vortices at the upper and lower surface of the cylinder. It is of interest to notice, however, that the drag coefficient is also dominated by a frequency of 2.43 Hz. This would not have been expected for stationary circular cylinders.

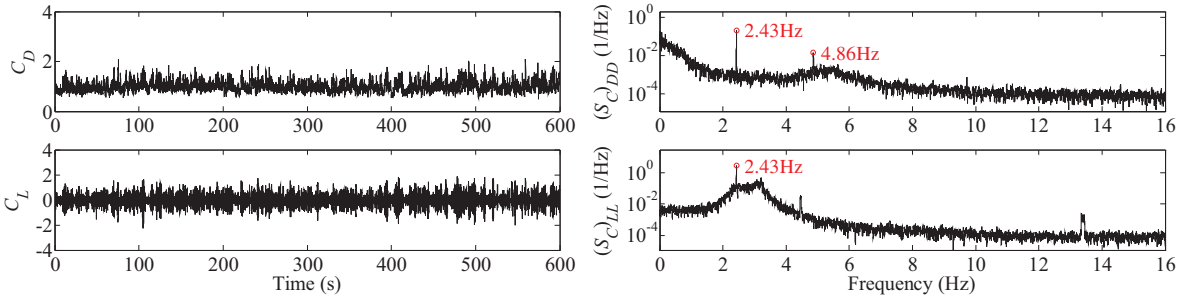

Figure 6 Drag and lift coefficients of the cylinder and the corresponding spectra: record 1

Figure 7 shows the acceleration of the cylinder due to wind loading shown in Figure 6 and the corresponding power spectra. The primarily in-plane vibration (a_z and a_y) is identified to be due to vortex shedding locked-in with the vibration of the structure. It is noteworthy that, in addition to the dominant frequency component at 2.43 Hz, the in-plane vibration also has a component at 4.86 Hz, which is twice the vortex-shedding frequency, despite the fact that this frequency is neither a natural frequency of the structure nor the vortex-shedding frequency. It is believed, therefore, that the in-plane vibration at 4.86Hz is due to a super-harmonic of the excitation at 2.43 Hz. It is of interest to notice that, since the drag coefficient has a significant frequency component at 2.43 Hz, the insignificant along-wind, out-of-plane, vibration also consists of a component at this frequency, which is not a natural frequency of the structure in this direction.

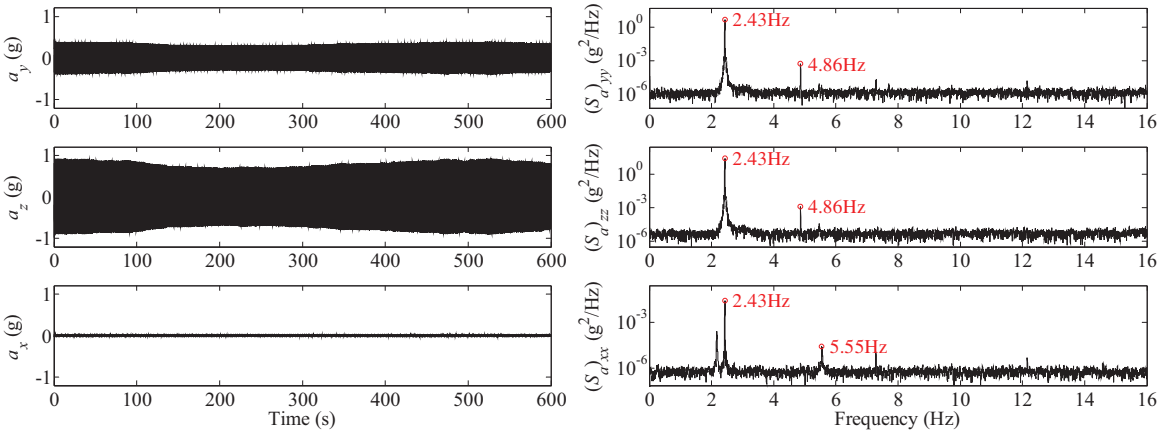

Figure 7 Acceleration time histories and the corresponding spectra: record 1

By comparing the lift coefficient time history shown in Figure 6 and the in-plane acceleration time histories shown in Figure 7, it is apparent that although the response of the structure is quite steady, the lift force acting on the cylinder at the pressure tap ring is not. This is further illustrated in Figure 8, in which can be seen that the lift force and the displacement at the location of the pressure tap ring are only intermittently synchronized due to the interaction of the cylinder and the turbulent wind.

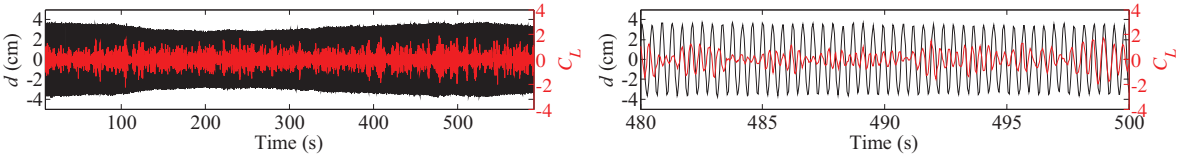

Figure 8 Cylinder displacement and lift coefficient at location of pressure tap ring: record 1

Figure 9 shows the cross-correlation coefficients of the pressures at 5 taps along two axial lines of the cylinder over a time lag of 5 seconds. The subscripts indicate the tap numbers. The measurement by tap number 36 is not used because this tap is determined to have malfunctioned. The coefficients are clearly those of narrow band processes with the same center frequency.

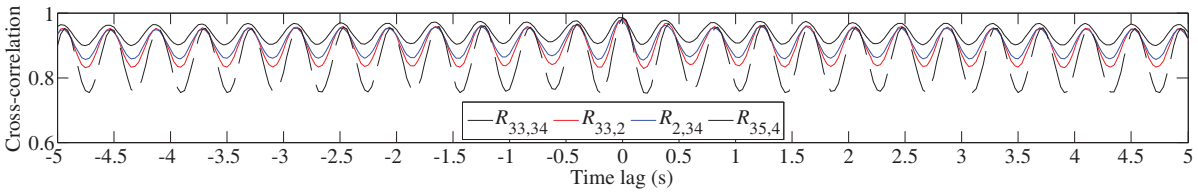

Figure 9 Cross-correlations of pressure measured along the axial direction of the cylinder: record 1

Figure 10 illustrates approximately one cycle of vibration at the pressure tap ring location and the corresponding pressure distribution on the surface of the cylinder, when the vibration and the lift force are nearly synchronized. It is apparent that the pressure distribution on the ring when the cylinder is at symmetric positions during upward and downward movements can be quite different, indicating different vortex shedding patters from the upper and lower surface primarily due to the existence of turbulence. Figure 11 illustrate the distribution of the mean pressure coefficients (C_p) over the 10-minute duration. It can be seen that for this particular record, the distribution of the mean pressure is quite symmetric about the horizontal plane through the centerline of the cylinder. It must be noted that, the pressure distributions illustrated in Figure 10 and Figure 11 might be biased by the reference pressure measured at the ground level and may be different from the static pressure at the height of the cylinder in a stable boundary layer, which is quite likely in this case as low turbulence intensity is a signature of stable boundary layers.

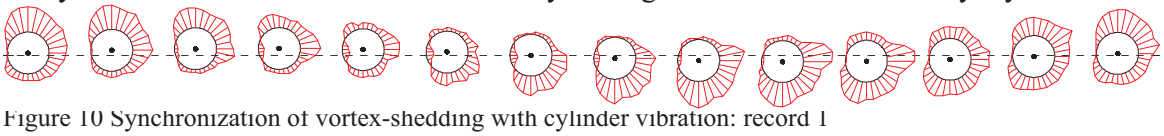

Figure 10 Synchronization of vortex-shedding with cylinder vibration: record 1

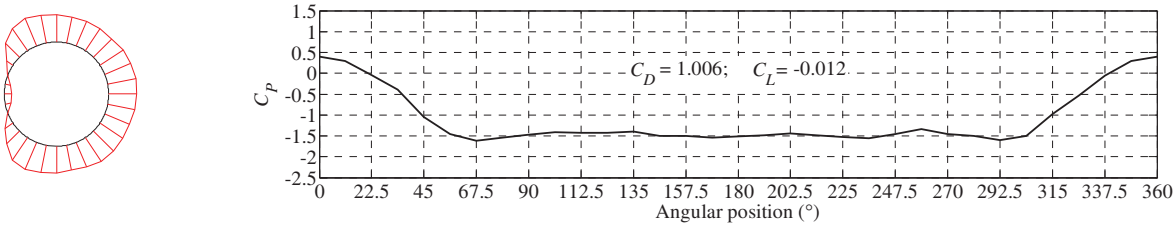

Figure 11 Mean pressure distribution at the pressure tap ring: record 1

According to Figure 5, the mean wind speed over the duration of record 2 is in the subcritical Reynolds number range. Figure 12 shows the drag and lift coefficients of the cylinder for this record and the corresponding spectra. It can be seen that neither the drag force nor the lift force acting at the location of the pressure tap ring have a dominant frequency component, but the lift force does have considerable contribution from components over a frequency band centered between 4 Hz and 5 Hz. This frequency band represents that of unorganized vortex-shedding off the surface of the cylinder. Figure 13 shows the acceleration response of the cylinder. It can be seen that the vibrations in both the in-plane and the out-of-plane directions are at small amplitudes, primarily in the first two modes in these directions.

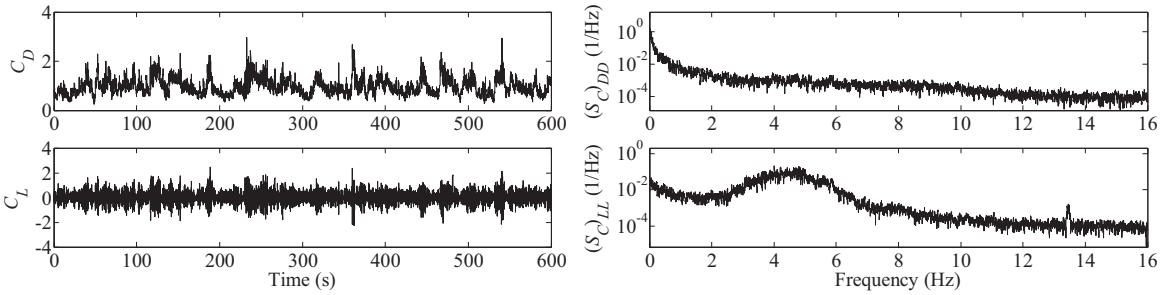

Figure 12 Drag and lift coefficients of the cylinder and the corresponding spectra: record 2

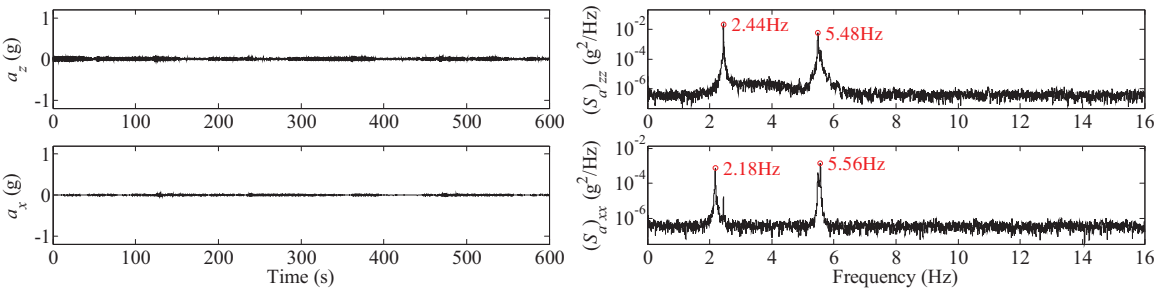

Figure 13 Acceleration time histories and the corresponding spectra: record 2

Figure 14 shows the cross correlation coefficients of the pressures at 5 taps along two axial lines along the cylinder over a time lag of 5 seconds. As expected, the pressures at the locations of the taps are the most correlated when the time lag is zero. The ripples at small time lags indicate the existence of the frequency band centered between 4 Hz and 5 Hz, which, as indicated by the spectra of the lift coefficient shown in Figure 12, is due to unorganized vortex shedding.

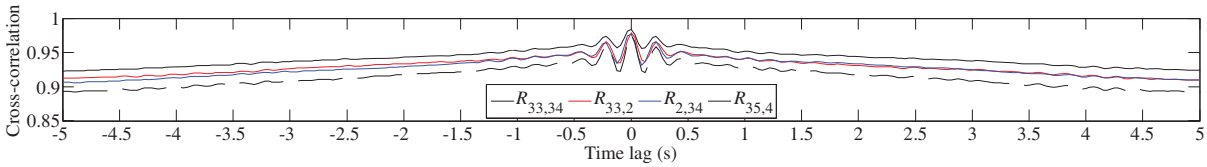

Figure 14 Cross-correlations of pressure measured along the axial direction of the cylinder: record 2

Figure 15 illustrate the distribution of the mean pressure coefficients for the duration of record 2. The angular position is measured clockwise relative to the would-be stagnation point if the cylinder were held stationary. An approximately symmetric pattern is again observed, indicating, on average, approximate symmetric separation of the flow from the upper and lower part of the cylinder during the duration of the record.

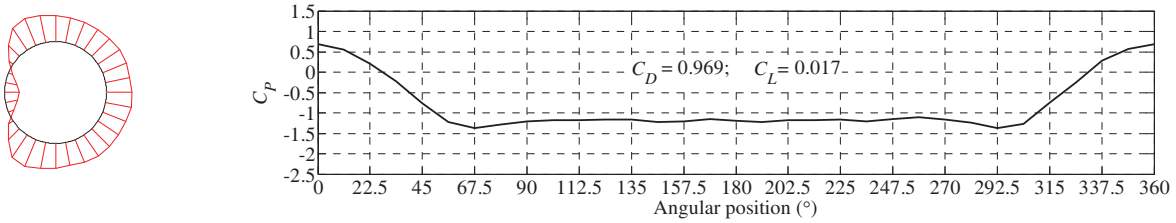

Figure 15 Mean pressure distribution at the pressure tap ring: record 2

According to Figure 5, the mean wind speed over the duration of record 3 is in the critical Reynolds number range. Figure 16 shows the drag and lift coefficients for this record and the corresponding spectra. The spectra of the coefficients show no sign of vortex-shedding, suggesting turbulent separation of the flow off the cylinder surface. Figure 17 shows the acceleration response of the cylinder. It can be seen that the vibrations in both the in-plane and out-of-plane directions are again dominated by the first two modes of the structure in these two directions.

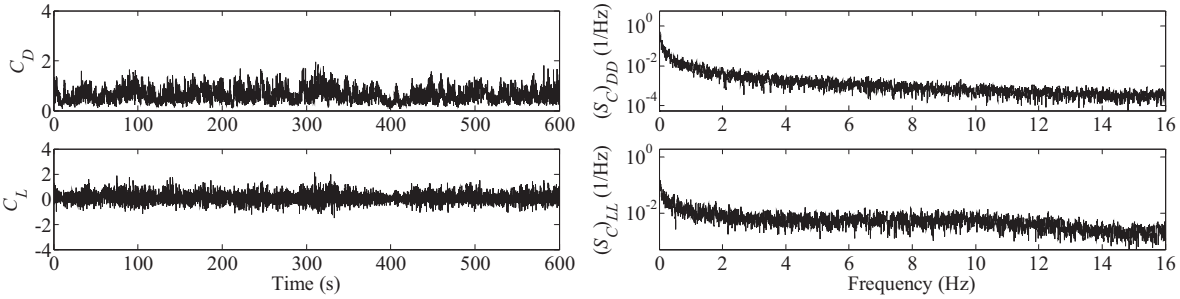

Figure 16 Drag and lift coefficients of the cylinder and the corresponding spectra: record 3

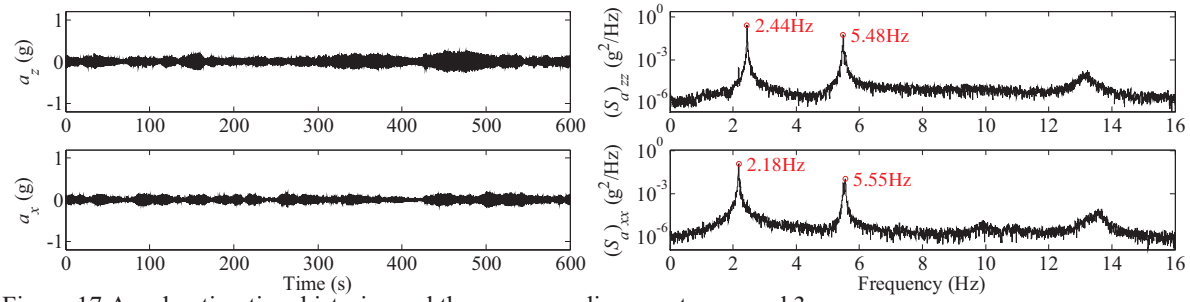

Figure 17 Acceleration time histories and the corresponding spectra: record 3

Figure 18 shows the cross-correlation correlations of the pressures at 5 taps along two axial lines of the cylinder over a time lag of 5 seconds. These are typical of the cross-correlations of correlated broadband processes.

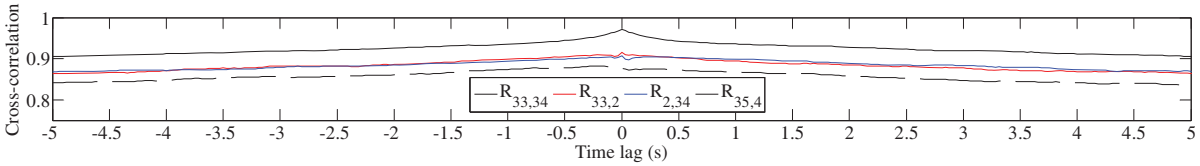

Figure 18 Cross-correlations of pressure measured along the axial direction of the cylinder: record 3

Figure 19 shows the distribution of the mean pressure coefficients for the duration of record 3. It is apparent that the mean pressures acting on the upper and lower parts of the cylinder are not symmetric. This indicates, on average, asymmetric separation of the flow from the oscillating cylinder in the critical Reynolds number range although the wind is approximately perpendicular to the cylinder axis.

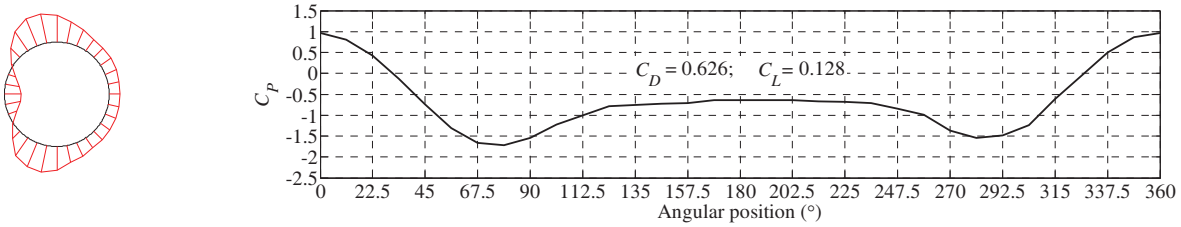

Figure 19 Mean pressure distribution at the pressure tap ring: record 3

The data show that the loading induced by wind oblique to the cylinder can have different characteristics from those of the loading by wind normal to the cylinder. As an illustration, Figure 20 shows the mean drag and lift coefficients against mean wind speed and the corresponding Reynolds number for a mean wind direction range of 55° to 65° relative to the cylinder. Both the force coefficients and the Reynolds number are computed based on the mean free-stream wind speed. The force coefficients show large scatter for low wind speeds. The reason for this scatter has not been positively identified and will be subjected to further investigation. The data does show, however, that the drag coefficient as a trend decrease consistently with wind speed when wind speed is higher than about 7.5 m/s, indicating that the critical Reynolds number range started at about this wind speed, which corresponds to a Reynolds number of 1.12×10^5.

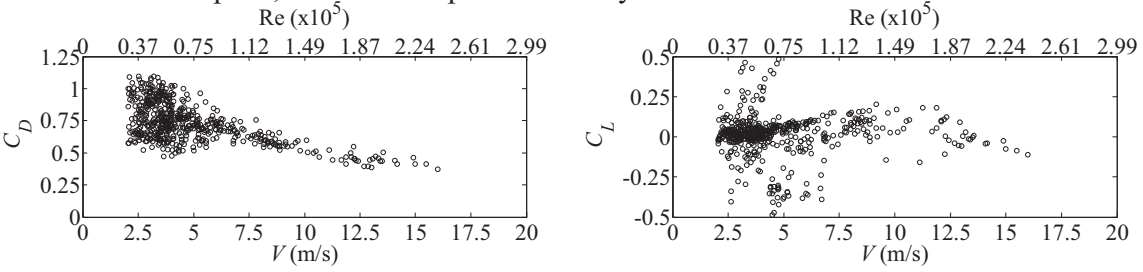

Figure 20 Mean drag and lift coefficients associated oblique to cylinder axis

In the following, a record with V= 11.27 m/s, β=64.5° and I_u=0.171, which is designated record 4, will be used to illustrate the interaction between the cylinder and oblique wind approaching from this direction. Figure 21 shows the time histories and the spectra of the drag and lift coefficients at the pressure tap ring. The spectra indicate that, in this case, the separation of the flow is also turbulent without regular vortex shedding. Figure 22 shows the acceleration response of the cylinder at the pressure tap ring. It can be seen that the low-amplitude response is dominated by the two lowest modes of the structure in the in-plane and out-of-plane directions.

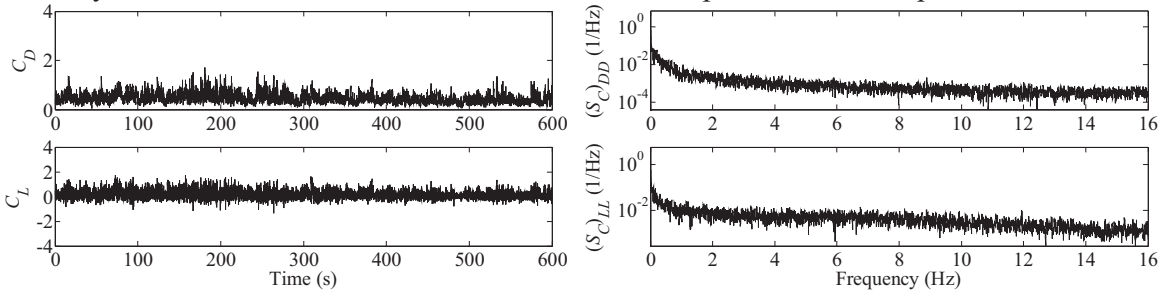

Figure 21 Drag and lift coefficients of the cylinder and the corresponding spectra: Record 4

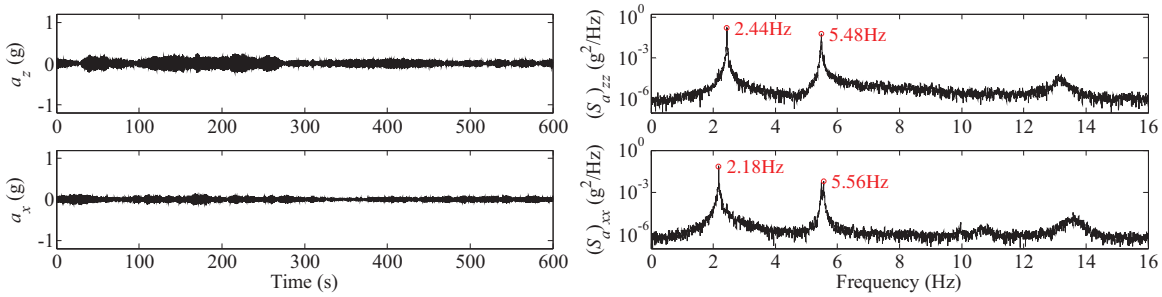

Figure 22 Acceleration time histories of and the corresponding spectra: record 4

Figure 23 shows the cross-correlation coefficients of the pressures at 5 taps along two axial lines of the cylinder over a time lag of 5 seconds. It is evident that the pressures at taps 33, 2 and 34 are the most correlated for zero time lag, indicating no apparent organized flow structure along these three taps. The figure also shows, however, that the maximum correlation between the pressures at taps 35 and 4 occurred for a time lag of ±0.125 second. This indicates the potential existence of an axial flow component along this line.

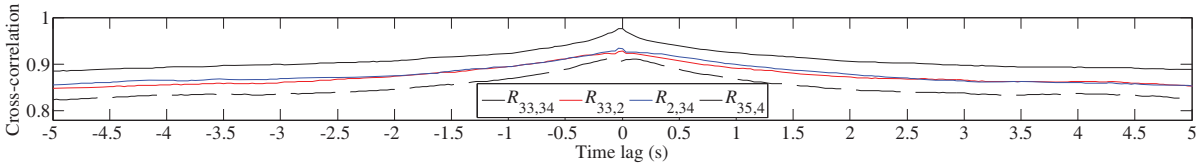

Figure 23 Cross-correlations of pressure measured along the axial direction of the cylinder: record 4

Figure 24 shows the distribution of the mean pressure for the duration of record 4. In this case, the mean pressures acting on the upper part and the lower part of the cylinder are not symmetric, indicating, on average, asymmetric separation of the flow from the oscillating circular cylinder when the oblique wind had mean wind speed in the critical Reynolds number range.

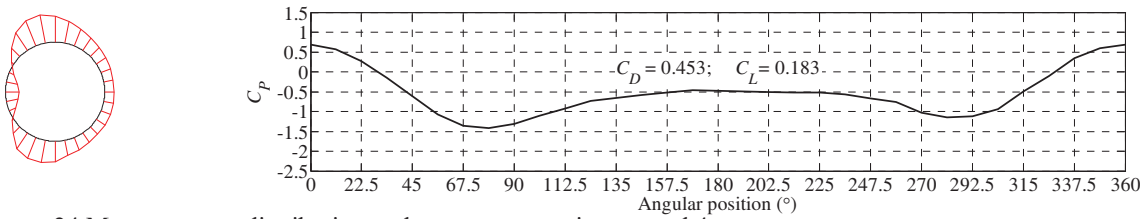

Figure 24 Mean pressure distribution at the pressure tap ring: record 4

5 CONCLUSIONS

A full-scale measurement campaign was conducted to study the dynamic interaction between wind and a circular cylinder. It is revealed that for wind both normal and oblique to the cylinder axis, the presence of turbulence in the free-stream wind shifts the transition from subcritical to critical Reynolds number range toward much lower Reynolds number than that at which the transition occurs in smooth flow. It was observed that when subjected to turbulent wind in the critical Reynolds number range, vortex-shedding does not occur and that in this Reynolds number range, the average flow separation lines on the upper and lower part of the circular cylinder surface are asymmetric about the horizontal plane through the centerline of the cylinder. The data also indicates the potential existence of an axial flow component in the wake of the cylinder when the wind is oblique to the cylinder axis.

6 ACKNOWLEDGEMENTS

The study presented herein is sponsored by the National Science Foundation of the United States through award number 0900643.

7 REFERENCES

1 Hikami Y, Shiraishi N. Rain-wind induced vibrations of cables in cable-stayed bridges. Journal of Wind Engineering and Industrial Aerodynamics. 1988;29:409-18.
2 Zuo D, Letchford CW. Wind-induced vibration of a traffic-signal-support structure with cantilevered tapered circular mast arm. Engineering Structures. 2010;32:3171-9.
3 Matsumoto M, Shirato H, Yagi T, Goto M, Sakai S, Ohya J. Field observation of the full-scale wind-induced cable vibration. Journal of Wind Engineering and Industrial Aerodynamics. 2003;91:13-26.
4 Zuo D, Jones NP. Interpretation of field observations of wind- and rain-wind-induced stay cable vibrations. Journal of Wind Engineering and Industrial Aerodynamics. 2010;98:73-87.
5 Cosentino N, Flamand O, Ceccoli C. Rain-wind induced vibration of inclined stay cables. Part I: Experimental investigation and physical explanation. Wind and Structures. 2003;6:471-84.
6 Cheng S, Larose GL, Savage MG, Tanaka H, Irwin PA. Experimental study on the wind-induced vibration of a dry inclined cable-Part I: Phenomena. Journal of Wind Engineering and Industrial Aerodynamics. 2008;96:2231-53.
7 Matsumoto M, Yagi T, Shigemura Y, Tsushima D. Vortex-induced cable vibration of cable-stayed bridges at high reduced wind velocity. Journal of Wind Engineering and Industrial Aerodynamics. 2001;89:633-47.
8 Zuo D, Jones NP. Wind tunnel testing of yawed and inclined circular cylinders in the context of field observations of stay-cable vibrations. Journal of Wind Engineering and Industrial Aerodynamics. 2009;97:219-27.
9 Cheng S, Tanaka T, Larose GL, Savage MG, Irwin PA, Jakobsen JB. Aerodynamic forces on an inclined circular cylinder. 5th International Colloquium on Bluff Body Aerodynamics and Applications. July 2004, 2004, Ottawa, Canada: 393-6
10 Yeo D, Jones NP. Investigation on 3-D characteristics of flow around a yawed and inclined circular cylinder. Journal of Wind Engineering and Industrial Aerodynamics. 2008;96:1947-60.
11 Blackburn HM, Melbourne WH. The effect of free-stream turbulence on sectional lift forces on a circular cylinder. Journal of Fluid Mechanics. 1996;306:267-92.
12 Zdravkovich MM. Flow around Circular Cylinders. New York: Oxford University Press; 1997.

The Seventh International Colloquium on Bluff Body Aerodynamics and Applications (BBAA7)
Shanghai, China; September 2-6, 2012

Unsteady wind force on an elliptic cylinder subjected to a short-rise-time gust from steady flow

Takashi Takeuchi [a], Junji Maeda [b], Kazuhiro Otsubo [b], Yasuyuki Shuto [c]

[a]*Kobe University, 1-1 Rokkodai-cho, Nada-ku, Kobe, Japan*
[b]*Kyushu University, 6-10-1 Hakozaki, Higashi-ku, Fukuoka, Japan*
[c]*Kyushu Electric Power Co., Inc., 6-10-1 Hakozaki, Higashi-ku, Fukuoka, Japan*

ABSTRACT: The properties of unsteady wind force on an elliptic cylinder under a rapid change from steady flow were investigated using a gust wind tunnel. As a result, we confirmed that the overshoot phenomenon of wind force occurred under a short-rise-time gust from steady flow as well as from calm. And it was found that the overshoot coefficient, defined by the ratio of maximum to a steady-state value of wind force, decreased with an increase in the ratio of the initial wind velocity to the target wind velocity. For each ratio of the initial wind velocity to the target wind velocity, the overshoot coefficient was determined by an expanded non-dimensional rise time composed of rise time, body size, and initial and target wind velocities.

KEYWORDS: Overshoot of wind force, Non-dimensional rise time, Gust wind tunnel test.

1 INTRODUCTION

A wind force acting on a structure under a gust with a very short rise time, which occurs in high winds associated with typhoons and tornadoes, differs from a quasi-steady aerodynamic force in consideration of a small turbulent flow, and occasionally reaches a large value not seen in a steady wind flow. Several reports have shown that an overshoot phenomenon bringing a much bigger wind force than in a steady flow occurs on a structure subjected to a short-rise-time gust. Taneda[1] investigated unsteady lift acting on an elliptic cylinder rapidly started at an angle of attack using a water tank test and reported that a remarkably big lift appeared just after starting. Sarpkaya[2] showed that the drag of a body increased by approximately 25 percent during the growth of the first pair of vortices as compared to a steady flow, using an impulsive flow test over circular cylinders in a vertical water tunnel, adding some results of potential flow analyses around the circular cylinders. Morison *et al.*[3] evaluated the force acting on a small cylinder in a flow with acceleration using a semi-empirical equation added to an inertia term proportional to flow acceleration. Nomura *et al.*[4] computed unsteady drag acting on a square cylinder under a sudden change of flow speed and reported that the drag component proportional to flow acceleration played quite an important role in the total unsteady drag when the flow speed was relatively low. Matsumoto *et al.*[5] measured transient drag on a two-dimensional cylindrical model under a suddenly-changing wind speed using a wind tunnel test with a working section of 200mm by 200mm square and reported an overshoot phenomenon in which the drag increased by approximately 20% compared to the force in a steady flow.

We have investigated the unsteady wind force on a body under a short-rise-time gust from calm using a specially-equipped wind tunnel, which could generate gusts with a rise time of 0.2 to 5 seconds from a flat calm by controlling the rotation speed of the blade rows. Takeuchi *et al.*[6] investigated the effects of the rise time of a step-function-like gust on the overshoot phenomenon of wind forces acting on a railcar-like body, and reported that the overshoot phenomenon was

more remarkable in the case of gusts with a shorter rise time. Takeuchi *et al.*[7] confirmed some overshoot phenomena of wind forces acting on an elliptic cylinder with some angles of attack, and reported that a non-dimensional rise time composed of rise time, body size, and target wind velocities considerably influenced the occurrence of the overshoot phenomenon. Takeuchi *et al.*[8] investigated the effect of the inertia force proportional to wind acceleration on the overshoot of wind force on an elliptic cylinder subjected to step-function-like gusts, and reported that the inertia force strongly influenced occurrence of the overshoot phenomenon in the case that the non-dimensional rise time was relatively small, but the overshoot phenomenon was due to other factors in the case of relatively large non-dimensional rise times.

Many of these reports have studied unsteady wind force acting on a body under a short-rise-time gust from calm. The unsteady wind force under a short-rise-time gust from steady flow has not been well studied. However, Tomokiyo *et al.*[9] investigated the features of the short-rise time wind gusts picked up from observation data of NeWMeK (Network for Wind Measurement in Kyushu, presented by Maeda & Ishida[10]), and reported that many of them were short-rise-time gusts from steady flow. Therefore, it is necessary to clarify the unsteady wind force on a body subjected to a short-rise-time gust from steady flow.

In this study, the properties of unsteady wind force on an elliptic cylinder under a short-rise-time gust from steady flow were investigated using wind tunnel tests. Short-rise-time gusts from steady flow were generated by the control of blade rows which were installed for generating a pulsation flow. We measured the unsteady drag and lateral forces on an elliptic cylinder under such gusts and organized the measured data by the non-dimensional rise time expanded to a short-rise-time gust from steady flow.

2 GENERAL SPECIFICATIONS OF THE WIND TUNNEL TEST

We used a wind tunnel of the Eiffel type at Kyushu University. The site plan of our testing system is illustrated in Figure 1a. The section area of the working space was 1.5m by 1.5m and the available length was 3m. The wind tunnel can generate a step-function-like gust to rise from a calm state by controlling the rotation of flat blade-rows. In this study, a short-rise-time gust from steady flow was generated by the following procedures. Firstly, we generated a steady flow with a constant wind velocity controlled by opening the blade rows partially. Secondly, we opened the blade rows quickly and fully, to generate a short-rise-time gust. An example of the time evolution of the wind velocity generated by control of the blade rows is shown in Figure 1b. The rise time of a gust, t_r, is defined as the time required for an approaching wind to reach a target wind, and the initial wind velocity, U_s, and the target wind velocity, U_t, are referred to as the initial and reached winds, respectively.

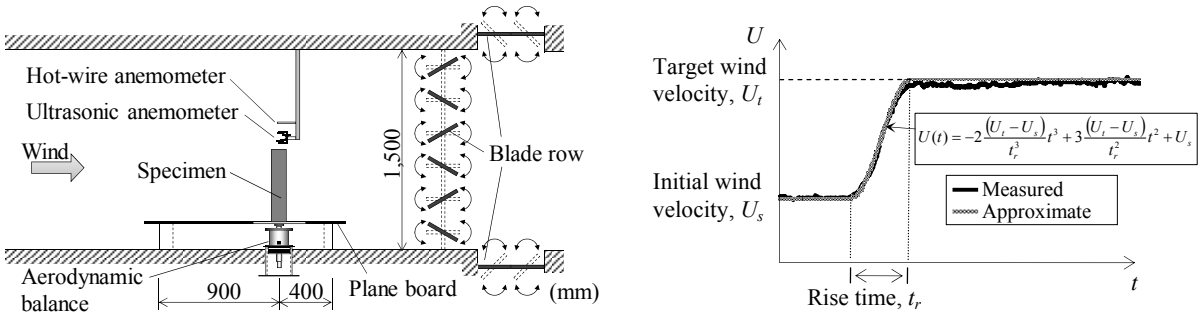

a) Site plan of wind tunnel. b) Time evolution of wind velocity.

Figure 1. Site plan of wind tunnel and time evolution of wind velocity.

In our earlier study, in which we generated step-function-like gusts from a calm state, we set the time required to open the blade rows as the rise time, because the rise time of a gust was almost equal to the time required to open the blade rows (Takeuchi *et al.*[7]). In this study, the rise time was decided by the following equation:

$$t_r = 2.348\,(t_{80} - t_{20}) \tag{1}$$

where t_{80} = the time for wind velocity to increase by 80% of the difference between U_s and U_t; and t_{20} = the time for wind velocity to increase by 20% of the difference.

The rise time, t_r, in Equation 1 was determined from the cubic function shown in Figure 1b which fits the time evolution of wind velocity. It should be noted that regarding the rise time of a short-rise-time gust from calm, t_r in this paper is different from that in our earlier study for the above reason. The wind velocity in the working space was confirmed by a hot-wire anemometer and an ultrasonic anemometer. The wind velocity was scanned at a frequency of 1000Hz.

We investigated some features of short-rise-time gusts generated by the above-mentioned

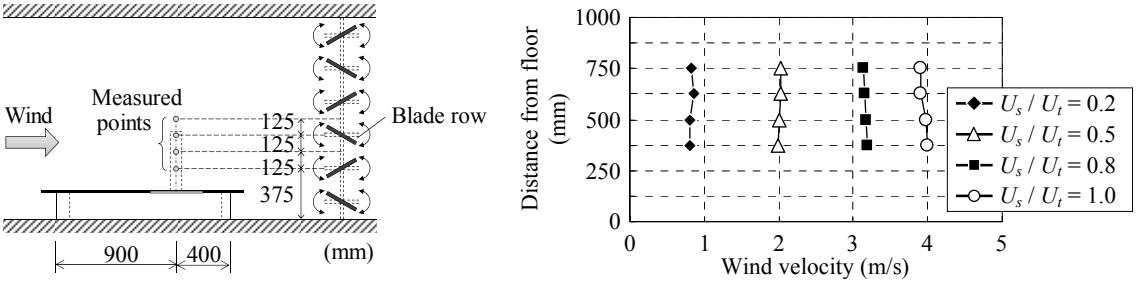

a) Positions of measured points. b) Averaged values of wind velocity.

Figure 2. Distribution of averaged values of wind velocity measured under steady flow controlled by opening blade rows.

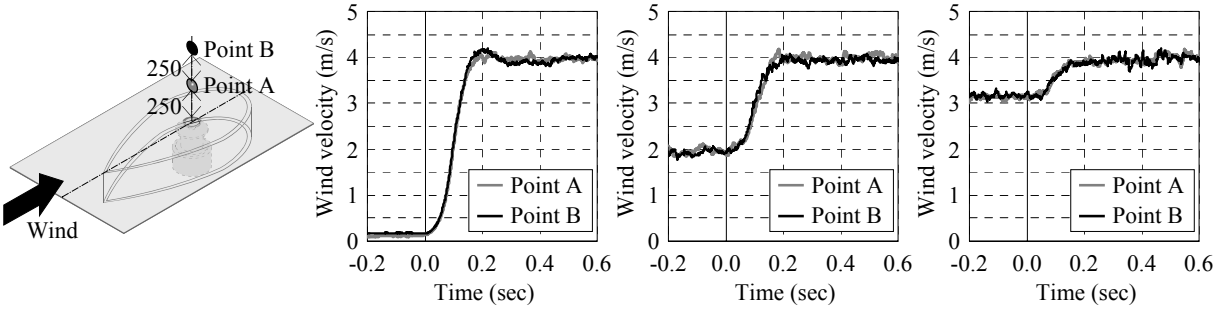

a) Positions of measured points. b) $U_s / U_t = 0.0$ c) $U_s / U_t = 0.5$ c) $U_s / U_t = 0.8$

Figure 3. Comparison of time evolutions of wind velocity measured at points A and B (U_t =4.0m/s, t_r =0.15sec).

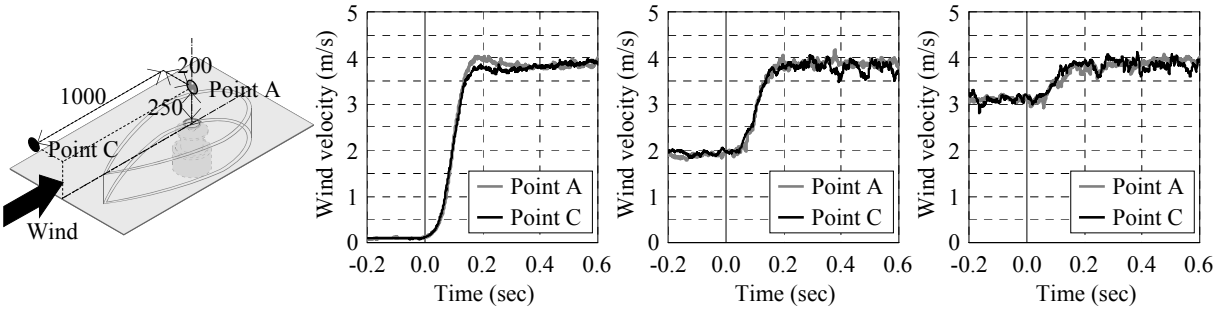

a) Positions of measured points. b) $U_s / U_t = 0.0$ c) $U_s / U_t = 0.5$ c) $U_s / U_t = 0.8$

Figure 4. Comparisons of time evolutions of wind velocity measured at points A and C (U_t =4.0m/s, t_r =0.15sec).

procedures. Figure 2 shows the distribution of the averaged values of wind velocity measured under steady flow controlled by opening the blade rows. We generated steady flows with 20%, 50%, 80% and 100% of wind velocity reached when the blade rows were opened fully, and measured wind velocity at 4 points over the aerodynamic balance, as shown in Figure 2a. Figure 2b indicates that the steady flow controlled by opening the blade rows was uniform. Figures 3 and 4 show the comparisons of the time evolutions of wind velocity measured at two points in the wind tunnel together under a short-rise-time gust. Figure 3 shows the comparisons of the time evolutions of wind velocity measured at points A and B over the aerodynamic balance, and indicates that they rose simultaneously under short-rise-time gusts from steady flow and calm. Figure 4 shows the comparisons of the time evolutions of wind velocity measured at point A and point C located 1000mm windward of point A, and indicates the same result as Figure 3. Thus, it was found that the wind velocity in the wind tunnel on the whole rose simultaneously under a short-rise-time gust from steady flow as well as under a short-rise-time gust from calm.

The specimens were two elliptic cylinders of axial ratio 2:1, both 500mm high, one 70mm and the other 140mm in major axis, as shown in Figure 5, and referred to as "Small-cylinder" and "Large-cylinder", respectively. They were fixed to the aerodynamic balance with a 45-degree angle of attack, and the drag and lateral forces acting on them were scanned at a frequency of 1000Hz. They were subjected to step-function-like gusts with a target wind velocity, U_t, between 2.0m/s and 7.0m/s, with the ratio of the initial wind velocity to the target wind velocity, U_s/U_t, between 0.0 and 0.9 and rise time, t_r, between 0.1sec and 1.4sec.

3 PROPERTIES OF UNSTEADY WIND FORCE ON ELLIPTIC CYLINDER UNDER SHORT-RISE-TIME GUST FROM STEADY FLOW

3.1 *Overshoot of wind forces*

Figures 6-9 show the time evolutions of the wind velocity, drag and lateral force on Large-cylinder, when the wind velocity reached 2.0m/s from 0.0m/s, 0.4m/s, 1.0m/s and 1.6m/s in a rise time of approximately 0.15sec. We confirmed that the overshoot phenomena of drag and lateral forces occurred under a rapid change from steady flow as well as from calm. But the peak of wind force changed with the initial wind velocity. The drag in the case of U_s = 0.0m/s had two peaks at approximately 0.1sec and 0.3sec. The first peak of drag in the case of U_s = 0.4m/s was smaller than that in the case of U_s = 0.0m/s. The drag in the cases of U_s = 1.0m/s and 1.6m/s had just one peak. Referring to Takeuchi *et al.*[8], it would appear that the first peaks of drag in the cases of U_s = 0.0m/s and 0.4m/s were caused by the inertia force proportional to wind acceleration. The inertia force and the wind acceleration decreased with an increase in the initial wind velocity, and the first peak of drag decreased with an increase in the initial wind velocity. In con-

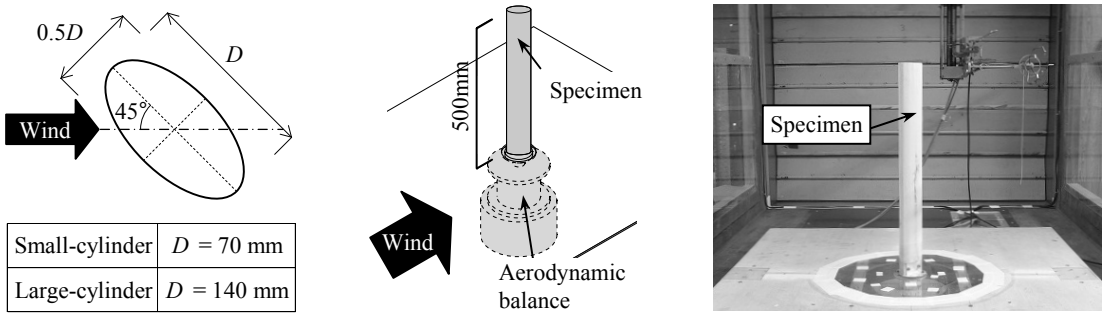

a) Section view of specimen b) Bird's-eye view c) Photograph of installation

Figure 5. Specimens.

trast, it is believed that the second peak of drag was due to unsteady vortex shedding. The value of the second peak of drag in the case of U_s = 0.0m/s was hardly different from that in the case of U_s = 0.4m/s. In cases where initial wind velocity was larger than 0.4m/s, the peak value decreased with an increase in the initial wind velocity.

The lateral force was little affected by the inertia force proportional to the wind acceleration,

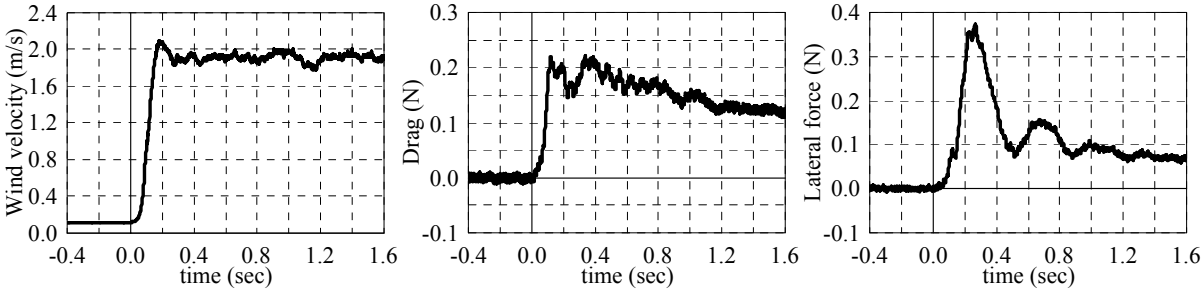

a) Wind velocity b) Drag c) Lateral force

Figure 6. Time history data of Large-cylinder (D =140mm, U_s =0.0m/s, U_t =2.0m/s, t_r =0.12sec).

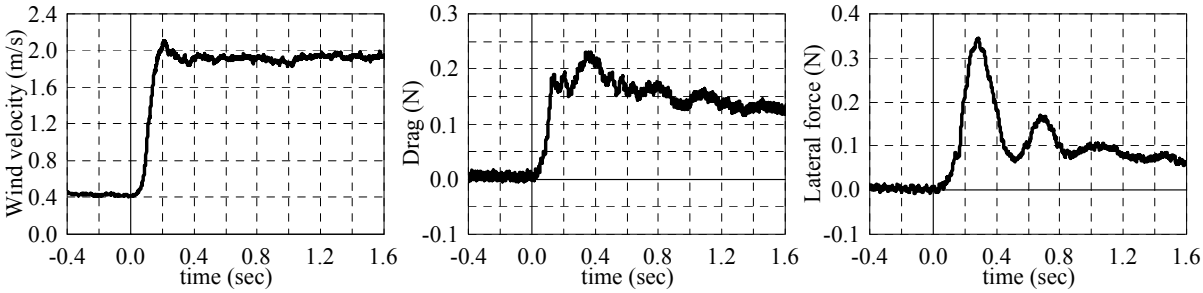

a) Wind velocity b) Drag c) Lateral force

Figure 7. Time history data of Large-cylinder (D =140mm, U_s =0.4m/s, U_t =2.0m/s, t_r =0.15sec).

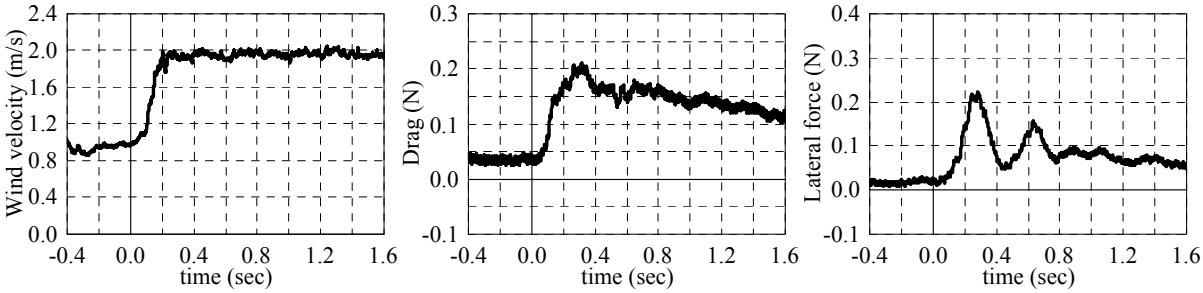

a) Wind velocity b) Drag c) Lateral force

Figure 8. Time history data of Large-cylinder (D =140mm, U_s =1.0m/s, U_t =2.0m/s, t_r =0.15sec).

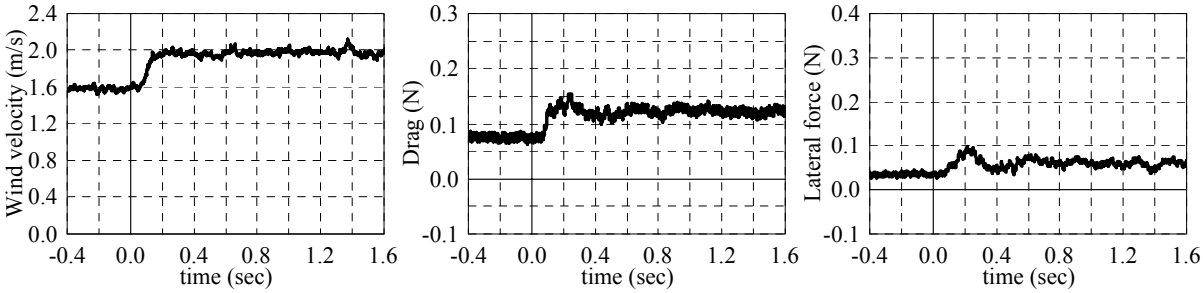

a) Wind velocity b) Drag c) Lateral force

Figure 9. Time history data of Large-cylinder (D =140mm, U_s =1.6m/s, U_t =2.0m/s, t_r =0.11sec).

and had just one peak due to unsteady vortex shedding. The peak value of lateral force decreased with an increase in the initial wind velocity as well as that of drag.

3.2 *Effects of parameters of short-rise-time gust on overshoot phenomenon*

Figure 10 shows the relationship between the overshoot coefficient and the rise time for Large-cylinder in the case of U_t = 3.0m/s and U_s / U_t = 0.0, 0.3 and 0.6. The overshoot coefficient is defined as the ratio of the peak value to the steady value, as shown in the following equation:

$$Overshoot\ coefficient = \frac{Peak\ wind\ \ force}{Steady\ wind\ \ force} \tag{2}$$

where the peak wind force is defined as the actual maximum force, and the steady wind force is defined as the mean over 20 seconds in a steady flow.

For each ratio of the initial wind velocity to the target wind velocity, both overshoot coefficients of drag and lateral force increased with a decrease in the rise time. Figure 11 shows the relationship between the overshoot coefficient and the target wind velocity for Large-cylinder in the case of t_r = approximately 0.15sec and U_s / U_t = 0.0, 0.3 and 0.6. Both overshoot coefficients of drag and lateral force increased with a decrease in the target wind velocity for each ratio of the initial wind velocity to the target wind velocity.

Figure 12 shows the relationship between the overshoot coefficient and the ratio of the initial wind velocity to the target wind velocity for Large-cylinder and Small-cylinder in the case of U_t = 3.0m/s and t_r = approximately 0.15sec. It was found that both overshoot coefficients of drag and lateral force decreased with an increase in the ratio of the initial wind velocity to the target wind velocity for each elliptic cylinder. And the overshoot coefficient of Large-cylinder was lar-

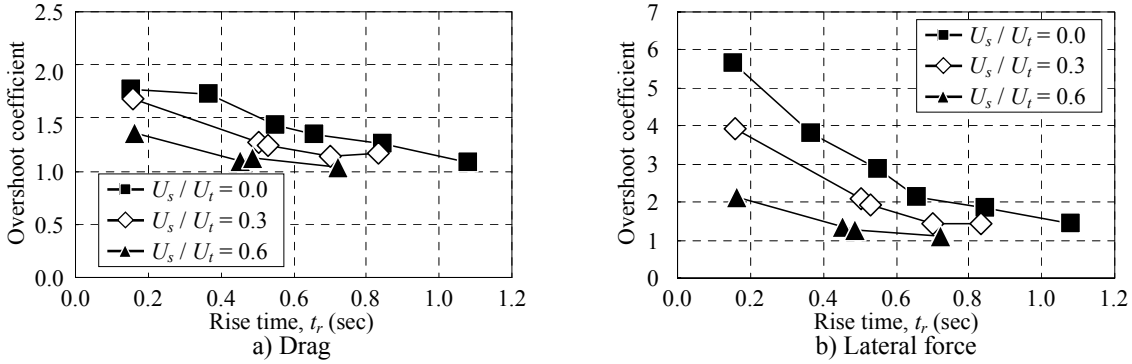

Figure 10. Overshoot coefficient with rise time (D =140mm, U_t =3.0m/s).

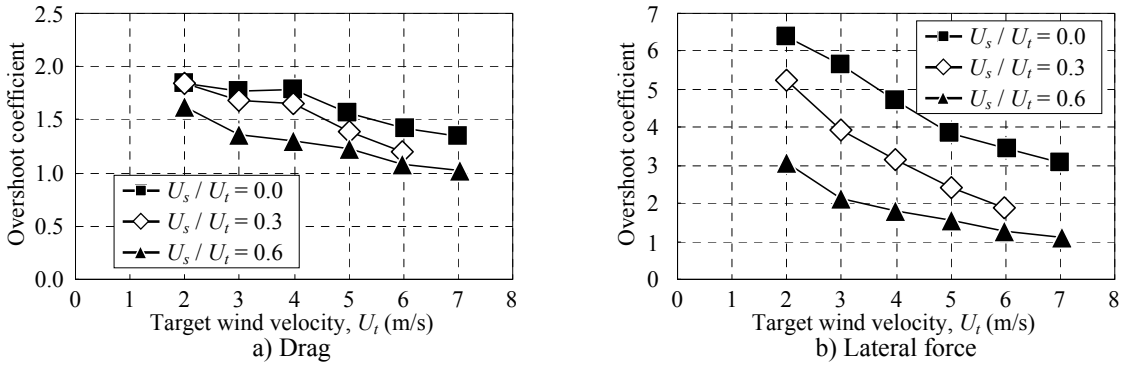

Figure 11. Overshoot coefficient with target wind velocity (D =140mm, t_r = approximately 0.15sec).

ger than that of Small-cylinder for all ratios of the initial wind velocity to the target wind velocity.

Figure 13 shows the overshoot coefficient for Large-cylinder and Small-cylinder in the case of t_r = approximately 0.15sec and the increase of wind velocity of 1.8m/s (U_s = 0.2m/s and U_t =2.0m/s; U_s = 1.2m/s and U_t =3.0m/s; U_s = 4.2m/s and U_t =6.0m/s). Even when the increase of wind velocity was the same, the overshoot coefficient decreased with an increase in the initial wind velocity or the target wind velocity.

3.3 *Relationship between overshoot coefficient and non-dimensional rise time*

In our earlier study, we reported that the overshoot coefficient of wind force on a body subjected to a short-rise-time gust from calm was determined by a non-dimensional rise time, which was composed of a rise time, a gust speed and the body size, as shown in the following equation (Takeuchi *et al.*[7]):

$$t_r' = \frac{U_t \cdot t_r}{d} \tag{3}$$

where U_t = the target wind velocity; t_r = the rise time; and d = a reference length (here, the length of the flow direction of the elliptic cylinder).

However, in this study, the overshoot phenomenon of wind force on a body subjected to a short-rise-time gust from steady flow was affected by the initial wind velocity, as previously mentioned. Thus, we need to consider the initial wind velocity to organize the overshoot coefficient of wind force on a body subjected to a short-rise-time gust from steady flow. In this study,

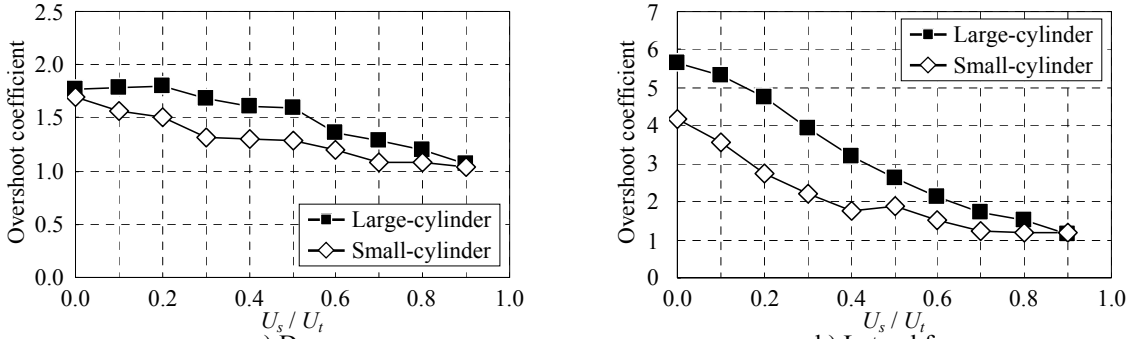

Figure 12. Overshoot coefficient with ratio of initial wind velocity to target wind velocity (U_t =3.0m/s, t_r = approximately 0.15sec).

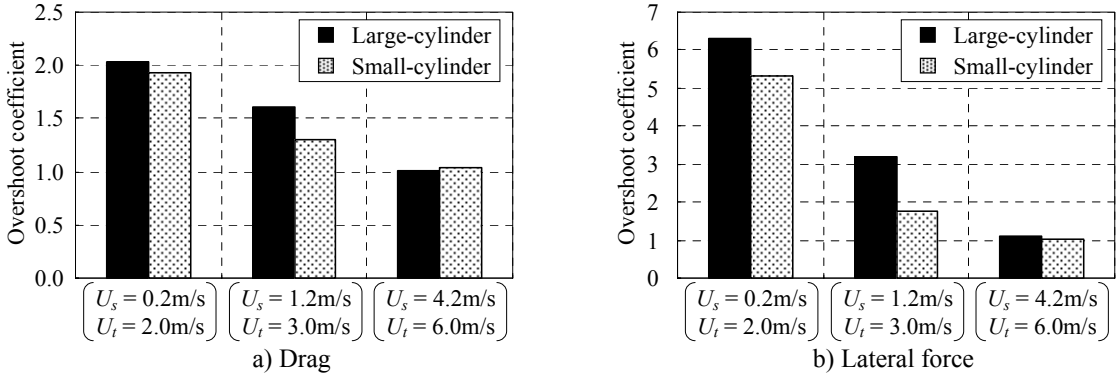

Figure 13. Overshoot coefficient in case of increase of wind velocity of 1.8m/s (t_r = approximately 0.15sec).

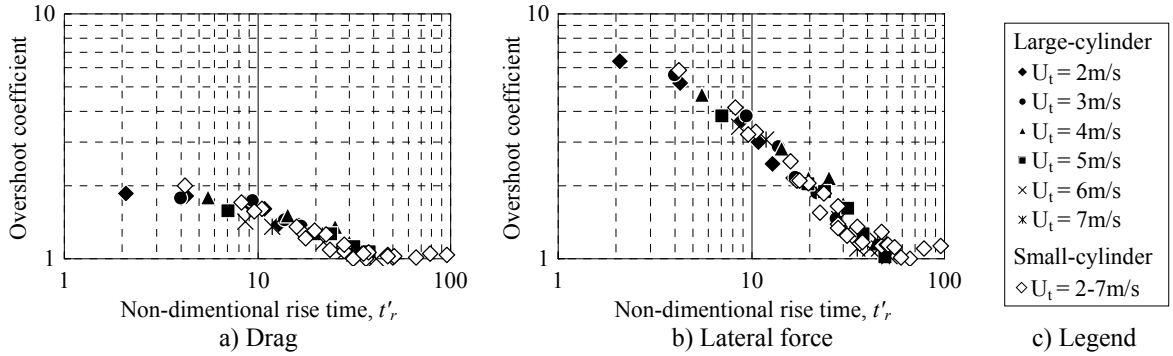

a) Drag b) Lateral force c) Legend

Figure 14. Relationship between overshoot coefficient and non-dimensional rise time (U_s / U_t = 0.0).

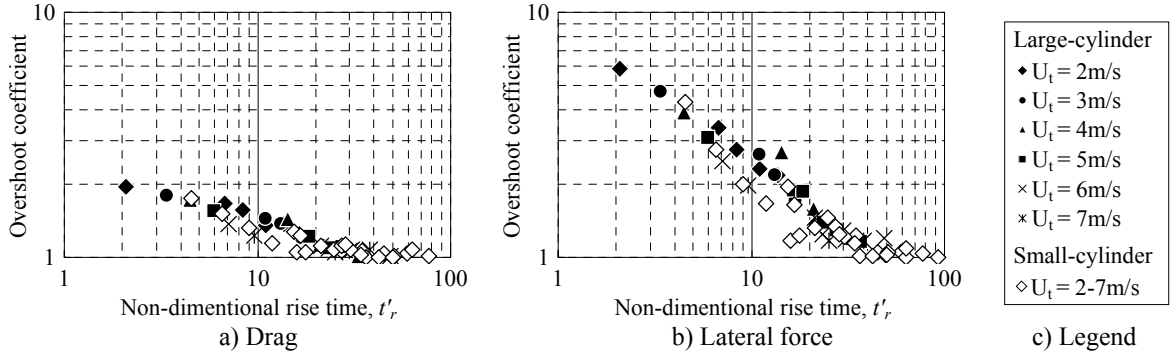

a) Drag b) Lateral force c) Legend

Figure 15. Relationship between overshoot coefficient and non-dimensional rise time (U_s / U_t = 0.2).

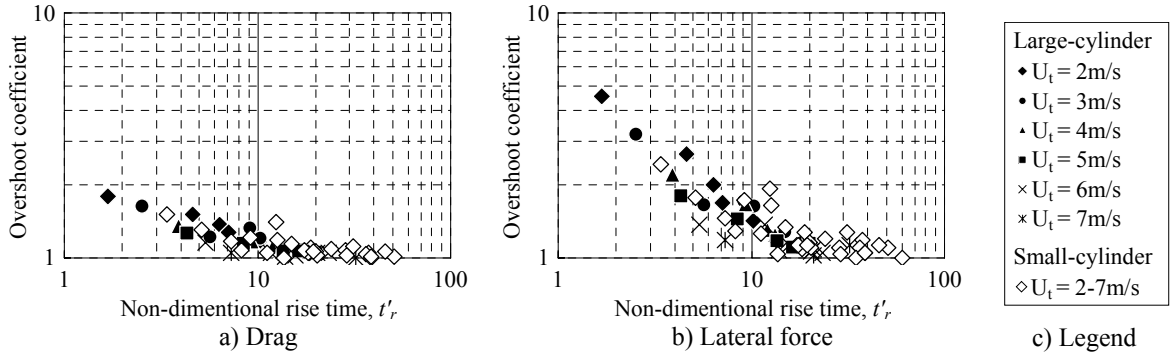

a) Drag b) Lateral force c) Legend

Figure 16. Relationship between overshoot coefficient and non-dimensional rise time (U_s / U_t = 0.4).

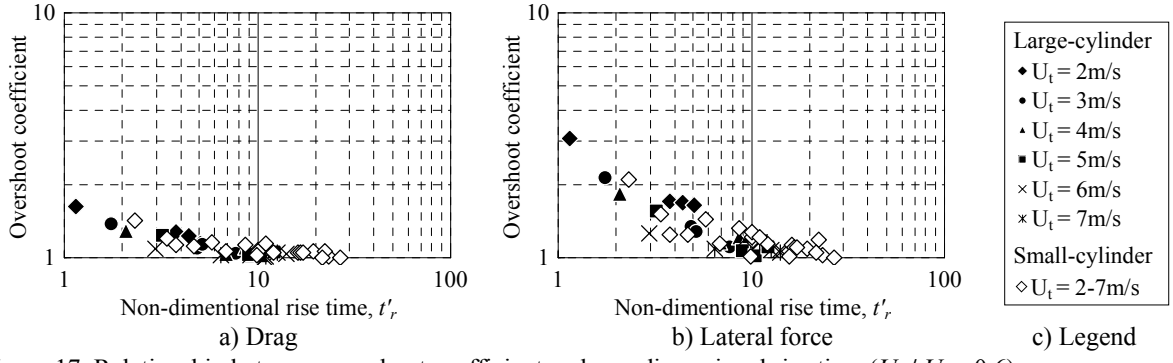

a) Drag b) Lateral force c) Legend

Figure 17. Relationship between overshoot coefficient and non-dimensional rise time (U_s / U_t = 0.6).

the non-dimensional rise time was expanded in consideration of the initial wind velocity as follows:

$$t_r' = \frac{(U_t - U_s) \cdot t_r}{d} \tag{4}$$

where U_s = the initial wind velocity. When $U_s = 0$, Equation 4 is the same as Equation 3.

Figures 14-17 show the relationships between the overshoot coefficients of drag and lateral force and the non-dimensional rise time obtained by Equation 4 in cases of $U_s / U_t = 0.0$, 0.2, 0.4 and 0.6, respectively. For each figure, the overshoot coefficients for Large-cylinder are plotted on one line regardless of the target wind velocity, and the overshoot coefficients for Small-cylinder are plotted on the line for Large-cylinder. Thus, for each ratio of the initial wind velocity to the target wind velocity, the overshoot phenomenon may be strongly affected by the non-dimensional rise time. And these figures show that the overshoot phenomenon was more remarkable in the case of a gust with the smaller ratio of the initial wind velocity to the target wind velocity. However, the variation in the overshoot coefficient increased with the ratio of the initial wind velocity to the target wind velocity. In future studies we will investigate the presence of a non-dimensional parameter associated with the overshoot phenomenon, additional to the non-dimensional rise time.

4 CONCLUSIONS

The properties of unsteady wind force on an elliptic cylinder under a rapid change from steady flow were investigated using wind tunnel tests. We introduced a procedure for generating short-rise-time gusts from steady flow by the control of blade rows which were installed for generating a pulsation flow. The following features of unsteady drag and lateral forces on an elliptic cylinder under such gusts were found:

1 It was confirmed that the overshoot phenomenon of wind force occurred under a short-rise-time gust from steady flow as well as from calm.
2 The overshoot coefficient, defined by the ratio of maximum to a steady-state value of wind force, decreased with an increase in the ratio of the initial wind velocity to the target wind velocity.
3 For each ratio of the initial wind velocity to the target wind velocity, the overshoot coefficient was determined by an expanded non-dimensional rise time composed of rise time, body size, and initial and target wind velocities. And it was shown that the overshoot phenomenon was more remarkable in the case of a gust with the smaller ratio of the initial wind velocity to the target wind velocity.

5 ACKNOWLEDGEMENTS

This study was supported by Grant-in-Aid for Scientific Research (B), No.22360230, Japan Society for the Promotion of Science.

6 REFERENCES

1 S. Taneda, The development of the lift of an impulsively started elliptic cylinder at incidence, Journal of the Physical Society of Japan, Vol. 33, No. 6, (1972) 1706-1711.

2 T. Sarpkaya, Separated Flow about Lifting Bodies and Impulsive Flow about Cylinders, AIAA Journal, Vol. 4, No. 3, (1966) 414-420.
3 J. P. Morison, M. P. O'Brien, J. W. Johnson and S. A. Schaaf, The force exerted by surface waves on piles, Petroleum Trans. AIME, 189, (1950) 149-154.
4 T. Nomura, N. Kitamura and T. Kitagawa, Characteristics of unsteady drag on a square cylinder under sudden change of wind speed, Proceedings of 3rd International Symposium on Computational Wind Engineering, 2000, pp. 3-6.
5 M. Matsumoto, M. Shimamura, T. Maeda, H. Shirato, T. Yagi, K. Hori, Y. Kawashima and M. Hashimoto, Drag forces on 2-D cylinders due to sudden increase of wind velocity, Proceedings of 12th International Conference on Wind Engineering, 2007, pp. 1727-1734.
6 T. Takeuchi, J. Maeda and H. Kawashita, The Overshoot of Aerodynamic Forces on a Railcar-like Body under Step-function-like Gusty Winds, Sixth International Colloquium on Bluff Body Aerodynamics & Applications, 2008, pp. 193-196.
7 T. Takeuchi, J. Maeda, T. Hayata and H. Kawashita, Effects of section size on aerodynamic forces on an elliptic cylinder under short-rise-time gusts, Proceedings of the 7th Asia-Pacific Conference on Wind Engineering, Taipei, 2009, pp. 731-734.
8 T. Takeuchi and J. Maeda, Effects of Inertia Force Proportional to Flow Acceleration on Unsteady Wind Forces Acting on an Elliptic Cylinder under Short-rise-time Gusts, Proceedings of 5th International Symposium on Computational Wind Engineering, USB flash memory (8pages), 2010.
9 E. Tomokiyo, J. Maeda and T. Takeuchi, Aerodynamic Definition of Wind Gust Affecting Overshoot of Wind Forces, Proceedings of the 21th National Symposium on Wind Engineering, 2010, pp. 179-184 (in Japanese).
10 J. Maeda and N. Ishida, Wind distribution analyses using a measurement array of high density, Proceedings of the 14th National Symposium on Wind Engineering, 1996, pp. 1–6 (in Japanese).

The Seventh International Colloquium on Bluff Body Aerodynamics and Applications (BBAA7)
Shanghai, China; September 2-6, 2012

Understanding rapid flow separation with spanwise variation

Jaime Wong, Jochen Kriegseis and David E. Rival

Dept. of Mech. Eng., University of Calgary, 2500 University Dr., Calgary, Canada

ABSTRACT: The current study investigates the influence of spanwise flow on three- dimensional vortex evolution. Using a robotic apparatus, a flapping motion was imposed on high aspect-ratio profiles. The flapping motion produced a spanwise variation in separation, and was reproduced for profiles with and without sweep to vary spanwise velocities. An analytical model for leading-edge vortex growth was proposed, based on the transportation of vorticity-containing mass through the shear-layer. When applied to the flapping motion, it was found that the analytical model predicted similar force coefficients with and without spanwise flow, which was confirmed by experiment. The model also predicted that the rate of vortex growth decreased with time in the presence of spanwise flow, although this could not be immediately verified experimentally.

KEYWORDS: Leading-edge vortex, spanwise flow, vortex modeling.

1 INTRODUCTION

Traditionally it is common to analyse flapping wings and rotating blade systems as a series of quasi-two-dimensional elements [1, 2]. However, flapping and rotating systems can exhibit large spanwise gradients in velocity and effective incidence. These spanwise gradients can couple with rapid flow separation to form highly three-dimensional vortex behaviour. The application of two-dimensional models to such highly three-dimensional flows will typically result in large errors when predicting aerodynamic performance [3]. Consider the case of a rotating blade, as on a wind turbine, experiencing a sharp-edged axial gust. The spanwise distribution of angle of attack $\alpha(r)$ from the base flow u_∞ takes the form $\arctan(u_\infty/\omega r)$. As shown in Figure 1, the change in effective incidence for a gust of strength $\Delta u = u_\infty$ would be greatest towards the root. Large, rapid changes in effective incidence towards the root ($r/R \approx 0$) can be expected to cause highly seperated flow, while this effect would diminish when moving towards the tip ($r/R \approx 1$). This can be compared to the root-flapping of a bird's wing. Changes in effective incidence would in this case grow towards the tip. At low speeds, where highly-separated flows are expected, gradients relating to vortical growth would increase towards the tip instead. In both scenarios, the low-momentum of separated flows would be small relative to coriolis and centripetal accelerations [4]. These accelerations would act to drive flow away from the root. Therefore, the direction of spanwise flow can coincide or oppose the gradient of effective incidence. The relationship between these two

effects, i.e. spanwise separation and coriolis/centripetal acceleration, is not immediately obvious.

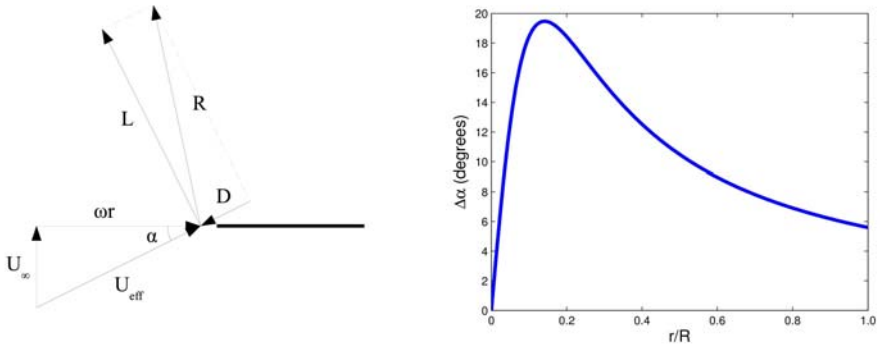

Figure 1: The velocity triangle and resulting forces for a rotating blade (left), and change in effective incidence as a function of span for a rotating blade subjected to a sharp-edged axial gust (right).

Of particular interest is how the leading-edge vortex (LEV) moves in the spanwise direction [5]. However, in highly three-dimensional cases, conventional blade-element schemes would fail to provide insight into spanwise transportation of vorticity. In the current study, analytical models for two- and three-dimensional vortex growth are proposed. These models are then compared with results obtained experimentally so as to verify the robustness of the model. Comparisons can be drawn from the relative influence of these sources of acceleration to spanwise velocity.

2 BACKGROUND

Consider the vorticity transport equation for an incompressible, barotropic fluid with conservative body forces:

$$\frac{\partial \vec{\omega}}{\partial t} + (\vec{u} \cdot \nabla)\vec{\omega} = (\vec{\omega} \cdot \nabla)\vec{u} + \nabla \times \left(\frac{\nabla \cdot \underline{\underline{\tau}}}{\rho} \right) . \tag{1}$$

The physical interpretation of each term from left to right can be described as: the changes in vorticity of the fluid due to unsteadiness, convection, vortex stretching through velocity gradients and the viscous diffusion of vorticity. Let us introduce a coordinate system set to a generic profile such that the z-direction is aligned with the blade span, and the x-direction with the blade chord, with the remaining y-coordinate then necessarily being normal to the blade surface, as shown in Figure 2. For the case of a simple plunging motion on a two-dimensional blade, a number of simplifications can be made. Firstly, viscous diffusion can be ignored under the assumption that timescales of diffusion are much larger than vortex growth itself. Furthermore, all gradients in the z-direction must necessarily be zero. The z-vorticity transport equation will subsequently reduce to:

$$\frac{\partial \omega_z}{\partial t} + u\frac{\partial \omega_z}{\partial x} + v\frac{\partial \omega_z}{\partial y} = 0 . \tag{2}$$

This is not conditional on a spanwise velocity field, caused for instance by a infinitely long wing of finite sweep, or on the existence of ω_x or ω_y. It follows that, after the elimination of z-gradient term, the remaining vortex stretching terms must sum to zero:

$$\omega_x \frac{\partial w}{\partial x} + \omega_y \frac{\partial w}{\partial y} = \left(\frac{\partial v}{\partial z} - \frac{\partial w}{\partial y} \right) \frac{\partial w}{\partial x} + \left(\frac{\partial w}{\partial x} - \frac{\partial u}{\partial z} \right) \frac{\partial w}{\partial y} = \frac{\partial w}{\partial x}\frac{\partial w}{\partial y} - \frac{\partial w}{\partial y}\frac{\partial w}{\partial x} = 0 \ . \tag{3}$$

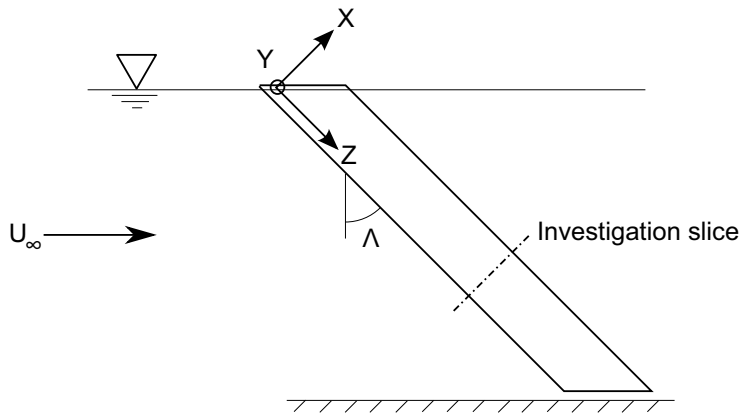

Figure 2: Coordinate system defined relative to a profile of sweep Λ in a quasi-two-dimensional arrangement, where the free surface and walls act as mirror planes.

As it is reasonable to assume a leading-edge vortex (LEV) would form parallel to the leading edge, it follows from equation (2) that the ω_z feeding the LEV would be confined to the $x - y$ plane. If the LEV is continually fed, it would grow until the vortex detaches and convects downstream. Thus, it may be conjectured that there is no two-dimensional mechanism from which one may stabilize the LEV. Consider now instead a three-dimensional case that is superficially similar, but where all gradients in the z-direction are non-negligible. A flapping wing would appear as a spanwise-dependent plunging motion. An order-of-magnitude argument can be made where ω_z is much larger than either ω_x or ω_y. In other words, the LEV can still be considered roughly parallel with the z-axis. The vorticity equation would then reduce to:

$$\frac{\partial \omega_z}{\partial t} + u\frac{\partial \omega_z}{\partial x} + v\frac{\partial \omega_z}{\partial y} + w\frac{\partial \omega_z}{\partial z} = \omega_z \frac{\partial w}{\partial z} \ . \tag{4}$$

Equation (4) introduces the ability for vorticity to be transported and stretched in the z-direction. In some circumstances, the vortex stretching term may be sufficiently large to cancel the convection terms. Only when those terms balance can $\partial \omega_z / \partial t$ be brought to zero and equilibrium be obtained. In other words, vortex stabilization must by definition require a three-dimensional flow. Planforms such as delta wings drain vorticity with spanwise flow to provide stable vortex lift under quasi-steady conditions. However, it is not clear what specific three-dimensional features, such as wing kinematics or shape, would result in an appropriate balance of vortex convection and stretching in highly-unsteady motions. This question ultimately motivates the development of the model described in the following section.

3 ANALYTICAL MODEL

3.1 *Two-Dimensional Case*

An analytical model for the unsteady lift on a plunging flat plate has been developed inspired by the work of Kaden [6]. As described in his model, the growth of a two-dimensional vortex can be attributed to the transport of vorticity-containing mass through the shear layer into the vortex in question. More recently, a model for the steady flux of vorticity in a shear layer has been tested by Sattari et al. [7]. The mass-flux into the LEV may therefore be described through conservation of mass for an incompressible fluid as:

$$m'(t) = \rho \int_0^t \int_0^d u(y,t)\ \mathrm{d}y\mathrm{d}t\ , \tag{5}$$

where $m'(t)$ is the vorticity-containing mass in the vortex per unit span, $u(y,t)$ is the shear-layer velocity profile and d is the shear-layer thickness. If the area of the vortex described by $m'(t)$ is then approximated as a roughly semi-circular shape attached to the blade, as in Figure 3, its radius $R(t)$ would be:

$$R(t) = \sqrt{\frac{2}{\pi}\frac{m'(t)}{\rho}}\ . \tag{6}$$

Knowing $m'(t)$, and thus $R(t)$, we may then compute the circulation of the vortex by the line integral of velocity around the vortex core:

$$\Gamma(t) = \oint \vec{u} \cdot \mathrm{d}\vec{l} = \pi\ u(d,t)R(t)\ , \tag{7}$$

where $u(d,t)$ is the velocity on the outer edge of the shear layer and the velocity along the profile surface is assumed zero. Recently it has been shown by Pitt-Ford and Babinksy that the bound circulation on flat plates in such unsteady conditions is negligible [8]. Thus, the LEV may be assumed to be the sole contributor of circulation. Lift may then be calculated, as a first approximation, by the Kutta-Joukowski equation. Difficulty now arises when attempting to predict the properties of the shear-layer growth from the bulk kinematics of the blade such as the plunge velocity $\dot{h}(t)$ and the effective incidence, $\alpha_{\text{eff}}(t) = \arctan(\dot{h}/u_\infty)$.

In the current model, the LEV is taken as a semi-circular shape located directly over the blade, while the shear layer exists on the outer radius of this semi-circle at position α_{eff}, as seen in Figure 3. The outer velocity $u(d,t)$ is determined by the superposition of three velocities: an acceleration around a cylindrical blockage of radius $R(t)$ at position α_{eff}; the induced velocity from the LEV itself; and the projection of the plunge velocity $\dot{h}$ onto the tangent of the semi-circle at α_{eff}:

$$u(d,t) = \underbrace{u_\infty \left(1 + \frac{R^2(t)}{r^2}\right) \sin(\alpha_{\text{eff}})}_{u_b} + \underbrace{\frac{\Gamma(t)}{2\pi r}}_{u_i} + \underbrace{\dot{h}\cos(\alpha_{\text{eff}})}_{u_p}\ , \tag{8}$$

where $r = R(t) + d$, u_b is the velocity component from blockage effects, u_i is the velocity component induced by the LEV, and u_p is component from the projection of the plunging motion. Furthermore, $u(0,t)$ is taken as the induced velocity component evaluated at $r =$

$R(t)$. From empirical observations, the shear-layer velocity profile was found to have an approximately sinusoidal transition from $u(0,t)$ to $u(d,t)$ such that:

$$u(y,t) = \frac{u(0,t) - u(d,t)}{2} \cos\left(\pi \frac{y}{d}\right) + \frac{u(0,t) + u(d,t)}{2} \ , \tag{9}$$

which then reduces the integral for vorticity-containing mass to:

$$m'(t) = \rho \int_0^t d \frac{u(0,t) + u(d,t)}{2} \ \mathrm{d}t \ . \tag{10}$$

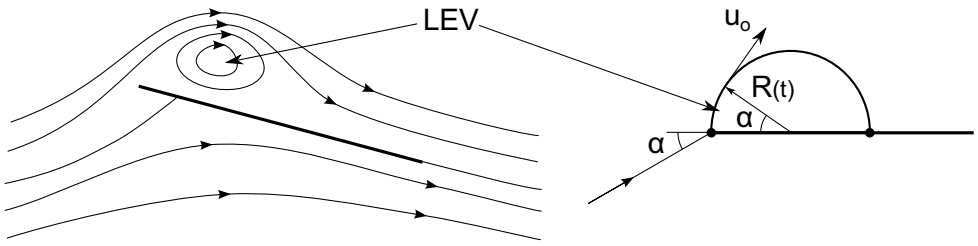

Figure 3: Comparison of the instantaneous streamline system (left) with the simplified model of a leading-edge stagnation point and semi-cylindrical blockage (right).

3.2 *Extension to the Three-Dimensional Case*

Given $\Gamma(t)$ is known for each two-dimensional slice, a blade-element scheme can be implemented to compute lift for three-dimensional motions. In the current study, a model was developed for the case of a high aspect-ratio blade far from the tip regions, such that three-dimensional effects were due exclusively to spanwise flow from sweep or centripetal/coriolis accelerations. In three dimensional flows, it is likely that flow near the blade can be broken into spanwise and chordwise components. While the chordwise-component of velocity contributes to vortex growth through the shear layer, the spanwise component serves to transport mass along the span only. We can revise the term for $u(d,t)$ such that:

$$u(d,t)\Big|_z = u_c \left(1 + \frac{R^2(z,t)}{r^2}\right) \sin(\alpha_{\text{eff}}) + \frac{\Gamma(z,t)}{2\pi r} + \dot{h}(z) \cos(\alpha_{\text{eff}}) \ , \tag{11}$$

where u_c is the chordwise component of u_∞ and α_{eff} is revised accordingly as $\arctan(\dot{h}/u_c)$. In addition, we must include an extra term for $m'(t)$ to account for the mass transfer through spanwise flow:

$$m'(t)\Big|_z = \rho \int_0^t \left(\frac{u(0,t) + u(d,t)}{2} d + \iint_R \vec{u}_s(z,t) \cdot \vec{n} \ \mathrm{d}A \right) \ \mathrm{d}t \ , \tag{12}$$

where z is the spanwise position, R is the surface swept by a semi-circular disc of radius $R(z,t)$ at the blade element z and $\vec{u}_s(z,t)$ is the spanwise component of velocity. It is worth noting that as gradients in the $z-$direction tend towards zero, equations (11) and (12) reduce to the two-dimensional cases represented by equations (8) and (10).

4 EXPERIMENTAL SETUP

Various blade motions were produced using a six degree-of-freedom hexapod manipulator, as shown in Figure 4. The hexapod was mounted over top of a custom water tunnel, which operated at 0.2m/s. A six-component ATI Gamma force/torque balance was flanged to the hexapod with a high aspect ratio flat blade of varying sweep $\Lambda = 0°$ and $-45°$ below. Each of the flat blades has a chord of 5cm measured normal to the leading edge, and a thickness of 3.12mm. In all test cases, the wing pierced the free-surface, which was considered as a mirror plane. Furthermore, the gap between the blade tip and tunnel floor was maintained under 3mm and therefore was similarly modeled as a mirror plane. The Reynolds number based on chord and freestream flow was $Re = 10,000$. Two test motions were considered. The first and most simple motion was of a sinusoidal-plunging movement as shown in equation (13):

$$\dot{h} = 0.1 \sin(2t) \ . \tag{13}$$

where $\dot{h}$ is the plunge velocity. This corresponds to a reduced frequency of:

$$k = \frac{\pi f c}{u_\infty} = 0.25 \ , \tag{14}$$

where f is the frequency of the motion. As a second case, a flapping motion described by equation (15) was considered. Kinematics were such that the plunging motion of case 1 was replicated at the 3/4 span, neglecting centripetal accelerations. The plate rotated about a virtual pin at the tunnel wall, by way of the programmable hexapod controller. The motion of case 2 took the form:

$$\dot{\theta} = 0.15 \sin(2t) \ . \tag{15}$$

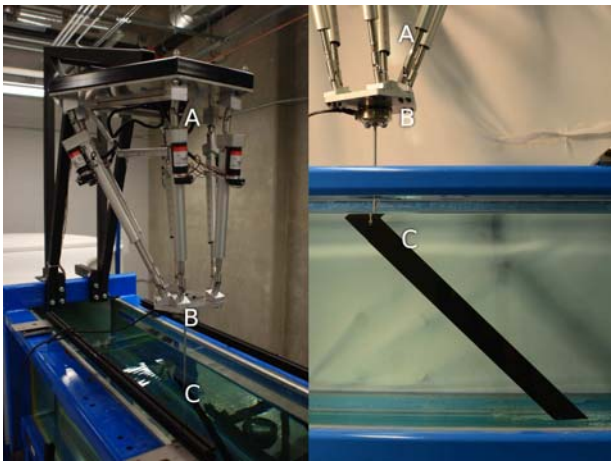

Figure 4: Experimental setup with high aspect ratio blade (A), 6-component balance (B), and hexapod manipulator (C) mounted to water tunnel.

5 RESULTS AND DISCUSSION

A comparison of the temporal evolution and spacial variation of vortex growth demonstrates the differences arising from spanwise flow in the flapping motion. Modeled vortex radii for flapping motion with and without sweep are compared in Figure 5. It can be seen that the rate of vortex growth slows with the period much more pronouncedly in the swept case than the unswept case. This suggests that vortex feeding and draining are tending towards similar rates. The mass flux through the shear-layer, which is roughly proportional to the shear-layer velocities shown in Figure 6, does not decrease with period. Therefore, mass transfer through spanwise flow becomes increasingly large, limiting vortex growth. If the rate of vortex growth would eventually decrease to zero, this would represent a stable vortex. Furthermore, the vortex is smaller in the swept case than in the unswept case across the entire span. This can be partially explained from the smaller chordwise velocity component u_c relative to the freestream velocity u_∞, limiting the rate of vortex feeding. However, since the vortex radius in the swept case is not simply a multiple of the unswept case as the change in chordwise velocity is, spanwise mass transfer towards the tip may also contribute to the smaller radius.

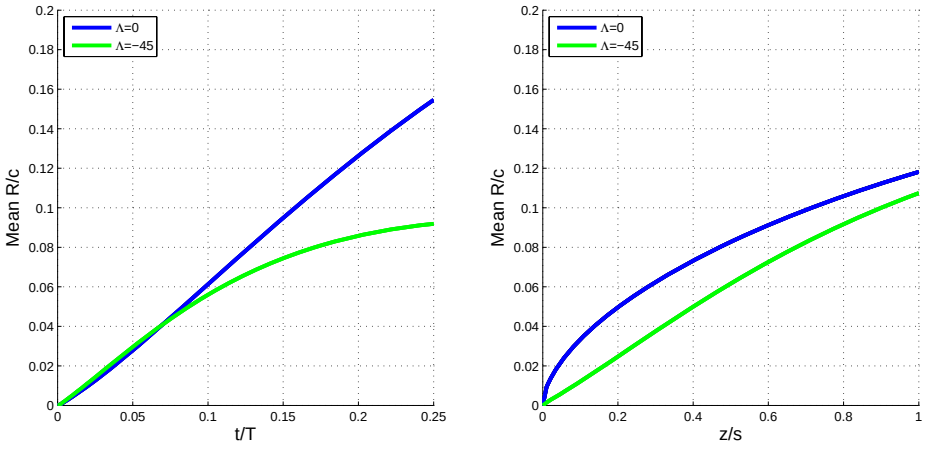

Figure 5: Modeled vortex radius as a function of period (left, averaged with span), and as a function of span (right, averaged with period).

To better understand the differences between swept and unswept cases, the individual components of shear layer velocity are compared in Figure 6. Note that the velocity component due to blockage effects is higher in the swept case than in the unswept case despite the smaller blockage radius. For this velocity component u_b, the effect of a smaller LEV radius in the swept case is balanced by a larger effective incidence. This effect of effective incidence can also be seen in the plunging component of velocity u_p. The equal induced velocity components u_i imply that unswept cases have a higher LEV circulation, given the larger vortex radius in unswept cases.

Measurements of lift coefficients show reasonable agreement with the analytical model for both two- and three-dimensional cases, shown in Figure 7. The largest discrepancies occur

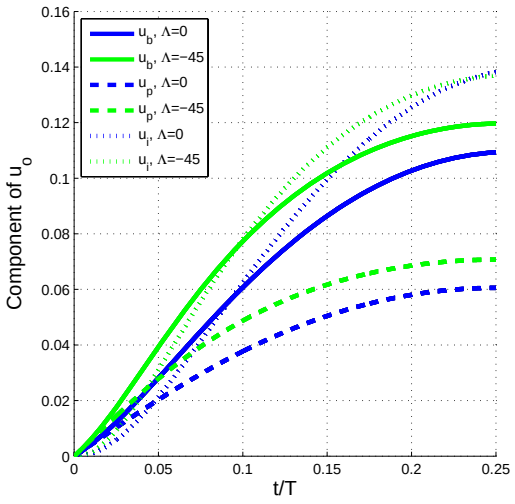

Figure 6: A comparison of terms contributing to $u(d, y)$ as a function of period, for cases with and without spanwise flow; u_b is velocity due to blockage, u_p is velocity due to plunging, and u_i is velocity induced by the LEV (see eq. (8)).

at $t/T = 0$, where the analytical model predicts a slope of zero. All measurements show a finite slope at $t/T = 0$, as the LEV begins to grow instantaneously. It is speculated that this effect is related to the vorticity-containing mass in the boundary layer contributing to the initial stages of LEV growth. Furthermore, agreement between the analytical model and measurements are also poor after one-quarter cycle, as the model cannot account for the vortex eventually detaching and convecting downstream.

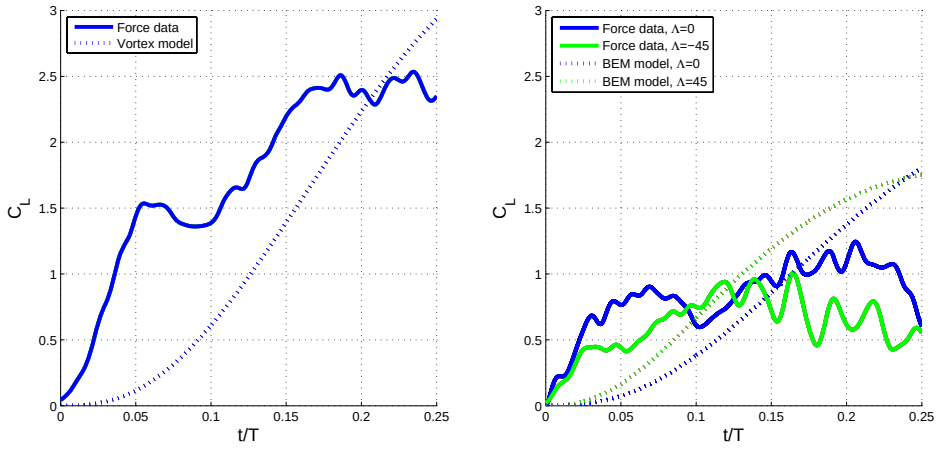

Figure 7: Lift coefficient as a function of period for plunging motion (left) and for flapping motion (right).

6 CONCLUSIONS

In this study, an analytical model for LEV growth has been developed and tested. When compared to physical measurements, rates of vortex growth between $0.05 \leq t/T \leq 0.2$ were reasonably accurate. Furthermore, the model predicted that the rate of LEV growth decreased across the first quarter period for a flapping motion in the presence of spanwise flow. This may contribute to vortex stability, however the reduction in vortex growth rate could not be immediately confirmed experimentally. The model was shown to be incapable of correctly predicting early-stage vortex growth. The model was also not developed to account for the eventual separation of the vortex from the profile. Nevertheless, the simple analytical description of the model and the ease of implementation are highly desirable. Future work will include verification that vortex growth can be limited by spanwise flow. Furthermore, the influence of an existing boundary layer on early-stage vortex growth and the influence of additional components of spanwise acceleration will be investigated.

REFERENCES

[1] H. Glauert. *Aerodynamic Theory*, volume IV, chapter Aeroplane Propellers. Springer, Berlin, 1935.

[2] J. Videler. *Avian Flight*. Oxford University Press, New York, 2005.

[3] J. Tangler and J. D. Kocurek. Wind turbine post-stall airfoil performance characteristics guidelines for blade-element momentum methods. 43rd AIAA Aerospace Sciences Meeting, Reno, Nevada, United States, January 2005.

[4] M. Hanson. *Aerodynamics of Wind Turbines*. Earthscan, London, 2008.

[5] H. Beem, D.E. Rival, and M.S. Triantafyllou. On the stabilization of leading-edge vorticies with spanwise flow. *Experiments in Fluids*, 51:511–517, 2012.

[6] H. Kaden. Aufwicklung einer unstabilen unstetigkeitsfläche. *Ing. Arch.*, 2:140–168, 1931.

[7] P. Sattari, D.E. Rival, R.J. Martinuzzi, and C. Tropea. Growth and separation of a start-up vortex from a two-dimensional shear layer. *Physics of Fluids*, 2012. (in revision).

[8] C.W. Pitt-Ford and H. Babinsky. Lift and the leading edge vortex. 50th AIAA Aerospace Sciences Meeting, Nashville, Tennessee, United States, January 2012.

The Seventh International Colloquium on Bluff Body Aerodynamics and Applications (BBAA7)
Shanghai, China; September 2-6, 2012

Effect of vortex-size around spike root and body base on possible hypersonic drag reduction

Shashank Khurana[a], Kojiro Suzuki[b], Ethirajan Rathakrishnan[c]

[a] *Graduate Student, Department of Advanced Energy, University of Tokyo, Japan*
[b] *Professor, Department of Advanced Energy, University of Tokyo, Japan*
[c] *Professor, Department of Aerospace Engineering, IIT Kanpur, India*

ABSTRACT: Large drag encountered by a blunt-nosed body, flying at a hypersonic speed, is primarily due to the high-pressure zone caused by the detached shock at the nose of the body. Spike has been identified as a passive technique to render the strong bow-shock at the nose to become weaker, thereby resulting in reduced pressure over the nose as a consequence of generated vortices, leading to drag reduction. However, all the previous studies were focused mainly on drag reduction quantification, without addressing the physical process causing the drag reduction. Therefore in the present work, attention is focused on understanding this aspect of the flow process at low Reynolds number (incompressible flow) and estimating its relevance for prospective hypersonic validity. It is known that the vortices at the attached end of the spike are responsible for reducing the high-pressure over the nose, leading to drag reduction. These vortices at the root of the spike would also influence the vortices at the base. It would be of great significance for drag reduction if the functional dependence of the size of these vortices on the Reynolds number can be established. Therefore, emphasis was focused on ascertaining the vortex size dependence, at the nose and at the base, on the flow Reynolds number and spike geometry, by visualizing the flow past a blunt-nose body with and without spike. Flow field around the blunt-nosed body, without spike and with spikes of various configurations, have been studied at Reynolds number 3170. It is found that there is a specific length-to-diameter ratio for every spike nose-configuration, resulting in the largest vortex at the spike base and at body base, for a given Reynolds number.

KEYWORDS: - Aerospike, Aerodynamics, Vortex-generation, Drag Reduction, Visualization

NOMENCLATURE

a - side of the square
d - spike diameter
D - body diameter
l - spike length
θ - spike nose-cone angle
φ - diameter
V - vortex length near fore-body nose

W - vortex length in wake region
CN- conical spike
FL- flat spike
HM- hemispherical spike
NS- no spike
SQ- square spike

1 INTRODUCTION

The drag reduction of a blunt-nosed body plays an important role in both low-speed and high-speed applications. This assumes a lot of importance in the case of hypersonic flying objects because of the extremely high drag caused by the high-pressure zone at the nose, owing to the blunt nature of the geometry. But the blunt shape is essential for the nose of the hypersonic vehicles to safeguard the body from ablation caused by aerodynamic heating. Considerable numbers of research articles are published in open literature with both experimental and computational studies on spiked blunt-nosed bodies at hypersonic Mach numbers [1]. For reducing the drag, secondary objects projecting ahead of the blunt nose (forward-facing) has been found to be an effective method. These secondary objects are termed spikes, in general. When a spike is fixed to a blunt nose, it essentially shifts the forward stagnation point away from the surface of the blunt nose, as shown in Figure 1. Because of this, the extent of the positive pressure zone over the blunt nose comes down consequently resulting in reduced drag. The flow process associated with the shifting of the stagnation point upstream of the blunt nose would result in weakening of the detached shock, and reduction of the extent of the zone influenced by the detached shock. However, for quantifying the dependence of the influence zone and the positive pressure zone over the nose, no information is available in the open literature. All the reasons given for the drag reduction, with the spikes, at hypersonic speeds are based on speculations about the zone of influence and the positive pressure zone over the nose, based on the end results obtained, mostly from direct measurements of force with wind tunnel balances. Therefore, there is an urgent need to understand the process associated with the flow over the basic body, with and without spike, for optimizing the spike geometry, resulting in efficient drag reduction. To gain an insight into the essential features of the flow physics associated with the drag reduction, it is essential to measure these parameters, if possible, directly. The present work is an attempt in this direction to assess and measure the extent of vortices near the fore-body stagnation area and in its wake, with and without spike, by direct means. For this, flow past the desired blunt-nosed body, with and without spikes, was visualized in a simple two-dimensional water channel, at a specific Reynolds number. The objective here is essentially to gain an insight into the important features governing the flow physics with the introdution of spike in front of the body nose, and its functional dependence on spike characteristics together with looking into the prospective application aspects governing the hypersonic flows.

Numerous researches in the past have proven that the positive pressure at the nose and the negative pressure at the base, together, amasses the large drag associated with blunt nosed bodies meant for high-speed applications. Therefore, it is essential to reduce the positive pressure at the nose and the negative pressure at the base to bring down the drag over the blunt nosed body. Vast quantity of studies, reported in literature, investigated these aspects of positive pressure at the nose and the negative pressure at the base, in isolation. For example, the first report in open literature which addresses both the nose and base fields is the work by Takama et.

al [2]. However, there is no direct address to the magnitude of the positive pressure at the nose and the base pressure at the rear, in this study. Also, the recent work of Kalimuthu et. al [3], though addressed drag reduction of blunt-nosed body, focuses mainly on reducing the positive pressure at the nose. It has been found that there is an optimum length for a spiked blunt-nosed body at a specified Mach number, resulting in maximum drag reduction. However except for the optimum length of the spike no information about the flow characteristics, causing the maximum drag reduction, was presented. From vortex dynamics, it is known that larger the vortex the higher is the suction caused by it. This feature is envisaged as the reason for the modification of the pressure flow field, resulting in maximum drag reduction. It can be visualized that if the suction caused by the vortex at the base end of the spike is large, the oblique shock formed at the spike tip and traveling towards the body nose will be attracted towards the body. If the suction created by the vortex is just enough to make the shock become tangential to the shoulder of the body, as illustrated in Figure 1, it would result in the optimum reduction of the pressure field over the body-nose, resulting in significant reduction of pressure drag. The subsequent work by Ashish and Rathakrishnan [4] is the first of its kind, which quantifies the shock strength, the base pressure field and the drag on a blunt nosed breathing body, by directly measuring the pressure distribution over the body and the drag force acting on it. In this work, a breathing blunt nose (BBN) concept has been employed successfully for reducing the drag at Mach 2. Sheard *et al.* [5] computed the flow normal to a cylinder, with hemispherical ends, using a spectral-element/Fourier method. They concluded that with variation in the ratio of cylinder length to diameter, the body varies smoothly from a sphere to a straight circular cylinder, providing an insight into the relationship between body topology and wake dynamics. Khurana *et al.* [6] performed the shallow water visualization experiments in a two-dimensional water channel around a blunt-nosed body, with and without spike, at Reynolds number 3070 and successfully captured the changes in flow field with the introduction of a spike, by quantification of different parameters namely zone of influence, pressure head and nose vortices.

It is also required to address the impact of introducing a spike on the flow field at the base area of the body. The higher the pressure field distributed over the nose area with spike at stagnation surface, the weaker will be the suction at the body base; consequently resulting in higher base pressure and a lesser pressure gradient in the flow direction for a lesser drag. Therefore, it will prove to be of great value and importance to understand the flow process responsible for total drag reduction (including nose and base) achieved with spike. Moreover, visualizing the vortex at the spike base at hypersonic Mach numbers is not possible because of extremely high inertia. Keeping this in mind the present work of vortex-size variation with spike-nose geometry and length-to-diameter ratio has been investigated in a water flow channel at Reynolds number 3170 and for different spike geometries shown in Figure 2.

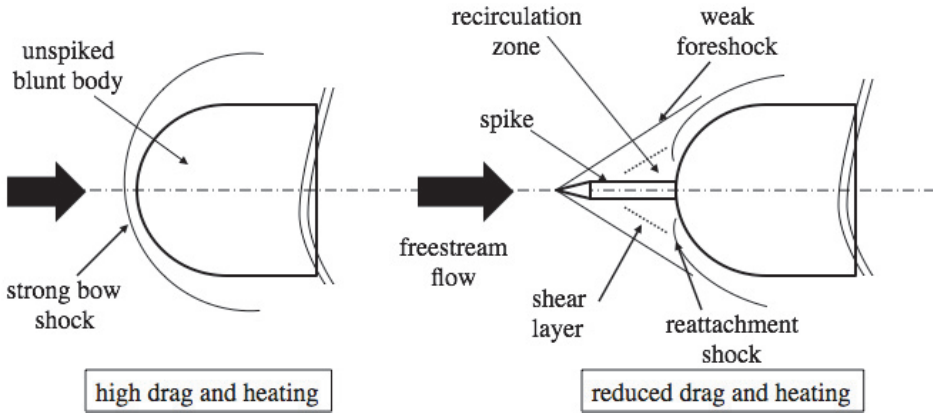

Figure 1. Spiked body concept.

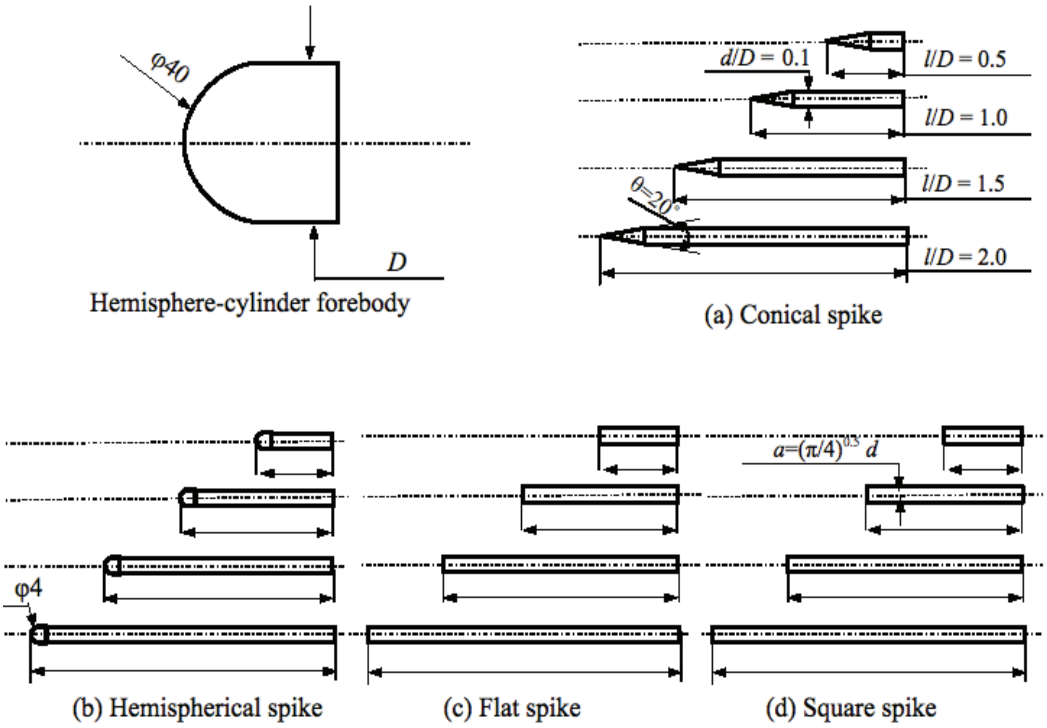

Figure 2. Test geometry with spike configurations.

2 EXPERIMENTAL SETUP

In the current investigation, the flow around a spiked body, comprising of vortices near the stagnation area, was visualized using a rectangular water flow channel [2,6,7,8] in the Suzuki K. Laboratory, The University of Tokyo. Schematic diagram and a pictorial view of the channel are shown in Figures 3(a) and 3(b), respectively. Water from the chamber, spills over the inclined plate and is conditioned using an array of wire-meshes, before reaching the downstream of the

test-section. The flow quality is ensured to be fairly uniform in the test-section. The velocity of the flow is measured using the floating-particle method technique, over the length of the test-section. The average of a set of 5 readings measured velocities is taken as the representative velocity of the flow. The test models and spike geometries were manufactured from ABS material for main body and Bakelite for spikes, using PC-controlled Modela MDX-504A (Roland DG Corporation) Rapid-prototyping machine available onsite in the laboratory (Fig. 2). The axis of the model was aligned parallel to the flow direction at the middle of test-section for every test. The model consists of a hemisphere-cylindrical fore-body with various spike-nose configurations (hemispherical, conical, flat and a specific case of square cross-section with side or equivalent diameter equal to $[(\pi/4)^{0.5}\, d]$. All the tests of the present study were carried out at Reynolds number 3170, based on the main body diameter. After the proper alignment has been ensured, some time is given for the flow to develop properly. The flow field in the test-section was ensured to be parallel and uniform by observing parallel streak lines of dye injected upstream of the empty test-section. Then the model was placed in the test-section and the flow field was recorded on a video camera (PANASONIC, Model DMC-ZX3) with resolution of 1280 x 720 and at 60 frames per second. The videos recorded clearly exhibit the flowfield comprising the vortices generated (V) at the body nose (spike base) and in the wake region (body base), as illustrated in Figure 4.

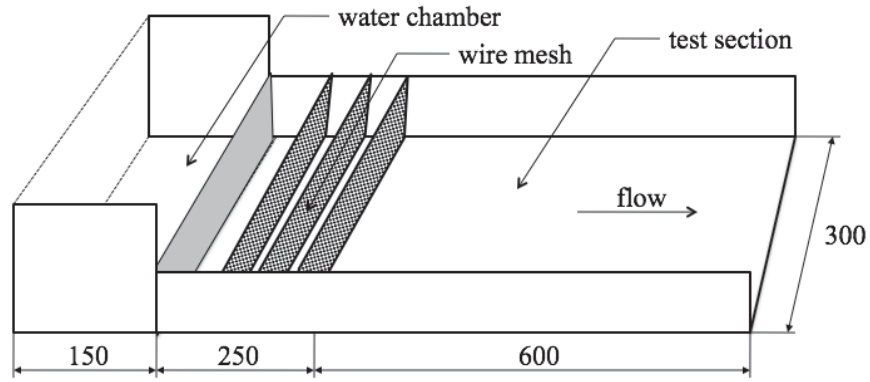

(a)

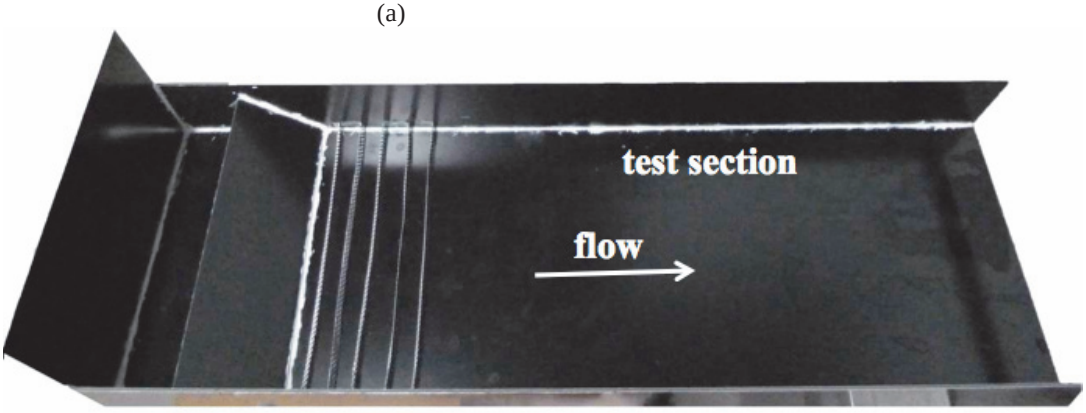

(b)

Figure 3. (a) Schematic diagram of the experimental set-up (dimensions in mm), (b) pictorial view of the set-up.

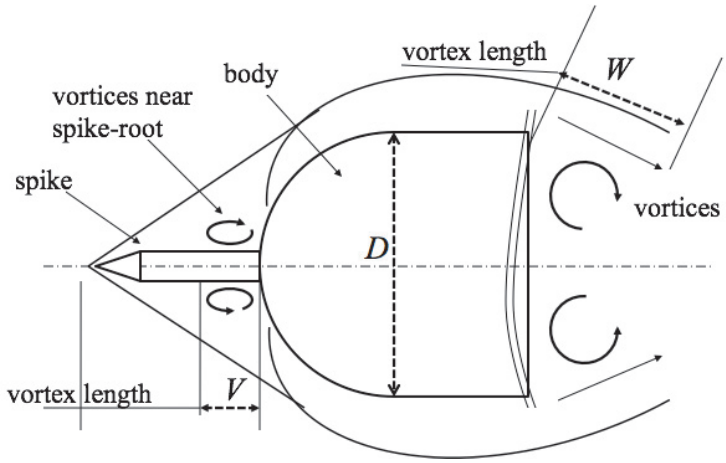

Figure 4. Flow field nomenclatures.

3 FLOW VISUALIZATION

The visualization results from the shallow water experiments have been presented in Figs. 5-8, with and without spike, for the varying length-to-nose-diameter ratios (l/D) from 0.5 to 2.0. Figure 5 shows the flow field for hemispherical-cylinder forebody with different spikes for l/D=0.5. The change in the streamlines after deflection from encountering an object (spike) in front of the nose can be easily concluded. The high pressure area that envelops the nose, is replaced by weak streamlines that gets deflected towards the shoulder of the body and again gets deflected towards the low pressure region of the wake. The flow field with different spikes, in front of the forebody for l/D=1.0, has been depicted in Figure 6. With the increase in l/D-ratio, the deflection of the streamline from the spike nose gets nearer to the shoulder of the forebody, confirming the suction that is created near the spike nose from the twin vortices on either sides. Together, the flow gets attracted towards the base of the body owing to the low pressure location in the wake. On further increasing the l/D-ratio to 1.5 (Fig. 7), it can be observed that the flow is nearly tangential to the forebody shoulder signifying an optimum value of l/D, for the generation of sufficiently larger vortices, which attracts the flow towards the nose-shoulder, thereby reducing the positive pressure on the nose. Beyond l/D=1.5, the flow starts dissipating at the spike nose, re-attaching near the spike root location resulting in negligible vortices. Contrary to this fact, the flow downstream of the forebody stays near to body base in the wake region, as the extent of vortices (low pressure region) behind the body decreases with increasing l/D-ratio.

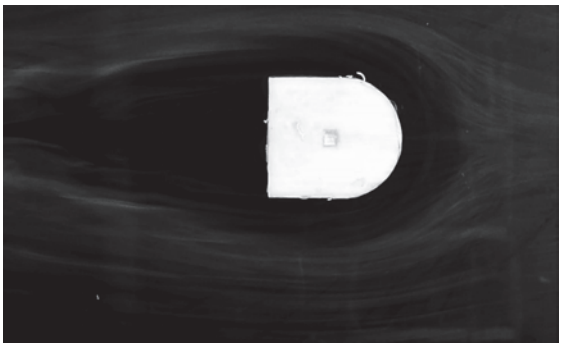

(i) No spike

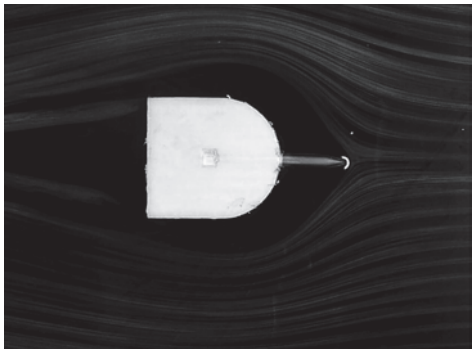

(ii) Conical spike

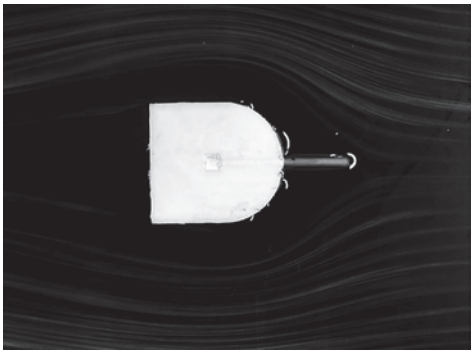

(iii) Hemispherical spike

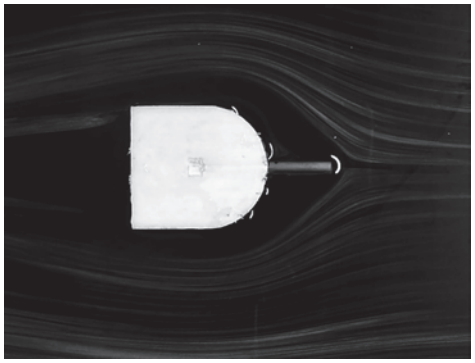

(iv) Flat spike

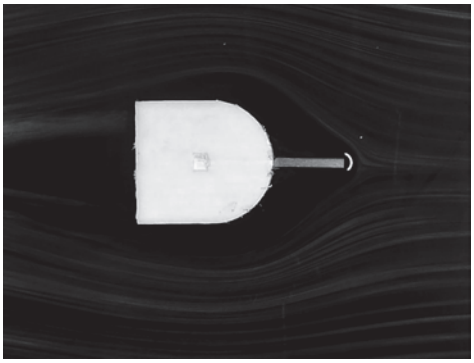

(v) Square spike

Figure 5. Flow field for various test cases for l/D=0.5

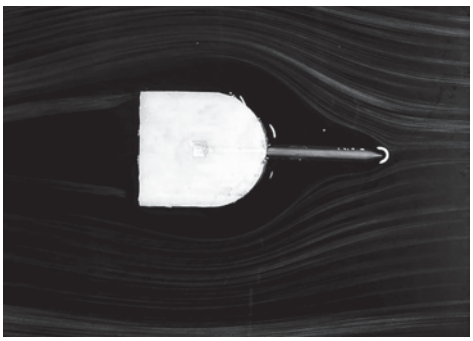

(i) Conical spike

(ii) Hemispherical spike

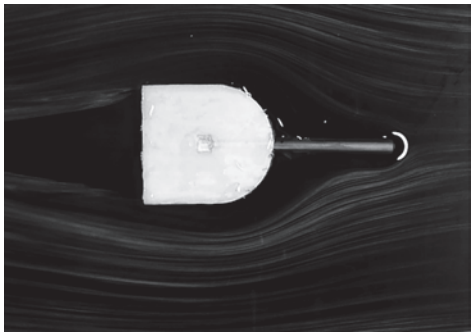

(iii) Flat spike

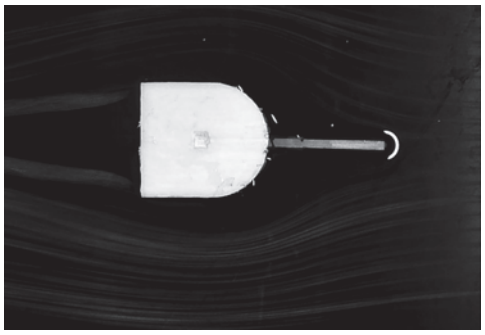

(iv) Square spike

Figure 6. Flow field for various test cases for l/D=1.0

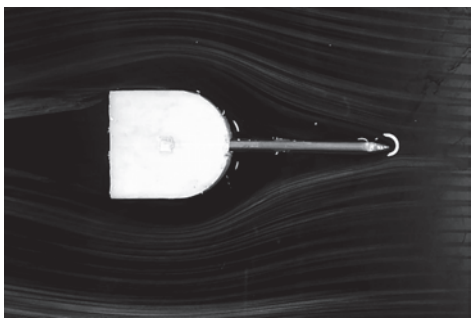

(i) Conical spike

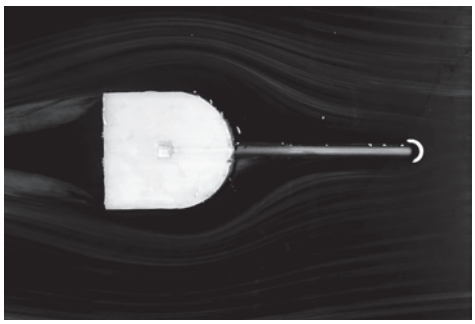

(ii) Hemispherical spike

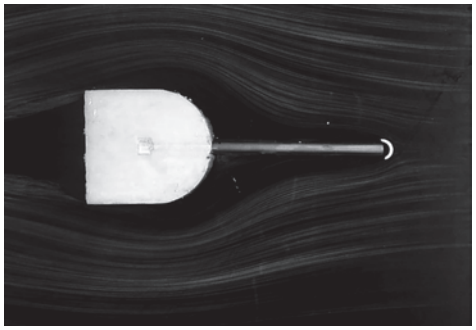

(iii) Flat spike

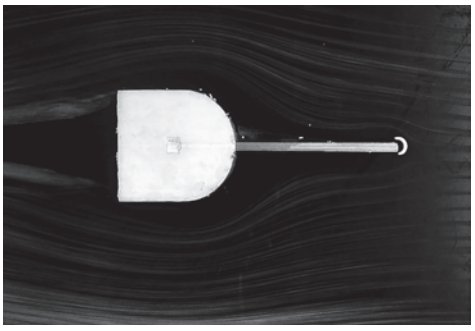

(iv) Square spike

Figure 7. Flow field for various test cases for l/D=1.5

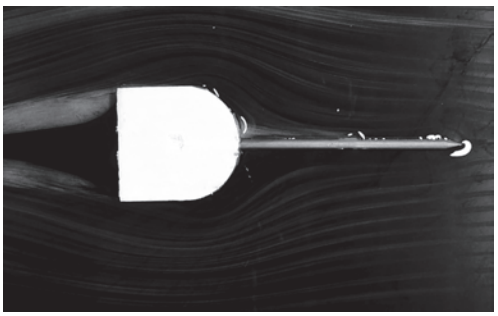

(i) Conical spike

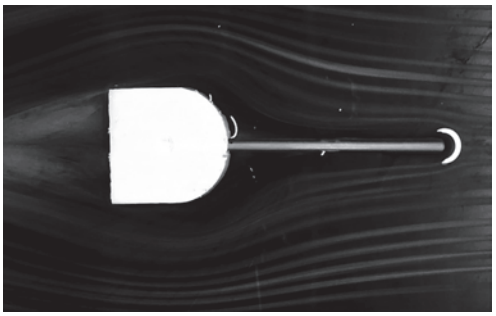

(ii) Hemispherical spike

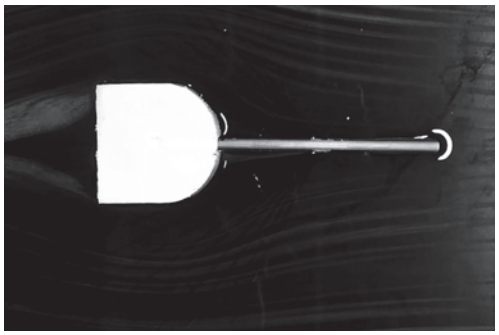

(iii) Flat spike

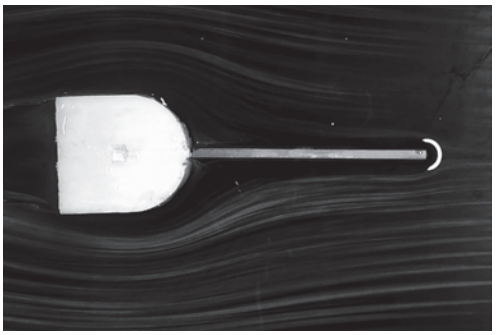

(iv) Square spike

Figure 8. Flow field for various test cases for l/D=2.0

4 RESULTS AND DISCUSSIONS

In the present investigation, the quantification of nose vortices around the spike root and stagnation area and those generated in the wake region have been completed. Figures 9 and 11 shows the flow field near-nose region with (l/D=1.5) and without spike and in the wake region with (l/D=2.0) and without spike respectively. These pictures of the flow field clearly exhibits the vortex length V and W, which were measured by projecting the visualization pictures on screen, for all the models studied. Figures 10 and 12 depicts the non-dimensional (V/D and W/D respectively) plots of vortex size variations with spike-nose configurations and different l/D-ratio around the nose and wake region. The ordinates of these graphs represent the non-dimensional lengths and the abscissa represents the type of spike-nose.

Considering the vortex-size variation around the nose, the representative and optimum l/D-ratio has been estimated to be 1.5 for the present case of Reynolds number. From Figure 10, it can be seen that a conical aerospike, irrespective of l/D-ratio, is incapable of generating vortices near the spike root, whereas a hemispherical spike reduces the zone of influence drastically (bringing the deflected flow near the shoulder). This may be envisaged as a direct indication of reduced positive pressure over the nose of the basic body. The generation of the vortices near the spike root results in low pressure recirculation region which attracts the deflected flow thereby keeping it near the shoulder. The radius of curvature of the approaching streamline is reduced; the deflection of the streamline is towards the shoulder of the basic body,

resulting in a narrow zone of the positive pressure hill at the nose. Therefore, integral of this positive pressure over the nose assumes lesser magnitude, compared to the positive zones for the spikes with conical or flat face, resulting in relatively smaller drag.

The wake-region behind the forebody is directly influence by the magnitude of the pressure on its nose and the deflection of the flow. The higher the magnitude of positive pressure on the nose, the stronger the deflection and larger the wake region, consequently resulting in increased drag. Figure 11 focusses on the flow field showing the wake region with (l/D=2.0) and without spikes and Figure 12 quantifies the magnitude of the vortex lengths by taking an average of the left and the right vortices (depicted in Fig. 11), generated on either side of the midspan, to avoid inaccuracy in case the wakes are not symmetrical. The equivalent vortex length is given by $\{(W_{right}+W_{left})/2\}$, which is plotted as a non-dimensional length (W/D) against the spike type for various l/D-ratios. From Figure 12, it can concluded that a spike (a forward-facing object in front of the nose), irrespective of its nose-type or size, is capable of reducing the low pressure void behind the forebody by significantly affecting the flow physics. For l/D=0.5, the deflection provided by the spike to the flow remains considerably away from the body and cannot reach the wake region inspite of the existing large suction zone at the base. Similar is the case with a conical spike, which provides large radius of deflection to the streamline. For a flat-faced spike, the radius of deflection gets reduced, resulting in lesser confinement zone of the wake vortices, where as hemispherical spike stands a sole candidate capable of positively affecting the wake region, and simultaneous reduction in drag.

About the practical application, considering the physics of flow around nose as well as base vortices, simultaneous action on both will provide the best solution for minimization of drag offered. This has been proved to be the function of forebody dimensions, flow velocity (Reynolds number) and spike configurations, which will hold its importance in deciding its utility for use in hypersonic conditions.

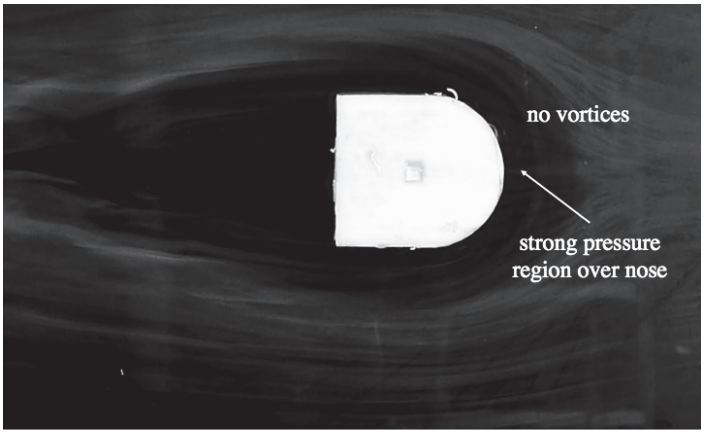

(i) No spike

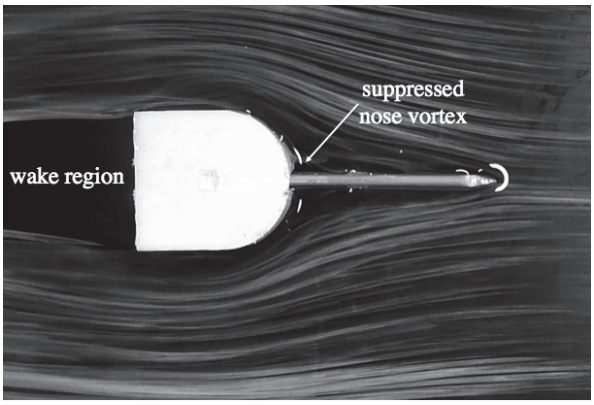

(ii) Conical spike

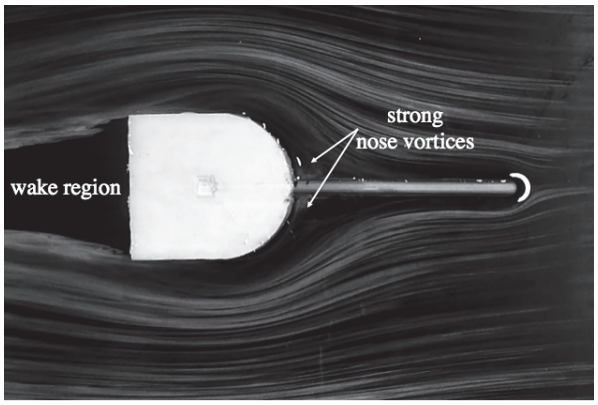

(iii) Hemispherical spike

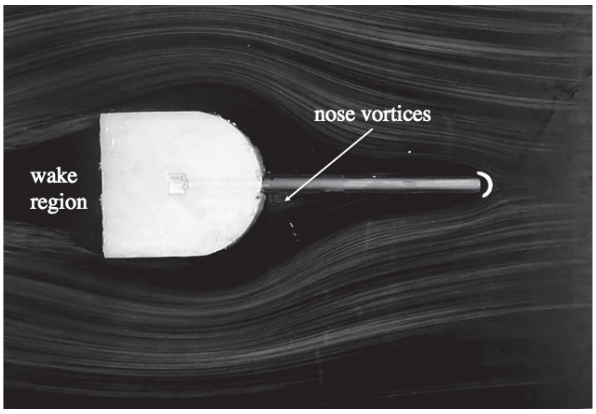

(iv) Flat spike

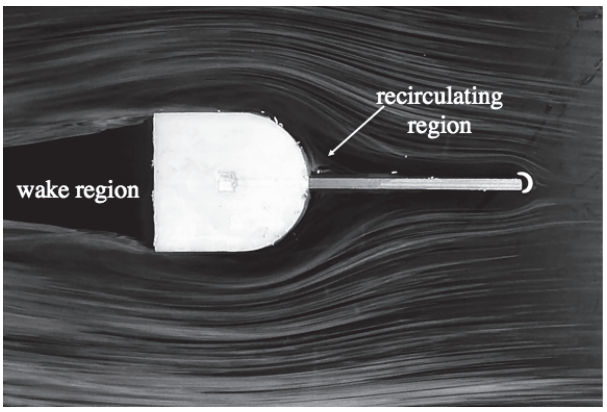

(v) Square spike

Figure 9. Flow field showing near-nose region with (l/D=1.5) and without spike.

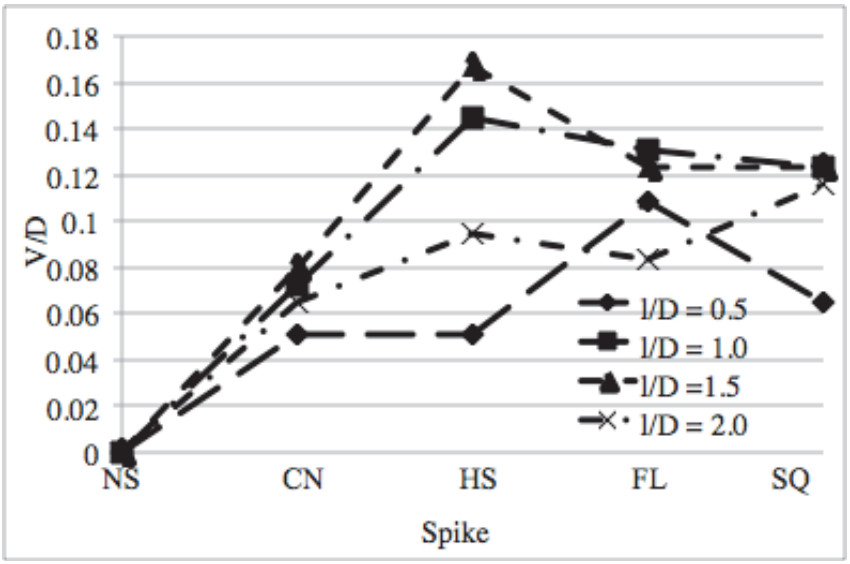

Figure 10. Vortex length variation around the nose for various spikes.

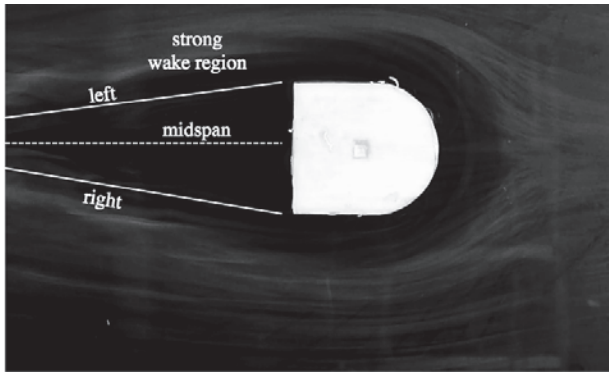

(i) No spike

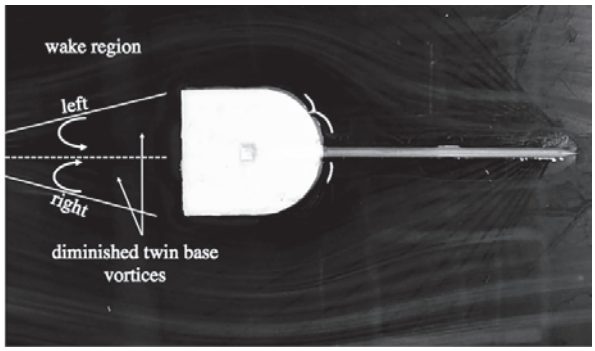

(ii) Conical spike

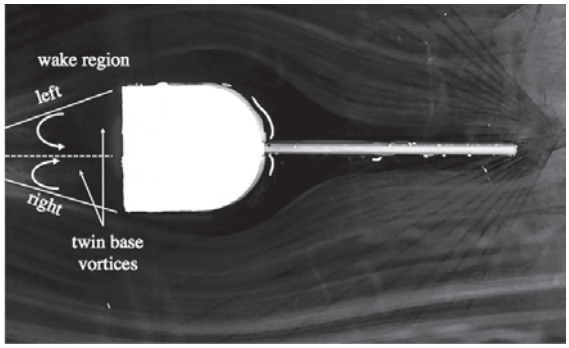

(iii) Hemispherical spike

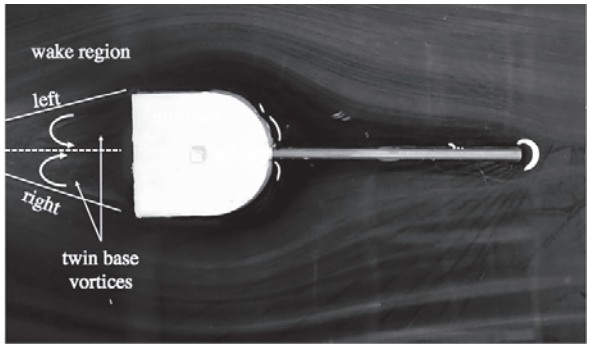

(iv) Flat spike

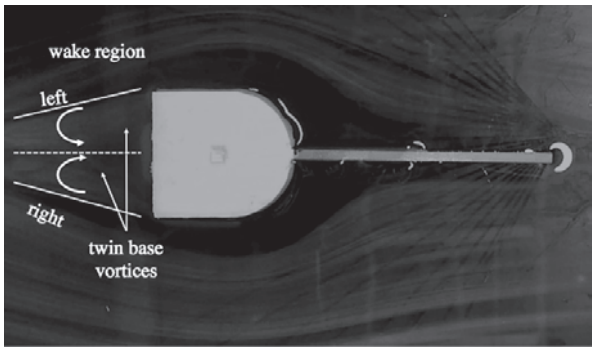

(v) Square spike

Figure 11. Flow field showing wake region with (l/D=2.0) and without spike.

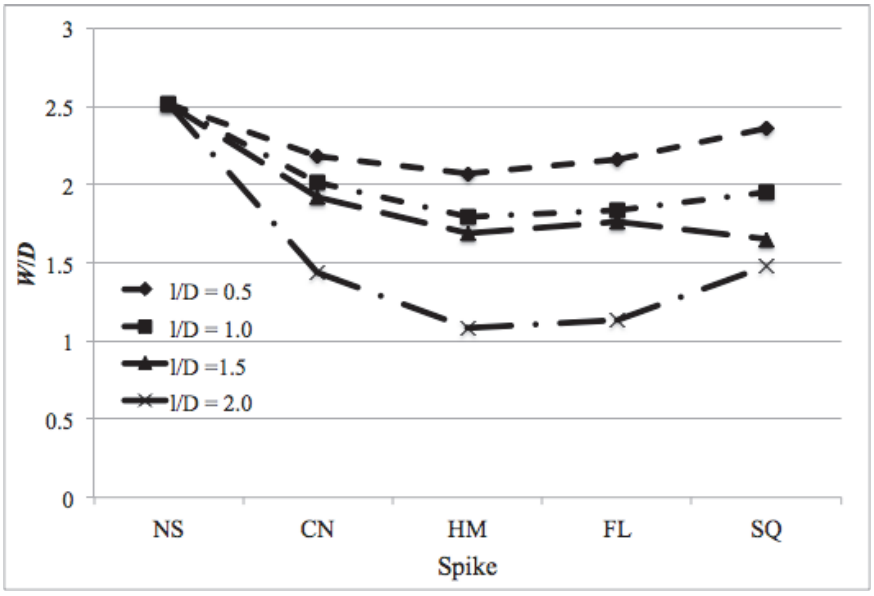

Figure 12. Vortex length variation around the base for various spikes.

5 UNCERTAINTY ANALYSIS

The velocity of the uniform flow in the water channel, before the conduct of the experiments, was measured by floating-particle method, by placing a small bit of paper on the surface of the flow and noting the time taken to traverse the length of the test-section. A set of 5 readings were taken, and the cumulative average of the same is taken as the representative value for the particular test case to calculate the flow Reynolds number, for this research to be conducted at Reynolds number 3170. The error in the measurement of the velocity was estimated to be within ±4%. The accuracy in the evaluation of characteristic lengths of the vortex zones from the captured videos near the nose and at the base, at a conservative estimate of ±2 pixels, stood at ±5%.

6 CONCLUSIONS

Flow around a blunt-nosed body without spike and with spike with different nose-configurations and varying spike length/body-nose-diameter ratios were visualized using a water flow channel. The vortices near the stagnation area of the spiked body and in the wake region were captured in the visualization. The flow field clearly exhibits the vortex characteristic lengths *V* and *W*. These parameters were measured by projecting the visualization pictures on a screen, for all the models studied. The results clearly show that, hemispherical nosed spike is a potential candidate from drag reduction point of view compared to the conical and flat nosed spikes. It is found that, there is a specific length-to-diameter ratio for every spike nose-configuration, resulting in the largest vortex at the spike base, at a given Reynolds number. Furthermore, the dependence of vortex at the base of the body has also been found to be a strong function of length-to-diameter ratio for spikes for the current low-speed incompressible flow. Larger the *l*/*D*-ratio weaker will be the vortices at the base and smaller will be the confinement zone of the wake region.

7 ACKNOWLEDGMENT

The authors would like to thank Mr. Yusuke Izumi for the help with the working of the Rapid prototyping machine and to Mr. Yasumasa Watanabe for the support extended with the preparation of the logistics during the conduct of the experiments.

8 REFERENCES

1 M.Y.M Ahmed and N. Qin, Recent advances in the aerothermodynamics of spiked hypersonic vehicles, Prog. Aerospace Sci. (2011) doi:10.1016/j.paerosci.2011.06.001

2 Y. Takama, K. Suzuki, and E. Rathakrishnan, Visualization and size measurement of vortex shed by flat and arc plates in an uniform flow, Int. Rev. Aerosp. Engg., 1 (2008) 55-60.

3 R. Kalimuthu and E. Rathakrishnan, Aerodynamic Characteristics of Blunt Nosed Body with and without Aerospike at Mach 5.87, Proc. 10th Asian Symposium on Visualization, 2010.

4 A. Vashishtha and E. Rathakrishnan, Breathing blunt-nose concept for drag reduction in supersonic flow, Proc. IMechE Part G: J. Aerospace Engineering, 223 (1) (2009) 31-38.

5 G. J. Sheard, M. C. Thompson, and K. Hourigan, Flow normal to a short cylinder with hemispherical ends, Phys. Fluids, 20 (2008); http://dx.doi.org/10.1063/1.2899782.

6 S. Khurana, K. Suzuki and E. Rathakrishnan, Flow field around a Blunted-nosed Body with Spike, Int. Jl. Jet Engines and Turbines, (2012) doi:10.1515/tjj-2012-0002.

7 H. Sharma, A. Vashishtha and E. Rathakrishnan, Twin vortex flow physics, Proc. IMechE Part G: J.Aerospace Engineering, 222 (2008) 783-788.

8 S. Khurana, K. Suzuki, K., Y. Watanabe and E. Rathakrishnan, Water-channel visualization of flow around a spiked body, Proc. 8th International Conference on Flow Dynamics, Sendai, Japan, 9th-11th November 2011.

The Seventh International Colloquium on Bluff Body Aerodynamics and Applications (BBAA7)
Shanghai, China; September 2-6, 2012

Excitation mechanism of rain-wind induced vibration of cables: unsteady and nonlinear aspects

Teng Wu [a], Ahsan Kareem [a], Shouying Li [b]

[a] *Nathaz Modeling Laboratory, University of Notre Dame, Notre Dame, IN, USA*
[b] *Wind Engineering Research Center, Hunan University, Changsha, China*

ABSTRACT: Two aerodynamic effects, i.e., unsteady and hysteretic behavior on the water rivulet along a stay cable are considered in the proposed analytical models for rain-wind induced vibration (RWIV). Neither the unsteadiness nor hysteresis can be considered using conventional quasi-steady (QS) model. The new analysis framework is also convenient to effectively take into account the turbulence effects in RWIV. Besides, the higher-order spectrum is utilized to detect the potential nonlinear interactions in RWIV. Numerical examples for unsteady and hysteretic considerations are illustrated based on the wind-tunnel data. The results are compared with the QS results.

KEYWORDS: Rain-wind induced vibration; Unsteadiness; Nonlinearity; Higher-order spectrum

1 INTRODUCTION

Among various wind-induced vibrations of cables of cable-stayed bridges (such as ice galloping, Karman vortex shedding induced vibration, wake induced vibration, vortex-induced oscillation at high wind velocity, rain-wind induced vibration (RWIV) etc.), RWIV is significant due to its large amplitude, frequent occurrence and low critical wind speed. Since the first observation of this phenomenon during the construction of a cable-stayed bridge (Hikami and Shiraishi 1988), focus has been on this topic to better understand and model these vibrations.

Though considerable research effort has been made, no consensus exists regarding the underlying mechanism due in part to the extremely complex nature of the gas-liquid-solid interaction. On the other hand, agreement exists among researchers regarding the formation of rivulet on the cable surface due to the rain and the attendant axial flow formation (Matsumoto et al. 2005) as two main factors responsible for RWIV. Predictive models have been established based on the quasi-steady (QS) assumption (e.g., Gu et al. 2009), where the rivulet formation on the cable is regarded as a dominant excitation factor. The QS assumption obviously leaves room for improvement due to extremely complicated flow field around the rivulet. For example, observation in wind tunnel has pointed out that the rain-wind induced vibrations have the self-excited characteristics (Verwiebe and Ruscheweyh 1998).

In this paper, the unsteady effect is considered with a scheme parallel to Scanlan's analysis framework of self-excited forces on bridge decks (Scanlan and Tomko 1971). The aerodynamic coefficients in the proposed unsteady model are first identified in the wind tunnel based on the measurement of the oscillatory pressure. On the other hand, RWIV is well recognized as a nonlinear interaction between the solid, liquid and air. However, neither the QS model, which is able to simulate static nonlinearity, nor the developed unsteady model, which is able to simulate the linear fluid memory effect, can take into account the hysteretic (dynamic) nonlinearity with the higher-order memory effect in the RWIV. As a result, a new analytical model based on the Moore-Penrose pseudoinverse identification scheme is developed to capture the nonlinear hysteretic aerodynamics of RWIV in this paper. A detailed discussion is given in the end of this paper to investigate the excitation mechanism of RWIV.

2 ANALYTICAL MODELS

This paper focuses on the analysis of the RWIV in plane, the consideration of the out-of-plane coupling effect is referred to the research work by Li et al. (2011).

2.1 *Conventional Quasi-Steady Model*

The basic assumption of the QS theory is that the wind velocity should be high enough where the unsteady aerodynamic forces acting on a oscillating structure could be modeled by utilizing the steady-state situation without the fluid memory consideration. Actually, an underlying assumption is that it is convenient to define the steady-state situation of the aerodynamic system (Van Oudheusden 1995). The main reason that the simulation fidelity is usually degraded as the QS model is applied to the torsional oscillation case is bacause it is intractable to define a steady-state situation for the torsional case as each point of the cross section has a different local relative angle of attack. Though it is never explicitly stated in the literature, the basis of the applicability of the QS assumption in the RWIV, where the torsional motion is critical, is that: (1) for the cable only one local relative angle of attack is sufficient to define the steady state of the cable since the rotational motion is uniquely determined by the rivulet position and (2) for the rivulet the rotational center is far from the geometric center where the situation approaches the translational case.

The QS based scheme recently developed treats the rivulet-cable system as a coupled one. A two dimensional model is applied to simulate the motions of cable and rivulet based on QS assumption. The coupled equations of motion are given as (Gu et al. 2009)

$$\ddot{y} + 2\xi_y \omega_y \dot{y} + \omega_y^2 y = -F_y / M \tag{1a}$$

$$m\left(\frac{D}{2}\right)\ddot{\theta} + F_0 sign(\dot{\theta}) + c_r\left(\frac{D}{2}\right)\dot{\theta} = F_r + m\ddot{y}\cos(\theta) - mg\cos(\varphi)\cos(\theta) \tag{1b}$$

where M is the mass per unit length of cable; y is the vertical displacement of cable; and ω_y and ξ_y are circular frequency and damping ratio of the cable, respectively; m is the mass per unit length of upper rivulet; θ is the position of the rivulet; c_r and F_0 are the linear damping coefficient and the Coulomb damping force between the rivulet and cable surface; and φ is the cable inclined angle; the aerostatic forces F_y and F_r are obtained based on QS assumption, which could be represented as

$$F_y = \frac{1}{2}\rho D U_{rel}^2 \left[C_L(\phi')\cos(\phi) + C_D(\phi')\sin(\phi)\right] \tag{2a}$$

$$F_r = \frac{1}{2}\rho R U_{rel}^2 \left[c_l(\phi')\cos(\phi') + c_d(\phi')\sin(\phi')\right] \tag{2b}$$

where D and R are the characteristic sizes of the cable and upper rivulet, respectively; ρ is the air density; C_L and C_D are lift and drag force coefficients of the cable, respectively; c_l and c_d are lift and drag force coefficients of the upper rivulet; ϕ represents the angle between relative wind velocity and x axis; and ϕ' the angle between relative wind velocity and position of upper rivulet.

2.2 *Unsteady model of RWIV*

The aerodynamic forces on the cable may be modeled well based on QS assumption since the RWIV usually happens at a high reduced wind velocity. However, the QS assumption is not appropriate for the upper rivulet since the flow around it usually becomes very unsteady, which could be observed form the intense changes of the pressure coefficients around the rivulet with

various locations, as shown in Fig. 1, where the data is obtained from the wind tunnel tests to be discussed in the following section. As indicated in the figure of wind pressure coefficients on cable, in the range of 25° to 58° for the angles of attack (also rivulet position) there is large difference between the pressures of the points before and after the rivulet, which may indicate the flow separates around the rivulet. After this range, the difference is gradually decreasing with respect to the increasing of angle of attack, which indicates the flow separates before the rivulet. The similar observation is also reported in recent literature (Gu et al. 2009). The wind pressure coefficient on rivulet further consolidates this observation. As indicated in the figure of wind pressure coefficients on rivulet, in the range of 25° to 58° for the angles of attack (also rivulet position) there is large difference between the pressures of the two portions of points on rivulet which are on windward side and on leeward side. The CFD results obtained from Direct Numerical Simulation (DNS) also show the similar behavior of flow around the rivulet (Li and Gu 2006). As indicated in the CFD results, the flow separates at the point of rivulet for both large and small angles of attack. However, when the angle of attack is small, the separation will reattach soon. This phenomenon is difficult to observe in the wind pressure coefficient results.

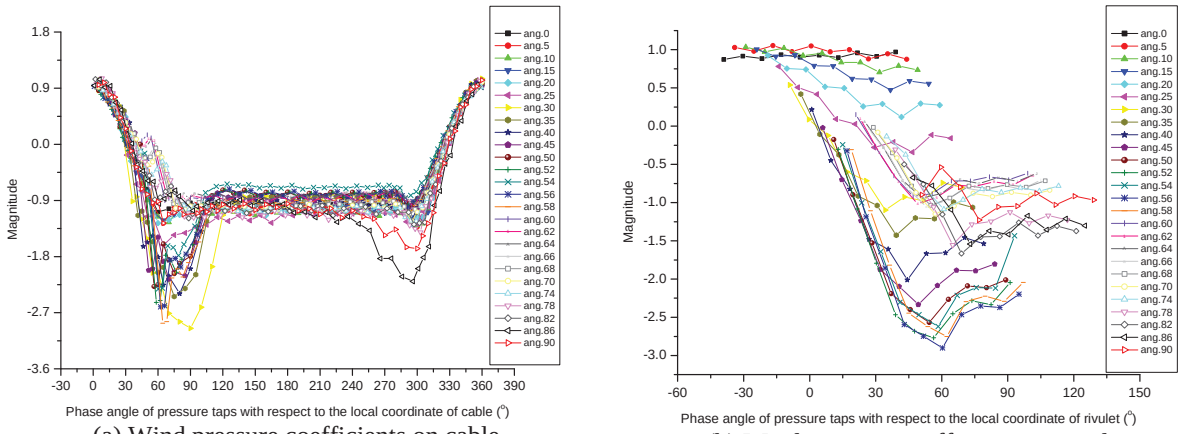

(a) Wind pressure coefficients on cable

(b) Wind pressure coefficients on rivulet

Figure 1. Wind pressure coefficients on cable and rivulet with different angles of attack.

These observations represent the extremely complicated interaction of the wind-rivulet-cable system especially around the rivulet. However, the averaged aerostatic force cannot take into account the unsteady effect since there is little discrepancy between lift and drag coefficients of the static and oscillatory situations. As a result, a more advanced unsteady model for RWIV is proposed in this paper. The unsteady aerodynamic load on the rivulet is represented as

$$F_r^u = \frac{1}{2}\rho R U^2 \left[c_d(\theta_0)\sin(\theta_0) + c_l(\theta_0)\cos(\theta_0)\right] + \left[-L\cos(\theta_0) + D\sin(\theta_0)\right] \tag{3}$$

$$L = \frac{1}{2}\rho U^2 (2R)\left[K_y H_{R1}^*(K_y)\frac{\dot{y}}{U} + K_{\tilde{\theta}} H_{R2}^*(K_{\tilde{\theta}})\frac{\dot{\tilde{\theta}}R}{U} + K_{\tilde{\theta}}^2 H_{R3}^*(K_{\tilde{\theta}})\tilde{\theta} + K_y^2 H_{R4}^*(K_y)\frac{y}{R}\right] \tag{4a}$$

$$D = \frac{1}{2}\rho U^2 (2R)\left[K_{\tilde{\theta}} P_{R2}^*(K_{\tilde{\theta}})\frac{\dot{\tilde{\theta}}R}{U} + K_{\tilde{\theta}}^2 P_{R3}^*(K_{\tilde{\theta}})\tilde{\theta} + K_y P_{R5}^*(K_y)\frac{\dot{y}}{U} + K_y^2 P_{R6}^*(K_y)\frac{y}{R}\right] \tag{4b}$$

where F_r^u represents the wind induced force on the rivulet using unsteady theory; θ_0 means the equilibrium potion of rivulet and $\tilde{\theta} = \theta - \theta_0$ is the dynamic circumferential displacement of rivulet on the cable; H_{R1}^*, H_{R2}^*, H_{R3}^*, H_{R4}^*, P_{R2}^*, P_{R3}^*, P_{R5}^* and P_{R6}^* are aerodynamic coefficients

(flutter derivatives) with respect to the reduced frequency $K_y = \omega_y R/U$ or $K_{\tilde{\theta}} = \omega_{\tilde{\theta}} R/U$. These aerodynamic coefficients play transfer-function roles in this unsteady model, e.g., H_{R1}^* takes into account the lift force exerting on the rivulet induced by the velocity of vertical vibration. In the case of bridge deck, usually some aerodynamic coefficients are negligible, e.g. the value of aerodynamic coefficient H_4^* of the vertical displacement is very small comparing to other aerodynamic coefficients because the aerodynamic stiffness is extremely small comparing to the bridge deck stiffness. However, this conclusion cannot apply to the RWIV system since the stiffness of rivulet is negligible as mentioned in the proceeding content.

2.3 *Nonlinear hysteretic model*

Recently, the nonlinear hysteretic behavior of bridge aerodynamics is observed and analyzed (Diana et al. 2010). Similar to the bridge deck, intense hysteretic behavior is observed in the wind-rivulet-cable interaction, which indicate that the higher-order memory in the wind-rivulet-cable system is another indispensable effect. Typically, the steady-state aerodynamic coefficients are modeled by a nonlinear polynomial in terms of the angle of attack. However, the hysteretic behavior can be best described by higher-order (nonlinear) polynomial involving the dynamic angle of attack (Resulting from turbulence components and deck motions) and its derivative, e.g. (Wu and Kareem 2012),

$$c_l^{hyst}(\tilde{\theta},\dot{\tilde{\theta}}) = \sum_{j,k}^{n} \eta_{j,k} \tilde{\theta}^j \dot{\tilde{\theta}}^k \tag{5}$$

where subscript "l" represents "L", "D" or "M", which denotes coefficients related to lift, drag and pitch, respectively; $\eta_{j,k}$ is the coefficient corresponding to $(j+k)^{th}$-order term; 2n is the highest order of the polynomial possible to parsimoniously model hysteretic behavior. The actual order of the model depends on the data used for fitting and the identification scheme used. Besides, the contributions of some of the terms in the polynomial may be negligible which leads to simplified expression. For example, for the lift coefficient of a stay cable of a cable-stayed bridge, the following model can represent the hysteretic behavior:

$$c_L^{hyst}(\tilde{\theta},\dot{\tilde{\theta}}) = \left[c_L(\theta_0)\right] + \eta_{0,0} + \eta_{1,0}\tilde{\theta} + \eta_{0,1}\dot{\tilde{\theta}} + \eta_{2,0}\tilde{\theta}^2 + \eta_{1,1}\tilde{\theta}\dot{\tilde{\theta}} + \eta_{3,0}\tilde{\theta}^3 + \eta_{4,0}\tilde{\theta}^4 \tag{6}$$

where the steady-state coefficient $c_L(\theta_0)$ corresponding to the equilibrium position is extracted from the constant term in order to emphasize the difference between the steady-state and the hysteretic cases.

3 PARAMETER IDENTIFICATION

3.1 *Wind tunnel test set-up*

The 'artificial' rivulet is applied in the wind tunnel test set-up since the pressure on the rivulet will be measured. Only the upper rivulet is simulated. The end plates are installed at each end of the two dimensional rigid cable to control the end flow condition. The rigid cable is mounted inside the wind tunnel to form a closed type test condition, which is presented in Fig. 2. Negligible turbulence is generated in the incoming laminar flow. The overall steady wind force on the cable-rivulet system and the pressures on cable and upper rivulet surfaces are measured under the forced pitching and plunging vibrations. The frequency of both pitching and plunging vibrations is 1 Hz. The double-amplitudes are 4 mm for pitching and 10 degrees for plunging. There are total four sections of the rigid cable in which the pressure taps are installed, and 63 pressure taps for each section. The position of these pressure taps is defined by the angle ψ, which is deter-

mined from the stagnation point to the center of taps. Since the pressure on the rivulet will be recorded, the sizes of rivulet and the corresponding cable are amplified comparing to the ones in the real world. The rigid cable is made of acryl glass with the diameter of 350 mm and the length of 1540 mm while the rigid rivulet is made of polyethylene. The shape of the rivulet is one section of arc of 42 mm which belongs to a circle with a 25 mm radius. The schematic illustrations of the test section coordinates, the rivulet and pressure holes positions, and the rivulet and cable sizes are presented in Fig. 3. The angle θ represents the position of upper rivulet and α the relative angle of attack induced by vertical motion of cable.

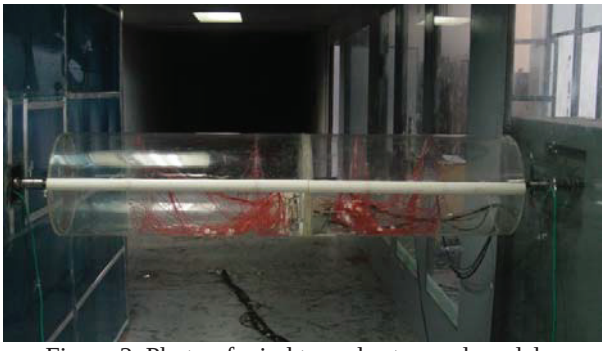

Figure 2. Photo of wind tunnel setup and model.

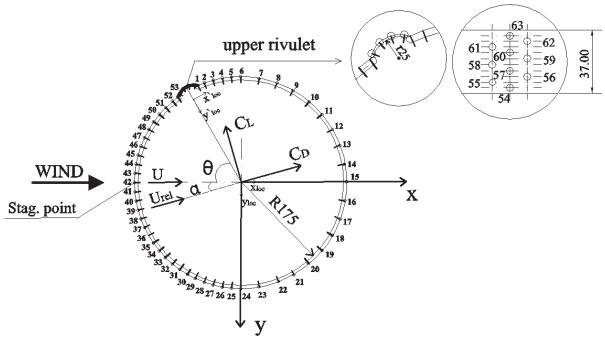

Figure 3. Coordinate system and arrangement of pressure taps.

3.2 *Steady-state coefficients utilized in quasi-steady model*

The steady-state coefficients for cable and rivulet are measured through wind tunnel experiment and shown in Fig. 4. In order to conveniently obtain their derivatives in terms of the angle of attack, which will be used in the calculation of RWIV, both of them are fitted using nonlinear least square technique.

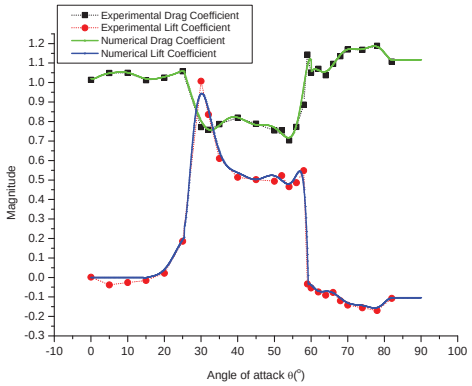

(a) Steady-state coefficients of cable

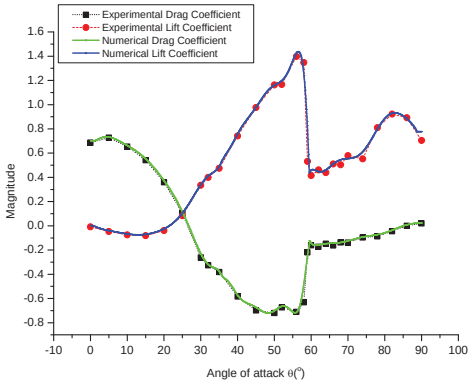

(b) Steady-state coefficients of rivulet

Figure 4. Experimental and numerical steady-state coefficients.

3.3 *Aerodynamic coefficients utilized in unsteady model*

The scheme based on the measurement of the oscillatory pressure is applied to extract the aerodynamic coefficients of the rivulet. A detailed validation procedure for the identified aerodynamic coefficients are carried out. For example, in order to validate the identification results based on pressure measurement, the forced oscillation scheme is also utilized for the cable. Fig. 5 shows

the identified aerodynamic coefficients (only aerodynamic coefficients for the lift force are presented here) of the upper rivulet. As shown in Fig. 5, the aerodynamic coefficients vary tremendously with respect to the wind angle of attack (e.g., the position of rivulet). The values of these aerodynamic coefficients become very large in the range of 58^{o}-62^{o}, which indicates the intense unsteady load in this range. This range is critical for RWIV since the existing of large negative slope of the life coefficient of cable which induced the large amplitude oscillation based on the galloping theory. Besides, the aerodynamic coefficient H_4^* of the vertical displacement is not negligible comparing to other aerodynamic coefficients, which indicates the large difference with bridge system. If the aerodynamic coefficients are presented utilizing Zasso's form (Zasso 1996), the identified aerodynamic coefficients per se straightforwardly show the intensive unsteadiness of the aerodynamic forces on the rivulet in the wind velocity range of interest.

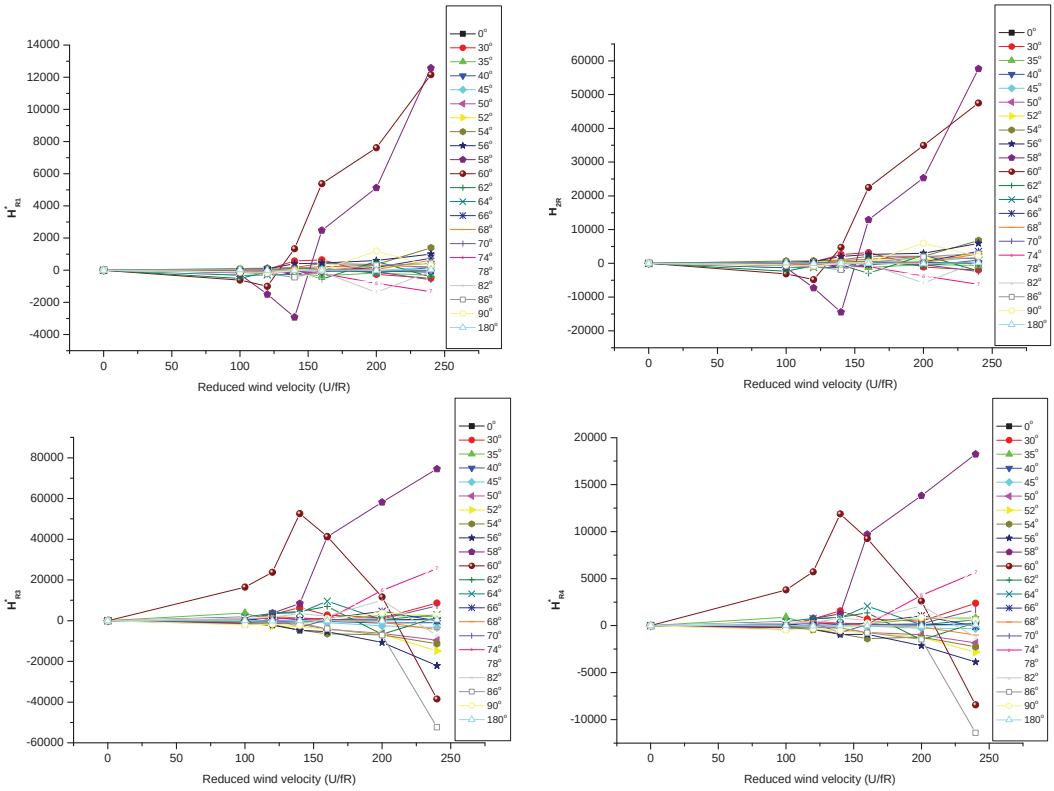

Figure 5. Identified aerodynamic coefficients for upper rivulet.

3.4 *Hysteretic loop utilized in nonlinear hysteretic model*

The Moore-Penrose pseudoinverse scheme is applied to identify the coefficients of the hysteretic numerical model. The hysteretic behavior in terms of steady-state coefficients and the numerical simulation results are shown in Fig. 6 (here only the lift coefficient are presented) at some certain reduced wind velocity. Because the facility in the wind tunnel can only oscillate with the maximum double-amplitude 10^{o}, the results shown in these figures are limited consideration of nonlinear hysteretic phenomenon of the RWIV.

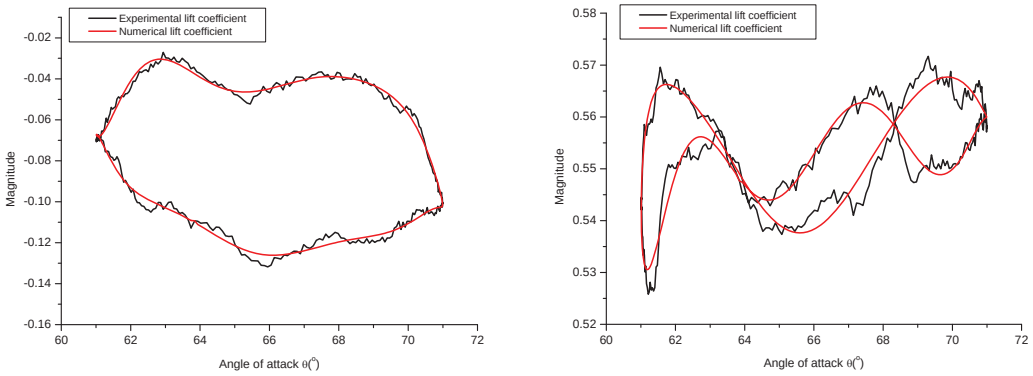

Figure 6. Hysteretic simulation of (a) cable and (b) rivulet (θ0=66o).

4 NUMERICAL EXAMPLE

The rivulet-cable model used in the numerical example is described in the proceeding section. Besides, the natural frequency of the cable is set the same with the frequency of forced vibration for aerodynamic coefficients identification. The mass and damping ratio of cable are 6 kg per unit length and 0.001, respectively. The linear damping coefficient and the Coulomb damping force between rivulet and cable are set as 0.0008 N·s/m^2 and 20% of the weight of rivulet, respectively. The mass of rivulet is set 0.0098 kg per unit length according to the density of water and the assumed area of the upper rivulet on the cable. Moreover, the reasonable range of the circumferential motion of rivulet is assumed between 0 to π/2. For the unsteady model, the equilibrium position needs to be determined firstly. The equilibrium position of the rivulet on the cable based on the QS model is utilized in this example. Although the equilibrium position based on QS assumption is somehow different with the observation in the wind tunnel, fortunately the results of unsteady model proposed in this paper are not sensitive to the equilibrium position of rivulet. As long as this equilibrium position in a reasonable range, the calculation of this unsteady model will converge to the same result. The equilibrium position of the rivulet on the cable based on the QS model could be replaced in the proposed unsteady model if reliable data based on the wind tunnel results are available. Some reliable records using an ultrasonic transmission thickness measurement system (UTTMS) are given in recent literature (e.g., Li et al. 2010).

A range of wind velocities are calculated for the RWIV utilizing these three models. The calculation responses of the cable based on the QS, unsteady and nonlinear hysteretic models at the wind velocity 9.5 m/s are shown in Fig. 7 while the responses of the rivulet are presented in Fig. 8.

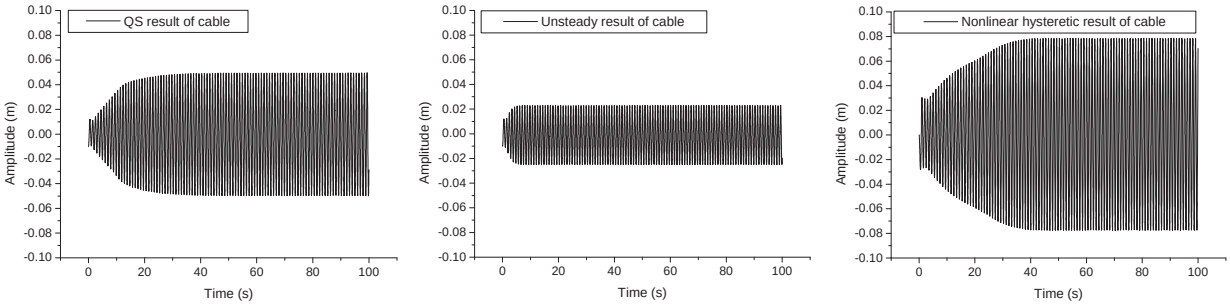

(i) QS model (ii) Unsteady model (iii) Nonlinear hysteretic model

Figure 7. Comparison of calculation results of the cable based on various models.

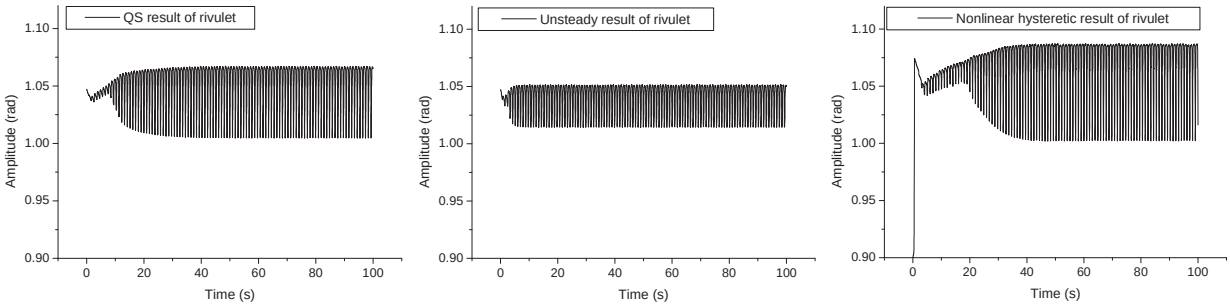

(i) QS model (ii) Unsteady model (iii) Nonlinear hysteretic model

Figure 8. Comparison of calculation results of the rivulet based on various models.

As shown in this figure, the vibration behaviors of the cable and rivulet obtained from QS, unsteady and nonlinear hysteretic models are similar while the vibration amplitude of unsteady results is smaller and the vibration amplitude of nonlinear hysteretic results is larger compared with the calculation based on the QS model. This comparison indicates that the linear unsteadiness will alleviate the RWIV while the nonlinear hysteretic behavior will intensify the responses of the rivulet-cable system.

Fig. 9 shows the comparison of the amplitudes of cable and the wind velocity range in which the large limited amplitude oscillation appears between numerical results based on QS and unsteady models (here the comparison with nonlinear hysteretic results are not presented due to the large number of computational work). As indicated in the figure, both of these models could obtain wind velocity limited and amplitude limited results. The limited wind velocity is almost the same for these two models while the limited amplitude obtained from unsteady model is just half of the one obtained based on QS model.

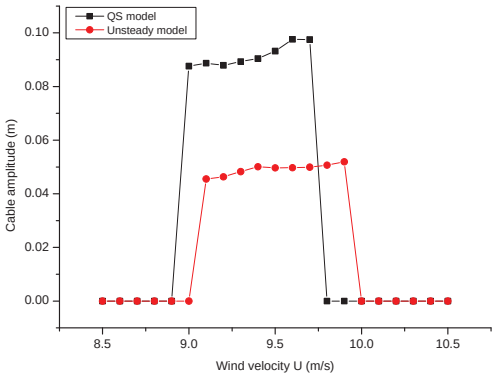

Figure 9. Comparison of cable responses based on QS and unsteady models.

It should be noticed that the oscillation frequency of the rivulet is set to be 1 Hz during the calculation process. In other words, the reduced frequency K_y and $K_{\tilde{\theta}}$ are not changed under a certain wind velocity. A more sophisticated procedure involving iterative calculation may give the unsteady results with higher accuracy, in which the oscillation frequency of the rivulet is treated as an unknown. However, based on the experience of the flutter analysis on bridge deck, this simplification will change the result negligibly. This unsteady model mainly focuses on the investigation of the wind induced force on the rivulet, while other parameters of the motion of rivulet especially the Coulomb damping force is very important and needed to be investigated in the future research.

Besides, although the turbulence has significant effect on the motion of the rivulet-cable system, this effect has not been well understood to date. It is challenging to take into account the

turbulence effect reasonably and conveniently based on the conventional QS model. On the other hand, this proposed unsteady model could effectively calculate the turbulence effect based on the hybrid scheme proposed by Chen and Kareem (2003). As the aerodynamic coefficients identified in the turbulent condition are available the effect of turbulence could be taken into account immediately with this proposed unsteady model.

5 DISCUSSION

One of the main features of RWIV is that the vibration is wind velocity and amplitude limited. Based on the observation of the lift coefficient curve, the mechanism of galloping is a reasonable explanation of RWIV phenomenon. Under this assumption, the effective cross-section of cable or the circumferential motion of rivulet on the cable is critical to the RWIV. Current coupling model based on the QS assumption successfully reproduce the wind velocity and amplitude limited characteristics of RWIV (e.g., Gu et al. 2009). However, it is not difficult to reproduce this "limited" property of RWIV regardless of the motion of rivulet. For example, with the assumption of the rivulet vibrating as a harmonic or a narrow banded stochastic process, the obtained results also present the "limited" feature in a similar range of wind velocity and with the same order of the magnitude of vibrating amplitude. Since the amplitude of RWIV is very sensitive to the test conditions (Gu and Du 2005), there is no strong evidence to support the superiority of any of these mentioned models with respect to reproducing the RWIV phenomenon.

Furthermore, even if the rivulet rests on the cable at the equilibrium position, which belongs to the classical galloping class, the calculation results of the example in this paper show that at the same range of wind velocity, the magnitude of the limited amplitude is in the same order as the harmonic/stochastic/QS results. Since the equilibrium position of the rivulet is changed as the wind velocity increasing, only in a certain range of wind velocity the position of rivulet is in the negative slope range of the lift coefficient where the large amplitude vibration occurs. The relatively small magnitude of the vibration amplitude for this "classical" galloping may result from the extremely narrow range of the negative slope of the lift coefficient. Assuming the cable vibrating harmonically, the amplitude of velocity of the cable, which contributes to the "relative" angle of attack, will be the amplitude of the displacement multiplied by the vibrating frequency. As a result, as the amplitude of the vibration increases, the "total" angle of attack is very easy to escape out of the negative slope range, especially for the large vibrating frequencies or high modes.

The higher-order spectrum could be utilized to analyze the data in RWIV (Wu and Kareem 2012). It is shown that there are intense nonlinear coupling and interactions that exist in RWIV. The harmonic distortion and super-harmonic (or sub-harmonic) behaviors could be a potentially convincing illustration of the appearance of the lower or higher frequency components in the aerodynamic forces on the cable or rivulet, where usually the axial flow theory is utilize (Matsumoto et al. 2005).

The current state of the art for the RWIV cannot predict the wind velocity range in which the large amplitude oscillation appears and the amplitude of the limited cycle oscillation with high accuracy. The main reason may be the inaccurate simulation of the forces exerting on the rivulet, which is the primary motivation of this research. The main objective of this paper is to reveal the mechanism of RWIV, especially the aerodynamic forces exerting on the rivulet. The effort of simulating the forces exerting on the rivulet with high fidelity is a promising venue of research to improve predictive capability of RWIV. The proposed unsteady model and nonlinear hysteretic model are more advanced and necessary. Other forces exerting on the rivulet especially the Coulomb damping force is also very important and needs to be investigated in the future research.

6 CONCLUDING REMARKS

It is shown that the flow around the rivulet in the rivulet-cable system is extremely complicated. Current model to calculate the rain-wind induced vibration (RWIV) is mainly based on the quasi-steady (QS) assumption, which is probably not appropriate for the circumferential motion of the rivulet on the cable. The unsteady model which parallels Scanlan's analysis framework for the bridge aerodynamics and the nonlinear hysteretic model which utilizing the Moore-Penrose pseudoinverse identification scheme are proposed in this paper. Both of these new models could take into account the unsteady effect of the aerodynamic forces exerting on the rivulet. Besides, the turbulence effect could be reasonably and conveniently considered with the unsteady model. The aerodynamic coefficients are identified based on the measured oscillatory pressure data. To the authors' knowledge, this is the first time that the aerodynamic force coefficients of rivulet are identified in the literature. The results of the QS, unsteady and nonlinear hysteretic models are significant different with each other. This comparison indicates that the linear unsteadiness will alleviate the RWIV while the nonlinear hysteretic behavior will intensify the responses of the rivulet-cable system. The unsteady aspects of the aerodynamic load on the cable are not considered in this paper for the sake of simplicity, however, it is straightforward to incorporate this effect in the proposed models.

7 ACKNOWLEDGEMENTS

The support for this project provided by the NSF Grant # CMMI 09-28282 which is gratefully acknowledged. The authors are also thankful to Mr. Wenfeng Sun, Hunan University for his help on a series of wind tunnel tests.

8 REFERENCES

1 Chen, X. and Kareem, A., 2003. Aeroelastic analysis of bridges: effects of turbulence and aerodynamic nonlinearities. *J. Eng. Mech.*, 129 (8), 885–895.
2 Diana, G., Rocchi, D., Argentini, T. and Muggiasca, S., 2010. Aerodynamic instability of a bridge deck section model: Linear and nonlinear approach to force modeling. *Journal of Wind Engineering and Industrial Aerodynamics*, v 98, n 6-7, 363-374.
3 Gu, M. and Du, X., 2005. Experimental investigation of rain-wind-induced vibration of cables in cable-stayed bridges and its mitigation. *Journal of Wind Engineering and Industrial Aerodynamics*, 93 (1), 79-95.
4 Gu, M., Du, X. Q. and Li, S. Y., 2009. Experimental and theoretical simulations on wind-rain-induced vibration of 3-D rigid stay cables. *Journal of Sound and Vibration*, 320 (1-2), 184-200.
5 Hikami, Y. and Shiraishi, N., 1988. Rain-wind induced vibrations of cables in cable stayed bridges. *Journal of Wind Engineering and Industrial Aerodynamics*, 29 (1-3), 409-418.
6 Li, H., Chen, W. L., Xu, F., Li, F. C. And O, J. P., 2010. A numerical and experimental hybrid approach for the investigation of aerodynamic forces on stay cables suffering from rain-wind induced vibration. *Journal of Fluids and Structures*, 26 (7-8), 1195-1215.
7 Li, S. and Gu, M., 2006. Numerical simulations of flow around stay cables with and without fixed artificial rivulets. *The Fourth International Symposium on Computational Wind Engineering (CWE2006)*, Yokohama, Japan, pp. 307-310.
8 Li, S. Y, Chen, Z. Q., Wu, T. and Kareem, A., 2011. On the Rain Induced Vibration of Cables. *Journal of Engineering Mechanics*, ASCE. Submitted.
9 Matsumoto, M., Yagi, T., Sakai, S., Ohya, J. and Okada, T., 2005. Steady wind force coefficients of inclined stay cables with water rivulet and their application to aerodynamics. *Wind and Structures*, 8 (2), 107-120.
10 Scanlan, R. H. and Tomko, J. J., 1971. Airfoil and bridge deck flutter derivatives. *J.Engrg. Mech .Div.ASCE*, 97(EM6), 1717-1737.
11 van Oudheusden, B. W., 1995. On the quasi-steady analysis of one-degree-of-freedom galloping with combined translational and rotational effects. *Nonlinear Dynamics*, 8, 435–451.
12 Verwiebe, C. and Ruscheweyh, H., 1998. Recent research results concerning the exciting mechanisms of rain-wind-induced vibrations. *Journal of Wind Engineering and Industrial Aerodynamics*, 74-76, 1005-1013.
13 Wu, T. and Kareem, A., 2012. Aerodynamics and Aeroelasticity of Cable-Supported Bridges: Identification of Nonlinear Features. *Journal of Engineering Mechanics*, ASCE. Submitted.
14 Zasso, A., 1996. Flutter derivatives: advantages of a new representation convention. *Journal of Wind Engineering and Industrial Aerodynamics*, 60, 35-47.

The Seventh International Colloquium on Bluff Body Aerodynamics and Applications (BBAA7)
Shanghai, China; September 2-6, 2012

Influence of dynamic properties and position of rivulet on rain-wind-induced vibration of stay cables

Wenli Chen[a,c], Shanran Tang[a], Hui Li[a] , Fengchen Li[b], Hui Hu[c]

[a] *School of Civil Engineering, Harbin Institute of Technology, Harbin, China*
[b] *School of Energy Science and Engineering, Harbin Institute of Technology, Harbin, China*
[c] *Department of Aerospace Engineering, Iowa State University, Ames, USA*

ABSTRACT: This paper combines experimental study and CFD simulation together to investigate the influence of dynamic properties and position of rivulet on rain-wind induced vibration (RWIV) of stay cables. The reproduction of the RWIV of a stay cable model is firstly carried out based on an artificial rainfall wind tunnel tests with an ultrasonic transmission thickness measurement system (UTTMS), which can obtain the characteristics of rivulets on the surface of the stay cable model. Based on the test results, the CFD simulations are next employed to study the aerodynamic influence of upper rivulet using different CFD models: the vibrating cable model with the moving upper rivulet and the vibrating cable model with the fixed upper rivulet. CFD simulations suggest that the existence of the upper rivulet do not sufficiently to excite RWIV. CFD simulations indicate that the presence of upper rivulet in certain region can significantly vary the aerodynamic force acting on cable. When the upper rivulet oscillates is in this specific range with the same frequency of cable, the aerodynamic resonant excitation will induce the occurrence of RWIV.

KEYWORDS: Stay cables, rain-wind-induced vibration, ultrasonic transmission thickness measurement system, CFD simulation, artificial rainfall wind tunnel tests and upper rivulet.

1 INTRODUCTION

Many studies have been carried out for the rain-wind induced vibration (RWIV) phenomenon in the past two decades through field measurements (Hikami and Shiraishi, 1988; Matsumoto *et al*, 2003a; and Zuo & Jones, 2010), wind tunnel tests (Matsumoto *et al*, 2003b; Flamand, 1995; Gu and Du, 2005, Cosentino *et al*, 2003), and theoretical analyses (Yamaguchi, 1990; and Peil, 2003). Study results indicate that water rivulet vibrations around the stay cable play a key role when RWIV occurs, indicating that it is necessary to investigate the characteristics of water rivulets around cables. Li *et al*. (2010a) employed an ultrasonic transmission thickness measurement system (UTTMS) based on the UT technique to obtain rivulet information. The shape, thickness, equilibrium position, oscillation amplitude, and frequency of water rivulets are obtained from the reconstructed images of the circumferential water rivulet distribution. In this paper, two types of CFD models are established and computed to verify the effect of upper rivulet oscillation.

2 WIND TUNNEL TESTS OF RWIV WITH UTTMS AND RESULTS

2.1 *Setup of experiment*

The wind tunnel test of RWIV of an inclined stay cable model is carried out in the TJ-1 atmosphere boundary layer wind tunnel located at Tongji University. The inclination angle of the cable

model α and the wind yaw angle β can be easily adjusted as shown in Figure 1(a). The length is 2.0 m and the diameter is 0.1 m for the cable model with a mass of 17.15 kg. The natural vibration frequency is 0.952 Hz and the damping ratio is 0.0017. The test measurement setup for the stay cable model with the UTTMS is shown in Figure 1 (b) and (c).

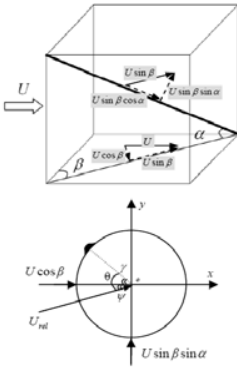

(a) Schematic diagram of the inclination angle

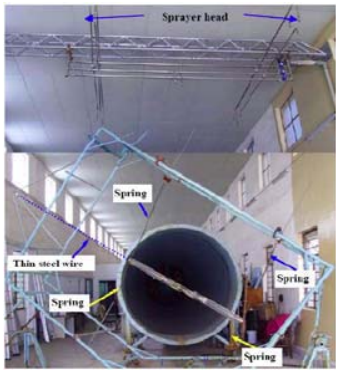

(b) Photograph of testing set-up of RWIV

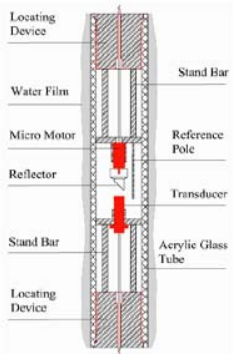

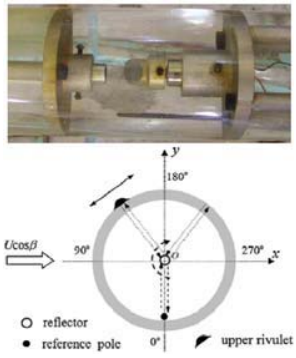

(c) Assemblage of UTTMS

Figure 1. Test measurement setup with UTTMS (Li and Chen, 2010a)

2.2 *Dynamic characteristics of cable vibration*

The reduced velocity and Reynolds number are respectively defined as U/fD and UD/ν, where U and ν are the wind speed and kinematic viscosity of the air, respectively. The test conditions of RWIV of cable are listed in Table 1.

Table 1 Test conditions of RWIV of stay cable

Wind speed (m/s)	Reduced velocity	Reynolds number	Rainfall intensity (mm/h)	Inclination Angle (°)	Yaw angle (°)
6-10	63-105	$(3.8\text{-}6.4)\times10^5$	20-60	30	20-25

According to previous study (Gu and Du, 2005), a rainfall intensity of 30mm/h with the inclination angle of 30° for two test cases (the yaw angles of 20° and 22.5° for the first and second tests, respectively) is employed. The cross-flow displacement amplitudes of cable versus wind velocity are shown in Figure 2. It can be seen that the RWIV occurs over the range of 6.76-8.04 m/s.

The time history and frequency response of cross-flow displacement at the velocity of 6.76 m/s, 7.72 m/s and 8.69 m/s are shown in Figure 3(a), (b) and (c), respectively.

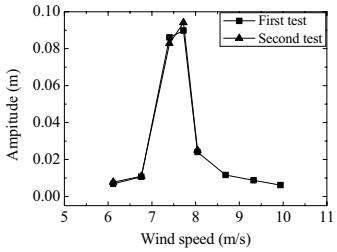

Figure 2. Amplitude versus wind speed

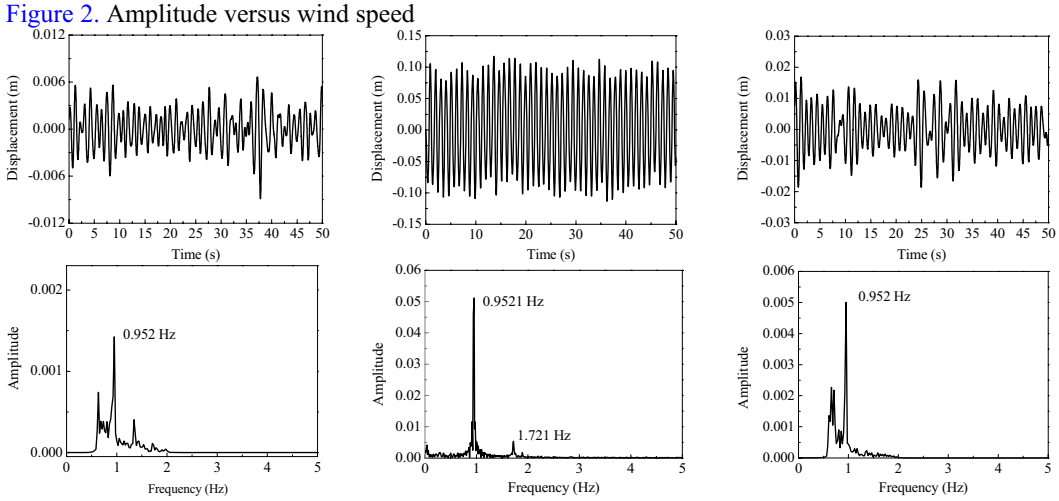

(a) 6.76 m/s (b) 7.72 m/s (c) 8.69 m/s

Figure 3. Time histories and frequency spectra of cable vibration

2.3 *Dynamic characteristics of water rivulets during RWIV*

Figure 4(a), (b) and (c) presents the water rivulets distribution on the surface measured by the UTTMS in the second test at the wind speeds of 6.76, 7.72 and 8.69 m/s, respectively. At the wind speed of 6.76 m/s, there are a number of continuous rivulets, while they do not flow along axial direction of the cable but slide to the windward side. At 7.72 m/s, the RWIV of the cable model occurs; at the same time, it can be seen that only one continuous upper rivulet forms and comes into a steady circumferential oscillation from Figure 4(b). The continuous lower rivulet also forms but barely moves in circumferential direction. As the wind speed continuously increases, no RWIV is observed, yet the upper rivulet still remains, but the steady circumferential oscillation of the upper rivulet gradually disappears as shown in Figure 4(c). Compared with Figure 4(b), the oscillation of the upper rivulet is quite different, i.e. one is disordered and unsystematic (Figure 4(c)), while the other is regular and behaves like a simple harmonic vibration (Figure 4(b)), although the state of the lower rivulet is almost the same.

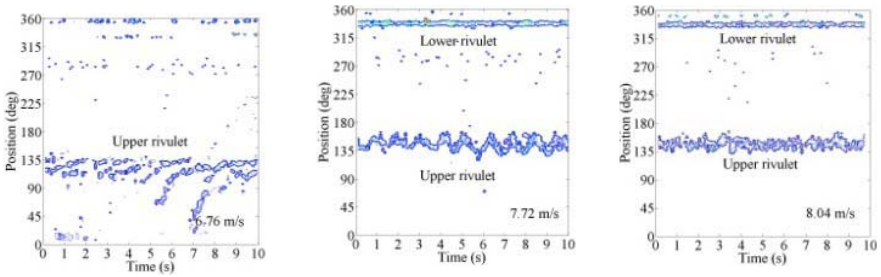

(a) 6.76 m/s (b) 7.72 m/s (c) 8.69 m/s

Figure 4. Water rivulet contour along circumferential direction measured by UTTMS

Figure 5 obviously indicate when the RWIV occurs the upper rivulet oscillation behaves large amplitude with one dominant frequency which is the natural frequency of the cable at the velocity of 7.72 m/s. At the velocity of 8.69 m/s, the cable vibration is disordered with no dominant frequency.

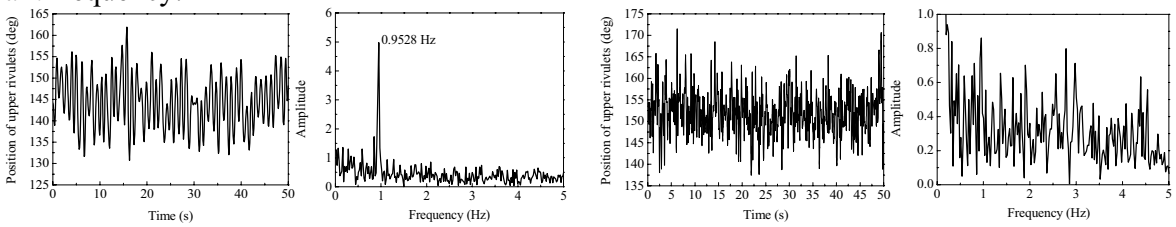

(a) 7.72 m/s (b) 8.69 m/s

Figure 5. Time histories and frequency spectra of rivulet oscillation

3 TWO-DIMENSIONAL CFD SIMULATIONS OF CABLE MODEL WITH UPPER RIVULET

3.1 *One degree-of-freedom cable model with an oscillating upper rivulet*

A mechanical model of cable is established as shown in Figure 6. The upper rivulet is given a pre-programmed harmonic oscillation expressed in Eq. (1) with the frequency same as cable vibration. The cable is considered as a one degree-of-freedom vibrating system under the aerodynamic lift force, and its dynamic equation is given in Eq. (2).

$$\theta = \mathrm{a}\sin(\omega t) + \theta_0,\ \mathrm{a}=10^\circ \tag{1}$$

$$\ddot{y} + 2\xi\omega\dot{y} + \omega^2 y = \frac{\rho R U_{rel}^2}{m_c} C_L(\theta) \tag{2}$$

where y is the displacement of cable in cross-flow direction; θ is the relative position angle between flow direction and upper rivulet; and θ_0 is the relative equilibrium angle of upper rivulet. $\xi = 0.17\%$ is the damping ratio and $\omega = 2\pi \times 0.952 = 5.98\,\mathrm{rad}/s$ is the natural circular frequency. m_c is the mass per unit length of the tested cable section model, which equals to 8.575 $\mathrm{kg/m}$. $R = 0.05$ m is the radius of cable. The above parameters are the same as those of the cable model used in the wind tunnel tests. ρ is the air density. $C_L(\theta)$ is the aerodynamic lift coefficient automatically computed by the FLUENT, which is a function of the angle θ. From Figure 1(a), the U_{rel} can be calculated as Eq. (3) by taking $\alpha = 30^\circ$, $\beta = 20^\circ$ and $U = 7.5\,\mathrm{m/s}$ which is in the range where RWIV occurs.

$$U_{rel} = \sqrt{(U\sin\alpha\sin\beta)^2 + (U\cos\beta)^2} = 7.16\ \mathrm{m/s} \tag{3}$$

The upper rivulet is represented by a rectangle with the height of 2 mm and the width of 8 mm in CFD simulations. Figure 7 shows the grid partition and the size of the fluid field in the CFD model. The number of triangular cells is roughly 60,000, and the first grid normal to the cable surface is set as 0.5 mm. The boundary conditions are defined as follows: left side is "velocity inlet"; right-hand side is "pressure outlet"; upper and lower sides are "symmetry", the cable and upper rivulet are considered as two separating "wall" surfaces. The shear stress transport (SST) $k-\omega$ turbulent model based on the Reynolds-averaged Navier-Stokes (RANS) method is employed to simulate the turbulent behavior of the flow. The time interval is set as 0.001 s, and dynamic meshing is applied because both cable and rivulet are moving in the flow field. Eq. (2) is solved by a user defined function (UDF) based on Newmark method to obtain the displace-

ment which defines the location of cable and rivulet in the problem domain. Moreover, the UDF also defines the oscillation of upper rivulet on the cable surface through Eq. (1).

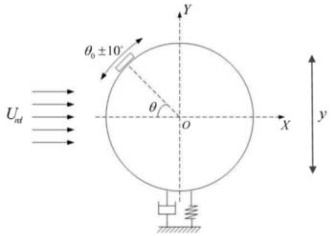

Figure 6. Dynamic model of vibrating cable with an upper rivulet

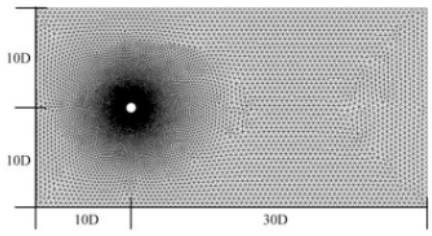

(a) Overall size of flow field (D=100mm)

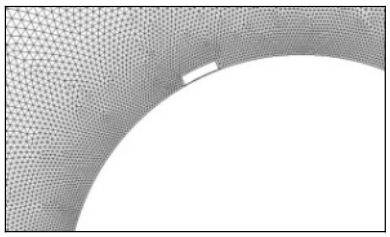

(b) Fractionate gain around the upper rivulet

Figure 7. Grid partition of CFD simulation

Three different conditions are chosen to study how the cable vibration is affected by different ranges of the oscillation of upper rivulet. The simulation results of the cases when equilibrium angles equal to 50°, 65° and 80°, are shown in Figure 8. In Figure 8(a) and (c), small vibrations with amplitude less than 5 mm are observed. Moreover, the displacement histories of the cable seem very random. Comparing with the large and systematic cable vibration captured in wind tunnel test (Figure 3(b)), CFD simulations indicate that RWIV does not occur when the relative equilibrium angles of upper rivulet is 50° or 80°.

A systematic and regular vibration of cable with large amplitude is only observed when the upper rivulet oscillates in the range of 55°-75° (Figure 8(b)). In this case, the amplitude increases to about 0.1 m when the vibration reaches its steady state, which agrees well with the observation in wind tunnel test (Figure 3(b)). Hence RWIV is also successfully reproduced by this CFD simulation with an upper rivulet oscillating harmonically in the same region.

The time histories and spectra of aerodynamic lift coefficients at the equilibrium angles of 50°, 65° and 80° are shown in Figure 9(a), (b) and (c), respectively. Since the amplitudes of lift coefficients are close, but the frequency components are different for three cases. When the equilibrium angles are 50°and 80°, the dominant frequencies do not include the natural frequency of the cable. But, for the equilibrium angle of 65°, the dominant frequencies are multiple of the natural frequency, also include the natural frequency. It is the mainly reason that the RWIV of the cable at this equilibrium angle can occur.

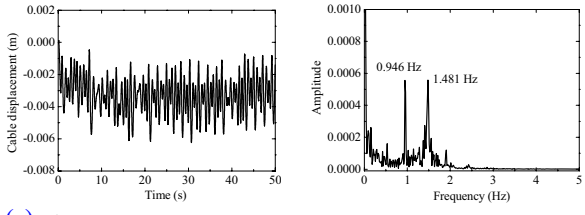

(a) $\theta_0 = 50^\circ$

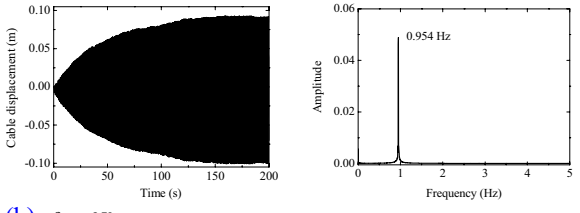

(b) $\theta_0 = 65^\circ$

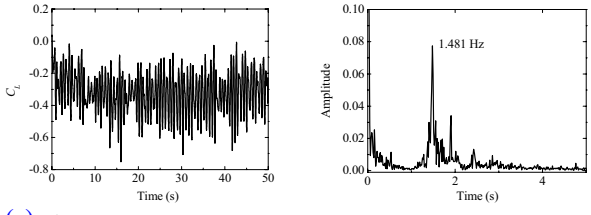

(a) $\theta_0 = 50^\circ$

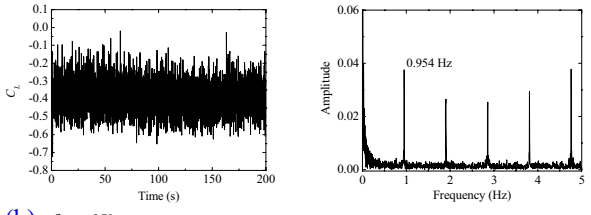

(b) $\theta_0 = 65^\circ$

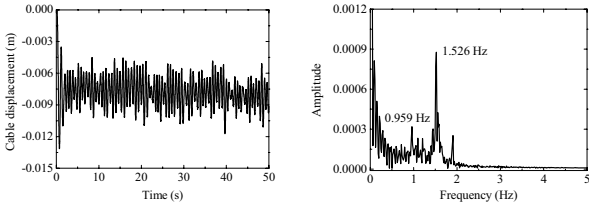

(c) $\theta_0 = 80^\circ$

Figure 8. Displacement response of the CFD cable model with an oscillating upper rivulet

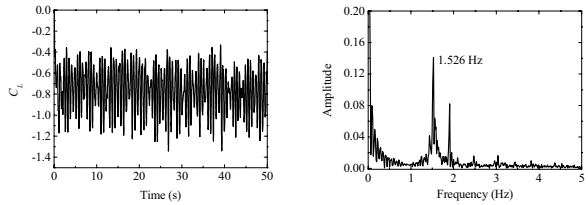

(c) $\theta_0 = 80^\circ$

Figure 9. Lift coefficients of the model with an oscillating upper rivulet

3.2 *One degree-of-freedom cable model with a fixed upper rivulet*

Similar CFD simulations are conducted using almost the same set-up as moving rivulet case except that the UDF only solves Eq. (2) for the displacement of cable and rivulet while the relative location between cable and the upper rivulet is fixed. The displacement history of the cable vibration illustrated in Figure 10 shows no RWIV exists when the upper rivulet is fixed at the position of 50°, 65° and 80°. All give the similar results that the amplitudes of the vibrations are much smaller than that of the RWIV observed in wind tunnel tests and Figure 8(b).

The time histories and spectra of aerodynamic lift coefficients at the fixed position angles of 50°, 65° and 80° are shown in Figure 14(a), (b) and (c), respectively. The lift coefficients do not represent the natural frequency of the cable for all cases and cannot induce the RWIV of the cable.

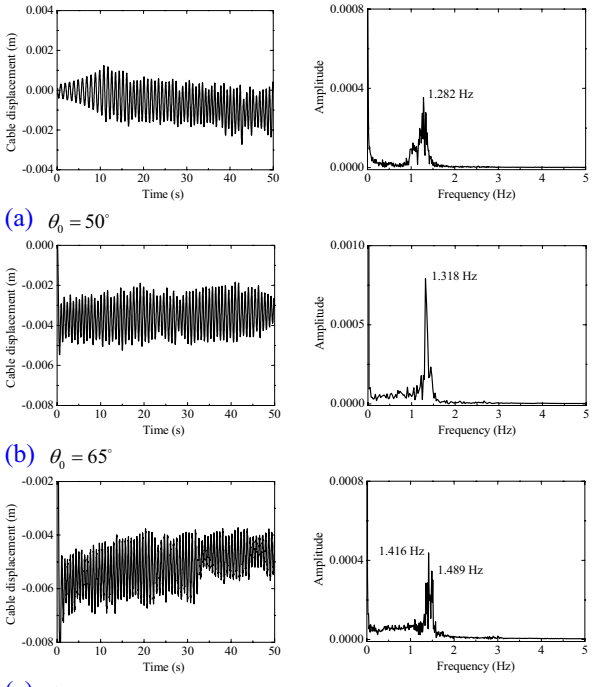

(a) $\theta_0 = 50^\circ$

(b) $\theta_0 = 65^\circ$

(c) $\theta_0 = 80^\circ$

Figure13. Displacement response of the CFD cable model with a fixed upper rivulet

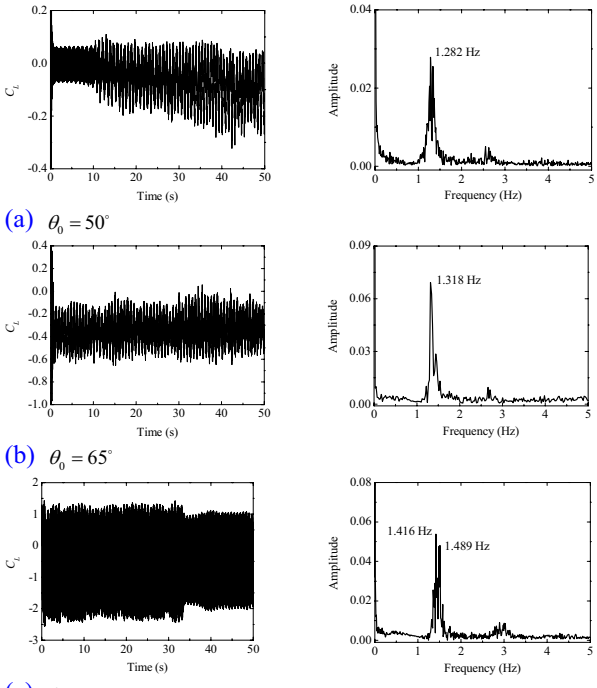

(a) $\theta_0 = 50^\circ$

(b) $\theta_0 = 65^\circ$

(c) $\theta_0 = 80^\circ$

Figure 14. Aerodynamic lift coefficients of the CFD cable model with a fixed upper rivulet

4 CONCLUSIONS

The wind tunnel test with UTTMS and CFD numerical simulation are carried out to investigate the influence of dynamic properties and position of rivulet on rain-wind-induced vibration of stay cables. The comprehensive study presented in this paper draws the following conclusions:

1. The experimental results indicate that when the RWIV occurs, the upper rivulets regularly oscillate following the natural frequency with large amplitude. At other cases when the RWIV does not appear, the upper rivulet does not form (low velocities) or irregularly vibrate with no dominant frequencies with small amplitude.

2. CFD simulations suggest that the existence of the upper rivulet do not sufficiently to excite RWIV. In order to excite RWIV, the upper rivulet should not only oscillate, but also oscillate in a certain region with the same frequency as that of cable vibration.

5 ACKNOWLEDGEMENTS

This research was funded by the National Natural Sciences Foundation of China (NSFC) (90815022, 51161120359 and 51008093). The authors gratefully acknowledge Prof. Yaojun Ge, Dr. Lin Zhao and the staff of the Wind Tunnel Laboratory of Tongji University of China for their assistance with this test.

6 REFERENCES

1 N. Coesentino, O. Flamand, C. Ceccoli, Rain-wind-induced vibration of inclined stay cables Part I: experimental investigation and physical explanation, Wind and Structures, 6(6) (2003) 471-484.
2 O. Flamand, Rain-wind-induced vibration of cables, Journal of Wind Engineering and Industrial Aerodynamics, 57 (1995) 353-362.
3 M. Gu, X. Q. Du, Experimental investigation of rain–wind-induced vibration of cables in cable-stayed bridges and its mitigation, Journal of Wind Engineering and Industrial , 93 (2005) 79-95.
4 Y. Hikami, N. Shiraishi, Rain-wind-induced vibrations of cables in cable stayed bridges, Journal of Wind Engineering and Industrial Aerodynamics, 29 (1988) 409-418.
5 F. C. Li, W. L. Chen, H. Li, R. Zhang, An ultrasonic transmission thickness measurement system for study of water rivulets characteristics of stay cables suffering from wind–rain-induced vibration, Sensors and Actuators A 159 (2010a) 12-23.
6 H. Li, W. L. Chen, F. Xu, F. C. Li, J. P. Ou, A numerical and experimental hybrid approach for the investigation of aerodynamic forces on stay cables suffering from rain-wind induced vibration, Journal of Fluids and Structures 26 (7-8) (2010b) 1195–1215
7 M. Matsumoto, H. Shirato, T. Yagi, M. Goto, S. Sakai, J. Ohya Field observation of the full-scale wind-induced cable vibration. Journal of Wind Engineering and Industrial Aerodynamics, 91 (2003a) 13-26.
7 M. Matsumoto, T. Yagi, M. Goto, S. Sakai Rain-wind-induced vibration of inclined cables at limited high reduced wind velocity region. Journal of Wind Engineering and Industrial Aerodynamics, 91 (2003b) 1-12.
8 U. Peil, N. Nahrath, Modeling of rain-wind induced vibrations, Wind and Structures 6(1) (2003) 41-52.
9 H. Yamaguichi, Analytical study on growth mechanism of rain vibration of cables, Journal of Wind Engineering and Industrial Aerodynamics, 33(1990) 73-80.
10 D. Zuo, J. P. Jones, Interpretation of field observations of wind- and rain-wind-induced stay cable vibrations, Journal of Wind Engineering and Industrial Aerodynamics, 98(2) (2010) 73-87

The Seventh International Colloquium on Bluff Body Aerodynamics and Applications (BBAA7)
Shanghai, China; September 2-6, 2012

Experimental study on the relation of water rivulet-Reynolds number effect-cable vibration

Qingkuan Liu, Yi Wang, Yunfei Zheng, Wenyong Ma

Wind Engineering Research Center, Shijiazhuang Tiedao University, 17 Northeast Second Inner Ring, Shijiazhuang, Hebei 050043 China

ABSTRACT: Rain-wind induced vibration of stay-cables is a worldwide problem of great concern in bridge engineering. In all factors that induce this vibration, water rivulet formed on cable surface in rainy and windy condition is considered as the most inportant one. Taking drag/lift force coefficients and vibration amplitudes in different Reynolds numbers as parameters, by wind tunnel tests, the influence of water rivulet on Reynolds number effect and mechanism of vibration caused by such facters were studied by means of force-measurement and vibration-measurement tests of stay-cable models with water rivulets attached in different positions. Resrults show that water rivulet has great influence upon changing rules of force coefficients with different Reynolds numbers; force coefficients value and changing rule have very close relationship with vibration.

KEYWORDS: stay cable; rain-wind induced vibration; wind force coefficients; water rivulet; Reynolds number

1 INTRODUCTION

Inclined cables often show violent vibration in rainy and/or windy days due to low structural damping. Among cable vibrations, rain-wind induced vibration is a worldwide problem, as its large amplitude and serious harm to cable-stayed bridges.

To make clear the mechanism and control methods of this vibration, by field observation[1-3],wind tunnel tests[4-11]and numerical analysis[12-13], reseach work have have been carried out for more than two decades, and galloping theory of water rivulet[4,14], high wind speed vortex induced vibration[5], water rivulet movement theory [6,7,9,15] have been put forward by different researchers.

In all the factors that induce this vibration, water rivulet formed on cable surface in rainy and windy condition is considered as the most inportant one, as it can change the cabel shape and wind force.

As we know that Reynolds number is a key parameter in study of fluid mechanics, particularly for the structures which have smooth surface, since flow fields around such structures vary with Reynolds number, as well as the aerodynamic force and vibration characteristics. In this research, from the viewpoint of Reynolds number effect, taking drag/lift force coefficients and vibration amplitudes in different Reynolds numbers as parameters, the influence of water rivulet on Reynolds number effect, the influence of Reynolds number on cable vibration were studied by means of force-measurement and vibration-measurement tests. The cable model used is a circular cylinder with water rivulets attached in different positions. The aim of this paper is tried to understand the mechanism of rain-wind induced vibration of stay-cables from the new viewpoint of Reynolds number effect.

2 WIND TUNNEL TEST

Two series of wind tunnel tests were performed to determine the exact relationship between Reynolds number effect and cable vibration. One series of tests is aerodynamic force measurements using fixed rigid cable models; the other one is vibration amplitude measurements using spring supported rigid cable models.

The wind tunnel used in this study is a open/closed circuit type with two sections, located at Shijiazhuang Tiedao University. The tests were performed using the small section of the wind tunnel, which is 2.2m in width and 2.0m in height and can reach a wind velocity up to 80m/s. The cable model in wind tunnel, the water position and shape are shown in Fig.1. The wind tunnel test cases are shown in Table 1.

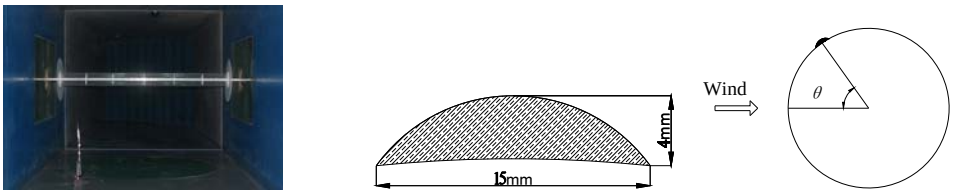

Fig.1 Cable model, water rivulet position and shape

Table1. Wind tunnel test cases

force-measurement test			vibration-measurement test		
θ(°)	*Re* range ($\times 10^5$)	*Re* step ($\times 10^5$)	θ(°)	*Re* range ($\times 10^5$)	*Re* step ($\times 10^5$)
10~70	8~15	1.0	10~50	8~15	1.0
				17~47	2.0
	17~47	2.0	52.5~70	8~21	1.0
				23~47	2.0

3 RELATION BETWEEN WATER RIVULET POSITION AND REYNOLDS NUMBER EFFECT

Drag and lift force coefficients of cable model with water rivulet in different positions are shown in Fig.2.

It can be seen that the Reynolds number effects of force coefficients have a very close relation with water rivulet position.

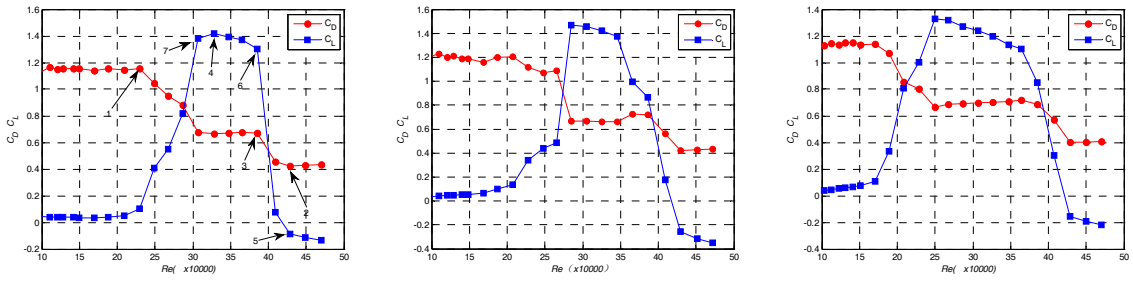

θ=10° θ=12.5° θ=15°

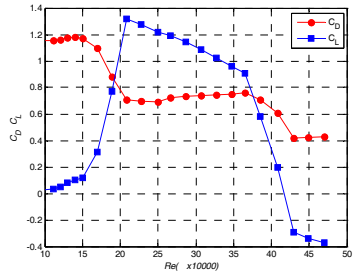

θ=17.5°

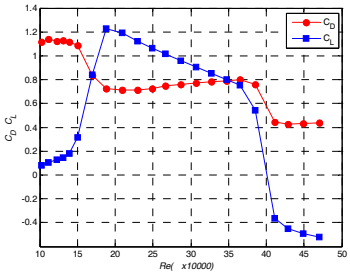

θ=20°

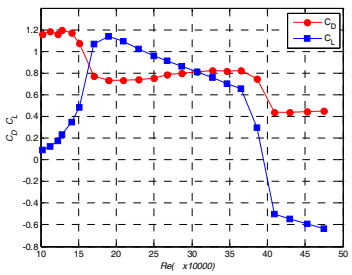

θ=22.5°

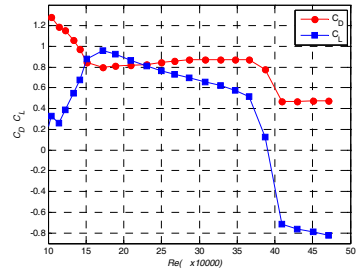

θ=25°

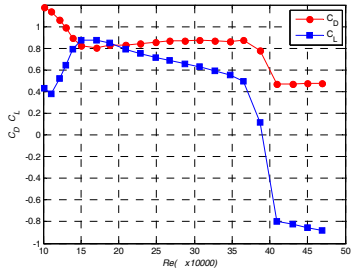

θ=27.5°

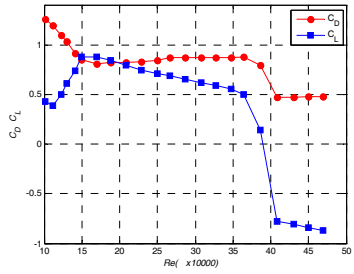

θ=30°

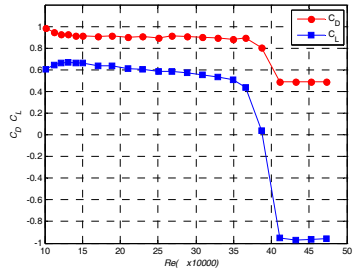

θ=32.5°

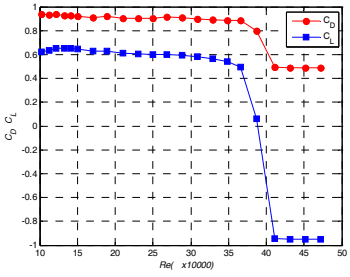

θ=35°

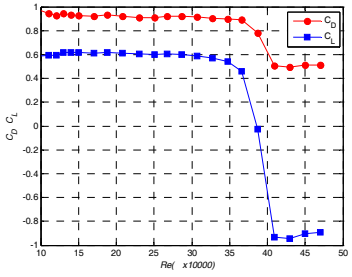

θ=37.5°

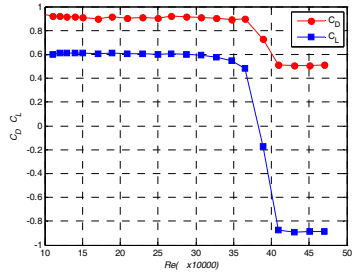

θ=40°

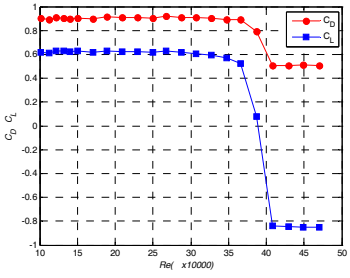

θ=42.5°

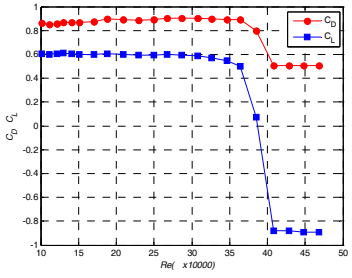

θ=45°

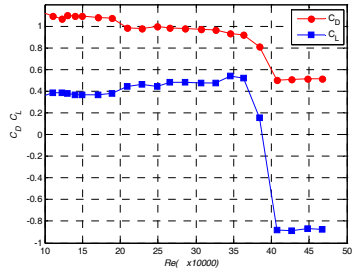

θ=47.5°

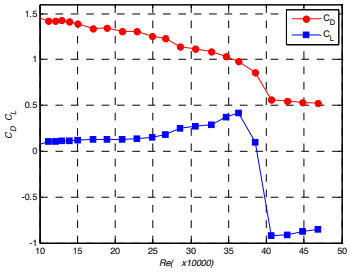

θ=50°

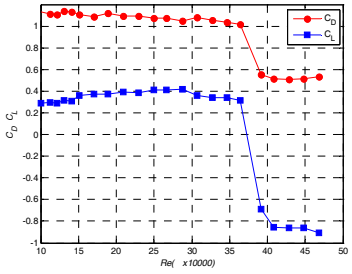

θ=52.5°

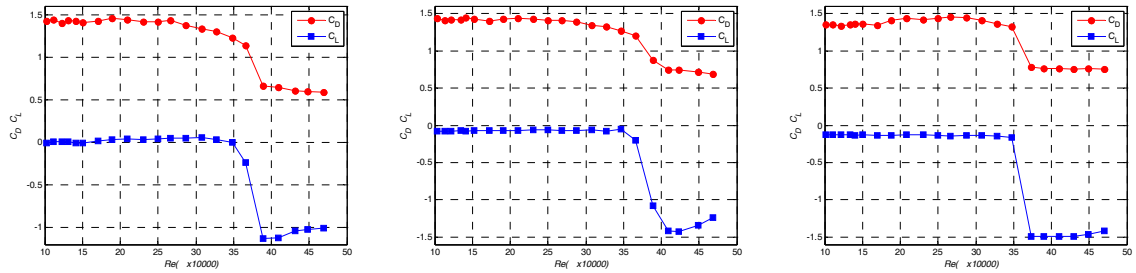

θ=55° θ=57.5° θ=60°

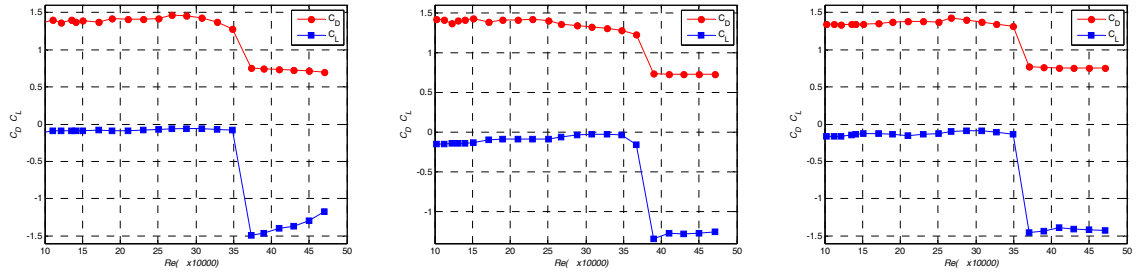

θ=62.5° θ=65° θ=67.5°

Fig.2 Drag and lift force coefficients of each water rivulet position

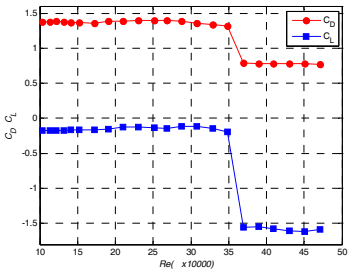

θ=70°

The results of Fig.2 can be classified into two types based on drag/lift force coefficients changing with Reynolds number, one type is results from water rivulet position θ=10° to θ=30°, the another type is other water rivulet positions.

In the first type, the changing rule of drag force coefficients with Reynolds number is steady-decreasing-steady-decreasing-steady, the changing rule of lift force coefficients is steady-increasing-steady-decreasing-steady. Refering to the changing rule of force coefficients of cable with smooth surface [19], it can be deduced that the first steady range of the two force coefficients belongs to subcritical Reynolds number range, and the following range belongs to critical Reynolds number range with the decreasing of drag force coefficient and increasing of lift force coefficient, the last steady range of the two force coeffients belongs to super-critical Reynolds number range.

In the second type, from the Reynold number range shown in the figures, the first stage of the two coefficients (drag force decreasing and lift force increasing) is not shown, the process of the two coefficients are steady-decreasing-steady.

Based on all the cases, defining the maximum of drag force coefficient as *Dmax* (ex. Point 1 in Fig.2, case of θ=10°), minimum of drag force coefficient as *Dmin* (Point 2), the drag force valve when it begins to decrease in the last decreasing stage as *Dst* (Point 3), the decreasing amplitude of drag force in the last decreasing stage as *DA* (drag force difference from Point 3 to Point 2), maximum of lift force as *Lmax* (Point 4), minimum of lift force as *Lmin* (Point 5), lift force value when it begins to decrease as *Lst* (Point 6), the decreasing amplitude of lift force in the last decreasing stage as *LA* (drag force difference from Point 6 to Point 5), the Reynolds number when drag force coefficient begins to decrease in the last stage as *Dstre* (Reynolds number of Point 3), Reynolds number when drag force coefficient gets its minimum as *Dminre* (Rey-

nolds number of Point 2), the distance of Reynolds number when drag force coefficient shows steady range as *Lpl* (Reynold number difference from Point 7 to 6), Reynolds number when lift force coefficient gets its maximum as *Ltre* (Reynolds number of Point 7), these parameters changing rule with water rivulet are concluded in Fig.3.

Base on Fig.2 and Fig.3, it can be seen that the change of water rivulet can induce obvious change of drag/lift force coefficients; the coefficients value and parameters above-mentioned are different in different water rivulet positions.

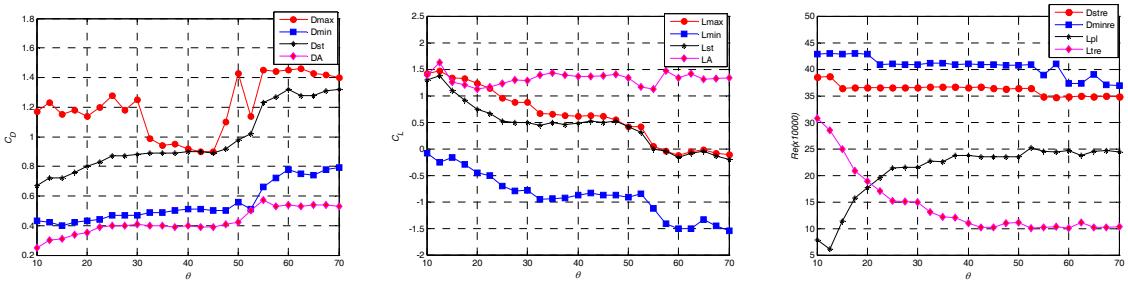

a Parameters of drag force coefficient b Parameters of lift force coefficient c Reynolds number of key point

Fig.3 Variation of force coefficient parameters with rivulet positions

4 RELATION BETWEEN WATER RIVULET POSITION AND AERODYNAMIC STABILITY

$dC_F/d\alpha$ and vibration amplitude of cable model with water rivulet in different positions are shown in Fig.4. Here, $dC_F/d\alpha$ is galloping coefficient, calculated from drag and lift force coefficients.

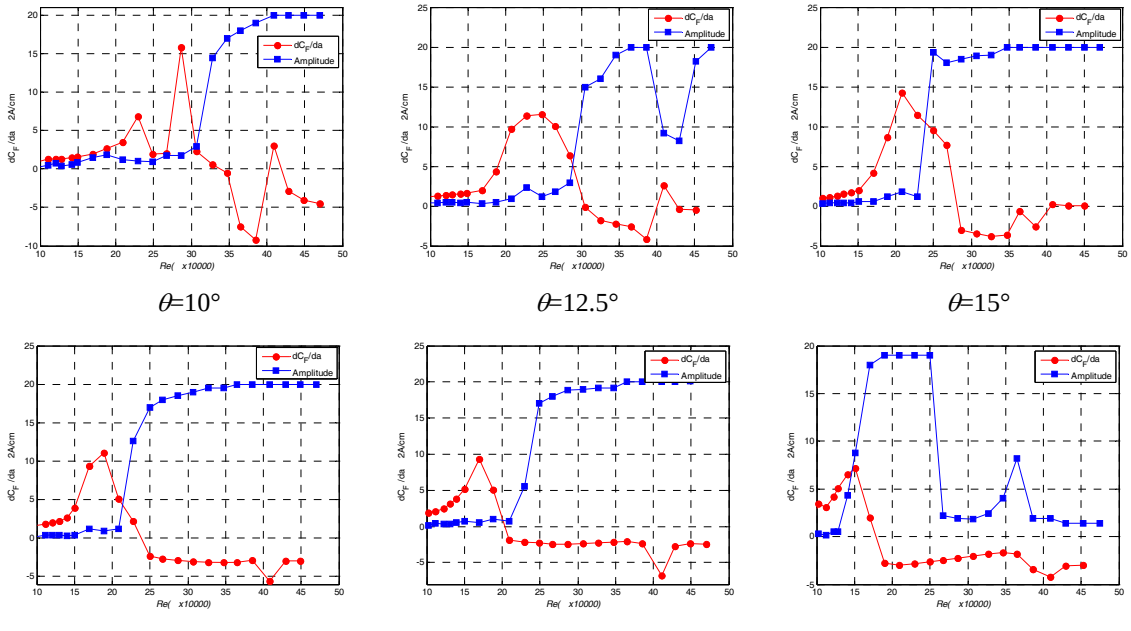

θ=10° θ=12.5° θ=15°

θ=17.5° θ=20° θ=22.5°

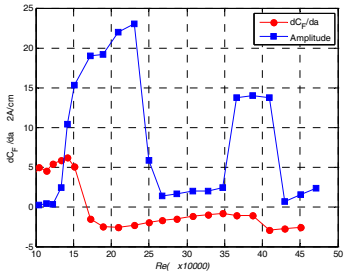

θ=25°

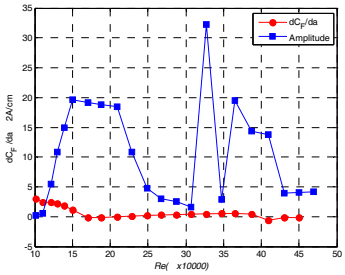

θ=27.5°

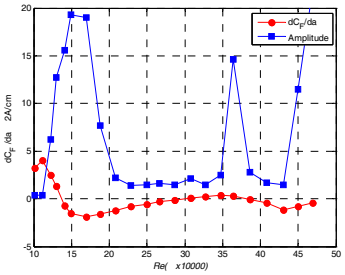

θ=30°

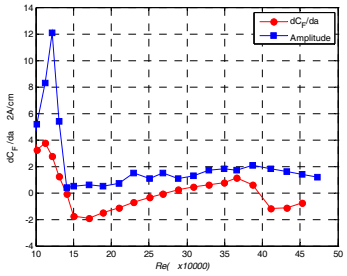

θ=32.5°

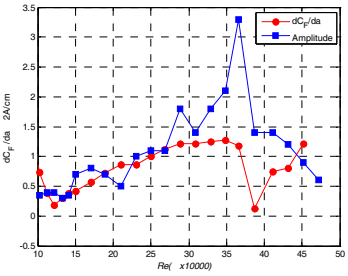

θ=35°

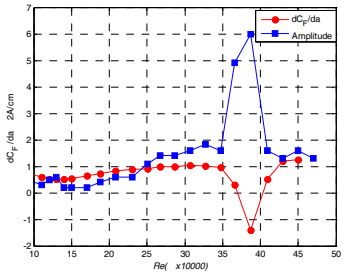

θ=37.5°

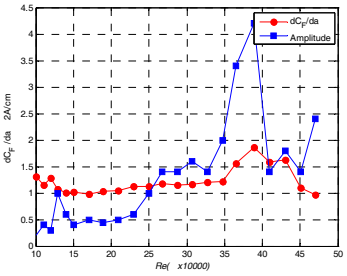

θ=40°

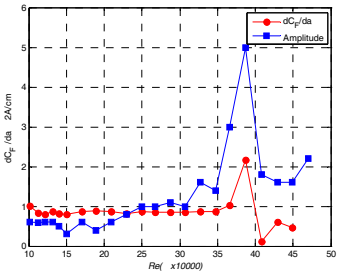

θ=42.5°

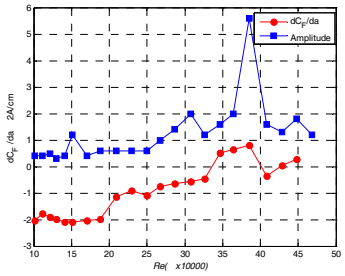

θ=45°

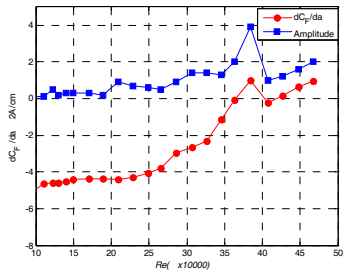

θ=47.5°

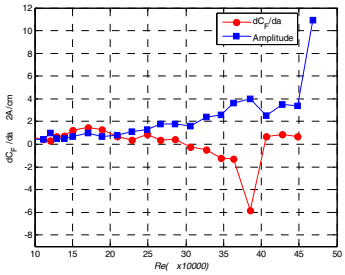

θ=50°

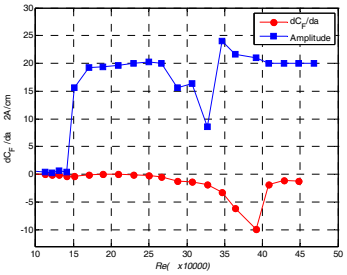

θ=52.5°

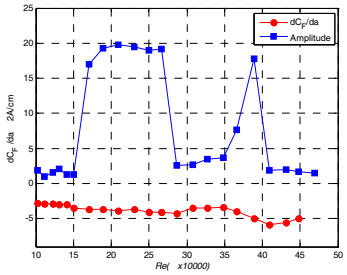

θ=55°

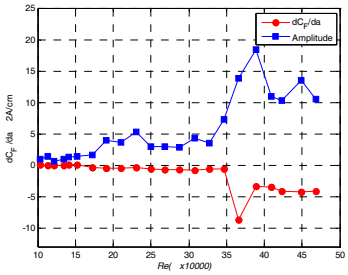

θ=57.5°

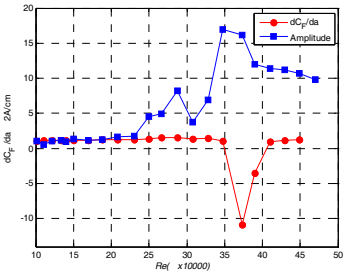

θ=60°

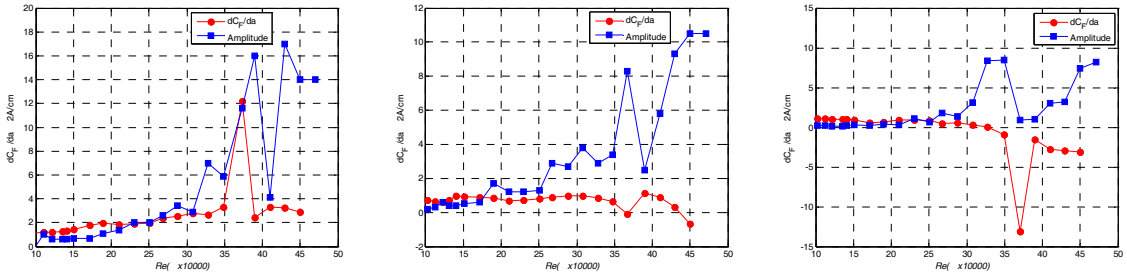

θ=62.5° θ=65° θ=67.5°

Fig.4 $dC_F/d\alpha$ and vibration amplitude of each water rivulet position

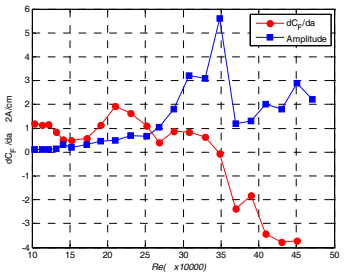

θ=70°

From Fig.4, it can be seen that there are two main vibration types of cable model.

When water rivulet is at a low position (θ is small), with the increasing of Reynolds number, drag force coefficient decreases and lift force coefficient increases dramatically. The similar critical Reynolds number effect occurs. The change of force coefficients induce minus $dC_F/d\alpha$. The large amplitude vibration of cable model under such condition can be explained by both critical Reynolds number effect and galloping.

When Reynolds number is relatively high (between 300000 and 450000), with the decreasing of drag force coefficient and lift force coefficient, varying amplitude vibrations of cable model occur for every water rivulet position test cases. The vibration under such condition is similar to the vibration induced by critical Reynolds number effect.

5 CONCLUSION

Base on Reynolds number effect, water rivulet effect on Reynolds number effect and mechanism of water rivulet effect on cable vibration are studied, the conclusions are as follows:

(1) Water rivulet can influnce the changing rule of force coefficients with Reynolds number; there is close relationship between cable vibration and coefficients value and their changing rules.

(2) In low water rivulet positions, with the increasing of Reynolds number, drag force decrease and lift force increase, the galloping coefficients are minus, cable shows large amplitude vibration. This vibration can be explained by Reynolds number effect and galloping.

(3) In high water rivulet positions, with the decreasing of drag force coefficient, lift force coefficient changes heavily; cable vibrates in different amplitude in each water rivulet position. The mechanism of these vibrations is similar to vibration induced by Reynold number effect.

6 ACKNOWLEDGEMENTS

This work was supported by National Science Foundation of China (50878135), New Century Training Program Foundation for Talents from the Ministry of Education of China (NCET-10-0130).

7 REFERENCE

[1] Irwin P A, Nedim A, Telang N. Wind induced stay cable vibrations-a case study [C]. Proceeding of the 3rd International Symposium on Cable Aerodynamics, Trondheim, 1999: 171-176.

[2] Matsumoto M, Shirato H, Yagi T, Goto M, Sakai S, Ohya, J. Field observation of the full-scale wind-induced cable vibration [J]. Journal of Wind Engineering and Industrial Aerodynamics, 2003, 91(1-2): 13-26.

[3] CHEN Zhengqing, LIU Chenyin, NI Yiqing, WANG Xiuyong, FU Xiaoning. Wind parameters in wind-rain induced stay cable vibration on Dongting Lake Bridge [J]. Journal of Railway Science and Engineering. 2004, 1(1)：52~57. (in Chinese)

[4] M. Matsumoto, T. Yagi, S. Sakai, J. Ohya, T. Okada. Steady wind force coefficients of inclined stay cables with water rivulet and their application to aerodynamics. Wind & Structures. 2005, 8(2) : 107-120.

[5] M. Matsumoto, T. Yagi, M. Goto, S. Sakai, Rain-wind-induced vibration of inclined cables at limited high reduced wind velocity region. Journal of Wind Engineering and Industrial Aerodynamics. 2003, 91: 1-12.

[6] N. Cosentino, O Flamaned, C . Ceccoli. Rain-wind-induced vibration of induced stay cables.Part I : Experimental investigation and physical explanation. Wind and Structure. 2003, 6 (6):471 ~ 484.

[7] GU Ming, DU Xiaoqing. Experimental-investigation of rain-wind-induced vibration of cables in cable-stayed bridges and its mitigation [J].Journal of wind engineering and Industrial Aerodynamics, 2005, 93:79~95.

[8] LI Yongle, LU Wei, TAO Qiyu, XIONG Wenbin. Study on rain-wind induced vibration of cables in cable-stayed bridges by wind tunnel test [J]. Experiments and Measur in Fluid Mechanics, 2007, 21(4): 36-40. (in Chinese)

[9] LIU Qingkuan. Experimental study on movement of water rivulet on cable surface in rain-wind induced vibration of stay-cables[J]. China Civil Engineering Journal. 2007, 40(7) : 62-67. (in Chinese)

[10] CHEN Wenli, LI Hui, LI Fengchen. An ultrasonic transmission thickness measurement system for rivulet on the stay cable under rain-wind induced vibration[J]. Earthquake Engineering and Engineering Vibration. 2009, 29(1):139-145. (in Chinese)

[11] DU Xiaoqing, GU Ming, QUAN Yong. Testing Study on Controlling Rain-wind induced Vibration of Cables of Cable-stayed Bridges[J]. Journal of Tongji University (Natural Science). 2003,31(11): 1266-1269. (in Chinese)

[12] LI Shouying, GU Ming, CHEN Zhengqing. An Analytical Model of Rain-wind-induced Vibration of Three-dimensional Continuous Stay Cable with Actual Moving Rivulet [J]. Journal of Hunan University (Naturnal Science), 2009. 36(2): 1-7. (in Chinese)

[13] LIU Qingkuan. Study on the mechanism of rain-wind induced vibration of cables on cable-stayed bridge using LES [J]. Engineering Mechanics. 2007,24(9)：134-139. (in Chinese)

[14] Y. Hikami, N. Shiraishi. Rain-wind induced vibrations of cables in cable stayed bridge. Journal of Wind Engineering and Industrial Aerodynamics, 1988, 29: 409~418.

[15] LIU Qingkuan, QIAO Fugui, ZHANG Feng. Effect of non-uniform rivulet movement on rain-wind induced vibration of stay-cables [J] Engineering Mechanics. 2008, 25(6): 234-240. (in Chinese)

[16] Miyata T, Yamada H, Hojo Y. Aerodynamic response of PE stay cables with pattern-indented surface [C]. Proceedings of International Conference on Cable-Stayed and Suspension Bridges (AFPC), Deauville, France, 1994: 515-522.

[17] Honda A, Yamanaka T, Fujiwara T, Saito T. Wind tunnel test on rain-induced vibration of the stay-cable [C]. Proceedings of International Symposium on Cable Dynamics, Liege, Belgium, 1995: 255-262.

[18] Cheng, S, Larose G L, Savage M G, Tanaka H, Irwin P A. Experimental study on the wind-induced vibration of a dry inclined cable--Part I: Phenomena [J]. Journal of Wind Engineering and Industrial Aerodynamics, 2008, 96(12): 2231-2253.

[19] LIU Qingkuan, ZHANG feng, MA Wenyong, WANG Yi. Experimental Study on Reynolds number Effect and Wind-induced Vibration of Stay cables [J]. Journal of Vibration and Shock. 2011, 30(12), 114-119 (in Chinese)

The Seventh International Colloquium on Bluff Body Aerodynamics and Applications (BBAA7)
Shanghai, China; September 2-6, 2012

Along-wind self-excited forces of two-dimensional cables under extreme wind speeds

Zhiwen Zhu

Center of Wind Engineering, Hunan University, Changsha, Hunan, China

ABSTRACT: Self-excited characteristics of cables under extreme wind speeds in along-wind direction currently is not clear, but may be of great interests for cable-supported bridge when dealing with flutter critical conditions. The flutter derivative with respect to along-wind aerodynamic damping is first derived according to the quasi-steady theory. For reduced wind speeds ranged from 53~1050, the flow fields around the along-wind forced vibration cable are simulated at Reynolds number of 5.18×105, followed by identifying flutter derivatives of P^*_1. The present results are in good agreement with the values from the quasi-steady theory, which suggests that the quasi-steady theory can be applied to obtaining flutter derivatives of P^*_1 at extreme wind condition. It is found that for cables under such condition, the vortex-induced forces dominate the variation of aerodynamic forces, and the self-excited forces can be negligible. Since the cable oscillation does not change the vortex-shedding frequency, it seems that the vortex-shedding pattern become very stable under extremely high wind speeds.

KEYWORDS: cable; along-wind vibration; self-excited forces; CFD; extreme wind; flutter derivatives.

1 INTRODUCTION

For cable-supported bridges with super-long spans, flutter instability at extreme wind condition may be a great concern. Normally, when carrying out flutter analysis, self-excited forces acting on bridge girders are always included, which can be determined through wind tunnel tests. However, it is found that the self-excited forces on cables are rarely considered among available references (Ge, 2008). But for super-long span bridges at flutter critical condition, the wind-induced forces on the cable may become significant since the increasing length and lower damping ratio of the cable. Based on this consideration, self-excited characteristics of cables in along wind under such kind of extreme wind condition should be first addressed.

It is well known that flow around circular cylinders show Reynolds-dependent characteristics, including vortex mode, separation point, mean and fluctuating drag and lift coefficients and so on. For flow around cables, such kind of characteristics always requires a full Reynolds simulation, which may help to provide meaningful results against the reality. This is also the case when dealing with cable aeroelasticity. If one considers a cable with diameter of 0.12m under extreme wind speeds, the corresponding Re number may be above 5×10^5, and if the cable oscillates at very low frequency, such as 0.1Hz, the resultant reduced wind speeds may be over several hundreds or even above thousand, which is far above the normal reduced wind speed relative to bridge girders elasticity. Meanwhile, under extreme wind speeds, the mean wind forces on the cable may be significantly large compared to the self-excited forces. Such kind of conditions almost prevents any test set and application dealing with identification of flutter derivatives of cables in wind tunnel.

The striking advantages of CFD in application to identification of flutter derivatives is that, neither test set nor model inertia forces are involved (Zhu, 2007). This helps to overcome many difficulties in wind tunnel test, and allows one to carry out self-excited simulations at the real Re

number under extreme wind speeds. In the following, one cable is picked up from a real bridge engineering, and is forced to undergo along-wind oscillation under high wind speeds. The flutter derivative of the cable corresponding to the along-wind degree of freedom is extracted, and compared to values from the quasi-steady theory.

2 FLUTTER DERIVATIVES OF CABLES IN QUASI-STEADY FORM

Under extreme wind speeds, the cables in cable-supported bridges are assumed to undergo small-amplitude vibration with a low frequency, which means a small velocity compared to the incoming wind. Therefor, the resultant wind angle of attack relative to cables will be small.

Consider a two-dimensional cable immerged in the incoming wind with velocity of U_∞, and oscillated both in along-wind direction and cross-wind direction, as shown in Figure 1. The synthesized wind velocity to the cable can be expressed as,

$$U_r = \sqrt{(U_\infty - \dot{p})^2 + \dot{h}^2} \approx U_\infty - \dot{p} \tag{1}$$

where $\dot{p}$ and $\dot{h}$ are the vibration velocities in along-wind and cross-wind directions on the coordinate system *oxy* with the *x* axis along the incoming wind, respectively. Obviously, Equation 1 recognizes the assumption that both $\dot{p}$ and $\dot{h}$ are small enough compared to incoming flow.

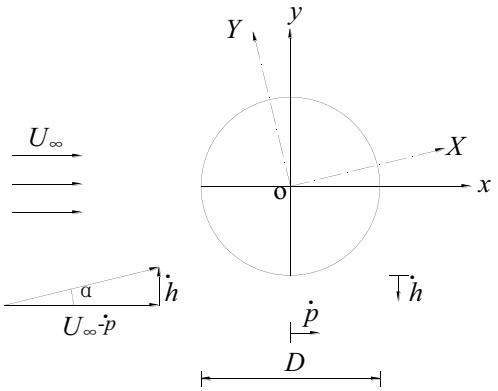

Figure 1 Cable in motion in incoming wind

The unsteady drag and lift forces acting on the cable can be rewritten as,

$$F_D = 0.5\rho U_r^2 D C_D(t) \tag{2a}$$

$$F_L = 0.5\rho U_r^2 D C_L(t) \tag{2b}$$

in which ρ denotes the air density; D the cable diameter; $C_L(t)$ and $C_D(t)$ are the unsteady lift and drag coefficients, and is depended on the relative wind angle of attack.

Under extreme wind speeds, the angle between the velocity of the cable and resultant wind velocity can be expressed as,

$$\alpha(t) = \tan^{-1}\left(\frac{\dot{h}}{U_\infty - \dot{p}}\right) \approx \frac{\dot{h}}{U_\infty - \dot{p}} \approx \frac{\dot{h}}{U_\infty} \tag{3}$$

with $\sin\alpha(t) \approx \alpha(t)$ and $\cos\alpha(t) \approx 1$ because of very small value of angle.

If one transfers Equation 2 onto the structural coordinate system OXY located at the center of the cable, with X axis along the synthesized wind direction, Equation 4 can be obtained as,

$$F_V = F_D \sin\alpha(t) + F_L \cos\alpha(t) \tag{4a}$$

$$F_H = F_D \cos\alpha(t) - F_L \sin\alpha(t) \tag{4b}$$

where F_V and F_H represent the wind forces normal to and along the resultant wind velocity, respectively.

This paper limits the study only on the along-wind oscillation and hence the drag force of the cable. Since the cable oscillates around the reference position with a small amplitude, Equation 4 can be expanded at the zero angle of attack based on Taylor's theory. If high-order terms are ignored, Equation 4b can be derived as,

$$\begin{aligned} F_H &= F_D - F_L\alpha(t) \\ &= 0.5\rho(U_\infty - \dot{p})^2 D\left[C_D(t) - C_L(t)\alpha(t)\right] \\ &= 0.5\rho(U_\infty - \dot{p})^2 D\left[C_{D0} + C_{D0}^{'}\alpha(t) - (C_{L0} + C_{L0}^{'}\alpha(t))\alpha(t)\right] \\ &= 0.5\rho(U_\infty - \dot{p})^2 DC_{D0} = 0.5\rho D(U_\infty^2 C_{D0} - 2U_\infty \dot{p} C_{D0}) \\ &= 0.5\rho D U_\infty^2 (C_{D0} - 2\frac{\dot{p}}{U_\infty} C_{D0}) \end{aligned} \tag{5}$$

in which C_{D0} and $C_{D0}^{'}$; C_{L0} and $C_{L0}^{'}$ are mean drag and lift coefficient, and their slopes at zero angle of attack, respectively.

It can be seen that the first term in Equation 5 is the drag force at steady state, while the second term represents the self-excited force induced by along-wind oscillation, which corresponds to aerodynamic damping as shown in the following.

In along-wind direction, if comparing the unsteady forces acting on the cables with the well-known Scanlan formulation (1971), the flutter derivative in along-wind direction can be obtained as,

$$P_1^* = -2C_{D0} / K \tag{6}$$

where $K = \omega D / U_\infty$ is the reduced frequency; $\omega = 2\pi f$ the circular frequency; f the cable vibration frequency.

3 NUMERICAL SIMULATION STRATEGIES

Under extreme wind speeds, the Re number is very high. If one considers the spanwise correlation of the flow and then performs full three-dimensional simulations, significantly high requirement will be put forward on computer resources. So, this paper limits the research only on the two-dimensional situation.

3.1 *The governing equations*

The two-dimensional incompressible flow around the circular cable cross section can be described by the unsteady Reynolds-averaged Navier-Stokes equations as follows,

$$\frac{\partial}{\partial x_i} u_i = 0 \tag{7}$$

$$\rho \frac{\partial}{\partial t} u_i + \rho \frac{\partial}{\partial x_j} \left(u_i u_j \right) = -\frac{\partial p}{\partial x_i} + \mu \frac{\partial}{\partial x_j} \left(\frac{\partial u_i}{\partial x_j} \right) + \rho \frac{\partial}{\partial x_j} \left(-\overline{u_i' u_j'} \right) \tag{8}$$

where μ denotes air viscosity; p and t are the pressure and time; u_i and u_i'; u_j and u_j' (i=1, 2 ; j=1, 2) represent the mean and fluctuating velocities along the axis in Cartesian coordinate system, respectively; $-\rho \overline{u_i' u_j'}$ the Reynolds stress.

If Eddy Viscosity Model is employed to close the equations, the Reynolds stress can be expressed as,

$$-\rho \overline{u_i' u_j'} = \mu_t \left[\frac{\partial u_i}{\partial x_j} + \frac{\partial u_j}{\partial x_i} \right] \tag{9}$$

where $\mu_t = \rho C_\mu k^2 / \varepsilon$ is the turbulent viscosity; C_μ the empirical constant; k the turbulent kinetic energy and ε the dissipation rate of turbulent kinetic energy.

The standard $k-\varepsilon$ model employs wall functions in near wall region in order to avoid fine mesh, which results in significant saving on computer power. It has been widely used in engineering practice due to its robust formation and lower computational overhead. However, such kind of treatment is not sufficient to resolve complex flow accurately. The model often over-predicts the turbulence near stagnation regions, and presents the length scale which is too large in adverse pressure gradient flow. In many engineering applications, it fails to represent flow field due to the presentation of swirling flows and curved boundary layers flows.

By defining the turbulent viscosity in form of $\mu_t = k / \omega$, and the dissipation rate per unit kinetic energy $\omega = \varepsilon / k$, the $k-\omega$ turbulence model, which have been developed to improve the performance of the standard $k-\varepsilon$ (Menter, 1994). It is observed that the standard $k-\varepsilon$ model performed well in the shear layer flow while the $k-\omega$ model is excellent near to the wall. This leads to the development of the Shear Stress Transport (SST) model combining the advantage of both models, in which the $k-\omega$ model is employed near the wall and the standard $k-\varepsilon$ model is used near the boundary layer edge. To achieve this, the $k-\omega$ model is multiplied by a blending function F_l and the $k-\varepsilon$ model by (1-F_l) such that F_l has a value of one near wall region and switches to zero at the boundary layer where $k-\varepsilon$ model is recovered. It is found that the SST $k-\omega$ model can predict better flow separation compared to both the $k-\varepsilon$ and $k-\omega$ models (Liaw, 2005).

3.2 *2.2 Numerical strategy*

The cable with a diameter of D=0.12m, is located near the center of the computational domain, with all of outer boundaries extended over 25D, as shown in Figure 2. Such domain arrangement

can largely avoid numerical interference coming from outside boundaries. Since the cable is forced to undergo imposed vibration in CFD simulation, dynamic mesh system will be activated in Fluent which requires a suitable grid arrangement. In order to ensure good mesh quality, the whole computational domain is divided into four zones. The Zone Z1 around the cable is covered with body-fitted structured quadrilateral girds, which will oscillate with the cable but the grids topological structure will not be changed all the time. In this zone, the mesh orthogonality is always kept, as shown in Figure3, which helps to improve the accuracy and capture flow features. The Zone Z2 is paved with unstructured triangle grids, and will be re-meshed after each time step as to reflect the displacement of cable. Re-mesh quality can be ensured based on suitable selection of spring constant in spring-based smoothing method. Zone Z3 is also covered with structured orthogonal quadrilateral girds, but Zone Z4 is paved with unstructured quadrilateral girds. The grids in Z3 and Z4 are fixed all the time although the cable is undergoing along-wind oscillation.

Three different grid systems are created, with the closest grid space near the cable wall of h_0=0.000005m, 0.0001m and 0.0002m, respectively, as shown in Table 1. For all grid systems, the adjacent cell expansion ratios are always controlled under 1.1, which provides a smooth grid dimension over the whole computational domain. The total number of cells is shown in Tab.1. Numerical simulations show that the maximum Y^+ values on the wall are less than one in all grid systems, which satisfy grid resolution requirement for the SST $k-\omega$ turbulent model. Figure 4 shows the Y^+ distribution around the cable for G1.

Temporal discretization of the governing equations is performed with a second-order implicit scheme, while the convective terms are approximated with a second-order upwind scheme. The SIMPLEC algorithm is used to decouple the pressure and velocities field.

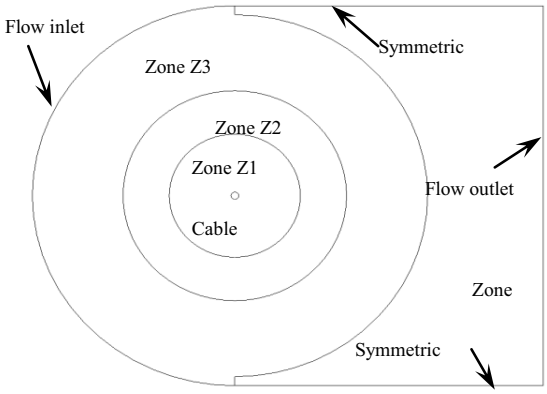

Figure 2 Partition and boundary conditions in computational domain

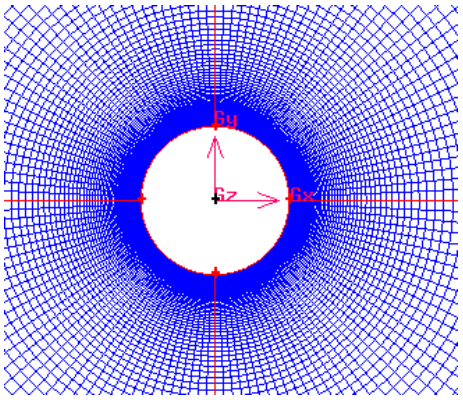

Figure 3 Grids arrangement around cable

Table 1. Grid parameters

Grid	h_0/m	Nodes	Y^+_{max}
G1	0.000005	26950	0.095
G2	0.00001	25270	0.22
G3	0.00002	23730	0.42

2.3 Cable motion and boundary conditions

In order to represent the body motion-induced forces acting on the cable and identify flutter derivatives, during CFD

simulations, the cable will undergo imposed along-wind sinusoidal vibration, i.e.,

$$p(t) = p_0 \sin(2\pi ft) \tag{12}$$

where p_0 is the vibration amplitude with a value of 0.025D, which is very small as to ensure small disturbance on flow field; f the vibration frequency. Since all simulations under different reduced wind speeds are performed at the same Re number, f needs to be changed as to obtain the desired reduced wind speeds.

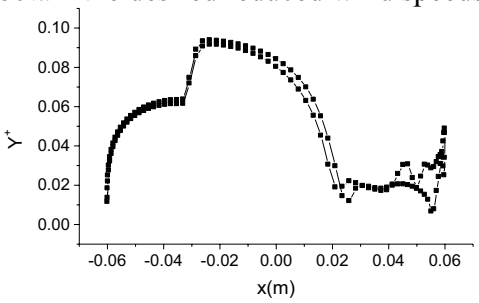

Figure 4 Y^+ values on cable surface of G1

In order to reflect surface roughness on the cable, a roughness height is assumed to be of 3×10^{-5}D (Poulin, 2007). Suitable boundary conditions are imposed on the computational domain, as shown in Figure 2. The flow inlet boundary is defined as velocity inlet with a value of 63m/s in horizontal direction (corresponds to the Reynolds number of 5.18×10^5), while flow outlet boundary is defined as the outflow boundary condition. The symmetric boundary condition is imposed on the top and bottom boundaries. As for the cable surface, no-slip condition is applied on it, which means the flow on the wall shares the same velocity as the cable when the cable undergoing imposed motion.

2.4 Grid-independence check

Simulation tests show that, even under extreme wind speeds, vortex shedding is still a dominating feature in flow around the cable. As to effectively capture vortex shedding, non-dimensional time step size is set to 0.01.

Define unsteady drag and lift coefficients on the cable as,

$$C_D = F_D / (0.5\rho U_\infty^2 D); \quad C_L = F_L / (0.5\rho U_\infty^2 D) \tag{13}$$

where F_D and F_L are drag and lift, which are positive in downstream and upside direction, respectively.

Grid check is performed for the fixed cable. Except the cable motion, boundary conditions and time step size will be the same. Data will be collected after 0.1s simulations as to avoid any influence from initial computation and thereafter the flow attains stable stage. As shown in Figure 5, time histories before 0.3s are force coefficients when the cable is fixed. It indicates that the flow around the cable experience a steady vortex shedding, with the St number indicated in Figure 4, which are slightly high compared to other reports (Norberg, 2003).

The results obtained on three different grid systems, including the mean drag and lift coefficients, RMS values of drag and lift coefficients, as well as the strouhal number are displayed in Figure 6. One can see that the results agree well with each other, especially the G1 and G2, which

means the simulation results will not be influenced by grid refinement. In this paper, G1 is selected for the further study on the moving cable.

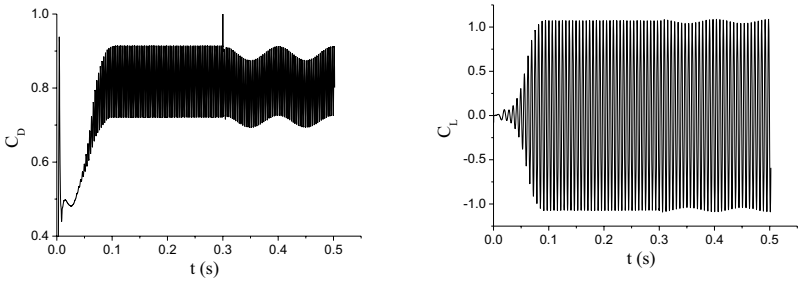

(a) (b)

Figure 5 Aerodynamic force time histories on cable

The mean drag coefficient from G1 is of 0.81, which matches well with the suggested value under extreme wind speeds (Poulin, 2007). This value will be used for the quasi-steady theory in the following.

Figure 7 is the vortex shedding plot around the fixed cable at four key states. It shows the vortex generation, elongation, shedding and drifting with the flow in the wake.

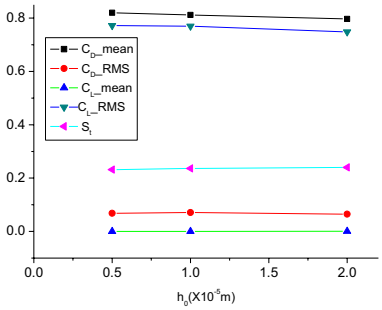

Figure 6 Aerodynamic coefficients and Strouhal number for flow around fixed cable

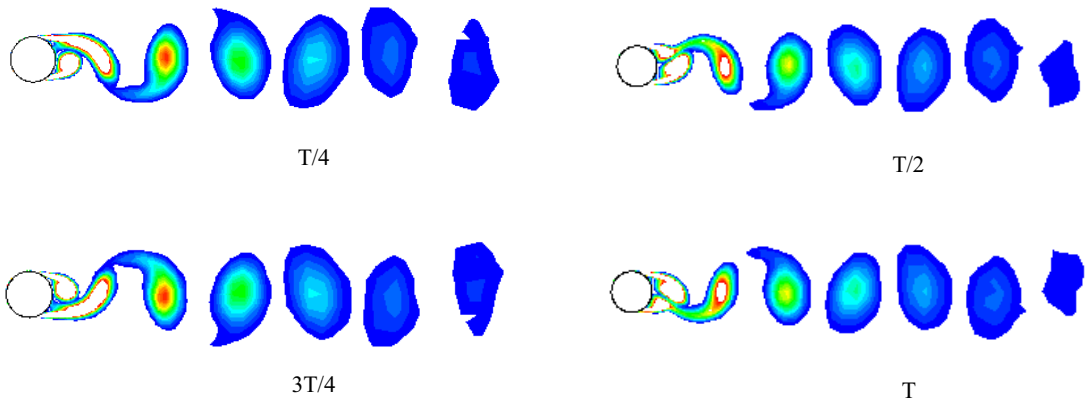

Figure 7 Vortex contour plot in wake of the fixed cable during one cycle of vortex shedding period

4 SIMULATIONS ON MOVING CABLE AND RESULTS

Considering simulations on the moving cable, enough time step simulations are first carried out for the fixed cable in order to establish a steady vortex shedding flow configuration, as shown in Figure 5. Then forced vibration is imposed on the cable, and force time histories are recorded on each time step. As shown in Figure 5 and more detailed in Figure 8, two cycles of data are plotted under the reduced wind speed v_r=53. Figure 9 also shows the total aerodynamic force time histories at a extreme high reduced wind speed of v_r=1050.

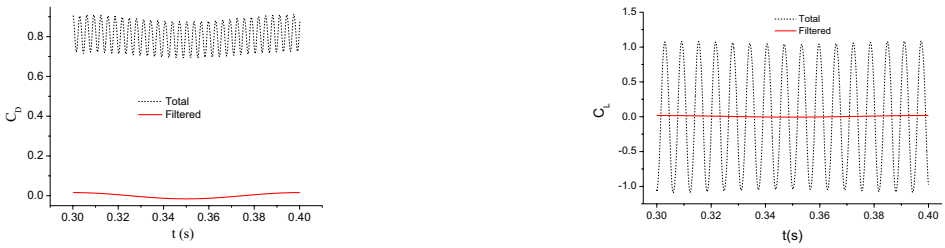

(a) (b)

Figure 8 Total and self-excited aerodynamic force time histories on forced vibration cables (V_r=53)

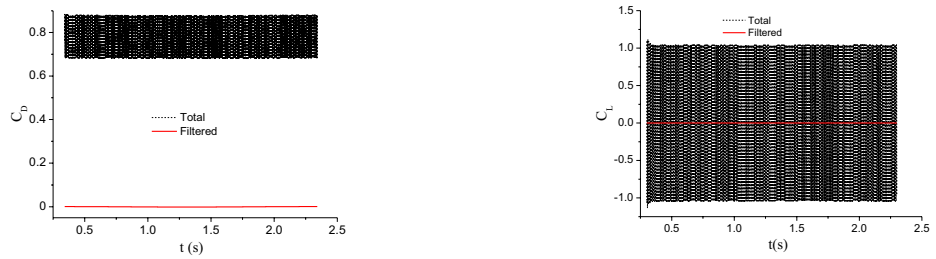

(a) (b)

Figure 9 Total and self-excited aerodynamic force time histories on forced vibration cables (V_r=1050)

Figures.8 and 9 appears that both of the total force time histories are formed by superposition of a high frequency wave on a low frequency oscillation. Frequency analysis indicates that two frequencies are included in the time histories, with the dominating one equals to the vortex shedding frequency, while the low one equals to the forced vibration frequency. It is worth noting that under such extreme wind speed, the oscillated cable still keeps its vortex shedding frequency as in the fixed situation. It seems that the vortex shedding mechanism will not be changed even the cable is under oscillation. Hence the vortex shedding mode is very stable under extreme wind speeds.

Based on assumption of linear superposition of aerodynamic forces, the self-excited forces can be separated from the total forces. Since the vortex-shedding frequency is significantly higher than the imposed motion frequency, the low-pass filtering technology can be used to obtain the self-excited forces, as shown in Figures.8 and 9. One can see that the self-excited mean and RMS value of drag is much smaller than the total one, while the RMS value of lift is significantly smaller than the total lift, especially at extreme high reduced wind speeds. In other words, the self-excited forces on the vibration cable are very small compared to the vortex-shedding forces. If comparing the self-excited drag coefficient with the mean total drag coefficient at the reduced

wind speed of 1050, one can conclude that the self-excited component may be negligible at extreme high wind speeds.

With the obtained self-excited drag time history, the flutter derivative of P^*_1 can be identified based on the least square method (Zhu, 2009). The present results are plotted against the quasi-steady ones from Equation 6 with C_d=0.81, as shown in Figure 10. One can see that the CFD results agree well with the quasi-stead theory. Hence if the self-excited drag force is considered under extreme wind speeds, the value of P^*_1 can be obtained straightforward from the quasi-stead theory.

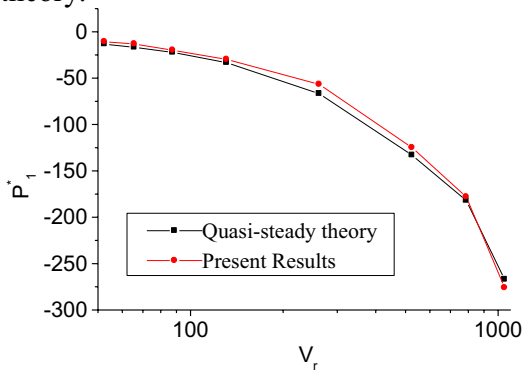

Figure 10 Identified flutter derivatives P^*_1 in comparison with quasi-steady theory

Table 2 also shows the value of KP^*_1, where $K=2\pi/v_r$ is the reduced frequency. If $C_{D0}=0.81$, the quasi-steady theory will give the value of $K\,P^*_1$= -1.62, which matches well with the present results at extreme high reduced wind speeds.

Table 2 CFD simulation cases and results

Vibration frequency/Hz	0.5	0.75	1	2	4	6	8	10
V_r	1050	788	525	263	131	88	66	53
K	0.006	0.009	0.012	0.024	0.048	0.072	0.096	0.12
$K\,P^*_1$	-1.65	-1.58	-1.5	-1.36	-1.42	-1.43	-1.25	-1.29

One striking feature in Figure 10 is that the P^*_1 become more negative with the increase of reduced wind speed, which means the aerodynamic damping relative to along-wind oscillation is always positive. It can be deduced that the one degree-of-freedom cable under along-wind oscillation is always stable.

Figure 11 shows the vortex-shedding patterns of the cable during one cycle of forced vibration, where T is the forced vibration period and denotes the cable coming back to the reference position. Since the vortex-shedding mechanism dominates the flow around the cable, the vortex street is apparent in the wake of vibration cable.

4 CONCLUSIONS AND REMARKS

The along-wind vibration of a cable is simulated by CFD method in this paper, with the following conclusions and remarks,

1) The identified flutter derivatives P^*_1 are in good agreement with the quasi-steady theory, which demonstrates the feasibility of CFD method to address the aeroelastic features of cables under extreme high wind speeds.
2) The quasi-steady theory, based on drag coefficient of 0.8, can provide a reasonable estimation

of the along-wind flutter derivatives of the cables at extremely high wind speeds.

3) It is found that under extreme wind speeds, the vortex shedding pattern will not be influenced by the cable vibration, and the vortex shedding still dominates the fluctuation on aerodynamic forces. It should be highlighted that the self-excited forces induced by along-wind vibration is negligible compared to the vortex-induced forces, i.e., the self-excited component may be negligible at extreme high wind speeds.
4) From aerodynamic point of view, the one degree-of-freedom cable oscillating in the along-wind direction is always stable, even under extreme high wind speeds.

If more computer resources are available, three-dimensional simulations may be carried out as to get further insight and extend the study to cross-wind vibration.

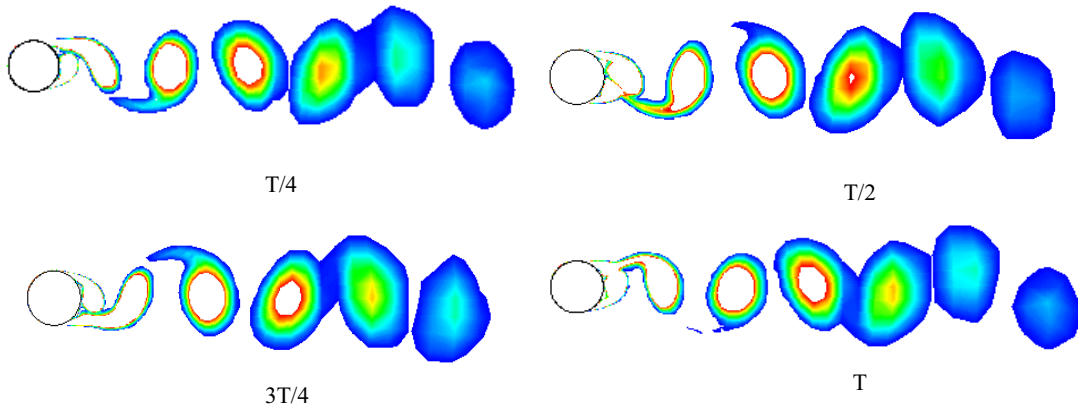

Figure 11 Snap shooting of vortex shedding of cables at four key states during one cycle of forced vibration

ACKNOWLEDGEMENTS

Financial support for this study is provided by Nation Natural Science Foundation of China (50978095) and Program for Changjiang Scholars and Innovative Research Team in University (IRT0917), to which the writers gratefully appreciate.

REFERENCES

1 Y.J. Ge, H.F. Xiang, Computational models and methods for the aerodynamic stability of long-span bridges, China Civil Engineering Journal, 2008, 41(2)96-93.(In Chinese)
2 K. F. Liaw, Simulation of flow around bluff bodies and bridge deck sections using CFD, University of Nottingham, School of Civil Engineering, 2005.
3 C. Norberg, Fluctuating lift on a circular cylinder: review and new measurements, Journal of Fluids and Structures, 2003,17: 57-96.
4 F. R. Menter, Two-Equation Eddy-Viscosity Turbulence Models for Engineering Applications, AIAA Journal, 1994, 32:269-289.
5 S. Poulin, A. Larsen, Drag loading of circular cylinders inclined in the along-wind direction, Journal of Wind Engineering and Industrial Aerodynamics, 2007, 95:1350-1363.
6 R.H.Scanlan, J. J.Tomko, Airfoil and bridge deck flutter derivatives, Journal of Engineering Mechanics, ASCE, 1971, 97(6)1717-1737.
7 Z.W. Zhu, M. Gu, Z. Q. Chen, Wind tunnel and CFD study on identification of flutter derivatives of a long-span self-anchored suspension bridge, Computer- Aided Civil and Infrastructure Engineering, 22 (2007) 541-554.
8 Z.W. Zhu, Z.Q. Chen, M. Gu, CFD based simulations of flutter characteristics of ideal thin plates with and without central slot, Wind and Structures, 2009, 12(1)1-19.

The Seventh International Colloquium on Bluff Body Aerodynamics and Applications (BBAA7)
Shanghai, China; September 2-6, 2012

Aerodynamic force coefficients of plain bridge cables in wet conditions

Giulia Matteoni[a,b], Christos T. Georgakis[b]

[a]*Department of Civil Enginering, Technical University of Denmark, Brovej, Building 118, Kgs. Lyngby, Denmark*
[b]*IPU, Building 404, Nils Koppels Allé, Kgs. Lyngby, Denmark*

ABSTRACT: In this paper, the aerodynamic forces and force coefficients from preliminary static wind tunnel tests on a plain cable in wet conditions are presented. The presented results are for several different relative cable wind-angles. A comparison is made with tests in dry conditions. In dry conditions, tests were performed for wind velocities between 2 and 31 m/s, whilst in wet conditions tests were performed for the range of wind velocities where rain rivulet formation was found possible, i.e. between 8-18 m/s. For all of the tested relative cable-wind angles in wet conditions, a reduction in the drag coefficient with increasing Reynolds number, accompanied by a near-zero lift coefficient, was observed. A theoretical evaluation of the aerodynamic damping assuming quasi-steady conditions reveals that changes in drag and lift coefficient are nonetheless not sufficient to generate negative aerodynamic damping. Analysis of the fluctuating lift component shows the presence of "enhanced" vortex shedding at specific wind velocities – similar to what might be observed in the presence of a tripping wire.

KEYWORDS: inclined bridge cable, yawed flow, drag, lift, rain, enhanced vortex shedding

1 INTRODUCTION

Rain-wind-induced vibrations (RWIVs) constitute 95% of all large amplitude vibrations of inclined bridge cables [1]. Vibrations may reach peak-to-peak amplitudes of 10 times the cable diameter, leading to serviceability issues and concerns over a much-decreased bending fatigue life for the cables. From both full scale and wind tunnel observations, it has been found that the vibrations occur mainly for cables declining in the wind direction, characterized by relative cable-wind angles Φ in the range of 60°-73°, under low to moderate rain intensities, in a restricted range of wind velocities of U = 5-18 m/s, and cable structural frequencies f = 0.6-3.3 Hz [2]. Physical parameters such as cable size and shape, surface roughness and wettability also affect the vibration mechanism [3]. Although the phenomenon is well known, the mechanisms that lead to this form of vibration are not thoroughly understood. Characterised by relatively low frequencies and large amplitudes of oscillation, RWIVs are generally not assumed to be a form of vortex-induced oscillation. Nevertheless, Matsumoto et al. [4] explained that wet bridge cables can undergo three types of unstable response, i.e. a "galloping type" which includes both divergent type galloping and velocity-restricted galloping, a "vortex shedding type" with a long period and a hybrid type. The galloping type response has been explained in terms of the negative slope in the lift coefficient with wind angle-of-attack, due to the formation of the upper water rivulet and/or the axial flow. Cosentino et al. [5] attributed RWIVs to the oscillation of the upper water rivulet on the vibrating cable model. They explained that during the cable's vibration cycle, the rivulet thickness, and the angular distance between the water rivulet and the stagnation line, changes as function of the cable's acceleration. When the rivulet reaches the farthest position from the flow stagnation line, it has gained its maximum thickness and the shear layer separating from the rivulet reattaches behind it, resulting in a single bubble on the cylinder surface. On the

other hand, when the upper rivulet is at the position nearest to the leading stagnation point, the rivulet thickness is minimum, and the shear layer separating from the rivulet does not reattach on the cylinder surface, leading to a flow pattern similar to that around a clean cylinder at a subcritical Reynolds number. Both explanations are inadequate though. For the stable formation of a balanced rain rivulet in the first case, cable wind angles-of-attack must remain in a very narrow range, thus eliminating the possibility for large changes in wind angle-of-attack. In the second case, the mechanism requires the relatively large oscillation of the cable, forfeiting any explanation of how the oscillation is initiated.

As RWIVs tend to occur for wind velocities that are generally lower than the maximum velocity used for the structural design of the cables and the bridge, the determination of the force coefficients of bridge cables in wet conditions has commonly been neglected. Nevertheless, these may vary significantly from those of dry cables. Furthermore, they may prove useful in the evaluation of the significance of the aforementioned additional effects in the mechanisms leading to RWIVs.

In the current work, the static forces and force coefficients of yawed full-scale bridge cable section models are determined from wind-tunnel tests, in both dry and wet surface conditions. From these tests, it is found that the measured forces on a wet cable differ from those of a dry cable. In particular, the drag coefficient is noticeably reduced, whilst the lift coefficient is near zero throughout the tested Re range – making the static cable model incapable of predicting negative aerodynamic damping. Furthermore, the fluctuating lift components are analysed and it is found that cable Strouhal numbers increase in wet conditions. Based on the measured drag and lift coefficients, as well as the observed Strouhal number, it is conjectured that the running water rivulets plays a similar role on the flow structure around the cable as a stationary tripping wire at a critical angular position from the flow stagnation line. Finally, the rain rivulet seems to generate a form of enhanced vortex shedding, which may contribute in some way to the initiation of the RWIV vibrations.

2 WIND TUNNEL TESTS

2.1 *Test setup*

Static wind tunnel tests were performed at the closed-circuit DTU/Force Climatic Wind Tunnel in Lyngby, Denmark. The wind tunnel features a test section of L×W×H =5m×2m×2m. Technical specifications of the wind tunnel are reported by Georgakis et al. [6]. The model (see Fig. 1) is a section of a prototype HDPE tube, with a nominal outer diameter of 160 mm, placed on an inner aluminium tube for increased stiffness. The measured roughness average of the cable model is R_a~1.8 μm. Aerodynamic forces at both cable ends were measured using 6-DOF force transducers, covered by HDPE dummy pieces of the same cable. For the tests performed in dry surface conditions, two configurations were tested, namely with and without end plates. When tested with end plates, the model was provided with circular end plates of diameter equal to 5 times the cable diameter, placed at a distance of approximately 90 mm from the walls, in order to minimize end effects. Wet tests were performed using the same model as in the dry state, but without end plates. At the upper end of the cable model, just above the measuring portion, two small diameter tubes were attached and connected to a water source placed outside the wind tunnel test chamber. In this way, a formed upper and lower water rivulet was simulated and allowed for a uniform rivulet along the full length of the cable model. Fig. 2 shows the test set-up in wet conditions. All tests were undertaken in smooth flow, i.e. for an along-wind turbulence intensity of I_u=0.5%, and for selected relative cable-wind angles Φ, defined as:

$$\Phi = \arctan\left(\frac{\sqrt{\tan^2\theta + \sin^2\beta}}{\cos\beta}\right) \qquad (1)$$

where θ is the vertical inclination and β is the horizontal yaw. In dry conditions, Φ=90º, 60º, and 55º were tested. In wet conditions, only Φ=60º and Φ=55º were investigated, as flow normal to the cable in wet conditions does not allow for the formation of a rain rivulet outside the wake. In dry conditions, the full wind tunnel velocity range up to 31 m/s was investigated. In wet conditions, the velocity range was restricted to the velocities at which rain rivulets could be formed, i.e. 8-18 m/s.

Figure 1. Full-scale, yawed cable model (dry tests).

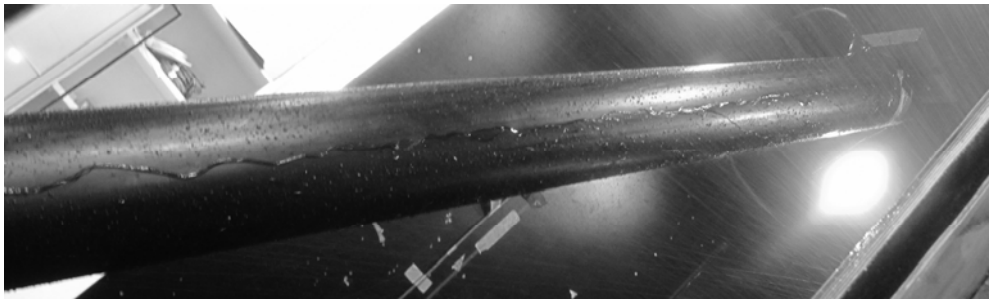

Figure 2. Full-scale yawed cable model (wet tests).

3 RESULTS

3.1 *Dry state*

The drag and lift coefficient components of dry inclined cables for the two selected relative cable-wind angles (Φ=60º and Φ=55º), together with cross-flow coefficients, are presented in Fig. 3. In cross flow, the blockage ratio was 8%, thus leading to the need for a drag coefficient correction following the Maskell III Method [7]. For the yawed cable tests, the wind tunnel blockage was lower than 2% and therefore no correction was needed.

The cable's aerodynamic damping is determined according to the general expression derived by Macdonald and Larose [8] for small (1-DOF) vibrations of a cylinder in a given plane. For

across-flow vibration (α=90°) and along-flow vibration (α=0°) the aerodynamic damping reduces to equations (2) and (3) respectively:

$$\xi_a = \frac{\mu \mathrm{Re}}{4m\omega_n} \frac{1}{\sin\phi}(C_D + \frac{\partial C_L}{\partial \alpha}) \qquad (2)$$

$$\xi_a = \frac{\mu \mathrm{Re}}{4m\omega_n}(2C_D \sin\phi + \frac{\partial C_D}{\partial \mathrm{Re}} \mathrm{Re} \sin\phi + \frac{\partial C_D}{\partial \phi}\cos\phi) \qquad (3)$$

where C_D, C_L are the cable's drag and lift coefficients, respectively, α is the wind angle-of-attack, Φ is the relative cable-wind angle, μ is the dynamic viscosity, m is the cable's mass and ω_n is the cable's circular frequency.

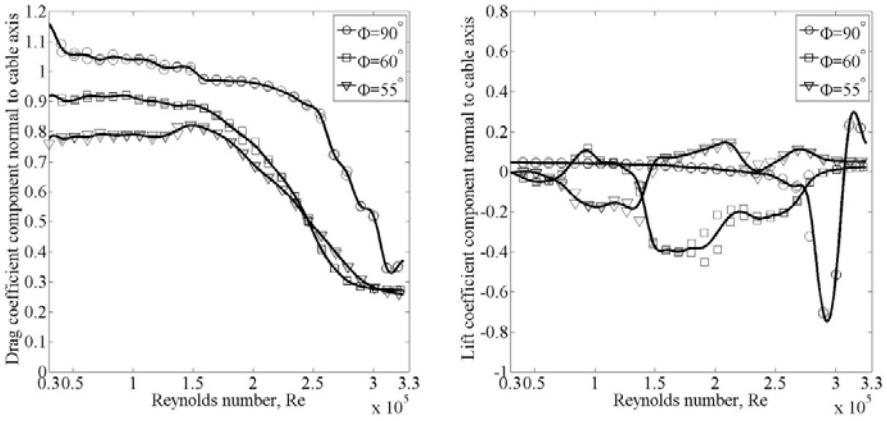

Figure 3. Drag and lift coefficient components for full-scale yawed cable model in dry conditions with end plates.

The across-flow (left) and along-flow (right) aerodynamic damping, normalized by the factor ($\mu/(4m\omega_n)$) and based on the drag and lift coefficient components in Fig. 3, are shown in Fig. 4. By neglecting the variation of the lift coefficient with angle-of-attack, the predicted across-flow aerodynamic damping is positive through the tested range of Reynolds number for all tested geometries. Similarly, neglecting the variation of the drag coefficient component with relative cable wind angle, leads to negative aerodynamic damping for Re=2.55×10^5-3.18×10^5 (Φ=90º), Re=2.27×10^5-2.83×10^5 (Φ=60º), Re=2.35×10^5-3.01×10^5 (Φ=55º).

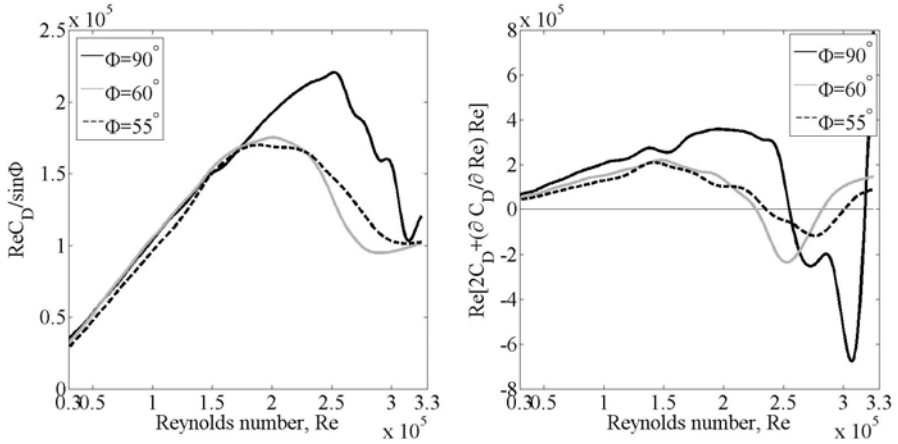

Figure 4. Across-flow and along-flow normalized aerodynamic damping for yawed cable model (dry conditions).

In Fig. 5, the drag and lift coefficient components for yawed cable models in dry conditions and in the absence of end plates are presented, for relative cable wind angles of Φ=90°, 60º and 55°. For all tested relative cable-wind angles, Φ, the drag and lift coefficient components are significantly changed in the absence of end plates. It is believed that varied three dimensional flow conditions must thus be responsible for the change in the aerodynamic behavior of the cable models, particularly when yawed. From Fig. 5 it is in fact observed that for flow normal to the cable axis, i.e. Φ=90º, the drag coefficient decreases through the full tested range of Reynolds numbers. For the yawed cases, the drag coefficient component normal to cable is continuously decreasing for Reynolds numbers higher than Re=1.61×10^5 (Φ=60º) and Re=1.06×10^5 (Φ=55º).

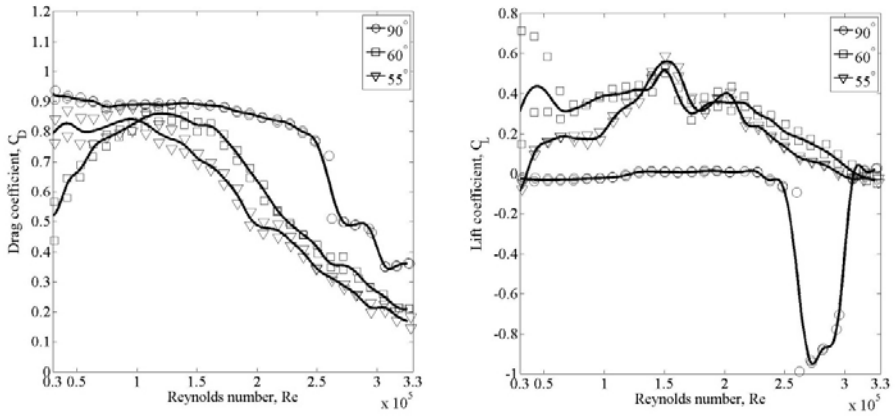

Figure 5. Drag and lift coefficient components for yawed cable model (dry conditions, no end plates).

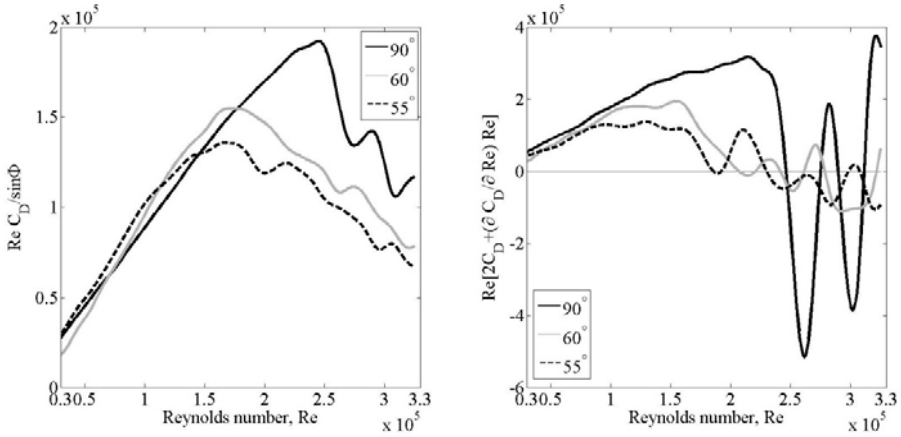

Figure 6. Across-flow and along-flow normalized aerodynamic damping for yawed cable model (dry conditions, no end plates).

Fig.6 is similar to Fig. 4, except that the results are for the dry tests with no end plates. Due to discontinuities in the slope of the drag coefficient components in the critical Re range, a change in the sign of the normalized aerodynamic damping is experienced. Negative aerodynamic damping is predicted for Re=2.46×10^5-2.75×10^5 and Re=2.90×10^5-3.11×10^5 (Φ=90º), Re=2.06×10^5-2.21×10^5 and Re=2.41×10^5-2.61×10^5 (Φ=60º), Re=1.86×10^5-1.92×10^5 and Re=2.30×10^5-2.98×10^5 (Φ=60º).

3.2 *Wet state*

In wet conditions, upper and lower water rivulets form when the wind velocity reaches the value of U=8 m/s (Re=0.80×10^5). This can be understood as the velocity at which there is a balance between the gravitational and the aerodynamic forces acting on the rivulet. At this stage the rivulets follow a slightly sinusoidal trajectory along the cable length. As the wind velocity is increased, the rivulets trajectory changes to a straight line. When the wind velocity overcomes the value of U=18 m/s (Re=1.8×10^5) the rivulets are disrupted, as all water is blown off of the cable.

Due to the presence of the water rivulets, the total force measured on the cable section at any time is comprised of an aerodynamic component and a gravitational component, as a result of the added weight of the water on the cable surface. The latter contribution was estimated based on the visually observed width and thickness of the upper and lower water rivulets along the cable length, which were equal to approximately 20 mm by 2 mm. This is in agreement with previous accounts, where the water rivulet base carpet width and hump height were estimated, depending on the rain intensity, to be in the range of 8-38 mm and 0.5-2mm, respectively, [9]. Thus, by assuming as observed that the weight of the water rivulets remains constant throughout the range of wind velocities - from their formation up to their disruption - the total added weight of water is 1 N/m. The drag and lift force components normal to the cable for relative cable-wind angle Φ=60° are presented in Fig. 7.

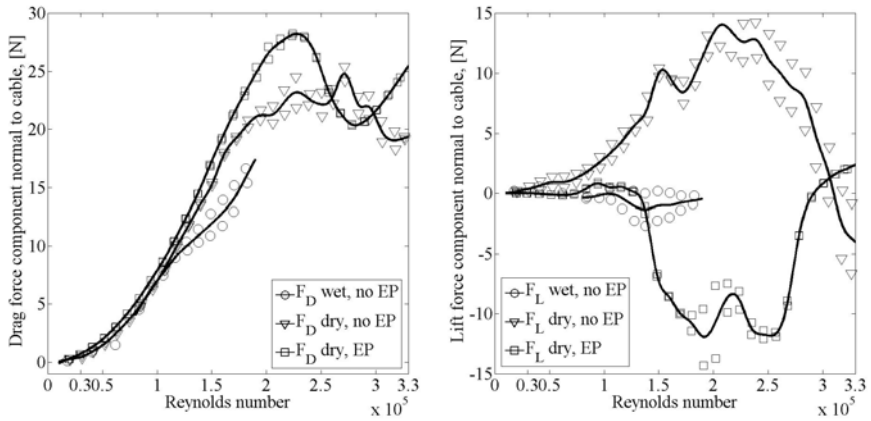

Figure 7. Drag (left) and lift (right) force component normal to cable (Φ=60º). EP refers to 'end plates'

For the dry tests with varying end conditions, it can be observed that the drag force components normal to cable generally follow each other in the subcritical Re range. Major deviations are observed though for Reynolds numbers higher than Re~1.6×10^5, i.e. in the critical Reynolds number range. In wet conditions, the drag force component normal to cable is generally equal to or lower than the respective force component in dry conditions, whilst the lift force component is near zero.

The drag and lift forces normal to the cable for relative cable-wind angle Φ=55° are reported in Fig. 8. Note that in wet conditions, for both Φ=60° and 55°, the total and purely aerodynamic force components do not differ significantly from each other, as the contribution of the projection of the added gravitation water weight along the two force components is lower than 0.52 N/m. Moreover, for Φ=55°, the angle between the gravitational force and the lift force component is 90°, thus making the total and the lift force components equal. The aerodynamic force components in wet conditions have been converted into aerodynamic force coefficients and presented in Figs. 9-10. In these figures, the drag and lift coefficient components normal to the cable axis obtained in wet surface conditions (with end plates) are compared with the respective force

components in dry surface conditions (with and without end plates) for the two yawed cable models.

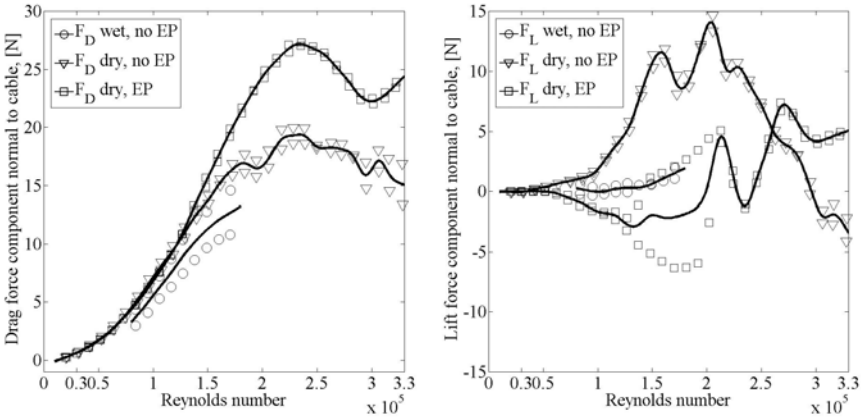

Figure 8. Drag (left) and lift (right) force component normal to cable (Φ=55º). EP refers to 'end plates'.

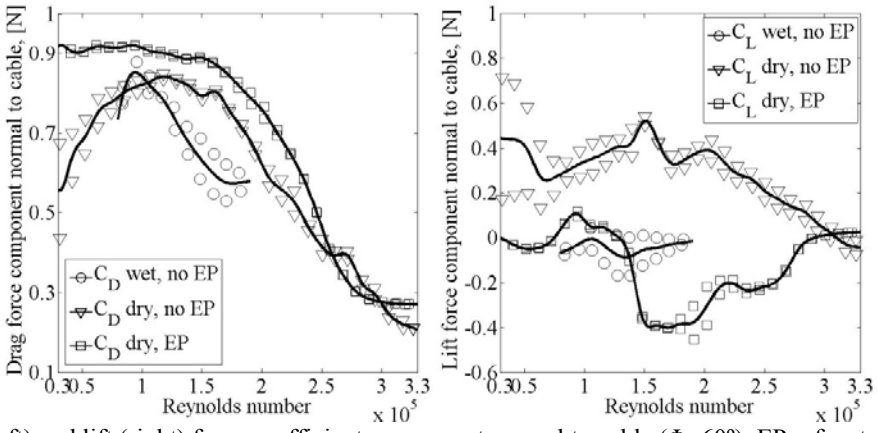

Figure 9. Drag (left) and lift (right) force coefficient component normal to cable (Φ=60º). EP refers to 'end plates'.

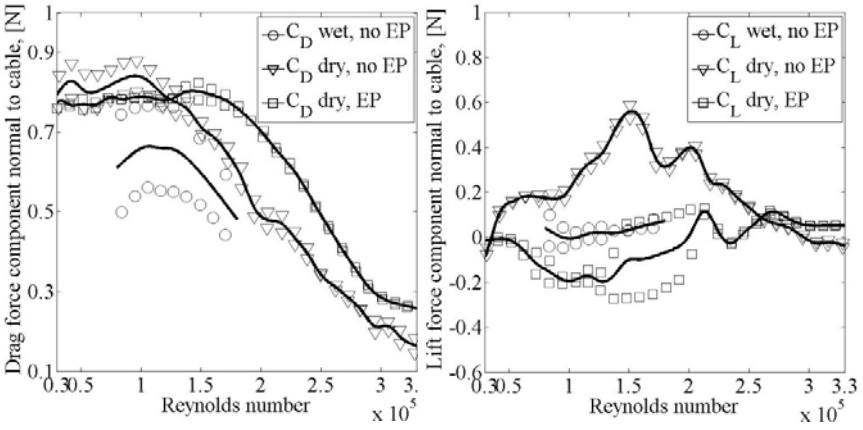

Figure 10. Drag (left) and lift (right) force coefficient component normal to cable (Φ=55º). EP refers to 'end plates'

In Figs. 11 and 12, the along-wind and across-wind normalized aerodynamic damping obtained in wet conditions (with end plates) and dry conditions (with and without end plates) for the two yawed cable models, is shown. For the case of Φ=60°, the across-wind and along-wind aerodynamic damping follows the same tendency as for the dry state, but it exhibits lower values. For

the case of Φ=55°, even if positive, the aerodynamic damping in wet conditions doesn't follow the same tendency as for the other tested cases in dry conditions.

It is apparent that the presence of water rivulets on a static yawed cable leads to a change in the flow structure around the cable (and thus in the drag and lift coefficient components), but it is not sufficient in itself to predict negative aerodynamic damping.

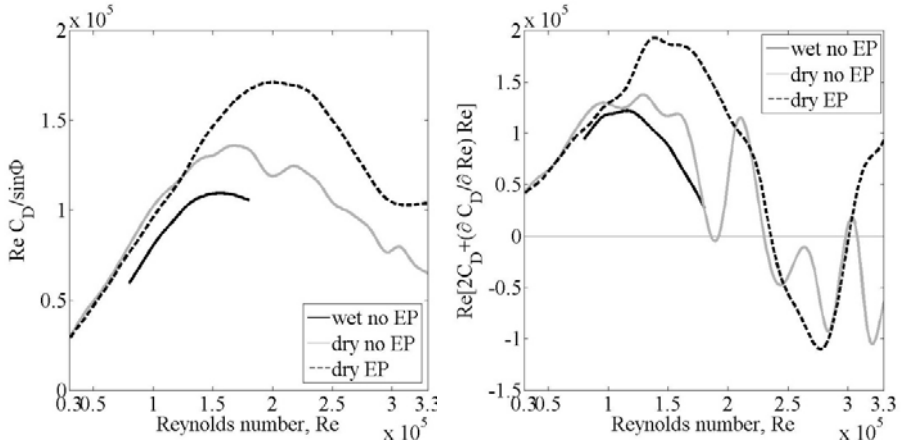

Figure 11. Across-wind (left) and along-wind (right) normalized aerodynamic damping for yawed cable model (Φ=60°). EP refers to 'end plates'

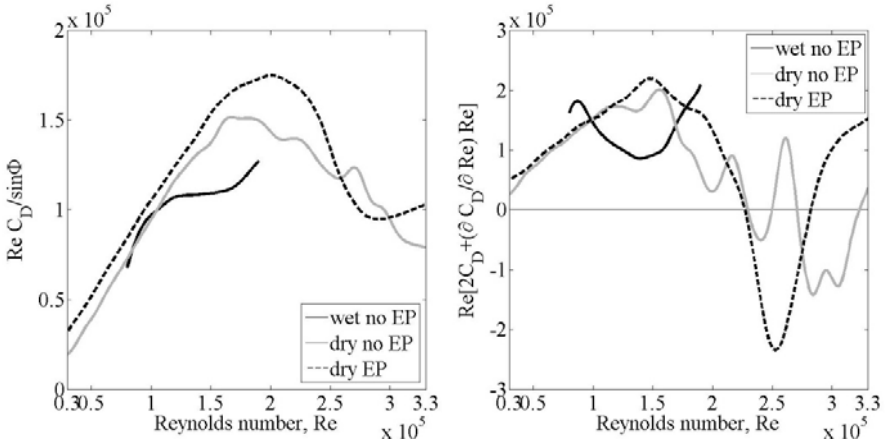

Figure 12. Across-wind (left) and along-wind (right) normalized aerodynamic damping for yawed cable model (Φ=55°). EP refers to 'end plates'

3.3 *Vortex shedding*

The RMS (Root Mean Square) values of the lift component normal to the cable (i.e. fluctuating lift) for varying Re values are reported in Fig. 13. For Φ=60° it is observed that in dry conditions the fluctuating lift coefficient exhibits an increase for Re~1.0-3.0×10^5, in both the presence and absence of end plates. In wet conditions, the fluctuating lift component peaks at between Re=1.3-1.4×10^5, whilst for Φ=60°, the fluctuating lift is considerably higher than in dry conditions, represented a form of enhanced vortex shedding. The same phenomenon, i.e. increase of the fluctuating lift for wet cylinders in comparison to the dry state, has been previously reported for the range of Reynolds numbers where the upper water rivulet reaches a critical angular position from

the flow stagnation line, but albeit for much lower Re numbers that examined here [10]. The increased RMS of the fluctuating lift for Φ=60° also qualitatively resembles the increased RMS response observed in certain cases when a cylinder is fitted with a flow tripping wire [11]. As it is unclear what initiates the RWIV, it is conjectured that the observed enhanced vortex shedding may trigger a response in higher cable harmonics or sub-harmonics. The driving mechanism may then migrate from vortex shedding to an aeroelastic mechanism.

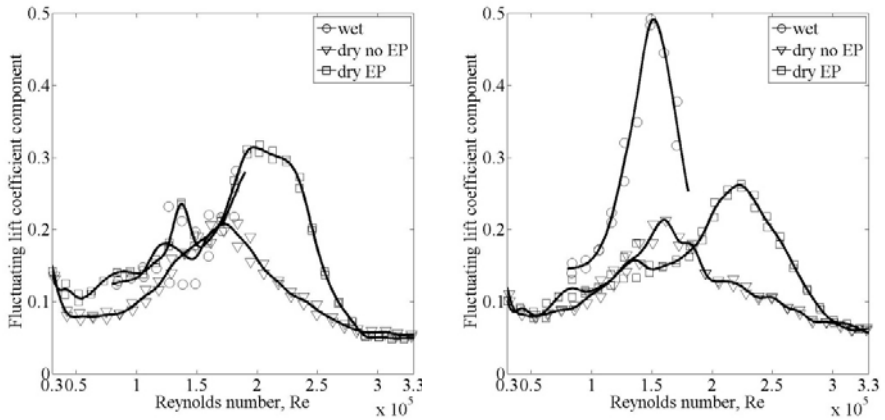

Figure 13. RMS fluctuating lift coefficient component normal to cable for Φ=60° (left) and Φ=55° (right).

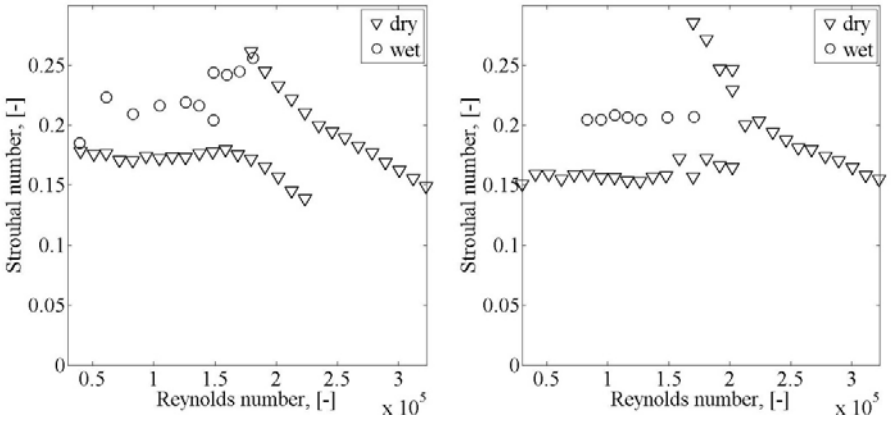

Figure 14. Strouhal number versus Reynolds number, Φ=60° (left) and Φ=55° (right), dry and wet conditions.

The Strouhal number versus Reynolds number is plotted for all of the tests in Figure 14. A linear trend is observed between the Strouhal frequency and Reynolds number in the PSD (power spectral density) of the lift coefficient component normal to cable for Φ=60° and Φ=55° in dry conditions, which disappears for Re~1.6×10^5 for both Φ=60° and Φ=55°. Additionally, in dry conditions and in the critical Reynolds number range, the lift's PSD exhibits local peaks at two separate Strouhal frequencies. In wet conditions, the same linearity is evident only for the test case Φ=55° throughout the full tested Re range. Moreover, in dry conditions, for both Φ=60° and Φ=55°, and for Reynolds numbers marking the start of the critical range (i.e. Re~1.6×10^5), local peaks in the PSD are observed for frequencies near zero. These may be associated with the occurrence of an alternating single separation bubble on one side of the cylinder, as reported by Nikitas et al. [12]. Finally, for both Φ=60° and Φ=55°, the Strouhal numbers measured in wet conditions are higher than in dry conditions and between 0.2 and 0.25. Again, this might be ex-

pected of a stationary cylinder with tripping wire fitted at a critical angular position from the stagnation line [11], [13].

4 CONCLUSION

Static forces and force coefficients of yawed full-scale bridge cable section models are determined from wind-tunnel tests, in both dry and wet surface conditions. In dry conditions, tests are performed for wind velocities between 2 and 31 m/s, while in wet conditions they are performed for wind velocities between 8 and 18 m/s. For the tested relative cable-wind angles, it is found that the drag coefficient of cables in wet conditions is reduced compared to a dry cable and the lift coefficient is near zero throughout the tested Re range. The changes in the aerodynamic coefficients in the range of Reynolds numbers in which the water rivulet can form cannot predict the generation of negative aerodynamic damping. Moreover, in wet conditions, the cable's Strouhal numbers are increased when compared to a dry cable. Based on the trend on the drag and lift coefficient, as well as of the Strouhal number, it is suggested that the running water rivulets plays a similar role on the flow structure around the cable as a stationary tripping wire fitted on the cable's surface. Finally, it is conjectured that an observed enhanced vortex shedding may contribute to the initiation of RWIV.

5 ACKNOWLEDGEMENTS

The authors would like to thank Femern A/S and Storebælt A/S for their financial support without which this work would not have been possible.

6 REFERENCES

1 P. Wagner, J.P. Fuzier, Health monitoring of structures-which solutions. Dissemination of the results of the IMAC European Project. 5th Int. Symposium on Cable Dynamics, Santa Margherita Ligure, 2003, pp. 333-340.
2 N.J. Gimsing, C.T. Georgakis, *Cable Supported Bridges, Concept and Design*, 3rd Edition, Wiley, 2012
3 O. Flamand, Rain-wind induced vibration of cables. J. Wind Eng. Ind. Aerodyn., 57 (1995) 353-362.
4 M. Matsumoto, T. Saitoh, M. Kitazawa, H. Shirato, T. Nishizaki, Response characteristics of rain-wind induced vibration of stay-cables of cable-stayed bridges. J. Wind Eng. Ind. Aerodyn. 57 (1995) 323-333.
5 N. Cosentino, O. Flamand, C. Ceccoli, Rain-wind induced vibration of inclined stay cables. Part I: Experimental investigation and physical interpretation. J. Wind and Structures, 6, (2003), 471-484.
6 C.T. Georgakis, H.H. Koss and F. Ricciardelli, Design specifications for a novel climatic wind tunnel for testing of structural cables, Proc. 8th Int. Symposium on Cable Dynamics, Paris, 2009, pp. 333-340.
7 K. Cooper, E. Mercker, J. Wiedemann, Improved blockage corrections for bluff bodies in closed and open wind tunnels., 10th International Conference Wind Engineering, Copenhagen, 1627-1634.
8 J.H.G. Macdonald, G.L. Larose, A unified approach to aerodynamic damping and drag/lift instabilities, and its application to dry inclined galloping. J. Wind Eng. Ind. Aerodyn., 22 (2006) 229-252.
9 C. Lemaitre, E. de Langre, P. Hémon, Rainwater rivulets running on a stay cable subjected to wind. European J. of Mechanics B/Fluids, 29 (2010) 251-258.
10 MD. Mahbub Alam, Y. Zhou, Turbulent wake of an inclined cylinder with water running. J. Fluid Mech. 58 (2007) 261-303.
11 F.S. Hover, H. Tved, M.S. Triantafyllou, Vortex-induced vibration of a cylinder with tripping wires. J. Fluid Mech. 448 (2001) 175-195.
12 N. Nikitas, J.H.G. Macdonald, J.B. Jakobsen, T.L. Andersen, Critical Reynolds number and galloping instabilities: experiments on circular cylinders, Experiments in Fluids, 52 (2012) 1295-1306
13 T. Igarashi, Effect of Tripping Wires on the Flow around a Circular Cylinder normal to an Airstream. Bulletin of JSME, 29 (1986) 2917-2924.

Comparison of several innovative bridge cable surface modifications

Kenneth Kleissl, Christos T. Georgakis

Department of Civil Engineering, Technical University of Denmark, Kgs. Lyngby, Denmark,
kenk@byg.dtu.dk, cg@byg.dtu.dk

INTRODUCTION

Over the last two decades, several bridge cable manufacturers have introduced surface modifications on the high-density polyethylene (HDPE) sheathing that is installed for the protection of inner cable strands or wires. The modifications are based on research undertaken predominantly in Europe and Japan, with two different prevailing systems: HDPE tubing fitted with helical fillets and tubing with pattern-indented surfaces. In the US and Europe, helical fillets dominate, whilst pattern indented surfaces are more common in Asia, particularly for long-span cable-stayed bridges.

Research into the effectiveness of helical fillets and pattern-indented surfaces has shown that, besides their purported ability to suppress rain-wind induced vibrations, they also modestly reduce drag forces at design wind velocities. This is of particular interest to bridge designers, as wind on stay planes of long-span bridges can now produce more than 50% of the overall horizontal load on the bridge (Gimsing and Georgakis, 2012). Recently, the authors presented a comprehensive comparative study of the aerodynamic performance of these existing cable surface modifications (Kleissl and Georgakis, 2011, 2012). The comparison helped to eliminate uncertainties in previous studies, due to the fact that several researchers, in different facilities, with varying wind-tunnel flow characteristics and performance, have developed each separately. During the study, the authors were able to document the performance advantages of each of the modifications, but often not to the levels that have been commonly reported.

Therefore, similarly to Yagi et al. (2011), several new surface modifications are proposed herewith, in an attempt to combine and enhance the performance advantages of each of the existing modifications. Each of the proposed modifications was investigated through wind tunnel testing. The resulting mean static force coefficients were obtained from wind tunnel tests, with the cables positioned normal to the wind, and were used as “gateway” criteria for the subsequent investigation of rain rivulet suppression.

SURFACE MODIFICATIONS

Several variations of the surface modifications tested are shown in Table 1. The code given to each modification is a combination of a letter assignment to a type of modification and a running index number, specifying an increase in the number of add-ons and/or roughness. Therefore, letters A and B relate to the application of discrete sharp-edged cylindrical protrusions or Cylindrical Vortex Generators (CVGs) in various patterned distributions. The smaller CVGs (models A1-A8) have a height of 2 mm (D/80) and a diameter of 8 mm (D/20), whilst the larger ones (models B1-B4) have a diameter of 14 mm (D/11). The CVGs were selected so as to generate a localised increase in streamwise vorticity in the form of a pair of counter-rotating vortices. Trough flow mixing, these enhance the near-wall streamwise momentum and thus delay the point of flow separation. The helical pattern with a 30-

degree pitch was adopted, thus introducing waviness into the separation line along the cable axis and a wavy wake structure, which is known to disturb vortex shedding, whilst increasing base pressure.

As the CVGs were not expected to sufficiently suppress rain rivulets, other modifications with the potential for drag-reduction were developed, primarily with rivulet suppression in mind. This first of these modifications involves elongated channels (models C1-C2). Here, a thermal procedure was employed in the generation of the modification, which resulted in protruding lips on each side of the channels. This was intentionally done, so as to increase the localised streamwise vorticity and introduce a wavy wake structure, whilst forming a barrier for rain rivulets running along the cable.

The next three modifications (models D-F) all involve the application of protruding strakes. The strake cross-section has a triangular shape with concave sides and a height of 6 mm, corresponding to 3.75% of the cable diameter. The concave sides have two intended functions. Firstly, they work as a ramp for rain rivulets, forcing water to leave the surface of the cable. Secondly, the concave sides and the sharp tip lead to stronger directional guidance of the remaining water along the strake. In models D1-D2 the strakes were arranged laterally in a staggered helical pattern with a 30-degree pitch. On model E the strakes were positioned circumferentially all around the cable at 1.25 D spacing along the cable. Model F replicates the typical fillet arrangement on current stay cables with helical fillets, leading to a double helix at a 45-degree pitch angle.

Model G was originally proposed and tested by Yagi et al. (2011) and involves 12 rectangular protrusions (7.5 x 5 mm) that are placed in a helical pattern, so as to hinder the formation of water rivulets, whilst reducing the drag through the disruption of vortex shedding.

Finally and for comparison, the most prevalent cable surfaces were also tested. These include plain, pattern-indented and twin helically filleted.

WIND TUNNEL TESTS

The comparative wind tunnel tests were performed at the $2x2m^2$ cross-section closed-circuit DTU/Force Climatic Wind Tunnel, located at Force Technology, Lyngby, Denmark. The flow conditions were measured with a cobra probe and turbulence intensities of 0.41-0.64% were found for 33/66/100% of the tunnel maximum flow velocity at the quarter point positions, both vertically and horizontally. When examining the yawed cable for rain rivulet suppression, the reported flow conditions are correct for the upwind end of the cable. The surface modified sectional cable models were all based on 160mm diameter original plain full-scale HDPE samples, supplied by bridge cable manufacturers. For the determination of the force coefficients, the models were placed horizontally, resulting in a near 2-D flow normal to the models. The force coefficients were measured with 6-DOF force transducers at each end of the cable. The force transducers were installed in between the cable model and supporting cardan joints fixed to the walls. End plates with a diameter of approximately five cylinder diameters were fitted close to the model ends to eliminate undesirable flow disturbances from the cable ends and cardan joints. Dummy tube pieces were mounted around the force transducers, leaving approximately a 2 mm gap to the cable model and extending beyond the end plates. During the tests, the wind velocity was increased by regular increments of approximately 1 m/s, up to the maximum wind-tunnel velocity of 32 m/s, allowing for supercritical Reynolds numbers to be reached for all test models. With an effective model length of 1.53 m, the aspect ratio was 9.6:1. The blockage ratios for all section models are 8% and the drag coefficients have been corrected with the Maskell III method, according to Cooper et al. (1999). The force coefficients are found according to $C_i=2F_i/\rho U^2DL$ where, F_d and F_l are the drag and lift forces, respectively. ρ is the air density, D is model diameter, L the model length and U the upstream undisturbed wind velocity.

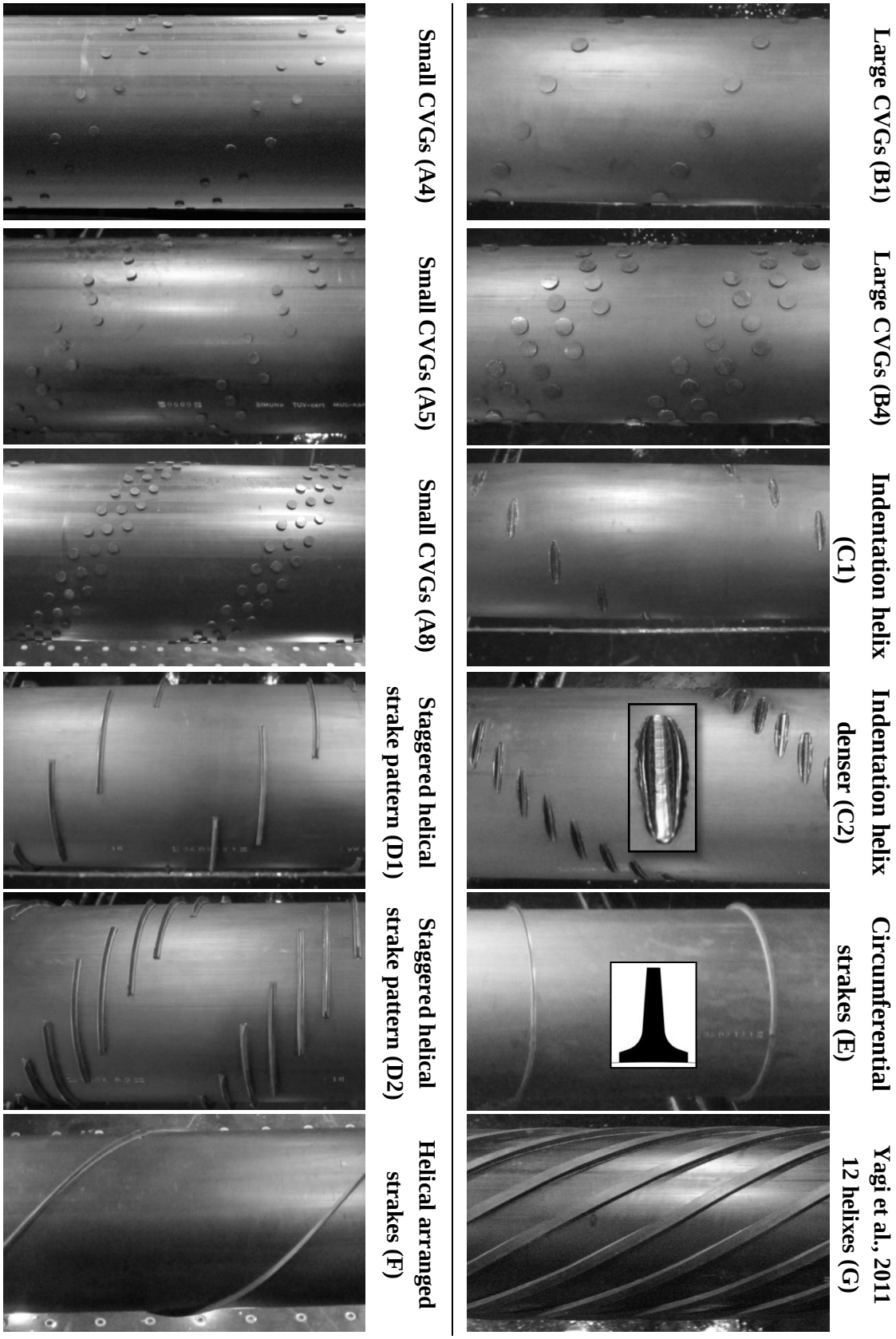

Table 1: Illustration of the different types of surface modifications tested.

RESULTS AND DISCUSSION

FORCE COEFFICIENTS

The average drag and lift coefficients obtained for all the tested models with CVGs applied are shown in Figure 1. For brevity only the results for the modifications shown in Table 1 are presented. Compared with the plain tubing, all of the models with CVGs experienced an earlier flow transition and a tendency for a near-constant drag coefficient in the supercritical region. With the appropriate number of CVGs, the flow transition occurs very gradually and with a minimum of lift force appearing. At the same time some of the tested modifications lead to a rather low supercritical drag coefficient. The best performance is obtained with test model A5, shown in Table 1. This model exhibits a near constant drag coefficient slope, resulting in a lift coefficient smaller than any of the currently applied surfaces. Throughout the tested supercritical Reynolds number range the drag coefficient remained below 0.59.

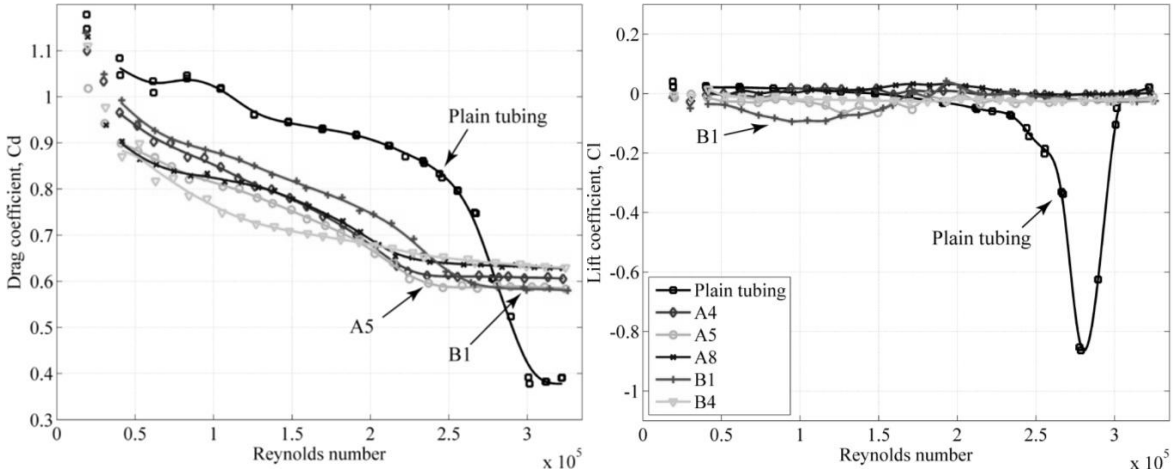

Figure 1. Drag (left) and lift (right) coefficients for the test models with CVG's.

The corresponding drag and lift coefficients for the remaining surface modified cable models, including the currently applied cables, are shown in Figure 2. Among these, model D2 and F appear successful in generating a gradual flow transition and sustaining near-zero lift coefficients. The drag optimised staggered strake arrangement of model D2 reaches a supercritical drag coefficient of 0.65, which is very similar to that of the pattern-indented cable surface. While the drag performance of the helical strake arrangement of model F is very similar to that of the currently applied cable with helical fillets. The reproduced cable surface with 12 rectangular helixes (G) proposed by in Yagi et al. (2011) resulted in a much larger drag coefficient than previously reported and was thus not further considered.

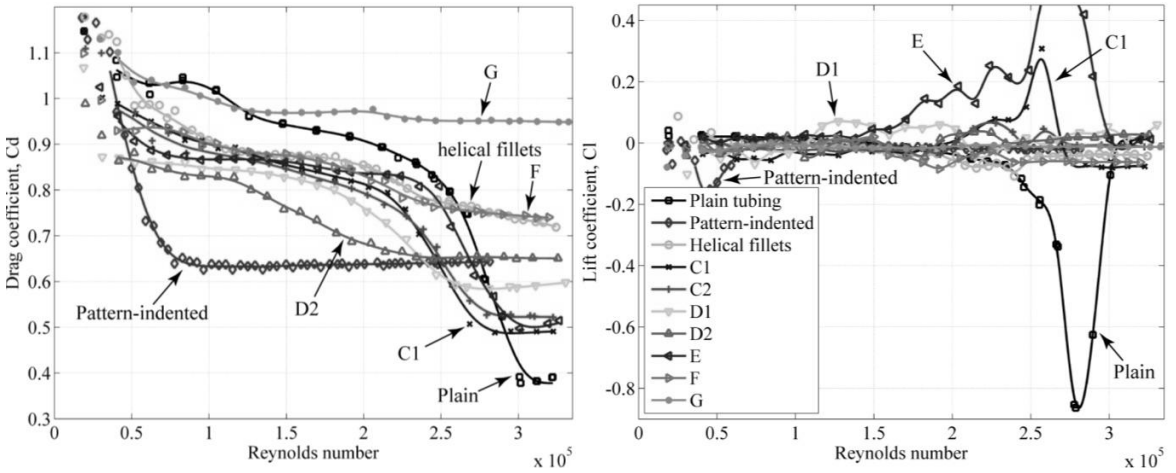

Figure 2. Drag (left) and lift (right) coefficients for the test models with indentations and strakes, compared with the currently applied cables having plain, pattern-indented, and helical fillets.

LIFT FORCE FLUCTUATIONS

A comparison of the fluctuating lift force between models was also made. With the test rig employed, only the total RMS lift fluctuations could be estimated. These are shown in Figure 3. Several of the tested models appear successful in generating small-scale vorticity, whilst avoiding any significant increase in lift force fluctuations. Among the models with CVGs, the smaller CVGs seem to perform best in this respect, with A5 having the best combination of low drag and lift. Model F exhibited the lowest level of lift fluctuations, whilst model D2 and the traditional helical fillets also performed well. The largest fluctuations were observed with the pattern-indented surface, with the lift experiencing a significant peak around Re~1.76×10^5.

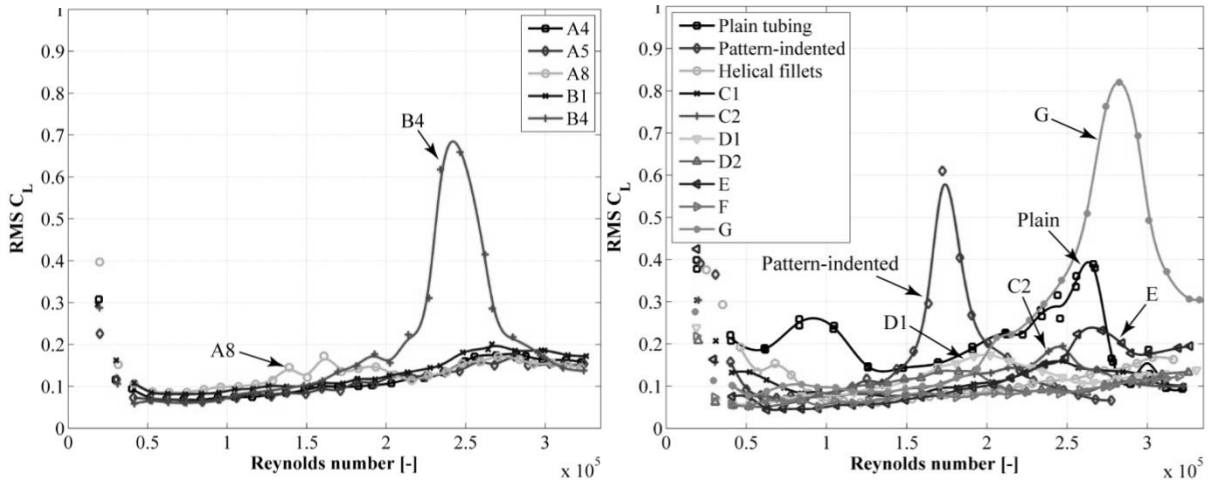

Figure 3. RMS values for the static lift force coefficients. Surface modified models with CVGs (left) and remaining surface modified models including currently applied cables (right).

RIVULET SUPPRESSION

Preliminary static tests on a plain cable showed that a lower rain rivulet formed for all tested wind velocities, while an upper rivulet only formed within the range of approximately 7-15m/s. Outside this range, the upper rivulet did not form as either gravity or the wind loading became dominant. As RWIVs typically occur within this velocity range, the presence of the upper rivulet is often considered critical for the generation of vibrations. The upper rain rivulet on a plain cable can be seen in Figure 4, whilst the lower rivulet is shown in Figure 5. All of the rivulet suppression tests were performed with the cable declining along the wind direction at a cable inclination angle of 40 degrees and with a yaw angle of +/- 22.5 degrees (relative to the along wind direction). In both situations the relative cable-wind angle is 45 degrees. See Kleissl and Georgakis (2012) for definition of angles.

The appearance and position of the rivulets were initially identified during simulation of uniform rain. Afterwards it was confirmed that by adding water only at the upper end of the cable, the same rivulets still formed along the full length of the cable. Based on this, it was decided that the inclined cable should consist of plain tubing at the upper part, where water was added, and then changed into the modified surface, in the central part of the section model, where the rivulets had been fully established. This allowed for a more conservative evaluation of the rivulet suppression ability of the modified cable surfaces.

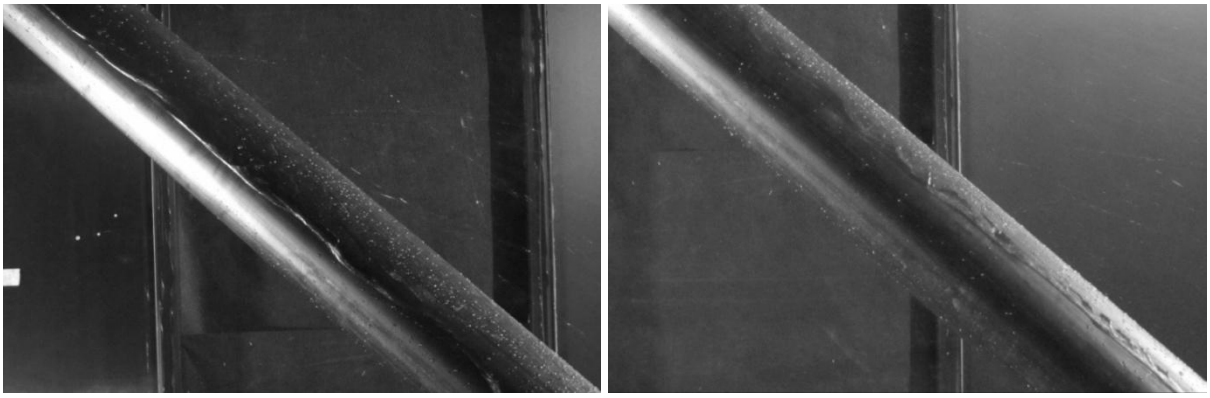

Figure 4. Plain tubing – strong presence of the upper rivulet. 8 m/s (left) and 14 m/s (right).

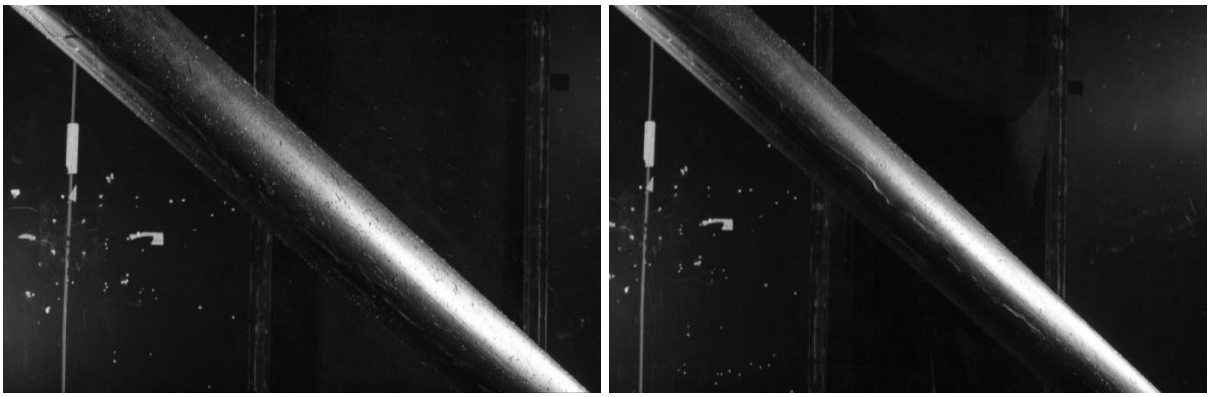

Figure 5. Plain tubing – strong presence of the lower rivulet. 8 m/s (left) and 14 m/s (right).

Figure 6 shows the upper rivulets forming on cable models A8 and B4. Neither of the two CVG sizes was capable of hindering the rivulets. Only minor rivulet disturbances were observed.

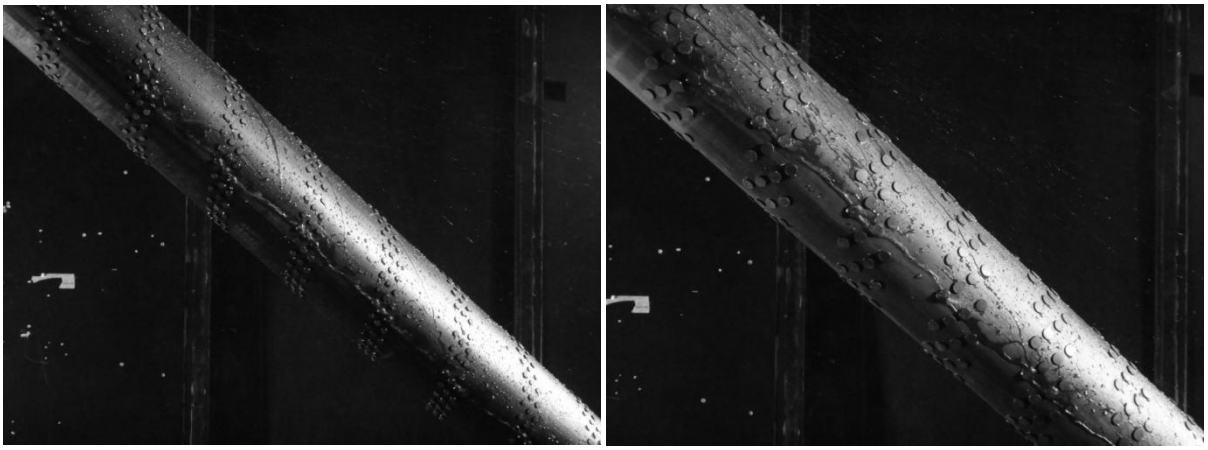

Figure 6. Strong presence of the lower rivulet at 14 m/s. Model A8 with small CVGs (left) and model B4 with larger CVGs (right).

Modified cable models C2 and model E are shown in Figure 7. Whilst neither of them completely suppressed the rivulets, the model with circumferentially arranged strakes (E) only experienced a weak upper rivulet. Although some of the water was knocked off of the surface, the strake arrangement failed to guide the remaining drops away from the point of balance, were the upper rivulet is stable.

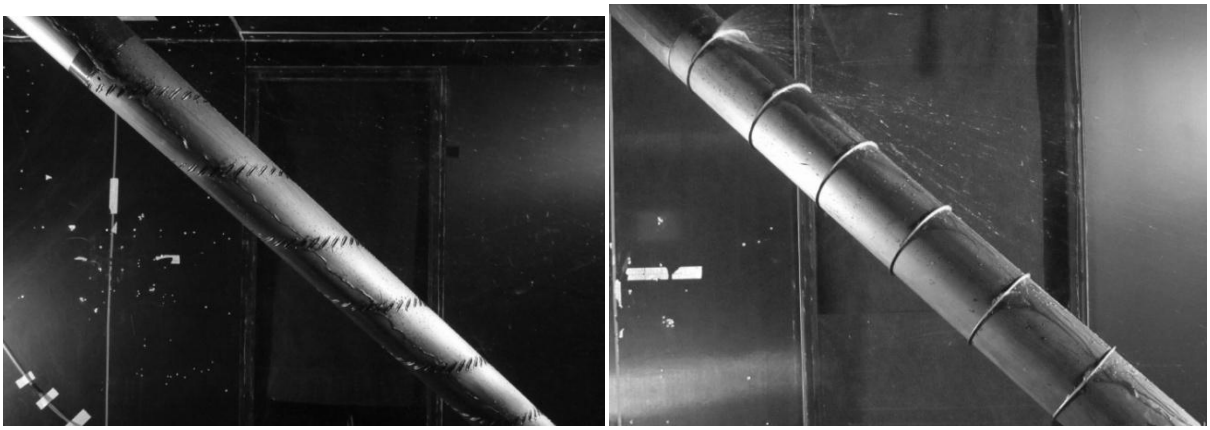

Figure 7. Lower rivulet forming on model C2 at 14 m/s (left) and model E with a weak upper rivulet at 14 m/s (right).

Figures 8-9 show how model D2, with the staggered arrangement of strakes, and model F, with helical strakes, both completely suppress the rivulets. In both cases the strakes work as ramps, which knock off the water rivulet from the surface of the cable.

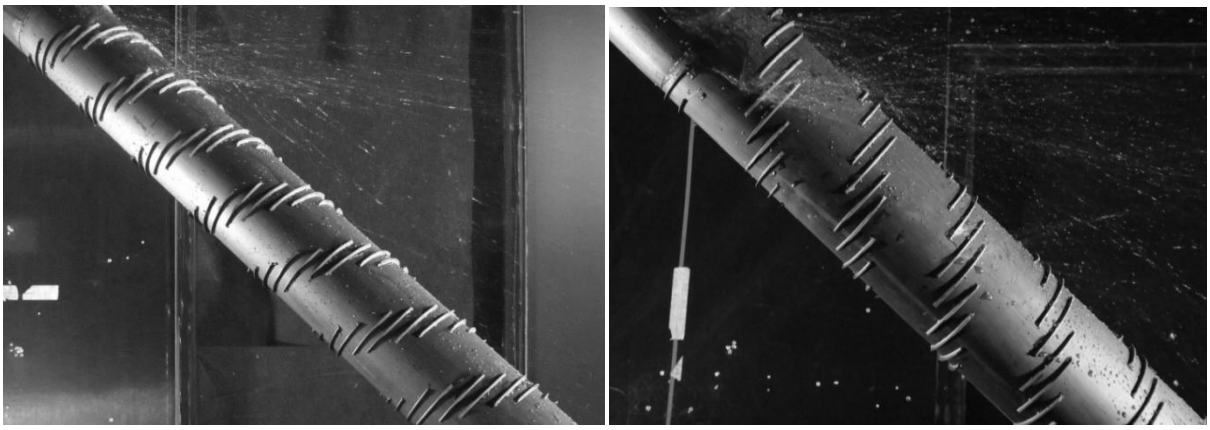

Figure 8. Model D2 completely suppressing the rivulets at all tested angles. Upper rivulet at 14 m/s (left) and lower rivulet at 14 m/s (right).

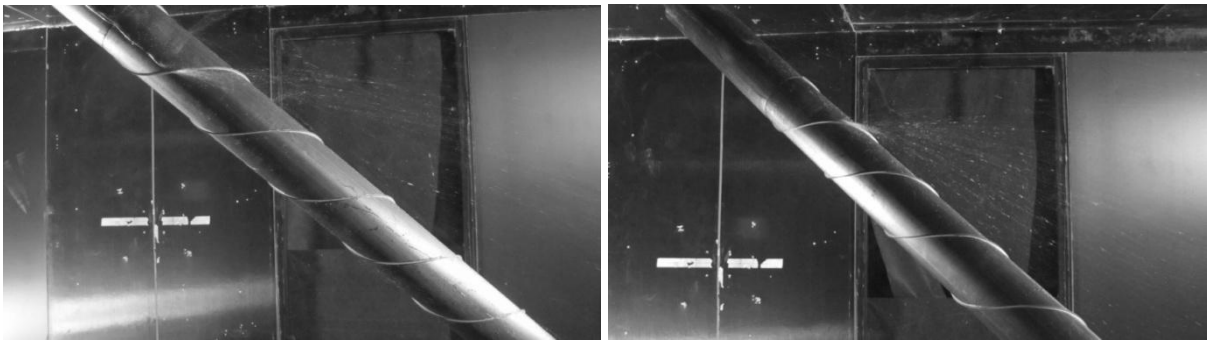

Figure 9. Model F with helical strakes completely suppressing the rivulets. Lower rivulet at 14 m/s (left) and upper rivulet at 14 m/s (right).

The cable with the currently applied helical fillets was found to be partly effective. Figure 10 shows how both a lower and upper rivulet could form despite the fillets' presence.

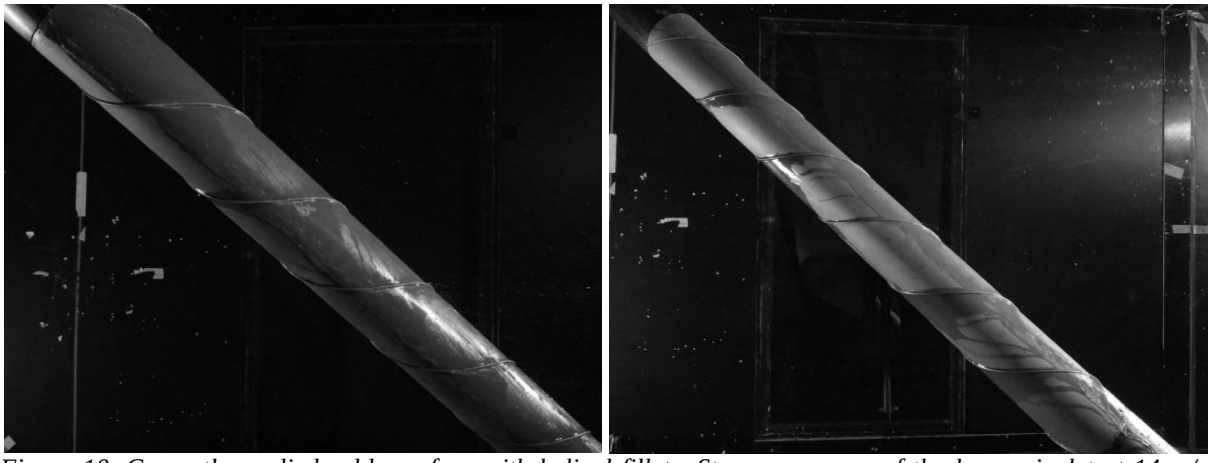

Figure 10. Currently applied cable surface with helical fillets. Strong presence of the lower rivulet at 14 m/s (left) and the upper rivulet at 14 m/s (right).

BRIEF CONCLUSION

Several novel and one previously proposed cable surface modification have been wind tunnel tested for the determination of aerodynamic force coefficients and rain rivulet suppression. Two of the proposed surface modifications outperform or match the current cables with helical fillets, both in drag reduction and rivulet suppression, whilst most of the other proposed modifications were unable to do both. While one of these newly proposed surfaces have similar drag coefficient to that of the current helically filleted cables, the other outperforms it and reaches a drag coefficient of only 0.65; at a level similar to that of the pattern-indented surface.

ACKNOWLEDGEMENTS

The authors would like to thank Femern A/S and Storebælt A/S for their financial support, without which this work would not have been made possible.

REFERENCES

Cooper, K., Mercke, E., Wiedemann, J., 1999. Improved blockage corrections for bluff-bodies in closed and open wind tunnels. Proc. of the 10th International Conference Wind Engineering, Copenhagen.

Gimsing, N.J., Georgakis, C.T., 2012. *Cable Supported Bridges, Concept and Design*, 3rd Edition, John Wiley & Sons

Kleissl, K., Georgakis, C., 2011. Comparison of the aerodynamics of bridge cables with helical fillets and a pattern-indented surface in normal flow. Proc. of the 13th International Conference on Wind Engineering, Amsterdam.

Kleissl, K. & Georgakis, C., 2012. Comparison of the aerodynamics of bridge cables with helical fillets and a pattern-indented surface. Journal of Wind Engineering and Industrial Aerodynamics, 104 - 106, 166 - 175.

Yagi, T., Okamoto, K., Sakaki, I., Koroyasu, H., Liang, Z., Narita, S. & Shirato, H., 2011. Modification of surface configurations of stay cables for drag force reduction and aerodynamic stabilization. Proc. of the 13th International Conference on Wind Engineering, Amsterdam, The Netherlands.

The Seventh International Colloquium on Bluff Body Aerodynamics and Applications (BBAA7)
Shanghai, China; September 2-6, 2012

Dynamic wind actions on catwalk structures

Soon-Duck Kwon[a], Hankyu Lee[b], Seungho Lee[a], Jonghwa Kim[b]

[a]*KOCED Wind Tunnel Center, Department of Civil Engineering*
Chonbuk National University, Chonju, Chonbuk, Korea
[b]*DM Engineering Co., 66-2, Bangi, Songpa, Seoul, Korea*

ABSTRACT: Wind tunnel tests and buffeting analyses were conducted to investigate wind induced responses of a catwalk structure of a suspension bridge. It was found from the wind tunnel tests that the Reynolds number effects on the aerostatic coefficients were negligible for the catwalk floor systems. Design formulae were proposed to estimate the aerostatic coefficients of catwalks with various solidity ratio and angle of attack. The buffeting analysis results revealed that tying the catwalk on an erecting main cable may be an effective structural countermeasure to reduce the lateral displacements of the catwalk.

KEYWORDS: Catwalk; Suspension bridge; Wind force; Wind tunnel test; Reynolds number.

1 INTRODUCTION

1.1 *Catwalk system*

Catwalk structures are temporary walkways that allow the erection of main cables in suspension bridges. As shown in Figs. 1 and 2, catwalk structures consist of a few ropes, wooden beams, wooden steps, and porous wire meshes at the bottom and sides. The ropes support a worker's weight, equipment for cable erection, and some wires forming main cable. The other components of catwalk are used for pedestrian comfort and safety. A pair of catwalk structures is generally installed along the main cables and linked at regular intervals by cross bridges.

Figure 1. Catwalk structure of Kwangyang Bridge.

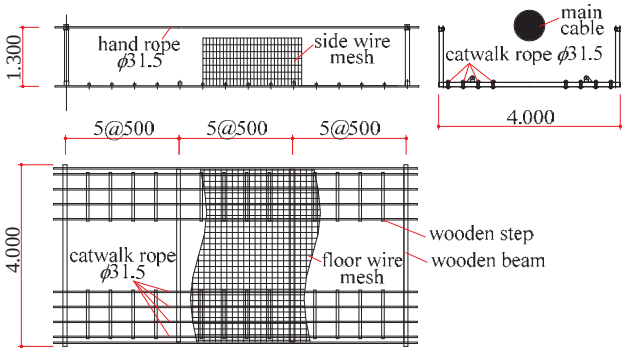

Figure 2. Details of the catwalk system.

The target model used in the present study was a catwalk structure derived from a design alternative of the Kwangyang Bridge, which has a main span length of 1,430 m (Fig. 1). The data used in this paper are not the actual properties of the Kwangyang Bridge catwalk but those of an alternative submitted to a design competition by DM Engineering Company.

As shown in Fig. 2, the width and height of the single side catwalk were 4.0 m and 1.3 m, re-

spectively. Each catwalk consists of 10 ropes with a diameter of 31.5 mm and a safety apparatus consisting of wire mesh, a wooden step, and a hand post. The solidity ratios of the side and bottom were 7% and 16%, respectively.

1.2 *Previous research and research objective*

The effects of wind on catwalk systems have not been well defined although many suspension bridges have recently been completed or are under construction worldwide (Tanaka 1998). Kawaguchi and Fukunaga (1995), Takeno et al. (1997), and Kitagawa (2004) suggested an erection plan for the catwalk structure in the Akashi Bridge. They assessed possible technical problems arising from the erection of the main cable such as the hauling system, erection sequence, static deformation, aerodynamic stability, arrangement of cross bridges, and vibration control measures. Matsuzaki et al. (1990) introduced the fabrication and erection of the prefabricated parallel wire strand used for most of the Honshu-Shikoku Bridges in Japan.

Shinichi et al. (1997) provided information for the design and construction of the catwalks for the Kurushima Bridges. They tested the effectiveness of stay ropes and guy ropes to mitigate vibrations of the catwalk using a 1/10 scaled structural model. Recently, Zheng et al. (2007) performed wind tunnel tests for the catwalks of the Runyang Bridges. Although they measured aerostatic force coefficients for various angles of attack and yaw angles, their tests were limited to a specific catwalk and did not provide general information for the aerodynamic forces acting on catwalk structures.

As a countermeasure to mitigate the lateral vibration of catwalks, additional storm ropes have been used to stabilize catwalk structures, which are sensitive to wind action due to their flexibility. The use of storm ropes, however, is associated with some disadvantages such as a protracted construction period, inconvenient navigation, and anchorage problems (Akiyama et al. 1999). Recently, additional guy ropes parallel to catwalk ropes or horizontal ropes connecting each catwalk have been adopted to reduce the horizontal vibrations caused by wind as well as by catwalk use (Hojo et al. 1995).

As summarized above, limited research has been conducted concerning the aerodynamic characteristics of catwalk structures. In particular, Reynolds number effects of porous catwalk structures have not been investigated. In this study, wind tunnel tests of two different scale models were performed in order to investigate the effects of the Reynolds number, main cable, and solidity ratio. Parameter studies of structural properties of catwalks and countermeasures to vibration were performed to examine the wind induced responses of catwalks by applying buffeting analysis in the time domain. This paper summarizes the technical results obtained from wind tunnel tests and buffeting analyses of catwalks.

2 EXPERIMENTAL SETUP

The parallel catwalks along the bridge axis are assumed to be aerodynamically independent of each other, because the porous catwalks were separated by more than 20 m. Consequently, wind tunnel tests were only conducted for a single catwalk.

Two rigid models with scale of 1/14 and 1/4 were fabricated and tested in wind tunnels to obtain the aerostatic force coefficients of the catwalk floor system. The solidity ratios of the model were varied by replacing porous wire mesh tied at steel frame. In order to investigate the Reynolds number effects, the aerostatic force coefficients of two different scaled models were measured at various wind velocities ranging from 5 to 30 m/s, which correspond to 1/84 to 1/4 of the Reynolds number of the actual catwalk.

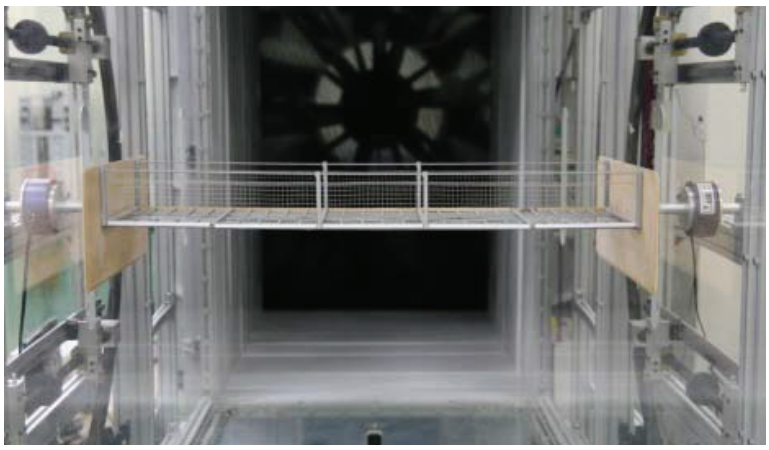

(a) 1/14 scale model in the small wind tunnel

(b) 1/4 scale model in the large wind tunnel

Figure 3. Catwalk models in the wind tunnels.

Fig. 3 shows the catwalk models installed on external force balances in the wind tunnels. The wind tunnel tests were carried out in two wind tunnels at the KOCED Wind Tunnel Center at Chonbuk National University in Korea. The 1/4 scale model tests were performed at the high speed test section of a closed return type wind tunnel. The size of the test section was 5.0 m wide × 2.5 m high × 20 m long, and the maximum wind speed was 31 m/s. The 1/14 scaled model was tested at the small wind tunnel with a test section of 1.0 m wide × 1.5 m high × 5 m long. The turbulent intensities of the large and small wind tunnels are less than 1% and 0.5% respectively.

The aerostatic forces acting on the models were measured using a pair of JR3 force balances that were capable of reading three forces and the associated three moments. The mean wind speed was measured using a pitot tube and a pressure transducer. The angle of attack was varied from -10 degree to +10 degree at 1 degree intervals. The correction for blockage effect was not done because blockage ratio of the models was less than 1%. The forces and moments were transformed into non-dimensional aerostatic coefficients using the following equations.

$$C_D = \frac{D}{\frac{1}{2}\rho V^2 H}, \quad C_L = \frac{L}{\frac{1}{2}\rho V^2 H}, \quad C_M = \frac{M}{\frac{1}{2}\rho V^2 H^2} \tag{1}$$

where, D is the drag force, L is the lift force, M is the pitching moment, V is the free stream wind speed, ρ is the air density and H is the height of the catwalk.

3 EXPERIMENTAL RESUTLS

3.1 *Effects of the Reynolds number*

The Reynolds number effects on the aerostatic coefficients were investigated using the two different scale models under uniform wind flow. The Reynolds numbers of the actual catwalk range from 4.3×10^5 to 2.6×10^6, while those of the scale models ranged from 3.1×10^4 to 6.5×10^5. The height of catwalk models was used for reference length evaluating the Reynolds numbers.

Fig. 4 shows that the Reynolds number effects on the aerostatic force coefficients were not significant for the catwalk floor systems. Lift coefficient and pitching moment coefficient were also found to be independent to the Reynolds number. In summary, the Reynolds number effect on aerostatic force coefficients of the catwalk system is negligible.

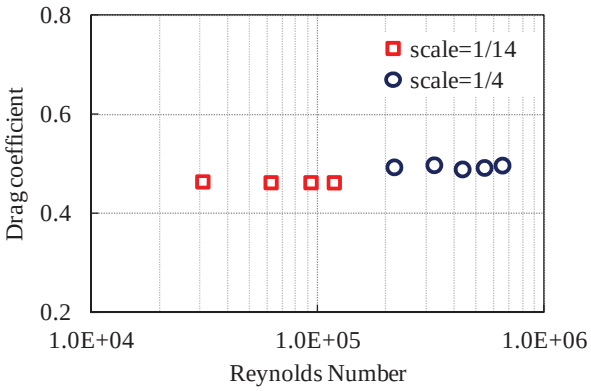

(a) Drag coefficient

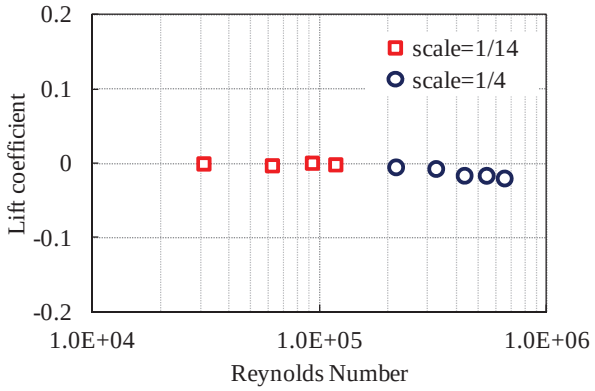

(b) Lift coefficient

Figure 4. Aerostatic force coefficient as a function of Reynolds number.

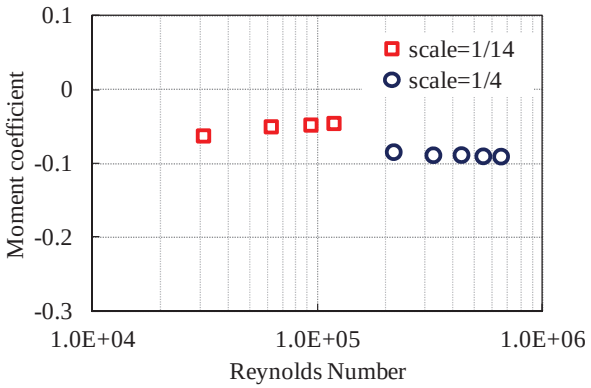

(c) Moment coefficient

Figure 4.

Figure 5. Catwalk with the main cable at its center.

3.2 *Effects of the main cable*

As the main cable erection work nears completion through air spinning, a strand bundle is placed inside of the catwalk, as shown in Fig. 5. Differences in the displacements between the main cable and the catwalk structure can occur under high winds because of discrepancy in stiffness. Consequently, the location of the main cable within the cross section of the catwalk shifts from the center point to the quarter point of the catwalk. These conditions were simulated in the wind tunnel tests, and the effects of the main cable presence on the aerostatic coefficients of the catwalk structure were investigated.

Fig. 6 shows the aerostatic coefficients of the catwalk without and with the main cable at the center point and quarter point. Although the aerostatic coefficients were slightly reduced in the presence of the main cable, the effects of the main cable on the aerostatic coefficients of the catwalk are negligible from a practical point of view.

3.3 *Effects of the solidity ratio*

The solidity ratios of a catwalk vary over a wide range depending on suspension bridges. The bottom solidity is generally higher than the side solidity. In order to investigate the effects of the solidity ratios on the aerostatic coefficients, wind tunnel tests were performed for solidity ratios

of the floor system ranging from 9% to 23.5% at the side and from 16% to 30.5% at the bottom. Most of the catwalk floor systems surveyed in this study was within the above ranges. The solidity ratios of the test model were changed by tying a proper porous wire mesh to frame of model.

The test results are shown in Fig. 6. It is clear from the figures that the side solidity ratio strongly affects the drag and moment coefficients but not the lift coefficient. In addition, the lift coefficient is only influenced slightly by the bottom solidity ratio but the drag and moment coefficients are not. From the above results, it is found that the drag and moment coefficients are a function of side solidity ratios, yet the lift coefficients are a function of bottom solidity ratio.

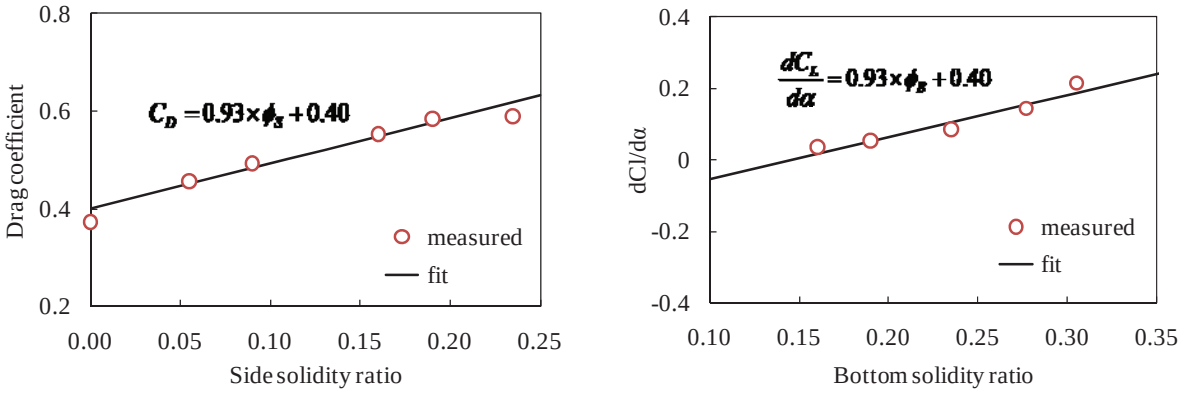

(a) Drag coefficient (b) Lift coefficient slope

Figure 6. Aerostatic Best fit lines of the aerostatic coefficients at attack angle of 0°.

3.4 *Design formulae for aerostatic coefficients*

From the results of wind tunnels tests for various solidity ratios of the catwalk, it is clear that the aerostatic coefficients are affected mostly by the solidity ratio of the floor system. As shown in Fig. 6, the drag coefficient and moment coefficient are almost linearly proportional to the side solidity ratio. Therefore, the following linear fit equations are proposed to estimate the aerostatic coefficients of a catwalk at attack angle of 0 degree as functions of the solidity ratios.

$$C_D = 0.93 \times \phi_S + 0.40 \tag{2a}$$

$$C_M = -0.32 \times \phi_S - 0.06 \tag{2b}$$

$$\frac{dC_L}{d\alpha} = 0.93 \times \phi_B + 0.40 \tag{2c}$$

$$C_L \approx \frac{dC_M}{d\alpha} \approx 0 \tag{2d}$$

where α is angle of attack, ϕ_S is the side solidity ratio, and ϕ_B is the bottom solidity ratio. In addition, the best fit equations for drag coefficients as a function of angle of attack and solidity ratio are given as follows.

$$C_D(\alpha, \phi_S) = 1.674 \times 10^{-3}\alpha^2 + 2.862 \times 10^{-4}\phi_S^2 + 0.470, \quad \phi_B = 16\% \tag{3a}$$

$$C_D(\alpha, \phi_B) = 1.977 \times 10^{-3}\alpha^2 + 1.597 \times 10^{-5}\phi_B^2 + 0.493, \quad \phi_S = 9\% \tag{3b}$$

4 WIND INDUCED RESPONSES

4.1 *Structural modeling and buffeting analysis*

The catwalk structural system was modeled using finite element based structural analysis software developed by DM Engineering Co. Isolated catwalk system neglecting the flexibility of the supporting towers was adopted at the analysis. The catwalk ropes were modeled by an elastic catenary element and cross bridges were modeled by a frame element. A total of 10 ropes at each side of the catwalk were considered to behave coincidently and were modeled as a single equivalent rope. The inertial effects of the wood steps, hand posts, and wire meshes were considered and their stiffness were neglected in the analysis.

To find the unstrained length and initial tension of ropes for the initial equilibrium configuration, present study used the TCUD (target configuration under dead loads) method that was an iterative numerical approach based on the Newton-Raphson method. Detail description of the TCUD method can be found in the reference (Kim and Lee 2001). By using the computed unstrained length and initial tension, the initial nonlinear static analysis was firstly conducted in order to include the influence of self weight on the deformations and internal forces of the catwalk structure, and then the free vibration analysis was done at next. The natural frequencies of the lowest four lateral modes were found to be 0.049 Hz, 0.097 Hz, 0.146 Hz, and 0.195 Hz. The lowest four vertical modes were 0.137 Hz, 0.194 Hz, 0.231 Hz, and 0.275 Hz.

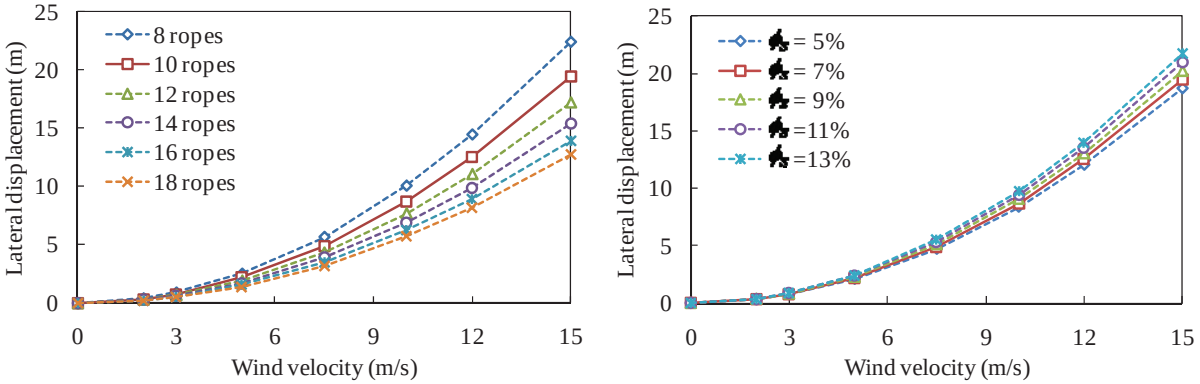

(a) Effect of the number of ropes (b) Effect of the side solidity ratio

Figure 7. Static lateral displacements of the catwalk under wind loads.

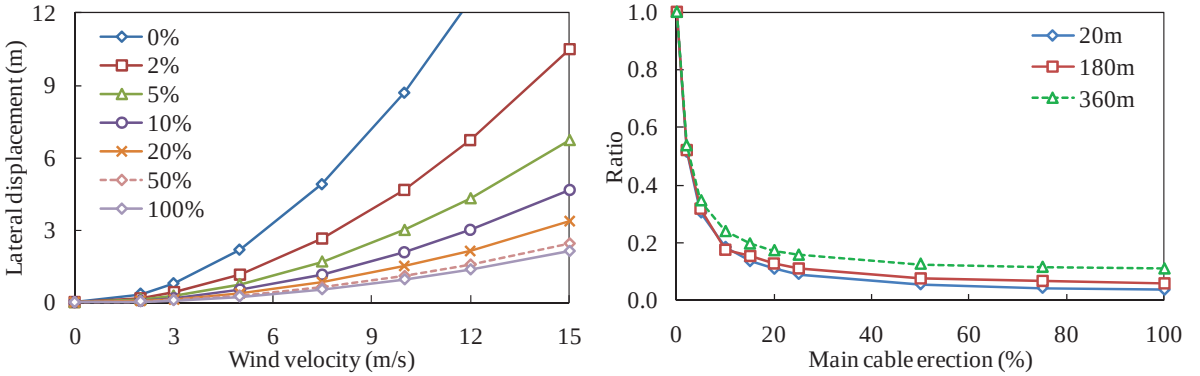

(a) Displacements as a function of the main cable erection ratio (b) Reduction ratio of displacements as a function of the tying interval

Figure 8. Static lateral displacements of the catwalk tied to the erecting main cable.

The horizontal and vertical components of turbulent wind velocities were generated by the ARMA technique considering special correlations along the bridge axis (Cao et al. 2000). Wind velocities were generated every 50 m along the bridge axis. A modal analysis combining the free vibration data and buffeting forces was performed to compute the catwalk displacements under turbulent winds. In the quasi-steady theory, the instantaneous forces acting on the moving catwalk structure are almost identical to the static forces at the same effective attack angle, and the phase lag between wind and moving body velocity is not considered. Aerodynamic damping was evaluated from the forced vibration tests (Kwon and Lee 2009).

4.2 *Static responses*

Fig. 7 shows the static lateral displacements of the catwalk under wind loads. The displacements gradually decrease as the number of ropes increases. However, the cross bridge intervals had a minor effect on the static lateral displacements. Static displacements slightly increased as the side solidity ratio was increased. This is because the drag coefficient increased by only 20% as the side solidity ratios increased from 5% to 13%.

Fig. 8(a) shows the static lateral displacements of the catwalk as a function of main cable erection completion. As the main cable erection was close to completion, the significantly increased stiffness of the main cable contributed to reduce the lateral displacement of the tied catwalk. Fig. 8(b) shows the effect of the tying interval between the catwalk and main cable on the lateral displacement. The lateral displacement can be effectively reduced by tying down the catwalk and main cable, regardless of the tying interval if the stress level of tying material is acceptable.

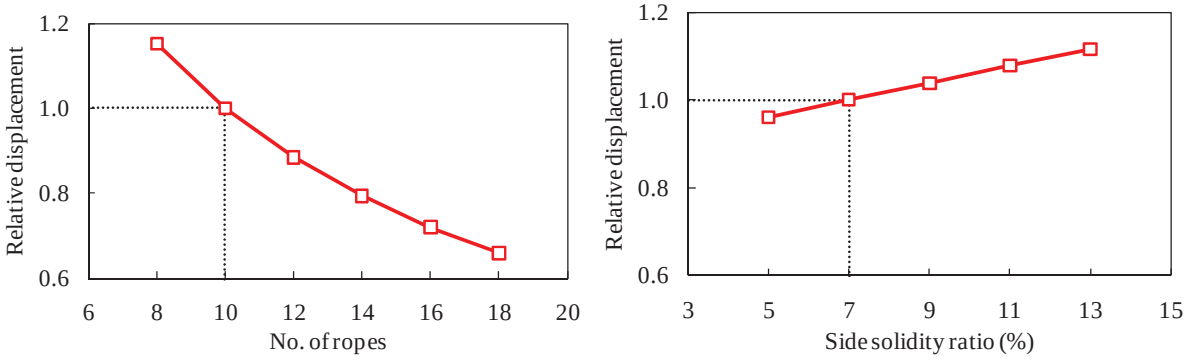

(a) Effect of the number of ropes (b) Effect of the side solidity ratio

Figure 9. Relative dynamic lateral displacements of the catwalk under turbulent winds.

4.3 *Dynamic responses*

Relative dynamic lateral displacements of the catwalk are given in Fig. 9. To allow a relative comparison of each structural type, the lateral displacements of the catwalks were normalized by dividing by the lateral displacement of the generic catwalk shown in Fig. 2. The dynamic displacements were significantly reduced as the number of ropes was increased. The cross bridge slightly contributed to reduce the lateral displacements. However, increasing the number of cross bridges may not be an effective way to reduce the lateral vibrations. The dynamic displacements also slightly increased as the side solidity ratio increased, as in the static evaluation results. In conclusion, the reduction of dynamic displacements can be effectively accomplished by increasing the number of ropes, that is, stiffening. However, the effect of the cross bridge interval on the vibration reduction is not significant.

5 CONCLUSIONS

Wind tunnel tests and buffeting analysis were performed in order to investigate wind induced responses of catwalk structures of a suspension bridge. The main findings of the present study are as follows.

The wind tunnel tests revealed that the Reynolds number effects on the aerostatic coefficients were negligible for the catwalk floor systems. The aerostatic coefficients of the catwalk were found to be consistent for practical purposes, regardless of the presence of the main cable inside the catwalk. Simple design formulae that are functions of the solidity ratios were proposed to estimate the aerostatic coefficients of the catwalk. It was found from the buffeting analysis that static and dynamic lateral displacements of the catwalk significantly decreased as the number of ropes increased. Lateral displacements were effectively reduced by tying down the catwalk and erecting a main cable.

6 ACKNOWLEDGEMENTS

This research was supported by the grant (09CCTI- A052531) from the Ministry of Land, Transport and Maritime of Korean government.

7 REFERENCES

Akiyama, M., et al. (1999). “Erecting technology for suspension bridge cables.” Bridge and Construction Engineering, 49(2), 2-7. (in Japanese).

Cao. Y., Xiang, H., and Zou, Y. (2000). “Simulation of stochastic wind velocity field on long-span bridges.” J. of Engineering Mechanics, 126(1), 1-6.

Hojo, T., Yamazaki, S., and Yamaguchi, H. (1995). “Experimental study on counter- measure for man-induced vibrations of catwalk without storm system.” J. of Structural Engineering, JSCE, 41A, 763-770. (in Japanese).

Kawaguchi, K., and Fukunaga, S. (1995). “Structure of Catwalk on the Akashi Kaikyo Bridge.” Honshi Tech. Report, Honshu-Shikoku Bridge Authority, 19(74) (in Japanese).

Kim, K. S., and Lee, H. S. (2001). “Analysis of target configuration under dead loads for cable-supported bridges.” Computer & Structures, 79, 2681-2692.

Kitagawa, M. (2004). “Technology of the Akashi Kaikyo Bridge.” Structural control and health monitoring, 11, 75–90.

Kwon, S. D., and Lee, S. H. (2009). “A simple apparatus for measuring self-excited wind forces on bridges.” Proceedings of 7th Asia-Pacific Conference on Wind Engineering, Taipei, 679-682.

Matsuzaki, M., Uchikawa, C., and Mitamura, T. (1990). “Advanced fabrication and erection techniques for long suspension bridge cables.” J. of Construction Engineering and Management, 116(1), 112-129.

Shinichi, H., et al. (1997). “Design and Construction of the Catwalks for the Kurushima Bridges.” Bridge and Foundation Engineering, 31(6), 13-19. (in Japanese).

Takeno, M., et al. (1997). “Cable erection technology for world’s longest suspension bridge - Akashi Kaikyo Bridge.” Nippon Steel Technical Report, 73, 59-70.

Tanaka, H. (1998). “Aeroelastic Stability of Suspension Bridges during Erection.” Structural Engineering International, 8(2), 118-123.

Zheng, S., Liao, H., and Li, Y. (2007). “Stability of suspension bridge catwalks under a wind load.” Wind and Structures, 10(4), 367-382.

The Seventh International Colloquium on Bluff Body Aerodynamics and Applications (BBAA7)
Shanghai, China; September 2-6, 2012

Wind tunnel tests for simulating large-amplitude, low-frequency galloping on overhead transmission lines

Hisato Matsumiya [a*], Takashi Nishihara [a]

[a] *Central Research Institute of Electric Power Industry, 1646 Abiko, Abiko-shi, Chiba-ken 270-1194, Japan * E-mail: hisato-m@criepi.denken.or.jp*

ABSTRACT: In order to carry out a complete investigation of the galloping phenomenon of overhead transmission lines under ice and snow accretion, the authors develop a modeling technique that enables physical simulation of the galloping motion of actual transmission lines in a wind tunnel. The test apparatus proposed here is composed of a transmission wire sector model supported in the wire axis direction by multiple elastic cords. This unique support allows the sector model to vibrate with large amplitudes at low frequencies in the vertical, horizontal, and torsional directions. Dynamic equations were derived for the large-amplitude motions of the model, and the frequency characteristics were examined theoretically and numerically. Free vibration tests in a wind tunnel were performed using a sector model of four-bundled conductors with dimensions identical to ACSR 410 mm^2 conductors. Observation of large amplitude galloping at low frequencies in these tests verifies the validity of this experimental technique and indicates that it is possible to fully discuss the galloping oscillation characteristics and unsteady aerodynamic forces during the vibration by using this technique.

KEYWORDS: Galloping, Overhead transmission lines, Sector model, Elastic rope

1 INTRODUCTION

The galloping phenomenon of overhead transmission lines is sometimes observed when they are subject to ice and snow accretion, which causes significant vertical oscillation with horizontal and torsional oscillation at low frequency. A considerable amount of research effort has been focused on this phenomenon [1] through studies such as field observation of full-scale transmission lines to investigate the actual characteristics of ice and snow accretion and analysis of the dynamic response of the lines caused by galloping [2-5]. While galloping of full-scale lines can be observed, it is difficult to identify in detail the conditions that induce galloping, e.g., accreted shape distribution and wind speed distribution. Furthermore, systematic clarification of the occurrence conditions and response characteristics is also difficult, because the structural conditions are difficult to alter and climate conditions in the observation period is limited. Thus, numerical analysis methods have been developed to simulate the dynamic response of lines under various conditions (structural characteristics, accreted shape, angle of attack, wind speed, etc.) [6-8]. Generally, aerodynamic forces are taken into account as quasi-steady forces [9] by using steady-state aerodynamic coefficients obtained from a wind tunnel test [10-12] and numerical fluid analysis [13,14]. However, it has been pointed out that the unsteady aerodynamic forces differ from the quasi-steady aerodynamic forces for large-amplitude motion: there is a significant difference in the aerodynamic moment [15,16]. Therefore, it is necessary to clarify the degree to which the simulation results are affected by this discrepancy.

Free vibration tests in a wind tunnel under definite input conditions offer an effective method for clarifying the occurrence conditions and response characteristics of conductor galloping. Furthermore, the influence of each individual condition can be clearly identified in the experiment, and the validity of the quasi-steady theory can be checked against the wind tunnel tests. Although some researchers have previously conducted free vibration tests in a wind tunnel [17-19], the oscillation amplitude has typically been limited to a comparatively small range because of experimental restrictions.

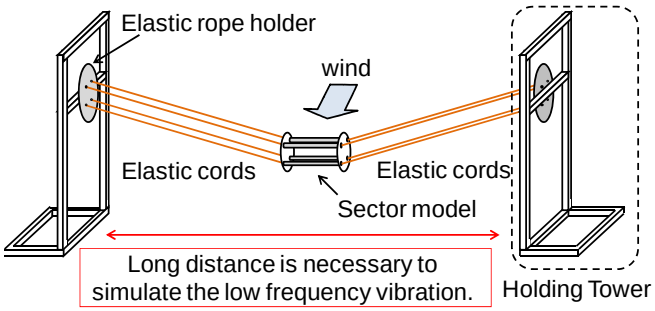

Figure 1 Elastic support technique of the sector model

Accordingly, the authors have developed a modeling technique that allows physical simulation of the galloping motion in actual overhead transmission lines. The sector model in the technique can oscillate in the vertical, horizontal, and torsional directions with large amplitude at low frequency, and the frequency of each motion can be selected arbitrarily and individually. This paper presents the details of this technique and the governing equations of motion of the sector model. The results of free vibration tests in a wind tunnel using this technique verify its applicability.

2 PROPOSED MODEL SUPPORT TECHNIQUE USING ELASTIC CORDS

2.1 *Model support technique*

The experimental technique proposed here is shown in Figure 1. This system is composed of a transmission wire sector model that is supported by multiple elastic cords extending in the direction of the wire axis. The technique described here is characterized via support from "long" elastic cords with "low" rigidity. This unique support method allows the sector model to vibrate with significant amplitude at low frequencies in the vertical, horizontal, and torsional directions. Furthermore, in this experimental system, the elastic cord holder on the holding tower can be rotated to adjust the angle of attack of the sector model.

2.2 *Governing equations of motion*

The equations of motion of the sector model can be derived using Lagrange's equation. The relevant parameters in this experiment are listed here and shown in Figure 2.

m	mass of the sector model [kg]
I	mass moment of inertia of the sector model [kgm^2]
B_r	radius of the elastic cord support on the sector model side [m]
D_r	radius of the elastic cord support on the holding tower side [m]
α_B	inclined angle of the elastic cord support on the sector model side [rad]
α_D	inclined angle of the elastic cord support on the holding tower side [rad]
L	horizontal length of the elastic cords [m]
H	sag (depth) of the sector model from the support point [m]
T	tension in the elastic cords [N]
EA	axial rigidity of the elastic cords [N]

The sector model is supported by eight elastic cords from the right and left sides, i.e., four elastic cords on each side. The distance between each elastic cord is B ($B=\sqrt{2}B_r$) on the sector

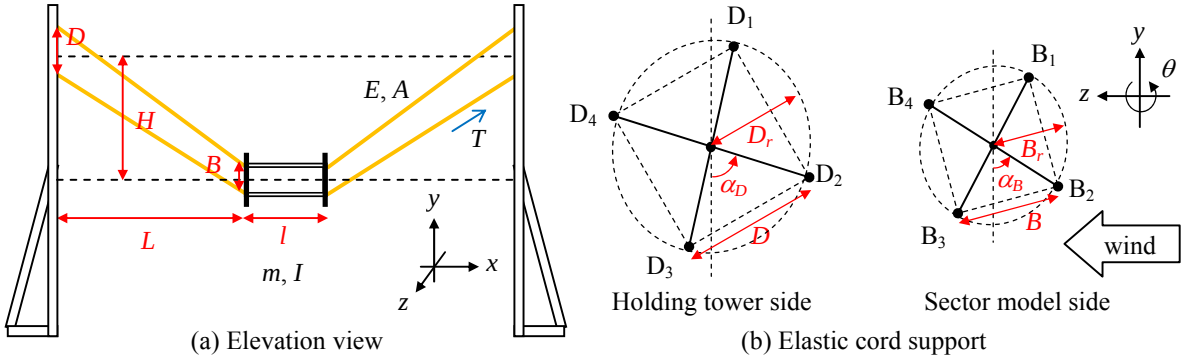

(a) Elevation view (b) Elastic cord support

Figure 2 Definition of each parameter

model side and D ($D=\sqrt{2}D_r$) on the holding tower side. It is assumed that all elastic cords are uniform and are set with same tension, and the weight of the elastic cords is ignored.

As shown in Figure 2 (b), the elastic cord support points on the holding tower side are defined as D_1 to D_4, and those on sector model side are defined as B_1 to B_4. When the sector model is in the stationary condition, the cord lengths $L^*_{i0}(i=1,2,3,4)$ (i.e., the distance from D_i to B_i) are described as follows.

$$L^*_{10}=\left\{L^2+\left(-H+B_r\sin\alpha_B-D_r\sin\alpha_D\right)^2+\left(-B_r\cos\alpha_B+D_r\cos\alpha_D\right)^2\right\}^{1/2} \tag{1}$$

$$L^*_{20}=\left\{L^2+\left(-H-B_r\cos\alpha_B+D_r\cos\alpha_D\right)^2+\left(-B_r\sin\alpha_B+D_r\sin\alpha_D\right)^2\right\}^{1/2} \tag{2}$$

$$L^*_{30}=\left\{L^2+\left(-H-B_r\sin\alpha_B+D_r\sin\alpha_D\right)^2+\left(+B_r\cos\alpha_B-D_r\cos\alpha_D\right)^2\right\}^{1/2} \tag{3}$$

$$L^*_{40}=\left\{L^2+\left(-H+B_r\cos\alpha_B-D_r\cos\alpha_D\right)^2+\left(+B_r\sin\alpha_B-D_r\sin\alpha_D\right)^2\right\}^{1/2}. \tag{4}$$

When the axial rigidity of the elastic cords is constant regardless of the rate of elongation, the initial lengths are

$$L_{i0}=\frac{EA}{T+EA}L^*_{i0}. \tag{5}$$

The vertical, horizontal, and torsional displacements from the stationary position during vibration of the sector model are y, z, and θ, respectively, and thus the lengths "L^*_i" at this time are described as follows:

$$L_1=\left\{L^2+\left(-H+y+B_r\sin(\alpha_B+\theta)-D_r\sin\alpha_D\right)^2+\left(z-B_r\cos(\alpha_B+\theta)+D_r\cos\alpha_D\right)^2\right\}^{1/2} \tag{6}$$

$$L_2=\left\{L^2+\left(-H+y-B_r\cos(\alpha_B+\theta)+D_r\cos\alpha_D\right)^2+\left(z-B_r\sin(\alpha_B+\theta)+D_r\sin\alpha_D\right)^2\right\}^{1/2} \tag{7}$$

$$L_3=\left\{L^2+\left(-H+y-B_r\sin(\alpha_B+\theta)+D_r\sin\alpha_D\right)^2+\left(z+B_r\cos(\alpha_B+\theta)-D_r\cos\alpha_D\right)^2\right\}^{1/2} \tag{8}$$

$$L_4=\left\{L^2+\left(-H+y+B_r\cos(\alpha_B+\theta)-D_r\cos\alpha_D\right)^2+\left(z+B_r\sin(\alpha_B+\theta)-D_r\sin\alpha_D\right)^2\right\}^{1/2}. \tag{9}$$

These lengths can then be used to derive the equations of motion. Lagrange's equation without a damping term is given by

$$\frac{d}{dt}\left(\frac{\partial T_v}{\partial\dot{q}}\right)-\frac{\partial T_v}{\partial q}+\frac{\partial(U_k+U_g)}{\partial q}=0. \tag{10}$$

Here, T_v is the kinetic energy of the sector model, U_k is the gravitational potential energy of the sector model, U_k is the elastic potential energy of the cords, and q is the displacement (y, z, and θ). Each energy term is described as follows:

$$T_v=\frac{1}{2}m(\dot{y}^2+\dot{z}^2)+\frac{1}{2}I\dot{\theta}^2,\ U_k=2\sum_{i=1}^{4}\frac{1}{2}\frac{EA}{L_0}\left\{L_i-L_0\right\}^2,\ U_g=mgy. \tag{11}$$

Here, g is gravitational acceleration. By substituting these equations into Equation (10), the differential equations for the vertical, horizontal, and torsional motion are

$$
\begin{aligned}
&m\ddot{y} + 2EA\{-H + y + B_r \sin(\alpha_B + \theta) - D_r \sin\alpha_D\}\left(L_{10}^{-1} - L_1^{-1}\right) \\
&\quad + 2EA\{-H + y - B_r \cos(\alpha_B + \theta) + D_r \cos\alpha_D\}\left(L_{20}^{-1} - L_2^{-1}\right) \\
&\quad + 2EA\{-H + y - B_r \sin(\alpha_B + \theta) + D_r \sin\alpha_D\}\left(L_{30}^{-1} - L_3^{-1}\right) \\
&\quad + 2EA\{-H + y + B_r \cos(\alpha_B + \theta) - D_r \cos\alpha_D\}\left(L_{40}^{-1} - L_4^{-1}\right) + mg = 0,
\end{aligned} \tag{12}
$$

$$
\begin{aligned}
&m\ddot{z} + 2EA\{z - B_r \cos(\alpha_B + \theta) + D_r \cos\alpha_D\}\left(L_{10}^{-1} - L_1^{-1}\right) \\
&\quad + 2EA\{z - B_r \sin(\alpha_B + \theta) + D_r \sin\alpha_D\}\left(L_{20}^{-1} - L_2^{-1}\right) \\
&\quad + 2EA\{z + B_r \cos(\alpha_B + \theta) - D_r \cos\alpha_D\}\left(L_{30}^{-1} - L_3^{-1}\right) \\
&\quad + 2EA\{z + B_r \sin(\alpha_B + \theta) - D_r \sin\alpha_D\}\left(L_{40}^{-1} - L_4^{-1}\right) = 0,
\end{aligned} \tag{13}
$$

$$
\begin{aligned}
&I\ddot{\theta} + 2EAB_r\{+(-H + y)\cos(\alpha_B + \theta) + z\sin(\alpha_B + \theta) + D_r \sin(\alpha_B - \alpha_D + \theta)\}\left(L_{10}^{-1} - L_1^{-1}\right) \\
&\quad + 2EAB_r\{+(-H + y)\sin(\alpha_B + \theta) - z\cos(\alpha_B + \theta) + D_r \sin(\alpha_B - \alpha_D + \theta)\}\left(L_{20}^{-1} - L_2^{-1}\right) \\
&\quad + 2EAB_r\{-(-H + y)\cos(\alpha_B + \theta) - z\sin(\alpha_B + \theta) + D_r \sin(\alpha_B - \alpha_D + \theta)\}\left(L_{30}^{-1} - L_3^{-1}\right) \\
&\quad + 2EAB_r\{-(-H + y)\sin(\alpha_B + \theta) + z\cos(\alpha_B + \theta) + D_r \sin(\alpha_B - \alpha_D + \theta)\}\left(L_{40}^{-1} - L_4^{-1}\right) = 0.
\end{aligned} \tag{14}
$$

2.3 *Adjustment technique of each frequency*

If $B_r = D_r$, $\alpha_B = \alpha_D$, and the motion is assumed to be infinitesimal, the frequencies are given by

$$
f_z = \frac{1}{2\pi}\sqrt{\frac{g}{H}},\ f_y = \frac{1}{2\pi}\sqrt{\frac{g}{H}}\sqrt{1 + \frac{EAH^2}{TL_g^2}},\ f_\theta = \frac{1}{2\pi}\sqrt{\frac{g}{H}}\frac{B_r}{R}\sqrt{1 + \frac{EAH^2}{2TL_g^2}}\ . \tag{15}
$$

Here, f_z, f_y, and f_θ are the frequencies of the horizontal, vertical, and torsional motion, respectively, L_g is the cord length ($=\sqrt{L^2 + H^2}$), and R is the radius of gyration of the sector model around the x axis ($=\sqrt{I/m}$). Then, the tension in the elastic cords T is

$$
T = \frac{mg}{8}\frac{L_0^*}{H}. \tag{16}
$$

The relationship between the frequencies and the parameters in Equations (15) and (16) show that each frequency, f_z, f_y, and f_θ, can be arbitrarily chosen by calibrating T, EA, and B_r, respectively. This adjustment technique is also applicable when $B_r \neq D_r$, $\alpha_B \neq \alpha_D$, and the motion is large. In that case, the torsional frequency can be adjusted through the choice of B_r or D_r. However, when $B_r \neq D_r$, the torsional motion is coupled structurally to the horizontal motion.

3 FREE VIBRATION TESTS IN A WIND TUNNEL

To verify the applicability of this experimental technique, free vibration tests in a wind tunnel were performed using a sector model of four-bundled conductors. The test conditions and free vibration test results are presented in this section.

3.1 *Test conditions*

3.1.1 *Wind tunnel facilities*

The tests were performed in an Eiffel-type wind tunnel with an axial fan at the Central Research Institute of Electric Power Industry (Figure 3). The outlet area of the wind tunnel is 1.6 m × 2.5 m (width × height), and the maximum wind speed is 17 m/s. The sector model was set up in the center of the wide open test space, 1.0 m in front of the outlet as shown in Figure 4. The variation of the wind speed was ±1.0%, and the turbulence intensity was less than 0.5% in a 1.2 m ×

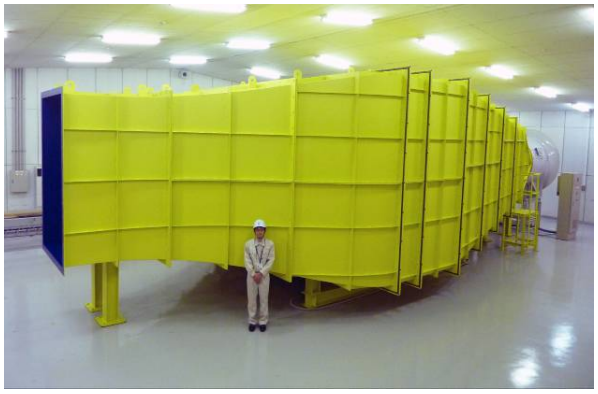

Figure 3 Overall view of wind tunnel

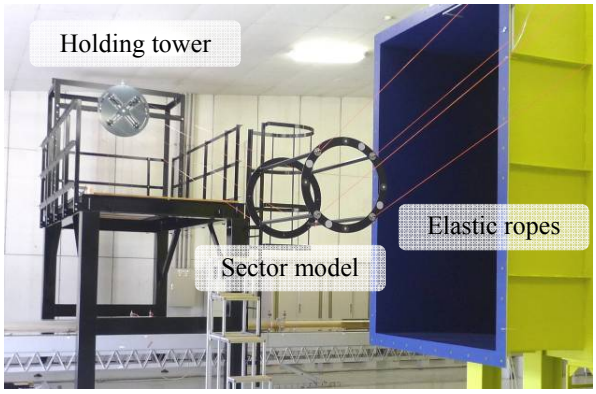

Figure 4 Experiment system

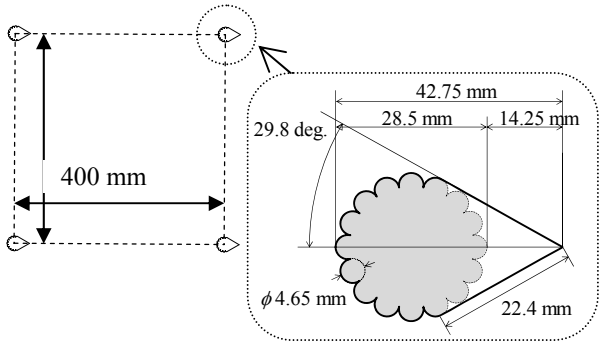

Figure 5 Cross-section of the sector model

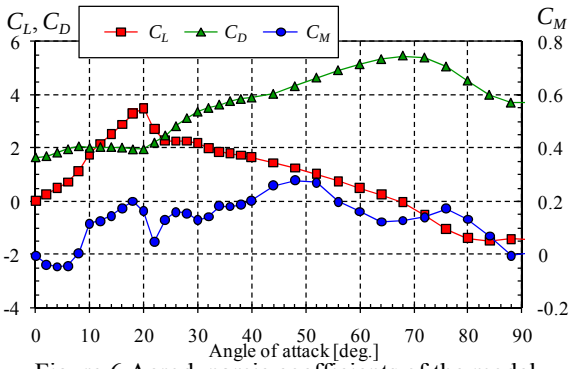

Figure 6 Aerodynamic coefficients of the model

2.0 m (width × height) area 0.5 m downstream of the outlet. The variation of the wind speed was ±1.0% in a 1.0 m × 1.5 m (width × height) area 2.5 m downstream of the outlet.

3.1.2 *Sector model shape and aerodynamic characteristics*

The four-bundled-conductor sector model had imitated snow accretion with a sharp triangular tip, the height of which was half the conductor diameter, as shown in Figure 5. The dimensions and weights of the model are identical to ACSR 410 mm^2 conductors with a span length l of 1.0 m. The angle of attack α was the same as α_B. The end plate was not installed this sector model because aerodynamic instability in the yaw rotation or spanwise directions may occur through the aerodynamic force on the end plate. The effect of the absence of the end plate should be discussed in future work.

The aerodynamic coefficients of the model in a wind speed of 10 m/s are shown in Figure 6 [12], and the aerodynamic coefficients fulfill the conditions of the Den Hartog criterion [10] in that the angle range is 20 to 24 degrees, which is just larger than the stalling angle. The definitions of the aerodynamic coefficients in this study are expressed as follows:

$$D_F = \frac{1}{2}\rho U^2 2D_l l C_D, L_F = \frac{1}{2}\rho U^2 2D_l l C_L, M_F = \frac{1}{2}\rho U^2 2D_l B_l l C_M. \quad (17)$$

Here, ρ and U are the air density [kg/m^3] and wind velocity [m/s], respectively. The mean value of the drag D_F [N], lift L_F [N], and pitching M_F [Nm] moments depend on the coefficients of the drag C_D, lift C_L, and moment C_M, respectively. The diameter of the conductor D_l is 0.0285 m, and the conductor center interval B_l is 0.40 m.

3.1.3 *Experimental set up and test cases*

Each of the eight elastic cords supporting the sector model was a two-bundled urethane rubber rope with a diameter of 3 mm. To discuss the vibration characteristics of a certain structural con-

dition (frequency and damping), free vibration tests should be performed by changing both the angle of attack and wind speed simultaneously. However, in this study, the purpose of the tests is mainly to verify the applicability of this experimental technique, free vibration tests were performed by changing the angle of attack and wind speed individually. In case 1, the angle of attack was set to about 20 degrees to fulfill the conditions of the Den Hartog criterion [9], and free vibration tests were conducted at various wind speeds. In case 2, the wind speed remained constant at U = 11.9 m/s, and tests were conducted at varying angles of attack. The other conditions for each case are shown in Table 1, along with the frequencies calculated by Equation (15).

Since the oscillation amplitude caused by galloping might have hysteresis characteristics, the dynamic response was measured in two ways for each wind speed (or angle of attack): after disengaging from the stationary position and after applying a large initial vibration. The vertical, horizontal, and torsional oscillating displacements were measured by a video tracking system with a frame rate of 60 Hz.

Table 1 Test conditions

Parameters	Case 1	Case 2
m	6.692 kg	6.692 kg
I	0.535 kg m^2	0.535 kg m^2
$B = D$	0.400 m	0.400 m
$\alpha_B = \alpha_D$	19.2 deg.	−0.8 to 29.4 deg.
L	6.293 m	6.255 m
H	1.696 m	1.657 m
T	31.5 N	32.0 N
EA	176.4 N	176.4 N
U	1.6–14.6 m/s	11.9 m/s
f_{y0}	0.449 Hz	0.452 Hz
f_{z0}	0.383 Hz	0.387 Hz
$f_{\theta 0}$	0.417 Hz	0.421 Hz

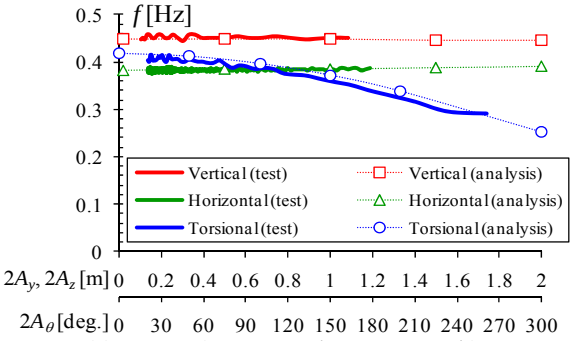

(a) Case 1 (α_B = 19.8 deg., U = 0 m/s)

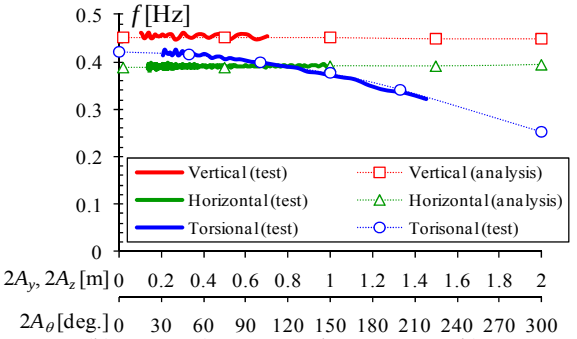

(b) Case 2 (α_B = −0.8 deg., U = 0 m/s)

Figure 7 Natural frequency characteristics

3.2 *Shift of natural frequency and structural damping with an increase in oscillation amplitude*

To investigate the natural frequency characteristics and structural damping, free vibration tests were conducted in a wind speed of 0 m/s. In these tests, the response was measured after applying an initial displacement in one direction only; a total of three measurement test were performed, one for each direction. The amplitude of the vertical, horizontal, and torsional displacements are defined as A_y, A_z, and A_θ, respectively. Figure 7 shows the natural frequency characteristics as a function of the total (peak-to-peak) oscillation amplitude of each degree of freedom. The results show a shift in the natural frequency with an increase in oscillation amplitude, and the torsional displacement frequency, in particular, decreases with an increase in the oscillation amplitude.

The relationship between the frequency and amplitude was also calculated analytically, and the results are plotted in Figure 7. Here, by using the Runge-Kutta method, the time-series behavior after the initial vibration, which has a specific amplitude for each degree of freedom, is calculated by Equations (12) to (14), which are non-damping equations of motion. A power spectrum analysis of the displacement data then shows the predominant frequency of each vibration for each amplitude. The analytically calculated frequency is in good agreement with the test results and therefore verifies the validity of the governing equations of motion in Section 2.2.

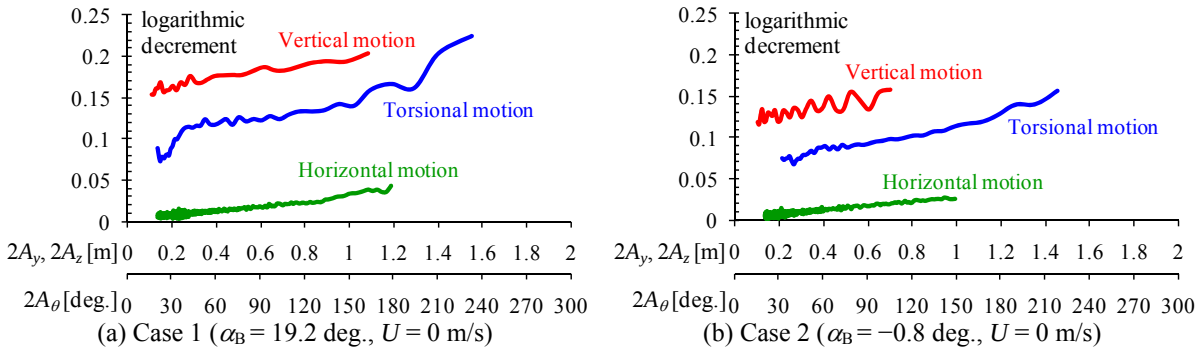

(a) Case 1 (α_B = 19.2 deg., U = 0 m/s) (b) Case 2 (α_B = −0.8 deg., U = 0 m/s)

Figure 8 Structural damping characteristics

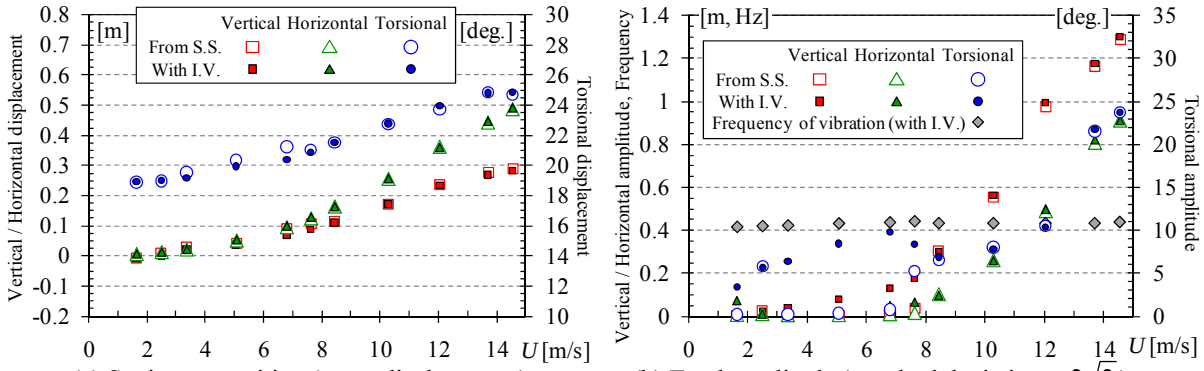

(a) Stationary position (mean displacement) (b) Total amplitude (standard deviation $\times 2\sqrt{2}$) and frequency of galloping oscillation

Figure 9 Test results at each wind speed in Case 1 (α = 19.2 deg.)

Figure 8 shows the structural damping characteristics, which also display a change with increasing oscillation amplitude. The structural damping of the vertical motion is the largest of the three directions because the elongation of the elastic cords is the longest. It was not possible to adjust the structural damping in the currently system, and thus, an adjustment technique will be developed in future work.

3.3 *Results of free vibration tests*

The results of the free vibration tests at each wind speed in Case 1 are shown in Figure 9. In these tests, "from S.S." indicates measurements of the response disengaged from the stationary state, and "with I.V." indicates measurements of the response after applying a large initial vibration. Figure 9(a) shows the stationary position at each wind speed that corresponds to the mean displacement from the stationary position in a wind speed of 0 m/s. The galloping oscillation observed in this tests had a steady amplitude and only one predominant frequency. Figure 9(b) shows the $2\sqrt{2}$ standard deviation, which corresponds to the total (peak-to-peak) amplitude, and also shows the frequency of the galloping oscillation. For some wind speeds in the range 1.6–7.6 m/s, galloping occurred when applying an initial vibration, although it did not occur from the stationary state. At wind speeds exceeding 7.6 m/s, the oscillation amplitude increased with increasing wind speed, with the vertical amplitude peaking at about 1.3 m and accompanied by horizontal and torsional oscillation. The vibration frequency was about 0.40–0.45 Hz. These results validate that the large-amplitude, low-frequency galloping observed in actual overhead transmission lines can be reproduced by using this experimental technique.

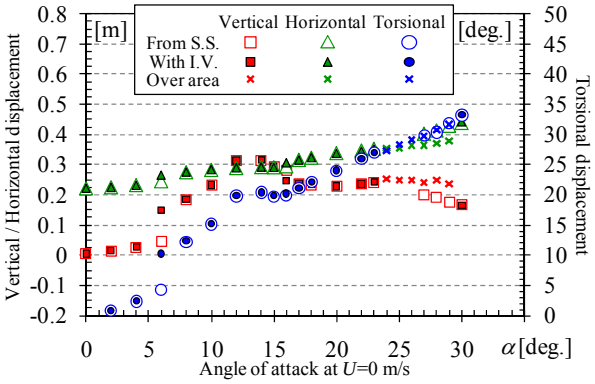

(a) Stationary position (mean displacement)

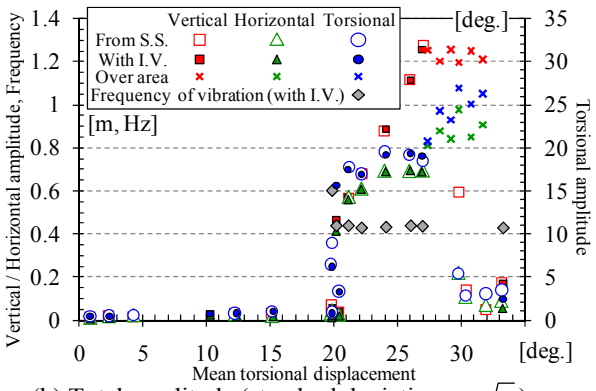

(b) Total amplitude (standard deviation $\times 2\sqrt{2}$) and frequency of galloping oscillation

Figure 10 Test results at each angle of attack in Case 2 (U = 11.9 m/s)

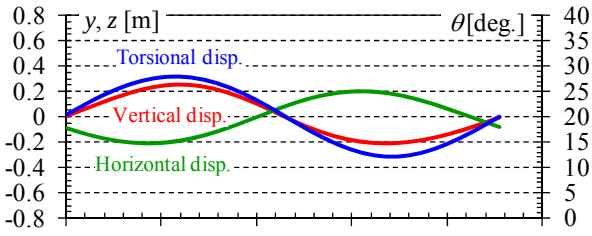

(a) Initial angle of attack α = 16 deg.

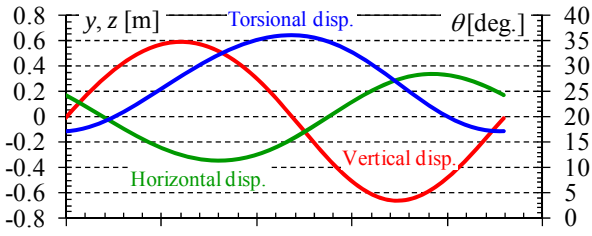

(b) Initial angle of attack α = 23 deg.

Figure 11 Time series of phase averaged displacement in Case 2

The results of the free vibration tests at each angle of attack in Case 2 are shown in Figure 10. The horizontal axis of Figure 10(a) represents the initial angle of attack at U = 0 m/s, which is the same value as the elastic cord support angle, and the horizontal axis of Figure 10(b) represents the mean torsional displacement. In some cases, the oscillation amplitude was larger than the area in which the wind speed distribution is approximately uniform. These cases are indicated as "over area" in Figure 10, and the actual value may differ from the represented value. As shown in Figure 10(a), the stationary angle to the wind is different from the initial angle of attack, especially in the case when the initial angle of attack is slightly less than the stalling angle (20 degrees). In contrast, as shown in Figure 10(b), when the stationary angle is larger than the stalling angle, galloping occurs. Figure 11 shows the phase averaged data of the galloping displacement in one period when the initial angle of attack α is 16 and 23 degrees in Case 2. The phase difference of each displacement varies with the initial angle of attack. In both cases, the torsional displacement range fulfills the Den Hartog criterion, and the mechanism of oscillation onset is thought to be essentially the same as "Den Hartog galloping" [1], which is the aeroelastic instability in a one-degree-of-freedom (vertical motion) only system. As above, a detailed discussion of the oscillation characteristics and onset conditions of galloping can be conducted by this experimental technique.

4 DISCUSSION ON UNSTEADY AERODYNAMIC FORCES

The quasi-steady aerodynamic forces can be calculated using the relative wind speed V_r and the relative angle of attack α_r as

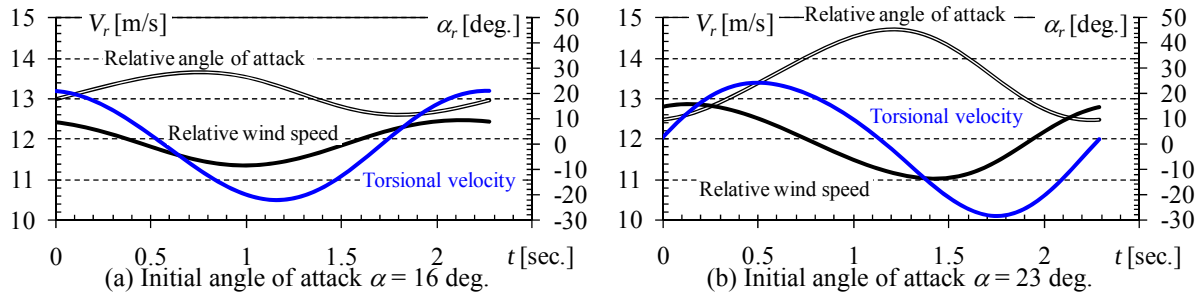

(a) Initial angle of attack $\alpha = 16$ deg. (b) Initial angle of attack $\alpha = 23$ deg.

Figure 12 Time series of relative wind speed, relative angle of attack, and torsional velocity in Case 2

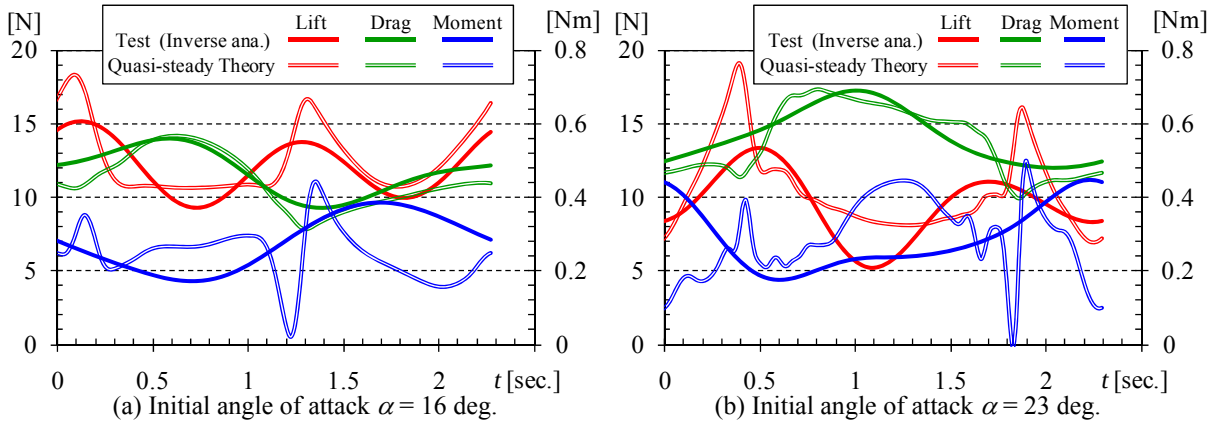

(a) Initial angle of attack $\alpha = 16$ deg. (b) Initial angle of attack $\alpha = 23$ deg.

Figure 13 Comparison of the aerodynamic forces obtained by inverse analysis of the free vibration tests and those calculated by quasi-steady theory in Case 2

$$V_r = \sqrt{(V - \dot{z})^2 + \dot{y}^2}, \alpha_r = \theta + \tan^{-1}\left(\frac{-\dot{y}}{V - \dot{z}}\right). \tag{18}$$

Furthermore, when the four-bundled conductor has a torsional velocity, each sub-conductor has a velocity in a circumferential direction. Thus, by using the aerodynamic coefficients [12], relative wind speed, and relative angle of attack of each sub-conductor, the quasi-steady aerodynamic force theory can calculate some effects of torsional velocity. Figure 12 shows a time series of the relative wind speed, relative angle of attack, and torsional velocity for Case 2.

In contrast, the unsteady aerodynamic forces acting on the sector model can be derived from an inverse analysis of the time-series displacements shown in Figure 11. In the inverse analysis, the structural characteristics are assumed to be expressed by Equations (12) to (14). Furthermore, the structural damping force is taken into account as an internal force. The total oscillation amplitude of each case is calculated by time-series displacements, and the value of the logarithmic decrement corresponding to the amplitude is derived from Figure 8. Figure 13 shows a comparison of the aerodynamic forces obtained by an inverse analysis of the free vibration tests and the quasi-steady aerodynamic forces that take into consideration the quasi-steady aero dynamic forces of each sub-conductor.

As shown in Figure 13, the drag data for both methods is in good agreement. The trend in the lift data is similar but the drastic changes seen in the quasi-steady forces are not present in the unsteady force calculation. Furthermore, there is a large discrepancy in the moment data. Although the reason for this discrepancy will be clarified in future work, the characteristics of the unsteady aerodynamic forces during large amplitude vibrations caused by galloping can be identified by the developed experimental technique.

5 CONCLUSION

The authors have developed and successfully implemented a modeling technique to physically simulate the galloping motion of actual overhead transmission lines in a wind tunnel at low frequency with a large amplitude. Furthermore, the technique allows the possibility of an in-detail discussion of the galloping oscillation characteristics and unsteady aerodynamic forces during the vibration. Future work will involve systematically determining the occurrence conditions and response characteristic of conductor galloping under definite input conditions: accretion shape, angle of attack, frequencies ratios, and wind speed. The results will then permit discussion of a model of the unsteady aerodynamic forces.

REFERENCES

1 CIGRE, State of the art of conductor galloping, CIGRE Technical Brochure, No. 322, TF B2.11.O6, 2007.
2 T. Yukino, K. Fujii and I. Hayase, Galloping phenomena of large bundle conductors observed on the full-scale test line, Proceeding of International Symposium on Cable Dynamics, pp. 557-563, 1995.
3 S. Morishita, K. Tsujimoto, M. Yasui, N. Mori, T. Inoue, K. Shimojima and K. Naito, Galloping phenomena of large bundle conductors experimental results of the field test lines, CIGRE, 22-04, 1984.
4 P. Van Dyke and A. Laneville, Galloping of a single conductor covered with a D-section on a high-voltage overhead test line, Journal of Wind Engineering and Industrial Aerodynamics, No. 96, pp.1141-1151, 2008.
5 H. Matsumiya, T. Nishihara, M. Shimizu and T. Yukino, Observation of galloping phenomenon of four-bundled conductors under ice accretion and its occurring condition, Journal of Structural Engineering. A, Vol. 58A, pp. 575-588, 2012. (in Japanese)
6 Y. M. Desai, P. Yu, A. H. Shah and N. Popplewell, Perturbation-based finite element analysis of transmission line galloping, Journal of Sound and Vibration, Vol. 191, pp. 469-489, 1996.
7 T. Ohkuma, J. Kagami, H. Nakauti, T. Kikuchi, K. Takeda and H. Marukawa, Numerical analysis of overhead transmission line galloping considering wind turbulence, Electrical Engineering in Japan, Vol. 131, Issue 3, pp. 19-33, 2000
8 M. Shimizu and J. Sato, Galloping observation and simulation of a 4-conductor bundle transmission line, Journal of Structural Engineering. A, Vol. 47A, pp. 479-488, 2001. (in Japanese)
9 J.P. Den Hartog, Mechanical Vibrations, McGraw-Hill, 1956.
10 M. Shimizu, T. Ishihara and P. V. Phuch, A wind tunnel study of aerodynamic characteristics of ice accreted transmission lines, 5th International Colloquium on Bluff Body Aerodynamics and Applications, pp. 369-372, 2004.
11 N. Propplewell, Quasi-steady aerodynamic data for moderate transition icing of a single conductor, 11th International Workshop on Atmospheric Icing of Structures, 2005.
12 H. Matsumiya, T. Nishihara and M. Shimizu, Aerodynamic characteristics of ice and snow accreted conductors of overhead transmission lines, Proceeding of 13th International Conference on Wind Engineering, 2011.
13 S. Oka and T. Ishihara, Numerical study on steady aerodynamic characteristics of ice accreted transmission lines, Proceeding of the fifth International Symposium on Computational Wind Engineering, 2010.
14 H. Matsumiya, Y. Eguchi and T. Nishihara, Large-eddy simulation on flow around ice and snow accreted conductors, CRIEPI Research Report, N11031, 2012. (in Japanese)
15 K. Kimura, M. Inoue, Y. Fujino, T. Yukino, H. Inoue and H. Morishima, Unsteady forces on an ice-accreted four-conductor bundle transmission line, Proceeding of 10th International Conference on Wind Engineering, pp. 467-472, 1999.
16 P. V. Phuch, T. Ishihara, Y. Fujino and M. Shimizu, A wind tunnel study on unsteady forces of ice accreted transmission lines, 5th International Colloquium on Bluff Body Aerodynamics and Applications, pp. 373-376, 2004.
17 O. Chabart and J.L. Lilien, Galloping of electrical lines in wind tunnel facilities, Journal of Wind Engineering and Industrial Aerodynamics, Volume 74-76, pp. 967-976, 1998.
18 K. Kimura, N. Tanaka, T. Fujino, T. Yukino and H. Inoue, Wind tunnel and analytical study on a section model of ice-accreted 4 bundled conductor transmission lines, Proceedings of the 6th East Asia-Pacific Conference on Structural Engineering and Construction, pp. 2293-2298, 1998.
19 M. B. Waris, T. Ishihara and M. W. Sarwar, Galloping response prediction of ice-accreted transmission lines, Proceedings of the 4th International Conference on Advances in Wind and Structures, pp. 876-885, 2008

The Seventh International Colloquiumon Bluff Body Aerodynamics and Applications (BBAA7)
Shanghai, China; September 2-6, 2012

Validation analyses of integrated procedures for evaluation of stability, buffeting response and wind loads on the Messina Bridge

A. Zasso[a], G. Diana[a], L. Rosa[a], A. Pagani[a], S. Stoyanoff[b], P.O. Dallaire[b], E. Vullo[c], D. Khazem[d], K.Serzan[d]
[a]*Politecnico di Milano,Dipartimento di Meccanica, Via G.LaMasa 1, Milano, Italy*
[b]*RWDI, 109 bd.de Bromont, Bromont, Québec J2L 2K7,Canada*
[a]*Stretto di Messina*
[d]*Parsons, 100 Broadway, New York, NY 10005, USA*

ABSTRACT: As a part of Messina Strait Bridge independent checking, numerical analysis was carried out to evaluate the bridge aerodynamic response and associated wind loads. The topic of this paper is a comparative presentation of the results obtained by RWDI and Politecnico di Milano (POLIMI) through independent theoretical and numerical methods, on the basis of an identical scheme of the structure and the same aerodynamic and wind turbulence properties.

KEYWORDS: Suspended bridge, Flutter, Stability analysis, Buffeting analysis, Wind Loads, Messina Strait Bridge

1 INTRODUCTION

The framework of the analysis consists in drawings provided by the bridge contractor Eurolink designers COWI, and mass distribution and structural model (eigenvalues and eigenvectors) as provided by Parsons Transportation Group (PTG), the Project Management Consultants for the Stretto di Messina Project. The behavior of the bridge under strong winds was predicted numerically based on experimental data from sectional model wind tunnel tests, carried out on a 1:45 scaled deck sectional model by Politecnico di Milano (POLIMI)and on a 1:100 scaled sectional and aeroelastic models of the tower by RWDI. Aerodynamic static coefficients of the twin main cables were supplied by the high Reynolds number sectional model tests performed on behalf of the bridge contractor Eurolink [Scheweand Jacobs, 2010].

The generalized coordinate numerical approach was applied allowing comparative verifications through independent analysis by RWDI and POLIMI on stability, buffeting and wind loads using similar, yet completely independent, numerical approaches and procedures.

2 THEORETICAL FRAMEWORK OF STABILITY AND RESPONSE ANALYSIS

Analyses were performed using modal approach, solving the bridge dynamics equations of equilibrium in generalized coordinates through the state space matrix of the first 100modes.
The aerodynamic stability of the structure was investigated using a numerical recursive method for taking into account the dependence of the reduced velocity in both the mean wind speed and the frequency of each mode. The aeroelastic terms were introduced by experimental coefficients (Flutter Derivatives).

The adopted numerical method allows for obtaining system eigenvalues as a function of the actual mean wind speed and the actual angle of attack (depending on the bridge average static configuration that is a non-linear function of the mean wind speed itself). Finally, the method

applies an innovative stability criterion focusing on the residual damping parameter, instead the traditional "flutter speed limit" criterion.

To describe the bridge response to turbulent winds, a time domain analysis was performed, based on time-space wind distributions in agreement with the local wind statistical parameters. Aeroelasticity effects were introduced with experimental Flutter Derivatives and buffeting loads were generated based on the quasi-static theory corrected with experimental aerodynamic admittances.

Based on the above theoretical background, independent solution methods were developed and implemented by POLIMI and RWDI producing two sets of “wind loads” that would cover fully the envelope of the expected time domain responses of the bridge to turbulent winds at the required limit states for structural design.

2.1 *Stability Analysis*

Using the described above theoretical framework, the stability analysis has been performed and its results compared to S.d.M. specifications. The stability of all important modes under wind action was verified.

The eigenvalues analysis takes into account the wind-structure aeroelastic effects using the Flutter Derivatives in order to simulate the state dependent forces and moments, accounting for the dependence of the local angle of attack and the frequency of every mode being analyzed. This procedure allows examining the evolution of the total modal damping (structural plus aerodynamic) as a function of the mean wind speed.

An innovative aspect of this independent check is that for the first time, according to S.d.M. specifications, in order to evaluate the stability performances of a suspended bridge, the key-factor of the analysis is the residual damping of each modes instead of the usual value of critical flutter velocity, corresponding to the lowest value of mean wind speed that causes the vanishing of the residual damping. The residual or total damping, also called “stability index”, is defined as $\alpha_i/\omega_i = f(V^*)$ where α_i and ω_i are the real and imaginary part of eigenvalues related to the i^{th} mode with frequency f_i being a function of the reduced velocity $V^*=V/(f_iB)$ (B is the deck width). It comprises structural and aerodynamic damping at given wind speed. Due to the relatively low level of the damping of each mode, this residual damping is the linearization of the theoretical modal damping without losing accuracy.

The residual damping is obtained solving the “Eigenvalues problem” of the coupled mechanic-aerodynamic system:

$$[m_s^*]\ddot{\underline{q}} + [r_s^*]\dot{\underline{q}} + [k_s^*]\underline{q} = \underline{F}_{Aero} = [\Phi]^T \underline{F}_{Aero}(V, V^*, \eta) \tag{1}$$

where $[m_s^*]$, $[r_s^*]$ and $[k_s^*]$ are the structural mass, damping and stiffness generalized matrixes. Structural damping ζ_s is set equal to 0.3% of critical for all deck and towers modes while for the main cables pure modes without deck motions, ζ_s = 0.03% representing the expected values for this structure and modes under consideration. The vector $\underline{q}$ and the matrix [Φ] contain respectively the modal coordinates and the modal vectors; $\underline{F}_{aero}(V,V^*,\eta)$ expresses the aeroelastic forces as a function of mean wind speed V(equal for each mode) and of the reduced velocity V^* that changes for each modes and the angle of attach η (due to mean wind static loads on the structure obtained by a non-linear iterative static procedure) that changes for each section.

The aerodynamic loads of each section were expressed using the Flutter Derivatives in the POLIMI convention[Zasso, 1996]. POLIMI used a modified formulation which includes the definition of an aerodynamic inertial matrix:

$$\begin{Bmatrix} F_y/qBL \\ F_z/qBL \\ F_\theta/qB^2L \end{Bmatrix}_{\substack{Deck\,section \\ Local}} = \left[M^*_{aero}\right] \begin{Bmatrix} \ddot{y} \\ \ddot{z} \\ \ddot{\vartheta} \end{Bmatrix}_{\substack{Deck\,section \\ Local}} + \left[R^*_{aero}\right] \begin{Bmatrix} \dot{y} \\ \dot{z} \\ \dot{\vartheta} \end{Bmatrix}_{\substack{Deck\,section \\ Local}} + \left[K^*_{aero}\right] \begin{Bmatrix} y \\ z \\ \vartheta \end{Bmatrix}_{\substack{Deck\,section \\ Local}} \tag{2}$$

where the aerodynamic matrixes are:

$$\left[M^*_{aero}\right] = -\begin{bmatrix} p_6^* \frac{\pi B}{2V^2} & p_4^* \frac{\pi B}{2V^2} & 0 \\ h_6^* \frac{\pi B}{2V^2} & h_4^* \frac{\pi B}{2V^2} & 0 \\ a_6^* \frac{\pi B}{2V^2} & a_4^* \frac{\pi B}{2V^2} & 0 \end{bmatrix} \quad \left[R^*_{aero}\right] = -\begin{bmatrix} -p_5^* \frac{1}{V} & -p_1^* \frac{1}{V} & -p_2^* \frac{B}{V} \\ -h_5^* \frac{1}{V} & -h_1^* \frac{1}{V} & -h_2^* \frac{B}{V} \\ -a_5^* \frac{B}{V} & -a_1^* \frac{B}{V} & -a_2^* \frac{B^2}{V} \end{bmatrix}$$

$$\left[K^*_{aero}\right] = -\begin{bmatrix} 0 & 0 & p_3^* \\ 0 & 0 & h_3^* \\ 0 & 0 & a_3^* B \end{bmatrix} \tag{3}$$

To consider the Flutter Derivatives not identified through Wind Tunnel tests ($a_{5,6}^*$; $h_{5,6}^*$;$p_{5,6}^*$) the quasi-static approximation using the static aerodynamic coefficients was adopted:

$$\begin{cases} \left\{a^*, h^*, p^*\right\}_6 = 0 \\ p_5^* = 2C_D \\ h_5^* = 2C_L \\ a_5^* = 2C_M \end{cases} \tag{4}$$

where C_D, C_L and C_M are respectively the drag, lift and moment aerostatic coefficients of the bridge deck section.

The same procedure is adopted for the main cables using the static coefficients provided by the dedicated wind tunnel tests [Schewe and Jacobs, 2010],and for the hangers considering only the drag contribution adopting a C_D derived from literature [Zdravkovich, 1997].

	C_{D0}	K_{D0}	C_{L0}	K_{L0}
Main Cables	0,52	0	0	-2.6767
Hangers	0,6	0	0	0

Table 2-1 Main Cables and hanger aerodynamic coefficients

The quasi-static approximation was also used for the two towers. Since their influence was judged small on stability estimation, the towers were included only for buffeting analysis in the POLIMI model. Given the same numerical model and solver was applied by RWDI, towers were included both into flutter stability and buffeting analyses.

Stability assessment was done using a modal approach on the basis of modal properties of the bridge provided by Parsons. The first mode becoming unstable is the first torsional anti-symmetric one (#4 - f = 0.080 Hz); Table 2-2reports a summary of the evolution of the residual damping at different angle of attach and at different mean wind speed value. Figure 2-1 shows the behavior of the first torsional anti-symmetric mode and the corresponding vertical and lateral modes those are directly involved in flutter. Results are presented considering or disregarding the main cables effect.

η[deg]	V_{fl}[m/s]		Wind speed[m/s]											
			10		44		47		54		60		75	
-4	∞	∞	1,25	1,36	2,86	3,20	3,04	3,41	3,46	3,87	3,79	4,25	4,39	4,98
-2	91	98	0,98	1,07	3,12	3,46	3,24	3,61	3,40	3,83	3,34	3,82	2,22	2,82
0	83	87	0,71	0,78	2,73	3,08	2,79	3,17	2,79	3,22	2,58	3,07	1,06	1,65
2	88	93	0,55	0,60	2,90	2,94	3,02	3,15	3,17	3,65	3,12	4,00	1,97	4,53
4	83	88	0,47	0,55	2,70	3,04	2,81	3,17	2,90	3,31	2,71	3,17	1,15	1,70

Table 2-2 Stability limit and residual damping of the 1st torsional mode with and without (gray cells) the main cables

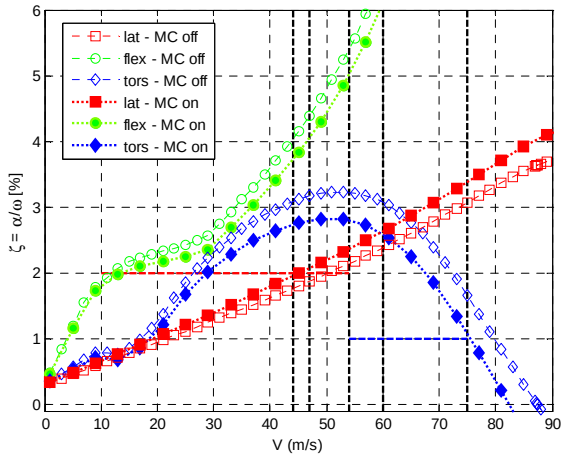

Figure 2-1 Residual damping of 1st lateral, vertical and torsional modes as functions of mean wind speed. Results of simulation with and without main cables. Assumed angle of wind attack 0°.

The project requests for aerodynamic specifications stability were satisfied for all fundamental modes controlling the deck stability at angle of attack η=0° as showed in Figure 2-2 that collects the evolution of all modes as requested by the project specification (modes: from 1 to 4 torsional asymmetric).The torsional instability is overcome at higher wind speed due to the regular positive aerodynamic damping shown by the asymptotic trend of the a^*_2 Flutter Derivatives at higher reduced velocity.

Due to negative lift coefficient of the Main Cables in twin configuration (as reported in Table 2-1) some higher cable modes show quite low damping. This problem must be addressed in the "Esecutivo" phase but it is easily resolvable.

Based on the same set of full data and theoretical framework, RWDI applied its procedure called "3D Flutter Analysis" [Stoyanoff, 1993] modified to include POLIMI's derivatives formulation. On the selected trial case at zero degree, mean angle of wind attack, almost identical residual damping traces (Figure 2-1) were predicted and critical flutter speeds within 2.5 m/sec.

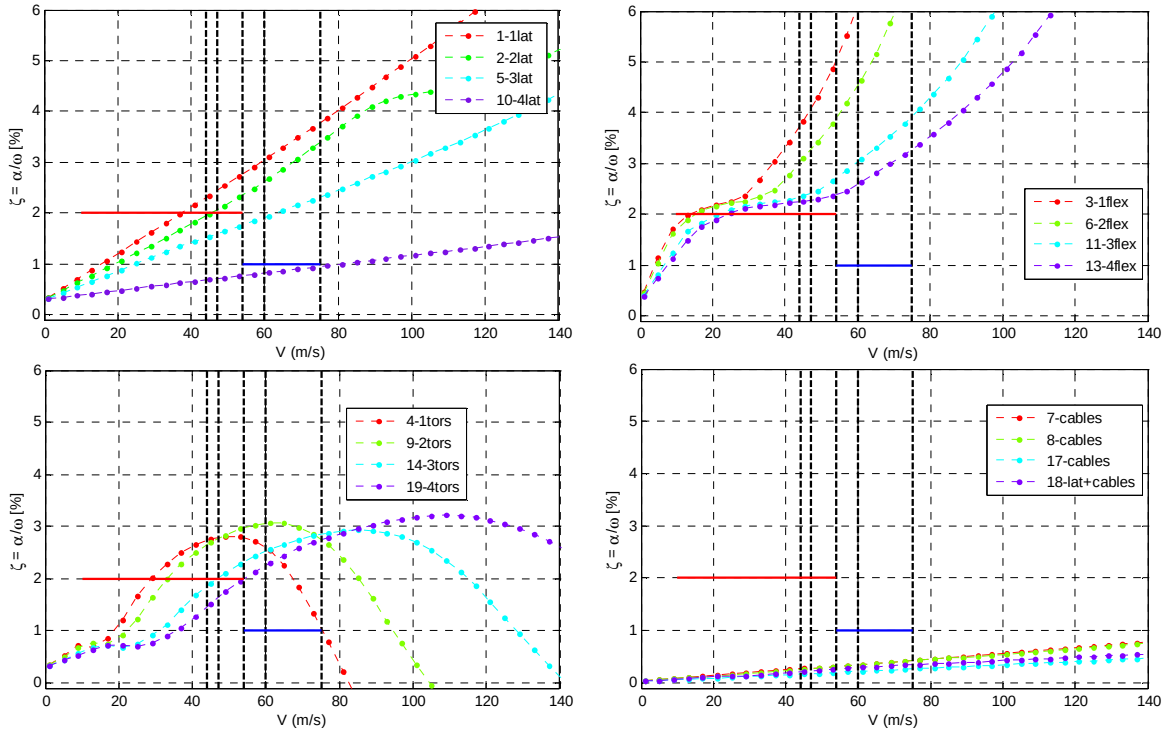

Figure 2-2.Instability coefficient vs. mean wind speed – Main cables + hangers ON – Modes by category.

2.2 *BUFFETING ANALYSIS*

Buffeting analysis has been performed with evaluation of displacements and accelerations distribution of the structure. The time histories of the bridge displacements and accelerations, together with the mean and turbulent wind components actions allow evaluation of the overall reference wind loads on the structure due to combined static and dynamic effects. The analysis has been performed using a linear integration analysis in time domain. RWDI's response solver uses a highly efficient "exact" integration method (Stoyanoff, 2001).

The buffeting analysis procedure entails the following steps:

- Choose a "wind grid" which covers the structure.
- Interpolate the bridge structure and the wind grid to locate the wind loads points of application.
- Generate wind time histories at all nodes get at previous step according with S.d.M. target turbulence properties
- Using these wind time histories, the Drag, Lift and Moment loads are expressed in the local frame of reference through the aerodynamic admittance functions define for each section and time step. As done for the Flutter Derivatives, the quasi-static approximation was used to extrapolate the aerodynamic admittance functions coefficients and cover for drag which was not experimentally identified. This simplification conserves the dependence from the angle of attach but obviously disregards the one to the reduced velocity.
- Integrate the equations of motion with buffeting loads obtained in the previous step.

Static force and moment coefficients on the towers were included based on the 1:100 sectional model test undertaken by RWDI (Stoyanoff et al, 2012).

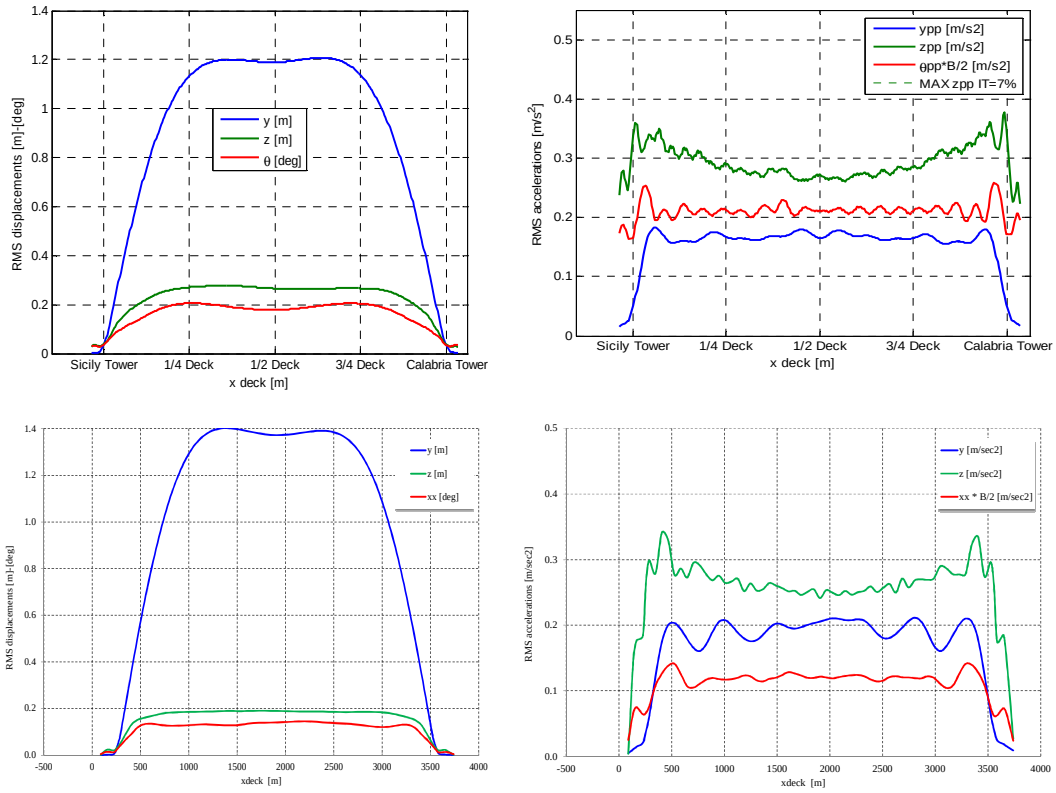

Table 2-3 Comparison between POLIMI (up)/RWDI (down) - rms displacements (left) and acceleration (right) of the deck in physical coordinates.

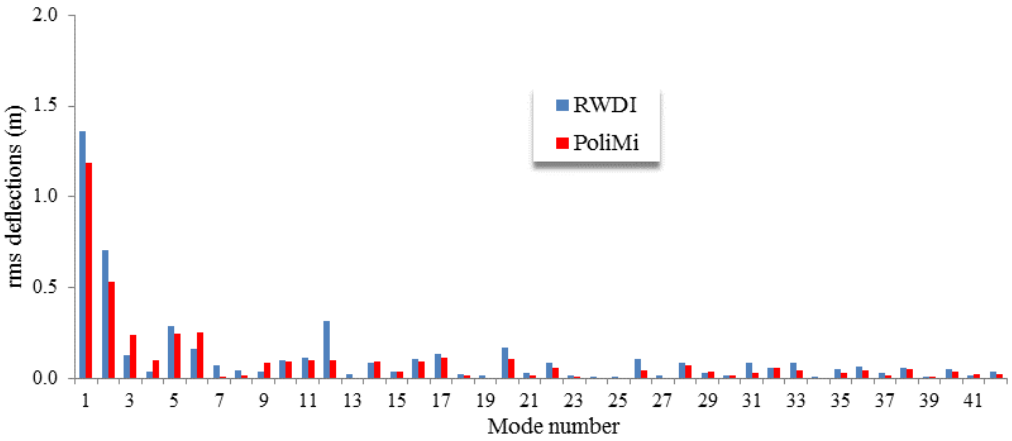

Table 2-4 Comparison between POLIMI /RWDI –modal rms. displacements for the first 50 modes

Figures 2-3 and 2-4 compare bridge response predicted by Polimi and RWDI at wind speed of 44 m/sec based on the same dynamic model and set of aerodynamic data. The observed differences were attributed to the different interpretations and simulations of the wind turbulence model and response analyses. These should outline the boundary of predictions for possible bridge responses.

3 WIND LOADS

3.1 *Time domain approach (POLIMI)*

The total loads on the bridge include stationary ones, due to the mean wind speed and time-averaged structure configuration and non-steady loads, caused by time dependent aeroelastic forces and by incoming turbulence fluctuations (buffeting forces). In response to these loads, the structure accelerations generate additional time dependent inertial forces. Performing the buffeting analysis, as describe in the previous paragraph, it is possible to calculate these loads at each simulation time step and for each section of the structure.

A common design practice is to express the effect of both steady and non-steady wind loads as equivalent wind loads (EWL), statically applied to the structure and taking into account also the dynamic effects of wind interaction. Different criterions were adopted in order to select these equivalent "scenarios" representative of critical loading.

A possible straightforward strategy is to select the loads combination determining the peak curvature values along the deck, main cable or tower sections, considering the direct link among structural curvatures and corresponding stresses in the structural components.

In order to calculate the structure time-space curvature distribution it's possible to take advantage of the modal approach due to the intrinsic separation of time and space domain functions, and writing the space partial derivative in terms of derivative of the eigenvectors as functions of the running space coordinate along the structure as follows:

$$\underline{x}(\zeta,t)=\left[\Phi(\zeta)\right]\underline{q}(t) \quad \rightarrow \quad \frac{\partial^2 \underline{x}}{\partial \zeta^2}=\left[\frac{\partial^2 \Phi}{\partial \zeta^2}\right]\underline{q}(t) \tag{5}$$

where $\underline{x}(\zeta,t)$ represent the time-space vector of the displacements, $[\Phi(\zeta)]$ the modal matrix of the eigenvectors and $\underline{q}(t)$ the vector of generalized coordinates. This vector of is a known function calculated from the buffeting response. It is possible now to select among the time-space curvature distributions, extreme values causing extreme stress conditions along the structure and to select those instantaneous configurations (and their associated equivalent static loads) as components of the relevant scenario of wind loading as required for structural design.

For instance, Figure 3-1shows,for the mean wind speed V=44m/s, one of the selected scenario in which the deck curvature in the horizontal plane reached extreme values (close to the north-west tower). The figure shows also the other curvatures (vertical and torsional) and the associated displacements simultaneously reached by the structure. The same figure shows finally the corresponding distribution of equivalent wind loads determining the over described extreme configuration described(external, inertial and total loads). It is important noting that wind loads causing maximum curvature are not caused by loads local extremes on a section, rather to overall load distributions along the deck, main cables and towers.

Proposed method supplies the "true" instantaneous distributions of external and inertial forces and moments determining the extreme bending or torsion curvatures which represent the loading condition at a selected limit state. They are derived straightforward from the time domain response analysis. Further work is ongoing to establish a probabilistic interpretation of these results.

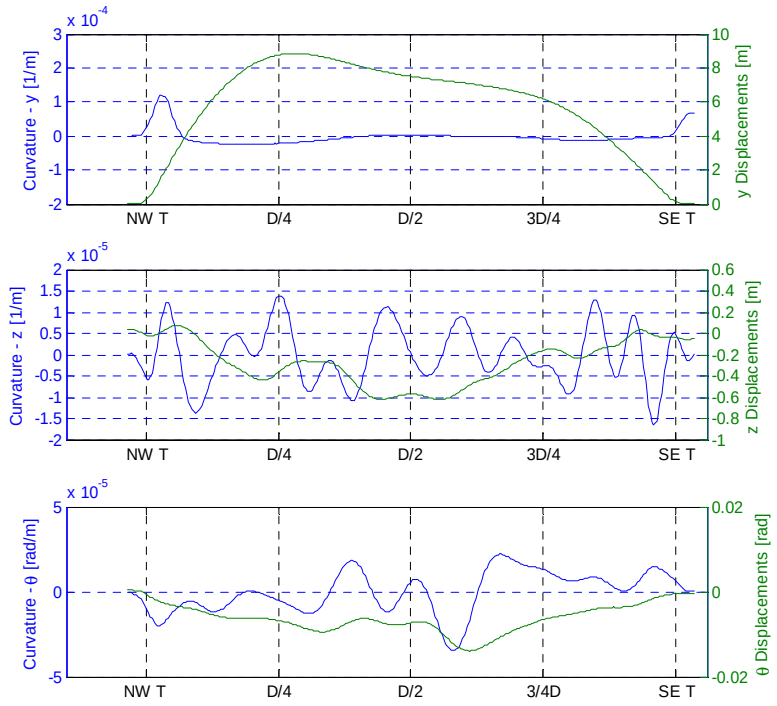

(a)

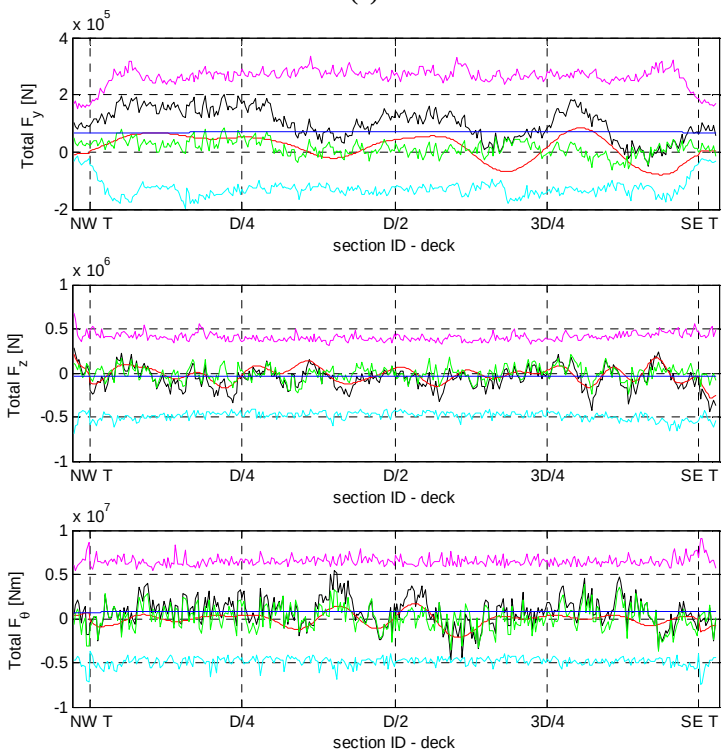

(b)

Figure 3-1 Snapshot of the scenario that represents the maximum curvature reached by the deck in the along wind direction. Also the other components (deflections, curvatures and loads in the crosswind direction and along the deck) are quoted. (a): curvature (blue), displacement (green). (b): total loads (black), inertial loads (red), buffeting loads (green), static loads (blue), max/min envelope loads on the total simulated time history(magenta/cyan).

3.2 *Wind Loads: modal participation approach based on top-bin sorting (RWDI)*

Wind loads were also developed by RWDI's independent procedure. The dynamic loads due to wind buffeting at various time instances tend to stress critically different bridge parts. They occur simultaneously with other static loads. It has been most convenient to designers to present wind loads as equivalent static loads. The dynamic wind loads are decomposed into various "snap-shot" equivalent-static load cases in order to cover likely critical conditions. Various combinations are developed with the load patterns being distributed lateral, vertical, longitudinal, and torsional loads.

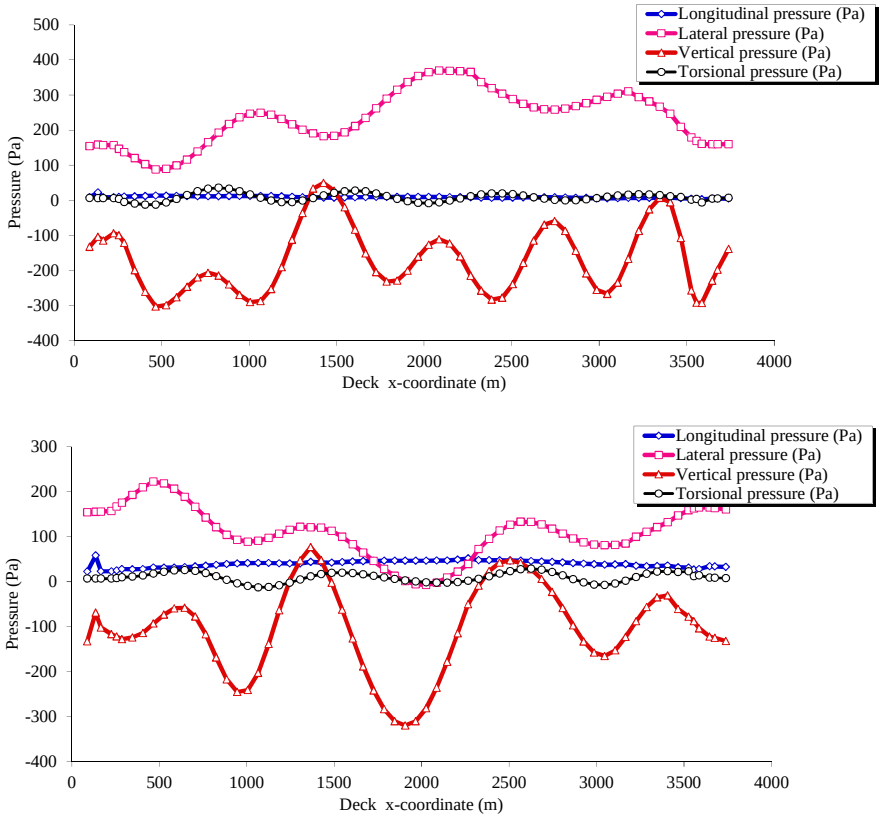

Figure 3.2 Equivalent static load distributions derived for the deck based on the modal participation factors identified from the top-bin sorting method. Longitudinal pressure (blue), lateral pressure (purple), vertical pressure (red) and torsional pressure (black) are given for the deck physical coordinates. UP: load distribution causing maximum lateral deflection. BOTTOM: load distribution causing maximum vertical negative deflection.

Whereas combining mean and direct wind gusts, and inertial loads is a straightforward procedure, the challenge is in defining the modal participation factors. One new technique can be applied where the time series of known responses at selected locations, e.g. on the deck near by the towers, are normalized and sorted. After normalization, the time histories of modal vectors will take values in the range of ±1 (in most cases only one of the boundaries will reach unity).The response then is divided into bins where the top-bin (for example from 0.99 to 1.0) will provide several sets of participation factors for simultaneously occurring lateral, vertical and torsional responses. Since RWDI's method for the response integration is in fact an exact solution in generalized coordinates, the modal participation factors are then directly obtained as required for load combinations.

Considering deflection only, on a long-span bridge typically are selected ¼, ½, and ¾ of the main span locations and time series of the overall response vectors produced. To examine differential responses, the cross-response vectors of (¼+½+¾)/3 and (¼-¾) span locations are also produced. Accepting then as a sorting objective to identify time instances of maximum and minimum deflections in along, lateral, vertical, and torsion direction would lead to about 50 load cases. Examples of load distributions on the deck causing maximum lateral and vertical deflections are given in Figure 3.2.

4 CONCLUSIONS

Considering stability in strong winds, reasonably similar results were predicted by the two independent analyses, confirming a high reliability of the applied experimental-numerical methodology. Based on the same structural and aerodynamic parameters, comparing the response predictions to turbulent winds, however larger scatters were found between the two independent solutions. This confirms the expectation of wider uncertainties depending on the actual implementation of the established methodological framework of increased complexity.

Concerning the wind loads, there is an ongoing development in both methodologies including the implementation of probabilistic interpretations with a reference to structural fatigue.

5 REFERENCE

Schewe, G. and Jacobs,M. Reynolds number-effects in flow around a Tandem-Cylinder from Re=10^5up to 6×10^6-Report from Wind Tunnel Tests at "D.L.R. Institute für Aeroelastik in Göttingen, Germany," 2010.

Zasso, A. Flutter Derivatives: advantages of a new representation convention. Journal of Wind Engineering and Industrial Aerodynamics 60, pp. 35–47, 1996.

Zdravkovich, M.M., Flow around circular cylinders. 2: Applications. Oxford: Oxford University Press, 1997.

Stoyanoff, S., Wind Induced Vibrations of Cable-Stayed Bridges, Ph.D. Thesis, Graduate School of Engineering, Kyoto University, Japan, 1993.

Stoyanoff, S. A unified approach for 3D stability and time domain response analysis with application of quasi-steady theory, Journal of Wind Engineering and Industrial Aerodynamics, v. 89, pp. 1591-1606, 2001.

Stoyanoff, S., Dallaire, P.O., Garber, J., Zasso, A., Diana, G., E. Vullo, Stretto, Khazem, D. and Serzan, K. Messina Strait Bridge - Confirmatory Wind Tunnel Testing of the Bridge Towers, submitted to BBAA7, Shanghai, China, September 22-23, 2012.

Unsteady buffeting prediction of bridges using proper orthogonal decomposition

Thai-Hoa Le[a)], Yukio Tamura[b)]

[a)] *Wind Engineering Research Center, Tokyo Polytechnic University*
1583 Iiyama, Atsugi-shi, Kanagawa 243-0297, Japan
[b)] *Department of Architectural Engineering, Tokyo Polytechnic University*
1583 Iiyama, Atsugi-shi, Kanagawa 243-0297, Japan

ABSTRACT: This paper presents the unsteady buffeting response prediction of bridges in the time domain using the proper orthogonal decomposition. Digital simulation of the turbulence wind fields is carried out at the bridge nodes using the spectral representation techniques via Cholesky decomposition and modal factorization. Covariance matrix-based proper orthogonal decomposition is used to decompose the unsteady buffeting forces via the impulse response functions, then formulate the buffeting response prediction of bridges in the time domain. The impulse response functions of unsteady buffeting forces are identified via aerostatic force coefficients and aerodynamic admittance functions. The Newton-beta integration method is also applied to obtain the buffeting response solution in the time domain. Numerical example of full-scale bridge is taken into account for illustration and discussions.

KEYWORDS: Buffeting analysis; Unsteady buffeting forces; Time domain; Proper Orthogonal Decomposition; Covariance proper transformation; Roger approximation

1 INTRODUCTION

Buffeting response prediction of long-span bridges subjected to the turbulent-induced forces (the buffeting forces) requires essential concern among wind-induced vibrations and their aerodynamic responses. General formulation and framework of the buffeting response prediction of bridges has been proposed by A.G. Davenport in the frequency domain (Davenport 1962). Recently, the state-of-the-art buffeting response analysis of bridges in coupling with the aeroelastic forces in the time domain has been carried out by some authors (ex., Boonyapinyo et al. 1999, Chen at al. 2000). Computational difficulties are to decompose spatially-correlated full-scale buffeting forces into the structurally generalized coordinates which are decomposed thanks to the structural modal transformation in order to estimate the generalized responses in the generalized coordinates and then the global responses of structures. In conventional methods in both the frequency-domain and the time-domain, the so-called joint acceptance function (JAF) has been used to decompose the full-scale buffeting forces into the structurally generalized coordinates.

Proper orthogonal decomposition (POD) (Lumley 1970), has been applied in many engineering fields (Liang et al. 2002). In the wind engineering topics, the proper orthogonal decomposition has been applied for analysis and order-reduced synthesis of the random pressure fields (Tamura et al. 1999), representation and simulation of the random fields (Tubino and Solari 2005), stochastic dynamic response (Carassale et al. 1999, Solari and Carassale 2000, Chen and Kareem 2005). Basing on the basic matrix of either the zero-time-lag covariance matrix or cross spectral density matrix of the random field, the proper orthogonal decomposition has been branched by either the covariance proper transformation or the spectral proper transformation. New approach of the gust response analysis of

structures has been proposed recently by Carassale et al. 1999 in which the structural modes decomposed by the structural modal transformation are associated with either the covariance turbulent loading modes or the spectral turbulent loading modes decomposed from proper transformations in order to determine the generalized responses and the global responses of structures. Combination manner between the structural modes and the turbulent loading modes for predicting the stochastic response of structures is named by Carassale et al. 1999 and Solari and Carassale 2000 as the double modal transformations (DMT). So far, almost literatures on the proper orthogonal decomposition application to the stochastic response of structures are formulated based on the spectral proper transformation in the frequency domain (Carassale et al. 1999, Solari and Carassale 2000, Chen and Kareem 2005). The frequency-domain buffeting response of long-span bridge using the spectral proper transformation has been formulated previously somewhere (ex., Tubino and Solari, 2007). The stochastic response of structures formulated in the time domain using the covariance proper transformation is very promising because of its direct and capable solutions for nonlinear problems and unsteady buffeting aerodynamics. However, digital simulation of the time series of the turbulence wind fields and the direct integration methods of generalized dynamic equations are usually required that are associated with time-consumed and difficult computation. Time-domain buffeting analysis is always promising for advanced treatment of nonlinear problems, unsteady buffeting response and buffeting-induced vibration countermeasures. Moreover, the unsteady buffeting forces in the time domain via the impulse response functions are better approach for the unsteady buffeting response problem due to its advantage for modeling so-called "memory effect" in the unsteady fluid that could capture the past history of response.

In the paper, the unsteady buffeting response prediction of bridges in the time domain using the proper orthogonal decomposition has been formulated. The spectral branched proper orthogonal decomposition has been used to digitally simulated the turbulence wind fields on the bridge, while the covariance branched proper orthogonal decomposition is used to decompose the unsteady buffeting forces via the impulse response functions, then the buffeting response prediction has been formulated in the time domain. The impulse response functions used for the unsteady buffeting forces have been estimated indirectly using the aerostatic force coefficients, the aerodynamic admittance functions and the Roger rational approximation. Buffeting responses of the bridges have been solved directly in the time domain using the Newton-beta integration technique. Numerical example of medium-span cable-stayed bridge has been taken into account for results and discussions.

2 UNSTEADY BUFFETING FORCES

The quasi-steady buffeting forces per unit deck length (lift, drag and moment) are determined due to the quasi-steady theory that is corrected by frequency-dependant aerodynamic admittance functions as follows (see Figure 1):

$$L_b(t)=\frac{1}{2}\rho U^2 B[C_L\chi_{Lu}(n)\frac{2u(t)}{U}+(C_L^{'}+C_D)\chi_{Lw}(n)\frac{w(t)}{U}] \quad (1a)$$

$$D_b(t)=\frac{1}{2}\rho U^2 B[C_D\chi_{Du}(n)\frac{2u(t)}{U}+(C_D^{'}-C_L)\chi_{Dw}(n)\frac{w(t)}{U}] \quad (1b)$$

$$M_b(t)=\frac{1}{2}\rho U^2 B^2[C_M\chi_{Mu}(n)\frac{2u(t)}{U}+C_M^{'}\chi_{Mw}(n)\frac{w(t)}{U}] \quad (1c)$$

where C_L, C_D, C_M: aerodynamic static coefficients (at balanced angle of attack); $C_L^{'}, C_D^{'}, C_M^{'}$: first-order derivatives; $\chi_{Fv}(n)\ (F=L,D,M;\upsilon=u,w)$: aerodynamic transfer functions between turbulent components and turbulent-induced forces (their absolute magnitudes refer as aerodynamic admittance functions).

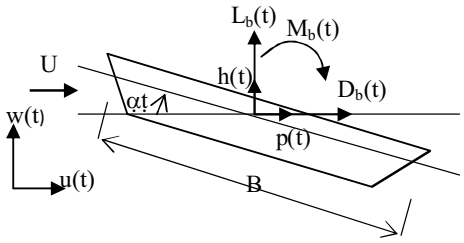

Figure 1. Buffeting forces on bridge deck

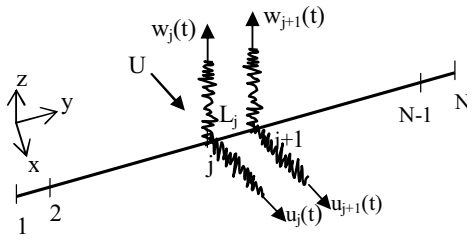

Figure 2. Turbulence wind fields

Quasi-steady buffeting forces, however, do not exactly reflect unsteady characteristics as nature of these random forces, which depend on not only geometric configuration of bridge decks, oncoming wind turbulence, but frequency-dependant parameters due to wind-structure interaction and bluff body flow. Additionally, it is indicated that unsteady fluid dynamics at low, medium flow velocity ranges must account for both past and present motion histories, thus the so-called "memory effect" of the unsteady fluid flow should be included in modeling of unsteady buffeting forces. So far, the unsteady buffeting forces can be determined via either the indicial response functions (Scanlan 1993) or the impulse response functions (Lin 1984, Chen and Kareem 2000) thanks to the convolution integration operation. Recently, the impulse response functions are usually used for modeling the unsteady buffeting forces in the time domain as follows:

$$L_b(t) = \frac{1}{2}\rho U^2 \{ \int_{-\infty}^{t} I_{Lu}(t-\tau)\frac{u(\tau)}{U}d\tau + \int_{-\infty}^{t} I_{Lw}(t-\tau)\frac{w(\tau)}{U}d\tau \} \quad (2a)$$

$$D_b(t) = \frac{1}{2}\rho U^2 \{ \int_{-\infty}^{t} I_{Du}(t-\tau)\frac{u(\tau)}{U}d\tau + \int_{-\infty}^{t} I_{Dw}(t-\tau)\frac{w(\tau)}{U}d\tau \} \quad (2b)$$

$$M_b(t) = \frac{1}{2}\rho U^2 \{ \int_{-\infty}^{t} I_{Mu}(t-\tau)\frac{u(s)}{U}d\tau + \int_{-\infty}^{t} I_{Mw}(t-\tau)\frac{w(\tau)}{U}d\tau \} \quad (2c)$$

where $I_{Lu}, I_{Lw}, I_{Du}, I_{Dw}, I_{Mu}, I_{Mw}$: impulse response functions which are usually obtained thanks to available admittance functions such following formulae as (Chen and Kareem 2002):

$$\bar{I}_{Lu} = 2BC_L\chi_{Lu}(n)\,;\ \bar{I}_{Lw} = B(C_L' + C_D)\chi_{Lw}(n) \quad (3a)$$

$$\bar{I}_{Du} = 2BC_D\chi_{Du}(n)\,;\ \bar{I}_{Dw} = B(C_D' - C_L)\chi_{Dw}(n) \quad (3b)$$

$$\bar{I}_{Mu} = 2B^2C_M\chi_{Mu}(n)\,;\ \bar{I}_{Mw} = B^2C_M'\chi_{Mw}(n) \quad (3c)$$

where $\bar{I}_{F\upsilon}$: Fourier transform of the impulse response functions ($F = L, D, M$ $\upsilon = u, w$) :

$$\bar{I}_{F\upsilon} = \int_0^{\infty} I_{F\upsilon}(t)e^{-i\omega t}dt = \int_0^{\infty} I_{F\upsilon}(s)e^{-iKs}ds$$

.

However, the aerodynamic admittance functions determined by either empirical formula or experimental measurement are expressed at discrete values of reduced frequency. Therefore, it is essential to approximate discrete frequency-dependant function to continuous one. Rational function approximation, known as the Roger's approximation is the mostly utilized for this purpose. Aerodynamic transfer functions can be expanded using rational function approximation:

$$\chi_{F\upsilon}(n) = A_{F\upsilon,1} + (iK)\sum_{j=1}^{m_{F\upsilon}} \frac{A_{F\upsilon,j+1}}{iK + d_{F\upsilon,j}} \quad (4)$$

where $A_{F\upsilon,1}, A_{F\upsilon,j+1}, d_{F\upsilon,j}$ frequency-dependant coefficients ($j = 1,2,\ldots,m_{F\upsilon}$) determined by nonlinear curve-fitting technique.

Then the impulse response functions and the unsteady buffeting forces (here only $I_{Lw}(s)$,

$L_{Lw}(t)$ are expended as example) can be determined as follows (Chen and Kareem, 2002):

$$I_{Lw}(s) = B(C_D + C_L^{'})\left[\left(A_{Lw,1} + \sum_{j=1}^{m_{Lw}} A_{Lw,j+1}\right)\delta(s) - \sum_{j=1}^{m_{Lw}} A_{Lw,j+1} d_{Lw,j} e^{-d_{Lw,j}s}\right] \quad (5a)$$

$$I_{Lw}(s) = \frac{1}{2}\rho U^2 B(C_D + C_L^{'})\left[\left(A_{Lw,1} + \sum_{j=1}^{m_{Lw}} A_{Lw,j+1}\right)\frac{w(t)}{B} - \sum_{j=1}^{m_{Lw}} \frac{d_{Lw,j}U}{B}\phi_{Lw,j}(t)\right] \quad (5b)$$

$$\dot{\phi}_{Lw,j}(t) = -\frac{d_{Lw,j}U}{B}\phi_{Lw,j}(t) + A_{Lw,j+1}\frac{w(t)}{U} \quad (5c)$$

where $\phi_{Fw,j}(t)$: augmented aerodynamic state coefficient.

3 PROPER ORTHOGONAL DECOMPOSITION

The main idea of the covariance matrix-based proper orthogonal decomposition and its covariance proper transformation is to find out a set of orthonormal basic vectors which can expand a multi-variate spatially-correlated random turbulent field into a sum of products of these basic orthogonal vectors (turbulent loading modes) and single-variate uncorrelated random processes (principal coordinates) based on the covariance matrix of this random field. The covariance matrix-based orthogonal vectors are found as the eigenvector solutions of the eigen problem of the zero-time lag covariance matrix $R_\upsilon(0)$ of N-variate random turbulent process $\upsilon(t)$:

$$R_\upsilon \Theta_\upsilon = \Gamma_\upsilon \Theta_\upsilon \quad (6)$$

where $R_\upsilon(0)$: zero-time-lag covariance matrix of $\upsilon(t)$; Γ_υ, Θ: covariance eigenvalue and eigenvector matrices $\Theta_\upsilon = [\theta_{\upsilon_1}, \theta_{\upsilon_2}, \ldots \theta_{\upsilon_N}]$, $\Gamma_\upsilon = diag(\gamma_{\upsilon_1}, \gamma_{\upsilon_2}, \ldots \gamma_{\upsilon_N})$. Because the zero-time lag covariance matrix is positive-definite symmetrical squared one, thus its covariance eigenvalues are real and positive, and covariance eigenvectors are also real, satisfy the orthonormal conditions:

$$\Theta_\upsilon \Theta_\upsilon^T = I; \ \Theta_\upsilon C_\upsilon \Theta_\upsilon^T = \Gamma_\upsilon \quad (7)$$

Then, the random turbulence field and its covariance matrix can be expressed such optimum approximation as follows:

$$\upsilon(t) = \Theta_\upsilon x_\upsilon(t) \approx \sum_{j=1}^{\tilde{N}} \theta_{\upsilon j} x_{\upsilon j}(t) \quad (8a)$$

$$R_\upsilon(0) = \Theta_\upsilon \Gamma_\upsilon \Theta_\upsilon^T(n) = \sum_{j=1}^{\tilde{N}} \theta_{\upsilon j} \gamma_{\upsilon j} \theta_{\upsilon j}^T \quad (8b)$$

where $\hat{x}_\upsilon(t) = \{\hat{x}_{\upsilon_1}(t), \hat{x}_{\upsilon_2}(t), \ldots, \hat{x}_{\upsilon_N}\}^T$: covariance matrix-based principal coordinates (shortly, the covariance principal coordinates) as the N-variate uncorrelated Gaussian random subprocesses that represents as image of the random turbulent field in the covariance-based space; $\tilde{N}$: number of truncated covariance eigenvectors ($\tilde{N} << N$). The covariance principal coordinates can be determined from observed data under following expression:

$$x_\upsilon(t) = \Theta_\upsilon^{-1}\upsilon(t) = \upsilon(t)\Theta_\upsilon = \sum_{i=1}^{N} \upsilon_i(t)\theta_{\upsilon i} \quad (9)$$

These approximations are known as the covariance proper transformation in the time domain. Two N-variate turbulent processes u(t), w(t) acting on the N structural nodes: $u(t) = \{u_1(t), u_2(t), \ldots, u_N(t)\}^T$ and $w(t) = \{w_1(t), w_2(t), \ldots, w_N(t)\}^T$ are represented under the zero-time lag covariance matrices $R_u(0), R_w(0)$.

Two N-variate Gaussian random turbulent processes u(t), w(t) can be transformed and approximated into the covariance principal coordinates due to the covariance proper transformation:

$$u(t) = \Theta_u x_u(t) \approx \sum_{j=1}^{\tilde{N}} \theta_{u_j} x_{u_j}(t) \quad (10a)$$

$$w(t) = \Theta_w x_w(t) \approx \sum_{j=1}^{\tilde{N}} \theta_{w_j} x_{w_j}(t) \quad (10b)$$

where $x_u(t), x_w(t)$: the covariance principal coordinates of u-,w-turbulences, respectively.

As the same way, the covariance matrices can be approximated as follows:

$$R_u(0) = \Theta_u \Gamma_u \Theta_u^{*T} \approx \sum_{j=1}^{\tilde{N}} \theta_{u_j} \gamma_{u_j} \theta_{u_j}^{*T} \quad (11a)$$

$$R_w(0) = \Theta_w \Gamma_w \Theta_w^{*T} \approx \sum_{j=1}^{\tilde{N}} \theta_{w_j} \gamma_{w_j} \theta_{w_j}^{*T} \quad (11b)$$

where $\Gamma_u, \Gamma_w, \Theta_u, \Theta_w$: covariance eigenvalues and corresponding covariance eigenvectors (or covariance turbulent modes) : $\Gamma_u = diag(\gamma_{u_1}, \gamma_{u_2}, ..., \gamma_{u_N})$, $\Gamma_w = diag(\gamma_{w_1}, \gamma_{w_2}, ..., \gamma_{w_N})$, $\Theta_u = \{\theta_{u_1}, \theta_{u_2}, ..., \theta_{u_N}\}^T$; $\Theta_w = \{\theta_{w_1}, \theta_{w_2}, ..., \theta_{w_N}\}^T$ determined from the covariance matrix-based proper orthogonal decomposition of the random turbulent processes u(t), w(t).

4 TURBULENCE WIND SIMULATION

In the unsteady buffeting response prediction of bridges, the turbulence wind fields u(t), w(t) require to be digitally simulated at the bridge nodes. Digital simulation techniques via the spectral representation can be used basing on Cholesky decomposition and modal factorization. The turbulence wind fields can be expressed in the frequency domain using the Cholesky decomposition as follows (Le 2007), see Figure 2:

$$\upsilon_j(t) = \sqrt{2(\Delta f)} \sum_{k=1}^{j} \sum_{l=1}^{\tilde{N}} |\sqrt{S_{\upsilon_j \upsilon_j}(f)} G_{jk}(f_{kl}) \cos(2\pi f_{kl} t + \phi_{kl}) \quad (12)$$

where $\upsilon_j(t)$: simulated turbulence process at node j ($\upsilon(t) = u(t), w(t)$) ; j: index of structural node; k: index of moving node; l: index of moving point in frequency range; $\tilde{N}$: number of frequency intervals; Δf : frequency interval $\Delta f = f_{up}/\tilde{N}$; f_{up} : upper cutoff frequency; f_{kl} : frequency point on frequency range $f_{kl} = (l-1)\Delta f + k\Delta f/N$; $S_{\upsilon_j \upsilon_j}(f)$: auto spectral density function of turbulence processes υ(u(t),w(t)) at bridge node j; $G_{jk_j}(f_{kl})$: coefficient matrix containing coherence values and dimension of bridge decks; N: number of deck nodes; ϕ_{kl} : random phase angles, uniformly distributed over [0,2π] generated randomly by the Monte Carlo technique.

One can use the modal factorization or the spectral matrix-based proper orthogonal decomposition to simulate the turbulence wind fields as following expression (Le 2007), see Figure 2:

$$\upsilon_i(t) = 2\sqrt{\Delta f} \sum_{j=1}^{\hat{N}} \sum_{l=1}^{\bar{N}} \psi_{\upsilon_j}(f_l) \sqrt{\lambda_{\upsilon_j}(f_l)} \cos(2\pi f_l t + \phi_l) \quad (13)$$

where Δf_l: frequency interval at point *l*; Δf : constantly frequency interval $\Delta f = f_{up}/\bar{N}$ and $f_l = (l-1)\Delta f$, f_{up} : upper cut-off frequency; $\psi_{\upsilon_j}(f_l)$: spectral vector of the turbulence process at frequency f_l; $\lambda_{\upsilon_j}(f_l)$: spectral eigenvalue of the turbulence process at frequency f_l; ϕ_l: phase angle considered as random variable uniformly distributed over [0,2π]. The random phase angles can also be digitally generated by the Monte Carlo technique.

Accuracy of simulated turbulence processes must be verified by comparing between power spectral densities of simulated processed and targeted power spectral densities, and between coherence of simulated processes and targeted coherence as well.

5 BUFFETING RESPONSE PREDICTION

Multi-degree-of-freedom motion (MDOF) equations of structures subjected to the full-scale buffeting forces can be expressed thanks to finite element method (FEM):

$$M\ddot{U} + C\dot{U} + KU = F_b(t) \quad (14)$$

where $U = \{h(t)^T, p(t)^T, a(t)^T\}$: displacement vector containing three vertical, lateral and rotational displacements; $\dot{U}, \ddot{U}$: velocity and acceleration vectors; $F_b(t)$: full-scale buffeting forces.

Structurally global responses can be expressed into the mass matrix-normalized generalized coordinates as follows:

$$U(t) = \Phi\xi(t) = \sum_{i=1}^{\overline{M}} \phi_i \xi_i \quad (15)$$

where $\xi(t) = \{\xi_1(t), \xi_2(t), ..., \xi_M(t)\}$: structural generalized coordinates; $\Phi = [\phi_1, \phi_2, ..., \phi_M]^T$: modal matrix; $\overline{M}$: number of truncated structural modes ($\overline{M} << M$);

Therefore, single-degree-of-freedom (SDOF) motion equation of the i-th generalized coordinate is determined:

$$\ddot{\xi}_i(t) + 2\zeta_i\omega_i\dot{\xi}_i(t) + \omega_i^2\xi_i(t) = \frac{1}{2}\phi_i^T \rho UB\left[C_u u(t) + C_w w(t)\right] \quad (16)$$

where ω_i, ζ_i : circular frequency, damping ratio of the i-th generalized coordinate.

Using the covariance proper transformation, the turbulence wind fields u(t), w(t) can be approximated by uncorrelated subprocesses and covariance eigenvectors (or covariance turbulent modes). Thus, the SDOF motion equation is expressed such following forms as:

$$\ddot{\xi}_i(t) + 2\zeta_i\omega_i\dot{\xi}_i(t) + \omega_i^2\xi_i(t) = \frac{1}{2}\rho UB\left[\phi_i^T C_u \sum_{j=1}^{\tilde{M}} \theta_{uj} y_{uj}(t) + \phi_i^T C_w \sum_{j=1}^{\tilde{M}} \theta_{wj} y_{wj}(t)\right] \quad (17a)$$

$$\ddot{\xi}_i(t) + 2\zeta_i\omega_i\dot{\xi}_i(t) + \omega_i^2\xi_i(t) = \frac{1}{2}\rho UB\left[\sum_{j=1}^{\tilde{M}} A_{uij} y_{uj}(t) + \sum_{j=1}^{\tilde{M}} A_{wij} y_{wj}(t)\right] \quad (17b)$$

where $A_{uij} = \phi_i C_u \theta_{uj}$; $A_{wij} = \phi_i C_w \theta_{wj}$: cross modal participation coefficients accounting for interaction between structural modes and covariance turbulent modes; C_u, C_w : full-scale force coefficients relating to wind velocity, aerodynamic force coefficients and deck length; $y_u(t) = \{y_{u_1}(t), y_{u_2}(t), ..., y_{u_N}(t)\}^T$, $y_w(t) = \{y_{w_1}(t), y_{w_2}(t), ..., y_{w_N}(t)\}^T$: covariance principal coordinates, which are determined from original turbulent fields as follows

$$y_u(t) = u(t)\Theta_u; \quad y_{u_j}(t) = u(t)\theta_{u_j} \quad (18a)$$

$$y_w(t) = w(t)\Theta_w; \quad y_{w_j}(t) = w(t)\theta_{w_j} \quad (18b)$$

Therefore, the SDOF motion equations associated with vertical, horizontal and rotation structural principal coordinates can be expressed as follows:

$$\ddot{\xi}_{hi}(t) + 2\zeta_{hi}\omega_{hi}\dot{\xi}_{hi}(t) + \omega_{hi}^2\xi_{hi}(t) = \frac{1}{2}\rho UB\left[\sum_{j=1}^{\tilde{M}} A_{uij}^L y_{uj}(t) + \sum_{j=1}^{\tilde{M}} A_{wij}^L y_{wj}(t)\right] \quad (19a)$$

$$\ddot{\xi}_{pi}(t) + 2\zeta_{pi}\omega_{pi}\dot{\xi}_{pi}(t) + \omega_{pi}^2\xi_{pi}(t) = \frac{1}{2}\rho UB\left[\sum_{j=1}^{\tilde{M}} A_{uij}^D y_{uj}(t) + \sum_{j=1}^{\tilde{M}} A_{wij}^D y_{wj}(t)\right] \quad (19b)$$

$$\ddot{\xi}_{ai}(t) + 2\zeta_{ai}\omega_{ai}\dot{\xi}_{ai}(t) + \omega_{ai}^2\xi_{ai}(t) = \frac{1}{2}\rho UB\left[\sum_{j=1}^{\tilde{M}} A_{uij}^M y_{uj}(t) + \sum_{j=1}^{\tilde{M}} A_{wij}^M y_{wj}(t)\right] \quad (19c)$$

where $A_{uij}^L, A_{wij}^L, A_{uij}^D, A_{wij}^D, A_{uij}^M, A_{wij}^M$: cross modal participation coefficients between structural modes and covariance turbulent modes which are correspondent to u-,w-turbulences and turbulent-induced lift, drag, moment $A_{uij}^L = \phi_{hi} C_u^L \theta_{uj}$; $A_{wij}^L = \phi_{hi} C_w^L \theta_{wj}$; $A_{uij}^D = \phi_{pi} C_u^D \theta_{uj}$; $A_{wij}^D = \phi_{hi} C_w^D \theta_{wj}$; $A_{uij}^M = \phi_{ai} C_u^M \theta_{uj}$; $A_{wij}^M = \phi_{ai} C_w^M \theta_{wj}$

The SDOF motion equations system is formulated in the time domain. Finding out solution of this system can be obtained based on the direct integration methods such as the Newmark-beta method, the fourth-order Runge-Kutta method and so on. Finally, the structural global responses (vertical, lateral and rotational displacements) of bridges can be determined based on the superposition principle as follows:

$$U_h = \sum_{i=1}^{\overline{M}_h} \phi_{hi}\xi_{hi}(t) \quad ; \quad U_p = \sum_{i=1}^{\overline{M}_p} \phi_{pi}\xi_{pi}(t) \quad ; \quad U_a = \sum_{i=1}^{\overline{M}_a} \phi_{ai}\xi_{ai}(t) \tag{20}$$

where U_h, U_p, U_a: global vertical, lateral and rotational displacements, respectively; ϕ_h, ϕ_p, ϕ_a: structural modes corresponding to three responses; $\overline{M}_h, \overline{M}_p, \overline{M}_a$: numbers of component modes in combination of responses.

6 RESULTS AND DISCUSIONS

A medium-span cable-stayed bridge has been taken for numerical example using the computational procedures. Span arrangement is 40.5+97+40.5=178m, while there are 30 total nodes in the bridge deck (nodes 8, 23 at pylons). The global responses of bridge are required to predict at the mean velocity range between 5m/s and 40m/s. 3-D frame model has built thanks to the finite element method (FEM), see Figure 3. First ten structural modes have been analyzed. Natural frequencies of the first ten structural modes vary between 0.61Hz and1.86Hz. Structural damping ratios are assumed to be 0.005 for all modes. Aerodynamic static coefficients of cross section at balanced attack angle and their first derivatives have been experimentally determined: $C_L = 0.158$, $C_D = 0.041$, $C_M = 0.174$, $C_L' = 3.73$, $C_D' \approx 0$, $C_M' = 2.06$. One-sided auto spectral density functions of u-, w-turbulent components are obtained due to the Kaimail's and the Panofsky's spectral models, respectively (Simiu and Scanlan 1976). Coherence function is applied the Davenport's empirical exponential function with decay factors with decay factors $c_u = 10,\ c_w = 6.5$ (Davenport 1962). Aerodynamic admittance function is used the Liepmann's empirical function as approximation of the Sears' function (Liepmann 1958), while the mechanical admittance function is determined corresponding to structural generalized coordinates.

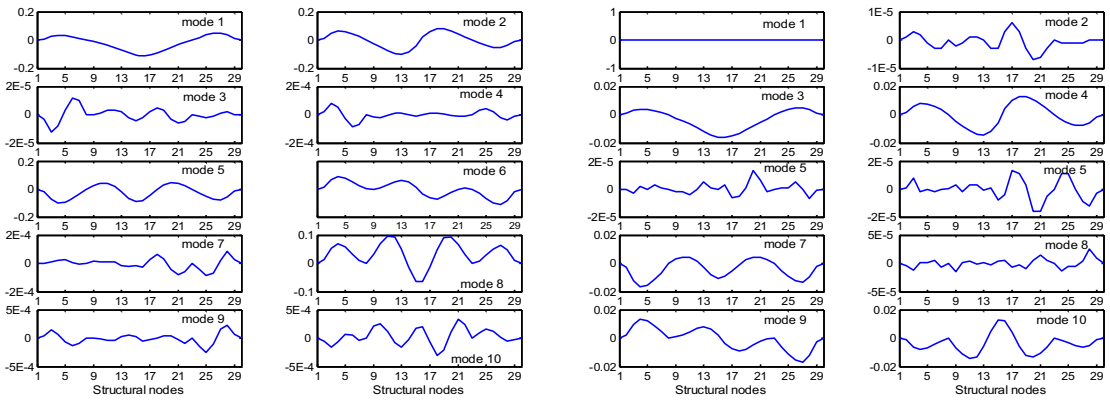

(a) Vertical modes (b) Rotational

Figure 3. Normalized bridge mode shapes : a. vertical modal displacement, b. rotational modal displacement

At the beginning, the turbulence wind fields at the 30 deck nodes $u(t) = \{u_1(t), u_2(t), \ldots, u_{30}(t)\}^T$ and $w(t) = \{w_1(t), w_2(t), \ldots, w_{30}(t)\}^T$ have been simulated using the above-mentioned digital simulation procedures. Figure 4 shows simulated turbulence processes at some deck nodes during 100-second interval, at the mean velocity U=20m/s (other simulated turbulence processes at other deck nodes and other wind velocities omitted for a sake of brevity).

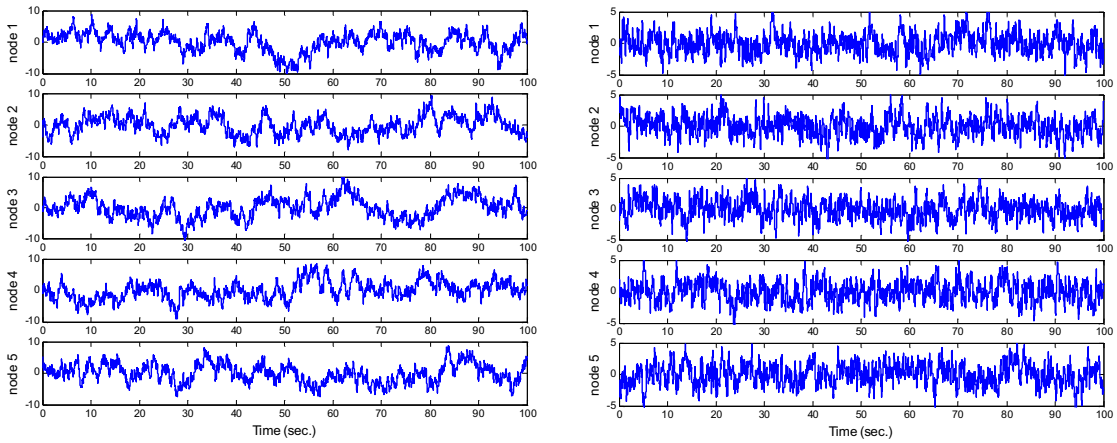

(a) u-turbulence (b) w-turbulence

Figure 4. Simulated turbulence processed at some deck nodes at mean velocity U=20m/s

Simulated turbulence fields u(t), w(t) have been used to formulate the zero-time-lag covariance matrix. The covariance eigenvectors (or covariance turbulence modes) and covariance eigenvalues have been found out. From the covariance eigenvalues, eigenvectotrs and the simulated turbulence wind fields, the covariance principal coordinates then can be determined. Figure 5 shows the first ten covariance turbulence modes of u-,w-turbulence wind fields.

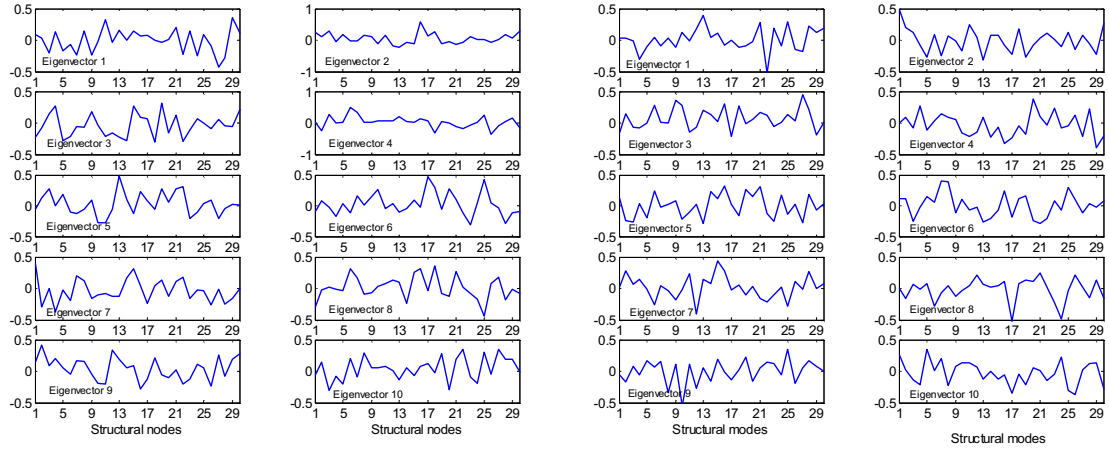

(a) u-turbulence (b) w-turbulence

Figure 5. Covariance turbulence modes of u-,w-turbulence wind fields

Time histories of the global buffeting responses of bridge (the vertical, rotational and lateral displacements) can be solved via the direct integration method. Figure 6 indicates the time histories of the vertical and rotational displacements at the main span's middle node No.15 at the wind velocity U=20m/s during the 100-second period. The maximum response values at all bridge deck nodes at all investigated mean wind velocities can be determined from these time histories of the global buffeting responses.

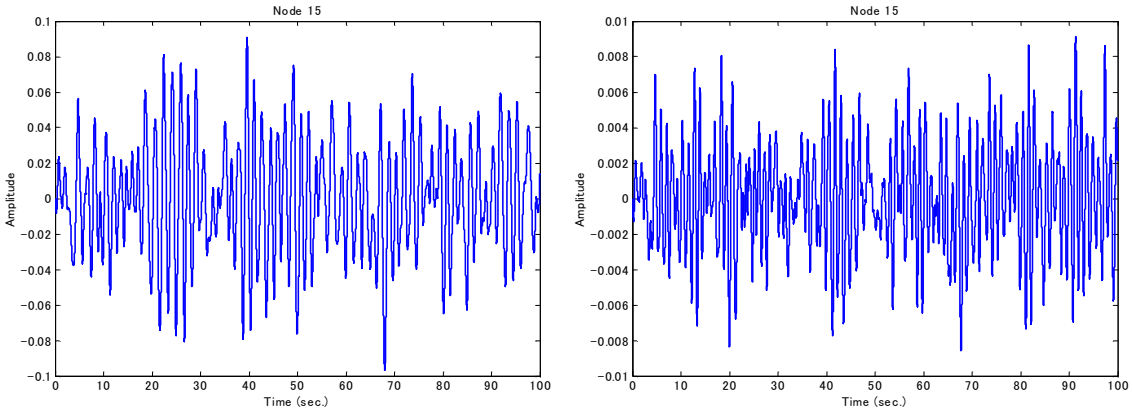

(a) Vertical displacement (b) Rotational displacement

Figure 6. Time histories of global buffeting responses at mid-span node 15 at mean velocity U=20m/s

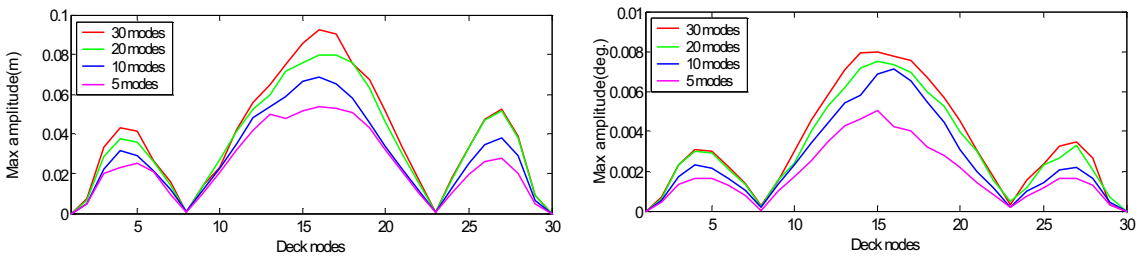

(a) Vertical displacement (b) Rotational displacement

Figure 7. Effect of number of turbulence modes on global responses at all deck nodes at mean velocity U=20m/s

Effect of number of the covariance turbulence modes on the buffeting responses of bridge has been investigated. Figure 7 indicates the maximum structural responses on the bridge deck at U=20m/s corresponding to number of the turbulence modes ($\tilde{M} = 30;20;10 and 5$, in which 30 modes imply for targeted response). Apparently, maximum buffeting responses reduce with respect to decrease of truncated number of the turbulence modes. Number of turbulence modes in some extent does influence considerably on the buffeting responses of bridge. Concretely, the maximum vertical amplitudes at midspan node 15 are 9.3cm (100%), 8.0cm (86%), 6.9cm (74%) and 5.3cm (57%) and the maximum torsional amplitudes at node 15 are 0.0078^0 (100%), 0.0075^0 (96%), 0.0071^0 (71%) and 0.0049^0 (63%) corresponding to 30, 20, 10 and 5 turbulence modes taken into account. Therefore, higher number of low-order covariance turbulence modes should be used for estimating the buffeting responses of bridge in the time domain.

7 CONCLUSION

New approach for the quasi-steady and unsteady buffeting response prediction of bridges has been formulated in the time domain using the covariance matrix-based proper orthogonal decomposition. Time histories of the turbulence wind fields on the bridge decks have been digitally simulated via the spectral matrix-based proper orthogonal decomposition. Effect of number of the covariance turbulence modes on the simulated turbulence wind fields and

global buffeting responses of bridges also is investigated accordingly. The computational procedure is promising for the both quasi-steady and unsteady buffeting response analysis of bridges in the time domain with its essential advantages to treat with aerodynamic and geometrical nonlinearities, and unsteady buffeting forces as well. Moreover, it seems that many number of the covariance turbulence modes should be required for more accurate estimation of the buffeting response of bridges. In the other words, the first covariance turbulence mode does not play significant role in its contribution for the buffeting response of bridges in the time domain.

ACKNOWLEDGEMENTS

This study was partially funded by the Ministry of Education, Culture, Sport, Science and Technology, Japan through the Global Center of Excellence Program, 2008-2012 which is acknowledged.

REFERENCES

V. Boonyapinyo, T. Miyata, H. Yamada, H., Advanced aerodynamic analysis of suspension bridges by state-space approach, J. Struct. Engrg., ASCE 125, 12(1999) 1357-1366.

L. Carassale, G. Piccardo, G. Solari, Double modal transformation and wind engineering applications, J. Engrg. Mech., ASCE 127, 5 (1999) 432-439.

X. Chen, M. Matsumoto, A. Kareem, Time domain flutter and buffeting response analysis of bridges, J. Engrg. Mech., ASCE 126, 1 (2000) 7-16.

X. Chen, A. Kareem, Advances in modeling of aerodynamic forces on bridges, J. Engrg. Mech., ASCE 128, 11(2002) 1193-1203.

X. Chen, A. Kareem, Proper orthogonal decomposition-based modeling, analysis, and simulation of dynamic wind load effects on structures, J.Engrg. Mech., ASCE 131, 4(2005) 325-339.

A.G. Davenport, Buffeting of a suspension bridge by storm winds, J. Struct. Div., ASCE 88, 3(1962) 233-268.

T.H. Le, Unsteady buffering forces and gust response prediction of bridges with proper orthogonal decomposition applications, Doctoral dissertation, Kyoto University 2007.

Y.C. Liang, P. Lee, W.Z. Lim, K. Lee, C.G. Wu, Proper orthogonal decomposition and its applications – part I: Theory, J. Sound Vib. 252, 3(2002) 527-544.

J.L. Lumley, Stochastic Tools in Turbulence, Academic Press 1970.

M. Matsumoto, H. Shirato, T.H. Le, Time and frequency domain gust response prediction using proper orthogonal decomposition, The 12th Int'l Conference on Wind Engineering (ICWE12), Cairne Australia, 2007, July 1-6.

G. Solari, L. Carassale, Modal transformation tools in structural dynamics and wind engineering, Wind & Structures, 3, 4 (2000) 221-241.

Y. Tamura, S. Suganuma, H. Kikuchi, K. Hibi, Proper orthogonal decomposition of random wind pressure field, J. Fluid Struct., 13 (1999) 1069-1095.

F. Tubino, G. Solari, Gust buffeting of long-span bridges: Double Modal Transformation and effective turbulence, J. Engrg. Struct. 29 (2007) 1698-1707.

The Seventh International Colloquium on Bluff Body Aerodynamics and Applications (BBAA7)
Shanghai, China; September 2-6, 2012

Prediction of buffeting response of long span bridges to transient nonstationary winds

Xinzhong Chen

Wind Science and Engineering Research Center, Department of Civil and Environmental Engineering, Texas Tech University, Lubbock, TX, USA

ABSTRACT: This paper presents a general frequency domain framework for predicting buffeting response of long span bridges to transient nonstationary winds. The wind speed field is described in terms of deterministic time-varying mean and evolutionary random fluctuations characterized by their evolutionary spectra. The static, self-excited and buffeting forces on bridges are modeled in static force coefficients, flutter derivatives and admittance functions with consideration of transient nonstationary winds. Formulations are presented for estimating the time-varying mean, evolutionary spectrum, variance and extreme response. The general characteristics of transient buffeting response are discussed using a long span suspension bridge as an example. The effectiveness and accuracy of the proposed framework is also confirmed through time domain Monte Carlo simulations.

KEYWORDS: Buffeting response; Nonstationary response; Bridge aerodynamics; Long span bridges; Wind loading.

1 INTRODUCTION

Current analysis frameworks for estimating wind-induced buffeting response of structures are generally based on the assumption of stationary wind excitations. The mean wind speed within a given time duration, say, 1 hour, is considered as a constant, and the wind fluctuation around its mean is modeled as a stationary random process. The stationarity assumption faces challenges in the cases such as hurricane or typhoon winds and thunderstorm downbursts, where the magnitude and direction of mean wind speed may change with time relatively rapidly, and the random wind turbulence may also show nonstationary characteristics.

Davenport and King (1993) illustrated the influence of storm duration on "build-up" of single torsional modal response of Golden Gate Bridge, and pointed out that the maximum response in a given storm may be greater than it would be in other storm having a higher wind speed but short duration. Chen (2008) developed an analysis framework for quantifying alongwind tall building response under transient nonstationary winds, and investigated the influence of time-varying mean wind speed, mean wind speed profile, and spatial correlation of wind fluctuations on building response. Kwon and Kareem (2009) introduced a general gust-front factor accounting for the extreme response of buildings under transient winds. The theory concerning structural response to nonstationary excitations (e.g., Lin and Cai 1995; Lutes and Sarkani 2004) has been used in earthquake engineering (e.g., Conte and Peng 1997; Michaelov et al. 2001; Barbato and Vasta 2010), but its applications in wind engineering has been very limited.

This paper presents a general frequency domain framework for predicting buffeting response of long span bridges to transient nonstationary winds. Formulations are presented for modeling static, self-excited and buffeting forces and for estimating the time-varying mean, variance and extreme response. The general characteristics of transient buffeting response are discussed using a long span suspension bridge as an example. Time domain Monte Carlo simulations are also performed to confirm the effectiveness and accuracy of the proposed framework.

2 THEORETICAL FRAMEWORK

2.1 *Equations of bridge motion*

A long span bridge subjected to wind excitation with the mean wind direction normal to the bridge deck axis is considered. At the spanwise location x, the deterministic time-varying mean wind speed is denoted by $U(x,t)$ with its random fluctuation components $u'(x,t)$ and $w'(x,t)$ in horizontal and vertical directions, respectively. $u'(x,t)$ and $w'(x,t)$ are regarded as zero mean evolutionary random processes with the underlying zero mean stationary random processes $u(x,t)$ and $w(x,t)$ and complex-valued deterministic modulation functions $g_u(x,\omega,t)$ and $g_w(x,\omega,t)$, respectively. $u'(x,t)$ and $u(x,t)$ are expressed in the general form of a Fourier-Stieltjes integral as

$$u'(x,t)=\int_{-\infty}^{\infty} g_u(x,\omega,t)e^{i\omega t}d\Theta_u(x,\omega)\,;\quad u(x,t)=\int_{-\infty}^{\infty} e^{i\omega t}d\Theta_u(x,\omega) \tag{1}$$

where $d\Theta_u(x,\omega)$ is complex-valued zero mean orthogonal increment random process

$$E[d\Theta_u(x,\omega)]=0;\ E[d\Theta_u(x,\omega)]=E[d\Theta_u^*(x,-\omega)];$$

$$E[d\Theta_u(x_1,\omega_1)d\Theta_u^*(x_2,\omega_2)]=S_u(x_1,x_2,\omega_1)\delta(\omega_1-\omega_2)d\omega_1 \tag{2}$$

$E[...]$ denotes the expectation or ensemble average; $\delta(...)$ represents the Dirac delta function; $S_u(x,\omega)=S_u(x,x,\omega)$ and $S_u(x_1,x_2,\omega)$ are the power spectral density (PSD) of $u(x,t)$ and cross PSD of $u(x_1,t)$ and $u(x_2,t)$; ω is frequency; superscript * denotes complex conjugate operator; and $i=\sqrt{-1}$.

The evolutionary PSD (EPSD) of $u'(x,t)$ and cross EPSD of $u'(x_1,t)$ and $u'(x_2,t)$ are then given as

$$S_{u'}(x,\omega,t)=|g_u(x,\omega,t)|^2\,S_u(x,\omega)\,;\quad S_{u'}(x_1,x_2,\omega,t)=g_u(x_1,\omega,t)g_u^*(x_2,\omega,t)S_u(x_1,x_2,\omega) \tag{3}$$

where $g_u(x,-\omega,t)=g_u^*(x,\omega,t)$. Similar formulations for $w'(x,t)$ and $w(x,t)$ can be given in terms of $d\Theta_w(x,\omega)$, $g_w(x,\omega,t)$, $S_w(x,\omega,t)$ and $S_w(x_1,x_2,\omega,t)$.

The aerodynamic forces on bridge deck, i.e., lift (downward), drag (downwind) and pitching moment (nose-up), can be separated into static (mean), self-excited and buffeting force components. It is assumed that the variation rate of time-varying mean wind speed is low enough such that the effects of transient aerodynamics can be neglected. Accordingly, the aerodynamic forces can be given in the same formulations as traditional time-invariant mean wind speed case, but with consideration of time-varying mean wind speed and evolutionary wind fluctuations. For instance, the static, self-excited and buffeting components of pitching moment per unit length of bridge deck are given as (e.g., Scanlan 1993; Chen and Kareem 2002)

$$M_s(x,t)=\frac{1}{2}\rho U^2(x,t)B^2C_M \tag{4}$$

$$M_{se}(x,t)=\frac{1}{2}\rho U^2(x,t)(2b^2)\left(kA_1^*\frac{\dot{h}}{U}+kA_2^*\frac{b\dot{\alpha}}{U}+k^2A_3^*\alpha+k^2A_4^*\frac{h}{b}+kA_5^*\frac{\dot{p}}{U}+k^2A_6^*\frac{p}{b}\right) \tag{5}$$

$$\begin{aligned}M_b(x,t)=\frac{1}{2}\rho U(x,t)B^2\int_{-\infty}^{\infty}[&2C_M\chi_{Mu}(x,\omega,t)g_u(x,\omega,t)e^{i\omega t}d\Theta_u(x,\omega)\\&+2C_M'\chi_{Mw}(x,\omega,t)g_w(x,\omega,t)e^{i\omega t}d\Theta_w(x,\omega)]\end{aligned} \tag{6}$$

where ρ is air density; $B = 2b$ is bridge deck width; C_M is static pitching moment coefficients; $C_M' = dC_M / d\alpha$; $A_i^*(i = 1-6)$ are flutter derivatives, which are function of reduced frequency $k = \omega b / U(x,t)$; $h(x,t)$, $p(x,t)$ and $\alpha(x,t)$ are bridge deck dynamic displacements around the statically deformed equilibrium at the spanwise location x in acrosswind, alongwind and torsional directions; χ_{Mu} and χ_{Mw} are aerodynamic admittance functions.

It is assumed that the time variation rates of mean wind speed and mean wind loading are low compared to the natural frequencies of the bridge, therefore the resulting bridge response can be calculated through quasi-static analysis. An iterative calculation procedure is need to solve this statically nonlinear problem as the static force coefficients are functions of angle of attack which is influenced by bridge deck rotation. The dynamic buffeting response around the statically deformed equilibrium is expressed in generalized modal responses. Following the finite element procedure, the equations of bridge motion can be expressed as follows in the generalized modal displacement vector $\boldsymbol{q}$ (e.g., Chen et al. 2000a and b)

$$\boldsymbol{M}\ddot{\boldsymbol{q}} + \boldsymbol{C}\dot{\boldsymbol{q}} + \boldsymbol{K}\boldsymbol{q} = \boldsymbol{Q}_{se} + \boldsymbol{Q}_b \tag{7}$$

$$\boldsymbol{M} = diag[m_j]; \quad \boldsymbol{C} = diag[2m_j\xi_{sj}\omega_{sj}]; \quad \boldsymbol{K} = diag[m_j\omega_{sj}^2] \tag{8}$$

$$\boldsymbol{Q}_{se} = \boldsymbol{A}_s(\omega,t)\boldsymbol{q}(t) + \boldsymbol{A}_d(\omega,t)\dot{\boldsymbol{q}}(t) \tag{9}$$

$$\boldsymbol{Q}_b = \int_{-\infty}^{\infty}\left(\boldsymbol{A}_{bu}(\omega,t)e^{i\omega t}d\boldsymbol{\Theta}_u(\omega) + \boldsymbol{A}_{bw}(\omega,t)e^{i\omega t}d\boldsymbol{\Theta}_w(\omega)\right) \tag{10}$$

where $\boldsymbol{M}, \boldsymbol{C}, \boldsymbol{K}$ are generalized mass, damping and stiffness matrices; $m_j, \xi_{sj}, \omega_{sj}$ are j-th generalized mass, damping ratio and frequency; $\boldsymbol{Q}_{se}$ and $\boldsymbol{Q}_b$ are generalized self-excited and buffeting force vectors; $\boldsymbol{A}_s(\omega,t)$ and $\boldsymbol{A}_d(\omega,t)$ are aerodynamic stiffness and damping matrices; $\boldsymbol{A}_{bu}(\omega,t)$ and $\boldsymbol{A}_{bw}(\omega,t)$ are buffeting force matrices; $d\boldsymbol{\Theta}_u(\omega)$ and $d\boldsymbol{\Theta}_w(\omega)$ are orthogonal increment random processes associated with horizontal and vertical wind fluctuation vectors, characterized by the spectral matrices, i.e.,

$$E[d\boldsymbol{\Theta}_u(\omega_1)d\boldsymbol{\Theta}_u^{T*}(\omega_2)] = \boldsymbol{S}_u(\omega_1)\delta(\omega_1-\omega_2)d\omega_1;\ E[d\boldsymbol{\Theta}_w(\omega_1)d\boldsymbol{\Theta}_w^{T*}(\omega_2)] = \boldsymbol{S}_w(\omega_1)\delta(\omega_1-\omega_2)d\omega_1 \tag{11}$$

and T denotes the matrix transpose operator.

The equations of bridge motion can be represented in the state-space format:

$$\dot{\boldsymbol{Y}} = \boldsymbol{A}(\omega,t)\boldsymbol{Y} + \boldsymbol{B}\boldsymbol{Q}_b \tag{12}$$

$$\boldsymbol{Y} = \begin{Bmatrix}\boldsymbol{q}\\ \dot{\boldsymbol{q}}\end{Bmatrix}; \quad \boldsymbol{A}(\omega,t) = \begin{bmatrix}\boldsymbol{0} & \boldsymbol{I}\\ -\boldsymbol{M}^{-1}[\boldsymbol{K}-\boldsymbol{A}_s(\omega,t)] & -\boldsymbol{M}^{-1}[\boldsymbol{C}-\boldsymbol{A}_d(\omega,t)]\end{bmatrix}; \quad \boldsymbol{B} = \begin{bmatrix}0\\ \boldsymbol{M}^{-1}\end{bmatrix} \tag{13}$$

At a given time instant, "frozen time", i.e., a given wind speed, the complex modal properties can be quantified through the solution of following complex eigenvalue problem:

$$\lambda_j\boldsymbol{\Gamma}_j = \boldsymbol{A}(\omega_j,t)\boldsymbol{\Gamma}_j; \quad \lambda_j = -\xi_j\omega_j + i\omega_j\sqrt{1-\xi_j^2}; \quad \boldsymbol{\Gamma}_j = \begin{Bmatrix}\boldsymbol{\Phi}_j\\ \lambda_j\boldsymbol{\Phi}_j\end{Bmatrix} \tag{14}$$

where λ_j and $\boldsymbol{\Phi}_j$ are j-th complex eigenvalue and eigenmode (mode shape) with their complex conjugates $\lambda_{j+N} = \lambda_j^*$ and $\boldsymbol{\Phi}_{j+N} = \boldsymbol{\Phi}_j^*$ (where N is the total number of modes considered); ω_j and ξ_j are j-th complex modal frequency and damping ratio. An iterative calculation is needed for the solution of this eigenvalue problem as $\boldsymbol{A}(\omega,t)$ involves the unknown frequency.

The corresponding eigenmode of $\boldsymbol{A}^T(\omega,t)$ is expressed as

$$\lambda_j \boldsymbol{\Psi}_j = \boldsymbol{A}^T(\omega_j,t)\boldsymbol{\Psi}_j; \quad \boldsymbol{\Psi}_j = \begin{Bmatrix} \boldsymbol{\Psi}_{ju} \\ \boldsymbol{\Psi}_{jd} \end{Bmatrix} \tag{15}$$

It is noted that each of the complex eigenvalues and modal shapes are determined using different system matrix defined at the corresponding modal frequency, i.e., $\boldsymbol{A}(\omega_j,t)$. Therefore, theoretically the orthogonal condition between different modal shapes does not exist, but can be considered to be approximately valid without introducing a noticeable influence on the system behavior. Accordingly, the equations of bridge motion can be represented in an equivalent frequency-independent format with $\boldsymbol{A}_{\text{ef}}(t)$ replacing $\boldsymbol{A}(\omega,t)$ (Chen 2006). This equivalent linear time-variant (LTV) bridge aeroelastic system is uniquely defined by the complex modal properties. Denote

$$\boldsymbol{\Gamma} = \begin{bmatrix} \boldsymbol{\Gamma}_1 & \boldsymbol{\Gamma}_2 & \dots & \boldsymbol{\Gamma}_{2N} \end{bmatrix} = \begin{bmatrix} \boldsymbol{\Phi} \\ \boldsymbol{\Phi}\boldsymbol{\Lambda} \end{bmatrix}; \boldsymbol{\Phi} = \begin{bmatrix} \boldsymbol{\Phi}_1 & \boldsymbol{\Phi}_2 & \dots & \boldsymbol{\Phi}_{2N} \end{bmatrix}; \boldsymbol{\Psi} = \begin{bmatrix} \boldsymbol{\Psi}_1 & \boldsymbol{\Psi}_2 & \dots & \boldsymbol{\Psi}_{2N} \end{bmatrix} = \begin{bmatrix} \boldsymbol{\Psi}_u \\ \boldsymbol{\Psi}_d \end{bmatrix} \tag{16}$$

the orthogonal condition leads to

$$\boldsymbol{\Psi}^T = \boldsymbol{\Gamma}^{-1}; \quad \boldsymbol{\Gamma}^{-1}\boldsymbol{A}_{\text{ef}}\boldsymbol{\Gamma} = \Lambda = diag[\lambda_j] \tag{17}$$

which can be used to determine $\boldsymbol{A}_{ef}(t)$ if needed.

2.2 *Frequency domain buffeting response analysis*

Introducing a transformation $\boldsymbol{Y}(t) = \boldsymbol{P}(t)\boldsymbol{R}(t)$, the state-space equation of motion becomes

$$\dot{\boldsymbol{R}}(t) = \boldsymbol{P}^{-1}(t)[\boldsymbol{A}_{\text{ef}}(t)\boldsymbol{P}(t) - \dot{\boldsymbol{P}}(t)]\boldsymbol{R}(t) + \boldsymbol{P}^{-1}(t)\boldsymbol{B}\boldsymbol{Q}_b(t) \tag{18}$$

If $\boldsymbol{P}(t)$ is a fundamental matrix, i.e., it satisfies the dynamic eigenvalue equation $\dot{\boldsymbol{P}}(t) = \boldsymbol{A}_{\text{ef}}(t)\boldsymbol{P}(t)$, the state-space equation leads to

$$\boldsymbol{Y}(t) = \boldsymbol{\Xi}(t,t_0)\boldsymbol{Y}(t_0) + \int_{t_0}^{t} \boldsymbol{\Xi}(t,\tau)\boldsymbol{B}\boldsymbol{Q}_b(\tau)d\tau \tag{19}$$

where $\boldsymbol{\Xi}(t,\tau) = \boldsymbol{P}(t)\boldsymbol{P}^{-1}(\tau)$ is state transition matrix; and $\boldsymbol{Y}(t_0)$ is the state vector at t_0.

The dynamic eigenvalue equation of the LTV system can be solved, for instance, using an approach introduced by Kloet and Neerhoff (2000), which is based on triangularization of system matrix by Riccati transformation. In this study, it is assumed that the variation rate of complex mode shape $\boldsymbol{\Gamma}(t)$ is relatively small, thus $\dot{\boldsymbol{\Gamma}}(t) \approx 0$, and the fundamental matrix can be approximately given by the "frozen time" complex eigenvalues and vectors as

$$\boldsymbol{P}(t) = \boldsymbol{\Gamma}(t)e^{\int_0^t \boldsymbol{\Lambda}(\tau)d\tau} \tag{20}$$

When the system is from "at rest" at $t = 0$, the generalized displacement and velocity vectors are given as follows based on Eq. (19):

$$\boldsymbol{q}(t) = \int_0^t \boldsymbol{h}_q(t,\tau)\boldsymbol{Q}_b(\tau)d\tau; \quad \dot{\boldsymbol{q}}(t) = \int_0^t \boldsymbol{h}_{\dot{q}}(t,\tau)\boldsymbol{Q}_b(\tau)d\tau \tag{21}$$

$$\boldsymbol{h}_q(t,\tau)=\boldsymbol{\Phi}(t)e^{\int_\tau^t \boldsymbol{\Lambda}(t)dt}\boldsymbol{\Psi}_d^T(\tau)\boldsymbol{M}^{-1};\quad \boldsymbol{h}_{\dot{q}}(t,\tau)=\frac{\partial \boldsymbol{h}_q(t,\tau)}{\partial t}\approx \boldsymbol{\Phi}(t)\boldsymbol{\Lambda}(t)e^{\int_\tau^t \boldsymbol{\Lambda}(t)dt}\boldsymbol{\Psi}_d^T(\tau)\boldsymbol{M}^{-1} \tag{22}$$

where $\boldsymbol{h}_q(t,\tau)$ and $\boldsymbol{h}_{\dot{q}}(t,\tau)$ are impulse response matrices for displacement and velocity.

The variance matrix of generalized displacement vector is then determined as

$$\boldsymbol{R}_q(t)=E[\boldsymbol{q}(t)\boldsymbol{q}^T(t)]=\int_0^t\int_0^t \boldsymbol{h}_q(t,t_1)\boldsymbol{R}_{Qb}(t_1,t_2)\boldsymbol{h}_q^T(t,t_2)dt_1dt_2 \tag{23}$$

$$\boldsymbol{R}_{Qb}(t_1,t_2)=\int_{-\infty}^{\infty}\boldsymbol{S}_{Qb}(\omega,t_1,t_2)e^{-i\omega(t_1-t_2)}d\omega \tag{24}$$

$$\boldsymbol{S}_{Qb}(\omega,t_1,t_2)=\boldsymbol{A}_{bu}(\omega,t_1)\boldsymbol{S}_u(\omega)\boldsymbol{A}_{bu}^{T*}(\omega,t_2)+\boldsymbol{A}_{bw}(\omega,t_1)\boldsymbol{S}_w(\omega)\boldsymbol{A}_{bw}^{T*}(\omega,t_2) \tag{25}$$

where $\boldsymbol{R}_{Qb}(t_1,t_2)$ and $\boldsymbol{S}_{Qb}(\omega,t_1,t_2)$ are the covariance matrix and cross EPSD between $\boldsymbol{Q}_b(t_1)$ and $\boldsymbol{Q}_b(t_2)$. It is assumed that *u*- and *w*-components of wind fluctuations are uncorrelated, while their correlation and cross spectrum can be readily incorporated in the formulations.

The EPSD matrix of the generalized displacement vector is determined as

$$\boldsymbol{S}_q(\omega,t)=\boldsymbol{H}_u(\omega,t)\boldsymbol{S}_u(\omega)\boldsymbol{H}_u^{T*}(\omega,t)+\boldsymbol{H}_w(\omega,t)\boldsymbol{S}_w(\omega)\boldsymbol{H}_w^{T*}(\omega,t) \tag{26}$$

$$\boldsymbol{H}_u(\omega,t)=\int_0^t \boldsymbol{h}_q(t,\tau)\boldsymbol{A}_{bu}(\omega,\tau)e^{-i\omega(t-\tau)}d\tau;\qquad \boldsymbol{H}_w(\omega,t)=\int_0^t \boldsymbol{h}_q(t,\tau)\boldsymbol{A}_{bw}(\omega,\tau)e^{-i\omega(t-\tau)}d\tau \tag{27}$$

and the integration of $\boldsymbol{S}_q(\omega,t)$ over the frequency gives $\boldsymbol{R}_q(t)$.

The time-varying variance and ESPD of any response of interest can be susequaently calculated. For a given response $v(t)=\boldsymbol{D}^T\boldsymbol{q}(t)$, these are

$$\sigma_v^2(t)=R_v(t)=\boldsymbol{D}^T\boldsymbol{R}_q(t)\boldsymbol{D};\quad \boldsymbol{S}_v(\omega,t)=\boldsymbol{D}^T\boldsymbol{S}_q(\omega,t)\boldsymbol{D} \tag{28}$$

and similar calculations for any response related to velocity response $\dot{\boldsymbol{q}}(t)$ can be made using the impulse response function matrix $\boldsymbol{h}_{\dot{q}}(t,\tau)$.

The extreme value of $v(t)$ within a time duration of *T*, i.e., $v_{\max}=\max\{v(t),0\le t\le T\}$, can be calculated through upcrossing rate analysis. Under the assumption of Poisson crossings, the cumulative distribution function (CDF) of the extreme response is calculated as

$$F_{\max}(v)=\exp\left(-\int_0^T \mu(v,t)dt\right);\qquad \mu(v,t)=\frac{1}{2\pi}\frac{\sigma_{\dot{v}}(t)}{\sigma_v(t)}\exp\left(-\frac{(v-\bar{v}(t))^2}{2\sigma_v^2(t)}\right) \tag{29}$$

where $\mu(v,t)$ is the crossing rate at level v; $\sigma_{\dot{v}}(t)$ is root-mean-square (RMS) value of $\dot{v}(t)$; and $\bar{v}(t)$ is the time-varying mean response. The mean extreme corresponds to a non-exceeding probability of 0.57 when the extreme distribution can be further modeled as a Gumbel-type distribution. The mean extreme subtracting the maximum of mean and then derived by the maximum of RMS response is referred to as peak factor for the transient response.

2.3 *Application to simplified cases*

Consider the case where the mean wind speed and wind fluctuations are expressed as

$$U(x,t)=U_{\max}U_0(x)d_m(t);\qquad u'(x,t)=u(x,t)d_u(t);\qquad w'(x,t)=w(x,t)d_w(t) \tag{30}$$

where $d_m(t)$, $d_u(t)$ and $d_w(t)$ are time-varying modulation functions for the mean wind speed and wind fluctuations; $U_{\max}$ is maximum mean wind speed over time and space; $U_0(x)$ defines the spanwise variation of the mean wind speed.

The PSDs and coherence functions of $u(x,t)$ and $w(x,t)$ are defined as

$$S_u(x_1,x_2,\omega)=\mathrm{coh}_u(x_1,x_2,\omega)S_u(\omega)I_{u0}^2(x_1)I_{u0}^2(x_2);\quad \mathrm{coh}_u(x_1,x_2,\omega)=\exp\left(-\frac{\lambda_u\omega\,|\,x_1-x_2\,|}{2\pi U_R}\right) \tag{31}$$

$$S_w(x_1,x_2,\omega)=\mathrm{coh}_w(x_1,x_2,\omega)S_w(\omega)I_{w0}^2(x_1)I_{w0}^2(x_2);\ \mathrm{coh}_w(x_1,x_2,\omega)=\exp\left(-\frac{\lambda_w\omega\,|\,x_1-x_2\,|}{2\pi U_R}\right) \tag{32}$$

where λ_u and λ_w are decay factors; $I_{u0}(x)$ and $I_{w0}(x)$ are functions to reflect the spatial variations of PSDs of wind fluctuations; and $U_R=U_{\max}[U_0(x_1)+U_0(x_2)]/2$. It is also assumed that the admittance functions are functions of reduced frequency $k=\omega b/(U_{\max}U_0(x))$, thus are functions of spanwise location x and frequency ω, but are independent of time t.

Accordingly, the buffeting force matrices are calculated as

$$\boldsymbol{A}_{bu}(\omega,t)=\boldsymbol{A}_{bu0}(\omega)d_m(t)d_u(t);\qquad \boldsymbol{A}_{bw}(\omega,t)=\boldsymbol{A}_{bw0}(\omega)d_m(t)d_w(t) \tag{33}$$

and the ESPD matrix of generalized displacement vector is estimated as

$$\boldsymbol{S}_q(\omega,t)=\boldsymbol{H}_{q0u}(\omega,t)\boldsymbol{S}_{Qbu}^{(0)}(\omega)\boldsymbol{H}_{q0u}^{T*}(\omega,t)+\boldsymbol{H}_{q0w}(\omega,t)\boldsymbol{S}_{Qbw}^{(0)}(\omega)\boldsymbol{H}_{q0w}^{T*}(\omega,t) \tag{34}$$

$$\boldsymbol{H}_{q0u}(\omega,t)=\int_0^t\boldsymbol{h}_q(t,\tau)d_m(\tau)d_u(\tau)e^{-i\omega(t-\tau)}d\tau;\quad \boldsymbol{H}_{q0w}(\omega,t)=\int_0^t\boldsymbol{h}_q(t,\tau)d_m(\tau)d_w(\tau)e^{-i\omega(t-\tau)}d\tau \tag{35}$$

$$\boldsymbol{S}_{Qbu}^{(0)}(\omega)=\boldsymbol{A}_{bu0}(\omega)\boldsymbol{S}_u(\omega)\boldsymbol{A}_{bu0}^{T*}(\omega);\quad \boldsymbol{S}_{Qbw}^{(0)}(\omega)=\boldsymbol{A}_{buw}(\omega)\boldsymbol{S}_w(\omega)\boldsymbol{A}_{bw0}^{T*}(\omega) \tag{36}$$

It is noted that the transient characteristics of response is reflected by the time dependence of $\boldsymbol{H}_{q0u}(\omega,t)$ and $\boldsymbol{H}_{q0w}(\omega,t)$. In the case of the time-invariant mean wind speed and stationary wind fluctuations, i.e., $d_m(t)=d_u(t)=d_w(t)=1$, $\boldsymbol{H}_{q0u}(\omega,t)$ and $\boldsymbol{H}_{q0w}(\omega,t)$, thus $\boldsymbol{S}_q(\omega,t)$ and $\boldsymbol{R}_q(t)$ approach to the steady-state values when time t is sufficiently large. The framework presented in this study reduces to that for multimode coupled buffeting analysis of bridge aeroelastic system under stationary winds (e.g., Chen and Kareem 2000a; Chen 2006). It is also worthy of noting that when the aerodynamic inter-modal coupling is negligible, $\boldsymbol{H}_{q0u}(\omega,t)$ and $\boldsymbol{H}_{q0w}(\omega,t)$ are diagonal matrices. The transient buffeting response of each mode can be estimated separately and then combined by using the square-root-of-sum-of-squares (SRSS) combination rule.

3 NUMERICAL EXAMPLES AND DISCUSSIONS

3.1 *A long span suspension bridge under nonstationary wind excitations*

A suspension bridge with a main span of nearly 2000 m was used as an example. The first 15 natural modes with frequencies ranging from 0.003 to 0.2 Hz were considered for describing the dynamic behavior of the bridge. The modal damping ratio was assumed to be 0.0032. For simplicity and without loss of generality, only the aerodynamic forces acting on the bridge deck were considered. The self-excited lift and pitching moment were calculated based on the flutter derivatives derived from Theodorsen function. The self-excited drag was evaluated based on the quasi-steady theory. The admittance functions used were based on Davenport's formula for drag with a decay factor of 8, and Sears function for lift and pitching moment. Two different joint acceptance functions were used for the buffeting force components associated with *u*- and *w*-components, respectively. The mean wind speed is uniform over the bridge span but with a time-varying amplitude, i.e.,

$$U_0(x)=1; \quad d_m(t)=\exp\{-(t-t_0)^2/2D_t^2\} \tag{37}$$

where t_0 is the time instance at which the wind speed reach its maximum; and D_t is wind storm duration parameter defining the time variation of wind speed.

The modulation functions of *u*- and *w*-components of wind fluctuations were identical to that of the mean wind speed, i.e., $d_u(t)=d_w(t)=d_m(t)$. The von Karman spectra were used to describe the underlying stationary wind fluctuations. The turbulence intensities and integral length scales were assumed to be 10 and 7.5%, and 80 and 40 m, for *u*- and *w*-components, respectively. The spectral characteristics of wind fluctuations were uniform over the bridge, i.e., $I_{u0}(x)=I_{w0}(x)=1$. The decay factors of the coherence functions for *u*- and *w*-components were $\lambda_u=\lambda_w=8$. Fig.1 shows the time modulation function $d_m(t)$ with t_0 =300 sec, and D_t =120, 180, 240 and 300 sec. A smaller value of D_t indicates a short duration of strong storm, i.e., a larger variation of mean wind speed.

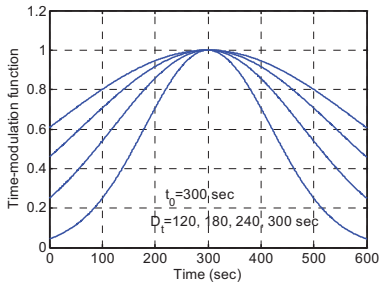

Figure 1. Time modulation function

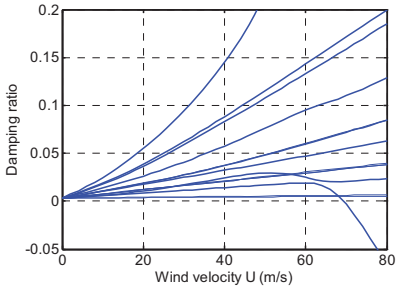

Figure 2. Modal damping ratio vs. mean wind speed

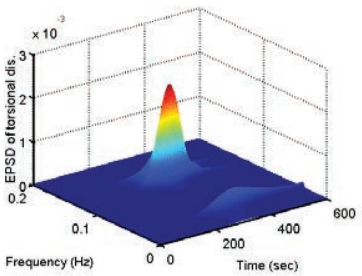

Figure 3. EPSD of torsional displacement at main span center

3.2 *Results and discussions*

The modal frequencies, damping ratios and complex modal shapes at different mean wind speeds are calculated, which are used to calculate the impulse response function matrix. Fig.2 shows the modal damping ratios at different mean wind speeds. The coupled flutter onset velocity is estimated to be 69.4 m/s. Fig.3 displays the EPSD of the torsional displacement at main span center with $U_{\max}=60$ m/s, $t_0=300$ sec, and $D_t=120$ sec. Fig.4 portrays the time-varying mean and RMS values of bridge deck displacements at center of main span. It is noted that the maximum RMS is delayed with respect to the time at which the mean wind speed reaches its maximum, which is due to transient effect of bridge dynamic system. The delay is more noticeable for lateral displacement that is dominated by first lateral mode with lower frequency and damping. Fig.5 shows the maximum values of static and RMS, and mean extreme (including static) response within 10 min at different spanwise location in terms of bridge deck vertical, lateral and torsional displacements. The results from ensemble average of 50 time domain simulation samples are also presented. The predictions in frequency and time domains are very agreeable.

The procedure for simulating the time history of transient response is essentially the same as that introduced in Chen et al. (2000b). The underlying stationary wind turbulence field is firstly generated based on their spectral characteristics using spectral representation method. The nonstationary wind turbulence field is then calculated by multiplying the modulation functions. The flutter derivatives, admittance functions and joint acceptance functions are represented as rational functions of reduced frequency. Based on the quasi-static assumption concerning the influence of time-varying mean wind speed on aerodynamics, the time histories of self-excited and

buffeting forces are generated and the resulting buffeting response is calculated using step-by-step solution of the dynamic equations.

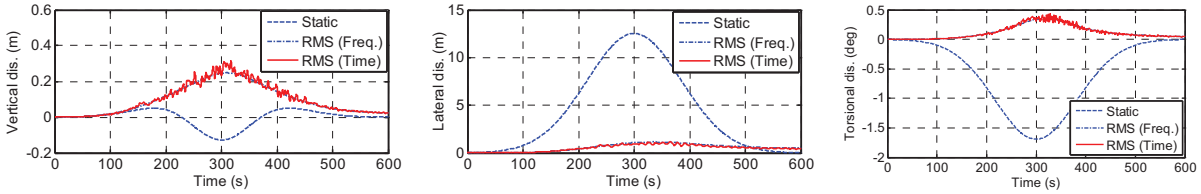

a) Vertical displacement (b) Lateral displacement (c) Torsional displacement

Figure 4. Time-varying mean and RMS values of bridge deck displacements at main span center

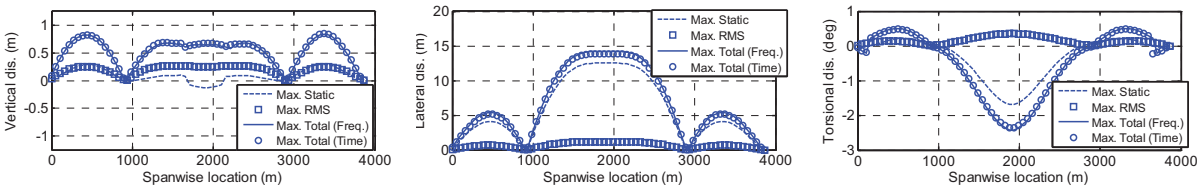

a) Vertical displacement (b) Lateral displacement (c) Torsional displacement

Figure 5. Maximum values of static, RMS and mean extreme (including static) response under transient wind

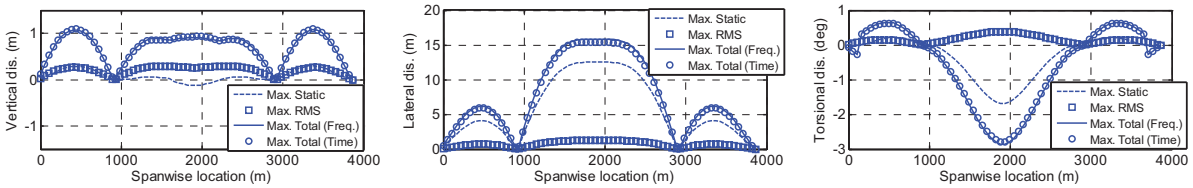

a) Vertical displacement (b) Lateral displacement (c) Torsional displacement

Figure 6. Static, RMS and mean extreme (including static) response under constant mean wind speed

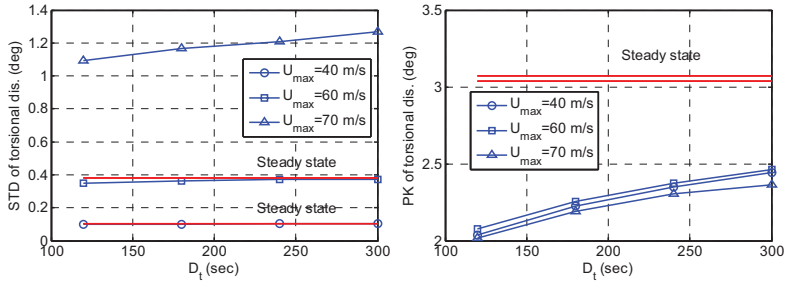

(a) RMS (b) Peak factor

Figure 7. Influence of storm duration parameter on torsional displacement at main span center

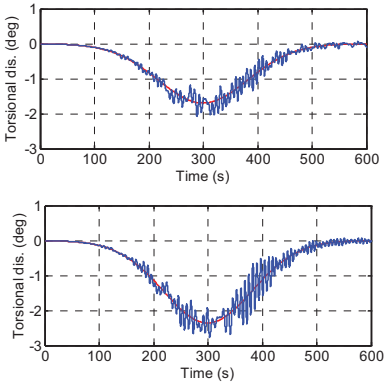

Figure 8. Time history samples of torsional displcament at U_{max}= 60 and 70 m/s

Fig.6 shows the steady state buffeting response when mean wind speed is a constant of 60 m/s, which corresponds to traditional buffeting analysis. Fig.7 is the predicted maximum RMS responses and peak factors at different values of D_t with $U_{\max} = 40$, 60 and 70 m/s and $t_0 = 300$ sec. It is obvious that the transient excitation results in reduced RMS response as compared to

steady state response. It is due to the lack of sufficient "build-up" time of response to reach the steady state level. At 70 m/s, the steady state buffeting response will be unstable as it exceeds the flutter onset speed. However, under the transient wind excitation the bridge shows stable response as the lack of sufficient "build-up" time of unstable response as shown in Fig.8. Take a single degree-of-freedom system as an example. The "build-up" time is the time required to make $\exp(-2\xi\omega t)$ close to zero in the case of positive damping, where ξ and ω are the system damping ratio and frequency. Clearly, a large value of $\xi\omega$, a shorter "build-up" time needed, and the RMS response becomes closer to the steady state value. Since the lateral displacement is dominated by lower frequency and with a lower modal damping, the transient effect is most significant. The build-up rate of unstable dynamic response is also proportional to the value of $\xi\omega$. At higher wind speeds with larger negative damping, the buffeting responses will develop into significant amplitudes even under transient wind excitations.

The extreme value and peak factor of transient buffeting response are significantly lower than those of stationary response. For instance of case with $U_{\max} = 60$ m/s, $t_0 = 300$ sec, and $D_t = 120$ sec, the peak factors of the bridge deck displacements in vertical, lateral and torsional directions at the main span center are 2.11, 1.43, and 2.08, respectively. These are 2.98, 2.68 and 3.07, respectively, in the case of steady state response under constant mean wind speed. The lower peak factor or extreme response is due to the fact that large response is only observed in a relatively short of time as compared to the stationary case where it occurs over the entire time duration. The crossing rate at a given response level is much lower than that of the state sate response.

4 CONCLUSIONS

This study presented a general frequency domain approach for quantifying buffeting response of long span bridges when subjected to transient nonstationary winds. The wind fluctuations were modeled as evolutionary random processes with time-varying mean. Formulations for calculating static, self-excited and buffeting forces were presented to account for the transient wind excitation. The bridge response to time-varying mean wind loading was determined through quasi-static analysis with an iterative procedure for solution of statically nonlinear problem. The dynamic bridge aeroelastic system was regarded as a linear time-variant system with slowly varying modal characteristics. The impulse response function matrix of the system was defined by the modal properties at "frozen time", which were determined through complex eigenvalue analysis at given mean wind speeds. Formulations were given for calculating the EPSD, time-varying RMS value, probability distribution of extreme response and peak factor. The traditional multi-mode coupled buffeting analysis framework to stationary wind excitation is the special case of the general framework presented in this study.

The analysis of buffeting response of the long span suspension bridge showed that transient wind excitation results in reduced RMS response attributed to the lack of sufficient "build-up" time of response to reach the steady state level. The lateral bridge deck displacement was more noticeably affected by the transient effect as it was dominated by the modal response with lower frequency and damping ratio. The duration of wind storm played a significant role in the generation of extreme buffeting response especially for very flexible structures with low frequency and damping. The extreme value and peak factor of transient response were much lower than those of steady-state response.

It is worthy of mentioning that the effects of transient aerodynamics, i.e., the potential changes in the aerodynamic force characteristics under transient winds, were neglected, which may be considerable in the case of rapidly varying transient winds. The information of transient

aerodynamics, when available, can be readily synthesized with the proposed approach and lead to a better prediction of structural response.

5 ACKNOWLEDGEMENTS

The support for this work was provided in part by NSF Grants CMMI-0824748 and CMMI-1029922, and is gratefully acknowledged.

6 REFERENCES

1 M. Barbato, and M. Vasta, Closed-form solutions for the time-variant spectral characteristics of non-stationary random processes, Probab. Eng. Mech., 25(2010), 9-17.
2 X. Chen, Analysis of long span bridge response to winds: building nexus between flutter and buffeting, J. of Struc. Eng., ASCE, 132(12)(2006), 2006-2017.
3 X. Chen, Analysis of alongwind tall building response to transient nonstationary winds, J. of Struct. Eng., ASCE, 134(5)(2008),782-791.
4 X. Chen, and A. Kareem, Advances in the modeling of aerodynamic forces on bridge decks, J. of Eng. Mech., ASCE, 128(11)(2002), 1193-1205.
5 X. Chen, M. Matsumoto, and A. Kareem, Aerodynamic coupling effects on flutter and buffeting of bridges, J. of Eng. Mech., ASCE, 126(1)(2000a), 17-26.
6 X. Chen, M. Matsumoto, and A. Kareem, Time domain flutter and buffeting response analysis of bridges, J. of Eng. Mech., ASCE, 126(1)(2000b), 7-16.
7 J. P. Conte, and B. F. Peng, Fully nonstationary analytical earthquake ground-motion model, J. Eng. Mech., 123(1)(1997), 15-24.
8 A.G. Davenport, and J.P.C. King, The influence of topography and storm structure on long span bridge behavior in wind, Proc. Int. Seminar on Utilization of Large Boundary Layer Wind Tunnel, Tsukuba, Japan, Dec., 1993, 11-21.
9 P. van der Kloet, and F. L. Neerhoff, Diagonalization algorithms for linear time-varying dynamic systems, Int. J. Systems Science, 31(8)(2000), 1053-1057.
10 D-K Kown, and A. Kareem, Gust-front factor: new framework for wind load effects on structures, J. Struct. Eng., ASCE, 135(6)(2009), 717-732.
11 Y. K. Lin, and G. Q. Cai, Probabilistic structural dynamics: advanced theory and applications, McGraw-Hill, New York, 1995.
12 L. D. Lutes, and S. Sarkani, Random vibration: analysis of structural and mechanical systems, Elsevier, 2004.
13 G. Michaelov, L. D. Lutes, and S. Sarkani, Extreme value of response to nonstationary excitation, J. Eng. Mech., 127(4)(2001), 352-363.
14 R. H. Scanlan, Problematic in formulation of wind-force models for bridge decks, J. of Eng. Mech., ASCE, 119(7)(1993), 1353-1375.

Wind tunnel test and the analysis of buffeting performance of f ree-standing tower of cable-stayed bridge under yaw wind

Xin Che [a], Jiawu Li[b], Dan Zhang [c]

[a]*Chang'an University, Nan'erhuan Road, Xi'an, Shaanxi, China*
[b]*Chang'an University, Nan'erhuan Road, Xi'an, Shaanxi, China*
[c]*Chang'an University, Nan'erhuan Road, Xi'an, Shaanxi, China*

ABSTRACT: This work is concerned with the aerodynamic characterization of a cable-stayed bridge tower in free-standing stage; experimental tests were performed at CA-1 wind tunnel (wind tunnel laboratory at Chang'an University, Xi'an, China) under turbulent flow condition. The aerodynamic behavior of the tower was investigated through full aeroelastic model in stand-alone configuration using a 1:50 scale. Aim of this paper is to discuss the buffeting character of a cable-stayed bridge tower at free-standing stage under yaw wind.

KEYWORDS: Free-standing; Tower; Aeroelastic model; Buffeting; Yaw wind

1. INTRODUCTION

A great number of cable-supported bridges across large rivers, lakes, sea bays and channels, have been built or are under construction since the completion of Shanghai Nanpu Bridge (a cable-stayed bridge with a main span of 423 m) in the earlier1990s. Among these bridges, Hongkong-Zhuhai-Macao Bridge, a key project across the LingDing Sea, is an extraordinary one in China for its steel structure for both bridge deck and towers, which results in lower structural damping compared with concrete structures. There are three bridges in this new road transport channel. The JiangHai Navigation Channel Bridge, a cable-stayed bridge with single-plane harp stayed cables, has three towers and six spans of 110+129+258+258+129+110=994 m, The deck is streamline closed box girder with two wind-fairings (4.5m high and 38.8 m wide). The three towers are, the central tower of 103.81m height and both side-towers of 102.55m height, of steel frame-structure .the configuration of the towers seem like a dolphin in the elevation plane. The cross section of tower's main column is rectangular, and the auxillary column is chamfered-corner rectangular (Layout and Typical sections of bridge tower are following Fig.1~2).

Buffeting is a kind of stochastic forced vibration and caused by the turbulence of incoming wind in conjunction with the so-called "rear wake induced turbulence". Buffeting is hence inevitable for any bridges exposed to the natural wind. Furthermore, buffeting may occur for the long-span bridges in strong-wind prevailing area. Such serious cause as strength and fatigue problems of structural components and instability of the vehicles traveling on the bridges may occur. Mitigated measures shall be introduced. For the great flexibility, modern long-span bridges are usually prone to strong winds induced damage, and the wind-resistant design becomes one of key issues for successful construction of bridges. Also for the tower, the higher the tower is, the slender the tower is. And the slender bridge tower is prone to aerodynamic problems connected to wind–structure interaction. For this reason, the design of these structures requires wind tunnel tests on scaled down models. At the free standing stage, the tower is of low stiffness and small damping without stay-cables system constraints, and wind-induced vibration will become one of the key factors in the design scheme. Therefore, prediction or evaluation of buffeting performances becomes very important for the towers of long-span bridges. Although many complicated approaches have been presented for the buffeting analysis (Scanlan and Gade,1977; Scanlan,1978b; Scanlan.,1978; Lin,1979;Scanlan andJones.,1990; Jain etal.,1996;Xu

etal.,1998;Boonyapinyo etal.,1999;Cai etal.,1999; Diana etal.,1999; Katsuchietal.,1999; Chen etal.,2000; Chen etal.,2001; Ding etal.,2002a; Zhu and Xu,2005;Xu and Zhu,2005), wind tunnel test of aeroelastic model will still be the most important approach in evaluating the wind-resistant performance of finalised scheme.

This paper discussed the buffeting character of a cable-stayed bridge tower at free-standing stage, wind tunnel tests on 1:50 aeroelastic model of tower were performed in the CA-1 wind tunnel (wind tunnel laboratory at Chang'an University, Xi'an, China) in turbulent flow. The model simulated the first four natural frequencies and mode shapes of the structure.

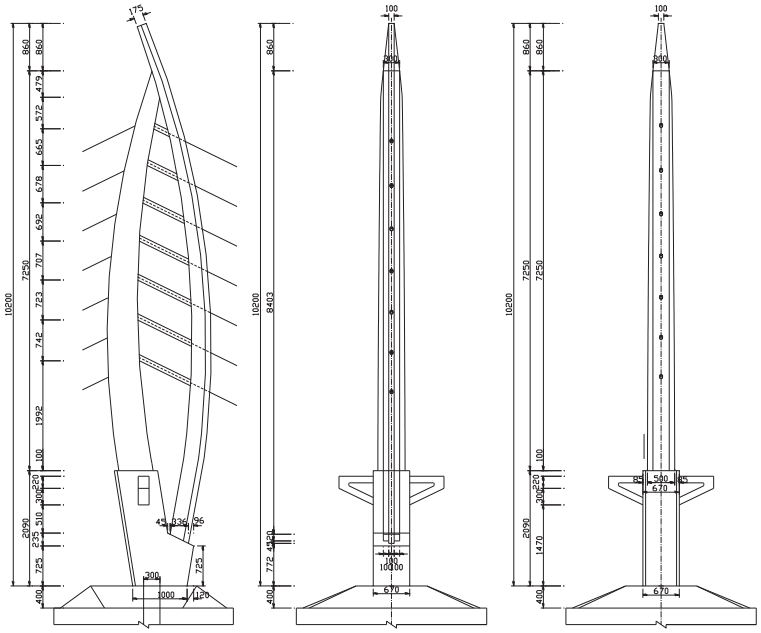

Fig 1. Layout of bridge tower（unit: cm）

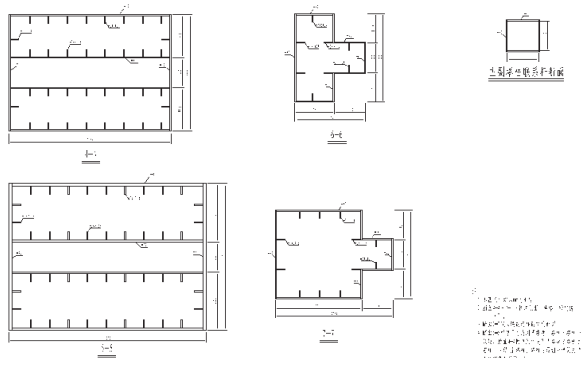

Fig 2. Typical section of bridge tower

2. MODAL ANALYSIS

The modal analysis of the bridge tower was carried out using a famous finite element program, ANSYS. The tower is completely consolidation at the bottom. The members of bridge tower were modeled with spatial beam elements. The natural frequencies of some major modes of free-standing tower are listed in Table 1. The fundamental frequencies and mode shapes are shown in Fig 3 for the tower.

Table 1. Dynamic properties of aeroelastic model

Modes	Computed frequency of prototype(Hz)	Design values(Hz)	Measured values (Hz)	Discrepancy (%)	Measured Damping ratio(‰)
L1	0.8293	5.32	5.37	0.94	6.00
LT1	1.5357	8.26	8.3	0.48	7.00
L2	3.0053	18.1	17.58	2.87	7.80
T1	3.6155	21.78	22.46	3.12	5.00

Note: L—Lateral bending of tower; LT—Longitudinal bending of tower; T—Torsional bending of tower; number—mode order.
From table 1, we can see that the errors of measured damping ratio are all within the scope of the permit.

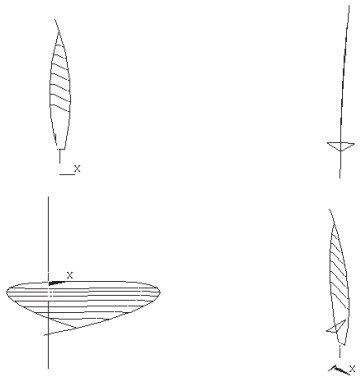

a. Lateral (0.8293Hz)

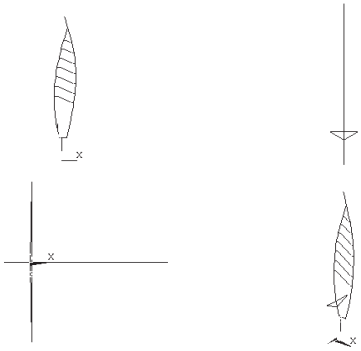

b. Longitudinal (1.5357Hz)

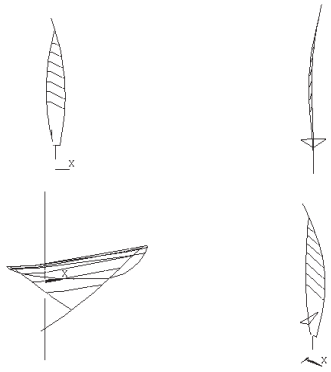

c. Lateral (3.0053Hz)

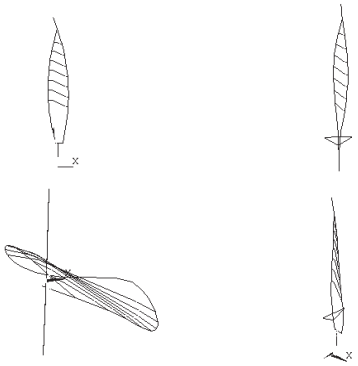

d. Torsional (3.6155Hz)

Fig 3. Fundamental modes of the tower

3. MODEL DESIGN AND MANUFACTURE

The full tower aeroelastic model test was carried out in the CA-1 wind tunnel, wind tunnel laboratory at Chang'an University. China. As shown in Fig 4. The wind tunnel is a large boundary layer wind tunnel with a closed testing section of 3 m width, 2.5m height and 15m length. The flow inside is driven by motor fans and circulates vertically. The achievable mean wind speed of empty wind tunnel ranges from 1.0 to 53 m/s, adjustable continuously.

The wind tunnel test of aeroelastic model not only require model and prototype meet geometrically similar, but also need to satisfy gravity, inertia parameters, elastic parameter, viscous parameters and damping parameters are consistent. This aeroelastic model meets the geometrically similar, inertia and damping parameters similar. A 1:50 scale full aeroelastic model of the tower was manufactured to reproduce the first four natural frequencies and mode shapes of the real structure. The similarity relations and the control parameters between aeroelastic model and prototype, we can refer to literature [1].

The model was comprised of steel core beam (simulating the tower stiffness), perspex coats (simulating the tower appearance) and plumbum compensating weights. The compensating weights were installed in the perspex coats to adjust the mass and mass moment of inertia of the tower. The perspex coats were connected to the core beam (We can refer to literature [8] for specific content.). As shown in Fig. 5 for the photo of the model in wind tunnel test.

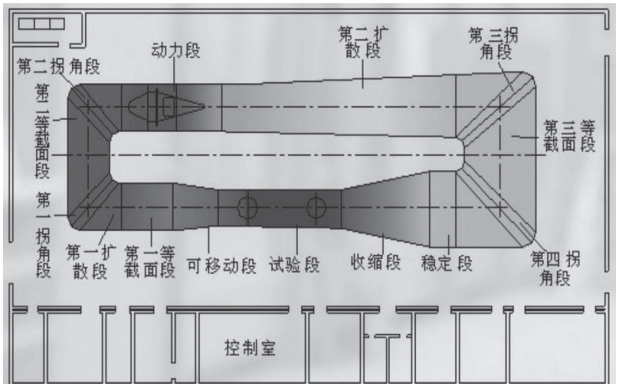

Fig 4. General layout of CA-1wind tunnel.

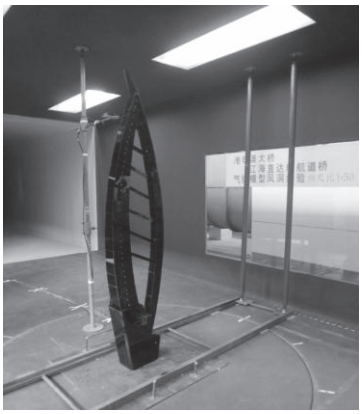

Fig 5. Photo of the model in wind tunnel test

4. MODAL CHECK OF THE AEROELASTIC MODEL

To ensure the accuracy of simulating the bridge dynamic properties, the modal parameters of the model, including natural frequencies, mode shapes and modal damping ratios of the model were carefully checked and compared with the design values.

Because of the small amplitude of vibration due to ambient excitation, the modal damping ratios of the mode were identified with conventional approach of free decay vibration stimulated with initial displacement for lower frequency modes or with initial impulse for higher frequency modes. The frequencies and modal damping of the free-standing state by this way are also listed in Table1. Furthermore, the modal damping ratios identified with free-decay vibration approach were between 0.5% and 2%, which were close to that suggested in the literature [5] for steel and concrete.

5. WIND PARAMETERS AT BRIDGE SITE

According to The Annual Report of Continuous Meteorological Observation and Wind Parameters Studies of the site of the Hong Kong-Zhuhai-Macao Bridge, the exponent (α) of mean wind profile at the bridge site is about 0.098, and the basic wind speed at the bridge site (U_{10}), namely the yearly-maximum 10-min averaged mean wind speed at 10m height corresponding to 120-year return period, is 47.2m/s. Thus, the design reference wind speed at deck level (33.8m above normal water level) for the service state (U_d) is as follows:

$$U_d = U_{10} \times (33.8/10)0.098 = 53.18 \text{m/s} \quad (1)$$

For construction state, the return period is taken as 10 years, and the corresponding design reference wind speed at deck level (U_{sd}) is determined as:

$$U_{sd} = 0.84 \times 53.18 = 44.67 \text{m/s} \quad (2)$$

The top of the tower is 107.81m above normal water level, and 65% height of the tower is 70.08m above normal water level, so the design reference wind speed of the tower is U_d=57.12m/s, For construction state, the corresponding design reference wind speed is U_{sd}=0.84×57.12=47.98m/s.

6. SIMULATION OF WIND FIELD

The atmospheric boundary layer was simulated in the CA-1 wind tunnel using spirelets, as shown in Fig 6. The simulated profiles of mean wind, along wind and vertical turbulent intensities are shown in Figs. 7–8. The fitted exponent of turbulent wind profile was 0.09.

Fig 6. Passive devices for simulation of turbulent wind field of boundary layer.

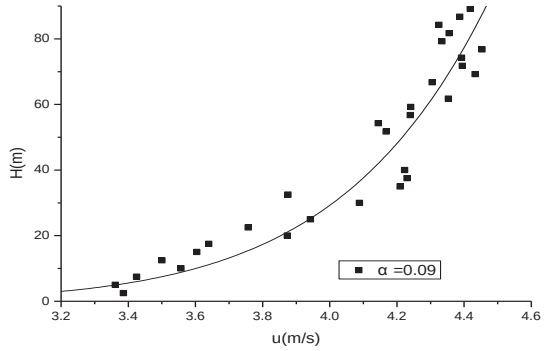

Fig 7. Mean wind profile of simulated wind field

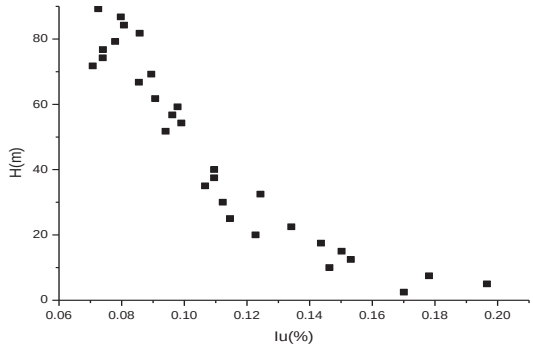

Fig 8. Turbulent intensity profile of simulated wind field

7. MAJOR TEST RESULTS

The case of tests is arranged as following, seven wind exposures(β), β =0°, 30°, 60°, 90°, 120°,150°,180° were considered(β -the angle between the direction of wind and the tower plane Fig 9).The test wind speed ranges from 0 to12m/s, it is corresponding to the speed ranges from 0 to 92.4m/s at the 65% height of tower.

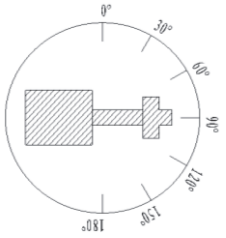

Fig 9.Section geometry and wind exposures

7.1 Variation of standard deviation of responses vs. wind yaw angle

From literature [8], we can know that for the construction state, the corresponding design reference wind speed is 47.98m/s.

Fig 10 shows, respectively, the test curves of the lateral, longitudinal and torsional standard deviations (σ_L, σ_{LT} and σ_T) at the top and at the 2/3 height of tower at the speed of 50m/s vs. wind yaw angle. It is found that the variation of buffeting response of free-standing tower with wind yaw angle is not monotonous. The standard deviation of displacement responses vs. wind yaw angle is very similar at the top and at the 2/3 height of tower. The lateral buffeting response on the top of the free-standing tower reach their minimal values (the top of tower is 0.015m, 2/3 height is 0.0006m) and maximal values (the top of tower is 0.0454m, 2/3 height is 0.0016m) at around 150°and 180°of wind yaw angle respectively, when the angle is over 150°, the response is increasing with wind angle. The longitudinal buffeting response gets their maximal values at around 90°of wind yaw angle.

a

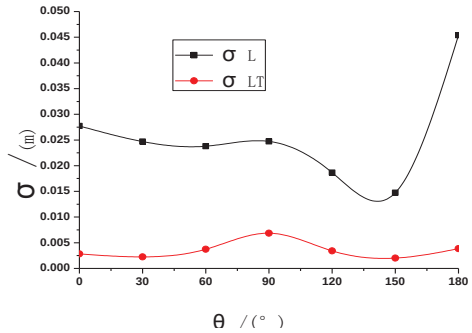

b

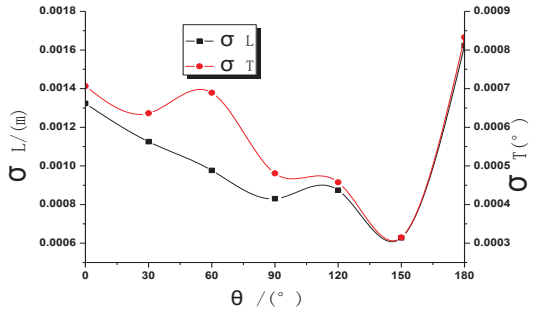

Fig 10. Variation of standard deviation of responses vs. wind yaw angle: (a) Top of the tower, (b) 2/3 height of the tower (v=50m/s)

For the tower is frame structure in longitudinal, its stiffness is significantly greater than the lateral stiffness. Therefore σ_L is much larger than σ_{LA}.

Also the torsional response is small, the standard deviation of displacement responses vs. wind yaw angle is very similar for torsional and lateral response, torsional buffeting response get their minimal values (0.00031°) at around 150° of wind yaw angle, and at around 180° achieve the maximal values (0.00083°). The torsional response curve has large fluctuation with wind angle.

a

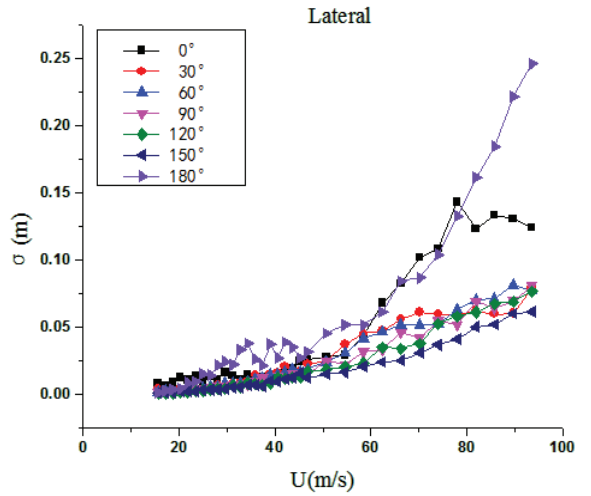

b

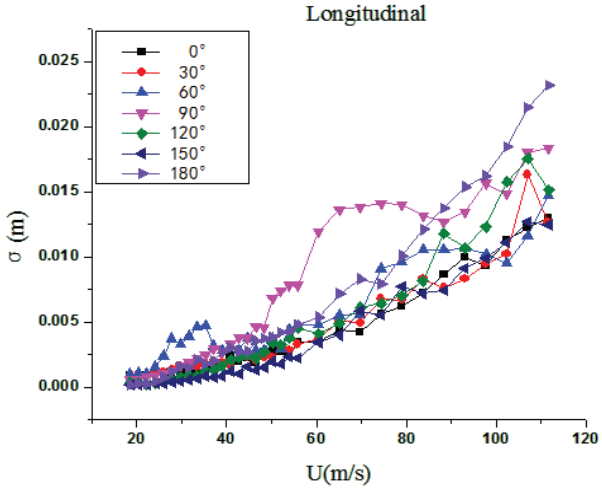

c

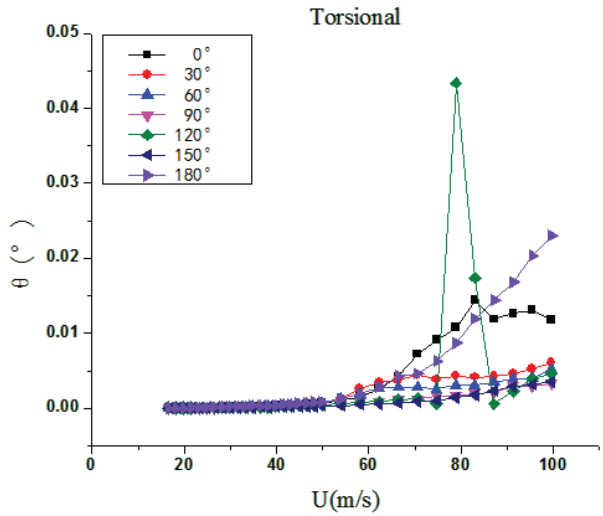

Fig 11. Variation of standard deviation of responses vs. wind speed:(a) lateral, (b) longitudinal, (c) torsional.

7.2 Variation of standard deviation of responses vs. wind speed

Fig 11.Shows, respectively, the test curves of the lateral, longitudinal and torsional standard deviations vs. mean wind speed (U), for the responses at top of the tower to turbulent wind with various wind yaw angles. From these figures, one can find by curve fitting that the buffeting responses of tower vary with wind speed at conic curves approximately, the maximal standard

deviations of the lateral, longitudinal and torsional responses at the tower top were about0.248, 0.025 m and0.045°, respectively, and the corresponding wind yaw angles were about 180° and 120°, respectively. The test results demonstrate that the most unfavorable buffeting responses of tower also occur in the yaw wind cases.

8. CONCLUSION

Wind tunnel tests are nowadays the most used and reliable method to evaluate the wind effects on slender structures that are sensitive to wind induced vibrations such as vortex shedding and galloping. This paper has presented a case study on a bridge tower where wind tunnel tests were carried out on a full tower aeroelastic model. The buffeting performance of free-standing tower of Jianghai Navigation Channel Bridge, a cable-stayed bridge, under yaw wind is investigated by means of wind tunnel test of aeroelastic model. It is very useful to understand the wind-induced vibration performance of free-standing tower in the construction states. Similarly, it is meaningful to ensure the safety of the long span bridges in construction states.

The following major conclusions can thus be drawn according to the results of wind tunnel test:

(1) The variation of buffeting response of free-standing tower with wind yaw angle is not monotonous.
(2) The lateral buffeting response on the top of the free-standing tower reach their minimal values and maximal values at around 150°and 180°of wind yaw angle respectively and the longitudinal buffeting response attain their maximal values at around 90°of wind yaw angle.
(3) The torsional buffeting response get their minimal values at around 150°of wind yaw angle, and at around 180°achieve the maximal values. And the response curve has large fluctuation with wind angle.
(4) Buffeting responses of the bridge to turbulent wind may reach the maximal values in yaw wind case. The normal wind case may not be the most unfavorable case.
(5) The buffeting response changes with the wind speed at a conic curve approximately.

9. ACKNOWLEDGMENTS

The work described in this paper is a part of a project supported by the Construction Commanding Office of Hongkong-Zhuhai-Macao Bridge, and is also financially supported by China Highway Planning and Design Institute, to which the writers are most grateful. Our sincerey thanks should also go to the Construction Commanding Office of Hongkong-Zhuhai-Maco Bridge for kindly supporting the wind-resistant research project of the bridge. Any opinions and concluding remarks presented in this paper are entirely those of the writers.

References:

1 Chen, X., Matsumoto, M., Kareem, A., 2000. Time domain flutter and buffeting response analysis of bridges. J. Eng. Mech. ASCE 126(1), 7–16.
2 Cai, C.S., Albrecht, P., Bosch, H.R., 1999. Flutter and buffeting analysis .I: Finite-element and RPE solution. J. Bridge Eng. ASCE 4(3), 174–180.
3 Scanlan, R.H., Jones, N.P., 1990. Aeroelastic analysis of cable-stayed bridges. J. Struct. Eng., ASCE 116 (2) , 1279–12 97.
4 Simiu, E., Scanlan, R.H., 1996. Wind Effects on Structures: Fundamentals and Applications to Design, thirded. Wiley, New York, USA.

5 Xiang, H.F., et al., 1996. Wind-resistant Design Guideline for Highway Bridges. China Communications Press (in Chinese).
6 Lin, Y.K., 1979. Motion of suspension bridges in turbulent winds. J. Eng. Mech. Div. ASCE 105(EM6), 921–932.
7 L.D. Zhu, M. Wang, D.L. Wang, Z.S. Guo, F.C. Cao, 2007. Flutter and buffeting performances of Third Nanjin Bridge over Yangtze River under yaw wind via aeroelastic model test. Journal of Wind Engineering and Industrial Aerodynamics 95(2007)1579–1606
8 Liu, J.X., Li, J.W., et al., 2011.Preliminary design for main construction of HZMB wind tunnel test for special structure special subject study report study on wind resistance of Jianghai navigation channel bridge-part V. Wind Tunnel laboratory of Chang'an University, Xi'an,China,2011
9 Zhu, L.D., Cao, Y.H., Ding, Q.S., et al., Buffeting Performance of Free-Standing Tower of Long-Span Cable-Stayed Bridge under Yawed Wind. J. Tongji Univ. 2005, 33 (7):880-884 (in Chinese)
10 Li, J.W., 2006. wind tunnel test for the tower of E'dong highway bridge in Hubei province. R. Wind Tunnel laboratory of Chang'an University, Xi'an, China, 2006.
11 Zhu, L.D., Wang, M., Guo, Z.S., et al., Buffeting Performance of double cantilever of long-span cable-stayed bridge under yawed wind. J. Engineering Mechanics.2006, 23 (4):86-92
12 Hu, Q. A., Qiao, Y. Q., Liu, J.X., Li, J.W., Buffeting performance of tower in construction state under yawed wind. J. Journal of traffic and Transportation Engineering, 2007, 8 (2):40-04
13 Xu,Y.L., Sun,D.K., Ko,J.M., Lin,J.H.,1988. Buffeting analysis of long span bridges:a new algorithm. Comput.Struct.68, 303-313.

Accurate equivalent static wind loads of lang-span bridges based on the displacement responses

Dong Rui Ge Yao-jun Yang Yong-xin
State Key Laboratory of Disaster Reduction in Civil Engineering, Tongji University
Room302, Bridge Building, Tongji University, 1239 Siping Road, Shanghai, P.R. China

ABSTRACT: Equivalent Static Wind load (ESWL) connects structure engineers and wind engineering researchers, and plays an important role in the field of civil engineering. The long-span bridge is a typical flexible line-like structure in horizontal direction. The displacements are usually the controlling responses in the structure design. Traditional ESWL calculating methods which are based on the most disadvantageous response of one node, such as the displacement in the mid-span or quarter-span, are single target methods. When putting the ESWLs calculated by the traditional single target methods on the bridge, except the most disadvantage node, the other nodes' responses are different from the real values. This paper firstly gets the modes and influence matrix using finite element method, then calculating the PSD matrix of the buffeting forces by coupled flutter and buffeting vibration method. According to random vibration theory and structure dynamics, the ESWLs of long-span bridges in vertical, horizontal and torsional can be expressed by the mode, influence matrix, aerodynamic mechanical admittance matrix, and PSD matrix of the buffeting forces. On the basis of the load-response relationship, the ESWLs calculated through the above method are the only accurate solution which based on the displacements of the bridge.

KEYWORDS: Equivalent static wind load, Long-span bridges, Displacement responses, Mode matrix, Influence matrix, Coupled flutter and buffeting vibration.

0. INTRODUCTION

Wind is the motion of air. Complex aerodynamic or/and aeroelastic forces can be produced when the air blows structures. When the structure stiffness is big, the wind effect is mainly static performance. On the contrary, the wind can induce significant dynamic responses. The long-span bridge is a typical line-like structure with small stiffness in horizontal, and buffeting effects can not be ignored in most cases. Estimating the buffeting responses of a long-span bridge is a complicated and difficult task, and can not be mastered by most structure engineers. So the wind engineers and researchers proposed the concept of ESWL (Equivalent Static Wind Load) to solve this problem. ESWL transfers the complex and difficult dynamic calculation into simple static analysis, and be accepted by most countries'/regions' wind load codes/specifications. ESWL can be defined as that the responses produced by the static ESWL are equal/approximate to the responses produced by the real wind load. Then the structure engineers can solve complex dynamic problems by using simple static analysis. ESWL has become the bridge which connected wind engineers and structure engineers, and plays an important role in practical projects.

The main traditional ESWL methods have GLF[1] (Gust Load Factor) method, LRC[2][3][4] (Load-Response Correlation) method, IWL (Inertia Wind Load) method, and LRC+IWL method[5][6][7]. All these methods are single-target methods. When putting the ESWLs which calculated by the above methods on the structures, only the response on the equivalent node is the same as the real one. Later Japanese researchers proposed Universal ESWL method[8]. This method firstly needs to take several different kinds of single-target ESWLs as the basic vectors of the multi-targets ESWLs. Then calculate the optimal coefficients fitting for the ultimate multi-targets ESWLs by the least square method. In fact, the Universal ESWL method is a numerical processing method and the physical meaning is not clear.

The displacement is usually the key response in the design of a long-span bridge. So, using the accurate ESWLs based on the displacement responses to design the long-span bridge can guarantee the safety of the

bridge design. Based on the long-span bridge's characteristics above, an accurate ESWL method based on the displacement responses is proposed in this paper. And a 300 meters simple bridge with ideal thin plate section is taken as an example to prove the validity and effectiveness of the method.

1. ESWLs BASED ON THE DISPLACEMENT RESPONSES

For linear MDOF (multi-degree-of-freedom) system, the governing equation of motion is

$$[M]\{\ddot{q}(t)\}+[C]\{\dot{q}(t)\}+[K]\{q(t)\}=\{F(t)\} \tag{1}$$

Where, $[M],[C],[K]$ are mass, damping, and stiffness matrices respectively; $\{q(t)\}$, $\{\dot{q}(t)\}$, $\{\ddot{q}(t)\}$, $\{F(t)\}$ are dynamic displacement, speed, acceleration and force vectors of the nodes respectively.

According to mode superposition method, $\{q(t)\}$ can be expressed by mode matrix $[\Phi]$ and modal coordinate vector $\{\xi(t)\}$

$$\{q(t)\}=[\Phi]\{\xi(t)\} \tag{2}$$

Submit equation (2) into equation (1), the linear MDOF system can be represented as

$$[I]\{\ddot{\xi}(t)\}+[\bar{M}]^{-1}[\bar{C}]\{\dot{\xi}(t)\}+[\bar{M}]^{-1}[\bar{K}]\{\xi(t)\}=[\bar{M}]^{-1}\{\bar{F}\} \tag{3}$$

Where, $[I]$, $[\Phi_q]^T[M][\Phi_q]=[\bar{M}]$, $[\Phi_q]^T[C][\Phi_q]=[\bar{C}]$, $[\Phi_q]^T[K][\Phi_q]=[\bar{K}]$ are identity matrix, general mass, damping, and stiffness matrices respectively; $[\Phi_q]^T\{F(t)\}=\{\bar{F}\}$ is the general node force vector.

Using normalized general mass matrix, then equation (3) can be represented as

$$[I]\{\ddot{\xi}(t)\}+[\Lambda_c]\{\dot{\xi}(t)\}+[\Lambda_\omega]\{\xi(t)\}=\{\bar{F}\} \tag{4}$$

Where, $[\bar{M}]^{-1}[\bar{C}]=[\Lambda_c]=\mathrm{diag}(2\zeta_1\omega_1\cdots 2\zeta_{\text{N-mode}}\omega_{\text{N-mode}})$, $[\bar{M}]^{-1}[\bar{K}]=[\Lambda_\omega]=\mathrm{diag}(\omega_1^2\cdots\omega_{\text{N-mode}}^2)$.

For equation (4), the modal coordinate vector can be obtained by Duhamel integral equation in time domain. Because it is time consuming in time domain, so, we solve equation (4) by frequency domain method. Fourier transformation is defined as

$$\bar{\xi}(\omega)=\int_{-\infty}^{+\infty}\xi(t)e^{-i\omega t}dt \tag{5}$$

Where, $i=\sqrt{-1}$ is imaginary unit.

Equation (4) is represented in frequency domain as

$$\left(-\omega^2[I]+i\omega[\Lambda_c]+[\Lambda_\omega]\right)\{\bar{\xi}(\omega)\}=[\Phi]^T\{\bar{F}(\omega)\} \tag{6}$$

Define $[H(\omega)]=-\omega^2[I]+i\omega[\Lambda_c]+[\Lambda_\omega]$ as frequency response function matrix. Then the response produced by dynamic loading can be obtained in frequency domain as

$$\{\bar{\xi}(\omega)\}=[H(\omega)]^{-1}[\Phi]^T\{\bar{F}(\omega)\} \tag{7}$$

Wind loading is one type of random dynamic loadings, so the wind induced responses should be represented in the form of RMS. According to equation (7), PSD matrix of the modal coordinate can be represented as

$$\left[S_{\xi\xi}(\omega)\right]=\left[H(\omega)\right]^{-1}[\Phi]^{T}\left[S_{FF}(\omega)\right][\Phi]\left[H(\omega)\right]^{-1*T} \tag{8}$$

Where, $\left[H(\omega)\right]^{-1*T}$ is complex conjugate transpose of matrix $\left[H(\omega)\right]^{-1}$.

The PSD of the displacement responses can be obtained from equation (2)

$$\left[S_{qq}\right]=[\Phi]\left[S_{\xi_i\xi_j}\right][\Phi]^{T} \tag{9}$$

So the covariance matrix of the displacement response can be expressed as

$$\left[\sigma_{qq}^{2}\right]=\left[\int_{0}^{+\infty}S_{qq}(\omega)d\omega\right] \tag{10}$$

Based on the load-responses relationship, displacement responses, the key dynamic responses of the structure, can be obtained as

$$\left\{\hat{R}\right\}=\left[I_q\right]\left\{F_R^{eq}\right\}=g\left\{\sigma_q\right\}=g\left\{\sqrt{\int_{0}^{+\infty}S_{qq}(\omega)d\omega}\right\} \tag{11}$$

Where, $\left\{\hat{R}\right\}$ is the dynamic displacement vector; $\left\{F_R^{eq}\right\}$ is the ESWLs vector; $\left[I_q\right]$ is the influence line matrix. In the calculation, we hypothesize the ESWL on the constraint note whose displacement response is zero, is zero, and the constraint notes are not included in equation (11). Then the ESWLs of the structure can be represented as

$$\left\{F_{R_i}^{eq}\right\}=g\left[I_q\right]^{-1}\left\{\sqrt{\int_{0}^{+\infty}S_{q_iq_i}(\omega)d\omega}\right\} \tag{12}$$

Where, g is the peak factor, and can take g = 3.5 in most cases. $\left[I_q\right]^{-1}$ is the flexibility matrix.

Equation (12) shows that the ESWLs have clear physical significance. If the mean wind loading is not considered, the ESWLs gotten from equation (12) are the only accurate ESWLs based on the displacement responses.

2. ACCURATE ESWLs OF LONG-SPAN BRIDGES BASED ON THE DISPLACEMENT RESPONSES

For long-span bridges, with the increase of the span, the structure stiffness becomes less and less smaller, and buffeting responses induced by wind load can not be ignored. Based on the analysis in part 1, we take the bridge deck as an example to calculate the ESWLs based on the displacement responses. The approach also applies to the bridge tower.

There are mainly three component forces on the bridge deck: lift force, drag force, and twist moment (Figure 1). The buffeting responses are calculated through coupled flutter and buffeting method[9][10][11][12]. Self-exited forces are estimated by Scanlan's calculation model[13] which contains 18 flutter derivatives. Buffeting forces are estimated by Davenport's buffeting calculation model[13]. For convenience, aerodynamic admittances are not considered in the buffeting calculation.

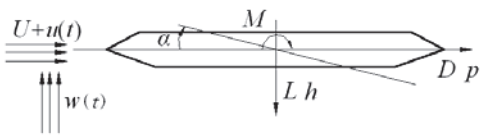

Figure 1. Freedoms and wind forces in the nodes of the bridge deck

The frequency response function can be represented as

$$\left[E_{ij}\right]=\left(-K^2\left[I\right]+iK\left(\left[\Lambda_c\right]-\frac{\rho(2B^4)K}{2}\left[A_{ij}\right]\right)+\left(\left[\Lambda_K\right]-\frac{(2B^4)K^2}{2}\left[B_{ij}\right]\right)\right) \tag{13}$$

Where, $K=\dfrac{\omega B}{U}$ is the reduced frequency; $\dfrac{\rho(2B^4)K}{2}\left[A_{ij}\right]$ and $\dfrac{(2B^4)K^2}{2}\left[B_{ij}\right]$ are aerodynamic damping and aerodynamic stiffness induced by self-exited forces. Detailed derivatives can be found in reference [11]. ω is the natural circular frequency; B is the width of the bridge deck; U is the mean wind speed; ρ is air density.

Matrix $\left[E\right]$ contains the influence of self-exited forces, so it is called aerodynamic frequency response function[14]. After getting the PSD of buffeting forces $\left[S_{b_ib_j}(\omega)\right]$, the PSD of the modal coordinate can be obtained by equation (8)

$$\left[S_{\xi_i\xi_j}\right]=\left(\frac{\rho B^4}{2U}\right)^2\left[E_{ij}\right]^{-1}\left[S_{b_ib_j}(\omega)\right]\left(\left[E_{ij}\right]^{-1}\right)^{*T} \tag{14}$$

So the PSD of the displacement responses in vertical, horizontal, and twist can be expressed as

$$\left(\left[S_{h_ih_j}\right]\quad\left[S_{p_ip_j}\right]\quad\left[S_{\alpha_i\alpha_j}\right]\right)=\left([Bh]\left[S_{\xi_i\xi_j}\right][Bh]^T\quad[Bp]\left[S_{\xi_i\xi_j}\right][Bp]^T\quad[\alpha]\left[S_{\xi_i\xi_j}\right][\alpha]^T\right) \tag{15}$$

For long-span bridges, the influence line functions in vertical, horizontal, and twist i.e. $\left[I_h\right]$, $\left[I_p\right]$, $\left[I_\alpha\right]$, are independent. The ESWLs in vertical, horizontal, and twist can be obtained through equation (12)

$$\left\{F_{L1}^{eq}\quad\cdots\quad F_{\text{LN-node}}^{eq}\right\}^T=g\left[I_h\right]^{-1}\left\{\sqrt{\int_0^{+\infty}S_{h_1h_1}(K)dK}\quad\cdots\quad\sqrt{\int_0^{+\infty}S_{h_{\text{N-node}}h_{\text{N-node}}}(K)dK}\right\}^T \tag{16-a}$$

$$\left\{F_{D1}^{eq}\quad\cdots\quad F_{\text{DN-node}}^{eq}\right\}^T=g\left[I_p\right]^{-1}\left\{\sqrt{\int_0^{+\infty}S_{p_1p_1}(K)dK}\quad\cdots\quad\sqrt{\int_0^{+\infty}S_{p_{\text{N-node}}p_{\text{N-node}}}(K)dK}\right\}^T \tag{16-b}$$

$$\left\{F_{M1}^{eq}\quad\cdots\quad F_{\text{MN-node}}^{eq}\right\}^T=g\left[I_\alpha\right]^{-1}\left\{\sqrt{\int_0^{+\infty}S_{\alpha_1\alpha_1}(K)dK}\quad\cdots\quad\sqrt{\int_0^{+\infty}S_{\alpha_{\text{N-node}}\alpha_{\text{N-node}}}(K)dK}\right\}^T \tag{16-c}$$

3. EXAMPLE OF ONE SIMPLE BRIDGE WITH IDEAL THIN PLATE SECTION

Due to the aerodynamic forces of the ideal thin plate having theory expression, we take a simple bridge with ideal thin plate section as an example to verify the validity and effectiveness of the method. The length of the simple bridge is L = 300m, and the width of the bridge deck is B = 40m. The stiffness of the bridge in vertical, horizontal, and twist are separately $EI_z = 2.1\times10^6$ MPa·m^4, $EI_y = 1.8\times10^7$ MPa·m^4, $GI_t = 4.1\times10^5$ MPa·m^4. The mass per unit length is m_{beam} = 20,000kg/m; the mass moment of inertia per unit length is $I_m = 4.5\times10^6$ kg·m^2/m; the air density is $\rho = 1.225$ kg/m^3; the modal damping ratios are assumed to 0.005.

The finite element model of the simple bridge is established by ANSYS software. The bridge deck is simulated by Beam 4 element, and the total bridge is divided into 30 finite elements. In the analysis, the elastic modulus is $E = 2.06\times10^{11}$ Pa, the shear modulus $G = 0.79\times10^{11}$ Pa. In the finite element model, there are relationships as follows:

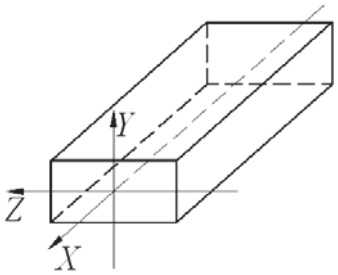

Figure 2. Directions of Beam 4 element

$$I_m = \int_A r^2 \cdot dm = \int_A r^2 \cdot d(A\rho) = \rho \int_A (y^2 + z^2) \cdot dA = \rho \left(\int_A y^2 \cdot dA + \int_A z^2 \cdot dA \right) = \rho (I_z + I_y) \quad (17)$$

From equation (17), we can get following equation

$$A_{beam} = m_{beam} / \rho = m_{beam} \Big/ \left(I_m \Big/ (I_z + I_y) \right) = m_{beam} (I_z + I_y) \Big/ I_m \quad (18)$$

Where, I_y , I_z are the inertia moment around Y and Z axis separately. A_{beam} is the section area of the bridge deck.

The boundary conditions of the simple bridge finite element model are as follows: For the left node, constrain UX, UY, UZ and RotX; For the right node, constrain UY, UZ and RotX. (X is the along bridge deck direction; Y is the vertical direction, and Z is the cross bridge deck direction.) The top 50 modes of the simple bridge are gotten using modal analysis. In the modal analysis, the mass matrix is consistent matrix, and the damping is not considered. The top 10 modes are shown in Table 1.

Table 1. Natural frequency and mode shape of simple bridge with ideal thin plate section

Mode No.	Frequence(Hz)	Mode shape	Mode No.	Frequence (Hz)	Mode shape
1	0.1786	1-S-V	6	1.5154	2-S-T
2	0.5033	1-S-T	7	1.5912	2-S-V
3	0.5179	1-S-L	8	1.7614	AD
4	0.7117	1-AS-V	9	2.0076	1-AS-L
5	1.0080	1-AS-T	10	2.0270	2-AS-T

V: vertical bending; T: torsion; L: lateral bending; S: symmetrical; AS: antisymmetrical; A: axial deformation

The self-exited forces of the bridge deck with ideal thin plate section can be expressed by Theodorson function: $C(k)=F(k)+ iG(k)$, and can also be represented using R. T. Jones's approximate expressions[15].

$$\begin{cases} F(k) = 1 - \dfrac{0.165}{1 + \left(\dfrac{0.0455}{k} \right)^2} - \dfrac{0.335}{1 + \left(\dfrac{0.03}{k} \right)^2} \\ G(k) = -\dfrac{0.165 \times 0.0455 / k}{1 + \left(\dfrac{0.0455}{k} \right)^2} - \dfrac{0.335 \times 0.03 / k}{1 + \left(\dfrac{0.03}{k} \right)^2} \end{cases} \quad (19)$$

Where, $k = \omega b/U = K/2$ is reduced frequency. Flutter derivatives of the ideal thin plate section bridge deck, i.e. H_i^*, A_i^* (i=1~4), can be obtained from equation (19).

$$\begin{cases} 4H_1^* = \dfrac{-2\pi F}{k}; & 8H_2^* = \dfrac{-\pi}{k}\left(1+F+\dfrac{2G}{k}\right) \\ 8H_3^* = \dfrac{-2\pi}{k^2}\left(F-\dfrac{kG}{2}\right); & 4H_4^* = 2\pi\left(\dfrac{1}{2}+\dfrac{G}{k}\right) \\ 8A_1^* = \dfrac{\pi F}{k}; & 16A_2^* = \dfrac{\pi}{k}\left(\dfrac{G}{k}+\dfrac{F-1}{2}\right) \\ 16A_3^* = \dfrac{\pi}{k^2}\left(F-\dfrac{kG}{2}+\dfrac{k^2}{8}\right); & 8A_4^* = \dfrac{-\pi G}{k} \end{cases} \tag{20}$$

The flutter derivatives obtained from equation (20) are shown in Figure 3.

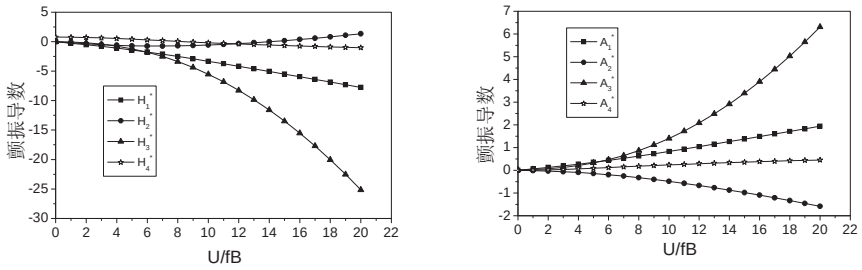

图 3　理想平板断面的颤振导数

Figure 3.　Flutter derivatives of the ideal thin plate section bridge deck

In order to calculate the buffeting responses, the aerodynamic parameters are taken the same values as reference [12]. The aerodynamic force coefficients in 0 wind attack angle are C_L = 0.128, C_D = 0.0697, C_M = –0.0074, $dC_L/d\alpha$ = –5.5577, $dC_D/d\alpha$ = 0.0 and $dC_M/d\alpha$ = 1.2662. The height of the bridge deck above the ground is z=60m. The roughness length is z_0=0.01m[16].

The Kaimal spectra[13] is chosen as the power spectra of the fluctuating wind in horizontal direction:

$$\frac{nS_{uu}(n)}{u_*^2} = \frac{200f}{(1+50f)^{5/3}} \tag{21}$$

Where, $f = \dfrac{nz}{U(z)}$ is the Monin (or similarity) coordinate; z is the height of the bridge deck above ground; $U(z)$ is the meaning wind speed at the height of z. $u_* = \dfrac{KU(z)}{\ln(\dfrac{z}{z_0})}$ is the friction velocity, a function of the surface roughness. $K \approx 0.4$ is the Karman constant. z_0 is the roughness length. n is the frequency of the fluctuating wind (Unit: Hz).

The Lumley – Panofsky spectra[13] is chosen as the power spectra of the fluctuating wind in vertical direction:

$$\frac{nS_{ww}(n)}{u_*^2} = \frac{3.36f}{1+10f^{5/3}} \tag{21}$$

The cross spectra can be expressed as

$$S_{uw}(n) = C_{uw}(n) + iQ_{uw}(n) \tag{22}$$

Where, $C_{uw}(n)$ is the cospectrum, choosing an empirical formula which is suitable for engineering applications; $Q_{uw}(n)$ is the quadrature spectrum which has not quantitative assessment, and be ignored in the calculation.

$$\frac{nC_{uw}(n)}{u_*^2} = \frac{14f}{1+9.6f^{2.4}} \tag{23}$$

The correlation in spanwise of the fluctuating wind can be expressed in conventional form[13] as

$$S\left(x_i, x_j, n\right) = S\left(n\right) e^{\frac{\lambda n}{U}\left|x_i - x_j\right|} \tag{24}$$

Where, $7 \le \lambda \le 21$, in the calculation $\lambda = 7$ considering the safety factor; x_i, x_j are the coordinate in the spanwise; $\left|x_i - x_j\right|$ is the length between x_i and x_j.

The maximal displacement responses of the simple bridge had all occurred in the mid-span, and the RMS of the displacement responses including 50 modes are shown in figure 4.

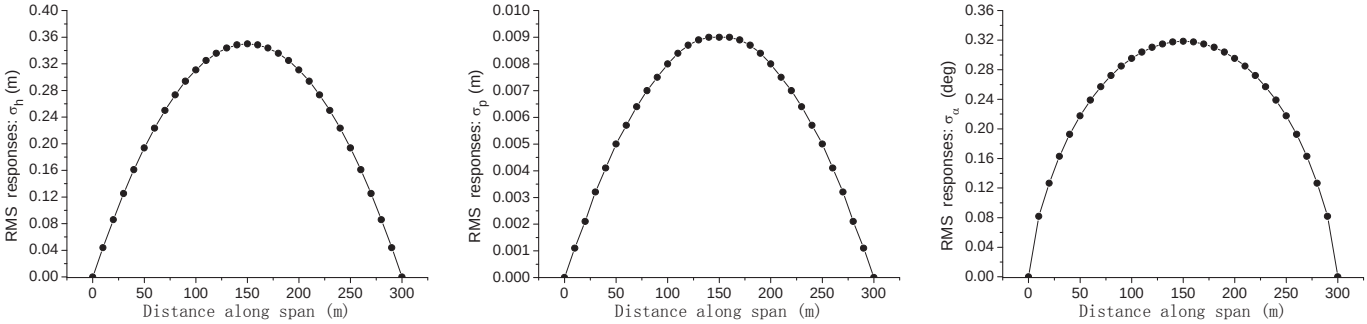

Figure 4. RMS of responses of the simple bridge with ideal thin plate section (50 modes)

According to equation (16), the accurate ESWLs of the simple bridge with ideal thin plate section in vertical, horizontal, and twist are shown in Figure 5 (exclude the mean wind load).

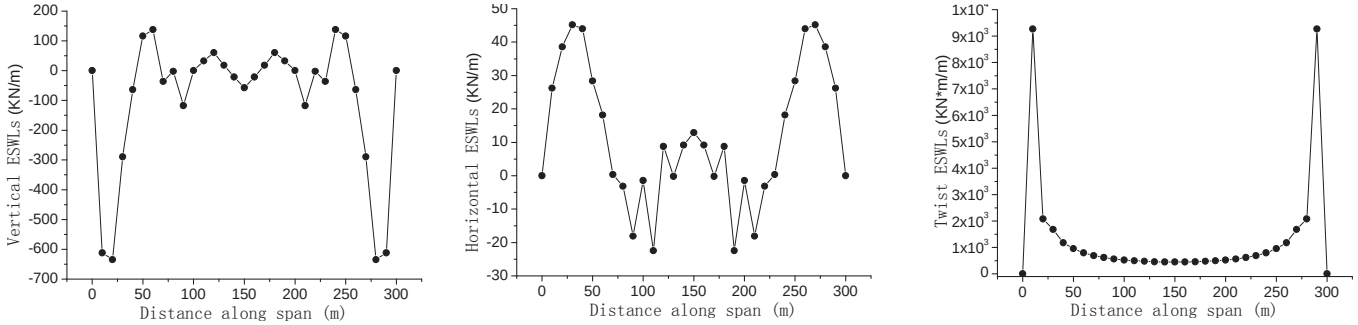

Figure 5. ESWLs of simple bridge with ideal thin plate section

In order to verify the validity of the method, we take the mid-span as an example to check the results. The influence lines of the mid-span are shown in figure 6. Put the ESWLs calculated by the method in this paper on the simple bridge, then the displacement responses can be obtained through static calculation. The results are shown in equation (24).

$$\hat{R}_h = 1.225m = 3.5\sigma_h;\ \ \hat{R}_p = 0.0316m = 3.5\sigma_p;\ \ \hat{R}_\alpha = 1.115m = 3.5\sigma_\alpha; \tag{24}$$

Equation (24) shows that the method proposed in this paper according to get equivalent static wind load on the structure, the structure of the displacement response and according to the theories of random vibration dynamic response of the structure of the get extreme value are exactly the same, so as to prove the correctness and effectiveness of this method.

The results show that the displacement responses calculated by ESWLs by method in this paper are the same as that calculated by the coupled flutter and buffeting analysis method. So the ESWL method in this paper is validity and effectiveness.

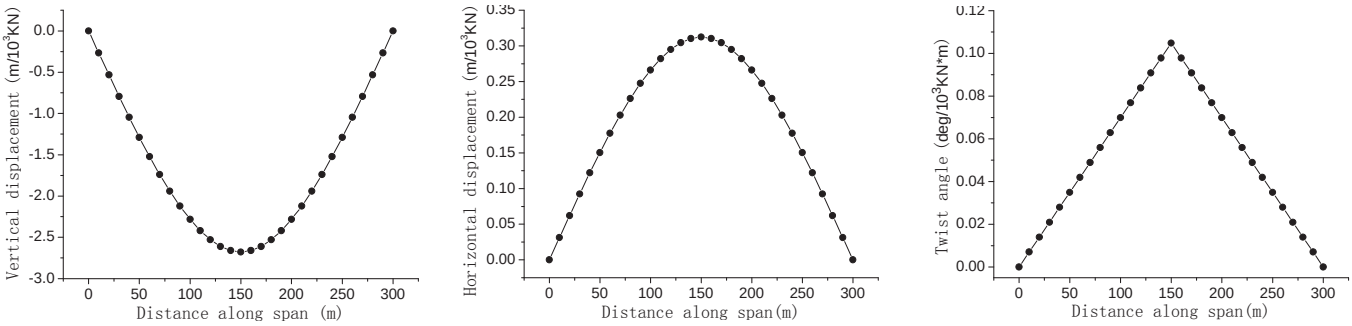

Table 6. Midspan influence line of the simple bridge with ideal thin plate section

4. CONCLUSION

According to the characteristics of the long-span bridge, one accurate ESWL method based on the displacement responses is proposed in this paper. This paper firstly calculates the mode and influence matrix using finite element method, then getting the PSD matrix of the buffeting forces by coupled flutter and buffeting vibration method. According to random vibration and structure dynamics, the ESWLs of long-span bridges in vertical, horizontal and torsional can be expressed by the mode matrix, influence matrix, aerodynamic mechanical admittance matrix, and PSD matrix of the buffeting forces. According to the load-response relationship, the ESWLs calculated through the method above are the only accurate solution which based on the displacements of the long-span bridge.

5. ACKNOWLEDGEMENT

Part of this work was sponsored by NSFC & JST joint funding program ‘New Strategy for Wind Disaster Risk Reduction of Wind Sensitive Infrastructures’. (Grant No. 51021140005). This support is gratefully acknowledged.

REFERENCES

[1]. Davenport A .G. Gust loading factors[J]. Journal of Structural Division, ASCE93(ST3), 1967: 11-34.

[2]. Kasperski, Niemann. The L. R. C.(Load-response-correlation)-method: A general method of estimating unfavorable wind load distribution for linear and non-linear structural behavior[J]. Journal of Wind Engineering and Industrial Aerodynamics,1992a,41-44: 1753-1763.

[3]. Kasperski, Niemann. Extreme wind load distributions for linear and nonlinear design[J]. Journal of Engineering Structure, 1992b,14(1): 27-34.

[4]. Kasperski, Niemann. Design wind loads for low-rise buildings: A critical review of wind load specification for industrial buildings[J]. Journal of Wind Engineering and Industrial Aerodynamics, 1996,61: 168-179.

[5]. Zhou, Y.，Gu, M.，Xiang, H. F. Alongwind static equivalent wind loads and responses of tall buildings, Part I: Unfavorable distributions of static equivalent wind loads[J]. Journal of Wind Engineering and Industrial Aerodynamics, 1999a,79: 135-150.

[6]. Zhou, Y., Gu, M., Xiang, H. F. Alongwind static equivalent wind loads and responses of tall buildings, Part II: Effects of mode shapes[J]. Journal of Wind Engineering and Industrial Aerodynamics, 1999b,79: 151-158.

[7]. Chen, X., Kareem, A. Equivalent static wind loads for buffeting response of bridges[J]. Journal of Structural Engineering, 2001,127: 1467-1475.

[8]. A.Katsumura, Y.Tamura, O.Nakamura. Universal wind load distribution simultaneously reproducing largest load effects in all subject members on large-span cantilevered roof[J]. Journal of Wind Engineering and Industrial Aerodynamics. 2007,95: 1145-1165.

[9]. N.P. Jones, R.H. Scanlan. Theory and Full-bridge Modeling of Wind Response of Cable-supported Bridges [J]. Journal of Bridge Engineering, 2001(6), 6: 365-375.

[10]. A. Jain, N.P. Jones, R.H. Scanlan. Coupled aeroelastic and aerodynamic response analysis of long-span Bridges [J]. Journal of Wind Engineering and Industrial Aerodynamics, 1996(60): 69-80.

[11]. A. Jain, N.P. Jones, R.H. Scanlan. Coupled Flutter and Buffeting Analysis of Long-span Bridges [J]. Journal of Structural Engineering, 1996(6): 716-725.

[12]. Ding Quan-shun. Refinement of coupled flutter and buffeting analysis for long-span bridges[D]. Doctoral dissertation. Shanghai: Tongji University, 2001. (in Chinese).

[13]. E. Simiu, R.H. Scanlan. Wind Effects on Structures (Third Edition)[M]. John Wiley & Sons, Inc. 1996.

[14]. Chen Wei. The study on the buffeting response spectrum of long-span bridges[D]. Doctoral dissertation. Shanghai: Tongji University, 1993. (in Chinese).

[15]. Li Guo-hao. Stability and vibration of bridge structures (Revised Edition)[M]. Beijing: China railway publishing house, 1996. (in Chinese).

[16]. Ministry of Communications of the People's Republic of China. Wind-resistent design specification for highway bridges (JTG/T D60-01-2004) [S]. Beijing: China Communations Press, 2004. (in Chinese).

Verification of time-domain buffeting theory and analysis of influence factors for long-span cable-stayed bridges

Wanshui HAN [a,*], Airong CHEN [b], Jiawu LI[a],Jianxin LIU[a]

[a]*Key Laboratory for Bridge and Tunnel of Shanxi Province, Chang'an University, China*
[b]*State Key Laboratory for Disaster Reduction in Civil Engineering, Tongji University, Shanghai, China*

ABSTRACT: In order to verify the current time-domain buffeting theory, the buffeting-induced structural displacements were measured in a full model test of the Hangzhou Bay Bridge. A time-domain buffeting analysis of aerodynamic forces on bridge deck, towers and main cables was performed to get the buffeting responses, where the aerodynamic admittance function was set as 1 and Sears, respectively, and the equivalent wind spectrum was used to calculate the buffeting loads while considering aerodynamic admittance function. Wind tunnel tests were carried out to study the spatial correlation, and the influences of Sears admittance function and spatial correlation on the buffeting responses were also investigated. The numerical results were compared with those of wind tunnel test. It shows that when the decay factor λ is 12.9, wind tunnel test results fall between buffeting responses with aerodynamic admittance being set to 1 and Sears, the results calculated with Sears function being on the unsafe side. Spatial correlation greatly influences buffeting responses, the buffeting responses can be reduced by about 13%~22% using the coefficient of spatial correlation obtained in wind tunnel test instead of that proposed in 《Wind-resistent Design Specification for Highway Bridges》. Analysis of the Hangzhou Bay Bridge shows that the current timedomain buffeting theory cannot predict bridge buffeting-induced responses accurately, certain discrepancy exists between the calculation and the tunnel test results.

Keywords: cable-stayed bridge; time-domain; buffeting analysis; aerodynamic admittance; Sears function; spatial correlation

1. Introduction

Due to diversity of factors involved in long-span bridges buffeting and comparatively complex theoretical analysis, so far there have been many proposed methods to predict buffeting response of long-span bridges (Aas-Jakobsena and Strommen,2001; Scanlan and Gade,1977; Scanlan,1977; Jain et al,1996; Ding,2001). Analysis in frequency domain is a conventional approach to predict the buffeting response. However, for a super long-span bridge, where highly nonlinear and coupled responses due to significant wind-structure interaction are encountered, the time-domain approach is more competitive. Long-span bridge nonlinear time-domain buffeting analysis consists of three key components: numerical simulation of wind field, expression of aerodynamic forces and calculation of buffeting responses. The overall stochastic wind field of long

span bridge was simulated by the improved WAWS in this paper while only the deck wind field was usually simulated in the former time-domain analysis. In the full model test of the Hangzhou Bay Bridge, the buffeting response of the full model was obtained under the action of the turbulent flow generated in the wind tunnel. Therefore, the analytical results will agree better with the experimental results if the wind-tunnel turbulence is used as the input. For that idea, records of wind tunnel turbulence of the full model test are analyzed to extract its statistical characteristics, which will in turn serve as the target input to the numerical simulation. Spatial correlation is an important factor that influences buffeting responses, however, data from field measurement of spatial correlation of natural wind are generally not available. Decay factor ranges from 7 to 20 and decay factor is set as 7 when there are not data from field measurement of spatial correlation, which is specified in《Wind-resistent Design Specification for Highway Bridges》. A study on spatial correlation of wind tunnel was carried out in the wind tunnel test. In order to evaluate the effect of the wind spatial correlation on buffeting responses, buffeting response analysis were conducted and decay factor was set as test result, 7 and 20 respectively in the course of wind field simulation. Buffeting analysis has been based on the quasi-steady theory considering Sears admittance function since Sears (Sears,1941) put forward the notion of aerodynamic admittance , however, the values calculated based on which are not always agreement with test results. How much the difference will be? Whether the influence of Sears admittance function to each component of buffeting responses (such as RMS of vertical, lateral, torsional displacements) will be similar? All of these will be investigated in this paper.

1. Turbulence characteristics

1.1. Characteristics of turbulence generated in the wind tunnel

Measured horizontal and upward wind spectrum in wind tunnel can be expressed by Eq.(1), the measured and fitted auto spectrum of *u* and *w* are shown in Fig.1 and Fig.2.

$$nS_a / u_*^2 = af / \left(1 + bf\right)^{cm} \tag{1}$$

where, the subscript *a* of *S* can be *u, v* or w, indicating the alongwind, horizontal and upward components of velocity fluctuations of wind turbulence, respectively; c=5/3 for the auto spectra; and a, b, *m* are the parameters fitted with non-linear least square method based on the measured spectral data.

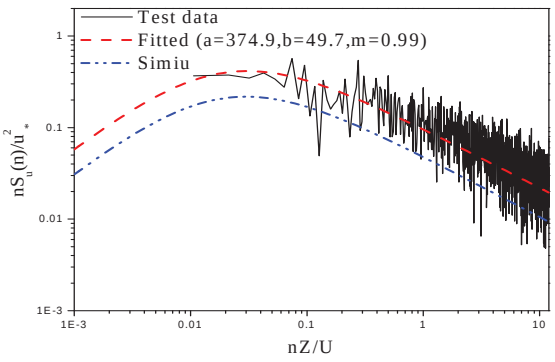

Fig.1. Auto spectra of component u

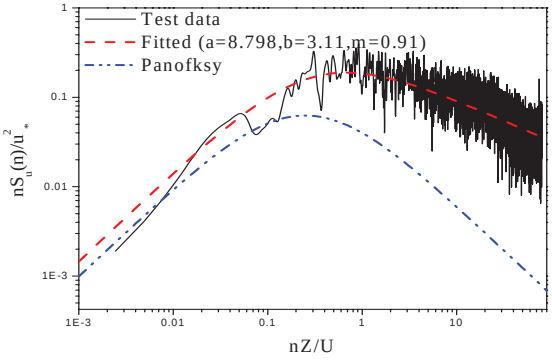

Fig.2. Auto spectra of component w

Co-coherence of wind is often expressed by an exponential function:

$$coh = \frac{S_{uu}^{C}(x_1, x_2, f)}{\sqrt{S_{uu}(x_1, f) S_{uu}(x_2, f)}} = \exp\left(-\lambda \frac{fD}{U}\right) \tag{2}$$

where, $S_{uu}(x_1, f)$ is the power spectrum of along wind-speed fluctuation u at x_1, $S_{uu}^{C}(x_1, x_2, f)$ is the real part of cross-spectrum of u between x_1 and x_2, λ the decay factor, f the frequency, $D = |x_1 - x_2|$ the transverse distance and U the mean wind speed.

A study on spatial correlation in wind tunnel was carried out in the full model test of the Hangzhou Bay Bridge . Spatial correlation is the function of f and D, In the measurement, D is set as 1.12、2.24、3.39 and 4.54m respectively, the least square method was used to achieve λ according Eq.(2), the decay factor λ ranges from 10.8 to 15.7 and the average of all data is 12.91.

2.3. Results of wind turbulence simulation and checks

The improved WAWS was chosen to simulate characteristics of wind field at Hangzhou Bay Bridge (Fig.3). The measured turbulence wind spectra and spatial correlation were used in the simulation. Main parameters in the simulation: K=0.4, z_0=0.03, U(55.41) = 40m/s; upper cutoff frequency ω_{up}=4π(rad/s).

Figs.4-6 show comparisons of target and simulated auto spectra, coherence function and correlation variance respectively by the improved WAWS. The spectra, coherence function and correlation variance of the simulated turbulence agree well with the input target on the whole.

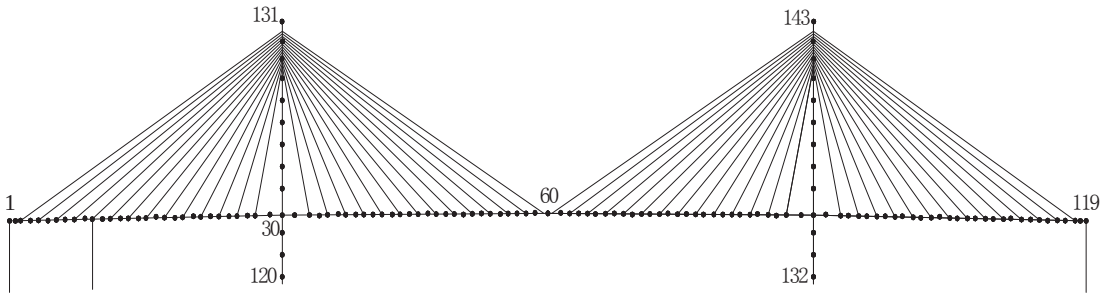

Fig.3. Layout of wind simulation points of Hangzhou Bay Bridge

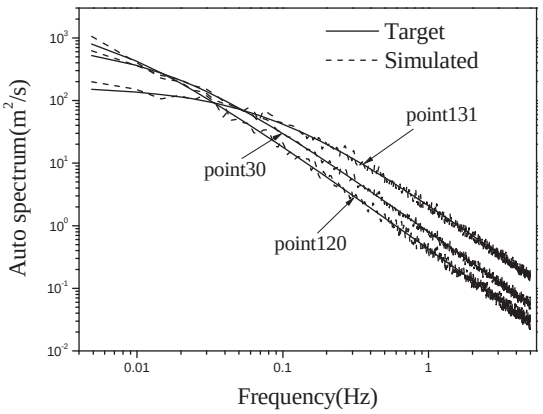

Fig.4. Auto-spectrum S_u

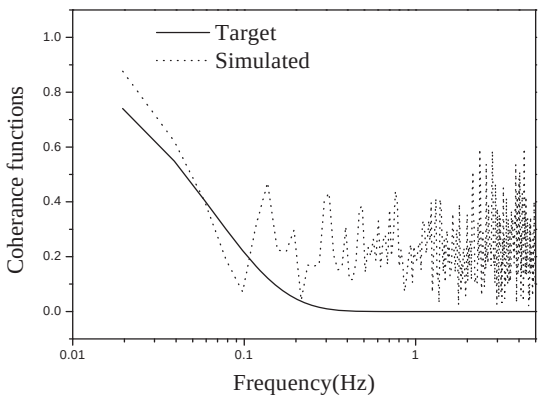

Fig.5. Coherence functions.

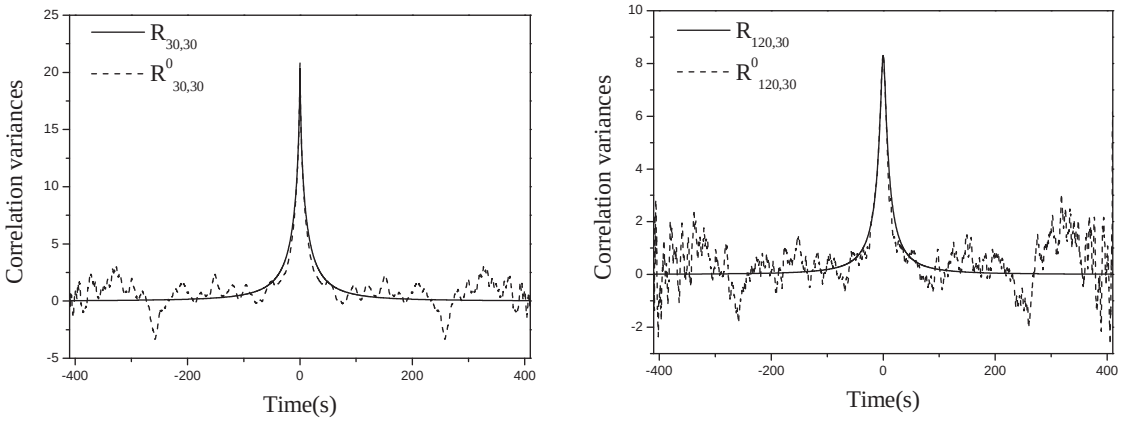

Fig.6. Comparison of simulated and target correlation variances by the improved method

2. Wind Tunnel Test and Analysis

Hangzhou Bay Bridge is a cable-stayed bridge with a span arrangement of 70+160+448+160+70 m, a twin girder steel deck, two inverted Y reinforced concrete pylons.

The full bridge aeroelastic model test was carried out in the TJ-3 Boundary Layer Wind Tunnel of the State Key Laboratory for Disaster Reduction in Civil Engineering at Tongji University. The model, shown in Fig.7, was manufactured at a geometric scale of 1:100. The total length and height of the model are 9.08m and 1.83m, respectively.

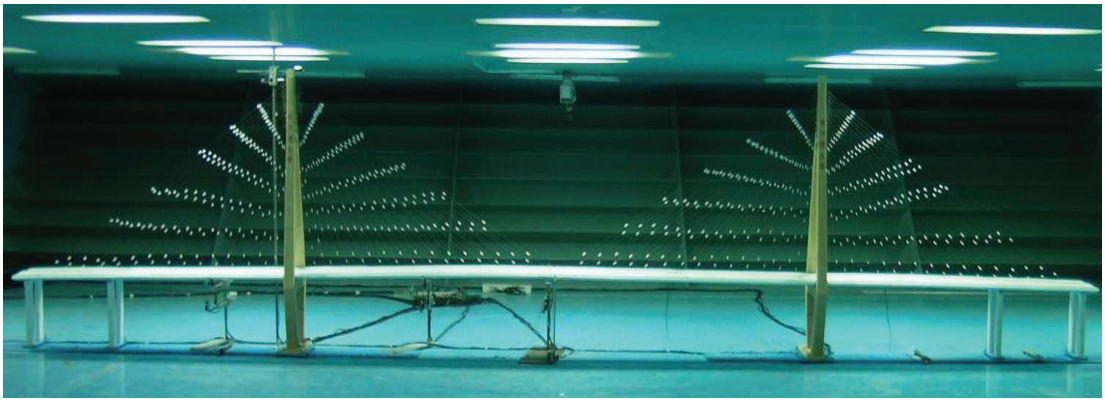

Fig.7. Full bridge aeroelastic model in TJ-3 Wind Tunnel

3. Buffeting-induced displacements test and analysis

3.1. Interaction between deck, towers and cables

In previous time-domain buffeting analyses, only deck wind field was simulated, this primarily owing to buffeting analytical method limitation. In this section, besides the buffeting forces and aeroelastic forces on the bridge deck, the buffeting forces on the towers and the cables are also included in the computation. The results are denoted by the term “full bridge”. The full-bridge results are then compared with those forces on the bridge deck only, both on the bridge deck and tower, and both on the bridge deck

and cable respectively. In this way, the interaction between the bridge deck, towers, and main cables can be examined.

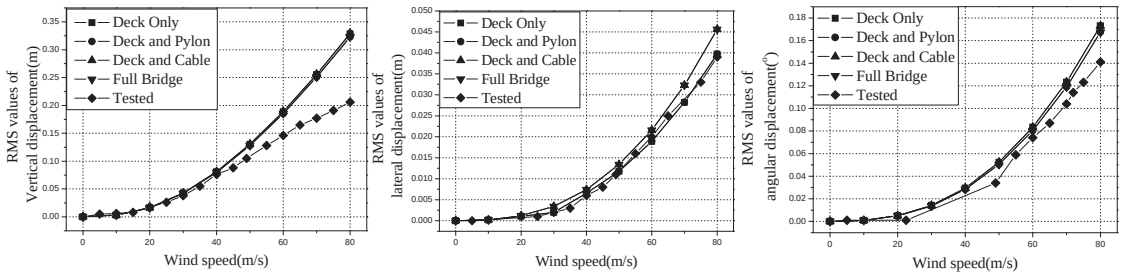

Fig.8. Comparisons of displacement responses RMS values at mid-span

Fig.8 shows the variable curves of mid-span's vertical, lateral and angular displacement RMS values for the full bridge, for the deck only, for both of the deck and tower, for both of the deck and cable and the test values. Table 1 presents comparisons of mid-span's lateral displacement RMS values for the full bridge, for the deck only the test values. As shown in the Fig.8 and Table 1, conclusions can be drawn as follows: 1), The buffeting forces on the cables and towers have a mild effect on the vertical and torsional displacement responses of the bridge deck at mid-span. 2), The buffeting forces on the towers contribute little to the lateral buffeting-induced responses of bridge deck. 3), Due to the consideration of buffeting forces on the main cables, the lateral displacement response of the bridge deck increases greatly. Take designed wind speed of 50m/s as an example, the full bridge lateral displacement response RMS value is 0.0134m, 13.8% larger than the value of 0.0118m if only taking deck wind field into consideration. Moreover, the differences become larger when wind speed increases. Therefore, the cable wind field must be taken into consideration, especially in the buffeting analysis of super long-span cable-stayed bridges whose cables are very long. 4) The displacement RMS values of deck at midspan are a little larger than wind tunnel test results and agree well with each other on the whole, especially for lateral and torsional displacement RMS values. For vertical displacement RMS values of mid-span, calculated values and test values have a good accordance at low wind speeds. The calculated vertical displacement RMS value at mid-span is 1.17 times larger than test values at design wind speed of 50m/s, whereas the difference become larger when wind speed increases.

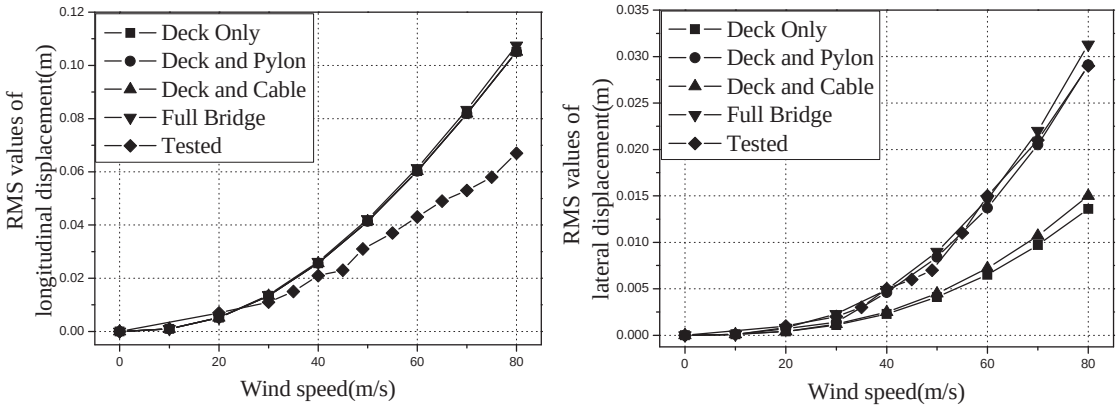

Fig.9. Comparison of displacement response RMS values at the top of pylon

Some conclusions can be found from Fig.9: 1), The buffeting forces on the cables have a little influence on lateral displacement at the top of pylon. At designed wind speed of 50m/s, the lateral displacement response RMS value with buffeting forces on the deck and cables is 0.0045m, 9.7% larger than the value of 0.0041m if only taking deck wind field into consideration. 2), The buffeting forces on the towers have a considerable influence on the lateral displacement RMS values. At designed wind speed of 50m/s, the full bridge lateral displacement response RMS value is 0.0084m, 104.8% larger than the value of 0.0041m if only taking deck wind field into consideration. 3) The full-bridge lateral displacement response RMS values at the top of pylon agree with the test values well while those forces on the bridge deck only are much smaller than the tested values. Therefore, ignorance of buffeting forces on pylon and cable will achieve insecure results.

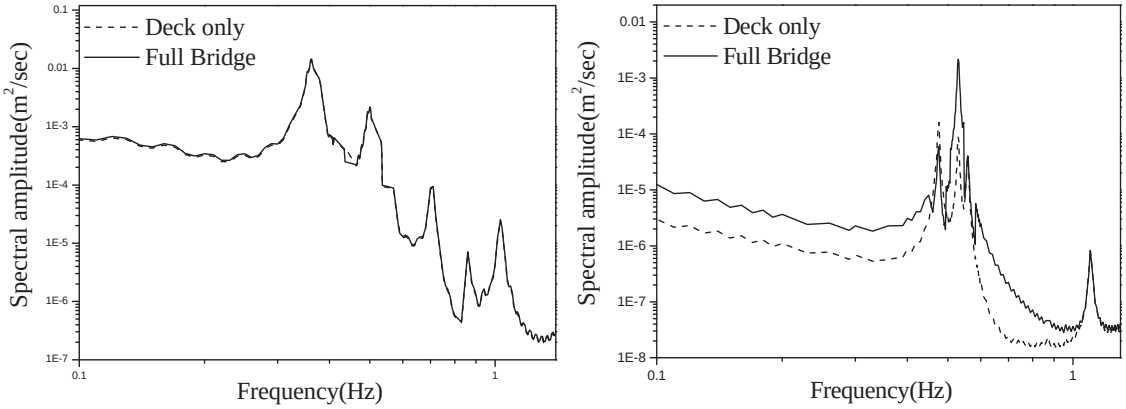

Fig.10. Comparison of power spectrum density of displacement response at the top of pylon

Table 1
Main modes of Hangzhou Bay Bridge

Mode	Frequency (Hz)	Mode type	Mode	Frequency (Hz)	Mode type
1	0.11186	LF	8	0.87337	A-L-1
2	0.36851	S-V-1	9	0.87611	A-V-2
3	0.47598	S-L-1	15	0.95133	S-T-1
4	0.50541	A-V-1	17	1.02839	S-V-3
5	0.53307	A-L(Tower)	23	1.16229	A-V-3
6	0.56004	S-L-2	24	1.41749	A-T-1
7	0.72903	S-V-2	25	1.45489	S-V-4

Note:S=Symmetrical; A=Antisymmetrical; LF=Longitudinal Floating; V=Vertical; T=Torsion; L=Lateral.

The spectra of the lateral and longitudinal displacement responses at the top of pylon are shown in Fig.10. The longitudinal displacement response spectra for the full bridge are almost agreement with the deck only. Five peak values occur in each power spectrum density curve VS the frequency of mode 2, 4, 7, 9, and 17. Moreover, the mode

types of these five peak values are all vertical symmetric bending or vertical dissymmetric bending of deck (Table 3). Therefore, can conclude that the longitudinal vibration of pylon mainly depend on the vertical vibration of deck. The lateral displacement response spectra for the deck only are obviously smaller than those for the full bridge. The former three peak values occur in each power spectrum density curve VS the frequency of mode 3, 5 and 6. The type of mode 5 is a dissymmetric lateral bending of pylon, but the type of mode 3 and 6 are both symmetric lateral bending of deck. Compared with the case only considering deck wind field, the contribution of mode 5 becomes more significant, and the contributions of mode 3 and 6 become weaker when taking full bridge into account.

3.2. Influence of aerodynamic admittance

Since Sears established the conception of aerodynamic admittance in 1940s, buffeting analysis is always carried out based on quasi-steady theory considering Sears admittance function. The difference in the actual value and the predicted value adopting Sears admittance function can't be ignored in practical projects. But how much the difference will be and how Sears function influence the displacement response (such as vertical, lateral and torsional displacement response RMS values) are still unknown to us. Therefore some researches are needed to resolve the above problems and are presented in this paper also.

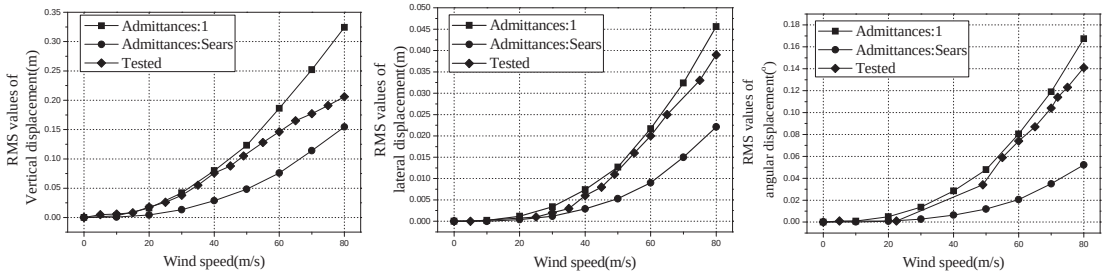

Fig.11. Comparison of displacement response RMS values at mid-span

Fig.11 show the buffeting responses at mid-span with and without consideration of Sears aerodynamic admittance. Some conclusions can be obtained thereinafter: 1), The RMS values considering Sears function are smaller than those without considering admittance function and the ones in wind tunnel. 2), The influence of Sears admittance function to each component of buffeting-induced displacement responses is different. Compared with vertical and lateral displacement responses, the ratios of torsional RMS values considering Sears admittance function to those without considering admittance function and the ones in wind tunnel are much smaller.

5. Conclusions

1) The buffeting forces on the cables and towers have a little effect on the vertical and torsional displacement responses of the bridge deck and the longitudinal responses of tower. The buffeting forces on the cables contribute mainly to the lateral responses of bridge deck while the buffeting forces on the towers can increase the lateral responses

of pylon significantly. Therefore, ignorance of buffeting forces on pylon and cable will achieve insecure results.

2) The calculated buffeting RMS values are slightly larger than wind tunnel test results and agree with the wind tunnel test results on the whole when admittance function is 1 and λ is 12.9. It is suggested that buffeting RMS values when admittance function is 1 and the value of λ is from field measurement can be served as controlling values in wind-resistance design when appropriate admittance function is not available.

Acknowledgements

The writers are grateful for the financial support from the National Natural Science Foundation of China under Grant NNSF-50478109.

References

[1] Aas-Jakobsena, K., Strommen, E.,2001. Time domain buffeting response calculations of slender structures . Journal of Wind Engineering & Industrial Aerodynamics 89, 341-364.

[2] Bucher, C. G., Lin, Y. K., 1988. Stochastic stability of bridges considering coupled modes .Journal of Engineering Mechanics 114(12), 2055-2071.

[3] Chen, X., Kareem, A., 2001. Equivalent static wind loads for buffeting response of bridges. J. struct. Engrg. 127(12), 1467-1475.

[4] Chen, A. R., Han, W. S., 2004. Technical report of wind tunnel study on wind-resistant performance of Hangzhou Bay Bridge. State Key Laboratory for Disaster Reduction in Civil Engineering (In Chinese).

[5] Communication Department of P. R. of China, 2004. (JTG/T D60-01-2004) Wind-resistant Design Specification for Highway Bridges, Beijing, China Communications Press (In Chinese).

[6] Deodatis, G., 1996. Simulation of ergodic multivariate stochastic processes. J. Engrg. Mech. 122 (8):778-787.

[7] Ding, Q. S., 2001. Refinement of coupled flutter and buffeting analysis for long-span bridges, Ph. D. Dissertation, Tongji University, Shanghai, China (In Chinese).

[8] Ding, Q. S., Chen, A.R., Xiang, H.F., 2006. Simulation of spatial fluctuating wind field on long span bridges. Chinese quarterly of Mechanics 27 (2):184-189 (In Chinese).

[9] Homles, J. D., 2002. Effective static 1oad distributions in wind engineering. J. Wind Engrg. Indust. Aerodyn. 90, 90-109.

[10] Jain, A., Jones , N. P., Scanlan, R. H., 1996. Coupled aeroelastic and aerodynamic response analysis of long-span bridges. Journal of Wind Engineering & Industrial Aerodynamics 60, 69-80.

[11] Sears, W. R., 1941. Some aspects of non-stationary airfoil theory and its practical application .Journal of Aeronautical Sciences 8, 104-108.

[12] Scanlan, R. H., Gade, R. H.,1977. Motion of suspended bridge spans under gusty wind. Journal of Structure Engineering 103 (9), 1867-1883.

[13] Scanlan, R. H., 1978. The action of flexible bridges under wind, II: buffeting theory. Journal of Sound and Vibration 60(2), 201-211.

Measurements of equivalent aerodynamic admittances of two separate and parallel bridge decks

Qi Zhou[a,b], Le-Dong Zhu[a,c], Peng-Jie Ren[a,c]
[a]*State Key Laboratory for Disaster Reduction in Civil Engineering, Tongji University, Shanghai, China*
[b]*Department of Civil Engineering, Shantou University, Guangdong, China,*
[c]*Key Laboratory for Wind Resistance Technology of Bridges of Ministry of Transport, Tongji University, Shanghai, China*

ABSTRACT: The concept of aerodynamic admittance functions was introduced into buffeting analysis of long-span bridges to consider the unsteadiness and spatial variation of wind turbulence and plays an important role in improving the accuracy of buffeting response. Because of the signature turbulence effect and aerodynamic interference effect, the aerodynamic admittance of bridge with two separated paralleled decks may no longer behave as Sears function. Taking Tanggu Haihe Bridge in Tianjin as an engineering back ground, the aerodynamic admittances of a semi-closed box deck a full-closed box deck were measured and analyzed in this article. Moreover, the aerodynamic interference effect on the equivalent aerodynamic admittance with different types of bridge decks at the windward or leeward position and with different distances between two decks were also investigated via wind tunnel test by the method of force measurement. The results show that the equivalent aerodynamic admittances of windward and leeward deck are quite different from that of single deck in their characteristics due to the aerodynamic interference effect. The aerodynamic interference effect on the $|\chi_D|^2$ curve is more significant than those on the $|\chi_L|^2$ and $|\chi_M|^2$ curves, and that on the leeward deck is much stronger than that on the windward deck. Furthermore, with variation of the ratios of D/B (the ratios of distance between two decks over the deck width), the aerodynamic interference may exert different effects on the equivalent aerodynamic admittances. For both of the $|\chi_D|^2$of the windward and leeward decks, the admittance curves approach to that of the single deck gradually with the increasing reduced frequency. And for the $|\chi_L|^2$ and $|\chi_M|^2$, there is no significant difference between the admittance curves of the windward deck and the single deck, whilst that of leeward deck are remarkable different from that of single deck, especially for the $|\chi_L|^2$ curves.

KEYWORDS: long-span bridge; wind tunnel test; aerodynamic admittance; signature turbulence effect; aerodynamic interference effect

1 INTRODUCTION

Buffeting is one of important types of wind-induced vibration of long-span bridges due to their flexibility and lower fundamental natural frequencies, and has been paid great attentions to in both wind engineering and bridge engineering fields. Up to now, apart from wind tunnel test means, various analysis methods have been developed for predicting buffeting responses of long-span bridges. The Davenport buffeting theory and linear self-excited aeroelastic force model introduced by Scanlan and his co-workers were generally accepted in the above analysis methods. In Davenport buffeting response prediction, Quasi-steady theory was employed to establish the buffeting forces on the bridge and aerodynamic admittance functions were introduced to consider the unsteadiness and spatial variation of wind turbulence surrounding bridge deck cross sections. The aerodynamic admittance can either be approximated as in Liepmanm(1952),Davenport(1962), Irwin(1977), or measured as in Holmes(1975), Kawatani & Kim (1992), Sankaran & Jancauskas(1992), Larose(1992) and Bogunovic Sears' function is most commonly used form of the lift aerodynamic admittance

of a thin airfoil in fully correlated gusts with sinusoidal fluctuations(Liepmanm 1952):

$$\left|\chi_L\left(f^*\right)\right|^2 = \frac{1}{1+2\pi^2 f^*} \tag{1}$$

where $|\chi_L|^2$ is the square of modules of equivalent aerodynamic admittances of lift; f^* is a reduced frequency $= fB/U$, U is the mean wind speed, and B is the whole width of the deck in this paper.

However, the buffeting forces in most of the current buffeting analysis are determined based on the quasi-steady theory, where, only the turbulence of incident wind is included. The signature turbulence caused by the interaction between structure and flow around it is normally ignored. Up to the present, the extent of signature turbulence effect on the bridge buffeting responses has not been understood yet and has rarely been investigated, although this issue was already regarded as one of major challenges in the prediction of long-span bridge response to wind (Jones 1999).

With the development of traffic flow, bridge with two separated paralleled decks has been built to accommodate the traffic requirement in long-span bridge engineering field, and it has been observed that aerodynamic interference phenomena exist between the two neighboring decks. And the interference behavior largely depends on the distance between the two decks (Honda et al., 1993; Larsen et al., 2000; Stoyanoff et al., 2003; Kimura et al., 2008). If the two bridge decks are close enough to each other, the surrounding flows around one bridge deck will be influenced by another, and vice versa. Consequently, the performance of cross-sectional aerodynamic admittance of each deck will be inevitably and significantly affected by another deck. However, Most of the conducted researches referred to above focused extensively on revealing the complicated behavior of the aerodynamic interference phenomenon, little research has been conducted to aerodynamic interference effect on the aerodynamic admittances, which may make significant effect on the buffeting response.

In this connection, the equivalent aerodynamic admittances are investigated in this study via force measurement wind tunnel tests of sectional model in turbulence flow. Because the signature turbulence is regarded to be much more significant for bridge decks with separate boxes than other types of decks, the existing and new Tanggu Haihe Bridge in Tianjin(see Figure 1), which are both cable-stayed single tower bridge with a main span of 310, are thus taken as a engineering back ground in this study. Furthermore, the aerodynamic interference effect on the equivalent aerodynamic admittances of bridge with two separated paralleled decks are also surveyed in these wind tunnel tests, which adopted seven D/Bs(the ratio of distance between two decks and deck width) conditions and six cases with the combinations of different type decks. The details of the research are to be introduced in the following sections.

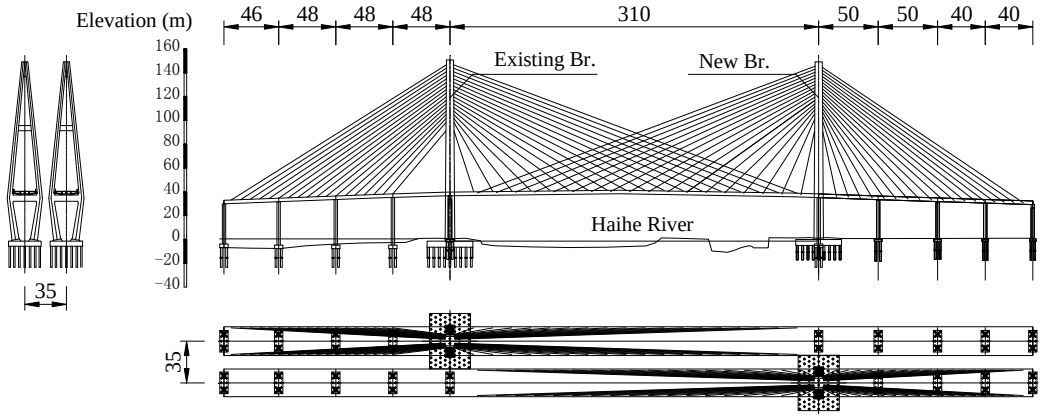

Figure 1 Layout of the existing and new Tanggu Haihe Bridge in Tianjin (Unit: m)

2 DESCRIPTION OF SECTIONAL MODEL TEST

The motionless sectional model tests for the equivalent aerodynamic admittances of the bridge deck were carried out in the TJ-2 Boundary Layer Wind Tunnel at a length scale of 1/60 and with turbulent intensities of 15%. In these wind tunnel tests, two types of sectional models, designed based on the existing and new Tanggu Haihe Bridge decks, were with the shape of semi- and full-closed box deck respectively(see Figure 2). The case simulating real Tanggu Haihe Bridge, full-closed box deck at windward and semi-closed box deck at leeward, is called as case FSD for short in this paper, and called as case SFD vice versa. Another two cases, two semi-closed box deck(case SSD) and two full-closed box deck(case FFD), are also investigated in order to reveal the relationship between aerodynamic interference effect and distance between two decks. And D/Bs of 0, 0.25,0.5,0.75,1,1.5,2 were adopted in these tests. Moreover, in order to compared with the cases mentioned above, two cases were also measured in additionally, and the case with single full-closed box deck is named as case FD, and likewise the case with single semi-closed box deck is called case SD in this paper.

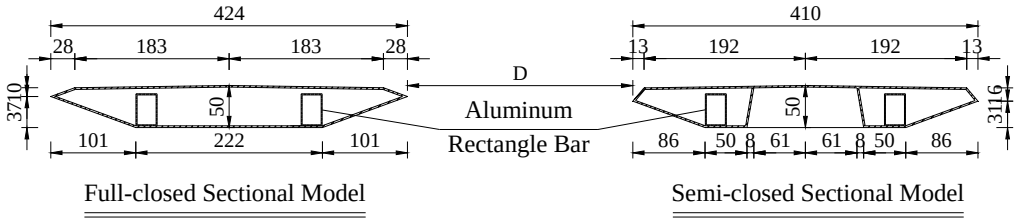

Figure 2 Measured segment of sectional model with semi- and full-closed box deck (Unit: mm)

Figure 3 Sectional model in TJ-2 Boundary Layer Wind Tunnel

Figure 3 shows the sectional model mounted in the TJ-2 wind tunnel. The sectional model was designed in such a way that the fluctuating forces could be synchronously measured in the test for the windward and leeward deck. Therefore, the sectional model was comprised of two measured segments and two upper compensatory segments. The windward segment and its upper compensatory segment were simulated the aerodynamic shape of windward bridge deck, and so does the leeward segment. The measured segment was made of wood and an aluminum link endplate, which was used to connect the measured segment to the balance. The measured segment of semi-closed box deck was 0.4m long (excluding the end plate), 0.05m high and 0.424m wide, and that of full-closed box deck also 0.4m long (excluding the end plate) and 0.05m high, but 0.41m wide. The total mass of the measured segments with

semi- and full-closed box are 1.01kg and 1.42kg, respectively. The aluminum end plate had a basic shape as same as the cross section shape of the measure segment, but its middle part was circular with a diameter as same as the force balance. Two upper compensatory segments were also 0.4m long and were made of same material, but empty inside for reducing weights.

Before the test, a steel frame for the installation of compensatory segments was mounted on the turntable at first. Two five-component force balances were then fixed separately on sectional steel bars with sliding grooves, and their surfaces was 0.3m upon the tunnel floor. Afterwards, to depress the disadvantageous effects of boundary layer above the tunnel floor and 3D flow around the lower end of the sectional model, a rectangular separating plate made of Perspex was then mounted upon the turntable with its bottom surface level a little bit lower than the top surface level of the force balance. In the middle region of the separating plate, there was an opening with a shape similar to the aluminum end plate of the measured segment, but a little bit larger than the latter. The separating plate must keep no touch to the top perceptional surface of the force balance. In the next step, two measured segment were vertically mounted on the force balances through the preset opening of the separating plate without any contact, and two upper compensatory segments were installed on the steel frame at their top ends and were kept a narrow gap of 1-2mm from the measured segment at their bottom ends. Finally two upper compensatory segments were connected to each other through the transverse link beam model to increase their stiffness. As a result, the fundamental natural frequencies of the measured segment with semi-closed box were 33Hz, 58Hz in the directions in and out of the deck plane(*F*x and *F*y), respectively, and 82Hz in torsional direction(*M*z). Consequently, the fundamental natural frequencies of the measured segment with full-closed box were 33Hz of *F*x, 50Hz of *F*y and 71Hz of *M*z. Both of the frequencies mentioned above were much higher than 15Hz calculated by the third vertical bending frequency of Tanggu Haihe Bridge and the frequency ratio of wind tunnel test.

3 RESULTS OF EQUIVALENT AERODYNAMIC ADMITTANCES

The spectra of buffeting drag (S_{DD}), lift (S_{LL}) and torsion moment (S_{MM}) on the bridge deck can be expressed with the following equations according to the quasi-steady theory (Chen et al. 2001):

$$\begin{aligned} S_{DD} &= (\rho UB/2)^2 \Big[4C_D^2 |\chi_{Du}|^2 S_{uu} + \left(-C_L + C_D^{'}\right)^2 |\chi_{Dw}|^2 S_{ww} \\ &\quad + 2C_D \left(-C_L + C_D^{'}\right)(\chi_{Du}^{*}\chi_{Dw} S_{uw} + \chi_{Du}\chi_{Dw}^{*} S_{uw}^{*}) \Big] \\ &= (\rho UB/2)^2 \Big[4C_D^2 S_{uu} + 4C_D \left(-C_L + C_D^{'}\right) C_{uw} + \left(-C_L + C_D^{'}\right)^2 S_{ww} \Big] |\chi_D|^2 \end{aligned} \tag{2}$$

$$\begin{aligned} S_{LL} &= \left(\frac{\rho UB}{2}\right)^2 \Big[4C_L^2 |\chi_{Lu}|^2 S_{uu} + \left(C_D + C_L^{'}\right)^2 |\chi_{Lw}|^2 S_{ww} \\ &\quad + 2C_L \left(C_D + C_L^{'}\right)(\chi_{Lu}^{*}\chi_{Lw} S_{uw} + \chi_{Lu}\chi_{Lw}^{*} S_{uw}^{*}) \Big] \\ &= (\rho UB/2)^2 \Big[4C_L^2 S_{uu} + 4C_L \left(C_D + C_L^{'}\right) C_{uw} + \left(C_D + C_L^{'}\right)^2 S_{ww} \Big] |\chi_L|^2 \end{aligned} \tag{3}$$

$$\begin{aligned} S_{MM} &= \left(\frac{\rho UB}{2}\right)^2 \Big[4C_M^2 |\chi_{Mu}|^2 S_{uu} + C_M^{'2} |\chi_{Mw}|^2 S_{ww} \\ &\quad + 2C_M C_M^{'} (\chi_{Mu}^{*}\chi_{Mw} S_{uw} + \chi_{Mu}\chi_{Mw}^{*} S_{uw}^{*}) \Big] \\ &= (\rho UB/2)^2 \Big[4C_M^2 S_{uu} + 4C_M C_M^{'} C_{uw} + C_M^{'2} S_{ww} \Big] |\chi_M|^2 \end{aligned} \tag{4}$$

where the superscript * indicates the conjugate operation; ρ is the density of air; C_D, C_L and

C_M are the aerodynamic coefficients of mean drag, lift and torsion moment, respectively; $C'_D = dC_D / d\alpha$, $C'_L = dC_L / d\alpha$; χ_{Du}, χ_{Dw}, χ_{Lu}, χ_{Lw}, χ_{Mu} and χ_{Mw} are the equivalent aerodynamic admittances, which are the function of $K=\omega B/U$, respectively; ω is circular frequency; S_{uu} and S_{ww} are auto spectra of fluctuating wind components u and w, respectively; S_{uw} and C_{uu}, are the cross spectrum and co-spectrum between u and w, respectively; $|\chi_D|^2$, $|\chi_L|^2$ and $|\chi_M|^2$ are the square of modules of equivalent aerodynamic admittances of drag, lift and torsion moment, respectively, considering the joint contribution of u and w.

Figure 4 shows the results of $|\chi_D|^2$, $|\chi_L|^2$ and $|\chi_M|^2$ of case FSD measured in the turbulence flow field with the mean attack angle of zero. The measured data are then fitted using the following target functions of fraction series of Eq.(5) for the incident turbulence contribution and of Eq.(6) for the signature turbulence contribution, respectively, and the corresponding fitted curves are also plotted in Figure 4.

$$|\chi_l|^2 = \frac{\alpha}{1+\beta K^r} \tag{5}$$

$$|\chi_s|^2 = \sum_{i=1}^{n} \frac{c_{1i} + c_{2i} K}{(K - c_{3i})^2 + c_{4i}} \tag{6}$$

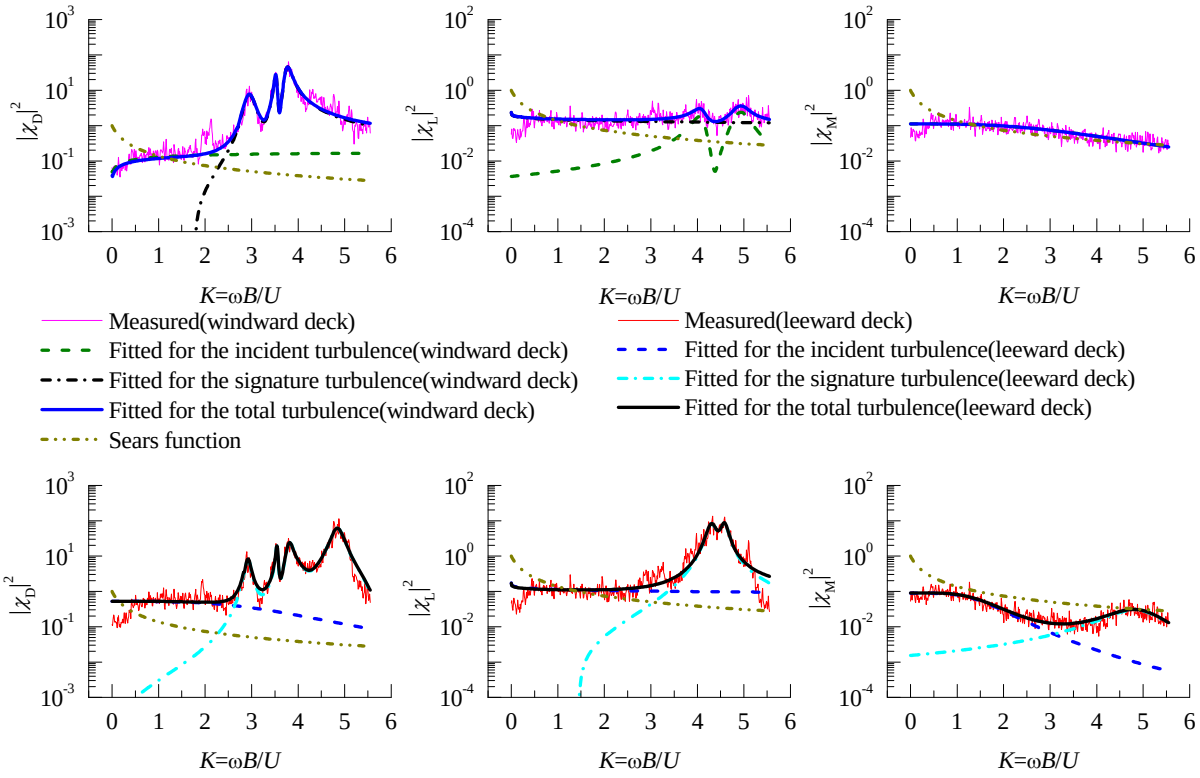

Figure 4 Measured and fitted equivalent aerodynamic admittances(EAA) of case FSD

From Figure 4, it can be seen that whatever windward deck or leeward deck, the tendencies of the measured equivalent aerodynamic admittances are not similar to that of Sears function. Due to the effect of signature turbulence, the $|\chi_D|^2$ and $|\chi_L|^2$ curves don't decrease with the increase of the reduced frequency, but generally, the $|\chi_M|^2$ curve still follows the reducing tendency as Sears function. In additional, the measured equivalent aerodynamic admittances are generally smaller than Sears function for K<1, and for K>1, the measured equivalent aerodynamic admittances of $|\chi_D|^2$ and $|\chi_L|^2$ are mostly somewhat much lager than Sears function whilst the $|\chi_M|^2$ of windward deck is close to Sears function and the $|\chi_M|^2$ of leeward deck is almost a bit little than Sears function. Furthermore, compared measured equivalent aerodynamic admittances of windward and leeward deck, the $|\chi_D|^2$ of windward and leeward deck have a similar characteristic that there are more than three significant peaks

at the range of K>3. Although the $|\chi_L|^2$ and $|\chi_M|^2$ of leeward deck are obviously influenced by the signature turbulence effect, that of windward almost does not affected by the signature turbulence.

Besides, it is found that for windward deck, the effect of signature turbulence makes the $|\chi_D|^2$ curve of having three significant peaks at about K=2.9, 3.5&3.8, and the $|\chi_L|^2$ curve of having two somewhat peaks appreciable peaks at 4&5, but doesn't influence the $|\chi_M|^2$ curve. For the leeward box, the effect of signature turbulence exerts remarkable influence on all the three equivalent aerodynamic admittances within the reduced frequency zone between 2.5 and 6, and makes the $|\chi_D|^2$ curve of having four peaks with a value much higher than 1.0 at about K= 2.9, 3.5,3.8 and 4.8, and influences the $|\chi_L|^2$ and $|\chi_M|^2$ curves of having a peak at about K=4.5 and 5, respectively. According to predecessors' research, the equivalent aerodynamic admittance of the signature turbulence is regarded to the aerodynamic shape of bridge deck and the inflow wind spectrum, Therefore, the equivalent aerodynamic admittances of incident and signature turbulence are fitted separated by different formula(Eq.(5) and Eq.(6), respectively) in Figure 4, and the result fitted for total turbulence is the sum of that of incident and signature turbulence.

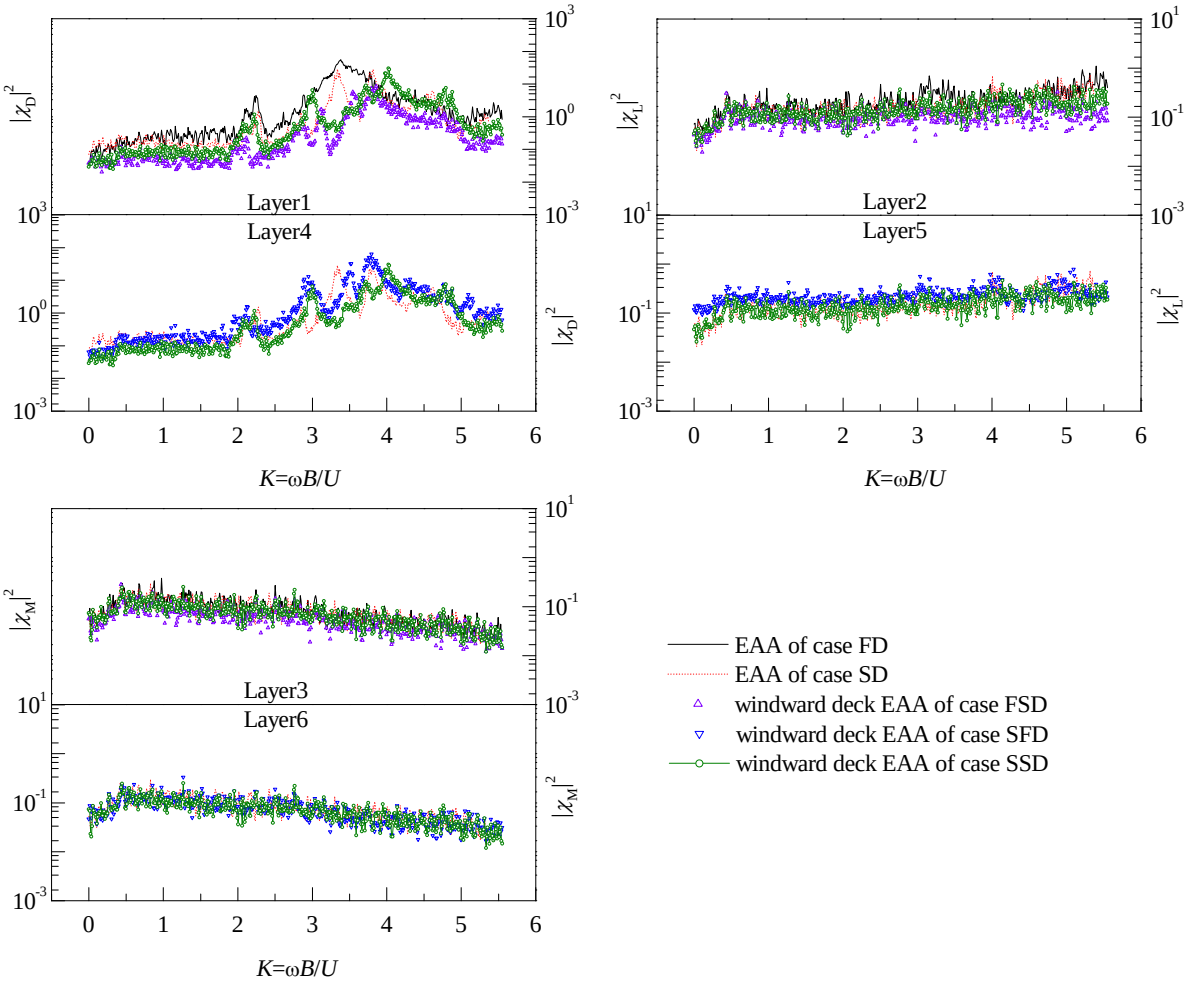

Figure 5 Comparison of equivalent aerodynamic admittances(EAA) of windward deck between different cases

4 EFFECT OF AERODYNAMIC INTERFRENCE

4.1 *Discussion of aerodynamic interference effect between different cases*

Figure 5 shows the comparison of the measured equivalent aerodynamic admittances of

windward deck between different cases. There are six layers of Figure 5 in which layer 1~3 present the measured $|\chi_D|^2$, $|\chi_L|^2$ and $|\chi_M|^2$ of windward deck in case FD, SD, FSD and SSD and layer 4~6 show that in case SD, SFD and SSD, respectively. From layer 1~3, compared between case FD and FSD or SD and SSD, it is found that the $|\chi_D|^2$ value of windward deck(case FSD or SSD) is remarkable smaller than that of single deck(case FD or SD), but $|\chi_L|^2$ and $|\chi_M|^2$ of windward deck are close to that of single deck. And there are three peaks of $|\chi_D|^2$ curve within case FSD whilst only two remarkable peaks within case FD, which can be explained that the signature turbulence contains more eminent reduced frequencies and wide range of affected frequency as a result of the aerodynamic interference effect. Furthermore, the $|\chi_D|^2$ curves of case FSD and SSD present similar peaks, thus it can be concluded that the equivalent aerodynamic admittance of different windward decks setting a same semi-closed box deck at leeward possess the alike signature turbulence effect. From layer 4~6, it is noticed that with different decks at leeward, the $|\chi_L|^2$ and $|\chi_M|^2$ curves of windward deck are approximate to each other, but for the $|\chi_D|^2$ curve, the semi-closed box deck at leeward exerts much more complicated signature turbulence effect than the full-closed box deck does. Therefore, we can concluded that leeward deck possessed significant signature turbulence effect will make more obvious aerodynamic interference effect on the windward deck.

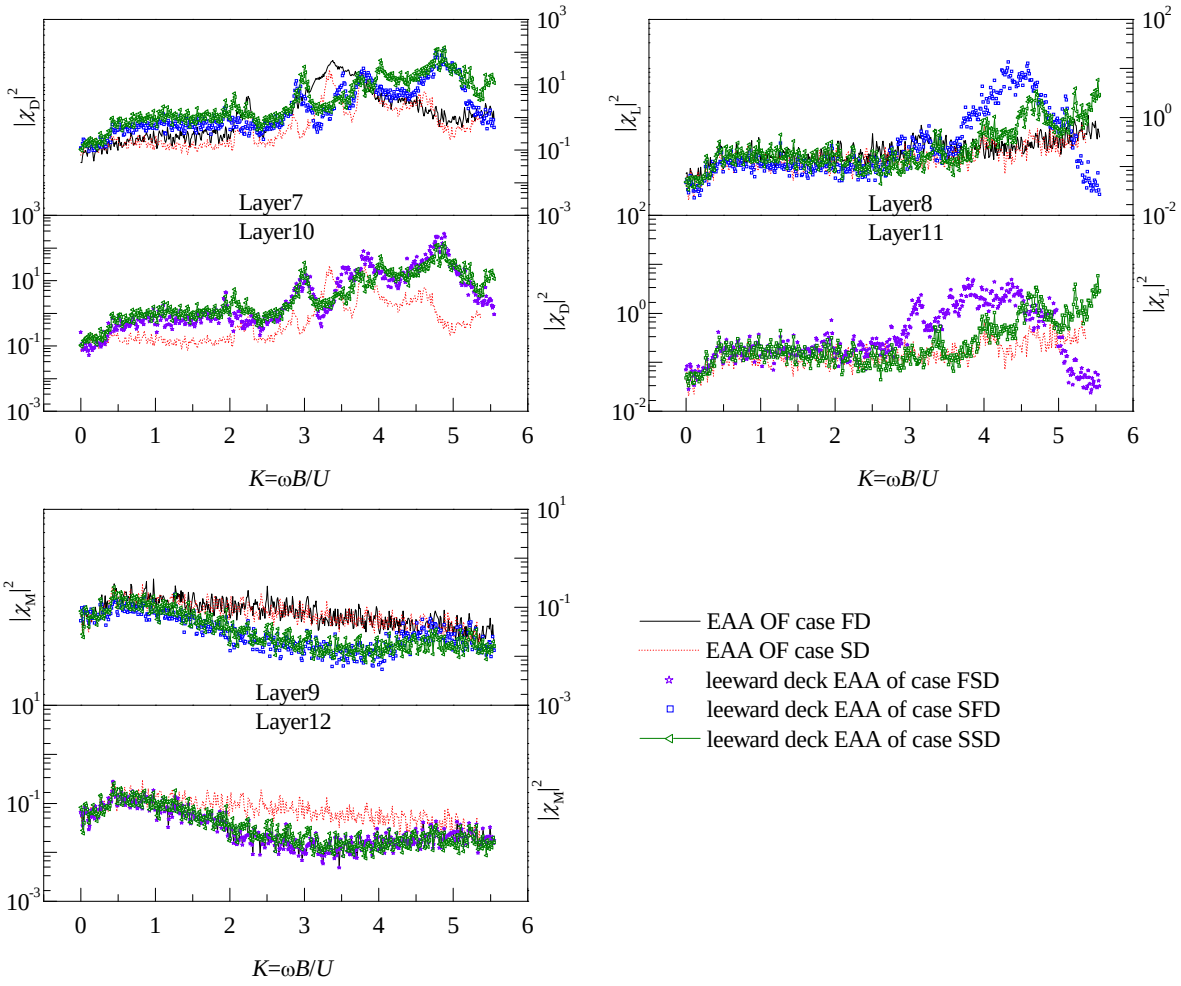

Figure 6 Comparison of equivalent aerodynamic admittances(EAA) of leeward deck between different cases

Figure 6 shows the comparison of the measured equivalent aerodynamic admittances of leeward deck with different cases. There are six layers of Figure 6 in which layer 7~9 present the measured $|\chi_D|^2$, $|\chi_L|^2$ and $|\chi_M|^2$ of leeward deck in case FD, SD, SFD and SSD and layer 10~12 show that in case SD, FSD and SSD, respectively. From layer 7~9, the equivalent aerodynamic admittances of leeward deck are remarkable different from that of single bridge

deck. For the $|\chi_L|^2$ and $|\chi_M|^2$ curves, there is no obvious peak in case FD/SD but a distinct peak at the approximation of K=5 in case SFD/SSD. For the $|\chi_D|^2$ curve, there is only one peak in case FD/SD but more than three peaks in case SFD/SSD. Consequently, the signature turbulence effect exerts a wider range of effect reduced frequency in case SFD/SSD than that in case FD/SD. Therefore, it can be further concluded that the equivalent aerodynamic admittance of bridge deck will greatly affected by the aerodynamic interference phenomenon caused by the windward deck. Moreover, compared with case SFD and SSD, because of a same bridge deck at windward, the aerodynamic interference effect on different leeward decks possess a similar behavior.

From layer 10~12, it is found that there is no obvious difference of the $|\chi_D|^2$ and $|\chi_M|^2$ curves of leeward deck between case FSD and SSD, but remarkable difference of the $|\chi_L|^2$ curve between case SD and FSD, SSD in high reduced frequency range. Because the semi- and full-closed box deck has a same width and height, the aerodynamic interference effects on the drag and torsional moment equivalent aerodynamic admittances are similar to each other. But for different bottom plates of decks, there is a remarkable difference of the lift equivalent aerodynamic admittance. The results above indicate that the same aerodynamic shape of bridge deck at windward will makes a similar aerodynamic interference effect on bridge deck at leeward, and vice versa.

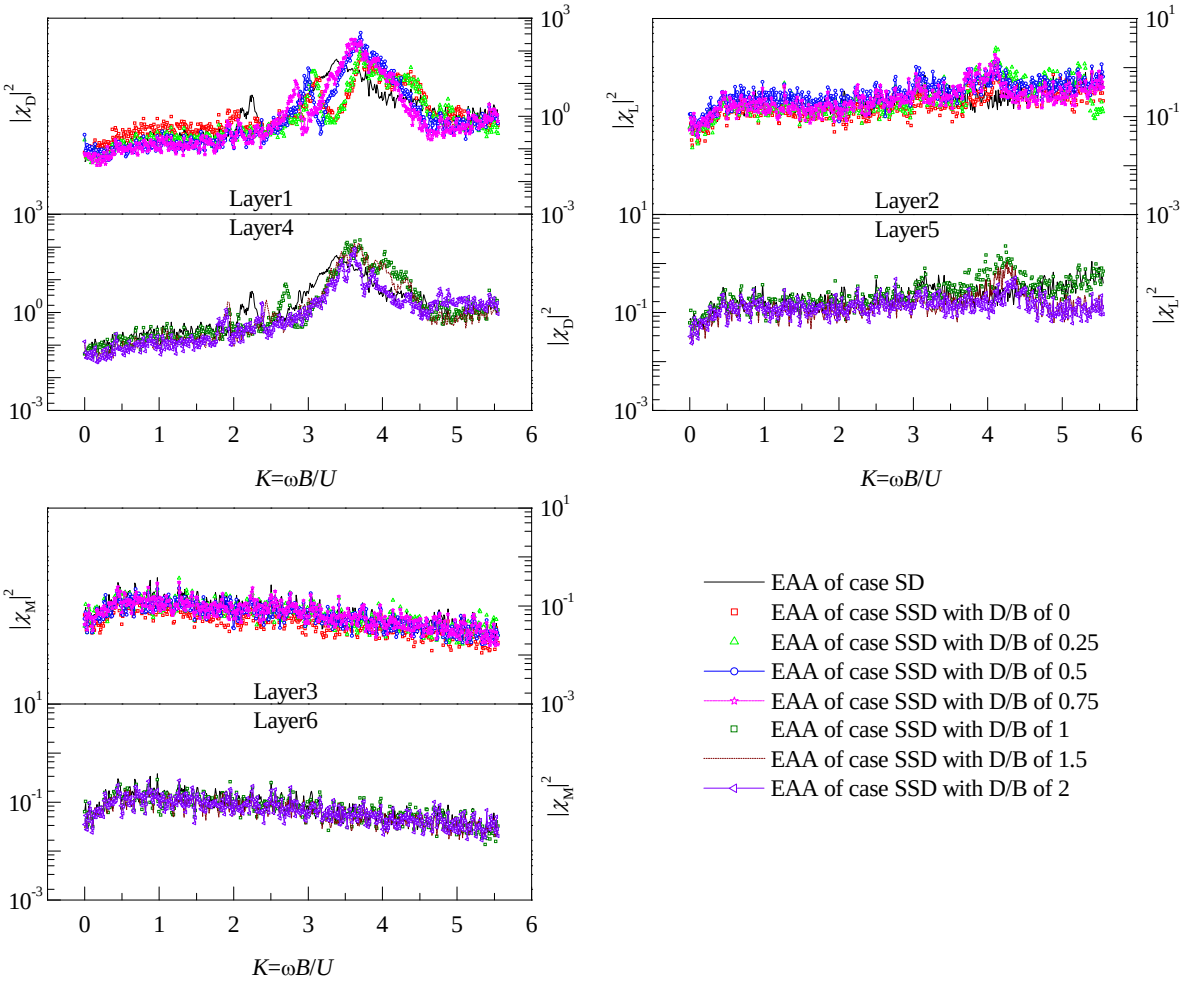

Figure 7 Comparison of equivalent aerodynamic admittances(EAA) of windward deck with different D/Bs

4.2 *Discussion of aerodynamic interference effect with different D/Bs*

Figure 7 shows the comparison of equivalent aerodynamic admittances of windward deck with different D/Bs of case SSD and that of case SD. In order to picture clearly, Figure 7 is

plotted out to six layers. Layer 1~3 present the measured results of windward deck in case SSD with D/B from 0 to 0.75 and the result of case SD, and layer 4~6 list that of leeward in case SSD with D/B from 1 to 2 and the result of case SD. From the $|\chi_D|^2$ curves in layer 1 and 4, it is interesting noticed that the drag equivalent aerodynamic admittance of windward deck with D/B of 0 is a little larger than that of other conditions. Compared with the results of case SD, the $|\chi_D|^2$ curves of case SSD are gradually approaching to that of case SD with the D/B increasing from 0 to 2. This variation indicates that the aerodynamic interference effect on the $|\chi_D|^2$ of the windward deck will become inconspicuous with the decreasing of the distance between windward and leeward deck. But in layer 2 and 5, we can found that the $|\chi_L|^2$ curves don't follow the change rule mentioned above. Meanwhile, compared with the $|\chi_L|^2$ of case SD affected by the signature turbulence inconspicuously, that of case SSD present somewhat signature turbulence effect with D/B>1. For the $|\chi_M|^2$ of case SSD in layer 3 and 6, there is no obvious difference in the comparison with case SD. Therefore, for windward deck, the drag equivalent aerodynamic admittance will get close to that of single deck gradually with the distance increasing, although it is a nonlinear change, but the lift and torsional moment equivalent aerodynamic admittances present no visible variety with the distance changing.

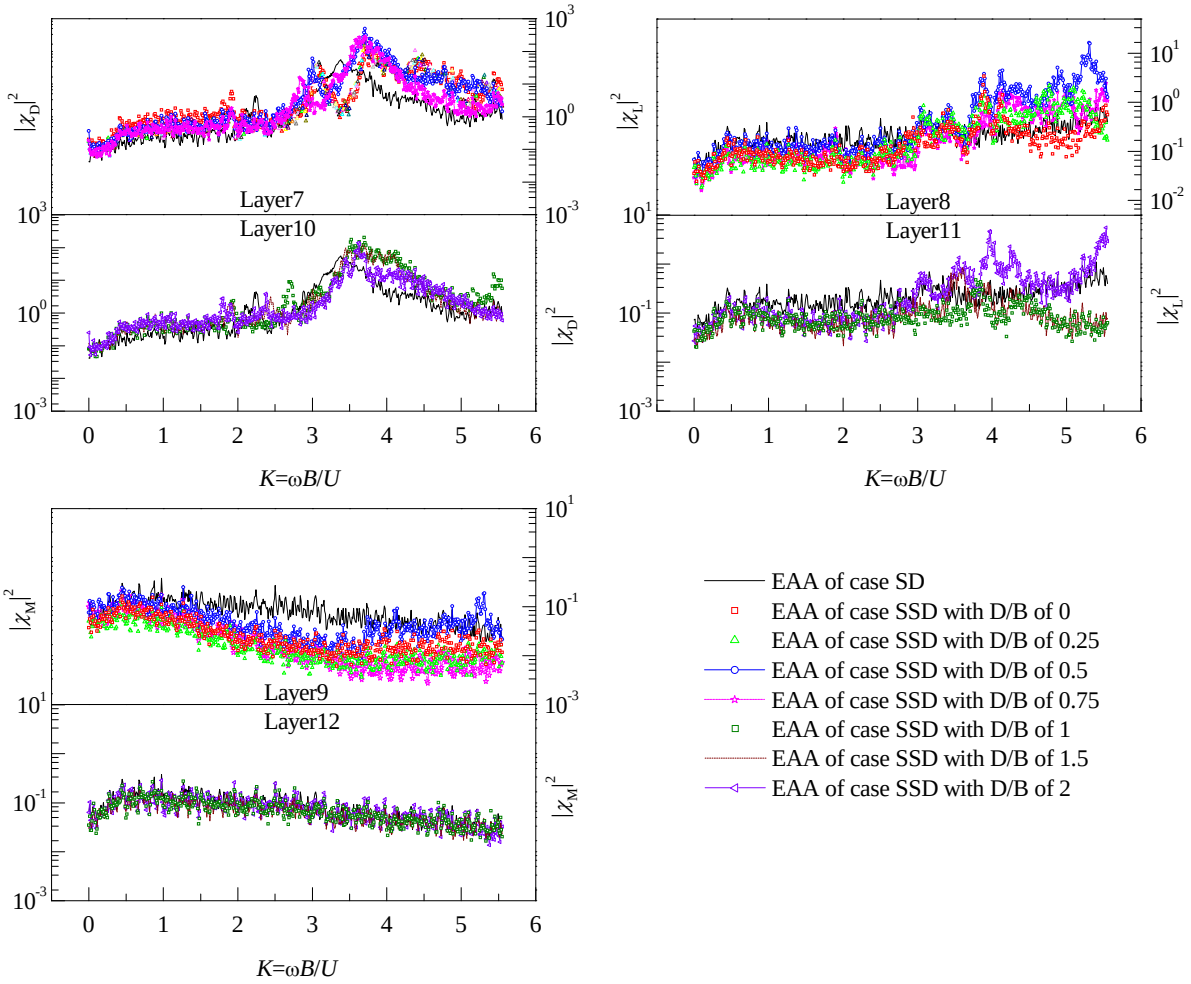

Figure 8 Comparison of equivalent aerodynamic admittances(EAA) of leeward deck with different D/Bs

Figure 8 shows the comparison of equivalent aerodynamic admittance of leeward deck with different D/Bs of case SSD and that of case SD, and is also plotted out to six layers. Layer 7~9 present the measured results of leeward deck in case SSD with D/B from 0 to 0.75 and the result of case SD, and layer 4~6 list that of leeward in case SSD with D/B from 10 to 12 and the result of case SD. From layer 7 and 10, the $|\chi_D|^2$ curves of case SSD also keep the change serially like that of windward deck with D/B increasing, but the signature turbulence

effect makes it much more nonlinear and complicated. In layer 2 and 5, due to intensely signature turbulence effect, the aerodynamic interference effect becomes disorderly and makes the $|\chi_L|^2$ curves greatly different from that of case SD. Consequently, although the distance equals zero in case SSD with D/B of 0, the signature turbulence still exerts the $|\chi_L|^2$ curves having more than two peaks at the range of K>3. In layer 9, the aerodynamic interference makes the $|\chi_M|^2$ curves of case SSD with D/B from 0 to 0.75 significant smaller than that of case SD. However in layer 12, the $|\chi_M|^2$ curves of case SSD with D/B>1 are almost equal to that of case SD which means that the aerodynamic interference effect can be ignored with the distance larger than a certain value. In general for leeward deck, with the change of distance between windward and leeward deck, the aerodynamic interference on the $|\chi_D|^2$ follows a certain variation like that of windward. presents disorderly and unsystematically on the $|\chi_L|^2$. Otherwise, the aerodynamic interference effect exerts the $|\chi_M|^2$ smaller than that of case SD with D/B<1, but can be ignored while D/B>1.

5 CONCLUDING REMARKS

The equivalent aerodynamics admittance of bridge with two separated paralleled decks are discussed in this paper. According to the discussion above, some conclusions can be drawn as follows:

The aerodynamic admittance curves don't always decrease with the reduced frequency increasing, which is different from the Sears function. Especially in high reduced frequency area, the signature turbulence effect exerts the aerodynamic admittance curves of windward deck of having some significant peaks, and makes that of leeward deck of having much more remarkable peaks. Otherwise, the measured equivalent aerodynamic admittances are generally smaller than Sears function for K<1, but much larger than Sears function at high reduced frequency due to the signature turbulence effect.

The aerodynamic interference phenomenon takes a great effect on windward and leeward deck and make their equivalent aerodynamic admittances tremendous different with that of single deck. The aerodynamic interference effect on the $|\chi_D|^2$ curve is serious than that on the $|\chi_L|^2$ and $|\chi_M|^2$ curves, and the aerodynamic interference effects on leeward deck are much more stronger than that on windward deck. Moreover, while the distance between windward and leeward deck changes, the aerodynamic interference may generate different effects on the equivalent aerodynamic admittances. For both the drag aerodynamic admittances of windward and leeward deck, the $|\chi_D|^2$ curves may approach to that of single deck gradually with the D/B increasing. For the lift and torsional moment aerodynamic admittances of windward and leeward deck, the $|\chi_L|^2$ and $|\chi_M|^2$ curves of windward deck don't behave any extraordinary difference from that of single deck, but that of leeward deck are quite different from that of single bridge especially the $|\chi_L|^2$ curves.

6 ACKNOWLEDGEMENTS

The work described in this paper was jointly supported by the Fundamental Research Fund for State Key Laboratories from the Ministry of Science and Technology of China (Grant No. SLDRCE08-A-02), and the National Nature Science Foundation of China (Grant 50978204). Any opinions and concluding remarks presented here are entirely those of the writers.

REFERENCES

A.G. Davenport, Buffeting of a suspension bridge by storm winds. Journal of the Structural Division, 88(1962,ST3), 233-268.

A. Honda, N. Shiraishi, M. Matsumoto, et al, Aerodynamic stability of Kansai International Airport access bridge. J. Wind Eng. Ind. Aerodyn. 49(1993), 533-542.

X. Chen and M. Matsumoto, Multimode coupled flutter and buffeting analysis of long span bridges, J. Ind. Aerodyn., 89(2001), 649-664.

E.D. Jancauskas and W.H. Melbourne, The aerodynamic admittance of two-dimensional rectangular cylinders in smooth flow. J. Ind. Aerodyn.,23(1986), 395-408.

H. Katsuchi, N.P. Jones and R.H. Scanlan. Multimode coupled flutter and buffeting analysis of the Akashi Kaikyo bridge. Journal of Structural Engineering, 125(1999), 60-70.

H.W. Liepmanm, On the application of statistical concepts to the buffeting problem. Journal of Aeronautical Science,19(1952),793-810.

J.D. Holmes, Prediction of the response of a cable-stayed bridge to turbulence. In Proceedings of 4th International Conference on Buildings and Structures, London, England. Cambridge: Cambridge University Press.

K. Kimura, K. Shima, K. Sano, et al, Effects of separation distance on wind-induced response of parallel box girders. J. Wind Eng. Ind. Aerodyn. 96(2008), 954-962.

M. Kawatani and H. Kim, Evaluation of aerodynamic admittance for buffeting analysis. J. Ind. Aerodyn.,41-44 (1992),613-624.

P. Irwin, Wind tunnel and analytical investigations of the response of Lions' Gate Bridge to turbulent wind. National Research Council of Canada, (1977), NAELTR-LA-210.

R. Sankaran and E.D. Jancauskas, Direct measurement of the aerodynamic admittance of two-dimensional rectangular cylinders in smooth and turbulent flows. J. Ind. Aerodyn.,41-42(1992),601-611.

S.V. Larsen, M.A. Astiz and G.L. Larose, Aerodynamic interference between two closely spaced cable supported bridges. In: Proceedings of the 4th International Colloquium on Bluff Body Aerodynamics and Applications, Bochum, 2000, pp. 33-37.

S. Stoyanoff, D. Kelly, P. Irwin, et al. Aerodynamic stability and wind loads of the Cooper River bridge replacement. In: Proceedings of the 11th International Conference on Wind Engineering, Rubbock, 2003, pp. 147-154.

The Seventh International Colloquium on Bluff Body Aerodynamics and Applications (BBAA7)
Shanghai, China; September 2-6, 2012

Effects of terrain proximity on the aeroelastic response of a bridge deck

Luigi Carassale [a], Andrea Freda [a], Michela Marrè-Brunenghi [a], Giovanni Solari [a]

[a] *Department of Civil, Environmental and Architectural Engineering, University of Genoa, Via Montallegro 1, Genoa, Italy*

ABSTRACT: Wind tunnel tests on sectional models are largely used to derive both aerodynamic forces and flutter derivatives of long-span bridge decks. The most common situation for this typology of bridges is to be far from the ground. Wind tunnel tests on sectional models are therefore generally carried out in a homogeneous and smooth flow. However, due to the possibility of channeling effects and a considerable turbulence intensity, the effects of terrain proximity deserve to be investigated if the bridge deck is close to the ground. The present paper reports the results of a wind tunnel test campaign aimed at the evaluation of wind actions and aeroelastic response of a bridge deck particularly close to the terrain. Wind tunnel tests are carried out both considering the classic configuration of isolated deck and simulating the terrain proximity with two different approaches. The results are compared.

KEYWORDS: Bridge deck, flutter, terrain proximity, wind-tunnel tests.

1 INTRODUCTION

The Marchetti Viaduct is a 290 m long arch bridge which will be built along the Milano – Novara highway, close to Ivrea, Italy. The bridge is composed by a single central arch with a trapezoidal section and the deck, which unusual width (B_p = 41 m) is coupled with a small height over the ground (H_p = 7 m, Fig. 1a). Such a configuration may emphasizes the aerodynamic interaction between the bridge and the terrain. Moreover, the noteworthy height of the side barriers, which is variable between 3 and 6.7 m, completes the picture of a project that is surely unconventional under the aerodynamic viewpoint.

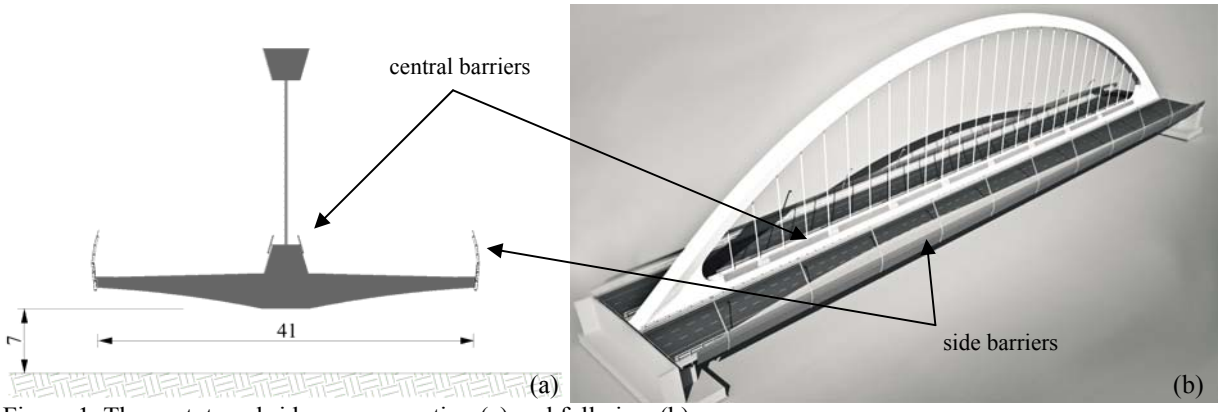

Figure 1. The prototype bridge: cross-section (a) and full view (b).

To investigate such a situation, static and aeroelastic sectional-model tests on the deck of the bridge have been conducted in the Wind Tunnel Laboratory at the Faculty of Engineering of the University of Genova, which working section is 1.7x1.35 m. Both static and aeroelastic wind

tunnel tests have been carried out considering three different arrangements: a) the deck is isolated, far from the ground, in a uniform flow; b) a rigid plate is installed under the deck, to simulate the wind channeling effect between the deck and the ground; c) the deck is placed at the scaled distance over an artificially-rough ground that generates a boundary layer coherent with the expected velocity profile for the bridge site.

The analysis of these different conditions is not traditional for sectional model tests, and the whole of these simulations provides an overview about how the effects involved by different configurations may change the aerodynamic response of the bridge.

2 WIND TUNNEL TESTS

2.1 *Experimental arrangement*

Static and aeroelastic wind tunnel tests have been carried out using the same sectional model, which has been realized in aluminium with a geometric scale equal to 1:150. The model has a length ℓ = 694 mm, and a width B = 274 mm ($\ell/B \simeq 2.5$). Static tests have been conducted separately on the sectional model of the arch but are not reported in the present paper.

The central and side barriers of the prototype are made of perforated steel plates, whose porosity changes as a function of the height over the deck. Moreover, their height changes with continuity along the length of the bridge (Fig. 1b). In the wind tunnel tests an average value of the side barriers height has been considered. Due to the impossibility of reproducing their actual geometry respecting the Reynolds number similarity, an equivalent solidity ratio of the barriers installed on the model has been selected to reproduce the head loss measured on a portion of the full-scale barrier. The head loss has been evaluated measuring the drag force acting on a portion of the real bridge barriers and on different grids suitable to be installed on the model. The grid that has been chosen to carry out the tests develops the correct drag force in the range of the velocities of interest (Fig. 2).

As introduced in Section 1, three different arrangements have been considered for wind tunnel tests. The first dealt with the isolated deck immersed in a homogeneous flow characterized by a turbulence intensity below 0.5%. This is the typical situation for testing sectional models. However, the closeness of the terrain for the real bridge may make the isolated-deck model not truly representative of the physical reality, due to the channeling of the flow between the deck and the terrain and the presence of a boundary layer characterized by high turbulence intensity. To investigate only the consequences of the channeling effects, a second setup was obtained installing a smooth, rigid plate below the model, at a distance corresponding to the height of the deck over the terrain (about 4.5 cm at 1:150 scale, Figs. 4b-6b). In this way the creation of a thick boundary layer was avoided. The real flow conditions have then been reproduced in the last setup using a suitable surface roughness to create a wind velocity profile and turbulence characteristics (Figs. 4c-6c).

The reproduced turbulent boundary layer is such that the mean wind velocity profile can be approximated by a power law with exponent α=0.27 (Fig. 3). Assuming a reference height equal to 10 m, corresponding to the average bridge deck height on the ground, the wind profile corresponds to a logarithmic law with roughness length equal to 0.2÷0.25 m, suitable for the site of prototype (i.e. countryside).

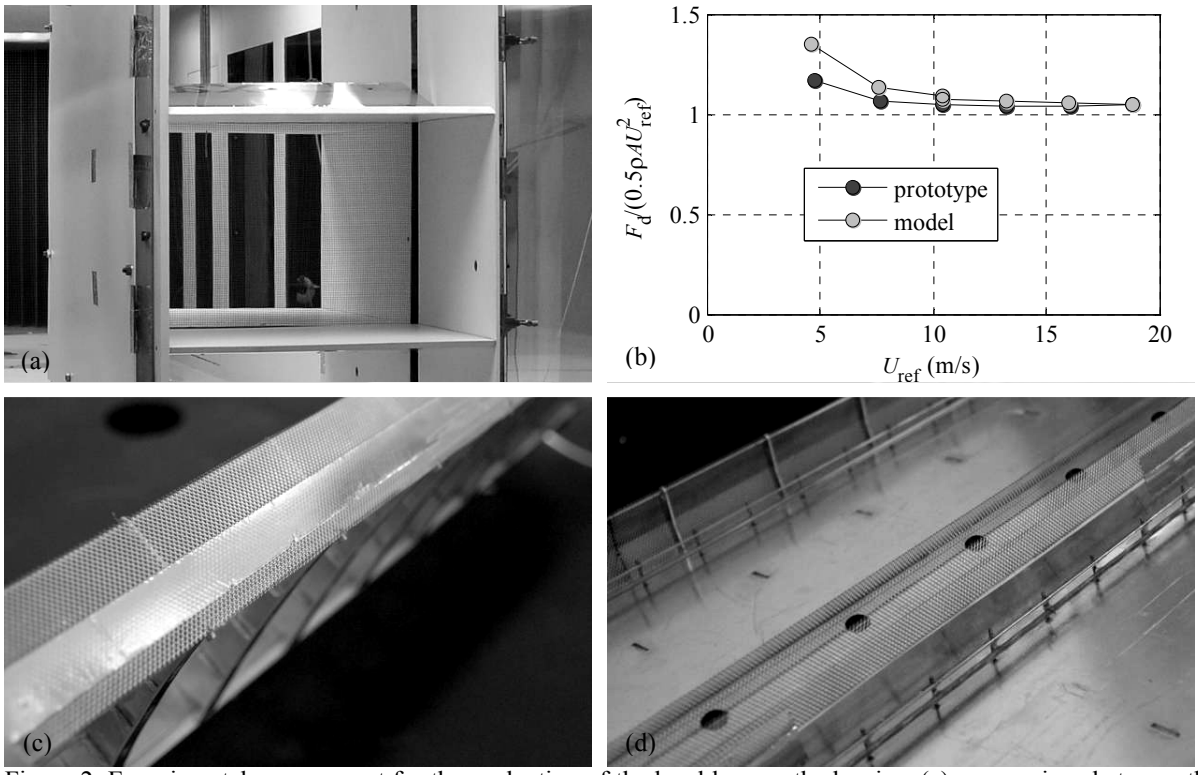

Figure 2. Experimental arrangement for the evaluation of the head loss on the barriers (a), comparison between the head loss on the prototype and the model grid (b), detail of the lateral (c) and central(d) barriers on the model.

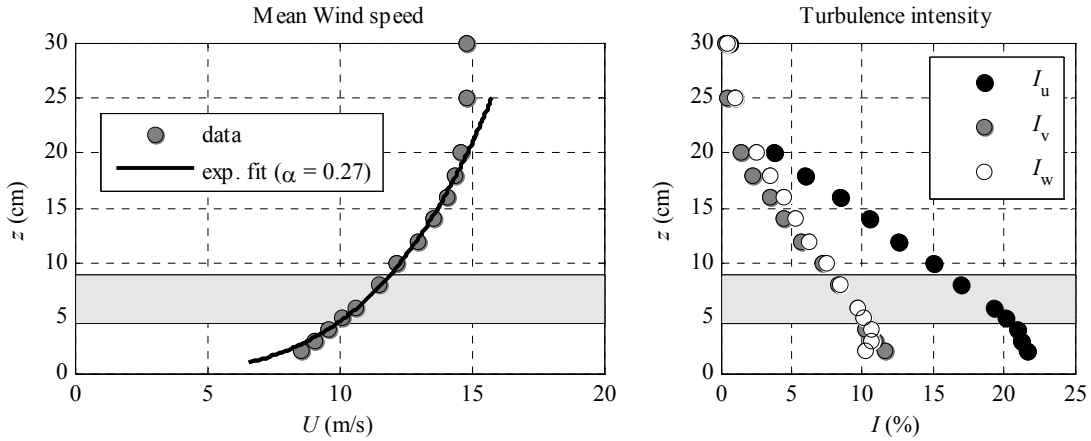

Figure 3. Main features of the boundary layer used in the third setup. The highlighted region is where the model is placed during tests.

2.2 *Static tests*

Static tests, aimed at the evaluation of the aerodynamic coefficients and wake parameters, have been carried out, with and without barriers, for a range of angles of attack between -10° and 10° in step of 1° (setups with and without plate) and with barriers between -5° and 5° in step of 1° (setup with boundary layer). Figure 4 shows the three different setups.

The drag, lift and torque aerodynamic coefficients are here defined based on the well-known expressions:

$$C_D = \frac{F_D}{0.5\rho U^2 B\ell}; \qquad C_L = \frac{F_L}{0.5\rho U^2 B\ell}; \qquad C_M = \frac{M}{0.5\rho U^2 B^2 \ell} \tag{1}$$

where F and M are the total force and the torque evaluated by measurements, ρ is the air density, U is the reference wind speed and the subscripts D, L, M stand for drag, lift and moment, respectively. The aerodynamic coefficients are constant for all practical purposes in the range of Reynolds numbers investigated during tests, i.e. $1.4 \cdot 10^5 \leq Re \leq 2.5 \cdot 10^5$ (based on the bridge width B).

Figure 4. Setups for static tests: isolated deck (a), deck close to plate (b), deck immersed in a boundary layer (c).

Figure 5 shows the drag, lift (positive upwards) and moment coefficients (positive nose up) for all the investigated configurations. From Figure 5 it is possible to infer that the barriers, the plate and the presence of a boundary layer influence significantly the aerodynamic coefficients. In particular, for the isolated deck, the introduction of the barriers enhances the dependency of the drag coefficient on the angle of attack, and tends to significantly reduce the values and the slope of both lift and moment coefficients; it also produces a stall at -5°.

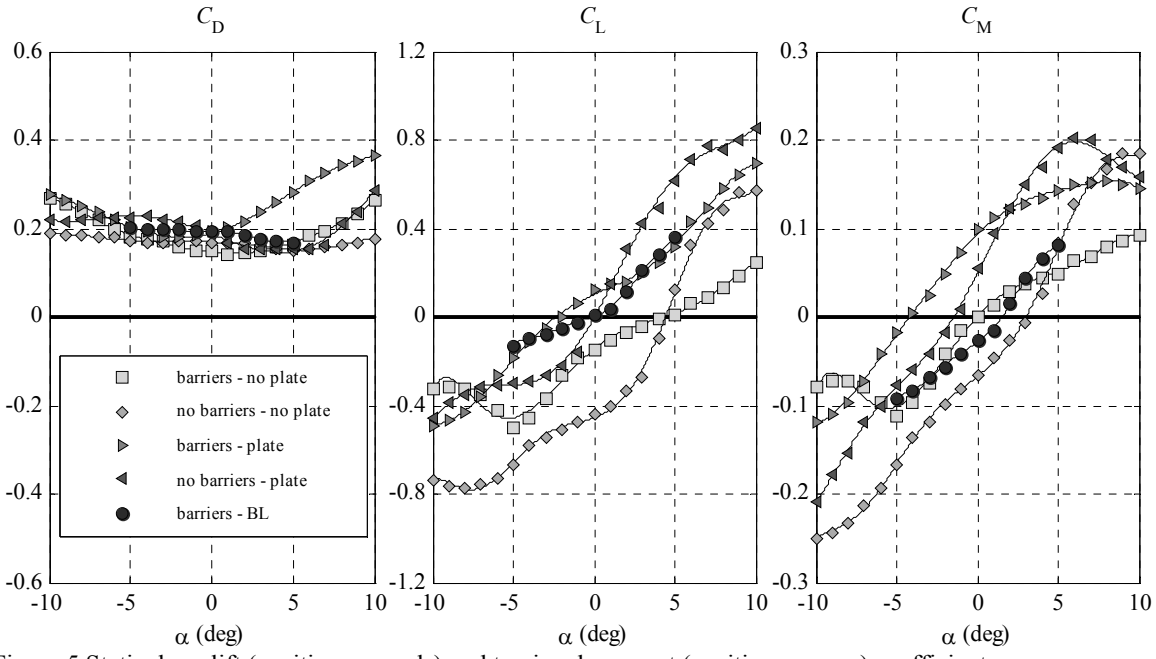

Figure 5 Static drag, lift (positive upwards) and torsional moment (positive nose up) coefficients.

The introduction of the plate to simulate the channeling effect due to the terrain mainly produces an increment of the drag coefficient for large angles of attack, and a shift of lift and moment coefficients (upwards for lift and nose-up for moment). The introduction of the plate

also anticipates the torsional stall for positive angle of incidence. The aerodynamic coefficients evaluated in presence of the turbulent boundary are obtained assuming as reference wind speed the averaged value where the deck is positioned (Fig. 3). The values of the actions evaluated in such a configuration are in between those evaluated in isolated conditions and with the plate. In particular, at zero angle of attack, the lift force becomes negligible as in the case with plate but without barriers.

2.3 *Aeroelastic tests*

Wind tunnel tests on the aeroelastic model have been carried out aimed at the evaluation of the flutter derivatives in the same configurations of static tests, but without changing the angle of attack. A classic 2 d.o.f. arrangement (i.e. heaving and pitching motion) has been considered. Figure 6 illustrates the wind tunnel setups. The aeroelastic derivatives have been extracted from the records of the free-decaying oscillatory motion from imposed initial conditions [1]. For each experimental setup and each wind velocity at least four repetitions have been carried out. Moreover, two sets of springs of different stiffness have been used to better explore different ranges of the reduced wind velocity. Table 1 shows the values of the spring stiffness k_s, the model mass and its moment of inertia, M and I respectively, the heaving and pitching natural frequencies f_h and f_α, and the corresponding damping ratios ξ_h and ξ_α.

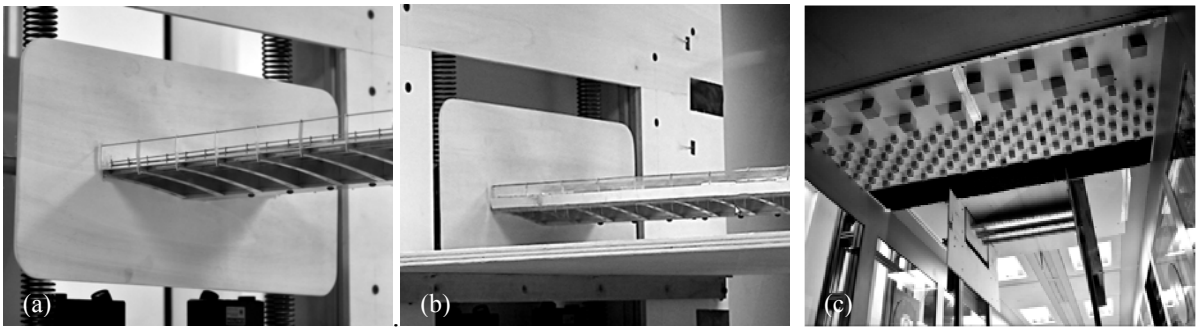

Figure 6. Experimental setups for aeroelastic tests: isolated deck (a), deck close to the plate (b) and deck immersed in the BL (c).

Table 1. Mechanical parameters for aeroelastic models.

Setup	k_s (kN/m)	M (kg)	I (kg m^2)	f_h (Hz)	f_α (Hz)	ξ_h (10^{-3})	ξ_α (10^{-3})
no barriers	1.21	5.52	6.41 10^{-2}	6.66	11.63	0.8	0.9
	7.54	5.99	6.92 10^{-2}	15.94	29.94	0.3	1.0
with barriers	1.21	5.60	6.49 10^{-2}	6.62	11.55	1.0	1.0
	7.54	6.08	7.03 10^{-2}	15.85	27.77	0.6	1.4

The estimation of the mechanical parameters during the tests has been made applying the algorithm proposed in [2]. The subsequent evaluation of the flutter derivatives has then been made applying the model proposed in [3], and considering $b = B/2$ as reference dimension.

The aeroelastic derivatives have been evaluated for reduced wind velocities up to U/(fB) = 16 and 9 (heaving motion and pitching motion respectively). As an example, Figure 7 shows, for the isolated deck without barriers, the aeroelastic derivatives H_1^*, A_1^* and A_2^* that plays an important role for torsional flutter (the direct derivative A_2^*) as well as for the coupled flutter (H_1^*, A_1^* and A_2^*) [4]. Small markers indicate the values obtained from single trials, large markers the mean values and lines the interpolating splines used for the subsequent stability analyses.

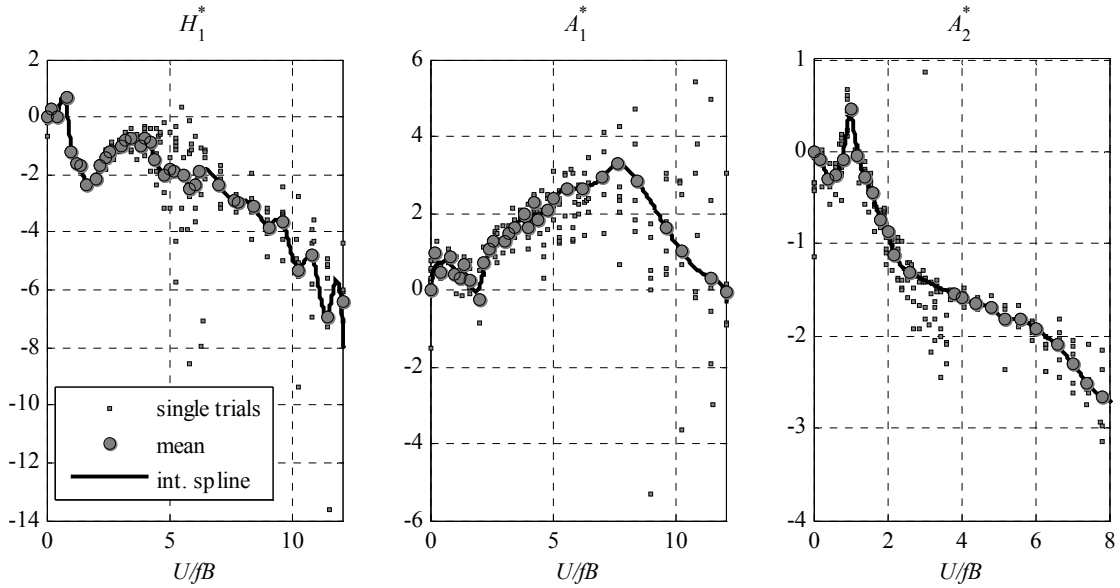

Figure 7. Flutter derivatives H_1^* A_1^* and A_2^* for the isolated deck (without barriers).

Figure 8 shows the standard deviation σ of the steady vibrations amplitude measured on the aeroelastic model (with barriers) as a function of the reduced velocity. It can be observed that the introduction of the plate deeply changed the torsional aeroelastic response of the model.

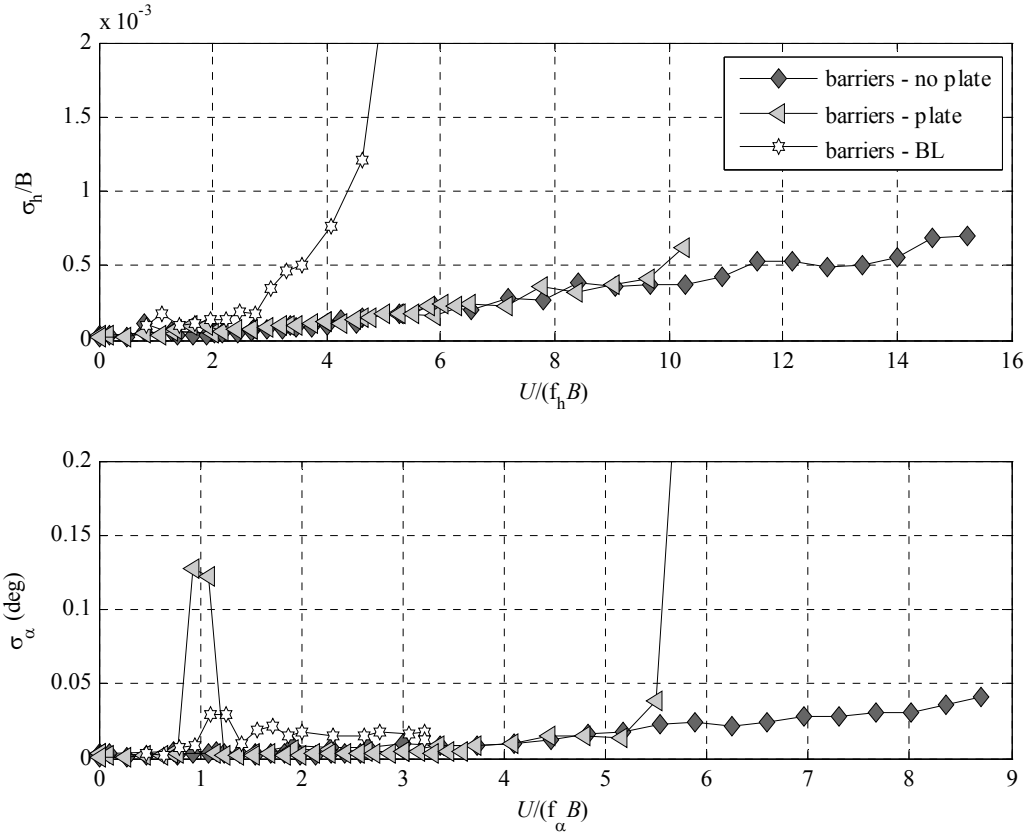

Figure 8. Amplitude of displacement of the bridge deck with barriers.

In particular, a significant vortex-induced vibration appeared at a reduced velocity roughly equal to 1, and the occurrence of diverging motion was anticipated at a reduced velocity equal to 5.5. On the other hand, the simulation of the terrain through a turbulent boundary layer reduced the torsional aeroelastic response, but significantly enhanced the heaving motion at lower reduced velocities.

3 DATA ANALYSIS AND DISCUSSION OF RESULTS

The aeroelastic derivatives obtained from wind tunnel tests have been used to carry out the stability analysis of the prototype bridge considering three modes of vibrations, namely the mode 2 (heaving, antisymmetric, 0.48 Hz) and the modes 6 and 7 (pitching, almost antisymmetric, 0.96 and 0.99 Hz, respectively). The introduction of a third mode, with respect to the classic formulation, has been made necessary due to the noteworthy similarity (both in mode shape and frequency) existing between modes 6 and 7. The other natural modes do not provide any significant contribution to the flutter mechanism.

Figure 9 shows the dependency on wind speed of the natural frequencies and damping ratios for the aforementioned prototype modes, considering the deck in isolated conditions, with and without the side barriers, and close to the plate (with barriers). From Figure 9 it can be inferred that the presence of the barriers does not affect significantly the evolution of the eigenfrequencies, but it anticipates the critical velocity from 233 to 217 m/s, as well as it shift the instability from the mode 2 (plunge, without wind) to the mode 6 (torsion, without wind).

The use of the plate to simulate channeling effects causes a significant reduction of the critical velocity for flutter, which is initiated by mode 6 as in the previous case. On the contrary, when simulating the terrain with a turbulent boundary layer (case not reported in Figure 9), no negative damping regions were found in the examined range of velocities.

Figure 9 also shows a region characterized by negative damping on pitching modes around 40 m/s. Such a region is due to a positive value of the aerodynamic derivative A_2^* (e.g. Fig. 7). This phenomenon, as already pointed out in [4], is characterized by an onset wind velocity nearly equal to the resonance velocity of Karman vortex shedding on the torsional mode, but in the present contest the response amplitude was limited as in classic vortex shedding, and such a region does not contribute to flutter instability. Confirmation of this fact is found in positive values of H_1^* in a range of reduced velocities for heaving motion corresponding to those of pitching motion (Fig. 7).

The aerodynamic coefficients derived through static tests have been used to evaluate the buffeting response of the bridge through a quasi-steady formulation, which is not reported in the present paper, and to check the applicability to the present case of the quasi-steady theory at high reduced velocities. Since the quasi-steady formulations can be referred to as a special case of unsteady forces when the frequency-dependent fluid memory effect is negligible, it is possible to correlate the static aerodynamic coefficients to the aeroelastic derivatives when the reduced frequencies tend to zero (i.e. high reduced wind velocities).

Based on the correlations between aeroelastic derivatives and quasi-steady aerodynamic force coefficients proposed in [5], Figure 10 shows the 6 aeroelastic derivatives that can be correlated to quasi-steady theory assuming a 2 d.o.f. heaving-pitching motion model. In Figure 10 the bridge deck is considered with barriers in the three different setups. The aeroelastic derivatives are plotted versus the reduced velocity; markers indicate results of aeroelastic tests, while values derived from aerodynamic coefficients (not dependent on frequency) are represented with horizontal lines of the same color.

It is necessary to point out that correlations between the flutter derivatives and the aerodynamic coefficients involves also an arbitrary length, often called characteristic radius,

whose definition is related to the contribution of the angular velocity of the body to the effective angle of incidence of the flow. The use the characteristic radius, hereinafter referred to as R_0, has been inspired by the use of the three-quarter chord point in airfoil flutter analysis, ands several values have been proposed in the literature based on the shape of the body, see [6] and [7] for references.

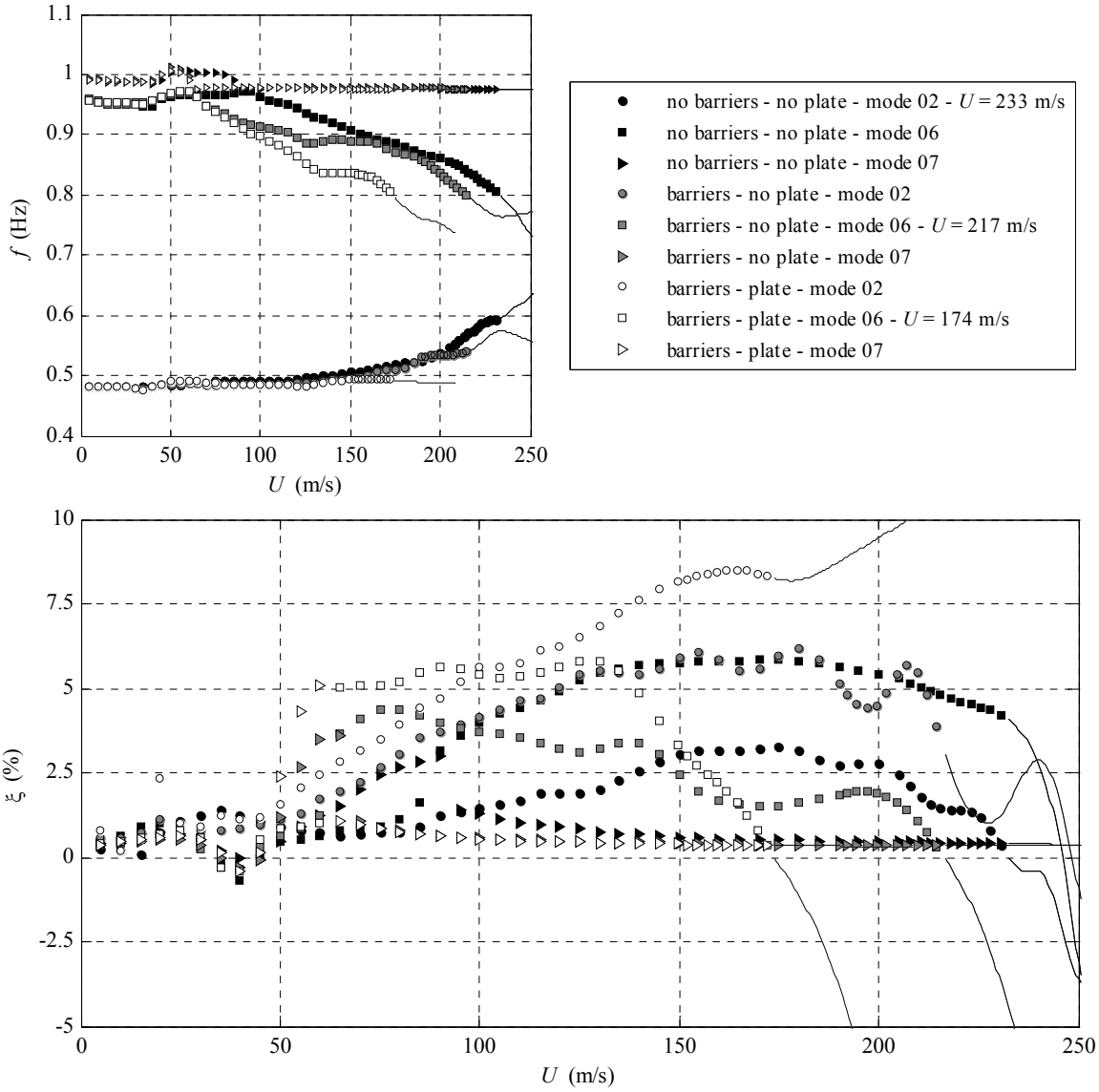

Figure 9. Isolated deck with and without barriers and deck with barriers close to plate: eigenfrequencies and damping ratios versus velocity.

The choice of the value of the characteristic radius is not obvious. In the present context, the linkage between the aeroelastic derivatives and the aerodynamic coefficients has been used to derive it, being involved in the relationships between H_2^* and $C_D + C_L'$ and between A_2^* and C_M'. Specifically, it has been evaluated by imposing the equivalence at higher reduced velocities on the term A_2^*. For the setups with installed barriers (Fig. 8), R_0 has been found always negative, varying from -0.3B to -2B (i.e. the reference point for velocity induced by the angular

velocity is aft of the pivot). Such a case is not common, but can be found in the literature (e.g. [8]).

To apply the quasi-steady theory, points represented in Figure 10 should tend to lines when the reduced velocity tends to the highest values. On the contrary, the comparison between experimental values of aeroelastic derivatives and values obtained from aerodynamic coefficients is far from being satisfactory in any case, confirming that the application of the quasi-steady theory to cases where torsional motion plays a fundamental role is questionable (e.g. [9]).

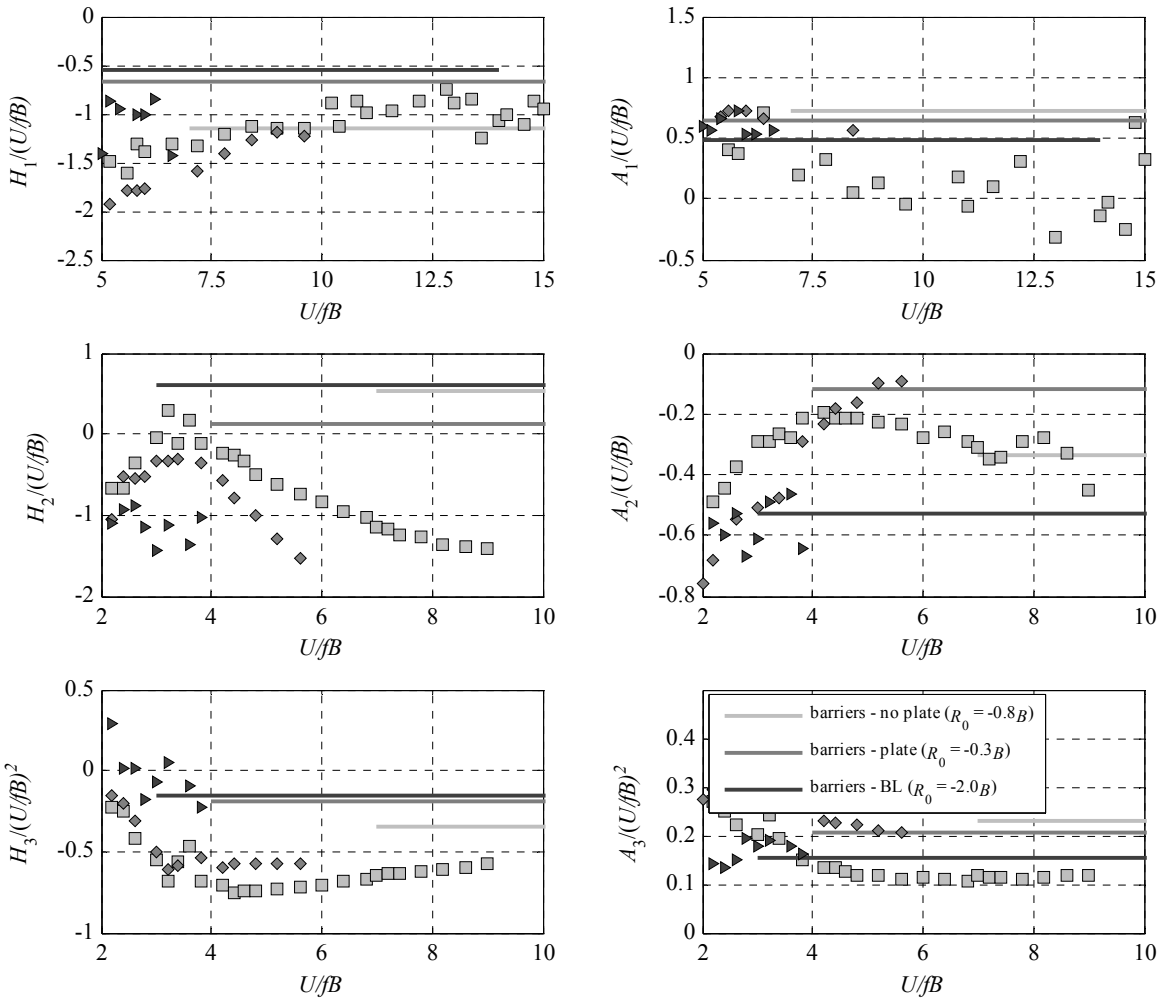

Figure 10. Aeroelastic derivatives derived from aeroelastic setups (markers) and based on aerodynamic coefficients from static tests (lines). The same color identifies the same experimental arrangement.

4 CONCLUSIONS AND PERSPECTIVES

Static and aeroelastic sectional wind tunnel tests have been carried out aimed at investigating the aerodynamic characteristics of a long-span bridge deck very close to the ground. Besides the classic configuration of isolated deck in uniform flow, the terrain proximity has been simulated with two different approaches, also considering the effects due to the barriers installed on the

bridge. The results highlight that the presence of the terrain and its modeling, as the presence of the barriers, implies deeply different aerodynamic behaviors.

It has been observed that the stability analyses carried out based on data derived considering the isolated deck do not lead to conservative values of the onset velocity for aeroelastic phenomena. Such an aspect points out that when channeling effects and the presence of a relevant boundary layer are not negligible, as for bridge decks close to the terrain, an investigation of the aerodynamic characteristics including the modeling of the boundary conditions is appropriate. Further researches are necessary to understand if some general trend can be derived, though.

Experimental results also confirm that the application of the quasi-steady theory to estimate the onset of instability is more than questionable for elongated bluff shapes.

5 REFERENCES

1 R. Scanlan and J. J. Tomko, Airfoil and bridge deck flutter derivatives, J. Eng. Mech. Div., ASCE, 97(6) (1971), 1717–1737.

2 G. Bartoli, S. Contri, C. Mannini and M. Righi, Toward an Improvement in the Identification of Bridge Deck Flutter Derivatives , J. Eng. Mech., ASCE, 135(8) (2009), 771-785.

3 E. Simiu and R. Scanlan, Wind effects on structures, 3rd Ed., John Wiley & Sons, New York, 1996.

4 M. Matsumoto, Aerodynamic damping of prisms, J. Wind Eng. Ind. Aerodyn., 59 (1996), 159–175.

5 X. Chen and A. Kareem, Advances in Modeling of Aerodynamic Forces on Bridge Decks, J. Eng. Mech., ASCE, 128(11) (2002), 1193-1205.

6 R.D. Blevins, Flow-Induced Vibration, 2nd Ed., Van Nostrand Reinhold, New York, 1990.

7 M. Paidoussis, S. Price and E. de Langre, Fluid-structure interactions: cross-flow-induced instabilities, Cambridge University Press, New York, 2011.

8 G. Diana, F. Resta and D. Rocchi, A new numerical approach to reproduce bridge aerodynamic non-linearities in time domain, J. Wind Eng. Ind. Aerodyn., 96 (2008) 1871–1884.

9 Y. Nakamura and T. Mizota, Torsional flutter of rectangular prisms, J. Eng. Mech. Div., ASCE, 101 (EM2) (1975), 125-142.

Research on combination coefficient of cross and torsional wind forces for high-rise buildings based on the copula method

Yalin Yan [a], Yi Tang [a], Xinyang Jin [a]

[a] *China Academy of Building Research, 30# East Road North 3rd Ring, Beijing, China*

Abstract: Through wind tunnel tests on 5 models whose side ratio ranked from 1:1~1:5 in different wind fields, based on the distribution induced by Copula method and Empirical distribution, the combination coefficients of the equivalent static cross wind force and torsional wind force were determined. By analysis, the time series of wind forces and responses in different directions shows that the random data nearly subject to normal distribution, while the Gumbel distribution is not so suitable for estimation for the random variable. And through calculation, the combinations are found between 0.5~0.7 while the cross direction is the leading, and 0.7~0.9 while the torsional direction is the leading. It is something like the combination coefficient defined in AIJ code.

Keyword: combination coefficient, copula method, normal distribution, AIJ code, wind tunnel test, Gaussian distribution

1 INTRODUCTION

Since Davenport gave a description for equivalent static wind load (ESWL) method, research on wind loads on buildings has been developing fast. Homels, Solari, Tumura, Kareem etc have done a lot of work on the alongwind, crosswind, and torsional wind load. In China, Ming Gu, Yin Zhou, YongQuan, Shuguo Liang also studied the mechanism of the wind on structures based on large amount of wind tunnel tests. Based on the test data and the real time pressure data of the actual structures, the actual responses of the structures are calculated through random vibration theory or collected by tests. However, it usually costs a lot of time and a lot of money and time to get the data. So the ESWL method has been discussed a lot. Usually, in the wind field the structures are loaded simultaneously from different directions, defined as along wind direction, cross wind direction and torsional direction. As a matter of factor, for simplicity it considers only along-wind load in many cases. One reason is the along wind direction is usually the proceeding direction for high-rise structures, that is, wind loads in other directions are negligible; another reason is that there is no suitable way to exactly combine loads in different directions. However, it may undervalue effects of wind for some structures. Isyumov (1982) suggested the square root of square sum (SRSS) method for the acceleration, so his method was based on the whole relative wind loads in alongwind and crosswind directions. Solari et al. (1998) erected an ellipse for the real loads in the alongwind and crosswind directions, and also he took the SRSS method. And in the AIJ code, the combination for different directions is defined, it considers the along wind and crosswind combination for rigid structures, and for the stiff structures along wind-crosswind combination, alongwind-torsional combination and crosswind-torsional combination are all considered. The combinations are based on the project experiences. So it is practical and reflects the real projects. However the

AIJ method is not so powerful for wind fields in other countries and there is not a reflection in theory. Gianni Bartoli(2011) suggested a new method based on the joint distribution of several random variables base on the copula method, which describes the combination of different directions with the aim function Z=X+Y. The conclusion is nearly the same as the AIJ method. At one aspect the method provides a probability analysis for the combination, whereas it didn't give the explanation for the aim function, and its analysis is based on the loads self and reflects little about the responses, so it is more fit for the rigid structures rather than the stiff.

There is less discussion about the combinations of different wind direction wind loads In China. The reason may be that it is more effective to analyze an actual project with the random vibration method if the structure is large, and there is no need to combine different direction actions while the scale is not so large. However, as the climate changes a lot, the structure's responses may be undervalued if the combinations are not considered. So this paper gives a description for the combination of different wind directions in China wind fields with a joint distribution probability density function.

Firstly, a combination model is created for the research on combination of different loads and the combination coefficient is defined. Then it introduces the way to get the joint distribution probability density function with the Copula function. And based to the wind tunnel tests on 5 models whose side ratio ranked from 1:1~1:5 in different wind fields in China, the combination of cross wind direction load and torsional direction load is discussed, it also proves that the displacement responses of the structures can be considered as subjected to Gaussian distribution. At last it makes a comparison between the combination coefficient calculated in this paper and AIJ code.

2 DATA MODEL FOR THE COMBINATION

The wind in the structures would be concentrated to six components. And in high-rise buildings, the proceeding components are in the direction of along wind, crosswind, and torsion. Wind data model one direction the is created with a random variable in this direction, and an estimated value that reflects some probability may calculated and used as the design value for projects, such as the along wind equivalent static wind load calculated in the code. However the variables in different directions may be not so relative that the estimation values in different directions would not take the same as the single direction if the probability is the same. So the combination are simply expressed as the formula as (1)

$$R = R_{Dir1} \text{"+"} \gamma R_{Dir2} \tag{1}$$

Where the '+' means liner combination. R represents the response. And Dir1 and Dir2 represent two orthogonal directions. According to some papers and the tests(Gianni Bartoli,2011) of the models, the relation of X and Y direction is found to be little enough to neglect. So the combination coefficients between X and Z directions and Y and Z directions are to be researched.

Define $Z = R_{Dir2} R_{Dir1}$, thus Z represents the response relationship between Direction1 and Direction2, for in statistic theory the product of two random variables represents the joint relationships.

The Chinese Code (2001) defines the calculation method the ESWL in the along wind direction, it defines the gust factor as 2.5, which implies the exceeding probability is 2.5% in a year. In that case, the two variables model should be defined the same as the single variable model. It is expressed as equation (2).

$$P(Z \le z_\alpha) = \int_{-\infty}^{\infty} \int_{-\infty}^{z_\alpha / r_2} f(r_1, r_2) dr_1 dr_2 = 97.5\% \tag{2}$$

Compare (2) with (1), it is easy to find relationship between z and responses in two directions as (3).

$$z_\alpha = \gamma r_{1\alpha} r_{2\alpha} \tag{3}$$

That is, the combination coefficient γ should be defined as (4)

$$\gamma = \frac{z_\alpha}{r_{1\alpha} r_{2\alpha}} \tag{4}$$

3 METHOD TO DETERMINE JOINT PROBABILITY DENSITY DISTRIBUTION FUNCTION

Conclusion can be got from the equation (2) that if $f(r_1, r_2)$ is certain then z_α can be defined. And another deduction is that if we know the distribution of $f(r_1, r_2)$, then we may make certain the distribution parameters. As a matter of fact, it is difficult to define the distribution for a two-dimensional distribution, but fortunately to simulate a one-dimension distribution is easier. As the one-dimension distribution for marginal density function is sure, a copula method will be used to combine two marginal density functions as a two-dimensional distribution function. The copula method should be introduced first.

2.1 Introductions to bivariate Copula

Copula-based approaches have been used for different statistical problems in many fields, such as economics, finance and hydrology. It combines two PDF through a tie function called copula function. The formula is can be described as (5).

$$F(x_1, x_2, \cdots, x_n) = C\left(F(x_1), F(x_2), \cdots, F(x_n)\right) \tag{5}$$

Where $F(x_1, x_2, \cdots, x_n)$ is the joint Cumulative distribution functions(CDF) of random variables($x_1, x_2, \cdots, x_n$) ; $F(x_i)$ is the CDF of random variable x_i (I=1,2,$\cdots$,n) and C is the copula function.

There exist some types of copula functions, which can be classified as ellipse copula and Archimedean copula. The usually used copula functions are listed. (6) is the Gaussian copula function and (7) is Gumbel copula function.

Gaussian copula

$$C(u_1, \cdots, u_n; \rho) = \Phi_\rho\left(\phi^{-1}(u_1), \cdots, \phi^{-1}(u_n)\right) \tag{6}$$

Here, $\Phi_\rho(\square)$ means the standard multivariate Gaussian CDF and $\phi(\square)$ is the Gaussian CDF

Gumbel copula

$$C(u_1, u_2; \theta) = \exp\left\{-\left[(-\ln u_1)^\theta + (-\ln u_2)^\theta\right]^{1/\theta}\right\} \tag{7}$$

Gaussian copula function is somewhat a simple method, for the joint PDF of the two variables which subject to Guassian distribution is just the bivariate Gaussian PDF. Gussian distribution reflects the strong relation in the middle part of the two variables. And Gumbel copula function reflects a strong relation in the tail.
Relationship between random variables is reflected by the parameters in the above formulae. It is very important to find the right copula function and parameter values to model the distribution of the wind-induced responses in two directions. However there is no fixed method to choose the copula, thus the parameters form parametric tests and two steps methods are adopted.

2.2 parametric tests

As there are parameters in different copula functions and in marginal functions, it is necessary to do parametric test for the CDF. The usually used method is the two step method, that is, firstly test the parameter for the marginal functions and then for copula functions.

In first step, maximum likelihood estimation was done. Formula(8) will be formulated to estimate the parameter v_i .

$$\hat{v}_i = \arg\max \sum_{i=1}^{T} \ln f_i\left(x_i; v_i\right) \tag{8}$$

Where $f_i\left(x_i; v_i\right)$ is the PDF for x_i ; $\hat{v}_i$ is the estimated value.

And in the second step,

$$\hat{\theta} = \arg\max \sum_{i}^{T} \ln c\left(F_1\left(x_1; \hat{v}_1\right), \cdots, F_1\left(x_{n1}; \hat{v}_n\right); \theta\right) \tag{9}$$

Where $c\left(u_1, u_2; \theta\right) = \dfrac{\partial C\left(u_1, u_2; \theta\right)}{\partial u_1 \partial u_2}$, T is the number of variables, in this paper, T=2.

The way is also named the inference functions for margins method.

2.3 copula choose method

As different copula functions are determined, the bivariate CDF is determined. For there are different CDF for different copula, it is necessary to find the most suitable one. One method to choose the suitable copula function is the KS (Kolmogorov-Smimov) check.

2.4 Determination of the bivariate joint probability density function

The marginal probability density function is simulated from the response data calculated using the original pressure data based on tunnel tests. And when the marginal functions and the copula function is determined, the CDF of the bivariables are determined. It will be calculated using the formula listed below.

$$f\left(x_1, x_2\right) = c\left(u_1, u_2; \theta\right) f_1\left(x_1\right) f_2\left(x_2\right) \tag{10}$$

Where $f_1(x_1)$, $f_2(x_2)$ are marginal distributions of x_1, x_2.

By the copula method and equation (11), the bivariate joint probability density function for Gaussian copula method is following.

$$f(x,y)=\frac{1}{2\pi\sigma_1\sigma_2\sqrt{1-\rho^2}}e^{-\frac{1}{2(1-\rho^2)}\left[\frac{(x-\mu_1)^2}{\sigma_1^2}-\frac{2\rho(x-\mu_1)(y-\mu_2)}{\sigma_1\sigma_2}+\frac{(y-\mu_2)^2}{\sigma_2^2}\right]} \tag{11}$$

3 WIND TUNNEL TESTS AND ANALYSIS

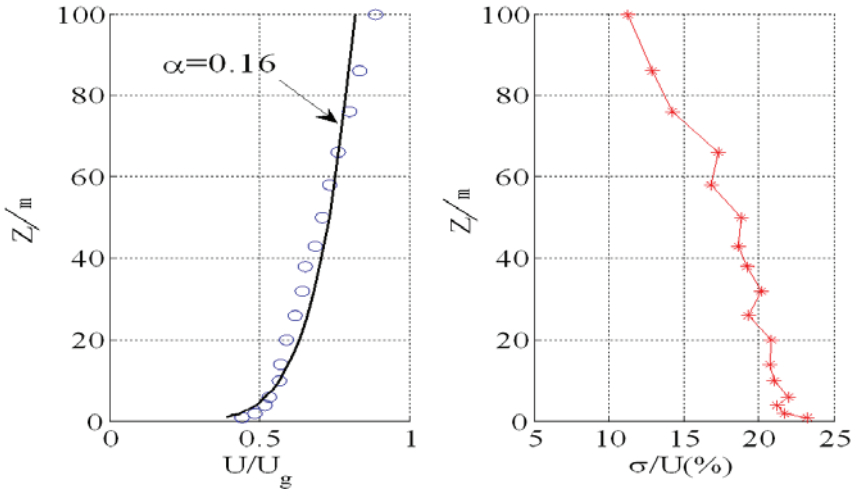

Fig 1 average wind speed and turbulence simulation in wind tunnel for field B

3.1 The basic test data

The tests were carried out in the wind tunnel in China Academy of Building Research. According to the Chinese Code, 'Load code for the design of building structures' GB50009-2001, wind fields A, B, C were simulated. Fig1 descripts the simulation of average wind speed and turbulence in wind tunnel for field B, where Z means the height from the ground. U_g means gradient velocity. U , σ means average wind speed and wind speed variance corresponding to z.

The models for test were made of ABS plates, and satisfy the similarity criteria and demand of rigidity and strength. Table1 shows the models data.

Table 1 the dimensions and test point's layout of the test models

Num.	Section	Height(H) (mm)	Breadth(B) (mm)	Depth(D) (mm)	Total number of test points (layer numbers×layer points numbers)
R1		600	100	400	216(9×24)
R2		600	100	300	216(9×24)
R3		600	100	200	216(9×24)
R4		600	100	150	324(9×36)
S4		600	100	100	180 (9×20)

3.2 The analysis of data

3.2.1 Responses time series in different directions

The responses time series in different directions are calculated in frequency domain, and translated into time domain by inverse Fourier translation (IFT). The equations for the movement of the high-rise buildings are as formula (14).

$$M\ddot{X}(t)+C\dot{X}(t)+KX(t)=F(t) \tag{12}$$

Where M is mass matrix, C is damper matrix and K is the stiffness matrix. F(t) is the force time series, and can be calculated by the sum of product of point pressures and area for the points. (14) can be translated into frequency domain.

$$M\ddot{X}(w)+C\dot{X}(w)+KX(w)=F(w) \tag{13}$$

Thus,

$$X(w)=H(iw)F(w) \tag{14}$$

Here,

$$H(iw)=\frac{1}{M^{*}w_n^2}\frac{1}{-\left(\frac{w}{w_n}\right)^2+i\left(\frac{w}{w_n}\right)+1} \tag{15}$$

w_n is the self-excited frequency of the structures.

$X(t)$ is then got from the IFT translation as formula.

$$X(t)=\frac{1}{2\pi}\int_{-\infty}^{+\infty}X(w)e^{iwt}dw \tag{16}$$

During computation, the modes are assumed to be separate and the first three modes are assumed to vibrate in along wind direction, cross wind direction and torsion direction. The periods follow the ratio as 0.77:0.85:1.

3.2.2 Marginal PDF determination

As for different directions of different models, the skewness and kurtosis of the wind forces were calculated and listed in Table2. Where x, y and represent along wind direction, cross wind direction and torsional direction. The K-S normality test results were also shown in Table 2.

Table 2 Standard variance, Skewness, Kurtosis and Normality test for displacement response

Model	Wind	Skewness	Kurtosis	Standard variance	Normality test

Mark								σ			（significance level）		
	field	x	y	θ	x	y	θ	x	y	θ	x	y	θ
R1	A	-0.12	-0.02	-0.04	2.96	2.93	2.86	0.19	0.23	0.15	0.001	0.2	0.113
	B	-0.13	0.11	0.02	2.91	3.21	2.99	0.14	0.14	0.09	0.006	0.002	0.2
	C	0.18	-0.08	0.03	3.04	2.94	3.18	0.19	0.21	0.12	0	0	0
R2	A	-0.02	0.06	0.22	3.08	3.05	2.83	0.27	0.38	0.16	0.2	0.2	0
	B	-0.05	-0.07	0.28	2.82	3.24	2.87	0.18	0.21	0.1	0.004	0.008	0
	C	-0.21	-0.1	0.2	3.22	3.27	2.87	0.23	0.29	0.14	0.005	0.002	0
R3	A	-0.13	0.12	0.22	2.88	2.67	2.75	0.29	0.62	0.12	0	0	0
	B	-0.04	0.09	0.18	2.99	2.68	2.76	0.21	0.35	0.08	0	0	0
	C	-0.03	0.1	0.17	2.93	2.62	2.62	0.28	0.42	0.11	0	0	0
R4	A	-0.02	0.06	0.02	3.01	3.05	2.95	0.19	0.19	0.15	0	0	0
	B	-0.1	0.05	0.06	2.89	3.19	3.11	0.14	0.11	0.1	0.001	0.007	0.103
	C	-0.2	-0.28	0.17	2.86	3.9	3.24	0.21	0.18	0.14	0	0	0
S4	A	0	-0.08	-0.33	3.17	3.04	4.4	0.3	0.73	0.05	0.001	0.011	0
	B	-0.03	-0.03	-0.03	2.72	2.8	4.15	0.24	0.5	0.04	0	0.007	0
	C	0.27	-0.08	-0.08	2.93	2.77	3.59	0.33	0.62	0.06	0	0	0

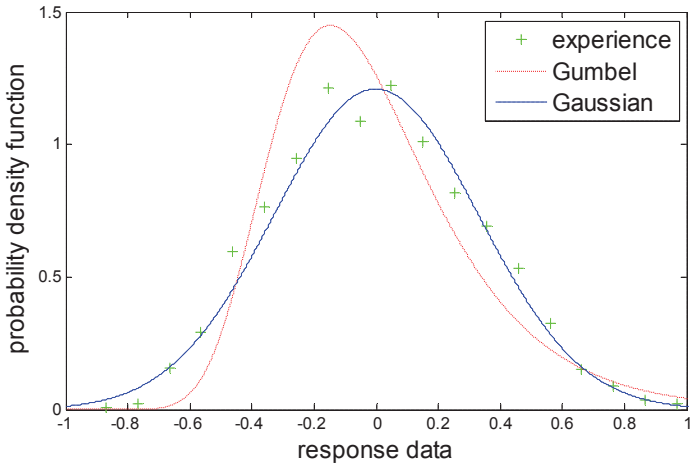

Fig 2 Comparison of different distributions

Table 3 Gumbel parameter estimation for displacement response

Model Mark	Wind field	Gumbel Parameter a			Gumbel Parameter b		
		x	y	θ	x	y	θ
R1	A	0.148	0.146	0.115	-0.085	-0.084	-0.066
	B	0.108	0.089	0.076	-0.062	-0.051	-0.044
	C	0.165	0.144	0.112	-0.095	-0.083	-0.065
R2	A	0.148	0.146	0.115	-0.087	-0.103	-0.067
	B	0.108	0.089	0.076	-0.065	-0.064	-0.043
	C	0.165	0.144	0.112	-0.088	-0.095	-0.055
R3	A	0.213	0.297	0.121	-0.123	-0.172	-0.070
	B	0.144	0.167	0.075	-0.083	-0.096	-0.043
	C	0.183	0.225	0.105	-0.105	-0.130	-0.061

R4	A	0.224	0.482	0.094	-0.129	-0.278	-0.054
	B	0.165	0.272	0.061	-0.095	-0.157	-0.035
	C	0.216	0.324	0.084	-0.125	-0.187	-0.048
S4	A	0.234	0.571	0.041	-0.135	-0.330	-0.024
	B	0.186	0.390	0.033	-0.108	-0.225	-0.019
	C	0.254	0.485	0.050	-0.147	-0.280	-0.029

As table2 shows, almost half of the wind forces are following Gaussian distribution through KS check. And there still exists a half which is not Gaussian distribution. So a Gumbel distribution was list out to check. Thus we get the Gumbel distribution parameters as Table 3.

Compare the Gumbel distribution and Gaussian distribution, Fig 2 is the comparison for the model S4 in filed C in x direction, where the label 'experience' represents data distribution acquired from the collected data directly, and 'Gaussian' and 'Gumbel' represent data distribution simulated as Gaussian distribution and Gumbel distribution. It is obvious that the data fit Gaussian distribution better than Gumbel distribution. And repeat the work, it finds that for all data that is not so good for Gaussian distribution in Table 3 is more accurate than Gumbel distribution. The Guassian distrution is then used for the marginal distributions.

3.2.3 Joint distribution and the combination coefficients

Use method mentioned in part 2, the joint PDF is regressed. Taking the simplicity and accuracy into account, the Gaussian copula is adopted for a strong relation between data located in the middle part of the marginal distribution, and Gumbel copula for that located in the tail. Thus the parameters for the both copula functions are listed in Table 3.

In order to check the data, the 'direct method'(Gianni Bartoli,2011) is used. Thus, the coefficients calculated by formula (4) are listed in table4

Table 4 Gumbel Parameter and Gaussian Parameter from calculation

Model Mark	Wind field	Gumbel Parameter $1/\theta$			Gaussian Parameter ρ		
		XY	$X\theta$	$Y\theta$	XY	$X\theta$	$Y\theta$
R1	A	1.01	1.10	1.01	0.00	0.18	0.02
	B	1.02	1.12	1.02	0.04	0.20	0.05
	C	1.04	1.10	1.08	0.07	0.13	0.15
R2	A	1.13	1.09	1.19	0.23	0.19	0.27
	B	1.05	1.10	1.16	0.15	0.17	0.23
	C	1.06	1.00	1.09	0.12	0.04	0.15
R3	A	1.00	1.02	1.48	0.04	0.03	0.52
	B	1.01	1.00	1.45	0.07	0.01	0.49
	C	1.02	1.08	1.38	0.08	0.11	0.46
R4	A	1.00	1.02	1.28	0.03	0.04	0.38
	B	1.04	1.03	1.36	0.09	0.09	0.44
	C	1.02	1.03	1.52	0.08	0.03	0.56

S4	A	1.00	1.02	1.56	0.02	0.02	0.56
	B	1.00	1.06	1.54	0.01	0.07	0.57
	C	1.02	1.06	1.51	0.08	0.08	0.54

Thus, using formula(4), the combination coefficients were computed and shown as table5.

Table 5 combination coefficients from different methods

Model Mark	Wind field	Gumbel Copula		Gauss Copula		Direct method	
		Y leading	Z leading	Y leading	Z leading	Y leading	Z leading
R3	A	0.230	0.807	0.604	0.923	0.90	0.82
	B	0.254	0.785	0.569	0.903	0.74	0.66
	C	0.264	0.764	0.545	0.882	0.78	0.95
R4	A	0.595	0.659	0.624	0.704	0.76	0.71
	B	0.704	0.729	0.683	0.727	0.71	0.84
	C	0.706	0.742	0.738	0.795	0.58	0.85
S4	A	0.126	0.914	0.586	0.970	0.74	0.95
	B	0.141	0.900	0.606	0.966	0.79	0.91
	C	0.133	0.882	0.581	0.957	0.68	0.94

From table 5, it is apparent the combination coefficients calculated by the Gaussian Copula method are more accurate than that by Gumbel method. In one sense it certificates Gaussian Copula method is more fit for the determination of joint probability density. Also from the table, if Y is the leading direction the combination coefficient is 0.54~0.74, and if Z is the leading direction the combination coefficient is 0.7~0.9. The result is different from the AIJ code. In AIJ code the combination coefficient is the same no matter which direction is the leading direction, and it does not give a constant exceeding probability. However if the leading direction is Y direction, then the combination coefficient of AIJ lies between 0.54~0.78 while the frequencies ratio is about 0.9, just the same as the result.

4 CONCLUSIONS

Through wind tunnel tests on 5 models whose side ratio ranked from 1:1~1:5 in different wind fields, based on the distribution induced by copula method and empirical distribution, the combination coefficients of the equivalent static cross wind force and torsional wind force were determined. By analysis, the time series of wind forces and responses in different directions shows that the random data nearly subject to normal distribution, while the Gumbel distribution is not so good for estimation for the random variable. And through calculation, if the frequency ratio is 0.85, the combinations are found between 0.5~0.7 while the cross direction is the leading, and 0.7~0.9 while the torsional direction is the leading. It is something like the combination coefficient defined in AIJ code.

REFERENCES:

[1] Davenport, A.G. The application of statistical concepts to the wind loading of structures. Proc. Inst. Civ. Eng. 19(1961), 449–472.

[2]G. Solari, L.C. Pagnini. Gust buffeting and aeroelastic behavior of poles and monotubular towers. Journal of Fluids and Structures 13 (1999), 877-905

[3] Shuguo Liang Shengchun Liu, Q.S. Li etc. Mathematical model of acrosswind dynamic loads on rectangular tall buildings. Journal of Wind Engineering and Industrial Aerodynamics 90 (2002) 1757-1770

[4] AIJ Recommendations for Loads on Buildings (2004 Edition)

[5] Gianni Bartoli, ClaudioMannini, TommasoMassai. Quasi-static combination of wind loads: A copula-based approach. J. Wind Eng. Ind. Aerodyn. 99 (2011) 672–681

[6] Ning Lin, Chris Letchford, Yukio Tamura etc. Characteristics of wind forces acting on tall buildings. Journal of Wind Engineering and Industrial Aerodynamics 93 (2005) 217-242

[7] Li Yanheng, Shi Baoping, Zhang Jian, The copula joint function and its application in probabilistic seismic hazard analysis, ACTA SEISMOLO GICA SINICA 30(2008) 292-301

[8] Quan Yong, Gu Ming. Analytical method of across-wind response and equivalent static wind loads of high-rise buildings. Engineering mechanics, 23(2006) 84-88

The Seventh International Colloquium on Bluff Body Aerodynamics and Applications (BBAA7)
Shanghai, China; September 2-6, 2012

Along-wind aerodynamic damping of high-rise buildings

Cao Huilan [a], Quan Yong [a], Gu Ming [a], Wu Di [a]

[a] *State Key Laboratory of Disaster Reduction in Civil Engineering, Bridge Building, Tongji University, No. 1239 Siping Road, Shanghai, China*

ABSTRACT: Along-wind aerodynamic damping ratios are identified from wind-induced responses of 46 aeroelastic models in simulated turbulent flow using the random decrement technique (RDT). Their validity is examined through comparison with previous research achievements and the results evaluated by quasi-steady theory. Based on the identified results, characteristics of along-wind aerodynamic damping of isolated high-rise buildings are studied. The effects of density ratio, generalized stiffness, structural damping ratio, aspect ratio, side ratio, roughness exposure, aerodynamically modified cross-sections and tapering on aerodynamic damping ratio of high-rise buildings are investigated. Results indicate that: aerodynamic damping ratio increases monotonically with reduced wind velocity; structural damping ratio, density ratio, side ratio, reduced wind velocity and aspect ratio are very important parameters for along-wind aerodynamic damping ratio, while no clear effect of generalized stiffness on aerodynamic damping ratio is observed. Aerodynamic damping ratio increases as corner-cut ratio or taper ratio increases; low corner-cut ratios significantly decrease aerodynamic damping; however, modifications of building corners and tapering are not always effective at reducing the aerodynamic damping of tall buildings. According to the database, an empirical aerodynamic damping function for high-rise buildings is proposed.

KEYWORDS: high-rise building; wind-induced vibration; aerodynamic damping; aeroelastic model; wind tunnel test; along-wind.

1 INTRODUCTION

Since structural damping ratio of high-rise building is always small and predominant frequency of aerodynamic force under strong wind is close to the natural frequency of structure, wind load would be one of the control loads in design of high-rise building for significant wind-induced response. In addition, coupling effect between incident turbulent flow and structure may generate negative aerodynamic damping, which would decrease total damping, and furthermore cause larger response. Generally, along-wind, across-wind and torsional structure motion all could induce aerodynamic damping. And aerodynamic damping in along-wind attracts researchers' attention most early.

Aerodynamic damping in along-wind can generally be estimated with satisfactory accuracy by adopting the quasi-steady theory. Based on it, Davenport (1979) [1] found ζ_a=0.0175 with $V/(f_0B)$=10, M/ρ_aB^2=182 and C_D~2. Holmes (1996, 2001) [2,3] estimated the aerodynamic damping in along-wind based on the assumption that the aerodynamic drag force is proportional to the square of the difference between the mean oncoming wind speed and the speed of the moving structure. Gabbai and Simiu (2010) [4] presented a methodology for estimating aerodynamic damping in which the relative wind speed with respect to the moving structure is modeled, more accurately, as the difference between the total oncoming wind speed and the speed of the moving structure. In addition, the structural motion is assumed to be proportional to the relative oncoming wind speed raised to powers larger than two. In theory, this methodology is more accurate than quasi-steady method and the method proposed by Holmes, but more complex.

There are also many researchers study along-wind aerodynamic damping of high-rise buildings through wind tunnel test. Marukawa (1996) [5] evaluated the aerodynamic damping of rectangular tall buildings from wind tunnel tests of aeroelastic model. Random decrement technique is used to analyze effects of side ratio, aspect ratio and structural damping ratio on along-wind aerodynamic damping. Cooper (1997) [6] studied the impact of motion amplitude on along-wind aerodynamic damping by forced vibration test. Besides, the aerodynamic damping obtained from aeroelastic response measurements was compared with those predicted by quasi-steady theory. The results indicated that aerodynamic damping ratios in this test are independent of motion amplitude. Quan (2002, 2004, 2005) [7,8,9] and Gu (2004) [10] proposed a formula for aerodynamic damping as a function of reduced velocity, roughness exposure and structural damping using RDT method. Zou (2003) [11] investigated the aerodynamic damping of an isolated rectangular high-rise building with side ratio of 2:1 at three reduced wind velocities. But up to now, existing researches only focus on one or a few influence factors and are far from systemization. Moreover, the research achievements are lack of comparison with each other and the theoretical results.

Generally, the use of aerodynamically modified cross-sections, such as slotted corners, chamfered corners and tapering, is an effective means to reduce the wind-induced response. However, modifications of building corners might not be entirely effective, as adverse effects may also occur (Kareem et al., 1999; Kim and Kawai, 1999) [12,13]. Kim and You (2002) [14] investigated the taper-ratio effect for reducing wind-induced excitations in along- and across-wind directions based on the force-balance test using rigid models with taper ratios of 5%, 10%, and 15%, and one basic model of a square cross-section without taper. They discovered that the tapering is more effective in reducing wind-induced excitations in the suburban flow environment than in the urban flow environment. They also showed that tapering reduces the across-wind responses more than the along-wind responses. And, compared with a basic model without a taper, the tapering is not always effective at reducing the wind-induced excitations of tall buildings. However, the literatures mentioned above could not systematically indicate the variation of wind-induced response of high buildings and aerodynamic damping. Huang (2003) [15] studied effects of modified cross-sections (corner-cut ratio of 10%) on along- and across-wind aerodynamic damping. Results showed that aerodynamic damping of high buildings with slotted corner and chamfered corner are much less than that of square high buildings, and in the view of engineering application, the aerodynamic damping in along- and across-wind all could be neglected for buildings with corner-cut ratio of 10%. However, up to the present, relevant researches all focus on rectangular building (Davenport, 1979; Marukawa, 1996; Quan, 2002, 2004, 2005; Gu, 2004; Zou, 2003 etc.). And whether theoretically or experimentally, quite limit studies are about the influence of corner-cut and tapering on aerodynamic damping. Therefore, further researches are needed to consider about these factors.

Along-wind aerodynamic damping ratios are identified from wind-induced response of 46 aeroelastic models in simulated turbulent flow. The effects of density ratio, generalized stiffness, structural damping ratio, aspect ratio, side ratio, roughness exposure and aerodynamically modified cross-sections and tapering on aerodynamic damping ratio of high-rise buildings are investigated. According to the database, an empirical aerodynamic damping function for high-rise buildings is proposed.

2 OUTLINE OF THE WIND TUNNEL TESTS

2.1 *Simulation of wind characteristics*

The test is carried out in TJ-1 Boundary Layer Wind Tunnel in Tongji University, whose working section is 1.8m in width, 1.8m in height and 18m in length, and the wind speed ranges from 3

to 32 m/s. Four kinds of wind conditions, corresponding to exposure category A, B, C and D in the Chinese code [16] are simulated in the wind tunnel at a length scale of 1/800. The exponents of the mean wind profiles for the exposure category A, B, C and D are 0.12, 0.16, 0.22 and 0.30, and the corresponding gradient heights are 300, 350, 400, 450m, respectively. The wind characteristics are achieved by a combination of turbulence generating spires, a barrier at the entrance of the wind tunnel, and roughness elements along the wind tunnel floor upstream of the model. The longitudinal turbulence intensities at the height of building (480m) are separately 9.23%、9.36%、9.52% and 9.78%, while the values at the height of roughness length are 18.52%、22.11%、27.07% and 27.50%. As profile of turbulence integral scale is difficult to be accurately simulated, the values at the 2/3 height of building for the exposure category A, B, C and D are respectively 229m, 231m, 285m, 274m. Figure 1 shows the simulated mean wind speed profiles and longitudinal component profiles of turbulence intensity, as wind speed profiles provided by Chinese code and turbulence intensity profile given by AIJ (2004) [17].

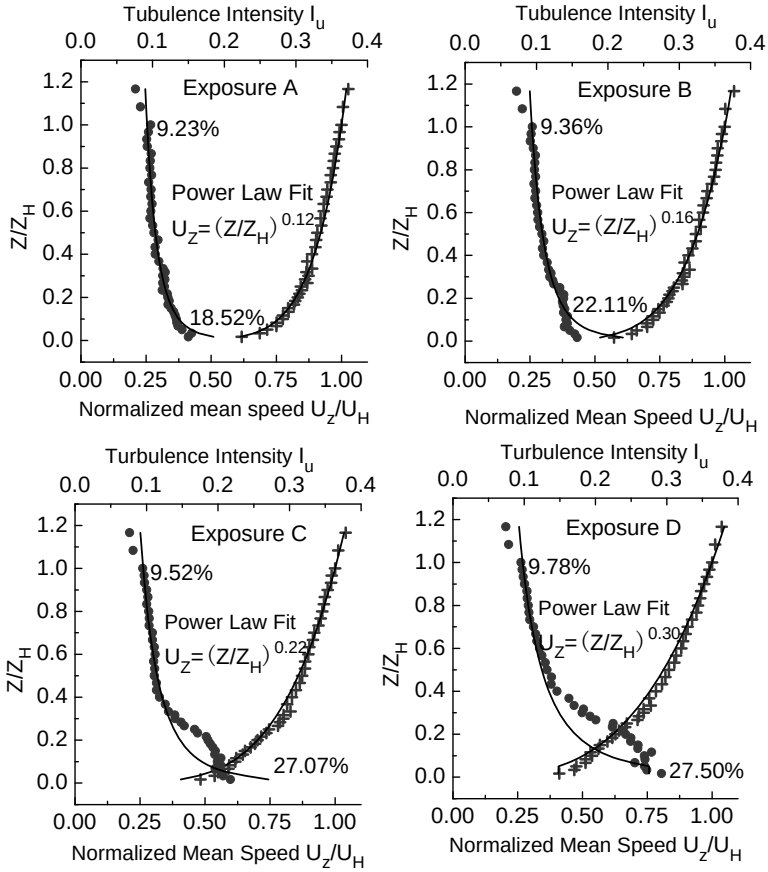

Figure 1 Profiles of wind velocity and longitudinal turbulence intensity

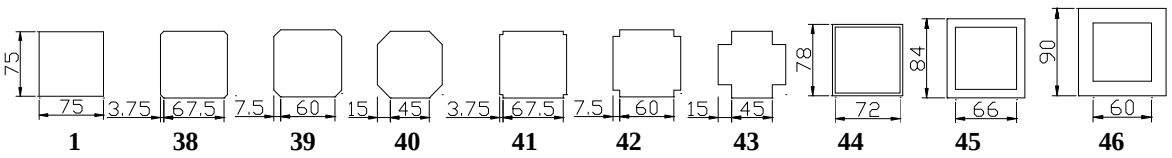

Figure 2 Model cross-sections (*mm*)

2.2 *Building models*

Length and velocity scale are separately 1/800 and 1/8. Dimensions of standard model are $0.075m \times 0.075m \times 0.6m$, with frequency of $13Hz$, density of $213Kg/m^3$ and generalized mass of $0.24Kg$. Corresponding to real structure, these parameters represent building with size of $60m \times 60m \times 480m$, natural frequency of 13 Hz, and density of $213Kg/m^3$. Generalized stiffness is selected to be 1600 Kg/s^2 according to natural frequency. In addition, structural damping ratio of standard model is taken as 1%, while density of air is $1.227Kg/m^3$.

Wind-induced responses of 46 high-rise buildings are measured from aeroelastic model wind tunnel test. The structure characteristic parameters are shown as Table 1. As to the other cases, the heights of models keep the same, and cross sections are changed according to aspect ratios and side ratios. The maximum block ratio of model to test section of wind tunnel is 2.22%. Case 38 to 46, cross sections are changed in accordance with corner-cut and taper ratios, considering one type of aerodynamically modification each case, as shown in Figure 2. The base is used to model the elastic parameters of buildings, as structural damping ratios are simulated by width of damping plates and their depth dipped into oil, while springs are used to achieve stiffness. In order to avoid energy transmission in the two orthogonal directions, one degree of freedom in horizontal direction is fixed. All of the models are built with base plates, hollow aluminum alloy as the cores, foamed plastics, light wood plates of 1mm thickness as their "clothes" and balancing weight. Two piezoelectric accelerometers with sampling frequency of $1000Hz$ are placed at the two ends inside windward surface, as sampling time set as 7 minutes.

Table 1 Wind tunnel test cases for high-rise buildings

Case	Model Height $H(mm)$	Roughness Exposure	Side Ratio B/D	Aspect Ratio $H/(BD)^{0.5}$	Structural Damping ζ_s (%)	Structure Density ρ_s (Kg/m^3)	Generalized Stiffness K (Kg/s^2)	Corner-cut or Taper Ratio
1-4	600	A,B,C,D	1	8	1	213	1600	0
5-12	600	B,D	1/3,3, 1/2,2	8	1	213	1600	0
13-18	600	B,D	1	5,10,12	1	213	1600	0
19-25	600	B,D	1	8	0.5,0.9,1.1,1.7 5,2.3,2.3,2.8	213	1600	0
26-31	600	B,D	1	8	1	360,255,160	1600	0
32-37	600	B,D	1	8	1	213	947,2130,3027	0
38-40	600	C	1	8	1	213	1592,1568,1472	5%-20%
41-43	600	C	1	8	1	213	1584,1536,1344	5%-20%
44-46	600	C	1	8	1	213	1600	1%-5%

3 TEST RESULTS

The generalized formula with four variables proposed by Tamura et al (1996) [18] is used to estimate damping from random acceleration responses.

$$a(\tau) = Ae^{-\zeta\omega\tau}\left(\cos\sqrt{1-\zeta^2}\,\omega_0\tau + B\sin\sqrt{1-\zeta^2}\,\omega_0\tau\right) \tag{1}$$

Firstly, amplitude dependent structural damping ratio is derived from free acceleration response. Then, RMS of wind-induced acceleration response after band-pass filtering is taken as the initial amplitude of RDT to calculate total damping ratio. Afterwards, structural damping ratio corresponding to this amplitude is derived through interpolation. The aerodynamic damping ratio ζ_a is

calculated by subtracting the value of structural damping ratio ζ_s from the value of total damping ratioζ, i.e. $\zeta_a = \zeta - \zeta_s$. Following research mainly focuses on the study of aerodynamic damping variation with density ratio, generalized stiffness, structural damping, aspect ratio, side ratio, roughness exposure, aerodynamically modified cross-sections and tapering.

3.1 *Verification of result*

Marukawa (1996) studied the effects of side ratio in the range of 0.33-3, aspect ratio from 4 to 6, and structural damping ratio of 0.5% to 2% on along-wind aerodynamic damping, and compared the results with that evaluated by quasi-steady theory. Here, the drag coefficient was derived from the mean displacement assuming that the wind force is distributed in proportion to the velocity pressure. Quan (2002, 2004) discussed impacts of exposure category (A、B、C、D) and structural damping on along-wind aerodynamic damping, and made comparison with Marukawa (1996). The validity of research results in this paper is examined through comparison with previous research achievements and the results evaluated by quasi-steady theory as shown in Figure 3, corresponding structure characters shown in Table 2.

As shown in Table 2 and Figure 3, there are certain differences between research results with different roughness exposures and model parameters. But in general, the results show a good agreement with previous research achievements and that derived by quasi-steady theory, especially with the result evaluated by quasi-steady theory.

Table 2 Structure parameters for tests

	Aspect Ratio $H/(BD)^{0.5}$	Side Ratio B/D	Roughness Exposure (α、I_h)	Model Height H (mm)	Length Scale	Structural Damping ζ_s	Structure Density ρ_s (Kg/m^3)
Standard Model	8	1	A、B、C、D	600	1/800	0.88%	213
Marukawa (1996)	6	1	α=0.167, I_h=10.7%	480	1/500	1%	200
Quan (2002)	6	1	A	600	1/500	0.6%	180
Quasi-steady Theory	$\zeta_a = \frac{1}{4\pi}\frac{\rho_a B^2}{M}\frac{V_H}{f_0 B}C_D$, as reduced velocity defined as $V_H/f_0(BD)^{0.5}$, derives $\zeta_a = = \frac{1}{4\pi}\frac{\rho_a}{\rho_s}\frac{B}{D}\frac{V_H}{f_0\sqrt{BD}}C_D$ (According to Marukawa (1996), for B/D =1, C_D=1.05; as to the Chinese code, for B/D =1, C_D=1.3)						

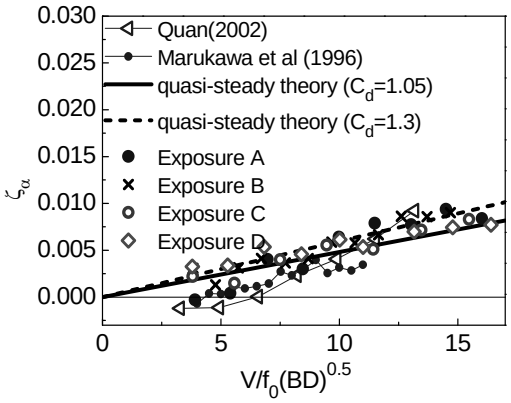

Figure 3 Comparison with research achievements and theoretical result

3.2 *Characteristics of aerodynamic damping*

3.2.1 *Effect of roughness exposure*

Figure 3 indicates the variation of aerodynamic damping ratio with reduced velocity $V_H/f_0(BD)^{0.5}$ in simulated turbulence wind environments A、B、C、D. The aerodynamic damping ratio in the along-wind in Figure 3 represents positive damping at reduced velocities of 4 or more, and it increases monotonically with reduced wind velocity. At low reduced wind velocities, aerodynamic damping ratios in exposure D are bigger than that in exposure category A. Furthermore, at reduced wind velocities of more than 10, aerodynamic damping ratios are apparently bigger than other cases. That is, aerodynamic damping ratio gradually increases slower with reduced velocity for exposure category A、B、C、D. But overall, wind environment has no clear effect on along-wind aerodynamic damping, as discrepancies are within 0.003. It may be caused by the similar profiles of wind velocity (Chinese code) and turbulence intensity (AIJ2004) for this height of building. So, the influence of roughness exposure still needs further research.

3.2.2 *Effect of side ratio B/D*

Figure 4 shows the variation of aerodynamic damping ratio with reduced velocity, as aspect ratio $H/(BD)^{0.5}$=8, structural damping ratio ζ_s =1%, side ratio B/D ranges from 0.33 to 3. The corresponding values obtained by quasi-steady theory are also provided in this Figure. Here, the drag coefficients adopt the values given in Marukawa (1996). Figure 4 indicates that side ratio is an important parameter for aerodynamic damping, as aerodynamic damping increases with side ratio, exclude the case with B/D=0.33. In most cases, aerodynamic damping increases monotonically with reduced wind velocity, except that it starts to decrease at reduced velocity of 8-10 for the case with B/D=0.33. For side ratios $B/D\geq1$, aerodynamic damping increases with side ratio; for side ratios $B/D\leq1$, there is no clear variation in aerodynamic damping ratio with side ratio. As to side ratios $B/D>1$, aerodynamic damping ratios derived from experiment are bigger than that evaluated by quasi-steady theory in exposure category B; and opposite phenomena can be observed in exposure category D. As to side ratios B/D=1, 0.5, aerodynamic damping ratios derived from experiment are a little bigger than that evaluated by quasi-steady theory, as discrepancies are within 0.002 in exposure category B and much less in exposure category D. Generally, there's no big difference between each other, so along-wind aerodynamic damping can be well predicted by quasi-steady theory for these cases. But as to the case of B/D=0.33, experimental values are much bigger than theoretical values. All in all, there is a much better agreement between aerodynamic damping evaluated from wind tunnel test and the theoretical value than that obtained by Marukawa (1996). This is because, reduced velocity adopted by Marukawa (1996) is $V_H/f_0(BD)^{0.5}$, while the one used for quasi-steady theory is V_H/f_0B.

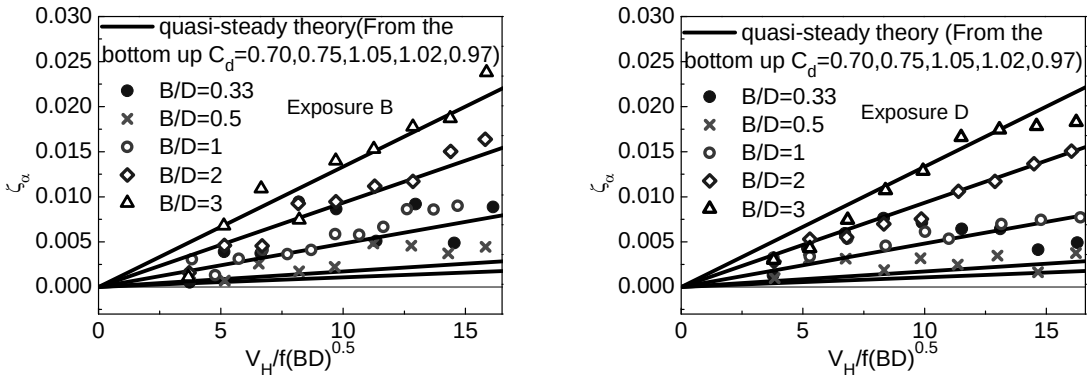

Figure 4 Effect of side ratio B/D ($H/(BD)^{0.5}$=8, ζ_s =1%)

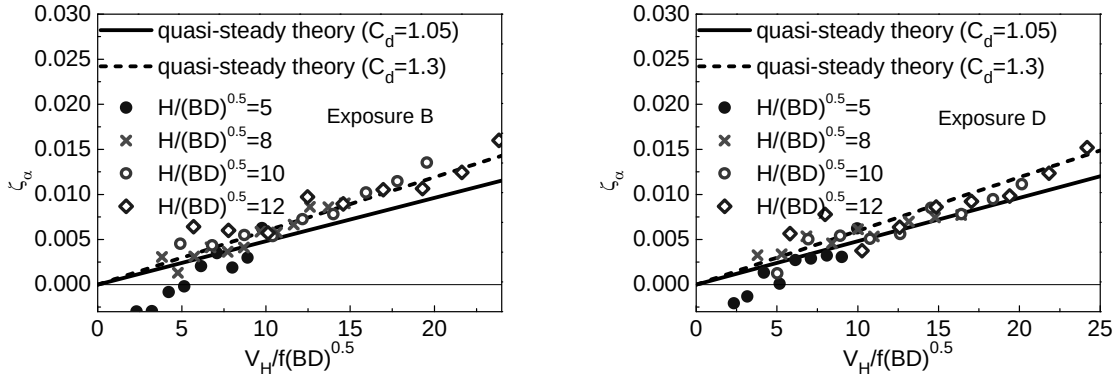

Figure 5 Effect of aspect ratio $H/(BD)^{0.5}$ (B/D=1, ζ_s=1%)

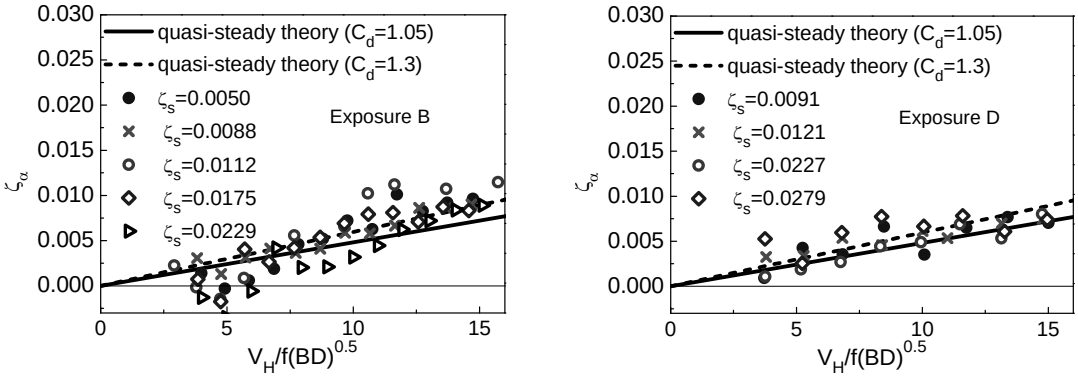

Figure 6 Effect of structural damping ζ_s (B/D=1, $H/(BD)^{0.5}$=8)

3.2.3 *Effect of aspect ratio $H/(BD)^{0.5}$*

Figure 5 shows the variation of aerodynamic damping ratio with reduced velocity, as side ratio B/D=1, structural damping ratio ζ_s =1%, aspect ratio $H/(BD)^{0.5}$ ranges from 5 to 12. Figure 5 indicates that aerodynamic damping ratio gradually increases slower with wind velocity as aspect ratio increases. At reduced wind velocitiy lower than 10, aerodynamic damping ratio increases as aspect ratio increases; while opposite trend is observed at reduced wind velocity higher than 10. Above all, the effect of aspect ratio is not so obvious, with difference not more than 0.003, and they can be relatively accurate evaluated by quasi-steady theory.

3.2.4 *Effect of structural damping ζ_s*

Figure 6 shows the variation of aerodynamic damping ratio with reduced velocity, as side ratio B/D=1, aspect ratio $H/(BD)^{0.5}$=8, structural damping ratios ζ_s ranges from 0.005 to 0.0279. At the same reduced velocity, difference of aerodynamic damping is about 0.005, which states unelectable effect of structural damping on aerodynamic damping. At low reduced wind velocity, aerodynamic damping generally decreases with structural damping; while the smaller the structural damping, the bigger the aerodynamic damping at high reduced wind velocity. The smallest aerodynamic damping ratio is observed when the structural damping ratio is 0.023. In addition, variations of aerodynamic damping for ζ_s=0.0091, 0.0121, 0.0227 in exposure category D are similar with cases of ζ_s=0.0088, 0.0112, 0.0229 in exposure category B.

3.2.5 *Effect of density ratio ρ_s/ρ_a*

Figure 7 shows the variation of aerodynamic damping ratio with reduced velocity when density ratio varies from 294 to 131. Density ratio has a clear effect on aerodynamic damping, with difference between 0.003 and 0.005 at the same reduced wind velocity. Aerodynamic damping ratio increases monotonically with density ratio. Moreover, the value derived in exposure category D is a little smaller than that in exposure category B.

3.2.6 *Effect of generalized stiffness K*

Figure 8 shows the variation of aerodynamic damping ratio with reduced velocity when generalized stiffness varies from 947 to 3027. As shown in Figure 8, no clear effect of generalized stiffness on aerodynamic damping is observed in the along-wind direction, with difference not more than 0.002. Likewise, aerodynamic damping ratio in exposure category D gradually increases slower with reduced velocity than in exposure category B. The values estimated in exposure category D are much closer to the values derived by quasi-steady theory, while much more discrepancies are observed in exposure category B.

3.2.7 *Effect of slot rate*

Figure 9 shows the variation of aerodynamic damping ratio with reduced velocity, as aspect ratios $H/(BD)^{0.5}$=8, structural damping ratio ζ_s=1%, side ratio B/D=1, slot rate ranges from 0% to 20%. The corresponding values obtained by quasi-steady theory are also provided in this Figure. Here, the drag coefficients adopt the value given in Marukawa (1996). Figure 9 indicates 5% and 10% slot rates significantly decrease aerodynamic damping, and this trend is more obvious at

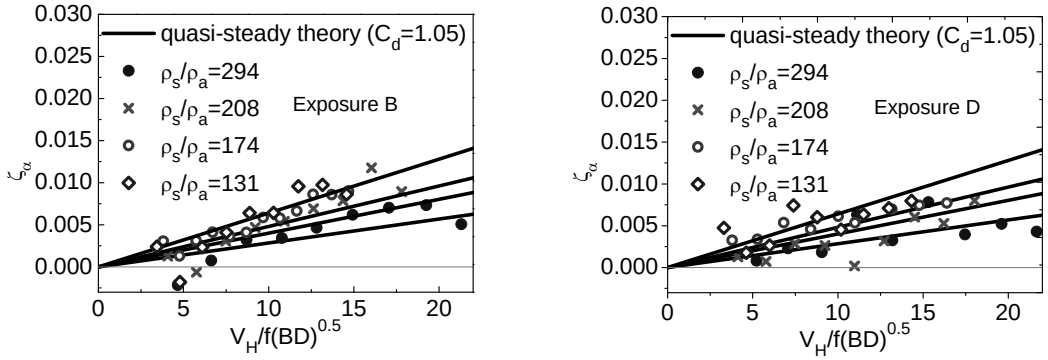

Figure 7 Effect of density ratio ρ_s/ρ_a

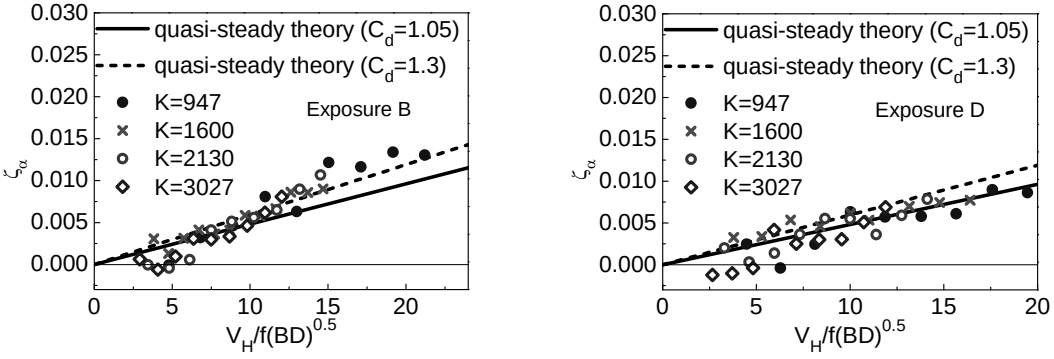

Figure 8 Effect of generalized stiffness *K*

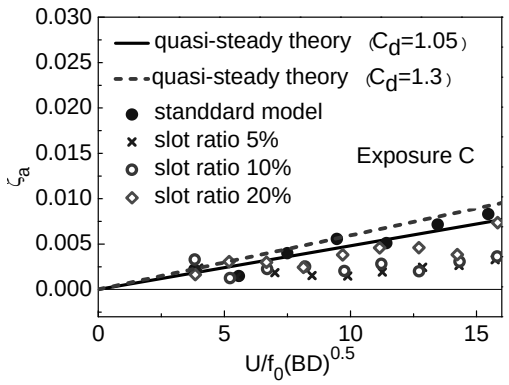

Figure 9 Effect of slot rate

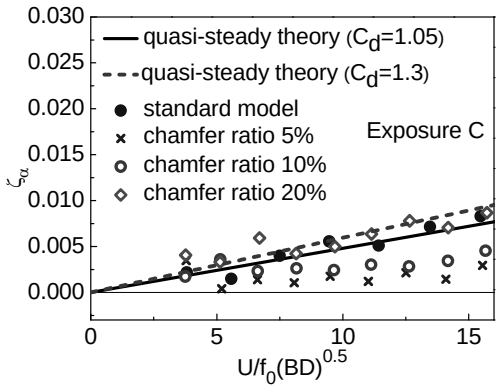

Figure 10 Effect of chamfer rate

higher reduced wind velocity. For slot rate of 20%, although it decreases in certain extend, but difference is not significant, i.e. larger slot does not lead to more decrease. Also in this case, decrease effect of aerodynamic damping strengthens as reduced wind velocity increases. In general, slot rates in certain range significantly decrease aerodynamic damping, especially for the case with slot rate of 5%.

3.2.8 *Effect of chamfer rate*

Figure 10 shows the variation of aerodynamic damping ratio with reduced velocity, as aspect ratios $H/(BD)^{0.5}$=8, structural damping ratio ζ_s=1%, side ratio B/D=1, chamfer rate ranges from 0% to 20%. The corresponding values obtained by quasi-steady theory are also provided in this Figure. As shown in Figure 10, 5% and 10% chamfer rates significantly decrease aerodynamic damping, and this trend is more obvious at higher reduced wind velocity. For chamfer rate of 20%, although it decreases in certain extend, but difference is not significant, which means larger chamfer is not always effective at reducing the aerodynamic damping of tall buildings. When chamfer rate varies from 5% to 20%, aerodynamic damping ratio increases as chamfer rate increases. As compared with cases with slotted corner, aerodynamic damping ratios of building with 5% chamfer rate are smaller than that with 5% slot rate, the opposite phenomena can be observed for chamfer rate 10% and 20%. Overall, the effects of slotted corner and chamfered corner on aerodynamic damping ratio are similar; for low corner-cut ratios, aerodynamic damping ratios are bigger with slotted corner, while for high corner-cut ratios, they are bigger with chamfered corner.

3.2.9 *Effect of tapering*

Figure 11 shows the variation of aerodynamic damping ratio with reduced velocity, as aspect ratios $H/(BD)^{0.5}$=8, structural damping ratio ζ_s=1%, side ratio B/D=1, taper rate ranges from 0% to 20%. The corresponding values obtained by quasi-steady theory are also provided in this Figure. As shown in Figure 11, taper rate of 1% reduces aerodynamic damping, but taper rate of 3% and 5% increase aerodynamic damping. When taper rate varies from 1% to 5%, aerodynamic damping ratio increases as taper rate increases. Therefore, tapering is not always effective at reducing the aerodynamic damping of tall buildings, as lower rates of tapering reduce aerodynamic damping and it will increase when taper rate exceeds 3%.

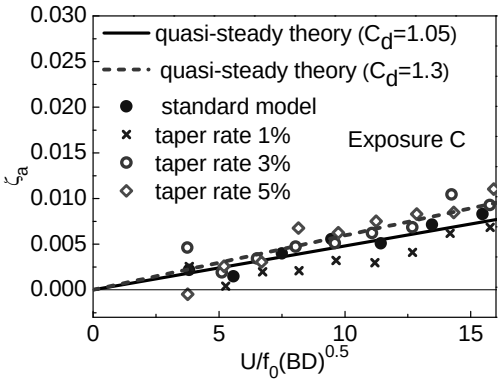

Figure 11 Effect of tapering

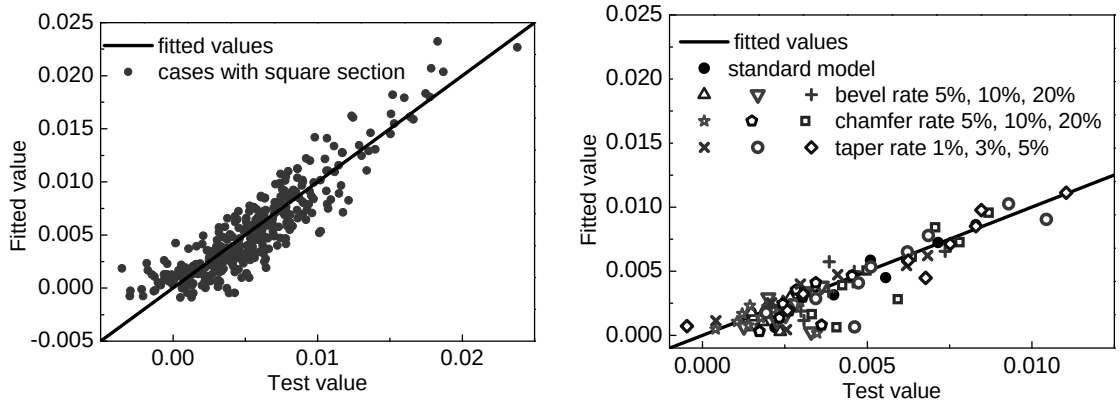

Figure 12 Comparison between fitted values and tested values for aerodynamic damping

3.3 *Formula fitting of aerodynamic damping ratio*

As described above, the aerodynamic damping ratios of high-rise building increase monotonically with reduced wind velocity. In most cases, they can be relatively accurate evaluated by quasi-steady theory. Research shows that structural damping ζ_s, density ratio ρ_s/ρ_a, side ratio B/D, reduced velocity $V_H/f_0(BD)^{0.5}$, aspect ratio $H/(BD)^{0.5}$, aerodynamically modified cross-sections and tapering are important effects for aerodynamic damping ratio in along-wind, while the influence of generalized stiffness and roughness exposure are not so significant. As quasi-steady theory only takes density ratio, side ratio, reduced velocity and drag coefficient into consideration, an empirical aerodynamic damping function for high-rise buildings, written as formula (2), is proposed according to the database after many times comparison. The conformity between aerodynamic damping ratios derived from wind tunnel test and by fitting is shown in Figure 12. Standard error for this for this empirical formula is

$$\delta_{\zeta a}=\sqrt{\frac{1}{N}\sum_{i=1}^{N}\left(\zeta_{a-calc}(i)-\zeta_{a-test}(i)\right)^2}=0.0018$$

Where, N is the number of case (415 for here); $\zeta_{a\text{-}calc}$ and $\zeta_{a\text{-}test}$ are separately the fitted values and tested values for aerodynamic damping.

$$\zeta_a = \lambda(\frac{1}{4\pi}\frac{\rho_a}{\rho_s}\frac{B}{D}\frac{\overline{U}}{f_0\sqrt{BD}}\zeta_s^{0.15}\left(\frac{H}{B}\right)^{0.5} C_D - 0.002) \tag{2}$$

Here, drag coefficient C_D adopts 1.05; λ is modification coefficient of cross section, as λ=1.0 for square building, with λ for other cases and corresponding standard error shown in Table 3.

Table 3 Fitting parameter of aerodynamic damping for corner-cut and tapering high-rise buildings

	Slot rate 5%	Slot rate 10%	Slot rate 20%	Chamfer rate 5%	Chamfer rate 10%	Chamfer rate 20%	Taper rate 1%	Taper rate 3%	Taper rate 5%
λ	0.38	0.44	0.75	0.30	0.53	1.10	0.71	1.17	1.26
$\delta_{\zeta ai}$	0.8×10^{-3}	1.2×10^{-3}	1.1×10^{-3}	1.2×10^{-3}	1.2×10^{-3}	1.7×10^{-3}	0.9×10^{-3}	1.5×10^{-3}	1.0×10^{-3}

4 CONCLUSION

46 aeroelastic model tests are conducted to study the effects of important factors on along-wind aerodynamic damping ratios using RDT method with four parameters. The influences of density ratio, generalized stiffness, structural damping ratio, aspect ratio, side ratio, roughness exposure, aerodynamically modified cross-sections and tapering on aerodynamic damping are investigated. All parameters of high-rise building, which could affect aerodynamic damping, are systematically taken into consideration. The following conclusion can be drawn:

1 Aerodynamic damping ratio gradually increases slower with reduced velocity in exposure category A、B、C、D. But overall, wind environment has no clear effect on along-wind aerodynamic damping, which may be caused by the similar profiles of wind velocity (Chinese code) and turbulence intensity (AIJ2004) for this height of building. So, the influence of roughness exposure still needs further research.
2 For side ratios $B/D\geq1$, aerodynamic damping ratio increases with side ratio; for side ratios $B/D\leq1$, there is no clear variation in aerodynamic damping ratio with side ratio. In addition, along-wind aerodynamic damping can be well predicted by quasi-steady theory.
3 Structural damping ratio and aspect ratio has great influence on aerodynamic damping. Aerodynamic damping ratio gradually increases slower with wind velocity as aspect ratio increases. At reduced wind velocity lower than 10, aerodynamic damping ratio increases as aspect ratio increases; while at reduced wind velocity higher than 10, opposite trend is observed.
4 Although density ratio and generalized stiffness all reflect in change of structural damping, the impact of density ratio is relatively significant while no clear effect of generalized stiffness can be observed.
5 The effects of slotted corner and chamfered corner on aerodynamic damping ratio are similar; aerodynamic damping ratio increases with corner-cut ratio, as corner-cut ratio of 5% and 10% significantly decrease aerodynamic damping, while there's little difference between square building and cases with corner-cut ratio of 20%.
6 Aerodynamic damping ratio increases as taper rate increases; taper rate of 1% reduces aerodynamic damping, but taper rate of 3% and 5% increase aerodynamic damping.
7 Modifications of building corners and tapering are not always effective at reducing the aerodynamic damping of tall buildings.

Structural damping ζ_s, density ratio ρ_s/ρ_a, side ratio B/D, reduced velocity $V_H/f_0(BD)^{0.5}$, aspect ratio $H/(BD)^{0.5}$, aerodynamically modified cross-sections and tapering are important effects for aerodynamic damping ratio in along-wind, while the influence of generalized stiffness is not

so significant. Through fitting of estimated aerodynamic damping ratios, an empirical aerodynamic damping function for high-rise buildings is proposed with taking effects of structural damping, aspect ratio and modification of cross section into quasi-steady theory.

5 ACKNOWLEDGEMENTS

The author would like to gratefully acknowledge the support of the National Natural Science Foundation of China (50878159, 90715040) and Special Research Fund for Doctoral Program of Senior School by the Minstry of Education of China (200802471005).

6 REFERENCES

[1] A.G. Davenport, The influence of Turbulence on the Aeroelastic Responses of Tall Structures to Wind, in IAHR-IUTAM Symp. Pract. Exp. with Flow Ind. Vib, Germany, Karlsruhe, University of Karlsruhe, 1979, pp.681-695.
[2] J.D. Holmes, Along-wind response of lattice towers—II: Aerodynamic damping and deflections, Eng. Struct., 18 (1996): 483-488.
[3] J.D. Holmes, Wind loading of structures, E & FN Spon, London, 2001.
[4] R.D. Gabbai and E. Simiu, Aerodynamic damping in the along-wind response of tall buildings, J. Struct. Eng., 136 (2010): 117-119.
[5] H. Marukawa, N. Kato, K. Fujii and Y. Tamura, Experimental evaluation of aerodynamic damping of tall buildings, J. Wind Eng. and Ind. Aerodyn., 59 (1996): 177-190.
[6] K.R. Cooper, M. Nakayama, Y. Sasaki, A.A. Fediw, S. Resende-Ide and S.J. Zan, Unsteady aerodynamic force measurements on a super-tall building with a tapered cross section, J. Wind Eng. and Ind. Aerodyn., 72 (1997): 199-212.
[7] 全涌, 超高层建筑横风向风荷载及响应研究, 上海, 同济大学, 2002.
Y. Quan. Across-wind loads and responses on super high-rise buildings, Shanghai, Tonji University, 2002.
[8] 全涌, 顾明, 方形断面高层建筑的气动阻尼研究, 工程力学, 21 (2004): 26-30+47.
Y. Quan and M. Gu, Wind tunnel test study of aerodynamic damping of super highrise buildings, Eng. Mech., 21(2004): 26-47.
[9] Y. Quan and M. Gu, Experimental evaluation of aerodynamic damping of square super high-rise buildings, Wind and Struct., 8(2005): 309-324.
[10] M. Gu and Y. Quan, Across-wind loads of typical tall buildings, J. Wind Eng. and Ind. Aerodyn., 92(2004): 1147-1165.
[11] 邹浩良, 梁枢果, 顾明, 高层建筑气动阻尼评估的随机减量技术, 华中科技大学学报 (城市科学版), 20 (2003): 30-33.
L.H. Zou, S.G. Liang and M. Gu, Evaluation of aerodynamic damping in wind-induced vibration of tall buildings by random decrement technology, J. Hu St. (Urban Science Edition), 20(2003): 30-33.
[12] A. Kareem, T. Kijewski and Y. Tamura, Mitigation of motions of tall buildings with specific examples of recent applications, Wind Struct., 3(1999): 201-251.
[13] Y.M. Kim and H. Kawai, Aerodynamic methods for reducing bending and torsional vibrations of tall building, Proc. 10th Int. Con. on Wind Eng., Denmark, Copenhagen, 1999, pp. 673– 667.
[14] Y.M. Kim and K.-P. You, Dynamic responses of a tapered tall building to wind loads, J. Wind Eng. and Ind. Aerodyn., 90(2002): 1771-1782.
[15] 黄鹏, 顾明, 全涌, 高层建筑气动阻尼的实验研究, 第十二届全国结构风工程学术会议, 2003, pp. 359-364.
P. Huang, M. Gu and Y. Quan, Wind tunnel study of aerodynamic damping of super high-rise buildings, Proc. 12th National Conf. on Struct. Wind Eng., 2003, pp. 359-364.
[16] GB50009-2001, 建筑结构荷载规范, 中国, 2001.
GB50009-2001, Architectural structure load standards load code, China, 2001.
[17] AIJ 2004 Recommendations for Loads on Building, Architectural Institute of Japan, 2004.
[18] Y. Tamura and S.Y. Suganuma, Evaluation of amplitude-dependent damping and natural frequency of buildings during strong winds, J. Wind Eng. and Ind. Aerodyn., 59 (1996): 115-130.

The Seventh International Colloquium on Bluff Body Aerodynamics and Applications (BBAA7)
Shanghai, China; September 2-6, 2012

A reliability approach for the wind-induced response assessment of tall buildings using the high frequency force balance

E. Bernardini [a], S.M.J. Spence [a], M. Gioffrè [b], A. Kareem [a]

[a] *NatHaz Modeling Laboratory, University of Notre Dame, Notre Dame IN, USA*
[b] *University of Perugia, via G.Duranti 93, Perugia, Italy*

ABSTRACT: The high frequency force balance is a versatile and widely used method for estimating the wind-induced response of tall buildings. Nevertheless, the estimates of the response parameters are inevitably affected by uncertainties essentially due to the lack of knowledge on the forces acting over the building height. Also, the usage the method is often hindered by the impossibility of considering more than three modes in the response assessment. In this paper a novel methodology is presented that allows to overcome the aforementioned shortcomings through the definition of a reliability framework in which the uncertainties arising from the use of the high frequency force balance are taken into account. The application to a case study building with coupled and non-linear modes shows the effectiveness of the method in providing safe estimates of the response parameters considering exclusively the base measurements.

KEYWORDS: Wind loading; Reliability models, Tall buildings, HFFB technique.

1 INTRODUCTION

The high frequency force balance (HFFB) is one of the most widely adopted techniques for the assessment of the wind-induced response of tall buildings, especially because the measurement of the base moments constitutes a relatively easy way to assess the overall action of the wind on the structure. Over the years, a number of methodologies have been proposed in the literature that are aimed at providing estimates of the structural responses commencing from the measured base moments. In most cases, this scope is attained through the identification of expressions that yield a set of correction coefficients that, applied to the three measured base moments, allow the estimation of the first three generalized forces [1, 2, 3, 4, 5]. These coefficients depend on the mode shapes of the building – therefore termed mode shape correction (MSC) coefficients – and on the pressure field acting over the building surface that, being unknown, has to be hypothesized. In the case of buildings with uncoupled fundamental modes it has been seen that these methodologies are able to provide good results in the estimation of structural response parameters [6, 7]. When the modes are coupled, in general, things become more involved and the estimates of the first three generalized forces and then of the response parameters are strongly affected by the assumptions made on the pressure field when estimating the MSC coefficients [6, 7]. It is worth underlining that, in any case, only the contribution of the fundamental modes is included in the response assessment: in general, while this is not a problem for the resonant response component, the background response can be affected by significant errors [8]. Indeed, it is common practice to use the HFFB technique only with the purpose of estimating the resonant response and not in order to obtain estimates of the background response. Different techniques that are not based on MSC coefficients, and are in general more complex from an applicative

point of view, have also been proposed [9, 10, 11]. In these cases, any number of modes can be included in the response calculation of the pressure field, but the necessity of hypothesizing the pressure field remains. Indeed, any method adopted for the assessment of the wind induced response starting from a set of base measurements is inevitably affected by what can be termed aerodynamic uncertainties [12], that is by the uncertainties generated by the lack of knowledge on the pressure field. These uncertainties propagate to the response parameter estimates, producing errors that can be significant [7], especially for tall buildings characterized by complex geometric shapes. As for the estimation of the mean response, when pressure measurements are unavailable the traditional approach consists in hypothesizing the distribution of the mean floor loads over the height of the building (linked to conventionally defined mean pressure profiles) and to calibrate it with the information at the base of the building [11]. In alternative, the method proposed in [13] exploits the definition of a power law model for the mean wind forces in order to define correction coefficients used to estimate mean values of the first three generalized forces. In any case, aerodynamic uncertainties result to be introduced also in the estimates of the mean responses.

A first step towards overcoming some of the aforementioned limitations of the HFFB technique has been proposed in [12], where the effect of the aerodynamic uncertainties on the resonant response was taken into consideration. In particular, a reliability framework was identified in which the aerodynamic uncertainties, and so their influence on the estimated response acceleration parameters, could be included.

The objective of this work is to further develop the approach proposed in [12]. This is done by firstly introducing a novel model for the probabilistic description of the mean. Secondly, a description of the correlation structure of the pressure field is carried out, which is more complete than the model presented in [12]. This allows the inclusion in the modal analysis of any number of modes, and therefore the probabilistic modeling of the total background response. To show the effectiveness of the proposed approach, a case study building characterized by a complex geometric form and non-linear coupled mode shapes is considered.

2 THE RELIABILITY FRAMEWORK

The aim of this section is to present the reliability framework in which the proposed approach for taking into account the aerodynamic uncertainties is set.

The fragility F for a generic response component R can be defined as the following conditional probability of exceedance of the response level $\widetilde{R}$ [14]:

$$F = P(R_{max} > \widetilde{R} \mid \mathbf{v}) \tag{1}$$

where $\mathbf{v} = \{U_H, \alpha\}$ is the vector of the hazard intensity with U_H the mean wind speed at the top of the building and α the wind direction while R_{max} is the peak value of the response process $R(t)$ for $t \in [0, T]$ where T is the observation period. The probability of exceedance $P_{f,R}$ can then be expressed in terms of the fragility as

$$P_{f,R} = \int_{D'} F(\mathbf{v}) \cdot p_{\mathbf{v}}(\mathbf{v}) d\mathbf{v} \tag{2}$$

where D' is the domain of all the possible hazard intensities while $p_{\mathbf{v}}$ is the probability density function of the hazard. Because $R(t)$ may be considered a stationary process, R_{max} with specified exceedance probability is given by:

$$R_{max} = \mu_R + g_R \sigma_R = \mu_R + \sqrt{g_{Rb}^2 \sigma_{Rb}^2 + g_{Rr}^2 \sigma_{Rr}^2} \tag{3}$$

where g_R is the peak value of the normalized (zero-mean and unit-variance) response process for $t \in [0, T]$, μ_R is the mean value, σ_R is the standard deviation while the subscript b and r indicate the background and resonant response component respectively. The estimates of μ_R and σ_R are traditionally considered unaffected by loading model uncertainties, resulting in a fragility only depending on g_R. Indeed, this is commonly done when choosing a deterministic model for the unknown pressure field over the building surface. On the other hand, if aerodynamic uncertainties are taken into account, the fragility can be re-written as:

$$F = 1 - \int_D p_{\mu g \sigma|\mathbf{v}}(\mu_{R,} g_R, \sigma_R) \cdot dD \tag{4}$$

where $p_{\mu g \sigma|\mathbf{v}}$ is the joint probability density function of μ_R, σ_R and g_R, conditional on the wind hazard intensity, and D is the domain where $R_{peak} < \tilde{R}$.
If the random variables μ_R, g_R and σ_R are considered independent, then

$$p_{\mu g \sigma|\mathbf{v}}(\mu_R, g_R, \sigma_R) = p_{\mu|\mathbf{v}}(\mu_R) p_{g|\mathbf{v}}(g_R) p_{\sigma|\mathbf{v}}(\sigma_R) \tag{5}$$

Therefore, to calculate the fragility it is necessary to estimate the marginal distributions $p_{\mu R}|\mathbf{v}(\mu_R)$, $p_{gR}|\mathbf{v}(g_R)$ and $p_{\sigma R}|\mathbf{v}(\sigma_R)$. The PDF $p_{gR}|\mathbf{v}(g_R)$ has been widely studied; under the hypotheses of stationary and Gaussian process, it can be expressed by the following

$$p_{gR|v}(g_R) = g_R \nu_0 T \exp\left[-1/2 g_R^2 - \nu_0 T \exp\left(-1/2 g_R^2\right)\right] \tag{6}$$

where v_0 is the mean zero-crossing rate, approximated by the first natural frequency of the building. Approaches for estimating the marginal distributions $p_{\mu R}|\mathbf{v}(\mu_R)$ and $p_{\sigma R}|\mathbf{v}(\sigma_R)$, are proposed in the following Section 3.

3 PROPOSED MODEL

3.1 *General features*

The aim of this section is to illustrate the proposed models for the propagation of the aerodynamic uncertainties in the floor loads to the structural mean and dynamic response. To reach this objective, models for the unknown floor loads (mean values and spectral structure) depending on a limited set of parameters are defined. Different values assumed by the parameters describe, although in an approximate fashion, all the possible floor load structures for every possible building and flow field. Secondly, the marginal PDFs and correlation structures for the random vectors collecting the parameters are assigned. If a large number of floor load structures would be known for buildings of different shapes and in different surrounding environments, the marginal PDFs of the governing parameters could be obtained by fitting the set of available data with the floor load model. Due to the insufficiency of this kind of data, the models for the statistical properties of the random parameters are only based on the knowledge of the physics of the problem, therefore it is of key importance that the governing parameters have a clear physical meaning.

3.2 *Model for the mean response*

With the aim of identifying the marginal PDF $p_{\mu R}|\mathbf{v}(\mu_R)$ introduced in Equation (5), in this section a probabilistic model of the unknown mean floor load distribution over the height of the building, calibrated through the five measured base reactions, is proposed. The basic idea is to use a Monte Carlo simulation to study the propagation of the uncertainties in the mean response parameters, μ_R, starting from the probabilistic description of a limited number of parameters that govern the mean floor load field.

3.2.1 *Model for the along-wind direction*

The floor loads in the along-wind direction, F_{Li}, $i = 1, \ldots, n$, where n is the number of the floors, are expressed in terms of the mean wind speed profile $U_i = U(z_i)$ and of the force coefficients in the along-wind direction c_{Li} at different heights z_i, as follows:

$$F_{L,i} = 1/2 \rho U_i^2 c_{Li} h_i L_{\alpha i} \tag{7}$$

where h_i is the height of the tributary area of the ith floor, $L_{\alpha i}$ is the width of the building orthogonal to the wind direction at height z_i and ρ is the air density. The mean wind speed profile indicated by the European Standards [15] is assumed. In this model, the vector of the random variables, $\{c_L\}$, contains the n values of the force coefficients, one for each floor:

$$\{c_L\} = \{c_{L1}, c_{L2}, \ldots c_{Ln}\} \quad \text{with} \quad c_{L,\min} \le c_{Li} \le c_{L,\max} \tag{8}$$

where $c_{L,min}$ and $c_{L,max}$ are the limits assigned to the force coefficients and can be fixed based on the knowledge of the physical phenomenon. The limits for the range of variability of the F_{Li} are consequently fixed and a range of possible values for the floor loads is obtained from Equations (7) and (8). Due to the lack of information on the actual value of the pressures over the building surface, a uniform distribution is adopted as marginal distribution for each random variable. As for the correlation structure of the random vector $\{c_L\}$, it can be observed that the degree of correlation among two force coefficients c_{Li} (at z_i) and c_{Lj} (at z_j) is in general very low if marked changes in the geometry of the building occur between the two floors at z_i and z_j. To account for this physical phenomenon, the floors of the building are grouped into n_g ideal sectors, based on the changes of geometry over the height of the building. Then, full correlation is assigned between all the force coefficients belonging to the same sector, while the coefficients of different sectors are considered uncorrelated. It should also be observed that the mean forces resulting from one realization of the random vector $\{c_L\}$ will not, in general, respect the base equilibrium conditions (shear and moment). To take this into account, only the randomly generated vectors that satisfy both the equilibrium equations (within a certain tolerance) are considered, while the others are rejected. As a result of this selection process, the marginal distributions of the c_{Li} are no longer uniform.

3.2.2 *Model for the across-wind direction*

For the across-wind direction the procedure adopted is substantially the same as for the along-wind direction. The floor load components, F_{Ci}, are defined in terms of the coefficients c_{Ci}, that can have positive or negative values. The following relation is adopted:

$$F_{C,i} = 1/2 \rho U_H^2 c_{Ci} h_i L'_{\alpha i} \tag{9}$$

where $L'_{\alpha i}$ is the width of the building parallel to the wind direction at height z_i. If the geometry of the building is symmetric with respect to a vertical plane containing the oncoming flow direction, the mean force coefficients are expected to be zero over the height of the building. Nevertheless, asymmetries in the geometry can generate non-zero mean across-wind forces. For this reason, the limiting values of c_{Ci} are set as $c_{C,max}$ and $c_{Cmin} = -c_{Cmax.}$. Considerations analogous to the along-wind case hold (the division of the buildings in sectors and the respect of the base equilibrium conditions).

3.2.3 *Model for the torsional component*

Because the torsional loads are generated by the two translational forces when their action is eccentric with respect to the vertical axis of the reference system, for the torsional component the random variables are the normalized eccentricities of the floor loads e^n_{si} ($s = x,y$) defined as:

$$e^n_{si} = e_{si} / L_{si} \tag{10}$$

where e_{si} is the eccentricity of the floor load F_{si} while L_{si} is the width of the building at the ith floor (in direction perpendicular to the s direction). At each floor, the hypothesized torsional force $F_{\theta i}$ can be calculated from:

$$F_{\theta i} = F_{yi} e^n_{xi} L_{xi} - F_{xi} e^n_{yi} L_{yi} \tag{11}$$

where the forces F_{yi} and F_{xi} are obtained by simply projecting the F_{Li} and F_{Ci}, generated as illustrated in 3.2.1 and 3.2.2, on the reference system xy. By fixing the limits for the values of the normalized eccentricities $e^n_{s,max}$ and $e^n_{s,min} = -e^n_{s,max}$ a range of possible values is obtained for the random variables. The limits for the values of the vector of the hypothesized torsional forces result from both the limits on the eccentricities and the limits obtained for the along and across-wind floor loads. Akin to what was done for the along- and across-wind coefficients, the generated aleatory vectors $\{e^n_x\}$ and $\{e^n_y\}$ are considered acceptable if the base torsional equilibrium equation is respected, otherwise they are rejected.

3.3 *Model for the dynamic response*

In this section, an approach for estimating the PDF of a response parameter standard deviation σ_R taking into account the propagation of aerodynamic uncertainties is proposed. Similarly to other methods that can be found in the literature, the proposed approach is based on the assumption of a model for the floor load spectral structure. However the method developed herein has three distinct advantages that make it particularly attractive: 1) all the components of the floor load spectral matrix $[S_F]$ are modeled: this allows to take into account any number of modes in the response estimate, without approximations on their shape; 2) the calibration of the spectra is different for each wind direction; 3) the model depends on a limited number of parameters; varying the parameter values all the possible spectral structures of the floor load can be (approximately) described. In particular, the third characteristic allows the model to be used for the estimation, through a Monte Carlo simulation, of the PDF of the response parameter standard deviation. To do this, probabilistic models have to be defined for the parameters that govern the spectral structure of the floor loads.

3.3.1 *Modeling of the floor load spectral structure*

In the proposed approach, the floor load spectrum S_{Fsphl}, i.e. the cross-spectrum between F_{sh} and F_{pl} ($s, p = x,y,\theta$ and $h,l = 1,\ldots,n$), is modeled according to the following expression:

$$S_{Fsphl}(f) = S_{FspHH}(f)\left(\frac{z_h}{H}\right)^{\gamma_s}\left(\frac{z_l}{H}\right)^{\gamma_p}\exp\left(-\frac{k_{zsp} f\left|z_h - z_l\right|}{U_H}\right) \tag{12}$$

where S_{FspHH} is the cross-spectrum between the two top floor forces in direction s and p, γ_s and γ_p are the coefficients that govern the variation of the intensity of the spectrum of the components s and p, respectively, over the height, k_{zsp} is the decay factor in the vertical direction that governs the cross-correlation between two spectra belonging to the sub-matrix $[S_{Fsp}]$ acting at different heights. Equation (12) is the extension to the case $s \neq p$ of the expression proposed in [5] for the spectra S_{Fsshl}.

The floor load spectra defined according to equation (12) depend on the values of the parameters k_{zsp}, γ_s and γ_p and also on the value of S_{FspHH}. In order to eliminate the dependency on S_{FspHH}, it is hypothesized that S_{FspHH} can be obtained by scaling with a proportionality factor, $\alpha_{sp}(f)$, the measured base moment spectrum S_{Msp} (cross-spectrum between the base moments M_s and M_p).

The proportionality factor $\alpha_{sp}(f)$ can then be determined by imposing the equilibrium at the base of the building, once the values for γ_s and k_{zsp} are chosen. In particular, it is imposed that the spectrum resulting from the integration of the spectra S_{Fsphl} over the building height coincides with the spectrum of the measured moments at the base S_{Msp}. The following equations are consequently obtained:

$$\alpha_{sp} = \left[\sum_{h=1}^{n} \sum_{l=1}^{n} \left(\frac{z_h}{H} \right)^{\gamma_s} \left(\frac{z_l}{H} \right)^{\gamma_p} \exp\left(- \frac{k_{zsp} f |z_h - z_l|}{U_H} \right) \right]^{-1} \qquad s, p = \theta \tag{13a}$$

$$\alpha_{sp} = \left[\sum_{h=1}^{n} \sum_{l=1}^{n} \left(\frac{z_h}{H} \right)^{\gamma_s} \left(\frac{z_l}{H} \right)^{\gamma_p} \exp\left(- \frac{k_{zsp} f |z_h - z_l|}{U_H} \right) z_h \right]^{-1} \qquad s = x, y \quad p = \theta \tag{13b}$$

$$\alpha_{sp} = \left[\sum_{h=1}^{n} \sum_{l=1}^{n} \left(\frac{z_h}{H} \right)^{\gamma_s} \left(\frac{z_l}{H} \right)^{\gamma_p} \exp\left(- \frac{k_{zsp} f |z_h - z_l|}{U_H} \right) z_h z_l \right]^{-1} \qquad s, p = x, y \tag{13c}$$

In this way, the dependency on S_{FspHH} is eliminated and all the spectra of the matrix $[S_F]$ can be modeled by fixing values for the 9 parameters γ_s and k_{zsp}.

3.3.2 *Response prediction*

The probabilistic approach illustrated in 3.3.1, being based on the modeling of the entire floor load spectral structure $[S_F]$, allows the assessment of any number of generalized force spectra as:

$$S_{Qij} = \{\Phi^i\}^T [S_F] \{\Phi^j\} \tag{14}$$

Therefore, any number of modes can be taken into account in the assessment of the structural response. Equation (14) will be used for the assessment of the resonant response, while to calculate the total background component of the response, R_b, the following expression will be adopted:

$$S_{Rb} = \{\Gamma_R\}^T [S_F] \{\Gamma_R\} \tag{15}$$

where S_{Rb} is the spectrum of the background response and $\{\Gamma_R\}$ is the vector of the influence coefficients of the response R.

3.3.3 *Modeling of the parameters*

In the proposed probabilistic model, the 9 parameters γ_s and k_{zsp} that govern the floor load spectrum model of Equation (12) are the components of a random vector whose marginal distribution and correlation structure have to be assigned. In this work, extending what proposed in [12], the marginal distributions of the governing parameters are obtained through the definition of analytical models describing the range of physically meaningful floor load correlation structures.

By observing that the value of k_{zss} is directly related, through the cross-power spectral densities S_{Fsshl}, to the level of correlation between the floor load F_{sh} (acting at z_h) and F_{sl} (at z_l), the distribution of k_{zss} can be chosen as to result in a uniform distribution of the correlation coefficient at a selected distance $D_{hl} = |z_h - z_l|$. The link between the correlation coefficient of the forces F_{sh} and F_{sl}, $r_{sshl} = \sigma^2_{sshl} / \sigma_{sshh}\sigma_{ssll}$, and the parameter k_{zss} can be found using Equation (12). With some simplifications it is possible to obtain:

$$r_{sshl} = \sigma^2_{sshl} / \sigma_{sshh}\sigma_{ssll} = \int_0^\infty S_{FssHH}(f)\exp(-k_{zss} f D_{hl} / U_H)df \Big/ \int_0^\infty S_{FssHH}(f)df \tag{16}$$

where σ^2_{sshh}, σ^2_{ssll} and σ^2_{sshl} are the variances and covariances of the forces $F_{sh}(t)$ and $F_{sl}(t)$. Having stated this, the marginal distribution of k_{zss} can be chosen as to result in a uniform distribution of the correlation coefficient between the floor loads at a selected distance D. In Equation (16), S_{FssHH} can be obtained by imposing the equilibrium of the moments at the base of the building. Considering for instance $s = x$, the relation

$$S_{Myy}(f) = \int_0^\infty \int_0^\infty S_{Fxxhl}(f) z_h z_l dz_h dz_l = \frac{S_{FxxHH}(f)}{H^{2\gamma_x}} \int_0^\infty \int_0^\infty z_h^{\gamma_x+1} z_l^{\gamma_x+1} \exp\left(\frac{-k_{zss} f |z_l - z_h|}{U_H}\right) dz_h dz_l \tag{17}$$

can be used to estimate S_{FxxHH} from the knowledge of the spectrum S_{Myy}. Analogous equations hold for the other components. It should be noted that the relation between the correlation coefficient and k_{zss} depends also on the value of γ_s, but this dependency is extremely weak and can therefore be neglected [17]. The choice of a uniform distribution for r_{sshl} ensures an impartial description of the unknown correlation between the forces, for which precise statistical information is extremely scarce. The proposed model for the marginal distribution of k_{zss} depends on D: it is suggested that this should be taken within the same order of magnitude of the average integral turbulence scales of the oncoming unsteady flow [12]. Considering the marginal distributions for the parameters k_{zsp}, with $s \neq p$, that govern the decay of the correlation between two floor loads acting in different directions, the simplest possibility is to assume their values as intermediate between k_{zss} and k_{zpp}. In this way, the k_{zsp} cease to be independent random variables. More in-depth studies on the nature of the cross-correlation between forces acting in different directions would be necessary in order to establish a more sophisticated model for these parameters.

Analogously to the k_{zsp}, the γ_s have a well-defined physical meaning: as their value passes from -1 to ∞ the energy of the floor loads progressively moves from the bottom to the top of the structure. Having said this, physically meaningful marginal distributions of the components γ_s can be obtained by imposing a suitable distribution of the value of the auto-spectrum S_{Fsshh} for each frequency (or of the floor load variance σ^2_{sshh}) at a fixed height $0 < z_d < H$. Exploiting indications in the literature concerning the most probable ranges of values for the floor load variances (normalized to the value at the top of the building), in [12] the authors suggested to assume for the floor load variance σ^2_{sshh} a PDF with uniform value between $\sigma^2_{sshh}(\gamma_s = 0)$ and $\sigma^2_{sshh}(\gamma_s = 0.5)$, and decreasing values outside this region. This leads to a distribution for the parameter γ_s which is well approximated by a lognormal distribution with mode = 0 and standard deviation of the associated normal distribution σ = 0.62. Further details on this model can be found in [12].

4 APPLICATION OF THE PROPOSED APPROACH TO A CASE STUDY

4.1 *Case study*

The Bank of China building, Hong Kong, is considered as a case study (Fig. 1). The footprint is square with a side of 52 m and the top floor height is 286 m. The geometry is irregular, with coupled and non-linear mode shapes (Fig. 1c): this is particularly interesting for the proposed application due to the fact that the use of the HFFB technique in presence of irregular shape and mode coupling can determine significant errors in the estimates of the floor loads [6]. Specific wind tunnel tests were carried out [16] using 126 pressure taps measuring synchronously the surface pressure for various wind directions, ranging from 0° to 360° with 10° increments, with a wind speed of 16 m/s and a sampling frequency of 250 Hz. The model length scale was 1/500.

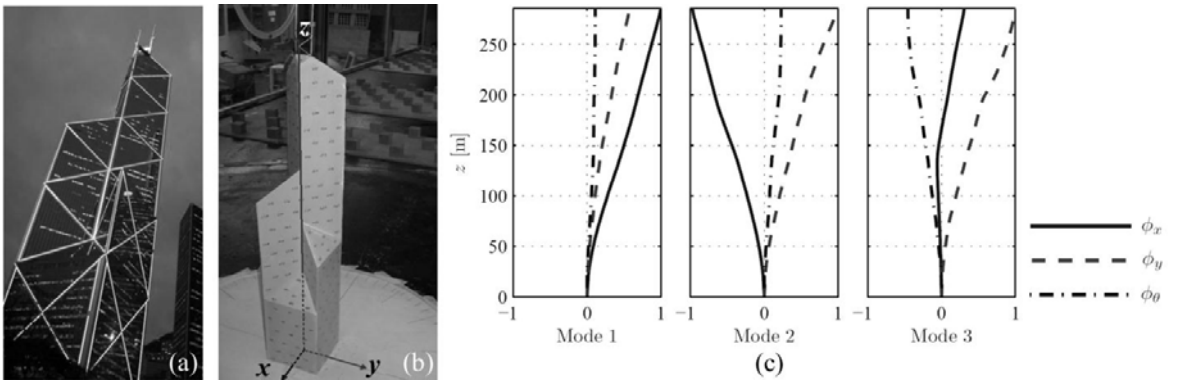

Figure 1. Bank of China building, Hong Kong (a); building model in the wind tunnel (b); mode shapes, with torsional component multiplied by 10 (c).

The pressures were then integrated to obtain virtual base moment measurements; the HFFB technique with the MSC scheme presented in [2] and the approach proposed in this paper were then applied to this virtual set of data to estimate the response parameters. The knowledge of the pressures allowed a reference solution to be determined, to which the approximated results obtained through the HFFB techniques can be compared. The response parameters which are taken into consideration are the top floor acceleration and displacement in the corner at (x_c, y_c) = (-26 m, 26 m). The results are referred to a wind speed of 55 m/s at prototype scale.

4.2 *Results*

For this application the random parameters γ_x, γ_y and γ_θ are assumed fully correlated. Also k_{zxx}, k_{zyy} and $k_{z\theta\theta}$ are assumed fully correlated, with zero correlation between the γ_s and the k_{zsp}. The following values have also been assumed: $D = H/8$, $c_{L,max} = 1.6$, $c_{L,min} = 1$, $c_{Cmax} = -c_{C,min} = 0.8$.

Figure 2 shows a complete overview of the conditional PDFs obtained for the peak values of the response. It is seen that both their mean and their standard deviation vary strongly with the wind angle, according to the directional behavior of the building. For the acceleration (Fig. 2(b)), a bigger spread is seen in the values of the standard deviation of the density functions, than for the displacements (Fig. 2(a)). This can be ascribed to the fact that the resonant response marginal distributions tend to have strong variations for different wind directions.

It is interesting to compare the proposed approach to traditional methodologies (i.e. the MSC approach) and to the reference solution. Figure 3 shows, for $\alpha = 300°$ and $U_H = 55$ m/s, the value of the fragility calculated for different intensities of the peak response. The reference solution is obtained considering the reference (deterministic) value of the standard deviation and of the mean. The solution obtained with the "traditional approach" has been determined through the use of the MSC approach of [2] for the standard deviation and with the approach proposed in [13] for the mean. In all cases the PDF for the peak factor is obtained through Equation 8. The presence of the aerodynamic uncertainties in the proposed approach causes the exceedance probability curve to be softer than the others, where only the uncertainties due to the aleatory nature of the wind loads are taken into account. For different wind directions, while the curves obtained with the traditional approach are not always close to the reference curves, and often lie on the unsafe side, for the proposed approach there is always a value of the fragility which is sufficiently low to give a conservative value of the peak response parameter. This is better seen from Figure 4, where the values of the peak response parameters are plotted for all wind angles and $F = 10\%$.

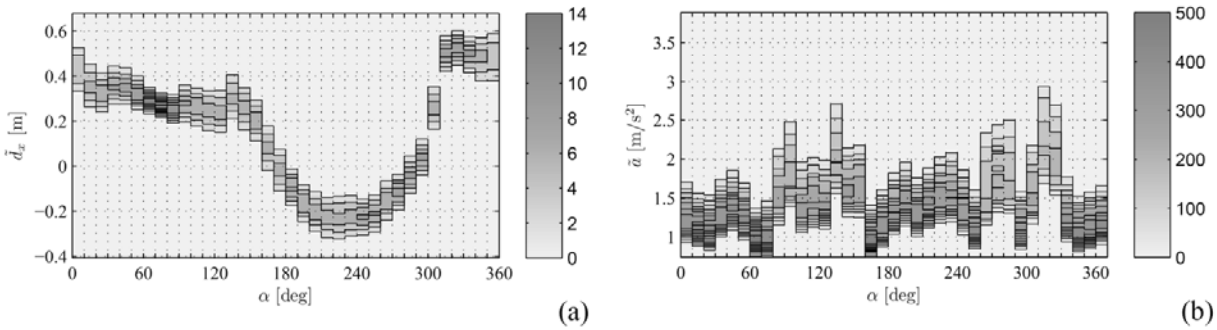

Figure 2. Estimated conditional PDFs of the peak values of the top floor *x*-displacement (a) and acceleration (b), for all wind angles and U_H = 55 m/s.

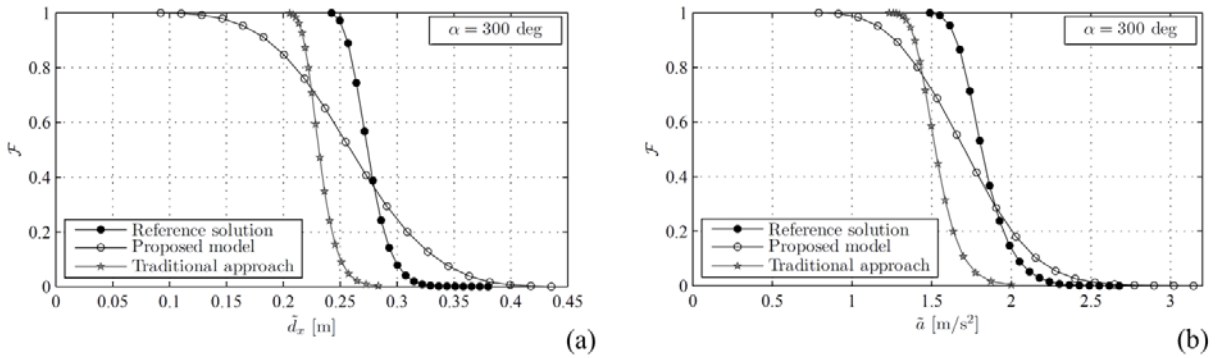

Figure 2. Fragility corresponding to different level of peak response for top floor corner *x*-displacement (a) and acceleration (b), for α = 300° and U_H = 55 m/s.

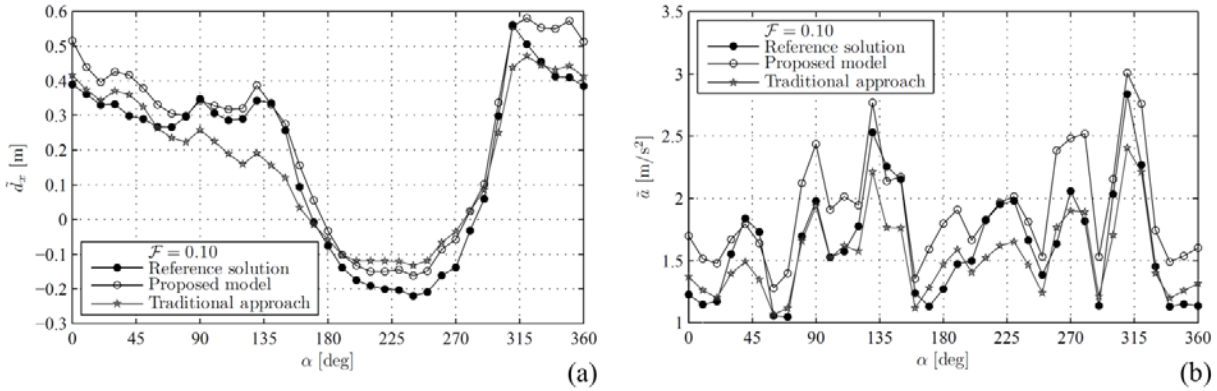

Figure 2. Value of the peak response of the top floor corner x-displacement (a) and acceleration (b) for all wind direction, U_H = 55 m/s and F = 0.10.

5 CONCLUSIONS

In this paper a new method for the estimation of the dynamic response of tall buildings based on HFFB measurements is presented. The methodology is set within a performance-based design framework and attempts to overcome the two fundamental shortcomings of the HFFB method, that is the necessity of making assumptions on the unknown floor loads spectral structure (that introduce aerodynamic uncertainties in the estimated responses) and the impossibility of taking into account higher mode contributions and mean values in the response estimates.

A novel probabilistic approach has been proposed for the assessment of the mean response. Also, for the dynamic response, a new model for the floor load spectral structure has been presented, that gives the possibility of including any number of modal contributions. Both models depend on a limited number of physically meaningful random parameters. By probabilistically modeling the random vector collecting these parameters, the propagation of the aerodynamic uncertainties to the response was achieved. A procedure for the probabilistic characterization of the random vector was presented that, being based on the physical meaning of the governing parameters, results to be independent of the mechanical and aerodynamic performance of the building under consideration. A novel fragility model incorporates both the modeled aerodynamic uncertainties and the aleatory nature of the wind load in the estimation of the peak responses.

An application of the model to a case study building with non-linear coupled modes was presented in terms of the exceedance probabilities of peak responses. A comparison to the traditional approach was made demonstrating the importance of the inclusion of aerodynamic uncertainties in the peak response estimation and the effectiveness of the proposed approach in providing safe design values for the response parameters.

REFERENCES

1. P.J. Vickery, S.C. Steckley, N. Isyumov and B.J. Vickery, The effect of mode shape on the wind induced response of tall buildings, in Proc. 5th U.S. National Conf. on Wind Engineering, Lubbock, Texas, 1985.
2. J. Holmes, Mode shape corrections for dynamic response to wind, Eng. Struct., 9 (1987) 210-212.
3. D. Boggs and J.A. Peterka, Aerodynamic model tests of tall buildings, J. Eng. Mech., 115 (1989) 618-635.
4. Y.L. Xu and K.C.S. Kwok, Mode shape corrections for wind tunnel tests of tall buildings, Eng. Struct., 15 (1993) 387-392.
5. X. Chen and A. Kareem, Equivalent static wind loads on buildings: new model, J. Str. Eng., 130 (2004) 1425-1435.
6. S.M.J. Spence, E. Bernardini and M. Gioffrè, Influence of the wind load correlation on the estimation of the generalized forces for 3D coupled tall buildings, J. Wind Eng. Ind. Aerodyn., 99 (2011) 757-766.
7. E. Bernardini, S.M.J. Spence and M. Gioffrè, Wind load correlation and its effects on the second order response properties of 3D coupled tall buildings, in Proc. 11th National Conf. on Wind Engineering, Spoleto, Italy, 2010.
8. S.M.J. Spence, M. Gioffrè and V. Gusella, Influence of higher modes on the dynamic response of irregular and regular tall buildings, in Proc. 6th Int. Colloquium on Bluff Bodies Aerodynamics and Applications (BBAA IV), Milan, Italy, 2008.
9. T. Ohkuma, H. Marukawa, K. Yoshie, H. Niwa, T. Teramoto and H. Kitamura, Simulation method of simultaneous time-series of multi-local wind forces on tall buildings by using dynamic balance data, J. Wind Eng. Ind. Aerodyn., 54/55 (1995) 115-123.
10. D.Y.N. Yip and R.G.J. Flay, A new force balance data analysis method for wind response predictions of tall buildings, J. Wind Eng. Ind. Aerodyn.,54/55 (1995) 457-471.
11. G. Solari, L. Pagnini and G. Piccardo, A numerical algorithm for the aerodynamic identification of structures, J. Wind Eng. Ind. Aerodyn., 69/71 (1997) 719-730.
12. E. Bernardini, S.M.J. Spence and M. Gioffrè, Dynamic response estimation of tall buildings with 3D modes: a probabilistic approach to the high frequency force balance method, J. Wind Eng. Ind. Aerodyn., In press (2012)
13. X. Chen and A. Kareem, Dynamic wind effects on buildings with 3D coupled modes: Application of high frequency force balance measurements, J. Eng. Mech.,131 (2005) 1115-1125.
14. S.M.J. Spence and M. Gioffrè, Large scale reliability-based design optimization of wind excited tall buildings, Prob. Eng. Mech.,28 (2012) 206-215
15. EN-1991-1-4, Eurocode 1, 2005: Actions on structures, 2005.
16. S.M.J. Spence, Time domain non-Gaussian optimization of wind excited tall buildings under vulnerability contraints, University of Florence and TU Braunschweig: PhD Thesis, 2009.
17. E. Bernardini, Reliability models for tall buildings with coupled modes: a probabilistic approach to the high frequency force balance technique, University of Perugia: PhD Thesis, 2012.

The Seventh International Colloquium on Bluff Body Aerodynamics and Applications (BBAA7)
Shanghai, China; September 2-6, 2012

The effects of freestream turbulence on wind-induced responses of tall buildings

Gang Hu, Q. S. Li

Department of Civil and Architectural Engineering, City University of Hong Kong, Tat Chee Avenue, Kowloon, Hong Kong

ABSTRACT: The turbulence characteristics of natural winds are usually described by turbulence intensity, turbulence scale, and wind velocity spectra. Turbulence intensity reflects fluctuations of wind velocity, which is affected by the degree of surface roughness of the earth. One of the most widely used scales is the integral length scale which is a representation of the average size of the most energetic turbulent eddies. In this paper, three tall buildings with different heights and typical height/width ratios are chosen to investigate the effects of turbulence integral length scale on along-wind responses of the tall buildings. Discussions on the influences of turbulence intensity to the along-wind structural responses are also presented. The results of this study indicate that as turbulence integral length scale increases, the along-wind responses of the tall buildings decrease while the along-wind responses increase obviously with the growth of turbulence intensity.

KEYWORDS: turbulence characteristics; turbulence integral length scale; turbulence intensity; tall building; along-wind response; wind spectra

1. INTRODUCTION

Wind flow in the atmospheric boundary layer of the earth is highly turbulent. As a result, wind loads acting on buildings and structures are significantly influenced by turbulence characteristics. Turbulence integral length scale and turbulence intensity are two main parameters to describe the characteristics of natural wind. Turbulence integral length scale is the measure of average size of the vortices. For wind flows, there are three turbulence integral length scales in three directions (longitudinal, lateral and vertical directions), namely, L_u^x, L_u^y, L_u^z, and they are often expressed as $L_u^y \approx 0.3-0.4L_u^x$, $L_u^z \approx 0.5-0.6L_u^x$ (Counihan 1975). Turbulence intensity is the ratio of the standard deviation of fluctuating component to the mean value of wind velocity. It is related to the surface roughness of the ground. Turbulence integral length scale and turbulence intensity can be defined as follows.

$$L_u^x = \frac{1}{\sigma_u^2}\int_0^\infty R_{u_1u_2}(x)dx \tag{1}$$

$$I_u = \sigma_u / \bar{U} \tag{2}$$

$R_{u_1u_2}(x)$ is the cross-correlation function of fluctuating wind speed component u at two points. σ_u is the standard deviation of wind speed, and $\bar{U}$ is mean wind speed. In boundary layer wind tunnel testing, how to control the value of turbulence integral length scale is a difficult problem. Varshney and Poddar (2011) conducted an investigation on controlling turbulence integral length scale values in a wind tunnel and showed that the integral length scale can be controlled using different combinations of passive devices. However, it is difficult or impossible to generate wind

flows with sufficiently large values of turbulence integral length scale in wind tunnels, even active devices are adopted.

During the past several decades, many researchers have conducted wind tunnel studies on the effects of turbulence on bluff bodies. Lee (1975a) reported that addition of turbulence to the flow causes an increase of base pressure and reduction of the drag of a two-dimensional square cylinder. His experiments showed the strength of the vortex shedding reduces as the growth of turbulence intensity. Lee (1975b) also investigated the effects of turbulence integral length scale on mean forces of square prisms and indicated that the mean drag is sensitive to the variation of turbulence scale when it is around the body size. In addition, at high values of turbulence integral length scale the drag tends to a constant value greater than that at low values. Tieleman and Akins (1990) analyzed the effects of incident turbulence on pressure distributions on rectangular prisms. Their results showed that the pressure coefficients on the side and rear faces of the prisms vary primarily with the energy associated with the small scale turbulence in the incident flow. Laneville (1990) investigated the effect of turbulence scale ratio on pressure coefficients of two dimensional square cylinders, finding that when turbulence scale ratio is larger than three, the turbulence scale effect on mean drag is evident and the magnitude of this effect is about 12%. Nakamura (1993) pointed out that turbulence intensity and turbulence integral length scale have significant effects on pressure coefficients on bluff bodies.

Besides the above studies carried out by wind tunnel experiments, other methods such as full-scale measurements, CFD and structural dynamic analysis were also applied to investigate the wind effect on tall building. It has been recognized that the most reliable evaluations of wind effects are obtained from measurements of prototype buildings. Li et al. (1998, 2004a, 2004b, 2005, 2006), Campbell et al. (2005), among others, have carried out full-scale measurements of wind effects on tall buildings. These investigations provided important validation of design procedures as well as examined structural behavior of tall buildings under wind actions. On the other hand, CFD method becomes more and more attractive to study wind effects on tall buildings (Swaddiwudhipong and Khan 2002; Huang et al. 2007; Tominaga et al. 2008; Braun and Awruch 2009; Huang et al. 2011; Hang and Li 2012) because of low cost compared with wind tunnel testing. In fact, CFD and structural dynamic analysis can overcome the limitations of generating wind flows with sufficiently large values of turbulence integral length scale. Therefore, structural dynamic analysis method is adopted in this paper to investigate the effects of freestream turbulence on wind-induced responses of tall buildings.

2. RELEVANT FACTORS AFFECTED BY TURBULENCE CHARACTERISTICS

Nakamura (1993) indicated that turbulence intensity and integral scale have remarkable effect on pressure coefficients on bluff bodies and concluded that absolute value of base pressure increases with integral scale for 3D square rod, as shown in Fig.1. The effect of turbulence intensity on drag coefficients on bluff bodies has been investigated in the past. The relation of turbulence intensity and drag coefficients (Simiu and Scanlan, 1996), as shown in Fig. 2, is employed in this study. The relationship between base pressure coefficient and drag coefficient is expressed in Eq. (3) (Petty 1979; Laneville 1990).

$$C_D = 0.9 - 0.82C_p \tag{3}$$

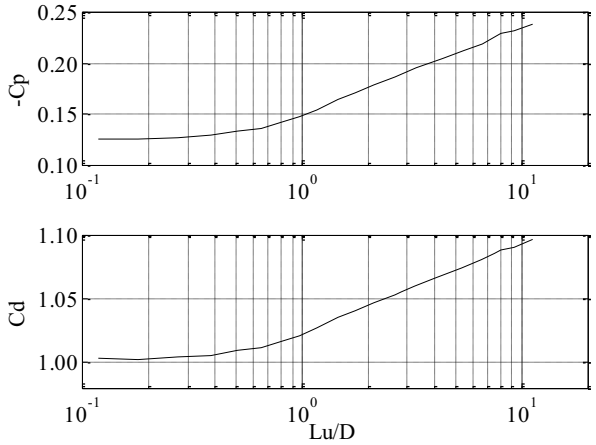

Figure 1. Pressure coefficient vs. turbulence integral scale

It can be seen from Fig. 1 that drag coefficient increases with turbulence integral scale significantly. The growth of drag coefficient will result in larger along-wind responses of

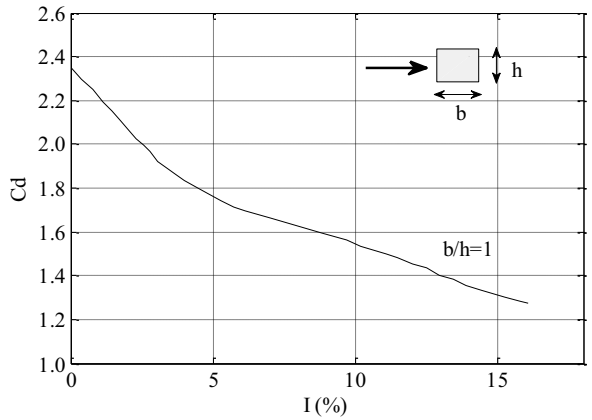

Figure 2. Drag coefficient vs. turbulence intensity (Simiu and Scanlan 1996)

tall buildings. Conversely, the increased turbulence intensity reduces the drag coefficient greatly, which will ultimately lead to the reduction of along-wind response of tall buildings.

In the computation of responses of long-span structures and high rise structures, spatial correlation of wind pressure cannot be ignored. For long-span structures, horizontal spatial correlation should be considered, and vertical spatial correlation can be neglected. On the contrary, for high rise structures, vertical spatial correlation must be taken into account, but horizontal spatial correlation may be ignored. Correlation coefficient ρ is the measurement of spatial correlation. Several empirical formulas for describing the correlation have been proposed. For example, Davenport (1967) presented a correlation function which is related to frequency n and distance between two points as follows:

$$\rho_{zz'}(z,z',n)=\exp(-C_z\frac{n\left|z-z'\right|}{\bar{v}_z})$$
$$\rho_{xx'}(x,x',n)=\exp(-C_x\frac{n\left|x-x'\right|}{\bar{v}_x}) \quad (4)$$

where C_z=7, C_x=8. These two formulas have considered several factors, such as frequency n, distances of two points and average wind speeds, but without turbulence integral scale. The following formulas include the effect of turbulence integral scale on correlation coefficient (Zhang, 2006).

$$\rho_z(z,z') = \exp(-\frac{|z-z'|}{L_z})$$
$$\rho_x(x,x') = \exp(-\frac{|x-x'|}{L_x}) \quad (5)$$

where L_z and L_x are vertical and horizontal turbulence integral scale, respectively. The relationship between correlation coefficient of two points with distance of 50m and turbulence integral scale is shown in Figure 3.

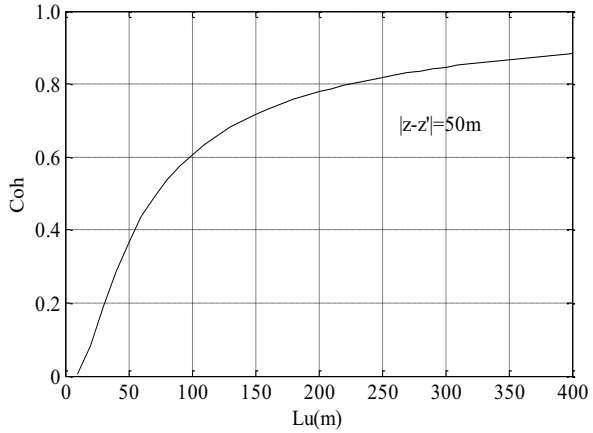

Figure 3. Correlation coefficient vs. turbulence integral scale

From Fig. 3, it can be seen that the correlation coefficient increases as turbulence integral scale increases. It is well known that the strengthening of correlation will lead to the increase of along-wind responses of tall buildings. In other words, an increase of turbulence integral scale may increase the along-wind responses.

Wind velocity spectrum varied with turbulence integral scale and turbulence intensity has significant effects on the wind-induced responses of tall buildings. There are many formulas that have been proposed to describe wind velocity spectrum. One of the widely-used wind velocity spectra was proposed by Von Karman, which is expressed as:

$$\frac{nS_u(n)}{\delta_u^2} = \frac{4\frac{nL_u}{u}}{\left[1+70.8\left(\frac{nL_u}{u}\right)^2\right]^{5/6}} \quad (6)$$

where n is the frequency; $S_u(n)$ is the power spectrum of wind velocity; δ_u is the standard deviation of fluctuating velocity; u is mean wind speed. L_u is the turbulence integral length scale. The variation of the wind velocity spectrum with turbulence integral length scale is presented in Fig. 4. In general, the fundamental frequencies of tall buildings arrange from 0.1 Hz to 2.0 Hz. Fig. 4 shows that the curves of the spectra shift to the left as turbulence integral scale increases, which means that the power of wind spectrum around fundamental frequencies reduces with the growth of integral scale. Thus, from this perspective, the increase of integral scale will result in the reduction of the along-wind responses of tall buildings.

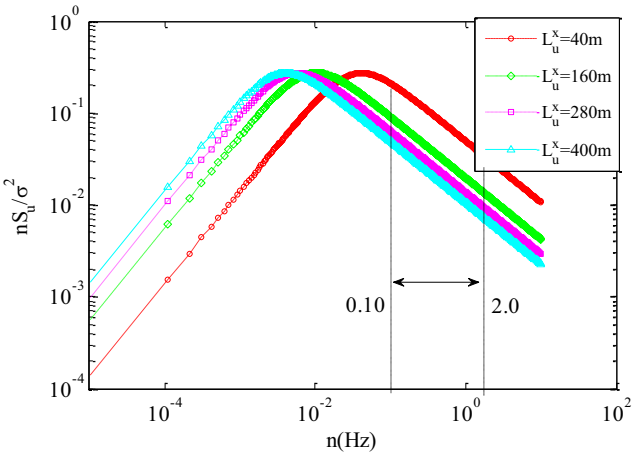

Figure 4. Von Karman spectra with different turbulence integral scales

Another form of Von Karman spectrum involved turbulence intensity is expressed as follow:

$$\frac{nS(z,n)}{v_*^2} = 0.475\beta(z)\frac{x}{(1+x^2)^{5/6}}$$
$$x = \frac{nL_x}{v}, L_x = \frac{vS(z,0)}{0.475\sigma_{vf}}, \sigma_{vf} = \beta(z)v_*^2, \beta(z) = \frac{(I\overline{v})^2}{v_*^2}, v_*^2 = K\overline{v}_{10}^2 \quad (7)$$

where L_x is turbulence integral length scale, I is turbulence intensity. In order to consider the effect of turbulence intensity on wind velocity spectrum, L_x and v_{10} are assumed as constants. The wind spectra with different turbulence intensities are plotted in Fig. 5. As turbulence intensity increases, the wind velocity spectra shift up. This illustrates the increasing power of wind spectra. Therefore, the addition of turbulence intensity will result in the growth of the along-wind responses of tall buildings.

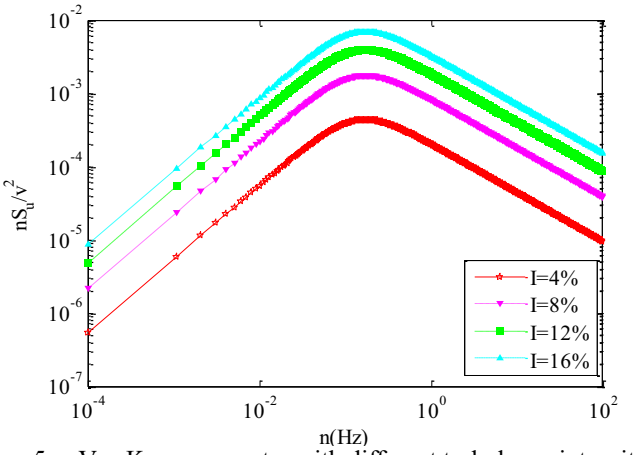

Figure 5. Von Karman spectra with different turbulence intensity

The effects of turbulence on drag coefficient, correlation coefficient and wind velocity spectrum have been discussed. The increase of turbulence integral length scale leads to the growth of drag coefficient and correlation coefficient, which will cause larger along-wind responses of tall buildings. Conversely, in the major frequency range of wind actions on tall

buildings (from 0.1 Hz to 2.0 Hz), the power of wind velocity spectrum reduces significantly as turbulence integral length scale increases, which will result in the reduction of the along-wind structural responses.

So, what on earth is the overall effect of turbulence integral length scale on the along-wind responses of tall buildings? This problem will be investigated in this paper through a detailed structural dynamic analysis. Similarly, the addition of turbulence intensity causes the decrease of drag coefficient but the increase of power of wind spectrum. The former will reduce the along-wind responses of tall building while the latter will increase the responses of tall buildings. This contradiction induces the uncertainty of the effect of turbulence intensity on the along-wind responses of tall buildings, which will also be investigated in this paper.

3. ALONG-WIND RESPONSES OF TALL BUILDINGS

A tall building can be simplified as a Multi-Degrees of Freedom (MDOF) System, the motion equation of a MDOF system subjected to random wind loads is:

$$[M]\{\ddot{y}\}+[C]\{\dot{y}\}+[K]\{y\}=\{F(t)\} \tag{8}$$

where [*M*], [*C*] and [*K*] are $N\times N$ order matrices of mass, damping and lateral condensed stiffness of the structure in along-wind direction. (*N* is the number of the total stories of a building). Since the order of the matrices defined in the above equation is high, the mode superposition method is used for evaluation of wind-induced response of a tall building. Assuming only the lowest N_k modes are considered in the computation, then the structural displacement vector $\{y\}$ is decomposed into

$$\{y\}=[\phi]\{q\}=\sum_{k=1}^{N_k}\{\phi_j\}q_k \tag{9}$$

where $[\phi]$ is the $N\times N_k$ mode shape matrix corresponding to the lowest N_k vibration modes. $\{q\}$ is the generalized displacement vector and q_k is the *k*-th component of vector $\{q\}$.

The power spectrum density (PSD) of the displacement responses at the location of the *i*-th floor (lumped mass) of the building would be

$$S_{yy}(y_{i,}\omega)=\sum_{j=1}^{N_k}\sum_{k=1}^{N_k}\phi_{ij}\phi_{ik}H_j^*(\omega)H_k(\omega)S_{f_jf_k}(\omega) \tag{10}$$

where

$$S_{f_jf_k}(\omega)=\frac{1}{M_j^*M_k^*}\sum_{i=1}^{N}\sum_{l=1}^{N}\phi_{ij}\phi_{lk}S_{F_iF_l}(\omega) \tag{11}$$

$S_{F_iF_l}(\omega)$ is the cross-PSD function of the local along-wind or across-wind load. The frequency response function $H_k(\omega)$ of the *k*-th vibration mode is

$$H_k(\omega)=(\omega_k^2-\omega^2+2i\xi_k\omega\omega_k)^{-1}, i=\sqrt{-1} \tag{12}$$

For tall building structures, the damping ratio is relatively small and the frequency response function distributes sparsely in the frequency domain, therefore the cross-correlation terms in Eq. (10) are usually neglected, which leads to the following approximate expression of Eq. (10)

$$S_{yy}(y_{i,}\omega)=\sum_{k=1}^{N_k}\phi_{ik}^2\left|H_k(\omega)\right|^2\frac{1}{(M_k^*)^2}\sum_{j=1}^{N}\sum_{l=1}^{N}\phi_{jk}\phi_{lk}S_{F_jF_l}(\omega) \tag{13}$$

The PSD of the acceleration response $\ddot{y}_i$ at the *i*-th floor (lump mass) of the building would be

$$S_{\ddot{y}\ddot{y}}(\ddot{y}_i,\omega)=\sum_{k=1}^{N_k}\omega_k^2\phi_{ik}^2\left|H_k(\omega)\right|^2\frac{1}{(M_k^*)^2}\sum_{j=1}^{N}\sum_{l=1}^{N}\phi_{jk}\phi_{lk}S_{F_jF_l}(\omega) \tag{14}$$

The RMS values of displacement response and acceleration response of a building structure would be

$$\sigma_{y_i}^2=\int_0^\infty S_{yy}(y_i,\omega)d\omega \tag{15}$$

and

$$\sigma_{\ddot{y}_i}^2=\int_0^\infty S_{\ddot{y}\ddot{y}}(\ddot{y}_i,\omega)d\omega \tag{16}$$

The along-wind load on each lumped mass can be expressed as

$$S_{F_{xi}F_{xj}}(z_i,z_j,f)=(\rho C_D)^2A_{z_i}A_{z_j}\overline{V}_{z_i}\overline{V}_{z_j}\sqrt{S_V(z_i,f)S_V(z_j,f)}Coh(z_i,z_j,f) \tag{17}$$

where $S_V(z_i, f)$ is the auto-power spectral density of the along-wind fluctuating wind speed, which can be represented by Von Karman spectrum.

4. VERIFICATION OF THE COMPUTATIONAL METHOD

For verification of the above method for calculating the along-wind responses of tall buildings, a typical rectangular building is chosen as a numerical example in this study. This rectangular tall building is a 30-storey steel structure with a cross-section area of $40m\times40m$ and $120m$ height, and the average mass density is approximate $187.5kg/m^3$. Wind tunnel test was carried out for this building to determine the wind forces on the building using pressure measurement technique, and the along-wind, across-wind and torsional responses of the building were calculated based on the model test results (Yoshida et al. 1992). The analytical model of the building for the dynamic analysis was simplified as a cantilever shear column with five lumped masses; each lumped mass has two translational degrees of freedoms (DOFs) in horizontal directions (X and Y direction) and one rotational DOF in vertical (Z) direction, as shown Fig.6. The vertical distribution of the lumped mass of this building is shown in Fig.6 (Yoshida et al., 1992). The fundamental natural frequency of this building is 0.336 Hz in the two translational directions. Damping ratio was assumed to be 1% for all the vibration modes (Wu and Li, 2008).

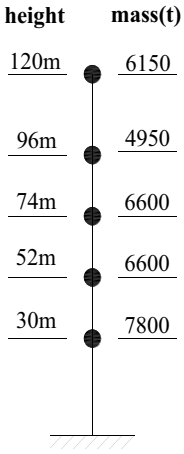

Figure 6. Simplified model of a tall building

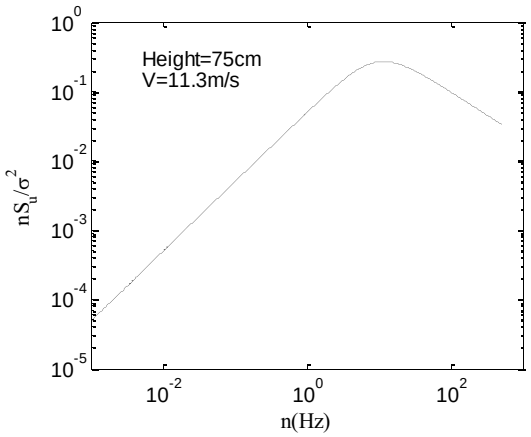

Figure 7. Power spectrum of wind speed in the wind tunnel testing

To examine the reliability of the computational method, two mean wind speeds atop the building, 20m/s and 30m/s, are chosen. The approaching wind direction is normal to one side of the square building. Comparison of the numerical predictions and wind tunnel test results are listed in table 1.

Table 1 Comparison between the numerical results and wind tunnel test results

Acceleration responses	$\sigma_{\ddot{y}}$ (gal)	
Wind speed	20m/s	30m/s
Numerical results	0.665	1.702
Wind tunnel results	0.620	1.913
Difference	7.26%	11.03%

As shown in table 1, the differences between the numerical results and wind tunnel test results are about 10%. Generally, such differences can be accepted in engineering practices, thus verifying the accuracy of the computational method.

5. EFFECTS OF TURBULENCE INTEGRAL LENGTH SCALE ON ALONG-WIND RESPONSES OF TALL BUILDINGS

To investigate the influences of turbulence integral length scale to the along-wind response of tall buildings, three square tall buildings with typical heights, 200m, 300m and 400m, are chosen as study objects, respectively. The models of the three tall buildings are simplified as cantilever shear columns with ten lumped masses; each lumped mass has two translational DOFs in horizontal directions and one rotational DOF in vertical direction. The average mass density is approximate 187.5kg/m^3, and the vertical distributions of the lumped mass of the buildings are shown in Fig. 8.

The fundamental natural frequency and mode shapes of the tall buildings can be calculated by the empirical formulas stipulated in the Chinese Load Code for The Design of Building Structures (2001). Damping ratio was assumed to be 1% for all the vibration modes. The parameters of these three buildings are listed in table 2.

Table 2 Parameters of three tall buildings

Height (H)	200*m*	300*m*	400*m*
Width (D)	40*m*	60*m*	80*m*
Fundamental frequency (f_1) (Hz)	0.200	0.133	0.100

Ten different values of turbulence integral scales at height of 30m above ground are chosen for the calculation, while L_u/D arranges from 1 to 10. In the computation, the variation of turbulence integral length scale with height was described by the empirical formula of AIJ Recommendations for Loads on Buildings (AIJ 2005). This code recommends the following formula.

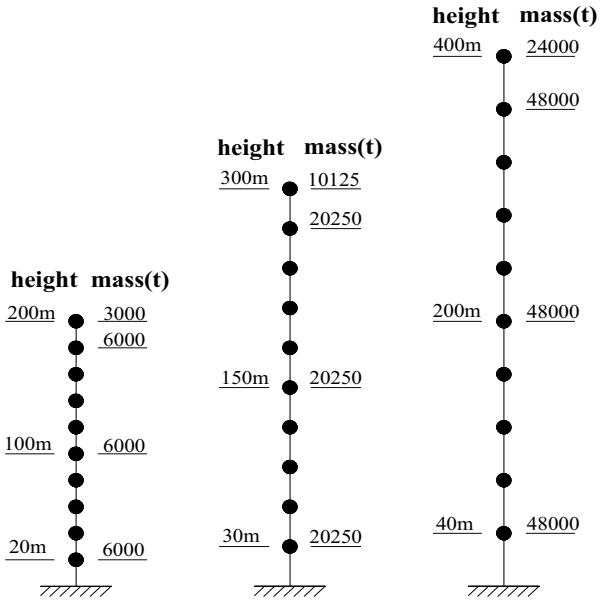

Figure 8. Three simplified models of the buildings

$$L_Z = \begin{cases} 100\left(\dfrac{Z}{30}\right)^{0.5} & 30\text{m}<Z \le Z_G \\ 100 & Z \le 30\text{m} \end{cases} \tag{18}$$

where Z (m) is height above ground; Z_G is a parameter determining the exposure factor. Turbulence integral length scale at one height calculated by this formula is a fixed value. However, the purpose of this paper is to discuss the variation of responses of tall buildings with various turbulence integral scales. So, different turbulence integral length scale profiles are required herein. In order to meet this requirement, the formula proposed by AIJ is modified as follows:

$$L_Z = L_{30}\left(\frac{Z}{30}\right)^{0.5} \tag{19}$$

where L_{30} is turbulence integral length scale at 30m. In this study, the values of L_{30}/D were selected to vary between 1 and 10, and then the integral length scale at other heights can be

calculated by this formula easily. Mean wind speeds at 10m height are supposed to be 20m/s and 40m/s, respectively. Based on the computational procedure presented previously, the along-wind responses of these three tall buildings are calculated, as shown in the following figures.

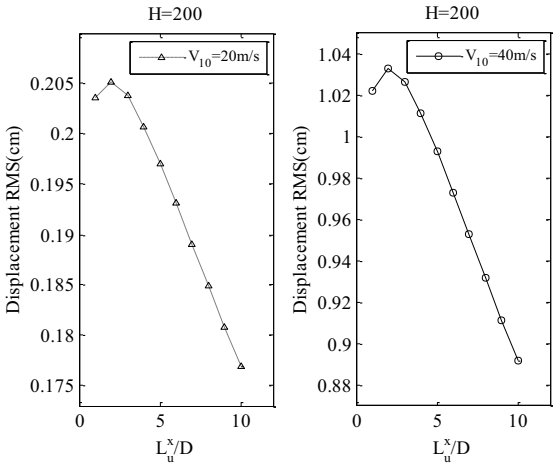

(a) Along-wind displacement responses

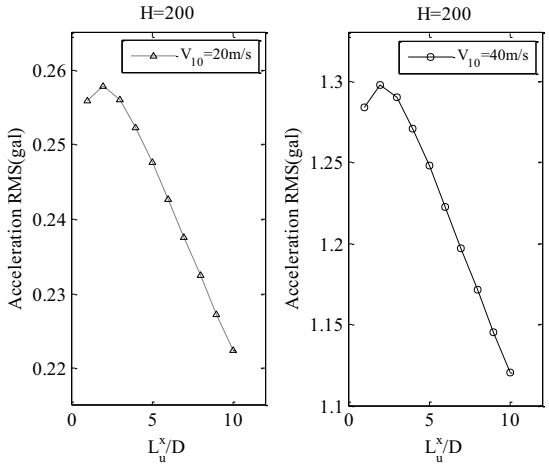

(b) Along-wind acceleration responses

Figure 9. Along-wind responses of a building (200m)

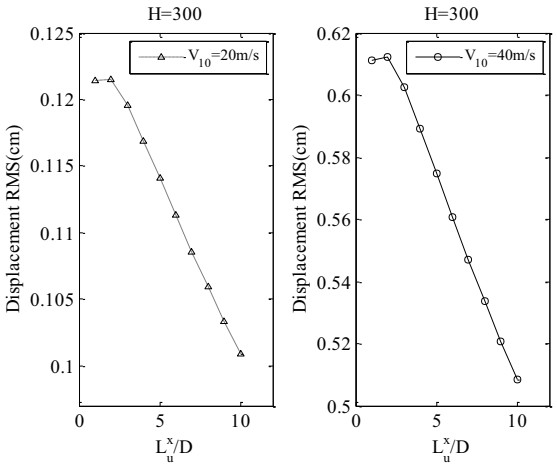

(a) Along-wind displacement responses

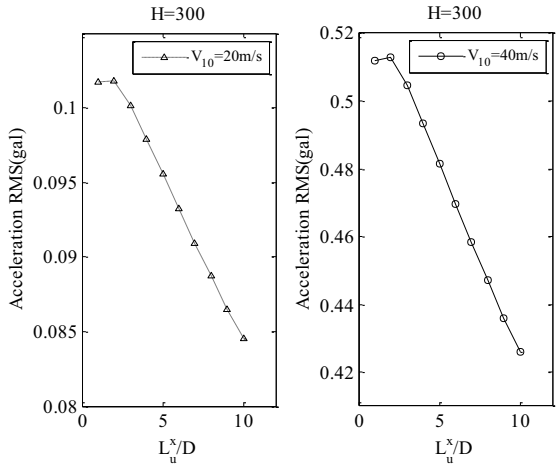

(b) Along-wind acceleration responses

Figure 10. Along-wind responses of a building (300m)

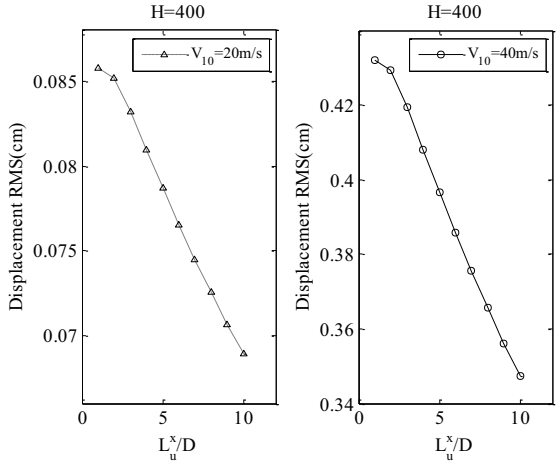

(a) Along-wind displacement responses

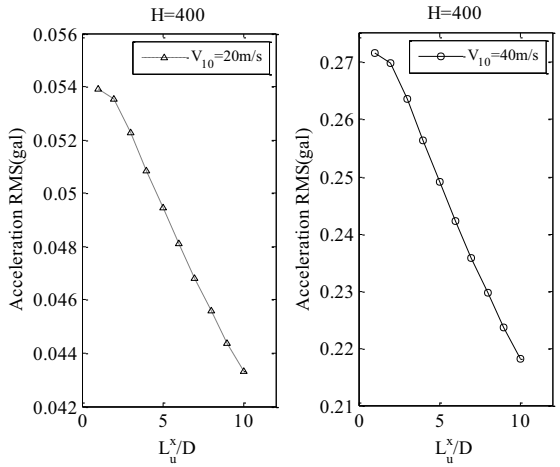

(b) Along-wind acceleration responses

Figure 11. Along-wind responses of a building (400m)

The above figures show the influences of turbulence integral length scale to the along-wind responses of three typical tall buildings with different heights under two wind speeds, namely,

20m/s and 40m/s. Fig. 9 presents the along-wind responses of a tall building where the building height is 200m. It can be seen from the figure that the along-wind responses increase with turbulence integral length scale when L_u/D is less than 2, then the responses reduce significantly with the increase of the integral scale when L_u/D is larger than 2. Similarly, Figs. 10-11 present the relationship between turbulence integral length scales and the along-wind responses of the tall buildings where the building heights are 300m and 400m, respectively. The effects of the integral scales on these two buildings are almost the same with those on the first building (200m). However, the uptrend of the structural responses when L_u/D is less than 2 becomes weaker gradually and eventually this uptrend is changed into downtrend as the building height increases. In conclusion, the along-wind displacement responses and acceleration responses decrease with the increase of turbulence integral length scale, although there are some uncertainties of small turbulence integral scales.

6. EFFECTS OF TURBULENCE INTENSITY ON ALONG-WIND RESPONSE OF TALL BUILDINGS

As discussed previously, the effects of turbulence intensity on drag coefficient and wind velocity spectrum are contradictory. Since these two factors have significant effects on the along-wind responses of tall buildings, it is necessary to examine the overall effects of turbulence intensity on the along-wind responses. Herein, turbulence intensities vary from 2% to 16%. Wind velocity spectrum employed in this study is Von Karman spectrum shown in Eq. (7). The relationship between turbulence intensity and drag coefficients is presented in Fig. 2. Based on the computational procedure given in section 3, the along-wind responses of the three tall buildings under wind actions with different turbulence intensities are shown in Figures 12-13 and Tables 3-4.

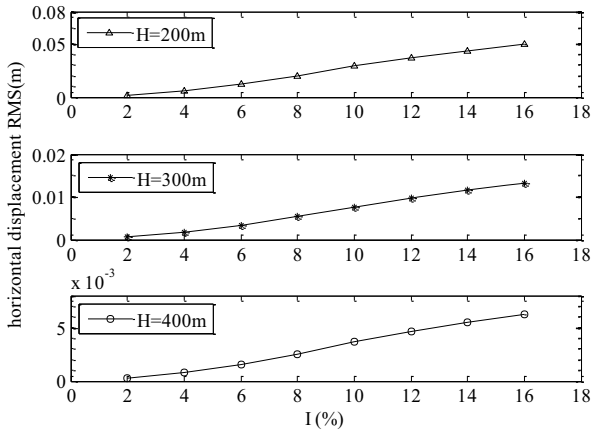

Figure 12. Along-wind displacements vs. turbulence intensities

Table 3 Along-wind displacements under different turbulence intensities

Along-wind displacements (cm)								
	Turbulence intensities							
Height(m)	2%	4%	6%	8%	10%	12%	14%	16%
200	0.2065	0.6385	1.2680	2.0230	2.8940	3.6470	4.3670	4.9740
300	0.0548	0.1694	0.3365	0.5369	0.7680	0.9679	1.1590	1.3200
400	0.0260	0.0804	0.1596	0.2547	0.3643	0.4591	0.5497	0.6261

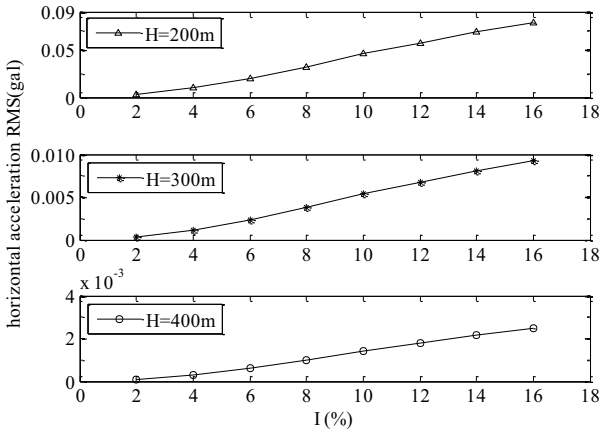

Figure 13. Along-wind accelerations vs. turbulence intensities

Table 4 Along-wind accelerations under different turbulence intensities

Along-wind acceleration (gal)								
	Turbulence intensities							
Height(m)	2%	4%	6%	8%	10%	12%	14%	16%
200	0.003261	0.01008	0.02003	0.03195	0.04571	0.0576	0.06897	0.07856
300	0.000384	0.00119	0.00236	0.00377	0.00539	0.0068	0.00813	0.00926
400	0.000103	0.00032	0.00063	0.00101	0.00144	0.0018	0.00217	0.00247

Fig. 12 shows that the along-wind displacements increase evidently as the addition of turbulence intensity. For the along-wind acceleration responses, there is the same trend as shown in Fig. 13. When turbulence intensity increases from 2% to 16%, the displacement and acceleration responses of the tall buildings raise almost 24 times. So, it is concluded that turbulence intensity has significantly effects on the along-wind responses of tall buildings.

7. CONCLUSIONS

The effects of turbulence on the along-wind responses of tall buildings have been investigated. It was found that turbulence integral length scale and turbulence intensity have significant effects on the along-wind responses of tall buildings. Some conclusions from this study are summarized below.

(1) Along-wind displacement responses and acceleration responses decrease with the increase of turbulence integral length scale, although there are some uncertainties of small turbulence integral scales.

(2) Along-wind displacement and acceleration responses increase evidently as the addition of turbulence intensity. Such effects are so remarkable that the responses rise almost 24 times when turbulence intensity increases from 2% to 16%. Consequently, the effects of turbulence intensity cannot be ignored in the determination of along-wind responses of tall buildings.

8. ACKNOWLEDGEMENTS

The work described in this paper was fully supported by a grant from the Research Grants Council of Hong Kong Special Administrative Region, China (Project No: CityU 117709).

9. REFERENCES

1. GB50009-2001 *Load Code for the Design of Building Structures*, China.
2. AIJ (2005), *Recommendations for Loads on Buildings*,
3. Braun, A.L. and Awruch, A.M. (2009), "Aerodynamic and aeroelastic analyses on the CAARC standard tall building model using numerical simulation", *Computers & Structures*., **87**(9-10), 564-581.
4. Campbell, S., Kwok, K.C.S. and Hitchcock, P.A. (2005), "Dynamic characteristics and wind-induced response of two high-rise residential buildings during typhoons", *J Wind Eng Ind Aerod*., **93**(6), 461-482.
5. Counihan, J. (1975), "Adiabatic atmospheric boundary layers: A review and analysis of data from the period 1880–1972", *Atmospheric Environment (1967)*., **9**(10), 871-905.
6. Davenport, A.G., The dependence of wind loads on meteorological parameters, Proceedings of the International Seminar of Wind Effects on Buildings and Structures, Ottawa, 1967.
7. D. G., Petty. (1979), "The effect of turbulence intensity and scale on the flow past square prisms", *J Wind Eng Ind Aerod*., **4**(3-4), 247-252.
8. Hang, J. and Li, Y. (2012), "Macroscopic simulations of turbulent flows through high-rise building arrays using a porous turbulence model", *Build Environ*., **49**(0), 41-54.
9. Huang, M.F., Lau, I.W.H., Chan, C.M., Kwok, K.C.S. and Li, G. (2011), "A hybrid RANS and kinematic simulation of wind load effects on full-scale tall buildings", *J Wind Eng Ind Aerod*., **99**(11), 1126-1138.
10. Huang, S., Li, Q.S. and Xu, S. (2007), "Numerical evaluation of wind effects on a tall steel building by CFD", *J Constr Steel Res*., **63**(5), 612-627.
11. Laneville, A. (1990), "Turbulence and blockage effects on two dimensional rectangular cylinders", *J Wind Eng Ind Aerod*., **33**(1-2), 11-20.
12. Lee, B.E. (1975a), "Some effects of turbulence scale on the mean forces on a bluff body", *J Wind Eng Ind Aerod*., **1**(0), 361-370.
13. Lee, B.E. (1975b), "The effect of turbulence on the surface pressure field of a square prism", *J Fluid Mech*., **69**(02), 263-282.
14. Li, Q.S., Fang, J.Q., Jeary, A.P. and Wong, C.K. (1998), "Full scale measurements of wind effects on tall buildings", *J Wind Eng Ind Aerod*., **74-76**(0), 741-750.
15. Li, Q.S., Wu, J.R., Liang, S.G., Xiao, Y.Q. and Wong, C.K. (2004a), "Full-scale measurements and numerical evaluation of wind-induced vibration of a 63-story reinforced concrete tall building", *Eng Struct*., **26**(12), 1779-1794.
16. Li, Q.S., Xiao, Y.Q., Wong, C.K. and Jeary, A.P. (2004b), "Field measurements of typhoon effects on a super tall building", *Eng Struct*., **26**(2), 233-244.
17. Li, Q.S., Xiao, Y.Q. and Wong, C.K. (2005), "Full-scale monitoring of typhoon effects on super tall buildings", *J Fluid Struct*., **20**(5), 697-717.
18. Li, Q.S., Fu, J.Y., Xiao, Y.Q., Li, Z.N., Ni, Z.H., Xie, Z.N. and Gu, M. (2006), "Wind tunnel and full-scale study of wind effects on China’s tallest building", *Eng Struct*., **28**(12), 1745-1758.
19. Nakamura, Y. (1993), "Bluff-body aerodynamics and turbulence", *J Wind Eng Ind Aerod*., **49**(1-3), 65-78.
20. Simiu, E. and Scanlan, R.H. (1996), *Wind effects on structures: fundamentals and applications to design*, John Wiley
21. Swaddiwudhipong, S. and Khan, M.S. (2002), "Dynamic response of wind-excited building using CFD", *J Sound Vib*., **253**(4), 735-754.
22. Tieleman, H.W. and Akins, R.E. (1990), "Effects of incident turbulence on pressure distributions on rectangular prisms", *J Wind Eng Ind Aerod*., **36, Part 1**(0), 579-588.
23. Tominaga, Y., Mochida, A., Murakami, S. and Sawaki, S. (2008), "Comparison of various revised k– ε models and LES applied to flow around a high-rise building model with 1:1:2 shape placed within the surface boundary layer", *J Wind Eng Ind Aerod*., **96**(4), 389-411.
24. Varshney, K. and Poddar, K. (2011), *Experiments on integral length scale control in atmospheric boundary layer wind tunnel*, Springer Wien
25. Wu, J.R. and Li, Q.S. (2008), "Wind-induced lateral-torsional coupled responses of tall buildings", *Wind Struct*., **11**(2), 153-178.
26. Yoshida, M., Kondo, K. and Suzuki, M. (1992), "Fluctuating wind pressure measured with tubing system", *J Wind Eng Ind Aerod*., **42**(1-3), 987-998.
27. Zhang, X.T. (2006), *Structural wind engineering*, China Architecture and Building Press, Beijing.

Experimental investigation on aerodynamic characteristics of various triangular-section high-rise buildings

Akihito Yoshida[a], Bandi Eswara Kumar[b], Yukio Tamura[c], Yong Chul Kim [d], Q. Yang[e]

[a] *Tokyo Polytechnic University, Atsugi, Kanagawa, Japan, yoshida@arch.t-kougei.ac.jp*
[b] *Tokyo Polytechnic University, Atsugi, Kanagawa, Japan, eswar@arch.t-kougei.ac.jp*
[c] *Tokyo Polytechnic University, Atsugi, Kanagawa, Japan, yukio@arch.t-kougei.ac.jp*
[d] *Tokyo Polytechnic University, Atsugi, Kanagawa, Japan, kimyc@arch.t-kougei.ac.jp*
[e] *Beijing Jiaotong university, Beijing, China, qshyang@bjtu.edu.cn*

ABSTRACT: Tall buildings are particularly prone to dynamic excitations such as those from natural disasters like strong winds and earthquakes, and this has become an especially important design issue with manhattanization. One way to minimize wind-induced vibrations of tall buildings is to focus more on their shapes in the design stage. This paper investigates variations in along-wind and crosswind overturning moment coefficients, power spectral densities, and trajectories of various wind force coefficients.

KEYWORDS: Overturning moment coefficients, trajectories, power spectral densities

1 INTRODUCTION

Helical models of square cross-section have shown good performance based on both safety and habitability criteria (Tamura et.al., 2010). The effects of building plan shape on aerodynamic forces and displacement response have been studied for super-high-rise buildings with square and triangular cross-sections with corner modifications (Hayashida et.al., 1990). Aerodynamic modification of building shape, such as by changing the cross-section with height through tapering, alters the flow pattern around tall buildings, which can reduce wind-induced excitations (Kim et.al., 2002). Many researchers have tested wind pressures on buildings with irregular plans (Amin et.al., 2008), buildings with different rectangular cross-sections (Lin et al., 2005), tapered building models with taper ratios of 5% and 10%, and building models with set-back at mid-height (Kim et.al., 2010). However, there have been very few studies on the aerodynamic characteristics of triangular-cross-section tall buildings with various configurations. The objective of this study was to investigate the aerodynamic characteristics for various triangular section models.

2 EXPERIMENTAL SETUP

Wind tunnel tests were conducted in a boundary layer wind tunnel at the Wind Engineering Research Center, Tokyo Polytechnic University, Japan. The wind tunnel test section was 19m long with a cross-section 2.2m wide by 1.8m high. Equilateral triangle models with a side dimension of 0.076m and a height of 0.4m were used. All the models had the same volume, and Straight Triangle, Corner cut, Clover, 60^{o}Helical, 180^{o}Helical and 360^{o}Helical models were tested to identify their aerodynamic characteristics. These models are shown in Figure 1. The experiments were conducted for an urban (power–law exponent, α=0.27) flow. A length scale of 1/1000 and a

time scale of 1/167 were assumed. The Reynolds number was about 9.6 × 10^4. The coordinate system adopted for the calculations is shown in Figure 2.

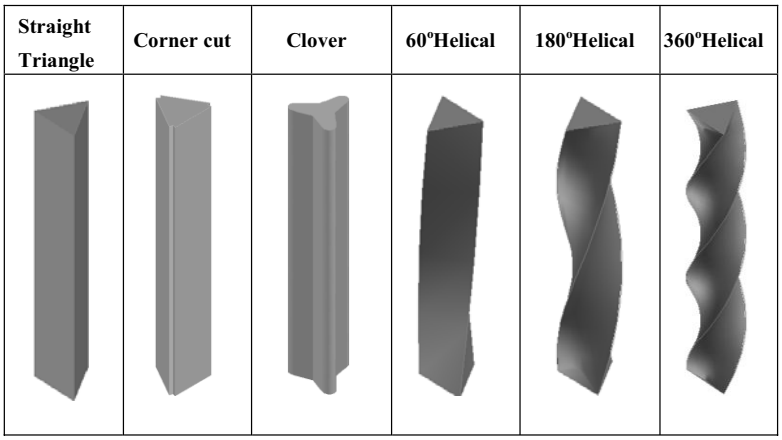

Figure 1. Schematic diagram of models.

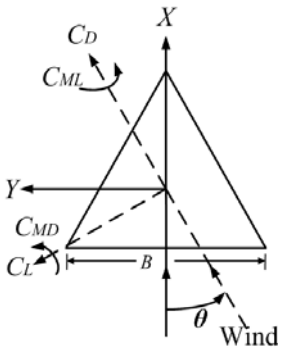

Figure 2. Coordinate system.

3 RESULTS AND DISCUSSIONS

3.1 *Mean overturning moment coefficients*

Overturning moment (OTM) coefficients in the along-wind and crosswind directions were calculated using the velocity pressure q_H at model height, width B and height H. Figure 3 shows the variation of mean along-wind OTM coefficient ($\overline{C}_{MD}$) and mean crosswind OTM coefficient ($\overline{C}_{ML}$) with wind direction (θ). $\overline{C}_{MD}$ values decrease and $\overline{C}_{ML}$ values increase as helical angle increases. The $\overline{C}_{MD}$ and $\overline{C}_{ML}$ values of the Corner cut model follow the same trend as the Straight Triangle model. The maximum and minimum values of $\overline{C}_{MD}$ for all the models are 0.64 and 0.3 for the Straight Triangle and Corner cut models. The maximum and minimum values of $\overline{C}_{ML}$ are 0.45 and -0.45 for the Straight Triangle model. For the 360° Helical model, the $\overline{C}_{ML}$ values are around 0.05~0.1 for all wind directions. The $\overline{C}_{ML}$ and $\overline{C}_{MD}$ values (around 0.1 and 0.4) for all the wind directions are almost constant for the 360°Helical model, as can be seen in Figure 3(b). For the Straight Triangle model, the minimum $\overline{C}_{MD}$ occurred at 60° wind direction and the curve is 'U'-shaped. Torsional moment coefficients are not discussed here in detail as these values were very small compared to the along-wind and crosswind force coefficients. They are almost 0 for the Straight Triangle, Corner cut and Clover models. The variation of mean drag and mean lift force coefficients were 1.2 and 0 for the Straight Triangle model at 0° wind direction, which is similar to the results of Kanda and Choi (1992).

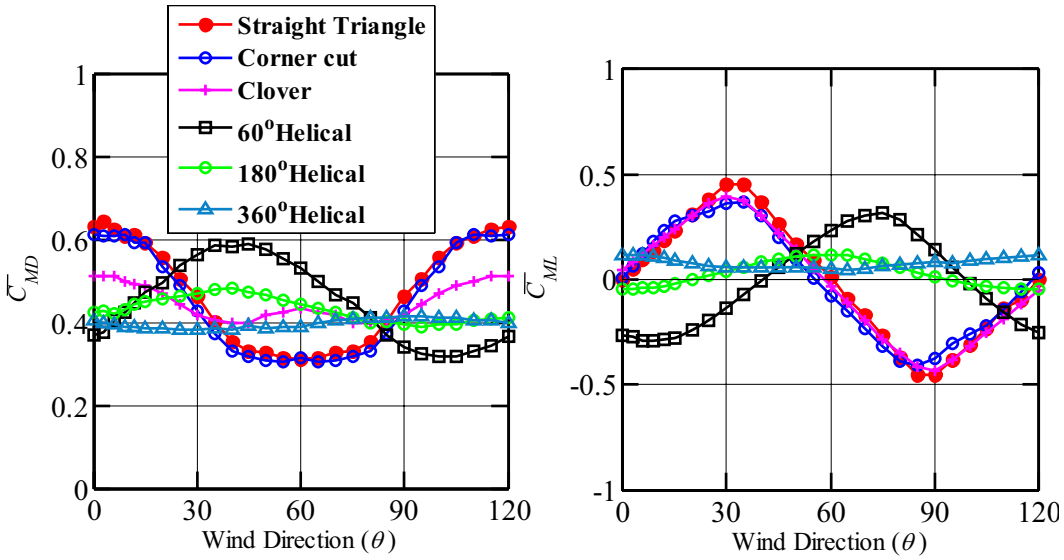

(a) Mean along-wind OTM coefficient (b) Mean crosswind OTM coefficient

Figure 3. Mean OTM coefficients.

3.2 *Fluctuating OTM coefficients*

Figure 4 shows the variation of fluctuating along-wind OTM coefficient (C'_{MD}) and fluctuating crosswind OTM coefficient (C'_{ML}) with wind direction (θ). For the 360°Helical model, the C'_{MD} values are almost 30% larger than the C'_{ML} values. The C'_{MD} and C'_{ML} values decrease as helical angle increases for the Straight Triangle model and the Helical models. The maximum and minimum values of C'_{MD} are 0.12 and 0.05 for the Straight Triangle model. The maximum and minimum values of C'_{ML} are 0.12 and 0.04 for the Straight Triangle and 360°Helical models. The maximum values of C'_{MD} and C'_{ML} are the same for the Straight Triangle model. The C'_{MD} and C'_{ML} values vary almost constantly for all wind directions for the 360°Helical model.

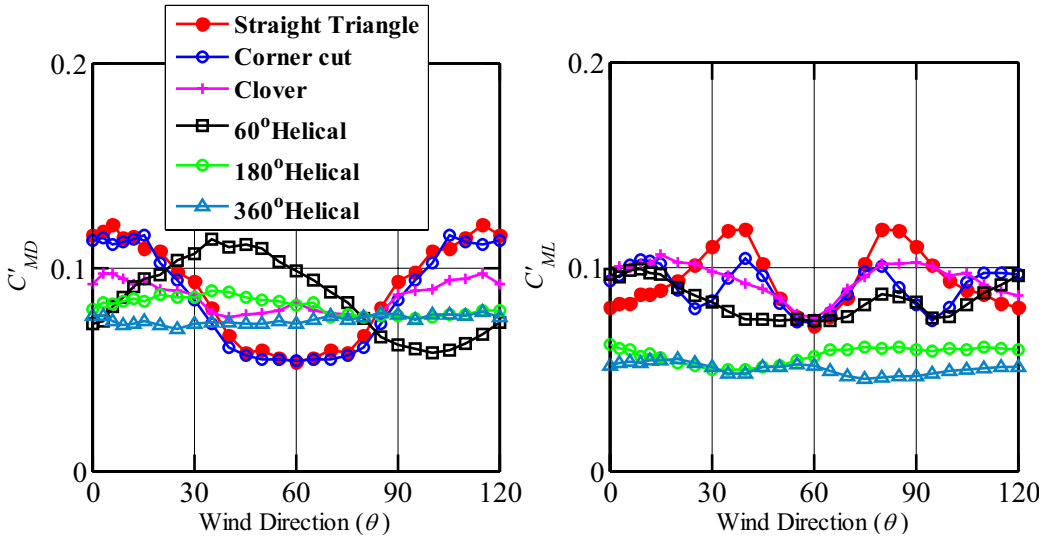

(a) Fluctuating along-wind OTM coefficient (b) Fluctuating crosswind OTM coefficient

Figure 4. Fluctuating OTM coefficients.

3.3 *Maximum fluctuating OTM coefficients*

Maximum fluctuating OTM coefficients in the along-wind and crosswind directions have been identified for all wind directions, as shown in Figure 5. The abscissa shows the various models. As it can be seen from Figure 5, the fluctuating OTM coefficients reduce as the helical angle increases in both the along-wind and crosswind directions. But in the along-wind direction, the maximum fluctuating OTM coefficient is almost the same as that for the Straight Triangle model. In the crosswind direction, the Clover model shows a slightly higher value than the Corner cut model.

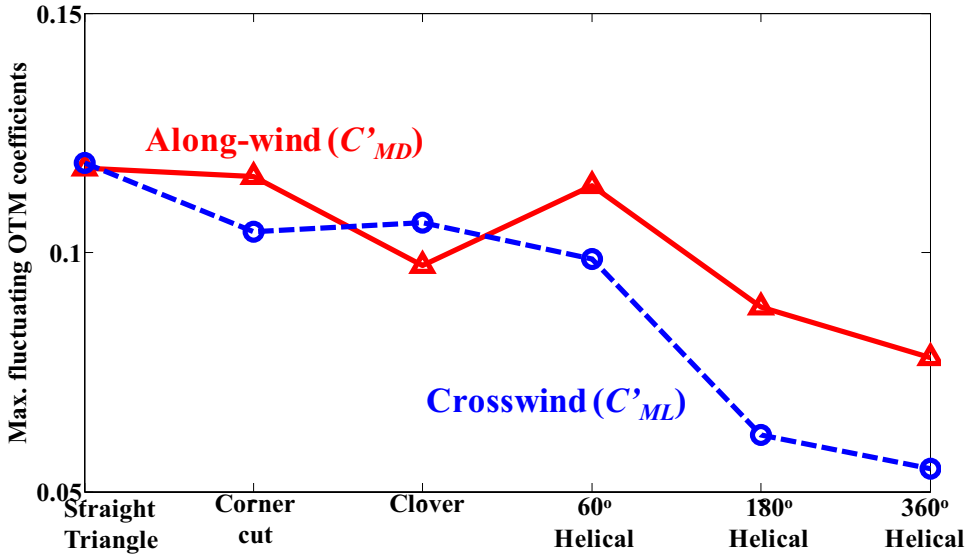

Figure 5. Maximum fluctuating OTM coefficients in along-wind and crosswind directions.

3.4 *Power spectral density for along-wind and crosswind OTM coefficients*

Figure 6(a) shows the along-wind power spectra, fS_{CMD}, for the wind directions corresponding to those where the maximum peak occurred for the crosswind spectra. Higher maximum peaks occurred for the Straight Triangle model than for all the other models. The 360°Helical model shows a smaller peak than the other models. Figure 6(b) shows the crosswind power spectra, fS_{CML}, for the wind directions at which the maximum peak occurred. The maximum peaks occurred for crosswind spectra at θ=0°, 0°, 15° 45°, 120° and 30° for the Straight Triangle, Corner cut, Clover, 60°Helical, 180°Helical and 360°Helical models. A sharp peak of crosswind spectrum is observed for the Straight Triangle, Corner cut and Clover models, but the maximum peak is observed for the Clover model. The sharp peak is reduced drastically for the Helical models as the helical angle increases, indicating that the shedding vortices are more disturbed than in the normal condition. As the helical angle increases, the peak shifts to higher reduced frequency ranges, and also the band width of the spectrum increases. But for the Corner cut and Clover models, the peak appears sharp and shifts towards slightly higher reduced frequency ranges than the Straight Triangle model.

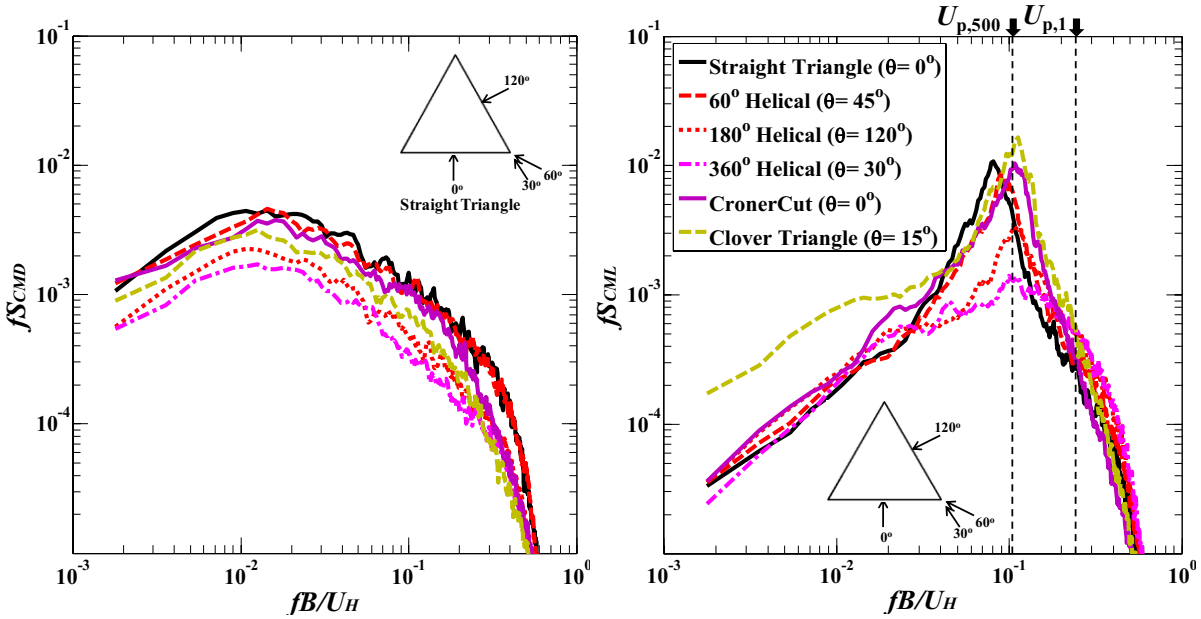

(a) Along-wind direction (b) Crosswind direction

Figure 6. Power spectral densities of along-wind and crosswind OTM coefficients.

Figure 7 compares in detail the square root of crosswind power spectra for the design wind speeds corresponding to a 500-year return period ($U_{p,500}$) and a 1-year return period ($U_{p,1}$). Here, the first natural frequency is assumed to be f_1=0.1Hz, and the design wind speeds are assumed to be $U_{p,500}$=71m/s and $U_{p,1}$=30m/s, respectively, in the Tokyo region. Then, the corresponding spectral values were calculated. The largest values decreased as the helical angle increased corresponding to $U_{p,500}$, but the largest value is shown for the Clover model. For $U_{p,1}$, the largest values become smaller than those for the Straight Triangle model. The Corner cut model shows the smallest value of all.

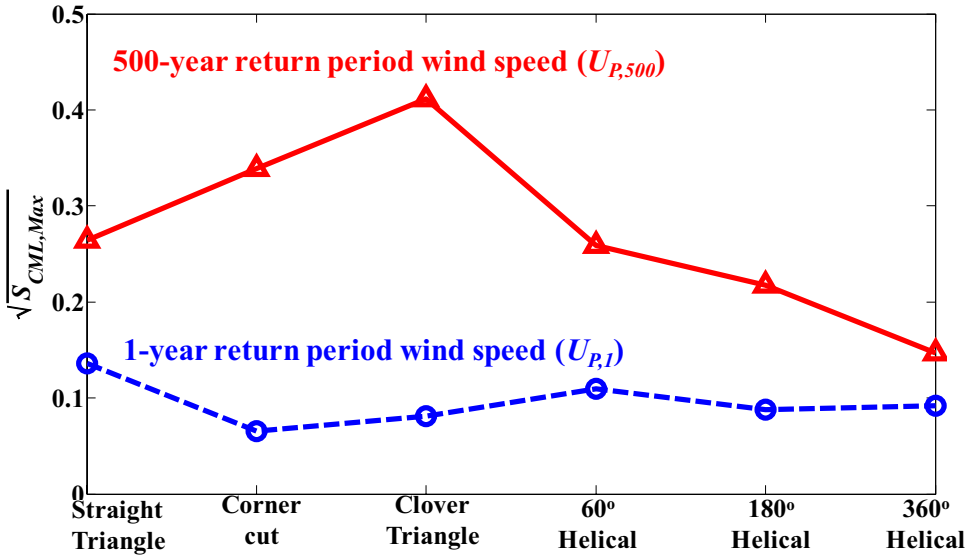

Figure 7. Peak spectral values in crosswind direction for 500-year and 1-year return periods.

3.5 *Trajectories of OTM coefficients*

Figures 8(a)-(e) show the trajectories of various OTM's for the Straight Triangle, Corner cut, Clover, 180°Helical and 360°Helical models. The values in parentheses are the wind directions for which the trajectories were obtained. These wind directions were selected where $\overline{C}_{ML}$ is zero for easy comparison of trajectory shapes. The trajectory of C_{MD}-C_{ML} for the Straight Triangle model shows a circular shape, showing that there is no correlation between them, but sometimes we can see some correlation for C_{MD}-C_{ML} and C_{MD}-C_{MT}. The 60°Helical model shows almost the same trend as the Straight Triangle model. For the 180°Helical model, we can see a higher correlation between C_{ML}-C_{MT}. But for the 360°Helical model, the trajectory is elliptic with some inclination angle indicating high correlation for C_{MD}-C_{MT} and C_{ML}-C_{MT}. For the Corner cut model, the trajectory size reduces to less than that for the Straight Triangle model and shows some correlation between C_{MD}-C_{ML}.

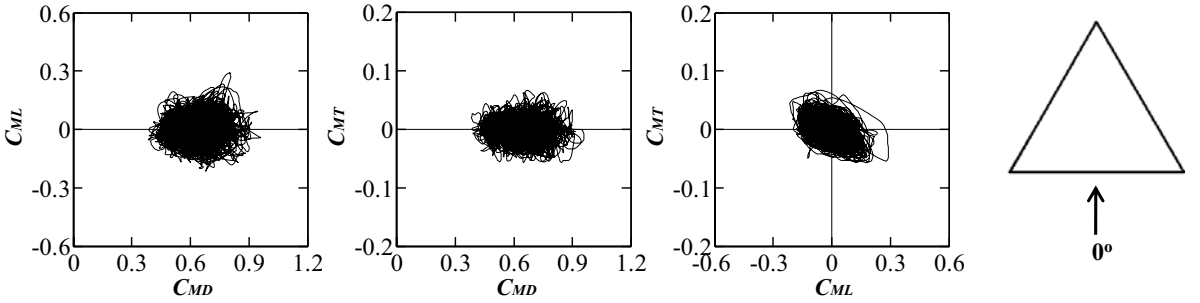

(a) Straight Triangle (θ=0°)

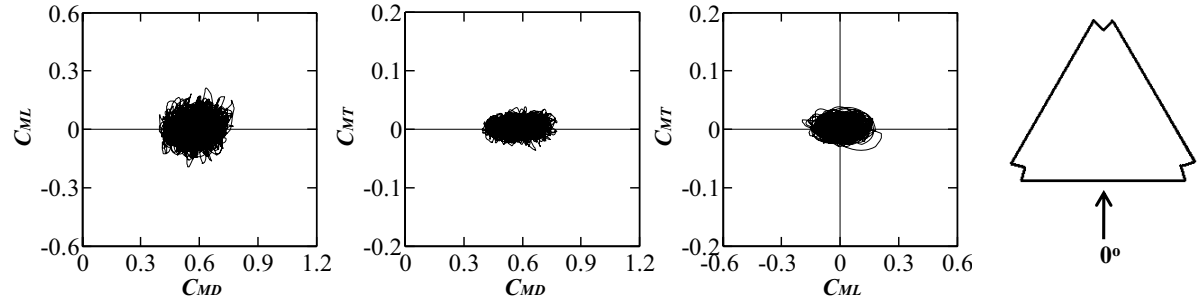

(b) Corner cut (θ=0°)

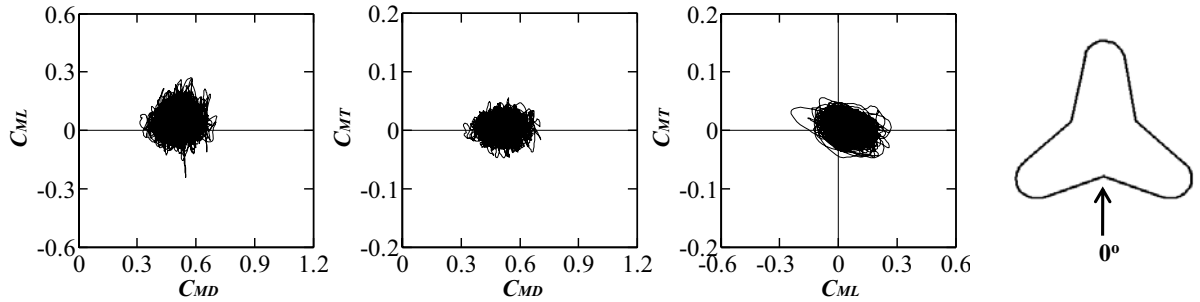

(c) Clover (θ=0°)

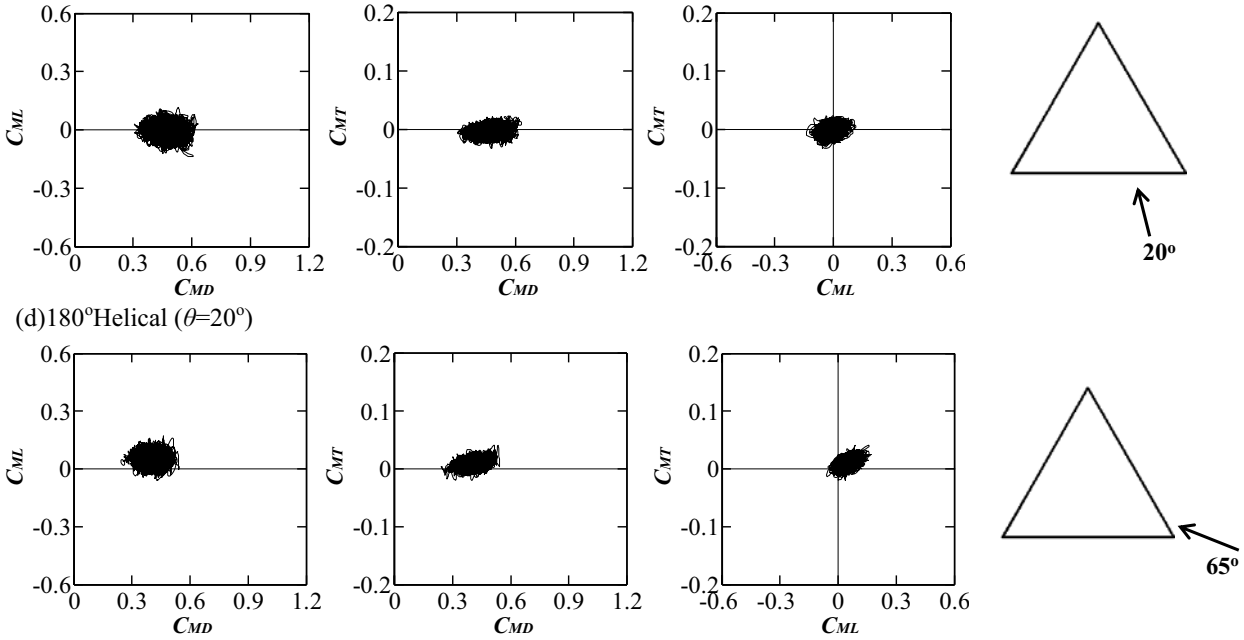

Figure 8. Trajectories of various wind force coefficients.

4 CONCLUSIONS

The aerodynamic characteristics of triangle section tall buildings with various configurations were investigated under urban flow conditions. The 360°Helical model showed lower values of C'_{ML} than all the other models. But, the Corner cut model showed a lower value than the Straight Triangle model in the crosswind direction. The maximum peak of the C_{ML} power spectra decreased as the helical angle increased, but the peak frequency shifted towards the higher reduced frequency ranges as the helical angle increased. The Clover model showed a larger peak than all the other models. The smallest crosswind spectral peak was shown for the 360°Helical model and the Corner cut model corresponding to $U_{p,500}$ and $U_{p,1}$. The 360°Helical model showed higher correlations for C_{MD}-C_{MT} and C_{ML}-C_{MT}.

5 ACKNOWLEDGEMENTS

This study was funded by the Strategic Japanese-Chinese Cooperative Program on “Science and Technology (S&T) for Environmental Conservation and Construction of a Society with Less Environmental Burden" (NSFC-JST) entitled "New Strategies for Wind Disaster Risk Reduction of Wind Sensitive Infrastructures" and Global Center of Excellence (Global COE), which is gratefully acknowledged.

6 REFERENCES

1 J-A., Amin, A-.K.,Ahuja, 2008, Experimental study of wind pressures on irregular plan shape buildings, BBAA VI, 20-24.

2 J., Kanda, H.,Choi, 1992, Correlating Dynamic Wind Force Components on 3-D cylinders, Journal of Wind Engineering and Industrial Aerodynamics 41-44, 785-796.

3 N., Lin, C., Letchford, Y., Tamura, B., Liang, O., Nakamura, 2005, Characteristics of wind forces acting on tall buildings, Journal of Wind Engineering and Industrial Aerodynamics 93, 217-242.

4 Y.C., Kim, J., Kanda, 2010, Characteristics of aerodynamic force and pressures on square plan buildings with height variations, Journal of Wind Engineering and Industrial Aerodynamics 98, 449-465.

5 Y.M., Kim, Ki-Pyo You, 2002, Dynamic responses of a tapered tall building to wind loads, Journal of Wind Engineering and Industrial Aerodynamics 90, 1771-1782.

6 Y.Tamura et al (2010), Aerodynamic characteristics of tall building models with various unconventional configurations, Proceedings of the 2010 Structures Congress.

The Seventh International Colloquium on Bluff Body Aerodynamics and Applications (BBAA7)
Shanghai, China; September 2-6, 2012

Tall building response evaluation to nonstationary winds b ased on multiple simulated samples

Guoqing Huang [a], Xinzhong Chen [b]

[a]*School of Civil Engineering, Southwest Jiaotong University, Chengdu, China*
[b]*Department of Civil and Environmental Engineering, Texas Tech University, Lubbock, TX, USA,*

ABSTRACT: This paper presents a time-domain approach for estimating alongwind load effects on tall buildings using multiple wind speed time history samples, which are simulated from evolutionary spectra of nonstationary wind fluctuations using the method developed by the authors (Huang and Chen 2009). The influence of transient wind loads on various responses including time-varying mean, root-mean-square value and peak factor is also studied. Further, a simplified model is proposed to describe the nonstationary wind fluctuation as a uniformly modulated process with a modulation function as the time-varying mean. Finally, the extreme response and peak factor are quantified based on the upcrossing theory of nonstationary process.

KEYWORDS: nonstationary winds; evolutionary; time domain; tall building; response

1. INTRODUCTION

The nonstationary extreme winds are responsible for damages of many buildings and other structures in US and around the world (e.g., Choi 2004). Characterizing and modeling these extreme winds have drawn more attention from meteorological and wind engineering communities. Based on full-scale observations, Fujita (1985 and 1990) characterized downbursts with unique mean wind speed vertical profiles, rapid time varying mean wind speeds, and spatially strongly correlated wind fluctuations. The physical simulation of nonstationary winds has been conducted (e.g., Letchford and Chay 2002). Although it is difficult to gauge the downbursts on site due to its small temporal and spatial scales, and random occurrences, limited full-scale measurements were obtained by Gast and Schroeder (2003) and (Choi, 2004). More information about characterization and simulation of the downbursts can be found in literature (e.g., Holmes an Oliver 2000; Mason et al. 2009).

These nonstationary extreme winds after removing mean values can be modeled as random processes which are often characterized in terms of time-varying spectra. The evolutionary power spectra density (EPSD) functions (e.g., Priestley 1981) prevail in engineering practice, especially for applications in stochastic structural dynamics, in that EPSD functions have similar physical significance for nonstationary processes as the traditional power spectral density (PSD) functions for the stationary processes. The adequate estimation of EPSDs will be essential for characterization, modeling and simulation of these processes and their effects on structures.

With better time-frequency resolution over other tools such as Wigner-Ville method and short-time Fourier Transform, wavelets have been adopted to develop EPSD estimation of nonstationary processes for both scalar case (Spanos and Failla 2004) and vector case (Huang and Chen 2009). Huang and Chen (2009) also applied this approach to full-scale downburst winds (Gast and Schroeder 2003), and analyzed their nonstationary characteristics.

Compared to considerable research on wind effects on structures under stationary boundary layer winds, the understanding of nonstationary extreme wind effects such as thunderstorm downbursts has been less developed. Chen and Letchford (2004) studied the building responses

in the time domain using a single sample of downburst wind. Holmes et al. (2005) computed the dynamic response spectrum of single-degree-of-freedom (SDOF) structures excited by a thunderstorm wind, which is similar to the response spectrum widely used in earthquake engineering. Recently, Chen (2008) developed a frequency domain framework for quantifying tall building response caused by nonstationary winds using the evolutionary spectra. Kwon and Kareem (2009) presented a general gust-front factor framework for modeling transient wind load effects on structures. Simulation of nonstationary winds based on the estimated EPSD offers a new opportunity to evaluate the nonstationary wind effects on buildings and improve the understanding of the interaction between the nonstationary wind and the structure.

In this paper, a time domain analysis framework is employed for estimating tall building response to nonstationary winds. This framework involves estimation of EPSD of nonstationary wind speed based on the method proposed by Huang and Chen (2009), simulation of nonstationary wind time history using spectral representation method (e.g., Deodatis 1996), calculation of time history of wind load, and determination of response history by using the step-by-step integration method. From multiple response time histories, the time-dependent statistics such as RMS and extreme value of response are determined. The results are compared with those obtained from the frequency domain analysis (Chen 2008). Further, a simplified model of nonstationary wind fluctuation is proposed, and the resulting building response is addressed. The influence of transient nature of nonstationary winds on the extreme value of building response, gust response factor (GRF) and peak factor is also studied. Finally, the extreme and peak factor of building response are quantified based on the upcrosssing theory of nonstationary processes.

As compared to the time domain response analysis using single sample of wind record (e.g., Holmes et al. 2005), the analysis using multiple samples presented in this study will provide the statistical information of responses. The time domain simulation also facilitates consideration of nonlinearities of the structures and wind loads over the frequency domain analysis (Chen 2008).

2. TIME DOMAIN RESPONSE ANALYSIS FRAMEWORK

Consider the alongwind response of a tall building under a nonstationary wind. The wind speed at elevation z, $U(z,t)$, can be decomposed into the time varying mean and fluctuation as

$$U(z,t) = \bar{U}(z,t) + u'(z,t) \tag{1}$$

where $u'(z,t)$ is modeled as an evolutionary process and expressed as $u'(z,t) = \int_{-\infty}^{\infty} e^{i\omega t} d\Theta(z,\omega,t)$, in which $i = \sqrt{-1}$; ω is circular frequency; $d\Theta(z,\omega,t)$ is complex-valued zero-mean orthogonal increment random process with the following properties

$$\begin{aligned} &E[d\Theta(z,\omega,t)] = 0; \quad d\Theta(z,\omega,t) = d\Theta^*(z,-\omega,t); \\ &E[d\Theta(z_1,\omega_1,t)d\Theta^*(z_2,\omega_2,t+\tau)] = S_u(z_1,z_2,\omega_1,t)e^{i\omega\tau}\delta(z_1-z_2)\delta(\omega_1-\omega_2)d\omega_1 d\omega_2 \end{aligned} \tag{2}$$

where $E[\ldots]$ is expectation or ensemble average; * denotes the complex conjugation; $\delta(\ldots)$ is Dirac delta function; τ is time lag; $S_u(z_1,z_2,\omega_1,t)$ is the cross EPSD between $u'(z_1,t)$ and $u'(z_2,t)$; and $S_u(z,\omega,t) = S_u(z,z,\omega,t)$ is EPSD of $u'(z,t)$.

Following the strip theory, the alongwind force per unit height at z is quantified as the summation of the time varying mean component, $\bar{P}(z,t)$, and fluctuating component, $P'(z,t)$,

$$\bar{P}(z,t) = 0.5\rho C_D B \bar{U}^2(z,t); \quad P'(z,t) = \rho C_D B \bar{U}(z,t) \int_{-\infty}^{\infty} \chi_D(\omega) e^{i\omega t} d\Theta(z,\omega,t) \tag{3}$$

where ρ is the air density; B is the building width; C_D is the drag coefficient; $\chi_D(\omega)$ is the complex-valued aerodynamic admittance function.

For tall buildings, the wind-induced response is usually dominated by fundamental modal responses and higher mode contributions can be neglected. The time varying mean and fluctuating component of the generalized force, $Q(t)$, in the fundamental mode are computed by

$$\bar{Q}(t) = \int_0^H \bar{P}(z,t)\Phi(z)dz; \quad Q'(t) = \int_0^H P'(z,t)\Phi(z)dz \tag{4}$$

where $\Phi(z) = (z/H)^{\beta}$ is modal shape; H is building height; and β is exponent (1.0-to 1.5.

The EPSD of the $Q'(t)$ can be given as (Chen 2008)

$$S_{Q'}(\omega,t) = \int_0^H \int_0^H (\rho C_D B)^2 \bar{U}(z_1,t)\bar{U}(z_2,t)\left(z_1/H\right)^{\beta}\left(z_2/H\right)^{\beta}\left|\chi_D(\omega)\right|^2 S_u(z_1,z_2,\omega,t)dz_1dz_2 \tag{5}$$

The mean speed is assumed as $\bar{U}(z,t) = \bar{U}_0(z)d(t)$, where $\bar{U}_0(z)$ is the vertical profile and $d(t)$ is the modulation function. A power law profile, $\bar{U}_0(z) = U_{\max}\left(z/H\right)^{\alpha}$, is considered in this study, where α is the profile exponent, and $U_{\max}$ is the maximum wind speed on $\bar{U}_0(z)$, i.e., wind speed at building top. Based on the study by Chen (2008), wind profiles were found to have little influence on the fundamental feature of the building dynamic response to transient winds.

Accordingly, the mean generalized force is given by

$$\bar{Q}(t) = Q_R d^2(t)/(1+2\alpha+\beta); \quad Q_R = 0.5\rho C_D BHU_{\max}^2 \tag{6}$$

The EPSD of fluctuation, $u'(z,t)$, is assumed to be same, i.e., $S_u(z,\omega,t) = S_u(\omega,t)$.

The coherence function between $u'(z_1,t)$ and $u'(z_2,t)$ is assumed as

$$\mathrm{Coh}(z_1,z_2,\omega) = S_u(z_1,z_2,\omega,t)/S_u(\omega,t) = \exp[-k_z\omega\left|z_1-z_2\right|/(2\pi U_{\max})] \tag{7}$$

where k_z is the decay factor.

The EPSD of the generalized force given by Eq. 5 can be reduced to

$$S_{Q'}(\omega,t) = 4Q_R^2 S_u(\omega,t)d^2(t)\left|\chi_D(\omega)\right|^2\left|J_z(\omega)\right|^2/U_{\max}^2 \tag{8}$$

where joint acceptance $\left|J_z(\omega)\right|^2 = (1+\alpha+\beta)^{-1}[1+k_z\omega H/(2\pi U_H)/(2.5+\beta)]^{-1}$ (Chen 2008).

For the purpose of simulating the time histories of the generalized force and building response, the EPSD of the generalized force is further approximated as

$$S_{Q'}(\omega,t) = 4Q_R^2 S_u(\omega,t)d^2(t)\left|\chi_D(\omega_1)\right|^2\left|J_z(\omega_1)\right|^2/U_{\max}^2 \tag{9}$$

where $\omega_1 = 2\pi f_1$ is the fundamental natural frequency of the building.

As compared to Eq. 8, although this approximation results in a different EPSD of the generalized force on other frequencies it leads to the almost same building response due to the property of the narrow band process of the building response around the building natural frequency. According to Eq. 9 and assuming the variation rate of $d(t)$ is relatively slow, the time history of the generalized force $Q'(t)$ can be directly related to $u_0'(t)$ by

$$Q'(t) = 2Q_R u_0'(t)d(t)\left|\chi_D(\omega_1)\right|\left|J_z(\omega_1)\right|/U_{\max} \tag{10}$$

where $u_0'(t)$ is a nonstationary wind fluctuation and characterized by its EPSD $S_u(\omega,t)$.

Hence, $Q'(t)$ can be generated by first simulating $u_0'(t)$ through its EPSD $S_u(\omega,t)$. It should be mentioned that a more accurate simulation of the time histories of $Q'(t)$ can be achieved based on Eq. 8 by using the rational function approximation (Chen et al. 2000).

With the knowledge of the time histories of the generalized force, the desired response can be determined using Newmark's method to solve the following equation of building motion

$$M[\ddot{q}'(t) + 2\xi\omega_1\dot{q}'(t) + \omega_1^2 q'(t)] = Q'(t) \tag{11}$$

where M, ξ, and $q'(t)$ are the fundamental generalized mass, damping ratio and displacement, respectively. In addition, the mean component of the generalized displacement can be directly computed from the quasi-static analysis as $\bar{q}(t) = \bar{Q}(t)/(M\omega_1^2)$.

The mean and dynamic components of other response, $R(t)$, are then given as

$$\bar{R}(t) = B\bar{q}(t); \quad R'(t) = Bq'(t) \tag{12}$$

where B is the modal participation coefficient.

The velocity and acceleration are of interest in habitability design and determined as

$$v(z,t) = \Phi(z)\dot{q}'(t) \approx \Phi(z)\omega_1 q'(t); \quad a(z,t) = \Phi(z)\ddot{q}'(t) \approx \Phi(z)\omega_1^2 q'(t) \tag{13}$$

Based on multiple response samples, instantaneous RMS, mean extreme values of response can be determined. In the next discussion, top displacement is normalized by $\bar{q}(t) = \bar{Q}(t)/(M\omega_1^2)$, which is the static displacement under load Q_R. The GRF and the peak factor are accordingly determined. The GRF is defined as the ratio of the mean extreme value of total response to the maximum static response. The peak factor is defined as the ratio of the mean extreme value of dynamic response to the maximum RMS response.

3. COMPARISON WITH FREQUENCY DOMAIN ANALYSIS

A shear building with a height of H =200 m and a square section of $B = D = 40$ m is studied. The fundamental modal frequency is given by the empirical formula $f_1 = 46/H$. The modal damping ratio is ξ =1%, and fundamental modal shape is assumed to be linear, i.e., β =1.0. The aerodynamic admittance function is given by Davenport's formula as

$$|\chi_D(\omega)|^2 = 2\lambda_y(1 - 1/\lambda_y + 1/\lambda_y e^{-\lambda_y}) \tag{14}$$

where $\lambda_y = k_y fD/U_{\max}$; k_y is decay factor and taken as 8. The power law exponent of mean wind speed profile is α =0.25. The decay factor for the coherence of wind fluctuation is $k_z = 8$.

The numerical example used by Chen (2008) for frequency domain analysis is reevaluated by the time domain approach presented here. The modulation function of the mean wind speed, $d(t)$, is shown in Figure 1(a). The mean wind speed at the building top is $U_{\max}$ = 40m/s. The wind fluctuation of this wind event is modeled as a uniformly modulated process from a stationary wind fluctuation. The stationary wind fluctuation is modeled by the von Karman spectrum with an integral length scale of 80 m and turbulence intensity of 15%.

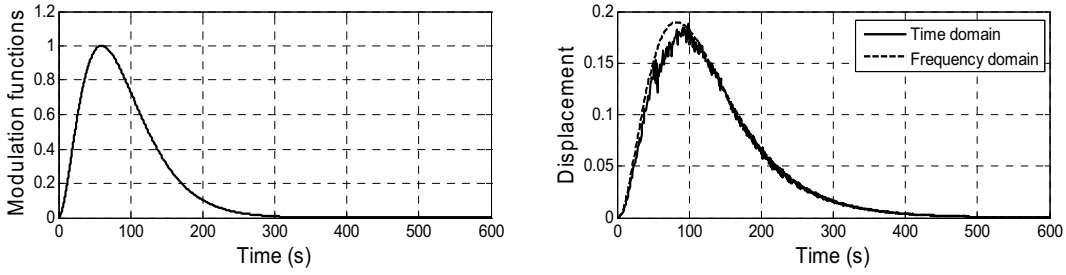

(a) Modulation function (b) Time varying RMS of top displacement

Figure 1 Comparison with frequency domain approach

A total of 100 time history samples of the wind fluctuation are generated through Monte Carlo simulation based on the spectral representation method (e.g., Deodatis 1996). The upper cutoff frequency is 10 Hz, and frequency increment is 0.00122 Hz. The generated time history samples have a time resolution of 0.05 s and time period of 819.2s. Based on multiple samples of the response time histories, the instantaneous RMS can be computed. The static and time varying RMS values of top displacement are shown and compared in Figure 1(b).

The results show that both approaches offer almost same results for time varying RMS value of response. This comparison also demonstrates the adequacy of the approximation in the generation of the time histories of the generalized force for the response prediction. From the analysis, the GRF and peak factor are calculated as 1.75 and 1.84, respectively.

4. RESPONSE TO WINDS GENERATED BY EVOLUTIONARY SPECTRA

4.1 *Characteristics of Transient Building Response*

In this case study, the full-scale measurement of a real flank downburst wind speed at height 15 m is used (Gast and Schroeder 2003). The time-varying mean and fluctuation components are derived using the discrete wavelet transform as described in Huang and Chen (2009), where wavelet was chosen as Daubechies wavelet (e.g., Daubechies 1992) of order 3 and decomposition levels were 5. The level 5 is equivalent to a window size of 32 s for the time-varying mean component with a frequency range below 0.016 Hz. The maximum time-varying mean wind speed is 32.15 m/s. Figure 2 shows the modulation function of the mean wind speed, $d(t)$, which is defined as the time-varying mean wind speed divided by the maximum wind speed. Based on the framework for estimating EPSD proposed by Huang and Chen (2009), the normalized EPSD of the wind fluctuation is shown in Figure 3, where length scale is $L_u = 168$ m. This length scale is derived from the corresponding stationary fluctuation of original nonstationary wind speed, as shown in next section.

Based on the modulation function of the mean wind speed and the estimated EPSD, the nonstationary wind time histories with a given maximum wind speed can be generated using the spectral representation method (e.g., Deodatis 1996). A total of 100 time history samples of the wind fluctuation are generated. The corresponding building responses are calculated.

From each sample of simulated response, the extreme value of response is quantified. Then the mean and RMS of the extreme values are calculated. In addition, responses of buildings with heights $H = 100$, 150, 250 and 300 m with $B = D = 40$ m are also investigated. The building natural frequency is $f_1 = 46/H$. Figure 4 shows the mean and RMS of extreme values of top displacements of the buildings. The building response at $U_{\max} = 32.15$ m/s directly using the original one wind speed record is also conducted for comparison. As shown in Figure 4, the results computed from the original sample locate in those obtained from the simulated samples. The slight difference between the response from original sample and averaged one from the multiple simulated samples is attributed to the difference in the spectral values around the natural frequency.

Figure 5 demonstrates the original sample of the nonstationary fluctuation with $U_{\max} = 32.15$ m/s and a simulated sample of the fluctuation with $U_{\max} = 40$ m/s. The static and RMS values of the normalized building top displacement are depicted in Figure 6. The maximum normalized static response is 0.4. It is observed that the maximum value of the RMS response appears slightly later than the static response reaches its maximum value. This time lag is also reported by other authors (e.g., Solomos and Spanos 1984; Chen 2008). The maximum RMS, mean extreme value, GRF and peak factor are summarized in the Table 1 (Case 1).

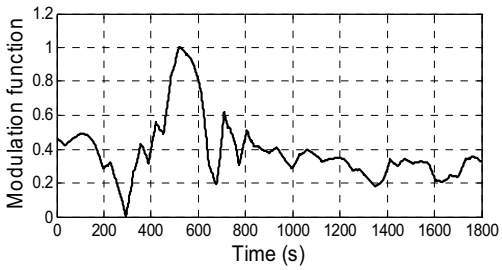

Figure 2 Modulation function from field observation

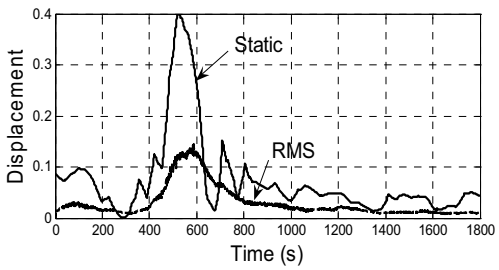

Figure 6 Static and RMS values of top displacement

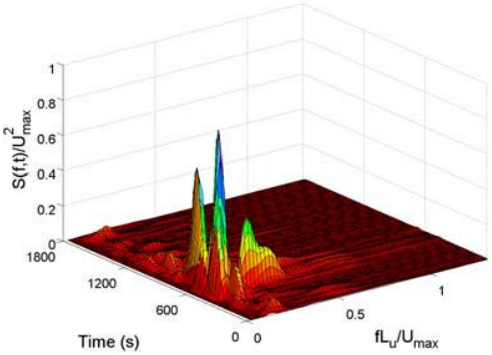

Figure 3 Normalized EPSD of the wind fluctuation

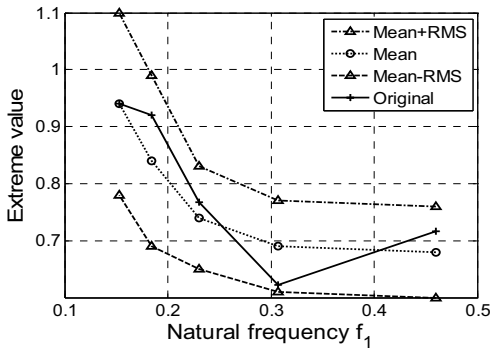

Figure 4 Comparison of building top displacement

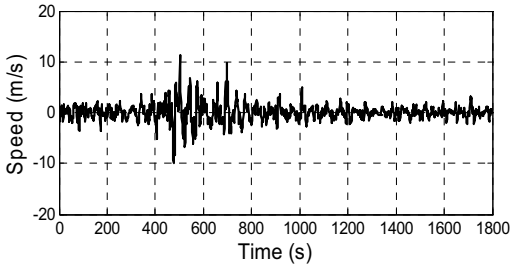

(a) The original sample ($U_{\max} = 32.15$ m/s)

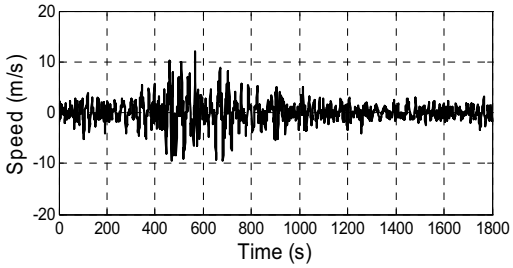

(b) A simulated sample ($U_{\max} = 40$ m/s)

Figure 5 Two samples of nonstatioanry wind fluctuation

Table 1. Comparison of different wind events

		Case 1	Case 2	Case 3	Case 4
Maximum RMS		0.144	0.157	0.147	0.154
Mean extreme	Time domain	0.63	0.66	0.62	0.88
	Upcrossing	0.64	0.70	0.65	0.93
GRF	Time domain	1.58	1.65	1.55	2.20
	Upcrossing	1.60	1.75	1.63	2.33
Peak factor	Time domain	1.60	1.66	1.50	3.12
	Upcrossing	1.67	1.91	1.70	3.44

Note: Case 1: time-varying mean + nonstationary fluctuation;
Case 2: time-invariant mean + nonstationary fluctuation;
Case 3: time-varying mean + simplified nonstationary fluctuation;
Case 4: time-invariant mean + stationary fluctuation.

4.2 *Influence of Time-Varying Mean Wind Speed*

To evaluate the influence of the time varying mean on the building response, the analysis using a time-invariant mean wind speed, i.e., $d(t)=1$, but same nonstationary wind fluctuation is also conducted. The previous case with time-varying mean wind speed and nonstationary wind fluctuation is referred to as "Case 1". The case discussed here is referred to as "Case 2". The time histories of total wind speed, which correspond to the wind fluctuation in Figure 5(b), is shown in Figure 7(a). The time-varying RMS values of top displacement are shown in Figure 7(b). The static top displacement is constant as 0.4. The maximum RMS, mean extreme value, GRF and peak factor are summarized in the Table 1. It is seen that the maximum value of RMS response is larger than that of Case 1. The main reason is attributed to slower fluctuation variation of the generalized force in Case 2, which needs less "build-up" time. This time is the one required to make $e^{-2\xi\omega_1 t}$ close unity (Chen 2008). Apparently, a large value of $\xi\omega_1$ requires less "build-up" time to reach the steady state response. Accordingly, the peak factor in Case 2 is also larger than that in Case 1 due to more developing time for the extreme value.

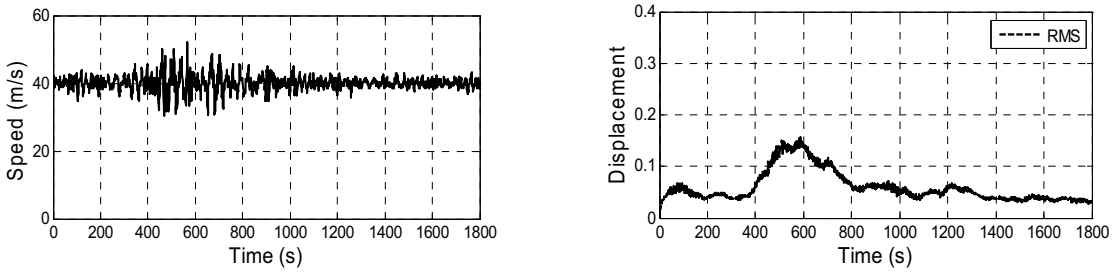

(a) A sample of total wind speed (b) RMS value of top displacement

Figure 7 Wind speed and building top displacement

5. A SIMPLIFIED MODELING OF NONSTATIONARY WIND FLUCTUATION

In engineering practice, the nonstationary wind fluctuation may be approximately modeled as a uniformly modulated process with its modulation function following the mean wind speed, i.e., $\bar{U}_0(t)=d(t)U_{\max}$ and $u_0'(t)=d(t)u(t)$.

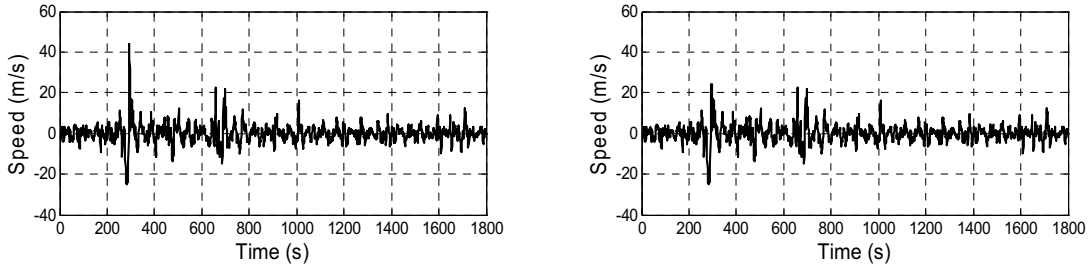

(c) $u_0'(t)=d(t)u(t)$ (d) $u(t)=u_0'(t)/d(t)$ without singular points

Figure 8 Derivation of the stationary fluctuation sample $u(t)$

The modulation function of the mean wind speed is shown in Figure 2. The wind fluctuation $u_0'(t)$ with $U_{\max}=32.15$ m/s is shown in Figure 5(a), which is derived by subtracting the time-varying mean from the original record. Based on this approximated model, stationary wind fluctuation $u(t)$ is obtained by dividing the original fluctuation sample $u_0'(t)$ with the corresponding modulation function, and then by removing few singular points, as shown in Figure 8(a) and (b). The PSD of the process $u(t)$, $S_u(f)$, is estimated and fitted with von Karman spectrum model. The length scale and turbulence intensity are 168 m and 15%, respectively. Figure 9 compared the PSD estimated from the sample and the one fitted by von

Karman spectrum. It can be seen that both have a satisfactory match around the frequency range of 0.15-0.25 Hz, which covers the fundamental frequencies of the tall buildings. The fitted spectrum is used to generate 100 samples of $u(t)$ and thus $u_0^{'}(t)$ for estimating the building response. This calculation is referred to as "Case 3".

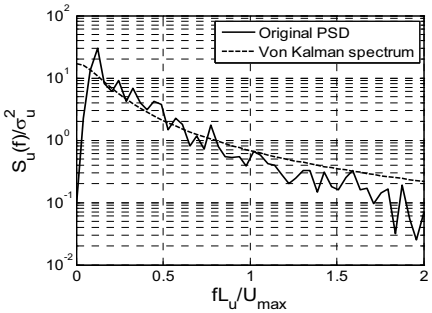

Figure 9 Comparison of normalized PSDs of stationary wind fluctuation

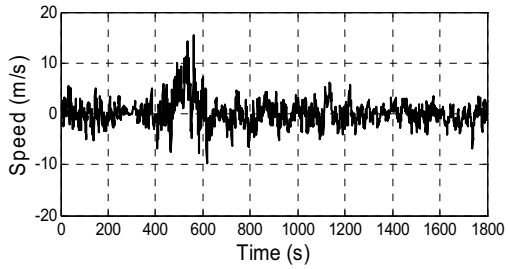

Figure 10 Sample of uniformly modulated fluctuation

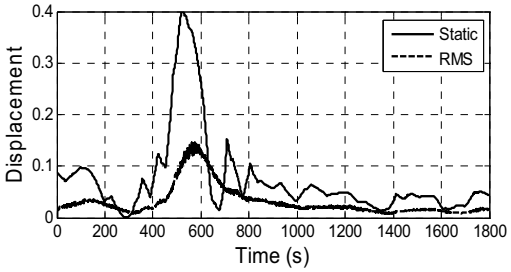

Figure 11 Static and RMS values of top displacement

Figure 10 shows one sample of the stationary fluctuation $u(t)$, and the corresponding uniformly modulated fluctuation $u_0^{'}(t) = d(t)u(t)$ with $U_{\max} = 40$ m/s. The time-varying static and RMS values of top displacement calculated from multiple samples are shown in Figure 11. The maximum RMS mean extreme, GRF and peak factor are summarized in Table 1 (Case 3).

The comparison between Cases 1 and 3 for other wind speeds is summarized in Table 2. The results in Tables 1 and 2 show that two different approaches in modeling the nonstationary downburst fluctuation have similar results in terms of the maximum RMS and the mean extreme value of the response, although they offer different time histories and time-varying RMS values. These two approaches generate different wind fluctuations and generalized forces. However, their spectra around the natural frequency are almost identical, which leads to almost equal response due to the property of the narrow-band filter of high-rise buildings. Hence, it may be practicable to model the nonstationary fluctuation as a uniformly modulated process with the modulation function of time-varying mean speed. However, for middle- and low-rise buildings, these approaches may not lead to similar responses because more frequency contents of wind loads will influence the response. In such a case, wind fluctuations generated from wavelets-based EPSD will offer more detailed time-frequency information of wind and wind load.

To further understand the transient wind load effect on the building response, the building response under stationary wind fluctuation $u(t)$ and mean wind speed of 40 m/s is also calculated. This is referred to as "Case 4". The maximum RMS, GRF and peak factor of three cases are summarized in Table 1. Compared to other three cases, the maximum RMS of Case 4 is almost identical, while the GRF and peak factor are much larger. The maximum RMS is mainly influenced by the wind fluctuation around the maximum mean wind speed. On the other hand, the extreme value as reflected by GRF and peak factor depends the time-varying RMS and the

time duration. Unlike Cases 1 to 3, Case 4 has a constant RMS and has a sufficient time to reach a larger extreme value. The influence of transient winds on the extreme response can also be well understood from the upcrossing theory, which is to be discussed in the next section.

Table 2 Comparison of Cases 1 and 3 under different wind speeds (H =200 m)

	$U_{\max}=40$ m/s		$U_{\max}=50$ m/s		$U_{\max}=60$ m/s	
	Case 1	Case 3	Case 1	Case 3	Case 1	Case 3
Maximum RMS	0.144	0.147	0.174	0.172	0.172	0.184
Mean extreme	0.63	0.62	0.68	0.65	0.68	0.68
GRF	1.58	1.55	1.70	1.63	1.70	1.70
Peak factor	1.60	1.50	1.61	1.47	1.63	1.52

6. EXTREME VALUE OF NONSTATIONARY RESPONSE BASED ON UPCROSSING RATE

The extreme value of a nonstationary Gaussian process $R(t)$ over a given time period T can also be estimated based on upcrossing theory. By "Poisson approximation of crossings", the mean upcrossing rate at level of r at any time t can be given by (e.g., Lutes and Sarkani 2004)

$$\nu(r,t)=\sigma_{\dot{R}}(t)/[2\pi\sigma_R(t)]\exp\left[-(r-\mu_R(t))^2/[2\sigma_R^2(t)]\right] \tag{15}$$

where $\mu_R(t)$ and $\sigma_R(t)$ are the time varying mean and RMS of $R(t)$, respectively; and $\sigma_{\dot{R}}(t)$ is the time varying RMS of $\dot{R}(t)$. As the building response $R(t)$ can be regarded as a narrow band process with the central frequency of the building natural frequency ω_1, $\sigma_{\dot{R}}(t)/\sigma_R(t)\approx\omega_1$.

The cumulative distribution function (CDF) of the extreme value of $R(t)$ over time period of T is given as (e.g., Lutes and Sarkani 2004)

$$Q_{\max}(r)=\exp[-\int_0^T\nu(r,t)dt]\approx\exp[-\exp(-\alpha_r(r-\hat{r}))] \tag{16}$$

The mode $\hat{r}$ and dispersion parameter $1/\alpha_r$ are determined by linearly fitting the curve $-\ln[-\ln(Q_{\max}(r))]$ as a function of r. The mean and RMS are subsequently quantified as

$$\mu_{r,\max}=\hat{r}+0.5772/\alpha_r,\quad \sigma_{r,\max}=\pi/(\sqrt{6}\alpha_r) \tag{17}$$

It is noted for a stationary process where $\nu(r,t)=\nu(r)$, the aforementioned formula reduces to that provided by Davenport (1964). The mean extreme values, corresponding GRFs and peak factors for these 4 cases are summarized in Table 1. It is seen that the results from the upcrossing approach is very close to those from the time domain simulation. It should be noted that the coefficient of variation of extreme value $\sigma_{r,\max}/\mu_{r,\max}$ for these 4 cases varies from 10% to 13%, which is close to that of the corresponding stationary case.

7. CONCLUDING REMARKS

A time domain analysis framework was presented for estimating tall building response excited by nonstationary wind events. Comparison with the frequency domain approach showed that the time domain approach offered very agreeable estimations of nonstationary response characteristics. Based on the simulated multiple samples of wind fluctuations and the calculated building responses, the transient nature in nonstationary wind was found to lead a smaller and lagged maximum RMS value and a smaller peak response due to less "build-up" time.

A simplified model was proposed to describe the nonstationary wind fluctuation as a uniformly modulated process with a modulation function as the time-varying mean. Response

analysis using this model illustrated that almost same response characteristics were obtained. This was attributed to the fact that the tall building response was dominated by the wind spectra around the natural frequency, which were almost unaffected by the approximate modeling. It should be noted that in the case of middle- and low-rise buildings, the simulation using wavelets-based EPSD will offer more detailed time-frequency information of nonstationary wind fluctuations and leads to more adequate estimation of their effects on buildings.

The approach based on the mean upcrossing rate of nonstationary process provided not only the similar extreme values of the response compared to those from the time domain simulation, but more detailed information of the influence of the instantaneous statistics on the extreme value. Compared to the corresponding stationary response, the nonstationary stationary response has a smaller peak factor and GRF due to insufficient time duration to develop extreme.

8 ACKNOWLEDGMENTS

The supports by "the Fundamental Research Funds for the Central Universities (No. SWJTU11CX018)" and the new faculty startup funds provided by Southwest Jiaotong University are gratefully acknowledged.

9 REFERENCES

1 L. Chen, and C. W. Letchford, Parametric study on the alongwind response of the CAARC building to downbursts in the time domain, J. Wind. Eng. Ind. Aerodyn., 92(9), (2004), 703-724.
2 X. Chen, Analysis of alongwind tall building response to transient nonstationary winds, J. Struct. Eng., 134(5), (2008), 782-791.
3 X. Chen, M. Matsumoto, and A. Kareem, Time domain flutter and buffeting response analysis of bridges, J. Eng. Mech., 126(1), (2000). 7-16.
4 E. C. C. Choi, Field measurement and experimental study of wind speed profile during thunderstorms, J. Wind. Eng. Ind. Aerodyn., 92, (2004), 275–290.
5 I. Daubechies, Ten lectures on wavelets, Society for Industrial and Applied Mathematics, Philadelphia, PA., (1992).
6 A. G. Davenport, Note on the distribution of the largest value of a random function with application to gust loading. Proc., Instit. of Civil Eng., 28, (1964), 187-196.
7 G. Deodatis, Non-stationary stochastic vector processes: seismic ground motion applications. Prob. Eng. Mech., 11, (1996), 149–68.
8 T. T. Fujita, Downbursts: meteorological features and wind field characteristics. J. Wind. Eng. Ind. Aerodyn., 36, (1990), 75–86.
9 K. D. Gast, and J. L. Schroeder, Supercell rear-flank downdraft as sampled in the 2002 thunderstorm outflow experiment. Proc., 11th Int. Conf. on Wind Eng., Lubbock ,TX, (2003), 2233-2240.
10 G. Huang, and X. Chen, Wavelets-based estimation of multivariate evolutionary spectra and its application to nonstationary downburst winds, Eng. Struct., 31(4), (2009), 976-989.
11 J. D. Holmes, G. Forristall, and J. McConochie. Dynamic response of structures to thunderstorm winds, Proc., 10th Americas Conf. on Wind Eng. (10ACWE) (CD-ROM), Baton Rouge, La., (2005), 1-6.
12 J. D. Holmes, and S. E. Oliver, An empirical model of a downburst, Eng. Struct., 22, (2000),1167–1172.
13 D. Kwon, and A. Kareem, Gust-front factor: new framework for wind load effects on structures. J. Eng. Struct., 135(6), (2009), 717-732.
14 C.W. Letchford, and M.T. Chay, Pressure distributions on a cube in a simulated thunderstorm downburst, Part B: moving downburst observations, J. Wind Eng. Ind. Aerodyn., 90, (2002), 733-753.
15 L. D. Lutes, and S. Sarkani, Random vibration: Analysis of structural and mechanical systems. Elsevier, NY, (2004).
16 M.S. Mason, G.S. Wood and D.F. Fletcher, Numerical simulation of downburst winds, J. Wind Eng. Ind. Aerodyn., (97), (2009), 523–539.
17 Priestley, M. B.. Spectral analysis and time series, Academic, NY, (1981).
18 G. P. Solomos, and P. D. Spanos, Oscillator response to nonstationary excitation, J. Appl. Mech., 51(4), (1984), 907-912.
19 P. D. Spanos, and G. Failla, Evolutionary spectra estimation using wavelets, J. Eng. Mech., 130(8), (2004), 952-960.

The Seventh International Colloquium on Bluff Body Aerodynamics and Applications (BBAA7)
Shanghai, China; September 2-6, 2012

A state-space model for the wind-induced response of tall buildings with errors in the lateral loading

Luca Caracoglia

Northeastern University, 360 Huntington Avenue, Boston, Massachusetts, USA

ABSTRACT: The dynamic response of a tall building due to turbulent wind is analyzed in this study. A model is proposed to account for errors in the lateral loading, for example emerging from aerodynamic modeling assumptions, used to estimate the load in a wind tunnel test of a scaled model. The buffeting response at full scale is predicted by considering a linear structure with primary bending planes, oriented as the vertical faces, and mean loading orthogonal to one of the faces. The CAARC benchmark building is employed in the simulations. The model is based on a state-space formulation, stochastic calculus and generalized Markov-type state vector with state augmentation.

KEYWORDS: Tall buildings, stationary dynamic response, lateral loading correlation error, stochastic calculus, Reduced Fokker-Plank Equation.

1 INTRODUCTION

Risk-based methods for estimating the wind loading response of tall buildings, accounting for uncertainty in the lateral loading estimation, have been recently proposed (Bashor & Kareem[1], Chen & Huang[2], Jain *et al.*[3], Norton *et al.*[4]). Nevertheless, most methods are developed for ad-hoc problems, such as a specific building or a given structural configuration. A new generalized framework for the simulation and analysis of wind-induced response of tall buildings, in which effects of "errors" in the estimation of the lateral loading are incorporated, is currently under investigation (e.g., Smith & Caracoglia[5]). The ultimate goal of the research is to develop algorithms for performance-based assessment of peak response under severe wind excitation with an application to structural serviceability.

The fundamental hypothesis of the proposed analysis framework requires "error" propagation to be directly incorporated into the dynamics of tall and flexible buildings. Errors in loading estimation can result from aerodynamic modeling assumptions or simplifications used to enable wind tunnel experimentation. A typical example, commonly encountered in the engineering practice during the interpretation of high-frequency force-balance (HFFB) data, is the need for compensation of the idealized mode shapes, assumed in an HFFB wind tunnel test, due to imperfect planarity of lateral modes in the full-scale structure (e.g., Tse *et al.*[6]).

In this paper a preliminary numerical model is presented and discussed. Lateral buffeting loading and stationary response are investigated. Quasi-steady approximation is used to derive the lateral loading model.

Due to parametric random error propagation, the stationary response of the building may deviate from standard second-moment random vibration theory. Therefore, the error-contaminated response is directly estimated from the joint-probability of an augmented state vector, which includes several state variables: generalized modal coordinates, turbulence variables, generalized correlation length of the lateral loading. The proposed model also builds on the results of a stochastic algorithm, proposed in recent years for uncertainty simulation and dynamic analysis of slender bridges (Caracoglia[7]).

2 THEORETICAL BACKGROUND

2.1 *Fluctuating wind loading and generalized response of the CAARC building*

This section describes the derivation of the state-space model for dynamic response in the time domain. This new model is derived from the standard approach for building aerodynamics in the frequency domain (e.g., Davenport[8], Melbourne[9], Kareem[10], Piccardo & Solari[11], Kareem[12]). The dynamics of a prototype tall building is studied under the general hypothesis of linear structural behavior. The prototype structure is modeled after the CAARC benchmark building (Melbourne[9]), with rectangular floor-plan of dimensions D_x and D_y and height h. Figure 1 shows a schematic of the building geometry and wind loading; the mean wind direction and mean loading plane is orthogonal to the vertical face of width D_y (Fig. 1b). Figure 1a also coincides with the along-wind loading plane and primary bending plane for the building. Quantities $x(z,t)$ and $y(z,t)$ are used to model the dynamic displacements in the primary bending planes of the structure, as indicated in Figure 1b. Torsional effects are neglected in this study.

The CAARC building mass is assumed as uniformly distributed along the height of the structure with $m(z)$ mass per unit height; the dynamic lateral response in the two primary lateral planes is represented by modal superposition, accounting for the fundamental modes only, as: $x(z,t)=\Phi_{1x}(z)D_x\xi_{1x}(t)$ along wind (Fig. 1b), and $y(z,t)=\Phi_{1y}(z)D_x\xi_{1y}(t)$ in the transverse direction; ξ_{1x} and ξ_{1y} are dimensionless modal coordinates; $\Phi_{1x}(z)$ and $\Phi_{1y}(z)$ are dimensionless mode shapes of the first two lateral modes with frequencies n_{1x} and n_{1y}, respectively. Modal damping ratios are ζ_{1x} and ζ_{1y} with respect to critical value. The plane of bending for mode "1y" is not shown in Figure 1a since it is orthogonal to the elevation plane in the figure.

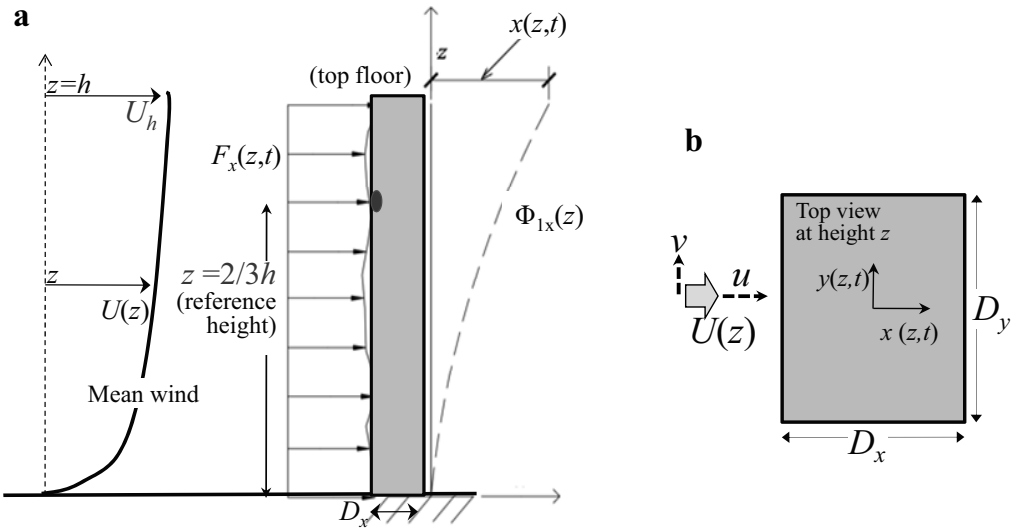

Figure 1. Schematic of the CAARC building with coordinate system and lateral wind loading: (a) lateral elevation view, (b) floor-plan view.

The fluctuating loading model operates in state space by assuming boundary layer wind with mean $U(z)$, stationary turbulence in the two directions, $u(z,t)$, $v(z,t)$ and quasi-steady aerodynamics (Fig. 1b). The along-wind and across-wind buffeting loading per unit height is written in the time domain as (Piccardo & Solari[11]):

$$F_x(z,t)=\frac{\rho D_x U^2(z)}{2}\left\{-2C_D\frac{\dot{x}(z,t)}{U(z)}+(\hat{C}_D-C_L)\frac{\dot{y}(z,t)}{U(z)}\right\}+\rho D_x U(z)C_D u(z,t) \tag{1}$$

$$F_y(z,t)=\frac{\rho D_x U^2(z)}{2}\left\{2C_L\frac{\dot{x}(z,t)}{U(z)}-(\hat{C}_L+C_D)\frac{\dot{y}(z,t)}{U(z)}\right\}+\frac{\rho D_x U(z)}{2}\left[2C_L u(z,t)+(\hat{C}_L+C_D)v(z,t)\right] \quad (2)$$

In equations above ρ=1.25 kg/m^3 is the air density. The "dot" symbol designates derivation with respect to time t. The static force coefficients per unit height are independent of z and are normalized with respect to width D_x: drag C_D per unit z and its derivative with respect to mean-wind direction $\hat{C}_D = dC_D/d\alpha$, "lift" (or transverse lateral force) C_L and $\hat{C}_L = dC_L/d\alpha$.

The mean wind velocity is referenced to the value at the top floor $z=h$ (U_h in Fig. 1a) $U(z)=U_h\Delta(z)$, with $\Delta(z)=(z/h)^g$ following a power-law velocity profile (as in Melbourne[9]). If modal superposition is employed, the previous equations can be rewritten as

$$F_x(z,t)=\frac{\rho D_x^2 U_h^{\,2}}{2}\Delta(z)\left\{-2C_D\frac{\Phi_{1x}(z)\dot{\xi}_{1x}}{U_h}+(\hat{C}_D-C_L)\frac{\Phi_{1y}(z)\dot{\xi}_{1y}}{U_h}\right\}+\rho D_x U_h\Delta(z)C_D u(z,t)$$

$$F_y(z,t)=\frac{\rho D_x^2 U_h^{\,2}}{2}\Delta(z)\left\{2C_L\frac{\Phi_{1x}(z)\dot{\xi}_{1x}}{U_h}-(\hat{C}_L+C_D)\frac{\Phi_{1y}(z)\dot{\xi}_{1y}}{U_h}\right\} \quad (3,4)$$

$$+\frac{\rho D_x U(z)\Delta(z)}{2}\left[2C_L u(z,t)+(\hat{C}_L+C_D)v(z,t)\right]$$

Modal superposition is used in Equations 3 and 4, under the hypothesis that modes "1x" and "1y" are purely planar, with mode shape $\Phi_{1x}(z)$ acting on the z-y plane and $\Phi_{1y}(z)$ on the z-x plane. Generalized forces (Q_{1x}, Q_{1y}) and modal masses (M_{1x}, M_{1y}) of "1x" and "1y" modes are:

$$Q_{1x}=\int_0^h \Phi_{1x}(z)F_x(z,t)dz, \qquad Q_{1y}=\int_0^h \Phi_{1y}(z)F_y(z,t)dz \quad (5,6)$$

$$M_{1x}=\int_0^h \left[\Phi_{1x}(z)\right]^2 m(z)dz, \qquad M_{1y}=\int_0^h \left[\Phi_{1y}(z)\right]^2 m(z)dz \quad (7,8)$$

If the dynamic response is expressed in terms of time $s=tU_h/D_x$ and dimensionless frequencies $K_{1x}=2\pi n_{1x}D_x/U_h$, $K_{1y}=2\pi n_{1y}D_x/U_h$, the generalized equations of modes "1x" and "1y" are

$$\xi_{1x}''+2(\zeta_{1x}+\mathrm{H}_{1x,1x}C_D)K_{1x}\xi_{1x}'+\mathrm{H}_{1x,1y}(C_L-\hat{C}_D)K_{1y}\xi_{1y}'+K_{1x}^2\xi_{1x}=\frac{\rho D_x^2 h C_D}{M_{1x}}\int_0^h \Delta(z)\hat{u}(z,s)\Phi_{1x}(z)\frac{dz}{h} \quad (9)$$

$$\xi_{1y}''+\left[2\zeta_{1y}+\mathrm{H}_{1y,1y}(C_D+\hat{C}_L)\right]K_{1y}\xi_{1y}'-2C_L\mathrm{H}_{1y,1x}K_{1x}\xi_{1x}'$$

$$+K_{1y}^2\xi_{1y}=\frac{\rho D_x^2 h}{M_{1y}}\left[C_L\int_0^h \Delta(z)\hat{u}(z,s)\Phi_{1y}(z)\frac{dz}{h}+(C_D+\hat{C}_L)\int_0^h \Delta(z)\hat{v}(z,s)\Phi_{1y}(z)\frac{dz}{h}\right] \quad (10)$$

In the previous equations the prime symbol designates derivation with respect to s; also, the turbulence components have been normalized as $\hat{u}=u/U_h$ and $\hat{v}=v/U_h$.

In Equations 10 and 11 fluid-structure coupling terms are introduced. These are derived from the quantities enclosed within braces in Equations 3 and 4; they become, for mode "1x" and "1y" respectively:

$$\mathrm{H}_{1x,1x}=\frac{\rho D_x^2 h}{2K_{1x}M_{1x}}\int_0^h \Delta(z)\left[\Phi_{1x}(z)\right]^2\frac{dz}{h},\qquad \mathrm{H}_{1x,1y}=\frac{\rho D_x^2 h}{2K_{1y}M_{1x}}\int_0^h \Delta(z)\Phi_{1x}(z)\Phi_{1y}(z)\frac{dz}{h} \tag{11}$$

$$\mathrm{H}_{1y,1y}=\frac{\rho D_x^2 h}{2K_{1y}M_{1y}}\int_0^h \Delta(z)\left[\Phi_{1y}(z)\right]^2\frac{dz}{h},\qquad \mathrm{H}_{1y,1x}=\frac{\rho D_x^2 h}{2K_{1x}M_{1y}}\int_0^h \Delta(z)\Phi_{1x}(z)\Phi_{1y}(z)\frac{dz}{h} \tag{12}$$

The loading terms on the right-hand side of Equations 9 and 10 are a function of along-wind and across-wind turbulence components at various z; loads may be simulated by separating the dependency on z and time s after rewriting the partially correlated turbulence-induced terms as equivalent fully correlated lateral loads, acting on a reduced "projected area", i.e., referenced to a Modal Correlation Length (MCL) in vertical direction. This principle has often been used in wind engineering and is compatible with the assumptions of the Equivalent Wind Spectrum Technique (Piccardo & Solari[11], Solari[13]). In the absence of loading errors, three MCLs are required by the model in Equations 9 and 10: $\Lambda_{1x,u}$, $\Lambda_{1y,u}$, $\Lambda_{1y,v}$. These quantities are dimensionless, normalized to the height h, and are computed by least-squares from:

$$\left[\Lambda_{1r,u}\right]^2=\int_0^h\int_0^h \Delta(z)\Delta(\upsilon)\Phi_{1r}(z)\Phi_{1r}(\upsilon)\exp\left[-\frac{2c_{z,u}n_{1r}}{U_h}\frac{|z-\upsilon|}{\Delta(z)+\Delta(\upsilon)}\right]\frac{dzd\upsilon}{h^2} \tag{13}$$

$$\left[\Lambda_{1y,v}\right]^2=\int_0^h\int_0^h \Delta(z)\Delta(\upsilon)\Phi_{1y}(z)\Phi_{1y}(\upsilon)\exp\left[-\frac{2c_{z,v}n_{1y}}{U_h}\frac{|z-\upsilon|}{\Delta(z)+\Delta(\upsilon)}\right]\frac{dzd\upsilon}{h^2} \tag{14}$$

Equation 13 is expressed in generic form with mode index "r" equal to x or y. For example, the square root of Equation 13, with $r=x$, is $0<\Lambda_{1x,u}\leq 1.0$, i.e., the MCL of the 1x-mode lateral loading (predominantly along-wind). In both Equation 13 and 14 the spatial coherence coefficients, $c_{z,u}=10$ and $c_{z,v}=6.67$, are defined in accordance with standard approaches. If Equations 13 and 14 are utilized, Equations 9 and 10 can be simplified as

$$\xi_{1x}''+2(\zeta_{1x}+\mathrm{H}_{1x,1x}C_D)K_{1x}\xi_{1x}'+K_{1y}\mathrm{H}_{1x,1y}(C_L-\hat{C}_D)\xi_{1y}'+K_{1x}^2\xi_{1x}=\frac{\rho D_x^2 h C_D}{M_{1x}}\Lambda_{1x,u}\hat{u}_{0.6h}(s) \tag{15}$$

$$\xi_{1y}''+\left[2\zeta_{1y}+\mathrm{H}_{1y,1y}(C_D+\hat{C}_L)\right]K_{1y}\xi_{1y}'-2C_L\mathrm{H}_{1y,1x}K_{1x}\xi_{1x}'$$
$$+K_{1y}^2\xi_{1y}=\frac{\rho D_x^2 h}{M_{1y}}\left[C_L\Lambda_{1y,u}\hat{u}_{0.6h}(s)+(C_D+\hat{C}_L)\Lambda_{1y,v}\hat{v}_{0.6h}(s)\right] \tag{16}$$

In Equations 15 and 16 the turbulence components are referenced to $z=0.6h\approx 2/3h$ (Solari[13]) as $\hat{u}_{0.6h}(s)=\hat{u}(z=0.6,s)$ and $\hat{v}_{0.6h}(s)=\hat{v}(z=0.6,s)$, as also schematically depicted in Figure 1a.

2.2 *Stochastic dynamics and state-space model*

The dynamic system of equations in the time domain $s=tU_h/D_x$ is transformed into a stochastic differential system of the Itô-type (Grigoriu[14]) to simulate effects of errors in the lateral loading.

In this study, random perturbation is applied to the MCL of the 1x-mode lateral loading, $\Lambda_{1x,u}$, in Equation 13 (with $r=x$), whereas quantities $\Lambda_{1y,u}$ and $\Lambda_{1y,v}$ are considered marginally affected by errors and, therefore, they are two deterministic constants. This perturbation is simulated by

replacing the deterministic quantity $\Lambda_{1x,u}$ in Equation 15 by $(\Lambda_{1x,u}+\lambda_u)$; λ_u is a zero-mean dimensionless random variable. The quantity $\Lambda_{1x,u}$, which is estimated through Equation 13, can be interpreted as the mean value of the MCL with λ_u being a measure of its error. As a result, while Equation 16 is still deterministic, Equation 15 is rewritten as

$$\xi_{1x}'' + 2(\zeta_{1x} + \mathrm{H}_{1x,1x}C_D)K_{1x}\xi_{1x}' + K_{1y}\mathrm{H}_{1x,1y}(C_L - \hat{C}_D)\xi_{1y}' + K_{1x}^2\xi_{1x} = \frac{\rho D_x^2 h C_D}{M_{1x}}\left(\Lambda_{1x,u} + \lambda_u\right)\hat{u}_{0.6h}(s) \tag{17}$$

The stochastic differential system is subsequently derived from Equations 16 and 17 in state-space form by simulating the time-dependent turbulence components $\hat{u}_{0.6h}$ and $\hat{v}_{0.6h}$ as the outputs of two auto-regressive filters as a function of s, applied to a scalar Wiener process of unit variance $W(s)$. This hypothesis enables the subsequent derivation of an Itô-type system:

$$d\hat{u}_{0.6h}(s) = -G_{1u}\hat{u}_{0.6h}(s)ds + G_{2u}dW(s) \tag{18}$$

$$d\hat{v}_{0.6h}(s) = -G_{1v}\hat{v}_{0.6h}(s)ds + G_{2v}dW(s) \tag{19}$$

In Equations 18 and 19, G_{1u}, G_{2u}, G_{1v} and G_{2v} are deterministic constants, which can be indirectly inferred from the power spectral density of turbulence (e.g., Caracoglia[7]) and are evaluated at z=0.6h. Equations 18 and 19 are written in differential form in accordance with Itô's differentiation rule.

Equations 18 and 19 are subsequently combined with Equations 16 and 17 and re-written in state-space form after augmentation (Grigoriu[14]) to obtain a stochastic differential system as a function of state vector **Z**(s). This vector is composed of physical states (generalized coordinates ξ_{1x}, ξ_{1y} and their derivatives), wind turbulence states ($\hat{u}_{0.6h}$ and $\hat{v}_{0.6h}$) and random variable λ_u. The stochastic differential equation, with $\mathbf{Z}(s)=[\xi_{1x}(s),\xi_{1y}(s),\xi'_{1x}(s),\xi'_{1y}(s),\hat{u}_{0.6h}(s),\hat{v}_{0.6h}(s),\lambda_u]^{\mathrm{T}}$ being a column vector and $s=tU_h/D_x$ a dimensionless time, is:

$$d\mathbf{Z}(s) = \mathbf{a}(\mathbf{Z}(s))ds + \sqrt{2\pi}\mathbf{d}dW(s) \tag{20}$$

In Equation 20, valid for for $s\geq 0$, **a** is a nonlinear (drift) function of **Z**(s) and $\mathbf{d} = \left[\mathbf{0}^{4\times 1}, G_{2u}, G_{2v}, 0\right]^{\mathrm{T}}$ is a scalar $n\times 1$ (diffusion) vector collecting some of the coefficients in Equations 18 and 19.

The dimension of the state vector is n=7. Initial conditions on **Z** at s=0 are irrelevant since the steady-state response (as $s\rightarrow+\infty$) is investigated. If the random state vector is relabeled as $\mathbf{Z}=[Z_1,..,Z_n]^{\mathrm{T}}$, **a**(**Z**) is

$$\mathbf{a} = \begin{bmatrix} Z_3 \\ Z_4 \\ -2K_{1x}(\zeta_{1x} + \mathrm{H}_{1x,1x}C_D)Z_3 - K_{1y}\mathrm{H}_{1x,1y}(C_L - \hat{C}_D)Z_4 - K_{1x}^2 Z_1 + \rho D_x^2 h C_D\left(M_{1x}\right)^{-1}\left(\Lambda_{1x,u} + Z_7\right)Z_5 \\ -\left[2\zeta_{1y} + \mathrm{H}_{1y,1y}(C_D + \hat{C}_L)\right]K_{1y}Z_4 - 2C_L\mathrm{H}_{1y,1x}K_{1x}Z_3 - K_{1y}^2 Z_2 + \dfrac{\rho D_x^2 h}{M_{1y}}\left[C_L\Lambda_{1y,u}Z_5 + (C_D + \hat{C}_L)\Lambda_{1y,v}Z_6\right] \\ -G_{1u}Z_5 \\ -G_{1v}Z_6 \\ 0 \end{bmatrix} \tag{21}$$

2.3 *Algorithm for assessing the joint-probability density function of the state vector*

The stationary joint-probability density function (PDF) of $\mathbf{Z}$, $p(\mathbf{z})$, can be determined from system 20 through the Reduced Fokker-Planck Equation (Grigoriu[14]) as $s\rightarrow+\infty$ and with r=4:

$$\sum_{j=1}^{n-1}\frac{\partial}{\partial z_j}\left[\mathrm{a}_j(\mathbf{z})p(\mathbf{z})\right]-\pi\sum_{j=r+1}^{n-1}\sum_{k=r+1}^{n-1}R_{jk}\frac{\partial^2 p(\mathbf{z})}{\partial z_j\partial z_k}=0 \tag{22}$$

The dependency on the time variable is irrelevant at steady-state; its explicit designation is omitted in the subsequent derivations. In Equation 22, $\mathbf{R}=\mathbf{d}^{\mathrm{T}}\mathbf{d}$ is a constant matrix with non-zero elements for $j>r$ and $k>r$. For the numerical solution of the previous equation the joint-PDF is first represented in terms of the probability potential (Lin & Cai[15]), $\varphi(\mathbf{z})$, as $p(\mathbf{z})=C_f\exp[\varphi(\mathbf{z})+\varphi_0]$ with C_f and φ_0 being two integration constants. These must satisfy the condition $\int..\int p(\mathbf{z})\mathrm{d}\mathbf{z}=1.0$. As a result, Equation 22 becomes

$$\sum_{j=1}^{n-1}\left[\mathrm{a}_j(\mathbf{z})\frac{\partial\varphi}{\partial z_j}+\frac{\partial\,\mathrm{a}_j(\mathbf{z})}{\partial z_j}\right]-\pi\sum_{j=r+1}^{n-1}\sum_{k=r+1}^{n-1}R_{jk}\left[\frac{\partial\varphi}{\partial z_j}\frac{\partial\varphi}{\partial z_k}+\frac{\partial^2\varphi}{\partial z_j\partial z_k}\right]=0 \tag{23}$$

A numerical algorithm has been developed to solve Equation 23, by adaptation of the approach proposed by Soize[16]. The numerical algorithm employs a Galerkin expansion for $\varphi(\mathbf{z})$: $\varphi(\mathbf{z})=\sum\kappa_{\boldsymbol{\beta}}h_{\boldsymbol{\beta}}(\mathbf{z})$. This expansion utilizes a basis of mutually-orthogonal Normalized Hermite Polynomials (NHP) $h_{\boldsymbol{\beta}}(z_1,..,z_j,..,z_n)=h_{\beta 1}(z_1)\times..\times h_{\beta j}(z_j)\times..\times h_{\beta n}(z_n)$ (Soize[16]). The degree of each scalar Hermite Polynomial (e.g., $h_{\beta 1}(z_1)$) is designated by its index (e.g., for $\beta_1=2$ $h_{\beta 1}(z_1)=(z_1^2-1)/\sqrt{2}$). The vector index $\boldsymbol{\beta}=(\beta_1,..,\beta_j,..,\beta_n)$ collects the degrees of each individual $h_{\beta j}$ function. The degree of each $h_{\boldsymbol{\beta}}$ is determined from $\sum\beta_j$, whereas a scalar index l=1 to $l=d_{\mathrm{NHP}}$ is used to label and group all the $\boldsymbol{\beta}$ vector indices in ascending order, based on degree and variables $z_1,..,z_n$.

The algorithm operates by exploiting the orthogonality of the NHPs with respect to the standard Gaussian vector of independent $\mathbf{z}$. The unknown coefficients of the series, $\kappa_{\boldsymbol{\beta}}$, are found by integration (Galerkin averaging) of Equation 23 with respect to the Gaussian vector over the multi-variable domain $\mathbf{z}$, after substituting $\varphi(\mathbf{z})=\sum q_{\boldsymbol{\beta}}h_{\boldsymbol{\beta}}(\mathbf{z})$.

If the series $\varphi(\mathbf{z})=\sum q_{\boldsymbol{\beta}}h_{\boldsymbol{\beta}}(\mathbf{z})$ is truncated to the first d_{NHP} terms ($\kappa_{\boldsymbol{\beta}}$), Equation 23 can be transformed into a non-linear homogeneous algebraic system of d_{NHP} equations. The expansion should preserve the features of the NHPs until the third degree to account for parametric non-Gaussian uncertainty propagation. The generic l-th scalar equation of this non-linear algebraic system is related to the generic vector index $\boldsymbol{\gamma}$ in the expansion, and is

$$\sum_{\boldsymbol{\beta}=(1,...,0)}\left(E_{\boldsymbol{\gamma}\boldsymbol{\beta}}-\pi E_{\boldsymbol{\gamma}(\boldsymbol{\beta})^j}\right)\kappa_{\boldsymbol{\beta}}-\pi\sum_{\boldsymbol{\beta}=(1,...,0)}\sum_{\boldsymbol{\varepsilon}=(1,...,0)}\kappa_{\boldsymbol{\beta}}\kappa_{\boldsymbol{\varepsilon}}G_{(\boldsymbol{\gamma}),\boldsymbol{\beta},\boldsymbol{\varepsilon}}=0 \tag{24}$$

In the previous equation the index $\boldsymbol{\gamma}$ varies from $\boldsymbol{\gamma}$=(1,..,0) (l=1) to $\boldsymbol{\gamma}$=(0,..,1,2) (l=116= d_{NHP}); $\kappa_{\boldsymbol{\beta}}$ and $\kappa_{\boldsymbol{\varepsilon}}$ denote the generic unwknown coefficients. The $E_{\boldsymbol{\gamma}\boldsymbol{\beta}}$ terms coincide with a series of scalar terms, which are evaluated by numerical integration, whearas the scalar $E_{\boldsymbol{\gamma}(\boldsymbol{\beta})j}$ and $G_{(\boldsymbol{\gamma}),\boldsymbol{\beta},\boldsymbol{\varepsilon}}$ can be found in closed form (details omitted for brevity). Equations 23 and 24 highlight the main advantage of the algorithm, which is superior to Monte Carlo simulation for solving Equation 20, since it enables the assessment of the joint-PDF directly in closed form.

3 NUMERICAL SIMULATIONS: CAARC BUILDING

3.1 *Description of full-scale building properties*

The geometric, dynamic and aerodynamic properties of the CAARC building are derived from Melbourne[9]. Reference geometric dimensions are D_x = 30.5 m, D_y = 45.7 m and h = 183 m (Fig. 1). The mass per unit height is constant with $m(z)$=220,800 kg/m. The natural frequencies are taken as n_{1x}=0.20 Hz and n_{1y}=0.22 Hz, respectively. Mode shapes are approximately linear with height (Melbourne[9]): $\Phi_{1x}(z)=(z/h)$ and $\Phi_{1y}(z)=(z/h)$. Modal damping ratios are assumed as $\zeta_{1x} = \zeta_{1y}$ = 0.01 for both modes. The aerodynamic coefficients per unit elevation are inferred from the original experimental data (Melbourne[9]), as described in Smith & Caracoglia[5], as: C_D=1.0, $dC_D/d\alpha$ = -1.1, C_L = -0.1, $dC_L/d\alpha$ = -2.2.

Two mean wind scenarios are investigated: U_h = 20 m/s (moderate wind) and U_h = 40 m/s (high wind) evaluated at mean roof height. The MCL for U_h = 20 m/s are $\Lambda_{1x,u}=\Lambda_{1y,u}$=0.17 and $\Lambda_{1y,v}$=0.21; those for U_h = 40 m/s are $\Lambda_{1x,u}$=0.23, $\Lambda_{1y,u}$=0.22 and $\Lambda_{1y,v}$=0.25. The power spectral densities of both $\hat{u}_{0.6h}$ and $\hat{v}_{0.6h}$ components are used to determine the parameters of Equations 18 and 19; densities are based on the Harris model.

In the case of the along-wind component $\hat{u}_{0.6h}$ (Fig. 1b) the energy of the spectrum has been linked to a dimensionless form of the Harris spectrum, based on the data in Melbourne[9], evaluated at z=0.6h:

$$S_{\hat{u}_{0.6h}}(K)=\frac{\left[I_u\right]^2}{\Delta_u(0.6h)U_h}\frac{960}{\left(2+\tilde{f}\right)^{5/6}},\qquad \tilde{f}=\frac{1600K}{2\pi D_x\Delta_u(0.6h)} \tag{25, 26}$$

with reduced frequency $K=2\pi nD_x/U_h$ and turbulence intensity I_u=11% at z=0.6h. For $\hat{v}_{0.6h}$ the same expression as in Equation 25 is used with I_v replacing the quantity enclosed within brackets. However, a reduction of transverse turbulence intensity is postulated: I_v=8%. The dimensionless parameters of the autoregressive turbulence models, derived for both U_h = 20 m/s and U_h = 40 m/s, are summarized in Table 1. Details on the derivation of these parameters are omitted for brevity.

Table 1. Parameters used for $\hat{u}_{0.6h}$ and $\hat{v}_{0.6h}$ in Equations 18 and 19.

U_h (m/s)	I_u	G_{1u}	G_{2u}	I_v	G_{1v}	G_{2v}
20	11%	0.356	0.121	8%	0.356	0.091
40	11%	0.294	0.082	8%	0.294	0.009

3.2 *Hermite-Polynomial Galerkin expansion*

Figure 2 shows the dimensionless scalar coefficients $\kappa_{\boldsymbol{\beta}}$, associated with each $h_{\boldsymbol{\beta}}$ term of the Galerkin expansion of $\varphi(\mathbf{z})$ and obtained by numerically solving the nonlinear system (24). In this figure the dynamic response of the CAARC building with reference wind speed U_h=20 m/s is analyzed. The NHPs are ordered in ascending order and in accordance with vector index $\boldsymbol{\beta}$. As outlined in Section 2.3 the scalar index $1 \le l \le 116$, shown on the horizontal axis of the graph, is used to identify each term of the expansion. In the figure the $\kappa_{\boldsymbol{\beta}}$ terms are divided by first, second and third degree. For example l=1 belongs to to $\boldsymbol{\beta}$=(1,0,..,0) and $h_{(1,0,0,0,0,0,0)}=z_1$, l=7 corresponds to $\boldsymbol{\beta}$=(2,0,..,0) and $h_{(2,0,0,0,0,0,0)}=(z_1^2-1)/\sqrt{2}$), l=34 to $\boldsymbol{\beta}$=(3,0,..,0) and $h_{(3,0,0,0,0,0,0)}=(z_1^3-3z_1)/\sqrt{6}$.

In Figure 2, two cases are depicted, the difference being related to the numerical integration limits on $\mathbf{z}$, which are used by Galerkin expansion to numerically evaluate $E_{\gamma\boldsymbol{\beta}}$ in Equation 24.

"Effective" integration limits must be pre-selected a priori on a hyper-cube of the whole domain **z** in the proximity of the origin and must account for the local features of the polynomial functions defined through the NHP. Preliminary simulations have suggested as acceptable limiting values $|z_j| \leq 0.50$ for each $j=1,..,n$ or $|z_j| \leq 0.25$ (Domain "b" in Fig. 2). Since the integration to determine the $E_{\gamma\beta}$ is conducted numerically, selection of integration limits and a suitable number of integration points (5E+5) is crucial.

From the analysis of Figure 2 it can be concluded that the main features of the solution are preserved between the two cases: the continuous line is related to limits $|z_j| \leq 0.50$ and the dashed line is obtained with $|z_j| \leq 0.25$.

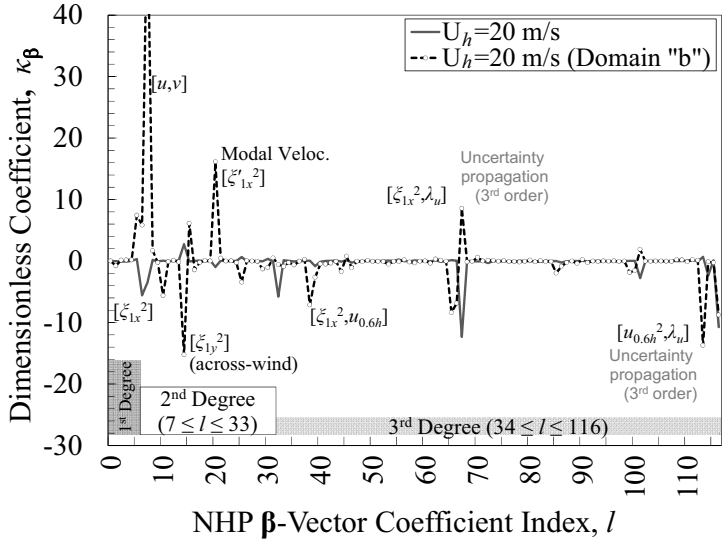

Figure 2. Normalized Hermite-Polynomials of the Galerkin expansion (U_h = 20 m/s).

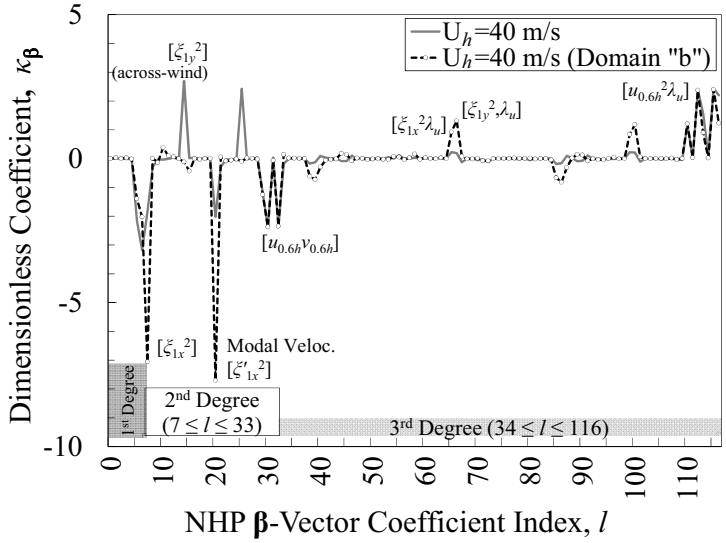

Figure 3. Normalized Hermite-Polynomials of the Galerkin expansion (U_h = 40 m/s).

A non-negligible variation in the magnitude of the κ_β parameters can be noticed in a few specific cases (e.g., l=5). Nevertheless, Figure 2 suggests that the proposed approach can replicate features typical of parametric uncertainty propagation; this observation is compatible

with the presence of non-negligible 3rd-degree polynomials in the figure, which are necessary to describe the non-Gaussian behavior in the state-space system. Figure 2 also shows that a limited number of $\kappa_{\boldsymbol{\beta}}$ terms are predominant in $\varphi(\mathbf{z})=\sum\kappa_{\boldsymbol{\beta}}h_{\boldsymbol{\beta}}(\mathbf{z})$ and, therefore, the joint-PDF; these are highlighted by indicating the corresponding state variables within brackets.

Similarly, Figure 3 depicts the numerical results obtained at large wind speed U_h=40 m/s for the same building type. The figure summarizes the results for both integration domains, i.e., limits $|z_j|\leq 0.50$ and $|z_j|\leq 0.25$ (Domain "b") imposed on each j=1,..,n. The vertical axis scale is not the same as in Figure 2.

Figure 3 tends to confirm the results at lower speed, since the same sub-set of relevant $\kappa_{\boldsymbol{\beta}}$ is observed; this fact suggests a preservation of the main features in the joint-PDF, which is numerically evaluated through $\varphi(\mathbf{z})=\sum\kappa_{\boldsymbol{\beta}}h_{\boldsymbol{\beta}}(\mathbf{z})$, if the mean wind speed U_h varies. Also, as U_h increases, the absolute value $|\kappa_{\boldsymbol{\beta}}|$ of the corresponding expansion terms (same $\boldsymbol{\beta}$) decreases. This remark is compatible with the fact that the overall load variance proportionally grows with U_h and turbulence energy.

3.3 *Integration constants of the joint-PDF*

From the discussion results in Figure 2 and Figure 3, it was inferred that the results obtained with the integration Domain "b" ($|z_j|\leq 0.25$) are preferable due to a more realistic combination of $\kappa_{\boldsymbol{\beta}}$, possibly more compatible with an actual full-scale scenario. This case is selected and analyzed in more detail in this section. The integration constants of the joint-PDF, $p(\mathbf{z})=C_f\exp[\varphi(\mathbf{z})+\varphi_0]$, C_f and φ_0, for both U_h=20 m/s and U_h=40 m/s are computed and shown in Table 2.

The quantities C_f and φ_0 depend on the random properties of λ_u, perturbing the $\Lambda_{1x,u}$. In this study, λ_u has zero mean and standard deviation $SD(\lambda_u)=0.25\Lambda_{1x,u}$ (25% of the mean value) This corresponds to $SD(\lambda_u)$=0.042 for U_h=20 m/s ($\Lambda_{1x,u}$=0.17) and $SD(\lambda_u)$=0.056 for U_h=20 m/s ($\Lambda_{1x,u}$=0.23).

The choice of employing two constants C_f and φ_0 is dictated by algorithmic efficiency. Since one condition can exclusively be imposed on the probability, $\int..\int p(\mathbf{z})d\mathbf{z}=1.0$, C_f and φ_0 are inherently dependent. In Table 2 φ_0 is initially pre-selected and C_f is subsequently determined. Even though some variability is observed in the table, the choice of an initial $\varphi_0<0$ leads to a more suitable, i.e., a finite value in C_f.

Table 2. Integration constants of $p(\mathbf{z})$, using Domain "b" solution in Figures 2 and 3

U_h (m/s)	Integr. limits	φ_0	C_f	φ_0	C_f	φ_0	C_f
20	$\lvert z_j\rvert \leq 0.25$	-1.83E+02	5.72E+00	4.76E+01	5.03E-29	0	8.37E-09
40	$\lvert z_j\rvert \leq 0.25$	-7.72E+00	1.50E-01	4.60E-01	7.20E-05	0	8.42E-05

(Note: j = 1,..,n-1)

4 CONCLUDING REMARKS

An analytically-based and numerically-implemented algorithm is proposed in this study for the simulation and analysis of modeling errors in the lateral buffeting loads for tall buildings. The model operates in time domain by employing state-space formulation and stochastic calculus techniques. The study shows that, if torsional effects are neglected, the buffeting response of a tall building can be successfully simulated. The paper demonstrates that it is possible to derive the joint probability density function of a generalized state vector, combining modal response with random turbulence and a random variable, which simulates errors in the modeling of the

correlation length of the loads. The algorithm enables the assessment of the joint-PDF directly by Galerkin expansion and is superior to "brute-force" Monte Carlo simulation, which operates by synthetically generating a series of realizations of the time-dependent response.

Buffeting response has been exclusively investigated at this stage. Preliminary results confirm the feasibility of this approach on a 183m building; sensitivity of the solution to the selection of integration domain limits has been noticed and is currently being considered for further investigation.

5 ACKNOLWDGEMENTS

This study was supported by the US National Science Foundation, CAREER Award 0844977. Findings, conclusions or recommendations are those of the author and do not necessarily reflect the views of the funding agency.

6 REFERENCES

1 R. Bashor and A. Kareem, Probabilistic performance evaluation of buildings: An occupant comfort perspective, Proc. 12th Int. Conference on Wind Engineering (12-ICWE), Cairns, Australia, July 1-6, 2007, pp. 1335-1342.
2 X. Chen and G. Huang, Evaluation of peak resultant response for wind-excited tall buildings, Engineering Structures, 31 (2009) 858-868.
3 A. Jain, M. Srinivasan and G.C. Hart, Performance based design extreme wind loads on a tall building, The Structural Design of Tall Buildings, 10 (2001) 9-26.
4 T. Norton, M.M. Abdullah and D. Stephens, Proposed methodology for performance-based vulnerability assessment of wind-excited tall buildings, In C.-K. Choi, J.D. Holmes, Y.-D. Kim and H.G. Kwak (Eds.), Fourth International Conference on Advances in Wind and Structures (AWAS'08), Techno-Press, South Korea, ISBN 978-89-89693-23-9-98530, Jeju Island, South Korea, 2008, pp. 1228-1246.
5 M.A. Smith and L. Caracoglia, A Monte Carlo based method for the dynamic "fragility analysis" of tall buildings under turbulent wind loading, Engineering Structures, 33 (2011) 410–420.
6 K.T. Tse, P.A. Hitchcock and K.C.S. Kwok, Mode shape linearization for HFFB analysis of wind-excited complex tall buildings, Engineering Structures, 31 (2009) 675-685.
7 L. Caracoglia, Effects of modeling and measurement errors on the aeroelastic response of flexible, long-span bridges, Proc. Fifth International Symposium on Computational Wind Engineering (CWE2010), Chapel Hill, North Carolina, USA May 23-27, 2010, pp. CD-ROM.
8 A.G. Davenport, Response of six building shapes to turbulent wind, Phil. Transaction of the Royal Society London Ser. A, 269 (1971) 385-394.
9 W.H. Melbourne, Comparison of measurements on the CAARC standard tall building model in simulated model wind flows, Journal of Wind Engineering and Industrial Aerodynamics, 6 (1980) 73-88.
10 A. Kareem, Lateral-torsional motion of tall buildings to wind loads, Journal of Structural Engineering, ASCE, 111 (1985) 2479-2496.
11 G. Piccardo and G. Solari, 3D wind-excited response of slender structures: closed-form solution, Journal of Structural Engineering, ASCE, 126 (2000) 936-943.
12 A. Kareem, Model for predicting the acrosswind response of buildings, Engineering Structures, 6 (1984) 136-141.
13 G. Solari, Equivalent Wind-Spectrum Technique: theory and applications, Journal of Structural Engineering, 114 (1988) 1303-1323.
14 M. Grigoriu, Stochastic calculus. Applications in science and engineering, Birkhäuser, Boston, MA, USA, 2002.
15 Y.K. Lin and G.Q. Cai, Probabilistic structural dynamics, McGraw-Hill, New York, New York, USA, 1995.
16 C. Soize, Steady-state solution of Fokker-Planck equation in higher dimension, Probabilistic Engineering Mechanics, 3 (1988) 196-206.

The Seventh International Colloquium on Bluff Body Aerodynamics and Applications (BBAA7)
Shanghai, China; September 2-6, 2012

Computational study of wind-fire-structure interactions and their impact on bushfire resistance design of housing

K.C.S. Kwok [a], Y. He [b], M. Poty [b]

[a] *Institute for Infrastructure Engineering, University of Western Sydney, Australia*
[b] *School of Computing, Engineering and Mathematics, University of Western Sydney, Australia*

ABSTRACT

This current paper presents the results of computational fluids dynamics (CFD) simulations of external flow over a cubic building block. The focus is given to the investigation of the domain size dependence of such simulations. This parametric study used a systematic examination of the pressure coefficient distribution around the block with stepwise variation in domain extensions in 4 directions relative to the block. The results revealed differences between the different domain expansions in each direction and the trend of a convergence. Dimensionless parameters were introduced to link the optimum domain size to the building size. The study identified the dominant direction that influences the domain dependence the most.

KEYWORDS: Domain dependence, sensitivity, pressure coefficient.

Nomenclature

C_p pressure coefficient
H characteristic building dimension (m)
H_i building size in i-direction (m)
P pressure (Pa)
s distance around the perimeter of building (m)
s^* non-dimensional distance =s/H
R Pearson correlation coefficient
T temperature (C, K)
t time (s)
U free stream velocity (m/s)
x, y, z coordinates of the computational domain (m)

Greek
α constant in the power law for wind velocity profile
Δ_i domain expansion in i-direction (m)
δ_i grid size in i-direction (m)

ρ density (kg/m^3)

Superscript
* non-dimensional parameter

1 INTRODUCTION

Bushfire is a natural phenomenon that occurs frequently in many places around the world, given favourable weather and fuel conditions, and ignition mechanisms naturally occurring, such as lightning, or man-made, such as fallen transmission lines. Most bushfires are dealt with and controlled by the various fire services at their early stages of development. However, bushfires which are difficult to control and with major fire runs, often in inaccessible areas, can develop into ragging catastrophic infernos causing widespread property damages and loss of lives, such as the recent Black Saturday Bushfire that claimed 173 lives and more than 2000 properties in Victoria, Australia on 7 February 2009 [1].

While considerable attention has been given to the principal agents of bushfire attack, including embers, radiant heat and flame contact [2], our knowledge about the characteristics of bushfire-enhanced winds and their impacts on buildings is relatively scarce. Early studies focused on the large scale, or meteorological scale interactions between wind and wild fires [3] and primarily on the effect of wind on fire spread [4]. Only recently, numerical investigations were conducted to study wind-bushfire-building interactions at the near ground level the scale comparable to building dimensions for different approach wind speeds and fire intensities [5-6]. The results demonstrated the exacerbation of wind conditions due to buoyancy effect created by a bushfire simulated as a line-like fire front. The fire-enhanced wind profile showed a significant increase in wind speed near the ground, and the speed-up effects were found to depend on the approach wind speed and the fire intensity. When the Silsoe 6 m cube was placed downstream from the fire front of a moderate intensity, the fire-enhanced wind caused a substantial increase in the positive windward wall pressures and a small decrease in the negative roof pressures, while the sidewall and leeward wall pressures remain relatively unchanged.

It is well known that the results of numerical simulations are grid dependent both in terms of grid cell size (or mesh resolution) and grid domain size [7-10]. Grid cell size sensitivity study using the particular numerical package, namely, the Fire Dynamics Simulator [11] has been investigated in a previous study [6]. Presented in the current paper is a continuous study on grid domain dependence.

1.1 *Grid dependence studies*

Murakami and Mochida [7] studied the behavior of an external flow over a cubic building. They focused on the influence of different mesh resolutions around the building, domain boundary conditions (free slip or non-slip conditions) and various wall functions (power or log law). Their investigations were carried out by comparing pressure coefficients, velocity vectors and solution or truncation errors between simulations and experiments. It was concluded that a mesh resolution in the order of $\delta x=H/24$ (or $\delta x=0.042H$), where H is the height of the cubic model, is necessary in windward building corner to avoid errors and behind the building to study the wake. Moreover, according to their results, it would be better to set the pressure rather than the velocity at domain boundary and the log law for wall condition shows better agreement with experiment.

In 1990, Baetke and Werner [12] studied external flow over a cubic building or over a square mounted rib respectively using a Reynolds averaged simulation scheme and a LES (Large Eddy

Simulation) simulation scheme. It was suggested that a mesh division of δx=19H/160 (or δx=0.12H), where H is the height of the rib, is necessary to obtain reasonable results.

More recently, He et al. [6] carried out a numerical study of wind-fire-building interactions. In their study a 6 meter cubic block was located downstream a fire bed and an external wind flow defined by $U_0(z)=U_r(z/z_r)^{\alpha}$ (where α=0.16, U_r=9.52 m/s and z_r=6 m). During this work, they began to simulate without fire and focused their study on grid dependence to find the mesh division which yields reasonably good agreement with experiments and is computationally economical. It was concluded that the optimum grid size was not necessarily the finest and the optimized grid size was δx=0.04H, similar to that found by Murakami and Mochida [7].

Yet, the domain dependence problem was often neglected. The computational domain was often set arbitrarily. It could cause serious errors because a non-appropriate domain size may overestimate or underestimate key parameters as pressure coefficient or flow velocity. He et al. [8] and Zhang et al. [9] studied particularly the domain dependence in building enclosure fire simulations. They carried out systematic investigations into the relationship between domain extension, vent opening size and the heat release rate of compartment fires. It was found that the necessary domain extension beyond the compartment boundary could be proportionally linked to the vent opening size and the heat release rate. Moreover the coefficient of proportionality depends on whether the fire is fuel controlled or ventilation controlled and the domain extension is more efficacious in the direction perpendicular to the vent opening.

Domain dependence study can be as dramatic as comparing between 2D and 3D simulations. Hostikka et al. [13] studied an external flow and fire behavior around a building block. Their primary interest is to examine the sensitivity of heat transfer (particularly radiant heat transfer) evaluation on grid dimension and grid density. They concluded that 3D domain is necessary for accurate evaluation of radiant heat transfer with grid size in the range of 0.02H<δx<0.04H.

The objective of the current study is to investigate the domain dependence problem in computational fluid dynamics studies of external flows using Fire Dynamic Simulator. The parameter of interest is the aerodynamic characteristics, or pressure coefficient distribution around a 6 m cube building block. This paper reports the first part of the study where no fire was involved.

2 METHODOLOGY

For carrying out this study, reference case was taken from He et al.'s simulation [6] using the Fire Dynamics Simulation 5 (FDS5) software. FDS5 solves numerically a form of the Navier-Stokes equations by employing Large Eddy Simulation (LES) scheme. This scheme uses a type of Smagorinsky k-ε model described in [11] to model the turbulence effect at the sub grid level and the core algorithm is a predictor-corrector scheme with second order accuracy in space and time [14].

He et al [6] have carried out a study to find the optimum grid size for a specified fire scenario. The same grid size was retained for the current study. Thus, during this investigation, multiple series of simulations with domain size extensions or contractions respectively in x, y and z directions were executed while keeping the same grid size. Each simulation has a domain size variation in only one direction to study the domain size dependence specifically in each direction. It was particularly important to take care of y direction, where the grid size is non-uniform, and keep the same mesh division around the building. So this parametric study uses a systematic examination of the results with stepwise variation in domain extension parameters. However this

stepwise variation, keeping the grid size constant, had to respect the restriction on cell numbers defined by the FDS User's Guide [10]. Thus the steps of domain size variation could not be maintained constant (Table 1). Moreover these domain extensions and contractions were described by non-dimensional parameters to allow future researchers to use the results for study with different building sizes.

The conclusion was obtained by comparing the predicted mean pressure coefficients in different cases and by identifying the parameters at which no significant difference occurs. The averaging was achieved by taking the predicted pressure during the quasi-steady period of simulation.

This domain dependence investigation was carried out firstly without involvement of fires. After finding the appropriate domain size, one more step was achieved. In order to observe the wind speed influence on the results, a simulation with variation in reference wind velocity was run. The criteria for determining the optimum domain size is that convergence is achieved in the predicted key parameter distributions, i.e. pressure coefficient distributions, within a prescribed relative error band and reasonable CPU time. The convergence is measured with two methods. On the one hand the Pearson correlation coefficient is calculated between the results of successive domain sizes simulations. On the other hand, the mean absolute pressure coefficient difference between results is also calculated.

2.1 *Domain description of the reference case*

As mentioned previously, reference case was taken from He et al.'s study [6]. The computational domain in reference case was a 40×30×18m rectangular space. A 6 meter cubic building block was located 25 meters downstream of the domain boundary. The origin of the *x*-*y*-*z* coordinate of the domain is set at the centre of the front base line of the building block as illustrate in Figure 1. Wind is blowing from left to right, along the positive *x* direction. The fire front of the bushfire, which is not involved during the first study step, is 3 m in width and runs in the entire domain in *y*-direction at the ground level. The trailing edge of this fire bed is located 20 meter upstream the left face of the building and the fire front is assumed stationary. The two domain boundaries in *y*-direction are closed and assumed slip conditions. The right and top boundaries are specified as "OPEN". All solid surfaces are specified smooth. The grid size in the reference case is 0.17, 0.24/0.42 and 0.15 m in *x*, *y* and *z* directions respectively. The grid size in *y* direction is non-uniform. A piecewise transformation was applied to achieve finer grid close to the building and relatively coarser grid further away from the building.

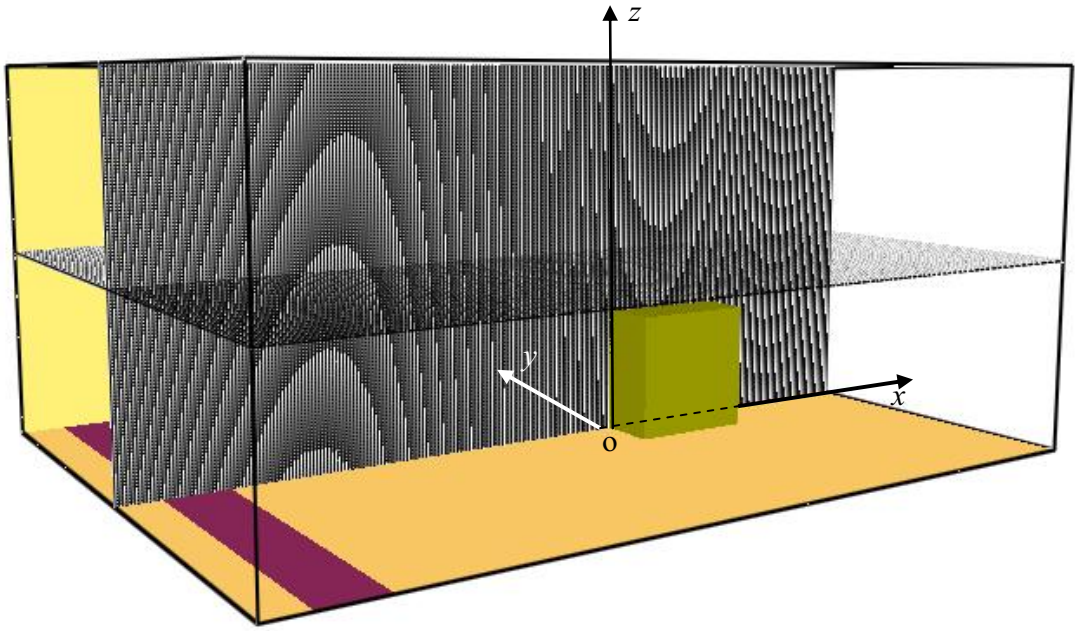

Figure 1. Computational domain and grid setup.

2.2 *Normalized parameters*

A group of normalize parameters are introduced to describe the dimension of the computation domain. The building block dimensions are defined as $H_x \times H_y \times H_z$. For the particular case investigated in the current study $H_x=H_y=H_z=H=6$ m. The domain expansion from the origin is denoted by Δx_+, Δx_-, Δy and Δz respectively in x_+, x_-, y and z directions. The domain expansion in y direction is symmetrical and in z is always positive. See Figure 2.

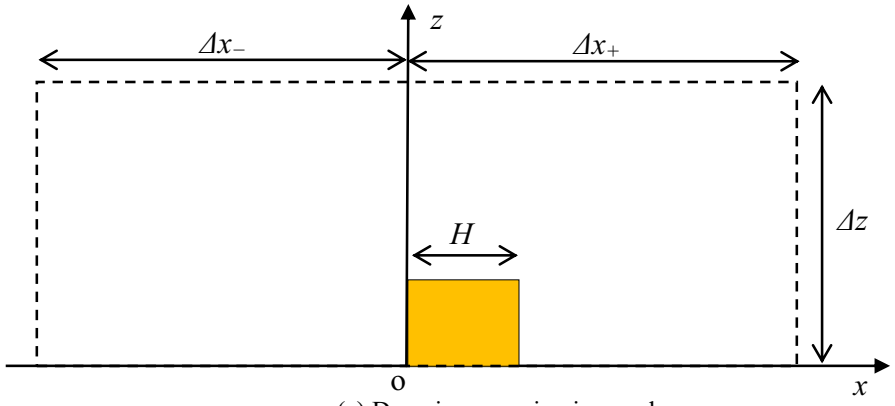

(a) Domain expansion in *x*-*z* plan

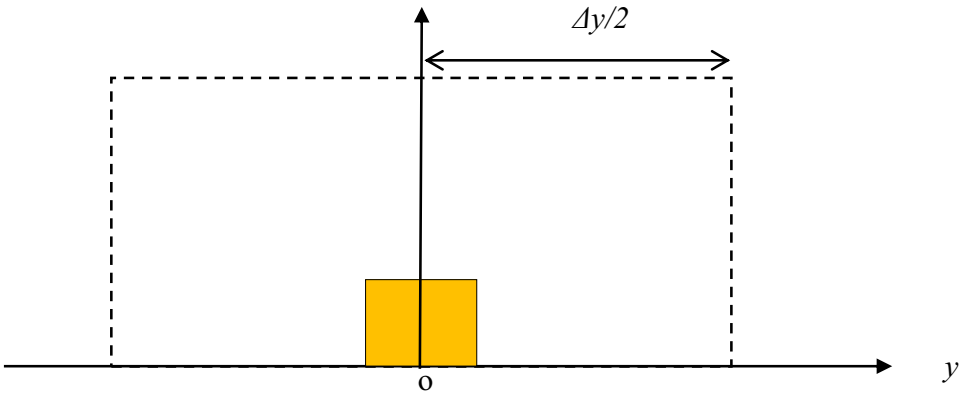

(b) Domain expansion in *y*-*z* plan

Figure 2. Illustration of computation domain and coordinate setup.

For ease in generalisation, the following non-dimensional parameters are introduced:

$$\Delta x_+^* = \Delta x_+/H; \qquad \Delta x_-^* = \Delta x_-/H; \qquad \Delta y^* = \Delta y/H; \qquad \Delta z^* = \Delta z/H \tag{1}$$

In addition, for the data presenting purpose, the non-dimensional parameter s^* is defined as $s^*=s/H$, where s is the distance measure from a reference point around the perimeter of the building block.

2.3 *Summary of simulation scenarios*

The domain expansion was undertaken in a stepwise manner in a series of simulations. From the reference case, domain expansion simulations are run. The major difficulty is to keep exactly the same grid size around the building. Moreover the number of cells in each direction has to be of the form $2^l3^m5^n$ where l, m and n are integers. So it is not possible to expand the domain arbitrarily whilst maintaining constant grid size. It is necessary to choose the domain size in function of the cell numbers permitted [10] to keep the same grid size. That explains why each domain extension in this study does not always use the same step. As regard y-direction and its non-uniform mesh division, it is not possible to keep the same grid size in the whole domain due to the piecewise linear transformation. Thus it was decided to keep the grid size unchanged close to the building. A summary of all the simulation scenarios are presented in Table 1.

Table 1. A Summary of simulation scenarios.

Simulation ID	Extensions	Domain size (m)			Grid size (m)		
		X	*Y*	*Z*	Δx	δy	δz
A	–[a]	40	30	18	0.17	0.24/0.42	0.15
B	Δx_+*≈1.8	36	30	18	0.17	0.24/0.42	0.15
C	Δx_+*≈3.3	45	30	18	0.17	0.24/0.42	0.15
D	Δx_+*≈4.17	50	30	18	0.17	0.24/0.42	0.15
E	Δx_+*≈5	54	30	18	0.17	0.24/0.42	0.15
F	Δx_-*=5	45	30	18	0.17	0.24/0.42	0.15
G	Δx_-*=3.5	36	30	18	0.17	0.24/0.42	0.15
H	Δy*=4	40	24	18	0.17	0.24/0.6	0.15
I	Δy*=6	40	36	18	0.17	0.24/0.375	0.15
J	Δy*=8	40	48	18	0.17	0.24/0.34	0.15
K	Δz*=3.6	40	30	21.6	0.17	0.24/0.42	0.15
L	Δz*=4	40	30	24	0.17	0.24/0.42	0.15
M	Δz*=3.375	40	30	20.25	0.17	0.24/0.42	0.15
N	Δz*=3.2	40	30	19.2	0.17	0.24/0.42	0.15
O	Δz*=2.5	40	30	15	0.17	0.24/0.42	0.15

a. Simulation scenario A is the reference case of which the domain dimensions are Δx_+*=2.5, Δy*=5, Δz*=3 and Δx_-*≈4.2.

3 RESULT AND DISCUSSION

3.1 *Sensitivity to downstream* (Δx_+) *expansion*

Presented in Figure 3 are the predicted pressure coefficient variations along the centerline and mid height of the cube. It can be observed from Figure 3 that a significant difference in pressure coefficient distribution if the x_+ domain size is varied. This phenomenon may be attributable to pressure boundary condition at the open boundary which was prescribed downstream of the domain. As such, the simulation of wake features and flow behavior behind the building block suffers a kind of truncation or discontinuity which resulted in higher pressure coefficient distribution above and behind the cube. When Δx_+^* is increased, the pressure coefficient distribution tends to settle asymptotically. Thus the domain has to be large enough in x_+ direction to allow the simulation to take the largest wake eddies into account.

It is also noticed from Figure 3 that the variation in domain expansion in x_+ direction hardly changes the shape of the distribution curve. Indeed, the Pearson correlation coefficients between successive simulations are all above 0.999 as shown in Table 2.

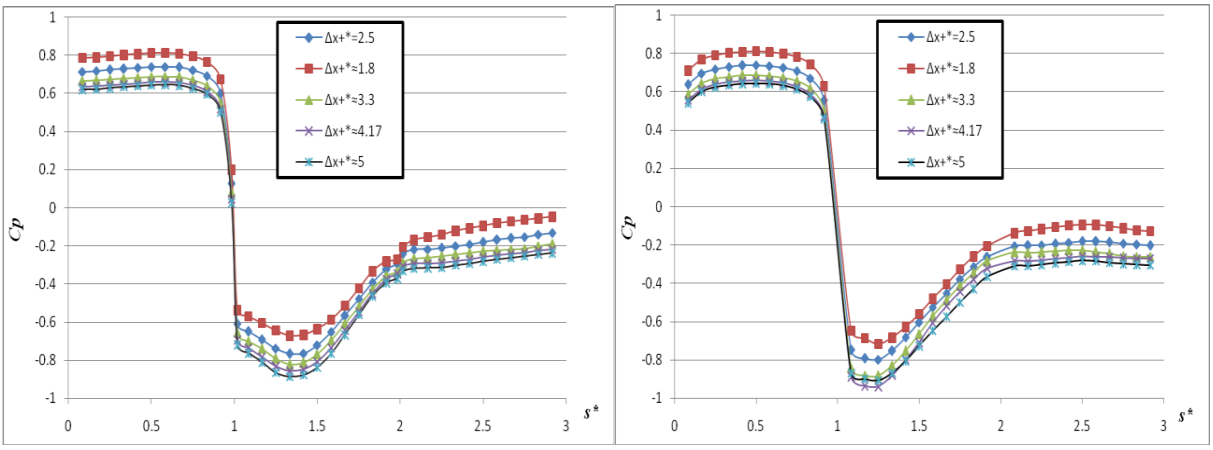

(a) Centerline variation. (b) Mid height variation.

Figure 3. Mean pressure coefficient in simulations with domain variation in x_+ direction.

Table 2. Correlation coefficients between successive simulations with increasing Δx_+^*.

Correlation between scenarios	R	
	Centerline	Mid height
A–B	0.99956	0.99965
A–C	0.99994	0.99961
C–D	0.99993	0.99981
D–E	0.99998	0.99929

3.2 *Sensitivity to upstream* (Δx_-) *expansion*

For the Δx_- study only two additional simulations were run and the results are presented in Figure 4. These simulations do not reveal any significant change in comparison with simulation scenarios involving domain variations downstream of the building block. Again the correlation coefficients between successive simulations are very high, as shown in Table 3.

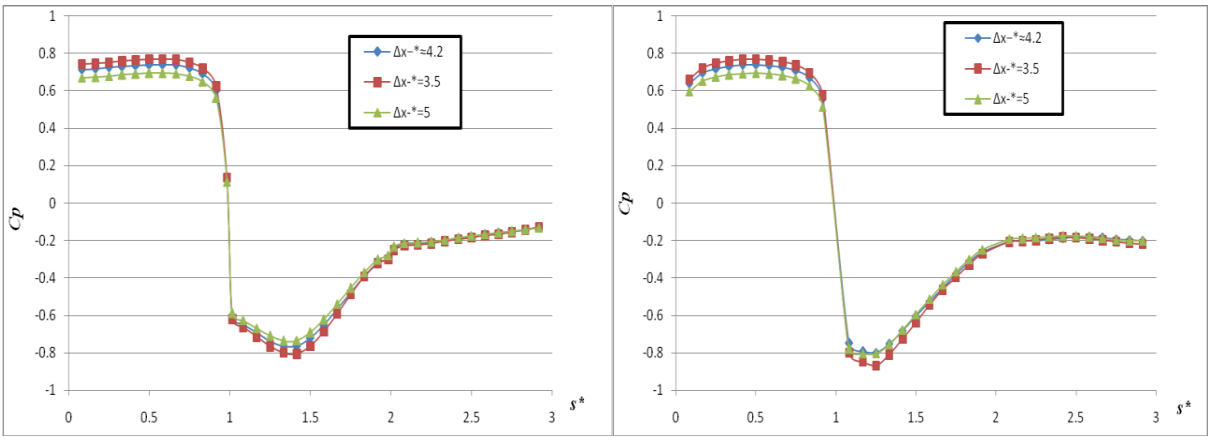

(a) Centerline variation. (b) Mid height variation.

Figure 4. Mean pressure coefficient in simulations with domain variation in x_- direction.

Table 3. Correlation coefficients between successive simulations with increasing Δx_{-}^{*}.

Correlation between scenarios	R	
	Centerline	Mid height
A–G	0.99994	0.99986
A–F	0.99998	0.99961

3.3 *Sensitivity to lateral* (Δy) *expansion*

In Δy variation simulation, the centerline pressure coefficient distribution does not show significant change, as revealed in Figure 5. However, in the side face, the pressure coefficient appears slightly lower when Δy^{*} is reduced. This is due to the Venturi effect between the building block and the non-slip closed boundary. Thus the domain has to be large enough to avoid this effect. It is seen from Figure 5 that the lateral dimension of Δy^{*}=5 (Case A) yielded reasonable results and any further expansion in y direction did not necessarily yield anything much different. Once more, it can be noted that the Pearson coefficient values are all higher than 0.999 and make the results reliable, as shown in Table 4.

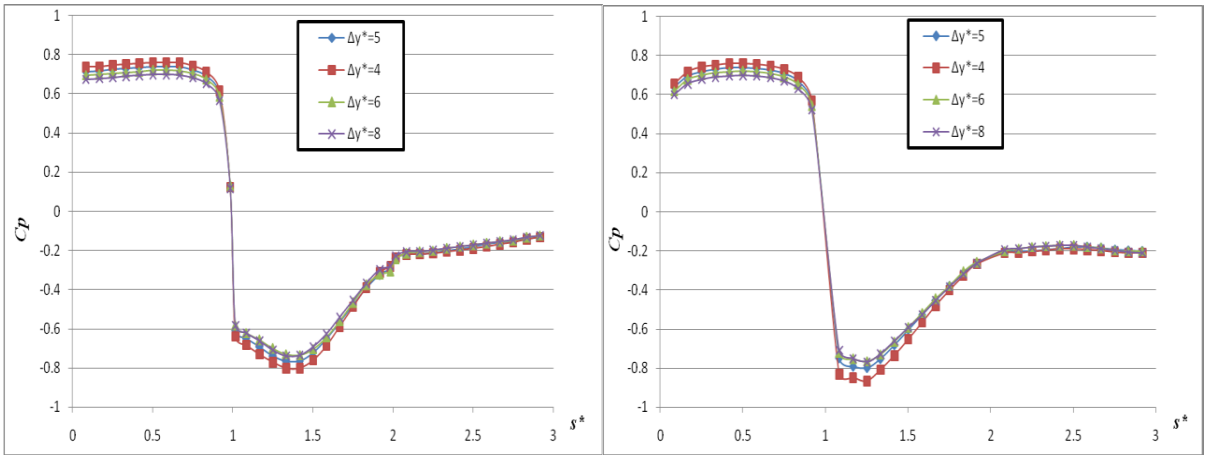

(a) Centerline variation. (b) Mid height variation.

Figure 5. Mean pressure coefficient in simulation of domain size variation in y direction.

Table 4. Correlation coefficients between successive simulations with increasing Δy^{*}.

Correlation between scenarios	R	
	Centerline	Mid height
A–H	0.99987	0.99980
A–I	0.99991	0.99992
I–J	0.99985	0.99996

3.4 *Sensitivity to vertical (Δz) expansion*

Finally, the sensitivity to vertical domain size was studied in the last 5 scenarios in which Δz^* was varied from 2.5 to 4. The results are shown in Figure 6. Initially for relatively small vertical size Δz^*=2.5 ~3.2, the predicted pressure coefficient was almost invariant. However, when Δz^* was increased from 3.2 to 3.375, the pressure coefficient distributions exhibited on the windward face noticeable increases whilst on the roof and the side walls noticeable drops, and then remained almost invariant for Δz^*>3.375. Such a trend of variation was also revealed in the correlation analysis as shown in Table 5 where the correlation coefficient between the predicted pressure coefficient distributions of Case M and Case N attains the lowest values for both the centreline and mid height measurements.

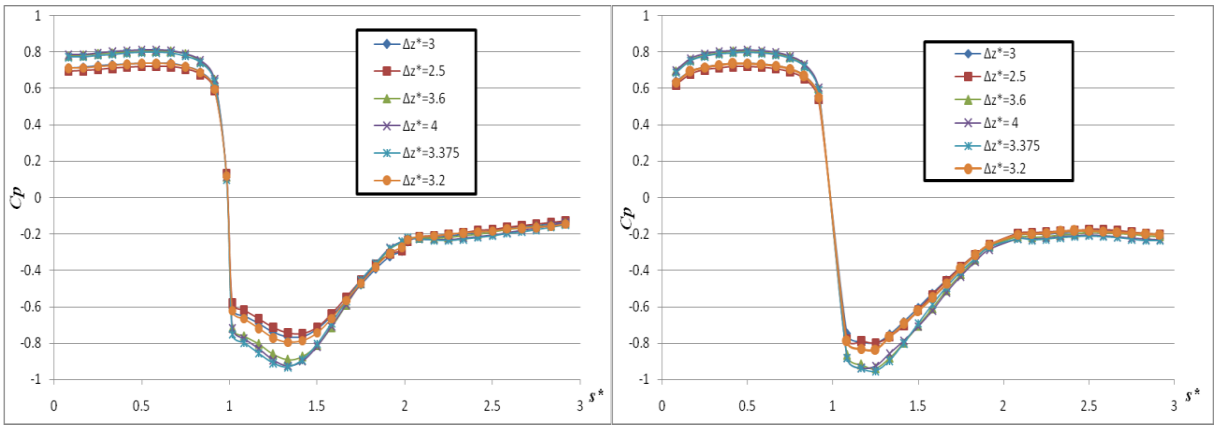

(a) Centerline variation. (b) Mid height variation.

Figure 6. Mean pressure coefficient in simulation of domain size variation in *z* direction.

Table 5. Correlation coefficients between successive simulations with increasing Δz^*.

Correlation between scenarios	*R*	
	Centerline	Mid height
A–O	0.99996	0.99982
A–N	0.99978	0.99982
N–M	0.99832	0.99967
M–K	0.99963	0.99980
K–L	0.99990	0.99984

4 CONCLUTION

A systematic examination of the mean pressure coefficient distribution in simulations with stepwise variation in each domain size has been carried out to examine the sensitivity of simulation outcome to computation domain size. As expected, the numerical simulation result of Fire Dynamics Simulator is domain dependent. In order of capture the effect of large eddies in the wake of a bluff body, sufficient domain space should be established around the bluff body. Based

on the result of the current study, a minimum domain size of 4 body length is recommended for both upstream and downstream of the body. Likewise, to avoid the "Venturi" effect, the total domain width in the lateral direction should be no less than 5 times of the body width, if the body is placed in the center location of the lateral direction. As for the vertical direction, the recommended domain height is greater than 3.5 times of the body height. The lateral and vertical domain requirement is consistent with the general requirement in wind tunnel model studies to keep the blockage ratio to be less than about 10%.

Finally, as the current study was undertaken for predominantly enclosure fire simulations, the optimum domain size is expected to be closely linked to the heat release rate or fire intensity when fires are involved. This aspect of the simulation is the subject of further studies.

5 REFERENCES

1. BCRC, *Victorian 2009 Bushfires Research Response: Final Report*. 2009, Bushfire Cooperative Research Centre: Melbourne.
2. Douglas, G., Tan, Z., Midgley, S., Short, L., *Bushfire building damage - A NSW perspective.* Proceedings of Royal Society of Queensland, 2009. **115**: p. 161-169.
3. Clark, T.L., Jenkins, M. A., Coen, J., Jackham, D., *A coupled atmospheric-fire model: convective feedback on fire line dynamics.* Journal of Applied Meteorology, 1996. **35**: p. 875-901.
4. Meroney, R.N. *Numerical Prediction of Fire Propagation in Idealized Wildland and Urban Canopies*. in *Proceedings of 12th International Conference on Wind Engineering (ICWE12)*. 2007. Cairns.
5. Kwok, K.C.S., He, Y., Douglas, G. B. *Wind impacts on fire spread and structural failure during bushfire in complex terrain*. in *Proceedings of 9th United Kingdom Conference on Wind Engineering*. 2010. Bristol, UK.
6. He, Y., Kwok, K. C. S., Douglas, G. B., Razali, I. M., *Numerical Investigation of Bushfire-Wind Interaction and Its Impact on Building Structure*, in *The 10th International Symposium on Fire Safety Science*. 2011, International Association for Fire Safety Science: Maryland, USA. p. 1449-1462.
7. Murakami, S., Mochida, A, *3-D Numerical simulation of airflow around a cubic model by means of the k-ϵ model.* Journal of Wind Engineering and Industrial Aerodynamics, 1988. **31**: p. 283-303.
8. He, Y., Jamieson, C., Jeary, A., Wang, J., *Effect of Computation Domain on Simulation of Small Compartment Fires*, in *Proceedings of the 9th International Symposium on Fire Safety Science*, B. Karlsson, Editor. 2008, International Association of Fire Safety Science: University of Karlsruhe, GERMANY. p. 1365-1376.
9. Zhang, X., Yang, M., Wang, J., He, Y., *Effects of Computational Domain on Numerical Simulation of Building Fires.* Journal of Fire Protection Engineering, 2010. **20**: p. 225-251.
10. Blocken, B., Stathopoulos, T., Carmeliet, J., *CFD simulation of the atmospheric boundary layer - wall function problems.* Atmospheric Environment, 2007. **41**: p. 238-252.

11. McGrattan, K., McDermott, R., Hostikka, S., Floyd, J., *Fire Dynamics Simulator (Version 5) User's Guide*. 2010, NIST Special Publication 1019-5, National Institute of Standards and Technology.
12. Baetke, F., Werner, H. , *Numerical simulation of turbulent flow over surface-mounted obstacles with sharp edges and corners.* Journal of Wind Engineering and Industrial Aerodynamics, 1990. **35**: p. 129-147.
13. Hostikka, S., Mangs, J., Mikkola, E., *Comparison of Two and Three Dimensional Simulations of Fires at Wildland Urban Interface*, in *Fire Safety Science – Proceedings of the 9th International Symposium on Fire Safety Science*. 2008, International Association for Fire Safety Science. p. 1353-1364.
14. McGrattan, K., Baum, H., Rehm, R., Mell, W., McDermott, R., *Fire Dynamic Simulator (Version 5) Technical Reference Guide*. 2010, NIST Special Publication 1018-5, National Institute of Standards and Technology.

The Seventh International Colloquium on Bluff Body Aerodynamics and Applications (BBAA7)
Shanghai, China; September 2-6, 2012

Nonlinear aerodynamic forces on square section: numerical study

Lin Huang [a], Haili Liao [b], Y. L. Xu [c]

[a] *School of Civil Engineering, Ningbo University of Technology, Ningbo, China*
[b] *School of Civil Engineering, Southwest Jiaotong University, Chengdu, China*
[c] *Department of Civil and Structural Engineering, The Hong Kong Polytechnic University, Hong Kong, China*

ABSTRACT: The paper presents a numerical simulation of nonlinear aerodynamic forces on square section by using computational fluid dynamic (CFD) method. The square section is subjected to a forced asymptotic transverse oscillation of varying amplitude. The aerodynamic forces on the square section are computed by multiple-domain mesh technique together with unstructured dynamic meshes. The instantaneous frequencies and amplitudes of lift force are identified from its time history by continuous wavelet transform (CWT) in terms of CWT ridges. The relationship between the non-dimensional amplitude and phase angle of frequency response component of lift force and the amplitude of forced oscillation is well demonstrated. Simulated results are compared with previous data at several reduced velocities. It shows that the proposed method can identify the general nonlinear features of aerodynamic forces in association with varying excitation amplitude.

KEYWORDS: square section; nonlinear aerodynamic force; large amplitude oscillation; numerical simulation; continuous wavelet transform; lock-in region

1 INTRODUCTION

For predicting wind-induced responses of long-span cable-supported bridges, the limitation of conventional linear aerodynamic methods has been recognized and nonlinear aerodynamic forces on the bridge attract more and more attentions [1]. Chen and Kareem [2, 3] separated the aerodynamic forces into the low- and high-frequency components in accordance with the effective angle of incidence. Diana et al. [4] proposed a rheological model in the time domain to reproduce nonlinear aerodynamic forces due to large changes in the angle of attack caused by turbulence and deck motion. They further carried out wind tunnel experiments to verify the rheological model [5]. Wu and Kareem [6] utilized artificial neural network framework with embedded cellular automata scheme to capture the hysteretic nonlinear behavior of aerodynamic systems.

This paper aims at investigating the relationship between the amplitude of aerodynamic forces on and the amplitude of forced oscillation of a bluff body, in which the square cylinder is selected. The nonlinear aerodynamic forces on the square cylinder forced in harmonic oscillation have been investigated through experiments [7, 8] and computational fluid dynamic (CFD) methods [9, 10]. The continuous wavelet transform (CWT) based on the complex Morlet wavelet [11] has been successfully applied to analyse the transient vibration behaviour of structures [12] and to detect structural damage [13]. However, the combination of these two problems to find the relationship between the amplitude of aerodynamic forces on and the amplitude of forced oscillation of a square section in this paper is original. The square section is subject to a forced asymptotic transverse oscillation of varying amplitude. The aerodynamic forces on the square sec-

tion are computed by the CFD method and are further analysed by using CWT. The captured features of the aerodynamic forces are compared with previous experiment and CFD results.

2 NUMERICAL SIMULATION OF NONLINEAR AERODYNAMIC FORCES

2.1 *Dynamic mesh algorithm*

To determine nonlinear aerodynamic forces on an oscillating square section of large amplitude with uniform flow inlets, a dynamic mesh algorithm called the domain decomposition algorithm [14] is used. Two-dimensional (2D) simulation is conducted and the computational domain is shown in Figure 1. The domain called the rigid boundary layer mesh region is connected with the square section and has the same movement as the square section during its oscillation. Very fine structured quadrangular meshes are used within this region. The domain called the dynamic mesh region is modified through the interface between this region and the rigid boundary layer mesh region while the square section is subjected to a forced oscillation. The initial triangular meshes are used in the dynamic mesh region and will be adjusted according to the early work of Batina [15] during the square section oscillation. The domain called the static mesh region is meshed by relatively coarse and fixed structured rectangular meshes.

2.2 *Governing equations*

The grid velocity $\boldsymbol{V}_{\mathrm{g}}$ of the moving mesh within the rigid boundary layer region can be determined by the boundary condition of the oscillating square section. The grid velocity $\boldsymbol{V}_{\mathrm{g}}$ of the moving mesh in the dynamic mesh region can be determined by the deformed and re-meshed grids. The grid velocity $\boldsymbol{V}_{\mathrm{g}}$ of the mesh within the static region is zero.

After $\boldsymbol{V}_{\mathrm{g}}$ is determined, the Reynolds-averaged Navier-Stokes (N-S) equations for 2D incompressible unsteady fluid, which will be solved by the finite volume method, are modified and given as:

$$\oint_{\Sigma} \rho\left(\boldsymbol{V}-\boldsymbol{V}_{g}\right)\cdot \boldsymbol{n}\mathrm{d}\Sigma = 0 \tag{1a}$$

$$\frac{\mathrm{d}}{\mathrm{d}t}\oint_{\Sigma} \rho u\mathrm{d}\Omega + \oint_{\Sigma} \rho u(\boldsymbol{V}-\boldsymbol{V}_{g})\cdot \boldsymbol{n}\mathrm{d}\Sigma + \oint_{\Sigma} (p+\frac{2}{3}\rho k)\boldsymbol{i}\cdot \boldsymbol{n}\mathrm{d}\Sigma = \oint_{\Sigma} \mu_{ef}\nabla v\cdot \boldsymbol{n}\mathrm{d}\Sigma \tag{1b}$$

$$\frac{\mathrm{d}}{\mathrm{d}t}\oint_{\Sigma} \rho v\mathrm{d}\Omega + \oint_{\Sigma} \rho v(\boldsymbol{V}-\boldsymbol{V}_{g})\cdot \boldsymbol{n}\mathrm{d}\Sigma + \oint_{\Sigma} (p+\frac{2}{3}\rho k)\boldsymbol{j}\cdot \boldsymbol{n}\mathrm{d}\Sigma = \oint_{\Sigma} \mu_{ef}\nabla v\cdot \boldsymbol{n}\mathrm{d}\Sigma \tag{1c}$$

where Ω represents the control volume of quadrangular/triangular meshes whose boundary is moving; Σ is the mesh boundary (one-dimensional) surface, whose outward unit normal vector is $\boldsymbol{n}$; $\boldsymbol{V}=u\boldsymbol{i}+v\boldsymbol{j}$ is the velocity vector of the fluid; p is the fluid pressure; k is the turbulent kinetic energy; $\mu_{ef}=\mu+\mu_t$ is the total fluid viscosity; and μ is the dynamic viscosity. The turbulent viscosity μ_t is obtained through a two-equation renormalization group (RNG) k-ε turbulence model [16]. Standard values are used for the model constants: C_{μ}=0.0845, $C_{1\varepsilon}$=1.42 and $C_{2\varepsilon}$=1.68. The grid velocity of the moving mesh is also introduced into the transport equations of k and ε. Advancement in time is accomplished by the first-order implicit Euler scheme. The pressure-implicit SIMPLE algorithm is used to solve the pressure-velocity coupling. The diffusive terms are solved by a second-order central difference scheme and the convection terms are computed by means of the second-order upwind scheme. The velocity field of the steady-state solution that satisfies the continuity condition is used as the initial condition of flow velocity field.

2.3 *Forced asymptotic oscillation*

Vortex-excited oscillation is an important instability phenomenon. The shedding vortex behind a bluff body can produce a lateral periodic force. Consequently, the vortex-excited oscillation is usually considered as a forced oscillation. Large and limited amplitude oscillation may occur once reduced velocity goes into the so-called lock-in region. Therefore, the square section is defined as a rigid body and is subjected to a forced asymptotic transverse oscillation of varying amplitude in this study. The oscillating displacement of the square section is expressed as $A(t)=D_{Af}(t)\sin(2\pi ft)$ where $D_{Af}(t)$ is the forced amplitude. $D_{Af}(t)$ is given by

$$D_{Af}(t)=\begin{cases} A_0 & 0\le t\le t_1, t\ge t_4 \\ A_0 e^{2\pi\lambda f(t-t_1)} & t_1\le t\le t_2 \\ A_0 e^{2\pi\lambda f(t_2-t_1)} & t_2\le t\le t_3 \\ A_0 e^{2\pi\lambda f(t_3-t)} & t_3\le t\le t_4 \end{cases} \tag{2}$$

where A_0 represents the initial amplitude of the harmonic oscillation; λ is a constant of very small value; and f is the frequency of forced oscillation.

2.4 *Definition of aerodynamic lift coefficient*

In present study, only unsteady lift force $F_L(t)$ (positive if upward) is investigated. The corresponding lift coefficient is defined as:

$$C_L(t)=\frac{F_L(t)}{0.5\rho U^2 H} \tag{3}$$

where H is the width of square section; and U is the mean speed of incoming flow.

3 IDENTIFICATION OF NONLINEAR AERODYNAMIC LIFT FORCE USING CWT

In CFD simulation, the lift coefficient $C_L(t)$ of the square section subjected to a forced asymptotic oscillation is basically asymptotic as well. If the force coefficient varies with time at a dominant frequency, it can be expressed by

$$C_L(t)=D_L(t)\cos[\varphi_L(t)] \tag{4}$$

where $D_L(t)$ and $\varphi'_L(t)$ are limited to slowly time-varying functions, $D_L(t)\ge 0$ and $\varphi_L(t)\in[0,2\pi]$ [17]. $D_L(t)$ is defined as the instantaneous amplitude of nonlinear aerodynamic lift. The corresponding instantaneous frequency of the nonlinear aerodynamic lift is introduced as

$$\omega_L(t)=\varphi'_L(t) \tag{5}$$

where the sign ' denotes the derivative with respect to time t. The CWT method with the complex Morlet wavelet is used to identify instantaneous features of nonlinear aerodynamic lift force, and the complex Morlet wavelet is given as

$$\psi(t)=\frac{1}{\sqrt{2\pi}}e^{-0.5t^2}\cdot e^{i\omega_c t} \tag{6}$$

where $\omega_c=2\pi f_c\ge 5.0$ and f_c is the centre frequency of the mother wavelet.

By applying the CWT with the complex Morlet wavelet to Equation (4), the first term of the wavelet transform can be approximated as [18]

$$T_{CL}(a,b)\approx 0.5D_L(b)e^{i\varphi_L(b)}\hat{\psi}^*\left[a\varphi'_L(b)\right] \tag{7}$$

where a is the scale parameter; b is the shift parameter in time; and $\hat{\psi}^*(\cdot)$ stands for complex conjugate of Fourier transform of $\psi(\cdot)$. For a mono-component signal, the modulus of the wavelet

transform $T_{CL}(a,b)$ is essentially maximum in the neighborhood of a curve $a_r(b)$, called the ridge of the wavelet transform, which satisfies the following condition [18].

$$a_r(b) = \frac{\omega_c}{\varphi'(b)} \tag{8}$$

The snake penalization method proposed by Carmona et al. [18] is selected in this study to search the ridge, by which the instantaneous frequency of nonlinear aerodynamic lift can be determined through Equation (8). On the other hand, the instantaneous amplitude of nonlinear aerodynamic lift force can be found from Equation (7) in terms of the modulus. The accuracy of the above-mentioned method for the determination of instantaneous features of nonlinear aerodynamic lift force is dependent upon the time and frequency resolutions, which are merely restricted by the mother wavelet resolution. For the complex Morlet wavelet, the time and frequency resolutions at a given frequency f_i in the CWT can be expressed as [19]

$$\Delta t_i = \frac{f_c}{\sqrt{2} f_i} \qquad \Delta f_i = \frac{f_i}{2\pi\sqrt{2} f_c} \tag{9}$$

Therefore, the centre frequency f_c of the mother wavelet is a critical parameter in defining the resolution capability. In this study, the wavelet entropy method proposed by Lin and Qu [20] is applied to determine the centre frequency f_c. The subsequent investigation reveals that the nonlinear aerodynamic lift coefficient may vary with time at several frequencies although the forced oscillation is at a single frequency. Therefore, the lift coefficient shall be expressed as

$$C_L(t) = \sum_{i=1}^{m_L} D_{Li}(t)\cos\left[\varphi_{Li}(t)\right] \tag{10}$$

The amplitude $D_{Li}(t)$ as well as the derivatives $\varphi'_{Li}(t)$ also slowly vary with time. The wavelet transform, being a linear transform, of the lift coefficient by using the Morlet wavelet yields

$$T_{CL}(a,b) \approx 0.5\sum_{i=1}^{m_L} D_{Li}(b)e^{\mathrm{i}\varphi_{Li}(b)}\hat{\psi}^*\left[a\varphi'_{Li}(b)\right] \tag{11}$$

After the ridges are found using the snake penalization method, the instantaneous frequency and amplitude for each of the concerned frequency components in the lift coefficient $C_L(t)$ can be determined. Phase angle $\varphi_{Li}(b)$ can be also determined from the complex function $T_{CL}(a,b)$.

4 NUMERICAL RESULTS AND DISCUSSIONS

4.1 *Numerical model of oscillating square section*

A square section of width H=0.15m is selected as an example. The whole computational domain is sketched in Figure 1 and the corresponding parameters defining three regions as described in Section 2.1 are also designated. The height of body-fitted meshes is about 1.5mm or 2.0mm. The initial computation meshes are shown in Figure 2, in which the rigid boundary layer region has 14,712 quadrangular meshes, the dynamic mesh region has 13,398 triangular meshes, and the static mesh region has 7,898 quadrangular meshes. The initial angle of attack at the equilibrium position is set as zero. The inflow is set as uniform flow with a mean speed U and a turbulence intensity of 0.5%. The reduced velocity $V_r=U/fH$ varies from 5.0 to 12.0, in which the frequency f of forced oscillation is 4.0Hz. The Reynolds number $Re=\rho UH/\mu$ also varies from 3.1×10^4 to 7.4×10^4. The initial amplitude A_0 of harmonic oscillation is 5mm. Parameters t_1, t_2, t_3 and t_4 in Equation (2) are set as $14/f$, $59/f$, $72/f$ and $119/f$, respectively. The iteration time step is 3×10^{-4}s.

4.2 *Characteristics of flow around the fixed square section*

To demonstrate the effectiveness of RNG *k-ε* turbulence model, the unsteady flow field around the fixed square section at zero incidence of wind is simulated. In this simulation, the computational meshes are as same as the meshes shown in Figure 2. The mean speed of incoming flow is U=4.2m/s and the Reynolds number is Re=4.3×10^4. The iteration time step is 3×10^{-4}s. The computed time-averaged velocity <u> along the centre line is shown in Figure 3 and compared with previous experiment and CFD results [21-24]. The computed results are in good agreement with experimental results and better than the previous computational results, but the size of reverse

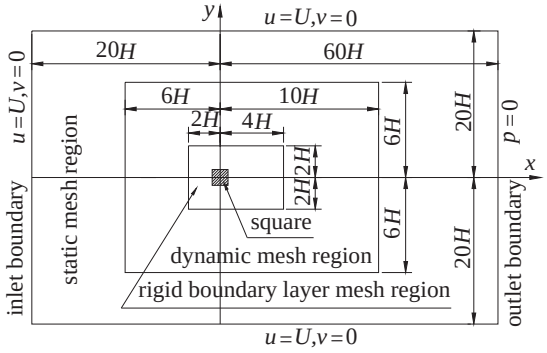

Figure 1 Sketch of computation domain

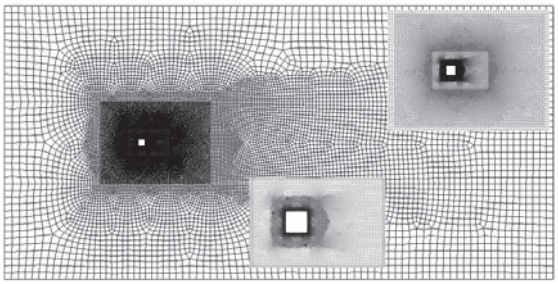

Figure 2 Initial computational meshes

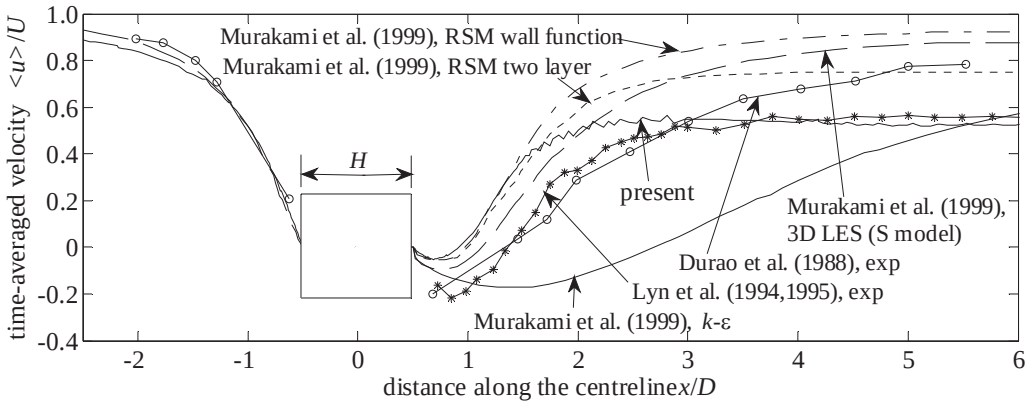

Figure 3 Comparison of time-averaged velocity <u> along the centerline

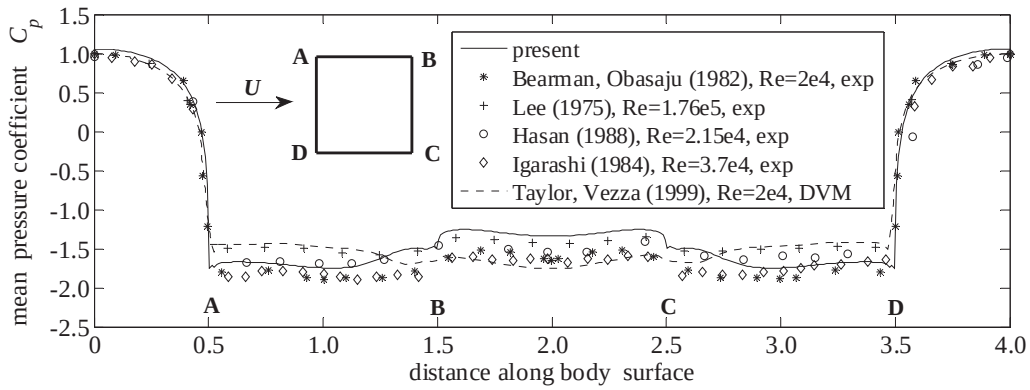

Figure 4 Mean pressure coefficient on body surface

flow region is smaller than experiment results. The latter may be induced by large turbulent viscosity in the RNG k-ε turbulence model. The mean surface pressure C_p around the square section is shown in Figure 4 and compared with previous experiment and CFD results [25-28, 10]. The corners of body are indicated in figure. The present results demonstrate a good agreement with experimental results. The Strouhal number of the fixed square section is St=0.129 by analyzing the present lift force time history. This is close to the experimental result St=0.12 [29] and the CFD results St=0.14 [9] and St=0.128 [10].

4.3 *Frequency response component of lift force on the oscillating square section*

As an example, the computed lift coefficient $C_L(t)$ is shown in Figure 5 at V_r=6, 7. The centre frequency of the complex Morlet wavelet is determined by using the wavelet entropy method [20]. The centre frequencies are set as f_c=4.0Hz and f_c=4.5Hz for V_r=6, 7, respectively. The corresponding scalograms obtained by CWT are shown in Figure 6. A unique ridge corresponding to the frequency response component of lift force can be found at V_r=7 since oscillation is in lock-in region. Two ridges can be observed at V_r=6 when the forced amplitude is small. One ridge is related to vortex-shedding frequency and the other is corresponding to frequency response component of lift force. As the forced amplitude gradually increases, oscillation will gradually go into lock-in region. Therefore, two ridges gradually merge into one at V_r=6 in Figure 6. This observation is in good agreement with the experiment result [7]. The ridge can be identified by snake penalization method [18].

The frequency response component of the lift coefficient can be expressed as

$$C_{Lf}(t)=D_{CLf}(t)\sin[2\pi ft+\beta_{CLf}(t)] \tag{12}$$

where the instantaneous amplitude $D_{CLf}(t)$ equals a certain value $D_{Li}(b)$ defined in Equation (11), such as $D_{L1}(b)$; phase angle $\beta_{CLf}(t)$ can be determined from $\varphi_{Li}(b)$ defined in Equation (11)， such

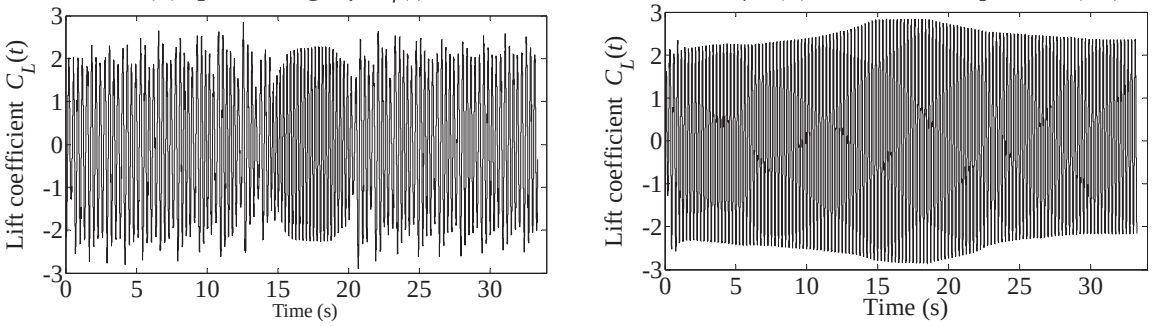

(a) Reduced velocity V_r=6 (b) Reduced velocity V_r=7

Figure 5 Computed lift coefficient

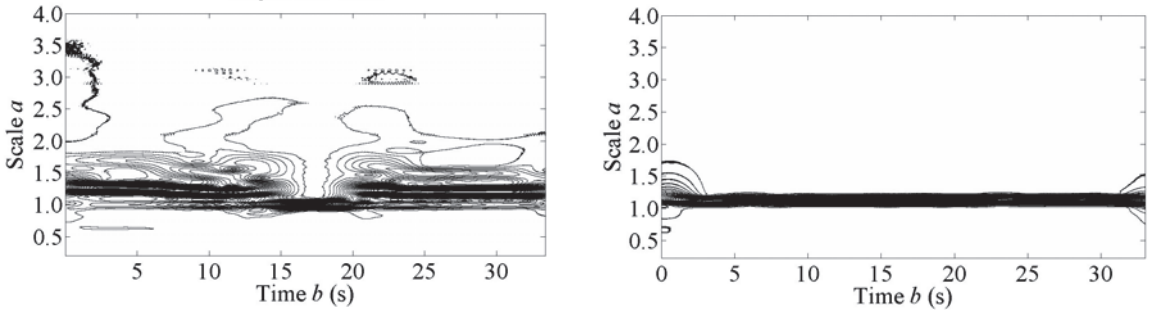

(a) Reduced velocity V_r=6 (b) Reduced velocity V_r=7

Figure 6 Scalogram of lift coefficient

as $\varphi_{L1}(b)$. Therefore, the instantaneous amplitude $D_{CLf}(t)$ and phase angle $\beta_{CLf}(t)$ of frequency response component can be determined from the corresponding wavelet ridge.

The instantaneous amplitude $D_{CLf}(t)$ and the corresponding phase angle $\beta_{CLf}(t)$ at different reduced velocities are shown in Figure 7 when the square section is subjected to a forced asymptotic transverse oscillation of varying amplitude defined in Equation (2). It is clear that the relation between instantaneous amplitude $D_{CLf}(t)$ and excitation amplitude $D_{Af}(t)$ is nonlinear. In general, the instantaneous amplitude $D_{CLf}(t)$ for reduced velocity V_r in lock-in region is larger than that for reduced velocity V_r outside lock-in region. An exceptional case is observed at V_r=6. When excitation amplitude is small, the instantaneous amplitude $D_{CLf}(t)$ at V_r=6 is relatively small. However, the instantaneous amplitude $D_{CLf}(t)$ rapidly increases when excitation amplitudereaches above 16mm. One can observe from Figure 6 that the oscillation in this case is gradually going into lock-in region. This reveals that the range of lock-in region increases with the

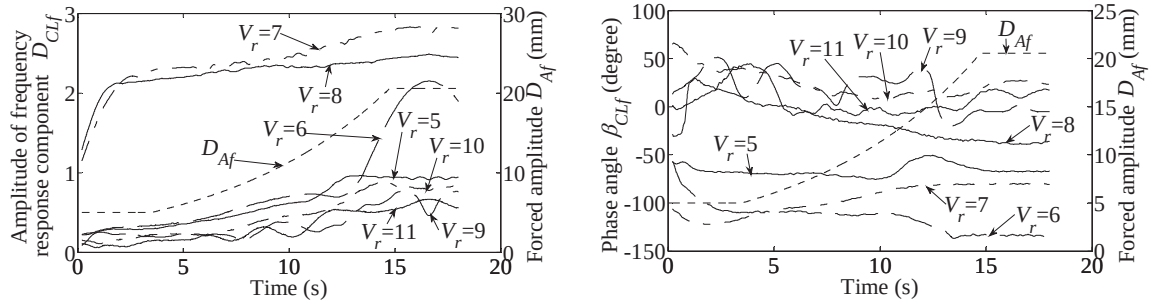

(a) Instantaneous amplitude $D_{CLf}(t)$ (b) Instantaneous phase angle $\beta_{CLf}(t)$

Figure 7 Simulated instantaneous amplitude and corresponding phase angle of frequency response component of lift coefficient at different reduced velocities

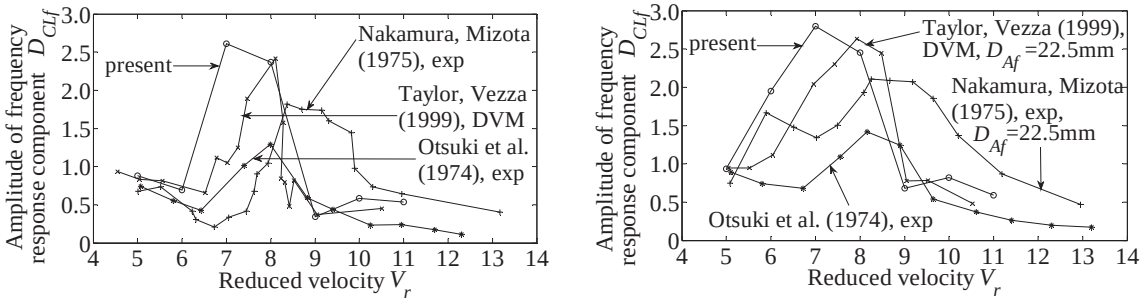

(a) Forced amplitude D_{Af}=15mm (b) Forced amplitude D_{Af}=20mm

Figure 8 Comparison of amplitude of frequency response component between present and previous results

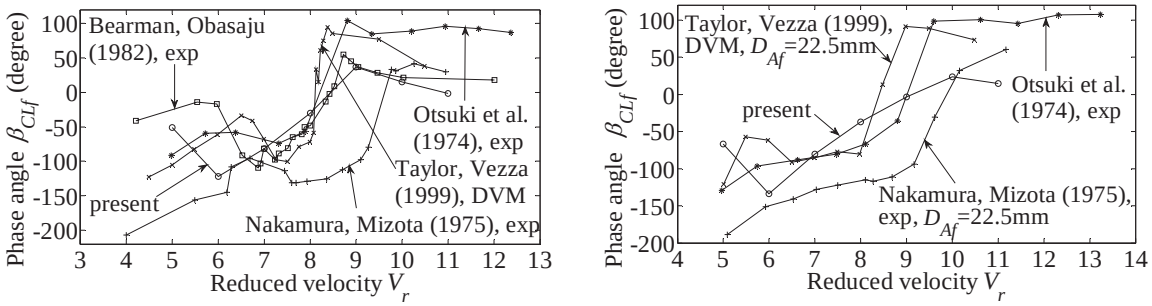

(a) Excitation amplitude D_{Af}=15mm (b) Excitation amplitude D_{Af}=20mm

Figure 9 Comparison of phase angle of frequency response component between present and previous results

increasing excitation amplitude. This observation is in good agreement with the experimental result of Otsuki et al. [7]. The phase angle $\beta_{CLf}(t)$ at different reduced velocities is relatively steady as excitation amplitude increases. The phase angle $\beta_{CLf}(t)$ is negative or positive for wind speed U below or above the resonance speed. It is clear that positive phase angle $\beta_{CLf}(t)$ is required for vortex-induced oscillation which only occurs once the reduced velocity goes into the lock-in region. Some values of instantaneous amplitude $D_{CLf}(t)$ and the corresponding phase angle $\beta_{CLf}(t)$ with varying reduced velocity V_r at several excitation amplitudes are compared with previous experiment and CFD results at the corresponding excitation amplitudes, as shown in Figure 8 and 9. The most noticeable feature is the sudden increase from negative to positive phase angle through the lock-in region. This feature is perfectly reproduced by the present method. The reduced velocity corresponding to the resonance speed is adjacent to 8.0 from Figure 8 and 9. This observation is supported by the previous experiment results, such as that given by Otsuki et al. [7]. The simulated general tendency of instantaneous amplitude $D_{CLf}(t)$ and phase angle $\beta_{CLf}(t)$ is in good agreement with the previous experiment and CFD results. Nevertheless, two typical discrepancies can be found. One lies in the lock-in region where the instantaneous amplitudes D_{CLf} of the present and previous data are distributed in a large range. The other lies in below or above lock-in region where the phase angle β_{CLf} of the present and previous data are also dispersed. These discrepancies will be discussed in Section 4.4.

4.4 *Discussions*

Since the instantaneous flow field around the square cylinder is highly three-dimensional (3D), the 2D CFD simulation cannot fully reproduce this feature. The previous CFD study [24] has obviously demonstrated that the spectrum shape of lift force from 2D simulation shifts from the spectrum of lift force obtained from the experiment [29] to a relative high vortex-shedding frequency. This may induce the peak of amplitude D_{CLf} from the CFD simulation appearing at a relative low reduced velocity while that from the experiment data lies at a relative high reduce velocity, as shown in Figure 8.

The spanwise correlation of the fluctuating surface pressure on the square cylinder has been early studied by wind tunnel experiments [26, 29, 30]. The experimental lift force on the square cylinder is actually a space-averaged value. The present 2D simulated lift force does not take the influence of spanwise correlation into account. This may cause large discrepancy between the simulation and experiment results. The experimental lift forces may be mainly affected by the spanwise correlation of the fluctuating surface pressure on the side surface of the square cylinder.

In the following, only the frequency response component $L_f(t)$ of lift force on the square cylinder will be discussed. For two points A and B on the top or bottom side surface of the square cylinder along the axial direction, assume that the correlation coefficient $R_{AB}(z,t)$ is independent on the time t during the square cylinder oscillation.

$$R_{AB}(z,t) \approx R_{AB}(z) \tag{13}$$

Further assume that the phase angle $\beta_{CLf}(t)$ defined in Equation (12) is also independent on the axial position. The frequency response component $L_f(t)$ can be expressed as

$$L_f(t) = 0.5\rho U^2 H^2 C_{Lf}(t) \int_0^L R_{AB}(z)\mathrm{d}z \tag{14}$$

Define the axial correlation length scale of the square cylinder C_R as

$$C_R = \int_0^L R_{AB}(z)\mathrm{d}z \tag{15}$$

The frequency response component of the experimental lift coefficient $C_{Lf,E}(t)$ is defined as

$$C_{Lf,E}(t) = \frac{L_f(t)}{0.5\rho U^2 H^2 L} \tag{16}$$

Therefore, the experimental $C_{Lf,E}(t)$ and the present 2D simulation $C_{Lf}(t)$ have relationship:

$$L \cdot C_{Lf,E}(t) = C_R \cdot C_{Lf}(t) \tag{17}$$

The expression of $C_{Lf,E}(t)$ can be expressed by Eq. (12) and the corresponding instantaneous amplitude is defined as $D_{CLf,E}(t)$. Assume that experimental phase angle equals the simulation one, the relationship between the experimental $D_{CLf,E}(t)$ and simulating $D_{CLf}(t)$ can be given as

$$L \cdot D_{CLf,E}(t) = C_R \cdot D_{CLf}(t) \tag{18}$$

In this expression, the amplitude $D_{CLf}(t)$ from the 2D CFD simulation cannot be directly compared with the experimental amplitude $D_{CLf,E}(t)$ since the experimental square cylinder is a fully 3D body. At the same time, the correlation length scale C_R is dependent on the length L of the square cylinder. The amplitude $D_{Lf,E}(t)$ may vary with length of square cylinder for the same experimental condition.

Otsuki et al. [7] investigated the square cylinder of width H=150mm and length L=660mm in a wind tunnel. Referring to the spanwise correlation distribution of fluctuating pressure of the square cylinder [26, 29], the correlation length scale C_R is approximately 3.2H for L/H=4.4. Therefore, the ratio of the experiment $D_{CLf,E}(t)$ to the 2D simulated $D_{CLf}(t)$ is about 0.73 from Equation (18). Other factors are also needed to be mentioned. For example, the method of subtraction of the inertia force from the measured data consisting of the aerodynamic force plus the inertia force may introduce some numerical errors, as pointed out by Otsuki et al. [7]. The spanwise correlation of phase angle $\beta_{CLf}(t)$ may also introduce some numerical errors. These factors may further decrease the ratio of the experiment data to the 2D simulation result.

By considering the above correlation coefficient and numerical errors, the present numerical results are acceptable. If 3D CFD simulation and more advance turbulent models are used, better simulation result can be expected.

5 CONCLUSIONS

(1) The proposed CFD simulation integrated with the CWT analysis can be used to determine nonlinear features of the aerodynamic forces on the square section in forced large amplitude oscillation. The simulated results are in good agreement with the previous experimental data and CFD results.

(2) The amplitude of aerodynamic forces on the square section depends on the amplitude of the forced oscillation in addition to reduced velocity.

ACKNOWLEDGMENTS

The authors are grateful for the financial support from the National Natural Science Foundation of China under Grant NNSF-90815016, Zhejiang Provincial Natural Science Foundation of China under Grant No. Y1111057 and Ningbo Natural Science Foundation of China under Grant No. 2008A610103.

REFERENCES

[1] A. Kareem, Numerical simulation of wind effects: A probabilistic perspective, Journal of Wind Engineering and Industrial Aerodynamics, 96 (2008) 1472-1497.

[2] X. Chen, A. Kareem, Nonlinear response analysis of long-span bridges under turbulent winds, Journal of Wind Engineering and Industrial Aerodynamics, 89 (2001) 1335-1350.

[3] X. Chen, A. Kareem, Aeroelastic analysis of bridges: Effects of turbulence and aerodynamic nonlinearities, Journal of Engineering Mechanics, 129 (2003) 885-895.
[4] G. Diana, F. Resta, D. Rocchi, A new numerical approach to reproduce bridge aerodynamic non-linearities in time domain, Journal of Wind Engineering and Industrial Aerodynamics, 96 (2008) 1871-1884.
[5] G. Diana, D. Rocchi, T. Argentini, S. Muggiasca, Aerodynamic instability of a bridge deck section model: linear and nonlinear approach to force modeling, Journal of Wind Engineering and Industrial Aerodynamics, 98 (2010) 363-374.
[6] T. Wu, A. Kareem, Modeling hysteretic nonlinear behavior of bridge aerodynamics via cellular automata nested neural network, Journal of Wind Engineering and Industrial Aerodynamics, 99 (2011) 378-388.
[7] Y. Otsuki, K. Washizu, H. Tomizawa, A. Ohya, A note on the aeroelastic instability of a prismatic bar with square section, Journal of Sound and Vibration, 34 (1974) 233-248.
[8] Y. Nakamura, T. Mizota, Unsteady lifts and wakes of oscillating rectangular prisms, Journal of Engineering Mechanics. Division, ASCE, 101 (1975) 855-871.
[9] S. Murakami, A Mochida, On turbulent vortex shedding flow past 2D square cylinder predicted by CFD, Journal of Wind Engineering and Industrial Aerodynamics, 54-55 (1995) 191-211.
[10] I. Taylor, M. Vezza, Calculation of the flow field around a square section cylinder undergoing forced transverse oscillations using a discrete vortex method, Journal of Wind Engineering and Industrial Aerodynamics, 82 (1999) 271-291.
[11] A. Grossman, J. Morlet, Decompositions of functions into wavelets of constant shape and related transforms, Mathematics and Physics, Lecture on Recent Results, (ed. L. Streit), World Scientific, Singapore, 135-165, 1985.
[12] M. Haase, J. Widjajakusuma, Damage identification based on ridges and maxima lines of the wavelet transform, International Journal of Engineering Science, 41 (2003) 1423-1443.
[13] R. O. Curadelli, J. D. Riera, D. Ambrosini, M. G. Amani, Damage detection by means of structural damping identification, Engineering Structures, 30 (2008) 3497-3504.
[14] Lin Huang, Haili Liao, Bin Wang, Yongle Li, Numerical simulation for aerodynamic derivatives of bridge deck, Simulation Modelling Practice and Theory, 17 (2009) 719-729.
[15] J. T. Batina, Unsteady Euler airfoil solutions using unstructured dynamic meshes, AIAA Journal, 28 (1990) 1381-1388.
[16] V. Yakhot, S. A. Orszag, Renormalization group analysis of turbulence I. Basic theory, Journal of Scientific Computing, 1 (1986) 3-51.
[17] R. A. Carmona, W. L. Hwang, B. Torrésani, Wavelet analysis and applications, vol. 9: Practical time-frequecny analysis, Academic Press, San Diego, USA, 1998.
[18] R. A. Carmona, W. L. Hwang, B. Torrésani, Characterization of signals by the ridges of their wavelet transform, IEEE Transactions on Signal Processing, 45 (1997) 2586-2590.
[19] T. Kijewski, A. Kareem, Wavelet transforms for system identification in civil engineering, Computer-Aided Civil and Infrastructure Engineering, 18 (2003) 339-355.
[20] J. Lin, L. Qu, Feature extraction based on Morlet Wavelet and its application for mechanical fault diagnosis, Journal of Sound and Vibration, 234 (2000) 135-148.
[21] D. A. Lyn, W. Rodi, The flapping shear layer formed by flow separation from the forward corner of a square cylinder, Journal of Fluid Mechanics, 267 (1994) 353-376.
[22] D. A. Lyn, S. Einav, W. Rodi, J. H. Park, A laser-Doppler velocimetry study of ensemble averaged characteristics of the turbulent near wake of square cylinder, Journal of Fluid Mechanics, 304 (1995) 285-319.
[23] D. F. G. Durao, M. V. Heitor, J. C. F. Pereira, Measurements of turbulent and periodic flows around a square cross-section cylinder, Experiments in Fluids, 6 (1988) 298-304.
[24] S. Murakami, S. Iizuka, R. Ooka, CFD analysis of turbulent flow past square cylinder using dynamic LES , Journal of Fluids and Structures, 13 (1999) 1097-1112.
[25] P. W. Bearman, E. D. Obasaju, An experimental study of pressure fluctuations on fixed and oscillating square-section cylinders, Journal of Fluid Mechanics, 119 (1982) 297-321.
[26] B. E. Lee, The effect of turbulence on the surface pressure field of a square prism, Journal of Fluid Mechanics, 69 (1975) 263-282.
[27] M. A. Z. Hasan, The near wake structure of a square cylinder, International Journal of Heat Fluid Flow, 10 (1989) 339-348.
[28] T. Igarashi, Characteristics of the flow around a square prism, Bulletin of JSME, 27 (1984) 1858-1865.
[29] B. J. Vickery, Fluctuating lift and drag on a long cylinder of square cross-section in a smooth and in a turbulent stream, Journal of Fluid Mechanics, 25 (1966) 481-494.
[30] R. H. Wilkinson, Fluctuating pressures on an oscillating square prism, Part II Spanwise correlation and loading, Aeronautical Quarterly, 32 (1981) 111-125.

The Seventh International Colloquium on Bluff Body Aerodynamics and Applications (BBAA7)
Shanghai, China; September 2-6, 2012

Flow above the free end of a surface-mounted square prism

N. Rostamy, J.F. McClean, D. Sumner, D.J. Bergstrom, J.D. Bugg

Department of Mechanical Engineering, University of Saskatchewan
57 Campus Drive, Saskatoon, Saskatchewan, Canada

ABSTRACT: The flow above the free end of a surface-mounted finite-height square prism was studied experimentally in a low-speed wind tunnel using particle image velocimetry (PIV). The prism was mounted normal to a ground plane and was partially immersed in a flat-plate turbulent boundary layer. Four finite square prisms of aspect ratios AR = 9, 7, 5 and 3 were tested at a Reynolds number of Re = 4.2×10^4. PIV velocity field measurements were made above the free ends in three vertical planes parallel to the mean flow direction at cross-stream locations of y/D = 0 (the flow centreline), 0.25, and 0.375 (where D is the side length of the square prism). The results show how the prism's aspect ratio influences the mean velocity field and the Reynolds stresses above the free end surface of the prism. A cross-stream vortex forms in the region of separated flow above the free end of the square prism, due to interaction between the separated flow from the leading edge of the prism and reverse flow over the free end. The centre of this vortex moves downstream and upwards as the aspect ratio is lowered. Another cross-stream vortex forms immediately behind the prism; the size and strength of this vortex increases as aspect ratio of the prism is lowered.

KEYWORDS: Bluff body, finite square prism, separated flow, vortex structures, particle image velocimetry

1. INTRODUCTION

The flow around surface-mounted circular cylinders and square prisms of finite height is more complex than the familiar case of a two-dimensional or "infinite" circular cylinder or prismatic body [1]. In engineering applications such as high-rise buildings, oil storage tanks, cooling towers, and chimneys, the flow fields of these prismatic structures are strongly three-dimensional due to the effect of the flow around the free end and the flow at the prism-wall junction.

A schematic of the flow past a surface-mounted finite-height square prism (of side length, D, and height, H), mounted normal to a ground plane and partially immersed in a flat-plate boundary layer (with thickness δ at the location of the prism), is shown in Figure 1. In this figure, x is the streamwise coordinate, y is the cross-stream coordinate, and z is the wall-normal coordinate. The flow field is influenced by the aspect ratio, AR (= H/D), the Reynolds number, Re (= DU_∞/ν, where U_∞ is the freestream velocity and ν is the kinematic viscosity), and the relative thickness of the boundary layer on the ground plane, δ/D or δ/H.

The flow field over and above the free end of the finite-height prism influences the flow pattern in the near-wake region, including the formation of a pair of mean streamwise trailing vortex structures in the upper wake and the downwash (downward-directed) flow associated with it. Few studies of finite circular cylinders and square prisms have examined, in detail, the flow separation on the free end and its potential for reattachment. Kawamura et al. [2] studied the flow pattern on the free ends of finite circular cylinders of AR = 8, 4 and 1 with δ/D = 1 at Re =

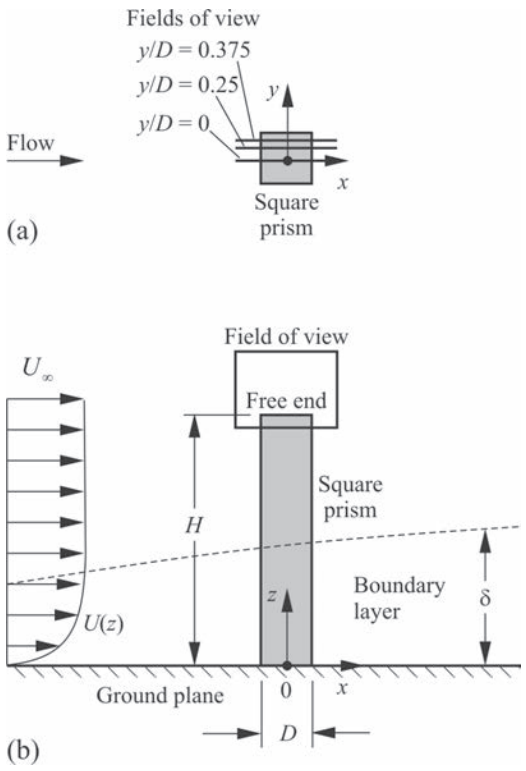

Figure 1. Schematic of the flow around a surface-mounted finite-height square prism partially immersed in a flat-plate boundary layer (with mean velocity profile, $U(z)$): (a) top view, showing the cross-stream positions of the fields of view for the particle image velocimetry (PIV) measurements; (b) side view, showing the field of view in the vicinity of the free end.

1.1×10^4 to 3.2×10^4. According to their flow visualization results, reattachment of the separated flow on the free end was sensitive to both AR and δ/H: reattachment of the flow on the upper surface occurred for the most slender and the least slender cylinders (for AR = 8 and δ/H = 0.125 and AR = 1 and δ/H = 1) but not for the intermediate cylinder (for AR = 4 and δ/H = 0.25). Leder [3] studied the flow past a finite circular cylinder of AR = 2 at Re = 2×10^5 and with δ/D = 0.008 using laser Doppler velocimetry (LDV). On the central vertical plane of the flow field, flow separated at the leading edge of the free end surface and reattached close to the trailing edge, at x/D = 0.34 (where x is measured from the centre of the cylinder). Weak recirculating flow was seen inside the time-mean separation bubble. Park and Lee [4] studied the flow around the free end of a finite circular cylinder of AR = 6 at Re = 7,500 using flow visualization, thermal anemometry, and particle image velocimetry (PIV). On the flow centreline, reattachment of the separated flow on the free-end surface was observed. Pattenden et al. [5] experimentally investigated the flow over a small-aspect-ratio surface-mounted finite circular cylinder of AR = 1 (well below a typical value for the critical aspect ratio), using PIV, surface flow visualization, and unsteady surface pressure measurements. Their results showed flow separation at the leading edge of the free end surface and, along the centreline, reattachment on the top of the circular cylinder at x/D = 0.17 (measured from the centre of the cylinder).

Recently, Krajnović [6] used large eddy simulation (LES) to study the flow around a finite circular cylinder with AR = 6, and reported that the flow on the top surface of the cylinder includes a large primary recirculation region and a secondary recirculation region. He showed

that the large recirculation region originates at the leading edge of the cylinder and reattaches at approximately 0.82*D* from the leading edge (i.e., at $x/D = 0.32$, as measured from the centre of the cylinder) in the streamwise direction and in the symmetry plane (y = 0). The results of his simulations disagree with the tip flow structure suggested by Roh and Park [7] but were in general agreement with the results of Pattenden et al. [5] and Kawamura et al. [2].

The above examples are all for the case of the finite circular cylinder. For the finite square prism, recent experimental studies have focused mostly on the wake dynamics [8–11], but without considering in depth the flow above the free end of the square prisms. In the present study, the flow field above the free-end surface of a surface-mounted, finite-height square prism was investigated in a low-speed wind tunnel using PIV. Of particular interest were the effects of prism aspect ratio on the flow field.

2. EXPERIMENTAL APPARATUS

The experiments were conducted in a low-speed closed-return wind tunnel with a test section of 1.96 m (length) × 0.91 m (height) × 1.13 m (width). The streamwise freestream turbulence intensity was less than 0.6% and the mean velocity non-uniformity outside the test section's wall boundary layers was less than 0.5%. An aluminum ground plane was installed on the floor of the wind tunnel test section and a fully developed turbulent boundary layer was produced on the ground plane at the location of the finite square prism.

Four different, smooth, aluminum square prism models, all of the same width, $D = 31.5$ mm, were tested. The free end of each prism was a flat surface with sharp perimeter edge. Each prism had a different height, giving prisms with AR = 9, 7, 5, and 3, similar to earlier experiments of [1,12]. The prisms were anodized flat black to minimize unwanted reflections from the laser light sheet used for the PIV measurements. Each prism was partially immersed in the turbulent boundary layer on the ground plane. The experiments were conducted at a freestream velocity of $U_\infty = 20$ m/s, giving a Reynolds number, based on prism width, of $\mathrm{Re} = 4.2\times10^4$.

The wind tunnel data were acquired using a computer with a 1.8-GHz Intel Pentium 4 processor, a National Instruments PCIe-6259 16-bit data acquisition board, and LabVIEW software. The freestream conditions were obtained with a Pitot-static probe, Datametrics Barocell absolute and differential pressure transducers, and an Analog Devices AD590 integrated circuit temperature transducer. To characterize the boundary layer on the ground plane, a boundary layer Pitot tube and an X-wire boundary layer probe were used to measure its mean velocity profile. At the location of the prism (with the prism removed), the boundary layer thickness was $\delta = 54$ mm providing a thickness-to-width ratio of $\delta/D = 1.7$ and a thickness-to-height ratio ranging from $\delta/H = 0.2$ (for AR = 9) to $\delta/H = 0.6$ (for AR = 3).

Velocity field measurements in the vicinity of the finite square prism were made with a PIV system. The laser light (532 nm) was supplied by a 200-mJ/pulse dual Nd:YAG Gemini PIV 15 laser from New Wave Research, which had a maximum pulse frequency of 15 Hz. A TSI light arm was used to deliver the laser beam from the laser to the light sheet optics. The light sheet optics included either −50-mm or −25-mm cylindrical lenses and 500-mm, 750-mm, or 1000-mm spherical lenses, depending on the location of the field of view. Images were acquired with a CCD camera (MegaPlus ES4020, double frames, 2048 × 2048 pixels) and captured by a 64-bit EDT PCI DV C-Link frame grabber on a computer workstation. The timing of the laser, camera, and frame grabber was controlled by a Berkeley Nucleonics 505-8C digital delay

generator synchronizer. The flow was seeded by atomized propylene glycol droplets produced by a theatrical fog machine.

PIV measurements were made above the free end surfaces of the prisms in vertical (*x*-*z*) planes located on the centreline of the model ($y/D = 0$) and at two offset locations ($y/D = 0.25$ and 0.375); the locations of these fields of view are shown in Figure 1. The light sheet optics were located above the wind tunnel test section and the laser light was directed through a small aperture in the test section roof and towards the ground plane. Each field of view was 61 mm × 61 mm (1.9*D* × 1.9*D*) yielding an image resolution of about 30 μm/pixel. For the tallest prism (of AR = 9), more than 25 fields of view were used to build a composite picture of the flow field upstream and downstream of the prism. For each field of view, an ensemble of 1,000 sample images was acquired from which the mean velocity vector field was determined. Image pairs were processed with a half-padded FFT cross-correlation algorithm, a relative maxima peak detection algorithm, and a Gaussian sub-pixel interpolation algorithm. A Hart correlation-based (CBC) validation method [13] with 50% overlap was used for reducing the sub-pixel errors and eliminating spurious vectors from the PIV results. The cellular neural network (CNN) method [14] together with dynamic threshold outlier identification was used as a post-interrogation algorithm to detect spurious vectors in PIV measurements. The fields of view were analyzed with interrogation areas of 64 × 64 pixels. A two-level analysis technique was used that halved the size during the second pass. In addition, a 50% interrogation area overlap was used in all cases. The resulting velocity vector fields contained approximately 63 × 63 velocity vectors with a vector spacing (spatial resolution) of approximately 0.03*D*. The uncertainty in the mean velocity measurements was estimated to be about 2%.

3. RESULTS AND DISCUSSION

Figure 2 shows the mean flow streamlines (obtained from the in-plane mean velocity components, $\overline{U}/U_\infty$, $\overline{W}/U_\infty$), on the wake centerline ($y/D = 0$) for each of the four prisms (of AR = 9, 7, 5, and 3). The mean fields are calculated from an ensemble of 1,000 instantaneous PIV velocity fields.

Upstream of the prism, for all four aspect ratios, part of the approach flow moves up and over the tip and separates from the leading edge of the free end. No flow reattachment occurs on the free end. The other part of the approach flow, closer to the ground plane, moves downwards as it nears the prism and recirculates upstream of the prism-wall junction. It is in this region where the familiar horseshoe vortex is located (although it cannot be discerned in Fig. 2). In the near-wake region, a strong downwash flow is observed immediately downstream of the free end in the near wake of the prism. The downwash originates downstream of the free-end recirculation zone, persists in the streamwise direction and descends into the central portion of the wake.

The mean streamlines show that part of the downwash flow is directed towards the ground plane and returns upstream to stagnate onto the rear surface of the prism; a large recirculation zone forms behind the prism. The rest of the downwash flow moves away from the prism into the far wake. A small vortex forms immediately downstream of the trailing edge of the free end. The size of the vortex is a function of the prism aspect ratio, such that the largest vortex occurs for the smallest aspect ratio (AR = 3, Fig. 2d). According to Figures 2a,b,c, for AR = 9, 7 and 5, respectively, some of the downwash flow is directed along the prism wall toward the ground plane, whereas for AR = 3 (Fig. 2d), flow moves upwards along the prism wall toward the free end, resulting in a larger vortex just below the free end.

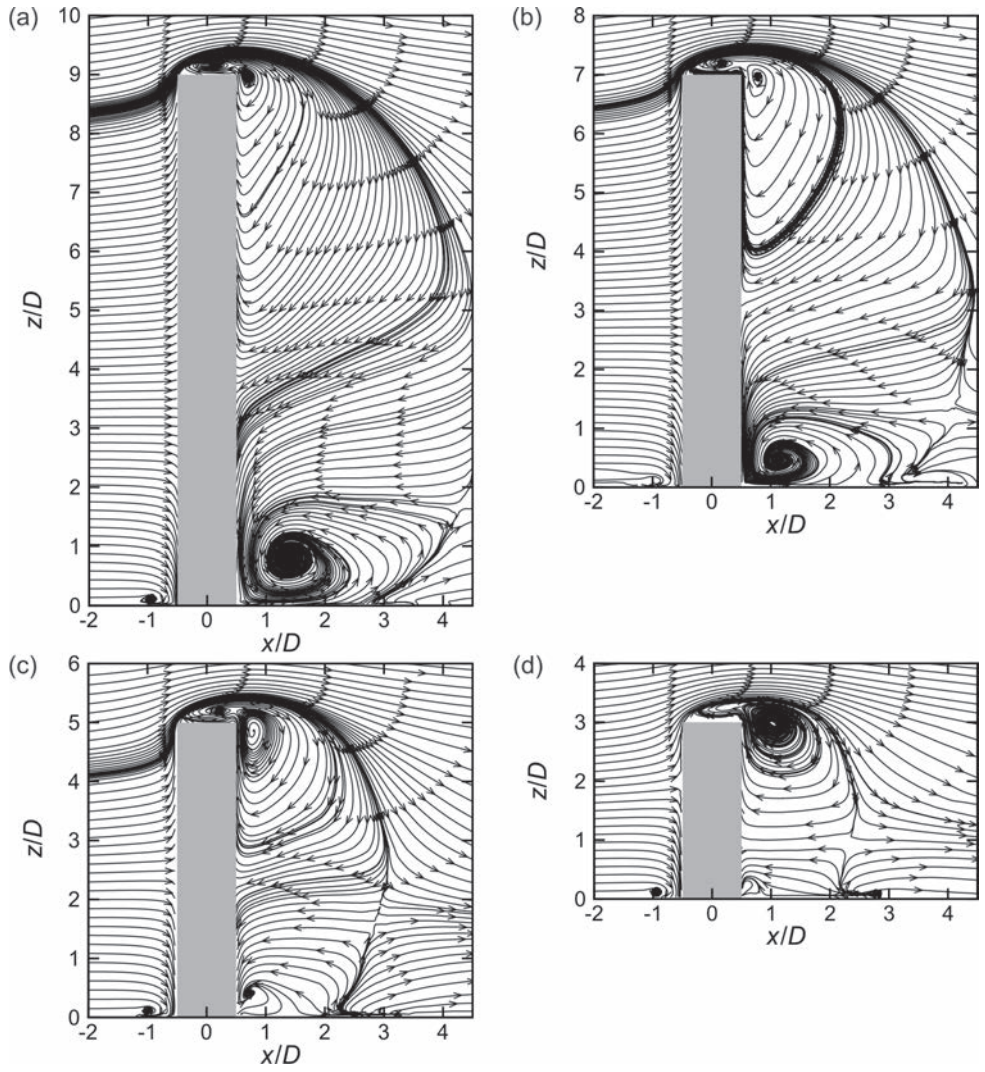

Figure 2. Mean streamlines in a vertical plane on the wake centerline (y/D = 0, the symmetry plane: (a) AR = 9; (b) AR = 7; (c) AR = 5; (d) AR = 3.

Another vortex, with CCW sense of rotation, can be found immediately behind the prism, near the prism-wall junction, for AR = 9 and 7 (Fig. 2a,b). This vortex is much weaker and nearly absent for the prisms of AR = 5 and 3 (Fig. 2c,d). The distinct near-wake structure for AR = 3, and to some extent for AR = 5, suggest the critical aspect ratio for these prisms is between AR = 5 and AR = 3.

Figure 3 shows an enlarged view of mean streamlines (on the flow centreline) and the CW vortex behind the square prism close to the trailing edge of the prism's free end surface. The size of the vortex is a function of aspect ratio, such that the largest vortex occurs for the smallest aspect ratio (AR = 3, Fig. 3d). This vortex is related to the flow direction along the rear surface of the prism (seen in Fig. 2). The centre of the vortex moves downstream as the prism aspect ratio decreases.

The mean streamlines above the free ends (on the flow centreline) of the square prisms are shown in Figure 4. Flow separating from the leading edge does not reattach onto the upper surface but extends into the near-wake region. Another small region of locally separated flow

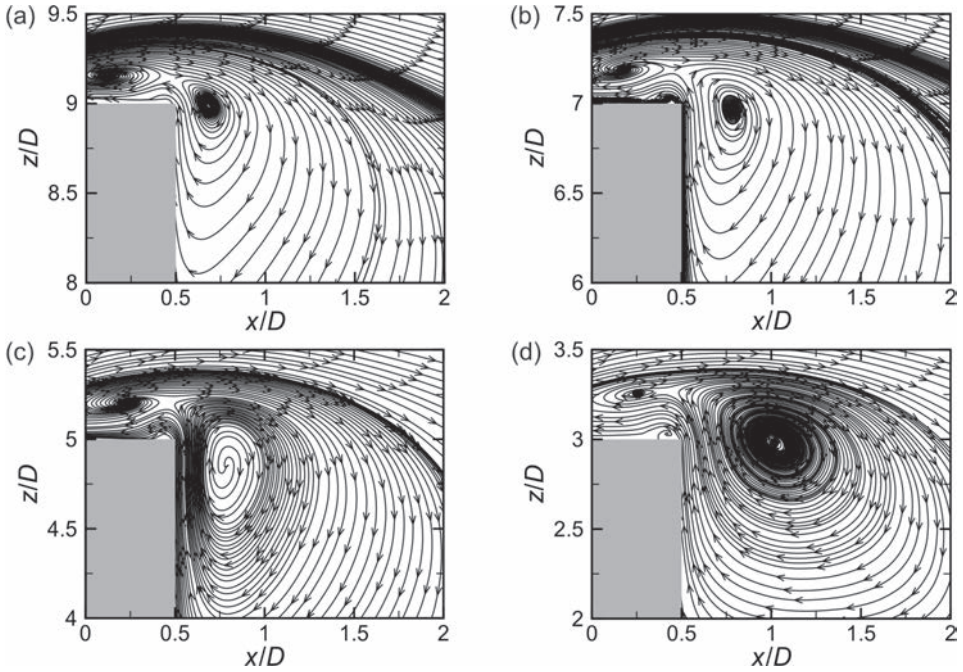

Figure 3. Mean streamlines immediately above and behind the prism, on the flow centreline (an enlargement of what is shown in Fig. 2): (a) AR = 9; (b) AR = 7; (c) AR = 5; (d) AR = 3.

may be seen on the upper surface just upstream of the trailing edge. A cross-stream vortex forms above the free end of the square prism, due to interaction between the separated flow from the leading edge of the prism and the reverse flow over the trailing edge. The role of the reverse flow coming up from the near wake of the prism and moving upstream over the free end surface is to form the vortices and saddle points in Figure 4. However, the behaviour of the reverse flow and its interaction with the separated flow changes with AR, and its overall behaviour is connected with the entire flow field around the prism. As seen in Figure 4, the centre of the cross-stream vortex moves downstream and upwards as the aspect ratio is lowered. Just behind this vortex, a saddle point is observed. As the aspect ratio is lowered, the locations of the vortex centre and saddle point are displaced farther away from the free end surface, moving from $z/D \approx 0.15$ above the surface for AR = 9 (Fig. 4a) to $z/D \approx 0.25$ for AR = 3 (Fig. 4d).

Contour plots of the streamwise turbulence intensity (u'/U_∞), above the free ends (on the flow centreline) of the finite square prisms are shown in Figure 5. This figure illustrates regions of elevated streamwise turbulence intensity above the free end surfaces that extend prominently downstream of the prisms. According to Figure 5, for all aspect ratios, the streamwise turbulence intensity level increases from its minimum value close to the free end surface to its highest level occurring along the shear-layer boundary between the outer flow and the mean recirculation zone. The maximum level of turbulence intensity for the prism of AR = 9 (Fig. 5a) is $u'/U_\infty \approx 0.43$, while for AR = 7, 5, and 3 (Fig. 5b,c,d) its value is $u'/U_\infty \approx 0.4$. For finite circular cylinders, however, the highest levels of u'/U_∞ are almost twice those for square prisms [15]. According to Figure 5, the region of highest level of u'/U_∞ is approximately located 0.2D to 0.3D above the free end surfaces of the square prisms and in the streamwise position range of x/D = −0.3 to −0.2.

Figure 6 shows the contours of the in-plane Reynolds shear stress field ($-\overline{u'w'}/U_\infty^2$) above the free end surfaces of the finite square prisms. The flow above the free end is characterized by

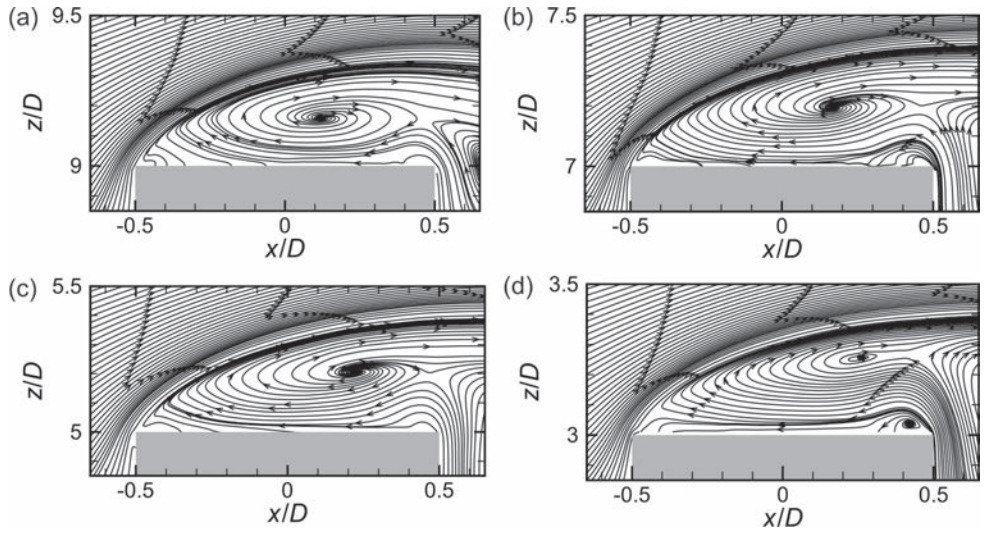

Figure 4. Mean streamlines above the free end on the flow centreline (an enlargement of what is shown in Figs. 2 and 3): (a) AR = 9; (b) AR = 7; (c) AR = 5; (d) AR = 3.

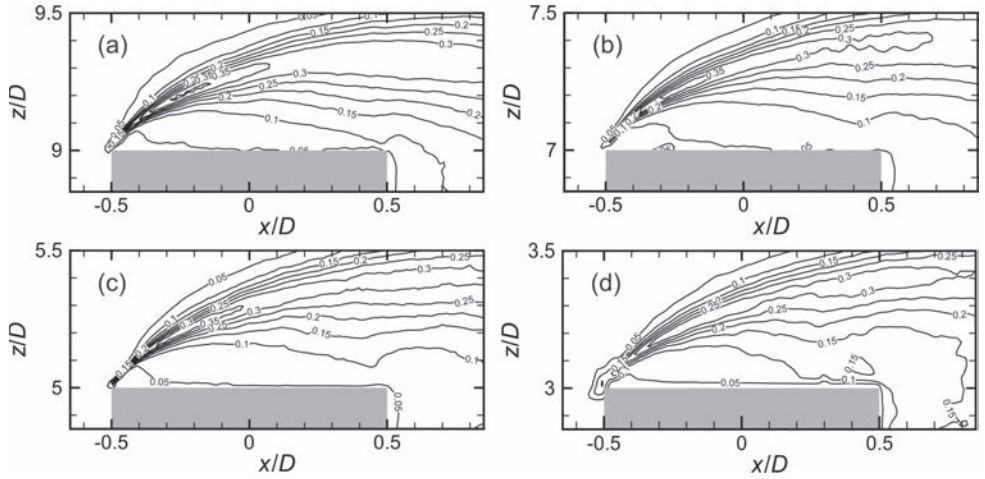

Figure 5. Streamwise turbulence intensity contours in a vertical plane on the wake centerline (y/D = 0, the symmetry plane): (a) AR = 9; (b) AR = 7; (c) AR = 5; (d) AR = 3.

two regions of elevated Reynolds shear stress: a region of negative shear stress above the free end that extends into the upper part of the near-wake region, and a region of positive shear stress originating from the leading edge and following the separated shear layer bounding the mean recirculation zone. The Reynolds shear stress behaviour does not change significantly as the aspect ratio of prism changes. However, as the prism aspect ratio increases, the region of negative Reynolds shear stress becomes wider so that for the prism of AR = 9 (Fig. 6a), the contour of negative Reynolds shear stress reaches the trailing edge of the free end surface.

Figure 7 shows the mean streamlines in three vertical (x-z) planes above the free ends of the square prisms; the three planes correspond to the three cross-stream positions of y/D = 0, 0.25, and 0.375 (illustrated in Fig. 1). According to Figure 7, the mean flow pattern above the free end of a square prism of a given aspect ratio changes considerably moving away from the

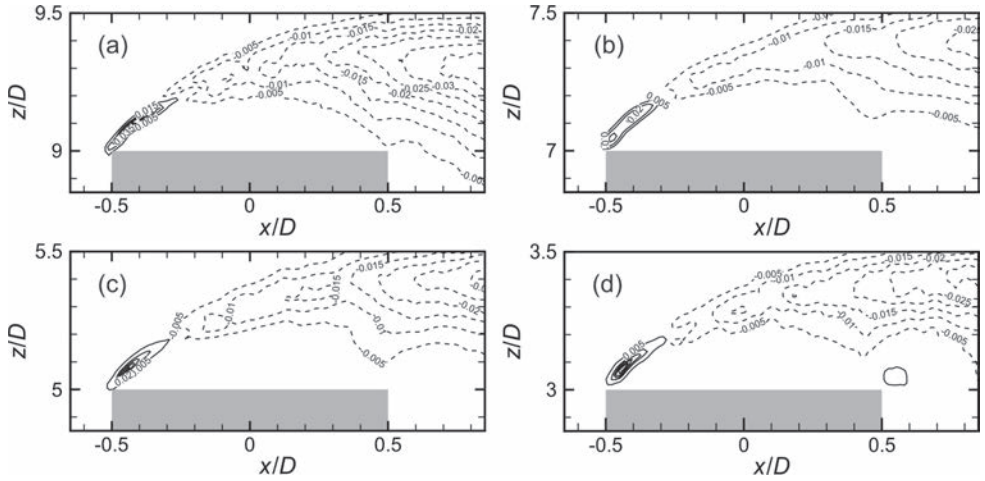

Figure 6. Reynolds shear stress contours in a vertical plane on the wake centerline (y/D = 0, the symmetry plane): (a) AR = 9; (b) AR = 7; (c) AR = 5; (d) AR = 3. Solid contour lines represent positive Reynolds shear stress, dashed contour lines represent negative Reynolds shear stress.

flow centreline. For the square prisms of AR = 9, 7, and 5, the cross-stream vortex seen at y/D = 0 (Fig. 7a,d,g), is absent away from the symmetry plane, however, the cross-stream vortex is still present at all the y/D positions considered for the prism of AR = 3 (Fig. 7j,k,l)). In addition, the reverse flow and its local separation from the trailing edge is more dominant for the prism of AR = 3 at different y/D locations (Fig. 7j,k,l), while for the more slender prisms (AR = 9, 7, and 5), the effect of the shear layer separated from the leading edge is more dominant than the reverse flow as the distance from the symmetry plane increases (Fig. 7a-i).

4. CONCLUSIONS

In the present study, the flow field above the free end surface of a surface-mounted finite square prism was investigated in a low-speed wind tunnel at Re = 4.2×10^4 using PIV. The prism was mounted normal to a ground plane and was partially immersed in a flat-plate turbulent boundary layer with δ/D = 1.7 at the location of the prism. Four prism aspect ratios were considered, AR = 9, 7, 5, and 3. PIV velocity measurements were made in vertical planes at the cross-stream locations of y/D = 0, 0.25, and 0.375 above the free end of the prism.

Flow separation occurs from the leading edge of the free end and the separated flow extends into the near-wake region. Unlike the circular cylinder case, there is no reattachment of the separated flow on the free end surface. A prominent CW vortex is found within the mean recirculation zone above the free end. A second CW vortex is found downstream in the upper part of the near wake. Elevated levels of turbulence intensity and Reynolds shear stress occur above the free end. The reverse flow and its local separation from the trailing edge of the free end surface was more dominant for the prism of AR = 3 at different cross-stream locations (y/D), while for prisms of AR = 9, 7, and 5, the effect of the shear layer separated from the leading edge was more dominant than the reverse flow as the cross-stream distance (y/D) increases. The results suggest a distinct flow pattern and behaviour for the finite square prism of AR = 3, and place the critical aspect ratio between AR = 3 and AR = 5 for these experimental conditions.

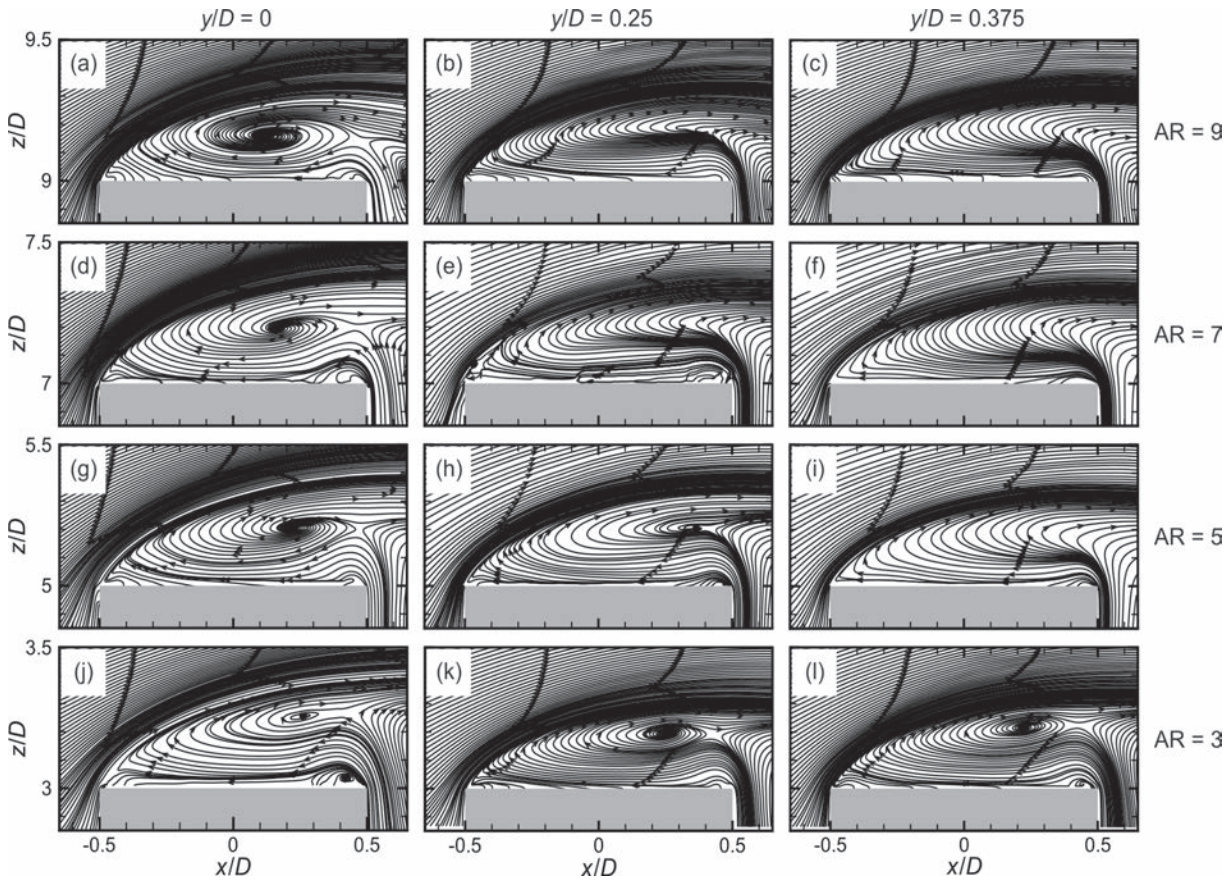

Figure 7. Mean streamlines for the flow over the free end of the finite square prism for aspect ratios of AR = 9 (first row, (a,b,c)), AR = 7 (second row, (d,e,f)), AR = 5 (third row, (g,h,i)), and AR = 3 (fourth row, (j,k,l)), for measurements made in vertical planes at y/D = 0 (left column, (a,d,g,j)), y/D = 0.25 (middle column, (b,e,h,k)), and y/D = 0.375 (right column, (c,f,i,l)).

ACKNOWLEDGMENTS

The authors acknowledge the support of the Natural Sciences and Engineering Research Council of Canada (NSERC). The assistance of D.M. Deutscher and Engineering Shops is gratefully acknowledged.

REFERENCES

1 D. Sumner, J.L. Heseltine, O.J.P. Dansereau, Wake structure of a finite circular cylinder of small aspect ratio, Exp. Fluids, 37 (2004) 720-730.
2 T. Kawamura, M. Hiwada, T. Habino, I. Mabuchi, M. Kumada, 1984, Flow around a finite circular cylinder on a flat plate, B. JSME, 27 (1984) 2142-2150.
3 A. Leder, 3D-flow structures behind truncated circular cylinders, Proceedings of FEDSM'03, 4th ASME-JSME Joint Fluids Engineering Conference, Honolulu, USA, Paper No. FEDSM2003-45083 (2003).
4 C.W. Park, S.J. Lee, Effects of free-end corner shape on flow structure around a finite cylinder, J. Fluids Struct., 19 (2004) 141-158.

5 R.J. Pattenden, S.R. Turnock, X. Zhang, Measurement of the flow over a low aspect ratio cylinder mounted on a ground plane, Exp. Fluids, 39 (2005) 10-21.
6 S. Krajnović, Flow around a tall finite cylinder explored by large eddy simulation, J. Fluid Mech., 676 (2011) 294-317.
7 S.C. Roh, S.O. Park, Vortical flow over the free end surface of a finite circular cylinder mounted on a flat plate, Exp. Fluids, 34 (2003) 63-67.
8 H.F. Wang, Y. Zhou, C. Chan, K.S. Lam, Effect of initial conditions on interaction between a boundary layer and a wall-mounted finite-length-cylinder wake, Phys. Fluids, 18 (2006) 065106.
9 H.F. Wang, Y. Zhou, C. Chan, T. Zhou, Momentum and heat transport in a finite-length cylinder wake, Exp. Fluids, 46 (2009) 1173-1185.
10 H.F. Wang, Y. Zhou, The finite-length square cylinder near wake, J. Fluid Mech., 683 (2009) 453-490.
11 J.A. Bourgeois, P. Sattari, R.J. Martinuzzi, Alternating half-loop shedding in the turbulent wake of a finite surface-mounted square cylinder with a thin boundary layer, Phys. Fluids, 23 (2011) 095101.
12 M.S. Adaramola, O.J. Akinlade, D. Sumner, D.J. Bergstrom, A.J. Schenstead, Turbulent wake of a finite circular cylinder of small aspect ratio, J. Fluid Struct., 22 (2006) 919-928.
13 D. Hart, PIV error correction, Exp. Fluids, 29 (2000) 13-22.
14 A.M. Shinneeb, J.D. Bugg, R. Balachandar, Variable threshold outlier identification in PIV data, Meas. Sci. Technol., 15 (2004) 1722-1732.
15 N. Rostamy, D. Sumner, D.J. Bergstrom, J.D. Bugg, An experimental study of the flow above the free ends of surface-mounted bluff bodies, Proceedings of ASME 2012 Fluids Engineering Summer Meeting, July 8-12, 2012, Rio Grande, Puerto Rico, Paper No. FEDSM2012-72028 (2012).

Simultations of flow around a three-dimensional square cylinder unsing LES and DNS

Tufan Arslan*, George K. El Khoury[a], Bjørnar Pettersen[a] and Helge I. Andersson[b]

*Department of Marine Technology
Norwegian University of Science and Technology, 7491 Trondheim, Norway
e-mail: tufan.arslan@ntnu.no,

[a] Department of Marine Technology
Norwegian University of Science and Technology, 7491 Trondheim, Norway
e-mails: george.e.khoury@ntnu.no, bjornar.pettersen@ntnu.no

[b] Department of Energy and Process Engineering
Norwegian University of Science and Technology, 7491 Trondheim, Norway
e-mails: helge.i.andersson@ntnu.no

Abstract. *The aim of the present study is to investigate the turbulent flow around a square cylinder. This is one of the most common studied bluff bodies. The unsteady flow is studied by using computational fluid dynamics (CFD) tools and different turbulence models. Simulation results are compared to laser doppler velocimetry (LDV) measurement data of the flow field published in the literature. The results are also compared with other numerical studies which can be used as verification. In addition, computed force coefficients are compared with experimental measurements.*

Keywords: LES, DNS, bluff body, numerical simulation, square.

1 INTRODUCTION

The flow past a square cylinder has been studied by many investigators for a long period of time. Large eddy simulation (LES) is a good approach for calculation of such unsteady turbulent flows which are three-dimensional and have strong separation and vortex shedding features. The flow past a square cylinder is often used as a benchmark case for testing various sub-grid scale models of LES, as in Sohankar et al. [1] and Rodi et al. [2]. The numerical results in the literature are comprehensive and it is often compared to the experimental works by Lyn et al. [3] and Durao et al. [4]. In more recent years Brun et al. [5] investigated the coherent structures in the flow around the square cylinder both numerically and experimentally. Fröhlich and Terzi [6] coupled LES and Reynolds-Averaged Navier-Stokes(RANS) to simulate the same flow. Filippini et al.[7] and Grigoriadis et al.[8] have investigated the flow around the square cylinder with LES model, Wissink [9], Djedini and Antonia[10] performed DNS.

The codes, FLUENT, MGLET and OpenFOAM have been used in present work for numerical simulations. These codes use the finite volume method to solve the Navier-Stokes equations. FLUENT (FL) is a commercial CFD software developed by ANSYS whereas OpenFOAM (OF) is an open-source code. MGLET is an in-house CFD code by Manhart [15] used for DNS.

2 FLOW CONFIGURATION AND COMPUTER EXPERIMENTS

2.1 Flow Model and Numerical Solution Procedure

In the present work, two different sub-grid scale models are used for LES simulations, i.e., the Smagorinsky's eddy-viscosity model (SM) and the kinetic energy transport model (KET). Simulation results from these two different models are compared with experimental results. For LES, two different Reynolds numbers have been studied, i.e Re=14000 and 21400. For DNS only the Re=14000 case is considered, The Reynolds number is based on the free-stream velocity (U_0) and the crosssection length of the square cross-section.

The governing equations solved in LES modeling are a set of filtered Navier-Stokes (N-S) equations. The continuity and filtered N-S equations can be written as

$$\frac{\delta \overline{u}_i}{\delta x_i} = 0 \tag{1}$$

and

$$\frac{\delta}{\delta t}\left(\overline{u_i}\right) + \frac{\delta}{\delta x_j}\left(\overline{u_i u_j}\right) = -\frac{\delta \overline{P}}{\delta x_i} - \frac{\delta \tau_{ij}}{\delta x_j} \frac{\delta}{\delta x_j}\left(\nu \frac{\delta \overline{u_i}}{\delta x_j}\right) \tag{2}$$

where the overbar points out the filtering operation. τ_{ij} is the subgrid-scale turbulent stress defined by

$$\tau_{ij} \equiv (\overline{u_i u_j} - \overline{u_i}\ \overline{u_j}) \tag{3}$$

and will to be modeled using the Smagorinsky model (SM). In the orginal eddy-viscosity model proposed by Smagorinsky [11], the subgrid-scale stresses are modeled using

$$\tau_{ij} - \frac{1}{3}\delta_{ij}\tau_{kk} = -2C_s\overline{\Delta^2}\left|\overline{S}\right|\overline{S_{ij}} \tag{4}$$

where C_s is the model coefficient (C_s =0.1~0.2), S_{ij} is the resolved rate-of-strain tensor, $\left|\overline{S}\right| = \sqrt{2\overline{S_{ij}}\,\overline{S_{ij}}}$ is its modulus and $\overline{\Delta} \equiv V^{1/3}$ where V is the volume of the cell. In the dynamic procedure, the model coefficient C_s is computed during the LES simulation (DSM) on-the-fly. Details of the procedure can be found in Germano et al. [12].

In the kinetic energy transport (KET) model, the unresolved stresses are modeled by solving a transport equation for the kinetic energy. More details can be found in Kim and Menon [13].

LESs are performed by the FL and OF software. FL employs a cell-centered finite-volume method that permits use of polyhedral cells. Higher order methods are used for discretization of the N-S equations. In order to ensure accuracy, efficiency and stability, bounded central-differencing is adopted to solve filtered momentum equations. This is a non-dissipative, second-order-accurate scheme combined with a nonlinear flux-limiter to suppress numerical oscillations. For pressure-velocity coupling, the PISO algorithm is used. The temporal discretization in the segregated solvers employs a fully implicit, three-level, second-order accurate scheme. The discretized equation system is solved using the point-wise Gauss-Seidel iterative algorithm with and acceleration of an algebraic multi-grid (AMG) method. More details can be found in Kim [14].

DNS calculations have been performed by the direct numerical simulation solver MGLET [15]. MGLET is a finite-volume code in which the Navier-Stokes equations are discretized on a staggered Cartesian mesh with non-equidistant grid-spacing. The discretization of advection and diffusion terms is second-order accurate. For time integration an explicit third-order Runge-Kutta scheme is used. The Poisson equation for the pressure is solved by an implicit procedure [16].

In the OpenFOAM (OF) finite volume open source code, the cell-centre values of the variables are interpolated at face locations using second-order central difference scheme for the diffusive terms. The convection terms are discretized by the so-called limited linear scheme, a second order accurate bounded total variational diminishing (TVD) scheme resulting from the application of the limiter (see Sweby[17]) to the central differencing. The advancement in time is obtained by the implicit two-step second order backward differentiation formula. The pressure-velocity coupling is applied via the pressure-implicit PISO algorithm, using predictor-corrector approach. The discretized equation system is solved by Preconditioned Conjugate Gradient (PCG) methods, see Jakobs [18].

2.2 Computational Domain, Grid and Boundary Conditions

Fig. (1) shows the the computational domain and its boundaries. The incoming flow velocity U_0 corresponds to Reynolds number 14000 and 21400 ($Re=U_0D/\nu$) where D is the crossection length of the square cylinder. The turbulence intensity of the incoming flow is 2% for Re=21400 and 6% for Re=14000 matching the turbulence level in the experimental circula-

tion tunnel. The outlet surface has zero pressure condition (atmospheric) as seen in Fig. (1). Simulations are performed with periodic conditions at the side walls. The cylinder surface is considered as no-slip wall. The upper and lower surfaces are defined as symmetry conditions.

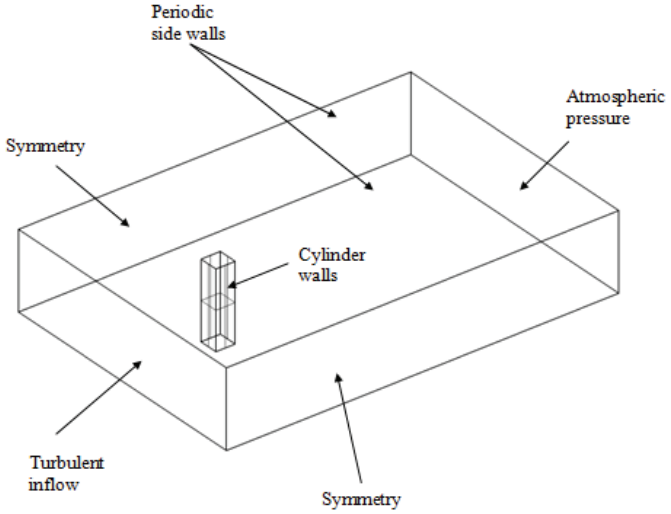

Figure 1. 3D Computational domain with boundary surfaces and its boundary conditions.

The size of the entire 3D computational domain can be seen in Fig. (2). The inlet and outlet are a distance 4.5D and 15D away from the rectangular section's front and back surfaces, respectively. The length of the cylinder in spanwise direction is 4D. The distance from the cylinder bottom and upper surface to the boundary surfaces of computational domain is 6.5D. The size of the computational domain is comparable with works reported in the literature [1], [2], [5], [7], [8].

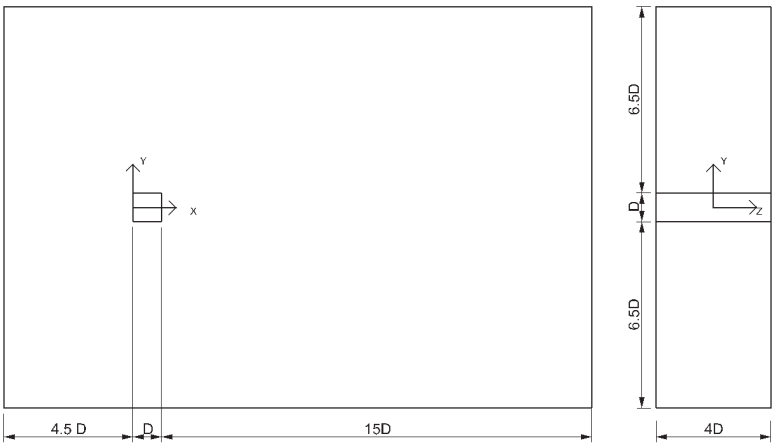

Figure 2. Size of the 3D computational domain.

In the LES calculations, a hexagonal type grid with unstructured quadrilateral type elements in streamwise and vertical direction (xy plane) is used as seen in Fig. (3a) and Fig. (3c). The grid is structured in spanwise direction (z direction). Close to the square cylinder wall, structured grid layers are employed in order to have sufficient small mesh size to resolve the

boundary layer (Fig. 3b.) The number of structured cells in these layers is 15 for the cylinder surface. The grid spacing normal to the wall for the first layer is 0.002D at the cylinder and expands out from the surface with the ratio equal to 1.2. Total number of elements in the 3D domain is varying from 1 to 4 million dependent on the expansion ratio from cylinder surface and resolution in the wake. Outside the hexahedral layer the quadrilateral elements in xy plane expand with the ratio 1.1 and reach the maximum size of 0.2D near the outer boundaries. This expansion is controlled in the wake region close to the rear of the cylinder (see Fig. 3a). The grid size is kept between 0.025D, 0.02D and 0.015D in this area for the meshes which has 1 million, 2 million and 4 million total elements respectively as seen in Table 1..The number of elements for discretizing the rectangular section with clustering towards the corners and element size in spanwise direction are showed in Table 1. The resulting y^+ values are in the order of 1 at the cylinder surface.

	Total number of elements	Number of elements in spanwise direction	Element size in wake region	Number of elements on the cylinder surface (crossection)
MESH1	1 million	30	0.025D	110x110
MESH2	2 milion	32	0.02D	120x120
MESH3	4 million	39	0.15D	140x140

Table 1: Computational grid resolution for LES calculations.

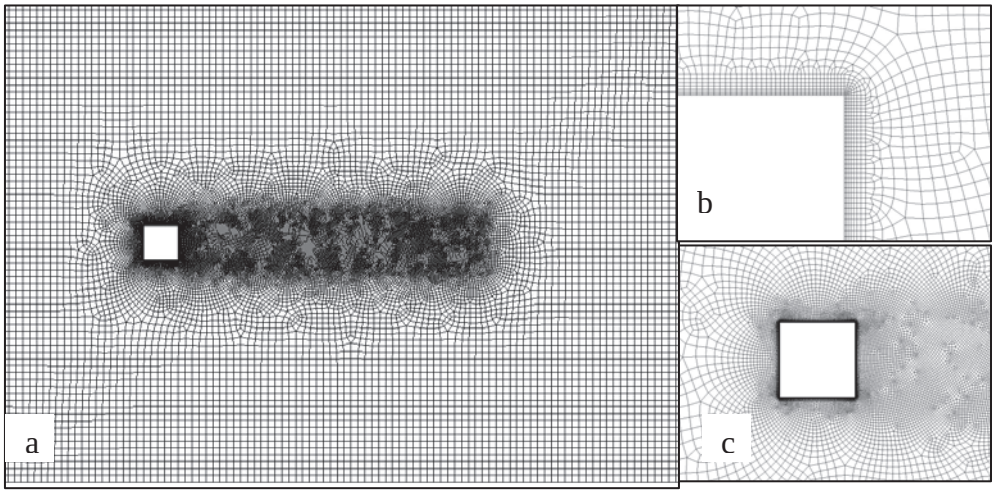

Figure 3. Cross-section of the 3D computational mesh, whole domain (a), around the trailing upper corner (b), around the square cylinder (c).

For DNS simulations, a structured mesh (850x450x400 elements) is used with the same domain size. In order to verify the current simulation is an sufficiently resolved direct numerical simulation, the Kolmogorov length scale η is estimated as $\varepsilon = (\nu^3 / \varepsilon)^{1/4}$, where the energy dissipation rate $\varepsilon = \nu\overline{(\partial u_i / \partial x_k)^2}$ is calculated from the simulation flow field. The local grid size Δ relative to Kolmogorov length scale is presented in Table 2 at different streamwise positions in the mid-section. The data in Table 2 shows that the adopted grid spacing is sufficiently fine to resolve almost all essential scales in the wake ($\Delta \sim< 7\eta$,). This value is slightly higher but comparable with results from literature, Khoury et.al. [19].

	X/D=1.5	X/D =2.5	X/D =4	X/D =9
Y/D=0.5	6.22	6.69	7.71	8.56
Y/D=0.375	6.04	6.84	8.11	8.97
Y/D=0.25	5.78	7.03	8.31	9.39
Y/D=0.125	5.71	7.20	8.36	9.11
Y/D=0	5.08	7.37	8.17	9.45

Table 2: Grid resolution $\Delta = \max(\Delta x, \Delta y, \Delta z)/\eta$ at various streamwise locations (Re=14000).

The time is non-dimensionalized by the uniform inlet velocity (U_0) and crossection length D as $T=tU_0/D$ and the simulations are carried out for T=140 in order to reach statistical convergence. The total simulation time corresponds to approximately 20 vortex shedding cycles. The Strouhal number, $St= fD/ U_0$ where f is the frequency, is gathered from the lift coefficient as a result of a FFT analysis. Mean drag and deviation of lift coefficients are calculated from the instantaneous forces.

3 RESULTS

In the LES calculations, at Reynolds number Re=21400, the effect of the temporal and spatial discretization on the simulation results is investigated by applying three different mesh sizes with different time steps. Beside this, the effect of the inlet turbulence level on the flow field has also been investigated.

Case No.	*mesh size (million)*	*time-step (seconds)*	*sub-grid scale*	*inlet turb.*	*Solver*	$\overline{C_D}$	C_L'	*St*
CASE-1	1	0.0004	SM	2 %	OF	2.15	1.37	0.135
CASE-2	1	0.00025	SM	2 %	OF	2.16	1.37	0.133
CASE-3	1	0.0001	SM	2 %	OF	2.15	1.45	0.137
CASE-4	2	0.00025	SM	2 %	OF	2.13	1.39	0.133
CASE-5	4	0.00025	SM	2 %	OF	2.13	1.36	0.133
CASE-6	1	0.00025	KET	2 %	OF	2.15	1.31	0.133
CASE-7	1	0.00025	SM	no turb.	OF	2.12	1.21	0.134
CASE-8	2	0.00025	SM	2 %	FL	2.21	1.4	0,133
CASE-9	1	0.00025	DSM	2 %	FL	2.21	1.45	0.073
CASE-10	1	0.00025	SM	2 %	FL	2.25	1.43	0.127
Exp. [3]						2.1		0.132
LES [1]	1	0.025	OEDSMF			2.09		0.132

Table 3: Mean drag and RMS of lift coefficients and Strouhal numbers (Re=21400).

The calculated lift and drag force coefficients in addition to the Strouhal numbers (based on lift coefficients) are compared with experimental data. In Table 3., the calculated mean drag coefficients, standard deviation of lift coefficients and Strouhal numbers are tabulated for 1, 2 and 4 million elements and different time steps (0.0001, 0.00025 and 0.0004 sec.). Use of SM, DSM and KET sub-grid scale models are also shown. In CASE-7, the incoming flow is considered smooth in order to investigate the effect of inlet turbulence (CASE-2). The re-

sults from FLUENT and OpenFOAM calculations are also compared. (CASE-2 vs. CASE-10 and CASE-4 vs. CASE-8)

For LES calculations at Reynolds number RE=14000, the computational mesh has one million elements (MESH1) and the time step is 0.00025 sec. The time and spanwise averaged streamwise velocity obtained by OpenFOAM using Smagorinsky sub-grid scale model is shown in Fig. 4 together with the DNS and experimental results. Here, U_0 is the free stream velocity and D is the length of the square cylinder crossection.

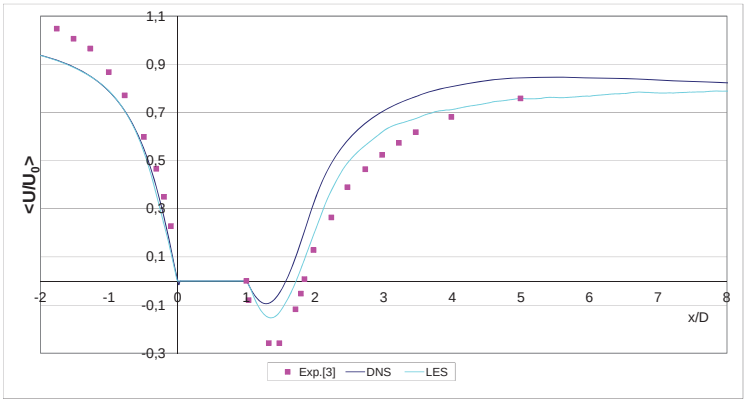

Figure 4. Time and spanwise averaged streamwise velocities at centerline in front and behind the square cylinder (Re=14000, MESH1).

As seen in Fig. (4), in LES, the minimum of the mean velocity in the near wake is estimated better than by DNS. This region is close to the center of the main vortex and kinetic energy has itsmaximum value. The fair prediction of the mean velocity may be due to underestimation of the velocity fluctuations because of slightly higher Δ values and the effect of unresolved small turbulent eddies in the wake region. However, as seen in Fig. (5), the time and spanwise averaged Reynolds normal stresses $< u'u' >$ agree well with experimental results for both DNS and LES. But the vertical component of Reynolds stresses $< v'v' >$ has been under-predicted in the near wake, 1.5D from origin of the coordinate system which is shown in Fig. (2). At the section 2.5D from origin, the $< v'v' >$ values have been predicted well for both DNS and LES but here $< u'u' >$ values are different from experimental results. Consequently, in the wake, Reynolds stresses have not been predicted well at the same time for both components. This results in the difference between calculations and experiments for the turbulent kinetic energy in the wake.

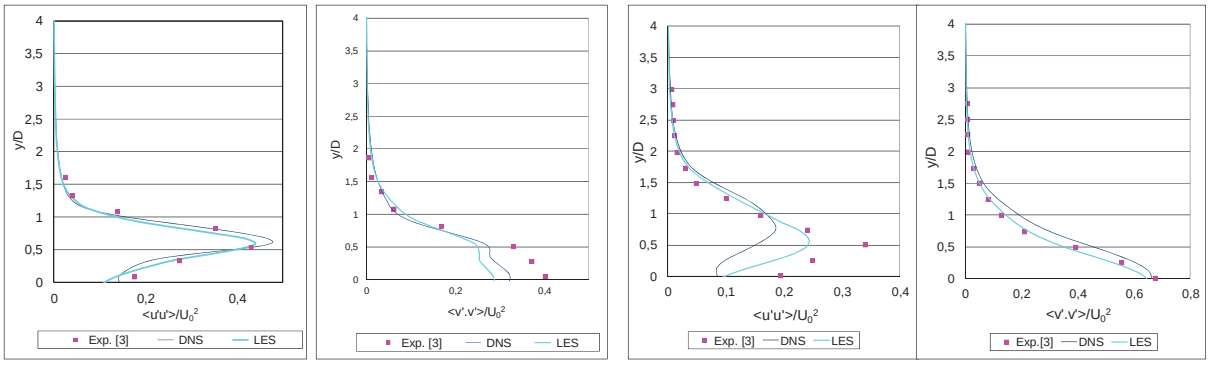

x/D=1.5 x/D=2.5

Figure 5. Time and spanwise averaged Reynolds normal turbulent stresses in the wake, Re=14000.

In Fig. (6), the measured (Durao et.al.[4]) and calculated turbulent kinetic energy contours by LES and DNS are plotted. The distribution of the turbulent kinetic energy, k, is calculated on the basis of local isotropy, i.e. $k = 3/4\left(\overline{u'^2} + \overline{v'^2}\right)$. The contours reveal distributions which are qualitatively similar to each other in the simulations and the experiment. The shear layer surrounding the recirculation bubble has intense velocity fluctuations and turbulent kinetic energy increase as the downstream distance increase, with maximum values around the center of the main circulation bubble.

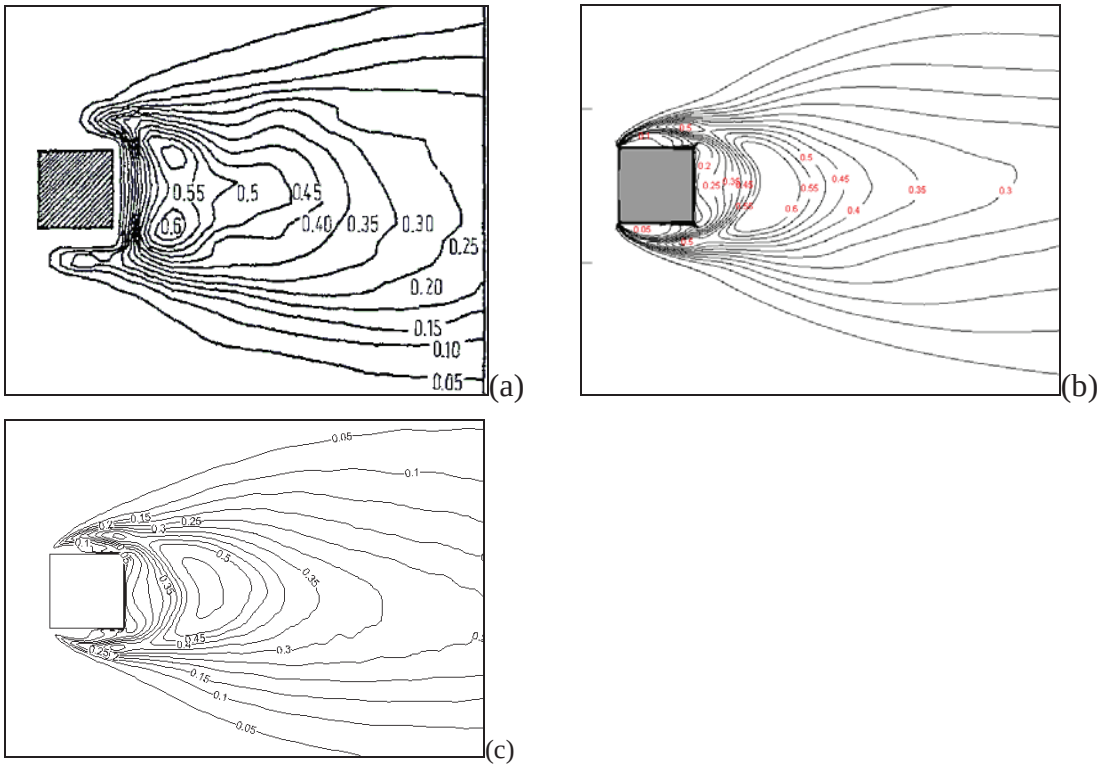

Figure 6 Spanwise averaged and normalized kinetic energy contours, (a) experiment [4] , (b) DNS and (c) LES at Re=14000.

In Fig. (7b), are shown experimental visualization results by Durao et.al[4] for Reynolds number Re=14000. Calculations of the instantaneous streamwise velocity contours have been performed by MGLET with DNS, and are shown in Fig (6 a). The streamwise velocity is normalized with free stream velocity (U_0) and spanwise averaged. Flow visualization has been made by injection of a solution of fluorescein-sodium at the upstream face of the cylinder. The calculated shear layer and vortex formation are very close to the experimental visualization as seen in Fig. (6)

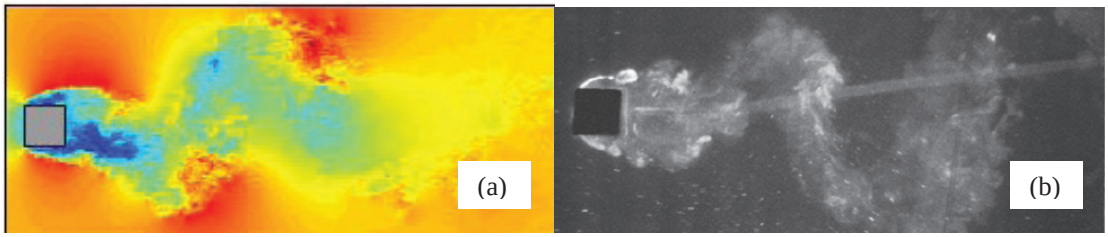

Figure 7. Instantaneous normalized streamwise velocity (U/U_0) contours by (a) DNS and (b) flow visualization experiments [4] for Re=14000.

4 CONCLUSIONS

- For Reynolds number Re=21400, the results from LES simulations with both codes and sub-grid scale models give good agreement with experimental data. One million elements and 0.0004 sec. time step size seem enough to predict acting forces and frequency of the lift with reasonable accuracy for the OF code. However the FL code gives poor results for the Strouhal number, and the mean drag coefficient is slightly over-predicted for coarse meshes (see CASE9 and CASE-10 in Table 3). The OF code seems less sensitive to grid resolution.
- Simulations show that the lift coefficient is sensitive to inlet turbulence level.
- For Reynolds number Re=14000, the variation of the streamwise component of the velocity is well predicted while the vertical component is underpredicted near the centerline in the wake ($y/D<0.5$) for both LES and DNS compared to experimental results. The calculated mean streamwise velocity is also underpredicted compared to experiments in the near wake and probably inside the separation bubble ($x/D<2$).
- DSM and KET which are more costly models, do not bring significant advantages for predicting drag and lift coefficients. The SM model can be used to simulate such flows.

ACKNOWLEDGEMENTS

Ph.D. research fellowship for the first author was provided by the Research Council of Norway. Computing time was granted by Research Council of Norway via NOTUR (The Norwegian Metacenter for Computational Science).

REFERENCES

[1] A. Sohankar, L. Davidson and C. Norberg. Large eddy simulation of flow past a square cylinder: comparison of different subgrid scale models. *Journal of Fluids Engineering*, **122**, 39–47, 2000.

[2] W. Rodi, J. H. Ferziger, M. Breuer and M. Pourquié. Status of large eddy simulation: Results of a workshop. *Journal of. Fluid Engineering*, **119**, 248-262, 1997.

[3] D. A. Lyn, S. Einav, W. Rodi and J. H. Park. A Laser-doppler velocimetry study of the ensemble-averaged characteristics of the turbulent near wake of a square cylinder. *Journal of Fluid Mechanics*, **304**, 285–319, 1995.

[4] D. F. G. Durao, M. V. Heitor and J. C. F. Pereira. Measurements of turbulent and periodic flows around a square cross-section cylinder. *Experiments in Fluids*, **1**, No. 5, 298-304, 1988.

[5] C. Brun, S. Aubrun, T. Goossens and P. Ravier. Coherent structures and their frequency signature in separated shear layer on the sides of a square cylinder. *Flow Turbulence and Combustion*, **81**, 97-117, 2008.

[6] J. Fröhlich and D. V. Terzi. Hybrid LES/RANS methods for the simulations of turbulent flows. *Progress in Aerospace Sciences*, **43**, 349–377, 2008.

[7] G. Filippini, G. Franck, N. Nigro, M. Sorti and J. D'elia. Large eddy simulations of the flow around a square cylinder, *Mecánica Computacional, Volume XXIV*, Buenos Aires, Argentina, November 2005.

[8] D. G. E. Grigoriadis, J. G. Bartzis and A. Goulas. LES of the flow past a rectangular cylinder using the immersed boundary concept, *International Journal for Numerical Methods in Fluids*, **41**, 615-632, 2003.

[9] D. Wissink. DNS of 2D turbulent flow around a square cylinder. *International Journal for Numerical Methods in Fluids*, **25,** 51-62, 1997.

[10] L. Djedini and R. A. Antonia. Shear layer instability in a low Reynolds number wake, *Proceedings of 8th International Symposium on Engineering Turbulence Modelling and Measurements*, ETMM8, ERCOFTAC, Marseille, France, 9-11 June 2010.

[11] J. Smagorinsky. General circulation experiments with the primitive equations. I. The basic experiment. *Monthly Weather Review*, **91**, 99–164, 1963.

[12] M. Germano, U. Piomelli, P. Moin and W. Cabot. A dynamic subgrid-scale eddy viscosity model. *Physics of Fluids*, **3**, 1760-1765, 1991.

[13] W. W. Kim and S. Menon. Application of the localized dynamic subgrid-scale model to turbulent wall-bounded flows. *Technical Report AIAA-97-0210*, 35th Aerospace Sciences Meeting, American Institute of Aeronautics and Astronautics, Reno, NV, January 6-9, 1997.

[14] S. –E. Kim. Large eddy simulation using unstructured meshes and dynamic subgrid-scale turbulence models. *Technical Report AIAA-2004-2548*, 34th Fluid Dynamics Conference and Exhibit, American Institute of Aeronautics and Astronautics, Portland, Oregon, June 28-July 1, 2004.

[15] M. Manhart. A zonal algorithm for DNS of turbulent boundary layers. *Computers and Fluids*, **33**, 435-461, 2004.

[16] H. Stone. Iterative solutions of implicit approximations of multidimensional partial differential equations. *SIAM, Journal of Numerical Analysis*, **5**, 530-538, 1968.

[17] P. K. Sweby. High resolution schemes using flux limiter for hyperbolic conservation laws. *SIAM, Journal of Numerical Analysis*, **21**, 995-1011, 1984.

[18] D. A. H. Jakobs. Preconditioned Conjugate Gradient methods for solving systems of algebraic equations. *Central Electricity Research Laboratories Report*, RD/L/N193/80, 1980.

[19] G. K. E. Khoury, H. I. Andersson and B. Pettersen. Crossflow past a prolate spheroid at Reynolds number of 10 000. *Journal of Fluid Mechanics*, **659**, 365–374, 2010.

The Seventh International Colloquium on Bluff Body Aerodynamics and Applications (BBAA7)
Shanghai, China; September 2-6, 2012

Wind pressure characteristics of square prism under non-stationary wind in multiple-fan wind tunnel

Yoshiyuki Tatewaki[a], Jun Kanda[b], Hitomisu Kikitsu[c], Yuan-Lung Lo[d]

[a] *Daiwa House Industry Co., Ltd., Kita, Osaka, Japan*
[b] *Nihon University, Chiyoda, Tokyo, Japan*
[c] *Building Research Institute, Tsukuba, Ibaraki, Japan*
[d] *University of Tokyo, Kashiwa, Chiba, Japan*

ABSTRACT: Statistical analyses of tornado-induced damages in Japan have been conducted and compared with Fujita Tornado Damage Scale for determining the parameters of tornado model. Based on determined parameters, tornados were scaled down and reproduced by tornado generator facilities for comparison with observed statistics. Then, by utilizing multiple-fan wind tunnel, non-stationary flow of tornado was simulated and wind pressure measurement of prism models under such flow was conducted to evaluate the distributions of wind pressure coefficients due to overshoot phenomenon observed in tornado-like wind velocities.

KEYWORDS: Tornado, Tornado model, Multiple-fan wind tunnel,
Tornado simulator, Non-stationary wind, Wind pressure characteristics

1 INTRODUCTION

Non-stationary winds induced by tornados have been investigated such as by Maeda et al ([5]) for overshoot phenomena of wind forces caused by gusty winds; by Ikeuchi et al ([2]) for the effect of wind direction changes. However, these investigations cannot be confirmed generally in the traditional turbulent boundary layer wind tunnels and many assumptions must be determined preliminarily. In this research, non-stationary wind direction change induced by tornados is focused. It is intended to clarify the effect on the prism models caused by such dramatic wind direction change by multiple-fan wind tunnel.

1.1 *General Instructions*

It was reported three casualties and one fully damaged building caused by gusty winds in Tokuno-jima, Kagoshima Prefecture on 11/18, 2012 ([8]). Generally speaking, the occurrence probability that tornado attacks one specific location is low and tornado-dependent wind resistant design for buildings is not provided in the current Japanese regulations. However, for nuclear power plants or long life structures, wind resistant design considering tornados that possess low occurrence probabilities must be considered. To include the observed tornado-induced damages in Japan, the practical tornado resistant design for important structures is essential and necessary.

In order to fully understand the tornado feature in Japan, including the wind speed profile and the wind direction change, the investigation is conducted as follows: (1) statistical studies on the recent tornado records for the specific virtual tornado model in Japan; (2) understanding the characteristics of tornado through reproducing tornado-like winds by tornado generator facilities; and (3) investigating the non-stationary effect of winds on prism models in a short period by utilizing multiple-fan wind tunnel in University of Tokyo ([7]).

2 PARAMETERS – *THEORETICAL TORNADO MODEL*

2.1 *Statistical Information of Tornado-induced Damage in Japan and Assumptions for Modeling*

Although plenty of reports or surveys have been carried out for investigation on tornado-induced damages in Japan, investigation items, such as damage path width or length, are judged subjectively based on the status of building damage appearances, which may sometimes results in significant biases for statistical studies. In order to avoid such data bias, this research utilized weather database since 1961 provided by Japan Meteorological Agency. The database includes all the tornado and downburst events. However, several assumptions are necessary for further investigations. The modeling of tornado in this research is assumed that counterclockwise Rankine tornado remains circular and moves constantly. And only horizontal wind speed component is investigated in this research.

2.2 *Time History and Occurrence Probability of Simulated Tornado Model*

Based on Fujita Tornado Damage Scale, Table 1 lists the recent records and the simulated models used in this research (VF). Applying the parameters of a simulated VF3 tornado in Table 1 as a Rankine tornado, Figure 1 shows the simulated time history and wind direction change. It is indicated that significant effects on structures can be considered resulted from the extremely high wind speed in the right side of the tornado and from the dramatic changes of wind speed and direction in a short period for the center of the tornado passing.

Table 1 Recent records and assumed tornado models

model	F scale	Wind speed (m/s)	movement (m/s)	radius (m)
Toyohashi	3	81	16.2	28.3
Mobara	3	81	20.9	80.0
Urawa	3	81	8.6	8.4
Saroma	3	81	28.8	30.2
Nobeoka	2	60	32.4	38.0
VF2	2	60	15.5	14.7
VF3	3	81	20.6	22.5
VF4	4	105	25.6	36.2
VF5	5	130	30.7	60.1

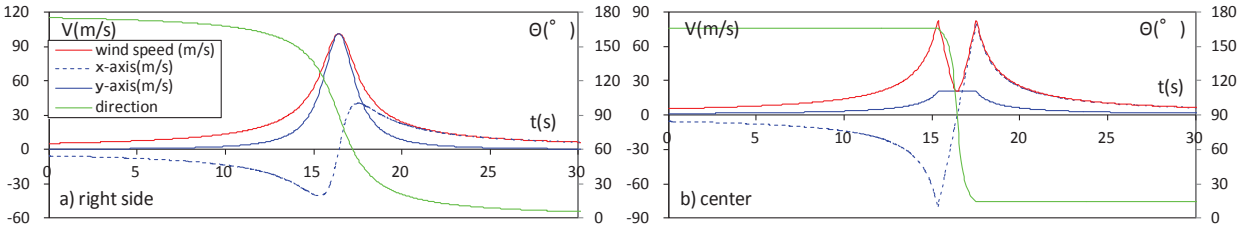

Figure 1 Wind speed and direction profile of assumed tornado model

Figure 2 shows the simulated parameters of tornado models in Table 1 and the ones suggested by American guideline, American National Standard for Estimating Tornado and Extreme Wind Characteristics at Nuclear Power Sites (ANSI/ANS-2.3-1983).
Comparing suggested tornado models by American standard and the simulated tornado models utilized in this research, it is known that the moving speed of the simulated one is 10% higher than American standard and the magnitude is only 25%. Based on this comparison, the simulated

tornado model specified in Japan is assumed F3 scale and the corresponding parameters are utilized for further experiments.

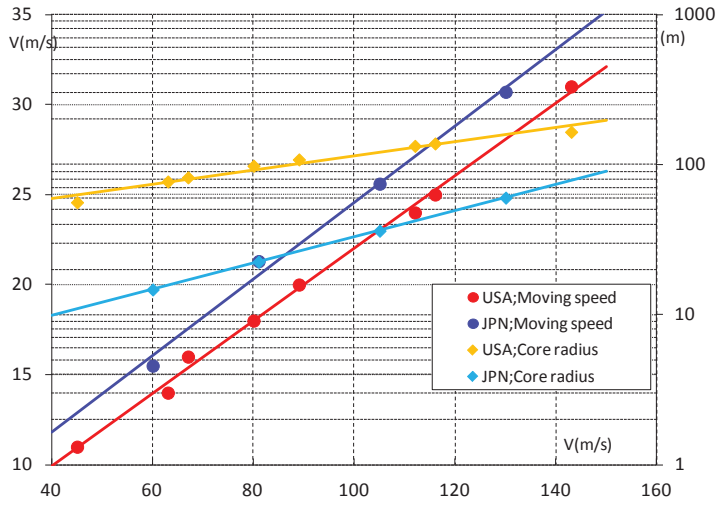

Figure 2 Comparison of assumed tornado models in Japan and suggested models by American standards

3 TORNADO REPRODUCTIONS BY TORNADO GENERATOR FACILITIES

To understand the characteristics of wind speed and wind direction changes of a tornado, a VF3 simulated tornado model mentioned in the previous section is simulated by the tornado generator facilities.

3.1 *Tornado Generator Facilities*

For the tornado generator facilities, the fan is hidden inside the main facility which can be driven by active control system to move constantly and straightly shown in Figure 3. 18 guide vans are set in the fan to generate rotary downward flows and the setting angle of vans tangent to the fan can be arbitrarily adjusted. The maximum moving speed of the main facility is 0.4m/sec. In this research, tornados with the setting angle of vans, 30°, and the rotation frequency of the fan, 8Hz, are generated for investigation of non-stationary wind flows. Sampling rate is 20Hz for 40 seconds for each sample.

Wind speed is measured from the center to the outer radius of a still simulated tornado. Figure 4 shows the wind speed profile along Z-Z axis of a still simulated tornado. The core radius is 100mm (R) and the tangent maximum wind speed is 4.29m/sec (V_m). However, the center of the simulated tornado is 10mm away from the centerline of the moving line of the experimental table.

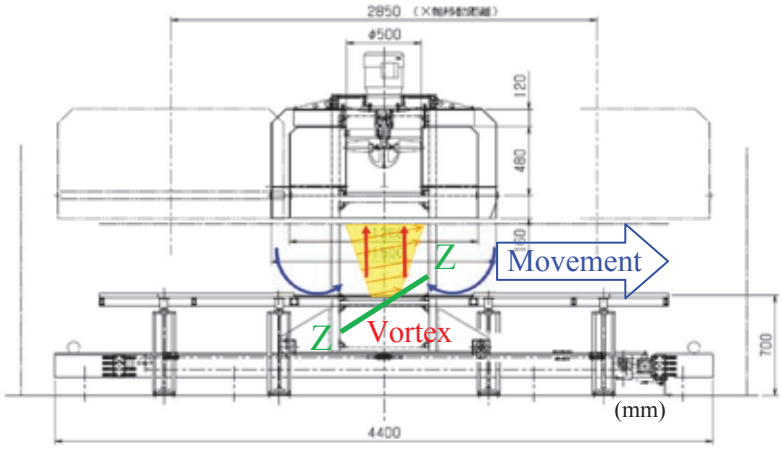

Figure 3 Tornado simulator with vortex generator

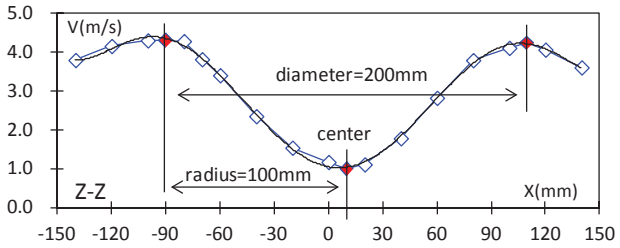

Figure 4 Wind speed distribution along Z-Z axis

3.2 *Characteristics of Wind Speed and Direction Changes of Tornado Winds*

Figure 5 shows the time histories of wind speeds and directions at the center of tornado and the right side of the moving path of the tornado when the moving speed is 0.1m/sec and 0.3m/sec (V_t). Wind speed measurements are conducted by I type hot-wire anemometers and Figure 5 shows the ensample average of 10 samples. From Figure 5, instead of Rankine tornado model, Shakeel's theoretical model ([4]) seems fit better to the experimental results (hereafter SA model). The formula to represent SA model are as follows.

Boundary layer thickness:

$$\delta(r') = \delta_0\left[1 - e^{-0.5r^2}\right] \tag{1-1}$$

Radial function:

$$r = {r'}/{r_{max}} \qquad \eta = {z}/{\delta} \tag{1-2}$$

T=tangential velocity component

$$T(\eta, r) = f(r) = 1.4\frac{V_{max}}{r}\left[1.0 - e^{-1.256r^2}\right] \tag{1-3}$$

W=vertical velocity component

$$W(\eta, r) = g(r) = 93.0r^3e^{-5r}V_{max} \qquad \eta > 1 \tag{1-4}$$

T=tangential velocity component

$$T(\eta, r) = f(r)[1 - e^{-\pi\eta}\cos(2b\pi\eta)] \quad (1\text{-}5)$$

R=radial velocity component

$$R(\eta, r) = f(r)[0.672e^{-\pi\eta}\sin\{(b+1)\pi\eta\}] \quad (1\text{-}6)$$

W=vertical velocity component

$$W(\eta, r) = g(r)[1 - e^{-\pi\eta}\cos(2b\pi\eta)] \qquad \eta \le 1 \quad (1\text{-}7)$$

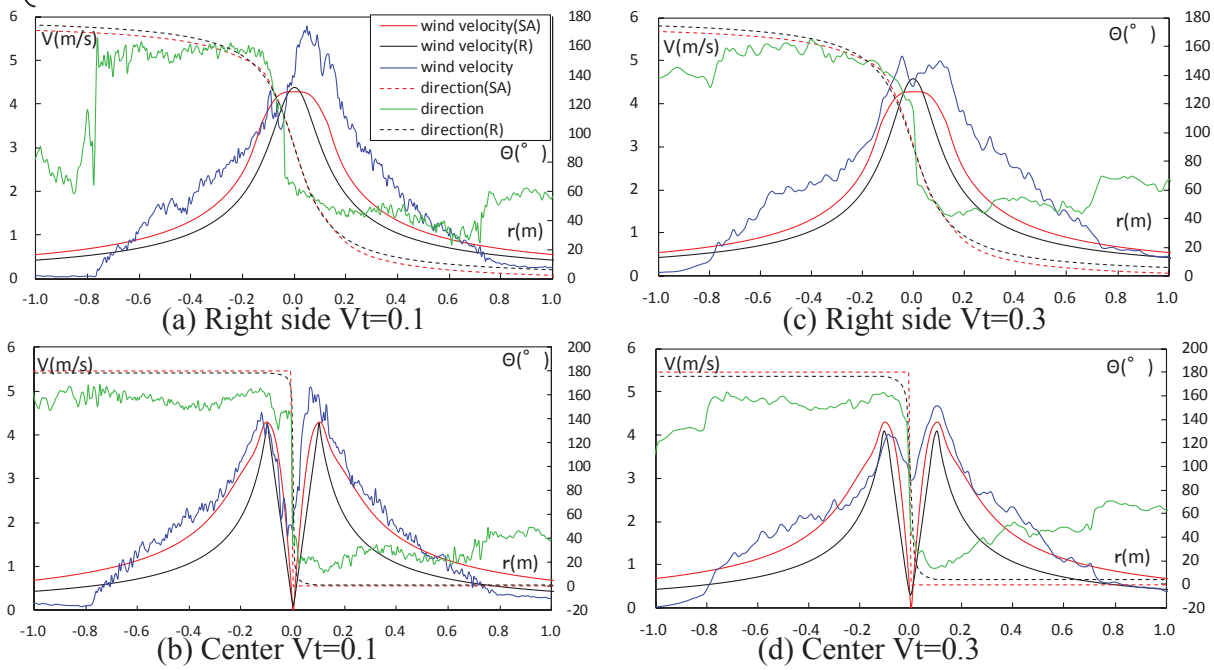

Figure 5 Time histories of measured wind speeds with the theoretical models

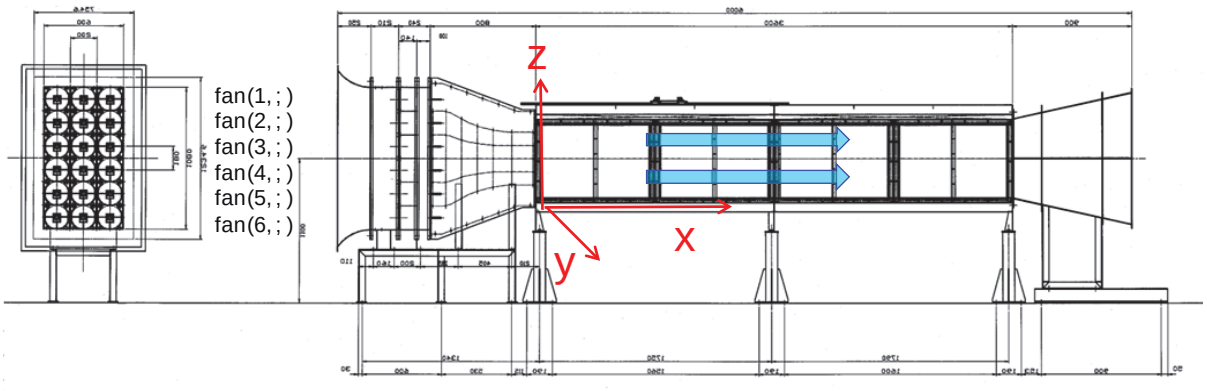

Figure 6 Diagram of multiple-fan wind tunnel and the coordinate system

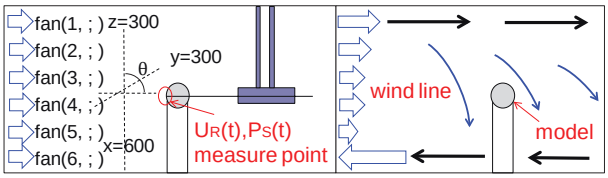

Figure 7 Mechanism of wind direction change and the measuring point

4 EXPERIMENT BY MULTIPLE-FAN WIND TUNNEL

4.1 *Simulation of Non-stationary Wind Flow based on Tornado Characteristics*

In order to investigate the non-stationary characteristics of a tornado, a multiple-fan wind tunnel is utilized to simulate part of the wind speed and direction profiles which are shown in Figure 5. A multiple-fan wind tunnel with 6×3 small fans is introduced in this research. As shown in Figure 6, fans are arranged in three vertical columns and each column contains six fans. Each fan can be actively controlled by computer independently. The rotation range of each fan is 0~3000rpm. By changing the input voltages of fans, non-stationary winds due to wind speed or direction changes can be simulated. To generate non-stationary wind flow caused by wind direction change, rotations of upper fans and lower fans can be controlled in the clockwise and counterclockwise direction. By balancing the rotation of these fans, stable wind direction change can be achieved. For the further measurement of wind speeds, the location with x=600mm, y=300mm, and z=300mm, is assumed as the measuring point. The mechanism of measurement is indicated as Figure 7.

Table 2 List of 9 types of non-stationary wind flows

stream type	⊿U(m/s)	⊿D(°)	⊿t(s)	remarks
st.1	–	–	–	stationary (0.9m/s)
st.2	–	–	–	stationary (2.2m/s)
st.3	1.2	–	1	velocity only
st.4	–	23.4	1	direction only
st.5	–	24.7	1	direction only (reverse)
st.6	1.5	22.0	1	vel & dir
st.7	1.2	18.8	1	vel & dir (reverse)
st.8	–	21.0	2	direction only
st.9	–	21.8	2	direction only (reverse)

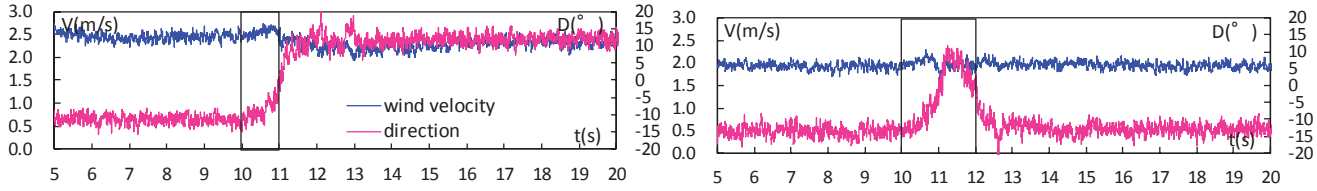

(a) Voltage of st.4 (b) Result of st.8

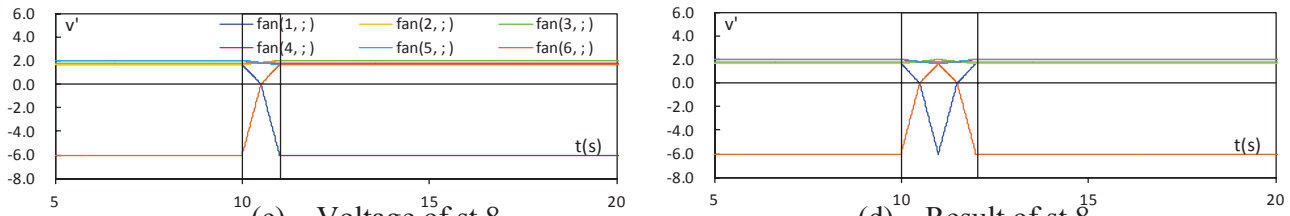

(c) Voltage of st.8 (d) Result of st.8

Figure 8 Examples of non-stationary wind flows, st4 and st8

To control each fan to generate non-stationary winds, it is necessary to vary the voltage in a short period. For the performance of fans in this research, the shortest period is 1 second. Further, to change the stationary status to non-stationary status (wind direction change here) which includes significant inverse rotation of fans, the wind speeds of fans are limited. In this research, the wind speed change is 50% of the maximum wind speed and 20° of the wind direction change.

Table 2 lists the simulated wind flow by multiple-fan wind tunnel. Wind flows st1 and st2 represent two stationary flows with two velocities; Wind flow st3 represents non-stationary flow with wind speed change of 1.2m/sec; Wind flows st4 and st5 represent two non-stationary flows with wind direction changes of 23.4° and 24.7° (reversely); Wind flows st6 and st7 represent non-stationary flows with both wind speed and direction changes; and Wind flows st8 and st9 represent the same condition as st4 and st5 but the period enlarges from 1 second to 2 seconds.
It is assumed that the downward wind direction change is indicated "-" and the upward direction is indicated "+". For non-stationary wind flows st3~st9, input voltages of fans arranged in the left column and right column are 60% of that in the middle column. Figure 8 shows the relationship of input voltage and wind speed and direction changes of st4 and st8 respectively. All the simulated wind flows remain uniform in the first 10 seconds and then start to change. An X type hot-wire anemometer is used for measurement in 1000Hz for 30 seconds. Ensample averaging is conducted by two records and moving averaging of every 200 samples is also executed.

4.2 *Distributions of Wind Speed and Direction*

In order to grasp the distributions of wind speed and direction of non-stationary wind flows inside the wind tunnel, a hot-wire anemometer is set at 25 grid measuring points shown as Figure 9. Interval of two neighboring measuring points is 25mm. Figure 10 shows the contour distributions of wind speed and direction of non-stationary st4. Each sub figure in Figure 10 represents the averaging result in certain period. It is indicated that the change of wind speed between two measuring points is less than 0.1m/sec and the wind direction change is quite stable.

4.3 *Wind Pressure Measurements on Square Prism Model*

As the results of circular prism model can eliminate the effect of velocity change ([7]), a square prism model is used to investigate the distributions of wind pressure coefficients due to non-stationary wind flow. The rotation of the square prism model is 5° and from 0°~45°. Wind pressures are recorded in 1000Hz for 30 seconds. Since the reference static wind pressure is different at different location in non-stationary wind flow, the reference static wind pressure measured on the wall of working sections of the wind tunnel is assumed for the calculation of wind pressure coefficients ([7]). The following equation is used for the definition of wind pressure coefficient.

$$C_p(t) = \frac{p'(t) - p_s(t)}{\frac{1}{2}\rho U_R(t)^2} \tag{2}$$

where $p'(t)$: measuring point; $p_s(t)$: reference static pressure; $U_R(t)$: basic wind speed.

It is known that the instantaneous maximum negative pressure around -1.2 is observed when the rotation angle is 15° ([3]). Figure 11 shows the dramatic large negative pressures when the wind direction changes in a very short period. Further, considering the wind direction change of 20° and the rotation angle of the model, the case of a 110° wind direction change can also be derived as shown in the diagram of Figure 12 and the time histories in Figure 13.

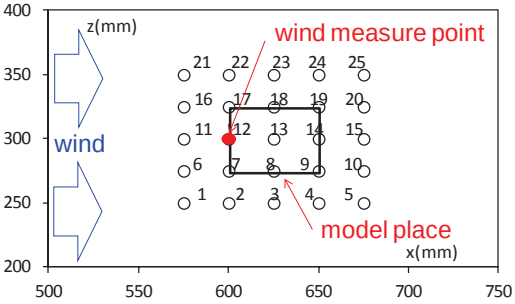

Figure 9 Measuring points inside the wind tunnel for wind velocity field

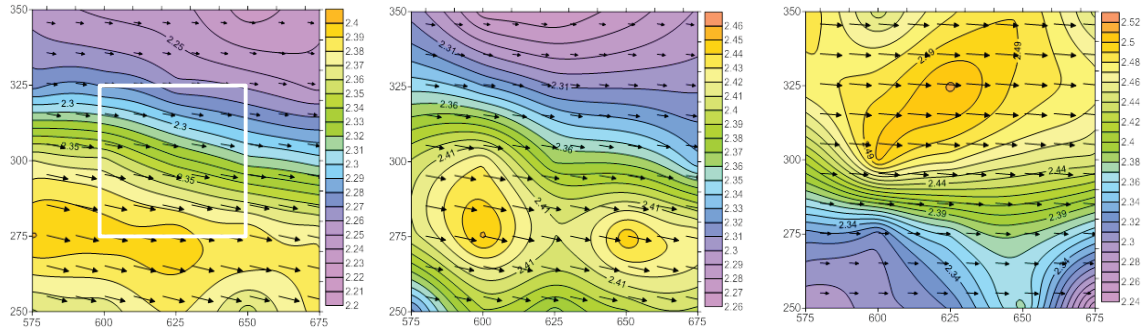

(a) 5-10s (b) 10-10.5s (c) 10.5-11s

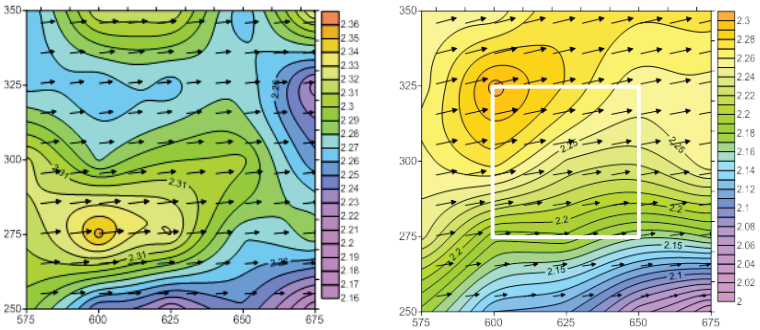

(d) 11-11.5s (e) 11.5-12s

Figure 10 Distributions of wind speed and direction of st4 non-stationary wind flow

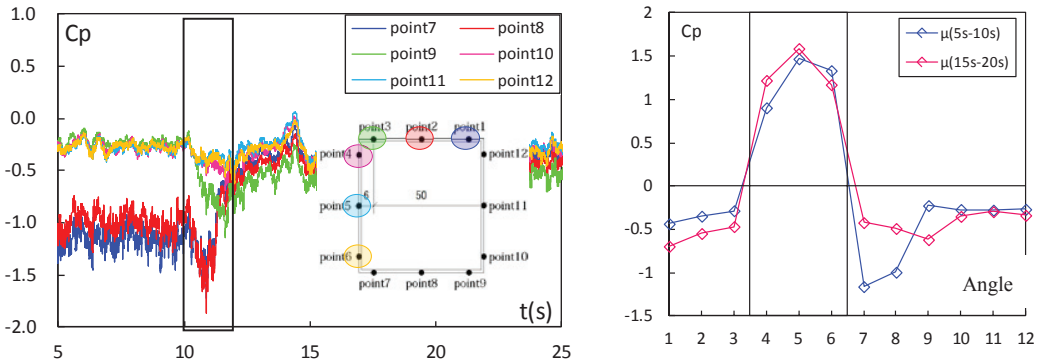

(a) Time-history (b) Average

Figure 11 Distribution of wind pressure coefficient of st5 flow with 5° rotation angle

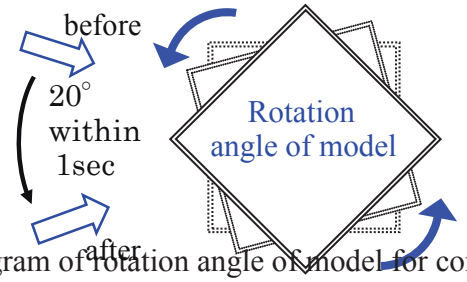

Figure 12 Diagram of rotation angle of model for continuous wind pressure coefficient measurements of 110°

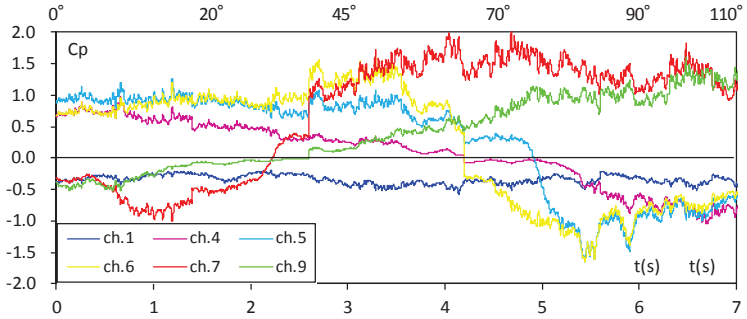

Figure 13 Derivation of wind pressure coefficients for each rotation angle for each pressure tubes

4.4 *Calculation of Wind Force Coefficients*

Wind force coefficients are derived by integrating wind pressures; however, due to the rotation of models, wind force coefficients are investigated in the x-direction and y-direction of the original model coordinates.

Figure 14 shows the wind force coefficient time histories in st4 flow for rotation angle of model equals 15° and 45°. It can be indicated clearly that instantaneous large wind forces shown in x-, y-, and torsion direction before and after the wind direction change. In this research, the shortest period is 1 second. Obvious overshoot phenomena cases are rare to investigate. Figure 15 shows respectively the obvious cases of wind speed change and wind direction change for st5 flow with 15° rotation angle and st4 flow with 10° rotation angle.

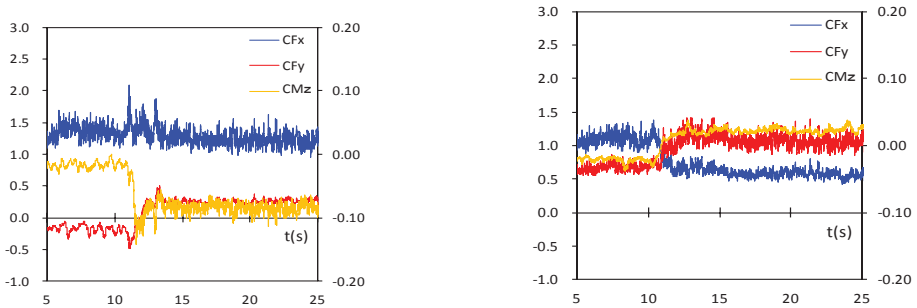

(a) Rotation angel 15° (b) Rotation angle 45°

Figure 14 Wind force coefficients of st4 with rotation angles

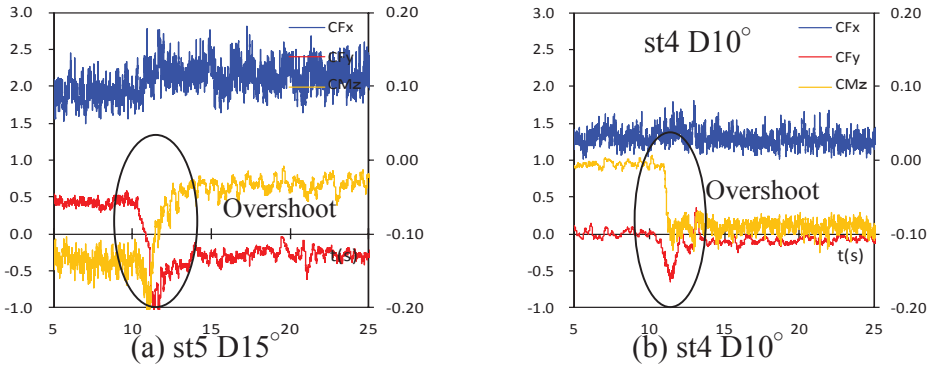

Figure 15 Observed examples of overshoot phenomena

5 CONCLUSIONS

Parameters of tornado model were first determined, based on statistical studies of recent tornado records in Japan. Then, tornado wind flow was simulated by tornado generator facilities and compared with theoretical tornado models. Nine types of non-stationary wind flows were simulated by multiple-fan wind tunnel for part of the tornado flow simulated in the generator facilities. Wind pressure measurements were then conducted under these types of non-stationary wind flows. From experimental results, it was indicated that large wind pressure coefficient around -1.2 were obtained when the rotation angle of model is 15° under wind direction change of 20° for a square prism model. And the overshoot phenomenon was also clearly observed. It is also indicated that a wind direction change of 110° can also be conducted by proper adjustment of rotation angle of the model and wind direction change. It may be anticipated that in the field scale, the effect on structures due to non-stationary wind flows is much more significant and essential.

ACKNOWLEDGEMENT

Grants-in-Aid for Scientific Research by JSPS are acknowledged for their financial support.

REFERENCES

1. M.E. Greenway, 1979, An analytical approach to wind velocity gust factors, J. Ind. Aerodyn., 5, p61-91
2. K. Idutu, J. Ikeuchi, T. Taniguchi, Y. Taniike, 2003, Study on the Wind Pressures due to Instantaneous Change of Wind Direction around a Cubic Model, Proceedings of AIJ Conference 2003 (in Japanese)
3. T. Ohkuma, J. Kanda, Y. Tamura, 2004, Wind Resistant Design of Structures, Kajima Co. (in Japanese)
4. A. Shakeel, Md. Ehtesham, 2009, Response of Transmission Towers Subjected to Tornado Loads, Proceedings of 7th Asia-Pacific Conference on Wind Engineering
5. J. Maeda, T. Takeuchi, 2010, Experimental Study of Unsteady Aerodynamic Forces – Properties of Unsteady Aerodynamic Forces under Wind Gust, Wind Engineers, JAWE, Vol.35, No.2 (in Japanese)
6. H. Kikitsu, P. P. Sarkar, Fred L. Haan, Jr., 2011, Experimental Study on Tornado-induced Loads on Low-rise Buildings Using a Large Tornado Simulator, Proceedings of ICWE13
7. R. Terai, J. Kanda, 2011, Non-stationary Wind Direction Simulation in Wind Tunnel with Computer-controlled Multiple Fans, Proceedings of ICWE13
8. Disaster on site report - On the gusty wind occurred in Tokunoshima, Kagoshima Prefecture on 18 November 2011, Naze observation station, Kagoshima regional meteorological agency (in Japanese)

The Seventh International Colloquium on Bluff Body Aerodynamics and Applications (BBAA7)
Shanghai, China; September 2-6, 2012

Wall-mounted finite cylinder wake structure modification due to boundary layer-wake interaction: Half-loop and full-loop coherent structure topologies

Z. Hosseini [a], J. A. Bourgeois [a], R. J. Martinuzzi [a]

[a]*University of Calgary, 2500 University Dr., Calgary, AB, Canada*

ABSTRACT: Earlier studies suggest that two types of shedding structures can be recognized in the wake of surface mounted cylinders. For height to width ratios lower than a critical limit, in the time averaged wake, a counter rotating vortex pair is present at the free-end. For taller cylinders another counter rotating pair is also noticed at the cylinder base. While some differences in the shedding process are discussed; due to insufficiently resolved data in spatial domain a detailed comparison of the three-dimensional turbulent field is not well documented. In addition to height to width ratio, boundary layer thickness can also change the wake structure; its effects, however, are not examined thoroughly. This work shows that the boundary layer has a key role on the shedding process. It is shown that even for a rather tall cylinder (significantly taller than the critical limit suggested in earlier work) both types of wakes can be observed depending on the boundary layer thickness. The three-dimensional phase averaged flow is reconstructed from planar PIV measurements and comparisons of the mean and dynamic wake structures are presented.

KEYWORDS: Bluff-body wake, turbulent boundary layer, coherent structure, counter rotating vortices, phase averaged flow.

1 INTRODUCTION

The prediction and control of wake transport processes requires an understanding of the turbulent coherent vortex structures due to the fundamental role they play in mixing and dispersion processes. The coherent structures in finite wall-mounted bluff body wakes give rise upon averaging to trailing streamwise vortex pairs [1-4]. In the vicinity of the obstacle tip, 'free-end' vortices induce downwash of flow toward the ground, while near the wall junction, 'junction' vortices induce upwash from below. As reported in [2-4], the junction vortex pair is not always present. The presence or absence of junction vortices can be of importance concerning safety for flow over stacks since the free-end vortex pair transports pollutants toward the ground when uninhibited by counter-rotating junction vortices. Similarly, the free-end downwash may be a concern in debris transport in strong winds over buildings which may endanger pedestrian traffic. Likewise, in combustor design using bluff-body flame stabilizer or fuel injection devices, the wall surface should be sheltered from hot gases in the core of the flow and a design ensuring junction vortices can meet this requirement.

While large differences in the mean and turbulent fields of the two wake types are observed (as discussed in [4] and presented in more details in the following), there is a lack of consensus on the parameters influencing the generation of these vortices. Sumner et al. [2] and Wang & Zhou [3], suggest that a sufficiently high aspect ratio h/d (where h is the height and d the width of the cylinder), will result in the presence of junction vortices. They, respectively, showed for circular- and square-cross-section cylinders that $h/d=3$ or less show dipole distributions of streamwise vorticity (only a free-end vortex pair) while $h/d=5$ or above show a quadrupole dis-

tribution of streamwise vorticity (free-end and junction vortex pairs). On the other hand, Wang et. al. [4] suggest that the boundary layer thickness (δ) plays an important role on presence of the upwash at the junction of the symmetry plane. They show for a cylinder with aspect ratio $h/d=5$ the upwash is present for a sufficiently thick boundary layer but it vanishes for a thin boundary layer. They suggest the effect of the boundary layer is less important for taller cylinders.

The present study aims to elucidate key role of the boundary layer by examining the flow around a rather tall building (with an aspect ratio clearly larger than the limit suggested in [2,3]) immersed in two very thin boundary layers with respect to the height. Using synchronized particle image velocimetry (PIV) and surface pressure measurements, the three-dimensional time averaged and phase averaged coherent structures in the wake of the cylinder are reconstructed and analyzed along with their respective velocity, vorticity, and Reynolds stress fields.

2 EXPERIMENTAL SETUP

The measurements were conducted in a suction type open-test-section wind tunnel shown in figure 1. A square cylinder with aspect ratio $h/d=8$ ($h=101.6mm$, $d=12.7mm$) was mounted on a sharp-leading-edge flat plate in the working section as shown in figure 2. The wake measurements were conducted for two turbulent boundary layers: the natural boundary layer developed over the flat plate and a tripped boundary layer with a $6.35mm$ rod positioned $1cm$ from the leading edge. The boundary layer thickness measured at the location of the obstacle ($x=200mm$ from the leading edge of the flat plate) with the cylinder removed was $\delta/h=0.09$ and 0.32 respectively. Boundary layer profiles and root-mean-square velocity fluctuations measured with hot-wire anemometers (TSI model 1210-20) are shown in figure 3. The free stream velocity was $U_\infty=15m/s$, corresponding to a Reynolds number $Re=U_\infty d/\nu=12,000$, with turbulent intensity of 0.8%. The measured Strouhal number was $St=fd/U_\infty=0.10 \pm 0.003$ with f the vortex shedding frequency. The Strouhal number was invariant with the change in boundary layer thickness.

A grid of several horizontal (x-y) and vertical (x-z) planes were measured using a LaVision FlowMaster high-frame-rate particle image velocimetry (PIV) system. These planar measurements are used to reconstruct the phase averaged three-dimensional flow. A pulse separation of $50\mu s$ was used and frame rates of 500 to $1000\ Hz$ captured 4 to 8 data points per shedding cycle. The estimated uncertainty on individual vector measurements is $\Delta u/U_\infty=\pm 0.025$. Conditional sampling (phase averaging) of the PIV measurements was performed using the fluctuating surface pressure difference on opposing sides of the obstacle at $z=h/2$ as the instantaneous phase of the shedding cycle. The sampling rate for the pressure is $10.24\ kHz$ and is sychronized with the PIV measurements using a TTL trigger. The shedding period is discretized into twenty equal phase steps, φ_n, ($\Delta\varphi = \pi/10$) between $\varphi=0$ and $\varphi=2\pi$. This number of bins was chosen as a compromise between statistical convergence and precision. A double decomposition ensemble average is undertaken for each phase step [5].

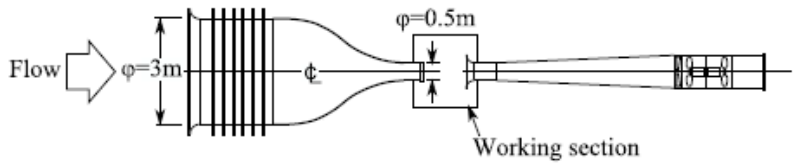

Figure 1. Schematic of the wind tunnel.

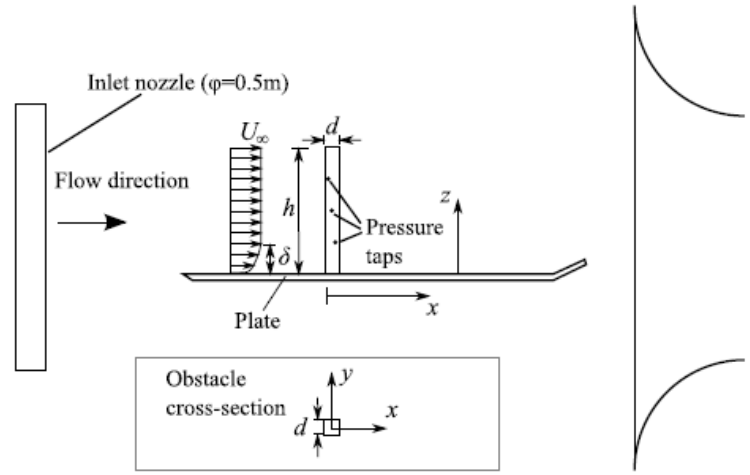

Figure 2. Schematic of the experimental setup inside working section (not to scale).

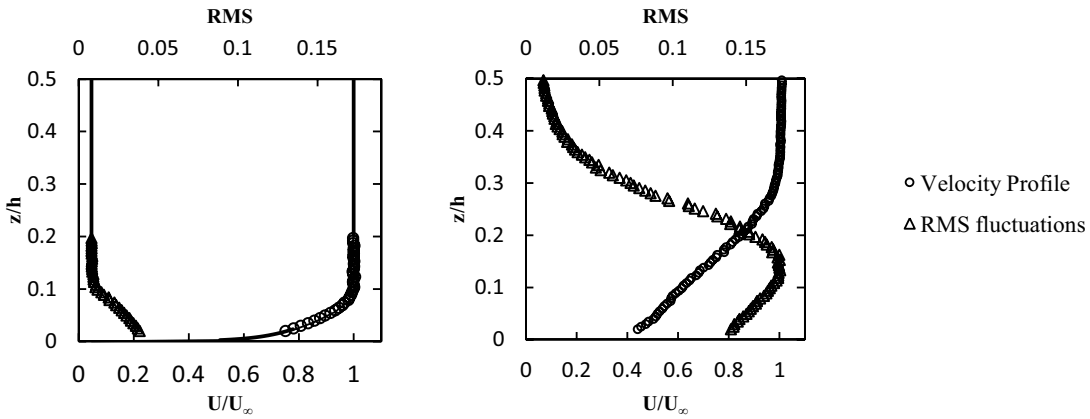

Figure 3. Natural and tripped boundary layer profiles and root-mean-square (RMS) velocity fluctuations at the location of the obstacle with the obstacle removed.

3 RESULTS

The boundary layer interactions with the vortex formation process results in topological differences both in the mean and dynamic fields. Figures 4 presents the mean sectional streamlines in the symmetry plane. For both the cases there is a downwash close to the free-end and an upwash in the base region at the junction. The separated streamlines from the free-end and the junction form a lee saddle point in the symmetry plane. The bifurcation lines extending from this saddle point separate the downwash region from the free-end and the upwash region near the mounting plate. For the thicker boundary layer (tripped case) the upwash at the junction is stronger thus the saddle point is located at a higher position. For the thinner boundary layer (untripped case), the upwash downstream of the saddle point is very weak. Similar observations were made in [4].

The mean streamlines at *z/h=0.25*, *0.50* and *0.75* are shown in figure 5. In general the recirculation regions are shorter in the tripped case. The largest difference is observed at the lower plane where for the untripped case the streamlines are diverging from the symmetry plane, in contrast to the tripped case where the streamlines converge onto the symmetry plane. The recirculation length is reduced largely for the tripped case while it stays almost the same as the middle plane in the untripped case.

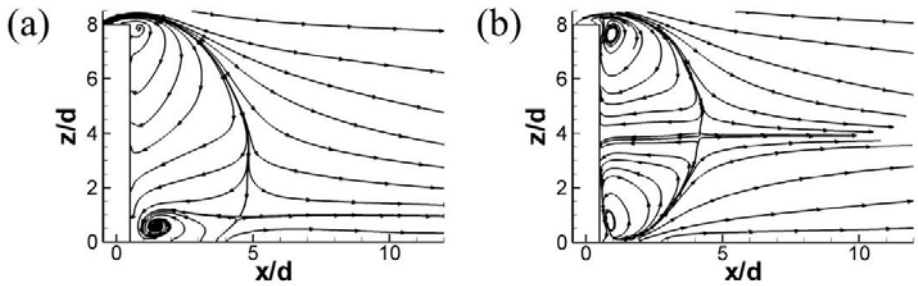

Figure 4. Mean flow streamlines in the symmetry plane for (a) untripped and (b) tripped cases. While the flow is similar close to the free-end, large differences are observed at lower heights.

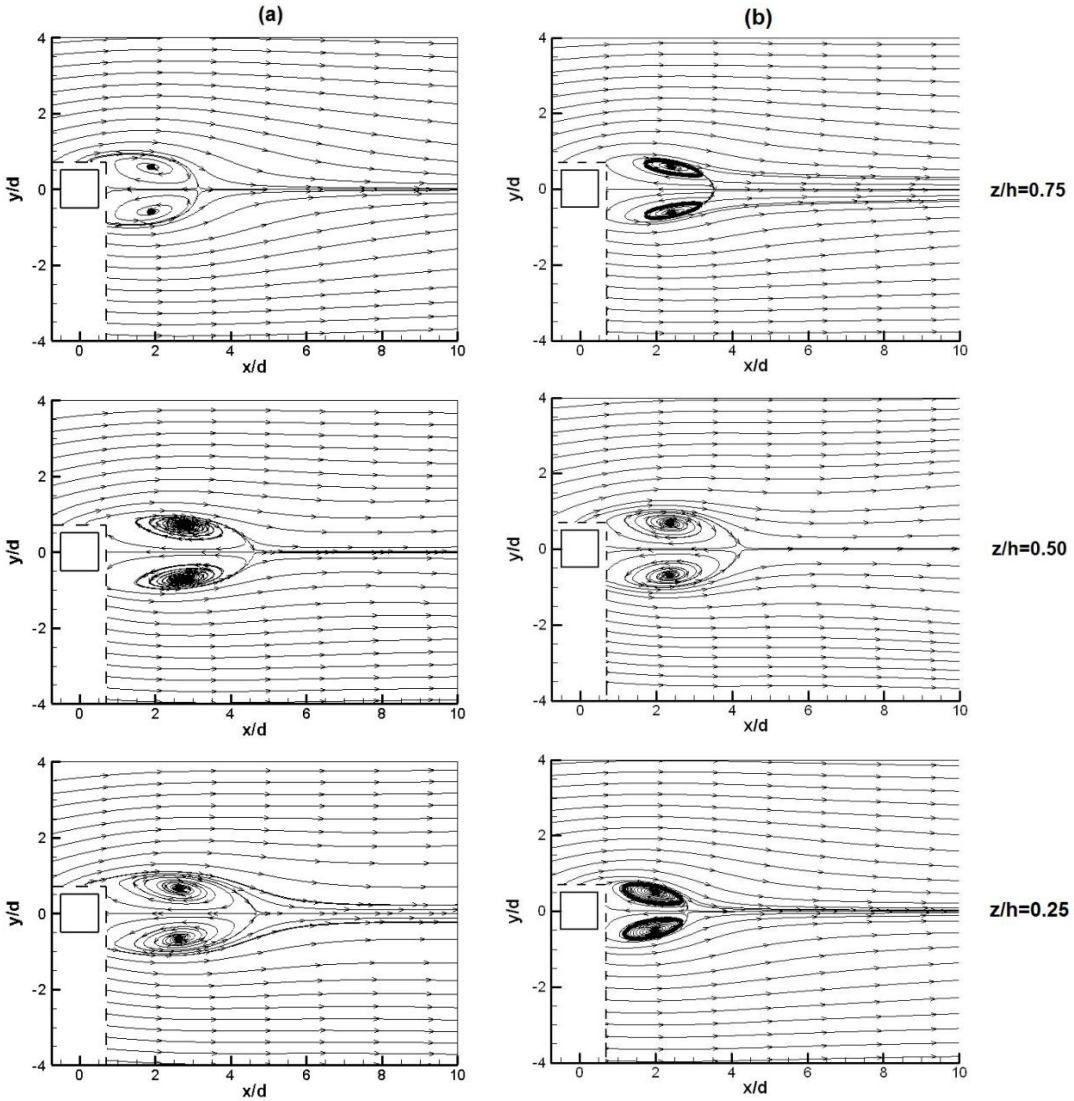

Figure 5. Mean flow streamlines in the symmetry plane for (a) untripped and (b) tripped cases. The largest differences are observed between the lower planes.

The mean vortex structures identified from λ_2-criterion [6] are shown in figures 6. For the untripped case a counter rotating vortex pair is present close to the free-end (dipole type). For the tripped case, on the other hand, another counter rotating vortex pair is also observed at the junction (quadrupole type). The free-end vortices look very similar both in strength and shape. In the tripped case, however, they are pushed up by the strong upwash induced by the junction vortices.

The rotation direction of these vortex pairs is such that the free-end pair induces a downwash and the junction pair induces an upwash in the wake. Thus a stronger upwash at the junction in the symmetry plane is due to the formation of the stronger junction vortices in the thicker boundary layer case.

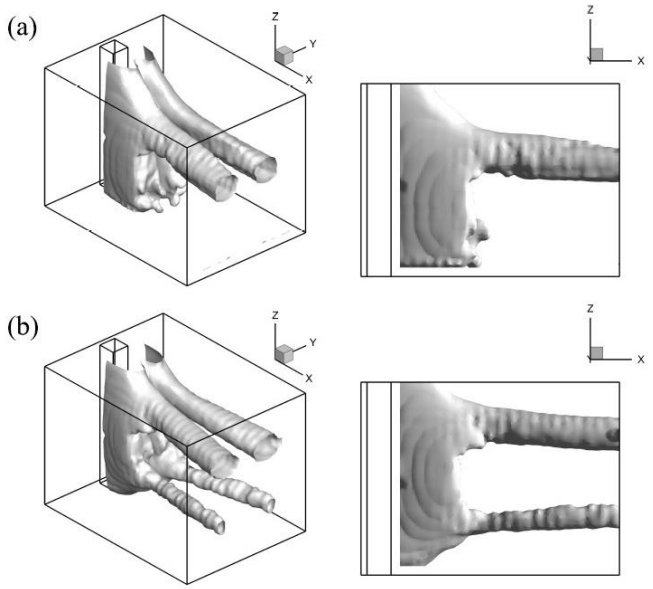

Figure 6. Mean vortex structure identified from $\lambda 2$-criterion for (a) untripped and (b) tripped cases which are respectively referred to as dipole and quadrupole wakes.

The differences indicated in the mean fields are due to different shed structures formed in each types of wake. To this end, a phase average decomposition is conducted to elucidate the typical wake and shed vortices structure. To justify the use of this decomposition the velocity fluctuations were measured at several spanwise and streamwise locations with a hot-wire anemometer. The power spectra along the span at $x/d=4$ and $y/d=2$, obtained from three realizations each *20* second long, is shown in figure 7. For all positions the power spectra exhibits a sharp and prominent peak at $St=0.102 \pm 0.003$ which is associated with the periodic vortex shedding. The peak is broadened at $z/h=0.25$ and *0.75* in the tripped case and $z/h=0.75$ in the untripped case; which is an evidence for a disruption of the regular von Karman structures that are shed parallel to the cylinder axis. It should be noted that the Strouhal numbers for both cases are very close. This is consistent with [7] where they examine the Strouhal number changes as a function of boundary layer thickness and show that at small boundary layer thickness to height ratios the Strouhal number remains constant.

Even though the Strouhal numbers for both the cases are the same, the power distributions are clearly different. The sharper peaks in the untripped case suggest that the shed structures have a clearer periodic behavior, i.e., the behavior is more similar to the periodic von Karman structures. Another difference is in the energy distribution. In the untripped case a significant portion of the energy is distributed among the low frequency fluctuations. The higher frequency fluctua-

tions, however, are less strong compared to the tripped case. This can also be seen in figure 8 where the symmetric and anti-symmetric parts of the pressure fluctuations are shown. The symmetric part is the sum of the pressure signals measured at the opposite faces of the obstacle and the anti-symmetric part is the difference. For a truly periodic shedding the pressures at either side are two periodic signals with 180^o phase shift. In a quasi-periodic shedding the sum represents the low frequency fluctuating part of the signal and the difference represents the high frequency fluctuations. Figure 8 shows that, the energy of the low fluctuations is slightly larger in the untripped case. The fluctuations in the anti-symmetric part, however, are stronger in the tripped case. It should be noted that with phase averaging only the periodic part of the high frequency fluctuations are categorized as coherent and the rest are assumed to be incoherent. As will be shown later, the coherent fluctuations obtained from phase averaging have the same level of energy and the difference is observed in the incoherent parts. These differences in the power distribution suggest that the shed structures behave differently.

Figure 9 shows the phase averaged vortical structures identified from λ_2-criterion. For both the cases the structures are shed alternatively from either side of the obstacle. In the dipole case the structure is connected to the ground almost vertically while is bent streamwise close to the free-end forming a half loop shape. In the tripped case, the shed structures are turned around both at the free-end and the junction forming a full loop shape. As shown in the figure the vertical part is called principal core and the streamwise part is called connector strand. The principal cores shed similar to the von Karman structures and thus they behave similarly. The connector strands, on the other hand, have a different form and thus their imprint is distinct. The broader peaks and higher level of non-periodic fluctuations in the tripped case, for example, are due to the presence of this non-von Karman type structures. By time averaging, connector strands give rise to streamwise vortex pairs. Thus time averaging of the half loop and full loop structures results in respectively the dipole and quadrupole wakes shown in figure 6.

To illustrate the significance of the shed structures in the turbulent field, contours of time-averaged squared lateral velocity fluctuations, $\overline{v'^2}$, as well as the recirculation region boundaries are plotted in figure 10 in three horizontal planes. The effect of the connector strands in the planes close to the strands, i.e., at *z/h=0.75* in the untripped case and *z/h=0.25* and *0.75* in the tripped case, can be seen as reducing the recirculation length and introducing three-dimensionality into the wake distribution. The recirculation length for a two-dimensional shedding is approximately the same as the vortex formation length, i.e., the distance downstream of the bluff body where the fluctuations reach the maximum value [8]. In these planes, however, the maximum fluctuation occurs farther downstream of the saddle point at the end of the recirculation region.

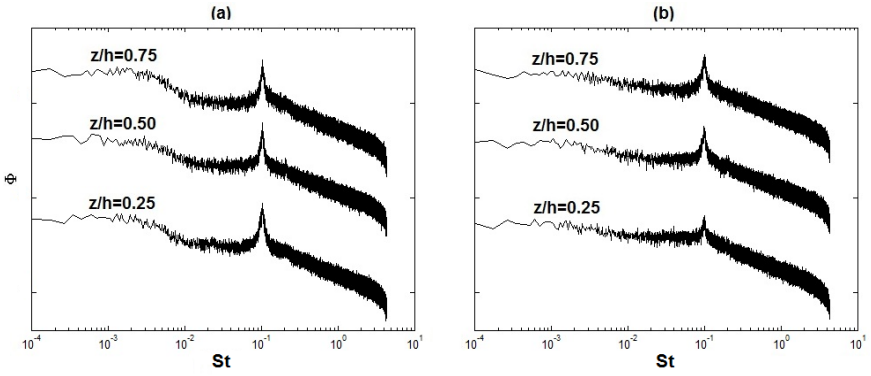

Figure 7. Power spectral density functions for (a) untripped and (b) tripped cases at *x/d=4* and *y/d=2*. Spectra at *z/h=0.50* and *0.75* are offset for clarity.

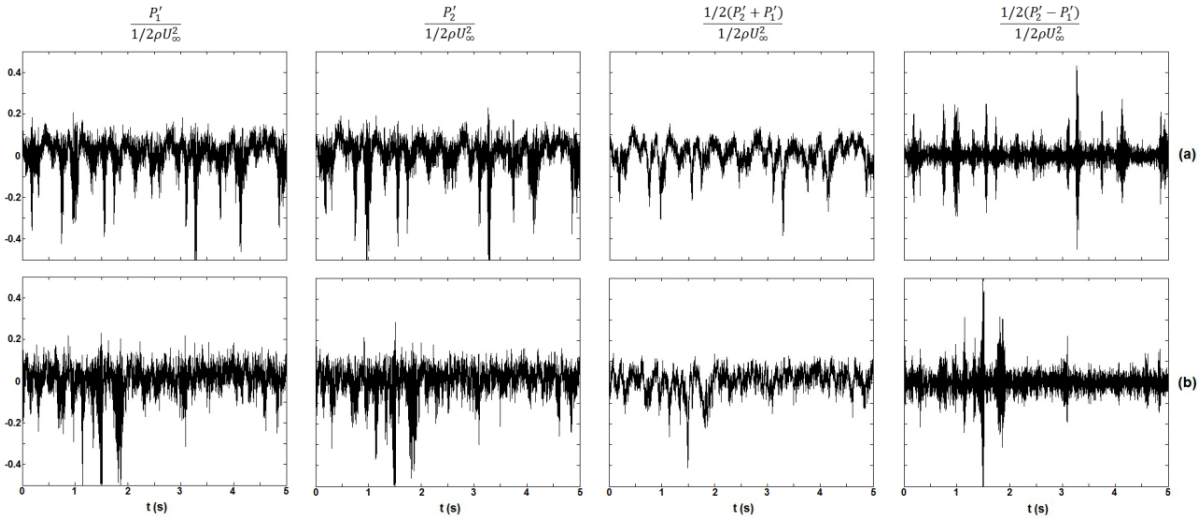

Figure 8. The pressure signals and the symmetric and anti-symmetric parts at z/h=0.25 for (a) untripped (b) tripped cases.

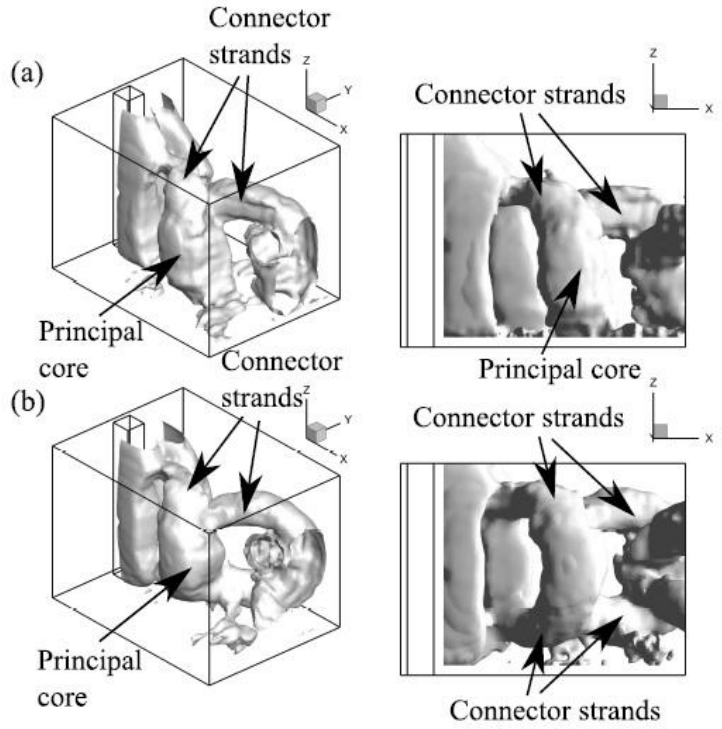

Figure 9. Half loop and full loop vortical structures, identified from $\lambda 2$-criterion, shed alternately from either side of the cylinder in (a) dipole (b) quadrupole wakes.

Another effect of the strands is decreasing the shear layer width and as discussed before enhancing the level of fluctuating energy. The maximum level of lateral fluctuations in the lower and upper planes in the tripped case is enhanced by more than 25% compared to the middle plane. Note that for the untripped case the connector strands are located at a lower position and thus this effect is not seen at *z/h=0.75*.

Figure 11 shows contours of $\overline{w'^2}$ at the symmetry plane. In the untripped case there is one maximum at the top while for the tripped case there are two maxima (with the same order of

magnitude) at the top and the bottom, close to the connector strands. Thus it can be concluded that the connector strands enhance the level of vertical fluctuations greatly. It should also be noted that for the present case, the full loop structures are almost symmetric and therefore the top and bottom strands act similarly.

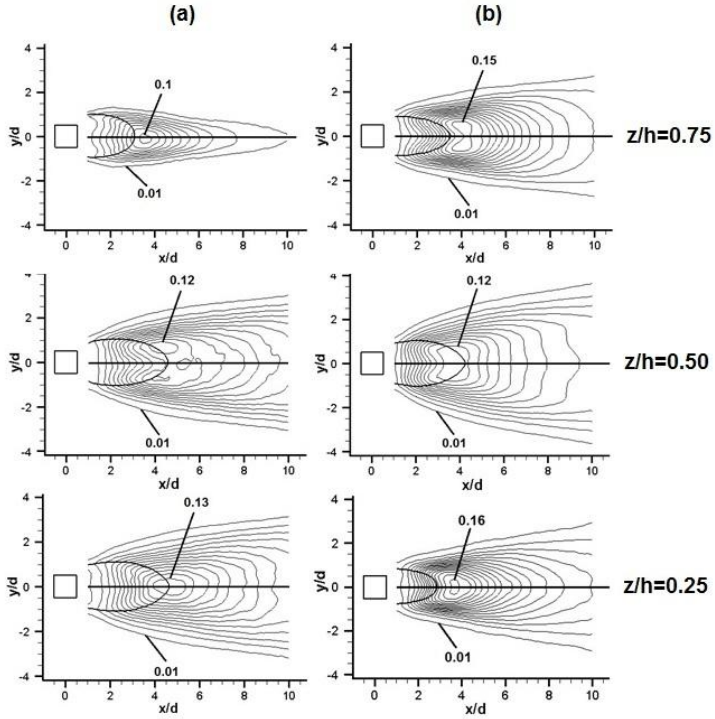

Figure 10. Contours of lateral fluctuations at *z/h=0.25*, *0.50* and *0.75* for (a) utripped and (b) tripped cases. The maximum fluctuation is located farther downstream of the end point of the recirculation region in the planes close to the connector strands.

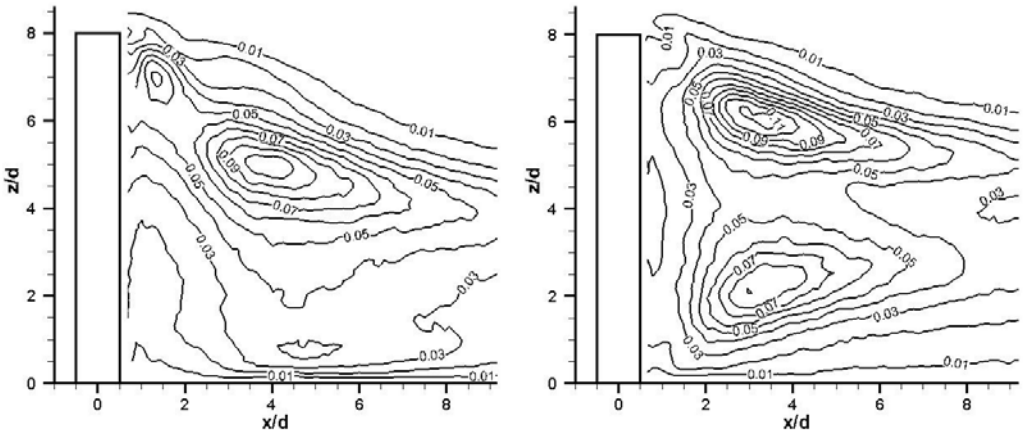

Figure 11. Contours of constant w'^2 for untripped (left) and tripped (right) boundary layers. The connector strands enhance the level of fluctuating energy.

From figures 10 and 11, it is concluded that in the planes close to the connector strands the total fluctuation level is increased. In figure 12 contours of total lateral fluctuations (repeated for the sake of comparison) as well as the coherent and incoherent parts are plotted for planes at

z/h=0.25 for both the wakes. This figure reveals that the increase in the lateral fluctuating level in the tripped case is due to the enhancement in the incoherent fluctuations, i.e., the parts that are not periodic as the regular von Karman structures. It could be argued that this increase could be due to the boundary layer effects since the tripped boundary layer is extended to this plane ($\delta/h=0.32$). Figure 13, however, shows that the same trend is observed in the plane close to the top strands, i.e. *z/h=0.75*, where compared to the middle plane the maximum level of incoherent fluctuations is larger. Thus the passage of the connector strands can be seen as an increase in the non-periodic fluctuating energy.

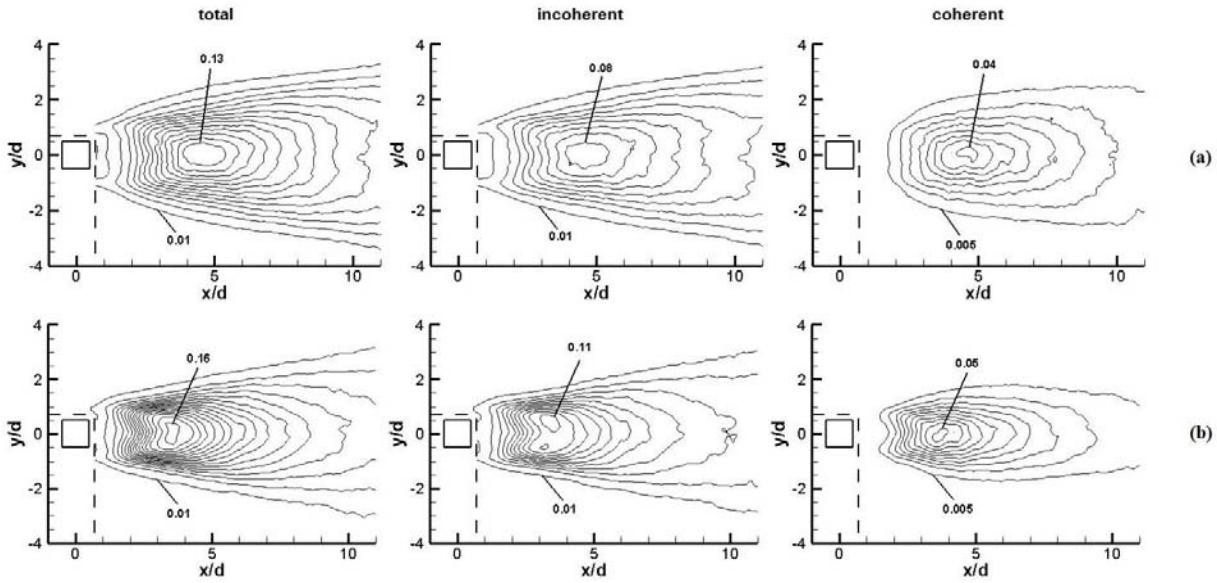

Figure 12. Decomposition of v'^2 into coherent and incoherent components for (a) untripped (b) tripped cases at *z/h=0.25*. The increase in the total fluctuating energy in the tripped case is mostly due to the increase in the non-periodic fluctuations which are categorized as incoherent in phase averaging.

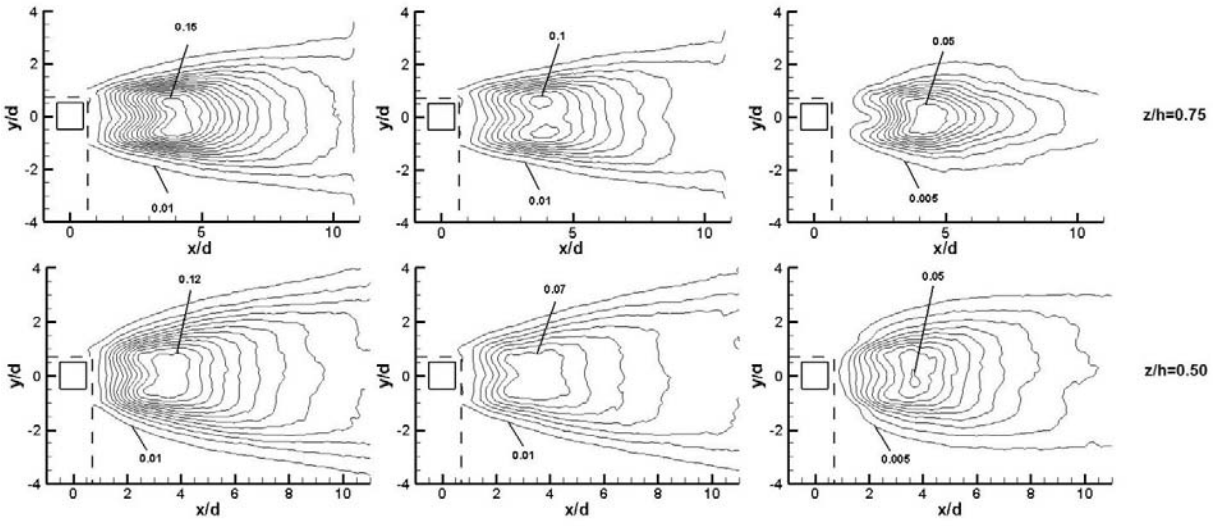

Figure 13. Decomposition of v'^2 into coherent and incoherent components for the tripped case.

4 CONCLUSION

The flow behind a tall square cylinder ($h/d=8$) mounted on a flat plate immersed in two thin boundary layers ($\delta/h=0.09$ and 0.32) is visualized using a 2-D PIV system. The three-dimensional phase averaged coherent structures are reconstructed from the velocity field at several horizontal and vertical planes measured simultaneously with the surface pressure as the reference signal. While the previous studies suggest that for cylinders immersed in thin boundary layers with aspect ratio taller than 3 the quadrupole wake is expected, the present work shows that depending on the boundary layer thickness both the wake types can form. This demonstrates the key role of the boundary layer even for boundary layers as thin as the ones considered here.

The shed structures form a half loop shape in the dipole wake and full loop shape in the quadrupole wake. The time averaging of these shed structures give rise to the different mean vortex distribution. The structures shed anti-symmetrically from either side of the obstacle and no evidence of symmetric shedding is observed.

The practical significance is in the large deviation of the wake distribution between the two cases. The rotation of the strands in the streamwise direction alters the mean and turbulent field greatly. The recirculation length is shortened and no longer coincides with the formation length as it does in two-dimensional shedding. The level of lateral fluctuating energy is increased by more than 25%; this increase is in the incoherent fluctuations. The distribution of the vertical velocity fluctuation is also altered highly. In the dipole wake only one maximum is observed close to the free-end while in the quadrupole wake another maximum with the same order of magnitude is observed close to the junction. Due to the large vertical velocities induced by the strands the wake width is reduced in the planes close to the strands.

All these effects are observed in the planes in proximity to the connector strands, i.e., $z/h=0.75$ in the dipole wake and $z/h=0.25$ and 0.50 in the quadrupole wake. Thus the largest difference between the two wakes is present at the lower plane, which is influenced by the strands in the quadrupole wake but remains undisturbed in the dipole wake. This is particularly important in predicting the wake load of tall buildings on pedestrians.

5 ACKNOWLEDGEMENTS

The authors would like to thank the Natural Sciences Engineering Research Council of Canada (NSERC) for their financial support of this work

6 REFRENCES

[1] J.A. Bourgeois, P. Sattari and R.J. Martinuzzi, Alternating half-loop shedding in the turbulent wake of a finite-surface-mounted square cylinder with a thin boundary layer, Physics of Fluids, 23 (2011).
[2] D. Sumner, J.L. Heseltine and O.J.P. Dansereau, Wake structure of a finite circular cylinder of small aspect ratio, Experiments in Fluids, 37 (2004) 720-730.
[3] H.F. Wang and Y. Zhou, The finite-length square cylinder near wake, Journal of Fluid Mechanics, 638 (2009) 453-490.
[4] H.F. Wang, Z. Zhou, C.K. Chan and K.S. Lam, Effect of initial conditions on interaction between a boundary layer and a wall-mounted finite-length-cylinder wake, Physics of Fluids, 18 (2006) 1-12.
[5] A.K.M.F. Hussain, Coherent structures-reality and myth, Physics of Fluids, 26 (1983).
[6] J. Jeong and F. Hussain, On the identification of a vortex, Journal of Fluid Mechanics, 285 (1995).
[7] H. Sakamoto and M. Arie, Vortex shedding from a rectangular prism and a circular cylinder placed vertically in turbulent boundary layer, Journal of Fluid Mechanics, 126 (1983) 147-165.
[8] B. Cantwell and D. Coles, An experimental study of entrainment and transport in the turbulent near wake of a circular cylinder, Journal of Fluid Mechanics, 136 (1983) 321–374.

The Seventh International Colloquium on Bluff Body Aerodynamics and Applications (BBAA7)
Shanghai, China; September 2-6, 2012

Experimental investigation on the aerodynamic behavior of square cylinders with rounded corners

Luigi Carassale [a], Andrea Freda [a], Michela Marrè Brunenghi [a],
Giuseppe Piccardo [a], Giovanni Solari [a]

[a] *Dept. of Civil Environmental and Geotechnical Engineering, University of Genova, Italy*

ABSTRACT: The influence of corner shaping on the aerodynamic behavior of square cylinders is studied through wind tunnel tests. Beside the sharp-edge corner condition considered as a benchmark, two different rounded-corner radii (r/b = 1/15 and 2/15) are studied. Global forces and surface pressure are simultaneously measured in the Reynolds number range between $2.5 \cdot 10^4$ and $1.8 \cdot 10^5$. The measurements are extended to angles of incidence between 0 and 45°, but the analysis and the discussion presented herein is focused on the low angle of incidence range. It is found that the critical angle of incidence where the flow reattaches on the lateral face exposed to the flow decreases as r/b increases and that an intermittent flow condition exists. In the case of turbulent incoming flow, two different aerodynamic regimes governed by the Reynolds number have been recognized.

KEYWORDS: Square cylinder, rounded corners, intermittence, Reynolds number effect

1 INTRODUCTION

A careful modeling of the corners shape of building and structural elements exposed to the wind has become a major objective for a wind-response-oriented optimal design. The introduction of rounded or chamfered corners has often the positive effect of reducing the drag force and the fluctuation of the transversal force due to vortex shedding [e.g. 1, 2], but can produce a relatively complicated aerodynamic behavior whose physical or numerical modeling may be challenging. In contrast to sharp-edge bodies, the absence of fixed separation points can introduce significant dependencies on the Reynolds number and on the characteristics of the incoming flow that must be taken into account during the design stage [e.g. 2 – 4].

The simplest and probably the most commonly investigate sharp-edge body is the square cylinder, thus it is the natural candidate to investigate the effect of corner shaping on the aerodynamic behavior of bluff bodies. With the twofold purpose of investigating the basic behavior of rounded corners and providing technical information useful for wind engineers, a series of wind-tunnel tests on square cylinders with rounded corners has been carried out. Rigid models of cylinders with two corner radii (r/b = 1/15 and 2/15), beside the sharp-corner case, have been realized and tested measuring the global forces and the pressure field along a cross-section. The considered Reynolds number range is between $2.5 \cdot 10^4$ and $1.8 \cdot 10^5$. Two levels of turbulence intensity (0.2% and 6%) in the incoming flow have been considered.

Section 2 provides a brief review of the current knowledge on the aerodynamic behavior of sharp-edge square cylinders, with particular reference to the qualitative description of the flow field for different angles of incidence. These concepts are then used as a guide for the interpretation of the experimental results presented in Section 3 and discussed in Section 4. Due to the space limitation, the discussion is focused on two specific phenomena that have been observed:

1) the intermittence of the vortex-shedding regime at the critical angle of incidence in smooth flow; 2) the inversion of the lift coefficient slope at zero angle of incidence in turbulent flow.

2 AERODYNAMIC BEHAVIOUR OF SHARP-CORNER SQUARE CYLINDERS

Sharp-edge square cylinders have been studied by several researchers who focused their attention on numerous aerodynamic parameters including pressure distribution, drag and lift forces, vortex shedding properties, as well as near wake velocity field [e.g. 5 – 11]. The flow pattern around a square cylinder is strongly dependent on the angle of incidence, α, and at least two characteristic flow regimes are clearly identified and separated by a critical angle of incidence, α_{cr} located about 12-15° [8]. For $\alpha < \alpha_{cr}$ the boundary layer on the lateral faces is completely separated, while for $\alpha > \alpha_{cr}$ the flow reattaches on the lateral face exposed to the wind forming a separation bubble [e.g. 10, 11]. A further sub-classification of the two mentioned regimes is possible [8], but is not relevant for the purpose of the present study. The subcritical regime ($\alpha < \alpha_{cr}$) is characterized by negative slope of the lift coefficient, which changes sharply to positive as α becomes grater than α_{cr}. Besides, the transition from the subcritical to the supercritical regime produces a rapid increment of the Strouhal number that corresponds to the reduction of the wake width due to the flow reattachment [6]. In the critical regime both the drag coefficient and the fluctuating lift coefficient have a minimum value. This scenario is not strongly modified by the Reynolds number and the characteristics of the incoming flow, even if some significant influence does exist. The thickening of the shear layers due to a small-scale free-stream turbulence promotes the formation of the separation bubble which tends to appear for smaller angle of incidence and to shrink towards the leading edge [6]. This mechanism is probably influenced by the Reynolds number as suggested in [4] for a the case of a 2:1 rectangular cylinder, however no effect has been revealed on square cylinders [9].

3 EXPERIMENTAL RESULTS

The experimental tests are carried out in the closed-circuit wind tunnel at the University of Genova with cross section 1700 × 1350 mm. The models are realized through the assemblage of aluminum plates, have a span length l = 500 mm and are mounted in cross-flow configuration on a force balance realized by six resistive load cells. End plates are installed at the extremities of the models to maintain a two-dimensional flow condition and separate the model from the boundary layer on the wind-tunnel walls. The mid-span cross section of the models is instrumented by a ring of N pressure taps (N ranges from 20 to 44 for the different tested models) connected through short tubes to 32-channel PSI pressure scanners mounted inside the model. Figure 1 shows the cross section of the tested cylinders and the reference system used for the presentation of the results. Beside the sharp-edge square cross section used as a benchmark test, two rounded-corner configurations with r/b = 1/15 and 2/15 (r and b being, respectively, the corner radius and the square size, Fig. 1) have been considered.

The force balance measurements are analyzed calculating the steady aerodynamic drag and lift coefficients (C_D and C_L) the Strouhal number (St) and the fluctuating lift coefficient (C_L^{rms}) defined as:

$$C_D = \frac{\mathrm{E}[D]}{0.5\rho blU^2} \qquad C_L = \frac{\mathrm{E}[L]}{0.5\rho blU^2} \qquad St = \frac{n_s b}{U} \qquad C_L^{rms} = \frac{\mathrm{E}\left[\left(L - \mathrm{E}[L]\right)^2\right]^{0.5}}{0.5\rho blU^2} \tag{1}$$

where D and L are, respectively, the measured drag and lift forces (Fig. 1), ρ the air density, U the undisturbed mean wind velocity; E[•] is the statistic average operator that is implemented as a time average adopting the hypothesis of ergodic behavior; n_s is the vortex shedding peak frequency estimated by fitting the Power Spectral Density (PSD) function of L through a Gaussian function in the neighborhood of its peak. Analogously, steady and fluctuating pressure coefficients are defined as

$$C_p = \frac{\mathrm{E}[p - p_0]}{0.5\rho U^2} \qquad C_p^{rms} = \frac{\mathrm{E}\left[\left(p - \mathrm{E}[p]\right)^2\right]^{0.5}}{0.5\rho U^2} \tag{2}$$

where p is the pressure measured on the body surface and p_0 is the static wind-tunnel pressure.

The influence of the Reynolds number (Re) is explored both varying the wind-tunnel velocity U in the range 5 – 25 m/s, as well as the body size b in the range 60 – 150 mm. No blockage correction has been adopted since the focus of the paper is the qualitative description of the behavior, which is not affected by slight modifications of the estimated numerical values.

Two conditions for the incoming flow have been considered: 1) smooth flow condition characterized by a turbulence intensity about 0.2%; 2) turbulent flow condition, produced through a grid realized by square bars, characterized by the intensity of the longitudinal turbulence I_u about 5% and integral length scale L_u about 20 mm. These parameters are substantially stable through the whole considered wind velocity range (Fig. 2).

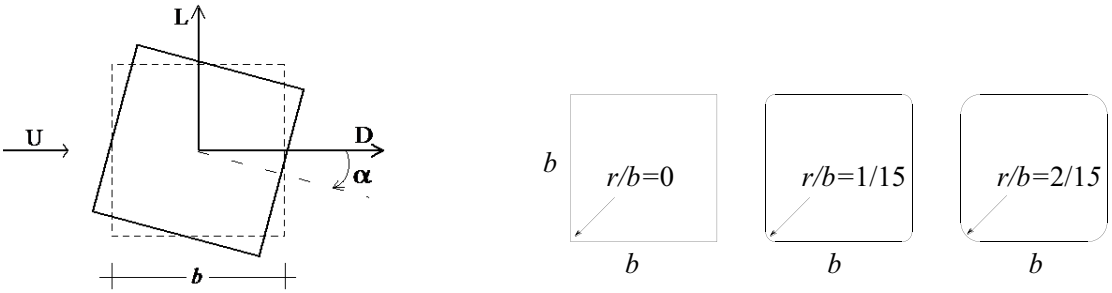

Figure 1. Experimental setup

Figure 3 shows the variation of C_D (a), C_L (b), St (c) and C_L^{rms} (d) with respect to the angle of incidence for the three considered models in smooth flow. No significant influence of the Re has been observed in the range between $2.69 \cdot 10^4$ and $1.65 \cdot 10^5$. It can be observed that the three models have a similar qualitative behavior characterized by the inversion of the lift slope for a critical angle of incidence, α_{cr}, that decreases as r/b increases. For $\alpha = \alpha_{cr}$ the steady drag and the fluctuating lift coefficients have a minimum value, while the Strouhal number increases sharply. For the sharp-corner model α_{cr} was found about 12° and is in substantial accord to previous experimentations (see [11] for a review of previous results). In the case of rounded-corner models it was found $\alpha_{cr} = 7°$ and 5° for r/b = 1/15 and 2/15, respectively. Tamura & Miyagi [2], working in similar flow conditions, found $\alpha_{cr} = 4°$ for r/b = 2.5/15.

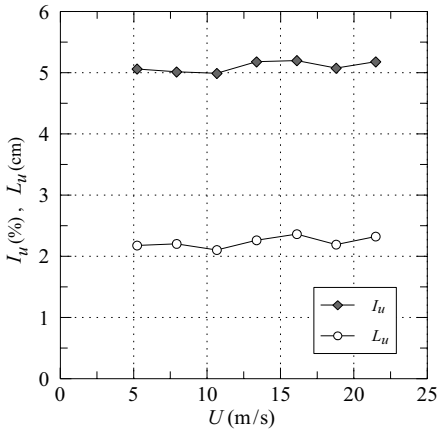

Figure 2. Intensity and integral length scale of the longitudinal turbulence in turbulent flow condition.

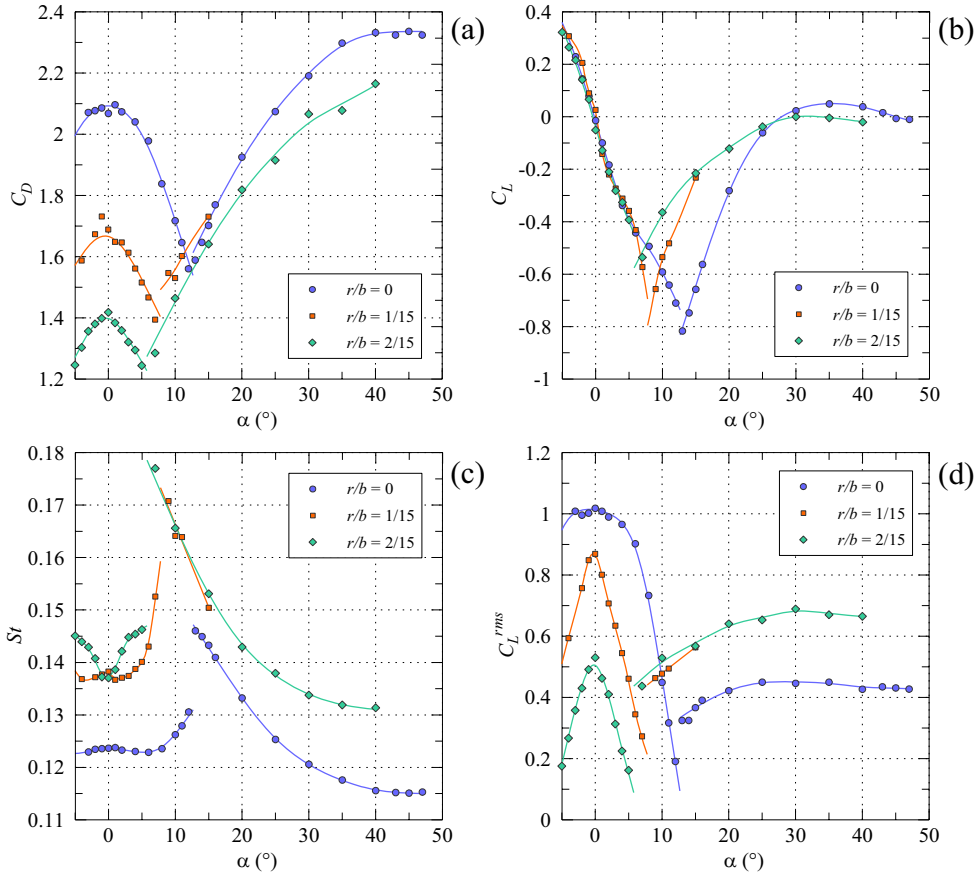

Figure 3. Steady drag (a) and lift (b) coefficients, Strouhal number (c) and fluctuating lift coefficient (d) in smooth flow condition.

Figure 4 shows the variation of C_D (a), C_L (b), St (c) and C_L^{rms} (d) with respect to the angle of incidence, for r/b = 2/15, in turbulent flow for Re between $2.49 \cdot 10^4$ and $1.81 \cdot 10^5$. For the tests corresponding to $Re = 2.49 \cdot 10^4$, $5.14 \cdot 10^4$, $7.81 \cdot 10^4$, a model with b = 75 mm was used, while a larger model with b = 150 mm was adopted for the other tests. A very strong dependency on Re

is observed for small angle of incidence. In particular two distinct behaviors can be observed, which are separated by a critical Reynolds number $Re_{cr} \simeq 5 \cdot 10^4$. These two regimes are referred to as subcritical ($Re < Re_{cr}$) and supercritical ($Re > Re_{cr}$).

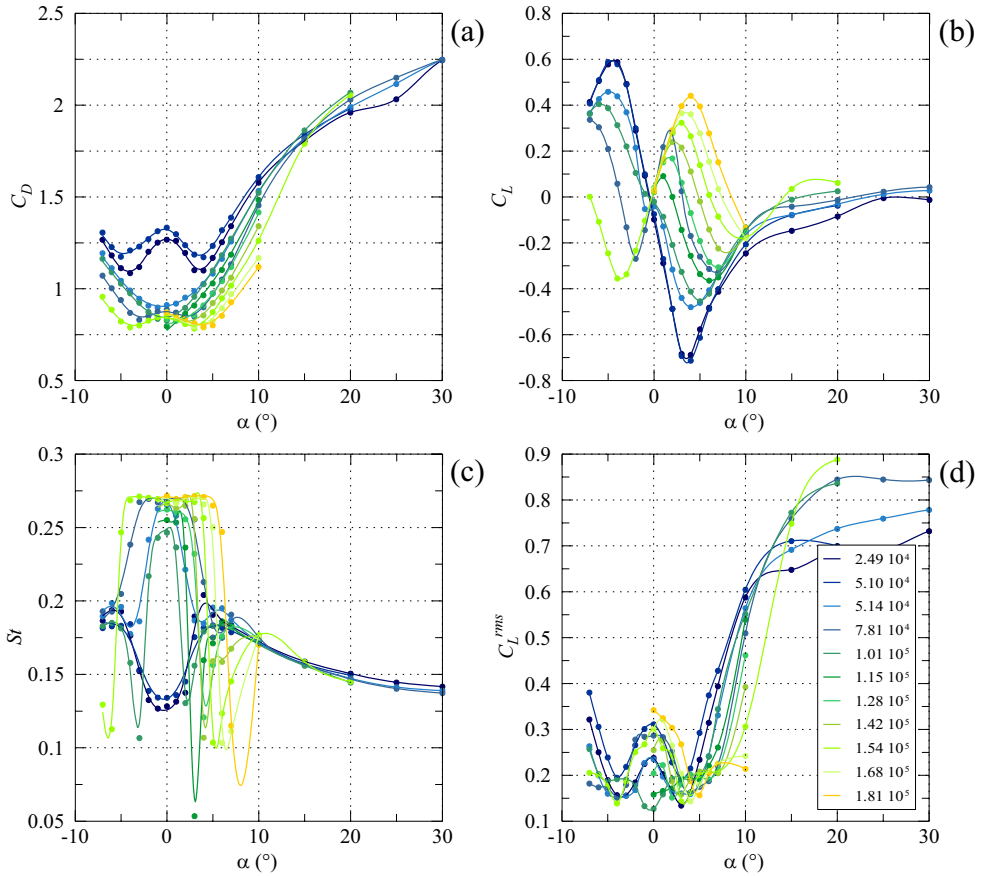

Figure 4. Steady drag (a) and lift (b) coefficients, Strouhal number (c) and fluctuating lift coefficient (d) in turbulent flow condition for $r/b = 2/15$ and different Reynolds numbers.

The results obtained for $Re = 2.49 \cdot 10^4$ and $5.10 \cdot 10^4$ are practically coincident even if are obtained using two different models (b = 75 mm and 150 mm, respectively) and are substantially similar to the results observed in smooth-flow condition. The steady drag coefficient for $\alpha = 0$ is about 1.3, (slightly lower than in smooth flow). The minimum value of the steady lift coefficient is about -0.7 and is obtained for $\alpha = 3$ - 4° (slightly before than α_{cr} in smooth flow); the Strouhal number is about 0.13 for $\alpha = 0$ and rapidly increases up to 0.18 for $\alpha = 4°$ (again not far from the values observed in smooth flow).

As Re increases, the steady lift slope for $\alpha = 0$ switches from negative to positive; further increments of Re have the result of extending the range of α for which a positive slope is observed. This trend seems quite regular with respect to Re, even if some small discrepancies between the behavior of the two models (different b) have been observed and may be related to the effect of the turbulence scale parameter L_u/b. The maximum value of the steady lift coefficient increases as Re increases and is obtained for larger and larger angles of incidence; for $Re = 1.82 \cdot 10^5$ the maximum C_L is about 0.45 and appears for $\alpha = 4°$. In the region where the steady lift slope is positive the Strouhal number is about 0.27 (approximately twice the value obtained in smooth flow) and is practically insensitive to Re. As the slope of C_L becomes negative, St drops to a very

low value about 0.10 and then recovers the trend observed in smooth flow for $\alpha > 10°$. The minimum value of the steady drag coefficient is reached for the angle of incidence corresponding to the maximum vales for C_L and St.

The supercritical regime has been observed only for $r/b = 2/15$, while for $r/b = 1/15$ only the subcritical regime has been observed for Re up to $2.32 \cdot 10^5$.

4 DISCUSSION

During the experimentation described in Section 3 two main issues clearly emerged and require a discussion. The former regards the sharp discontinuity of the aerodynamic behavior observed for $\alpha = \alpha_{cr}$ in smooth-flow condition. The latter issue is related to the two distinct flow behaviors observed for different Re in turbulent flow for $r/b = 2/15$.

4.1 *Discontinuity of the aerodynamic behavior at the critical angle of incidence in smooth flow*

For the case of sharp-corner square cylinders, the existence of two flow regimes separated by the critical angle of incidence has been clearly documented through accurate flow visualization techniques [8, 10]. The qualitative similarity of the behavior observed for the three tested models suggests that a modification of the corner geometry (within the considered limits) does not produce qualitative variations of the flow pattern, but rather modifies the limit of existence of the flow regimes known for the sharp corner case. In particular the increment of r/b produces a reduction of α_{cr}.

The transition between these two regimes is due to the reattachment of the mean flow on the lateral face exposed to the wind, generating a separation bubble; however to the authors' knowledge the unsteady nature of this transition has never been carefully investigated. Figure 5 shows a time-frequency analysis of the lift force measured in smooth flow on the sharp-edge model (a) and rounded-corner models with $r/b = 1/15$ (b) and 2/15 (c) for $\alpha = \alpha_{cr}$. The colormaps represent the amplitude of the wavelet transform of L, plotted with respect to the time t and the frequency n non-dimensionalized through b and U; the mother wavelet used for the analysis is an analytic Morlet type; the lift coefficient is reported below the maps for reference. The length of the considered time windows is 800 non-dimensional time units, which roughly correspond to 120 cycles of vortex shedding. From the wavelet maps it can be observed that the vortex-shedding peak frequency changes with time fluctuating between the values reported in Figure 3 for angles just before and after α_{cr}. This result suggests that the wavelet maps can be employed to study, from a qualitative point of view the stability of the two concurrent flow regimes (subcritical and supercritical) that appear in the neighborhood of α_{cr}, as well as the transition from one regime to the other. The comparison of the three wavelet maps reveals that the flow around the sharp-corner cylinder tends to have smooth and frequent transitions between the two flow regimes giving rise to a behavior that may be identified as irregular vortex shedding (Fig. 5a). On the contrary, in the case of rounded-corner cylinder with $r/b = 2/15$, a proper intermittent behavior has been found as documented in Figure 5c, where the transition between supercritical to subcritical, as well as from subcritical to supercritical regime is clearly visible. The transitions are very sharp and the time in which the system remains stable in a regime is relatively long (in Figure 5c the length of the subcritical phase corresponds to about 50 cycles of vortex shedding).

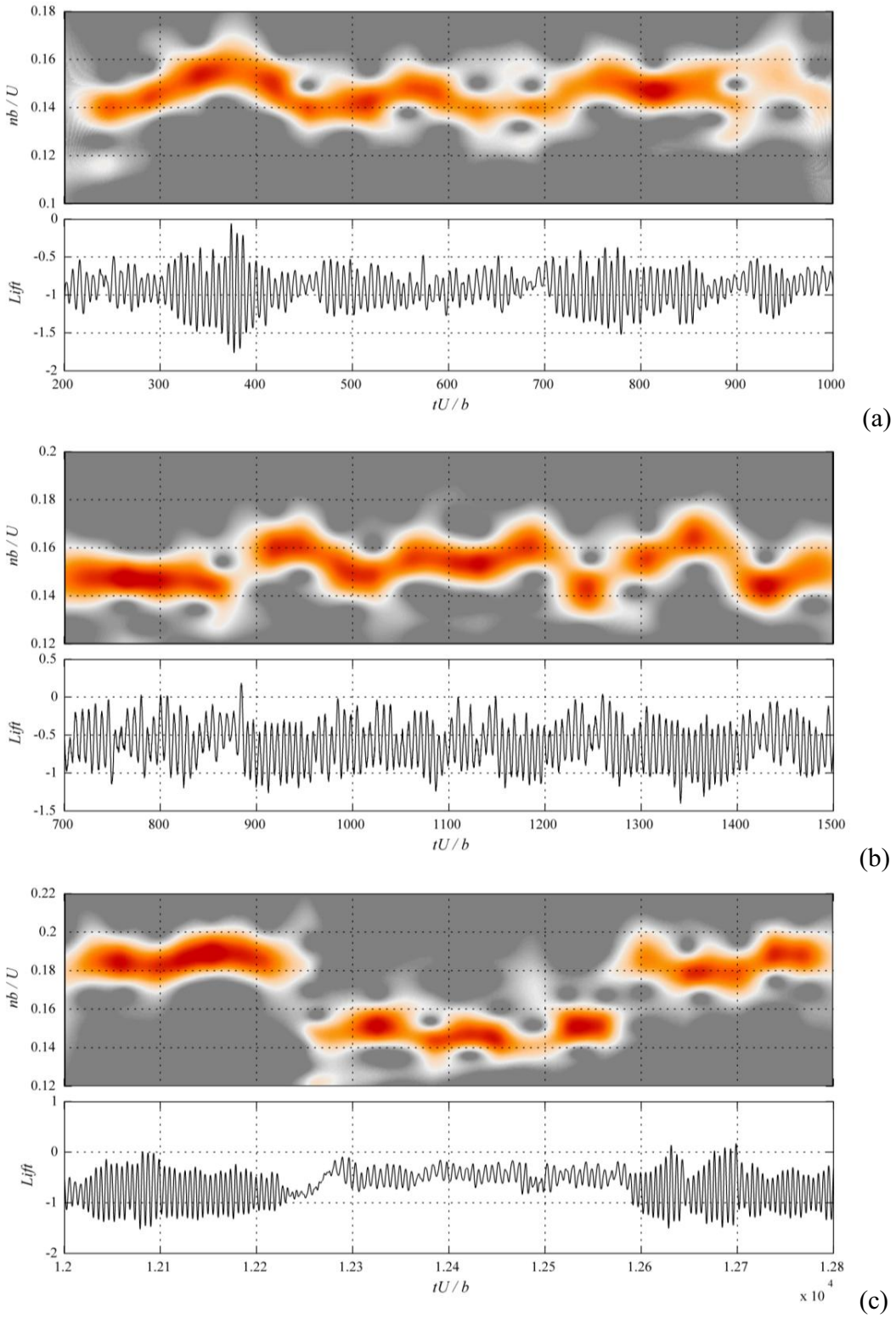

Figure 5. Wavelet map and time history of the lift coefficient for sharp corners (a), r/b = 1/15, r/b = 2/15 (c).

4.2 *Inversion of the lift slope at small angle of incidence in turbulent flow*

The analysis of the results obtained in turbulent flow for the rounded cylinder with $r/b = 2/15$ suggests the existence of two flow regimes for small angle of incidence, whose transition is governed by the Reynolds number.

On the basis of aerodynamic coefficients and Strouhal number, it may be deduced that in the subcritical *Re* regime the aerodynamic behavior is similar to the one observed in smooth-flow condition, even if the sharp transition with intermittence for $\alpha = \alpha_{cr}$ described in Section 4.1 does not take place. This analogy (which implies the conclusion that the free-stream turbulence has a limited effect in the subcritical *Re* regime) can be verified by comparing the mean and fluctuating pressure coefficients obtained in smooth and turbulent flow for $\alpha = 0$ and different *Re* (Fig. 6). In particular it can be observed that C_p obtained in turbulent flow and subcritical regime (Fig. 6c, *Re* $= 2.49 \cdot 10^4$ and $5.10 \cdot 10^4$) is very similar to C_p obtained in smooth flow (Fig. 6a), which is substantially independent of *Re*; the same analogy also applies to the fluctuating pressure coefficients (Fig. 6b and d).

For small angles of incidence the passage to the supercritical *Re* regime deeply changes the aerodynamic behavior: the steady drag coefficient drops to values about 0.7 (Fig. 4a), the steady lift slope switches to positive (Fig. 4b) and the Strouhal number doubles (Fig. 4c). The steady pressure coefficient (Fig. 6c) is strongly dependent on *Re*, whose increment has two major effects: 1) the suction near the leading edges increases; 2) the point on the lateral faces where the base pressure is recovered moves upstream. As far as the fluctuating pressure coefficient is concerned (Fig. 6d) an increment of *Re* produces: 1) a reduction of the pressure fluctuation by the midpoint of the lateral faces; 2) an increment of the pressure fluctuation near the trailing edges; 3) an increment of the pressure fluctuation on the leeward face. The above observations suggest that in the supercritical *Re* regime the flow reattaches on the lateral faces even for $\alpha = 0$ forming two the separation bubbles that shrink towards the leading edges as *Re* increases.

Figure 7 shows the steady pressure coefficient for smooth flow (Fig. 7a) and turbulent flow (Fig. 7c), as well as the respective fluctuating coefficients (Fig. 7b and d) for $\alpha = 4°$. It can be observed that while in smooth flow condition the pressure field is only slightly modified by passing from $\alpha = 0$ to $\alpha = 4°$, in case of turbulent flow the modifications are relevant and can be summarizes as: 1) near the lower (in Fig. 7) leading edge the pressure field is independent of *Re* and the separation bubble tends to shirk as α increases likewise it happens for the sharp-corner cylinder for $\alpha > \alpha_{cr}$; 2) near the upper leading edge the steady pressure field is strongly dependent on *Re* and the point where the base pressure is recovered shifts downstream. A further increment of α prevents the flow reattachment on the leeward lateral face and produces a flow pattern similar to the one observed in smooth flow for $\alpha > \alpha_{cr}$. The angle of incidence for which this transition arises corresponds to the maximum of the steady lift coefficient and is strongly dependent on *Re*.

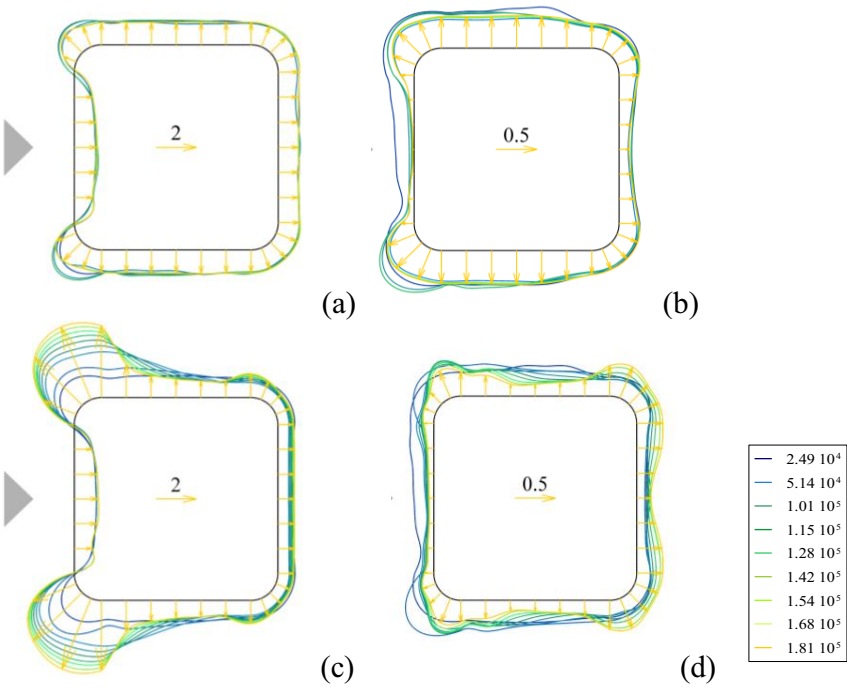

Figure 6. Pressure coefficients for $\alpha = 0$. Smooth flow C_p (a) and C_p^{rms} (b); turbulent flow C_p (c) and C_p^{rms} (d).

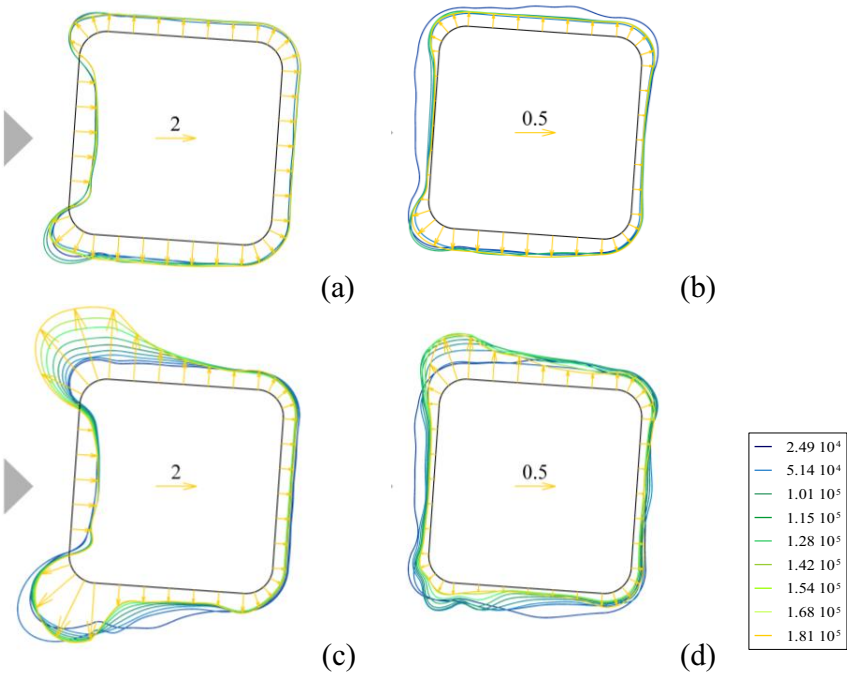

Figure 7. Pressure coefficients for $\alpha = 4°$. Smooth flow C_p (a) and C_p^{rms} (b); turbulent flow C_p (c) and C_p^{rms} (d).

5 CONCLUSIONS

The effects of corner shaping on the aerodynamic behavior of square cylinders have been investigated through the analysis and discussion of wind-tunnel experiments. It has been found that rounded corners promote the reattachment of the flow on the lateral faces producing 1) a reduction of the critical angle of incidence α_{cr}, 2) an intermittent behavior for $\alpha = \alpha_{cr}$, 3) the inversion of the lift slope for small angles of incidence. This latter effect has been observed only for r/b = 2/15, however it cannot be excluded that it may appear also for smaller r/b ratios at sufficiently high Reynolds numbers.

The technical implications of the mentioned effects are important due to the large variation of the aerodynamic coefficients, as well as in relation to galloping instability. From the results obtained in smooth flow it can be concluded that the classical galloping model (based upon a quasi-steady assumption) cannot be adopted due to the observed intermittent behavior. On the other hand, the results obtained in turbulent flow reveal that the lift coefficient or rounded corner cylinders can be negative or positive for different *Re* and that, in supercritical *Re* regime, the necessary condition for galloping (negative lift slope) does not appear at $\alpha = 0$, but in a range between 5° and 10°.

REFERENCES

1. K.C.S. Kwok, P.A. Wilhelm, B.G. Wilkie, Effect of edge configuration on wind-induced response of a tall buildings, Engineering Structures, 10 (1988), 135-140.
2. T. Tamura, T. Miyagi, The effect of turbulence on aerodynamic forces on a square cylinder with various corner shapes, Journal of Wind Engineering and Industrial Aerodynamics, 83 (1999), 135–145.
3. T. Tamura, T. Miyagi, T. Kitagishi, Numerical prediction of unsteady pressures on a square cylinder with various corner shapes, Journal of Wind Engineering and Industrial Aerodynamics, 74-76 (1998) 531-542.
4. G.L. Larose, A. D'Auteuil, Experiments on 2D rectangular prisms at high Reynolds numbers in a pressurised wind tunnel, Journal of Wind Engineering and Industrial Aerodynamics, 96 (2008), 923-933.
5. B.J. Vickery, Fluctuating lift and drag on a long cylinder of square cross-section in a smooth and in a turbulent stream, Journal of Fluid Mechanics, 25 (1966), 481–494.
6. B.E. Lee, The effect of turbulence on the surface pressure field of a square prism, Journal of Fluid Mechanics, 69 (1975), 321–352.
7. A. Okajima, Strouhal numbers of rectangular cylinders. Journal of Fluid Mechanics, 123 (1982), 379–398.
8. T. Igarashi, Characteristics of the flow around a square prism, Bulletin of JSME, 27 (1984), 1858–1865.
9. Y. Nakamura, Y. Ohya, The effects of turbulence on the mean flow past two-dimensional rectangular cylinders, Journal of Fluid Mechanics, 149 (1984), 255-273.
10. R.F. Huang, B.H. Lin, S.C. Yen, Time-averaged topological flow patterns and their influence on vortex shedding of a square cylinder in crossflow at incidence, Journal of Fluids and Structures, 26 (2010), 406–429
11. R.F. Huang, B.H. Lin, Effect of flow patterns on aerodynamic forces of a square cylinder at incidence, Journal of Mechanics, 27 (2011), 347-355.

The Seventh International Colloquium on Bluff Body Aerodynamics and Applications (BBAA7)
Shanghai, China; September 2-6, 2012

POD analysis of the finite-length square cylinder wake

Wang Hanfeng

School of Civil Engineering, Central South University, Changsha, China

ABSTRACT: The near wake of a wall-mounted finite-length square cylinder with H/d = 7 is measured with PIV in three spanwise planes, i.e. near cylinder free end, at mid span and near the flat wall. The Reynolds number based on freestream velocity and cylinder width is 9300. Proper orthogonal decomposition (POD) technique is utilized to analyze the experimental data. Under the effects of free-end downwash flow, the near wake is highly three dimensional and drastically different from that of a 2D cylinder. The turbulent kinetic energy distributes over more POD modes relative to 2D cylinder wake. Low-dimensional model is not applicable to reconstruct this 3D flow. Both symmetrical and anti-symmetrical vortices structures occur in the finite-length cylinder wake, which can be identified based on the coefficients of the first two POD modes.

KEYWORDS: Bluff body, Finite-length cylinder, Wake, PIV, POD.

1 INTRODUCTION

The flow around a two-dimensional (2D) cylinder has long been the subject of extensive study. However, in engineering applications, the cylinder like structures are often finite in length (or height), with one end free and other end mounted on the ground, such as aerodynamic forces on high-rise buildings, plume behaviors behind chimneys, etc. Due to the effects of cylinder free end and boundary layer, the flow around a finite-length cylinder differs drastically from that behind a 2D cylinder[1, 2]. The near wake of a wall-mounted finite-length cylinder is characterized by the presence of two pairs of longitudinal tip and base vortices, in addition to the possible spanwise Karman vortex shedding. The interactions between these three types of vortices complicate the flow and make it highly three dimensional. The tip vortices are associated with the downwash flow behind cylinder free end[3, 4]. The base vortices depend on the conditions of the boundary layer where the cylinder mounted. When the boundary layer thickness is negligibly small, the base vortices will not present[4, 5].

The near wake of a finite-length cylinder depends strongly on H/d, where H and d are cylinder characteristic height and width, respectively. When H/d falls below a critical value, vortex shedding changes from antisymmetrical to symmetric[5-7]. The critical value is 2~6, depending on factors such as the boundary layer thickness and incoming turbulence intensity[6, 8]. Wang & Zhou[2] measured the near wake of finite-length square cylinder with H/d = 3, 5 and 7. They found both symmetrical and anti-symmetrical vortex shedding can be observed throughout cylinder span for all tested H/d. At mid-span of the cylinder with H/d = 7, which is larger than the critical value proposed, there are still more than 10% of instantaneous vortices are symmetrically arranged.

The proper orthogonal decomposition (POD) is a quantitative and an unbiased method that has been increasingly applied in conjunction with instantaneous whole-filed measurement techniques such as PIV for identifying the coherent structures. The POD technique provides an optimal set of basis function (POD mode) from an ensemble of data to reconstruct the coherent structures as mixtures of POD modes. This method has been successfully used in various types of flows, such as jets, mixing layers, channel flows and cylinder wakes. Detailed information about POD in fluid dynamics may be found in Sirovich[9].

The present paper aims to reveal the difference between the near wake structure of wall-mounted square cylinder with $H/d = 7$ and 2D one using PIV and POD techniques. From the PIV data, the time-averaged velocities, and other turbulent statistical quantities were obtained. Comparisons are also made in the context of POD mode and mode energy distribution to highlight the three dimensional effects for the wall-mounted finite-length cylinder wake.

2 EXPERIMENTAL DETAILS & POD METHOD

2.1 *Experimental setup*

All experiments were conducted in a closed-loop low-speed wind tunnel with a 2.4m long test section of 0.6m×0.6m. The flow velocity in the test section was uniform to 0.1% and the longitudinal turbulence intensity was less than 0.4%. A flat plate of 0.5m in width and 1.2m in length was installed in the test section with its upper surface 0.15m from the bottom wall. The leading edge of the flat plate was rounded to avoid flow separation. A square cylinder with a width d = 20mm was placed at the centerline, 0.3m downstream from the leading edge of the plate, as shown in figure 1. The H/d was 7. All measurements were conducted at a free-stream velocity $U_\infty = 7\text{ms}^{-1}$, corresponding to a Reynolds number $\text{Re}_d \equiv U_\infty d/\nu = 9300$, where ν is the kinematic viscosity of fluid. A LDA was used to document the boundary layer at the cylinder axis. The boundary layer disturbance thickness (δ) was estimated to be 27mm so that $\delta/d \approx 1.35$. Considering the thickness of the boundary layer, it may result in pronounced upwash flow and associated base vortices[10]. A nominal 2D square cylinder (with $H/d \approx 28$) wake was also measured at the same Re_d for comparison.

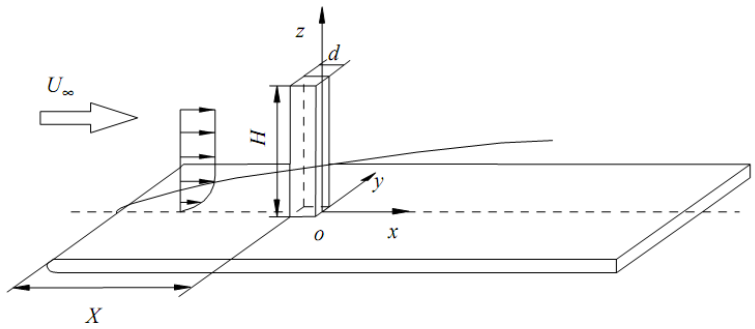

Figure 1. Experimental setup and the definition of coordinate system.

2.2 *PIV measurements*

A Dantec standard PIV2100 system was used to measure both the instantaneous and time-averaged flow fields. Flow illumination was provided by two NewWave standard pulse laser sources of a 532 nm wavelength, each with a maximum energy output of 120 mJ pulse^{-1}. Particle images were taken using one CCD camera (HiSense type 13, gain×4, double frames, 1280×1024 pixels). Synchronization between image taking and flow illumination was provided by the Dantec FlowMap Processor (PIV2001 type). PIV measurements were performed in three (x, y) planes at $z^* = 1$, 3.5 and 6, i.e. 1d above the flat plate, cylinder mid-span and 1d lower than the free end. The superscript asterisk in present paper indicates normalization by U_∞ and/or d. The image magnification was 148 μm/pixel. In processing PIV images, an interrogation area of 32×32 pixels was used with a 50% overlap in both directions, producing 78×62 in-plane velocity vectors. For each case, a total of 1500 PIV images were captured to calculate time-averaged velocities and Reynolds stresses and perform POD analysis.

2.3 *POD method*

The snapshot POD method, proposed by Sirovich[9], was employed to analysis the PIV data. By this method, each instantaneous PIV data is considered a snapshot of the flow field. The present snapshot POD follows the procedure outlined by Meyer *et al.*[11]. The first step is to calculate the mean velocity field, which can be considered the zero mode of POD. The rest of analysis works on the fluctuation parts of the velocity components (u_i^n, v_i^n), where u and v denote the fluctuation velocity in streamwise and lateral directions. Index n runs through the N snapshots, and i runs through the M positions of velocity vectors in a given snapshot.

All fluctuating velocity components from N snapshots are arranged in a matrix U as:

$$U = \left[u^1, u^2 \ldots u^N\right] = \begin{bmatrix} u_1^1 & u_1^2 & \ldots & u_1^N \\ \vdots & \vdots & \vdots & \vdots \\ u_M^1 & u_M^2 & \ldots & u_M^N \\ v_1^1 & v_1^2 & \ldots & v_1^N \\ \vdots & \vdots & \vdots & \vdots \\ v_M^1 & v_M^1 & \ldots & v_M^1 \end{bmatrix} \tag{1}$$

The autocovariance matrix C is created as $C=U^TU$. A set of N eigenvalues λ^i and corresponding set of eigenvectors A^i which satisfy $CA^i = \lambda^i A^i$ are evaluated. The eigenvalues are ordered by decreasing value as $\lambda^1 > \lambda^2 > \ldots > \lambda^N > 0$. The normalized POD modes φ^i are constructed from the projection of the eigenvectors A^i as:

$$\varphi^i = \frac{\sum_1^N A_n^i u^n}{\left\| \sum_1^N A_n^i u^n \right\|}, \qquad i = 1, 2, \ldots N \tag{2}$$

Each snapshot can be expanded in a series of the POD modes with expansion coefficients a_i for each φ^i. The coefficients a_i also called POD coefficients, are determined by projecting the fluctuating part of the velocity field onto the POD modes $a^n = \Psi^T u^n$, where $\Psi = [\varphi^1, \varphi^2 \ldots \varphi^N]$. Then, the expansion of the fluctuation part of a snapshot n is obtained from:

$$u^n = \sum_{i=1}^{N} a_i^n \varphi^i \tag{3}$$

Readers may refer to Sirovich[9] and Meyer *et al.*[11] for more details of the POD method.

3 RESULTS & DISCUSSIONS

Figure 2 presents the contours of $\overline{U^*}$, $\overline{u^*_{rms}}$, $\overline{v^*_{rms}}$ and $\overline{u^*v^*}$ at $z^* = 6$ and 3.5 for a finite-length cylinder with $H/d = 7$, together with those for a 2D square cylinder at the same Re_d for comparison. The overbar denotes time-average and the subscript *rms* indicates the root-mean-square value of fluctuation velocity. The results at $z^* = 1$ are qualitatively similar to those at $z^* = 3.5$ thus not present here. The streamwise extent of the reverse flow zone at mid-span, indicated by the bold line in figure 2(i), is far larger than that of 2D cylinder (figure 2a). A shorter reversed flow zone implies stronger entrainment of high-speed free-stream fluid into the wake, i.e. stronger vortex shedding. The maximum values of $\overline{u^*_{rms}}$, $\overline{v^*_{rms}}$ and $\overline{u^*v^*}$ at the mid-span (figure 2 j, k & l) are about

one-half of those for a 2D cylinder at the same Re_d (figure b, c & d), which also suggests that the vortex shedding is less organized in a finite-length cylinder wake. Near the free end (z^*=6), all the contours appear to converge towards the centerline with increasing x^* due to downwash flow from the free end, which differ not only quantitatively but qualitatively from those at mid-span. Under the effect of free-end downwash flow, the reverse flow zone at $z^* = 6$ shrinks significantly relative to that at mid-span, while still far larger that of 2D cylinder.

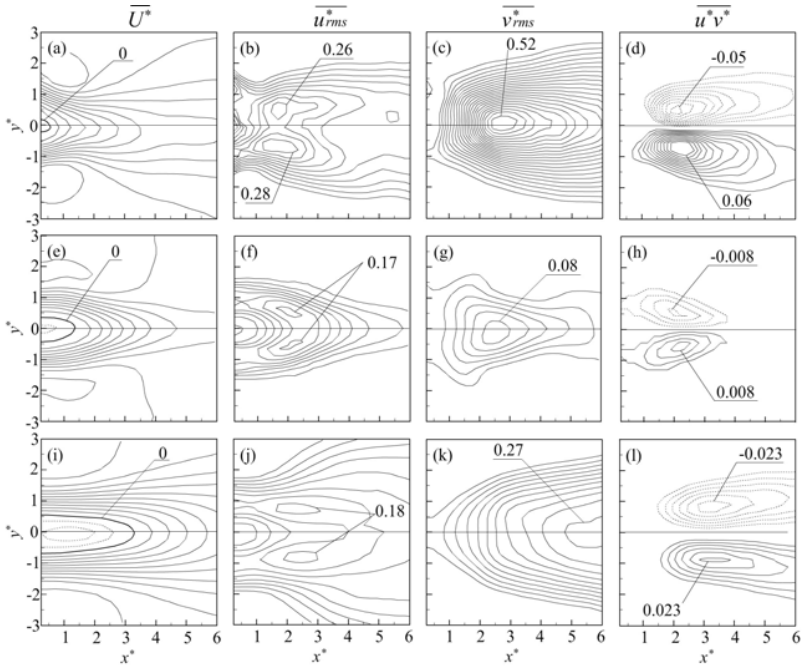

Figure 2. The contours of $\overline{U^*}$, $\overline{u^*_{rms}}$, $\overline{v^*_{rms}}$ and $\overline{u^*v^*}$. (a-d) 2D square cylinder; (e-h) $z^* = 6$, for $H/d = 7$; (i-l) $z^* = 3.5$, for $H/d = 7$. (a, e & i) Contour interval = 0.1; (b, f & j) 0.02, 0.02, 0.02; (c, g & k) 0.02, 0.01, 0.02; (d, h & l) 0.005, 0.002, 0.004.

To reveal the three-dimensionality of vortex structures for finite-length cylinder, POD analysis was applied in spanwise planes of different z^*. Since the sample size or number of snapshots necessary to obtain converged POD analysis was about 1000[12], the 1500 PIV records at each spanwise position for present experiments are sufficient. POD analysis was also applied for a 2D square cylinder wake at the same Re_d for comparison.

Figure 3 shows the first 3 modes of u^*, v^* and ω_z^* for a 2D square cylinder wake. The contour structures of Mode1 and 2 are highly correlated. Particularly, Mode 2 can be regards as a streamwise shift of Mode 1, with the phase difference of about 1/4 shedding circle. These observations are similar to those in a 2D square cylinder wake[13]. For Mode1 and 2, the contours of ω_z^* with positive and negative values present alternating pattern. This pattern inherently resembles the alternating Karman vortex structure. The pattern of Mode 3 is drastically different from those of the first two modes, as shown in figure 3. The contours of $\phi_{w_z}^*$ are somewhat symmetrical about the wake centerline. However, the strength of Mode3 is far weaker than Mode 1 and 2, with the maximum of $\phi_{w_z}^*$ less than 5% of those for the first two modes, which may suggest that its contribution to the total fluctuation energy is limited.

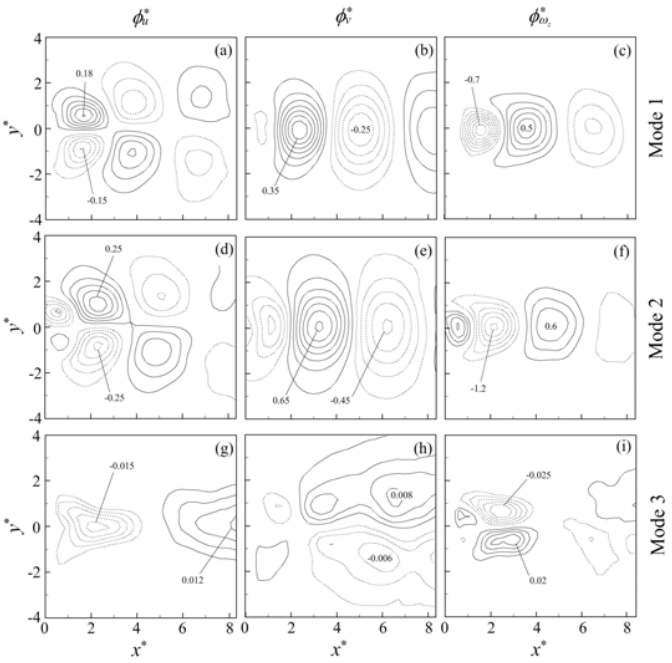

Figure 3. Contours of the first three POD modes in a 2D square cylinder wake: φ_u^*, φ_v^* and $\varphi_{w_z}^*$.(a) Contour interval = 0.03, (b) 0.05, (c) 0.1, (d) 0.05, (e) 0.1, (f) 0.2, (g) 0.003, (h) 0.002 and (i) 0.005.

Figures 4 & 5 present the first three modes in the finite-length cylinder wake at z^* = 6 and 3.5. The results at z^* = 1 are qualitatively similar to those at z^* = 3.5, thus not present here. At z^* = 6, i.e. 1d lower than the free end, Wang & Zhou[2] found over 55% spanwise vortices are symmetrical or approximately symmetrical. They ascribed this observation to the free-end downwash flow, which tends to change vortex shedding from anti-symmetrical to symmetrical. For a wall-mounted finite-length circular cylinder (H/d = 7, Re_d = 1060), Okamoto & Sunabashiri[5] suggested the anti-symmetrical vortex shedding vanishes at 0.5d lower than the free end. For the present finite-length square cylinder wake, Wang & Zhou[2] suggested that about 13% of vortices at 1d lower than the free end are anti-symmetrical. Drastically different from that of 2D cylinder wake, the contours of $\phi_{w_z}^*$ of Mode 1 is symmetrical about the centerline, as shown in figure 4(c). Although $\phi_{w_z}^*$ of Mode 2 is also approximately symmetrical about the centerline, its structure does not correlate with Mode1. The contours of $\phi_{w_z}^*$ for the first two modes converge towards the centerline, accord with the behavior of time-averaged quantities as shown in figure 2(e-h). For Mode3, the structure becomes more complicated and less organized.

At z^* = 3.5, i.e. the cylinder mid-span, the positive and negative $\phi_{w_z}^*$ contours for the first two modes occur alternately along centerline (figure 5c & f), generally similar to those of 2D cylinder wake. However, a close look at the topology may find that the contours are stretched in transverse direction and the local extreme values occur symmetrically on both sides of the centerline (figure 5c & f), which are far different from those of 2D cylinder wake (figure 3 c & f). The transverse stretched $\phi_{w_z}^*$ contours of the first two energetic modes are ascribed to the free-end downwash flow, which tends to entrain fluid from near the free end and separate the shear layers from both sides of the cylinder. The structure of Mode3 for finite-length cylinder (figure 5g-i) is drastically different from that of 2D cylinder. It is interesting that, a close resemblance

can be observed between Mode 1 at $z^* = 6$ (figure 4a-c) and Mode 3 at $z^* = 3.5$ (figure 5g-i) except the opposite sign.

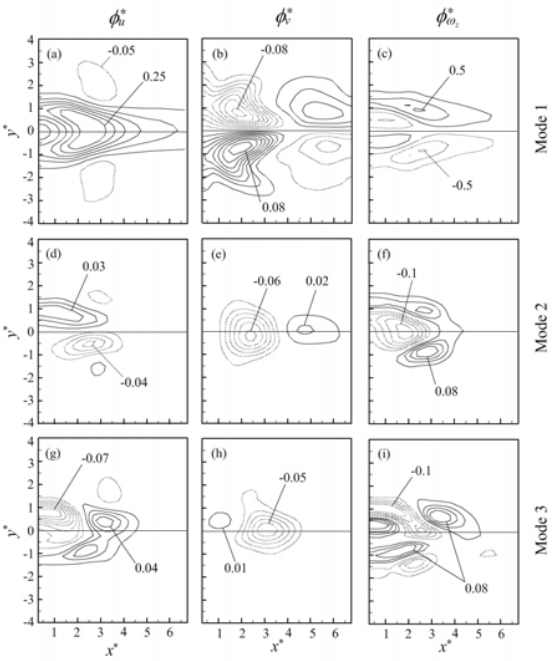

Figure 4. Contours of the first three POD modes of φ_u^*, φ_v^* and $\varphi_{w_z}^*$ at $z^* = 6$ for $H/d = 7$ (a) Contour interval = 0.05, (b) 0.01, (c) 0.2, (d) 0.01, (e) 0.01, (f) 0.02, (g) 0.01, (h) 0.01 and (i) 0.02.

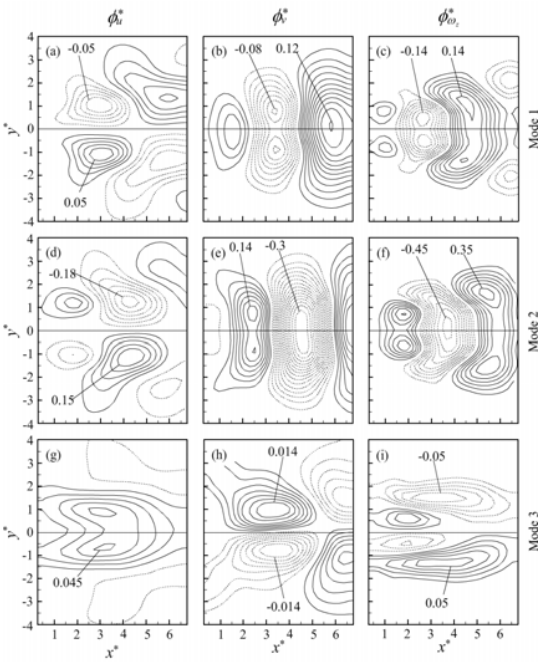

Figure 5. Contours of the first three POD modes of φ_u^*, φ_v^* and $\varphi_{w_z}^*$ at $z^* = 3.5$ for $H/d = 7$ (a) Contour interval = 0.01, (b) 0.02, (c) 0.02, (d) 0.03, (e) 0.02, (f) 0.05, (g) 0.01, (h) 0.002 and (i) 0.01.

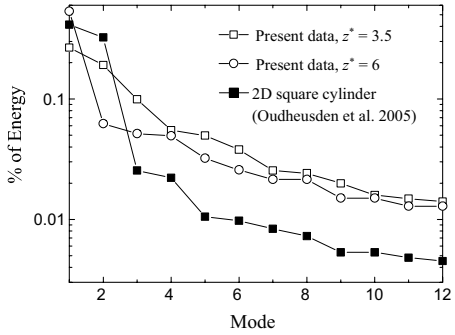

Figure 6. Fractional contribution to the turbulent kinetic energy by different mode.

The fractional contributions to the turbulent kinetic energy (TKE) from different modes are illustrated in figure 6. For the 2D square cylinder at $Re_d \approx 10000$[13], the fractional contribution reduces quickly with increasing mode number. Over 73% (41.3% + 32.4%) TKE is from the first two modes, suggesting the near wake is dominated by the alternating Karman vortex shedding. The TKE from the symmetrical Mode 3 diminishes remarkably to about 2.5%. For the present finite-length cylinder, at $z^* = 3.5$, the first two modes account for 45.9% (the first and second modes contributes 26.7% and 19.2%, respectively) of total TKE, significantly smaller than that for 2D cylinder wake. Contrary to the reduced contribution of the first two modes, the TKE contributions from higher modes are larger than the corresponding values for 2D cylinder. Particularly, the TKE from the symmetrical Mode 3 is 10% at $z^* = 3.5$, which suggests that symmetrical vortex shedding is still remarkable. This observation accord with the finding proposed by Wang & Zhou[2] that about 10% vortex shedding is symmetrically arranged at cylinder mid-span. The TKE contributions from Mode 1 and 2 are close to each other for 2D cylinder wake, which is also observed at the mid-span for $H/d = 7$. This observation may because the first two modes are highly correlated. However, the TKE contribution at $z^* = 6$ is completely different. First, the TKE from the symmetrical Mode 1 is over 54%, which is far larger than that at mid-span. Second, the TKE from Mode 2 is about only 1/10 of that from Mode 1, suggesting the near wake at $z^* = 6$ is dominated by Mode 1 which represent the effects of free-end downwash flow, as shown in figure 4(a-c). Figure 6 also suggests that, the TKE distributes over more modes for the finite-length cylinder wake than for 2D cylinder wake. For example, for 2D cylinder wake, the first two modes account for over 70% of total TKE, while at mid-span of $H/d = 7$, it needs 6 modes to contribute 70% of total TKE.

In view of the small TKE contribution from Mode 3 and other higher modes in 2D cylinder wake, the instantaneous velocity field can be reconstructed with a low-order flow model incorporating only the time-averaged and the first two POD modes[13] via:

$$u_{LOM} = \overline{U} + a_1\phi^1 + a_2\phi^2 \tag{4}$$

$$a_1 = \sqrt{2\lambda_1}\sin\theta, \quad a_2 = \sqrt{2\lambda_2}\cos\theta \tag{5}$$

where u_{LOM} is the instantaneous velocity field and θ is the vortex-shedding phase angle (Durao et al. 1988). The coefficient a_1 and a_2 are not independent, but forms an ellipse in the (a_1, a_2) plane. The cross plot of a_1 and a_2, normalized by their own eigenvalues, is shown in figure 7. For the 2D square cylinder wake, as shown in figure 7(a), the cross plot of normalized (a_1, a_2) approximately forms a circle, confirms the relation shown in Eqs. (4 & 5). As shown in figure 7(a), the observed scatter of the data point around the theoretical circle can be an indication of cycle-to-cycle variations of the vortex shedding process, induced by small scale fluctuations or turbu-

lence[13]. This scatter reduces with decreasing Re_d. Ma & Karniadakis[14] found the cross plot of (a_1, a_2) forms nearly an ideal circle and not scattering presents at Re_d = 185.

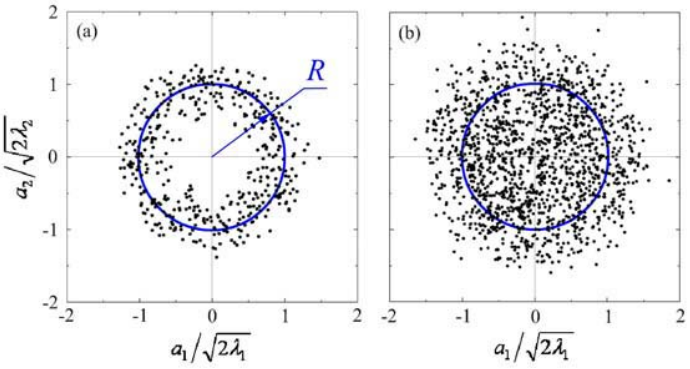

Figure 7. Snapshot mode coefficient correlation (a) 2D cylinder wake, (b) at mid-span for H/d = 7.

For the present finite-length cylinder, at z^* = 3.5 (figure 7b), the points distribute more dispersedly in (a_1, a_2) plan relative to that of 2D cylinder wake. Considering the Re_d is the same for figure 7(a & b), the dispersion in figure 7(b) may be ascribed to the different vortex shedding mechanism in a finite-length cylinder wake. As shown in figure 6, at z^* = 3.5, since the first two modes accounts for less than half of total TKE, the low-order model may be not applicable. It is worth mentioning that, each point in figure 7 indicates a snapshot. For the points near the origin point (as shown in figure 7b), the TKE contributions from the first two modes are quite limited, because of the small absolute values of a_1 and a_2. For theses snapshots, the main TKE are from Mode 3 and other higher modes, which are less organized. One the other hand, for the points away from the origin point, most TKE are from the first two modes.

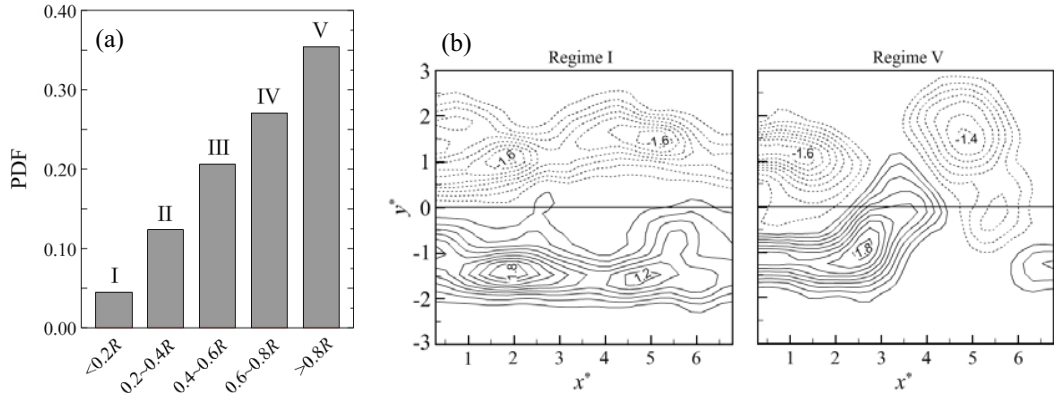

Figure 8. PDF of different flow regimes and typical instantaneous vorticity contours for Regime I and V. (a) PDF distribution; (b) normalized vorticity contours for Regime I and Regime V, contour interval = 0.2

Since the vortices in mode 1 and mode 2 are stagger arranged, different from those in mode 3 and other higher modes, it may be possible to use the distance between the snapshot point and origin point to classify the instantaneous flow status. Five regimes are classified based on this distance, i.e. <0.2R, 0.2~0.4R, 0.4~0.6R, 0.6~0.8R and >0.8R. The probability density function for these five regimes determined from 1500 instantaneous snapshots is shown in figure 8(a). Figure 8(b) presents two typical instantaneous vorticity contours for Regime I and V, respectively. For Regime I, the most TKE are from mode 3 and other higher modes; while for Regime V, most TKE are from the first two modes. Since the flow structure of the first two modes is different from that of the other higher modes, as shown in figure 5, the corresponding flow structures for Regimes I and V are also different (figure 8b). For Regime I, the shear layers from both

sides of the cylinder do not roll into successive vortices and the near wake is symmetrical about the wake centerline. For Regime V, the near wake is dominated by stagger arranged vortices, similar to those observed in 2D cylinder wake.

4 CONCLUSIONS

The near wake of a wall-mounted finite-length cylinder has been measured with PIV and analyzed using POD technique. The cylinder aspect ratio H/d = 7. PIV measurements were conducted in spanwise planes at z^* = 1, 3.5 and 6. The following conclusions may be drawn from the analysis of the data:

(1) The flow depends strongly on the spanwise position, the contours of $\overline{U^*}$, $\overline{u^*_{rms}}$, $\overline{v^*_{rms}}$ and $\overline{u^*v^*}$ converge towards wake centerline near the free end (z^* = 6), which is significantly different from those at mid span. Under the effects of free-end downwash flow, the streamwise extend of reverse flow zone at most spanwise positions of present tested finite-length cylinder is larger than that for 2D cylinder, and the magnitudes of $\overline{u^*_{rms}}$, $\overline{v^*_{rms}}$ and $\overline{u^*v^*}$ are significantly suppressed, especially near the free end.

(2) At the mid span of H/d = 7, although the vortical structures of the first two POD modes are staggered arranged along wake centerline and highly correlated with each other, somewhat similar to those in 2D cylinder wake, the vorticity contours are stretched in lateral direction with the local extreme values occur symmetrically on both sides of centerline. Near the free end, i.e., z^* = 6, the structure of first POD mode is completely different from that of higher modes.

(3) For finite-length cylinder wake, the TKE distributes over mode POD modes relatively to that of 2D cylinder wake. Instantaneous vortex shedding patterns can be classified based on the coefficients of the first two POD modes. Both symmetrical and anti-symmetrical vortex shedding occurs in the near wake at z^* = 3.5.

5 ACKNOWLEDGEMENTS

The author wish to acknowledge support given to them from the National Natural Science Foundation of China through grants 51108468.

6 REFERENCES

1 D. Summer, J.L. Heseltine and O.J.P. Dansereau, Wake structure of a finite circular cylinder of small aspect ratio, Exp. Fluids, 2004(37) 720–730.
2 H.F. Wang and Y. Zhou, The finite-length square cylinder near wake, J. Fluid Mech., 2009(638) 453-490.
3 F. Etzold and H. Fiedler, The near-wake structure of a cantilevered cylinder in a crossflow, Z. Flugwiss., 1976(24) 77–82.
4 C.W. Park and S.J. Lee, Free end effects on the near wake flow structure behind a finite circular cylinder, J. Wind Engng Ind. Aerodyn., 2000(88) 231–246.
5 T. Okamoto and Y. Sunabashiri, Vortex shedding from a circular cylinder of finite length placed on a ground plane, J. Fluids Engng., 1992(114) 512–521.
6 H. Sakamoto and M. Arie, Vortex shedding from a rectangular prism and a circular cylinder placed vertically in a turbulent boundary layer, J. Fluid Mech., 1983(126) 147–165.
7 R.J. Pattenden, S.R. Turnock and X. Zhang, Measurements of the flow over a low-aspect-ratio cylinder mounted on a ground plane, Exp. Fluids, 2005(39) 10–21.
8 T. Kawamura, M. Hiwada, T. Hibino, I. Mabuchi and M. Kumada, Flow around a finite circular cylinder on a flat plate, Bull. JSME, 1984(27) 2142–2150.
9 L. Sirovich, Turbulence and the dynamics of coherent structures, Quart Appl Math., 1987(45) 561–590.

10 H.F. Wang, Y. Zhou, C.K. Chan and K.S. Lam, Effect of initial conditions on interaction between a boundary layer and a wall-mounted finite-length-cylinder wake, Phys. Fluids, 2006(18) 065106.
11 K.E. Meyer, J.M. Pedersen and O. Özcan, Turbulent Jet in crossflow analyzed with Proper Orthogonal Decomposition, J. Fluid Mech., 2007(583) 199-228.
12 S.S. Paul, M. Agelinchaab and M.F. Tachie, Flow around finite circular and square cylinder in an open channel, ASME 2009 Fluids Engineering Division Summer Meeting, Aug. 2-6, 2009, Vail, Colorado USA.
13 B.W. Oudheusden, F. Scarano, N.P. Hinsberg and D.W. Watt, Phase-resolved characterization of vortex shedding in the near wake of a square-section cylinder at incidence, Exp. Fluids, 2005(39) 86-98.
14 X. Ma and G. Karniadakis, A low-dimensional model for simulating three dimensional cylinder flow, J. Fluid Mech., 2002(458) 181-190.

The Seventh International Colloquium on Bluff Body Aerodynamics and Applications (BBAA7)
Shanghai, China; September 2-6, 2012

Effects of corner recession modification on aerodynamic coefficients of square tall buildings

Zhang Zhengwei[a,b], Quan Yong[a], Gu Ming[a], Tu Nankun[a], Xiong Yong[c]

a Sate Key Laboratory for Disaster Reduction in Civil Engineering , Tongji University , Shanghai, China

b School of Architecture Engineering, Nantong University, Nantong, China

c Sichuan Road & Bridge Co., Ltd, Chengdu, China, bluer.xiong@gmail.com

ABSTRACT: With high frequency force balance (HFFB) technique, 14 square tall buildings models with recessed corners were tested in two different simulated wind fields to obtain aerodynamic forces. The effects of turbulence intensities and corner recession ratios on mean and RMS coefficients of the aerodynamic base moment and torque in typical wind directions were analyzed. The test results indicate that two types of corner recession have dramatic effects on the aerodynamic coefficients of base moment and torque, and the model with a corner recession ratio of 7.5% is the best one to cut down the aerodynamic forces coefficients. Empirical formulae are fitted for aerodynamic force coefficients of square tall buildings with different corner recession ratios, which provide technical support for the revisions and supplements of load codes.

KEYWORDS: aerodynamic force coefficients, corner recession, empirical formula, HFFB technique, tall building, wind tunnel test.

1 INTRODUCTION

With enormous utilization of light-weight and high-strength materials, super-tall buildings are becoming ever-increasingly high, flexible, and low in damping. These flexible structures are totally sensitive to dynamic wind load, which plays a significant role in the structure design and should be put more emphasis. Across-wind response of super-tall buildings gradually exceeds along-wind response as their heights increase, which is the crux of structural wind-resistant design [1]. Besides, comfort problem is becoming more and more serious especially under strong winds. Recently, primary wind-induced vibration control measures of super-tall building consist of structure measures, mechanical treatments and aerodynamic wind-resistant measures [2], which play an essential role in initial project design of the super tall building to vitally reduce wind load and wind-induced response [3]. Corner recession modification serves as one type of typical aerodynamic measures for high-rise buildings. Melbourne and Cheung [4], Miyashita etc [5], Gu and Quan [6] have discussed the effects of corner recession modification on aerodynamic characteristics for high-rise buildings through high frequency balance test and aeroelastic model test, and point out that corner recession modification basically reduces the peak value of power spectra densities for across-wind base moment, and that the model with corner recession ratio of 10% greatly reduces the peak value of spectrum for aerodynamic force. Besides, Kawai [7] has discussed the effects of corner recession modification on aerodynamic instability of square and rectangular models, and states that corner recession ratio of 5% would effectively prevent aerodynamic aeroelastic divergence, especially for the square model; however, as for high side-length ratio of rectangular section corner modification measure is not effective in preventing divergence. Irwin [8], Suresh etc [9] have discussed characteristics of wind load of Taipei 101

building, and these research results indicated that it is the double corner recession modification that reduces RMS of across-wind aerodynamic force by 40%, along-wind mean wind load by 20% and total base moment by 25%. Moreover, Tse etc [10] investigate the impact of aerodynamic modifications on the building economics of tall structures and indicate that corner recession models act more effectively than corner cutting model in decreasing base moment. Those researches primarily aim at wind-induced effect of models with specific corner recession ratio, especially the aerodynamic power spectra of across-wind response and wind-induced response, and the author gave some qualitative conclusions, however, there existed no comprehensive empirical formula portraying the effect of aerodynamic modification measures on square building which can be directly applied as standard.

In this paper, 14 square tall buildings models were tested to determine the effects of two types of corner recession modification on characteristics of aerodynamic force. In order to provide technical support for the revisions and supplements of load codes, empirical formulae for effect of corner recession modification on base aerodynamic coefficients are provided by using the nonlinear least-squares method. However, due to space constraints, only the preliminary results are given in this paper to illustrate the influences of corner recession modification on coefficients of base moment and torque. The effects on power spectra of base moment and torque will be discussed in other future papers.

2 WIND TUNNEL TESTS AND RESULTS

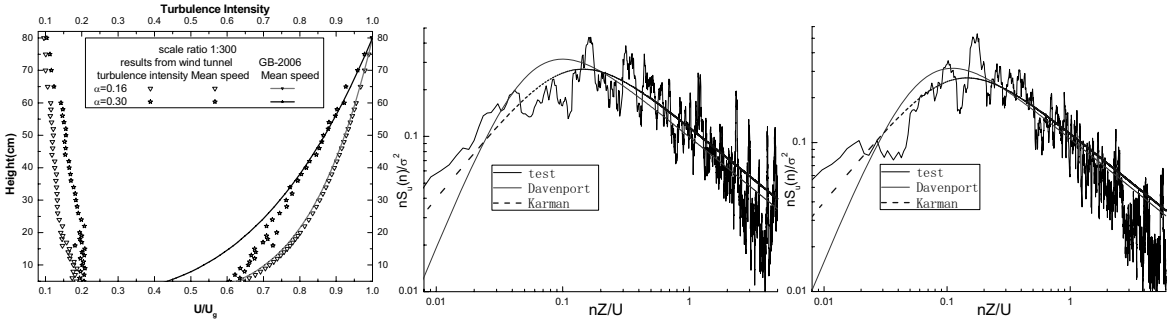

(a) Mean wind speeds and turbulence intensity profiles
(b) PSD of turbulence at height of 60 cm in terrain B (c) PSD of Turbulence at height of 60 cm in terrain D
Fig.1. Simulated wind parameters of the terrain categories B and D

This test is carried out in TJ-1 Boundary Layer Wind Tunnel, whose working section is 1.8m in width and 1.8m in height, and the wind speed ranges continuously from 3 to 32m/s. With passive simulation method, i.e., different arrangement of three devices (turbulence generating spires, barrier and roughness element) in wind tunnel [11], the wind characteristics are achieved to simulate two kinds of wind conditions, corresponding to terrain categories B and D in the wind tunnel at a length scale of 1/300 in accordance with Chinese code [12]. Fig 1 shows simulated wind parameters of the terrain categories B and D where z is height; U stands for wind speed; U_g represents height for gradient wind; $S_u(n)$ is power spectra of wind speed, and σ^2 represents mean square value of wind speed; n is frequency. The turbulence intensity 60 cm above model is 12.6% and 16.5% for the two categories of terrain, respectively, and turbulent integral scale at the same height is according 34 cm and 36 cm (in wind tunnel), corresponding to actual turbulent integral scale 100 m and 110 m, respectively. Despite mean wind profiles at one-third height

for terrain categories D was larger than normative standard values, this error can be ignored since the contribution to base moment made by aerodynamic force below one-third height of this building is less than 5%.

The two types of cross-section modified by corner recession shown in Fig. 2 consist of type I and type II (double concave corner) developing from the fundamental type I. The corner recession ratio is defined as

$$\gamma_c = b / B \tag{1}$$

where B denotes section width, and b is cutting length of corner recession.

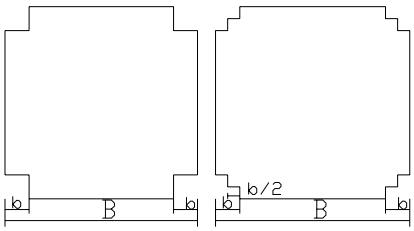

(a) type I (corner recession) (b) type II (double corner recession)
Fig. 2.Cross sections of the building models

Table 1 Testing cases

Types of corner recession	Corner recession ratio $\gamma_c = b / B$	Wind angle	Test wind speed(m/s)	Terrain
type I	0%,5%,7.5%,10%,12.5%,15%,20%,30%	0~45°	6, 8	B, D
type II	0%,7.5%,10%,12.5%,15%,20%,30%	0~45°	6, 8	B, D

The aluminum tube, whose cross-section area is 50mm×50mm, height is 600mm and thickness is 1mm, serves as mandrel to provide rigidity, and external foam was employed to satisfy different shape parameters for building simulation, ensuring little mass but large stiffness for models and enough high natural frequency for balance-model system. Additionally, in order to ensure the validity of the test data and precision of the measured signal, final test result is average of the two sets of test data under wind speed 6 m/s and 8 m/s, and all of the test data is used to fit the empirical formulae. Besides, the calculation program is employed to serve as automatic recognition of the modal parameters (free vibration frequency and damping ratio) for balance system according to output time-history data of high frequency force balance, and aerodynamic base moment decoupled from output of high frequency force balance signals is then revised, and the details of modified process is shown in paper [13]. The work cases is shown in table 1, and there exists totally 14 different models (13 model with corner recession modification and basic model with no corner recession modification whose dimension is 600mm×120mm×120mm) having been tested in terrain categories B and D. Owing to symmetry of square section 5° serves as a wind angle interval and wind range is from 0° to 45°. Moreover, the measuring range of base (torque) moments is 30 Nm, and the measuring precision is 0.004 Nm, and sampling frequency is 600 Hz, and sampling time is 60 s.

Non-dimensional coefficients of base aerodynamic force are defined as:

$$\bar{C}_{M_D} = \bar{M}_D / q_H BH^2, C'_{M_D} = \sigma_{M_D} / q_H BH^2, C'_{M_L} = \sigma_{M_L} / q_H BH^2, C'_{M_T} = \sigma_{M_T} / q_H B^2 H \tag{2}$$

where $q_H = 0.5\rho U_H^2$ is the dynamics pressure at the top of buildings, and B represents building width normal to the approaching flow, and H stands for the height of the building, and U_H is the wind velocity at the top of buildings. In addition, M_D is the mean base moment in along-wind;

σ_{MD}, σ_{ML} and σ_{MT} are the RMS values of the base moment for along-wind, across-wind and torsion direction, respectively; C_{MD} is the mean coefficients of along-wind base moment, C'_{MD}, C'_{ML} and C'_{MT} are the RMS coefficients of the base moment for the along-wind, across-wind and torsion direction, respectively.

To illustrate the effect of different corner recession ratio on coefficients of base moment, the correction factor is defined as:

$$\eta_{MD}(\gamma_c) = C_{MD}(\gamma_c) / C_{MD0} \tag{3}$$

$$\eta'_{Ml}(\gamma_c) = C'_{Ml}(\gamma_c) / C'_{Ml0},\ l = D,L,T \tag{4}$$

where $\eta_{MD}(\gamma_c)$ stands for correction factor for mean coefficients of along-wind base moment; C_{MD0} and $C_{MD}(\gamma_c)$ represent mean coefficients of along-wind base moment with corner recession and with no recession, respectively. Additionally, $\eta'_{Ml}(\gamma_c)$ represents correction factor for RMS coefficients of base moment (torque). C'_{Ml0} and $C'_{Ml}(\gamma_c)$ are RMS coefficients of base moment (torque) with corner recession and with no recession, respectively. Besides, subscript 0 represents basic square model with no corner recession and subscripts D, L, and T denote along-wind, across-wind, and torsional directions, respectively.

In order to facilitate the engineering application, empirical formulae for effect of corner recession modification on coefficients of base moment and torque are provided by using the nonlinear least-squares method. Moreover, error rate facilitating quantitative analysis is defined as follows:

$$\text{Error ratio=(Fitted result-Testing result)/Testing result} \times 100\% \tag{5}$$

3 EXPERIMENT RESULT

3.1 *Mean coefficients of base moment*

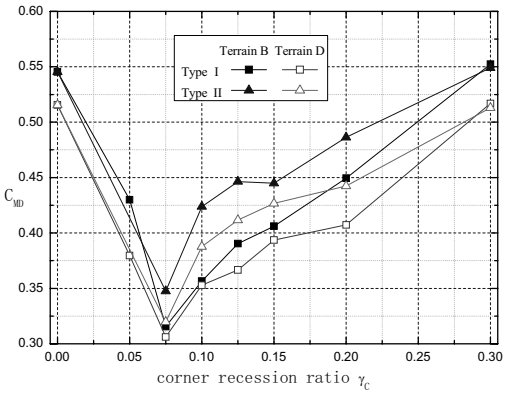

Fig. 3. Effect of corner recession ratio on the mean coefficient of along-wind base moment

Fig. 3 illustrates the effect of corner recession ratio γ_c on C_{MD} of square model, where corner recession ratio 0 represents basic model with no corner recession. Seen from Fig.3, mean coefficients of base moment of models with no corner recession in terrain categories B and D are 0.55 and 0.52, respectively. With corner recession ratio increasing from 0% to 7.5%, C_{MD} decrease gradually and it reaches the minimum when γ_c is 7.5%. C_{MD}, however, would conversely increases if γ_c continues to grow over 7.5%, and processing to C_{MD0} when γ_c reaches 30%. In

sum, C_{MD} can be diminished when γ_c ranges from 0% to 30%, and reaches its minimum at the point 7.5%, roughly equivalent to 60% of C_{MD0}. Despite C_{MD} tested from terrain categories D is lower than the one from terrain categories B, effect of terrain categories B and D on C_{MD} is not obvious in error allow range. That regularity of the vortex shedding has been transformed and leeward negative pressure has been then reduced may explain for the phenomenon that the influence of two types of corner recession on C_{MD} is basically the same. Besides, type I corner recession is more effective than type II at reducing mean coefficients of base moment.

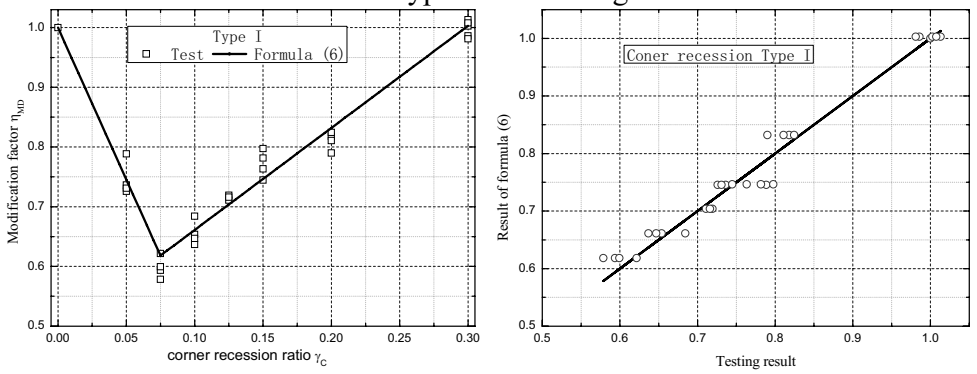

(a) Corner recession type I

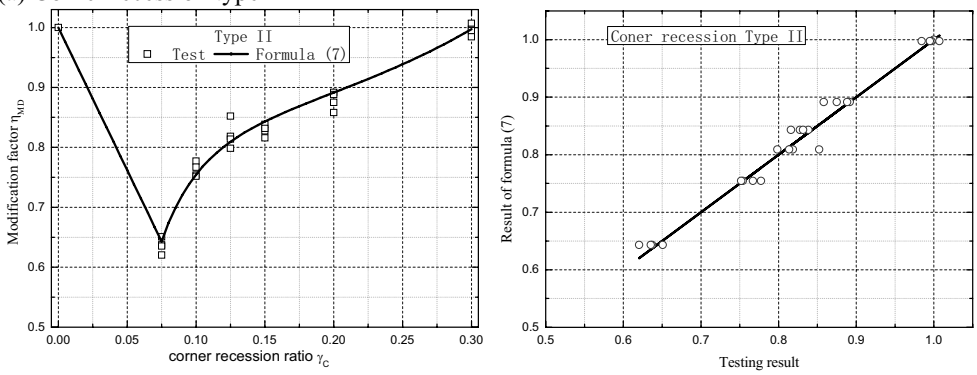

(b) Corner recession type II

Fig. 4. Comparison of Modification factor η_{MD} between the testing results and corresponding fitted ones

Empirical formulae are derived by nonlinear least-squares method technique, expressed as:

$$\eta_{MD} = \begin{cases} 1.0 - 5.1\gamma_c, & 0 \le \gamma_c < 7.5\% \\ 0.49 + 1.7\gamma_c, & 7.5\% \le \gamma_c \le 30\% \end{cases}, \ Type\ I \tag{6}$$

$$\eta_{MD} = \begin{cases} 1.0 - 4.8\gamma_C, & 0 \le \gamma_C < 7.5\% \\ 0.89 + 4.55\gamma_C^3 - 0.0014\gamma_C^{-2}, & 7.5\% \le \gamma_C \le 30\% \end{cases}, \text{Type Ⅱ} \tag{7}$$

Fig. 4 portrays the distinction between test and calculation results obtained from formulae (6) and (7). The average of the error rate of calculation results obtained from formula (6) is 0.46% and RMS is 3.08%, and as for formula (7) the average and RMS of the error rate are 0.08% and 4.36%, respectively.

3.2 *RMS coefficients of along-wind base moment*

Fig. 5 illustrates the effect of corner recession ratio γ_c on C'_{MD} of square model. With corner recession ratio increasing, C'_{MD} firstly decreases, then increases, and finally decreases. C'_{MD} appears to be roughly equivalent to 80% of C'_{MD0} when γ_c=30%, and reaches its minimum when 7.5%, and probably equals 55% of C'_{MD0} when 7.5%. In brief, corner recession ratio ranging from 0 to 30% can reduce C'_{MD} and further increasing corner recession ratio over 7.5% is really ineffective at reducing C'_{MD}. Finally, effect of two types of corner recession on C'_{MD} is basically the same whether in terrain categories B or D.

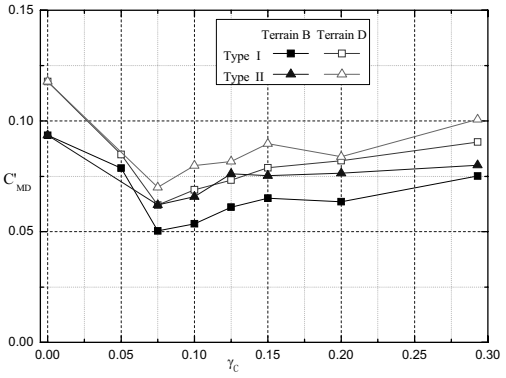

Fig. 5. Effect of corner recession ratio on the RMS coefficient of along-wind base moment

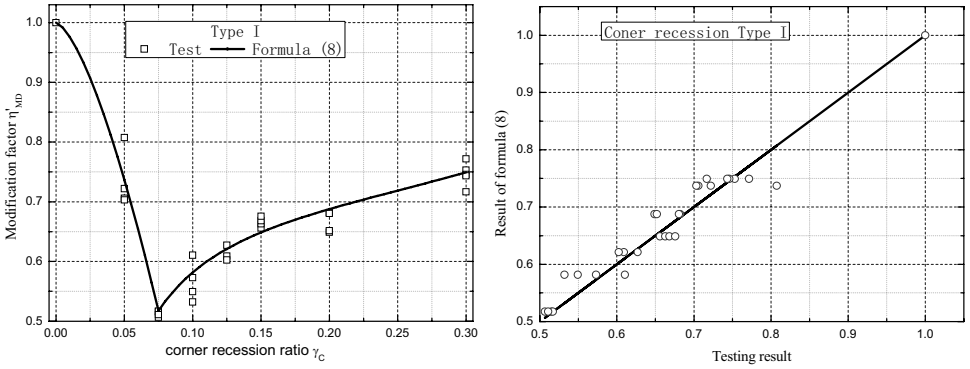

(a) Corner recession type I

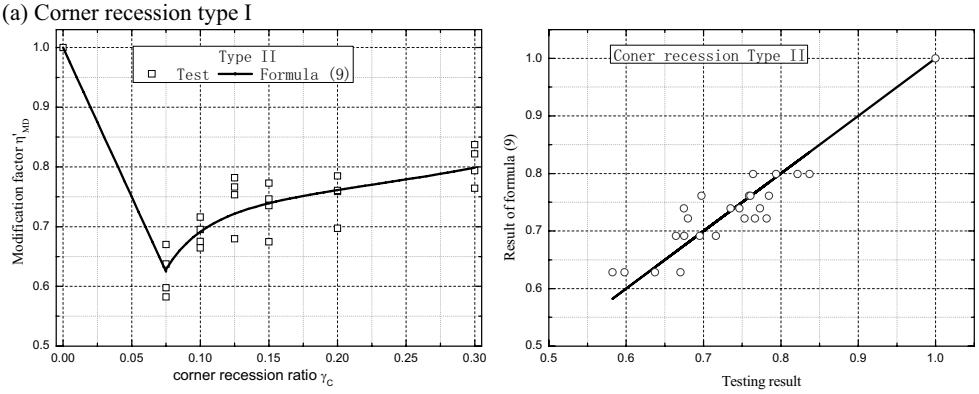

(b) Corner recession type II

Fig. 6. Comparison of Modification factor η'_{MD} between the testing results and corresponding fitted ones

Piecewise function is adopted in fitting process because regular pattern of C'_{MD} in 0-7.5% is not consistent with that in 7.5%-30%. Empirical formulae reflecting the effect of two types of corner recession modification on C'_{MD} are shown as:

$$\eta'_{MD}=\begin{cases}1-24\gamma_c^{1.5}, & 0\le\gamma_c<7.5\%\\ 0.77+1.6\gamma_c^{3}-0.02/\gamma_c, & 7.5\le\gamma_c\le 30\%\end{cases},\quad \text{Type Ⅰ} \tag{8}$$

$$\eta'_{MD}=\begin{cases}1-5\gamma_c, & 0\le\gamma_c<7.5\%\\ 0.77+1.4\gamma_c^{3}-0.0008\gamma_c^{-2}, & 7.5\le\gamma_c\le 30\%\end{cases},\quad \text{Type Ⅱ} \tag{9}$$

Fig. 6 presents the comparison between testing results and the corresponding fitted ones obtained from formula (8) and (9). The average of the error rate of corresponding fitted results obtained from formula (8) is -0.18%and RMS value is 3.71%; the average and RMS of the error rate obtained from formula (9) are 0.21% and 4.86%, respectively.

3.3 *RMS coefficients of base across-wind moment*

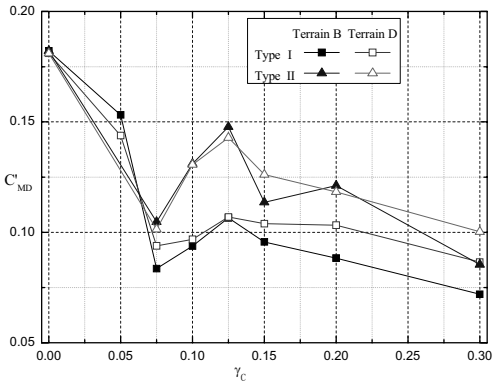

Fig. 7. Effect of corner recession ratio on the RMS coefficient of across-wind base moment

Fig. 7 illustrates the effect of corner recession ratio γ_c on C'_{ML} of square model. With corner recession ratio increasing, C'_{ML} firstly decreases, and then increases, and finally conversely decreases. C'_{ML} dramatically and sharply drops when γ_c=7.5%, and gradually increases with γ_c varying from 7.5% to 12.5%, and then decreases when γ_c grows over 12.5% whose decrease amplitude is relatively small. The essential change in vortex shedding would explain for this variation rule of C'_{ML} after γ_c grows over 7.5%. In brief, C'_{ML} can be diminished with γ_c varying from 0 to 30%, and appears to be roughly equivalent to 65% of C'_{ML0} when γ_c=7.5%. However, further increasing γ_c is really ineffective at reducing C'_{ML}. Besides, the effect of two types of corner recession on C'_{ML} are basically the same whether in terrain categories B or D, but decreasing amplitude of C'_{ML} induced by type I is larger than that of type II, whose usable area is larger than type I as for the same γ_c.

Despite the absence of test data on 5% for C'_{ML} of type II, linear function is adopted in fitting process for type II in 0~7.5% because the regularity in both types are similar.

Empirical formulae for the effect of corner recession modification on C'_{ML} are provided as:

$$\eta'_{ML}=\begin{cases}1-92\gamma_c^{2}, & 0\le\gamma_c<7.5\%\\ 11\gamma_c e^{-7\gamma_c}, & 7.5\le\gamma_c\le 30\%\end{cases},\quad \text{Type Ⅰ} \tag{10}$$

$$\eta'_{ML}=\begin{cases}1-5.5\gamma_c, & 0\le\gamma_c<7.5\%\\ 1/(6.4-3.55\gamma_c^{-0.5}+0.62/\gamma_c), & 7.5\le\gamma_c\le 30\%\end{cases},\text{Type Ⅱ} \tag{11}$$

Fig. 8 presents the distinction between test and calculated results obtained from formula (10) and (11). The mean error rate of fitted results obtained from formula (10) is 0.16% and RMS is 7.1%, and as for formula (11) mean and RMS of error rate are -0.96% and 6.39%, respectively, demonstrating high precision of formula.

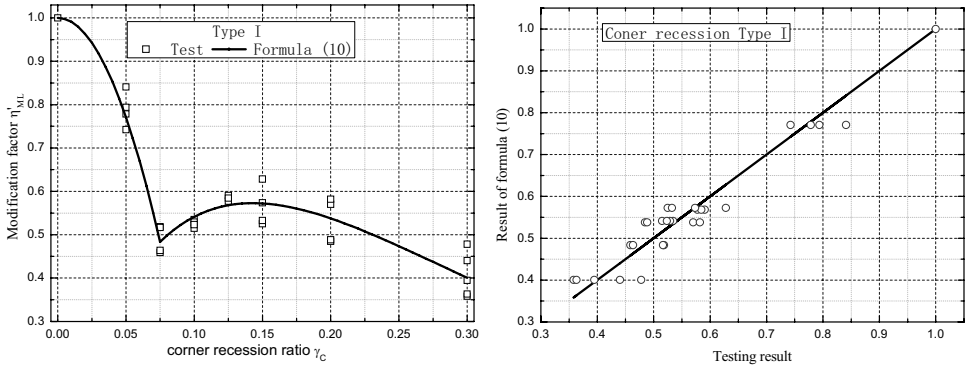

(a) Corner recession type I

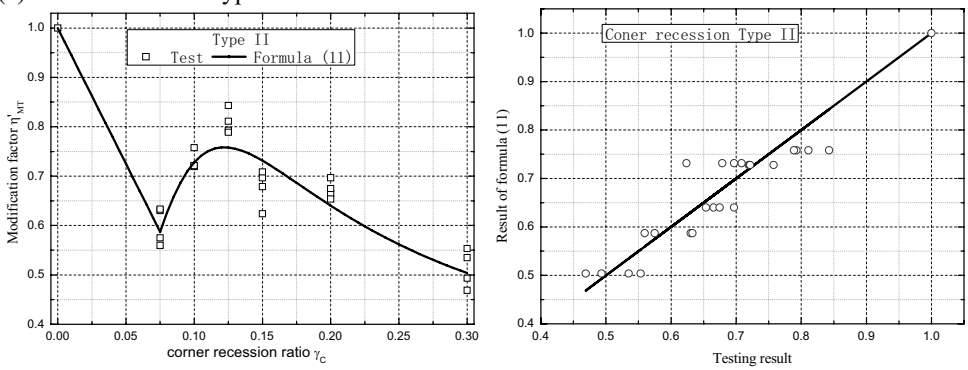

(b) Corner recession type II

Fig. 8. Comparison of Modification factor η'_{ML} between the testing results and corresponding fitted ones

3.4 *RMS coefficients of base torque*

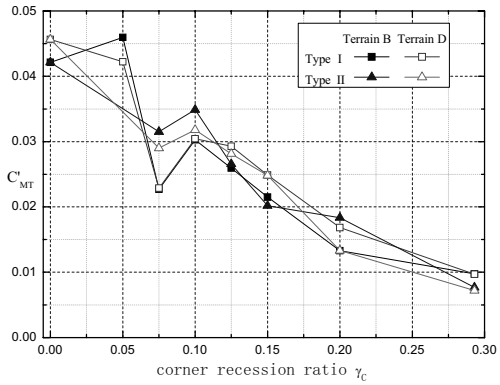

Fig. 9. Effect of corner recession ratio on the RMS coefficient of base torque

Fig. 9 illustrates the effect of two types of corner recession on RMS coefficients of base torque C'_{MT} of square model. Seen from Fig.9, if corner recession ratio varies between 0 and 5%, corner recession modification basically has no influence on C'_{MT}. However, C'_{MT} dramatically decrease with corner recession ratio increasing over 5%, and both of two types of corner recession have such effectiveness that C'_{MT} is less than 25% of C'_{MT0} when γ_c is 30%. Besides, effect of two types of corner recession on C'_{MT} are basically the same whether in terrain categories B or D.

Empirical formulae for the effect of corner recession modification on C'_{MT} are provided as:

$$\eta'_{MT} = e^{-5.6\gamma_c}, \qquad \text{Type I}, \quad 0 \le \gamma_c \le 30\% \tag{12}$$

$$\eta'_{MT} = 1 - 3.5\gamma_c + 7\gamma_c^3, \qquad \text{Type II}, \quad 0 \le \gamma_c \le 30\% \tag{13}$$

Fig. 10 presents comparison between test values and fitted ones obtained from formula (12) and (13), and calculation results evenly distributed in two side of test level, demonstrating these formulae both is concise and meet the requirements for engineering application.

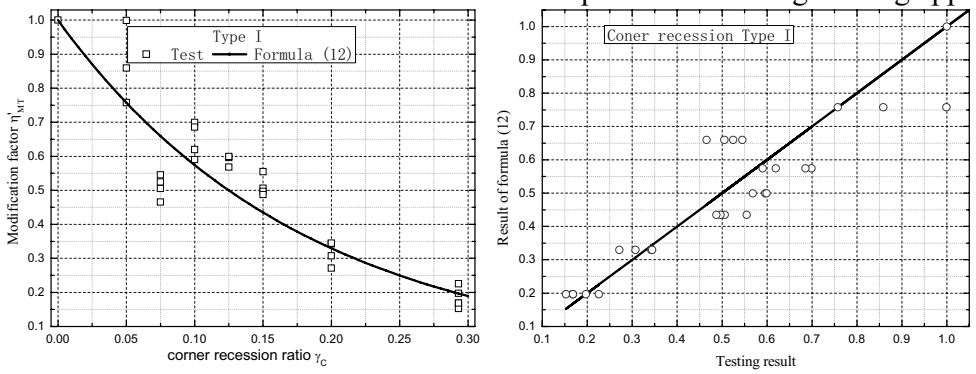

(a) Corner recession type I

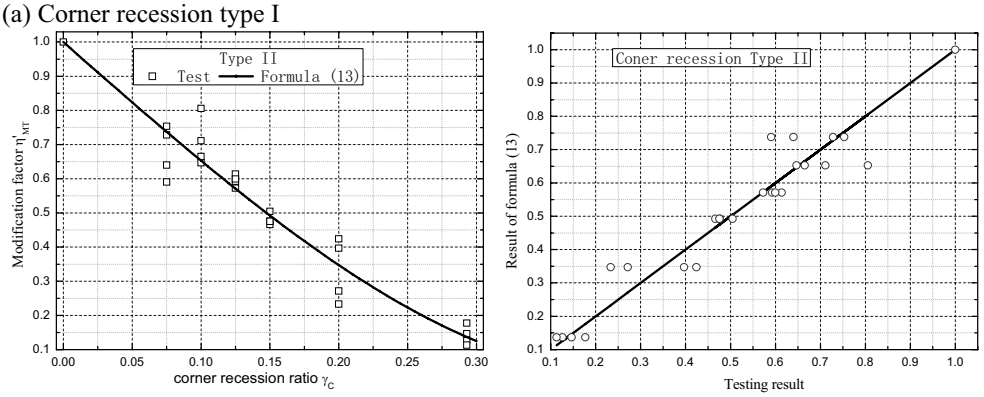

(b) Corner recession type II

Fig. 10. Comparison of modification factor η'_{MT} between the testing results and corresponding fitted ones

4 CONCLUSIONS

This paper presents the test results of 14 rigid models with corner concession of square tall buildings with high frequency force balance (HFFB) technique in two simulated wind field conditions, and analyzes the effects of corner concession modification on the coefficients of base moment and torque. The main findings of the present study are summarized as follows:

(1) Both type I and type II corner recession measures can reduce the coefficients of base moment and torque of square high-rise building, and the corner recession rate of 7.5% is the most effective and optimal.

(2) Each of regularity in the coefficients of base moment and torque for along-wind, cross-wind and torsion direction is different. For any kind of aerodynamic coefficients two types of corner concession measures have the same regularity, insensitive to turbulence intensity of wind field condition.

(3) The precision and applicability of the empirical formulae for the coefficients of aerodynamic force were verified, which provides technical support for the revisions and supplements of load codes.

5 ACKNOWLEDGMENTS

This research was supported by the National Natural Science Foundation of China (Grant Nos. 50878159 and 90715040).

6 REFERENCES

1 M. Gu. The research process and basic scientific issues about civil structures. Science Press, Beijing, 2006

2 Kareem, T. Kijewski, Y. Tamura. Mitigation of motions of tall buildings with specific examples of recent applications , Wind and Structures, 3(1999) 201-251.

3 M. GU, Z.W. Zhang, Y. Quan, Y. Xiong. Aerodynamic Measures for Mitigation of Across-wind Responses of Super Tall Buildings: State of the Art, Journal of Tongji University: Natural Science, (submitted) (in Chinese).

4 N.H. Melbourne, J.C.K. Cheung. Designing for serviceable accelerations in tall buildings, Proceedings of the 4th International Conference on Tall Buildings, Hong Kong and Shanghai, 1988, pp.148-155.

5 K. Miyashita, J. Katagiri, O.Nakamura, et al. Wind induced response of high rise building: effects of corner cuts or opening in square building, Journal of Wind Engineering and Industrial Aerodynamics, 50(1993) 319-328.

6 M. Gu, Y. Quan. Across-wind loads of typical tall buildings, Journal of Wind Engineering and Industrial Aerodynamics, 92(2004) 1147-1165.

7 H. Kawai. Effects of corner modifications on aeroelastic instabilities of tall buildings, Journal of Wind Engineering and Industrial Aerodynamics, 74-76(1998) 719-729.

8 P.A. Irwin. Bluff body aerodynamics in wind engineering, Journal of Wind Engineering and Industrial Aerodynamics, 96(2008) 701–712.

9 K.K. Suresh, P.A. Irwin, A. Davies. Design of tall building for wind: wind tunnel vs. codes/standards , Proceedings of the 3rd National Conference on Wind Engineering, Calcutta, India, 2006,pp.318-325.

10 K.T. Tse, P.A. Hitchcock, K.C.S. Kwok, et al. Economic perspectives of aerodynamic treatments of square tall buildings, Journal of Wind Engineering and Industrial Aerodynamics, 43(2009) 1973-1983.

11 Chinese Code for Loading on Buildings and other Structures, GB50009-2001, 2006(in Chinese).

12 P. Huang, Y. Quan, M. Gu. Research of passive simulation method of atmospheric boundary layer in TJ-2 wind tunnel, Journal of Tongji University :Natural Science ,1999 ,27(2) :136-144(in Chinese).

13 M. GU, Z.W. Zhang, Y. Quan, Y. Xiong. RMS values of base torsional moment coefficients of tall buildings with square and rectangular cross-sections, Journal of Vibration and Shock, 30 (2011) 1-5 (in Chinese).

The Seventh International Colloquium on Bluff Body Aerodynamics and Applications (BBAA7)
Shanghai, China; September 2-6, 2012

Large-eddy simulation of reactive pollutant dispersion in a street canyon using a subgrid scale variance model of concentration field

Hideki Kikumoto [a], Ryozo Ooka [b]

[a]*The University of Tokyo, 4-6-1 Komaba, Meguro-ku, Tokyo, Japan*
[b]*IIS, The University of Tokyo, 4-6-1 Komaba, Meguro-ku, Tokyo, Japan*

ABSTRACT: Bi-molecular reactions can affect the transport of air pollutants in urban street canyons. In numerical simulations, we need to evaluate the correlation between the concentrations of the reactants to know the reaction rate. In this paper, we examine the effects of the subgrid scale (SGS) on the reaction rate in large-eddy simulations (LESs). LESs coupled with an SGS variance model are used to study the dispersion of both inert and reactive pollutants in a simulated street canyon. First, we conduct simulations of an inert pollutant at different grid resolutions. The results of these simulations demonstrate the validity of our model for calculating the variance of concentration at the SGS. Second, we apply the model to the dispersion of reactive pollutants. The correlations of the SGS variances become relatively large in a free shear layer at the height of the canyon. However, the SGS variance is very small and has a negligible impact on the mean concentrations of pollutants within the canyon.

KEYWORDS:
Pollutant dispersion; Street canyon; Chemical reaction; LES; Subgrid-scale variance

1 INTRODUCTION

To address an increasing number of air quality issues, many previous studies have evaluated pollutant flow and dispersion in urban areas. Street canyons are a common component of urban areas, and numerous studies have used CFD (computational fluid dynamics) simulations to explore the fundamental characteristics of air pollutant dispersion in street canyons. Additionally, recent increases in computing power have allowed for the development of numerical simulations with high computational loads. In response, engineers and scientists have started to employ large-eddy simulations (LESs) to study the urban atmospheric environment.

Some attempts have been made to extend CFD simulations to the transport of reactive pollutants. For example, Baker et al. [1] and our group [2] have applied LESs with reaction rate models to the dispersion of reactive pollutants in urban street canyons. In these studies, the variance of pollutant concentrations was not considered at the subgrid scale (SGS), which means that the authors assumed perfect mixing of pollutants at the SGS. However, additional studies have reported the influence of the segregation of pollutants at the SGS on the reaction rate [3].

This study aims to assess the influence that the variance of the concentrations at the SGS has on the dispersion of reactive pollutants in an urban street canyon. To evaluate this system, an LES model was coupled with an SGS variance model. To confirm the performance of our model, we initially studied the dispersion of an inert pollutant in an urban street canyon. We then ap-

plied the model to the dispersion of a pollutant that undergoes a bi-molecular reaction in the canyon.

2 MODEL DESCRIPTION AND NUMERICAL METHOD

2.1 *LES model of the flow field*

We employed a one-equation model for LES proposed by Yoshizawa and Horituti [4]. The model simultaneously solves the transport equation for the kinetic energy at the SGS k_{SGS} and the filtered velocities $\bar{u}_i\ (i=1,2,3)$. The equations of the model become

$$\frac{\partial \bar{u}_i}{\partial x_i} = 0, \tag{1}$$

$$\frac{\partial \bar{u}_i}{\partial t} + \frac{\partial \bar{u}_i \bar{u}_j}{\partial x_j} = -\frac{\partial \bar{p}}{\partial x_i} + \frac{\partial}{\partial x_j}\left(-\tau_{ij} + \frac{2}{Re}\bar{D}_{ij} \right), \tag{2}$$

$$\tau_{ij} - \frac{1}{3}\delta_{ij}\tau_{kk} = -2\nu_{SGS}\bar{D}_{ij}, \tag{3}$$

$$\nu_{SGS} = C_1 \Delta k_{SGS}^{1/2}, \tag{4}$$

$$\frac{\partial k_{SGS}}{\partial t} + \frac{\partial \bar{u}_j k_{SGS}}{\partial x_j} = 2\nu_{SGS}\bar{D}_{ij}^{\,2} - C_2\frac{k_{SGS}^{3/2}}{\Delta} + \frac{\partial}{\partial x_j}\left[\left(\frac{1}{Re} + C_3 \Delta k_{SGS}^{1/2} \right)\frac{\partial k_{SGS}}{\partial x_j} \right]. \tag{5}$$

In these equations, τ_{ij} is the Reynolds stress at the SGS; D_{ij} is the strain-rate tensor; Re is the Reynolds number; ν_{SGS} is the eddy viscosity coefficient at the SGS; Δ is the grid width; and C_1, C_2 and C_3 are the model coefficients.

2.2 *SGS variance model*

The filtered mass conservation of pollutants becomes

$$\frac{\partial \bar{c}_m}{\partial t} + \frac{\partial \bar{u}_j \bar{c}_m}{\partial x_j} = \frac{\partial}{\partial x_j}\left[\left(\frac{1}{ReSc} + \frac{\nu_{SGS}}{\sigma_{tc}} \right)\frac{\partial \bar{c}_m}{\partial x_j} \right] + \bar{R}_m, \tag{6}$$

where Sc is the Schmidt number, σ_{tc} is the turbulent Schmidt number at the SGS, and R_m is the source/sink term due to the reactions.

In this study, we considered the following bi-molecular reaction:

$$c_1 + c_2 \rightarrow c_3. \tag{7}$$

Reaction rates for the reduction of c_1 and c_2 and the corresponding production of c_3, are defined as

$$\bar{R}_1 = \bar{R}_2 = -\bar{R}_3 = -D_{a1}\overline{c_1 c_2}, \tag{8}$$

where D_{a1} is the first Damköhler number. The filtered product of c_1 and c_2 can be approximated by the following equation:

$$\overline{c_1 c_2} = \bar{c}_1 \bar{c}_2 + \overline{c_1'' c_2''}, \tag{9}$$

where x" is the SGS variance of x. Following Meeder and Nieuwstadt [3], we employed the transport equation of the SGS correlation described in Equation (10). We numerically integrated it with the governing equations for the flow and the grid scale (GS) concentration fields

$$\frac{\partial \overline{c_1"c_2"}}{\partial t}+\frac{\partial \bar{u}_j \overline{c_1"c_2"}}{\partial x_j}=2\frac{\nu_{SGS}}{\sigma_{tc}}\frac{\partial \bar{c}_1}{\partial x_j}\frac{\partial \bar{c}_2}{\partial x_j}+\frac{\partial}{\partial x_j}\left[\left(\frac{1}{ReSc}+\frac{\nu_{SGS}}{\sigma_{tc}}\right)\frac{\partial \overline{c_1"c_2"}}{\partial x_j}\right]-C_4\overline{c_1"c_2"}\frac{k_{SGS}^{1/2}}{\Delta}, \tag{10}$$

where C_4 is a model coefficient.

To validate the performance of the SGS variance model, we carried out a numerical experiment to evaluate the dispersion of a sole scalar without reaction. In this case, $D_{a1} = 0$ and Equation (10) reduces to

$$\frac{\partial \overline{c"^2}}{\partial t}+\frac{\partial \bar{u}_j \overline{c"^2}}{\partial x_j}=2\frac{\nu_{SGS}}{\sigma_c}\left(\frac{\partial \bar{c}}{\partial x_j}\right)^2+\frac{\partial}{\partial x_j}\left[\left(\frac{1}{ReSc}+\frac{\nu_{SGS}}{\sigma_c}\right)\frac{\partial \overline{c"^2}}{\partial x_j}\right]-C_4\overline{c"^2}\frac{k_{SGS}^{1/2}}{\Delta}. \tag{11}$$

For this simulation, we set $c_1 = c_2 = c$.

2.3 *Computational details*

Figure 1 shows an illustration of the street canyon model with an aspect ratio of unity. It has a uniform shape along the y-axis, and the computational domain has a size of $2H$ (x) x $2H$ (y) x $2H$ (z). A line source of c or c_2 is set at the bottom of the canyon along the center. For the case involving the reactive pollutant, the inflow supplies a constant concentration of c_1 into the domain.

Periodic boundary conditions are applied for all components of the flow fields, both in the stream-wise and span-wise directions. This means that infinitely long street canyons line up continuously along the x-axis. A constant pressure difference is imposed between the inflow and outflow of the computational domain. The upwind wind direction is set to be perpendicular to the street canyon. We carried out the simulation under an isothermal condition.

Calculation conditions are listed in Table 1. The Reynolds number is approximately 1.5×10^5 and is defined with a building height of H and reference velocity of U_{upw}. We set the model constants to be $Sc = 1.0$, $\sigma_{tc} = 0.5$, $C_1 = 0.05$, $C_2 = 1.0$, $C_3 = 0.1$ [4], and $C_4 = 1/Sc$ [5]. Table 2 shows the grid resolutions used in the simulations. We used all of the resolutions for the simulations of the inert pollutant dispersion, whereas only GR32 was employed for the reactive pollutant dispersion. All of the statistics in this paper were averaged along the y-axis because of the uniform shape along the street canyon.

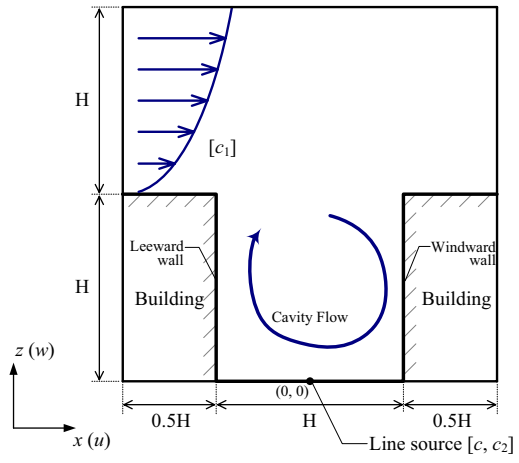

Figure 1. Schematic diagram of the analytical model.

Table 1. Calculation conditions.

Time Marching	PISO (SOR) [6]
Time Discretization	Adams-Bashforth, Crank-Nicolson (Diffusion term in GS NS equation)
Space Discretization	2nd order Central Difference, FCT scheme (Advection terms in scalar transport equations) [7]
Inflow B.C.	Vel., k_{SGS}: Periodic; Conc.: $c = 0.0$, $c_{1,\,in} = C_0$, $c_{2,\,in} = c_{3,\,in} = 0.0$; Pressure: $p_{in} = p_{out} + 1.2 \times 10^{-2} U_{upw}^{-2}$; SGS conc. variance: Constant (= 0.0)
Outflow B.C.	Vel., k_{SGS}: Periodic; Conc., SGS conc. variance: Gradient-zero
Side B.C.	Periodic
Top B.C.	Vel.: u, v = free-slip, $w = 0$; k_{SGS}, Conc., SGS conc. variance: Gradient-zero
Wall and Ground B.C.	Vel.: linear-1/7 power law; k_{SGS}, Conc., SGS conc. variance: Gradient-zero
Line Source	Conc.: Constant flux (c, c_2)

Table 2. Grid partitionings.

Case	All*	Target canyon**
GR32	64 x 32 x 48	32 x 32
GR64	128 x 64 x 96	64 x 64
GR128	256 x 128 x 192	128 x 128

*N (x) x N (y) x N (z); ** N (x) x N (z) ($z < H$)

3 RESULTS AND DISCUSSION

3.1 *Grid resolution and flow field*

We initially checked the dependency of the flow field on the grid resolution. Statistics relating to the velocities are normalized by the mean velocity at z/H = 2.0 (U_{upw}) in each case.

Figure 2 shows the profiles of the mean stream-wise velocities at three locations. An increase of grid resolution results in high wind-speeds just above the canyon, which makes the cavity eddy stronger in the high resolution case. The difference between the stream-wise velocities for GR128 and GR64 is smaller than the difference between GR64 and GR32. This means that the sensitivity of the flow field to the grid resolution becomes low at a resolution of approximately H/128.

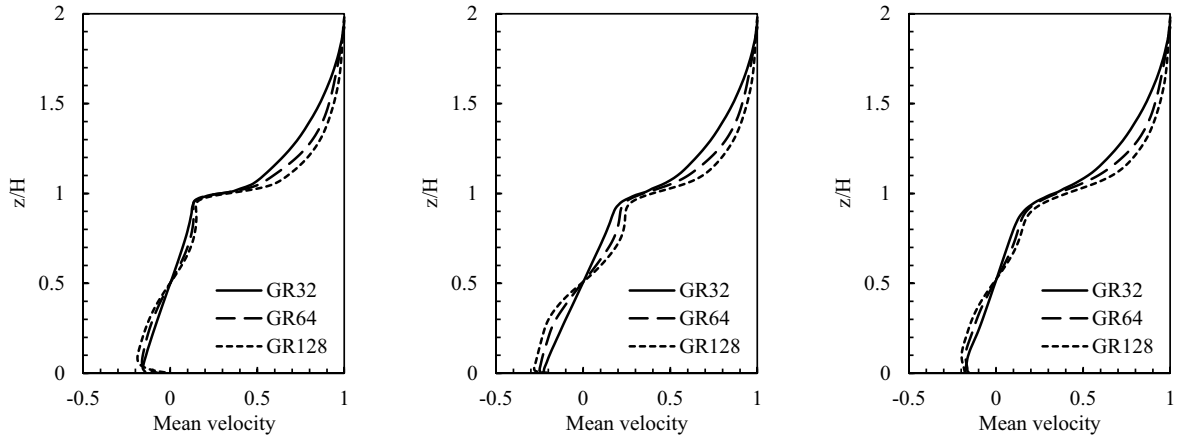

Figure 2. Mean velocity in the stream-wise direction. All variables are normalized by U_{upw}.

The higher resolution enables a larger amount of kinetic energy to be contained in the GS. Therefore, RMS (root-mean-square) values of the filtered velocities become high in GR128 and low in GR32 (Figs 3 i) and ii)). Consequently, the kinetic energy at the SGS (k_{SGS}) is the lowest in GR128 (Fig. 3 iii)).

3.2 *Grid resolution and inert scalar field*

Before accounting for the reactivity of pollutants, we conducted dispersion simulations for an inert pollutant at the three different grid resolutions. Concentrations presented in this section are normalized by C_n:

$$C_n = Q_e / U_{upw} HL, \tag{12}$$

where Q_e is the emission rate of the pollutant and L is the length of the street canyon.

Figure 4 shows the mean concentration profiles for the inert pollutant. The mean concentration is high along the lower part of leeward wall because it is in the direct downwind region of the line source. Some differences of the mean concentrations are apparent for the different grid resolutions; however, the trend of the dependency on the grid resolution is not clear compared to the flow field in the previous section.

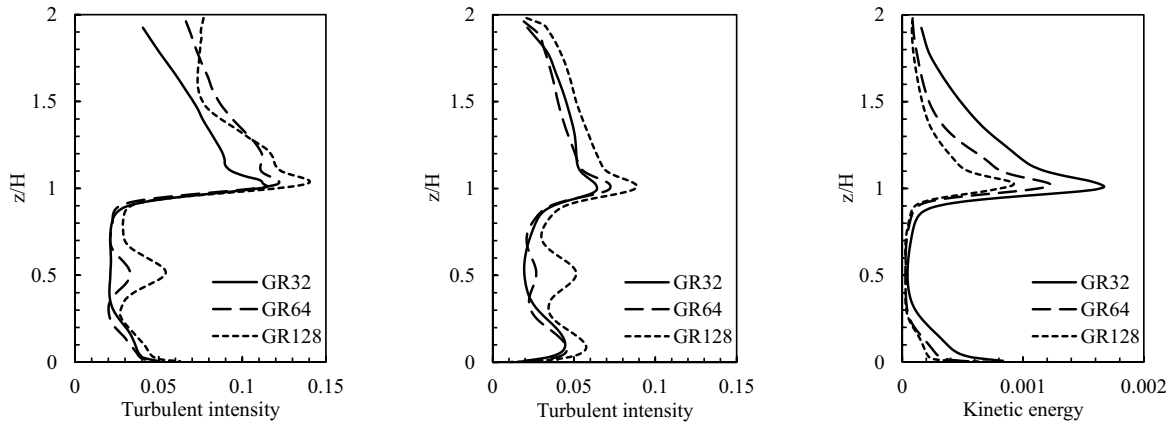

i) RMS $\overline{u}$ ii) RMS $\overline{w}$ iii) k_{SGS}

Figure 3. Turbulent intensity at the GS and kinetic energy at the SGS at x/H = 0.0 (Center). All variables are normalized by U_{upw}.

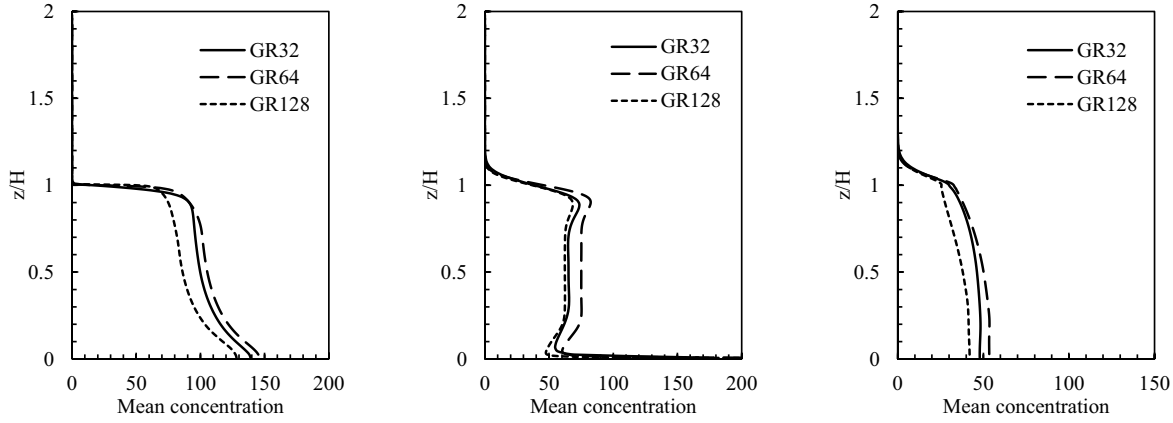

i) x/H = -0.5 (Leeward wall) ii) x/H = 0.0 (Center) iii) x/H = 0.5 (Windward wall)

Figure 4. Mean concentration normalized by C_n.

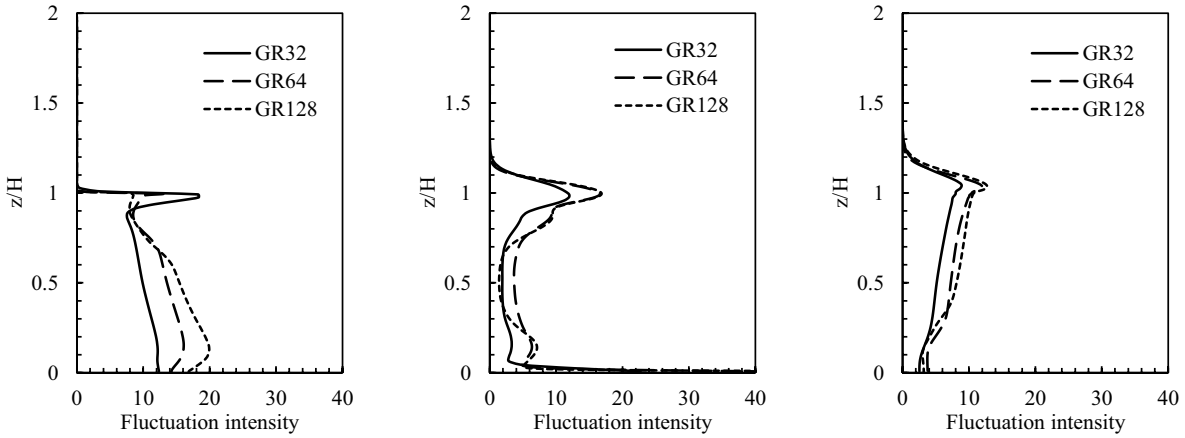

i) x/H = -0.5 (Leeward wall) ii) x/H = 0.0 (Center) iii) x/H = 0.5 (Windward wall)

Figure 5. Concentration fluctuation intensity at the GS ($\sigma_{c,GS}$) normalized by C_n.

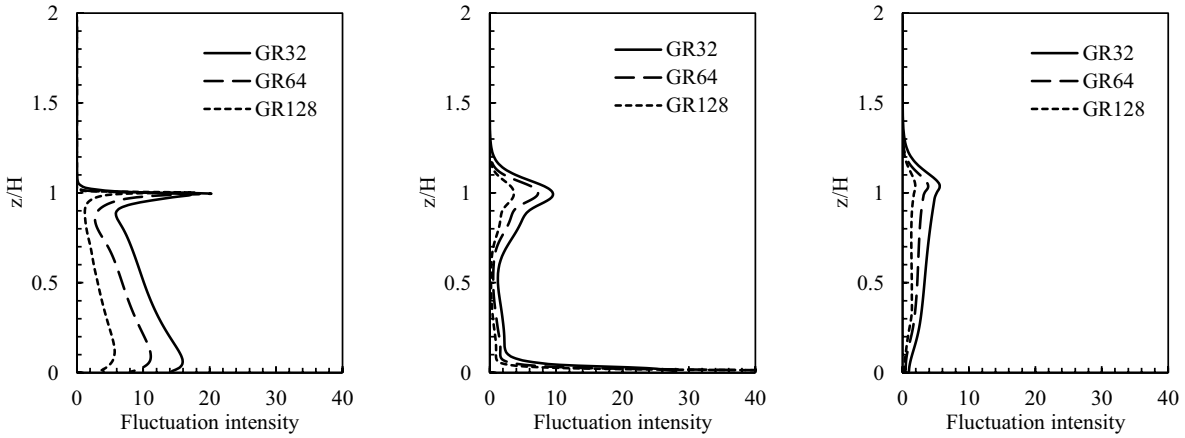

i) x/H = -0.5 (Leeward wall) ii) x/H = 0.0 (Center) iii) x/H = 0.5 (Windward wall)

Figure 6. Concentration fluctuation intensity at the SGS ($\sigma_{c,SGS}$) normalized by C_n.

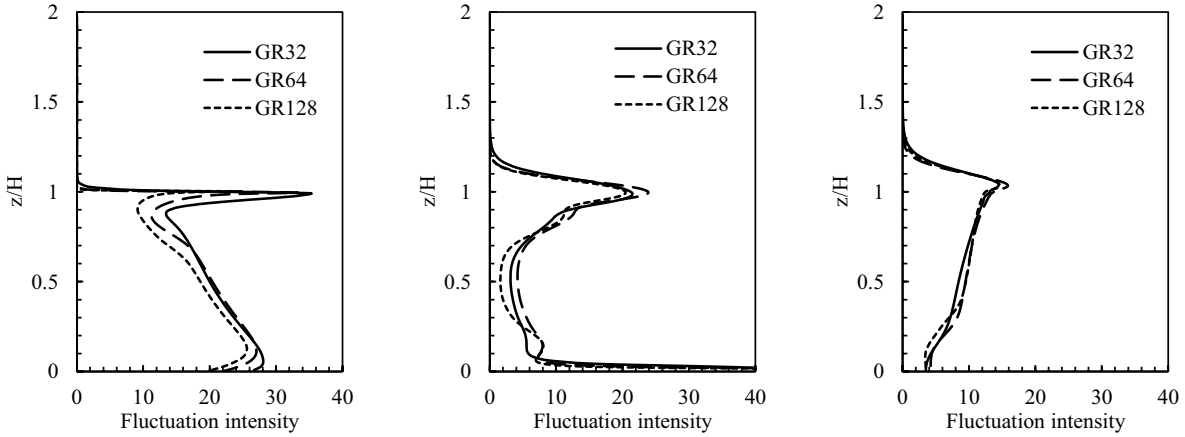

i) x/H = -0.5 (Leeward wall) ii) x/H = 0.0 (Center) iii) x/H = 0.5 (Windward wall)

Figure 7. Total concentration fluctuation intensity at the GS and SGS normalized by C_n.

Figures 5 and 6 show the concentration fluctuation intensities at the GS $\sigma_{c,GS}$ and SGS $\sigma_{c,SGS}$, respectively. Here, $\sigma_{c,GS}$ is the RMS of the filtered concentration, and $\sigma_{c,SGS}$ is the mean value of $\overline{c''^2}^{1/2}$. The higher resolution also makes it possible to have more concentration fluctuation energy at the GS. Therefore, $\sigma_{c,GS}$ is highest in GR128 and lowest in GR32, and $\sigma_{c,SGS}$ shows the opposite behavior. Additionally, $\sigma_{c,SGS}$ is greater than $\sigma_{c,GS}$ on the leeward wall for GR32 because the region is near the line source.

We defined the total fluctuation intensity of the concentration σ_c as the sum of $\sigma_{c,GS}$ and $\sigma_{c,SGS}$. Although some discrepancies remain near the top of the leeward wall, Figure 7 shows that σ_c becomes comparable for the three grid resolutions. This means that our SGS variance model worked well to evaluate the variance of the concentration field at the SGS.

3.3 *Influence of SGS variance on the dispersion of reactive pollutants*

To evaluate the effect of the reaction between c_1 and c_2, we compared two different cases. The first case accounts for the SGS correlation of c_1 and c_2 to calculate the reaction rates using Equation (10), and the second case neglects it. Concentrations are normalized by C_0, or the concentration of c_1 in the inflow. D_{a1} has a value of approximately 1.3, and it is defined using U_{upw}, H and C_0. This value of D_{a1} agrees well with the actual values reported for the reaction between ozone and nitrogen monoxide in urban canyons [2]. The results described in the previous sections demonstrate that sensitivity to the grid resolution remains high for GR32. However, we elected to use this resolution for this portion of the study because we expected that the influence of the SGS variance model would be largest in the case of the lowest resolution.

Figure 8 shows the distributions of the mean concentrations of c_1 and c_2 for the case that includes the SGS variance model. As the reaction proceeds, the concentrations of c_1 and c_2 are reduced in the canyon (Eq. (7)).

The presence or absence of the SGS variance model resulted in small differences between the mean concentrations, as shown in Figure 9. This is because the contribution of the SGS correlation to the reaction rate is very small relative to the product of the filtered concentrations (Eq. (9)). Figure 10 shows that the SGS correlation becomes large at a value of approximately z/H = 1.0 due to the strong mixing of c_1 and c_2. However, the correlation is a small percentage of the product of the filtered concentrations in most regions in the canyon.

4 CONCLUSIONS

To study the dispersion of both inert and reactive pollutants in an urban street canyon, we used LESs that were coupled with an SGS variance model. The model solves the transport equations of the variance or the correlation of pollutants at the SGS with the equations of the filtered concentrations.

First, we validated the performance of the model by evaluating the concentration fluctuations at the SGS for changing grid resolutions. Three resolutions of averaged grid widths (H/32, H/64 and H/128) were employed, where H is the height of the canyon. The concentration fluctuation intensity at the GS was small for the coarse grid case. This was due to the expansion of the filtering width. However, the SGS variance model could estimate the variance lost in the filtering operation. From this result, we concluded that the model could reliably calculate the SGS variance of the concentrations.

Second, we investigated the effect of the SGS variance of concentrations on dispersion for the case of bi-molecular reactions. We carried out simulations at a grid resolution of H/32 and either included or excluded the SGS variance model. The correlations of concentration variations at the SGS of reactive pollutants became relatively large at the height of the canyon. This was because

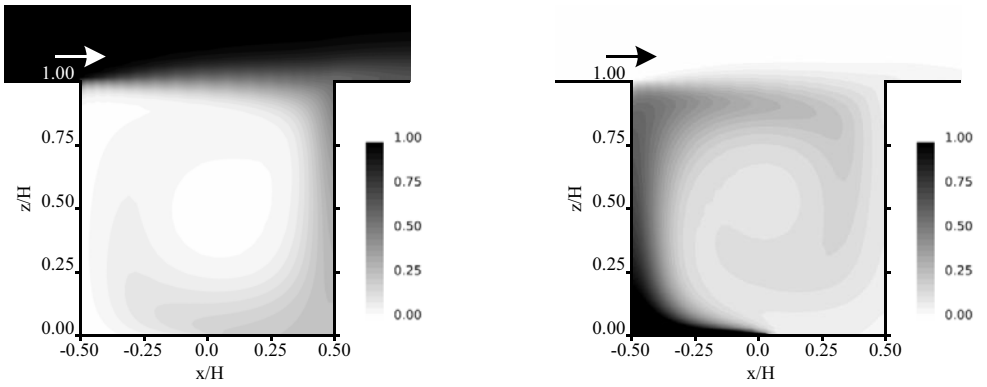

i) c_1 ii) c_2

Figure 8. Distributions of the mean concentration of reactive pollutants for the case which accounts for the correlation of c_1 and c_2 at the SGS. These concentrations are normalized by C_0.

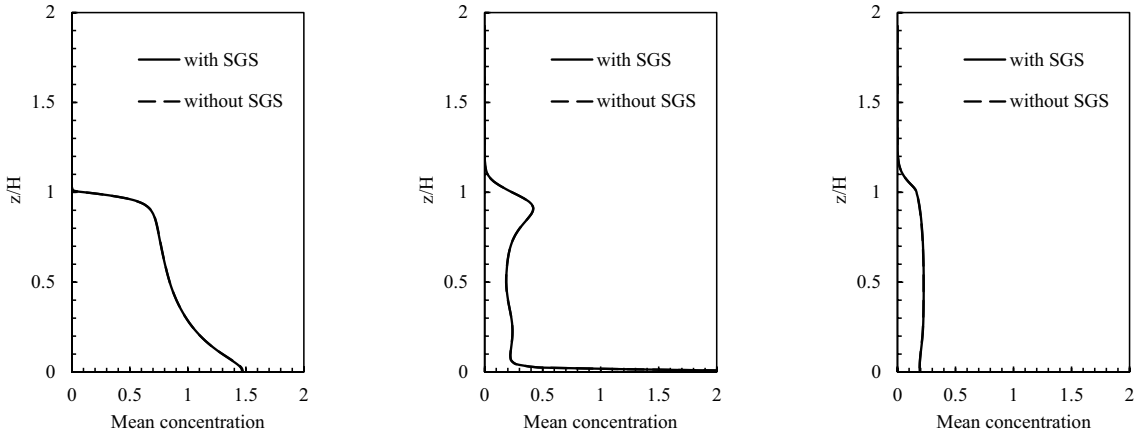

i) x/H = -0.5 (Leeward wall) ii) x/H = 0.0 (Center) iii) x/H = 0.5 (Windward wall)

Figure 9. Comparison of the mean value of c_2 between two cases with and without the SGS variance model. The concentrations are normalized by C_n.

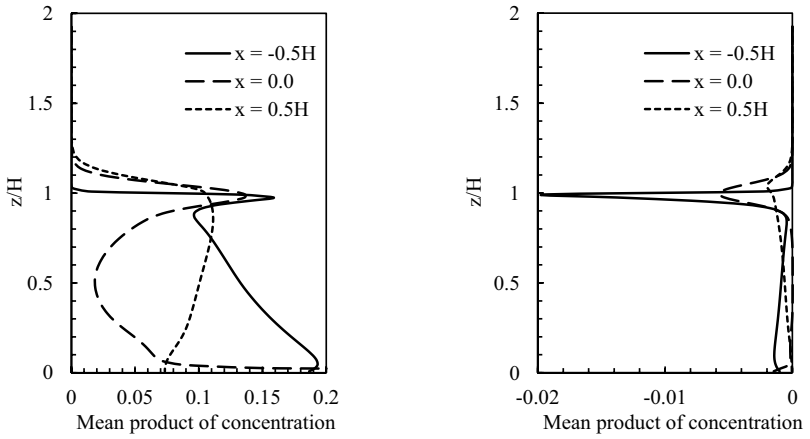

i) $\langle \bar{c}_1 \bar{c}_2 \rangle$ ii) $\langle \overline{c_1" c_2"} \rangle$

Figure 10. Mean product of the reactive pollutant concentrations in the GS and the SGS normalized by C_0.

the two pollutants (one came from above the canyon and the other from inside the canyon) were well mixed by the turbulence at this location. However, we found that the SGS variance was too small to make a significant difference in the mean concentrations of pollutants in the canyon.

REFERENCES

1 J. Baker, H.L. Walker and X. Cai, A study of the dispersion and transport of reactive pollutants in and above street canyons – a large eddy simulation, Atmospheric Environment 38 (2004) 6883-6892.
2 H. Kikumoto and R. Ooka, A study on air pollutant dispersion with bimolecular reactions in urban street canyons using large-eddy simulations, Journal of Wind Engineering and Industrial Aerodynamics (2012), doi:10.1016/j.jweia.2012.03.001.
3 J.P. Meeder and F.T.M. Nieuwstadt, Large-eddy simulation of the turbulent dispersion of a reactive plume from a point source into a neutral atmospheric boundary layer, Atmospheric Environment 34 (2000) 3563-3573.
4 A. Yoshizawa and K. Horiuti, A Statistically-Derived Subgrid-Scale Kinetic Energy Model for the Large-Eddy Simulation of Turbulent Flows, Journal of the Physical Society of Japan 54 (1985) 2834-2839.
5 C. Jimenez, F. Ducros, B. Cuenot and B. Bedat, Subgrid scale variance and dissipation of a scalar field in large eddy simulations, Physics of Fluids 13 (2001) 1748-1754.
6 R.I. Issa, Solution of the implicitly discretised fluid flow equations by operator-splitting, Journal of Computational Physics 62 (1986) 40-65.
7 S.T. Zalesak, Fully multidimensional flux-corrected transport algorithms for fluids, Journal of Computational Physics 31 (1979) 335-362.

The Seventh International Colloquium on Bluff Body Aerodynamics and Applications (BBAA7)
Shanghai, China; September 2-6, 2012

CFD modelling of flow and dispersion in the built environment: different RANS models and a first attempt to use URANS

M. Chavez [a], T. Stathopoulos [a], A. Bahloul [b]

[a]*Department of Building, Civil and Environmental Engineering, Concordia University,Montreal, Canada*
[b]*Institut de recherche Robert-Sauvé en santé et en sécurité du travail, Montreal, Canada*
**Corresponding email: mau_chav@encs.concordia.ca*

ABSTRACT: Air pollution is a global phenomenon which has been the subject of study for several years. Pollutants released from rooftop stacks have a tendency to re-enter the same building or an adjacent building in the near vicinity. Complexities in airflow and pollutant transport due to terrain conditions, local topography and buildings make it very difficult to assess plume concentrations. This paper will analyse the role of the unsteady flow and its influence on pollutant dispersion. The effect of a building located upstream to an emitting building which has a roof stack, will be tested in a boundary layer wind tunnel and compared with computational fluid dynamics simulation (CFD). The most used approach for turbulent flow simulation is the Reynolds-averaged Navier-Stokes (RANS) equations. However, it was confirmed that important inaccuracies for dispersion prediction especially in the near-field of an emitting building are usually obtained by RANS. The reason is attributed to the RANS incapability to capture the inherent unsteadiness of flow in the wake of buildings. The influence of different turbulence models was evaluated but no clear improvement to compensate the mentioned inaccuracy was noticed. The effect of unsteady RANS (URANS) was also analyzed in an exploratory way.

KEYWORDS: CFD, Dispersion; Multiple buildings; Pollutants re-ingestion; Schmidt number; Wind tunnel.

1. Introduction

Air pollution is a global phenomenon which has been the subject of study for several years. Complexities in airflow and pollutant transport due to terrain conditions, local topography and buildings make it very difficult to assess plume concentrations (Saathoff et al., 2009). In the built environment increasing exhaust emissions from institutional, industrial buildings and vehicular traffic are inevitable. Toxic and odorous emissions affecting the urban environment and degrading human health are present in every city. One on the most common urban pollution phenomenon is associated with contaminants released from rooftop stacks. Depending on the average airflow, the turbulence of flow and the building-generated turbulence, pollutants can be trapped in recirculation zones and affect sensitive areas as, for example, fresh air intakes. This closed circuit path is known as re-ingestion of pollutants.

In the past, studies performed by Wilson et al., 1998 and Stathopoulos et al., 2008 showed that the presence of a taller upstream building produces higher concentrations on the rooftop of the emitting building. Currently, ASHRAE 2007 gives guidelines for determining plume dilutions for an isolated building without considering the effects of adjacent buildings and local turbulence. Studies performed by Hajra et al., 2010 have shown that ASHRAE 2007 predicts rather unrealistic and overly conservative dilutions. More recently, CFD has been a useful tool in as-

sessing plume dilutions in the built environment. However, CFD simulations require validations with field and wind tunnel measurements.
This paper presents wind tunnel data for tracer gas released from rooftop stack 0.005 m height (full scale equivalent to 1 m) and exhaust momentum ratio M = 1.7. The spacing between the buildings, for a two-building configuration, was fixed to 0.1 m (20 m) and the stack location placed in the middle of the symmetry plan on the roof of downstream building. Results are compared to CFD simulations using different turbulence models.

2. Wind tunnel simulation of building exhaust and dispersion

The wind tunnel experiments were carried out in the open circuit boundary layer wind tunnel at Concordia University, Montreal, Canada. The wind tunnel is 1.8 m by 1.8 m in cross-section and 12.2 m in length. The buildings tested in the wind tunnel were made of timber on a 1:200 scale. According to Snyder, 1981 while modelling non-buoyant plume exhaust, certain criteria should be satisfied:

· Geometric similarity
· Building Reynolds Number > 11.000
· Stack Reynolds Number > 2.000
· Similarity of wind tunnel flow with atmospheric surface layer
· Equivalent stack momentum ratio.

Tracer gas consisting of a mixture of Sulphur hexafluoride (SF_6) and Nitrogen was released from a roof stack of an emitting building named B1. A multi-syringe pump was used to collect the gas samples to determine the concentration of effluents at various receptors with a sampling time of 2 minutes. A Gas Chromatograph (GC) was used to assess the gas concentrations that were collected using syringe samplers. The velocity at building height was measured to be 6.2 m/s in the wind tunnel. The buildings were considered to be in an urban terrain with a power law exponent of 0.31 (Simiu and Scanlan, 1996). Additional details on the experimental conditions used in this study are described in Stathopoulos et al., 2008.

The pollutant dispersion was evaluated in terms of normalized dilution following the formulation suggested by Wilson (1979):

$$D_N = (D_r Q)/(U_H H^2) \quad (1)$$

where $D_r = C_e / C_r$ is the dimensionless concentration coefficient at the coordinate location (receptor), C_e = contaminant mass fraction in exhaust (ppm), C_r = contaminant mass fraction at the coordinate location (ppm), Q is the flow rate at the exhaust (m^3/s), H is the B1 height (H=0.075 m) and U_H the wind speed at the B1 height. The momentum ratio at the stack outflow is $M=V_e/U_H = 1.7$ (where V_e is the exhaust velocity). Receptors for concentration measurements were distributed on the roof of the emitting building along and across wind direction, as shown in Figure 1.

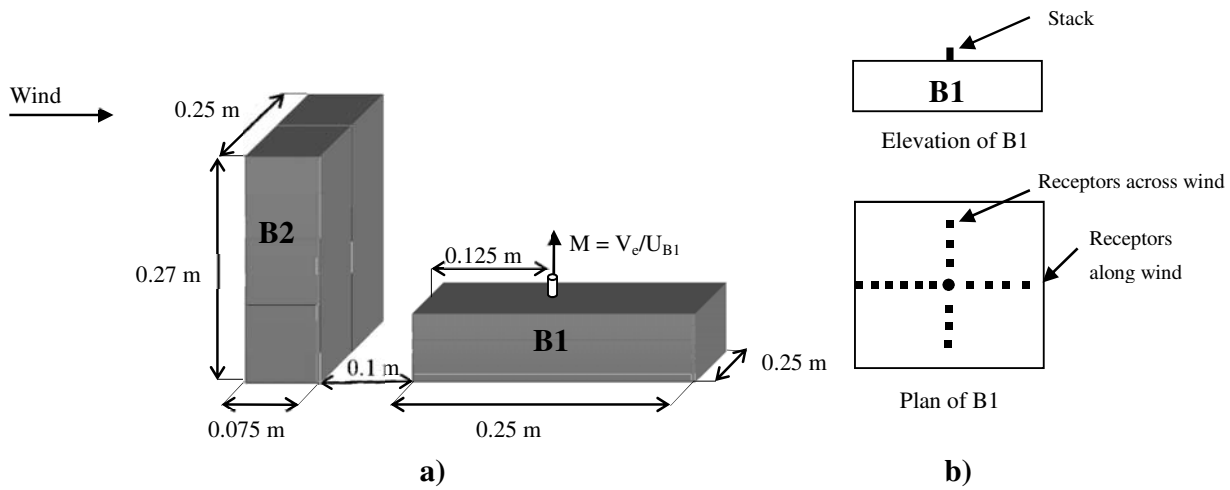

Figure 1: a) Schematic representation of an emitting builng (B1) with an upstream building (B2). b) Location of receptors on roof of the emitting building.

Figure 2 shows the profiles of mean velocity (a) and turbulence intensity quantities (b) measured at the wind tunnel. These profiles will be used to specify the inlet condition in the numerical model. The mean velocity profile was approximated by power law exponent of 0.31, which corresponds to an urban terrain. The velocity at the building B1 height (H = 0.075 m) was $U_H = 6.2$ m/s.

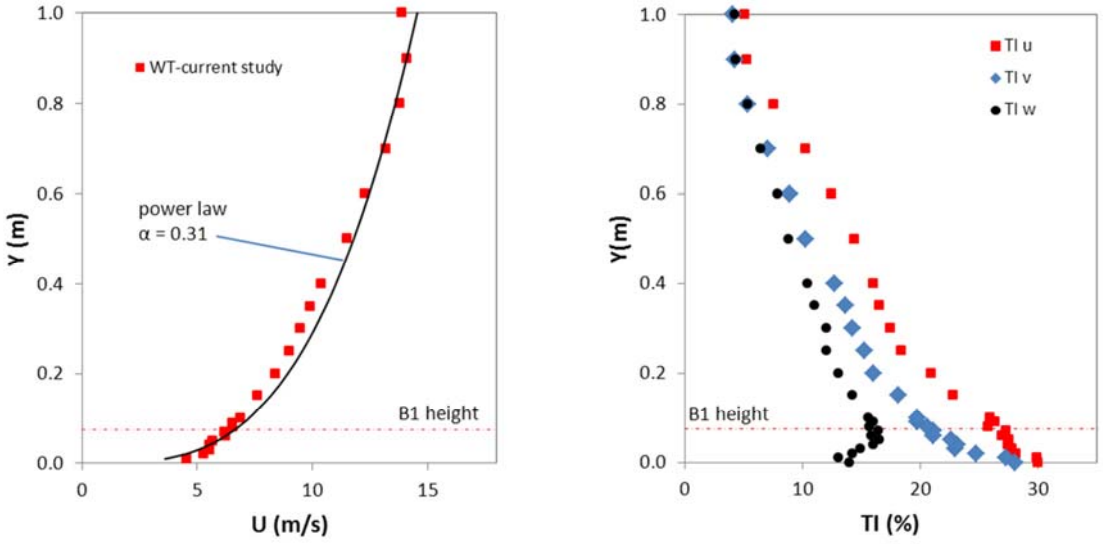

Figure 2. Atmospheric boundary layer profiles from wind tunnel. a) mean velocity b) turbulence intensity

The measured turbulence intensity profiles are converted in a turbulent kinetic energy (k) profile using two approaches. Option-1: k is calculated from turbulent intensity measurements in the wind tunnel considering the three components of fluctuating velocities $\langle u' \rangle, \langle v' \rangle$ and $\langle w' \rangle$ assuming $\langle u' \rangle = TI_u U/100$. Option-2: k is calculated assuming isotropic turbulence and only x component, $\langle u' \rangle$, of the measured component is used (van Hooff and Blocken, 2010). In order to

specify these profiles in the numerical model, a function of height (Y(m)) k defined as polynomial of degree 5 was developed for each option. The impact of this difference will be evaluated in the next section. The two options of k are as follows:

Option 1: $k = \frac{1}{2}(\langle u' \rangle^2 + \langle v' \rangle^2 + \langle w' \rangle^2)$ (2)

Option 2: $k = \frac{3}{2}\langle u' \rangle^2$ (3)

As shown in Figure 3 option-2 presents a relatively high value of k in the low level of the boundary layer, as compared with option-1. The dissipation rate profile (ε) was defined as $\varepsilon = u^{*3}/\kappa y$ where κ is the von Karman constant (0.42) and u* is the friction velocity obtained from the equation $u(y)/u^* = 1/\kappa(\ln(y/y_o)$ with roughness length $y_o = 0.0033$ m. At the model scale of 1:200, the equivalent full-scale roughness length is 0.66 m, which is at the low end of the expected range for an urban environment ($0.5 \text{ m} < y_o < 1.5$ m) (Stathopoulos et al. 2004).

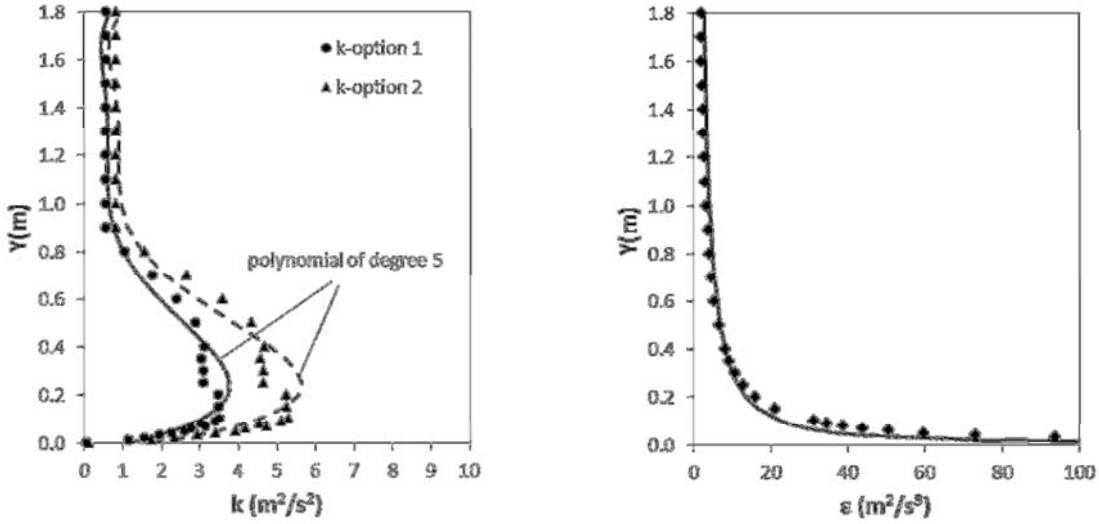

Figure 3. Turbulence kinetic energy and dissipation profiles evaluated from wind tunnel data.

3. CFD simulations

3.1 Description of cases considered

Dispersion was evaluated using two cases: an isolated emitting building (B1) and a two building configuration (B2 upstream of B1). A schematic representation of the latter was presented in Figure 1. The dimensions of each building used are provided in Table 1.

Table 1. Building models for CFD and wind tunnel experiments

Building	Height (m)	Width (m)	Length (m)
B1	0.075 (15)	0.25 (50)	0.25 (50)
B2	0.27 (54)	0.25 (50)	0.075 (15)

NB: Width refers to across wind dimension

3.2 Computational model and boundary conditions

The numerical model was constructed principally using structured hexahedra grids since it has been proved that this mesh style provides the best computational results (Hefny and Ooka, 2009). Due to the circular section of the stack an unstructured wedge grid was used in its vicinity. Three meshes were tested: mesh 1, 2 and 3 with 885,044, 2,388,057 and 3,398,121 cells respectively. The near wall region was modeled using the semi-empirical formulation called "wall function" which requires a y^+ between 30 and 300 (Fluent, 2006). Figure 4 shows dilution comparisons obtained by the three meshes. No difference in dilution at the roof level of B1 was detected using mesh 2 and 3. In consequence, mesh 2 was selected to continue the study. The inlet profile of turbulence intensity, k, was tested using the two options shown previously. Figure 5 shows no relevant impact on the dilution values at the roof level of B1. Therefore, option-1 was used in this study since it provides more physically correct prediction of k.

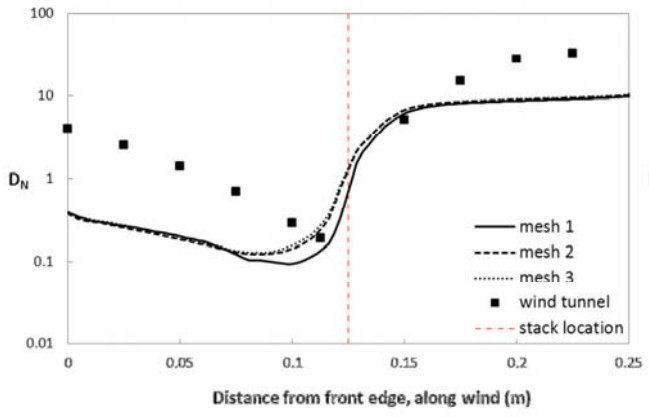

Figure 4. Effect of mesh on D_N

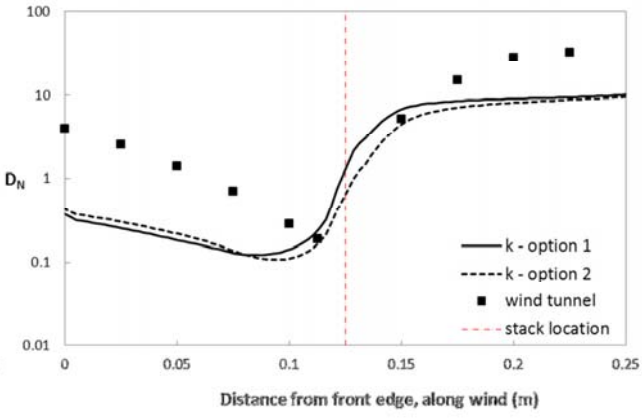

Figure 5. Effect of turbulence intensity profile on D_N

The bottom surface (i.e ground) is specified as a rigid plane with an aerodynamic roughness length y_o defined previously. In Fluent this roughness length is implemented by the sand-grain roughness height k_s (m) which can be defined using the function developed by Blocken et al. (2007): $k_s = 9.793y_o/Cs$, where Cs is a roughness constant. Considering the default value of Cs equal to 0.5, k_s should be specified as 0.0646 m. However, this value is limited to the distance z_p of the centroid of the first cell to the bottom domain (e.g $z_p = 0.00187$ m) as imposed by Fluent. The effect of this limitation is translated as streamwise changes in the inlet vertical profile. However, these effects are minimized considering the significant turbulence induced by the upstream building.

Top and sides of the domain were modelled as no slip walls in order to respect the wind tunnel conditions. At the outlet an outflow (zero gradient) condition was specified, to generate a fully-developed flow.

Turbulent Schmidt number (Sc_t) is necessary to solve the transport mass equation in CFD prediction of dispersion with RANS and is defined as the ratio of turbulent momentum diffusivity (eddy viscosity) to the turbulent mass diffusivity ($Sc_t=\nu_t/D_t$). In Fluent Sc_t must be declared as an input before any calculation or else the default value is 0.7. Past studies have shown the depend-

ence of Sc_t on simulation of pollutant dispersion from isolated buildings (Tominaga and Stathopoulos, 2007; Chavez et al., 2011) and hence the present work pays special attention to Sc_t values.

4. Results and discussion

This section has three parts:
1. Dilution prediction at the roof of B1 using RANS when it is isolated.
2. Dilution prediction at the roof of B1 using RANS when a tall building (B2) is placed upstream of B1.
3. Flow simulation for a single cube in a fully developed channel flow. This simulation was inspired on the work carried out by Iaccarino et al. (2003) and is presented in this study to confirm that it is possible to capture the vortex shedding in the wake of buildings using unsteady RANS (URANS).

In the following subsections, different turbulence models will be evaluated in order to compare their performance for dispersion prediction in the near-field of a source.

4.1 B1 isolated

Firstly a flow and dispersion around an isolated building with a roof stack (B1) was performed. The results were compared with experimental data obtained by the authors for an identical configuration. The computations were carried out using different turbulence models: the standard k-ε (std), the standard k-ε with modified constants proposed by Yan et al. (2009) (std-modified), the realizable k-ε using two turbulent Schmidt numbers, Sct = 0,1 and 0,3 (rlz-sct = 0.1, rlz-sc t = 0,3), the renormalization group (rng) and the Reynolds stress-model (rsm).

Figure 6 a) and b) compares the dilution values streamwise and spanwise from the roof stack of B1. Firstly, it is observed that in general no significant difference on dilution values among all turbulence models tested is registered. Thus, for this case, no clear statement can be made against or for a particular turbulence model. The computed dilutions are similar very near the stack but are mostly underestimated downstream the stack and overestimated upstream the stack. Clearly the computed values become completely out of range near the windward edge. This indicates that practically no species is trapped in the front edge recirculation zone, as it seems to happen with the experimental results. In the crosswind plotting line, dilution is also overestimated by all turbulence models. Only the rlz turbulence model when using Sc_t different from the default value (0.7) shows relatively better results, especially downstream the stack and in the crosswind direction where $Sc_t = 0.3$ seems to be appropriated. It is interesting to notice that upstream the stack a low Sc_t tries to correct the predicted dilution by reducing diffusion of species whereas downstream the stack a low Sc_t increase diffusion. This is exactly what it is needed to improve the agreement with experimental data; however calibration of numerical dispersion simulations using different Sc_t cannot be generalized because it is highly case dependent. The effect of reducing Sc_t for dispersion when using RANS has already been presented in various previous publications (Di Sabatino et al. 2007; Tominaga and Stathopoulos, 2007; Blocken et al. 2008; Chavez et al. 2011).

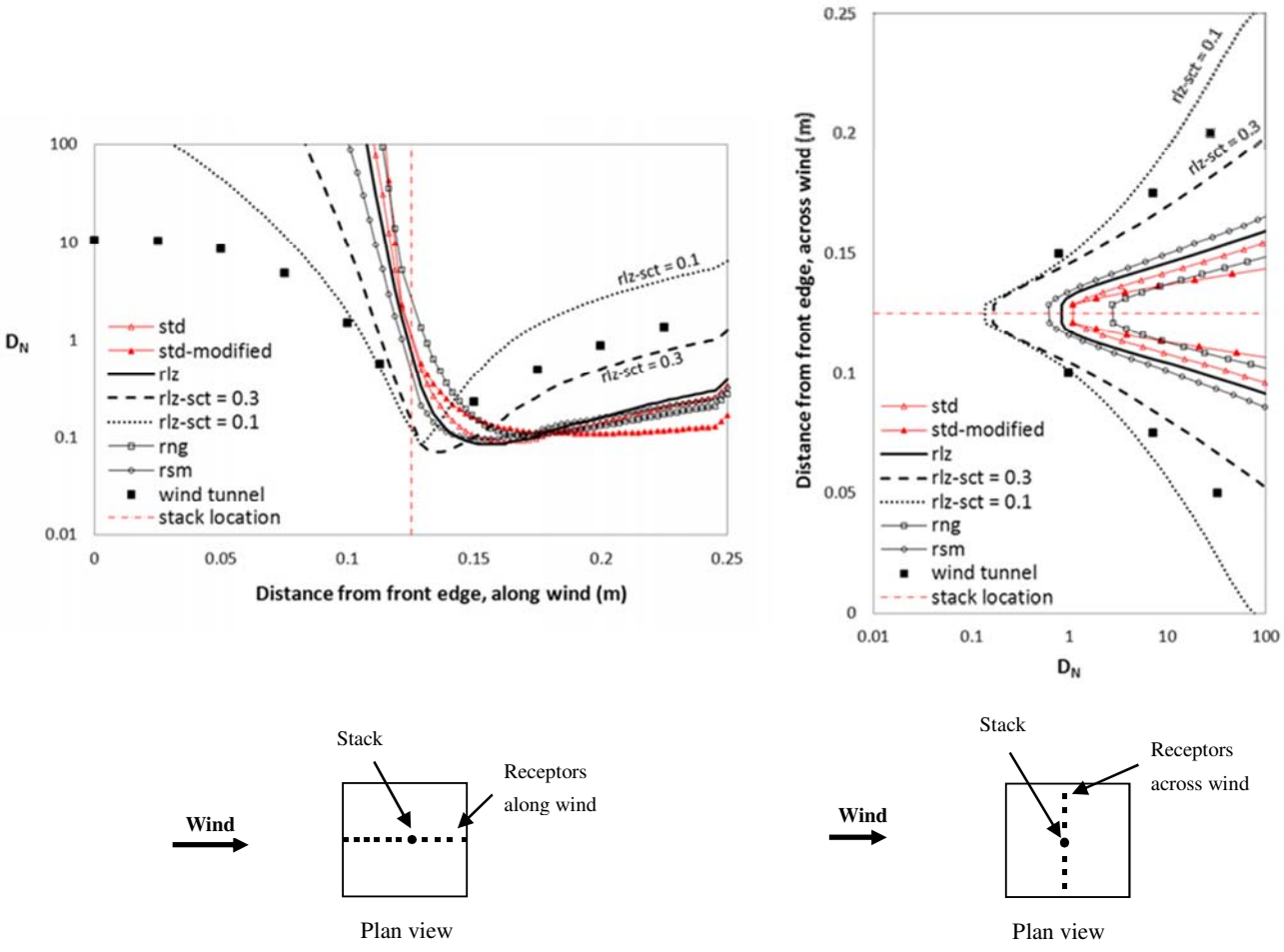

Figure 6: Steady simulations for an isolated building (B1) using different turbulence models. Dilution values at roof level a) along direction b) across wind direction.

4.2 B1 with an upstream building (B2)

The present case considers the emitting building B1 with an adjacent building (B2) placed upstream. The streamwise and spanwise distribution of dilution at the roof of B1 is presented in Figure 7 a) and b). Observing only the experimental results, and comparing with the isolated case, it can be seen that the presence of the upstream building changes significantly the dilution field in the near field. Downstream the stack the values of dilution increase almost two orders of magnitude and upstream the stack dilution decrease less than one order of magnitude. Dilution distribution spanwise from the stack also change and relatively low values are registered when B2 is added. This shows that the velocity field, which is characterized by a predominant upwind flow, tends to trap the species between the two buildings instead of dragging them downstream with the mean stream. This was also observed in previous cases (e.g. Chavez et al. 2012).

In terms of computed dilution values, similarly to the isolated case, no significant differences are registered among the turbulence models tested. In general, the computed dilution values have

better agreement downstream the stack but it remains significantly underestimated upstream the stack. The specification of a low Sc_t value produces an interesting improvement in terms of predicted values upstream the stack; however it has a very little effect downstream the stack. It is observed that along the crosswind plotting line Sc_t = 0.1 and 0.3 present practically same results on dilution values.

The discrepancies found on dilution values at roof level of B1, when B2 is placed upstream are probably due to the inherent fluctuations in the wake of B2, which are not detected by RANS as mentioned by Tominaga and Stathopoulos (2009). These fluctuations are characterized by unsteady vortical structures which interact with each other and with the surroundings playing a fundamental roll in the transport mechanism of pollutants. Consequently, steady RANS will reproduce poor prediction accuracy of dilution in regions where mixing is caused by the advection of generated eddies into the wake.

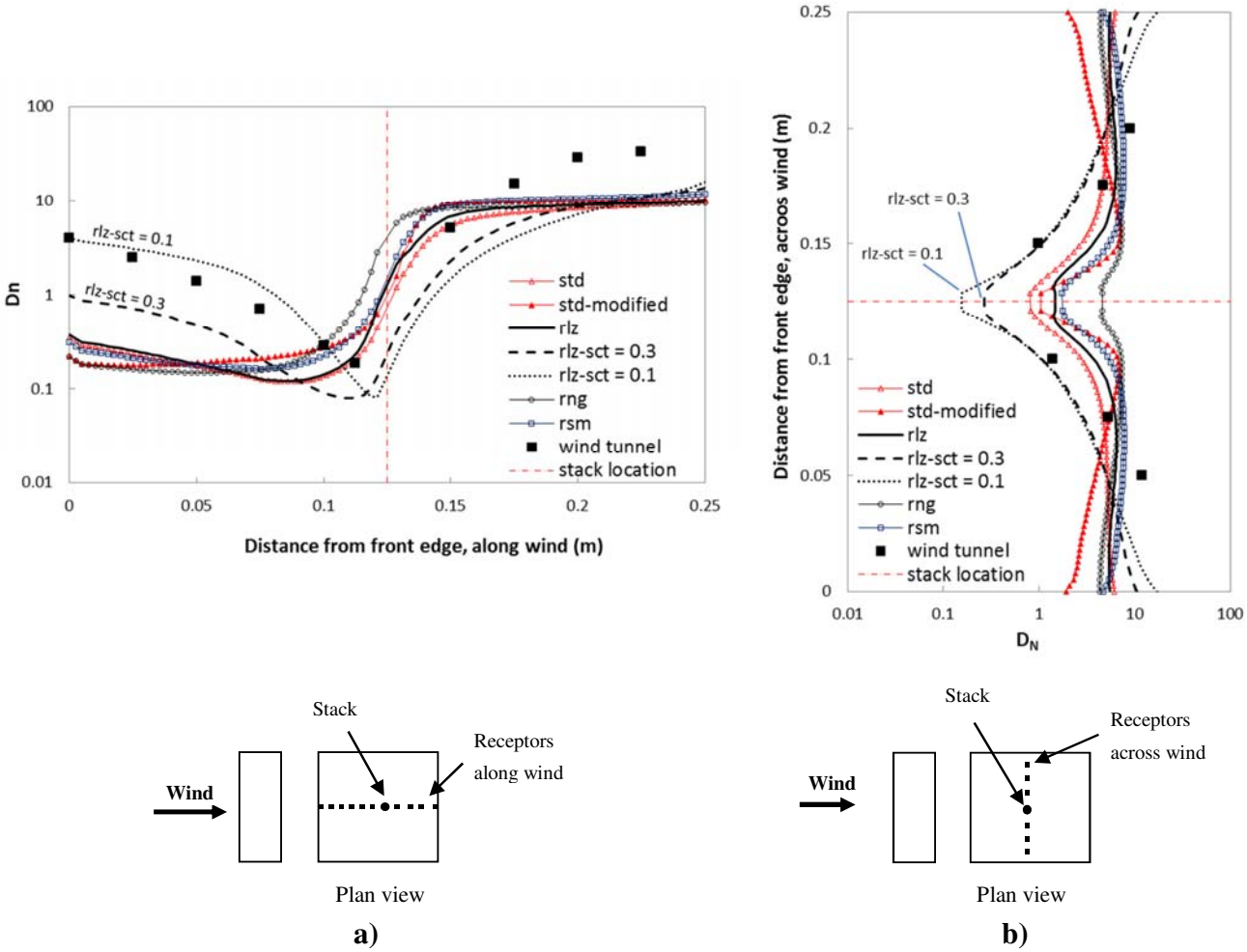

Figure 7. Normalized dilution at roof level of an emitting building with an upstream building. a) along wind b) across wind

4.3 URANS simulation

To gain insight into the numerical modelling of flow around bluff bodies using the unsteady RANS approach (URANS), a basic literature case represented by a cube in a channel flow was

reproduced and analyzed. One of the well-known experimental results for such idealized problem is that developed and documented by Hussein and Martinuzzi (1996).
The model corresponds to a surface-mounted cube (0.25x0.25x0.25 m) in a fully-developed channel flow. The dimensions of the channel were specified as 10h x 7h and 2h height, where h is the height of the cube (0.25 m). The inlet conditions correspond to a fully developed channel velocity profile as the measured by Hussein and Martinuzzi (1996). The channel walls were specified as walls with no slip condition. The grid was built using hexahedral elements only with strong clustering close to the walls to capture the near-wall turbulent regions. The y+ for all walls was kept below 4 in order to apply the "enhanced wall treatment" available in Fluent (Fluent, 2006). Initially, a very large time step was specified until convergence condition (10^{-5}) was reached. Then a very small time step (t = 10^{-3}s) combined with a small unsymmetric perturbation in the velocity field was imposed to perform the simulation. The latter condition is suggested to "trigger" the unsteadiness, since otherwise the symmetric geometry and flow would not allow the formation of vortices (Iaccarino et al. 2003).

Figure 8 shows the existence of unsteadiness in the wake of the cube. Four instances within T, which is the time period for a complete cycle of vortex generation, are presented as streamlines at the cube half height. The side-to-side oscillations of flow are characterised by vortical structures interacting with each other within the wake of the cube but with a limited time life because they vanish after detaching. These results support the idea that URANS can capture coherent vortex shedding that occur in a flow around cubic obstacles.

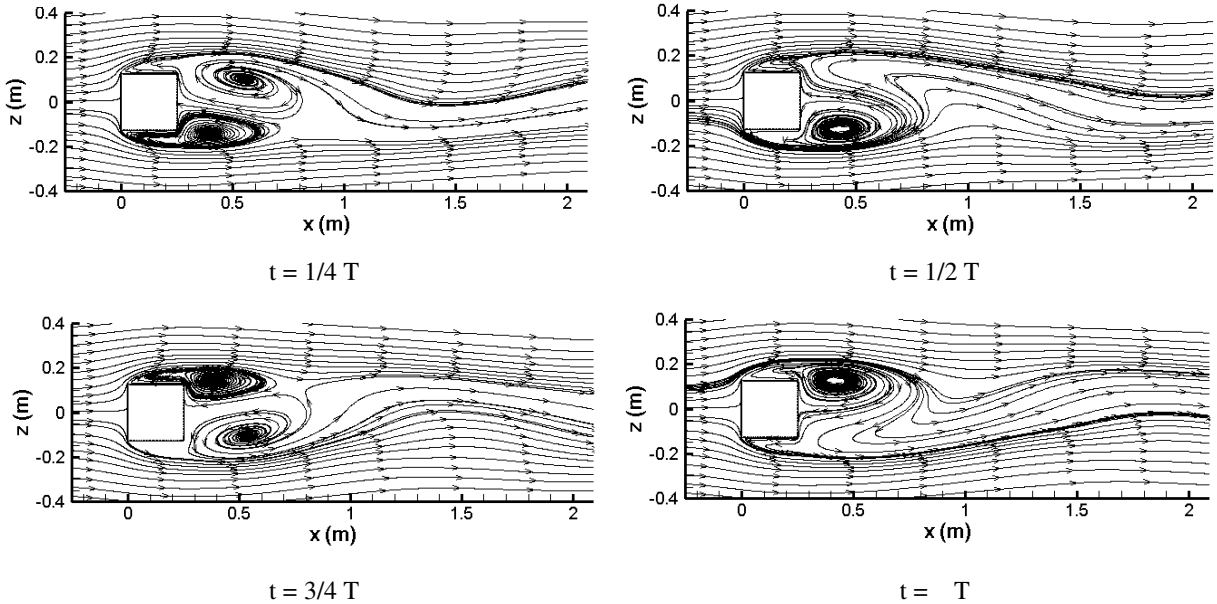

Figure 8. Planview of streamlines for a flow around a cube using URANS approach.

Figure 9 a) and b) shows the distribution of velocity Ux (streamwise) and Uz (spanwise) in the wake of the cube. Practically no change is experienced with either steady or unsteady simulation for Ux. On the other hand, an oscillation is noticed for Uz within the wake of the cube, as expected. These fluctuating velocities, which are not captured by steady RANS simulation, probably explain the inaccuracy experienced in preceding comparisons. The next step of this study is

to apply same methodology as it was carried for the cube but for the two-building configuration. It is expected to find significant flow unsteadiness, which could explain the underestimation of dilution registered using RANS.

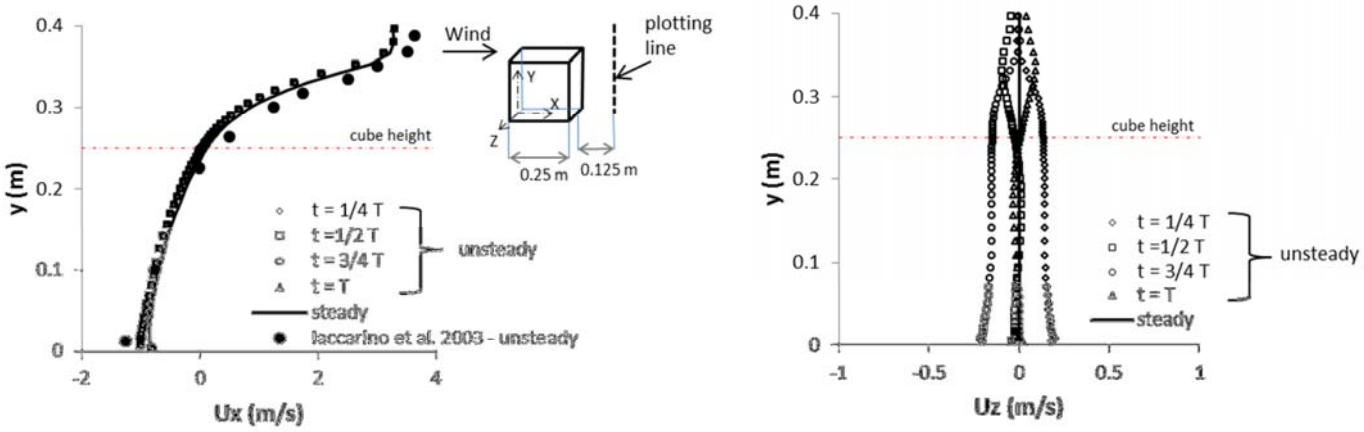

a) **b)**

Figure 9. Velocity profile within the wake of the cube. a) Ux m/s (streamwise). b) Uz m/s (spanwise)

5.- Conclusions

This work has investigated the distribution of dilution of pollutants at roof level of an emitting building. Two cases were considered: the emitting building as isolated and with a taller upstream building. Comparisons between wind tunnel data and CFD simulations confirmed that in general RANS underestimate dilution in the near field of a source in both cases. For the isolated building case dilution prediction is characterized by an overestimation upstream the stack and an underestimation downstream the stack. It was confirmed that low values of Sc_t can partly compensate the mentioned inaccuracy by increasing species diffusion upstream and in the lateral direction. For the two-building configuration, dilution is generally underestimated along the streamwise and lightly overestimated in the lateral direction. The "calibration" using low Sc_t is also confirmed. Discrepancies may be explained by the inaccuracy of steady RANS to capture unsteadiness in the wake of the taller building. In order to gain insight into unsteady simulation of flow around an obstacle, URANS approach confirmed the existence of coherent vortical structures in the wake of a building.

References

ASHRAE, 2007. Building air intake and exhaust design. ASHRAE Applications Handbook, Chapter 44, American Society of Heating, Refrigerating and Air-Conditioning Engineering Inc., Atlanta, USA.

Blocken, B., Stathopoulos, T., Carmeliet, J., 2007. CFD simulation of the atmospheric boundary layer: wall function problems. Atmospheric Environment 41, 238-252.

Blocken, B., Stathopoulos, T., Saathoff, P., Wang, X., 2008. Numerical evaluation of pollutant dispersion in the built environment: comparisons between models and experiments. Journal of Wind Engineering and Industrial Aerodynamics 96, 1817- 1831.

Chavez, M., Hajra, B., Stathopoulos, T., Bahloul, A. 2011. Near-field pollutant dispersion in the built environment by CFD and wind tunnel simulations. Journal of Wind Engineering and Industrial Aerodynamics, 99 (4), 330-339.

Chavez, M., Hajra, B., Stathopoulos, T., Bahloul, A,. 2012. Assessment of near-field pollutant dispersion: Effect of upstream buildings. Journal of Wind Engineering & Industrial Aerodynamics, doi:10.1016/j.jweia.2012.02.019

Cheng, Y., Lien, F.S., Yee, E., Sinclair, R., 2003. A comparison of large eddy simulations with a standard k −ε Reynolds-averaged Navier Stokes model for the prediction of a fully developed turbulent flow over a matrix of cubes. Journal of Wind Engineering and Industrial Aerodynamics, 91, 1301-1328.

Di Sabatino, S., Buccolieri, R., Pulvirenti, B., Britter, R., 2007. Simulations of pollutant dispersion within idealized urban-type geometries using CFD and integral models. Atmospheric Environment, 41,8316–8329.

Fluent 6.3 User's guide, Fluent Inc., Lebanon, 2006.

Hajra, B., Stathopoulos, T., Bahloul, A., 2010. Assessment of pollutant dispersion from rooftop stacks: ASHRAE, ADMS and wind tunnel simulation. Building and Environment, 45, 2768-2777.

Hefny M, Ooka R., 2009. CFD analysis of pollutant dispersion around buildings: effect of cell geometry. Building and Environment, 44(8), 1699-1706.

Hussein, H.J., Martinuzzi, R.J., 1996. Energy balance for the turbulent flow around a surface mounted cube placed in a channel. Physics of Fluids, 8 (3), 764-780

Iaccarino, G., Ooi, A., Durbin, P.A., Behnia, M., 2003. Reynolds averaged simulation of unsteady separated flow. International Journal of Heat and Fluid Flow, 24, 147-156.

Saathoff, P., Gupta, A., Stathopoulos, T., Lazure, L., 2009. Contamination of fresh air intakes due to downwash from a rooftop structure. Journal of Air & Waste Management Association, 59, 343–353.

Simiu, E., Scanlan, R. H., 1996. Wind effects on structures: fundamentals and applications to design. 3rd Edition, Wiley Interscience Publication, USA.

Snyder, W. H., 1981. Guidelines for fluid modelling of atmospheric diffusion. EPA office of Air quality, planning and standards, Research Triangle Park, USA, EPA-600/8-81-009.

Stathopoulos T., Lazure L., Saathoff, P., Gupta, A. 2004.The effect of stack height, stack location, and roof top structures on air intake contamination -A laboratory and full scale study. IRSST research report R-392, Institut de recherche Robert-Sauvé en santé et en securité du travail, Montréal, Canada.

Stathopoulos, T., Hajra, B., Bahloul, A., 2008. Analytical evaluation of dispersion of exhaust from rooftop stacks on buildings. IRSST research report R-576, *Institut de recherche Robert-Sauvé en santé et en sécurité du travail*, Montreal, Canada.

Tominaga, Y., Stathopoulos, T., 2007. Turbulent Schmidt numbers for CFD analysis with various types of flowfield. Atmospheric Environment, 41, 8091-8099.

Tominaga, Y., Stathopoulos, T., 2009. Numerical simulation of dispersion around an isolated cubic building: Comparison of various types of k-ε models. Atmospheric Environment, 43, 3200-3210.

van Hooff T, Blocken B, 2010. On the effect of wind direction and urban surroundings on natural ventilation of a large semi-enclosed stadium. Computers & Fluids, 39, 1146-1155.

Wilson, D. J., Fabris, I, Ackerman M Y., 1998. Measuring adjacent effects on laboratory exhaust stack design. ASHRAE Transactions, 88 (1), 513-533.

Wilson, D.J. 1979. Flow patterns over a flat roofed buildings and application to exhaust stack design. ASHRAE Transactions, 85(2), 284-295.

Yang, Y., Gu, M., Chen, S., Jin, X., 2009. New inflow boundary conditions for modelling the neutral equilibrium atmospheric boundary layer in computational wind engineering, Journal of Wind Engineering and Industrial Aerodynamics, 97, 88-95.

The Seventh International Colloquium on Bluff Body Aerodynamics and Applications (BBAA7)
Shanghai, China; September 2-6, 2012

Recent advancement from flow and dispersion studies around bluff bodies for urban environment applications

Silvana Di Sabatino [a], Riccardo Buccolieri [a], Pietro Salizzoni [b]

[a] *Dipartimento di Scienze e Tecnologie Biologiche ed Ambientali, University of Salento, Lecce, Italy*
[b] *Laboratoire de Mécanique des Fluides et d'Acoustique, University of Lyon Ecole Centrale de Lyon, France*

ABSTRACT: This paper reviews recent studies pertaining to flow and pollutant dispersion around buildings and complex geometries (real cities). Field/laboratory experiments and numerical simulations (mainly Computational Fluid Dynamics, with attention to Large Eddy Simulation approach) performed by us as well as by other researchers who have looked at flow, turbulence, dispersion and ventilation around bluff bodies are considered. We attempt to review state of the art results considering that the urban complexity is not only due to the packing density, but also spatial building-height variability, thermal properties, the presence of vegetation. These findings are discussed in light of recent advances of operational urban dispersion models.

KEYWORDS: flow and dispersion, modelling, experiments, city breathability, urban models

1 INTRODUCTION

Health risks associated with exposure to pollutant concentrations in cities have motivated research to improve numerical models for local air quality. One of the difficulties arises from the complexity of the urban form which continues to be a challenge for modellers. An urban canopy consists of a large collection of buildings, trees and other obstacles affecting transport and distribution of scalars (pollutants, temperature, humidity etc.). A large number of experiments and simulations of flow around bluff bodies has been performed to understand the wide range of complex flow phenomena. This has led to the development and improvement of obstacle resolving models, such as Computational Fluid Dynamics (CFD) models.

Most of the studies have been performed separately depending on the specific application and a comprehensive overview is still missing. In this context, the paper reviews and summarizes some of the most recent advances in numerical (with attention to the Large Eddy Simulation techniques) and experimental findings obtained by us as well as by other researchers who have looked at flow and turbulence around single and groups of bluff bodies to adequately predict pollutant dispersion at the micro-scale. These advances are examined in light of the development of recent operational dispersion models, which are commonly used to determine the exposure of the population to pollutants in urban areas and to develop strategies for its reduction.

2 BUILDING AND STREET SCALE

2.1 *Flow and dispersion around isolated buildings*

Several studies, both numerical and experimental, were carried out in the past analyzing flow and dispersion in flat terrain and around bluff bodies (buildings). Among the pioneering studies,

Riddle et al. (2004) considered the simulation of the dynamics of the basic atmospheric boundary layer using a CFD code and an integral, operational model for the prediction of gas dispersion for neutral stability and flat terrain situations. Overall, they proposed to artificially increase the plume dispersion by reducing the typical turbulent Schmidt number Sc_t value in order to increase the turbulent diffusion near the ground in the Reynolds-averaged Navier–Stokes (RANS) k-ε model. Similar analyses and results were performed by Di Sabatino et al. (2007, 2008a). The work by Tominaga & Stathopoulos (2009) is one of the more systematic attempt to examine prediction accuracy of flow and dispersion around a cubic building for several wind directions using various k-ε models, comparing numerical results with wind-tunnel data. As for the flat terrain cases, the standard k-ε model provided inadequate results for the concentration field, because it cannot reproduce the basic flow structure, such as the reverse flow on the roof.

Only very recently, there has been an increasing interest in using Large Eddy Simulation (LES) models which, although computationally expensive, have the advantage over RANS in that they explicitly resolve the majority of the energy carrying eddies and the internally or externally induced periodicity involved, whereas only the universal small scale eddies are modelled. Following Tominaga & Stathopoulos (2010), Gousseau et al. (2011a, 2012) compared the convective and turbulent mass fluxes predicted RANS and LES for isolated buildings and analyzed the turbulent mass transport mechanism by unsteady concentration and velocity statistics. They showed that RANS models predict erroneous convective fluxes and are largely outperformed by LES in terms of prediction accuracy of mean concentration. Calculated results by Yoshie et al. (2011) confirmed better agreement of LES results with experiments.

2.2 *Flow and dispersion within urban street canyons*

Several works have been performed to understand flow and dispersion in urban street canyons. Most of the researches focused on the idealized case of an infinitely long street, within which a recirculating flow develops, driven by an external wind blowing perpendicularly to the street axis. These studies have provided fundamental knowledge on flow dynamics and pollutant dispersion in presence of obstacles for several engineering applications and for the optimization of the urban comfort. Moving from this basic knowledge, recent studies have been focusing on more complex phenomena. Among these we focus here on the effects induced by varying wind directions on the flow within a street canyon and at the intersection of two or more canyons. The effect of vegetation and buoyancy is also taken into account.

Reviews of recent progress in CFD and operational modelling of wind field and pollutant transport can be found in Vardoulakis et al. (2003) and Li et al. (2006). More recently, Blocken et al. (2011) and Chavez et al. (2011) reviewed various aspects of outdoor air pollution modelling through CFD in the urban environment which included isolated buildings, airborne particles in dense urban areas etc. Recent studies pertaining to CFD modelling techniques to assess pollutant dispersion in different street canyons have been reviewed by Hajra (in press), who discussed modeling technique advantages and demerits. This study shows that the future of CFD is bright and in the coming years LES model is more likely to be used due to its computational preciseness despite increased computer simulation time (Tominaga & Stathopoulos, 2011).

2.2.1 *Wind direction and street intersections*

Most of the studies have been devoted to the case of a wind blowing perpendicularly to the street axis since it is widely believed to maximize the retention time of pollutants. However, field experiments and numerical simulations have demonstrated that if the street is sufficiently long, the wind blowing along the street causes an accumulation of pollutants and the resulting concentra-

tion at the downwind end of the street can exceed that produced when a similar wind blows perpendicular (e.g. Berkowicz et al., 1996; Soulhac & Salizzoni, 2010; Hang et al, 2012). The evaluation of the advective fluxes along the canyon is then essential to predict and model the wide range of dispersion conditions that can occur within a street canyon.

A review of experimental studies of the flow induced in a street by an external wind blowing at an arbitrary angle is given in Ahmad et al. (2005) and described as a complex 3D helicoid. Soulhac et al. (2008) have shown that certain aspects of the flow can be obtained from the linear superposition of two asymptotic cases - flow parallel to the street and flow perpendicular to the street - providing an analytical model wind velocity along the street axis spatially averaged over the transverse street section. This result is the basis for finer parametric modeling approach for the exchange phenomena of pollutant, heat or momentum between the urban canopy and the overlying atmosphere (Cantelli et al., 2011; Soulhac et al., 2011).

Advective transfer along the street axis within a street of finite length causes dynamical effects within a street intersection. A detailed review on the state of the art has been given by Tiwary et al. (2011). Numerical simulations, wind tunnel and field experiments have provided a detailed picture of some of the major flow mechanisms that occur (e.g. Soulhac et al, 2009, Carpenitieri et al, 2019) showing that, even for simple configurations, the flow structure is very complicated, with significant variation of local averages of pollutant concentrations and even larger instantaneous variations, due to both wind direction variations and local smaller scale turbulence.

2.2.2 *Thermal effects*

To date relatively few studies investigated the role of heat fluxes in urban canyons, which are generated by temperature difference between the canyon walls and the air within the canyon. The temperature difference is typically induced by the direct solar radiation and can reach over tens of degrees in summer (Offerle et al., 2007). Thermal fluxes generate buoyancy forces within the canyon which have a relevant influence on the flow within it, especially in low wind conditions.

First studies were performed numerically by Sini et. al. (1996) and Kim & Baik (2001) and experimentally by Kovar-Pankus et al. (2002). Full scale experiments were performed in central Nantes (France) by Idczac et al. (2007) and in central Gothenburg (Sweden) by Offerle et al. (2007). Recently, numerical studies of these phenomena have captured increasingly interest. Memon et al. (2010) developed a two-dimensional k-ε turbulence model with a Renormalization Group (RNG) closure scheme to assess the impact of the street canyon aspect ratio and wind speed on the intensity of heat. The street canyon model was validated by comparing results with reported wind tunnel data and similar numerical models (e.g. Uehara et al., 2000; Kim & Baik, 2001; Xie et al., 2007). Results uncovered the importance of street canyon aspect ratio and wind speed on urban heating and that urban cool island (i.e., daytime lower temperatures in an urban area) may be associated with direct ground heating. Another recent contribution was given by Defraeye et al. (in press) who proposed an adjusted wall function for temperature intended for forced-convective heat transfer at surfaces of bluff bodies. Finally Cheng & Liu (2011) performed LES simulations to examine characteristics of flows and pollutant dispersion in two-dimensional urban street canyons of aspect ratio equal to one in neutral, unstable, and stable thermal stratifications. While pollutants tend to be well mixed in street canyons in neutral and unstable conditions, improved pollutant removal in unstable conditions was observed due to the enhanced roof-level buoyancy-driven turbulence. Similar results were found by Cai (2012).

2.2.3 *Effects of vegetation*

To complete the picture, one should also consider how urban vegetation affects urban canopy flows, the microclimate and air pollution levels. Although particle deposition on plant surfaces removes pollutants from the atmosphere, thus reducing their concentration, it also should be noted that trees themselves act as obstacles to airflow decreasing air exchange with the above roof level atmosphere. Many research studies are underway to determine the role of vegetation in urban microclimates (e.g CODASC Database, 2008; Mochida et al., 2008; Buccolieri et al., 2009; 2011). In numerical simulations using CFD models, trees have been modelled as porous media to which is associated a pressure loss according to the specific tree porosity. Typically, a modification to the governing equation is done by adding a momentum sink term. The interpretation of concentration results is done by looking at modifications that the flow undergoes in presence of trees. Though numerical studies using LES type of models should be employed (Salim et al., 2011; Park et al., 2011), RANS CFD simulations suggest that the presence of trees in the canyon break the main vortex structure expected in the tree-free cases and modifies the corner vortices at the street ends thus reducing mass exchanges with the various openings, therefore in first approximation dilution is much reduced. Real-city applications have further complications and both buildings and trees have to be considered together (Buccolieri et al., 2011).

3 DISTRICT SCALE

3.1 *The influence of building geometry and arrangements on pollutant dispersion*

When the urban rough surface interacts with the atmospheric flow above it, the disturbed flow field can become extremely complex depending on the obstacles' geometry, spacing and the spatial arrangement. Nowadays, several high-quality experimental and numerical data sets are available in the literature. Street-level pollutant concentrations have been proven to be attributable to several factors such as wind direction and velocity, street canyon aspect ratios, the presence of street intersections and upstream buildings, building roof geometry (Yassin, 2011), building packing density etc. In this context, a recent contribution has recently been made by the COST Action 732 (2005-2009, http://www.mi.uni-hamburg.de/Home.484.0.html) numerical team which has highlighted current potential and pitfalls of CFD models using data from the Mock Urban Setting Test (MUST) wind tunnel experiments (Bezpalcova, 2007). In addition, the CEDVAL dataset (2006-2009) have been recently studied by several authors in the context of model validation (e.g. Di Sabatino et al., 2008a; Franke et al., in press).

Even though different attempts were made to improve the capability of RANS models by modifying model parameters to improve their capability to reproduce real wind flow fields, turbulence and concentration patterns (e.g. Solazzo et al., 2009), interest in LES is increasing. Spatial distribution of the turbulent scalar flux inside building arrays by comparing the numerical results obtained by LES and RANS computations have confirmed what found for simple street canyon model, that is RANS underestimates turbulence diffusion in the building canyon when compared with LES due to the difference in the representation of turbulent scalar flux (Tominaga & Stathopoulos, in press). Another recent comparison between LES and RANS (Gousseau et al., 2011b) has further shown by comparison with wind tunnel experiments in Montreal that the performance of the standard k-ε model strongly depends on the turbulent Schmidt number, whose optimum value is case-dependent and unknown a priori. In contrast, LES showed a better performance without requiring any parameter input to solve the dispersion equation. As an example

Figure 1 (left) shows that even in presence of symmetrical geometry, the instantaneous concentrations can be asymmetric, which can be captured only by using the LES approach.

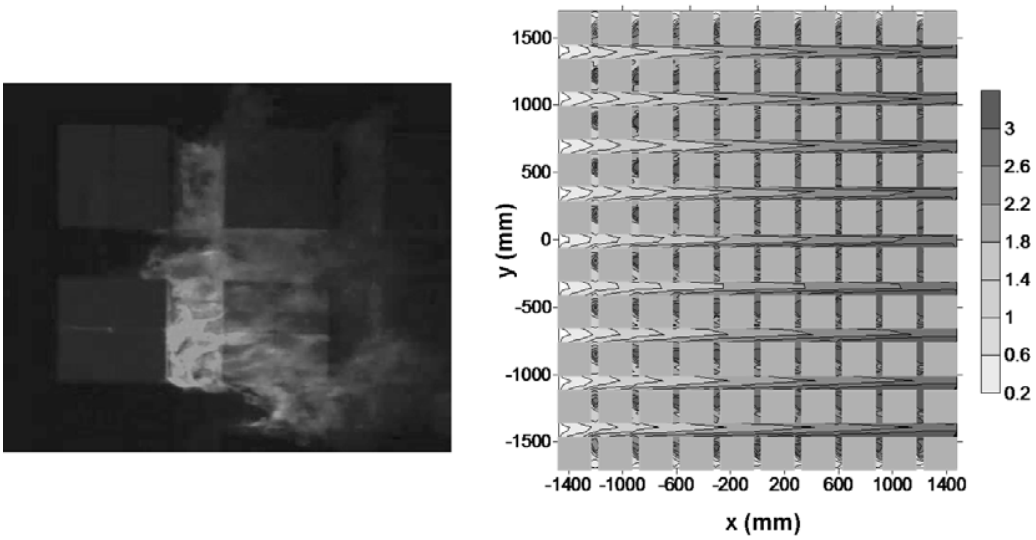

Figure 1. Visualization of a passive scalar injected by a line source at ground level within a regular obstacle array (left) and example of a map of normalized mean age of air (right). The wind blows from the left.

3.2 *City breathability*

An approach to determine street level pollutant dilution has recently been offered by the implementation of building ventilation concepts previously used to evaluate indoor exposure (Chen, 2009). Among the most recent studies, Hang et al. (2012) analyzed the nature of the flow being advected into the city from its surrounding rural areas using the concept of local mean age of air (Etheridge & Sandberg, 1996), which intuitively represents the time taken by an air parcel to reach a given place after it enters the city. A poorly ventilated region, as occurs at the end of the array (Figure 1, right) implies a large mean age, i.e. air mass takes a long time to reach a given region and therefore pollutant removal will be slower. Buccolieri et al. (2010) introduced the expression city breathability to describe this effect. Those authors set a conceptual frame to interpret pollution concentration levels in urban-like geometries using a bulk flow balance approach to calculate flow rates by means of RANS CFD simulations. Wind tunnel and numerical simulations analyses suggested a way to classify city's neighbourhoods into three groups: sparse, compact and very compact cities. Further, the presence of a low spatial building-height variability (a negative effect with respect to city breathability) and a low value of built-up area index (positive effect) together with the intracity variability of city morphometry is expected to be relevant for city breathability and still needs to be quantified (Di Sabatino et al., 2010).

4 URBAN DISPERSION MODELLING

As discussed above, CFD codes have been proven to be successful in predicting flow and dispersion at city scale by resolving the flow and dispersion down to the building scale. However, when a district of hundreds of streets and a large amount of the pollutant emissions have to be considered, CFD requires still unfeasible computational costs for operational purposes. Alterna-

tive approaches have then to be adopted and operational dispersion models are commonly used to determine the population's exposure to pollutants and to develop strategies for its reduction. We discuss here four different simulation strategies: Coupling dispersion models with diagnostic flow models, Street network models, Canopy models and Adapted Gaussian models. The models are hereafter presented for decreasing computational costs, which is strictly associated to the accuracy adopted in the description of details the urban geometry and of the velocity field within it.

4.1 *Coupling dispersion models with diagnostic flow models*

This method aims in reproducing the local urban geometry with high accuracy. The modeling chain can be directly fed with Geographic Information System (GIS) data of the buildings. Pollutant concentrations are obtained by coupling a Lagrangian dispersion model with velocity field predictions obtained by diagnostic models. These can be eventually modified using analytical corrections to better simulate the recirculation zones developing in the wakes of buildings and obstacles (Kaplan & Dinar, 1996). Examples of this approach are given by Moussafir et al. (2004) and Tinarelli et al. (2007), which present simulations of pollutant dispersion around isolated buildings or in groups of buildings in domains with lengths scales of few hundreds of meters. The computational cost are significantly lower than those needed to run simulations with prognostic CFD codes but not sufficiently low to use this model for simulations of multiple sources over a whole district or to run simulations over a whole year.

At larger scales, that span between the district and the city scale, when it is not possible to represent the details of recirculation zone developing within canyons and building wakes, the velocity field within the urban area can be reconstructed by correcting the output of a mass-consistent diagnostic model with analytical solution of the spatial averaged velocity within the urban canopy (Cionco, 1965; Macdonald et al., 1998). These velocity fields can then be used to run Gaussian puff dispersion models (e.g. Chang et al, 2005).

4.2 *Street network models*

Further reduction of the computational costs can be achieved adopting a street network approach. These are box models at heart but formulated with explicit modelling of the exchange of flow and pollutant fluxes at urban intersections and capable of providing a detailed concentration field at the street scale over a whole urban district. These models adopt a simplified description of the urban canopy. The streets in a district are modelled as a simplified network of connected street segments represented by boxes, whose mass exchanges are modelled by means of parametric laws. The flow within each street is driven by the external wind and the pollutant is assumed to be uniformly mixed over the street. In order to compute the mean concentration within each street, these models account for three transport mechanisms: the convective mass transfer along the streets (Soulhac et al., 2008) due to the mean wind along their axis, the turbulent transfer across the interface (Salizzoni et al., 2009) between the streets and the atmosphere, the convective transport at street intersections (Soulhac et al., 2009). An example of implementation of this approach is provided by Soulhac et al. (2011). Recent studies have evaluated the performances of this approach both against laboratory experiments (Carpentieri et al, in press) and field experiments (Soulhac et al, 2012). These approaches provide reliable results for high density canopy, and the width of the building blocks exceeds that of the streets separating them, as for most central part of European cities. Their performances decrease in case of sub-urban districts, when the spacing between the buildings increases, the physical limits of the street volume becomes unclear and the flow field within the street is strongly coupled with that of the atmosphere just above.

4.3 *Canopy models*

Much effort has been done in order to relate mass, heat and momentum exchanges between an urban canopy and the overlying atmosphere to spatially averaged characteristics of the urban geometry. As an example we cite here Di Sabatino et al. (2008b) who have recently proposed a modelling approach for the computation of the spatially-averaged flow field, where the average is defined at the neighbourhood scale, between 0.2 up to 10km. The novel idea is the description of the drag forces in terms of height dependent morphological parameters based on detailed knowledge of building geometry. This is nowadays available in digital format (Digital Elevation Models) which can be easily analyzed using image processing techniques (Di Sabatino et al., 2010). The goal is the development of a fast model for the prediction of the flow and pollutant concentration fields at the neighbourhood scale taking into account building arrangement in terms of porosity parameters and spatial building height variability. In terms of computational costs canopy models are similar to street network models. However, canopy models loose details in the spatial resolutions of the concentration fields, since they are not able to grasp the flow details in the streets at the local scale or the channelling effect occurring along the axes of the street canyons. Their application can be however particularly interesting in sub-urban areas or in general in district with mow density of buildings, which have proven to be critical for street network approach.

4.4 *Adapted Gaussian models*

For short-range local problems (up to about 5km), simple Gaussian models are used. It is accepted that in urban areas these models can still be applied when pollutants disperse above the buildings or when the dimensions of the cloud are much bigger than the dimensions of the obstacles. Under such conditions classical Gaussian models may still play a role as screening tools but lack the potential for realistic predictions (COST Action 732).

The performances of these models can however be significantly improved by accurately correcting the plume spreading parameterizations implemented in it with specific semi-empirical relations. In particular, at the micro-scale the retention of pollutant within the recirculating flow structures in building wakes and street canyons, that inhibit street ventilation and enhances ground level concentrations, can be computed as the sum of two components: the background concentration due to street canyon trapping effect and the concentration related to the direct contribution of vehicles emissions within the street (e.g. Hertel & Berkowicz, 1989; Schuluman et al., 2000). Further, at slightly large scales the enhanced lateral spreading of a pollutant plume due to increased plume meandering in the buildings wakes can be efficiently simulated with simple parametric relations linking the intensity of the turbulent fluctuations to the time averaged later spread of the plume (e.g. Venkatram et al., 2004). At the district scale, similar corrections for the parameterization of the plume can be taken into account to model the enhanced diffusivity within the roughness sub layer (Raupach et al., 1991; Rotach, 1993; Salizzoni et al., 2009), taking advantage of the fact that turbulent characteristics have proven to be almost uniform with height (Venkatram et al., 2005). It is worth mentioning however, that these approaches are reliable mainly in case of sparse obstacle arrays, and not in dense packed obstacle array, where the channelling of pollutant along the street axes is one of the main transfer process (Garbero, 2010).

5 CONCLUSIONS

This short review tried to show recent advancement from flow and dispersion studies around bluff bodies for urban environment applications. The focus was to select some very recent works in this area. Until now a large number of experiments and simulations of flow around bluff bod-

ies has been performed to improve fluid dynamics around obstacles and to understand the wide range of complex flow phenomena. Physical simulation studies in wind tunnels show a high potential since the influence of bluff body's geometry, presence of obstacles etc. can be investigated by controlling each parameter independently. This has also led to the development and improvement of obstacle resolving models, such as CFD, with LES more likely to be used in future owing to its accuracy.

Up to now computational dispersion models have been proven to be successful in predicting flow and dispersion at city scale by resolving the flow and dispersion down to the building scale. However, when a district of hundreds of streets is considered and a large amount of the urban pollutant emissions has to be taken into account, the application of CFD codes requires computational costs that are still unfeasible for operational purposes. In this context, operational dispersion models are commonly used to determine the exposure of the population to pollutants in urban areas and to help develop strategies for its reduction.

REFERENCES

K. Ahmad, M. Khare and K.K. Chaudhry, Wind tunnel simulation studies on dispersion at urban street canyons and intersections - a review, Journal of Wind Engineering and Industrial Aerodynamics, 93 (2005) 697-717.

R. Berkowicz, F. Palmgren, O. Hertel and E. Vignati, Using measurements of air pollution in streets for evaluation of urban air quality - meteorological analysis and model calculations. Science of the Total Environment, 189/190 (1996) 259-265.

K. Bezpalcova, Physical Modelling of Flow and Diffusion in Urban Canopy, PhD Thesis, Faculty of Mathematics and Physics, Charles University in Prague, 2007.

B. Blocken, T. Stathopoulos, J. Carmeliet and J.L.M. Hensen, Application of computational fluid dynamics in building performance simulation for the outdoor environment: An overview, Building Performance Simulation, 4 (2011) 157-184.

R. Buccolieri, C. Gromke, S. Di Sabatino and B. Ruck, Aerodynamic effects of trees on pollutant concentration in street canyons, Science of the Total Environment, 407 (2009) 5247-5256.

R. Buccolieri, M. Sandberg and S. Di Sabatino, City breathability and its link to pollutant concentration distribution within urban-like geometries, Atmospheric Environment, 44 (2010) 1894-1903.

R. Buccolieri R., S.M. Salim, L.S. Leo, S. Di Sabatino, A. Chan, P. Ielpo, G. de Gennaro and C. Gromme, Analysis of local scale tree-atmosphere interaction on pollutant concentration in idealized street canyons and application to a real urban junction, Atmospheric Environment, 45 (2011) 1702-1713.

X. Cai, Effects of differential wall heating in street canyons on dispersion and ventilation characteristics of a passive scalar, Atmospheric Environment, 51 (2012) 268-277.

A. Cantelli, P. Monti and G. Leuzzi, The role of geometric factors in urban canyon modeling: new parametrisations and sensitivity analysis, Proc. 14th Conference on Harmonisation within Atmospheric Dispersion Modelling for Regulatory Purposes, Kos, Greece, 2-6 October 2011

M. Carpentieri, A. Robins and S. Baldi, Three-dimensional mapping of air flow at an urban canyon street intersection, Boundary-Layer Meteorology, 133 (2009) 277-296.

M. Carpentieri, P. Salizzoni, A. Robins and L. Soulhac, Evaluation of a neighbourhood scale, street network dispersion model through comparison with wind tunnel data, Environmental Modelling and Software, (in press) http://dx.doi.org/10.1016/j.envsoft.2012.03.009

M. Chavez, B. Hajra, T. Stathopoulos and A. Bahloul, Near-field pollutant dispersion in the built environment by CFD and wind tunnel simulations, Journal of Wind Engineering and Industrial Aerodynamics, 99 (2011) 330-339.

J.C. Chang, S.R. Hanna, Z. BoyBeyi and P. Franzese, Use of Salt Lake City URBAN 2000 field data to evaluate the Urban Hazard Prediction Assessment Capability (HPAC) dispersion model, Journal of Applied Meteorology, 44 (2005) 485-501.

Q. Chen, Ventilation performance prediction for buildings: a method overview and recent applications, Building and Environment, 44 (2009) 848–858.

W.C. Cheng and C.H. Liu, Large-eddy simulation of turbulent transports in urban street canyons in different thermal stabilities, Journal of Wind Engineering and Industrial Aerodynamics, 99 (2011) 434-442.

R. Cionco, A mathematical model for air flow in a vegetative canopy, Journal of Applied Meteorology, 4 (1965) 517-522.
CEDVAL Dataset, (1996-1999) http://www.mi.uni-hamburg.de/cedval
CODASC Database, Concentration Data of Street Canyon, (2008) http://www.codasc.de
T. Defraeye, B. Blocken and J. Carmeliet, CFD simulation of heat transfer at surfaces of bluff bodies in turbulent boundary layers: Evaluation of a forced-convective temperature wall function for mixed convection, Journal of Wind Engineering and Industrial Aerodynamics, (in press) http://dx.doi.org/10.1016/j.jweia.2012.02.001
S. Di Sabatino, R. Buccolieri, B. Pulvirenti and R. Bitter, Simulations of pollutant dispersion within idealised urban-type geometries with CFD and integral models. Atmospheric Environment, 41 (2007) 8316-8329.
S. Di Sabatino, R. Buccolieri, B. Pulvirenti and R.E. Bitter, Flow and pollutant dispersion in street canyons using FLUENT and ADMS-Urban. Environmental Modeling & Assessment, 13 (2008a) 369-381.
S. Di Sabatino, E. Solazzo, P. Paradisi and R. Bitter, A simple model for spatially-averaged wind profiles within and above an urban canopy, Boundary-Layer Meteorology, 127 (2008b) 131-151.
S. Di Sabatino, L.S. Leo, R. Cataldo, C. Ratti and R.E. Bitter, Construction of digital elevation models for a southern European city and a comparative morphological analysis with respect to Northern European and North American cities, Journal of Applied Meteorology and Climatology, 49 (2010) 1377-1396.
D. Etheridge and M. Sandberg, Building Ventilation: Theory and Measurement, John Wiley & Sons, Chichester, 1996.
J. Franke, M. Sturm and C. Kalmbach, Validation of OpenFOAM 1.6.x with the German VDI guideline for obstacle resolving micro-scale models, Journal of Wind Engineering and Industrial Aerodynamics, (In press) http://dx.doi.org/10.1016/j.jweia.2012.02.021
V. Garbero, P. Salizzoni and L. Soulhac, Experimental study of pollutant dispersion within a network of streets, Boundary-Layer Meteorology, 136 (2010) 457-487.
P. Gousseau, B. Blocken and G.J.F. van Heijst, CFD simulation of pollutant dispersion around isolated buildings: On the role of convective and turbulent mass fluxes in the prediction accuracy, Journal of Hazardous Materials, 194 (2011a) 422-434.
P. Gousseau, B. Blocken, T. Stathopoulos and G.J.F. van Heijst, CFD simulation of near-field pollutant dispersion on a high-resolution grid: A case study by LES and RANS for a building group in downtown, Atmospheric Environment, 45 (2011b) 428-438.
P. Gousseau, B. Blocken and G.J.F. van Heijst, Large-Eddy Simulation of pollutant dispersion around a cubical building: Analysis of the turbulent mass transport mechanism by unsteady concentration and velocity statistics, Environmental Pollution, 167 (2012) 47-57.
B. Hajra, Recent studies in CFD modelling of pollutant dispersion in street canyons, Building Simulation, (in press) DOI 10.1007/s12273-011-0048-1
J. Hang, Y. Li, R. Buccolieri, M. Sandberg and S. Di Sabatino, On the contribution of mean flow and turbulence to city breathability: the case of long streets with tall buildings, Science of the Total Environment, 416 (2012) 362-373.
O. Hertel and R. Berkowicz, Modelling pollution from traffic in a street canyon. Evaluation of data and model developement. Tech. rep., DMU Luft A-129, NERI, 1989.
H. Kaplan and N. Dinar, A Lagrangian dispersion model for calculating concentration distribution within a built-up domain, Atmospheric Environment, 30 (1996) 4197-4207.
J.J. Kim and J.J. Baik, Urban street-canyon flow with bottom heating, Atmospheric Environnment, 35 (2001) 3395-3404.
A. Kovar-Panskus, L. Moulinneuf, E. Savory, A. Abdelqari, J.F. Sini, J.M. Rosant, A. Robins and N. Tony, A wind tunnel investigation of the influence of solar induced wall-heating on the flow regime within a simulated urban street canyon, Water, Air and Soil Pollution, Focus 2, (2002) 329-358.
M. Idczac, P. Mestayer, J.M. Rosant, J.F. Sini and M. Violeeau, Micrometeorological measuraments in a street canyon during joint ATREUS-PICADA experiment, Boundary-layer Meteorology, 124 (2007) 25-41.
X.-X. Li, C.-H. Liu, D.Y.C. Leung and K.M. Lam, Recent progress in CFD modelling of wind field and pollutant transport in street canyons, Atmospheric Environment, 40 (2006) 5640-5658.
R. Macdonald, R. Griffiths and D. Hall, An improved method for estimation of surface roughness of obstacle arrays, Atmospheric Environment, 32 (1998) 1857-1864.
R.A. Memon, D.Y.C. Leung and C.H. Liu, Effects of building aspect ratio and wind speed on air temperatures in urban-like street canyons, Building and Environment, 45 (2010) 176-188.
A. Mochida, Y. Tabata, T. Iwata and H. Yoshino, Examining tree canopy models for CFD prediction of wind environment at pedestrian level, Journal of Wind Engineering and Industrial Aerodynamics, 96 (2008) 1667-1677.
J. Moussafir, O. Oldrini, G. Tinarelli, J. Sontowski and C. Dougherty, A new operational approach to deal with dispersion around obstacles: the MSS (Micro-Swift-Spray) software suite, Proc. 9th Int. Conf. on Harmonisation within Atmospheric Dispersion Modelling for Regulatory Purposes, 2004, vol. 2, pp. 114-118.

B. Offerle, I. Eliasson, C.S.B. Grimmond and B. Holmer, Surface heating in relation to air temperature, wind and turbulence in an urban street canyon, Boundary-Layer Meteorology, 122 (2007) 273-292.
M. Park, A. Hagishima, J. Tanimoto and K. Marita, Numerical simulation of dispersion in urban street canyons with avenue-like tree plantings: Comparison between RANS and LES, Building and Environment, 46 (2011) 1735-1746.
M.R. Raupach, R.A. Antonia and S. Rajoplan, Rough-wall turbulent boundary layers, Applied Mechanics Review, 44 (1991) 1-25.
M. W. Rotach, Turbulence close to a rough urban surface. Part I: Reynolds Stress, Boundary-Layer Meteorology, 65 (1993) 1-28.
A. Riddle, D. Carruthers, A. Sharpe, C. McHugh and J. Stocker, Comparisons between FLUENT and ADMS for atmospheric dispersion modelling, Atmospheric Environment, 38 (2004) 1029-1038.
S.M. Salim, S.C. Cheah and A. Chan, Effect of urban vegetation on outdoor thermal environment: Field measurement at a scale model site, Building and Environment, 56 (2012) 38-46.
P. Salizzoni, R. Van Liefferinge, L. Soulhac, P. Mejean and R.J. Perkins, Influence of wall roughness on the dispersion of a passive scalar in a turbulent boundary layer, Atmospheric Environment, 43 (2009) 734-748.
L.L. Schuluman, D.G. Strimaitis and J.S. Scire, Development and evaluation of the PRIME plume rise and building downwash model, Journal of the Air and Waste Management Association, 50 (2000) 378-390.
J.F. Sini, S. Anquentin and P.G. Mestayer, Pollutant dispersion and thermal effects in urban street canyons, Atmospheric Environnment, 30 (1996) 2659-2677.
E. Solazzo, X. Cai and S. Vardoulakis, Improved parameterisation for the numerical modelling of air pollution within an urban street canyon, Environmental Modelling & Software, 24 (2009) 381-388.
L. Soulhac, R.J. Perkins and P. Salizzoni, Flow in a street canyon for any external wind direction, Boundary-Layer Meteorology, 126 (2008) 365-388.
L. Soulhac, V. Garbero, P. Salizzoni, P. Mejean, and R.J. Perkins, Flow and dispersion in street intersections, Atmospheric Environment, 43 (2009) 2981-2996.
L. Soulhac and P. Salizzoni, Dispersion in a street canyon for a wind direction parallel to the street axis, Journal of Wind Engineering and Industrial Aerodynamics, 98 (2010) 903-910.
L. Soulhac, P. Salizzoni, R.J. Perkins, The model SIRANE for atmospheric urban pollutant dispersion; Part I, presentation of the model, Atmospheric Environment, 45 (2011) 7379-7395.
L. Soulhac, P. Salizzoni, P. Mejean, D. Didier and I. Rios, The model SIRANE for atmospheric urban pollutant dispersion; Part II, validation of the model on a real case study, Atmospheric Environment, 49 (2012) 320-337.
G. Tinarelli, G. Brusasca, O. Oldrini, D. Anfossi, S. Trini Castelli and J. Moussafir, Micro-Swift-Spray (MSS): a new modelling system for the simulation of dispersion at microscale. General description and validation, In C. Borrego and A.N. Norman (Eds), Air Pollution Modelling and its Applications XVII, 2007, Springer, pp. 449-458.
A. Tiwary, A. Robins, A. Namdeo and M. Bell, Air flow and concentration fields at urban road intersections for improved understanding of personal exposure, Environment International, 37 (2011) 1005-1018.
Y. Tominaga and T. Stathopoulos, Numerical simulation of dispersion around an isolated cubic building: Comparison of various types of k–ε models, Atmospheric Environment, 43 (2009) 3200-3210.
Y. Tominaga and T. Stathopoulos, Numerical simulation of dispersion around an isolated cubic building: model evaluation of RANS and LES, Building and Environment, 45 (2010) 2231-2239.
Y. Tominaga and T. Stathopoulos, CFD modeling of pollution dispersion in a street canyon: Comparison between LES and RANS, Journal of Wind Engineering and Industrial Aerodynamics, 99 (2011) 340-348.
Y. Tominaga and T. Stathopoulos, CFD Modeling of pollution dispersion in building array: evaluation of turbulent scalar flux modeling in RANS model using LES results, Journal of Wind Engineering and Industrial Aerodynamics, (in press) http://dx.doi.org/10.1016/j.jweia.2012.02.004
K. Uehara, S. Murakami, S. Oikawa and S. Wakamatsu, Wind tunnel experiments on how thermal stratification affects flow in and above urban street canyons, Atmospheric Environment, 34 (2000) 1553-1562.
S. Vardoulakis, B.E. Fisher, K. Pericleous and N. Gonzalez-Flesca, Modelling air quality in street canyons: A review, Atmospheric Environment, 37 (2003) 155-182.
A. Venkatram, V. Isakov, J. Yuan and D. Pankratz, Modeling dispersion at distances of meters from urban sources, Atmospheric Environment, 38 (2004) 4633-4641.
A. Venkatram, V. Isakov, D. Pankratz, and J. Yuan, J., Relating plume spread to meteorology in urban areas, Atmospheric Environment, 39 (2005) 371-380.
X. Xie, C.H. Liu, D.Y.C. Leung and M.K.H. Leung, Impact of building facades and ground heating on wind flow and pollutant transport in street canyons, Atmospheric Environment, 41 (2007) 9030-9049.
M.F. Yassin, Impact of height and shape of building roof on air quality in urban street canyons, Atmospheric Environment, 45 (2011) 5220-5229.

R. Yoshie, G. Jiang, T. Shirasawa and J. Chung, CFD simulations of gas dispersion around high-rise building in non-isothermal boundary layer, Journal of Wind Engineering and Industrial Aerodynamics, 99 (2011) 279-288.

The Seventh International Colloquium on Bluff Body Aerodynamics and Applications (BBAA7)
Shanghai, China; September 2-6, 2012

Large Eddy Simulation of concentration fluctuations in an urban street canyon

P. Moonen [a,b], V. Dorer [a,b], J. Carmeliet [a,b]

[a] *Empa, Swiss Federal Laboratories for Materials Science and Technology, Dübendorf, Switzerland*
[b] *ETH, Swiss Federal Institute of Technology Zürich, Zürich, Switzerland*

ABSTRACT: We examine some statistical properties of the concentration field, developing from the steady release of tracer gas at street level in an urban street canyon. To that extent, detailed time-resolved numerical simulations of coupled flow and dispersion are conducted. The numerical model was extensively validated by comparing the predicted time-averaged concentrations to wind tunnel measurements. In this paper, we employ the validated model to assess the time-averaged concentration, the variance and the probability density function (PDF) at various locations in the urban street canyon. The PDF in the mid-plane of the street canyon was found to be wider and more uniform at near-ground locations close to the leeward wall, and narrower and more pronounced at locations higher above the ground and closer to the windward wall. A wider PDF implies that both the mean concentration and the variance are higher, and that longer time periods are needed to determine these quantities at a given confidence level. This observation has an immediate impact on the sensor location and averaging time for siting monitoring networks, and affects the assessment and planning of pollutant mitigation strategies.

KEYWORDS: Computational Fluid Dynamics (CFD), Large Eddy Simulation (LES), dispersion, statistical analysis, average, variance, probability density function (PDF).

1 INTRODUCTION

Thus far, pollutant dispersion studies have mainly focused on mean concentrations and their spatial distribution for a wide range of configurations and emission scenarios. Studies providing statistical information on air pollutant concentration are rare. Nevertheless, their significant added value was demonstrated in a wind tunnel study by Pavageau and Schatzmann (1999), and discussed again in e.g. Schatzmann and Leitl (2011). They showed that statistical information can help to improve our understanding of dispersion mechanisms, and can assist to suggest specifications regarding e.g. sensor location and averaging time for siting monitoring networks. Compared to wind tunnel studies, performing numerical simulations has the advantage that full-field data of all quantities of interest are available over the considered period of time.

In Moonen et al. (2012a), we assessed the performance of a numerical model to accurately simulate pollutant dispersion in an urban street canyon with tree planting. Detailed time-resolved numerical simulations of coupled flow and dispersion were conducted and compared to corresponding wind tunnel measurements (Gromke and Ruck 2007, 2009). The model performance was assessed in several steps, ranging from a qualitative comparison to measured concentration

profiles, over statistical data analysis by means of scatter plots and box plots, up to the calculation of objective validation metrics, and was found to be excellent.

The goal of the current study is to employ the validated model to assess the statistical properties of the concentration field. We focus on an isolated urban street canyon with near-ground released traffic emissions, under perpendicular approach flow. The numerical model is described in Section 2. Section 3 summarizes the main conclusions of the validation study. In Section 4, the statistical properties of the concentration field are analyzed. We concentrate on three quantities of interest, namely the time-averaged concentration field, its variance and corresponding probability density function.

2 NUMERICAL MODEL

2.1 *Domain dimensions*

We perform detailed unsteady simulations of a dispersion experiment, conducted in the atmospheric boundary layer wind tunnel of the University of Karlsruhe, Germany. We focus on a 1:150 scaled isolated street canyon under perpendicular approach flow conditions. The street canyon consists of two parallel buildings of 0.12 x 0.12 x 1.2 m (L_x x L_y x L_z), and positioned 0.12 m apart in streamwise direction (x). In this way, a street canyon with $W/H = 0.12/0.12 = 1$ and $L/H = 10$ is formed ($H = 0.12$ m), see Figure 1. The cross sectional dimensions of the numerical domain are taken equal to the dimensions of the wind tunnel, namely 2 m wide by 1 m high, hereby accurately reproducing the experimental blockage ratio of 7.2%. The total streamwise length of the domain is 25 H (3 m), and consists of an approach flow region of 7 H (0.84 m), a model region of 3 H (0.36 m) and a wake region of 15 H (1.8 m). The position of the upstream domain boundary coincides with the entrance of the wind tunnel test section, i.e. where velocity profiles have been measured. The downstream distance is chosen in accordance with the best practice guidelines, formulated as outcome of COST Action 732 (Franke et al. 2011).

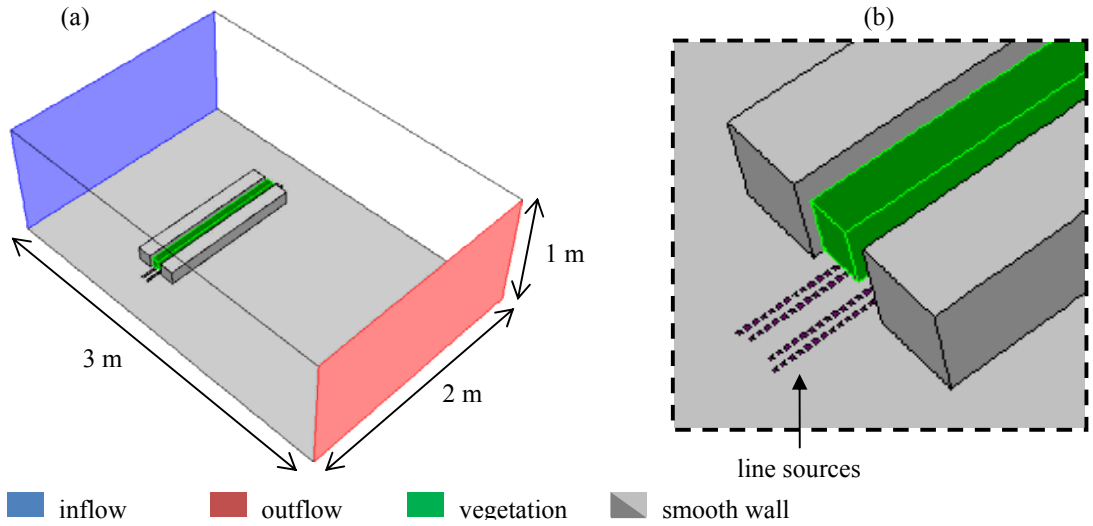

Figure 1. Layout of the computational domain.

2.2 *Boundary conditions*

We simulate the flow in an atmospheric boundary layer wind tunnel, in absence of temperature effects. Boundary conditions (BCs) are chosen accordingly.

No-slip conditions are imposed along the *top, bottom and lateral boundaries* of the domain, corresponding to flow along the smooth wind tunnel walls. The same BC is applied for the surfaces of the canyon model. All walls are considered impermeable for species transport.

At the *inflow boundary*, the measured vertical profiles of mean flow speed $u(y)$ and turbulence intensity $I(y)$ can be well approximated by power-law correlations with exponents $k_u = 0.3$ [-] and $k_I = 0.65$ [-], respectively (Moonen et al. 2012a):

$$\frac{u(y)}{u(y_H)} = \left(\frac{y}{y_H}\right)^{k_u} \tag{1}$$

$$\frac{I(y)}{I(y_H)} = \left(\frac{y + y_d}{y_H}\right)^{k_I} \tag{2}$$

with $u(y_H) = 4.65$ m/s the mean flow speed and $I(y_H) = 16.3\%$ the turbulence intensity at reference height $y_H = H$ and $y_d = 0.02$ m a parameter representing the peak in turbulence intensity at the top of the roughness elements. Time-dependent inlet conditions are generated from the measured mean profiles by means of Ansys' inbuilt spectral synthesizer (Ansys Inc. 2009). In this method, the fluctuating velocity components are computed by synthesizing a divergence-free velocity-vector field from the summation of (100) Fourier harmonics. The inflowing fluid is dry air at 293.15 K with zero background tracer concentration.

On the *outflow boundary*, a zero diffusive flux is imposed for all flow variables in the direction normal to the exit plane. This means that the conditions of the outflow plane are extrapolated from within the domain and have no impact on the upstream flow. This assumption is valid for fully-developed flows.

The *line source* is modeled as a series of equidistantly-spaced point sources at ground level, as in the experiment. The individual hypodermic tubes have been approximated by square inflow boundaries, each 0.005 x 0.005 m^2. The imposed flow rate and concentration are equivalent to the experimental conditions, namely a mixture of 7000 cm^3/min dry air ($\rho = 1.225$ kg/m^3, $\mu = 1.7894\ 10^{-5}$ kg/(m·s), molecular weight of 28.966 kg/kgmol) and 6.5 cm^3/min SF_6 ($\rho = 6.164$ kg/m^3, $\mu = 1.42\ 10^{-4}$ kg/(m·s), molecular weight of 146.05499 kg/kgmol). The properties of air are taken from the inbuilt material database (Ansys Inc. 2009). The ones of SF_6 are compiled from various literature sources. SF_6 is considered as an inert gas (i.e. chemical reactions are not modeled). Because of the larger surface area of the individual point sources in the CFD model, the exhaust momentum is lower than in the experiment. This is compensated by adding a source term to the vertical momentum equation in the cells in direct contact with the source. Note that other researchers (Gromke et al. 2008, Salim et al. 2011a,b) proposed more simplified modeling strategies for the line source and reported a qualitatively good agreement with the experimental results. Since SF_6 is about 6 times heavier than air, gravitational effects need to be included in the model.

2.3 *Computational grid*

In LES, the computational grid acts as a filter. The turbulent structures larger than the grid size (i.e. the large eddies) are resolved, while the smaller ones are modeled. Small eddies are more isotropic. Cubic elements have an equal filter length in the three principal directions, and are

thus the -optimal element type for resolving turbulent structures with LES. The grid employed in this study is therefore entirely built up with this element type.

Since uniform grid refinement rapidly results in a prohibitively large number of elements for grids consisting of cubic elements, we developed and validated an algorithm that systematically refines the grid – in all three dimensions – towards regions of interest (Moonen et al. 2012b). The final grid consists of 1'226'062 perfectly cubic elements. The element size gradually reduces from $H/3$ (= 0.04 m) in the bulk up to $H/24$ (= 0.005 m) in the region of interest. The employed element size in the region of interest is about 2 times smaller than the one obtained by sensitivity analysis (Salim et al. 2011a) and about 2.5 times smaller than the recommended maximal grid size for isolated buildings (Franke et al. 2011) and street canyons (Bartzis et al. 2004).

2.4 *Solution method*

The three-dimensional Navier-Stokes equations, the continuity equation and the species transport equation were solved using the commercial CFD code Ansys Fluent 12.1 that employs the control-volume technique. The staggered pressure-based solver was selected. For the unsteady LES simulations, closure was obtained by means of the dynamic Smagorinsky-Lilly subgrid-scale model (Lilly 1992). The subgrid-scale turbulent Schmidt number was dynamically updated, obviating the need to prescribe a default value. Near-wall modeling was performed using the law-of-the-wall. It was verified that the instantaneous $y+$ values in the region of interest did not exceed 60, i.e. the limit of validity of the selected near-wall modeling approach (Ansys Inc. 2009). Pressure-velocity coupling was taken care of by the SIMPLEC algorithm (Vandoormaal and Raithby 1984). Pressure interpolation was performed by means of the PRESTO! scheme (Peyret 1996). Green-Gauss cell-based gradient evaluation was employed. The third-order MUSCL discretization scheme (Van Leer 1979) was used for the convection terms of the governing equations. By default, second-order accuracy is used for the viscous terms. Second order implicit time integration is employed.

2.5 *Initialization, solution and termination criterion*

The simulations were initialized from a preliminary RANS simulation. An LES time step of 0.00125 s was selected, resulting in cell Courant numbers below 2.5. Typically 100 iterations were required per time step, until the desired level of convergence was reached, i.e. constant residuals of 10^{-4} or less for all equations (Franke et al. 2011). The residuals are defined as the imbalance of the conservation equations, summed over all elements. These values are scaled and the scaled values are used in the code as a measure of the iteration convergence (Ansys Inc. 2009). We reached 10^{-4} for the species transport equation, 10^{-9} for the continuity equation and machine precision ($<10^{-12}$) for the three momentum equations.

All simulations were run on the ETH Brutus cluster (17'000 cores, peak performance 180 TF). Typically, one time step (0.00125 s) required 1.6 hours of CPU time. A stable flow pattern is reached after 10 s (8000 time steps), corresponding to more than 15 domain flow-through times. Statistics were collected during the subsequent 8000 time steps (10 s). In section 4, we will show that the considered time period (10 s in the reduced-scale model, or 25 minutes in full scale) is sufficient to obtain converged statistics in the largest part of the domain. We will show that, for specific locations and applications, even longer averaging times are required.

3 MODEL VALIDATION

The model performance was analyzed in detail in Moonen et al. (2012a). In this section, we only summarize the main conclusions of the comparison between the results, based on the model described in Section 2, and the corresponding wind tunnel measurements by Gromke and Ruck (2007, 2009). The comparison focused on the mean near-wall pollutant concentration, normalized according to:

$$c^+ = \frac{cu_H H}{Q/\ell} \tag{3}$$

with c [-] the measured concentration, u_H [m/s] the mean streamwise flow velocity at height H [m] in the undisturbed approach flow and Q/ℓ [m^2/s] the tracer gas source strength per unit length, with Q being 6.5 cm^3/min SF_6 mixed with 7000 cm^3/min dry air and ℓ = 1.42 m.

Figure 2a and b depict scatter plots of the mean normalized concentration at the leeward and windward wall of the street canyon, respectively. Predicted and observed data have been paired in space and are plotted against each other. Information on the spatial location is retained, and is represented by the different marker types (*, x, + and . for z/H = 0, ±1.25, ±3.75 and ±4.9, respectively). Points on the diagonal indicate a perfect match between simulations and measurements. The two dotted lines bound the region where measured and simulated data differ by less than a factor two.

Figure 2a shows a good degree of correlation between model results and measurements at the leeward wall. A detailed analysis of the different datasets reveals that the simulated mean normalized concentration in the center of the street canyon ('*'; $z/H = 0$) is consistently higher than the observations, while the simulated concentrations at the edges of the street canyon ('.'; $z/H = \pm 5$) are consistently lower than the observations. The mean normalized concentrations at the windward wall are significantly lower than at the leeward wall, and are systematically overpredicted by the model (Figure 2b). Note that this discrepancy does not necessarily imply poor model performance. As will be shown in the next section, the specific temporal flow features in the areas where the largest discrepancies occur necessitate the acquisition of extremely long time series in order to arrive at statistically relevant quantities. The latter condition applies both to measurements and to time-resolved simulations.

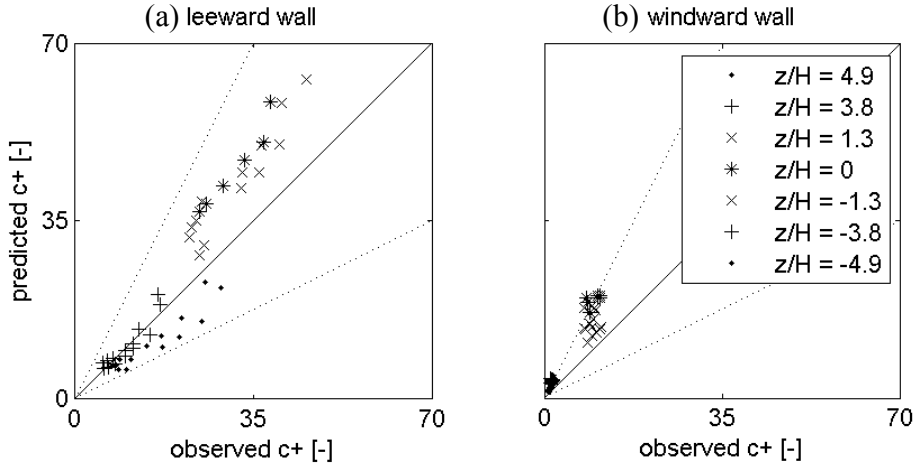

Figure 2. Predicted versus observed mean normalized concentration near (a) the leeward wall and (b) the windward wall of a street canyon. Marker types indicate the spatial location.

4 ANALYSIS OF TEMPORAL FLOW FEATURES

4.1 *Time series*

Figure 3 depicts the temporal evolution of the normalized concentration at a typical near-ground location in the street canyon (solid line). Periods characterized by a relatively low scalar concentration alternate with sudden peaks of high concentration. The short duration of these peaks, i.e. on the order of a few milliseconds, necessitates employing small time steps in the simulation (in this case $\Delta t = 0.00125$ s). The intermittent time between two high-concentration events does not seem to follow a regular pattern. The concentration history at a specific point is the result of the contaminated fluid parcels that reach that point over time. The peak concentrations originate from fluid parcels whose trajectory passed through the scalar source. The lower intermediate concentration is representative for the background concentration after mixing.

Two additional statistical quantities are shown on Figure 3, namely the cumulative mean (dashed line) and the cumulative standard deviation (dotted line). The cumulative mean is calculated according to:

$$c^+_{avg}(t) = \frac{1}{t - t_0}\int_{t_0}^{t} c^+(t)dt \tag{4}$$

and the cumulative standard deviation is obtained as:

$$c^+_{std}(t) = \sqrt{\frac{1}{t - t_0}\int_{t_0}^{t} \left(c^+(t) - c^+_{avg}(t)\right)^2 dt} \tag{5}$$

where the onset of the averaging period (t_0) is taken 10 s after the start of the simulation, to avoid including transitional affects.

From Figure 3, it is clear that both quantities gradually strive towards a constant value. The true mean and standard deviation theoretically require considering an infinitely long time series. In practice however, it can be noticed that their magnitude hardly changes after $t = 16$ s. The considered time interval of 10 s (25 min in full scale) is therefore sufficiently long to study the concentration fluctuations at this spatial location. As will be shown in Section 4.3, points at different spatial locations have different requirements regarding the time period to reach representative statistical quantities. Considering higher order moments generally also implies acquiring longer time series.

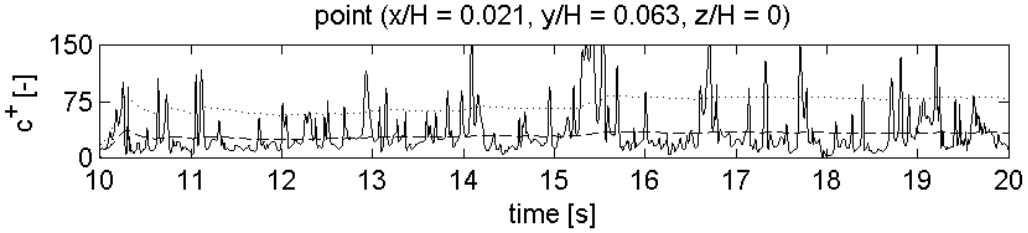

Figure 3. Temporal evolution of the mean normalized concentration at a point in the street canyon (solid line) and the corresponding cumulative mean (dashed line) and cumulative standard deviation (dotted line).

4.2 *Mean and standard deviation*

Figure 4 depicts the ten-second mean (left) and standard deviation (right) of the normalized concentration in every cell along the mid-plane ($z/H = 0$) of the urban street canyon. The flow direction of the standing vortex is schematically indicated as well. The tracer sources are pairwise clustered around $x/H = \pm 0.2$, leading to a locally increased mean normalized concentration in the cells above the sources. The tracer sources around $x/H = -0.2$ receive already contaminated air from the tracer sources around $x/H = +0.2$, explaining the location of the maximum tracer gas concentration. The concentration rapidly decreases with increasing distance from the tracer sources (along a streamline) due to mixing and dilution. The highest mean normalized concentrations are found near the ground and at the lower part of the leeward wall.

Although the source strength is uniform in time, the standard deviation of the concentration fluctuations in the air above the sources is larger than at any other place in the considered cross section (Figure 4). This clearly demonstrates the unsteadiness of the flow. Since the line source is composed of a series of point sources, turbulent fluctuations can easily cause a fluid parcel to travel either above the source or immediately next to it. The local instantaneous concentration therefore varies between zero and the source strength, resulting in a high standard deviation.

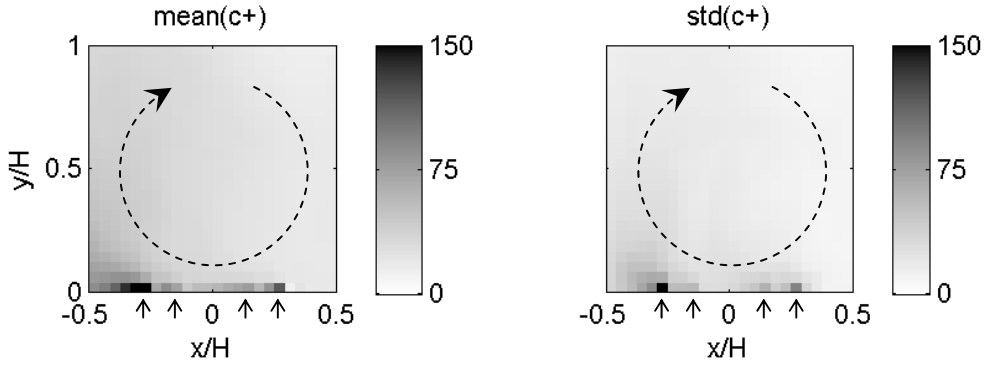

Figure 4. Mean and standard deviation of the normalized concentration in the mid-plane of the street canyon (z/H = 0). The standing vortex and the position of the tracer sources are schematically depicted as well.

4.3 *Probability density function*

Time-resolved simulations can offer interesting information beyond first order statistics. Figure 5 depicts probability density functions (PDFs) at 9 locations in the center plane of the urban street canyon ($z/H = 0$). The PDF gives the relative likelihood that a certain normalized concentration is found at that specific location. From Figure 5, it is clear that the shape of the probability density function is highly location-dependent. Distributions near the leeward wall are consistently wider than distributions near the windward wall, and the width of the PDF decreases with increasing height above the ground. Moreover, the normalized concentration with the highest likelihood is higher for wider distributions. These observations are in agreement with the observed patterns of mean concentration and standard deviation (see Section 4.2, Figure 4).

Statistical principles state that the width of the PDF, or more precisely the variance, is proportional to the required sampling time for determining a statistical quantity such as the mean, with a given level of confidence. In other words, a long time period needs to be considered at locations where the variance is high. The observed spatial variability of the variance of the PDF im-

plies that very long time series are required at locations near the ground and near the leeward wall, while locations higher above the ground and closer to the windward wall require shorter time series for the same level of accuracy. These observations have important consequences when comparing CFD results to full-scale field data: the turbulent time scales governing dispersion might exceed the time period over which quasi-stable conditions can reasonably be expected to occur in the field. Measurement sensor locations should therefore be selected with care, preferentially avoiding regions characterized by a high variance.

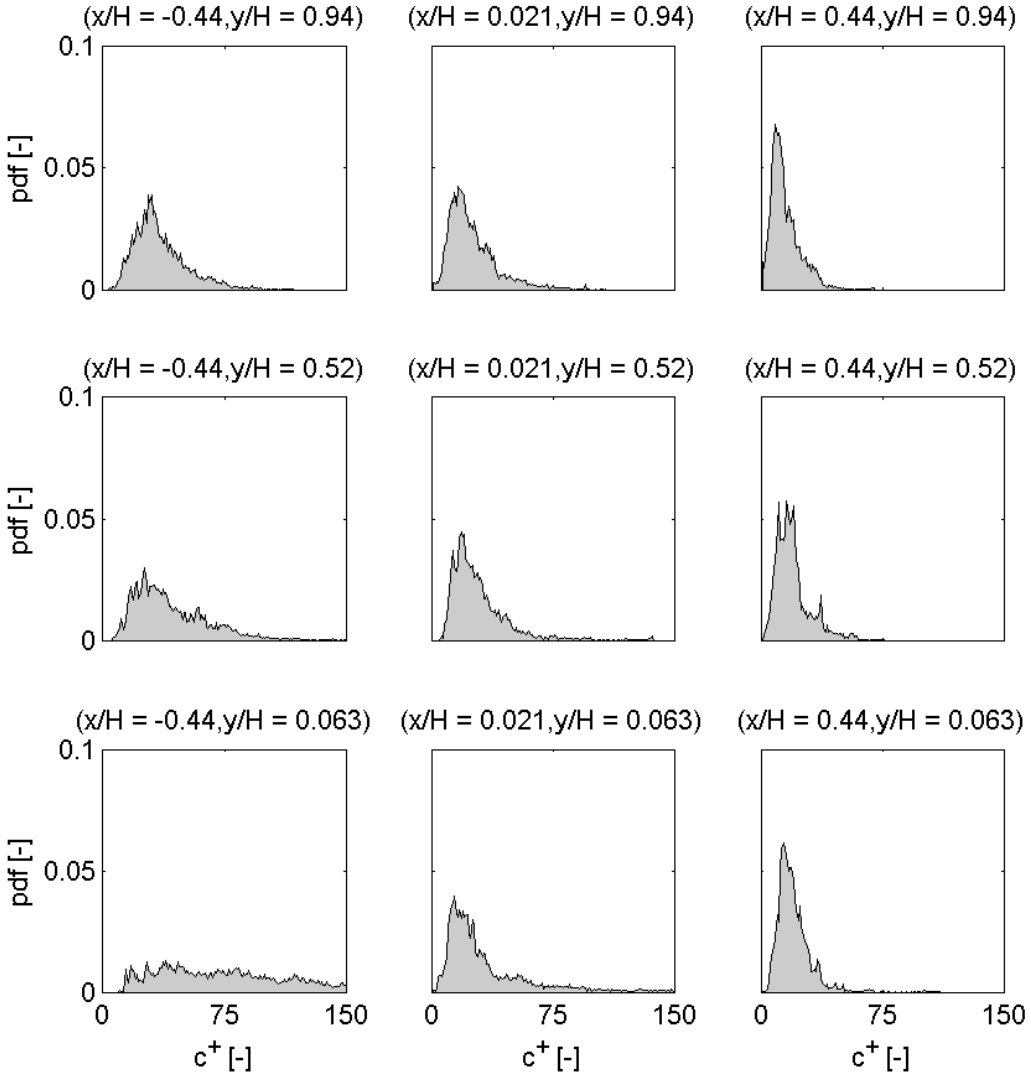

Figure 5. Probability density function (PDF) of normalized concentration at several location along the mid-plane of the street canyon (z/H = 0). Bin size is one unit of normalized concentration.

5 CONCLUSIONS

Unsteady simulations of coupled flow and dispersion inside a street canyon were performed and some statistical properties of the concentration field were analyzed. We focused on the time-averaged concentration, the variance and the probability density function (PDF) at various locations in the urban street canyon. The following observations were made:

- The region in the immediate neighborhood of the pollutant source is not only characterized by a high mean concentration, but also by a large variance.
- The PDF in the mid-plane of the street canyon was found to be wider and more uniform at near-ground locations close to the leeward wall, and narrower and more pronounced at locations higher above the ground and closer to the windward wall.
- At locations characterized by a wide PDF, long time periods are needed to determine statistical quantities, such as the mean and the variance, at a given confidence level.

We have shown that carefully conducted numerical simulations are capable to provide accurate and detailed information on concentration fluctuations in urban street canyons, at high spatial and temporal resolution. The results in this paper clearly illustrate the need for sufficiently long averaging times in unsteady numerical simulations, and, by analogy, also in wind tunnel tests and during field campaigns. We believe these observations are relevant to all modelers and experimentalists, involved in pollutant dispersion research.

6 REFERENCES

Ansys Inc., Ansys Fluent 12.0 User's Guide, 2009a.

Ansys Inc., Ansys Fluent 12.0 Theory Guide, 2009b.

Bartzis, J.G., Vlachogiannis, D. and Sfetsos, A., 2004. Thematic area 5: Best practice advice for environmental flows. The QNET-CFD Network Newsletter 2 (4), 34-39.

Franke, J., Hellsten, A., Schlünzen, H. Carissimo, B., 2011. The COST 732 Best Practice Guideline for CFD simulation of flows in the urban environment: a summary, International Journal of Environment and Pollution 44(1-4), 419-427.

Gromke, C., Ruck, B., 2007. Influence of trees on the dispersion of pollutants in an urban street canyon—Experimental investigation of the flow and concentration field, Atmospheric Environment 41, 3287–3302

Gromke, C., Ruck, B., 2009. On the impact of trees on dispersion processes of traffic emissions in street canyons, Boundary-Layer Meteorology 131, 19-34.

Gromke, C., Buccolieri, R., Di Sabatino, S., Ruck, B., 2008. Dispersion study in a street canyon with tree planting by means of wind tunnel and numerical investigations – Evaluation of CFD data with experimental data, Atmospheric Environment 42, 8640–8650.

Lilly, D. K., 1992. A proposed modification of the Germano subgrid‐scale closure method, Physics of Fluids A 4, 633-635.

Moonen, P., Gromke, C., Dorer, V., Carmeliet, J., 2012a. Performance assessment of a model for simulating dispersion in an urban street canyon with tree planting. 5th International Building Physics Conference (IBPC5), Kyoto, Japan, May 28-31, 2012.

Moonen, P., Dorer, V., Carmeliet, J., 2012b. Effect of flow unsteadiness on the mean wind flow pattern in an idealized urban environment. Journal of Wind Engineering and Industrial Aerodynamics. (doi:10.1016/j.jweia.2012.01.007)

Pavageau, M., Schatzmann, M., 1999. Wind tunnel measurements of concentration fluctuations in an urban street canyon. Atmospheric Environment 33, 3961-3971.

Peyret, R., 1996. Handbook of Computational Fluid Mechanics. Academic Press Limited, USA.

Salim, S.M., Buccolieri, R., Chan, A., Di Sabatino, S., 2011a. Numerical simulation of atmospheric pollutant dispersion in an urban street canyon: Comparison between RANS and LES. Journal of Wind Engineering and Industrial Aerodynamics 99(2-3), 103-113.

Salim, S.M., Chan, A., Cheah, S.C., 2011b. Numerical simulation of atmospheric pollutant dispersion in tree-lined street canyons: Comparison between RANS and LES. Journal of Building and Environment 46(9), 1735-1746.

Schatzmann, M., Leitl, B., 2011. Issues with validation of urban flow and dispersion CFD models. Journal of Wind Engineering and Industrial Aerodynamics 99(2-3), 169-186.
Vandoormaal, P., Raithby, G.D., 1984. Enhancements of the SIMPLE Method for Predicting Incompressible Fluid Flows. Numerical Heat Transfer 7, 147-163.
Van Leer, B., 1979. Towards the ultimate conservative difference scheme. V - A second-order sequel to Godunov's method. Journal of Computational Physics 32, 101-136.

The Seventh International Colloquium on Bluff Body Aerodynamics and Applications (BBAA7)
Shanghai, China; September 2-6, 2012

Physical and numerical modelling of dust dispersion in the leeward zone of two single-standing buildings

Cornelia Wevers, Rüdiger Höffer

Wind Engineering and Fluid Mechanics, Ruhr-Universität Bochum,
Universitätsstraße 150, Bochum, Germany

ABSTRACT: The aim of this work is to define a model setup for a suitable and economical prediction of dust/particle dispersion and deposition around buildings driven by an atmospheric boundary layer (ABL) flow. The dispersion behind two different single buildings is modelled physically and numerically. The numerical simulations with gas and particle dispersion show different results in comparison to the physical tracer gas experiments. The normalised concentrations behind the single cube are overpredicted and underpredicted behind the single-standing hall with an open leeward side. The used wind tunnel technique does not allow the simulation of particle settling, in contrasts the numerical simulation is able to model particle deposition using different particle diameters in the gravity field, which is shown in a pre-study.

KEYWORDS: dispersion, particle transport, CFD, wind tunnel, Eulerian, Lagrangian

1 INTRODUCTION

To model dust/particle dispersion and deposition from diffuse sources in the atmospheric flow physical and numerical simulations were combined and used together in this study. In the past, several researchers investigated numerical simulation approaches for urban pollution dispersion in comparison to physical models [1], either for gaseous pollutants [2,3,4] or for particle dispersion [5,6]. Numerical CFD calculations need to be compared to physical experiments to ensure a proper prediction of the target values and to proof the suitability of the numerical model and the dispersion characteristics. But before adopting a physical model for validation purpose it needs to be validated and tested itself. For this reason first a geometrically simple test case, namely a cubic building with a pollution source on the building top is used to validate the experimental set up for dispersion modelling (cf. Fig. 1 Case1). The dispersion process itself depends on the flow field and in detail on the existent turbulence quantities. In a previous work the validation of the computed wind field around bluff buildings using the commercial code ANSYS CFX and the same simulation setup compared to this study were performed with the VDI Guideline 3783-9 (VDI = The Association of German Engineers), [7]. This validation shows a suitable agreement between the experimental and numerical predicted velocity components within a given range [8,9]. The target values of this work are the nondimensional concentration distributions. For that reason the validation test case from the wind tunnel model, the cube, is also used for CFD calculations in order to compare the computed concentration values with the performed experiments. As idealised case of use a leeward open industrial hall (Case 2 in Fig. 1) with a source inside was placed in the ABL-flow. In real live such buildings dusty goods like construction or soil materials are handled and storage. Due to the wind around and through the halls emitted particles are transported outwards and interact with the environment. The other way around, numerical calculations were used to find appropriate and optimal measurement positions in the wind tunnel for detect the concentration distribution behind the buildings.

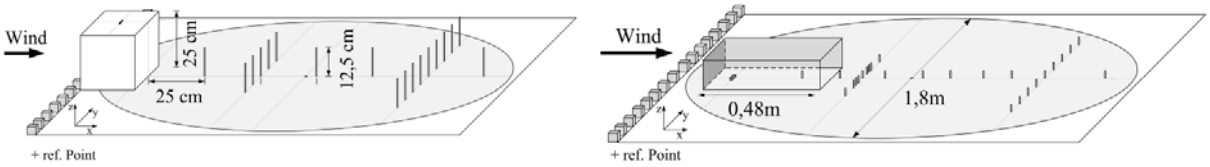

Figure 1. Left: cube with source on the top (Case 1), right: leeward open hall with source inside (Case 2).

One main disadvantage of the physical approach is the difficulty of modelling particle tracking because of the scaling requirements (see Chapt. 2.1.2). Thus, the physical experiments were performed using a tracer gas, assuming that very small dust particles are suspended in air and not affected by gravity. The same tracer gas approach (EULERIAN model) is then used in the numerical calculation for comparison. In contrast the advantage of the numerical model is the possibility to simulate particle transport in real scale while using a LAGRANGIAN model approach. Therefore, at first, gravity-free dispersion simulations with uniform particles were performed and compared to the tracer gas approach. Afterwards, simulations with gravity and different particle diameters were done in order to model particle deposition. The physical plausibility of the simulated particle behaviour is analysed heuristically in a first step.

2 DESCRIPTION OF THE PHYSICAL AND NUMERICAL MODELS

2.1 *Physical model*

2.1.1 *Boundary conditions and measurement techniques*

The physical tracer gas experiments are performed in the boundary layer wind tunnel of the Ruhr-Universität Bochum. The oncoming turbulent flow is generated using a COUNIHAN-setup [10] and corresponds to an atmospheric wind over urban terrain with a real roughness length z_0 = 0.1m (geometrical scale 1:200). In Figure 2 the dots show measured flow characteristics, like vertical velocity profile and turbulence quantities in x-direction [11].

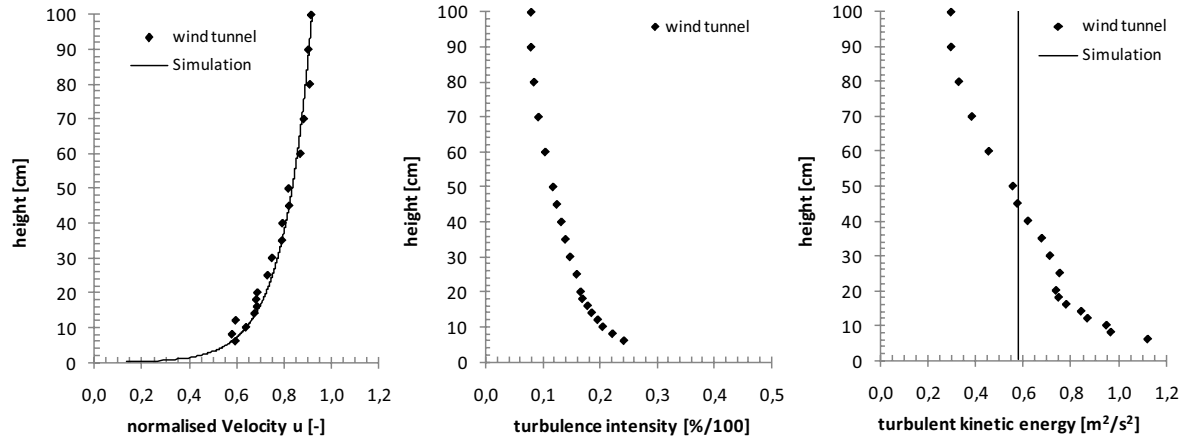

Figure 2. Characteristics of the turbulent boundary layer flow in the wind tunnel [11] and used inlet conditions for the numerical approach, left: velocity profile, middle: turbulence intensity, right: turbulent kinetic energy (all in x-direction).

The dust phase is modelled with Sulfurhexafluorid (SF6) diluted in Nitrogen (N2) to achieve the same fluid capacity like air. The source is geometrically modelled in such a way, that the mo-

mentum flux densities of the tracer and of the air flow in source height are almost equal. For both cases, the concentrations were measured along three axes, two laterals and one longitudinal (see Figure 1) in certain heights with an Electron Capture Detector (ECD). Under consideration of all fluid parameters the local concentrations $\rho_{SF6,i}$ are measured and normalised with a reference velocity u_{ref}, height z_{ref} and the source mass flow $\dot{m}_{Q,SF6}$ to a nondimensional concentration coefficient C_i:

$$C_i = \left(\rho_{SF6,i}\, u_{ref}\, z_{ref}{}^2\right) / \dot{m}_{Q,SF6} \tag{1}$$

For testing the repeatability and independency from the measured values of the parameters variations of the experiments were made with different flow velocities, source strengths and measurement times.

2.1.2 *Scaling requirements for particle simulation*

The basic principle of a boundary layer wind tunnel test is to scale the wind field so that a certain similarity of wind velocity profile, turbulence intensity and turbulent length scales exists compared to the real wind [12]. One measure for similarity between real and model scale flow is the Flow-REYNOLDS-Number $Re_F = \rho_f\, u\, L/\eta_f$, using a reference velocity u, a characteristic building length L and the fluid density ρ_f as well as the dynamic fluid viscosity η_f. It is usually not possible to match the real Re_F-Number in the experiments, but to ensure a similarity of the flow around bluff buildings $Re_F \geq 10\,000$ is recommended in the literature for the experiments [13].

Physical experiments with particles were done in the past either for saltation of scaled snow [14,15] or for analysis of real sand motion [16,17,18]. In case of modelling aeolian particle motion requirements for particle scaling in a wind tunnel simulation are summarized e.g. by Kind [19], White [20] and Durán et al. [21]. Kind performed a similarity analysis and stated out, that "it will often be impracticable to simultaneously satisfy all the simulation requirements […]", therefore compromises are necessary [19, p. 219]. There are three particle movement modes which develop due to the wind shear stress on the grain surface and due to atmospheric turbulence: suspension (free flight), saltation (short jumps on a surface) and creep or reptation [22]. The main influence on the mode is given by the ratio between particle size, particle settling velocity, particle spin, wind shear stress and turbulence intensity. Therefore, as scaling requirement, e.g. the ratio between the particle settling velocity and a reference velocity should be equal in real and model scale [19]. The similarity of the aerodynamic behaviour of the free flying particles is characterized amongst others by the Particle-REYNOLDS-Number $Re_p = \rho_f\, u_P\, d_P/\eta_f$, which describes the inertial and viscous effects at the scale of a grain. In case of fine sand (quartz, $d = 300\mu m$) the deposition velocity is $u_p = 3m/s$ [21] and the corresponding Particle-REYNOLDS-Number is $Re_p = 58.3$ ($\gg 1$, turbulent regime).

The consideration of all requirements can make it nearly impossible to find a proper material, which matches all requirements for modelling suspension, deposition and saltation simultaneously in a scaled physical wind tunnel experiment. Therefore, in general, only physical gas simulations are performed and then in the numerical approach discrete particles are considered. The development of the numerical set up is still progressing.

2.2 *Numerical model*

2.2.1 *Meshes, flow boundary conditions and simulation settings*

For both Case 1 and Case 2, the geometries and meshes were build regarding the used wind tunnel models and following the recommendations of Franke et al. [23]. In Case 1 the height of the cube is $H_{C1} = 25cm$, the width (W_{C1}) and the length (L_{C1}) are equal. For Case 2 the building height is $H_{C2} = 12cm$ and the size ratio is $H_{C2} : W_{C2} : L_{C2} = 1:2:4$. Block-structured hexahedral

volume meshes are generated with a maximum cell-growing ration of 1:1. The meshes were refined iteratively until the target values did not change much anymore. For the particle simulation in real scale the mesh was exported with a building height H_{C2} = 24m. Therefore Case 1 has c.a. 1.4Mio cells and Case 2 has c.a. 5.3Mio cells. The inlet profiles for velocity, turbulent kinetic energy (TKE) and its dissipation are modelled according to the method proposed by Richards et al. [24] to match the results of the performed physical simulations, see Figure 2. The lateral sides, the bottom and the building surfaces are defined as walls. The top boundary has a constant shear velocity in order to keep the vertical velocity profile as much as possible constant in horizontal direction [25]. The outlet has a relative static pressure of 0Pa. All numerical simulations were performed as REYNOLDS-Averaged NAVIER-STOKES (RANS) simulations with the Standard k-ε turbulence model using the commercial code ANSYS CFX 12.1. For the approximation of the convective terms the High-Resolution scheme is used, and the truncation error is set for the maximum residuals to 10^{-6} within 1000 iteration steps. The iteration convergence is observed using monitor probes behind the buildings.

2.2.2 *Modelling the dust dispersion*

The physical experiments for modelling the transport of the dust material use a tracer gas method as mentioned before. In order to use these experiments for comparison the dust in the numerical simulations is modelled in two ways. The first way describes the tracer as gas, like in the physical model, using an additional transported scalar variable (EULERIAN approach) and the standard gradient-diffusion-hypothesis (SGDH) for the scalar fluxes [26]. They are modelled amongst others using the turbulent eddy viscosity ν_t and the turbulent SCHMIDT-number Sc_t. The latter one describes the scale between the turbulent viscosity and turbulent diffusivity, thus the scale of transport values between momentum exchange and mass exchange [27]. Although Sc_t is not a constant [28,29], it is used as a constant in the gradient-diffusion-hypothesis. A proper value choice is an actual discussion of research [3,4,29,30]. The choice should be made case dependent. In this study the turbulent SCHMIDT-number is Sc_t = 0.9 and will be not vary for this study. The transport properties for the scalar are the same like for air at 25°C, which is defined as fluid for the whole domain. The source mass flow and velocity of the tracer are set with respect to the wind tunnel experiments. For analysis the nondimensional concentration is calculated with Equation (1). The second way to model the tracer is to track discrete particles in the continuous air phase using the RANS-calculated flow field (LAGRANGIAN approach). With EULER-forward integration of the particle velocity in discrete points the particles are moved along paths through the domain. The particle velocity itself is calculated from an analytical solution of the particle momentum equation, which sums all forces acting on a spherical particle [31]. The most relevant force is the drag force, which is calculated using STOKES-law in Equation (2). This includes the velocities of the fluid u_f and of the particle u_P as well as the particle diameter d_P, the dynamic viscosity η and the correction factor C_{cor}, which depends on the Particle-REYNOLDS-Number, used model from SCHILLER & NAUMANN in [32,31].

$$m_P \frac{du_P}{dt} = 3\pi\eta d_P C_{cor}(u_F - u_P) \tag{2}$$

Additionally the stochastic “discrete droplet” model from Gosman and Ioannides [33] is used to calculate the turbulent diffusion of each particle due to turbulent eddies with a characteristic fluctuation velocity u_i', length ℓ_e and lifetime τ_e:

$$u_i' = \Gamma\left(\overline{u_i'^2}\right)^{1/2} = \Gamma(2k/3)^{1/2} \quad ; \quad \ell_e = \left(C_\mu^{3/4} k^{3/2}\right)/\varepsilon \quad ; \quad \tau_e = \ell_e/(2k/3)^{1/2} . \tag{3}$$

The variable Γ denotes a normal distributed random number, k the local TKE, its dissipation ε and C_μ a constant [31]. For suspension modelling 80,000 numbers of positions with particles of diameter d_p = 2.5µm (quartz ρ_P = 2650kg/m^3) and a mass flow of $m_{Q,P}$ = 0.2kg/s were injected inside the hall (real scale sized). The maximum tracking time was set to 24 hours with an integration time step per particle of Δt = 1s. The nondimensional concentration C_i (Equ. (4)) is calculated comparable to Equation (1) using the averaged volume fraction from Equation (4). The summation is performed over all particles and time steps in a control volume CV and stored in each vertex; Δt is the particle integration step, N_P is the particle number rate, m_P is the particle mass and Φ_P the volume fraction [31].

$$C_i = \left(\overline{\Phi}_{P,i}\, u_{ref}\, z_{ref}{}^2\right) \Big/ \left(m_{Q,P}/\rho_P\right) \quad \text{with} \quad \overline{\Phi}_{P,i} = \sum\left(\Delta t\, m_P\, N_P\, \Phi_P\right) \Big/ \sum\left(\Delta t\, m_P\, N_P\right) \tag{4}$$

3 RESULTS AND DISCUSSION

3.1 *Independency of the flow-REYNOLDS-number and of the model scale*

The dependency of the inflow velocity, more precisely of the flow-REYNOLDS-number *Re*, and of the model-scaling was tested and analysed. The physical experiments were performed with a *Re* - number around *Re* = 42000 with $u_{ref} \approx$ 5m/s (> 10000, cf. 2.1.2). The normalised numerical results for gas and particle dispersion are not affected by different inlet velocities above a critical minimum velocity (e.g. model scale: $u_{ref} \approx$ 2,5m/s results in an undeveloped flow field). The normalised results of the gas dispersion are also not influenced by different scaling (model scale = wind tunnel scale and real scale). But, as expected, the particle simulations show clearly the necessity of particle scaling. When using the same particles (size and material) the normalised concentration distributions show higher values in model scale simulations compared to the real scale simulations. The particle size is too huge in the ratio to the model scale domain size and yields to higher concentrations by calculation of the volume fraction in Equation (4). Therefore, all numerical simulations were performed in real scale and not in wind tunnel model scale.

3.2 *Comparison of the normalised concentrations*

3.2.1 *Cubic building (Case 1)*

The flow and dispersion around the cubic building is one of the benchmark geometries in the German VDI Guideline 3783-12 for physical wind tunnel tests. Figure 3 demonstrate the concentration distributions behind the cube along the measurement axes, and Figure 4 shows the normalised concentration contours in the middle vertical plane. The conducted physical experiments give almost satisfying results compared to this guideline. It can be stated that the physical wind tunnel set up is able to reproduce the dispersion process behind the cube. In contrast to this, the numerical approaches overestimate the concentration by far in longitudinal direction and underestimate the lateral dispersion. Similar results were also found for isolated sources e.g. by Blocken et al. [4] and Gousseau et al. [34] and seem to be characteristically for a RANS SGDH approach. On the one hand several researchers found a high dependency of such results on the turbulent SCHMIDT-number Sc_t, as discussed in Chapter 2.2.2, so that a variation of Sc_t could lead to some improvement of the results. But on the other hand, to vary this number is not always a solution. For example Rossi et al. [29] pointed out, that the discrepancies "may reflect the inadequacy of the SGDH model in capturing the complex features of the scalar dispersion process, which cannot be compensated by adjusting the Schmidt number value." [29, p. 3]. In addition, the source on the top lies in a highly turbulent zone where an unsteady recirculation bubble influences the source, which cannot be captured by a RANS model.

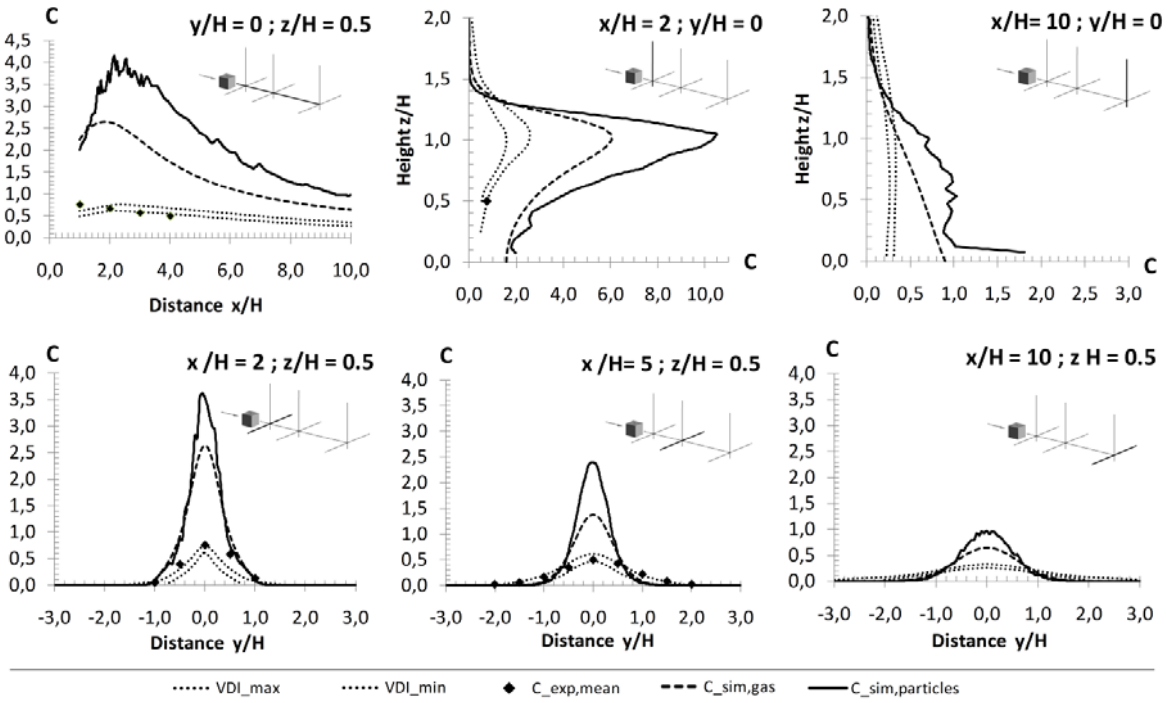

Figure 3. Longitudinal, vertical and horizontal concentration distribution behind the cube.

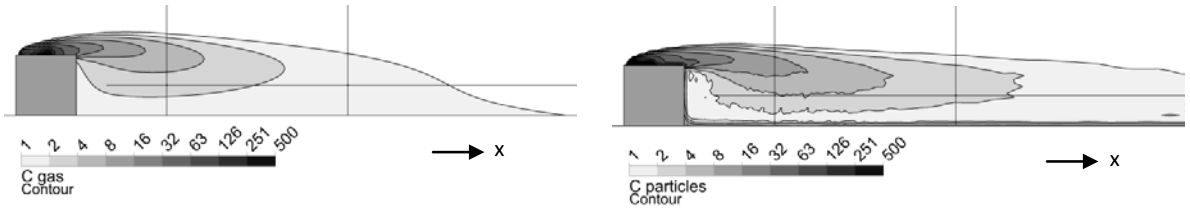

Figure 4. Simulated normalised concentration in the middle vertical plane, left: gas concentration, right: particle concentration; the straight lines determine the position of measurement axes.

3.2.2 *Leeward open hall (Case 2)*

Behind the hall with an open leeward side the normalised concentrations are compared along the three axes. Figure 5 shows in the first row the concentrations at height z = 0.5H and in the second row at height z = 0.25H. In general, the quantitative concentration distribution characteristics can be predict by the numerical approaches, but the gas simulation as well as the particle simulation underestimates the concentration values of the physical experiment, particularly inside the building (Figure 5 first column, negative x direction). This is strongly in contrast to the results of Case 1, where all numerical results are overpredicted compared to the physical measurements.

The dispersion in and outside the hall is mainly influenced by the recirculation zone behind the building, which leads to an interaction of the outer and inner flow field. Inside the hall the velocity and the pressure is low compared to the outer regime. The wake is pulling the dust out from the interior along the building walls (Fig. 6) and most of the dust (gas or particle mass) escapes the hall in the upper corners as well as close to the bottom (Fig. 7).

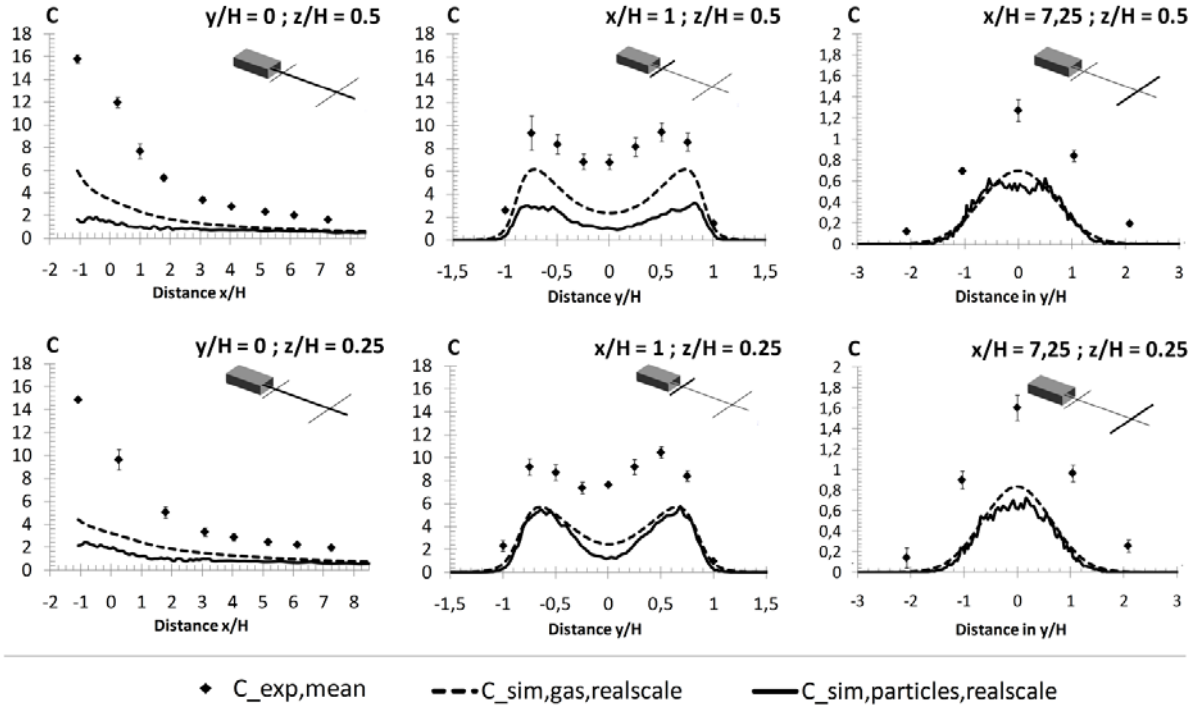

Figure 5. Comparison of normalised concentration distribution behind building "Case 2" along three measurement axes in two different measurement heights; all numerical simulations are run in real scale.

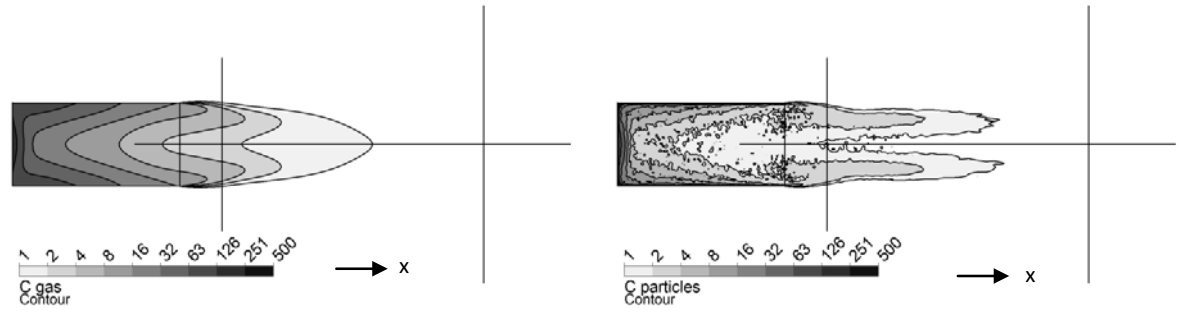

Figure 6. Bird eyes view on simulated normalised concentration contours in horizontal plane in height z/H=2, left: gas concentration, right: particle concentration; the straight lines determine the position of measurement axes.

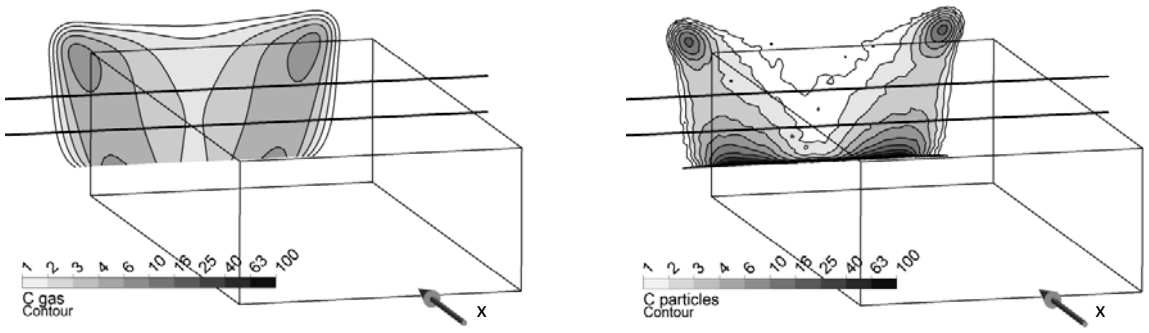

Figure 7. Simulated normalised concentration contours in vertical plane x/H = 1 behind the opening, left: gas concentration, right: particle concentration; the straight lines determine the measurement axes z/H = 0.5 and z/H = 0.25.

The wake re-enters the building from all sides in the middle and lower area of the opening and transports air and partially dust back into the hall. Inside of this recirculation, particulary in the two lateral vortices, the dust is stored and the concentration is higher, see middle column in Figure 5. This recirculation is a highly turbulent and non stationary process, occurring and collapsing or meandering, as could be seen in laser light sheets during the physical experiments. This unsteadiness may cause the high discrepancies, especially along the lateral axes, between the physical and numerical approach, because in the performed RANS simulation the recirculation is of steady state. So there is less lateral mixing and more dilution of the concentration from the building interior to the outer region compared to the physical results.

3.3 *Retention time of the particles and particle deposition*

The Lagrangian approach is able to provide information about the time resolved particle motion and particle deposition, when gravity is acting on the particles. In Case 2 the particles moves from the source to the opening in about 10 minutes, for u_{ref} = 10m/s. The longest retention time is about 30 minutes. In the presented results no gravity was activated and all particles had the same size. Figure 8 shows particle tracks of a performed numerical sand simulation with gravity and different particle diameter. Particles in suspension mode are usually smaller than 20µm and are kept aloft by turbulent eddies, grains between 20-70µm develop short term suspension which reaches distances of tens to hundred meters [35]. Sand grains with a size of 70-100µm are transported mainly in a series of short jumps (saltation) in a layer close to the bottom, in which the vertical component of wind velocity due to turbulence has no effect on the particle trajectories [36]. If the particle size is larger than 500µm the grains are moved in contact with the surface by reptation and creep. This physical behaviour was reproduced in a first numerical approach and shows acceptable results compared to literature (Fig. 8 right).

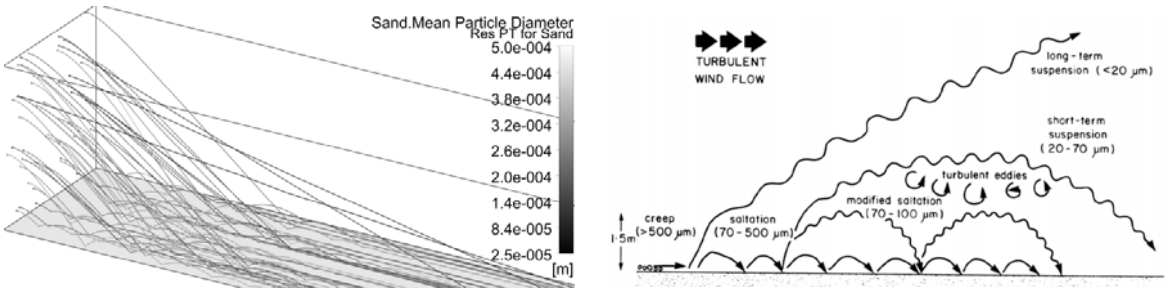

Figure 8. Particle tracks of aeolian sand, left: numerical simulation of sand particles in an empty domain (light = small 50µm – dark = large 250-500µm diameter, right: scheme of aeolian particle transport [Pye, 1987].

4 CONCLUSION AND OUTLOOK

The comparison of the numerically calculated concentration distributions in the leeward zones of two different buildings with results from wind tunnel measurements indicates a completely different behaviour of the models while using almost the same simulation settings. In case of a cubic building with one local source on the top a high overestimation of the concentrations in longitudinal direction and an underestimation of the lateral dispersion are found. In contrast to this, the numerical results of the concentration distribution behind the open hall show better agreement but underestimate the concentration distribution in longitudinal direction. It can be stated that the dispersion behind an idealised geometry with a locally placed source in a highly turbu-

lent zone is more difficult to predict than the dispersion behind a more complex case. Such results were also found by other researchers, e.g. [4]. In case of an open hall the source itself is diffuse and the dispersion process is affected mainly by the recirculation behind the hall. It is not possible to generalise the suitability of a RANS model for dispersion modelling. It depends on the type, location and surrounding of the source. Large Eddy Simulation gives better results compared to physical experiments for pollution dispersion [37,38], but it is not a useful alternative until today because of the required high expenses in calculation time and computer power. The comparison of the flow field and turbulence quantities is matter of future works in order to define more precisely the transport mechanisms. The time resolved LAGRANGIAN particle model provides more detailed information about the particle transport compared to the EULERIAN approach, like tracking time or particle-wall interaction. In future work, the deposition and interaction of the particles with the walls shall be modelled/improved, to analyse e.g. the retention effect of dust in such a hall. But particle erosion and accumulation is difficult or rather impossible to model. One alternative to the LAGRANGIAN approach could be the use of an EULERIAN Multiphase model, like the Algebraic Slip Model, which is commonly used for snow modelling [39,40].

5 REFERENCES

1 X.X. Li, C.-h. Liu, D.Y.C. Leung and K.M. Lam, Recent progress in CFD modelling of wind field and pollutant transport in street canyons, Atmospheric Environment 40 (2006), pp. 5640–5658.
2 R.E. Britter and S.R. Hanna, Flow and dispersion in urban areas, Annual Review of Fluid Mechanics 35 (2003), pp. 469–496.
3 S. Di Sabatino, R. Buccolieri, B. Pulvirenti and Britter R., Simulations of pollutant dispersion within idealised urban-type geometries with CFD and integral models, Atmospheric Environment 41 (2007), pp. 8316–8329.
4 B. Blocken, T. Stathopoulos, P. Saathoff and X. Wang, Numerical evaluation of pollutant dispersion in the built environment: Comparisons between models and experiments, Journal of Wind Engineering and Industrial Aerodynamics 96 (2008), pp. 1817–1831.
5 P. Witt, K. Carey and T. Nguyen, Prediction of dust loss from conveyors using computational fluid dynamics modelling, Applied Mathematical Modelling 26 (2002), pp. 297–309.
6 C. Gorlé, J. van Beeck, P. Rambaud and G. van Tendeloo, CFD modelling of small particle dispersion: The influence of the turbulence kinetic energy in the atmospheric boundary layer, Atmospheric Environment 43 (2009), pp. 673–681.
7 VDI-Guideline 3783 Part 9, Environmental meteorology - Prognostic microscale wind field models - Evaluation for flow around buildings and obstacles, 2005.
8 C. Wevers, J. Franke and R. Höffer, Validierung von CFD-Simulationsprogrammen anhand der VDI Richtlinie 3783, Fachteil WTG, Bauingenieur 83 (2008), pp. 2–5.
9 J. Franke and M. Sturm, Einfluss der Wahl des Koordinatensystems in der VDI Richtlinie 3783/9 auf die Validierung numerischer Strömungssimulationen, WTG-Fachteil, Bauingenieur 85 (2010), pp. 1–3.
10 J. Counihan, An improved method of simulating an atmospheric boundary layer in a wind tunnel, Atmospheric Environment (1967) 3 (1969), pp. 197–214.
11 F. Kipsch, Geschwindigkeits- und Druckmessmethoden für Modellversuche der Gebäudeaerodynamic im Grenzschichtwindkanal, Diploma Thesis, Bochum, Ruhr-Universtität Bochum, Windingenieurwesen und Strömungsmechanik, 2010.
12 VDI-Guideline 3783 Part 12, Environmental meteorology - Physical modelling of flow and dispersion processes in the atmospheric boundary layer - Application of wind tunnels, 2000.
13 WTG-Merkblatt, Windkanalversuch in der Gebäudeaerodynamic, 1994.
14 T. Okaze, A. Mochida, Y. Tominaga, M. Nemoto, T. Sato, Y. Sasaki and K. Ichinohe, Wind tunnel investigation of drifting snow development in a boundary layer, In Proc. 13th International Conference on Wind Engineering, ICWE13, Amsterdam, Multi-Science Publishing Co Ltd, 2011.
15 G. Kimbar and A. Flaga, Wind tunnel tests of snow load redistribution on large span flat roofs, In Proc. 13th International Conference on Wind Engineering, ICWE13, Amsterdam, Multi-Science Publishing Co Ltd, 2011.

16 M. Creyssels, P. Dupont, A. Ould El Moctar, A. Valance, I. Cantat, J. Jenkins, J. Pasini and Rasmussen. K.R, Saltating particles in a turbulent boundary layer: experiment and theory, Journal of Fluid Mechanics 625 (2009), pp. 47–74.
17 Z. Dong, X. Liu, H. Wang and X. Wang, Aeolian sand transport: a wind tunnel model, Sedimentary Geology 2003 (161), pp. 71–83.
18 L. Xianwan, L. Sen and S. Jianyou, Wind tunnel simulation experiement of mountain dunes, Journal of Arid Environments 42 (1999), pp. 49–59.
19 R. Kind, A critical examination of the requirements for model simulation of wind-induced erosion/deposition phenomena such as snow drifting, Atmospheric Environment 10 (1976), pp. 219–227.
20 B.R. White, Laboratory Simulation of Aeolian Sand Transport and Physical Modeling of Flow Around Dunes, Annals of Arid Zones 35 (1996), pp. 187–213.
21 O. Durán, P. Claudin and B. Andreotti, On aeolian transport: Grain-scale interactions, dynamical mechanisms and scaling laws, Aeolian Research 3 (2011), pp. 243–270.
22 K. Pye and H. Tsoar, Aeolian sand and sand dunes, Springer, Berlin, 2009.
23 J. Franke, A. Hellsten, H. Schlünzen and B. Carissimo, Best practice guideline for the CFD simulation of flows in the urban environment, COST Action 732, Quality assurance and improvement of microscale meteorological models, COST office, Brussels, 2007.
24 P.J. Richards and S.E. Norris, Appropriate boundary conditions for computational wind engineering models revisited, Journal of Wind Engineering and Industrial Aerodynamics (2011), pp. 257–266.
25 D.M. Hargreaves and Wright N. G., On the use of the k-ε model in commercial CFD software to model the natural atmospheric boundary layer, Journal of Wind Engineering and Industrial Aerodynamics 95 (2007), pp. 355–369.
26 J.H. Ferziger and M. Peric, Computational Methods for Fluid Dynamics, Springer, Berlin, 2001.
27 K. Koeltzsch, The height dependence of the turbulent Schmidt number within the boundary layer, Atmospheric Environment 34 (2000), pp. 1147–1151.
28 Y. Tominaga and T. Stathopoulos, CFD Modeling of Pollution Dispersion in Street Canyons: Evaluation of turbulent scalar flux modeling in RANS model using LES results, In Proc. 13th International Conference on Wind Engineering, ICWE13, Amsterdam, Multi-Science Publishing Co Ltd, 2011a.
29 R. Rossi and G. Iccarino, Numerical simulation of scalar dispersion downstream of a square obstacle using gradient-transport type models, Atmospheric Environment (2009), doi:10.1016/j.atmosenv.2009.02.044.
30 M. Chavez, B. Hajra, T. Stathopoulos and A. Bahloul, Near-field pollutant dispersion in the built environment by CFD and wind tunnel simulations, Journal of Wind Engineering and Industrial Aerodynamics 99 (2011), pp. 330–339.
31 ANSYS Inc., ANSYS-CFX Solver Theory Guide, Release 12.0, ANSYS Inc., Canonsburg, PA 15317, 2009.
32 AEA Technology Engineering Software Ldt., CFX-TASCflow, Computational Fluid Dynamics Software, Theory Documentation Version 2.12, AEA Technology Engineering Software Ldt., Canada, 2002.
33 A.D. Gosman and E. Ioannides, Aspects of Computer Simulation of Liquid-Fueled Combustors, Journal of Energy 7 (1993), pp. 482–490.
34 P. Gousseau, B. Blocken and G.J. van Heijst, Pollutant dispersion around isolated buildings: on the prediction of convective and turbulent mass fluxes by LES and RANS, In Proc. 13th International Conference on Wind Engineering, ICWE13, Amsterdam, Multi-Science Publishing Co Ltd, 2011.
35 K. Pye, Aeolian dust and dust deposits, Acad. Press, London, 1987.
36 N. Lancaster, Sedimentary Processes, Aeolian Processes, In K. Macdonald, I. Plimer, R. Cocks und R. Selley (Ed.), Encyclopedia of Geology, Elsevier, 2004.
37 S.M. Salim, R. Buccolieri, A. Chan and S. Di Sabatino, Numerical simulation of atmospheric pollutant dispersion in an urban street canyon: Comparison between RANS and LES, Journal of Wind Engineering and Industrial Aerodynamics 99 (2011), pp. 103–113.
38 Y. Tominaga and T. Stathopoulos, CFD modeling of pollution dispersion in a street canyon: Comparison between LES and RANS, Journal of Wind Engineering and Industrial Aerodynamics 99 (2011b), pp. 340–348.
39 M. Naaim, F. Naaim-Bouvet and H. Martinez, Numerical simulation of driting snow: erosion and deposition models, Annals of Glaciology 26 (1998), pp. 191–196.
40 Y. Tominaga, T. Okaze and A. Mochida, CFD modeling of snowdrift around a building: An overview of models and evaluation of a new approach, Building and Environment 46 (2011c), pp. 899–910.

CFD simulations of pollutant gas dispersion with different buoyancies around an isolated building

Yoshihide Tominaga and Lin Guo-Cheng

Department of Architecture and Building Engineering, Niigata Institute of Technology, Kashiwazaki, Niigata, Japan

Abstract

CFD simulations are performed for flow and dispersion fields around an isolated cubic building model with tracer gases exhausted behind it. The tracer gases have three different buoyancies due to density differences with ambient air. Therefore, they behave as neutral, buoyant and dense gases. Two modeling approaches, steady RANS and LES, are adopted and compared. For the neutral gas case, all the RANS computations show very large concentrations near the floor, which did not appear in the experimental and LES results. The same tendency is observed for the buoyant gas case. These high concentrations are mainly caused by underestimation of turbulent diffusion behind the building. On the other hand, since the density gradient is negative (stable) in the dense gas case, the discrepancy in steady-RANS is not noticeable. The difference between the two modeling approaches for the dense gas case is relatively small compared with those for the neutral and buoyant gases.

Keywords: CFD, Dispersion, Buoyancy, Building, Turbulence model

1 INTRODUCTION

Prediction of contaminant dispersion around buildings is one of the most important subjects in the fields of wind engineering, air-conditioning engineering, etc. A number of investigations have been carried out for predicting turbulent diffusion around buildings using wind tunnel tests. However, there are several difficulties and limitations with wind tunnel tests in comprehending the very complicated turbulent diffusion process around buildings located in atmospheric boundary layers.

Numerical methods based on CFD (Computational Fluid Dynamics) for simulating flow and diffusion fields have developed rapidly as a new analysis tool for wind engineering. Much research has been conducted on pollutant dispersion around buildings using the CFD technique (e.g. Blocken et al., 2008; Tominaga and Stathopoulos, 2010). Most of these previous studies have treated tracer gases as neutrally buoyant (passive) scalar (e.g. Hanna et al., 2004). Even when using a lighter or heavier tracer gas than air in an experiment, buoyancy effect of pollutants on a dispersion field has not been explicit in many cases. However, negative or positive buoyancies in pollutants have a large influence on flow and dispersion fields (Gavelli et al., 2008; Meroney, 2010; Hu et al., 2011).

In the present study, CFD simulations are performed for flow and dispersion fields around an isolated cubic building model, where the tracer gases are exhausted from behind the building. The tracer gases are treated as neutral, buoyant or dense compared with ambient air. Various turbulence models including two modeling approaches, steady Reynolds-averaged Navier-Stokes (RANS) and Large-Eddy Simulation (LES), are used and compared. Effects of pollutant buoyancies on the prediction results by various models are investigated by comparison with wind tunnel experiment results.

2 FLOW AND DISPERSION FIELD

2.1 *Target configuration*

The target configuration was determined based on the experiment reported in Tominaga et al. (1992, 1997). Figure 1 illustrates the flow situation analyzed here. A cubic building model 0.2m high was located in the turbulent boundary layer. Here, x_3 is the vertical direction. The Reynolds number based on $<u_b>$ and H is 5.7×10^3. It was confirmed in preliminary experiments that Reynolds number effect is small. A square-shaped gas source with a side length of 0.025H was set at ground level in the recirculation region behind the cube. Exit gas speed $<w_s>$ was $0.5<u_b>$. The cases compared in this study are listed in Table 1. The densimetric Froude numbers Fr_d, defined by Eq. (1), for the buoyant and dense gas cases were determined so that their absolute values were identical.

$$Fr_d = \frac{g\Delta\rho H}{\rho_a < u_b >^2} \qquad (1)$$

where ρ_a is ambient air density; ρ_s is gas density; $\Delta\rho = \rho_s - \rho_a$.

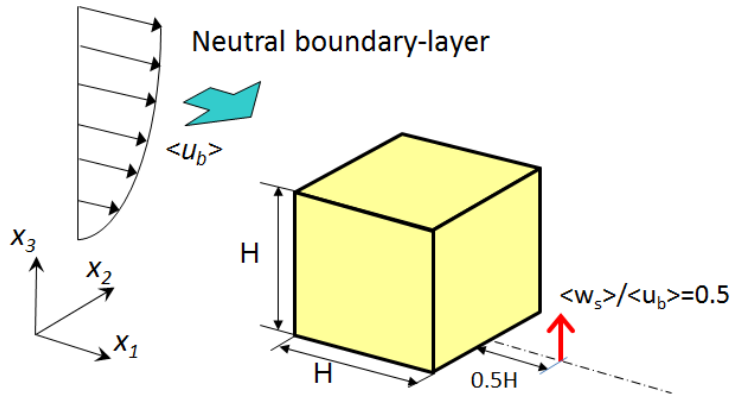

Figure 1. Model flowfield.

Table 1. Cases investigated.

Case	ρ_s/ρ_a	Fr_d	
1	1.0	0.0	neutral gas
2	0.3	-8.6	buoyant gas
3	1.7	+8.6	dense gas

2.2 *Experimental setup*

Experiments were carried out in the boundary layer wind tunnel at the Institute of Industrial Science, the University of Tokyo. The power law exponent of the vertical profile of the inflow velocity was 0.25. The streamwise turbulent intensity at building height H was approximately 20%. The upwind mean velocity at building height H was 0.4 m/s. The neutral gas C_2H_4 was used as a tracer gas. In order to take into account negative and positive buoyancies shown in Table 1, a mixture of He and C_2H_4 and of SF_6 and C_2H_4 were used for the buoyant and dense gases, respectively. Concentration measurements were performed using a high-speed total Hydro-Carbon Analyzer (Technica; H-THCA-01). Wind velocity was measured by a split fibre probe (Dantec Dynamics; 55R55) and a CTA module, which can discern the three-dimensional components of velocity vector. Sampling frequency was set to 10Hz to obtain 4,096 data for each measuring point.

3 COMPUTATIONAL SETUP

3.1 *Numerical methods*

The commercial software ANSYS FLUENT 13.0 was used for both RANS and LES computations based on a control volume approach for solving flow and concentration equations (FLUENT Inc., 2010).

1) RANS: Three types of turbulence models were used and compared: the standard k-ε model (SKE), the RNG k-ε model (RNG) (Yakhot et al., 1992) and the realizable k-ε model (RLZ) (Shih et al., 1995). All model constants were set to be the default values in the software. All the transport equations were discretized using a second-order upwind scheme. The SIMPLE algorithm was used for pressure-velocity coupling. The generation of turbulent kinetic energy due to buoyancy was included in the k equation by default of the software. Although the buoyancy effect on ε was also included, it was confirmed that its effect on the results was negligible.

2) LES: Two types of sub-grid scale (SGS) eddy viscosity models were used: the standard Smagorinsky model (SS; Smagorinsky 1963) with the empirical constant C_S=0.12 (Tominaga 2008a) and the dynamic Smagorinsky SGS model (DS; Germano et al. 1991). The filtered equation was discretized using a bounded central-differencing scheme. Time integration was second-order implicit. The computations were conducted for 800 non-dimensional time units t* (=t×<u_b>/H), which corresponds to 400 s in real time scale, to determine the time-averaged values. It was confirmed that the statistical results were almost repeatable over a longer averaging period.

3.2 *Domain, computational grid and boundary conditions*

The boundary conditions were set following basic guidelines (Tominaga et al., 2008b). The computational domain covered a volume of 21H(x_1)×13H(x_2)×6.5H(x_3). This domain was discretized into 1,112,200 hexahedral grids. These conditions were the same in both computations. Turbulence in the exhaust outlet flow was not considered.

1) RNG: The vertical distributions of <u_1>, k and ε at the inflow boundaries were based on the experiment. For the ground surface, the wall functions were modified for roughness, specified by an equivalent sand-grain roughness height k_s and a roughness constant C_r. k_s was defined using the function proposed by Blocken et al. (2007): k_s=9.793z_0/C_r. The value of z_0 was estimated by the velocity profile obtained by the experiment.

2) LES: A time-dependent inlet profile was generated by using the vortex method with a number of vortices N_v=190 (Gousseau et al., 2011). For the boundary condition at the solid walls (floor and building surfaces), a logarithmic-law was assumed.

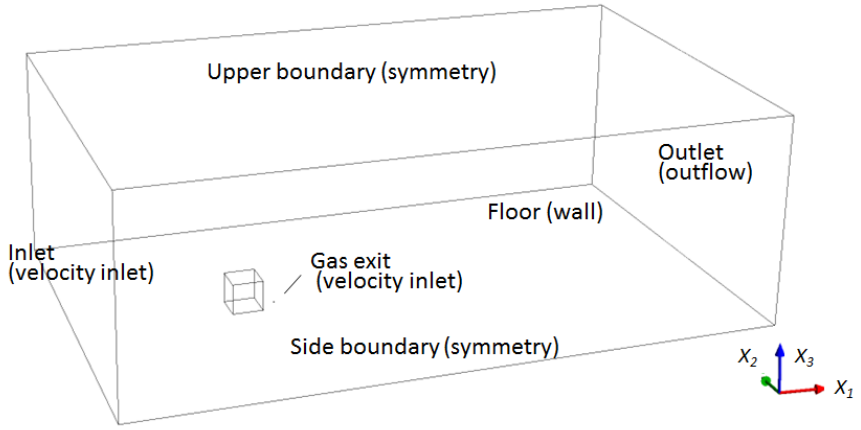

Figure 2. Computational domain.

4 RESULTS AND DISCUSSION

4.1 *Neutral gas case*

Figure 3 compares the contours of the time-averaged velocities of streamwise component ($<u_1>$) at the central section. Three computational results by the RANS approach show stronger reverse flow and longer reattachment length behind the building than those by two LES computations. In the RANS computations, the strongest recirculation flows are predicted by RNG and the weakest by SKE. The choice of SGS model in LES hardly influences the velocity predictions. The small recirculation region behind the building in the LES cases are mainly due to the fact that the periodic velocity fluctuation behind the building is well reproduced in comparison with RANS, as pointed out in previous studies (e.g. Tominaga et al. 2008a).

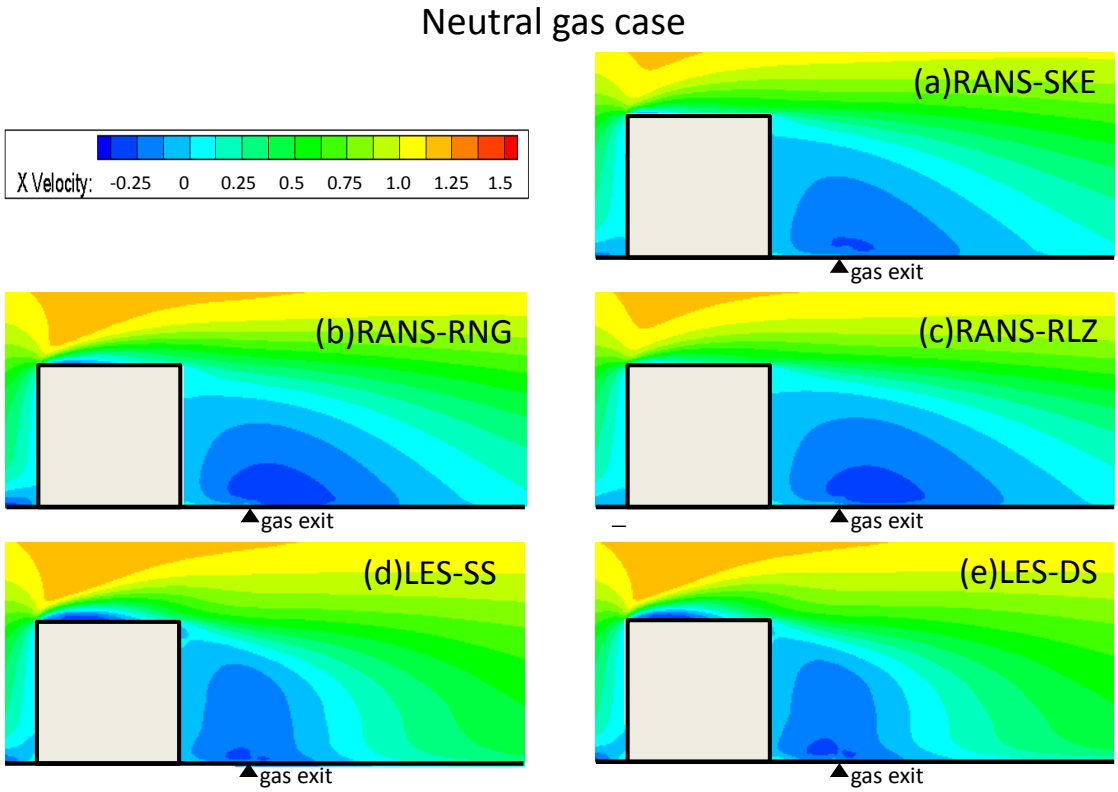

Figure 3. Contours of time-averaged streamwise velocity $<u_1>/<u_b>$ at center section: (a) RANS-SKE; (b) RANS-RNG; (c) RANS-RLZ; (d) LES-SS; (e) LES-DS.

Figure 4 shows the time-averaged concentrations at the center section. There is no significant difference among the general distributions of all models. It should be noted that the contour obtained by the experiment may give different expression from those of CFD because the experimental measuring pitch was coarse. In all the results, concentrations from the source exit are advected by the recirculation flow behind the building, and a high concentration region appears windward of the exit. The two LES cases predict smaller spread of concentration leeward of the exit in comparison with RANS. This difference between LES and RANS is mainly caused by the fact that the turbulent diffusion in the wake region is underestimated and the convective transport is dominant in RANS, as previously mentioned.

Figure 5 compares the vertical distributions of concentration at the mid-point between the building and the exit. All RANS computations show extremely large concentrations near the floor, which differs from the experiment and LES. The concentrations obtained by the two LES cases are lower and are closer to that of the experiment than those by RANS.

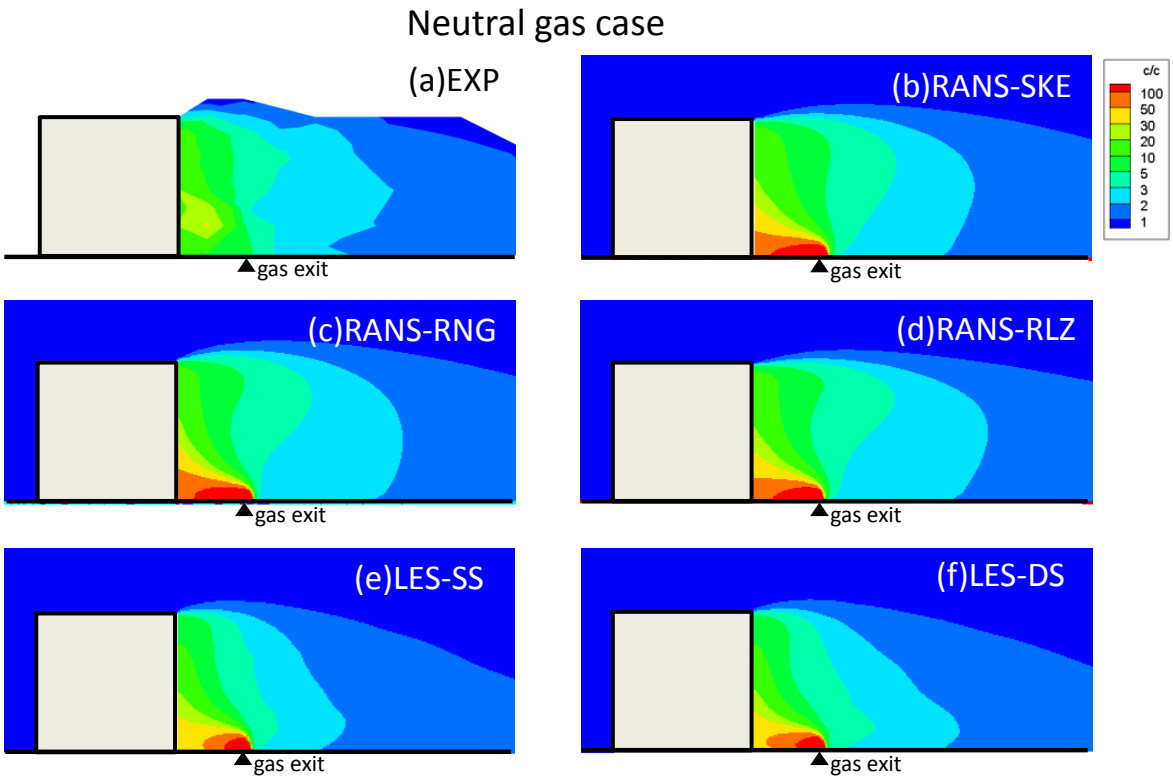

Figure 4. Contours of time-averaged concentration <c>/<c_0> (at center section): (a) experiment; (b) RANS-SKE; (c) RANS-RNG; (d) RANS-RLZ; (e) LES-SS; (f) LES-DS.

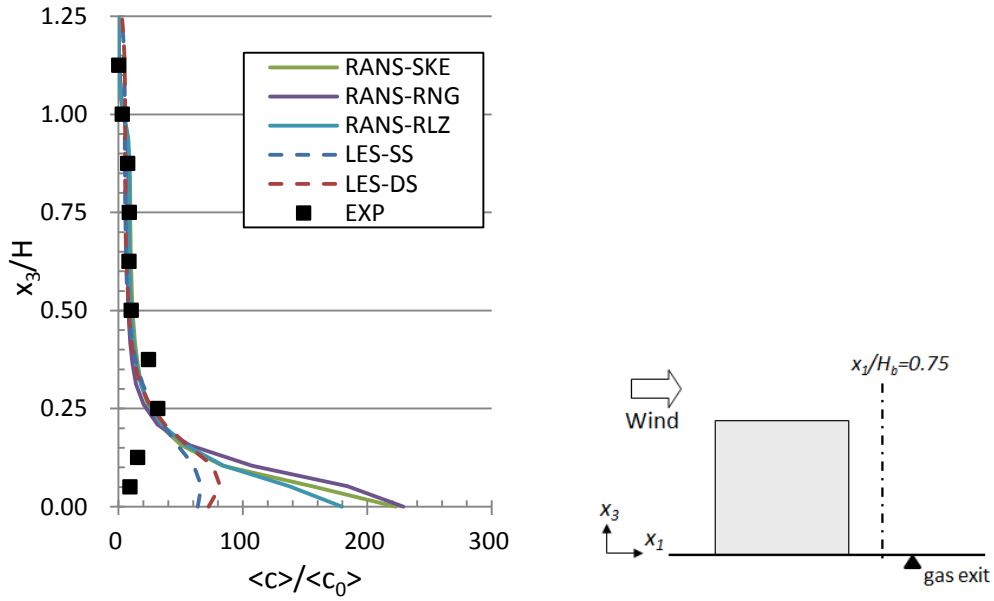

Figure 5. Vertical distributions of time-averaged concentration <c>/<c_0>.

4.2 *Buoyant and dense gas cases*

Only the RANS-RLZ and LES-DS cases, which show the best results for the neutral gas case for each modeling approach, are compared. Time-averaged concentration in the buoyant gas case is illustrated in Figure 6. The experimental results show that the concentration for the buoyant gas case is very low windward of the exit in comparison with that for the

neutral gas case. The concentration at the lower part of the wake region is especially low. These results are clearly affected by the positive buoyancy of the tracer gas. Although both CFD results reproduce this tendency due to buoyancy, the predicted upward spreads of the concentrations are smaller than those of the experiment. The vertical distribution of the time-averaged concentration along the line between the exit and the building is also shown in Figure 6. LES-DS succeeds in reproducing the tendency of the concentration to decrease near the floor as in the experiment, while the concentration increases as the position approaches the floor in the RANS-RLZ case. However, the concentration is underestimated by both models in the upper part.

The time-averaged concentration for the dense gas case is shown in Figure 7. The experimental results show very high concentrations in the lower part of the wake region. An extraordinarily high concentration region occurred near the floor windward of the source exit. This tendency is well reproduced in both CFD results. The vertical distribution of the time-averaged concentration is also indicated in Figure 7. The difference between the two models is small, and they both reproduce the tendency for the concentration to increase rapidly as the position approaches the floor. The difference between the prediction accuracies for the buoyant and dense gases can be explained as follows: For the buoyant gas, the flow field is more diffusive than for the neutral gas, because the density gradient is positive (unstable) in most of the wake region. Therefore, the previously-mentioned underestimation of turbulent diffusion behind the building in RANS acts more significantly than for the neutral gas. On the other hand, since the flow field is stable due to negative buoyancy and turbulent diffusion is suppressed for the dense gas, no such discrepancy occurs for RANS. Therefore, the difference between the two models is relatively small compared with the neutral and buoyant gas cases.

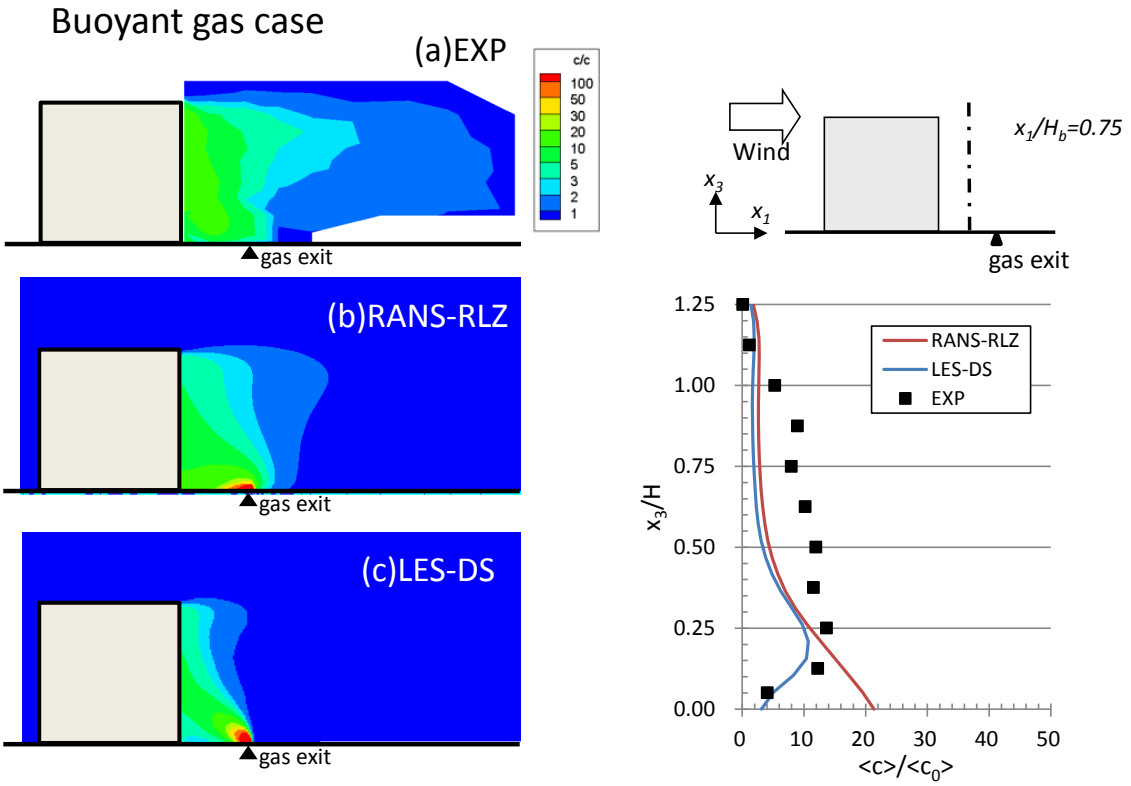

Figure 6 Time-averaged concentration <c>/<c_0> with buoyant gas. Left: Contour at center section obtained from (a) Experiment; (b) RANS-RLZ; and (c) LES-DS. Right: Comparison of vertical distributions at indicated line behind a building.

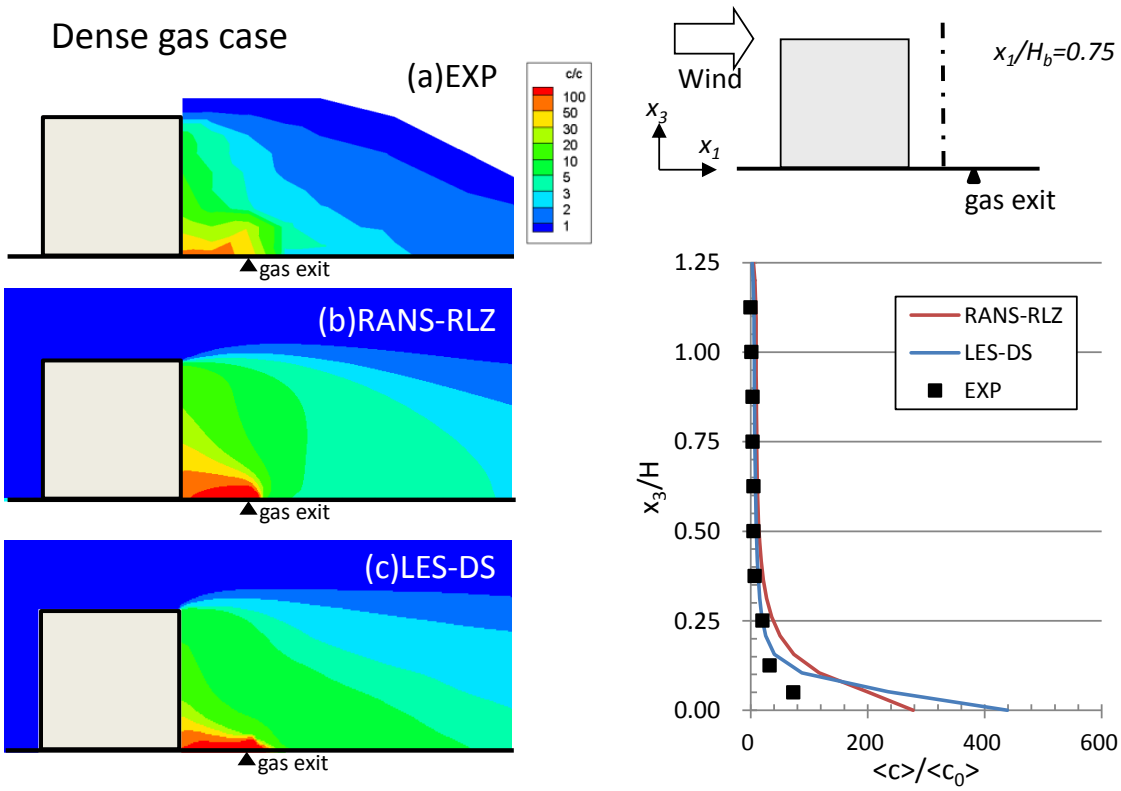

Figure 7. Time-averaged concentration <c>/<c_0> with dense gas. Left: Contour at center section obtained from (a) Experiment; (b) RANS-RLZ; and (c) LES-DS. Right: Comparison of vertical distributions at indicated line behind a building.

5 CONCLUSIONS

CFD simulations were performed for flow and dispersion fields around a cubic building model, in which the tracer gases were exhausted behind the building. The tracer gases were of three different densities, behaving as neutral, buoyant or dense gases. Two modeling approaches, steady RANS and LES, were used and compared. For the neutral gas, all RANS computations showed very large concentrations near the floor, which did not appear in the experimental and LES results. The same tendency was observed in the results for the buoyant gas. These high concentrations appearing in steady-RANS computations were mainly caused by underestimation of turbulent diffusion behind the building. On the other hand, since the density gradient was negative (stable) and turbulent diffusion was suppressed in the dense gas case, there was no noticeable discrepancy for steady-RANS. Therefore, the differences between the two models were relatively small in comparison with those for the neutral and buoyant gases. Detailed explanation on the influence of buoyancy effects on prediction accuracy will be presented in the final presentation.

NOMENCLATURE

c : concentration
<c_0>: standard gas concentration (=$q/(\langle u_b \rangle H^2)$)
<f> : ensemble average value of f
Fr_d :densimetric Froude Number (=$g\Delta\rho H/\rho_a \langle u_b \rangle^2$)
g : gravitational acceleration
H : building height
k : turbulent kinetic energy
q : gas emission rate

t^* : non-dimensional time unit ($=t<u_b>/H$)
u_i : three components of wind velocity
u_b : inflow velocity at building height H
w_s : exit velocity
x_i : three components of spatial coordinates (i=1,2,3: streamwise, lateral, vertical)
ρ_a : ambient air density
ρ_s : gas density

REFERENCES

Blocken B, Stathopoulos T, Carmeliet J. 2007. CFD simulation of the atmospheric boundary layer: wall function problems. Atmospheric Environment 41, 238-252.

Blocken, B., Stathopoulos, T., Saathoff, P. and Wang, X., 2008. Numerical evaluation of pollutant dispersion in the built environment: comparisons between models and experiments. Journal of Wind Engineering and Industrial Aerodynamics 96, 1817-1831.

ANSYS Inc., 2010. ANSYS FLUENT 13.0 Users guide. FLUENT Inc., Lebanon.

Gavelli, F., Bullister, E. and Kytomaa, H., 2008. Application of CFD (Fluent) to LNG spills into geometrically complex environments. Journal of Hazardous Materials 159, 158-168.

Germano, M., Piomelli, U., Moin, P., Cabot, W.H., 1991. A dynamic subgrid-scale eddy viscosity model. Physics of Fluids A3, 1760-1765.

Gousseau, P., Blocken, B., & van Heijst, G. J. F., 2011. CFD simulation of pollutant dispersion around isolated buildings: on the role of convective and turbulent mass fluxes in the prediction accuracy. Journal of Hazardous Materials 194, 422-434.

Hanna, S., R., Hansen, O., R., Dharmavaram, S., 2004. FLACS CFD air quality model performance evaluation with Kit Fox, MUST, Prairie Grass, and EMU observations. Atmospheric Environment 38, 4675-4687.

Hu ,L.H., Xu, Y., Zhu, W., Wu, L., Tang F, Lu K.H. 2011. Large eddy simulation of pollutant gas dispersion with buoyancy ejected from building into an urban street canyon. Journal of Hazardous Materials 192, 940-948.

Meroney, R. N., 2010. CFD prediction of dense gas clouds spreading in a mock urban environment. The Fifth International Symposium on Computational Wind Engineering (CWE2010), Chapel Hill, North Carolina, USA, May 23-27, 2010.

Smagorinsky, J., 1963. General circulation experiments with the primitive equations I. The basic experiment. Monthly Weather Review 91, 99-164.

Shih, T.H., Liou, W. W., Shabbir, A., Yang, Z. and Zhu, J., 1995. A new k-ε eddy viscosity model for high Reynolds number turbulent flows. Computers and Fluids 24, 227-238.

Tominaga, Y. Murakami, S., Mochida, A., Shibuya, A., Noguchi, Y., 1992. Wind tunnel tests on turbulent diffusion and concentration fluctuation of buoyant gas near building. Proceedings of 12th National Symposium on Wind Engineering, 119-124. (in Japanese)

Tominaga, Y., Murakami, S., Mochida, A., 1997. CFD Prediction of Gaseous Diffusion around a Cubic Model using a Dynamic Mixed SGS Model based on Composite Grid Technique. Journal of Wind Engineering and Industrial Aerodynamics 67&68, 827-841.

Tominaga, Y., Mochida, A., Murakami, S., Sawaki, S., 2008a. Comparison of various revised k-ε models and LES applied to flow around a high-rise building model with 1:1:2 shape placed within the surface boundary layer. Journal of Wind Engineering and Industrial Aerodynamics 96, 389-411.

Tominaga, Y., Mochida, A., Yoshie, R., Kataoka, H., Nozu, T., Yoshikawa, M., Shirasawa, T., 2008b. AIJ guidelines for practical applications of CFD to pedestrian wind environment around buildings. Journal of Wind Engineering and Industrial Aerodynamics 96, 1749-1761.

Tominaga, Y., Stathopoulos, T., 2010. Numerical simulation of dispersion around an isolated cubic building: Model evaluation of RANS and LES. Building and Environment 45, 2231-2239.

Yakhot, V., Orszag, S.A., Thangam, S., Gatski, T.B., Speziale, C.G., 1992. Development of turbulence models for shear flows by a double expansion technique. Physics of Fluids A4, 1510–1520.

The Seventh International Colloquium on Bluff Body Aerodynamics and Applications (BBAA7)
Shanghai, China; September 2-6, 2012

Analysis of unsteady concentration and flow statistics around an isolated building by Large-Eddy Simulation

P. Gousseau [a], B. Blocken [a], G.J.F. van Heijst [b]

[a] *Building Physics and Services, Department of the Built Environment, Eindhoven University of Technology, P.O. Box 513, Eindhoven, The Netherlands*
[b] *Fluid Dynamics Laboratory, Department of Applied Physics, Eindhoven University of Technology, P.O. Box 513, Eindhoven, The Netherlands*

ABSTRACT: Large-Eddy Simulation is used to simulate wind-induced pollutant dispersion from a vent on the roof of a cubical building. The profiles of the computed mean value and standard deviation of the concentration in the wake of the building are compared to wind-tunnel measurements and good agreement is found. The velocity and concentration values at two monitoring points located in the shear layer developing above the roof have been sampled at each time step of the simulation. The statistics are presented and analyzed to provide insight into the dispersion process. In particular, the fact that the turbulent mass flux in the streamwise direction is directed from the low to high levels of mean concentration (counter-gradient mechanism) is explained.

KEYWORDS: Urban wind flow; scalar transport; turbulent mass flux; counter-gradient diffusion; turbulent Schmidt number.

1 INTRODUCTION

Computational Fluid Dynamics (CFD) is increasingly used to predict pollutant dispersion around buildings and in cities (e.g. Tominaga et al., 1997; Blocken et al., 2008; Gromke et al., 2008; Tominaga and Stathopoulos, 2010; Gousseau et al., 2011a; Gousseau et al., 2011b; Tominaga and Stathopoulos, 2011). Overall, it has been confirmed that Large Eddy Simulation (LES) is inherently more accurate than the Reynolds-Averaged Navier-Stokes (RANS) turbulence modeling approach for modeling wind flow and dispersion in urban environments (e.g. Tominaga and Stathopoulos, 2010; Gousseau et al., 2011a; Gousseau et al., 2011b; Tominaga and Stathopoulos, 2011).

Most of the two-equation RANS turbulence models like the standard or realizable k-ε models compute the turbulence-induced transport of concentration – and more generally, of scalars – based on the gradient of the mean value, with the so-called gradient-diffusion (GD) hypothesis, also called first-order closure:

$$\overrightarrow{Q_{a,t}} = -D_{a,t}\nabla A \tag{1}$$

where $\overrightarrow{Q_{a,t}}$ is the turbulent flux of a, $D_{a,t}$ is the turbulent diffusivity and $A=\langle a \rangle$ is the mean value of a. However, some recent studies (Rossi et al., 2010; Gousseau et al., 2011b) have shown that this hypothesis is not valid in the streamwise direction for dispersion around an isolated building. In this case, above roof level, the turbulent mass flux is directed backwards, i.e. from the low to high levels of mean concentration, in contradiction with Equation 1. This so-called counter-gradient (CG) mechanism of turbulent transport has also been reported in the literature for various cases such as a ground-level line source in a street canyon (Simoëns and Wallace,

2008), a line source in a turbulent boundary layer (Raupach and Legg, 1983; Lavertu and Mydlarski, 2005), or a stratified shear flow (Meroney, 1976).

The CG mechanism cannot be reproduced by RANS models which use Equation 1 to model the turbulent mass transport. Therefore, more elaborate models are needed. To support the choice of the existing appropriate model or to develop a new one, a more complete understanding of the physical mechanism of dispersion around bluff bodies is needed. The present study aims at exploring this mechanism with LES. Since the turbulent mass flux in a given direction is equal to the covariance of velocity and concentration, the observation of the statistics of these variables allows providing insight into the dispersion process and in particular to aid in explaning the CG mechanism in the streamwise direction.

The case under study corresponds to a wind-tunnel experiment which is briefly described in the next section together with the numerical model used. The experimental results are used to validate the CFD results in section 3. Next, the CFD simulations are used to monitor velocity and concentration statistics in two points located in the shear layer developing above the roof of the building, and the results are analyzed in the framework of turbulent mass transport.

2 NUMERICAL MODEL

2.1 Domain, grid and boundary conditions

The wind-tunnel experiment by Li and Meroney (Li and Meroney, 1983a; Li and Meroney, 1983b) has been reproduced with the Ansys 12.1 CFD code. It involves a cubical building model (height H=0.05m) immersed in a turbulent atmospheric boundary layer (ABL) with a mean velocity profile corresponding to a power law with an exponent equal to 0.19 and an aerodynamic roughness length z_0=7.5×10^{-5}m. Wind direction is perpendicular to the windward façade. At the center of the roof, helium is emitted by a 5mm diameter circular exhaust with a low velocity ratio M=0.19 (M=W_e/U_H where W_e is the vertical exhaust velocity and U_H is the mean velocity in the approaching ABL at building height). The Reynolds number based on H and U_H is equal to 1.1×10^4.

The computational domain is shown in Figure 1a. Its dimensions are 26H×11H×6H in the streamwise (x), lateral (y) and vertical (z) direction, respectively, following the COST Action 732 (Franke et al., 2007) and AIJ (Tominaga et al., 2008) guidelines. The ground and building walls are defined as no-slip walls. At the top and sides of the domain, symmetry boundary conditions are set. Zero static pressure is imposed at the outlet face of the domain. At the inlet, unsteady perturbations are super-imposed on the prescribed mean velocity profile by the vortex method (Mathey et al., 2006) with a number of vortices equal to 190. This technique also requires the vertical profiles of turbulent kinetic energy and dissipation rate, which are prescribed based on the experiments.

The computational grid has been created with the surface grid-extrusion technique (van Hooff and Blocken, 2010). It counts 1,480,754 cells in total and the building is discretized into 32 cells in the vertical direction and 25 cells in the lateral and streamwise directions (Fig. 1b). The monitoring points P1 and P2 are also shown in Figure 1b. P1 is located at x/H=1; y/H=0; z/H=1.24 and P2 at x/H=2; y/H=0.25; z/H=1.24.

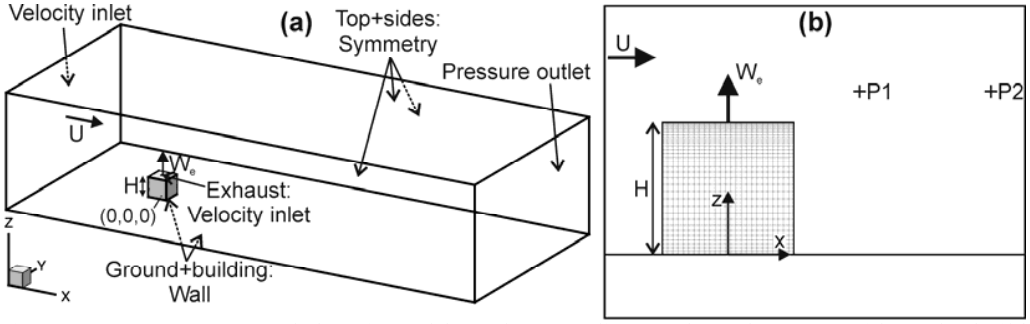

Figure 1. (a) Computational domain and boundary conditions. (b) Side view: grid on the building surface (total number of cells: 1,480,754) and location of the two monitoring points P1 and P2.

2.2 LES and dispersion modeling

In the remainder of the paper, the Reynolds decomposition is used for all variables; for example a is decomposed into its time-average component $A=\langle a \rangle$ and its fluctuation a' such that $a=A+a'$. Furthermore, in what follows, the overbar is used to symbolize the spatial-filtering operator. Note that it will be used only in this section and will be omitted in the remaining of the paper.

LES has been used with the dynamic Smagorinsky subgrid-scale (SGS) model (Smagorinsky, 1963; Germano et al., 1991; Lilly, 1992): the Smagorinsky coefficient C_s which allows computing the SGS turbulent viscosity is evaluated at each time step, based on the smallest resolved scales of motion.

The Eulerian approach has been adopted to compute the transport of the tracer gas concentration (c). In the filtered dispersion equation, the SGS mass flux $\overrightarrow{q_{SGS}}$ stands for the effects of the smallest scales of motion on the dispersion process. It is assumed to be proportional to the gradient of resolved concentration:

$$q_{SGS,i} = \overline{u_i c} - \overline{u}_i \overline{c} = -D_{SGS} \frac{\partial \overline{c}}{\partial x_i} \tag{2}$$

where D_{SGS} is the SGS diffusivity, computed with a dynamic procedure in the similar way as C_s (Moin et al., 1991).

The turbulent mass flux $\overrightarrow{Q_t}$ is the combined effect of the concentration and velocity fluctuations, plus the mean SGS mass flux:

$$Q_{t,i} = \langle \overline{u}_i' \overline{c}' \rangle + \langle q_{SGS,i} \rangle \tag{3}$$

Reference concentration (C_0) and flux (Q_0) are used to make the variables non-dimensional. These quantities are defined by:

$$C_0 = \frac{Q_e}{H^2 U_H} \tag{4}$$

$$Q_0 = C_0 \times U_H \tag{5}$$

where Q_e is the pollutant exhaust rate.

Discretization of the filtered momentum equation is performed with a second-order accurate bounded central-differencing scheme. A second-order scheme is used for the spatial derivatives of the other equations (energy, concentration). Pressure interpolation is second order. The non-iterative time advancement scheme is used for the unsteady solver, with the fractional step meth-

od for pressure-velocity coupling (Kim and Moin, 1985). One single outer iteration is performed per time step, allowing reduction of the computational time needed for the simulation. A fixed time step Δt^*=0.066 in non-dimensional time units ($\Delta t^* = \Delta t \times U_H/H$, where Δt is the physical time step) has been set. After an initialization period, which allows losing the dependence on the non-physical initial state, averaging is performed during t^*=1,584. The data at the monitoring points are stored at each of these 24,000 time steps.

3 MEAN CONCENTRATION AND TURBULENT MASS FLUX

The profiles of the non-dimensional concentration coefficient ($K=C/C_0$) and the non-dimensional standard deviation of concentration ($c_{rms}/C_{1G}=(<c'^2>)^{1/2}/C_{1G}$) obtained with LES along three vertical lines (x/H=1; 3; 5) in the vertical mid-plane are compared to the wind-tunnel measurements in Figure 2. The standard deviation of concentration is normalized by the mean ground concentration value at x/H=1 and y/H=0 (C_{1G}). Along these three lines, a good agreement is obtained for K (Fig. 2a). Close to the building, at x/H=1, the LES results over-estimate the concentration fluctuations (Fig. 2b). Along the two other lines, there is a very close agreement.

Contours of the different turbulent mass flux components are depicted in Figure 3. In this figure, the isolines $\partial C/\partial x_i$=0 in the corresponding directions are also shown (dashed lines) and, in circles, the sign of $\partial C/\partial x_i$ for each zone delimited by the dashed line. As far as the vertical and lateral components of the turbulent flux ($Q_{t,z}$ and $Q_{t,y}$) are concerned, the contours in Figures 3c and 3d show that turbulent mass transport operates as a diffusion mechanism directed from the high towards the low concentration values, i.e. from the centerline of the plume to its outer edges. In the streamwise direction, however, the mechanism is different. In the horizontal plane z/H=1.25 for example, and more generally in the large region above the roof level colored in light gray in Figure 3a, the streamwise turbulent mass flux is negative, i.e. directed towards the high levels of K. In this region where the turbulent mass flux and the mean concentration gradient are of the same sign, the CG mechanism of turbulent mass transport is present. Another CG zone is present in the near-wake of the building where both $Q_{t,x}$ and $\partial C/\partial x$ are positive.

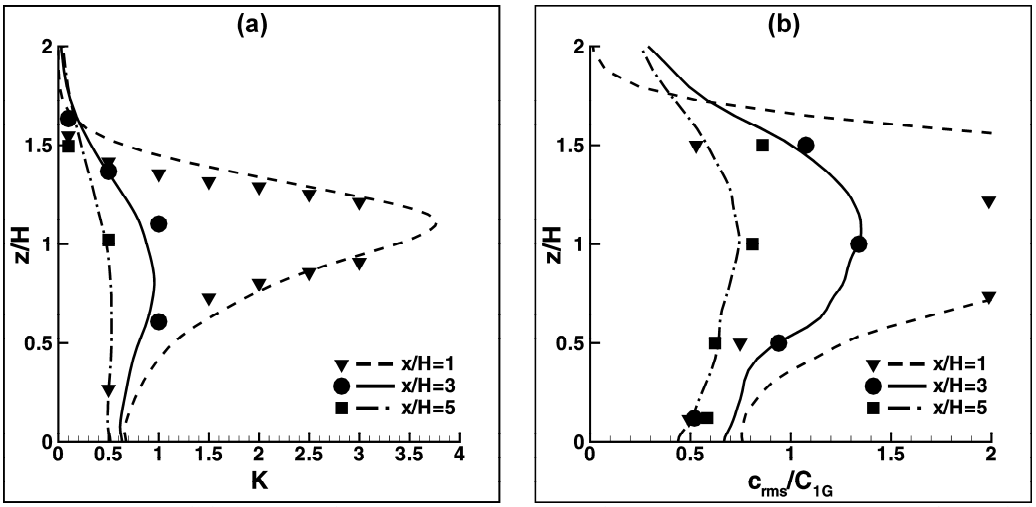

Figure 2. CFD validation: profiles of (a) non-dimensional concentration coefficient $K=C/C_0$ and (b) standard deviation of concentration normalized by C_{1G} along three vertical lines in the plane y/H=0. Symbols: wind-tunnel measurements (Li and Meroney, 1983a; Li and Meroney, 1983b); lines: LES of this study.

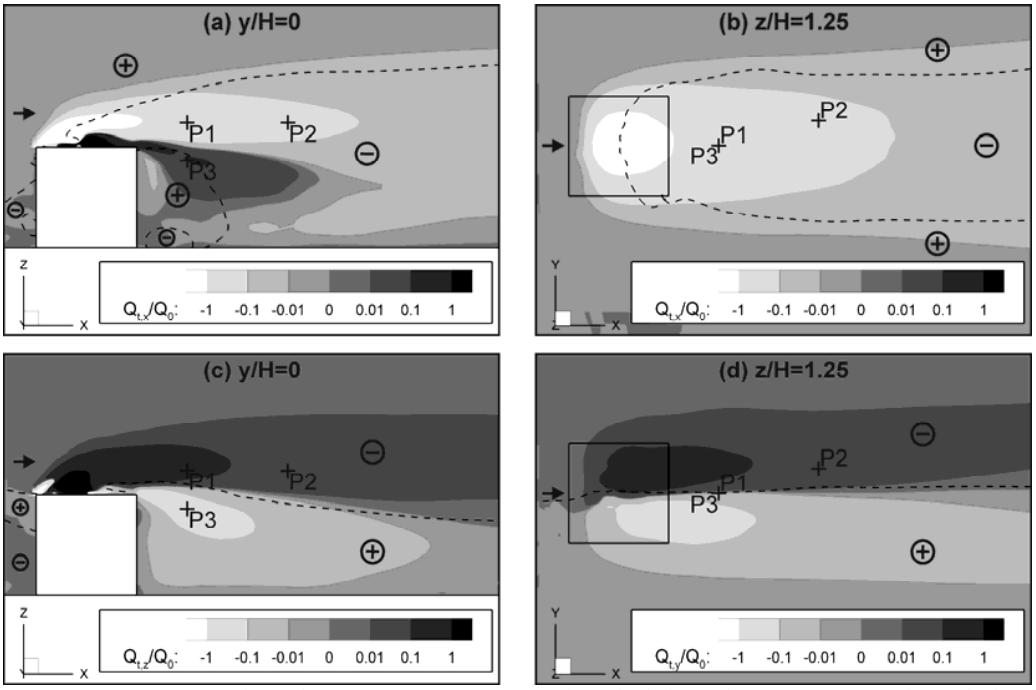

Figure 3. Contours of the (a,b) streamwise, (c) vertical, and (d) lateral components of the turbulent mass flux vector. The dashed lines represent the isolines $\partial C/\partial x_i$=0 in the corresponding direction: (a,b) x_i=x, (c) x_i=z, (d) x_i=y. On each side of the isoline, the sign of $\partial C/\partial x_i$ is indicated in circles (+: positive; -: negative). The CG mechanism of turbulent mass transport is characterized by $Q_{t,i}$ and $\partial C/\partial x_i$ of the same sign for a given direction

4 CONCENTRATION AND VELOCITY STATISTICS AT THE TWO MONITORING POINTS

The resolved concentration (c) and velocity components (u, v, w) have been recorded at the two monitoring points at each of the 24,000 time steps of the simulation. For the four variables of interest, the range of the non-dimensional fluctuations (a'_k/a_{rms}, where k is the sample number and the subscript rms indicates the standard deviation,) has been divided into 50 equal intervals I_i (i=1,…,50) and the frequency f_i of occurrence of a'_k/a_{rms} belongs to I_i has been calculated to build the histogram of frequency distribution:

$$f_i = \frac{n_i}{N} \quad (i = 1,...,50) \tag{6}$$

where n_i is the number of samples such as a'_k/a_{rms} belongs to I_i and N is the total number of samples.

The histograms for point P1 are shown in Figure 4. The histogram of concentration fluctuations (Fig. 4a) has an exponential-like shape, which indicates that P1 is most of the time characterized by a low background concentration level and the occurrence of rare but extremely high peaks of concentration (the kurtosis of the frequency distribution is high). Approximately 60% of the samples are of negative fluctuation and the average is raised by peaks of c' reaching up to 13 times the standard deviation. This asymmetry around the mean is quantified by the high skewness value. This shape of frequency distribution corresponds to measurements by Fackrell and Robins (Fackrell and Robins, 1982) far from the ground in the case of an elevated point source and was attributed to the meandering motion of the plume caused by large turbulent eddies.

Here, the largest turbulence scales are of the order of the cube size, larger than the size of the plume at P1, and tend to move the plume as a block, resulting in the high intermittency observed at this monitoring point.

The frequency distribution of u'/u_{rms} shows negative skewness (Fig. 4b): among the samples, the majority is of positive fluctuation but some of them are characterized by a large negative u'. The opposite holds for the vertical velocity fluctuations, whose frequency distribution is right-tailed (Fig. 4d). Considering that P1 lies in the vertical symmetry plane of the computational domain, it is logical that the frequency distribution of v'/v_{rms} is symmetric with respect to its zero mean (Fig. 4c).

A similar approach can be used to analyze the statistics of the variables two by two. The bivariate histograms have been built for the three couples of variables (c'/c_{rms}; $u_i'/u_{i,rms}$). For example, for two variables a and b, the range of the non-dimensional fluctuations has been divided into an arbitrary number of intervals (here: 20), say I_i for a'_k/a_{rms} and J_j for b'_k/b_{rms}. For given i and j, the frequency $f_{i,j}=f(I_i,J_j)$ is the ratio of the number of samples $n_{i,j}$ for which a'_k/a_{rms} belongs to I_i and simultaneously b'_k/b_{rms} belongs to J_j to the total number of samples N:

$$f_{i,j} = \frac{n_{i,j}}{N} \quad (i, j = 1,...,20) \tag{7}$$

Each of the four combinations of signs of (c'/c_{rms}; $u_i'/u_{i,rms}$) is associated with a specific event of pollutant transport. Observing the bivariate histograms gives therefore an indication of which events are the most frequent among the samples and/or contribute most to the turbulent flux. This so-called quadrant analysis was first introduced for momentum transfer (Shaw et al., 1983) but is also widely used in the case of scalar dispersion (Chen, 1990; Cheng and Liu, 2011). The definitions of the quadrants are shown in Table 1, together with the name given to the corresponding event in the vertical direction, for which quadrant analysis is often used. Note that this nomenclature can also be used here for the lateral direction, considering the symmetry of our problem. The frequency of occurrence of a given quadrant Q_m is equal to the sum of the frequencies of the intervals which compose Q_m. This frequency multiplied by the average of $u_i'c'$ on Q_m ($<u_i'c'>_{|Qm}$) gives the contribution of the quadrant Q_m to the turbulent flux in the direction i.

Table 1. Numbering and definitions of the quadrants. The names of the corresponding events hold for the vertical direction, following (Chen, 1990).

Quadrant	u_i'	c'	Name (z-direction)
Q1	>0	>0	Ejection
Q2	<0	>0	Inward interaction
Q3	<0	<0	Sweep
Q4	>0	<0	Outward interaction

The contours of $f_{i,j}$ in the planes (c'/c_{rms}; $u_i'/u_{i,rms}$) for P1 are shown in Figure 5. In the streamwise direction (Fig. 5a), the most frequent situation among the samples is simultaneously $u'>0$ and $c'<0$ (Q4): 46% of the samples are in this zone. Nevertheless, the most important contribution to the total turbulent flux is due to Q2, for which the frequency (27%) is lower than for Q4 but for which the individual contributions $u'c'$ are on average higher in magnitude. The contributions of Q1 and Q3 are minor in this case, both in terms of frequency and magnitude. The dominant contributions of Q2 and Q4, where u' and c' are of opposite signs, result on average in a negative turbulent flux $<u'c'>$. Concerning the lateral direction, the frequency distribution of (c'/c_{rms}; v'/v_{rms}) is approximately symmetrical with respect to the axis $v'=0$, leading to a zero turbulent mass flux in the lateral direction (Fig. 5b). Concerning the vertical direction, sweeps (Q3)

are the most frequent events of vertical mass transfer at P1 (Fig. 5c); they correspond to downward motions of fresh air. However, the calculation of the contribution of each quadrant to $Q_{t,z}$ shows that the dominant contribution is made by ejections (Q1), which occur less often but are more intense.

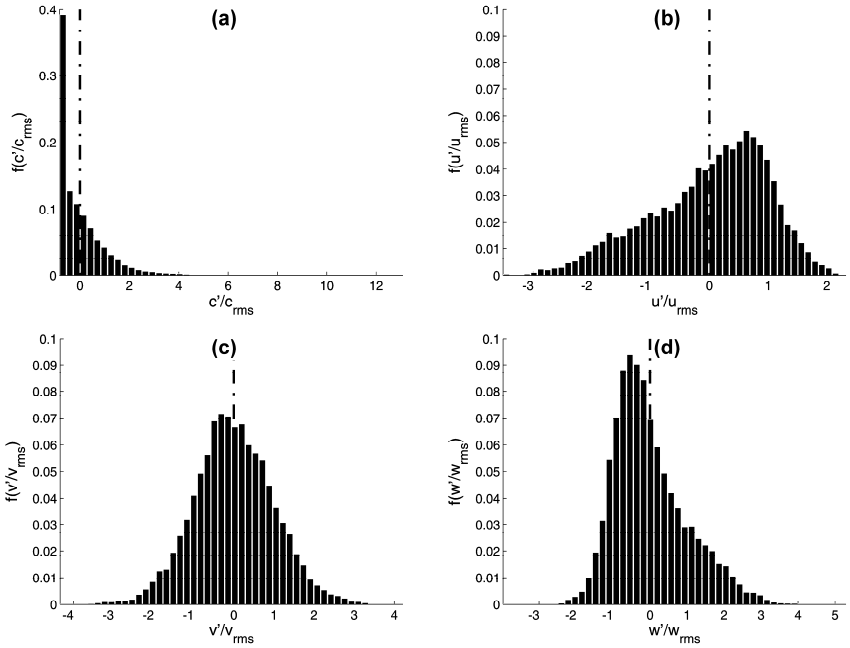

Figure 4. Point P1: frequency distribution histograms of (a) c'/c_{rms}, (b) u'/u_{rms}, (c) v'/v_{rms}, and (d) w'/w_{rms}. For each variable, the x-axis limits correspond to the minimum and maximum sample values. The dashed line indicates the mean (zero) values of the fluctuations. Mean values: K=3.00; U/U_H=0.84; V/U_H=0.01; W/U_H=-0.11.

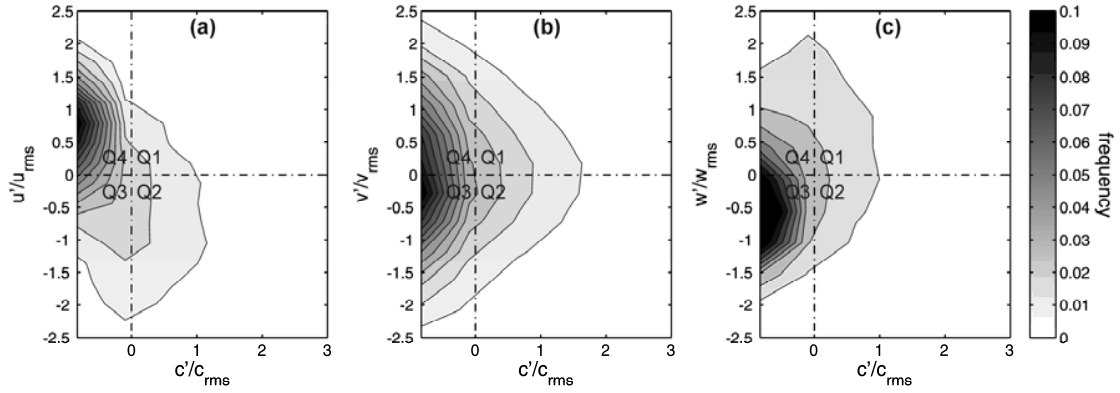

Figure 5. Point P1: bivariate histogram of frequency distribution for (a) (c'/c_{rms}; u'/u_{rms}), (b) (c'/c_{rms}; v'/v_{rms}), and (c) (c'/c_{rms}; w'/w_{rms}).

Figure 6a shows the frequency distribution of c'/c_{rms} for P2. The trend is similar as for P1, with even higher values of skewness and kurtosis, because of the off-center position of the sampling point at which the plume intermittency is higher (Fackrell and Robins, 1982). Approximately 65% of the samples have concentration values between zero and one third of the mean concentration value at this point. The velocity fluctuations in the x- and z-directions also have similar frequency distributions as those at P1, with a negative and positive skewness, respective-

ly. The main difference with point P1 is the asymmetry of the histogram of v'/v_{rms}, quantified by the non-zero skewness. This feature is due to the position of P2 out of the symmetry plane of the geometry.

The bivariate histogram of (c'/c_{rms}; v'/v_{rms}) is similar in shape to the one of (c'/c_{rms}; w'/w_{rms}) (Figs. 7b,c): a large majority of the samples belongs to Q3 and the main contribution to the mass flux is due to intense ejections corresponding to quadrant Q1. Hence, both $Q_{t,y}$ and $Q_{t,z}$ are positive at P2. Concerning the streamwise direction, the bivariate histogram (Fig. 7a) is similar in shape to the one at P1. Note that the intense Q2 events in the x-direction coincide with Q1 events in the y- and z-directions (not shown here).

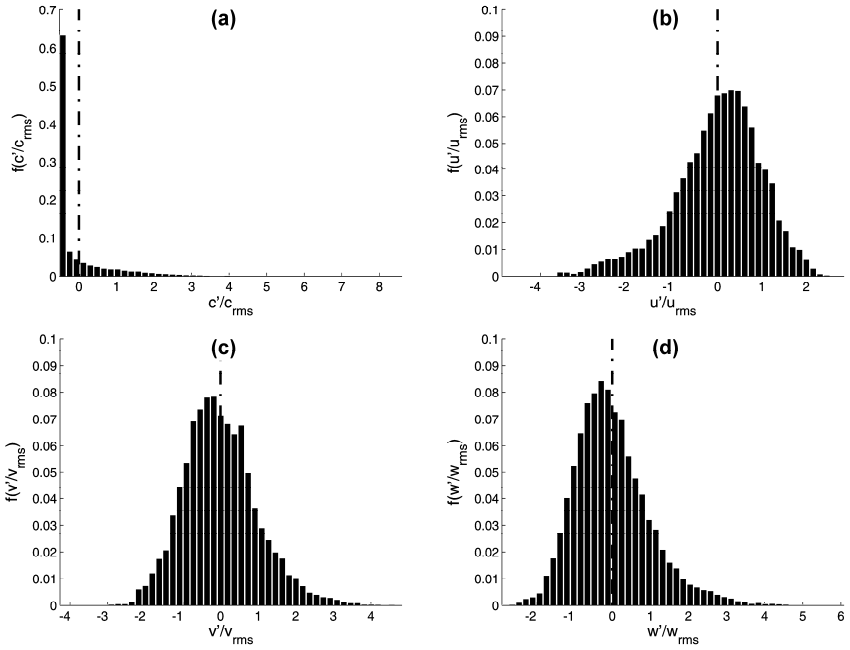

Figure 6. Point P2: frequency distribution histograms of (a) c'/c_{rms}, (b) u'/u_{rms}, (c) v'/v_{rms}, and (d) w'/w_{rms}. For each variable, the x-axis limits correspond to the minimum and maximum sample values. The dashed line indicates the mean (zero) values of the fluctuations. Mean values: K=0.50; U/U_H=0.94; V/U_H=-0.04; W/U_H=-0.08.

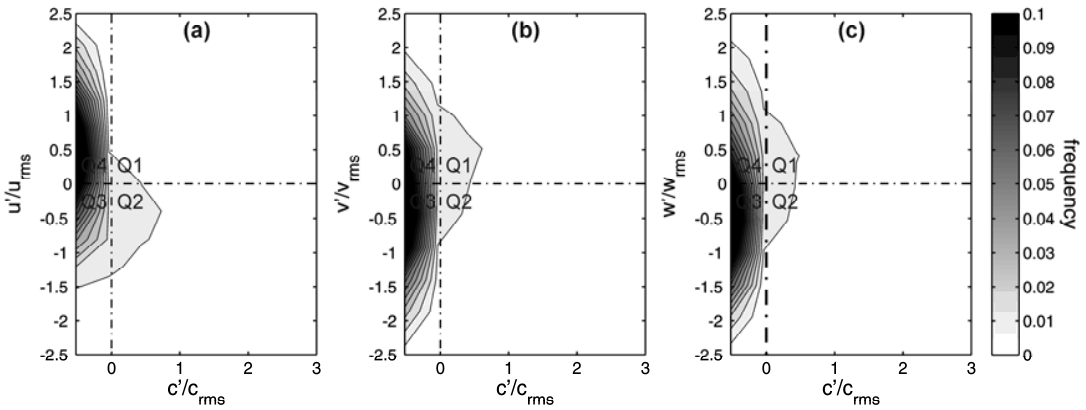

Figure 7. Point P2: bivariate histogram of frequency distribution for (a) (c'/c_{rms}; u'/u_{rms}), (b) (c'/c_{rms}; v'/v_{rms}), and (c) (c'/c_{rms}; w'/w_{rms}).

5 DISCUSSION AND CONCLUSIONS

Large-Eddy Simulation of pollutant dispersion around an isolated cubical building has been performed. The results have been compared with wind-tunnel measurements in terms of mean and standard deviation of concentration in the wake of the building and a fairly good agreement has been found between numerical and experimental values.

The velocity and concentration statistics have been reported for two points located in the shear layer developing above roof level. At this location, vortical structures generated at the front corner of the building and which are transported downstream are responsible for the meandering motion of the plume (see (Gousseau et al., 2012) for a further analysis of the flowfield). This could be observed in the histogram of frequency distribution of the concentration fluctuations at these two points: the exponential shape traduces the low background concentration and the occurrence of rare but intense peaks of concentration. The vortical structures also affect the frequency distributions of the velocity components by creating non-zero skewness. This holds also in the shear layers developing on the sides of the building (point P2). The bivariate analysis showed that for a given sign of c' there is a preferred sign of u_i' which is more likely to occur. In the streamwise direction, it was shown at P1 and P2 that c' and u' most of the time have opposite signs, leading on average to a negative turbulent mass flux $Q_{t,x}$ and explaining the CG mechanism in this zone.

It has been shown that specific unsteady events govern turbulent mass transport, which explains the failure of the first-order closure model (Eq. 1). If used, this model should be adapted to reproduce the CG mechanism of turbulent mass transport – for example by taking out the minus sign from the right-hand side of Equation 1 – and to take into account the flow anisotropy, by use of a diffusivity vector.

6 REFERENCES

B. Blocken, T. Sathopoulos, P. Saathoff and X. Wang, Numerical evaluation of pollutant dispersion in the built environment: Comparisons between models and experiments, Journal of Wind Engineering and Industrial Aerodynamics, 96 (2008) 1817-1831.

F. Chen, Turbulent characteristics over a rough natural surface. Part I: Turbulent structures, Boundary-Layer Meteorology, 52 (1990) 151-175.

W.C. Cheng and C.H. Liu, Large-Eddy Simulation of flow and pollutant transports in and above two-dimensional idealized street canyons, Boundary-Layer Meteorology, 139 (2011) 411-437.

J.E. Fackrell and A.G. Robins, Concentration fluctuations and fluxes in plumes from point sources in a turbulent boundary layer, Journal of Fluid Mechanics, 117 (1982) 1-26.

J. Franke, A. Hellsten, H. Schlünzen and B. Carissimo, Best practice guideline for the CFD simulation of flows in the urban environment, COST Action 732, 2007.

M. Germano, U. Piomelli, P. Moin and W.H. Cabot, A dynamic subgrid-scale eddy viscosity model, Physics of Fluids, A 3 (1991) 1760-1765.

P. Gousseau, B. Blocken, T. Stathopoulos and G.J.F. van Heijst, CFD simulation of near-field pollutant dispersion on a high-resolution grid: a case study by LES and RANS for a building group in downtown Montreal, Atmospheric Environment, 45 (2011a) 428-438.

P. Gousseau, B. Blocken and G.J.F. van Heijst, CFD simulation of pollutant dispersion around isolated buildings: On the role of convective and turbulent mass fluxes in the prediction accuracy, Journal of Hazardous Materials, 194 (2011b) 422-434.

P. Gousseau, B. Blocken and G.J.F. van Heijst, Large-Eddy Simulation of pollutant dispersion around a cubical building: Analysis of the turbulent mass transport mechanism by unsteady concentration and velocity statistics, Environmental Pollution (2012), doi: 10.1016/j.envpol.2012.03.021.

C. Gromke, R. Buccolieri, S.D. Sabatino and B. Ruck, Dispersion study in a street canyon with tree planting by means of wind tunnel and numerical investigations - Evaluation of CFD data with experimental data, Atmospheric Environment, 42 (37) (2008) 8640-8650.

J. Kim and P. Moin, Application of a fractional step method to incompressible Navier-Stokes equations, Journal of Computational Physics, 59 (1985) 308-323.

R.A. Lavertu and L. Mydlarski, Scalar mixing from a concentrated source in turbulent channel flow, Journal of Fluid Mechanics, 528 (2005) 135-172.

W.W. Li and R.N. Meroney, Gas dispersion near a cubical model building – Part I. Mean concentration measurements, Journal of Wind Engineering and Industrial Aerodynamics, 12 (1983a) 15-33.

W.W. Li and R.N. Meroney, Gas dispersion near a cubical model building – Part II. Concentration fluctuation measurements, Journal of Wind Engineering and Industrial Aerodynamics, 12 (1983b) 35-47.

D.K. Lilly, A proposed modification of the Germano subgrid-scale closure method, Physics of Fluids, A 4 (1992) 633-635.

F. Mathey, D. Cokljat, J.P. Bertoglio and E. Sergent, Assessment of the vortex method for large eddy simulation inlet conditions, Progress in Computational Fluid Dynamics, 6 (2006) 58-67.

R.N. Meroney, An algebraic stress model for stratified turbulent shear flows, Computer and Fluids, 4 (1976) 93-107.

P. Moin, K. Squires, W. Cabot and S. Lee, A dynamic subgrid-scale model for compressible turbulence and scalar transport, Physics of Fluids, A3-11 (1991) 2746-2757.

M.R. Raupach and B.J. Legg, Turbulent dispersion from an elevated line source: measurements of wind-concentration moments and budgets, Journal of Fluid Mechanics, 136 (1983) 111-137.

R. Rossi, D.A. Philips and G. Iaccarino, A numerical study of scalar dispersion downstream of a wall-mounted cube using direct simulations and algebraic flux models, International Journal of Heat and Fluid Flow, 31 (2010) 805-819.

R.H. Shaw, J. Tavangar and D.P. Ward, Structure of the Reynolds stress in a canopy layer, Journal of Climate and Applied Meteorology, 22 (1983) 1922-1931.

S. Simoëns and J.M. Wallace, The flow across a street canyon of variable width—Part 2: Scalar dispersion from a street level line source, Atmospheric Environment, 42 (2008) 2489-2503.

J. Smagorinsky, General circulation experiments with the primitive equations. I. The basic experiment, Monthly Weather Review, 91 (1963) 99-164.

Y. Tominaga, S. Murakami and A. Mochida, CFD prediction of gaseous diffusion around a cubic model using a dynamic mixed SGS model based on composite grid technique, Journal of Wind Engineering and Industrial Aerodynamics, 67 & 68 (1997) 827-841.

Y. Tominaga, A. Mochida, R. Yoshie, H. Kataoka, T. Nozu, M. Yoshikawa and T. Shirasawa, AIJ guidelines for practical applications of CFD to pedestrian wind environment around buildings, Journal of Wind Engineering and Industrial Aerodynamics, 96 (2008) 1749-1761.

Y. Tominaga and T. Stathopoulos, Numerical simulation of dispersion around an isolated cubic building: model evaluation of RANS and LES, Building and Environment, 45 (10) (2010) 2231-2239.

Y. Tominaga and T. Stathopoulos, CFD modeling of pollution dispersion in a street canyon: Comparison between LES and RANS, Journal of Wind Engineering and Industrial Aerodynamics, 99 (2011) 340-348.

T. van Hooff and B. Blocken, Coupled urban wind flow and indoor natural ventilation modelling on a high-resolution grid: A case study for the Amsterdam ArenA stadium, Environmental Modelling & Software, 25 (2010) 51-65.

The Seventh International Colloquium on Bluff Body Aerodynamics and Applications (BBAA7)
Shanghai, China; September 2-6, 2012

A review of cases of vortex shedding excitation in bridges: Sectional models testing

J. Á. Jurado[a], R. Sánchez[b], S. Hernández[c], F. Nieto[d], I. Kusano[e]

[a,b,c,d,e] *School of Civil Engineering. University of La Coruña, Campus Elviña 15071 La Coruña, Spain*

ABSTRACT: Vortex shedding excitation frequently occurs in cable supported bridges. Even other types of bridges such as beam or arch bridges suffer this phenomenon during or after construction. It is well-known that a bluff body sheds alternating vortices with frequency *n*, which mainly depends on the Reynolds number and body geometry. Vortices induce transverse forces on the body with the same frequency. In many cases of flexible and slender structures with a small damping, these forces may produce unacceptable vibrations. This paper reviews several bridges where this phenomenon was important and explains the approaches used to study the instability and the solutions to improve the behavior of the structures. Then several sectional models of long span bridges have been tested in the wind tunnel of the School of Civil Engineering at the University of La Coruña for the vortex shedding excitation.

KEYWORDS: Vortex shedding, Bridges, Deck Sectional Models, Wind Tunnel

1 VORTEX SHEDDING FUNDAMENTALS

Vortex shedding is perhaps one of the most studied phenomena of fluid mechanics, especially its interaction with circular cylinders; see for example Goswami *et al*. [1]. When a vortex is formed on one side of a body, it immediately increases flow velocity on the opposite side, which results, according to Bernouilli theory, in a pressure reduction. Under certain conditions such as a case of a cylinder, the vorticity in the shear layers of the body becomes periodic forming alternating vortices downstream. The periodic vortex street causes a fluctuating force on the body. If it is flexible or supported flexibly, an interaction takes place between downstream flow and body displacements. These periodic vortices are called Von Karman Vortex Street, named after Von Karman who studies the phenomenon around 1910. The fundamentals of this phenomenon can be found in classical literature such as Simiu & Scanlan [2] and Dyrbye & Hansen [3].

Vortex shedding can not be explained without taking into account of air viscosity. Air particles in contact with the body surface adhere to it, which produces the boundary layer; however, due to its mass, air undergoes inertial effect according to Newton's law and Navier-Stokes equations. The relationship between inertial and viscous effects is defined by Reynolds number, $Re = \rho UL/\mu$ (ρ, air density, μ, air viscosity, L, main dimension, U, velocity). The separation point of the boundary layer is the key to explain the body behavior immersed in a flow. When there is a surface body with high curvature, such as circular cylinder, the separation point changes with regard to *Re*, which produces very

different effects. The structures in civil engineering generally use bluff body sections that have separation points always at sharp corners, and therefore vortex shedding does not vary with *Re*. Although some bridge decks consisted of aerodynamic boxes with curved edges have different behavior when *Re* changes. This is a problem for carrying out wind tunnel testing, and it obliges us to use large scale models.

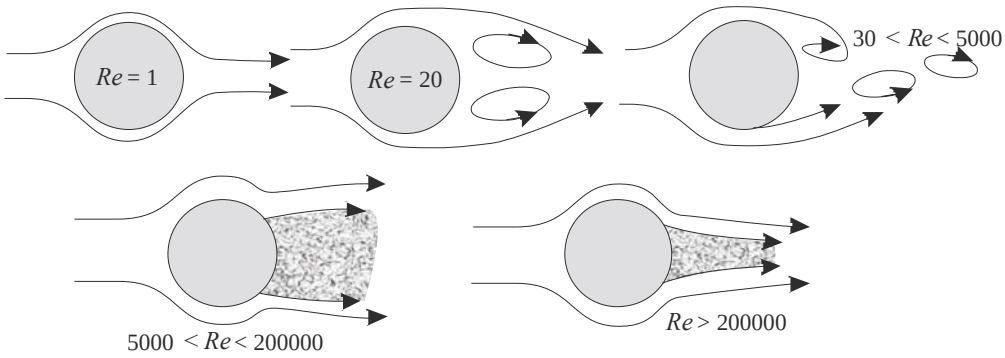

Figure 1. Reynolds dependency of the cylinder wake

Another determining parameter in order to study vortex shedding phenomenon is the Strouhal number $St=nD/U$ (n, vortex frequency). It is of a particular interest to establish a relationship between flow velocity and the frequency of the fluctuating forces on the body, which will permit the definition of a critical velocity at which vortex shedding frequency is close to a natural frequency of the structure. The Strouhal number is approximately constant. It has been evaluated for a great number of cross sections, and it takes values from 0.2 and 0.1 depending on the geometry. The value is greater if the section is rounded like a circular cylinder and lower if it is square like a flat plate. In the cases of flexible structures with a small damping, these forces can produce large vibrations. The greatest displacement occurs when the vortex frequency is close to the structural natural frequency. When this coupling takes place, the vortex shedding frequency does not change with the wind velocity in a significant range, which is called lock-in.

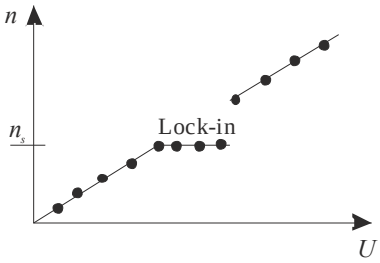

Figure 2. Lock-in effect when vortex frequency n is close to natural frequency of the body n_s.

Relating structural damping and mass with vibrations due to vortex shedding and air displaced, the Scrouton number can be established as $Sc=2\delta m/(\rho L^2)$. (δ, logarithm decrement damping, m, vibrating structural mass). This parameter is used to determine whenever structures are prone to suffer vibrations due to vortex shedding. Whenever Sc is high, structural damping and mass prevail over displaced air, so the structure should not have problems of vibrations. As soon as Sc reduces, the displaced air may induce negative

damping that nullifies the structural damping and induces stationary vibrations with high amplitude.

Other factors such as the turbulent scale of wind or the number and the shape of near bodies play an important role on wake behavior and structural excitation by vortex shedding. Long-scale turbulence means that wind velocity varies with a slow fluctuation, not allowing the vibrations to grow. When bodies are placed in a way that one follows the other such as the case of twin box decks (see Figure 3), or set of cables, the possibilities of vortex shedding increase, which also depends on the separation between bodies. The bodies may behave as a single body if the separation is small, while they behave as different bodies if the separation is sufficiently large. There are intermediate cases depending on the turbulence.

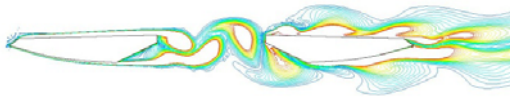

Figure 3. Vortex shedding of a twin box

2 VORTEX SHEDDING EXCITATION IN BRIDGES

Historically, many bridges have had vortex shedding vibration problems (Jurado et al. [4]). The first example was the clear vertical oscillations that the old Tacoma Narrows Bridge showed days before the collapse caused by flutter instability. Another veteran bridge like the Golden Gate Bridge suffered also this effect previously to its deck reinforcement. More modern bridge like Kessock Bridge, a cable stayed bridge in Scotland or Great Belt suspension bridge in Denmark showed this behavior. Not only cable supported bridges but also, continuous truss bridges like the one over Niterói River in Brasil showed this interaction with the wind. Moreover, the arch of Alconétar Bridge in Spain had big oscillations during the construction. A review of these cases helps us to explain the details of the phenomenon showing the best solutions to mitigate the vibrations.

Figure 4. From left to right: Kessock Brige, Great Belt Bridge, Niterói Bridge, Alconétar Bridge

Kessok Bridge has two planes of cable stayed and a 240 m of main span with an open cross section deck shown in figure 5. Since vibrations of large amplitude appeared during its construction, tuned mass dumpers (TMD) were installed. At the beginning of 90's monitoring measurements were registered and several events with large peak dynamic displacements were observed. For a wind velocity of about 21 m/s, the first mode of 0.51

Hz frequency were excited with large amplitude. Also in another occasion, the first torsional mode of 0.74 Hz frequency was excited. The Owen at al. [5] investigation concluded that TMDs did not succeed in limiting the response of the bridge to the desired level.

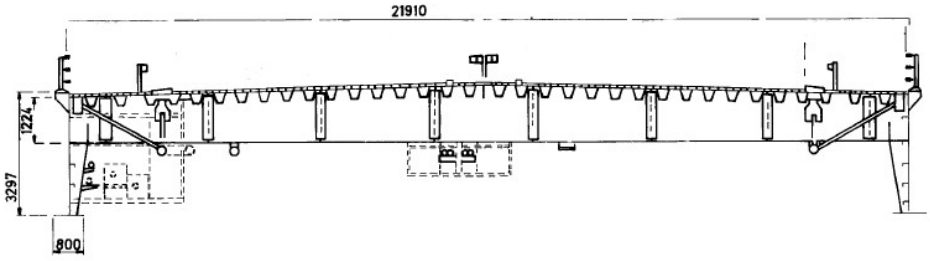

Figure 5. Open cross section of the Kessock Bridge

The Great Belt Suspension Bridge in Denmark also suffered vortex-shedding oscillations during last construction phases of the girder, before the application of the roadway surfacing. In January of 1998 a monitoring structural system of several accelerometers was installed (Larsen at al. [6]). At the same time the wind conditions at the bridge site were measured. The registered events of vortex shedding were for a mean velocity of $5 < U < 13$ m/s. The excited vertical modes were the third (0.13 Hz), the fifth (0.209 Hz), and the sixth (0.242 Hz). All the events had a reduce velocity $1 < U/nB < 1.5$. Its deck width measured $B = 31$m. These results were in agreement with the 1/80 sectional model. The structural analysis indicated that the vibrations were insignificant for structural safety, although they could cause bad sensations for the users. Thus a system of guide vanes was designed for mitigating the oscillations (see Figure 6). The rms of the vertical displacements of a 1/60 sectional model with guide vanes resulted almost null.

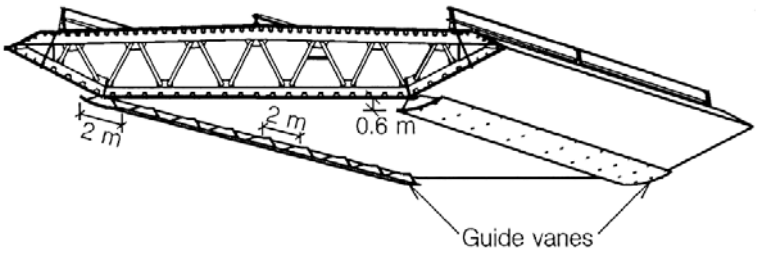

Figure 6. Bridge deck of Great Belt Bridge with guide vanes

The Rio Niterói Bridge has three continuous spans (200/300/200 m) of steel twin-box-girder. Since its opening to traffic in 1973, this non-cable-supported bridge also suffered several vortex shedding oscillation events for mean wind velocities close to 60 km/h. The figure 7 shows the bluff body cross section of the bridge deck which causes lock-in instability with big amplitudes. Considering that the natural frequency of the first excited bending mode is 0.32Hz, the Strouhal number results in around 0.14. An interested study for reducing the oscillation by active and passive control devices using TMDs was conducted by Battista & Pfeil [7]. They used structural optimization to design the TMD properties, achieving to avoid the coupling between the vortices and the structural motions.

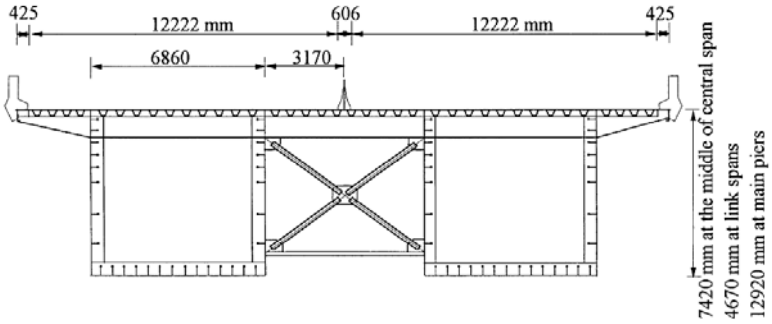

Figure 7. Steel twin-box-girder of Rio Niterói Bridge

The vortex shedding excitation also took place during the construction of the Alconétar Arch. As can be observed in figure 8, the bridge has two arches supporting two superior decks with 220 m of span length. The oscillations occurred when the first arch was closed, before the columns and deck where built. The mean wind velocity was estimated around 30 Km/h and the excited vibration mode was non-symmetrical with a frequency of 0.70 Hz. A 1/20 fixed sectional model, and 1/15 elastic model were tested in an aerodynamic wind tunnel; see Barrero et al. [8]. These experiments showed that the Strouhal number for the twin box section was 0.15. The solution to avoid the vibrations was to install guide vanes, which are small plates welded to the steel boxes. This type of aerodynamic appendages resulted easy to build and it reduced the oscillation amplitudes to an acceptable level. The complete arch bridge has no problems of wind structure interaction because its stiffness and damping of the complete structure is much greater than the isolate arches.

Figure 8. Arches of Alconétar Bridge.

The observation of these examples shows that non-aerodynamic sections of the Kessock Bridge, Niterói Bridge and Alconétar Arch, with twin boxes sections in the Niterói and Alconétar cases have tendency to vortex shedding excitation. Also the more aerodynamic

deck of the Great Belt Bridge generates the effect, but not a dangerous amplitude for the structure. TMDs installation is a suitable solution for bridges with bluff body sections in spite of maintenance problems; however, it is generally recommendable to use aerodynamic appendages. It is the case of the guide vanes of the Great Belt Bridge, or the welded plates of Alconétar arch section.

3 WIND TUNNEL TESTING

There are several ways to determine the wind speed for vortex shedding excitation and to evaluate if the oscillation amplitude is dangerous for the structure. Numerical methods based on CFD analysis have nowadays great expectation and give rapid results, but wind tunnel testing has been the most reliable way of studying the phenomenon. There are researches using complete models, taut-strip models and sectional models. Full models have to maintain the Froud number $Fr = U^2/Dg$ (g is the gravity), resulting that the velocity scale is the root of scale length; thus the velocity is very low in the wind tunnel. This generates low Reynolds numbers and inaccurate results for vortex shedding simulation. Taut-strip models are complicated compared to sectional models that are the most common way of studying vortex excitation. Larsen et al. [5] shows results for the Great Belt Bridge vortex shedding using three types of testing.

The sectional model validity is based on the dynamic similarity. The results in the wind tunnel can be apply to the real bridge if there is a geometric similarity and Reynolds number related to the air flow around the real obstacle is the same. The differential equation of the body displacement oscillating laterally respect to the air flow can be written:

$$m\left(\frac{d^2y}{dt^2} + 2\pi n\xi\frac{dy}{dt} + (2\pi n)^2 y\right) = F\left(\rho, \mu, U, D, n, y, \frac{dy}{dt}, \frac{d^2y}{dt^2}\right) \quad (1)$$

Where m is the mass per unit length, y is the lateral displacement, t the time, n the structural frequency, ξ the damping ratio, F the force per unit length which depends on the fluid properties. Using dimensionless parameters, it can be written:

$$\frac{d^2\eta}{d\tau^2} + 2\pi\xi\frac{d\eta}{d\tau} + (2\pi)^2\eta = \frac{\frac{1}{2}\rho U^2}{mn^2}F\left(Re, \frac{nD}{U}, \eta, \frac{d\eta}{d\tau}, \frac{d^2\eta}{d\tau}\right) \quad (2)$$

The Reynolds number dependency is small if the body has sharp corners, so the problem depends of the reduce frequency nD/U and of the parameter $\rho U^2/(mn^2)$. As ρ is the same value in model and real prototype, the velocity, mass and frequency scales must verify $(\lambda_U)^2=\lambda_m(\lambda_n)^2$ and keep nD/U, $\lambda_U=\lambda_n\lambda_L$. Both relations set up that mass scale must be the square of length scale $\lambda_m=(\lambda_L)^2$. For example, these similarity requirements were considered in the sectional model of the Alconétar Bridge arch [7] (see figure 9). When the length scale was fixed as λ_L = 1/15 because of the wind tunnel dimensions, the mass scale was defined as λ_m = 1/225. Then the stiffness of the suspension system determines that λ_n =3.31 and the velocity scale was calculated by $\lambda_U=\lambda_n\lambda_L$=1/4.5.

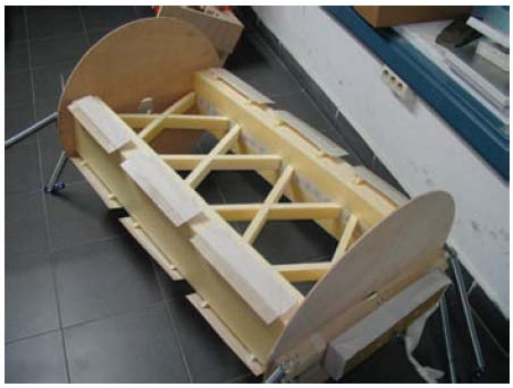

Figure 9. Sectional model of the arch with guide vanes

An interesting research about vortex shedding excitation for the twin box deck of the Stonecutters Bridge (Figure 10) in Hong Kong was done by Larose et al. [9]. In the study, a greater than usual sectional model scale of 1/20 was tested. The aim was to achieve a greater Reynolds number to compare the results with that of smaller scale. The results showed considerable differences with respect to a previous study using a 1/80 sectional model, mainly when the model is tested with aerodynamic appendages. If the wind velocity is the same, and the scale model is greater, the required frequency of the model at vortex shedding excitation decreases because the reduced frequency, *nB/U* should be constant during the phenomenon. The model weight was 215 Kg with the aspect ratio of 5:1, and the suspension system could vary the vertical frequency between 7 and 10 Hz. The damping was 1% log. dec. The tests were carried out in a smooth flow at 0º attack angle in a 9m x 9m wind tunnel of the National Research Council of Canada. The results showed clear vortex shedding peak at 0.35 of reduce velocity. The Strouhal number measured in the wake had two peaks for 0.20 and 0.14. The sectional model also was tested with guide vanes and it was checked that these aerodynamic appendages successfully mitigated the excitation.

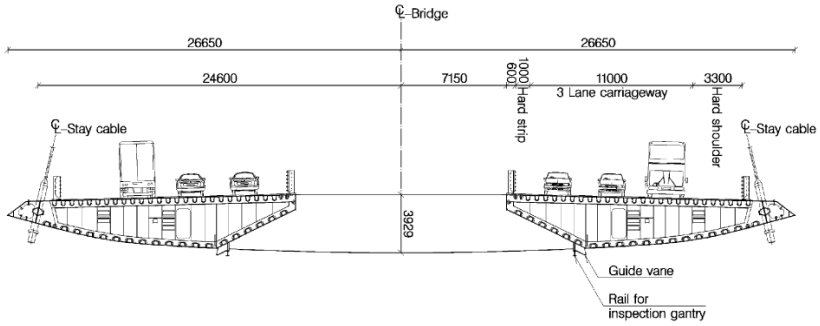

Figure 10. Stonecutters Bridge deck cross section.

4 SECTIONAL MODELS TESTED AT THE UNIVERSITY OF LA CORUÑA

Several experiments of vortex shedding on sectional models have been carried out in the wind tunnel of the School of Civil Engineering at the University of La Coruña. For determining the Strouhal number, it is useful to test the sectional model supported by a very

stiff system built by bars connected to load cells. A Fourier transform of the alternating forces measured by load cells permits to identify the force peak for vortex shedding and the greatest peak force at the natural frequency of the model. As figure 11 shows, both peaks values increase with the wind velocity. At lock-in both peaks overlap and the highest amplitude force appears.

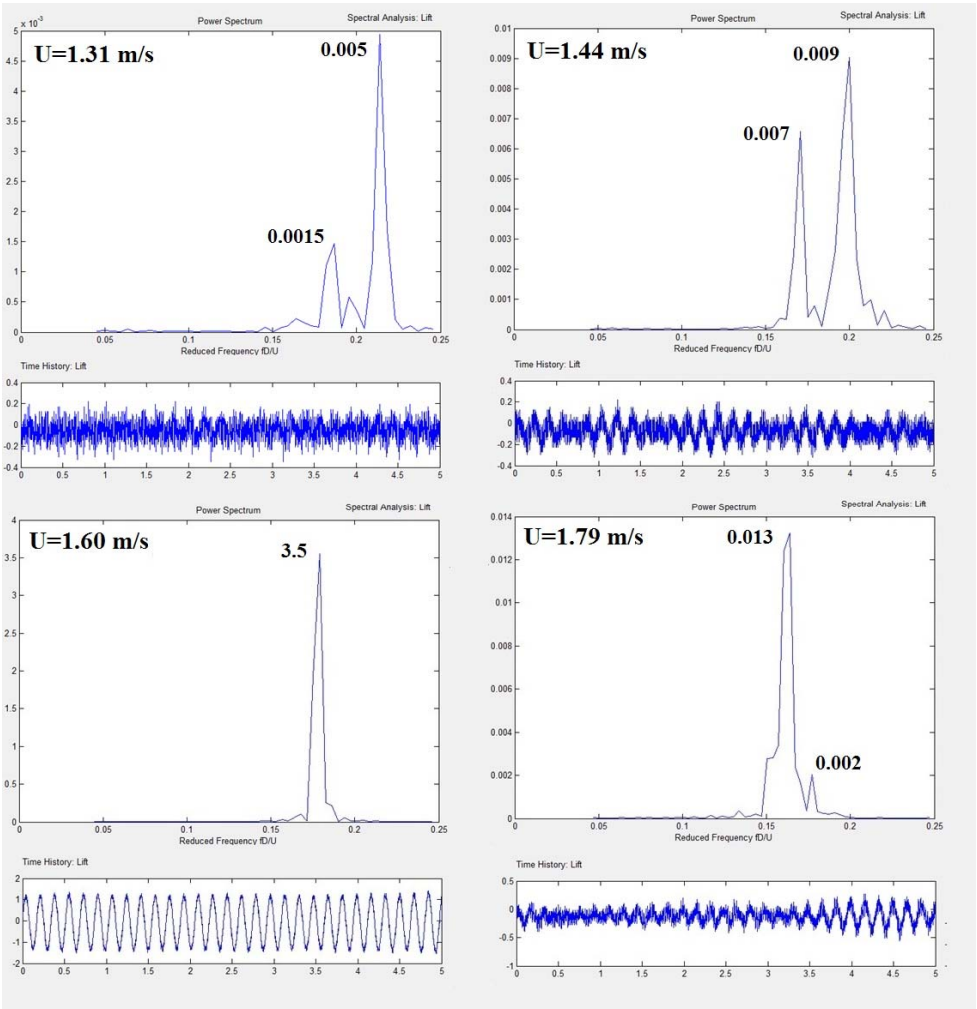

Figure 11. Vertical force Fourier transform on a sectional model with rigid support.

A graph that represents the vortex shedding frequency peaks as function of the value *U/D* permits the calculation of the Strouhal number value, which is the slop of the line. The figure 12 shows three sectional models: the twin-box deck of the Stonecutters Bridge (λ_L = 1/80), the single-box of the Miradoiros Project Bridge in La Coruña (Spain) (λ_L = 1/100) (Jurado et al. [10]), and the stress ribbon footbridge of Cuenca in Spain (λ_L = 1/10) (Jurado et al. [11]). For the case of the twin-box sectional model, the table 1 indicates a good agreement for the lift peaks at lock-in with regards to the results of Larose et al. [8]

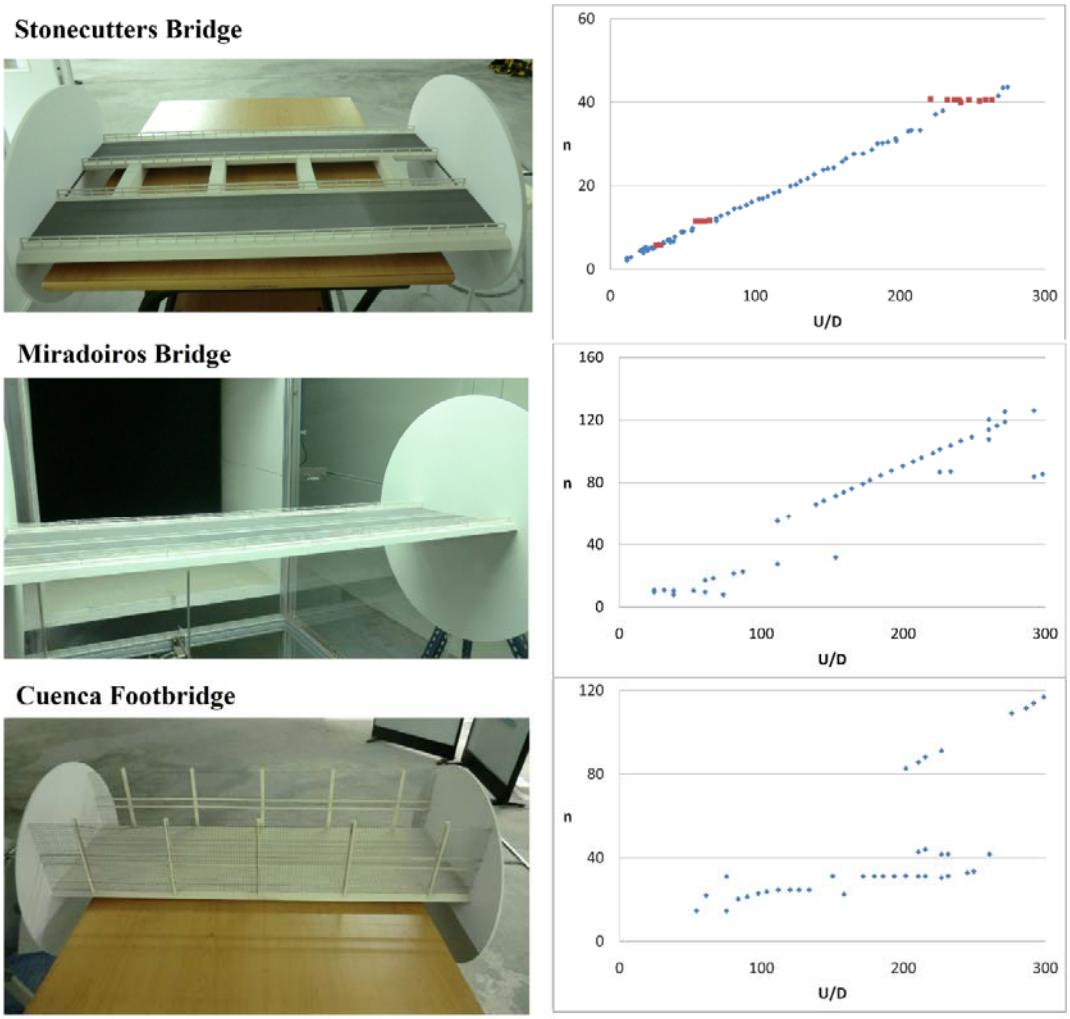

Figure 12. Frequency *n* of vortex shedding with regard to *U/D* for three sectional models.

Table 1. Strouhal number for the tween-box deck.

	U	*n*	*D*	*St*	(*St* Larose et al.[8])
	(m/s)	(Hz)	(m)		
First Lock-in	1.604	5.859	0.049	0.179	0.20
Second Lock-in	3.586	11.597	0.049	0.158	0.14

5 CONCLUSIONS

Vortex shedding fundamentals have been explained to understand several cases of bridges that suffered this effect.

The observation of these examples shows that non-aerodynamic sections, mainly with twin boxes have tendency for vortex shedding excitation. Also more aerodynamic sections could generate the phenomenon, as in the case of the Great Belt Bridge deck.

TMDs installation is a suitable solution for bridges, but it creates maintenance problems. It is generally recommendable to use aerodynamic appendages as guide vanes.

Testing sectional models is the most common way of studying vortex excitation. Several cases have been explained.

The Fourier transform of the lift force on a stiff sectional model is useful to determine the frequency of vortex shedding and the lock-in effect. The procedure has been used with several sectional models in the wind tunnel of the School of Civil Engineering at the University of La Coruña.

6 ACKNOWLEDGMENTS

This research has been funded by the Spanish Ministry of Economy and Competitiveness under project BIA2010-19989.

7 REFERENCES

1 I. Goswami, R.H. Scanlan, N.P. Jones, Voretex-Induce Vibrations of Circular Cylinders. I:Experimental Data. J. Eng. Mechanics, Vol.119 No 11, November (1993) 2270-2287.
2 E. Simiu, R.H. Scanlan, (1996). Wind effects on Structures. John Wiley & Sons, New York.
3 C. Dyrbye, S.O. Hansen, (1997) Wind Loads on Structures. John Wiley, Chichester.
4 J.Á. Jurado, S. Hernández, F. Nieto, A. Mosquera (2011) Bridge Aeroelasticity, Sensitivity Analysis and Optimal Design. Wit Press, Sothampton, Boston ISBN: 978-1-84564-056-9.
5 J.S. Owen, A.M. Vann, J.P. Davies, A. Blakeborough, The prototype testing of Kessock Bridge: response to vortex shedding. J. of Wind Engineering and Industrial Aerodynamics 60 (1996) 91-108
6 A. Larsen, S. Esdahl, J.E. Andersen, T. Vejrum. Storebelt Suspension bridge - vortex shedding excitation and mitigation by guide vanes. J. of Wind Engineering and Industrial Aerodynamics 88 (2000) 283-296.
7 R.C. Battista, M.S. Pfeil, Reduction of vortex-induced oscillations of Rio Niterói bridge by dynamic control devices. J. of Wind Engineering and Industrial Aerodynamics 84 (2000) 273-288.
8 A. Barrero, G. Alonso, J. Meseguer, M.A. Astiz, (in Spanish) Ensayos en túnel de viento de un modelo aeroelástico del arco del puente sobre el río Tajo "Arcos de Alconétar", Hormigón y Acero nº 245, (2007) 33-40.
9 G.L. Larose, S.V. Larsen, M. Hui, A.G. Jensen, Sectional model experimentes at high Reynolds number for deck of 1018 m span cable-stayed bridge. Eleventh International Conference on Wind Engineering, Lubbock, Texas, 2-5 June (2003).
10 J.Á. Jurado, S. Hernández, A. Baldomir, F. Nieto, Aeroelastic Analysis of Miradoiros Bridge in La Coruña (Spain). 5th European & African Conference on Wind Engineering. Florence Italy 19-23 July (2009).
11 J.Á Jurado, L. Romera, A. Baldomir, S. Hernández, Non-lineral dynamic analysis for studding the aeroelastic behavior of a stress ribbon pedestrian bridge in Cuenca (Spain). 13th International Conference on Wind Engineering Amsterdam The Netherlands, 10-15 July (2011).

A new approach to identifying aeroelastic parameters in nonlinear vortex induced force model

Xiangying Weng[a], Yaojun Ge[a, b], Haixing Chen[a]

[a] *Department of Bridge Engineering, Tongji University, Shanghai, China*
[b] *State Key Laboratory for Disaster Reduction in Civil Engineering, Tongji University, Shanghai, China*

ABSTRACT: A new approach for extracting the aeroelastic parameters in semi-empirical nonlinear vortex induced force model is proposed based on the nonlinear least squares fitting. The approach consists of obtaining an approximate analytic solution to modified motion equation with homotopy analysis method and making use of genetic algorithms to conduct nonlinear fitting. Additionally, the concept of limit cycle for Van der Pol oscillator is employed to give the preliminary ranges of parameters to be extracted. Verification of the effectiveness and accuracy of the proposed methodology was conducted through numerical simulations in which both time histories with and without noise perturbation were adopted . Finally, wind tunnel tests of a streamlined bridge deck were carried out and the aeroelastic parameters in vortex induced force model were identified by the proposed method.

KEYWORDS: Parameter identification; Aeroelastic parameters; Vortex induced force model; Van der Pol oscillator; Genetic algorithms; Limit cycles;

1. INTRODUCTION

Vortex-induced vibration(VIV) is a phenomenon that occurs when the vibration of a body immersed in a flow is governed by the action of the vortices periodically shedding from its own surface. As a self-excited system, one of the most prominent features of VIV is the existence of limit cycle in its phase space. Noticing this characteristic, Scruton[1], Simiu and Scanlan[2], and Larsen[3] et al proposed a set of single degree-of-freedom(SDOF) models based on the Van der Pol oscillator in which a single dynamic equation with aeroelastic forcing terms on the right hand side of the equation are used to describe this kind of vibration. These analytic vortex-induced force models commonly contain reduced frequency dependent areoelastic parameters which need to be extracted from wind tunnel tests. It is obvious that the accuracy of extracted aeroelastic parameters has a direct effect on the prediction of the prototype vortex-induced response. Consequently, an efficient method for identifying aeroelastic parameters in the SDOF vortex-induced force model is demanded. Work focusing on this aspect has already been reported in several literatures. Ehsan and Scanlan[4] proposed a method which consists of conducting a decay-to-resonance model test at wind speed in lock-in region after imposing the model a higher initial displacement. Gupta et al.[5] described a technique for this extraction based on the theory of invariant imbedding. It is essentially a kind of nonlinear least squares fitting method which inherently makes the fitting results dependent on a set of initial values. Unfortunately, the appropriate initial values corresponding to the global optimum aren't easy to be known preliminarily. By introducing the quasi-linear approximation to the Van der Pol equation, Marra et al.[6] suggested an alternative identification procedure based on the method of slowly varying parameters and verified its validness. Zhou[7] obtained the analytic formulation of vortex-induced response also based on the slowly varying parameters method. But it was found that the power spectral density of the extracted vortex-induced force contained an additional frequency component besides the

prominent mechanical frequency corresponding to the Strouhal frequency. In this paper, a new identification procedure is proposed for the extraction of the aeroelastic parameters in the semi-empirical nonlinear vortex-induced force model.

2. SDOF MODEL FOR BRIDGE DECK VOTEXT INDUCED VIBRATION

Among the proposed SDOF models, the so called semi-empirical nonlinear model proposed by Scanlan[8] is widely adopted to estimate of the response of VIV because of its accuracy and simplicity. This SDOF model has the general form as follows:

$$m(\ddot{x} + 2\xi\omega_n\dot{x} + \omega_n^2 x) = \frac{1}{2}\rho U^2(2D)\left[Y_1(K)\left(1 - \epsilon\frac{x^2}{D^2}\right)\frac{\dot{x}}{U} + Y_2(K)\frac{x}{D} + C_L(K)\sin(\omega_s t + \psi)\right] \quad (1)$$

In Equation(Eq.) (1), m=mass per unit span; ξ=mechanical damping ratio; ω_n=natural circle frequency in rad/sec; U=flow velocity in the lock-in region; $x, \dot{x}, \ddot{x}$ represent displacement, velocity and acceleration, respectively; D=a characteristic length of bridge deck section; ω_S=circular frequency of vortex shedding; ψ=initial phase angle of the harmonic force. $K = \omega_n D/U$ is the reduced frequency during vortex-induced vibration. The remaining notations $Y_1(K), \epsilon, Y_2(K), C_L(K)$ are aeroelastic parameters that need to be extracted from wind tunnel tests. In practical usage, the instantaneous fluctuating lift force term, namely $1/2\rho U^2(2D)C_L(K)\sin(\omega_s t + \psi)$, is often neglected since it is generally smaller than the aerodynamic lift caused by the motion of the body[4]. Thus at the lock-in region, Eq.(1) can be reduced to the flowing form:

$$m(\ddot{x} + 2\xi\omega_n\dot{x} + \omega_n^2 x) = \frac{1}{2}\rho U^2(2D)\left[Y_1(K)\left(1 - \epsilon\frac{x^2}{D^2}\right)\frac{\dot{x}}{U} + Y_2(K)\frac{x}{D}\right] \quad (2)$$

Obviously, Eq.(2) shows aspects of Van der Pol oscillator. Making some proper transformations to Eq.(2), a Van der Pol oscillator would be obtained. Initially, making the variables in Eq.(2) dimensionless by introducing follow definitions:

$$\eta = \frac{x}{D}, \qquad s = \frac{Ut}{D}, \qquad K_n = \frac{\omega_n D}{U}, \qquad m_r = \frac{\rho D^2}{m}, \qquad \dot{\eta} = \frac{d\eta}{ds} \quad (3)$$

Eq. (2) becomes:

$$\ddot{\eta} - \mu_1\left(1 - \frac{\mu_2}{\mu_1}\eta^2\right)\dot{\eta} + \mu_3\eta = 0 \quad (4)$$

where

$$\mu_1 = -\left(2\xi K_n - m_r Y_1(K)\right) \quad (5)$$

$$\mu_2 = m_r Y_1(K)\epsilon \quad (6)$$

$$\mu_3 = K_n^2 - m_r Y_2(K) \quad (7)$$

Eq.(4) conforms with the constitution of a Van der Pol oscillator. Analyzing the system described by Eq.(4), one could find the oscillating behavior depends on the parameters μ_1 and μ_2. When μ_1 and μ_2 have different signs, in other words one of the two is positive while the other is negative, the vibrational amplitude will either becomes zero or proceeds to a divergent level. Consequently, μ_1 and μ_2 have the same sign which means both of them are positive or negative. Reviewing the existing literatures on aeroelastic parameters of vortex-induced force model, the coefficients relating to the linear and nonlinear damping force terms $Y_1(K)$ and ϵ are mostly positive. It is subsequently acceptable assuming these two parameters are positive. Therefore, define a substitution:

$$y = \sqrt{\frac{\mu_2}{\mu_1}}\eta \quad (8)$$

We obtain a classical Van der Pol-type oscillator:

$$\ddot{y} - \mu_1(1 - y^2)\dot{y} + \mu_3 y = 0 \tag{9}$$

where $\dot{y} = dy/ds$.

3. APPROXIMATE ANALYTIC SOLUTION TO VAN DEL POL OSCILLATOR

Van der Pol oscillator is a subject that has been well studied in the field of science and engineering. It is a nonlinear self-excitation system while exhibiting a characteristic of self-sustained periodic oscillation. The accurately analytic solution to this system is still an unsolved problem. Methodologies documented in the literature on this subject include perturbation method, KBM method, the harmonic balance method and so on. Solutions from these schemes are essentially approximate, and the feasibility of these solutions require the precondition of small parameters. An alternatively analytic method, the so-called homotopy analysis method[9], has been recently proposed to obtain the analytically serial solution to free oscillations of self-excited system. As it is described about this method that the requirement of small parameters is unnecessary and it is convenient to get higher-order analytic approximation. In this work, we adopt this method to obtain the approximate analytic solution to Eq.(4).

Initially, define new notations to Eq.(9):

$$\tau = \omega s, \qquad y(s) = a u(\tau) \tag{10}$$

Under the definition of Eq.(10), Eq.(9) could be rewritten as follows:

$$\omega^2 u''(\tau) + \mu_3 u(\tau) = \mu_1 \omega [1 - a^2 u^2(\tau)] u'(\tau) \tag{11}$$

Following the basic ideas and approaches of homotopy analysis method[9], a second order approximation could be obtained:

$$u^{(2)}(\tau) = \mathrm{Cos}[\tau]\left(1 - \frac{13\mu_1^2}{192\mu_3}\right) + \mathrm{Sin}[\tau]\left(-\frac{3\mu_1^3}{128\mu_3^{3/2}} + \frac{3\mu_1}{8\sqrt{\mu_3}}\right)$$
$$+\mathrm{Sin}[3\tau]\left(\frac{\mu_1^3}{128\mu_3^{3/2}} - \frac{\mu_1}{8\sqrt{\mu_3}}\right) + \frac{3\mathrm{Cos}[3\tau]\mu_1^2}{32\mu_3} - \frac{5\mathrm{Cos}[5\tau]\mu_1^2}{192\mu_3} \tag{12}$$

$$a = 2 + \frac{\mu_1^2}{96\mu_3} \tag{13}$$

$$\omega = \sqrt{\mu_3} - \frac{\mu_1^2}{16\sqrt{\mu_3}} \tag{14}$$

Substituting the above three equations into Eq.(10), the second order approximation to Eq.(9) becomes:

$$y^{(2)}(s) = a\mathrm{Cos}[\omega s]\left(1 - \frac{13\mu_1^2}{192\mu_3}\right) + a\mathrm{Sin}[\omega s]\left(-\frac{3\mu_1^3}{128\mu_3^{3/2}} + \frac{3\mu_1}{8\sqrt{\mu_3}}\right)$$
$$+a\mathrm{Sin}[3\omega s]\left(\frac{\mu_1^3}{128\mu_3^{3/2}} - \frac{\mu_1}{8\sqrt{\mu_3}}\right) + a\frac{3\mathrm{Cos}[3\omega s]\mu_1^2}{32\mu_3} - a\frac{5\mathrm{Cos}[5\omega s]\mu_1^2}{192\mu_3} \tag{15}$$

Using the symbolic calculation software, higher-order approximations could be easily obtained. The fact that small damping in bridge deck VIV, equivalently the small magnitude of μ_1, makes the selection of second order approximation be reasonable. So we choose second order approximation in this work.

With the obtained analytic approximation, Eq.(15), as the estimated displacement, the objective function of this extraction problem could be expressed by following equation:

$$f(\mu_1, \mu_3) = \sum_{i=1}^{N} \left(y^m(s) - y^e(\mu_1, \mu_3, s) \right)^2 \tag{16}$$

in which $y^m(s)$ and $y^e(\mu_1, \mu_3, s)$ are the measured and the estimated displacement response, respectively. *N* denotes the total number of samples used for parameters identification, and *s* represents the dimensionless sampling time. It is easy to understand that the extraction of these two parameters is equivalent to obtain the minimum value of the function $f(\mu_1, \mu_3)$ within the ranges of μ_1 and μ_3. Thus, this identification problem is essentially an optimization problem under certain initial conditions.

4. GENETIC ALGORITHMS FOR AEROELASTIC PARAMETERS IDENTIFICATION

As it has been mentioned in the previous section, extraction of aeroelastic parameters, μ_1 and μ_3, in the semi-empirical SDOF model is a nonlinear optimization problem whose dependence on initial values has a direct effect on the results. As a general rule of thumb the objective functions of many nonlinear optimization problems possess a large number of local minima and maxima. For arbitrarily given initial values, the results extracted by classical gradient related methods may be just a local optimum but global optimum. Classical schemes include Newton's method, quasi-Newton method, gradient descend method and so on. Being aware of the difficulties of finding global optimum, some heuristic search strategies have been proposed to solve this problem in a more or less intelligent way.

A genetic algorithm[10] which will be adopted in this article is one of these heuristic search strategies that mimics the process of natural evolution. After deciding the genetic representation of the solution domain and the fitness function, a classical genetic algorithm consists of four parts, namely initialization, selection, reproduction and termination. Specifically, a set of individually initial solutions are randomly produced in the range of solution domain, and then the better solutions are selected as the parents to breed the next generation according to the value of fitness function, and in the reproduction step, a new generation representing averagely better solutions are produced through a series of genetic operations, namely crossover and mutation, and finally when the above evolutionary process reaches the termination conditions including a satisfactory fitness level or a maximum number of generations, the global optimum could be obtained in a great probability. Repeating this heuristic search certain times, the best individual among these times could be identified as the global optimum.

Following the previous introductions, a program was developed to search an optimal solution to Eq.(16).

5. NUMERICAL SIMULATIONS

The feasibility of making use of genetic algorithms combining with the approximately analytic formulation to identify the areoelastic parameters in SDOF model needs to be verified to evaluate its performance. Besides, it should be remarked that the measured data from wind tunnel tests or field observations are inevitably contaminated by noise. Therefore, both samples with and without noise perturbations should be adopted to justify the effectiveness of this methodology. In these numerical simulations, the values of parameters μ_1 and μ_3 were set as 0.70 and 1280, respectively[5]. Approximate solution to Eq.(9) at the tenth-order obtained by the homotopy analysis method was employed as the non-contaminated time history $y^{ms}(s)$.Additionally, a Gaussian white noise was added to simulate a noisy process $y^{mn}(s)$ maintaining a noise-to-signal ratio of 0.5%. The inherent parameters of a genetic algorithm were set as follows: the population size $M = 50$, the crossover probability $P_c = 0.7$, the

mutation probability $P_m = 0.05$, the maximum iteration times $N = 300$. Another necessity for genetic algorithms is having a preliminary information on the solution domain so as to capture the global optimum within the restricted ranges. In this numerical simulation, we set the lower and upper bounds of μ_1 as 0 and 1, respectively. Of course, a wider domain could also be adopted, but it should be remembered that the wider the provided domain is, the more rapidly the computing resources increase. Taking the fact of μ_3 approximating to squared oscillating circle frequency which enormously influences the sum of squared residuals into account, a wider range of $[30^2, 40^2]$ was selected for μ_3 with the purpose of detecting the performance of developed genetic algorithm program. In the selection operator, the linear ranking selection combining with elitist model was adopted to avoid the premature convergence. In this simulation, fitness function is defined as a reciprocal of the objective function.

$$F(\mu_1, \mu_3) = \frac{1}{f(\mu_1, \mu_3)} \tag{17}$$

where $f(\mu_1, \mu_3)$ is the sum of squared residuals defined in Eq.(16). To this definition, the greater the fitness function of an individual is, the greater its selection probability is. Taking account of the degree of nonlinearity of this optimization problem and the fact that heuristic search method may failure in achieving the global optimum with a certain possibility, conducting a certain times of simulation is necessary for obtaining the results as optimal as possible. This simulation was conducted both 30 times for two cases to determine and compare the extracted parameters.

For the simulation results of non-contaminated sample, it was found that the estimated values converged to the true value with a high accuracy and ratio. Both the two identified parameters varied a little in all 30 times simulations. And the finally determined values corresponding to minimum of the sum of squared residuals almost exactly equaled the true values, $\mu_1 = 0.7084$ and $\mu_3 = 35.7771^2 \approx 1279.994$. The accuracy of this simulation result demonstrated the effectiveness of this method adopted in smooth signal processing.

However, in analyzing the simulation results of noisy sample we found that the estimated value of μ_1 dispersed a lot, whereas μ_3 almost kept constant with maximum variation less than 0.3% with respect to its true value. Thus, an identification error for μ_1 is defined:

$$e_{\mu_1}(\%) = 100\frac{|\mu_1^t - \mu_1^e|}{\mu_1^t} \tag{18}$$

in which superscript "t" denotes the "true value" of μ_1 whereas the superscript "e" denotes the estimated value from the simulation.

Table 1. Identification results of noisy sample

Identification error	Times
$e_{\mu_1} \leq 10\%$	9
$10\% < e_{\mu_1} \leq 15\%$	7
$e_{\mu_1} > 15\%$	14

Based on the principle of minimizing the sum of squared residuals, equivently maximizing the fitness function, the best simulation results could be determined from these 30 times simulations. And the finally determined values for μ_1 and μ_3 were 0.6300 and 1279.96, respectively. An emphasis should be made at this point that the final determination of the estimated values from the repeated simulations is not based on the identification error defined in Eq.(18) but the sum of squared residuals. Comparing to the original values of $\mu_1 = 0.7$ and $\mu_3 = 1280$, one could find that the error in parameter μ_3 was almost negligible, yet the error in μ_1 was calculated as 10%. The reason for this enormous change of μ_1 due to the added noise with relatively small noise-to-signal ratio could be attributed to the sensitive dependence of amplitude on damping parameter μ_1. Hence, the consequence of the limit cycle which directly depends on the amplitude being destroyed by the added noise affects the extracted value of μ_1 to a high extent. Figure 1 shows the estimated displacement responses calculated with the extracted parameters $\mu_1 = 0.6300$, $\mu_3 = 1279.96$ and the originally noisy signal.

The consistence of the oscillatory behavior generated by the estimated formula and original data verifies the effectiveness of this identification method to some extent.

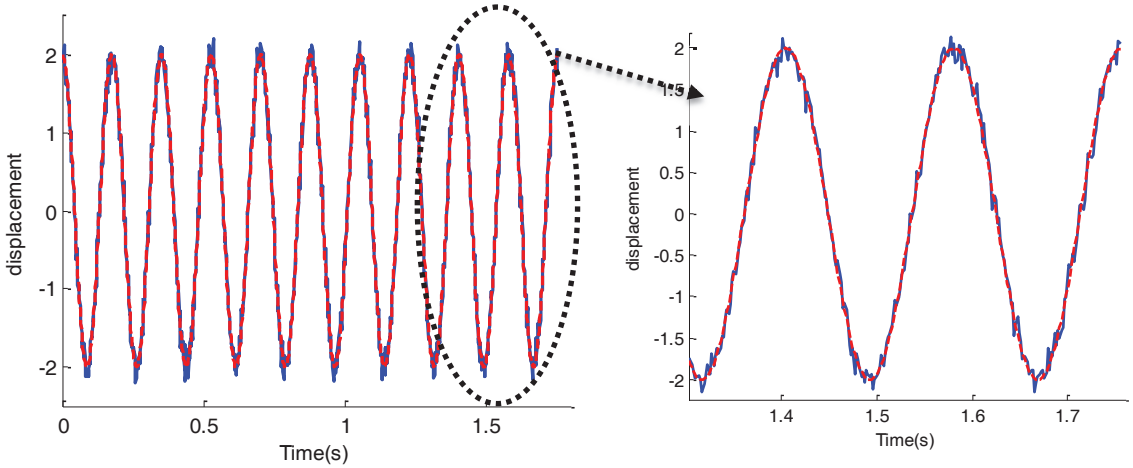

Figure 1. Estimated $y(s)$(red dotted line) and simulated noisy $y^{mn}(s)$(blue continuous line)

6. WIND TUNNEL TESTS

6.1 *Outline of wind tunnel tests*

To evaluate further the applicability of this method for the extraction of aeroelastic parameters in SDOF force model, wind tunnel tests of a streamlined bridge deck section(Figure 2) were conducted.

The tests were carried out in TJ-3 Boundary Layer Wind Tunnel of Tongji University. The facility is a closed-circuit wind tunnel, with a working section of 15m wide, 2m high, and 14m long and wind velocity ranging from 1.0m/s to 17.6m/s. In tests, an decomposable elastic suspension system was developed. In order to reduce aerodynamic end effects, two Plexiglas end plates were fixed to the both longitudinal ends of the section model. Restraining the lateral DOF, only the vertical and torsional DOFs were interested in the tests. The bridge section model was elastically suspended by 8 springs. Figure 3 shows the setup of this tests.

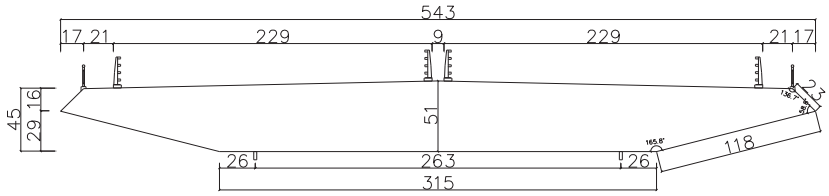

Figure 2. Streamlined box gird section model for wind tunnel tests

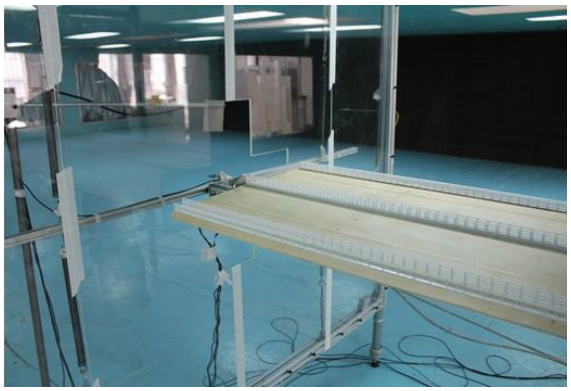

Figure 3. Setup of wind tunnel tests

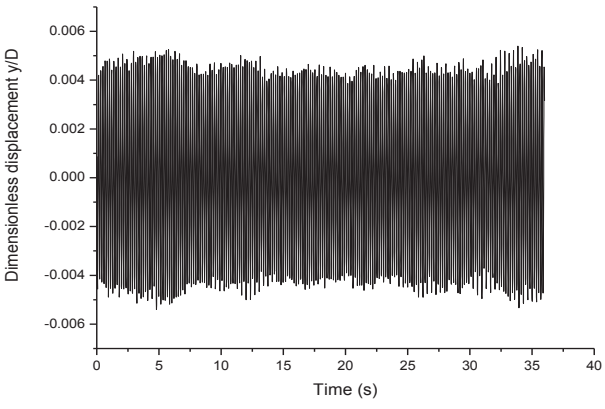

Figure 4. Vertical VIV displacement time history

The tests were conducted in smooth flow. The main parameters of the section model were as follows: the width $D = 0.543\text{m}$, the height $H = 0.051\text{m}$, the longitudinal length of the section model $L = 1.70\text{m}$, the total mass of the section model and the components of the suspension system vibrating in the vertical direction $m = 10.1\text{kg}$, the first vertical vibrational frequency $f = 5.664\text{Hz}$, the mechanical damping ratio $\xi = 1.25\%$. The phenomenon of synchronization was observed at the wind velocity of $U = 6.0\text{m/s}$. Under this condition, the reduced frequency corresponding to this wind velocity was $K_n = 3.221$.

Measurements of displacement time histories of the section model were accomplished with 2 laser displacement transducers. A sampling rate of 100Hz was used to acquire displacement data with 3,600 sample points in each time history.

6.2 *Test results and determination of the ranges of desired parameters*

Figure 4 shows a dimensionless vertical VIV displacement time history of this streamlined bridge deck section model at a wind velocity of $U = 6.0\text{m/s}$. It is this one that is used to extract the areoelastic parameters with the scheme proposed in the previous sections.

First of all, a transformation of the quantities from dimensional ones to their dimensionless counterparts was accomplished according to Eq.(3). With neglect of the second order of μ_1 in Eq.(13), a constant amplitude of 2 could be obtained from the dimensionless Van der Pol equation, namely Eq.(4). As it has been established in Eq.(8), the relationship of μ_1 and μ_2 in terms of amplitude could be approximated to:

$$\sqrt{\frac{\mu_2}{\mu_1}} = \frac{2}{A_t} \tag{19}$$

where A_t is the dimensionless amplitude of the test results. Considering the minor differences among every amplitude, mean value of all peaks and troughs could be used alternatively. Therefore, the estimated displacement responses corresponding to this actual situation is:

$$y^e(\mu_1, \mu_3, s) = \frac{y^{(2)}(s)}{\sqrt{\frac{\mu_2}{\mu_1}}} \tag{20}$$

For the parameters inherent to the genetic algorithms, most of them kept the same as that has been described in section 5, while the solution domains for the desired parameters μ_1 and μ_3 still need to be paid more attention.

Noticing the negligible frequency shift, linear aeroelastic stiffness in Eq.(7), $-m_r Y_2(K)$, could be asserted sufficiently small in most cases. Consequently, the lower and upper boundaries of μ_3 could be determined around the value of squared reduced frequency, namely K_n^2. In this work, we choose 3^2 and 4^2 as the lower and upper boundaries for μ_3, respectively.

Relatively, it is more difficult to obtain a preliminary information on the solution domain of parameter μ_1. Although difficulties exist, it is of importance that one should provide an appropriate range for μ_1 due to its direct effect on the final extraction of the original nonlinear aeroelastic damping parameters $\mathrm{Y}_1(K)$ and ϵ. In terms of Van der Pol equation (Eq.(9)), μ_1 is the parameter that indicates the nonlinearity and the strength of the damping. The fact that Van der Pol system satisfies the Liénard's theorem ensures that there is a limit cycle in the phase space. With the variation of parameter μ_1, the behavior of Van der Pol system runs from near-harmonic oscillations for μ_1 close to zero to relaxation oscillations when μ_1 tends to infinity[11]. Thus, the effect of different magnitudes of parameter μ_1 on the behavior of Van der Pol system could also be observed from the shape of limit cycle. Inversely, the rough ranges of parameter μ_1 may be determined by comparing the limit cycle of the measured data with the ones corresponding to different magnitudes of parameter μ_1.A methodology was proposed in Ref.(11) for approximately calculating the amplitude and form of limit cycles of weakly nonlinear Liénard's systems.

Following the procedures presented in the article[11], an alternative representation of Eq.(9) with time variable being implicit could be written as follows:

$$\delta\delta' + \mu_1(1-y^2)\delta + \mu_3 y = 0 \tag{21}$$

where $\delta(y) = \dot{y}(s)$, $\delta(y)\delta'(y) = \ddot{y}(s)$ and $\delta'(y) = d\delta/dy$. It is obvious that Eq.(21) is equivalent to Eq.(9). Being aware of the conservation of mechanical energy(Eq.(22)) in a half oscillation, a transformation to Eq.(21) could be derived in the form of Eq.(23).

$$E = \frac{\delta^2 + \mu_3 y^2}{2} \tag{22}$$

$$S(a) = \int_{-a}^{a} \frac{dE}{dy} dy = \int_{-a}^{a} -\mu_1(1-y^2)\delta dy = 0 \tag{23}$$

Based on the condition of Eq.(23), an approximation to the limit cycles and amplitude up to the Nth order in small parameter μ_1 could be assumed:

$$\delta(y) = \delta_0(y) + \sum_{n=1}^{N} \mu_1^n \delta(y) \tag{24}$$

As reported, the second order is accurate enough to describe the limit cycle of Van der Pol system with small parameter[11]. Therefore, In this work we choose the second order solution to form the limit cycle of Eq.(21), which will be listed below. Details of derivation and calculation could be retrieved to the Ref.(11).

$$\delta_0(y) = \sqrt{\mu_3(4-y^2)} \tag{25a}$$

$$\delta_1(y) = \frac{1}{4} y(4-y^2) \tag{25b}$$

$$\delta_2(y) = \frac{2+y^2}{96\sqrt{\mu_3}}(4-y^2)^{\frac{3}{2}} \tag{25c}$$

Assemble Eq.(25) to generate the second approximation of limit cycles:

$$\delta^{(2)}(y) = \delta_0(y) + \mu_1\delta_1(y) + \mu_1^2\delta_2(y) \tag{26}$$

With the approximation of $\mu_3 \approx K_n^2$, plotting the limit cycles of different μ_1 within the weakly nonlinear regimes is realizable, as showed in Figure 5. Thanks to the smoothness of the acquired displacement time histories, the limit cycle for the test results is also plotted with the velocity derived by central difference method.

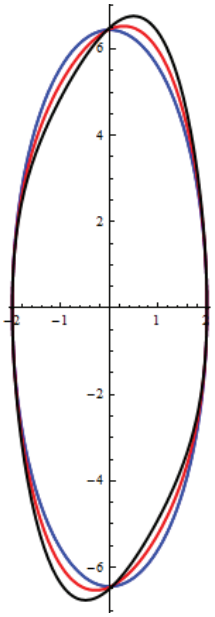

Figure 5. Limit cycles for Eq.(18) with: $\mu_1 = 0$(blue), $\mu_1 = 0.5$(red), and $\mu_1 = 1$(black)

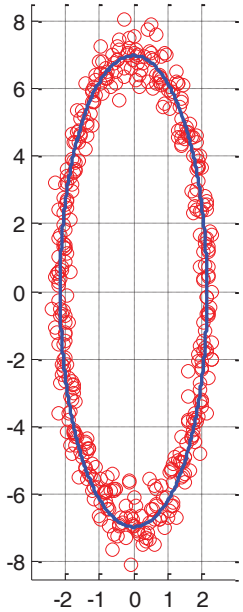

Figure 6. Limit cycle for measured data: test results(red circle), fitted cycle(blue line)

Figure 6 shows the limit cycle roughly fitted with the test results. It is obviously that the major axis of the ellipse approximately coincides with vertical axis of the coordinate system. Combining the displayed limit cycles for different values of μ_1, a choice of the range [0, 0.5] for μ_1 is made with some certainty.

So far all the demanded parameters for genetic algorithms have yet been decided.

6.3 *Simulation results and determination of the aeroelastic parameters*

With the displacement signal presented in Figure.4 as original data, simulation were carried out 50 times with the purpose of verifying the stability of estimated results. Most of these 50 times simulations converged to the same result of $\mu_1 = 0.394$ and $\mu_3 = 3.24^2$. Figure 7 shows good consistence between the estimated time histories of displacement and the measured one, which demonstrates the precision and effectiveness of the identification method.

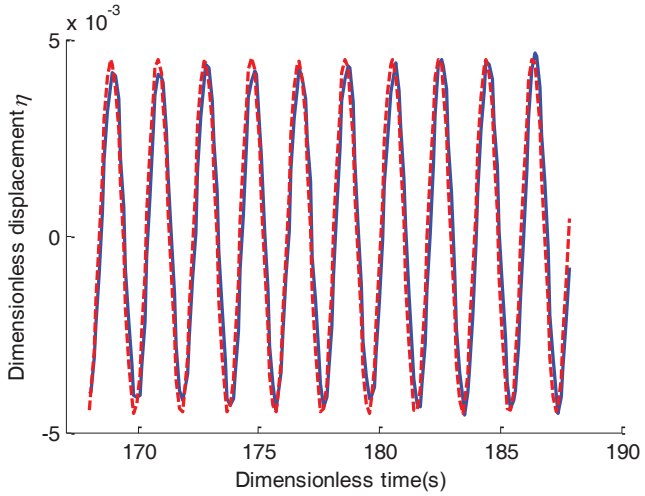

Figure 7. A section of estimated(red) and measured(blue) displacement time histories

As $\mu_1$has been extracted, μ_2 could be successively calculated according to Eq.(19) with dimensionless amplitude A_t being 4.5031×10^{-3}.

$$\mu_2 = \mu_1 \left(\frac{2}{A_t}\right)^2 = 77720.96 \tag{27}$$

Combining the definitions of μ_1, μ_2, μ_3 in Eqs5, 6 and 7, determinations of aeroelastic parameters of the SDOF vortex induced force model are realizable. With dimensionless structural parameters listed in previous sub-section, table 2 summarizes the identified and calculated results for this bridge deck section model.

Table 2. Identified and calculated parameters of SDOF vortex induced force model

μ_1	μ_2	μ_3
0.394	77720.96	3.24^2
$Y_1(K)$	ϵ	$Y_2(K)$
7.65	163772	-1.98

7. CONCLUSTIONS

A transformation of the semi-empirical nonlinear vortex induced force model to classical Van der Pol oscillator was made at the first step of this work, with subsequently replacing the original aeroelastic parameters with a new set of three characteristic parameters inherent to Van der Pol oscillator. An operation of substitutions of variables further simplified the equation with parameter μ_2 being implicit. Based on the obtained equation, homotopy analyses method

was adopted to estimate the displacement response.

The objective function on the basis of minimizing the sum of squared residuals was constructed to perform a nonlinear fitting. Taking account of the initial value dependence nature and the difficulties of providing appropriate initial boundaries of the nonlinear fitting method, a heuristic search method, namely a genetic algorithm, was selected and developed. The results of a numerical simulation with given values of parameters verified the effectiveness of the suggested procedure to some extent.

Wind tunnel tests of a streamlined bridge deck section model were then conducted in the TJ-3 boundary wind tunnel in Tongji University. A limit cycle in phase space for the measured displacement response was obtained to make a comparison with the limit cycles for given values of μ_1. Following the previous process, a determination of a range of μ_1 is accomplished. The consistence between estimated displacement response and measured counterpart shows the effectiveness of the proposed methodology in the usage of practical wind tunnel tests. The extracted parameters μ_1, μ_2 and μ_3 give a direct way to finally identify the desired aeroelastic parameters in semi-empirical nonlinear vortex induced force model.

Acknowledgement
This work has been supported by

8. REFERENCES

1. Scruton, C., On the wind-excited oscillations of stacks, towers and masts1963.
2. Simiu, E. and R.H. Scanlan, Wind effects on structures: an introduction to wind engineering1986: John Wiley.
3. Larsen, A., A Generalized-Model for Assessment of Vortex-Induced Vibrations of Flexible Structures. Journal of Wind Engineering and Industrial Aerodynamics, 1995. 57(2-3): p. 281-294.
4. Ehsan, F., Vortex - Induced Vibrations of Flexible Bridges. Journal of Engineering Mechanics, 1990. 116: p. 1392.
5. Gupta, H., P.P. Sarkar, and K.C. Mehta, Identification of vortex-induced-response parameters in time domain. Journal of Engineering Mechanics-Asce, 1996. 122(11): p. 1031-1037.
6. Marra, A.M., C. Mannini, and G. Bartoli, Van der Pol-type equation for modeling vortex-induced oscillations of bridge decks. Journal of Wind Engineering and Industrial Aerodynamics, 2011. 99(6–7): p. 776-785.
7. Zhou, T., L.-D. Zhu, and Z.-S. Guo, Parameters identification of nonlinear empirical model for vortex-induced vibration (VIV). Zhendong yu Chongji/Journal of Vibration and Shock, 2011. 30(3): p. 115-118+144(in Chinese).
8. Scanlan, R.H., State-of-the-art methods for calculating flutter, vortex-induced, and buffeting response of bridge structures, 1981.
9. Liao, S.J., An analytic approximate approach for free oscillations of self-excited systems. International Journal of Non-Linear Mechanics, 2004. 39(2): p. 271-280.
10. Holland, J.H., Genetic algorithms. Scientific American, 1992. 267(1): p. 66-72.
11. López, J.L. and R. López-Ruiz, Approximating the amplitude and form of limit cycles in the weakly nonlinear regime of Liénard systems. Chaos, Solitons & Fractals, 2007. 34(4): p. 1307-1317.

The Seventh International Colloquium on Bluff Body Aerodynamics and Applications (BBAA7)
Shanghai, China; September 2-6, 2012

Vortex-induced vibration prediction of long-span bridges considering imperfect correlation of aerodynamic forces

Li Mingshui [a], Sun Yanguo [a], Liao Haili [a]

[a] *Research Centre for Wind Engineering, Southwest Jiaotong University, Chengdu, China*

ABSTRACT: Periodical wake vortices may cause vortex induced vibration (VIV) of a long span bridge, the vortex-induced aerodynamic forces produced by vortices are partial correlation along the span. Based on Scanlan's semi-empirical linear and nonlinear models, the correlation of vortex-induced aerodynamic forces along span is studied respectively in frequency domain, and reduced factor of vortex-induced response between two-dimensional model to three-dimensional prototype structure is defined, and the methodology for extending the test results of section model into prototype structure by considering partial correlation of vortex-induced aerodynamic force along span is discussed. Validity of proposed theory is proved by sectional model tests and observed results in field.

KEYWORDS: Vortex-induced vibration; long span bridge; linear and nonlinear force models; partial correlation; wind tunnel testing.

1 INTRODUCTION

Vortex-induced vibration (VIV) of line-like structures, such as flexible long-span bridge, is one of the most common aeroelastic phenomena due to wind-structure interaction at relative low wind speeds. In the recent decades, obvious vortex-induced vibration has been observed in many long-span bridges (Kumarasena 1991, Larsen 2000, Fujino 2002). Various mathematical models that reflect the main aspects of the vortex-induced response of bluff bodies have been proposed (Hartlen & Currie, 1970, Iwan & Blevins, 1974, Scanlan, 1981, Larsen 1995), and most of these models were developed for the 2-D model. Elastically-mounted, rigid, section model (2-D) wind tunnel testing technique becomes a general methodology to investigate VIV of long-span bridges. However, the vortex-induced aerodynamic force produced by vortices is imperfect correlation along the span (Williamson 1988, Miller 1994). Consistence between the observation of prototype bridge and predictions based on 2-D model testing is still uncertain due to contribution of spatial spanwise correlation of vortex-induced aerodynamic forces (Wilkinson 1981). There is still lack of comprehensive theory to extend the test results of section into prototype bridge vibration because of the fact that the existence of mode shapes and the nonlinear vortex-induced forces are not fully correlated along the span, although several researchers tried to study it (Ehsan and Scanlan 1990, Zhu 2005, Xian 2008).

Two methods for considering the effect of imperfect span-wise correlation of aerodynamic forces on the vortex-induced response of long-span flexible bridges are described in this paper. These methods are based on semi-empirical linear and nonlinear mathematical model respectively. Validity of proposed theory is proved by sectional model tests and observed results in field.

2 LINEAR METHOD

2.1 *Linear model description*

By considering the existence of phase-difference along the span, the across-flow vortex-induced vibration of a rigid bluff body based on Scanlan's semi-empirical linear force model (1981) should take the form (here take the lift as an example):

$$m(\ddot{y} + 2\zeta\omega_0\dot{y} + \omega_0^2 y) = \frac{1}{2}\rho U^2 D[Y_1(K)\frac{\dot{y}}{U} + Y_2(K)\frac{y}{D} + \frac{1}{2}C_L(K)\sin(\omega t + \psi(x))] \quad (1)$$

Where, m=mass of per unit span length; ζ=damping ratio-to-critical; $\omega 0$=mechanical circular frequency; ρ=air density; U=the velocity of wind flow; D=across-flow dimension of section; $y(x,t)$=the vortex-induced vibration of the body, x=along-span degree-of-freedom; $K=\omega D/U$, ω is vortex shedding frequency that satisfies the Strouhal relation $2\pi S=\omega D/U$ (S is Strouhal number) ; $Y_1(K)$, $Y_2(K)$, $C_L(K)$ and $\psi(x)$ are unknown parameters to be identified by experiments. The vertical motion y at the location x along the deck can be expressed as:

$$y(x,t) = \phi(x)\xi(t)D \quad (2)$$

In which, $\phi(x)$=mode shape; ξ=generalized coordinate. The dimensionless form of the mathematical model can be written as the following equation by inserting Eq.2 into Eq.1, multiplying both sides by $\phi(x)$ and integrating over the span length L,

$$\ddot{\xi}(s) + (2\zeta K_0 - \frac{\rho D^2}{2m_{eq}}Y_1)\dot{\xi}(s) + (K_0^2 - \frac{\rho D^2}{2m_{eq}}Y_2)\xi(s) = \frac{\Gamma F(s)}{\vartheta} \quad (3)$$

Here,

$$s = \frac{Ut}{D};\ \Gamma = \frac{\rho D^2 C_L}{4m_{eq}};\ \vartheta = \frac{1}{L}\int_{-L/2}^{L/2}\phi^2(x)dx;\ m_{eq} = \frac{M}{L\vartheta};\ M = \int_{-L/2}^{L/2} m(x)\phi(x)^2 \mathrm{d}x;$$

$$F(s) = \frac{1}{L}\int_{-L/2}^{L/2}|\phi(x)|\sin[Ks + \psi(x)]\mathrm{d}x$$

The correlation of $F(s)$ along the span is studied in following. $F(s)$ can be written in the form:

$$F(s) = \frac{1}{L}\int_{-L/2}^{L/2}|\phi(x)|f(s,x)\mathrm{d}x \quad (4)$$

Where, $f(s,x)=\sin[Ks+\psi(x)]$, the correlation of $F(s)$ can be expressed as:

$$R_{F(\tau)} = \frac{1}{L^2}\int_{-L/2}^{L/2}\int_{-L/2}^{L/2}|\phi(x_1)|\cdot|\phi(x_2)|R_{f(\tau)}dx_1dx_2 \quad (5)$$

Fourier transform is applied in both sides of above equation：

$$S_F(\omega) = \frac{1}{L^2}\int_{-L/2}^{L/2}\int_{-L/2}^{L/2}|\phi(x_1)|\cdot|\phi(x_2)|\cdot S_f(\omega,|x_2 - x_1|)dx_1dx_2 \quad (6)$$

Correlation function of three-dimensional spectrum can be written as (Houblt 1958):

$$R(M,M',\omega) = S_F(M,M',\omega)/S(\omega) \quad (7)$$

Here, M and M' represent any two points in 3-D space, Eq.6 can be rewritten as follow by using Eq.7,

$$S_F(\omega) = \frac{1}{L^2}\int_{-L/2}^{L/2}\int_{-L/2}^{L/2}\left|\phi(x_1)\right|\cdot\left|\phi(x_2)\right|\cdot R(\omega,\left|x_2 - x_1\right|)\mathrm{S}(\omega)dx_1 dx_2 \tag{8}$$

Where $S(\omega)$=power spectrum of vortex induced force at any cross section of span; correlation function R is independent with frequency ω, as vortex induced vibration is always one participation mode at lock-in. Eq.8can be written as follow:

$$S_F(\omega) = R_F \mathrm{S}(\omega) \tag{9}$$

$$R_F = \frac{1}{L^2}\int_{-L/2}^{L/2}\int_{-L/2}^{L/2}\left|\phi(x_1)\right|\cdot\left|\phi(x_2)\right|R(\left|x_2 - x_1\right|)dx_1 dx_2 \tag{10}$$

Auto-convolution Integral of mode shape is pre-defined as following form (Li and Tanaka 1996):

$$\theta(\Delta x) = 2\int_{-L/2}^{L/2-\Delta x}\left|\phi(x)\right|\cdot\left|\phi(x+\Delta x)\right|dx \tag{11}$$

The reduced relation of vortex induced forces between two-dimensional and three-dimensional is $F=\Phi\cdot f$. After inserting Eq.11 into Eq.10, and extracting square root of Eq.9. Reduced factor Φ, representing the transformation of vortex induced response between two-dimensional and three-dimensional, is defined as,

$$\Phi = 1/L\sqrt{\int_0^L \theta(\Delta x)R(\Delta x)d\Delta x} \tag{12}$$

Where $R(\Delta x)$ is correlation function of vortex-induced aerodynamic force along span, Δx is spacing along span. It is obvious that reduce factor belongs to the range of (0,1].

The Eq.3 can be written in the following form,

$$\ddot{\xi}(s) + (2\zeta K_0 - \frac{\rho D^2}{2m_{eq}}Y_1)\dot{\xi}(s) + (K_0^2 - \frac{\rho D^2}{2m_{eq}}Y_2)\xi(s) = \frac{\Gamma\Phi\sin[Ks+\psi_0]}{\vartheta} \tag{13}$$

The simplified form of Eq.13 can be rewritten as,

$$\ddot{\xi}(s) + 2\gamma\hat{K}_0\dot{\xi}(s) + \hat{K}_0^{\,2}\xi(s) = \frac{\Gamma\Phi}{\vartheta}\sin[Ks+\psi_0] \tag{14}$$

In which,

$$2\gamma\hat{K}_0 = 2\zeta K_0 - \frac{\rho D^2}{2m_{eq}}Y_1;\quad \hat{K}_0^{\,2} = K_0^2 - \frac{\rho D^2}{2m_{eq}}Y_2 .$$

The amplitude of the generalized coordinate can be calculated by:

$$\xi(s) = \frac{\Gamma\Phi}{\vartheta\hat{K}_0^2}\frac{\sin[Ks-\theta]}{\sqrt{(1-\beta_v^2)^2 + (2\gamma\beta_v)^2}} \qquad \theta = \arctan\frac{2\gamma\beta_v}{1-\beta_v^2} \quad (\beta_v = K/\hat{K}_0) \tag{15}$$

2.2 *Application of linear method*

As there is no correlation function available for the concerned bridge, the correlation function proposed by Wilkinson (1981) based on pressure measurement on square cylinder is used in present analysis (Fig. 1):

$$R(\Delta x) = \exp[-f_1(\eta)(\frac{\Delta x}{D})^{f_2(\eta)}] \tag{16}$$

Here, η is non-dimensional amplitude, $f_1(\eta)$ and $f_2(\eta)$ are fitted as the following functions (Ehsan 1990):

$$f_1(\eta) = \frac{0.052}{0.298+\eta^{0.25}} \qquad f_2(\eta) = \frac{0.065}{0.042+\eta} \tag{17}$$

For section model case, the reduced factor varies with length of model and amplitude. The mode shape function is $\phi(x)=1$, $\theta(\Delta x)$ and $R(\cdot)$ can be calculated by Eqs.11 and 16 respectively. The reduced factor Φ is then obtained fromEq.12. Fig. 2 shows the reduced factors of section model varying with length of model and amplitude. For prototype or full bridge model of long span suspension bridge, the mode shape function of first symmetric vertical (V-S-1) mode can be simplified as $\phi(x)=\cos(\pi \cdot x/L)$. The reduced factor can also be obtained from above mentioned equations. Fig. 3 shows the reduced factors for prototype bridge or full bridge model varying with length and amplitude (V-S-1).

The amplitude derived from section model testing can be interpreted into prototype bridge by the following iteration equation:

$$A_{pi+1} = nA_m \cdot \frac{\Phi_{pi}\vartheta_m}{\Phi_m\vartheta_p} \tag{18}$$

In above, n is model scale, A is amplitude, m and p represent model and prototype.

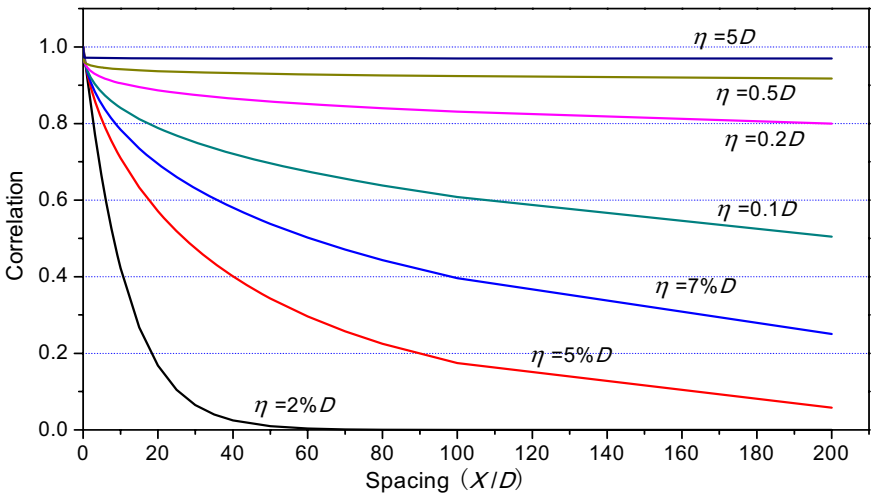

Fig. 1 Examples of correlation curves (Wilkinson, 1981)

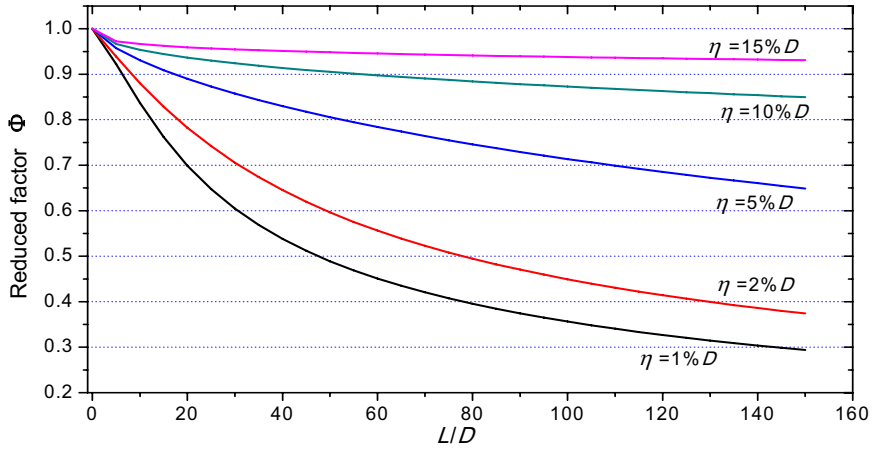

Fig. 2 Reduced factors for section model, $\phi(x)=1$

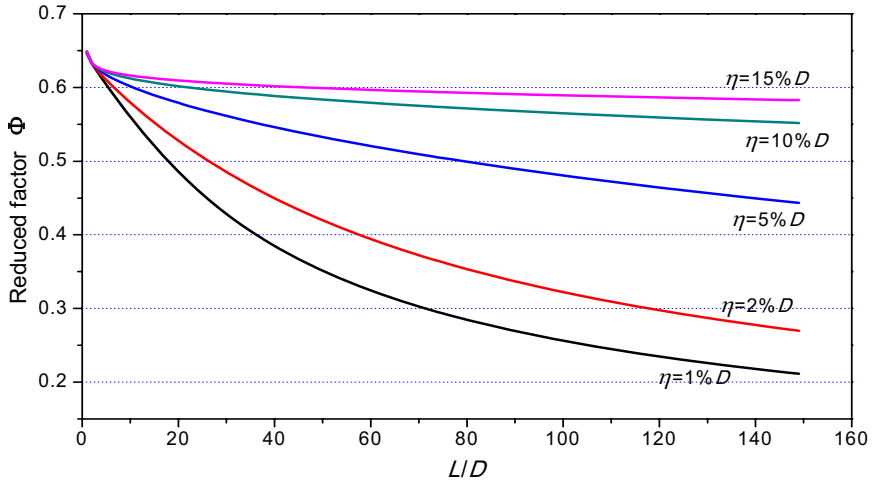

Fig. 3 Reduced factors for suspension bridge (V-S-1)

The maximum amplitude of prototype bridge can be found by Eq.16 after several iteration. Special attention is required that the amending for mode shape has been finished in the first iterative process, and it shouldn't be included in the rest iterative processes. It means that the iterative equation of the rest processes can be written as

$$A_{pi+1} = nA_m \Phi_{pi} / \Phi_m$$

3 NONLINEAR METHOD

3.1 *Nonlinear model description*

Scanlan (1981) proposed a semi-empirical nonlinear model. In this model, a linear mechanical oscillator is subjected to a forcing function which is assumed to be the sum of a motion-induced component and a direct vortex shedding component:

$$m(\ddot{y}+2\zeta\omega_0\dot{y}+\omega_0^2 y)=\frac{1}{2}\rho U^2(2D)\left[Y_1(K)\left(1-\varepsilon(K)\frac{y^2}{D^2}\right)\frac{\dot{y}}{U}+Y_2(K)\frac{y}{D}+\frac{1}{2}C_L\sin(\omega t+\theta)\right] \tag{19}$$

The parameters Y_1, ε, Y_2, C_L and θ in this model should be estimated by section model wind tunnel testing. Several methods for estimating the parameters were outlined by Scanlan (1981) Ehsan (1990) and Li (1995) etc. The other notations in Eq.19 denote the same means as Eq.1.

At lock-in, it is assumed that the parameters of aerodynamic stiffness term Y_2 and instantaneous lift coefficient C_L are very small compared to aerodynamic damping term Y_1. It means Y_2= C_L =0. Although an elastic suspended section model is assumed to behave in a two dimensional manner, it is actually a three-dimensional object so that the aerodynamic force are not perfectly correlated along its length. In the case of an actual bridge, the vortex-induced aerodynamic force introduced by vortices is imperfect correlation along the span. Thus Y_1 and ε estimated from section model testing actually represent these forces in an average sense only, they may be varied with the location x along the span. Thus, the modified model can be expressed as:

$$m(\ddot{y}+2\zeta\omega_0\dot{y}+\omega_0^2 y)=\rho UD\left[Y_1(K,x)\left(1-\varepsilon(K,x)\frac{y^2}{D^2}\right)\frac{\dot{y}}{U}\right] \tag{20}$$

The non-dimensional form of the model should be written in the following form by non-dimensional process and introducing generalized coordination ξ(*t*):

$$m\phi(x)\left(\ddot{\xi}(t)+2\zeta\omega_0\dot{\xi}(t)+\omega_0^2\xi(t)\right)=\rho UD\left[Y_1(K,x)\left(1-\varepsilon(K,x)\phi^2(x)\xi^2\right)\phi(x)\dot{\xi}\right] \tag{21}$$

Multiplying both sides by ϕ(*x*) and integrating over the span *L* of the deck:

$$M\left(\ddot{\xi}(t)+2\zeta\omega_0\dot{\xi}(t)+\omega_0^2\xi(t)\right)=\rho UD\int_0^L\left[Y_1(K,x)\left(1-\varepsilon(K,x)\phi^2(x)\xi^2(t)\right)\phi^2(x)\dot{\xi}(t)\right]dx \tag{22}$$

Where *M* is the generalized mass, $M=\int_{-L/2}^{L/2}m(x)\phi(\mathrm{x})^2\mathrm{dx}$.

3.2 *Section model case*

For section model case, the mode shape function is ϕ(*x*)=1, the reduced factor varies with length of model and amplitude. The mathematic model can be written as following by inserting ϕ(*x*)=1 into Eq.22.

$$M\left[\ddot{\xi}(t)+2\zeta\omega_0\dot{\xi}(t)+\omega_0^2\xi(t)\right]=\rho UDLF(t) \tag{23}$$

Here, $F(t)=\frac{1}{L}\int_{-L/2}^{L/2}f(\mathrm{t,x})\mathrm{dx}$, $f(t,x)=Y_1(K,x)\left[1-\varepsilon(K,x)\xi^2(t)\right]\dot{\xi}(t)$.

The correlation of *F*(*s*) is studied by using the similar method as last chapter (Eqs.5-9). The reduced relation of vortex induced aerodynamic forces between two-dimensional and three-dimensional is still F=Φ·f. Reduced factor Φ of vortex induced response between two-dimensional and three-dimensional is defined as follow:

$$\Phi=\sqrt{\frac{1}{L^2}\int_{-L/2}^{L/2}\int_{-L/2}^{L/2}R(\Delta x)dx_1dx_2} \tag{24}$$

Eq.23 can be rewritten as the following form by using correlation function proposed by Wilkinson,

$$M\left[\ddot{\xi}(t)+2\zeta\omega_0\dot{\xi}(t)+\omega_0^2\xi(t)\right]=\Phi\rho UDLY_1'\left[1-\varepsilon'\xi^2(t)\right]\dot{\xi}(t) \tag{25}$$

It is worth mentioned that the parameters of $Y_1'$and ε' in this equation are based on absolute two-dimensional estimation. It may be quiet different with the one estimated from section model wind tunnel testing. After analyzing the right side of Eq.22, it is clearly that the parameter ε is constant and retains its two-dimensional value and parameter Y_1 has the same reduced factor with vortex induced force. It means that,

$$Y_1'=Y_1/\Phi \qquad \varepsilon'=\varepsilon \tag{26}$$

If the net energy loss or gain per cycle is zero at lock-in,

$$\int_0^T\left[2M\zeta\omega_0-\Phi\rho UDLY_1\left(1-\varepsilon\xi^2(t)\right)\right]\cdot\dot{\xi}^2(t)dt=0 \tag{27}$$

Assuming that the generalized coordinate is sinusoidal, i.e. $\xi(t)=\xi_0\cos(\omega t)$, then,

$$\xi(t)=\xi_0\cos(\omega t);\quad \int_0^T\dot{\xi}^2(t)dt=\pi\omega\xi_0^2;\quad \int_0^T\dot{\xi}^2(t)\xi^2(t)dt=\frac{\pi}{4}\omega\xi_0^4$$

The energy condition leads to the following expression for the amplitude of the generalized coordinate ξ_0,

$$\xi_0=2\sqrt{\frac{\Phi Y_1'-\dfrac{2M\zeta\omega}{\rho UDL}}{\Phi Y_1'\varepsilon'}} \tag{28}$$

In which, $M=mL$. Lets $m_r=\rho D^2/m$, Eq.28 can be rewritten as:

$$\xi_0=2\sqrt{\frac{1}{\varepsilon'}}\left(1-\frac{2\zeta K}{m_r\Phi Y_1'}\right)^{1/2} \tag{29}$$

3.3 *Prototype bridge*

In the case of an actual bridge, it has an infinite set of modes. The mode shape function $\phi(x)$ of the bridge should be gained by mode analysis. For arbitrary $\phi(x)$, the vertical displacement at lock-in can be calculated using the condition that net energy loss or gain per cycle is zero. The energy condition leads to the following expression for the amplitude of the generalized coordinate ξ_0:

$$\xi_0=2\sqrt{\frac{\displaystyle\int_0^L Y_1\phi^2(x)\frac{dx}{L}-\frac{2M\zeta K}{\rho D^2L}}{\displaystyle\int_0^L Y_1\varepsilon\phi^4(x)\frac{dx}{L}}} \tag{30}$$

Ehsan (1990) proposed a roughly method to account for the imperfect correlation of aerodynamic forces along the span. The similar method with linear theory (Chapter 2) and Duhamel Integral theory are applied in this study. Eq.22 can be rewritten as follow:

$$M\left(\ddot{\xi}(t)+2\zeta\omega_0\dot{\xi}(t)+\omega_0^2\xi(t)\right)=\rho UD\left(\int_0^L Y_1\phi^2(x)dx-\int_0^L Y_1\varepsilon\phi^4(x)dx\xi^2(t)\right)\dot{\xi}(t) \tag{31}$$

According to Duhamel Integral theory, mode shape function ϕ(x) can be seen as input function, and correlation function R(Δx) can be treated as response functions. The mathematic model can be written as following form:

$$M\left(\ddot{\xi}(t)+2\zeta\omega_0\dot{\xi}(t)+\omega_0^2\xi(t)\right)=\rho UDL\left(Y_1'\Phi_2-Y_1'\varepsilon'\Phi_4\xi^2(t)\right)\dot{\xi}(t) \tag{32}$$

Where

$$\Phi_2=\sqrt{\frac{1}{L^2}\int_{-L/2}^{L/2}\int_{-L/2}^{L/2}\phi^2(x_1)\phi^2(x_2)R(\Delta x)dx_1dx_2}$$

$$\Phi_4=\sqrt{\frac{1}{L^2}\int_{-L/2}^{L/2}\int_{-L/2}^{L/2}\phi^4(x_1)\phi^4(x_2)R(\Delta x)dx_1dx_2} \tag{33}$$

The energy condition leads to the following expression for the amplitude of the generalized coordinate ξ_0:

$$\xi_0=2\sqrt{\frac{\Phi_2Y_1'-\dfrac{2M\zeta\omega}{\rho UDL}}{\Phi_4Y_1'\varepsilon'}} \tag{34}$$

Eq.34 can be re written as,

$$\xi_0=2\sqrt{\frac{\Phi_2}{\varepsilon'\Phi_4}}\left(1-\frac{2\zeta K}{m_r\Phi_2Y_1'}\int_0^L\phi^2(x)dx\right)^{1/2} \tag{35}$$

If the parameters of the model indentified from sectional model testing are available, the vortex induced response of bridge can be estimated by using Eq.35 and taking into account the imperfect spanwise correlation of aerodynamic forces.

3.4 *Application of nonlinear method*

For section model, $\phi(x)=1$, $\theta(\Delta x)=2(L-\Delta x)$, and the reduced factor can be obtain by inserting it into Eq.24:

$$\Phi=\sqrt{\frac{1}{L^2}\int_0^L 2(L-x)R(\Delta x)d\Delta x} \tag{36}$$

Lets $z=\Delta x/L$ and $\hat{L}=L/D$, the non-dimensional form of Eq.36 can be expressed as follow：

$$\Phi(\hat{L})=\sqrt{\int_0^1 2(1-z)\exp[-f_1(\eta)\cdot(\hat{L}z)^{f_2(\eta)}]dz} \tag{37}$$

For prototype or full bridge model of long span suspension bridge, the mode shape function of first symmetric vertical can be assuming as the form $\phi(x)=\cos(\pi\cdot x/L)$. The reduced factor can be obtained by inserting it into Eq.33:

$$\Phi_2 = \sqrt{\frac{1}{L^2}\int_0^l 2\int_{-L/2}^{L/2-\Delta x} \cos^2(\frac{\pi \cdot x}{L}) \cdot \cos^2(\frac{\pi \cdot (x+\Delta x)}{L}) dx \cdot \exp[-f_1(\eta) \cdot (\Delta x / D)^{f_2(\eta)}] d\Delta x}$$

$$\Phi_4 = \sqrt{\frac{1}{L^2}\int_0^l 2\int_{-L/2}^{L/2-\Delta x} \cos^4(\frac{\pi \cdot x}{L}) \cdot \cos^4(\frac{\pi \cdot (x+\Delta x)}{L}) dx \cdot \exp[-f_1(\eta) \cdot (\Delta x / D)^{f_2(\eta)}] d\Delta x} \quad (38)$$

Lets $\hat{x} = x / L$, the non-dimensional form of Eq.38 can be written as：

$$\Phi_2 = \sqrt{2\int_0^1 \int_{-1/2}^{1/2-z} \cos^2(\pi \hat{x}) \cdot \cos^2(\pi(\hat{x}+z)) d\hat{x} \cdot \exp[-f_1(\eta) \cdot (\hat{L}z)^{f_2(\eta)}] dz}$$

$$\Phi_4 = \sqrt{2\int_0^1 \int_{-1/2}^{1/2-z} \cos^4(\pi \hat{x}) \cdot \cos^4(\pi(\hat{x}+z)) d\hat{x} \cdot \exp[-f_1(\eta) \cdot (\hat{L}z)^{f_2(\eta)}] dz} \quad (39)$$

4 CASE STUDY

Obvious vortex induced vibration (VIV) was observed during sectional model testing and prototype for the Deer Isle-Sedgwick bridge in the third vertical mode. Details of the testing are given by Ehsan (1988) and Kumarasena (1989). The estimated parameter values at K=0.929 and ζ=0.00625 were Y_1=10.54 and ε=228.7. The main span of the bridge is 329.2m long; the deck is 1.98m deep. The mass ratio was computed to be m_r=0.001348. The peak-to-peak amplitude derived from section model testing is interpreted into prototype bridge with linear VIV theory and nonlinear VIV theory are 0.076m and 0.101m respectively by considering imperfect correlation of vortex-induced aerodynamic force along span. The amplitude observed in the field is 0.096m. It's obvious that the proposed response estimation method yields very reasonable results.

5 ACKNOWLEDGEMENTS

Financial support from National Natural Science Foundation of China (Project No 50978223) is appreciated.

6 REFERENCES

[1] Kumarasena T., Scanlan R. H. and Ehsan F., 1991. Wind-induced motions of Deer Isle bridge. Journal of Structural Engineering, 117(11): 3356-3374.
[2] Larsen A., Esdahl S., Andresen J. E., Vejrum T., 2000. Storebaelt suspension bridge-vortex shedding excitation and mitigation by guide vanes. Journal of Wind Engineering and Industrial Aerodynamics, 88: 283–296.
[3] Fujino Y., Yoshida Y., 2002. Wind-Induced Vibration and Control of Trans-Tokyo Bay Crossing Bridge. Journal of Structural Engineering, 128(8): 1012-1025.
[4] Hartlen R T, Currie I G., 1970. Lift-oscillator model of vortex-induced vibration. Journal of the Engineering Mechanics, 96(5): 577-591.
[5] Iwan W. D., Blevins R. D., 1974. A model for the vortex-induced oscillation of structures. Journal of Applied Mechanics, 41(3): 581-586.
[6] Scanlan R. H., 1981. On the state-of-the-arts methods for calculation flutter, vortex-induced vibration and buffeting response of bridge structures, FHWA/RD-80/050, National technical information service, Springfiled.
[7] Larsen A., 1995. A generalized model for assessment of vertex-induced vibrations of flexible structures. Journal of wind engineering and industrial aerodynamics, 57(2-3): 281-294.

[8] Williamson, C. H. K. (1988), "The existence of two stages in the transition to three dimensionality of a cylinder wake", Physics of Fluids, 31, 3165-3168.
[9] Miller, G.D. and Williamson, C. H. K. (1994), "Control of three-dimensional phase dynamics in a cylinder wake", Experiments in Fluids, 18-26.
[10]Wilkinson R H., 1981. Fluctuating pressures on an oscillating square prism: Part II: Spanwise correlation and loading. Aero. Quarterly, 32 (2): 111-125.
[11]Ehsan F, Scanlan R H., 1990. Vortex-induced vibrations of flexible bridges. Journal of Engineering Mechanics, 116: 1392-1410.
[12]Zhu Le-dong., 2005. Mass simulation and amplitude conversion of bridge sectional model test for vortex excited resonance (in Chinese). Engineering mechanics, 22(5): 204-208.
[13]Xian R., 2008. Spanwise vortex-induced vibration research of long-span bridge girder, PhD dissertation, Southwest Jiaotong University, Chengdu, China. (in Chinese)
[14]Houblt J G., 1958. On the response of structural having multiple random inputs, WGLR-Jahrbuch.
[15]Li Ming-shui, Tanaka H., 1996. Extended joint acceptance function for buffeting analysis. Journal of Wind Engineering and Industrial Aerodynamics, 64: 1-4.
[16]LI Ming-shui, HE De-xin., 1995. Parameter Identification of Vortex-Induced Forces on Bluff Bodies. Acta Aerodynamica Sinica, 13(4): 396-404.
[17]Ehsan F., 1988. The vortex-induced response of long suspended-span bridges. PhD dissertation, Johns Hopkins University, Baltimore, Md, USA.
[18]Kumarasena T, Scanlan R H, Morris G R., 1989. Deer Isle bridge: Field and computed vibrations. Journal of Structure Engineering, 115(9): 2313-2328.

The Seventh International Colloquium on Bluff Body Aerodynamics and Applications (BBAA7)
Shanghai, China; September 2-6, 2012

Experimental study of vortex-induced vibrations on H-shaped sections

Abraham S. Corriols [a], Miguel A. Astiz [a], Antonio Barrero [a]
[a] *Technical University of Madrid, Prof. Aranguren s/n, Spain*

ABSTRACT: Experimental results of aeroelastic tests carried out with H-section models, aiming to study in detail the aeroelastic phenomena associated with vortex shedding, are presented through this paper. Such phenomena led to the oscillations of Alconétar arch bridge during its construction in 2006. The facility used is a small, simple wind tunnel built at the Ignacio Da Riva Institute, School of Aeronautics, Technical University of Madrid. Also a comparison with data from rectangular tandem section tests that conform to the geometry of the bow section of the Alconétar Bridge and some conclusions are outlined.

KEYWORDS: Aerodynamics, Vortex shedding, Vibration, Tandem section, H-shaped section

1 INTRODUCTION

The oscillations observed in the Alconétar steel arch bridge during its construction in January 2006 before placing the superstructure [1], led to the initiation of a research aimed at studying in detail the aeroelastic phenomena related to the vortex shedding that resulted in such an event [2].

Figure 1. Alconétar bridge during erection (left) and cross-section with main dimensions (right)

The maximum amplitude reached was 80 cm on the vertical axis [1]. The box depth corresponding to the maximum amplitude value is D=2.41 m, the box width is B=1.2m and the total width is W=7.74 m, giving a side ratio of W/D = 3.21. Measured wind speeds during the Alconétar Bridge vibration episode did not exceed 30 km/h, so the corresponding reduced frequency was close to 0.21, typical from a H-shaped section with the same side ratio. [3]. The modal mass is 1,133 kg/m and the damping ratio of critical, 0.003.

It is well known that bluff bodies behave very differently than streamlined bodies with the passage of air flow. In high curvature surfaces, an adverse pressure gradient is added to the retardant action of friction surface, which can cause the flow to be interrupted and retreat to a region adjacent to the surface. This results in the emergence of a back flow region, and a detached boundary layer appears below. For sufficiently high Reynolds numbers (say, above 10^3), the region due to the separation flow becomes unstable and an oscillating wave composed of large-scale eddies, known as Von Karman vortex street, is formed downstream of the body.

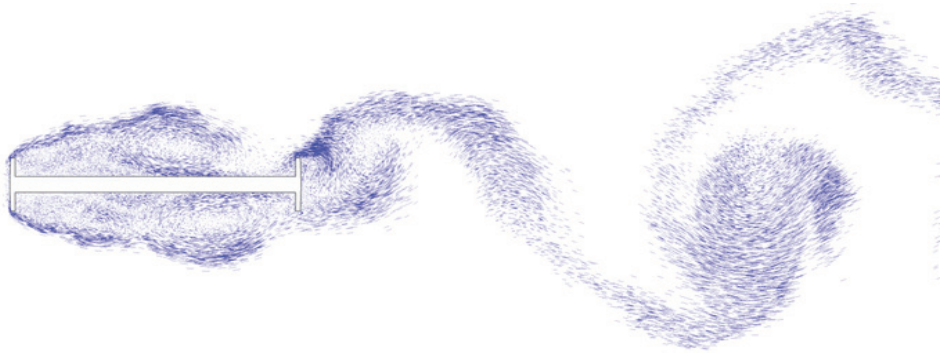

Figure 2. Visualization of the vortex shedding phenomenon through a numerical simulation code

The vortex shedding typically develops with great regularity showing a dominant frequency, which is characterized by the Strouhal number, according to the following expression:

$$St = \frac{fD}{U_\infty} \tag{1}$$

where D is the section depth, and U_∞, the speed of the current incident. The Strouhal number (St) mainly depends on the geometry of the object.

When the natural frequency of the structure is close to the value of the vortex shedding frequency, the periodic forces caused by the alternate shedding can give rise to resonance oscillations, resulting in a complex coupling between the motion of the structure and the wake pattern (e.g., the spacing between the vortices can change). Usually these type of oscillations are classified as instability induced excitations (IIE) [3]

When analysing the effect of vortex-induced oscillations, it is important to note that the amplitude of the structure is self-limited [3]. There is an upper threshold with a maximum equal to the vertical dimension of the body. Nevertheless, these types of oscillations can be considered as problematic for the serviceability of the structure. Thus, it is necessary to limit the level of vibrations in structures to ensure an appropriate standard of comfort for the users and avoid fatigue damage over time.

2 EXPERIMENTAL SET-UP

Tests were conducted in a small, simple wind tunnel built at the Ignacio Da Riva Institute, School of Aeronautics, Technical University of Madrid (see fig. 2). The installation has a rotor capable of generating an air flow that can reach a maximum speed of 1.40 m/s, driven by an AC motor. The regulation of the flow speed is achieved through a variable transformer capable to get speed increments of 0.01 m/s (the same as the tolerance of the hot wire anemometer used for

measuring the flow speed values). A laser device to measure the oscillation amplitudes of the models is employed. An oscilloscope has been connected in order to allow a better visualization of periodic movements.

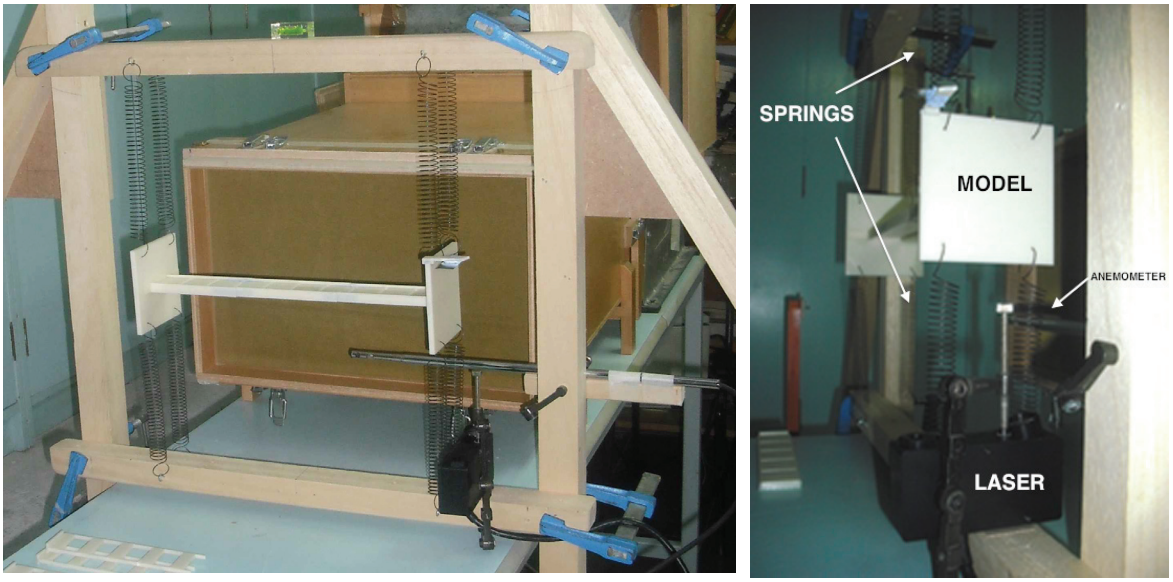

Figure 3. General view of the installation (left). Detail of springs, laser and hot wire anemometer (right)

Eight springs support the model elastically normal to the air flow. Linearity of the mechanical properties for every model was checked. These properties ready for testing are listed in Table 1.

Compared to the real section of Alconétar Bridge, it has a scale factor of 1/240. The Reynolds number range is between 67 and 930. Typical Reynolds numbers for real bridges are between 10^5 and 10^7, so it creates a turbulent wake behind the section. For Reynolds numbers less than 10^3 as the case is, viscous forces are still important, so it will be necessary to consider this fact to draw the appropriate conclusions and compare the results with other tests performed.

3 MODELS TESTED

Table 1 summarizes the geometry properties of the models used, being W/D the width/depth ratio corresponding to each model.

Table 1. Geometry of models tested

Model	Length (L) mm	Width (W) mm	Depth (D) mm	W/D
H-SHAPED 2.0	300	20	10	2.0
H-SHAPED 2.5	300	25	10	2.5
H-SHAPED 3.0	300	30	10	3.0
H-SHAPED 4.0	300	40	10	4.0
H-SHAPED 5.0	300	50	10	5.0
H-SHAPED 6.0	300	60	10	6.0
H-SHAPED 7.5	300	75	10	7.5

Dynamic properties to characterize frequency and damping for each W/D ratio are presented below.

Table 2 summarizes dynamic parameters of models tested

MODEL	W/D -	D m	f Hz	m Kg/m	.ξ %	m* -	m*ξ -
H-SHAPED 2.0	2.0	0.01	4.73	0.1017	0.110	813.5	0.8957
H-SHAPED 2.5	2.5	0.01	4.69	0.1031	0.107	825.1	0.8830
H-SHAPED 3.0	3.0	0.01	4.80	0.0982	0.131	785.4	1.0296
H-SHAPED 4.0	4.0	0.01	4.76	0.1011	0.131	809.1	1.0568
H-SHAPED 5.0	5.0	0.01	4.76	0.1046	0.101	837.2	0.8456
H-SHAPED 6.0	6.0	0.01	4.75	0.1038	0.141	830.5	1.1705
H-SHAPED 7.5	7.5	0.01	4.80	0.1042	0.133	833.3	1.1091
H-SHAPED 4.0 POROSITY 0%	4.0	0.01	4.33	0.0994	0.076	794.8	0.6065
H-SHAPED 4.0 POROSITY 10%	4.0	0.01	4.60	0.0867	0.129	693.5	0.8397
ALCONÉTAR BRIDGE	3.21	2.41	0.70	1131	0.300	153.9	0.4616

where W/D=width/depth ratio; f=the vibration frequency of the model; m=linear mass associated to the model; ξ=damping ratio; m*=mass ratio (=m/ρD^2); m*ξ=reduced damping. In order to achieve a realistic comparison, not only depending on the W/D ratio, similar values of damping ratio in all models have been sought. In this case, the values are all close to unity.

A model with a porosity ratio of 10% (related to overall surface and distributed in hollow strips parallels to the air flow direction) has also been tested, in order to compare the amplitude of oscillations with solid models. Also another model with a lower reduced damping (m*ξ) have been considered to check the dependency of the amplitude of oscillations as a function of reduced damping. Lastly, real data from Alconétar Bridge are also included.

Figure 4. Model with of W/D=4.0 and porosity ratio of 10% ready to be tested

4 RESULTS

Figure 5 shows a series of plots corresponding to the amplitude spectrum of lift coefficient oscillations (left) and temporal registration of vertical movements (right) that identify the process of vortex-induced vibration of the model with a W/D = 4.0, for a given range of air flow speeds. Frequency range of the spectrum is 20 Hz, and the time interval considered is one minute, always leaving two minutes at each speed interval prior to the start of data recording to ensure that the steady state is reached.

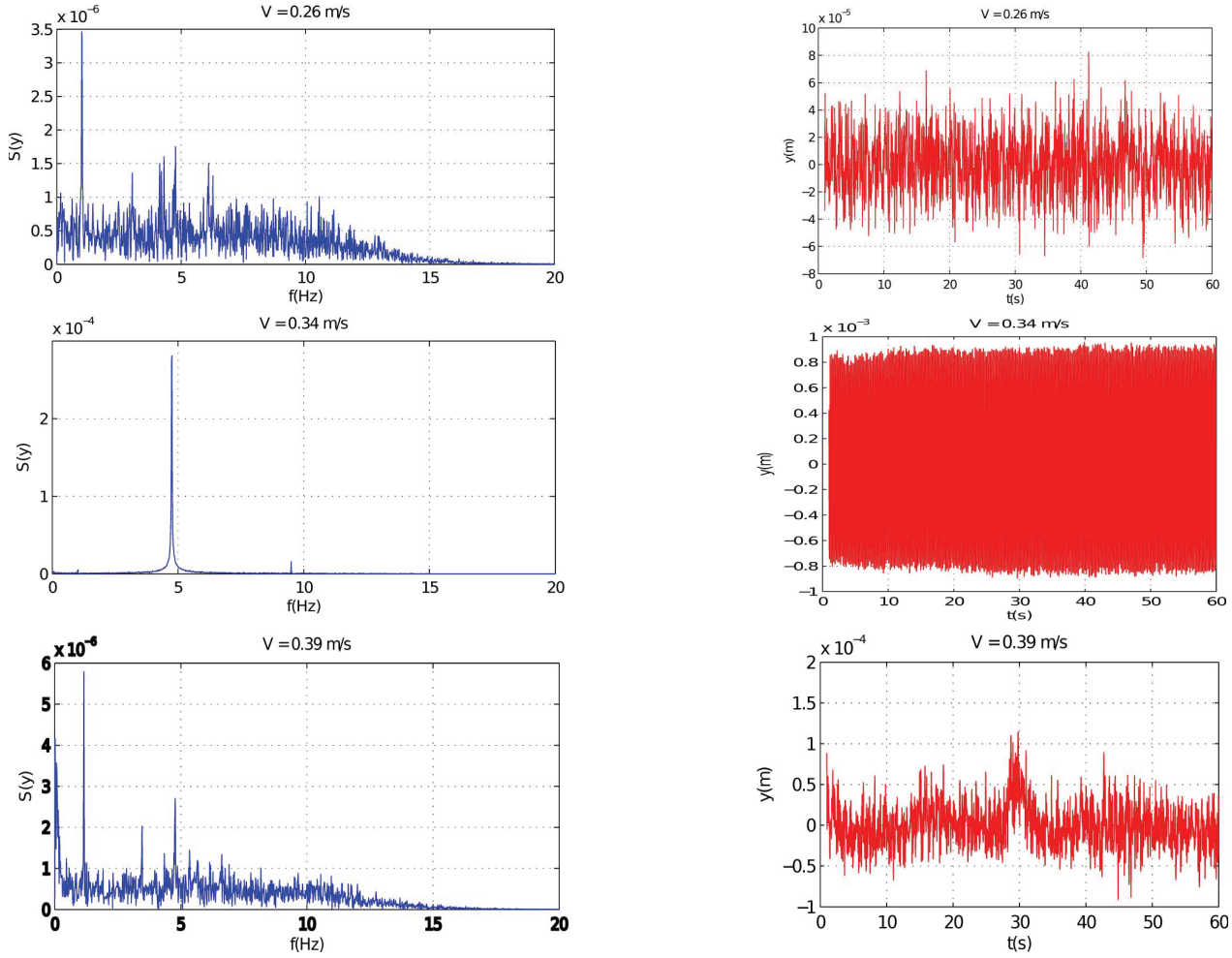

Figure 5. Amplitude spectrum of lift coefficient oscillations (left) and temporal register of vertical displacements within the wind speed range of VIV (right). Model with side ratio of W/D=4.0

Figure 5 (v = 0.26 m/s) shows that the excited frequency range is quite broad, which indicates that the model is vibrating slightly. However, there is no coupling between the natural vibration frequency and the vortex shedding frequency. The oscillations are small, not exceeding the threshold of $6 \cdot 10^{-5}$ m of amplitude (y/D<0.6%). As the wind speed increases, the vortex shedding frequency approaches the natural frequency. Oscillations become more regular and their amplitude increases, reaching a value close to 10^{-4} m (y/D = 1.0%) for an air flow speed value of 0.28 m/s. This value can precisely be considered as the starting speed of vortex-induced vibration phenomenon (v_0), which occurs within an air flow speed range between 0.28 m/s and 0.37 m/s. Critical air flow speed (v_{crit}) is 0.34 m/s, associated to the peak value of vertical oscillations, around $9 \cdot 10^{-4}$m (y/D = 9%). From 0.37 m/s, air flow speed considered as the end of the coupling phenomenon (v_e), small peaks in the spectrum different to the natural oscillation frequency begin to appear, decreasing the amplitude of the oscillation gradually and losing the regularity simultaneously, turning back to the prior oscillation state.

Figure 6 shows the root mean square (RMS) of the amplitude of oscillation as a function of the reduced speed for each model. The range of reduced speeds in which the phenomenon of vortex-induced vibration (VIV) occurs when the W/D ratio varies from 2.0 to 7.5, is between 3.0 and 15.5. For the comparison to be effective and not depend only on the W/D ratio, similar low values of damping ratio (or Scruton number, which is an equivalent parameter) in all models has been sought to achieve.

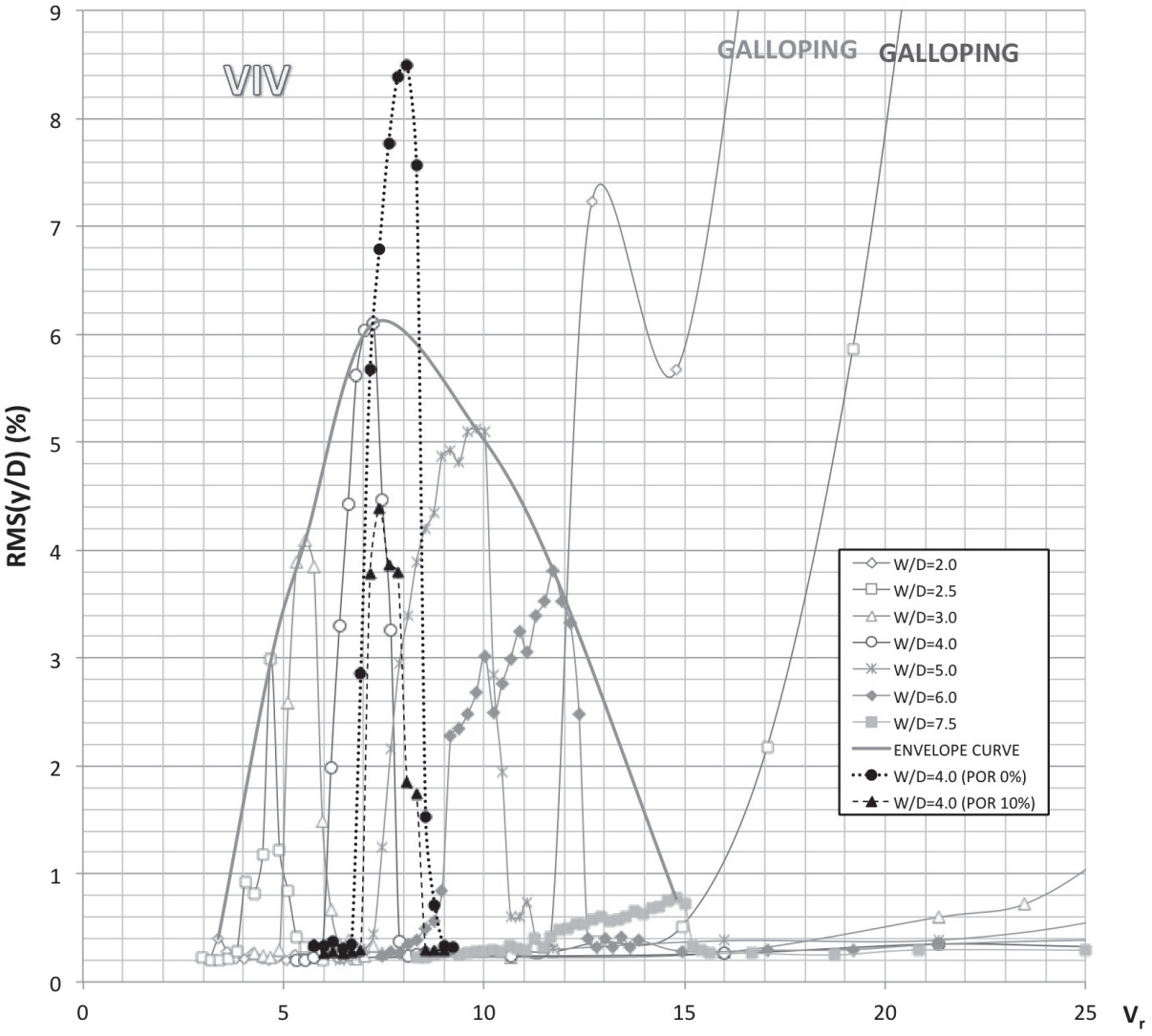

Figure 6. RMS non-dimensional amplitude (RMS(y/D)%) as a function of the reduced speed, v_{red} of models tested

Table 3 collects the most important data represented in figure 6.

Table 3 summarizes main results extracted from the tests

MODEL	$v_{red,crit}$ -	$v_{red,0}$ -	$v_{red,e}$ -	Band-width	$RMS(y)_{max}$(%) -	Sc -
H-SHAPED 2.0	3.38		3.81	0.64	0.40	11.26
H-SHAPED 2.5	4.69	3.17	5.50	1.70	2.99	11.10
H-SHAPED 3.0	5.54	3.80	6.40	1.50	4.09	12.94
H-SHAPED 4.0	7.25	4.90	7.89	1.92	6.10	13.28
H-SHAPED 5.0	9.81	5.97	10.66	3.41	5.12	10.63
H-SHAPED 6.0	11.73	7.25	12.58	3.63	3.81	14.71
H-SHAPED 7.5	14.79	8.95	15.20	3.74	0.08	13.94
H-SHAPED POROSITY 0%	8.08	6.93	8.61	1.68	8.49	7.62
H-SHAPED POROSITY 10%	6.96	6.82	9.02	2.20	4.39	11.23
ALCONÉTAR BRIDGE	≈5.0	-	-	-	≈16.60	5.80

where $v_{red,crit}$=critical reduced wind speed ($v_{red,crit}$=U/fD, being U=air flow speed corresponding to the maximum amplitude of oscillation); $RMS(y)_{max}$=root mean square of the maximum amplitude of oscillation; $RMS(y/D)_{max}$ (%)=root mean square of non dimensional maximum amplitude; Sc=Scruton number ($Sc = 4\pi m^*\xi$)

The most important fact to note is the variation of the maximum response as a function of W/D ratio. As shown in figure 6, the response increases as the W/D relationship increases, up to a maximum, which reaches a non dimensional amplitude of 6.10%for a given side ratio of W/D=4.0. From this value, the response amplitude decreases while W/D increases, so that, with a side ratio of 7.5, the effects of vortex-induced vibrations on the H-shaped section are not significant. The evolution of the response and its dependence on W/D can be explained by the coalescence phenomena of vortices that occur when the air flow interacts with the model [4]. It has been shown that models with W/D=2.0 and W/D=2.5 experience vibrations associated with the phenomenon of transverse galloping at excessively high reduced speeds. It would be interesting to test other models at higher speeds, and thus verify if they might undergo transverse galloping as well at certain air flow speeds.

Figure 7 shows the critical reduced speed, $v_{red,crit}$, the onset reduced speed, $v_{r,0}$, and the ending reduced speed, $v_{red,e}$, as a function of the W/D ratio. All these parameters keep a linear dependence on the W/D ratio. Expressions obtained by least squares adjustment are also given by the following expressions:

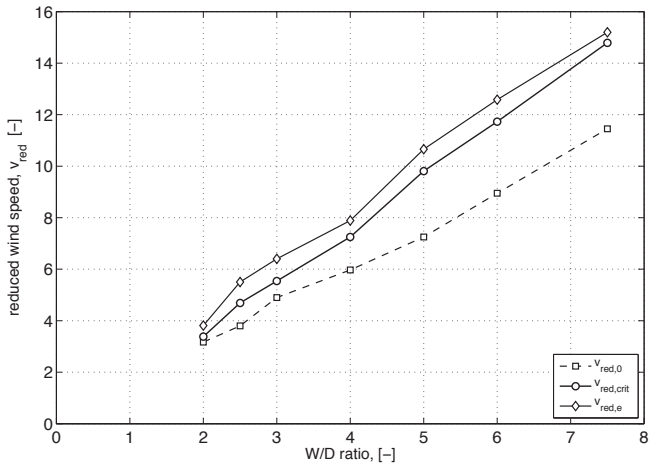

Figure 7. Reduced speeds as a function of W/D ratio for H-shaped section models

$$v_{red,crit} = 2.06 \cdot \frac{W}{D} - 0.67 \quad (2)$$

$$v_{red,o} = 1.47 \cdot \frac{W}{D} - 0.18 \quad (3)$$

$$v_{red,e} = 2.05 \cdot \frac{W}{D} - 0.08 \quad (4)$$

H-shaped section models represent a transition between rectangular sections and two prisms in tandem arrangement. In this case, the vortex shedding pattern presents a peculiar behaviour as described below and depicted in figure 8 with the aid of a CFD code, a very useful tool for understanding the vortex shedding mechanism. For small side ratios the central spacing between section borders do not have any influence and behaves as an equivalent rectangular section. For side ratios greater than 2.0, vortex shedding mechanism responds to the ILEV type [3] That is due to the appearance of convection cells in the upper and lower gap, which maintains the detached boundary layer and favours the formation of impinging leading edge vortices along the surface (ILEVcc). This effect is less important as the side ratio increases. Furthermore, according to figure 8, with side ratios between 2.0 and 4.0, a transition zone between normal ILEV pattern and that caused by convection cells (ILEVcc) gives rise to a dual vortex shedding frequencies, thus we conclude that the resonant effect may occur for two different horizontal wind speeds.

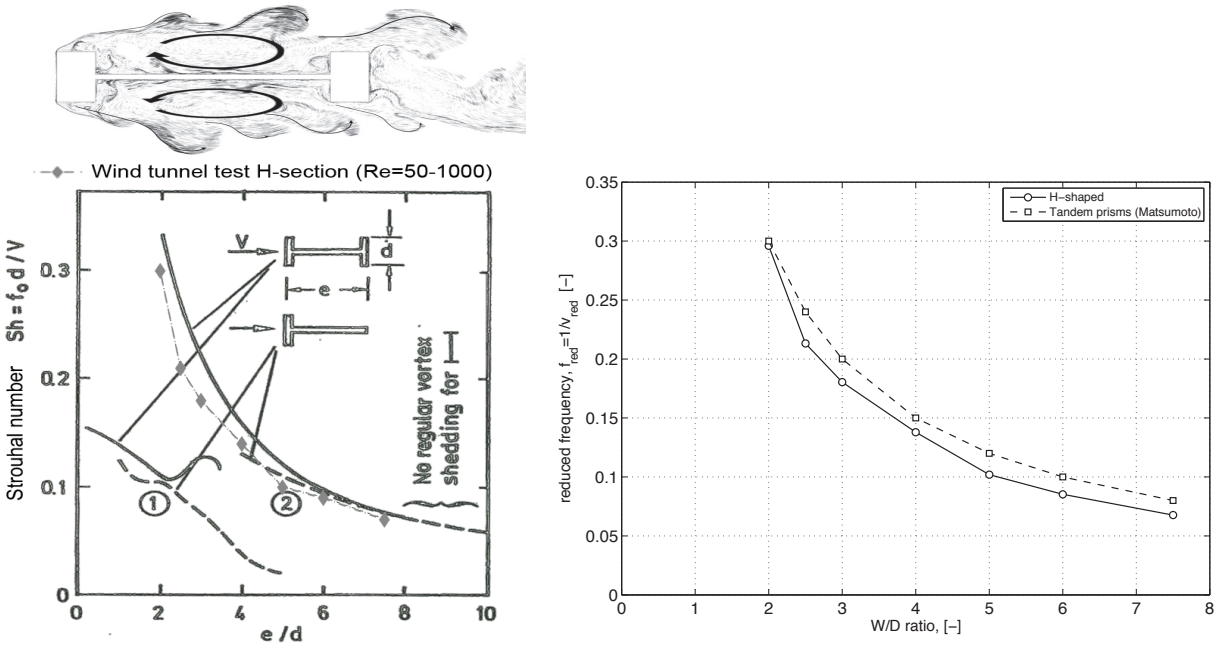

Figure 8. CFD flow visualization and Strouhal number for different H-section side ratios (After [5], p. 129), with present results added (left). Reduced frequency of VIV p as a function of W/D ratio (right)

5 COMPARISON WITH OTHER EXPERIMENTAL RESULTS

Experimental wind tests similar to that described in this paper were carried out by Matsumoto and other researchers with rectangular sections in tandem configuration [4] are shown in figure 9. The model tested consist in two prisms in tandem arrangement with W/D=4.0, B/D=1.0 and a splitter plate behind the prism downstream. Two vortex shedding patterns are identified: the movement induced excitation (MIE) and Karman Vortex (KV). MIE pattern can be associated to the ILEV mechanism, as described previously.

The upper curve on the right (see figure 8) corresponds to the onset reduced frequency ($f_{red,o}=1/v_{red,o}$) of MIE vibrations type, characterized by Matsumoto and experienced by rectangular tandem sections. Their values are very close to the lower curve, which relates the reduced

frequency with the W/D ratio for H-shaped section models. Results for H-shaped section correlate well with those obtained by the Japanese researcher.

Figure 9 shows the value of non dimensional amplitude, η/D, based on the reduced speed obtained by Matsumoto [4]. Peaks amplitudes are located close to 15%. In the case of H-shaped sections, the maximum peak amplitude registered was 9.0% for 'H-SHAPED W/D=4.0' and 12.1% for 'H-SHAPED W/D=4.0 POROSITY=0%'. The maximum RMS value was 6.1% and 8.5%, respectively. Both models have the same geometry but different values of reduced damping: m*ξ=1.06 for 'H-SHAPED W/D=4.0' and m*ξ=0.61 for 'H-SHAPED W/D=4.0 POROSITY=0%'. Matsumoto's model has a total value (two prisms) of m*ξ=1.66 (m*δ=5.2 per prism, being δ=2πξ). The larger reduced damping is, the smaller the smaller amplitudes of oscillation are. However, H-shaped section and two prisms in tandem cannot be compared, since their force coefficients are not equivalent and the amplitude of oscillation significantly depends on the lift coefficient as well.

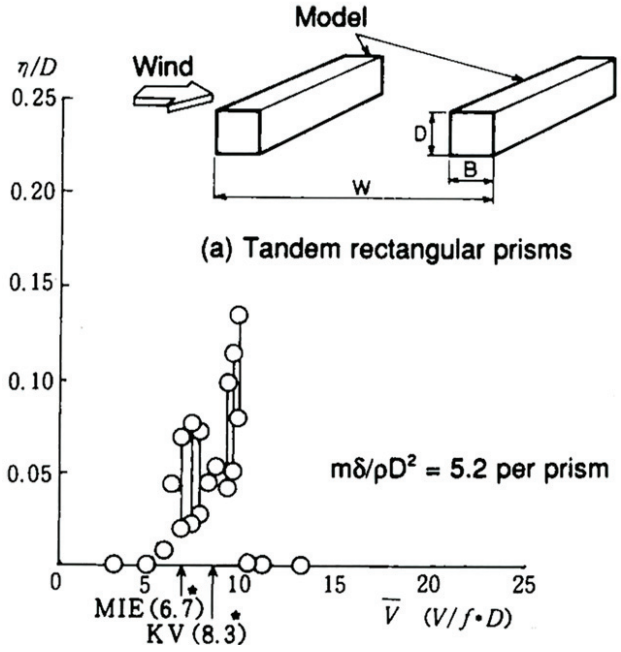

Figure 9. Non dimensional amplitude of oscillation as a function of reduced speed for prisms in tandem arrangement (from [4])

6 CONCLUSIONS

Vortex-induced vibrations identified in the H-shaped section models are not due to alternating shedding of vortices, or Von Karman vortices (KV, according to the description made by Matsumoto in [4]) as it might be initially thought, but an excitation induced by the movement of the structure itself. The vortices originated from the interaction between the air flow and the studied section also come into play different from alternating shedding of vortices. As in the rectangular tandem sections, the aerodynamic forces acting on the H-shaped section models seem to be largely conditioned by the section oscillations.

This issue highlights the importance to understand the mechanism that causes the aerodynamic phenomenon and thus take the required measurements to eliminate or minimize vibrations as they can endanger the integrity of certain structures such as bridges, if the circumstances occur. The vibration episode of Alconétar Bridge might be explained through two possible vortex shedding patterns analyzed herein.

7 ACKOWLEDGEMENTS

The authors would like to thank Ignacio Da Riva Institute staff for their kindness and availability to perform the wind tests.

8 REFERENCES

[1] M.Astiz, Estudio de las Vibraciones de los Arcos de Alconétar, Hormigón y Acero, 4/2006 (2006) 41-50.

[2] A. S. Corriols. Estudio de las Vibraciones Inducidas por Vórtices en Puentes Arco (Master Thesis), Technical University of Madrid, 2010.

[3] E. Naudascher, D. Rockwell, Flow-Induced Vibrations. An Engineering Guide 1st ed. (reprint), Dover Publications, Inc., Mineola, NY, USA, 2005, Chaps. 3, 4, 6 & 9.

[4] T. Takeuchi, M. Matsumoto, Vortex-induced oscillations of tandem rectangular bluff bodies, Wind Engineering, Thomas Telford, London, 1993, 421-430.

The Seventh International Colloquium on Bluff Body Aerodynamics and Applications (BBAA7)
Shanghai, China; September 2-6, 2012

Effects of balusters on vortex-induced vibration of a bluff bridge deck section

Qing-hai Guan [a], Jia-wu Li [a], Chun-ping Guo [a], Jian-xin Liu [a], Xi-ji Xing [a]

[a] *School of Highway, Chang'an University, Xi'an, China*

ABSTRACT: The vortex shedding response of a bluff bridge girder deck with and without balusters has been investigated by numerical simulation and wind tunnel experiments with the objective of identifying the mode of vortex excitation and effects of balusters on vortex-induced vibration of bridge deck. Tests on 2 spring suspended models revealed different vortex response. This process is likely to render the blunt bridge girder deck with balusters more susceptible to vortex shedding excitation than the bare section. Measurement of the fluctuating pressure around the deck surface indicates that vortices shed from the downstream section with balusters have greatly contributed to the vertical vortex-induced vibration, while the bare section (i.e. without balusters) pressure fluctuations over the entire upper and lower surface have little contribution to the vortex response.

KEYWORDS: Bluff bridge deck; Balusters; Vortex-induced Vibration; Fluent; Wind tunnel test; Surface pressure measurement

1 INTRODUCTION

Vortex-induced vibration which is prone to occur is one of the wind-induced vibration phenomenon. For many years, lots of researchers have fully proved that the vortex response has a strong dependence on the shape of structures. Kubo et al. [1] had investigated the air flow characteristics of the torsional vortex-induced vibration of a π section with C/D = 0.5 and C/D = 2, where C is the length of the cantilever and D is the π section height. The results show that the flow separation in the C/D = 0.5 is more obvious than C/D = 2, that is, the more blunt π section is, the more serious separation. Nagao and co-workers [2] studied effects of handrails on the vortex-induced oscillations, the conclusion is that the handrails can amplify the vertical vortex-induced vibration, and in torsional vortex-induced vibration, the interaction of the separated flow and handrails can not only weaken the formation of vortices shedding, but also reduce the self-excited forces.

In order to analyze influences of balusters on vortex response of the bridge deck, this present paper makes a research on vortex-induced vibration response of a bluff bridge girder deck with and without balusters, and explains the differences of both vortex response through an analysis of surface pressure distribution.

2 VORTEX EXCITATION OF BRIDGE DECKS

The test section is based on a bluff bridge deck section with flanges (Fig. 1). As a trapezoidal box shape, Von Karman type vortices are expected to form and to be shed at regular time intervals in the downstream box as illustrated in the snapshots taken from a detached eddy simulation of the air flow, Fig. 2.

Fig. 2 indicates that the flow separation of two kinds of section is fairly different. The balusters have a great impact on the vortex shedding. Vortices of bare section are much less than vortices of section with balusters. The vortex shedding process of section with balusters may, if could allow to occur, lock-in with a vertical eigenmode, and thus excite vertical vortex-induced oscillations.

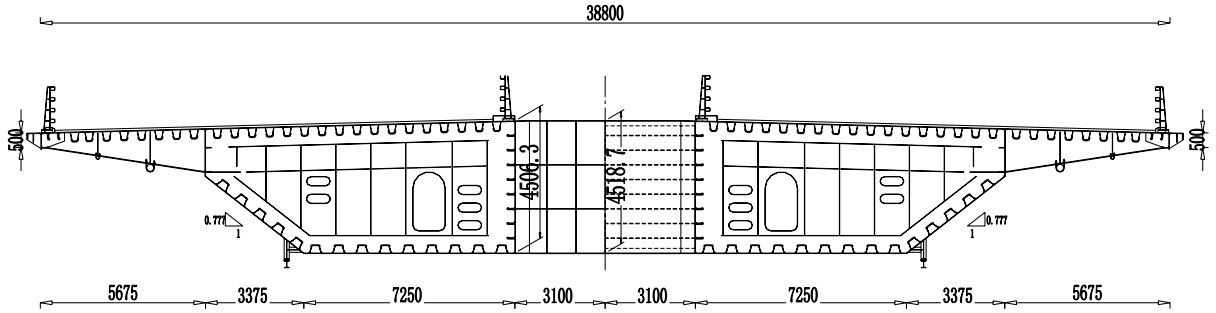

Fig. 1. Section of a box bridge girder. 38.8 meters wide (B), 4.5 meters high (H), the aspect ratio H/B = 1: 8.62. There are four balusters with the height of 1.5m along the bridge cross section.

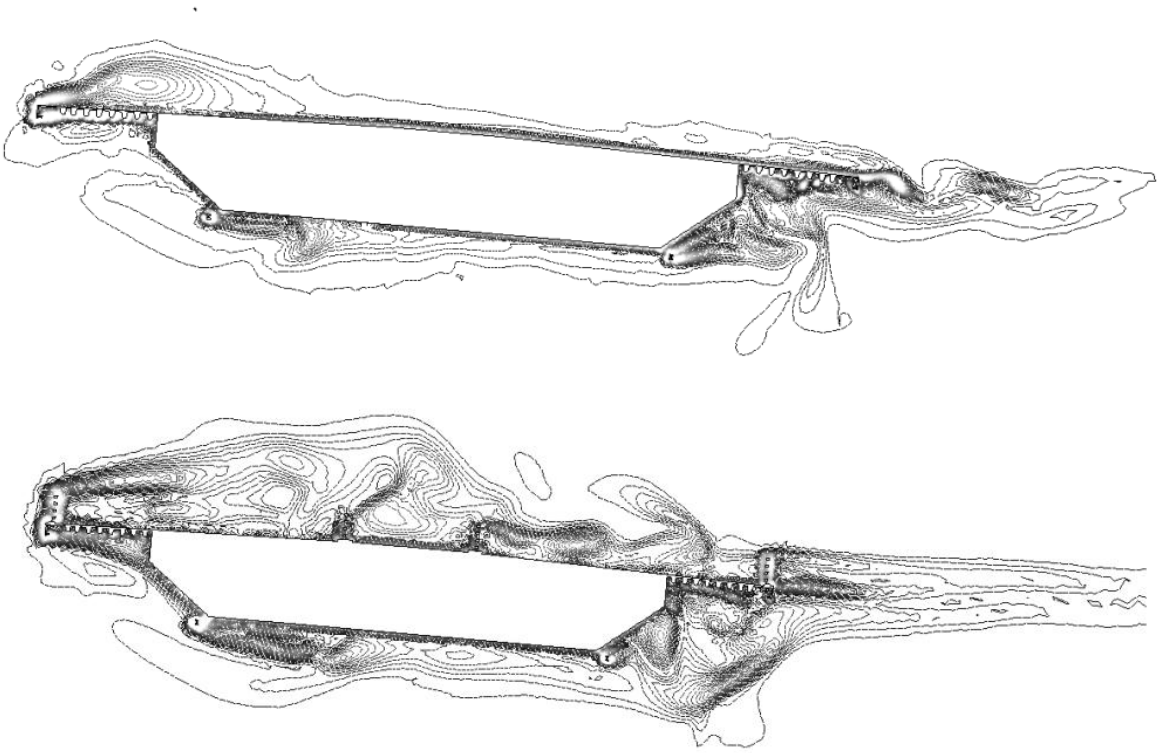

Fig. 2. Detached eddy simulation of the air flow about the bridge deck cross section with and without balusters. Angle of attack α = +5deg, wind speed is 15 m/s. Bare section, i.e. without balusters (top), section with balusters (bottom).

3 VERTEX SHEDDING TESTS

The vortex response of two sections, as shown in Fig. 3, were test during standard 1:20 scale section model wind tunnel experiments conducted in CA-1 wind tunnel which is a closed circuit wind tunnel with test section of 3.0m × 2.5m. Tests on the section with balusters under the uniform flow revealed a vertical response peak of 5% root mean square (rms) amplitude of the section depth H at a non-dimensional wind speed U/fB ≈ 1.88, while no vertex-reduced vibration happened in the bare section. Experimental studies had shown that the section with balusters excited two lock-in districts of vertical vortex-induced vibration. Larsen and his co-workers [3] also obtained the similar results in a 1 : 80 scale wind tunnel tests of a twin box bridge deck section.

The present paper focuses on the latter vortex-reduced vibration because the latter amplitude is fairly larger than the former. In order to understand the vortex response difference of the two sections, surface pressure measurements should be conducted.

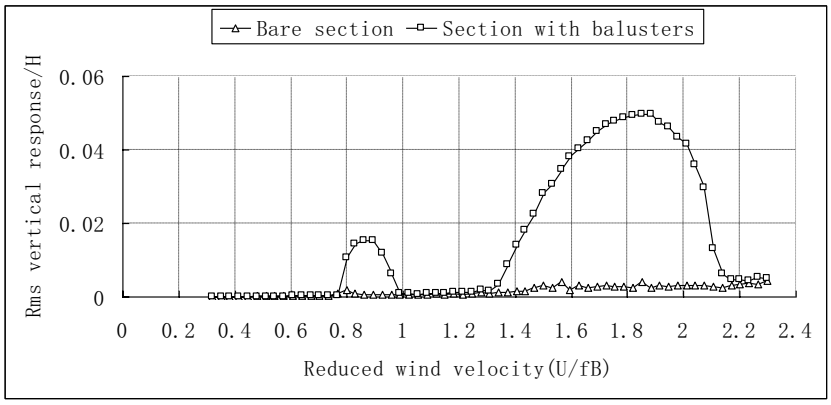

Fig. 3. Vortex response of the two kinds of section. 1:20 scale section model is supported by a 4.04 Hz spring suspension having a nominal structural damping ζ = 0.3% relative-to-critical. Angle of attack α = +5deg, U is wind speed, f is vertical frequency and B is the overall deck width.

4 SURFACE PRESSURE MEASUREMENTS

The surface fluctuating pressure status gave an opportunity to look further into the vortex dynamics through high frequency pressure measurements made at 120 taps (Fig. 4) mounted with the box section circumference. Two electronic pressure scanning valves manufactured by the PSI company in U.S were used to measure the fluctuating pressure around the two kinds of section. The range of each electronic pressure scanning valve is ±10 inch water column. There are 64 channels on a single valve and the measurement time delay is not greater than 3.2×10^{-3}s, it is considered that every channel is measured simultaneously.

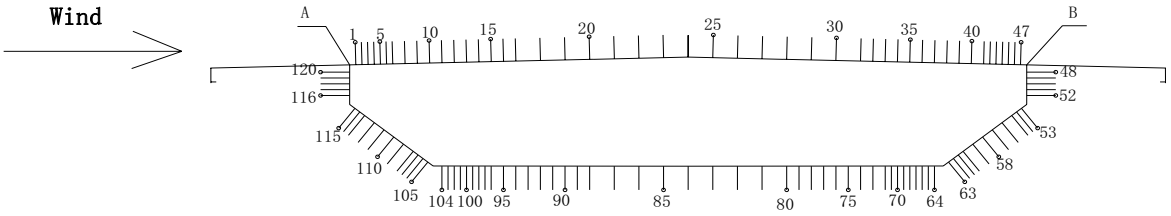

Fig. 4. Arrangement of pressure taps.

4.1 *Mean pressure coefficient*

Fig. 5 compares the mean pressure coefficient between the bare section and section with balusters at the non-dimensional wind speed U/fB ≈ 1.88. The presence of balusters does not change the mean pressure distribution of soffit plate (Fig. 5 bottom), but significantly change the pressure distribution on the upper surface (Fig. 5 top). When introducing the balusters it is noted that the adverse pressure gradient on the upper surface (x/D ≈ 0.25 ~ 0.76) of bare section vanish. In other words, the air flow separation on the upper surface come earlier owing to effects of balusters. Boundary layer separation would lead to vortex shedding, and vortex-induced forces from periodic vortex shedding would have contributed to the vortex-induced oscillations.

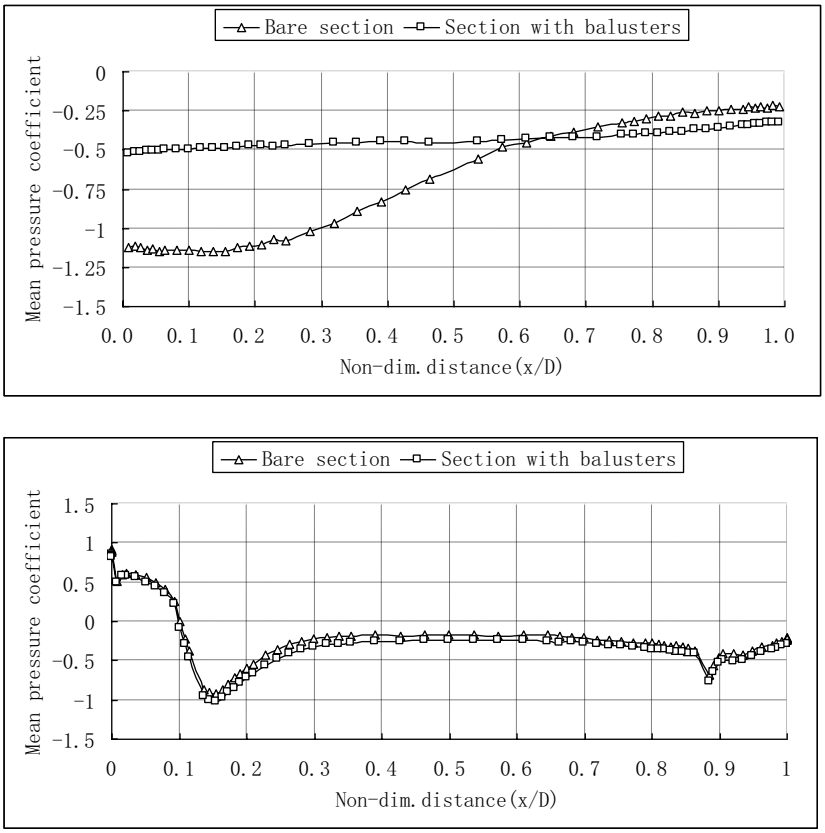

Fig. 5. Mean surface pressure coefficient of the two kinds of section at U/fB ≈ 1.88. Upper surface (top) and lower surface(bottom).

4.2 *Rms pressure coefficient*

With reference to the response diagram in Fig. 6, corresponding normalized rms pressure coefficient distributions obtained for the bare section and the section with balusters were obtained through the calculation of surface pressure time-history of every tap. Analysis of the rms pressure coefficient can find the critical region of vortex-induced vibration. In particular, fairly large rms pressures which result from the adverse pressure gradient are observed on the central upper surface of bare section(x/D = 0.32~0.68). Observing the difference between the bare section and section with balusters rms pressure coefficients, it is noted that the strong pressure fluctuation of bare section on the upper surface vanish due to the existence of the balusters, but the fluctuating pressures are significantly increased in the downstream zone of the upper surface, especially in the region x/D = 0.76~1.00. When introducing the balusters it is noted that the pressures on the entire lower surface are markedly increased. The Rms pressure coefficients of the entire lower surface have increased by 2 times when going from no balusters to having balusters. Comparing the downstream zone pressure distributions for the bare section and section with balusters, it is evident that the presence of balusters has strengthened the pressure fluctuation significantly, giving evidence that the downstream zone of deck have great contribution to the vertical vortex-induced response.

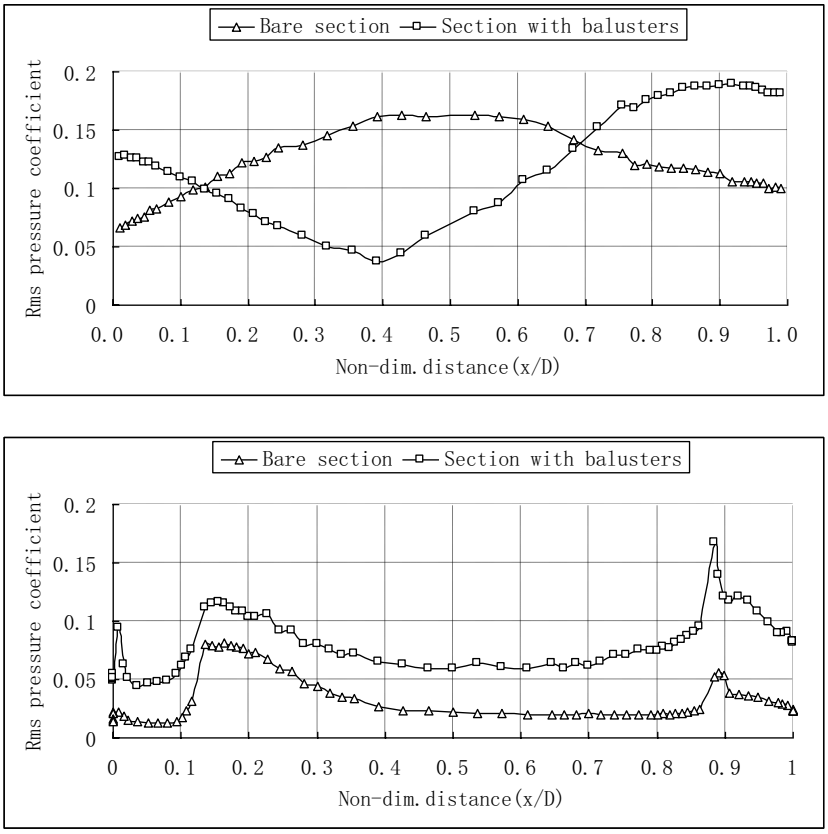

Fig. 6. Rms surface pressure coefficient of the two kinds of section at U/fB ≈ 1.88. Upper surface (top) and lower surface(bottom).

5 AERODYNAMIC FORCES

In this paper, aerodynamic forces in wind-axis coordinate system were obtained from the recorded pressure signals by using a method of surface pressures integration [4]. Aerodynamic force of a single pressure tap means aerodynamic force of the area which the tap represents, the total aerodynamic force is got by summarizing all the single taps.

Fig. 7 compares lift force time-history between bare section and section with balusters, and the curves of lift force power spectral density are shown in Fig. 8. For the section with balusters, a sinusoidal curve of lift force is shown in Fig. 7 (right) and a 4.04Hz harmonically lift force is noted in Fig. 8 (right). When the balusters are removed, Fig.7 (left) and Fig. 8 (left), the sinusoidal lift force and the distinct harmonic lift force altogether disappear, bearing evidence that the aerodynamic force of exciting vertical vortex-induced vibration is lift force. Vertical vertex-reduced vibration can be study through analysis of the changing of lift force because the vibration is caused by lift force.

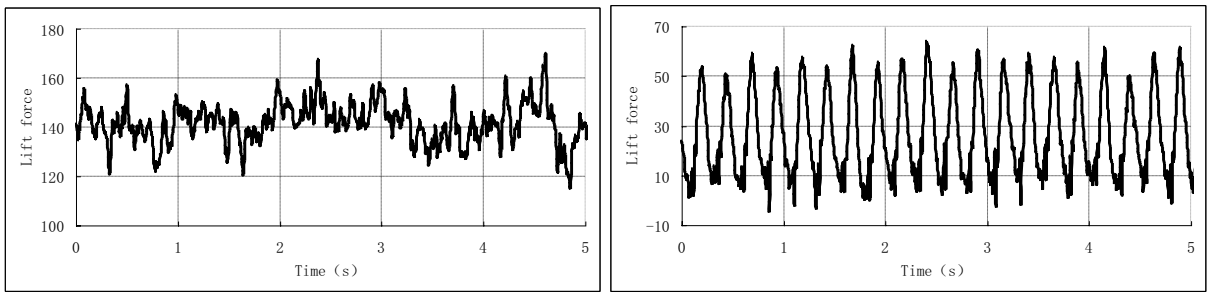

Fig. 7. Lift force time-history of the two kinds of section at U/fB ≈ 1.88. Bare section (left) and section with balusters (right).

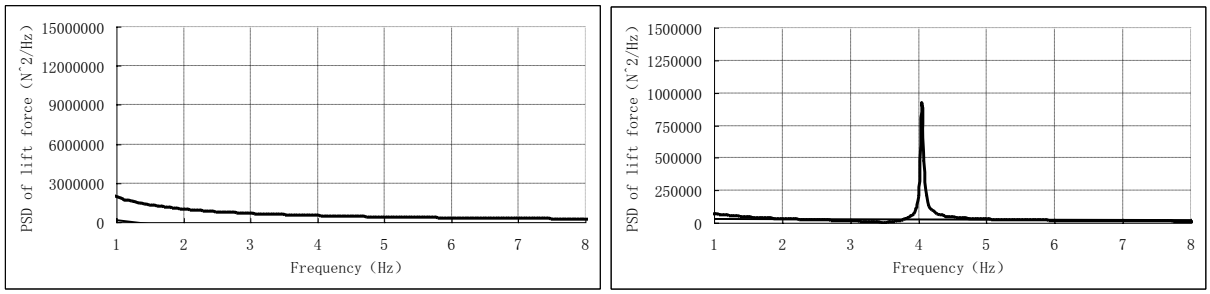

Fig. 8. Lift force power spectral density of the two kinds of section at U/fB ≈ 1.88. Bare section (left) and section with balusters (right).

Fig. 9 shows Karl Pearson correlation coefficient between local lift force and total lift force. The contribution of the local lift force to vortex-reduced vibration, as shown in fig.10, can be obtained through the multiplication of local rms lift force and the correlation coefficient between local lift force and total lift force.

From Fig 9 it is noted that the correlation between local lift force and total lift force in the downstream zone have markedly increased due to the role of balusters. For the section with balusters, as shown in Fig. 10, the upper surface of the region x / D = 0.68 ~ 0.99 and the lower surface of the region x / D = 0.35~0.98 have a greater contribution to vertical vertex-reduced vibration, and the contribution of upper surface is significantly larger than the lower surface.

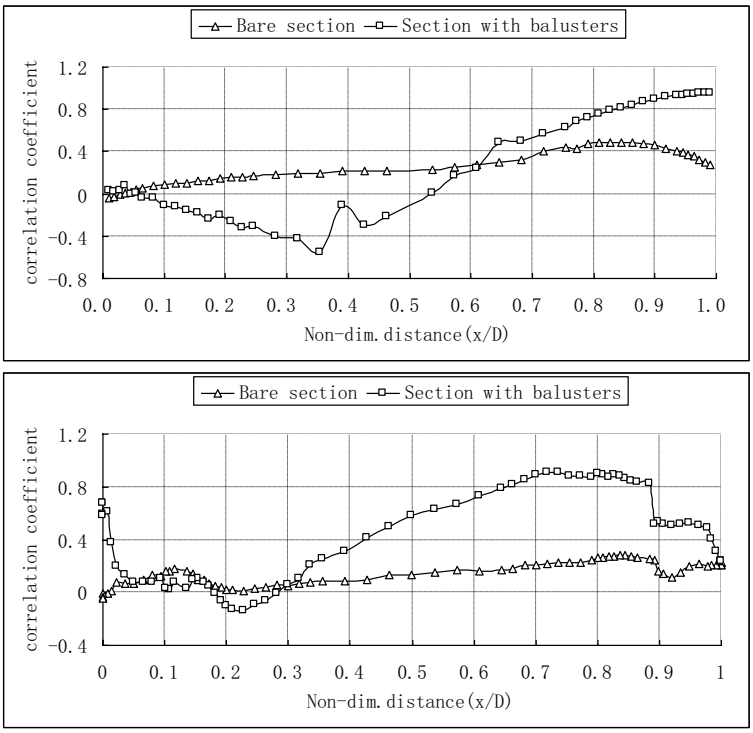

Fig. 9. Karl Pearson correlation coefficient of local lift force and total lift force at U/fB ≈ 1.88. Upper surface (top) and lower surface (bottom).

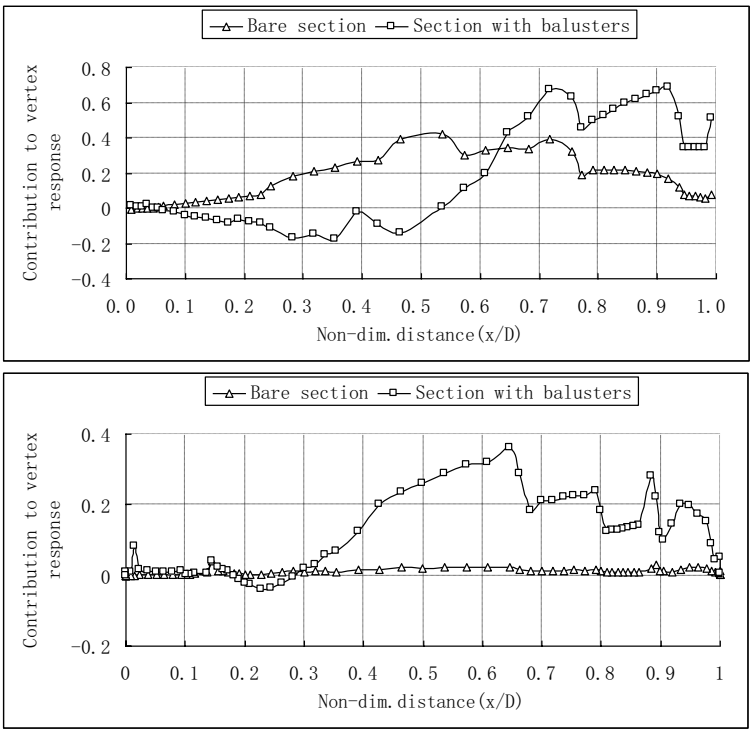

Fig. 10. Contribution of the local lift force to vortex-reduced vibration at U/fB ≈ 1.88. Upper surface (top) and lower surface(bottom).

6 CONCLUSIONS

The present paper has examined vertical vortex response of a bluff bridge deck with a view to unveil the excitation mechanism of balusters on vortex-induced vibration of bridge deck. The following is concluding remarks about vortex response of the bridge deck section with and without balusters.

1) The balusters of bridge deck significantly affect the mean pressure distribution of the upper surface, but the lower surface mean pressure distribution will not be change by balusters. The balusters of bridge deck will not only dramaticlly affect the upper surface pressure fluctuation but also the lower surface pressure fluctuation.

2) It is concluded that vortex excitation of deck with balusters is likely to be stronger than vortex excitation of bare deck, as the deck with balusters fluctuating pressures originating from the vortex impinging on the downstream box are larger than the fluctuating pressures of bare deck.

3) The balusters of bridge deck stimulate the vertical vortex-reduced vibration. It may achieve the purpose of suppression of vortex-induced vibration through partially sealing the balusters. In order to verify the suppression effect of partially sealing the balusters, it is necessary to carry out wind tunnel tests.

ACKNOWLEDGEMENTS

The National Natural Science Foundation of China (Grant No. 51078038) is gratefully acknowledged for their financial support.

REFERENCES

[1] Y. Kubo, K. Kimura, K. Sadashima, Y. Okamoto, E. Yamaguchi, K. Kato. Aerodynamic performance of improved shallow π shape bridge deck. Journal of Wind Engineering and Industrial Aerodynamics, 2002, Vol. 90, pp. 2113-2125

[2] F.Nagao, H.Utsunomiya, E. Yoshioka, A. Ikeuchi, H. Kobayashi. Effects of handrails on separated shear flow and vortex-induced oscillation. Journal of Wind Engineering and Industrial Aerodynamics, 1997, Vol. 69-71, pp. 819-827

[3] A.Larsen, M.Savage, A.Lafreniere, M. C.H. Hui, S. V. Larsen. Investigation of vortex response of a twin box bridge section at high and low Reynolds numbers. Journal of Wind Engineering and Industrial Aerodynamics, 2008, 96: 934-944

[4] LI Jia-wu, LIN Zhi-xing, JIN Ting, Application of pressures integration in effects of bridge decks. Journal of Vibration Engineering, 2006, vol.19, pp. 505-508

Investigation of vortex-induced vibration of twin box girders

Shujin Laima [a], Hui Li [b], Wenli Chen [c]

[a] *School of Civil Engineering, Harbin Institute of Technology, Harbin, China, laimashujin@126.com*
[b] *School of Civil Engineering, Harbin Institute of Technology, Harbin, China, lihui@hit.edu.cn*
[c] *School of Civil Engineering, Harbin Institute of Technology, Harbin, China, cwl_80@hit.edu.cn*

ABSTRACT: Dynamic wind tunnel tests of twin box girders with a space ratio of L/D=1.70 have been performed in this study. The results show that although the strength of the vortex is very weak under stationary conditions, it gives rise to vortex-induced vibrations with a lock-in range of $0.570 \leq U_r \leq 0.668$ in dynamic testing. To further study the flow characteristics around the twin box girder when undergoing vortex-induced vibration, a hybrid method combining experiments with numerical simulations is employed. The energy transfer between the flow and motion of the body, and evolution of flow patterns over vortex-induced vibration process are analyzed based on the computational results. The results indicate that with an increase in oscillation amplitude, strong vortices form in the gap between the two box girders. These vortices impinge on the windward wall of the downstream box girder and cause the flow to separate and re-attach periodically around the windward corners of the downstream box girder.

KEYWORDS: twin box girders; vortex-induced vibration; vortex structures;

1 INTRODUCTION

With increases in the spans of bridges, bridges become more flexible and have small damping. Therefore, the bridges more readily oscillate dramatically when subjected to wind. In order to improve the aerodynamic stability of long-span bridge, twin-separated box steel girder configuration may be a good choice. For the kind of bridge, the bridge deck is composed of two parallel longitudinal girders with an open space between them. The two parallel girders are connected by transverse cross-beams. Now some super-long span bridges have chose this section configuration, for instance, Xihoumen suspension Bridge (main span: 1650m, China), Hong Kong Stonecutters cable-stayed Bridge (main span: 1018m, China), Gwangyang suspension Bridge (main span: 1545m, Korea). Although it is proved that twin-separated box girder has higher critical flutter speed than single box girder (Ge and Xiang, 2009), the flow characteristics around the bridge deck become more complicated due to the effects of gap between two separated box girders.

It is well known that when the vortex shedding frequency is close to the natural frequency of the body, it can cause vortex-induced resonance. Although vortex-induced vibration is limited amplitude vibration and does not cause collapse for the bridge, it can result in large displacements and discomfort to the drivers. In addition, the vortex-induced oscillations commonly occur in the low wind speed region, so the occurrence probability of vortex-induced vibration is high, resulting in long-term fatigue damage. The main objective of the paper is to investigate the flow characteristics around twin box girders and deeply understand the mechanism of vortex-induced vibration of twin box girders.

2 EXPERIMENTAL INVESTIGATION OF VORTEX-INDUCED VIBRATIONS OF TWIN BOX GIRDERS

2.1 *Experiment set-up*

The experiments are conducted in a closed circuit wind tunnel, which has a small rectangle testing section of 4 m in width, 3 m in height and 25 m in length and a large rectangle testing section of 6 m in width, 3.5 m in height and 50 m in length (see Figure 1). In the small testing section, the maximum wind velocity can be 50 m/s, the turbulence intensity of the free stream can be no stronger than 0.46% and the non-uniformity of free-stream is less than 1%. In this study, all experiments are carried out in the small testing section.

The model is composed of two parallel box girders with an open space of L=150 mm. The two parallel girders are connected by transverse cross-beams every 360 mm. The length and height of the model are 1440 mm and 87.55 mm, respectively. Detailed geometry of the section model is shown in Figure 2. In the dynamic test, the modal is supported by 8 springs allowing a vertical degree of freedom with a natural frequency of 4.272 Hz and damping ratio of 0.21%. The lower surface of the section model is 1.20 m from the bottom of the wind tunnel. The geometric blockage ratio in the testing section is 2.9%; thus the blockage effects are negligible.

Two one-dimensional hotwire probes (Dantec 55P11) are used in the experiment. One is placed at 1.5 m upstream from the leading edge of the section to measure the oncoming free-stream velocity, while the other probe is moved to different locations near the section model to obtain the vortex-shedding information. The sampling frequencies of both hotwire probes were set at 1 kHz.

When carrying out the vortex-induced vibration test, the inflow velocity is increased stepwise, and the increment of each step is approximately 0.05 m/s over the range of 2.19≤U≤2.65 m/s (1.3e5≤Re≤1.59e5).

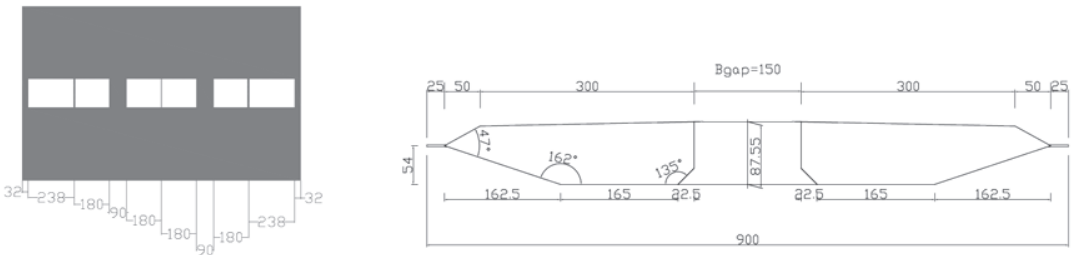

(a) Top view (b) Side view

Figure 1Geometry information of the section model

2.2 *Vortex-induced response*

Figure 2 presents the time history of vertical acceleration when the twin box girder is undergoing vortex-induced vibrations. The vertical displacement of oscillation is obtained by integrating the vertical acceleration twice. Figure 3 shows the relationship between the RMS of displacement response and reduced wind velocity ($U_r = U/f_{\text{vertical}}B$, in which U_r is the reduced wind velocity and f_{vertical} is the vertical nature frequency of the model). The response amplitude increases in two steps with an increase in the reduced inflow velocity up to U_r=0.650. Over the range of 0.57≤U_r≤0.603, the amplitude increases extremely slowly, whereas over the range of 0.616≤U_r≤0.650, the amplitude increases very rapidly. At U_r=0.668, the amplitude undergoes a small reduction. When the reduced inflow velocity increases to 0.689, the amplitude of vortex-induced vibration abruptly drops to zero, which suggests that the vortex exciting force suddenly

disappears. In the whole process of vortex-induced vibration, the largest RMS of non-dimensional displacement, RMS(y)/D, is 0.029 at U_r=0.650, which is much smaller than that of rigid cylinders, where the maximum is 0.11 at the same Skop-Griffin parameter of S_G=1.875 (Sarpkaya, 2004). In the range of 0.57≤U_r≤0.603, the vortex-shedding frequency is controlled by the oscillation frequency of the body, which is identical to the natural vertical frequency of the system. Beyond this range, the vortex-shedding frequency follows Strouhal's law. The variation of the dimensionless vortex-shedding frequency with the reduced wind velocity is shown in Figure 4.

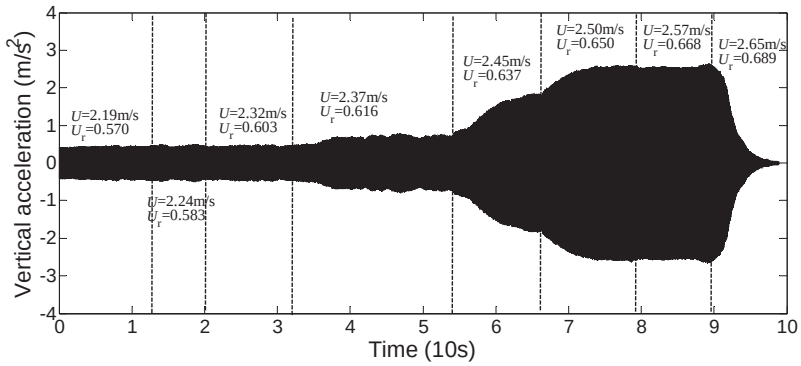

Figure 2. Time histories of vertical acceleration.

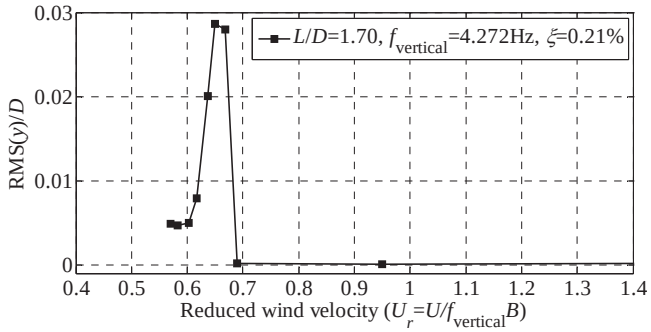

Figure 3. Vortex response of the twin separated box girders.

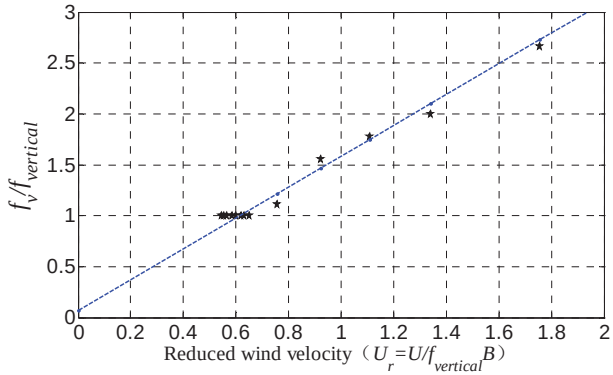

Figure 4. Variation of the dimensionless vortex-shedding frequency with the reduced wind velocity (f_v is the vortex-shedding frequency).

3 NUMERICAL INVESTIGATION OF VORTEX-INDUCED VIBRATIONS OF A TWIN BOX GIRDER

3.1 *Computational method*

In the wind tunnel test, the motion of a structure is easy to measure. However, it is very difficult to accurately measure the fluid structures of a flow field, which usually requires very expensive instrument, e.g., PIV. To obtain characteristics of flow structures when the body is undergoing vortex-induced vibration, a hybrid method that combined experiments with numerical simulations (Li et al., 2010) is employed in this paper. For the problem of flow-induced vibration of a bluff body, the analytical model includes two parts: one is fluid dynamics based on the incompressible Navier-Stokes equations; and the other is the dynamics based on the equation of the motion of the body. The two parts are coupled through the no-slip condition, i.e., the velocities of the fluid and the body are identical at the interface. In traditional computational process, the fluid and structure motion equations are solved simultaneously. For the hybrid method, the motion of the structure is already known, which is first obtained from the wind tunnel test or field monitoring, i.e., the flow velocities on the interface are also known. Therefore, the flow-induced vibration problem becomes a moving boundary problem of the flow. Only fluid dynamic equations need to be solved and the motion of the interface is measured from the wind tunnel test or field monitoring, so it is more accurate than the traditional computational method to obtain the flow characteristics.

The computational domain is discretized with an unstructured mesh, as shown in Figure 5. The majority of y^+ values, which are nearest to the wall, are in the range of 0.105-1.2 (only 5.67% of y^+ values higher than 1.2).The numerical simulations are performed with ANSYS CFX 11 code based on the finite volume method. The large eddy simulation (LES) with a Smagorinsky subgrid scale model is employed in the computational process. The advection term is discretized using the Central Difference Scheme in the spatial domain, and the transient term is discretized by the Second Order Backward Euler Scheme in the time domain. The time step is set at 0.001s, and the convergence criteria is such that if the RMS of normalized residual taken over the whole domain is less than 10^{-4}, the iteration process stops.

At the inlet boundary, a steady uniform flow velocity is given. At the outlet boundary, an opening pressure condition is applied, and for the upper and lower surfaces of the computational domain, symmetric conditions are employed.

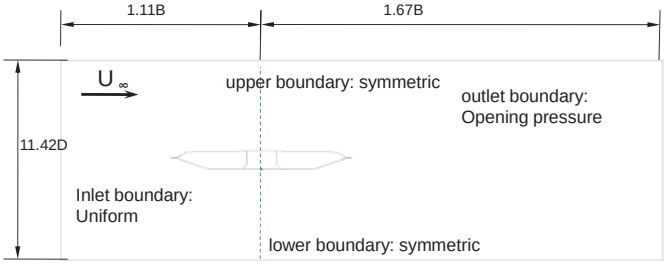

Section view of computational domain

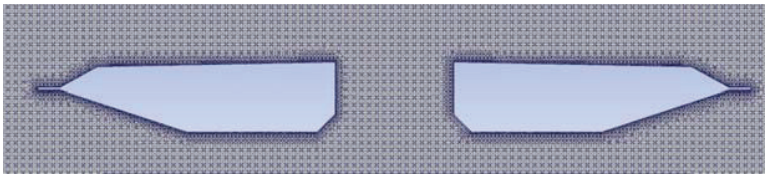

Mesh

Figure 5. Section view and mesh of the computational domain.

3.2 *Energy transfer between flows and the twin box girder*

In the vortex-induced vibration process, if the work performed by the aerodynamic force on the body is positive, i.e., the energy of flows is transferred to body, the vibration of the body will gradually increase. The energy transfer is mainly influenced by the amplitude of the fluctuating force and the phase between the fluctuating force and body motion.

The aerodynamic force is calculated by integrating the surface pressure of the twin separated box girders. Lift force coefficient per length is defined as:

$$C_{\mathrm{L}} = \frac{F_L}{\frac{1}{2}\rho_{air} U^2 BL}, \tag{1}$$

where, C_{L} is the lift force coefficient, F_{L} is the lift force, U is the inflow velocity, B is the width of model and L is the length of the model.

The phase between the lift force and vertical displacement is calculated by the following equation:

$$\theta(\omega) = \begin{cases} \arccos \dfrac{real(P_{ly}(\omega))}{\sqrt{\left(real(P_{ly}(\omega))\right)^2 + \left(imag(P_{ly}(\omega))\right)^2}} & if\ imag(P_{ly}) \geq 0 \\ -\arccos \dfrac{real(P_{ly}(\omega))}{\sqrt{\left(real(P_{ly}(\omega))\right)^2 + \left(imag(P_{ly}(\omega))\right)^2}} & if\ imag(P_{ly}) < 0 \end{cases}, \tag{2}$$

where, $\theta(\omega)$ is the phase lag between lift force and vertical displacement, P_{ly} is the cross power spectrum of lift force and vertical displacement and ω is the circular frequency of vertical vibration (ω is equal to the oscillation frequency).

The total work of lift force performed on the twin box girder is obtained as follows:

$$W = \frac{1}{N}\int_{y(KT)}^{y(KT+NT)} F_L dy, \tag{3}$$

where, W is the work of lift force on the body, T is the period of vertical vibration and K and N are the numbers of cycles.

Figure 6 shows the mean lift force coefficient, RMS of fluctuating lift force coefficient, phase angle between lift force and vertical displacement and work of lift force acting on the twin box girder at U_{r}=0.570, 0.583, 0.603, 0.616 and 0.650. At U_{r}=0.570, 0.583 and 0.603, the phase between lift force to vertical displacement are -72.0°, -95.0° and -110.0°, respectively, which are nearly in phase with the vertical velocity of body vibration, indicating that the aerodynamic lift force mainly provides negative damping characteristics. However, the net work acting on the structure is very low, which is attributed to a small-fluctuation lift force, so the amplitude of vibration is small at the beginning of oscillation. At U_{r}=0.650, although the phase of the lift force to vertical displacement is about -144.0°, which deviates from the direction of the vertical velocity, the large-fluctuation lift force resulted in large work of lift force on the body, so a dramatic response of the body is observed. It is found that the phase lags between lift force and vertical displacement are very different from those for a circular cylinder, in which phase lags are less than 45.0° in initial branch of oscillation, and lead to an increase in oscillation (Feng, 1968). Unlike a circular cylinder, no phase jump over the vortex-induced vibration process appears for the box girder.

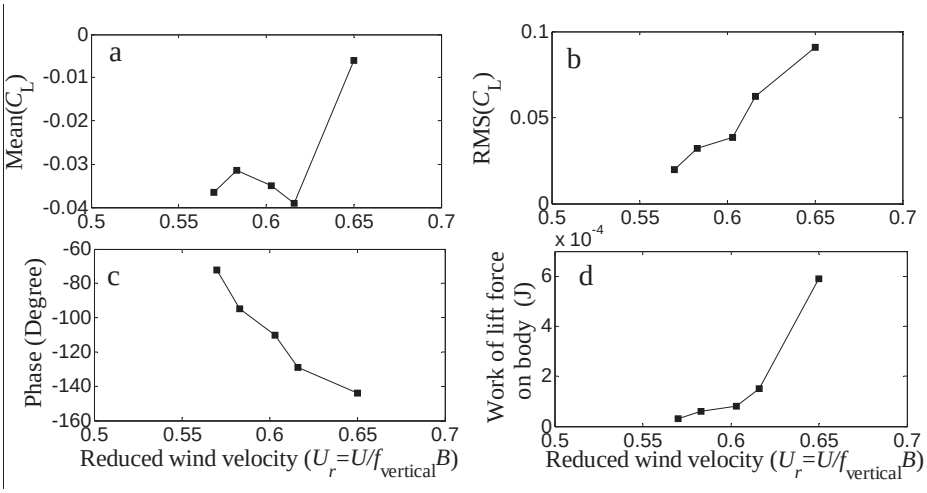

Figure 6. Lift force characteristics and work performed by the lift force at U_r=0.570, 0.583, 0.603, 0.616 and 0.650. (a) mean lift force coefficients, (b) RMS of fluctuating lift force coefficient, (c) phase between lift force and displacement, and (d) work performed by the lift force

The work of lift force on the body can also be rewritten as:

$$W_k = \frac{1}{N}\int_{y(KT)}^{y(KT+NT)} \int_S \left\{ -p\delta_{jk} + 2\mu\left(\frac{\partial u_j}{\partial x_k} + \frac{\partial u_k}{\partial x_j} \right) \right\} n_j dS dy$$

$$= \int_S \frac{1}{N}\int_{y(KT)}^{y(KT+NT)} \left\{ -p\delta_{jk} + 2\mu\left(\frac{\partial u_j}{\partial x_k} + \frac{\partial u_k}{\partial x_j} \right) \right\} n_j dy dS \qquad (4)$$

To obtain the energy transfer over the whole surface of the body, a work density function $P(x,y,z)$ on the surface of the twin box girder is defined as:

$$P(x,y,z) = \frac{1}{N}\int_{y(KT)}^{y(KT+NT)} \left\{ -p\delta_{jk} + 2\mu\left(\frac{\partial u_j}{\partial x_k} + \frac{\partial u_k}{\partial x_j} \right) \right\} n_j dy. \qquad (5)$$

The work density of flow over the surface of the twin box girder at U_r=0.570 and U_r=0.650 at z=630 mm is shown in Figure 7. The positive values of the work density show that the flow energies are transferred to body, while the negative values indicate that the energy of body motion is transferred to the flows. At U_r=0.570, the beginning of vortex-induced vibration, the energy of flows is transferred to the body in the regions of X/B=[0.217 0.412] for the lower surface and X/B=[0.190 0.450] for the upper surface due to the influence of shedding vortices in the near wake. However, for the case of U_r=0.650 (the amplitude of response is largest), besides the work density becoming much larger, the region where the energy of the flows transfers to the body is located mainly near the gap. This implies that the vortices in the gap play a critical role to vortex-induced vibrations of twin box girders.

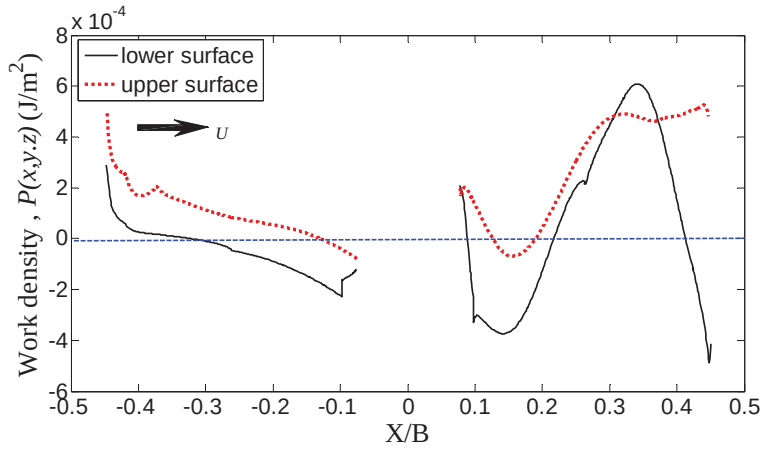

(a)

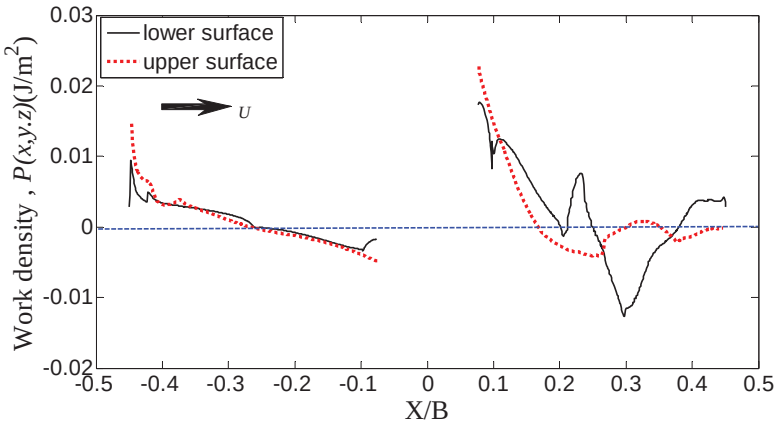

(b)

Figure 7. Work density over the surface of the twin box girder at z=630 mm (a) U_r=0.570, and (b) U_r=0.650.

3.3 *Flow pattern evolution when the twin box girder undergoes vortex-induced vibration*

In the vortex-induced vibration process, the structure motion and vortex interact with each other, forming a feedback loop system. Therefore, the vortex structure and vortex-shedding modes have significant effects on the structural oscillation. Although the vortex structures can be recognized according to many criteria, for example, Q-criterion (Hunt, 1988), Δ-criterion (Dallmann,1983, and Chong, 1990), λ_2-criterion (Jeong and Hussain, 1995), etc. , there still lacks a common agreement, and these methods have their respective advantages and limitations. In this study, the λ_2-criterion is selected to obtain the vortex structure. Jeong and Hussain (1995) argued that, if discarding unsteady straining and viscous effects, the existence of a minimum pressure value and existence of a vortex core are consistent. By taking the gradient of the Navier-Stokes equation and decomposing it into symmetric and asymmetric parts, the following equation can be deduced:

$$\frac{DS_{ij}}{Dt} - \nu S_{ij,kk} + \Omega_{ik}\Omega_{kj} + S_{ik}S_{kj} = -\frac{1}{\rho} p_{,ij} \tag{6}$$

where, S_{ij} is the strain tensor, $S_{ij} = \frac{1}{2}\left(\frac{\partial u_i}{\partial x_j} + \frac{\partial u_j}{\partial x_i}\right)$, Ω_{ij} is the rotation tensor, $\Omega_{ij} = \frac{1}{2}\left(\frac{\partial u_i}{\partial x_j} - \frac{\partial u_j}{\partial x_i}\right)$ and $p_{,ij}$ is the Hessian pressure.

The occurrence of a local pressure minimum in a plane requires two positive eigenvalues of the tensor $p_{,ij}$. Discarding the first term of Eq.(6), which represents an unsteady irrotational straining effect and the second term, which represents viscous effects, yields only $S^2+\Omega^2$ to determine the existence of a local pressure minimum. Therefore, the vortex core definition criterion is that the vortex is the location with two negative eigenvalues of $S^2+\Omega^2$. Assuming λ_1, λ_2 and λ_3 are the eigenvalues of $S^2+\Omega^2$ and $\lambda_1 \geq \lambda_2 \geq \lambda_3$, the vortex identification criterion is equivalent to the condition that $\lambda_2 < 0$.

Figure 8 presents the vortex core structures at U_r=0.570 and U_r=0.650. At the initial stage of vortex-induced vibration, i.e., U_r=0.570, the body motion leads to the boundary layers of the upstream box girder becoming unstable and generates vortices on the upper and lower sides of the gap. It is worth noting that these vortices are generated due to the flow by the body motion disturbance rather than the direct interaction of the upper and lower shear layers. The shedding vortices propagate downstream along the upper and lower surfaces of the downstream box girder and then merge with the vortices generated in the inclined regions of the downstream box girder. Finally, the merging vortices are shed alternately in the near wake of the downstream box girder with the 2S shedding mode, i.e., when the displacement is largest, the single vortex sheds from the opposite side. Due to the asymmetrical geometry of the wind nose (inclined regions of box girder), asymmetrical vortex structures are generated in the upper and lower sides of the near wake. For the lower side of the nose, the width of the inclined plane is very long ($L_{inclined}/B$=0.18), so the nascent vortex on the lower side of the wake is long and narrow, and the energy distribution of the vortex is not uniform. This special kind of vortex structure results in instability of the primary vortex on the upside of wake and rapid translation into 3-D structures. However, for the upper side of the nose, the dimensionless width of the inclined plane $L_{inclined}/B$ is only 0.056, so the primary vortex is more regular and stays stable when propagating downstream.

When the amplitude of the vortex-induced vibration is largest, the vortex-shedding phenomena and vortex structures change significantly. The interaction between the upper and lower boundary shear layers of the upstream box girder is enhanced through the gap, and thus, strong vortices generate around the gap. These vortices propagate downstream along the surfaces of the downstream box girder and finally break into small vortices in the nose region. In the near wake of the downstream box girder, because of body motion disturbance, the primary vortices, which appear at the initial stage of vortex-induced vibrations, disappear, and the flow transforms into turbulent flow. As shown in Figure 9, the vortex-shedding phenomena around the gap are very complicated. As the body reaches its maximum displacement, the nascent vortex of the side impinges on the windward wall of downstream box girder and cuts off the vorticity supply of the opposite vortex, so a free vortex forms. In addition, the flow from the opposite side separates around the windward corner of the downstream box girder and a new vortex begins to form at that moment. After approximately 1/4 of a cycle, i.e., the displacement of body is zero, the separated flow begins to re-attach, and the flow re-attaches on the surface of the downstream box girder completely as the body reaches the maximum displacement on the same side.

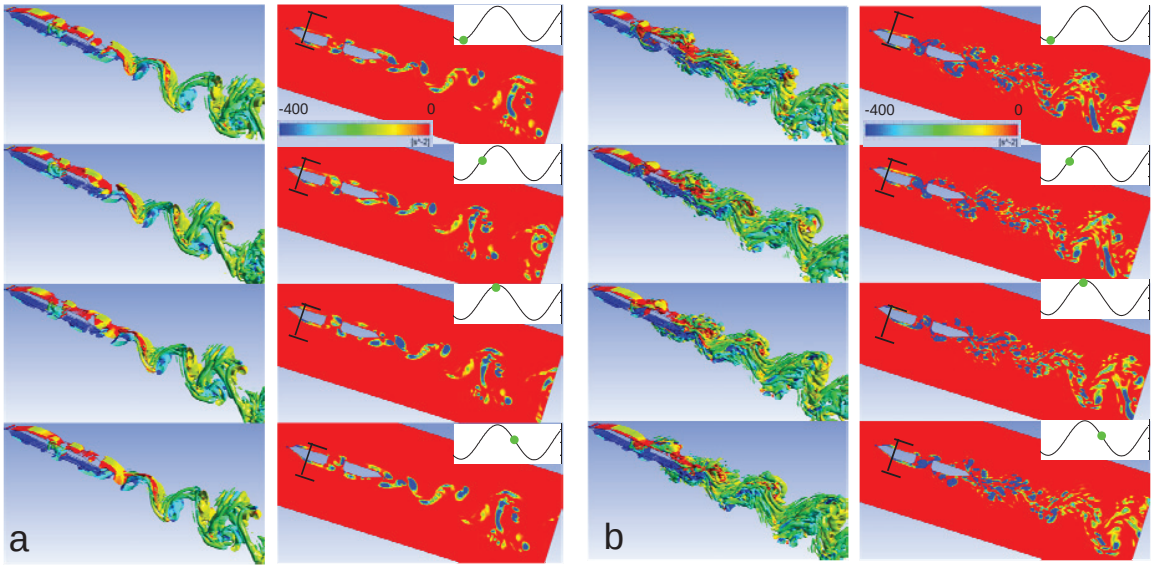

Figure 8. Vortex core structures, Left: Iso-surfaces of λ2=-10[s^-2]; Right: the contour plots of λ2 at section of Z=630 mm (a) Ur=0.570 and (b) Ur=0.650.

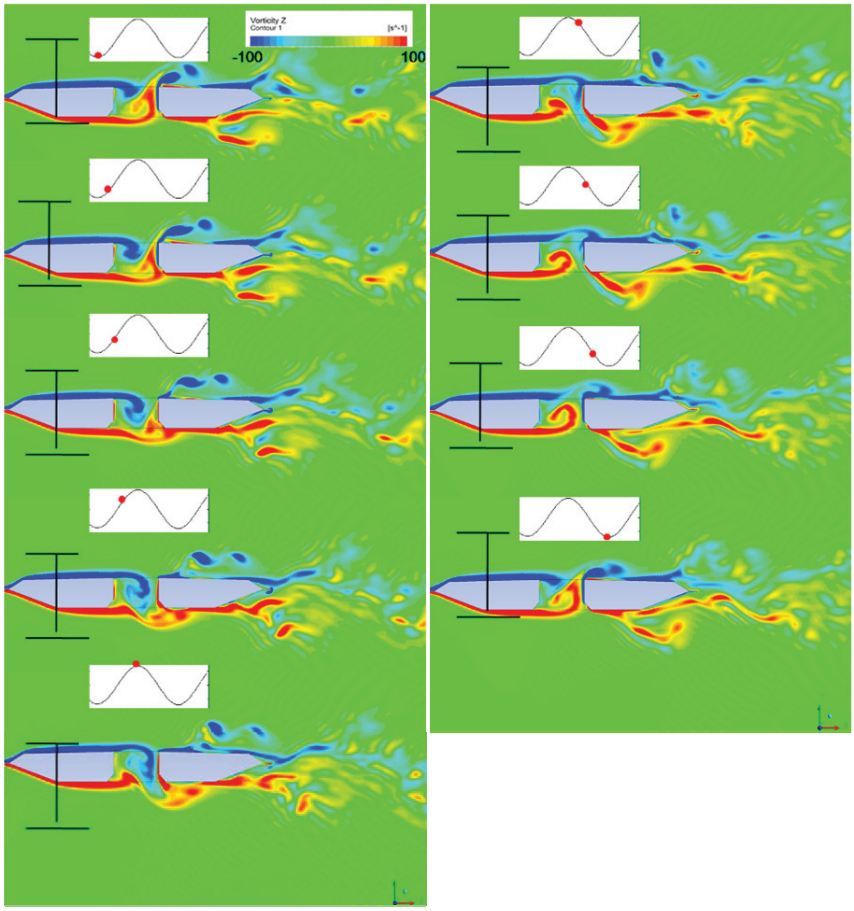

Figure 9. Instantaneous vorticity contours in a periodic vibration at z=630 mm.

4 CONCLUSION

The experimental investigations of vortex-induced vibrations of a twin box girder model with a gap ratio L/D=1.70 are carried out in this study. The following conclusions can be obtained:

Under stationary conditions, there is no occurrence of regular Karman vortices in the gap, but regular vortex-shedding phenomena with St=0.15 appear in the near wake of the downstream box girder. Although the strength of the primary vortex is very weak in the stationary test, vortex-induced vibration of the twin box girder occurs in the dynamic test. The synchronization range is $0.570 \leq U_r \leq 0.668$. Furthermore, the largest RMS of non-dimensional displacement is only 0.029 at U_r=0.650, which is much smaller than that of circular cylinders.

A hybrid method is employed to investigate the flow characteristics around the twin box girders when undergoing vortex-induced vibrations. The results show that the regular vortices are generated only in the near wake of the downstream box girder with the 2S shedding mode at the initial stage of vortex-induced vibration. However, as the amplitude of oscillation becomes large, strong vortices are generated in the gap and the flow of near wake transforms into turbulent flow. The vortices impinge on the windward wall of the downstream box girder when propagating downstream and cause the flow to separate and re-attach periodically around the windward corners of the downstream box girder. Due to the effects of vortices in the gap, the pressure shows high fluctuating characteristics near the windward corner of the downstream box girder. The energy of body oscillation is generated mainly by the pressures of these regions.

5 ACKNOWLEDGEMENTS

This study is financially supported by the NSFC under grant No. 90815022 and grant No. 51161120359.

6 REFERENCES

Chong, M.S., Perry, A.E., Cantwell, B.J., 1990. A general classification of three-dimensional flow fields. Physics of Fluids A 2(5), 261-265

Dallmann, U., 1983. Topological structures of three-dimensional flow separations, DFVLR, Rep.No. 221-82-A07, Göttingen, West Germany

Feng, C.-C., 1968. The measurement of vortex-induced effects in flow past stationary and oscillating circular and d-section cylinders. Master's Thesis, Department of Mechanical Engineering, The University of British Columbia, Canada.

Ge, Y.J., Xiang, H.F., Bluff body aerodynamics application in challenging bridge span length, BBAA VI International Colloquium on: Bluff Bodies Aerodynamics & Applications, Milano, Italy, July, 20-24 2008

Hunt, J.R.C., Wary, A.A., Moin, P., Eddies, 1988. streams and convergence zones in turbulent flows. Center of Turbulence Research Report CTR-S88, 193-208

Jeong, J., Hussain, F., 1995. On the identification of a vortex. Journal of Fluid Mechanics 285, 69-94

Li, H., Chen, W.L., Xu, F., Li, F.C., Ou, J.P., 2010. A numerical and experimental hybrid approach for the investigation of aerodynamic forces on stay cables suffering from rain-wind induced vibration, Journal of Fluids and Structures 26, 1195–1215

Sarpkaya, T., 2004. A critical review of the intrinsic nature of vortex-induced Vibrations, Journal of Fluids and Structures 19, 389–447

Experimental study on vortex resonance of streamline-like bridge deck section

Cui Xin [a], Li Jiawu [a], Liu Jianxin [a]

[a] *College of Highway, Chang'an University, Xi'an 710064,China*

ABSTRACT: In order to study the vortex-induced vibration and characteristics of high-order torsion vortex-induced vibration in streamline-like bridge deck section, model with pressure taps supported by spring was made for wind tunnel test, which included the torsion amplitude and time-history wind pressure in each tap. Based on the analyses of vibration spectrum in two vortex vibration areas, pressure fluctuation spectrum in each tap, and Strouhal number, this paper reveals the micro-characteristics of double vortex vibration area. This investigation indicates the possibility that occurrence of high-order vortex-induced vibration in streamline-like bridge section can be forecasted by analyzing surface pressure fluctuation spectrum of models; what is more, it is predicable to analyze the proportion of energy for the amplitude of model. Due to the same Strouhal number at same attack angle, we can decide whether the critical wind speed is lower than designed through forecasting critical wind speed of vortex-induced vibration under high speed wind.

KEYWORDS:Bridge engineering, Vortex-induced vibration, Wind tunnel test , Pressure fluctuation, High-order

1 INTRODUCTION

Contrast with vortex-induced vibration occurred in low wind, flutter attracts more attention rather than vortex-induced vibration under high speed wind in academic circles for a long time. With a lower critical wind speed in low-order modal, vortex-induced vibration takes a long time to accumulate energy. On the other hand, since vortex-induced vibration accumulates energy fast with a high critical wind in high-order modal [1], it is possible to stimulate vortex vibration in a short time and even cause aerodynamic instability. Therefore, concentration should be paid on high frequency vortex-induced vibration.

Second-order or higher order modal vortex-induced vibration has been found in the wind tunnel test of Tokyo Bay Aqua-Line Bridge [2]. For Jiaojiang Second Bridge, vortex-induced vi-

bration appeared twice in high speed wind range from 19m/s to 27m/s in +3 attack angle; torsion vortex-induced vibration appeared twice only in high speed wind range from 32m/s to 36m/s [3]. Except for vortex-induced vibration in base-order modal, there is possibility occurring vortex-induced vibration in the situation that critical wind speed is less than designed. Therefore, studying vortex vibration performance of common streamline-like section of long-span bridges, this paper introduces vortex-induced vibration phenomena under high speed wind, using time-history pressure of surface taps to analyze vortex vibration performance of the section.

2 TEST BACKGROUND

Taking a bridge as an example, the section deck model was tested in CA-1 wind tunnel at Chang'an University. In the scale of 1:25, the model is placed aluminum alloy skeleton inside, cowered by hard plastic, filled in bubble, with the width of 1.2 meters.

Vibration test and pressure test were conducted simultaneously. Fig.1 shows the arrangement of model in wind tunnel. Hanged by springs, two-dimension rigid section model is used for vibration test, with two supporting arms to limit the degree-of-freedom only in vertical and torsion. Depending on vibration signal sent from four acceleration sensors installed at rigid supporting arms, we can simulate the frequency in damp ratio of 0.5% and wind speed ratio of 1:4.

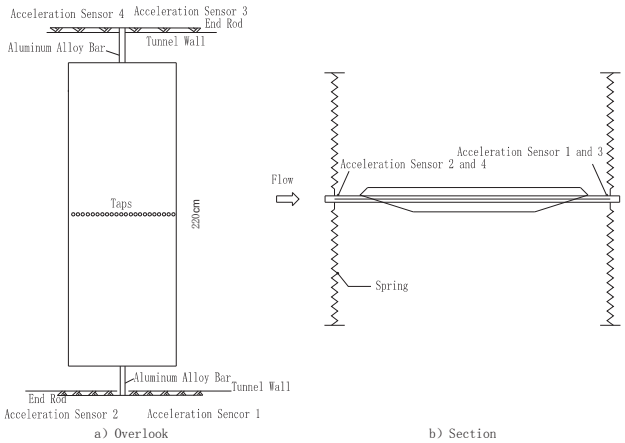

Fig.1 Arrangement of wind tunnel test

With 88 taps in the middle, which each diameter is 1mm, the model can meet the requirement of pressure test. Fig.2 displays the distribution of surface pressure taps.

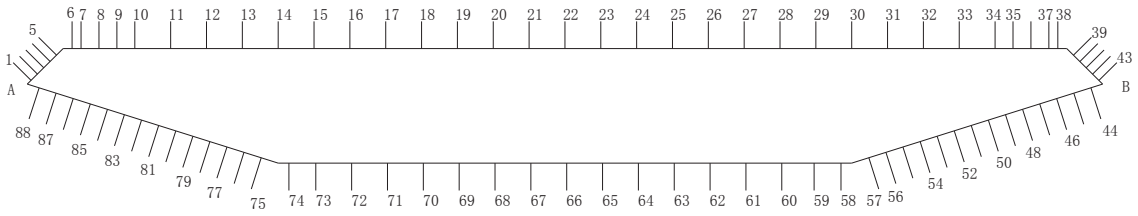

Fig.2 Taps distribution

We tested the model in the uniform flow at attack angles which were +5°、+3°and 0°. The results demonstrates that vortex-induced vibration occurred when attack angle was +3°, and there were two areas of vortex vibration. Accordingly, this paper studies the two areas in the condition of +3°attack angle.

2.1 Relationship between Wind Speed and Amplitude

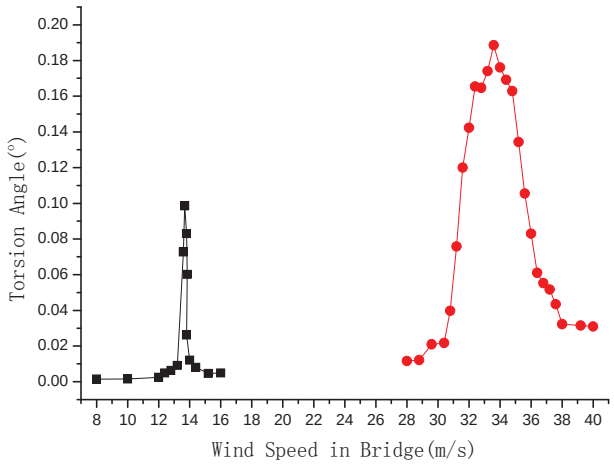

Fig.3 Relationship between amplitude and wind speed

Fig.3 shows the relationship between amplitude and wind speed. The amplitude here means standard deviation of time-history torsion angle under each wind speed. From Fig.3, vortex-induced vibration occurred twice when the wind speed ranges from 8.0m/s to 40.0m/s. The first one occurred in low wind speed from 12m/s to 16m/s. The second occurred in high wind speed, which range is 29.6m/s~40m/s. Apparently, the range of vortex vibration is wider under high speed wind, and the amplitude difference is more as well. The first maximum amplitude occurred when the wind speed was 13.6m/s under torsion angle of 0.1°, and the second maximum amplitude occurred when the wind speed was 33.6m/s under torsion angle of 0.19°,which shows the difference between two maximum amplitude is almost double. Since the speed range of the sec-

ond vortex vibration is 29.6m/s~40.0m/s, which is contained in the range of checking wind speed of the bridge, there is great possibility of occurring vortex vibration in reality.

2.2 Spectrum

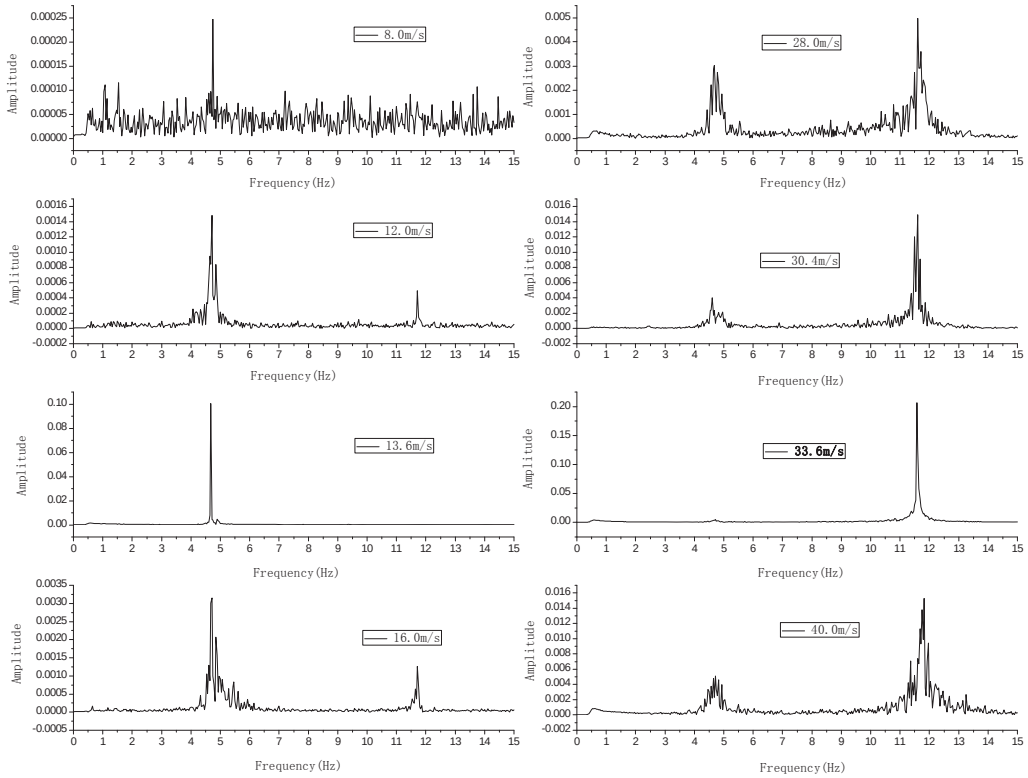

Fig.4 Torsion vibration spectrum

Fig.4 shows vibration spectrum of the model under eight different speeds of wind, including different wind speeds when the model was vibrationless, beginning vortex vibration, appearing the maximum amplitude, and has finished vortex vibration. Following the increase of wind speed, the vibration is getting intense when the frequency around 4.7Hz to 11.6Hz in two vortex vibration area. The dominant frequency is 4.7Hz in first vibration area, and is 11.6Hz in the second. After that, the vibration grows to be much intense, which becomes the max in the wind speed of maximum amplitude. The frequency becomes complex after the vortex-induced vibration ended, which indicates that the model restarted normal vibration. Containing high level of energy, the two vortex-induced vibration shows similar spectrum, with the frequency of 4.7Hz and 11.6Hz. When the wind speed is low, energy of the model increase gradually since 4.7Hz

vortex shedding frequency is same with the first-order torsion frequency; when the wind speed is high, the same phenomenon happened in the frequency of 11.6Hz.

2.3 Spectrums of each tap pressure fluctuation

The spectrum of time-history pressure reflects the characteristic of pressure fluctuation at each surface tap, and indicates the relationship between surface pressure and vibration [5].

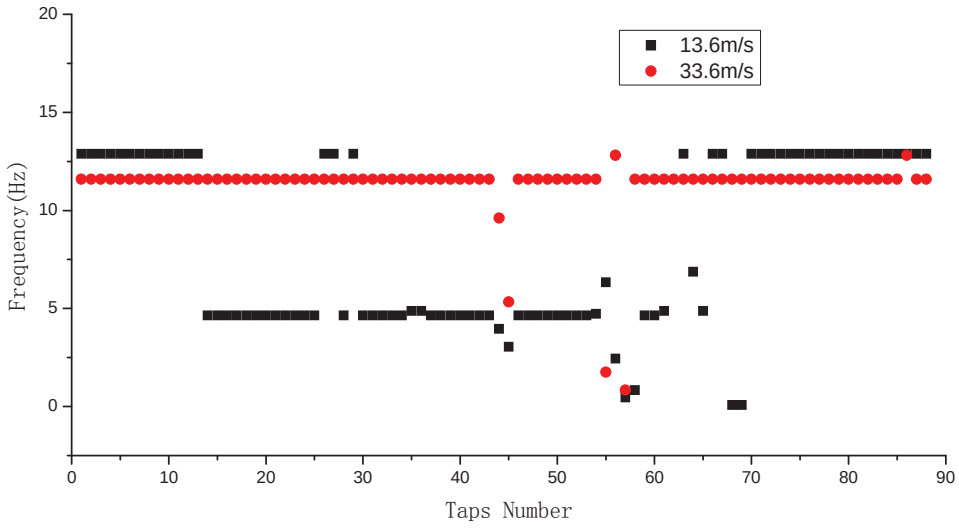

Fig.5 Frequency at the highest amplitude in spectrum

Fig.5 shows the frequency at the highest amplitude in pressure fluctuation spectrums. Only 1/2 surface taps shows 4.7Hz dominant frequency, with most of the other half centers in high frequency, and a small part disperses in different frequency, when the first vortex-induced vibration occurred (13.6m/s). Almost the all surface taps shows 11.6Hz dominant frequency when the second vortex-induced vibration occurred (33.6m/s).

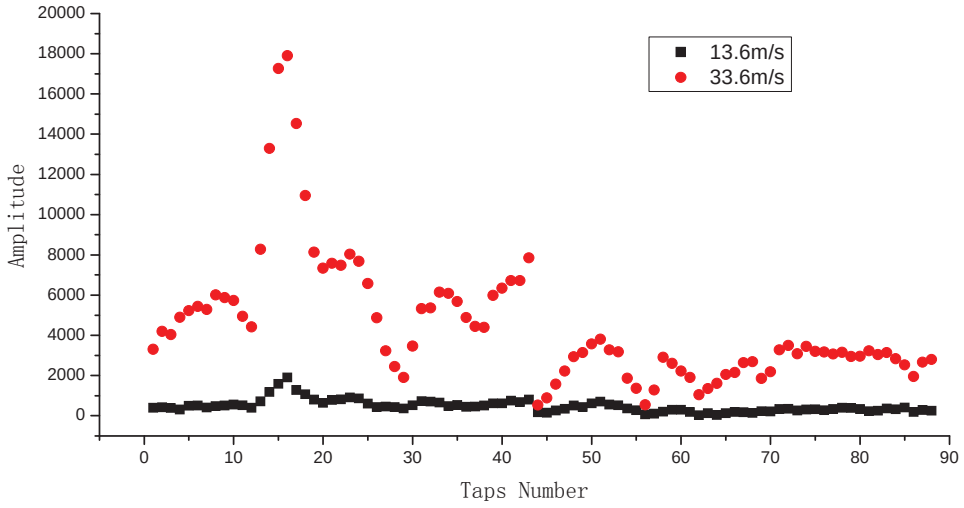

Fig.6 Amplitude of each tap vortex shedding frequency

Fig.6 depicts the spectrum amplitude of the vortex shedding under the wind speed of 13.6m/s and 33.6 m/s respectively. It is observed that the energy of the vortex shedding of the second spectrum amplitude is significantly bigger than that of the first one, which is also the case in Fig.5. This is because most of the excellence frequencies concentrate on vortex shedding frequency under the wind speed of 33.6m/s, which is dispersed under 13.6 m/s. Therefore the energy of vortex frequency is also dispersed under the wind speed of 13.6 m/s, which leads to a significantly smaller amplitude.

The above analysis reveals that airflow spiral produced by airflow crossing the section contains a variety of energy frequencies. When one vortex frequency corresponds with the frequency of the structure, vortex-induced vibration occurs. The amplitude of vortex-induced vibration is influenced by the proportion of energy of vortex frequency, and the energy of vortex frequency is determined by the frequency composition of all vortex and its degree of concentration in section tail. To illustrate, energy concentrates around 4.7 Hz and 12.5 Hz to a large extent under the 13.6 m/s wind speed, which incurred vortex-induced vibration at the structure frequency of 4.7 Hz. However, since some energy around the vortex shedding around 12.5 Hz is dispersed, the amplitude under the wind speed of 13.6m/s is significantly smaller than that of 33.6m/s. Meanwhile, since vortex shedding frequency consists of some high frequency, it is likely to bring out structure high frequency vortex-induced vibration: the structure experiences another vortex-induced vibration under the wind speed of 33.6m/s.

2.4 Strouhal Number

Under certain conditions, fluid on the surface will induce interchanging vortex shedding, which puts merged objects in the fluid under a force vertical to the flow. Both the direction and magnitude of the force change in a complicated manner with time. Its main frequency and vortex shedding frequency f and incoming flow velocity U, the characteristic size of the objects D meets Strouhal relationship.

$$S_t = \frac{fD}{U} \tag{1}$$

Fig.4 shows the main frequency and corresponding wind speed of the two vortex-induced vibration, which could be used to calculate the Strouhal number St. according to Eq.2. In the calculation, the characteristic size is the height of the beam. The Strouhal numbers in the two vortex-induced vibrations are listed in Table.1.

Table.1 St. Number of two vortex-induced vibration

No.	Test Wind Speed (m/s)	Vortex Shedding Frequency (Hz)	St. Number
1	3.4	4.7	0.165
2	8.4	11.6	0.165

Table.1 tells us that under the same attacking angle, the St. Number is fixed. Provided that there is a large component of high frequency vortex in the wake, a preliminary prediction of vortex vibration critical wind speed could be made according to the St. Number obtained in low wind speed, which casts light upon the whether the structure is safe.

3 CONCLUSIONS

- Time-history surface pressure is very informative. According to an analysis into the frequency composition of section surface pressure spectrum, a preliminary prediction to the possibility of vortex-induced vibration in high wind speed and its amplitude could be achieved.
- A disturbance of the concentration of each tap pressure fluctuation dominant frequency on first-order torsion frequency, which causes a dispersion on different frequencies, could weaken the amplitude of vortex-induced vibration.

4 REFERENCES

1 XIAN Rong，Liao HAi-li，LI Ming-shui. Analysis of vortex-induced vibration of large-scale section model of girder in wind tunne[J]. Journal of Experiments in Fluid Mechanic, 2009,23（4）：15-20.

2 FUJINO Y.Wind-induced vibration and control of Tran-Tokyo Bay Crossing Bridge[J].Journal of Structure and Engineering,2002,8: 1012-1025.

3 MENG Xiao-liang, ZHU Le-dong, DING Quan-shui. Vortex Vibration Performance of Colse Partly Separation Double Box Bridge Section Influenced by Maintenance Rail Position[C]. The 14 th national structure wind engineering conference proceedings,2009,Beijing

The Seventh International Colloquium on Bluff Body Aerodynamics and Applications (BBAA7)
Shanghai, China; September 2-6, 2012

Multi-mode vortex-induced vibration of a long rectangular shallow beam

Zhenqing Chen[a], Xugang Hua[a], Wen Chen[a], Zhiwen Huang[a],

[a] *Wind Engineering Research Center, Hunan University, Changsha, China*, *zqchen@hnu.edu.cn*

ABSTRACT: Two sectional models with the same side ratio of B/D=6 but different length scales are used to investigate the characteristics of multi-mode vortex-induced vibration (VIV) for long-span suspension bridges. The models are elastically suspended with springs of varying stiffness and a total of 11 cases are tested in smooth flow. Strouhal number of the models is found to be constant for all the cases regardless of model vibration frequency and model length scale. The vertical maximum non-dimensional amplitudes of each model are almost the same for different vibration frequencies, but the vertical amplitudes between the two models differ significantly. It is also observed that the torsional amplitudes drastically reduce with torsional frequency. A novel multi-elastically supported shallow beam is proposed as a simplified aeroelastic model of suspension bridge, which is capable of reproducing as many as closely-spaced vertical modes of suspension bridges. Ideally important modes of the aeroelastic model are expected to be excited in turn so as to further explore the multi-mode vortex-induced vibration of suspension bridges, in particular to study the effects of span-wise correlations of vortex-shedding forces on VIV under different vibration modes.

KEYWORDS: Vortex-shedding; Vortex-induced vibration; Suspension bridge; Aeroelastic model; Shallow section.

1 INTRODUCTION

Multi-mode vertical vortex-induced vibration (VIV) has been observed on several steel box girder suspension bridges with main spans over 1500m. Under varying wind velocity, different natural modes of a suspension bridge may be excited in turn following the Strouhal law and vibration frequency usually lies between 0.2Hz and 0.4Hz [1~3]. Analytical and experimental predication of the VIV amplitudes for every candidate vertical mode is a serious concern for wind-resistant design of suspension bridges. The vertical modes of a suspension bridge have the two salient features. They are closely-spaced such that there may exists more than ten modes in the frequency ranges of interests. The second feature is that the equivalent modal mass for every mode is nearly the same and approximately equals to the sum of stiffening girder and two main cables. As an example, Table 1 lists the modal characteristics of the first 8 vertical modes for a typical steel box suspension bridge with main span of about 800m. There are as many as 8 modes in the frequency range from 0.12Hz to 0.69Hz with an average increment of 0.07Hz, and the frequency distribution characteristics of suspension bridges differs from that of simply-supported beams (increase in a squared law) and that of taut strings (increase in a linear law).

The steel box girder in suspension bridges may be considered as a shallow beam and its height is usually about 4m. For such a shallow section, Strouhal number St is rarely below 0.1. The onset velocity of VIV does not exceed 25m/s, the maximum wind velocity for bridges open to traffic, when f<0.6Hz. The modes with frequency from 0.2Hz to 0.4Hz have VIV onset velocity of about 6~12m/s and are therefore most easily excited by vortex shedding than lower-order

modes. On the other hand, the limiting value of VIV amplitude is mainly determined by the maximum acceleration, and therefore it decreases with modal frequency. As a result, restricting the VIV amplitudes for higher-order modes is more rigorous than that of lower-order modes, and worthy of more attention.

Table 1 Modal parameters of the first 8 vertical modes for a suspension bridge with a main span of 800m

Mode number	Frequency (Hz)	Mode shape	Equivalent modal mass[1] (t/m)	Onset velocity of VIV[2] (m/s)
2	0.1181	1st asymmetrical vertical	37.1	3.44
3	0.1710	1st symmetrical vertical	33.8	4.98
5	0.2354	2nd symmetrical vertical	33.9	6.85
6	0.2645	2nd asymmetrical vertical	35.4	7.72
13	0.3588	3rd symmetrical vertical	33.8	10.5
18	0.4648	3rd asymmetrical vertical	46.0	13.6
26	0.5621	4th symmetrical vertical	33.8	16.3
34	0.6900	4th asymmetrical vertical	34.1	20.1

[1] The mass of stiffening box girder and the two main cables are 27.7t/m and 5.9t/m, the equivalent modal mass for every approximately equals to the sum of stiffening girder and the two main cables except for mode 18.
[2] Evaluated according on height of stiffening girder D=3.5m and a nominal value of Strouhal number St=0.12

2 EXISTING METHOD FOR MULTI-MODE VIV

2.1 *Mathematical model of VIV*

Excessive vortex-induced vibration may cause fatigue problems of structure and user comfort, and it is therefore necessary to limit the vibration amplitude. However accurate prediction of VIV amplitudes remains a difficult problem and the existing mathematical models are mainly semi-analytical and semi-experimental. The *empirical linear model* developed by Simiu and Scanlan in 1986 is chosen to discuss the multi-mode vortex-induced vibrations. The cross-wind dimension D of the cylinder (the box-girder height in the context of suspension bridges), is taken as characteristics length. The equation of motion of the cylinder during lock-in can be written as

$$m(\ddot{y}+2\varsigma\omega_n\dot{y}+\omega_n^2 y)=\frac{1}{2}\rho U^2 2D\left[Y_1(K_1)\frac{\dot{y}}{U}+Y_2(K_1)\frac{y}{U}\right]+\frac{1}{4}\rho U^2(2D)C_L(K_1)\sin(\omega_n t+\varphi) \tag{1}$$

where m is the cylinder mass per unit length; ρ is the mass density of air; U is the wind velocity; K_1, defined as $D\omega_n/U$, is the reduced frequency with ω_n being the natural frequency of cylinder; $Y_1(K_1)$, $Y_2(K_1)$ and $C_L(K_1)$ describe the aerodynamic damping, aerodynamic stiffness and motion-independent vortex-shedding forces at lock in, and they are functions of reduced frequency K_1. By defining the non-dimensional amplitude $\eta=y/D$, the steady solution for equation (1) can be expressed as

$$|\eta|=\frac{\rho D^2 C_L}{2m\sqrt{\left(K_0^2-K_1^2\right)^2+\left(2\gamma K_0 K_1\right)^2}} \tag{2}$$

$$K_0^2=K_1^2-\frac{\rho D^2}{m}Y_2(K_1) \qquad \gamma=\frac{1}{2K_0}\left[2\varsigma K_1-\frac{\rho D^2}{m}Y_1(K_1)\right] \tag{3, 4}$$

By analog, equation (2) may be regarded as the response of single degree-of-freedom (SDOF) system with reduced modal frequency K_0 and modal damping ratio of γ under forced sinusoidal

excitation with frequency K_1; during lock in, K_1 decreases with wind velocity U and the maximum vibration amplitude η develops when $K_1=K_0$. By this analogy, one can identify the aerodynamic parameters $Y_1(K_1)$, $Y_2(K_1)$ and $C_L(K_1)$ from the experimental K_1-η curve obtained from sectional model wind tunnel tests. The Simiu-Scanlan model only predict the the maximum amplitude for $K_1=D\omega_n/U$, and it cannot also provide the range of wind velocity at lock-in.

The VIV amplitude described by equations (2)~(4) are implicit functions of aerodynamic parameters $Y_1(K_1)$, $Y_2(K_1)$ and $C_L(K_1)$. Substituting equations (3) and (4) into equation (2) yields

$$|\eta| = \frac{C_L}{2\sqrt{Y_2^2 + \left(2K_1^2 S_C - Y_1\right)^2}} \tag{5}$$

where S_C is the Scruton number defined as $S_C=m\varsigma/\rho D^2$.

The vibration frequency remains constant for the full lock-in range and it equals to the structural frequency, that is $\omega_n=2\pi f$. The relationship between the apparent Strouhal number and K_1 is

$$S_t = \frac{fD}{U} = \frac{K_1}{2\pi} \tag{6}$$

By letting $Y_1=Y_2=0$, equation (5) reduces to the case of the most *simple linear model* of vortex-shedding forces considering only the motion-independent term. In such case, the solution of VIV amplitude reduces to

$$|\eta|_L = \frac{C_L}{16\pi^2 S_t^2 S_C} \tag{7}$$

where $|\eta|_L$ represents the solution of SDOF system for the *simple linear model* of vortex shedding. It is clear that the non-dimensional amplitude is in inverse proportion with S_t^2 and S_C for the *simple linear model*.

2.2 *Prediction for multi-mode VIV*

The existing method for predicting the lock-in wind velocity as well as vibration amplitude for every possibly-excited mode bases its theoretical foundation on equation (7). In more detail, experimental results of vortex-induced vibration for a particular mode is determined by sectional model wind tunnel tests while those for the remaining modes is evaluated by equations (6) and (7). The procedure is as follows.

(1) Conduct sectional model tests for one particular mode P to determine the St number, lock-in range and maximum vibration amplitude η_P for that mode.

(2) Assume St is constant and calculate the wind velocity of VIV for remaining modes, for example mode Q, as follows

$$V_Q = V_P \cdot \frac{f_P}{f_Q} \tag{8}$$

where V_P may be the onset wind velocity of VIV, wind velocity interval of VIV and wind velocity of VIV with maximum vibration amplitude.

(3) If the modal damping ratios are the same for all modes, it is obvious that η is in inverse proportion with equivalent modal mass m. As such, the relationship of vibration amplitude between mode P and mode Q is given as

$$\eta_Q = \eta_P \cdot \frac{m_P}{m_Q} \tag{9}$$

where m_P and m_Q are the equivalent modal mass for modes P and Q. Equation (9) is only valid for the *simple linear model* of vortex-shedding force, and may become invalid for the *empirical linear model* of Simiu-Scanlan type if Y_1 and Y_2 are non-trivial.

(4) Consider further correction of vibration amplitude due to three-dimensional mode shape as well as the span-wise correlation of vortex-shedding forces. One noticeable example is the correlation method developed by Ruscheweyh which has been included in the Eurocode [4, 5]. However, Ruscheweyh's method is suitable for chimneys and other vertical structures. Chimneys may experience vortex-induced vibration for the first or second modes, which differs appreciably from higher-modes of long-span suspension bridges. Investigation on span-wise correlation of vortex-shedding forces for higher-modes is very rare if not none. The current Chinese code for wind-resistant design of highway bridges does not consider the correction of vibration amplitude due to imperfect correlation of vortex-shedding forces.

A series of investigations are underway to develop method for predicting maximum vibration amplitudes for higher-order modes of suspension bridges. Some key issues needing further research are summarized as follows:

(1) Variation of *St* number with vibration frequency for the same model;
(2) Variation of VIV amplitude with vibration frequency for the same *Sc* number;
(3) Effect of aerodynamic damping on VIV for different modes;
(4) Equability of modal damping ratio for different modes;
(5) Span-wise correlation of vortex-shedding forces under different mode shapes;
(6) Determination of allowable vibration amplitude for higher-order mode.

In the following, selected results for (1) and (2) are presented and discussed.

3 WIND TUNNL TESTS OF RECTANGULAR SECTIONS AT DIFFERENT VIBRATION FREQUENCY

As a first step for studying the multi-mode vortex-induced vibrations, two rectangular sectional models having the same side ratio of B/D=6 but different length scale are elastically suspended by springs with varying stiffness to simulate different vibration modes. The wind tunnel tests are conducted in the high-speed test section of HD-2 wind tunnel at the Hunan University, the dimension of the test section is 3m(W)×2.5m(H)×17m(L).

3.1 *Section models and experimental setup*

The side ratio of both sectional models is 6, and the length of the models is 1.54m. The model A has a height of 12cm and a width of 72cm while the model B has a height of 6.7cm and a width of 40cm. The inner part of the model is constructed with mental materials to have sufficient rigidity while the surface of the model is covered with ABS plates to ensure the smoothness of the surface. Large plates are connected at both model ends to improve the flow conditions. As shown in Figure 1, the model is elastically suspended in wind tunnel by springs, and the model may move in vertical and torsional directions but the motion in along-wind direction is restrained by a long steel wire. The incoming wind velocity is recorded by Croba. The model displacements at upstream and downstream locations are measured by two laser displacement transducers, the model accelerations at upstream and downstream locations are measured by two micro-accelerometers. The test is conducted in smooth flow (with turbulent intensity less than 1% for mean wind velocity larger than 3m/s) and only zero wind attack angle is considered.

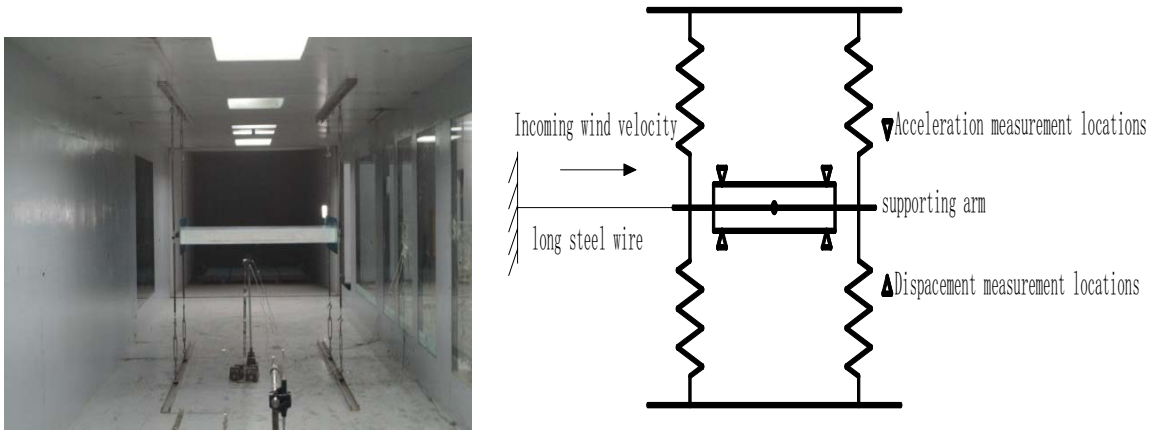

Figure 1. Elastically-suspended section model and its supporting frames

3.2 *Data processing*

The data are recorded after the model vibration become stable. The sampling frequency is 100Hz and sample duration exceeds 45s for each record. For each test case, the wind velocity, two accelerations and two displacements are measured. The two displacements $u_1(t)$ and $u_2(t)$ (or accelerations) are used to calculate the vertical and torsional displacements, as follows.

$$h(t)=\frac{1}{2}\left(u_1(t)+u_2(t)\right) \qquad \alpha(t)=\frac{1}{2L}\left(u_1(t)-u_2(t)\right) \tag{10}$$

where L is the half of distance of measurement points of laser transducer. The standard deviation of the response is calculated from vertical and torsional displacements.

3.3 *Experimental results*

A total of 11 testing cases is carried out, 8 for the model A and 3 for the model B. The experimental parameters of each case for the model A and the model B are summarized in Table 2 and Table 3. The equivalent modal mass for each case are precisely calculated based on finite element modal analysis of the free vibration system consisting of rigid sectional model, springs, connecting arms and long steel-wire, and the results are shown in the tables.

Table 2. Experimental parameters for the model A

Test case	6	1	7	2	8	3	4	5
Vertical frequency f_v (Hz)	2.25	2.44	2.95	3.34	3.96	4.95	5.86	6.98
Vertical damping ratio (%)	0.16	0.25	0.16	0.25	0.16	0.25	0.25	0.25
Total physical mass (Kg)	21.0	19.4	22.3	20.6	21.5	19.9	23.0	22.2
Equivalent modal mass (Kg)	18.9	17.7	18.8	18.0	18.3	17.7	18.6	18.1
Sc number	1.32	1.63	1.31	1.66	1.28	1.63	1.71	1.67
Torsional frequency f_T (Hz)	5.27	4.54	7.03	6.10	10.55	9.16	10.4	12.6
Torsional damping ratio (%)	0.31	0.43	0.30	0.42	--	--	--	--
f_T/f_V	2.34	1.86	2.38	1.83	2.66	1.85	1.77	1.81

Table 3 Experimental parameters for the model B

Test case	9	10	11
Vertical frequency f_v (Hz)	2.42	3.54	5.03
Vertical damping ratio (%)	0.19	0.25	0.25
Total physical mass (Kg)	9.67	10.20	10.89
Equivalent modal mass (Kg)	7.63	8.16	7.89
Sc number	1.71	2.41	2.33
Torsional frequency f_T (Hz)	5.08	7.52	9.57
Torsional damping ratio (%)	0.26	0.29	0.26
f_T/f_V	2.10	2.12	1.90

Wind tunnel experiments for the 1st~5th cases of the model A are first carried out and the vertical damping is 0.25%. For each case, two vertical VIV and two torsional VIV develop with increase of wind velocity. The variation of non-dimensional vertical displacement is shown in Figure 2. The first vertical VIV for the five cases are very similar; the second vertical VIV for the 3rd~5th cases are very similar but differs from those for the first and second cases. The anomaly in the second vertical VIV for both cases is probably caused by the simultaneous occurrence of vertical and torsional VIV such that vertical VIV transits into torsional VIV. In order to validate this assumption, three additional cases with larger torsional-to-vertical frequency ratio are tested. It is observed that the second VIV for the 6th~8th cases is very similar to those of the 3rd~5th cases.

It is also important to mention that the torsional vibration amplitude reduces drastically with torsional model frequency, and that the model with the case 8 does not develop torsional vibration even at the lower damping ratio of 0.16%. As there is no interference between vertical VIV and torsional VIV for the 3rd~8th cases, it is believed that the experimental vertical VIV data are reliable for these cases.

Wind tunnel experiments for the model B are then conducted for the 9th~11th cases. Due to the large value of torsional-to-vertical frequency ratio, vertical VIV and torsional VIV are well separated. The results of vertical VIV are shown in Figure 3.

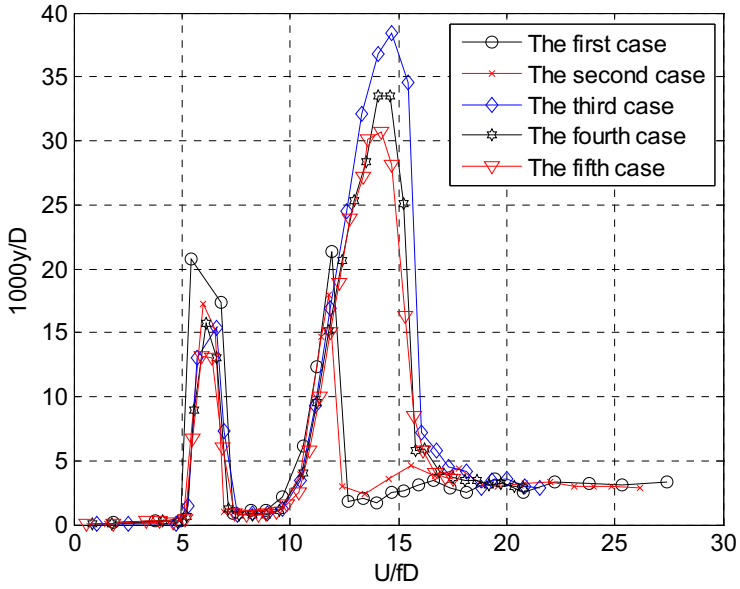

Figure 2. Variation of non-dimension vertical amplitude for the model A

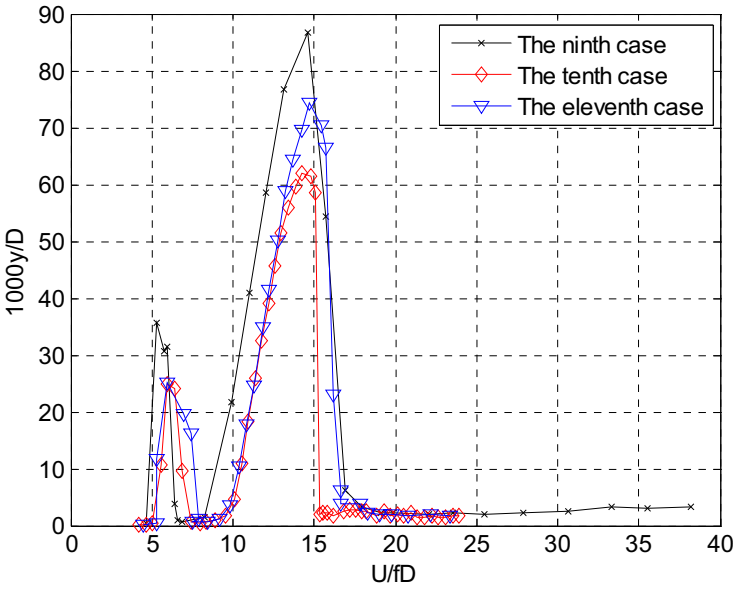

Figure 3. Variation of non-dimension vertical amplitude for the model B

3.4 *Analysis and discussion*

(1) There are two obvious vertical VIV for all the cases of the model A and the model B. The *St* numbers for all the 11 cases are calculated from onset wind velocity of two vertical VIV. The mean value of *St* numbers for the first and the second VIV are 0.206 and 0.107, respectively, and their stand deviation is 0.01 and 0.003. It is found that *St* numbers of the first and second vertical VIV are almost the same for all the cases. Vibration frequency and length scale of the model have minor effects on *St* number. Therefore it is reasonable and of sufficient accuracy to derive the wind velocity of VIV of other modes simply based on experimental data on one particular mode. The mechanism associated with the development of two vertical VIV rather than a single VIV remains further investigations.

(2) The mass *m* and damping ratio ς vary slightly for all the cases, and therefore the corresponding *Sc* number will be slightly different, as shown in Tables 2 and 3. In order eliminate the effect of *Sc* numbers on vibration amplitude, the *Sc* number for the 6th case is taken as reference value, and vibration amplitude for other cases of the model A are normalized with respect to the 6th case. As the vibration amplitude is inversely proportional to *Sc* number, the *Sc*-corrected non-dimensional vibration amplitude for all other cases is calculated as

$$|\eta|_n' = |\eta|_n \cdot \frac{S_{cn}}{S_{c6}} \tag{11}$$

where the subscript *n* represent the case *n*; $|\eta|'$ is the *Sc*-corrected vibration amplitude. The variations of *Sc*-corrected vibration amplitude for the model A are show in Figure 4. After correction, the discrepancy in vibration amplitude is further reduced for the model A. Figure 5 shows the *Sc*-corrected vibration amplitude for the model B where the 9th case is taken as reference. Both Figures 4 and 5 imply that vibration frequency does not have important effects on vibration amplitude. It may be concluded the assumption *that the non-dimensional vibration amplitudes for different vertical VIV modes of a bridge is the same* is valid and of sufficient accuracy for practical applications. However, the VIV torsional amplitude reduces drastically with torsional frequency,

and the above assumption is completely invalid for torsional VIV; however this observation appears to be consistent with realistic situations where the actual bridges rarely develop torsional VIV for higher modes. Further investigations are needed to better understand torsional VIV.

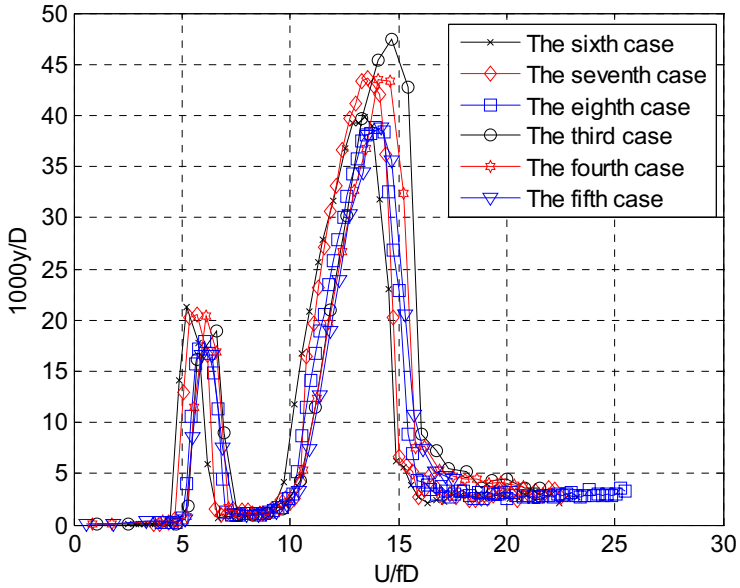

Figure 4. Variation of *Sc*-corrected vertical amplitude for the model A

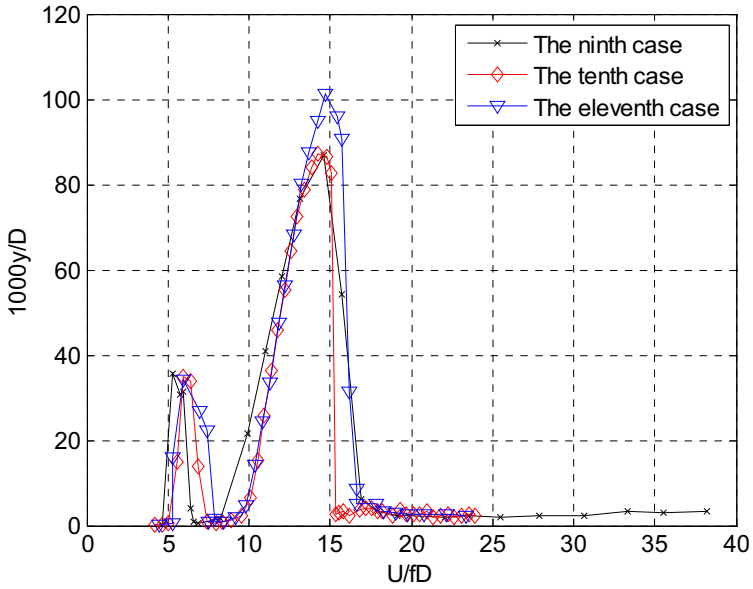

Figure 5. Variation of *Sc*-corrected vertical amplitude for the model B

(3) The *St* number for the second VIV is nearly half that for the first VIV. If the *simple linear model* of vortex-shedding forces stands, the maximum amplitude for the second VIV will be theoretically four that for the first VIV. However, the maximum amplitude for the second VIV is about two that for the first VIV, implying the *simple linear model* is insufficient. Due to the incorporation of Y_1 and Y_2 in the *empirical linear model* of Simiu-Scanlan type, the vibration am-

plitude is not simply in inverse relation with St^2. It may be concluded equation (7) is not of sufficient accuracy for structures with shallow cross sections.

(4) While the different cases of each model A or B have almost the same vibration amplitudes, the difference in vibration amplitude between the model A and the model B is quite large. The average non-dimensional amplitudes of the two vertical VIV for the model A is 19.28 and 45.02, while those for the model B is 35.97 and 91.71. The vibration amplitude for the model B with smaller scale doubles. Detailed comparisons are given in Table 4. Larger and smaller models will be used to further quantify the effect of length scales on vertical VIV amplitudes.

Table 4 Comparison of *Sc*-corrected non-dimensional amplitude for the models A and B

	L (m)	B (m)	D (m)	The first vertical VIV		The second vertical VIV	
				Re number	Mean maximum amplitude $1000\eta/D$	*Re* number	Mean maximum amplitude $1000\eta/D$
Model A	1.54	0.72	0.12	9.7E3~5.0E4	19.28	2.0E4~1.1E5	45.02
Model B	1.54	0.40	0.67	3.4E3~1.1E4	35.97	6.4E3~2.5E4	91.71
A/B	1.00	1.79	1.79	2.87 ~4.51	0.426	3.13~4.30	0.379

4 NOVEL MULTI-ELASTICALLY SUPPORTED AEROELASTIC MODEL

In order to investigate the span-wise correlations of vortex-shedding forces for different vibrational mode shapes as well to directly measure the vertical VIV amplitudes for every mode, an aeroelastic model capable of reproducing closely-spaced vertical modes is necessary. A scaled aeroelastic model of the full bridge may fulfill such requirement, but it is practically infeasible due to the small scale ratio, usually at the order of 1/200. The taut-strip model is capable of reproducing a pair of vertical and torsional modes of suspension bridges and can be used to investigate the flutter characteristics. The stiffness of the taut-strip model is provided by two internal parallel taut strings, and the vertical frequencies of the taut strings increase linearly with model number. For example, if the first vertical frequency is f_1, the modal frequencies of other higher-order modes will be $2f_1$, $3f_1$, $4f_1$, …. Such frequency distribution is not the case for the vertical modes of suspension bridges, as exemplified in Table 1.

In this study, a novel multi-elastically supported scaled aeroelastic model of shallow beam is proposed as simplified representation of a suspension bridge, which is capable of reproducing as many as closely-spaced vertical modes of suspension bridges The method for design such a model is developed. In the aeroelastic model of this kind, only the stiffening girder is included, and the girder model is elastically supported by springs at multiple locations. The key in developing the new aeroelastic model is to determine the appropriate number of elastic supports as well as the support stiffness with the assumed mode shape method.

An aeroelastic model of rectangular cross section with the side ratio B/D=6 has been designed and constructed, and hopefully very important mode of the aeroelastic model may be excited by vortex-shedding one by one to further understand the variation of vibration amplitude for different vertical modes. The model is 8m long, 2cm high and 12cm wide. The model is intended to simulate multiple vertical modes of a suspension bridge with main span of 1600m. Froude number is followed in the model design. The stiffness of the rectangular cylinder is provided by a thin steel plate, while the outer configuration is made by foam materials. The modal frequencies and mode shapes of the spring-supported aeroelastic model will be tested by sinusoidal excitation and will be compared with finite element predictions to evaluate the shear effect of shallow beam on higher modes. The carefully-calibrated aeroelastic model tests will be finally conducted in the smooth and turbulent flows to measure the VIV vibration amplitude of each mode as well

as to investigate the relationship between vibration amplitude and other (structural and wind) influencing parameters. The experiments will be conducted in the new 8.5m(W)×2m(H)×15m(L) test section of the HD-2 wind tunnel. Many investigations are still underway.

5 ACKNOWLEDGEMENTS

The work is supported by the Natural Science Foundation of China (NSFC), and a key project from Ministry of Transportation of China.

6 REFERENCES

1 A. Larsen, S. Esdahl, J.E. Andersen and T. Vejrum, Storebalt suspension bridge-vortex shedding excitation and mitigation by guide vanes, Journal of Wind Engineering and Industrial Aerodynamics. Vol. 88, 2000, 283-296.
2 H. Li, S. Laima, J.P. Ou, X.F. Zhao, W.S. Zhou, Y. Yu, N. Li, Investigation of vortex-induced vibration of a suspension bridge with two separated steel box girders based on field measurements , Engineering Structures 33 (2011) 1894–1907.
3 Z.Q. Chen, Bridge Wind Engineering, China Communications Press, Beijing, 2004.
4 R. Ruscheweyh, Practical experience with vortex-induced vibration, Journal of Wind Engineering and Industrial Aerodynamics, 1990, 33: 211-218
5 Eurocode 1: Actions on structures - General actions - Part 1-4:Wind actions, Annex E, prEN 1991-1-4,January 2004.

The Seventh International Colloquium on Bluff Body Aerodynamics and Applications (BBAA7)
Shanghai, China; September 2-6, 2012

Benchmark wind tunnel study of wind loading on rectangular sign structures

Delong Zuo, Douglas A. Smith, Kishor C. Mehta

Wind Science and Engineering Research Center, Texas Tech University, Mail Box 41023, Lubbock, TX, USA

ABSTRACT: Wind-tunnel tests were conducted to study wind loading on elevated rectangular sign structures of various configurations. Based on these tests, the wind-induced force and moment acting on the sign models were evaluated. The data obtained from the wind tunnel tests were analyzed in the context of the results of previous wind tunnel tests as well as those of a full-scale investigation. It is revealed that the configuration of the rectangular sign faces significantly affects the loading on these structures. It particular, the outcomes of the present study indicate that the torque acting on rectangular sign structures is overestimated by a standard that guides the design of such structures.

KEYWORDS: rectangular sign, wind loading, wind tunnel tests.

1 INTRODUCTION

Rectangular boxes and plates are frequently used as signs to display information and to function as a structural component. These sign systems with rectangular faces are structurally quite simple: They usually consist of a rectangular sign board or box and a simple support, such as a mono-pole or a truss. In some other cases, the rectangular signs are simply fixed to the ground. Despite the structural simplicity of these structures and that fact that rectangular boxes and plates are among bluff bodies of the simplest shapes, the wind loading of sign structures can be complex and is dependent on the size of the sign, the ratios between the three dimensions of the sign, whether the sign is elevated or located on the ground and, in the case of elevated sign, the amount of the clearance between the sign and the ground.

Perhaps due to the perceived simplicity of the structure, to date, very few studies have been dedicated to expressly investigate the wind loading of sign structures. Previous studies related to wind loading of rectangular sign structures evolved from wind tunnel experiments conducted in smooth, uniform flow (e.g., the early work done by Flachsbart, as summarized in [1]) to turbulent uniform flow (e.g., [2]) to both wind tunnel and full-scale studies in turbulent boundary layer flow (e.g., [3-9]). Most of these studies, however, were conducted to study wind loading on free-standing walls, which resemble a class of rectangular signs on the ground. Only very few studies (e.g., [5, 9]) were dedicated to the study of sign structures, and the focus of these studies were on signs formed by thin plate-like rectangular elements. This paper presents the outcomes of a benchmark study, which is a subset of a more comprehensive research effort, conducted to assess wind loading on sign structures of a number of configurations. These outcomes are interpreted in the context of the results from previous studies on wind loading on rectangular sign structures and the specifications of design standard.

2 EXPERIMENTAL CONFIGURATIONS

2.1 *Models*

Models of four sign structures with rectangular sign faces were tested in the wind tunnel at a length scale of 1:50. The first has a single-plate of 3 mm in thickness, which will subsequently be referred to as the single-plate sign model. The second is composed primarily of two parallel thin plates of 3 mm in thickness as the sign faces, which will be referred to as the double-plate sign model. This model is open on all sides, and the two sign faces are connected by eight 6mm by 6 mm struts, four at the top and the other four at the bottom of the sign at equal spacing. The third is a model also composed of two thin plates of 3 mm in thickness as the sign faces, but these two plates form a $30°$ angle instead of being parallel to each other. The two faces of this model are also connected by eight 6mm by 6 mm struts, four at the top and the other four at the bottom of the sign at equal spacing. This model will be subsequently referred to as the V-shaped sign model. The fourth is cubic in shape with all the sides closed, which will subsequently be referred to as the box sign model. The sign double-plate, the V-shaped and the box sign models were printed out by a three-dimensional printer, and the sign face of the single-plate sign model was an aluminum plate. All four sign models were supported by a circular steel rod of 0.95 cm in diameter. Figure 1 schematically shows the configuration and major dimensions of the models. In this figure, $b = 15.2$ cm, $h = c = 7.6$ cm, and $t = 3.7$ cm. At a length scale of 1:50, these dimensions correspond to full-scale sign faces with a width of 7.6 m and a height of 3.8 m. In current design practices, sign structures are often characterized by their aspect ratio (b/h) and clearance ratio ($h/(h+c)$). These specimens represented sign models with an aspect ratio of 2 and a clearance ratio of 0.5.

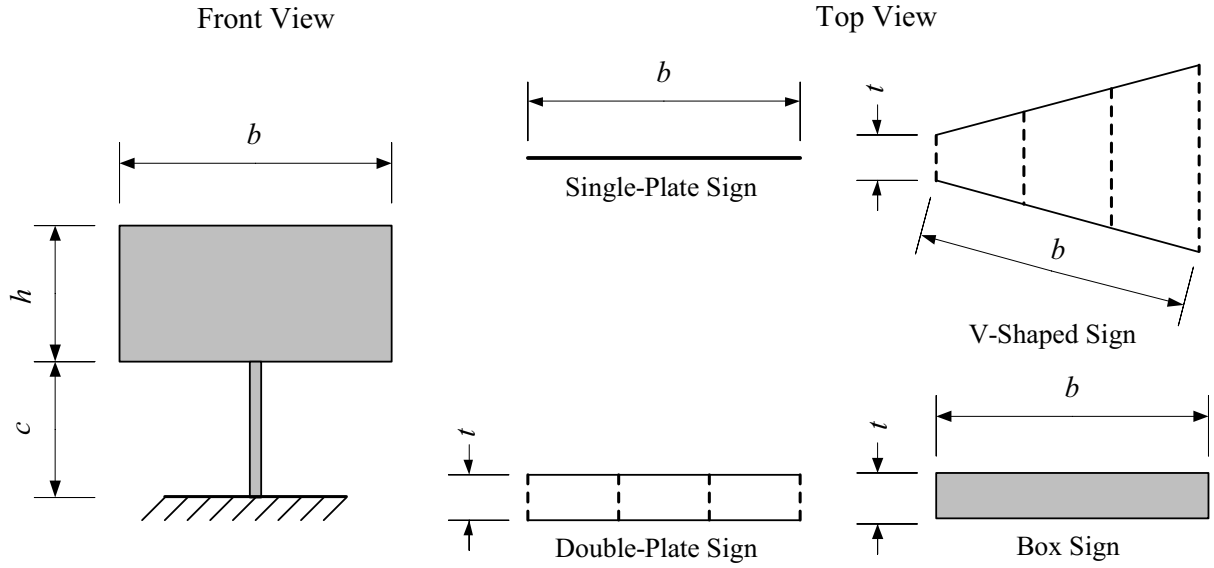

Figure 1 Sign models tested in the wind tunnel (not to scale)

2.2 *Simulation of boundary layer*

A wood grid system right outside of the settling chamber of the wind tunnel, a barrier upstream of the boundary layer section and a combination of a carpet and wood blocks were used to simulate atmospheric boundary flows representing those over exposure C specified by the loading standard published by American Society of Civil Engineers [10] (subsequently referred to as ASCE 7-10). Figure 2 shows the mean wind speed profile of the simulated atmospheric bounda-

ry layer at a length scale of 1:50. In this graph, the mean wind speeds at the measurement heights were normalized by that measured at a height of 0.2 m above the wind tunnel floor. A least-squares fit of the height against mean wind speed assuming that the profile is logarithmic in nature yields an equivalent full-scale roughness length value of $z_0 = 0.015$ m, which is close to the representative roughness length scale associated with exposure *C* specified by ASCE 7-10. Also shown in Figure 2 is the estimated auto-spectral density function of the along-wind speed at a height of 0.2 m above the wind tunnel floor as well as the corresponding Kaimal spectrum ([11]) at this height. In this figure, n is frequency, U is the mean wind speed, σ_u is the standard deviation and $S_n(n,z)$ is the auto-spectral density function. It can be observed that the simulated boundary layer has slightly higher energy content at higher frequencies and slightly lower energy content at lower frequencies than the flow represented by the Kaimal spectrum. This is a typical shortcoming of larger scale wind tunnel simulations.

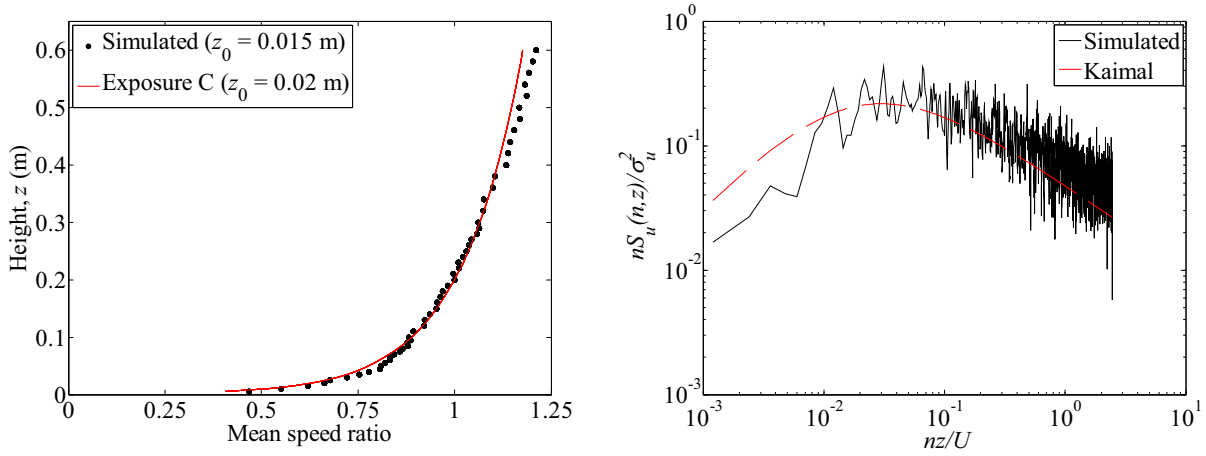

Figure 2 Mean wind speed profile of boundary layer flow and spectrum of along-wind speed at a height of 0.2 m above wind tunnel floor

2.3 *Measurements*

During the tests, the rods that supported the sign models were clamped to a six-component force transducer (ATI Industrial Automation, Inc. Gamma series, calibration SI-32-2.5), which has a resonance frequency of more than 1000 Hz for all components, for direct measurements of the forces and moments acting on the sign structure models. The mean test wind speed was approximately 10 m/s at a height of 20 cm above the wind tunnel floor, which is equivalent to 40 m/s at 10 m above ground level. The reference wind speeds for calculation of the reference dynamic pressure were measured by a Cobra probe (Turbulent Flow Instrumentation, series 100), which was placed at a position that was at the same height as the top of the sign model and at least one sign face width away from the side of the model. The single-plate, double-plate and box sign models were tested for 6 orientations represented by yaw angles of $0°$ to $75°$ at a $15°$ increment, relative to the mean direction of the wind, respectively; and the V-shaped sign model was tested for 13 orientation represented by yaw angles of $-90°$ to $90°$ at a $15°$ increment. Figure 3 schematically indicates the definition of the yaw angle (β) for the four types of sign models tested. For the V-shaped sign model, clockwise rotation of the sign axis relative to the direction normal to the wind direction results in positive yaw angles and counterclockwise rotation result in negative yaw angles. In addition to testing the whole sign models, a separate series of tests were also performed for the supporting rods without the sign faces attached. With the reasonable assumption that the effect of the secondary flow induced by the rod can be neglected, this enables estimation of the net forces and moments acting on the sign faces only.

All the measurement channels were sampled at a frequency of 250 Hz. Ten tests were conducted for each sign configuration as well as the rod to facilitate estimation of the coefficients representing the wind-induced forces and moments. The duration of each test is 72 seconds, which is equivalent to 15 minutes at full-scale.

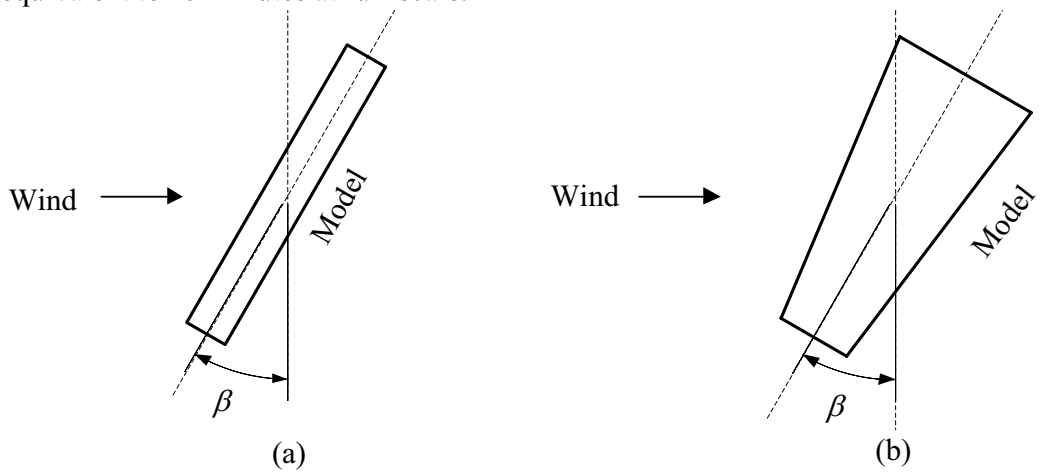

Figure 3 Definition of yaw angle for (a) single-plate, double-plate and box signs and (b) V-shaped sign

3 RESULTS

3.1 *Mean force and eccentricity coefficients*

To estimate the mean force coefficients, the forces acting on the sign structure models and those acting on the supporting rods were first evaluated independently. For all specimens, the forces measured by the two orthogonal axes of the force transducer were decomposed into an along-wind drag component and a cross-wind lift component. The mean drag and lift forces acting on the rod are estimated as the mean value of the drag and lift force time histories obtained from 10 tests of the rod. These mean drag and lift forces acting on the rod are subtracted from the drag and lift force time histories obtained from the 10 tests of each sign structure model to yield time histories of the net drag and lift forces acting on the faces of this sign model. These net drag and lift time histories were then used to compute the resultant net horizontal force, which will subsequently be denoted $F_i(t)$, in which i is the test number and t is time. For each net force time history, the corresponding force coefficient time history is estimated as

$$C_{Fi}(t) = \frac{F_i(t)}{\frac{1}{2}\rho U^2 A} \tag{1}$$

where ρ is the air density calculated based on the temperature, barometric pressure and relative humidity measured in the wind tunnel, U is the mean wind speed measured at the height of the top of the sign, and A is the area of the sign faces. For each sign model, a 15-minute mean force coefficient, $\overline{C}_{Fi} = \text{mean}(\overline{C}_{Fi}(t))$ is computed based on time histories obtained from each individual test. The mean force coefficient of a sign model is then estimated as the average of these 10 15-minute mean force coefficients. That is

$$\overline{C}_F = \frac{1}{10}\sum_{i=1}^{10} \overline{C}_{Fi} \tag{2}$$

Figure 4 shows the mean force coefficients of the four sign models tested for the yaw angles tested. It can be seen that the mean aerodynamic behavior of the 4 sign models were quite different. While the largest mean force coefficient for all four models are expectedly associated with smaller absolute values of yaw angles, the detailed evolution of these mean force coefficients with the yaw angle is quite model dependent. For the single-plate sign model and the box sign model, the mean force coefficients remain mostly constant for yaw angles of $0°$ to $30°$. At yaw angles of $45°$ and above, however, these two models behaved very differently due to the difference in the depth of the signs. In particular, while the single-plate sign is seen to attain a maximum mean force coefficient at a yaw angle of $45°$, the mean force coefficient of the box-sign at a yaw angle of $45°$ is much smaller than those at yaw angles of $0°$ to $30°$. By comparison, the evolution of the mean force coefficients of the double-plate sign is quite similar to that of the single-plate sign except that the existence of a second rectangular plate make the mean force coefficients of the double-plate sign slightly lower at yaw angles of $0°$, $15°$ and $45°$ and slightly higher yaw angles of $30°$, $60°$ and $75°$ than those of the single-plate sign at the corresponding yaw angles. By contrast, the loading of the V-shaped sign model is the most different from that of the other three sign models due to the fact that the orientation of this sign relative to wind is asymmetrical about the yaw angle of zero degree.

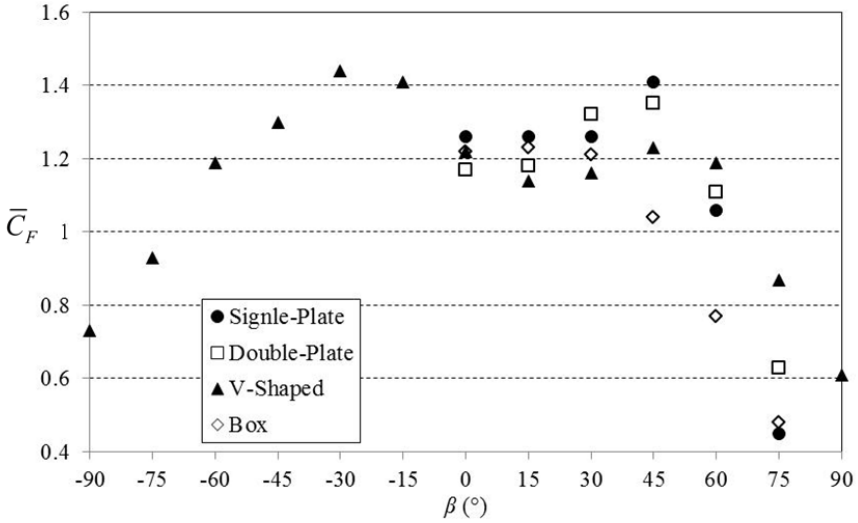

Figure 4 Mean force coefficient vs. yaw angle

While the mean force coefficients of the single-plate, double-plate and V-shaped sign models shown in Figure 4 are quite similar to those reported by Letchford [5] and Warnitchai [9] for corresponding equivalent sign models tested at the same yaw angles in similar simulated boundary layers flows, it is noteworthy that, as can be observed in , the critical (i.e., maximum) force coefficient of the box sign model, which was not tested by either Letchford [5] or Warnitchai [9], is considerably lower than those of the other three sign models, which are quite similar. This suggests that closing the sides of rectangular sign structures results in reduction of wind loading of these structures. Also, in the standards and specifications that guide the design of rectangular sign structures (e.g., [10]), the force coefficients are mostly derived based on wind tunnel tests of single-plate sign models, this means that the currently design practice likely overestimates the wind loading on box sign structures.

Table 1 Critical mean force coefficients

	single-plate	double-plate	V-shaped	box
$(\overline{C}_F)_{\max}$	1.41	1.35	1.44	1.23

To characterize the mean torque acting on the sign structure due to wind loading, an eccentricity coefficient, which is the moment arm of the torque normalized by the width of the sign model, is defined as:

$$C_{ei}(t) = \frac{T_i(t)}{F_i(t)b} \tag{3}$$

where $T_i(t)$ is the time history of the torque acting on the base of the supporting rod during the ith test run. For each sign model, a 15-minute mean eccentricity coefficient, $\overline{C}_{ei} = \text{mean}(\overline{C}_{ei}(t))$ is computed based on time histories obtained from each individual test. The mean force coefficient of a sign model is then estimated as the average of these 10 15-minute mean force coefficients. That is

$$\overline{C}_e = \frac{1}{10}\sum_{i=1}^{10}\overline{C}_{ei} \tag{4}$$

Figure 5 shows the mean eccentricity coefficients of the four sign models tested for the yaw angles tested. It can be seen that the difference in the mean force coefficients of the 4 sign models were also present in the wind-induced torque acting on them. It can be seen that for the single-plate, double-plate and box sign models, the mean eccentricity coefficients exhibit a general trend of increasing with increasing yaw angle. For yaw angles of $0°$ and $15°$, the mean eccentricity coefficients of the single-plate, double-plate and box sign models are almost the same. With increasing yaw angle, the mean eccentricity coefficients of the single-plate and double-plate sign models become much higher than those of the box sign model at the corresponding yaw angles, with the double-plate sign having the largest mean eccentricity coefficient at a given yaw angle. Compared with these three sign models, the behavior of the torque acting of the V-shaped sign model is much more complex again owning to the fact that the orientation of this sign relative to wind is asymmetrical about the yaw angle of zero degree.

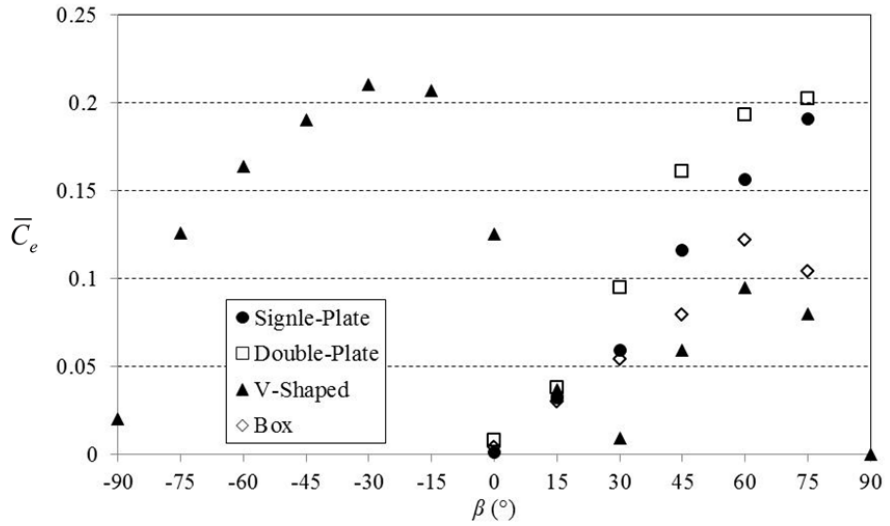

Figure 5 Mean eccentricity coefficient vs. yaw angle

Table 2 Critical mean eccentricity coefficients

	single-plate	double-plate	V-shaped	box
$(\overline{C}_e)_{\max}$	0.19	0.20	0.21	0.12

3.2 *Force and eccentricity coefficients based on extreme values*

In addition to the mean coefficients, the measurements made in the tests were also used to estimate the pseudo-steady force coefficients. For each sign model, at each yaw angle, the maximum force coefficients was identified based on the force coefficient time history obtained from each test. the 10 maximum force coefficients were then fitted to a type I Fisher-Tippett extreme value distribution using the Lieblein method [12]. The mode and dispersion of the fitted extreme value distribution were used to estimate the mean hourly extreme force coefficient as

$$\hat{C}_F = \text{mode}_{10\text{ minute}} + [0.577 + \ln(6)] \times \text{dispersion}_{10\text{ minute}} \tag{5}$$

The pseudo-steady force coefficient is then estimated as

$$\tilde{C}_F = \frac{\hat{C}_F}{G^2} \tag{6}$$

where G is the gust factor calculated based on the expression [13]

$$G = 1 + 0.42\ln(3600/t_0) \tag{7}$$

In this study, t_0 is taken as 3 seconds, the gust factor obtained using equation (7) therefore represents that associated with 3-second gusts.

Figure 6 shows the pseudo-steady force coefficients of the four sign models against the yaw angles. The mean force coefficients based on full-scale equivalent 15 minute records and the pseudo-steady force coefficients based on hourly extreme values are comparable since both time durations fall in the spectral gap (e.g., [14]). Comparison of Figure 6 with Figure 2 reveals that for the critical loading cases associated with small yaw angle (i.e., less then $60°$), the pseudo-steady force coefficients for all four models are close to the corresponding mean force coefficients. At larger yaw angles, the pseudo-steady force coefficients for a given sign model differs from the corresponding mean coefficients because for these yaw angles, the effect of the structure-induced turbulence becomes more pronounced.

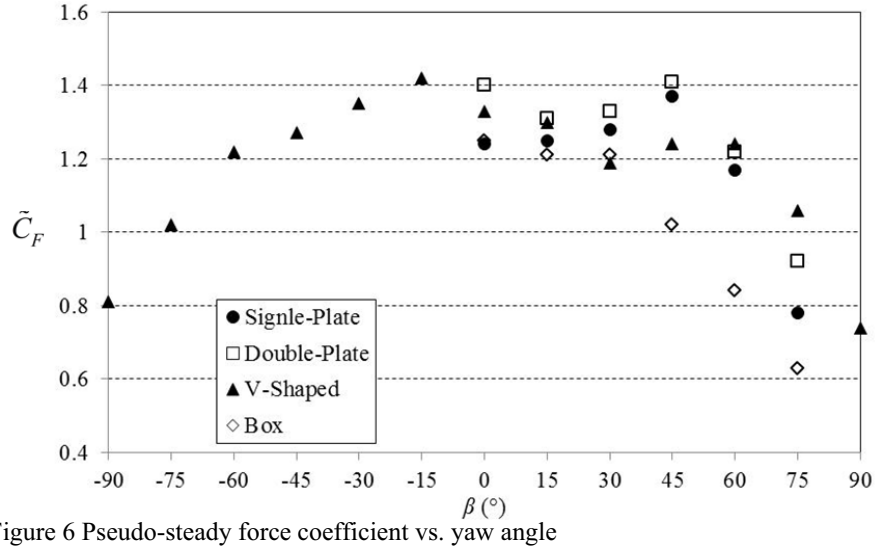

Figure 6 Pseudo-steady force coefficient vs. yaw angle

Table 3 lists the critical pseudo-steady force coefficients for the four sign models tested. It is apparent again that while the critical pseudo-steady force coefficients of the single-plate, double-plate and V-shaped sign models are close, that of the box sign model is considerably lower. This again suggest that it is likely to be conservative if force coefficients derived based on study of wind loading on single-plate signs are used to design box sign structures.

Table 3 Critical pseudo-steady force coefficients

	single-plate	double-plate	V-shaped	box
$(\tilde{C}_F)_{\max}$	1.37	1.41	1.42	1.25

Using the same procedure used to estimate the hourly extreme force coefficients, the hourly mean extreme force ($\hat{F}$) and absolute torque ($|\hat{T}|$) acting on a sign model. These mean extreme values can then be used to estimate a mean extreme value based eccentricity coefficient for this sign model:

$$\tilde{C}_e = \frac{|\hat{T}|}{\hat{F}b} \tag{8}$$

Figure 7 shows the mean extreme value based eccentricity coefficients against the yaw angles tested. It is evident that for the single-plate, double-plate and box sign models, the eccentricity coefficients increase with increasing yaw angle. It also can be seen that except for the case of zero yaw angle, for the same yaw angle, the single-plate and the double-late sign models have higher eccentricity coefficients than the box sign model. In addition, the graph suggests that, as in the case of mean eccentricity coefficient, the relationship between the mean-extreme value based eccentricity coefficients of the V-shaped sign and the yaw angles are much more complex.

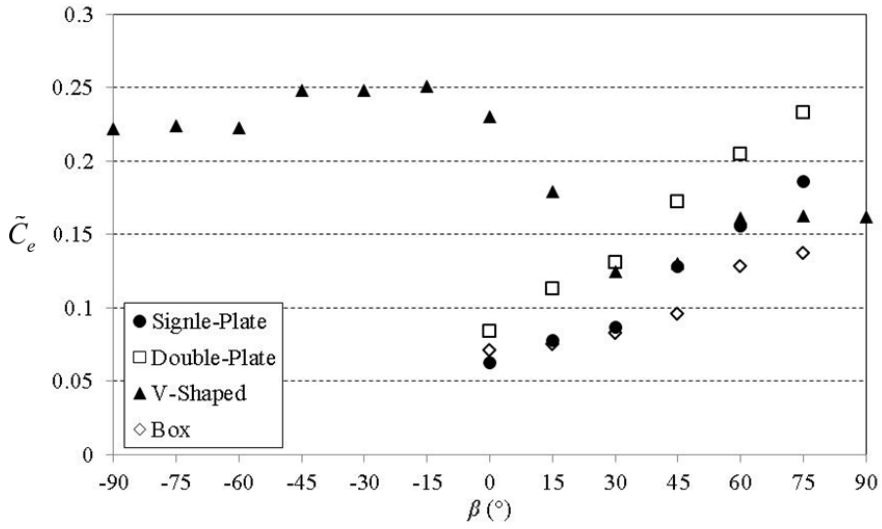

Figure 7 Mean extreme value based eccentricity coefficient vs. yaw angle

For a typical design situation, the design extreme torque is likely calculated based on the design extreme force, which is the maximum extreme force for all the possible yaw angles. For codification purposes, an alternative synthesized eccentricity coefficient can be defined as

$$\tilde{C}_e' = \frac{|\hat{T}|}{\hat{F}_{\max} b} \tag{9}$$

in which $\hat{F}_{\max}$ is the maximum of the mean extreme force for all wind directions.

Figure 8 depicts the synthesized eccentricity coefficients against the yaw angles. This graph indicates that for a given yaw angle, the two sign models consist of two plates as sign faces, i.e., the double-plate sign and the V-shaped sign generally have larger synthesized eccentricity coefficients. It also suggested that although the synthesized eccentricity coefficients of the single-plate sign model and the box sign model are close for small yaw angles (i.e., up to $30°$), with increasing yaw angle, the synthesized eccentricity coefficients of the single-plate sign model becomes much larger than the corresponding ones of the box sign model.

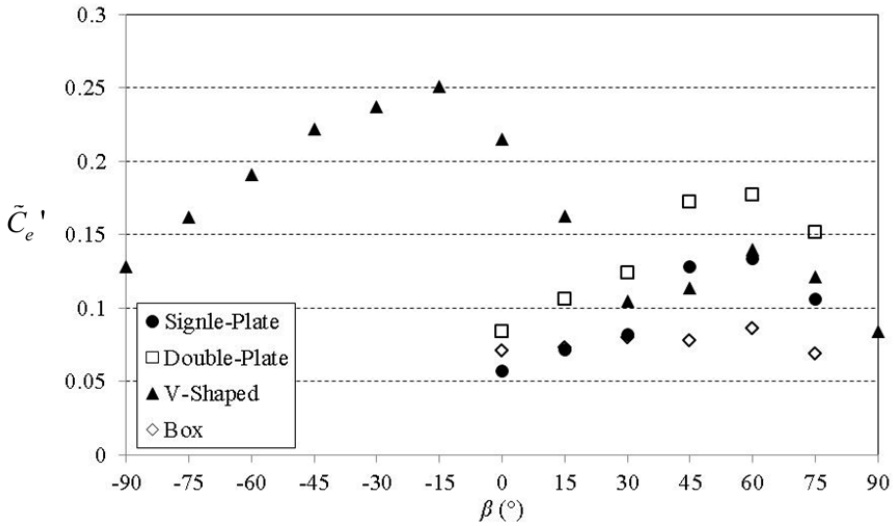

Figure 8 synthesized eccentricity coefficient vs. yaw angle

Table 4 lists the critical (i.e., maximum) synthesized eccentricity coefficients for the four sign models tested. Except that of the V-shaped sign model, these synthesized eccentricity coefficients are smaller than that specified in a typical standard. For example, in ASCE 7-10, the eccentricity coefficient recommended for the design of rectangular sign structures is 0.2. This value is obviously overly conservative for box sign structures similar to full-scale equivalent of the box sign model tested in the wind tunnel.

Table 4 Critical synthesized eccentricity coefficients

	single-plate	double-plate	V-shaped	box
$(\tilde{C}_e')_{max}$	0.13	0.18	0.25	0.09

4 CONCLUSIONS

Models of four types of sign structures with rectangular faces are tested in a wind tunnel as a benchmark study of wind loading on rectangular sign structures. The data obtained from the wind tunnel tests were used to evaluate the wind-induced force acting on the models represented by mean and pseudo-steady force coefficients of these four types of structures as well as the wind-induced torque about the vertical sign axis represented mean and mean-extreme loading based eccentricity coefficients. It is revealed that for the four models with the same sized sign faces, different configuration of the signs can result in quite different loading on the structures. In particular, it was found that rectangular sign structures with all sides closed are subjected to less wind loading in terms of both horizontal force and torque about the vertical axis than are

signs consisting of either a single-plate or two plates with open sides. This means that design specifications derived based on study of wind loading of single-plate sign structures can potentially overestimate the wind force acting on box type sign structures. In addition, the outcome of the study also suggests that current design practice potentially overestimate the torque acting on many types of rectangular sign structure.

5 REFERENCES

1 Simiu E, Scanlan RH. Wind effects on structures. 3rd edition ed. New York, NY, USA: John Wiley and Sons; 1996.

2 Bearman PW. An investigation of the forces on flat plates normal to a turbulent flow. Journal of Fluid Mechanics. 1971;46:177-98.

3 Letchford CW, Holmes JD. Wind loads on free-standing walls in turbulent boundary layers. Journal of Wind Engineering and Industrial Aerodynamics. 1994;51:1-27.

4 Letchford CW, Robertson AP. Mean wind loading at the leading ends of free standing walls. Journal of Wind Engineering and Industrial Aerodynamics. 1999;79:123-34.

5 Letchford CW. Wind loads on rectangular signboards and hoardings. Journal of Wind Engineering and Industrial Aerodynamics. 2001;89:135-51.

6 Robertson AP, Hoxey RP, Richards PJ. Design code, full-scale and numerical data for wind loads on free-standing walls. Journal of Wind Engineering and Industrial Aerodynamics. 1995;57:203-14.

7 Robertson AP, Hoxey RP, Short JL, Ferguson WA, Blackmore PA. Wind loads on boundary walls: Full-scale studies. Journal of Wind Engineering and Industrial Aerodynamics. 1997;69-71:451-9.

8 Robertson AP, Hoxey RP, Richards PJ, Ferguson WA. Full-scale measurements and computational predictions of wind loads on free-standing walls. Journal of Wind Engineering and Industrial Aerodynamics. 1997;67-68:639-46.

9 Warnitchai P, Sinthuwong S, Poemsantitham K. Wind Tunnel Model Tests of Large Billboards. Advances in Structural Engineering. 2009;12:103-14.

10 ASCE. Minimum Design Loads for Buildings and Other Structures (ASCE7-10). Reston, VA, USA: American Society of Civil Engineers; 2010.

11 Kaimal JC, Wyngaard JC, Izumi Y, Coté OR. Spectral characteristics of surface-layer turbulence. Quarterly Journal of the Royal Meteorological Society. 1972;98:563-89.

12 Lieblein J. (1974). Efficient methods of extreme value methodology. (NBSIR 74-602). Washington, DC., National Bureau of Standards.

13 Cook NJ. The Designer's Guide to Wind Loading of Building Structures, Part 2: Static structures. London: BRE/Butterworths; 1990.

14 Holmes JD. Wind loading of structures. 2nd ed. London and New York: Taylor & Francis; 2007.

The Seventh International Colloquium on Bluff Body Aerodynamics and Applications (BBAA7)
Shanghai, China; September 2-6, 2012

Instantaneous forces and moments on inclined flat plates

Xavier Ortiz, Arman Hemmatti, David Rival, David Wood
Dept Mechanical and Manufacturing Engineering, University of Calgary, Canada

ABSTRACT: This work was motivated by the need to improve knowledge of extreme wind loads on photovoltaic structures mounted on flat roofs at the high angles required in high latitudes. Traditionally these loads have been assessed from pressure distributions on model installations in an atmospheric boundary layer tunnel. Because we have no access to such a facility and because of concern over the possible interaction of lift and drag in producing the overturning moment, it was decided to measure the instantaneous forces and moments on model flat plates over a range of inclination and distance from the floor. The average lift and drag agree well with the available measurements in ESDU 70015 [1]. The instantaneous forces appear most complex for the smaller aspect ratios. As the wind tunnel floor is approached, there is a reduction in high frequency components. It is shown that the centre of the late is close to the centre of pressure for nearly all cases, but the fluctuation level of the pitch (overturning) moment is large.

KEYWORDS: Flat plate lift and drag, instantaneous forces, PV wind loads, unsteady moments

1 INTRODUCTION

This paper is motivated by the need to understand the extreme wind loads on photovoltaic (PV) modules and arrays retrofitted to flat roofs at high angles of inclination. PV arrays can be installed in either closed or open frames; only open frames are considered here. The support structures or frames are usually held in place using ballast, or occasionally by anchoring. The usual recommended ballast of approximately 100 kg per m^2 of PV area (which equates to 100 kg per 170 W of maximum electricity production) has exceeded the structural loading capacity of the roof for a number of potential installations around Calgary.

These wind loadings can be estimated using international standards, but neither the standard CEN/EN1991-1-4 [2] nor ASCE/SEI 7-10 [3], give explicit guidance for calculating the wind load. For Canada, the National Building Code [4] and the Alberta Building Code [5] are similarly unspecific regarding wind loads on PV structures mounted on flat or pitched roofs. The Dutch standard NVN 7250-2007 [6], gives specific guidance for determining forces and moments exerted on PV modules and arrays mounted on flat roofs, based on the pressure coefficients obtained from the experiments at TNO on PV arrays with an inclination angle of 35°. Blackmore [7] is a guide to calculate wind loads in UK, but it is not included in the standard BS 6399 Part 2 [8]. None of these standards uses direct force or moment measurements of individual modules.

Most wind engineering studies have concentrated on measuring the average pressure distribution on model modules and arrays and inferring the overturning moments, eg Miller & Zimmerman [9] and Tieleman *et al.* [10]. Some authors, eg Chevalier and Norton [11] measured the moments as well, but the data is limited: the pitch (overturning) moment was not reported. More recently, Radu *et.al.* [12] determined wind force coefficients on solar collector arrays mounted on a typical five story building.

Between 2005 and 2008, the European Active Roofer program carried out wind tunnel experiments in pitched and flat roofs to determine the wind loads. Those results were incorporated in the latest version of NVN 7250 [6] and Ref. [7]. Geurts and van Bentum [13] show how to use Ref. [2] to calculate wind loads on PV arrays mounted on flat roofs.

All the published studies determine wind loads on PV structures as function of average pressure coefficients, in order to incorporate these values into the equations specified in the current standards. Given the advent of accurate, fast response force and torque sensors, such as the one described in the next section, it is now easy to measure the wind loads directly, and so avoid some of the potential errors involved in inferring forces and moments from measured pressures. For example Ref. [6] assumes the centre of pressure of an inclined module is at the equivalent of the quarter-chord position, and assumption we show below to be significantly in error at high angles.

Flat plates are also the fundamental geometries for a number of other wind engineering and aerodynamic applications. For example, it is common in wind turbine design to account for blade behaviour at high angles by invoking the lift and drag properties of a thin flat plate at the appropriate aspect ratio, *AR*. The determination of the forces on, and flow around such plates has received little attention since the pioneering experiments of Fage & Johansen [14]. It is to be expected that the vortex shedding processes depend sensitively on aspect ratio and, of course the wake flow impinges on downwind modules. Investigation of the vortex dynamics is underway but is not reported herein.

2 WIND TUNNEL EXPERIMENTS

Wind tunnel experiments have been carried out in the Environmental Wind Tunnel at University of Calgary. This tunnel has a cross-section of 0.76 m x 1.37 m. The nominal wind speed was 19 m/s measured using a pitot-static tube connected to a micro-manometer. The model sizes were chosen to keep the blockage below 3.5 %. Table 1 shows the eight different *AR*s that were tested. $AR = 0.6$ represents a typical single PV module in "portrait" orientation, $AR = 1.66$ is the same module in "landscape", while $AR = 3.6$ (see Figure 1(a)) represents an array of six modules in portrait, a common grouping. Measurements were made at eleven different angles of attack, α (0°, 25°, 35°, 40°, 45°, 50°, 55°, 60°, 70°, 80°, 90°) and five different clearances between the model and the wind tunnel floor, *H*. In practice, the wind direction can vary significantly from being parallel to the *x*-axis as indicated in Figure 1, but this is the only direction studied so far.

The flat plates were attached to a sting to simulate an open support structure. The selected sting was an aluminum symmetrical streamline strut tubing of very high rigidity with chord of 68.5 mm and maximum thickness of 29 mm. Instantaneous forces and moments were measured by an ATI multi-axis force/torque sensor holding the sting to a solid frame. The force sensing ranges was 65 N in the x-direction and the y-direction, and, 200 N in the z-direction as defined in Figure 1. The moment sensing range was 5 Nm. Resolution was 1/80 N for force and 10/13333 Nm for torque. The frequency response was up to 40 kHz per channel. The sensor output signal in the range of +/- 10 V was connected to a National Instruments data acquisition board NI-DAQ USB 6212. The resolution of the board is 16 bit. One bit is used to transmit the sign (+ or -) of the signal, the other 15 are used to digitize the instantaneous value per channel, corresponding to a resolution of 0.61 mV. The sampling rate was 1 kHz. Forces and Moments were recorded for 60 s using the NI LabView Signal Express Software. MatLab was used for data reduction.

The $\boldsymbol{x}$ co-ordinate (and drag) is in the free-stream direction, $\boldsymbol{y}$, the direction of lift, is normal, and $\boldsymbol{z}$ is the spanwise direction parallel to the shortest side of the models for $AR < 1$ and the longest side when $AR > 1$, as shown in Figure 1(a). All moments are about the centre of the flat plate.

Forces and Moments acting on the sting were measured prior the tests with the flat plate to allow these to be subtracted from the averaged measurements.

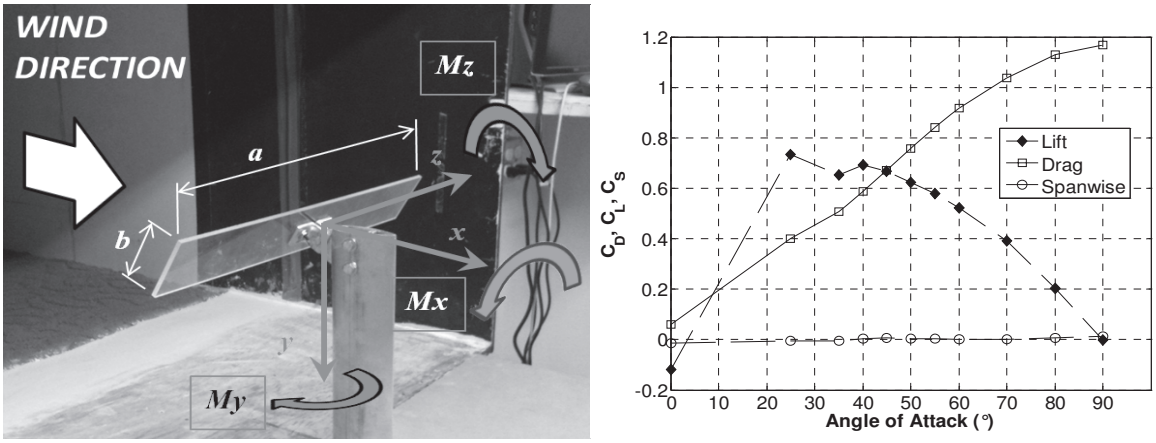

(a) (b)

Figure 1: (a) Experimental stand showing a flat plate of AR = 3.58; (b) Force coefficients as a function of angle of attack for AR =3.58 in the free-stream .

The experimental set-up was checked by measurements of normal plates in the free stream. The mean results are summarized in Table 1 where the drag coefficient is compared to the equation given by ESDU [1]:

$$C_D = \quad 1.11 + 0.02(a/b + b/a) \tag{1}$$

C_S is the spanwise force coefficient, C_L is the lift force coefficient, a is the breadth and b is the height of the flat plate. Re is the Reynolds number based on the shortest dimension at each AR. Equation (1) expresses the fact that, in the absence of Re effects, the drag on a normal plate of $AR = a/b$, is the same as on a plate of the "complementary" $AR = b/a$.

Table 1: Measured forces and moments on a normal flat plate in the free stream.

AR	a(m)	b(m)	Re	C_D	C_D from Eq. (1)	C_L	C_S
0.40	0.094	0.232	1.18×10^5	1.077	1.157	0.0168	0.0124
0.60	0.142	0.236	1.78×10^5	1.074	1.145	0.0164	-0.023
1.00	0.168	0.168	2.10×10^5	1.067	1.140	0.0096	-0.030
1.66	0.236	0.142	1.78×10^5	1.081	1.145	0.0111	-0.015
2.48	0.232	0.094	1.18×10^5	1.101	1.157	0.1133	0.0004
3.58	0.364	0.101	1.27×10^5	1.169	1.178	0.0023	-0.014
6.00	0.400	0.066	8.27×10^4	1.155	1.225	0.0201	0.0039
9.00	0.457	0.051	6.39×10^4	1.182	1.281	0.0227	0.0148

All entries in the last column should be zero. They are not, but are significantly smaller than the drag coefficient. The measured C_D is in reasonable agreement with Equn (1); the difference is 6.9% at the lowest AR and 7.7% at the highest.

Additional measurements of the average force coefficients as a function of angle of attack α, for AR =3.58 are shown in Fig.1(b). The results are unremarkable but further demonstrate the adequacy of the experimental arrangement. Similar data were obtained for all plates.

3 TIME-AVERAGED RESULTS

Figures 3 and 4 summarize the time-averaged results in terms of the mean lift and drag coefficients determined using the model surface area *ab*, *not* the projected area. Figure 3 shows the free stream results where it can be seen that the low AR plates exhibit a local peak in lift around 45°. This peak disappears at higher AR. Although not shown, the lift (L) and drag (D) closely follow the relation $\tan \alpha = D/L$ that comes from assuming that the loads are due solely to the pressure distribution.

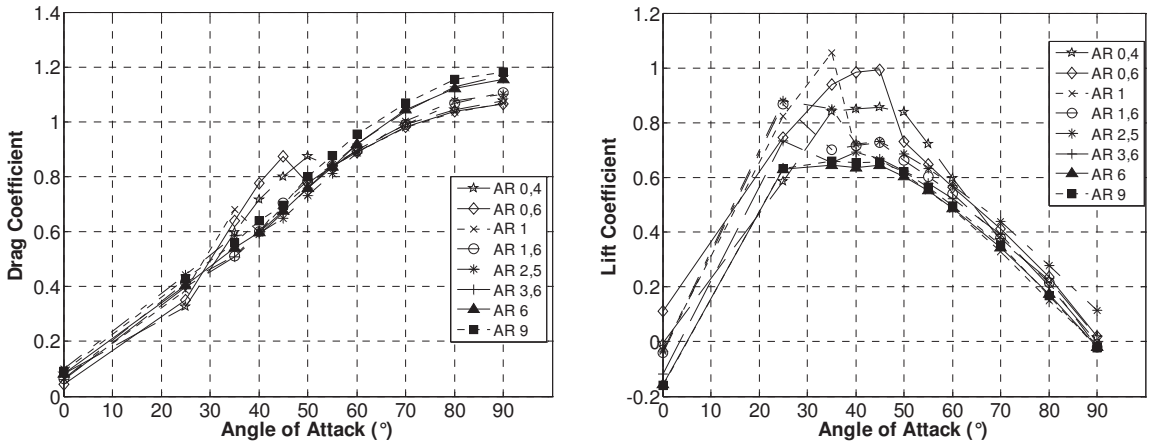

Figure 3: Free stream Drag and Lift coefficient as a function of AR and α.

Figure 4 shows the same coefficients at closest proximity to the tunnel floor. In all cases the drag is reduced but the lift behaviour is more complex and non-monotonic in AR.

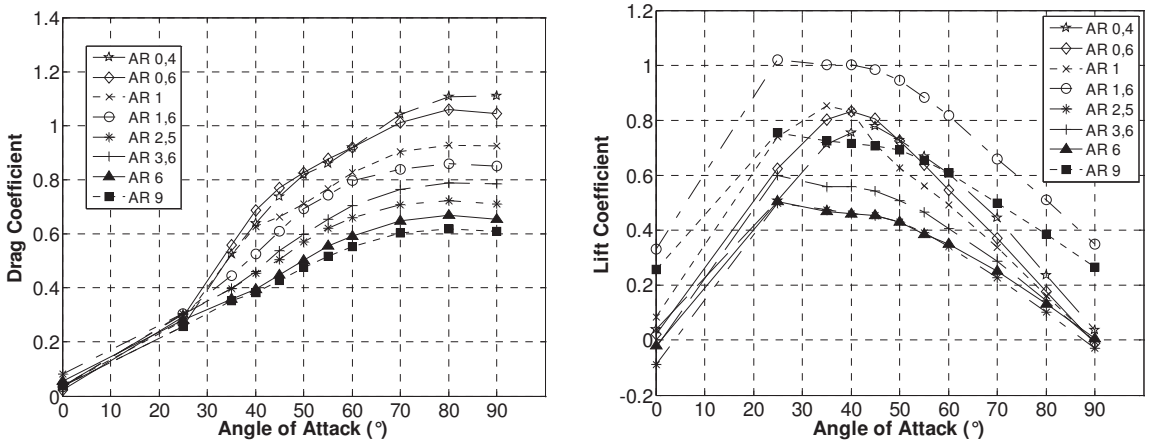

Figure 4: Drag and Lift coefficient at Minimum Clearance as a function of AR and α.

4 INSTANTANEOUS RESULTS

The following figures show a small sample of the extensive time-dependent measurements. Figures 5 and 6 show typical traces of the instantaneous drag for two widely different *AR*s in the free-stream and at mimimum clearance. There are clearly dominant frequencies in all traces but the free stream traces have more high frequency content. This may be due to the increased importance of sting drag which is a subject of current experimentation.

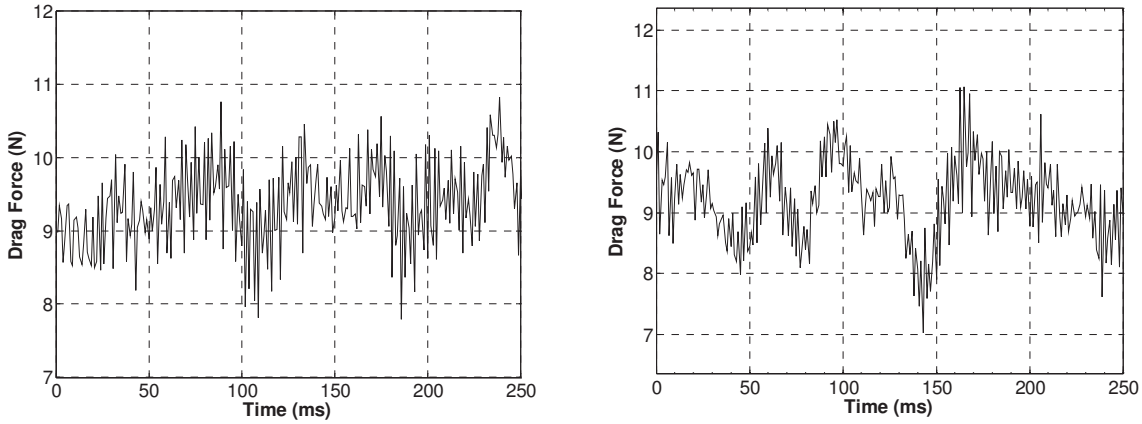

Figure 5: Instantaneous drag in the free stream and at minimum clearance for $AR = 0.60$ and $\alpha = 90°$.

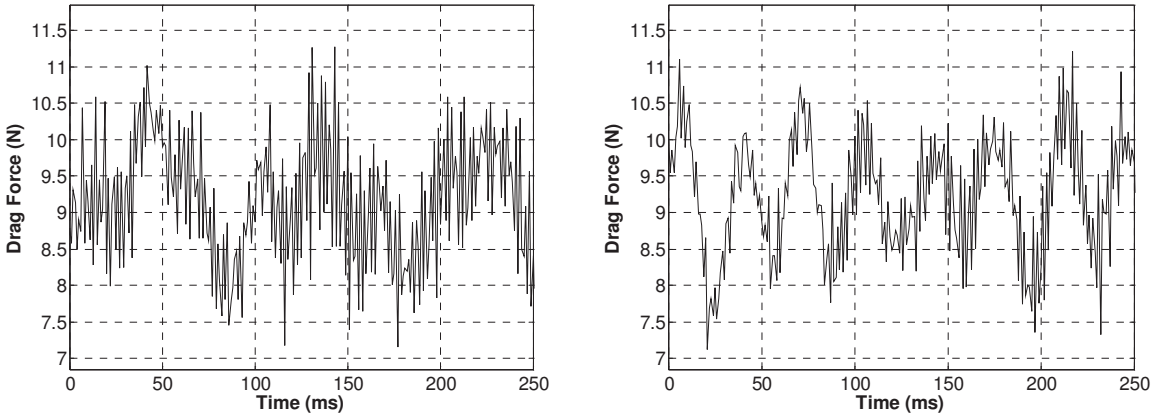

Figure 6: Instantaneous drag in the free stream and at minimum clearance for $AR = 3.58$ and $\alpha = 90°$.

Similar traces for the pitch moment for $AR = 0.6$ in Figure 7 again show the high frequency content in the free-stream is reduced at minimum clearance.

The dominant frequencies are clearly seen in the spectral densities in Figures 8 and 9. In figure 8, the peaks in the drag spectra at 11 and 18 Hz are replicated in the pitch moment as is the (probable) second harmonic at 22 Hz, although to a lesser extent. The strong peak in the drag only around 30 Hz is thought to be due to vortex shedding from the sting and will be investigated further with new, thinner stings.

The spectra become simpler as the *AR* decreases, Figure 9, as is evident from the previous figures, although the strong 30 Hz component remains.

One major advantage of measuring the moments directly is that assumptions need not be made about the location of the centre of pressure as is done in most standards covering wind loads on PV structures.

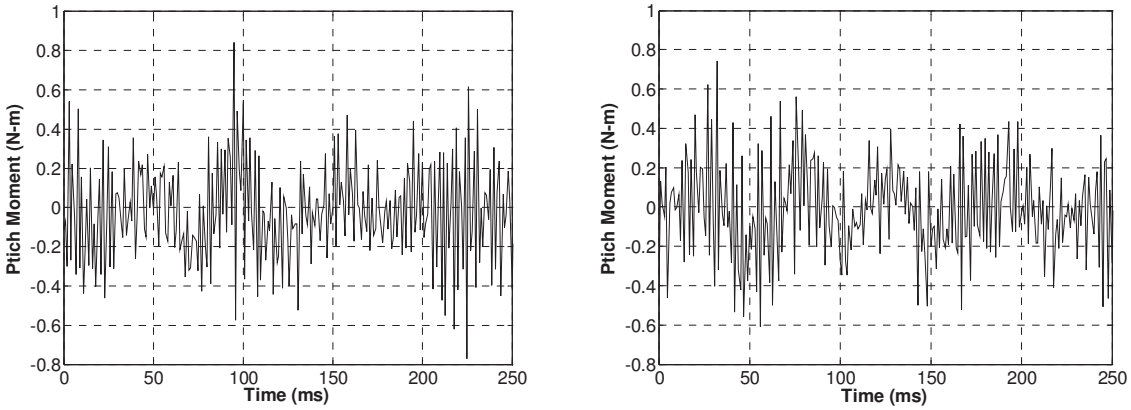

Figure 7: Instantaneous pitch moment in the free stream and at minimum clearance for $AR = 0.6$ and $\alpha = 90°$.

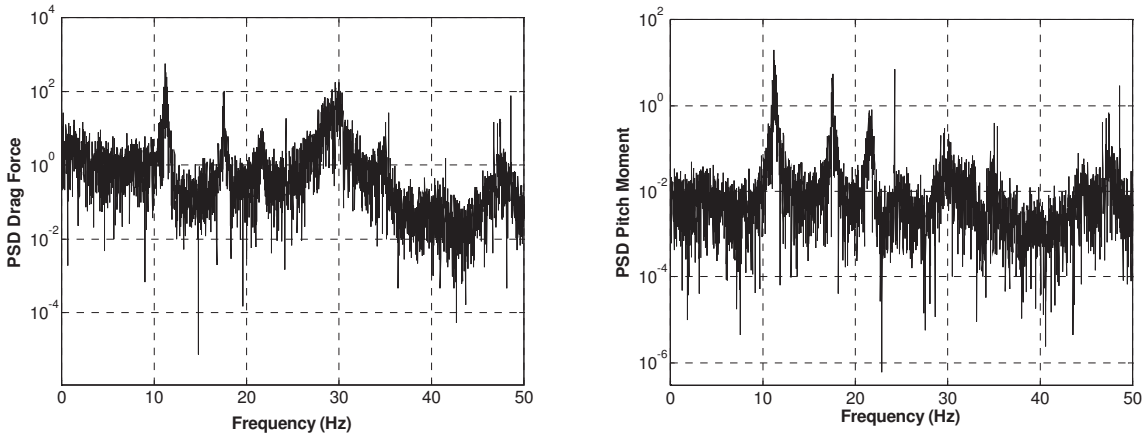

Figure 8: Power spectral density of drag and pitch moment in the free-stream for $AR = 0.6$ and $\alpha = 90°$.

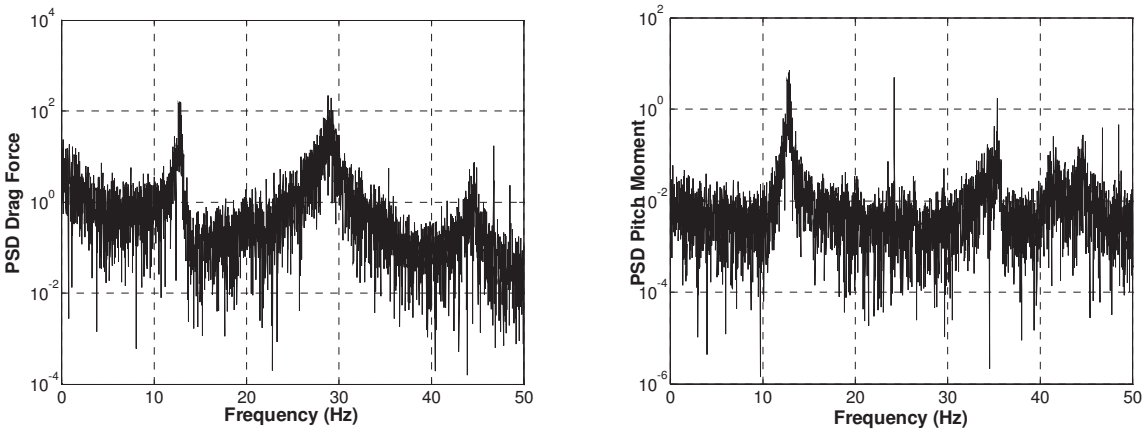

Figure 9: Power spectral density of drag and pitch moment in the free-stream for $AR = 3.58$ and $\alpha = 90°$.

Figure 10 shows the average free-stream and minimum clearance pitch moments compared to those calculated from the mean forces assuming the centre of pressure was the midpoint of the

plate. Although this assumption over-estimates the pitch moment at minimum clearance, it is remarkably accurate. Perhaps of greater significance for wind engineering purposes are the large variations in the instantaneous moments as indicated by the 95% intervals for the measurements. This suggests that the relationship between mean moment and the extreme moment at extreme wind speed needs re-evaluation.

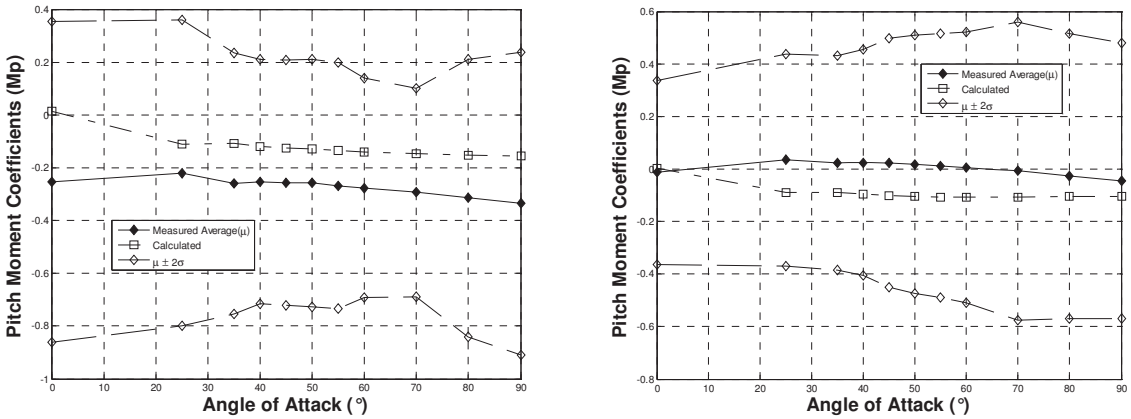

Figure 10: Mean pitch moment in the free-stream and at minimum clearance for AR= 3.58 and α=90°. The solid diamonds show the actual moment, the open squares show the moment calculated from the mean forces by assuming the centre of pressure is the middle of the plate. The open diamonds indicate the fluctuation level as measured by the position of two standard deviations from the mean.

5 CONCLUSIONS

The present experiments have investigated the instantaneous forces on thin, rectangular flat plate over a wide range of aspect ratios, angles of attack, and distances from the wind tunnel floor. The primary application was to determine extreme wind loads on photovoltaic structures at high angles. The mean forces agree well with the expectations of two-dimensionality and with the available previous measurements, mainly on normal flat plates in the free stream. In the free stream, an increase in aspect ratio increased the low frequency contribution to the instantaneous drag and simplified the spectra. As the wind tunnel floor is approached, the high frequency fluctuations reduce significantly. It is not clear, however, at this stage the extent to which the relatively thick sting contributed to these variations. For example, removing some of the high frequency content of the forces may be due to the reduced effect of the sting. Surprisingly the assumption that the centre of the plate is also the centre of pressure is remarkably accurate for the entire angle of attack range that was studied given the large fluctuation levels in the instantaneous pitch moments.

ACKNOWLEDGMENTS

This work is supported by the Canadian National Science and Engineering Research Council under the Industrial Research Chairs and Discovery programs.

REFERENCES

1 ESDU 70015, Fluid Forces and Moments on Flat Plates, Engineering Sciences Data Unit, ESDU International, London, UK, September, 1970
2 CEN/EN1991-1-4 EUROCODE 1: Actions on Structures – – Part1-4: General Actions - Wind Actions, European Committee for Standardization, Europe, 2005.
3 ASCE/SEI 7-10: Minimum Design loads for buildings and other structures. American Society of Civil Engineers, USA, 2010.
4 National Building Code of Canada, Canadian Commission on Building and Fire Codes, National Research Council of Canada, Twelfth Edition, Canada, 2005.
5 Alberta Building Code, National Research Council of Canada, Canada, 2006.
6 NVN 7250-2007-Zonne-energiesystemn – Integratie in daken en gevels – Bouwkundige aspecten, Nederlands Normalisatie-instituut, The Nederlands, 2007.
7 P. Blackmore, Wind Loads on Roof-based Photovoltaic Systems. BRE Digest 489. Building Research Establishment BRE, Center for Structural and Geotechnical Engineering, UK, 2004.
8 British Standard BS 6399 Part 2: 1995, Loading for Buildings, Part 2. Code of practice for wind loads, UK, 1995.
9 R. D. Miller, D.K. Zimmerman, Wind Loads on Flat Plate Photovoltaic Array Fields, JPL Contract No. 954833, Low Cost Solar Array Project Engineering Area, Phase III Final Report, USA, April, 1981.
10 H.W. Tieleman, R.E. Akins, P.R. Sparks, An Investigation of Wind Loads on solar collectors, College of engineering, Virginia Polytechnic Institute and State University, Blacksburg, Virginia 24061, USA, January, 1980.
11 H.L. Chevalier, D.J. Norton, Wind Loads on Solar-Collector Panels and Support Structure. Texas A&M University, Contract No. EY-76-S-05-5130, USA, October, 1979.
12 A. Radu, E. Axinte, C. Theohari, Steady Wind Pressures on Solar Collectors on Flat-Roofed Buildings, Journal of Wind Engineering and Industrial Aerodynamics, 23(1986) 249-258.
13 C.P.W. geurts, C.A. van Bentum, Wind Loads on Solar Energy Roofs, TNO Built Environment and Geosciences, Delft, The Netherlands, HERON Vol.52 (2007) No.3.
14 A. Fage, F.C. Johansen, On the Flow of Air Behind and Inclined Flat Plate of Infinite Span, Proceedings of the Royal Society of London. Series A, Containing Papers of a Mathematical and Physical Character, Vol. 116, No. 773 (Sep.1, 1927), pp. 170-197.

The Seventh International Colloquium on Bluff Body Aerodynamics and Applications (BBAA7)
Shanghai, China; September 2-6, 2012

Wind tunnel studies on the effects of porous elements on the aerodynamic behavior of civil structures

M. Belloli[a], D. Rocchi[a], L. Rosa[a], A. Zasso[a]

[a] Politecnico di Milano, Dipartimento di Meccanica, via La Masa 1, 20156 Milano, Italy

ABSTRACT: This paper deals with the role of the porosity on the aerodynamic behavior of two civil structures: the Spire, a tall slender tower 80.44m high, and the buttresses of a tall building. The Spire is an original architectonic complement. Its covering, made of perforated steel plates, forms and intricate three-dimensional spiral characterized by five different diameters. The buttresses connect the building core around one fourth of its height to viscous dampers at their bottom, in order to increase the overall damping value of the building. The geometry of the buttresses is characterized by a variable cross-section along the longitudinal axis, permeable to the air. Wind tunnel tests on a 1:50 scaled rigid and aeroelastic model of the Spire and on a 3:10 scaled sectional model of the buttress were carried out in order to investigate the aerodynamic behavior of the structures using different geometry of the porosity or replacing with not-porous surfaces. The analysis carried out highlights the great influence of the porosity in the dynamic response of both structures, mainly in relation to vortex shedding induced vibrations.

KEYWORDS: Porous surface; Vortex Shedding; Wind Tunnel Tests; Wind Loads; Aeroelastic Model; High Slender Tower.

1 INTRODUCTION

Nowadays porosity has a wide range of application in engineering and civil fields. In agricultural, porous screens have been largely used for many years in many functions: temperature regulating, shading, wind-breaking, anti-hail, anti-frost or for preventing the entrance of insects or birds. In some ventilation system, screens are used to control dust as filter function. As an alternative to these historical functions, the porosity finds new applications in civil structures. In fact modern buildings have required to reach higher energetic standards and this is achieved not only, using new construction materials, but also applying accessory elements to the structures. Porous structural elements are ones of the most common, since they have many functionalities: architectural design, temperature regulating function, shading function, wind-breaking effect and, last but not least, vortex shedding mitigation.

In literature there are many experimental and numerical CFD studies about flow through porous surface, e.g. [1,2,3]. Most of them regard wind loads on structures such as greenhouses, panels or roof [4,5,6,7,8,9]; these results reveals that the wind loads on perforated structure are generally lower than those on same non-porous surfaces. More systematic studies regard flow around porous cylinders [10,11]: in particular they show how vortex shedding can be reduced or suppressed manipulating the flow around the cylinder through the application of suction or blowing. Not a great number of experimental data are on the contrary available about wind interaction with permeable accessory elements in civil structures. For instance some recent studies attest that the porosity of a surface could modifies the wake formation and reduces the intensity of the vortex shedding and the overall crosswind load [12,13].

This paper deals with the role of the porosity on the aerodynamic behavior considering as illustrative examples two civil structures: the Spire, a tall slender tower 80.44m high, and the buttresses of a tall building. Wind tunnel tests were carried out in order to investigate the aerody-

namic behavior of the structures using different geometry of the porosity or replacing with not-porous surfaces. This analysis is very interesting as the structures could be subjected to atmospheric icing which can make non-porous parts of the perforated panels and so change their aerodynamic behavior.

1.1 *The Spire*

The Spire, which is erected on the top of a 139m new tall building, consists of a supporting lattice framework structure 80.44m high, covered with perforated steel plates. Considering the height of the building, the Spire maximum elevation from the ground is 220m (Figure 1). The external cover is not regular, but forms an intricate three-dimensional spiral characterized by five different diameters which decrease along the height of the structure. Changing the diameter along the height of the structure mitigates the vortex shedding phenomenon, but in the present case each section of the spire has an adequate length to introduce energy to the whole system and to induce oscillations of the spire to lead to fatigue damages [14,15].

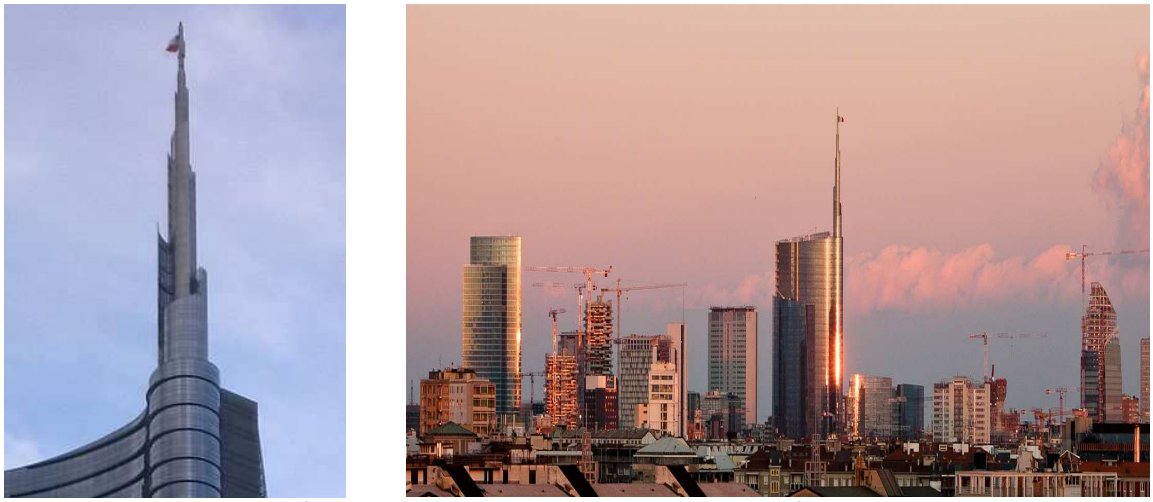

Figure 1. The Spire at the top of the new tall building. Its maximum elevation from the ground is 220m.

1.2 *The buttress*

The second structure studied in this paper are the long buttresses of a tall building, Figure 2(a). This building is an office tower 220m tall and it has a rectangular floor plan of 61.5m x 24m. The tower is characterized by two couples of external steel buttresses inclined with respect to the vertical axis and connected to the tower core around one fourth of its height along the front and the back facades. The buttresses are connected to their bottom ends to viscous dampers in order to increase the overall damping value of the building with respect to the minor side, providing beneficial effect to the base moment.

The length of the buttress is 61.6m end connections included. Their geometry is characterized by a variable cross-section along the longitudinal axis made by 3 Circular Hollow Section (CHS) interconnected rigidly by steel plates (Figure 2(b)); between the transverse connections the area within the three longitudinal CHS is permeable to the air. At mid span the three CHS reach the maximum c/c distance of 1.2m (see section 3, Figure 2); whereas at the two ends the three sections converge into a single circular tube (see sections 1 and 2, Figure 2).

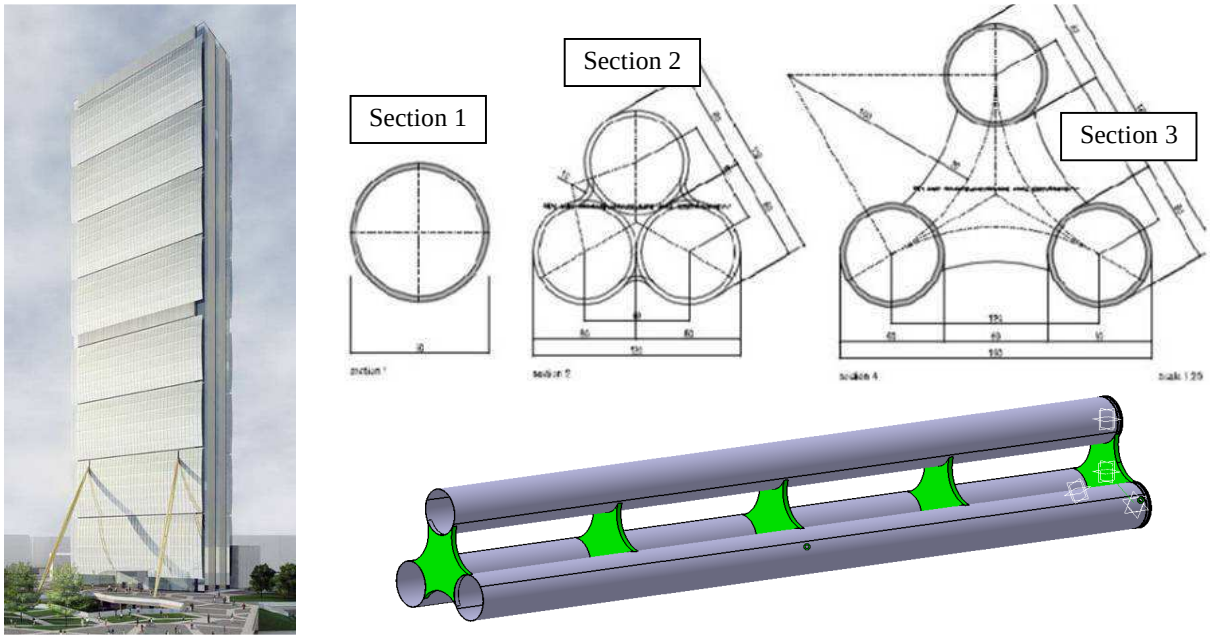

Figure 2. The 220m high tall building. (a) Global view. (b) Buttress geometry and transverse typical sections. The 3D view represents the central part of the buttress (section 3).

2 EXPERIMENTAL SET-UP

Wind tunnel tests were performed at the 1.5MW closed-circuit wind tunnel at the Politecnico di Milano, Italy. The large dimensions of the boundary layer test section (4m high, 14m wide and 36m long) allows a very large geometry scale to be used while maintaining lower blockage effects. The tests were performed in smooth flow condition (turbulence intensity I_u< 2%) which is considered on the safe side with respect to instability and vortex shedding excitation.

2.1 *The model of the Spire*

The experimental tests were performed using two models of the Spire: a rigid and an aeroelastic model. In this work we will focus on the results obtained on the aeroelastic model. A comparison between the results from the two models, to verify the presence of possible aeroelastic effects, can be found in [16], while a study about the local wind loads on the permeable panels by means of pressures measurements can be found in [17]. The large dimensions of the test section allowed to choose a geometry scale λ_L = 1/50. The aeroelastic model was designed as a spine model, adopting the Froude similitude criteria for scale reduction: the elastic properties of the real structure were reproduced by means of an aluminum bar made up by rectangular section of four different dimensions. An external cover, constituted of 16 modules, was adopted to reproduce the wind interaction shape and to match the correctly scaled mass. A more detailed description about the aeroelastic model set-up can be found in [17], while Figure 3(a) shows the model in the test section. Great care was taken for scaling the external surface geometry and porosity: in order to guarantee the kinematic similitude the perforated panels must be scaled not geometrically but the same loss coefficient must be maintained [7]. The loss coefficient k is defined as:

$$k = \frac{p_u - p_d}{\rho U^2 / 2} \tag{1}$$

being p_u and p_d respectively the upstream and the downstream static pressure on either side of the grid, ρ is the density of the air and U is the mean wind speed. This coefficient is a indicator of the resistance to flow through a porous surface, including the effects of the open area β (defined as the ratio between the area open to through flow and the total area of the panel) as well as the shape of the perforations. The pressure loss coefficients were evaluate experimentally in a smaller wind tunnel, in which its entire round cross section (diameter = 400mm) was covered by the grid being tested.

(a) (b)

Figure 3. (a) The aeroelastic model in wind tunnel test section. (b) The perforated panels on the real structure.

In the real structure the panels have round hole perforation (radius 7.5mm) with triangular pitch of 21mm, Figure 3(b). Their open area β is 46.3% and the loss coefficient k varies between 4.5 and 4.8 (experimentally evaluated). On the models round hole perforated plates with radius 0.4mm and triangular pitch of 1mm were used. These plates were electrical discharge machining formed, they had an open area β=58% and a loss coefficient k very close to the real structure ($4<k<4.5$).

Global forces measurement is carried out by means of a dynamometric six-components force-balance linked at the base of the model. The exposure angle and the reference system is shown in Figure 4(a).

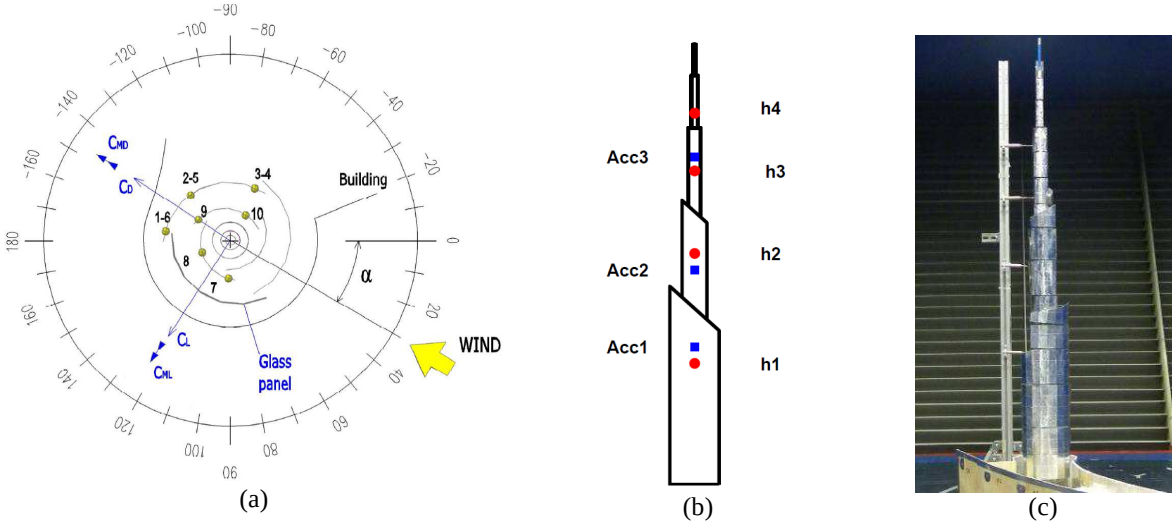

(a) (b) (c)

Figure 4. (a) Exposure angle and reference system. (b) Heights of the cobra probes (h) and the accelerometers (Acc). (c) The aeroelastic model made completely non-porous.

The model was instrumented with 6 accelerometers fixed on the structural bar in order to monitor the accelerations according to its bending modes (*x*-dir and *y*-dir). Vortex shedding excitation was investigated using four Cobra Probes, a multi-hole pressure probe developed by Turbulent Flow Instrumentation (TFI). They were fixed downwind the Spire at the heights shown in Figure 4(b); the same figure shows the positions of the accelerometers. In order to evaluate the effects of the porosity on the wind loads as well as the vortex shedding excitation, some tests were duplicated making impermeable the entire external surface of the aeroelastic model, Figure 4(c). Great care has been taken in order to keep the surface roughness unchanged adding the tape on the external surface.

2.2 *The model of the buttress*

The tests were carried out on a sectional model of the buttress (3/10 geometric scaled, aspect ratio L/B=6) realized in carbon fiber. The model is rigid and it was elastically suspended to realize a one degree of freedom system able to vibrate orthogonally to the incoming mean wind direction (cross flow direction), Figure 5. Structural modal damping was kept as low as possible in order to highlight the VIV phenomenon and it was adjustable by adding damping to the model through eddy current dampers or viscous dampers. In this way it was possible to change the Scruton Number and to investigate the oscillation amplitudes as a function of this parameter.

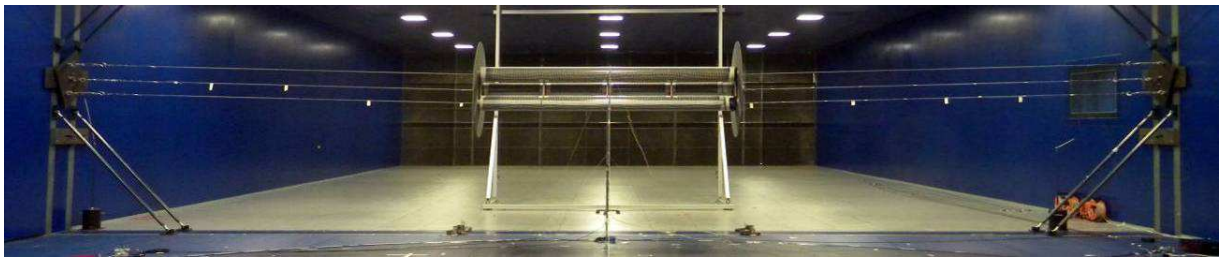

Figure 5. Overall view of the suspended model in the test section for dynamic tests.

Tests were performed at 3 angles of attack α, in according with Figure 6(a) and on different layouts. Porous screens: the gap between the cylinders is closed by a porous screen, Figure 6(b). Solid screens: the gap between the cylinders is completely closed, Figure 6(c). Different model surface finishing were also tested.

(a) (b) (c)

Figure 6. Sectional model of the buttresses. (a) Cross-section and wind direction angle. (b) Open, porous screens. (c) Close, solid screens.

3 RESULTS

The analysis has demonstrated that the permeability has a great importance on the aerodynamic behavior of both structures. In the following the main results from the experimental wind tunnel tests are presented.

3.1 *The Spire*

Figure 7 shows the overall wind load at the base of the aeroelastic model of the Spire. The results are expressed in terms of the drag coefficient $C_D(\alpha)$ and $C_L(\alpha)$, Equation (2), where F_D is the drag force and F_L is the lift (side) force function of the exposition angle α, q_H is the mean wind pressure at the base of the Spire and A_{rif} is the reference area. The peak factor method for Gaussian process has been used for the evaluation of the peak values.

$$C_{D,L}(\alpha) = \frac{F_{D,L}(\alpha)}{q_H A_{rif}} \tag{2}$$

The figure shows the along-wind component $C_{D,}$ Figure 7(a) and the cross-wind component C_L, Figure 7(b), of the overall wind load measured at the base of the aeroelastic model of the Spire in the in-service configuration (perforated panels) and making not-porous all the panels (close configuration). Due to the three dimensional external shape of the covering both coefficients manifest a great variability changing the exposition angle α. Considering the drag coefficient C_D, the non-porous configuration shows a moderate increment of the mean value and a higher increment of the peak values. In particular at α=-30deg and α=-60deg the mean value is almost the same, but the peak value is nearly doubled. The effect of the porosity on cross wind coefficient is more relevant. The non-porous Spire does not manifest a modification in mean value, which stays close to zero, on the contrary the peak values show a great increment: the maximum peak occurs about at a=-90 deg, where its value is about ten-times larger than the equivalent from porous panels. The analysis of the wind load coefficients reveals that making non-porous the panels slightly increases the along-wind force on the structures and generates a strong cross-wind dynamic load. The increment of the cross wind dynamic is strictly linked to a strong vortex shedding excitation, described in the next paragraph.

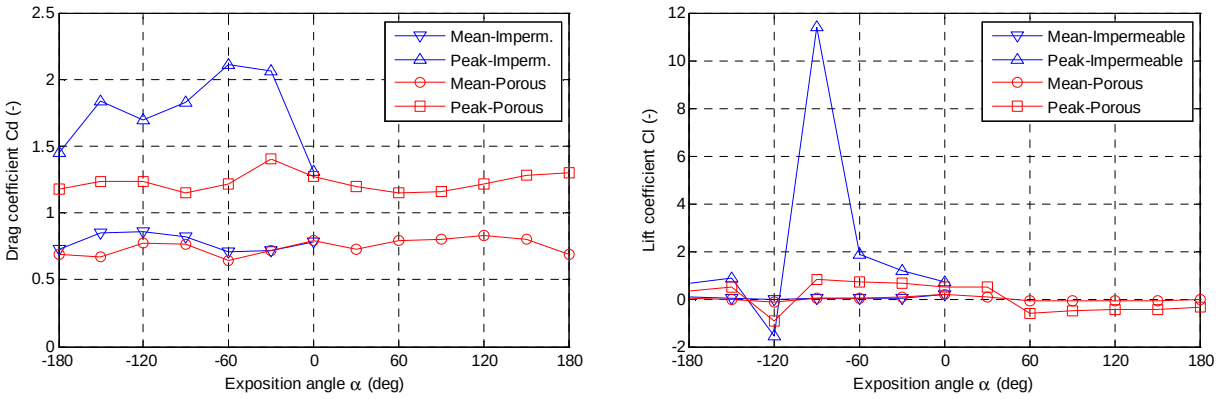

Figure 7. Overall wind load at the base of the Spire, smooth flow. Comparison between porous and non-porous panels. (a) Drag coefficient, C_D. (b) Lift coefficient, C_L (Note the difference in the y-axis scale).

The vortex shedding investigation has been performed analyzing the cross-wind velocities downwind the Spire measured by the four cobra probes. In the discussion of the results the cross-wind velocity v_i refers the probe at height h_i placed downwind a section of the Spire characterized by a diameter D_i. Figure 8 shows the spectra of the cross-wind velocities *vi* in the wake of the Spire the porous panels. The test speed was selected in order to generate from the section *D*2 a vortex shedding resonant with the first vibration mode of the structure (*f*1=5.09Hz). The peak at the frequency *f*1 in the spectra of the component *v*2, Figure 8(c), confirms this condition.

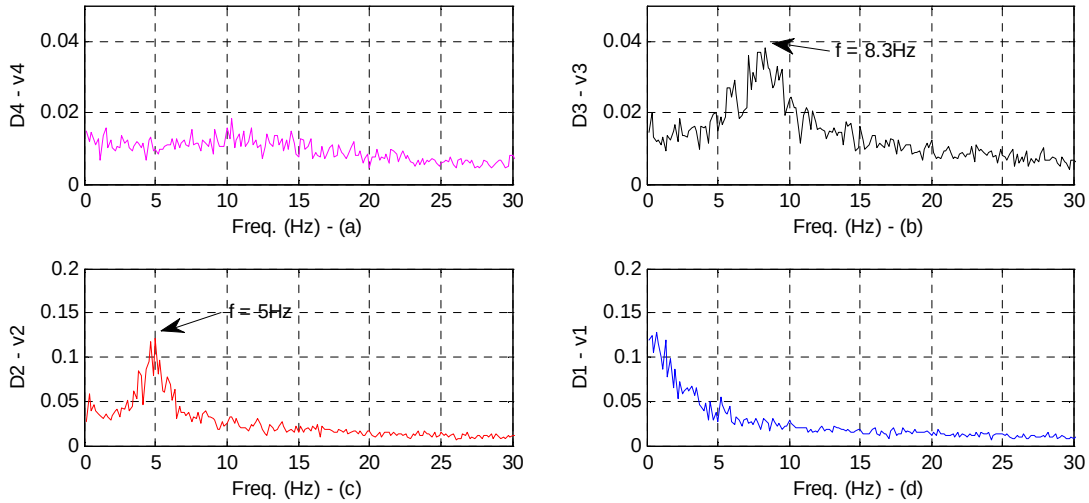

Figure 8. Aeroelastic model with porous panels. U=2.18m/s, SF. Spectra of the cross-wind velocities v_i downwind the Spire (Model scale data).

The section *D*2 has a full length scale of about 20m, a quarter of the total height of the structure, making its length not negligible compared with the respective mean diameter of about 5m. For this reason, even if changing the diameter along the height of the structure is known that mitigates the vortex shedding phenomenon, this section could have an adequate length to introduce enough energy to whole structure and induce vibrations [14,18,19]. The previous assumption, generally valid for non-porous circular surfaces, is disproved in the present case inspecting the spectra of the cross-wind velocities at the other levels. The excitation of the whole structure due to vortex shedding phenomenon is excluded by the following considerations: the spectra of the component *v*3, Figure 8(b), shows a peak at the Strohual frequency of the section *D*3 (*f*=8.3 Hz) and not at the first natural frequency of the model. The peaks in the spectra have a broad bandwidth, indicating a vortex shedding not fully synchronized. Lastly the crosswind displacements time histories calculated from the integration of the accelerometers signals are very low at all the levels considered (the maximum full scale peak to peak displacement is 5mm) and no regular vibrations are visible. On the contrary, the aerodynamic behavior of the Spire completely non-porous is totally different. Figure 9 shows the spectra of the cross-wind velocities *vi* in the wake of the Spire fully non-porous. The test speed was selected in order to have a vortex shedding generated by the section *D*3 resonant with the first vibration mode of the structure (*f*1=4.5Hz). The clear narrow bandwidth peak at the frequency *f*1 in the spectra of the component *v*3, Figure 9(b), confirms this condition. A narrow bandwidth peak at the same frequency is also present in the spectrum of the component *v*4, Figure 9(a), while downwind the sections at the lower levels, *D*1 and *D*2, a peak is also present but it is located at the Strohual frequency of the section and not at the first natural frequency of the model, Figure 9(c-d). This analysis reveal that vortex shedding induced vibration is now present, but due to the very low wind speed the energy introduced is not enough to induce an important vibration of the entire Spire.

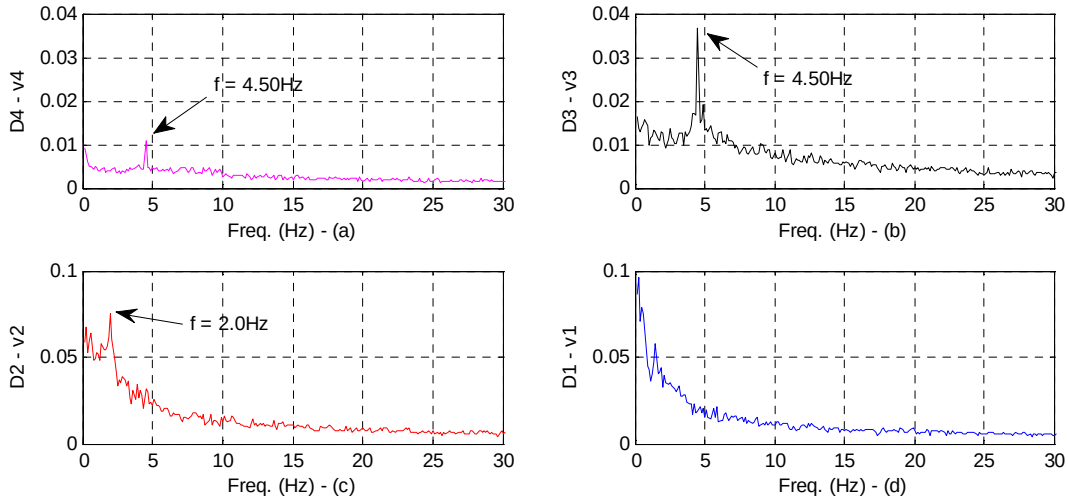

Figure 9. Aeroelastic model with panels fully non-permeable. U=1.28m/s, SF. Spectra of the cross-wind velocities v_i downwind the Spire (Model scale data).

The top-Spire cross-wind time history displacement calculated from the integration of the accelerometers shows an evident constant vibration of the Spire due the vortex shedding excitation. The vibration is small, 2mm model equal to 100mm full scale, nevertheless since the low but very frequent wind speed, it could be enough to lead to fatigue damages to the structure.

The absence of a vortex induced vibration on the permeable structure is given by the porosity: a detailed analysis by means of pressure measurements conducted in [16] has shown that permeability reduces the wind load because the air flows through the holes of the permeable panel, tending to equalize the mean pressure and attenuate the peak across the panel. As a consequence the vortex shedding excitation is strongly reduced.

3.2 *Isozaki tower buttresses*

Vortex induced vibration (VIV) tests were performed on the sectional model of the buttress. Aim of the tests was to compare the aerodynamic behavior of the buttresses using different screens layouts, different porosity in the area permeable to the air and different surface roughness. Aerodynamic stability of the buttress shape has been also investigated by studying the aerodynamic damping trend increasing the mean wind speed. The results are presented in function of the Scruton Number, defined as Eq.(3), where m is the mass per unit length of the body, h_s critical damping ratio, ρ is the air density and B is the overall dimension of the cross section.

$$Sc = \frac{2\pi m h_s}{\rho B^2} \tag{3}$$

The “solid screens” layout (Figure 6(c)) was firstly investigated. This configuration highlighted significant problems related to the fluid-structure interaction. In particular, considering the angle of attack α=-30deg (Figure 6(a)), the model showed significant vortex induced vibrations with also the presence of instability phenomena that led to large uncontrolled flow-induced vibrations unsuitable at low Scruton number (Sc=0.1, Figure 10(a)) and even at high value of Scruton number (u/B=4.5% at Sc=23, where u is the experimental displacement and B the model characteristic dimension, Figure 10(b)). Oscillations were still present even if the Scruton number was increased up to 50.

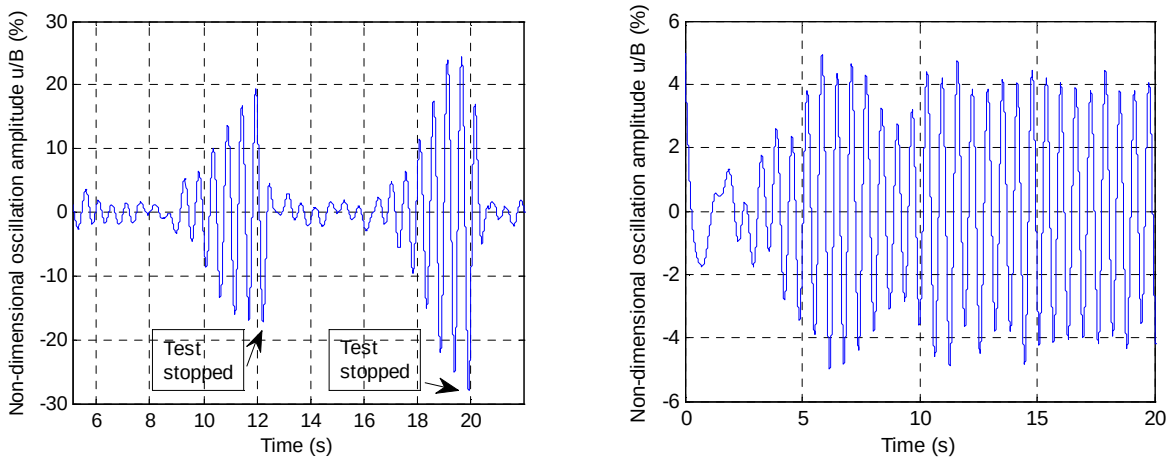

Figure 10. (a) Solid screens layout , α=-30deg, instability and VIV. (a) *Sc*=0.1. (b) *Sc*=25.

The choice was to use porous screens as an alternative configuration to the "solid screens". These screens have round hole perforation (radius 5mm) with triangular pitch of 14mm and porosity β=46%. This layout was stable at the angles of attack α=0deg and α=30deg, while vortex induced vibrations were still present at α=-30deg. Figure 11(b) shows the non-dimensional oscillation amplitude *u/B* (%) function of the Scruton Number *Sc:* it is possible to see that increasing the structural damping to provide a Scruton number higher than 12 the oscillations stopped. The stability of the structure was checked also changing the surface roughness of the model.

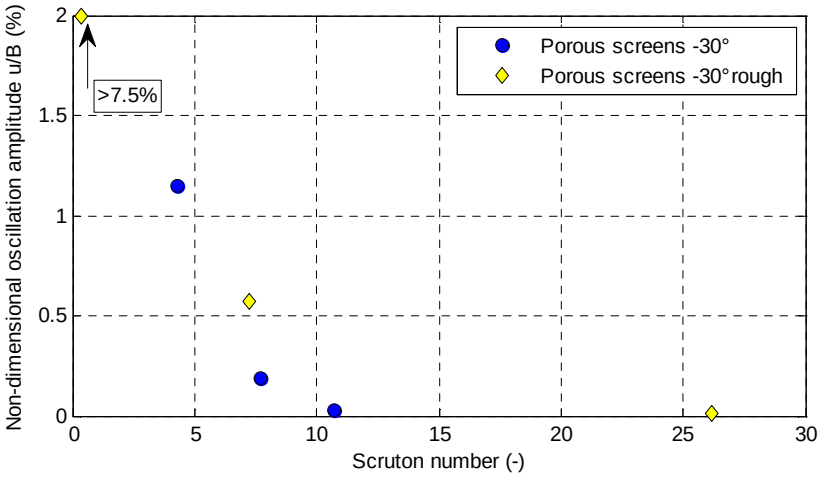

Figure 11. Porous screens layout, α=30deg. VIV in function of Scruton number at the most critical angle of attack.

4 CONCLUSIONS

The analysis has demonstrated that the permeability has a great importance on the aerodynamic behavior of the structures considered in the present work. Tests showed that the porosity of the external surface gives advance on both the mean load reduction as well vortex shedding attenuation. This is due to the passage of the flow through the panels which modifies locally the pressure distribution and, as a result, the wind loads and the dynamic response of the whole

structure. The realistic relevance of this analysis is even that the structures, due to their position, can be subjected to atmospheric icing which can make non-porous parts of the external panels.

In particular, the Spire with porous external panels is not affected by vortex shedding induced vibrations. since the energy introduced by the wind is not enough the induce a synchronous vibration of the entire structure. On the contrary the Spire fully non-porous suffers of a strong vortex shedding induced vibration which, due to the presence of four different diameter along the height, occur in a wide range of wind speeds.

The second structure studied were the long buttresses of a tall building. Also in this case the porosity of the screen between the cylinders gave stability to the structure which, if completely closed, suffered of significant vortex induced vibrations with also the presence of instability phenomena.

5 REFERENCES

1. M. Teitel, D. Dvorkin, Y. Haim, J. Tanny and I. Seginer, Comparison of measured and simulated flow through screens: Effects of screen inclination and porosity, Biosystems Engineering, 104 (2009), pp. 404-416.
2. J. L. Santiago, F. Martin, A. Cuerva, N. Bezdenejnykh and A. Sanz-Andres, 'Experimental and numerical study of wind flow behind windbreaks', Atmospheric Environment, 41 (2007), pp. 6406-6420.
3. A. F. Miguel, 'Airflow through porous screens: From theory to practical considerations', Energy and Buildings, 28 (1998), pp. 63-69.Briassoulis, D., A. Mistriotis, and A. Giannoulis, Wind forces on porous elevated panels. Journal of Wind Engineering and Industrial Aerodynamics, 2010. 98(12): p. 919-928.
4. D. Briassoulis, A. Mistriotis and A. Giannoulis, 'Wind forces on porous elevated panels', Journal of Wind Engineering and Industrial Aerodynamics, 98 (2010), pp. 919-928.
5. A. P. Robertson, P. Roux, J. Gratraud, G. Scarascia, S. Castellano, M. Dufresne de Virel and P. Palier, 'Wind pressures on permeably and impermeably-clad structures', Journal of Wind Engineering and Industrial Aerodynamics, 90 (2002), pp. 461-474.
6. C. W. Letchford, 'Wind loads on rectangular signboards and hoardings', Journal of Wind Engineering and Industrial Aerodynamics, 89 (2001), pp. 135-151.
7. C. W. Letchford, A. Row, A. Vitale and J. Wolbers, 'Mean wind loads on porous canopy roofs', Journal of Wind Engineering and Industrial Aerodynamics, 84 (2000), pp. 197-213.
8. G. M. Richardson, 'A permeable windbreak: its micro-environment and its effect on structural loads', Journal of Agricultural Engineering Research, 38 (1987), pp. 65-76.
9. J. C. K. Cheung and W. H. Melbourne, 'Wind loading on a porous roof', Journal of Wind Engineering and Industrial Aerodynamics, 29 (1988), pp. 19-28.
10. J. H. M. Fransson, P. Konieczny and P. H. Alfredsson, 'Flow around a porous cylinder subject to continuous suction or blowing', Journal of Fluids and Structures, 19 (2004), pp. 1031-1048.
11. L. Mathelin, F. Bataille and A. Lallemand, 'Near wake of a circular cylinder submitted to blowing - II: Impact on the dynamics', International Journal of Heat and Mass Transfer, 44 (2001), pp. 3709-3719.
12. C. Zheng and Y. Zhang, 'Numerical investigation of wind-load reduction for a high-rise building by blowing control', Jianzhu Jiegou Xuebao/Journal of Building Structures, 31 (2010), pp. 176-181.
13. H. Baek and G. E. Karniadakis, 'Suppressing vortex-induced vibrations via passive means', Journal of Fluids and Structures, 25 (2009), pp. 848-866.
14. P. A. Irwin, 'Wind engineering challenges of the new generation of super-tall buildings', Journal of Wind Engineering and Industrial Aerodynamics, 97 (2009), pp. 328-334.
15. M. P. Repetto and G. Solari, 'Wind-induced fatigue collapse of real slender structures', Engineering Structures, 32 (2010), pp. 3888-3898.
16. M. Belloli, L. Rosa and A. Zasso, 'Wind loads and vortex shedding analysis on the effects of the porosity on an high slender tower', submitted to: Journal of Wind Engineering and Industrial Aerodynamics (2012).
17. M. Belloli, L. Rosa and A. Zasso, 'A comparative study of the wind loads on a slender tower with porous surface', submitted to: Wind and Structure (2011).
18. Y.-M. Kim, K.-P. You and N.-H. Ko, 'Across-wind responses of an aeroelastic tapered tall building', Journal of Wind Engineering and Industrial Aerodynamics, 96 (2008), pp. 1307-1319.
19. K. Shimada and K. Hibi, 'Estimation of wind loads for a super-tall building (SSH)', The Structural Design of Tall Buildings, 4 (1995), pp. 47-60.

The Seventh International Colloquium on Bluff Body Aerodynamics and Applications (BBAA7)
Shanghai, China; September 2-6, 2012

Aerodynamic coefficients for iced lattice tower models

Jarosław Bęc [a], Tomasz Lipecki [b], Ewa Błazik-Borowa [c]

[a]*Lublin University of Technology, 40 Nadbystrzycka St, Lublin, Poland*
[b]*Lublin University of Technology, 40 Nadbystrzycka St, Lublin, Poland*
[c]*Lublin University of Technology, 40 Nadbystrzycka St, Lublin, Poland*

ABSTRACT: Aerodynamic forces on lattice tower-like structures have been measured in wind tunnel. The parameters of the incoming flow have been modified with use of sets of elements forming boundary layer. Three types of shafts have been used in measurements. Aerodynamic forces have been measured and aerodynamic coefficients have been calculated as functions of wind attack angle. The measurements have been made for bare structures, and for structures with cover modeling icing. The influence of wind structure on the functions of aerodynamic coefficients has been analyzed.

KEYWORDS: lattice towers, wind action, aerodynamic coefficients, icing, wind tunnel, boundary layer.

1 INTRODUCTION

Wind action on lattice structures is well understood and described in standards [1], [2], [3], [4]. The problem has been often analyzed numerically [5] or by experiments in wind tunnels [6]. However, in this paper wind inflow structure influence on wind action on vertical lattice structures like towers or shafts of guyed masts has been analyzed.

The results obtained with tests carried out in boundary layer wind tunnel have been presented here. The experiment contains measurements of aerodynamic forces performed with use of five component aerodynamic balance. Different cases of flow structure and various angles of wind attack have been used in the research. Such parameters as vertical mean wind speed profile, turbulence intensity profile and wind PSD functions have been used to characterize various flows.

The paper presents result of wind tunnel measurements for three lattice towers. Wind action analysis has been made with respect to the following parameters: 1. shaft cross-section (square or triangular), 2. members cross-sections (legs and bracing of square or circular cross-sections). Tests have been made for bare structures and with respect to icing on structures. Additional measurements of wind fields behind each model have been made, as well.

2 RESEARCH DESCRIPTION

The experiments have been carried out in the boundary layer wind tunnel in Wind Engineering Laboratory in Cracow, Poland. The geometry and the dimensions of the wind tunnel have been shown in Figure 1.

The modeling of the boundary layer in the wind tunnel is realized with use of nets, spires, barriers of various heights, and mechanically adjustable blocks. Forty five combinations of these elements have been analyzed. The elements forming boundary layer have been presented in Table 1 and in Figure 2. One of the boundary layer settings has been shown in Figure 2. The more detailed description of the research on wind structure in the wind tunnel of Cracow University of Technology is presented in [7].

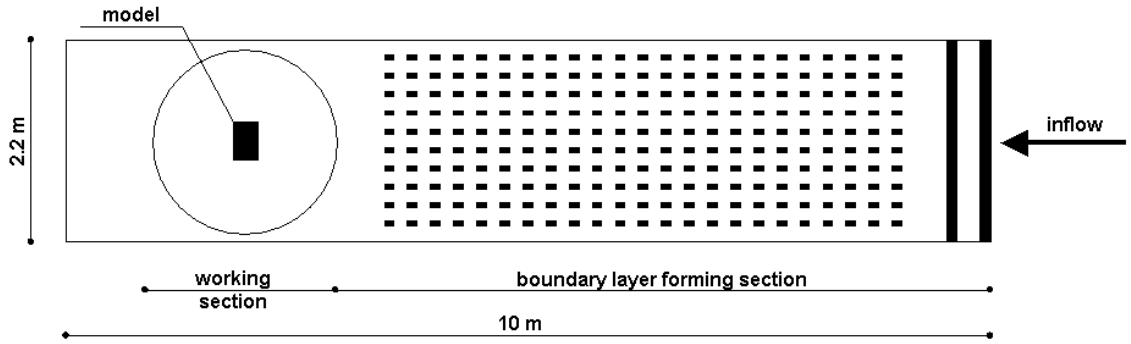

Figure 1. Working section of the wind tunnel with model.

Table 1. Elements forming boundary layer

Element types		Height	
Spires	80 cm	100 cm	120 cm
Spatial Flat	iv8 it8	iv10 it10	iv12 it12
Barriers	20 cm	30 cm	40 cm
Zigzag Even	bz2 br2	bz3 br3	bz4 br4
Blocks	0 cm kl0	10 cm kl10	20 cm kl20

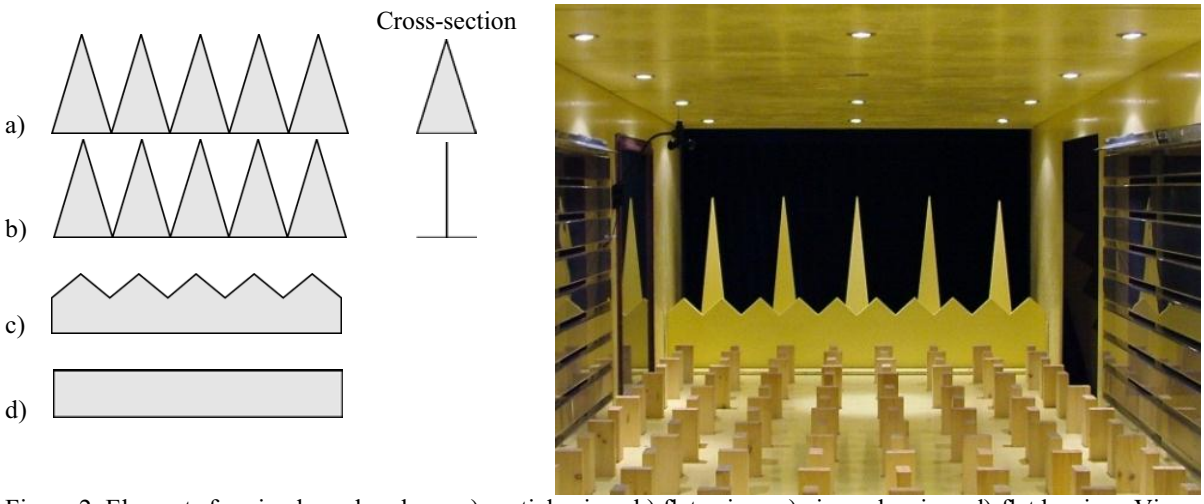

Figure 2. Elements forming boundary layer a) spatial spires, b) flat spires, c) zigzag barriers, d) flat barriers. View of the set of the elements in the wind tunnel.

Measurements have been made with use of six sets of elements forming boundary layer. These sets had been selected out of 45 tested settings giving various types of modeled terrain roughness. The selection has been made to obtain most differing parameters of the wind structures. The following parameters had been taken into account: vertical mean wind profile, turbulence intensity profile and wind frequency spectrum. Vertical mean wind profiles in the wind tunnel have been approximated with the following power-law formula [6]:

$$u(z) = k \cdot z^{\alpha} \quad \text{for} \quad z > z_{\min} \tag{1}$$

where k and α are the values obtained with least square method, z is the height above wind tunnel floor measured in cm. The wind profile coefficients have been reduced to make the wind

speed at the height of 70 cm equal in each wind speed profile. The wind speed obtained with the formula (1) is expressed in m/s. The calculated values of wind speed profile parameters have been presented in Table 2.

Table 2. Parameters for selected vertical mean wind profiles.

Profile	Symbol	k	α	z_{min}
1	bz2kl0	4.26	0.20	1.70
2	iv10bz4okl0	2.52	0.32	0.55
3	it10bz3kl0	2.99	0.28	0.85
4	iv10bz2okl10	1.63	0.42	0.25
5	it10bz3kl20	1.05	0.52	0.10
6	iv10bz4okl20	0.93	0.55	0.07

Vertical profiles of turbulence intensity and functions of wind spectrum have been approximated similarly. Graphs of vertical profiles of mean wind speed and turbulence intensity for six analyzed cases are presented in Figure 3.

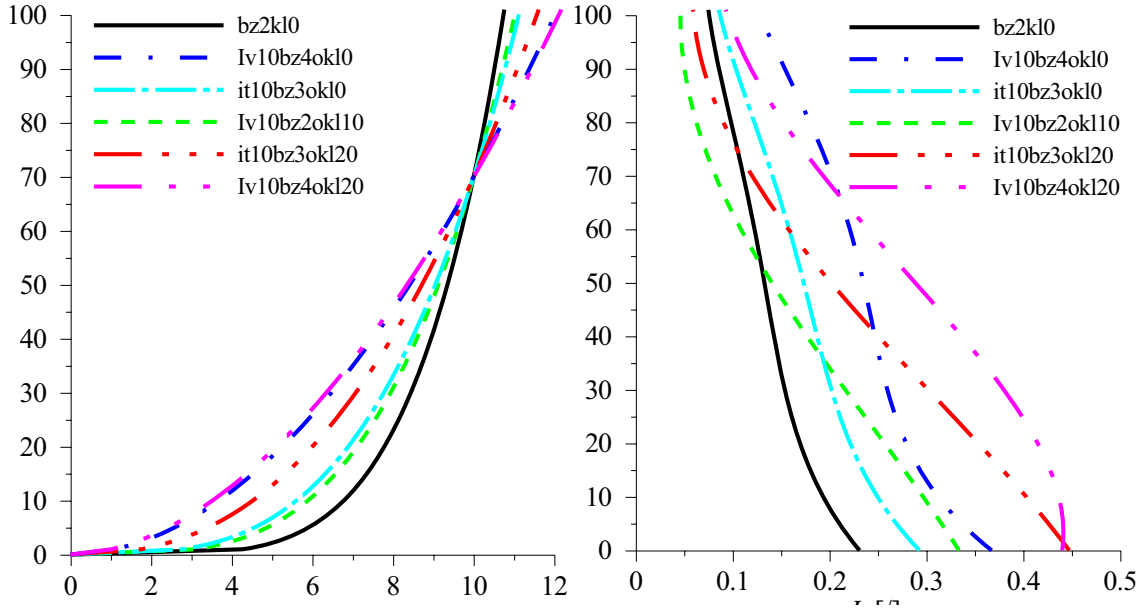

Figure 3. Vertical profiles of mean wind speed (left) and turbulence intensity (right).

Three lattice tower-like models of 1 m height and 10 cm shaft cross-section side dimensions with square or triangular shaft cross-sections, rectangular or circular cross-section members have been used. The models have been placed vertically on rotating table in the working section of the wind tunnel. The dimensions and characteristics of three models are collected in Table 3. The views of the models are presented in Figure 4.

Table 3. Parameters obtained for selected vertical mean wind profiles.

Model	Shaft shape	Member	Member cross-section	Material
m_kw_10x10_kw	Square 10 cm×10 cm×100 cm	Legs Bracing	Square 10 ×10 mm Square 5 ×5 mm	Aluminum Brass
m_kw_10x10_cicr	Square 10 cm×10 cm×100 cm	Legs Bracing	Circular 10 mm Circular 5 mm	Aluminum Aluminum
m_tr_10x10_circ	Triangular 10 cm×10 cm×100 cm	Legs Bracing	Circular 10 mm Circular 5 mm	Aluminum Brass

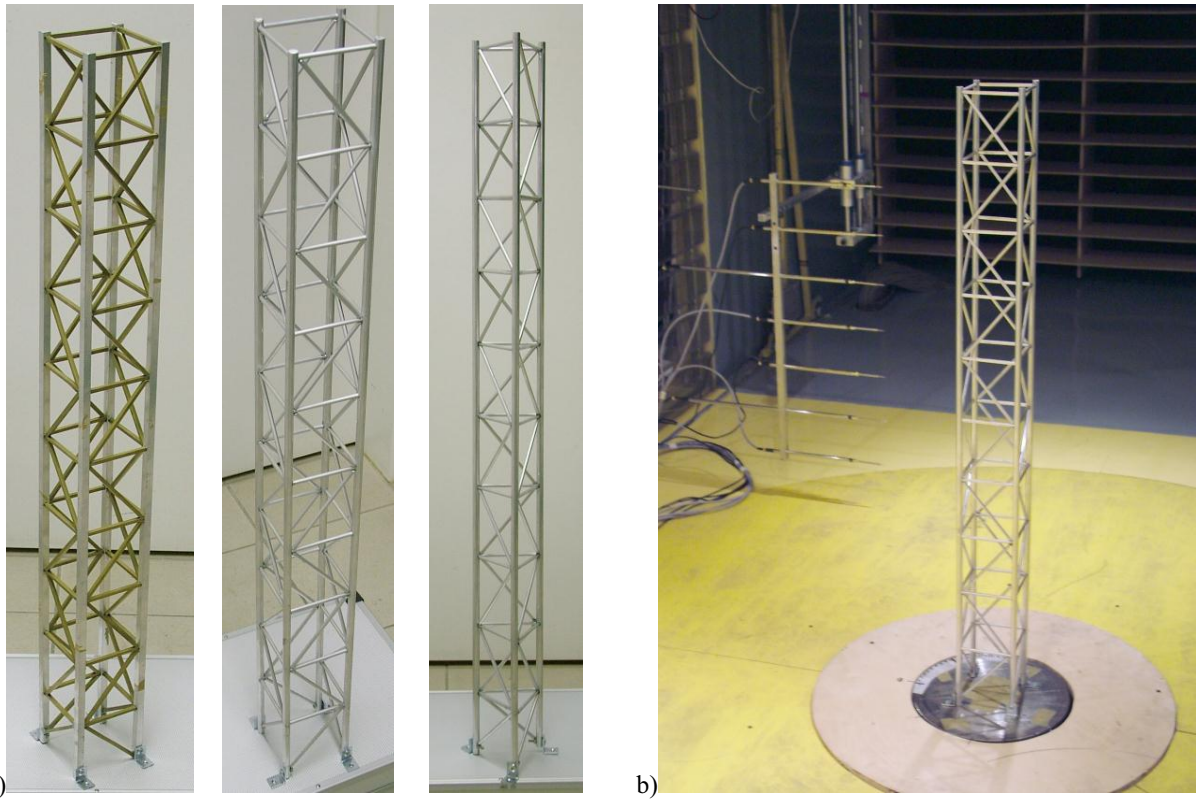

Figure 4. a) Lattice towers models, b) wind tunnel set-up with X hot-wire anemometers.

Each of the models has been used for further analysis of wind action on the iced structures. Icing has been modeled with use of the gypsum cover formed on structures. The gypsum layer modeling icing has been obtained with sinking models repeatedly in the liquid gypsum plaster. Then the models have been hanged in horizontal position to form asymmetric coating. Additional layers of the icing model have been made with pouring the liquid gypsum plaster on the lattice models. The process of ice cover modeling has been shown in Figure 5.

Figure 5. Forming of ice cover model.

One of the models and the model with the cover modeling icing set in the wind tunnel has been shown in Figure 6.

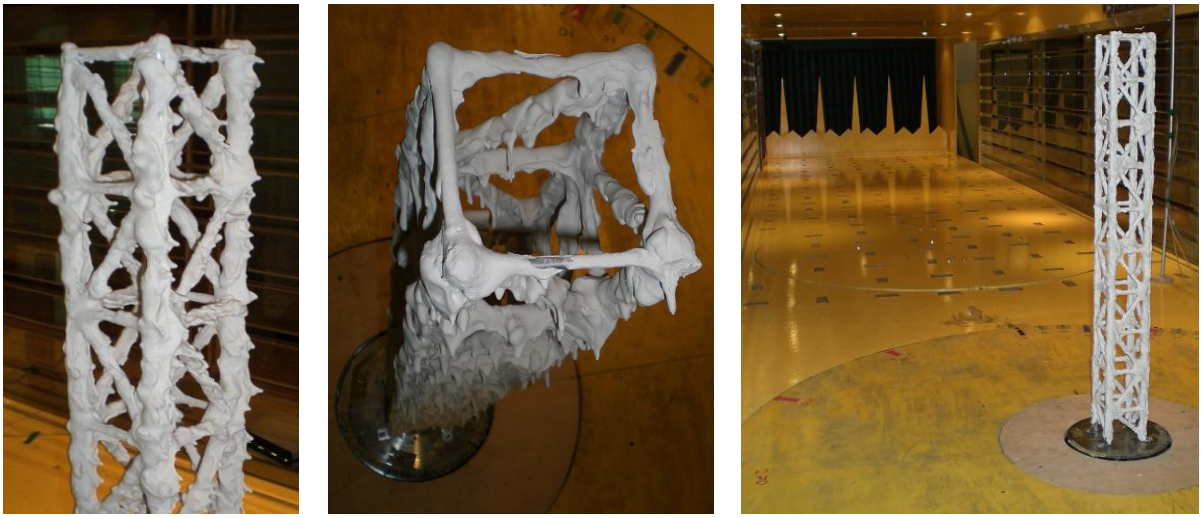

Figure 6. Lattice tower models with the cover modeling icing.

The angle of wind attack in the analysis has been changing from 0˚ to 90˚ for rectangular towers and from 0˚ to 120˚ for triangular ones (with the step of 5˚). The measurements for the iced models have been performed at angles from 0˚ to 180˚ due to non-symmetric ice cover.

The wind attack angle 0˚ refers to the mean wind speed direction perpendicular to one side of the lattice shaft (Fig. 7).

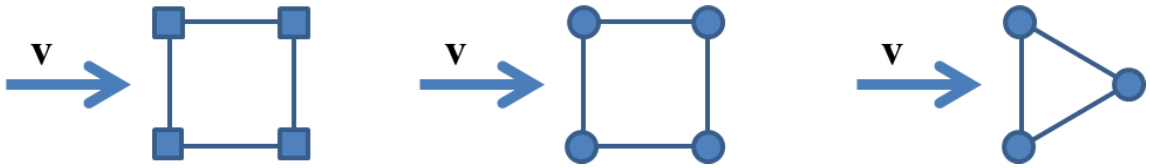

Figure 7. Models setting at wind attack angle 0˚.

3 RESULTS

The measurements have been made with use of five component aerodynamic balance. The following aerodynamic forces have been measured: drag ($\mathbf{P_x}$ – along mean wind speed) and lift ($\mathbf{P_y}$ – horizontal, perpendicular to drag force) and three components of aerodynamic moment. The setting of aerodynamic forces in respect to mean wind speed has been presented in Figure 8.

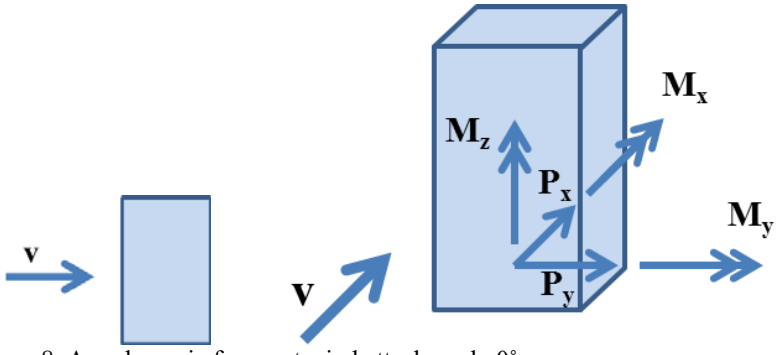

Figure 8. Aerodynamic forces at wind attack angle 0˚.

Functions of aerodynamic forces in reference to wind attack angle have been obtained for each model. Exemplary functions of aerodynamic forces are shown in Figure 9.

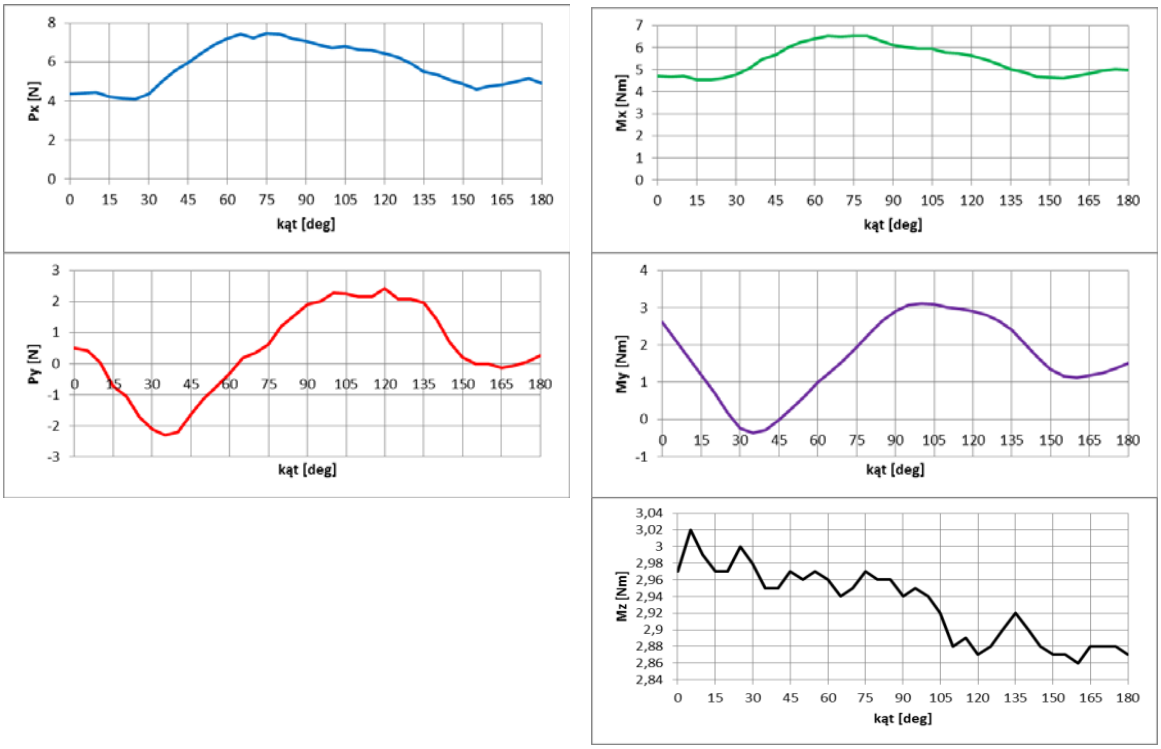

Figure 9. Exemplary functions of aerodynamic forces (*l1_tr_10x10_cir_bz2okl0*) – triangular shaft with ice cover, wind profile *bz2okl0*.

On the basis of measured aerodynamic forces in reference to wind attack angle, the aerodynamic coefficients have been calculated, for both types of structures: bare and with cover modeling icing. The values of aerodynamic coefficients have been obtained by dividing respective aerodynamic force by the value of the reference pressure measured at the height of 71 cm in the working section of the wind tunnel in undisturbed flow in front of models. Such reduction of aerodynamic coefficients allows estimation of wind structure influence on the results. The following formula has been used [6],[8]:

$$C = F \Big/ \left(\frac{1}{2} \rho v^2 \right) \tag{2}$$

where: C is aerodynamic coefficient (C_x, C_y, C_{Mx}, C_{My} or C_{Mz}), F is the value of the respective aerodynamic force at the given wind attack angle (P_x, P_y, M_x, M_y or M_z), ρ – air density, v – reference wind speed.

There have been aerodynamic coefficients presented in the next figures. The graphs are shown for each structure model, bare and iced, for all of the selected cases of sets of elements forming boundary layer with respective wind structures. Aerodynamic coefficients for bare structures have been shown in Figures 10-12. The graphs of aerodynamic coefficients for models with ice cover have been shown in Figures 13-15.

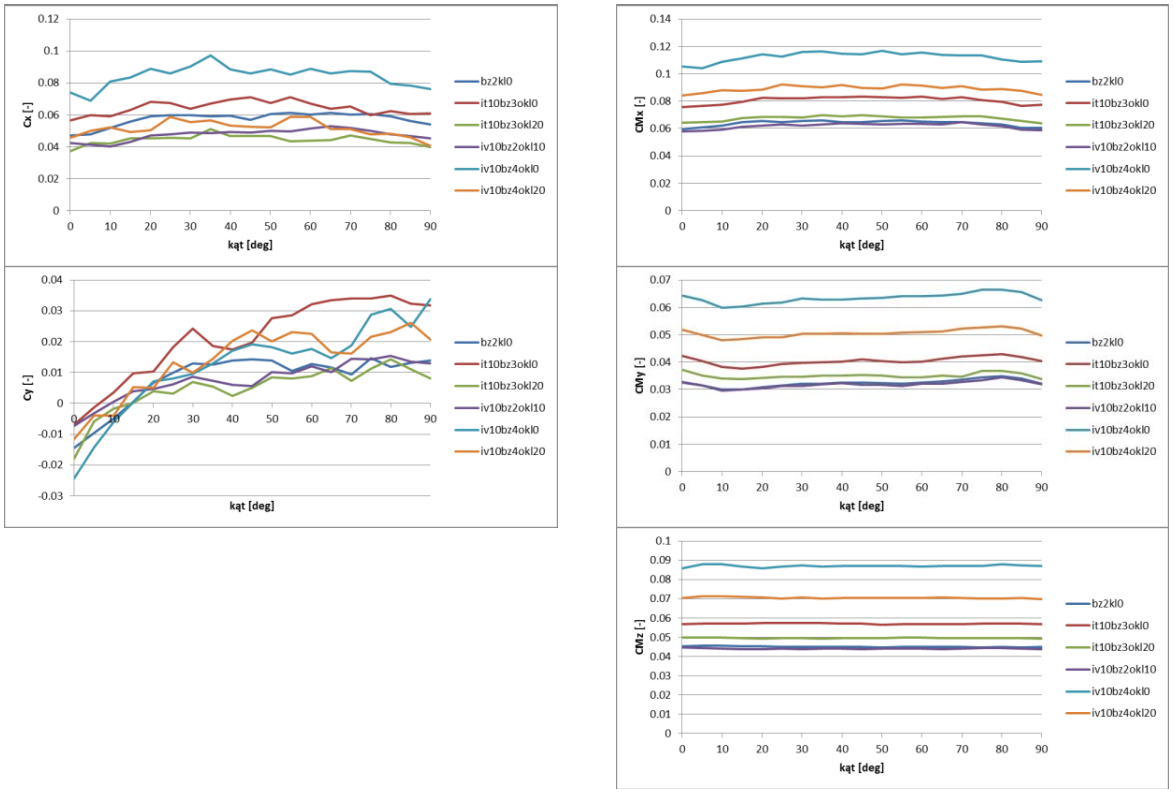

Figure 10. Aerodynamic coefficients – model *m_kw_10x10_cir*.

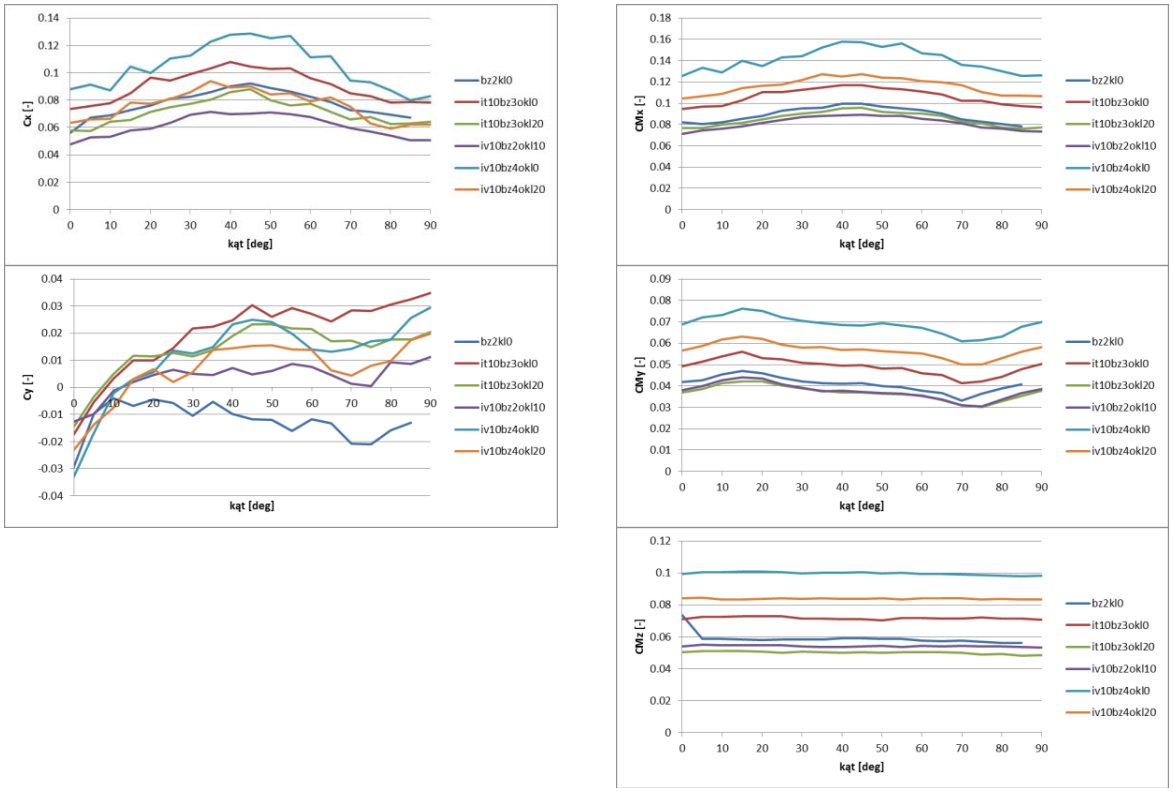

Figure 11. Aerodynamic coefficients – model *m_kw_10x10_kw*.

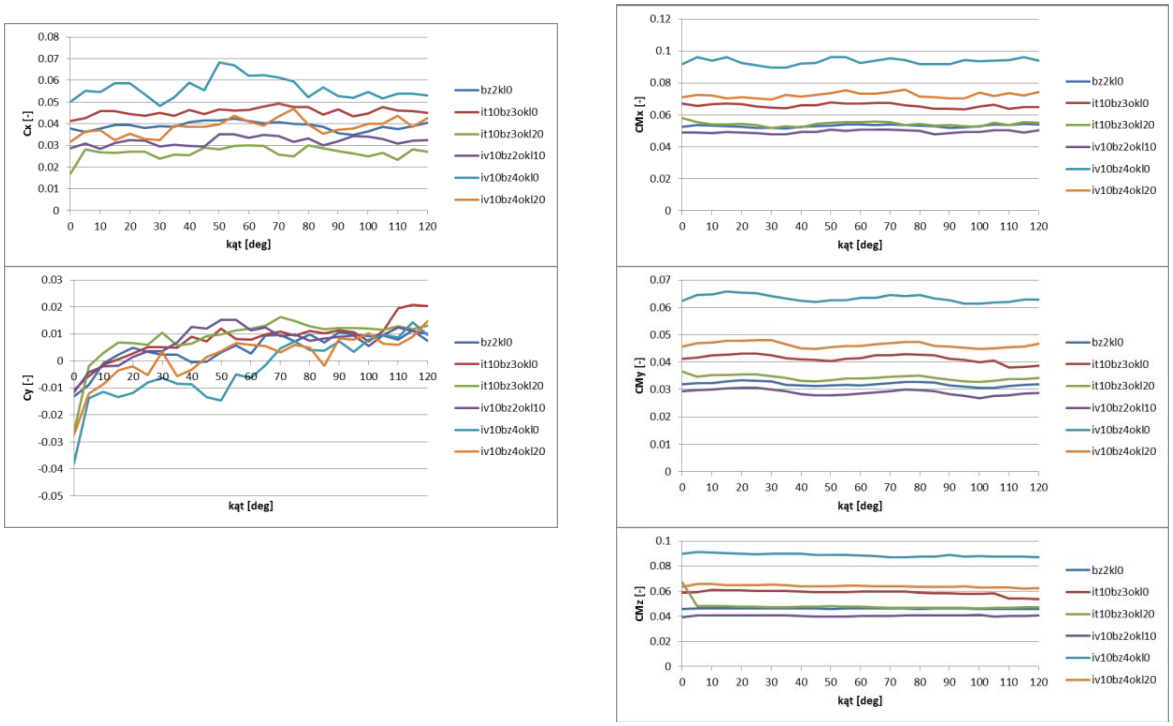

Figure 12. Aerodynamic coefficients – model *m_tr_10x10_cir*.

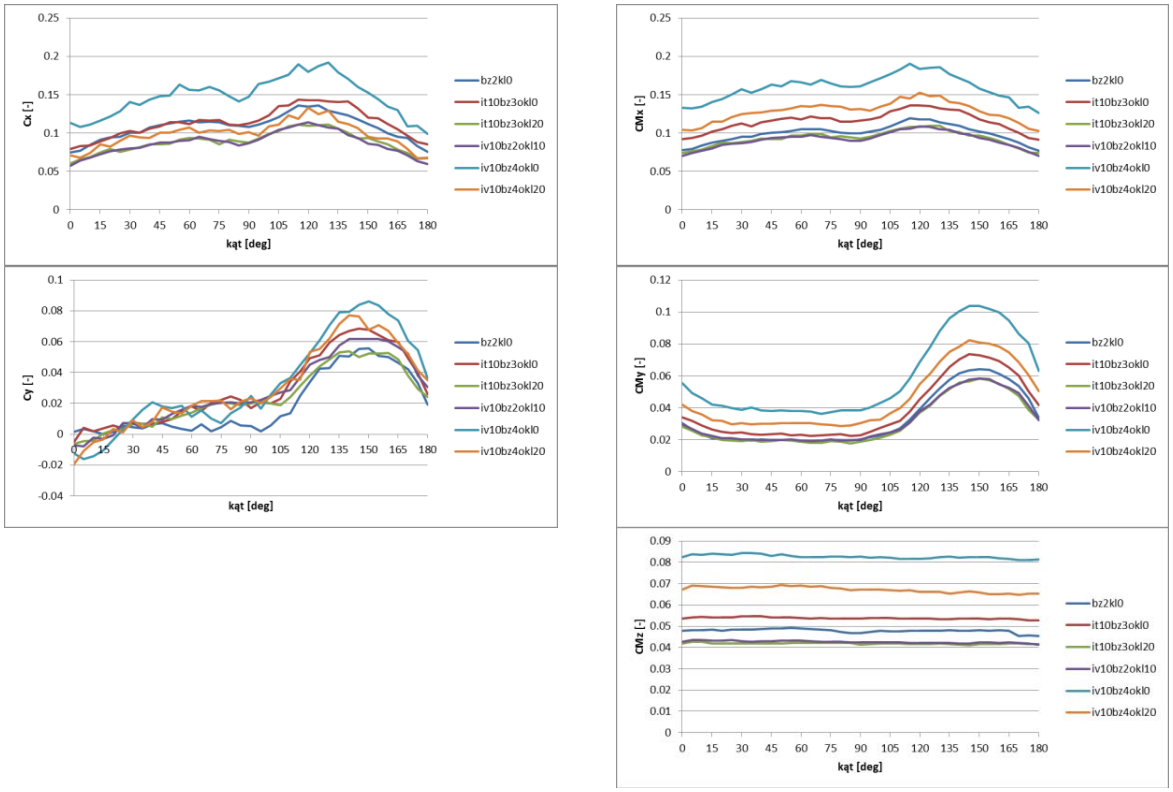

Figure 13. Aerodynamic coefficients – model *m_kw_10x10_cir* with ice cover.

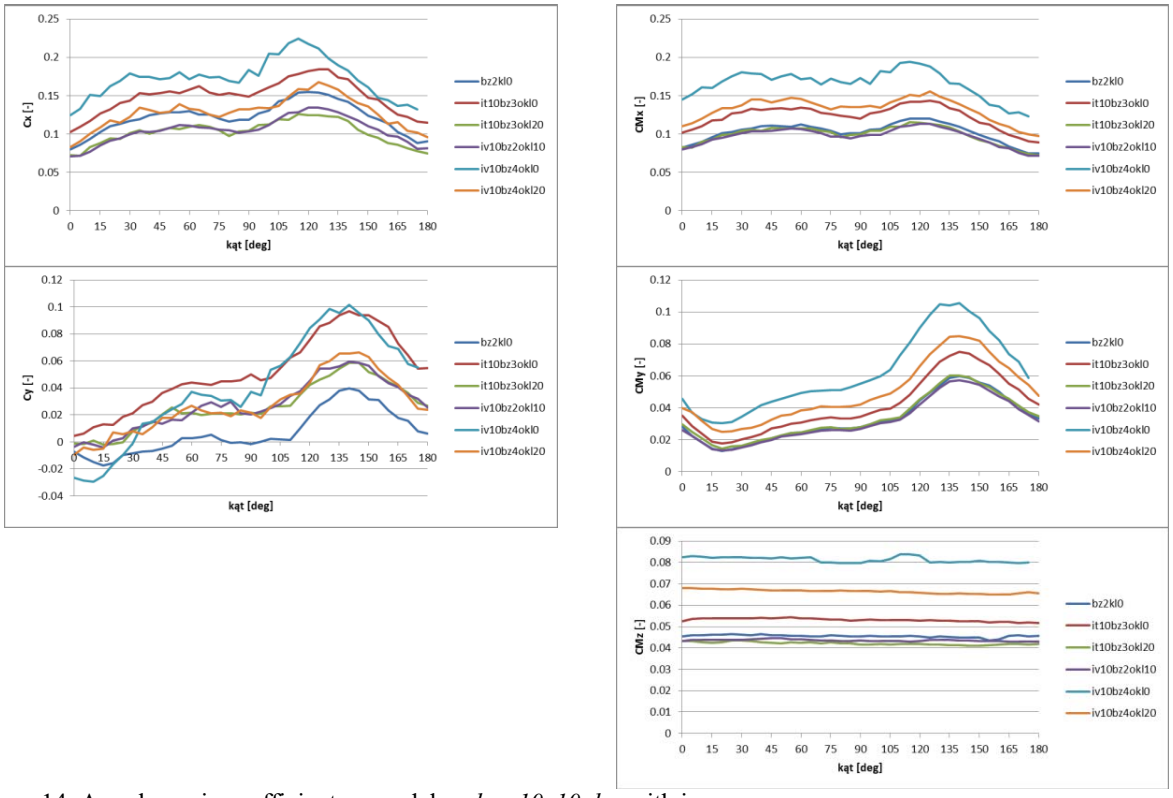

Figure 14. Aerodynamic coefficients – model *m_kw_10x10_kw* with ice cover.

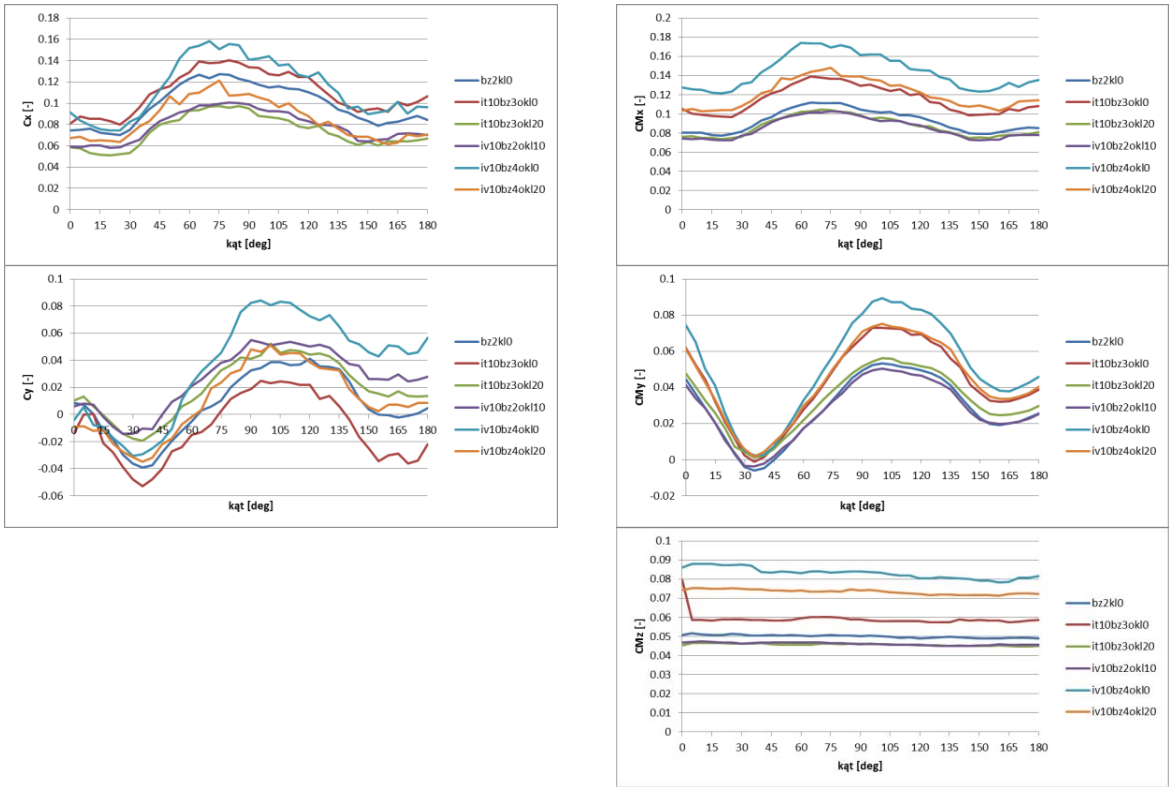

Figure 15. Aerodynamic coefficients – model *m_tr_10x10_cir* with ice cover.

The results show significant influence of wind structure on the wind forces and aerodynamic coefficients for such structures. The icing influence is clearly visible as qualitative and quantitative change in obtained functions. The shape of graph for iced structures is changed as the result of asymmetric ice cover.

4 CONCLUSIONS

The following conclusions can be drawn out:
- Wind load depends on the wind inflow structure.
- Wind action on shafts made with rectangular cross-section members is bigger than with cylindrical ones.
- Icing changes the area subjected to wind action, so the wind action is bigger, as well.
- It is impossible distinguish the influence of each of wind structure parameters to the wind action based on wind tunnel tests only. Supplementary numerical simulation can give a solution to the problem.

5 ACKNOWLEDGEMENTS

The work was prepared within Ministry of Science and Higher Education research project – No. N506 267337.

6 REFERENCES

1 EIA/TIA-222F: Structural Standards for Steel Antenna Towers and Antenna Supporting Structures, Electronic Industries Association, 2001.
2 ENV 1991-2-7. Eurocode 1: Basis of design and actions on structures – Part 2-4: Actions on structures – Wind actions, CEN 1995.
3 ENV 1993-3-1, Eurocode 3. Design of steel structures. Towers and masts, CEN 1997
4 ESDU 81028: Lattice structures. Part 2: Mean fluid forces on tower-like space frames, ESDU International LTD 1981.
5 E. Błazik-Borowa, J. Bęc, P. Wielgos, Calculating Aerodynamic Coefficients for Shafts of Guyed Masts, Environmental Effects On Buildings, Structures And People, Lublin 2007.
6 A. Flaga, Inżynieria wiatrowa. Podstawy i zastosowania, Arkady, Warszawa, 2008.
7 J. Bęc, T. Lipecki, E. Błazik-Borowa, Research on Wind Structure in the Wind Tunnel of Wind Engineering Laboratory of Cracow University of Technology, Journal of Physics: Conference Series 318 (2011) 072003, doi: 10.1088/1742-6596/318/7/072003
8 A. Flaga, E. Błazik-Borowa, J. Podgórski, Aerodynamika smukłych budowli i konstrukcji prętowo-cięgnowych, Wydawnictwo Politechniki Lubelskiej, 2004.

Wind tunnel measurements of aeroelastic guyed mast models

Jarosław Bęc [a], Tomasz Lipecki [b], Ewa Błazik-Borowa [c]

[a]*Lublin University of Technology, 40 Nadbystrzycka St, Lublin, Poland*
[b]*Lublin University of Technology, 40 Nadbystrzycka St, Lublin, Poland*
[c]*Lublin University of Technology, 40 Nadbystrzycka St, Lublin, Poland*

ABSTRACT: Dynamic response of guyed masts models to the wind action in the wind tunnel has been analyzed in the paper. Accelerations and forces in guys have been measured. Spectra of the response have been calculated. The influence of the wind structure on the response has been analyzed. The results obtained with experiments have been compared with the ones coming from numerical analysis.

KEYWORDS: guyed masts, wind action, wind tunnel, boundary layer, dynamic response.

1 INTRODUCTION

Analysis of the dynamic response of guyed masts has been presented in this paper. The problem can be approached in two ways, experimentally or numerically. The measurements can be made in-situ or on models in wind tunnel. Here in this paper, the results from the wind tunnel measurements of two guyed masts models have been presented. Triangular and rectangular shaft masts have been modeled and measured. The research consists of measurements of time series of accelerations in selected points located on the mast models and measurements of force time series in guys. Three cases of approaching flow structure have been used in experiment. Various wind profiles, turbulence intensity profiles and power spectral density functions have been obtained with sets of elements forming boundary layer. Various angles of wind attack have also been considered. The results obtained with experiments have been compared with the results coming from numerical analysis.

2 RESEARCH DESCRIPTION

The experiments have been carried out in the boundary layer wind tunnel of the Wind Engineering Laboratory in Cracow, Poland. The scheme of the working section of the wind tunnel has been presented in Figure 1.

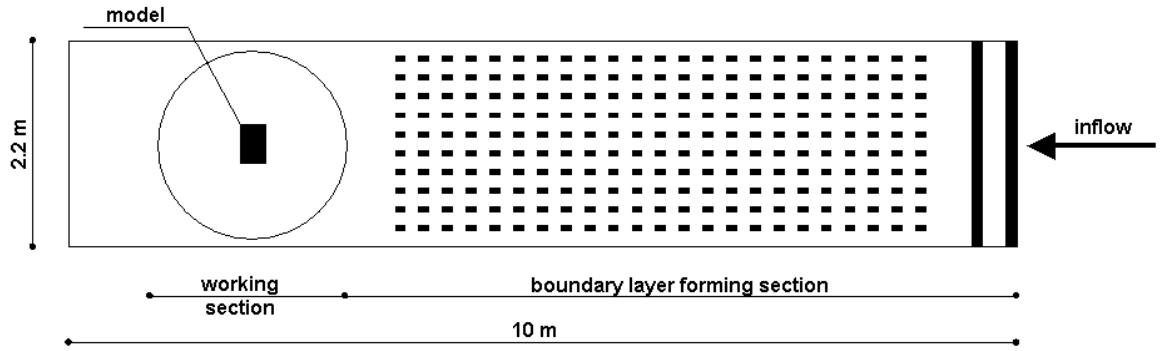

Figure 1. Working section of the wind tunnel with model location.

The influence of wind characteristics such as vertical mean wind speed profiles, turbulence intensity profiles and wind PSD functions on the response of structure models has been examined.

The measurements of masts models have been carried out for three setting of elements forming boundary layer. The settings have been selected with most varying values of obtained wind structure parameters. The following cases, out of 45 all tested ones and 6 previously used in wider analyses, have been selected for this research:

- *bz2kl0* – zigzag barrier of 20 cm height, no blocks (profile nr 1);
- *it10bz3kl0* – T-shape cross-section spires of 100 cm height, 30 cm zigzag barrier, no blocks (profile nr 3);
- *iv10bz4kl20* – triangular cross-section spires of 100 cm height, 40 cm zigzag barrier, blocks set at 20 cm (profile nr 6).

Vertical mean wind profiles measured in the wind tunnel have been approximated with the power-law formula [1]:

$$u(z) = k \cdot z^{\alpha} \quad \text{for} \quad z > z_{\min} \tag{1}$$

where k and α are the values obtained with least square method, z is the height above wind tunnel floor measured in cm. The wind profile coefficients have been reduced to make the wind speed at the height of 70 cm equal in each mean wind speed profile. The wind speed obtained with the formula (1) is expressed in m/s. The calculated values of wind speed profile parameters have been presented in Table 1.

Table 1. Parameters for selected vertical mean wind profiles.

Profile	Symbol	k	α	z_{min}
1	*bz2kl0*	4.26	0.20	1.70
3	*it10bz3kl0*	2.99	0.28	0.85
6	*iv10bz4okl20*	0.93	0.55	0.07

Similar procedure has been used in approximation of other wind structure parameters. The more detailed description of the research on wind structure in the wind tunnel of Cracow University of Technology is presented in [2].

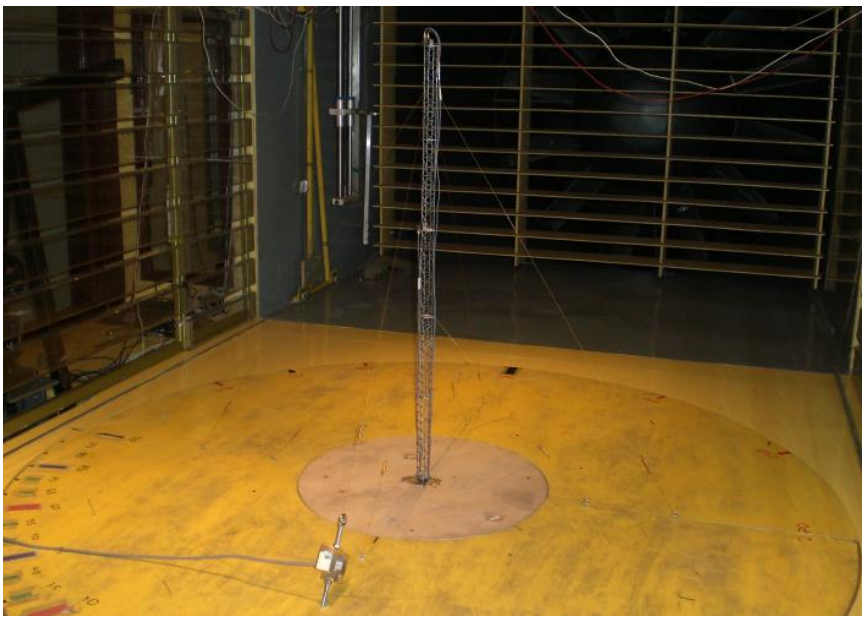

Figure 2. Guyed masts model in the wind tunnel.

Guyed masts have been placed vertically on rotating table in the working section of the wind tunnel. The response of two models have been measured:

- M1 (*m_tr_2x2_circ*) of triangular shaft cross-section (three planes of guys);
- M2 (*m_kw_2x2_circ*) of rectangular shaft cross-section (four planes of guys).

The view of the M1 model in the wind tunnel is presented in Figure 2. Both models are made from steel members of circular cross-section. Shaft legs are made of the 2 mm diameter rods, bracing – of rods of the 1 mm diameter. Each model is supported at the base (free rotations) and with use of two levels of guys made of steel wire of the 0.25 mm diameter. The guys are connected to the shafts at the levels of 40 cm and 90 cm with the guy yaw angles of 45° and 60°, respectively. The side dimension of each shaft cross-section is equal to 2 cm. The overall height of each model is 1 m.

The analysis has been made for various rotations of models with angle of wind attack varying from 0˚ to 180˚ with the step of 45˚ for rectangular mast model and 30˚ in the case of the triangular model. The exemplary shaft rotations with mean wind direction and the directions of measured accelerations have been presented in Figure 3.

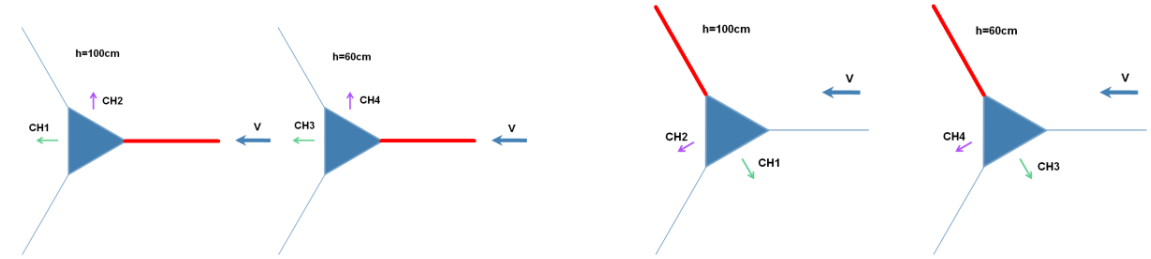

Figure 3. Exemplary rotations of triangular cross-section shaft mast: 0° – left, 120° – right.

The measurements have been made at 16 mean wind speed steps changing from 0 m/s to about 20 m/s.

2.1 Accelerations

The measurements of acceleration have been made in two perpendicular directions (along and across wind tunnel in base position) at two levels of each model: at the top (h=100 cm) and in the middle of upper span (h=60 cm).

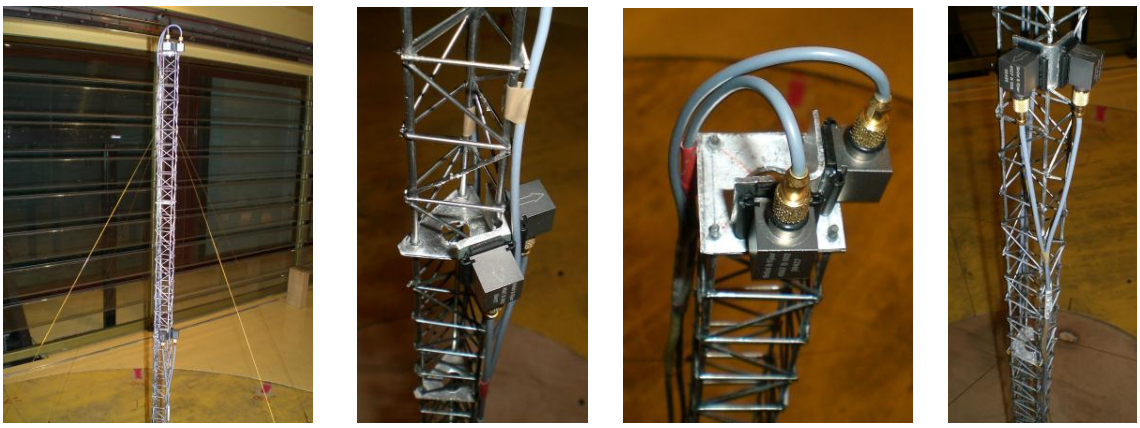

Figure 4. Accelerometers mounted at the mast model structure.

Brüel&Kjær accelerometers 4507B-002 connected to the PULSE measuring system have been used. The instrumentation of the model in wind tunnel is shown in Figure 4.

The measurements have been made with the sampling frequency 8192 Hz. The saved time series lasted for about 20 s for each analyzed case. The accelerations have been measured simultaneously with measuring of forces in guys and mean wind speeds.

2.2 Forces in guys

Hottinger S2/100 force transducer has been used in these measurements. The range of measured forces is -100 ÷ +100 N for this transducer. Time series of forces in guys under wind action have been measured. Forces in both upper (*og*) and lower (*od*) guys have been measured. Various characteristic positions (rotations) of the mast have been considered, allowing analysis of the guys at the windward and leeward sides of the mast. The measurements have been made simultaneously with measurements of accelerations with use of accelerometers, wind speed fields with use of hot wire anemometers and mean wind speeds with use of pressure scanner. Simultaneous recording allows further analysis of correlations of wind speeds in turbulent flows and the effects of its action on guyed masts. The mounted force transducer has been shown in Figure 5.

Figure 5. Force transducer for measuring forces in guys.

3 RESULTS

Time series of the accelerations at selected points of the models have been obtained. Accelerations in two perpendicular directions at the top of the model M1 are presented in Figure 6.

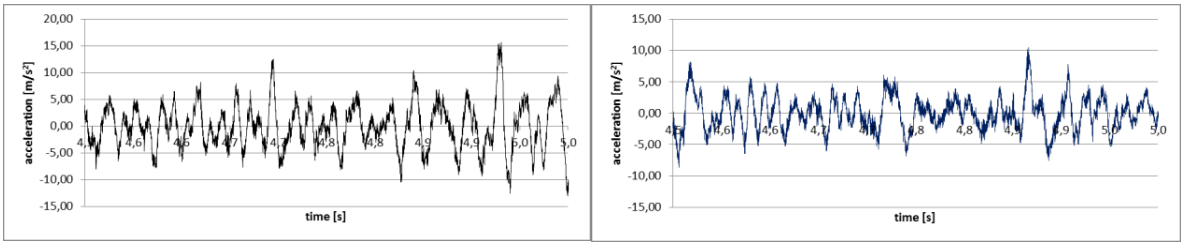

Figure 6. Exemplary time series of accelerations: along mean wind (left) and cross-wind (right) components.

There have been shown exemplary time series of accelerations in Figure 7 for the steps of mean wind speeds selected out of 16 measured ones. There are 6 s views on the left and 0.5 s zooms on the right presented for each time series.

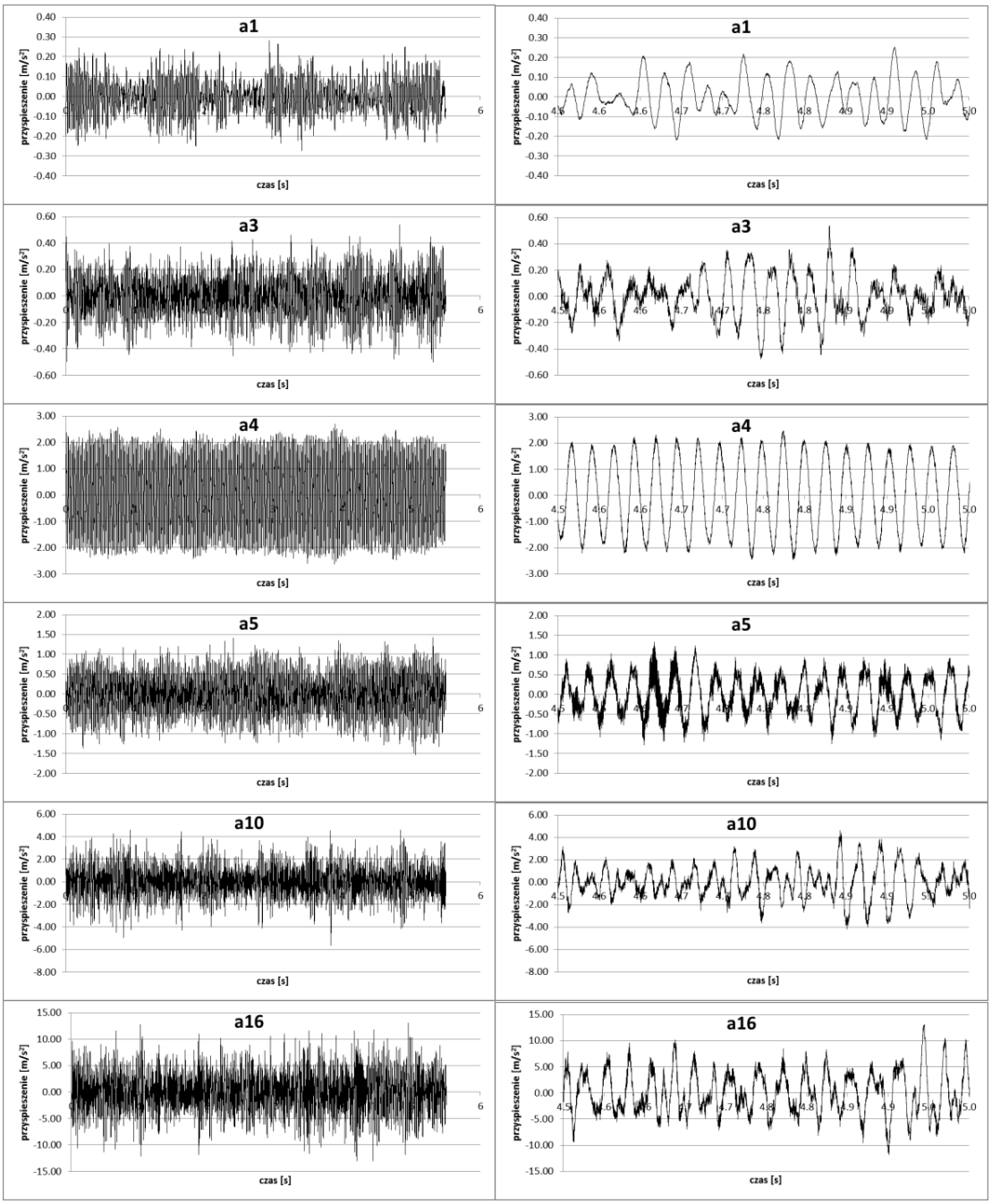

Figure 7. Along wind accelerations for triangular shaft model at the top of the structure (*od_m_tr_2x2_circ-bz2kl0*).

Spectral analysis of the measured variation of acceleration has been made as the next step of the research. Power spectral density functions have been calculated with use of the HBM Catman software. PSD functions have been presented in graphs. Exemplary graphs, respective to the time

series presented previously, have been shown below. Whole calculated spectrum is presented on the left, and 100 Hz zoom is shown on the right in Figure 8.

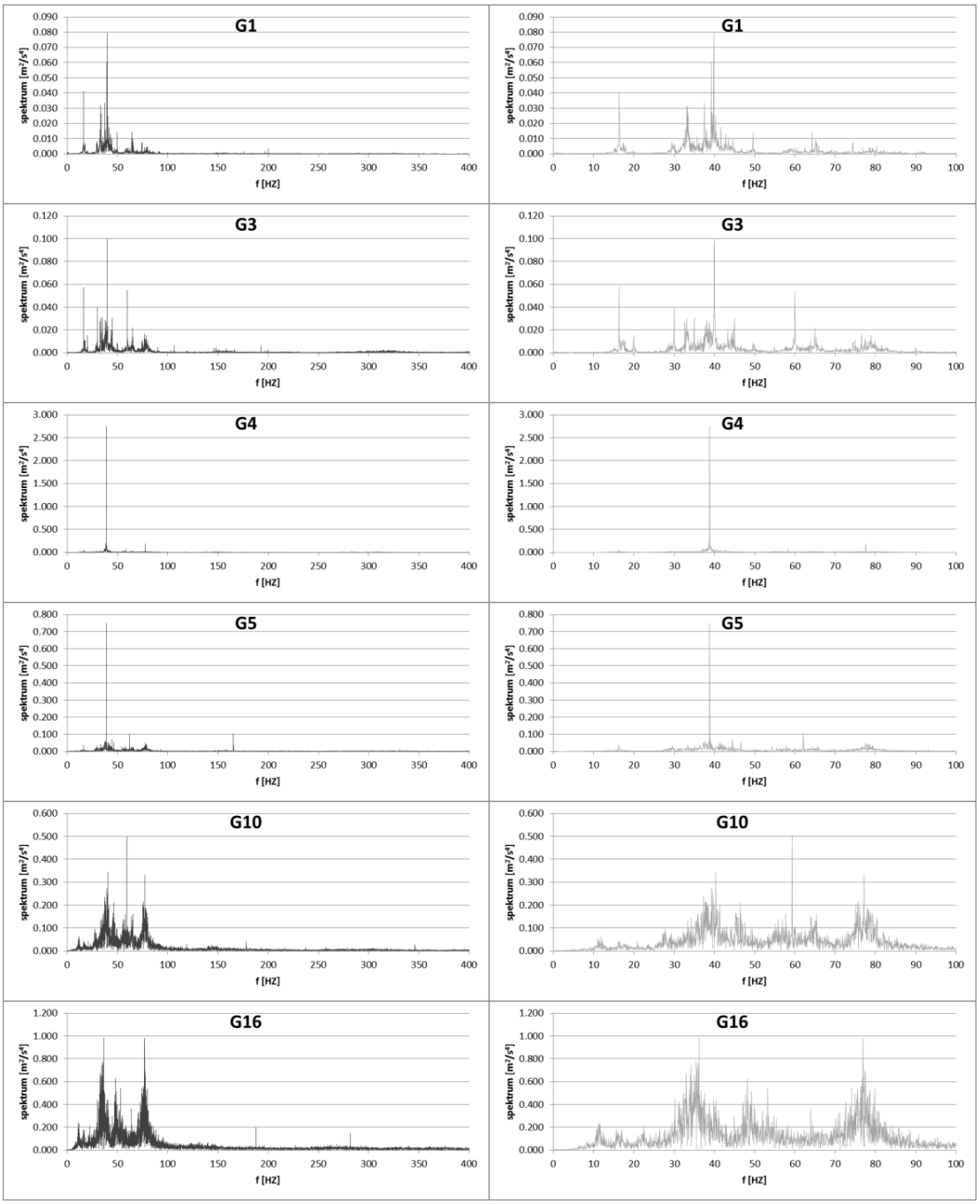

Figure 8. PSD functions for along wind accelerations measured at the top of triangular shaft model (*od_m_tr_2x2_circ-bz2kl0*).

Similar graphs, as for the accelerations, have been made for the forces in guys of the mast models. Exemplary graphs of force time series for the lower guy have been presented in Figure 9. There are 20 s long time series presented on the left, and 1 s zooms shown on the right.

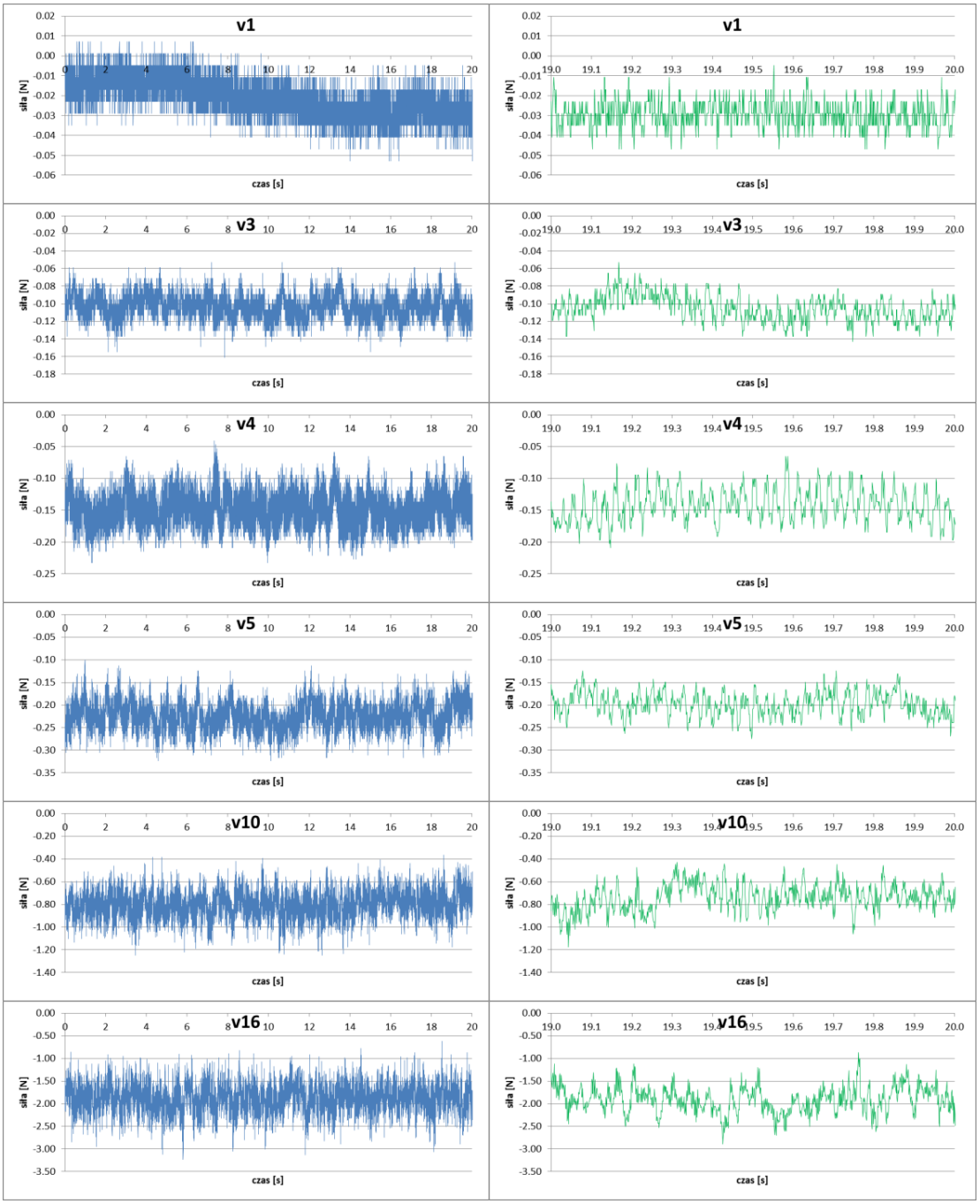

Figure 9. Time series of forces in lower windward guy of triangular shaft model (*od_m_tr_2x2_circ-bz2kl0*).

Spectral analysis of the guy force variations has been made. Exemplary graphs of PSD functions, respective to the time series of force variations in guys, have been presented in Figure 10. The graphs of PSD functions are shown in the same manner as for accelerations.

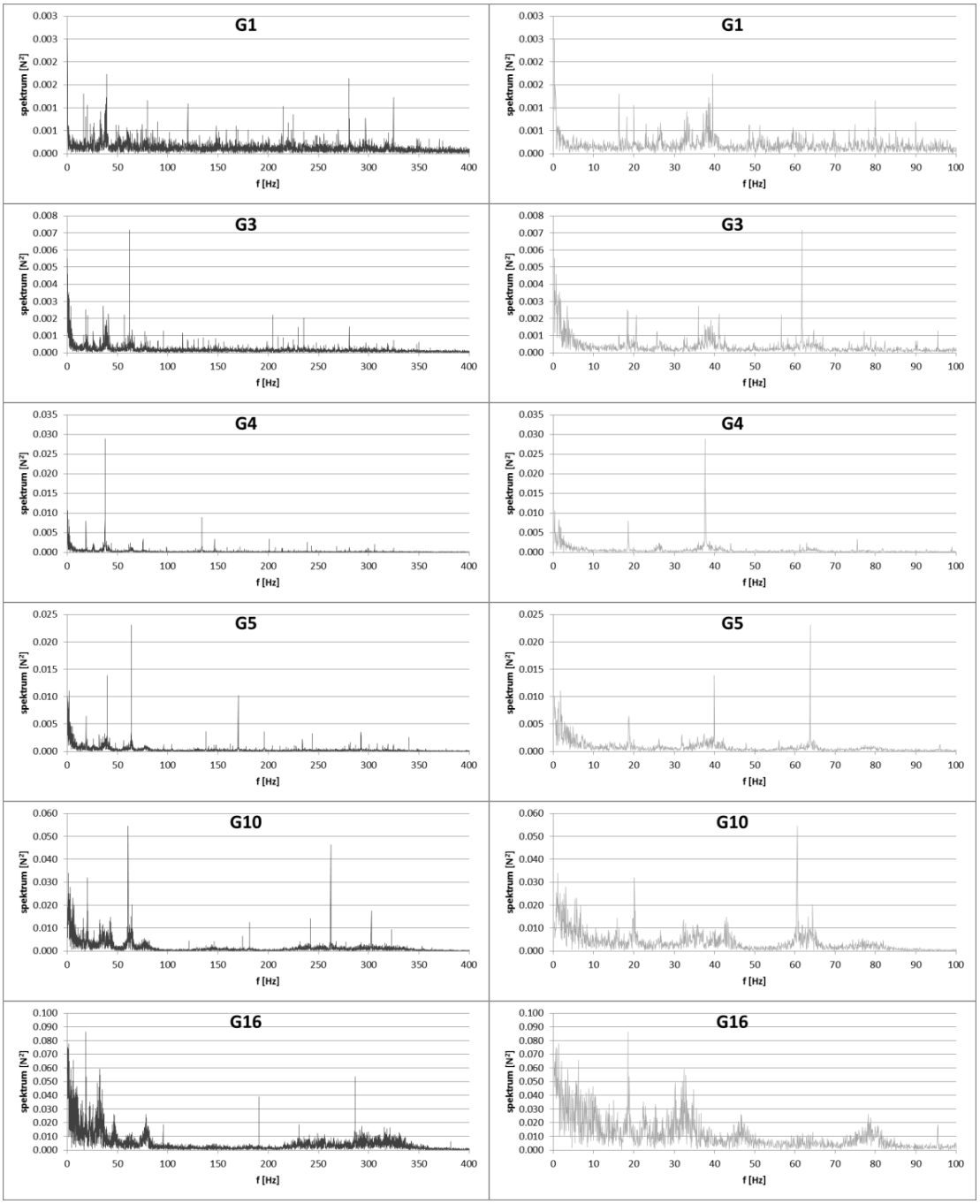

Figure 10. PSD functions for force variations of lower guy in triangular .

The results have been compared with the ones obtained with use of FEM calculations. Own software [3, 4] based on commercial system ALGOR has been used. The wind action has been modeled according to quasi-steady theory [5].

Displacements in selected points of mast structure have been obtained. Exemplary time series of displacements coming from calculations at the top of the mast model have been presented in Figure 11.

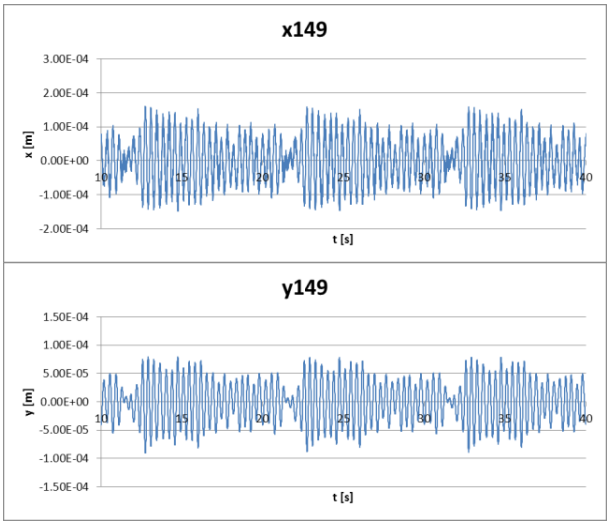

Figure 11. Exemplary time series of displacements of two perpendicular displacements on the top of the mast model.

Double differentiation has led to accelerations. Exemplary time series of along wind accelerations have been presented in Figure 12.

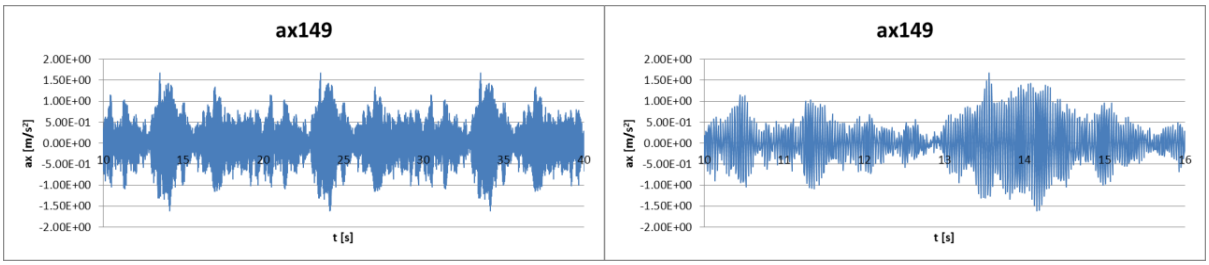

Figure 12. Exemplary time series of along wind accelerations: 30 s long time series (left), 6 s zoom (right).

Amplitudes of accelerations and their standard deviations have been compared with results obtained with measurements at the 8th wind speed level from wind tunnel tests (Fig. 13). The wind speed in numerical analysis has been set approximately equal to the mean wind speed in measurements at this mean wind speed step (v≈10 m/s).

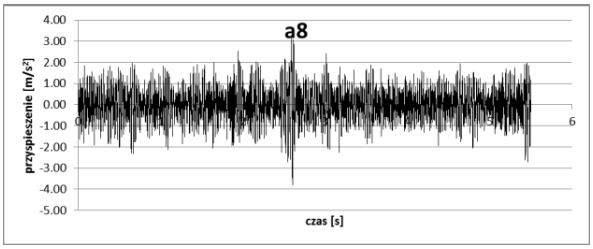

Figure 13. Exemplary time series of along wind accelerations from measurements at 8th mean wind speed step.

The obtained time series of accelerations from numerical analysis are in good accordance with the results from measurements in the wind tunnel. Amplitudes of accelerations in numerical analysis reach about 1.6 m/s^2. Similar values have been noticed in the wind tunnel tests. Amplitudes are usually only slightly higher in measurements than the ones obtained in numerical analy-

sis. There may be values of accelerations exceeding 3 m/s^2 coming from the stronger wind gust observed at short period of time. However, this is not changing the overall picture significantly, and the preliminary verification is proved for measurements versus numerical analysis.

4 CONCLUSIONS

The following conclusions can be drawn out of the presented results:

- Amplitudes of accelerations grow rapidly to about 2 m/s^2 in the case *a4*. Then they are getting smaller to about 1 m/s^2 and in the next steps they constantly grow with the wind speed increase.
- There is one dominating frequency in the case *a4* observed in the graphs of time series of accelerations. This frequency can also be observed in the PSD function graphs.
- The results of measurements allow us to mark the wind speed in this case as the critical one.
- The graphs of guy forces show both frequencies that have been observed in acceleration graphs for shafts and new frequencies that can be distinguished, as the ones referring to guys vibrations only, since they have not been observed before.

Wind parameters have significant influence on guyed masts response. Accelerations measurements allow recognition of mode shapes of vibrations. Different shapes of shaft cross-section of masts only slightly affect the wind field behind models in comparison to the flow without mast models placed in the wind tunnel. High slenderness of the shafts may be responsible for this result.

5 ACKNOWLEDGEMENTS

The work was prepared within Ministry of Science and Higher Education research project – No. N506 267337.

6 REFERENCES

1 A. Flaga, Inżynieria wiatrowa. Podstawy i zastosowania, Arkady, Warszawa, 2008.
2 J. Bęc, T. Lipecki, E. Błazik-Borowa, Research on Wind Structure in the Wind Tunnel of Wind Engineering Laboratory of Cracow University of Technology, Journal of Physics: Conference Series 318 (2011) 072003, doi: 10.1088/1742-6596/318/7/072003
3 J. Bęc, A. Flaga: Aerodynamic Analysis of Guyed Masts, Proc. 4th Symposium "Environmental Effects on Buildings and People", Cracow, Lublin, Susiec, June 16-18, 2004
4 J. Bęc, A. Flaga: Guyed Masts Subjected to Wind and Other Environmental Actions, Proc. the 4th European & African Conference on Wind Engineering, July 11-15, 2005, Prague, Czech Republic
5 A. Flaga, Quasisteady theory in aerodynamics of slender structures, Sonderforschungsbereich 151 – Tragwerksdynamik, Berichte Nr. 25, Ruhr Universität Bochum, Germany

The Seventh International Colloquium on Bluff Body Aerodynamics and Applications (BBAA7)
Shanghai, China; September 2-6, 2012

Aeroelastic behavior of complex lighting poles and antenna masts

Cung Huy Nguyen [a], Andrea Freda [a], Giuseppe Piccardo [a], Giovanni Solari [a], Federica Tubino [a]

[a] *Department of Civil, Environmental and Architectural Engineering, University of Genoa, Via Montallegro 1, Genoa, Italy*

ABSTRACT: This paper presents the analytical and experimental studies of aeroelastic behavior of slender structures, particularly of lighting poles and antenna masts with distributed eccentricities. Critical conditions of coupled galloping and of generalized Den Hartog's criterion are derived in closed form. An application of the method on a real structure indicates the significance of the aerodynamic eccentricities, upper vibration modes, and coupling between the translational components of the motion. Additionally, in case of such a structure, it is pointed out that carrying out the classic simplified SDOF (single degree of freedom) stability analysis may lead to considerable errors in the prediction of instability conditions.

KEYWORDS: Aeroelasticity, steady-state theory, galloping, tubular poles, antenna masts, critical velocity, wind-tunnel test

1 INTRODUCTION

Tubular poles may appear as simple structures that can be modeled, very easily, by a cantilever beam with one or more concentrated masses usually at their top; unfortunately, this is often the concept that inspires the usual static engineering calculations. A deeper reflection on this structural type, however, points out totally different characteristics. The structures are built in such a large and growing number to represent a relevant economic problem in spite of a low single cost. They are characterized by an increasing height, lightness, slenderness and complicated shapes that make them extremely sensitive to complex wind-excited and aeroelastic responses and require refined analyses to capture their physical behavior (Fig.1). An impressive number of collapses that increasingly involve these constructions, frequently due to wind-excited fatigue [1], emphasize their susceptibility to wind actions and their potentially dangerous role in the anthropogenic territory.

A dominant property that joins engineering calculations and refined evaluations carried out in the literature on tubular poles is their idealization as polar symmetric structures. This is definitely not correct due to several peculiar features of these structures, such as stairs, cable bundles, or solar panels, usually applied to the shaft, lighting devices, top balcony, antennas and parabolas that are often put eccentrically with respect to the axis of the shaft, and cylinder hulls, which ever more frequently cover the transmission devices, endowed with non circular sections due to construction imperfections. One or the whole of these situations give rise to mass and shape eccentricities, which make these structures complex, both in mechanical and in aerodynamic terms, and sensitive to potential instabilities due to aeroelastic critical phenomena.

Review in literature shows that there are few studies on this issue, both in theoretical and experimental aspects. Solari and Pagnini [2] analyzed the wind-excited response and the galloping of lighting poles and antenna masts with distributed concentrated masses, upper modes and coupling between alongwind and crosswind vibrations, without considering eccentricities. Cara-

coglia and Jones [3] studied the galloping and buffeting responses of poles with a luminaire at the top; the effect of eccentric aerodynamic loads at the level of the luminaire is taken into account, but the main pole is considered as polar symmetric structure.

(a) (b) (c) (d)

Figure 1. Typical lighting poles and antennas masts

To clarify the role and the importance of the above remarks, this paper introduces a theoretical framework to evaluate the aeroelastic performance of slender structures with distributed eccentricities, particularly of lighting poles and antenna masts. A quasi-steady theory is first developed that takes into account the variations of mass, width of cross section, aerodynamic coefficients, eccentricity, and wind velocity along the structure; besides, upper modes of vibration and coupling effects among such modes are considered; aeroelastic instability conditions are determined in the state space. Starting from this formulation, and introducing suitable conditions, analytical solutions for the critical velocity of coupled and uncoupled systems are then derived.

As an example, this formulation is applied to a real telecommunication antenna mast, in which typical distributed eccentricities, such as stairs, cable bundles and masts are considered. This structure reveals the occurrence of unusual aeroelastic instabilities that emphasize the role of the upper modes, of the coupling between crosswind and alongwind vibrations, of the distribution of the eccentricities along the structural height.

2 GENERAL FORMULATIONS

Let us consider a vertical tubular pole idealized as a vertical cantilever beam with longitudinal axis z passing through the stiffness center of the cross section. The structural motion at height z is defined by two horizontal displacements x and y and a torsional rotation θ. The structure has height L, mass per unit length $m(z)$, width of cross section $b(z)$. The wind direction is horizontal and makes an angle α with axis x (Fig.2).

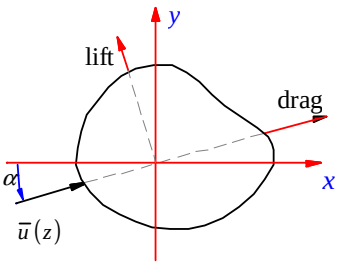

Figure 2. Wind action on a structural body.

To perform the stability analysis, the forces given rise from the mean wind velocity, atmospheric turbulence and vortex shedding are ignored. Then, the equations of motion can be expressed in principal coordinates as follows [4]:

$$\tilde{\mathbf{M}}\ddot{\mathbf{P}}(t)+\tilde{\mathbf{C}}\dot{\mathbf{P}}(t)+\tilde{\mathbf{K}}\mathbf{P}(t)=\tilde{\mathbf{F}}_a(t) \tag{1}$$

where $\mathbf{P}(t)$ is the generalized displacements vector; $\tilde{\mathbf{M}}$=diag($\tilde{m}_i$), $\tilde{\mathbf{C}}$ = diag($2\tilde{m}_i\xi_i\omega_i$), and $\tilde{\mathbf{K}}$=diag($\tilde{m}_i\omega^2{}_i$) are respectively the generalized mass, structural damping, stiffness matrices, in which $\tilde{m}_i$, ξ_i, ω_i are correspondingly the generalized mass, structural damping coefficient, and natural frequency associated with i-th mode (i=1,2…); whereas $\tilde{\mathbf{F}}_a(t)$ is the vector of generalized aeroelastic wind actions:

$$\tilde{\mathbf{F}}_a(t)=\int_0^L \mathbf{\Psi}^T(z)\mathbf{f}_a(z,t)\,dz \tag{2}$$

in which $\mathbf{\Psi}(z)$=[$\boldsymbol{\psi}_1(z)$ $\boldsymbol{\psi}_2(z)$ …] is the modal matrix where $\boldsymbol{\psi}_k(z)$ = [$\psi_{kx}(z)$ $\psi_{ky}(z)$ $\psi_{k\theta}(z)$]^T ; $\mathbf{f}_a(z,t)$=[$f_{ax}(z)$ $f_{ay}(z)$ $f_{a\theta}(z)$]^T is the vector of aeroelastic wind actions. By adopting the quasi-steady theory, it follows that:

$$\mathbf{f}_a(z,t)=-\frac{1}{2}\rho\bar{u}^2(z)b(z)\mathbf{R}^T\mathbf{c}_a(z)\mathbf{R}\mathbf{\Psi}(z)\dot{\mathbf{P}}(t) \tag{3}$$

where ρ is the air density, $\bar{u}(z)$ is the mean wind velocity profile ; $\mathbf{c}_a(z)$ and $\mathbf{R}$ are the aerodynamic coefficient and rotation matrices, respectively:

$$\mathbf{c}_a(z)=\begin{bmatrix} 2c_d(z) & c_d'(z)-c_l(z) & -R_0(z)\left(c_d'(z)-c_l(z)\right) \\ 2c_l(z) & c_d(z)+c_l'(z) & -R_0(z)\left(c_d(z)+c_l'(z)\right) \\ 2b(z)c_m(z) & b(z)c_m'(z) & R_0(z)b(z)c_m'(z) \end{bmatrix};\quad \mathbf{R}=\begin{bmatrix} \cos\alpha & \sin\alpha & 0 \\ -\sin\alpha & \cos\alpha & 0 \\ 0 & 0 & 1 \end{bmatrix} \tag{4}$$

in which $c_d(z)$, $c_l(z)$, and $c_m(z)$ are the mean drag, lift, and torsional moment coefficients, respectively, estimated through static tests in wind tunnel ; $R_0(z)$ is the characteristic radius of the cross section; dealing with a compact section, it is reasonably assumed as equal to zero [5-6].

Substituting Eq.(3) into Eq.(2), then Eq.(2) into Eq.(1) and rearranging in state space form, it leads to:

$$\dot{\mathbf{p}}=\tilde{\mathbf{A}}\mathbf{p} \tag{5}$$

where

$$\mathbf{p}=\begin{bmatrix}\mathbf{P}\\ \dot{\mathbf{P}}\end{bmatrix};\quad \tilde{\mathbf{A}}=\begin{bmatrix}\mathbf{0} & \mathbf{I}\\ -\tilde{\mathbf{M}}^{-1}\mathbf{K} & -\tilde{\mathbf{M}}^{-1}\left(\tilde{\mathbf{C}}+\tilde{\mathbf{C}}_a\right)\end{bmatrix} \tag{6}$$

in which $\tilde{\mathbf{C}}_a$ is the generalized aerodynamic damping matrix:

$$\tilde{\mathbf{C}}_a=\frac{1}{2}\rho\int_0^L \bar{u}(z)b(z)\mathbf{\Psi}^T(z)\mathbf{R}^T(z)\mathbf{c}_a(z)\mathbf{R}\mathbf{\Psi}(z)dz \tag{7}$$

The dynamical system represented by Eq.(5) is asymptotically stable if and only if all the real part of the eigenvalues of matrix $\tilde{\mathbf{A}}$ are negative [7]. Such an eigenvalue problem to find the con-

dition for the instability occurrence is normally solved through a numerical procedure. Particularly, neglecting the torsional rotation component and assuming that the resultant 2 DOFs coupled system is endowed with a set of couples of orthogonal modes having the same frequencies, i.e. $\omega_{2k-1}= \omega_{2k}$ (k = 1,2,…), this problem can be solved in closed form and the eigenvalues of the matrix $\tilde{\mathbf{A}}$ are given by [4, 8]:

$$\begin{aligned}\lambda_{1,2} &= i-\xi_{2k}+\frac{\rho b(z_e)\bar{u}(z_e)}{8\tilde{m}_{2k,eq}\omega_{2k}}\left(-\operatorname{tr}\tilde{\mathbf{C}}_{a,2k,eq}\pm\sqrt{\operatorname{tr}^2\tilde{\mathbf{C}}_{a,2k,eq}-4\det\tilde{\mathbf{C}}_{a,2k,eq}}\right)\\ \lambda_{3,4} &= -i-\xi_{2k}+\frac{\rho b(z_e)\bar{u}(z_e)}{8\tilde{m}_{2k,eq}\omega_{2k}}\left(-\operatorname{tr}\tilde{\mathbf{C}}_{a,2k,eq}\pm\sqrt{\operatorname{tr}^2\tilde{\mathbf{C}}_{a,2k,eq}-4\det\tilde{\mathbf{C}}_{a,2k,eq}}\right)\end{aligned} \tag{8}$$

where i is the imaginary unit; z_e is a reference height; $\tilde{m}_{2k,eq}$ and $\tilde{\mathbf{C}}_{a,2k,eq}$ are the equivalent mass and aerodynamic matrix related to mode 2k-th, respectively:

$$\tilde{m}_{2k,eq}=\frac{\int_0^L m(z)\left\|\boldsymbol{\Psi}_{2k}(z)\right\|^2 dz}{\int_0^L\left\|\boldsymbol{\Psi}_{2k}(z)\right\|^2 dz}\ ;\ \tilde{\mathbf{C}}_{a,2k,eq}=\int_0^L \boldsymbol{\Pi}_{2k}^T(z)\mathbf{c}_a(z)\boldsymbol{\Pi}_{2k}(z)dz \tag{9}$$

in which $\mathbf{c}_a$ is the aerodynamic matrix achieved by dropping the third column and row in the aerodynamic matrix $\mathbf{c}_a(z)$ given in Eq.(4), and $\boldsymbol{\Pi}_{2k}(z)$ is a functional matrix associated with the 2k-th mode given by:

$$\boldsymbol{\Pi}_{2k}(z)=\sqrt{\frac{\bar{\mu}(z)b(z)}{\bar{\mu}(z_e)b(z_e)\int_0^L\left\|\boldsymbol{\Psi}_{2k}(z)\right\|^2 dz}}\mathbf{R}\boldsymbol{\Psi}_{2k}(z) \tag{10}$$

where $\|\boldsymbol{\Psi}_{2k}(z)\|$ denotes the norm of the mode shape $\boldsymbol{\Psi}_{2k}(z)$ and $\bar{\mu}(z)$ is a suitable non-dimensional function expressing the shape of the mean wind velocity profile, e.g. a power or logarithm law:

$$\bar{u}(z)=\bar{u}(z_e)\frac{\bar{\mu}(z)}{\bar{\mu}(z_e)} \tag{11}$$

As a result, the necessary condition for instability is represented by the simultaneous satisfaction of the following two equations:

i) $\operatorname{tr}\tilde{\mathbf{C}}_{a,2k,eq}<0$ (12)

ii) $\operatorname{tr}\tilde{\mathbf{C}}_{a,2k,eq}\geq 0>\det\tilde{\mathbf{C}}_{a,2k,eq}$ (13)

The critical velocity at the reference height z_e associated with such two conditions is given by:

i) $$\bar{u}_{cr,2k}(z_e)=\begin{cases}-\dfrac{8\omega_{2k}\xi_{2k}\tilde{m}_{2k,eq}}{\rho b(z_e)\,\mathrm{tr}\,\tilde{\mathbf{C}}_{a,2k,eq}} & for\ \ \mathrm{tr}^2\,\tilde{\mathbf{C}}_{a,2k,eq}-4\det\tilde{\mathbf{C}}_{a,2k,eq}\le 0\\ -\dfrac{8\omega_{2k}\xi_{2k}\tilde{m}_{2k,eq}}{\rho b(z_e)\left[\mathrm{tr}\,\tilde{\mathbf{C}}_{a,2k,eq}-\sqrt{\mathrm{tr}^2\,\tilde{\mathbf{C}}_{a,2k,eq}-4\det\tilde{\mathbf{C}}_{a,2k,eq}}\right]} & for\ \ \mathrm{tr}^2\,\tilde{\mathbf{C}}_{a,2k,eq}-4\det\tilde{\mathbf{C}}_{a,2k,eq}>0\end{cases} \tag{14}$$

ii) $$\bar{u}_{cr,2k}(z_e)=-\frac{8\omega_{2k}\xi_{2k}\tilde{m}_{2k,eq}}{\rho b(z_e)\left[\mathrm{tr}\,\tilde{\mathbf{C}}_{a,2k,eq}-\sqrt{\mathrm{tr}^2\,\tilde{\mathbf{C}}_{a,2k,eq}-4\det\tilde{\mathbf{C}}_{a,2k,eq}}\right]} \tag{15}$$

It is worth noting that the eigenvalues derived in Eq.(8) and the instability conditions given in Eq. (12)-(15) take into account the variation along the whole structures of the width of cross section $b(z)$, mass per unit length $m(z)$, aerodynamic coefficients $\mathbf{c}_a(z)$, and mean wind velocity $\bar{u}(z)$. So, they constitute the generalization of the solutions given in literature, e.g. in [8], in which those structural and aerodynamic parameters were assumed to be constant. Moreover, focusing on the sole oscillation corresponding to crosswind modes, the galloping analysis of a SDOF system can be derived as a particular case of Eqs.(12) and (13). This can be done by setting α=0 and by considering only the element (2,2) of matrix $\tilde{\mathbf{C}}_{a,2k,eq}$. Consequently, the necessary condition for galloping occurrence it the k-th mode in the crosswind direction results:

$$\left(c_d+c_l'\right)_{k,eq}<0 \tag{16}$$

where $(c_d+c'_l)_{k,eq}$ is the equivalent galloping coefficient in the k-th mode obtained from the second equation of Eq.(9):

$$\left(c_d+c_l'\right)_{k,eq}=\int_0^L\left[c_d(z)+c_l'(z)\right]\Pi_k(z)\,dz \tag{17}$$

in which $\Pi_k(z)$ is a function related to the k-th mode:

$$\Pi_k(z)=\frac{\bar{\mu}(z)b(z)\psi_k^2(z)}{\bar{\mu}(z_e)b(z_e)\int_0^L\psi_k^2(z)\,dz} \tag{18}$$

The critical velocity corresponding to k-th mode at the reference height z_e is provided by:

$$\bar{u}_{cr,k}(z_e)=-\frac{4\omega_k\xi_k\tilde{m}_{k,eq}}{\rho b(z_e)\left(c_d+c_l'\right)_{k,eq}} \tag{19}$$

For a particular case in which $m(z)$, $b(z)$, $c_d(z)$, $c'_l(z)$, and $\bar{u}(z)$ are constant, then $(c_d+c'_l)_{k,eq}$ is equal to $(c_d+c'_l)$; furthermore, the critical velocity related to the first crosswind mode is resulted in:

$$\bar{u}_{cr,1}=-\frac{4\omega_1\xi_1 m}{\rho b\left(c_d+c_l'\right)} \tag{20}$$

which is the one given by Den Hartog.

Consequently, Eq.(16) and Eq.(19) are the generalizations of the classical galloping analysis.

It is worth noting that once the critical wind velocity at the reference height z_e is determined, thanks to Eq.(11), a critical wind profile is established.

3 CASE STUDY

An infinite series of different lighting poles and antennas masts exists in reality. The theoretical framework described above is applied herein to study the aeroelastic behavior of a particular type of real structure. This structure is an antenna mast whose total height is h = 30 m and it is composed by two steel shafts with circular sections (Fig.3). The first shaft, which is referred to as main shaft, is 24 m long. The outer diameter of its section, whose thickness is 5 mm, varies from 950 mm at the bottom to 350 mm at the top. The cables attached along this shaft have a distributed mass per unit length 5 kg/m. The second shaft, put above the first one, is 6 m long, and it carries 6 antennas; the total weight of this shaft is 540 kg. Its section has constant outer diameter 193.7 mm, and it is 7.1 mm thick. A stair is placed along the whole structure and has a unit mass per length 7 kg/m. The structural damping for each mode is assumed as 0.5%. The additional stuffs such as the stair, cables, and antennas give rise to a distributed mass eccentricity; instead, they are assumed to be ineffective to the structural stiffness. Besides, the pole is located at a terrain characterized by a roughness length z_0=0.3 m, and the mean wind velocity is assumed to follow the logarithm law.

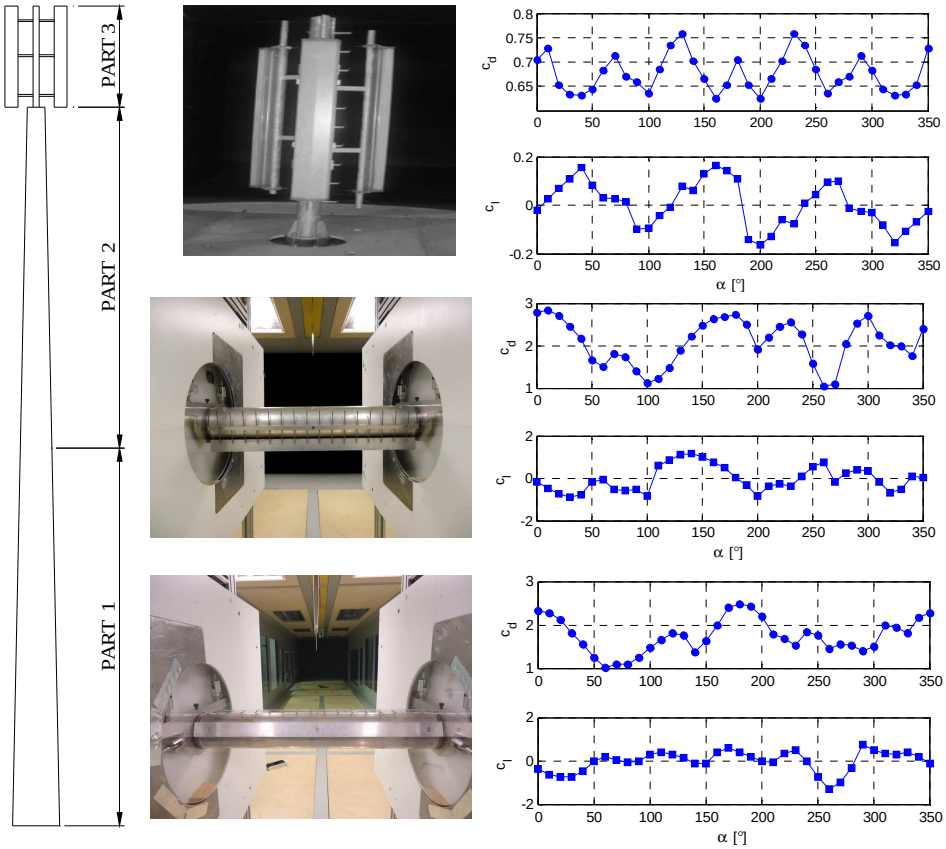

Figure 3. Sectional models of wind tunnel test and aerodynamic coefficients.

The static aerodynamic coefficients have been determined by wind tunnel tests. The tests on the main shaft have been conducted in the wind tunnel of the Faculty of Engineering of the University of Genoa. Since the outer diameter of the main shaft varies significantly from 950 mm to 350 mm, measurements have been carried out by dividing this shaft into two uniform parts with geometric scales 1:5 and 1:10. The angle of attack has been varied with 10° steps. For the top shaft, the results achieved from previous experiments performed in the wind tunnel of Milan Polytechnic have been used. All results pointed out that the Reynolds numbers do not affect considerably the aerodynamic coefficients. Fig.3 shows the drag and lift coefficients for each part of the pole.

4 NUMERICAL RESULTS AND DISCUSSIONS

The modal analysis provides the first four natural frequencies: $n_{1,2}$=0.774 Hz, $n_{3,4}$=3.628 Hz. The corresponding mode shapes are plotted in Fig.4. The eccentricity does not change the substantial similarity between couples of natural frequencies in translational directions, but it couples the corresponding mode shapes.

In the stability analysis, the Den Hartog's criterion is preliminarily utilized for each of three parts of the pole. Next, the instability conditions presented in the previous section for the SDOF and the 2DOF systems, i.e. uncoupled and coupled vibrations, are applied.

The analysis is carried out by taking into account the variation along the whole structure of the mass, width, mean wind velocity and aerodynamic coefficients. Two cases are considered, namely the shaft without eccentricity and with an eccentricity varying along its height. By employing Eq.(9), it results in that $\mathrm{tr}\tilde{\mathbf{C}}_{a,2k,eq}$ is always positive. Then Eqs.(13), (15), (16), and (19) are applied to determine the instability conditions and the critical velocities for both SDOF and 2DOF systems. The critical velocity is evaluated at the reference height fixed z_e=10 m. Any critical velocity larger than 200 m/s is disregarded. It is found that, on one hand, the presence of the distributed eccentricity, which is small as compared with the pole diameter, does not influence the aeroelastic response. On the other hand, the following remarks are highlighted.

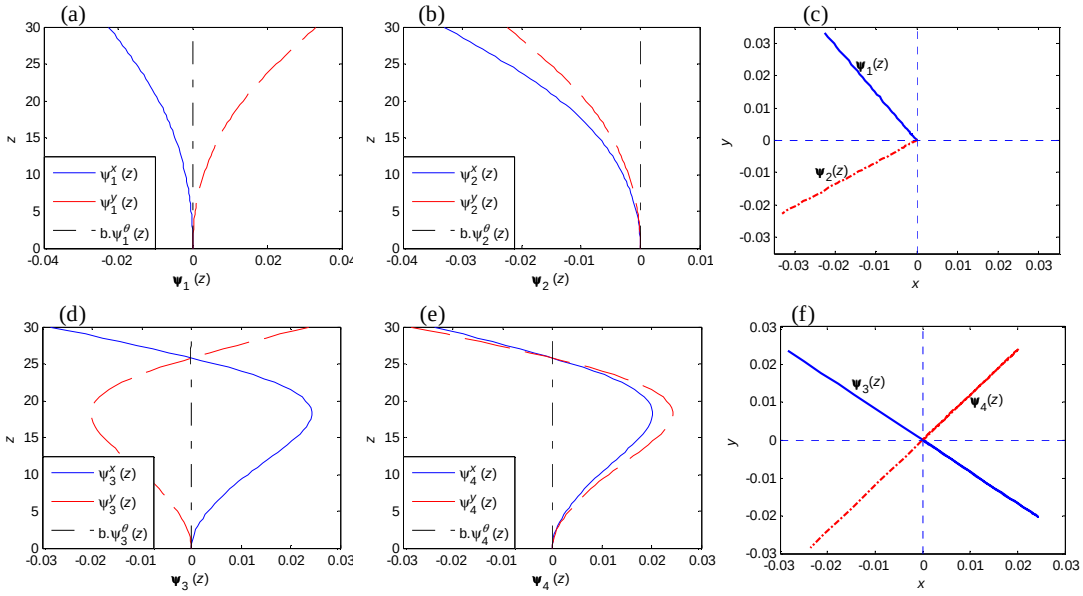

Figure 4. First four mode shapes : (a) first mode; (b) second mode; (c) first and second modes top view; (d) third mode; (e) fourth mode; (f) third and fourth modes top view

Firstly, Fig.5a shows the values of $(c_d+c'_l)$ for each of the three parts of the pole; Fig. 5b shows the values of $(c_d+c'_l)_{k,eq}$ provided in Eq.(17) for the first two crosswind modes. It can be seen that, according to the Den Hartog's criterion for each of three single parts, part 1 can gallop at wind attack angles 240° and 250°; part 2 at 0°, 100°, 120°, and 240° ; part 3 at 180° and 190°. However, applying the generalized Den Hartog's criterion given by Eq.(16), in which the shaft is considered in its whole, the structure can gallop at only 3 wind attack angles 180°, 190° and 240°. Moreover, the structure can be unstable not only in the first crosswind mode (mode 2 in Fig.2) but also in the second crosswind mode (mode 4 in Fig. 2). This latter case occurs for the angle of attack 240° where it cannot gallop in the first crosswind mode. Therefore, carrying out the galloping analysis only for first crosswind mode of a SDOF system can be unsafe.

Secondly, Fig.6a shows the necessary condition for instability of a 2DOF system, i.e. $\det\tilde{\mathbf{C}}_{a,2k,eq} < 0$, and Fig.6b presents the critical velocities for the 2DOF coupled system (Eq.(15)) in comparison with those for the SDOF uncoupled one (Eq.(19)). That the instability can occur in the third and fourth coupled modes reconfirms the importance of the higher modes in the stability analysis. Moreover, at the angle 180°, the SDOF model provides the critical velocity 37.03 m/s, while the 2DOF model gives a higher value, 40.52 m/s; in this case, carrying out a SDOF galloping analysis, as in the common practice, provides a result on the safe side. The situation changes at the angle 190°, where the critical velocity of a 2DOF system is 23.87 m/s, considerably lower than the value 36.12 m/s provided by a SDOF galloping analysis. This huge error (34%) stresses the significance of coupling the crosswind component of the motion with the alongwind one. In other words, neglecting such coupling as usual may give rise to unsafe evaluations. The difference between the above two critical velocities may result from the internal resonance due to the equality of two translational modes.

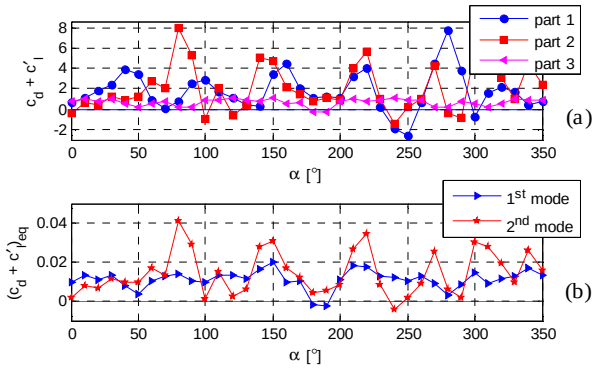

Figure 5: Galloping condition for SDOF system: Den Hartog'creterion (a); generalized Den Hartog's criterion (b)

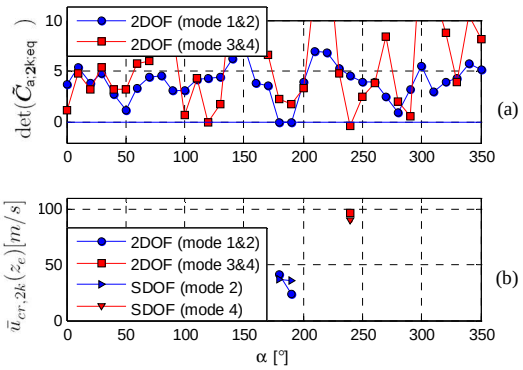

Figure 6. (a) Necessary conditions for 2DOF galloping; (b) Critical velocities.

Thirdly, in the first crosswind mode of a SDOF system, and in the first two modes of a 2DOF system, the galloping occurs only at the angles 180° and 190°, at which the top antennas part (part 3) is potentially unstable. This emphasizes the role of the antennas in the instability of the whole structure. To investigate deeper this role, the analysis is replicated by rotating the top part with an angle θ varying from 0° to 350°, with respect to the main pole, with an increment of 10°. Fig.7a shows, for each the angles of attack α, the minimum critical velocity corresponding to all the rotation angles θ. It can be witnessed that the structure is potentially unstable with different critical velocities for different position of the antennas part. In the meanwhile, for each angle θ, Fig.7b plots the minimum critical velocity corresponding to all the attack angles α. From this, the worst position of the top part respect to the main shaft that the critical velocity is smallest corresponds to θ=310°. This means that the antennas should not be put in such a position during the construction. In addition, due to the resonant coupling between the first two translational modes, the critical velocities of a 2DOF system are not always close to those of a SDOF system; even more, in some cases, e.g. at θ=0°, 140°, 150°, they are seriously lower than those of a SDOF system. Besides, the structure is unstable in the 4th uncoupled mode and in the 3rd and 4th coupled modes at all rotating angles θ while it is still stable in the lower modes at θ equal to 30°, 40°, 100°, 110°, 200°, 230°, 240°, and 330°. In summary, this study points out that, on one hand, the effect of the top antennas part on the stability of whole pole is noteworthy. On the other hand, it is confirmed that neglecting the alongwind component of the response, i.e. considering only the crosswind SDOF instability with different modes may lead to remarkable errors being fatal to the structure.

Lastly, to understand deeper the influence of the antennas part on the structural stability, the analysis is repeated by covering the antennas with a cylinder, as it is shown in Fig.1d. For this cylinder, c_d=0.74, and c_l=c'_d=c'_l=0. Fig.8a plots the necessary instability conditions (tr$\tilde{\mathbf{C}}_{\boldsymbol{a},2k,eq}$ is absent in this figure since it is positive for every k) while Fig.8b shows the critical velocities for the 2DOF coupled system in comparison with those for the SDOF uncoupled one. It can be seen that the instability phenomenon occurs only at 240° for the second crosswind mode in the case of a SDOF system and in the second two modes in the case of a 2DOF system. This phenomenon disappears at the lower modes. Furthermore, the critical velocities given by the SDOF and 2DOF models are coincident with the value 64.3 m/s. It can be concluded that the cover cylinder does not only create a positive aerodynamic damping that makes the structure more stable, but it can also decouple the aeroelastic motions in translational directions. It should be observed, however, that these considerations apply to perfectly circular cylinders. Recent experiences showed that this situation is definitely not guaranteed. In some limit cases values of the lift coefficient in the order of 0.4 have been detected. This creates a further sort of complexity that can modify also the stability conditions of the pole.

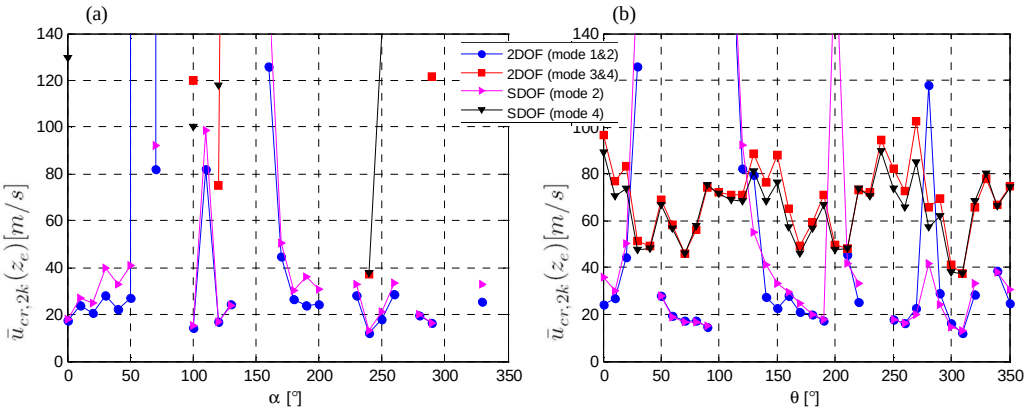

Figure 7. Minimum critical velocity by rotating the antennas part

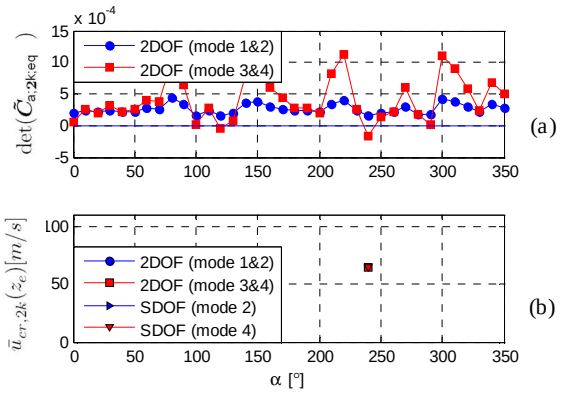

Figure 8. Conditions for 2DOF galloping with the cover cylinder: necessary condition (a); critical velocity (b)

5 CONCUSIONS AND PERSPECTIVES

This paper establishes a general theoretical framework to study the aeroelastic instability of slender structures with distributed eccentricities. Neglecting torsion and focusing on the internal resonance of translational oscillations, an analytical solution for coupled instability conditions is formulated, which generalizes some previous results available in literature. The classic galloping condition for a SDOF system vibrating in the crosswind direction is obtained as a particular case.

An application of presented method to a real telecommunication antenna mast points out the importance of the aerodynamic eccentricities, of the upper modes of oscillation, and of the coupling between the crosswind and alongwind components of the motion. A comparison between the results provided herein and the classical engineering approaches emphasizes that relevant errors may occur, especially for particular sets of parameters and specific configurations. In such conditions the structure may exhibit very low critical galloping velocity able to produce unexpected damages and collapses. This might explains a lot of damages and collapses that these structures often suffer without clear and suitable explanations.

Showing the potentiality for the occurrence of critical situations unpredictable by means of classic models, this paper can be regarded as a preliminary step towards more refined analyses that may confirm the results provided herein.

The first and most important point is to study the reliability of the proposed theory by carrying out suitable aeroelastic wind tunnel tests and comparing the results obtained with monitored structures and the engineering evidence. Such study cannot avoid the investigation of the role of the turbulence, neglected herein by considering only smooth flows.

A second point to be inspected is a generalization of this study from the aeroelastic instability conditions to the wind-excited response [9, 10] and fatigue [11, 12]. Even far from unstable behavior, slender structures with distributed eccentricities are traditionally calculated without considering such eccentricities, crosswind response and upper modes. The results provided in this paper point out that all these aspects might strongly increase design wind loads, making the current design approaches for these structures seriously unsafe.

6 REFERENCES

[1] M.P. Repetto and G.Solari, Wind-induced fatigue collapse of real slender structures. Engineering Structures, 32 (2010), 3888-3898.

[2] G. Solari and L.C. Pagnini, Gust buffeting and aeroelastic behaviour of poles and monotubolar towers. Journal of Fluids and Structures, 13, 7-8 (1999), 877-905.

[3] L. Caracoglia and N.P. Jones, Numerical and experimental study of vibration mitigation for highway light poles, Engineering Structures, 29 (2007), 821–831
[4] C.H. Nguyen, Aerodynamic and aeroelastic analysis of complex structures. Ph.D. Thesis, University of Genoa, 2012, in progress.
[5] R.D. Blevins and W.D. Iwan, The Galloping Response of a Two Degree-of- Freedom System. Journal of Applied Mechanics, ASME, December (1974), 1113- 1118.
[6] Y. Nakamura and T. Mizota, Torsional Flutter of Rectangular Prisms. Journal of Engineering Mechanics Division, ASCE, 101 (1975), 125-142.
[7] L. Meirovitch, Elements of vibration analysis (2nd edition), McGraw-Hill, 1986.
[8] G. Piccardo G, L. Carassale and A. Freda, Critical conditions of galloping for inclined square cylinders. Journal of Wind Engineering and Industrial Aerodynamics, 99 (2011), 748-756.
[9] G. Piccardo and G. Solari, 3-D gust effect factor for slender vertical structures, Probabilistic Engineering Mechanics, 17, (2002) 143-155.
[10] M.P. Repetto and G. Solari, Equivalent static wind actions on vertical structures, Journal of Wind Engineering and Industrial Aerodynamics, 92 (2004), 335-357.
[11] M.P. Repetto and G. Solari, Closed form solution of the alongwind-induced fatigue damage of structures. Engineering Structures, 31 (2009), 2414-2425.
[12] M.P. Repetto and G. Solari, Engineering methods for evaluating the alongwind-induced fatigue of structures. Journal of Engineering Structures, ASCE, (2012), in press.

The Seventh International Colloquium on Bluff Body Aerodynamics and Applications (BBAA7)
Shanghai, China; September 2-6, 2012

Design wind loads of wire mesh claddings and their fatigue behavior considering structural non-linearities

Frank H. Kemper[1], Markus Feldmann[2]

[1,2]*RWTH Aachen University, Institute for Steel Structures, Aachen, Germany*

ABSTRACT: Cladding elements made of prestressed, permeable wire meshes are for different reasons challenging with respect to their aerodynamic load-response behavior. On the one hand, the aerodynamic admittance is dominated by the flow resistance of the mesh and its individual location on the buildings surface. On the other hand, the wind excited stress range spectra may lead to structural failures caused by fatigue, therefore a proper determination of the expected gust induced vibrations and a subsequent stress analysis of the geometric non-linear structure is necessary. By means of wind tunnel tests and a sophisticated analytical model of the non-linear dynamic structure, a realistic design concept has been derived to allow a closed form structural dimensioning.

KEYWORDS: Permeable Structures, Gust Response, Geometric non-linearity, Fatigue Design

1 INTRODUCTION

Permeable cladding structures are part of modern architectural concepts. In most cases only simplest static load assumptions are considered for their design, i.e. a consideration as a free standing element. However, the complexity of the actual installation position and the thereby caused interaction with a closed inner façade lead to a significantly modified aerodynamic impact. Especially for permeable elements with high porosity, general rules are rare.

Wind affected structures generally have to withstand fluctuating load cycles. For an appraisement whether the resulting stress range spectra may lead to structural failures during the designed lifetime, standard methods are still rare because the influencing parameter are manifold. A realistic determination of structural stress range spectra provoked by the natural wind, needs profound knowledge about the statistical properties of the wind flow at the considered site, as well as about the dynamic structural behavior. Eventually, the interpretation of the resulting structural responses in terms of stress amplitudes $\Delta\sigma$ and associated frequencies of occurrence $N(\Delta\sigma)_{Life}$ over the expected lifetime are the main task to allow fatigue verifications. The complexity of the topic increases significantly, when the usual linearized considerations are not sufficient anymore. In the present paper the fatigue behavior of geometrically non-linear elements under gusty wind loads is considered.

2 WIRE MESH CLADDINGS

Cladding structures made of wire mesh are part of modern architectural concepts and they are used both as an amendment of conventional closed façades and as sole building closure (e.g. for car parks). In Figure 1 an innovative cladding concept is shown, thereby the permeable wire mesh webs are installed in front of the glazed façade.

[1]kemper@stb.rwth-aachen.de

Figure 1. Exemplary Wire Mesh Cladding Structure at the Los Angeles Police Department, USA

2.1 Static Wind Force Description

2.1.1 Simplified Load Considerations

For the calculation of the static wind forces, the aerodynamic characteristics of the used meshes and the influence of the installation position at the building have to be known. In case of multi-layered cladding systems, where the outer skin is made of a permeable mesh structure and the inner one is impermeable, the distance between both is an important additional parameter for the load determination.

Approximative values for the design of mesh elements, a simple accumulation of the flow resistances leads to conservative results. Taking the example of the multi-layered cladding, the flow resistance consists of the mesh resistance and the resistance of the inner barrier. The first effect can be approximated by the Bernoulli Equation under consideration of the pressure loss coefficient of the mesh (1). Hence, the acting local wind speed u_i can be determined to:

$$\frac{\rho}{2} \cdot u_\infty^2 = (1 + \zeta_{Mesh}) \cdot \frac{\rho}{2} \cdot u_i^2 \rightarrow u_i = u_\infty \cdot \sqrt{\frac{1}{1 + \zeta_{Mesh}}} \tag{1}$$

The computation of local loads can be performed based on the mesh force coefficient and the local flow velocity v_i. Due to the second resistance effect (closed inner wall), generally an additional reduction of the local flow speed can be expected.

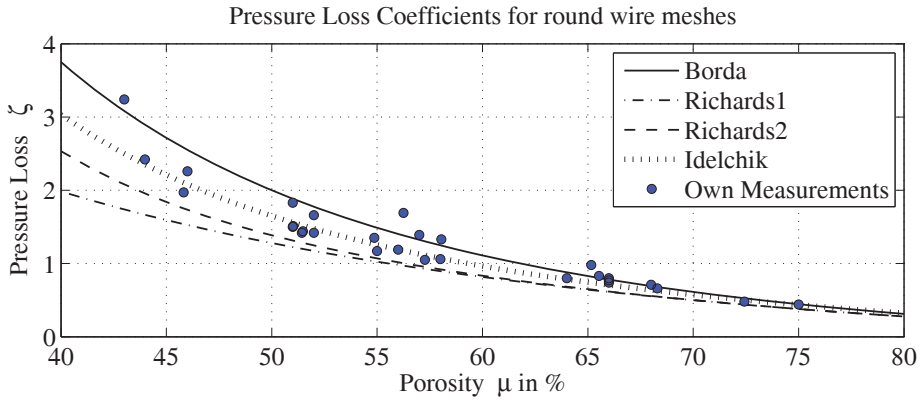

Figure 2. Pressure Loss Coefficients ζ of round Wire Meshes, Comparison of own Measurements and Data from other Authors

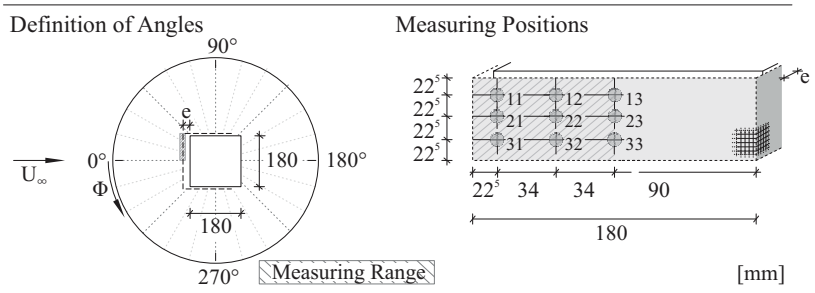

Parameter					
α = 0,16	h_{ref} = 90 mm	$I_{u,ref}$ = 0,17	λ_{Geo} = 1:250	Φ_{Range} = 0°-360°	ζ_{Mesh} = 1.3
e = 3-20 mm	u_{ref} = 12 m/s	L_{ux} = 400 mm	λ_{Time} = 1:100	ΔΦ = 15°	

Figure 3. Illustration of the Wind Tunnel Model and Definition of Measurement Parameters, Angles and Measuring Positions

2.1.2 BLWT Investigations

More detailed information about the directional wind load components (due to the mesh resistance as well as due to the inner blockage) can be achieved based on experiments in the boundary layer wind tunnel. With this aim, a model of a building with multi-layered cladding system and variable distance between the cladding layers has been build in a scale of M1:250 (s. Fig. 4). For the measurements, a circular mesh cut-out has been connected to a high precision force balance ($F_{max} = 0.5$N). The position of the force balance was variable in 9 positions.

In order to allow a statistic analysis of the extreme wind induced forces, for each wind direction 30 independent runs have been performed. For a unique formulation of the location dependent wind load effects but independent of the mesh resistance, a flow parameter α_{local} is introduced, which represents the flow resistance caused by the impermeable inner wall. Generally, the wind load effect is formulated as:

$$\alpha_{local} \cdot c_{f,Mesh} = \frac{1+\zeta_{Mesh}}{q} \cdot \frac{F_{local}}{A} = \frac{F_{local}}{q_{local} \cdot A} \tag{2}$$

Under consideration of an Extreme Value distribution Type I, the peak values for the locational flow parameter α_{local} can be computed based on the well-known *Cook-Mayne* [3] method, whereat the force coefficient c_f refers to the mean wind load admittance of the mesh. Altogether,

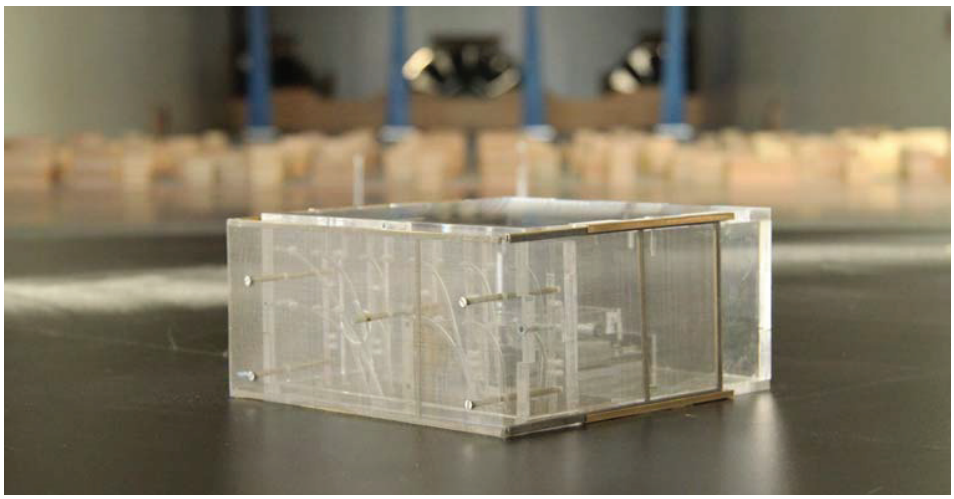

Figure 4. Windtunnel Model of a closed Building with permeable outer Cladding in a scale of 1:250

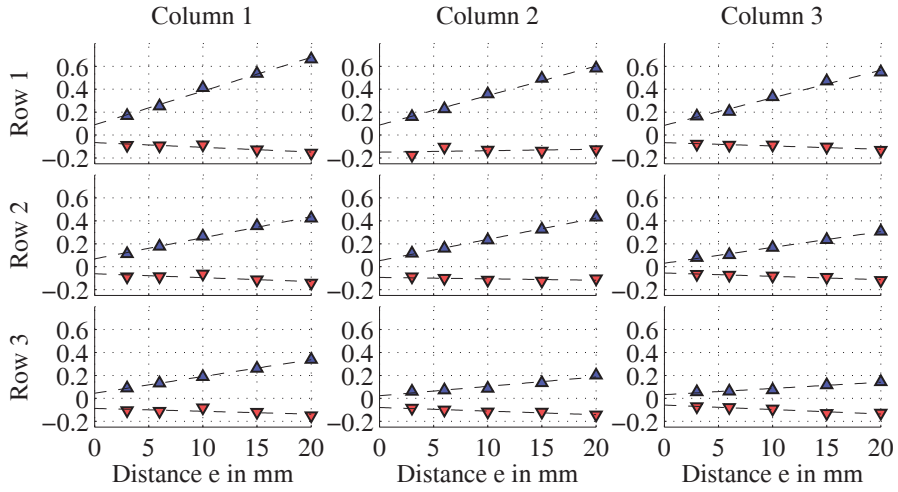

Figure 5. Characteristic Values $\hat{\alpha}$ and $\check{\alpha}$ for a mesh with a Pressure Loss Coefficient $\zeta_{Mesh} = 1.3$ for different Cladding Positions, dependent on the Distance e between Mesh and inner Cladding

the following formulas have been used for the analysis:

$$\hat{\alpha}_{local} = (1+\zeta_{Mesh}) \cdot \frac{mean(\hat{F}_i) + 0.636 \cdot std(\hat{F}_i)}{q_p(z = H_{OK}) \cdot c_f \cdot A} \tag{3}$$

$$\check{\alpha}_{local} = (1+\zeta_{Mesh}) \cdot \frac{mean(\check{F}_i) - 0.636 \cdot std(\check{F}_i)}{q_p(z = H_{OK}) \cdot c_f \cdot A} \tag{4}$$

In Figure 6 the results for $\hat{\alpha}$ are plotted, dependent on the wind direction and the distance between the cladding layers in model scale. Obviously, the perpendicular and nearly perpendicular flow towards the mesh ($\Theta \approx 0° - 20°$) is most unfavorable for the positive force in wind direction. With increasing distance between mesh and closed inner façade, as well as with increasing

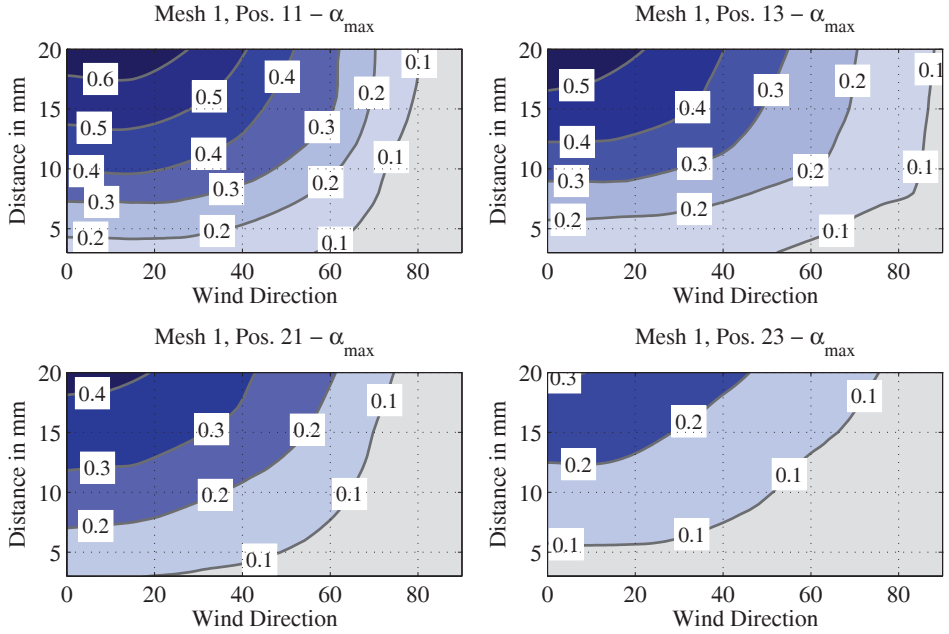

Figure 6. Characteristic Flow Parameter $\hat{\alpha}$ for the building with double-layered Cladding System, dependent on the Layer Distance e and the Direction of Flow Θ, Pressure Loss Coefficient $\zeta_{Mesh} = 1.3$

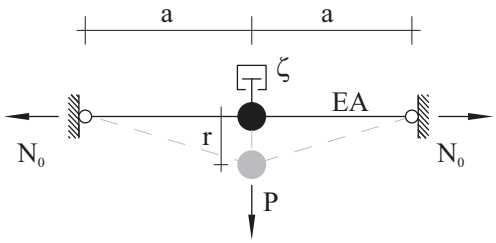

Figure 7. Duffing Oscillator as a 1 DOF Modell for the Dynamic Behaviour of prestressed Cladding Webs

wind direction, the wind positive wind force decreases. Appreciable negative wind forces only occur for wind angles above $\Theta \approx 45$, but the amplitude is commonly not decisive.

3 GEOMETRIC NONLINEAR STRUCTURAL BEHAVIOUR

The dynamic behavior of prestressed line-like elements can be described by a nonlinear single degree of freedom oscillator. As the resisting force is a polynomial with first and third order terms in r, this kind of oscillator is denoted as *Duffing-Oscillator* (s. Fig. 7). According to the geometric nonlinear kinematic, the deflection r of a Duffing-Oscillator leads to an elastic (additional) strain:

$$\varepsilon = \frac{\left(a^2+r^2\right)^{1/2}-a}{a} = \left[1+\left(\frac{r}{a}\right)^2\right]^{1/2} - 1 \tag{5}$$

Due to the increment of strain, the inner force N growths, compared to the prestressing force N_0:

$$N = N_0 + \varepsilon EA = N_0 + EA\left\{\left[1+\left(\frac{r}{a}\right)^2\right]^{1/2} - 1\right\} \tag{6}$$

The associated restoring force F_R of the Duffing-Oscillator can be determined by [1]:

$$\begin{aligned} F_R(r) &= 2\cdot N sin\phi = 2\cdot N\frac{r}{\left(a^2+r^2\right)^{1/2}} \\ &= 2\cdot N_0\cdot\frac{r}{a}\left[1+\left(\frac{r}{a}\right)^2\right]^{-1/2} + 2EA\cdot\frac{r}{a}\left\{1-\left[1+\left(\frac{r}{a}\right)^2\right]^{-1/2}\right\} \end{aligned} \tag{7}$$

Obviously, the response behavior from *Duffing-Oscillators* is dominated by the initial force N_0, the longitudinal elasticity EA and the span-width $2\cdot a$. The decisive parameter which combines the mentioned values is the degree of nonlinearity δ. It can be expressed as [5]:

$$\delta \approx \frac{EA}{2a^2N_0} \tag{8}$$

For fatigue verifications, not only the extreme values are relevant, but also the distribution of amplitudes has to be considered. For this aim, it is suggested to make use of advanced stochastic methods. Classical stochastic linearization approaches utilize an optimization of the expected value between the nonlinear and the linear stiffness to minimize the divergence of an equivalent linear system to the original system, in a least-square sense [8]. As a results a single equivalent structural frequency ω_{eq} can be found. This approach generally leads to a correct representation of the spectral energy and the increased structural frequencies, but underestimates the spectral

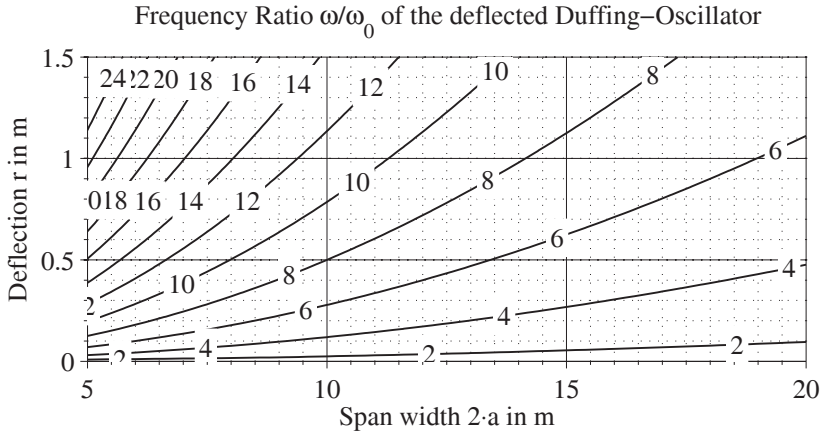

Figure 8. Increase of structural frequency of a Duffing-Oscillator dependent on span-width $2 \cdot a$ and applied deflection r

bandwidth (especially for slightly damped systems) [2]. Therefore *Miles* [7] and *Spanos* [9] used a concept, based on a linear differential equation of motion with a random expression for the amplitude dependent structural frequency (Equivalent Linear System, ELS). Transferring these concepts and extending them to stochastic wind loads with non-zero means leads to good approximations of the spectral system response, as well. Due to the analytic approach, they are advantageous compared to transient methods in case of structures which can be reduced to a single degree of freedom system.

In this paper, the ELS method is presented. The amplitude related structural frequency $\omega(A)$ can be obtained from:

$$\ddot{r} + 2\zeta\omega_0\dot{r} + \omega^2(A) \cdot r = f(t) \tag{9}$$

Hence, the differential equation of motion (9) represents a system of linear single degree of freedom oscillators. The Eigenfrequency ω is dependent on the deflective amplitude A and the expected frequency of its occurrence $P_n(A)$. According to [7], [9],[6] probability distribution can be expressed for a clear white noise excitation as:

$$P(A) = \frac{2\pi\omega_0^2\,(A + \delta \cdot A)}{\omega(A)} \cdot e^{-\frac{A^2\left(\delta \cdot A^2 + 2\right)}{4 \cdot \sigma_0^2}} \quad \text{and} \quad P_n(A) = \frac{P(A)}{\int_0^\infty P(a)da} \tag{10}$$

A dynamically excited Duffing-Oscillator changes its frequency continuously, the amplitude related detuning can be expressed analytically [1]:

$$\frac{\omega(A)}{\omega_0} = \sqrt{1 + \frac{3}{4}\delta A^2} \tag{11}$$

In Figure 8 exemplarily the increase factors of the structural frequency $\omega(A)/\omega$ are plotted over the system span width and the applied deflection.
The approximate PSD of the structural deflective response $S_{aa}(\omega)$ can now be computed according to:

$$S_{aa}(\omega) = \int_0^\infty \frac{S_{ff}(\omega)}{\left(\omega^2\,(A) - \omega^2\right)^2 + \left(2\zeta\omega_0\omega\right)^2} \cdot P_n(A)dA \tag{12}$$

Although equation 10 is only exact for a white noise excitation with zero expectation, it has been used as an approximation here, whereat the variance σ_0^2 of the process has been derived by a

linear spectral computation with the actual force spectrum (based on a *Kaimal* PSD of the wind velocity).

Wind gust effects generally come along with a significant mean load component. The structural vibrations then take place around the resulting average deflection. To incorporate those effects alternatively in the before described computation algorithm, firstly the static displacement r_{stat} has to be computed based on the associated load situation:

$$F_{stat} = 2 \cdot N_0 \cdot \frac{r_{stat}}{a} + (EA - N_0) \cdot \left(\frac{r_{stat}}{a}\right)^3 \tag{13}$$

Due to the static deflection, the structural stiffness increases. Subsequently, all dynamic computations acc. to Equations (11) to (12), may be used with the associated structural characteristics of the modified system (denoted by the index "1"), i.e. the Eigenfrequency ω_1 and the variance σ_1^2. Consistently, in Equation 12 the varying structural frequency is to be computed for $A_1 = A + r_{stat}$.

4 DETERMINATION OF NONLINEAR RESPONSES WITH STOCHASTIC METHODS

The geometric non-linear behavior can be considered analytically based on the findings of section 3. Typical prestressed cladding constructions show degrees of non-linearity between $\delta = 50$ and $\delta = 100$. In this section, the presented ELS method has been performed for structures with different degrees of non-linearity under varying load cases. As a load scenario, a 10 min gust impact has been considered, whereat for the aerodynamic admittance, different local flow coefficients have been taken into account. All associated properties are listed in Table 1.

As a first result, the power spectral densities of the structural deflections are plotted in Figure 10, as a comparison between the ELS method to conventional time based methods. The spectral results reveal the accuracy of the analytic method with respect to the predicted response behavior. In section 5, the consequence of the method, related to the fatigue prediction is investigated.

5 FATIGUE BEHAVIOUR AND STRUCTURAL INFLUENCE ON THE LIFETIME

Making use of a PSD based cycle count algorithm which is able to interpreted processes with arbitrary bandwidth, namely the *Dirlik*-algorithm [4], the rain-flow cycle count succeeds with frequency based responses. Even in case of nonlinear structures, the Rainflow classification can be performed based on the (with the prior described methods) computed power spectral density $S_{uu}(\omega)$.

The applicability of the presented methodology is illustrated by exemplary computations of flexible cladding elements (membrane structures) with different, realistic mechanical parameters. By means of these results, it is demonstrated how the different parameters influence the expectable damage and the fatigue life respectively.

So far, only the impact of a short-termed extreme wind on the stress range distribution has been considered. For the computation of the expected design life-time under fatigue aspects, the prevalent wind events during the foreseen lifetime have to be taken into account as well.

Table 1. Overview of Aerodynamic and Mechanic Properties of the Exemplary Computations

System	α_{local}	δ	System	α_{local}	δ	System	α_{local}	δ
S01-LC1	0.05	0.4	S02-LC1	0.05	4.0	S03-LC1	0.05	40
S01-LC2	0.5	0.4	S02-LC2	0.5	4.0	S03-LC2	0.5	40
S01-LC3	2.0	0.4	S02-LC3	2.0	4.0	S03-LC3	2.0	40

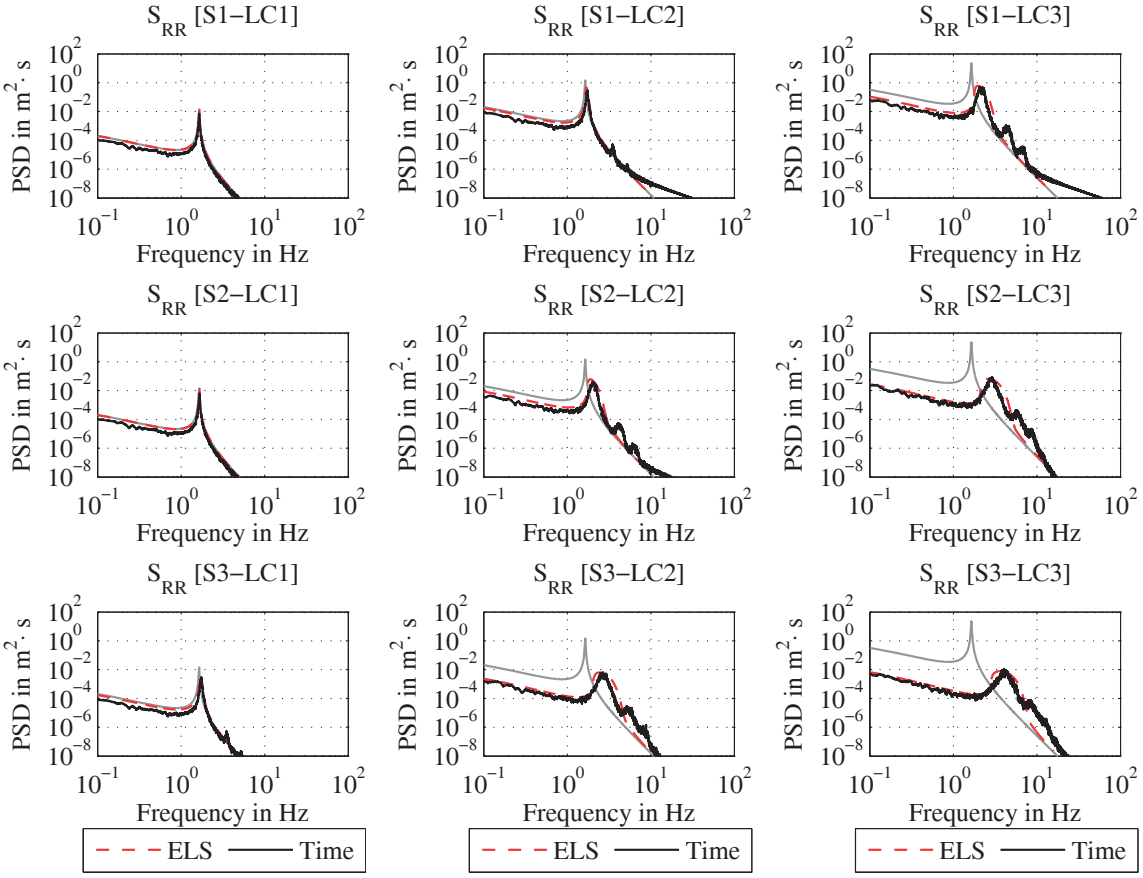

Figure 9. PSD of deflective Response for different Structures with ELS and transient Computation

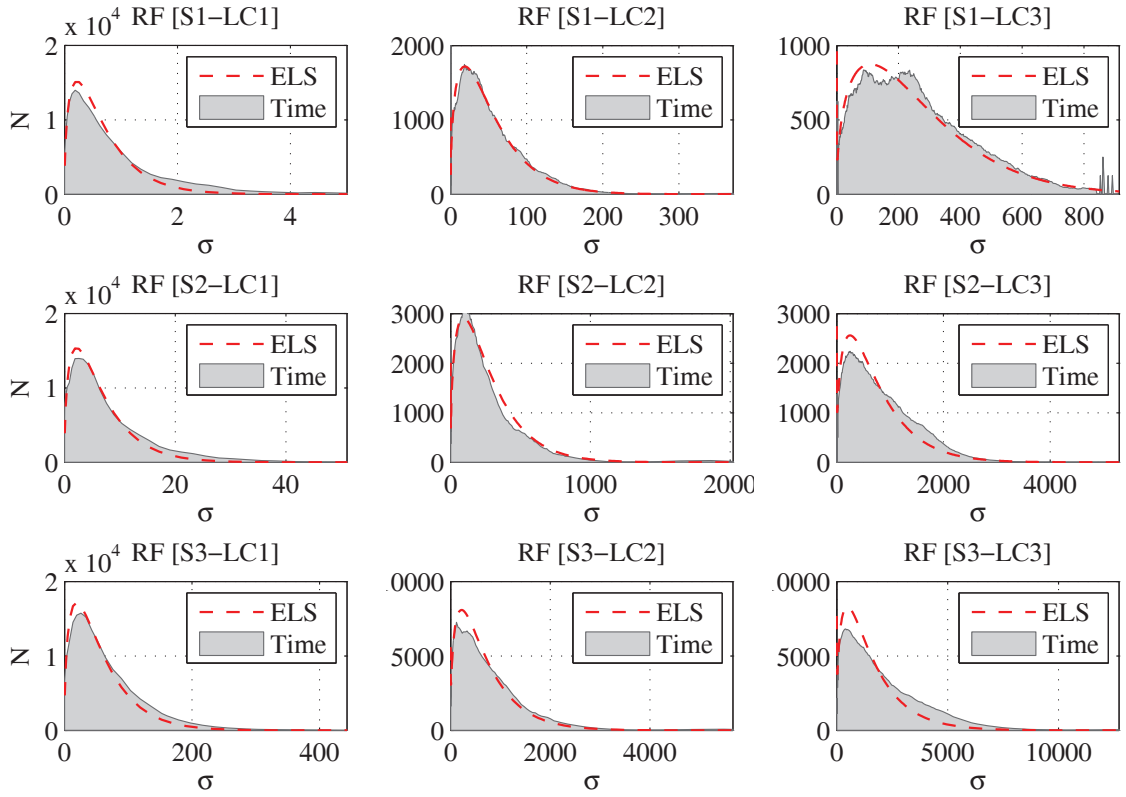

Figure 10. Stress Range Spectra (Rainflow Method) of ELS and transient computed Responses

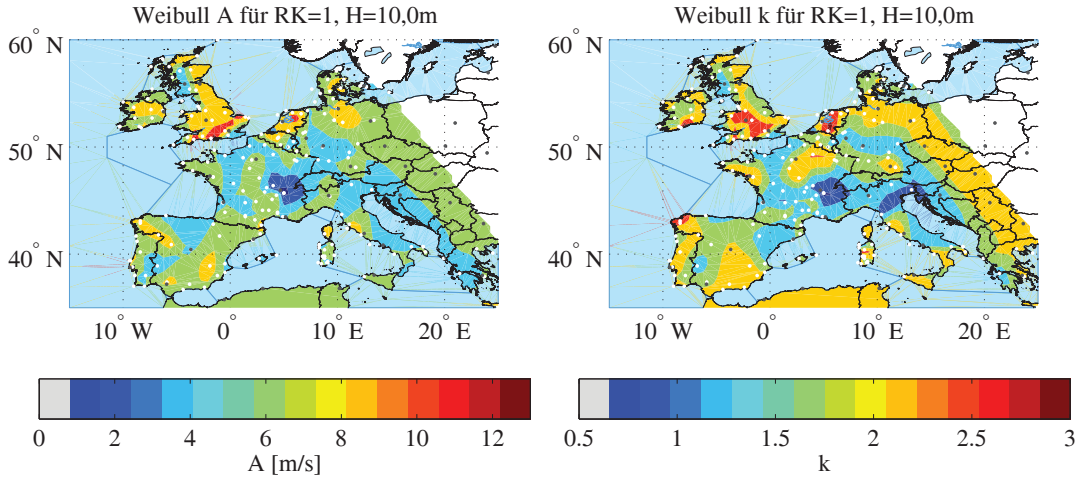

Figure 11. Weibull Parameter for Europe, Roughness Category 1 (Data Source: European Wind Atlas [10])

Merging all before described influence parameters, the stress range spectra can be computed by the following expression:

$$N(\Delta\sigma)_{Life} = \int_0^{\overline{u}} \frac{T_{Life}}{T_{ref}} \cdot f(u) \cdot N(\Delta\sigma, u) du \tag{14}$$

where: T_{Life} is the designed Lifetime, T_{ref} is the average time of the mean wind speed, $f(u)$ is the probability density function of the wind velocity and $N(\Delta\sigma, u)$ is the stress range spectra for a given mean wind speed within the average time period.

The probability density function for the frequency of occurrence of mean wind speeds can be derived based on the *Weibull*-Distribution:

$$f(\overline{u}) = \frac{k}{A}\left(\frac{\overline{u}}{A}\right)^{k-1} exp\left[-\left(\frac{\overline{u}}{A}\right)^{k}\right] \tag{15}$$

where: A is the scale and k is the form parameter of the distribution. Site dependent values for these parameters can be taken from e.g. the European Wind Atlas [10]. In Fig. 11, exemplarily the parameters A and k (cumulated over all directions) are plotted in the map of Europe for the roughness category 1 ($z_0 = 0.05m$), for a height of 10m and for an average period of $T = 1$ hour.

Based on the appropriate assumptions for the site dependent extreme wind impact and the probability of exceedance of the prevalent wind speeds, a realistic consideration of fatigue impact is possible. Using the direction related Weibull Parameter, even a directional design is possible.

The fatigue verification now succeeds with common methods, like *Miner*-Rule for a linear damage cumulation with an appropriate s-N-Curve. In most cases the s-N-Curve should be obtained from dynamic fatigue tests, as general notch cases are not classified for crimped wires.

6 CONCLUSIONS

Static wind load assumptions have been derived for permeable cladding structures, installed as an outer skin in front on conventional, closed façades. Based on simplified models of the total pressure drop and the extended Bernoulli equation, conservative loads can be determined. Additional wind tunnel results show a good concordance of the local flow parameter α_{local}.
With respect to the structural investigations, it has been shown, that reliable fatigue verifications based on cumulative damage predictions are possible by means of closed form spectral methods,

even for highly nonlinear structures. The chosen method, the equivalent linearization approach, leads to appropriate estimations of the increased structural frequencies of geometrical nonlinear systems under loading, as well as of the obtained damage prognoses. The presented examples emphasize the complexity of the topic and the effects of the various structural and aerodynamic parameters with respect to the expected fatigue life.

REFERENCES

[1] J. Argyris and H.-P. Mlejnek. *Computerdynamik der Tragwerke*, volume III of *Die Methode der finiten Elemente*. Vieweg, Braunschweig, studienausg. edition, 1997.

[2] R. Bouc. The power spectral density of response for a strongly non-linear random oscillator. *Journal of Sound and Vibration*, (175):317–331, 1994.

[3] N. J. Cook and J. R. Mayne. A novel working approach to the assessment of wind loads for equivalent static design. In *Journal of Industrial Aerodynamics*, volume 4, pages 149–164. ELSEVIER SCIENCE BV, 1979.

[4] T. Dirlik. *Application of computers to fatigue analysis*. PhD thesis, Warwick University, Warwick, 1985.

[5] F. H. Kemper, M. Feldmann, and J. Kuck. Stochastic vibrations of prestressed membrane cladding elements. In Michael Brennan, editor, *RASD*. Synergie Lymington Ltd, Lymington and UK, 2010.

[6] Y. K. Lin. *Probabilistic Theory of Structural Dynamics*. McGraw-Hill Book Company, New York, 1967.

[7] R.N Miles. Spectral response of a bilinear oscillator. *Journal of Sound and Vibration*, (163):319–326, 1993.

[8] J.B Roberts and P.D Spanos. *Random vibration and statistical linearization*. Dover books on engineering. Dover Publ, Mineola and NY, 2003.

[9] P. D. Spanos, I.A Kougioumtzoglou, and C. Soize. On the determination of the power spectrum of randomly excited oscillators via stochastic averaging: An alternative perspective. *Probabilistic Engineering Mechanics*, (26):10–15, 2011.

[10] I. Troen and E. L. Petersen. *European wind atlas*. Risø National Laboratory, Roskilde, 1989.

The Seventh International Colloquium on Bluff Body Aerodynamics and Applications (BBAA7)
Shanghai, China; September 2-6, 2012

Statistics and analysis of typhoons landing and failure mechanism of coastal low-rise buildings in China

Yimin Dai [a] ,Xuguang Yan[b] ,Xiangjun Wang[c],SUN Hongxin[d], Li Yonggui[e]

[a] *School of Civil Engineering,Hunan University of Science and Technology,Xiangtan,china*
[b] *School of Civil Engineering,Hunan University of Science and Technology,Xiangtan,china*
[c] *School of Civil Engineering,Hunan University of Science and Technology,Xiangtan,china*
[d] *School of Civil Engineering,Hunan University of Science and Technology,Xiangtan,china*
[e] *School of Civil Engineering,Hunan University of Science and Technology,Xiangtan,china*

ABSTRACT: In order to reveal the status of typhoon landfall in China coastal areas, the coastal areas and frequency of typhoon landing were compared with the statistical analysis in the paper for nearly 50 years; combined with the wind pressure of low-rise buildings under typhoon in China's coastal, structures damage of low-rise buildings were investigated. The results show that, the southwest coast of Guangdong landfall the largest number of typhoon landing, while the coastal areas of Fujian and Zhejiang have larger number of strong typhoons; turbulence great impact on surface air pressure; It was also found that the high suction pressure zones occurred around the windward roof edges at a wind azimuth of 45^0,and wind pressure along the roof corner just behind the roof ridge. The results of the present study are expected to be useful for the future development of a simple approximate formula for the low-rise buildings of the coastal area for design use.

KEYWORDS: Typhoon ;Low-rise buildings; Hurricane; wind pressure; failure mechanism.

1 INTRODUCTION

A full-length paper should have a short introduction. This should state the reasons for the work, with brief reference to previous work on the subject.

Typhoon (tropical storms and strong tropical storm) is an extreme climate which originated in tropical ocean between latitudes 5^0 ~20^0 and have great destructive, belonging to one of the severe natural disasters. The intensity of typhoon is one of the largest sea area in the Western Pacific, typhoon frequently attacks in China's coastal areas, China is also one of the few countries most severely affected by the Typhoon [1].

Wind resistance capacity of 0oastal residential wall in China is 12-level design, the strength design value of the walls are about 327kg/m^2, and negative pressure of roof about 43kg/m^2. Positive wind pressure of super- typhoon “SaoMai” reached 510~900kg/m^2, roof negative pressure up to 67~118kg/m^2, which greatly exceeded the design limit value of the low-rise buildings at china coastal, Typhoon “SaoMai” caused heavy casualties, which collapsed 39,000 houses and killed 144 people in Zhejiang Province [2~3]. Previous wind statistics show that the damage of low-rise buildings caused losses were more than half of the total losses .Therefore, researching of low-rise building on wind resistance possesses important practical significance [4~7].

2 NEARLY 60 YEARS LANDED IN COASTAL AREAS OF CHINA TYPHOON

Fujian ,Guangdong and Zhejiang Provinces ,suffered most landing typhoons during the past 60 years from 1950 to 2011.Most of the landing typhoons originated from northwest Pacific at east of Philippine, with northwest path as the main track. On the average, 5 typhoons every year landed or impacted china coast areas during the past 60 years, with a relatively big inter annual change and slight upward trend. Most of the impacting typhoons mainly occurred in July to September, showing a normal distribution with August as the centre.

we can see the following conclusions:

(1) Number of landing Typhoon from 1949-2006 in coastal marine areas of Guangdong were a total of 211 typhoons, each year average 3.64, followed by Hainan Province, 135 typhoons, the average was 2.33.But in the 5 years, total of 46 of Landfalling typhoons from 2007 to 2011, the average annual number of 9.2 typhoons.
(2) Compared to 1949-2006 strong typhoon data for more than 50 years, number and frequency of strong typhoons nearly 5 years landing and affecting along the coast appear Increasing trends in china.

Extensive disaster investigation shows that:

(1) Improper location: many houses built in the Typhoon-prone landed in empty fields, the region of villages and towns, offshore marine and upwind or higher ground, when the Typhoon landed, the geographical landform withstand wind loads of very large, very easily lead to collapse or damage of low-rise buildings.
(2) Improper design: wind damage of low-rise buildings of 1 or 2 independent houses account for a large proportion.
(3) Improper construction: construction of residences is not code for building construction, without structural design basic concepts of security, poor construction program, construction technology and construction techniques ,which led to the current poor quality of residential houses in coastal areas, and cause poor wind resistance capacity.

3 STUDY ON THE FAILURE MECHANISM OF COASTAL RESIDENTIAL WIND

According to the damage investigations,most damage to houses was restricted to the envelope of building, in particular to roof sheathing.which indicate that an improvement in wind resistance of the building's envelope will result in a significant reduction in overall economic losses.Failure mechanism of houses along the coast storms due to the Typhoon-prone area residential dwellings along the coast a large number of broad, each time the storms as a result of the economic problems, and also the essential problem facing social and political stability, so there is a need for low-rise buildings in storms damage mechanism of further scientific research.

Fig.1 Hurricane of a low-rise building in China coastal areas

Figure 2 show that[11], most damage to houses was restricted to the envelope of building, suggesting that coastal dwellings destroyed upwind wind-related, and roof more easily damaged than the walls.

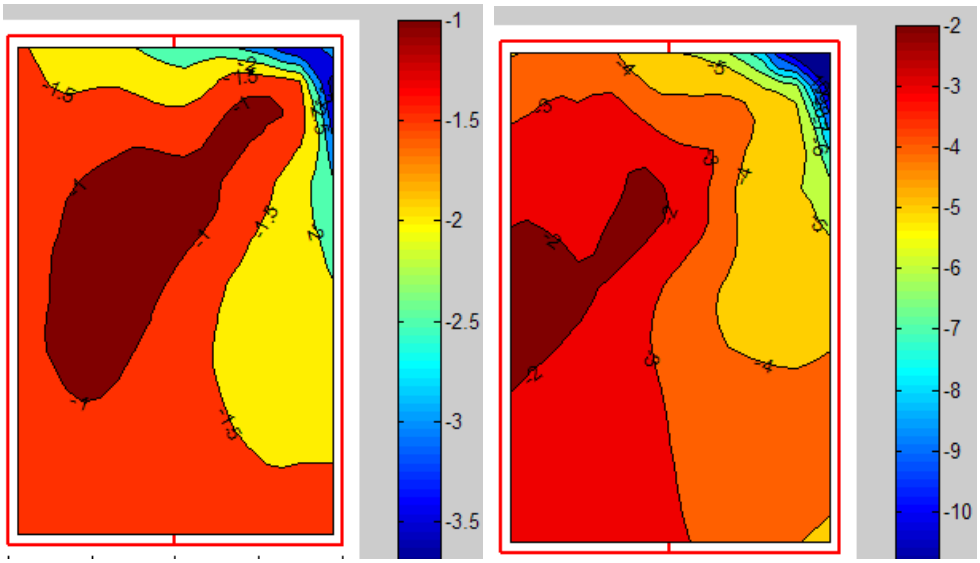

a) Cp_{mean} b) Cp_{min}

Fig.2 Hurricane of a low-rise building in China coastal areas[11]

The results [8~11]show that, The entire roofs of the full-scale low rise building experience negative mean and minimum pressures regardless of the incident wind direction. The angular position of highest (mean and peak) suction do follow the vortex core position closely. It was found that the high suction pressure zones occur round the windward roof edges.The roof corner just at the windward end of the roof exhibit the highest minimumu pressure coefficients.The regions are expected to be the most vulnerable for wind induced roof damage in severe windstorms.strong suction and high pressure regions on the the leading edges and roof-corner regions were induced by the updrafts and downdrafts of wind flows near the eye of the typhoon. The highest negative mean pressure coefficients observed was -3.34.It occurred at a wind azimuth of 45^0,and the corresponding minimum pressure coefficients was -10.64.

CONCLUSIONS

(1) Some practical cosiderations and tasks in the development for wind- resistance design of low-rise buildings have been examined in this paper, author suggest that we should increase wind resistance design standard of coastal low-rise buildings in China.

(2) Strong suction and high pressure regions on the the leading edges and roof-corner regions were induced by the updrafts and downdrafts of wind flows near the eye of the typhoon.

(3) This article analyzes the main problems in practical construction of the coastal buildings in China, and puts forward improving measures for the improvement of current design of low rise buildings in China coast.

ACKNOWLEDGEMENTS

Finanical support is gratefully acknowledged from Teaching and Research Reform Project of Hunan University of Science and Technology (Number:J11216) and Department of transportation major projects of science and technology (2011318824140).

REFERENCES

1 FU Guohong.Study on wind load characteristics and Typhoon-resistant design of low-rise buildings[D].Hangzhou .Zhejiang University,2002:1~3

2 WANG Wei-guo,WANG Xiu-rong, XU Ying-long.Characteristics of super-typhoon“SaoMai”and benefits of forecast service. Journal of Natural Disasters, 2008,17(3):106-112

3 CHEN Xiang. Analysis of Devastating“Sangmei”Typhoon No·0608 in Fujian, Journal of Subtropical Resources and Environmen,2007,2(3):36-43

4 XUE genyuan,YU Shanxian. Damage characteristias of Typhoon Rananim and primary research on typhoon disasters in Zhejiang Province. Journal of Natural Disasters, 2006,16(4):39-47

5 LIU Qiaohui, ZHENG Youfei1,SONG Yajie. Statistical analysis of typhoon landing and impacting Fuding area ofFujian Province during 1948-2007. Journal of Natural Disasters ,2011, 20(1):130-134

6 SONG Fang-fang,OU Jin-ping. Investigation and analysis of structures damage caused by typhoon“Hagubit”. Journal of Natural Disasters,2010,19(4):9-17

7 XU An,FU Jiyang,ZHAO Ruohong.Field measurements of typhoons according to civil engineering research. Journal of Acta Aerodynamica Sinica,2010,28(1):24-32

8 LI Qiusheng, DAI Yimin, LI Zheng nong.Surface layer wind field characterics during severe typhoon“Hagupit”landfalling. Journa of Building structures,2010,4(31):54-62

9 LI Qiusheng, DAI Yimin, LI Zheng nong. Wind pressures on the building surface during severe typhoon“Hagupit”. Journa of Building structures,2010,4(31):62-69

10 DAI Yimin, LI Qiusheng, LI Zheng nong.Experiment study of wind pressures on a low-rise full-scale building.China Civil Eingeering Journa,2008, 41(6): 9-15

11 DAI Yimin, LI Qiusheng, LI Zheng nong. Wind loads on low-rise buildings－ Study on variation of near ground wind profiles.China Civil Eingeering Journal, 2009,3(42):44-51

The Seventh International Colloquium on Bluff Body Aerodynamics and Applications (BBAA7)
Shanghai, China; September 2-6, 2012

Field measurements of wind loads on an instrumented low-rise building during typhoons and comparison with wind tunnel test results

Q. S. Li [a, b], S. Y. Hu[b], Y. M. Dai[b]

[a] *Department of Civil and Architectural Engineering, City University of Hong Kong, Tat Chee Avenue, Kowloon, Hong Kong*
[b] *Key Laboratory of Building Safety and Energy Efficiency of Ministry of Education, College of Civil Engineering, Hunan University, Changsha 410082, P.R. China*

ABSTRACT: A full-scale moveable instrumented low-rise building has been constructed and implemented to monitor wind velocity field and associated building surface pressures during typhoons. The major objective of the field study is to further understand typhoon-generated wind characteristics and wind effects on the low-rise building under extreme wind conditions during typhoon landfalls. This paper presents a combined study of field measurements and wind tunnel tests. Detailed analysis of the mean, standard deviation and negative peak pressures measured on a roof corner zone of this building is conducted to investigate the pressure distribution characteristics in conical vortex region under oblique approaching wind directions. The field measurement results reveal that the windward leading edges on the corner area are consistently subjected to the most severe suction pressures for quartering winds. The measured extreme peak pressures are compared with those stipulated by ASCE 7-10 Standard. It is found that the measured extreme peak pressures at the windward leading edge area on the corner are significantly larger in absolute value than those determined by ASCE 7-10. Moreover, the effect of spatial and time average on the peak pressures on the corner zone is discussed. On the other hand, wind tunnel tests are performed to assess the wind effects on the experimental building. Comparison of the full-scale measurements and the model test results of negative peak and fluctuating pressure coefficients near the roof corner, roof ridges and leading edges shows distinct discrepancies. In general, the wind tunnel tests underestimate the real negative peak and fluctuating pressure coefficients on the roof corner zone for quartering winds. The outputs of this comprehensive study are expected to provide useful information for the wind-resistant design of low-rise buildings in typhoon-prone regions.

KEYWORDS: low rise building, typhoon, field measurement, wind tunnel test, wind-induced pressure, flat roof.

1 INTRODUCTION

Full-scale measurement is considered to be the most reliable method for evaluating wind effects on buildings and structures. There have been a number of field studies of wind effects on low-rise buildings conducted in the past several decades, including Aylesbury building field experiment (Eaton and Mayne,1975), the Silsoe structure building field experiment (Richardson et al.1990) and the Texas Tech University (TTU) Building filed experiment (Levitan and Mehta 1992a,1992b). The collected wind pressures on full-scale low-rise buildings were also used to validate the accuracy of wind tunnel test results, as reviewed by Uematsu and Isyumov (1999).

For example, the Aylesbury building measurement program provided wind pressure data for validation of wind tunnel experimental results (IAWE Aylesbury comparative experiment) using 1:100 models at 17 laboratories worldwide (Sill et al., 1992). The Silsoe structure building experiment provided the wind loads on a steel, gable-roof, and portal framed structure for verifying model test data (Richardson et al., 1994, 1995, 1997). In particular, several wind tunnel studies (e.g., Cocharan and Cermark, 1992; Okada and Ha, 1992; Endo et al., 2006) for the TTU Building have been conducted, and detailed comparisons with the full-scale measurements have been made. However, there are distinct discrepancies between the full-scale measurements and the wind tunnel test results of negative peak and fluctuating pressure coefficients near roof corners and roof leading edges.

More recently, field measurements on the Kern P. Pitts Centre provided valuable information of external pressure distributions and characteristics recorded during the passage of three cyclones in the proximity of the building (Caracoglia and Jones, 2009). In particular, the extensive Florida Coastal Monitoring Program currently being undertaken by three institutions in the USA focuses on monitoring of near-surface hurricane wind characteristics and wind pressures on residential low-rise buildings (Aponte, 2006). However, full-scale measurements of wind loads on low-rise buildings have rarely been conducted under strong windstorm conditions such as in eye-walls of hurricanes or typhoons. Consequently, there is lack of wind-induced pressure data on low-rise buildings under extreme wind conditions during typhoon landfalls. Obviously, there is an urgent need to enhance our understanding of turbulence structure of typhoons and the mechanisms for generations of extreme suctions in the region of flow separation or conical vortex. In this connection, a full-scale moveable instrumented low-rise building has been constructed and implemented to monitor wind velocity field and associated building surface pressures during typhoons. The major objective of the field study is to further understand typhoon-generated wind characteristics and wind effects on the low-rise building under extreme wind conditions during typhoon landfalls.

This paper is organized into four sections. Section 2 briefly describes the full-scale and wind tunnel measurement program for obtaining wind pressures on the instrumented low-rise building. Section 3 presents the measurement results from the instrumented building during the passage of several typhoons. Detailed analysis of the mean, standard deviation and negative peak pressures measured on a roof corner zone are conducted to investigate the pressure distribution characteristics in conical vortex region under oblique approaching wind directions. The measured extreme peak pressures are compared with those stipulated by ASCE 7-05 Standard. Furthermore, the effect of spatial and time average on the peak pressures on the corner zone is discussed. Moreover, wind tunnel tests are performed to assess the wind pressure distributions on the experimental building. The model test results are then compared with the field measurements to evaluate the accuracy of the model test results. Section 4 summarizes the major findings and conclusions from this combined full-scale measurement and wind tunnel test study.

2 FULL-SCALE AND WIND TUNNEL MEASUREMENT PROGRAMS

2.1 Full scale measurement

The monitoring station of the moveable instrumented building consists of a 6.0×4.0×4.0m flat-roof low-rise building and a 10m high meteorological tower located seven meters away from the building, as shown in Figure 1. Eighty differential pressure transducers (Setra model 264 or 265) with three types of measurement ranges of ±1250 Pa, ±2500 Pa and ±6250 Pa were used to measure the surface pressures on the building. A CR-5 PC based central recording monitoring

system which can simultaneously record data from 60 channels was used to measure wind speed, wind direction and pressure data. The pressure transducers and anemometers were sampled at 20 Hz. A more detailed description of the measurement system can be found in Li et al. (2009). The field measurements of wind speeds and wind pressures on the buildings were conducted under strong windstorm conditions such as in the eye-walls of Typhoons Hagupit and Chanthu. The information on the tracks of these typhoons and the building site is shown in Figure 2. This paper presents the selected results of the pressure data measured from nine taps on a roof corner and six taps at mid span of the experimental building, as shown in Figure 3. These corner taps are distributed in grids of 3 columns and 3 rows in two orthogonal directions. The tap locations nearest the roof edges are 0.12m from the edges. Tap12 indicates a tap located at row 1 and column 2 on the corner, as illustrated in Figure 3. Pressure coefficient is defined as follows:

$$C_p(t) = \frac{p(t) - p_s}{1/2\rho U_{ref}{}^2} \tag{1}$$

where $p(t)$ is the external pressure at a point of interest, p_s is the free stream static pressure or reference static pressure, ρ and U_{ref} are the air density and 10-minute mean wind speed at 10m height (reference height), respectively. The mean, standard deviation and peak pressure coefficients were calculated based on the measured pressure data. The pressure data presented in this paper were measured when the 10-min average wind speed at 10m height was larger than 8m/s (i.e., for dynamic pressure >40.2Pa).

Figure 1. The moveable instrumented building

Figure 2. Track of typhoons and location of the instrumented building

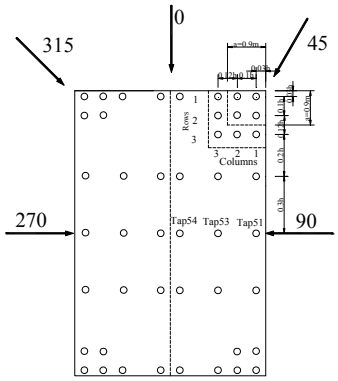

Figure 3.The locations of pressure taps and definition of incident wind direction

2.2 Wind tunnel test

The wind tunnel test was conducted at the Wind Tunnel Laboratory of Building and Environment of Hunan University. The wind tunnel is an open circuit tunnel with a working section of 3 meters wide and 2.5 meters high. With consideration of the size of the full-scale building, a geometric scale of 1:20 of the low-rise building was selected for the wind tunnel study.

For the critical wind directions (0°-90°) where the building roof was subjected to the most severe suctions, the terrain exposures at the building site can be categorized as coastal terrain and open land terrain, respectively. Therefore, the boundary layer wind flows for coastal terrain and open land terrain in the wind tunnel test were simulated based on the recorded profiles during typhoons and the terrain conditions around the instrument building site. The mean longitudinal wind speed and turbulence intensity profiles for the coastal terrain and the open land terrain, including the field measured profiles and those simulated for the wind tunnel test, are shown in

Figure 4 and Figure 5, respectively, for comparison purposes. The model scale mean wind speed profile was normalized by the mean wind speed at 0.5 meter height which corresponds to 10 meter full-scale height in order to compare the profile with the field measured profile. It can be seen from these figures that the mean wind speed profiles simulated for the model test are in good agreement with the field measured profiles. The mean wind speed profiles for the coastal terrain are well matched by a simple logarithmic profile with a roughness length z_0 ranged from 0.0027-0.0033m. A power-law exponent (α**)** 0.12 represents a mean value for the profiles over the coastal terrain. The simulated turbulence intensities for the coastal terrain were slightly larger than the measured ones. The mean value of the surface roughness length for the wind tunnel test was 0.03m which was close to the field measured mean value of 0.02m for the open land terrain. The power law exponent (α**)** was found to be 0.16 for this terrain. The model scale Jensen Number ranged from 133 to 1200 which was in accordance with the full-scale Jensen Number. The Reynolds Number based on the full-scale building height is 10^6 while it is 10^5 in the wind tunnel test.

Model and full-scale normalized longitudinal velocity spectra at 10m height are presented in Figure 6 for comparison purposes. Figure 6 shows that the full-scale velocity spectrum measured within the eye-wall region of Typhoon Chanthu follows a Karman-type spectrum in the main frequency range. Meanwhile, the model scale spectra are in good agreement with the full-scale spectrum in the main frequency range, implying that the spectral characteristics of a strong typhoon can be reproduced in the wind tunnel test. There are three interdependent scaling factors; length, velocity and time. The length scaling was fixed by the 1:20 scale model. The mean longitudinal mean wind speed at the reference height of the model test for the coastal terrain and the open land terrain were 7.93m/s and 8.45m/s, respectively. The mean longitudinal wind speed at the reference height of 10m in full-scale was typically between 10 and 40m/s during the typhoons. Thus, the velocity scaling is about 1:5. This means that the sampling period of 6s in the model test is equivalent to a 10min period recording in full-scale.

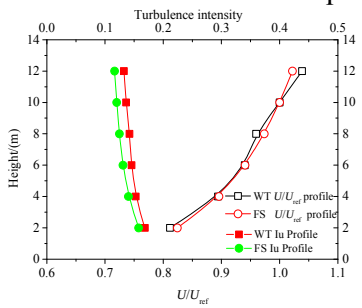

Figure 4. Mean wind speed and turbulence intensity profiles for the coastal terrain

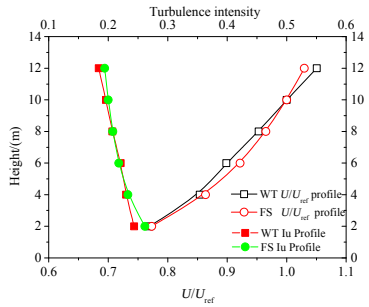

Figure 5. Mean wind speed and turbulence intensity profiles for the open land terrain

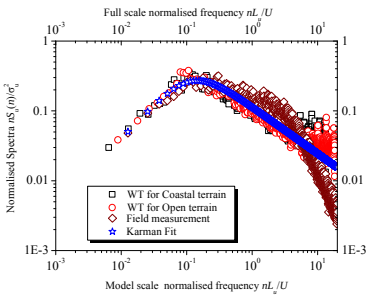

Figure 6.Comparison of the field measured spectra to those simulated in the wind tunnel test at 10m height

3 PRESSURE RESULTS AND DISCUSSIONS

3.1 *Wind pressures in conical vortex region*

Variations of the mean, negative peak and rms pressure coefficients at the windward leading edge on the corner (Tap12, Tap13 and Tap21, Tap31) with the mean incident wind direction are presented in Figure 7(a) through 7(c), respectively. The mean pressure coefficient distributions for all the taps were similar. The negative peak pressure coefficients and rms pressure

coefficients at Tap12 and Tap21 were consistently subjected to the most severe suction pressures around 20°-60°. The minimum negative peak pressure coefficient at Tap21 was found to be -13.5. Conical vortices were believed to form on the roof corner region, which produced the worst severe suctions on the corner for quartering winds. This observation is consistent with those obtained from other low-rise buildings (Tieleman et al. 1994; Kawai and Nishimura, 1996; Zhao, 1997; Banks et al., 2000; Wu et al., 2001; Blessing et al., 2009). Such extreme suctions occurring on roof corner zones and roof edges are the primary causes of roof damages of low-rise buildings during hurricanes and typhoons (Holmes, 2001).

The availability of the field measurements of wind pressure results from this experimental building provides an excellent opportunity for comparisons with the provisions of wind codes and standards to assess the suitability of the codes of practice. Comparisons between the measured pressures and those derived from ASCE 7-10 Standard (2010) are presented in Figure 7 (b). It should be noted that the pressure coefficients stipulated in the ASCE were determined based on 3 sec gust wind speed. Hence, appropriate transformations are necessary in order to make meaningful comparison with the field results which were determined based on 10 min mean wind speed data. The value determined from ASCE 7-10 Standard is -9.25 for the corner zone, which was converted from -2.8 stipulated in the Standard by consideration of a gust pressure factor of 1.51^2=2.28 (converting 3s gust speed to 10min mean wind speed) and the associated adjustment factor was 1.45 for the reference height and terrain exposure. The pressure coefficients measured at Tap12 and Tap21 on the corner are significantly larger in absolute value than that stipulated in ASCE 7-10 for the corner zone.

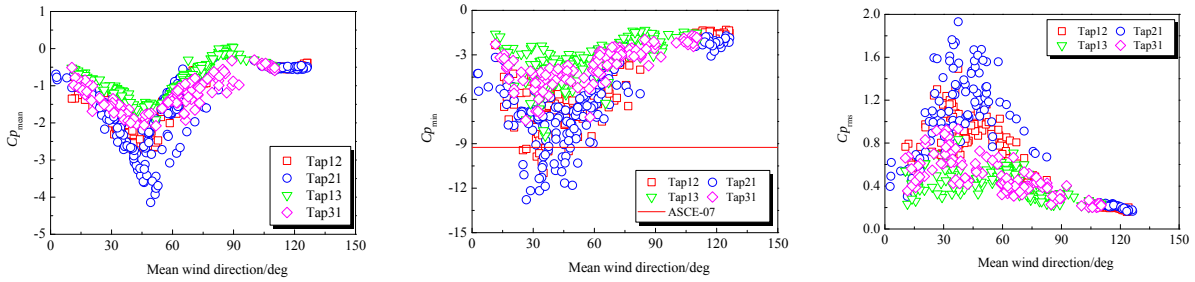

(a) Cp_{mean} (b) Cp_{min} (c) Cp_{rms}

Figure 7 Variations of pressure coefficients with mean wind direction for the taps on the roof corner

3.2 *Area-averaged pressure coefficients*

The design wind loads on roof member and cladding stipulated in current codes or standards are made up of the most critical area averaged pressure coefficients specified as functions of tributary area. Area-averaged pressure coefficients and the duration for determination of peak wind loads are key factors for evaluation of wind loads on roof members and claddings.

Firstly, the correlations of pressure coefficient in the corner zone were investigated. The correlations of pressure coefficient indicate how well the pressures are related in space under the conical vortex flow. The correlations between Tap 11, Tap 13, on the short-span leading edge of the roof, and Tap 31, on the long-span leading edge, with the other corner taps are shown in Figure 8. It can be seen from the figure that the pressures at Tap 11 are reasonably correlated with other taps in row 1 (above 0.85 for Taps 12, 13) and are also related to those in column 1 on the diagonally opposite edge (above 0.75 for Taps 21 and 31). In general, it appears that there are higher correlations at most locations in the corner area. These results indicate that both edges are affected by the generation of delta wing vortices. Therefore, the area-averaged pressures on the corner area can be obtained by adding up the pressures measured at all the taps, weighted by the respective tributary areas involved the taps. As an example, corner leading edge area I includes

Tap11, Tap 21 and Tap 31 and corner area II covers the cross-area of row 2 and column 2, while corner area III with 1.44m^2 includes the nine taps marked as the dotted square, as shown in Figure 3.

The variations of the negative peak pressure coefficient at the corner leading edge area I, corner area II and corner area III with the mean wind direction are presented in Figure 9. As expected, the largest peak coefficients in absolute value occurred at the windward leading edge on the corner area zone for wind attacking angles around 20°-45°. The minimum peak negative pressure coefficient on the corner leading edge area I was found to be -9.9 which was slightly larger in absolute value than that stipulated in ASCE 7-10 Standard (2010) for corner zones.

For investigation of the area and time averaged effects on peak pressures, the pressure data on the roof corner zone with 1h record duration under a quartering wind around 45° with mean wind speed 18.3m/s were selected herein as a case study. The effects of time and area average on the negative peak pressure coefficients on the corner zone are presented in Figure 10. The minimum peak pressure coefficients decreased generally with an increase in time average (T). But, the peak pressure coefficients stabilized around 3s average time. As expected, the area averaged peak negative pressure decreased considerably when the area increased.

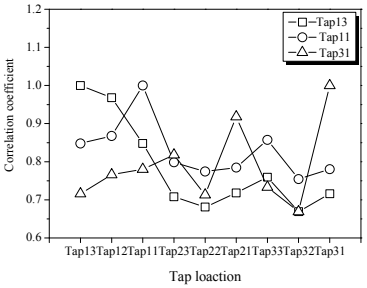

Figure 8. Correlation coefficients between Taps 13, Tap11 and Tap 31 with the other taps in the corner zone

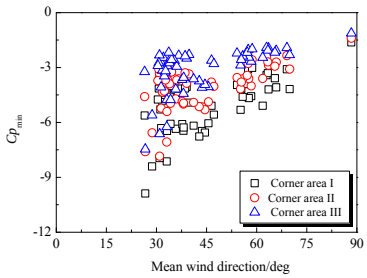

Figure 9. Variation of negative peak pressure coefficients on the corner area with mean wind direction

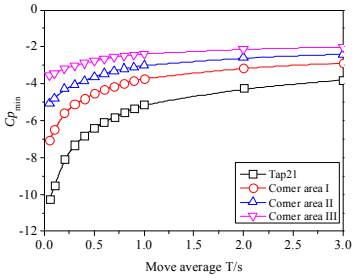

Figure 10. Effects of time and area averaging on negative peak pressure coefficients at Tap21 and in the corner area

3.3 *Wind tunnel results and comparison with the full-scale measurements*

3.3.1 *Wind pressures coefficients on the roof*

The comparisons of the mean, negative peak and rms pressure coefficient distributions along the mid-plane section across the roof between the full-scale and model-scale tests for an angle of approaching wind of 90° are shown in Figure.11 (a) through 11 (c), respectively. It can be seen from these figures that the model-scale mean pressure coefficients are in good agreement with the field measured values except for the mean pressures coefficients at the leading edge. Moreover, the field measured negative peak and rms pressure coefficients in magnitude at the leading edge are slightly higher than the wind tunnel results. It was found that the field measured peak suction pressure coefficient of -2.85 was observed near the leading edge area of the roof, while the peak suction pressure coefficients were -2.05 and -2.59 observed for the coastal terrain and the open land terrain, respectively. The discrepancies between the model-scale and full-scale negative peak and rms pressure coefficients at the leading edge of the roof may be caused by several factors, such as non-stationary wind characteristics during typhoons and Reynolds number effects etc. These results indicate that wind tunnel tests may underestimate the fluctuating and negative peak pressures at the leading edge of the flat roof under separation bubble.

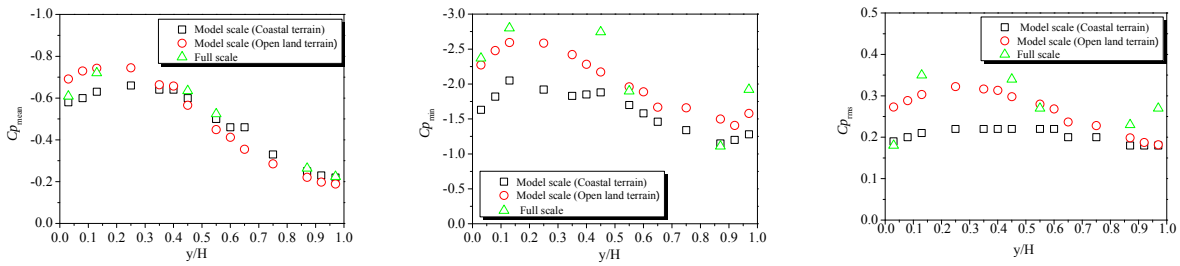

(a)Cp_{mean} (b)Cp_{min} (c)Cp_{rms}

Figure 11. Comparison of pressure coefficients along the centerline on the roof between the field and wind tunnel measurements (at wind direction of 90 degree)

The comparisons between the full-scale and model-scale measurements of the mean, negative peak and rms pressure coefficients at Tap12 are shown in Figure.12 (a) through 12(c). For the mean pressure coefficients, the smoother (coastal) terrain model test results are closer to the full-scale data. High magnitudes of the mean pressure coefficients are observed for angles of attack from 30° to 60°, as shown in Figure 12(a). It is found that the wind tunnel test underestimated the negative peak and rms pressure coefficients in the roof corner region in comparison with the full-scale results for the critical wind angles, as depicted in Figure 12(b) and 12(c). Besides the critical wind direction range (from 0° to 90°), the negative peak and rms pressure coefficients measured in the wind tunnel test for the open terrain are higher in magnitude than the full-scale values. The similar observations were made for Tap21 as shown in Figure13 (a)-13(c). The results displayed in Figures 12 and 13 indicated that the wind tunnel test underestimated the highest fluctuating and peak pressure coefficients near the edges of the roof corner zone under conical vortices. The distinct discrepancies may be attributed that it is difficult to fully simulate the realistic wind characteristics during typhoons in a conventional wind tunnel.

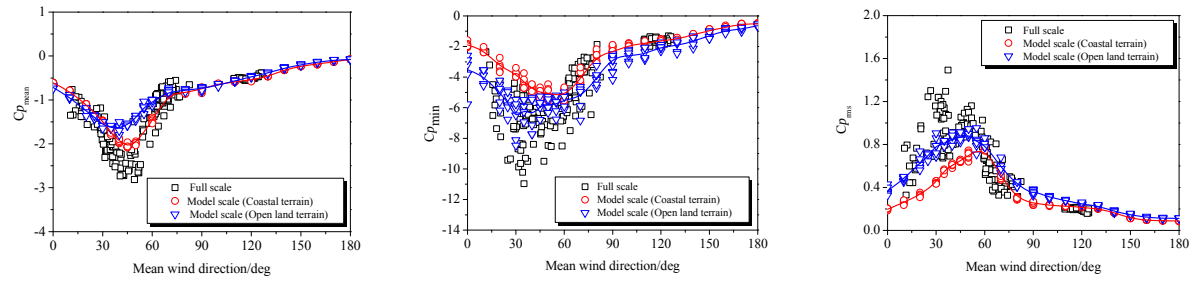

(a) Cp_{mean} (b) Cp_{min} (c) Cp_{rms}

Figure 12. Comparison of the mean, peak and rms pressure coefficients at the roof corner tap12 between the field and wind tunnel measurements

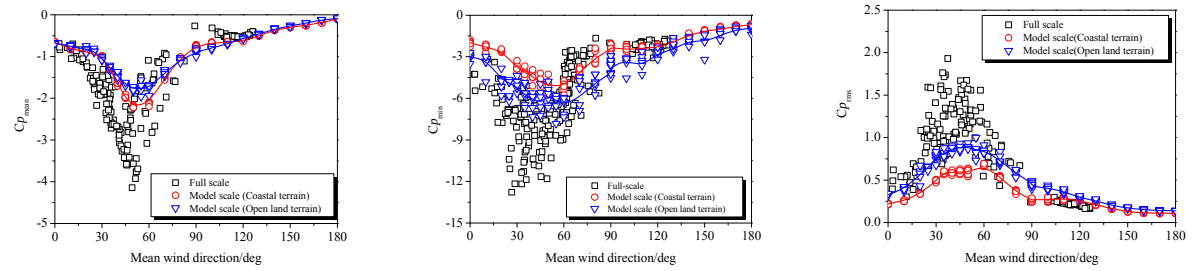

(a) Cp_{mean} (b) Cp_{min} (c) Cp_{rms}

Figure 13. Comparison of the mean, peak and rms pressure coefficients for the roof corner tap21 between the field and wind tunnel measurements

3.3.2 Probability density function

The probability density functions of pressure coefficient for Tap21, corner area I and corner area III obtained from the full-scale measurements and the wind tunnel test for approaching wind direction of 45° were estimated as shown in Figure.14 (a) through 14(c), respectively. It obviously appears that the probability distributions of the field measured pressures at the corner tap and on the corner areas are more highly skew than those of the wind tunnel test, corresponding to skewness to the left. The differences in the tail of the probability density functions indicate that the wind tunnel test underestimate the negative peak pressures. Meanwhile, the probability distributions of the field measured pressures significantly deviate from the Gaussian distribution, demonstrating that the probability distributions of the pressures in a conical vortex flow region are non-Gaussian.

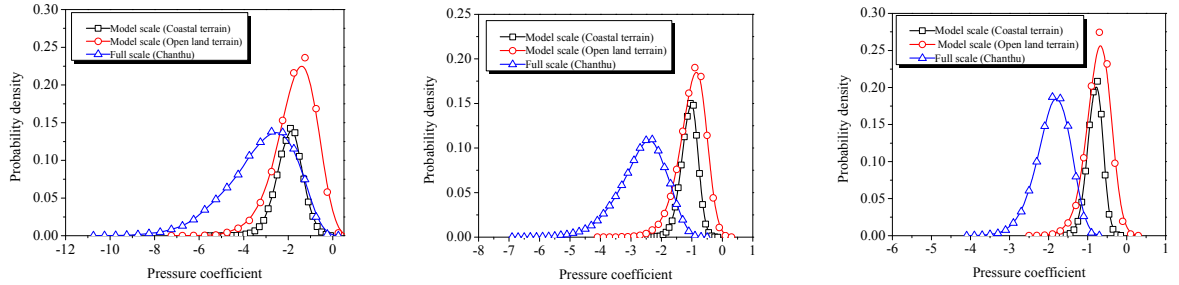

(a)Tap 21 (b) Corner area I (c) Corner area III

Figure 14.Comparison of probability density of pressure coefficient for Tap21, areas I and II between the full-scale and wind tunnel measurements (for wind direction of 45 degree)

3.3.3 Spectral analysis

The representative spectra of fluctuating pressures for Tap21, corner area I and corner area III, which were obtained from the full-scale measurements and the wind tunnel test, are shown in Figure 15(a) through 15(c), respectively. The comparison shows that the field measured spectral amplitudes are higher than these of the model test results for Tap 21. The spectra measured from the open terrain are closer to the full-scale spectra than those obtained from the coastal terrain, implying that the real wind flows were more turbulent than those from the coastal terrain. The agreement of the spectra is better for corner area III than other two cases. This suggests that as the increase of the considered area for determination of wind loads on it, more accurate area-averaged wind pressures may be obtained.

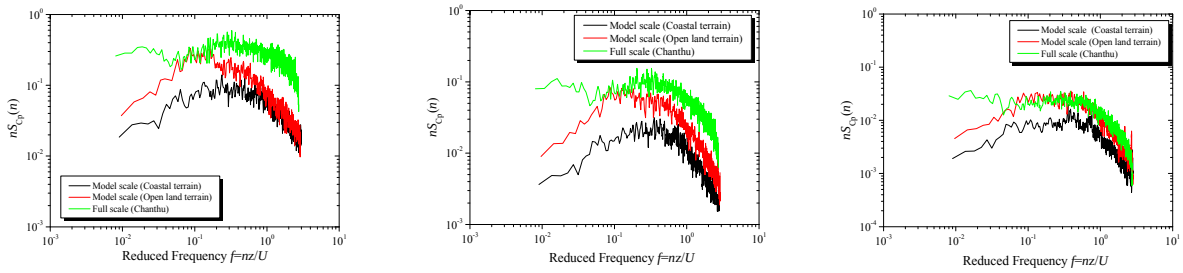

(a)Tap 21 (b) Corner area I (b) Corner area III

Figure 15. Comparison of spectra of pressure coefficient for corner Tap21 and corner areas between the full-scale and wind tunnel measurements (for wind direction of 45 degree)

4 CONCLUSIONS

A combined study of field measurement and wind tunnel test was conducted to investigate the wind loads on a low-rise building during typhoons. The major conclusions of this study are summarized as follows:

(1) The windward leading edges on the corner area were consistently subjected to the most severe suction pressures for quartering winds. The measured minimum peak pressure coefficient was -13.5 and the associated minimum peak pressure coefficient at the windward corner leading edge area was -9.9. The measured extreme peak pressures at the windward leading edge area on the corner were significantly larger in absolute value than those from ASCE 7-10 Standard. These findings imply that the peak uplift loads prescribed in ASCE 7-10 for components and cladding may be non-conservative for low-rise buildings during typhoons.

(2) Comparison of the full-scale measurements and wind tunnel test results of negative peak and fluctuating pressure coefficients near the roof corner, roof ridges and roof leading edges showed distinct discrepancies. This implied that the conventional wind tunnel techniques cannot reproduce the highest peak and fluctuating pressure coefficients on roof regions under conical vortices or separation bubbles for extreme wind conditions.

5 ACKNOWLEDGEMENTS

The work described in this paper was fully supported by a grant from the “985” Project of Hunan University and grants from City University of Hong Kong (Project No. 7002661 and 7002748).

6 REFERENCES

ASCE/SEI 7-10, Minimum Design Loads for Buildings and Other Structures. American Society of Civil Engineers, Reston, VA, 2010.

Aponte, L., Measurement hurricane wind pressure on full-scale residential structures: analysis and comparison to wind tunnel studies and ASCE-7. Ph.D. Dissertation. Gainesville, University of Florida. Department of Civil and Coastal Engineering, 2006.

Banks, D., Meroney, R.N., Sarkar, P. P., Zhao, Z., Wu, F., Flow visualization of conical vortices on flat roofs with simultaneous surface pressure measurement, J. Wind Eng. Ind. Aerodyn., 84(2000) 65-85.

Blessing, C., Chowdhury, A. G, Lin, J., Huang, P., Full scale validation of vortex suppression techniques for mitigation of roof uplift, Engineering Structures, 31 (2009) 2936-2946.

Caracoglia, L., Jones, N. P., Analysis of full-scale wind and pressure measurements on a low-rise building, J. Wind Eng. Ind. Aerodyn., 97 (2009) 157-173.

Cochran, L.S., Cermak, J.E., Full-scale and model cladding pressures on the Texas Tech University Experimental Building, J. Wind Eng. Ind. Aerodyn., 44 (1992) 1589-1600.

Eaton, K.J., Mayne, J.R., The measurement of wind pressures on two storey houses at Aylesbury, J. Wind Eng. Ind. Aerodyn., 1 (1975) 67-109.

Endo, M., Bienkewicz, B., Ham, H. J., Wind-tunnel investigation off point pressure on TTU test building, J. Wind Eng. Ind. Aerodyn., 94 (2006) 553-578.

Holmes, J.D., Wind Loading of Structure. New York: Spon, 2001.

Levitan, M.L., Mehta, K.C., Texas tech field experiments for wind loads part I: Building and pressure measuring system, J. Wind Eng. Ind. Aerodyn., 43 (1992) 1565-1576.

Levitan, M.L., Mehta, K.C., Texas tech field experiments for wind loads part II: Meteorological instrumentation and terrain parameters, J. Wind Eng. Ind. Aerodyn., 43 (1992) 1577-1588.

Li, Q.S., Hu, S.Y., Da, Y.M., Li, Z.N., Extreme-value analysis for field measured peak pressure coefficients on a low-rise building. In Proc: The seventh Asia-Pacific Conference on Wind Engineering, Taipei, Taiwan, 2009, pp269-276.

Okada, H., Ha, Y.C., Comparison of wind tunnel and full-scale pressure measurement tests on the Texas tech building, J. Wind Eng. Ind. Aerodyn., 43 (1992) 1601-1612.

Richardson, G.M., Robertson, A.P., Hoxey, R. P., Surry, D., Full-scale and model investigations of pressures on an industrial/agricultural building, J. Wind Eng. Ind. Aerodyn., 36 (1990) 1053-1062.

Richardson, G.M., Surry, D., The silsoe structures building: comparison between full-scale and wind-tunnel data, J. Wind Eng. Ind. Aerodyn., 51 (1994) 157-176.

Richardson, G.M., Blackmore, P.A., Silsoe structures building: comparison of 1:100 model-scale data with full-scale data, J. Wind Eng. Ind. Aerodyn., 57 (1995) 191-201.

Richardson, G.M., Hoxey, R.P., Robertson, A.P., Short, J.L., The silsoe structures building: comparisons of pressures measured at full scale and in two wind tunnels, J. Wind Eng. Ind. Aerodyn., 72 (1997) 187-197.

Sill, B.L., Cook, N.J., Fang, C., Aylesbury comparative experiment, A final report, J. Wind Eng. Ind. Aerodyn., 43 (1992) 1553-1564.

Tieleman, H.W., Surry, D., Lin, J.X., Characteristics of mean and fluctuating pressure coefficients under corner (delta wind), J. Wind Eng. Ind. Aerodyn., 52 (1994) 263-275.

Okada, H., Ha, Y.C., Comparison of wind tunnel and full-scale pressure measurement tests on the Texas tech building, J. Wind Eng. Ind. Aerodyn., 43 (1992) 1601-1612.

Uematsu Yasush, Isyumov Nicholas, Wind pressures acting on low rise buildings, J. Wind Eng. Ind. Aerodyn., 82 (1999) 1-25.

Wu, F., Sarkar, P.P., Mehta, K. C., Zhao, Z., Influence of incident wind turbulence on pressure fluctuations near flat-roof corners, J. Wind Eng. Ind. Aerodyn., 89 (2001) 403-420.

Zhao. Z., Wind flow characteristics and their effects on low-rise buildings, Ph.D. Dissertation, Lubbock, Texas Tech University, Civil Engineering, 1997.

The Seventh International Colloquium on Bluff Body Aerodynamics and Applications (BBAA7)
Shanghai, China; September 2-6, 2012

Field measurement of wind loads on low-rise building with adjustable roof pitch

Wang Xu, Huang Peng, Gu Ming

State Key Laboratory of Disaster Reduction in Civil Engineering, Tongji University, Shanghai, China

ABSTRACT: A low-rise building and a tower were constructed near Shanghai Pudong International Airport by East China Sea to study the characteristics of wind field and wind pressure on the roof of the building. The remarkable feature of the test building is that the roof pitch can be adjusted range from 0° to 30°, so that the wind pressure for different roof pitches can be analyzed. In this paper, the time-histories of three pieces of ten-minute wind pressures were analyzed with different roof pitches at 0°, 10° and 20° respectively, and then comparison was done with a wind tunnel test on a rigid model of 1:30 scale. It indicates that distributions of the mean and fluctuating pressure agree well with those of the wind tunnel test results. The non-Gaussian feature of the pressure is investigated. It is shown that there exists a linear relation between the skewness and kurtosis, and the fitting formulae are presented at 0, 10, and 20 pitches.

KEYWORDS: field measurement, test building with adjustable roof pitch, low-rise building, pressure coefficient, wind tunnel test, non-Gaussian.

1 INTRODUCTION

Wind is a part of our daily lives. While wind can be beneficial to humankind's enterprises, it can also be extremely destructive to buildings and other structures we build on the earth[1]. According to the survey of wind hazard, the main reason results in causalities and property losses is the damage and collapse of the low-rise buildings at villages and small towns, especially in China. So it is necessary to improve wind resistance capacity of low-rise buildings based on field measurement and thus reduce property losses attacked by severe wind.

The last three decades of the twentieth century were notable for a number of full-scale studies of wind loads on low-rise buildings. In these studies, advantage was taken of the considerable developments that had taken place in electronic instrumentation, and provided a vast body of data which challenged wind tunnel modeling techniques. In the early 1970s, the BRE(Building Research Establishment) in the UK commenced a program of full-scale measurements on a special constructed experimental building with two stories at Aylesbury, England[2]. The building had the unique feature of a roof pitch which was adjustable between 5°and 45°. In the late 1980s, another famous full-scale experiment on low-rise building was set up in Lubbock, Texas, USA[3,4]. The building had a small steel shed of height, 4.0m, and plan dimensions, 9.1and 13.7m and a near-flat roof. The building had the unique feature of being mounted on a turntable, thus enabling control of the building orientation relative to mean wind direction. Almost at the same time, a new full-scale experiment was commenced in Silsoe, UK[5,6]. The building was a larger steel portal-framed structure, 24m long, 12.9m span, and 4m to the eaves, with a 10 degrees roof pitch, located in open country. The building had unique capacity of being fitted with both curved and sharp eaves. At the beginning of twentieth century, a 6m cube has been constructed at Silsoe Research Institute in an open country exposed position in order to provide a facility for fundamental studies of the interactions between the wind and a structure[7,8]. The building had the feature of the changes in roof pressure brought about by pitching the cube for-

wards by 2.5° and 5°. At the late of 2000s, the researchers from Hunan University in China put forward the idea of removable building and successfully developed field measurement of wind loads on that building[9,10]. The main feature is that the building can be moved to the typhoon landed areas, which makes more opportunities to carry out field measurement during typhoon. The building for field measurement in this paper is built near Shanghai Pudong International Airport by East China Sea. The size of the plane of the building is 10m×6m and the height of the eave is 8m. The feature of this building is that the pitch of roof can be changed. The roof pitch can be adjusted between 0°and 30° by using the lifting device. The architectural appearance of the pitch-changed building is designed according to the common characteristics of the low-rise buildings at villages in Southern China. Therefore, the research results have important significances to the wind resistance study of low-rise buildings in China.

2 THE FULL-SCALE FACILITY

2.1 *Introduction of full-scale building*

Pudong district in Shanghai is the area where strong wind, especially strong typhoons, frequently occurs each year. So a field laboratory had been set up by State Key Laboratory of Disaster Reduction in Civil Engineering of Tongji University to study the turbulence characteristics near ground and wind effects on low-rise buildings in the field. The field laboratory is located on flat area close to the Yangtze river estuary, and in the vicinity of Shanghai Pudong International Airport(see Figure 1). It consists of a test building and a meteorological tower(see Figure 2).This laboratory features many capabilities not found in past full-scale experiments. The notable feature of the test building is that its roof pitch can adjust from 0° to 30°. Figure 3 shows the full-scale building respectively with 0° and 30° roof pitch.

Figure 1. Location of test building

Figure 2. Landform around test building

(a)0°

(b)30°

Figure 3. Full-scale low-rise experimental building

Figure 4 shows the essentials of the design. The hinged design method was used for the connections of the roof and the girder of ridge. With the lifting of girder by two sets of worm and worm wheel, the roof pitch will change correspondingly.

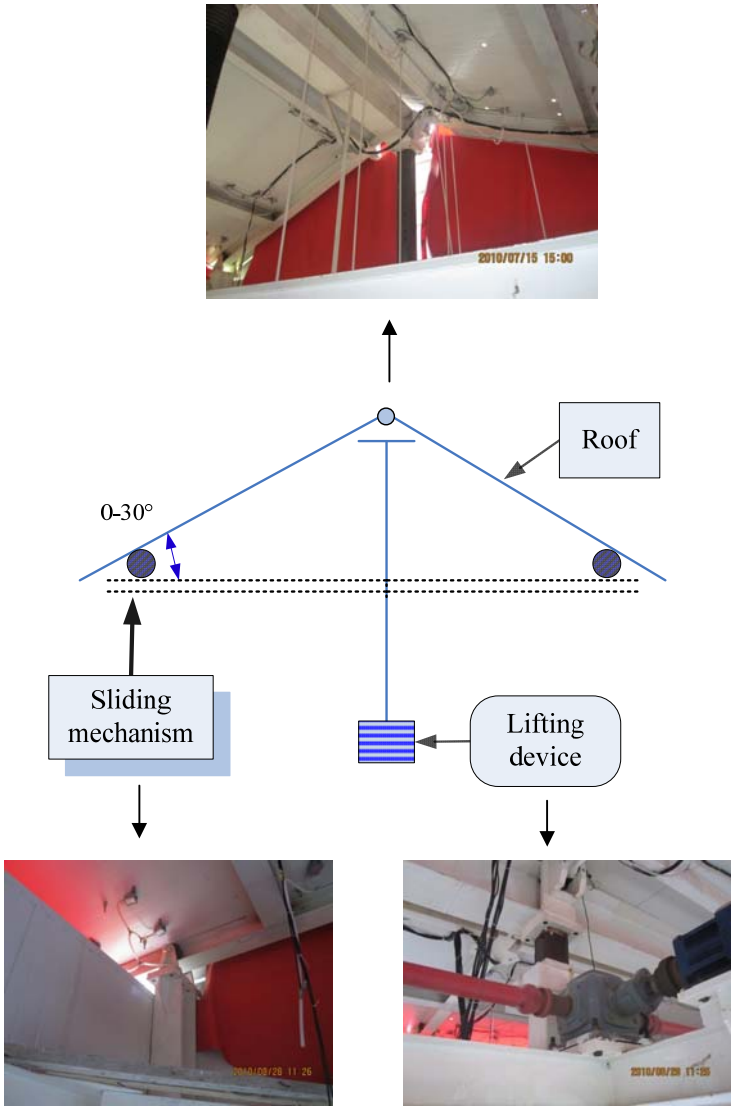

Figure 4. Elevating system

2.2 *Field instruments*

According to the demand of the field experiment, the anemometers type of R.M. Young 81000, R.M. Young 85106, R.M. Young 05305V are installed respectively at the level of 10m, 20m, 30m and 40m, see Figure 5. The sample frequency of R.M. Young 85106 is 1Hz, and those of the other two types are 20Hz. Micro differential pressure sensors supplied by Shuangqiao Sensor measurement and control technology Co. Ltd are installed on the roof of the test building to study local wind pressure in the field. Figure 6 shows the photo of the pressure sensors.

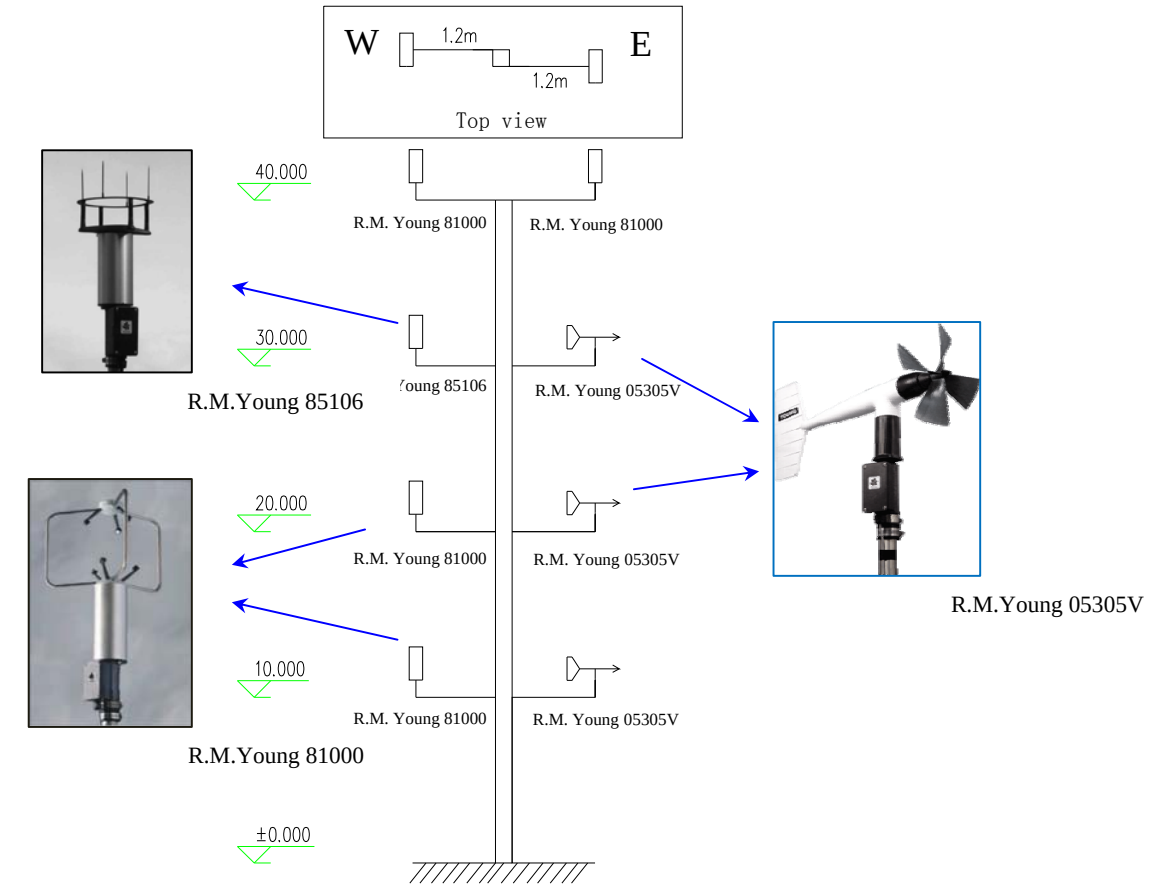

Figure 5. The arrangements of anemometers

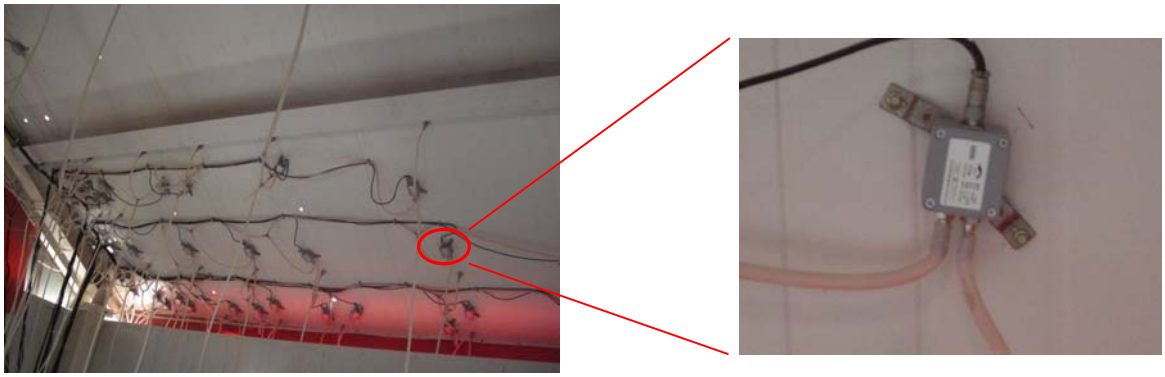

Figure 6. Micro differential pressure sensors

Figure 7 shows the pressure measurement system of field experiment in this paper. A valve is added to prevent rainwater from damaging the sensors.

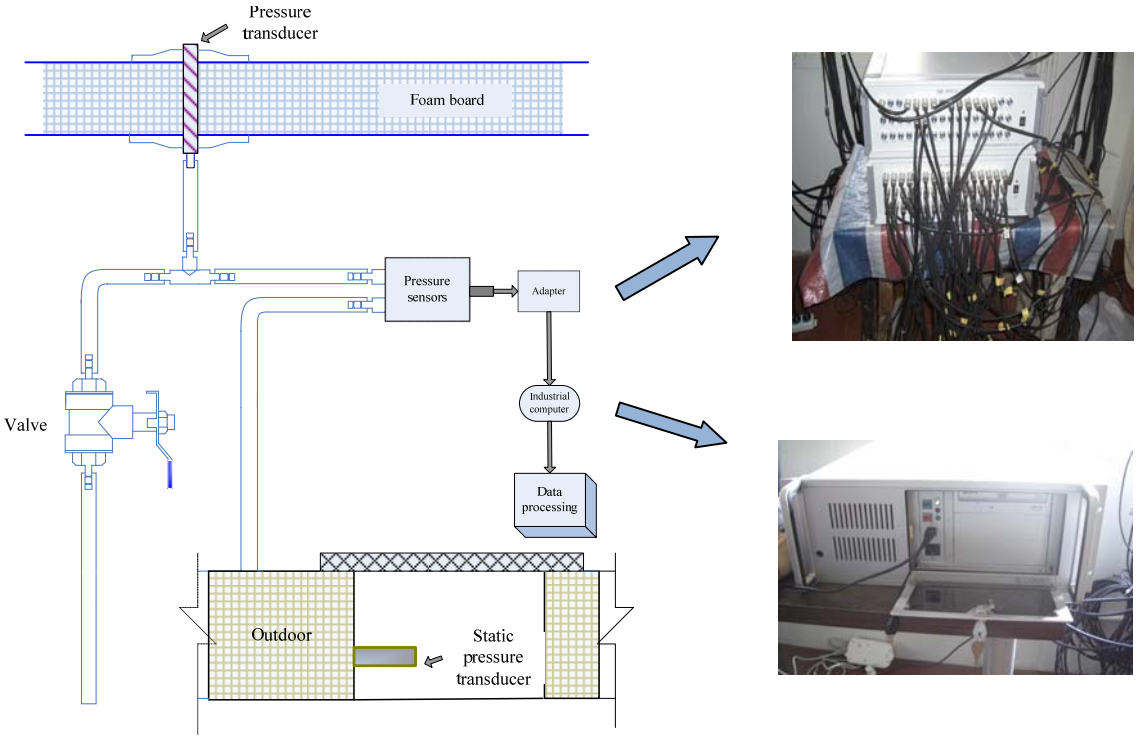

Figure 7. Pressure measurement system

2.3 *Layout of pressure measurements*

Figure 8 shows the positions of pressure transducers, there are ninety-four taps on the roof. There are more pressure transducers installed at north-east corner of the roof than other regions because of the frequently emerge of southeast wind in Shanghai.

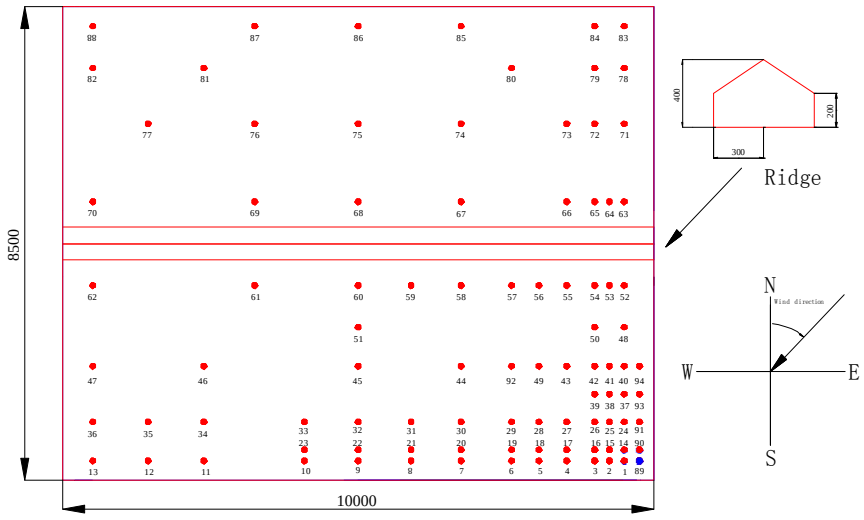

Figure 8. Layout of pressure measurements on test building

3 TEST RESULTS

In order to compare the wind pressure on the roof between full-scale experiment and wind tunnel test, wind tunnel test was made with a rigid model of 1:30 scale based on full-scale test building. The test is carried out in TJ-2 Boundary Layer Wind Tunnel in Tongji University, whose working section is 3m in width, 2.5m in height and 15m in length. Wind condition corresponding to roughness exposure B in the Chinese code [11] is simulated in the wind tunnel at a length scale of 1/50. Table 1 shows the parameters of field measurement and wind tunnel test.

Table 1. Cases of field measurement and wind tunnel test

Parameters	FS1	FS2	FS3	WT1	WT2	WT3
Test type	Full-scale	Full-scale	Full-scale	Wind tunnel	Wind tunnel	Wind tunnel
Scale proportion	1:1	1:1	1:1	1:30	1:30	1:30
Roof pitch	0°	10°	20°	0°	10°	20°
Mean wind speed at eave	8.58 m/s	9.95m/s	9.97m/s	9.02m/s	9.02m/s	9.02m/s
Mean wind direction	41°	34°	43°	40°	35°	45°
Turbulence intensity	0.233	0.158	0.221	0.247	0.245	0.241
Frequency（Hz）	20	20	20	312.5	312.5	312.5
Sample time and data length	10min 12000	10min 12000	10min 12000	38.4s 12000	38.4s 12000	38.4s 12000

The surface pressure on the body is usually expressed in the form a non-dimensional pressure coefficient[12]. A general time-varying pressure coefficient C_{p_i} is as follows:

$$C_{p_i} = \frac{p_i - p_\infty}{p_0 - p_\infty} \tag{1}$$

where p_i is the pressure of tap i; p_0 is a total reference pressure; p_∞ is a static reference pressure. In this paper, the mean wind speed was measured at height of the eave of test building.

3.1 *Pressure distribution on roof surface*

In order to compare the results, Figure 9 shows the contour graph of mean wind pressure on the roof based on two types of experiments, and Figure 10 shows the contour graph of fluctuating wind pressure. It indicates that the distributions of mean and fluctuating pressure agree well with those of the wind tunnel test results. No matter field or wind tunnel experiment, we can see there are two pairs of conical vortices occurred at the windward of roof as well as the backside of ridge. In these regions, negative pressure is larger than that in other regions.

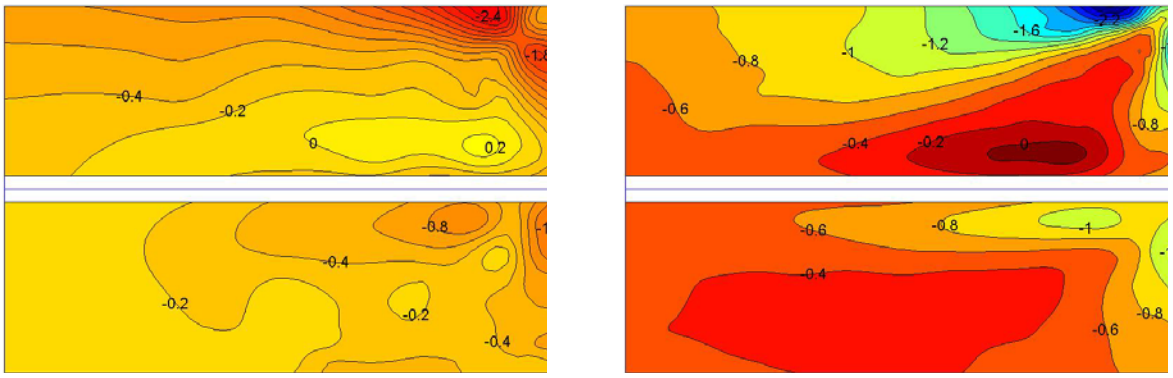

FS1 WT1

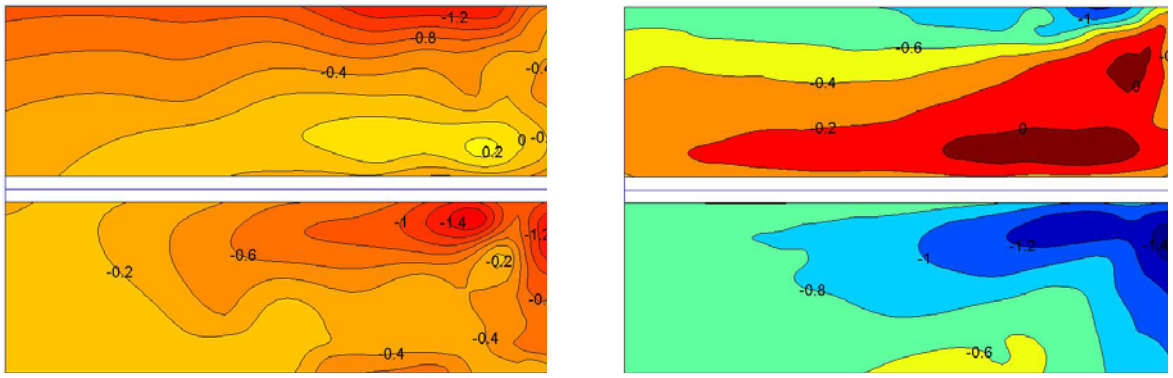

FS2 WT2

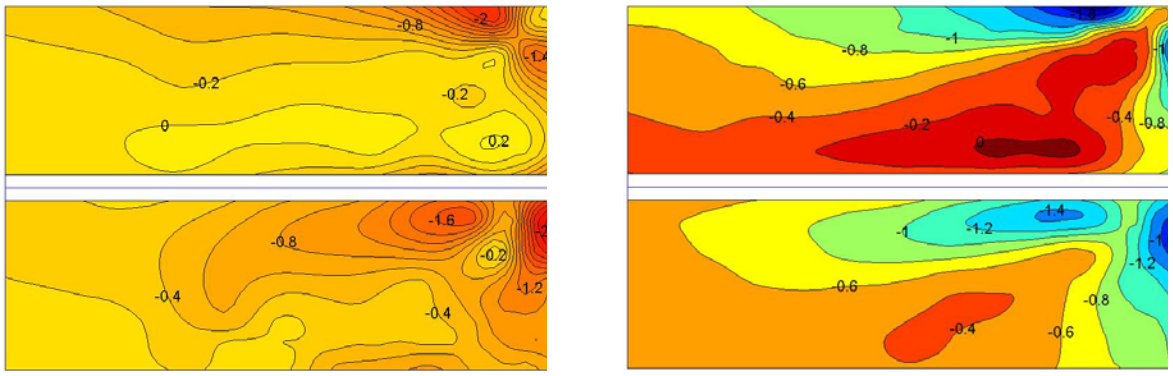

FS3 WT3

Figure 9. Contours of mean wind pressure coefficients

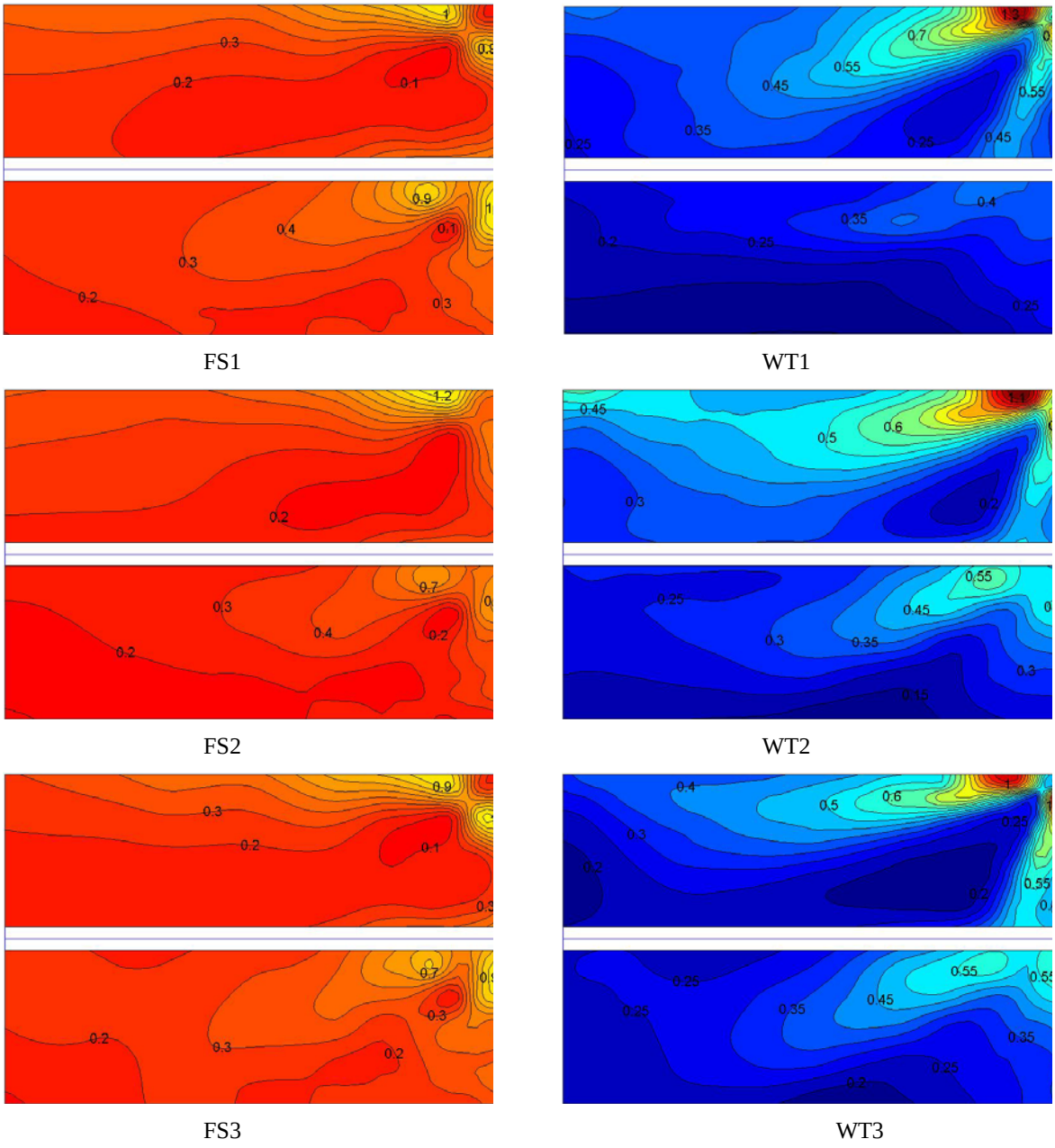

Figure 10. Contours of rms wind pressure coefficients

3.2 *Mean and peak wind pressure coefficients along middle line*

In order to study the influence of the roof pitch on the wind pressure, the pressure coefficients of the nine taps along the central line are analyzed, which are taken advantage of the field data FS1, FS2 and FS3 in Table 2. Figure 11 shows the mean, fluctuating and peak values of wind pressure along the middle line changing with the roof pitch. First of all, we can see from Figure 11(a), in the windward region, the mean negative pressure is maximum at the 0 ° and minimum at 20 °, but contrary to the leeward area. The results in Figure 11 (b) is the same as Figure 11 (a), fluctuating wind pressure increases with the roof pitch decreases in the windward region, in contrast to

the leeward regional conclusions. It can be seen obviously from Figure 11(c), the maximum wind pressure at 20° is significantly smaller than these at the other two roof pitch, while Figure 11(d) shows the minimum value is at 0 °. In summary, the roof pitch has a significant influence on the roof surface wind pressure, not only on the mean wind pressure, but also on the fluctuating and peak wind pressure. The wind pressure changes significantly because the air flow pattern and the internal structural properties of vortex on the roof surface vary with the roof pitch.

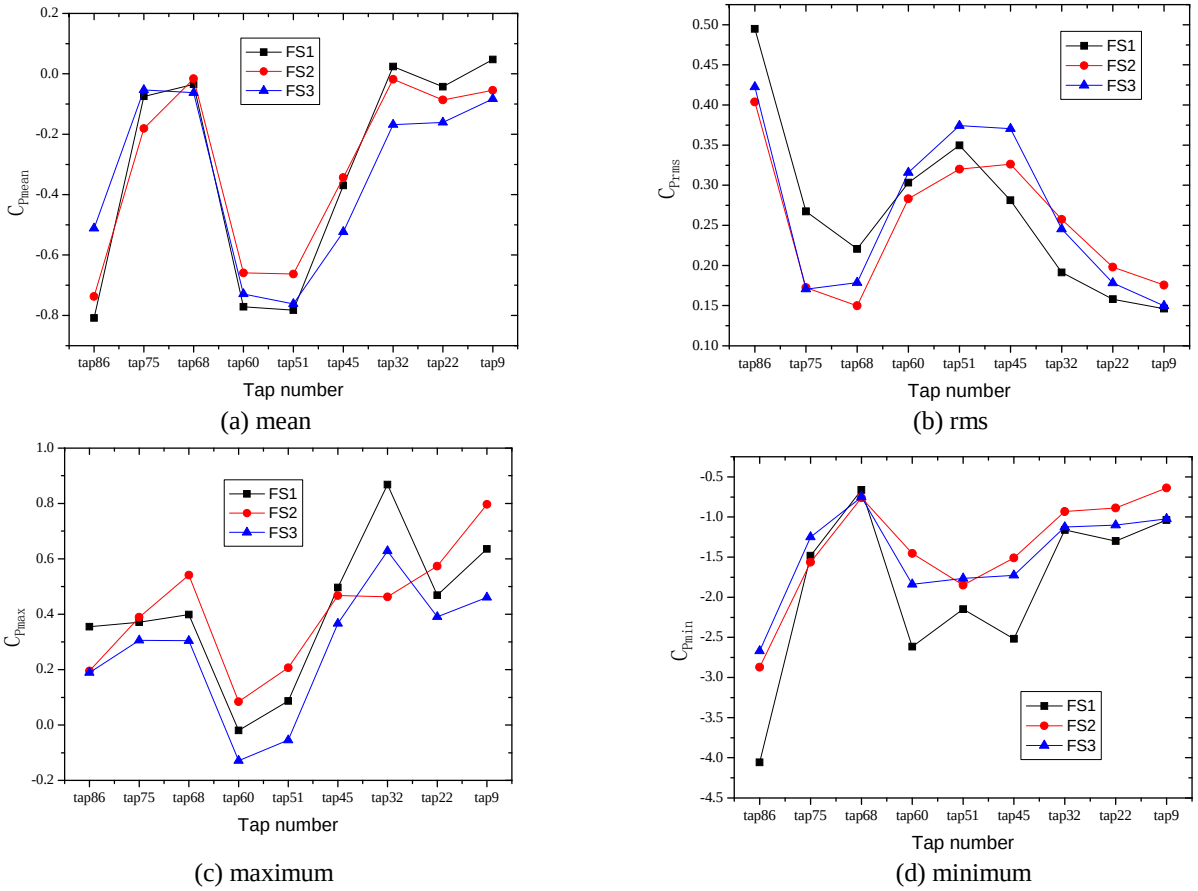

(a) mean (b) rms

(c) maximum (d) minimum

Figure 11. Mean and peak wind pressure coefficients along central line

3.3 *Non-Gaussian features of fluctuating wind pressure*

The assurance of safety and reliability of buildings requires estimation of the extremes of the applied load effects. If the statistical description in a system differs significantly from Gaussian, conventional methodologies with implicit assumption of Gaussian may no longer be valid requiring a non-Gaussian estimation framework. This is particularly important when considering the extremes, which are sensitive to the tail regions of the probabilistic description of non-Gaussian processes. For instance, the local pressure fluctuations measured at corners as well as other separation flow regions of roofs of low buildings are found to be highly non-Gaussian [13,14]. Thus, it is necessary to carry out the study on non-Gaussian features of fluctuating wind pressure.

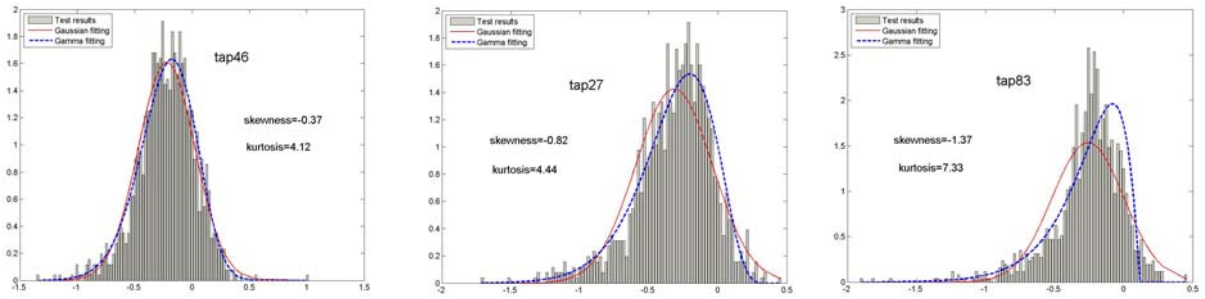

(a) (b) (c)

Figure 12. Probability distribution of wind pressure

Due to space limitation, only the probability distribution of fluctuating pressure for typical measured taps under working condition of FS1 has been given in Figure 12. We can see the local fluctuating pressure measured at the windward of the roof as well as the backside of the ridge is found to be highly non-Gaussian. The absolute value of skewness and kurtosis in these regions are obviously larger than that in other regions. The probability distribution of fluctuating pressure agrees well with Gaussian processes when skewness is larger than -0.5, and has better agreement with Gamma distribution when the value of skewness is between -1 and -0.5, nevertheless neither of the distributions is in accordance with the measured data.

The value of skewness and kurtosis are sensitive to the tail regions of the probabilistic distribution of non-Gaussian processes, and the relation between skewness and kurtosis is very important for the study on the extremes of the applied load effects. Figure 13 shows the relation between the measured results. It shows that there is a linear relation between the skewness and kurtosis, and the fitting formulae are presented between skewness and kurtosis at 0°, 10°, and 30° pitches. To evaluate the precision of the fitting functions, the theoretically calculated and the fitted values of kurtosis in all work cases are also compared in Figure 13. It can be seen from Figure 13 that the fitted values can be reliably used for evaluating the theoretically calculated values.

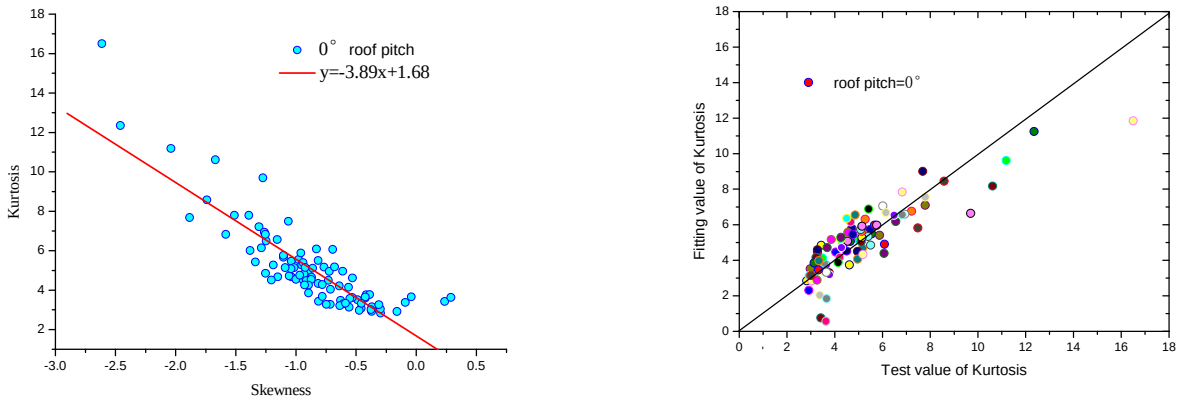

(a) roof pitch=0°

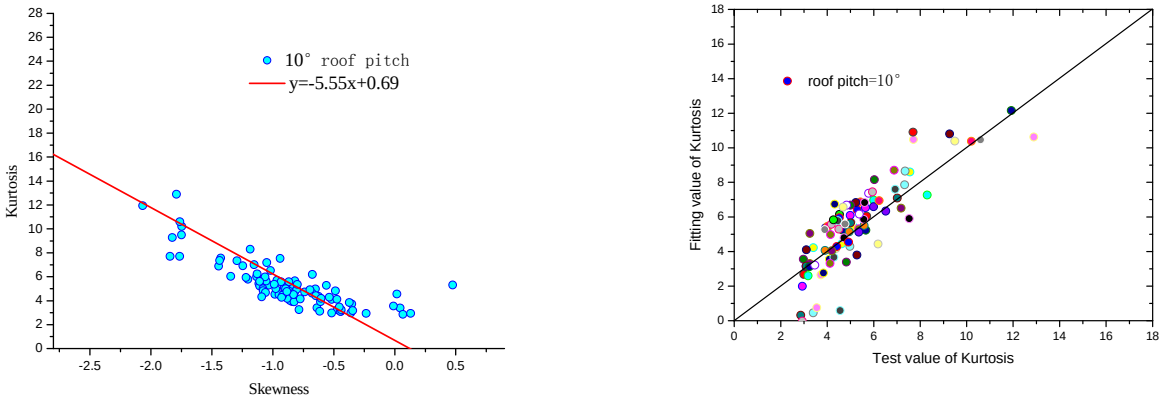

(b) roof pitch=10°

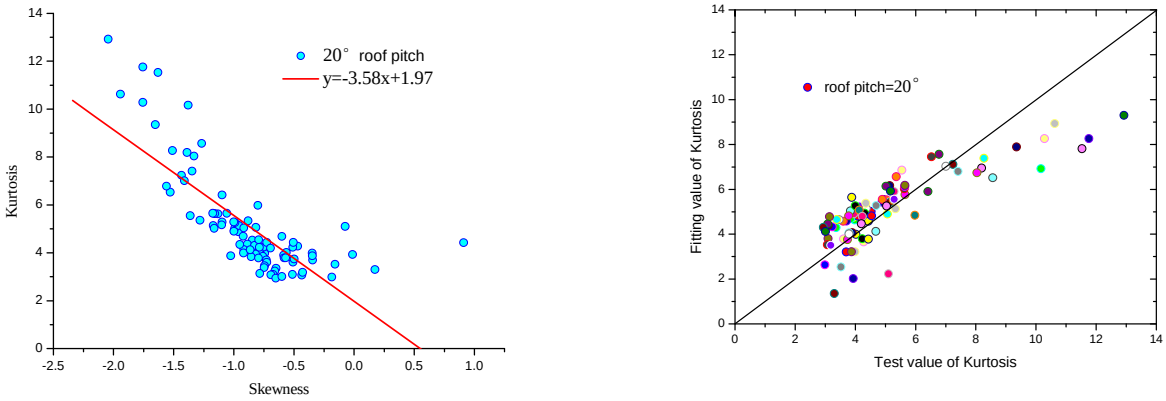

(c) roof pitch=20°

Figure 13. Variation of skewness with kurtosis

4 CONCLUSIONS

The characteristics of wind pressure on the roof of the test building are studied. The main results are as follows:

(1) The trend of average and fluctuating wind pressure distribution tested by the filed measurement is consistent with that by wind tunnel test.

(2) The probability distribution of fluctuating pressure agrees well with Gaussian processes when the skewness is larger than -0.5, while has better agreement with Gamma distribution when the value of skewness is between -1 and -0.5, nevertheless neither of the distributions are in accordance with the measured data.

(3) There exists a linear relation between the skewness and kurtosis, and the fitting formulae are presented between skewness and kurtosis with 0, 10, and 30 pitches, which will be helpful to the calculation of the extreme of wind pressure.

5 ACKNOWLEDGEMENTS

The author would like to gratefully acknowledge the support of the National Natural Science Foundation of China (51178352, 90715040).

6 REFERENCES

[1] Zhongshan Zhao. Wind Flow Characteristics and their effects on low-rise buildings, Texas Tech University, 1997.
[2] K.J. Eaton, J R Mayne, The measurement of wind pressures on two-story houses at Aylesbury, J. Wind Eng. and Ind. Aerodyn., 1(1975): 67- 109.
[3] M.L. Levitan, K C Mehta, Texas tech field experiments for wind loads: Part 1. Building and pressure measuring system, J. Wind Eng. and Ind. Aerodyn., 43(1992): 1565-1576.
[4] M.L. Levitan, K C Mehta. Texas tech field experiments for wind loads: Part II. Meteorological instrumentation and terrain parameters, J. Wind Eng. and Ind. Aerodyn., 43(1992): 1577-1588.
[5] R.P. Hoxey, P.J. Richards, Full-scall wind load measurements point the way forward, J. Wind Eng. and Ind. Aerodyn., 57(1995): 215-224.
[6] P.J. Richards, R.P. Hoxey, B.S.Wanigaratne, The effect of directional variations on the observed mean and rms pressure coefficients, J. Wind Eng. and Ind. Aerodyn., 54/55(1995):359-367.
[7] P.J. Richards, R.P. Hoxey, Flow reattachment on the roof of a 6m cube, J. Wind Eng. and Ind. Aerodyn., 94(2006): 77–99.
[8] M. Sterling, C.J. Baker, R.P. Hoxey, Short term unsteady wind loading on a low-rise building, Wind and Structures. 6(2003): 403-418.
[9] Yimin Dai, Qiusheng Li, Zhengnong Li, Experimental study of wind pressures on a low-rise full-scale building, China Civil Engineering Journal. 41(2008): 9-13.
[10] Yimin Dai, Zhengnong Li, Qiusheng Li, Wind loads on low-rise buildings: study on variation of near ground wind profiles, China Civil Engineering Journal, 42(2009): 42-48.
[11] GB50009-2001, Architectural structure load standards load code, China, 2001.
[12] J.D. Holmes, Wind loading of structures, E & FN Spon, London, 2001.
[13] T.Stathopoulos, PDF of wind pressures on low-rise buildings, J Struct Eng ASCE, 106(1980):973–90.
[14] K.S. Kumar, T Stathopoulos, Synthesis of non-Gaussian wind pressure time series on low building roofs, Engineering Structures, 21 (1999):1086–1100.

Wind-induced torsional aerodynamic loads on low and medium height buildings

M. Elsharawy, T. Stathopoulos and K. Galal

Faculty of Engineering and Computer Science, Concordia University, Montréal, QC, Canada

ABSTRACT: Since there is limited information about wind-induced torsional loads on buildings, wind tunnel tests were carried out on a series of buildings with low and medium heights. Four buildings (scale 1:400), having the same horizontal dimensions but different heights (6, 12, 25 and 50 m), were tested in a simulated open terrain exposure for different wind directions (i.e. from 0^o to 180^o every 15^o). The synchronized wind pressure measurements on the rigid building model allowed estimating the instantaneous shear forces and torsional moments. All results were normalized and presented in terms of mean and peak values of shear and torsional coefficients representing two load cases (torsion and shear load). Furthermore, the experimental results were compared with the existing torsion- and shear-related provisions in the National Building Code of Canada (NBCC 2010), the American Society of Civil Engineers Standard (ASCE/SEI 7-10) and the European Code (EN 1991-1-4). The results demonstrated significant discrepancies among the provisions of these wind standards from one side and the wind tunnel results from another in evaluating torsional wind loads on low and medium height buildings. The findings of this study could assist to improve the analytical methods to evaluate wind-induced torsional loads on low and medium height buildings.

KEYWORDS: Torsion, wind loads, codes, low buildings, medium height buildings, structural design

1 INTRODUCTION

The common characteristics of wind-induced loads on building envelopes continuously vary in temporal and spatial dimensions. The variation of local wind pressures on building claddings and the total effective wind forces (base shear/overturning moment) on the main structural building systems of low and medium rise buildings have been investigated extensively in the past few decades (Krishna, 1995, Stathopoulos and Dumitrescu, 1989, and Sanni et al, 1992). However, studies on wind-induced torsional loads on low and medium height buildings are very limited. Discrepancies have been found when wind-induced torsional load provisions for low and medium height buildings in three well known building codes and standards (American, Canadian, and Eurocode) were compared by Elsharawy et al. 2011. Wind-induced torsion has been measured in the wind tunnel for three low-rise buildings with different aspect ratios (length/width = 1, 2, and 3) in open terrain exposure by Isyumov and Case, 2000. The study suggested that applying partial wind loads, similar to those implemented for the design of tall buildings, would improve the design of low buildings until more pertinent data become available. Recently, three low rise buildings having the same horizontal dimensions but different roof angles (0^o, 18.4^o, and 45^o) located in open terrain exposure were tested by Elsharawy et al. 2012. The results were also compared to the current wind load provisions and it was found that the American standard introduces torsional moment in line with the experimental data, while the Canadian and Eurocode provisions underestimate the torsional moment on low buildings.

In the current study, wind-induced torsional loads on low and medium height buildings were examined in the boundary layer wind tunnel. Building model (scaled at 1:400) has been used to represent four actual buildings having the same horizontal dimensions but with different heights. All buildings were tested in open exposure for different wind directions. The synchronized wind tunnel measurements were presented in terms of shear, and torsional coefficients. Furthermore, the experimental results were compared with wind provisions in the NBCC 2010, ASCE/SEI 7-10 and EN 1991-1-4.

2 WIND TUNNEL STUDIES

All experiments were carried out in a boundary layer wind tunnel with a working section approximately 12.2 x 1.80 m and an a adjustable roof height ranging between 1.4 and 1.8 m. A turntable of 1.2 m diameter is located on the test section of the tunnel and allows testing of models for any wind direction. A new automated Traversing Gear system has been installed to give the capability of measuring wind characteristics at any spatial location around a building model inside the test section. A geometric scale of 1:400 has been recommended for the simulation of the most important variables of the atmospheric boundary layer under strong wind conditions.

2.1 Building models

The basic building model used for the experiments was fabricated from plexiglass and scaled at 1:400. Figure 1 shows the model and the location of 146 pressure taps on its side walls. The roof does not have any pressure taps, since the uplift force does not contribute to torsion or horizontal shear forces. The model was tested at different building heights representing four actual buildings with heights (6, 12, 25 and 50 m). Model dimensions and the tested building heights are given in Table 1.

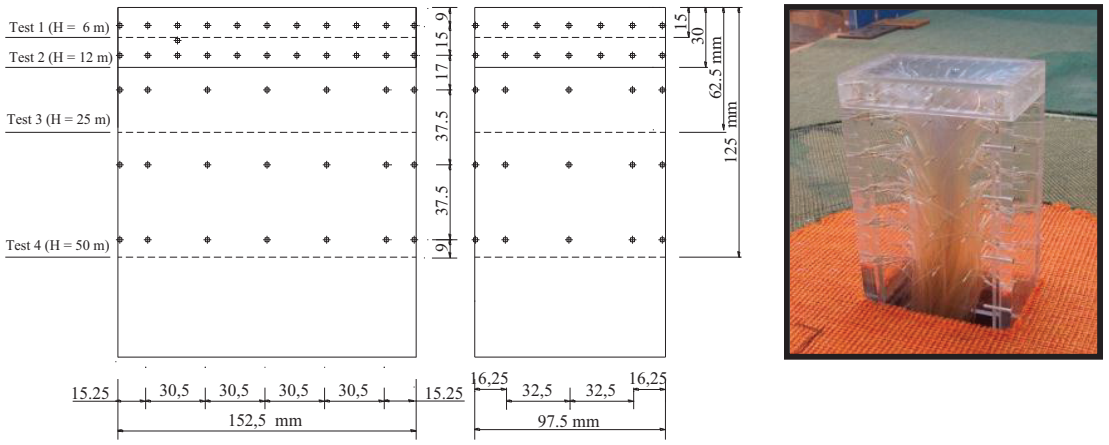

Figure 1. Building model and 146 pressure taps location.

Table 1. Model dimensions and Building heights tested

Building	Dimensions	
	Scaled (1:400, mm)	Actual (m)
Width (B)	97.5	39
Length (L)	152.5	61
Tested heights (h)	15, 30, 62.5, 125	6, 12, 25, 50

2.2 Terrain simulations

An open-country exposure was simulated in the wind tunnel. Figure 2 shows the flow approach profiles of mean wind velocity and turbulence intensity measured using a 4-hole Cobra probe (TFI) for the simulated terrain exposure. The gradient wind velocity is 13.6 m/s at a height of z_g=70 cm. The power law exponent for the wind velocity profiles simulated in these tests was 0.16. Although, it is not common for medium height buildings to be situated in open terrain, this exposure was used as a kind of conservatism since higher loads are expected to act on buildings. The pressure measurements on the models were conducted using a system of miniature pressure scanners from Scanivalve (ZOC33/64Px) and the digital service module DSM 3400. All measurements were synchronized with a sampling rate of 300Hz on each channel for a period of 27 sec (i.e. about 1 hour in full scale).

2.3 Analytical approach

Figure 3 shows a schematic representation of external pressure distributions on building envelope at a certain instant, the exerted shear forces (F_X, F_Y) and torsional moment (M_T). Pressure measurements are scanned simultaneously. The instantaneous wind force at each pressure tap is calculated according to

$$f_{i,t} = (p_{i,t} \times A_{effective}) \qquad f_{j,t} = (p_{j,t} \times A_{effective}) \qquad (1)$$

where $P_{i,t}$, and $P_{j,t}$ are instantaneous pressures measured at each pressure tap. The wind forces exerted at pressure tap locations in X- and Y-directions are noted by $f_{i,t}$ and $f_{j,t}$, respectively. For each wind direction, the horizontal force components in X- and Y-directions, and the total base shear, are evaluated according to

$$F_X = \sum_{i=1}^{N} f_{i,t} \qquad F_Y = \sum_{j=1}^{M} f_{j,t} \qquad V = \sqrt{F_X^2 + F_Y^2} \qquad (2)$$

where N and M are the numbers of the pressure taps on the longitudinal and transverse directions, respectively. All these forces are normalized with respect to the dynamic wind pressure at the mean roof height as follows:

$$C_{vx} = \frac{F_x}{q_h B\, h} \qquad C_{vy} = \frac{F_Y}{q_h B\, h} \qquad C_V = \frac{V}{q_h B\, h} \qquad (3)$$

Where q_h = dynamic wind pressure at mean roof height (kN/m^2), B = minimum horizontal building dimension (m), and h = mean roof building height (m). The torsional coefficients (C_T) and equivalent eccentricity (e) are evaluated based on

$$C_T = \frac{M_T}{q_h B\, h\, L} \qquad e(\%) = \frac{M_T}{L * V} \times 100 \qquad (4)$$

where L= building length

NBCC 2010 specifies wind loads on low buildings (mean roof height, h < 10 m, or h < width, B and h < 20 m) and medium-height rigid buildings (h < 60 m, h/B < 4, lowest natural frequency, f_n > 1 Hz). On the other hand, ASCE/SEI 7-10 identifies low buildings as (h < 18 m and h < B) and medium-height rigid buildings as having f_n > 1 Hz. In EN 1991-1-4, low buildings were defined as those with h < 15 m while buildings with frames, structural walls with h less than 100 m are introduced structurally as rigid buildings. In this study all tested buildings were assumed to be structurally rigid and follow the limitations stated in the three wind load standards.

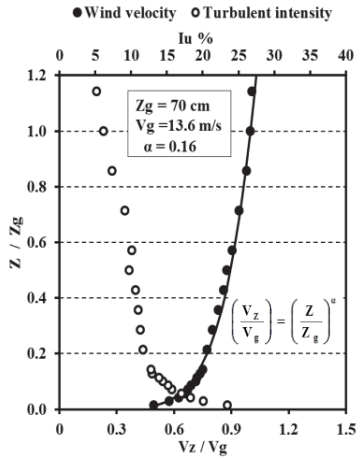

Figure 2. Wind velocity and turbulence intensity profiles for open terrain exposure.

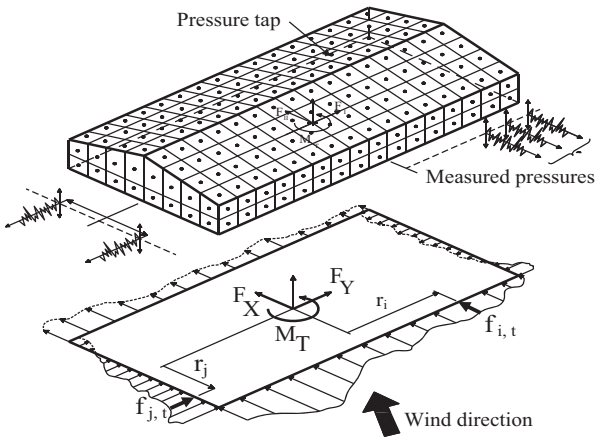

Figure 3. Instantaneous wind pressure distributions, generated wind forces (F_X, F_Y) and torsional moment (M_T).

3 COMPARISON WITH PREVIOUS STUDIES

A comparison with a previous study by Amin and Ahuja, 2012 for building (L = 37.5, B = 15, h = 90 m, scale 1:300, 140 pressure taps) was made using the wind tunnel measurements for building model (L = 61 m, B = 39 m, h = 50 m, scale 1:400, 146 pressure taps). Figure 3 shows the evaluated mean torsion for both buildings for different wind directions. The mean torsion coefficient was calculated based on the following formula

$$C_{T\,Mean} = \text{Mean Base Torsion} / (q_h BhL) = (\sum_{i=1}^{i=n} C_{P\,\text{Mean}}\ x\ A_{effective}\ x\ r_i) / BhL \qquad (5)$$

Where n=number of pressure taps, $C_{P\ Mean}$ = mean pressure coefficient, $A_{\ effective}$= presented area by the pressure tap, r_i = the distance between pressure tap and the building center.

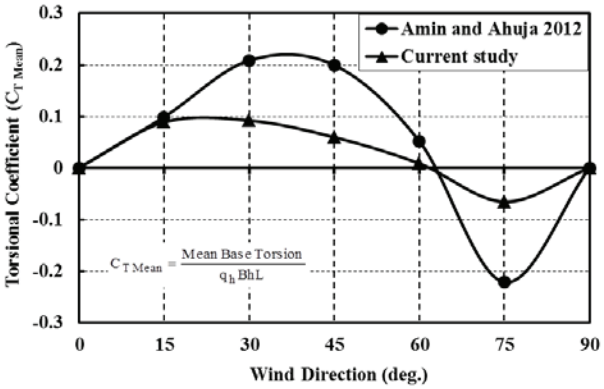

Figure 3. Mean torsional coefficient measured by Amin and Ahuja, 2012 and the current study

Data show relatively good agreement for the variation of the mean torsional coefficient measured in the two studies. The differences seen between the two studies for some wind directions may be attributed to the difference in building dimensions, the scale used, the number of pressure taps.

4 EXPERIMENTAL RESULTS

4.1. Variation of torsion and shear coefficients:

Figure 4 shows the variation of mean and peak shear coefficients (C_{vx}, C_{vy}) with wind direction for the two buildings (6 and 50 m) tested in simulated open-country exposure. The maximum shear forces in x-direction occur for wind directions from 0^o to 45^o; while in y-direction when wind is almost perpendicular to building face, i.e. 90^o. For the tested buildings, the peak shear coefficients have increased by about 50% with increasing building heights form 6 to 50 m.

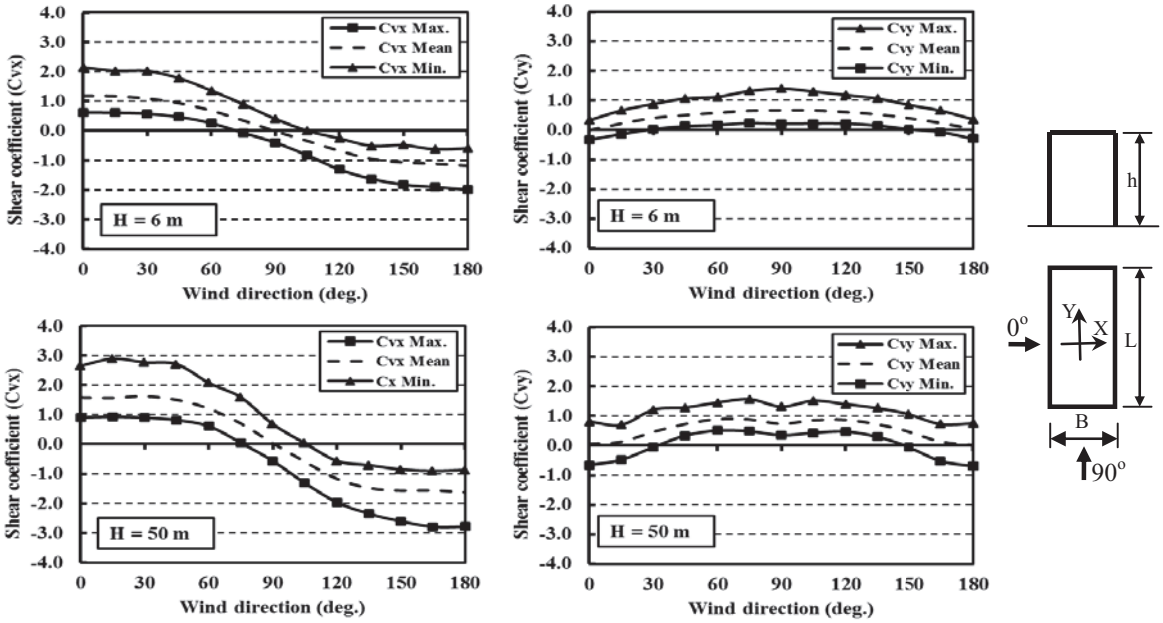

Figure 4. Variation of shear coefficients (C_{VX}, C_{VY}) with wind direction for building models corresponding to 6 and 50 m heights.

Although, the determination of the shear coefficient is important to propose equivalent wind loading, identification of horizontal distribution of these wind loads on building structural system still requires information about the torsional moment. The variation of mean and peak torsional coefficients with wind direction is presented in Figure 5 for buildings (6, 12, 25, and 50 m) in open-country terrain exposure. As a result of the building models having symmetric shapes, mean torsions are zero for wind directions perpendicular to building face, i.e. 0^o and 90^o. However, there are significant maximum and minimum torsional coefficients for these wind directions due to the lack of wind pressure correlation over the building envelope in the horizontal direction. The maximum torsional moment occurs for wind directions from 15^o to 45^o for the first three buildings (6, 12, 25 m) while for the 50 m building, two peaks appear at wind directions 30^o and 75^o. This may be attributed to different characteristics of wind flow interactions with buildings with height lower than 25 m compared to buildings with heights greater than 25 m. For better understanding in this regard, a flow visualization study is scheduled as a part of future tasks in the current research project.

4.2. Most critical torsion and shear coefficients

As it is very well known, the distribution and the magnitude of wind forces on building envelope are linked to the magnitude of torsional moment. Therefore and based on the wind tunnel measurements, two load cases are presented. Case A shows maximum torsion ($C_{T\ Max.}$) and corresponding shear ($C_{V\ Corr.}$) while Case B shows maximum shear ($C_{V\ Max.}$) and corresponding torsion ($C_{T\ Corr.}$). For simplicity, torsional loads can be treated analytically by introducing wind forces (V) with equivalent eccentricity (e) as shown in Figure 6. Tables 2

and 3, for Case A and Case B, show the evaluated coefficients for the critical wind directions for which the maximum torsion and shear were measured. For the 50 m building height, the most critical torsional moments have been measured for wind azimuths 30^o and 75^o. Thus, it quite significant for the wind provisions to cover these critical torsions for achieving the anticipated proper design for low and medium height buildings.

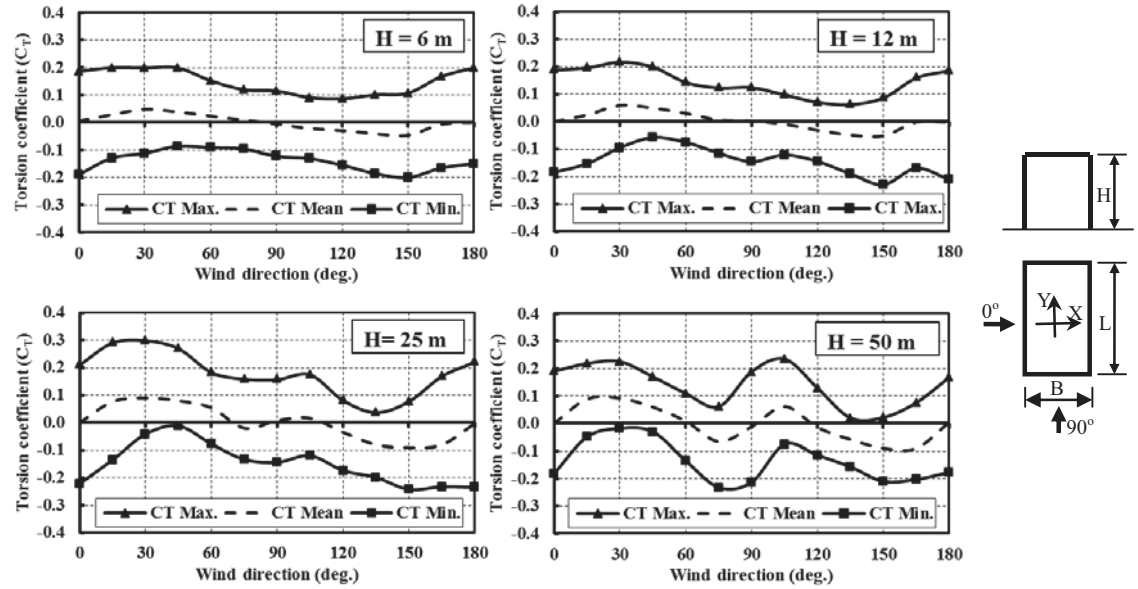

Figure 5. Variation of mean and peak torsion coefficients with wind direction for four different building heights (6, 12, 25 ,and 50m)

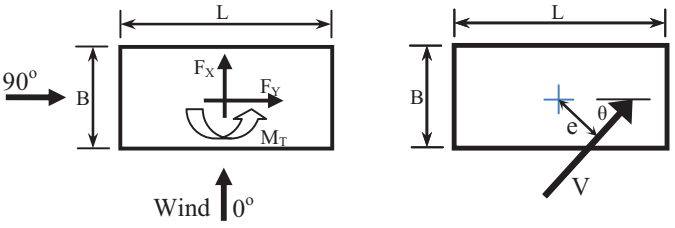

Figure 6. Horizontal wind force and torsional moment and its equivalent eccentric force.

The maximum equivalent eccentricity has been reported of about 16% of building largest horizontal dimension for building with height 50 m. The maximum ratio between the corresponding shear (associated to maximum torsion, Case A) to the maximum base shear (full load - Case B) was 74% for the 25 m high building. As indicated in many past wind tunnel studies, wind-induced torsion always exists even for wind direction for which the maximum full shear force occurs. The current study demonstrates that maximum shear is mostly associated with equivalent eccentricity about 5%. This is in line with the following statement given in ASCE/SEI 7-10, (Commentary part, C27.4.6),

> "*...wind tunnel studies often show an eccentricity of 5% or more under full (not reduced) base shear. The designer may wish to apply this level of eccentricity at full wind loading for certain more critical buildings even though it is not required by the standard. The present more moderate torsional load requirements can in part be*

justified by the fact that the design wind forces tend to be upper-bound for most common building shapes."

Table 2. Case A: Maximum torsion ($C_{T\,Max.}$) and corresponding Shear ($C_{V\,corr.}$)

Building height (m)	Wind tunnel measurements				
	Wind azimuth	$C_{T\,Max.}$	$C_{V\,Corr.}$	θ	*e (%)*
6	30^o	0.20	1.40	89.90^o	14.20
12	30^o	0.22	1.65	71.35^o	13.30
25	30^o	0.24	2.00	77.13^o	11.80
50	30^o	0.23	1.90	72.35^o	11.92
50	75^o	0.23	1.50	23.67^o	15.32

Table 3. Case B: Maximum shear ($C_{V\,Max.}$) and corresponding torsion ($C_{T\,corr.}$)

Building height (m)	Wind tunnel measurements				
	Wind azimuth	$C_{V\,Max.}$	$C_{T\,Corr.}$	θ	*e (%)*
6	0^o	2.15	0.04	88.61^o	1.96
12	15^o	2.40	0.05	84.60^o	2.66
25	30^o	2.71	0.15	84.80^o	5.50
50	15^o	2.90	0.16	87.01^o	5.42

5 INSTANTANEOUS WIND FORCES ON BUILDING SURFACES

The wind flow characteristics (i.e. attached flow, separation, and reattachment) around buildings are critical for the determination of torsional moment (M_T). The non-uniform distribution of the generated wind loads in the horizontal directions is the main reason for generating torsional moment. Figure 7 shows measured integrated wind forces on building with height 25 m in X and Y axes for the critical wind directions, i.e. 0^o, 90^o, and 30^o as the peak torsional moment occurs.

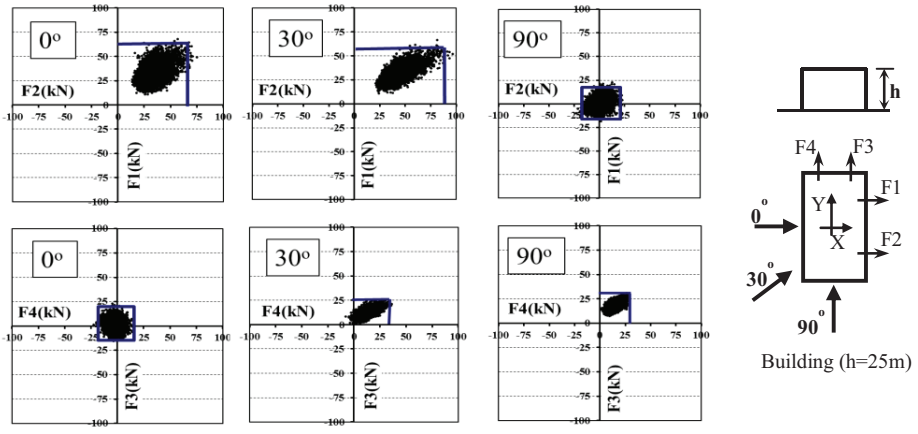

Figure 7. Horizontal forces in X and Y directions for azimuths 0^o, 30^o, and 90^o for which maximum torsions were measured for building with height = 25 m.

Since all buildings have symmetric shapes and structural systems, the center of rigidity is located at the middle of building plan. Identification of the wind forces (F1 to F4) around the vertical building axis may allow better understanding for the relation between the generated torsion and wind direction. In case of perpendicular wind (0^o and 90^o), the forces (F1 and F2) vary with the same magnitude ranges and the trend line for these values has almost slope 1:1, and the correlation coefficient is very small (0.003). Similarly, the F3 and F4 values vary in

the same manner for the same wind directions. This justifies the fact of the zero mean-torsion measured while having relatively maximum and minimum torsions for these wind directions. For wind direction 30^o, the magnitude range of (F_2) generated on the side close to wind is about double the force range of (F_1) generated on the far side. The trend line for the F1 and F2 values has slope equal to 2:3 while the correlation coefficient is 0.38. Accordingly, this could explain why the maximum torsion occurs for wind direction 30^o.

6 CODE PROVISION COMPARISONS WITH WIND TUNNEL RESULTS

The results of the wind tunnel tests (Case A and Case B) for the tested building heights were compared to the values for base shear force and torsional moment evaluated by NBCC 2010, ASCE/SEI 7-10 and EN 1991-1-4.

6.1. NBCC 2010

In NBCC 2010, the static method (called herein NBCC 2010-S1) is introduced for low buildings while the simplified method (called herein NBCC 2010-S2) is proposed for rigid buildings with intermediate height. The static method calculations for the torsional and shear coefficients were derived based on figure I-7 of NBCC 2010, Commentary I, where the external peak (gust) pressure coefficients (C_pC_g) are provided for low buildings. Likewise, for the simplified method, the external pressure is taken from Figure I-15, Commentary I. Partial and full load cases were considered to estimate maximum torsion and corresponding shear, as well as maximum shear and corresponding torsion. Calculations were carried out considering the open terrain exposure. Static method values were increased by 25% to eliminate the implicit reduction (0.8) due to directionality issue.

6.2. ASCE/SEI 7-10

The three analytical procedures stated in ASCE/SEI 7-10 to evaluate wind loads were applied for this comparison. The envelope method (ASCE 7-10-E) appropriate for low buildings ($h < 18$ m and $h < B$) where h and B are the mean roof height and the least horizontal dimension respectively, figure 28.4-1 is used to get the external pressure coefficients (GC_{pf}). The basic (transverse) and torsional load cases presented in ASCE 7-10, figure 28.4-1 are used to estimate the maximum torsional moment and the maximum base shear. Directional methods-Part 1 and Part 2 (called in this paper ASCE 7-10-D1 and ASCE 7-10-D2), proposed in ASCE/SEI 7-10 to be used for all building heights, are also considered in this comparison. External pressure coefficients were collected from figure 27.4-1. Pressure coefficients are provided in table 27.6-1 for buildings with height up to 48.8 m. ASCE 7-10 calculations were carried out considering the open terrain exposure C. Also, the directional factor was taken as 1.

6.3. EN 1991-1-4

The Eurocode defines one unified analytical method that can be used for predicting the wind forces on all building types regardless of height. Torsional effects are taken into account by applying non-uniform pressures and forces, as shown in EN 1991-1-4, Figure 7.1. A triangular wind load is applied on the windward surface with a rectangular load on the leeward face of the building. External pressure coefficients for vertical walls of rectangular plan buildings are calculated using Figure 7.5 and Table 7.1 available in section 7, while for the external pressure of duo-pitch roofs, values are provided in the same section (Figure 7.8 and Table 7.4a).

All ASCE/SEI 7-10 values were multiplied by 1.51^2 and EN 1991-1-4 values by 1.06^2 in order to consider the effect of the 3-sec and the 10-min wind speed respectively in comparison to the mean-hourly wind speed in NBCC 2010.

Figure 8 summarizes the results for Case A (see Table 2). Peak torsional coefficients, corresponding shear, and equivalent eccentricity are evaluated either by the wind tunnel study or by the provisions of standards considered. Case B (see Table 3) comparison results, maximum shear, corresponding torsion and equivalent eccentricity are presented in Figure 9.

In the first instance, European code shows very good agreement with torsions measured in the wind tunnel for low and intermediate height buildings, see Figure 8. However, the applied wind load (i.e. corresponding shear) and the corresponding equivalent eccentricity are different from the measured values, given that torsional coefficients are always products of force coefficients times eccentricities. For low buildings, the envelope method in ASCE/SEI 7-10 shows relatively good agreement with the measured torsion, although decreasing the eccentricity from about 18% to 15% will improve its performance. Also, the static method in NBCC 2010 underestimates torsion on low buildings significantly. On the other hand for medium height buildings, the wind load procedures in the NBCC 2010 and the ASCE/SEI 7-10 overestimate torsion in some case significantly. Regarding Case B, Figure 9 indicates clearly that the static and envelope methods for low buildings in NBCC 2010 and ASCE/SEI 7-10 respectively succeed to predict maximum shear forces. All other methods in the three provisions overestimate shear forces on low and medium height buildings, as shown in Figure 9. Based on the results presented in Figures 8 and 9, it could be recommended that applying 75% of the full wind loads (i.e. maximum shear measured in Case B) with equivalent eccentricity 15% will improve torsion evaluation for low and medium height buildings.

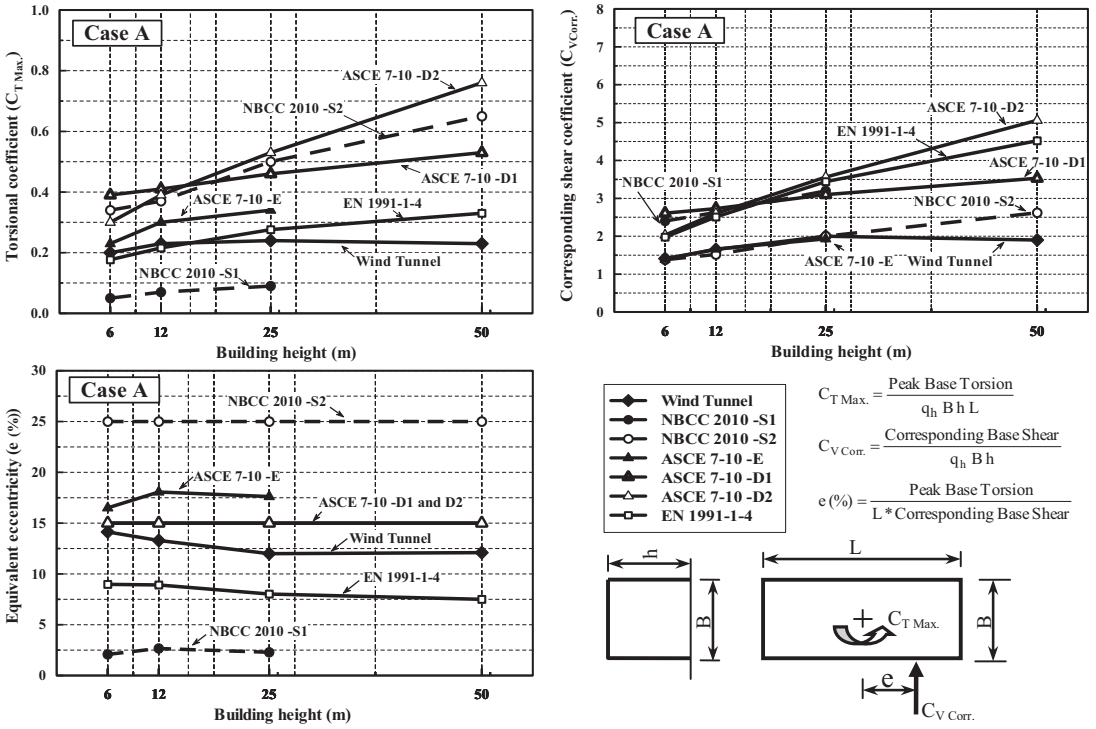

Figure 8. Comparison of torsional load case evaluated by NBCC 2010, ASCE/SEI 7-10, and wind tunnel tests (Case A: maximum torsion and corresponding shear)

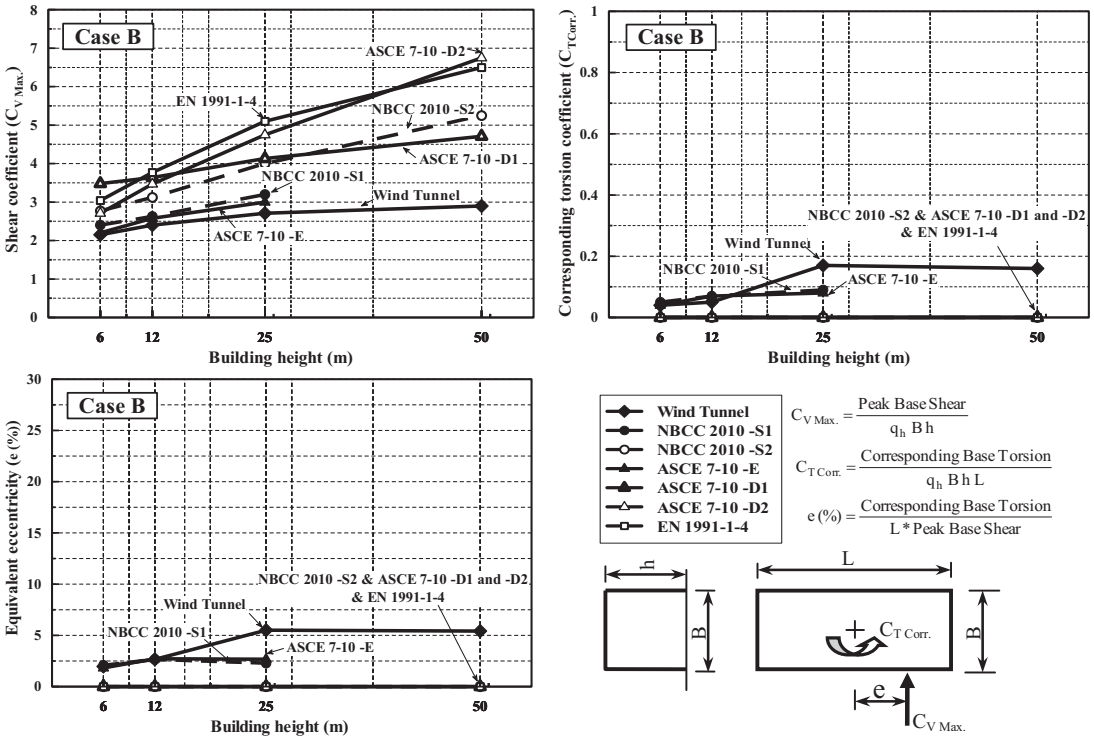

Figure 9. Comparison of shear load case evaluated by NBCC 2010, ASCE/SEI 7-10 and wind tunnel tests (Case B: maximum shear and corresponding torsion).

7 CONCLUSIONS

Wind-induced torsion was measured in the wind tunnel for four buildings having the same horizontal dimensions with different heights ranged from 6 m to 50 m. In addition, the experimental results were compared with wind provisions in NBCC 2010, ASCE/SEI 7-10 and EN 1991-1-4. The comparison results demonstrate the following:

a) For low buildings:
- The static method in NBCC 2010 underestimates torsion significantly.
- The envelope method in ASCE/SEI 7-10 shows relatively good agreement with the measured torsion.
- EN 1991-1-4 shows good agreement with the wind tunnel results.

b) For intermediate height buildings:
- Wind load procedures in NBCC 2010 and ASCE/SEI 7-10, overestimate torsion while EN 1991-1-4 shows good agreement with the wind tunnel results.

Until more experimental data become available, it could be recommended that applying 75% of the full wind loads with equivalent eccentricity 15% will improve torsion evaluation for low and medium height buildings.

8 ACKNOWLEDGMENT

The authors are grateful for the financial support received for this study from the Natural Sciences and Engineering Research Council of Canada (NSERC).

9 REFERENCES

1 NBC2010, User's Guide – NBC 2010, Structural Commentaries (part 4), Issued by the Canadian Commission on Buildings and Fire Codes, National Research Council of Canada, 2010.
2 ASCE/SEI 7-10, Minimum design loads for buildings and other structures. Published by the Structural Engineering Institute of ASCE, Reston, VA, 2010.
3 EN 1991-1-4, 2005. Eurocode 1, 2005: Actions on Structures – General actions – Part 1-4: Wind actions, European Standard
4 P. Krishna, Wind loads on low-rise buildings – a review. Journal of Wind Engineering and Industrial Aerodynamics, 1995, 54-55, 383-396.
5 T. Stathopoulos and M. Dumitrescu-Brulotte, Design recommendations for wind loading on buildings of intermediate height, Canadian Journal of Civil Engineering, 1989, 16, 910-916.
6 R. A. Sanni, D. Surry, and A. G. Davenport, Wind loading on intermediate height buildings, Canadian journal of civil engineering, 1992, 19,148-163.
7 M. Elsharawy, T. Stathopoulos, and K. Galal, Evaluation of wind-induced torsional loads on buildings by north American and European codes and standards, Proceedings of the 2011 Structures Congress, Sponsored by ASCE/SEI, Las Vegas, Nevada, USA, 2011, April 14-16.
8 N. Isyumov and P. C. Case, Wind-Induced torsional loads and responses of buildings, in: Proceedings of the 2000 Structures Congress, Sponsored by ASCE/SEI, Philadelphia, Pennsylvania, USA, 2000, May 8-10.
9 M. Elsharawy, T. Stathopoulos, and K. Galal, Wind-Induced torsional loads on low buildings, Journal of Wind Engineering and Industrial Aerodynamics, 2012, http://dx.doi.org/10.1016/j.jweia.2012.03.011.
10 J. A. Amin and A. Ahuja, Wind-induced mean interference effects between two closed spaced buildings, KSCE Journal of Civil Engineering, 2012, 16 (1), 119-131.

Wind pressure acting on flat roofed buildings

X.K. Jing[a], Y.Q. Li[a, b]

[a]*Department of Building Engineering, Tongji University, Shanghai, China*
[b]*State Key Laboratory for Disaster Reduction in Civil Engineering, Tongji University, Shanghai, China*

ABSTRACT: The wind pressure distributions on flat roofed steel frame buildings with and without parapet are studied by wind tunnel tests. At first, the magnitudes and distributions of the mean, fluctuating and minimum wind pressure coefficients on the surface of the models are analyzed. Then, wind pressure distributions derived from wind tunnel test and main country codes are compared in transverse wind direction, not considering wind-induce internal pressure and gust effect factor due to such low-rise building with enough rigidity. Finally, the characteristics of the proper orthogonal decomposition results of the measured wind pressure field are analyzed. The investigation can provide some basic understanding and reference for clauses about wind loads.

KEYWORDS: Flat-roofed buildings; parapet; wind tunnel test; wind pressure distribution; shape coefficient; code; proper orthogonal decomposition

1 INTRODUCTION

Flat roofs with and without parapet are widely used for commercial and residential low-rise buildings with steel frames Their relatively light dead and flexibility make them susceptible to wind load. There have been relatively few studies on the effects of parapet on wind load for low-rise building, this is likely due to the conclusion in Ref [1] that the code provisions for buildings without parapet are equally applicable to buildings with parapet, which may lead to unnecessary cost waste in structural design. The current codes have no recommendations about considering the effects of parapet in wind-resistant design. The present study is first to examine the general distribution of wind loads on flat-roofed buildings with and without parapet, secondly to compare wind pressure distribution obtained from wind tunnel test and main country codes, and thirdly to analyze the characteristics of the proper orthogonal decomposition results of the measured wind pressure field.

2 EXPERIMENTAL PROCEDURE

The experiments were carried out in the Boundary Layer Wind Tunnel at State Key Laboratory for Disaster Reduction in Civil Engineering at Tongji University. The wind tunnel working section is 2.5m high, 3m wide and 15m long. The exposure category of the ground roughness can be regarded as Category B according to *Load code for the design of building structures* GB50009-2001 of china [2]. Model A without parapet and model B with 1.2m high parapet commonly used in China were made at a geometric scale of 1:40, and they have the same full scale dimensions. Figure 1 shows the prototype buildings. 235 taps were arranged on the roof and walls of the models to measure wind pressure simultaneously. Due to wind load on parapet is beyond the scope of this study, no tap was arranged on the parapet. Figure 2 shows the layout of pressure taps on the roof and walls. The wind attack angle is varied from 0^o to 360^o in 45^o in steps (Figure 2). Wind speed and corresponding velocity pressure at the eave heights of the models are taken as the reference wind speed and reference pressure in analyzing the wind pressure coefficients. The reference wind speed at the reference height is near to 8m/s.

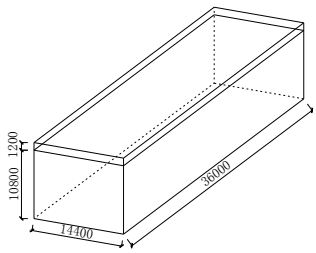

Figure 1. Prototype of flat-roofed buildings

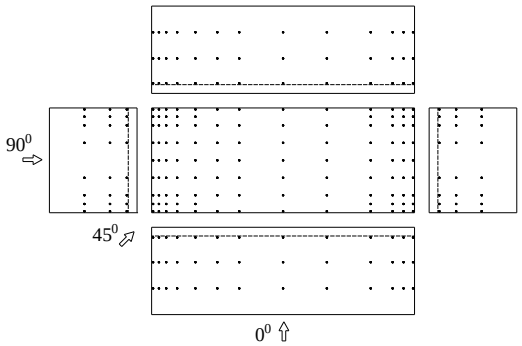

Figure 2. Layout of pressure taps for the models

3 RESULTS AND DISCUSSION

3.1 *The characteristics of wind pressure*

Figure 3 and figure 4 show the magnitudes and distributions of mean and fluctuating wind pressure coefficients on model A and model B with 0^0, 45^0, and 90^0 wind directions, respectively, in consideration of the symmetric conditions of the models. The distributions of mean wind pressure coefficient on the walls of model B are similar to those of model A, and the magnitudes of mean wind pressure coefficient on the walls of model B are close to those of model A in the same wind direction. Wind pressure on the walls is little affected by the presence of parapet. The distributions of mean wind pressure coefficient on the roofs of model A and model B are similar in the same wind direction; however a significant decrease in the magnitudes of wind pressure coefficient on the roof of model B, compared with those of model A, is observed due to the presence of 1.2m parapet. The effects of parapet on the roof and the walls are consistent with the findings in Ref [3]. The magnitudes and distributions of fluctuating wind pressure coefficients on model B are similar to those of model A in the same wind direction.

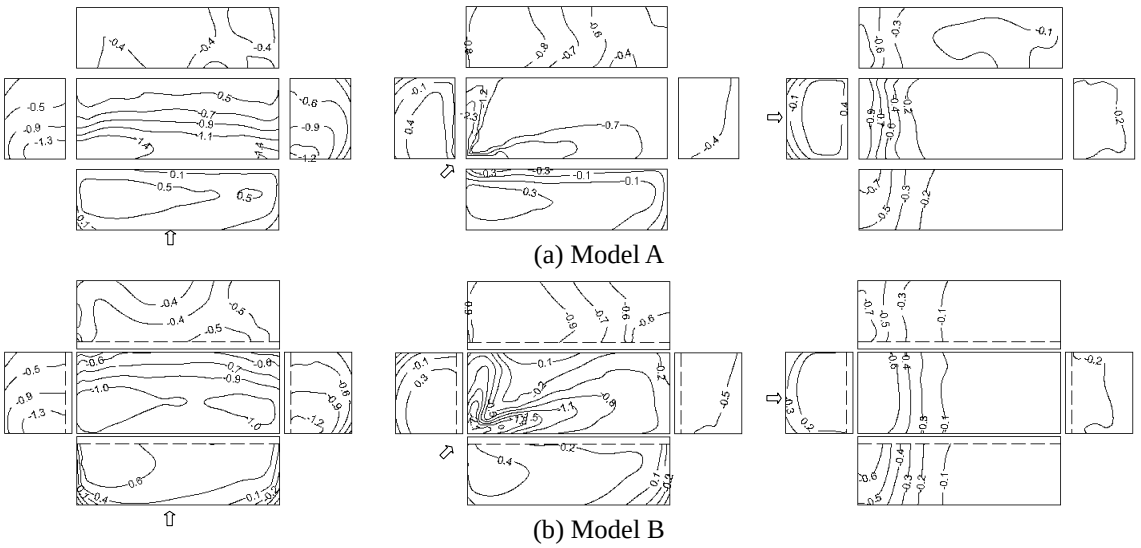

(a) Model A

(b) Model B

Figure 3. Mean wind pressure distributions

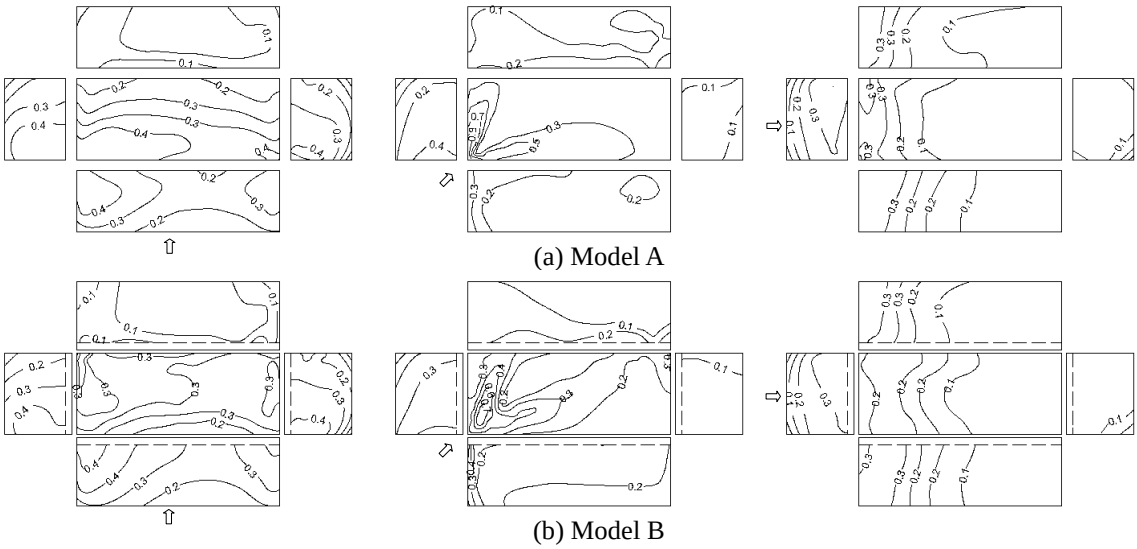

(a) Model A

(b) Model B

Figure 4. Fluctuating wind pressure distributions

The variations of the instantaneous pressure distribution on the roofs of the two models in 45^0 wind direction with time from $t= T_{max}-5\Delta t$ to $t= T_{max}+6\Delta t$ are shown in figure 5, where T_{max} represents the time when the maximum peak suction is observed at the reference height during the whole record. These results show that the pressure distribution, which causes very severe suctions in the leading edge and corner regions, last only 4-6 time steps, or 0.2-0.3s in very case that was tested. The pressure distributions on the roofs change significantly with time during such a short period around $T_{max.}$ The area of severe suctions at $t= T_{max}$ is small as up to 0.5m×1m, which covers the connections in self-drilling screws of profiled steel sheets commonly used in China. These results indicate that the time and/or spatial averages of wind fluctuations lead to a remarkable decrease in the peak suction.

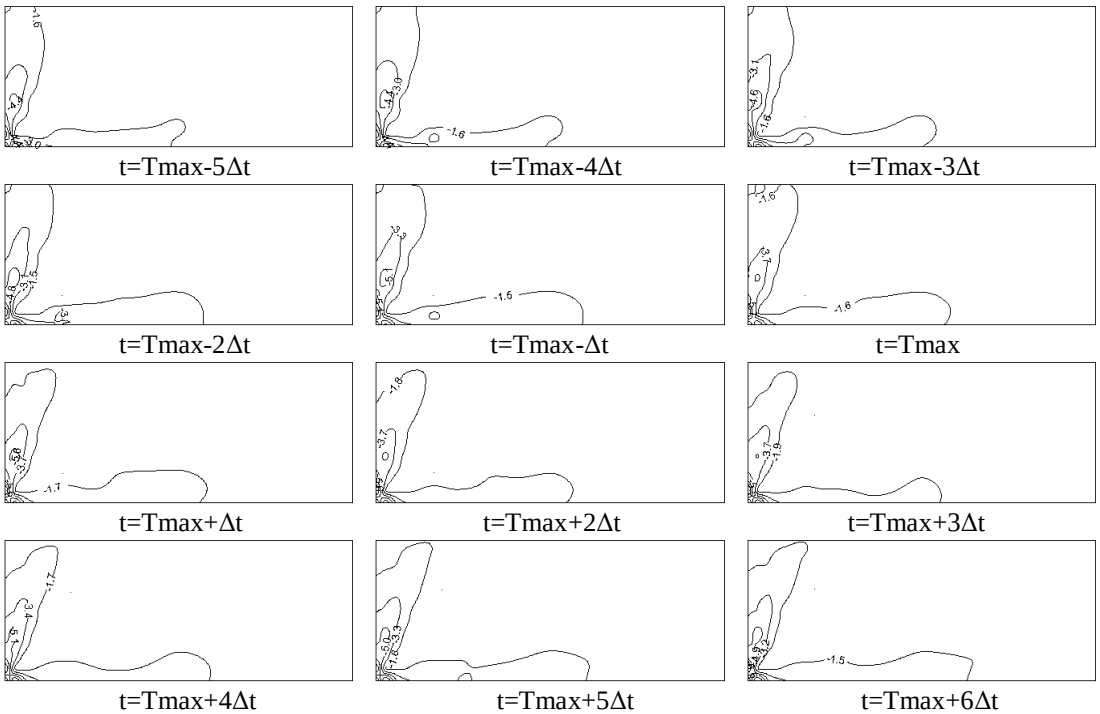

(a) Roof without parapet

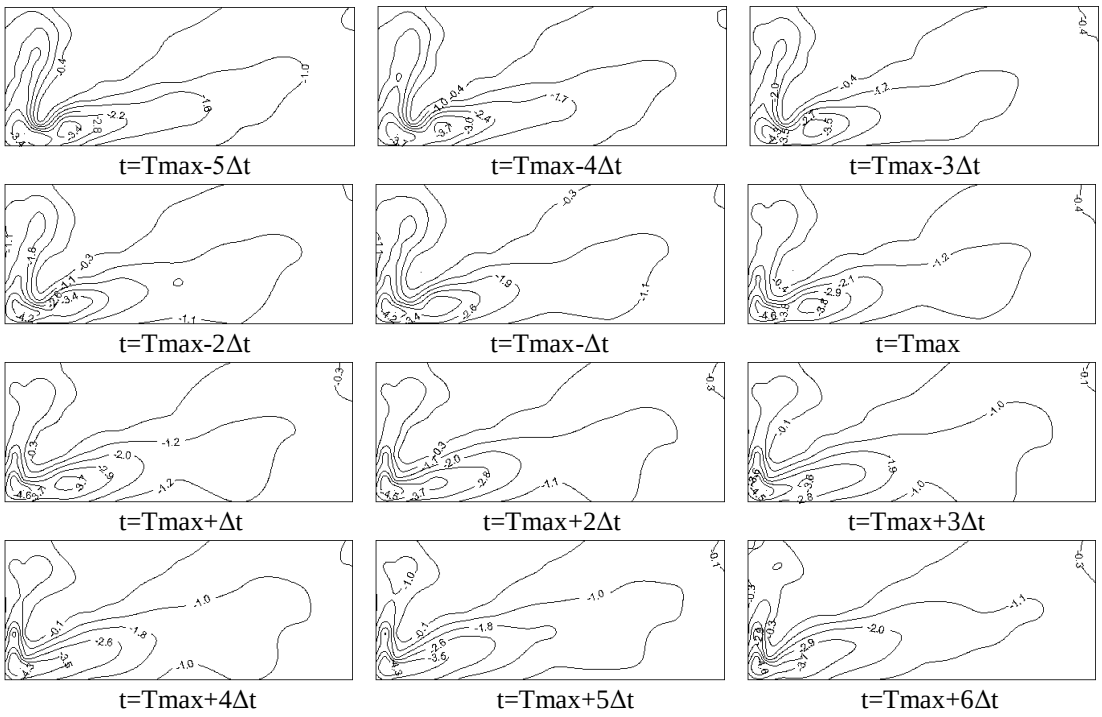

(b) Roof with parapet

Figure 5. Variations of the instantaneous pressure distribution on the roofs in 45^0 wind direction

3.2 *Comparison with current codes*

The magnitude and distribution of wind pressure on model A in transverse wind direction, obtained from wind tunnel test is compared with those from current codes, including GB 50009-2001, *Architectural Institute of Japan Recommendations for Loads on Buildings* AIJ2004 [4], *Minimum Design Loads for Buildings and Other Structures* ASCE/SEI7-05 of American [5] and *Structural Design Actions* AS/NZS1170.2:2002 of Australian/New Zealand [6]. Not considering wind-induce internal pressure and gust effect factor due to such low-rise building with enough rigidity, design wind pressure from current codes can be estimated in uniform equation as:

$$w_d = 0.5\rho_{air} v_d^2 C_s C_h \tag{1}$$

where, w_d is design wind pressure; ρ_{air} is the air density, , which normally lies in the range 1.20 to 1.25 kg/m^3; v_d is design wind speed, determined by the height, exposure category, time duration and return period. C_s is the shape coefficient a modifying coefficient for the place of the point on the surface; C_h is the height coefficient, a modifying coefficient for the height of the point. In AIJ2004 and AS/NZS1170.2:2002, C_h is concluded in the calculation of v_d, which has little effect on wind pressure on such low-rise building.

The parameters of the estimation on design wind pressures from different country codes are given in table 1. Wind pressures in all codes are evaluated at an elevation of 10 m. Time duration of wind speed in GB 50009-2001 and AIJ2004 are 10 minutes; while 3 seconds in ASCE/SEI7-05 and AS/NZS1170.2:2002. Return period of wind speed in AIJ2004 is 100 years; while 50 years in other codes. Conversion coefficients of time duration and return year are used in determination of wind speed between different codes. The zone of the shape coefficient, C_s, in table 1 is shown in figure 6. H is the eave height of the building and a equals to 1.44 m according to ASCE/SEI7-05. For the flat-roofed building, the shape coefficient distributions from GB 50009-2001 are the same as those from AIJ2004. The roof end, windward wall end and leeward wall end suffered higher pressure are considered in

ASCE/SEI7-05. The shape coefficients decreasing along wind direction on the roof and side walls are considered in AS/NZS1170.2:2002, which is more consist with experimental results.

Table 1. The parameters of the estimation on design wind pressures from different country codes

Parameters			GB 50009-2001	AIJ2004	ASCE/SEI7-05	AS/NZS1170.2:2002
Wind speed at 10 m height (m/s)			23.71	26.08	35.09	35.09
C_h			1.022	1.009	1.017	1.008
v_d (m/s)			23.71	26.31	35.09	35.72
C_s	Windward wall	W	+0.80	0.60	+0.48	+0.80
		WE	+0.80	0.60	+0.72	+0.80
	Leeward wall	L	-0.50	-0.40	-0.34	-0.50
		LE	-0.50	-0.40	-0.51	-0.50
	Side wall	S1	-0.70	-0.70	-0.53	-0.65
		S2	-0.70	-0.70	-0.53	-0.50
	Roof	R1	-0.60	-0.87	-0.81	-1.10
		R2	-0.60	-0.87	-0.81	-0.80
		R3	-0.60	-0.87	-0.81	-0.50
		R1E	-0.60	-0.87	-1.26	-1.10
		R2E	-0.60	-0.87	-1.26	-0.80
		R3E	-0.60	-0.87	-1.26	-0.50

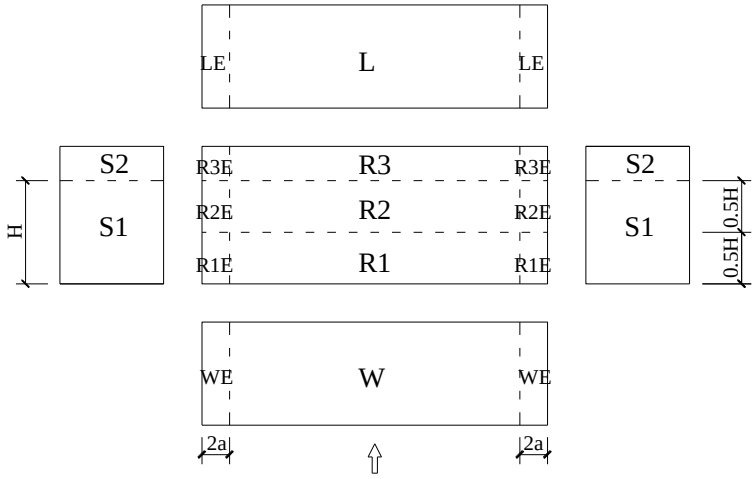

Figure 6. The zone of the shape coefficient according to the codes

The comparison of design wind pressure from different country codes with experimental results is shown in figure 7. Load combination coefficient, 1.4, is considered by GB 50009-2001 to compare with design wind pressure by other codes. Experimental results show that the wind pressures on the windward wall and the leeward wall are close to constant; while the wind pressures on the roof and the side walls decrease along wind direction. Wind pressures on the windward wall and the leeward wall obtained from GB 50009-2001, ASCE/SEI7-05 and AS/NZS1170.2:2002 are much larger than experimental results, which may result from two factors: (1) larger shape coefficient on the windward wall given by the codes; (2) 3-s wind speed, close to gust wind speed, used in ASCE/SEI7-05 and AS/NZS1170.2:2002. Wind pressures on the windward wall and the leeward wall obtained from AIJ2004 are relatively close to experimental results. Wind pressures on side walls and the roof obtained from GB 50009-2001 and AIJ2004 are somewhat smaller than experimental results, not considering higher suction on the windward end. Although wind pressure on the

roof obtained from ASCE/SEI7-05 is much larger than experimental result, it does not reflect actual wind pressure distribution. Wind pressure distributions on the roof and side walls given by AS/NZS1170.2:2002 are suitable to experimental results. The reason of larger wind pressure on the roof and side walls given by AS/NZS1170.2:2002 than experimental results is mainly 3-s wind speed in AS/NZS1170.2:2002.

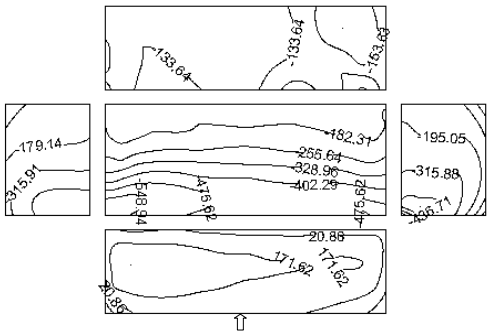

(a) Mean wind pressure at 10 m height based on wind tunnel test

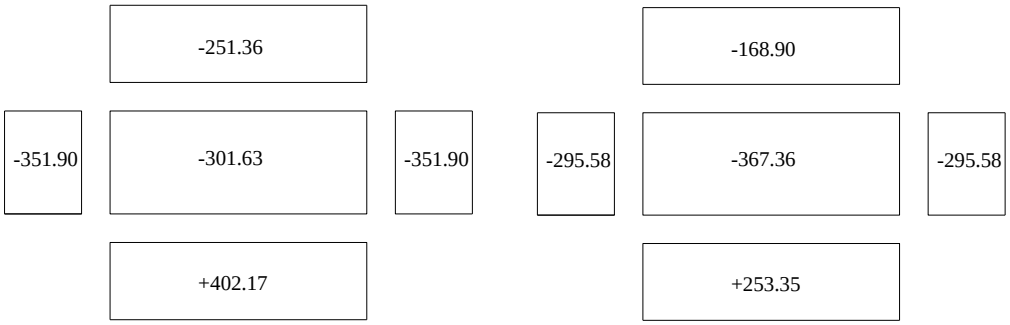

(c) Wind pressure from GB 50009-2001 (d) Wind pressure from AIJ2004

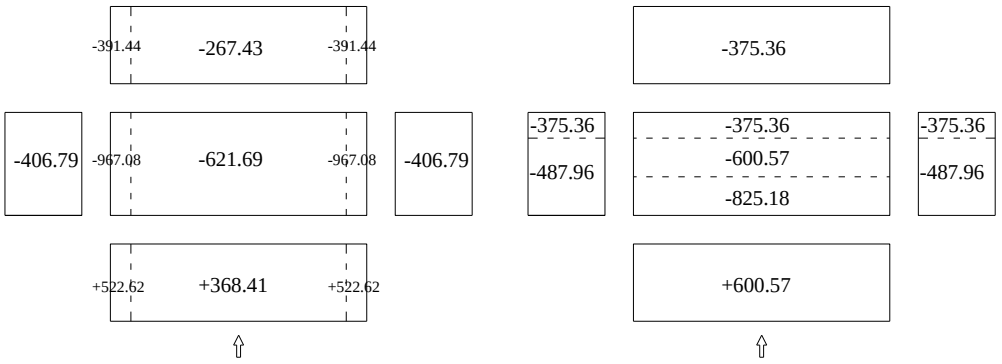

(e) Wind pressure from ASCE/SEI7-05 (f) Wind pressure from AS/NZS1170.2:2002

Figure 7. The comparison of design wind pressure from different country codes with experimental results

3.3 *The characteristics of proper orthogonal decomposition*

Proper Orthogonal Decomposition (POD) is a method used to derive the most efficient coordinate system for observing individual phenomena [7]. It can be applied to the analysis of random phenomena. As an example, contribution proportion of each mode from proper orthogonal decomposition on model B is given in table 2. It can be seen that, when wind direction is 90^0, the contribution of the first mode, as well as the cumulative contribution of the first several modes is a little larger in comparison with the results corresponding to 0^0 or 45^0 wind direction. For an expected cumulated contribution approximate to 90%, at least

more than 50 modes should be considered. The first twelve eigenvectors of the measured wind pressure on model B in 90^0 wind direction are shown in figure 8. The contribution proportions of each mode to the global wind pressures field are given in the brackets under the contours of corresponding mode. Wind pressure on the model has good spatial correlation. The first several modes give a global description of wind pressure distribution on the model surface, while the other high-order modes just represent local distributions.

Table 2. Eigenvalues, proportions and cumulative proportions for the pressure field on model B

Mode	0^o			45^o			90^o		
	Eigen -value	Proport -ion(%)	Cumulative proportion (%)	Eigen -value	Proport -ion (%)	Cumulative proportion (%)	Eigen -value	Proport -ion (%)	Cumulative proportion (%)
1	40.98	17.44	17.44	41.39	17.61	17.61	49.48	21.05	21.05
2	21.82	9.29	26.72	27.24	11.59	29.20	21.56	9.17	30.23
3	18.43	7.84	34.57	26.03	11.08	40.28	17.18	7.31	37.54
4	15.10	6.43	40.99	15.56	6.62	46.91	13.60	5.79	43.33
5	13.91	5.92	46.91	10.10	4.30	51.20	12.31	5.24	48.56
6	10.90	4.64	51.55	9.06	3.85	55.06	10.14	4.32	52.88
7	8.69	3.70	55.25	8.21	3.49	58.55	8.37	3.56	56.44
8	8.36	3.56	58.81	6.83	2.90	61.45	6.65	2.83	59.27
9	6.11	2.60	61.41	6.02	2.56	64.01	5.77	2.45	61.73
10	5.63	2.40	63.80	4.89	2.08	66.10	4.97	2.12	63.84
20	1.96	0.83	76.73	1.72	0.73	77.47	1.86	0.79	75.74
50	0.53	0.23	89.17	0.54	0.23	89.58	0.57	0.24	87.97
100	0.17	0.07	95.87	0.17	0.07	96.02	0.22	0.09	95.26
150	0.09	0.04	98.48	0.08	0.03	98.50	0.10	0.04	98.43
200	0.03	0.01	99.72	0.03	0.01	99.66	0.03	0.01	99.74
230	0.01	0.00	99.98	0.02	0.01	99.97	0.01	0.00	99.99
235	0.01	0.00	100.00	0.01	0.00	100.00	0.00	0.00	100.00

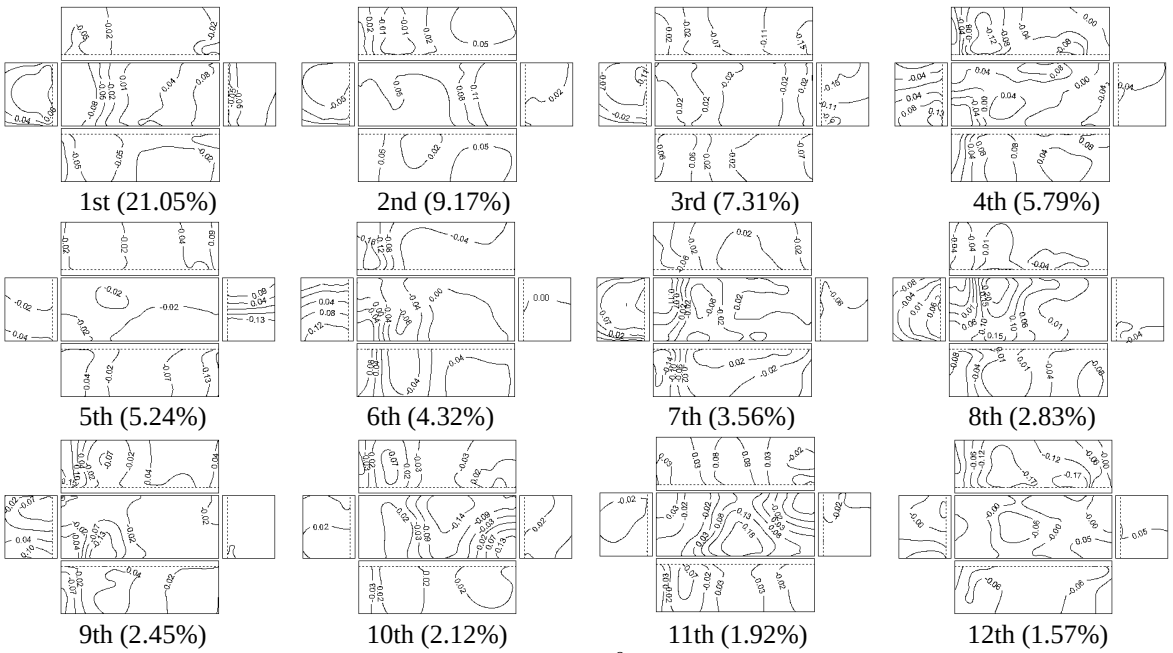

Figure 8. First twelve modes from POD on model B in 90^o wind direction

4 CONCLUSIONS

Flat-roofed buildings with and without parapet have been tested in a wind tunnel to investigate the characteristics of wind pressure distribution. 1.2m high parapet, commonly

used in China, reduces mean suctions and extreme suctions by up to 50% on the roof edges, and wall loads remain unaffected by the presence of parapet. The variations of the instantaneous pressure distribution with time indicate that the time and/or spatial averages of wind fluctuations leads to a remarkable decrease in the peak suction. Wind pressure distributions on the flat roofed steel frame building without parapet in transverse wind direction given by AS/NZS1170.2:2002 are suitable to experimental results that wind pressures on the windward wall and the leeward wall are close to constant; while the wind pressures on the roof and the side walls decrease along wind direction. Wind pressure on the models has good spatial correlation. The first several modes give a global description of wind pressure distribution on the model surface, while the other high-order modes just represent local distributions.

5 ACKNOWLEDGEMENTS

The authors are grateful to the Research Fund of State Key Laboratory of Disaster Reduction in Civil Engineering (No.SLDRCE09-B-01) and Kwang-Hua Fund of College of Civil Engineering, Tongji University.

6 REFERENCES

1 H.J. Leutheusser. Parapets improve roof wind loading. The Consulting Engineer, 1964, p.94-96.
2 Load code for the design of building structures GB 50009-2001. Beijing: China Architecture and Building Press, 2006
3 T. Stathopoulos, The effect of parapets to wind loads of low-rise buildings. Symposium on designing with the wind, Centre Scientifique et Technique du Batiment, Nantes, France, 1981
4 Architectural Institute of Japan Recommendations for Loads on Buildings(English Version),2004
5 Minimum Design Loads for Buildings and Other Structures, ASCE/SEI7-05, A.S.C.E., New York, 2006
6 Structural Design Actions, Part 2: Wind Actions, AS/NZS 1170.2.2002, Standards Australia, 2002
7 Y. Tamura and S. Suganuma, Proper orthogonal decomposition of random wind pressure field. Journal of Fluids and Structures, 13 (1999) 1069-1095

The Seventh International Colloquium on Bluff Body Aerodynamics and Applications (BBAA7)
Shanghai, China; September 2-6, 2012

Internal pressure in real flexible porous buildings: A design perspective

Guha T. K.[a], Sharma R. N. [a], Richards P. J. [a]

[a]*Department of Mechanical Engineering, The University of Auckland, New Zealand*

ABSTRACT: Analytical and associated numerical investigations of the fluctuating internal pressures induced through a dominant opening in real buildings with leaky and flexible envelopes are undertaken. The damping effect of these factors both separately and in combination are quantified using Root Mean Square (RMS) internal pressure coefficients and equivalent damping ratios for a range of envelope flexibilities and background porosities for the case of the Texas Tech University (TTU) test building. In particular, the equivalent damping ratio and the RMS internal pressure coefficient for the TTU building with a flexibility parameter of 2 and porosity ratio of 20% is found to be around 4 times higher and 27% lower than for a rigid non-porous TTU building. Simulated ratios of the RMS internal pressures and the peak spectral response of internal pressure for leaky and flexible buildings to that of rigid, nonporous envelopes are presented in non-dimensional format for a range of building volumes, opening areas and porosity ratios. Additionally non-dimensional charts of the RMS internal to external pressure ratios for real flexible and leaky envelopes are presented in a form suitable for design purposes.

KEYWORDS: Internal Pressures, Envelope Flexibility, Background Leakage.

1 INTRODUCTION

Buildings in real life, excepting special circumstances, have flexible and leaky envelopes. Flexibility and background leakage are known to act as dampers to internal pressure fluctuations induced through a dominant opening in the building. This has been demonstrated previously by wind tunnel [1,2] and full-scale studies [3] that dealt with these two factors separately. Theoretical models [2,4], in accordance with the experimental predictions, that take into account the effect of either of these factors in isolation have also been proposed.

Research, both theoretical and experimental, into the combined effect of leakage and flexibility, as occurs in most real buildings, has received comparatively little attention [5]. In fact, many studies of internal pressure in the past have tended to neglect their effects altogether. While theoretical studies have been limited by the lack of knowledge of the structural characteristics of the envelope (such as stiffness) and the distribution of the leakages arising out of normal construction tolerances, experimental research has suffered mainly from the difficulties in the similarity based modeling such as the lack of suitable materials to simultaneously satisfy the mass and stiffness scaling of such a realistic scenario. Even fewer, if at all any, has been the quantitative studies of the combined effect of these two factors in moderating the fluctuating and peak internal pressure response compared to that for a rigid, non-porous building; an issue this paper attempts to address from a design perspective.

While full-scale measurements of internal pressure in real flexible and leaky buildings for a range of internal volumes and opening sizes under strong wind conditions offer a promising alternative, they are expensive, time consuming and resource intensive. Additionally controlling

the different factors such as the extent of flexibility and leakage in the building envelope presents difficulties in full-scale. This paper thus uses analytical modeling and associated numerical simulation technique to quantify the damping effects of envelope porosity and flexibility on the fluctuating internal pressure response. The damping influence of flexibility and background leakage are exhibited separately and in combination for different envelope flexibilities and porosities for the case of the Texas Tech University (TTU) test building [6] with an opening in terms of the simulated Root Mean Square (RMS) internal pressure coefficients and equivalent damping ratios. Results of the RMS and peak spectral response of internal pressure for leaky and flexible buildings in comparison to that of rigid, nonporous envelopes (of the same nominal internal volume and opening size) are presented in non-dimensional format for realistic values of non-dimensional parameters S^*,Φ_5 [7] and porosity ratio (r) [2]. Design charts of the RMS internal to external pressure ratios are also presented for ranges of S^*, Φ_5 and r in a form suitable for design purposes.

2 GOVERNING EQUATIONS

Internal pressure induced in a building is described using an air slug/jet oscillating through the opening, being forced by the turbulent external pressures against an air-spring inside the building volume and damped by the irrecoverable loss of energy due to viscous and radiation effects. Further damping is imparted by flexibility and background leakage in the envelope of real buildings. Such buildings usually behave quasi-statically to fluctuations in the onset wind, meaning structural displacements are linearly proportionally to the applied load at all times. Hence they are considered as static structures. The leakages in the building envelope are found to behave quasi-steadily to onset turbulence, low pass filtering the external pressure fluctuations beyond a critical frequency [2] that is dependent on the mean internal-external pressure difference and the total leakage area in the surface.

Figure 1 provides a schematic representation of a real flexible and leaky building with an opening for which a general equation of the internal pressure response is provided.

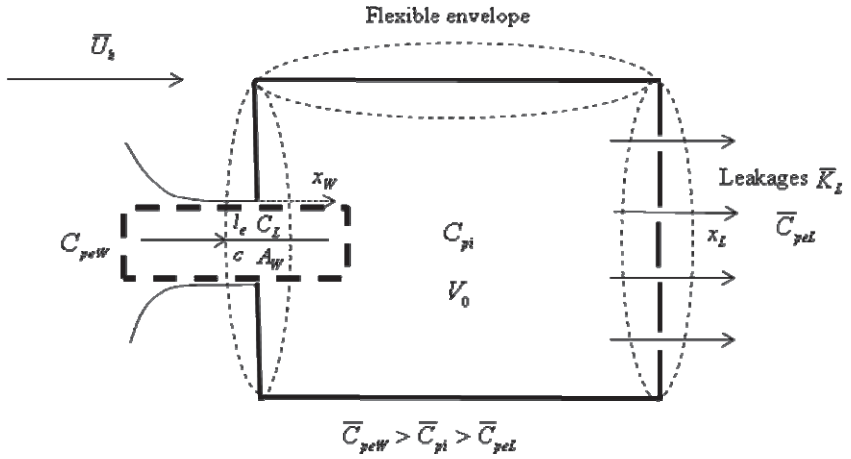

Figure 1. Schematic of a real flexible and leaky building with an opening

The unsteady equation of motion of the air-slug oscillating through the windward dominant opening under the fluctuating internal and external pressures (represented by the coefficients C_{pi} and C_{peW} respectively) and damped by energy losses through the opening, takes the form:

$$\rho_a l_e c A_W \ddot{x}_W + \frac{1}{2}\rho_a c A_W C_L |\dot{x}_W| \dot{x}_W = c A_W q\left(C_{peW} - C_{pi}\right) \tag{1}$$

where ρ_a, l_e, c and A_W are the density of air, effective length of the air slug, flow contraction coefficient and area of the opening respectively, C_L is the loss coefficient of flow through the opening, q is the ridge height dynamic pressure derived from the ridge height wind velocity $\overline{U}_h$ and $\dot{x}_W$, $\ddot{x}_W$ are the velocity and acceleration of the oscillating air-slug respectively.

The quasi-static response (i.e. displacement and its temporal derivatives) of the building envelope to fluctuating internal pressures in terms of the non-dimensional volume change (υ) can be written as

$$\upsilon = \frac{qC_{pi}}{K_B} + 1; \dot{\upsilon} = \frac{q}{K_B}\dot{C}_{pi}; \ddot{\upsilon} = \frac{q}{K_B}\ddot{C}_{pi} \tag{2}$$

where K_B is the bulk modulus of the building envelope. The quantity υ can be defined as V/V_0 where V is the instantaneous volume and V_0 is the nominal volume of the building.

The quasi-steady equation of motion through the leakages lumped together with predominant damping is given by

$$\frac{\rho_a}{2} A_L \overline{K}_L \dot{x}_L |\dot{x}_L| = q A_L \left(C_{pi} - \overline{C}_{peL}\right) \tag{3}$$

where $\overline{K}_L \approx 1/c^2$ and A_L and are the steady-state loss coefficient and area of the lumped leakage and $\dot{x}_L$ is the flow velocity through it for a mean leeward external pressure coefficient $\overline{C}_{peL}$.

Conservation of mass inside the building volume determined by the continuity equation with an isentropic pressure-volume relationship is given by

$$C_{pi} = \frac{\gamma P_a}{qV_0}\left[c A_W x_W - A_L x_L - V_0(\upsilon - 1)\right] \tag{4}$$

where γ =1.4 is the ratio of specific heat capacities for an isentropic process and P_a is the atmospheric pressure.

The governing equation of internal pressure in a quasi-static flexible and leaky building with an opening can be deduced from Equations 1-4 as

$$\begin{aligned} &\frac{\rho_a l_e V_e}{\gamma c A_W P_a}\ddot{C}_{pi} + C_L \frac{\rho_a q V_e^2}{2\left(\gamma A_W P_a\right)^2}\left|\dot{C}_{pi} + \frac{A_L \gamma P_a \overline{U}_h}{qV_e}\sqrt{\frac{C_{pi} - \overline{C}_{peL}}{\overline{K}_L}}\right|\left(\dot{C}_{pi} + \frac{A_L \gamma P_a \overline{U}_h}{qV_e}\sqrt{\frac{C_{pi} - \overline{C}_{peL}}{\overline{K}_L}}\right) \\ &+ \frac{\rho_a \overline{U}_h l_e}{2qc\sqrt{\overline{K}_L\left(C_{pi} - \overline{C}_{peL}\right)}}\left(\frac{A_L}{A_W}\right)\dot{C}_{pi} + C_{pi} = C_{pe} \end{aligned} \tag{5}$$

where V_e is the effective volume of the cavity and equal to V_0 (the nominal cavity volume) for a building with rigid envelope and equal to $V_0(1+b)$ for a flexible envelope, where $b = \gamma P_a / K_B$ is the ratio of the bulk modulus of air to that of the building envelope.

The Helmholtz frequency (f_{HH}) of internal pressure oscillations is given by

$$f_{HH} = \frac{\omega_{HH}}{2\pi} = \frac{1}{2\pi}\sqrt{\frac{\gamma c A_W P_a}{\rho_a l_e V_e}} \tag{6}$$

where ω_{HH} is the corresponding angular frequency. It can be noted from Equation 6 that the effect of envelope flexibility is associated with a corresponding reduction in the Helmholtz frequency of the system (due to increase in the value of parameter b and hence effective volume V_e).

Putting b = 0 and A_L = 0 in Equation 5 leads to Sharma & Richards' [8] form of the well known dynamic equation of internal pressure for a rigid non-porous envelope originally proposed by Holmes [7].

A non-dimensional form of Equation 5 based on the parameters S^* [$=\left(A_W^{3/2}/V_e\right)\left(a_s/\overline{U}_h\right)^2$], Φ_5 [$=\lambda_U/\sqrt{A_W}$], porosity ratio r [$=A_L/A_W$] and a non-dimensional time t^* [$=t\overline{U}_h/\lambda_U$] is given by

$$\frac{C_I}{cS^*\phi_5^2}\frac{d^2C_{pi}}{dt_*^2} + \frac{C_L}{4\left(S^*\phi_5\right)^2}\left|\frac{dC_{pi}}{dt_*} + 2\left(\frac{A_L}{A_W}\right)S^*\phi_5\sqrt{\frac{C_{pi}-\overline{C}_{peL}}{\overline{K}_L}}\right|\left(\frac{dC_{pi}}{dt_*} + 2\left(\frac{A_L}{A_W}\right)S^*\phi_5\sqrt{\frac{C_{pi}-\overline{C}_{peL}}{\overline{K}_L}}\right)$$
$$+\left(\frac{A_L}{A_W}\right)\frac{C_I}{\phi_5 c\sqrt{\overline{K}_L\left(C_{pi}-\overline{C}_{peL}\right)}}\frac{dC_{pi}}{dt_*} + C_{pi} = C_{pe} \tag{7}$$

where C_I = $\sqrt{\pi/4}$ is the inertia coefficient of flow through the opening, a_s is the speed of sound and λ_U is the longitudinal integral length scale of turbulence at the building ridge height. It should be noted that S^*, as defined here, intrinsically incorporates the effect of envelope flexibility through usage of an effective volume (V_e) instead of the nominal building volume (V_0). For given values of C_I, c, C_L and $\overline{K}_L$, Equation 7 can be solved to yield the response of internal pressure as a function of S^*, Φ_5 and r.

3 QUANTIFICATION OF THE EQUIVALENT DAMPING RATIO (ζ_{eq})

It is a common practice to quantify all the damping effects of internal pressure fluctuations using the loss coefficient C_L. Attempts have been made in the past to match the predicted resonant response to the measured value by altering the value of C_L until a match is obtained. A review of such investigations and the values of C_L thus obtained are discussed by Holmes and Ginger [9]. A wide scatter of values ranging from 1.2 to 100 is observed in these studies. This brings forth the question as to whether C_L is being overloaded with the damping effects of other factors when it is solely meant to quantify the energy losses at the opening. While some of the values reported in literature, such as C_L=1.2, have been supported by CFD studies [8] of internal pressure involving rigid non-porous buildings with effects of other dampers eliminated, the particularly high values such as 44 and 100 used for spectral matching in some studies [3,10] seems unrealistic. The possibility of damping due to envelope compliance and leakage in the model and/or full-scale buildings seems to have been intrinsically included in C_L leading to such unrealistically high values.

It is therefore physically more realistic to quantify the effect of the different dampers operating separately or in combination using as equivalent damping ratio (ζ_{eq}). This can be done by re-

writing the governing equation of internal pressure (Equation 5) in the standard single degree-of-freedom dynamic system

$$\frac{1}{\omega_{HH}^2}\ddot{C}_{pi}+\frac{c_j}{k}\dot{C}_{pi}+C_{pi}=C_{pe} \tag{8}$$

where c_j is the damping coefficient and k is the stiffness of the air mass-spring system. The equivalent damping ratio (ζ_{eq}) can then be defined by comparing Equations 5 and 8, giving

$$\zeta_{eq}=\frac{c_j}{k}\frac{\omega_{HH}}{2}=\frac{1}{2}\sqrt{\frac{\gamma c A_W P_a}{\rho_a l_e V_e}}\left[\begin{array}{l} C_L\dfrac{\rho_a q V_e^2}{2(\gamma A_W P_a)^2}\left|\dot{C}_{pi}+\dfrac{A_L\gamma P_a\overline{U}_h}{qV_e}\sqrt{\dfrac{C_{pi}-\overline{C}_{peL}}{\overline{K}_L}}\right|\left\{1+\dfrac{A_L\gamma P_a\overline{U}_h}{qV_e\dot{C}_{pi}}\sqrt{\dfrac{C_{pi}-\overline{C}_{peL}}{\overline{K}_L}}\right\} \\ +\dfrac{\rho_a\overline{U}_h l_e}{2qc\sqrt{\overline{K}_L(C_{pi}-\overline{C}_{peL})}}\left(\dfrac{A_L}{A_W}\right)\end{array}\right] \tag{9}$$

For non-leaky envelopes (A_L=0), the equivalent damping ratio (ζ_{eq}) simplifies to

$$\zeta_{eq}=\frac{c_j}{k}\frac{\omega_{HH}}{2}=C_L\frac{\rho_a q V_e^2}{2(\gamma A_W P_a)^2}\frac{1}{2}\sqrt{\frac{\gamma c A_W P_a}{\rho_a l_e V_e}}\left|\dot{C}_{pi}\right| \tag{10}$$

The damping effects of envelope flexibility and background leakage can then be quantified individually or in combination using ζ_{eq} by a spectral match of the solutions of Equation 5 and 8 by switching on and off the effect of the relevant dampers (i.e. flexibility and leakage). Such damping ratios (ζ_{eq}) with intrinsically loaded effects of flexibility and/or leakage provide for a better parameter than loss coefficient (C_L) to quantify the effect of the different dampers.

4 ANALYTICAL EXAMPLE USING THE TTU TEST BUILDING

An analytical example for the effect of envelope flexibility and background leakage on the fluctuating internal pressure response is provided for a building similar in dimensions to the TTU test building with a windward dominant opening (area ratio of 5%) under the following basic conditions:

V_o = 497m^3; A_W = 1.94m^2; $l_e=\sqrt{\pi A_W/4}$; c = 0.6; C_L= 1.2; $\overline{K}_L$ = 2.78; $\overline{U}_h$ = 30m/s;
$\overline{C}_{peW}=\overline{C}_{pi}$ = 0.7; $\overline{C}_{peL}$ = -0.3; I_u= 0.20; ρ_a = 1.185kg/m^3; γ = 1.4; P_a = 101.3KPa

Numerical simulations of Equations 5 and 8 using a fourth-order Runge-Kutta method with adaptive time-stepping capability were used for quantitative analysis and comparison. The external pressure coefficient time history used to force the internal pressure response was obtained by applying an aerodynamic admittance and random phase to the Fourier coefficients derived from the Kaimal spectrum using an Inverse Fast Fourier Transform (IFFT) technique.

4.1 *Effect of envelope flexibility*

The effect of flexibility on internal pressure for the non-porous TTU test building with a windward dominant opening is studied by varying the parameter b from 0 to 2 in steps of 0.5, i.e. from a rigid to a relatively flexible envelope system. Figure 2a presents the simulated internal pressure coefficient spectra for b = 0, 1 and 2.

Table 1. Effect of flexibility on damping w.r.t. spectral response at resonance

b	0	0.5	1.0	1.5	2.0
c_j/k	0.005	0.008	0.013	0.018	0.022
ζ_{eq}	0.038	0.049	0.069	0.086	0.096

The overall damping of the system at resonance is found to increase with flexibility in the building envelope. The associated reduction in the Helmholtz frequency from 2.4Hz down to 1.3Hz is also evident in the figure for an increase in b from 0 to 2. The increased damping effect of envelope flexibility is further confirmed in Table 1 which shows an increase in the quantities c_j/k (damping term in Equation 8) and ζ_{eq} with b. A spectral match between the solutions of Equations 5 and 8 was used to estimate these quantities.

An increase in the equivalent damping ratio (ζ_{eq}) by a factor of 2.5 is observed for an increase in b from 0 to 2. The decrease in the Helmholtz frequency with flexibility is however neglected in this analysis in order to study the effect of flexibility induced damping in isolation.

The effect of the decrease in the Helmholtz frequency with flexibility and its effect on the internal pressure resonant response in terms of the overall damping using the concept of equivalent damping ratio is shown in Table 2. In this case, an iterative process was used to estimate the quantities c_j/k and ζ_{eq} until a match between the RMS internal pressures and gain of internal to external pressure at resonance as predicted by Equations 5 and 8 were obtained.

The increased damping effect of envelope flexibility notwithstanding the shift (decrease) in the Helmholtz frequency towards the more energy containing region of the external pressure forcing spectrum is evident from the values of c_j/k and ζ_{eq} in Table 2. The reduction in Helmholtz frequency with envelope flexibility is found to partially compensate for the increased internal pressure damping in a flexible envelope, e.g. 6% when reduction the in Helmholtz frequency due to flexibility is accounted for in Table 2 against 9.6% when not considered in Table 1 for b=2.

Table 2. Effect of flexibility on damping w.r.t. equivalence of the RMS internal pressure

b	0	0.5	1.0	1.5	2.0
c_j/k	0.005	0.006	0.007	0.008	0.008
ζ_{eq}	0.038	0.047	0.051	0.057	0.060

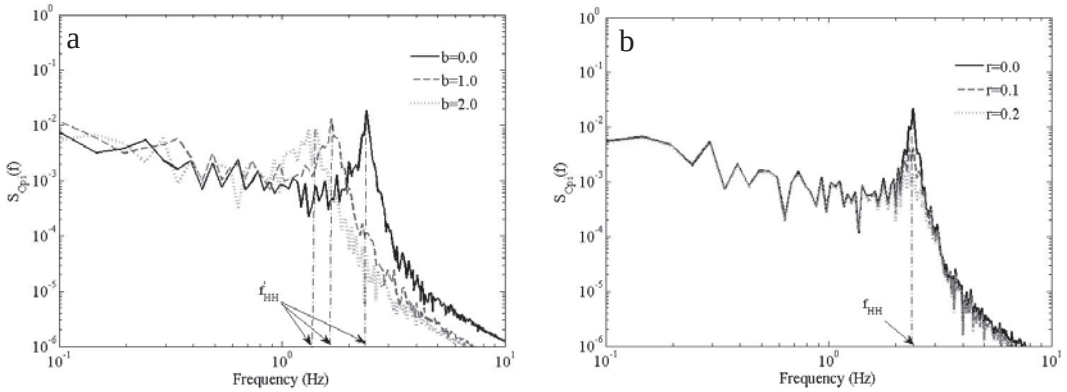

Figure 2. Simulated internal pressure coefficient spectra for the TTU building with (a) varying envelope flexibility and (b) varying envelope porosity

4.2 *Effect of background porosity*

The effect of background porosity on the internal pressure response for the rigid TTU test building with a windward dominant opening is studied by varying the porosity ratio r ($=A_L/A_W$) from 0 to 0.2 in steps of 0.05, i.e. from a non-porous to a relatively porous envelope system. Figure 2b presents the simulated internal pressure coefficient spectra for r = 0, 0.1 and 0.2.

Increase in envelope porosity is expectedly found to further limit the amplitude of internal pressure fluctuations at resonance. Thus the peak spectral response is found to have decreased by a factor of 15 with increase in porosity from 0 to 20%. The corresponding equivalent damping ratio is found to increase from around 3.8% for a non-porous building to around 11% for a porosity ratio of 20%. This will decrease the RMS and peak internal pressures to a great extent compared to the non-porous model predictions.

4.3 *Combined effect of envelope flexibility and background porosity*

The combined influence of envelope flexibility and background porosity, as occurs in most real building envelopes, is further investigated for the TTU setup using the same range of flexibility parameter b and porosity ratio r as discussed in the preceding sections. Figures 3a, b and c presents a measure of the quantities c_j/k, ζ_{eq} and RMS internal pressure coefficient ($\widetilde{C}_{pi}$) respectively as a function of the parameters b and r, visualized as 3-D surface plots.

The extent of the damping imparted by the two factors is evident in the plots. Particularly, the equivalent damping ratio for the TTU building with damping parameters b=2 and r=20% is found to be around 4 times higher compared to a rigid non-porous TTU building envelope. The corresponding RMS internal pressure coefficient (≈0.19) is found to decrease by around 27% for the flexible (b=2) and porous (r=20%) envelope compared to the rigid non-porous case (≈0.26).

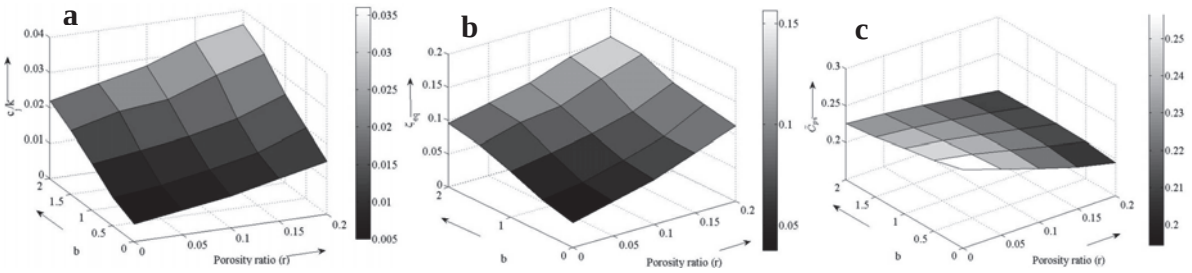

Figure 3. Simulated (a) c_j/k (b) Equivalent damping ratio (ζ_{eq}) and (c) RMS internal pressure coefficient for the TTU building as a function of envelope flexibility parameter, b, and background porosity ratio, r.

5 DESIGN APPROACH FOR INTERNAL PRESSURES IN REAL BUILDINGS

Recent internal pressure research [9,10] has been directed towards putting the dominant opening case in a non-dimensional format for useful design solutions. These studies have however looked into rigid non-porous envelope systems. This paper attempts to extend the work by incorporating the effects of envelope flexibility and background porosity into the ambit of the internal pressure design process. This is accomplished by numerically simulating the non-dimensional design Equation 7 for a range of realistic design parameters S^*, Φ_5 and r. Results are presented in the form

of non-dimensional design charts. It is worth noting that an experimental validation of the predictions of Equation 7 have been provided in Guha et al. [2] for selected cases of S^*, Φ_5 and r.

Typical values of the parameters S^* and Φ_5 for usual buildings encountered during normal design practices under wind speed conditions of 30-50m/s range from 0.1 to 15 and 10 to 100 respectively [11]. While values of S^* for small rigid structures of the size of garden-sheds at design wind speeds are usually around 10-15, a value of b (= $\gamma P_a/K_B$) around 2-5 for statically flexible large-span low-rise structures such as portal framed industrial buildings would render values of S^* to be less than 5. Hence S^* values of up to 5 are used in the current analysis. Values of Φ_5 are based on typical longitudinal integral length scales of 25-100m at the building ridge height of 5-7m in open and suburban terrains [11]. Porosities of buildings in the temperate climates of Australia/New Zealand are usually less than a conservative estimate of r=20% used in the current analysis. Figures 4a-d present the ratio of the simulated RMS internal pressure coefficients of leaky and flexible building to rigid non-porous envelopes as a function of the porosity ratio (r) for Φ_5 values 10, 20, 50 and 100 respectively.

The moderating effect of the background porosity on the internal pressure response is evident in all cases. The effect is more pronounced for higher porosity ratios (r) and larger Φ_5 (corresponding to smaller opening sizes). This is due to the reduced resonant response of internal pressure in smaller opening area-internal volume systems in which further damping effect of background porosity becomes significant. Reduction in the RMS internal pressure response for such cavity-opening systems with large S^* (i.e. small effective volume) is found to occur by as much as 50-70% compared to the non-porous building envelope at porosities beyond 10%.

For a given dominant opening size i.e. Φ_5 and porosity ratio (r), the RMS internal pressure ratios are found to decrease with decrease in effective building volume (i.e. large S^*). This is due to the moderating effect of background porosity and the associated reduction in the fluctuating internal pressure response becoming more pronounced for smaller building volumes.

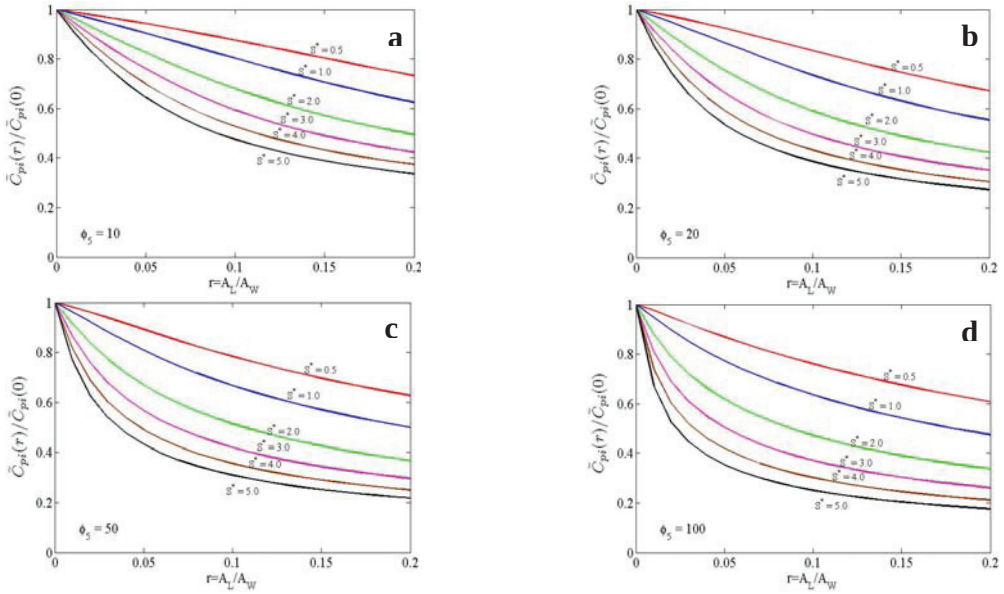

Figure 4. Simulated RMS internal pressure ratios for flexible and leaky envelopes to that for rigid non-porous buildings as a function of the porosity ratio for Φ_5= (a) 10 (b) 20 (c) 50 (d) 100

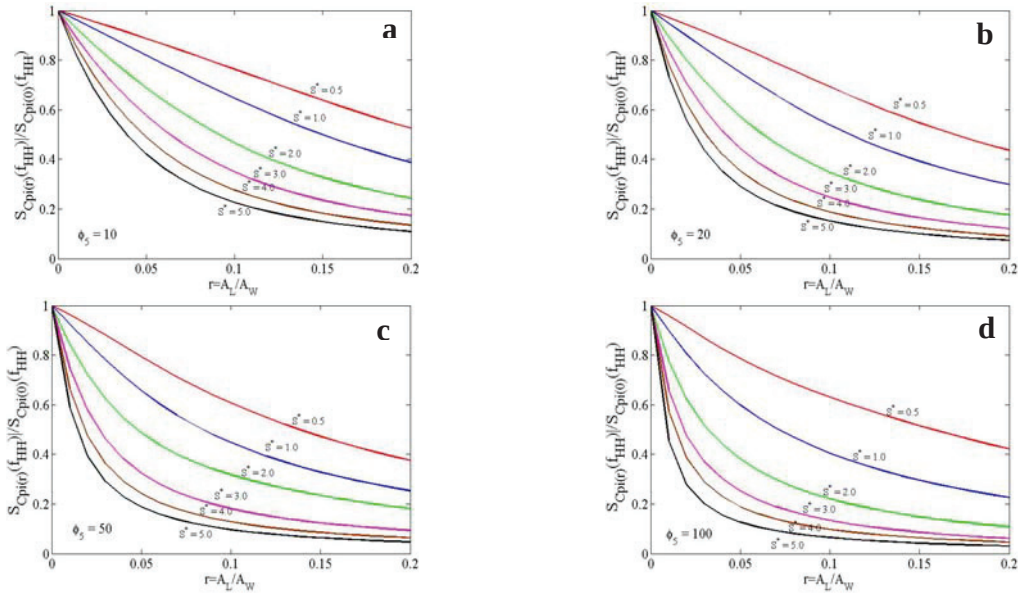

Figure 5. Simulated spectral ratios of internal pressure for flexible and leaky envelopes to that for rigid non-porous buildings for different building porosity ratios for Φ_5= (a) 10 (b) 20 (c) 50 (d) 100

Figure 5a-d reinforces the fore-going discussion by showing the ratio of the peak spectral response (at resonance) of the fluctuating internal pressure for different S^* and r for Φ_5 values of 10, 20, 50 and 100 respectively. Similar observations as in Figure 4 can be made.

Efforts into developing a suitable design solution of internal pressure by incorporating the damping effects of envelope flexibility and background leakage are made in Figure 6a-d by presenting the RMS internal to external pressure coefficient ratios as a function of S^* and r for Φ_5 values of 10, 20, 50 and 100 respectively.

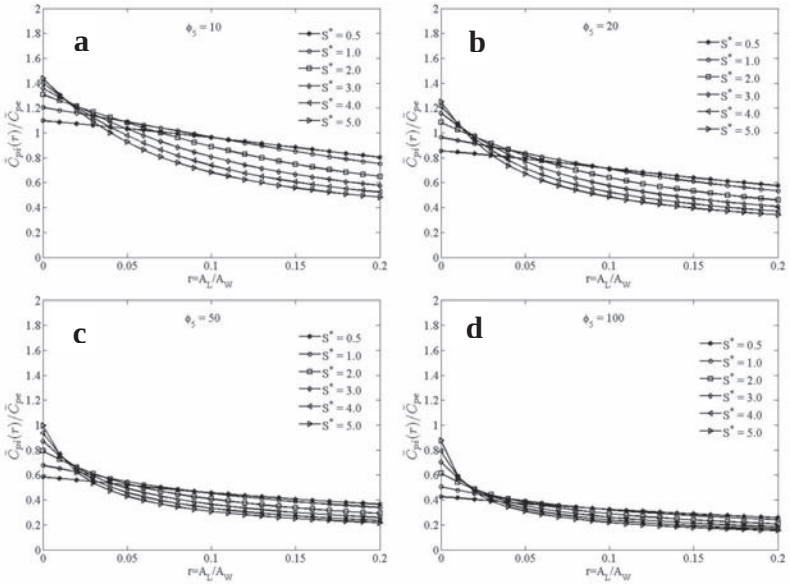

Figure 6. Simulated RMS internal to external pressure coefficient ratios for a range of building volumes and opening areas for different building porosity ratios for Φ_5= (a) 10 (b) 20 (c) 50 (d) 100

The moderating effects of envelope flexibility (small S^*) and background porosity (larger r) is clearly evident in all the plots. For a given opening size (Φ_5), the RMS internal to external pressure coefficient ratio is found to be higher for smaller volumes (larger S^*) up to a porosity ratio of around 5%, beyond which the RMS ratios are higher for larger volumes. This, as explained before, is due to the damping effect of background porosity gaining more prominence than the resonant response of internal pressure in smaller building volumes compared to the larger ones.

6 CONCLUSIONS

An analytical and numerical study of the fluctuating internal pressures induced through a dominant opening in real buildings with leaky and flexible envelopes is carried out. The increase in magnitude of the equivalent damping ratio with increase in envelope flexibility and background leakage is exhibited for the case of TTU test building using different values of flexibility and leakage parameter. In particular, the equivalent damping ratio for the TTU building with a flexibility parameter of 2 and porosity ratio of 20% is found to be around 4 times higher than for a rigid non-porous TTU building. The corresponding RMS internal pressure coefficient for such a building configuration is found to be about 27% less than the rigid non-porous building case.

Simulated ratios of the Root Mean Square (RMS) internal pressures and the peak spectral response of internal pressure for leaky and flexible buildings to that of rigid, nonporous envelopes presented in non-dimensional format also exhibit the damping influence of envelope flexibility and leakage. Non-dimensional charts of the RMS internal to external pressure ratios are presented for a realistic range of building volumes, opening areas and background porosities by incorporating the damping effect of flexibility and leakage in a form suitable for design purposes.

7 REFERENCES

1 Pearce, W., Sykes, D. M., 1999. Wind tunnel measurements of cavity pressure dynamics in a low-rise flexible roofed building. Journal of Wind Engineering and Industrial Aerodynamics 82 (1999) 27-48.

2 Guha, T. K., Sharma, R. N., Richards, P. J., Internal pressure dynamics of a leaky building with a dominant opening. Journal of Wind Engineering and Industrial Aerodynamics 99 (2011) 1151-1161.

3 Ginger, J. D., Mehta, K. C., Yeatts, B. B., Internal pressures in a low-rise full scale building. Journal of Wind Engineering and Industrial Aerodynamics 72 (1997) 163- 174.

4 Vickery, B. J., Internal pressures and interactions with the building envelope. Journal of Wind Engineering and Industrial Aerodynamics 53 (1994) 125-144.

5 Guha, T. K., Sharma, R. N., Richards, P. J., On the internal pressure dynamics of a leaky and flexible low rise building with a dominant opening, in: Proc. 13th Int. Conf. on Wind Eng., Amsterdam, Netherlands, July 2011.

6 Yeatts, B. B., Mehta, K. C., Field experiments for building aerodynamics. Journal of Wind Engineering and Industrial Aerodynamics 50 (1993) 213-224.

7 Holmes, J. D., 1979. Mean and fluctuating internal pressure induced by wind, in: Proc. 5th Int. Conf. on Wind Eng., 435-450, Colorado State University, USA, 1979.

8 Sharma, R. N., Richards, P. J., Computational modelling of the transient response of building internal pressure to a sudden opening. Journal of Wind Engineering and Industrial Aerodynamics 72 (1997) 149-161.

9 Holmes, J. D., Ginger, J. D., Internal Pressures-The Dominant Opening Case-A Review, in: Proceedings of the 9th UK Conference on Wind Engineering, Bristol, UK, 2010.

10 Ginger, J. D., Holmes, J. D., Kim, P. Y., Variation of internal pressure with varying sizes of dominant openings and volumes. Journal of Structural Engineering 136 (2010) 1319-1326.

11 Ginger, J. D., Holmes, J. D., Kopp, G. A., Effect of building volume and opening size on fluctuating internal pressures. Wind and Structures, An International Journal 11 (2008) 361-376.

The Seventh International Colloquium on Bluff Body Aerodynamics and Applications (BBAA7)
Shanghai, China; September 2-6, 2012

Coupled vibration between wind-induced internal pressures and large span roof for a two-compartment building with openings

Yu Xianfeng, Quan Yong, Gu Ming

State Key Laboratory of Disaster Reduction in Civil Engineering, Tongji University, Shanghai, China

ABSTRACT: The equations governing wind-induced internal pressure responses for a two-compartment building are derived based on some reasonable assumptions when the roof responds in dynamic and quasi-static manners, respectively. The gain functions, power spectra, and RMS values of internal pressure coefficients in both compartments are numerically analyzed. The results show that the dynamic model must be used to calculate the responses of internal pressure when the roof is flexible, while the simplified quasi-static model can be used for rigid roof. With increased roof natural frequency, all the three resonance frequencies of the "internal pressures - roof" coupled system increase; the peak internal pressure response also increases at the first two frequencies, but decreases at the third resonance frequency; the RMS internal pressure coefficients also increase, but their difference decreases.

KEYWORDS: building with internal partitioning and openings, wind-induced internal pressure, roof flexibility, governing equations, gain functions, coupled system.

1 INTRODUCTION

The dominant openings might be created due to either impact of flying debris or failure of windows and doors in severe wind storms. In the laminar uniform wind, an initial internal pressure overshoot which is higher than the mean external pressure at the opening will be produced when a sudden opening is created, then the response of internal pressure will exhibit damped oscillation, and it finally will keep constant with the external pressure. However, the overshoot phenomenon existed in smooth flow is lost amidst fluctuating turbulent wind in real life [1]. The steady-state internal pressure response for a building with a dominant opening can also be described with the Helmholtz acoustic resonator model. The resonance phenomenon will be occurred if there is sufficient energy at the Helmholtz frequency for the external pressure at the opening. So it will have a profound effect on building safety.

The effect of structure flexibility on internal pressure has been studied a lot for the single-cell building with a dominant opening. Vickery [2] treated the building deflections as quasi-static and suggested an effective volume method to consider the effect of building flexibility. Sharma and Richards [3] derived an equation governing the internal pressure for a building with a dominant opening and flexible roof, but the effect of external pressure on the roof movement failed to be considered. Yu et al [4] further considered the joint action of external and internal pressures on roof, and presented a linear internal pressure model. Sharma [5] derived an equation governing the response of internal pressure in any flexible building. Furthermore, a non-linear internal pressure governing equation was presented when the roof structure responds in a quasi-static manner, and the roof is under the joint action of external and internal pressures. Guha [6] derived an equation governing the internal pressure for a building with a dominant opening and flexible roof, however only considered the effect of internal pressure on roof. The studies of wind-induced internal pressures for a two-compartment building are much less compared with the single-cell building. Sharma [7] presented linearized equations governing the internal pressures for

a rigid and non-leaky two-compartment building. Yu et al [8] developed non-linear governing equations by considering the effect of background leakage. However, there are no theoretical and experimental studies on the effect of roof flexibility.

In this paper, the equations governing wind-induced internal pressure responses for a two-compartment building when the roof responds in dynamic and quasi-static manners is derived. Then, the gain functions, roof displacement, power spectra and RMS values of internal pressures are numerically analyzed.

2 GOVERNING EQUATIONS FOR A FLEXIBLE BUILDING

2.1 *Basic assumptions*

The object is a two-compartment building with flexible roof. There is an opening in the windward wall and an opening in the partition wall, and there are no background leakages. Besides, some reasonable assumptions are made as follows:

(i) The wall is rigid, while the roof is flexible.
(ii) The partition wall only plays a role of wind shield, but it doesn't provide support to the roof.
(iii) The roof behaves linearly.
(iv) The roof will produce a tiny rotation angle in theory for the fluctuating internal pressure in the compartment without an external opening is a little higher than that in the other one. However, it can be ignored for the roof is large and the wall is rigid.
(v) Internal pressures are completely relevant in their own compartments. This is the precondition for the theory of the internal pressure response and has already been validated by experiments [9].
(vi) The adiabatic law is applied for air in both compartments. It means the state equation gov erning the variation of the internal air pressure and density becomes:

$$P_i / \rho_i^{\gamma} = \mathrm{C} \tag{1}$$

where γ is the specific heat ratio for adiabatic air and is generally equal to 1.4, C is a constant, and P_i , ρ_i are the internal air pressure and density, respectively. After differentiating both sides of equation (1) and simplifying it, then:

$$dP_i = \frac{\gamma P_a}{\rho_i} d\rho_i \tag{2}$$

where P_a is the atmospheric pressure, which is the steady-state internal pressure.

2.2 *Governing equations*

The simplified model of internal pressures for a two-compartment building with flexible roof and openings is shown in Fig. 1. P_W , P_{i1} and P_{i2} are the transient wind pressures of windward wall, compartment 1 and compartment 2, respectively. L_{e1} and L_{e2} are the effective lengths of "air slugs" in the opening 1 and 2. A_{o1} and A_{o2} are the areas of the opening 1 and 2. $\forall_{01}$ and $\forall_{02}$ are the internal volumes of compartment 1 and 2, $\forall_0 = \forall_{01} + \forall_{02}$. c_1 and c_2 are the flow coefficients at the opening 1 and 2. C_{L1} and C_{L2} are the loss coefficients at the opening 1 and 2. m_r , k_r and ς_r are the mass, stiffness and damping ratio of the roof, respectively. A_{r1} and A_{r2}

are the roof areas of compartment 1 and 2, $A_r = A_{r1} + A_{r2}$. x_1 and x_2 are the displacements of "air slugs" in the opening 1 and 2, x_r is the displacement of flexible roof.

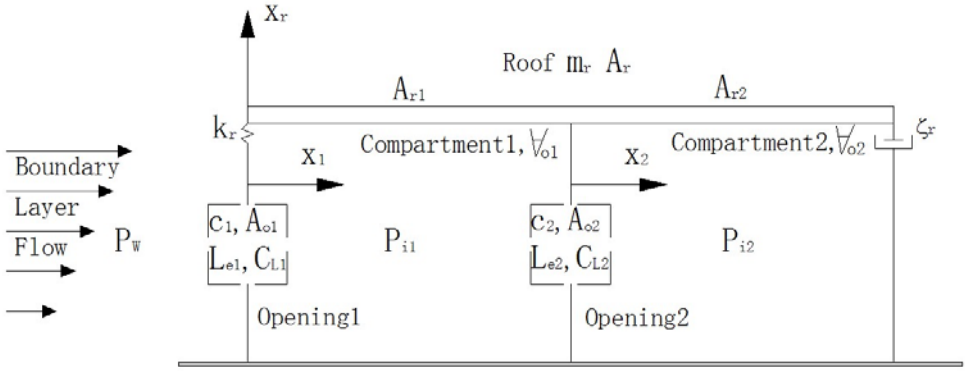

Figure 1. Model of a two-compartment building with linearly flexible roof structure

According to the unsteady form of the Bernoulli equation [2], the relationship between the airflow rate and the transient pressure drop for opening 1 is given by:

$$\rho_a L_{e1} c_1 A_{o1} \ddot{x}_1 + \frac{1}{2}\rho_a c_1 A_{o1} C_{L1} |\dot{x}_1| \dot{x}_1 = c_1 A_{o1} q_0 \left(C_{PW} - C_{Pi1}\right) \tag{3}$$

Similarly, the relationship between the airflow rate and the transient pressure drop for opening 2 is given by:

$$\rho_a L_{e2} c_2 A_{o2} \ddot{x}_2 + \frac{1}{2}\rho_a c_2 A_{o2} C_{L2} |\dot{x}_2| \dot{x}_2 = c_2 A_{o2} q_0 \left(C_{Pi1} - C_{Pi2}\right) \tag{4}$$

where $C_{Pi1} = P_{i1} / q_0$ and $C_{Pi2} = P_{i2} / q_0$ are the transient internal pressure coefficients of compartment 1 and compartment 2, $C_{PW} = P_W / q_0$ is the transient external pressure coefficient on the windward wall. ρ_a is the air density, $q_0 = \frac{1}{2}\rho_a U_0^2$ is the reference dynamic pressure of the approaching flow.

The changes in volumes of both compartments are:

$$\Delta\forall_1 = \forall_1 - \forall_{01} = A_{r1} x_r - c_1 A_{o1} x_1 + c_2 A_{o2} x_2 \tag{5}$$

$$\Delta\forall_2 = \forall_2 - \forall_{02} = A_{r2} x_r - c_2 A_{o2} x_2 \tag{6}$$

Then, according to the assumption (vi):

$$-q_0 \frac{\Delta C_{pi}}{\Delta\forall} \approx -q_0 \frac{dC_{pi}}{d\forall} = \frac{\gamma P_a}{\forall_0} \tag{7}$$

Substation of equations (5) and (6) into equation (7), and let $\upsilon = \frac{\forall}{\forall_0} = 1 + \frac{x_r}{H}$, $\dot{\upsilon} = \frac{\dot{x}_r}{H}$, $\ddot{\upsilon} = \frac{\ddot{x}_r}{H}$, there are:

$$C_{Pi1}=\frac{\gamma P_a}{q_0 \forall_{01}}\left[c_1 A_{o1} x_1 - c_2 A_{o2} x_2 - A_{r1} H(\upsilon - 1)\right] \tag{8}$$

$$C_{Pi2}=\frac{\gamma P_a}{q_0 \forall_{02}}\left[c_2 A_{o2} x_2 - A_{r2} H(\upsilon - 1)\right] \tag{9}$$

where H is the ridge height of the building.

Simultaneously solving equations (8) and (9) results in:

$$x_1=\frac{q_0 C_{Pi1}\forall_{01}+q_0 C_{Pi2}\forall_{02}}{\gamma P_a c_1 A_{o1}}+\frac{A_r H(\upsilon-1)}{c_1 A_{o1}} \tag{10}$$

$$x_2=\frac{q_0 C_{Pi2}\forall_{02}}{\gamma P_a c_2 A_{o2}}+\frac{A_{r2} H(\upsilon-1)}{c_2 A_{o2}} \tag{11}$$

Derivation of both sides of equations (10) and (11) leads to:

$$\dot{x}_1=\frac{q_0 \dot{C}_{Pi1}\forall_{01}+q_0 \dot{C}_{Pi2}\forall_{02}}{\gamma P_a c_1 A_{o1}}+\frac{A_r H\dot{\upsilon}}{c_1 A_{o1}} \tag{12}$$

$$\dot{x}_2=\frac{q_0 \dot{C}_{Pi2}\forall_{02}}{\gamma P_a c_2 A_{o2}}+\frac{A_{r2} H\dot{\upsilon}}{c_2 A_{o2}} \tag{13}$$

$$\ddot{x}_1=\frac{q_0 \ddot{C}_{Pi1}\forall_{01}+q_0 \ddot{C}_{Pi2}\forall_{02}}{\gamma P_a c_1 A_{o1}}+\frac{A_r H\ddot{\upsilon}}{c_1 A_{o1}} \tag{14}$$

$$\ddot{x}_2=\frac{q_0 \ddot{C}_{Pi2}\forall_{02}}{\gamma P_a c_2 A_{o2}}+\frac{A_{r2} H\ddot{\upsilon}}{c_2 A_{o2}} \tag{15}$$

Substation of equations (12~15) into equations (3~4) yields:

$$\begin{aligned}&\frac{\rho_a L_{e1}\forall_{01}}{\gamma P_a c_1 A_{o1}}\ddot{C}_{Pi1}+\frac{\rho_a L_{e1}\forall_{02}}{\gamma P_a c_1 A_{o1}}\ddot{C}_{Pi2}+\frac{\rho_a L_{e1}\forall_0}{c_1 A_{o1} q_0}\ddot{\upsilon}+\\&\frac{\rho_a C_{L1}\forall_0{}^2}{2(c_1 A_{o1})^2 q_0}\left|\frac{q_0\forall_{01}\dot{C}_{Pi1}+q_0\forall_{02}\dot{C}_{Pi2}}{\gamma P_a \forall_0}+\dot{\upsilon}\right|\left(\frac{q_0\forall_{01}\dot{C}_{Pi1}+q_0\forall_{02}\dot{C}_{Pi2}}{\gamma P_a\forall_0}+\dot{\upsilon}\right)+C_{Pi1}=C_{PW}\end{aligned} \tag{16}$$

$$\begin{aligned}&\frac{\rho_a L_{e2}\forall_{02}}{\gamma P_a c_2 A_{o2}}\ddot{C}_{Pi2}+\frac{\rho_a L_{e2}\forall_{02}}{c_2 A_{o2} q_0}\ddot{\upsilon}+\\&\frac{\rho_a C_{L2}\forall_{02}{}^2}{2(c_2 A_{o2})^2 q_0}\left|\frac{q_0\dot{C}_{Pi2}}{\gamma P_a}+\dot{\upsilon}\right|\left(\frac{q_0\dot{C}_{Pi2}}{\gamma P_a}+\dot{\upsilon}\right)+C_{Pi2}-C_{Pi1}=0\end{aligned} \tag{17}$$

Equations (16~17) are the general equations governing the internal pressure responses for a two-compartment building with flexible roof.

When the roof of the building is rigid, i.e. $\upsilon = 1$, $\dot{\upsilon} = 0$ and $\ddot{\upsilon} = 0$, the equations (16~17) can be simplified as follows:

$$\frac{\rho_a L_{e1} \forall_{01}}{\gamma P_a c_1 A_{o1}} \ddot{C}_{Pi1} + \frac{\rho_a L_{e1} \forall_{02}}{\gamma P_a c_1 A_{o1}} \ddot{C}_{Pi2} + \frac{\rho_a C_{L1} q_0 \forall_{01}^{\ 2}}{2(\gamma P_a c_1 A_{o1})^2} \left| \dot{C}_{Pi1} + \frac{\forall_{02}}{\forall_{01}} \dot{C}_{Pi2} \right| \left(\dot{C}_{Pi1} + \frac{\forall_{02}}{\forall_{01}} \dot{C}_{Pi2} \right) + C_{Pi1} = C_{PW} \tag{18}$$

$$\frac{\rho_a L_{e2} \forall_{02}}{\gamma P_a c_2 A_{o2}} \ddot{C}_{Pi2} + \frac{\rho_a C_{L2} q_0 \forall_{02}^{\ 2}}{2(\gamma P_a c_2 A_{o2})^2} \left| \dot{C}_{Pi2} \right| (\dot{C}_{Pi2}) + C_{Pi2} - C_{Pi1} = 0 \tag{19}$$

If the damping coefficients in equations (18) and (19) are linearized, they will become the internal pressure governing equations presented by Sharma [7]. Thus, the Sharma's governing equations [7] are a special case of the equations (16) and (17) derived in this paper.

2.2.1 *Responses of internal pressure when the roof responds in a dynamic manner*

In reality, many large span industrial building, their component structures, in particular the roof, exhibit greater flexibility than the wall. So they will behave in a dynamics manner in strong wind. As for a two-compartment building shown in Fig. 1, the response of the roof to the internal pressures will be governed by:

$$m_r \ddot{x}_r + 2m_r \zeta_r \omega_r \dot{x}_r + m_r \omega_r^2 x_r = A_{r1} q_0 C_{Pi1} + A_{r2} q_0 C_{Pi2} \tag{20}$$

The non-dimensional form of the equation (20) is:

$$\ddot{\upsilon} = \frac{q_0 \left(A_{r1} C_{Pi1} + A_{r2} C_{Pi2} \right)}{m_r H} - 2\zeta_r \omega_r \dot{\upsilon} - \omega_r^2 \left(\upsilon - 1 \right) \tag{21}$$

Equations (21) and (16~17) are the dynamic model of internal pressures for a two-compartment building with flexible roof. The equation (21) can be solved simultaneously with equations (16~17) to obtain the coupling responses of internal pressures and roof for specified parameter conditions.

2.2.2 *Responses of internal pressure when the roof responds in a quasi-static manner*

The dynamics model (Equations (21) and (16~17)) is a second-order differential equations, and it is hard to be solved for its complexity.

When the natural frequency of the roof is larger than the first expected Helmholtz frequency, the internal pressure responses are dominated by average and background components, while the resonance component can be ignored for its little contribution. Thus, the roof deflection is proportional to the applied load at all times [2], i.e. a quasi-static manner [3].

$$\upsilon = 1 + \frac{q_0 (C_{pi1} + C_{pi2})}{k_b} \tag{22}$$

where $k_b = (2\pi f_r)^2 \forall_0 m_r / A_r^2$ is the building bulk modulus defined as the ratio of increase in pressure to volumetric strain.

Substitution of the time derivation of υ into equations (16~17), and let $b = \gamma P_a / k_b$, yields:

$$\frac{\rho_a L_{e1}\left(\forall_{01}+b\forall_0\right)}{\gamma P_a c_1 A_{o1}}\ddot{C}_{Pi1}+\frac{\rho_a L_{e1}\left(\forall_{02}+b\forall_0\right)}{\gamma P_a c_1 A_{o1}}\ddot{C}_{Pi2}+\frac{\rho_a C_{L1} q_0}{2(\gamma P_a c_1 A_{o1})^2}\cdot$$
$$\left|\left(\forall_{01}+b\forall_0\right)\dot{C}_{Pi1}+\left(\forall_{02}+b\forall_0\right)\dot{C}_{Pi2}\right|\left[\left(\forall_{01}+b\forall_0\right)\dot{C}_{Pi1}+\left(\forall_{02}+b\forall_0\right)\dot{C}_{Pi2}\right]+C_{Pi1}=C_{PW} \tag{23}$$

$$\frac{\rho_a L_{e2}\forall_{02}(1+b)}{\gamma P_a c_2 A_{o2}}\left(\ddot{C}_{Pi2}+\frac{b}{1+b}\ddot{C}_{pi1}\right)+$$
$$\frac{\rho_a C_{L2} q_0 \forall_{02}{}^2(1+b)^2}{2(\gamma P_a c_2 A_{o2})^2}\left|\dot{C}_{pi2}+\frac{b}{1+b}\dot{C}_{pi1}\right|\left(\dot{C}_{pi2}+\frac{b}{1+b}\dot{C}_{pi1}\right)-C_{Pi1}+C_{Pi2}=0 \tag{24}$$

Equations (23~24) are the quasi-static model of internal pressures for a two-compartment building with flexible roof. It is actually an approximate model of the dynamic model when the natural frequency of roof is considerably larger than the lower Helmholtz frequency.

3 NUMERICAL EXAMPLE

Take a two-compartment building as an example to analyze the dynamic and quasi-static responses of internal pressure. The two-compartment building is similar as the TTU test building, whose basic parameter values are as follows:

$\forall_{01}=200m^3$, $\forall_{02}=300m^3$, $A_{o1}=2m^2$, $A_{o2}=2m^2$, $L_{e1}=\sqrt{\pi A_{o1}/4}$, $L_{e2}=\sqrt{\pi A_{o2}/4}$, $c_1=0.6$, $c_2=0.6$, $C_{L1}=1.2$, $C_{L2}=1.2$, $\bar{U}_0=30m/s$, $\gamma=1.4$, $P_a=101300Pa$, $\rho_a=1.22kg/m^3$, $A_{r1}=50m^2$, $A_{r2}=75m^2$, $H=4m$, $m_r=3500kg$, $\varsigma_r=0.1$, $\omega_r=2\pi f_r$, $f_r=$3Hz, 5Hz, 7Hz, 10Hz.

The time history of wind speed can be simulated by the superposition of the harmonic [10] based on Davenport spectrum, and then the time history of external pressure coefficient at the windward opening can be further obtained according to the quasi-steady theory. The responses of internal pressure can be calculated by inputting the external pressure coefficient obtained in last step into the governing equations derived in the present paper. The simulated wind speed and its verification are shown in Fig. 2.

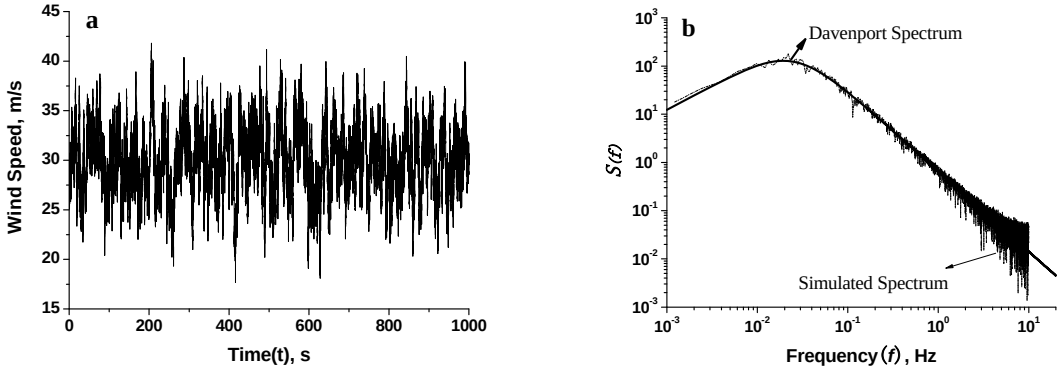

Figure 2. (a) Simulated time-history wind speed and (b) its verification

The gain functions of internal pressures calculated from the dynamic and quasi-static models for different roof flexibilities are shown in Fig. 3, in which Figs 3a,b,c,d are the results of compartment 1 and Figs 3e,f,g,h are the results of compartment 2. The two-compartment building

with flexible roof and openings is similar to a coupled dynamic system which contains three "mass-spring-damping" subsystems. It can be seen from Fig.3 that three resonance peaks are evident from dynamic analysis while only two resonance peaks are obtained from quasi-static analysis. Furthermore, the first two resonance frequencies obtained from dynamic analysis is the same as that obtained from quasi-static analysis. Besides, the internal pressure response in compartment 2 is higher than that in compartment 1 calculated from both models. However, the third resonance peak gradually disappears when the roof natural frequency gradually becomes larger, and the gain function obtained from the dynamic model is gradually consistent with that from quasi-static model.

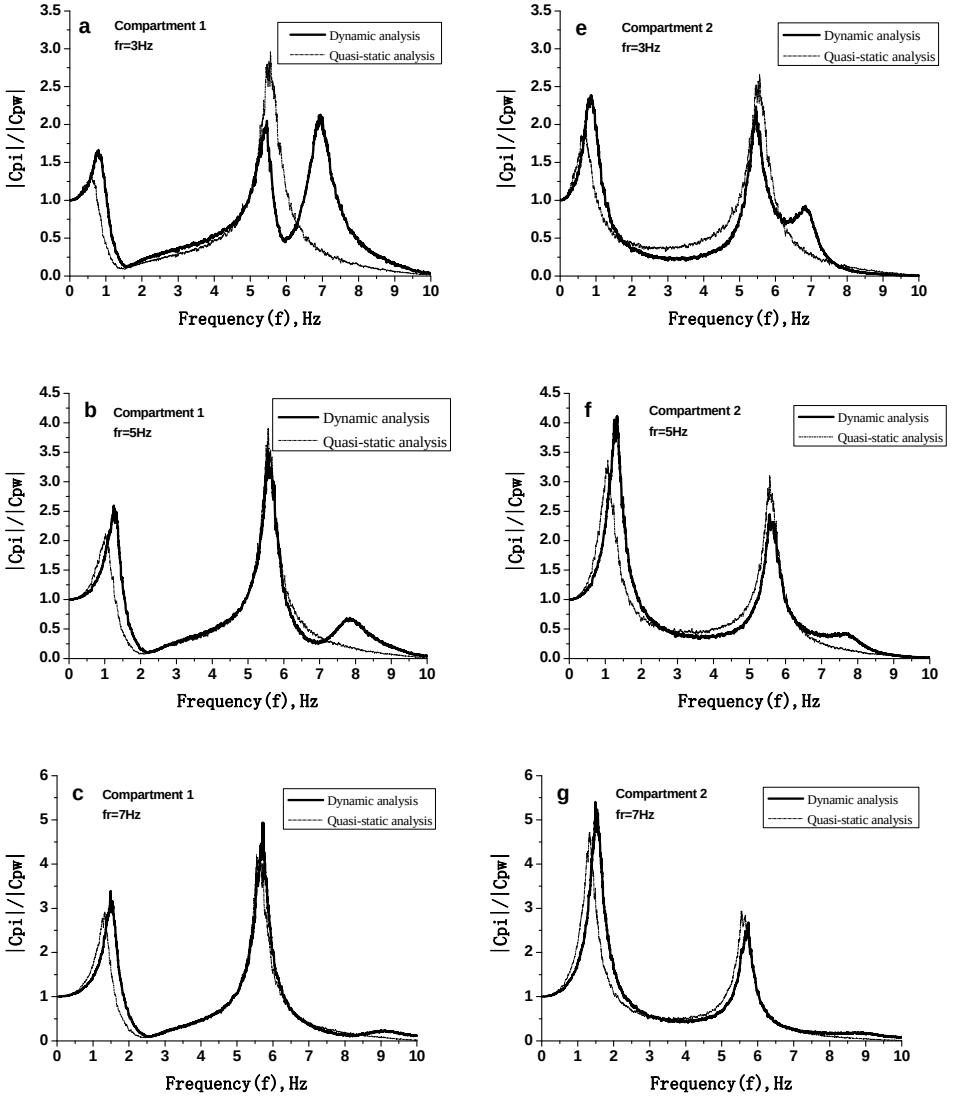

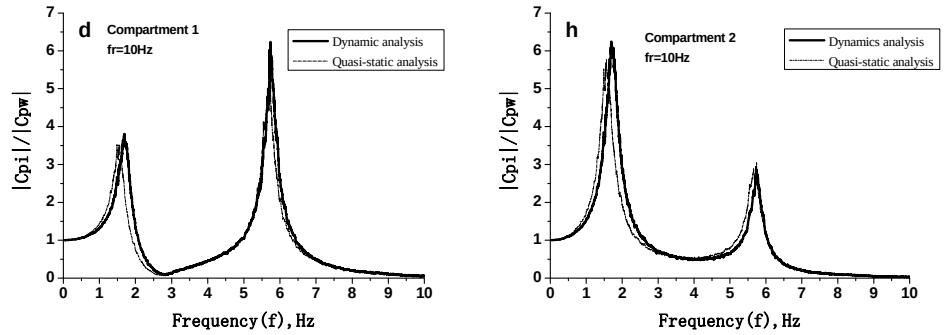

Fig 3. Gain function of internal pressure for dynamic and quasi-static analysis

The gain functions of internal pressures in both compartments, the roof displacement over external pressure at the windward opening calculated from dynamic model for different roof natural frequencies are shown in Fig.4. It is shown from Figs 4a,b that three resonance frequencies of the "internal pressure - roof" coupled system increase with increased roof natural frequency. The first two resonance peaks of internal pressure are also increase with increased roof natural frequency, while the third resonance peak decreases and finally disappears. It is shown from Fig 4c that the restoring force of the roof increases with increased roof natural frequency at the first two resonance frequencies, and the restoring forces at the first resonance frequency are much larger than these at the last two resonance frequencies.

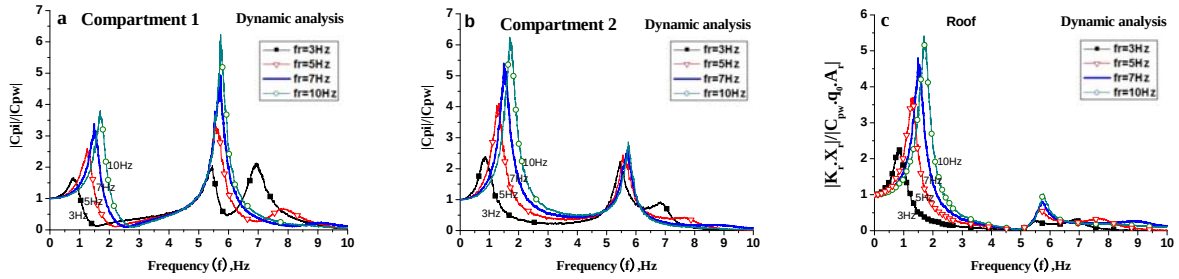

Figure 4. Gain function of (a) internal pressure for compartment 1 (b) internal pressure for compartment 2 and (c) roof displacement over external pressure for different roof flexibilities

The power spectra of internal pressure coefficients in both compartments obtained from the dynamic model for different roof flexibilities are shown in Fig.5. It is shown that the resonance energy of internal pressure in compartment 2 at the first resonance frequency is higher than that in compartment 1 for all kinds of roof flexibilities. The resonance energies of internal pressure in both compartments at the third resonance frequency decrease with increased roof natural frequency. This is in agreement with the analytical results of Fig.3.

The RMS internal pressure coefficients in both compartments and RMS roof displacement for different roof flexibilities are list in Table 1. It is shown that the RMS internal pressure coefficient in compartment 2 is large than that in compartment 1. The RMS internal pressure coefficients obtained from both models increase with increased roof natural frequency, but their difference decreases. It is because with increased roof natural frequency, i.e. the roof flexibility gradually decreases, the additional damping also decreases. Moreover, the RMS value of the roof displacement decreases with increased roof natural frequency.

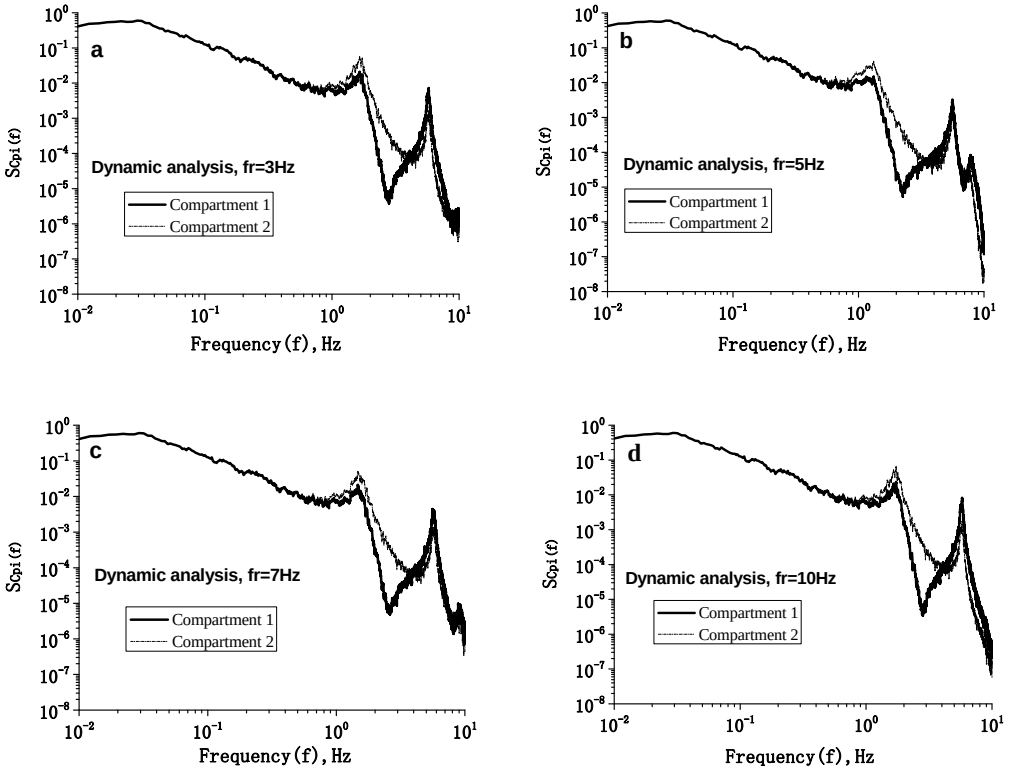

Figure 5. Power spectra of internal pressure coefficients in both compartments

Table 1. RMS internal pressure coefficients in bot compartments and RMS roof displacement for different roof flexibilities

Roof frequency	$\tilde{C}_{pi}$ (Dynamic analysis)		$\tilde{C}_{pi}$ (Quasi-static analysis)		$\tilde{x}_r$ (Dynamic analysis)
	Compartment 1	Compartment 2	Compartment 1	Compartment 2	
3 Hz	0.236	0.250	0.233	0.248	0.0136
5 Hz	0.243	0.262	0.242	0.261	0.0051
7 Hz	0.247	0.269	0.246	0.269	0.0026
10 Hz	0.251	0.274	0.249	0.273	0.0013

4 CONCLUSIONS

As for a two-compartment building with flexible roof and openings, the equations governing wind-induced internal pressure responses are derived based on some reasonable assumptions when the roof responds in dynamic and quasi-static manners. The unsteady form of the Bernoulli equation, the law of mass conservation, and adiabatic equation are used for the derivation. A two-compartment building similar to the TTU test building is taken as an example to analyze the characteristics of gain functions, power spectra and RMS values of the internal pressure coefficients and roof displacement. Some main conclusions are drawn:

(1) The governing equations derived in the present paper can be used to analyze the internal pressure responses for a two-compartment building with flexible roof and openings. The dynamic model must be used to calculate the responses of internal pressure when the roof is flexible, otherwise, the simplified quasi-static model can be instead.

(2) The first two resonance frequencies of the “internal pressure - roof” coupled system obtained from the dynamic model is consistent with that obtained from the quasi-static model. The internal pressure response in compartment 2 is larger than that in compartment 1. When the roof natural frequency gradually becomes larger, the gain functions obtained from the dynamic model are gradually in accord with these from the quasi-static model.

(3) With increased roof natural frequency, the three resonance frequencies increase, and the first two resonance peaks of internal pressure are also increase, while the third resonance peak decreases and finally disappears. Besides, the restoring forces of the roof at the first two resonance frequencies also increase with increased roof natural frequency.

(4) The RMS internal pressure coefficient in compartment 2 is large than that in compartment 1. The RMS internal pressure coefficients obtained from both the dynamic and quasi-static models increase with increased roof natural frequency, but their difference decreases. Moreover, the RMS value of the roof displacement also decreases with increased roof natural frequency.

5 ACKNOWLEDGEMENTS

We gratefully acknowledge the joint support of the Key Project of the Major Research Program of Chinese National Natural Science Foundation (Grant No. 90715040) and the General Program of Chinese National Natural Science Foundation (Grant No. 50878159).

6 REFERENCES

1 Stathopoulos, T., Luchian, H. D., 1989. Transient wind-induced internal pressures. Journal of Engineering Mechanics 115, 1501-1514.

2 Vickery, B. J., 1986. Gust-factors for internal-pressures in low rise buildings. Journal of Wind Engineering and Industrial Aerodynamics 23, 259-271.

3 Sharma, R. N., Richards, P. J., 1997. The effect of roof flexibility on internal pressure fluctuations. Journal of Wind Engineering and Industrial Aerodynamics 72, 175-186.

4 Yu Shice. Wind-induced internal pressure of structure with openings and its coupuling effect with flexible roof.[PhD Thesis]. Zhejiang: Zhejiang University, 2006.53~56. (in Chinese)

5 Sharma, R. N., 2008. Internal and net envelope pressures in a building having quasi-static flexibility and a dominant opening. Journal of Wind Engineering and Industrial Aerodynamics 96,1074-1083.

6 Guha, T. K., Sharma, R. N., Richards, P. J., 2011. On the internal pressure dynamics of a leaky and flexible low rise building with a dominant opening. in: Proceedings of the 13th Int. Conf on wind Engineering, Amsterdam, Netherlands.

7 Sharma, R. N., 2003. Internal Pressure Dynamics with Internal Partitioning. in: Proceedings of the 11th International Conference on Wind Engineering, Lubbock Texas.

8 Yu Xianfeng, Gu Ming, Quan Yong, et al., 2012. Study on response of wind-induced internal pressure for structure with internal partitioning and an opening when considering background porosity, Acta Aerodynamica Sinica 30, 240-245. (in Chinese)

9 Holmes, J. D., 1979. Mean and fluctuating internal pressures induced by wind. in: Proceedings of the 5th Int Conf on Wind Engineering, Fort Collins,USA.

10 Wang Zhihong, 1994. Simulation of wind loading. Journal of building structures 15, 44-52. (in Chinese)

The Seventh International Colloquium on Bluff Body Aerodynamics and Applications (BBAA7)
Shanghai, China; September 2-6, 2012

Ground roughness effects on internal pressures and local roof wind forces of building exposed to tornado-like flow

Geetha Rajasekharan Sabareesh [a], Masahiro Matsui [b], Yukio Tamura [c]

[a]*Tokyo Polytechnic University, Atsugi, Kanagawa, Japan, sabareesh@arch.t-kougei.ac.jp*
[b]*Tokyo Polytechnic University, Atsugi, Kanagawa, Japan, matsui@arch.t-kougei.ac.jp*
[c]*Tokyo Polytechnic University, Atsugi, Kanagawa, Japan, yukio@arch.t-kougei.ac.jp*

ABSTRACT: Tornadoes pose serious threat to buildings and structures. Reducing the risk to building structures requires the understanding of tornado-structure interaction, the surface and internal pressures developed and the net wind loads acting on the building. In the present investigation an attempt is made to investigate the effect of ground roughness on the internal pressure developed inside a building model exposed to a stationary vortex generated by a tornado-like flow simulator at Tokyo Polytechnic University. Results show that the internal pressures decrease in magnitude with introduction of roughness, whereas the resulting local roof forces increase in magnitude with introduction of roughness.

KEYWORDS: Tornado, Ground Roughness, Swirl Ratio, Building Structures, Internal Pressure

1 INTRODUCTION

The real time investigations on the nature of tornadoes are impractical because of unpredictability, short life span and danger. Many strategically important buildings such as Nuclear power plants and hospitals should be designed against tornado wind. Every year Japan experiences around 17~20 tornadoes, distributed over the mainland, though some recent studies by Tamura et al. predicts as high as 35-40. Though the human fatalities associated with tornado-occurrence in Japan are very less, the damage to building roofs and walls and the building as a whole is extensive. On an average 385 residential structures are partly or completely damaged due to tornadoes in Japan every year, Niino et al (1997). Recently several strong tornadoes attacked Japan at Nobeoka and Hokkaido in 2006.

Wind pressure studies estimated from boundary layer wind tunnels along with full-scale studies are used in building codes. But in local disturbances like a tornado, where there is a rotational wind component together with a significant vertical component of velocity, the nature and distribution of pressures and resulting wind loads will be quite different from a straight line wind. This demands the analysis of tornado-structure interaction different from a boundary layer phenomenon.

A comprehensive investigation will be possible only through a thorough understanding of the damage characteristics, the failure modes of structures in a tornado wind, the commonly occurring structural damages, the relation between the tornado parameters and type of structures that failed etc. Based on this knowledge based information, identical conditions need to be simulated in situ for careful and systematic velocity and pressure measurements and estimate the tornado wind loads varying the geometrical and dynamic parameters influencing tornado-building

interaction to gain a clear insight into the underlying mechanism that inflict damage. This in turn could help the broader aim of tornado wind resistant building design.

During the past few decades, there have been attempts to simulate tornado-like flow situations in laboratory and expose scaled building models to the vortex-type flow [Chang (1971), Jischke & Light (1983), Mishra et al (2008), Haan et al (2010), Yang et al (2011)]. Many of these studies were limited to the surface pressures on buildings under these extreme flow-regimes. But recently, attempts are done to understand the internal pressures developed under such flow situations [(Kikitsu et al (2011), Sabareesh et al (2011)].

Internal pressure studies become significant in the view of openings created on the building walls under such local disturbances like a tornado. The internal pressures will respond to the changes in external pressures, if the opening porosity is higher.

2 EXPERIMENTAL SETUP

In the present work an attempt is made to determine the internal pressures and resulting local roof wind force for a building under tornado-like flow and exposed to two different terrain conditions.

The tornado-like flow simulator at Tokyo Polytechnic University that could generate a stationary tornado-like flow was used. The tornado-like flow generator is essentially the same as used in Sabareesh et al. (2012) with the confluence height being reduced to 200mm for the present case. The parameters governing tornado-like flow has been found to be in close agreement with those that are attainable in other laboratory simulator flows as explained in Sabareesh et al. (2012).

The building model was of size 30mm x 30mm x 15 mm, and was located at the centre of the simulator floor. A square central hole constituting an opening porosity of 3.9% was kept open in the building wall. The definition of opening porosity in the present case is the ratio of opening area to single wall area. A volume chamber was placed beneath the simulator floor as per the requirements to scale the internal volume to maintain similarity in dynamic response of volume between full scale and model scale, see Figure 1.

Two different terrain conditions were used for this study. The first was a plain floor without any roughness, which can be categorized as a near smooth terrain, the second used a 5mm artificial grass carpet on the simulator floor, see Figure 2. The roughness in the second case can be estimated as typically about $1/30^{th}$ of the height of roughness element (Leslie, 1977), or using a procedure described in Counihan (1971) which results in an effective roughness in the range of Z_0 =0.17~0.28mm. The effects under two different swirl ratio cases are discussed.

Figure 1. Scaled volume chamber

Figure 2. Building model exposed to artificial roughness

2.1 *Velocity Measurements*

The variation of velocity field to the rotating flow determines the type of flow field in the simulator. The scalar component of velocity was measured at definite radial locations from the simulator centre to the periphery and simultaneously at different heights above the floor in these radial locations. A multi-channel thermistor type anemometer probe which can measure simultaneously the mean component of velocity at different locations was used for this purpose.

With increase in roughness the outer boundary of core thickens, and the higher velocity region shifts up to greater heights above the floor of simulator. A lower mean velocity region can

be observed close to the ground with increase in surface roughness. Away from the core regions, the effect of surface roughness on mean velocity was negligible.

Also it is observed that the core updraft velocity increases with increase in roughness as shown in Figure 3 for different swirl ratios.

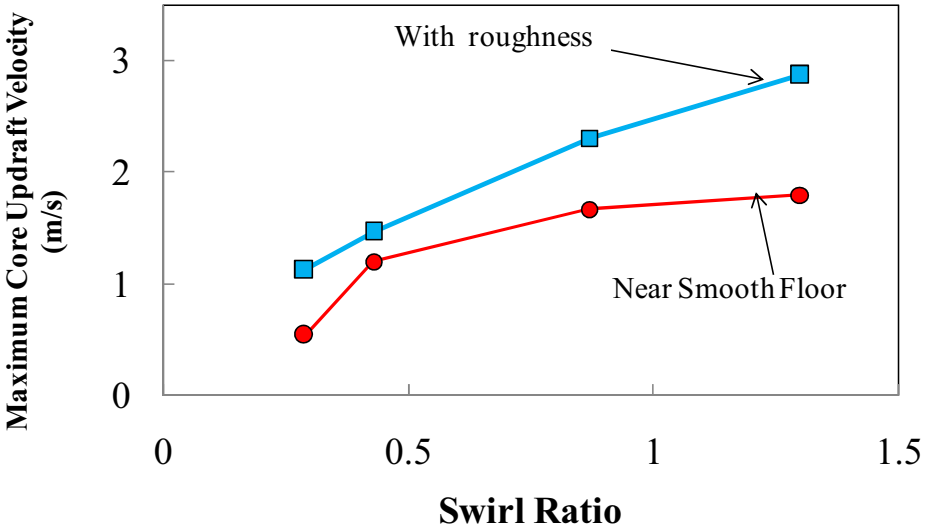

Figure 3Variation of core updraft velocity with roughness at different swirl ratio

2.2 *Pressure Measurements*

Simulator floor was fitted with pressure taps on its surface. The building model was also fitted with pressure taps in the inside apart from the outer pressure taps. Synthetic resin tubes 1m long connected each pressure tap with the pressure measurement scan valve, which is capable of simultaneously measuring the pressures at these taps.

Pressure sensors were employed, which could simultaneously measure pressures at multiple points. Sampling frequency of data points was 700 Hz. Measured voltage signals were transformed to time series of wind pressures. Effects of tube system were removed by analyzing the transfer function of tube system and eliminating it from the raw wind pressures.

Internal pressures were simultaneously measured at 10 pressure taps distributed evenly inside the building model and the volume chamber and numerically averaged. There were a total of 25 pressure taps distributed on the roof external face. The pressure coefficient (Cp_j) at any point' $_j$' is defined by equation (1).

$$Cp_j = \frac{P_j - P_\infty}{q_r} \tag{1}$$

Where, 'q_r' is the reference dynamic pressure obtained from velocity at roof height. 'P_∞' is the reference static pressure measured far from simulator centre.

Minimum values (*Cpi (minimum*) of the internal pressure coefficients were obtained. The time scale was obtained employing the ratio between the core radius of the tornado vortex and maximum wind speed in the flow region (approx. 2.4m/s). Using this time scale, the full scale equivalent of model scale time was estimated for the entire length of pressure data assuming a F3 tornado having a core size of 30m and maximum wind speed of 92m/s. The time histories corresponding to 1minute in full scale from a conservative view point were measured for 21

samples. The minimum values in the time history were obtained independently for each of these 21 segments. The average of the minimum values of the 21 segments defines the minimum peak pressure coefficient presented in the results.
The net local roof force coefficients per unit area around a point '*j*' $C_{F(t)}$ was derived as the difference between external, $Cpe_{j(t)}$ and internal, $Cpi_{(t)}$ pressure coefficients,

$$C_{F_{(t)}} = Cpe_{j(t)} - Cpi_{(t)}$$

3 RESULTS AND DISCUSSIONS

The roughness heights are normalized with respect to building height.

Analysing the effect of roughness, it was found that for both the swirl ratio examined with increase in roughness, the minimum value of peak internal pressure coefficients showed a decrease in magnitude, see Figure 4. This may be because the flow gets retarded near the surface layers as observed from the velocity distribution near the surface in presence of roughness, see Sabareesh et al(2012). This inturn reduces the pressure coefficients across the building surface and interiors. Roughness on the ground reduces the near ground velocities, which tends to decrease in magnitude the external pressures on building walls outside the opening. This in turn reduces the internal pressure coefficients inside the building, as the internal pressures respond to the changes in external pressure when the opening porosity is higher.

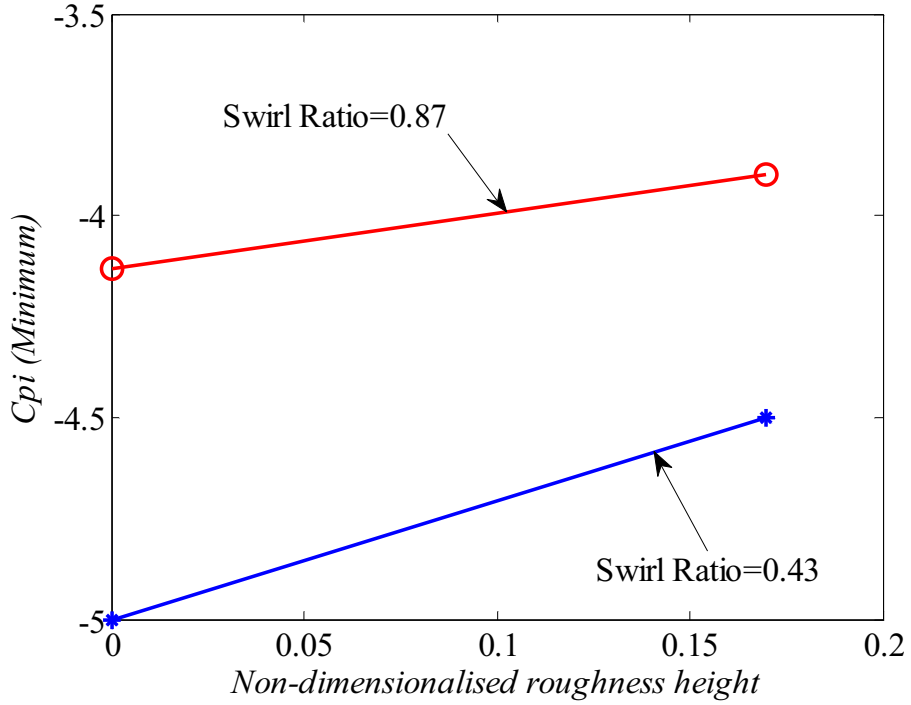

Figure 4. Variation of minimum internal pressure coefficient with terrain condition

Comparing the variation of external pressure coefficients with the internal pressure coefficients, see Figure 5, it is found that with introduction of roughness the external pressure coeffi-

cients show a steeper descent in magnitude compared to the internal pressure coefficients showing that the decrease in internal pressure within the building model is rather gradual.

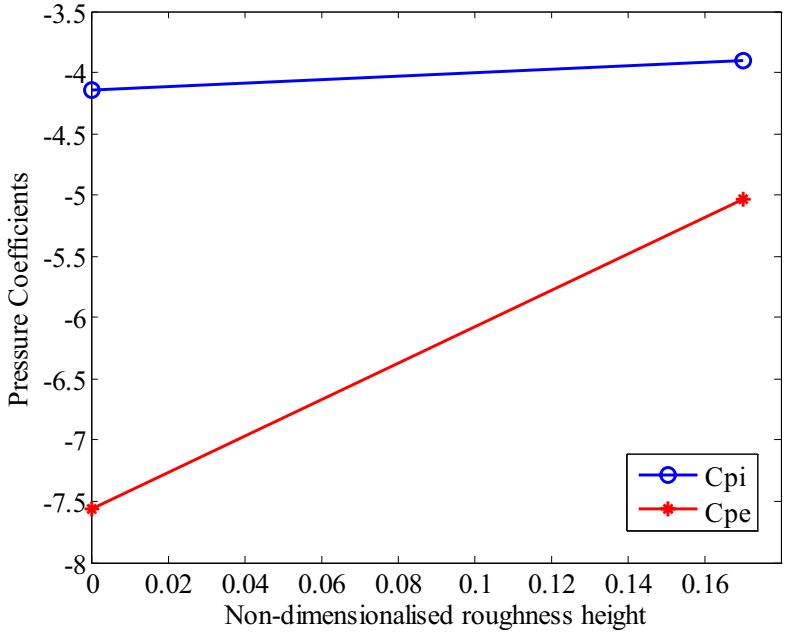

Figure 5. Variation of minimum pressure coefficients with terrain condition

Analyzing the Helmholtz frequency for the flow through the openings, see Figure 6, it is found that with increase in roughness the peak of Helmholtz resonance slightly shifts to the higher frequency side.

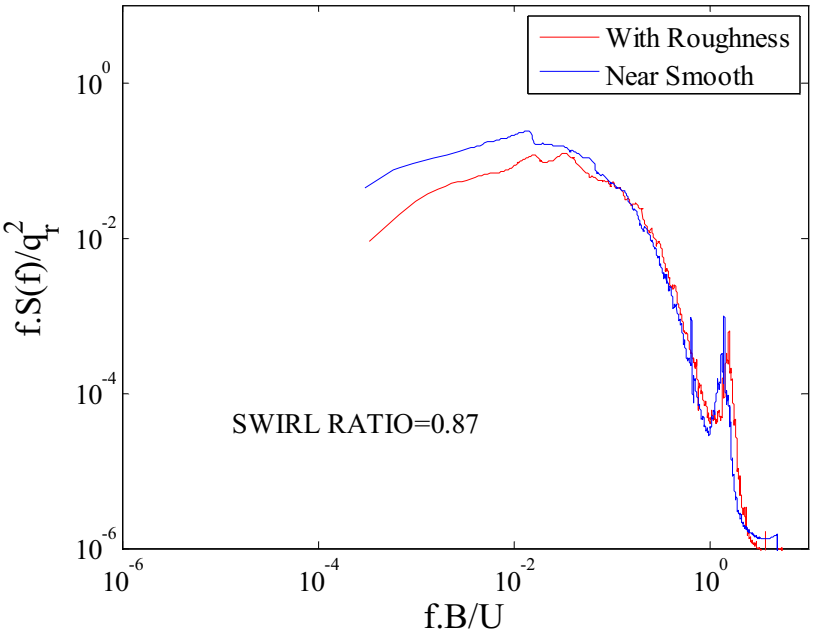

Figure 6. Variation of Helmholtz resonance with introduction of roughness

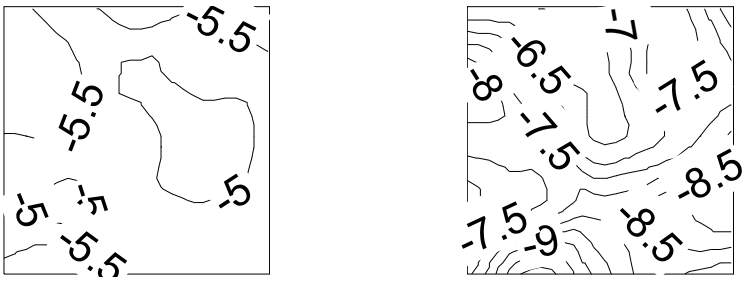

(a) (b)

Figure 7 Local roof wind force coefficient (a) Smooth Terrain (b) With roughness

Figure 7 shows the local wind force coefficient contours on the building roof for the two roughness cases at Swirl ratio S=0.87. The effects on the local roof wind force were the opposite of that experienced for the internal pressures. The smoother terrain case experienced lower magnitude local roof wind force compared to the rougher terrain. This may be attributed to the increase in core updraft velocity associated with increase in terrain roughness which increases the magnitude of suction forces on roof surfaces. These effects repeated for the two swirl ratios examined.

3.1 *Conclusions*

1. With the introduction of roughness the internal pressures decrease in magnitude irrespective of swirl ratio.
2. External pressures shows higher decrease compared to internal pressures with the introduction of roughness.
3. Helmholtz resonance shows a shift in peak to the higher frequency side with introduction of roughness.
4. The net roof force increase in magnitude with introduction of roughness.

4 ACKNOWLEDGEMENTS

This study was funded by the Ministry of Education, Culture, Sports, Science and Technology Japan, through the Global Center of Excellence Program, 2008-2012, which is gratefully acknowledged.

5 REFERENCES

1. Chang, C.C., 1971, Tornado wind effects on buildings and structures with laboratory simulation. In: Proceedings of Third International Conference on Wind Effects on Buildings and Structures, Tokyo, Japan, 151–174.
2. Church, C. R., Snow, J.T., and Agee, E. M., 1979. Characteristics of Tornado-Like Vortices as a Function of Swirl Ratio: A Laboratory Investigation, American Meteorological Society, vol. 36, 1755-1774
3. Counihan, J., 1971. Wind tunnel determination of the roughness length as a function of the fetch and the roughness density of three-dimensional roughness elements. Atmospheric Environment 5,637-642
4. Ginger, J. D., Mehta, K. C., Yeatts, B. B., 1997. Internal pressures in a low-rise full-scale building, Journal of Wind Engineering and Industrial Aerodynamics 72, 163-174.
5. Ginger, J.D., Letchford, C.W., 1999. Net pressures on a low-rise full-scale building, Journal of Wind Engineering and Industrial Aerodynamics 83,239-250.

6. Haan, F.L. Jr, Balaramudu, V.K., Sarkar,P.P., 2010. Tornado-induced wind loads on a low rise building. Journal of Structural Engineering, 106-116.
7. Jischke, M.C., Light, B.D., 1983. Laboratory simulation of tornadic wind loads on a rectangular model structure, Journal of Wind Engineering and Industrial Aerodynamics 13, 371-382.
8. Kikitsu.H, Sarkar,P.P, Haan, F.L. Jr., 2011. Experimental study on tornado-induced loads of low-rise buildings using a large tornado-simulator.In Proc of 13th International Conference on Wind Engineering
9. Leslie, F.W., 1977. Surface roughness effects on suction vortex formation. a laboratory simulation, Journal of Atmospheric Sciences 34, 1022-1027.
10. Mishra, A.R., James, D.L., Letchford, C.W., 2008. Physical simulation of a single-celled tornado-like vortex, Part B: Wind loading on a cubic model. Journal of Wind Engineering and Industrial Aerodynamics, 96, 1258-1273.
11. Geetha Rajasekharan Sabareesh, Masahiro Matsui, Yukio Tamura, 2011.Dependence of surface pressures on a cubic building in tornado-like flow on building location and ground roughness. Journal of Wind Engineering and Industrial Aerodynamics, 103, 50-59
12. Sabareesh.G.R, Masahiro Matsui, Yukio Tamura, 2011. Characteristics of internal pressure and resulting roof wind force in tornado-like flow. In Proc of 13th International Conference on Wind Engineering
13. Yang, Z., Sarkar, P., Hu, H., 2011, An experimental study of a high-rise building model in tornado-like winds, Journal of Fluid and Structures 27, 471-486.

The Seventh International Colloquium on Bluff Body Aerodynamics and Applications (BBAA7)
Shanghai, China; September 2-6, 2012

Numerical simulation of pressure and flow field in large group of low-rise buildings

Yong Chul Kim [a], Akihito Yoshida [a], Yukio Tamura [a],
Hirotoshi Kikuchi [b], Kazuki Hibi [b],

[a] *Tokyo Polytechnic University, 1583 Iiyama Atsugi, Kanagawa, Japan*
[b] *Shimizu Corporation, 3-4-17 Etchujima, Koto-ku, Tokyo, Japan*

ABSTRACT: The pressure and flow field around a target low-rise model immersed in a large group simulating various area densities were investigated using three-dimensional numerical RANS turbulence models. Wind pressure coefficients obtained from the numerical results were compared with those of wind pressure measurements, and the flow fields around the model were compared with those obtained from flow visualization. The results show that for the wind pressure coefficients for the isolated model, more reasonable results were obtained when the rng k-ε model was used, but there was little difference between turbulence models for the target model in a large group. For the flow field around the model, the RANS turbulence models were able to reproduce the overall flow pattern generally, even though some differences were found.

KEYWORDS: Group of low-rise buildings; Computational fluid dynamics; Wind pressure measurement; Flow visualization

1 INTRODUCTION

As low-rise buildings are normally built in large groups, the flow field around a low-rise building of interest is totally different from that around an isolated building. The significance of this different flow field should be focused on not only from structural but also from environmental viewpoints because the flow field determines wind pressure distributions and the degree of scalar dispersion. Flow field conditions are strongly dependent on building geometry and arrangement characteristics, more or less incident flow conditions, by interacting and overlapping, which governs the wind force/pressure characteristics as well as the nature of ventilation and dispersion of pollutants in urban street canyons.

Wind pressure measurements for a low-rise building in a large group have been performed by many researchers (Sun et al., 2008; Kim et al., 2011, 2012). Sun et al. (2008) investigated peak pressure coefficients through a number of wind tunnel tests, and reported that shielding effects generally depend on area density and relative height ratio between the target building and surrounding buildings, and although the shielding effects were significant in most cases, the positive peak wind pressure coefficients were increased by 100% in some cases. Most recently, Kim et al. (2011, 2012) measured fluctuating wind pressures applied to a cubical low-rise building immersed in various area densities and long upstream distances under suburban flow conditions. After a detailed examination of wind pressures and forces characteristics, methodologies of wind load estimation were suggested based on the interference factor for the structural frame and zoning interference factor for components and cladding.

The remarkable growth in computer technology has enabled increasing application of numerical simulations to a large group of low-rise buildings to the problems including wind loads,

flow conditions and pollutant dispersion. Much of the works have focused on investigating the flow and pollutant dispersion problems within urban street canyons using the RANS turbulence model. Chang and Meroney (2003) investigated the effect of surrounding buildings with different separation distances on flow distributions and transport from steady point sources of pollutants, or chemical and biological agents, in an idealized urban environment. Lien and Yee (2004) studied the neutrally-stratified flow within and over a large group of 3-dimensional cubical buildings using two turbulence models: the standard k-ε model and the Kato-Launder k-ε model. Santiago et al. (2007) examined the wind flow and pollutant dispersion inside and above a three-dimensional cubic array to describe and explain the flow structure and tracer dispersion using the standard k-ε turbulence model.

Most recent numerical studies have discussed flow and pollutant dispersion, and although some previous studies have discussed the pressure and flow field for a target low-rise building in large group, the simulated area density was very limited, mostly an area density of 25%. The purpose of the present study was to investigate the pressure and flow field for a target low-rise building immersed in various area densities ranging from 6% to 44% by comparing numerical results with wind pressure measurements and flow visualizations using a DPIV system. For the numerical simulation, three-dimensional RANS turbulence models were implemented.

2 WIND TUNNEL TEST AND COMPUTATIONAL FLUID DYNAMICS

Wind tunnel tests were conducted at the Tokyo Polytechnic University in Japan. A 0.1m cubical building model was used for the target low-rise building, and the same sized cubes made of wood were used as dummy models. Area density, C_A, was defined as the ratio of the area covered by the building to the building lot area, and varied as 6%, 11%, 16%, 25%, and 44%. A schematic of the wind tunnel test is shown in Figure 1, and the experimental procedures were as follows.

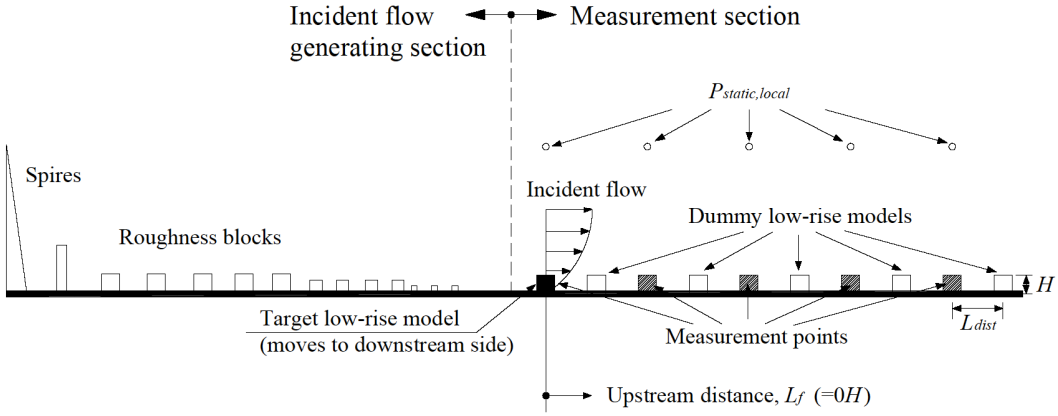

Figure 1. Schematic of wind tunnel test

As shown in Figure 1, half the wind tunnel was used as an incident flow generating section using spires, barriers, and three different-sized blocks. The incident flow was measured at L_f=0H. To clarify the effect of surrounding buildings, the wind pressure measurement of the isolated model was conducted at L_f=0H. After arranging the dummy low-rise models, the wind pressure measurements for the target model were conducted by moving it downstream at specified intervals determined by area density. Here, the term “target model” is used to indicate the model surrounded by dummy low-rise models in order to differentiate it from “isolated model”. In previous studies,

the dummy models were arranged on the upstream side while the target model was fixed at a position. But in the present study, the target model was moved to the downstream side, which makes the changes of wind pressures and flow conditions more understandable depending on various area densities and upstream distances. The number of measurement points was dependent on area density, and there were 9 measurement points for area densities of 11%, 16%, and 44%, and 6 measurement points for area densities of 6% and 25%. 125 pressure taps were installed, and all pressures were measured simultaneously using a multi-channel pressure measurement system, and the tubing effects were numerically compensated using the gain and phase shift characteristics of the pressure measurement system. As an incident flow, a turbulent boundary layer representing a suburban area with a power-law exponent of 0.2 (U_H≈7.2m/s, $I_{u,H}$≈23%) was simulated as shown in Figure 2 (thick solid line). The Reynolds number based on U_{ref} and B was about 5×10^4, and the wind direction was fixed at 0˚, with the incident wind normal to the model surface.

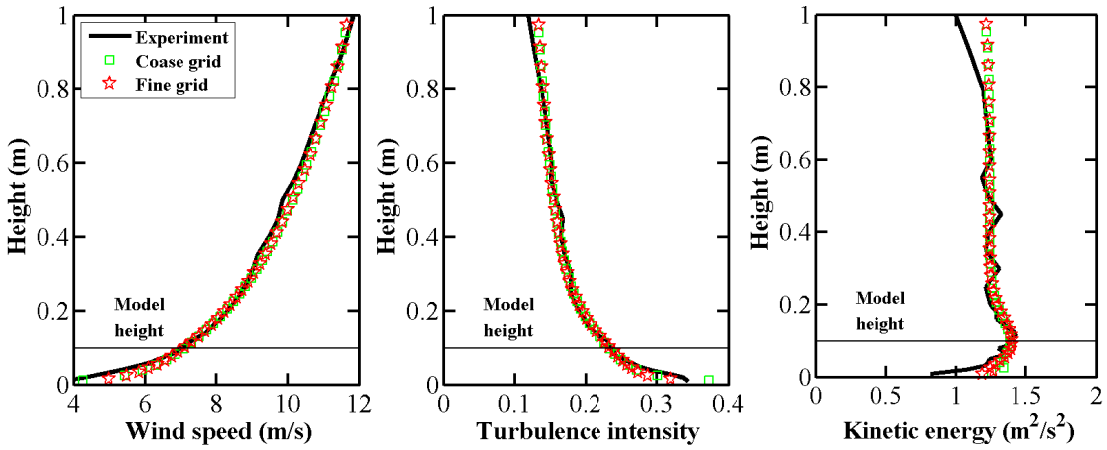

Figure 2. Comparison between incident flow conditions from wind tunnel test and simulation

Flow visualization using a Dynamic Particle Image Velocimetry (DPIV) system was carried out in a Boundary Layer Wind Tunnel at Shimizu Institute of Technology, Japan. The system consisted of a high-speed digital video camera, a double pulse ND: YAG laser, and a particle generator. Tracer particles were discharged from the particle generator, which was located at the end of the group of low-rise buildings, and then circulated in the wind tunnel. The particles were illuminated by a pulsed laser light sheet. The image size was adjusted to be large enough to adequately capture the flow field. A pixel resolution of 800×600 was used, and 2000 pictures were taken, resulting in sampling frequencies of 1000 frames per second. The measuring time was set to 2.95 seconds (5900 pictures).

Fluent, included in the package of ANSYS 13.0, was used to carry out all numerical simulations based on the finite volume method. In the present study, well-known turbulent Reynolds Averaged Navier-Stokes (RANS) models, the standard k-ε model and the rng k-ε model, were used for the turbulent flow of an incompressible viscous fluid. The modified law-of-the-wall function was used in combination with RANS turbulence models. As input parameters for the modified law-of-the-wall function, K_S and C_S needed to be input to the solver, and K_S and C_S were determined using the incident flow from the wind tunnel test considering the relationship between K_S and z_0 for the fully rough regime (Blocken et al., 2007). The obtained z_0 for the incident flow was 4.76×10^{-4}, and using C_S =1, K_S was set to 0.001 for the wind tunnel's floor roughness condition. Note that this K_S was smaller than y_P, which is the distance from the floor to the center point P of the wall adjacent to the cell. The boundary conditions of the two sides and the

top were modeled as slip walls, and the free outlet boundary condition was used. Inlet profiles for streamwise mean wind speed, turbulent kinetic energy, and turbulent dissipation rate were simulated using a user-defined function. Turbulent kinetic energy was obtained considering only the streamwise fluctuating component, and turbulent dissipation rate was obtained assuming local equilibrium of $G_k=\varepsilon$ (Tominaga et al., 2008). Lateral and vertical wind speeds were assumed to be zero. For the isolated model, two grid systems were employed: a coarse grid with y^+ larger than 61 and a fine grid with y^+ larger than 30. The simulated profiles at the model position in the empty three-dimensional computational domain are shown in Figure 2 for the fine and coarse grids, and show good agreement with incident flow from the wind tunnel test regardless of the y^+ values. Here, the reference wind speed U_{ref} means the mean wind speed at the model position. Other important computational conditions and the position of the target model are summarized in Table 1. For the isolated model, two grids were employed to examine the grid dependence of the results, and for the target model, the computational domain was reduced considering the symmetry condition. One example of a grid for the target model when C_A=25% is shown in Figure 3.

Table 1 Computational conditions

		C_A=0%	C_A=6%	C_A=11%	C_A=16%	C_A=25%	C_A=44%
Computational Domain (X×Z×Y, unit: H)		21×10×7	49×10×2	51×10×1.5	51×10×1.25	49×10×1	51×10×0.75
Target Model Position (L_f, unit: H)		0	8 and 24	6 and 24	5 and 25	8 and 24	6 and 24
Pressure-velocity Coupling		SIMPLE					
Spatial Discretization		QUICK					
Convergence Criteria		Continuity: 10^{-6} Others: 10^{-6}					
Grid Number (X×Z×Y)	Coarse Grid	60×33×39	293×19×41	336×16×41	352×14×41	395×12×41	416×9×41
	Fine Grid	117×47×52					
y^+	Coarse Grid	$61<y^+<263$	$57<y^+<395$	$54<y^+<398$	$62<y^+<400$	$54<y^+<401$	$27<y^+<420$
	Fine Grid	$30<y^+<357$					
y_P (simulation scale, m)	Coarse Grid	0.00514	0.00629				
	Fine Grid	0.00262					
Grid Expansion Factor (y_i/y_{i+1})		Less than 1.2					

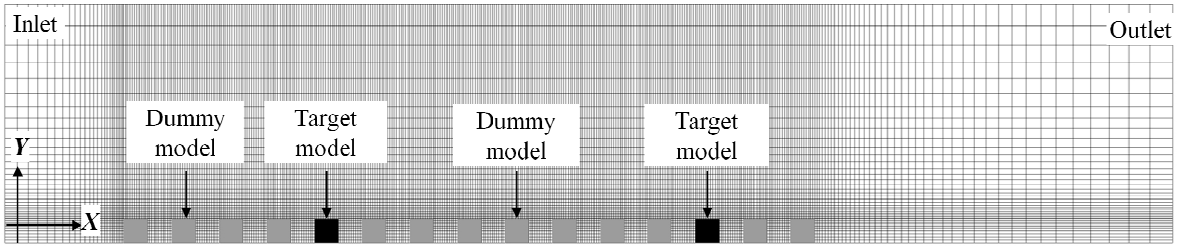

Figure 3. Grid for target model when C_A =25%

3 RESULTS AND DISCUSSION

3.1 *Results for isolated model*

Mean wind pressure coefficients are defined as:

$$\overline{C}_p = \frac{\overline{P} - \overline{P}_{ref}}{0.5\rho U_{ref}^2} \tag{1}$$

where, $\overline{P}$ is the time-averaged surface pressure and $\overline{P}_{ref}$ is the time-averaged reference static pressure in the computational domain, which is at exactly the same position as the pitot tube in the wind tunnel test.

Figure 4 compares the mean wind pressure coefficients from the wind tunnel test with the simulation results from the coarse and fine grids. Differences are observed near the stagnation point on the windward surface and on the leading edges of the roof and side surfaces where large suctions occur due to the separated shear layer. On the leeward surface, the simulation results show slightly larger values than the experimental values (smaller absolute value). From the different turbulence models, clear differences are also observed near the stagnation point and leading edges. For the standard k-ε model, the mean wind pressure coefficient near the stagnation point is larger than unity, which is theoretically impossible and which is also much larger than the experimental values. Contrary to the results of the standard k-ε model, those of the rng k-ε model show relatively good agreement with the experimental results on the windward surface. On the side surfaces, the variation trend of the rng k-ε model is similar to that of the experimental value, but the values are much larger than the experimental results and the standard k-ε model results. Focusing on the smallest mean wind pressure coefficient (larger absolute value), it seems that the standard k-ε model results in more reasonable but slightly conservative values. There is little difference between the pressure coefficients on the leeward surface given by the two turbulence models, and it is interesting to note that almost the same results were obtained for the two different grids, although the fine grid gives slightly larger absolute values.

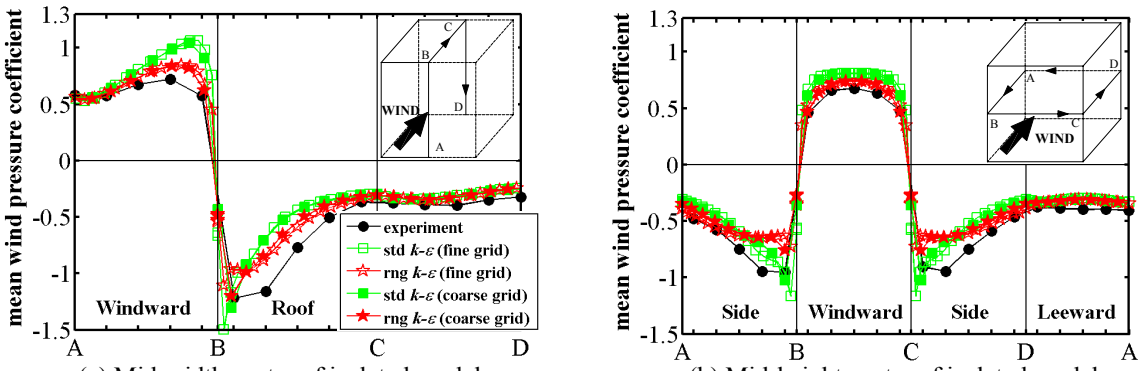

(a) Mid-width center of isolated model (b) Mid-height center of isolated model

Figure 4. Comparison of mean C_p for isolated model

Wind pressure coefficients at mid-width center were compared quantitatively using three statistical parameters, normalized mean square error (NMSE, Eq. (2)), fractional bias (FB, Eq. (3)), and correlation coefficients (R), and the results are summarized in Table 2. For comparison, the numerical results corresponding to pressure tap positions were selected. NMSE indicates a value of normalized discrepancies between the computed and experimental values, and FB gives

information about overestimation (negative value of FB) or underestimation (positive value of FB).

$$NMSE = \frac{1/n\sum_{i=1}^{n}(E_i - C_i)^2}{1/n\sum_{i=1}^{n}(E_i C_i)} \quad (2); \qquad FB = \frac{(E_i - C_i)}{0.5(E_i + C_i)} \quad (3)$$

As shown in Table 2, the NMSE of the rng k-ε model is very small compared to those of the standard k-ε model on the windward and roof surfaces, while that on the leeward surface is almost the same. As expected, the FB of the windward surface is negative, while those of the roof and leeward surfaces are positive, meaning that the numerical results are overestimated for the windward surface and underestimated for the roof and leeward surfaces. The FB of the rng k-ε model is smaller than that of the standard k-ε model, showing especially large differences on the windward surface. Like NMSE, FB shows little difference on the leeward surface. Similar observations can be made for correlation coefficient R. Considering the different grids, NMSE and FB obtained from the coarse grid are smaller than those obtained from the fine grid, implying that the numerical results from the coarse grid better correspond to the experimental results, but the differences between them are not significant. The statistical parameters at mid-height center show a similar trend to the mid-width center, generally showing numerical results from the coarse grid using the rng k-ε model in better correspondence with the experimental values.

Table 2 Comparison of normalized mean square error (NMSE), fractional bias (FB) and correlation coefficient (R)

		NMSE		FB		R for all points	
		std k-ε	rng k-ε	std k-ε	rng k-ε	std k-ε	rng k-ε
Fine Grid	Windward Surface	0.1	0.01	-0.23	-0.09	0.90	0.97
	Roof Surface	0.15	0.06	0.36	0.23		
	Leeward Surface	0.04	0.04	0.21	0.19		
Coarse Grid	Windward Surface	0.08	0.01	-0.21	-0.06	0.91	0.97
	Roof Surface	0.12	0.06	0.26	0.2		
	Leeward Surface	0.03	0.04	0.18	0.18		

Using the numerical results obtained from the rng k-ε model with the coarse grid, prediction of peak pressure coefficients on the windward and roof surfaces were attempted, considering that the largest maxC_p occurred on the windward surface (maxC_p≈2.95) and the smallest minC_p occurred on the roof surface (minC_p≈-4.75). The largest maxC_p was obtained near the stagnation point, and the smallest minC_p was obtained at pressure tap near the edges. For the pressure taps shown as solid thick lines in Figure 5, the relationship between normalized turbulent kinetic energy (k/U_{ref}^2) and fluctuating wind pressure coefficients (rmsC_p) were examined, and the results are shown in Figure 5. There is a clear linear relationship between them, implying that rmsC_p can be estimated by k/U_{ref}^2. From these relationships, peakC_p values were obtained from various peak factors (g). The comparisons are shown in Figure 6, showing good agreement with the experimental data when $g_{\max}$=5 for windward and $g_{\min}$=-6 for roof surface.

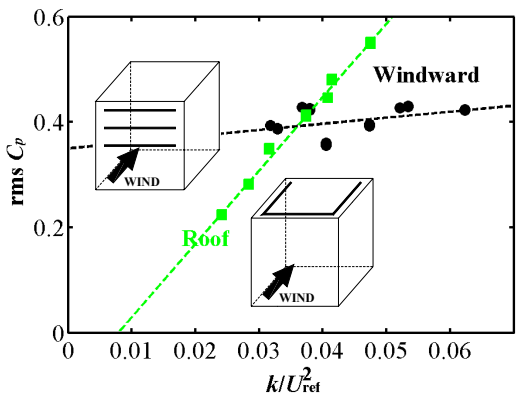

Figure 5. Relationship between k/U_{ref}^2 and rmsC_p

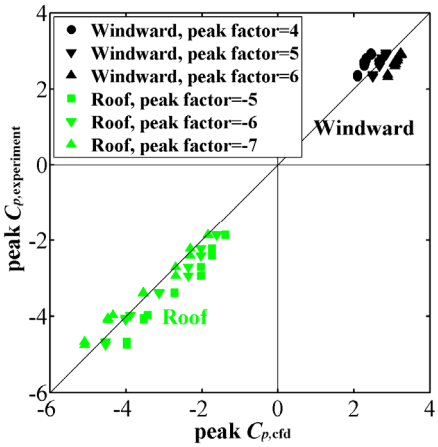

Figure 6. Comparison of peakC_p from numerical and experimental results

The flow conditions on the roof are shown in Figure 7 using contours of mean wind speed and streamlines for the coarse grid. The black rectangle indicates the isolated model, and the gray region in Figure 7(a) indicates a mask region where the particles cannot be captured by the high-speed digital video camera. From the DPIV result in Figure 7(a), it is not clearly ascertained but there is a reverse flow region on the roof. This region is well reproduced by the rng k-ε model (Fig. 7(c)), but not by the standard k-ε model (Fig. 7(b)).

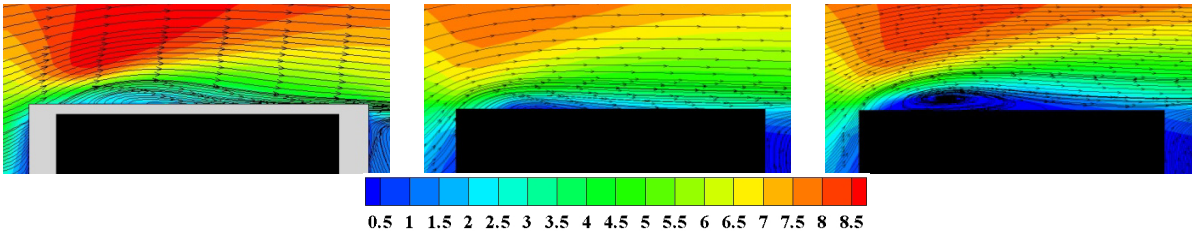

(a) DPIV (b) Standard k-ε (c) Rng k-ε

Figure 7. Contours of wind speed and streamlines on roof of isolated model

The flow fields measured and simulated at mid-height center are shown in Figure 8 for the coarse grid. The three black rectangles indicate half the isolated model adjusted to the same scale, making direct comparison possible. The flow field including the circulation in the wake seems to be simulated appropriately, but some differences were found. The circulation center (red solid circle) and wake center (red solid square) move to the downstream side for the simulation results, and the deviation is more for the rng k-ε model. There is reversed flow on the side surface for the rng k-ε model as on the roof, and these reverse flows are responsible for the larger mean wind pressure coefficient

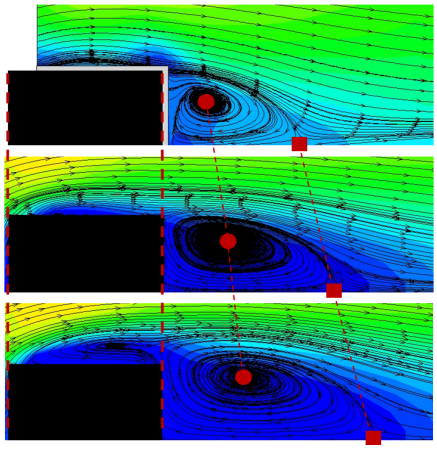

(a) DPIV

(b) Standard k-ε

(c) Rng k-ε

Figure 8. Comparison of flow field of isolated building for mid-height center

(smaller absolute value) on the leading edge on the roof and side surfaces, as shown in Figure 4. The results for the flow fields of the fine grid show a similar trend.

Summarizing the above results, it was found that there is clear dependence of wind pressure on the turbulence models, but little dependence on grid, meaning that the numerical simulations for the grids with (30~61)<y^+ result in almost identical results. Thus, the simulation of the target model surrounded by a large group of dummy models was conducted for the grid with (30~62)<y^+<(roughly 400).

3.2 *Results for target model*

Figure 9 shows the variation of mean wind pressure coefficients derived from wind tunnel tests (solid and open circles), the standard k-ε model (solid and open squares), and the rng k-ε model (solid and open stars) at mid-width and mid-height center at L_f/H=8 and 24 for various area densities. Note that as only half of the target model was used in the simulation, the results from half the windward and leeward surfaces were used for the mid-height center. For all area densities, the variation trends of the numerical results along the two centers are similar to the experimental results, and correspondence becomes better at higher area density. For example, the mean wind pressure coefficients on the windward surface decrease with area density, and at higher area density the coefficients at all surfaces become similar. However, large differences were found near the separation region on the roof and side surfaces as for the isolated model, showing larger values than the experimental results (smaller absolute value). But the differences in the turbulence models are generally small for all surfaces at different upstream distances, showing similar degrees of correspondence to the experimental results.

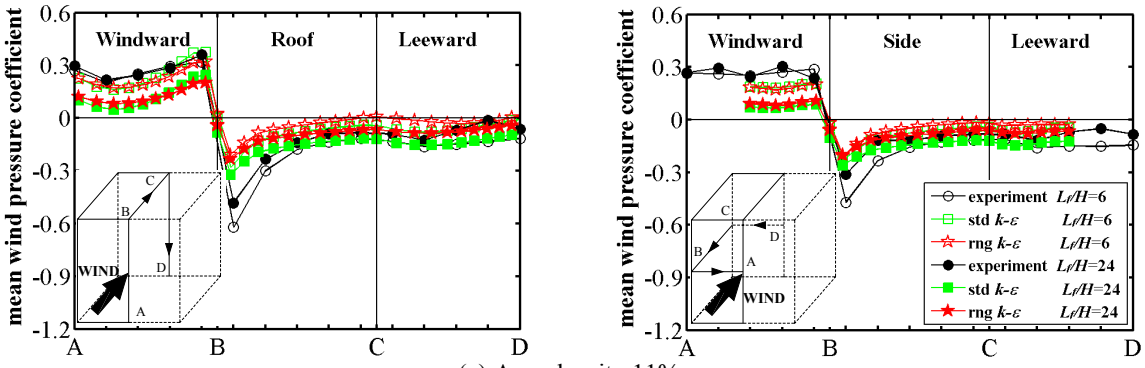

(a) Area density 11%

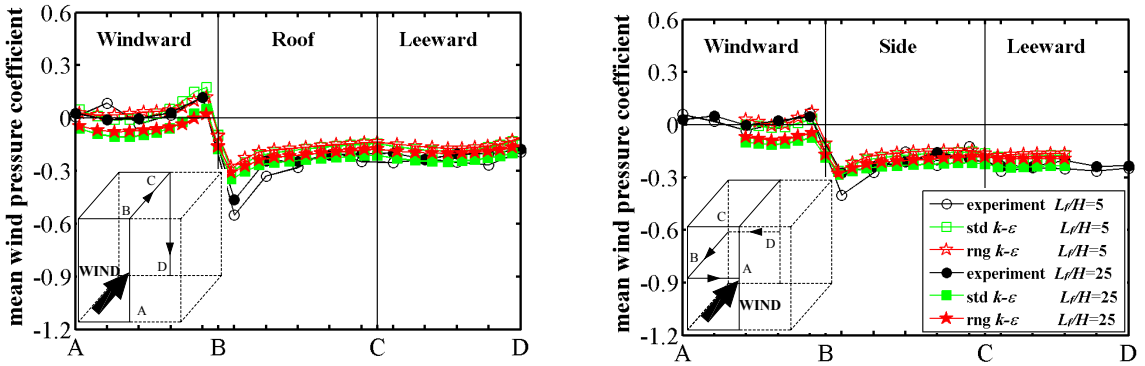

(b) Area density 16%

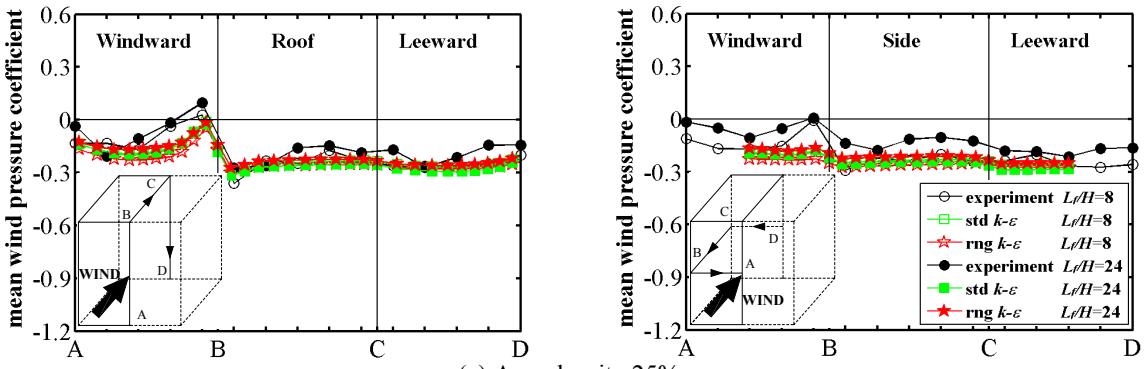

(c) Area density 25%

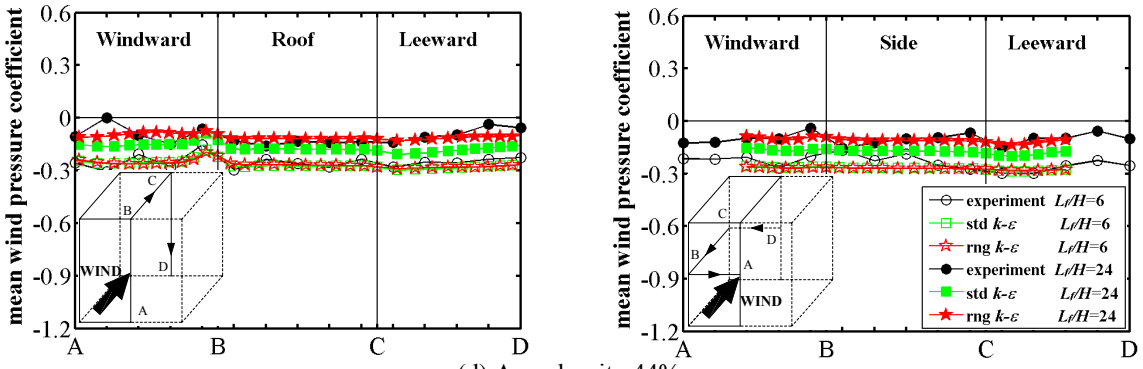

(d) Area density 44%

Figure 9. Comparison of meanC_p for various area densities (Mid-width center (left) and mid-height center (right))

3.3 Flow over large group of low-rise buildings

The variations of mean wind speed and turbulence intensity are shown in Figure 10. In simulation and experiment, the profiles were measured without the target model, and in the wind tunnel tests the profiles were measured from 0.1m (model height) to 0.4m using hot wire. The mean wind speed profiles from the wind tunnel tests and simulations agree well with each other, showing little differences depending on the turbulence models. But in the turbulence intensity profiles, the turbulence intensity for the standard k-ε model is slightly higher than that for the rng k-ε model when the height is less than 0.4, and is more consistent with the wind tunnel test results. The profiles from the standard k-ε model seem to be more similar to the wind tunnel test results. For other area densities, similar results with a similar degree of correspondence to the experimental results were obtained.

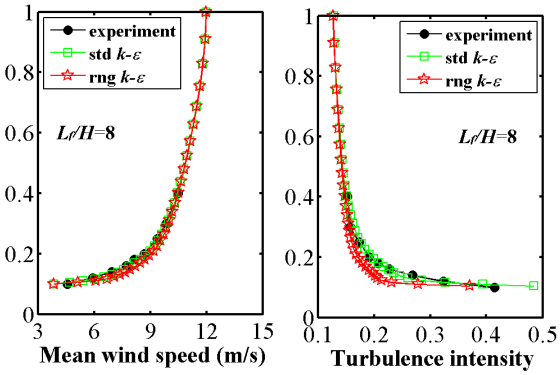

Figure 10. Comparisons of mean wind speed and turbulence intensity profiles at C_A=25%

4 CONCLUSIONS

Mean wind pressure coefficients of the isolated model obtained from the rng k-ε turbulence model match well with those from the pressure measurement. However, the differences in turbulence models were small for the target model in a large group, and the correspondence to experimental data was generally good, still showing some discrepancy near a large suction area. Using a limited number of pressure taps on the windward and roof surfaces, the prediction of peakC_p was attempted, and the results agreed with the experimental results, once the peak factors were given appropriately. For the flow field, the RANS turbulence models were able to reproduce the overall flow pattern around the model generally, but some differences were found i.e., the rng k-ε model provided reasonable simulation near the regions where large suctions occur, and in other many regions the standard k-ε model gave more similar results to experiment.

5 ACKNOWLEDGEMENTS

This study was funded by the Ministry of Education, Culture, Sports, Science and Technology, Japan, through the Global Center of Excellence Program, 2008-2012. The authors gratefully acknowledge their support.

6 REFERENCES

1 Blocken, B., Carmeliet, J., Stathopoulos, T., CFD evaluation of wind speed conditions in passages between parallel buildings-effect of wall-function roughness modifications for the atmospheric boundary layer flow, J. Wind Eng. Ind. Aerod., 95 (2007) 941-962.
2 Chang, C.H., Meroney, R.N., Concentration and flow distributions in urban street canyons - wind tunnel and computational data, J. Wind Eng. Ind. Aerod., 91 (2003) 1141-1154.
3 Kim, Y.C., Yoshida, A., Tamura, Y., Characteristics of surface wind pressures on low-rise building immersed in large group of surroundings, Eng. Struct., Vol. 35 (2011) 18-28.
4 Kim, Y.C., Yoshida, A., Tamura, Y., Influence of surrounding buildings on wind loads acting on low-rise building, J. Struct. Eng., ASCE, (To be published) (2012)
5 Lien, F.S., and Yee, E., Numerical modeling of the turbulent flow developing within and over a 3-D building array, Part I: A high-resolution Reynolds-Averaged Navier-Stokes approach, Boundary-Layer Meteorol., 112 (2004) 427-466.
6 Santiago, J.L., Martilli, A., Martin, F., CFD simulation of airflow over a regular array of cube. Part I: Three-dimensional simulation of the flow and validation with wind-tunnel measurements, Boundary-Layer Meteorol., 122 (2007) 609-634.
7 Sun, Y., Tamura, Y., Quan, Y., Matsui, M., The interference effect of surrounding roughness on wind pressures of rectangular prism, 6th Int. Colloquium Bluff Bodies Aerody. Appl., 2008, pp. 1-10.
8 Tominaga, Y., Mochida, A., Yoshie, R., Kataoka, H., Nozu, T., Yoshikawa, M., Shirasawa, T., AIJ guidelines for practical applications of CFD pedestrian wind environment around buildings, J. Wind Eng. Ind. Aerod. 96 (2008) 1749-1761.

The Seventh International Colloquium on Bluff Body Aerodynamics and Applications (BBAA7)
Shanghai, China; September 2-6, 2012

Experimental simulation of downburst-generated wind loading on building structure

Honghai Li [a], Jinping Ou [a, b]

[a] *School of Civil Engineering, Harbin Institute of Technology, Harbin Heilongjiang Province, China*
[b] *Faculty of Infrastructure Engineering, Dalian University of Technology, Dalian Liaoning Province, China*

ABSTRACT: This paper figures the resulting wind loading on a building structure, as observed in the wind tunnel. In the laboratory, the natural downburst downdraft phenomenon and spreading out is replicated using a round jet impinging onto a flat plate. An extensive experimental simulation was conducted to study the effects of the static downburst at various distances from the prismatic building structure to the jet. The outcome is better understanding of wind loading on buildings produced by downburst generated outflows and this paper evaluates the reliability of experimental simulation to simulate downburst type wind loads on buildings.

KEYWORDS: wind loading; downburst; building aerodynamics; impinging wall jet model

1 INTRUDUCTION

Downburst is a weathering phenomenon occurred within a thunderstorm. When the severe convection of atmosphere developed into the vigorous stage, the weight of the precipitation acts to accelerate the air downwards. In the regions where the thunderstorm happens frequently, the strong downward air current could get together in a very short time and suddenly hit the ground surface, the diffusion of the reflected air is expanding in all directions with high wind velocity. So, the downburst is characterized by an intense localized downwards and an outburst of strong winds near the ground.

Fujita described downburst as a small downdraft having an outburst of damaging winds with the horizontal extent of the damaging winds being less than 4 km [1]. A strong downburst can result in damaging winds near 75 m/s. Vickery & Twisdale found that up to 75% of the peak gust wind speeds occurred during thunderstorms [2]. This kind of disaster can destroy the main body of the structures and their exterior-protected construction both. The annual insured property loss from thunderstorm winds in the U.S.A. is $1.4 billion on an average. Almost all of the damages due to thunderstorms can be assumed to be caused by intense downdraft winds, downbursts.

2 DOWNBURST MODEL

Two methods have been used in general to simulate and study downburst outflow characteristics. These are the impinging wall jet model and the “ring vortex” model (Fig. 1).

There is a steady flow against a flat plate in the impinging wall jet model. This impingement gives rise to a wall jet. As air touches the ground, the vertical component of the wind decelerates downwards and the horizontal component of the wind accelerates outward from the impact center. So, the impact pressure field is generated. However, there are no hydrostatic pressure changes in this model.

In the second type of model, the downwards flow shapes into a vortex ring before approaching the ground. After touchdown, it is the radial outflow, which influences the surface structures. In conclusion the first model seems to replicate the effects of downburst better. The schematic of a wall jet for JAWS is shown in Figure 2 [3].

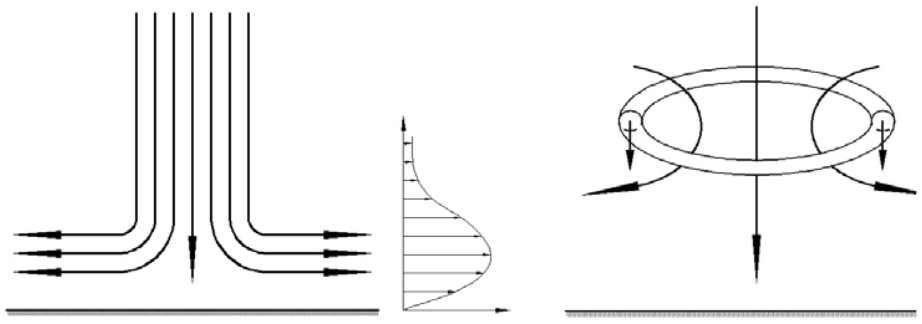

Figure 1 downburst model (a) impinging wall jet model (b) ring vortex model

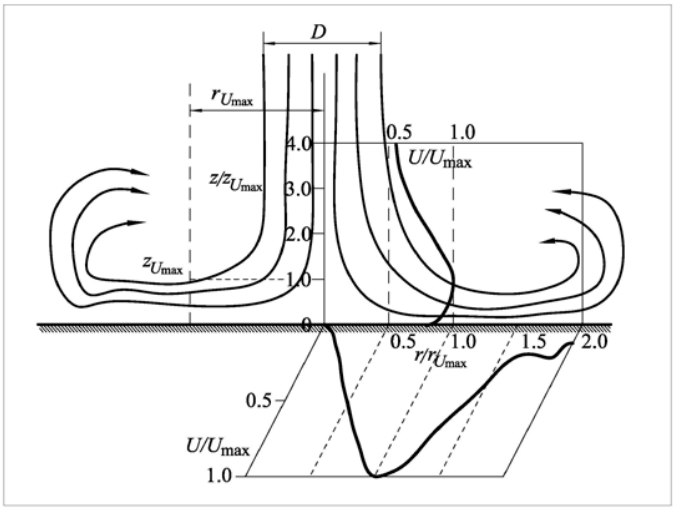

Figure 2 JAWS downburst Schematic [3]

3 EXPERIMENTAL SIMULATION

The current research focuses on the simulation of a stationary downburst using experimental methods.

Compared with the natural boundary layer type wind flow, the extent of work done to study the effects of downburst wind on civil engineering structures is very limited. Only a few case studies on downburst-generated wind loading on building structures have been found in the literature.

The first to use an impinging jet model to simulate downburst were Selvam and Holmes [4]. And then, Holmes [5] and Letchford and Illidge [6] undertook physical model studies of a jet impinging on a wall to study topography effects in downburst. Savory et al. [7] also studied the effects of failure of lattice transmission towers due to tornado and downburst induced wind loading. Sengupta et al. [8] studied the pressure distribution on a cubic building. Chay and Letchford

[9] also studied the effects of stationary jet on cubic building models and used a translating jet (which was moved manually) to see the effects to jet translation speeds [10]. Sengupta and Sarkar [11-13] have reported their findings on laboratory and numerical simulation of both static and translating downbursts and compared them to wind loads on cubic as well as tall buildings due to a translating tornado using the Tornado/Downburst Simulator in the WiST laboratory at Iowa State University. Lin and Savory [14], Kim and Hangan [15] have studied the outflow velocity characteristics and the effects of these wind fields over buildings.

Because the downburst is sudden and random occurrence in nature, there is currently no field data available for study. So, the only possible mechanism to study the effects of downburst type of wind loads on buildings is through laboratory simulation. The primary objective of the present work was to perform a systematic parametric study of laboratory simulation of stationary downburst using an impinging jet to determine the pressure distribution on cube-shaped buildings. The effects of the building's location with respect to the center of the downburst were the main focus of the parametric study.

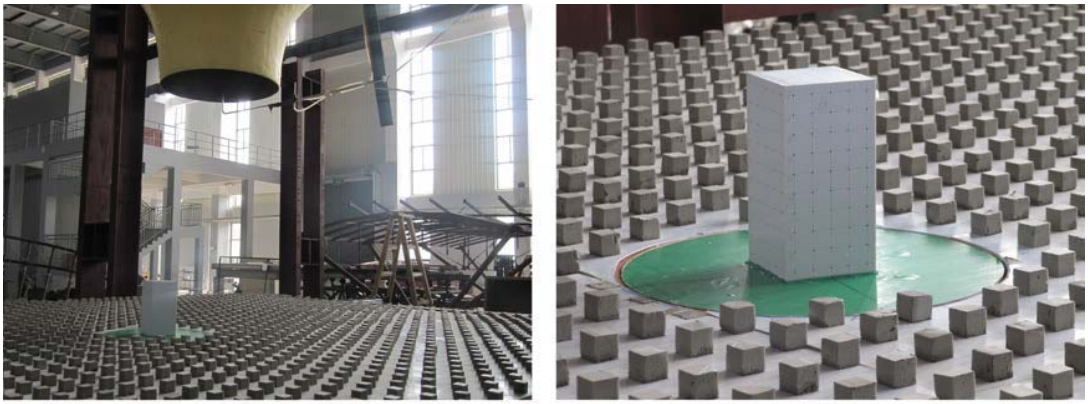

(a) (b)

Figure 3 (a) the equipment of the experimental simulation (b) model building dimensions and pressure tap locations

The experimental setup is shown in Figure 3(a). Here the downburst is modeled as an impinging jet coming out of a pipe and hitting against on a flat wooden board placed below. Roughness elements situated on the plate uniformly could establish the essential coincidence between the experimental simulation and the downburst wind practical condition. The diameter (D) of injection nozzle used to generate the impinging jet was 500 mm. The height (H) of the injection nozzle from the ground board was 1000 mm. So, H/D = 2 was resulted. And the impinging jet velocity was used, V = 10 m/s. This resulted in a Reynolds number of 3.45×10^5 based on the diameter of injection nozzle (D). The building model was made of rigid plastics. The structure is designed as a high-rise building and the size is set as 100 mm (W, 0.1D) × 100 mm (L, 0.1D) × 200 mm (H, 0.2D). The main focus of the parametric study was the location with respect to the center of the downburst of the building model. For the current work, L1 = 0 mm (0D), L2 = 250 mm (0.5D), L3 = 300 mm (0.6D), L4 = 400 mm (0.8D), L5 = 450 mm (0.9D), L6 = 500 mm (1.0D), L7 = 550 mm (1.1D), L8 = 600 mm (1.2D), L9 = 750 mm (1.5D) were used as a series of the various distances from the model to the injection nozzle.

Digital pressure transducers were used to measure the pressures on the surface of the building model. Pressure taps were uniform distributed on the building model that were tested on the front, back, left, right and top surfaces. A total of 225 pressure taps were used with 25 taps on the top surface and 50 taps on the each surface of the others. The arrangement of pressure taps for the building model is shown in Figure 3(b). Four 64-channels scanning valve pressure trans-

ducers were used to measure both the static and fluctuating pressures on the building model. And the sampling rate to acquire the data was 312.5Hz.

4 RESULTS AND DISCUSSION

The pressure coefficient Cp was normalized with the impinging jet velocity V, where Cp is defined as:

$$C_P = \frac{P - P_s}{0.5\rho V^2} \tag{1}$$

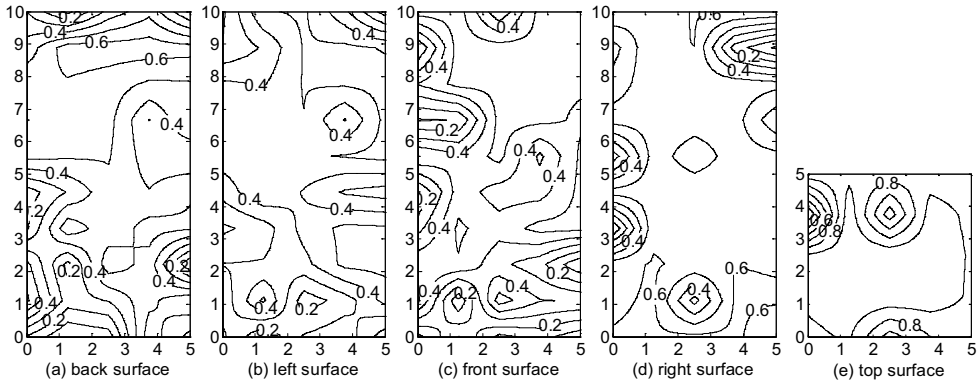

Figure 4 pressure coefficient for building model at 0D

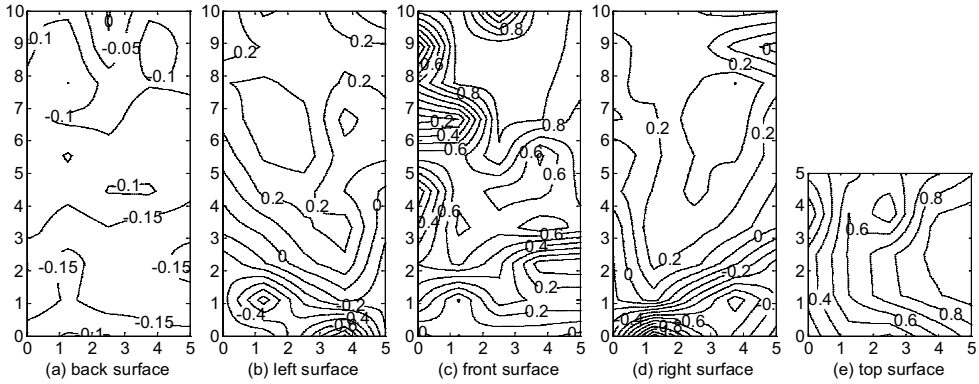

Figure 5 pressure coefficient for building model at 0.5D

The building model is placed directly under the direct impact of the jet downdraft in Figure 4. The impinging jet downwards reaches the top of the building model before attacking on the plate. Not only is the top surface subjected to a significant amount of negative lift, but also the other surfaces are suffering the pressure of the downburst wind.

At location 0.5D (Fig. 5), same as the building location 0D, there is no flow separation on the top of the building model. The top surface is still partly under the injection nozzle and the pressure distribution is still positive. But the pressure on the back surface is reduced obviously and the wind loadings on the left and right surfaces are decreased slightly. Meanwhile, the front surface is endured stronger wind and the pressure is raised perpendicularly.

As mentioned above, the building model is subjected to a downward force on the top surface and a positive pressure on the front surface. This wind loading generated by downburst is different from those produced by natural wind with a regular straight line type flow, and is not considered in the current design practice.

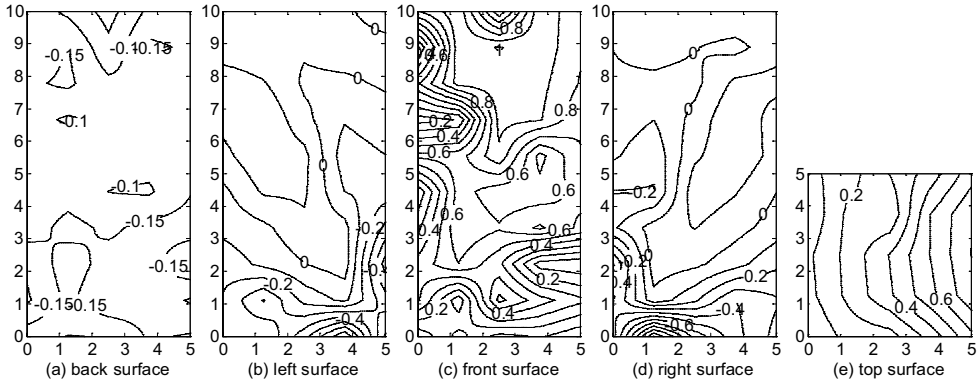

Figure 6 pressure coefficient for building model at 0.6D

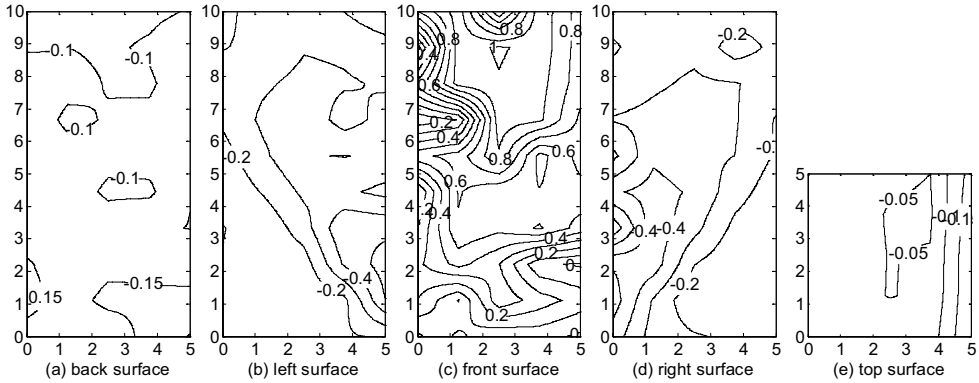

Figure 7 pressure coefficient for building model at 0.8D

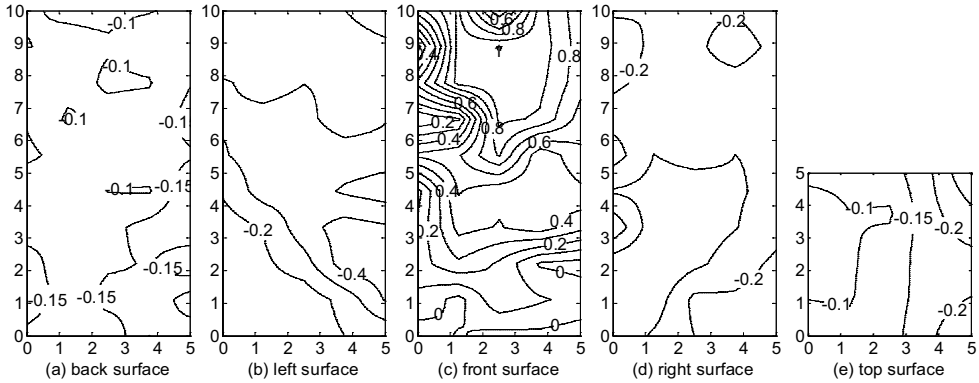

Figure 8 pressure coefficient for building model at 0.9D

When the building model is at a distance of 1.0D from the center location of the injection nozzle, the front surface is subjected to higher positive pressures. Though the pressure distribution on the back surface of the building model is identical almost, there is some difference on the

top surface and the left and right side faces. It can be seen that the pressure distributions are observed to change: the suction or negative pressure is generated (Figs 6-11).

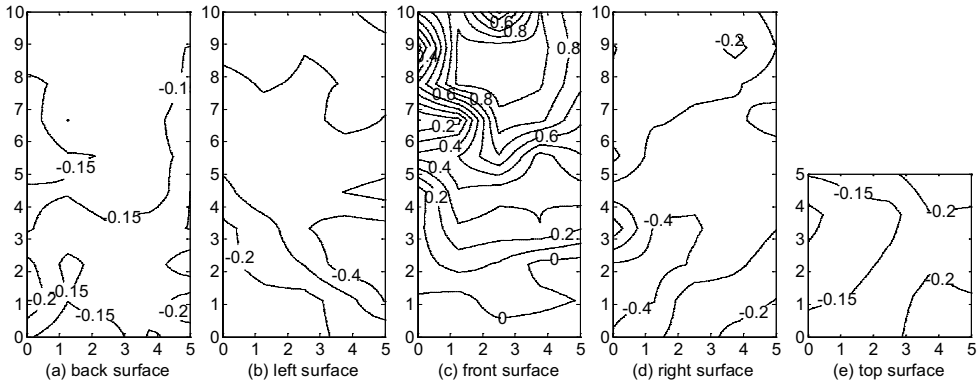

Figure 9 pressure coefficient for building model at 1.0D

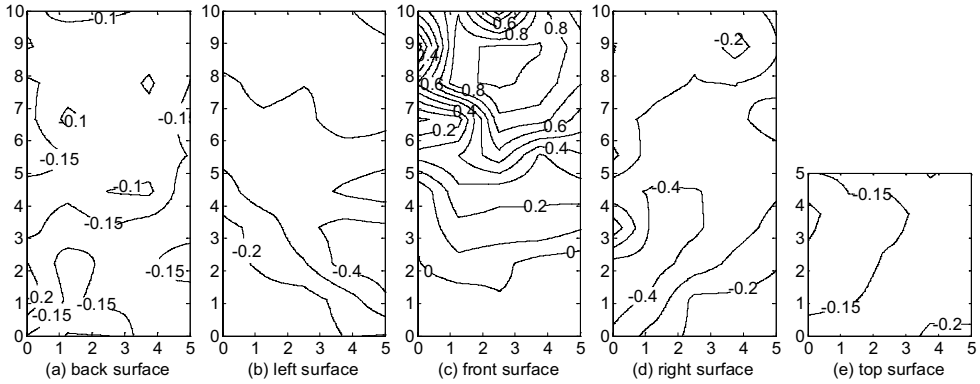

Figure 10 pressure coefficient for building model at 1.1D

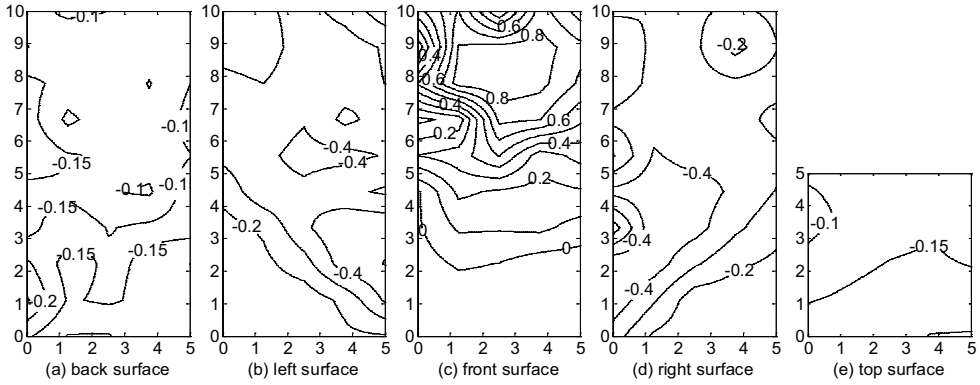

Figure 11 pressure coefficient for building model at 1.2D

When the building is placed at 1.5D (Fig. 12), the positive pressure on the front surface is reduced clearly and the negative pressure on the left and right side face and the top surface is decrease appreciably. So the effect of downburst on the building model is turn to be weakened.

Based on the experimental simulation results, four conclusions can be made with respect to the wind loading generated by downburst on the surface of the prismatic building structure.

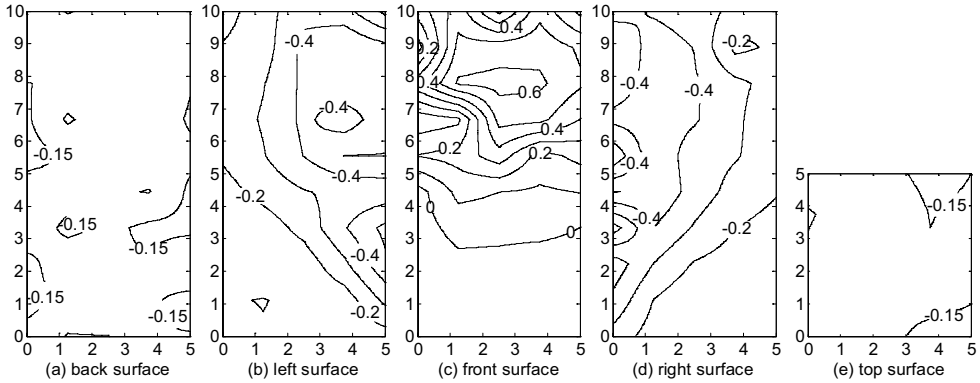

Figure 12 pressure coefficient for building model at 1.5D

The first is that the building is subjected to the maximum wind pressure when it is exactly under the injection nozzle (0D). (Fig. 13)

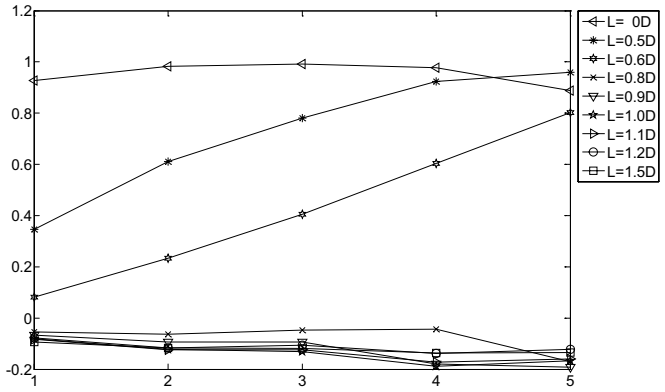

Figure 13 pressure coefficient on top surface

Secondly, the maximum positive pressure on the building is generated when the building is located at 1D from the center of the impinging jet. (Fig. 14)

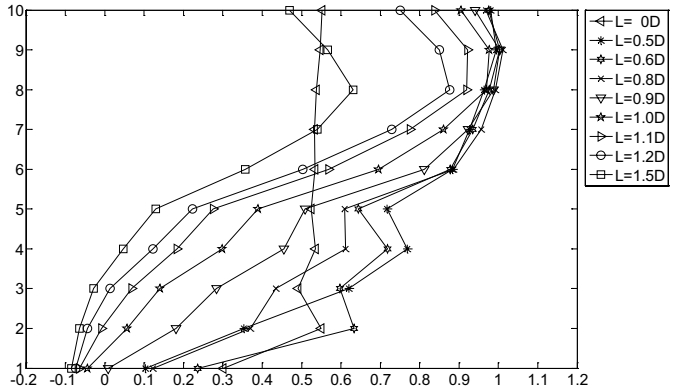

Figure 14 pressure coefficient on the front surface

Thirdly, the pressure distributions on the left and right surfaces are converted form positive pressure to negative pressure for building location 0.8 D and beyond from the center of the injection nozzle. (Fig. 15-16)

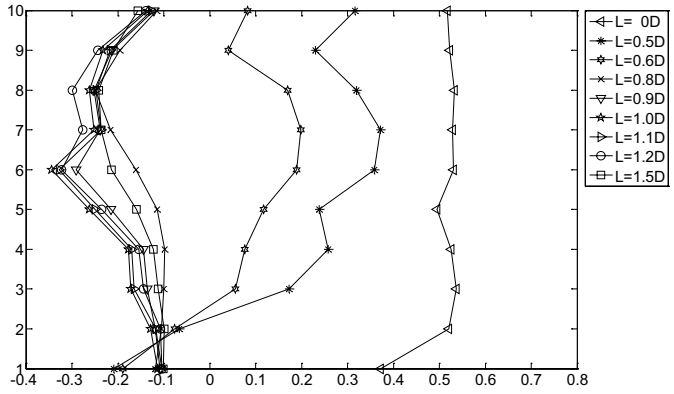

Figure 15 pressure coefficient on the left surface

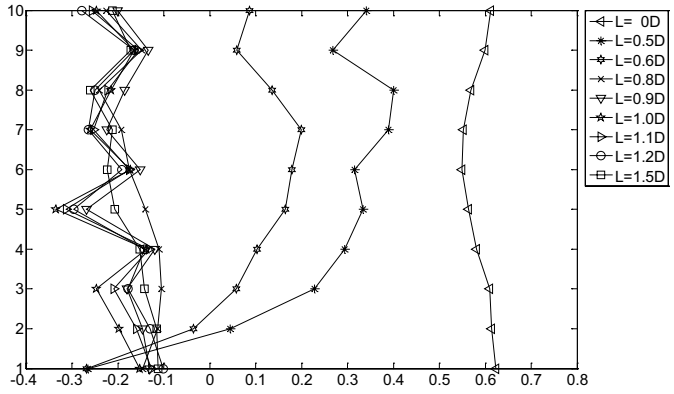

Figure 16 pressure coefficient on the right surface

Fourthly, the wind loading on the back surface is smaller than the other surfaces all but the placed 0D. (Fig. 17)

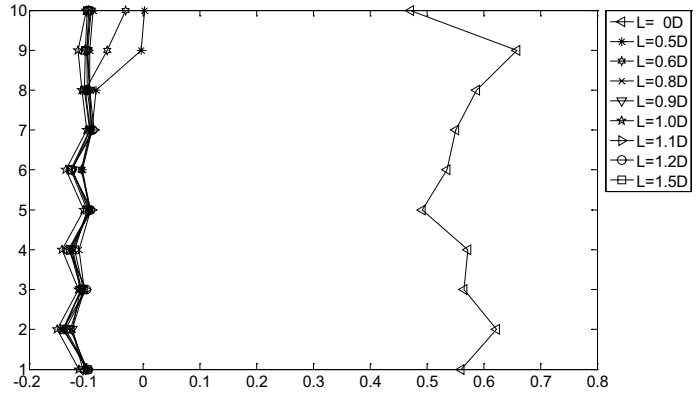

Figure 17 pressure coefficient on the back surface

The maximum and the mean values of pressure coefficients on the surfaces of the building model are given in table 1.

Table 1. the maximum and the mean values of pressure coefficients on the building surfaces

Loca-	Back surface		Left surface		Right surface		Front surface		Top surface	
tions	Max	Mean	Max	Mean	Max	Mean	Max	Mean	Max	Mean
L=0	0.6589	0.5617	0.5371	0.5083	0.6233	0.5874	0.5517	0.5105	0.9910	0.9532
L=250	-0.1405	-0.0844	0.3717	0.1992	0.4005	0.2351	0.9950	0.7311	0.9593	0.7242
L=300	-0.1392	-0.0958	0.1982	0.0664	-0.2678	0.0683	1.0037	0.7600	0.8015	0.4250
L=400	-0.1242	-0.1005	-0.2483	-0.1473	-0.2404	-0.1594	1.0114	0.6964	-0.1698	-0.0756
L=450	-0.1256	-0.1067	-0.2911	-0.1837	-0.2683	-0.1740	1.0026	0.6104	-0.1912	-0.1253
L=500	-0.1511	-0.1178	-0.3439	-0.2076	-0.3352	-0.2128	0.9773	0.5250	-0.1892	-0.1381
L=550	-0.1404	-0.1050	-0.3280	-0.1962	-0.3124	-0.2000	0.9221	0.4479	-0.1716	-0.1326
L=600	-0.1361	-0.1059	-0.3231	-0.2026	-0.2954	-0.1994	0.8762	0.3953	-0.1377	-0.1117
L=750	-0.1287	-0.1070	-0.2416	-0.1653	-0.2598	-0.1808	0.6308	0.2562	-0.1361	-0.1201

5 SUMMARY AND CONCLUSIONS

The primary mission of this work presented here was to subject an impinging jet to simulated downburst winds and to test a prismatic building model to study the aerodynamic loading.

Wind loadings on the building model at various distances from the center of the injection nozzle were studied. It was found that the top surface experienced a significant amount of pressure when it is straight under the center of the impinging jet. A symbol change in the loads on the building was generated by varying the distance. When the model placed at 1.0D, the wind loadings are somewhat greater than the other locations. This should be paid more attention in the practical engineering of the downburst-prone areas.

6 ACKNOWLEDGEMENTS

This research has been made possible through funding from the National Key Technology R&D Program (No. 2006BAJ03B04) for the 11th five-year plan. The information of the downburst was generously provided by Chao Li and Yang Zhao. Fei Wu's help are also acknowledged.

7 REFERENCES

1 T.T. Fujita, The downburst: microburst and macroburst, University of Chicago Press, 1985, 23.
2 P.J. Vickery and L.A. Twisdale, Analysis of thunderstorm occurrences and wind speed statistics, J. Wind Eng. Ind. Aerodyn., 1995, 55, 813-821.
3 M.R. Hjelmfelt, The Microbursts of 22 June 1982 in JAWS, J. Atmospheric Sciences, 1987, 44(12), 1646-1665.
4 R.P. Selvam and J.D. Holmes, Numerical simulation of thunderstorm downdrafts, J. Wind Eng. Ind. Aerodyn., 1992, 41-44, 2817-2825.
5 J.D. Holmes, Modeling of extreme thunderstorm winds for wind loading of structures and risk assessment, Wind Engineering into the 21st Century, Proc. of the 10th Intl. Conf. on Wind Eng. eds. A. Larsen *et al*., Denmark, June 1999, 1409−1415.
6 C.W. Letchford, and G. Illidge, Turbulence and topographic effects in simulated thunderstorm downdrafts by wind tunnel jet. Wind Engineering into the 21st Century, Proc. of the 10th Intl. Conf. on Wind Eng. eds. A. Larsen *et al*., Denmark, June 1999, 1907-1912.

7 E. Savory, *et al*., Modeling of a tornado and microburst-induced wind loading failure of a lattice transmission tower. Engineering Structures, 2001, 23, 365-375.
8 A. Sengupta, *et al*., Numerical and physical simulation of thunderstorm downdraft winds and their effects on buildings, 1st Americas Conference on Wind Engineering, Clemson, SC, 2001.
9 M.T. Chay and C.W. Letchford Pressure distributions on a cube in a simulated thunderstorm downburst, Part A: stationary downburst observations, J. Wind Eng. Ind. Aerodyn., 2002, 90, 711-732.
10 C.W. Letchford and M.T. Chay, Pressure distributions on a cube in a simulated thunderstorm downburst, Part B: moving downburst observations, J. Wind Eng. Ind. Aerodyn., 2002, 90, 733-753.
11 A. Sengupta and P.P. Sarkar, Physical and numerical simulation of microburst-like wind: A study of flow characteristics and surface pressures on a cube, Proc. 3rd Indian National Conf. on Wind Engineering, Kolkata, India, 2006.
12 A. Sengupta, *et al*., Transient loads on buildings in microburst and tornado winds, Proc. 4th Intl. Symp. on Computational Wind Engineering, Japan, 2006.
13 A. Sengupta and P.P. Sarkar, Computational and experimental simulation of static and transient loads on buildings in microburst winds. Proc. 12th Intl. Conf. on Wind Eng., Cairns, Australia, 2007.
14 W.E. Lin and E. Savory, Large-scale quasi-steady modeling of a downburst outflow using a slot jet, Wind and Structures. 2006, 9, 209-220.
15 J. Kim and H. Hangan, Numerical simulation of impinging jets with application to downbursts, J. Wind Eng. Ind. Aerodyn., 2007, 95, 279-298.

The simulation of non-synoptic effects for wind damage studies

Matthew Haines [a], Mark Sterling [a], Andrew Quinn [a]

[a] *School of Civil Engineering, The University of Birmingham, UK*

ABSTRACT: This paper presents a brief analysis of the pressure distribution on a physical model building (scale 1:1000) arising as a result of the passing of a non stationary gust front. The gust front is generated using the University of Birmingham's "downburst" simulator. Issues and challenges relating to the simulation of such pressures in a flow field akin to a moving downburst are briefly discussed. There is tentative evidence to suggest that there are differences in the pressure distribution arising as a result from a non stationary gust front compared to boundary layer flow. However, these differences are far from conclusive.

KEYWORDS:thunderstorm, downburst

1 INTRODUCTION

It is now an accepted fact that the disruption and economic losses arising as a result of extreme storms are increasing at a significant rate ABI (2005). There is also tentative evidence to suggest that these storms are increasing in frequency and magnitude due primarily to climate change effects, although it is acknowledged that such evidence is far from conclusive (Kasperki, 1998). Any increases in magnitude and frequency of extreme storms are likely to result in serious damage to the urban infrastructure, the world economy and society as a whole. In European terms, it is predicted that by 2080, there will be an increase in "wind-related insured losses from extreme European storms by at least....€25-30bn" (ABI, 2005) . However, it is perhaps worth noting that these estimates do not take into account society's increasing exposure to extreme storms, due to growing populations, wealthier populations and increasing assets at risk, e.g., ".. if Hurricane Andrew had hit Florida in 2002 rather than 1992, the losses would have been doubled, due to increase coastal development and rising asset values." (ABI, 2005).

Within the last few years, thunderstorm downburst type events have received considerable interest (Chay and Letchford (2002a), Lin and Savory (2006), McConville et al. (2009)). Figure 1a illustrates that severe thunderstorms can produce a streamwise velocity distribution which differs from the typical boundary layer flow.

In order to assess the potential damage that could be caused by these extreme wind events a number of studies have examined the wind loading present during an extreme event, for example Chay and Letchford (2002a) studied the flow around a simple cube. Mason (2009) examined the effect of surface roughness on the flow characteristics and noted the importance of possible Reynolds number effects. Sterling et al. (2011) discussed the multiple scales that could be used when interpreting physical simulations and as a resulted noted that it can be difficult to ensure that the scaling requirements of ISO2009, i.e., "for thunderstorms...wind methods should be used that adequately generate the spatial and temporal variation of wind speeds and turbulence characteristics within such systems" occur in simulations. Work by Sterling and co-workers (McConville et al. (2009); Sterling et al. (2011)) has sought to examine such events using physical experiments at relatively large scale in order to try and minimise the problems associated with scaling and it is with such experiments that the current work is concerned.

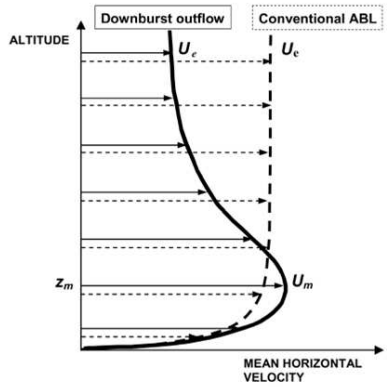

(a) Streamwise vertical profile

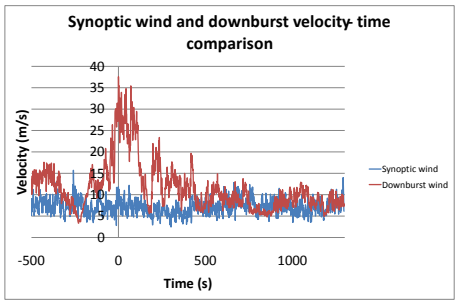

(b) Synoptic and downburst velocity time history

Figure 1: (a) A schematic illustration of the mean streamwise velocity profile corresponding to a 'typical' downburst and a typical boundary layer wind. (Lin and Savory, 2006). (b) A comparison of a synoptic and downburst wind velocity time history.

1.1 *Flow around simple structures*

Figure 2 illustrates the distribution of pressure coefficient (C_p) over the central portion of a cubic structure arising as a result of a typical boundary layer flow normal to a cube. The pressure coefficient is defined as:

$$C_p = \frac{p - p_{ref}}{\frac{1}{2}\rho_{ref} {V_{ref}}^2} \tag{1}$$

where p is the pressure in the location being measured, p_{ref} is a reference pressure taken outside of the flow, ρ_{ref} is the density of the air and V_{ref} is typically taken to be the mean velocity at an equivalent height of $10m$ above the ground.

The flow around a simple cube in a boundary layer flow has been studied in a number of wind tunnel and full scale experiments including but not limited to Baines (1963), Castro and Robins (1977), Hunt (1982) and Hölscher and Niemann (1998). As illustrated in figure 2 the (mean) pressure distribution on the windward wall of a cube in boundary layer flow has a positive mean C_p value, with a slight increase as the leading edge of the cube is approached. There is then a sharp reduction in C_p associated with flow separation on the leading edge of the cube, resulting in a region of high negative pressure which gradually reduces as the windward edge is approached. Flow reattachment then occurs and towards the leeward edge of the roof and on the leeward wall there is a slight negative mean C_p value.

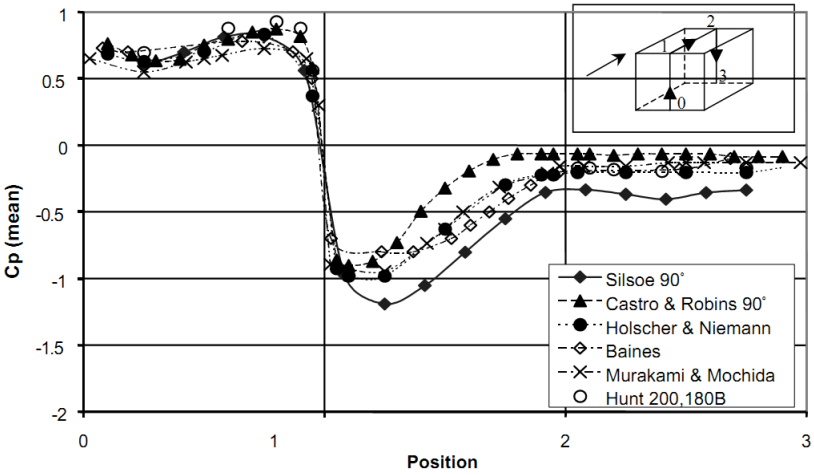

Figure 2: Vertical central section mean pressure coefficients with the wind normal to one face (0^o). From Richards et al. (2001)

There have also been a number of full scale tests on cubic structures. Richards et al. (2001) and Hoxey and Richards (2002) examined the flow structure around a full scale simple cube in synoptic wind flow conditions in a wind tunnel and a full-scale in a rural sight located in Bedfordshire, England.

Chay and Letchford (2002a), Chay and Letchford (2002b) and Mason et al. (2009) have previously looked at the flow around a simple cube in a simulated downburst outflow. Chay and Letchford (2002a) used a stationary wall jet in order to simulate the impinging nature of the flow but did not create the ring vortex structure observed by Fujita (1985) in a full scale downburst. At a distance of $\frac{X}{D} = 1$ (where X is the distance from the centre of the impingement and D is the diameter of the nozzle), the general trend of the pressure coefficients over the windward wall and leeward wall of the building were found to resemble cubes placed in boundary layer flow (albeit with differences in magnitude). Noticeable differences over the roof were found. However, it should be stressed that the results varied with respect to different X/D values.

Chay and Letchford (2002b) used a translating jet and more successfully produced the pressure field seen in a downburst. However because of the non-stationarity of the data a direct comparison to previous boundary layer flow tests could not be made. For low translating speeds no downburst gust front was formed and the profile of the event closely matched the stationary jet case. However when translating speeds were increased a gust front was formed and previous assumptions regarding the quasi-steady nature of the jet broke down. As a result using the standard pressure coefficient definition seen in equation (1) was not appropriate.

Instead the following definition of pressure coefficients was used which took into account the translating velocity component of the flow:

$$C_{PE}(t) = \frac{P(t) - P_{ATMOS}}{\frac{1}{2}\rho V^2_{EAVES,\frac{X}{D}}} \tag{2}$$

$V^2_{EAVES,\frac{X}{D}}$ is the smoothed eaves height velocity and it was calculated from V_{ref} by fitting a polynomial to the time history.

Chay and Letchford (2002b) also looked at taking into account the static pressure variation caused by the passage of the translating jet. This gave the only the wind induced forces on the structure, internal pressures were assumed to reach equilibrium with their surroundings. The

following equation was used:

$$C_{PE}(t) = \frac{P(t) - \overline{P_{STATIC,\frac{x}{D}}}}{\frac{1}{2}\rho V^2_{EAVES,\frac{x}{D}}} \tag{3}$$

Where $P_{STATIC,\frac{x}{D}}$ was modelled using a study of P_{STATIC} in the translating jet. However this had little effect on the values of the pressure coefficients for the largest magnitude pressues and suctions compared with equation (2).

The above treatment resulted in the transient wall jet event closely matching the pattern of pressure coefficients found in boundary layer flow for the windward and near the leading edge of the roof. However the magnitude of the pressure and suction coefficients were found to be far greater in the translating flow than the stationary wall jet case. It was also found that the surface pressures on the cube were well correlated for the translating wall jet flow.

Since these experiments there has been little in the way of examination of downburst flow around simple or complex structures in a physical simulation. There has however been more recent interest in using numerical modelling to look at wind loading on more complex structures. Chen and Letchford (2004) used a numerical model based upon empirical models of downbursts and then examined the impact on models of a cantilevered tower. The examination of downburst loading on transmission lines has also attracted interest within the numerical modelling community because of the destructive impact downburst events have on such structures. Shehata et al. (2005), Shehata and Damatty (2007), Shehata and Damatty (2008) and Fu et al. (2010) looked at transmission line failure with reasonable success at simulating the failure of a section of transmission line which had already failed.

There have also been a limited number of full scale measurements. Lombardo (2009) examined the response of the Texas Tech. Wind Engineering Research Field Laboratory (WERFL) in downburst winds.

2 THE BIRMINGHAM SIMULATOR

The Birmingham downburst simulator consists of nine axial flow fans each with a cross sectional area of $0.85m^2$ used to direct air downwards into a transition section which narrows to a circular cross section of diameter 1m. The latter is suspended $2m$ above the floor. This opening can be closed with the use of a series of flaps and opened suddenly to create a pulse of air which then travels to the ground and spreads out horizontally as a vortex, in a similar manner to downburst outflow (illustrated in figure 3). Further information can be found in McConville et al. (2007) and McConville et al. (2009). In order to simulate the translating aspect of a downburst two tracks were positioned on the ground and a translating rig built which passed under the simulator, the opening mechanism was automated to release when the rig was at a specific distance from the centre of impingement.

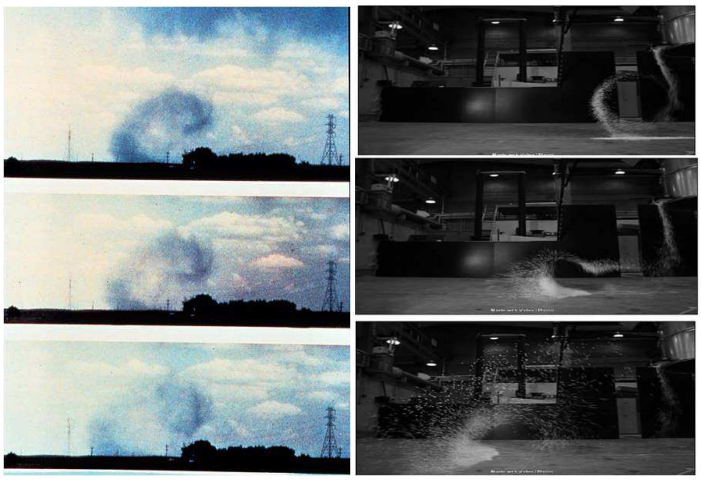

(a) NOAA photo library Image ID: nssl0106

(b) The Birmingham downburst simulator

Figure 3: A visual comparison between an actual downburst event and a physical simulation.

Since the experiments undertaken by McConville et al. (2007; 2009) a number of modifications have been made. These include the addition of a translating platform with false floor to enable different surface roughness effects to be studied as well as making it far simpler to examine the velocity flow field of the simulator.

3 DATA COLLECTION METHODS

A $244 \times 98 \times 104mm$ model was pressure tapped down the centreline so that the pressure field around the centre of the simulated downburst could be studied. The arrangement of the pressure taps can be seen in figure 4.

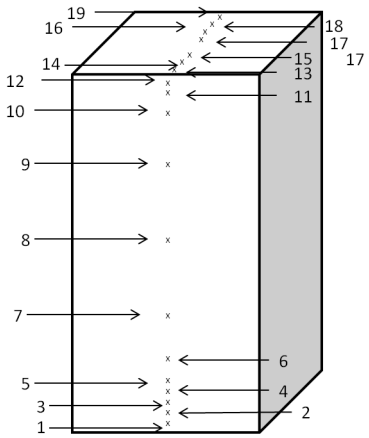

Figure 4: The arrangement of pressure taps on the model building

The location of the pressure taps is defined in terms of distance from the ground on the windward face measured around a line extending over the central portion of the building. For example, a tap on the windward face at the base would have a position of $0mm$ while a tap on the base of the leeward face would have a position of $592mm$. In what follows the location of the taps have been expressed in terms of a normalised distance, i.e., the distance from the base of the building at the leading edge divided by $592mm$. Hence, the location of the taps shown in figure 4 are: tapping 2 (0.0338), 4 (0.0676), 8 (0.2061), 10 (0.3784), 12 (0.4037), 13 (0.4206), 15 (0.4747), 16 (0.5000), 17 (0.5253), 19 (0.5794), 22 (0.6149) and 24 (0.7872).

Hjemfelt (1988) found that for the JAWS project data that the maximum wind speed occurred at a height of $80m$ and a distance of $1.5km$ from the centre of impingement. Using these values a very rough scaling parameter for height can be found. In the simulator peak wind speed occurred at a height of $20mm$, which gives a (vertical) length scaling of $1 : 4000$. However there is an inconsistency in length scaling if the downburst diameter is examined. The

average downburst diameter found by Hjemfelt (1988) was 1.8km, the diameter of the downburst simulator was $1m$, giving a length scaling of $1:1800$. This inconsistency highlights one of the difficulties in simulating downburst winds, it is exceedingly difficult to produce a flow field which matches a real world situation. Therefore the results below should be treated with caution, they may not be entirely representative of a full scale downburst wind striking a cube at full scale.

4 RESULTS

Preliminary investigations of the wind induced pressure field on a simple structure indicated that the use of a translating platform raised an important issue in terms of the wind loading experienced by the building, i.e., once the release mechanism had been fired the fans continued to rotate (due to the inertial of the fans it was not possible to stop rotation instantly). Hence, as the building moved through the jet a positive pressure field around the entire building was created and as such the flow field was considered not to be representative of a 'typical' downburst. Hence, in order to general a more appropriate simulation it was decided the building would remain stationary.

Figure 5 illustrates the pressure coefficient time series for three pressure taps located around the building arising as a result of a passing gust front associated with the ring vortex. The mechanism for generating the gust front is outlined in McConville et al. (2009). The building is located at a normalised distance of $\frac{X}{D} = 1.4$ from the centre of the impingement. The pressure coefficient is calculated using equation (1) but with V_{ref} taken as the peak velocity associated with the gust front at an equivalent height of $10m$ above the ground. In order to smooth the data an ensemble average of 5 velocity times series were used and a 50 point moving average time wind implemented (in keeping with McConville (2008)). This yielded a value of V_{ref} equal to $15ms^{-1}$.

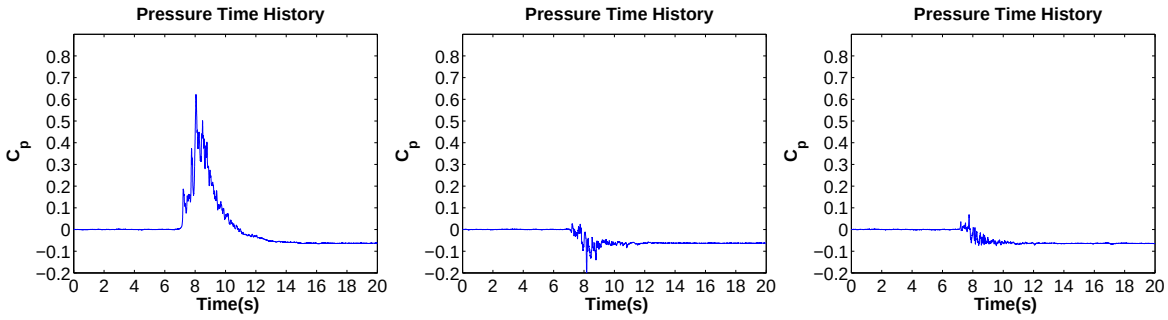

(a) C_p time history at tapping 8 (b) C_p time history at tapping 16 (c) C_p time history at tapping 24

Figure 5: Pressure time histories at the centres of the windward,roof and leeward faces

Figure 5a is illustrative of the general trend in pressure with respect to time for all of the taps on the windward face. The only difference between the windward face pressure taps is the magnitude of the pressure coefficients, which is greater at the lowest height of $20mm$ and reduces with height.

At the centre of the roof (figure 5b) there is a slight reduction in C_p values, possibly indicative of flow separation occurring on the edge between the windward face and the roof. A comparison between figures 5 and 2 illustrates the differences between the C_p values of boundary layer and downburst flow. It would appear that flow separation is far less obvious in the downburst case than for boundary layer flow. As a result of this the recovery on the leeward side of the building back to atmospheric pressure is not as noticeable as the boundary layer case. However, it needs to be appreciated that the pressure coefficients in figures 2 and 5 are not directly comparable but the comparison is somewhat instructive.

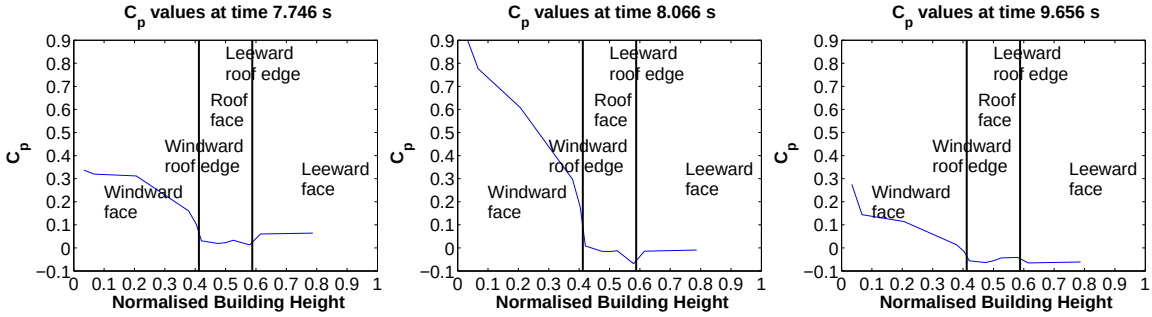

(a) C_p variation at different heights time 7.746*s* (b) C_p variation at different heights time 8.066*s* (c) C_p variation at different heights time 9.656*s*

Figure 6: Variation of C_p at different vortex locations (times)

Figure 6 illustrates the values of C_p across the various faces of the model at different phases of the vortex interaction with the building. In order to estimate the location of the vortex with respect to time, a crude form of PIV was used (see figure 3b).

A general trend across all phases of the interaction is the reduction with height of C_p coefficients on the windward face of the building. The exact trend varies depending on the degree of interaction of the building with the vortex: figure 6a illustrates the time at which the vortex is just impacting on the front face of the building. The vortex at this stage has fully developed but has yet to interact wholly with the building, hence relatively constant values of C_p over a proportion of the windward face can be observed. In figure 6b the vortex is fully interacting with the building and it is hypothesised that the vertical velocity profile seen in figure 1a will have developed against the windward face. Compared to figure 6a there is a slight decrease in the value of pressure coefficients on the roof of the building. In both their is a reduction on the roof-leeward edge of the building before rising again on the leeward face of the building and staying roughly on the leeward face. After the vortex has passed the values of the pressure coefficients on the windward face reduce to around the values seen as the vortex began to interact, only with a trend more similar to that seen when the vortex was interacting. The pressure coefficients on the roof and leeward face are roughly constant with a slight drop on the windward-roof edge and a slight raise on the roof-leeward edge, which is in contrast to the reduction seen at other points of the vortex interaction.

5 CONCLUSION

From a relatively low resolution study of the pressure field around a modelled high rise structure in a downburst flow it would appear that there are some differences between the established C_p loadings seen in a boundary layer flow and the simulated downburst used in this study. One of the most notable differences is the effect of the large (non-stationary) gust front. The pressure time histories on the model building showed a general trend of having a large positive C_p value on the windward face of the building with a slight negative C_p value on the roof and leeward faces. The largest C_p values were seen when the vortex was interacting most strongly with the building with the weakest seen after the vortex had passed over the building.

5 REFERENCES

ABI, 2005: Financial risks of climate change. ABI, URL `http://www.climatewise.org.uk/storage/610/financial_risks_of_climate_change.pdf`, [Online; downloaded 19th March 2010].

Baines, W., 1963: Effects of velocity distribution on wind loads and flow patterns on a building. *Symposium No. 16, Wind effects on Buildings and Structures*, England, Wind effects on Buildings and Structures.

Castro, I. and A. Robins, 1977: The flow around a surface mounted cube in uniform and turbulent streams. *Journal of fluid mechanics*, **79(2)**, 307–335.

Chay, M. and C. Letchford, 2002a: Pressure distributions on a cube in a simulated thunderstorm downburst, part a: stationary downburst observations. *Journal of wind engineering and industrial Aerodynamics*, **90**, 711–732.

Chay, M. and C. Letchford, 2002b: Pressure distributions on a cube in a simulated thunderstorm downburst, part b: moving downburst observations. *Journal of wind engineering and industrial Aerodynamics*, **90**, 733–753.

Chen, L. and C. Letchford, 2004: A deterministic-stochastic hybrid model of downbursts and its impact on a cantilevered structure. *Engineering Structures*, **26**, 619–629.

Fu, D., F. Yang, Q. Li, and J. Yang, 2010: Simulations for tower collapses of 500kv zhengxiang transmission line induced by the downburst. *2010 international conference for power transmission*, China Electric Power Research Institute, Qinghe, Beijing, China, CSEE and ISEE/PES.

Fujita, T., 1985: Downburst: Microburst and macroburst. *University of Chicago Press, IL*, pp. 122.

Hjemfelt, M. R., 1988: Structure and life cycle of microburst outflows observed in colarado. *Journal of Applied meteorology*, **27**, 900–927.

Hölscher, N. and H.-J. Niemann, 1998: Towards quality assurance of for wind tunnel tests: a comparastive testing program of the windtechnologische gesellschaft. *Journal of wind engineering and industrial dynamics*, **74-76**, 599–608.

Hoxey, R. P. and P. Richards, 2002: A six metre cube in an atmospheric boundary layer flow, part one full scale and wind tunnel results. *Journal of wind and structures*, **5(2-4)**, 165–176.

Hunt, A., 1982: Wind-tunnel measurements of surface pressures on cubic building models at several scales. *Journal of wind engineering and industrial dynamics*, **10**, 137–163.

Kasperki, M., 1998: Climate change and design wind load concepts. *Wind and structures*, **1(2)**, 145–160.

Lin, W. and E. Savory, 2006: Large-scale quasi steady modelling of a downburst outflow using a slot jet. *Wind and structures*, **9**, 419–440.

Lombardo, F., 2009: Analysis and interpretation of thunderstorm wind flow and its effects on a bluff body. Ph.D. thesis, Texas Technical University, [PhD thesis available from Atmospheric Science group, Texas Techincal University].

Mason, M., 2009: Simulation of downburst wind fields. Ph.D. thesis, University of Sydney, 265 pp., [Available from University of Sydney, School of Civil Engineering].

Mason, M., D. James, and C. Letchford, 2009: Wind loading on a cube subject to a pulsed wall jet simulation of a stationary downburst. *Wind and structures*, **12(1)**, 77–88.

McConville, A., 2008: The physical simulation of thunderstorm downbursts. Ph.D. thesis, University of Birmingham, 236 pp., [Available from University of Birmingham, Department of Civil Engineering, Edgbaston Birmingham, B15 2TT].

McConville, A., A. Sterling, and C. Baker, 2009: The physical simulation of thunderstorm downdrafts using an impinging jet. *Wind and structures*, **12(2)**, 133–149.

McConville, A., M. Sterling, and C. Baker, 2007: An introduction to the scaling issues associated with the physical simulation of thunderstorm downbursts. *In Proceedings of the 12th International Conference on Wind Engineering*, Cairns Australia, ICWE, 1431–1438.

Richards, P., R. Hoxey, and L. Short, 2001: Wind pressures on a 6m cube. *Journal of wind engineering and industrial dynamics*, **89**, 1553–1564.

Shehata, A. and A. E. Damatty, 2007: Behaviour of guyed transmission line structures under downburst wind loading. *Journal of Winds and Structures*, **10**, 249–269.

Shehata, A. and A. E. Damatty, 2008: Failure analysis of a transmission tower during a microburst. *Journal of Winds and Structures*, **11(3)**, 193–208.

Shehata, A., A. E. Damatty, and E. Savory, 2005: Finite element modelling of transmission line under downburst wind loading. *Journal of Finite Element in Analysis and Design*, 71–89.

Sterling, M., C. Baker, M. Haines, and A. Quinn, 2011: Scaling a thunderstorm downburst simulator. *In Proceedings of the 13th International Conference on Wind Engineering*, RAI, Amsterdam, The Netherlands, ICWE.

The Seventh International Colloquium on Bluff Body Aerodynamics and Applications (BBAA7)
Shanghai, China; September 2-6, 2012

An initial study of the aerodynamics of photovoltaic panel arrays mounted on large flat-roofs

R. Nicolas Pratt [a] & Gregory A. Kopp [a]
[a]*Boundary Layer Wind Tunnel Laboratory, Faculty of Engineering, University of Western Ontario, London, ON, Canada*

ABSTRACT: Pressure and velocity measurements, acquired during wind tunnel testing, associated with a PV array mounted on a low-rise building during a southern wind have been presented. The mean flow field outside the separation bubble was found to be similar to a bare roof. Peak uplifts were characterized by large suctions over the top to centre of the upper side of the panel. Positive vertical velocity fluctuations and streamwise gusts were also found to be correlated with peak events

KEYWORDS: Wind loads; solar arrays; low-rise buildings; aerodynamics; turbulent flow

1 INTRODUCTION

An initial study of the aerodynamics of roof-mounted photovoltaic (PV) arrays has been undertaken, with the goal of understanding and mitigating the aerodynamic loads, most importantly uplift, which act on such arrays. Existing published work on the subject is mainly limited to investigations of the aerodynamic loads, without extensive discussion on the aerodynamic mechanisms. This work builds on pressure experiments previously conducted at the Boundary Layer Wind Tunnel Laboratory (BLWTL) at the University of Western Ontario (UWO) [1]. This previous work involved extensive pressure measurements acquired during wind-tunnel testing and provided significant insight into the flow field which develops over a roof-mounted PV array. To further elucidate the aerodynamic mechanisms associated with wind loading on PV arrays we conducted experiments using synchronized time-resolved particle image velocimetry (TR-PIV) and pressure measurements. The use of PIV allows the spatial development of the flow field to be examined in greater detail than is possible with pressure measurements alone.

Several studies [2,3,4,5] report the effect of shielding by leading rows of panels on trailing rows whereby loads were reduced on the trailing rows of panels. The use of the term shielding should be used with some caution as, shown by Kopp *et. al.*,[1] shielding (implying a reduction in uplift for panels downstream of one another) is highly dependent on not only the wind direction but also the area of the roof under consideration. A north wind, for example, led to positive mean loads on the first few leading edge panels which are in the separation bubble; downstream of the bubble net uplifts were observed to increase as the as the wind moves over the array. Hence, although panels are in the wake of leading panels, no shielding effect was observed for this flow direction.

The primary basis for our study is the work of Kopp *et al.*,[1] which indicated that two critical wind directions (those resulting in the highest uplift) exist for roof mounted PV arrays: Southern winds (170°-180°) and northern cornering winds (30°-60°). These two wind directions were observed to be critical for area-averaged pressure coefficients over various panel areas. For northern cornering winds, the peak loads arose from the interaction of the corner vortex (i.e., the so-

called “delta-wing” vortex formed at the corner of the building) with the array. The peak uplifts for southern winds most often occurred in the first two southern rows. These rows were located within the separation bubble that forms when the flow separates from the southern edge of the roof. Hence the flow in the separation bubble at the height of the array was travelling upstream relative to the freestream velocity, resulting in uplift on the panels. Peak events were characterized by peak factors approaching 10, indicating the rarity of these events. In the reattached region, for southern winds, the panels experienced a net down-force. For a north wind (0°) essentially the opposite effect occurred; panels within the separated region experienced a net down-force, while panels downstream of reattachment experienced a net uplift. The mechanisms that resulted in the peak loads on solar panels are still unclear, although it was suggested [1] that higher turbulence levels being convected above the roof on rare occasions could be related to the peak loads.

Our study will focus on the flow-field that develops during southern winds. South winds are of interest as this represents one of the critical wind directions for panel uplift identified in Kopp *et al* [1]. In particular, they observed that peak uplifts occur within the separation bubble (approximately located in the first 3 rows of panels). By focusing initially on the southern winds it is possible to avoid the complications that would be associated with performing PIV during the cornering wind events, which would likely necessitate the use of either stereoscopic or dual-plane PIV to resolve the three dimensionality of the flow. Similarly, this experiment will focus of on the model north-south centerline to minimize any error associated with out of plane velocity components; while the mean velocity in the cross-stream direction is zero due to symmetry, although turbulence is, of course, always three-dimensional.

2 EXPERIMENTAL SETUP

2.1 *Model details*

The model used in the present experiments is the same 20° tilt angle model used by Kopp *et al.* [1]. The model is a 1:30 scale low rise building to which an array consisting of 12 rows of 12 modules each of which was chord mounted on the roof (i.e., the width in the north south direction when mounted on the roof); noting that the modules normally tilt towards the south in the northern hemisphere. In the geometrical description of the building and PV array that follows all units are in full-scale. The roof height, H, of the building is 7.3 m. The chord of the modules is 1.00 m, and the length is 1.65 m. Rows were modeled without gaps hence each row was 20 m long. The ground clearance is 0.16 m and the distance between the rows is 1.68 m. The roof setback was 2.9 m. For full details of the model design refer to Kopp *et al* [1].

The blockage for the model was less than 3%, while the roof height based Reynolds number was 1.9×10^5. Full-scale Reynolds numbers would be larger by the length scale multiplied by the velocity scale, so the present experiments are about two orders of magnitude low (while still remaining about one order of magnitude higher than the minimum allowed in the ASCE # 67 [6]).

2.2 *Terrain simulation*

The experiments were conducted in a simulated open country terrain characterized by a roughness length, z_0, of 0.03 m. The terrain simulation was achieved by matching the wind tunnel profiles to the ESDU mean profiles, ESDU turbulence intensities and ESDU velocity spectra [7, 8,

9]. There was excellent agreement between experimental and target mean and intensity profiles. The agreement between the measured and target spectra were also reasonable given the large scale of the flow simulation. For a comparison of measured profiles and spectra with the ESDU profiles refer to Kopp *et al* [1]. Testing was conducted in the Boundary Layer Wind tunnel I at UWO which has a working cross section of 3.4 m wide and a variable height, nominally 2.4 m at the measurement location, with an upstream fetch of 39 m.

2.3 *Surface pressure measurements*

Pressure measurements were made along the top and bottom surface of the panels along the north-south centreline. For each panel 3 taps were located on the top surface while 1 tap was placed on the bottom surface. The location of the 12 pressure taps is shown in Figure 1. Pressure measurements were made at a sample rate of 500Hz and low-pass filtered at 200 Hz. Full details of the pressure measurement system and pressure tubing can be found in Ho *et al* [10].

The measured pressures were referenced to the dynamic pressures at the upper level of the wind tunnel where the flow is uniform with low turbulence levels. The pressure coefficients were then re-referenced to the dynamic pressure at roof height using mean velocity profiles which were established without the building in the tunnel.

2.4 *Particle Image Velocimetry measurements*

In order to investigate the flow field with both good spatial and temporal resolution the TR-PIV system developed at UWO's BLWTL was utilized to measure the flow field velocity. The system consists of a double-head diode-pumped Q-switched, Nd:YLF laser operating at 1000 Hz. The seeding particles used in this study were created by atomizing olive oil. Images were captured using two Photron FASTCAM-1024PCI CMOS cameras operating in tandem. The cameras have a spatial resolution of 1024x1024 pixels and are able to stream individual images to a PC at 1000 Hz, giving a sampling rate of 500 Hz for velocity data. Full details of the TR-PIV system can be found in Taylor *et al* [11]. The experimental setup, showing the position of the cameras and the laser sheet illuminating the field of view shown in Figure 2.

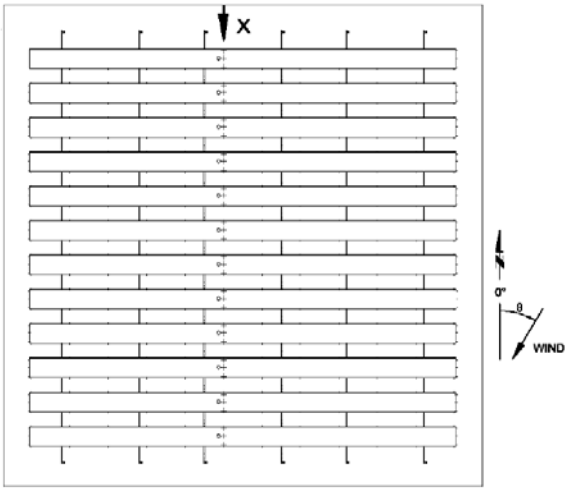

Figure 1. Sketch of the array layout with coordinate definition (x) and wind direction (θ). Taps on the uppers surface of the panels are marked with '+', while taps on the underside are marked with '○'.

Figure 2. Photograph of experimental setup showing positioning of cameras and laser sheet

2.5 *Synchronization of pressure and velocity data*

One of the difficulties in these experiments was the synchronization of the pressure and velocity data, given that both the pressure data acquisition system (DAQ) and the PIV system were both designed to operate independently of each other. Synchronization was achieved by connecting the PIV camera triggers to the pressure DAQ analog input. As both the pressure DAQ and camera triggers operate at 500 Hz, on separate clocks, some ambiguity was expected in the synchronization. Based on the first and last peaks of the camera trigger signal the start and finish of the PIV operation could be determined and then the pressure time history was trimmed to match the PIV data series. However, after this process the pressure time series contained 11 more data points than the PIV measurements; thus there is an uncertainty of 22 ms between the pressure and velocity data; this uncertainty is less than 0.015% of the entire sampling period. To overcome this uncertainty vector fields during peak events were compared to pressure distributions over the 11 data point uncertainty range to subjectively determine the correct synchronization. This issue will be corrected in future experiments.

After synchronization the pressure and velocity time series were approximately 160 s long. Assuming a full-scale gust speed of 45 m/s at 10 m (giving a velocity ratio of 1:2.6), the resultant full-scale sampling period is approximately ½ an hour.

3 STATISTICAL DESCRIPTION

3.1 *Flow field*

As discussed large peak uplifts have been observed within the separation bubble for a southern wind direction (180°). In this section we discuss the features of the leading edge flow field associated with a southern wind. The mean streamwise velocity profiles are plotted in Figure 3 while the vertical velocity profiles are shown in Figure 4. The velocities are normalized by the roof-height velocity (U_H) while the lengths are normalized by the roof height, H. While it has been shown that normalized pressure data for a separating-reattaching flow collapses if the streamwise distance is normalized by reattachment length [12], the presence of the panels perturbs the reattaching shear layer such that the reattachment location is ambiguous, and as such the roof height was seen as a more appropriate normalizing scale. As shown in Figures 5 and 6 the outer flow field at the leading edge is similar to that of a typical separating-reattaching flow, however, it is clear that within the separation bubble the flow is significantly altered. The separation bubble is essentially divided by the panels into three smaller recirculation zones, with the additional complication of flow separating from the trailing edge of each panel and entering into the subsequent recirculation region. From a visual inspection of the streamlines it appears that the large scale (that associated with building rather than the panels) separated shear layer has reattached by the 3rd to 4th downstream panel (~ 0.8-1.0 H). Both the reattachment length and height of the separation bubble are similar to what would be observed over a bare-roofed low-rise building (not shown here).

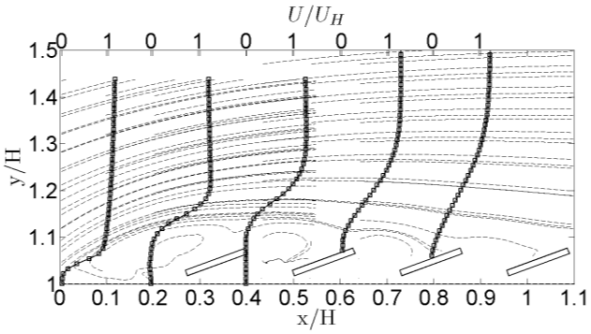

Figure 3. Mean streamwise velocity profiles for a wind direction of 180°. Streamlines are shown by the dashed lines for reference.

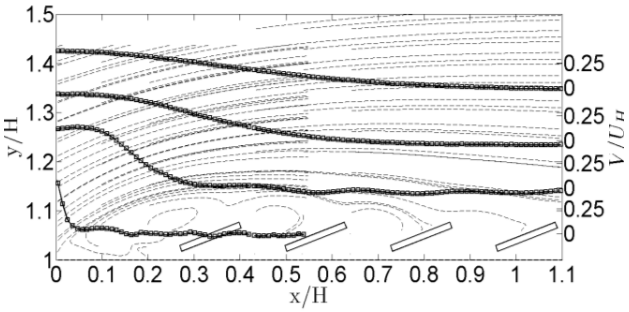

Figure 4. Mean vertical velocity profiles for a wind direction of 180°. Streamlines are shown by the dashed lines for reference.

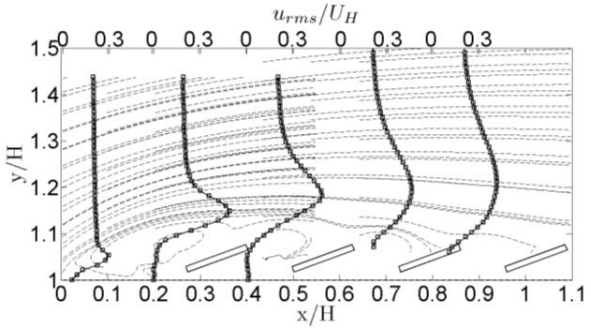

Figure 5. RMS streamwise velocity profiles for a wind direction of 180°. Streamlines are shown by the dashed lines for reference.

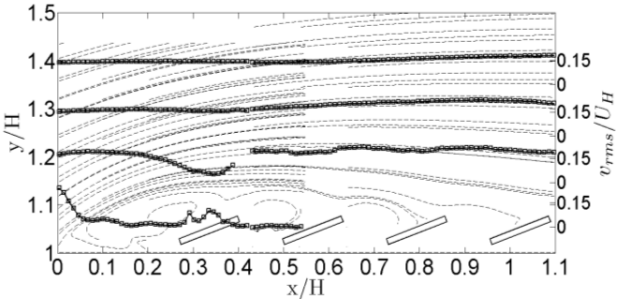

Figure 6. RMS vertical velocity profiles for a wind direction of 180°. Streamlines are shown by the dashed lines for reference.

Root mean square (rms) streamwise and vertical velocity profiles are shown in Figures 7 and 8 respectively. The maximum streamwise rms velocities are associated with the separating shear layer and are approximately twice the magnitude of the maximum vertical rms velocities. The vertical rms velocities are almost constant outside the separation bubble.

3.2 *Pressure field*

Figure 3.5 shows the mean pressure coefficients (Cp_{mean}) for the point pressures along the centerline and the net pressure coefficient for the ring of four taps around each panel's centerline. Figure 3.6 shows the corresponding RMS pressure coefficient (Cp_{rms}) for the centerline taps and centerline net pressures. Figure 3.7 shows the peak pressure coefficients (Cp_{min}) for the centerline net pressures. The mean, RMS, and peak pressure coefficients all appear to follow the same trend, the peaks all occur on the first southernmost panel followed by a monotonic reduction along the array (with the exception of the absolute peak at the 3rd southernmost panel). The distinction between the panels within the separation bubble and those in the reattached flow zone is clear from the stabilization of in mean, rms and peak pressure coefficients by the 3rd to 4th southernmost panels. Furthermore peak factors,

$$g = \frac{|Cp_{min} - Cp_{mean}|}{Cp_{rms}} \quad (1)$$

shown Figure 10 exhibit a peak around reattachment. Kopp *et al.* noted that towards the leeward side of the array for a southern wind the loads become similar to those observed or an equivalent ground-mounted system [1].

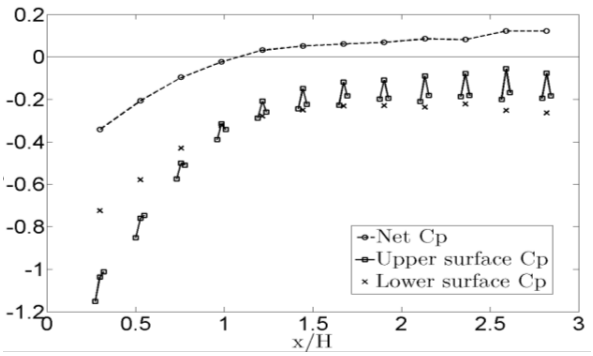

Figure 7. Mean pressure coefficients for a wind direction of 180°.

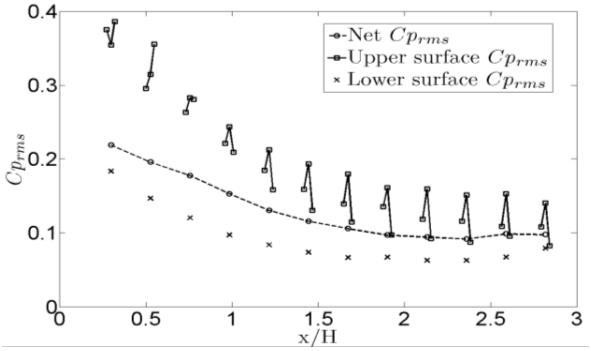

Figure 8. RMS pressure coefficients for a wind direction of 180°.

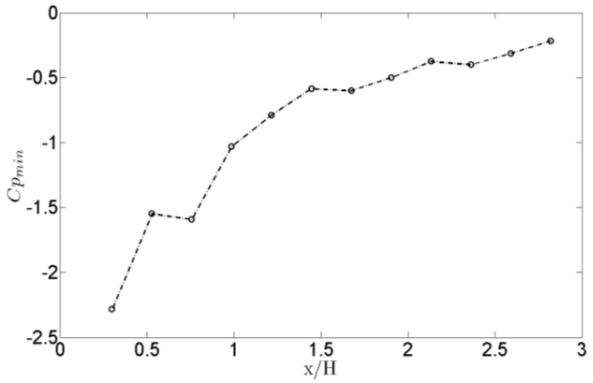

Figure 9. Peak pressure coefficients for a wind direction of 180°.

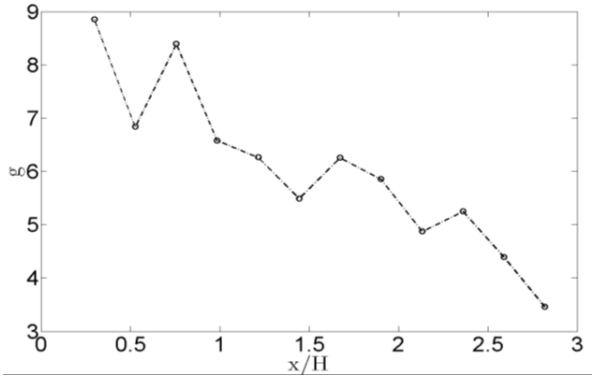

Figure 10. Peak factors for a wind direction of 180°.

4 PEAK UPLIFT EVENTS

A primary concern in our experiments was the determination of the aerodynamic mechanisms associated with the peak uplift events. As the highest uplift is experienced by panels within the separation bubble, caused by the flow separating from the leading edge of the building, the pressure and velocity fields associated with peak events was investigated for the 2nd southernmost panel, located at ~0.6 *H*. The pressure field for the 1st peak event is shown in Figure 11. The 1st peak uplift event is clearly dominated by the high suction at the upper side of the top of the panel. The suctions at the centre and bottom of the top of the panel are also almost double their mean values. In contrast the pressure on the lower surface of the panel exhibits only a minimal deviation from the mean. Streamwise and vertical velocity profiles for the 1st peak are shown in Figure 12; the associated vector field is also shown with the mean velocity subtracted to accentuate the velocity fluctuations. The flow field associated with the 1st peak shows large vertical fluctuations near the top of the panel which could explain the large suctions in this region. Near the lower edge of the panel large velocity fluctuations are not evident. The 1st peak also appears to be associated with only a mild streamwise gust.

The pressure field for the 2nd peak event is shown in Figure 13. As with the 1st peak, the 2nd peak is characterized by a strong suction on the upper side of the top panel. The lower portion of

the top of the panel also exhibits an increased suction, however, this is less pronounced than at the top of the panel. The suction on the underside of the panel is also moderately increased during the 2nd peak, relative to the mean. Examining the velocity profiles during the 2nd peak, shown in Figure 14, the extent of vertical fluctuations in the vicinity of the panel is less than during the 1st peak however large vertical fluctuations are observed ~0.1 *H* above the panel's lower edge. As with the 1st peak the 2nd peak appears to be correlated with a mild streamwise gust.

In contrast with the first two peaks the pressure field during the 3rd peak, shown in Figure 15, is characterized by strong suctions at not only the top of the upper surface, but also near the centre of the top surface of the panel. Suction at the bottom of the top surface and the underside of the panel are also moderately increased. Turning to the velocity profiles associated with the 3rd peak, shown in Figure 16, large vertical fluctuations are again evident with maximum vertical velocities approaching the reference speed above the top of the panel. There also appears to be a negative streamwise fluctuation above the panel associated with the 3rd peak in addition to a strong streamwise gust in the freestream further above the panel.

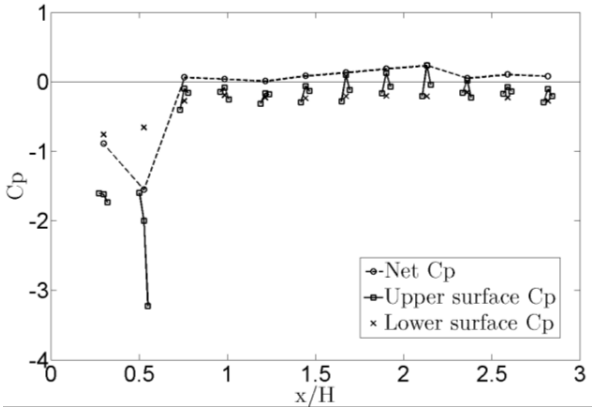

Figure 11. Instantaneous pressure coefficients during 1st peak uplift event on the 2nd southernmost panel for a wind direction of 180°.

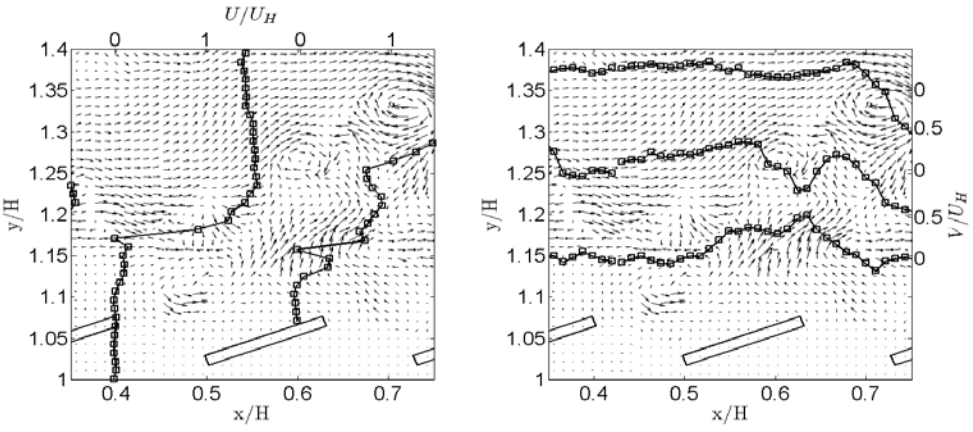

Figure 12. Instantaneous streamwise and vertical velocity profiles during 1st peak uplift event on the 2nd southernmost panel for wind direction of 180°. Vector field shows fluctuating component of velocity only.

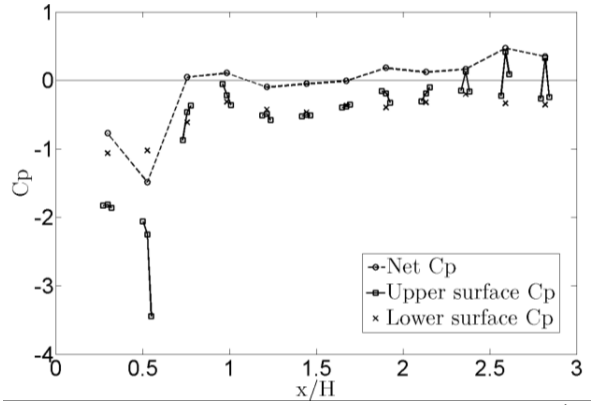

Figure 13. Instantaneous pressure coefficients during 2nd peak uplift event on the 2nd southernmost panel for a wind direction of 180°.

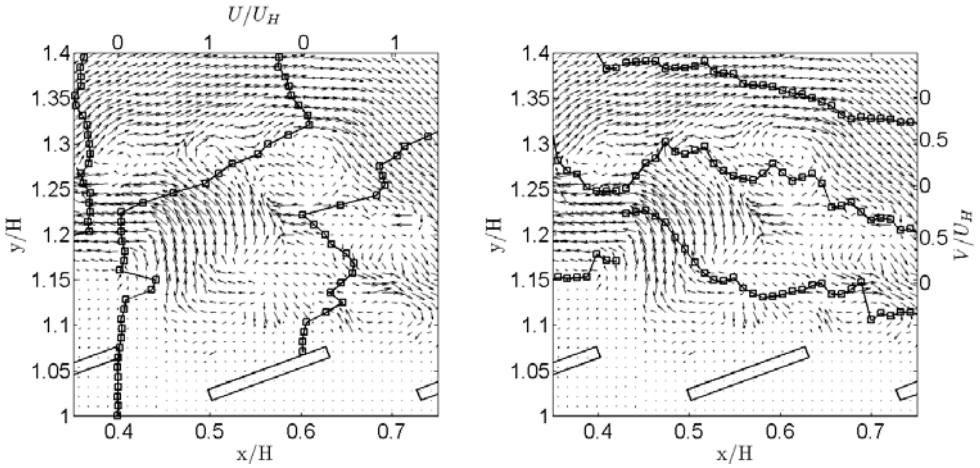

Figure 14. Instantaneous streamwise and vertical velocity profiles during 2nd peak uplift event on the 2nd southernmost panel for a wind direction of 180°. Vector field shows fluctuating component of velocity only.

The vector maps for the first 3 peaks on 2nd southernmost panel all show some level of vortex activity, to quantify these vortices instantaneous swirling strength maps were calculated, shown in Figure 17. While vorticity has traditionally been used to identify vortices, vorticity also identifies regions of shear. Thus, strong shear layers will often mask vortices in vorticity maps. Swirling strength on the other had isolates swirling motion associated with vortices from pure shear [13]. From Figure 4.8 it is clear that while vortices are certainly present during peak events they appear uncorrelated in strength, size, and location with peak uplift events.

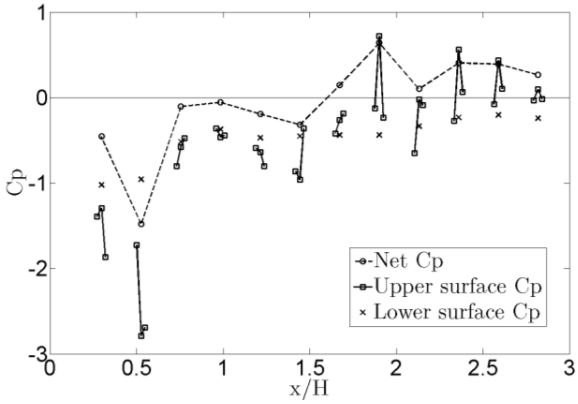

Figure 15.Instantaneous pressure coefficients during 3rd peak uplift event on the 2nd southernmost panel for a wind direction of 180°.

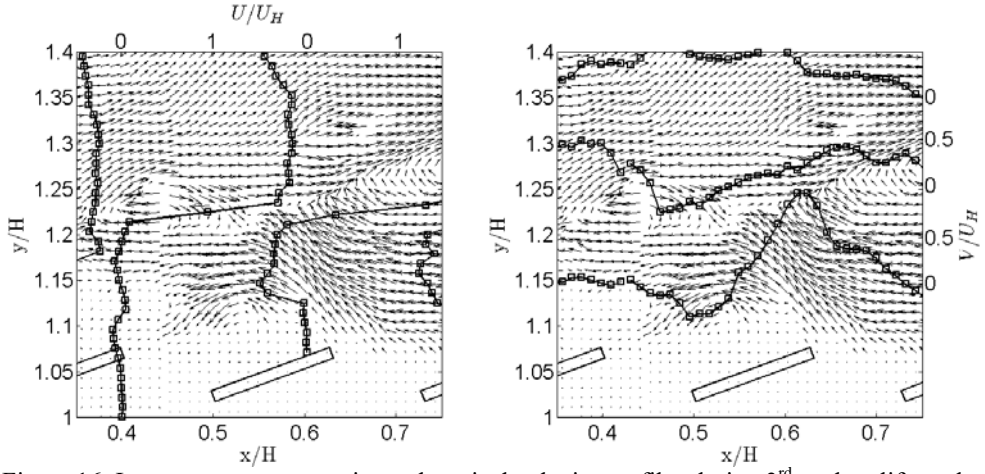

Figure 16. Instantaneous streamwise and vertical velocity profiles during 3rd peak uplift on the 2nd southernmost panel event for a wind direction of 180°. Vector field shows fluctuating component of velocity only.

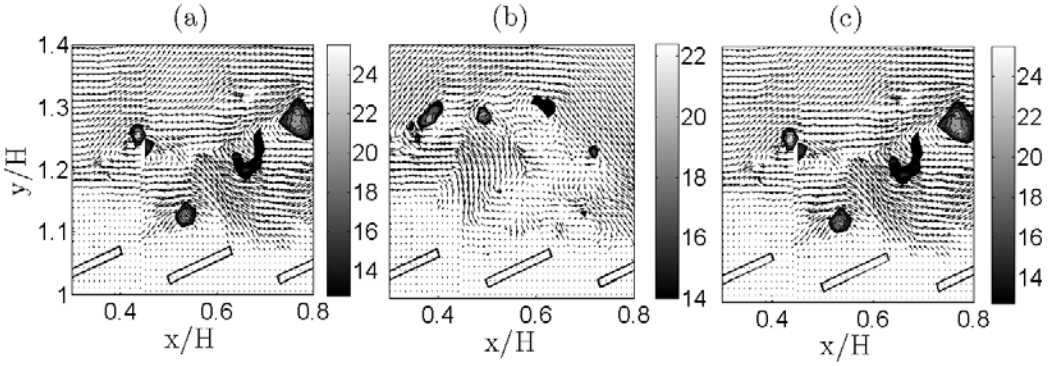

Figure 17. Instantaneous swirling strength maps for (a) 1st peak , (b) 2nd peak and (c) 3rd peak uplift on the 2nd southernmost panel for a wind direction of 180°. Vector field shows fluctuating component of velocity only.

5 CONCLUSIONS

We have presented both pressure and velocity measurements associated with a PV array mounted on a low-rise building during a southern wind. It was found that the separating-reattaching

flow caused by the flow separating at the leading edge of the building was similar to that observed for a bare-roof building in that the height and length of the separation bubble were close to what one would expect for a similar bare-roofed building. The details of the flow within the separation bubble were of course different from a bare-roof building due to the presence of the panels.

The pressure and flow fields associated with peak uplift events on panels within the separation bubble were also examined as these panels experience some of the largest loads seen by the entire array. It was found that the peak events were characterized by large suctions over the top to centre of the upper side of the panel. While suctions also increased towards the bottom of the panel topside as well as the panel underside these increases were much less pronounced. Large positive vertical velocity fluctuations were found to be well correlated with peak uplifts along with mild to strong streamwise gusts further above the panels. While vortices appear in the vicinity of panels experiencing peak uplifts, these vortices seem uncorrelated with the peaks as the size, strength and location of these vortices vary significantly from peak to peak.

6 ACKNOWLEDGEMENTS

This research was supported by NSERC, under the Discovery Grants program. The second author (GAK) gratefully acknowledges the many interesting discussions and enthusiastic support provided by Mr. Chris Tilley and Mr. Rob Ward of SunLink Corporation, and also for the use of the wind tunnel models, which were developed for testing of SunLink's system.

7 REFERENCES

1 G. A. Kopp, S. Farquhar and M. J. Morrison, Aerodynamic mechanisms for wind loads on tilted, roof-mounted, solar arrays, J. Wind Eng. Ind. Aerodyn., submitted.
2 C. P. W. Guerts and C. A. van Bentum, Wind load on active roofs, TNO Report 2006-D-R0203, Delft, The Netherlands, 2006.
3 H.W. Tielman, R.E. Akins and P. R. Sparks, An investigation of wind loads on solar collectors, Report VPI-E-80-1, Virginia Polytechnic Institute and State University, Blacksburg, Virginia, 1980.
4 A. Radu, E. Axinte, and C. Theohari , Steady wind pressures on solar collectors on flat-roofed buildings, J. Wind Eng. Ind. Aerodyn., 23 (1986) 249-258.
5 H. Ruscheweyh and R. Windhövel, Wind loads at solar and photovoltaic modules for large plants, In Proc. of the 13th International Conference on Wind Engineering, Amsterdam, The Netherlands, 2011.
6 ASCE No. 67, Wind Tunnel Studies of Buildings and Structures, ASCE Manuals and Reports on Engineering Practice No. 67, American Society of Civil Engineers, Reston, Virginia, 1999.
7 Engineering Data Science Unit, Strong winds in the atmosphere boundary layer. Part 1: Mean-hourly wind speeds, Data Item 82026, 1982.
8 Engineering Data Science Unit, Strong winds in the atmosphere boundary layer. Part 2: Discrete gust speeds, Data Item 83045, 1983.
9 Engineering Science Data Unit, Characteristics of atmospheric turbulence near the ground, Data Item 74031, 1974.
10 T.C.E. Ho, D. Surry, D. Morrish and G.A. Kopp, The UWO contribution to the NIST aerodynamic database for wind loads on low buildings: Part 1. Archiving format and basic aerodynamic data, J. Wind Eng. Ind. Aerodyn., 93 (2005) 1-30.
11 Z. J. Taylor, R. Gurka, G. A. Kopp, and A. Liberzon, Long-Duration Time-Resolved PIV to Study Unsteady Aerodynamics, IEEE Transactions on Instrumentation and Measurement, 59 (2010) 3262-3269.
12 A. Roshko, J. Lau, Some observations on transition and reattachment of a free shear layer in incompressible flow. Proceedings of the Heat Transfer and Fluid Mechanics Institute18 (1965) 157–167.
13 R. Adrian, K. Christensen, Z. Liu, Analysis and interpretation of instantaneous turbulent velocity fields. Experiments in Fluids, 29 (2000) 275–290.

The Seventh International Colloquium on Bluff Body Aerodynamics and Applications (BBAA7)
Shanghai, China; September 2-6, 2012

Discussion of design wind force coefficients for hyperbolic paraboloid free roofs

Fumiyoshi Takeda [a], Tatsuya Yoshino [b], Yasushi Uematsu [c]

[a] *Structural Engineer, Technical Research Center, R&D Division, Taiyo Kogyo Corporation, 3-20, Syodai-Tajika, Hirakatashi, Osaka, Japan*
[b] *Researcher, Technical Research Center, R&D Division, Taiyo Kogyo Corporation, 3-20, Syodai-Tajika, Hirakatashi, Osaka, Japan*
[c] *Professor, Department of Architecture and Building Science, Tohoku University, Sendai, Japan*

ABSTRACT: The present paper discusses the design wind force coefficients for hyperbolic paraboloid (hereafter "HP") free roofs constructed of membrane structures, based on a structural analysis for various conditions as well as on a CFD analysis. The application of the wind force coefficients obtained from wind tunnel experiments with rigid models is investigated. The influences of roof deformation on the wind forces and the resultant load effects are also investigated.

KEYWORDS: Wind force coefficient, Hyperbolic paraboloid roof, Membrane structure, Wind tunnel experiment, CFD (Computational Fluid Dynamics), Structural analysis.

1 INTRODUCTION

The purpose of the present study is to propose the design wind force coefficients providing the equivalent static wind loads on HP-shaped membrane structures, in which the dynamic load effect is considered appropriately. Pun and Letchford (1993) reported the analysis of an HP-shaped tension membrane roof subjected to fluctuating wind loads (Ref. 1). To the authors' best knowledge, few studies of wind loads on HP-shaped membrane free roofs have been done since. Even for free roofs of the other shapes, the number of studies on the wind loads is quite limited. Recently, Nagai et al. (2012) (Ref. 2) have investigated the wind loads on a horn-shaped membrane structure.

The authors have carried out a series of wind tunnel experiments and CFD analyses to investigate the wind forces on rigid free roofs with various configurations, i.e. gable, troughed, mono-sloped, and HP-shaped roofs (Ref. 3, 4). Figure 1(a) shows an HP-shaped rigid model used in the wind tunnel experiments. Based on the results, we have proposed the design wind force coefficients for HP free roofs (Ref. 5), assuming that the roof is supported by the four corner columns (see Fig. 1(b)), in which the axial forces involved in the columns are regarded as the

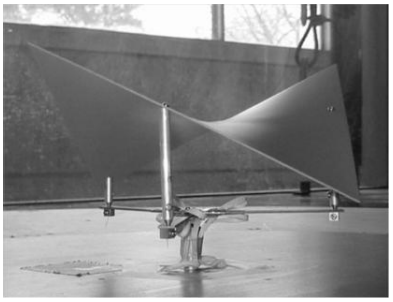

(a) Picture of an HP model

(b) Four corner columns

Figure 1. Experimental model and a supporting system

most important load effect for discussing the design wind force coefficients.

In practice, however, there are many other supporting systems, such as a 'post and guy cable system'. Moreover, the membrane roof is not rigid but rather flexible, the deformation of which is larger than that of conventional roofs such as metal roofs. Therefore, regarding the application of the proposed wind force coefficients, the following questions have arisen: (i) Can they be applied to membrane structures with the other supporting systems? The structural characteristics such as arrangement and stiffness of the members may affect the responses significantly (Ref. 6); (ii) Can they be applied to flexible roofs that deform under wind loading? The roof deformation may change the wind force significantly; (iii) Do they overestimate or underestimate the wind loads for suspension structures?

Therefore, the present paper investigates these subjects, based on structural analyses of the roofs with three types of structural systems and CFD analyses of the wind forces on the deformed roof. Finally, a discussion is made of the design wind force coefficients.

2 DEFINITION OF WIND FORCE AND MOMENT COEFFICIENTS

2.1 *Roof types*

Three models (Models A - C) with different rise/span (or sag/span) ratios have investigated in previous studies (Fig. 2). Focus is on the model A in the present study. The plan of the roof is a square of 15 m by 15 m, and the mean roof height H is 8 m in full scale.

2.2 *Definitions*

Figure 3 shows the definition of the aerodynamic forces and moments, where D and L represent the drag and lift, respectively; M_x and M_y are the moments about the x and y axes, respectively. These values are normalized as follows:

$$C_D = \frac{D}{q_H ha} \quad C_L = \frac{L}{q_H S} \quad C_{Mx} = \frac{M_x}{q_H Sa} \quad C_{My} = \frac{M_y}{q_H Sa} \qquad (1), (2), (3), (4)$$

where q_H = reference velocity pressure at the mean roof height; h = difference in height for the roof ; a = horizontal (projection) width of the roof; and S = projection area of the roof. For the purpose of simplicity, the design wind force coefficients on the roof are specified by two uniformly distributed values (C_{NW} and C_{NL}) over the windward and leeward halves (Fig. 4), which are defined by

$$C_{NW} = \frac{N_W}{q_H S/2} \quad C_{NL} = \frac{N_L}{q_H S/2} \qquad (5), (6)$$

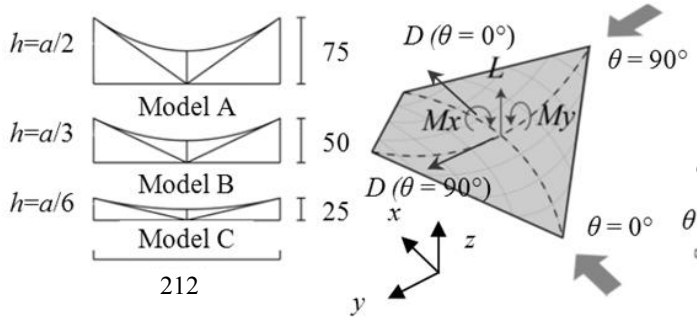

Figure 2. Roof shapes (mm)

Figure 3. Definition of D, L, M_x and M_y

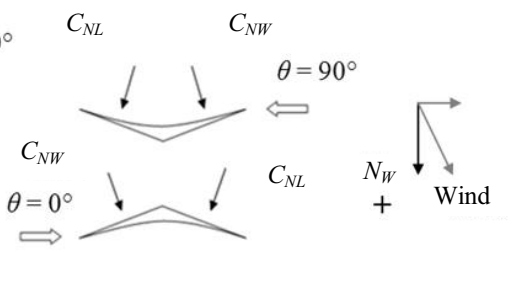

Figure 4. Dimensions of C_{NL} and C_{NW}

where N_W and N_L represent the normal wind forces, positive downward, on the windward and leeward halves, respectively. The coefficients C_{NW} and C_{NL} can be represented by C_L and C_{My} for the wind direction $\theta = 0°$ as follows:

$$C_{NW} = -C_L - 3\sqrt{2}C_{My} \quad C_{NL} = -C_L + 3\sqrt{2}C_{My} \qquad (7), (8)$$

3 WIND TUNNEL EXPERIMNET

3.1 *Arrangement and Procedure*

The wind tunnel model is made of 1 mm thick acrylic plate with a geometric scale of 1/100. Figure 1(a) shows a model mounted on the force balance that was designed, built and gauged for this experiment. The Y-shaped force balance is made of 1.2 mm thick phosphor bronze in order to measure the lift L and the aerodynamic moments M_x and M_y (Ref. 5). The experiments were carried out in a boundary layer wind tunnel with a working section 1.4 m wide, 1.0 m high and 6.5 m long at the Department of Architecture and Building Science, Tohoku University, Japan. A turbulent boundary layer with a power law exponent of α = 0.18 for the mean velocity profile was generated on the wind tunnel floor. The turbulence intensity I_u and longitudinal length scale L_x of the flow at a height of z = 100 mm are 0.17 and 0.16 m, respectively. The measurements were carried out at a wind speed of $U_H \approx 6$ m/s at the mean roof height H. The design wind speed is assumed 31.5 m/s, as a typical value of strong wind events; therefore, the velocity scale is approximately 1/5.25. The geometric scale of the model and the velocity scale yield a time scale of approximately 1/19. The wind direction θ is changed from 0° to 90° at a step of 15°. The outputs of the strain meters were sampled simultaneously at a rate of 200 Hz for a period of 32 sec, which approximately corresponds to 10 min in full scale. The measurements were repeated six times under the same condition. The statistics of the aerodynamic coefficients are evaluated by applying ensemble average to the results of the six consequence runs. Figure 5 shows a phase-plane representation of the C_L - C_{My} relation when θ = 0°. The circle in the figure represents a condition where the C_L value becomes an extreme (the maximum and minimum peak) in each run. It is seen that the peak values of C_L and C_{My} do not necessarily occur at the same time. The envelope of the trajectory is approximated by a hexagon as shown in Figure 6.

4 PROPOSED DESIGN WIND FORCE COEFFICIENTS

4.1 *Design wind force coefficients*

The authors have proposed a procedure to obtain the design wind force coefficients (Ref. 5),

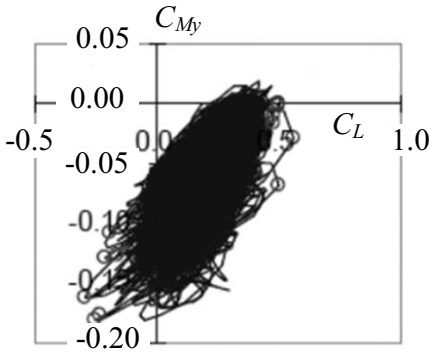

Figure 5. C_L- C_{My} trajectory for Model B (h/a = 1/3)

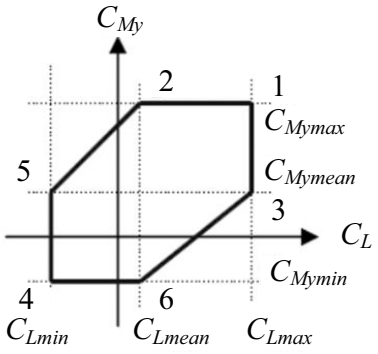

Figure 6. Model of the envelope of C_L-C_{My} trajectory

Table 1. Basic values of the wind force coefficients

Apex	Combination of C_L and C_{My}/C_{Mx} *1)	Wind direction $\theta = 0°$		Wind direction $\theta = 90°$	
		C_{NW0}	C_{NL0}	C_{NW0}	C_{NL0}
1	$C_{Lmax} + C_{Mymax}/C_{Mxmax}$	-0.65	-0.72	-0.37	0.11
2	$C_{Lmean} + C_{Mymax}/C_{Mxmax}$	-0.31	-0.38	0.02	0.50
3	$C_{Lmax} + C_{Mymean}/C_{Mxmean}$	-0.40	-0.97	-0.89	0.63
4	$C_{Lmin} + C_{Mymin}/C_{Mxmin}$	0.80	-0.67	-0.56	2.31
5	$C_{Lmin} + C_{Mymean}/C_{Mxmean}$	0.35	-0.22	0.12	1.63
6	$C_{Lmean} + C_{Mymin}/C_{Mxmin}$	0.39	-1.08	-1.17	1.70

*1) Using C_{My} for $\theta = 0°$, C_{Mx} for $\theta = 90°$

assuming that the roof is rigid and simply supported by the four corner columns. The procedure is summarized as follows. Focus is on the incremental axial forces induced in the columns by the wind forces as one of the most important load effects for evaluating the wind force coefficients. The incremental axial forces are computed for the combination of C_L and C_{My} (for $\theta = 0°$) or C_{Mx} (for $\theta = 90°$) at each apex of the hexagon as shown in Figure 6. The roof is divided into two areas, i.e. the windward and leeward halves, and the design wind force coefficient is assumed constant in each area. The design wind force coefficients C^*_{NW} and C^*_{NL} for these halves are presented as follows:

$$C^*_{NW} = \frac{\gamma C_{NW0}}{G_f} \qquad C^*_{NL} = \frac{\gamma C_{NL0}}{G_f} \tag{9), (10}$$

where C_{NW0} and C_{NL0} are the basic values, computed from Equations (7) and (8), respectively, by using a combination of C_L and C_{My} (or C_{Mx}) at each apex of the hexagon. Table 1 summarizes the values of C_{NW0} and C_{NL0} at the six apexes for two wind directions, i.e. $\theta = 0°$ and $\theta = 90°$ (see Fig. 4). In the study, two sets of the C_{NW0} and C_{NL0} values are selected from the six sets at the apexes, which induce the maximum tension and compression in the columns.

The value of γ in Equations (9) and (10) is a correction factor for the influence of wind direction (Ref. 5). It is obtained by calculating the ratio of the actual maximum or minimum axial force in a wind direction range of 0° ± 45° (WD1) or 90° ± 45° (WD2) to the predicted value from C_{NW0} and C_{NL0}. In practice, the value of $\gamma = 1.0$ is used in the present study, because the maximum tension and compression are induced when $\theta = 0°$ for WD1 and $\theta = 90°$ for WD2. Note that this is not the case for gable and troughed roofs (Ref.3). G_f is the gust effect factor for considering the dynamic load effect. The value of $G_f = 2.0$ is used for evaluating the design wind force coefficients in this study.

5 EFFECT OF ROOF SUPPORTING SYSTEM

5.1 *Analytical models*

Three structural systems are often used for membrane structures, i.e. frame, suspension and air-supported types. Focus is on the frame and suspension types in the present analyses. Figure 7 shows the analytical models. In Frame-model 1 (F1 model), the roof structure is constructed of the perimeter girders and binding beams, which divide the roof area into twelve zones (Fig. 7(a)). The frame is covered with pre-stressed membrane. The pre-stress is 4 kN/m both in the warp and fill (weft) directions of membrane. The warp direction is shown in Figure 7(b). The fill direction is perpendicular to the warp direction. The self-weight of membrane is assumed 12 N/m^2. Frame-model 2 (F2 model) consists of the perimeter girders and pre-stressed membrane (Fig. 7(b)). In

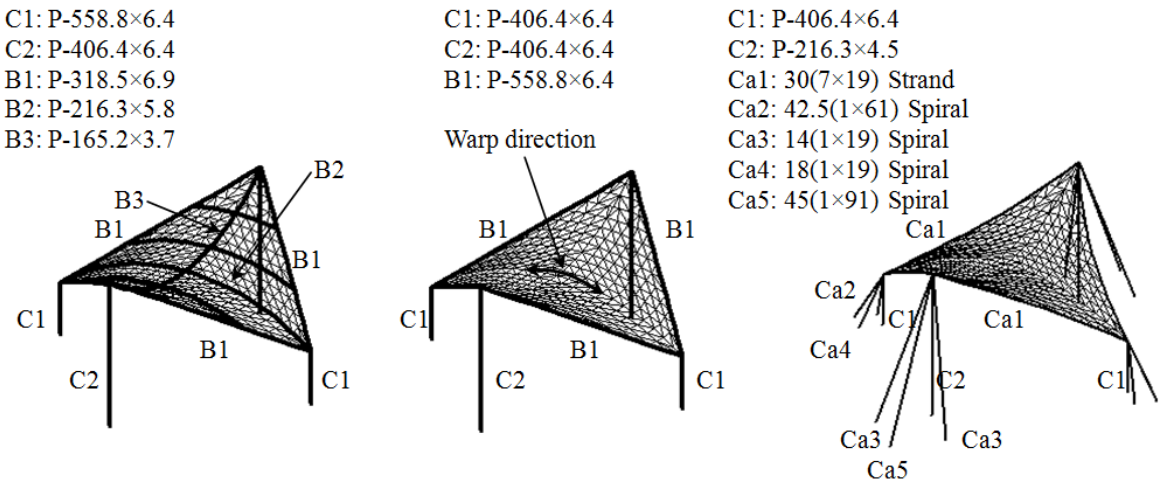

(a) Frame-model 1 (F1) (b) Frame-model 2 (F2) (c) Suspension-model (S1)

Figure 7. Analytical models

Table 2(a). Membrane (t: Thickness)

Tensional stiffness:	$E_w \times t$ = 1284.67 kN/m (Warp)
	$E_f \times t$ = 861.024 kN/m (Fill)
Poisson's ratio:	ν_w = 0.85 (Warp) ν_f = 0. 57 (Fill)
Shear modulus:	$G \times t$ = 56.9766 kN/m

Table 2(b). Cable

Elastic modulus:	$E = 1.37 \times 10^8$ kN/m^2 (Strand)
	$E = 1.57 \times 10^8$ kN/m^2 (Spiral)

Table 2(c). Beam and Post

Elastic modulus:	$E = 2.05 \times 10^8$ kN/m^2
Poisson's ratio:	$\nu = 0.3$

these Frame-models, the roof girders are supported by the four corner columns. On the other hand, Suspension-model (S1 model) consists of the curved perimeter cables and pre-stressed membrane; the roof is supported by the posts and guy cables at the four corners, as shown in Figure 7(c). The column bases of the F1 and F2 models are fixed, while the posts of the S1 model are pin-supported. The connection of elements in the F1 and F2 models is rigid. The material of the columns, beams, posts and cables is steel; that of the membranes is PTFE-coated glass fiber plain-weave fabric. The projection area of the S1 model is approximately 82% of that of the Frame models because of the curved perimeters. The S1 model is the most flexible among these three models, which causes the largest deformation to the roof under wind loading. On the other hand, the F1 model is relatively rigid. Moreover, the roof membrane slightly deforms in the downward direction due to the self-weight. Therefore, the initial shapes of these three roofs are slightly different from each other due to the difference in the supporting system.

5.2 *Structural analyses*

The structural analyses are conducted by using a program named MAGESTIC, in-house software of Taiyo Kogyo Corp., based on a finite element method with the Newton-Raphson method, in which the geometrical nonlinearity is taken into account. The membrane material is assumed orthotropic and elastic. Furthermore, it is assumed that the membrane carry only tension; in other words, it does not resist compression and bending moment. The design wind speed is 31.5 m/s. The corresponding velocity pressure is 605 N/m^2. The six wind force coefficients calculated from the C_{NW0} and C_{NL0} values in Table 1 for each wind direction are used in order to find the critical condition that gives the maximum load effect; they are provided by the combination of C_L and C_{My} (or C_{Mx}) corresponding to the six apexes of the hexagon. In the analyses, the stresses

are calculated based on the Building Standard Law of Japan and Design Standard for Steel Structures published by the Architectural Institute of Japan. For the membranes and cables, tensile stresses are calculated from the tensile forces; for the beams and columns, the extreme fiber stresses are calculated by combining the axial forces and bending moments; for the posts of the S1 model, axial stresses are calculated from the axial forces. The allowable stresses and

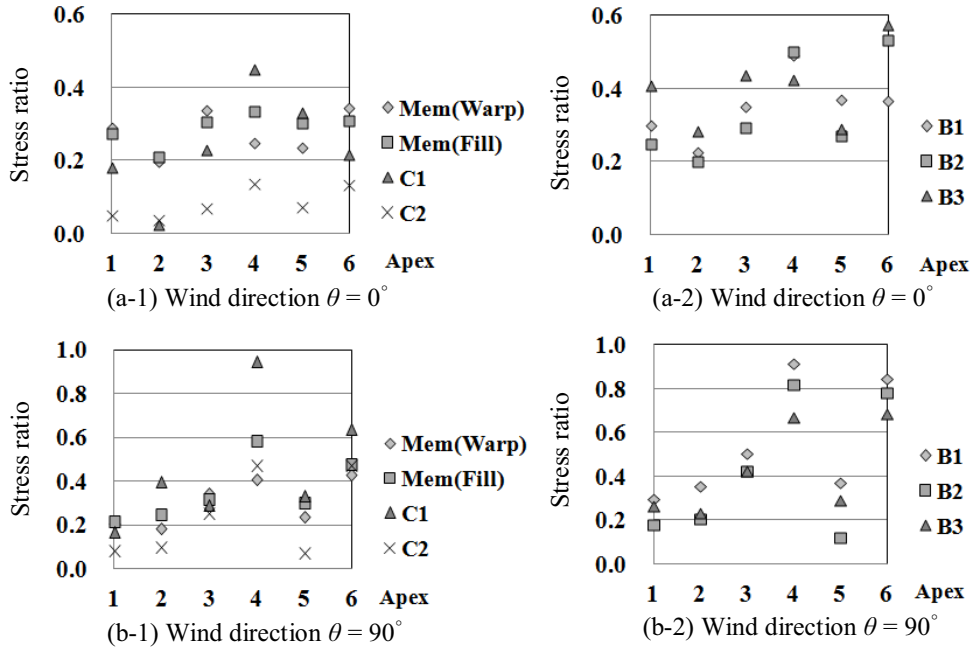

(a-1) Wind direction $\theta = 0^{\circ}$ (a-2) Wind direction $\theta = 0^{\circ}$

(b-1) Wind direction $\theta = 90^{\circ}$ (b-2) Wind direction $\theta = 90^{\circ}$

Figure 8. Stress ratio for Frame-model 1 (F1)

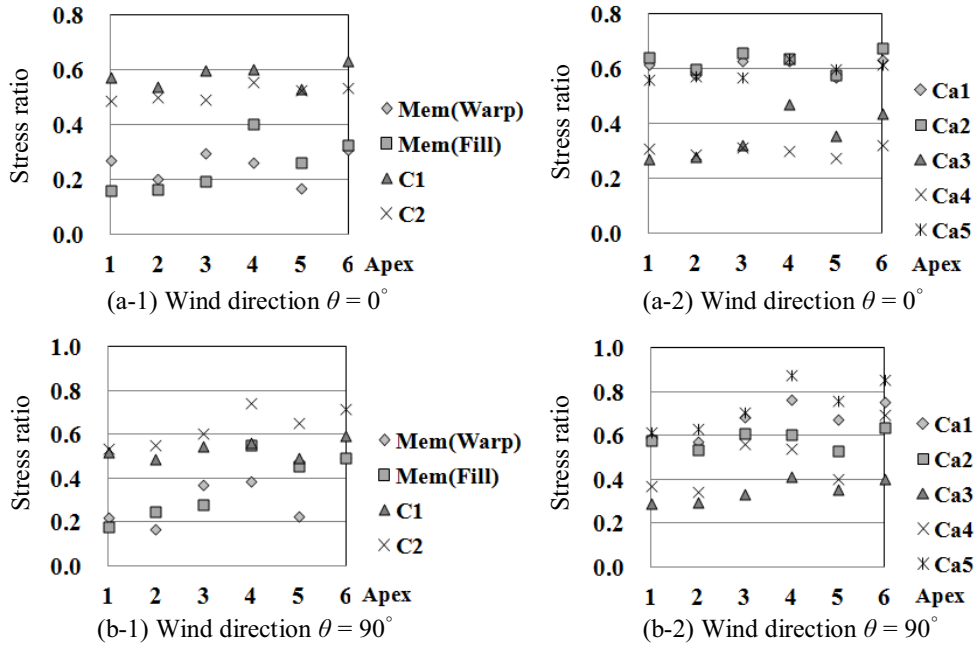

(a-1) Wind direction $\theta = 0^{\circ}$ (a-2) Wind direction $\theta = 0^{\circ}$

(b-1) Wind direction $\theta = 90^{\circ}$ (b-2) Wind direction $\theta = 90^{\circ}$

Figure 9. Stress ratio for Suspension model (S1)

Table 3. Load combination providing the maximum stress

Model	Wind direction	Member	Maximum Apex	Expected Apex	Ratio
F1	0°	Mem (Warp)	6	3	1.38
		B2	6	4	1.06
		B3	6	3	1.36
F2	0°	Mem (Warp)	6	3	1.01
		B1	6	4	1.03
S1	0°	Mem (Warp)	6	3	1.18
		C1	6	4	1.05
		Ca1	6	4	1.01
		Ca2	6	3	1.06
		Ca4	6	3	1.07

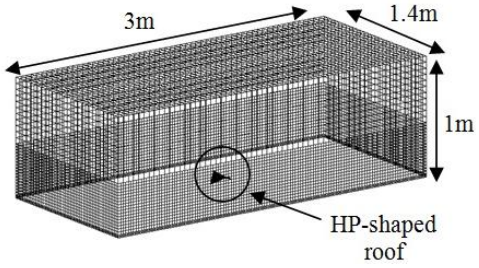

Figure 10. Numerical model

material constants (Table. 2) are also determined based on the Law and Standard. Moreover, the ratio of the computed stress to the allowable stress is calculated, which is called 'stress ratio' in the present paper. The each member size is determined so that the stress ratios are less than 1.0. Figure 8 and 9 shows the results of structural analyses for the F1 and S1 model, respectively. In the figures, the maximum stress ratios for the members, i.e. membrane (Mem), cable, column, beam and post, are shown for the six apexes of the hexagon in Figure 6.

5.3 *Load effects*

The design wind force coefficients are provided by the two combinations of C_L and C_{My} (or C_{Mx}) so that the incremental axial force induced in the columns becomes the maximum compression and tension. In this HP-shaped roof case, the two combinations are the ones corresponding to Apexes 3 and 4 for the wind direction $\theta = 0^o$ and Apexes 4 and 6 for the wind direction $\theta = 90^o$. The combination corresponding to one of the two Apexes (hereafter called "expected Apex") is expected to become the critical condition for the stress ratio of the members.

In Figures 8 and 9, the results for the wind direction $\theta = 90^o$ indicate that the stress ratio of them becomes the maximum for the combination of C_L and C_{Mx} corresponding to Apex 4 or 6 (hereafter called "maximum Apex"). On the other hand, for the wind direction $\theta = 0^o$, the stress ratio does not necessarily becomes the maximum for the combination of C_L and C_{My} corresponding to the Apex 3 or 4. Similar feature is also observed for F2 model. Such cases are summarized in Table 3. In the table, the load combination (i.e. the maximum Apex number) that provides the maximum stress in the member is shown, together with the ratio of the maximum stress to that corresponding to the expected Apex 3 or 4. The ratios for 'Mem' and B3 of F1 model are approximately 1.4, while the ratios range from 1.0 to 1.2 for the other members. The reason why the load combination other than the Apex 3 or 4 induces the maximum stress in the member is not clear at present. However, this may be due to the difference in stress distribution in the roof structure between rigid and flexible roofs. These results suggest that the design wind force coefficients proposed before will be improved so that they can be applied to flexible roofs.

6 EFFECT OF ROOF DEFORMATION

6.1 *CFD analyses of wind forces for the initial roof shapes*

First, CFD analysis is performed for the initial roof shapes of the F1, F2 and S1 models (hereafter "CFD1"). A three dimensional analysis with RANS (Reynolds Averaged Navier-Stokes) model is made by using an open source software named 'OpenFOAM version 1.5' in

Table 4. Boundary condition

Surface at X_{min} (Inlet)	Wind speed: $U_Z = U_{ref} \times (Z/Z_{ref})^{\alpha}$ U_{ref} = 8 m/s; Z_{ref} = 0.6 m; α = 0.18 Turbulence intensity: Experiment values (See Table 5.)
Surface at X_{min} (Outlet)	Surface pressure at outlet: 0 Pa
Surface at X_{min}, Y_{max}, Z_{max}	Free-slip wall
Surface at Z_{min}	No-slip wall
HP surface	No-slip wall

Table 5. Turbulence intensity at inlet

Z (m)	I_u
0 ~ 0.01	0.186
~ 0.02	0.179
~ 0.03	0.186
~ 0.05	0.172
~ 0.10	0.158
~ 0.20	0.111
~ 0.30	0.087
~ 0.40	0.063
~ 0.50	0.047
~ 1.00	0.035

order to calculate the mean C_D, C_L and C_{My} (or C_{Mx}) values. The computational domain is 1.0 × 1.4 × 3.0 m, in which an HP-shaped roof with the same configuration that we used in the wind tunnel experiment is placed as shown in Figure 10. The computation is based on a finite volume method, in which the SIMPLE (Semi-Implicit Method for Pressure Linked Equations) algorithm and the RNG (Re-Normalization Group) k-ε model are used. The boundary condition is summarized in Table 4. The turbulence intensity obtained from the wind tunnel experiment is used (Table 5). The distributions of the wind force coefficients obtained from CFD1 for θ = 0° are shown in Figure 11. Figure 12 shows a comparison for the mean C_L and C_{My} values between experiment and CFD1, and the mean C_D value from CFD1. The values for the S1 model are corrected for the difference in the roof area. It is seen that the results of CFD1 capture the general trend of the experimental results.

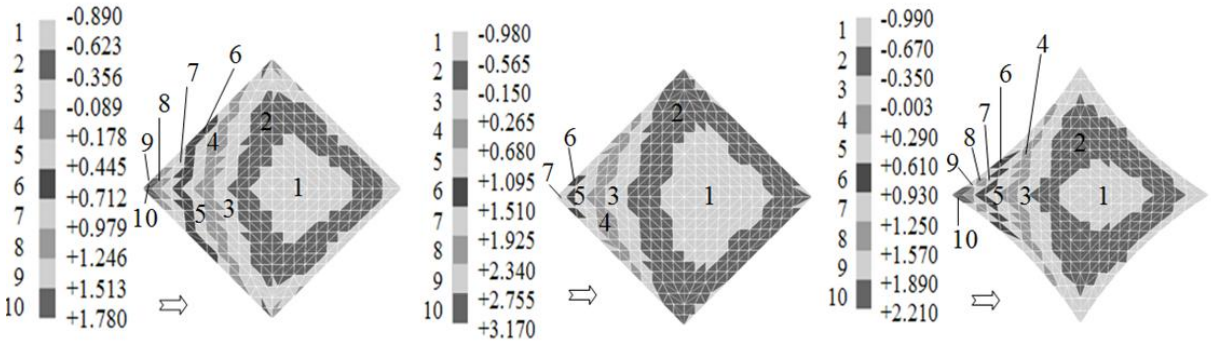

(a) F1 model (θ = 0°) (b) F2 model (θ = 0°) (c) S1 model (θ = 0°)

Figure 11. Wind force coefficients obtained from CFD1 for the initial roof shape

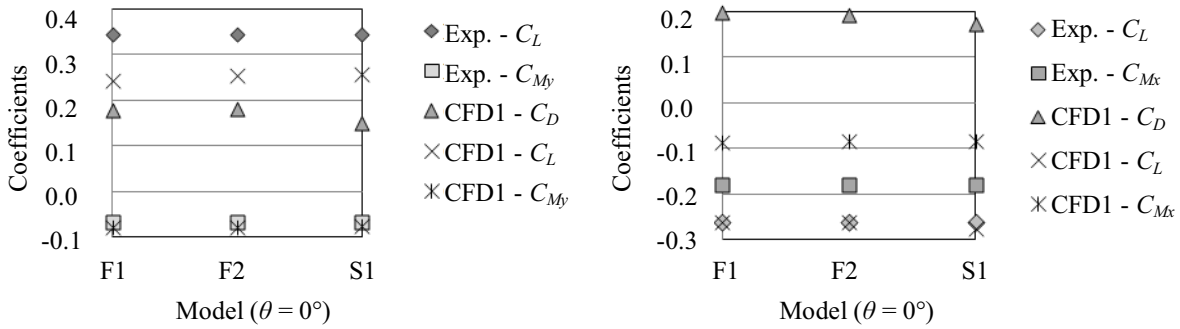

Figure 12. Comparison between experiment and CFD1 for the mean aerodynamic coefficients

6.2 *Effect of roof deformation on the wind forces*

The structural analysis is performed with the mean wind force coefficients obtained from CFD1 (hereafter "SA1"). The design wind speed is 31.5 m/s in the same way as Section 5.2. However, the value of G_f = 1.0 is used to obtain the time-averaged deformation. Then, CFD analysis is again performed for the deformed roofs obtained from SA1 (hereafter "CFD2"). The cross-sections of the roofs are shown in Figure 13. Figure 14 shows the distributions of the mean wind force coefficients on the deformed roofs. Comparing the results with those in Figure 11, it can be seen that the region of upward wind forces expands in the leeward division for the F2 and S1 models. This indicates that the roof deformation in the upward direction causes an increase in the wind force on the roof. Figure 15 shows a comparison for the mean C_D, C_L, and C_{My} values between CFD1 and CFD2. In the figure, the C_L and C_{My} values obtained from CFD2 for F2 and S1 models are approximately 4% to 18% larger than those from CFD1. These features may be caused by the expansion of the upward wind force region that is accompanied by the change of curvature of the membrane surface. Similar feature is observed for the wind direction θ = 90°.

The structural analysis is again made with the mean wind force coefficients obtained from CFD2 (hereafter "SA2"). Figure 16 shows the ratio of the maximum stress obtained from SA2 to that from SA1 for θ = 0°. It is seen that the stresses obtained from SA2 are generally larger than those from SA1. The ratios for the F1 model are up to 1.08, while those for the F2 and S1 models are up to 1.13. Similar feature is also observed for the wind direction θ = 90°. This feature may be related to the increase in the lift coefficient C_L, as shown in Figure 15. Moreover, the feature may be related to the arrangement and stiffness of the elements. From these results, a correction factor for the effect of roof deformation should be introduced in the proposed wind force coefficients.

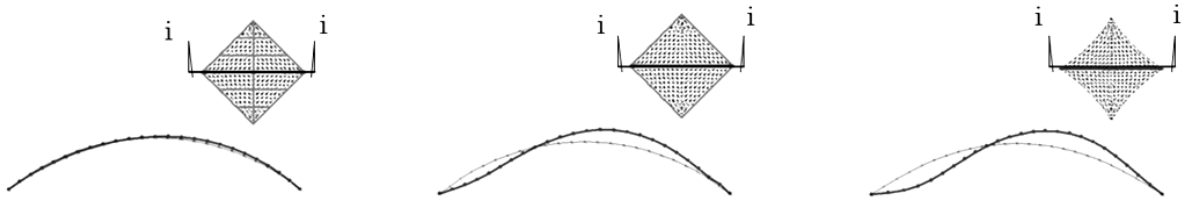

(a) F1 model (b) F2 model (c) S1 model

Scale factor for the displacement: 5 times

Figure 13. Cross-sections (i - i) of the deformed roofs obtained from SA1 for the wind direction θ = 0°

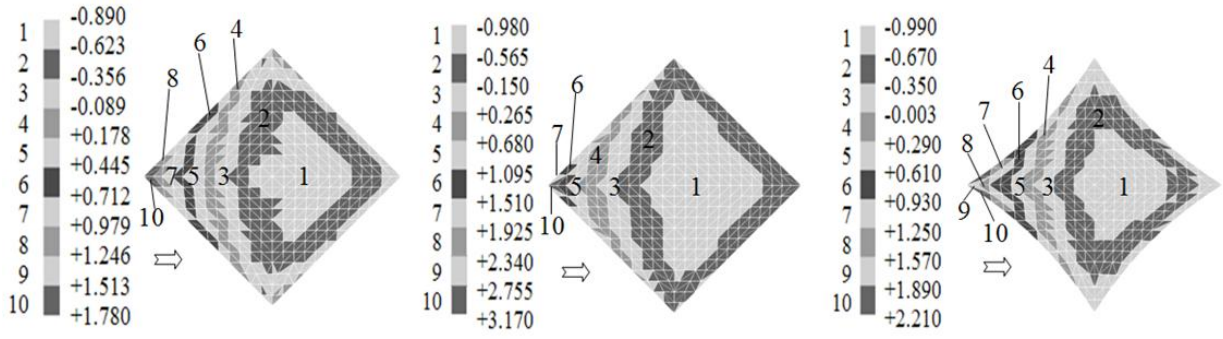

(a) F1 model (θ = 0°) (b) F2 model (θ = 0°) (c) S1 model (θ = 0°)

Figure 14. Wind force coefficients obtained from CFD2 for the deformed shape

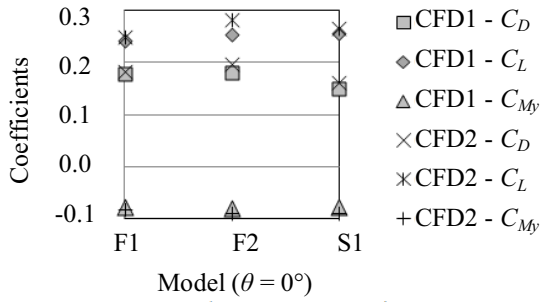

Figure 15. Comparison between CFD1 and CFD2

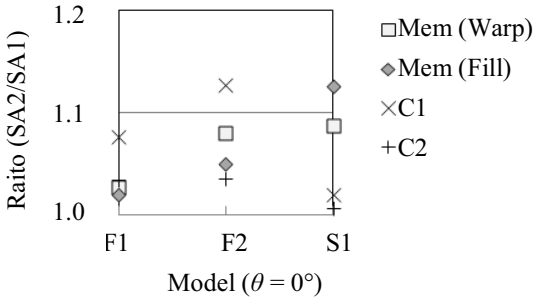

Figure 16. Ratio of the maximum stress obtained from SA2 to that from SA1

7 CONCLUDING REMARKS

The application of the design wind force coefficients obtained from the wind tunnel experiments with rigid models of HP-shaped free roofs to membrane structures has been investigated numerically, based on structural and CFD analyses. Focus is on the supporting system and roof deformation. Three types of membrane structure are considered, i.e. two frame types and one suspension type. First, the structural analyses are performed with the previously proposed design wind force coefficients to investigate the effects of supporting systems on the load effects. The maximum stress ratios for the members are calculated to identify the critical condition providing the maximum load effects. The results suggest that the previously proposed design wind force coefficients should be improved so that they can be applied to membrane roofs. Then, the mean wind forces coefficients on the initial HP-shaped roofs are computed numerically. The structural analysis is made with the mean wind force coefficients obtained from the CFD analysis to predict the time-averaged deformation of the membrane roofs. The CFD analysis on the deformed roofs is performed again. Moreover, the structural analysis is made again with the computed mean wind force coefficients on the deformed roofs. Finally, the load effects obtained from the second structural analyses are compared with those of the first structural analyses. The results indicate that a correction factor for the effect of roof deformation should be introduced in the wind force coefficients.

8 REFERENCES

1 P.K.F. Pun and C.W. Letchford, Analysis of a tension membrane hypar roof subjected to fluctuating wind loads, Third Asia-Pacific Symposium on Wind Engineering, Hong Kong, December 13-15, 1993.
2 Nagai Y., Okada A., Kanda M., Miyasato N. and Saitoh M., Study on wind response on horn-shaped membrane structure, Journal of Structural and Construction Engineering, AIJ, 2012, Vol.77 No.672, pp. 211-219.
3 Uematsu Y., Iizumi, E. and Stachopoulos, T., Wind force coefficients for designing free standing canopy roofs, Journal of Wind Engineering and Industrial Aerodynamics, 2007, Vol.95, pp.1486-1510.
4 Takeda F., Yoshino T. and Uematsu Y., Wind force coefficients for the design of a hyperbolic paraboloid free roof, Proceeding of the International Association for Shell and Spatial Structures (IASS) Symposium, Shanghai, China, 2010.
5 Uematsu Y., Arakatsu F., Matsumoto S. and Takeda F., Wind force coefficients for the design of a hyperbolic paraboloid free roof, Proceeding of Seventh Asia-Pacific Conference on Wind Engineering (APCWE-VII), Taipei, Taiwan, 2009.
6 Takeda F., Yoshino T. and Uematsu Y., Wind force coefficients for the design of a hyperbolic paraboloid free roof, USB flash drive of the 13th International Conference on Wind Engineering, Amsterdam, The Netherlans, 2011.

The Seventh International Colloquium on Bluff Body Aerodynamics and Applications (BBAA7)
Shanghai, China; September 2-6, 2012

Wind force characteristics of scaffoldings with sheets

Feng Wang [a], Yukio Tamura [b], Akihito Yoshida [c], Rei Okada [d]

[a]Tokyo Polytechnic University, Kanagawa, Japan, feng@arch.t-kougei.ac.jp
[b]Tokyo Polytechnic University, Kanagawa, Japan, yukio@arch.t-kougei.ac.jp
[c]Tokyo Polytechnic University, Kanagawa, Japan, yoshida@arch.t-kougei.ac.jp
[d]Tokyo Polytechnic University, Kanagawa, Japan, rei@arch.t-kougei.ac.jp

ABSTRACT: Wind loads have a very severe effect on the stability of scaffolding, especially when is covered with sheets of 0% porosity, which significantly changes the wind forces acting on it. Wind tunnel experiments were carried out based on a prototype of scaffolding attached to a medium-height building, and covered with sheets of 0% porosity. Wind force characteristics of scaffoldings with sheets for different building opening ratios and scaffolding arrangements were studied. For most scaffolding arrangements, both maximum positive and minimum negative wind force coefficients tended to be smaller when the building opening ratio was increased. When scaffolding was arranged on one side or encompasses half the building, local wind force coefficients of the scaffolding sheets were more sensitive to changes of building openings.

Keywords: Scaffolding sheet; Wind force coefficient; Wind tunnel experiment; Building opening ratio; Scaffolding arrangement.

1 INTRODUCTION

Scaffolding is a temporary structure used to support people and material in the construction or repair of buildings and other large structures. It is usually a modular system of metal pipes or tubes. For safety, environmental and noise considerations, it is commonly net clad or sheet clad. On construction sites, scaffolding collapses sometimes occur due to strong wind when the scaffolding is covered with sheets of 0% porosity, which significantly increases the wind forces acting on it (Katsutoshi Ohdo, 2005). Furthermore, buildings of different structural types have different kinds of wall openings during construction stages, which also significantly affect wind forces (F. Yue, 2005; Yasumichi Hino, et al, 2005). Thus, the influence of building opening ratios should be considered in the design stage when estimating wind forces acting on scaffolding. For different construction sequences and engineering needs, for a common rectangular section building, scaffolding arrangements vary from one side to all four sides, which affect the wind flow between building and scaffolding (Yasumichi Hino, et al, 2005).

In this study, wind tunnel experiments were carried out based on a prototype of scaffolding attached to a medium-height building, and covered with sheets of 0% porosity. A systemic study of the influence of different building openings on wind forces acting on scaffolding covered with sheets was conducted, and scaffolding arrangements were also taken into account.

2 EXPERIMENT SETUP

The experiments were carried out in the Boundary Layer Wind Tunnel of the Tokyo Polytechnic University, Japan. Two scaffolding sheet models 5mm thick and 0.363m high were selected to

simulate 0% porosity sheets covering scaffolding, attached to a medium-height building with 1/75 geometric scale.

304 pressure taps were arranged on both outer and inner sides of the two sheet models (Sheet A and Sheet B). 4 building opening ratios and 6 scaffolding arrangements were considered. Building opening ratios ϕ_B for Models B0, B20, B40, B80 were 0%, 20% 40%, 80%, respectively, and two dummy models (no pressure taps) of sheets were used in some scaffolding arrangements. Fig. 1 shows experiment pictures. Fig. 2 shows building models and scaffolding arrangements.

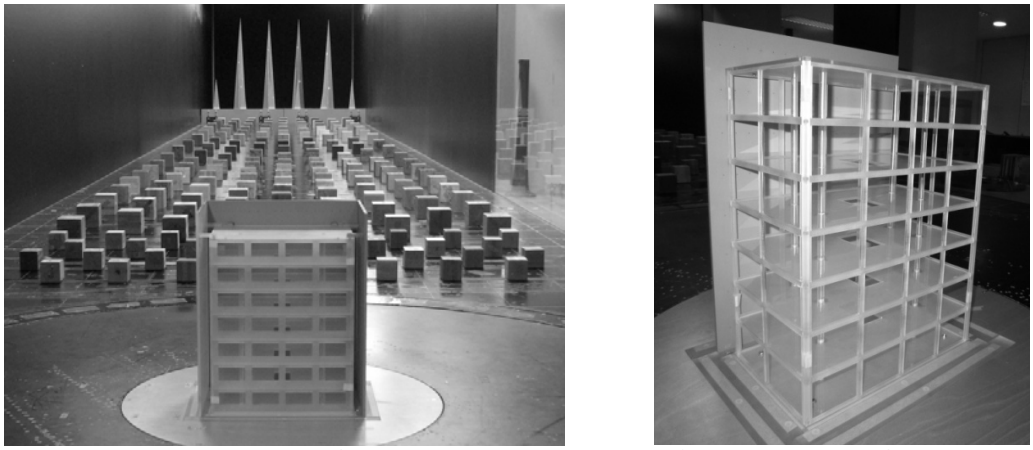

(a) U1 arrangement, ϕ_B =40% (b) I1 arrangement, ϕ_B =80%

Fig.1 Experiment pictures

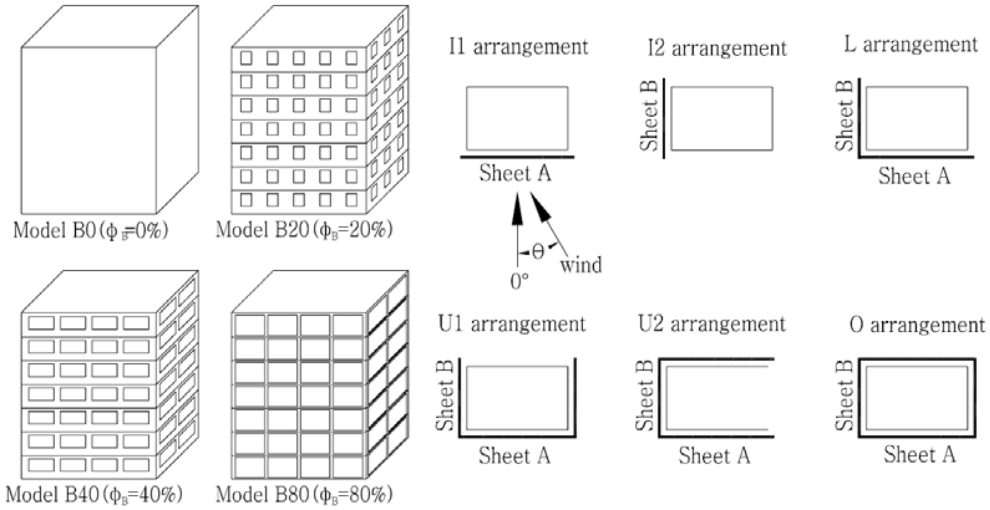

(a) Building models (b) Scaffolding arrangements

Fig. 2 Building models and scaffolding arrangements

Reference wind pressures recorded by a pitot tube and pressure data were simultaneously collected at 781.25Hz for a sampling period of 20 seconds for each sample, corresponding to 26Hz and 10 minutes in full scale. Wind direction was changed at intervals of 5 degrees for each test case. The top wind speed, U_H, was used to obtain the wind pressure coefficients. A turbulent boundary layer with a power-law exponent, α, of 0.2 (U_H≈8.8m/s, $I_{u,H}$≈21%) was simulated (Fig. 3). Experimental cases are shown in Table 1.

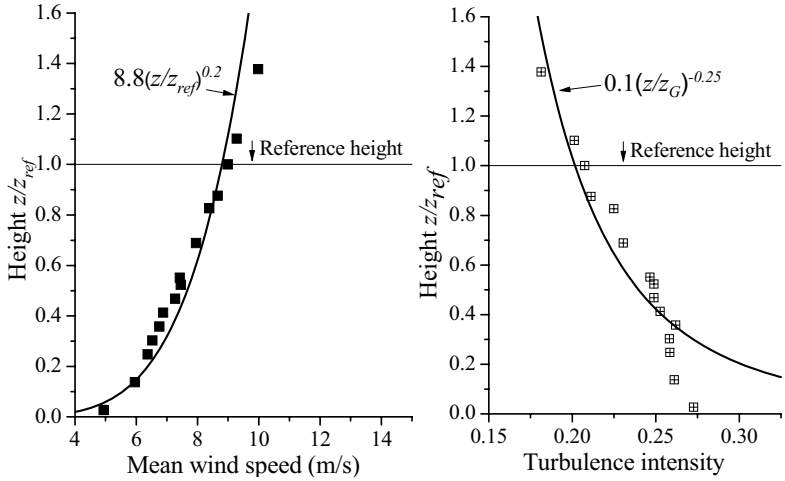

Fig. 3 Mean wind speed and turbulence intensity profile

Table 1 Experimental cases

Scaffolding arrange-ments	Building models	Wind directions
I1	Model B0, B20, B40, B80	0°~180°
I2	Model B0, B80	90°~270°
L	Model B0, B20, B40, B80	0°~360°
U1	Model B0, B20, B40, B80	0°~360°
U2	Model B0, B80	0°~360°
O	Model B0, B20, B40, B80	0°~360°

3 RESULT

Wind pressures measured on the models were expressed in the form of a non-dimensional pressure coefficient, defined as:

$$C_{p,\ outer} = \frac{P_{outer} - P_0}{0.5\rho U_H^2} \qquad C_{p,\ inner} = \frac{P_{inner} - P_0}{0.5\rho U_H^2} \tag{1}$$

where $C_{p,outer}$ and $C_{p,inner}$ are the wind pressure coefficients of the model's outer and inner surfaces, respectively, P_0 is the static reference pressure, U_H is the mean longitudinal wind speed at the reference height(model top) and ρ is air density. Wind force coefficient $C_f = C_{p,outer} - C_{p,inner}$, namely, net pressure coefficient. Thus, the positive wind force coefficient direction is from outside to inside. The maximum and minimum peak wind force coefficients are expressed as $C_{f,max}(i,\theta,\phi_B)$ and $C_{f,min}(i,\theta,\phi_B)$, respectively, where i and θ indicate the i-th pressure tap and the approaching wind direction, and ϕ_B is building opening ratio.

3.1 *Local mean wind force coefficient*

3.1.1 *Local mean wind force coefficient distribution*

The maximum local mean C_f usually occurs near wind direction 45 degrees for scaffolding arrangement I1. Fig. 4 shows the local mean C_f distribution of model Sheet A for scaffolding arrangement I1 and wind direction 45 degrees. The maximum local mean C_f occurs at the top corner of the model when ϕ_B (building opening ratio) increases, and the value of the maximum local mean C_f becomes smaller, from 2.6 decreasing to 1.8 at the corner of the model.

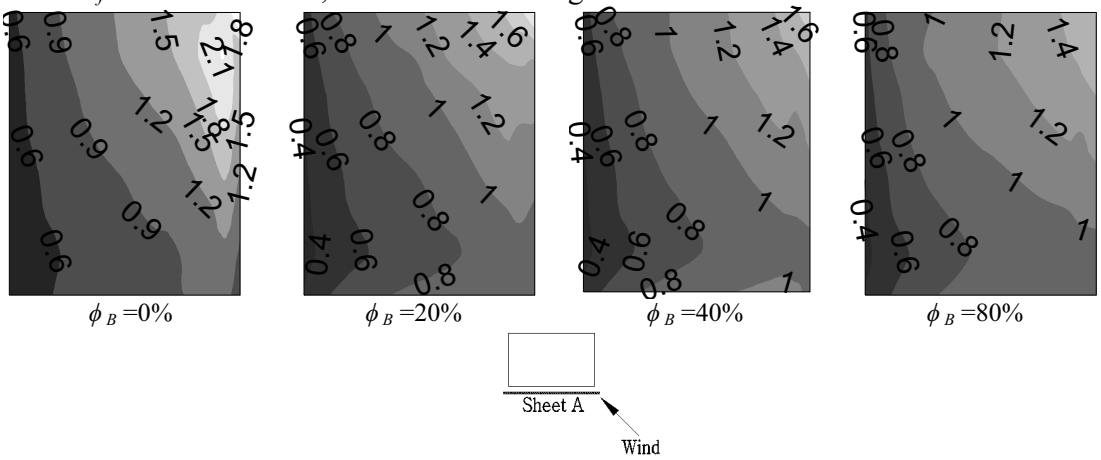

Fig.4 Local mean wind force coefficient distribution, arrangement I1, 45 degrees (Sheet A)

The minimum local mean C_f was found near wind direction 90 degrees, with wind flow almost parallel to the scaffolding sheet. When ϕ_B increased from 0% to 80%, local mean C_f became smaller, and was from -1.2 to -1.3 at the top corner. Thus, when ϕ_B increases, the changing tendencies of both the maximum and minimum local mean C_f are decrease.

Fig. 5 shows the distribution of mean $C_{p,outer}$ and $C_{p,inner}$ of Sheet A for different ϕ_B(0% and 80%). It shows almost the same distributions of $C_{p,outer}$, but for $C_{p,inner}$, they are quite different in both values and distribution. When ϕ_B increases from 0% to 80%, the mean $C_{p,inner}$ at the corner changes from -1.8 to around -0.8. When ϕ_B increases, the mean $C_{p,inner}$ increases and the mean $C_{p,outer}$ remains almost the same. Thus, the mean net pressure coefficients become smaller, namely, local mean C_f tend to be smaller.

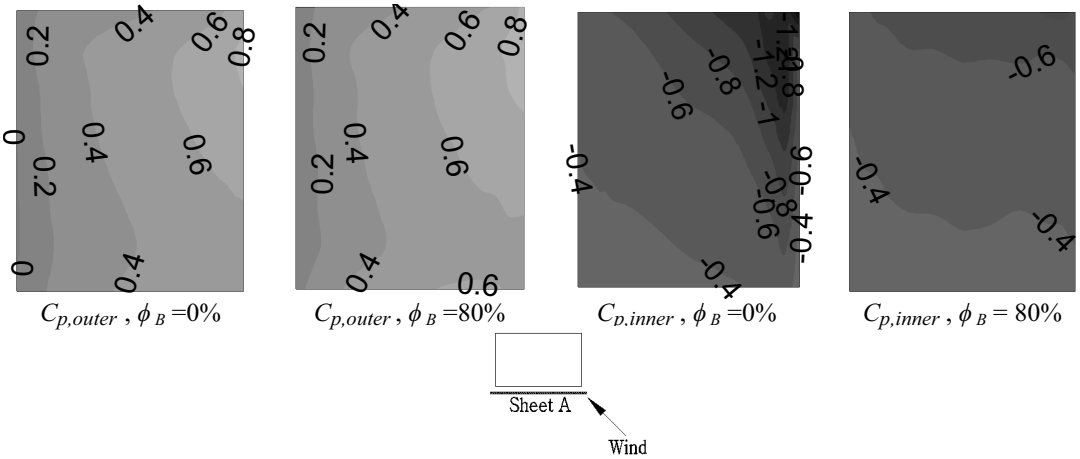

Fig.5 Mean wind pressure coefficient distribution of outer and inner surface, arrangement I1, 45 degrees (Sheet A)

For other scaffolding arrangements, both the maximum and minimum local mean C_f positions are usually located on the top layer or side edge. From the experimental results, the distribution and tendency of local mean C_f on model Sheet B is similar to that on model Sheet A, except that the maximum value is smaller.

Unfavourable wind direction is the direction that causes a maximum or minimum local mean C_f on the models. When the scaffolding arrangement was I1, I2, L, or U1, the unfavourable wind directions changed within the range of ±25º for different ϕ_B. This means that the opening ratio of the building didn't greatly change the unfavorable wind direction for these arrangements. When the scaffolding arrangement was U2 or O, the unfavourable wind directions changed a lot within the range of ±80º for different ϕ_B.

3.1.2 *Local fluctuating wind force coefficients*

The standard deviation values show the fluctuating characteristic of C_f. Fig. 6 shows the local fluctuating C_f distribution of arrangement I1 of Sheet A. 45 and 90 degrees are unfavourable wind directions for the maximum positive and minimum negative local mean C_f, respectively. When ϕ_B changes from 0% to 80%, the maximum local fluctuating C_f becomes smaller (from 1.0 to 0.5) at wind direction 45 degrees but becomes larger (from 0.7 to 0.8) at wind direction 90 degrees. When ϕ_B=0%, maximum local fluctuating C_f occurs at wind direction 45 degrees, but when ϕ_B=80%, maximum local fluctuating C_f occurs at wind direction 90 degrees. Thus, building opening ratio significantly affects the fluctuating characteristic of C_f.

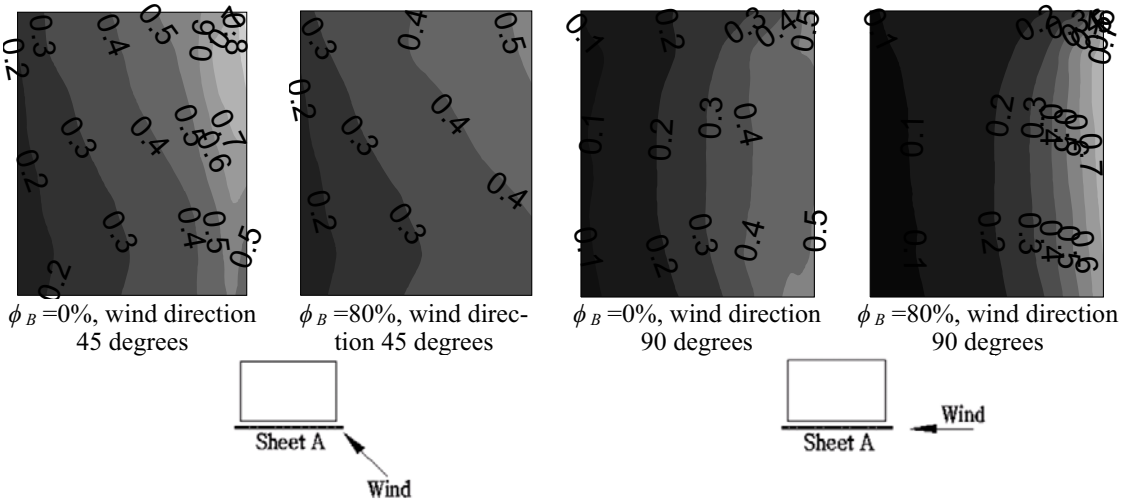

ϕ_B =0%, wind direction 45 degrees | ϕ_B =80%, wind direction 45 degrees | ϕ_B =0%, wind direction 90 degrees | ϕ_B =80%, wind direction 90 degrees

Fig.6 Local fluctuating wind force coefficient distribution, arrangement I1 (Sheet A)

The maximum local fluctuating C_f usually occurs on the top layer or side edge of the model. When scaffoldings is in O arrangement, which all four sides of the building encompassed, the value of local fluctuating C_f is almost unchanged by the effect of ϕ_B.

3.2 *Local peak wind force coefficient*

An "Equivalent time averaging" method was used to determine the wind load acting on a finite area from point pressure. 0.0038s corresponding to 0.11s in full scale was, used for time averaging. The peak force coefficients were calculated by the "Cook-Mayne method" using the maximum values (for positive wind force coefficient) and minimum ones (for negative wind force coefficient) of 10 samples.

3.2.1 *Local peak wind force coefficient distribution*

Local $C_{f,max}$ and $C_{f,min}$ distribution was similar to local mean C_f distribution. Both maximum and minimum peak values usually occurred on the top layer or side edge of the model in most scaffolding arrangements. Usually, the maximum local $C_{f,max}$ occurred when ϕ_B =0% and the minimum local $C_{f,min}$ occurred when ϕ_B =80%. Fig. 7 shows the local $C_{f,max}$ distribution of Sheet A of all wind directions when ϕ_B =0%. Fig. 8 shows the local $C_{f,min}$ distribution of Sheet A of all wind directions when ϕ_B =80%. Scaffolding arrangements I1, L and O represent the conditions of a building single side clad, half clad and completely clad a building, respectively. The figures show that both maximum and minimum local peak values were smaller for arrangement O than for arrangements I1 and L. The maximum local $C_{f,max}$ of arrangement I1 is 7.6, larger than the value 6.2 for arrangement L, the minimum local $C_{f,min}$ for arrangements I1 and L are both -6.4.

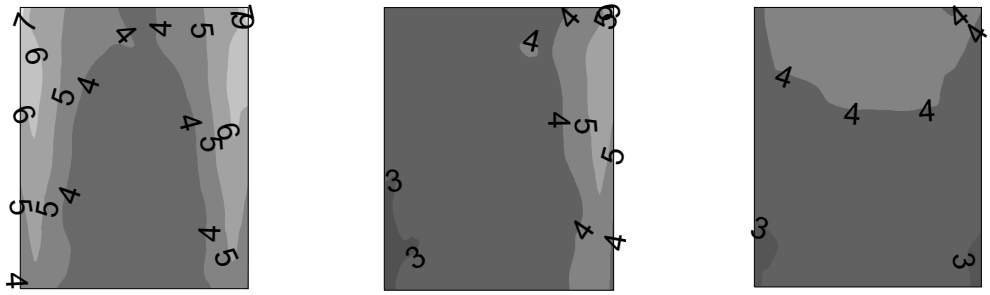

Arrangement I1 Arrangement L Arrangement O

Fig.7 Local $C_{f,max}$ distribution, ϕ_B =0%, all wind directions (Sheet A)

Arrangement I1 Arrangement L Arrangement O

Fig.8 Local $C_{f,min}$ distribution, ϕ_B =80%, all wind directions (Sheet A)

3.2.2 *Effect of building opening ratio and scaffolding arrangement*

Fig. 9 compares the maximum local $C_{f,max}$ *(i,θ)* and minimum local $C_{f,min}$ *(i,θ)* of model Sheet A for different building opening ratios. For arrangement I1, when ϕ_B increases from 0% to 80%, the maximum local $C_{f,max}$ *(i,θ)* becomes smaller, changing from 7.6 to 5.3, and the minimum local $C_{f,min}$ *(i,θ)* also becomes smaller, from -5.4 to -6.4. For arrangement L, when ϕ_B increases from 0% to 80%, the maximum local $C_{f,max}$ *(i,θ)* becomes smaller, changing from 6.2 to 4.2, and the minimum local $C_{f,min}$ *(i,θ)* also becomes smaller, from -5.6 to -6.4. For arrangements U1 and U2, both the maximum local $C_{f,max}$ *(i,θ)* and minimum local $C_{f,min}$ *(i,θ)* are almost unchanged, within the range of ±0.3 for different ϕ_B. For arrangement O, when ϕ_B increases from 0% to 80%, the maximum local $C_{f,max}$ *(i,θ)* becomes smaller, changing from 4.4 to 4.2, but the minimum local $C_{f,min}$ *(i,θ)* becomes larger, changing from -4.6 to -4.

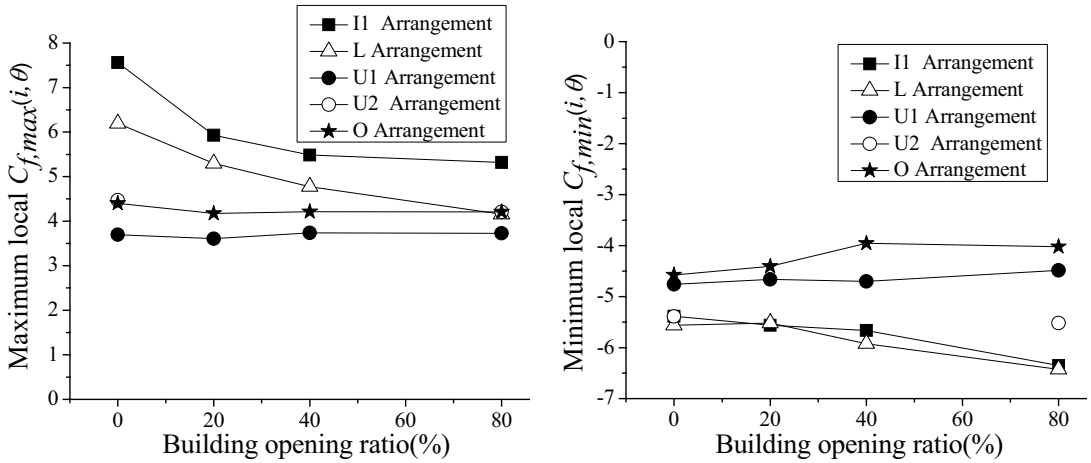

Fig. 9 Maximum local $C_{f,max}$ (i,θ) and minimum local $C_{f,min}$ (i,θ) for each building opening ratio (Sheet A)

From Fig. 10, it is clear that when ϕ_B increases from 0% to 80%, for arrangements I1 and L, the absolute values of both the maximum local $C_{f,max}$ (i,θ,ϕ_B) and minimum local $C_{f,min}$ (i,θ,ϕ_B) become significantly smaller, with a largest difference of 2.3. For arrangements U1, U2 and O, the maximum local $C_{f,max}$ (i,θ,ϕ_B) and minimum local $C_{f,min}$ (i,θ,ϕ_B) vary within the range of ±0.6 for different ϕ_B. Thus, for scaffolding arrangement I1 or L, the local peak $C_f(i,\theta)$ is more sensitive to building openings than for arrangements U1, U2 and O.

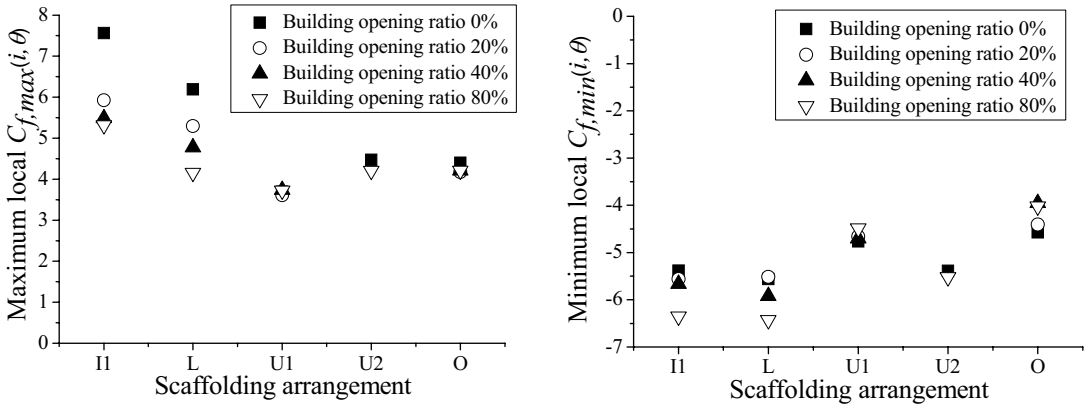

Fig. 10 Maximum local $C_{f,max}$ (i,θ) and minimum local $C_{f,min}$ (i,θ) for each scaffolding arrangement (Sheet A)

Fig. 11 shows local $C_{f,max}$ (i,θ) for wind direction ϕ_B= 0%. For scaffolding arrangements I1 and L, the maximum local $C_{f,max}$ (i,θ) are larger. For arrangement U1, the maximum local $C_{f,max}$ (i,θ) is smaller than those for the other arrangements. The maximum local $C_{f,max}$ (i,θ) of arrangements I1, L and U2 occur near wind direction 45 degrees. For scaffolding arrangements U1 and O, the maximum local $C_{f,max}$ (i,θ) were found near wind direction 0 degrees.

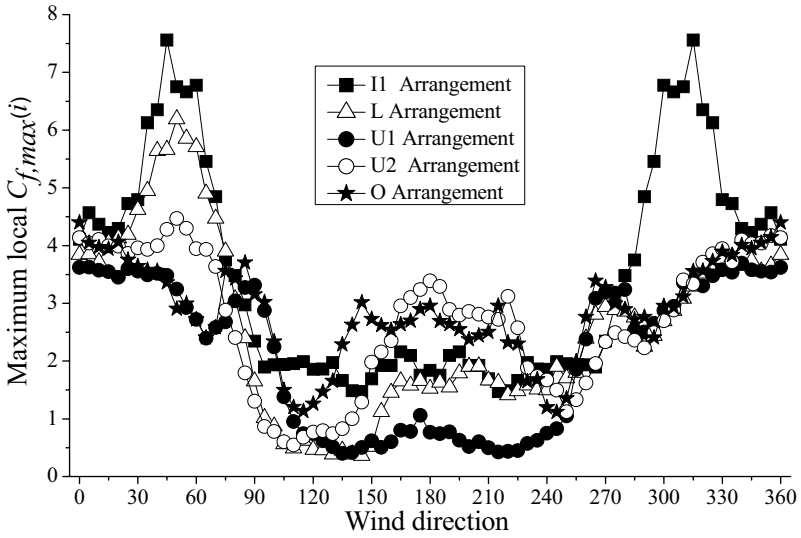

Fig. 11 Maximum local $C_{f,max}(i)$ for each wind direction, φ_B =0%(Sheet A)

3.2.3 *Comparison of model Sheets A and B*

The previous section discussed the characteristics of wind force acting on model Sheet A. This section compares model Sheets A and B. For scaffolding arrangements I(I1 or I2), L, and O, the distributions and changing tendencies of wind force on model Sheet B are similar to those on model Sheet A. Table 2 compares local $C_{f,max}(i,\theta,\phi_B)$ and $C_{f,min}(i,\theta,\phi_B)$ for model Sheets A and B. For arrangements I and L, the maximum local $C_{f,max}(i,\theta,\phi_B)$ value for Sheet A is larger than for Sheet B, but the minimum local $C_{f,min}(i,\theta,\phi_B)$ value is almost the same. For arrangement O, the absolute value of both maximum local $C_{f,max}(i,\theta,\phi_B)$ and minimum local $C_{f,min}(i,\theta,\phi_B)$ of Sheet B is smaller than of Sheet A, with a difference of around 0.5.

Table 2 Maximum local $C_{f,max}(i,\theta,\phi_B)$ and minimum local $C_{f,min}(i,\theta,\phi_B)$ of model Sheet A and Sheet B

Scaffolding arrangement	Maximum local $C_{f,max}(i,\theta,\phi_B)$		Minimum local $C_{f,min}(i,\theta,\phi_B)$	
	Sheet A	Sheet B	Sheet A	Sheet B
I1 or I2	7.6	6.6	-6.4	-6.5
L	6.2	4.6	-6.4	-6.4
U1	3.7	4.1	-4.8	-6.4
U2	4.5	4.1	-5.5	-4.2
O	4.4	4	-4.6	-4.1

For arrangements U1 and U2, the absolute values of both the maximum local $C_{f,max}(i,\theta,\phi_B)$ and the minimum local $C_{f,min}(i,\theta,\phi_B)$ of Sheet A is larger for arrangement U2 and that of Sheet B is larger for arrangement U1. For scaffolding arrangement U1, scaffolding sheets are located on both two adjacent sides of Sheet A, which diminish the absolute value of both the maximum local $C_{f,max}(i,\theta,\phi_B)$ and minimum local $C_{f,min}(i,\theta,\phi_B)$ of Sheet A. For Sheet B in arrangement U2, the absolute value of the minimum local $C_{f,min}(i,\theta,\phi_B)$ of Sheet B is also smaller due to the existence of the two adjacent side sheet models. Sheet A in arrangement U2 and Sheet B in arrangement U1 are the conditions with only one adjacent side scaffolding sheet model, which is similar to arrangement L.

3.3 *Total panel force coefficient*

For most wind load recommendations for scaffoldings, the resultant wind force F is calculated by a equation including three components: a velocity pressure, a reference area of scaffolding and a wind force coefficient C_f. C_f is usually used as a total panel C_f. In this study, the total panel C_f of each experimental case was calculated.

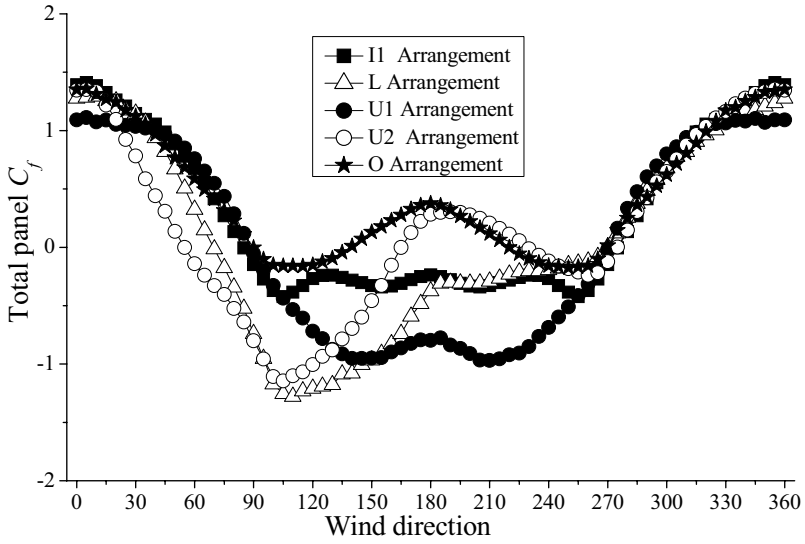

Fig. 12 Total panel C_f for each wind direction, φ_B =0%(Sheet A)

Fig. 12 shows the total panel C_f of model Sheet A for different scaffolding arrangements and each wind direction. Maximum positive total panel C_f occurs at wind direction near 0 degrees for each scaffolding arrangement, and its value is around 1.3 to 1.4, except for arrangement U1, which is 1.1. Minimum negative total panel C_f occurs at wind directions between 105 and 115 degrees for most scaffolding arrangements, except arrangement U1 at 150 degrees. The values are quite different. The minimum negative total panel C_f of arrangement L is the smallest, at around -1.3.

For other building opening ratios, the tendency of most scaffolding arrangements for both maximum positive and minimum negative total panel C_f become smaller when ϕ_B increases from 0% to 80%, but arrangement O has the inverse effect and becomes larger. Model Sheets B and A have the same tendencies as these results.

4 CONCLUDING REMARKS

Wind force characteristics of scaffoldings with sheets for different building opening ratios and scaffolding arrangements were studied from wind tunnel experiment results. The conclusions are:

(1) Local peak wind force coefficients usually occur on the top layer or side edge of a scaffolding sheet, and are significantly affected by building opening ratio. For most scaffolding arrangements, both maximum positive and minimum negative wind force coefficients tend to become smaller when building opening ratio increases.

(2) When scaffolding is arranged on one side or encompasses half a building, local wind force coefficients of scaffolding sheets are more sensitive to change of building openings. When scaf-

folding does not completely encompass a building, wind loads on the scaffolding sheet are larger.

5 ACKNOWLEDGEMENTS

This study was funded by the Ministry of Education, Culture, Sports, Science and Technology, Japan, through the Global Center of Excellence Program, 2008-2012, which is gratefully acknowledged.

6 REFERENCES

[1] F. Yue, Y. Yuan, G. Q. Li, K. M. Ye, Zh. M. Chen, and Zh. P. Wang, Wind Load on Integral-Lift Scaffolds for Tall Building Construction，Journal of Structural Engineering, 131(2005)816-824.
[2] H. Irtaza, R.G.Beale, M.H.R.Godley, A wind-tunnel investigation into the pressure distribution around sheet-clad scaffolds, Journal of Wind Engineering and Industrial Aerodynamics, 103(2012)86-95
[3] K. Ohdo, S. Takanashi, Y. Hino, K. Saito, Measurement of wind load acting on the scaffolds, Specific Research Reports of the National Institute of Industrial Safety, NIIS-SRR-NO.31, 2005 (in Japanese), pp. 9-18.
[4] Y. Hino, S. Phongkumsing, Study on the Estimation Method of Wind Pressure Acting on the temporary Scaffolds, Specific Research Reports of the National Institute of Industrial Safety, NIIS-SRR-NO.31, 2005 (in Japanese), pp. 27-42.

The Seventh International Colloquium on Bluff Body Aerodynamics and Applications (BBAA7)
Shanghai, China; September 2-6, 2012

Towards a better understanding of pressure equalization

Carine van Bentum [a], Ivo Kalkman [a], Chris Geurts [a,b]

[a] *TNO, Delft, The Netherlands*
b Eindhoven University of Technology, Dept. of the Built Environment, the Netherlands

ABSTRACT: A series of wind tunnels tests are presented on a cube, equipped with a permeable outer layer. The influences of cavity depth and opening width have been investigated. This research shows that a wind direction of 75 degrees with respect to the considered panel gives the highest differential pressures relevant for cladding. For smooth flow conditions uniform cavity flows are found, with local effects at the openings in the reattachment zones. Large gaps and small cavity depths have a positive effect on pressure equalization. However, the varied gap width and cavity depth in the current study show minimal effects. It is possible that measures leading to significant effects are outside the range of current practice.

KEYWORDS: Local wind loads, pressure equalization, building facades

1 INTRODUCTION

Rain screen facades are being applied frequently. The façade consists of an air tight inner layer, a cavity (usually partially filled with thermal insulation) and a permeable outer layer. This outer layer can be made of a variety of materials, e.g. natural stone, wood or metal. The permeability allows the pressures over the cladding to equalize. This minimizes the pressure difference over the cladding, thus preventing rain ingress, and reducing the local wind loads. As a result, relative lightweight solutions for the façade and its fixings can be applied. The extent of pressure equalization is sensitive to the detailing of the façade. A number of parameters, such as cavity depth, opening ratios, the extent to which compartments are realized in the cavity, and the complexity of the flow nearby the building influence the pressure distributions over the façade. The relation between these parameters and the pressure distributions are not explicitly known, which makes it difficult to accurately predict the differential pressure over individual façade elements.

The majority of research on pressure equalization has been carried out with respect to rain penetration. The relevant pressures in those studies is the pressure at the windward side of a building, which is the driving force for wind-driven rain. Brown et al. (1991) conclude that the cavity volume should be minimized to improve the speed of pressure equalization, since it reduces the amount of airflow required. Studies of Inculet & Davenport (1994) and Van Schijndel & Schols (1998) show that the higher frequency pressures (>0.1-1.0 Hz) are more damped than the lower frequency pressures.

For wind loads on permeable façades the pressure in the separation zones at the side faces of the building is of relevance. From wind tunnel tests, carried out by Gerhardt & Kramer (1983) and Gerhardt & Janser (1994), it was concluded that the detailing of the extremities, open or closed, has a major effect on the pressure equalization and the differential pressures near corners. The largest mean differential pressures are found at the reattachment point, where the mean external pressure has its minimum. For peak pressures, the largest differential pressure occurs near the

leading edge, where the flow is fully separated. Both for the means and peaks, smooth flow leads to the highest values. A good correlation between cavity flow and external flow is found for small gap widths where the gap flow resistance is high.

Cheung and Melbourne (1988) have performed an extensive wind tunnel study on permeable roofs where they varied the porosity of the roof and the cavity volume. The effect of the internal volume depends upon the distance from the leading edge and of the porosity. Except for regions very close to the leading edge (x/L<0.02), a combination of high porosity and small internal volume leads to the highest reduction in mean differential pressures. The effect of the internal volume on the peak differential pressures is small.

A simple test has been set up to separately investigate these parameters. This paper focusses on the effect of the cavity volume and opening width on the wind loading of façade elements.

2 EXPERIMENTAL SET-UP

A research project has been set up in the Netherlands, to understand the local wind loads of rain screen facades. A full scale, in-situ, test has been started on a 150 m high building in Rotterdam, and both CFD and wind tunnel work has been planned. This paper deals with a wind tunnel test in which parametric studies are carried out. The wind tunnel experiments were carried out in the open circuit atmospheric boundary layer (ABL) wind tunnel of TNO in the Netherlands. Pressure measurement have been performed on a floating cube with dimensions 60x60x60 cm positioned at half tunnel height (h_{ref}). Measurements were done with a smooth up-stream fetch and no roughness elements. The oncoming flow was measured above the center of the turntable with a one-component Dantec Dynamics hot wire anemometer. Ten measurements were performed with a 500 Hz sampling frequency for a total period of approximately 41 s. At a velocity of 15.16 m/s (+/- 0.04 m/s) the turbulence intensity was 0.38% (+/- 0.05%). The main flow properties are given Figure 1.

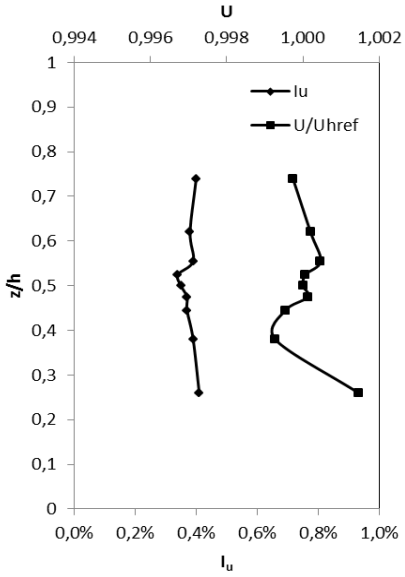

Figure 1. Main flow properties

The cube consists of an airtight inner cube and an outside layer. This layer consists of flat plates with open joints of 8 mm width. Figure 2 gives the outline of the cube. External pressures

and cavity pressures, and flow speeds in the cavity have been measured at different angles of attack. The reference dynamic pressure and oncoming flow velocity (U_{ref}=14.9 m/s) have been measured using a pitot static probe at half the height of the model. The pressures were simultaneously sampled at 20Hz. For every wind direction, 32 time series of 60 s each have been obtained.

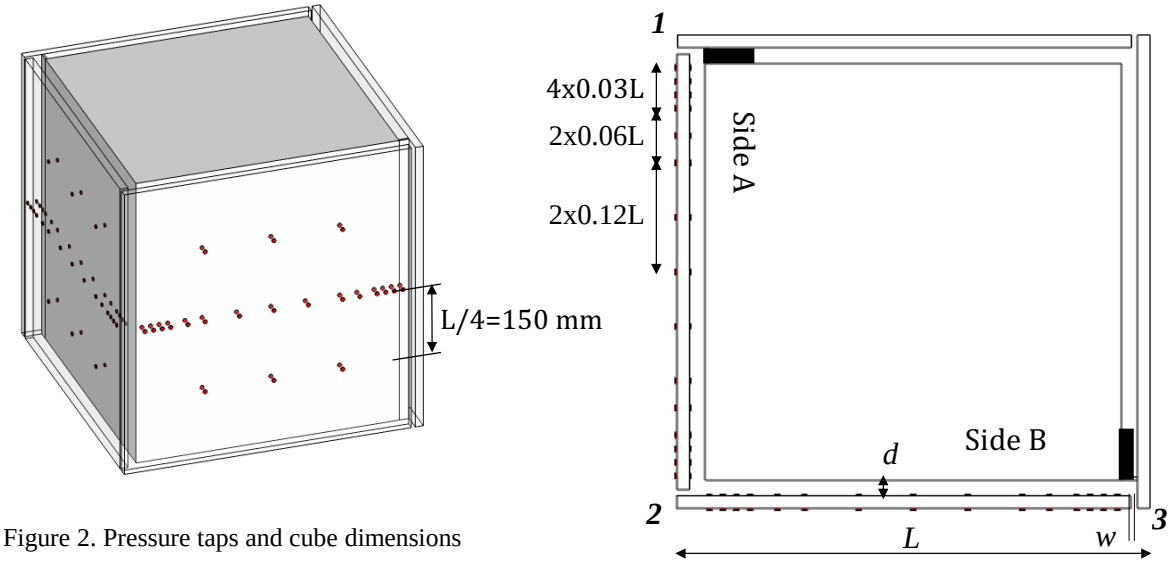

Figure 2. Pressure taps and cube dimensions

Mean, standard deviation and peak pressure coefficients are derived for each of these series according to:

$$C_p(\theta,t) = \frac{p(\theta,t) - p_a(\theta,t)}{\frac{1}{2}\rho U_{ref}^2} \quad (1)$$

Of which both mean values $\bar{C}_p$ and peak-values $\hat{C}_p$ are presented. Using the time signals of external p_e and cavity pressures p_c, time series of the differential pressure were derived. The resulting differential pressure coefficients C_{pdiff} are given by:

$$C_{pdiff}(\theta,t) = \frac{p_e(\theta,t) - p_c(\theta,t)}{\frac{1}{2}\rho U_{ref}^2} \quad (2)$$

Negative values correspond to a direction pointing outwards of the cube and positive values towards the cube.

The purpose of this paper is to show the effects of opening size and cavity width on the peak differential pressures. To study these effects, the configurations described in table 1 have been used. C0 consists of measurements of external pressures only on a closed cube. The basic configuration is C1A, with a gap width of 8 mm and a cavity depth of 20 mm. These sizes correspond on a 1:1 scale to measures found in current practice. The effects of the gap width and cavity depth are investigated by applying the other configurations of table 1.

Table 1. Configurations

Configuration	Gap width	Cavity depth	Outer dimensions	Opening 1	Opening 2	Opening 3
	w (mm)	*d* (mm)	*L*x*L* (mm)	*x*/*L* (-)	*x*/*L* (-)	*x*/*L* (-)
C0 (closed)	0	0	600x600	-	-	-
C1A (reference)	8	20	600x600	-0.97	-0.03	0.97
C1D	4	20	600x600	-0.97	-0.03	0.97
C1E	16	20	600x600	-0.96	-0.04	0.96
C1F	8	10	580x580	-0.97	-0.03	0.97
C1G	8	40	640x640	-0.97	-0.03	0.97

3 RESULTS

Results are presented for two sides of the cube (referred to as side A and side B, see figure 2), for approach flow directions towards those sides. This section starts with the external pressure distribution over C0, the closed cube. Subsequently, the pressure distributions over the outer layer and cavity are given for reference case C1A, followed by data obtained after varying the opening width and cavity depth.

3.1 *Cube without openings (C0)*

The mean external pressure coefficients of the closed cube are given in figure 3 for 4 angles of attack, zero being the direction perpendicular to side B. For the purpose of this study, the negative external peak pressure coefficients are of main interest. The mean peak external pressure coefficients are given in figure 4. The approach flow direction of 15 degrees give the largest external loads on side A. Note that these values correspond to approach flow direction of 75 degrees for side B, because of symmetry over the diagonal.

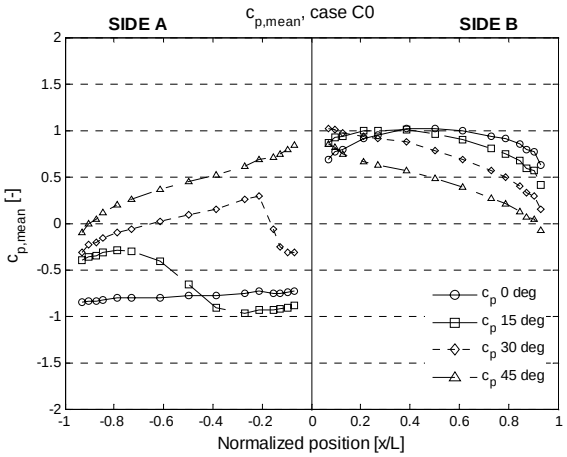

Figure 3: Mean pressure coefficient

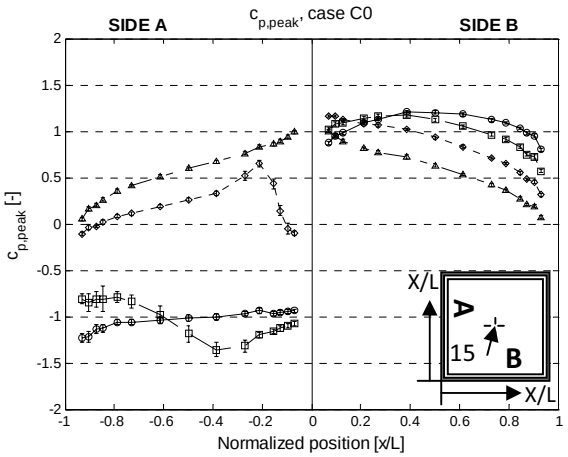

Figure 4: Peak pressure coefficient

The mean pressure distributions show that the positive pressure coefficients decrease with increasing angle of attack, while simultaneously there is a shift of the maximum value towards the leading edge. At side A, the flow direction of 15 degrees show a clear separation zone, as well as reattachment. The mean peak pressure coefficients (0,1s peaks) are slightly higher, and have their maximum of -1.4 at x/L=-0.39 by 15 degrees angle of attack. At the reattachment zone high standard deviations are found, which affect the mean peak pressure coefficients of this flow direction.

The values for this cube have been compared with earlier reported values in literature. Unfortunately, no values for a non-surface mounted "floating" cube could be found by the authors. Data considered are surface mounted cubes and 2-dimensional cylinders with square cross-section. Measurements of the pressure distribution around square cylinders in turbulent flow have been presented by Lee (1975). A cube in uniform flow has been reported by Baines (1965).

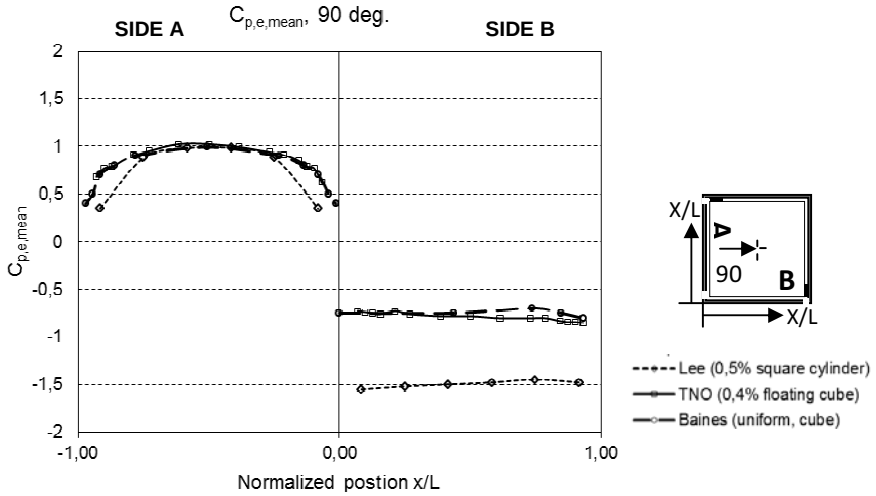

The floating cube is best comparable with a surface-mounted cube in uniform flow field and end effects dominate the flow.

3.1 *Differential pressures over a permeable layer: the reference case*

The reference case has 3 openings (see figure 2): one at the leading edge of side A (2), one at the trailing edge of A (1) and one at the trailing edge of side B (3). Figure 5 shows the mean values of the external pressure coefficients and the cavity pressure coefficients for 4 angles of attack. The flow directions contain the highest pressures for side A (15 degrees) and B (75 degrees). The external pressure is not affected by the openings, resulting in the same external pressure coefficients as for the closed cube. At side A, the cavity pressures are dominated by opening 1, whereas at side B, the cavity pressures are determined by both openings (2 and 3). As expected the pressure in the cavity is uniform, except from local effects near the openings.

Figure 6 presents the mean peak pressure coefficients. Due to higher external pressures at the openings, the mean peak pressure coefficients of the cavities are higher than the mean pressure coefficients. Since the turbulence is low, the effect is rather small. As already concluded by Geurts (2000, 2005) pressure equalization is a very fast process and all external fluctuations are immediately followed by the cavity. The mean peak pressure coefficients of the separated flow near the leading edge (flow directions 15 degrees for side A and 75 degrees for side B) increase a bit more. The largest difference occurs where the flow is reattached and high standard deviations (not shown here) are found.

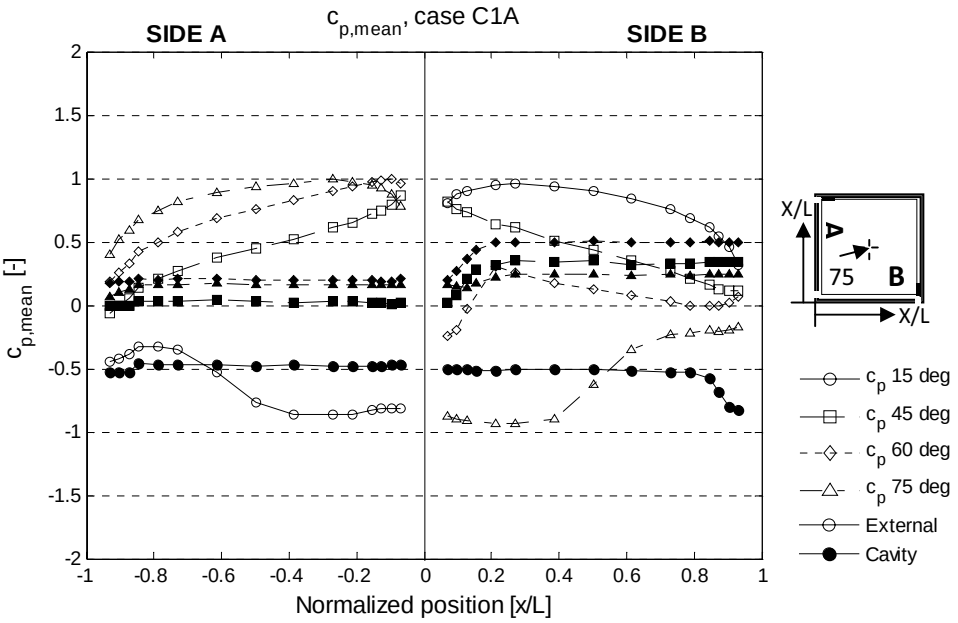

Figure 5: Mean pressure coefficients of reference case

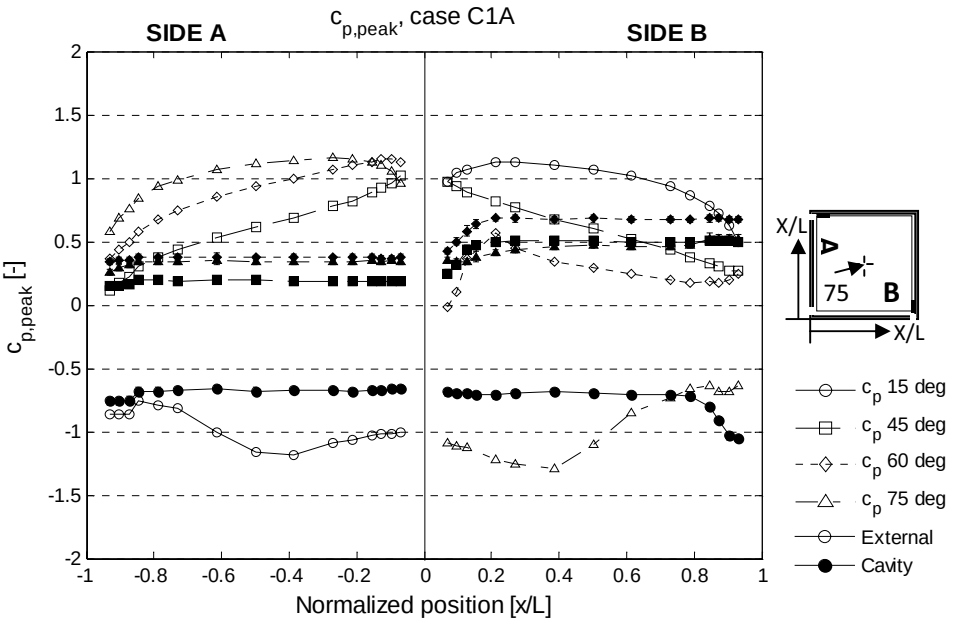

Figure 6: Mean peak pressure coefficients of reference case

For cladding the differential pressure is the most interesting one. The mean peak differential pressure coefficients are shown in figure 7. Negative values correspond to a direction pointing outwards of the cube and positive values towards the cube. On side A the cavity pressures have the same sign as the external pressures and lower differential pressures are found. On side B the opposite is true and the differential pressures are higher than the external pressures.

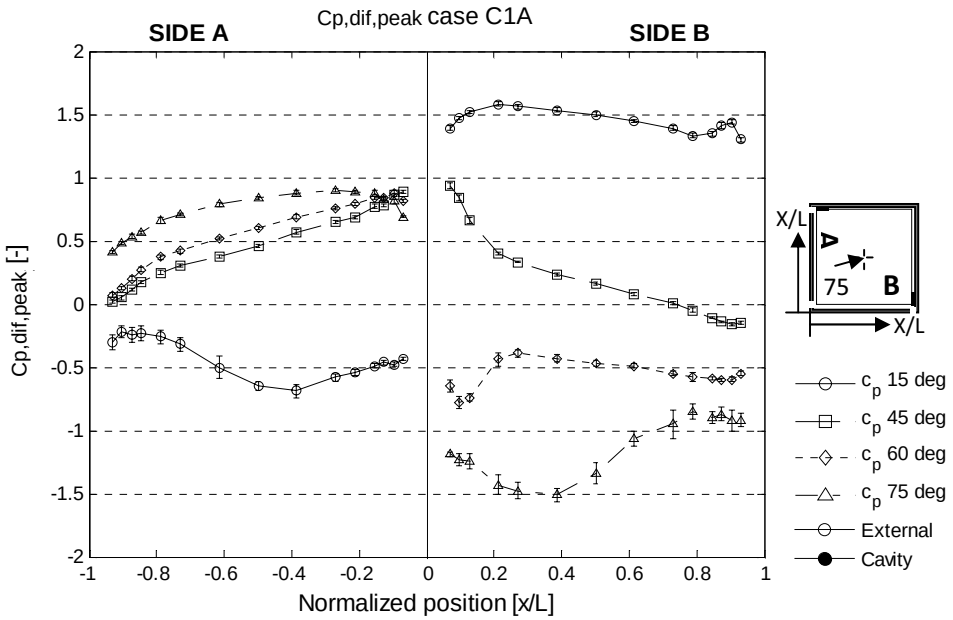

Figure 7: Mean peak differential pressure coefficients of reference case

Of the 4 considered wind directions, the highest outward pointing differential pressures are found for 75 degrees approach flow. On the leading edge the external pressure contributes for 2/3 in this pressure, on the trailing edge the cavity pressure and external pressure contribute equally.

3.2 *Effect of gap width (C1D, C1A, C1E)*

Three series of measurements have been conducted to investigate the effect of the gap width between de panels on the pressure distributions in the cavity. The gap width was varied between 4, 8 and 16 mm. Results are presented here for the approach flow direction of 75 degrees (figures 8 and 9). At this approach direction, the largest differential pressures have been measured in the reference case (with the 8 mm gap width).

Due to a higher flow resistance, the lowest pressures in the cavity and accordingly the highest differential pressures are expected with the smallest gap widths. Figure 8 does not show this effect: the smaller gap of 4 mm width gives similar values as the 8 mm gap at side A. However, it does show the opposite effect for the 16 mm gap where lower differential pressures are found. Side B results in higher mean differential pressure coefficients with increasing gap width. Since a wider gap leads to better pressure equalization at opening 2, a higher cavity pressure is present. The external underpressure combined with the cavity overpressure results in higher differential pressures over the outer layer.

The mean peak coefficients (figure 9) are even harder to compare for the different gap widths. Higher gap widths result in higher standard deviations in the cavity near opening 3 and near opening 2 to lesser extent. These local effects disturb the mean peak differential pressure coefficients and a trend is no longer visible. Figures 8 and 9 show that a more distinguished gap width difference is necessary to determine the gap width effect.

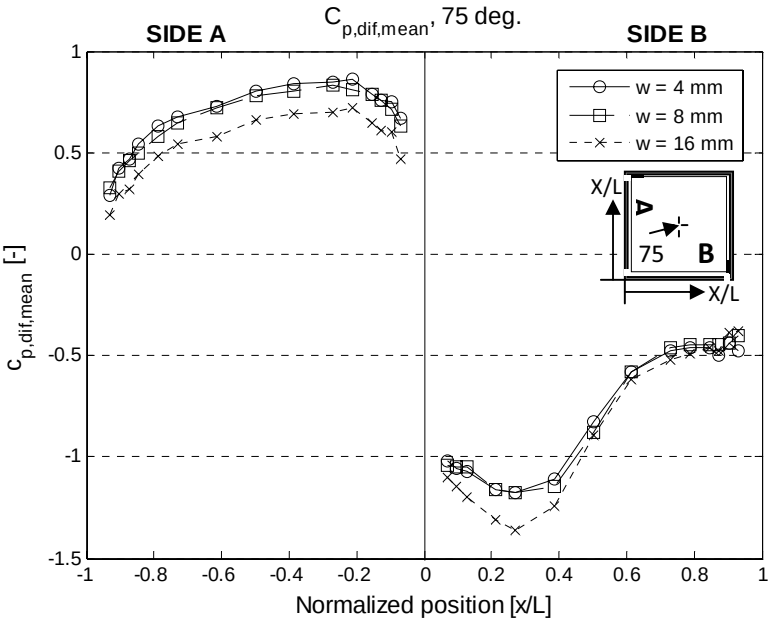

Figure 8: Mean pressure coefficient with varying gap width

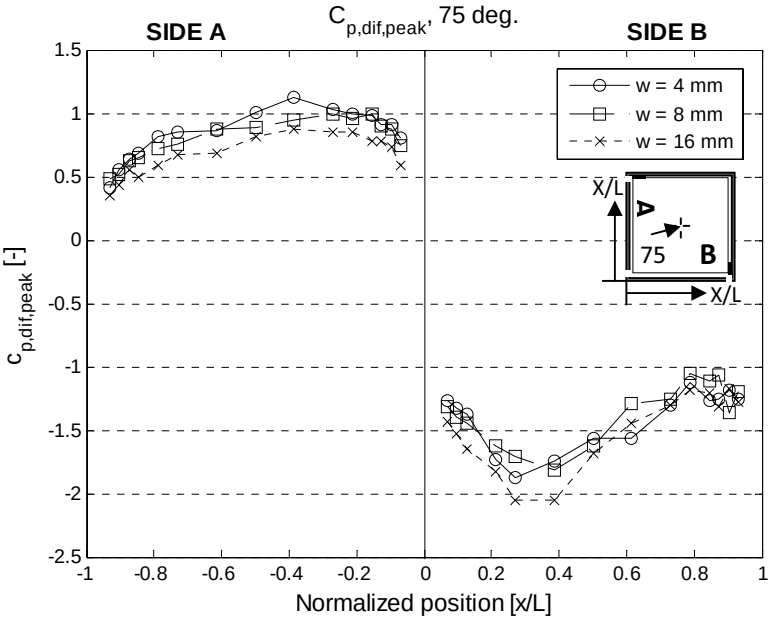

Figure 9: Mean peak pressure coefficient with varying gap width

3.1 *Effect of cavity depth (C1F, C1A, C1G)*

Again, three series of measurements have been conducted to investigate the effect of the cavity depth on the pressure distributions in the cavity. The cavity depth was varied between 10, 20 and 40 mm. Results are presented for the 75 degrees flow direction, that gave the highest differential

pressures for the reference case (with the 20 mm cavity depth). Unfortunately, also in this study the differences in cavity depth seem not distinguished enough to show clear effects. Brown et.al (1991) conclude that smaller cavity volumes, and thus smaller cavity depths, enhance pressure equalization and will lead to the smallest differential pressures. The mean pressure coefficients on the windward side show this trend, but very little (see figure 10). Side B shows the opposite effect due to the opposite sign of the pressures (externally and in the cavity).

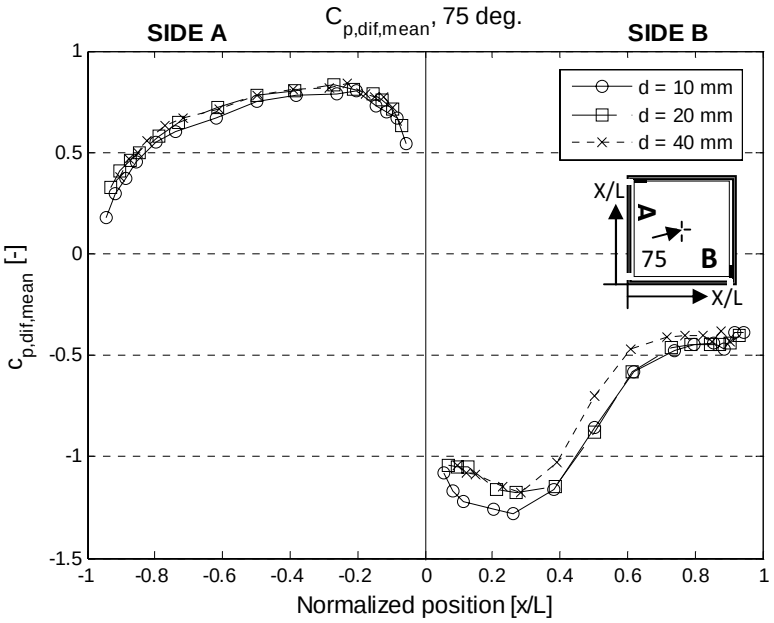

Figure 10: Peak pressure coefficient with varying cavity depth

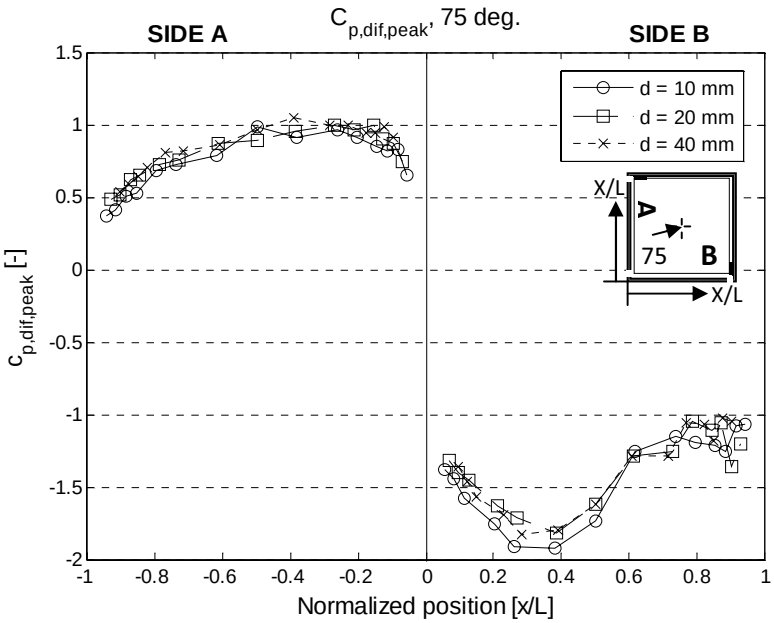

Figure 11: Peak pressure coefficient with varying cavity depth

The mean peak pressure coefficients show hardly any difference between the 3 cavity depths (figure 11). Like a large gap width a small cavity depth results in high standard deviations in the cavity near opening 3 and local effects disturb the flow pattern.

4 CONCLUSIONS

Measurements are performed on a cube with an airtight inner cube and an outside layer with open joints of 8 mm width and a cavity depth of 20 mm. These sizes correspond on a 1:1 scale to measures found in current practice. In smooth flow conditions a wind direction of 75 degrees with respect to the considered panel gives the highest differential pressures relevant for cladding. In general uniform cavity flows are found, with local effects at the openings in the reattachment zones. For unfavorable flow configurations, with overpressure in the cavity, the contribution of the cavity pressure to the total pressure difference is large. For the considered configurations between 1/3 and 1/2.

Large gaps and small cavity depths have a positive effect on pressure equalization. However the varied gap width and cavity depth in the current study are not distinguished enough to come up with final conclusions. It is possible that the measures for which the effects are clearly visible are outside the range of current practice. The tests in the next phase of this research should give an answer to that question.

Further research is ongoing, in which more configurations are being tested in turbulent flow conditions. Also upscaling to building level and validation with full scale measurements are part of the research program.

5 ACKNOWLEDGEMENTS

This research project is a collaboration of DHV, which took the initiative for the full scale measurements, Blitta, Centrum Natuursteen, Kenniscentrum Gevelbouw and TNO.

6 REFERENCES

1 Brown, W.C., M.Z. Rousseau, W.A. Dalgliesh, 1991. Field testing of pressure equalized rainscreen walls. Exterior Wall Symposium, Precast Concrete, Masonry and Stucco, 59-69.

2 Cheung, J.C.K., W.H. Melbourne, 1988. Wind loading on a porous roof, Journal of Wind Engineering and Industrial Aerodynamics 29, 19 – 28.

3 Gerhardt, H.J., F. Janser, 1994. Wind loads on permeable façades. Journal of Wind Engineering and Industrial Aerodynamics 53, 37 – 48.

4 Inculet, D.R., A.G. Davenport, 1994. Pressure equalized rainscreen: A study in the frequency domain. Journal of Wind Engineering and Industrial Aerodynamics 53, 63 – 87.

5 Schijndel, A.W.M. van, S.F.C Schols, 1998. Modeling pressure equalization in cavities. Journal of Wind Engineering and Industrial Aerodynamics 74-76, 641 – 649

6 Lee B.E., 1974, The effect of turbulence on the surface pressure field of a square prism, J. Fluid Mech, vol 69, part 2, 263-282

7 Baines, W.D, 1965. Effects of velocity distribution on wind loads and flow patterns on buildings. Proceedings of Symp. 16, Wind effects on buildings and structures, National Physical Laboratory England

8 Geurts, C.P.W., P.W. Bouma, A. Aghaei, 2005. Pressure equalization of brick masonry walls, in: Proceedings of the 4th European-African Conference on Wind Engineering, published on CD rom, Prague.

9 Geurts, C.P.W., 2000. Wind loads on permeable roof covering products, in: Book of abstracts of the Fourth colloquium on bluff body aerodynamics and applications, Ruhr Universität Bochum, 511-514.

The Seventh International Colloquium on Bluff Body Aerodynamics and Applications (BBAA7)
Shanghai, China; September 2-6, 2012

Wind force and wind-induced vibration characteristics of slender beam with angle cross-section

Toshio Tsurumi [a] Junji Katagiri [a] Takeshi Ohkuma [b]

[a] *Urban Environment Research Center, Izumi Sohken Engineering Co.,Ltd.,51 Minamisode Sodegaura Chiba, Japan*
[b] *Institute of Technology, Kanagawa University, 3-27-1 Rokkakubashi Kabagawa-ku Yokohama Kanagawa, Japan*

ABSTRACT: This paper investigates the characteristics of wind forces and wind induced vibrations on L-130x130x9 angle members used as members for large towers through wind forces tests and vibration tests in a wind tunnel using section models. It is thus clarified that unstable aerodynamic vibrations such as vortex induced vibrations, galloping and flutter occur in the angle member.

KEYWORDS: Angle cross-section member, Wind tunnel test, Wind force, Wind-induced vibration, Aerodynamic damping

1 INTRODUCTION

Angle-cross section members have been used in a lot of open structures such as transmission towers, radio towers and canopy roofs. Members of large open type structures in particular have large aspect ratios (ratio of length to width), so their natural frequencies are low and/or their critical damping ratios are small. For such members, vibrations induced by vortex shedding or self-exited vibrations may occur frequently under the design wind speed, which may cause fatigue damage or loosening of bolts at connections. To avoid these problems, characteristics of wind-induced vibrations need to be clarified and estimated in the design stage.

Cook[1], Modi et al.[2] and Okajima et al.[3] studied the relationship between the characteristics of mean wind forces on beams with angle sections and wind angles of attack (wind direction). However, there have been few studies on fluctuating wind forces in these members, and they did not provide enough information to estimate wind responses analytically.

Wardlaw[4], Modi et al.[2] and Okajima et al.[3] studied wind-induced vibrations in angle members. They suggested that vortex-induced vibration, galloping and/or flutter could occur in angle members. However, some of these vibration modes did not agree with the real vibration modes of angle members in open structures. Thus, the characteristics of real vibrations are not clarified by these results.

This paper discusses the characteristics of wind forces and wind induced vibrations on L-130x130x9 angle members usually used as members for large towers, through wind force tests and vibration tests in a wind tunnel.

2 OUTLINE OF WIND TUNNEL TESTS

2.1 *Wind force test*

An Eiffel type wind tunnel with a cross section 2.2m wide by 1.8m high was used.

The section of the model used in this study was L-130x130x9, which was the same as that of a full-scale member. The model was 1m long with end plates 0.5m in diameter, as shown in Figure 1(a). Wind forces were obtained from simultaneous wind pressure measurements at 37 points set on the center of the span (see Figure 1(b)). Approaching wind flow was generated by a turbulence grid. The mean wind speed profiles were almost constant. The wind turbulence intensity was about 5% and the turbulence scale was 0.12m. Wind direction was defined as shown in Figure 2. Wind tunnel tests were carried out for wind directions from 45^{o} to 225^{o} taking the section's symmetry into consideration. Wind speed was 4m/s. Sampling frequency of wind pressure was 500Hz and sampling length was 130seconds.

2.2 *Vibration test*

The wind tunnel cross section for the vibration test was 0.4m wide by 1.8m high. The model's section was the same as that of the wind force test model. The model was 0.4m long with end plates 0.45m in diameter. The model setting system is outlined in Figure 2. The vibration model was supported by 4 coil springs and vibration normal to the springs was fixed by long piano wires. It seemed that the effect due to the wires was negligible for target vibrations. Critical damping ratio was controlled by a damping system made up of a plate and silicon oil. The mass and mass inertia moment of the model were 17.9kg/m and $0.058 kgm^2/m$, respectively. These values were the same as those of the full-scale member.

The characteristics of the model's vibration modes were set according to those of the vibration mode obtained from the eigenvalue of a fixed beam of L-130x130x9 section and 8m span. The eigenvalues were calculated by the finite element method (FEM). Table 1 shows the obtained 1st to 4th mode eigenvalues. The 1st mode vibration swayed toward the weak axis and the 2nd mode one was coupled vibration between sway toward the strong axis and torsion. The 4th mode was also coupled vibration between sway toward the strong axis and torsion. The 3rd one swayed toward the weak axis with a node in the center of the span. The natural frequencies of the 3rd and4th modes were twice that of the 2nd mode, so it seemed that the 3rd and 4th mode vibrations did not occur within the design wind speed. In consequence, the target vibrations in the tests were the 1st and 2nd mode vibrations. The 1st and 2nd mode vibration tests were carried out respectively in order to clarify their vibration characteristics.

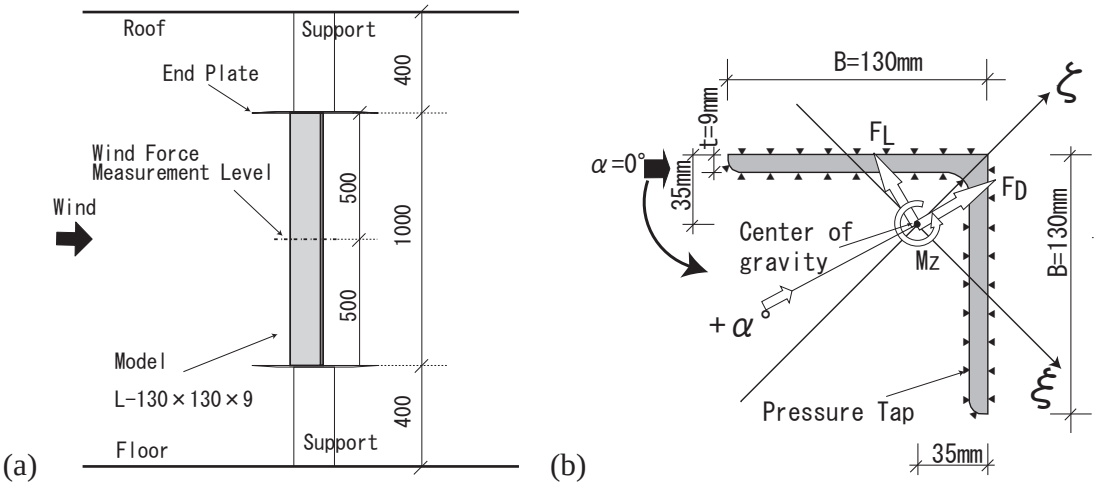

Figure 1. Wind force test model (a) Set up of wind force test model (b) Arrangement of wind pressure points and definition of wind direction

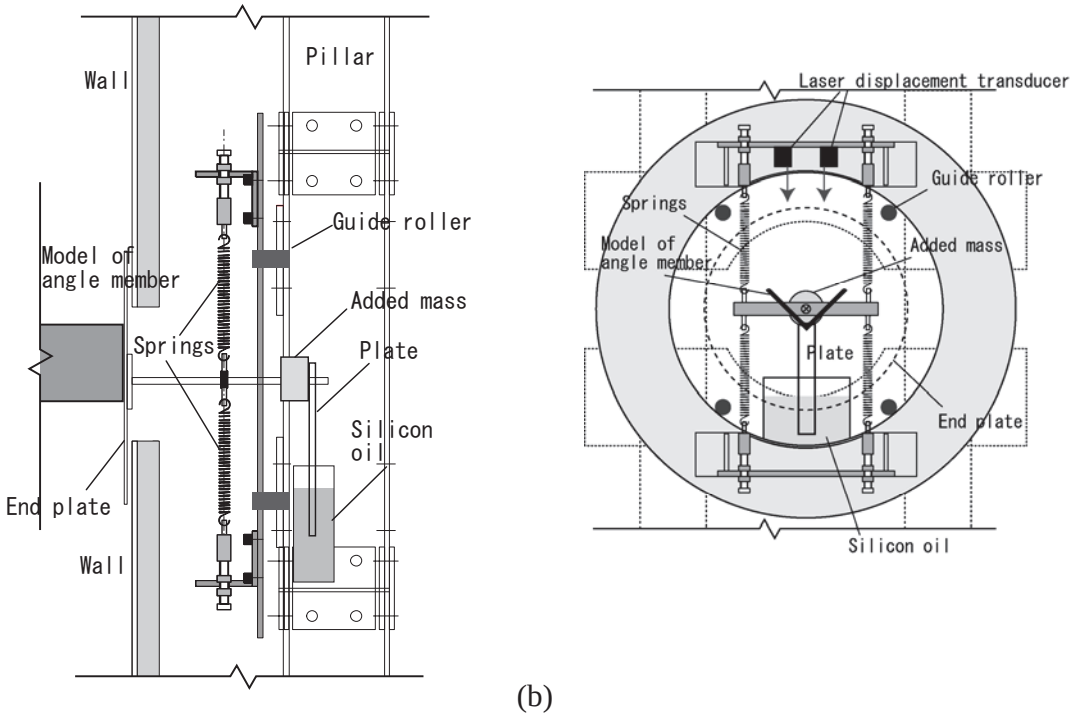

Figure 2. Wind vibration test system (a) View from leeward side, (b) Side view

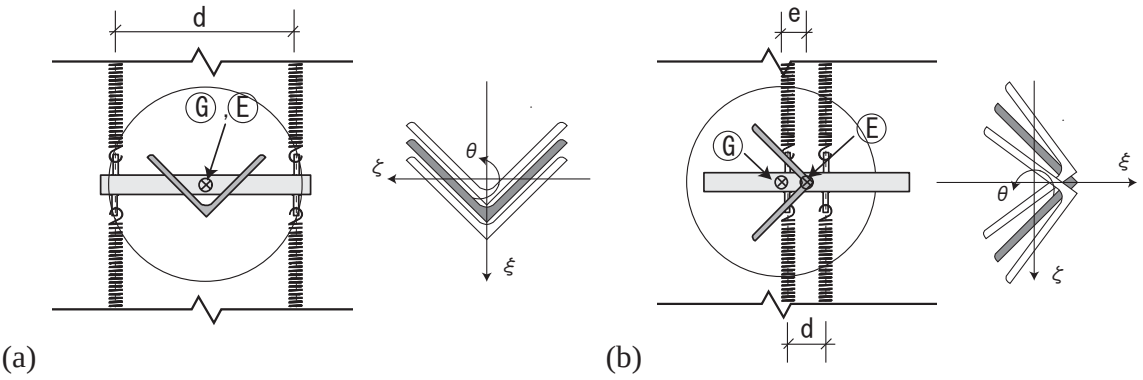

Figure 3. Set up of vibration model and vibration mode of model (a) 1st mode (b) 2nd mode

Table 1. Natural frequency and mode vector of FEM analysis and vibration model

Mode	Result of FEM analysis				Vibration test model			
	n_0 (Hz)	u_ξ	u_ζ	u_θ (rad/m)	n_0 (Hz)	u_ξ	u_ζ	u_θ (rad/m)
1st	7.7	1.0	0.0	0.0	6.5	1.0	0.0	0.0
2nd	11.7	0.0	1.0	8.8	6.2	0.0	1.0	5.2
3rd	21.3	1.0	0.0	0.0	-	-	-	-
4th	23.3	0.0	1.0	-22.0	-	-	-	-

The center of gravity of the model agrees with the center of stiffness for the 1st mode vibration model, supported with coil springs. The distance *d* between the coil springs was 0.28m, which was the maximum distance to produce high torsional frequency in the vibration system

(see Figure 3(a)). The resulting torsional frequency was 15Hz, being almost twice the 1st mode frequency. Therefore, it seemed that the effect of torsional vibration upon the 1st mode vibration was negligible.

The 2nd mode vibration test model was set such that the distance *e* between its center of gravity and center of stiffness was 0.042m, which was the same as the full-scale value. The distance *d* between coil springs was 0.061m (see Figure 3(b)).

Figure 3 and Table 1 show the characteristics of the 1st and the 2nd mode vibrations for the section model, where u_ξ, u_ζ and u_θ are the mode vectors for the weak axis, strong axis and rotation axis, respectively, and n_0 is the modal natural frequency. For the 2nd modal vibration, the vector for the rotation axis was smaller than the target value. However, the characteristics of coupled vibration were evaluated accurately enough by the model.

The critical damping ratio of the model was adjusted by silicon oil and the number of plates submerged in silicon oil (see figure 2). The critical damping ratios in the experiments were adjusted in the rage from 0.1% to 1%. The ratios were measured by free vibration tests in the no-wind condition. The experimental wind speed of the vibration tests were in the range from 3m/s to 20m/s. The model displacements were measured by two raiser displacement transducers at each end sides of the vibration system. The sampling frequency of displacement was 200Hz and the measurement time was 80 seconds for each case.

3 RESULTS OF WIND FORCE TEST AND DISSCUSSION

3.1 *Characteristic of mean wind force coefficient*

Figure 4(a) shows mean drag force coefficients C_{FD}, mean lift force coefficients C_{FL} and mean torsional moment coefficients C_{MZ} at the middle span of the section model, as defined by Equation 1.

$$C_{FD} = \frac{F_D}{qB}, C_{FL} = \frac{F_L}{qB}, C_{MZ} = \frac{M_Z}{qB^2} \tag{1}$$

where F_D is mean drag force; F_L is mean lift force; M_Z is mean torsional moment; q is dynamic pressure; and B is reference width 0.13m.

The mean drag force coefficients were large, being about 2.2 for wind directions of about 45°, 85° and 180° The minimum value was about 1.0 for a wind direction of about 135°. The mean lift force coefficients varied widely with change of wind direction. The maximum value was about 3 for a wind direction of 135 ° and the minimum value was about -3 for a wind direction of about 100°.

The mean drag force coefficients agreed with the values obtained by Modi et al. [2] and Okajima et al. [3], except for wind directions in the range from 45° to 80°, where the values obtained from this study were smaller. This difference is probably due to the difference of sectional edge shape of the model, arising from the difference of back pressure.

Figure 4(b) shows the values of Den Hartog's criterion obtained from Equation 2, which showed large negative values of about -12 for a wind direction of 137°. This direction is normal to the weak axis, so galloping may occur in this case.

$$A_F = C_{FD} + \frac{\partial C_{FL}}{\partial \alpha} \tag{2}$$

where α is the wind direction.

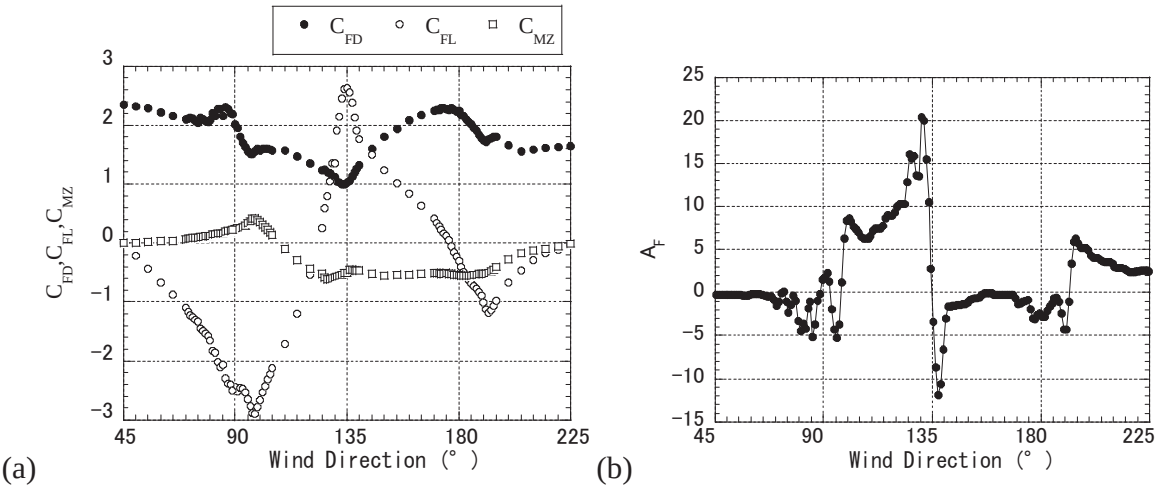

(a) (b)

Figure 4 Mean wind force (a) Mean wind force coefficient (b) Den Hartog's criterion

3.2 *Characteristics of modal fluctuating wind force coefficient*

The characteristics of modal fluctuating wind force coefficients derived from Equation 3 and 4 are discussed.

Figure 5 shows the modal fluctuating wind force coefficients of the *i* th mode C'_{Fi} versus wind direction.

$$C'_{Fi} = \frac{\sigma_{Fi}}{qB} \tag{3}$$

$$\sigma_{Fi} = \sqrt{\overline{F_i(t)^2}} = \sqrt{\overline{\left(F_\xi(t)u_{\xi i} + F_\zeta(t)u_{\zeta i} + M_Z(t)u_{\theta i}\right)^2}} \tag{4}$$

where $F_i(t)$ is modal wind force and subscript *i* is modal number; and $F_\xi(t)$, $F_\zeta(t)$ and $M_Z(t)$ are the fluctuating wind forces for the weak axis, the strong axis and torsion, respectively.

The 1st and 2nd modal fluctuating wind force coefficients showed large values for wind directions of 85° and 140° to 180° .

The 1st modal fluctuating wind force coefficients show the same values as the 2nd ones for wind directions of about 85°, but the 1st modal fluctuating wind force coefficients are larger than the 2nd ones for wind directions of 140° to 180°.

Figure 6 shows the power spectral densities of modal fluctuating forces.

The power spectral densities of the 1st and the 2nd modal fluctuating forces for wind directions of 85° and 175° show a dominant peak at a non-dimensional frequency of 0.12. These peaks are due to vortex shedding from the model. The peak value of the 2nd modal fluctuating force is larger than the value of the 1st one for a wind direction of 85°, and the peak values of the 1st and the 2nd modal fluctuating forces show almost the same values for wind direction 175°. Judging from these power spectral densities, vortex induced vibration may occur for wind directions of about 90° and 150° to180°.

Modi et al. [2] and Okajima et al. [3] indicated that across-wind vibrations due to vortex occurred for wind directions of 45°, 75° and 165° in vibration tests. The result for the wind direction of 165° is the same as the result foreseen from this study. However, the peaks of power spectral densities are not dominant for wind directions of 45° and 75° in this study, so there are

few possibilities of across-wind vibration due to shedding vortex. These differences between the results obtained from this study and those obtained from Modi et al. [2] and Okajima et al. [3] seem to be due to the shape difference of the model's edge.

Figure 6(c) and (d) shows the modal fluctuating forces for wind direction of 95° and 135° where large displacements occurred in the vibration tests. The power spectral densities of the 1st and the 2nd modal fluctuating forces for a wind direction of 95° show a blunt peak at a non-dimensional frequency of 0.12, unlike the peaks for a wind direction of 85°. The power spectral densities of the 1st modal fluctuating force for a wind direction of 135° show a blunt peak at a non-dimensional frequency of 0.2, which is about twice those for wind directions of 85° and 175°.

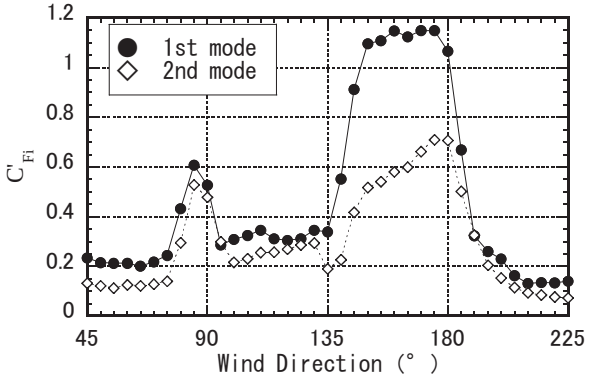

Figure 5. Modal fluctuating wind force coefficient

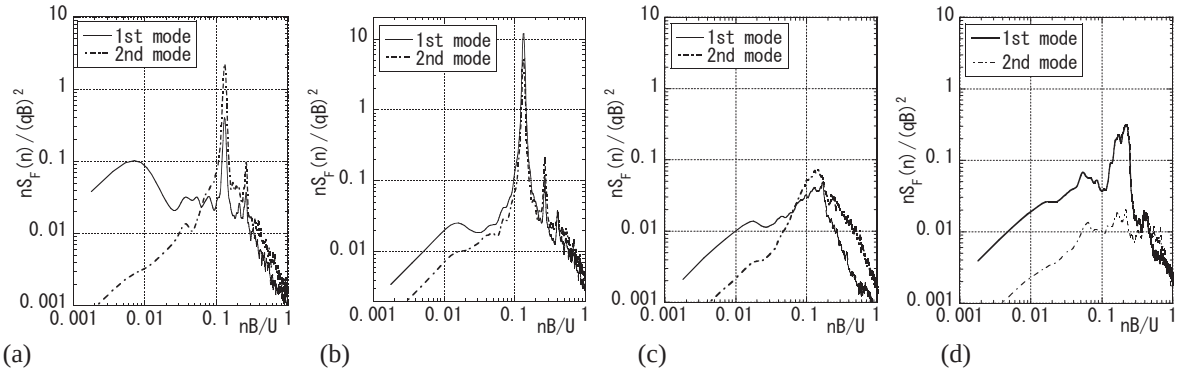

Figure 6. Non-dimensional power Spectral Densities of modal fluctuating wind force (a) Wind Direction 85° (b) Wind Direction 175° (c) Wind Direction 95° (d) Wind Direction 135°

4 RESULT OF VIBRATION TEST AND DISCUSSION

4.1 *Measurement result of response displacement*

Figure 7 shows some examples of standard deviations of response displacement obtained from vibration tests. The test results shown in Figure 9 are selected for the following reasons: (1) Wind directions are 85° and 175° where the power spectral densities have dominant peaks due to shedding vortex in the force tests and vortex-induced vibration occurs clearly in the vibration tests. (2) Wind direction is 135° , which is normal to weak axis, where the Den Hartog's criterion

had negative and large values in the force tests and galloping occurred in the vibration tests. (3) Wind direction is 95° where the 2nd vibration mode occurred divergently in the vibration tests.

Standard deviations of response displacement obtained from the force vibration theory, Equation 5, 6 and 7, by using fluctuating modal forces are also shown in Figure 7.

$$\sigma_i = \sqrt{\int_0^\infty S_{Fi}(n) \mid H_i(n) \mid^2 \, dn} \tag{5}$$

$$\mid H_i(n) \mid^2 = \frac{1}{(2\pi n_i)^2 M_i \left[\left\{ 1-(n/n_i)^2 \right\}^2 + 4h_i^2 (n/n_i)^2 \right]} \tag{6}$$

$$M_i = M(u_\xi^2 + u_\zeta^2) + Iu_\theta^2 \tag{7}$$

where $S_{Fi}(n)$ is the ith modal power spectral density; $|H_i(n)|^2$ is the ith mechanical admittance; M_i is the ith modal mass; n_i is the ith natural frequency; h_i is the ith modal critical damping ratio; M is the mass of the model; and I is the mass moment of inertia of the model.

In the 1st modal vibration test, large displacements occurred at non-dimensional wind speed 7 for wind direction 175°. The values obtained from the vibration tests were larger than the estimated values by the aforementioned theory for critical damping ratio 0.23%. However, for critical damping ratios larger than 0.49%, the two displacements were almost the same. The same characteristic of displacements was indicated for wind directions of 150° to 180°, where the power spectral densities of the 1st modal fluctuating forces had dominant peaks. On the other hand, the power spectral density of the 1st modal fluctuating force also had a dominant peak for wind direction 85°. However, self-excited vortex vibration did not occur.

The displacements of the 1st mode for wind direction 135°, where the Den Hartog's criterion had negative and large values, increased suddenly with increasing wind speed for non-dimensional wind speeds more than 15, so this vibration was galloping. This tendency was clearer where the critical damping ratio was less than 0.42%. The critical galloping non-dimensional wind speed was larger than about 9, as obtained from Equation 8 where A_F is -5 and h_1 is 0.2%.

$$U_C = \frac{4M\omega_1 h_1}{\rho B \mid A_F \mid L} \tag{8}$$

where ω_1 is the 1st modal angular frequency; h_1 is the 1st modal critical damping ratio; ρ is air density; and L is model length.

In the 2nd modal vibration test, the displacements for wind direction 85° were larger than the estimated values from the force vibration theory regardless of critical damping ratio values. For critical damping ratio 0.18%, the vibration translated into divergent vibration from self-excited vortex vibration. For critical damping ratio 0.4%, displacements at non-dimensional wind speeds more than 15 increase rapidly with increase of wind speed. Taking the 2nd mode shape into consideration, self-excited vortex vibration and flutter could occur for wind direction 85°.

On the other hand, displacements are almost the same as the estimated values for wind direction 175°.

Flutter occurred without regard to critical damping ratio values for wind direction 95°. The critical flutter wind speed was non-dimensional wind speed 10 for critical damping ratio 0.1% and as the critical damping ratio became larger, the critical flutter wind speed became higher.

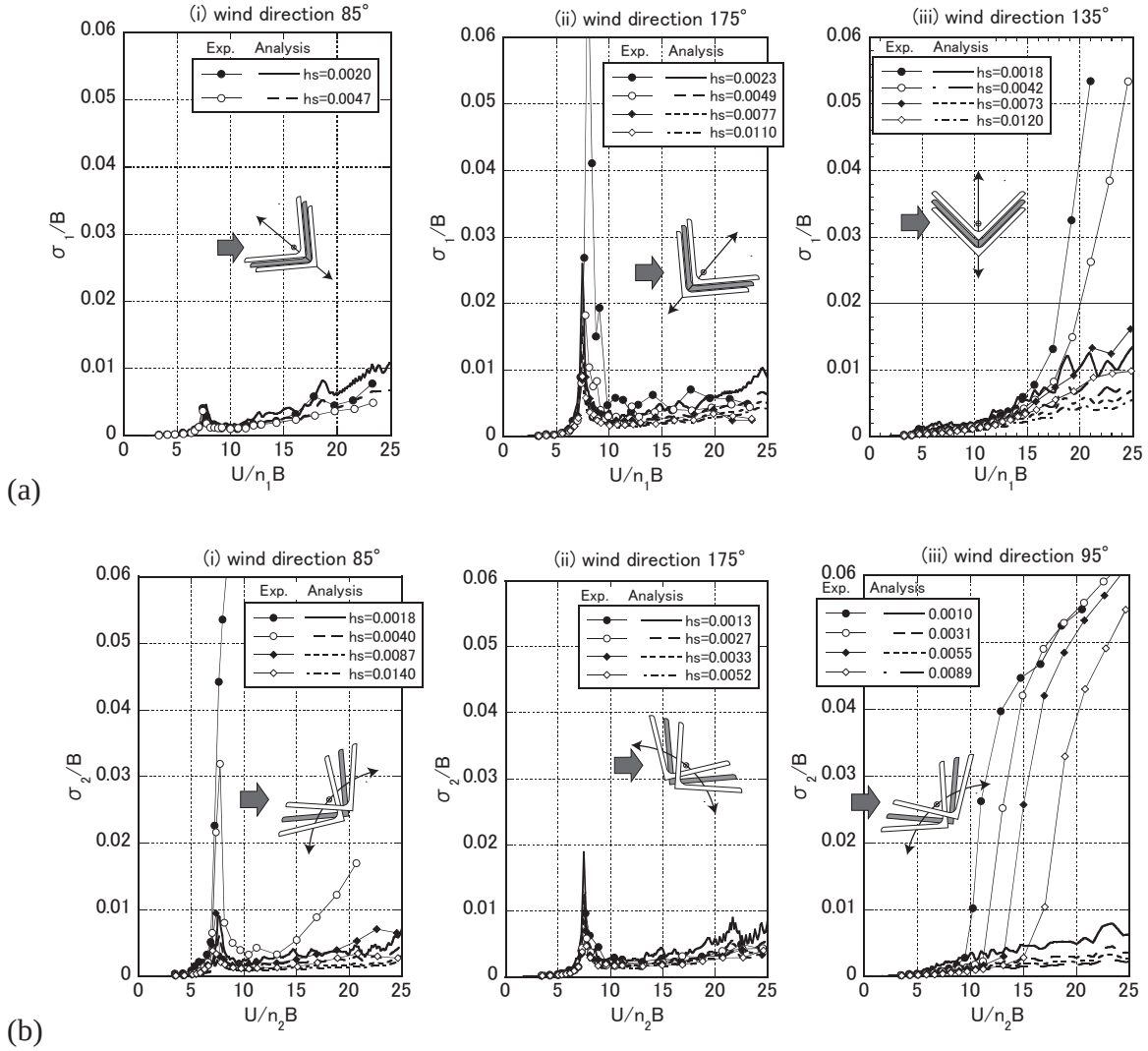

Figure 7. Results of standard deviations of response displacement form vibration test (a) 1st mode vibration, (b) 2nd mode vibration

4.2 *Aerodynamic damping ratio*

The vibration test suggested that galloping for wind direction 135° in the 1st mode occurred and flutter for wind direction 95° in the 2nd mode occurred. We discuss aerodynamic damping ratios estimated by the random decrement method (RD method) for these wind directions. However, these power spectral densities of fluctuating wind forces had a peak because the shedding vortex added a peak of components of natural frequency. Therefore, the time series obtained from the RD method is approximated by Equation 9. Equation 9 gives equivalent modal damping ratio, so aerodynamic damping ratio was one that was deducted from the critical damping ratio of the model from the equivalent modal damping ratio.

$$C(\tau) = a_I \exp(-h_{eqI}\omega_I\tau)\cos(\omega_I\tau + \varphi_I) + a_{II} \exp(-h_{eqII}\omega_{II}\tau)\cos(\omega_{II}\tau + \varphi_{II}) \quad (9)$$

where h_{eq} is equivalent critical damping ratio; and a and φ are constants.

Figure 8 shows aerodynamic damping ratio.

For the 1st mode for wind direction 135°, aerodynamic damping ratios are negative at non-dimensional wind speeds more than 17. The aerodynamic damping ratio derived from Equation 10 is also shown in Figure 8(a) where A_F was -5. Galloping can be estimated over non-dimensional wind speed 20 by quasi-steady theory.

$$h_a = \frac{\rho B |A_F| UL}{4M\omega_1} \quad (10)$$

For the 2nd mode for wind direction 95°, aerodynamic damping ratios are negative at non-dimensional wind speeds more than about 10 and the vibration is a coupled one. So, this vibration seems a flutter which is mainly controlled by aerodynamic forces subjected to the one side plate almost parallel to the wind direction. In this connection, the aerodynamic damping ratios for the 2nd mode were calculated from the result obtained from forced vibration tests for 2-dimensional rectangular cylinders[5].

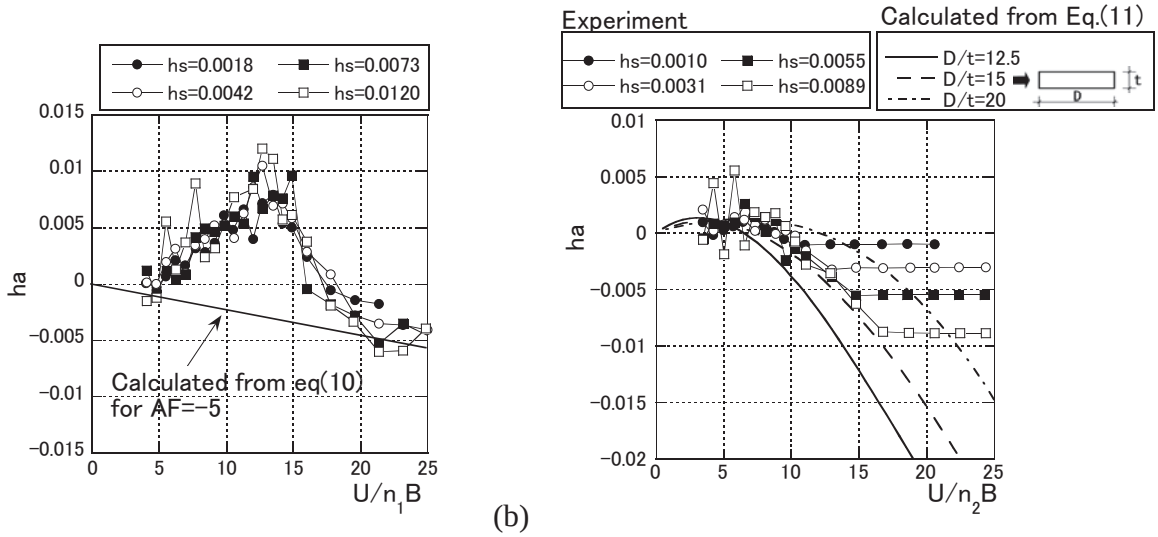

Figure 8. Estimated results of aerodynamic damping ratio (a) 1st mode vibration for wind direction 135°, (b) 2nd mode vibration for wind direction 95°

$$\begin{aligned} h_a &= -\frac{1}{16}\frac{\rho}{\rho_b}U^{*2}C_{FI} \\ &= -\frac{1}{16}\frac{\rho}{\rho_b}U^{*2}\left[C_{LCI}u_\zeta + C_{MCI}u_\theta\right] \\ &= -\frac{1}{16}\frac{\rho}{\rho_b}U^{*2}\left[(2H_1^*u_\zeta + H_2^*u_\theta)u_\zeta + (A_1^*u_\zeta + \frac{A_2^*}{2}u_\theta)u_\theta\right] \end{aligned} \quad (11)$$

where C_{FI} is out-of-phase component of unsteady aerodynamic force coefficient (motion-induced force coefficient); C_{LCI} and C_{MCI} are unsteady lift force coefficient and unsteady torsional moment coefficient during coupled vibration, respectively; H_1^*, H_2^*, A_1^* and A_2^* are aerodynamic derivatives[5]; $U^*=U/\omega_2 b$; $b=D/2$; and D is depth of rectangular cylinder.

Figure 8(b) shows the aerodynamic damping ratio obtained from vibration tests and the result derived from Equation 11. The test result is in good agreement with the values obtained from Equation 11 where the ratio of width to thickness of a plate is 15. The ratio of width to thickness(t:see Figure 1) of one side plate of the angle model is 14.4. Therefore, it seems that the vibrations are due to the same factor as that causing plate flutter.

5 CONCLUSIONS

This study investigated the characteristics of wind forces and wind-induced vibrations on L-130x130x9 angle member usually used as members for large towers, through wind force tests and vibration tests in a wind tunnel.

(1) In the 1st mode vibration, the self-excited vortex vibration occurs at non-dimensional wind speed 7 for wind direction 175°. For wind direction 135°, galloping occurs in the case of low critical damping ratios at non-dimensional wind speed over 15.
(2) In the 2nd mode vibration, the self-excited vortex vibration occurs at non-dimensional wind speed 7 for wind direction 85°. For wind direction 95°, flutter occurs for more than non-dimensional wind speed 10 without regard to critical damping ratio values.

6 REFERENCES

[1] Cook., N.J., The designer's guide to wind loading of building structures Part 2 Static structures, BRE press
[2] Modi, V.J., Slater, J.E., Unsteady aerodynamics and vortex induced aeroelastic instability of a structural angle section, Journal of Wind Engineering and Industrial Aerodynamics, 11(1983) 321-334
[3] Okajuna, A., Ueno, H., Nishi, T., Harada, H., Yano, K., Uno, T., Study on aeroelastic characteristics and aeroelastic instability of structural L-shaped, T-shaped and cross-shaped section, 12th National Symposium of Wind Engineering, 149-154 (in Japanese)
[4] Wardlaw, R.L., Wind-induced vibrations of slender beams with angle cross-sections, Wind Effects on Buildings and Structures, 1967, 739-772
[5] Matsumoto, M., Kobayashi, Y., Niihata, Y., Shirato, H., Hamasaki, H., Flutter mechanism and its stabilization of bluff bodied, Proceeding of 9th ICWE, 1995, 827-838

The Seventh International Colloquium on Bluff Body Aerodynamics and Applications (BBAA7)
Shanghai, China; September 2-6, 2012

Accurate simulations of surface pressure fluctuations and flow-induced noise near bluff body at low mach numbers

Y. P. Wang [a], J. Chen [b], H. C. Lee [b] K. M. Li [b]

[a]*School of Automotive Engineering, Wuhan University of Technology, Wuhan, Hubei, China*
[b]*School of Mechanical Engineering, Purdue University, West Lafayette, IN, USA*

ABSTRACT: For low Mach number flow around a bluff body, the far-field sound pressure is mainly dominated by dipole sources. The dipole sources are induced by the unsteady surface pressure distributions due to the presence of a turbulent boundary layer in the vicinity of the solid body. The far-field sound pressure can be calculated by integrating the time derivative of the wall-pressure fluctuations at the surface of the rigid body. Recent development in computational fluid dynamics (CFD) brings a powerful tool for predicting unsteady turbulent flow fields and the generation mechanism of aerodynamic noise. The present study investigates the use of an improved CFD method to accurately simulate the flow fields near a solid body. In particular, a large eddy simulation technique is adopted to predict the unsteady surface pressure fluctuation. The influences of various subgrid-scale models and near-wall treatments are investigated. The information of the flow field is then used to calculate the far field sound pressures. Extensive computations have been conducted to calculate the noise induced by the flow over a circular cylinder and an automobile's rear view mirror. The calculated sound pressure levels have been shown to agree well with published experimental results.

KEYWORDS: Low Mach Number Flow, Dipole, CFD, Aerodynamic Noise, Subgrid-scale model, Near-wall Treatment.

1 INTRODUCTION

For low Mach number flow around a solid body, the far-field sound pressure is dominated by dipole sources and quadrupole components play little role in the total sound field [1][2]. The dipole sources are created by unsteady surface pressure distributions due to the presence of a turbulent boundary layer in the vicinity of the solid body. The far-field sound pressure can be calculated by integrating the time derivative of wall-pressure fluctuations at the surface of the rigid body [3][4]. Recent developments in the field of computational fluid dynamics (CFD) have provided a powerful tool for predicting unsteady turbulent flow fields and the generation mechanism of aerodynamic noise. The direct numerical simulation (DNS) approach [5] solves the Navier–Stokes equation "exactly" in the temporal-spatial domain (resolving to the smallest scale). To avoid the extremely high computational cost associated with DNS, temporal development of averaged field parameters can be assessed using unsteady Reynolds-averaged Navier–Stokes (U-RANS) equations. Appropriate turbulence closure models are then required to close these equations. Different turbulence closure models, ranging from simple algebraic models to more complicated ones involving multiple equations [6], are applied to simulate flow-induced aerodynamic noise [7]-[9].

An alternate approach is to apply the large eddy simulation (LES) methodology [10] where large energy-containing scales of the flow fields are computed numerically and flow parameters

in unresolved subgrid scales are modeled by a subgrid-scale (SGS) model. Among the various proposed SGS schemes[10]-[12], the most popular model is the eddy-viscosity type developed by Smagorinsky [13], where the model constant can either have a static value or be determined dynamically (see detailed discussion in section 2). LES generally provides better accuracy than U-RANS for flows that feature unsteady components and large-scale eddies. When LES is used to simulate a flow field for analyzing flow-induced noise, it is very important to select an appropriate SGS model. This is because mid-to-high frequency noise is generated by turbulent structures of a very fine resolution at the subgrid scale, and the energy contained in the SGS eddies may be comparable to the acoustic energy.

The performance of SGS models can usually be appraised by a priori or a posteriori tests, as suggested by Piomelli et al. [14]. The validity of static and dynamic Smagorinsky-type SGS models for LES simulations has been well established using either numerical simulations or experimental results on homogenous isotropic turbulence [10][12]. LES simulations show that the dynamic Smagorinsky model gives better prediction results as compared to the static Smagorinsky model for predicting aerodynamic noise generated by an automobile's rear-view mirror [15]. However, a priori tests on SGS models of a homogenous but less complicated, time-evolving, anisotropic, turbulent flow field show that the dynamic Smagorinsky model, as well as several other advanced SGS models, do not always yield numerical results that are better than those predicted by the static Smagorinsky model [16]. It is therefore important to examine the performance of a number of SGS models and establish guidelines for their use in studying flow-induced noise at low Mach numbers.

The current study is also motivated by the need to reduce the cabin noise level in automobiles operating at cruising speeds. The aerodynamic noise inside the cabin increases considerably with the vehicle's speed. This type of flow-induced noise has broadband spectral content ranging from tens of Hertz at low frequencies to a few hundreds or thousands of Hertz at mid-to-high frequencies. This is attributed to time-varying flow separations and the breaking of large vortical structures into fine turbulent structures. The low frequency noise is generated by periodic convection of large-scale vortices over the open cavities where an unsteady shear flow exists, e.g., buffeting noise due to an open sunroof or window. The high frequency noise is induced by the shedding of unsteady vortices due to the interaction between body details, e.g., the flow interaction between the outside rear-view mirror and the A-pillar. This type of aerodynamic noise is a major contributor to the total noise levels inside the passenger cabins of vehicles. It can cause passenger discomfort, and more importantly, it may lead to driver fatigue. Therefore, it is crucial for the success of automobile development to predict the aerodynamic noise at the design stage and control it within an acceptable level. In the past few years, some researchers have incorporated the boundary element formulation in Curle's analogy [17]–[19] to predict aerodynamic noise for a non-compact solid body interacting with flow at low Mach numbers. However, we adopt a different route by examining the accuracy of the flow fields to address the weakness of the traditional approach at high Helmholtz numbers. We note that the first requirement for predicting the sound fields accurately is to develop an effective and precise numerical scheme to simulate the unsteady flow fields.

This paper aims to assess the effectiveness of combinations of SGS models and near-wall treatments in predicting aerodynamic noise. We conduct LES simulations on 2D and 3D canonical problems. The simulations are configured in such a way that the results can be directly compared with well-documented acoustic measurements. This evaluation is expected to aid the selection of effective simulation tools at the design stage for predicting flow-induced noise. The paper is organized as follows. A brief review of LES is given in section 2. Following that, the simulation results of flow over a 2D cylinder and 3D generic side-view mirror model are discussed in sections 3 and 4; comparisons of the experimental data are also presented therein. Conclusions and future prospects are presented in the final section.

2 UNSTEADY FLOW SIMULATION BY LES FOR PREDICTING FLOW-INDUCED NOISE—A REVIEW

In LES, a filtering operation is applied initially to field variable $g(\mathbf{x},t)$ to obtain its resolved component $\tilde{g}(\mathbf{x},t)$ in the spatial domain$D$:

$$\tilde{g}(\mathbf{x},t)=\int_D g(\mathbf{x}-\mathbf{x}',t)G_\Delta(\mathbf{x}')\,d\mathbf{x}' \tag{1}$$

where $\mathbf{x}=(x_1,x_2,x_3)$ denotes the coordinates, t is time, and $G_\Delta(\mathbf{x})$ is the filtering kernel with a characteristic length scale Δ. The representative flow variable $g(\mathbf{x},t)$ can be either the flow velocity $u_i(\mathbf{x},t)$ or the instantaneous pressure$p(\mathbf{x},t)$. For low Mach number (incompressible) flow, $\tilde{u}_i(\mathbf{x},t)$ and $\tilde{p}(\mathbf{x},t)$ can be solved using the filtered incompressible Navier–Stokes equations [20]:

$$\begin{cases}\dfrac{\partial\tilde{u}_i}{\partial x_i}=0\\[2ex]\dfrac{\partial\tilde{u}_i}{\partial t}+\tilde{u}_j\dfrac{\partial\tilde{u}_i}{\partial x_j}=-\dfrac{1}{\rho}\dfrac{\partial\tilde{p}}{\partial x_i}+\nu\dfrac{\partial^2\tilde{u}_i}{\partial x_j\partial x_j}-\dfrac{1}{\rho}\dfrac{\partial\tau_{ij}}{\partial x_j}\end{cases} \tag{2}$$

where ρ is the fluid density and τ_{ij} is the subgrid-scale stress given by

$$\tau_{ij}\equiv\widetilde{u_iu_j}-\tilde{u}_i\tilde{u}_j, \tag{3}$$

and the subscripts *i*, *j* = 1, 2, 3 (free indexes of index notation) represent the respective components along the coordinate axes x_1,x_2, and x_3. Once the SGS stress given in equation (3) is modeled properly, e.g., using the resolved parameters $\tilde{u}_i(\mathbf{x},t)$ and $\tilde{p}(\mathbf{x},t)$, it can be solved using equation (2). Then, the instantaneous flow fields are approximated by their resolved counterparts, namely,

$$u_i\simeq\tilde{u}_i(\mathbf{x},t) \tag{4a}$$

and

$$p\simeq\tilde{p}(\mathbf{x},t) \tag{4b}$$

The predominant influence of the SGS stress on the resolved flow field parameters is reflected in the transport of kinetic energy from large resolved scales to the small unresolved subgrid scales [20],[21]. As a result, accurate modeling of the SGS stress is crucial for the success of LES in predicting the flow fields. Among the various SGS models that have been proposed [10]-[12], the most popular model is the eddy-viscosity type wherein the deviatoric part of the SGS stress is given by

$$\tau_{ij}-\frac{1}{3}\tau_{kk}\delta_{ij}=-2\nu_r\tilde{S}_{ij} \tag{5a}$$

where, δ_{ij} is the Kronecker delta function, ν_r is the subgrid-scale eddy viscosity, and the resolved strain is given by

$$\tilde{S}_{ij}=\tfrac{1}{2}(\partial\tilde{u}_i/\partial x_j+\partial\tilde{u}_j/\partial x_i) \tag{5b}$$

where the repeated subscript *k* in the tensor represents the sum of the respective components from 1 to 3 (summation index of index notation).

The Smagorinsky model [13] is typically used for this class of approximations for the SGS stress, in which the eddy viscosity is

$$\nu_r=\left(C_S\Delta\right)^2\tilde{S} \tag{6a}$$

where C_S is the Smagorinsky coefficient, and the magnitude of the resolved strain, $\tilde{S}$, is calculated as

$$\tilde{S}=\sqrt{2\tilde{S}_{ij}\tilde{S}_{ij}} \tag{6b}$$

In the traditional (static) Smagorinsky–Lilly model, C_S usually takes a static value of 0.16 in

many practical situations simulated using scale invariant models [22]. However, the value of this Smagorinsky coefficient is questionable in highly complex flow problems [12]. A dynamic approach is proposed to determine the local value of C_S by applying a second filtering operation at a scale of $\alpha\Delta$ where α is usually taken as 2 [23],[24]. This approach is referred to as the (standard) dynamic Smagorinsky model. Other approaches to model C_S and τ_{ij} have been proposed [10] - [12]. Some of these advanced models have been incorporated into commercial CFD programs. Users may choose a specific SGS model to simulate different flow problems.

Once the unsteady flow field is determined from LES, the Ffowcs Williams–Hawkings (FW-H) acoustic analogy [25] can be applied to compute the far-field sound pressure for flow over the rigid body, where the dipole term is dominant over the monopole and quadrupole terms. Then, the FW-H equation can be simplified as follows [26]:

$$p'(\mathbf{x},t)=\frac{1}{4\pi c_0}\int_S \frac{(x_i-y_i)n_i}{r^2}\frac{\partial p(\mathbf{y},\tau)}{\partial t}dS(\mathbf{y})+\frac{1}{4\pi}\int_S \frac{(x_i-y_i)n_i p(\mathbf{y},\tau)}{r^3}dS(\mathbf{y}) \tag{7}$$

where c_0 is the speed of sound in air, τ is the emission time ($\tau = t - r/c_0$), r is the distance between the source and the receiver, and $\mathbf{y}$ is the source on the surface of the rigid body S.

An accurate prediction of surface pressures in an unsteady flow field is crucial for the successful prediction of the far-field aerodynamic noise [15]. Flow fields in the viscous near-wall regime must be treated properly because of the distribution of dipole-type sources located on rigid surfaces. The presence of small but dynamically important eddies in the near-wall region demands that LES meets a number of challenging requirements. The computational grid must be sufficiently fine to resolve at least 80% of the energy-containing flow eddies. In addition, grid cells of high aspect ratio in the near-wall regime should be avoided [27]. Estimation suggests that an extremely fine grid is needed to accurately predict the surface pressure fluctuation, and the number of required grid points is proportional to the second power of the flow Reynolds number, which is comparable to the grid requirement in DNS [28]. It is evident that LES becomes increasingly impractical for fully resolving the near-wall regime in high Reynolds number flows.

To extend the applicability of LES at high Reynolds number flows, the dynamic effects of a semi-viscous near-wall layer can be estimated by means of a simple model that leads to an approximate boundary condition for LES at the outer regions; thus, the need to construct very fine grid points near the wall surface is avoided [29]-[31]. Among the various options proposed, the "wall-function" (WF) method uses an assumed instantaneous velocity profile between the nodes closest to the wall and the wall surface. A commonly used velocity profile is the Werner–Wengle wall function [32], which assumes a 1/7th power law outside the viscous sublayer interfaced with the linear profile within the viscous sublayer,

$$u^+(y^+)=\begin{cases} y^+ & \text{if} \quad y^+ < 11.8 \\ 8.3(y^+)^{1/7} & \text{if} \quad y^+ > 11.8 \end{cases} \tag{8a}$$

Here, $u^+ = u/u_\tau$, and u is the resolved velocity tangential to the wall at the nearest point. The non-dimensionalized distance y^+ measured from the wall is given by

$$y^+ = u_\tau y/v \tag{8b}$$

where u_τ is the friction velocity, y is the normal distance measured from the cell centers, and v is the kinematic viscosity of the fluid. The tangential velocity can be related to the wall shear stress by integrating the velocity profile given in equation (8a) over the distance between the first cell and the wall surface. A detached eddy simulation (DES), which matches U-RANS simulation for the near-wall layer and is equivalent to LES in the outer region, is also frequently used. The LES-WF combination and the DES method have been used to study unsteady separated flows in channels and over cylinders at high Reynolds numbers [29]-[31],[33].

3 FLOW OVER CIRCULAR CYLINDER

Flow over a 2D circular cylinder is a canonical problem for studying the unsteady effect of flow over a solid body and the induced aerodynamic noise. We simulate air flow with a free stream velocity $U_0 = 69.2$ m s^{-1} over a cylinder with diameter $D = 19$ mm; Reynolds number $Re = U_0 D / \nu \approx 90{,}000$. These parameters are set such that they are identical to the values in the experimental study conducted by Revell et al. [34]. The computational domain extends from $-8.5D$ (upstream) to $+20.5D$ (downstream) with the origin set at the center of the cylinder. As suggested by Kim [35],[36], the distance between the top and the bottom of the computational domain is $21.0D$. An O-mesh topology is applied around the cylinder for better quality mapping of computational results. Thus, a fine mesh of 94,651 quadrilateral cells are employed, with a total of 360 mesh nodes in the circumferential direction and 80 mesh nodes in the radial direction. Numerical accuracy is checked by having a finer mesh consisting of 162,543 quadrilateral cells and a coarser grid consisting of 47,449 quadrilateral cells. Surface pressure and skin friction coefficient of the circular cylinder on different computational grids are compared in figure 1 and figure 2. As shown in figure 1 and 2, the fine and finer grid results are in good agreement, proving that the resolution is sufficient for an LES [47]. An additional comparison of the results between different meshes is presented in Table 1, where drag coefficients are compared. The difference in drag coefficient between fine and finer grids is approximately 0.4%. Thus, fine computational grid is used for the entire analysis.

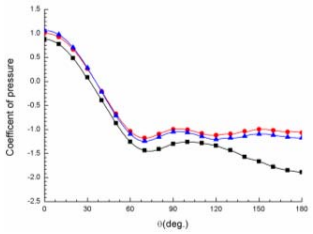

Figure 1. Distribution of average coefficient of pressure C_p over surface of circular cylinder ($\theta = 0^\circ$ is leading edge and $\theta = 180^\circ$ is trailing edge). Square: coarse grids; Triangle: fine grids; Circle: finer grids.

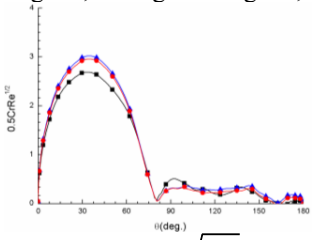

Figure 2. Distribution of scaled skin-friction coefficient $Cr\sqrt{Re}\ /\ 2$ (where $Cr{=}2\tau_w / (\rho U_0^2)$ and τ_ω is local wall shear stress) over circular cylinder. Square: coarse grids; Triangle: fine grids; Circle: finer grids.

	Number of cells	LES SLM+WF $\overline{C}_d$
Coarse	47,449	0.82
Fine	94,651	1.26
Finer	162,543	1.265

Table 1. Comparisons of drag coefficient on different computational grids.

In this set of numerical simulations, the boundary conditions are (i) no-slip and no-penetration conditions on the cylinder surface, (ii) a uniform free stream velocity with no perturbations at the inlet boundary, (iii) a constant free stream pressure on the outlet boundary, and (iv) free-slip conditions on the upper and lower boundaries of the computational grids. To predict the sound pressure, an implicit pressure-based finite volume method is used to solve the incompressible Navier–Stokes equations (equation 2) on the unstructured grids. The numerical solver in Fluent

CFD software is used for the present study. The discretized transport equations are advanced in time using the non-iterative time-advancement (NITA) algorithm. In addition, the fractional-step method (FSM) is chosen so that the momentum equations are decoupled from the continuity equation. To avoid numerical diffusion, the convection terms in all transport equations are discretized using bounded central-differencing schemes (BCD). Thus, this methodology preserves the non-dissipative properties of the fluid flow and avoids possible unbounded solutions and non-physical oscillations caused by other central-differencing schemes. Furthermore, the diffusion terms are discretized using a central-differencing scheme of second-order accuracy. The unsteady pressure is interpolated using PRESTO (PREssure STaggering Option), available in Fluent.

In LES the timescale of the smallest resolved eddies determines the time step needed. According to Kim and Mohan [35], the smallest resolved eddy, ℓ, should be set approximately at $\ell = 0.05D$ and the corresponding characteristic velocity, u', at $0.2U_0$. A non-dimensional time step, $U_0 \Delta t / D = 0.0036$ (Δt~1×10^{-6} s), is used to ensure that the maximum local Courant-Friedriches-Lewy (CFL) number does not exceed 1.5 in most grid points of the computational domain. Although using this time resolution to predict sound pressure is a second-order approach, it has been demonstrated that the numerical solutions are as accurate as those directly computed by a sixth-order compressible flow solver in the frequency range in which the numerical method accurately resolves the flow structures [15].

To obtain converged results, it is essential that the CFL criterion is met. In fact, the CFL number reflects the portion of a cell that a fluid traverses by advection in one time step. The Courant number should preferably be chosen to be less than 1.5 in order to reduce oscillations and numerical dispersion and improve accuracy. In general, each cell in the computations has a different CFL number. A summary of statistical data used in our numerical simulations shows that over 95% of cells have CFL numbers that are less than 1.5.

In the present study, we investigate the importance of simulation methods in efficiently and accurately predicting the aerodynamic noise in low Mach number flows. In particular, a variety of SGS models are used in LES and DES to obtain the time histories of flow fields over a circular cylinder. Predictions from the following models are compared: (i) Smagorinsky–Lilly model (SLM, equation (6) with $C_S = 0.16$), (ii) wall-function equation (8) along with Smagorinsky–Lilly model (SLM+WF), (iii) dynamic kinetic energy subgrid-scale model (DKESM), (iv) wall-adapting local eddy-viscosity model (WALEM), (v) renormalization group model (RNGM) [37], (vi) dynamic Smagorinsky–Lilly model (DSLM) [37], and (vii) DES with Spalart-Allmaras RANS model and Smagorinsky–Lilly model [37].

The prediction results are evaluated by comparing them with the experimental data obtained by Cantwell and Coles [38]. As shown in figure 3, the pressure coefficients predicted by DKESM, WALEM, and RNGM are less than the measured data in most angular positions. On the other hand, DSLM performs better than DKESM, WALEM, and RNGM. DSLM underpredicts as compared to the experimental data when $\theta < 120^\circ$ but overpredicts when $\theta > 120^\circ$. DES predictions are generally less accurate than those of LES when θ is small, but DES yields improved results near the trailing edge when $\theta > 110^\circ$.

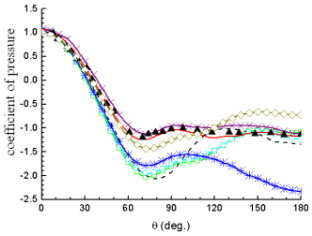

Figure 3. Distribution of average coefficient of pressure C_p over surface of circular cylinder ($\theta = 0^\circ$ is leading edge and $\theta = 180^\circ$ is trailing edge). Solid triangle: experimental data [Ref. 38]; solid line: SLM+WF; cross: SLM; square: DKESM; circle: WALEM; asterisk: RNGM; diamond: DSLM; dashed line: DES.

The remaining two models, SLM and SLM+WF, both give excellent predictions C_p, although the predictions of SLM+WF are marginally better than those of SLM. However, it is interesting to note that SLM alone does not yield better predictions for the coefficient of mean skin friction (figure 4). Thus, SLM+WF out of all the methods tested is the best numerical model for accurately predicting the coefficient of skin friction. Both DKESM and WALEM agree closely with the experimental data. The prediction of RNGM is of the same order of accuracy as that of SLM. DSLM performs marginally better than RNGM and SLM and generally underpredicts the coefficient of mean skin friction at the leading edge.

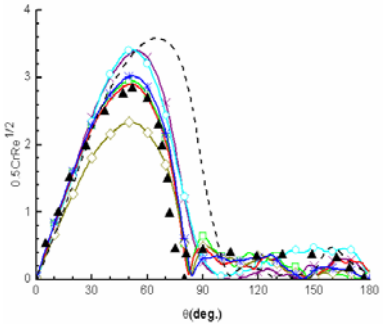

Figure 4. Distribution of scaled skin-friction coefficient over circular cylinder. Solid triangle: experimental data [Ref. 39]; solid line: SLM+WF; cross: SLM; square: DKESM; circle: WALEM; asterisk: RNGM; diamond: DSLM; dashed line: DES.

The Strouhal number ($St = fD/U_0$) for the shedding frequency of vortices, mean and r.m.s. drag coefficients ($\overline{C}_d$ and $\sqrt{C_d^2}$), lift coefficients ($\sqrt{C_l^2}$), and angle of flow separation (θ_s) are also used as benchmark parameters for evaluating the quality of the CFD results. The predicted values of these parameters are listed in table 2 for comparison with the experimental data. Except for the r.m.s. drag coefficient, the SLM+WF model agrees better with the measured data. All other models give comparable results for these parameters. The predictions according to LES with different subgrid models are consistently better than the DES predictions in all parameters except the Strouhal number. However, the computational cost for LES is generally higher than that for DES.

		St	$\overline{C}_d$	$\sqrt{\overline{C_d^2}}$	$\sqrt{\overline{C_l^2}}$	θ_s
Experimental Data		0.18-0.19 [Ref. 40]	1.0-1.4 [Ref. 38]	0.18 [Ref. 41]	0.45-0.60 [Ref. 40]	78° [Ref. 39]
LES	SLM+WF	0.173	1.26	0.26	0.55	80°
	SLM	0.230	1.06	0.25	0.52	82°
	DKESM	0.126	0.96	0.25	0.47	83°
	DSLM	0.226	0.86	0.25	0.46	84°
	WALEM	0.235	0.85	0.24	0.39	84°
	RNGM	0.230	0.78	0.21	0.31	103°
DES		0.205	0.8	0.21	0.35	99°

Table 2: Comparisons of simulation results with experimental data.

The comparisons indicate that SLM+WF shows better agreement between the predictions and the experimental data. The SLM differs from SLM+WF only in terms of the respective near-wall treatments. As shown in the computational results, the interaction between the flow and the solid surface greatly affects the accuracy of the numerical model. This result indicates the superior performance of the analytical integration of the power law in the velocity distribution for the near-wall treatment in dealing with separating flows.

Thus, in light of the comparisons described above, SLM+WF is suitable for performing LES to compute unsteady lift and drag forces on a circular cylinder as well as to predict the surface

pressure and mean drag and the point of flow separation on the cylinder's surface. Furthermore, by substituting pressure into equation (7), the flow-induced noise can be calculated for an observer located at the far field. Before we proceed, it is of interest to demonstrate the correlation between the flow fields and acoustic field by examining snapshots of flow fields. Figure 5(a) and (b) shows the instantaneous streamlines and pressure distribution in the vicinity of the circular cylinder, where a periodic flow pattern is identified. This repeated alternate shedding of vortices suggests that the frequency of the far-field sound pressure can be characterized by the Strouhal number of the flow (corresponding to a frequency of 625 Hz and period of 0.0016 s).

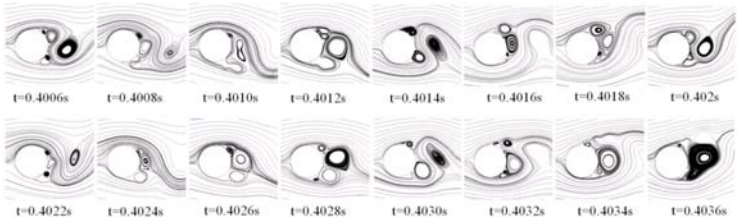

(a) Instantaneous streamlines

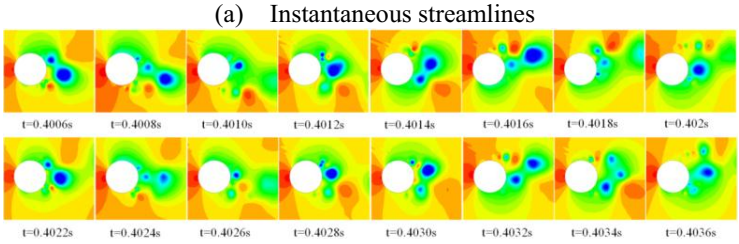

(b) Instantaneous static pressure

Figure 5. Predictions of instantaneous flow field from LES simulations (SLM+WF). (a) Instantaneous streamlines; (b) instantaneous static pressure.

To further support the above observation, time histories of the lift coefficient and the surface pressure at selected points on the cylinder's surface are analyzed (results not shown here for brevity). It is noted that the magnitudes of the lift force and surface pressures vary sinusoidally with a dominant period of approximately 0.0016 s, which is consistent with the change in flow patterns observed in figure 5. However, the phase angles of the surface pressures at different locations differ because the surface pressures change both spatially and temporally. In figure 6, we plot the power spectral density of the lift coefficient of the cylinder versus Strouhal number, and a distinct peak is observed at $St = 0.173$. Figure 7 shows spectra of relative surface pressure levels, L, at three azimuthal locations of 10°, 90°, and 160°, where L is defined as

$$L = 20 \log \; p / p_{ref} \tag{9}$$

with the reference pressure $p_{ref} = 2 \times 10^{-5}$ Pa. Figures 6 and 7 show the broadband characteristics of the lift force and surface pressure. These are largely due to the presence of a turbulence field in the flow around the cylinder.

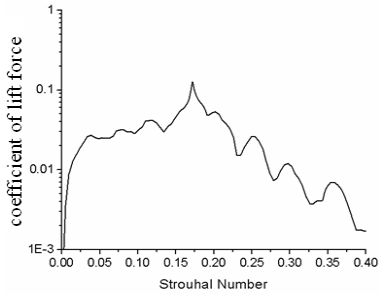

Figure 6. Lift coefficient of 2D cylinder versus Strouhal number.

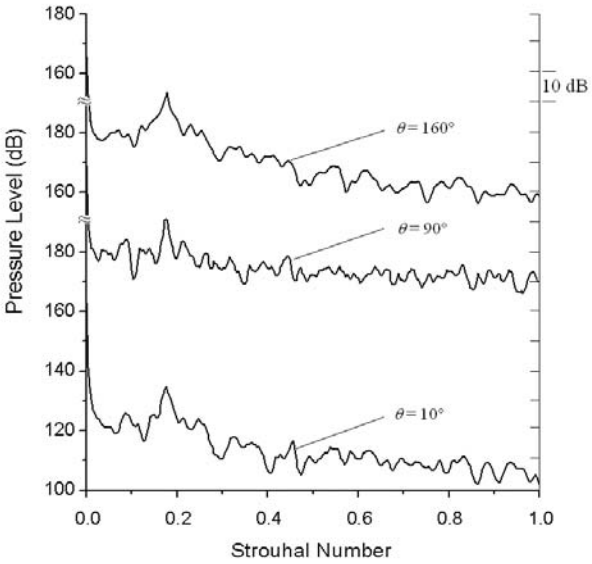

Figure 7. Spectra of relative surface pressure levels at three selected locations on surface of circular cylinder. Results are from LES predictions using SLM+WF.

Next, we compare the predictions of noise induced by this flow over a 2D circular cylinder with experimental results. The data is from Revell et al. [34], where a microphone is used to measure a sound field $128D$ away from the longitudinal axis at an angle $\theta = 90°$ in an acoustic wind tunnel. The tests are conducted at a Mach number of 0.2 ($U_0 \approx 69.2$ m s^{-1}) and Reynolds number of 89,000. The flow simulations and acoustics analysis are repeated under identical conditions. The numerical results are presented in terms of the overall sound pressure level (OASPL):

$$\mathrm{OASPL} = 10\log\left[\sum_i 10^{SPL_i/10}\right] \tag{10}$$

where SPL_i represents the far-field sound pressure level at the receiver location for the ith frequency band.

The relative sound pressure level SPL is represented by equation (9) where p is replaced with the far-field acoustic pressure in the time domain, which is computed via equation (7) using the time histories of the surface pressure predicted by CFD. The narrow-band acoustic pressures in the frequency domain can then be computed from the time-domain data by means of fast Fourier transform (FFT). Summing contributions from all frequency bands leads to the OASPL given in equation (9). Recall that the integration given in equation (7) is performed over a 3D surface. Hence, a further assumption is needed to compute the sound fields based on the 2D input data. To allow a reasonable comparison between numerical and experimental results, a source correction length (SCL) is introduced where the sound sources are assumed to be perfectly correlated within the SCL region but uncorrelated outside it. Based on the strategy employed by Cox et al. [42], the SCL region can be adjusted for evaluating its effect on the predicted OASPL. For a Reynolds number of 90,000, Norberg [40] suggests that the SCL can be set experimentally as $3.16D$. Here, according to the conclusion of Orselli et al. [8], the SCL of $5.0D$ provides the best agreement with the experimental results for 3D flow over a long cylinder of length $25.3D$. The OASPLs obtained from the LES using SLM+WF and DES are 101.9 dB and 102.09 dB, respectively, compared to the experimental data 100 dB obtained by Revell et al. [34]. This further supports the notion that, in order to predict flow-induced noise at a far-field location, accurate predictions of the near-field unsteady flow fields are essential.

4 FLOW OVER CIRCULAR CYLINDER

In the previous section, the 2D simulation results suggest that LES with SLM+WF agrees better with the experimental data. In this section, this approach is extended to a 3D model problem. In particular, we consider the noise induced by flow over a generic side-view mirror mounted on a flat plate. The flow has a free stream velocity U_1=39 m s^{-1} and a Reynolds number Re =5.2×10^5. As shown in figure 8, the generic side-view mirror consists of a half-cylinder of diameter D=0.2 m and height H=0.2 m. A quarter sphere is placed on top of a half-cylinder, making the total height $1.5D$. The mounting plate has a width of $8D$ and a length of $12D$. The side mirror is located centrally at $4.5D$ downstream of the plate's leading edge.

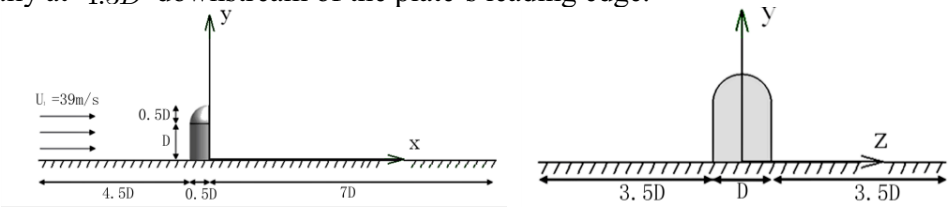

Figure 8. Geometry of generic side-view mirror.

The numerical solver is set similar to the 2D case described in section 2. The computational mesh is composed of a structured grid with a multi-block arrangement. A total of three different computational grids are created using ICEM-HEXA software [43]. The purposes of having three different computational grids (Coarse, Fine, and Finer) are to ensure that the results obtained are grid independent. There are 2.3million of nodes in the coarse computational domain, 5.2million of nodes in the fine computational domain and 7.2million of nodes in the finer computational domain. Figure 9 shows the surface pressure coefficient at different sensor position for coarse, fine and finer meshes. Fine and finer mesh produce similar results, meaning that the results obtained is converged and is grid independent. Thus, fine mesh is be used throughout the entire analysis. The height and circumferential direction of the cylinder surface in the fine grid computational domain are discretized by 100 nodes, and the first off-wall node is located 2×10^{-4} m away from the solid surface along the normal direction, n, of the local wall. A fine mesh is extended in the wake of the mirror for a distance of $10D$ as measured from the mirror's rear face. The mesh is progressively coarsened from the vicinity of the mirror to the domain boundary, where the mesh size is set from 0.01 m to 0.1 m.

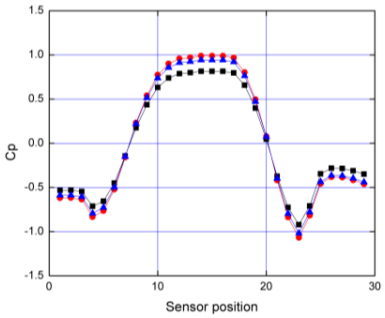

Figure 9. Comparison of time-mean pressure coefficient on three different computational grids. Square: coarse grids; Triangle: fine grids; Circle: finer grids.

The boundary conditions are as follows: (i) no-slip and no-penetration conditions on the generic mirror and the flat plate, (ii) a uniform free stream velocity with no perturbations at the inlet boundary, (iii) a constant free stream pressure at the outlet boundary, and (iv) free-slip conditions at the top and two lateral sides of the computational domain. The flow fields and fluctuating pressures are computed by SLM+WF. To improve numerical efficiency, a steady RANS approach is first employed to initialize the transient computations. The pressure time histories are then calculated and recorded after an initial transient period ($\sim 90D/U_1 = 0.46s$) with a time step

of 5×10^{-5} s for a period of 0.85 s, i.e., the recording time period is between $90D/U_1$ and $255D/U_1$. The time-domain pressures are then converted to frequency-domain pressures by standard FFT numerical routines. These results are then compared later with the published experimental data [44] and DES predictions [45].

For ease of comparison, figure 10 gives the locations of multiple pressure transducers for measuring surface pressures. The measured mean surface pressures (circles) from transducers 1 to 34 are presented in figure 11. The predictions of LES with SLM+WF and DES, also shown in figure 11, show reasonable agreement with the measurement results. The predicted mean pressure from LES and DES over the mirror front side (locations 10–25) shows good agreement with the measured results. Sensors at locations 1–9 and 30–34 are deployed downstream of the separation line where the flow has complex temporal-spatial characteristics, and thus, it is difficult to obtain ideal agreement with the experimental data. DES underpredicts the mean pressure at these locations, whereas LES (with SLM+WF) overpredicts. At locations 5 and 28 the underprediction from DES is more pronounced, which is attributed to a misrepresentation of the separation zone, as highlighted by Ask and Davidson [46]. LES with SLM+WF provides accurate predictions at these two locations.

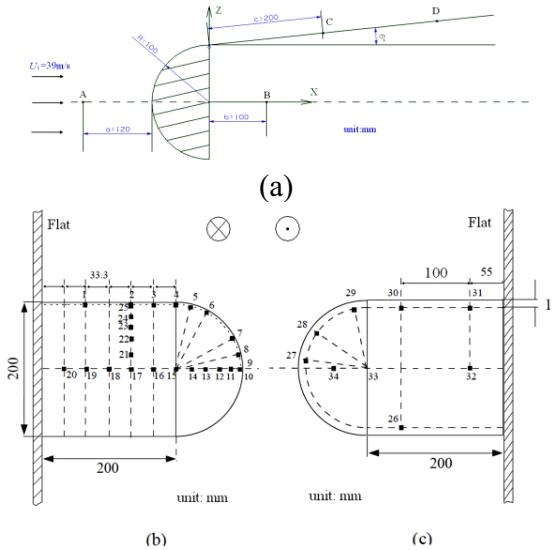

Figure 10. Locations of pressure measurements on plate surface (A, B, C, and D) and mirror surface (1–34) of generic side-view mirror model: (a) top, (b) front, and (c) rear view.

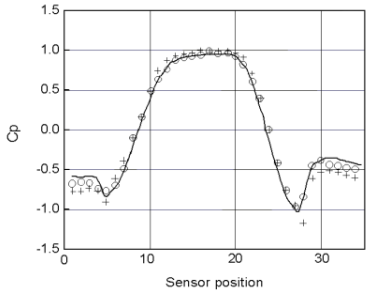

Figure 11. Comparison of predicted and measured time-mean pressure coefficient. Circle: experimental; solid line: LES + wall function; cross: DES.

The breaking vortex behind the side mirror will induce air noise and may trigger vibration of the exterior structure. Thus, it is necessary to evaluate the capacity of a variety of simulation schemes to accurately predict surface pressure fluctuation. The simulation results are compared with the experimental data [43] and the numerical results from DES [45]. Again, the relative

pressure level, which is defined in equation (9), is used for the presentation of data. Figure 12 shows comparisons of experimental measurements with numerical predictions at four selected locations (A–D, figure 11). Predictions of the surface pressures according to SLM+WF agree well with the experimental data for all these locations. At the upstream location A, numerical predictions according to DES provide the worst results, with discrepancies in excess of 40 dB even at low frequencies. Numerical predictions according to SLM and DSLM are somewhat better than those of DES, but the errors are typically more than 25 dB at high frequencies.

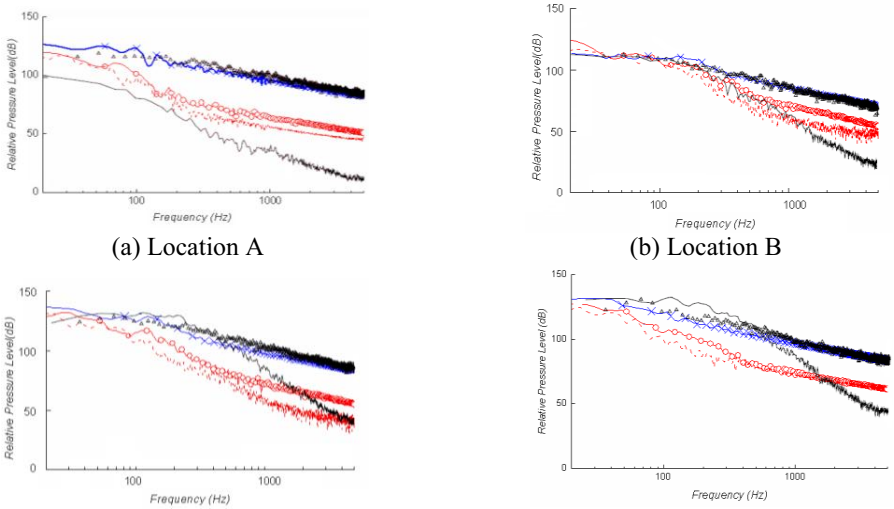

(a) Location A (b) Location B

(c) Location C (d) Location D

Figure 12. Predicted and measured relative pressure levels [equation (9)] at various locations. Cross: SLM+WF; circle: SLM; solid line: DES; dashed line: DSLM; triangle: experimental [Ref. 44].

The propagation of sound is computed at four receiver locations, shown in figure 13. The far-field acoustic pressures at the same locations are measured by Rung et al. [45], and the comparison is shown in figure 14. It is evident that the LES with SLM+WF offers the best predictions at these four locations. DES significantly underpredicts SPL, particularly at high frequency range (>300 Hz), which may contribute to the underprediction of unsteady pressure level (thus dipole strength in equation (7)) at high frequency (figure 14). LES with DSLM overpredicts SPL at the same high frequency range, which further demonstrates the inadequacy of the dynamic Smagorinsky SGS model in simulating unsteady surface pressure fluctuation.

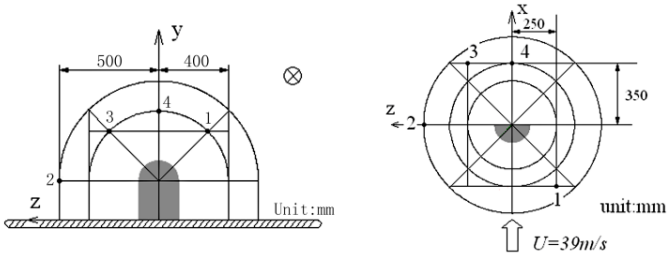

Figure 13. Locations of microphones (1–4) employed by Rung et al. [Ref. 45] for far-field acoustic measurements.

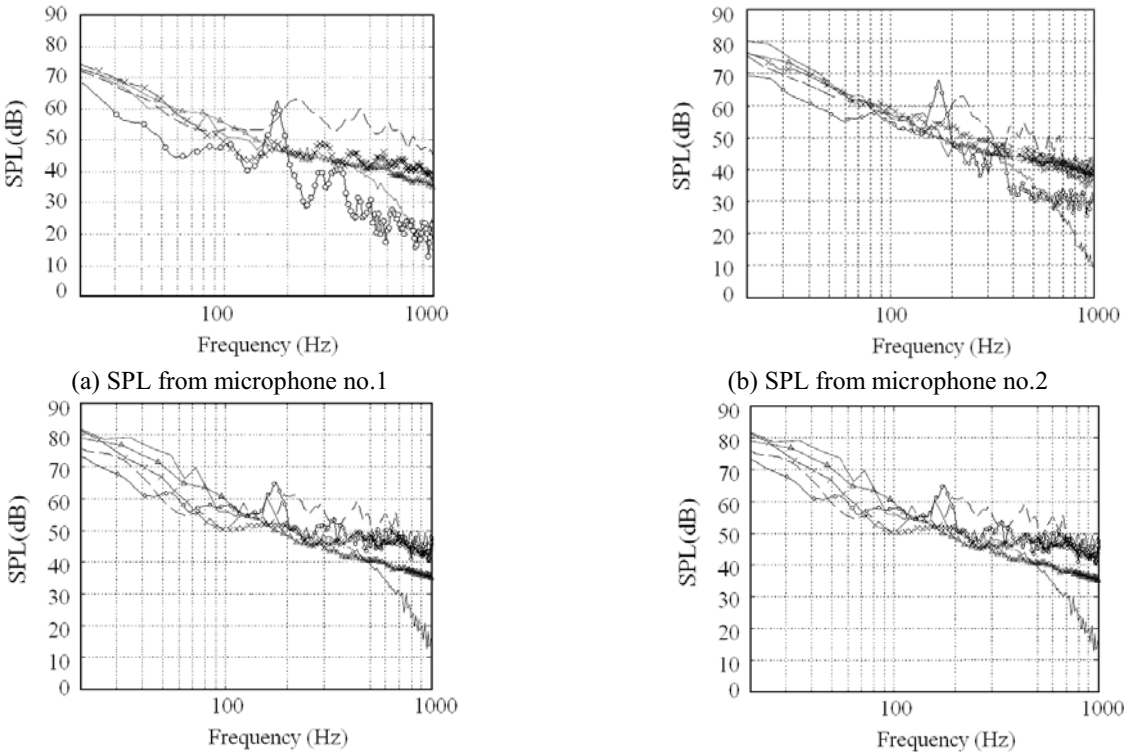

(a) SPL from microphone no.1

(b) SPL from microphone no.2

(c) SPL from microphone no.3

(d) SPL from microphone no.4

Figure 14. Predicted and measured sound pressure level (SPL) at various observer locations. Cross: SLM+WF; circle: SLM; solid line: DES; dashed line: DSLM; triangle: experimental.

5 CONCLUSIONS

In this study, the implications of various SGS models and near-wall treatment schemes used in LES of low Mach number flows are investigated for the accurate prediction of unsteady flow fields and far-field acoustic fields. The unsteady LES predicts surface pressure fluctuations, which gives a distribution of the dominant dipole source. The far-field acoustic fields are assessed using the FW-H analogy. Benchmark studies are conducted on flow over a 2D cylinder and a generic side-view mirror model. Numerical predictions of various schemes are compared with the measured surface pressure and far-field acoustic data. It is identified that LES combined with the Smagorinsky–Lilly SGS model ($C_S = 0.16$) and the Werner–Wengle wall function provides the best predictions in a wide frequency range (10–1000 Hz). On the other hand, the DES approach (a combination of RANS in the near-wall regime and LES in the outer regime) considerably underpredicts the unsteady surface pressure and acoustic field at high frequencies (>300 Hz). Advanced SGS models such as the dynamic Smagorinsky model show no superiority over the other models in predicting surface pressure fluctuations. These results aid the selection of appropriate CFD techniques for accurately simulating low Mach number flows. The technique identified in the present study is currently being applied to investigate the aerodynamic noise of automobiles operating at cruising speeds, including low frequency buffeting noise due to flow over open cavities and high frequency noise associated with the breaking of large-scale vortical structures.

6 ACKNOWLEDGEMENTS

The research was supported by “the Fundamental Research Funds for the Central Universities” (2012-IV-068) and China Scholarship Council of the National Natural Science Foundation of China (NSFC 50975083).

7 REFERENCES

[1] M. S. Howe, Acoustics of Fluid-Structure Interactions, Cambridge University Press, 1998, Chap. 3.
[2] S. Ogawa, and T. Kamioka, Review of Aerodynamic Noise Prediction Using CFD, SAE Paper 1999-01-1126.
[3] M. Wang, J. B. Freund, and S. J. Lele, Computational Prediction of Flow-Generated Sound, Annual Review of Fluid Mechanics, Vol. 38, 2006, pp. 483-512.
[4] C. H. Tsai, L. M. Fu, Y. L. Huang, and J. C. Leong, Computational Aero-acoustic Analysis of a Passenger Car with a Rear Spoiler, Applied Mathematical Modeling, Vol. 33, 2009, pp. 3661-3673.
[5] P. Moin and K. Mahesh, Direct Numerical Simulation: A Tool in Turbulence Research, Annual Review of Fluid Mechanics, Vol. 30, 1998, pp. 359-378.
[6] T. Cebeci, Turbulence Models and Their Application. Efficient Numerical Methods with Computer Programs, Springer-Verlag, New York 2004.
[7] K. J. Karbon, and U. D. Dietschi, Computational Analysis and Design to Minimize Vehicle Roof Rack Wind Noise, SAE Paper 2005-01-0602.
[8] R. M. Orselli, J. R. Meneghini, and F. Saltara, Two and Three-Dimensional Simulation of Sound Generated by Flow around a Circular Cylinder, AIAA 2009-3270.
[9] Y. Li, N. Kasaki, S. Tsunoda, etc., Evaluation of Wind Noise Sources Using Experimental and Computational Methods, SAE Paper 2006-01-0343.
[10] M. Lesieur, and O. Metais, New Trends in Large-eddy Simulations of Turbulence, Annual Review of Fluid Mechanics, Vol. 28, 1996, pp. 45-82.
[11] R. Rogallo, and P. Moin, Numerical Simulation of Turbulent Flows, Annual Review of Fluid Mechanics, Vol. 16, 1984, pp. 99-137.
[12] C. Meneveau, and J. Katz, Scale-invariance and Turbulence Models for Large-eddy Simulation, Annual Review of Fluid Mechanics, Vol. 32, 2000, pp. 1-32.
[13] J. Smagorinsky, General Circulation Experiments with the Primitive Equations, Part 1: the Basic Experiment, Monthly Weather Review, Vol. 91, 1963, pp. 99-164.
[14] U. Piomelli, P. Moin, and J. F. Ferziger, Model Consistency in Large Eddy Simulation of Turbulent Channel Flows, Physics of Fluids, Vol. 31, 1988, pp. 1884-1891.
[15] K.H. Chen, J. Johnson, U. Dietschi, and B. Khalighi, Automotive Mirror Wind Noise Simulations and Wind Tunnel Measurements, AIAA 2008-2906.
[16] J. Chen, J. Katz, and C. Meneveau, The Implication of Mismatch between Stress and Strain-Rate in Turbulence Subjected to Rapid Straining and Destraining on Dynamic LES Models, Journal of Fluids Engineering, Vol. 127, 2005, pp 840-850.
[17] T. Takaishi, M. Miyazawa, and C. Kato, A Computational Method of Evaluating Noncompact Sound Based on Vortex Sound Theory,Journal of the Acoustical Society of America, Vol. 121, 2007, pp. 1353-1361.
[18] C. Schram, A Boundary Element Eextension of Curle's Analogy for Non-Compact Geometries at Low-Mach Numbers, Journal of Sound and Vibration, vol. 322, 2009, pp. 264-281.
[19] Y. Khalighi, A. Mani, F. Ham, and P. Moin, Prediction of Sound Generated by Complex Flows at Low Mach Numbers, AIAA Journal, Vol.48, 2010, pp.306-316.
[20] S. Pope, Turbulent Flows, Cambridge University Press, Cambridge, 2000.
[21] U. Piomelli, W. H. Cabot, P. Moin, and S. Lee, Subgrid-Scale Backscatter in Turbulent and Transitional Flows, Physics of Fluids, A3 (7), 1991, pp. 1766-1771.
[22] D. Lilly, The representation of Small-scale Turbulence in Numerical Simulation Experiments, In Proc. IBM Scientific Computing Symp. Environ. Sci., 1967, p. 195.
[23] M. Germano, Turbulence: the Filtering Approach, Journal of Fluid Mechanics. Vol. 238, 1992, pp. 325-335.
[24] M. Germano, U. Piomelli, and W. Cabot, A Dynamic Subgrid-scale Eddy Viscosity Model, Physics of Fluids, A3, 1992, pp. 1760-1765.
[25] J. E. Ffowcs Williams, and D. L. Hawkins, Sound Generation by Turbulence and Surfaces in Arbitrary Motion, Proceedings of the Royal Society of London , Vol. A- 264, 1969, pp. 321-342.
[26] S. E. Kim, Y. Dai, E. K. Koutsavdis, S. Sovani, N. A. Kadam, and K. M. R. Ravuri, A Versatile Implementaiton

of Acoustic Analogy Based Noise Prediction Method in a General-Purpose CFD Code, AIAA Paper 2003-3202.
[27] A. Travin, M. Shur, M. Strelets and P. Spalart, Detached-Eddy Simulation Past a Circular Cylinder, Flow Turbulence and Combustion, Vol. 63, 1999, pp. 293-313.
[28] J. S. Baggett, J. Jimenez, and A. G. Kravchenko, Resolution requirements in large-eddy simulations of shear flows. Annual Research Briefs, Center for Turbulence Research, NASA Ames/Stanford Univ., 1997, pp.51-66.
[29] M. Breuer, Numerical and Modeling Influences on Large Eddy Simulations for the Flow Past a Circular Cylinder, International Journal of Heat and Fluid Flow, Vol. 19, 1998, pp. 512-521.
[30] P. Catalano, M. Wang, G. Iaccarino, and P. Moin, Numerical Simulation of the Flow Around a Circular Cylinder at High Reynolds Numbers, International Journal of Heat and Fluid Flow, Vol. 24, 2003, pp. 463-469.
[31] L. Temmerman, M. A. Leschziner, C. P. Mellen, and J. Frohlich, Investigation of Wall-Function Approximation and Subgrid-Scale Models in Large Eddy Simulation of Separated Flow in a Channel with Streamwise Periodic Constrictions, International Journal of Heat and Fluid Flow, Vol. 24, 2003, pp. 157-180.
[32] H. Werner, and H. Wengle, Large-eddy Simulation of Turbulent Flow over and Around a Cube in a Plate Channel, 8th Symposium on Turbulent Shear Flows, 1991, p. 155–168.
[33] J. Ziefle, S. Stolz, and K. Kleiser, Large-eddy Simulation of Separated Flow in a Channel with Streamwise-Periodic Constrictions, AIAA Journal, Vol. 46, 2008, pp. 1705-1718.
[34] J.D. Revell, R.A. Prydz, and A.P. Hays, Experimental Study of Airframe vs. Drag Relationship for Circular Cylinders, Lockheed Report 28074, Final Report NASA Contract NAS1-14403, 1977.
[35] S. E. Kim and L. S. Mohan , Prediction of Unsteady Loading on a Circular Cylinder in High Reynolds Number Flows using Large Eddy Simulation, Proceedings of 24th Int. Conf. Offshore Mech. and Artic Eng., OMAE 2005, Halkidiki, Greece, June 12-17, 2005.
[36] S. E. Kim, "Large Eddy Simulation of Turbulent Flow Past a Circular Cylinder in Subcritical Regime", AIAA 2006-1418, 44th AIAA Aerospace Science Meeting and Exhibit, Reno, NV, 9-12 Jan., 2006.
[37] Fluent User Manual, Fluent Inc. 2006-09-20.
[38] B. Cantwell, and D. Coles, An Experimental Study of Entrainment and Transport in the Turbulent Near Wake of Circular Cylinder, J. Fluid Mech., Vol.136, pp.321-374,1983.
[39] E. Achenbach, Distribution of Local Pressure and Skin Friction in Cross Flow Around a Circular Cylinder up to $Re = 5 \times 10^6$, J. Fluid Mech., Vol. 34, 1968, pp. 625-639.
[40] C. Norberg, Fluctuating Lift on a Circular Cylinder: Review and New Measurement, J. Fluids and structures, Vol.17, No.1, 2002, pp.57-96.
[41] G.S. West, and C.J. Apelt, Measurement of Fluctuation Pressures and Forces on Circular Cylinder in the Reynolds Number. 10^4 and 2.5×10^5, J. Fluids and Structures, Vol.7, No.3, 1993, pp.227-244.
[42] J.S. Cox, K.S. Brentner, and L. Rumsey, Computational of Vortex Shedding and Radiated Sound for a Circular Cylinder: Subcritical to Transcritical Reynolds Numbers, Theoretical and Computational Fluid Dynamics, Vol.12, No.4,1998,pp.223-253.
[43] ICEM-CFD user manual, SAS IP, Inc. 2009.
[44] R. Hold, A. Brenneis, and A. Eberle, Numerical Simulation of Aeroacoustic Sound Generated by Generic Bodies Placed on a Plate: Part I - Prediction of Aeroacoustic Sources, 5th AIAA/CEAS Aeroacoustics Conference. Seattle, Washington, 10-12 May 1999, AIAA-99-1896.
[45] Th. Rung, D. Eschricht, J. Yan, and F. Thiele, Sound Radiation of the Vortex Flow Past a Generic Side Mirror, 8th AIAA/CEAS Aeroacoustics Conference & Exhibit, Breckenridge, Colorado, 17-19 June 2002 AIAA 2002-2549
[46] J. Ask and L. Davidson. "=The Sub-critical Flow past a Generic Side Mirror and its Impact on Sound Generation and Propagation"=, 12th AIAA/CEAS Aeroacoustics Conference. Cambridge, Massachusetts, 8-10 May 2006, AIAA 2006-2558.
[47] S. Krajnovic, S. Sarmast, B. Basara. "Numerical Investigation of the Flow Around a Simplified Wheel in a Wheelhouse", Journal of Fluid Engineering, Vol. 133, No.111001, pp.1-12

The Seventh International Colloquium on Bluff Body Aerodynamics and Applications (BBAA7)
Shanghai, China; September 2-6, 2012

Three-dimensional forced oscillation technique in flutter assessment

Gergely Szabó [a], Miklós Pálossy [b], László Szecsányi [c]

[a]*Phd student, Ustokos u. 4 Szolnok, Hungary*
[b]*Chief designer, Than Karoly Str. 3-5, Hungary*
[c]*Design engineer, Than Karoly Str. 3-5, Hungary*

ABSTRACT: In this paper a novel approach for bridge deck flutter assessment is introduced. The classical forced oscillation technique was updated by using advanced three-dimensional CFD simulation instead of 2D sectional studies. The whole bridge deck wall boundary was given a forced oscillation in airflow according to the relevant rotational and bending modes. The advanced CFD modeling required the development of the modal derivatives that can be used to calculate the critical wind speed as by using the classical flutter derivatives. An aeroelastic wind tunnel model was constructed, specially dedicated to the validation of the numerical solution. Good agreement between the measured and simulated results was found. After the validation the technique was applied on a footbridge with a main span of 120m.

KEYWORDS: Three-dimensional study, CFD, modal derivatives, bridge flutter

1 INTRODUCTION

In classical flutter prediction of bridges the flutter derivatives theory is applied mainly. These derivatives are calculated by considering a section of the bridge deck. Nowadays, however, really complex bridges are built in geometry, therefore their simplification into a section is not easy to make in some cases. Therefore, the authors of this paper have invested a lot into the application of three-dimensional flutter simulation [2], in which a fluid-structure interaction (FSI) simulation of a three-dimensional bridge deck was studied. Such work can mainly be found for aircraft wings [1]. As a thee-dimensional FSI simulation requires tremendous amount of computational time, a new approach was developed for flutter study of complex structures. In this approach the three-dimensional flow field around the oscillating bridge deck can be taken into account and the niceties of the forced vibration method can be kept too. The forced oscillation of the 3D bridge deck leads to new derivatives that will be referred to as modal derivatives later.

2 DEVELOPMENT OF THE MODAL DERIVATIVES

In this chapter the development of the modal flutter derivatives will be presented. First of all a full aeroelastic wind tunnel model is shown as a validation for the novel method. A three-dimensional CFD model and the necessary parameters of the simulation will be shown that are necessary for calculating the modal derivatives. The formulation of these modal derivatives as well as their application in the critical wind speed evaluation will be finally presented.

2.1 *Full aeroelastic wind tunnel model*

In Figure 1 the fully aeroelastic wind tunnel model is shown that was constructed in order to validate the numerical solutions. This model is an individual mechanical system for validation

only and is not a scaled model of any real bridge structure. The bridge is made up by using an aluminum core beam on which balsa elements are fixed. The cross section can be seen in Figure 2. The contour of the model represents an idealized streamlined boxed bridge deck cross section. This section was chosen because it was believed to be handled properly with simpler turbulence models and coarse CFD mesh. The core beam is fully constrained at both ends. There are six steel wires working like stay cables. These wires were softened by introducing spring elements (stiffness is 230N/m) in order to make the bridge more flexible. The model can be seen in Figure 3. The elastic modulus of the aluminum is 2.06E10 N/m², the density is 2500kg/m³. The density of the balsa coating is 123kg/m³.

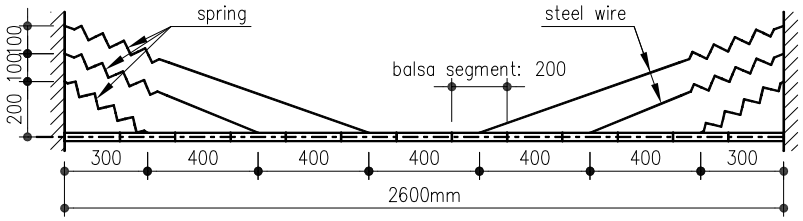

Figure 1. Side view of the aeroelastic wind tunnel model.

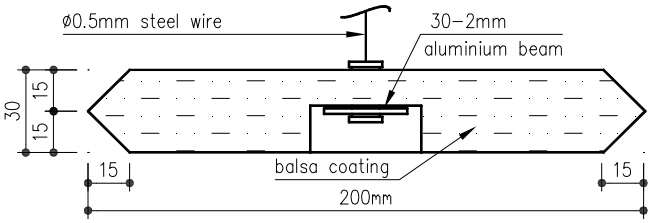

Figure 2. Cross section of the aeroelastic model.

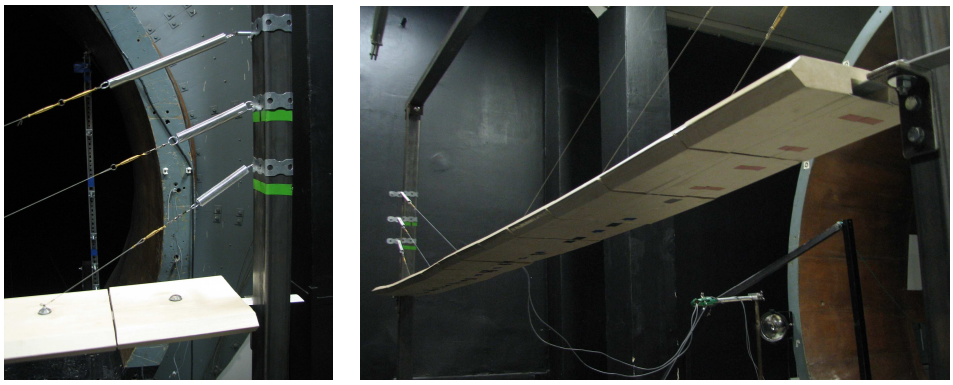
Figure 3. Bridge model mounted in the wind tunnel.

At the middle balsa element of the bridge, at both sides of the segment two piezoelectric accelerometers were fixed for monitoring the vertical motion. For the wind-off case the natural frequencies and logarithmic decrement values were measured. The first vibration mode was a symmetrical heave motion of the bridge deck with a natural frequency of 1.62Hz. For the flutter analysis the first torsion mode is dominant, which was the fifth one with a natural frequency of 5.55Hz. The logarithmic decrement for this mode was δ=0.02. These parameters were used for tuning the mechanical FEM model. During the measurement the wind speed was incrementally increased. The high frequency vibrations caused by the vortex shedding were ignored and the flutter phenomenon was only considered. The tests were done under low turbulence level. The critical wind speed was 9.7m/s with a coupled flutter motion.

2.2 *Three-dimensional CFD model*

The aerodynamic characteristics of the bridge deck were modeled by using CFD. The mesh and the domain is show in Figure 4. The ANSYS-CFX was utilized. The computational mesh was carefully optimized in order to save computational time and maintain the accuracy of the results. The number of cells used is 49.816, where the in-plane cell number is 958 and there are 52 divisions along the bridge axis.

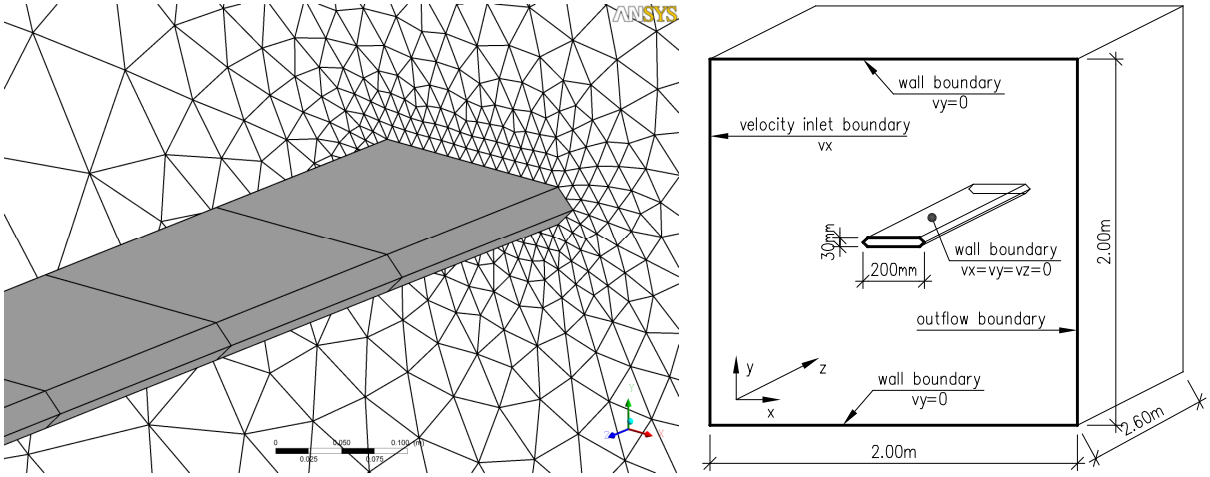

Figure 4. CFD mesh around the aeroelastic bridge model with the boundary conditions.

The novel approach requires the arbitrary motion of the bridge deck that is feasible by using user defined functions. Every cell node position of the bridge boundary can be defined as a function of time, therefore any kind of three-dimensional shape can be defined. In Figure 5 a rotated bridge shape in illustrated. The mesh deformation is solved by the software by using spring stiffness analogy. The initial (no deformed) mesh quality can be preserved by defining increased spring stiffness in the vicinity of the bridge boundary. In case of a section model the forced oscillation is performed with translational and rotational degrees of freedoms. In case of a 3D boundary, however, the relevant heave and torsion mode shapes are used that will be shown later. As usual, a reduced inflow velocity range (4, 8, 12, 16 and 20) is considered. The oscillating frequency was 6.00 Hz in each case. The time step was chosen as 0.0008 s. In Figure 6 the flutter derivatives are shown. The flutter derivatives were determined with an ordinary 2D section model with 12590 cells that is not shown here. The derivatives were also determined using the result of the 3D mesh; the lift force and moment signals of the middle section along the bridge axis were considered where the motion amplitudes reach their maximal values.

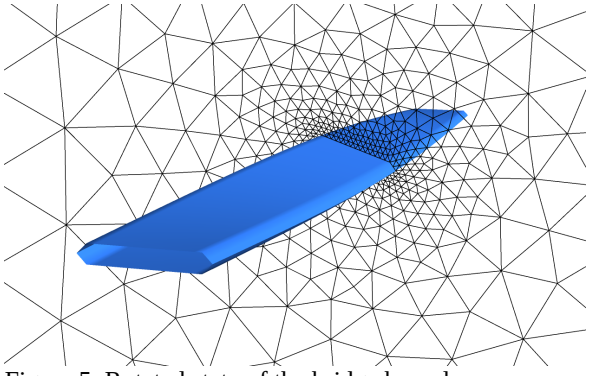

Figure 5. Rotated state of the bridge boundary.

In Figure 6 the flutter derivatives belonging to the 2D and 3D meshes can be seen. Although the 3D mesh is much coarser than the 2D one, it succeeds to provide accurate flutter derivatives. Therefore, the 3D mesh is considered to be appropriate for the novel technique. As a streamlined cross section is investigated the derivatives of the flat plate theory are also illustrated.

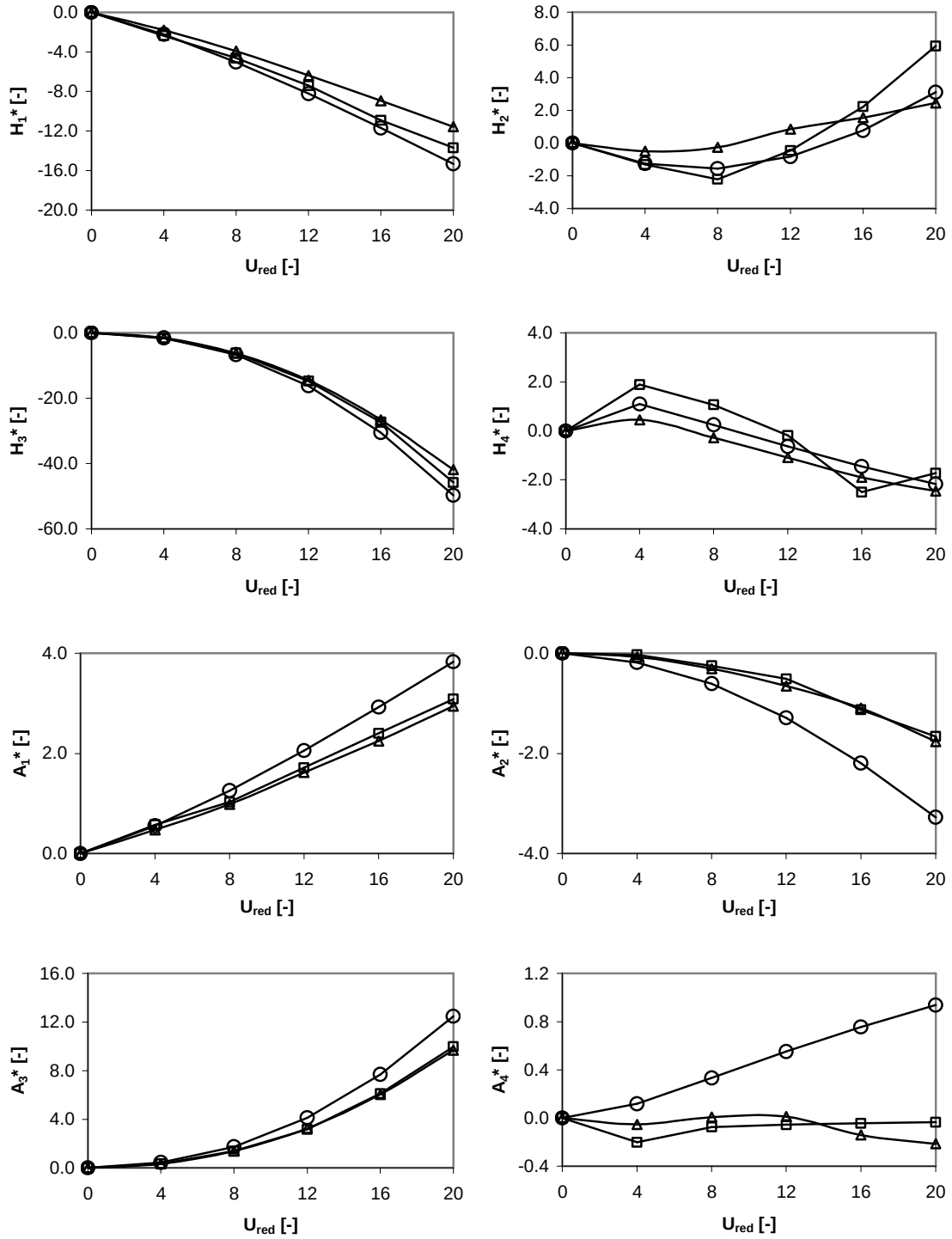

Figure 6. Flutter derivatives of the bridge (Circle: Flat plate theory, Rectangle: CFD_2D, Triangle: CFD_3D).

2.3 *Mathematical background of flutter prediction*

In classical flutter prediction the following eigenproblem is to be solved (1). In case of a 2DOF system the problem can be solved according to [3]. If the system is considered as a system with a series of segments (see Figure 7), the (1) solution can be extended.

$$\left|(1+\mathrm{i}\gamma)\mathbf{K}-\omega^2\left[\mathbf{M}+\mathbf{L}(U_{red})\right]\right|=0 \tag{1}$$

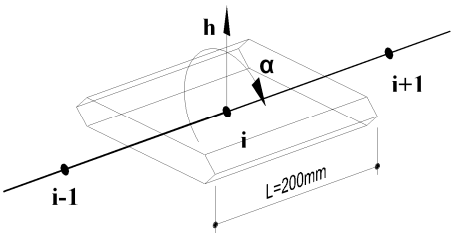

Figure 7. A 200mm long segment of the aeroelastic bridge model.

The aeroelastic wind tunnel model can be regarded as a system with 13 nodes, as 13 balsa segments are attached to the main beam. The load matrix in (1) can be rewritten in (2).

$$\mathbf{L}=\pi\rho b^2\begin{bmatrix} c_{hh} & bc_{h\alpha} & & & & & & n=1 \\ bc_{\alpha h} & b^2c_{\alpha\alpha} & & & & & & n=1 \\ & & \ddots & & & & & \vdots \\ & & & \ddots & & & & \vdots \\ & & & & c_{hh} & bc_{h\alpha} & & n=13 \\ & & & & bc_{\alpha h} & b^2c_{\alpha\alpha} & & n=13 \end{bmatrix} \tag{2}$$

In (2) the aeroelastic bridge is considered as a bridge deck with 13 nodes, with a lift force and a moment at each node. Therefore the size of the **L** matrix is 26x26 in this case. By seeking the solution in the form (3) according to the modal analysis, and using expressions in (4), the (5) eigenproblem is to be solved now.

$$\tilde{\mathbf{x}}=\mathbf{V}\tilde{\mathbf{y}} \tag{3}$$

$$\mathbf{V}^{\mathrm{T}}\mathbf{L}\mathbf{V}=\mathbf{A},\quad \mathbf{V}^{\mathrm{T}}\mathbf{M}\mathbf{V}=\mathbf{E},\quad \mathbf{V}^{\mathrm{T}}\mathbf{K}\mathbf{V}=\left\langle\omega_{0r}^2\right\rangle \tag{4}$$

$$\left|(1+\mathrm{i}\gamma)\left\langle\omega_{0r}^2\right\rangle-\omega^2\left[\mathbf{E}+\mathbf{A}(U_{red})\right]\right|=0 \tag{5}$$

In (5) **V** contains two column vectors belonging to the chosen mode shapes. In (4) **E** is the unity matrix, ω_{0r} is the r_{th} natural circular frequency of the bridge structure. The solution process of the (5) system is the same as in case of a 2DOF system. On top of all, the size of the (5) equation in case of two mode shapes is also the same as that of the 2DOF system. In [3] similar approach can be found for involving the bridge deck as a three-dimensional spatial system. It can be seen that if the flutter derivatives as functions are known for a certain bridge shape, the critical wind speed can be calculated for the bridge structure. This can be done by reducing the bridge into a 2DOF system or by using the mode shapes and natural frequencies in the framework of the modal analysis. The main shortcoming of the above described method is that the three-dimensional flow field is reduced into a set of two-dimensional flows that is the flow parallel

with the bridge axis is neglected. On top of all if the cross section is not constant along the bridge axis for instance, the flutter derivatives have to be determined at several cross sections, resulting in a tedious calculation process.

2.4 *Formulation of the modal derivatives*

In this section the advantages of the flutter derivatives theory and the three-dimensional CFD modelling are combined in order to develop a novel technique. The flutter condition is assumed to show harmonic motion; therefore the analysis is obvious to carry out in the frequency domain as in case of the classical flutter calculation. In (5) matrix **A** can be compiled easily, as **L** and **V** matrices are known for a certain fixed U_{red} value. In order to replace the two-dimensional CFD simulations with the advanced three-dimensional simulation, the **A** matrix should be examined in detail; after multiplying the **L** matrix by **V** matrix, **A** reads (6).

$$\mathbf{A} = \pi\rho b^2 \begin{bmatrix} \sum_i v_{hi}^2 \cdot c_{hh} & b \cdot \sum_i v_{hi} \cdot v_{\alpha i} \cdot c_{h\alpha} \\ b \cdot \sum_i v_{hi} \cdot v_{\alpha i} \cdot c_{\alpha h} & b^2 \cdot \sum_i v_{\alpha i}^2 \cdot c_{\alpha\alpha} \end{bmatrix} \tag{6}$$

The elements of the **A** matrix are terms c_{ii} multiplied by the elements of the mode shape vectors. The main goal is to compile the **A** matrix based on the result of the three-dimensional CFD simulation instead of the 2D ones. As mentioned earlier the ANSYS-CFX enables the user to define arbitrary motion of the bridge deck. The 3D CFD model was tested and the flutter derivatives were extracted by defining translational and rotational spatial deformation of the bridge boundary (see Figure 6). The ways of prescribing this motion is explained here in detail. Obviously the first translational and rotational mode shapes were used, as these contribute to the flutter motion.

In Figure 8 the two relevant mode shapes are shown with the corresponding natural frequencies. The calculation of the mode shapes and frequencies were done by using FEM model of the aeroelastic wind tunnel model.

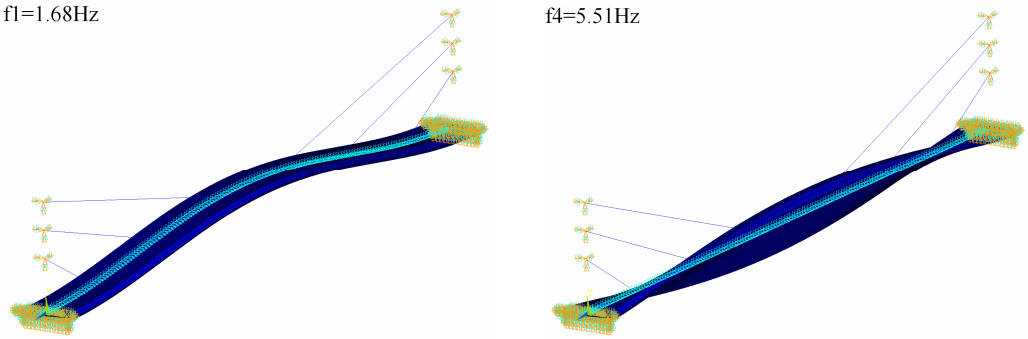

Figure 8. The two relevant dynamic mode shapes.

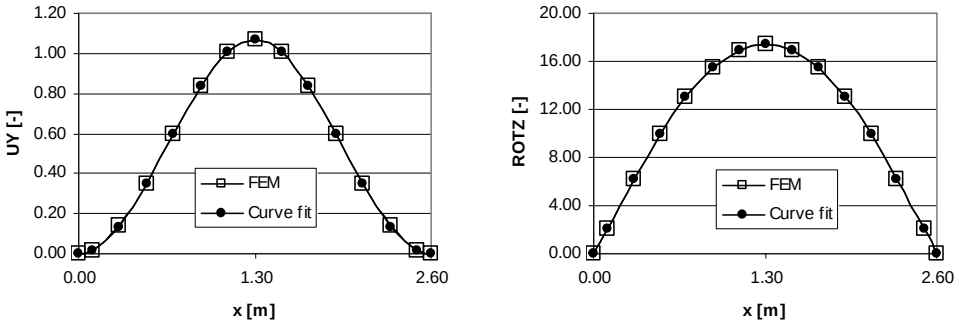

Figure 9. Heave (UY) and torsion (ROTZ) mode shape values used for the calculation.

It is necessary that the bridge boundary is given a predefined motion as a function of time and space. In Figure 9 the discrete mode shape values of the FEM model are fitted by analytical functions. The motion in time is written by using harmonic function. The translational function of the bridge deck is written in (7), where the vertical position of every point (h) is defined at location (z) and at time (t). Likewise the rotation can be written (8), from which vertical and horizontal components can be derived. The maximal translational amplitude at the middle of the deck is h_0=20mm, the maximal rotational amplitude is α_0=0.1744 (10°).

$$h(z,t) = \left[1 - \cos(z\,2\,\pi/L))\right] \cdot h_0 / 2 \cdot \sin(\omega\, t) \tag{7}$$

$$\alpha(z,t) = \left[\sin(z\,\pi/L))\right] \cdot \alpha_0 / 2 \cdot \sin(\omega\, t) \tag{8}$$

When the three-dimensional bridge deck is oscillated according to the certain mode shapes, the aerodynamic forces belonging to the i_{th} node (see Figure 7) can be calculated. There are 13 moment and 13 lift force signals at each simulation case. In Figure 10 the moment functions are shown (U_{red}=8) at i=1,4 and 7 sections.

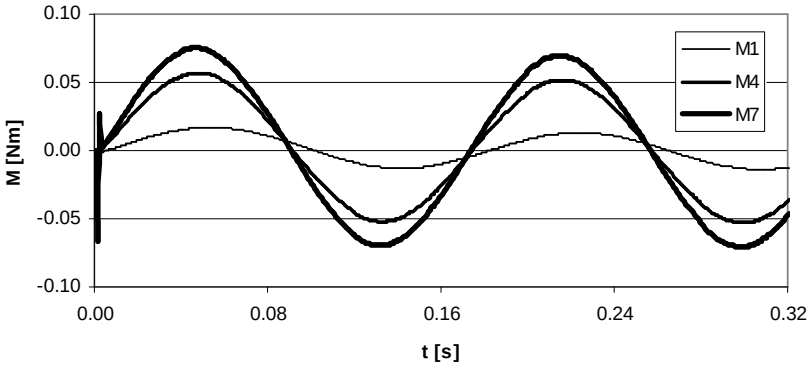

Figure 10. Moment signals at deck element 1, 4 and 7 (U_{red}=8).

Based on the aerodynamic forces and moments in relation with the modal oscillation, (6) equation can be rewritten as (9). The over hat denotes that the $\hat{\mathbf{A}}$ matrix is written by using the mode shape vectors.

$$\hat{\mathbf{A}} = \pi\rho b^2 \cdot \begin{bmatrix} \hat{c}_{hh} & b \cdot \hat{c}_{h\alpha} \\ b \cdot \hat{c}_{\alpha h} & b^2 \cdot \hat{c}_{\alpha\alpha} \end{bmatrix} \tag{9}$$

The elements of matrix $\hat{\mathbf{A}}$ can be compiled analogously as shown in [3], but instead of using the flutter derivatives of a 2D section of the bridge new terms are to be used. In (8) these new flutter derivatives are introduced, that are extracted based on the results of the modal oscillation of the 3D CFD model, therefore can be called as modal (flutter) derivatives. As the 3D bridge is oscillated according to the selected mode shape vectors, the resulting force and moment signals at each i_{th} element of the bridge deck can be assumed to be proportional to the mode shape values at the same locations. Thus, the force and moment signals are to be multiplied by the mode shape values only at once, contrary to the case of the **A** matrix in (6). The summation in (6), thus, can be substituted by summing up the forces and moments multiplied by the relevant mode shape values at the i_{th} location.

$$\hat{H}_1^* = -U_{red}^2 \cdot \frac{\max\left[\sum_i v_{hi} \cdot F_{hi}(t)\right]}{q \cdot B \cdot (2\pi)^2 \cdot (h_0/\hat{h})/B} \sin(\beta) \qquad \hat{H}_2^* = -U_{red}^2 \cdot \frac{\max\left[\sum_i v_{hi} \cdot F_{\alpha i}(t)\right]}{q \cdot B \cdot (2\pi)^2 \cdot (\alpha_0/\hat{\alpha})} \sin(\beta)$$

$$\hat{H}_3^* = U_{red}^2 \cdot \frac{\max\left[\sum_i v_{hi} \cdot F_{\alpha i}(t)\right]}{q \cdot B \cdot (2\pi)^2 \cdot (\alpha_0/\hat{\alpha})} \cos(\beta) \qquad \hat{H}_4^* = U_{red}^2 \cdot \frac{\max\left[\sum_i v_{hi} \cdot F_{hi}(t)\right]}{q \cdot B \cdot (2\pi)^2 \cdot (h_0/\hat{h})/B} \cos(\beta)$$

$$\hat{A}_1^* = -U_{red}^2 \cdot \frac{\max\left[\sum_i v_{\alpha i} \cdot M_{hi}(t)\right]}{q \cdot B^2 \cdot (2\pi)^2 \cdot (h_0/\hat{h})/B} \sin(\beta) \qquad \hat{A}_2^* = -U_{red}^2 \cdot \frac{\max\left[\sum_i v_{\alpha i} \cdot M_{\alpha i}(t)\right]}{q \cdot B^2 \cdot (2\pi)^2 \cdot (\alpha_0/\hat{\alpha})} \sin(\beta)$$

$$\hat{A}_3^* = U_{red}^2 \cdot \frac{\max\left[\sum_i v_{\alpha i} \cdot M_{\alpha i}(t)\right]}{q \cdot B^2 \cdot (2\pi)^2 \cdot (\alpha_0/\hat{\alpha})} \cos(\beta) \qquad \hat{A}_4^* = U_{red}^2 \cdot \frac{\max\left[\sum_i v_{\alpha i} \cdot M_{hi}(t)\right]}{q \cdot B^2 \cdot (2\pi)^2 \cdot (h_0/\hat{h})/B} \cos(\beta) \qquad (8)$$

Finally, the maximum values of these functions are taken, as in case of the extraction of the classical flutter derivatives. If necessary, the summed force and moment functions can be filtered in order to remove the high frequency components that are irrelevant in flutter analysis. In (8) $\hat{h}$ and $\hat{\alpha}$ are the maximum values of the mode shape vectors (Figure 8 and 9), respectively, β is the phase shift between the force or moment functions and the translational or rotational oscillations, $q = 0.5\rho U^2$ is the dynamic pressure, where U is the flow speed, ρ is the air density. In Figure 11 the logarithmic decrement of damping can be seen by using the classical and the novel methods. The flutter speed is 8.7m/s with the classical method, and 9.2m/s using the novel one.

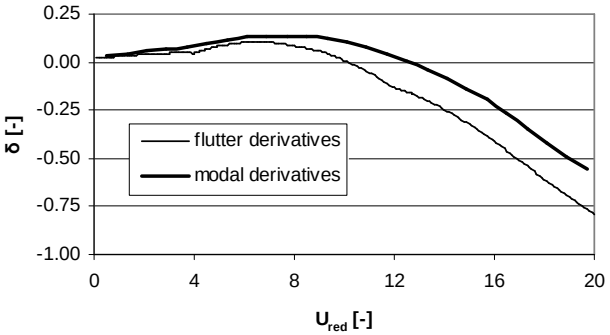

Figure 11. Logarithmic decrement damping versus reduced wind speed.

3 APPLICATION OF THE MODAL DERIVATIVES

3.1 *Introduction of the investigated footbridge*

The previously introduced modal derivatives method is applied on a footbridge with a main span of 120m, which was completed in 2011 at Szolnok city, Hungary. The bridge structure is shown in Figure 12. The stiffening girder is a truss structure with two upper and one bigger lower chord. The stiffening girder is supported by two steel arches that are tilted outwards. The modeling process is completely the same as in case of the previously detailed case study. The FEM model provided the natural frequencies and the mode shape vectors. The heave frequency is 1.67Hz, the rotational is 2.02Hz.

Figure 12. Picture of the investigated bridge structure and the two relevant mode shapes.

The CFD mesh can be seen in Figure 13. The CFD modelling required simplification of the stiffening girder. The spatial trusses were substituted with an equivalent longitudinal object, enabling the CFD mesh be simply extruded. The vertical elements of the handrails were also replaced with longitudinal elements. The cell number was limited to 775300. The in-plane cell number is 38765 and there are 20 divisions along the bridge axis.

In accordance with the modal derivatives method, the forced vibration method was used according to the two relevant mode shapes. The reduced velocity range was 4-20 with a step of 4. The oscillation frequency was 2.00 Hz in each case. The inflow velocity was varied from 4.80 up to 24.00. The reference width was 0.60 m. The rotational oscillation shape with the streamlines at U_{red}=8 can be seen in Figure 14. The heave mode shape is also asymmetrical as the rotational one.

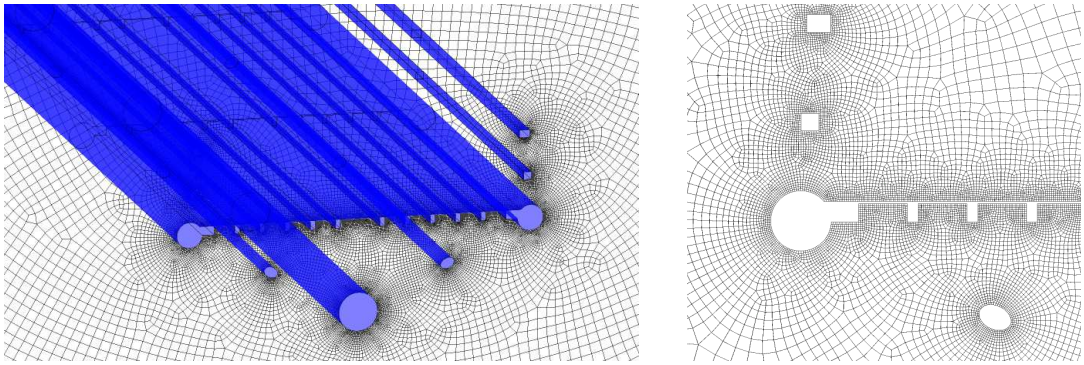

Figure 13. CFD mesh of the bridge structure.

The critical wind velocity was determined by using the classical approach according to expressions (2) and (5) giving a critical wind speed of 146m/s. The novel approach provided a value of 171m/s, which is higher by 17 percent than the classical one.

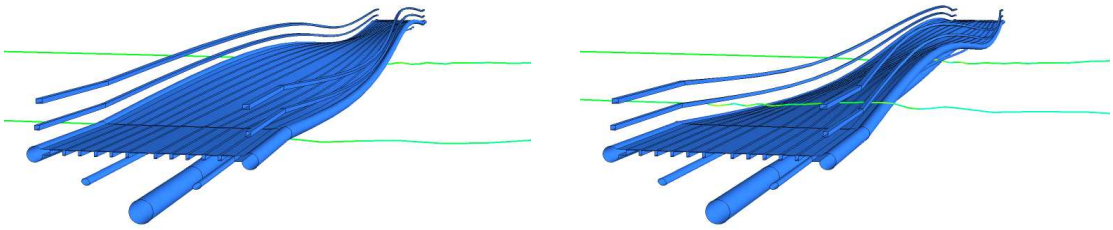

Figure 14. Streamlines around the rotated bridge deck (U_{red}=8).

4 CONCLUSIONS

In this paper a novel technique for flutter prediction of bridge decks has been shown. The method is strongly based on the ANSYS-CFX CFD code, in which arbitrary three-dimensional motion can be defined as a function of time. The 3D bridge deck is considered as a series of segments, on which the lift force and moment signals can be collected. These time functions were properly multiplied by the corresponding elements of the dynamic mode shape vectors and summed up, giving the modal derivatives. The modal derivatives can be used in the framework of the classical procedure of the critical wind speed. The modal derivatives were tested in a case study; a full aeroelastic wind tunnel model was considered. The critical wind speed by using the modal derivatives (9.2 m/s) was closer to the measured one (9.7 m/s) than by using the classical method (8.7 m/s). The method was also tested on a completed pedestrian bridge. The critical wind speed by using the modal derivatives was higher than that of the classical method, as in case of the case study. To conclude, the modal derivatives approach can be a tool in bridge flutter study of structures with complex geometry. In our future work the effects of turbulence will be taken into consideration.

5 REFERENCES

The authors are grateful for the support of the Department of Fluid Mechanics (University of Technology and Economics, Budapest), CFD.hu Ltd., Pont-TERV Ltd. and the INNOCSEKK foundation (NKTH, Hungary).

6 REFERENCES

Journals

1 Wang Y., Lin Y.: Combination of CFD and CSD packages for fluid-structure interaction, Journal of Hydrodynamics, 20(6):756-761, (2008).

Monographs, Multi-author volumes, Proceedings

2 G. Szabó, G. Kristóf, Three-dimensional numerical flutter simulation, The Fifth International Symposium on Computational Wind Engineering (CWE2010), Chapel Hill, USA, May 23-27, 2010.

3 U. Starossek, Bridge Flutter Prediction with Finite Beam Elements in Complex Notation. Seventh International Conference on Computing in Civil and Building Engineering, Seoul, Korea, 1997.

The Seventh International Colloquium on Bluff Body Aerodynamics and Applications (BBAA7)
Shanghai, China; September 2-6, 2012

Probability evaluation of flutter failure for long-span bridges

Lingyao Li [a,c], Yaojun Ge [b], Gonglian Dai [a]

[a]*Department of bridge Engineering, Central South University, China*
[b]*State Key Labrotary for Desaster Reduction in Civil Engineering, Tongji University, China*
[c]*National Engineering Laboratory for High Speed Railway Construction, Central South University, China*

ABSTRACT: Previous researches found that the moment method is on the unsafe side for structural reliability evaluation compared with the result using Monte Carlo (MC) method for low failure probability events such as flutter instability. In this paper a quadratically asympototic integral method based on the direct calculation of probability density was proposed in probabilistic evaluation of four parameters of flutter failure mode which was compared with MC method. The fourteen domestic long-span bridges were utilized to validate the proposed algorithm. The results showed that the flutter failure probability based on the proposed method is more reliable and safer than that based on MC method. Of course, this method proposed here involves the calculation about the first-order and second-order derivatives of logarithm of probability density function (PDF) for random variables so that it is not fit in those situations such as unknown PDF of random variables or very complex derivatives.

KEYWORDS: Long-span bridge, Flutter vibration, Flutter failure, Probability evaluation, Monte Carlo method, Quadratically asympototic integral method.

1 INTRODUCTION

Probability and statistics design method is more reasonable than empirical coefficient design method used in the estimation of flutter failure probability for long-span bridges. Since most of these parameters involved in the prediction are physically uncertain variables and/or subjectively assumed values because of a lack of complete knowledge, it would make more sense to carry out a probabilistic reliability analysis to determine a probability of the bridge flutter failure. Over the years various reliability theories have been proposed for the study of failure probabilities of complex systems, since in many cases an exact numerical calculation is not possible. The first paper, in which approximate methods were proposed, is Freudenthal (A.N. Freudenthal, 1956). The basic idea in this article is to approximate the probability content of a failure region by linearizing the boundary of the region at a point, where the "local" failure probability is maximal. This method is described there only for normal and lognormal random variables, but in principle it is applicable for arbitrary distributions with continuous probability densities.

Hasofer and Lind (A.M. Hasofer and N.C. Lind, 1974) proposed for the case of standardized independent random variables a so-called reliability index β for the failure domains. This index β is the distance of the failure domain to the origin and is not an extimate for the failure probability. But, in consequence of that paper, many papers were published, where approximations for the failure probability were derived by linearizing the failure boundary at the points with minimal distance to the origin, giving $\Phi(-\beta)$ as approximation in the case of normal random variables. Later, also quadratic approximations for the boundary were proposed (B. Fiessler, H.J. Neumann and R. Rackwitz, 1979). All these methods were based on heuristic arguments and no clear mathematical justification was given.

When these approximation methods can not provide ideal probability density distribution, the failure probability of structure can be calculationed by directly integral of PDF of random variables in failure margin. Then Breitung (K. Breitung, 1984) showed with methods of asymptotic analysis that for certain methods a mathematical basis can be found. He proved that the asymptotic relative error of quadratic approximations converges to zero, i.e. these approximations are asymptotically exact and the problem of convergence would not be easy to occur.
In the present paper, a reliability analysis model is formulated by considering four random variables, which are mutually indepent, and the safety margin which is also a random variable and depends only on the stochastic nature of these variables. Though the probability of failure from the safety margin may be efficiently determined by some approximate reliability methods or by applying simulation techniques such as the MC method, the quadratically asympototic integral method is applied here and extensively explained through some sample calculations of 14 long-span bridges in China compared with MC method.

2 FLUTTER FAILURE EVALUATION METHODS

2.1 *Limit state function of flutter failure*

For the sake of comparing and analysising, a flutter reliability model established by Prof. Ge Yaojun was utilized in this study. The corresponding limit state function is represented by the critical flutter speed U_{cr} minus the extreme wind speed U_c (Y.J. Ge, H.F. Xiang, H. Tanaka, 2000)

$$f(U_{cr}, U_c) = U_{cr} - U_c \tag{1}$$

the probability model of the critical flutter speed U_{cr} and the extreme wind speed U_c can be expressed respectively as

$$U_{cr} = C_w U_f \tag{2}$$

$$U_c = G_s U_b \tag{3}$$

where U_f = basic flutter speed which is experimentally determined with some uncertainties of the structural properties; C_w = wind conversion factor from a scaled model to the prototype structure; U_b = basic wind speed at the bridge deck location; and G_s = gust speed factor for taking account of the influence of wind gust speed and its horizontal correlation.
Substituting Eqs.(2) and (3) into Eq.(1), the safety margin Z is now defined as a function which denpends on the stochastic nature of a basic variable vector $X = (C_w, U_f, G_s, U_b)$ as

$$Z = f(X) = C_w U_f - G_s U_b \tag{4}$$

where the above four random variables may be described as normal distribution, log-normal distribution, log-distribution and Gumbel distribution respectively. Since f is a non-linear function and the random variables are not all distributed normally, the failure probability can not be gained directly by using PDF of normal distribution. So many algorithms are applied such as a first-order reliability method (FORM) and a second-order reliability method(SORM) etc. Here the probability was calculated by applying both quadratically asympototic integral method and MC method.

2.2 *The MC method*

A procedure based on th MC method was implemented to allow for the direct numerical estimation of the probability without first-order reliability approximation. Standard algorithms for MC statistical analysis were considered (C. Bucher, 2009). A standard MC procedure was employed and a large sample of computer generated events (1×10^6) was used to estimate probabilities.
A fatal deficiency existing in the MC method is the enormous simulation number when the failure probability of structure is less than 1×10^{-3}. Therefore, the MC method is usually used to validate those proposed methods.

2.3 *The quadratically asympototic integral method*

The general procedure of quadratically asympototic integral method can be resolved into three parts. Firstly, it considers direct integral of probability density function (PDF) in failure region so that non-convergence of calculation can rarely happen. Secondly, it considers direct integral nearby most probable point of structural failure mainly contributes to the evaluation of failure probability. Finally, its direct integral is in fact an asympototic integral by Taylor series quadratical development for logarithm of PDF of random variables and performance function. The derived quadratic hypersurface is applied in approximating practical failure surface. And then the integral is finished by use of the definition of first-order and second-moment and second-order and second-moment methods.
A likelihood function h(x) of PDF is defined by

$$h(x)=ln(f(x)) \tag{5}$$

The performance function of structure is defined as $Z = g_X(X)$ and the random variables $X = (X_1, X_2, \cdots, X_n)^T$'s joint PDF is defined as $f_X(x)$, then the probability of failure by flutter can be written in the form (K. Breitung, 1984,1989)

$$p_f = \int_{g_X(x)\le 0} f_X(x)dx = \int_{g_X(x)\le 0} \exp[\ln f_X(x)]dx = \int_{g_X(x)\le 0} \exp[h(x)]dx \tag{6}$$

h(x) is expanded into Taylor series at x^*, which is a poin on limit state surface and taken to the quadratic term as

$$\begin{aligned} h(x) &\approx h(x^*) + (x-x^*)^T \nabla h(x^*) + \frac{1}{2}(x-x^*)^T \nabla^2 h(x^*)(x-x^*) \\ &= h(x^*) + \frac{1}{2}\nu^T B\nu - \frac{1}{2}(x-x^*-B\nu)^T B^{-1}(x-x^*-B\nu) \end{aligned} \tag{7}$$

where

$$\nu = \nabla h(x^*) \tag{8}$$

$$B = -[\nabla^2 h(x^*)]^{-1} \tag{9}$$

Substituting Eq. (7) into Eq. (6), the failure probability p_f is now given as

$$p_f \approx f_X(x^*)\exp\left(\frac{\nu^T B\nu}{2}\right) \times \int_{g_X(x)\le 0}\exp\left[-\frac{1}{2}\left(x-x^*-B\nu\right)^T B^{-1}\left(x-x^*-B\nu\right)\right]dx \tag{10}$$

Applying the Chokesky decomposition, the matrix B can be defined as $B=AA^T$ and then defining $X-x^*-B\nu=AY$, the failure probability p_f is now defined as

$$p_f \approx \sqrt{\det B}\, f_X(x^*)\exp\left(\frac{\nu^T B\nu}{2}\right)\int_{g_Y(y)\le 0}\exp\left(-\frac{y^T y}{2}\right)dy \tag{11}$$

Corresponding performance function Z at x^* can be defined as

$$\begin{aligned} Z_Q &= (AY+B\nu)^T\nabla g_X(x^*) \\ &\quad +\frac{1}{2}(AY+B\nu)^T\nabla^2 g_X(x^*)(AY+B\nu) \\ &= \left(Y+A^T\nu\right)^T A^T\nabla g_X(x^*) \\ &\quad +\frac{1}{2}\left(Y+A^T\nu\right)^T A^T\nabla^2 g_X(x^*)A\left(Y+A^T\nu\right) \end{aligned} \tag{12}$$

Let be unit vector

$$\alpha_X = -\frac{A^T\nabla g_X(x^*)}{\left\|A^T\nabla g_X(x^*)\right\|} = -\frac{A^T\nu}{\left\|A^T\nu\right\|} = -\frac{A^T\nu}{\beta_L} \tag{13}$$

By structuring an orthogonal matrix $H=[H_1,H_2,\cdots,H_{n-1},\alpha_X]$ using α_X, Y space is orthogonally transformed into U space in the form

$$Y=HU \tag{14}$$

Z_Q can be expressed as

$$\begin{aligned} Z_Q &= \left\|A^T\nabla g_X(x^*)\right\|\left(\beta_L-U_n-\frac{1}{2}\tilde{U}^T H^T QH\tilde{U}\right) \\ &\approx \left\|A^T\nabla g_X(x^*)\right\|\left[\beta_L-U_n-\frac{1}{2}V^T\left(H^T QH\right)_{n-1}V\right] \end{aligned} \tag{15}$$

where $\tilde{U}=(U_1,U_2,\cdots,U_n-\beta_L)^T=\left(V^T,U_n-\beta_L\right)^T$.

Substituting Eq. (14) into Eq. (11), the quadratic failure probability p_{fQ} is derived as

$$\begin{aligned} p_{fQ} &= \sqrt{\det B}\, f_X(x^*)\exp\left(\frac{\nu^T B\nu}{2}\right)\int_{g_U(u)\le 0}\exp\left(-\frac{u^T u}{2}\right)du \\ &= (2\pi)^{1/2}\sqrt{\det B}\, f_X(x^*)\exp\left(\frac{\nu^T B\nu}{2}\right)\int_{g_U(u)\le 0}\varphi_n(u)du \end{aligned} \tag{16}$$

Then, the quadratically asympototic integral failure probability applying directly the result of SORM in Gauss space is expressed as

$$p_{fQ} = \frac{p_{fL}}{\sqrt{\det\left[I - \beta_L \left(H^T Q H\right)_{n-1}\right]}} \tag{17}$$

where p_{fL} is first order asympototic integral failure probability (K.M. Breitung, 1994)

$$p_{fL} = (2\pi)^{n/2} \sqrt{\det B}\, f_X(x^*) \exp\left(\frac{v^T B v}{2}\right) \Phi(-\beta_L) \tag{18}$$

3 FLUTTER PROBABILITY FOR 14 LONG-SPAN BRIDGES

The results of the numerical simulations for 14 bridges are summarized in Table 1. In this table the flutter failure probability computed by both the quadratically asympototic integral method and MC method was compared. The minimum failure probabilities is less than 1×10^{-7} . Most result using the quadratically asympototic integral method is larger than that using MC method. That is the result using the quadratically asympototic integral method emphasis on safety compared with that using MC method.

Table 1. Flutter failure probability of 14 Long-span bridges using two methods

Serial number of bridges	Quadratically asympototic integral		MC		Relative error of failure probability
	Reliability index β	Failure probability Pf	Reliability index β	Failure probability Pf	%
1	3.05	1.16E-03	3.03	1.21E-03	-4.87
2	4.23	1.16E-05	4.24	1.09E-05	6.51
3	2.64	4.09E-03	2.66	3.85E-03	6.30
4	5.12	1.55E-07	5.13	1.42E-07	9.51
5	3.25	5.82E-04	3.25	5.75E-04	1.19
6	2.65	3.97E-03	2.67	3.80E-03	4.43
7	5.32	5.07E-08	5.34	4.56E-08	11.26
8	3.64	1.37E-04	3.66	1.27E-04	8.07
9	3.82	6.57E-05	3.85	6.02E-05	9.06
10	3.09	9.99E-04	3.11	9.31E-04	7.31
11	4.34	7.27E-06	4.36	6.58E-06	10.54
12	3.40	3.39E-04	3.41	3.21E-04	5.63
13	2.59	4.86E-03	2.61	4.58E-03	6.17
14	2.82	2.40E-03	2.84	2.25E-03	6.77

4 CONCLUSIONS

For very small probability case, a quadratically asympototic integral method has been presented for the consideration of flutter failure of long-span bridges compared with MC method. The proposed method gives asymptotic approximations for failure probabilities without using any transformation of the probability space and any cumulative distribution function of random variable. Some sample calculations using 14 long-span bridges were introduced to demonstrate its effectiveness. It was found that most of failure probabilities using the proposed method were generally larger than that using MC method. The approximation may emphasis on safety compared with that using MC method.

5 REFERENCES

1 A.N. Freudenthal, Safety and the probability of structural failure, Transactions of the ASCE, 121(1956) 1337-1397.
2 A.M. Hasofer and N.C. Lind, An exact and invariant first-order reliability format, Journal of the Engineering Mechanics Division ASCE, 100(1974) 111-121.
3 B. Fiessler, H.J. Neumann and R. Rackwitz, Quadratic limit states in structural reliability, Journal of the Engineering Mechanics Division ASCE, 105(1979) 661-676.
4 Y.J. Ge, H.F. Xiang and H. Tanaka, Application of a reliability analysis model to bridge flutter under extreme winds, J. Wind. Engrg. Ind. Aerodyn., 86 (2000) 155-167.
5 C. Bucher, Computational analysis of randomness in structural mechanics, Taylor Francis Group, London, UK, 2009.
6 K. Breitung, Asymptotic approximation for multinormal integrals, Journal of Engineering Mechanics, 110(1984) 357-366.
7 K. Breitung, Asymptotic approximation for probability integrals, Probability Engineering Mechanics, 4(1989) 187-190.
8 K.M. Breitung, Asympotic approximation for probability integrals, Springer-Verlag, Berlin, 1994.

The Seventh International Colloquium on Bluff Body Aerodynamics and Applications (BBAA7)
Shanghai, China; September 2-6, 2012

Influences of local vibrations of cables on flutter behaviors of cable-stayed bridges

De-Can Yang [a] , Yao-Jun Ge [b] , Hai-Fan Xiang [b]

[a] *Department of Road & Bridge Engineering, Wuhan University of Technology, Wuhan 430063, China*
[b] *State Key Laboratory for Disaster Reduction in Civil Engineering, Tongji University, Shanghai 200092, China*

ABSTRACT: The effects of local vibrations of cables on flutter behaviors of cable-stayed bridges are investigated by using the 3D flutter analysis method. The cables are treated as multi-link model, instead of single link model, and therefore can show the lateral degrees of freedom along the cables. After simulating the structural damping, the flutter behaviors including local vibration effects of cables for an example bridges, Yangpu Bridge in China, are investigated based on the 3D flutter analysis method. The calculated results show that for the Yangpu cable-stayed bridge with a 602m main span, the flutter critical wind velocity can be increased by 20.2% with the consideration of local vibration effects of cables and the aerodynamic forces acting on cables. The mechanisms of the local vibration effects of cables are also discussed in this paper.

KEYWORDS: cable-stayed bridges; flutter analysis; single-link model; multi-link model; lateral vibrations of cables

1 INTRODUCTION

The aeroelastic interaction between the flowing air and the cables of the cable-stayed bridges must exist and will exhibit some influences on the flutter behaviors of the bridge structures. The aeroelastic effects of cables include the aerodynamic forces acting on cables, the local vibrations of cables, and their interaction. The aerodynamic forces on cables are generally neglected due to the belief of their insignificant effects. For a long-span cable-stayed bridge, the effects of cable local vibrations on flutter should be investigated because the dense cable system of a cable-stayed bridge can form one or more powerful wind-resisting cable planes. The local vibrations of these cables as tightly tensioned chords can significantly impact the bridge-and-wind interaction. This interaction can be taken into account by using the flutter analysis method with the cable model which can show the local vibration shapes of cables.

The three-dimensional (3D) flutter analysis of bridges is based on structural 3D finite element (FE) models and the action of self-excited aerodynamic forces (Ge, 2008) [1]. Many researchers have contributed to the bridge 3D flutter analysis. Xie and Xiang (1985) [2] proposed the state apace method. Agar (1989) [3] treated the flutter as a 2M-order eigenvalue problem. Chen (1994) [4] proposed a multi-mode search method based on the modal analysis method. Namini, et al (1992) [5] presented the pK-F method, to solve the flutter equations. Ge (2000) [6] proposed a full mode method to abstract the eigenvalues and eigenvectors without the need to select the participating modes. All these methods treated the cable as a single-link model and therefore cannot consider the local vibrations of cables.

Cheng (1999) [7] took the aeroelastic effects of cables into account by using a finite strip model (Lau, et al, 2000) [8] of the deck and the pK-F solving method. The lateral degrees of

freedom of cables are represented by sinusoidal generalized coordinates. However, since the modes representing the local vibration of cables are usually far away from the principal modes of bridges and cannot be selected by the pK-F method, the pK-F method cannot take into account of the effects of cable local vibrations very well.

If a method intends to take into account the cable lateral vibration effects, the method has to both include the degrees of freedom reflecting the cable local vibrating shapes and have the ability to abstract the modes of cable local vibrations as well as the bridge principal modes. Yang (2005, 2011)[9, 10], Hua (2007)[11] separately proposed a method to conduct the bridge 3D flutter analysis by using the commercial FE software (ANSYS)[12], which is based on the existing functions of the software. This method could model the cable as a multi-link model with consideration of the geometric stiffness to show the lateral degrees of freedom along the cable and therefore make it possible to take the lateral vibration effects of cables into account. By taking an actual cable-stayed bridge with a middle span length of 602m as an example, this paper focuses to calculate the effects of local vibrations of cables on flutter critical state by the 3D finite element method for the flutter analysis.

2 3D FLUTTER ANALYSIS OF CABLE-STAYED BRIDGE

An example bridge needs to be employed to illustrate the 3D flutter analysis of cable-stayed bridges (Yang 2005, 2011) [9, 10]. The Yangpu Bridge, opened to traffic in 1993, in Shanghai, China, has twin towers, twin cable planes and composite girders. The bridge spans over the Huangpu River by its main span of 602m. It was the longest span of cable-stayed bridges in the world when it was completed and opened to traffic. It has a span length pattern of 99+144+602+144+99 m. The cross section of the deck applies an open-style composite girder. It has two separate steel boxes of 2.67m deep and 1.5m wide each with a composite precast prestressed concrete deck slab of 0.26m deep. The overall width of the bridge deck is 32.5m. The FE model was established using the structural data used by Ding (2001, 2002) [13, 14]. The structural FE model is shown in Figure 1.

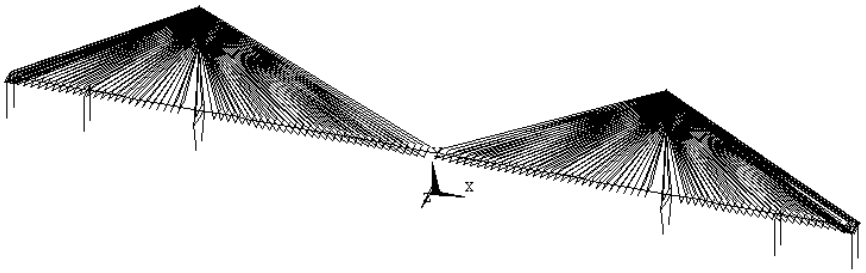

Figure 1. FE model of Yangpu Bridge with span pattern of (99+144+602+144+99) m

The mode damping ratio of the Yangpu cable-stayed bridge can be simulated by 1%. The two-parameter Rayleigh damping (Clough 1993) [15] can cover two main participative modes. After the damping is simulated, the structural natural modes with the designed damping can be obtained. Using the data of flutter derivatives of the Yangpu Bridge deck, as same as in Ding 2001, 2002 [13, 14], the flutter analysis can be carried out, in which each cable with the top end connecting to the tower and the bottom end to the girder, is simulated as a single link model. The calculated results without local vibration shapes of cables (single-link model) and without aerodynamic forces acting on cables are listed in Table 1. The flutter mode is initiated from the

structural inherit mode of the first symmetric torsion and companied with the second symmetric vertical deck bending. The mode shape of the flutter critical state is shown in Figure 2.

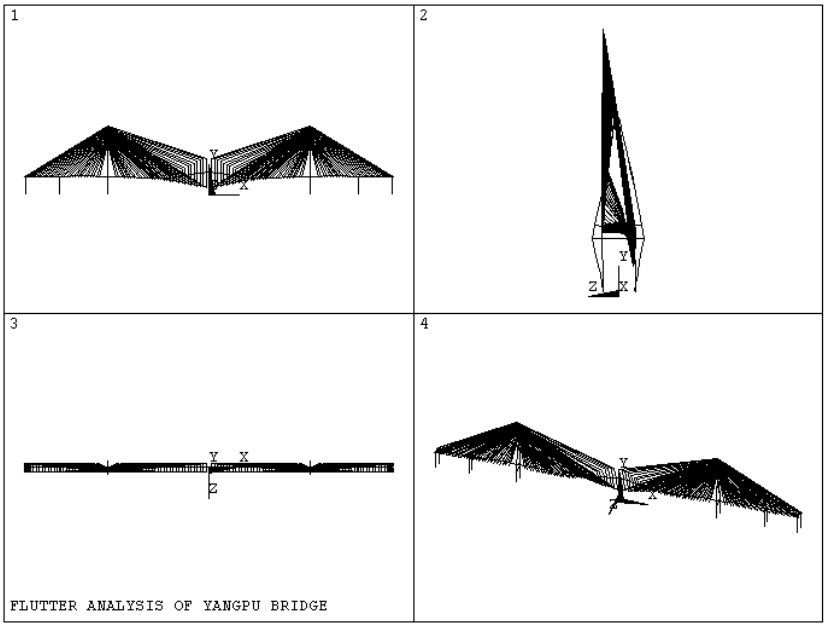

Figure 2. Mode shape of flutter critical state for Yangpu Bridge
(single-link model, 1st symmetric torsion complex mode)

3 MULTI-LINK MODEL OF CABLES

When a cable-stayed bridge is vibrating, each cable vibrates locally and laterally as a tensioned chord in addition to the vibration as a straight link member along with the movement of the 3D spatial bridge structure. The single-link model, as shown in Figure 3 (a), cannot reveal the behavior of the local vibrations of cables. Instead, it can only reflect the global movement as a straight member connecting with the tower and the deck of the bridge structure. The multi-link model, as shown in Figure 3 (b), which includes the degrees of freedom reflecting the local vibrations of cables, can be introduced to take into account the lateral vibrations of cables. The geometric stiffness must be included for the multi-link model in order to avoid the zero lateral stiffness of intermediate nodes of a cable.

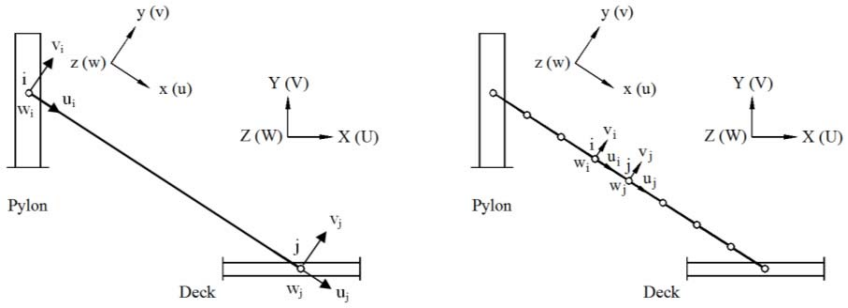

(a) Single-link model (b) Multi-link model

Figure 3. Single-link and multi-link models of a cable

It is the lower local vibrating modes of cables that impact the dynamic behaviors of the whole bridge including the flutter behaviors. The model with 8 links in a cable can well reflect two half-sinusoids with 4 links in each. For the first mode, it is more perfect to display a half-sinusoid with 8 links. So, the 8-link model for a cable is appropriate.

4 EFFECTS OF LOCAL VIBRATIONS OF CABLES

Take the Yangpu Bridge as an example again. The flutter analysis is carried out based on the multi-link model. The earliest flutter critical state is still the vibration shape dominated by the first symmetric deck torsion. The calculated results by using the multi-link model are listed in Table 1. This table also shows the results of the single-link model and as well as the results considering of aerodynamic forces on cables for comparison. Figure 4 shows the mode shape of the flutter critical state of the first symmetric torsion of the Yangpu Bridge by using multi-link model which considers the aerodynamic forces acting on cables.

Table 1 Effects of cable local vibrations and cable aerodynamic forces on flutter critical state of Yangpu Bridge

Critical Wind Velocity (m/s) / Frequency (Hz)		Local Vibrations of Cables	
		Without (Single-Link Model)	With (Multi-link Model)
Aerodynamic Forces Acting on Cables	without	76.33 / 0.49044	84.36 / 0.50877
	with	77.88 / 0.48963	91.74 / 0.50104

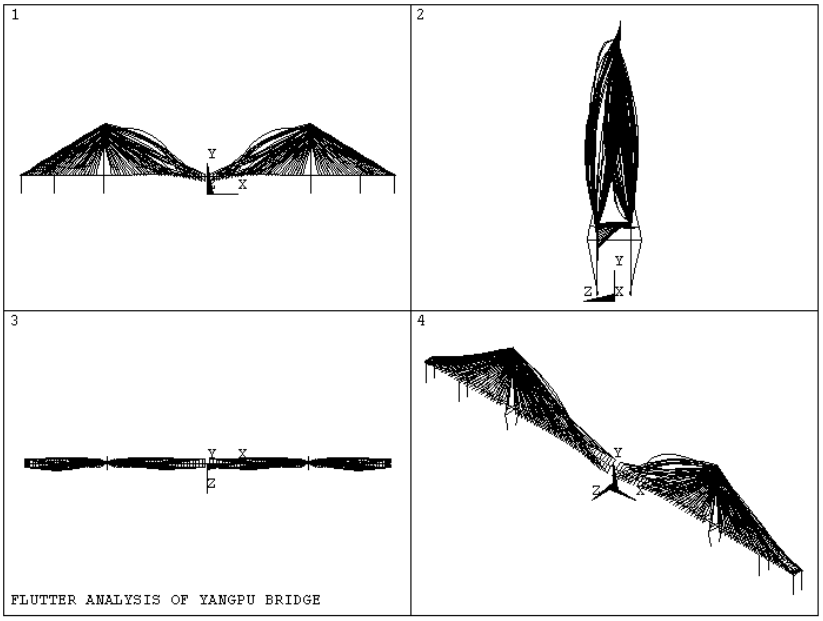

Figure 4. Mode shape of flutter critical state of 1st symmetric torsion of Yangpu Bridge (multi-link model, 8-link for each cable)

From Table 1, without the aerodynamic forces on cables but with the lateral vibrations of cables, the flutter critical wind velocity is increased by 10.5%. Without the lateral vibrations of cables but with the aerodynamic forces on cables, it is increased by 2.0%. When both the aerodynamic forces and the lateral vibrations of cables are considered, the flutter critical wind velocity is increased by 20.2%, from 76.33 to 91.74 m/s. It can be seen there exists an interaction

between the aerodynamic forces and the lateral vibrations of cables. The emergence of the cable lateral vibration shapes intensifies the action of the aerodynamic forces on cables, and therefore intensifies the absorption of the aerodynamic positive damping for cables.

5 EXPLANATION FOR MECHANISM

The mechanism of the effects of local vibrations of cables on the flutter characteristics of cable-stayed bridges can be further explained as follows.

After the introduction of the multi-link model, the increase of the flutter frequency is caused by the increase of the certain structural natural mode frequency since the flutter mode is originated from a certain structural natural mode.

The increase of the flutter frequency will generally cause the increase of the flutter critical wind velocity since the flutter derivatives, which represent the aerodynamic forces between the structure and the flow around it, are related to the reduced wind velocity defined as the actual wind velocity over the vibrating frequency. Therefore, the flutter with a higher vibrating frequency needs a higher wind velocity to activate.

However, the increasing extents in the wind velocity and the frequency should match each other according to the definition of the reduced wind velocity. But in this example, the increasing extent of the critical wind velocity predicted by the multi-link model is far more than that by the single-link model.

In fact, the flutter vibration shape of the first symmetric torsion in the multi-link model is much different from that in the single-link model in addition to the difference of the flutter frequencies. In the flutter vibration shape of the multi-link model (Figure 4), many first-order cable lateral vibration shapes emerge. Consequently, the component of the deck torsional displacement is decreased and is submerged in the lateral vibration shapes of stay cables. On the other hand, the flutter vibration shape in the single-link model is represented by simple torsional displacements of the deck. It is known that the aerodynamic negative damping should be absorbed by the deck torsional displacements, while the lateral vibration shapes of cables can only absorb aerodynamic positive damping. This is the very reason why the flutter critical wind velocity is much increased in the multi-link model.

In summary, the increase of the flutter critical wind velocity due to the effects of the aerodynamic forces on cables is limited. Only when the multi-link model is employed and the lateral vibration shapes emerge as a result, can the increase extent be significant due to the decrease of the component of the deck torsional displacements. The change of the critical wind velocity due to the change of the critical frequency is secondary. The decreasing extent of the deck torsional displacements is related to the participating extent of lateral vibration shapes of cables, namely the coinciding extent of lateral vibrating primary frequencies of cables as tension chords and the fundamental deck torsion frequencies of bridge structures.

6 CONCLUSIONS

Based on the developed method, the aeroelastic effects of cables on flutter behaviors are investigated by using the actual bridge examples. According to the analysis results, some conclusions can be summarized as follows:

(1) With the aerodynamic forces acting on cables but without the consideration of the local vibrations of cables, the flutter critical wind velocity can be increased by 2.0% for the cable-stayed bridge with a 602m middle span. This is because the cable aerodynamic forces only

include the positive aerodynamic damping but do not include the aerodynamic stiffness.

(2) Without the aerodynamic forces but with the local vibrations of cables, the flutter critical wind velocity can be increased by 10.5%. The participation of the cable vibrations weakens the component of torsional displacements of the deck in flutter mode. The emergence of local vibration shapes of cables increase the ability for the bridge to absorb positive damping; while the weakening of the deck torsional displacements decreases the ability for the bridge to absorb the negative damping.

(3) With both the aerodynamic forces and the lateral vibrations of cables, the flutter critical wind velocity can be increased by 20.2%, which is remarkable and much larger than the sum of both separate effects. The apparent impact reveals the interaction relationship between the aerodynamic forces and the local vibrations of cables.

ACKNOWLEDGEMENTS

The research described in this paper was partially supported by Natural Science Foundation of China, under the Grant No. 51178367. Dr. Q.S. Ding provided the ANSYS command flow of structural FE model and the data of flutter derivatives of Yangpu Bridge. These supports are gratefully acknowledged.

REFERENCES

1 Ge, Y. J., and Xiang, H. F. (2008). "Computational models and methods for aerodynamic flutter of long-span bridges", Journal of Wind Engineering and Industrial Aerodynamics, Vol. 96, No. 10-11, pp. 1912-1924.
2 Xie, J. M. and Xiang, H. F. (1985). "State-space method for 3-D flutter analysis of bridge structures", Proceeding of Asia pacific symposium on wind engineering, India, pp. 169-276.
3 Agar, T. J. A. (1989). "Aerodynamic flutter analysis of suspension bridges by a modal technique", Engineering Structures, Vol. 11, No.2, pp. 75-82.
4 Chen, Z. Q. (1994). "The three dimension analysis and behaviors investigation on the critical flutter state of bridges", International symposium on cable-stayed bridges, Shanghai, China.
5 Namini, A. H., Albrecht, H., and Bosch, H. (1992). "Finite element-based flutter analysis of cable-suspended bridges", Journal of Structural Engineering, ASCE, Vol. 118, No. 6, pp. 1509-1526.
6 Ge, Y. J. and Tanaka, H. (2000). "Aerodynamic flutter analysis of cable-supported bridges by multi-mode and full-mode approaches", Journal of Wind Engineering and Industrial Aerodynamics, Vol. 86, No. 2-3, pp. 123-153.
7 Cheng, S. H. (1999). Structural and Aerodynamic Stability Analysis of Long-span Cable-stayed Bridges, Ph. D. Dissertation, Carleton University, Ottawa, Canada.
8 Lau, D. T., Cheung, M. S., and Cheng, S. H. (2000). "3D flutter analysis of bridges by spline finite-strip method", Journal of Structural Engineering, ASCE, Vol. 126, No. 10, pp. 1246-1254.
9 Yang, D.C. (2005). Three-Dimensional Flutter Analysis of Long Span Bridges with Aeroelastic Effects of Cables, Ph. D. Dissertation, Tongji University, Shanghai, China (in Chinese).
10 Yang, D. C. Ge, Y. J. Xiang, H. F. and Ma, Z. J. (2011) "3D flutter analysis of cable supported bridges including aeroelastic effects of cables", Advances in Structural Engineering, Vol. 14, No.6, pp.1129-1147.
11 Hua, X.G., Chen, Z.Q., Ni, Y.Q., and Ko, J.M. (2007). "Flutter Analysis of Long-span Bridges Using ANSYS", Wind and Structures, Vol. 10, No. 1, pp. 61-82.
12 ANSYS, Inc. (2004). ANSYS Structural Analysis Guide, SAS IP Inc.
13 Ding, Q.S. (2001). Fine Analysis of Coupling Flutter and Buffeting Responses for Long-span Bridges Ph. D. Dissertation, Tongji University, Shanghai, China (in Chinese).
14 Ding, Q. S., Chen, A. R., and Xiang, H. F. (2002). "Coupled flutter analysis of long-span bridges by multimode and full-order approaches", Journal of Wind Engineering and Industrial Aerodynamics, Vol. 90, No. 12-15, pp. 1981-1993.
15 Clough, R. W. and Penzien, J. (1993). Dynamics of Structures, Second Edition, McGraw-Hill, Inc., New York.

The Seventh International Colloquium on Bluff Body Aerodynamics and Applications (BBAA7)
Shanghai, China; September 2-6, 2012

The nonlinear aerodynamic stability of long-span bridges: post flutter

Wang Qi [a], Liao Hai-li [a]

[a] *Research Centre for Wind Engineering, Southwest Jiaotong University, Chengdu, China*

ABSTRACT: The linear flutter analytical method can't give the reasonable explanation to post flutter status of bridges. Based on the nonlinear MIAF expressions, the nonlinear vibration differential equation can describe the aerodynamic stability of bridge under different amplitudes and reduced frequency. The nonlinear aerodynamic coefficients in the expression can be represented by the amplitude and initial phase of harmonic components. The nonlinear aerodynamic stability analysis had been performed in state space using the 4th Runge-Kutta algorithm, and the results indicated that the girder of long span bridge would appear different motion types in post flutter, including the convergence motion, the divergence motion and the identical amplitude oscillation. The girder of long span bridge can keep the identical amplitude oscillation status at different amplitude conditions, and the only requirement is the equilibrium in the aerodynamic works.

KEYWORDS: post flutter; nonlinear aerodynamic coefficient; nonlinear aerodynamic stability

1 INTRODUCTION

The motion-induced aerodynamic force (MIAF) in Scanlan's expression is only the function of reduced frequency, and is independent with the amplitude of bridge girder, and there are no nonlinear items and variables in the expression. According to the linear stability theory, there is only a critical status in flutter equation, thus it can't give the further results about aerodynamic stability of bridges especially in the post flutter status. Indeed, the large amplitude oscillation of Tacoma Bridge is typical motion of post flutter, although its collapse was only explained for flutter. The stability status or motion status in post flutter of long span bridges needs to be investigated by the means of nonlinear differential equation considering the nonlinear MIAF.

For the issue of large amplitude oscillation of Tacoma Bridge, several researchers analyzed the aerodynamic mechanism based on nonlinear aerodynamic force and nonlinear vibration theory. Steinmann[2] proposed an aerodynamic force expression of Tacoma deck in 1954, then Böhm[1] studied the nonlinear oscillation of Tacoma Bridge, and interpreted that the large amplitude oscillation of Tacoma Bridge was a limit cycle oscillation. Piccardo[3] also studied the nonlinear vibration of Tacoma Bridge by using Steinmann's expression, and obtained the wind speed 17.44m/s under the limit cycle oscillation of this bridge. Xu[4,5] deduced an expression of nonlinear aerodynamic force and nonlinear vibration equation, and obtained the nearly same critical wind speed as Piccardo under limit cycle oscillation state. Due to the restriction of wind tunnel test technique in acquiring nonlinear aerodynamic force, other bridges are scarcely studied on its nonlinear aerodynamic force or the post flutter state. Diana [6-8] studied nonlinear aerodynamic force of Messina Bridge girder, and indicated that the neglect of nonlinear component of aerodynamic force could lead to unsafely side for aerodynamic instability. Liao[9] found the distinct 8-shape aerodynamic hysteresis loops of streamline box

girder under the larger pitching amplitude, which means that the aerodynamic forces can provide both the positive and negative works within one vibration period. And the 8-shape aerodynamic hysteresis loops also gave a favorable support of limit cycle oscillation of long-span bridge. Chen[10] indicated that the soft flutter phenomenon of long-span bridge was a typical nonlinear vibration, and he used Von Del Pol equation to describe the phenomenon and the nonlinear MIAF of bridge girder.

The other researches on nonlinear aerodynamic oscillation of flexible and long-span structures, were mainly focused on the galloping, such as iced transmission line. Den Hartog[11,12] studied the galloping of iced transmission line in details first time, and proposed the analysis method of galloping using semi-steady theory. Pakinson[13] studied the galloping theory of square column in details. He studied the process of square column galloping by aero-elastic model wind tunnel tests, and found the leap and hysteresis phenomenon in galloping under different reduced frequency. Novak[14], based on SDOF torsional vibration model, studied the galloping of square column in details. His theoretical researches can be correspondent with the wind tunnel test results conducted by Pakinson. The galloping theory based on the semi-steady has developed greatly, the main reason is the simplification of nonlinear aerodynamic force. Lift and pitching moment acting on a transmission line, or square column, has been described only as the function of incidence angle, namely the aerodynamic force can be expressed only with incidence angle.

Although the nonlinear aerodynamic force of bridge girder can be described at very low reduced frequency, under which the aerodynamic hysteresis loop is almost a single curve (this phenomenon was verified in wind tunnel test by Diana[6] and Liao[9]), the bridge may occur flutter at a common reduced frequency, under which the aerodynamic hysteresis is loop.

Combining with the nonlinear MIAF expressions[15], the nonlinear vibration differential equation can describe the aerodynamic stability of bridge girder under different amplitudes and reduced frequency, especially the large amplitude oscillation in the post flutter status of bridges. The nonlinear aerodynamic stability analysis had been performed in state space by using the 4th Runge-Kutta algorithm, and the results indicated that the girder of long span bridge would appear different motion types in post flutter, including the convergence motion, the divergence motion and the identical amplitude oscillation (limit cycle oscillation). The girder of long span bridge can keep the identical amplitude oscillation status at different amplitude conditions, and the only requirement is the equilibrium in the aerodynamic works.

2 AERODYNAMIC FORCE AND COEFFICIENTS

2.1 *Typical aerodynamic force*

Based on the results of the wind tunnel tests, the empirical mathematic model[15] was proposed to describe the nonlinear MIAF under different conditions by using Taylor expanding. Before the analysis, the typical aerodynamic forces under different conditions were selected from the reference paper [16], and one of them represented the special energy inputting to the girder. The outline of the deck cross section is shown in Fig.1, and the wind tunnel test was interpreted in the reference paper [9] and [16]. The selected aerodynamic forces were presented in the form of hysteresis loop, and all of them with the same static incidence angle +5 degree. The forces were shown in Fig.2 ~ Fig.5 respectively and the illustration were as follows.

The aerodynamic force in Fig.2 was obtained under the condition of 10° amplitude and $\pi/5$ reduced frequency, and defined as the case-1. The direction of rotation is counter clock,

which indicates the aerodynamic work is negative. The aerodynamic force in Fig.3 was obtained under the condition of 10° amplitude and π/8 reduced frequency, and defined as the case-2. Varying with the decrease of reduced frequency, the hysteresis loop became the 8-shape, which means that the aerodynamic forces can provide both the positive and negative works within one vibration period. The area of clockwise is less than the c counter-clockwise, namely the negative one is greater than the positive one a little. The aerodynamic force in Fig.4 was obtained under the condition of 10° amplitude and π/10 reduced frequency, and defined the case-3, and the negative work is less than the positive work a little while the *K* decreasing. The aerodynamic force in Fig.5 was obtained under the condition of 20° amplitude and π/10 reduced frequency, and defined the case-4, and positive one is more greater than the negative one while the amplitude increasing.

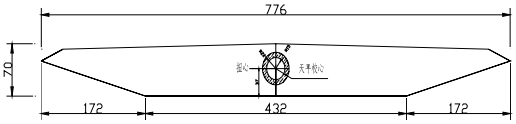

Fig. 1. The cross-section of test model

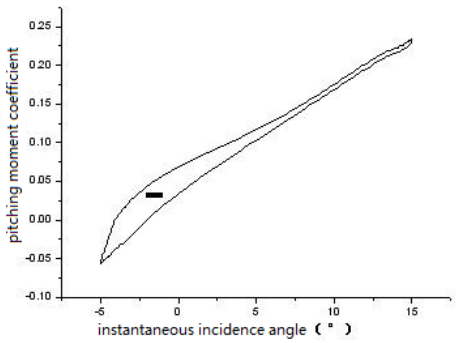

Fig.2 the hysteresis loop of pitching moment coefficient (case-1: *K*=π/5, Amplitude=10degree)

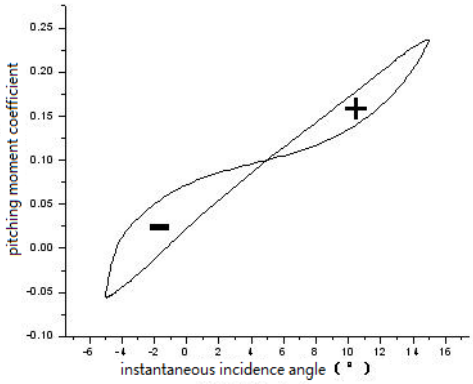

Fig.3 the hysteresis loop of pitching moment coefficient (case-2: *K*=π/8, Amplitude=10degree)

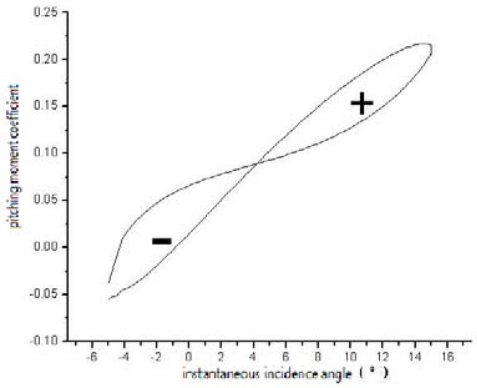

Fig.4 the hysteresis loop of pitching moment coefficient (case-3: K=π/10, Amplitude=10degree)

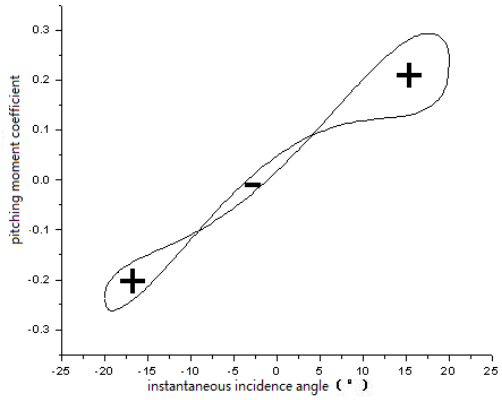

Fig.5 the hysteresis loop of pitching moment coefficient (case-4: K=π/10, Amplitude=20degree)

2.2 *Aerodynamic coefficient*

The aerodynamic coefficients were obtained by the method proposed in reference paper[15], and expressed as follows.

$$C^k_{\dot\alpha^m\alpha^n}=\frac{X^k_{TM}k!}{\omega^m}\sin(\theta^k_{TM}+\frac{n\pi}{2}) \tag{1}$$

In which, k=1,2……n, is the order of nonlinear harmonic components; m is the nonlinear aerodynamic coefficient order which represents the derivative order of velocity and displacement. X^k_{VL} is the pitching amplitude of the k^{th} order torsional pitching moment harmonic component and θ^k_{VL} is the initial phase angle.

If taking the first five orders in aerodynamic coefficient, the C_M can be written as,

$$\begin{aligned}C_M=&C^1_{\dot\alpha}\dot\alpha+C^1_{\alpha}\alpha\\&+\frac{1}{2}C^2_{\dot\alpha^2}\dot\alpha^2+C^2_{\alpha\dot\alpha}\dot\alpha\alpha+\frac{1}{2}C^2_{\alpha^2}\alpha^2\\&+\frac{1}{6}C^3_{\dot\alpha^3}\dot\alpha^3+\frac{1}{2}C^3_{\alpha\dot\alpha^2}\dot\alpha^2\alpha+\frac{1}{2}C^3_{\alpha^2\dot\alpha}\dot\alpha\alpha^2+\frac{1}{6}C^3_{\alpha^3}\alpha^3\\&+\frac{1}{24}C^4_{\dot\alpha^4}\dot\alpha^4+\frac{1}{6}C^4_{\alpha\dot\alpha^3}\dot\alpha^3\alpha+\frac{1}{4}C^4_{\alpha^2\dot\alpha^2}\dot\alpha^2\alpha^2+\frac{1}{6}C^4_{\alpha^3\dot\alpha}\dot\alpha\alpha^3+\frac{1}{24}C^4_{\alpha^4}\alpha^4\\&+\frac{1}{120}C^5_{\dot\alpha^5}\dot\alpha^5+\frac{1}{24}C^5_{\alpha\dot\alpha^4}\dot\alpha^4\alpha+\frac{1}{12}C^5_{\alpha^2\dot\alpha^3}\dot\alpha^3\alpha^2+\frac{1}{12}C^5_{\alpha^3\dot\alpha^2}\dot\alpha^2\alpha^3+\frac{1}{24}C^5_{\alpha^4\dot\alpha}\dot\alpha\alpha^4+\frac{1}{120}C^5_{\alpha^5}\alpha^5\end{aligned} \tag{2}$$

In order to show the coefficients clearly, Table 1 gives the correspondence of the coefficients and characters. The coefficients of aerodynamic force shown in Figs. 2-5 were illustrated in Tables 2-5.

Table 1 Correspondence of the coefficients and characters

	D1	*D2*	*D3*	*D4*	*D5*	*D6*
C1	$C^1_{\dot{\alpha}}$	C^1_{α}				
C2	$C^2_{\dot{\alpha}^2}$	$C^2_{\alpha\dot{\alpha}}$	$C^2_{\alpha^2}$			
C3	$C^3_{\dot{\alpha}^3}$	$C^3_{\alpha\dot{\alpha}^2}$	$C^3_{\alpha^2\dot{\alpha}}$	$C^3_{\alpha^3}$		
C4	$C^4_{\dot{\alpha}^4}$	$C^4_{\alpha\dot{\alpha}^3}$	$C^4_{\alpha^2\dot{\alpha}^2}$	$C^4_{\alpha^3\dot{\alpha}}$	$C^4_{\alpha^4}$	
C5	$C^5_{\dot{\alpha}^5}$	$C^5_{\alpha\dot{\alpha}^4}$	$C^5_{\alpha^2\dot{\alpha}^3}$	$C^5_{\alpha^3\dot{\alpha}^2}$	$C^5_{\alpha^4\dot{\alpha}}$	$C^5_{\alpha^5}$

Table 2 Aerodynamic coefficients for case-1

	D1	*D2*	*D3*	*D4*	*D5*	*D6*
C1	-0.0061	0.7576	0.0000	0.0000	0.0000	0.0000
C2	0.0041	0.0500	-0.6016	0.0000	0.0000	0.0000
C3	0.0039	-0.0473	-0.5667	6.9572	0.0000	0.0000
C4	-0.0058	-0.0144	0.8540	2.1116	-125.5797	0.0000
C5	-0.0015	0.0370	0.2227	-5.4456	-32.7507	800.7876

Table 3 Aerodynamic coefficients for case-12

	D1	*D2*	*D3*	*D4*	*D5*	*D6*
C1	-0.0034	0.7311	0.0000	0.0000	0.0000	0.0000
C2	0.0007	0.1651	-0.0701	0.0000	0.0000	0.0000
C3	0.0066	-0.1245	-0.6803	12.7382	0.0000	0.0000
C4	-0.0028	-0.0144	0.2916	1.4759	-29.8426	0.0000
C5	-0.0111	0.0737	1.1382	-7.5422	-116.4733	771.8068

Table 4 Aerodynamic coefficients for case-3

	D1	*D2*	*D3*	*D4*	*D5*	*D6*
C1	0.0029	0.6873	0.0000	0.0000	0.0000	0.0000
C2	0.0044	0.2381	-0.2920	0.0000	0.0000	0.0000
C3	0.0085	-0.0772	-0.5607	5.0724	0.0000	0.0000
C4	-0.0088	-0.0232	0.5804	1.5230	-38.1319	0.0000
C5	0.0136	0.2087	-0.8938	-13.7102	58.7196	900.7039

Table 5 Aerodynamic coefficients for case-4

	D1	*D2*	*D3*	*D4*	*D5*	*D6*
C1	0.0081	0.7103	0.0000	0.0000	0.0000	0.0000
C2	0.0041	0.0450	-0.2679	0.0000	0.0000	0.0000
C3	-0.0118	0.0228	0.7776	-1.5007	0.0000	0.0000
C4	0.0007	0.0004	-0.0459	-0.0270	3.0179	0.0000

C5	0.0014	0.0070	-0.0934	-0.4621	6.1378	30.3609

3 NONLINEAR DIFFERENTIAL EQUATION AND SOLUTION

3.1 *Nonlinear differential equation.*

Based on the direct Taylor expanding of nonlinear MIAF, and combined with the free vibration equation of the dynamic system, the nonlinear differential equation was constructed to describe the nonlinear aerodynamic stability of bridge girder. Because of the nonlinear items and variables in this equation, the limit cycle, the convergence motion and the divergence motion may exist under a special condition, which can prediction the motion of long bridges at the post-flutter status.

Taking an example of aerodynamic moment under torsional motion condition, the nonlinear differential Eq. can be written as follows:

$$\ddot{\alpha}+(2\xi_\alpha\omega_\alpha-\eta)\dot{\alpha}+(\omega_\alpha^2-\mu)\alpha=0 \tag{3}$$

In above, $\eta=f(\dot{\alpha},\alpha),\mu=g(\dot{\alpha},\alpha)$, and both of them are the nonlinear function of motion variables of bridge girder. Considering the motion variables (velocity and displacement) in the wind tunnel tests are certain values, and the parameter η and μ is also a certain value, and the solution of Eq. 3 in the different case only represents the tendency of girder motion with a special condition (including the dynamic parameters and initial motion parameters).

Because the 2nd order variables in Eq. 3 could bring on the difficult in solving, the state variables, which can reduce the order of the variables, are introduced, thus the equation can be transformed to the 1st order in the state space,

$$\dot{Y}=\begin{bmatrix}\dot{y}_1\\ \dot{y}_2\end{bmatrix}=\begin{bmatrix}\dot{\alpha}\\ \ddot{\alpha}\end{bmatrix}=\begin{bmatrix}y_2\\ -(2\xi_\alpha\omega_\alpha-\eta)y_2-(\omega^2-\mu)y_1\end{bmatrix}=\begin{bmatrix}\dot{\alpha}\\ -(2\xi_\alpha\omega_\alpha-\eta)\dot{\alpha}-(\omega^2-\mu)\alpha\end{bmatrix} \tag{4}$$

$$Y_0=\begin{bmatrix}y_1(0)\\ y_2(0)\end{bmatrix}=\begin{bmatrix}\alpha_0\\ \dot{\alpha}_0\end{bmatrix} \tag{5}$$

Giving the initial condition, the Eq. 3 can be solved using the 4th Runge-Kutta algorithm, and the results show the locus of the motion, which represent the motion status in post flutter.

3.2 *Solving conditions*

The general nonlinear differential equation to investigate the nonlinear aerodynamic stability of bridge girder under the special condition is shown below,

$$\ddot{\alpha}+2\xi\omega\dot{\alpha}+\omega^2\alpha=pC_M^T(\alpha,\dot{\alpha}) \tag{6}$$

where $p=\frac{1}{2}\rho U^2\mathrm{B}^2L\Big/I_m$ is the merging term, and the ρ=air density, *U*= wind speed, *B*= girder width, *L*= girder length, I_m= mass moment of inertia, ξ=damping ratio，ω=cycle frequency. $C_M^T(\alpha,\dot{\alpha})$ is the pitching moment coefficient of the different cases illustrated in Tables 2-5.

The standard form of solution in state space is as follow,

$$\dot{Y}=\begin{bmatrix}\dot{y}_1\\ \dot{y}_2\end{bmatrix}=\begin{bmatrix}\dot{\alpha}\\ \ddot{\alpha}\end{bmatrix}=\begin{bmatrix}y_2\\ -2\xi\omega y_2-\omega^2y_1-pC_M^T\end{bmatrix}=\begin{bmatrix}\dot{\alpha}\\ -2\xi\omega\dot{\alpha}-\omega^2\alpha-pC_M^T\end{bmatrix} \tag{7}$$

The initial condition in solution is ,

$\alpha_0 = 0$， $\dot{\alpha}_0 = 0.1745\omega$

The width of the girder in analysis is 0.776m, and considering the 2D analysis assumption the length is 1.0m. The other initial parameters for 4 cases are listed in Table 6.

Table 6 Parameters in different cases

	ω(rad/s)	2ξω	U(m/s)	I_m(Kgm^2)	p(/s^2)
Case1	12.13	0.01	15	1.0	82.987
Case2	10.12	0.01	20	2.0	73.766
Case3	8.11	0.01	20	2.5	59.013
Case4	8.11	0.01	20	8.0	18.442

4 NONLINEAR AERODYNAMIC STABILITY OF POST FLUTTER

The different motion corresponding to the differential equation can be desicribed in solution curve and phase plane diagram. Generally, the analysis results can express as follows: the positive work in the hysteresis loop is less than the negtive one, the motion of bridge girder will converge, see in Fig.6 and Fig.7. On the other hands, the motion will converge while the aerodynamic positive work is greater than the negative one, see in Fig.8. The identical amplitude oscillation could appear while the energy which structure consumed is equal to the aerodynamic energy, as shown in Fig.9. Because the area of positive work is almost equal to negative work in case-3, the speed of convergence is slow down dramatically, and the amplitude trends to the identical. The larger mass moment can consume the more aerodynamic energy in one period, and the identical amplitude oscillation can also occur even if the positive aerodynamic work is larger than the negative one. For case-4, if the I_m become the twice of the original one, and the amplitude will be identical, and the girder could occur limit cycle oscillation, see Fig.10

On the contrary, if the structural stiffness is so small, or the mass moment is too small to consume the aerodynamic energy in one period, the displacement of bridge girder increases vary rapidly, and the aerodynamic negative damping and structural damping can't consume the positive energy in time, even if the negative work is larger than the positive one, the girder motion will divergence directly as show in Fig. 11. In fact, because of the exist of 8-shape loop under different conditions, the motion of bridges girder may tend to the limit cycle oscillation, and may convert to different amplitude depending on wind speed. Of course, the girder could also occur the direct divergence while the positive aerodynamic energy increasing.

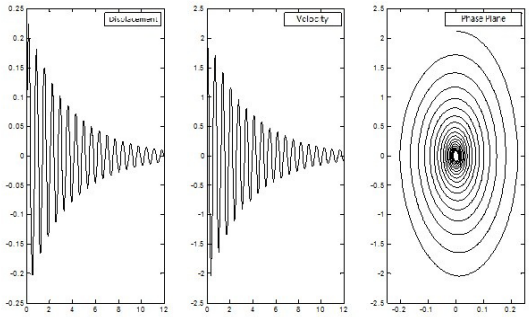

Fig.6 The solution curve and the phase plane diagram (case-1)

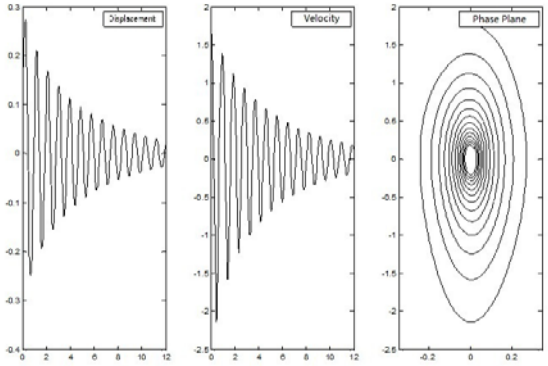

Fig.7 The solution curve and the phase plane diagram (case-2)

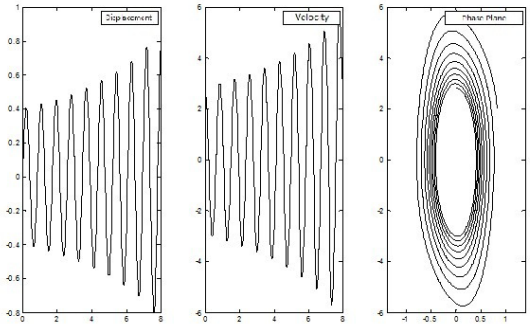

Fig.8 The solution curve and the phase plane diagram (case-4)

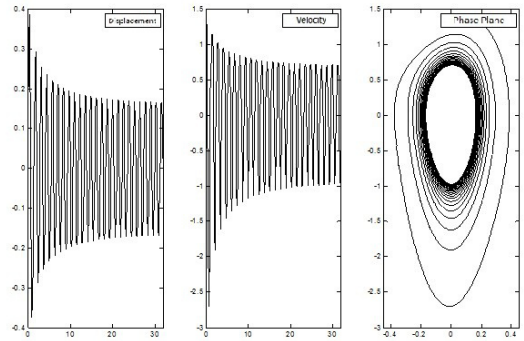

Fig.9 The solution curve and the phase plane diagram (case-3)

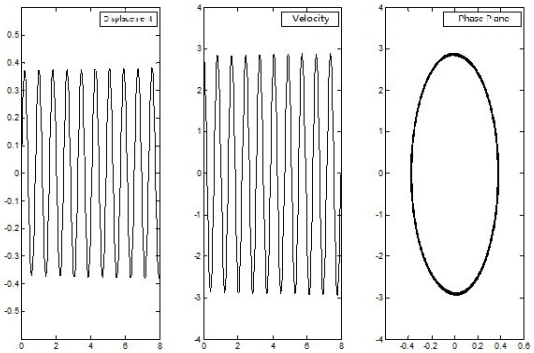

Fig.10 The solution curve and the phase plane diagram (case-4, I_m=16)

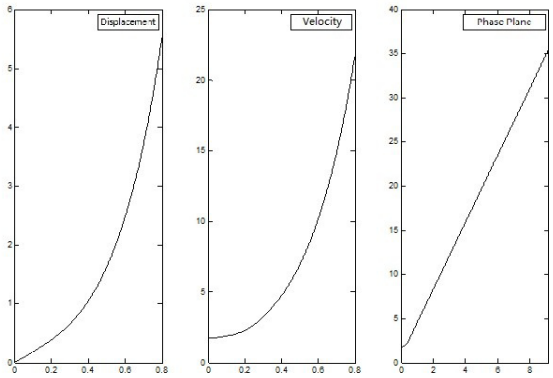

Fig.10 The solution curve and the phase plane diagram (case-2, I_m=1)

5 CONCLUSIONS

By introducing nonlinear MIAF expressions, nonlinear vibration differential equation can describe the aerodynamic stability of bridge girder under different amplitudes and reduced frequency, especially the large amplitude oscillation in the post flutter status of bridges. The nonlinear aerodynamic stability analysis had been solved in state space by using the 4th Runge-Kutta algorithm, and results show that the girder of long span bridge would appear different motion types in post flutter, including the convergence motion, the divergence motion and the identical amplitude oscillation (limit cycle oscillation). The motion of bridges girder may tend to the limit cycle oscillation, and convert to different amplitude due to 8-shape loop under different conditions. The girder can also occur the direct divergence while the positive aerodynamic energy increasing.

6 ACKNOWLEDGEMENTS

The paper is based on the project: The study on nonlinear motion-induced aerodynamic force and nonlinear aerodynamic stability of long-span bridge, which is supported by the Major Research plan of the National Natural Science Foundation of China (Grant No. 90815016).

7 REFERENCES

[1] Böhm V. F., Berechnugn nichtlinearer aerodynamisch erregter schwingungen von Hangebrücken[J]. Der Stahlbau, 7:207-215. 1967.
[2] Steinmann D. G., Hangebrücken-Das aerodynamicsche problem und seine lösung[J]. Acier-Steel-Stahl, 19(10-11):495-542.1954.
[3] Piccardo G., A methodology for the study of coupled aeroelastic phenomena[J]. J Wind Eng Indus Aerodynamic, 48:241-252. 1993
[4] Xu X., Cao Z., New expressions of nonlinear aerodynamic forces in civil engineering[A]. Proceedings of ICNM-3, Shanghai University Press: 396-401. 1998
[5] Xu X., Cao Z., Linear and nonlinear aerodynamic theory of interaction between flexible structure and wind[J], Applied Mathematics and Mechanics, 22(12): 57-65.2002
[6] Diana G, et al., Aerodynamic hysteresis: wind tunnel tests and numerical implementation of a fully nonlinear model for the bridge aeroelastic forces[C]. Proceedings of the 4th International Conference on Advance in

Wind and Structural-08, 944-960. Jeju, Korea.2008
[7] Diana G, et al., A new numerical approach to reproduce bridge aerodynamic non-linearities in time domain[J]. Journal of Wind Engineering and Industrial Aerodynamics 96, 1871-1884. 2008.
[8] Diana G, et al., Aerodynamic instability of a bridge deck section model Linear and nonlinear approach to force modeling[J]. Journal of Wind Engineering and Industrial Aerodynamics 98, 363-374.2010
[9] Liao H., Wang Q., Aerodynamic hysteresis effects of thin airfoil and streamline box girder under large amplitude oscillation[C]. In: Proceedings of the ICWE 13, Amsterdam NL., 2011
[10] Chen A., Ma R., Self-excited force model and parameter identification for soft flutter[C]. In: Proceedings of the ICWE 13, Amsterdam NL., 2011
[11] Den Hartog, J. P., Transmission line vibration due to sleet. Transaction of AIEE, 51, Part 4: 1074-1086, 1932.
[12] Den Hartog, J. P., Mechanical Vibrations. New York, McGraw Hill. 1956.
[13] Parkinson G. V., Smith J. D., The square prism as an aeroelastic nonlinear oscillator. Quart. J. Mech. Appl. Math., 17:225-239. 1964.
[14] Novak M., Aeroelastic galloping of prismatic bodies. ASCE J. Eng. Mech., 96:115-142.1969.
[15] Liao H., Wang Q., Study on the empirical mathematical model of nonlinear motion-induced aerodynamic force of bridge girder[C]. In: Proceedings of the BBAA 7, Shanghai China, 2012
[16] Wang Q., The study on nonlinear motion-induced aerodynamic force and nonlinear aerodynamic stability of long-span bridge girder [D]. Southwest Jiaotong University: Doctor Degree Dissertation, 2011.

The Seventh International Colloquium on Bluff Body Aerodynamics and Applications (BBAA7)
Shanghai, China; September 2-6, 2012

Eco-generation of energy from flutter based on energy-recycling mechanism

Kanjuro Makihara [a]

[a]*Tohoku University, 6-6-01 Aramaki-Aza-Aramaki, Aoba-Ward, Sendai, Japan*

ABSTRACT: This paper presents a harvesting system that extracts electrical energy by effectively using wing flutter, which is called eco-generation or energy-harvesting. This study utilizes the quasi-steady aerodynamic theory and FEM for simulating the dynamics of a plate wing. The use of piezoelectric patches and switching circuits can lead to effective harvesting from supersonic flutter. We evaluated our switching harvesting approach in supersonic flutter. Our harvesting system via wing flutter can generate 10 times more energy than a conventional harvesting system.

KEYWORDS: Eco-Generation, Flutter, Energy-Harvesting, Energy-Recycling, Piezoelectric

1 INTRODUCTION

The interaction between the structural motion of a wing and the aerodynamic load exerted on the wing can cause flutter phenomenon. It is a self-excited aeroelastic phenomenon that occurs in wings, thin walls, and so on. Wing flutter can be found most frequently within a high-speed, i.e., transonic, supersonic, and hypersonic flow (Dowell, 1966).

Eco-generation or energy-harvesting is a process by which energy is extracted from various sources and stored for future use, such as solar energy, tidal energy, piezoelectricity, thermoelectricity, and kinematic energy. Energy-harvesting techniques are expected to be of vital importance in the future when fossil fuel reserves will exhaust completely. Among the various sources mentioned above, this study focuses on harvesting energy from vibrating structures using piezoelectricity. Sodano et al. (2003) reviewed investigations of piezoelectric energy-harvesting techniques. Lesieutre et al. (2003) discussed the damping associated with harvesting electrical energy from a mechanically excited piezoelectric structure. Cornwell et al. (2005) developed an approach to improve energy output by using a tuned auxiliary structure. Because of the interest in the use of wind in harvesting energy, various studies and investigations were conducted by researchers, as discussed below. Erturk et al. (2010) employed the lumped-parameter model that entails energy-harvesting from aeroelastic vibration of a two-degree-of-freedom system. Robbin et al. (2006) discussed vortex-induced oscillations of piezoelectric cantilevers located behind bluff bodies. Isogai et al. (2003) conducted a study on a power generation system that extracts wind energy from flutter of a binary elastic system.

So far, wing flutter has been considered as a phenomenon that should be avoided, especially in aerospace engineering. However, adding electromotor or piezoelectric transducers to wings under aeroelastic vibrations is a feasible method for harvesting energy, as Isogai (2010), verified in simulation and experiments. We introduce an energy-harvesting system that extracts electrical energy from wing flutter using piezoelectric materials and a switching circuit. The effective use of wing flutter changes our perception of it; from being a destructive phenomenon as it was formerly known to be to being useful in various applications.

2 WING FLUTTER MODEL

2.1 *Outline of tail wing of rocket*

We focus on harvesting energy from wing flutters of sounding rockets (National Research Council Board, 2009). Japan Aerospace Exploration Agency has developed a sounding rocket S-310, which we consider as an example in our research. This rocket is 310 mm in diameter, and can reach an altitude of 150 km. The rocket attains approximately Mach 4.6 in 23 seconds, which indicates that it flies at a supersonic speed during most of its flight. Thus, it can be subject to supersonic flutter during the flight of the sounding rocket. The rocket has four tail wings made of a solid titanium plate (Fig. 1) flying at a supersonic speed. We include a cantilevered-plate wing to investigate the harvesting of energy from wing flutter. Piezoelectric patches are attached to the wing surface to generate electrical energy from the wing motion. In reality, patches attached to the wing surface may adversely affect fluid dynamics because they cause discontinuity of the wing surface. Furthermore, the patches may be adversely affected by the heat generated by aerodynamic interference. However, in this study, we do not consider these issues.

2.2 *Derivation of aerodynamic pressure for flutter analysis*

The flow velocity field, (u_1, u_2, u_3), is written as

$$u_1 = 0, \quad u_2 = U + \tilde{u}_2, \quad u_3 = \tilde{u}_3. \tag{1}$$

Here, U is the steady flow in the direction x_2. It is assumed that the variation of velocity is sufficiently small, compared with the steady flow. The continuous equation is

$$\frac{\partial \rho}{\partial t} + \frac{\partial}{\partial x_j}\left(\rho u_j\right) = 0. \tag{2}$$

The conservation of momentum is

$$\frac{\partial u_i}{\partial t} + u_j \frac{\partial u_i}{\partial x_j} = -\frac{1}{\rho}\frac{\partial p}{\partial x_i}. \tag{3}$$

The variation of velocity occurs in an adiabatic reversible manner, and the law of conservation of energy in an isentropic process can be written as

$$\frac{1}{2}u_i u_i + \frac{a^2}{\gamma - 1} = \frac{1}{2}U^2 + \frac{a_\infty^2}{\gamma - 1}. \tag{4}$$

The inner-product with u_i of Eq. (3) yields

$$u_i\left(\frac{\partial u_i}{\partial t} + u_j \frac{\partial u_i}{\partial x_j}\right) = -u_i\left(\frac{1}{\rho}\frac{\partial p}{\partial x_i}\right) = -\frac{u_i}{\rho}\left(\frac{\partial p}{\partial \rho}\right)_s\left(\frac{\partial \rho}{\partial x_i}\right) = -\frac{u_i}{\rho}a^2\left(\frac{\partial \rho}{\partial x_i}\right). \tag{5}$$

The substitution of Eq. (2) to Eq. (5) becomes

$$u_i\left(\frac{\partial u_i}{\partial t} + u_j \frac{\partial u_i}{\partial x_j}\right) = a^2\left(\frac{1}{\rho}\frac{\partial \rho}{\partial t} + \frac{\partial u_k}{\partial x_k}\right). \tag{6}$$

By substituting Eq. (1) in Eq. (6), and exchanging right and left terms, we get

$$a^2\left(\frac{1}{\rho}\frac{\partial\rho}{\partial t}+\frac{\partial u_2}{\partial x_2}+\frac{\partial u_3}{\partial x_3}\right)=(U+u_2)\left\{(U+u_2)\frac{\partial u_2}{\partial x_2}+u_3\frac{\partial u_2}{\partial x_3}\right\}+u_3\left\{(U+u_2)\frac{\partial u_3}{\partial x_2}+u_3\frac{\partial u_3}{\partial x_3}\right\}$$
$$+(U+u_2)\frac{\partial u_2}{\partial t}+u_3\frac{\partial u_3}{\partial t}. \tag{7}$$

The variation symbol, $(\tilde{\bullet})$, is removed. The substitution of Eq. (1) to Eq. (4) yields

$$a^2=a_\infty^2\left[1-\frac{\gamma-1}{2}M_\infty^2\left\{2\frac{u_2}{U}+\left(\frac{u_2}{U}\right)^2+\left(\frac{u_3}{U}\right)^2\right\}\right]. \tag{8}$$

By combining Eqs. (7) and (8), we obtain

$$a_\infty^2\left[1-\frac{\gamma-1}{2}M_\infty^2\left\{2\frac{u_2}{U}+\left(\frac{u_2}{U}\right)^2+\left(\frac{u_3}{U}\right)^2\right\}\right]\left(\frac{1}{\rho}\frac{\partial\rho}{\partial t}+\frac{\partial u_2}{\partial x_2}+\frac{\partial u_3}{\partial x_3}\right)=(U+u_2)\frac{\partial u_2}{\partial t}+u_3\frac{\partial u_3}{\partial t}$$
$$+(U+u_2)\left\{(U+u_2)\frac{\partial u_2}{\partial x_2}+u_3\frac{\partial u_2}{\partial x_3}\right\}+u_3\left\{(U+u_2)\frac{\partial u_3}{\partial x_2}+u_3\frac{\partial u_3}{\partial x_3}\right\}. \tag{9}$$

In Eq. (9), we omit higher variation terms than the first-order because $(u_i/U)\ll 1$;

$$\left(M_\infty^2-1\right)\frac{\partial u_2}{\partial x_2}+M_\infty^2\frac{\partial u_2}{\partial t}-\frac{\partial u_3}{\partial x_3}=\frac{1}{\rho}\frac{\partial\rho}{\partial t}. \tag{10}$$

The velocity potential, $\phi=\phi(x_2,x_3,t)$, is introduced as

$$\frac{\partial\phi}{\partial x_2}\equiv u_2,\quad \frac{\partial\phi}{\partial x_3}\equiv u_3. \tag{11}$$

By using D'Alembert's method without the time variation, a general solution can be expressed as

$$\phi\equiv F(x_2-\lambda x_3)+G(x_2+\lambda x_3),\quad \lambda\equiv\sqrt{M_\infty^2-1} \tag{12}$$

These functions F and G hold constant values along lines $x_2\pm\lambda x_3=const.$, respectively, Boundary condition at wing surface $w=0$ is

$$-\lambda\frac{\partial}{\partial x_2}\{F(x_2-\lambda x_3)\}|_{w=0}=U\frac{\partial w}{\partial x_2}. \tag{13}$$

Ashley and Zartarian (1956) developed the piston theory under the notion that at high Mach numbers the shock waves and expansion fans on an airfoil form at small angles to the undisturbed flow. The stream wise gradients are small compared to gradients perpendicular to the flow. Normal fluid velocity produced by the wing's motion results from Eq. (13) as

$$u_3=\frac{\partial w}{\partial t}+\left(U\frac{\partial w}{\partial x_2}\right) \tag{14}$$

Considering Eqs. (3) and (10) to (14), the pressure is expressed as

$$\frac{p}{p_\infty}=\left(1+\frac{\gamma-1}{2}\frac{w}{a_\infty}\right)^{(2\gamma)/(\gamma-1)}\approx 1+\gamma\frac{w}{a_\infty}+\frac{\gamma(\gamma+1)}{4}\left(\frac{w}{a_\infty}\right)^2+\frac{\gamma(\gamma+1)}{12}\left(\frac{w}{a_\infty}\right)^3. \tag{15}$$

When high order terms are truncated, the low-order aerodynamic pressure is described by

$$p - p_\infty = \frac{2q}{\lambda}\left[\frac{\partial w}{\partial x_2} + \left(\frac{\lambda^2 - 1}{\lambda^2}\right)\frac{1}{U}\frac{\partial w}{\partial t}\right]. \tag{16}$$

Other parameters are defined in Appendices A and B. Assuming that the pressure is exerted on both sides of the wing, we can express the resultant pressure $p_a(x, y, t)$ exerted on the wing as

$$p_a(x_1, x_2, t) \equiv -\frac{4q}{\lambda}\left[\frac{\partial w}{\partial x_2} + \left(\frac{\lambda^2 - 1}{\lambda^2}\right)\frac{1}{U}\frac{\partial w}{\partial t}\right]. \tag{17}$$

3 FLUTTER HARVESTING WITH PIEZOELECTRIC PATCHES

3.1 *Equations of motion for wing dynamics*

Piezoelectric patches shown in Fig. 1 are assumed to be polarized in the thickness direction (x_3 direction) and isotropic in the in-plane direction ($x_1 - x_2$ plane). Hence, their constitutive equations (Jaffe et al., 1971) are given by

$$\sigma_p = \mathbf{c}_p^D \varepsilon_p - \mathbf{h} D_3,\ E_3 = -\mathbf{h}^{\mathrm{T}} \varepsilon_p + \beta_{33}^S D_3. \tag{18}$$

The stress–strain relation of a wing is written as

$$\sigma_w = \mathbf{c}_w \varepsilon_w. \tag{19}$$

The linear strain-displacement relation based on the Kirchhoff–Love assumption is

$$\varepsilon = -x_3\left[\frac{\partial^2}{\partial x_1^2}, \frac{\partial^2}{\partial x_2^2}, 2\frac{\partial^2}{\partial x_1 \partial x_2}\right]^{\mathrm{T}} w(x_1, x_2, t). \tag{20}$$

On the surface of the wing, n_{p} pieces of piezoelectric patches are attached, and the j th patch ($1 \le j \le n_p$) is attached at positions $x_{1Sj} \le x_1 \le x_{1Ej}$, $x_{2Sj} \le x_2 \le x_{2Ej}$, and $x_{3Sj} \le x_3 \le x_{3Ej}$. To ensure the generality of this theoretical analysis, a multiple-input–multiple-output system is considered. Using Hamilton's principle, we construct

$$\int_{t_1}^{t_2}\left[\delta T_w - \delta U_w + \sum_{j=1}^{n_{\mathrm{p}}}(\delta T_{pj} - \delta U_{pj}) + \delta W\right]\mathrm{d}t = 0, \tag{21}$$

where virtual work δW can be written as

$$\delta W \equiv \int_S \delta w[f(x_1, x_2, t) + p_a(x_1, x_2, t)]\,\mathrm{d}S + \sum_{j=1}^{n_{\mathrm{p}}} V_j \int_{S_{pj}} \delta D_{3j} g_j(x_1, x_2, x_3)\,\mathrm{d}S. \tag{22}$$

Here, $f(x_1, x_2, t)$ is the external force normal to the wing and V_j is the voltage applied to the j th piezoelectric patch as a generalized external force. The finite element method (FEM) element proposed by Adini, Clough, and Melosh that is known as the ACM element (Zienkiewicz and Taylor, 1985), which is a four-node non-conforming plate element, is employed to discretize the partial derivative equations of motion. From Eqs. (17)–(22), the equation of motion for the cantilevered wing with multiple piezoelectric patches attached to it can be expressed as

$$\mathbf{M}\ddot{\vec{y}} + (\mathbf{K} + \psi\mathbf{A})\vec{y} = \mathbf{B}\vec{Q} + \vec{f}, \tag{23}$$

$$\vec{V} = -\mathbf{B}^{\mathrm{T}}\vec{y} + \mathbf{C}^{-1}\vec{Q}. \tag{24}$$

We perform the modal transformation

$$\vec{y} = \mathbf{\Phi}\vec{\eta}, \tag{25}$$

and introduce the modal damping in Eq. (23) as

$$\ddot{\vec{\eta}} + \mathbf{\Xi}\dot{\vec{\eta}} + (\mathbf{\Omega} + \psi\mathbf{\Phi}^{\mathrm{T}}\mathbf{A}\mathbf{\Phi})\vec{\eta} = \mathbf{\Phi}^{\mathrm{T}}\mathbf{B}\vec{Q} + \mathbf{\Phi}^{\mathrm{T}}\vec{f}. \tag{26}$$

This eigenvalue problem is solved for the homogenous part of Eq. (23) with $\psi = 0$.

3.2 *Switching eco-generation and circuit enhancement*

A conventional energy-harvesting device that employs piezoelectric materials to generate energy includes a vibrating piezoelectric structure and an energy storage system (Priya and Inman, 2003). The energy generator is composed of piezoelectric materials, which are attached to the structure, and a harvesting circuit. Circuit A shown in Fig. 2 is a conventional harvesting circuit consisting of a diode bridge of four diodes. The diode bridge is connected to the piezoelectric materials and it provides a mechanism for current rectification. This harvesting system is used in many vibration systems; however, it does not satisfactorily harvest electrical energy.

To enhance the energy-harvesting performance, we use the energy-recycling semi-active approach (Onoda et al, 2003) as an effective energy-harvesting mechanism. This approach involves the use of Circuit B, which is connected to the piezoelectric material, as shown in Fig. 3. The circuit has only two diodes and a selector switch. The selector switch is connected to point 1 or 2 to control the current flow. According to our previous study (Onoda et al, 2003), the advanced energy-recycling approach can simultaneously manage multiple circuits and piezoelectric patches. This type of energy-harvesting was described in (Makihara et al, 2006). Because our semi-active method just changes the switch connection to point 1 or 2 in Fig. 3, it never increases the vibration energy by its switching action. Hence, our semi-active approach is safer than other active approaches that usually involve a risk of instability such as spillover.

As will be seen later, in flutter problems, modal frequencies can shift according to dynamic pressure. Therefore, sophisticated controls based on modal decomposition are impractical. One way of implementing switching controls without modal information is to adopt an approach based on the direct velocity feedback method (Balas, 1979). The control reads that switching point should be changed according to the strain at the position of piezoelectric patch.

4 NUMERICAL ANALYSIS OF FLUTTER HARVESTING

4.1 *Wing flutter design*

We carried out numerical simulation of the energy-harvesting on the plate wing (Fig. 1). The wing was made of a titanium alloy (Ti-6Al-4V). This configuration is essentially a simpler model of the S-310's tail wing for explaining the harvesting performance on which we focus in this study. The wing was rigidly supported on one of its boundaries, i.e., $\psi = 0$. A piezoelectric patch was attached at $0 \le x_1 \le 0.15$ and $0.28 \le x_2 \le 0.46$ on the wing. The total resistance in the circuit was $30\,\Omega$, and the piezoelectric capacitance C_p was 1.17×10^{-6} F. Without considering the aerodynamic influence, the first and second mode frequencies of the open circuit (i.e., constant charge) were 43.0 Hz and 84.5 Hz, respectively. The simulation parameters are listed in Table 1. These parameters were determined on the basis of the materials used in the investigation to carry out realistic simulations. This study focuses on the energy harvested from wing flutter via

piezoelectric patches. We here explain the harvesting mechanism shown in Circuit B (Fig. 3) using a single-degree-of-freedom (SDOF) system, as this system is comprehensible. Figure 4 shows a schematic of the single-mode vibration in energy-harvesting.

4.2 *Eigenvalue analysis for flutter phenomenon*

Equation (23) can be reduced into an eigenvalue problem:

$$\left|\mathbf{K}+\psi\mathbf{A}-\mu\mathbf{M}\right|=0, \tag{27}$$

where μ is a complex eigenvalue. Because the eigen-analysis is performed on a no-control system, the control input and the external disturbance are neglected. Figure 4 plots eigenvalues as a function of the dynamic pressure parameter ψ. The curves of the two values of the real part approach each other as ψ increases. When $\psi=2.86\times10^{6}$, the two values of the real part can be combined as $\mathrm{Re}[\mu]=1.86\times10^{3}$. At this critical value of ψ the wing experiences a flutter phenomenon. This figure shows the loci of only the first and second modes. Since this critical value indicates the smallest dynamic pressure among all critical values, we focus on the relation between only two vibration modes.

4.3 *Flutter harvesting simulation*

We simulated flutter dynamics in the case that a white noise force was exerted on the wing surface. The power spectral density (PSD) per unit frequency of white noise had a constant nonzero value in the range of 30 to 100 Hz and a value of 0 in the rest of the frequency range. Therefore, the frequency range of the nonzero PSD covered the first and second modes.

The history of wing dynamics at a critical dynamic pressure with Circuit B is shown in Fig. 5. The wing tip displacement increases due to the wing flutter phenomenon. Following the displacement, the piezoelectric voltage also increases. Then, the stored voltage increases and harvested energy is accumulated. The stored voltage in the harvesting device is shown to have a step-like curve, which is characteristic of harvesting systems that use diode bridges. Figure 6 shows the magnified view of voltage in the two harvesting systems with Circuit A and Circuit B for $C_s=1.17\times10^{-6}$. The harvesting system with Circuit B outperforms in harvesting energy from wing flutter. Figure 7 presents a comparison of the energy harvested by the two systems with $C_s=1.17\times10^{-6}$. Our harvesting system with Circuit B can generate 10 times more electrical energy than the system with Circuit A. The generation ratio, i.e., 10 times, is quite a striking and attractive number as a powerful energy harvester. Our harvesting system shows potential and is effective because it takes advantage of the wing flutter that has thus far been considered as destructive.

5 CONCLUSIONS

Eco-generation from the flutter phenomenon of a plate wing is studied using the quasi-steady aerodynamic theory and the finite element method. The wing is modeled as sounding rockets' wings. We harvest electrical energy from supersonic flutter by using piezoelectric patches and electric devices. To assess their harvesting performances, we simulate flutter dynamics of the plate wing to which piezoelectric patches are attached. We demonstrate that our harvesting sys-

tem can generate 10 times more electrical energy from wing flutter than conventional harvesting systems can. We expect that our proposed technique will be applicable to various energy-harvesting systems, and we anticipate that it will be the basis for further studies in this field. More experimental validation is essential for assessing the harvesting performances, and an experiment is currently being carried out for this purpose.

6 REFERENCES

1. H. Ashley and G. Zartarian, Piston theory - a new aerodynamic tool for the aeroelastician, J. Aeronautical Sci., 23 (1956) 1109-1118.
2. M.J. Balas, Direct velocity feedback control of large space structures, J. Guid. Control, 2 (1979) 252-253.
3. P.J. Cornwell, J. Goethal, J. Kowko and M. Daminakis, Enhancing power harvesting using a tuned auxiliary structure, J. Intel. Mat. Sys. Struct., 16 (2005) 825-834.
4. E.H. Dowell, Nonlinear oscillations of a fluttering plate, AIAA J., 4 (1966) 1267-1275.
5. A. Erturk, W.G.R. Vieira, C.De Marqui and D.J. Inman, On the energy harvesting potential of piezoaeroelastic systems, Appl. Phys. Lett., 96 (2010) Article No. 184103.
6. K. Isogai, Theoretical and experimental study of elastically supported flapping wing power generator, Proc. Int. Conf. AIMM 10, (2010).
7. K. Isogai, M. Yamasaki and T. Asaoka, Application of CFD to design study of flutter-power-generation, Special Pub. National Aerospace Lab., 57 (2003) 106-111.
8. B. Jaffe, W.R.Jr. Cook and H. Jaffe, Piezoelectric ceramics, Academic Press, London, (1971).
9. G.A. Lesieutre, G.K. Ottman and H.F. Hofmann, Damping as a result of piezoelectric energy harvesting, J. Sound Vib., 269 (2003) 991-1002.
10. K. Makihara, J. Onoda and T. Miyakawa, Low energy-dissipation electric circuit for energy-harvesting, Smart Mater. Struct., 15 (2006) 1493-1498.
11. National Research Council Board, Sounding rockets; their role in space research, General Books LLC, Tennessee, USA, (2009).
12. J. Onoda, K. Makihara and K. Minesugi, Energy-recycling semi-active method for vibration suppression with piezoelectric transducers, AIAA J., 41 (2003) 711-719.
13. S. Priya and D.J. Inman, Energy harvesting technology, Springer Company, New York, (2009).
14. W.P. Robbins, D. Morris, I. Marusic and T.O. Novak, Wind-generated electrical energy using flexible piezoelectric materials, Proc. ASME, IMECE, (2006).
15. H.A. Sodano, G. Park and D.J. Inman, A review of power harvesting using piezoelectric materials, Shock Vib. Digest, 36 (2003) 197-206.
16. O.C. Zienkiewicz and R.L. Taylor, The finite element method, McGraw-Hill Book Company, Berkshire, England, (1985).

7 ACKNOWLEDGEMENTS

This research was supported by a Grant-in-Aid for Young Scientists (A) (No. 23686125) from the Japan Society for the Promotion of Science.

8 APPNDIX A. DEFINITION OF TERMS

$$\sigma_p \equiv \begin{Bmatrix} \sigma_1 \\ \sigma_2 \\ \tau_{12} \end{Bmatrix}, \epsilon_p \equiv \begin{Bmatrix} \epsilon_1 \\ \epsilon_2 \\ \gamma_{12} \end{Bmatrix}, \mathbf{h} \equiv \begin{Bmatrix} h_{13} \\ h_{13} \\ 0 \end{Bmatrix}, \mathbf{c}_p^D \equiv \frac{c_p^D}{1-\nu_p^2} \begin{bmatrix} 1 & \nu_p & 0 \\ \nu_p & 1 & 0 \\ 0 & 0 & \frac{1-\nu_p}{2} \end{bmatrix}, \mathbf{c}_w \equiv \frac{c_w}{1-\nu_w^2} \begin{bmatrix} 1 & \nu_w & 0 \\ \nu_w & 1 & 0 \\ 0 & 0 & \frac{1-\nu_w}{2} \end{bmatrix}$$

$$g_j(x_1,x_2,x_3) \equiv \left[H(x_1-x_{1Sj})-H(x_1-x_{2Ej})\right]\times\left[H(x_{2j}-x_{2Sj})-H(x_2-x_{2Ej})\right] \times\left[H(x_3-x_{3Sj})-H(x_3-x_{3Ej})\right]$$

$$T_w \equiv \int_V \frac{\rho_w}{2}\left(\frac{\partial w}{\partial t}\right)^2 \mathrm{d}V, U_w \equiv \int_V \frac{\sigma_w^{\mathrm{T}}\epsilon_w}{2}\mathrm{d}V, T_{pj} \equiv \int_{V_{pj}} \frac{\rho_{pj}}{2}\left(\frac{\partial w}{\partial t}\right)^2 g_j \mathrm{d}V, U_{pj} \equiv \int_{V_{pj}} \frac{(\sigma_p^{\mathrm{T}}\epsilon_p + E_3 D_3)}{2}\mathrm{d}V$$

$$\mathbf{M} \equiv \sum_{\text{ele}} \int_{V+V_p} \rho \mathbf{N}_{\mathrm{F}}^{\mathrm{T}} \mathbf{N}_{\mathrm{F}}\, \mathrm{d}V, \mathbf{K} \equiv \sum_{\text{ele}} \int_{V+V_p} x_3^2 \mathbf{B}_{\mathrm{F}}^{\mathrm{T}} \tilde{\mathbf{c}} \mathbf{B}_{\mathrm{F}}\, \mathrm{d}V, \mathbf{A} \equiv \sum_{\text{ele}} \int_S \mathbf{N}_{\mathrm{F}}^{\mathrm{T}} \frac{\partial \mathbf{N}_{\mathrm{F}}}{\partial x_2}\mathrm{d}S$$

$$\mathbf{B} \equiv \sum_{\text{ele}} \int_{V_p} \left(\frac{x_3}{S_{\text{ele}}}\right) \mathbf{B}_{\mathrm{F}}^{\mathrm{T}} \mathbf{h}\, \mathrm{d}V, \mathbf{C}^{-1} \equiv \sum_{\text{ele}} \int \left(\frac{x_3 \beta_{33}^S}{S_{\text{ele}}}\right) \mathrm{d}x_3, \mathbf{B}_{\mathrm{F}} \equiv \left[\frac{\partial^2 \mathbf{N}_{\mathrm{F}}}{\partial x_1^2}, \frac{\partial^2 \mathbf{N}_{\mathrm{F}}}{\partial x_2^2}, 2\frac{\partial^2 \mathbf{N}_{\mathrm{F}}}{\partial x_1 \partial x_2}\right]^{\mathrm{T}}$$

$$\psi \equiv \frac{4q}{\lambda},\ q \equiv \frac{1}{2}\rho_\infty U^2,\ M_\infty \equiv \frac{U}{a_\infty}$$

$$\mathbf{\Phi} \equiv [\varphi_1, \varphi_2, \ldots, \varphi_n],\ \mathbf{\Omega} \equiv \text{diagonal}[\omega_k^2],\ \mathbf{\Xi} \equiv \text{diagonal}[2\zeta\omega_k]$$

Table 1. Parameters of titanium wing and piezoelectric patch

	Titanium wing	Piezoelectric	unit
Piezoelectric coefficient	–	4.67	10^8 V/m
Dielectric coefficient	–	1.95	10^7 Vm/C
Density	4.47	8.10	10^3 kg/ m^3
Young's modulus	11.3	6.40	10^{10} N/ m^2
Poisson's ratio	0.31	0.32	–
Area	370×490	154×175	mm×mm
Thickness	6.75	0.5	mm

NOMENCLATURE

a_∞	speed of sound in air
c	Young's modulus
D_3 , E_3	electric displacement and field
$\vec{f}$	external disturbance vector
$\mathbf{F}$	feedback matrix
h_{13}	piezoelectric coefficient
n_p	number of piezoelectric
$\mathbf{N}_F$	shape function of FEM
p	pressure exerted on plate
p_∞	air pressure
$\vec{\eta}$	modal displacement vector
$\vec{Q}$	electric charge vector
T_w	kinetic energy of wing
T_{pj}	kinetic energy of j th piezoelectric
U	flight speed
U_w	strain energy of wing
U_{pj}	mechanical and electrical energy of j th piezoelectric
$\vec{V}$	voltage vector of piezoelectric
w	x_3-directional displacement
$\vec{y}$	FEM displacement vector
β_{33}^S	dielectric coefficient
ε , σ	strain and stress vectors
ρ , ν	density and Poisson's ratio
ρ_∞	air density
ζ	modal damping ratio
γ	ratio of specific heat

superscript

D	constant electric displacement
S	constant strain
T	transpose

subscript

p	piezoelectric patch
pj	j th piezoelectric patch
w	wing structure without piezoelectric

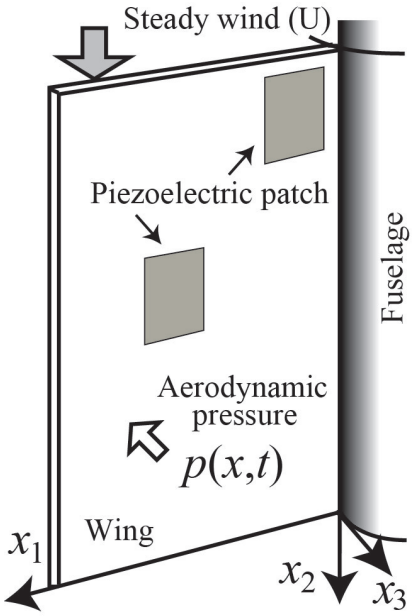

Figure 1. Tail wing subject to flutter and piezoelectric patches attached to wing

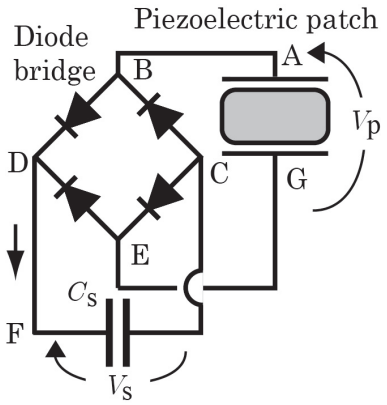

Figure 2. Circuit A: Conventional harvesting

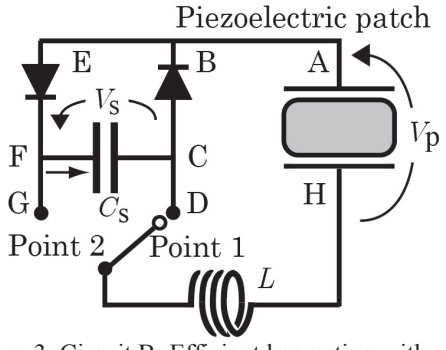

Figure 3. Circuit B: Efficient harvesting with energy-recycling mechanism

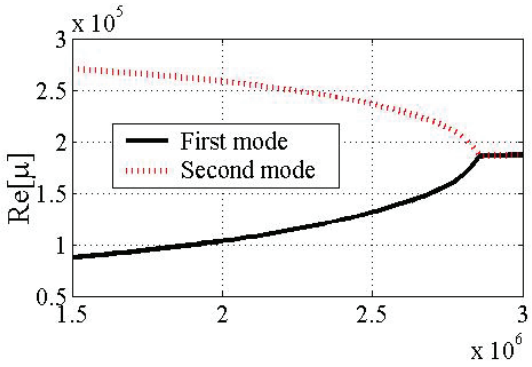

Figure 4. Eigenvalues as a function of dynamic pressure

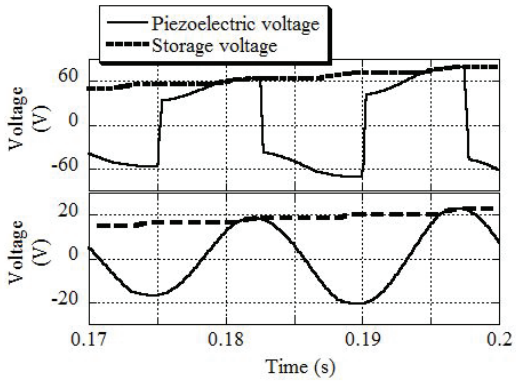

Figure 6. Magnified view of voltages (Upper: energy-harvesting, Lower: conventional)

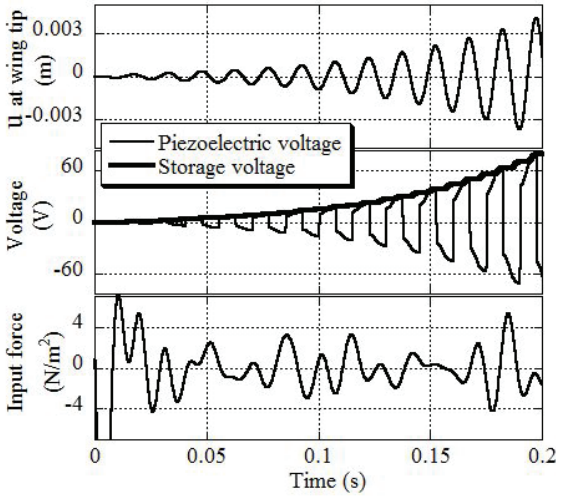

Figure 5. History of wing at critical dynamic pressure with energy-harvesting

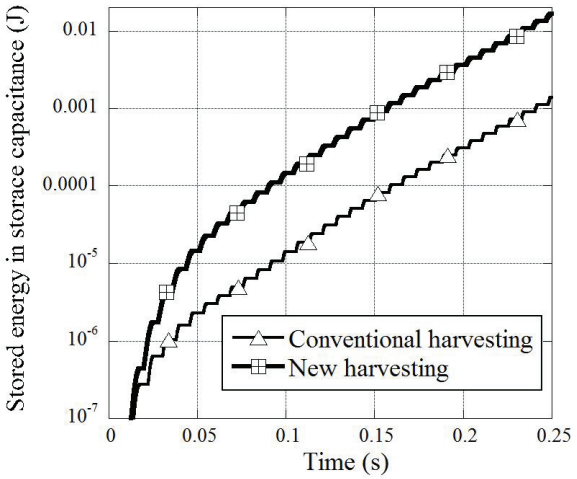

Figure 7. Comparison of stored energy in harvesting systems ($C_s = 1.17 \times 10^{-6}$)

The Seventh International Colloquium on Bluff Body Aerodynamics and Applications (BBAA7)
Shanghai, China; September 2-6, 2012

Wind energy harvesting at elevated bridges

Hosung Song[a], Seungho Lee[a], Bon-Sung Ku[b],
Ju-Yong Eum[b], Soon-Duck Kwon[a]

[a] *KOCED Wind Tunnel Center, Department of Civil Engineering, Chonbuk National Univ., 664-14, Dukjin, Chonju, Chonbuk, Korea*
[b] *Expressway & Transportation Research Institute, Korea Expressway Corp., 50-5, Dongtan, Hwaseong, Kyongki, Korea*

E-mail: sdkwon@chonbuk.ac.kr

ABSTRACT: This paper presents overall procedure for wind energy harvesting at elevated bridge in order to enable the self powered bridge. The test bed bridge was carefully selected from short term wind data measured at 86 sites considering wind energy potential and safety issues for traffic. The position of wind turbine around bridge girder was chosen from the CFD analysis and wind tunnel tests, where wind speed boosted 17~27% by oncoming wind. Two small wind turbines and associate monitoring system for wind data and electric power have been installed at the concrete girder of an elevated bridge over 57m above ground. Monitoring results for recent two months reveals a high correlation between the wind speed probability distribution and actual generated electric power. Long term monitoring of wind data and electric power is ongoing for further investigation.

KEYWORDS: Wind Energy, Bridge, Wind Turbine, Wind Tunnel Test.

1 INTRODUCTION

In modern bridges, electricity is needed for service and maintenance such as traffic control, lighting, and structural health monitoring. However, it is not easy to supply electricity to bridges in remote area. The cost for electric grid connection is $50/m in Korea, and is not acceptable for many bridges in rural or mountain area. One feasible way is to provide the harvested electricity from ambient energy sources to rechargeable battery equipped at bridges. Wind has an advantage of a continuous source of energy. The traditional wind turbines convert the ambient wind flows into useful electrical energy.

Elevated bridges are good places for wind energy harvesting because of escalated wind speed from the ground. Wind speed is also increased at elevated bridges which cross a valley or canyon, producing a convergence of streamlines. When wind turbines are installed at bridge girder, the major concerns for bridge are probable wind forces increase, mechanical vibration and wind-induced vibrations. In case of short and mid span bridges, wind induced vibrations and mechanical vibrations may be not significant because of its stiffness. The additional wind forces at the bridges introduced by wind turbines seem to be negligible compared with self load and other live loads.

In the first step for realizing the self powered bridges, an elevated concrete bridge with sufficient stiffness has been selected and equipped two different types of small wind turbines. This paper presents overall numerical and experimental results of site selection, position of wind turbine, monitoring system and short term measurement at field.

2 WIND RESOURCE ASSESSMENTS

2.1 *Long term estimation of wind resource*

While field observation of wind data at a specific site is the best solution for accurately assessing the wind energy potential, it is generally not feasible to acquire sufficient long-term wind data for the site. To overcome this problem, the Measure–Correlate–Predict (MCP) method has generally been used to estimate the long-term wind data at the target site from the wind data at the reference site. The fundamental principle behind MCP is that the wind at a new "test site" can be predicted on the basis of comparisons with data from a long-term "reference" site, which is located somewhere in the general vicinity [Manwell, *et al*., 2001].

When we obtained sufficient number of wind data at target site from the MCP method, we need to model the wind speed using probability distributions. The Weibull distribution is widely used in practical application. However, it is not acceptable at some case that the sources of wind are two or more. If probability density function of wind speed reveals two peaks, it is suitable to use the conventional Weibull distribution, and the mixed probability distribution seems to be solution. These two probability distributions are explained at next section.

Once the probability distribution is determined, next step for wind energy assessment is combining and integrating the probability distribution and power performance curve of the selected wind turbines. The output electrical power can be expressed as

$$E = T \int_0^\infty P(v) f_v(v) dv \tag{1}$$

where, v is wind speed, $P(v)$ is power performance curve of wind turbine, f_v is probability density function, and T is time period. T is 8760(=365×24) hours for calculating annual energy production (AEP).

2.2 *Probability distributions of wind speed*

The two parameter Weibull is a flexible distribution that is useful frequency distributions of wind speeds. The probability density function (PDF) of the Weibull distribution is expressed as

$$f_v(V) = \frac{k}{c}\left(\frac{V}{c}\right)^{k-1} exp\left\{-\left(\frac{v}{c}\right)^k\right\}, \qquad \text{for } V>0 \tag{2}$$

where, c>0 is the scale parameter, and k>0 is the shape parameter of the distribution. The following shape and scale parameters can be calculated from the maximum likelihood method.

$$k = \left[\frac{\sum_{i=1}^n v_i^k \ln(v_i)}{\sum_{i=1}^n v_i^k} - \frac{\sum_{i=1}^n \ln(v_i)}{n}\right]^{-1} \tag{3a}$$

$$c = \left(\frac{1}{n}\sum_{i=1}^n v_i^k\right)^{\frac{1}{k}} \tag{3b}$$

where, v_i is the wind speed in i^{th} time step, and n is the number of data points.

A mixture density is a probability density function that is linear combination of other probability density functions. Suppose that $v_i (i = 1,2)$ are independently distributed as two-parameter Weibull $f(v,c,k,)$, a random variable v that is distributed as v_i with mixing parameters ω_i is said to have a two-component mixture Weibull distribution. The PDF of v, which depends on five parameters (c_1,k_1,c_2,k_2,ω), is given by [Carta, *et al*., 2007]

$$f_v(c_1, k_1, c_2, k_2, \omega) = \omega f_{v1}(c_1, k_1) + (1-\omega) f_{v2}(c_2, k_2) \tag{4}$$

where, $v > 0$, $c_1,k_1,c_2,k_2 > 0$, and $0 \le \omega \le 1$. Parameter estimation method consists of finding the values of the parameters (c_1,k_1,c_2,k_2,ω), which maximize the function of log-likelihood is given by

$$Maximise \ \ln L_v(c_1,k_1,c_2,k_2,\omega)$$
$$= \sum_{i=1}^{n} \ln\left\{\omega\left[\frac{k_1}{c_1}\left(\frac{v_i}{c_1}\right)^{k_1-1}\exp\left\{-\left(\frac{v_i}{c_1}\right)^{k_1}\right\}\right] + (1-\omega)\left[\frac{k_2}{c_2}\left(\frac{v_i}{c_2}\right)^{k_2-1}\exp\left\{-\left(\frac{v_i}{c_2}\right)^{k_2}\right\}\right]\right\} \quad (5)$$

3 SELF POWERED BRIDGE

3.1 *Site survey*

Short term wind speeds measured at 86 bridges were used to find a test bed bridge site for wind energy harvesting. The wind data on bridge were measured for one year in order to investigate the effect of side wind on vehicle runnability [KEC, 2009]. These were the only reliable wind data for bridges in mountainous region where local topographical effect dominated. The strong seasonal variations of the measured short term wind speeds were interpolated comparing the wind data at nearby local weather station.

Bridges near residential area and overpass were eliminated from test bed site to avoid any civil complaint and traffic danger. Figure 1 shows the average wind speeds measured at several highway bridges. All bridges except the first one were located at mountainous area. Though the Seohae Bridge revealed the highest average wind speed, it was discarded from the candidate bridge because of high traffic volume.

The KJC Bridge shown in Figure 2 was finally selected as test bed for wind energy harvesting because of its relatively high wind speed, stiff girder and low traffic volume. The KJC Bridge, located in Yangyang, Kangwon, Korea which was north eastern part of South Korea. Annual average wind speed of the bridge was 4.38m/s. Single span length and width of the prestressed concrete box girder were respectively 57m and 11.3m. Height of the superstructure was 57m from ground. Wind barrier of 3m high has been installed at southwest side of the bridge for traffic safety.

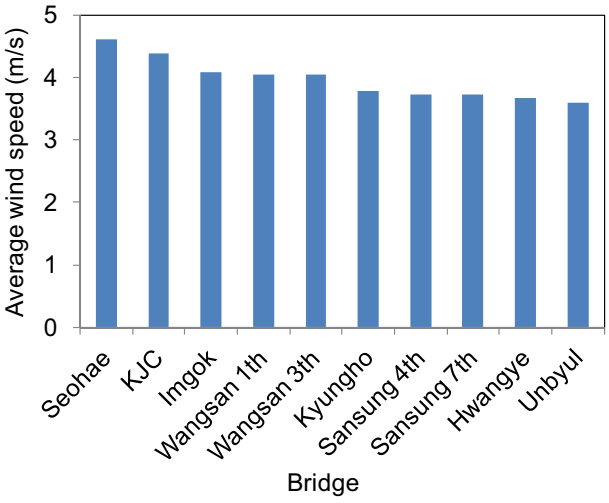

Figure 1. Average wind speed measured at highway bridges in Korea.

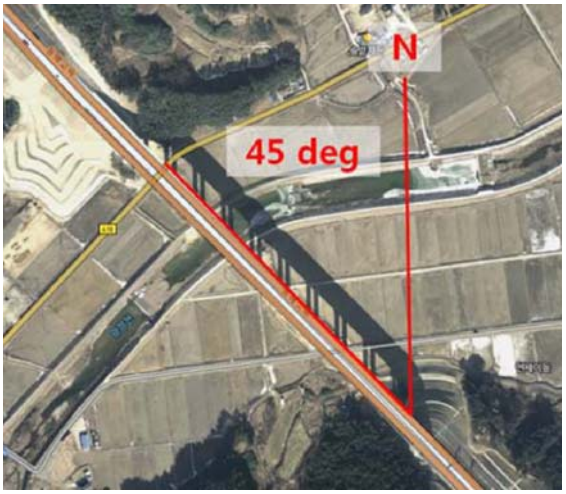

Figure 2. Aerial view of the KJC Bridge.

3.2 *Wind data at test bed bridge*

10 minutes averaged wind speed and direction of the KJC Bridge were measured from June 2007 to May 2008 to obtain the basic data for assessment of traffic safety. KJC Bridge was tilted 45 degrees from the north. As shown in Figure 3, the main wind direction represented frequency of more than 50% from the southeast that was perpendicular to the bridge. These wind direction was good to install wind turbines near the side surface of bridge girder.

The MCP interpolation was not carried out because of poor correlation among wind speed at the bridge and those at nearby weather stations. The wind speed and directions at the bridge seemed to be strongly influenced by local topography. Table 1 shows annual mean wind speed, power density, and Weibull scale and shape parameters above the girder of KJC Bridge, which were respectively 4.38m/s, 173W/m^2, 4.95 and 1.9. The graphical representation of the same data in the table is given in Figure 3. Figure 4 shows probability distribution function for the observed wind speed above the girder from June 2007 to May 2008.

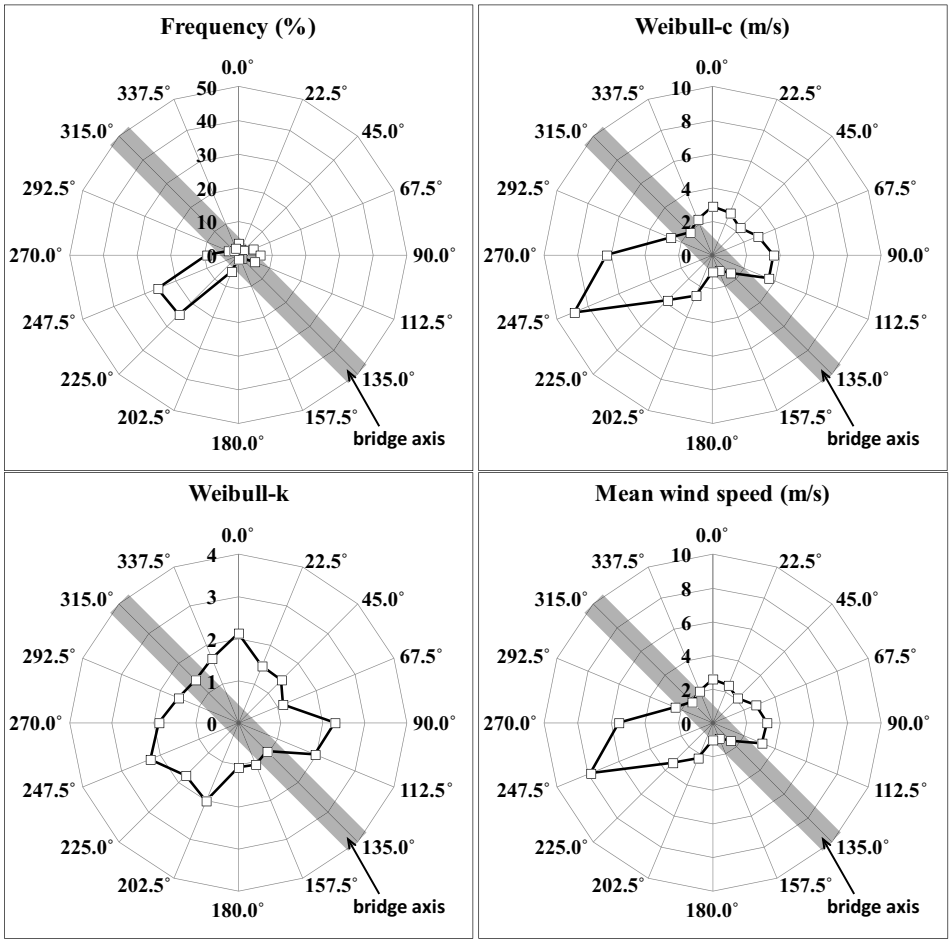

Figure 3. Wind characteristics of KJC Bridge. Marks represent the values evaluated from the measured wind data, and the shaded area represents bridge axis.

Table 1. Wind characteristics above the girder from June 2007 to May 2008.

No.	Angle (°)	Frequency (%)	Weibull-c (m/s)	Weibull-k	Mean wind speed (m/s)	Power Density (W/m²)
1	0 (North)	3.5	2.9	2.13	2.60	19

2	22.5	1.8	2.7	1.46	2.41	24
3	45	2.0	2.3	1.44	2.08	16
4	67.5	4.7	2.9	1.14	2.77	58
5	90	6.4	3.6	2.29	3.21	34
6	112.5	5.2	3.6	1.97	3.16	38
7	135	1.4	1.5	0.96	1.50	14
8	157.5	1.1	1.0	1.07	1.00	3
9	180 (South)	1.2	1.0	1.06	1.02	3
10	202.5	5.3	2.6	2.01	2.27	14
11	225	24.9	3.8	1.77	3.36	51
12	247.5	25.9	8.9	2.27	7.84	503
13	270	9.4	6.3	1.89	5.58	216
14	292.5	3.3	2.7	1.54	2.42	23
15	315	1.9	1.9	1.44	1.74	9
16	337.5	2.2	2.3	1.65	2.03	12
Mean	-	-	4.95	1.9	4.38	173

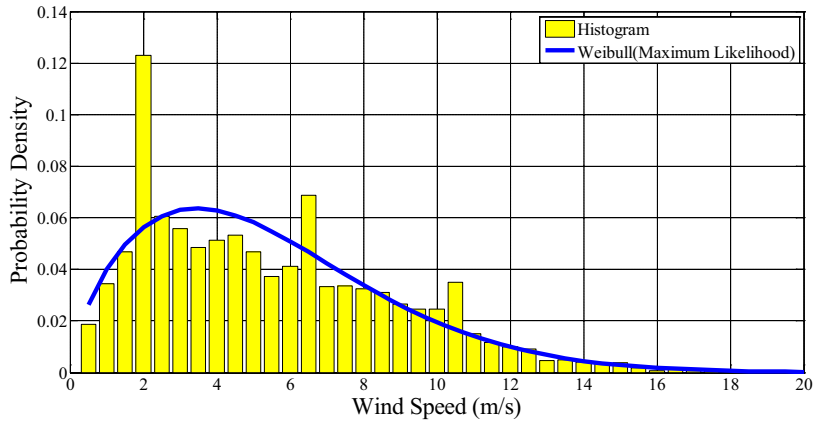

Figure 1. Probability density function for the observed wind speed above the girder from June 2007 to May 2008.

3.3 *Estimation of annual energy prediction at test bed bridge*

By applying the measured wind data and associate Weibull distribution into the Equation (1), annual energy production of a turbine equipped at bridge girder was roughly estimated. In the study, a wind turbine with rated power of 2.4kW was assumed to be installed at bridge. The power performance curve of the target wind turbine, Skystream3.7, is shown in Fig. 5. Fig. 6 shows estimation of energy production for the observed wind speed above the girder from June 2007 to May 2008. In this case, the annual energy production estimated from histogram was 3.26 MWh, and that from Weibull distribution was 3.21 MWh. The Weibull distribution could be effectively used for estimating energy production at present wind data.

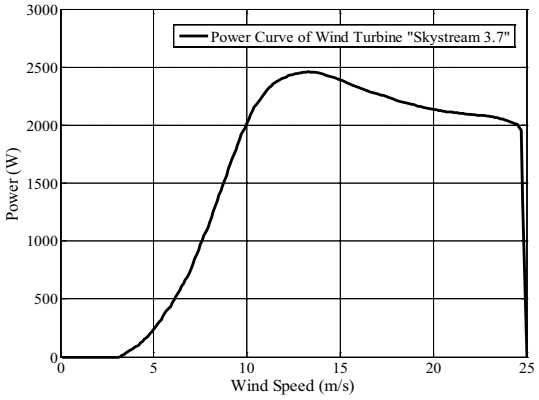

Figure 5. Power performance curve of Skystream3.7 wind turbine

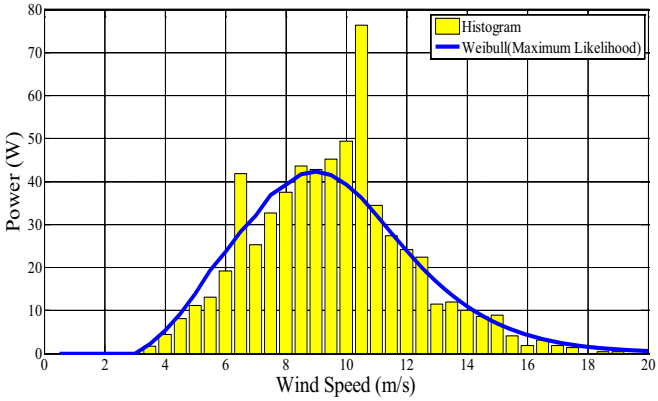

Figure 6. Estimation of energy production from the observed wind speed from June 2007 to May 2008

4 PLACING WIND TURBINES AT BRIDGE GIRDER

It was very important to decide where the wind turbines were installed at bridge girder. The electric output power might be varied depending on position of the wind turbine because wind speeds around the girder are different at point by point. However wind flow field near the girder was complicated and was dependent on girder shape. Accordingly, numerical simulation based on computational fluid dynamics (CFD) analysis was first performed, and then wind tunnel test were carried out in order to investigate wind speed, wind direction and turbulent intensity around the bridge girder.

4.1 *Numerical simulation*

For the selection of the optimal installation location for wind turbines, CFD analysis was performed to examine the flow field around the bridge girder prior to wind tunnel test. A commercial CFD software, FLUENT, on supercomputer in Korea Institute of Science and Technology Information was used in the analysis. Conditions and results of analysis are as follows.

In the two dimensional CFD analysis, a typical the bridge girder section at center span was adopted and pier was not modeled. Uniform wind speed of 30m/s was applied to the input domain regardless of height variation. Wind barrier installed at west side of the girder was included in the modeling. Transmittance of the wind barrier (wind speed passing wind barrier per basic wind speed) was set at the rate of 50%. Analysis was performed for two different wind directions; the southwest direction and the northeast direction. In former case, wind flow passed through the wind barrier at windward edge.

Figure 7 shows analysis results for two different wind directions. From the figures, wind speed just near the bridge girder decreased significantly, yet wind speed increased at beneath or above the girder height. Both safety of traffics and power efficiency of wind turbine were considered in determination of wind turbine position. Positions above the girder slab were excluded from the installation place for wind turbine to prevent any effects on high speed traffics passing the bridge. In the beneath of the girder, the wind speed at 13m beneath the bridge slab was respectively 17% and 2% higher than oncoming wind speed. In the figure, “x” mark denotes possible position of wind turbine to get more electric energy and less effect on traffics. Figure 8 shows variation of wind speed along height from leeward and windward edges of slab. It is apparent from the figure that wind speed boosts up at a few meters depart from the girder.

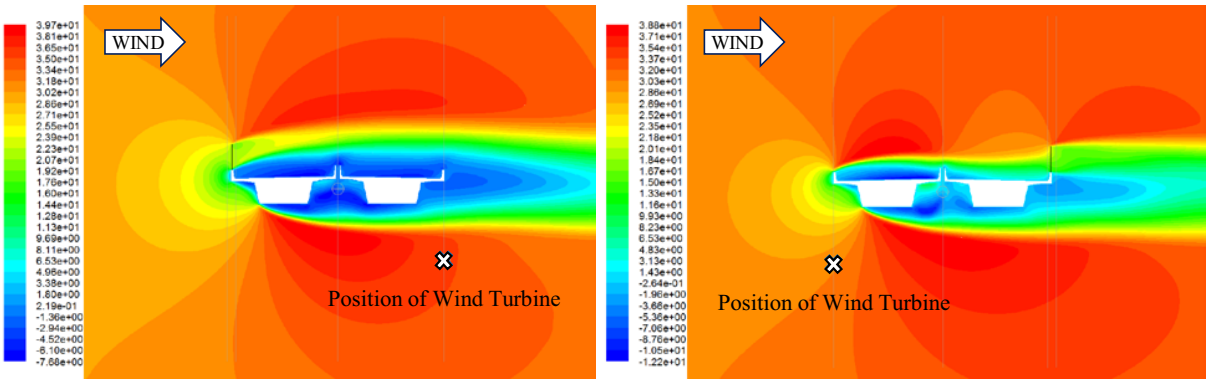

Figure 2. Contour of x-direction wind speed. left: wind barrier at windward edge, right: wind barrier at leeward edge.

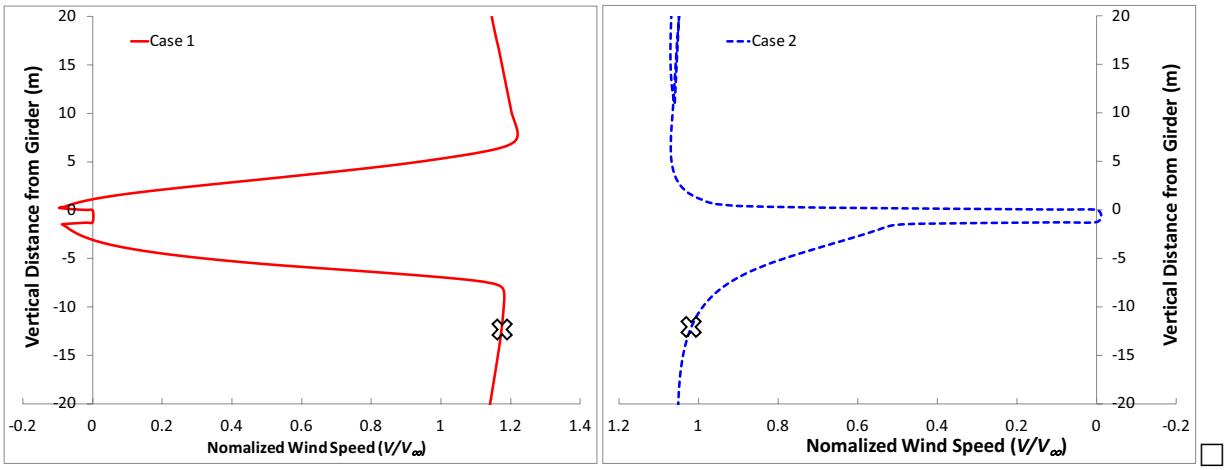

Figure 3. Variation of wind speed along height (a) from windward edge of slab, (b) from leeward edge of slab.

4.2 *Wind Tunnel test*

Wind tunnel test of single span bridge was performed at KOCED Wind Tunnel Center in Chonbuk National University. Model scale was 1:15. Wind speeds were measured at total 113 points near the bridge girder to investigate the flow field. Figure 9 shows the bridge model in the wind tunnel.

This closed return type vertical returning wind tunnel has two test sections. The tests were carried out at the high speed test section of 5m(W) × 2.5m(H) × 20m(L). The wind tunnel has five fans and motors with 275 KW each. The free stream velocity of this low speed test section ranges from 0.5 m/s to 31m/s. The mean velocity of the free stream flow was made by using two pitot tubes and pressure transducers (Setra 239). A temperature and humidity sensors (Vinotech GHP-20R) was used to evaluate air density. DANTEC CTA-90C10 constant temperature anemometer incorporated with DANTEC 55P11 hotwire sensors was used to measure the turbulent wind velocity near the bridge girder. At each measurement, velocity data for 100 seconds were acquired at a 6 kHz sampling rate.

Figure 10 shows wind speed contour around bridge girder measured from wind tunnel test. Undisturbed input wind speed was 10m/s. The wind speed at 10m beneath from bridge slab was 27% higher than oncoming wind speed. Turbulent intensity at the position was 4.1%. Finally it

was decide to install the wind turbine at 10m beneath the bridge slab to get more electric energy and not to disturb the passing traffics.

Figure 4. 1/15 scale model of single span bridge in wind tunnel.

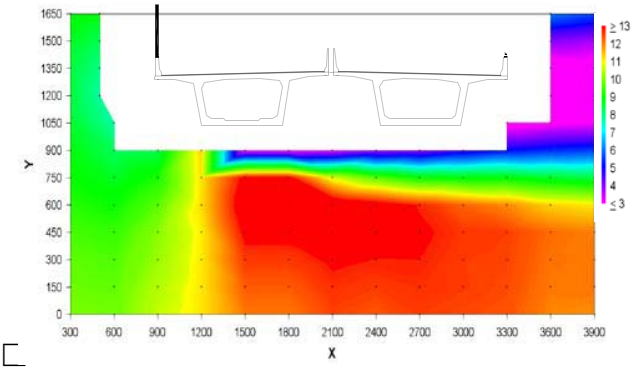

Figure 5. Wind speed measured at wind tunnel test.

5 FIELD MEASUREMENTS AND RESUTLS

5.1 *Wind turbines*

As shown in Figure 11, two wind turbines have been installed at 10m beneath the bridge slab of the KJC Bridge. The first wind turbine has three blades in horizontal axis. Diameter and rated power are respectively 3.7m and 2.4kW. The second one is Savonius type vertical axis turbine with 2kW rated power. Diameter and height of the second one are 0.8m and 1.4m respectively. Self weights of the two wind turbines excluding tower were 93kg and 140kg respectively.

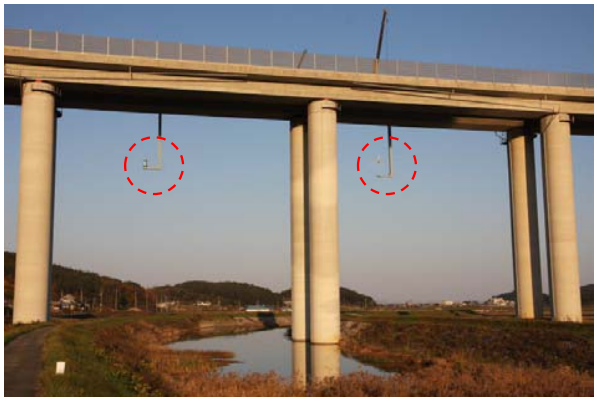

Figure 6. Tow wind turbines installed at the KJC Bridge.

Figure 7. Monitoring system at bridge site.

5.2 *Monitoring system*

Monitoring system shown in Figure 12 was designed and installed at the bridge to measure wind data as well as generated electric power. Total three cup anemometers provided by NRG System were equipped at the bridge; two at near each wind turbines, and one at 10m above bridge slab to measure undisturbed wind speed. Two digital power meters provided by LSIS were used to measure the electric voltage, current and power from wind turbines. All data from

electric power meters, anemometers, wind direction sensors, temperature sensor, relative humidity sensor and barometric pressure sensor have been recorded at the data logger, and periodically transmitted to remote computer at KOCED Wind Tunnel Center in Chonbuk National University through cellular network.

5.3 *Short term monitoring results*

The wind data and electric power at the KJC Bridge for every 10 minutes from 2/1/2012 to 3/31/2012 were measured by using the monitoring system. Figure 13 shows the frequency of occurrence and mean wind speed as function of wind direction. Wind shows strong directionality in southwest as was expected from the wind data at 2007~2008.

Table 3 summarizes the energy production during two months monitoring. It is clear from table that the mixture Weibull distribution reveals more accurate estimation of energy production compared with the conventional Weibull distribution. Power estimation error for the Weibull distribution was 6.4% but the mixture Weibull distribution showed 1.4% error in the estimation. The superiority of mixture Weibull distribution compared with conventional Weibull distribution can be clearly seen at Figure 14.

When we compare the recently observed two months data and those at the same period in 2008, there is some difference between two results. The generated electric power was less than expected one because of mainly poor average wind speed compared with that at 2008. Average wind speed at 10m above slab was 5.48 m/s at 2008 but decreased to 4.75 m/s at 2012. Moreover the wind speed at 10m beneath the slab was about 3% less than that at 10m above the slab.

Table 3. Wind energy production for two months from February to March.

Period	Location	Average speed (m/s)	Power density (W/m^2)	Energy production (kWh)	
				Weibull	Mixture Weibull
2/1/2008~3/31/2008	above slab	5.48	227	701	734
2/1/2012~3/31/2012	above slab	4.75	165	642	668
	beneath slab	4.61	95	414	434
				440 (measured)	

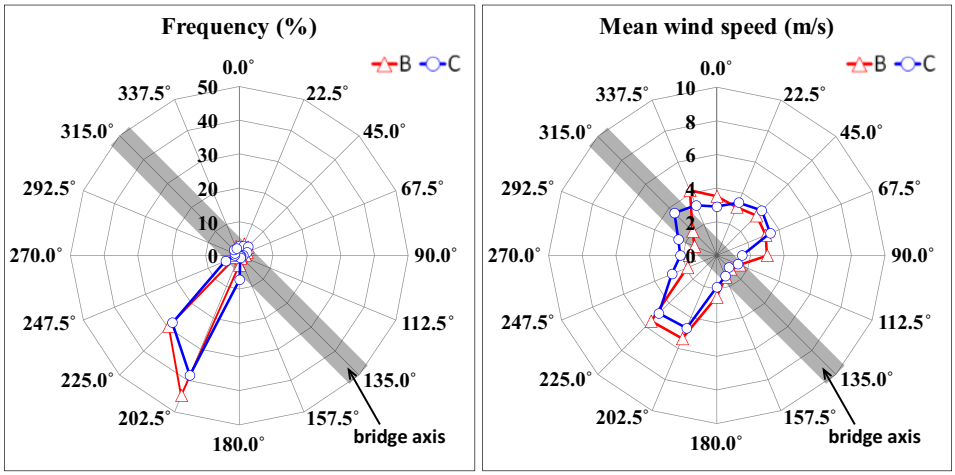

Figure 8. Wind characteristics observed at 2/1/2012~3/31/2012. B: above slab, C: near wind turbine.

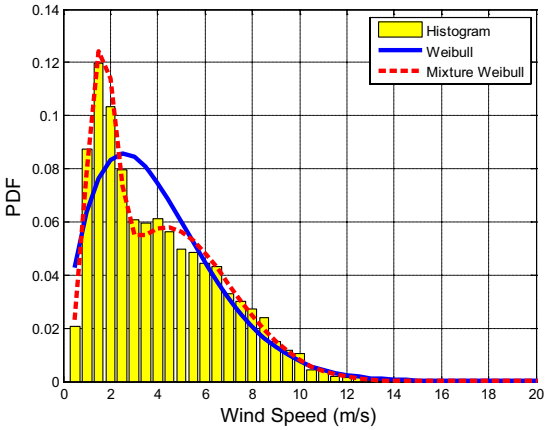

Figure 14. PDF of two months wind speed at wind turbine in 2012.

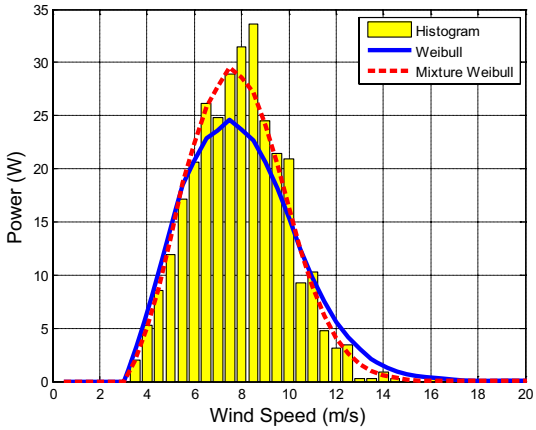

Figure 15. PDF of two months energy production for a skystream3.7 wind turbine in 2012.

6 CONCLUDING REMARKS

This paper presents design, analysis, test, installation and monitoring of wind turbine equipped at elevated bridge in order to enable the self powered bridge. Two small wind turbines have been installed beneath the bridge girder that was selected from 86 sites considering wind energy potential and safety of passing traffics. The installation position of wind turbine near the bridge girder was chosen from the CFD analysis and wind tunnel tests, where wind speed boosted 17~27% by oncoming wind. Monitoring results for recent two months reveals a high correlation between the wind speed probability distribution and actual generated electric power.

7 REFERENCES

1 A.M. Razali and A.A. Salih, Combining Two Weibull Distributions Using a Mixing Parameter, European Journal of Scientific Research, Vol.31, No.2 (2009) 296-305.
2 J.A. Carta and P. Ramirez, Analysis of two-component mixture Weibull statistics for estimation of wind speed distributions, Renewable Energy, 32 (2007) 518–531.
3 J.F. Manwell, A.L. Rogers, J.G. McGowan and B.H. Bailey, An offshore wind resource assessment study for New England, Renewable Energy, 27 (2002) 175-187.
4 M. EI-Gammal, H. Hangan and P. King, Control of vortex shedding-induced effects in a sectional bridge model by span-wise perturbation method, Journal of Wind Engineering and Industrial Aerodynamics, Vol.95 (2007) 663-678.
5 S.D. Kwon, Uncertainty analysis of wind energy potential assessment, Applied Energy, 87 (2010) 856–865.
6 S.D. Kwon, S.H. Lee, and H.K. Lee, Aerodynamic Retrofit of Bridge and Energy Harvesting by Small Wind Turbines, Journal of Korean Society of Civil Engineering, Vol.30, 1A (2010) 27-33.
7 T.J. Chang, Y.T. Wu, H.Y. Hsu, C.R. Chu and C.M. Liao, Assessment of wind characteristics and wind turbine characteristics in Taiwan, Renewable Energy, 28 (2003) 851-871.
8 T.P. Chang, Estimation of wind energy potential using different probability density functions, Applied Energy, 88 (2011) 1848–1856.
9 E. Simiu and T. Miyata, Design of Buildings and Bridges for Wind, Wiley. 2006.
10 IEC, Wind turbines. Part 12-1: Power performance measurements of electricity producing wind turbines, IEC 61400-12-1, International Electro-technical Commission, 2005.
11 KEC, The Report of Analysis and Design for Installing Wind Barrier at High Wind Speed Site, Korea Expressway Corporation, 2009 (in Korean).

The Seventh International Colloquium on Bluff Body Aerodynamics and Applications (BBAA7)
Shanghai, China; September 2-6, 2012

A parametric study of wind-induced flutter of piezoelectric patches for energy harvesting

J. M. McCarthy [a], A. Deivasigamani [a], S. Watkins [a], S. J. John [a], F. Coman [b]

[a] *RMIT University, School of Aerospace, Mechanical & Manufacturing Engineering, PO Box 71, Bundoora, Victoria 3083, Australia*
[b] *FCST Pty., PO Box 122, South Carlton, Victoria 3053, Australia*

ABSTRACT: A study of key parameters affecting flutter characteristics and power output levels from a thin piezoelectric patch immersed in a parallel, smooth flow was examined. The piezoelectric patch vibration amplitudes were augmented through the use of a polymeric "leaf", freely hinged to the trailing edge of the patch. The leading edge of the patch was rigidly clamped to a relatively narrow, rectangular support that extended across the wind-tunnel test domain, giving effectively a two-dimensional testing scenario. The influence of clamping base geometry on the flutter characteristics was evaluated. It was found that the stream-wise dimension of the rectangular clamp had little effect, whilst an increasing cross-stream dimension tends to delay the onset of flutter. Stream-wise proximity experiments were conducted with two leaf-stalk systems, and it was found that there exists a point tandem and downstream of a fluttering leaf-stalk system, whereby a second leaf-stalk can output more than 40% more power than when alone.

KEYWORDS: piezoelectric, energy harvesting, flow-induced flutter, vortex shedding

1 INTRODUCTION

A fluttering leaf on a tree, a vibrating automobile antenna, or blinds flapping in the wind; all of these seemingly trivial events actually reveal a complex engineering and scientific problem: fluid-flow induced flutter. Traditionally, flutter has been considered a detriment to structural integrity, and engineers would design the structure to obviate flutter occurrence. In fact, much research has been conducted to comprehend the underlying mechanisms of an object fluttering in a fluid flow (e.g. Lord Rayleigh 1879; Theodorsen 1935; Kornecki *et al.* 1976; Fredericks *et al.* 1986; Huang 1995; Paidoüssis 1998; Zhang *et al.* 2000; Argentina & Mahadevan 2005; Paidoüssis *et al.* 2011).

Recently, however, there has been a realization that flutter could be exploited for the purposes of energy harvesting, using thin, flexible piezoelectric materials immersed in a fluid flow. Flutter is related to resonance of the system, and thus the amplitudes of an object in flutter become large. In order to extract large amounts of energy from a piezoelectric material large mechanical strain must be applied, and if this can be induced by flutter then energy can be extracted from a fluid flow. One of the first known attempts in the laboratory environment to realize this concept was by Allen & Smits (2001); where flutter of a thin, polyvinylidene-fluoride[1]-laden membrane was induced by introducing an upstream vortex-shedding, bluff body. The vortices would impinge on the flexible membrane, and due to the imposed pressure gradients, would cause time-varying membrane deformation according to the vortex shedding frequency of the bluff body. This method of flutter excitation is classed by Naudasher & Rockwell (1980) as Extraneously Induced Excitation, or EIE; flutter is induced from external pressure gradients caused by turbulence or vortices. Taylor *et al.* (2001) carried out a similar study, whereby a bluff body was used

[1] Polyvinylidene-fluoride (PVDF) is a flexible, isotropic piezoelectric material.

to excite undulations of the so-called piezoelectric "eel" within a water flow; however, they focused their attention on optimizing the electrical subsystem. Pobering & Schwesinger (2004) suggest two designs that exploit vortex shedding in a water flow; along with a simplified analysis, they state that such a piezoelectric system, when scaled up, could have a higher power density than that of a conventional wind turbine.

Dickson (2008) envisioned a piezoelectric flutter system that would not only be efficient, but aesthetically-pleasing and safe; a tree-like construct with multiple piezoelectric "stalks" with polymeric "leaves" attached the stalks – figure 1 shows this concept.

Figure 1. The piezoelectric "tree" concept proposed by Dickson (2008).

Li & Lipson (2009) initiated research on this concept, by starting with a single piezoelectric, cantilevered leaf and stalk system in parallel, laminar flow. There was no vortex-shedding bluff body in this study, as flutter in this type of arrangement is meant to be self-induced. Naudasher & Rockwell (1980) classified this type of flutter excitation as Movement Induced Excitation, or MIE. Here, flutter is caused by a small perturbation of the membrane in the flow and further growth of this instability. Most theoretical and numerical studies in the past have focused on this type of flutter (see: references 1-9), because the instability growth and mechanisms by which the flutter initiates are still not quite fully understood. An important parameter to consider with this type of flutter is the critical flutter speed (U_c), which is the flow speed at which flutter of the membrane starts. In their studies, Li & Lipson (2009) examined different piezoelectric-stalk lengths, as well as different leaf geometries. They found that a triangular-shaped leaf coupled with a piezoelectric short stalk in the vertical configuration (Fig. 2b), gave the highest power output when properly load-matched, at a wind speed of 8.0m/s.

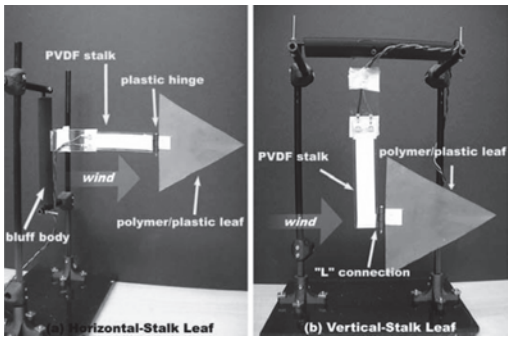

Figure 2. The two different piezoelectric leaf and stalk arrangements used by Li & Lipson (2009, Fig. 5).

They concluded that the hinge might play a significant role in amplifying the vibrations of the piezoelectric stalk, though no analysis was carried out.

Bryant *et al.* (2011) looked at the aerodynamic interaction between two piezoelectric/leaf beams, and the subsequent influence on the power output. The stalks were constructed of thin steel with a piezoelectric patch bonded along their length. In their experiments, one piezoelectric/leaf beam was placed at a fixed point in a laminar-flow wind tunnel, and another identical replica was placed downstream at varying stream-wise and cross-stream locations. It was found that when the second beam was placed aligned and downstream of the first beam, it could produce up to 30% more power in tandem than when alone. At all times, the frequencies of the beams were monitored, and the resistive load adjusted accordingly in order that the maximum power from each beam was always attained. The reason this was done is because there exists, for a given flutter frequency and piezoelectric capacitance value, an optimum load resistance value that will permit maximum power to be extracted (see Li and Lipson 2009; Roundy *et al.* 2003; Sodano *et al.* 2004). Nevertheless, real-world deployment of these piezoelectric/leaf devices would demand that minimal power is consumed by the device itself (i.e. would operate with a high efficiency), and it is unknown if the benefits of an active resistance tuning circuit would outweigh the performance degradation in terms of power output; Roundy & Zhang (2005) investigated active-tuning of a piezoelectric device via active mechanical resonance tuning and it was found that active tuning never resulted in a net power output increase, but active electrical tuning was not examined.

Such devices are likely to be "driven" by the atmospheric wind which is inherently turbulent and may approach from a wide range of angles, thus simulations or laboratory experiments in (usually) smooth flow may not give correct predictions of power outputs. Wind conditions vary widely with geographical location, notwithstanding the prevalence of local wind effects within urban settings. For instance, in Melbourne, Australia, the average wind speed in the Greater Metropolitan area as modeled by the Sustainable Energy Authority Victoria (2003) is 3.0m/s at a geometric height of 65 meters. However there are wind over- and under-speed effects, that occur due to topography and/or building proximity effects, hence the average wind speed may be far removed from the local speed.

Here, we aim to investigate the effect of the leading-edge geometry on U_c, as this has not been quantified in previous analyses. We also, for a given leaf area and aspect ratio, examine the power output effects of two of these piezoelectric beams in proximity with each other. Unlike Bryant *et al.* (2011), this will be done with a predetermined, load-matched circuit resistance that will remain unchanged during the course of the experiments.

2 METHOD

2.1 *Wind Tunnel Calibration and Setup*

The wind tunnel utilized in the experiments is a subsonic, closed-circuit design with an octagonal test section, measuring 1320mm high by 1070mm wide. A honeycomb mesh and an anti-turbulence screen, plus a 4:1 contraction ratio inure the test-section incoming airflow. A 134-horsepower DC motor powers a six-bladed fan, giving a maximum tunnel flow speed of approximately 45m/s. According to previous calibration work, the free-stream longitudinal turbulence intensity was much less than 3% (Creazzo 1999). A pitot-static tube installed that linked to an MKS Baratron® was used for velocity measurements, according to a standardized air density value of 1.23kg/m^3. A simple error analysis was carried out, in order to determine the impact of standardizing the density across a large range of tests, and a maximum error of 0.5% in velocity

measurements was obtained. Tunnel blockage due to the experimental setup was also found to be negligible.

Due to the electrical nature of the experiments, the wind-tunnel electromagnetic noise (EMI) was evaluated so that a signal-to-noise ratio could be estimated and any destructive interference identified and attenuated. First, the coaxial, shielded cable for the experiments was connected to a 20MHz oscilloscope, and the other end left free near the wind tunnel (but not contacting the wind tunnel, so as to avoid an 'antenna' effect). The wind tunnel was ramped up to a wind speed of 14.6m/s and voltage curve observed, with no noticeable peaks occurring throughout the frequency sweep range. Next, a piezoelectric element was mounted in the wind tunnel, and the shielded cable connected to the electrodes. The voltage curve was then observed with no wind speed, and a small peak of the order 2.5-10mV was appearing at a frequency of 40Hz, presumably stemming from the fluorescent lights in the room. Finally, the voltage curve was evaluated for a piezoelectric element in flutter, initiated by the airflow in the wind tunnel traveling at around 5.1m/s. The voltage peaked at 3-3.2V, at a frequency of around 7.1Hz, the flutter frequency of the piezoelectric element. Therefore, the signal-to-noise ratio was deemed large enough that no further action was required.

2.2 *Base Clamping Geometry Experimental Setup*

In order to assess the influence that the clamping geometry could potentially have on the critical flutter speed, a quick parametric study that included varying the length and width of the rectangular clamp was carried out. Figure 3 shows a diagrammatic of the clamp cross-section characteristic dimensions.

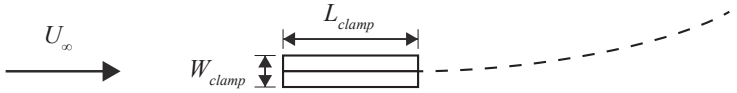

Figure 3. The base clamping setup, showing the clamping length, L_{clamp}, and the clamping width, W_{clamp}. The dashed line illustrates the test specimen, and the free-stream uniform flow is denoted by U_∞.

The test specimen was chosen based on tests performed elsewhere, and consisted of a polypropylene membrane that was 248mm long by 60mm wide by 0.35mm thick, placed well outside of the tunnel boundary layer. The membrane was clamped at its leading edge so that the effective length was 236mm. The membrane material density is 995kg/m^3 and the elastic modulus is 1261MPa. A stand was installed in the wind-tunnel test section to fix the top of the clamping base, and the bottom was fastened to the wind-tunnel floor. Guying wire was used so that there would be no transverse vibrations of the clamp in the flow, as shown in figure 4.

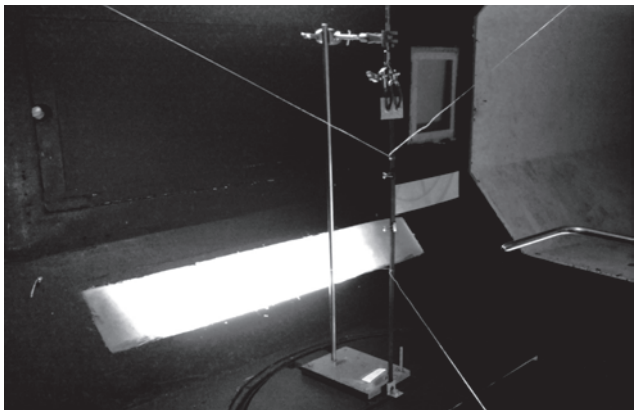

Figure 4. A photograph of the clamping geometry sensitivity tests wind-tunnel setup.

The clamping base was fabricated out of two lengths of 1.25mm-thick steel; one 600mm-long strip that extended from the stand to the wind-tunnel floor, and a 100mm strip that would be fastened to the other strip with the specimen clamped in between (Fig. 4). The baseline width of the clamping base was 3.5mm, and the baseline length was 12mm.

The base clamping length was varied first, while keeping the clamping width at the baseline dimension. The length was varied from the baseline value to 70mm. Then, the clamping width was altered while keeping the baseline length dimension; the width was varied from 3.5mm to 12.5mm. For each dimension, the wind speed was ramped up slow enough so as to ensure steady-state flow, and the membrane start-up flutter wind speed was recorded. A Reynolds number range of 129,000-214,000 was observed in the testing, based on the membrane effective length.

2.3 *Proximity Testing Experimental Setup*

Due to their flexibility, durability and relatively low cost, PVDF piezoelectric patches were utilized (Measurement Specialties, Inc., LDT1-028K/L type) in these experiments. The length, width and thickness of the piezoelectric patch are 72mm, 16mm and 205 !m respectively. These patches were the same ones used by Li & Lipson (2009) in their work. Bryant *et al.* (2011) utilized Lead-Titanium-Zirconate (PZT) patches bonded to their steel beams, which are capable of outputting higher power but are generally less durable than PVDF.

The leaves used for the experiments were fabricated from 0.35mm-thick polypropylene (whose properties are mentioned in section 2.2). The shape of the leaf is an isosceles triangle with dimensions of 80mm by 80mm (base by height), as this is the shape and area that caused the PVDF's to output the highest power in previous work (Li and Lipson 2009). The leaf and piezoelectric stalk were coupled with a plastic revolute hinge, which would allow free rotation of leaf about the vertical axis. The mass of the hinge was 0.009kg. The leading edge of the piezoelectric stalk was securely clamped and the leaf end was free. The clamping length utilized for these experiments was 12mm. This length was chosen in order to securely hold the leads and wires attached to the PVDF stalk. The clamping strips were bolted to the wind-tunnel floor and ceiling, and guyed to the sidewalls to prevent any transverse oscillations. The clamping base was also taped, so as to prevent the piezoelectric electrodes from contacting the metal. The overall length (L) of the system with the piezoelectric stalk, leaf, hinge and the clamping length were measured to be 180mm.

In order to determine the optimum placement of these leaf-stalk systems in a given volume, two such systems were placed co-linearly in the wind tunnel and the stream-wise distance be-

tween them (*d*) varied, see figure 5. The separation distance was normalized by a single leaf-stalk length such that it is expressed as (*d/L*). At first, the two devices were positioned with a normalized separation distance of 1.0. Subsequently, the separation distance was increased to 2.0 and 3.0. This was done to examine the aerodynamic effects of the upstream leaf-stalk system on the downstream one. The wind speed range considered here was 3-8m/s. Figure 6 shows a photograph of the wind-tunnel setup.

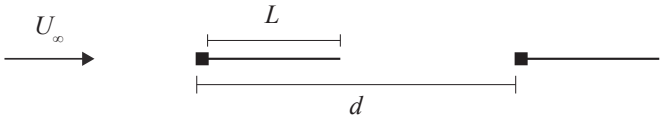

Figure 5. A cross-section schematic of the co-linear proximity experiments, showing the relevant parameters.

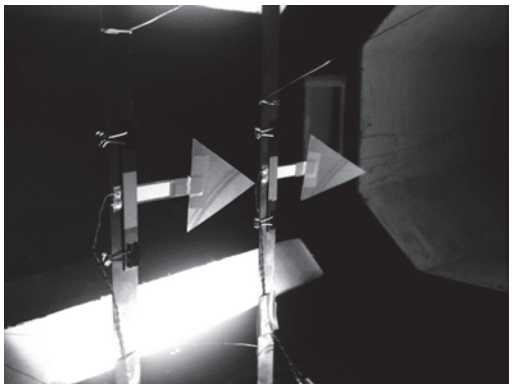

Figure 6. A photograph of the proximity experimental setup in the wind tunnel.

The piezoelectric stalks were connected to a simple parallel electrical circuit. The load resistance used for this experiment was 5.6MΩ. This value was experimentally obtained by recording the power output from a single leaf-stalk system across various load resistances in parallel (R_L); from 1.0MΩ to 60MΩ, at a constant wind speed of 5.0m/s. The voltages from the piezoelectric stalks were measured using a differential probe (Elditest, GE8115) which has a high internal resistance (60MΩ) compared to the load resistance. The data from the differential probe was sent to a DAQ board (National Instruments, BNC2110) and the RMS voltage (V_{RMS}) of the AC waveform was calculated in one-second intervals using LabView®.

The electrical power generated in one second of leaf-stalk flutter is given by equation 1 (Bryant *et al.* 2011):

$$P_i = \frac{V_{RMS_i}^2}{R_L} \tag{1}$$

Then, the total average power generated over the 30-second data acquisition window was calculated as:

$$P_{ave} = \frac{1}{30}\sum_{i=1}^{30} P_i \tag{2}$$

3 RESULTS AND DISCUSSIONS

3.1 *Clamping Base Geometry Sensitivity*

Figures 8 and 9 show the experimental results for the sensitivity of the critical flutter speed to the clamping length and width dimensions, respectively. The critical flutter speed is normalized by the critical flutter speed observed with the baseline clamp dimensions. The ordinate axis is plotted as such, for clarity.

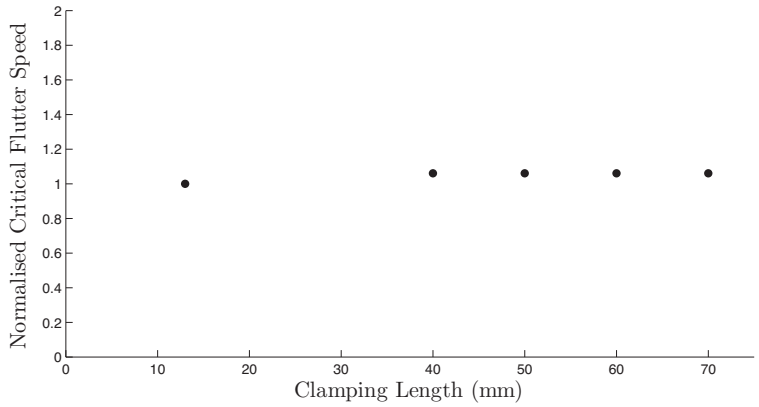

Figure 8. Clamping length sensitivity results.

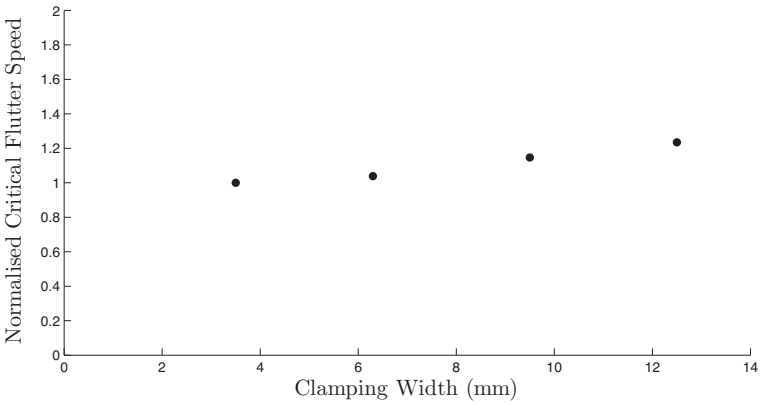

Figure 9. Clamping width sensitivity results.

Altering the length of the clamping base does not seem to affect the critical flutter speed of the membrane. This could mean that the stream-wise boundary layer manifesting on the clamp topology is not causal to membrane flutter, at least for the Reynolds number range experienced. However, if the length of the clamping base were to greatly increase, assuming a constant width, the membrane root would then by definition encounter a thicker boundary layer, since the boundary layer thickness varies as the square root of distance from the leading edge (e.g. see Anderson 2007, chpt. 18). Additionally, depending on the state of the boundary layer at the root location of the membrane, whether laminar or turbulent, the critical flutter speed may change.

The clamping width does seem to affect the membrane critical flutter speed. Considering previous theoretical treatments of flutter (e.g. Kornecki *et al.* 1976; Argentina and Mahadevan 2005), one major assumption made is that the clamped leading edge of the membrane is infinitely stiff, yet infinitesimally thin. Of course, this is very difficult to achieve in practice, and it can

be seen that as the width of the clamp deviates upwards from the infinitesimal value, there comes an increase in critical flutter speed. This could be attributed to vortex shedding off of the clamp at a frequency other than the membrane natural frequencies, thereby causing destructive interference and henceforth a damping effect. However, once a clamping width that generates shed vortices at a frequency equal to the membrane natural frequency is deployed, it is anticipated that the critical flutter speed would decrease dramatically.

3.2 *Proximity Experimental Results*

Figure 10 presents the proximity testing results for the downstream leaf-stalk. The output power is normalized by the power extracted with no upstream leaf-stalk (P_{baseline}) present, and this quantity is plotted against the wind speed.

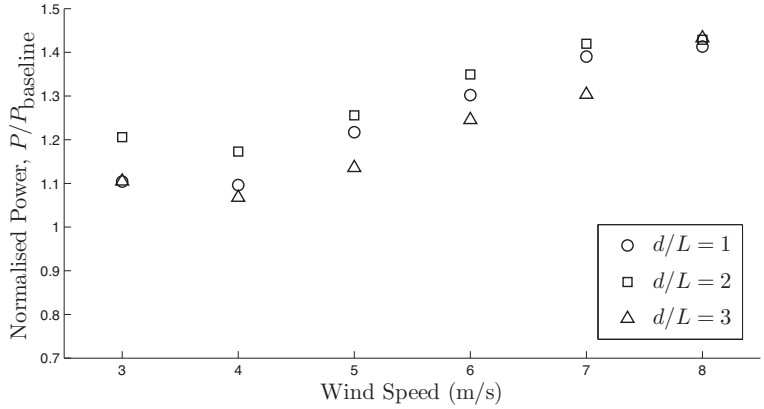

Figure 10. The downstream leaf-stalk power output as a function of wind speed for multiple separation distances.

A maximum normalized power of more than 1.4 is being obtained at 8.0m/s, even though the load resistance was optimized for a wind speed of 5.0m/s; this suggests that there is potential for even higher power outputs from the downstream leaf-stalk, should an actively-tuned load resistance be used. Bryant *et al.* (2011) obtained a trailing leaf-stalk normalized power of 1.3, for a wind speed of around 6-7m/s, so the results obtained here agree quite well. This correlation is despite a smaller cantilever length, different piezoelectric material and configuration, a different leaf shape, and a leaf area less than half of what Bryant *et al.* (2011) use. This strongly suggests that the increase in output power is purely an aerodynamic phenomenon, and not a structural dynamic one. Also, the flutter type occurring in this wind speed range is steady state, limit-cycle, sinusoidal; elsewhere it was determined by power spectral analysis that this flutter type contains the most bending energy at the discrete membrane natural frequencies (Alben and Shelley 2008). Once the flutter transitions to chaotic, stochastic motion with random snap-through events (Connell and Yue 2007), the maximum attainable power decreases and response becomes more broadband. It can be seen in figure 10 that for d/L = 1 and 2, the normalized power approaches a maximum. However, for d/L = 3 the normalized power growth rate is instead increasing. It could be that for separation distances of 1 and 2, transition to the chaotic flutter regime is starting and thus the power output has reached a peak. It is also interesting to note the local minimum transpiring at a wind speed of 4.0m/s – this is most likely due to anti-resonance occurring between the upstream leaf-stalk vortex shedding frequency and the flutter frequency of the downstream leaf-stalk.

Figure 11 shows the normalized power plotted against the normalized separation distance, for wind speeds of 3.0 and 8.0m/s. Clearly, there is a maximum occurring at a separation distance of 2 for a wind speed of 3.0m/s, but there is no global maximum occurring with a wind speed of 8.0m/s.

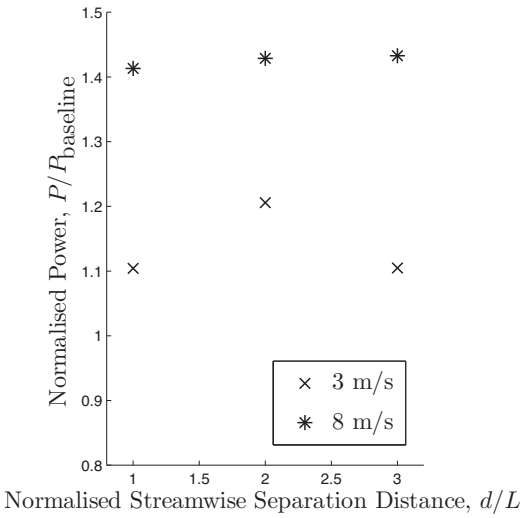

Figure 11. The normalized power plotted against the normalized separation distance for the minimum and maximum wind speeds tested.

Evidently, optimum increased power output is occurring for the downstream leaf-stalk at a normalized separation distance of 2, as this is also what Bryant *et al.* (2011) found. However, the coalescence of the normalized power output across the separation distances for a wind speed of 8.0m/s is intriguing. Perhaps the higher kinetic energy in the flow sustains the advection of the shed vortices from the upstream leaf-stalk flutter and delays transition to chaotic flutter, which was found to occur at wind speeds slightly greater than 8.0m/s for a single leaf-stalk. Further work would entail flow visualization using a dual smoke wire approach.

4 CONCLUSIONS

The sensitivity of the critical flutter speed to the clamping geometry was first examined. The results suggested that the clamping length has little or no effect on the critical flutter speed, and that an increasing clamping width tends to delay the onset of flutter. These results only hold for parallel, laminar flow; it would be erroneous to extrapolate to turbulent flow, and also the effect of the wind approaching from any direction hasn't been quantified. That said, any future work concerning piezoelectric fluttering systems could benefit from the findings, especially if there is a need to control the critical flutter speed, or perhaps minimize it.

Proximity testing, investigating exclusively the effect of a tandem configuration in the streamwise direction, was carried out. Results agree well with findings reported elsewhere for similar wind speeds tested. It is found that for wind speeds of 3-7m/s, a normalized separation distance of 2 causes the greatest increase in power output from the downstream leaf-stalk system, over a 40% increase. A wind speed of 8.0m/s caused a coalescence of the normalized power across the range of separation distances, and it is speculated that the increased kinetic energy in the flow

more readily sustains the advection of the vortices shed from the upstream leaf-stalk system, such that the transition of the downstream leaf-stalk system to chaotic flutter is impeded.

5 REFERENCES

1 M. Paidoüssis, Fluid-Structure Interactions - Slender Structures and Axial Flow, Elsevier Academic Press, 1998, Vol. 1.
2 M. Paidoüssis, S.J. Price and E. de Langre, Fluid-Structure Interactions - Cross-Flow-Induced Instabilities, Cambridge University Press, 2011.
3 Lord Rayleigh, Proc. Lond. Math. Soc., 1879, Vol. X, pp. 4-13.
4 T. Theodorsen, General Theory of Aerodynamic Instability and the Mechanism of Flutter, NACA Tech. Rep. No. 496, 1935.
5 A. Kornecki, E.H. Dowell and J. O'Brien, On the aerodynamic instability of two-dimensional panels in uniform incompressible flow, Journal of Sound and Vibration, 2 (1976), 163-178.
6 W. Frederiks, H.C.J. Hilberink and J.A. Sparenberg, On the Kutta condition for the flow along a semi-infinite elastic plate, Journal of Engineering Mathematics, 20 (1986), 27-50.
7 L. Huang, Flutter of Cantilevered Plates in Axial Flow, Journal of Fluids and Structures, 9 (1995), 127-147.
8 J. Zhang, S. Childress, A. Libchaber and M. Shelley, Flexible filaments in a flowing soap film as a model for one-dimensional flags in a two-dimensional wind, Nature, 408 (2000), 835-839.
9 M. Argentina and L. Mahadevan, Fluid-flow-induced flutter of a flag, Proceedings of the National Academy of Sciences of the United States of America, 6 (2005), 1829-1834.
10 J.J. Allen and A.J. Smits, Energy Harvesting Eel, Journal of Fluids and Structures, 3-4 (2001), 629-640.
11 E. Naudascher and D. Rockwell, Oscillator-model approach to the identification and assessment of flow-induced vibrations in the system, Journal of Hydraulic Research, 18 (1980), 59-82.
12 G.W. Taylor, J.R. Burns, S.M. Kammann, W.B. Powers and T.R. Welsh, The energy harvesting Eel: A small subsurface ocean/river power generator, IEEE Journal of Oceanic Engineering, 4 (2001), 539-547.
13 S. Pobering and N. Schwesinger, A novel hydropower harvesting device, International Conference on MEMS, NANO and Smart Systems, ICMENS 2004, August 25 - August 27, pp. 480-485.
14 R.M. Dickson, New Concepts in Renewable Energy, Lulu Enterprises Inc., 2008.
15 S. Li and H. Lipson, Vertical-stalk flapping-leaf generator for wind energy harvesting, ASME Conference on Smart Materials, Adaptive Structures and Intelligent Systems, SMASIS2009, September 21 - September 23, pp. 611-619.
16 M. Bryant, R. Mahtani and E. Garcia, Synergistic Wake Interactions in Aeroelastic Flutter Vibration Energy Harvester Arrays, ASME Conference on Smart Materials, Adaptive Structures and Intelligent Systems, SMASIS2011, September 18 - September 21, pp. 1-7.
17 S. Roundy, P.K. Wright and J. Rabaey, A study of low level vibrations as a power source for wireless sensor nodes, Computer Communications, 26 (2003), 1131-1144.
18 H.A. Sodano, G. Park and D.J. Inman, Estimation of electric charge output for piezoelectric energy harvesting, Strain, 40 (2004), 49-58.
19 S. Roundy and Y. Zhang, Toward self-tuning adaptive vibration based micro-generators, Proceedings of SPIE, Smart Structures, Devices, and Systems II, Vol. 5649 (2005), pp. 373-348.
20 Sustainable Energy Authority Victoria, Victorian Wind Atlas (Cartographic Material), 2003.
21 J. Creazzo, The interaction between a non-imbedded longitudinal vortex and turbulent boundary layer under the influence of a stream-wise pressure gradient, PhD thesis, RMIT University, 1999.
22 J.D. Anderson Jr., Fundamentals of Aerodynamics, 4th edn., McGraw-Hill, New York, 2007
23 S. Alben and M.J. Shelley, Flapping states of a flag in an inviscid fluid: Bistability and the transition to chaos, Physical Review Letters, 100 (2008), 074301-1 – 4.
24 B.S.H. Connell and D.K.P. Yue, Flapping dynamics of a flag in a uniform stream, Journal of Fluid Mechanics, 581 (2007), 33-67.

The Seventh International Colloquium on Bluff Body Aerodynamics and Applications (BBAA7)
Shanghai, China; September 2-6, 2012

The flight of roofing tiles during strong winds

Richards P. J. [a], Norris S. E. [a]

[a]*Department of Mechanical Engineering, The University of Auckland, New Zealand*

ABSTRACT: Roof tiles are a common type of windborne debris and have been associated with significant damage during several severe storms. They have sufficient mass to do damage and sufficient area to accelerate quickly. Trajectory analysis is conducted for tiles breaking free from several generic buildings with a variety of roof slopes. These show that the upward flow around the windward eaves can lift a tile over the building, from which point it can be carried well downwind. The range and speed achieved under these conditions is much greater than would occur if the tile was released from the same height well away from the building. With steeper roofs a stronger gust is required to lift the tile over the roof but if this occurs, then the range is extended beyond than which would occur with the same gust but a shallower roof. It is shown that the flight of roofing tiles depends very strongly on the point of origin and the wind direction.

KEYWORDS: Windborne debris, roofing tiles.

1 INTRODUCTION

During extreme wind events considerable damage may be caused either directly or indirectly by windborne debris. In assessing the failures of structures during windstorms, Minor *et al.* [1] observed that windows were traditionally designed for wind pressures, but that breakage from impacts by windborne debris was the most common failure mechanism. While breaking a window may not be too important in itself, such breakages can result in internal building pressures that significantly increase the net load on building components, such as the roof, which in some cases my result in structural failure. In addition, since strong winds are often associated with heavy rainfall, a broken window can allow the ingress of water, leading to considerable damage to contents or structure. In 1974 Tropical Cyclone Tracey devastated Darwin in northern Australia. Walker [2] noted that “pressurisation of buildings following failure of windward windows, generally due to windborne debris,” was one of the major factors contributing to the widespread damage. Two decades later such debris related failures remained a problem, with Minor [3], referring to the damage inflicted by Hurricane Andrew in 1992, commenting “With few exceptions, glazing systems performed poorly, largely due to the impact of windborne debris, and damage to building contents was extensive”.

2 COMMON TYPES OF DEBRIS

The relevant source and type of debris varies greatly. Minor *et al.* [4] concluded that with tornadoes the most prevalent type of windborne debris in residential areas was timber from wood frame houses, whereas Minor [1] discusses several situations where roof gravel caused extensive glass breakages on high rise buildings, but also notes that investigations in south Florida following Hurricane Andrew tended to point to roofing tiles as the most prevalent type of windborne debris. He points out that initially the Dade County Building Code Committee chose a roofing

tile as the design missile for testing purposes but then recognised that it would be difficult to define a representative tile and almost impossible to propel a tile repeatedly with the same orientation and at the same speed as part of a standard test, and so ultimately the committee chose a 9 lb '2 × 4' timber instead. This test projectile is essentially the same as the 4 kg timber member with nominal cross-section of 100 × 50 mm, which first appeared in the Darwin Area Building Manual in 1976 and is still included in the Australia/New Zealand wind loading standard AS/NZS1170.2 [5]. For tropical cyclone affected areas this standard requires that internal pressure resulting from a dominant opening must be applied unless windows, doors and cladding up to a height of 25 m can be shown to be capable of resisting impact loading from windborne debris equivalent to:

1. Timber member of 4 kg mass with a nominal cross-section of 100 mm × 50 mm impacting end on at 0.4 V_R for horizontal trajectories and 0.1 V_R for vertical trajectories and
2. Spherical steel ball 8 mm diameter (approximately 2 grams mass) impacting at 0.4 V_R for horizontal trajectories and 0.3 V_R for vertical trajectories

where V_R is the regional wind speed, based on 3-second gust wind data. These test projectiles represent both roof gravel and larger debris such as tiles or chunks of framing timber.

Skerlj et al. [6], while analysing the damage caused by Hurricane Charley in 2004, noted "Single family residences constructed with clay tile roof covers performed poorly when mortar was used to attach the tiles to the roof structure as opposed to mechanical fasteners (i.e. nails or screws). Failed roof tiles can, and often do, become airborne and create additional damage by impact to either other sections of the roof from which they originate or to adjacent buildings." They also note that shutters significantly reduced damage in areas where tile roofs were common and that this went beyond just shielding the windows.

Following Tropical Cyclone Yasi, which affected northern Queensland in February 2011, Boughton et al. [7] made the following observations regarding the range of materials that had become windborne debris:

- Detached roof tiles had impacted other parts of the roof from which they had been removed and nearby buildings. Tiles were observed to have broken windows and penetrated steel roofing and wall cladding.
- Some pieces of timber close to the size of the standard test piece were observed. Some of these had penetrated the outer cladding of buildings but a few had made it into the inside other than through windows. One piece was observed to have come through a roof.
- Very large pieces of buildings had become windborne debris. These items included large assemblies of roofing and battens, significant portions of the roof structure, whole sheds and a complete shipping container.

3 ROOF TILES AS DEBRIS

It is apparent from the above comments that roof tiles are a significant form of windborne debris. This significance can be attributed to a number of factors including:

- Where roof tiles are used there are many hundreds, if not thousands, of individual pieces that have the potential to become a missile with a mass of several kilograms and an area large enough to attract sufficient aerodynamic drag.
- One tile pulling free is likely to lift its neighbour(s) and hence encourage others to break free in turn.
- The starting point for a roof tile trajectory is an elevated location which means that they can fly a reasonable distance.

- When roofing tiles are pulled free from their fixings they are likely to be in a region of flow where the velocity is locally accelerated. Hence the tile may achieve speeds which are higher than if they were simply released into the wind at that height.
- Most tiles are removed from the windward sloping section of the roof. The flow in this region will have an upward component and so tiles can be accelerated upwards in the early stages of a flight and hence can achieve greater distances.

4 SIMPLIFIED TRAJECTORY ANALYSIS

The ability of any piece of debris to accelerate and become a dangerous projectile can be partially characterised by the ballistic coefficient $B=C_D\rho A/(2m)$, where C_D is the average drag coefficient, ρ is the air density, A is the maximum face area (m^2) and m the mass (kg). Some typical values are given in Table 1, where the drag coefficient values are based on [8]. It includes the two standard test projectiles from the Australia/New Zealand Wind Loading Standard AS/NZS 1170.2 [5], a couple of typical roofing tiles, a lighter clay tile and a heavier concrete tile, and a section of roofing which has been arbitrarily assumed to be 3 m × 2.4 m and made up of 35 kg of roofing iron and 85 kg of attached timber battens and roofing framework.

Table 2 presents some calculated results for these five pieces of debris after a 20 m flight during a 50 m/s wind gust. This distance was chosen as a typical spacing of houses in a suburban area. For these simple calculations the wind is assumed to be uniform and the object is approximated as compact debris, that is no consideration is made of the orientation of the object.

The following points may be noted:

- All flights last less than 3 s (common design gust duration).
- All horizontal speeds are in excess of 40% of the gust speed (as used in [5]) and the four larger projectiles have reached 51-62% of the gust speed.
- The steel balls, which represent gravel or similar debris, have fallen 12 m and so would need to originate from a multi-storey building but the other projectiles have only fallen between 3.6 m and 6.2 m and so could originate from a single storey house.
- For such short flights the vertical speed is much less than the horizontal speed.

The tiles and timber projectiles have impact energies between 1 and 2 kJ, which is sufficient to do some damage, but perhaps more concerning is the corrugated iron and timber roof which has 60 kJ of energy on impact.

Table 1. Typical Windborne Debris Characteristics

	m (kg)	A (m^2)	C_D	B (m^{-1})
Steel Ball	0.002	5.03×10^{-5}	0.5	0.008
Clay Tile	2.3	0.1	0.9	0.024
Concrete Tile	4.5	0.14	0.9	0.017
Timber	4	0.2	0.8	0.025
Roof	120	7.2	0.9	0.033

Table 2. Data at x = 20 m during a 50 m/s gust

	Time (s)	Horizontal speed (m/s)	Height dropped (m)	Vertical speed (m/s)	Kinetic energy (J)
Steel Ball	1.7	20.2	-12.0	-13.3	0.6
Clay Tile	1.1	28.5	-4.7	-7.8	1006
Concrete Tile	1.3	25.8	-6.2	-9.2	1692
Timber	1.1	28.8	-4.5	-7.6	1776
Roof	1.0	31.0	-3.6	-6.7	60301

5 DETAILED TRAJECTORY ANALYSIS

Although the simple trajectory analysis in the previous section can provide some indication of the relative hazard posed by various types of debris the situation is far from reality. As noted earlier, when tiles break free from a roof they are immediately immersed in a complex 3-dimensional flow field. In order to assess the likely impact of this flow field the trajectory modelling program developed by Richards et al. [9] has been modified to incorporate a non-uniform flow field which has been computed using computational fluid dynamics (CFD). It is assumed that the flow field isn't modified by the debris and is simply a function of the building geometry. It is also assumed that the flight of a roofing tile occurs during a gust which has sufficient duration for it to totally envelope the building and hence the flow field may be approximated by a steady flow of the same strength. In the current study three gable ended buildings have been considered. Each is gable ended, has a length of 18 m, width of 12 m and an eaves height of 3 m, but they have roof slopes of 14°, 18.4° and 26.6°, which are slopes of 1 in 4, 1 in 3 and 1 in 2 respectively. With these roof slopes the buildings have ridge heights of 4.5, 5 and 6 m. Figure 1 illustrates the flow field around the 6 m ridge height building with the wind perpendicular to the ridge, it clearly shows the upward flow on the windward slope and the wake behind the building.

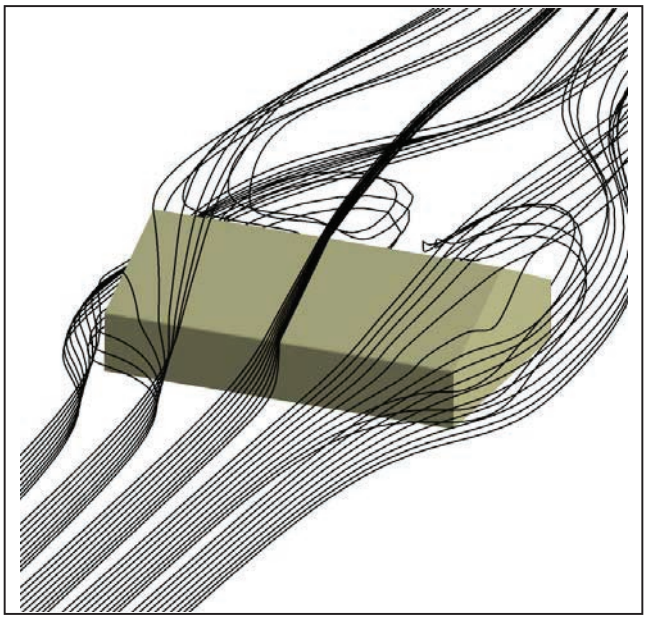

Figure 1. Streamlines around the 6 m ridge height building. Wind direction is perpendicular to the ridge.

5.1 *CFD modeling of the flow field*

The turbulent atmospheric flow around the buildings was modeled using the ANSYS CFX 13.0 CFD package as a steady flow approximated by the Reynolds Averaged Navier-Stokes equations. Different meshes were used for each building and flow direction, a 50 m high domain was used that extended 50 m upstream, 100 m downstream, and 50 m laterally from the center of the building, resulting in a 150 m × 100 m × 50 m domain for the cases when the building was aligned with the flow, and 150 m × 150 m × 50 m domain for the quartering flow. An unstructured mesh was used containing approximately 7.5×10^5 nodes, with inflation layers being used on the building and ground surfaces. The centre of the building is at co-ordinate (50,50,0).

At the upstream boundary, profiles of the velocity and turbulence scalars were prescribed using the velocity at the eaves height of the building (3 m) as the reference and with a roughness length appropriate for suburban terrain of $z_0 = 0.2$ m. Within the computational domain the ground was set as a no-slip wall with a roughness length of 0.01 m (appropriate for open terrain), since the suburban roughness elements (houses) were being explicitly modeled. The boundary for the building was set as a smooth no-slip wall, the top (and side surfaces when present) to symmetry planes, and the outlet was modeled as a constant pressure boundary with the velocity and turbulence fields having a zero-gradient normal to the boundary.

The turbulence was modeled using the SST two equation turbulence model [10], and the velocity field was discretized using the CFX solver's 'higher order differencing' scheme [11], a flux limited scheme that approaches second order with mesh refinement. For reasons of stability the turbulence scalars were discretized using first order upwinding. A convergence criterion of 10^{-6} was applied to the RMS residuals, resulting in the RMS residuals for a run being reduced by approximately 5 orders of magnitude.

The solution was interpolated onto a regular mesh, to allow easy interpolation of flow field data by the trajectory modeling code, with the velocities being non-dimensionalized with respect to the reference velocity at 3 m elevation (the height of the eaves). Within the trajectory code the wind velocity vector at each location was determined by tri-linear interpolation between the data points supplied by the CFD modeling, which is then scaled by the reference gust wind speed.

5.2 *Computed trajectories with the wind perpendicular to the ridge*

Figure 2 illustrates the central plane flow patterns of the 4.5 and 6 m ridge height buildings with the wind perpendicular to the ridge. With the steeper roof the flow on the windward slope has a much stronger upward component and this extends out over the much larger wake. However numerical experiments showed that with this steeper slope, if a clay tile (as specified in Table 1) broke free from the windward eaves then it would fall back onto the roof unless the gust wind speed was in excess of 60 m/s, while for a concrete tile the wind needed to exceed 70 m/s. In contrast a gust of only 35 m/s would lift a clay tile over the ridge of the 4.5 m high building and only 40 m/s for the concrete tile.

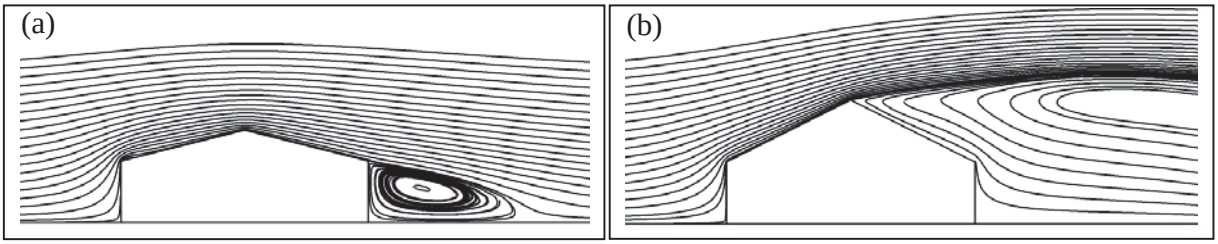

Figure 2. Streamlines on the central plane of (a) the 4.5 m and (b) 6 m ridge height buildings.

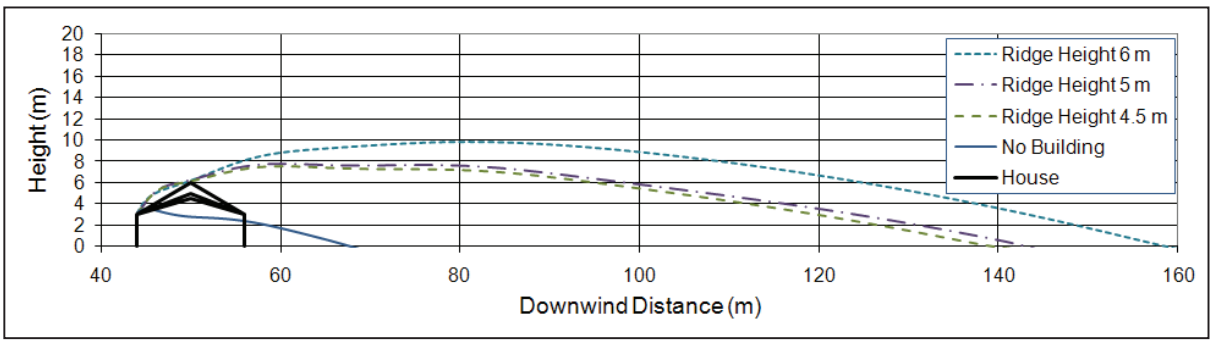

Figure 3. Computed trajectories of clay tiles originating from the windward eaves during a 65 m/s gust. Wind direction is perpendicular to the ridge.

Figure 3 shows the trajectories of clay tiles released from the windward eaves of the three buildings during a 65 m/s gust in comparison with that which occurs from the same height and in the same wind well away from a building. With this strong gust the flow over all of the buildings lifts the tiles well above the no building case and carries these tiles a long distance downstream. Without the influence of a building the tile falls to the ground about 24 m downwind, whereas even the lowest slope helps to carry the tile over 90 m and the steepest slope extends this to about 110 m. Since one cannot easily define the orientation of the tile at the moment it breaks free from its fixings a variety of release orientations have been tried and those shown here seemed to give the longest flights. Other orientations are likely to result in shorter flights or even the tile landing back onto the surface from which it has just broken free.

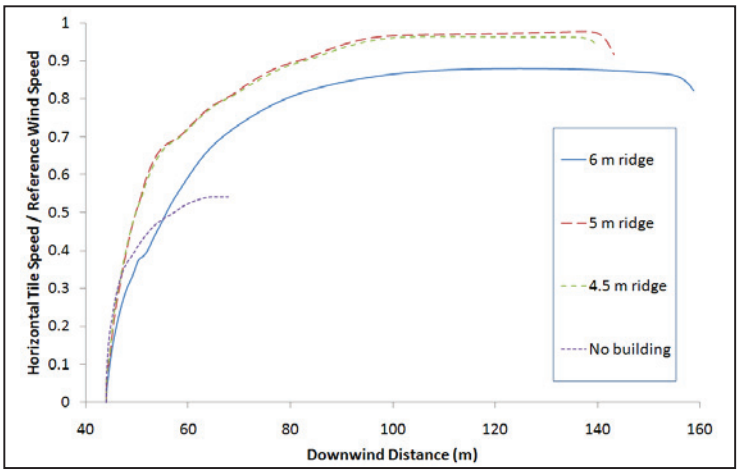

Figure 4. Ratio of clay tile horizontal speed to the reference gust speed (65 m/s at 3 m height) as a function of downwind distance.

Figure 4 shows the variation of horizontal velocity with downwind distance for these four cases. Without the influence of a building the velocity increases to just over 50% of the reference gust speed before it hits the ground. Since in this paper the reference velocity used is that at the eaves height (3 m), then this corresponds to about 35% of the gust speed at 10 m height in suburban terrain. This is slightly less than the 40% prescribed as a testing regime in AS/NZS 1170.2 [5]. However the results show that with the influence of a building not only the range but the velocity can be considerably higher. In all three building cases the maximum horizontal velocity attained

is over 80% of the reference gust speed and in two cases over 95%. This occur both because the flow field is modified, with some parts having higher speeds than the approach flow, and because the tile is lifted by the flow up and over the building to heights it wouldn't otherwise reach. With the 6.5 m ridge height case the highest velocity encountered by the tile is almost 80 m/s but it appears that the higher roof slope means that the velocities are lower in the early part of the trajectory. If the tiles reach about 95% of the 3 m gust speed then this corresponds to almost 70% of the 10 m gust speed, which is considerably higher than the testing regime in AS/NZS 1170.2. It may be noted that in the latter stages of the trajectory, as the tile drops into the wake and the slower flow near the ground, the velocity begins to decrease but this effect is fairly small.

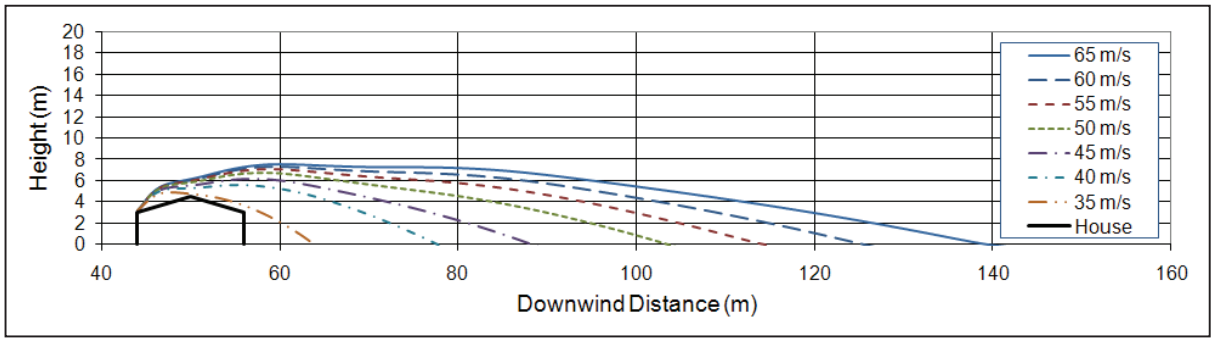

Figure 5. Computed trajectories of clay tiles originating from the windward eaves of the 4.5 m building with various gust wind speeds. Wind direction is perpendicular to the ridge.

Figure 5 shows the computed trajectories of clay tiles originating from the centre of the windward eaves of the 4.5 m high building assuming a range of gust wind speeds. As might be anticipated the stronger gusts lift the tiles more and carry then a much greater distance. With the weakest gust the tile barely clears the ridge and quickly drops into the wake of the building and falls to the ground. In Figure 6 the ratio of the tile's horizontal speed to the gust wind speed shows that not only does a weaker gust induce lower speeds but even the proportion is lower. With a 35 m/s gust the tile barely exceeds 40% of the gust speed whereas at 65 m/s the tile reaches 95% of the gust speed.

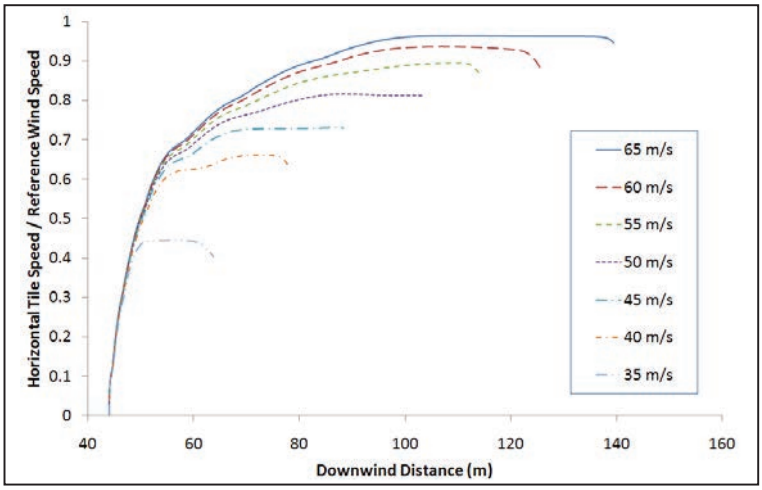

Figure 6. Ratio of clay tile horizontal speed to the reference gust speed as a function of downwind distance for the same cases as in Figure 5.

One of the consequences of this observation is the marked increase in the hazard posed by tiles as the gust speed increases. Not only are tiles more likely to be broken free from their fixings as the speed increases, but should this occur they will be projected over longer distances and at markedly higher speeds. In addition the flatter trajectory at higher gust speeds increases the chance that the tile might hit another building at a height where it might break a window. For example if one assumes that windows are located between 0.8 and 2.0 m above the ground, then with a 40 m/s gust the tile's path is only between these heights from 16 to 20 m downwind of the leeward wall, in contrast with a 65 m/s gust the tiles path falls between these heights from 60 to 68 m downwind of the leeward wall, doubling the downwind range band and hence approximately doubling the chance of an impact on a window.

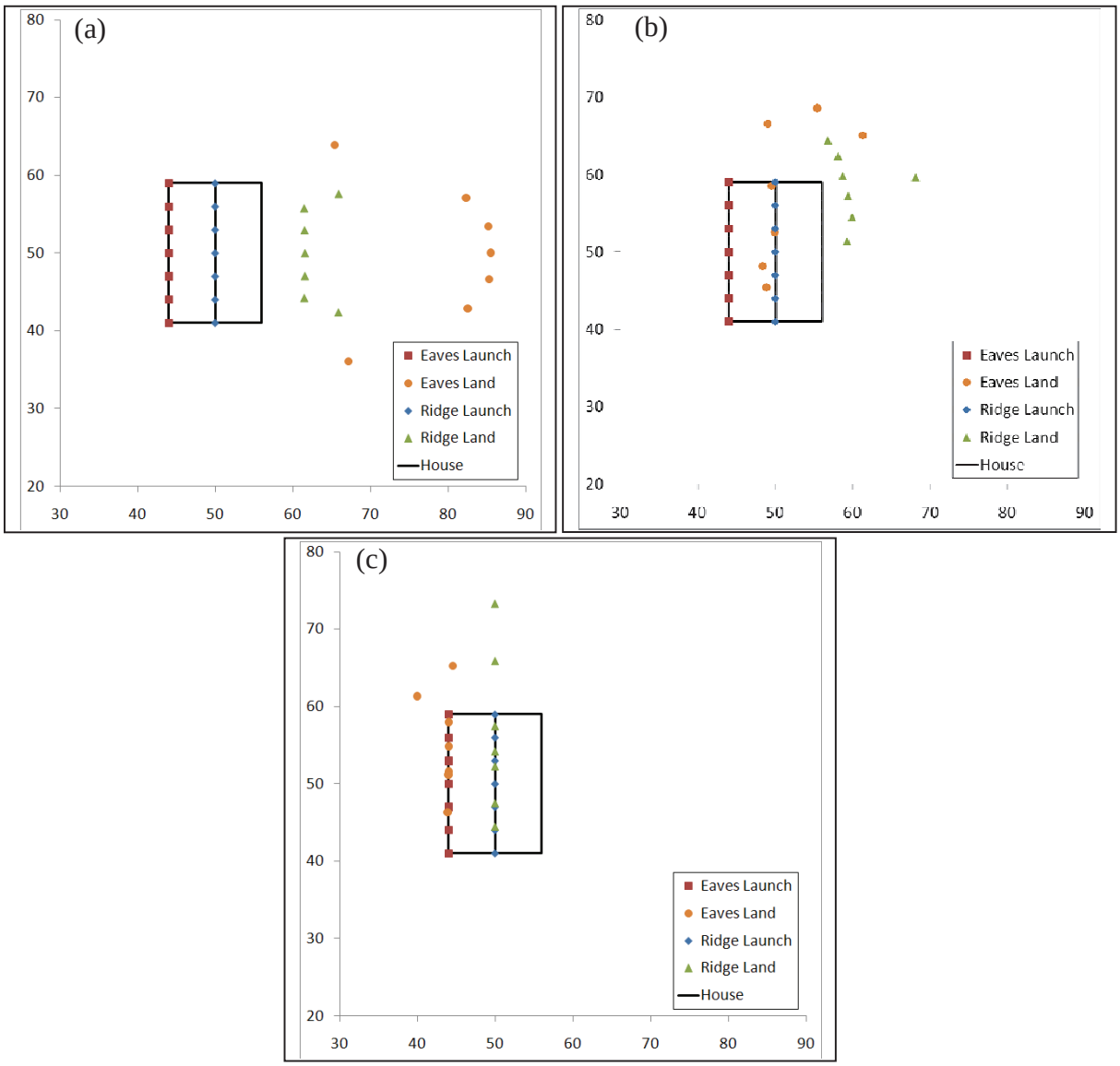

Figure 7. Computed landing locations for concrete tiles originating from various points on the 4.5 m ridge height building during a 50 m/s gust. Wind directions: (a) perpendicular, (b) 45° and (c) parallel to the ridge.

5.3 *The influence of wind direction and point of origin on trajectories.*

In the previous section only winds perpendicular to the ridge and tiles originating from the centre of the windward eaves have been considered. In order to assess the influence of wind direction and point of origin on the trajectories, flow fields have been computed with the wind at 45° and parallel to the ridge. The data presented in Figure 7 is for the heavier concrete tile, specified in Table 1, breaking free from the 4.5 m ridge height building during a 50 m/s gust. Fourteen release points have been considered, seven evenly spaced along the windward eaves and seven evenly spaced along the ridge. This figure shows both the points of origin and the landing points on plan views of the building and surroundings. With the wind perpendicular to the ridge, Figure 7(a), all fourteen tiles are carried clear of the building, with those originating from the eaves, but not at the corners, travelling a significant distance downwind. This occurs because the eaves are a region of relatively fast upward flow. At the corners the tiles are carried wide of the building but do not experience the same uplift and hence fall to ground sooner. Similarly those tiles originating from the ridge do not experience a strong uplift and hence fall into the wake and land close to the building. With the quartering wind case, Figure 7(b), four of the tiles from the eaves fall back onto the roof and the other three from the eaves are only carried about 10 m from the building. All of the ridge tiles are carried clear of the building but it is only the tile from the windward gable end that is carried any distance from the building and even this is quite moderate. In a similar manner with the wind parallel to the ridge, Figure 7(c), it is only the tiles from the two ends which are carried away from the building. In this case the tile that is carried furthest downwind originates from the ridge at the windward gable.

Overall these results show that should a tile break free from its fixing, the distance it is likely to travel will be strongly influenced by the wind direction and the local flow it encounters in the early stage of its trajectory. It is particularly, where there is a strong upward flow around the point of origin, that the tile is both lifted up and accelerated.

6 CONCLUSIONS

Roof tiles are a common type of windborne debris and have been associated with significant damage during several severe storms. They have sufficient mass to do damage and sufficient area to accelerate quickly. Trajectory analysis has been conducted for tiles breaking free from several generic buildings with a variety of roof slopes. These show that the upward flow around the windward eaves can lift a tile over the building, from which point it can be carried well downwind. The range and speed achieved under these conditions is much greater than would occur if the tile was released from the same height well away from the building. With steeper roofs a stronger gust is required to lift the tile over the roof but if this occurs then the range is extended beyond than which would occur with the same gust but a shallower roof. It has been shown that the flight of roofing tiles depends very strongly on the point of origin and the wind direction.

7 REFERENCES

1. Minor, J.E., Mehta, K.C. and McDonald, J.R., Failures of Structures due to Extreme Winds, ASCE J. Struct. Div. 98(ST11), 1972, 2455-2471
2. Walker, G.R., The application of wind engineering technology to the mitigation of damage to housing from tropical cyclones – An Australian achievement, Int. Conf. on Impact of Disasters, Los Angeles, USA, 1991.
3. Minor, J.E., Windborne debris and the building envelope. J. Wind Eng. Ind. Aerodyn., 53(1-2), 1994, 207-227.
4. Minor, J.E., McDonald, J.R. and Mehta, K.C., The tornado, an engineering oriented perspective, NOAA Technical Memorandum ERL NSSL-82, National weather Service, NOAA, Washington, DC, 1978.
5. Australia/New Zealand Standard AS/NZS 1170.2:2011, Structural Design Actions, Part 2: Wind actions, 2011.
6. Skerlj, P., Kleinn, J., Castella, H., Thomas, S., Hurricane Charley, August 10-15, 2004, Post-storm damage survey, PartnerRe, 2004.
7. Boughton, G.N., Henderson, D.J., Ginger, J.D. Holmes, J.D., Walker, G.R., Leitch, C.J., Somerville, L.R., Frye, U., Jayasinghe, N.C., Kim, P.Y., Tropical Cyclone Yasi – Structural damage to buildings, James Cook University, Cyclone Testing Station, Technical Report No. 57, 2011.
8. Lin, N., Simulation of windborne debris trajectories, MSc Thesis, Texas Tech University, 2005.
9. Richards, P.J., Williams, N., Laing, B., McCarty, M., Pond, M., "Numerical Calculation of the 3-Dimensional Motion of Wind-borne Debris", *J. Wind Eng. Ind. Aerodyn.*, **96**, 2188-2202, 2008.
10. Menter, F.R., "Two-equation eddy-viscosity turbulence models for engineering applications", AIAA J. **32**(8), 1598-1605, 1994.
11. Barth, T.J., and Jesperson, D.C, "The Design and Application of Upwind Schemes on Unstructured Meshes", AIAA Paper 89-0366, 1989.

The Seventh International Colloquium on Bluff Body Aerodynamics and Applications (BBAA7)
Shanghai, China; September 2-6, 2012

Modeling vegetation in Wind Engineering wind tunnel studies

Christof Gromke

Building Physics and Services, Eindhoven University of Technology, Den Dolech 2, Eindhoven, The Netherlands
Institute for Hydromechanics, Karlsruhe Institute of Technology KIT, Kaiserstrasse 12, Karlsruhe, Germany

ABSTRACT: A vegetation modeling approach for Wind Engineering wind tunnel studies is presented. The approach is based on fluid dynamical similitude. It enables the small-scale modeling of different vegetation types, e.g. trees, shrubs, hedges, forests and field crops. Its suitability and applicability is demonstrated by wind tunnel pollutant dispersion investigations. To this end, tree-avenues in an urban street canyon were modeled and their effect on pollutant concentration was investigated. The experiments substantiate the modeling approach to be practicable for wind tunnel studies and suggest to provide small-scale results which can be reliably transferred to full-scale.

KEYWORDS: vegetation, wind tunnel, similarity, trees, street canyon, tree-avenue

1 INTRODUCTION

The transfer of small-scale wind tunnel findings to full-scale requires the adherence to similitude which is expressed by similarity criteria. Whereas for investigations of buildings and civil engineering structures classical bluff body aerodynamic similarity criteria are well-defined and proved in practice, rather few knowledge and experience is available for the appropriate modeling of vegetation. In contrast to classical bluff body structures, vegetation is permeable to wind and from a general fluid mechanical point of view, a highly complex porous medium consisting of stems, branches, stalks and leafs or needles, all giving rise to the development of boundary layers. Flow past porous bodies differs essentially from flow past non-porous bodies. Wakes extend further downstream, recirculation zones are, in case they exist, detached from the leeward body side and skin friction contributes considerably to the overall drag due to large volume specific surface areas. Skin friction can no longer be neglected as with bluff bodies, where the pressure difference on the windward and leeward sides dominates the drag. Moreover, vegetation is relatively flexible and susceptible for oscillating motions giving rise to fluid-structure interactions. Trees adjust their shape when subjected to wind and show varying aerodynamic properties when exposed to moderate and strong winds [1], [2], [3]. Consequently, principles and similarity criteria of classical bluff body aerodynamics cannot carried forward directly to the modeling of vegetation.

In the following, after a short review of existing wind tunnel vegetation modeling approaches, a new approach is introduced. The modeling approach is validated using the results from wind tunnel experiments of pollutant dispersion in urban street canyons with tree-avenues.

2 REVIEW OF WIND TUNNEL VEGETATION MODELING APPROACHES

So far, only a few wind tunnel studies have been performed which explicitly include the small-scale aerodynamic modeling of vegetation. In these studies, vegetation has often been represented by model railway scenery accessories, e.g. [4], [5]. Moreover, brushes, metal screens, boughs, cotton balls, wooden pegs, matches and plastic stripes have been utilized [6]. Most of these materials have been used to model wind shelterbelts rather than single trees or forest stands. [6] investigated wind and turbulence characteristics in and above a model forest. The forest was assembled by tree models made up of plastic bough imitations and validated by arguing that drag coefficients and general wake characteristics agree well with those of real trees. In another study, [7] used pipe cleaners to simulate wind shelterbelts consisting of conifers. Attention was paid to comply with the Jensen number (ratio of shelterbelt height H to aerodynamic roughness length z_0) which was considered to be the dominating similarity criterion. Flow and stem ground-level bending moment measurements were performed by [8] at an aeroelastic forest model. The tree models were developed by Gardiner in Edinburgh (UK) according to aerodynamic and structure dynamical similarity criteria. The trees were made of injection-molded Nylon-66 stems with low density Polyethylene branch elements. Special attention was given to the branch element design in order to realize appropriate drag coefficients. Furthermore, tree model mass and stiffness were adjusted to match the natural sway frequency. [9] investigated flow fields in forest clearings in a wind tunnel study. Their forest was made of flexible tree models with eigenfrequency of 2.2 Hz. The foliage was modeled by plastic stripes which were attached to two interwounded steel wires forming the tree trunk. This approach allowed to simulate distinct leaf area densities or indices. More recently, [10] and [11] employed metallic mesh rings to model a forest. Their aim was to simulate the mean flow and turbulence characteristics in the above canopy region in order to study the exchange of biogenic emission with the atmosphere. By comparison with full-scale measurements, they concluded that their forest model satisfactorily simulates the mean flow and turbulence structure in the above canopy region. A further example for the modeling of forest stands can be found in [12]. In this study an open-porous foam material (foam 10 ppi - pores per inch) was used and the storm stability of the near forest edge region was investigated. Their results showed that the design of the near forest edge region is crucial for its storm stability. [13] found that the drag coefficient of model railway scenery conifer trees lies in the range for natural conifer trees and employed a wind tunnel forest set up of those tree models to validate numerical simulations of flow over forest clearings. [14] built wind tunnel tree models using filamentous materials which were enlaced and formed to porous crowns of spherical shape. Different porosities were realized by the amount of filamentous material used to form the crown. They demonstrated that the approach enables the aerodynamic modeling of trees in terms of drag and wake characteristics.

3 MODELING APPROACH

3.1 *Vegetation modeling approach*

Tree-avenues were modeled for wind tunnel investigations of pollutant dispersion in urban street canyons. For this purpose, a line-like lattice cage construction of street canyon length with equally sized cells was built and filled with a filamentous synthetic wadding material (Figure 1). Trunks were not modeled as they are fairly small compared to the crowns and their influence on the flow past trees is negligible.

The approach allows to model tree-avenues of different stand density (trees per unit length) and crown porosity (pore volume fraction), see also [15], [16]. Different stand densities can be realized by filling every nth cell (n = 1, 2, 3, …) and different crown porosities by filling the cells with defined masses of the wadding material. For the present study, tree-avenues of maximum stand density (n = 1) and crown porosities with pore volume fractions of P_{Vol} = 97.5% and P_{Vol} = 96.0%, typical for deciduous trees, e.g. [17], [18], were realized.

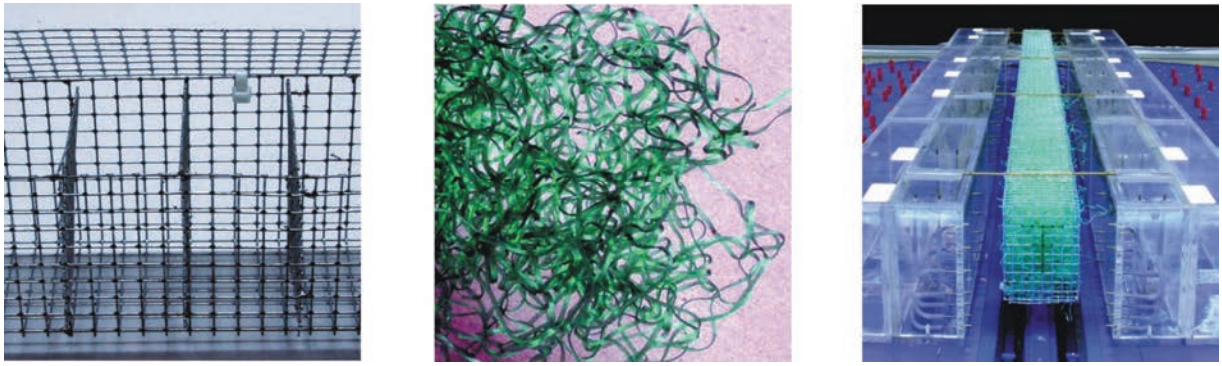

Figure 1. Close-up of lattice cage, filamentous wadding material, and street canyon model with tree-avenue.

In addition to the pore volume fraction, the texture of porous media, i.e. the form, arrangement and size distribution of the pores and their wall roughness as well as their orientation to the flow influence the wind permeability. A definite measure for the permeability of porous media is given by the pressure loss coefficient λ [m^{-1}]. The pressure loss coefficient is determined in forced convection flows, see Figure 2 (left), according to

$$\lambda = \frac{\Delta p_{st}}{p_{dyn}\, d} = \frac{p_{windward} - p_{leeward}}{0.5\, \rho\, u^2 d} \tag{1}$$

where Δp_{st} is the static pressure drop [Pa] over the porous media of streamwise thickness d [m], p_{dyn} is the dynamic pressure [Pa] and u is the bulk velocity [ms^{-1}].

Figure 2 (right) shows the measured pressure loss coefficients λ for different flow speeds. No pronounced dependency of λ on u is visible for both porosities. The slight decreases in λ with increasing u for P_{Vol} = 96.0% is attributed to viscous effects. A deformation or compaction of the wadding material samples was not observed in the tested flow speed range. From these measurements, the pressure loss coefficients were determined to λ = 80 m^{-1} and λ = 200 m^{-1} for the tree model crowns of high (P_{Vol} = 97.5%) and low (P_{Vol} = 96.0%) porosity, respectively.

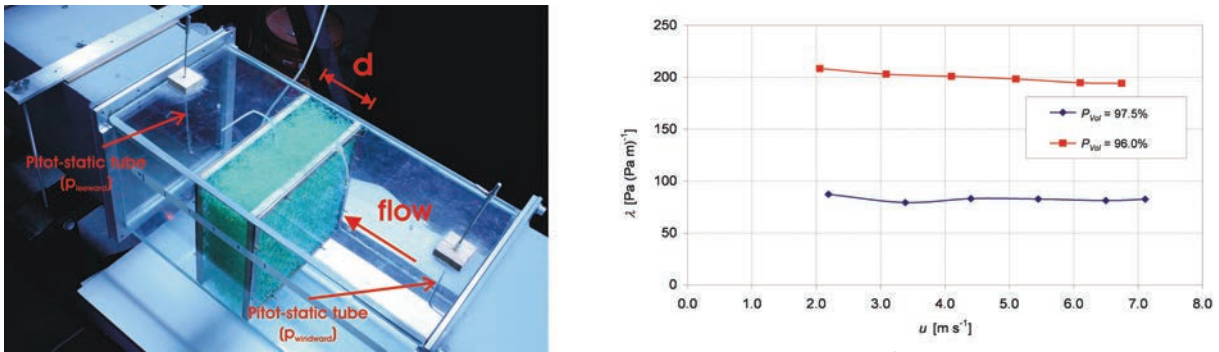

Figure 2. Forced convection flow setup for measuring pressure loss coefficient λ [m^{-1}], and pressure loss coefficient λ vs. flow speed u.

As already stated in the introduction, fluid dynamical similarity is required in order to transfer the wind tunnel model results to full-scale. In the present modeling approach, a similarity criterion is established based on energy considerations. Postulating equality in the normalized static pressure drops $\Delta p_{st}/p_{dyn}$ for forced convection flows in full-scale (fs) and in small-scale (ss), i.e.

$$\left[\frac{\Delta p_{st}}{p_{dyn}}\right]_{fs} = \left[\frac{\Delta p_{st}}{p_{dyn}}\right]_{ss} \tag{2}$$

ensures that the flow potential energy which is extracted by the resistance of the porous media relative to the flow kinetic energy is equal in both scales. This gives with Equation 1

$$\frac{\lambda_{fs}}{\lambda_{ss}} = \frac{d_{ss}}{d_{fs}} = M \tag{3}$$

with M [-] the wind tunnel model scale.

Applying Equation 3 to the tree models, results with the wind tunnel model scale M = 1:150 in up-scaled pressure loss coefficients of $\lambda_{fs} = 0.53$ m^{-1} and $\lambda_{fs} = 1.33$ m^{-1}. For the purpose of comparison and validation, pressure loss coefficients λ of vegetation shelterbelts formed by broad-leaved trees measured in forced convection flows by [19] are provided in Table 1. It has to be noted that these shelterbelt values are the most appropriate data available as pressure loss coefficients of tree crowns lack.

Table 1. Pressure loss coefficients λ [m^{-1}] for leaved vegetation shelterbelts [19].

density ρ_S [a]	1.33	1.00	0.67
poplar	1.2 - 3.6	0.8 - 2.4	0.5 - 1.5
Norway maple	1.5 - 3.5	1.1 - 2.5	0.7 - 1.6
field maple	4.7 - 8.9	3.5 - 6.9	2.2 - 4.0
small-leaved lime	1.5 - 4.0	0.9 - 2.3	0.4 - 1.5
bird cherry	1.5 - 13.4	1.2 - 6.5	0.6 - 3.1

[a] density ρ_S refers to the branch arrangement in the shelterbelt. $\rho_S = 1.00$ is the 'normal density'.

From Table 1 it can be seen that the up-scaled tree model pressure loss coefficients λ_{fs} are in agreement with the values of [19] for thinned out shelterbelts ($\rho_S = 0.67$). The reason for employing the thinned out values is that the branch and foliage arrangement in ground-near shelterbelts of rather shrub-like stature appears to be denser and more uniform than in elevated tree crowns. In elevated tree crowns, most of the foliage is concentrated at the crowns' envelopes whereas the crowns' interiors are almost empty. Based on this argument it is hypothesis that the thinned out shelterbelt pressure loss coefficients are more adequate for the validation.

3.2 *Urban street canyon model*

The line-like lattice cage was positioned in a generic urban street canyon model with aspect ratios W/H = 1 and L/H = 10 (H = 0.12 m). The whole setup was placed in a wind tunnel and subjected to perpendicular approaching flow simulating an urban-type atmospheric boundary layer of model scale M = 1:150 (Figure 3). For more detailed information on the boundary layer wind tunnel characteristics, the reader is referred to [20] or to the internet database CODASC - Concentration Data of Street Canyons [21].

The Reynolds number Re based on the velocity u_H of the undisturbed flow at building height H is equal to 37000, ensuring a Reynolds number independent flow field. Traffic emis-

sions were simulated by tracer gas emitting line sources according to functional principle described in [22]. Sulfur hexafluoride SF_6 was used as tracer gas. Measurement taps were applied along the leeward and windward canyon walls (hereafter referred to as wall A and wall B, respectively) to sample the near-façade canyon air. Mean concentrations were measured with Electron Capture Detection (ECD), model Meltron LH108. The measured concentrations c [-] were normalized according to

$$c^+ = \frac{c\, u_H\, H}{Q_T / l} \tag{4}$$

where QT/l [$m^3 s^{-1} m^{-1}$] is the tracer gas source strength per unit length.

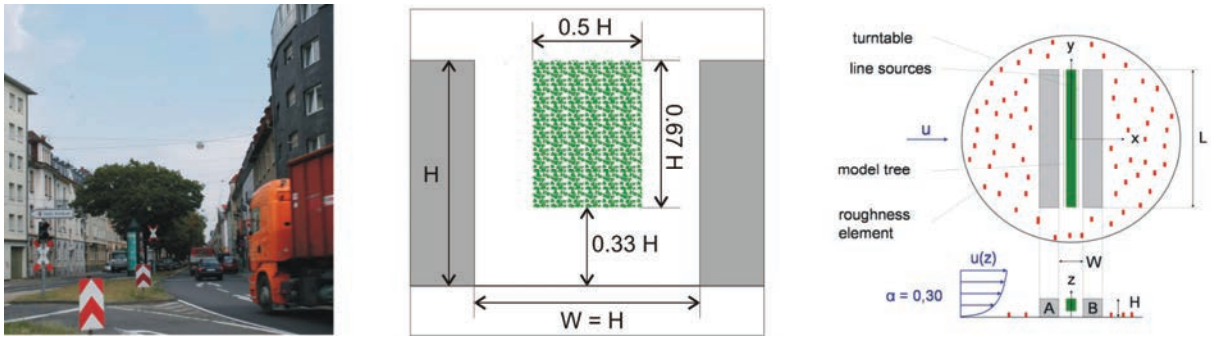

Figure 3. Urban street canyon with tree-avenue and geometry of generic model setup.

4 APPLICATION TO POLLUTANT DISPERSION STUDIES

Figure 4 shows contour plots of normalized pollutant concentrations c^+ [-] at the canyon walls A and B for tree-avenues of maximum stand density (n = 1). Starting with the tree-free street canyon at the top (a), tree crowns with decreasing permeability, i.e. increasing pressure loss coefficients λ were investigated, with λ_{ss} = 80 m^{-1} in (b) and λ_{ss} = 200 m^{-1} in (c). Finally, in (d), the tree-avenue model was formed by a solid block corresponding to an infinite pressure loss coefficient. The latter was considered as a limiting case revealing the highest possible concentrations. Please note that the vertical dimension z [m] and the along street dimension y [m] are normalized by the building height H and that only one half of the building walls is shown (-5 < y/H < 0) utilizing symmetry.

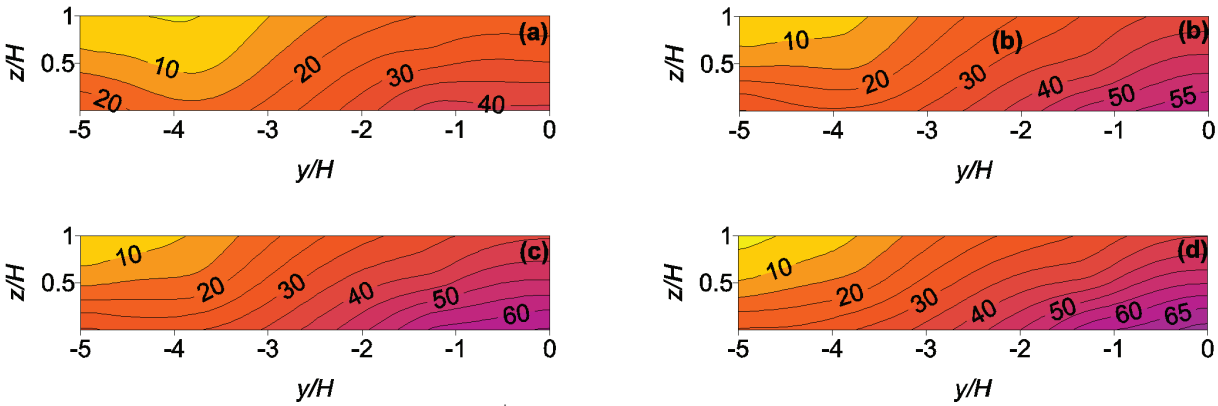

Figure 4. Normalized pollutant concentrations c^+ [-] at building wall A for (a) tree-free street canyon, (b) tree crown with λ_{ss} = 80 m^{-1}, (c) tree crown with λ_{ss} = 200 m^{-1}, and (d) solid block ($\lambda_{ss} = \infty$).

The contour plots of Figure 4 reveal the general implications of tree-avenues and crown permeability on traffic pollutant concentrations in urban street canyons. At the leeward canyon wall A, increasing traffic pollutant concentrations with decreasing crown permeability, i.e. increasing pressure loss coefficient λ, are visible. Both the wall average pollutant level and the peak concentration increase continuously.

In order to understand the influence of tree-avenues on the canyon wall concentrations, it is useful to consider the dominating flow and dispersion processes in the tree-free street canyon first. The flow field in the tree-free street canyon is dominated by two vortex structures, the canyon vortex and the corner eddies. Driven by the above roof wind, a clockwise rotating canyon vortex forms and entrains air into the street canyon in front of the windward wall B. On the reverse flow from wall B to wall A, the canyon vortex accumulates traffic exhaust emissions. Thus, the upward flow in front of the leeward wall A contains increased pollutant concentrations which are then partially entrained and mixed into the above roof wind before re-entrained into the street canyon again. At the street ends additional air exchange is provided by the corner eddies leading to reduced pollutant concentrations [23], [24]. In street canyons with tree-avenues, flow and pollutant dispersion are also dominated by the canyon vortex and corner eddies as was found by Laser Doppler velocimetry (LDV) measurements [23] and by CFD simulations [25], [26], [27]. However, the presence of trees leads to smaller flow velocities inside the street canyon and modified air exchange with the surroundings at the canyon roof and ends. Smaller flow velocities implicate a reduced volume flux of the canyon vortex. Consequently, the traffic exhaust emissions are less diluted and the concentrations in the upward flow in front of the leeward wall A are higher. The contour plots of Figure 4 indicate that these effects are stronger pronounced with decreasing crown permeability, resulting in continuously increasing traffic pollutant concentrations at the leeward wall A. Additionally, the tree crowns partly block the corner eddies and reduce the lateral air exchange which is reflected by increased concentrations at wall A close to the street canyon ends.

Figure 5 summarizes the influence of tree-avenues on pollutant concentrations at wall A. Shown are the relative changes $\Delta c/c_{ref}$ [%] in wall average and peak concentrations with crown permeability λ [m^{-1}] according to

$$\frac{\Delta c}{c_{ref}} = \frac{c_{trees} - c_{tree-free}}{c_{tree-free}} . \tag{5}$$

Steady increases in wall average and peak concentrations with increasing pressure loss coefficient can be seen. The incremental increases are strongest for small values of λ. For larger pressure loss coefficients, the wall average and peak concentrations asymptotically approach their upper limits given by the solid block tree model (dashed lines in diagram).

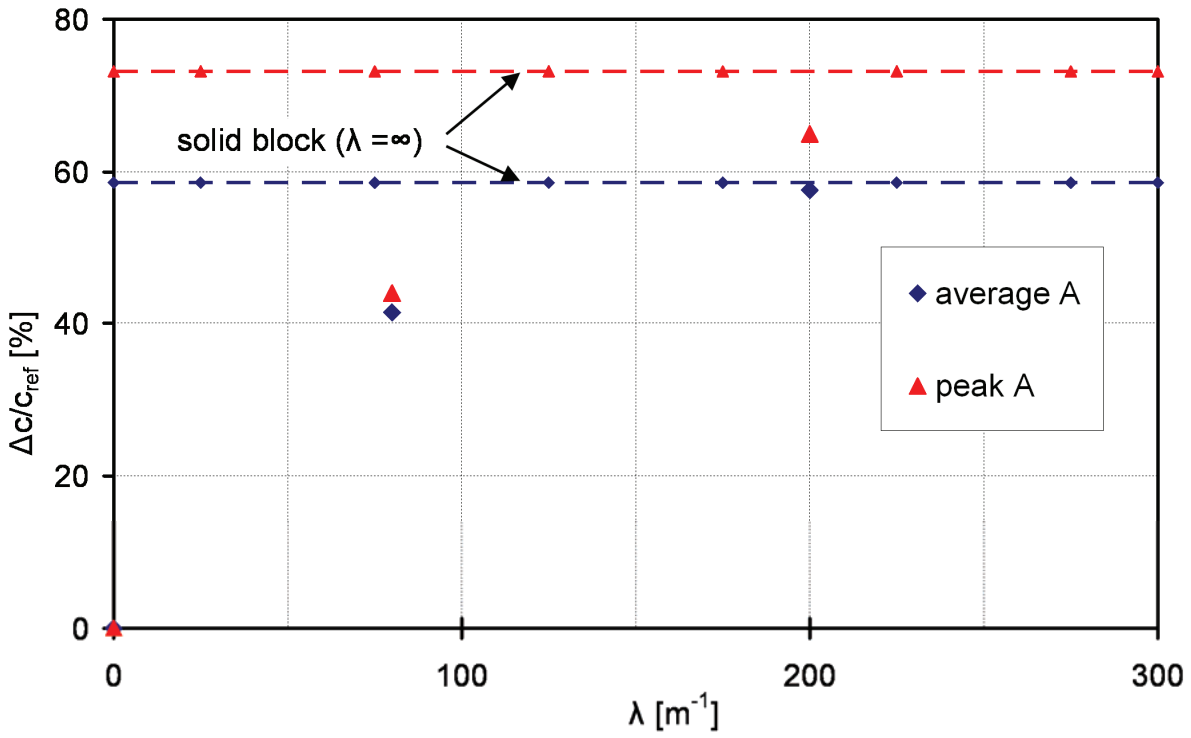

Figure 5. Rel. changes $\Delta c/c_{ref}$ [%] in wall average and wall peak concentrations with crown permeability λ [m^{-1}].

5 CONCLUSIONS

A new vegetation modeling approach was introduced and successfully applied in Wind Engineering small-scale pollutant dispersion studies. The transferability of the small-scale wind tunnel results to the full-scale was ensured by compliance with fluid dynamical similitude requirements. The permeability to wind was identified as relevant for the aerodynamic of vegetation. Consequently, the similarity criterion was set up based on the pressure loss coefficient which is a measure for permeability.

In this study, the modeling approach was employed to model tree-avenues in an urban street canyon and to study pollutant dispersion. The wind tunnel dispersion experiments a posteriori proved the vegetation modeling approach to be practicable and provided strong evidence for its reliability. Beyond the scope of the investigation presented herein, the approach can also be applied to other vegetation types, such as single trees, shrubs, hedges, forest stands or field crops, in diverse Wind Engineering wind tunnel studies, concerning e.g. pedestrian wind comfort or wind loads on structures.

AKNOWLEDGEMENT

The author is indebted to Prof. Bodo Ruck, head of the Laboratory of Building- and Environmental Aerodynamics at the Institute for Hydromechanics of the Karlsruhe Institute of Technology (KIT) for supervising the work. The German Research Foundation DFG (Deutsche Forschungsgemeinschaft) is acknowledged for financial support (grant-no. Ru 345/28).

REFERENCES

1 B. Ruck, Über die Aerodynamik der Bäume, In: C. Egbers, L. Jehring, T. von Larcher, B. Ruck, A. Leder, D. Dopheide (Ed), Proc. 13. GALA-Fachtagung Lasermethoden in der Strömungsmesstechnik, Brandenburg University of Technology, Cottbus, Germany, 2005, pp. 49.1-49.7.

2 M. Rudnicki, S.J. Mitchell, M.D., Novak, Wind tunnel measurements of crown streamlining and drag relationships for three conifer species. Canadian J. Forest Research 34 (2004) 666-676.

3 S. Vollsinger, S.J. Mitchell, K.E. Byrne, M.D. Novak, M. Rudnicki, Wind tunnel measurements of crown streamlining and drag relationships for several hardwood species. Canadian J. Forest Research 35 (2005) 1238-1249.

4 W. Agster, B. Ruck, The influence of aerodynamic properties of forest edges and stands on the pressure pattern within a forest, In B. Ruck, C. Kottmeier, C. Mattheck, C. Quine, G. Wilhelm, (Ed), Int. Conf. Wind Effects on Trees, Karlsruhe, Germany, 2003, pp. 25-32.

5 C, Frank, B. Ruck, Numerical study of the airflow over forest clearings. Forestry 81 (2008) 259-277.

6 R.N. Meroney, Characteristics of wind and turbulence in and above model forests. J. App. Meteorol. 7 (1968) 780-788.

7 R.N. Meroney, Wind-tunnel simulation of the flow over hills and complex terrain. J. Ind. Aerodyn. 5 (1980) 297-321.

8 G.R. Stacey, R.E. Belcher, C.J. Wood, B.A. Gardiner, Wind flows and forces in a model spruce forest. Bound.-Layer Meteorol. 69 (1994) 311-334.

9 J.M. Chen, T.A. Black, M.D. Novak, R.S., Adams, A wind tunnel study of turbulent airflow in forest clearcuts, In M.P. Coutts J. Grace (Ed) Wind and Trees. Cambridge University Press, Cambridge, 1995, pp. 71-87.

10 S. Aubrun, B. Leitl, Development of an improved physical modelling of a forest area in a wind tunnel. Atmos. Env. 38 (2004) 2797-2801.

11 S. Aubrun, R. Koppmann, B. Leitl, M. Möllmann-Coers, A. Schaub, Physical modelling of a complex forest area in a wind tunnel - comparison with field data. Agricult. Forest Meteorol. 129 (2005) 121-135.

12 M. Zaschke, B. Ruck, A wind tunnel investigation of the flow across a forest edge, 12th Int. Conf. on Wind Engineering, Cairns, Australia, 2007, pp. 1055-1062.

13 C, Frank, B. Ruck, Numerical study of the airflow over forest clearings. Forestry 81 (2008) 259-277.

14 C. Gromke, B. Ruck, Aerodynamic modeling of trees for small scale wind tunnel studies. Forestry 81 (2008) 243-258.

15 C. Gromke, A vegetation modeling concept for Building and Environmental Aerodynamics wind tunnel tests and its application in pollutant dispersion studies. Environ. Poll. 159 (2011) 2094-2099.

16 C. Gromke, B. Ruck, Pollutant concentrations in street canyons of different aspect ratio with avenues of trees for various wind directions. Bound.-Layer Meteorol., in press.

17 G. Gross, A numerical study of the air flow within and around a single tree. Bound.-Layer Meteorol. 40 (1987) 311-327.

18 B. Ruck, F. Schmidt, Das Strömungsfeld der Einzelbaumumströmung - Abschätzung von Depositionswahrscheinlichkeiten für Feinsttröpfchen. Forstwissenschaftliches Centralblatt 105 (1986) 178-196.

19 F. Grunert, D. Benndorf, K. Klingbeil, Neuere Ergebnisse zum Aufbau von Schutzpflanzungen. Beiträge für die Forstwissenschaft 18 (1984) 108-115.

20 C. Gromke, B. Ruck, Die Simulation atmosphärischer Grenzschichten in Windkanälen, In C. Egbers, L. Jehring, T. von Larcher, B. Ruck, A. Leder, D. Dopheide (Ed) Proceed. 13. GALA-Fachtagung Lasermethoden in der Strömungsmesstechnik, Brandenburg University of Technology, Cottbus, 2005, pp. 51.1-51.8.

21 CODASC, Concentration Data of Street Canyons. Internet database. Karlsruhe Institute of Technology KIT, Germany, 2008, www.codasc.de.

22 R.N. Meroney, M. Pavageau, S. Rafailidis, M. Schatzmann, Study of line source characteristics for 2-D physical modelling of pollutant dispersion in street canyons. J. Ind. Aerodyn. 62 (1996) 37-56.

23 C. Gromke, B. Ruck, Influence of trees on the dispersion of pollutants in an urban street canyon - experimental investigation of the flow and concentration field. Atmos. Environ. 41 (2007) 3387-3302.

24 C. Gromke, B. Ruck, Effects of trees on the dilution of vehicle exhaust emissions in urban street canyons. Int. J. Environ. Waste Management 4 (2009) 225-242.

25 M. Balczó, C. Gromke, B. Ruck, Numerical modeling of flow and pollutant dispersion in street canyons with tree planting. Meteorol. Zeit. 18 (2009) 197-206.

26 R. Buccolieri, C. Gromke, S. Di Sabatino, B. Ruck, Aerodynamic effects of trees on pollutant concentration in street canyons. Science Tot. Environ. 407 (2009) 5247-5256.

27 C. Gromke, R. Buccolieri, S. Di Sabatino, B. Ruck, Dispersion modeling study in a street canyon with tree planting by means of wind tunnel and numerical investigations - Evaluation of CFD data with experimental data. Atmos. Environ. 42 (2008) 8640-8650.

A numerical tree canopy model and its application in computational wind engineering simulation

Yi Yang[ab], Tim K.T. Tse[b], Xinyang Jin[a], Liguo Yang[a] and Ming Gu[c]

[a]*Center of Wind Engineering Research, China Academy of Building Research, Beijing, China*
[b]*Department of Civil and Environmental Engineering, The Hong Kong University of Science and Technology, Clear Water Bay, Kowloon, Hong Kong, China*
[c]*State Key Laboratory for Disaster Reduction in Civil Engineering, Tongji University, Shanghai, China*

ABSTRACT: Existing turbulence model had been improved by introducing additional source/sink terms in the governing equations to appropriately consider the effect of tree canopy on the wind environment flow. The new source term model S_ω for the turbulence frequency ω equation in the SST k-ω model was proposed and numerically verified through the simulation of the windbreak flow firstly. Then it was adopted in the wind environment optimal design of the twin high-rise buildings of CABR (China Academy of Building Research). With the new inflow boundary conditions developed in the previous studies, it was concluded that the theoretically reasonable source term model was applicable for modeling the tree canopy flow and could get relatively better results.

KEYWORDS: wind environment, numerical simulation, SST k-ω model, additional source/sink term, high-rise building, optimization design.

1. INTRODUCTION

In studies on wind environment around buildings, usually the influence of vegetation cover cannot be ignored. The windbreak formed by the vegetation cover increases the wind drag and subsequently reduces the downstream wind speed effectively. Vegetation cover and its influences on surface roughness have therefore induced considerable complexity to computational modeling of airflow.

For large-scale atmospheric flows, the broad characteristics of flow are concerned most, and the modified wall function considering roughness modification can be then used to model the near ground flow. From the viewpoint of numerical simulation, the wall function has substantially reduced the excessive grid requirement, particularly in the viscous sub-layer. It is however that this method is not suitable for modeling the near ground canopy flow since the use of roughness parameters in the modified law of the wall provides no information of the turbulence structure within the canopy region in terms of the vegetation-related parameters, such as leaf area density (LAD) [1].

In focusing on surface flow complexity, plant drag can be accounted for by incorporating surface roughness parameters and/or introducing additional source/sink terms[1-4]. As such, modified transport equations can be derived to establish mean momentum, turbulent kinetic energy and turbulent kinetic dissipation rate.

In this paper, a more appropriate source term S_ω in the k-ω model has been deduced through the theoretical analogy with the two turbulence models, i.e. the k-ε model and the k-ω model. The new source term S_ω for the SST k-ω model was numerically verified by comparing the numerical results with the mean velocity profiles at different downstream locations of the vegetated windbreak experiment conducted by Kurotani et al.(2002)[5]. At last, the proposed source term model was adopted in the wind environment optimal design of the twin high-rise buildings of China Academy of Building Research (CABR). The effects of tree canopy on the wind flow in the passage formed by the two closely arranged buildings

was numerically investigated and then compared with the situation without the tree canopy. In the numerical simulations, the new inflow boundary conditions proposed by Yang et al. (2008, 2009, 2012)[6-8] are used to model the equilibrium ABL. By using this new inflow boundary condition profiles, the stream-wise errors can be significantly reduced if a good fit between the inflow profiles and the model was used [9]. Based on the results of the numerical simulation, technical measures to ameliorate the unfavorable wind environment were then suggested.

2. TURBULENCE MODELS AND ADDITIONAL SOURCE/SINK TERMS

2.1 *k-ω model*

For the k-ω model [10], the governing equations for the turbulent kinetic energy k and turbulence frequency ω can be expressed as follows:

$$\frac{\partial k}{\partial t}+\frac{\partial u_i k}{\partial x_i}=\frac{\partial}{\partial x_j}(\frac{\nu_t}{\sigma_k}\frac{\partial k}{\partial x_j})+P_k-Y_k+S_k \tag{1}$$

$$\frac{\partial \omega}{\partial t}+\frac{\partial u_i \omega}{\partial x_i}=\frac{\partial}{\partial x_j}(\frac{\nu_t}{\sigma_\omega}\frac{\partial \omega}{\partial x_j})+P_\omega-Y_\omega+S_\omega \tag{2}$$

where P_k and P_ω represents the production terms of k and ω, and Y_k and Y_ω are the effective dissipation terms due to turbulence. The S_k and S_ω are the additional source/sink terms of the k and ω transport equations, respectively. The turbulent viscosity is computed by combining k and ω as follows:

$$\nu_t=\frac{k}{\omega} \tag{3}$$

2.2 *Additional source/sink terms model of the SST k-ω model*

The k-ω based SST model developed by Menter (1994)[10] employs the k-ω model near the surface and the k-ε model in the free-shear layers. A blending function is adopted to bridge these two models. The SST k-ω model takes into account of the transport of the turbulent shear stress and gives accurate predictions of the onset and the amount of flow separation under adverse pressure gradients[10]. In view of its relatively high efficiency for numerical simulation and accurate solution, the SST k-ω model was adopted in this study.

The plant effects were accounted for by introducing the additional source/sink terms in the mean momentum, the turbulence kinetic energy k and turbulence frequency ω equations in the SST k-ω model, which is more suitable for blunt body flow, compared with the standard k-ε model [6]. The expressions of the additional source/sink terms have been proposed by a number of researchers [2-4]. Mochida et al. (2006)[10] conducted a numerical study and compared the performances of different forms of additional source/sink terms on the tree canopy flow.

For the k-ε model, the source/sink terms accounting for the plant drag are expressed as follows [12]:

$$S_{ui}=-C_d A u_i U \tag{4}$$

$$S_k = C_d A \beta_p U^3 - C_d A \beta_d U k \tag{5}$$

$$S_\varepsilon = C_d A \alpha_p \beta_p \frac{\varepsilon}{k} U^3 - C_d A \alpha_d \beta_d \frac{\varepsilon}{k} U k \tag{6}$$

In Eqs. (4)-(6), C_d is the drag coefficient; A is the leaf area density (LAD) (m^2m^{-3}); u_i is the velocity component of i direction; where $U=|u_i u_i|^{1/2}$ is the absolute value of the spatially averaged wind speed. β_p was the fraction of mean flow kinetic energy being converted to wake-generated energy by canopy drag, and β_d was the magnitude of energy losses from interactions with obstacles. For the standard k-ε model, the typical values of β_p and β_d are 1 and 4, respectively [13]. α_p and α_d are the adjustable model constants, and the analytical values are both 1.5. For the SST k-ω model, the values of α_p and α_d are modified to 3.2 and 0, respectively [1][14].

Due to the relationship between the SST k-ω model and the standard k-ε model, the source/sink terms of the mean momentum and k equations in the standard k-ε model, i.e. Eqs. (4) and (5), can be adopted in the SST k-ω model directly. While, for the source/sink term of the ω equation, almost no theoretical expression can be referred to directly. For example, Pattanapol et al. (2008) adopted the equation of S_ε as the form of the expression of S_ω directly only through a simple linear transformation between ε and ω.

Theoretical derivation had been conducted to obtain a reasonable source term S_ω as Eq.(7)[15].

$$S_\omega = C_d A(\alpha_p - 1)\beta_p \frac{\omega}{k} U^3 - C_d A(\alpha_d - 1)\beta_d \frac{\omega}{k} U k \tag{7}$$

The newly-derived source term S_ω of Eq. (7), which was deduced from the turbulence model equations, will be employed along with the source/sink terms of S_u and S_k in the numerical simulation of windbreak flow in the next section.

3. NUMERICAL VERIFICATION

3.1 *Model Setup*

Kurotani et al. (2002)[5] performed a field experiment of vegetated windbreak flow and the experimental results are available in the website (http://www.aij.or.jp/). Based on the experimental results, Mochida et al. (2006)[12] carried out a series of parameter optimization studies on the additional source/sink terms of k-ε model.

The experiment and the numerical simulations conducted by Mochida et al. (2006)[12] were referred to, and a corresponding 2D numerical model was built. The dimensions of the rectangular computational domain were 100m(L)×100m(W), which could be referred to Franke et al. (2007)[16]. The domain was discretized by structural grids and the finest mesh grid close to the ground was set as 0.1 m. The total amount of cells was 50,000. The present work was conducted using the CFD code Fluent 6.3 (Fluent Inc.). The effect of tree canopy on the wind flow was modeled by adding the source/sink terms of S_u, S_k and S_ω (i.e. Eqs. (4), (5) and (7)) into the momentum, k and ω equations, respectively, using the user defined functions (UDF). The flow was assumed incompressible and steady, and the SIMPLE algorithm was used for pressure-velocity coupling. The second order upwind difference scheme, QUICK, was adopted for all the convective terms in the momentum equation and turbulence model equations. The diffusive terms were discretized by second order central difference scheme. The flow field was initiated by the inlet boundary condition. The

convergence criteria of the scaled residuals for all variables and the continuity equation were set as 10^{-4}. To obtain convergent results, although the convergence criteria were achieved, additional iterations were performed to ensure a stable convergence over a sufficient period.

The numerical simulations on different mesh resolutions were performed at the onset to check the requirement of mesh independence. Four variations of mesh densities, which was similar to that was adopted in Yang et al. (2009)[7], were investigated. It was concluded that the CFD simulation results under the present settings were independent of the mesh resolution. The mean velocity profiles obtained from the current numerical simulation at different locations downstream of the vegetated windbreak were compared with the experimental data [5] and acceptable results have been obtained [15].

3.2 *Modeling of equilibrium atmospheric boundary layer*

The modeling of equilibrium atmospheric boundary layer (ABL) was an important precondition for a proper numerical simulation of flows around buildings[17]. The most important requirement of equilibrium ABLs was the horizontal homogeneity, which means that the stream-wise gradients of all variables should be zero.

The issue of generating an equilibrium ABL was investigated from the viewpoint of the turbulence model. The approximate solution to the standard k-ε model was derived based on the assumption of the local equilibrium of turbulence, and then a new set of inflow turbulence boundary conditions for modeling equilibrium ABL was proposed [6][7]. The application of the new inflow boundary conditions was further extended to the SST k-ω model for modeling equilibrium ABL [8]. The performance and applicability of this new set of inflow boundary condition have been recently validated [9][18], and it has been adopted in the numerical simulations of ABL transport phenomena [19-21].

The first step of the numerical verification was the simulation of simple boundary layer flow in an empty domain to confirm whether the equilibrium ABL is adequately generated. The boundary conditions of the numerical model were stipulated in Table 1. The parameters in the inflow boundary conditions were referred to the experiment of Kurotani et al. (2002) and the numerical simulations by Mochida et al. (2006)[11], in which u=5.6m/s, H_b=9m, α=0.22, D_1=-8.94$m^{4-\alpha}/s^4$, D_2=53.4 m^4/s^4.

Numerical simulation shows that both the mean velocity and turbulent kinetic energy profiles were sustained satisfactorily throughout the whole domain under the present inflow turbulence boundary conditions [7][15].

Table 1. Boundary conditions of the numerical model

Location	Boundary conditions	
Inflow face	Defining the mean velocity (u), TKE (k) and turbulence frequency (ω)	$u = u_b(z/H_b)^{\alpha}$, $v = 0$, $w = 0$; $k = \sqrt{D_1 z^{\alpha_i} + D_2}$, $\omega = \varepsilon / \left(C_\mu \cdot k\right)$; where $\varepsilon = \alpha_i C_\mu^{\frac{1}{2}} (u/z)\sqrt{D_1 z^{\alpha_i} + D_2}$
Outflow face	Fully developed outflow	$\frac{\partial}{\partial x}(u, v, w, k, \omega) = 0$
Upper face of computational domain	Free slip	$w = 0$, $\frac{\partial}{\partial y}(u, v, k, \omega) = 0$
Side faces of computational domain	Free slip	$v = 0$, $\frac{\partial}{\partial y}(u, w, k, \omega) = 0$
Ground surface boundary	wall	No slip wall with wall roughness modification, roughness height Ks=0.05m and roughness constant Cs=0.5

4. APPLICATION

4.1 *Introduction*

The assessment and modification research of wind environment of the high-rise buildings Silvertop Towers had been reported by Blocken et al. (2004)[22]. CFD simulation was demonstrated being an effective method for such assessment [23].

The method of introducing the additional source/sink terms in governing equations to appropriately consider the tree canopy effect are further applied to the wind environment optimization of the high-rise buildings of China Academy of Building Research (CABR).

The new mansion of CABR (i.e. the left building in Figure 1) was built close to the existing building, and both were 80m in height (h). Due to the limited site area, the minimum width of the passage, b_{min}, is only about 15m. Therefore, the ratio of b_{min}/h was as small as 0.19. This narrow passage formed by two closely arranged high-rise buildings will be the main entrance of CABR in the future.

Due to lack of obstacles in front of the buildings, moreover, the passage being towards the local dominant wind direction in the whole year, therefore, the pedestrian wind environment was deteriorated in windy days for the wind speed in the passage being accelerated apparently. In order to quantitatively evaluate the pedestrian wind environment comfort and safety around the buildings, particularly at the narrow passage, a detailed wind tunnel test and numerical simulations had been carried out.

According to the wind tunnel test and the numerical simulations, the maximum wind speed ratio C_u, which was defined as the ratio of the local mean wind speed U_p to the undisturbed wind speed U_f at the pedestrian level., i.e., $C_u=U_p/U_f$, could reach 1.8. Combining with the local wind climate statistic data, it resulted that the peak wind speed was as high as the Beaufort scale 8. The probability of occurrence of such high wind speed in the passage was estimated to be nearly 8 times per year. That implied the wind environment in the passage does not satisfy the basic requirements of safety and comfort for pedestrians.

4.2 *Wind environment optimization design*

In order to ameliorate the unfavorable wind environment, additional optimization scheme in cooperation with architects have been performed. Some remedial measures were suggested, for example, a large billboard as high as 9m was planned to set up in front of the windward opening of the passage as a windbreak, and the semi-opened corridor on the ground floor of the new mansion was recommended to be closed and used as pedestrian pathway, as depicted in Figure 2.

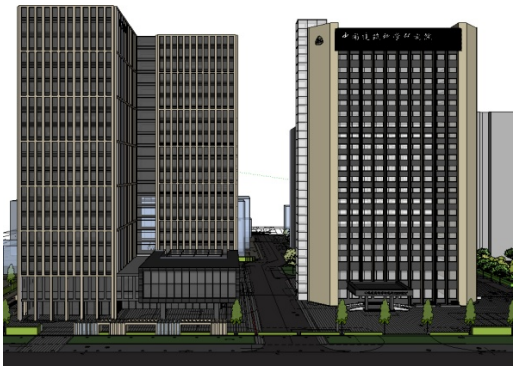

Figure 1. Scheme of the new building of CABR

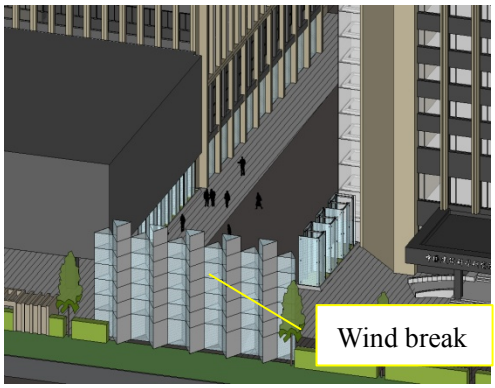

Figure 2. The optimization measures of alleviating unfavorable wind

Though the proposed measures can potentially ameliorate the high wind speed environment at some extent, further numerical simulation (numerical model see Figure 3)

showed that the wind speed at the pedestrian level still tended to unfavorable. This is because the major characteristic of the narrow passage formed by the two high-rise buildings largely remains unchanged.

For example, the big billboard can successfully block off strong wind from north in the downstream near field but the flow separated over the billboard was speeding up and reattaching farther downstream, as reported in Figure 4. Therefore the high wind speed environment in the southern end of the passage was not mitigated and may even be worse in some situations as demonstrated here. Consequently, optimizing the quality of the wind environment around the building, in particular the passage was challenging for wind engineers.

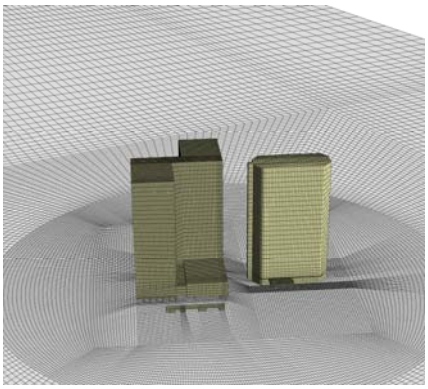

Figure 3. Grid discretization of the numerical model of CABR buildings

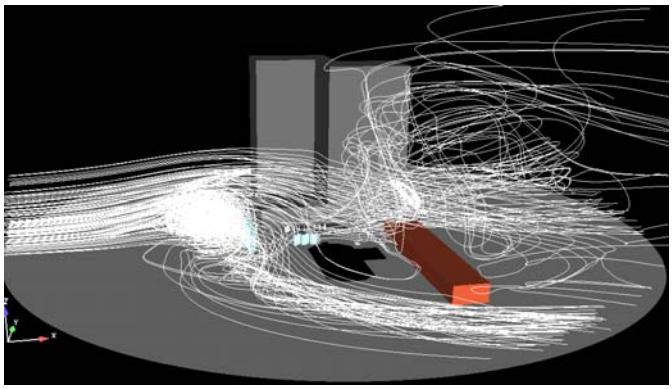

Figure 4. The wind flow streamlines around the building under the north wind

4.3 *Application of the tree canopy in the optimization design*

4.3.1 *Numerical model*

The idea of installing tree canopy in the passage acting as a "soft" windbreak was then proposed and the numerical simulation was carried out. The full scale 3D model of CABR buildings was built according to the architectural design. Some unnecessary architectural details and features were simplified to avoid over-weighted calculation load. The dimensions of the computational domain were set as 720m x 1360m x 560m (i.e. W x L x H), resulting in the blockage ratio of the domain being smaller than 3%.

The grid discretization scheme was designed to achieve a balance between the precision of numerical results and the computational time. The whole domain was divided into two parts as showed in Figure 3 and then hexahedron cells were adopted for both internal and external parts' discretization. The size of the smallest cells close to the building boundaries in the internal part was approximately 0.5m. This scheme gives the total grid cells of about 2 million.

The boundary conditions were set following the expressions in Tab.1, while the two constants of k, D_1 and D_2 were changed slightly in consideration of the local wind terrain feature. Here they were defined as: D_1=-8.93$m^{4-\alpha}/s^4$, D_2=53.1 m^4/s^4; where α=0.22.

In the numerical model, a line of tree canopy was set in the middle of the passage, as illustrated in Figure 5(b). The dimensions of the tree model were 50.0m(L)×1.0m(W) ×1.5m(H). The drag coefficient C_d and LAD of the tree model were 0.8 and 1.17m^2/m^3, respectively. The details of the tree windbreak can be referred to the paper of Kurotani et al. (2002)[5].

4.3.2 *Calculation results*

Figure 5 illustrates the comparisons of the wind velocity ratios C_u at the pedestrian level

before and after setting up the vegetated windbreak in the center of the passage subject to the north wind. It can be clearly seen from the figure that the high wind velocity ratio (i.e. C_u >1.5) was restrained and the area with high wind velocities, especially in the southern part of passage, was reduced significantly after the tree canopy was "planted"(Figure 5 (b)). Therefore, it could partly overcome the negative influence brought by the installation of the windbreak at the northern end as showed in Figure 4.

Numerical simulations exhibited the effects of the tree canopy partly eliminating the unfavorable strong pedestrian wind and improving the wind environment in the passage. Based on the numerical results, a proposal of ameliorating the wind environment of this development project was presented. A line of tree canopy in the middle of the passage with properly designed windbreak facilities installed at the northern end of the passage can effectively reduce the high wind speed and avoid the unfavorable wind environment.

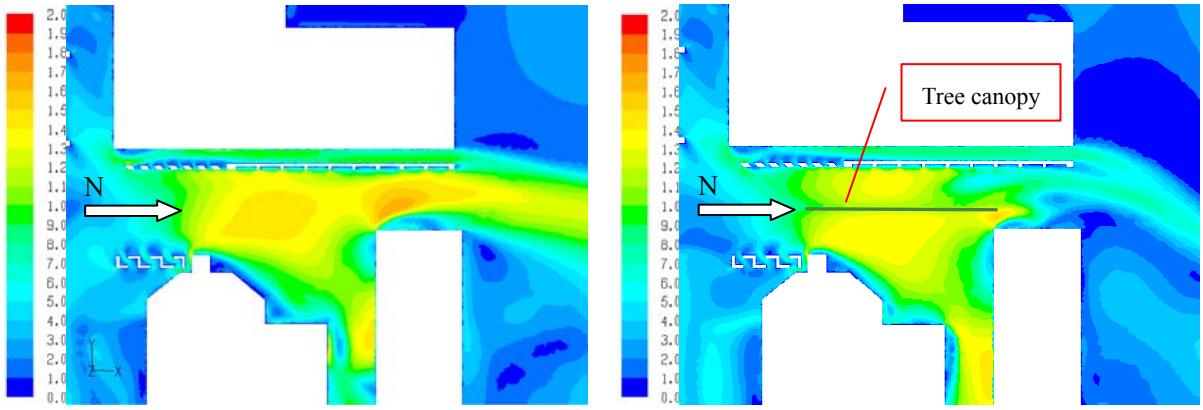

(a) Without the central vegetated windbreak (b) With the central vegetated windbreak

Figure 5. Comparisons of the contours of the wind velocity ratios C_u at the pedestrian level before/after setting the vegetated windbreak in the center of the passage

5. CONCLUSIONS

Existing turbulence model has been improved in order to appropriately consider the effect of tree canopy on the wind environment flow, which is realized by introducing additional source/sink terms in the governing equations. The new source term model S_ω for the turbulence frequency ω equation in the SST k-ω model was derived through the theoretical analogy. Its applicability and performance were numerically verified by performing the simulation of the windbreak flow. Then the proposed source term model was adopted in the wind environment optimal design of the twin high-rise buildings of CABR.

Using the new inflow boundary conditions developed in the previous study to model the equilibrium atmospheric boundary layer, it was concluded that the theoretically reasonable source/sink term model of the SST k-ω model was applicable for the modeling of tree canopy flow. Though some optimization works of the parameters in the model have been performed to achieve better results, the authors believe that more refined study will be helpful for further improving the numerical accuracy.

6. ACKNOWLEDGEMENT

The study reported in this paper is partly carried out under the support of the RGC General Research Fund, HKSAR Project No. 9041338. Financial supports of this study from the National Natural Science Foundation of China under Grant No. 50708014, 51178441 and the National Key Technology R&D Program during the 11th Five-Year Plan Period under Grant No. 2006BAJ02A05 are gratefully appreciated.

7. REFERENCES

1 Pattanapol W., Wakes Sarah J., Hilton Michael J. and Dickinson Katharine J.M., Modeling of Surface Roughness for Flow over a Complex Vegetated Surface, International Journal of Mathematical, Physical and Engineering Sciences, 2008, 2(1), 18-26.

2 Svensson et al., A Two-Equation Turbulence Model For Canopy Flows, J. Wind Eng. Ind. Aerod., 1990, 35, 201-211.

3 Green, S. R., Modelling Turbulent Air Flow in a Stand of Widely-Spaced Trees, PHOENICS Journal Computational Fluid Dynamics and its Applications, 1992, 5, 294-312.

4 Liu J., et al., E-ε Modelling of Turbulent Air Flow Downwind of a Model Forest Edge, Boundary-Layer Meteorol., 1996, 77, 21-44.

5 Kurotani Y., Kiyota N. and Kobayashi S., Windbreak effect of Tsuijimatsu in Izumo Part 2, Summaries of technical papers of annual meeting, AIJ Environmental Engineering I (in Japanese), 2002,745–746.

6 Yang W., Quan Y., Jin X.Y., Tamura Y., Gu M., Influences of equilibrium atmosphere boundary layer and turbulence parameter on wind loads of low-rise building, J. Wind Eng. Ind. Aerodyn., 2008, 96, 2080-2092.

7 Yang Y., Gu M., New inflow boundary conditions for modeling the neutral equilibrium atmospheric boundary layers in Computational Wind Engineering:II, submitted to J. Wind Eng. Ind. Aerodyn, 2012.

8 Yang Y., Gu M., Chen S.Q. and Jin X.Y., New inflow boundary conditions for modeling the neutral equilibrium atmospheric boundary layers in Computational Wind Engineering, J. Wind Eng. Ind. Aerodyn., 2009, 97 (2), 88‐95.

9 O'Sullivan,J.P., Archer, R.A. and Flay, R.G.J., Consistent boundary conditions for flows within the atmospheric boundary layer, J. Wind Eng. Ind. Aerodyn., 2011, 99,65–77.

10 Menter, F.R., Two-equation eddy-viscosity turbulence models for engineering applications, AIAA J., 1994, 32 (8), 1598‐1605.

11 Mochida A., Yoshino H., Iwata T. and Tabata Y., Optimization of Tree Canopy Model for CFD Prediction of Wind Environment at Pedestrian Level, The Fourth International Symposium of Computational Wind Engineering , Yokohama, 2006, 561-564.

12 Mochida A., Tabata Y.,Iwatab T. and Yoshino H., Examining tree canopy models for CFD prediction of wind environment at pedestrian level, J. Wind Eng. Ind. Aerodyn., 2008, 99, 1667–1677.

13 Sogachev, A. and O. Panferov, Modification of two-equation models to account for plant drag, Boundary-Layer Meteorol., 2006, 121, 229-266.

14 Neary, V.S., Numerical solution of fully developed flow with Vegetative Resistance, Journal of Engineering Mechanics, 2003, 129, 558-563.

15 Yang Y., Jin X., Tim K.T. Tse et al., Verification of a tree canopy model and an example of its application in wind environment optimization, Wind and Structures, 2012, Vol.15, No.5, 2012.

16 Franke, J., Hellsten, A., Schlünzen, H., Carissimo, B., Best Practice Guideline for the CFD Simulation of Flows in the Urban Environment, COST Office, Brussels, 2007, http://www.mi.uni-hamburg.de/Official-Documents.5849.0.html

17 Blocken, B., Stathopoulos, T., Carmeliet, J., CFD simulation of the atmospheric boundary layer: wall function problems, Atmospheric Environment, 2007, 41 (2), 238–252.

18 Gorlé, C., van Beeck, J., Rambaud, P., Dispersion in the Wake of a Rectangular Building: Validation of Two Reynolds-Averaged Navier-Stokes Modelling Approaches, Boundary-Layer Meteorol., 2010, 137(1), 115-133.

19 Barić, E., Džijan, I., Kozmar, H., Numerical simulation of wind characteristics in the wake of a rectangular building submitted to realistic boundary layer conditions, Transactions of Famena, 2010, **34**(3), 1-10.

20 Kozmar, H., Wind-tunnel simulations of the suburban ABL and comparison with international standards, Wind and Structures, 2011, 14 (1), 15-34.

21 Labovský, J. and Jelemenský, L., Verification of CFD pollution dispersion modelling based on experimental data, Journal of Loss Prevention in the Process Industries, 2011, 24 (2), 166-177.

22 Blocken B., Roels S., Carmeliet J., Modification of pedestrian wind comfort in the Silvertop Tower passages by an automatic control system, J. Wind Eng. Ind. Aerodyn., 2004, 92(10), 849-873.

23 Blocken B, Carmeliet J., Pedestrian wind conditions at outdoor platforms in a high-rise apartment building: generic sub-configuration validation, wind comfort assessment and uncertainty issues, Wind and Structures, 2008, 11(1), 51-70.

The Seventh International Colloquium on Bluff Body Aerodynamics and Applications (BBAA7)
Shanghai, China; September 2-6, 2012

Aerodynamic characteristics of trees for green roofing systems

Jinxin Cao [a], Yukio Tamura [b], Akihito Yoshida [c]

[a]*Tokyo Polytechnic University, Kanagawa, Japan, jinxin@arch.t-kougei.ac.jp*
[b]*Tokyo Polytechnic University, Kanagawa, Japan, yukio@arch.t-kougei.ac.jp*
[c]*Tokyo Polytechnic University, Kanagawa, Japan, yoshida@arch.t-kougei.ac.jp*

ABSTRACT: Three tree species appropriate for intensive green roofs with different aerodynamic forms were tested through a boundary layer wind tunnel experiment, including one deciduous tree, one coniferous tree and one broadleaf evergreen tree. Drags and over-turning moments under different wind speeds were measured; wind-speed-specific frontal areas and tip displacements were recorded. Even considering frontal area reduction due to increasing wind speeds, drag coefficients decrease with increase in wind speed for deciduous and coniferous trees. The effect of crown porosity varies among tree species.

KEYWORDS: tree; drag coefficient; over-turning moment coefficient; wind-speed-specific frontal area; wind tunnel experiment.

1 INTRODUCTION

Green roofing systems are lightweight, engineered roofing systems that allow for the propagation of rooftop vegetation while protecting the integrity of the underlying roof (Earth Pledge Foundation, 2004). There are two main classifications of green roofs: extensive and intensive. Extensive green roofs have a thin substrate layer with low-level planting, typically sedum or lawn, and can be very lightweight in structure. Intensive green roofs have a deeper substrate layer to allow deeper rooting plants such as shrubs and trees to survive (Castleton, 2010). The likelihood of tree failure in green roofing systems is high since trees on the tops of buildings are exposed to higher wind velocities than those on the ground. Therefore, wind loads on trees and their mitigation is an important issue in the design and maintenance of green roofing systems.

During past decades, the effects of wind forces on trees have been studied from the viewpoint of forest stability. Mayhead (1973) was among the first to systematically present drag coefficients for various British forest tree species based on through wind tunnel measurements. Rudnicki et al. (2004) and Vollsinger et al. (2005) also studied the relationship between crown streamlining and drag in a wind tunnel for several young hardwood species and juvenile conifers. Of these studies, Rudnicki et al. (2004) was the first to identify wind speed specific crown frontal area simultaneously with crown drag, while crown frontal areas in still air were used before. Recently, researches relating to wind forces on real urban trees were conducted through wind tunnel experiments (Ishikawa, 2006) and field measurements (Takamori et al, 2003; Kane and Smiley, 2006; Kane et al, 2008; Koizumi et al, 2010) to determine how to prevent wind damage to them. Although field measurements tended to overcome the size restriction of wind tunnel testing, it was difficult to record the reconfigurations of trees.

The goal of this study was to evaluate drag and over-turning moment coefficients, reconfigurations and deflections of different trees. Drag coefficients based on frontal areas in still air and wind-speed-specific frontal areas were both determined; Over-turning moment coefficients based on frontal areas in still air and aerodynamic centers were provided. Other parameter considered was crown porosity as affected by crown pruning.

2 METHODS AND MATERIALS

2.1 *Trees*

Three trees including one deciduous tree, Rose of Sharon (*Hibiscus syriacus*) (HS); one coniferous tree, Emerald Cedar (*Thuja occidentalis 'Smaragd'*) (TO); and one evergreen tree, Japanese Holly (*Ilex crenata*) (IC), were chosen, as shown in Figure 1. The criteria for choice of tree species were: (1) suitable for green roofs and (2) representatives of different types of trees, especially from the aerodynamic viewpoint. Table 1 summarizes morphometric data for each species, including tree geometries, main characteristics of branching habits and foliage textures. Trees were cut just above the root flare and mounted to the five-component force balance. Rotation of the bottom of stems was not allowed after the mounting.

2.2 *Measurements*

Wind tunnel experiments were carried out in a Boundary Layer Wind Tunnel at Tokyo Polytechnic University, Japan. The test section was 2.2m wide by 1.8m high. Drag and over-turning moment data measured through a five-component commercial force balance where the tree was mounted and the reference wind pressure recorded at 1.2m above the wind tunnel floor were simultaneously collected at 500Hz and the sampling time for each run was 10 minutes. Two digital cameras were installed, one downstream of the tree and the other outside the wind tunnel, to capture the frontal areas and deformations after each run for each intended wind speed respectively.

(a) HS (b) TO (c) IC

Figure 1. Experimental trees

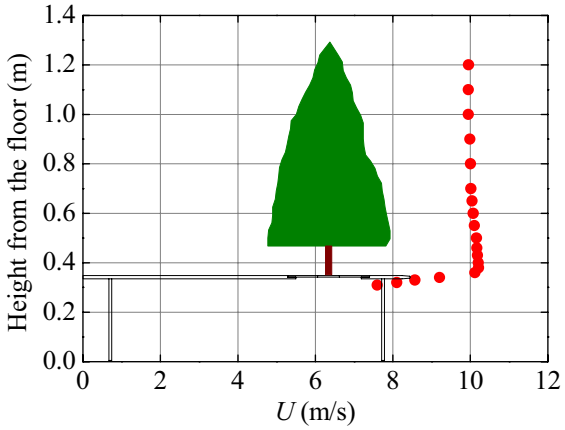

Figure 2. Uniformity of mean wind speed (U=10 m/s)

Table 1. Tree geometries and tree forms

Item		HS	TO	IC
Tree geometry	Height (H: m)	1.24	0.98	0.40
	Width (B: m)	0.53	0.45	0.42
	Caliper (b: cm)	2.3	3.7	3.3
	Frontal area (As: m^2)	0.15	0.33	0.11
	Volume (V_0: cm^3)	555	2280	930
	Porosity (VP: %)	/	97.1	96.6
Branching habit	Crown shape	upright	pyramidal	round
	Trunk and Branches	multi-trunked	with a single leader	clumping stems
Foliage texture	Leaf shape	rhomboid	scale-like	obovate
	Leaf margin	dentate	entire	serrulate

Uniform flow fields were adopted. Wind speeds ranged from 5m/s to 15m/s, the maximum wind speed in this wind tunnel, with 1m/s interval. The uniformity of the wind speed at the measurement position is shown in Figure 2 and a 30cm-high end plate was used to compensate for the non-uniform wind flows near the wind tunnel floor. The exposed part of force balance was covered by the wooden cover with a streamlined shape attached to the end plate.

2.3 *Variation in crown porosity*

The original crown porosities were reduced by pruning the branches several times using thinning pruning method (ANSI, 2001) which only removed small-diameter branches along the outside of the crown and almost kept the post-pruning crown dimensions. Four pruning for TO (Fig. 3) and three pruning for IC (Fig. 4) were conducted. The pruning dose (volumes of pruned branches and leaves) were measured using a water-displacement method after each tree pruning.

The original volume of each tree was V_0, and the volume after each pruning was V_i, (i was the times of pruning) and pruning dose (PD) (Table 2) was performed using:

$$PD = \frac{V_0 - V_i}{V_0}\left(i = 1, 2, ..., N\right) \tag{1}$$

The imaginary solid volumes V_E (gross volume) formed by the boundary of the tree structure were estimated by the special software "Tree analyzer 1.20" (Phattaralerphong and Sinoquet, 2005) through eight photos of the tree structure taken from 8 directions.The 3D crown porosity (VP) (Table 1, 2) was defined by the ratio between the volume of the trees and V_E:

$$\mathrm{VP} = \frac{V_E - V_i}{V_E}\left(i = 0, 1, ..., N\right) \tag{2}$$

(a) VP = 97.1% (b) VP = 97.8% (c) VP = 98.2% (d) VP = 98.7% (e) VP = 99.1%

Figure 3. Variation of shape of TO due to crown porosity (VP)

(a) VP = 96.6% (b) VP = 96.9% (c) VP = 97.1% (d) VP = 97.5%

Figure 4. Variation of shape of IC due to crown porosity (VP)

Table 2. Tree volumes after pruning

Tree	Item	Pruning 1	Pruning 2	Pruning 3	Pruning 4
TO	Volume (V0: cm3)	1730	1400	1020	720
	Porosity (VP)	97.8	98.2	98.7	99.1
IC	Volume (V0: cm3)	855	775	690	
	Porosity (VP: %)	96.9	97.1	97.5	

2.4 *Calculations*

E value, an alternative measure of crown reconfiguration suggested by Vogel (1984), represents the exponent to which the wind speed must be raised to be directly proportional to either the drag coefficient or the drag divided by the square of wind speed:

$$\frac{F_{\mathrm{D}}}{U^2} \propto U^E \tag{3}$$

where F_{D} is measured mean drag and U is measured mean wind speed.

Two sets of results for mean drag coefficients (Fig. 7) for each tree ($C_{\mathrm{D,U}}$ and $C_{\mathrm{D,S}}$) were calculated based on wind-speed-specific frontal areas and frontal areas in still air.

$$C_{\mathrm{D,U}} = \frac{F_{\mathrm{D}}}{0.5\rho U^2 A_{\mathrm{U}}} \tag{4}$$

$$C_{\mathrm{D,S}} = \frac{F_{\mathrm{D}}}{0.5\rho U^2 A_{\mathrm{S}}} \tag{5}$$

where ρ is air density calculated using readings from a barometer and thermometer before each experimental run; A_{U} and A_{S} are wind-speed-specific frontal areas of trees and frontal areas of trees in still air, respectively.

Overturning moment coefficients C_{M} at the bottom of tree stems were calculated based on frontal areas in still air as follows:

$$C_{\mathrm{M}} = \frac{M_{\mathrm{OT}}}{0.5\rho U^2 A_{\mathrm{S}} H} \tag{6}$$

where M_{OT} is measured mean overturning moment and H is the height of tree in still air.

The distance between stem base and the height of aerodynamic center of trees (H_{C}) can be identified based on:

$$H_{\mathrm{C}} = \frac{M_{\mathrm{OT}}}{F_{\mathrm{D}}} = \frac{0.5\rho U^2 A_{\mathrm{S}} H \cdot C_{\mathrm{M}}}{0.5\rho U^2 A_{\mathrm{S}} \cdot C_{\mathrm{D,S}}} = \frac{C_{\mathrm{M}} H}{C_{\mathrm{D,S}}} \tag{7}$$

and the non-dimensional height of the aerodynamic center of the trees (α_{C}) were normalized by the height of the tree in still air:

$$\alpha_{\mathrm{C}} = \frac{H_{\mathrm{C}}}{H} = \frac{C_{\mathrm{M}}}{C_{\mathrm{D,S}}} \tag{8}$$

3 RESULTS AND DISCUSSIONS

3.1 *Force and wind speed relationship*

Fig. 5 shows the relationship between drag force and wind speed for the three trees, including the experimental data and curve fit using power function. *E* values are -0.36, -0.29 and -0.01 for HS, TO and IC respectively.

Although the aerodynamic forms of HS and TO are totally different, including branching habit and leaf texture as indicated in Table 1, their *E* values do not show a large difference. However, the *E* value for IC, close to 0, is different from the previous two trees. This is mainly due to higher branch stiffness of IC and its reconfiguration is limited compared to HS and TO. It can be concluded that other than morphological differences among species, *E* values, which reflects the ability of reconfiguration, are mainly affected by the branch stiffness.

3.2 *Frontal area and wind speed relationship*

The wind-speed-specific frontal areas of the three trees and corresponding curve fits are shown in Fig. 6. The high capacity for reconfiguration of HS showed the largest exponent -0.20, while the exponent was -0.07 for TO. IC presented a positive power exponent of 0.04, which indicates that the frontal area slightly increased with increase in wind speed. This is mainly because the high frequency movements of branches and leaves at large wind speeds cannot be identified by the relatively low-frequency digital camera and overlapping in photographs was available.

When the wind speed increased from 5m/s to 15m/s, frontal areas decreased by 20% for HS from $0.15m^2$ to $0.12m^2$, and 10% for TO from $0.33m^2$ to $0.30m^2$, and the values kept constant for IC. Unlike HS and TO, the reconfiguration of both branches and leaves of IC was not obvious because of the smaller size of the crown; the less flexible branches and leaves do not easily change their shapes.

3.3 *Deflection of tree*

The tip displacements normalized by the tree height as well as the fitted curves are presented in Figure 7. The maximum relative displacement x_{top}/H for HS was the largest among the three species, 0.3 when the wind speed was 15m/s and the values for TO and IC were 0.17 and 0.03, respectively. Although the quantity of the wind-speed-specific tip displacement for HS was around twice that of TO, the exponents for the curve fitting were almost the same: 1.58 and 1.57. Moreover, since the power exponent for IC was 3.78, which was close to 4, pure bending theory for a rigid body in which the second-order derivative of the deformation was proportional to horizontal force seemed to be appropriate for it.

3.4 *Drag coefficient*

Two sets of results for mean drag coefficients (Fig. 8) for each tree were calculated. For HS and TO, it can be seen that even drag coefficients based on wind-speed-specific frontal area also decreased with increase in wind speed. This indicates that wind-speed-specific frontal area is not the only parameter to affecting drag coefficients, but that there are other factors caused by reconfiguration of trees.

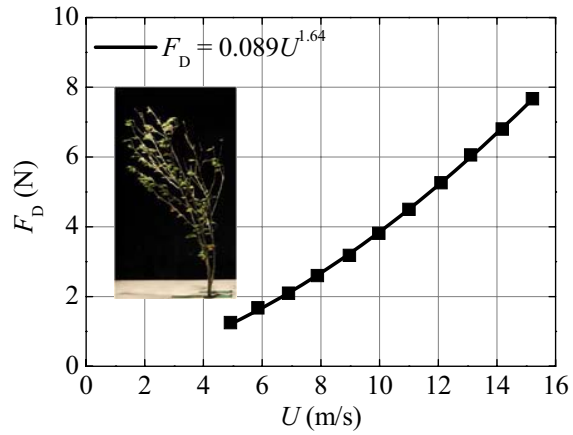

(a) HS

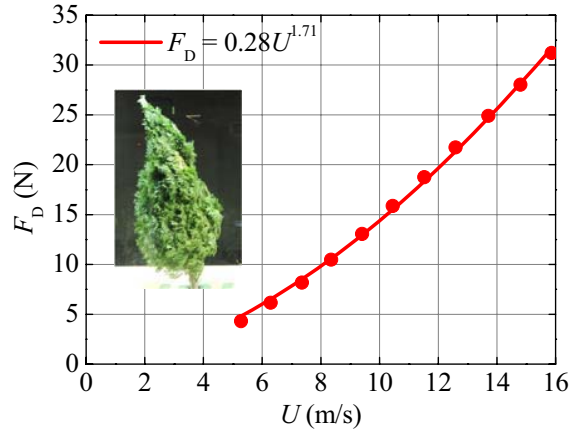

(b) TO

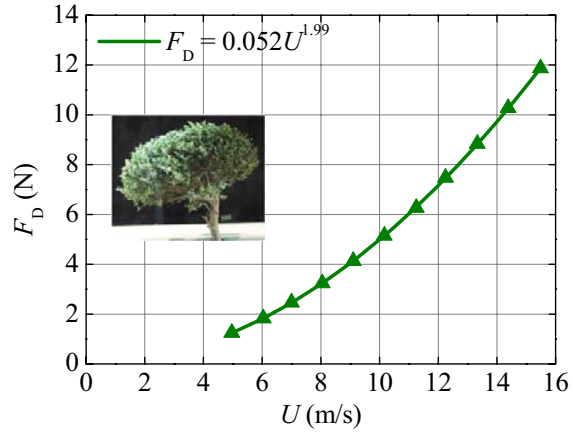

(c) IC

Figure 5. Variation of mean drags due to mean wind speeds

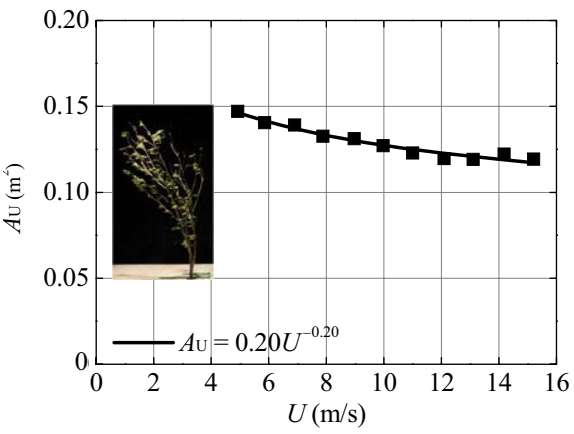

(a) HS

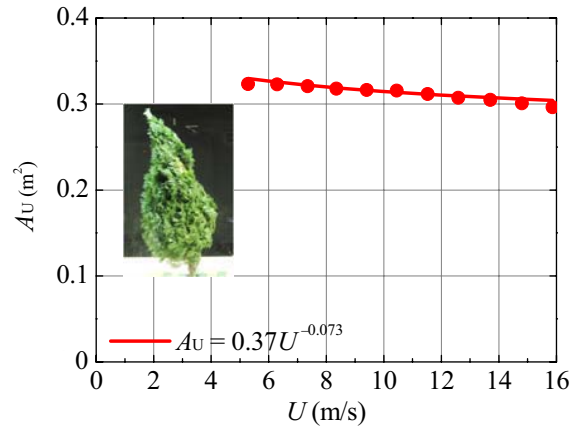

(b) TO

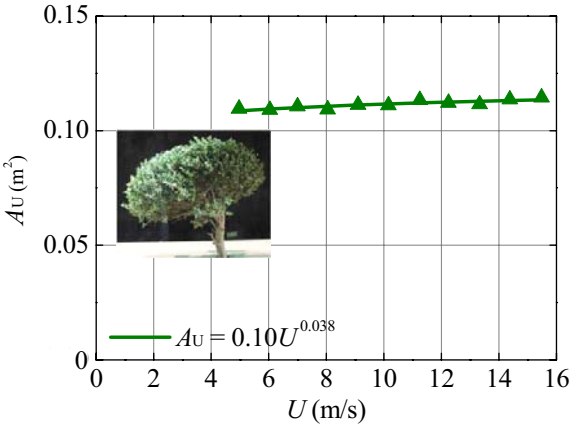

(c) IC

Figure 6. Variation of wind-speed-specific frontal areas due to mean wind speeds

As expected, drag coefficients for HS and TO based on frontal area in still air decreased more rapidly with increase in wind speed and were consistently smaller than those calculated based on wind-speed-specific frontal area. For wind speeds from 5m/s to 15m/s, for HS, the drag coefficients based on wind-speed-specific frontal area decreased by 20% from 0.61 to 0.49, while those based on frontal area in still air decreased by 36% from 0.59 to 0.38; for TO, the

values based on wind-speed-specific frontal area decreased by 12% from 0.83 to 0.73, while those based on frontal area in still air decreased by 19% from 0.83 to 0.67. For IC, drag coefficients keep constant around 0.79.

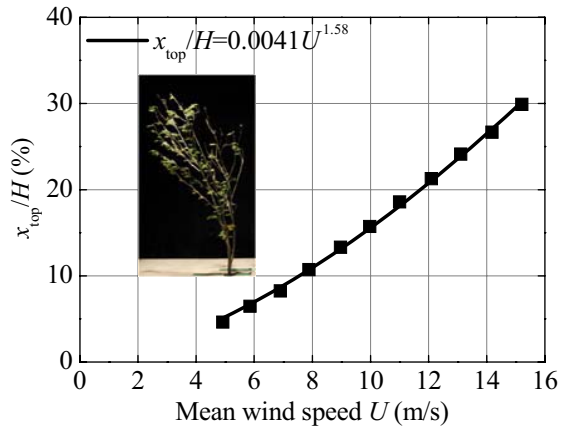

(a) HS

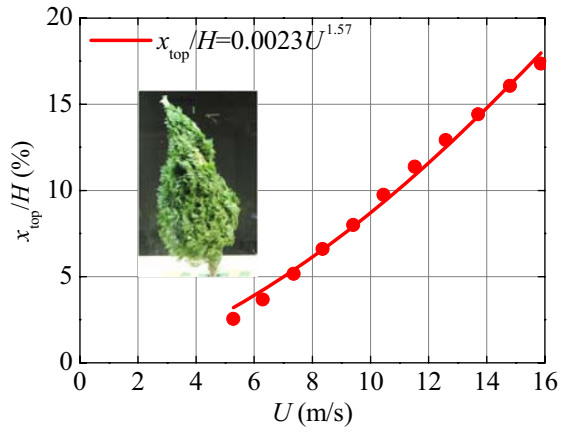

(b) TO

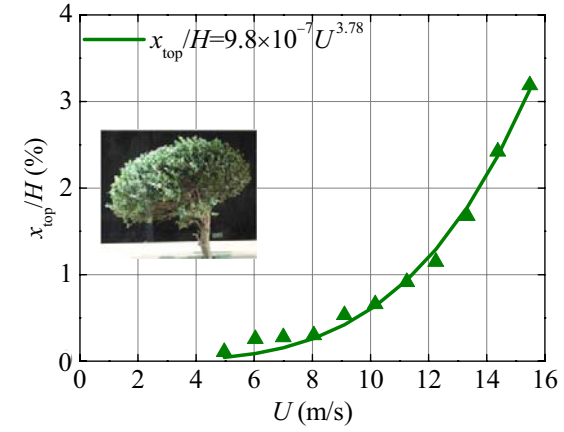

(c) IC

Figure 7. Variation of tip displacements due to mean wind speeds

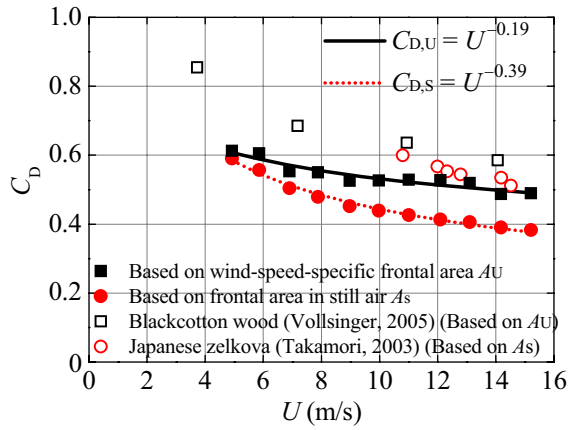

(a) HS

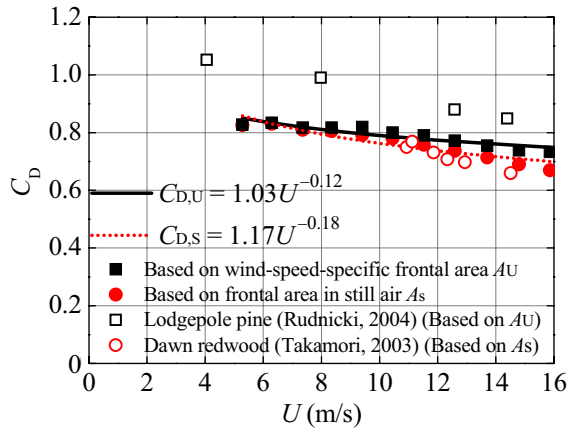

(b) TO

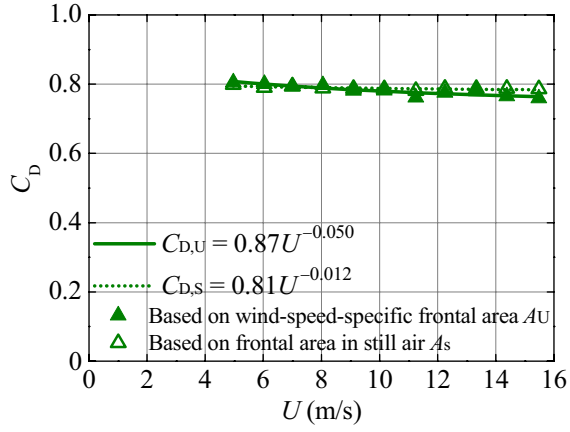

(c) IC

Figure 8. Mean drag coefficients

The exponents for the fitted curves using $C_{D,U}$ values based on wind-speed-specific frontal area of the three trees were -0.19, -0.12 and -0.05. Since the only difference between the two sets of drag force coefficients was the area used for calculation, the discrepancy in the exponents of the curve fitting for the two sets of data can be reflected by the exponents of the curve fitting for wind-speed-specific frontal area. The exponents for wind-speed-specific frontal area were -0.20, -0.07 and 0.04; thus, the exponents for $C_{D,S}$ values based on still air area were -0.39, -0.19 and -0.01.

Drag coefficients of HS and TO have been compared with those obtained from similar researches on real trees. Two deciduous trees, Blackcotton wood (Vollsinger, 2005) and Japanese zelkova (Takamori, 2003), and two coniferous trees, Lodgepole pine (Rudnicki, 2004) and Dawn redwood (Takamori, 2003), in a similar wind speed range were chosen for comparison. The results showed that the present data for both HS and TO were comparable to the previous data. For HS, the values ranged from 0.49 to 0.61 were between the reported range from 0.51 to 0.85; and the range from 0.73 to 0.83 for TO was also located in the range for previous data from 0.66 to 1.05, which validate the reasonableness of the present data.

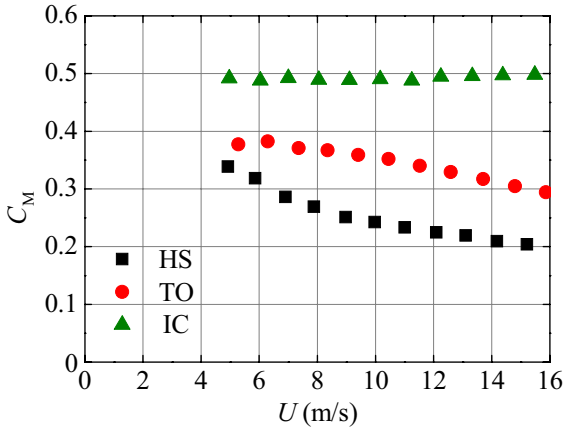

Figure 9. Mean overturning moment coefficients

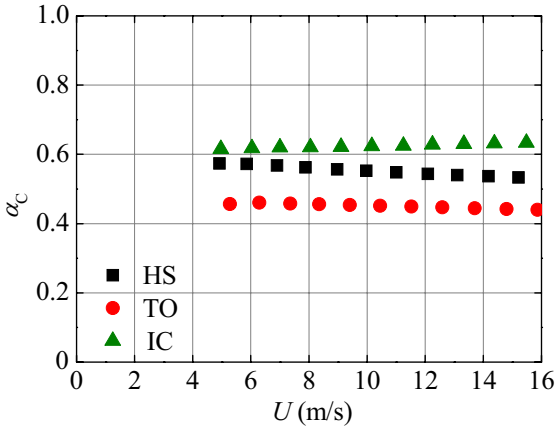

Figure 10. Relative height of aerodynamic centers

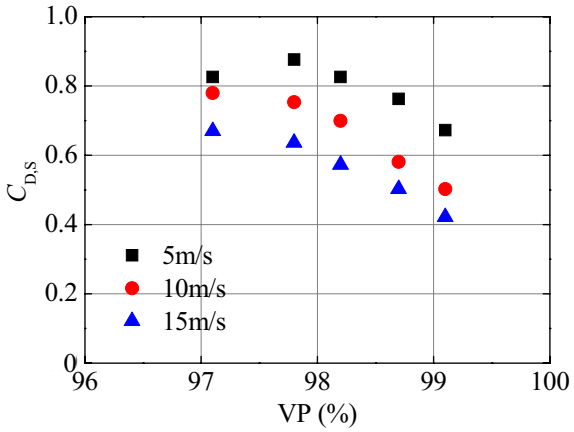

(a) TO

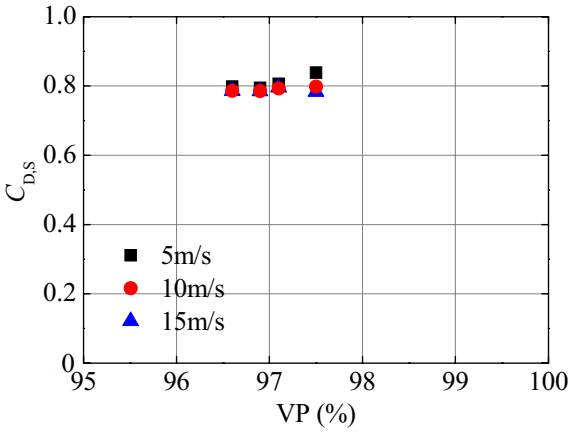

(b) IC

Figure 11. Effect of crown porosity on mean drag coefficients

3.5 *Aerodynamic center*

Results of overturning moment coefficients calculated based on frontal area in still air and relative height of the aerodynamic center are shown in Figures 9 and 10, respectively. The relationships between overturning moment coefficients and wind speeds for the three species were similar to the results for drag coefficients.

Aerodynamic center was mainly affected by the distribution of the crown structures and differed among tree species. Among the three experimental trees, the maximum value of α_C, 0.62, was recorded for IC, since the main crown was located at the upper part of the tree and left trunk only at half the bottom. TO has the smallest value of aerodynamic center, 0.45, since the crown has a conical shape and the main crown was distributed at the lower part of the crown. For HS which has a relatively uniform distribution in branch and leaves from top to bottom compared with the previous two species, the values ranged from 0.53 to 0.57.

3.6 *Effect of crown porosity*

Figure 11 shows the effect of crown porosity on drag coefficients of the tree in terms of the crown porosities and the values for the wind speeds of 5m/s, 10m/s and 15m/s were chosen. For TO, when the wind speed was low (5m/s), the drag coefficients first increased with increase in crown porosity and then decreased. This tendency never took place and drag coefficients gradually decreased with increase in crown porosity for high wind speed (10m/s and 15m/s). For IC, although the values at different wind speeds slightly changed, values for the same wind speed did not differ with change in crown porosity.

4 CONCLUDING REMARKS

Aerodynamic characteristics including drag and over-turning moment coefficients and plant forms of three trees, suitable for green roofing system were investigated through wind tunnel experiments. Variations of drag, frontal area, tip displacement and drag and over-turning moment coefficient due to mean wind speed were mainly discussed. The effect of crown porosity, view angle and turbulence intensity were investigated. The main conclusions are summarized as follows:

(1) The Vogel exponents were -0.36 and -0.29 for HS and TO, and -0.01 for IC. The power exponents fitting the relationship between wind-specific frontal areas and wind speed were -0.20, -0.07 for HS and TO, and 0 for IC. The discrepancy between Vogel exponents and power exponents for frontal areas indicated that there were parameters other than area reduction due to reconfiguration that affected the reduction of drag forces. The power exponents for the curve fitting of tip displacements of the three trees were 1.58, 1.57 and 3.78, respectively. Pure bending theory for a rigid body seems to be appropriate for IC since the value was close to 4.

(2) Even considering area reduction due to wind speed, mean drag coefficients decreased with increase in wind speed from 0.61 to 0.49 for HS, from 0.83 to 0.73 for TO, which were comparable to those of previous researches. Values for IC kept constant at around 0.79. The aerodynamic center was mainly affected by the distribution of the crown structures and differed among tree species.

(3) The effect of crown porosity differed among tree species and wind speeds. For TO, unfavorable porosity occurs with maximum drag coefficients with low wind speed while porosity has little effect on IC.

5 ACKNOWLEDGEMENTS

This study was funded by the Ministry of Education, Culture, Sports, Science and Technology, Japan, through the Global Center of Excellence Program, 2008-2012, which is gratefully acknowledged.

6 REFERENCES

1 American National Standards Institute (ANSI A300 Part1), 2001. American national standard for tree care operations – Tree, shrub and other wood plant maintenance – Standard practices (Pruning). Tree Care Industry Association, Manchester, NH.
2 Castleton, H. F., Stovin, V., Beck, S. B. M., Davison, J. B., 2010. Green roofs; building energy savings and the potential for retrofit. Energy and Building 42, 1582-1591.
3 Earth Pledge Foundation, 2004. Green Roofs - Ecological Design and Construction. Schiffer Publishing.
4 Ishikawa, H., et al, 2006. Flow around a living tree. JSME International Journal (Series B) 49, 1064-1069.
5 Kane, B. and Smiley, E.T., 2006. Drag coefficients and crown area estimation of red maple. Canadian Journal of Forest Research 36(8), 1951-1958.
6 Kane, B., Pavlis, M., Harris, J. R. and Seiler, J. R., 2008. Crown reconfiguration and trunk stress in deciduous trees. Canadian Journal of Forest Research 38(6), 1275-1289.
7 Koizumi, A., 2010. Evaluation of drag coefficients of poplar-tree crowns by a field test method. Journal of Wood Science 56(3), 189-193.
8 Mayhead, G. J., 1973. Some drag coefficients for British forest trees derived from wind tunnel studies. Agricultural Meteorology 12, 123-130.
9 Phattaralerphong, J. and Sinoquet, H., 2005. A method for 3D reconstruction of tree crown volume from photographs: assesment with 3D-digitized plants. Tree Physiology 25, 1229-1242.
10 Rudnicki, M., Mitchell, S. J. and Novak, M. D., 2004. Wind tunnel measurements of crown streamlining and drag relationships for three conifer species. Canadian Journal of Forest Research 34, 666-676.
11 Takamori, K., Nishimura, H. and Nomura., H., 2003. Wind force on several trees. Proceedings of AIJ coference, 79-80.
12 Vogel, S., 1984. Drag and flexibility in sessile organisms. American Zoologist 24 (1), 37-44.
13 Vollsinger, S., et al, 2005. Wind tunnel measurements of crown streamlining and drag relationships for several hardwood species. Canadian Journal of Forest Research 35, 1238-1249.

The Seventh International Colloquium on Bluff Body Aerodynamics and Applications (BBAA7)
Shanghai, China; September 2-6, 2012

Numerical simulation of flow past discrete coniferous trees

F.M. Fang [a], C.C. Liang [b], J.Y. Chung [c], C.Y. Yen [d], Y.C. Li [e], C.H. Chen [f]

[a-d] *Dept of Civil Engg., National Chung Hsing University, 250 Kuo Kuang Road, Taichung, Taiwan*
[e] *Architecture & Building Research Institute, 200, Sect. 3, Beisin Road, Sindian, Taiwan*
[f] *Dept. of Civil & Environmental Engg., National University of Kaohsiung, Kaohsiung, Taiwan*

ABSTRACT: The study is to establish a numerical model, capable of correctly predicting flows past discrete coniferous trees so as to provide a handy tool for pedestrian wind analysis during the preliminary design for local wind environments. Besides numerical computations, wind tunnel measurements were also performed to guide and confirm the numerical simulations. Results showed that the tree factor, to be applied in the numerical flow computations, generally increased with increases of the volume ratio and horizontal thickness of the tree body. Based on a calibrated relationship of the tree factor, numerical computations were further performed to simulate flow past an isolated tree and dual trees. The predicted downstream wind speed profiles showed good agreements compared to the measurement results.

KEYWORDS: numerical simulation, wind tunnel measurement, pedestrian wind, coniferous tree.

1 INTRODUCTION

Planting trees in building areas can not only upgrade the local landscape but to some extent improve the wind environment, particularly regarding the reduction of wind speed at the pedestrian level. Therefore, how to analyze the wind flow in areas with discrete trees becomes an important task for the designers during the planning stage. Physically, the flow pattern around a tree may appear somewhat different from that around a solid (impermeable) body due to its porous nature. As a portion of wind passes through the tree, the shedding vortices can interact with the penetrating flow and disturb the formation of the downstream wake. Intuitively, the extent of this interaction effect may depend on the porosity and thickness of the tree.

To analyze the flow past discrete trees, wind tunnel model experiments are mostly employed. Besides the amount of human labor and time required in the execution of experimental work, however, technical difficulties (such as the scale effect) are generally encountered. In contrast, the adoption of numerical simulations can be another alternative for the flow analysis. Due to significant advancements of computer hardware and software, the application of numerical simulations becomes more and more popular in dealing with such flow problems as it is considered relatively more economical. Although it is presently impractical to simulate the flow around porous trees by taking into account the detail geometry of leaves and twigs since it involves a great deal of computing time, a second choice may be to find out a factor that physically reflect their existence in the computations.

Accordingly, the goal of the study is to establish a numerical model, capable of adequately predicting flows past discrete trees so as to provide a handy tool for pedestrian wind analysis during the preliminary design for local wind environments. Besides numerical computations, wind tunnel measurements were also performed to confirm and guide the numerical simulations.

2 RELATED STUDIES

Most of the previous related work concentrated on the studies in the research areas of forestry and meteorology. The main focus was to investigate the global wind flow characteristics around group trees in forest territories. Based on a global approach, the three-dimensional wind flow analyses were generally simplified into a two- or even one-dimensional problem depending on the spatial distributions of local group trees. Typically, Finnigan [1] stated that the surface wind flow region could be divided into a canopy and a surface sublayer. By field investigations, Raupach *et al.* [2] indicated that the pattern of turbulent flow characteristics within the canopy sublayer was close to that of a mixing-layer flow. A description of wind speed profile was then proposed by Raupach *et al.* [3] based on wind tunnel results. Similar profiles in forest territories were also brought out by Mihailovic *et al*. [4]. Based on the wind tunnel results, Massman [5] proposed a leaf area index (LAI) and discussed its influence on the associated wind speed profiles, surface shear velocities and roughness heights. Additionally, Novak *et al.* [6] found that a change of the spatial density of trees in a forest could affect the local mean and turbulent flow characteristics, mainly dominated by large-scale turbulence eddies. Further results of wind tunnel experiments of wind flow past a single layer and a double layer of plants by Boldes *et al*. [7] revealed that mixing flows occurred in the wake region and produced bleed flows due to the effect of large-scale eddies. Moreover, Flesch & Wilson [8, 9] carried out wind tunnel experiments to investigate the protected area as well as the extent of wind speed reduction downstream of group trees.

There are also several typical studies related to wind past trees by using numerical analysis. For instance, Shaw & Schumann [10] proposed an inclusion of a source term in the momentum equations to physically reflect the tree effects. The introduced drag term was the product of the drag coefficient (c_D), leaf density (a) and combined velocity (V). Wilson and Flesch [11] used a two-dimensional numerical model to simulated the flow past forests. The predicted wind speed profiles were in good agreements with the in-field results by Raynor [12]. By performing large eddy simulations, Su *et al*. [13] predicted neutrally stratified flows past forests. Patton & Davis [14] also carried out large eddy simulations to investigate the dispersion mechanism of chemicals in forests. Watanable [15] performed large eddy computations to examine the turbulence structure above forests. Moreover, Sládek *et al*. [16] investigated numerically the two- and three dimensional wind fields of boundary-layer flows past forests in complicated land territories.

3 NUMERICAL METHOD

In the study, a weakly-compressible-flow method [17] together with large-eddy-simulations is used in the numerical simulations. To simulate turbulence effect in the flow, a subgrid-scale turbulence model by Smagorinsky [18] is applied. In the computations, a finite-volume approach is adopted. For spatial volumes wholly occupied by air, the governing continuity and momentum equations in index forms are respectively as

$$\frac{\partial \overline{p}}{\partial t} + \frac{\partial}{\partial x_j}(\rho c^2 \overline{u_j}) = 0 \tag{1}$$

$$\frac{\partial \overline{u_i}}{\partial t} + \frac{\partial \overline{u_i}\,\overline{u_j}}{\partial x_j} = -\frac{\partial}{\partial x_j}\left(\frac{\overline{p^*}}{\rho}\right) + \frac{\partial}{\partial x_j}\left(\frac{\tau_{ij}}{\rho}\right) \tag{2}$$

where t and x indicate time and spatial coordinates; c, ρ , u and p denote respectively sound speed, air density, flow velocity and pressure; “bar” means spatial average and the subscripts in-

dicates spatial indices; $p^* = p + (\rho/3)\overline{u_i' u_i'}$; τ is the combination of the viscous and subgrid-scale stress, in which the subgrid-scale diffusion coefficient is expressed as [18]

$$v_t = (C_S \Delta)^2 (\frac{S_{ij}}{2})^{0.5} \qquad \text{with} \qquad S_{ij} = (\frac{\partial \overline{u_j}}{\partial x_i} + \frac{\partial \overline{u_i}}{\partial x_j}) \tag{3}$$

where Δ denotes the characteristic length of the computation cell and C_S is the Smagorinsky constant.

For the computational cells partially occupied by leaves and twigs, by neglecting sway motion of the tree body the momentum equation is modified by adding a source term as [10]

$$\frac{\partial \overline{u_i}}{\partial t} + \frac{\partial \overline{u_i}\,\overline{u_j}}{\partial x_j} = -\frac{\partial}{\partial x_j}(\frac{\overline{p^*}}{\rho}) + \frac{\partial}{\partial x_j}(\frac{\tau_{ij}}{\rho}) + (f_D)_i \tag{4}$$

$$\text{with} \quad \overrightarrow{f_D} = \left[-C_D a u \left|\overrightarrow{V}\right|, -C_D a v \left|\overrightarrow{V}\right|, -C_D a w \left|\overrightarrow{V}\right| \right]^T \tag{5}$$

where C_D is the drag coefficient and a is the leaf surface area per unit volume.

4 WIND TUNNEL EXPERIMENTS

Since the factor of leaf surface area per unit volume (a value) cannot not be easily measured, a new parameter is proposed and is defined as

$$C_{Da} = C_D a \tag{6}$$

To investigate how C_{Da} varied with the conditions of trees, wind tunnel experiments were performed. In the experiments, a rectangular panel (D = 0.28 m) with a number of parallel coniferous leaf strings was set in the direction perpendicular to the uniform approaching flow (see Figs. 1 and 2； U_0 = 10 m/s). Hot-film anemometry was adopted to measure the downstream cross-sectional mean and root-mean-square velocity profiles. On the other hand, a series of numerical simulations with a number of guessed C_{Da} values were performed in parallel. By comparing with the measurement profiles corresponding to a prescribed thickness (B) and volume density of trees (γ), the C_{Da} value that lead to the best agreement between the measurement and calculated profiles was then obtained. Figure 3 illustrates a typical example of the velocity profile comparisons.

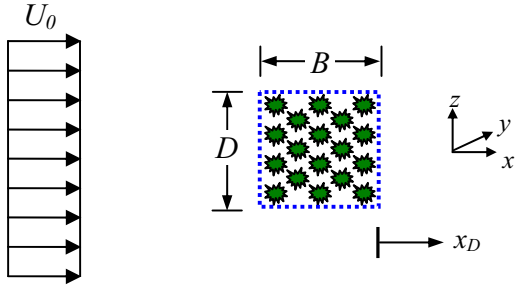

Figure 1. Schematic of experiments.

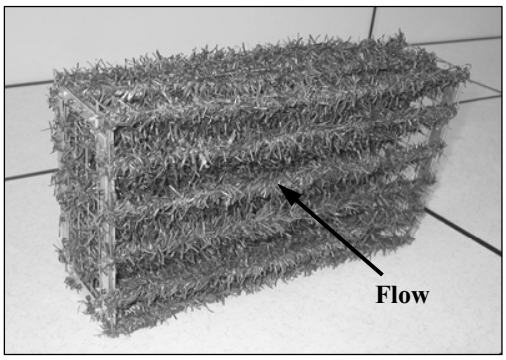

Figure 2. Panel of tree strings.

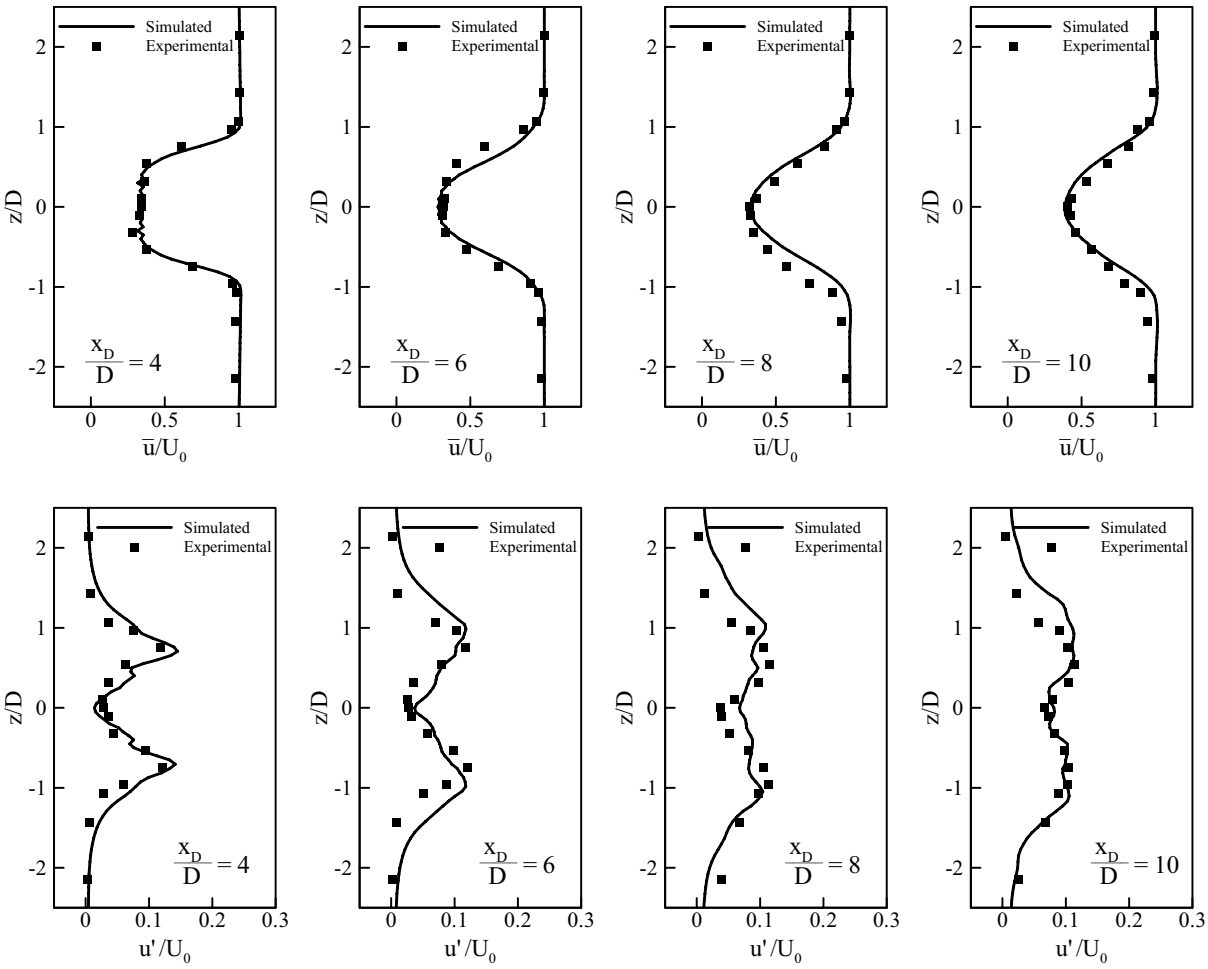

Figure 3. Comparison of cross-sectional mean and root-mean-square velocity profiles behind a square tree panel. (B/D = 0.5, γ = 0.3%, C_{Da} = 1.75)

Accordingly, Fig. 4 depicts the contour plot of the C_{Da} value in relation to the panel thickness (B) and volume ratio of tree body (γ). The general tendency shows that an increase of the

panel width or the volume ratio results in an increase of the C_{Da} value, except when B and γ are about 0.3D and 0.75%. In addition, the variation of C_{Da} appears insignificant as B is greater than $2D$.

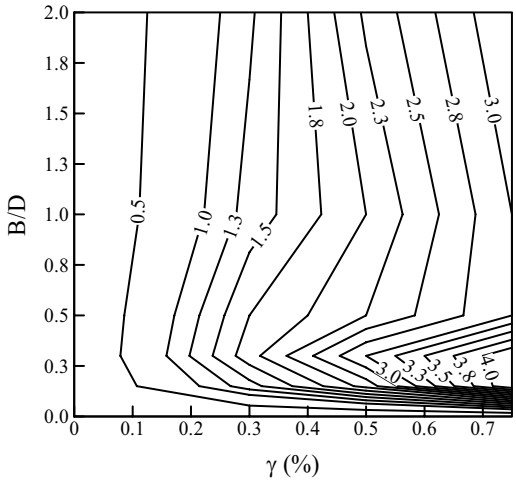

Figure 4. Contours of C_{Da}.

5 FLOW SIMULATIONS

Based on the result in Fig. 4, simulations were conducted further to examine the validity of the calibrated C_{Da} variations. In the computations, a uniform approaching flow is selected (U_0 = 10 m/s). Parallel wind tunnel experiments were also carried out to measure the downstream velocity profiles for comparisons.

5.1 *Uniform flow past an isolated coniferous tree with a conical shape*

Figure 5 depicts the schematic of the three-dimensional problem. In the computation, the tree body was divided into several layers, and the C_{Da} values associated with the grid cells in each layer were taken from the calibration contour plot (Fig. 4) according to the horizontal thickness and volume ratio of the tree body.

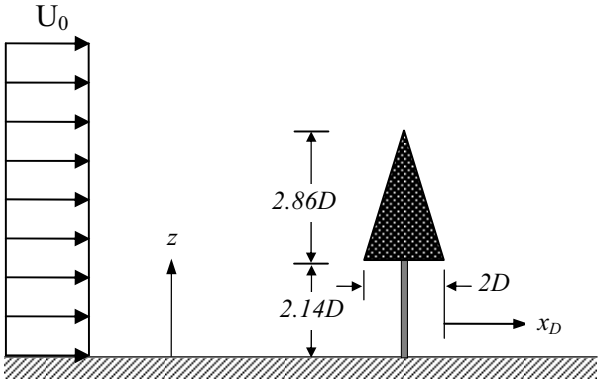

Figure 5. Schematic of flow past an isolated tree body with a conical shape.

The comparisons of mean and root-mean-square velocity profiles at a typical downstream cross-section (x_D = 6*D*) are shown in Fig. 6. The spatial correlation coefficient of the cross-sectional velocity variations between the experimental and calculated results are respectively 0.976 and 0.916, indicating that the simulations well predicted the flow.

(a) Mean profiles (correlation coefficient = 0.976)

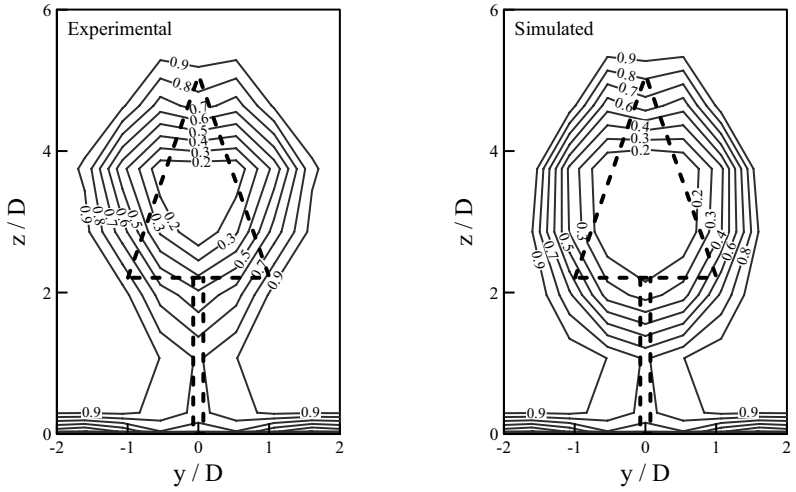

(b) Root-mean-square profiles (correlation coefficient = 0.916)

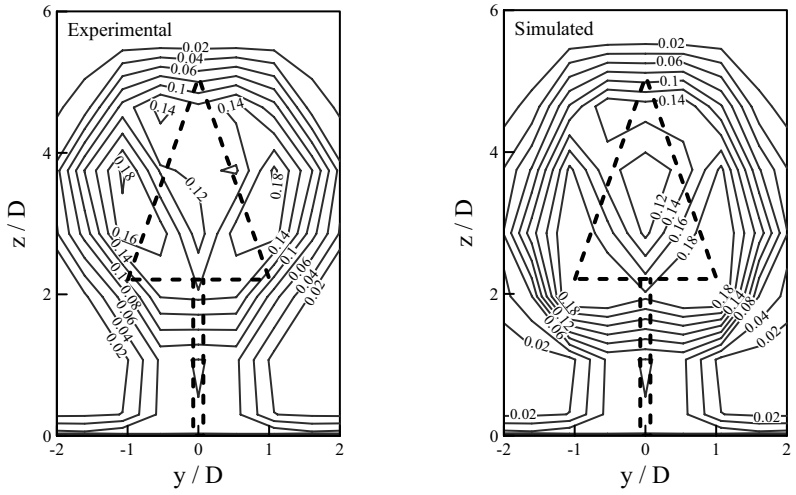

Figure 6. Comparison of cross-sectional mean and root-mean-square velocity profiles of an isolated tree (x_D = 6*D*).

5.2 *Uniform flow past dual coniferous trees in a tandem arrangement*

An additional flow computation was conducted to simulate a uniform flow past dual coniferous trees in a tandem arrangement with an edge-to edge distance of 2*D* (see Fig. 7). The comparison shows in Fig. 8 that the agreement between the measurement and the predicted results at a typical cross-section (x_D = 6*D*) appears fairly good. The spatial correlation coefficients are respectively 0.976 for the mean profiles and 0.916 for the root-mean-square profiles.

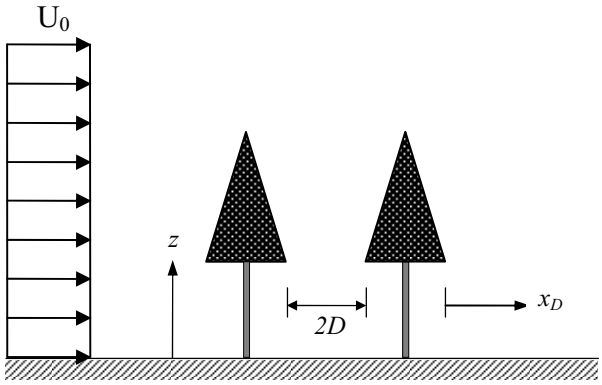

Figure 7. Schematic of flow past dual trees in a tandem arrangement.

(a) Mean profiles (correlation coefficient = 0.985)

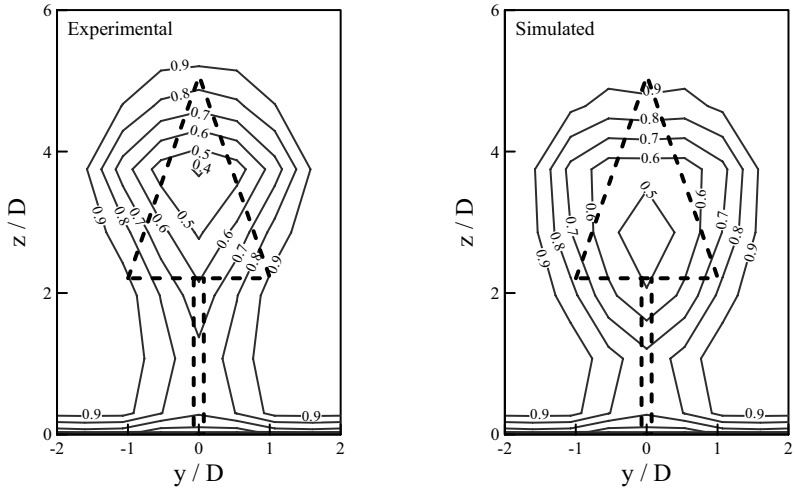

(b) Root-mean-square profiles (correlation coefficient = 0.901)

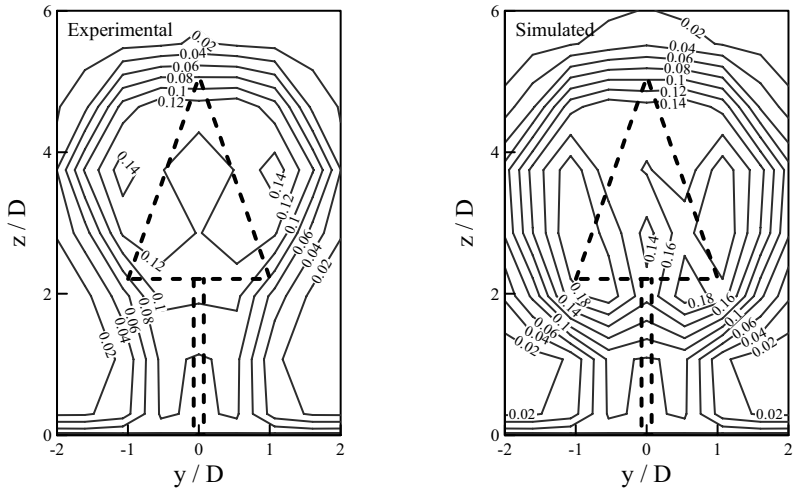

Figure 8. Comparison of mean and root-mean-square velocity profiles of dual trees in a tandem arrangement ($x_D = 6D$).

5.3 *Uniform flow past dual coniferous trees in a side-by-side arrangement*

A uniform flow past dual coniferous trees in a side-by-side arrangement with an edge-to-edge transverse distance of *0.5D* was further simulated numerically. The comparisons in Fig. 9 show that at a typical downstream cross-section (x_D = *0.6D*), again, the predicted mean and fluctuating velocity profiles are predicted with acceptable accuracy.

(a) Mean profiles (correlation coefficient = 0.939)

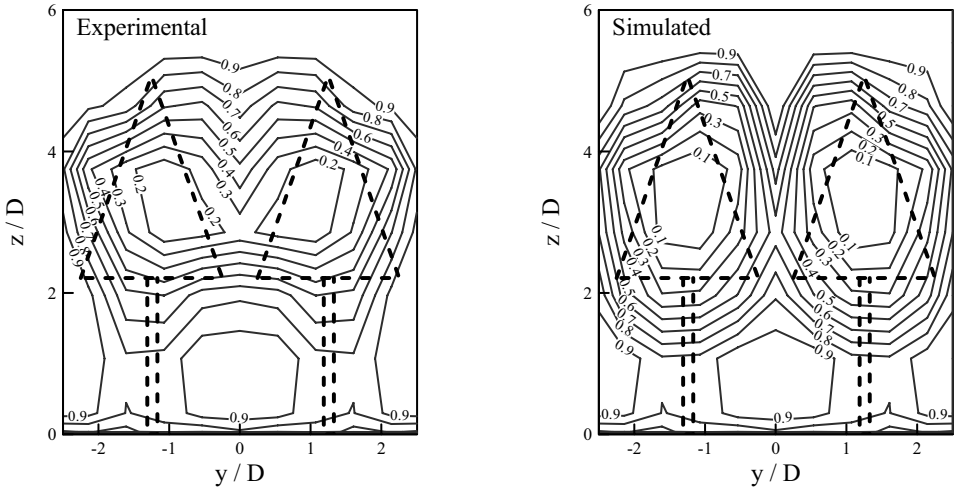

(b) Root-mean-square profiles (correlation coefficient = 0.854)

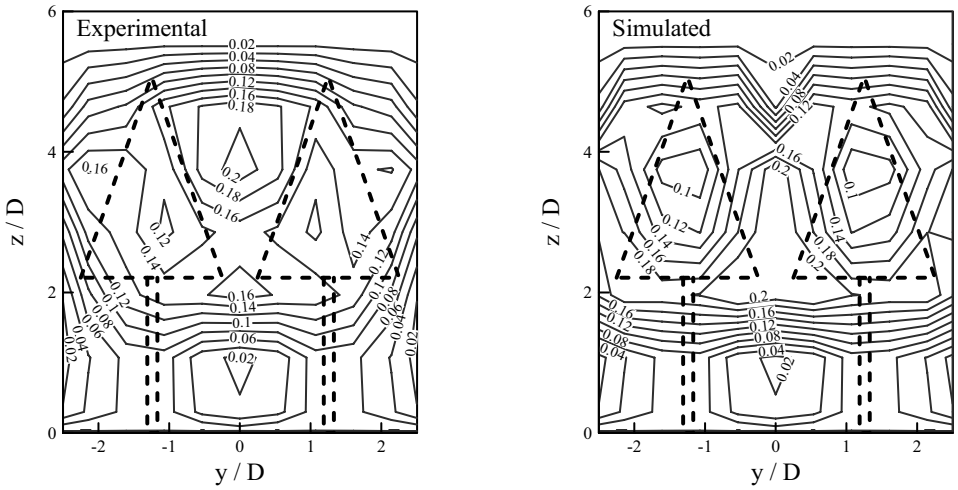

Figure 9. Comparison of mean and root-mean-square velocity profiles of dual trees in a side-by-side arrangement (x_D = 6*D*).

6 DISCUSSIONS

Different from the analysis of flow past group trees, the present study attempted to investigate the effect of discrete trees in more detail so as to provide extensive information regarding the local tree characteristics. Although the sway motion of trees due to wind action could affect the neighboring flow behavior [8, 9, 11], it was not considered in the study to simplify the analysis.

The basic concept of the proposed procedure to determine the C_{Da} variation is that as the wind flow impinges the tree body, the effect of the tree is mainly controlled by the volume ratio of local leaves and twigs as well as the horizontal thickness. As the numerical flow simulations in the three examples were successfully applied, it indicates that the C_{Da} variation (Fig. 4) can be used to simulate flows past discrete trees with adequate accuracy.

The result in Fig. 4 also indicates that as the thickness of the tree body exceeds $2D$(D = 0.28 m), the variation of C_{Da} appears insignificant. It reveals that the relation can be adopted in cases with a larger size of discrete trees.

Finally, it interesting that C_{Da} varies significantly when B and γ are near $0.3D$ and 0.75% . In the wind tunnel experiments, however, the range of the volume density (γ) was limited up to 0.75%. Additional studies will be needed to investigate this issue in a more extensive manner.

7 CONCLUSIONS

A method of identifying the tree factor was proposed. By comparing with the measurement results of the velocity profiles downstream of rectangular tree panels, the C_{Da} value associated with the thickness (B) and volume ratio (γ) of the tree body was calibrated numerically by a try-and-error procedure. Accordingly, the variation of C_{Da} in relation to B and γ was presented.

Based on the calibrated contour plot of C_{Da}, simulations of uniform flows past an isolated tree, and dual trees in a tandem and a side-by-side arrangement were performed to examine the validity of the numerical method. The comparisons, in terms of the downstream mean and root-mean-square velocity profiles indicated that the flows were well predicted. Several conclusions are drawn as follows:

1. The general tendency shows that an increase of the thickness or the volume ratio results in an increase of the C_{Da} value, except when B and γ are about $0.3D$ and 0.75% respectively.
2. When B exceeds $2D$, the variation of C_{Da} appears insignificant.
3. As the sway motions of trees can be neglected, the calibrated variation of C_{Da} can be readily applied to simulate flows past discrete trees with adequate accuracy.

8 ACKNOWLEDGEMENTS

The study was cordially sponsored by National Science Council in Taiwan (Grant No. NSC 100-2221-E-005-068).

9 REFERENCES

1 J. Finnigan, Turbulence in plant canopies, Annu. Rev. Fluid Mech., 32 (2000) 519-571.
2 M.R. Raupach, R.A. Antonia and S. Rajagopalan, Rough-wall turbulent boundary layers, Appl. Mech. Rev., 44 (1991) 1-25.
3 M.R. Raupach, P.A. Coppin and B.J. Legg, Experiments on scalar dispersion within a model plant canopy. Part I: The turbulence structure, Bound.-Lay. Meteorol., 35 (1986) 21-52.
4 D.T. Mihailovic, B. Lalic, B. Rajkovic and I. Arsenic, I., A roughness sublayer wind profile above non-uniform surface, Bound.-Lay. Meteorol., 93 (1999) 425–451.
5 W. Massman, A comparative study of some mathematical models of the mean wind structure and aerodynamic drag of plant canopies," Bound.-Lay. Meteorol., 40 (1987) 179-197.
6 M.D. Novak, J.S. Warland, A.L. Orchaansky, R. Ketler, and R. Green, R., Wind tunnel and field measurements of turbulent flow in forests. Part I: Uniformly thinned stands, Bound.-Lay. Meteorol., 95 (2000) 457-495.

7 U. Boldes, J. Colman and D.L.J. Maranon, Field study of the flow behind single and double row herbaceous windbreaks, J. Ind. Aerodyn., 89 (2001) 665-687.
8 T. K. Flesch and J.D. Wilson, Wind and remnant tree sway in forest cutblocks. I. Measured winds in experimental cutblocks, Agr. Forest Meteorol., 93 (1999) 229-242.
9 T. K. Flesch and J.D. Wilson, Wind and remnant tree sway in forest cutblocks. II. Relating measured tree sway to wind statistics, Agr. Forest Meteorol., 93 (1999) 243-258.
10 R.H. Shaw and U. Schumann, Large-eddy simulation of turbulent flow above and within a forest, Bound-Lay. Meteorol., 61 (1992) 47-64.
11 J. D. Wilson and T. K. Flesch, Wind and remnant tree sway in forest cutblocks. III. A windflow model to diagnose spatial variation," Agr. Forest Meteorol., 93 (1999) 243-258.
12 G.S. Raynor, Wind and temperature structure in a coniferous forest and a contiguous field," Forest Sci., 17 (1971) 351-363.
13 H.B. Su, R.H. Shaw, K.T. Pawu, C.H. Moeng and P.P. Sullivan, Turbulent statistics of neutrally stratified flow within and above a sparse forest from large-eddy simulation and field observations, Bound.-Lay. Meteorol., 88 (1998) 363-397.
14 E.G. Patton and K.J. Davis, Decaying scalars emitted by a forest canopy: A numerical study," Bound.-Lay. Meteorol., 100 (2001) 91-129.
15 T. Watanabe, Large eddy simulation of coherent turbulence structures associated with scalar ramps over plant canopies," Bound.-Lay. Meteorol., 112 (2004) 307-341.
16 I. Sladek, T. Bodnar and K. Kozel, On a numerical study of atmospheric 2D and 3D-flows over a complex topography with forest including pollution dispersion, J. Ind. Aerodyn., 95 (2007) 1424-1444.
17 C.C.S. Song and M. Yuan, A weakly compressible model and rapid convergence methods, J. Fluid E.-T. ASME, 110 (1988) 441-455.
18 J. Smagorinsky, General circulation experiments with primitive equations, Month Weather Rev., 91 (1963) 99-164.

The Seventh International Colloquium on Bluff Body Aerodynamics and Applications (BBAA7)
Shanghai, China; September 2-6, 2012

Aerodynamics of high-speed trains in confined spaces

Tim Gilbert, Chris Baker, Andrew Quinn, Mark Sterling

School of Civil Engineering, University of Birmingham, Edgbaston, Birmingham, UK

ABSTRACT: In confined spaces the air movements around high speed trains may be amplified. Moving-model aerodynamic experiments were undertaken to identify the fundamental changes to train-induced air movements by firing a 1/25th scale high-speed train past instrumented walls and through box-shaped tunnels. The effect of confinement on velocities in the boundary layer and wake are assessed. Moreover the peak gusts are analysed using a prescribed European methodology to determine whether confined spaces cause the flow to exceed acceptable criteria. All results showed significant increases in velocity in the near wake, with the gusts exceeding allowable limits of velocity at positions extending far from the train side. The pressure transient increased in magnitude with increasing confinement, although the increases were lower than those predicted by European standards.

KEYWORDS: High-speed trains, aerodynamics, confined spaces, pressure, slipstream.

1 INTRODUCTION

This paper will analyse the flow around a German ICE-2-style high-speed train passing through confined spaces formed by various combinations of walls and ceilings, both at a fundamental and an applied level. This information is useful for assessing resilience and safety on routes where confined sections may amplify the flow. Tests were undertaken at the TRAIN Rig moving-model aerodynamic facility in Derby (UK), owned and operated by the University of Birmingham. It has 150m long tracks and can propel reduced scale model vehicles to speeds of up to 75m/s. A large dataset was collected, from which a small subset will be analysed in this paper.

The methodology is described in Section 2. Slipstream and wake velocities will be presented in Sections 3 and 4, with emphasis placed on the fundamental changes caused by the confined cases. Section 5 examines the peak gusts at 'human height' at the trackside, using the European slipstream methodology set out by the 'Technical Specification for Interoperability' (TSI) for high-speed rolling stock ([1]). The TSI rules apply to any train operator seeking regulatory acceptance for operating high-speed services between national borders, so it is very relevant to the developing trans-European interoperable high-speed rail network. Section 6 builds on a recent observation by [2] that the predictive equations for loading on objects caused by train-induced pressure changes in [3] may need revising. A revision would have a direct impact on the structural engineering costs of trackside infrastructure ([4,5]).

2 METHODOLOGY

Experiments were commissioned at the TRAIN Rig moving-model facility. A four-coach ICE-2 shaped train was used, pictured in Figure 1 below. It was built to 1/25 scale with equivalent full-scale length 106m. The test Reynolds number was 9 million based on the train model length and test speed of 32±1m/s.

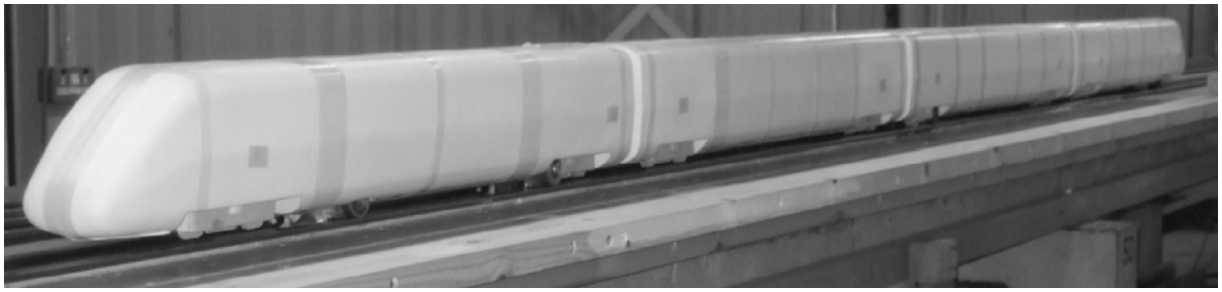

Figure 1: Photograph of the ICE-2 shaped model train.

The choice of facility was inspired by the need to measure velocities in areas within which such concerns as space for equipment, logistical issues, and health and safety considerations would be limiting factors for commissioning full-scale tests. The ability to account for relative movement between the train and the walls is a particular strength of the TRAIN Rig over wind tunnels. Other benefits of the facility compared to full-scale tests include the ability to control the speeds with little deviation between runs, to obtain data quickly and inexpensively, and to prevent changes in the background environment from occurring unpredictably and suddenly.

The ICE-2 train was selected as there is a wealth of empirical data against which to validate the results. There are several unique flow features related to the geometry, making the results specific to the train. An often crucial area is the nose and tail since the pressure and wake depend on the tail geometry. [6] discusses the flow differences between train geometries in detail.

Figure 2 below shows a general arrangement of structures, probes and pressure tappings. All measurements in this paper are written as full-scale equivalent dimensions (scale factor 25). There are three coordinate systems: ‘y’ originates from the surface of the train at its widest point; ‘y(r)’ from the top-centre of the nearest rail; ‘y(c)’ from the track centre; ‘z’ from the top of the rail. The ‘x’ axis extends through the page, with the origin aligned to the train nose (predicted to ±15cm accuracy at full-scale). Table 1 explains the structure configurations. The photographs in Figures 3 (a) and (b) show the structures as built. Every probe has a corresponding open air ‘reference case’ for comparative purposes. The probes were repositioned for Case W2 so its own reference case called ‘OA2’ is provided.

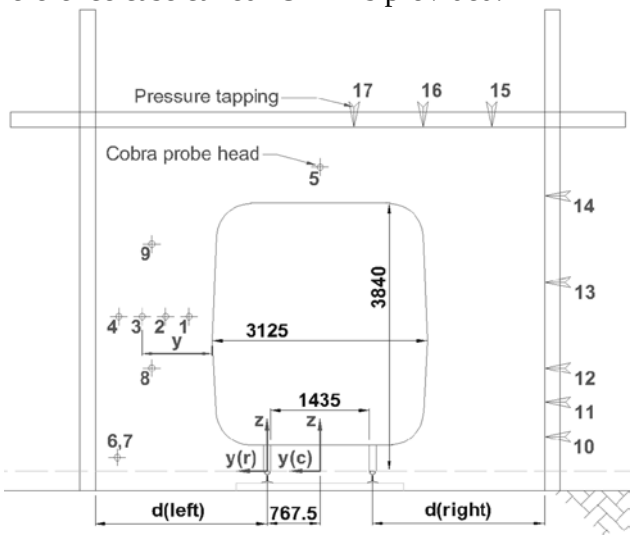

Figure 2: General arrangement of structures and instrumentation.

Table 1: Details of the test cases and structure geometries.

Case	Name	d(left) (m)	d(right) (m)	z (m)	Length[(1)] (m)	Ref. Case
OA1	Open air characterization for cases W1 W3 B1 B2.					
W1	2.5m walls	2.5	2.5	*No roof, walls 6.75m high*	8	OA1
W3	Asymmetrical walls		1.5			
B1	8m long box[(2)]		2.5	5		
B2	2m long box[(2)]		2.5		2	
OA2	Open air characterization for case W2					OA2
W2	2m walls	2	2	*No roof, walls 6.75m high*	8	

Notes:
(1) The structure length is written in model scale metres.
(2) The box edges are sealed.

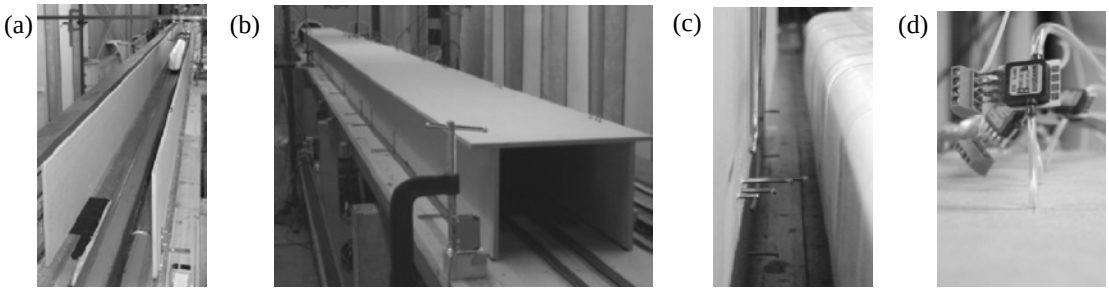

Figure 3: (a) Case W1, (b) Case B1, (c) Pressure tappings, (d) Cobra Probe heads

The probes which provide results relevant to this paper are included in Table 2 which describes their geometries. 'TFI' Cobra Probes (Figure 3(c)) measured the slipstream and wake velocities in three dimensions, and the static pressure. They were chosen because of their suitability for model-scale testing; their calibrated frequency responses are greater than 2000Hz; their accuracies are ±2%, and their 2.54mm head diameters are small and unobtrusive. The drawback is the 45 degree 'cone of acceptance' which limits the range of detection. If flow goes outside the range the data for that scan is replaced with zeros. The size of the ensemble (i.e. number of nonzero values per x-position) thus varied with distance, meaning that the ensemble was low around the first carriage where the flow was highly three-dimensional but rose to 80-100% in the wake where the flow was mainly longitudinal. For this reason the paper will not plot slipstream velocities upstream of the nose where data retention was poor. Pressure tappings were installed on the structure surfaces (Figure 3(d)). For all instruments the data were sampled at 5000Hz and low-pass filtered depending on the analysis requirements. Table 2 only describes the most relevant dimensions, but Figure 2 provides the necessary measurements to transfer geometries between coordinate systems.

Table 2: Description and positions of the instrumentation.

Probe	Type	Description	Case OA1/W1/W3/B1/B2				Case OA2/W2		
			y (m)	y(r) (m)	y(c) (m)	z (m)	y (m)	y(r) (m)	z (m)
1	Cobra	Boundary layer 1 $y_{wall}/5$ [(1)]	0.34			2.25	0.24		
2	Cobra	Boundary layer 2 $2y_{wall}/5$	0.69			2.25	0.48		
4	Cobra	Boundary layer 4 $4y_{wall}/5$	1.36			2.25	0.97		
6	Cobra	Trackside gusts			3	0.2		1.5	0.5

10-15	Tapping	Wall		2.5, 2, 1.5 (from right rail)		0.5, 1, 1.5, 2.75, 4			

Notes:
(1) The measurement y_{wall} represents the distance between the 'y' axis origin and the left wall, i.e. the gap between the train side and the wall. The probes are positioned in one fifth increments of y_{wall}.

3 THE BOUNDARY-LAYER

It is important to first validate the data. Figure 4 below plots the open air slipstreams (from OA2) against empirical data, closely following the analysis techniques used in the empirical tests. The data referred to as 'Baker' in Figure 4 (a) was reported in [7]. Hot-wire anemometers were used, and the positions differed very slightly (see legend for y-values); otherwise the test parameters were identical. The RAPIDE data in Figure 4 (b) was reported in [8] and comprised seven passes of an eight-car ICE-2 train measured by Gust anemometers, and seven passes of an ICE-2 model at the TRAIN Rig measured by Hot-wire anemometers. The train end at x=106m is denoted by a vertical dashed line. In Figure 4 (b) there are two 'train end' lines which represent the four and eight car trains respectively.

(a) Comparison with [7] (z=2.25m)

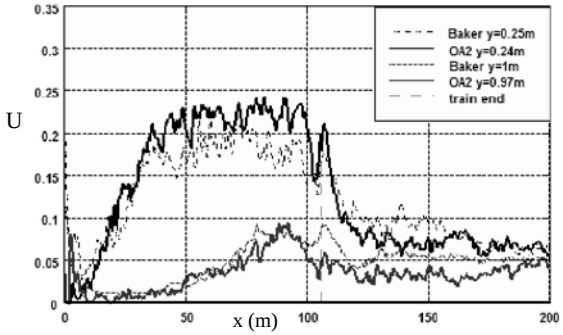

(b) Comparison with [8] (y(r)=1.5m, z=0.5m)

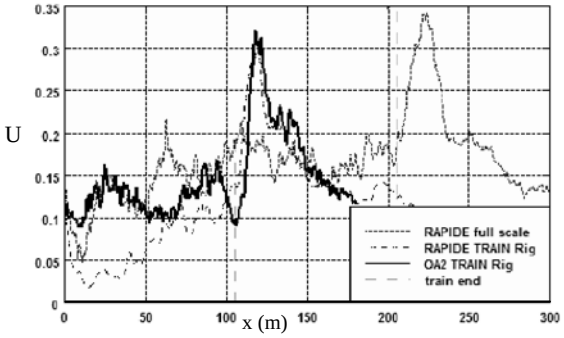

Figure 4: Comparisons of slipstream velocities with empirical data.

The Cobra Probes detect higher boundary layer velocities than previous model-scale tests, but this appears to be valid because agreement with the full-scale boundary layer in Figure 4 (b) is closer. The peak gust behind the tail is 6% lower than full-scale and has a shorter duration.

Moving on to the new results, a selection of boundary layer resultant velocities at half-train-height is shown in Figures 5-6 for a range of experimental configurations, and featuring Probes 1, 2 and 4. The slipstream data were low-pass filtered to 1000Hz using a Butterworth filter. They were non-dimensionalised by dividing by train speed (32m/s). The boundary layer extends from x=0-106m with the train end bounded by a vertical dashed line. A small section of the wake is shown. As stated previously the probe positions in Figures 5 and 6 differ, so comparisons may be made with the reference cases but not between Figures.

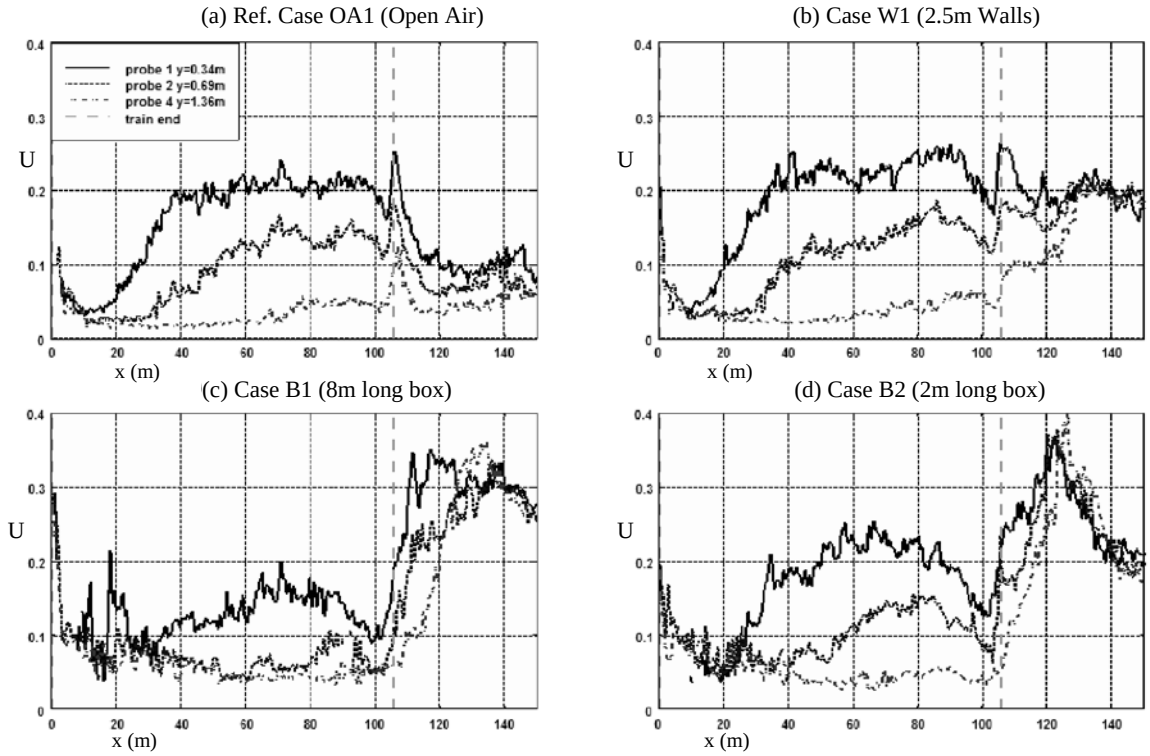

Figure 5: Boundary layer resultant velocities at z=2.25m. Reference case is OA1.

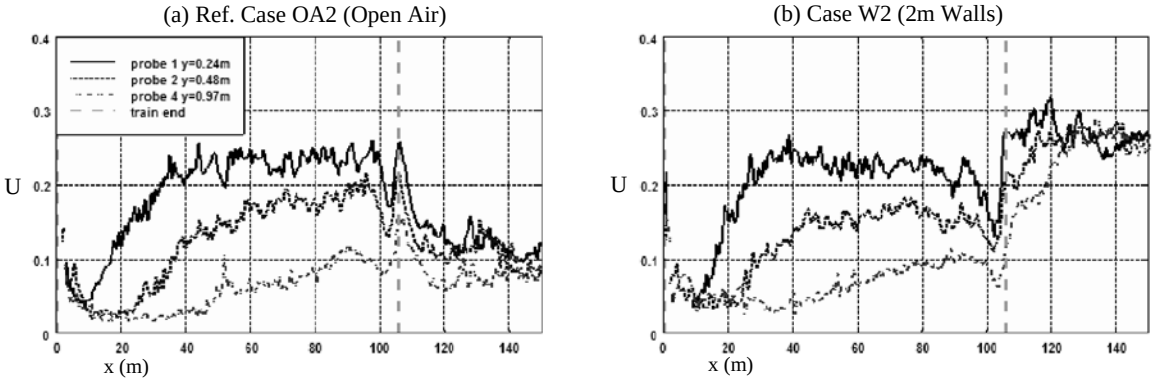

Figure 6: Boundary layer resultant velocities at z=2.25m. Reference case is OA2.

The results show that the boundary layer grows towards an equilibrium velocity, before falling off just upstream of the peak in the tail. For the wall cases the boundary layers develop very similarly to the open air cases. When the flow is enclosed by sealed boxes B1 or B2 it does not reach equilibrium because there are strong pressure gradients along the whole train length. In the short box the pressure gradients are more localized to the train ends so the velocity more closely resembles the results from unsealed configurations. The velocity gradient with respect to y (distance from train side) differs between the long and short boxes, which is likely related to the reduced cumulative effect of wall friction on the flow.

4 THE WAKE

A selection of resultant wake velocities is shown in Figures 7-8. The slipstream data were low-pass filtered to 1000Hz using a Butterworth filter. Only Probes 1 and 6 are shown. Probe 1 is quite representative of the z=2.25m group of boundary layer probes as Section 3 showed them collapsing into one curve. Probe 6 represents the wake at a low height further from the train side. Velocities are non-dimensionalised by dividing by train speed.

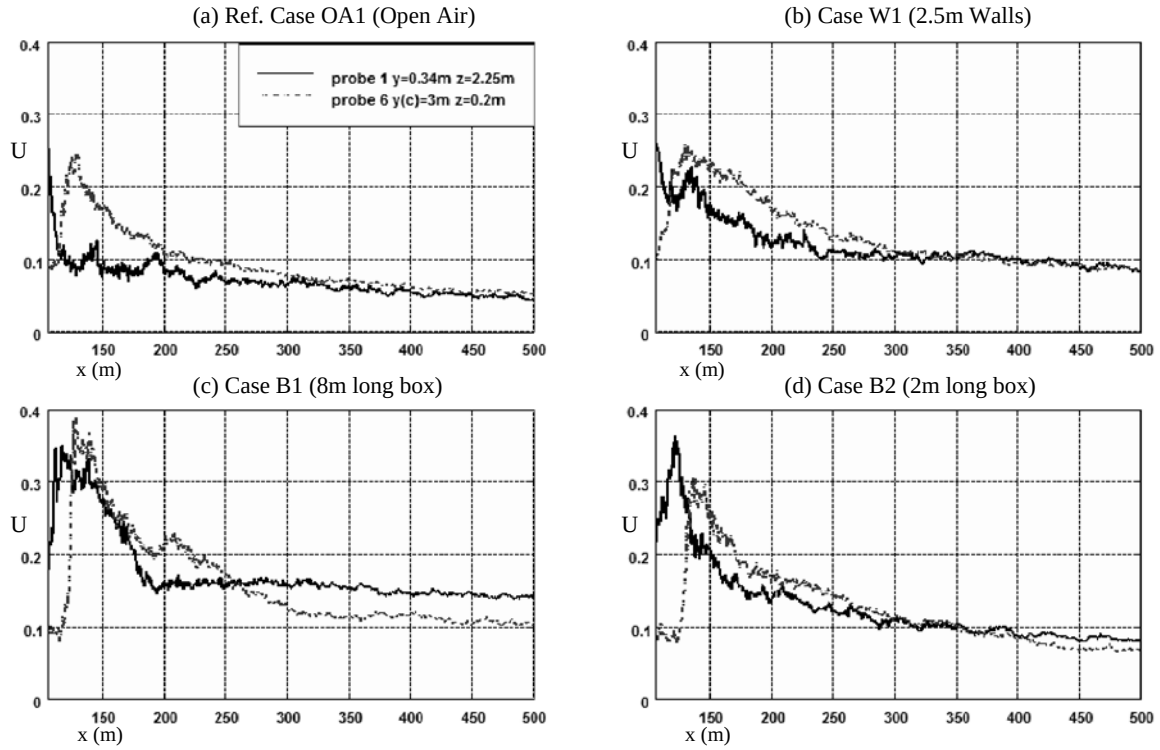

Figure 7: Wake resultant velocities. Reference case is OA1.

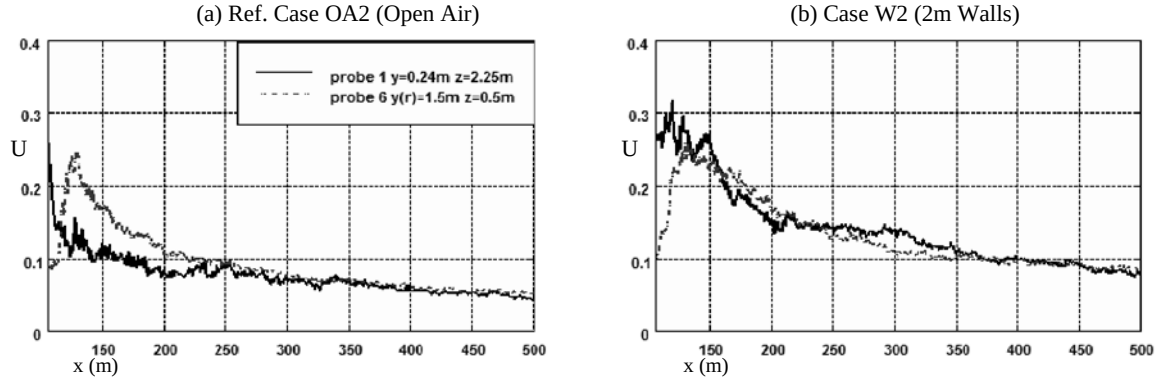

Figure 8: Wake resultant velocities. Reference case is OA2.

The results show the gust magnitudes significantly increasing relative to open air gusts in all confined cases except W1. In all cases the duration of the gust is greatly increased, which is likely due to containment of the trailing vortices behind the train which reduces their spatial

dissipation. Even at 500m the velocities are still higher than the open air cases. The signals from Probes 1 and 6 converge, suggesting the flow becomes somewhat one-dimensional and fills the space. They decay together exponentially. Case B1 (Probe 1) does not fit this description, as it seems that the decaying velocity is met by a continuous flow of air being drawn through the box long after the train has passed. It is not known if this effect is as pronounced at full-scale.

Probe 6 is laterally further from the train side than Probe 1, so predictably the near wake peak gust occurs later. We may also examine height effects by comparing Probe 6 and Probe 4 as they are at nearly the same lateral position. For reader reference Probe 4 is plotted in Figures 5-6 above. In the open air Probe 6 captures higher gusts due to the proximity to the 'trailing edge' of the tail, where the large-scale vortices are released. In the Wall and Box cases Probes 4 and 6 show closer agreement with each other, suggesting that the vortex structure fills more vertical space with increasing confinement.

5 LOW HEIGHT GUSTS

Probe 6 at y(c)=3m and z=0.2m (in Cases OA1, W1, W3, B1, B2) could be taken to represent a trackside worker standing at a continuous walkway as trains pass, with the probe roughly at the position of their centre-of-gravity. When Probe 6 is at y(r)=1.5m and z=0.5m (in Cases OA2, W2) it could represent a worker standing on the edge of a ballast shoulder. Note that for these tests the ballast itself was not simulated, meaning the ground profile was flat.

The aforementioned TSI [1] rules will be used to assess low-height gusts. It specifies an acceptable limit on the slipstream of 22m/s (by the trackside). Assessment requires ≥20 measurements to be made with the train speed very close to the design speed, and at full scale next to straight, ballasted track. Each run must be measured at ≥10Hz then filtered with a 1 second window moving-average filter. The maximum velocities of each run form an ensemble from which the mean $\bar{u}$ and standard deviation σ may be calculated. The overall U(TSI) gust value is obtained by summing $\bar{u} + 2\sigma$ of the peak values.

The TSI method is designed and optimized for ideal running conditions. One of these idealized test requirements is that the train must be running in the open air with no obstructions. This means excessive velocities may occur in certain confined spaces. These results will provide an insight into how much the limits might be exceeded in confined spaces, but this paper will not go as far as recommending actions.

The chosen analysis method emulates that used in AeroTRAIN [9]. The data was low-pass filtered and re-sampled down to 1250Hz (50Hz * model scale). A moving-average filter then smoothed the runs to 25Hz (1 second * model scale). The assumption is that the characteristic lengths and durations of the gusts are exactly 1/25th of full scale. This is obviously not the case as Reynolds number effects are non-linear, so there will be some over- or under-smoothing caused by the filter, compared to the full-scale equivalent filter.

Peak gust values from individual runs are plotted in Figure 9 and separated by test case. Note that Figures 7-8 above show the corresponding ensemble average time histories as dotted lines. Table 3 summarizes the results of the analysis.

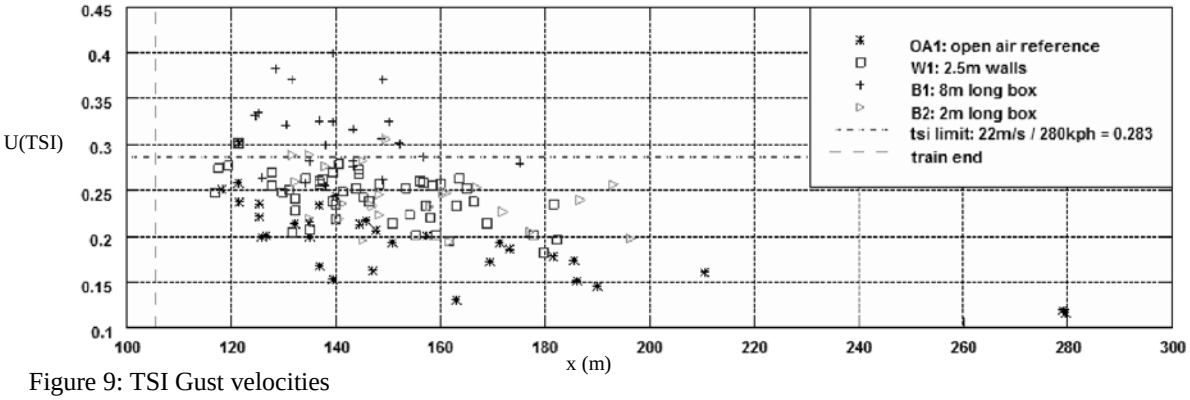

Figure 9: TSI Gust velocities

Table 3: Results of the TSI analysis applied to slipstream gusts at low heights.

Test case	Number of runs (n)	Mean ($\bar{u}$)	Standard deviation (σ)	U(TSI) ($\bar{u} + 2\sigma$)	Increase on open air (%)	Position of U(TSI) from x=0 (m)	Runs exceeding 22m/s limit (%)	Standard error of U(TSI) ($2\sigma/\sqrt{n}$)[(1)] (%)
Probe at y(c)=3m, and z=0.2m. Conforms to TSI. Plotted in Figure 9.								
OA1	32	0.20	0.04	0.28	--	157	3%	1.42
W1	50	0.24	0.03	0.29	4% on OA1	146	2%	0.84
B1	25	0.31	0.04	0.39	39% on OA1	129	60%	1.6
B2	25	0.24	0.03	0.3	7% on OA1	155	13%	1.2
Probe at y(r)=1.5m, and z=0.5m. Not plotted.								
OA2	36	0.23	0.06	0.34	--	139	*No prescribed limits*	2
W2	50	0.33	0.03	0.4	18% on OA2	122	*No prescribed limits*	0.84

Notes:
(1) The standard error is multiplied by two because U(TSI) is calculated by $\bar{u} + 2\sigma$.

Before drawing any conclusions the open air U(TSI) value should be validated. Unfortunately there aren't any directly comparable empirical tests, but the most similar is reported in [10]. Full-scale measurements of 16-car double-unit ICE-2 trains were undertaken at a position corresponding to OA1, providing a dataset of 32 passes (exactly the same as OA1), with a U(TSI) of 0.28. Although the values agree, one would expect the moving-model value to be slightly lower due to the shorter train model length. Nevertheless we may conclude that the combined mean and standard deviation of the gusts give close enough values to what would be measured at full-scale.

Moving on to the confined cases, all found higher U(TSI) values than the open air reference cases. The U(TSI) value for Case W1 was above the allowable limit of 0.283, but interestingly just 2% of the individual runs had exceeded this limit, i.e. fewer of them than OA1. On closer inspection this is because σ is lower than OA1 whilst $\bar{u}$ is higher. This is a curiosity of the TSI method. The 8m long Box (B1) found greater gust magnitudes than the 2m long box (B2). Table 3 also shows how the position of the peak gust varies; the gusts generally occur closer to the train tail as confinement increases, although this is less-so for short structures.

6 THE PRESSURE TRANSIENT

The final point of discussion addresses transient pressure loads on stationary structures. [2] recently showed that a moving-model Class 390 UK train caused pressure loads on low, short vertical walls that were significantly lower than the Eurocode ([3]) predicted loads when they were close to the side of the train. This was mainly because UK trains have smaller cross-sectional areas than the continental trains that the code equations were derived from. The code equations originated from CFD 'Panel method' simulations. The data is shown in Figure 10 (a). the paper proposed a less conservative 'National Annex' to the code for British infrastructure, based on this and other results. It was also recommended that further experiments are carried out at the TRAIN Rig on continental gauge trains to replace "the less reliable data in the current code", referring at least to the CFD-derived data.

These new experimental results allow an early indication to be made on how the pressure varies with lateral distance, and whether the current code accurately predicts the loads for larger continental rolling stock in this situation. The pressure is presumed to be scalable and sufficiently Reynolds number independent, as proven in [11]. In what follows the analysis method set out in [2] will be performed on just the vertical wall data. These experiments represent a worst case scenario; the walls are little-affected by end and edge effects, the train is distinctly wider than most high-speed trains, and it has a wedge-shaped nose, so overall the ICE-2 produces higher pressure transients than modern 'streamlined' rolling stock. The analysis involves first obtaining the maximum and minimum pressures by averaging the pressure 5m in front of and behind the nose location where the pressure crosses zero. For consistency with [2] the mean wall pressure is calculated by measuring the bending moment about the base of the maximum and minimum pressures at each of the five tapping positions, and rearranging the cantilever bending moment equation so that $\omega = 2M/L^2$, in which L=4m, and ω is the non-dimensional uniformly distributed load (Cp/m). This 'moment method' predicts slightly higher loads than a 'normal' integration of pressure tappings but agrees to one decimal place. Figure 10 (b) below shows the maximum and minimum pressures plotted against the predictive curve from [3]. Note that the predictive curve does not extend closer than y(c)=2.3m.

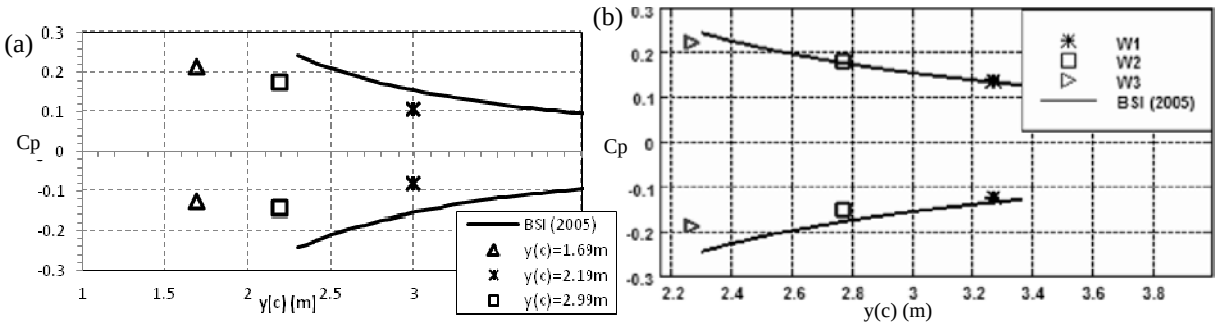

Figure 10: Wall surface pressures plotted against BSI (2005) ([3]) predictive curves, (a) Class 390, Baker et al (2012a), (b) ICE-2, Current tests.

It is clear that despite the worst case scenario the predictive curve for high-speed trains still predicts higher loads than it should for close wall distances, although the agreement is better at greater distances. Cost-savings may be possible through revising and updating the code. Please note this paper is not assuming cost savings are linked only with relaxations of standards. It may emerge that 'dynamically sensitive' structures or similar might require more stringent standards in a revised code, which may save money through reduced failures.

7 CONCLUSIONS

- The TRAIN Rig can measure slipstreams which compare well with full-scale values.
- Boundary layer velocities do not increase significantly with confinement. When sealed box cases were tested the boundary layer growth was suppressed due to steep pressure gradients along the boundary layer.
- Walls 2.5m or closer from the nearest rail increase the durations of the peak gusts behind the tail of the train, and in some cases their magnitudes.
- The addition of a ceiling to form a box further increases the durations of the gusts, as well as their magnitudes. The box represents a worst case.
- The peak-to-peak pressure change increases with confinement, with implications on the transient loads on structures.
- This paper presents just a small subset of the data that were collected. More detailed analysis of the data will be disseminated in the future, along with the results from follow-up experiments and CFD simulations.

8 ACKNOWLEDGEMENTS

Many thanks to RSSB who gave us authorization to use their pressure data. Tim would like to thank his co-authors for their support for this paper and his ongoing PhD. Thanks also to our colleagues David Soper, Sarah Jordan, and Francesco Dorigatti for their various roles in making these tests convenient and possible.

9 REFERENCES

[1] EU Technical Specification For Interoperability Relating to the 'Rolling Stock' Sub-System of the Trans-European High-Speed Rail System, Directive 96/48/EC, 2008/232/EC, 2008.
[2] C. Baker, S. Jordan, T. Gilbert, A. Quinn and M. Sterling. Transient aerodynamic pressures and forces on trackside and overhead structures due to passing trains. Part 2 standards applications, unpublished manuscript, University of Birmingham, 2012.
[3] Railway applications — Aerodynamics — Part 4: Requirements and test procedures for aerodynamics on open track, BS EN 14067-4:2005+A1:2009, BSI, 2005.
[4] Eurocode 1, Actions on structures – Part 2: Traffic loads on bridges, BS EN 1991-2:2003, BSI, 2003.
[5] EU Technical Specification For Interoperability Relating to the 'Infrastructure' Sub-System of the Trans-European High-Speed Rail System, Directive 96/48/EC, 2008/217/EC, 2008.
[6] C. Baker. Full scale measurement and analysis of train slipstreams and wakes: Part 1 Ensemble averages, unpublished manuscript, University of Birmingham, 2012.
[7] C. J. Baker, S. J. Dalley, T. Johnson, A. Quinn and N. G. Wright. The slipstream and wake of a high speed train, Proc. IMechE Part F: Journal of Rail and Rapid Transit, 215, 83-99, 2001.
[8] J. Temple and S. Dalley. RAPIDE Project: Analysis of the slipstream data, AEA Technology Rail, Report number AEATR-T&S-2001-197, 2000.
[9] M. Sima, E. Grappein, M. Weise, N. Paradot, M. Hieke, C. Baker, R. Licciardello and M. Couturier. Presentation of the EU FP7 AeroTRAIN project and first results, Proceedings 9th World Congress on Railway Research, Lille, May 22-26 2011.
[10] C. Baker. Full scale measurement and analysis of train slipstreams and wakes: Part 2 Gust analysis, unpublished manuscript, University of Birmingham, 2012.
[11] T. Johnson and S. Dalley. 1/25 scale moving model tests for the TRANSAERO project, In "TRANSAERO A European initiative on transient aerodynamics for railway system optimization", pp123-125, Springer-Verlag Berlin, 2002, ISBN 3-540-433136-3.

The Seventh International Colloquium on Bluff Body Aerodynamics and Applications (BBAA7)
Shanghai, China; September 2-6, 2012

Wind loads and coupling vibration of wind-vehicle-bridge system in the process of two trains passing each other

LI Yongle, XIANG Huoyue, Wu Mengxue, QIANG Shizhong

(*Department of Bridge Engineering, Southwest Jiaotong University, Sichuan Chengdu 610031, China*)

ABSTRACT: Under lateral wind action, wind loads on vehicles and bridge can be changed dramatically when two trains pass each other. Taking a long-span suspension bridge as a practical example, the aerodynamic coefficients of vehicles and bridge were measured by wind tunnel tests with section models of vehicle and bridge. The coupling vibration of wind-vehicle-bridge (WVB) system was simulated for the process of two trains passing each other. The responses of vehicles and bridge were investigated to demonstrate the effects of the spacing of two trains, wind speed and vehicle speed. The analysis results indicate that the sudden change of wind loads on leeward vehicles can considerably increase the lateral response of leeward vehicles.

KEYWORDS: two trains passing each other; wind-vehicle-bridge system; coupling vibration; wind load; wind tunnel test.

1 INTRODUCTION

Lateral wind is one of the most important influencing factors on train running performance. Many wind-induced accidents of rail vehicles have been reported all over the world. With higher train speed and lighter vehicle body, train is more sensitive to strong lateral winds. In the process of high speed train running along a flexible bridge under lateral winds, there is the interaction among wind, vehicle, and bridge, which represents the coupling vibration of WVB system.

Diana and Cheli[1] studied the interaction of wind, vehicle and bridge, in which the wind force was simplified as additional transverse force. Xia[2]and Guo[3] et al. further studied the effect of fluctuating wind. Ge et al[4-5]. developed above works by measuring aerodynamic coefficients, which considered the interaction between bridge and vehicle. Li et al. [6-9] presented a relatively better WVB system model, which well reflected the aerodynamic coupling relationship between wind, vehicle and bridge, and considered the geometric and mechanical coupling relationships between bridge and vehicle.

High-speed vehicles running on bridge deck are subjected to side force and overturning moment under strong lateral wind. The wind loads of leeward vehicles are abruptly decreased due to the wind-shielding effect of windward vehicles at the beginning of two trains passing each other. When leeward vehicles are out of the shelter of windward vehicles at the end of two trains passing each other, the wind loads on leeward vehicles are suddenly increased. In the process of two trains passing each other, the leeward vehicles experience a sudden wind loads reduction and loading again, which is dangerous for vehicle safety. In addition, leeward vehicles change the aerodynamic ambient flow around windward vehicles and bridge, so the wind loads on windward vehicles and bridge also have a sudden change. The sudden change of wind loads in the process of two trains passing each other could result in the increase of responses of vehicle and bridge, and would become a controlling factor for the safety of WVB system.

In the present study, the bridge and vehicle aerodynamic coefficients in the process of two trains passing each other were tested by wind tunnel testing to study the effect of sudden change of wind loads. The responses of vehicle and bridge were calculated by BANSYS (Bridge Analysis System), addressing the effects of distance between two trains, wind speed and vehicle speed.

2 WIND TUNNEL TEST FOR WIND LOADS ON VEHICLES AND BRIDGE DECK

At the present time, bridge and vehicles are regarded as two separate subsystems in the most vehicle-bridge coupling vibration analysis, so respective wind loads on the two subsystems must be determined with consideration of aerodynamic interaction between them[9]. Crossed Slot System[10] was employed to measure aerodynamic coefficients of bridge deck and vehicle. The wind tunnel tests included two kinds of track arrangements on deck (shown in Figure.1), i.e., the space of 3.5m between two trains in case 1, and 29.5m in case 2, and three different angles of attack (-3°, 0°, +3°). Both vehicle and bridge section models are in scale of 1:55, with length of 2.1m. The aerodynamic coefficients at angle of attack of 0°are shown in table 1.

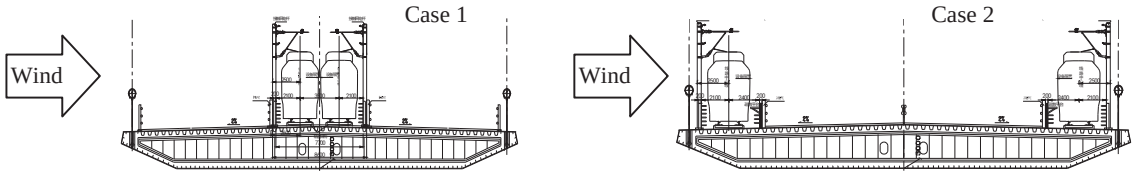

Figure.1 Two kinds of track arrangements on deck

The table 1 shows that local wind field of bridge deck determines the real aerodynamic forces of vehicles as a result of the vehicles submerged in the aerodynamic ambient flow of bridge, leading to obvious differences of aerodynamic coefficients of vehicle and bridge in various combination. The drag and lift coefficients of leeward vehicles decrease dramaticlly when the two trains are passing each other, meanwhile, the aerodynamic coefficients of windward vehicles and bridge also have a certain degree of change. The influence of two trains passing each other on wind loads of bridge and vehicle is more significant in the case 1 of track arrangement.

The bridge structure form has an effect on the aerodynamic forces of vehicle, at the same time, the vehicle has an influence on the aerodynamic forces of bridge, because the interaction between them is significant.

Table.1 Aerodynamic coefficients of box section in 0°

		Track arrangement case 1 (3.5m)			Track arrangement case 2 (29.5m)		
		C_D	C_L	C_M	C_D	C_L	C_M
One train passing	Leeward vehicle	0.5859	0.4398	——	0.5225	0.3207	0.0151
	Windward vehicle	0.6669	0.5160	——	1.0404	0.2629	-0.0151
	Bridge I	0.8913	-0.1026	-0.0564	0.9119	-0.2617	-0.0320
	Bridge II	0.8585	-0.0251	-0.0552	0.7361	0.1742	-0.0261
Two train passing each other	Leeward vehicle	0.0790	0.1757	0.0151	0.2536	0.0405	——
	Windward vehicle	0.7254	0.4718	——	1.0252	0.2383	——
	Bridge	0.9069	-0.0841	-0.0620	0.7992	0.0093	-0.0340

Note: ‘Bridge I’ means aerodynamic coefficients of bridge with leeward vehicle, ‘Bridge II’ means aerodynamic coefficients of bridge with windward vehicle, ‘——’means the aerodynamic forces are too small to measure.

3 ANALYSIS METHOD OF COUPLING VIBRATION OF WVB SYSTEM

Random cross-wind velocity field is usually simulated as a stationary Gaussian stochastic processe by spectral representation method. Vehicle can be modeled as a mass-spring-damping system with 23 degrees of freedom. Bridge analysis model can be established by the finite element method. Bridge and vehicle can be regarded as two subsystems. The motion equations of wind-vehicle-bridge system are as follows.

$$\mathbf{M}_b\ddot{\mathbf{u}}_b + \mathbf{C}_b\dot{\mathbf{u}}_b + \mathbf{K}_b\mathbf{u}_b = \mathbf{F}_{stb} + \mathbf{F}_{bub} + \mathbf{F}_{seb} + \mathbf{F}_{vb}$$

$$\mathbf{M}_v\ddot{\mathbf{u}}_v + \mathbf{C}_v\dot{\mathbf{u}}_v + \mathbf{K}_v\mathbf{u}_v = \mathbf{F}_{stv} + \mathbf{F}_{buv} + \mathbf{F}_{sev} + \mathbf{F}_{vv}$$

Where the subscript b and v indicate the bridge and vehicle, respectively; $\mathbf{F}_{st}$, $\mathbf{F}_{bu}$, and $\mathbf{F}_{se}$ are the static wind loads, buffeting wind loads and self-excited loads, respectively; $\mathbf{F}_{vb}$, $\mathbf{F}_{bv}$ denote the interaction forces between vehicle and bridge. The displacement response of bridge under static wind loads is equivalent to change the track irregularity, thus affecting the vehicle vibration. The equilibrium position of bridge under static wind loads should be treated as the initial state in the direct integral calculation of system motion equation. The expression of static and buffeting wind was refered to the literature [9].

The aerodynamic coefficients of one train passing are used before and after the two trains passing each other, and the aerodynamic coefficients of two trains passing each are adopted in the process of two trains passing each other, the specific aerodynamic coefficients are shown in table 1. The lateral and vertical fluctuating wind speeds are determined by the position of the vehicle. In the calculation of the buffeting force of vehicle and bridge, the fluctuating wind of vehicle is similar to the bridge. The self-excited force of train is ignored in WVB system because the width of vehicle is lesser, and the section is bluff body. The wind loads of bridge are accordingly changed with the motion of vehicle in the process of two trains passing each other in addition to the vehicle wind loads.

4 ANALYSIS OF TWO TRAINS PASSING EACH OTHER

4.1 *Engineering example*

A suspension bridge which have three-spans continuous steel box girder is investigated in the process of two trains passing each other, and the combination of span is 212m++600m+212m (as shown in Fig.2). The track layout form on the deck is shown in Fig.3. The width of deck is 35.5m, and the height is 3.0m. The aerodynamic coefficients in table 1 were adapted.

The fluctuating wind velocity was simulated by using spectral representation method. The horizontal and vertical fluctuating wind velocity field which included 105 wind speed simulation points evenly distributed along the girder were simulated respectively. The space of wind speed simulation points is 10m, and the space in tower is similar to girder, but the horizontal and crosswise fluctuating wind velocity field along towers included 15 wind speed points. The wind velocity spectrum comes from literature [12].

The B type vehicle of urban rail transit was employed, and the composition of the train is 2× (M+T+T+M). The rail irregularities was simulated by American level 6 spectrum, and the dynamic time history analysis of spatial step is 0.2 m, the damping ratio is 0.5% [12].

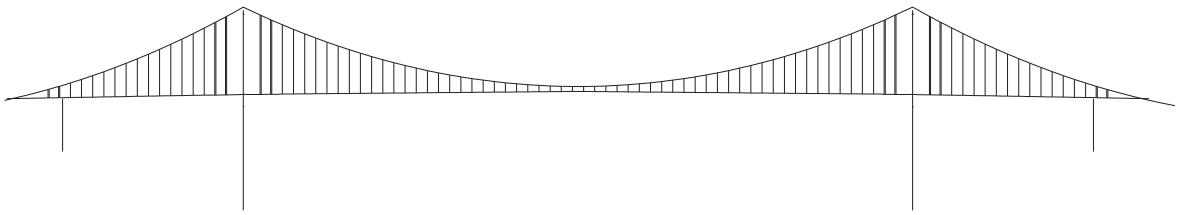

Figure.2 Overall Structure arrangement

4.2 *Effect of vehicle speed*

Two trains entering into bridge at the same time in opposite directions at various vehicle speeds were analyzed by method of coupling vibration of WVB according to case 1 (as shown in figure.1) under the wind speed of 30m/s. The lateral acceleration of 1st vehicle and 8th vehicle of the leeward trains at different speeds for two trains passing each other is shown in Figure.2 and Figure.3. It shows that there are two peaks at the beginning and end of two trains passing each other in the mid-span due to the effect of sudden change of wind loads. The maximum acceleration of vehicle at different speeds is shown in table 2. The effect of sudden change of wind loads in leeward vehicle is larger than windward vehicle, leading to the larger acceleration of leeward vehicle. The lateral acceleration of vehicle increases with increasing speed of leeward and windward vehicle, it suggests that the higher speed is, the stronger effect of sudden change of wind loads is.

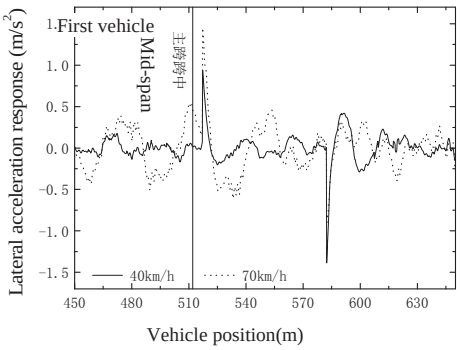

Figure.3 Response of lateral acceleration of first vehicle

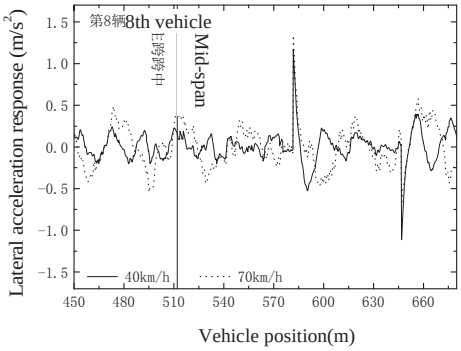

Figure.4 Response of lateral acceleration of 8th vehicle

Table.2 Response of acceleration at various vehicle speeds

Vehicle speed(/km/h)		40	50	60	70	80
Leeward vehicle	Lateral acceleration(m/s^2)	1.566	1.488	1.258	1.840	1.793
	Vertical acceleration(m/s^2)	1.841	1.869	1.693	1.861	1.710
Windward vehicle	Lateral acceleration(m/s^2)	0.472	0.534	0.680	0.854	0.995
	Vertical acceleration(m/s^2)	1.809	1.850	1.692	1.831	1.812

4.3 *Effect of wind speed*

Two trains entering into bridge at the same time in opposite direction at various wind speeds were analyzed by method of coupling vibration of WVB according to case 1 (as shown in Figure.1) under the vehicle speed of 80km/h. The acceleration of windward vehicle at wind speed of 20m/s is shown in figure 4. From the Fig. 4 we can see that the lateral and vertical acceleration don't have a remarkable change, which suggests that the effect of sudden change of wind loads of windward vehicle is limited with two trains passing each other (about 23s). The lateral and vertical displacements in the two trains passing each other at various wind speed is shown in figure 5, the figure shows lateral and vertical response bridge increased with higher wind speeds, the bridge response did not happen significant mutations at the two trains passing each other(about 510m～650m).

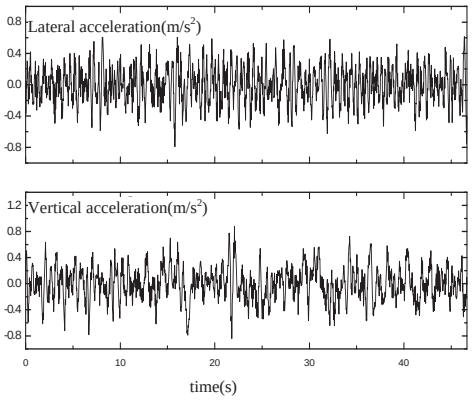

Figure.4 Acceleration of windward vehicle

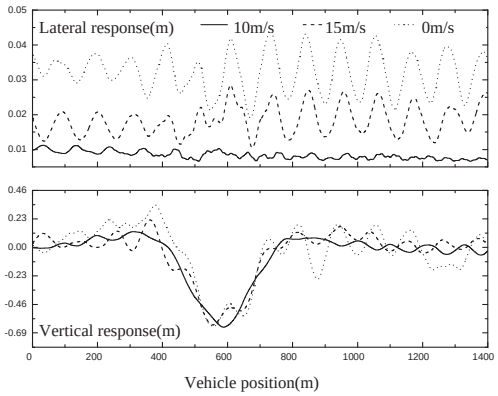

Figure.5 Response of displacement in midspan

The responses of vehicle and bridge at different wind speeds is shown in the table 3, the lateral acceleration of leeward vehicle is increased significantly with increasing wind speed, but the lateral acceleration of windward vehicle is only increased slightly, although the acceleration of bridge was accompanied with the wind velocity increased and bigger, the acceleration value is small. For this reason, the effect of sudden change of wind loads was a controlling factor for the leeward vehicle, the lateral vibration of bridge is limited devoted to the response of vehicle. The vertical acceleration is increased significantly with increasing wind speed, corresponding to the acceleration of vehicle is significant increased, but the vertical acceleration of vehicle (as shown in Table 3) wasn't significantly changed with increasing speed. Therefore, the vertical vibration of bridge under the strong cross-wind has a great contribution to the vertical acceleration of vehicle, but the vehicle speed is limited.

Table.3 Response of acceleration for vehicle and bridge in various wind speed

Wind speed(m/s)		10	15	20	25	30
Leeward vehicle	Lateral acceleration(m/s^2)	0.837	0.836	0.810	1.017	1.793
	Vertical acceleration(m/s^2)	0.743	1.022	0.999	1.561	1.710
Windward vehicle	Lateral acceleration(m/s^2)	0.806	0.806	0.850	0.886	0.995
	Vertical acceleration(m/s^2)	0.948	1.036	0.916	1.412	1.812
Maximum lateral acceleration in midspan(m/s^2)		0.054	0.064	0.063	0.065	0.142
Maximum vetical acceleration in midspan(m/s^2)		0.133	0.215	0.441	0.773	1.180

4.4 *Effect of the distance between two trains*

Another type of track arrangement (in Fig.1 case 2) was analyzed by method of coupling vibration of WVB under the vehicle speed of 80km/h, the responses of vehicle and bridge at different wind speeds were shown in the table 4, the vertical acceleration of vehicle and vertical acceleration of leeward vehicle in the two cases was similar in table 3 and table 4, but the transverse acceleration of leeward vehicle has significant difference with increasing wind speed, the lateral acceleration of leeward vehicle was slowly increased with the wind velocity increased, this suggested that the effect of sudden change of wind loads in the two trains passing each other is more weaker with the intervals of two trains as a result of effect of covering for windward vehicle.

Table.4 Acceleration of vehicle under different wind speed

Wind speed(m/s)		10	15	20	25	30
Leeward vehicle	Lateral acceleration(m/s^2)	0.838	0.837	0.811	0.873	1.201
	Vertical acceleration(m/s^2)	0.764	0.975	0.914	1.437	1.645
Windward vehicle	Lateral acceleration(m/s^2)	0.807	0.821	0.841	0.867	0.949
	Vertical acceleration(m/s^2)	0.897	1.002	0.984	1.591	1.779

CONCLUSION REMARKS

Some conclusions are drawn in this section on basis of wind tunnel tests and above calculation analysis.

1. the vehicle and bridge aerodynamic coefficients have an obvious effect on different combination of vehicle and bridge, the drag and lift coefficients in leeward vehicle are abruptly decreased when the two trains passing each other, and the aerodynamic coefficients of vehicle and bridge in windward have a change to some degree, the alteration of vehicle and bridge should be considered in the coupling vibration of WVB system for the process of two trains passing each other.
2. The vehicle speed and wind speed is higher, the effect of sudden change for horizontal acceleration of vehicle is stronger. The horizontal response in leeward is a controlling factor when the two train passing each other.
3. The vertical wind-induced vibration of bridge has a significant influence on the vertical response of vehicle in windward and leeward, but the effect of vehicle speed is limited.
4. The shielding effect of windward vehicle could be reduced with the increase of horizontal distance between two vehicles when the two trains passing each other.

ACKNOWLEDGEMENT

This work was supported by the Natural Science Foundation of China (50508036), The Ministry of Education New Century Excellent Talent Support Plan (NCET-06-0802), Sichuan Outstanding Youth Discipline Leaders Plan (2009-15-406).

REFERENCE

[1] G.Diana, F.Cheli. Dynamic interaction of railway systems with large bridges[J]. Vehicle System Dynamics,1989,Vol,18(1),pp:71-106.

[2] Xia He, Guiping Yan, yingjun Chen. Dynamic Responses of Train and Cable-Stayed Bridge System Unde Wind Action[J] .Journal of Northern Jiaotong University.1995, Vol. 19(2) ,pp:131-136.

[3] Xiangrong Guo, Qingyuan Zeng. Analysis of critical wind speed for running trains on a schemed Yangtze River Bridge at Nanjing on Jing-Hu high speed railway line[J]. Journal of the China Railway Society. 200l, Vol. 23(5) , pp:75-80.

[4] Yumei Ge, Yongle Li, Xiangdong He. Study on Wind-Induced Loads of Train-Bridge System by Wind Tunnel Test[J]. Journal of Southwest Jiaotong University[J]. 2001. Vol. 36(6) ,pp:612-616.

[5] Yumei Ge, Shuhua Zhou, Longan Li. Coupled vibration of train and cable-stayed bridges with the efects of wind[J]. Journal of Southwest Jiaotong University. 2001. Vol. 36(4) ,pp:369-373.

[6] Yongle Li, Shizhong Qiang, Haili Liao. 3-D coupled vibration of wind-vehicle-bridge system[J]. China Civil Engineering Journal, 2005, Vol. 38(7) ,pp: 61-64.

[7] Y.L. Xu, W.H.Guo, Dynamic analysis of coupled road vehicle and cable-stayed bridge systems under turbulent wind[J]. Engineering Structures, 2003, Vol. 25 ,pp: 473-486.

[8] C.S. Cai and S.R. Chen. Framework of vehicle–bridge–wind dynamic analysis[J]. Journal of Wind Engineering and Industrial Aerodynamics, 2004, Vol. 92 , pp: 579–607.

[9] Yongle Li, Shizhong Qiang, Haili Liao and Y.L. Xu. Dynamics of wind-rail vehicle-bridge systems, Journal of Wind Engineering and Industrial Aerodynamics[J]. 2006, Vol. 93, pp: 483-507.

[10] Yongle Li, Haili Liao, Shizhong Qiang. Study on aerodynamic characteristics of the vehicle-bridge system by the section model wind tunnel test[J]. Journal of The China Railway Society.2004, Vol. 26(3) , pp: 71-75

[11] Yongle Li, Haili Liao and Shizhoing Qiang. Simplifying the simulation of stochastic wind velocity fields for long cable-stayed bridges[J]. Computers and Structures,2004, Vol. 82, pp: 1591-1598.

[12] JTG/T D60-01—2004 Wind resistant design specification for highway bridge [S].Beijing: China Communications Press, 2004, p:46.

The Seventh International Colloquium on Bluff Body Aerodynamics and Applications (BBAA7)
Shanghai, China; September 2-6, 2012

Wind tunnel test study the influence of wind screen on wind pressure distribution above railway tracks

Xiang Huoyue, Li Yongle, Chen Ning, Liao Haili

Department of Bridge Engineering, Southwest Jiaotong University, Chengdu 610031, China

ABSTRACT: In order to investigate the wind screen to effects of distribution on wind pressure above tracks, the wind pressure coefficients profile were tested by the wind tunnel testing used the wind pressure row tube, and numerical simulation was carried out at the same time to contrast with wind tunnel testing, the effects of wind screen arrangements, heights of wind screen, the line structure types such as the ground roadbeds, high embankments and bridges were discussed about the distribution of wind pressure on tracks, and the mechanism of aerodynamics was analyzed. It shows that the wind pressure value above tracks are significant decreased by wind screen in windward; the wind screens in leeward increased the negative pressure above tracks; in the three line structure forms, the wind pressure value above tracks on bridge are maximum, the energy dissipations are minimum, and the energy dissipations in high embankment are maximum, meanwhile, the wind pressure coefficients on catenary are decreased when the wind screens installed on high embankment.

KEYWORDS: wind screen; wind pressure coefficients; wind tunnel testing; line structure forms

1 INTRODUCTION

In recently, wind-induced accidents of trains have been reported around the world from time to time. For instance, there have been more than 30 wind-induced accidents of trains since 1872 in Japan[1, 2] (statistics to 2006). In 2005, Shinkansen train “Rice 14”of East Japan Railway Company was derailed as a result of encountering cross-wind which was much lower than the warning wind speed[3]. In China, more than 110 rail vehicle (statistics to 2002) rollover accidents by cross winds have been reported on the Lan-Xin Railway since 1959[4], in 2007, a 5807 times train from Urumchi to Aksu was derailed by 13 class gale leaded to four deaths and more than 30 injured. Beijing-Shanghai (or Jing-Hu) high-speed railway has been built along the annual maximum wind speed greater than 20m/s, the number of occurrences is about 19.2[5]. In summary, it is very necessary for gale district railway to set up the precautions such as wind screens, it’s one of the efficient measures for vehicle safety, wind screens were installed one or two sides along the railway to create a local environment of relatively low wind speed for trains.

Wang et al.[4] indicated that the heights of windbreak wall should be 2.4m above rail top, the construction cost per kilometer will be decreased by 33%. Ge and Jiang[6] studied the wind velocity reduced ratio in Lan-Xin railway by full-scale measurements, their results showed that the speed of the wind behind the 3m high windbreak is smaller than that outside the windbreak and the shielding scope of windbreak exceeds 38m when wind speed is 20m/s. A series of wind tunnel testing are conducted in Japan, the result shows that the effects of wind screen on the reduction of aerodynamic forces depends on the heights of wind screen, solidity ratios, configurations of vehicles and infrastructures[7, 8]. Numerical simulations were also conducted to understand the wind shield effect of wind screen. Bobi et al.[9] used the method of Navier-Stokes simulation to study the different wind screen shapes, obtained global values of efficacy greater than 90% in both viaduct and embankment situations. Jiang and Liang[10] studied the effects of the vehicle

aerodynamic performance caused by the change of height and position of wind-break wall, the result shows that position vs. height was approximately cubic polynomial relations.

In conclusion, the related research in China focused on the heavy windbreak wall in Nan Xing railway, researched on light wind screen and its mechanism is relatively limited, and the research results of foreign is difficult of direct reference. The Jing-Hu high-speed railway located in the eastern coastal of china where is vulnerable to the attack of typhoon and strong monsoon, so it is necessary to set up wind screen in the high wind speed regions. Three line structure types were chosen from Jing-Hu high speed railway: the ground roadbed, high embankment and 32m span bridges, were respectively made the wind tunnel test model. The wind pressure coefficients in different wind screens were tested, discussed the effects of arrangements, heights, line structure types, and analyzed the aerodynamic mechanism of wind screen.

2 WIND TUNNEL TESTING

Strong lateral wind can affect substantially the performance of the running train, the wind screen can change the ambient flow field above the railway, furthermore influence the wind loads acting on vehicles. Three types of infrastructure forms are adopted in this study, bridge, high embankment and ground roadbed.

The test of wind pressure distributions was conducted in XNJD-3 wind tunnel with a scale of 1:15, the end-plate was set up along the side of models to reduce the effect of flow around, because the width of the model is 3m while the width of the wind tunnel is 22.5m. The wind pressure pipe was vertical to flows installed in columns, and was vertical extended 0.05m to reduce the disturbing effect of pillar. There are 16 measuring points in the center of tracks with a measuring spacing of 0.03m below height of 0.25m, other spacing was 0.04m (shown in figure 1). The wind pressure coefficient profile of the center of tracks can be obtained by the synchronous acquisition system.

A pitot tube was placed in undisturbed flows to test the static pressure and velocity, if the static pressure in upper stream was considered as a reference point, then the wind pressure coefficient can be expressed as:

$$C_{pi} = (P_i - P_\infty) / 0.5\rho V_\infty^2 \qquad (1)$$

Where P_i is value of wind pressure in ith wind pressure pipe (total pressure); P_∞ is static pressure in reference point of upper stream; V_∞ is velocity of upper stream; ρ is the air density; It should be noted that wall pressure coefficient is relative to the shape of the structure reflecting the surface wind load distribution on the structure, but C_{pi} is the relatively wind pressure coefficient reflecting distribution of the flow field and the total energy.

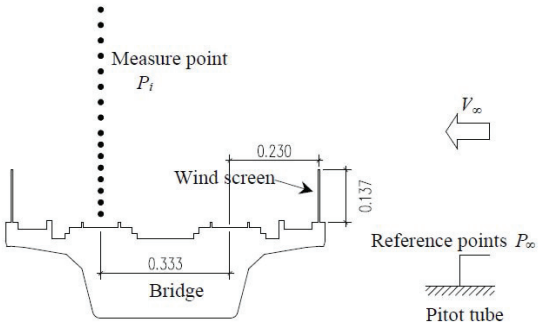

Figure.1 Schematic diagram of wind pressure profile test schemes on bridge (unit: m)

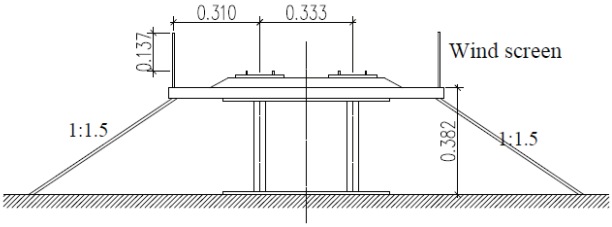

Figure.2 Wind tunnel test model of high embankment (unit: m)

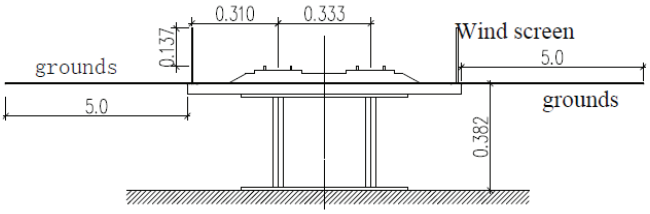

Figure.3 Wind tunnel test model of ground roadbed (unit: m)

the wind pressure coefficient profile in the center of tracks on windward side and leeward side was tested with different wind screens height and arrangement on three typical line construction forms (as shown in figure.1～figure.3) for the Beijing-Shanghai high-speed railway, the specific case is shown in table 1.

Table.1 Wind tunnel test cases

infrastructure scenario	height of wind screen(unit:m)	Arrangement of wind screen
bridge	0.0、1.72、2.05	one side, both side
high embankment	0.0、1.60、2.05	one side, both side
ground roadbed	0.0、1.60、2.05	one side, both side

Noted: the height above orbital plans is the wind screen height, 0.0 is no wind screen, and one side is no windward wind screen.

3 RESULT ANALYSIS

The numerical simulation was firstly conducted at the same time for typical case, compared the results of wind tunnel test and CFD, and on that basis, the mechanism of aerodynamics was analyzed, the wind pressure distributions above tracks were discussed in different arrangements, heights and line structure types.

3.1 *Comparison of the wind tunnel test and CFD*

A 2D wind pressure distributions with a scale of 1:15 was simulated using CFD with a 2.05m height wind screen set on the bridge (as shown in figure 1) to validate this paper test method, the turbulent model is the SST k-ω, boundary layer thickness refer to the literature [11], the grid number is approximately 76 thousand, the comparison of numerical simulation by steady analysis and wind tunnel test is shown in figure 4, which shows that the CFD simulation results well agree with the wind tunnel test in windward tracks, although there has certain differences in the leeward side tracks, but the law are similar; In addition, the wind pressure coefficient in scope of

shading is smaller than external flow by the reason of energy dissipation of turbulence according to the ideal fluid Bernoulli Equation. Therefore, the wind pressure distributions tested by row tube is feasible.

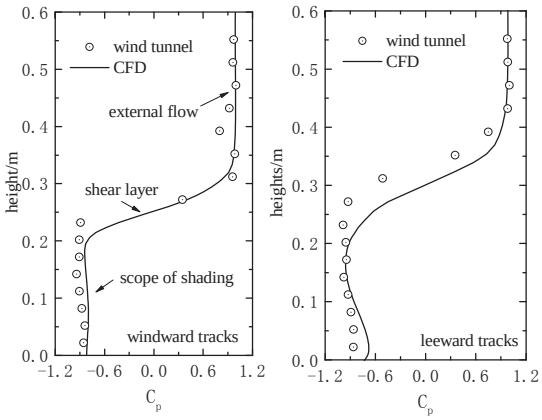

Figure.4 Comparison of wind tunnel test with CFD

3.2 *Effects of windscreen arrangement*

Comparison of wind pressure coefficient profile, setting one side, both side and without wind screen with a height of 2.05m on the bridge is shown in figure 5 to investigate the effect of windscreen arrangement. The value of pressure in the center of tracks was reduced as the wind screen was set on one side or both sides. Compared the wind pressure coefficients with one side and both side cases, it is easy to learn that both side case were increased with respect to one side case in the scope of shading. Because the leeward wind screen blocked the around flow coming from windward wind screen, which increased the backflow above tracks, increased the pressure coefficient, and reduced the energy dissipation in scope of shading.

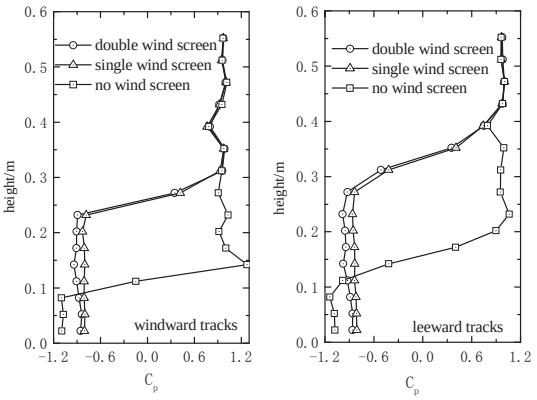

Figure.5 Effects of position of wind screen

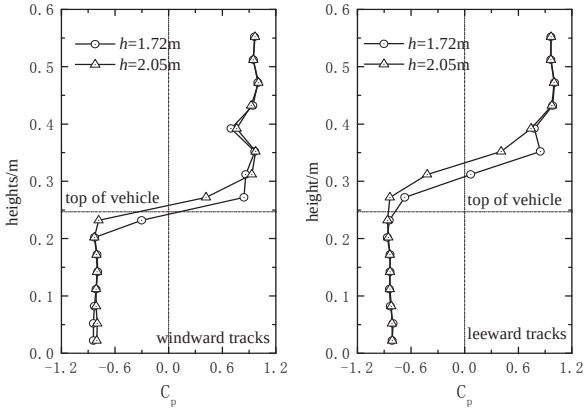

Figure.6 Effects of height of wind screens

3.3 *Effects of height*

The wind pressure profile of two heights of wind screens (1.72m and 2.05m) on one side is shown in figure 6 to investigate the effects of height. It shows that the change law of wind pressure coefficient profile is similar, and the height of the shear layer increased with the height of wind screen increasing. The height of vehicles in practice is generally in 3.5m to 4.0m such as

the vehicle of CRH2 is 3.7m above orbital plane with a value of 0.247m after scale. There is negative pressure in the windward tracks beneath the height of vehicles when the heights of wind screen are 2.05m. But the vehicles are partly subjected to positive pressure when the heights of wind screen are 1.72, and smaller than 2.05m. The shear layer of wind pressure coefficients in leeward wind screen are above the top of vehicle, and there has little difference in the scope of shading. Therefore, the wind shield of 1.72m wind screen is better than 2.05m if the wind pressure coefficient is considered as evaluation index.

3.4 *Effects of line structure type*

The profile of wind pressure distributions in bridges (shown in figure 1), high embankment (shown in figure 2), grounds roadbed (shown in figure 3) was tested to check the effect of line structure type. The wind pressure distributions for three kinds of infrastructure forms with wind screen set on one side are shown in figure 7. It shows that the wind pressure coefficient in bridge is largest, while the high embankment is smallest, it because the effect of slope in high embankment leads to change the attacks of wind, and improved the height of shear layer, meanwhile, the wind pressure coefficients on catenary was decreased when the wind screens is installed on high embankment.

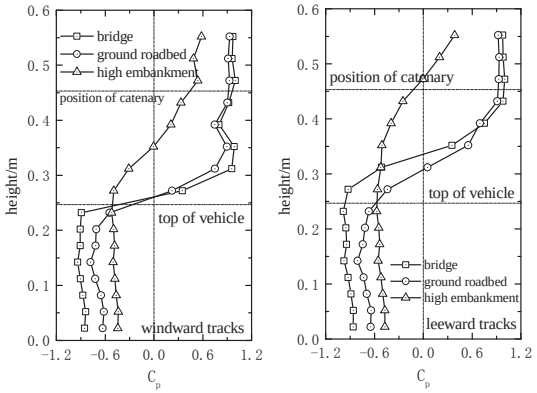

Figure.7 Effects of line structure types with wind screens

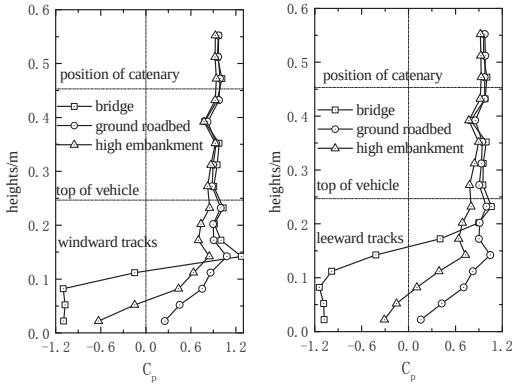

Figure.8 Effects of line structure types without wind screens

The wind pressure coefficient above tracks in different line structure types without wind screen were compared from the perspective of energy dissipation as shown in figure 8. Combined with figure 7, it is easy to learn that that the line structure types have a significant effect on the wind shield of wind screen, the distribution of wind pressure above tracks without wind screen have a remarkable difference, the energy dissipation in high embankment is maximum, the bridge is minimum. Therefore, it should be pay attention to the adverse effect of sudden change of vehicle wind load as a result of the change of line structure types.

4 CONCLUSION

The wind tunnel test has been performed investigating the effects of the wind screen on the three line structure types as well as an analysis of the flow field distribution, and derived the following conclusions.

1. The existence of windward wind screen reduced the wind pressure value, and the shear layer height increases with the height of the wind screen.

2. the wind pressure distribution have a significant difference in varied lines structure type, and the difference of energy dissipation is obvious, the energy dissipation is minimum on the bridge, is maximum on high embankment which can reduce the wind pressure coefficients on catenary.

ACKNOWLEDGMENT

This work was supported by the Natural Science Foundation of China (50508036), The Ministry of Education New Century Excellent Talent Support Plan (NCET-06-0802), Sichuan Outstanding Youth Discipline Leaders Plan (2009-15-406), Southwest Jiaotong University Ph.D Candidate Innovation Fund is gratefully acknowledged.

REFERENCE

[1] M Suzuki, K Tanemoto, A T Maeda. Aerodynamic characteristics of train/vehicles under cross winds [J]. Journal of Wind Engineering and Industrial Aerodynamics, 2003, Vol. 91, pp: 209-218.

[2] Qingkuan Liu, Yanliang Du, Fugui Qiao. Train-crosswind and strong wind countermeasure research in Japan[J]. Journal of the China Railway Society, 2008, Vol. 30(1), pp:82-88. (in Chinese)

[3] Xuesong Jin, Jun Guo, Xinbiao Xiao, et al.Key scientific problems in the study on running safety of high speed trains[J].Engineering Mechanics,2009, Vol. 26(S2) , pp:8-21.(in Chinese)

[4] Houxiong Wang, Zhu Gao, Shudong Wang, et al.A study on height of wind break wall[J]. China Railway Science, 1990, Vol. 11(1) , pp:14-23(in Chinese)

[5] Qiang Zhang, Xianwei Yang, Yongshan Zhang, et al. The analysis of the distribution characteristics of severe precipitation frequency and strong wind frequency along the high speed railway from Beijing to Shanghai[J]. Meteorological Science and Technology, 2003, Vol. 31(1) , pp:45-49(in Chinese)

[6] Shengchang Ge, Fuqiang Jiang. Analyses of the causes for wind d isaster in strong wind Area along Lanzhou - Xinjiang railway and the effect of windbreak[J].Journal of railway Engineering Society, 2009, Vol. 128(5) , pp:1-4. (in Chinese)

[7] T Fujii, T Maeda, H Ishida, et al. Wind-induced accidents of train/vehicles and their measures in Japan[J]. Quarterly Report of RTRI (Railway Technical Research Institute) (Japan), 1999, Vol. 40(1) , pp:50-55.

[8] T Maeda. Wind-induced accidents of train/vehicles and their countermeasures [C]. Probabilistic Mechanics and Structural and Geotechnical Reliability, Proceedings of the Specialty Conference, Worcester, MA, USA, 1996,pp:70-73:

[9] De Dios Sanz Bobi J, B Suarez, J G Nunez, et al. Protection high speed trains against lateral wind effects[C]. ASME International Mechanical Engineering Congress and Exposition, Proceedings, Lake Buena Vista, FL, United states, 2010,pp: 771-780.

[10] Cuixiang Jiang, Xifeng Liang. Effect of the vehicle aerodynamic performance caused by the height and position of wind-break wall[J]. China Railway Science, 2006, Vol. 27(2) , pp:66-70. (in Chinese)

[11] Lin Huang. Ananlysis of vehicle-bridge vibration under train induced wind and natural wind [D]. Chendu: Southwest Jiaotong University,2007, pp:30. (in Chinese)

The Seventh International Colloquium on Bluff Body Aerodynamics and Applications (BBAA7)
Shanghai, China; September 2-6, 2012

Evaluation of crosswind effects on rail vehicles through moving model experiments

F. Dorigatti [a], A.D. Quinn [a], M. Sterling [a], C.J. Baker [a]

[a] *School of Civil Engineering, University of Birmingham, Birmingham, UK*

ABSTRACT: This paper presents the results obtained from two series of tests on scale-model rail vehicles, one in static and the other in moving model conditions. The experiments were carried out at the TRAIN (TRansient Aerodynamic INvestigation) rig using the recently developed crosswind generator. A 1:25 scale model of a Class 390 Pendolino train was tested on a flat ground scenario in correspondence of a 30° yaw angle. The Reynolds number was of the order of 2×10^5. The surface pressure on the train leading car was monitored in correspondence of 110 tapping points using a novel onboard stand-alone measuring system. An evaluation of the mean values for the local pressure coefficient shows limited differences between static and moving model tests only in correspondence of a restricted number of tapping points. A comparison in terms of overall mean aerodynamic coefficients indicates a good agreement between the two sets of results.

KEYWORDS: Crosswind, rail vehicles, moving model tests, static tests, mean pressure coefficient, mean aerodynamic load coefficients

1 INTRODUCTION

A train travelling through a natural turbulent crosswind is surrounded by a complex flow field which leads to a series of steady and unsteady aerodynamic forces and moments. These aerodynamic loads may induce significant changes in the vehicle dynamic behaviour in comparison to a no-crosswind condition and, in the presence of strong winds, serious accidents may happen because the train stability has been compromised [1]. To prevent the occurrence of such events, in the last two decades a series of specific methodologies have been developed for assessing the stability of trains in crosswinds [2, 3]. These methodologies are currently applied within the rolling stock certification process [4, 5] and rely on a numerical-experimental approach. While the vehicle dynamics and the characteristics of the natural wind are simulated numerically, the information regarding the wind-vehicle interaction is provided as an external input to the model in form of dimensionless aerodynamic coefficients. Such parameters depend on the train geometry and are typically obtained through wind tunnel experiments on static scale models, which represent the standard technique of investigation [4, 5]. These type of experiments have the significant advantage that they can be treated as conventional wind tunnel tests and, as such, can be carried out in traditional environmental wind tunnel facilities. However, by their very nature they do not simulate the movement of the train relative to the ground; the importance of this on the overall forces/moments acting on the train still remains largely unresolved [6].

Different studies have been undertaken in the past for evaluating the impact that the vehicle movement simulation has on the crosswind loads on trains. Since the mid 1980's the problem was approached from an experimental perspective and a number of moving model test campaigns were carried out [7, 8, 9, 10]. Despite the differences in these experiments, three common elements can be identified. Firstly, a test methodology based on carrying out series of multiple

runs was adopted. This was essential in order to collect a proper amount of data for enabling stable ensemble averages of the time histories to be calculated. Secondly, in the vast majority of the cases, the tests took place in existing wind tunnel facilities, where specifically designed propulsion systems (either mechanical [7, 8, 10] or gravity based [9]) had been integrated for providing the vehicle movement. Finally, the measuring systems employed during the tests all measured the overall forces and moments acting on the moving vehicle through the use of internal strain gauge balances. The outcomes from these previous moving model test campaigns do not appear to be entirely consistent. Bocciolone *et al.* [9] found no relevant discrepancies between aerodynamic loads on a train measured in stationary and moving model conditions, whereas Baker [7] and Humphreys [8] found the opposite. However, a close examination of data which did show an effect of the vehicle movement simulation yielded no definitive trends. Such inhomogeneity suggests a limited level of reliability associated with the results and was one of the motivations for the current work.

Considering the numerous issues associated with a moving model test campaign, recently, an alternative approach based on CFD analyses has been used [11]. However, before quantitative conclusions can be drawn based on numerical results, it is essential to assess the level of accuracy of CFD when applied to moving vehicles. Such a comparison requires detailed and reliable experiment data, some of which will be outlined below.

This paper presents the results obtained from a measurement campaign on scale-model rail vehicles in crosswinds, which was undertaken as part of the EU-funded AeroTRAIN project. Two series of experiments were carried out, one under static conditions and the other in moving model conditions. Contrary to previous moving model campaigns, the measuring system used for these tests monitored the local pressure distribution on the train surface rather than the overall aerodynamic loads on the vehicle. This approach enables a first comparison between static and moving tests results to be made with consideration to local values of the mean pressure in different areas of the train. By integrating the pressure distribution, a further comparison can be arranged in terms of steady overall aerodynamic loads. In what follows, the details of the examined test case, together with the characteristics of the facility, as well as of the measuring system and of the methodology, are described in section 2. Section 3 illustrates the results in terms of local values of the mean pressure coefficient and also of overall steady aerodynamic loads. Side force, lift force and rolling moment coefficients are considered and a comparison between static and moving tests is discussed. Finally, some concluding remarks are drawn in section 4.

2 EXPERIMENTAL CAMPAIGN

All of the experiments outlined below were carried out at the University of Birmingham's TRAIN (TRansient Aerodynamic INvestigation) rig (the distinctive features of which are outlined in section 2.1). A 1:25 scale model of a Class 390 Pendolino train was used for the tests. It comprised a full reproduction of the leading car followed by a dummy half trailing car: the leading vehicle was the object of investigation, while the partial second coach was provided to ensure realistic flow around the length of the train (Fig. 1a). For the purpose of the present work a Flat Ground (FG) scenario (i.e. no representation of the ballast was included) and a yaw angle (i.e. the angle between the direction of travel and the relative impacting wind) of 30° were examined. An onset turbulent crosswind characterized both series of tests, static and moving. Such flow simulation was provided by a crosswind generator that has been developed as part of this project. A more in depth description of this apparatus, as well as of the flow characteristics, is reported in what follows. The Reynolds number, based on the train height and the wind speed relative to the vehicle, was of the order of 2×10^5.

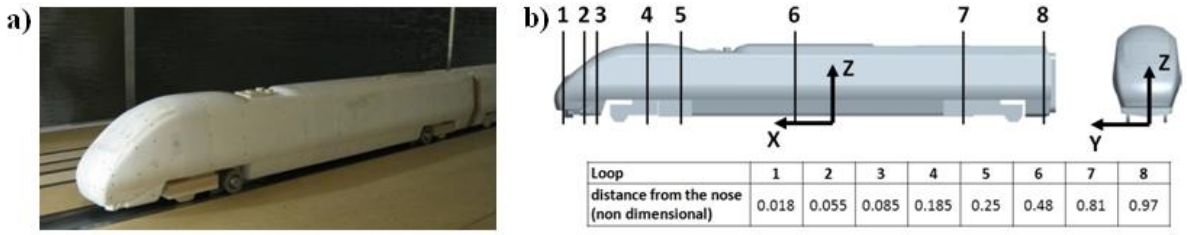

Loop	1	2	3	4	5	6	7	8
distance from the nose (non dimensional)	0.018	0.055	0.085	0.185	0.25	0.48	0.81	0.97

Figure 1. a) Photograph of the Class 390 Pendolino model (1:25 scale). b) Reference system and position of the loops of pressure taps on the leading car.

2.1 *The TRAIN rig*

The TRAIN rig is a research facility specifically dedicated to undertaking moving model tests on scale model vehicles in open-air, crosswinds and tunnels [12]. It is situated in Derby (UK) and was designed and built by British Rail Research at the end of 1980's [13]. The rig consists of a series of three straight parallel tracks, 150 meters long, equipped with a mechanical propulsion system that can catapult a 1/25 scale model up to 75 m/s. The acceleration mechanism employs a series of pre-tensioned elastic ropes driven by pulleys, while the brake is based on the use of a piston deformable tube. The facility was acquired by the University of Birmingham Centre for Railway Research and Education (BCRRE) in 2009. Since then, the capability of performing moving model experiments in crosswinds has been improved through the design and installation of a new crosswind generator.

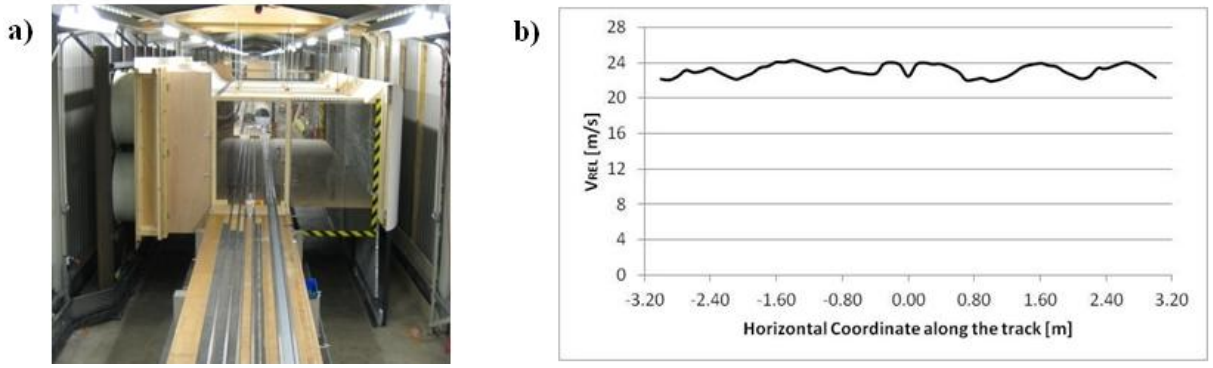

Figure 2. a) TRAIN rig internal view: new crosswind generator. b) Mean wind velocity relative to a train travelling at 20m/s c.a. and experiencing a 30° yaw angle: horizontal profile at 3m full scale equivalent height.

The new system, consists of a series of 16 axial flow fans positioned at the trackside and arranged in two rows of eight units each. The fans operate in sucking-mode and generate an airflow directed perpendicularly to the direction of travel. Such flow is enclosed in a tests section spanning a portion of the tracks 6.4m long (indicated in what follows as L_{CW}). A photograph of the new crosswind generator is shown in Figure 2a. Before the static and moving model test campaigns started, a dedicated session was carried out in order characterize the properties of the simulated crosswind in terms of mean speed, turbulence intensity and static pressure. The spanwise average of the mean wind speed (U) and turbulence intensity (I_U), measured at 3m full

scale equivalent height, are approximately 12m/s and 16%, respectively. The mean velocity profile of the relative wind, as seen by a train travelling through the crosswind section at approximately 21 m/s (thus in correspondence to a 30° yaw angle) is illustrated in Figure 2b.

2.2 *Measuring Instrumentation*

The experimental data collected during the tests comprised of both trackside and onboard measurements. The trackside measurements included the data regarding the ambient conditions (temperature, barometric pressure and relative humidity), the crosswind properties (velocity and static pressure within the air-channel) and the train speed (for moving model tests only). The ambient conditions were monitored using an Oregon Scientific BAR208HGA weather station and a GBP3300 digital barometer. Localized measurements of the flow speed and static pressure within the crosswind section were recorded using a set of Series 100 cobra probes (by Turbulent Flow Instrumentation Ltd) and a Pitot-static tube in combination with differential pressure transducers HCLA02X5PB (by Sensortechnics GmbH). An acquisition system run by a laptop computer was employed and data were sampled at 1KHz over a time interval of 60s. During moving model tests, the vehicle speed at the entry and exit of the crosswind generator was measured by two sets of photoelectric position finders and reflectors.

The onboard measurements consisted mainly of the surface pressures detected on the train model. For moving model tests, they included also the output signal from a light detector. The employment of an onboard stand-alone measuring system is essential in order to enable moving model experiments. Unlike what had been done in the past, the system used for these tests monitored the local pressure distribution on the train surface rather than the overall aerodynamic loads on the vehicle. It is a purpose-built measuring system, which employs a series of miniaturized ultra-low differential pressure transducers HCLA12X5PB (by Sensortechnics GmbH) in combination with a stand-alone data logger. The data logger has a 16-bit resolution, is capable of monitoring 16 channels at a maximum sampling rate of 4KHz and presents an extremely compact design that makes it suitable to be accommodated inside the scale train model. The surface pressure was measured only on the first vehicle, which was equipped with eight loops of pressure taps distributed along its length for a total of 110 measuring positions (Fig. 1b). A series of silicon tubing connected the tapping points to the pressure ports of the transducers. Having 15 channels of the data logger available to pressure measurements, the same number of transducers was used. This enabled the pressure taps of each single loop to be monitored simultaneously. A light detector was connected to the sixteenth channel of the data logger. Having set a series of light sources at specified locations along the track, during the moving model tests the signal from such sensor provided a number of ‘position markers’. They were used while post-processing the data for trimming the records from the raw data and thus isolate the portion of time histories associated to the train travelling within the crosswind section.

2.3 *Experimental setup and test methodology*

The test procedure for static tests was similar to the standard methodology commonly adopted for wind tunnel experiments. The train model was mounted statically inside the air-channel and rotated with respect to the oncoming wind in order to simulate the required yaw angle (30°). Time histories of the surface pressure on the train were recorded during a time window of 60s at a sampling rate of 4KHz. It is worth noting that, having the design of the crosswind generator optimized for moving model tests, a number of restrictions were imposed on the static tests. The dimensions of the model coupled with the limited extension of the air-channel in the along-wind direction (i.e. transversally to the track) meant that the nose of train was positioned close to the

channel inlet (i.e. at a distance of approximately 0.2m). This positioning compromised the possibility of a freestream flow upstream the model and determined a high sensitivity of the pressure field on the nose of the train to minor alterations in the environment external to the air-channel. In addition, a gradient in the along-wind direction was identified by the experimental data collected during the flow characterization, either for the streamwise mean wind velocity (negative gradient) or for the static pressure (positive gradient). All these aspects were taken into account during the data processing and also within the uncertainty analysis. They led to an estimate of the experimental error for the static tests slightly larger than in moving model conditions (Fig. 6).

During the moving model experiments the train was run through the crosswind section at approximately 20.8m/s (±0.6m/s). For analysis purposes the wind velocity was doubled averaged, i.e., both in time (averaged over the measurement time) and spatially (spanwise) along the measurement domain, yielding a value of 12m/s. Hence, the required yaw angle was 30° ±1°. Considering a total span of the air-channel (L_{CW}) of 6.4m, a train travelling at the specified speed spent approximately 0.3s within the crosswind section. With an acquisition data rate of 4 KHz, this corresponded to approximately 1200 samples. A high variability was observed in the time histories of the surface pressure associated to different runs (Fig. 3b). This suggesting that no reliable indication could be obtained from the analysis of individual runs, a data analysis method based on ensembles of runs was adopted for the moving model tests [14]. For the experiments reported in this paper, a sensitivity study indicated that 15 runs were required for obtaining stable ensemble averages. Figure 3 presents an example of the results obtained by applying this moving model test procedure, with consideration of one single pressure tap on loop 2 (on the nose of the train according to Figure 1b).

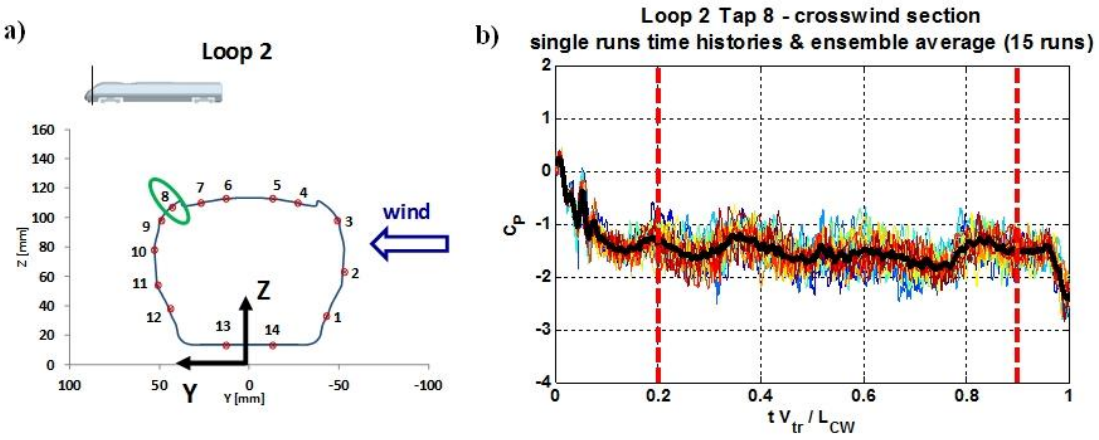

Figure 3. a) Loop 2: cross-section and taps' distribution. b) Single runs time histories (thin lines in grey colors) and ensemble average time history (thick line in black) trimmed within the crosswind section: C_P with respect to non-dimensional time (the vertical dotted lines denote the portion of time history considered for calculating the mean pressure coefficient).

3 RESULTS AND DISCUSSION

3.1 *Stationary pressure distribution*

In this section the data concerning the pressure distribution on the train are presented in terms of non-dimensional pressure coefficients. Considering each tapping point *i* on the train surface, the

instantaneous value of the pressure coefficient at a generic time t is indicated as C_{Pi} and defined as:

$$C_{Pi}(t) = \frac{P_i(t) - P_0}{0.5\rho V_{rel}^2} \quad (1)$$

where $P_i(t)$ is the instantaneous value of the actual pressure, measured at the tapping point i, P_0 is the reference pressure, ρ is the crosswind air density and V_{rel} is the reference wind velocity relative to the train.

The reference pressure (P_0) adopted in this study, either in static or moving conditions, consists in the estimated double average static pressure: during any single run, the wind static pressure at a number of measuring positions were recorded over a 60s time interval. Selecting one of these positions as a reference, and averaging the data over the entire time interval, a local mean value for the static pressure during each run was calculated. The reference pressure P_0, as defined in the above, corresponds to the spanwise average extrapolated from such local mean value. It was obtained using a spanwise average-to-local ratio based on data obtained during the full flow characterization. For static tests only, an additional correction was applied to the reference static pressure calculated as explained in the above. Considering that different loops of tappings were at considerably different distances from the inlet, such correction was adopted to take into account the along-wind static pressure gradient (see Section 2.3). For the moving model experiments, the Cobra probe used for monitoring the reference wind conditions was positioned 0.2m upstream the track centreline, at 3m full scale equivalent height. During the static tests, although still at the same height, the probe was set close to the channel inlet and on the side with respect to the model.

For static tests, the relative wind corresponds to the absolute crosswind. Hence, the reference relative wind velocity (V_{rel}) coincided with the reference crosswind streamwise velocity, indicated as U. Both the definition and the process according to which U was calculated were consistent with those for the reference pressure. A local mean was calculated time averaging the 60s velocity time history recorded by the reference Cobra probe (the same that provided the data for the crosswind static reference pressure). The reference crosswind streamwise velocity (U) is the spanwise average extrapolated from such local mean velocity. Once again it was based on a spanwise average-to-local ratio obtained from the flow characterization data. An along-wind velocity gradient correction was applied when processing the data from static tests.

The results reported in what follows are relative to a stationary aerodynamic condition. Hence, they are expressed in terms of a mean pressure coefficient, $\bar{C}_{Pi}$, where i corresponds to a particular tapping point. For the static tests, the average was calculated over the entire 60s time interval, which corresponded to the full length of time histories recorded for the surface pressure. For the moving model tests, it was obtained considering only the central portion of the ensemble average time history relative to the crosswind section (noted by vertical dotted lines on Figure 3b). The transitions experienced by a running train at the entry and exit of the crosswind section determined a series of unsteady fluctuations respectively in the initial part and in the tail of the ensemble average time history. As not representative of a stationary aerodynamic condition, such effects were not taken into account in the analysis reported here.

Figures 4 and 5 present the mean pressure coefficient distribution in correspondence of two loops of pressure taps, loop 2 on the train nose and loop 6 approximately in the centre of the leading car. A comparison between static and moving tests results is outlined. Error bars are included in the figures to represent the experimental error that has been estimated through an uncertainty analysis (not discussed in the current paper). As specified above, experimental data for the surface pressure were collected for all the eight loops of tappings shown in Figure 1a. For

purposes of discussions, however, two cross-sections were selected to provide a significant example of different surface pressure conditions experienced along the vehicle.

On the nose of the train (Fig. 4) positive values of $\bar{C}_P$, which indicate a stagnation region, are shown on the windward side and also on the roof windward corner. Negative values of $\bar{C}_P$, which instead indicate suction, characterize the leeward side, the underbody region and also the roof leeward corner, with an evident suction peak arising in correspondence of the latter. Significantly reduced magnitudes of $\bar{C}_P$, for both positive and negative values, and also a partially different trend are outlined at the centre of the train leading car (Fig. 5). Similarly to what observed for loop 2, the results relative to loop 6 show areas of suction that embrace both the leeward side and the underbody region. A stagnation region is still present on the windward side, within which a uniform surface pressure is indicated by the very similar $\bar{C}_P$ values in correspondence of taps 1 and 2. The pressure distribution on the roof presents the main variations with respect to what found on the train nose: in the centre of the leading car the roof is entirely characterized by an area of suction, which shows a peak in correspondence of the windward corner.

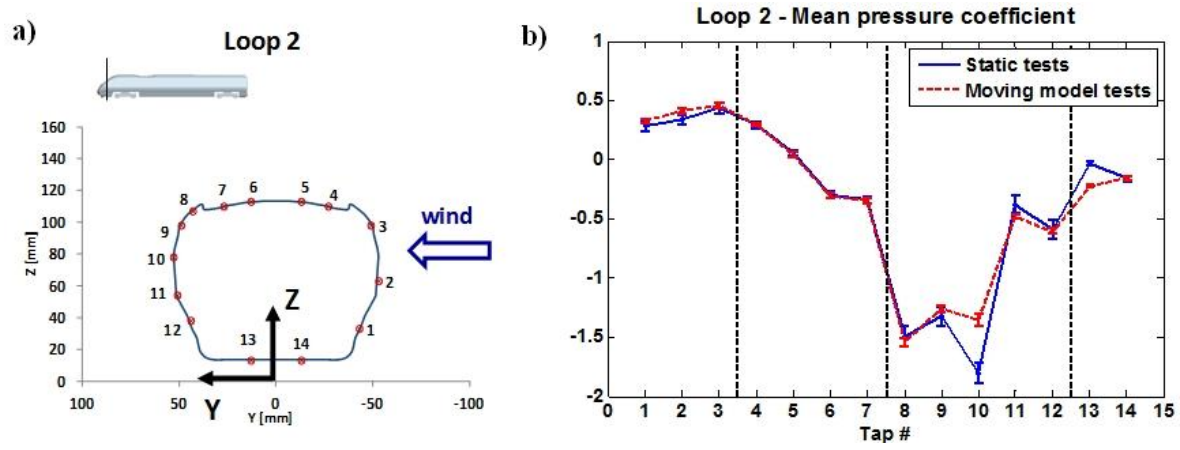

Figure 4. Mean pressure distribution over loop 2 on the nose of the train: Static vs Moving model tests comparison (Class 390 Pendolino, 1:25 scale, 30° yaw angle, FG scenario)

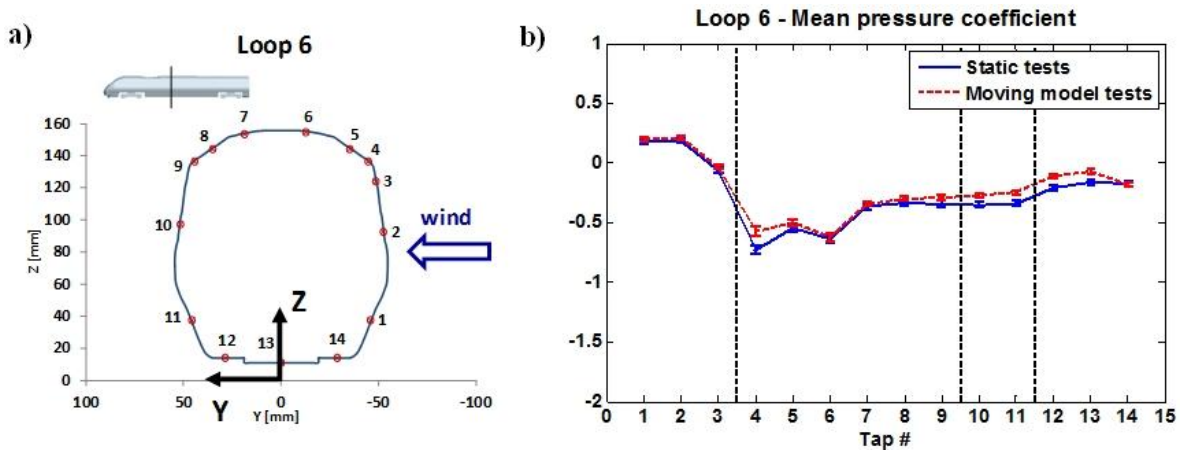

Figure 5. Mean pressure distribution over loop 6 in centre of the leading car: Static vs Moving model tests comparison (Class 390 Pendolino, 1:25 scale, 30° yaw angle, FG scenario)

These results appear consistent with those reported by previous studies on trains which presented similar streamlined designs and were investigated at a 30° yaw angle [11, 15]. The stagnation on the windward side, which on the nose extends also to part of the roof, is determined by the relative crosswind directly impinging the train surface. The suction peak on the nose leeward side is compatible with the presence in that area of one (or more) vortex attached to the train surface. This being supported not only by the magnitude of the suction highlighted in Figure 4 on tap 8, 9 and 10, but also by the fluctuations observed in the time histories of the surface pressure and reflected by high values of standard deviation (not shown here). Moving towards the rear of the train, the data for the adjacent loops of tappings (not shown here) denotes a progressive attenuation in the intensity of this low pressure peak. Such a trend supporting the hypothesis of the vortices mentioned in the above progressively rolling up and moving away from the train surface. A smooth pressure distribution on the leeward side, still associated to a suction region but showing no peak, is reached already in correspondence of loop 4 (Fig. 1a) by where, hence, a complete detachment of the vortical structures seems to have occurred. A region of uniform low pressure is maintained on the leeward side from that section up the rear of the leading vehicle, as reflected by the results relative to the centre of the first car (Fig. 5). The suction peak observed on loop 6, in correspondence of the roof windward corner, suggests in that area the presence of a further vortex. The data from adjacent measuring sections seems to indicate that this vortex is rolling up on the roof. While moving towards the rear, it is drifting progressively from the windward edge to the centerline of the roof, and then it detaches from the train.

The comparison between static and moving model tests indicate good correspondence between the two cases. If the estimated measurement accuracy is taken into account, the majority of the data show a level of agreement that appears somehow remarkable. There are local differences that do not fall within the margin of experimental error. They tend to occur in correspondence of the suction peaks. Nevertheless, it is worth noting that they can be found only for a limited number of tapping points. The trend of the pressure distribution shows a good agreement between static and moving model test results. In correspondence of all the examined loops of pressure taps, the position and extension of the stagnation regions and of the suction peaks are very similar, and also the magnitude of such peaks is comparable. No major differences, hence, can be inferred with regard to the characteristics of the flowfield surrounding the train.

3.2 *Mean aerodynamic load coefficients*

The mean aerodynamic load coefficients for the side and lift forces, and for the rolling moment are presented in this section. Such coefficients are indicated in what follows as $\bar{C}_Y$, $\bar{C}_Z$ and $\bar{C}_{Mx}$, respectively. They were calculated by discrete integration of the pressure distribution over the entire leading car, according to the following equations:

$$\bar{C}_Y = \frac{1}{A_{ref}} \Sigma_i \bar{C}_{Pi} A_i \left(\mathbf{n}_i \bullet \mathbf{y} \right); \quad \bar{C}_Z = \frac{1}{A_{ref}} \Sigma_i \bar{C}_{Pi} A_i \left(\mathbf{n}_i \bullet \mathbf{z} \right); \quad \bar{C}_{Mx} = \frac{1}{A_{ref} H_{ref}} \Sigma_i \bar{C}_{Pi} A_i \left| \mathbf{d}_i \times \mathbf{n}_i \right| \tag{3}$$

In Equation 3, $\bar{C}_{Pi}$ is the mean pressure coefficient as defined in the previous section. A_i and $\mathbf{n}_i$ represent, respectively, the area and the normal unit vector associated to each flat surface into which the train geometry has been discretized. The discretized geometry adopted for the integration was the same for both the static and moving model tests pressure data. **d** is the vector directed from the longitudinal axis X to the center of such flat surfaces *i*, while **y** and **z** are the unit vectors associated to the Y and Z axes, respectively (Fig. 1b). A_{ref} is the reference area, assumed as the nominal side area of the leading car and equivalent to 77m^2 at full scale, while H_{ref} is the reference height and corresponds to a full scale equivalent of 3.1m. The convention for positive

directions defined in accordance to the reference system specified in Figure 1a (for the rolling moment following the 'right-hand screw rule').

A comparison between the results obtained from static and moving model tests is illustrated in Figure 6. The differences appear to be very limited. In particular, whereas the experimental accuracy is taken into consideration (i.e. by specifying error bars on the figure), it can be appreciated how the discrepancies fall well within the estimated margin of error.

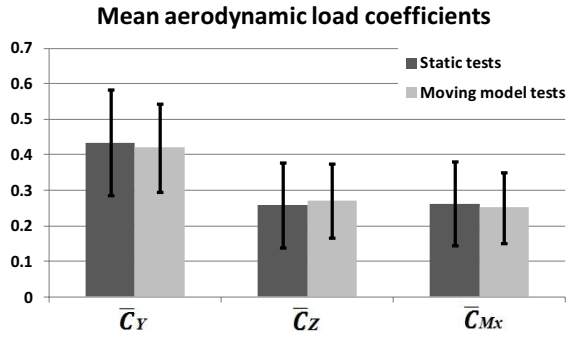

Figure 6. Mean aerodynamic load coefficients for the side force, lift force and rolling moment: Static vs Moving model tests comparison (Class 390 Pendolino, 1/25th scale, 30° yaw angle, FG scenario)

4 CONCLUSIONS

This paper has presented the results from an experimental campaign aimed to assess the effect of the vehicle movement simulation on the train aerodynamics in crosswinds. The existing TRAIN rig moving model test facility was updated by installing a new crosswind generator. A novel test methodology based on the use of an onboard pressure measuring system was developed. The combination of such factors enabled a rather extensive set of data to be collected through both static and moving model experiments. A Class 390 Pendolino scale model was tested on flat ground scenario at a 30° yaw angle. A first comparison, concerned with the mean pressure coefficient on the train leading car, shows limited differences between static and moving model tests. A second analysis, focused on the mean aerodynamic load coefficients, indicates non-significant impact of the vehicle movement on such parameters. Additional studies are ongoing. A further data analysis is investigating the unsteady aerodynamic effects. Also, the experimental results are being shared and used within the AeroTRAIN consortium for CFD benchmarking.

5 ACKNOWLEDGEMENTS

This paper describes some work undertaken in the context of the AeroTRAIN project, Aerodynamics: Total Regulatory Acceptance for the Interoperable Network (www.triotrain.eu).
AeroTRAIN is a collaborative project –medium-scale focused research project supported by the European Commission under the 7th Framework Programme, contract number: 233985, and coordinated by UNIFE, the European Rail Industry. The authors wish to express their gratitude to the numerous people that provided invaluable help and assistance with the TRAIN rig development and the experimental campaign: Dr S.C.Jordan, Mr. T.Gilbert and Mr. D.Soper, Mr. M.Vanderstam and the technical staff of the Civil Engineering Laboratory of the University of Birmingham, Derwent Patterns Ltd, Mr. M.Entezami and Dr C.W. Pope.

6 REFERENCES

1 Baker, C.J., Cheli, F., Orellano, A., Paradot, N., Proppe, C., Rocchi, D., 2009. Cross-wind effects on road and rail vehicles. Vehicle System Dynamics: International Journal of Vehicle Mechanics and Mobility 47, 983 - 1022.

2 Cheli, F., Corradi, R., Diana, G., Ripamonti, F., Rocchi, D., Tomasini, G., 2007. Methodologies for assessing trains CWC trhough time-domain multibody simulations, in: Proceedings of the 12th International Conference on Wind Engineering.

3 Baker, C.J., 2010. The simulation of unsteady aerodynamic cross wind forces on trains. Journal of Wind Engineering and Industrial Aerodynamics 98, 88-99.

4 CEN, 2010. Railway Applications - Aerodynamics - Part 6: Requirements and test procedure for cross wind assessment, EN 14067-6, Brussels.

5 EC, TSI - Technical Specification for Interaoperability of the trans-European high-speed rail system, in 'Rolling stock' Sub-System. 2008, Official Journal of the European Union. p. 193-195.

6 Baker, C.J., Humphreys, N.D., 1996. Assessment of the adequacy of various wind tunnel techniques to obtain aerodynamic data for ground vehicles in cross winds. Journal of Wind Engineering and Industrial Aerodynamics 60, 49-68.

7 Baker, C.J., 1986. Train aerodynamic forces and moments from moving model experiments. Journal of Wind Engineering and Industrial Aerodynamics 24, 227-251.

8 Humphreys, N.D., 1995. High Cross Wind Gust Loads on Ground Vehicles from Moving Model Experiments. University of Nottingham, Nottingham, UK.

9 Bocciolone, M., Cheli, F., Corradi, R., Muggiasca, S., Tomasini, G., 2008. Crosswind action on rail vehicles: Wind tunnel experimental analyses. Journal of Wind Engineering and Industrial Aerodynamics 96, 584-610.

10 Li, Y., Hu, P., Zhang, M., Liao, H., 2009. Wind tunnel tests with moving vehicle model for aerodynamic forces of vehicle-bridge systems under crosswind, in: Proceedings of the The Seventh Asia-Pacific Conference on Wind Engineering, APCWE-VII.

11 Cheli, F., Rocchi, D., Schito, P., Tomasini, G., 2011. Steady and moving high-speed train crosswind simulations. Comparison with wind-tunnel tests, in: Proceedings of the 9th World Congress on Railway Research, WCRR 2011.

12 Quinn, A.D. The TRAIN (Transient Railway Aerodynamics INvestigation) Rig. 2009-2011 19/02/2012]; Available from: http://www.windresearch.org/mmr.html.

13 Pope, C.W. The simulation of flows in railway tunnels using a 1/25th scale moving model facility. in Aerodynamics and Ventilation of Vehicle Tunnels, p 709-737, edited by Alex Haerter, published by Elsevier, 1991.

14 Baker, C.J., et al., The slipstream and wake of a high-speed train. Proceedings of the Institution of Mechanical Engineers, Part F: Journal of Rail and Rapid Transit, 2001. 215(2): p. 83-99.

15 Hemida, H., Krajnovic, S., 2009. Exploring flow structure around a simplified ICE2 train subjected to a 30 degrees side wind using LES. Engineering Applications of Computational Fluid Mechanics 3, 28-41.

The Seventh International Colloquium on Bluff Body Aerodynamics and Applications (BBAA7)
Shanghai, China; September 2-6, 2012

CFD aerodynamic assessment of deck alternatives for a cable-stayed bridge

Felix Nieto [a], Santiago Hernández [a], Ibuki Kusano [a], José Á. Jurado [a]

[a] *School of Civil Engineering – University of La Coruna, Campus de Elviña s/n, Spain*

ABSTRACT: The present document reports the CFD analyses carried out for a set of four different deck cross-sections considered at the preliminary design of the Forth Replacement Crossing: a single box girder with and without wind shields and a twin box girder with and without wind shields. In order to assess the aerodynamic performance of these alternative designs the force coefficients, the shelter provided by the wind shields and the low-speed vortex shedding response of the static deck have been computed. The results obtained are compared with experimental data available in the literature for similar cross-sections finding a good general agreement. It can be concluded that CFD can provide designers with valuable qualitative information at an early design stage for the set of alternative designs considered.

KEYWORDS: CFD, force coefficients, wind shields, vortex shedding, cable-stayed bridges.

1 INTRODUCTION

Focusing on the wind action response, at the early design stage of long span bridges several alternatives for the deck are usually considered. The expected aerodynamic and aeroelastic response must be assessed in order to choose the most feasible alternative for each specific project. Usually engineers rely on previous experiences with similar cross-sections and only in the most challenging projects it is possible to test in the wind tunnel some of the considered preliminary designs. On the other hand, the use of computer-based aerodynamic analysis in real cases is scarce in spite of the growing number of applications in recent times [1, 2].

The aim of the present work is to employ CFD tools to assess the aerodynamic response of two deck types considered at the early design stage of the Forth Replacement Crossing. In order to recreate the constraints in the real design process, where the available resources are limited, 2D models with a limited size are employed. In the absence of published experimental data of the considered cross-sections the results are partially validated using experimental results of similar decks available in the literature. It must be remarked that this application aims to qualitatively evaluate the aerodynamic response of the set of cross-sections and to identify potential problems to focus on in a comprehensive wind tunnel campaign of a candidate design. It is out of discussion the requirement of extensive experimental campaigns to ascertain the performance of any bridge final design. Finally, it is worth recalling that the alternative selected by Transport Scotland for the final design of the Forth Replacement Crossing was the single box girder with wind shields [3].

2 ANALYSIS STRATEGY

2.1 *Deck types*

Two different deck types, from the ones considered for the Forth Replacement Crossing two corridor functional cross section, have been chosen as the specimens for this study: namely, single

box girder (SBG) and twin box girder (TWBG). The data required for the geometric definition of the cross sections of the aforementioned deck types have been obtained from published documents [4, 5] while the geometric definition of the 50% porosity wind shields has been obtained from Ozkan et al. [6] .

In the forthcoming sections the results obtained computationally for the two different deck types, with and without wind shields (WS standing for wind shields and BD standing for bare deck respectively), are going to be presented. This means that a benchmark of four different configurations will be analysed. In figure 1 the geometric definition of the cross sections studied suited with wind shields can be inspected (dimensions in m at real scale). It can be remarked that the purpose of the simulations has been to reproduce numerically the real sectional model wind tunnel tests at a 1:80 geometric scale.

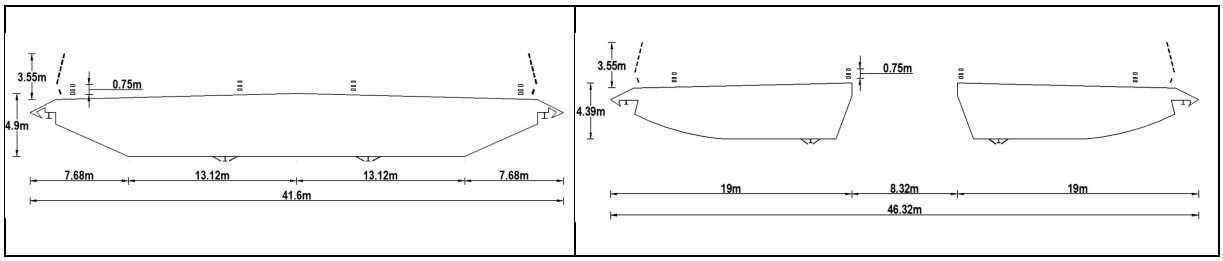

Figure 1. Geometry of the deck types

2.2 *Aerodynamic assessment approach*

The first step to ascertain the aerodynamic response of the set of considered deck types has been the computation of the force coefficients.

$$C_d = \frac{D}{\frac{1}{2}\rho U^2 B}; \quad C_l = \frac{L}{\frac{1}{2}\rho U^2 B}; \quad C_m = \frac{M}{\frac{1}{2}\rho U^2 B^2} \tag{1}$$

In fact, force coefficients play a very significant role because to avoid one degree of freedom instability the first derivative of lift and moment coefficients must be positive according to the criteria of figure 2; additionally, the greater the value of those derivatives is the lower the flutter critical wind speed of the structure is [7, 8]. Moreover, the force coefficients allow the quantification of the effect caused by the wind shields in the overall aerodynamic performance of each particular cross-section, for instance in the increase of the drag coefficient or the changes in the slope of the lift and moment coefficients.

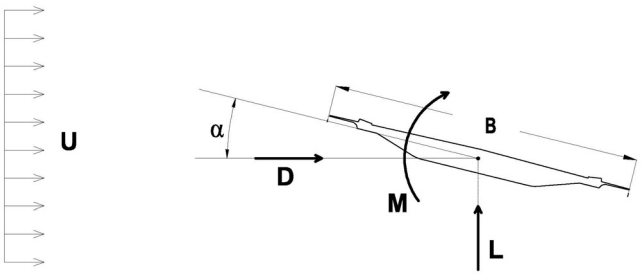

Figure 2. Sign criteria for the force coefficients

Besides this, the computer simulations also allow the evaluation of the level of shelter created by the wind shields in the vehicles' circulation zone on the deck.

Another critical issue to be addressed in the conceptual design stage of a cable supported bridge is the risk of low-speed vortex shedding excitation. In this study a number of flow velocities are considered in the unsteady simulations carried out, and the effect of the wind shields in the oscillatory lift forces suffered by the deck has been analysed.

In this work the CFD simulations for the single box girder are in the Reynolds number range (4.33e+04, 5.3e+05) based on the girder width, while for the twin box girder deck the Reynolds number based on the one box chord length is in the range (1.19e+04, 2.37e+05). It has been assumed that the deck is static throughout the simulations.

3 COMPUTATIONAL MODELLING

The flow around the deck has been computed using the incompressible, unsteady Reynolds averaged Navier-Stokes equations in 2D and the $k-\omega$ SST turbulence model has been chosen. Dirichlet conditions are imposed at the inlet and outlet while no-slip boundary condition has been imposed at the deck surface and the upper and lower limits of the fluid domain as the purpose of the simulations is to reproduce real sectional wind tunnel tests. The corners are modelled as perfectly sharp. The turbulent intensity prescribed at the inlet is 1.1% while the turbulent length scale is about 0.1 times the width of the single box girder design [9]. The flow domain considered in this work is 26.9*B* by 3.8*B* (being *B* the single box girder width), similar to existing wind tunnel facilities.

A commercial finite volume solver has been used to numerically evaluate the flow field. A quadrilateral mesh using the map scheme near walls, and pave scheme in the main part of the flow domain, was utilised. As the target of this study is the preliminary analysis of a set of tentative designs it has been intended to avoid high density meshes. Additionally it has been intended to employ only one mesh for each deck type with similar temporal and spatial discretization, thus the boundary layer grid resolution has been a compromise between the requirements associated to each Reynolds number. As a consequence the ratio of the height of the first grid layer attached to the deck and the single girder width is δ_1/B =5.8e-5 for all the cases analyzed, which is close to the value prescribed by Ribeiro [10] and one order of magnitude higher than the values adopted by Mannini and co-workers [11] and Fransos and Bruno [12]. In tables 1 and 2 the time averaged values of $y^+ = \delta_1 u_\tau / \nu$ ($\overline{y^+}$) averaged along the boxes, the traffic barriers and the windward wind shield are presented along with the time averaged maximum value of y^+ ($\overline{y^+_{max}}$) for the same parts of the deck.

Table 1. Single box girder grids y^+ characteristics

	SBG_BARE			SBG_WS		
	Re=4.3e+4	*Re*=1.0e+5	*Re*=5.2e+5	*Re*=4.3e+4	*Re*=1.0e+5	*Re*=5.2e+5
$\overline{y^+}$ box	0.05	0.11	0.49	0.07	0.10	0.41
$\overline{y^+_{max}}$ box	0.30	0.60	2.81	0.56	0.88	2.92
$\overline{y^+}$ traffic barriers	0.14	0.28	0.85	0.11	0.19	0.67
$\overline{y^+_{max}}$ traffic barriers	0.64	1.20	3.44	0.61	1.22	3.25
$\overline{y^+}$ windward WS				0.24	0.49	1.54
$\overline{y^+_{max}}$ windward WS				0.73	1.47	3.95

Table 2. Twin box girder girders y^+ characteristics

	TWBG_BARE			TWBG_WS		
	Re=1.2e+4	*Re*=4.7e+4	*Re*=2.4e+5	*Re*=1.2e+4	*Re*=4.7e+4	*Re*=2.4e+5
$\overline{y^+}$ windward box	0.05	0.14	0.62	0.05	0.13	0.57
$\overline{y^+_{max}}$ windward box	0.22	0.70	2.52	0.23	0.80	2.50
$\overline{y^+}$ leeward box	0.05	0.14	0.48	0.03	0.08	0.25
$\overline{y^+_{max}}$ leeward box	0.27	0.78	2.57	0.19	0.62	1.77
$\overline{y^+}$ traffic barrier	0.12	0.33	1.04	0.08	0.19	0.57
$\overline{y^+_{max}}$ traffic barrier	0.43	1.18	3.43	0.41	1.17	3.32
$\overline{y^+}$ windward WS				0.17	0.49	1.61
$\overline{y^+_{max}}$ windward WS				0.55	1.51	4.13

4 GRID AND TIME-STEP REFINEMENT

As a first step in the verification of the numerical simulations a grid and time-step refinement study has been carried at *Re*=5.3e5 and 0º angle of attack for both single box girder arrangements and at *Re*=2.4e5 for the twin box girder with and without wind shields, in order to analyze the changes in several variables.

Regarding the spatial discretization study, in tables 3 to 6 the main characteristics of the set of grids considered are presented along with the results obtained for the mean force coefficients (C_d, C_l and C_m) and the standard deviation of the fluctuating force coefficients (C'_d, C'_l and C'_m). The number of cells is increased by a factor of 1.5 while the characteristics of the structured layer attached to the deck, described in the previous section, are the same in all the cases.

Table 3. Grid refinement study of the single box girder without wind shields

Mesh	total cells	total nodes	δ_1/B	Incr *s*	C_d	C_l	C_m	C'_d	C'_l	C'_m
coarse	173396	175396	5.8E-05	2.88E-03	0.069	-0.071	0.018	0.0008	0.0005	0.00004
medium	257717	262242	5.8E-05	2.88E-03	0.069	-0.073	0.017	0.0012	0.0114	0.0025
fine	378123	381099	5.8E-05	2.88E-03	0.069	-0.087	0.016	0.0018	0.0010	0.0002

Table 4. Grid refinement study of the single box girder with wind shields

Mesh	total cells	total nodes	δ_1/B	Incr *s*	C_d	C_l	C_m	C'_d	C'_l	C'_m
coarse	219414	222275	5.8E-05	2.88E-03	0.143	-0.223	-0.013	0.0049	0.0126	0.0026
medium	349250	352322	5.8E-05	2.88E-03	0.142	-0.223	-0.013	0.0058	0.0158	0.0034
fine	511717	514949	5.8E-05	2.88E-03	0.145	-0.227	-0.011	0.0060	0.0169	0.0037

Table 5. Grid refinement study of the twin box girder without wind shields

Mesh	total cells	total nodes	δ_1/B	Incr *s*	*St*	C_d	C_l	C_m	C'_d	C'_l	C'_m
coarse	171705	174350	5.8E-05	2.53E-03	0.149	0.136	-0.140	0.033	0.0327	0.2677	0.0200
medium	255248	258626	5.8E-05	2.53E-03	0.151	0.140	-0.131	0.030	0.0318	0.2815	0.0231
fine	384587	387368	5.8E-05	2.53E-03	0.149	0.132	-0.134	0.031	0.0340	0.2385	0.0267

Table 6. Grid refinement study of the twin box girder with wind shields

Mesh	total cells	total nodes	δ_1/B	Incr s	C_d	C_l	C_m	C'_d	C'_l	C'_m
coarse	230611	233501	5.8E-05	2.53E-03	0.130	-0.087	0.026	0.0064	0.0222	0.0061
medium	345674	348613	5.8E-05	2.53E-03	0.132	-0.084	0.027	0.0063	0.0230	0.0063
fine	508476	511641	5.8E-05	2.53E-03	0.132	-0.081	0.028	0.0064	0.0288	0.0073

From the results presented in the tables above it can be concluded that there are not substantial differences in the mean values of the force coefficients obtained with the medium and fine grids for the single box girder with wind shields, and the twin box girder deck with and without wind shields. Therefore the medium mesh will be used in the simulations hereafter. It is worth remarking that for the single box girder without wind shields there is a non-negligible difference in the value computed for the mean lift coefficient as a 20% discrepancy exists between the medium and fine mesh results, furthermore the standard deviation of both lift and moment coefficients is about one order of magnitude lower when the fine grid is adopted. Further studies are required to set an accurate spatial discretization for the single box girder case without wind shields, nevertheless at the present stage of the investigation it has been decided to adopt the medium mesh to keep coherency with the other cases studied, in the understanding that the level of accuracy can be compatible with the purpose of this work, which is the preliminary assessment of a set of alternative designs. The twin box girder without wind shields shows a strong vortex shedding; thus the Strouhal number (St) has been included in table 5 for comparison.

For the ascertaining of the time step adequacy, the mean values and standard deviation of the force coefficients are computed using the medium grid, considering two different non-dimensional time steps: 2.88e-03 and 1.44e-03, for the single box girder cases, and 2.53e-03 and 1.23e-03 for the twin box girder cases. The results are presented in tables 7 to 10.

Table 7. Time step refinement study of the the single box girder without wind shields

Mesh	δ_1/B	Incr s	C_d	C_l	C_m	C'_d	C'_l	C'_m
medium	5.80E-05	2.88E-03	0.069	-0.073	0.017	0.0012	0.0114	0.0025
medium	5.80E-05	1.44E-03	0.069	-0.069	0.017	0.0017	0.0117	0.0024

Table 8. Time step refinement study of the the single box girder with wind shields

Mesh	δ_1/B	Incr s	C_d	C_l	C_m	C'_d	C'_l	C'_m
medium	5.80E-05	2.88E-03	0.142	-0.223	-0.013	0.0058	0.0158	0.0034
medium	5.80E-05	1.44E-03	0.144	-0.224	-0.009	0.0055	0.0136	0.0030

Table 9. Time step refinement study of the the twin box girder without wind shields

Mesh	δ_1/B	Incr s	St	C_d	C_l	C_m	C'_d	C'_l	C'_m
medium	5.80E-05	2.53E-03	0.151	0.140	-0.131	0.030	0.0318	0.2815	0.0231
medium	5.80E-05	1.26E-03	0.153	0.133	-0.153	0.026	0.0338	0.2671	0.0235

Table 10. Time step refinement study of the the twin box girder with wind shields

Mesh	δ_1/B	Incr s	C_d	C_l	C_m	C'_d	C'_l	C'_m
medium	5.80E-05	2.53E-03	0.132	-0.084	0.027	0.0063	0.0230	0.0063
medium	5.80E-05	1.26E-03	0.133	-0.083	0.026	0.0059	0.0182	0.0051

For the twin box girder without wind shields a 17% difference in the mean lift coefficient along with a 5% difference in the mean drag coefficient have been found while the Strouhal number and the standard deviation of the three force coefficients are in good agreement. These differences are considered assumable at the present stage for the intended purposes of the investigation. For the other three deck types, no substantial discrepancies are presented. As a consequence 2.88e-03 and 2.53e-03 non-dimensional time steps are selected for the computation of the complete set of mean force coefficients which are going to be presented next. However for the low-speed vortex shedding simulations 1.44e-03 and 1.26e-03 non-dimensional time steps have been chosen for the sake of higher accuracy in evaluating this unsteady response.

5 NUMERICAL EVALUATION OF THE FORCE COEFFICIENTS

5.1 *Single box girder with and without wind shields*

In figure 4 the computed mean force coefficients of the single box girder deck with and without wind shields at *Re*=5.2e5 are presented along with the experimental force coefficients of section H4.1 of the candidate cross-sectional shapes considered in the early design of the Great Belt Bridge [13] for validation.

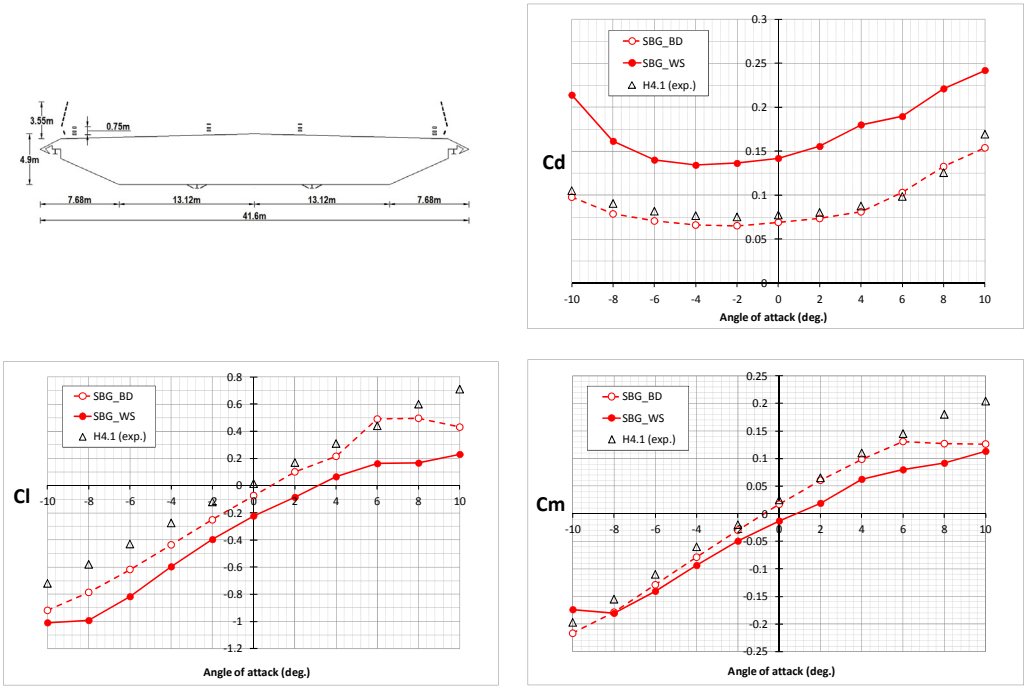

Figure 4. Force coefficients of the single box girder with and without wind shields

From figure 4 it can be concluded that mean force coefficients of the single box girder without wind shields are in good agreement with the experimental data of the H4.1 section. This is important due to the poor results of the grid convergence study for this particular deck type. Besides this the wind shields cause an important increment in the drag coefficient, which is about twice the drag coefficient for the bare section at 0º angle of attack. Furthermore the lift co-

efficient shifts down about 0.15 units keeping the same slope in the range of angles of attack (-8º, 6º) and the slope of the moment coefficient decreases slightly.

5.2 *Twin box girder with and without wind shields*

The computed mean force coefficients at *Re*=2.4e5 for the twin box girder deck types are presented in figure 5. In this case, the experimental force coefficients of two twin box girder decks as the Xihoumen Bridge [14], with a geometrical arrangement similar to the studied specimen, and the Stonecutters Bridge [15], with curved box lateral plates, are also included for the sake of indirectly validating the numerical results.

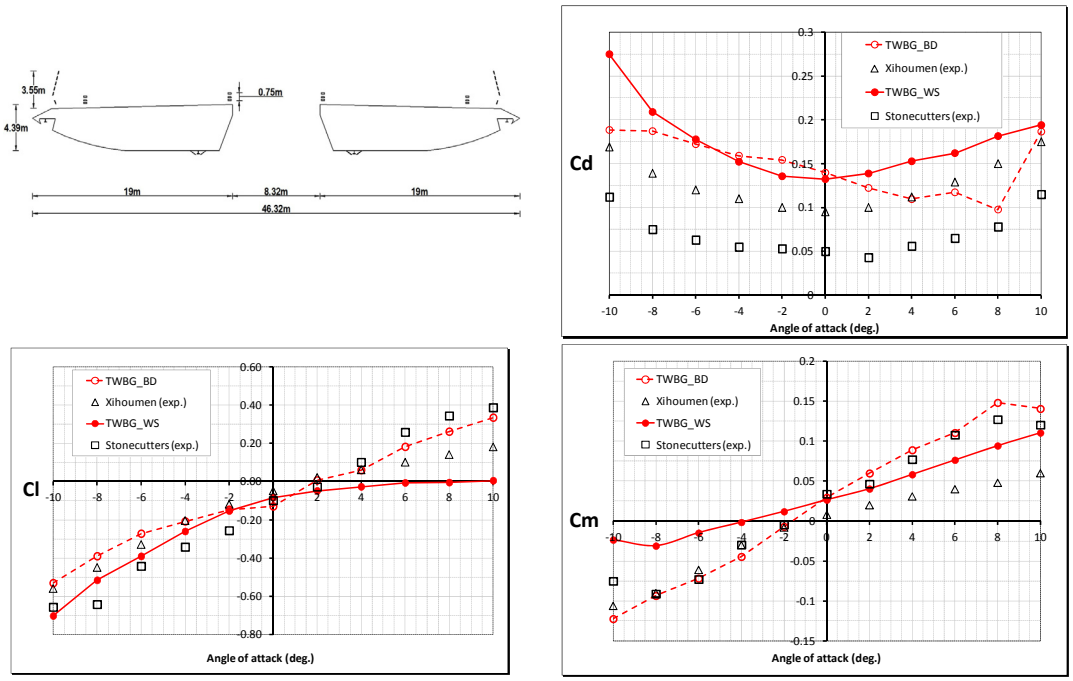

Figure 5. Force coefficients of the twin box girder with and without wind shields

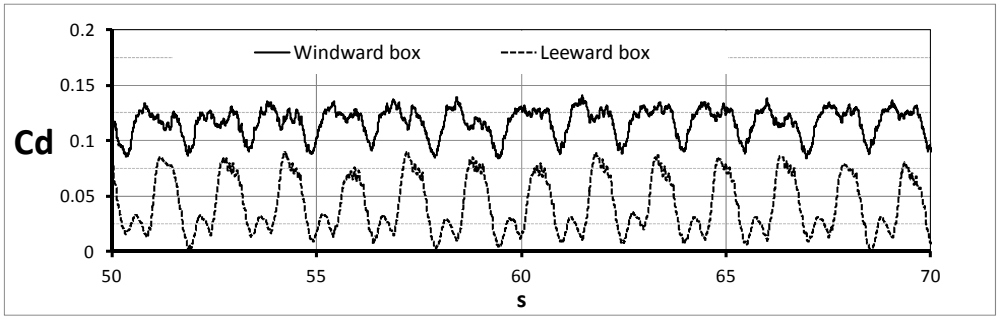

Figure 6. Time history of the disaggregated drag coefficient for TWBG without wind shields at -4º angle of attack.

The twin box girder without wind shields shows lift force coefficient close to the Xihoumen Bridge in the range of angles of attack between -10º and 4º and the differences increase for higher angles of attack. The computed moment coefficient shows good agreement with the Xihoumen Bridge experimental data from -10º to -2º angle of attack. Besides this, for the positive angles of attack the computational results are in agreement with lift and moment coeffi-

cients of the Stonecutters Bridge. Nevertheless it must be remarked the abnormal patter of the drag coefficient which is far from the parabolic shape typical of this force coefficient. Another important characteristic is the high value of the drag coefficient which is similar to the values of the wind shield configuration for the angles of attack between -8º and 2º. Analyzing the computed disaggregated drag forces acting on the windward and leeward boxes it has been found that they are nearly in phase as it can be perused in figure 6. In the absence of a precise experimental validation, this result must be taken as a work hypothesis to be confirmed in the experimental wind tunnel tests to carry out in case of this alternative progressing along the design process.

On the other hand the drag coefficient computed for the twin box girder with wind shields shows a parabolic shape, with values higher than those corresponding to the Xihoumen Bridge. The effect caused by the wind shields in the lift coefficient is the decrement in the slope of the Cl for the positive angles of attack. Regarding the moment coefficient, the wind shields cause the decrement of the coefficient slope for the complete range of studied angles of attack.

6 SHELTER EFFECT OF WIND SHIELDS

The purpose of windshielding in bridges is to provide shelter to vulnerable vehicles, in order to avoid restrictions in bridge operation such as the imposition of lane closures [16].

For the single box girder and the twin box girder alternatives for the Forth Replacement Crossing, computational simulations were carried out for a 3.0 m/s flow speed, which corresponds to a 26.3 m/s free stream velocity at real scale, which is above the wind speed values triggering restrictions in the operation of long span bridges. In figure 7 the normalized wind velocities (ratio of the velocity magnitude to the reference velocity at any point) fields between wind shields are presented for both the single box girder and the twin box girder deck types. The origin of coordinates x and y is set at the connection between the windward wind shield and the box deck. In the charts the horizontal and vertical coordinates are normalized employing the height of the wind shield (H)

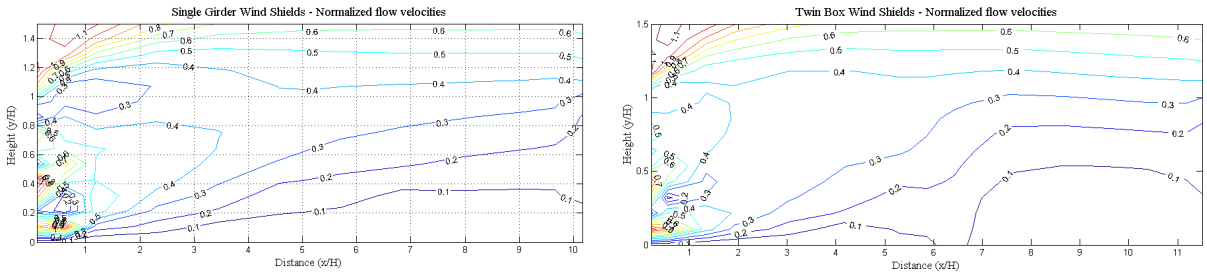

Figure 7. Normalized flow velocities at 0º angle of attack.

The numerical results are compared with the experimental tests reported by Kwon and coworkers [17] who tested an expanded metal barrier with a porosity ratio of 53.7% and a folded porous plate with a porosity ratio of 50% at a 1:10 geometric scale. The numerical results are about a 15%-20% lower that the normalized velocities obtained in the wind tunnel. This can be due to several causes: in the experimental tests the size of the mesh and the holes of the porous plate were not scaled to prevent scale effects, furthermore in the wind tunnel tests only a windward barrier was considered, nevertheless in the present computation both windward and leeward barriers along with the four traffic barriers have been included in the model, which justifies an additional decrement in the flow velocities. Additional studies are required for an accurate as-

sessment of the shelter provided by the wind shields as Reynolds number effects cannot be dismissed beforehand.

7 VORTEX SHEDDING RESPONSE

The preliminary assessment of the vortex-induced vibration risk of the different deck types proposed for the Forth Replacement Crossing at the early design stage has an obvious interest as it would allow the identification of potential aerodynamic concerns. Special attention must be paid to the twin box girder arrangement as bridges with this configuration such as the Stonecutters [18] or the Xihoumen [19] Bridges required mitigation strategies to tackle this phenomenon.

Several simulations considering a static deck have been carried out at low speed and 0º angle of attack for the set of deck types considered in this work. The fluctuating lift coefficient has been analyzed in order to identify strong peaks on the spectrum, indicative of vortex shedding excitation risk. For the single box girder with and without wind shields the fluctuating lift coefficient does not show important peaks on the spectrum. However for the twin box configuration without wind shields a single and extremely high pick has been identified at a *St* between 0.152 and 0.160 for all the flow velocities considered (0.75 m/s, 1.25 m/s, 1.75 m/s, 2.25 m/s and 3 m/s) which clearly indicates a vortex excitation risk and is in agreement with the experimental results reported in the literature. On the other hand, when the twin box girder is fitted with wind shields, it does not show a single strong peak in the spectrum of the lift coefficient for the same set of wind speeds. This indicates a beneficial effect of the wind shields in the vortex shedding response of twin box decks as it has been reported by Ge and co-workers [19].

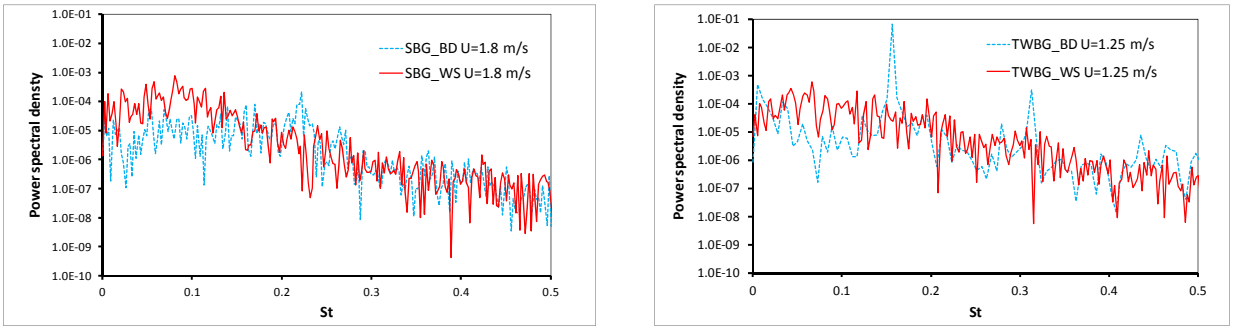

Figure 8. Power spectral density of the fluctuating lift coefficient at 0º angle of attack for the single box girder and the twin box girder with and without wind shields.

8 CONCLUSIONS

CFD techniques have been employed to study the aerodynamic response of two different deck types, with and without wind shields. The force coefficients have been computed, along with the shelter provided by the wind barriers and the vortex shedding response at low-speed.

The verification studies have shown a poor grid convergence for the single box girder without wind shields and some discrepancies were found for the twin box girder without wind shields refining the time step. On the other hand both decks fitted with wind shields showed a good grid and time step convergence.

The force coefficients for the decks without wind shields presented results close to other designs whose experimental data are available in the literature, except for the drag coefficient of the twin box which must be further studied. The decks fitted with wind shields showed a strong increment in the drag coefficient and a slight decrement in the slopes of lift and moment coefficients.

The shelter provided by the 50% porosity wind shields is higher than the existing results in the literature. However, the presence of the leeward wind shield and the traffic barriers justifies lower wind speeds at deck level.

Vortex shedding excitation risk was detected for the twin box girder without wind shields which is in agreement with the published literature. Also the beneficial effect of the wind shields has been pointed out, which is also in agreement with the results published for the Xihoumen Bridge.

9 ACKNOWLEDGEMENTS

This work has been partially founded by the Spanish Ministry of Economy and Competitiveness under project BIA2010-19989. The work carried out by the research assistant A. Troche in preparing the grids for this investigation is acknowledged.

10 REFERENCES

1 T. Vejrum, D.J. Queen, G.L. Larose and A. Larsen. Further aerodynamic studies of Lions' Gate Bridge – 3 lane renovation. J. Ind. Aerodyn., 88(2-3) (2000) 325-341.

2 I.J. Taylor, M. Vezza and I. Salisbury. Numerical investigation of the effects of pedestrian barriers on aeroelastic stability of a proposed footbridge. J. Ind. Aerodyn., 96(12) (2008) 2418-2437.

3 S. Kite, M. Carter and B. Minto. Design of the Forth Replacement Crossing, Scotland, UK. Proc. Sixth New York City Bride Conference, New York, USA, 2011.

4 Transport Scotland. Forth Replacement Crossing: Main Crossing (Bridge) Scheme Assessment Report Development of D2M Alternatives; 2009.

5 Hussain N. Boutique Footbridges to Major Crossings. Middle East Bridges Design and Engineering Summit, Abu Dhabi, UAE; 2009.

6 E. Ozkan, D. Rocchi, A. Allsop, S. Kite, A. Zasso and B. Minto. The aerodynamic performance of Forth Replacement Crossing. Proc. 13th Int. Conf. on Wind Engineering, Amsterdam, The Netherlands, 2011.

7 Larose GL, Livesey FM. (). Performance of streamlined bridge decks in relation to the aerodynamics of a flat plate. Journal of Wind Engineering and Industrial Aerodynamics 1997; 69-71: 851-860.

8 Diana G, Belloli M, Rocchi D, Resta F, Zasso A. Sensitivity analysis on the effects of different aerodynamic devices on the behaviour of a bridge deck. 12th International Conference on Wind Engineering, Cairns, Australia; 2007.

9 L. Bruno, S. Khris and J. Marcillat. Contribution of numerical simulation to evaluating the effect of section details on the aerodynamic behavior of a long-span bridge deck. Proc. 10th Int. Conf. on Wind Engineering, Copenhagen, Denmark, 1999.

10 A.F.P. Ribeiro. Unsteady RANS modeling of flow past a rectangular 5:1 cylinder: investigation of edge sharpness effects. Proc. 13th Int. Conf. on Wind Engineering, Amsterdam, The Netherlands, 2011.

11 C. Mannini, A. Soda, R. Vob and G. Schewe. Unsteady RANS simulations of flow around a bridge section. J. Ind. Aerodyn., 98(12) (2010) 742-753.

12 D. Fransos and L. Bruno. Edge degree-of-sharpness and free-stream turbulence scale effects on the aerodynamics of a bridge deck. J. Ind. Aerodyn., 98(10-11) (2010) 661-671.

13 T.A. Reinhold, M. Brinch and A. Damsgaard. Wind tunnel tests for the Great Belt Link. Proc. Aerodynamics of Large Bridges, Copenhagen, Denmark, 1992.

14 Z.T. Zhang, Z.Q. Chen, X.G. Hua, C.G. Li and Y.J. Ge. Investigation of turbulence effects on torsional divergence of long-span bridges by using dynamic finite-element method. J. Bridge Eng., 15(6), (2010) 639-652.

15 Fok CH, Kwok KCS, Qin XR, Hitchcock PA. (). Sectional Pressure Tests of a Twin-deck Bridge: Part 2: Effects of Gap-width on a Twin –deck Configuration. Proc. 11th Australasian Wind Engineering Society Workshop, Darwin, Australia; 2004.

16 Wyatt TA. Recent British developments: Windshielding of bridges for traffic. Proceedings of the first international symposium on aerodynamics of large bridges, Copenhagen, Denmark; 1992.

17 S.D. Kwon, D.H. Kim, S.H. Lee and H.S. Song. Design criteria of wind barriers for traffic. Part 1: wind barrier performance. Wind and Structures , 14(1) (2011) 55-70.

18 Larsen A, Savage M, Lafrenière A, Hui MCH, Larsen SV. Investigation of vortex response of a twin box bridge section at high and low Reynolds numbers. Journal of Wind Engineering and Industrial Aerodynamics 2008; 96: 934-944.

19 Y.J. Ge, Y. Yang and F. Cao. VIV sectional model testing and field measurements of Xihoumen Suspension Bridge with twin box girder. Proc. 13th Int. Conf. on Wind Engineering, Amsterdam, The Netherlands, 2011.

The Seventh International Colloquium on Bluff Body Aerodynamics and Applications (BBAA7)
Shanghai, China; September 2-6, 2012

Two dimensional numerical simulations of vortex-induced vibration responses of H-shaped bridge deck

Zhiwen Liu[a], Zhengqing Chen[b], Steve C.S.Cai[c]

[a] *Dept. of Civil Eng., Hunan University, Changsha, Hunan, China*
[b] *Dept. of Civil Eng., Hunan University, Changsha, Hunan, China*
[c] *Dept. of Civil and Environmental. Eng., LSU, Baton Rouge, LA, USA*

ABSTRACT: Two dimensional numerical simulations of vortex-induced vibration response of H-shaped bridge deck with 2DOF was conducted with the techniques of dynamic mesh and UDF in Fluent software. The energy of the vertical vibration mode and torsional vibration mode were also calculated to investigate to the energy transition mechanism from one vibration mode to another vibration mode. Numerical results show that the drag coefficient and Strouhal number of the stationary H-shaped bridge deck agree well with the results reported by Larsen. The lock-in of the vertical vibration mode of the H-shaped bridge deck was found when the reduced wind velocity is in the range from 1.23 to 2.43. The flutter critical reduced wind velocity of the H-shaped bridge deck is about 5.26, which corresponding to flutter critical wind velocity of 12.5m/s for the original H-shaped bridge deck. When the reduced wind velocity is 5.26 and 6.31 separately, the energy of the H-shaped section with 2DOF is dominated by the vertical vibration mode firstly, then the energy of it in the torsional vibration mode increase dramatically and the flutter instability occurred.

KEYWORDS: numerical simulation; vortex-induced vibration; H-shaped bridge deck; energy of vibration mode; dynamic mesh; UDF

1 INTRODUCTION

Vortex-induced vibrations (VIV) are motions induced by the vortex shedding behind the bluff bodies. VIVs can occur in many engineering situations, such as large span bridge decks, offshore structures, and other engineering structures. The famous first Tacoma Narrows Bridge main deck exhibited the vortex-induced vibrations after opening to the traffic, which was finally destroyed by wind (Billah K.Y., et al., 1991). With the development of computational performance of computers, the numerical methods on VIVs of structures with sample geometry shapes, such as circular section, square section and rectangular section are used by many researchers (Murakami S., et al., 1997; Owen J.S., et al., 2007; Placzek A., et al., 2009; Sarwar M.W., Ishihara T., 2010, Liu Z.W., 2011). The aerodynamics and structural responses of four generic cross-section shapes developed from the well-known plate girder section of the first Tacoma Narrows bridge were investigated by Larsen with discrete vortex methods (Larsen A., 1998). The aerodynamic performance of the main deck of the first Tacoma Narrows bridge was investigated by many researchers (Matsumoto M., et al., 2008).

In present paper, a new gird generation method was developed to simulate vortex-induced vibrations of H-shaped bridge deck of Tacoma Narrows Bridge with two-degree-of-freedom (2DOF). The energy of the vertical vibration mode and torsional vibration mode were also calculated to investigate to the energy transition mechanism from one vibration mode to another vibration mode.

2 NUMERICAL METHODS

2.1 *Governing equations*

The fluid flow computation is in the framework of the finite volume method (FVM). The Reynolds-averaged Navier-Stokes (RANS) equations can be written as

$$\frac{\partial u_i}{\partial x_i} = 0 \tag{1}$$

$$\frac{\partial}{\partial t}(\rho u_i) + \frac{\partial}{\partial x_j}(\rho u_i u_j) = -\frac{\partial p}{\partial x_i} + \frac{\partial}{\partial x_j}(2\mu S_{ij} - \rho\overline{u'_j u'_i}) \tag{2}$$

where u, p present the time-average value of velocity and pressure; μ is the molecular viscosity, and S_{ij} is the mean stress tensor. The small-scale fluctuations of velocity relating to the turbulence are reduced as $\overline{u'_j u'_i}$, which is referred to as the Reynolds stresses.

The shear stress transport (SST) $k-\omega$ turbulence model was used in the present work. It models the Reynolds stresses with two transport equations for the turbulent kinetic energy k and the specific dissipation rate ω. The SST $k-\omega$ model shows good performance in predicting the adverse pressure gradient flows. The unsteady segregate solution was adopted in the calculations. The SIMPEC algorithm was used to solve the pressure-velocity coupled equations. The implicit first-order scheme was used for the unsteady terms. The PRESTO algorithm was used for pressure terms. The third-order upwind difference scheme QUICK was applied to the convection terms in the momentum equations and the k and the ω transport equations.

2.2 *Modeling of fluid-structure interaction*

The elastically mounted cylinder with 2DOF under the vortex-induced forces can be idealized as shown in Figure 1. The differential equations governing the vortex-induced vibration of the 2DOF system with damping are given as follows,

$$m\ddot{y} + c_y\dot{y} + k_y y = F_y(t) \tag{3}$$

$$I_m\ddot{\alpha} + c_\alpha\dot{\alpha} + k_\alpha\alpha = M_\alpha(t) \tag{4}$$

where m is the mass of the structure, c_y is the vertical damping, k_y is the vertical stiffness of the structure, y is the vertical displacement, respectively. I_m is the inertial moment of mass, c_α is the torsional damping, k_α is the torsional stiffness of the structure, α is the rotational displacement. $F_y(t)$ is the lift force in y direction, and $M_\alpha(t)$ is the torque around the z axis, which can be obtained by conducting fluid analysis around the structure section.

To analyze the structural response of the two-degree-of-freedom system, the equations of structural motion were integrated using Newmark-β method. The computational flow chart of numerical simulation of VIV of H-shaped bridge deck with 2DOF used in present paper is given in Figure 2.

2.3 *Geometry and mesh generation*

The original Tacoma Narrows bridge deck was chosen to investigate the wind-induced vibration responses with numerical methods given in present paper. The geometry and structural data of the original Tacoma Narrows bridge deck were taken from the paper by Larsen (Larsen A., 1998). The main parameters of the main deck are given in Table 1.

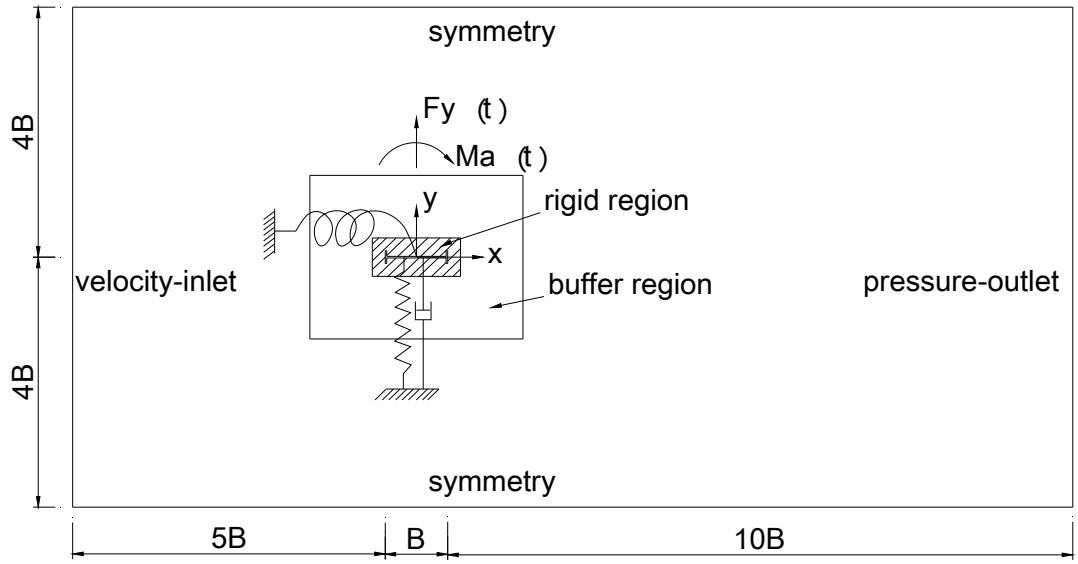

Figure 1 VIV model, computational region and boundary condition of the H-shaped bridge deck

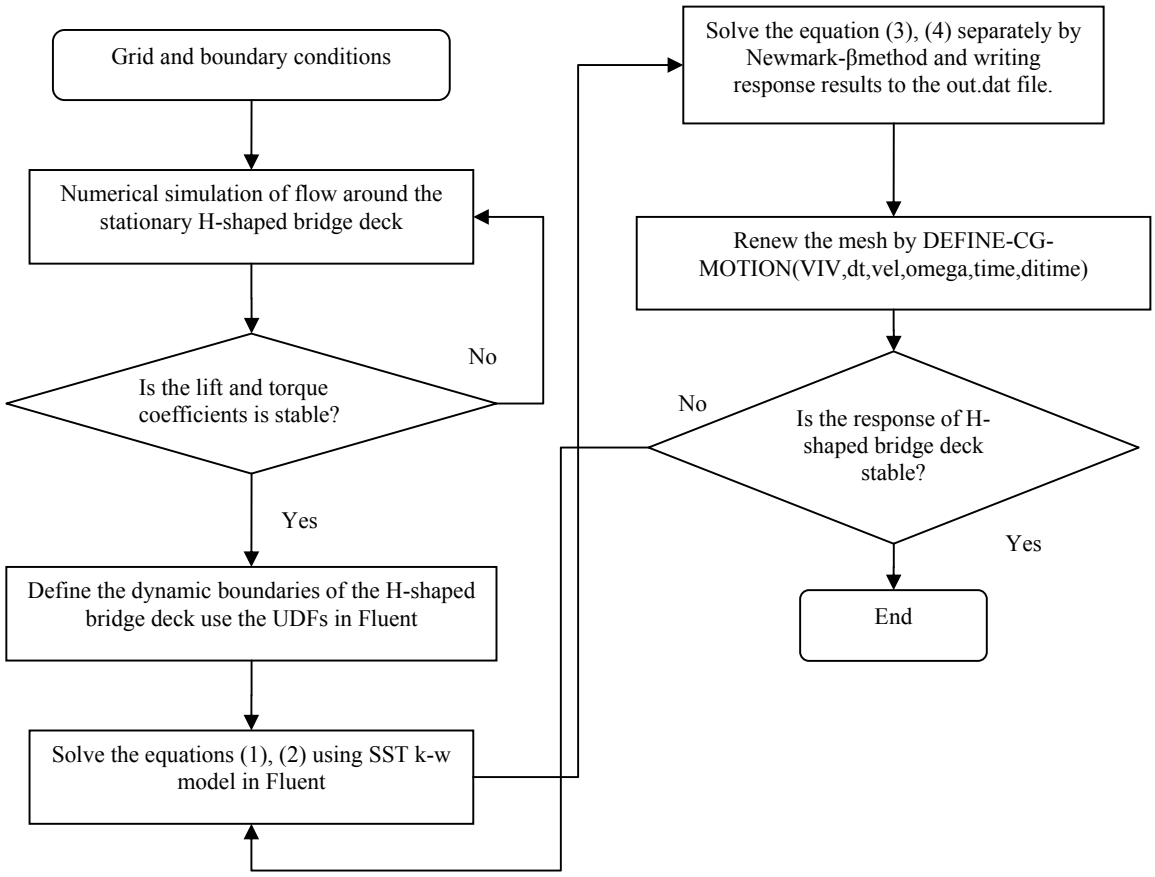

Fig. 2 Flow chart of numerical simulation of VIV of H-shaped bridge deck with 2DOF

Table 1 Main parameters of H-shaped deck of 1st Tacoma Narrows Bridge (Larsen A., 1998)

Parameters	Unit	Original value	Scale	Model value
The width of the deck, B	m	11.887	1/50	0.23774
The height of the deck, H	m	2.40	1/50	0.048
The mass per meter of the deck, m	kg/m	4.25×10^3	$1/50^2$	1.70
The inertial mass per meter of the deck, I_m	$kg\cdot m^2/m$	177.73×10^3	$1/50^4$	0.02844
The first asymmetric vertical vibration frequency, f_h	Hz	0.13	10/1	1.3
The first asymmetric torsional vibration frequency, f_α	Hz	0.20	10/1	2.0
Ratio of wind velocity, λ	/	/	1/5	/
The damping ratio, ξ	%	0.005	1.0	0.005

The computational region and boundary conditions of the H-shaped bridge deck are shown in Figure 1. As shown in Figure 1, the whole computational domain was divided into three different blocks, namely, rigid region, buffer region and stationary region. The displacements and velocities of the rigid region are same as that of the H-shaped bridge deck. The region between the rigid region and the stationary region was modeled as buffer region in which the mesh can be renewed at each time step. The turbulence intensity was of the order of 0.5% at the velocity inlet boundary. And the inlet velocity was in the range from 0.38m/s to 3.0m/s, which corresponding to the reduced wind velocity V/f_hB from 1.23 to 9.71. Symmetry condition was used for the top and bottom sides of the computational domain. The outflow condition was used for the right side of the outlet boundary of the computational domain. The no-slip wall condition was used for the H-shaped bridge deck.

A block-structured grid was used with coarser structured mesh in the stationary region, and the unstructured mesh was used for the buffer region between the stationary region and the rigid region of the computational domain, whereas fine structured mesh was used for the rigid region near the H-shaped bridge deck. The height of the first layer of the mesh near the H-shaped bridge deck is $\delta = 0.0017B$. An overview of the grid of the region is shown in Figure 3(a), and the local view of the mesh around the H-shaped bridge deck is shown in Figure 3(b).

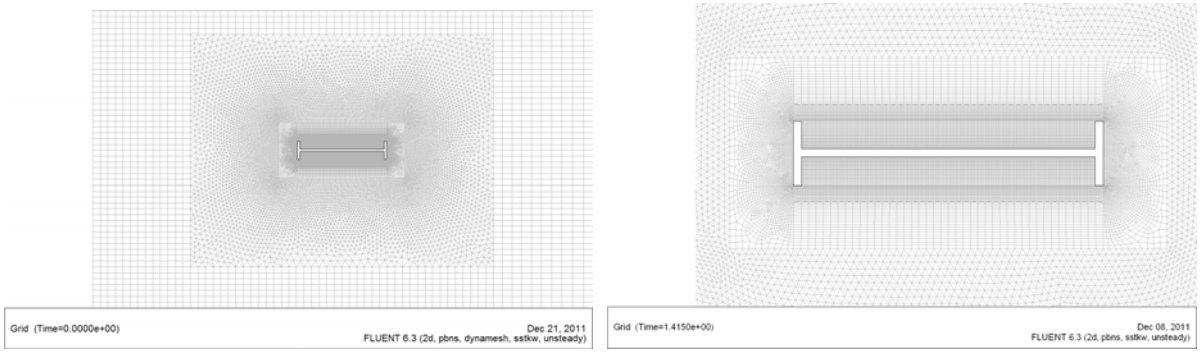

(a) general mesh (b) local mesh near the section

Figure 3 Mesh of the computation region of the H-shaped bridge deck

3 NUMERICAL RESULTS

3.1 *Numerical simulation of flow around the stationary H-shaped bridge deck*

To verification the accuracy of the mesh, the numerical simulations of flow around the stationary H-shaped bridge deck were conducted firstly. The inlet velocity was 10m/s, and symmetry condition was used for the top and bottom sides of the computation domain. The pressure outlet condition was used for the right side of the outlet boundary of the computational domain. The no-slip wall condition was used for the H-shaped bridge deck. The aerostatic coefficients and FFT of the lift coefficients of the H-shaped section are given in Figure 4.

From the Figure 4, it can be seen that the drag coefficient of it is 0.238 with the reference width of B, which is slightly less than the result of Cd=0.28 reported by Larsen (Larsen A.,1998). The Strouhal numbe is about St=fH/V=0.1219, which is slightly larger than the result of St=0.11 given by Larsen (Larsen A.,1998).

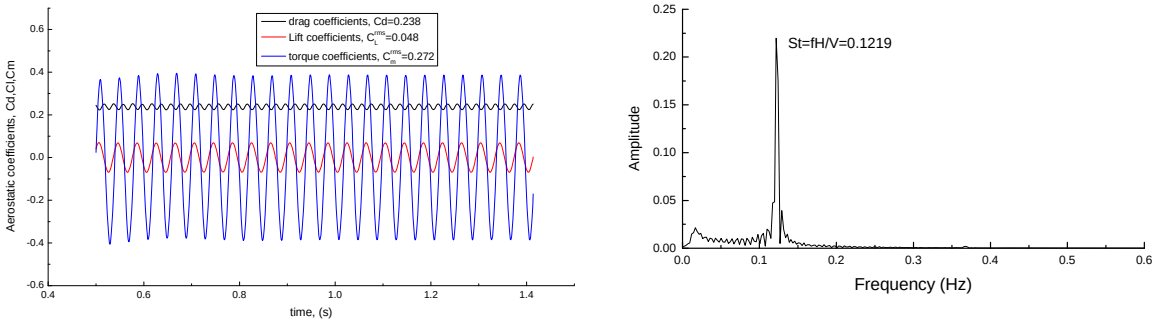

(a) aerostatic coefficients, Cd, Cl, and Cm (b) FFT of lift coefficients

Figure 4 Aerostatic coefficients and FFT of the H-shaped section

3.2 *Numerical simulation of wind-induced vibration of the oscillating H-shaped bridge deck*

The numerical simulations of wind-induced vibration of the H-shaped section with 2DOF were conducted with the method given in present paper under the wind velocity of from 0.38 to 3.0m/s. Fig. 5 gives the time history of wind-induced vibration responses of the H-shaped bridge deck of the first Tacoma Narrows bridge for the wind velocity of 0.57m/s, 0.75ms, 2.50m/s, and 3.0m/s.

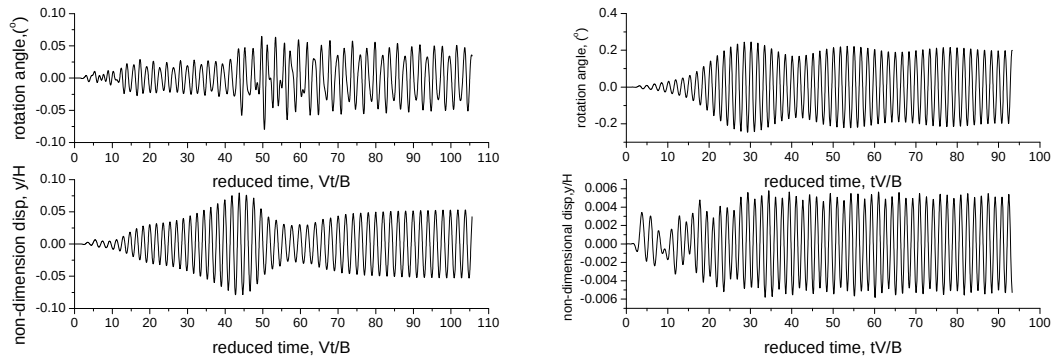

(a) $V_m = 0.57m/s$ (b) $V_m = 0.75m/s$

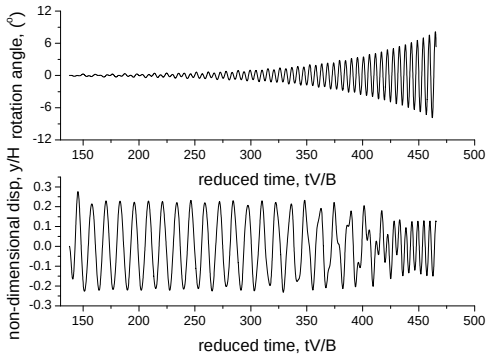

(c) $V = 2.5m/s$

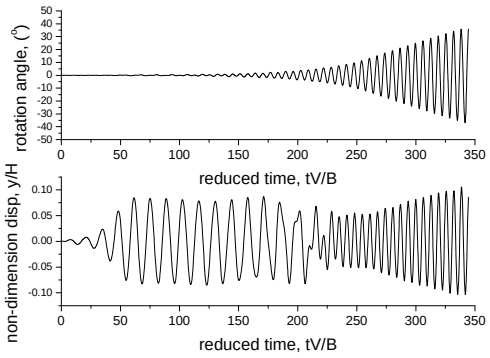

(d) $V = 3.0m/s$

Figure 5 Time history of wind-induced vibration responses of the H-shaped bridge deck with 2DOF

The wind-induced vibration responses of the H-shaped bridge deck with 2DOF are given in Figure 6. From the Figure 6(a), it can be seen that the VIV of the heaving vibration mode of the H-shaped bridge deck was found, and the lock-in reduced wind velocity located from1.23 to 2.43, which corresponding to the wind velocity from 1.90 to 3.75 m/s for the prototype bridge. The maximum RMS value of the non-dimensional displacement is about 0.04 when the wind velocity for the numerical model is 0.57m/s. At this wind velocity, the maximum amplitude is about 0.06H (H is the height of the H-shaped section). As shown in Figure 6(b), the torsional vibration angle of the H-shaped bridge deck increasing suddenly when the wind velocity is about 2.5m/s, which means that the flutter critical wind velocity is about 2.5m/s for the numerical model. The flutter critical wind velocity is about 12.5m/s for the original Tacoma Narrows bridge deck, which is less than the wind velocity of 18.7m/s (Matsumoto M., et al., 2008).

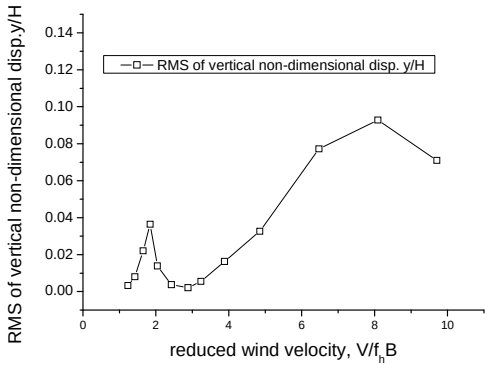

(a) Vertical responses of the H-shaped bridge deck

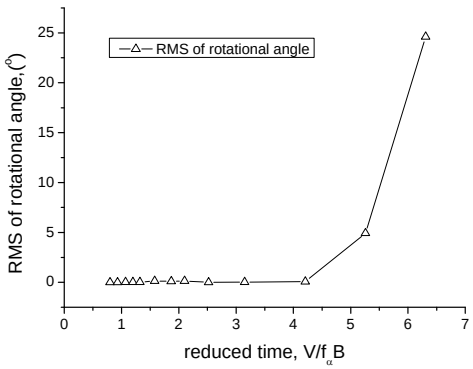

(b) Torsional responses of the H-shaped bridge deck

Figure 6 Wind-induced vibration responses of the H-shaped bridge deck with 2DOF

3.3 *Energy transformation of VIV of the H-shaped bridge deck*

The energy transformation from one vibration mode to another one was calculated to investigate the mechanism of VIV of the H-shaped bridge deck with 2DOF. The energy of the vertical vibration mode and rotation vibration mode of the VIV of the H-shaped bridge deck are defined as follows,

$$E_1 = (m\dot{y}^2 + ky^2)/2.0 \tag{5}$$

$$E_2 = (I_m\dot{\alpha}^2 + k_a\alpha^2)/2.0 \tag{6}$$

where m is the mass structure, k is the spring stiffness of the bridge deck in vertical direction, y and $\dot{y}$ are the vertical vibration displacement and velocity separately, E_1 is the energy of the structure system of the vertical vibration mode. I_m is the inertial moment of the mass of the bridge deck, k_α is the spring stiffness in torsional direction of the bridge deck, α and $\dot{\alpha}$ are the rotation angle and angular velocity separately, E_2 is the energy of the structure system of the torsional vibration mode.

The total energy of the VIV of the H-shaped bridge deck is given as follows,

$$E = E_1 + E_2 \tag{7}$$

where E is the total energy of the H-shaped bridge deck with 2DOF.

The time history of energy of the vertical vibration mode and rotation vibration mode of the H-shaped bridge deck for wind velocity of 0.51m/s to 3.0m/s are given in the Figure 7.

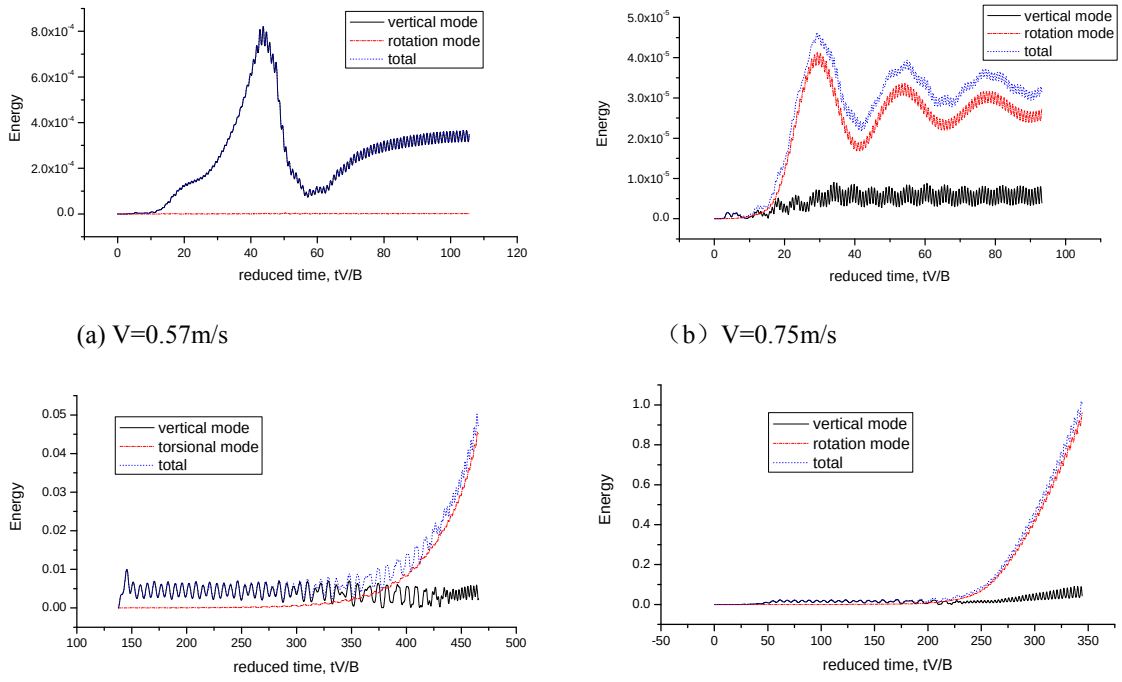

(a) V=0.57m/s　　（b）V=0.75m/s

（c）V=2.5m/s　　（d）V=3.0m/s

Figure 7 Time history of the energy of the H-shaped bridge deck with 2DOF

As shown in Fig.7, the energy of the H-shaped bridge deck with 2DOF is mainly dominated by the vertical vibration mode when the wind velocity is in the range from 0.38 to 0.63m/s. While the energy of it is mainly dominated by the torsional vibration mode when the wind velocity is in the range from 0.75 to 1.0m/s. The energy of the H-shaped bridge deck with 2DOF is mainly dominated by the vertical vibration mode when the wind velocity is in the range from 1.2 to 2.0m/s. When the wind velocity is 2.5m/s and 3.0m/s separately, the energy of the H-shaped bridge deck with 2DOF is dominated by the vertical vibration mode firstly, then the energy of it in the torsional vibration mode increase sharply and the flutter instability occurred.

4 CONCLUSIONS

The gird generation method and UDF (User defined function) program developed in present paper was used to simulate the wind-induced vibration of the H-shaped bridge deck with 2DOF. The wind-induced vibration responses of the H-shaped bridge deck with 2DOF were calculated to investigate the VIV responses and flutter instability of it. Numerical results show that the drag coefficient and Strouhal number of the stationary H-shaped bridge deck agree well with the results reported by Larsen. The lock-in of the vertical vibration mode of the H-shaped bridge deck was found when the reduced wind velocity is in the range from 1.23 to 2.43. The flutter critical reduced wind velocity of the H-shaped bridge deck is about 5.26, which corresponding to flutter critical wind velocity of 12.5m/s for the original H-shaped bridge deck. When the reduced wind velocity is 5.26 and 6.31 separately, the energy of the H-shaped section with 2DOF is dominated by the vertical vibration mode firstly, then the energy of it in the torsional vibration mode increase sharply and the flutter instability occurred.

5 ACKNOWLEDGEMENTS

This research works has been supported by National Natural Science Foundation of China （No.51178181）.

6 REFERENCES

1. Billah K.Yusuf, Scanlan Robert H., Resonance, Tacoma Narrows bridge failure, and undergraduate physics textbooks, Am. J. Phys, 59(2) (1991)118-124
2. Murakami S., Mochida A., Sakamoto S., CFD analysis of wind-structure interaction for oscillating square cylinders, Journal of Wind Engineering and Industrial Aerodynamics, 72(1997)33-46
3. Owen J.S., Hargreaves D.M., Bridge deck aero-elasticity: Comparisons of the computational models with Wind Tunnel Test, ICWE12, Cairns, Australia, (2007)151-158
4. Placzek A., Sigrist J.F., Hamdouni A., Numerical simulation of an oscillating cylinder in a cross-flow at low Reynolds number: Forced and free oscillations, Computers & Fluids 38(2009)80-100
5. Sarwar M.W., Ishihara T., Numerical study on suppression of vortex-induced vibrations of box girder bridge section by aerodynamic countermeasures, Journal of Wind Engineering and Industrial Aerodynamics, doi:10.1016/j.jweia.2010.06.001
6. Liu Z.W., Chen Z.Q., Cai Steve C.S., Two dimensional numerical simulations of vortex-induced vibrations of rectangular section with aspect ratio of 4, 13th International Conference on Wind Engineering, Amsterdam, the Nrtherlands, 2011
7. Larsen Allan, Advances in aeroelastic analyses of suspension and cable-stayed bridges, Journal of Wind Engineering and Industrial Aerodynamics, 74-76(1998)73-90
8. Matsumoto Masaru, Yagi Tomomi, et al., Vortex-induced vibration and its effect on torsional flutter instability in the case of B/D=4 rectangular cylinder. Journal of wind Engineering and Industrial Aerodynamics, 96(2008)971-983

The Seventh International Colloquium on Bluff Body Aerodynamics and Applications (BBAA7)
Shanghai, China; September 2-6, 2012

Numerical simulation of hydrodynamic loading on submerged rectangular bridge decks

Chia-Ren Chu[1], Chih-Jung Huang[1], Tso-Ren Wu[2], Chung-Yue Wang[1]

[1]*Department of Civil Engineering, National Central University, Tao-Yuan, Taiwan, R.O.C.*
[2]*Institute of Hydrological and Oceanic Sciences, National Central University, Taiwan, R.O.C.*

ABSTRACT: This study used a Large Eddy Simulation (LES) model to investigate the hydrodynamic forces on fully submerged bridge decks. The numerical simulation was verified by comparing with the experimental results and was used to examine the influences of the deck Froude number and blockage ratio on the drag and lift coefficients of the bridge deck. The results demonstrate that the force coefficients are dependent on the deck Froude number. The drag coefficient increases as the blockage ratio increases for low Froude number, and dramatically increases, due to the wave induced drag, for high Froude number. On the other hand, the lift coefficient is a function of the submergence ratio of the deck. The downward velocity above the bridge deck and the asymmetric pressure distribution on the upper and lower sides of the deck generate a negative lift force on the bridge deck.

KEYWORDS: Bridge deck, Froude number, drag coefficient, lift coefficient, blockage ratio.

1 INTRODUCTION

The hydrodynamic loading on the bridge body is an essential parameter for evaluating bridge safety, especially when a bridge deck is entirely submerged in the river flow during flood events. The drag and lift forces can be calculated as:

$$F_D = C_D \frac{1}{2} \rho U_o^2 A \tag{1}$$

$$F_L = C_L \frac{1}{2} \rho U_o^2 A \tag{2}$$

where C_D is the drag coefficient, C_L is the lift coefficient, ρ is the density of water, U_o is the free-stream velocity of the undisturbed flow, and A is the frontal area of the bridge body. The drag and lift coefficients are functions of the bridge shape, attack angle and the Reynolds number of the flow (Hamill, 1999).

For fully submerged bridge decks, due to the presence of a free surface and the complicated interaction between the bridge structure and river flow, the drag and lift coefficients are difficult to determine. In previous studies, Naudascher & Medlarz (1983) measured the drag coefficient of a girder bridge and found that the wave motion and vortex formation between the girders generated a peak loading on the bridge deck. Malavasi & Guadagnini (2003) used dynamometers to measure the hydrodynamic forces on partially and fully submerged bridge decks with a rectangular cross-section. Their results revealed that the drag and lift coefficients were dependent on the Reynolds number and submergence ratio of the bridge deck. The submergence ratio is defined as:

$$h^* = \frac{H_o - h}{D} \tag{3}$$

where H_o is the water depth of undisturbed flow, D is the thickness of the bridge deck, and h is the distance from the channel floor to the underside of the deck (see Fig. 1). They also point out that the drag and lift coefficients significantly deviated from the corresponding values in an unbounded domain. In another paper, Malavasi & Guadagnini (2007) used a laboratory flume to study the interaction between a free surface flow and a rectangular cylinder in the water. They found that the rectangular cylinder created a blockage effect on the water flow, and the Reynolds number and the blockage ratio together affected the hydrodynamic loading on the cylinder. The blockage ratio is defined as the ratio of the frontal area of the bridge to the channel cross-sectional area.

On the other hand, Malavasi & Trabucchi (2008) used a three-dimensional k-ε turbulence model to investigate the proximity effects of a solid wall on the wake flow of a rectangular cylinder (aspect ratio L/D = 3) placed above a solid wall with different gap ratios h/D (h is the distance of the lower side of the cylinder to the wall). Their simulation results showed that the drag and lift coefficients increased as the gap ratio, S/D, decreased.

However, the above studies only covered a narrow range of flow conditions. Whether their results could be applied to other flow conditions (for example, supercritical flow) still needed to be examined. This study used a Large Eddy Simulation (LES) model to investigate the interactions between a free surface flow and fully submerged bridge decks. A series of numerical simulations were carried out to clarify the influences of the Froude number, the blockage ratio and the submergence ratio on the force coefficients of the bridge deck.

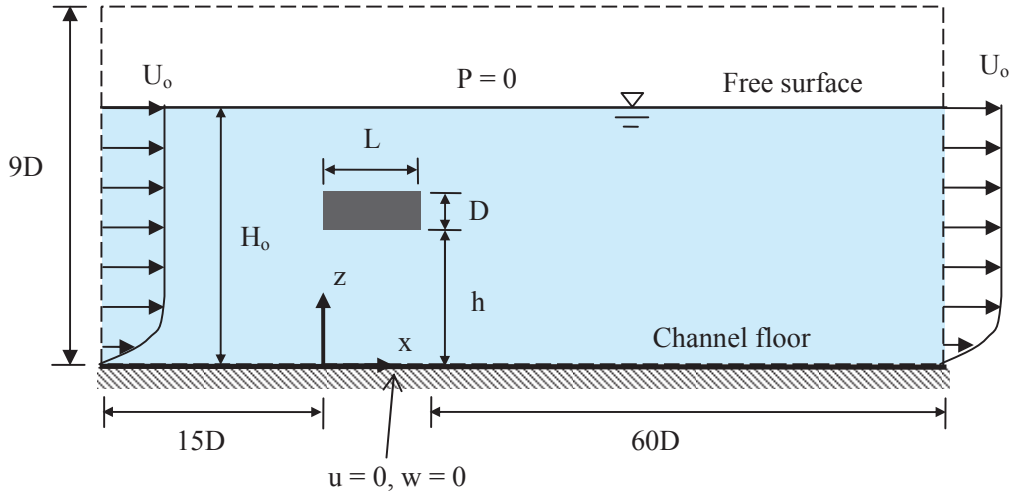

Figure 1. Schematic diagram of a fully submerged rectangular bridge deck.

2 NUMERICAL MODEL

This study used a Large Eddy Simulation (LES) model to simulate the flow field around the bridge deck. The fluid motion was simulated by solving the continuity equation and the Navier-

Stokes equations. The free surface was tracked by the Volume of Fluid (VOF) algorithm. The governing equations can be expressed as:

$$\frac{\partial \bar{u}_i}{\partial x_i} = 0 \tag{4}$$

$$\frac{\partial \overline{\rho u_i}}{\partial t} + \frac{\partial \rho \overline{u_i u_j}}{\partial x_j} = -\frac{\partial \bar{P}}{\partial x_i} + \rho g \delta_{i3} + \frac{\partial}{\partial x_j}\left[\mu_{eff}\left(\frac{\partial \overline{u_i}}{\partial x_j} + \frac{\partial \overline{u_j}}{\partial x_i}\right)\right] \tag{5}$$

where the subscripts i, j = 1, 2 represent the x and z directions, respectively; t is the time, $\bar{u}$ and $\bar{P}$ are the filtered velocity and pressure, ρ is the density of water, g is the gravitational acceleration, and μ_{eff} is the effective viscosity, defined as:

$$\mu_{eff} = \mu + \mu_{SGS} \tag{6}$$

where μ is the dynamic viscosity of water, and μ_{SGS} is the viscosity of sub-grid scale turbulence, defined as:

$$\mu_{SGS} = \rho(C_s \Delta_s)^2 \sqrt{2\bar{S}_{ij}\bar{S}_{ij}} \tag{7}$$

where C_s is the Smagorinsky parameter, S_{ij} is the rate of strain, and Δ_s is the characteristic length of the spatial filter:

$$\Delta_s = 2(\Delta x \Delta z)^{1/2} \tag{8}$$

In this study, the value of the Smagorinsky parameter was set to be $C_s = 0.30$. In addition, the projection method (DeLong, 1997) was used to solve the Poisson Pressure Equation (PPE) and to decouple the velocity and pressure in the Navier-Stokes equations. The water surface was simulated by the Volume of fluid (VOF) method (Hirt & Nichols, 1981).

$$\frac{\partial f_m}{\partial t} + \nabla \cdot (f_m \mathbf{u}) = 0 \tag{9}$$

The value of $f_m = 1$ corresponds to a cell full of water; and $f_m = 0$ represents the cell is full of air. Further details of the numerical model can be found in Wu & Liu (2009).

3 RESULTS AND DISCUSSIONS

In order to demonstrate the accuracy of the numerical model, the present Large Eddy Simulation (LES) model was compared with the experimental results of Malavasi & Guadagnini (2007). A stationary, rectangular cross-sectional bridge deck (thickness D = 0.06 m, length L = 0.18 m, aspect ratio L/D = 3) was placed above the channel floor. The deck was fixed in the channel and parallel to the channel floor. The distance from the channel floor to the underside of the deck was h = 0.14 m (see Fig. 1). The width of the bridge deck was equal to the width of the channel, and the flow direction was parallel to the length of the bridge deck. The bridge pier was not considered in this study. The water depth of undisturbed flow was in the range of $H_o = 0.17 \sim 0.5$ m, upstream velocity $U_o = 0.2$ m/s, the submergence ratio $h^* = (H_o - h)/D = 0.5 \sim 5.0$, the blockage ratio Br = 0.12 ~ 0.35. The Reynolds number $Re = U_o D/\nu = 1.2 \times 10^4$, and the Froude number $Fr = U_o/(gH_o)^{1/2}$ was in the range of Fr = 0.09 ~ 0.15. In order to examine the influence of the flow velocity on the force coefficients of the bridge deck, Malavasi & Guadagnini (2003) defined a deck Froude number as:

$$Fr_D = \frac{U_o}{\sqrt{gD}} \tag{10}$$

where D is the thickness of the bridge deck.

The drag and lift coefficients were computed from the pressure distribution around the cylinder and compared with the experimental results of Malavasi & Guadagnini (2007). As shown in Figure 2, the simulation results of the uniform grid (936 x 110) and the non-uniform grid (496 x 110) both are close to the measured drag and lift coefficients. The biggest difference for the time-averaged drag coefficient was 1.9%. In order to reduce the computing time, the non-uniform grid was used for the rest of the simulation.

Figure 2(a) depicts that the drag coefficient C_D increased as the submergence ratio, h^*, increased in the range of $0 \le h^* < 1.0$. This is because the bridge deck was partially submerged and the frontal area of the deck under the water surface increased as h^* increased. However, the value of C_D decreased as the submergence ratio, h^*, increased when $h^* \ge 1.2$. Malavasi & Guadagnini (2007) explained this trend by asserting that the variations of h^* induced the change in the blockage ratio, and the increasing blockage ratio resulted in the increase of the drag coefficient.

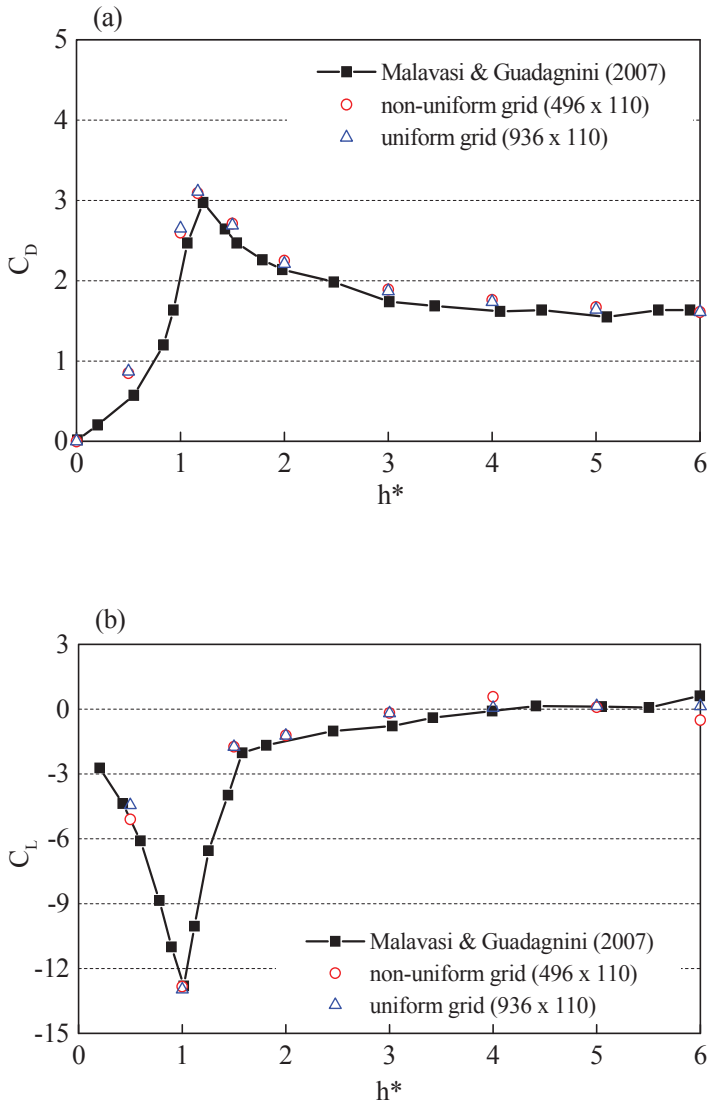

Figure 2. Comparison of model predictions and experimental results of Malavasi & Guadagnini (2007): (a) drag coefficient; (b) lift coefficient.

However, the submergence ratio and the blockage ratio were related to each other in the experimental conditions of Malavasi & Guadagnini (2007). Discriminating the influences of the blockage ratio and the submergence ratio on the drag coefficient can be difficult.

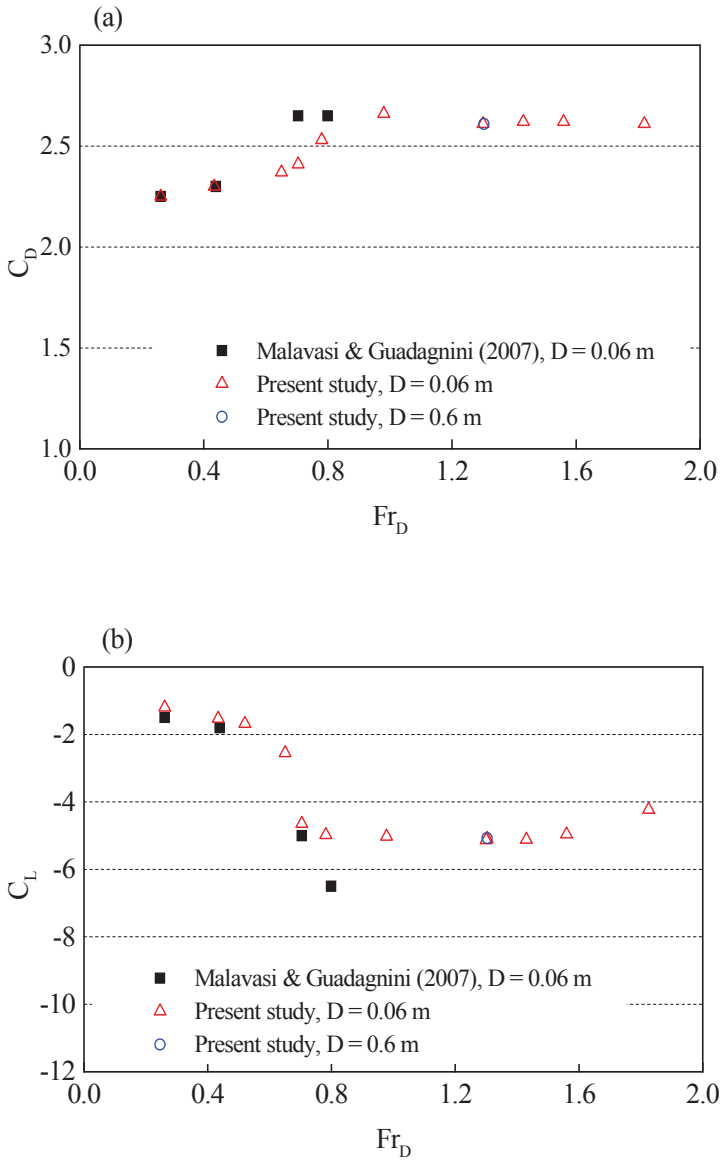

Figure 3. Relationship between force coefficients and deck Froude number for submergence ratio h* = 2.0, and blockage ratio Br = 0.23: (a) drag coefficient; (b) lift coefficient.

On the other hand, Figure 2(b) shows that the lift coefficient, C_L, was negative and decreased as the submergence ratio, h^*, increased in the range of $0 \le h^* \le 1.0$. This is due to the negative pressure (suction) produced by the separation bubble only occurred on the lower side of the deck when $h^* < 1.0$. When the deck was fully submerged ($h^* \ge 1.2$), the lift coefficient, C_L,

increased until it approached zero ($h^* \geq 3.5$). It was easy to understand this phenomenon because the pressure coefficients, C_p, became symmetric on the upper and lower sides when the water surface no longer influenced the separation flow on the upper side of the deck.

The drag and lift coefficients of the present study were plotted against the deck Froude number in Figure 3. The submergence ratio was $h^* = 2.0$, the aspect ratio was L/D = 3, and the blockage ratio was Br = 0.23. The Reynolds number was $Re = 1.2 \times 10^4 \sim 6.54 \times 10^4$, and the Froude number based on water depth H_o, $Fr = U_o/(gH_o)^{1/2}$, was in the range of Fr = 0.13 ~ 0.88. Namely, the channel flows were all sub-critical flows. However, the flow condition covered sub-critical flow to super-critical flow while using the deck Froude number ($Fr_D = 0.26 \sim 1.82$).

Figure 3(a) shows that when $Fr_D < 0.50$, the computed drag coefficient, $C_D = 2.25$, was close to the value $C_D = 2.0$~2.2 suggested by Hamill (1999) for bridge deck design. But the value of C_D increased slightly as the deck Froude number increased, and became a constant $C_D = 2.6$ when $Fr_D > 0.80$. In addition, the lift coefficient suddenly decreased from $C_L = -1.5$ to $C_L = -5.0$ when the deck Froude number was $Fr_D > 0.80$ (see Fig. 3(b)). This implied that there was a flow transition when the deck Froude number increased from 0.50 to 0.80.

The time-averaged water surface curves of different deck Froude numbers are shown in Figure 4. The gray area represents the location of the bridge deck. The location of the water surface was determined by setting the volume fraction $f_m = 0.5$. The water surface was smooth and undisturbed for low Froude number ($Fr_D \leq 0.52$). However, due to the back-water effect, the water surface was levitated in front of the bridge deck and suddenly dropped behind the deck when the Froude number was $Fr_D \geq 0.78$. This was the reason that the drag and lift coefficients went through a transition as the deck Froude number increased. The flow condition transformed from a sub-critical flow to a trans-critical flow as the deck Froude number increased from $Fr_D \leq 0.52$ to $Fr_D \geq 0.78$. The trans-critical flow covered the near-critical flow ($0.8 < Fr_D < 1.0$), critical flow ($Fr_D = 1.0$) and super-critical flow ($Fr_D > 1.0$).

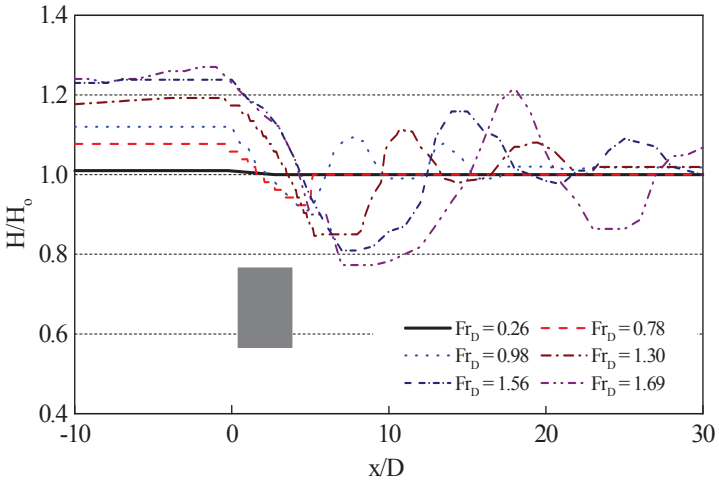

Figure 4. Water surface variations of different deck Froude numbers for h* = 2. The gray area represents the location of the bridge deck, x is the distance from the leading edge of the deck.

It should be noted that, for trans-critical flows, the height of the water surface above the deck and the amplitude of the surface disturbance increased as the deck Froude number increased. The surface disturbance behind the deck gradually decreased as the water flowed downstream. This is similar to the ship wave generated by a moving object near the water surface (Bal, 2008). The increase of the drag coefficient from $C_D = 2.2$ to $C_D = 2.6$, as the flow condition changed from sub-critical flow to trans-critical flow, was due to the wave-induced drag.

Figure 5 compares the distribution of the time-averaged pressure coefficients on the upper and lower sides of the deck for $Fr_D = 0.26$, 0.78 and 1.30, $h^* = 2.0$. The spatial average pressure coefficients were $C_{p3} = -2.01$, 0.66, 0.92 on the upper sides and $C_{p4} = -3.21$, -4.32, -4.17 on the lower sides, respectively. As can be seen in Figure 5, the pressure coefficients C_{p4} on the lower side of the deck were all negative and were close to each other for different Froude numbers. But the pressure coefficients $C_{p3} < 0$ on the upper side of the deck for the sub-critical flow ($Fr_D = 0.26$) and $C_{p3} > 0$ for the trans-critical flows ($Fr_D \geq 0.78$). The positive pressure coefficient, C_{p3}, was caused by the downward flow above the bridge deck. This positive pressure on the upper side together with the negative pressure on the lower side engendered a large downward force on the deck (negative lift coefficient C_L).

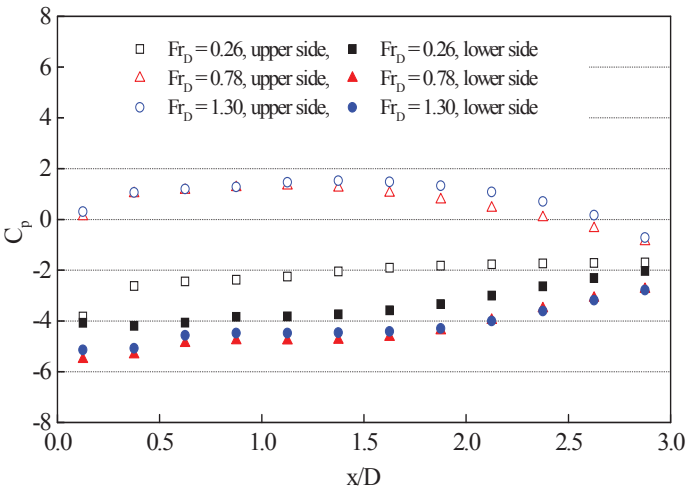

Figure 5. Distribution of time-averaged pressure coefficients on the upper and lower sides of the deck for $Fr_D = 0.26$, 0.78 and 1.30. The submergence ratio h* = 2.

Besides the Froude number effect, the force coefficients were influenced by the blockage ratio. This section focuses on the blockage effect on the force coefficients. The deck thickness D = 0.06 m, length L = 0.18 m (aspect ratio L/D = 3), and the free-stream velocity $U_o = 0.20$ m s^{-1} were kept constant throughout the simulation. The Reynolds number was $Re = 1.20 \times 10^4$, and the deck Froude number was $Fr_D = 0.26$. The variation of the blockage ratio included two different simulation series. The first simulation series kept the distance from the channel floor to the underside of the deck constant (h = 0.14 m), while changing the water depth $H_o = 0.23 \sim 0.50$ m. This was similar to the experimental setup of Malavasi & Guadagnini (2007). The submergence ratio was in the range of $h^* = 1.0 \sim 6.0$, and the blockage ratio was $Br = 0.12 \sim 0.26$. The second

simulation series changed the water depth, H_o and the height above the channel floor, h, while keeping the submergence ratio ($h^* = 2.0$) constant. The blockage ratio was in the range of Br = 0.05 ~ 0.20.

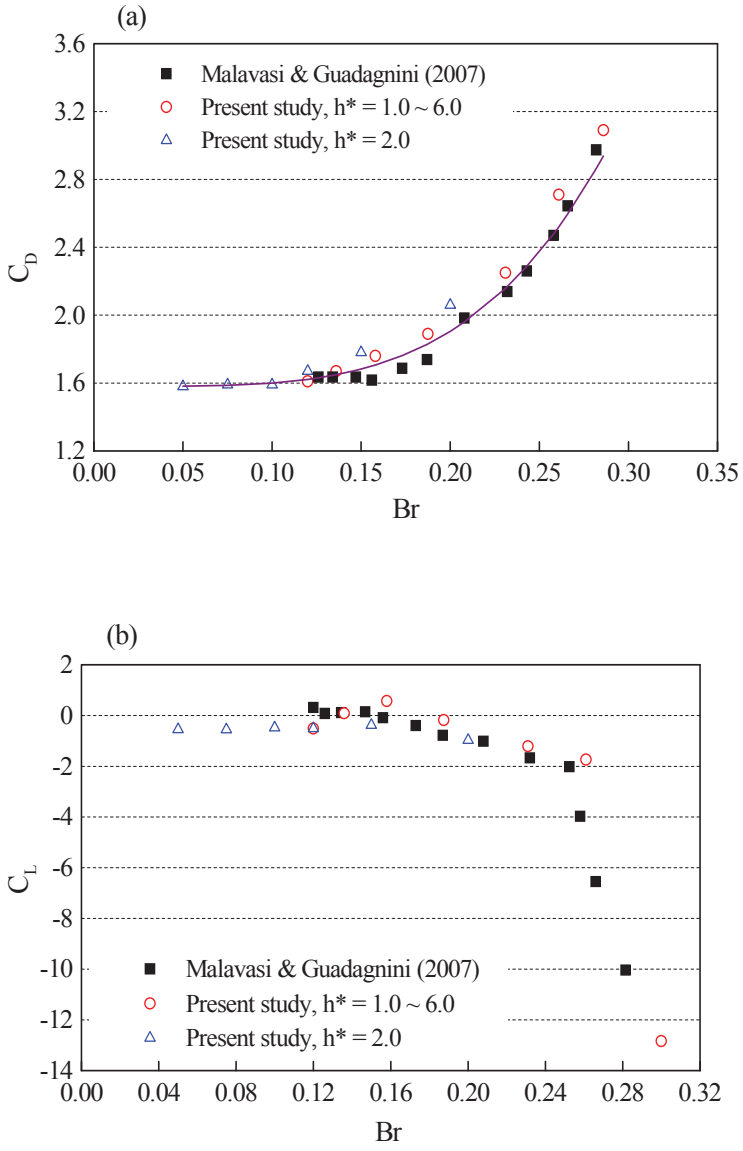

Figure 6. Relationship between force coefficients and blockage ratio for $Fr_D = 0.26$: (a) drag coefficient; (b) lift coefficient. The line is the prediction of Eq. (11).

The force coefficients were plotted against the blockage ratio in Figure 6. The flow condition was sub-critical flow ($Fr_D = 0.26$). The experimental results of Malavasi & Guadagnini (2007) were also plotted in the figure for comparison. Note that in Figure 6(a), the relationship between the drag coefficient and the blockage ratio was independent of the submergence ratio h^* for sub-

critical flow. The drag coefficient was a constant C_D = 1.6 when the blockage ratio was Br < 0.14. When Br > 0.14, the value of C_D increased from 1.6 to 2.8 as the blockage ratio Br increased. This is because the pressure difference between the frontal and rear faces of the deck increased by the blockage effect, and higher pressure drop resulted in a greater drag on the deck. In other words, the drag coefficient C_D = 2.0~2.2 suggested by Hamill (1999) may not be applicable for bridge decks with a large blockage ratio (Br > 0.23) or in trans-critical flows ($Fr_D \geq 0.78$). An empirical equation between the drag coefficient, C_D, and blockage ratio Br can be found by least square regression:

$$\frac{C_D}{C_{Do}} = 1.0 + \alpha \cdot Br^n \tag{11}$$

The parameters α =128.4, n = 4.0 and C_{Do} = 1.58 is the drag coefficient of rectangular cylinders of aspect ratio L/D = 3 in an unbounded domain. The coefficient of determination was R^2 = 0.938. This equation could be used to compute the drag coefficients of fully submerged bridge decks ($h^* > 1$) with a rectangular cross-section in sub-critical flows.

On the other hand, Figure 6(b) shows that the lift coefficient, C_L, decreased as the blockage ratio increased. The lift coefficient was $C_L > -2.0$ when the blockage ratio Br < 0.25. This is because the water surface restricted the development of separation flow on the upper side of the deck, and resulted in the asymmetric pressure distribution on the upper and lower sides of the deck. However, the negative lift coefficient became fairly large ($C_L < -3.0$) when the blockage ratio Br > 0.25. When the blockage ratio Br > 0.25, even in sub-critical flows, the pressure distribution is similar to trans-critical flow shown in Figure 5. The spatial average pressure coefficients, C_{p3}, on the upper side of the deck were positive, together with the negative pressure on the lower side generated a large downward force on the deck.

4 CONCLUSIONS

This study used a Large Eddy Simulation (LES) model and the Volume of fluid (VOF) method to investigate the interactions between the free surface flows and fully submerged bridge decks. The model prediction was verified by comparing it with the experimental data of Malavasi & Guadagnini (2007). The numerical model then was used to calculate the hydrodynamic forces on bridge decks of rectangular cross-section. The results indicated that the drag and lift coefficients were dependent on the deck Froude number, $Fr_D = U_o/(gD)^{1/2}$. The water surface was flat and undisturbed for sub-critical flow ($Fr_D \leq 0.52$). When the deck Froude number was $Fr_D \geq 0.78$, the water surface rose up in front of the submerged deck and dropped behind the deck, created a large surface disturbance.

In addition, the drag coefficient remained a constant C_D = 1.6 when Br < 0.14, and the value of C_D increased as the blockage ratio, Br, increased for sub-critical flows ($Fr_D \leq 0.52$). For trans-critical flows ($Fr_D \geq 0.78$), due to the wave-induced drag, the drag coefficient was larger than that for sub-critical flows with the same blockage ratio. Furthermore, the lift coefficient was a function of the deck Froude number, Fr_D, and the submergence ratio, h^*. This is because the separation shear flow on the upper side of the deck was constrained by the water surface and resulted in an asymmetric pressure distribution on the upper and lower sides of the deck. For trans-critical flows and submergence ratio h^* = 2.0, the downward flow above the deck produced positive pressures on the upper side of the deck and subsequently generated a large negative lift force on the deck.

5 ACKNOWLEDGEMENTS

The financial support from the China Engineering Consultants Inc. (CECI) of Taiwan, R.O.C. under grants no. 99932 is gratefully appreciated.

6 REFERENCES

1 S. Bal, Prediction of wave pattern and wave resistance of surface piercing bodies by a boundary element method, Inter. J. of Numerical Methods in Fluids, 56 (2008) 305-329.
2 M. DeLong, Two examples of the impact of partitioning with Chaco and Metis on the convergence of additive-Schwarz preconditioned FGMRES. Technical Report LA-UR-97-4181, Los Alamos National Laboratory, 1997, New Mexico, USA.
3 L. Hamill, Bridge Hydraulics, E & FN Spon, London, UK. 1999, p.344.
4 C.W. Hirt and B.D. Nichols, Volume of fluid (VOF) method for the dynamics of free boundaries. J. of Computational Physics, 39 (1981) 201-225.
5 S. Malavasi and A. Guadagnini, Hydrodynamic loading on river bridges. J. of Hydraulic Engineering, 129(11), (2003) 854-861.
6 S. Malavasi and A. Guadagnini, Interactions between a rectangular cylinder and a free-surface flow. J. of Fluids and Structures, 23 (2007) 1137-1148.
7 S. Malavasi and N. Trabucchi, Numerical investigation of the flow around a rectangular cylinder near a solid wall. Conference Proceeding of Bluff Bodies Aerodynamics & Applications, Milano, Italy, 2008, pp.20-24.
8 E. Naudascher and H.J. Medlarz, Hydrodynamic loading and backwater effect of partially submerged bridges. J. of Hydraulic Research, 21(3) (1983) 213–232.
9 T.-R. Wu and P. L.-F. Liu, Numerical study on the three-dimensional dam-break bore interacting with a square cylinder, In P. Lynett (Ed.), Symposium of Nonlinear Wave Dynamics, World Scientific, Singapore, 2009, pp. 281-303.

Flutter stability studies of Great Belt East Bridge and Tacoma Narrows Bridge by CFD numerical simulation

Hao Zhan[a],Tao Fang[b]

[a]*China Railway Major Bridge Reconnaissance & Design Institute Co., Ltd.,China*

[b]*School of Civil Engineering and Mechanics, Huazhong University of Science and Technology,China*

ABSTRACT: In the paper, by secondary development of commercial computational fluid dynamics software FLUENT, establish two-dimensional bending and torsional fluid-structure interaction numerical model to calculate flutter critical wind speed of Great Belt East Bridge and Tacoma Narrows Bridge.According to time histories of vertical displacements and torsional displacements, we can judge flutter critical wind speed and flutter modality. The numerical results show:when the wind speed is more than 63m/s, Coupled vertical-torsional flutter is found in Great Belt East suspension bridge; When the wind speed is more than 8m/s, Torsional dominated flutter is found in Tacoma Narrow Bridge. Critical wind speed of flutter by numerical simulation is in agreement with wind tunnel test.At the same time, this paper uses numerical wind tunnel technique displays the vortex drift along the beam, reveals the interaction between the main beam and vortex motion is one of the reasons leading to divergent vibration.

KEYWORDS: fluid-structure interaction,divergent vibration,vortices movement bending-torsional coupled flutter,torsional dominated flutter,critical flutter wind speed

1 INTRODUCTION

Flutter is a complex physical phenomenon,It is basically divided into two categories in term of aerodynamic.There is no flow separation phenomenon in streamlined profile object, such as aircraft wings in small angle of attack.When flutter happen at the situation we call it classical flutter.It is first flutter.Second flutter is related with the flow separation and vortex formation. It is likely to occur in the lifting surface in large angle of attack or no streamlined profile building structures.It is called stall flutter.

Bridge flutter is a divergent self-excited vibration, which can potentially result in catastrophic failure of a structure.It is mainly due to vibration of the structure can absorb the energy in the flow air and the energy is greater than energy dissipation of the structural damping in the vibration.There are two types of flutter phenomena in bridge structure: One is bending-torsional coupled flutter another is separated flow flutter. Bending and torsion coupled flutter is generally occurs in the streamlined beam.The majority of bridge deck is non-streamlined. Flow separation phenomenon occur at the corners of the deck where vortex shedding is generated, then single degree of freedom of torsional flutter is likely to occur. It is separated flow flutter.

In the paper,by secondary development of commercial computational fluid dynamics software FLUENT, establish two-dimensional bending and torsional fluid-structure interaction numerical model to calculate flutter critical wind speed of Great Belt East Bridge and Tacoma Narrows Bridge. According to time histories of vertical displacements and torsional displacements, we can judge flutter critical wind speed and flutter modality.It is critical flutter wind speed when the main beam start divergence vibration under a certain wind speed.

2 NUMERICAL SIMULATION

2.1 Great Belt East Bridge and Tacoma Narrows Bridge

As shown in Figure 1.,Figure 2. and Figure 3., Great Belt East Bridge has a main span of 1624m. The semi-streamlined steel box deck is 31m wide and 4.34m high. Tacoma Narrows Bridge was constructed as a 1660 meter long suspension bridge with a main span of 853 meters, the third longest suspension bridge in the world at that time.The bridge deck was 11.9 meter wide, supported by two 2.45 meter deep plate girders(I-girders).At November morning 7 in 1940,A wind of 16-19m/s was blowing,The segments of the span were heaving periodically up and down in fifth antisymmetric vertical mode as much as 0.9m for about 3 hours, with oscillation frequency of 0.6-0.63Hz.At 10 clock in morning,one middle girder suspender root breaking,suddenly antisymmetric vertical vibration change into the antisymmetric torsional vibration, frequency is 0.23Hz,soon after,change to 0.2Hz, amplitude is bigger and bigger (approximately 8 meters),until the deck began to sway with an amplitude of about 45 degree, suspenders break,bridge deck steel fracture and ruined, falling to the valley[1][2].

Figure 1. Great Belt East Bridge [1]

Figure 2. Tacoma Narrows Bridge[2]

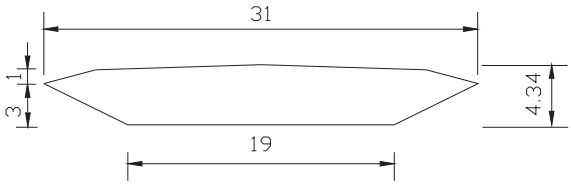

(1) Great Belt East Bridge

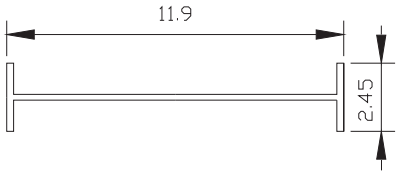

(2) Tacoma Narrows Bridge

Figure 3. Girder Cross-sections(m)

2.2 Numerical simulation principle

The structure is regarded as mass, spring and damping system.Schematic diagram of numerical simulation is shown in Figure 4.The governing structural equation for the one-degree-of-freedom heaving mode and torsional mode is shown as (1),(2).

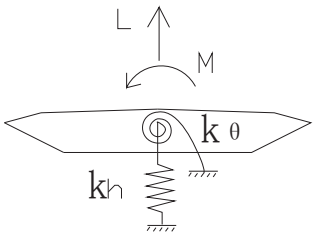

(1) Great Belt East Bridge

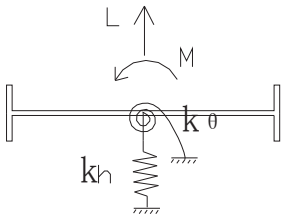

(2) Tacoma Narrows Bridge

Figure 4. Schematic diagram of numerical simulation

$$m\ddot{y} + c_h\dot{y} + k_h y = F_h \quad (1)$$

$$I_\theta\ddot{\theta} + c_\theta\dot{\theta} + k_\theta\theta = M_\theta \quad (2)$$

Where m is the mass per unit length of the body, I_θ is the mass moment of inertia. k_h is the translational spring stiffness, k_θ is the rotational spring stiffness. c_h and c_θ is the structural damping coefficients. F_h and M_θ is the fluid forces. y denotes the transverse location of the centre of the body and θ denotes the rotational angle of the body around elastic centre.The governing equations of the incompressible flow is the continuity equation and the Navier-Stokes equations as (3),(4).

$$\nabla\cdot\vec{V} = 0 \quad (3)$$

$$\frac{\partial\vec{V}}{\partial t} + (\vec{V}\cdot\nabla)\vec{V} = -\frac{1}{\rho}\nabla p + \mu\nabla^2\vec{V} \quad (4)$$

Where ρ is the density of the fluid. $\vec{V}, p, t$ denote the velocity vector,pressure,time respectively[3].

Solve equation (3),(4),obtain pressure and velocity around object,calculate aerodynamic force acting on the object. This can be done by FLUENT. Then extract lift and moment into vibration equation (1) (2) and solve the vibration equation by Newmark method.The velocity is assigned to the object and simulate object move by FLUENT dynamic mesh technique. This can be done by secondary development of FLUENT which program code is embedded to the FLUENT by user defined function(UDF).

2.3 Numerical simulation model

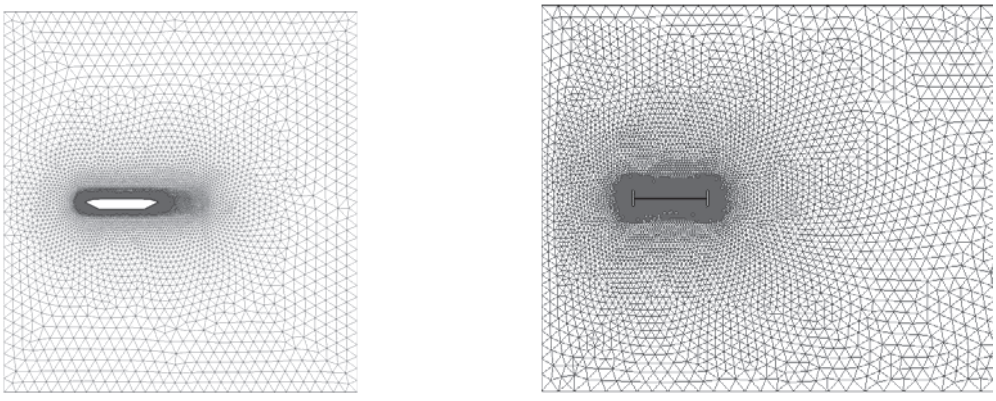

(1) Great Belt East Bridge (2) Tacoma Narrows Bridge

Figure 5. Whole mesh

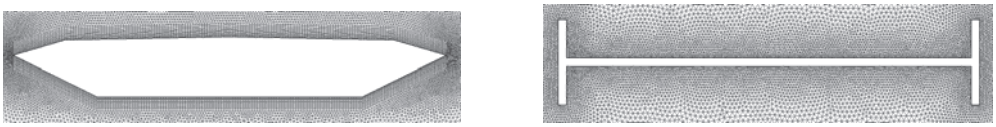

(1) Great Belt East Bridge (2) Tacoma Narrows Bridge

Figure 6. Local mesh

Computational grid is shown in Figure 5. and Figure 6..The flow runs from the left to the right.The inflow boundary is specified with the inflow velocity. On the right exit boundary,it is specified with free flow.The upper and lower borders is specified with the wall. The no-slip boundary condition is employed on the body surface. Fine grid is created near the body and the grid becomes gradually coarser in the far field. Navier-Stokes equations are solved by using finite volume method,second-order upwind difference form and SMPLEC algorithm. RNG turbulence model is used in Great Belt East Bridge and the LES turbulence model is used in Tacoma Narrows Bridge. Properties of the suspension Bridge is shown in Table 1.

Table 1. Properties of the suspension Bridge [3][4]

parameters	unit	Great Belt East Bridge	Tacoma Narrows Bridge
Mass per unit length	kg/m	23687	4250
Mass moment of inertia	kgm/m	$2.501x10^6$	177730
Natural vertical frequency	Hz	0.097	0.13
Natural torsional frequency	Hz	0.27	0.2
vertical damping ratio		/	0.005
Torsional damping ratio		/	0.005

The vertical damping ratio and torsional damping ratio of Great Belt East Bridge are $1.59x10^{-3}$ and $3.18x10^{-4}$ respectively in the paper.

3 NUMERICAL SIMULATION RESULTS

3.1 The Great Belt East Bridge

3.1.1.Time histories of Lift coefficient and moment coefficient

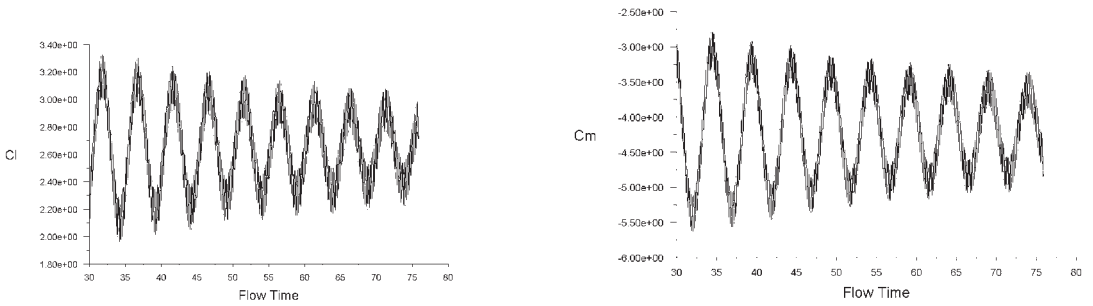

（1）v=60m/s

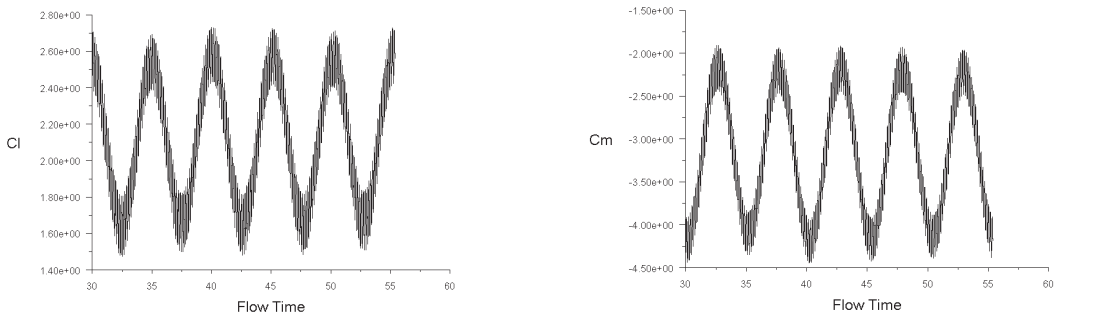

（2）v=63m/s

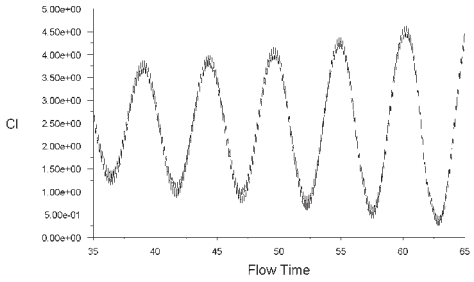

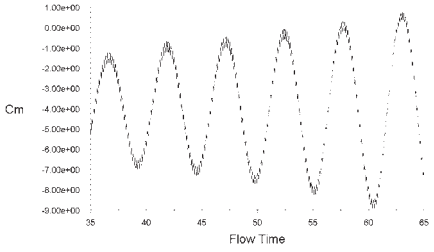

（3） v =65m/s

Figure 7. Time histories of Lift coefficient

Figure 8.Time histories of moment coefficient

As shown in Figure 7. and Figure 8.,We can see the force acting on the deck at different wind speed.When the wind speed is 60m/s,The force acting on the deck gradually decreased. When the wind speed is 63m/s,The force acting on the deck remain almost same. When the wind speed is 65m/s,The force acting on the deck gradually increased.

3.1.2 Time histories of displacements

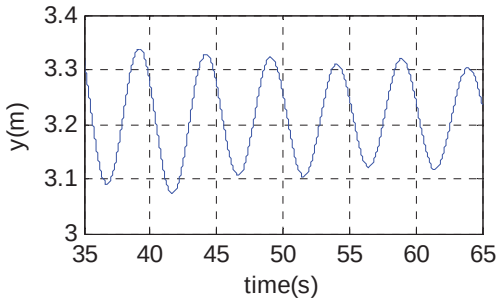

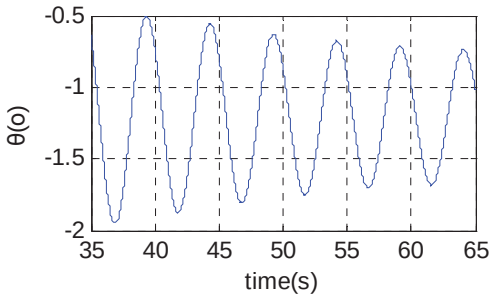

v=60m/s

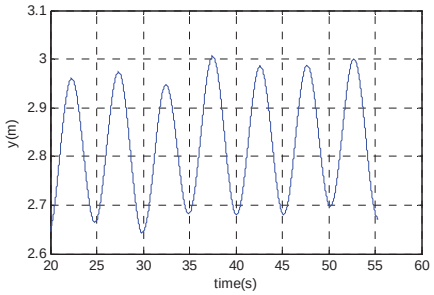

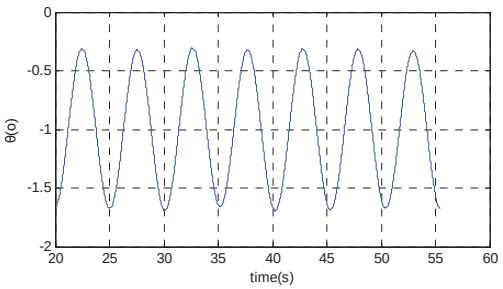

v=63m/s

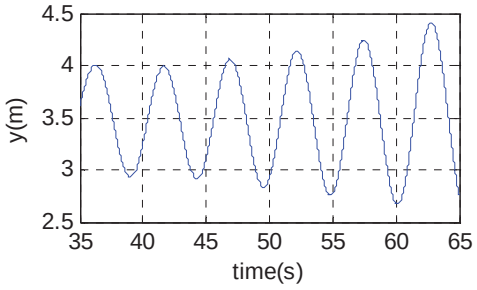

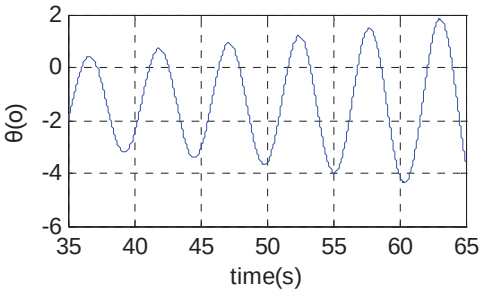

v=65m/s

Figure 9.Time histories of vertical displacements

Figure 10.Time histories of torsional displacements

Figure 9.and Figure 10. show the displacements change of deck at different wind speed.When the wind speed is 60m/s , vertical and torsional displacements gradually decreased.When the wind speed is 63m/s ,vertical and torsional displacements remain almost same.When the wind speed is 65m/s, vertical and torsional displacements gradually increased. Divergent coupling vibration between vertical-bending model and torsional mode of deck is found when the wind speed is over 63m/s. Vertical vibration frequency and the torsional vibration frequency are about 0.2Hz,which is between the vertical and torsional natural frequencies. As shown in Table2.,Critical wind speed of flutter by numerical simulation is in agreement with wind tunnel testing.

Table 2. Critical wind speed of flutter[3]

source	critical wind speed of flutter（m/s）
wind tunnel testing (section model)	74
numerical simulation	63—65

3.1.3. Contours of vorticity magnitude at different times

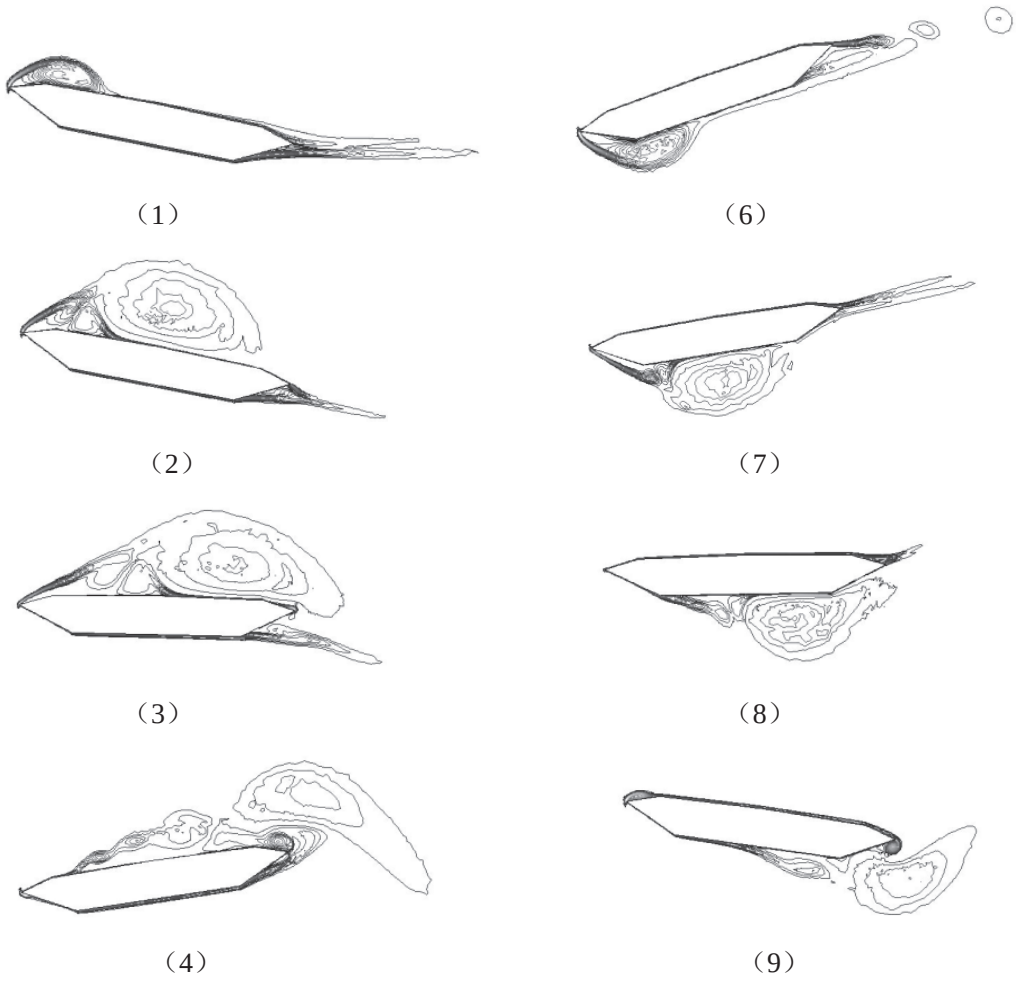

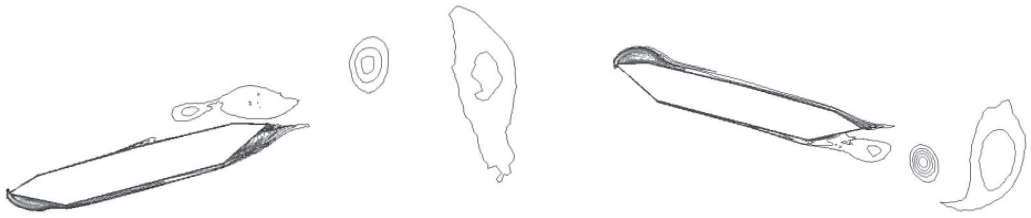

（5） （10）

Figure 11. Contours of vorticity magnitude at different times

As illustrated in Figure 11., we can see the movement of object is driven by vortex. Rotate clockwise and drift along the lower part of the main beam,main beam rotate counterclockwise,vortex rotate counterclockwise and drift along the upper part of the main beam,main beam clockwise torsion.The interaction between the main beam and vortex motion lead to divergent vibration.

3.2 Tacoma Narrows Bridge

3.2.1 Time histories of Lift coefficient and moment coefficient

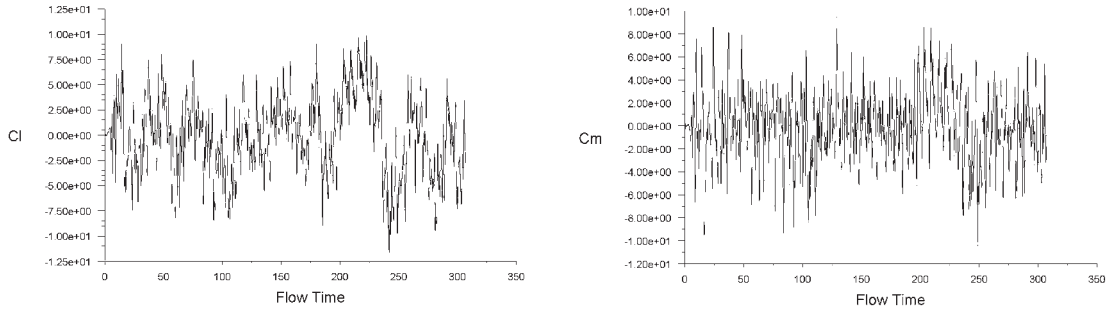

（1）v =8m/s

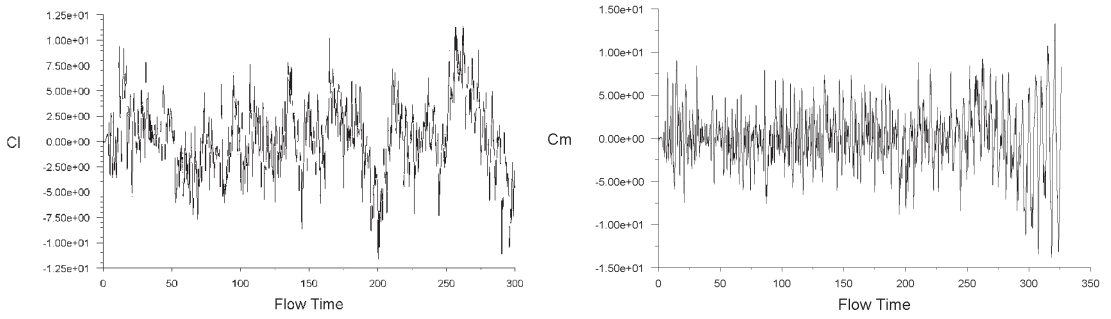

（2） v =10m/s

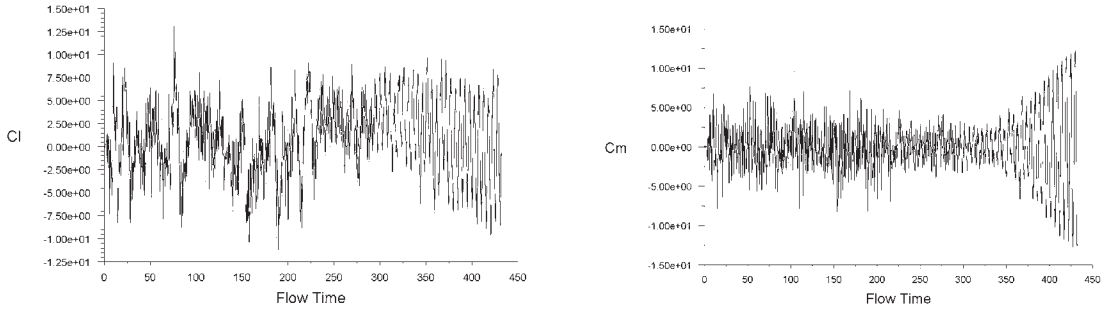

（3）v =12m/s

Figure 12. Time histories of Lift coefficient Figure 13.Time histories of moment coefficient

As shown in Figure 12. and Figure 13.,We can see the force acting on the deck at different wind speed.When the wind speed is 8m/s,The force acting on the deck remain almost same.When the wind speed is 10m/s or 12m/s,The force acting on the deck gradually increased.

3.2.2 Time histories of displacements

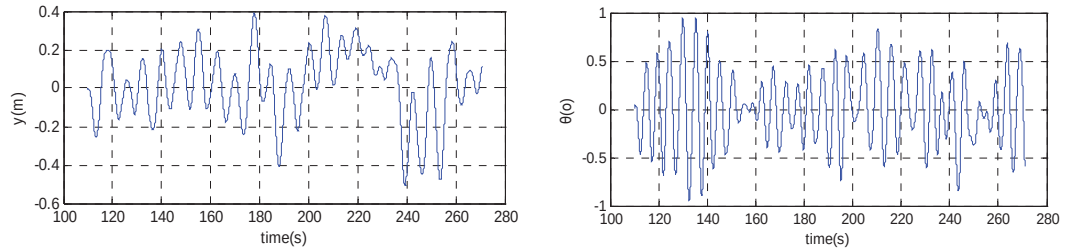

（1） v =8m/s

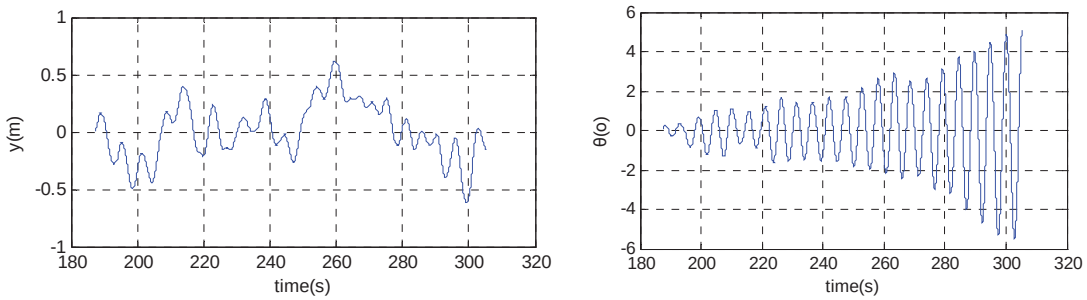

（2） v =10m/s

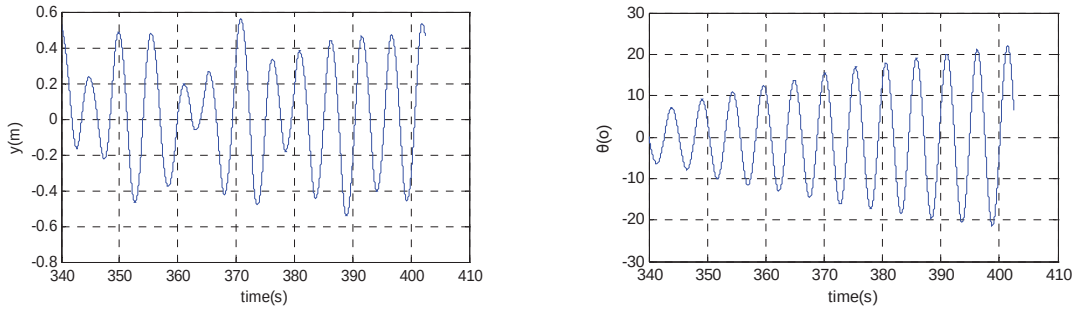

（3）v =12m/s

Figure 14.Time histories of vertical displacements Figure 15.Time histories of torsional displacements

Figure 14. and Figure 15. shows the beam displacement under different wind speeds. When the wind speed is 8m/s, vibration is limit, vertical displacement does not exceed 0.4m, torsional angles degree is less than 1 degrees; When the wind speed is 10m/s, The maximum vertical displacement is 0.4m, The maximum torsion angle is above 5 degree and increases with time; When the wind speed is 12m/s, torsional vibration divergence is evident. the oscillation frequency is 0.2Hz, the same as torsional frequency of the structure. As Table 3. shows,Critical wind speed of flutter by numerical simulation is in agreement with wind tunnel test.

Table 3. Critical wind speed of flutter(m/s) [4]

result	Tacoma Narrow Bridge
wind tunnel test	11.5
numerical simulation	8—10

3.2.3. Contours of vorticity magnitude at different times

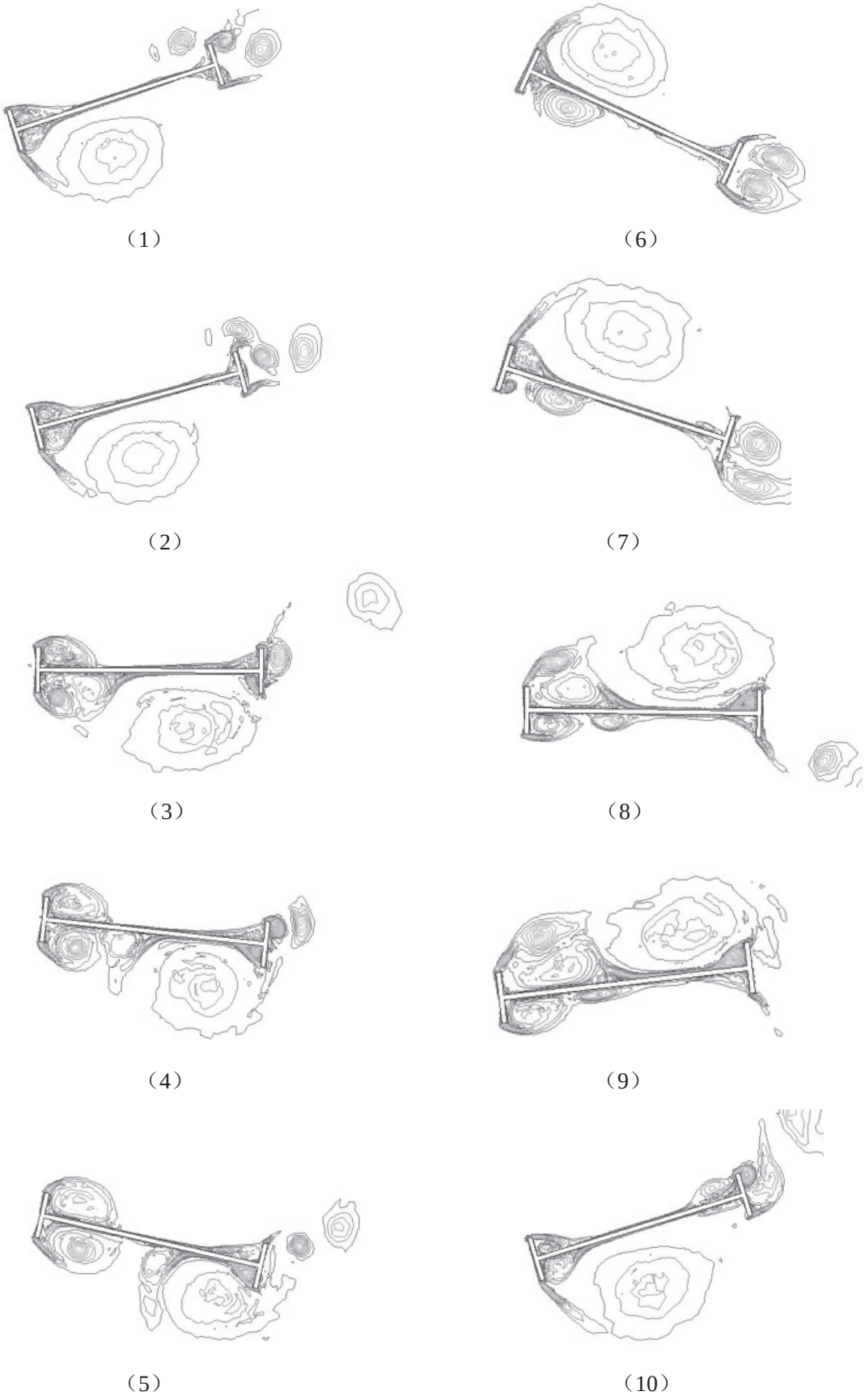

Figure 16. Contours of vorticity magnitude at different times

As illustrated in Figure 16., it is noted that H shaped section movement is drive by vortex. Vortex is generated by upstream end and continuous development, movement, The vortex experienced a complete cycle from developing, moving and ultimately shedding. Actions on structures also completed a cycle of evolution. If we effectively prevent the large-scale vortex formation, twisting instability can be controlled in a certain extent. Tacoma bridge girder design is obvious defect: width span ratio of the stiffening beam is small, torsional rigidity is weak, On both sides there is windtight bluff body longeron, It is easy to cause the aeroelastic instability.So we might increase the cross-sectional size to get sufficient torsional rigidity and adopts a streamline cross section shape and ventilated structure to prevent large vortex formation.

4 CONCLUSION

By numerical simulation analysis can we get the following conclusions:

(1) Critical flutter wind speed by numerical simulation is in agreement with wind tunnel test.

(2) Bending-torsional coupled flutter is found in Great Belt East suspension bridge. Flutter frequency is between the vertical natural frequency and torsional natural frequency of structure. Torsional domined flutter is found in Tacoma Narrow Bridge. Flutter frequency is the same as torsional natural frequency of structure.

(3) The interaction between the main beam and vortex motion is one of the reasons leading to divergent vibration.

5 REFERENCES

[1]M.Matsumoto,K.Mizuno,K.Okubo,Flutter instability and recent development in stabilization of structures.Journal of Wind Engineering and Industrial Aerodynamic 95(2007) 888-907

[2]R.H.Plaut,Snap loads and torsional oscillations of the original Tacoma Narrows Bridge,Journal of Sound and Vibration 309(2008) 613-636

[3]J.B.Frandsen,Numerical bridge deck studies using finite elements.Part I:flutter Journal of Fluids and Structures 19（2004）171-191

[4]Allan Larsen.Advances in aeroelastic analyses of suspension and cable-stayed bridges. Journal of Wind Engineering and Industrial Aerodynamics 74-76(1998) 73-90

Direct simulation method for flutter stability of bridge deck

Xiaobing Liu[a,b] Zhengqing Chen[b] Zhiwen Liu[b]

[a]*Shijiazhuang Tiedao University, Shijiazhuang, China*
[b]*Hunan University, Changsha, China*

ABSTRACT: A direct simulation method for flutter stability of bridge deck was developed based on CFD software Fluent. Flutter stability of two representative sections, rectangular section and streamlined section, was simulated by using this method. The validity of the simulation method was verified by comparison of simulation result and wind tunnel test result.

KEYWORDS: Bridge Deck Flutter Stability Direct Simulation

1 INTRODUCTION

Bridges become more and more flexible with the increase of span. Wind–resistant design of bridge becomes more and more important. Flutter is a kind of divergent vibration style which may occur for long-span flexible bridges. The flutter of bridge decks can be classified into two categories. One is single-degree torsional flutter which may occur for bridge decks with sharp angles. The other is bending-torsional coupled flutter which may occur for bridges with streamlined decks. Flutter may destroy bridge. Therefore, it is very necessary to ensure that the flutter critical wind speed is higher than flutter checking wind speed in design stage of long-span bridges. At present, there are two main simulation methods for flutter stability of bridge deck. One is based on flutter derivatives which are gotten by simulated forced motion of bridge deck. The flutter critical wind speed of bridge deck is calculated by using the flutter derivatives. The other one is direct simulation method. The vibration displacements of bridge deck in different wind speed are simulated. The flutter critical wind speed of bridge deck is gotten by checking vibration displacements. In the past, researches paid more attention to the first simulation method [1-7], while less attention to on direct simulation method [8-9]. The study on direct simulation method is almost based on self-written program which is short of applicability.

In recent years, with rapid development of computer technique, some universal CFD software, such as Fluent, CFX, and so on, were adopted by bridge design organization because of good interface, convenient pre-processor and post-processor, open secondary developing function and so on. It is meaningful to perform direct simulation of flutter stability based on these universal CFD software to evaluate the flutter critical wind speed of the bridge deck in preliminary design stage. In present paper, a direct simulation method for flutter stability of bridge deck was developed based on CFD software Fluent. Flutter stability of two representative sections, rectangular section and streamlined section, was simulated by using this method. The validity of the simulation method was verified by comparison of simulation result and wind tunnel test result.

2. DIRECT SIMULATION METHOD

First of all, the bridge deck is simplified to bending-torsional two degree spring-mass-damping system. The dynamic equation is as follows:

$$m\ddot{h}(t)+c_h\dot{h}(t)+k_h h(t)=L(t) \qquad I\ddot{\alpha}(t)+c_\alpha\dot{\alpha}(t)+k_\alpha\alpha(t)=M(t) \tag{1}$$

where $\ddot{h}(t)$, $\dot{h}(t)$ and $h(t)$ are instantaneous bending acceleration, bending velocity and bending displacement; $\ddot{\alpha}(t)$, $\dot{\alpha}(t)$ and $\alpha(t)$ are instantaneous torsional acceleration, torsional velocity and torsional displacement; $L(t)$ and $M(t)$ are instantaneous lift force and torque on bridge deck.

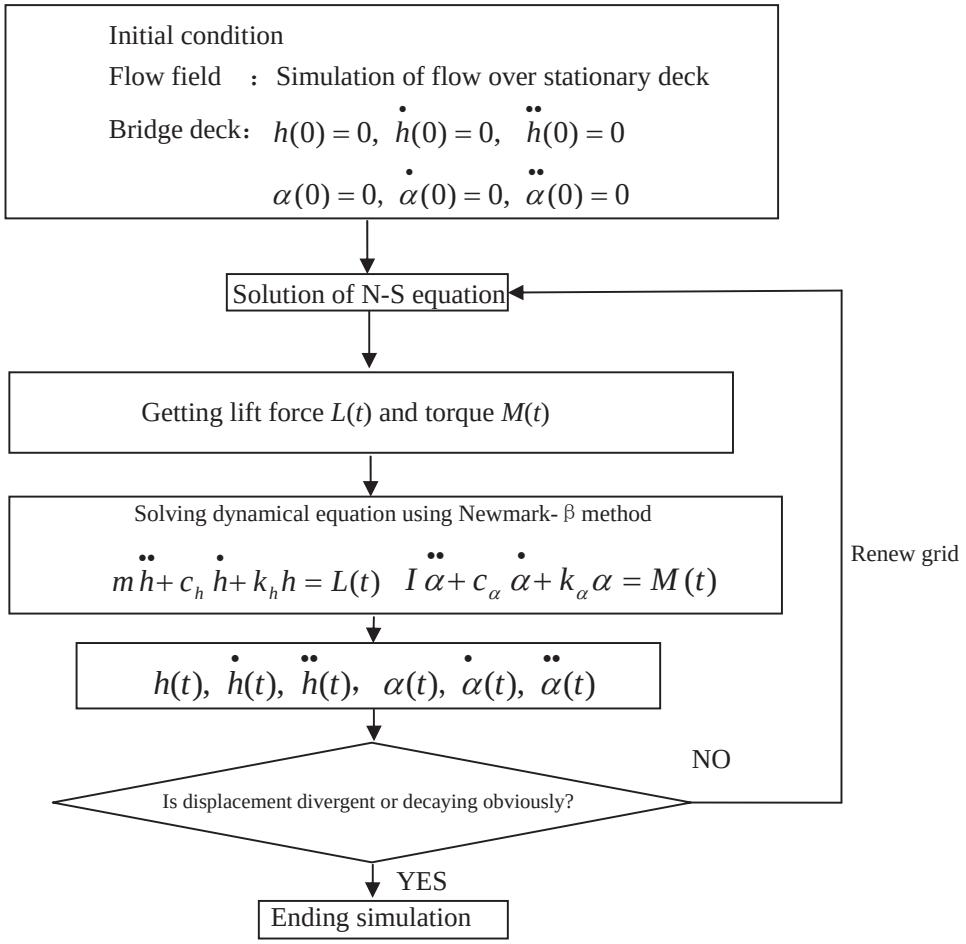

Figure 1 Procedure of direct simulation in every wind speed

The bridge deck vibration displacements under several wind speeds need to be calculated in direct simulation method. In order to improve efficiency, the flutter critical wind speed can be estimated through Wind–resistant Design Specification for Bridge at first. Then the direct

simulation can be carried out around the estimated wind speed. The procedure of direct simulation in every wind speed is shown in Figure 1. Firstly, flow around static bridge deck is performed. When the flow is stable, the bending degree and torsional degree are unrestricted. Before first calculating time step, the preliminary value of bending acceleration, bending velocity, bending displacement, torsional acceleration, torsional velocity and torsional displacement are set to zero. For every time step, the fluid control equation, Navier-Stocks equation is solved and the lift force and torque on the bridge deck is gotten, then the bending and torsional displacements can be obtained by solving equation (1) using *Newmark-β* method. Simulation in given wind speed ends if the displacement divergent or decaying obviously.

3. SIMULATION MODEL

In present paper, flutter stability of two representative sections, rectangular section and streamlined section, was simulated. The dimensions of these two representative sections are shown in Figure 2. The width and height of rectangular section are 30cm and 6cm. The width and height of streamlined section are 40.392cm and 6cm. The numerical simulation region and boundary condition are shown in Figure 3. The simulation region is two dimensional rectangular region. The distance between inlet and middle point of simulation region is 10times the width of section. The distance between outlet and middle point of simulation region is 20 times the width of section. The distance between top wall and bottom wall is 20 times the width of section The boundary conditions are set as follows: velocity inlet boundary condition for inlet; outflow outlet boundary condition for outlet; free-slip wall boundary condition for top and bottom wall; no-slip wall boundary condition for surface of deck section.

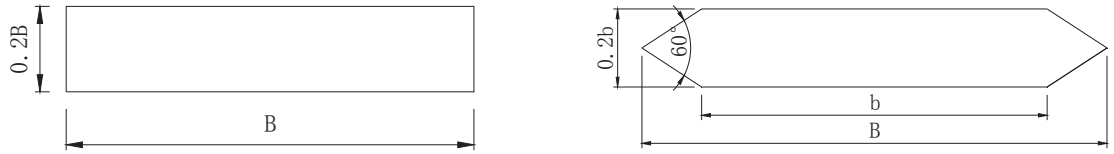

(a) rectangular section (b) streamlined section

Figure 2 Dimension of two representative sections

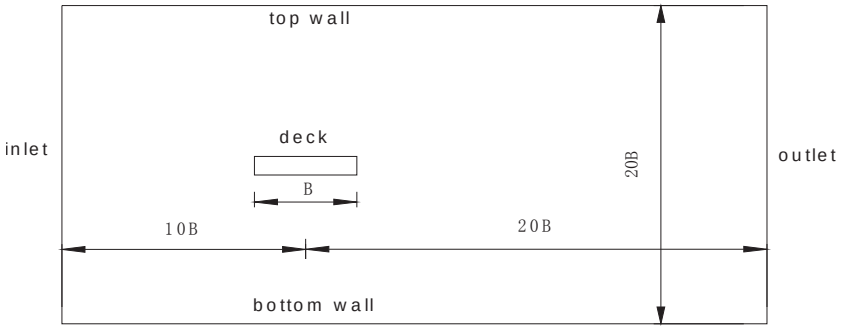

Figure 3 Numerical simulation region and boundary condition

Figure 4 and Figure 5 shows numerical grid of the two sections. Rigid mesh grid is used in inner region. Stationary mesh grid is used in outer region. Between the rigid mesh grid and stationary mesh grid is dynamic mesh grid. The width and height of rigid mesh are about two times and one time the width of section, respectively. Both the width and height of dynamic mesh grid are about six times the width of section. When deck section vibrates, the rigid mesh grid follows the deck section synchronously; the static grid keeps stationary; the shape and dimension of dynamic mesh changes constantly. The number of mesh grid for rectangular section and streamlined section are about 76800 and 62300, respectively. In region which is far away the section, the size of mesh grid is big comparatively. In region which is near the section, the size of mesh grid is small comparatively.

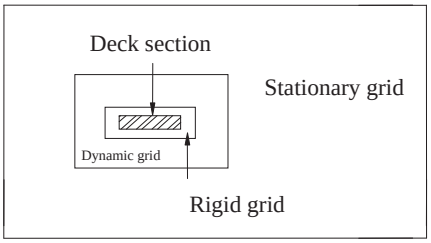

Figure 4 illustration of numerical grid division

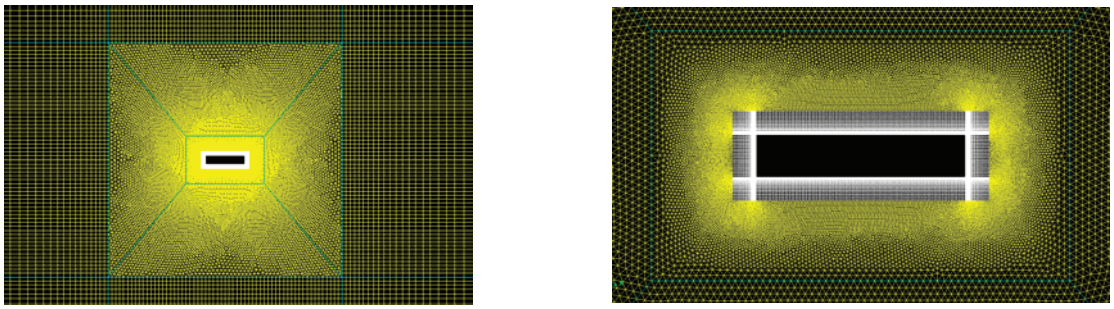

(a) rectangular section

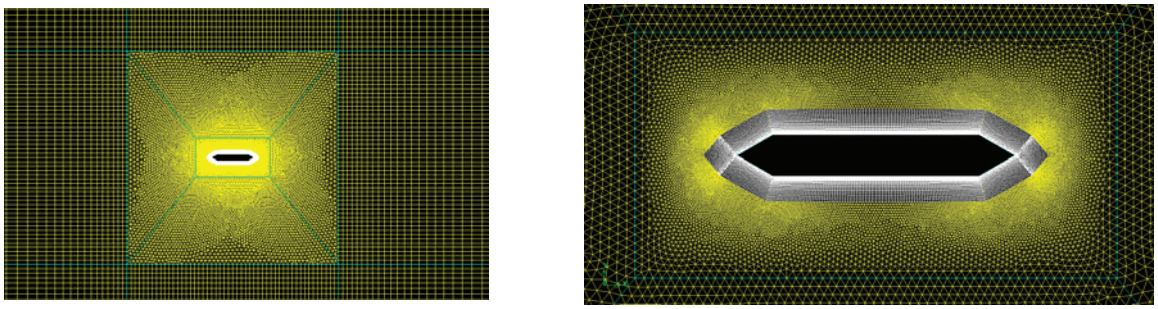

(b) streamlined section

Figure 5 Numerical grid of two representative sections

In order to validate the direct simulation result, wind tunnel tests were performed to measure the flutter stability of these two sections. The photos of wind tunnel tests are shown in Figure 6. The length of sectional model is 1.5 meter. The test parameters, including model mass, mass moment of inertia, bending vibration frequency, torsional vibration frequency and damping ratio, are

listed in Table 1. The direct numerical simulation parameters are in accordance with wind tunnel test parameters. The only difference is that the mass and mass moment of inertia per unit length are used in direct numerical simulation.

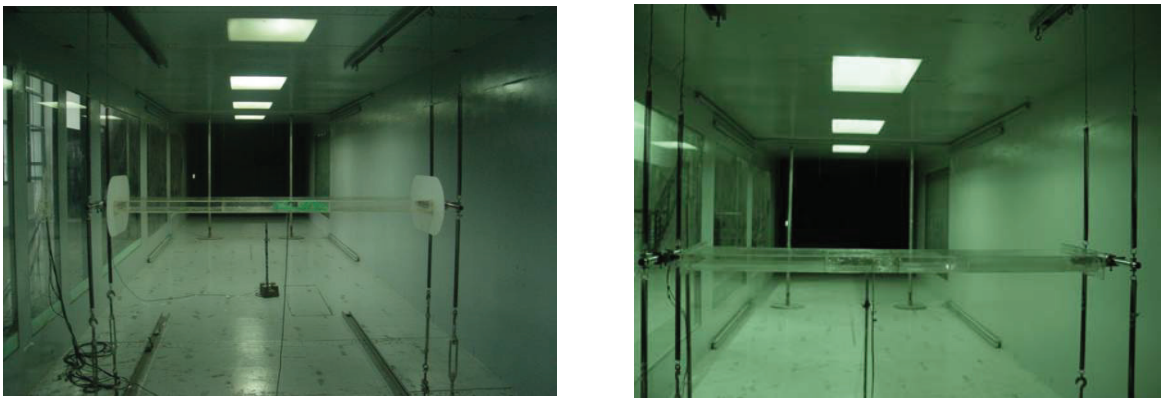

(a) rectangular section (b) streamlined section

Figure 6 Photo of wind tunnel test

Table 1 Parameters of wind tunnel test

section type	m(kg)	I(kg m^2)	f_h (Hz)	f_α (Hz)	ξ_h	ξ_α
rectangular section	11.89	0.1280	3.13	6.64	0.3%	0.3%
streamlined section	13.38	0.1505	2.54	5.27	0.3%	0.3%

4 SIMULATION RESULT

Figure 7 and Figure 8 show curves of torsional angular displacement versus time history of streamlined section and rectangular section, respectively. Figure 9 shows amplitude spectrum of curves of torsional angular displacement versus time history. In these figures, the reduced wind speed is defined as follows:

$$V_r = \frac{U}{f_t B} \tag{2}$$

Where U is incoming wind speed, ft is torsional vibration frequency of model, B is width of model.

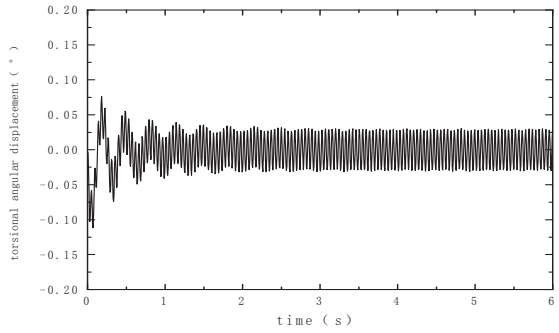

(a) Vr=10.80

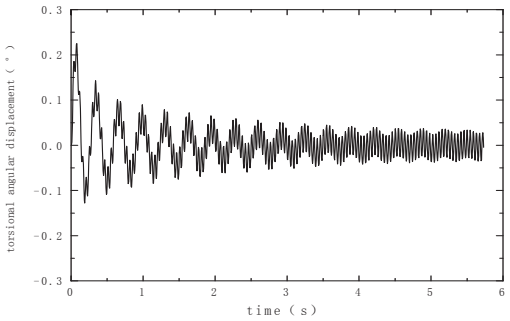

(b) Vr=11.27

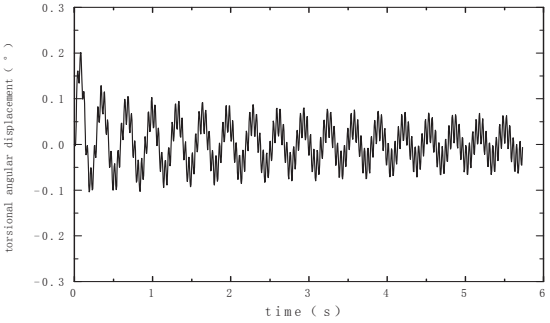

(c) Vr=11.51

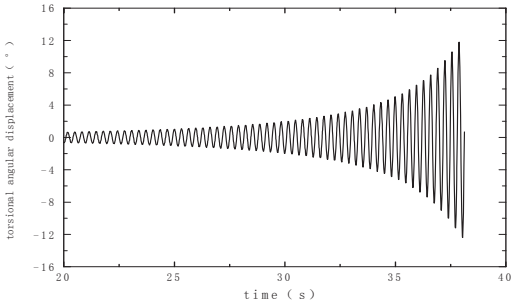

(d) Vr=11.74

Figure 7 Curves of torsional angular displacement versus time history of streamlined section

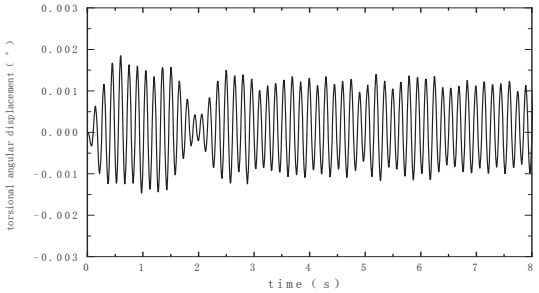

(a) Vr=3.29

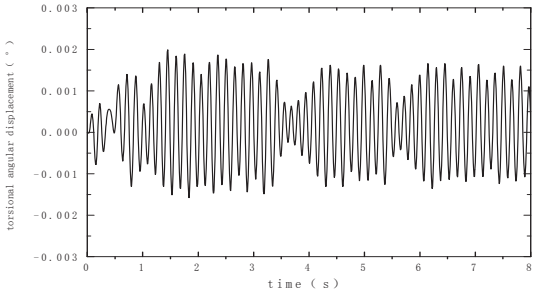

(b) Vr=3.77

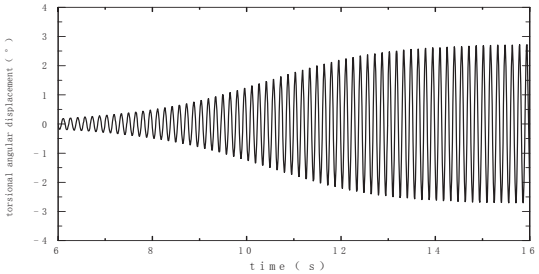

(c) Vr=4.00

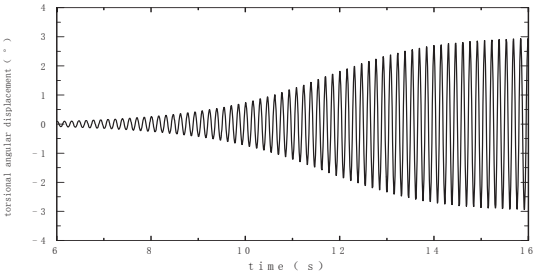

(d) Vr=4.24

Figure 8 Curves of torsional angular displacement versus time history of rectangular section

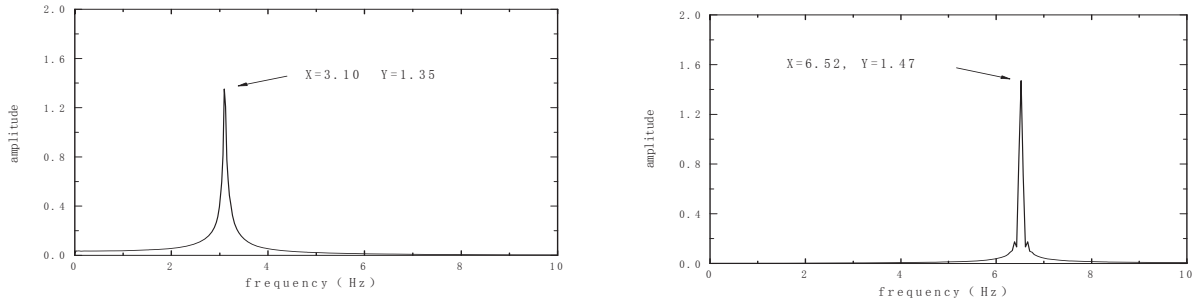

(a) Streamlined section Vr=11.74 (b) rectangular section Vr=4.0

Figure 9 Amplitude spectrum of curves of torsional angular displacement versus time history

From Figure7 and Figure 9(a), it can be seen that: (1) when reduced wind speed is less than11.51, torsional angular displacement of streamlined section is decreasing with increase of time. This illustrates that the total damping of model is positive. (2)When reduced wind speed is less than11.51, with increase of reduced wind speed, torsional angular displacement of streamlined section is decreasing slowly. This suggests that although the total damping of model is positive, the absolute value of total damping becomes small with increase of reduced wind speed. (3)When reduced wind speed reaches to 11.74, torsional angular displacement of streamlined section is increasing with the increase of time. This illustrates that the total damping of model changes from positive to negative. Flutter critical wind speed is around 11.74. (4) When flutter occurs, the torsional vibration frequency is 3.10Hz. This frequency is between natural bending vibration frequency and torsional vibration frequency. This suggests that flutter style for streamlined section is bending-torsional coupled flutter.

From Figure8 and Figure 9(b), it can be seen that: (1) When reduced wind speed is less than3.77, torsional angular displacement of rectangular section is very small and is decreasing with the increase of time. This illustrates that the total damping of model is positive. (2) When reduced wind speed reaches to 4.0, torsional angular displacement of rectangular section is increasing dramatically with increase of time. What is different from streamlined section is that vibration amplitude of rectangular section keeps a constant value at last. When reduced wind speed continues to increase, the amplitude increases to a greater constant value. This illustrates that the flutter critical wind speed of rectangular section is around 4.0. The rectangular section shows obvious soft flutter characteristic. (3) When flutter occurs, the torsional vibration frequency is 6.52Hz. This frequency is very close to nature torsional vibration frequency. This suggests that flutter style for rectangular section is single-degree torsional flutter.

In Table 2, direct numerical simulation result and wind tunnel test result were compared. It can be seen that direct simulation results are in good agreement with wind tunnel test results. This shows that the direct simulation method used in present paper is correct.

Table2. Compare of wind tunnel test result and direct simulation result

section type	flutter stability	wind tunnel test	direct simulation
rectangular section	non dimensional flutter critical wind speed	4.00	3.77~4.00
	flutter frequency (Hz)	6.63	6.52
streamlined section	non dimensional flutter critical wind speed	10.67	11.51~11.74
	flutter frequency (Hz)	3.99	3.10

5 CONCLUSION

In present paper, a direct simulation method for flutter stability of bridge deck was developed based on CFD software Fluent. Flutter stability of two representative sections, rectangular section and streamlined section, was simulated by using this method. The validity of the simulation method was verified by comparison of simulation result and wind tunnel test result. In further study, the flutter stability of bridge deck with more complex geometry, such as Π-shaped section, separate twin box section and so on, will be calculated using this simulation method.

6 REFERENCES

[1] Walther J H, Larsen A. Two dimensional discrete vortex method for application to bluff body aerodynamics. Journal of Wind Engineering and Industrial Aerodynamics, 1997, 67-68: 183-193

[2] Larsen A, Walther J H. Aeroelastic analysis of bridge girder sections based on discrete vortex simulations. Journal of Wind Engineering and Industrial Aerodynamics, 1997, 67-68: 253-265

[3] Fujiwara A, Kataoka H, Ito M. Numerical simulation of flow field around an oscillating bridge using finite difference method. Journal of Wind Engineering and Industrial Aerodynamics, 1993, 46-47: 567-575

[4] Vairo G. A numerical model for wind loads simulation on long-span bridges. Simulation Modelling Practice and Theory, 2003, 11(5-6): 315-351

[5] Cao Fengchan, Xiang Haifan, Chen Airong. Numerical Assessment of Aerodynamic Derivatives of Thin Flat Plates. Journal of Tongji University. 1999, 27(2): 131-135

[6] Zhu Zhiwen, Chen Zhengqing, Chen Weifang. Assessment of Aerodynamic Derivatives of the Ideal Flat Plate Based on the Moving Grid Method., Journal of National University Of Defense Technology. 2002, 24(3): 13-17

[7] Zhou Zhiyong, Chen Airong Xiang Haifan. Assessment of Aerodynamic Derivatives and Critical Wind Speed of Flutter of Bridge Decks by Discrete Vortex Method. Journal of Vibration Engineering. 2002, 15(3): 327-331

[8] Selvam R P, Govindaswamy S, Bosch H. Aeroelastic analysis of bridges using FEM and moving grids. Wind and Structures, 2002, 5(2-4): 257-266

[9] Frandsen J B. Numerical bridge deck studies using finite elements. Part Ⅰ: flutter. Journal of Fluids and Structures, 2004, 19: 171-191

The Seventh International Colloquium on Bluff Body Aerodynamics and Applications (BBAA7)
Shanghai, China; September 2-6, 2012

Computational analysis of VIV observed on existing bridges

Abraham S. Corriols [a], Guido Morgenthal [b]
[a] *Technical University of Madrid, Prof. Aranguren s/n, Spain*
[b] *Bauhaus University of Weimar, Marienstraße 13A, Germany*

ABSTRACT: This paper presents Computational Fluid Dynamics simulations of two existing bridges which exhibited vortex-induced vertical vibrations: Alconétar upper steel arch bridge (2006, Cáceres, Spain, 220 m main span) and the Volgograd Bridge (2009, Volgograd, Russia, 155 m main span). The Vortex Particle Method is used for the analysis.

KEYWORDS: Aerodynamics, Vortex shedding, Vibration, CFD, Bridge, Volgograd, Alconétar

1 INTRODUCTION

Vortex shedding from bridge cross sections can lead to significant aerodynamic excitation of the structure. This is a limited amplitude phenomenon, which however can be critical to the serviceability of the bridge or lead to fatigue damage. For structures sensitive to vortex shedding an adequately realistic assessment of the problem is required.

Traditional wind tunnel testing of all alternatives is often dismissed in early design stages unless in the case of large-scale or other high-profile bridge projects. Various analytical models exist for assessing vortex-induced vibrations (VIV), however these are of limited use for complex bridge deck geometries. Numerical simulations of the fluid flow provide a further method for modelling the physical problem. Such methods are gaining popularity in the field of civil engineering because of their growing reliability provided by the implementation of new computational methods and the availability of more powerful computational resources.

2 GENERAL APPROACH TO THE AERODYNAMIC PROBLEM

2.1 *Vortex shedding phenomenon*

Dynamic actions due to wind flow are usually associated with long span bridges such as suspension and cable stayed bridges. The design optimization has resulted in a reduction of the cross section depth to decrease its weight and static wind loads. However, this also brings increased flexibility and the likelihood of dynamic effects at lower wind speeds if the geometry of the cross section is not adequate. In particular, a characteristic of the aerodynamic problems in the range of low wind speeds is that of the vortex induced vibrations (VIV). When the wind impinges on a body with sharp edges, a shear layer separation is produced resulting in vortical structures, which are displaced downstream, as the air is a viscous fluid. These vortical structures induce differences in pressure between the upper and lower body surface, which result in aerodynamic forces. If the frequency of generation is near the natural frequency of the structure, a phenomenon of resonance or coupling between the two frequencies occurs, initiating a process whose vibrational amplitudes, although limited, can have serious consequences by affecting serviceability conditions, or even be the main cause of its long-term decline and decrease their service life.

$$St = \frac{fs\,D}{U} \tag{1}$$

where St=Strouhal number; f_s=vortex shedding frequency; D=cross-sectional dimension perpendicular to the wind direction.

The Strouhal number relates the vortex shedding frequency with the incident wind speed, and depends mainly on the geometry of the section and the Reynolds number. In bridge aerodynamics, the latter parameter is usually always greater than 10^5, so the Strouhal number is not strongly conditioned by the Reynolds number. Furthermore, the shear layer is controlled by the sharp edges of the section, and not by the fluid flow regime [1].

The VIVs are associated with a single mode of vibration, so this is a decoupled phenomenon. It can result in vertical movement or rotations, depending on which natural frequency is being excited. The cases included in this study correspond to vertical vibrations, because bridges with high torsional stiffness have higher torsional natural frequencies, thus implying wind speeds well above the normal values. Nevertheless, there are cases, like the Bay Bridge in Tokyo, that have suffered vibrations associated with vortex shedding and whose primary mode of torsion was close to vertical modes [2].

The primary goal is the identification of the critical wind speed which gives rise to resonance phenomena between the vortices generated and the natural frequency of the bridge. Once the Strouhal number associated with a given geometry and the vortex shedding frequency matches the natural frequency, the critical velocity is estimated by the following expression:

$$fs \approx fn \quad \Rightarrow \quad v_{crit} = \frac{fs\ D}{St} \tag{2}$$

where fs=vortex shedding frequency; fn=natural vibration frequency of the bridge; v_{crit}=critical wind speed; D=cross-sectional dimension perpendicular to the wind direction; St=Strouhal number.

The study of fluid-structure interaction tends to classify the VIV phenomenon as an instability induced by the fluid (Instability Induced Excitation, IIE) [1], where the influence of movement of the structure in the steady state over the aerodynamic forces responsible for this movement is irrelevant, partly because these vibrations are of limited amplitude. At the time when the vibrations exceed a certain maximum amplitude (usually given as limit cross-sectional transversal dimension), the process of generation and shed of vortex along the wake becomes unstable causing the excitatory action to disappear. The same happens if the wind speed generates a shedding frequency outside the interval of resonance of the bridge natural frequency (f_n), which traditionally is considered limited between the values of $0.8f_n$ and $1.2f_n$.

The resonance phenomena which gives rise to VIV can be avoided by furthering the vortex shedding frequency from to the considered natural frequency. This last parameter is determined by its mass and mechanical stiffness, in turn conditioned by resistant and constructive criteria, so it seems more logical to act on the cross section. The key is to design an efficient geometry so that the resonant phenomenon can only occur with high wind speeds that fall outside the range of average wind speeds of where the bridge stands. The VIV only takes place when the wind regime is more or less regular and average speed remains substantially constant for a given time, usually greater than 20-30 minutes.

To simplify the analysis, the majority of the models consider that the aerodynamic forces act over the static section, and the parameters that identify the phenomenon, e.g. Strouhal number and force coefficients, are obtained from wind tunnel static testing. Simple or regular geometries values (circle, square, rectangle, U-sections) are reflected in various standards and publications, such as the Eurocode (EN 1991 1-4), the British Design Manual for Roads & Bridges (BS 49/01) and the Canadian Highway Bridge Design Code (CAN/CSA-S6-06) . Different expressions to obtain the maximum vibration amplitude of the oscillations associated with VIV are also includ-

ed. Nevertheless, the parameters for sections of irregular or complex geometry are not included, and their estimation from static tests turns more complicated because several vortex shedding frequencies converge and it is not possible to distinguish which one is the main one.

This fact is also evident in sections whose aspect ratio (B/D) is greater than 2.0, since the evolution pattern of the wake does not obey the classical Von Karman vortex street (KV). Vortical structures generated in leading edge are not able to pass over the entire width of the section without causing its reattachment on its surface, resulting in a release pattern known as impinging leading edge vortex (ILEV) [1,3]. It has been found that the regularity of vortical structures shedding in the ILEV pattern are more affected by the movement of the section configuration than in the KV pattern. The static consideration of the aerodynamic forces is less accurate, although it remains valid. Nevertheless, the critical speed should be determined by other tests rather than static tests. The phenomenon of vortex induced vibrations is still regarded as an induced instability excitation (IIE), according to the classification criteria offered by Rockwell and Naudascher [1], but the change in the shedding pattern as a result of the oscillations of the section in its interaction with the wind in the range of resonant frequencies, identified as movement-induced excitation (MIE) [1] can not be ignored.

For regular sections, the Strouhal number is very similar to the reduced frequency corresponding to the moving section. However, in the cases of asymmetric, twin tandem, multibox and other complex sections, this does not hold true. Consequently, it is more accurate to use the reduced frequency parameter, f_{red}, to refer to the relationship between the vortex shedding frequency and incident wind speed on any type of wind tunnel test, being the Strouhal number equal to the value of reduced frequency referred only to static wind tunnel tests.

$$f_{s,red} = \frac{fs\,D}{U} \qquad Static\ tests \Rightarrow f_{red} \equiv St \tag{3}$$

In order to avoid this drawback, forced wind tunnel tests can be addressed, assigning a frequency oscillation similar to their natural frequency and moderate amplitude of vibration. A value between 0.1D and 0.2D (D, cross-sectional transversal dimension) is often used because the maximum amplitudes of oscillation of the phenomena of VIV on bridges studied stand close to these values.

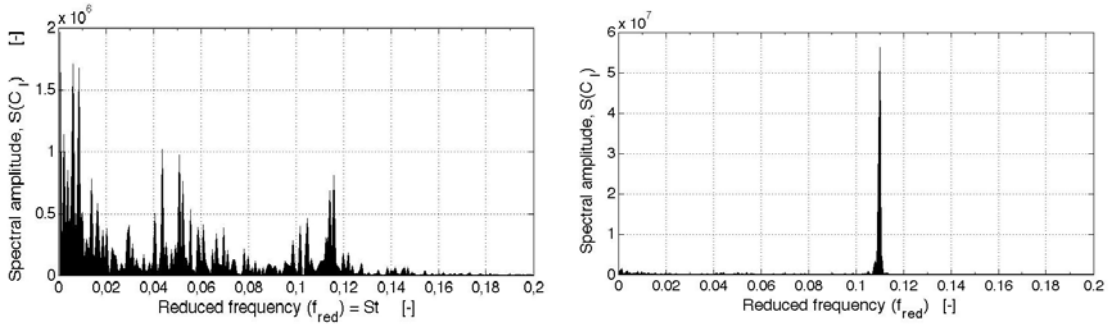

Figure 1. Spectral amplitudes of lift coefficient for a static numerical simulation (left) and a dynamic (right).

It is also possible to achieve dynamic wind tunnel tests, assigning the model the corresponding mechanical properties of stiffness and mass, thus representing the real bridge for its scale, by the progressive increase in wind speed up to the point of resonance and critical speed, where the models vibrate regularly. Following increasing wind speed, the resonance disappears and the models cease to experience these vibrations.

2.2 *Numerical simulations*

In this study several simulations of flow past bodies have been performed using a technique based on the Vortex-In-Cell (VIC) method. This is a hybrid particle-mesh algorithm that uses a discretization of the vorticity field and particles through a Lagrangian scheme for solving the Navier-Stokes equations describing fluid motion, while allowing high-resolving simulations resolution with a reasonable computational cost. To model the diffusion term in the Navier-Stokes expression, the random walk method is applied, which has been very successful in some fields of engineering, such as bridge aerodynamics. A comprehensive description of the simulation method can be found in [4] and in previous publications referenced in the mentioned document.

The use of numerical simulation methods are useful to achieve optimal geometric design of the cross section in those bridges that may be subjected to aerodynamic problems during its construction and service. It replaces or reduces aerodynamic tests necessary to verify the performance of several alternatives, thereby reducing cost and time, making it possible to extend its application to minor bridges that would not initially be tested. Although aerodynamic testing is essential for bridges with special features, the results can be compared with numerical simulations that can be carried out simultaneously.

This paper presents a computational analysis of the phenomenon of VIV in real bridges that have experienced an episode of vibrations of this type, and a comparison of critical speed values of wind and amplitudes of oscillation recorded.

3 THE VOLGOGRAD BRIDGE

3.1 *Outline of the vibration episode*

On May 20th, 2010, the new bridge over the Volga River in the city of Volgograd was closed to traffic because it was swinging dangerously due to the wind regime existing in the area. According to meteorological data, average speeds between 11.6 m/s and 15.6 m/s were recorded with a direction deviated 7 degrees from the normal direction to the longitudinal axis of the bridge. This suggested that it could be an episode of vertical vortex induced vibrations; there are other conditions surrounding the phenomenon that lead to the same hypothesis:

- Relatively low average wind speeds and constant regime with little turbulence, caused by the orography. The great width of the Volga River helps direct the wind along the smooth surface provided by the water.
- The oscillation frequency coincides with the fundamental frequency of vertical vibration of the bridge, indicating that there was a phenomenon of resonance or coupling between these frequencies associated to the vortex shedding.
- The amplitudes of vibration were limited (not exceeding one meter) according to the observations made by people who witnessed the phenomenon. The image recordings made during the development of the phenomenon were used to estimate the vibration amplitudes more accurately, reaching around 65-70 cm.

Initially, there was speculation on the fact that the vibrations could be caused by a moderate earthquake, alone or in coalition with the wind, although this hypothesis was discarded because an earthquake would not correspond to the development of the vibrations. The board swung slowly and regularly for about four hours, while the oscillations due to earthquakes are more irregular (incorporating various frequencies) and generally only last for so long.

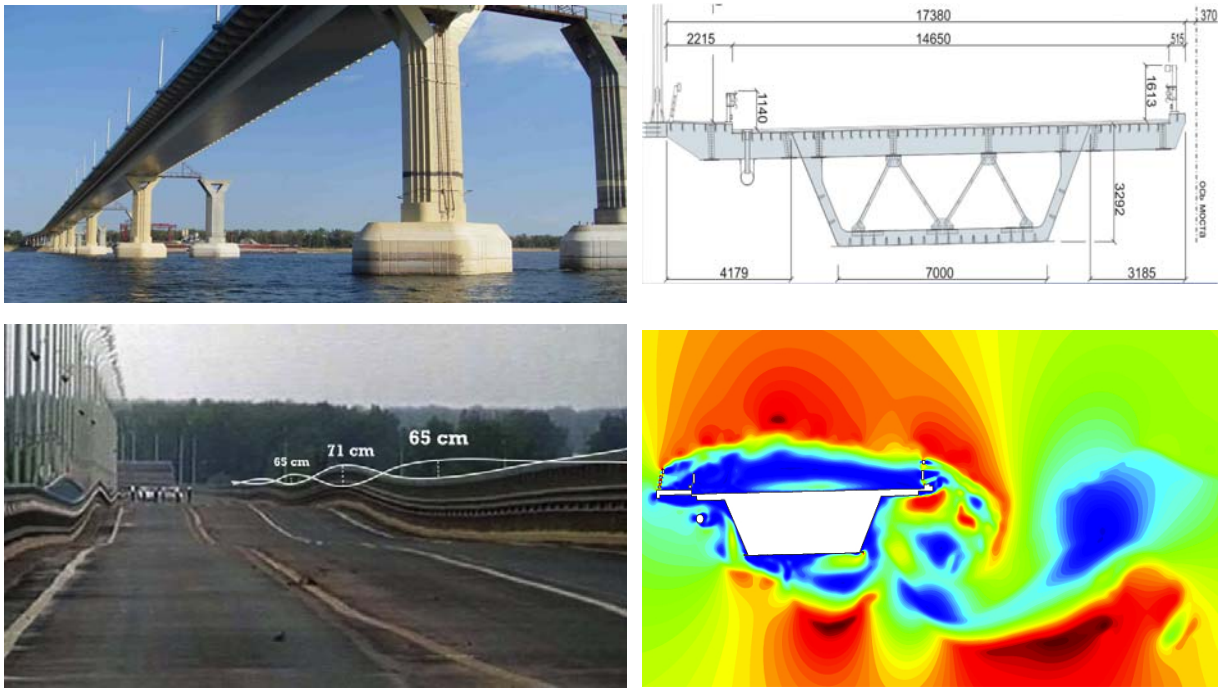

Figure 2. Volgograd Bridge. Top, left: General view. Top, right: cross-section dimensions of bridge deck. Bottom, left: video snapshot showing the vortex-induced oscillations episode (20th, May, 2010). Bottom, right: Velocity field visualization frame, obtained from the numerical simulation carried out.

A special commission was created to examine the state of the structure to check for damage that could keep the bridge from safely reopening. The bridge was reopened to pedestrians and passenger vehicle traffic five days later. However, traffic from heavy vehicles was not allowed until August 25th, 2010, once the bridge was examined in detail and no external or internal damage in the structure was found. After phenomenon experienced by the bridge, a monitoring system along the bridge to control its possible movements, and a weather station for the continued observance of the weather conditions in the area were implemented. An intervention plan was also designed so that emergency departments could act quickly if the phenomenon recurred. At the same time, wind tunnel tests on sectional models were carried out in Central Aero-Hydrodynamics Institute (TsAGI), near Moscow, to study the problem in detail. In recent years, a number of cable-stayed and girder bridges over rivers with wide channels that run through vast plains have been built in Russia. The aerodynamic problems observed on the bridge of Volgograd have focused attention on the remaining bridges of similar properties that may be subjected to the same problems. On March 2011, the bridge over the Volga River near Kineshma became the sixteenth bridge tested at the TsAGI wind tunnels.

3.2 *Numerical simulations*

The bridge, inaugurated in October 2009, is the only structure to cross over the Volga in the region, in addition to the existing dam on the Volga Hydroelectric Power Station, near the city. It has a total length of 7110 m, including the flyovers. The middle section overpasses the Volga and is composed of seven spans of 155 m length each. The cross section is a steel box of 10.02 m wide, with an upper and lower width of 7.00 m; 7.44 m if the overall width, which forms the base, is taken into account. The deck has two flies over the box on both sides of 4.179 m and

3.185 m, so that the total bridge width is 17.38 m. It has two traffic lanes separated by a barrier free median, and a strip for pedestrian traffic. There are two guardrails at each along each side of the bridge and an additional one to separate the vehicle traffic from pedestrians. The deck has an inclination of 1.1 degrees counter-clockwise about its longitudinal axis, so that its horizontal dimension parallels the wind direction at 17.25 m.

Figure 3. Flow visualization through vortex streaks and effective dimensions of cross-section with bars

Figure 3 shows the interaction of the fluid stream with the section through the vortex streaks generated by the simulation code. During the interaction process, three points of particular importance can be identified: (1) the detachment of the shear layer, which reattaches again on the lower surface, resulting in the pattern known as ILEV; (2) the actual detachment of the fluid shear layer. On the upper surface, the interaction between the fluid and the structure is similar, generating a release ILEV type pattern that is maintained along the entire width; (3) the final take-off of the fluid stream at the top of the section and its junction with the bottom which will cause a series of vortex structures of certain regularity throughout the wake downstream. It somehow determines the cyclic variations of pressure on the two surfaces of the section and therefore the aerodynamic forces acting on it.

The Strouhal number defines the frequency of generation of said vortical structures, and hence the frequency of variation of the aerodynamic forces responsible for the vibrations. The fluid-structure interaction mechanism in sections of complex geometry can be likened to what occurs in a rectangular section of dimensions B* x D*. To do this, these parameters must first be identified. B* represents the distance between the point of origin of the interaction of the surface of shorter length (1), which will condition the process and the final release point of the shear layer (2), that will subsequently converge with the other part of the fluid flow after passing the obstacle represented by the cross section. D* is the dimension perpendicular to the flow direction, causing the separation of the fluid flow. Figure 4 represents the Strouhal number against the B/D for rectangular sections, according to results of several investigators collected by Deniz & Staubli [3]. Results obtained by numerical simulation (Vortex Particle Method, VPM) of static tests have been added. The two different lines obtained for relations B/D between 2.0 and 5.0 confirm the coexistence of two patterns of evolution: the pure ILEV type, which identifies the lowest values, and another pattern closer to the KV type, where the shear layer reattachment on the surface of the body occurs alternately, resulting in higher values of the Strouhal number. When the section vibrates, the latter is favoured.

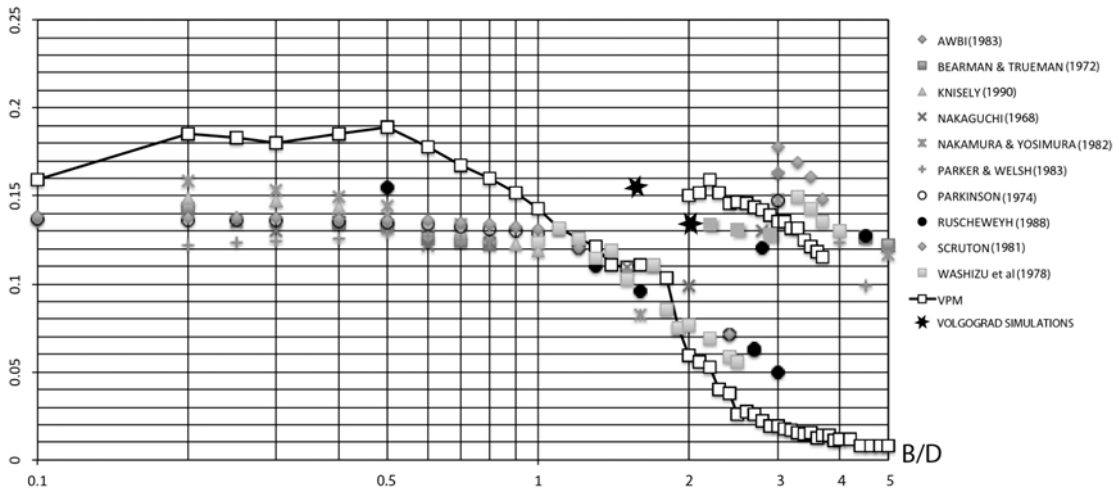

Figure 4. Strouhal number as a function of the side ratio, B/D, after [2] with present results added

Furthermore, higher Strouhal numbers correspond to lower wind speeds, and therefore have greater probability of occurrence. For B/D ratios exceeding 2.0, the lower Strouhal numbers are less than 0.06, which would require an average wind speeds too high for the associated release pattern to be given in most of the bridge sections. The Reynolds number corresponding to the numerical simulations is of $2.24 \cdot 10^6$. Although its influence on the Strouhal number is not as significant in bluff bodies, there can be some slight variation.

To analyse the VIV episode suffered by the Volgograd Bridge, two types of two-dimensional numerical simulations have been performed, using the cross section of the bridge with barriers and without them. The contours of both have been identified, which represent the surface exposed to the air stream and define a simple degree of freedom model where the only motion possible is vertical displacement. The natural frequency of the structure associated with the first vertical vibration mode is 0.42 Hz, and the mode shape is defined as a sinusoidal function, with the maximum in the centre span. The damping ratio relative to critical used is ζ=0.003, a typical value for steel bridges. The corresponding sectional mass is 2,500 kg/m, its effective width B* is 17.25 m. The effective vertical dimension D* is 3.61 m for the section without barriers, and 4.82 m for the section with barriers, being the B*/D* ratio of 2.06 and 1.54. Strouhal numbers obtained from static tests are 0.133 and 0.155, respectively. Both are represented in figure 4 and keep some consistency with the other values showed.

Figure 5 shows the evolution of the root mean square values (RMS) of the vibration amplitude as a function of the reduced wind speed of the two cases studied. To achieve a better comparison between them, the vertical dimension D of 3.61m in both cases has been considered, so that the Strouhal number of the barrier section is 0.116 instead of 0.155. The VIV takes place in the section with barriers in the low wind speed range of 6.60 and 9.60, corresponding to a wind speed of 10.0 m/s and 14.50 m/s. The critical speed is estimated around 13.0 m/s, the point where the structure reaches its maximum semi-amplitude vibration. This speed is included in the range of average speeds measured in the area between 11.6 m/s and 15.6m/s. The RMS value is estimated at 0.32 m, while the maximum value registered in the simulation is of 0.53 m. The temporal evolution of lift coefficient for this case is shown in figure 5. To determine the RMS value, the temporal force register has been filtered using a frequency range between and $1.1f_s$ $0.9f_s$, being f_s vortex shedding frequency calculated through the Fourier transform. Its value is RMS,Cl=0.55.

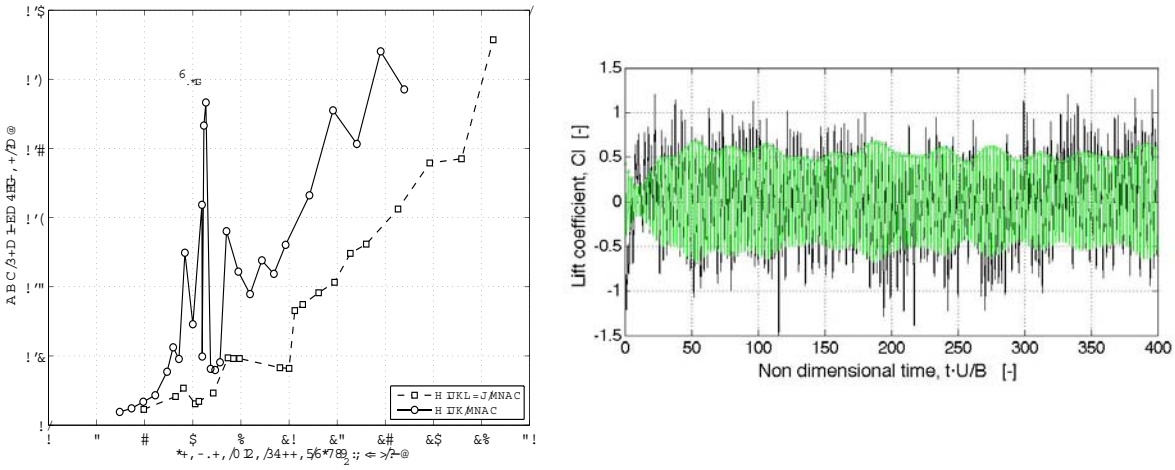

Figure 5. RMS semi-amplitude corresponding to the cases modeled (left), and lift coefficient history of the section with bars (right)

These figures are an accurate estimation of the values recorded during the vibration episode in May 2010, oscillations with a maximum amplitude of 0.71 m (0.36 m semi-amplitude), were reached. From 14.50 m/s, the amplitudes of vibration progressively increases as the wind speed increases, thus indicating the starting of another aerodynamic effect such as galloping, which leads to the dynamic instability of the structure if a certain speed is exceeded.

In the case of simulation of the section without barriers, the presence of VIV phenomenon is not detected as in the previous case, but a tendency to suffer obvious galloping effects as speed increases it is also checked. An interval in the curve where there is a sharper increase in the amplitude of vibration (between the values of reduced wind speed of 6.85 and 10.0) can be identified as a possible VIV effect.

A summary of previous results is shown in Table 1.

Table 1. Summary of results: Volgograd

2D model	B	D	B*	D*	B*/D*	St (D*)	vcrit	MAX (y)	RMS(y)	RMS(Cl)	Cd
	m	m	m	m	-	-	-	m	m	-	-
without bars	17.25	3.61	7.44	3.61	2.06	0.133	11.3	0.26	0.097	0.11	1.13
with bars	17.25	4.83	7.44	4.83	1.54	0.116	12.9	0.53	0.32	0.55	1.46

where B=section width; D=section depth; B*=section effective width; D=section effective depth; St=Strouhal number (static sectional simulation); vcrit=critical wind speed; MAX (y)=maximum semi-amplitude of oscillation; RMS(y)=root mean square referred to the semi-amplitude of oscillation; RMS(Cl)=root mean square of lift coefficient, $Cl=Fl/(1/2\rho U^2 D)$, with Fl=lift force; U=wind speed, ρ=air density, and D=3.61m for both cases; $Cd=Fd/(1/2\rho U^2 B)$, drag coefficient, with Fd=drag force.

The code employed also allows a numerical simulation based on a multimodal quasi-3D scheme. It is possible to discretize the total length of the bridge through slices of a given length and assign geometric and mechanical characteristics associated with each mode (frequency, mass, damping and mode shape). The fluid-structure interaction is developed in each slice independently of the others, i.e., there is no aerodynamic interference between the different slices. However, the movements of each slice depend on each other because there is a

structural connection between them, and this in turn influences the process of interaction with the fluid flow. This additional tool allows for a more detailed study of the interaction problem, and is especially useful when the bridge has variable sections along its longitudinal axis, as its geometry greatly influences the generation and development of the vortices during interaction. The correlation between oscillations of each of the sections will be smaller if the coupling phenomenon occurs at different rates in each of them, and therefore the vibration amplitudes will in principle be lower.

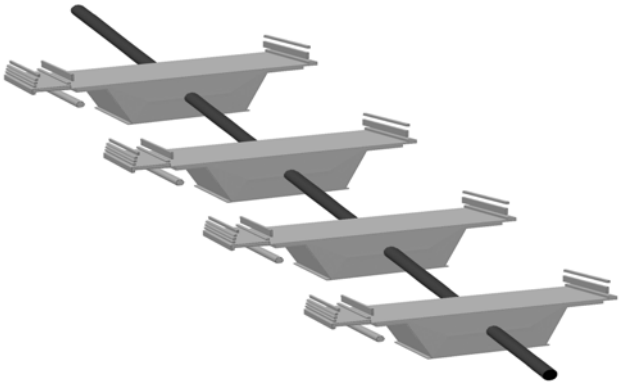

Figure 6. Draft of the quasi-3D scheme of the Volgograd Bridge composed by several slices

The Volgograd Bridge has a constant section and the slices considered in the quasi-3D scheme are closely correlated, because the lock-in occurs at the same speed throughout them. In this case only the simulation of the section with barriers has been carried out. The total length of the central span of 155 metres is discretized into 16 slices, 9 m each except those located at the boundaries, which are of 10 m. The maximum semi-amplitude vibration is 0.41 m, and the RMS value is 0.30 m, results close to the two-dimensional case; RMS value of lift coefficient is 0.54.

4 ALCONÉTAR BRIDGE

4.1 *Outline of the vibration episode*

The oscillations of Alconétar Bridge due to vortex shedding took place on January 2006 during the bridge erection, once the arch was completed. Two rectangular variable depth boxes in tandem arrangement braced by X-trusses formed each of the two arches. The maximum amplitude reached was 80 cm on the vertical axis and seriously threatened the structural stability of the arch [5,6]. The braces managed to resist the wind action. The box depth corresponding to the maximum amplitude value is D=2.41 m, the box width is B=1.2m and the total width is W=7.74 m, giving a side ratio of W/D = 3.21. Measured wind speeds during the Alconétar Bridge vibration episode did not exceed 30 km/h, so the corresponding reduced frequency was close to 0.21, typical from a H-shaped section with the same side ratio. [3]. The modal mass is 1,133 kg/m and the damping ratio of critical, 0.0048.

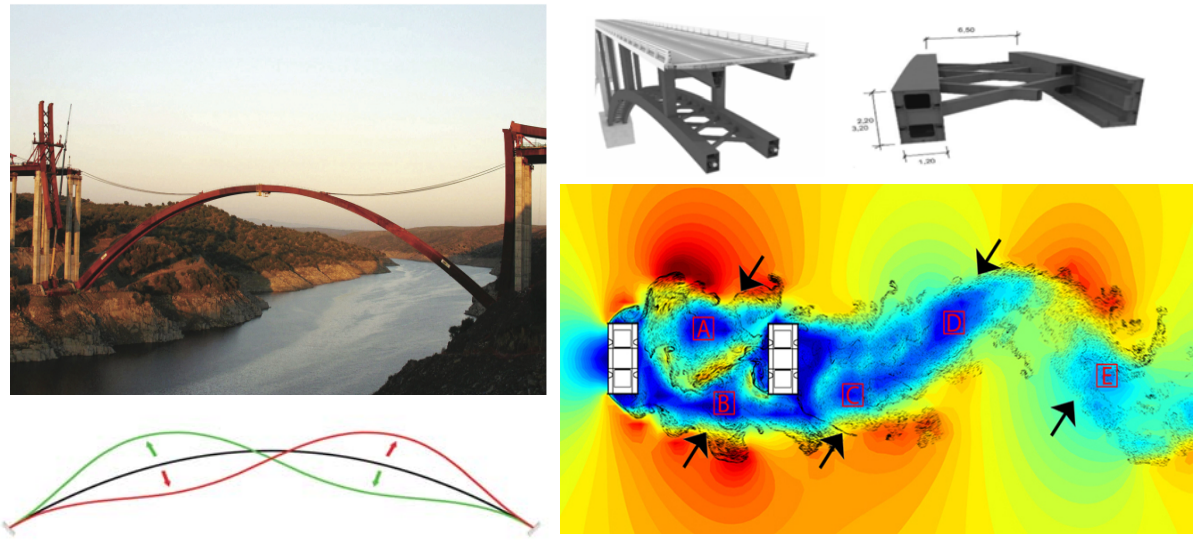

Figure 7. Alconétar Bridge. Top, left: the bridge under erection. Bottom, left: mode shape of the first vertical vibration mode of the single arch. Top, right: 3D bridge scheme, with main dimensions. Bottom, right: velocity field visualization from the simulation.

4.2 *Numerical simulations*

Two cross-section variants are studied for Alconétar Bridge: the twin steel box section with two little rectangles in the middle that represents the braces, and the cross-section without the influence of these elements. To identify the lock-in effects and thus the vortex-shedding phenomenon, a certain range of wind speeds are employed in the numerical simulation process. The Alconétar Bridge does not have a conventional H-section because the X-trusses connecting the twin boxes do not occupy the whole space between them. It can be thought that the vortex shedding mechanism obeys a tandem configuration, as previously seen, having a spacing ratio of (W-2B)/D = 2.21.

The main results are collected in Table 2.

Table 2. Summary of results: Alconétar

2D model	B	D	B*	D*	B*/D*	St (D*)	vcrit	MAX (y)	RMS(y)	RMS(Cl)	Cd
	m	m	m	m	-	-	-	m	m	-	-
without braces	7.74	2.41	1.20	2.41	0.5	0.140	11.81	0.43	0.29	1.4- 1.3	2.4-0.3
with braces	7.74	2.41	1.20	2.41	0.5	0.140	11.81	0.34	0.18	0.85-1.1	1.8-0.2

where B=section width; D=section depth; B*=section effective width (one box); D=section effective depth (one box); St=Strouhal number (static sectional simulation); vcrit=critical wind speed; MAX (y)=maximum semi-amplitude of oscillation; RMS(y)=root mean square referred to the semi-amplitude of oscillation; RMS(Cl)=root mean square of lift coefficient, $Cl=Fl/(1/2\rho U^2 D^*)$, with Fl=lift force; U=wind speed, ρ=air density, and D=2.41m; $Cd=Fd/(1/2\rho U^2 B^*)$, drag coefficient, with Fd=drag force. The dual values of RMS(Cl) and Cd correspond to the upstream section and the downstream section, respectively.

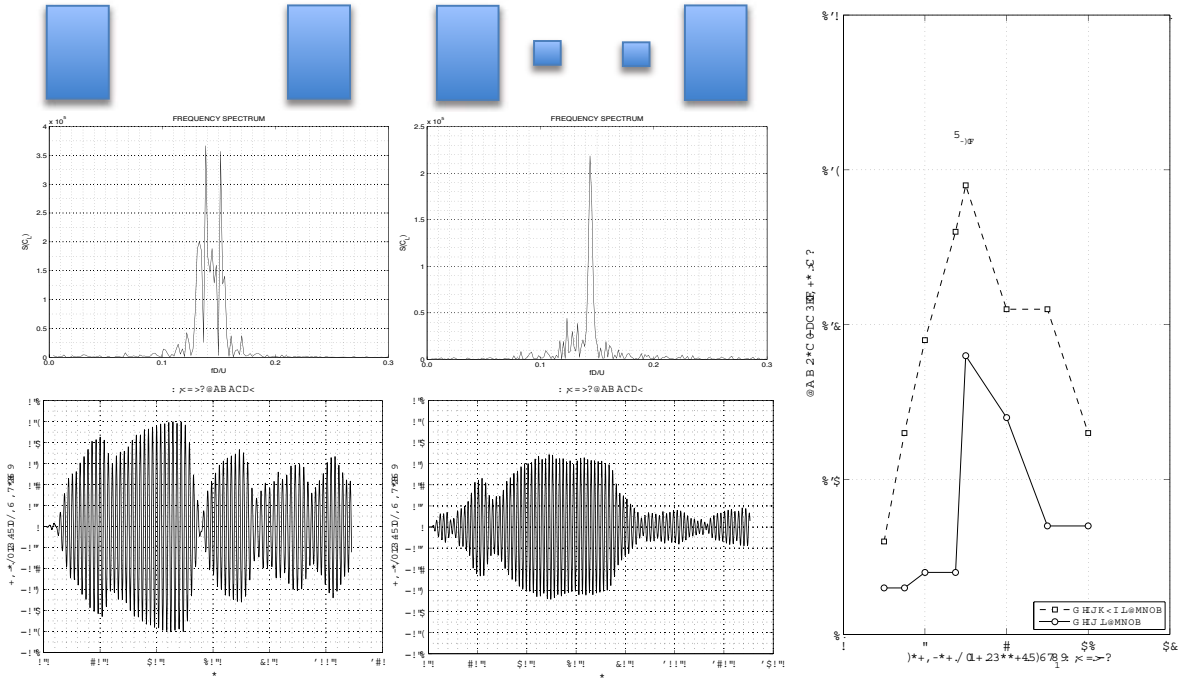

Figure 8. Comparison of frequency spectrum and vertical displacements of the two cross-section variants (with and without braces) (left); semi-amplitudes corresponding to these numerical simulations (right)

According to the results of the simulations the reduced frequency is 0.14 for both sections (without and with braces), and hence the estimated critical wind speed is:

$$!!!\ "\ !\quad !"\ !\quad !\ !!\ "\ !!\ "\ !!!!!\overset{!}{\Rightarrow}\ !!!!!\ !"\#\$\ !\ \frac{!\ "\ !!}{!\ !\ "\#}\ !\ \frac{!\ !!\ "\ !!\ !!\ "}{!\ !!\ "}\ !\quad !\ "\ !!\ !\quad !\ !\quad !\quad !\ "\ !!\ !\ "\quad !\ ! \tag{3}$$

Figure 7 c) shows the simulation of vortex shedding process in a rectangular prism with a side ratio B/D = 0.5, and its interaction with another twin section situated downstream. The vortex pattern for both sections corresponds to the KV. For a specific spacing ratio between 2.5D and 3.0D, vortices shed from upstream prism coalesce with those being formed downstream, thus leading to a resonance phenomenon. However, some arguments suggest that the vortex shedding pattern is closer to the H-section rather than the tandem configuration:

- The braces partially occupy the gap between the two boxes, interceding in the vortices convection process and thus hindering the coalescence phenomenon. In addition to that, the varying depth of the boxes results in different shedding frequencies, which are not excited by the same wind speed.
- The critical wind speed below 30 km/h, as measured during the excitation episode, does not correspond to the critical wind speed estimated for the tandem configuration.
- Wind tunnel sectional tests were carried out resulting in a measured Strouhal number of 0.15, closer to that of the tandem configuration. However, it is necessary to point out that three-dimensional effects must be taken into account: the fact that the wind speed is not homogeneous along its axis, the varying depth (D = 3.2 m in abutments and D=2.2 m in the central point) and the bracing configuration can greatly influence the resonance phenomenon.

The more homogeneous the bridge is, the more representative the sectional wind tunnel tests are. The specifications mentioned previously cause the vortex shedding mechanism to have a significant three-dimensional component, which must be taken into account. As a consequence, a full-bridge wind tunnel test should be conducted to consider all of these properties and experimentally corroborate the above results arisen.

5 COUNTERMEASURES

5.1 *Volgograd Bridge*

Wind tunnel sectional model tests conducted confirmed that the oscillations suffered by the Volgograd Bridge were due to a problem of aerodynamic resonance, and it was decided to place three sets of dynamic dampers in its three main spans. Technical work began in mid-summer 2011 and was completed in October. The total cost was about 112 million roubles (3.8 billion US dollars), accounting for 4.5% of total budget of the bridge (2,500 million roubles, 84 million US dollars). The traffic was not interrupted during the assembly process.

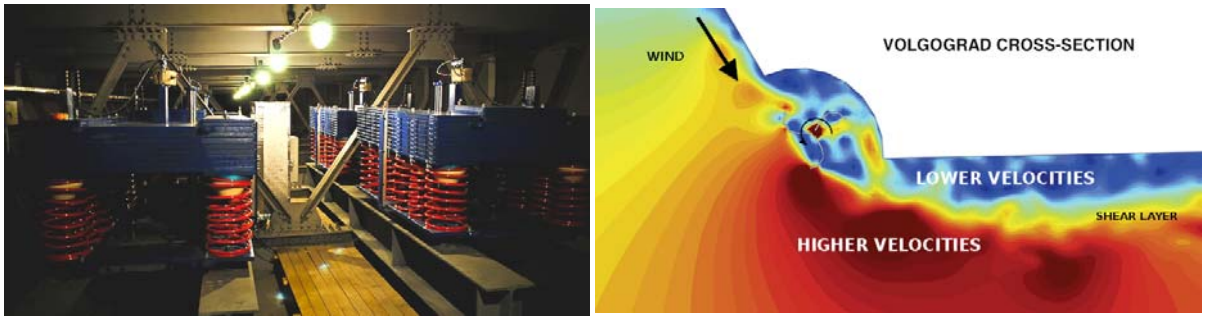

Figure 9. Damping system assembled inside Volgograd Bridge (left). Improvement of bridge behavior against VIV effects by adding a Savonius type turbine on the lower corner of the cross-section (right)

No major vibrations since the dampers were added have been detected. A similar solution was adopted in Niterói Bridge in 2004 to end the nagging vibrations that were given from time to time. [7] Volgograd Bridge has thus become the first continuous deck bridge in Russia to adopt this solution. The damper system becomes an expensive alternative to reduce these effects and avoid the lock-in phenomenon with other natural frequencies that could be excited. An adequate aerodynamic study of the section prior to its erection could have raised the choice of a more efficient geometry against the effects of VIV. Figure 9 shows an example of an alternative section tested using the simulation code in which a small Savonius type turbine is added to the lower corner of the box section.

This configuration would modify the vortex-shedding pattern allowing the maximum amplitude to decrease to a half of the amplitude associated to the standard section (0.20 m). Moreover, this solution would have permitted the small-scale energy generation that could contribute to the bridge illumination and other small necessities related to its maintenance. It is also planned to build a second bridge deck next to the current in the future, so its influence over the aerodynamic actions have also been studied using the simulation code. As shown in Figure 10, the location of a second section reduces the amplitude of vibration of the initial section.

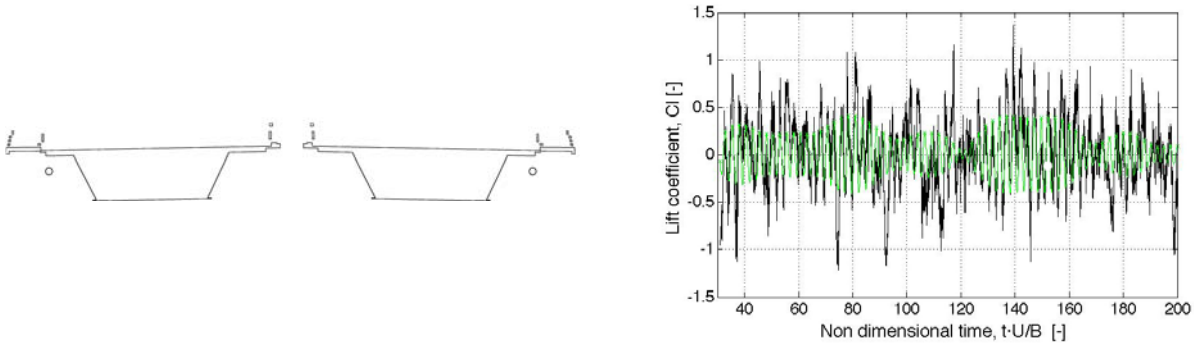

Figure 10. Double deck configuration of Volgograd Bridge (left) and lift its lift coefficient evolution (right)

For a critical wind speed of 13m/s, the RMS amplitude is 0.14 m while it was 0.32 m for the standard section. The lift coefficient is 0.24, not considering the contribution of the lift forces of the right section (downstream).

5.2 *Alconétar Bridge*

A number of deflectors were welded along the section arch in order to modify its geometry and, consequently, avoid the lock-in phenomenon. After placing the two upper decks above the arches, its global stiffness, mass and geometry were modified so that the Bridge is safe from suffering any VIV problem.

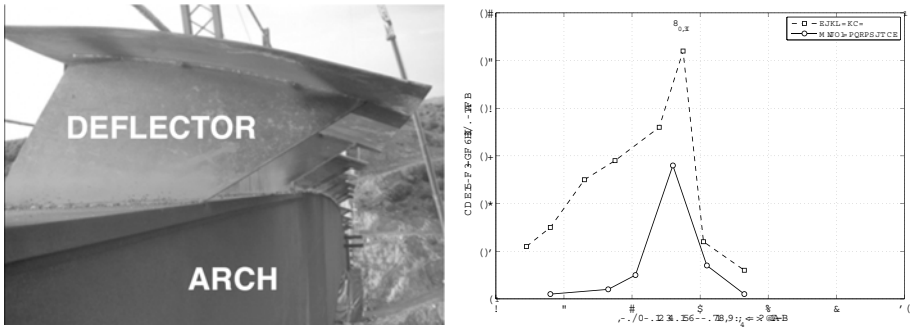

Figure 11. Deflectors added to Alconétar Arch Bridge (left) and maximum semi-amplitude value as a function of the reduced wind speed for the standard cross-section and with deflectors (right)

6 CONCLUSIONS

The vibrations suffered by some bridges have been controlled by the addition of tuned mass dampers. Examples include the steel girder bridges of Rio Niterói (1980, Niterói, Brazil, 300 m main span) [7] and the Trans-Tokyo Bay Bridge (1997, Tokyo Bay, Japan, 240 m main span) [2]

On the contrary, computational methods are aimed to identify the potential problem in early design stages, and thus avoid subsequent interventions (e.g. installation of damper devices) which have major economic implications, unless strictly necessary for other reasons.

The maximum amplitude has been successfully reduced for both cases. As for the Volgograd Bridge, it has been seen that the presence of a twin girder deck next to the existing one would lead to a notable reduction in the maximum vibration amplitude. This additional deck is planned to be constructed in the future.

The influence of the braces geometry together with the twin box cross-section of Alconétar Bridge is not very clear. It is important to analyse the influence of the solidity ratio of the horizontal strip that braces the two sections in tandem arrangement, since this parameter determines the force coefficient and therefore the amplitude of oscillation of the VIV phenomena. Therefore, a deeper study should be conducted.

7 REFERENCES

[1] E. Naudascher, D. Rockwell, Flow-Induced Vibrations. An Engineering Guide 1st ed. (reprint), Dover Publications, Inc., Mineola, NY, USA, 2005, Chaps. 3, 4, 6 & 9.

[2] Y. Fujino, Y. Yoshida, Wind-Induced Vibration and Control of Trans-Tokyo Bay Crossing Bridge, Journal of Structural Engineering, ASCE, 128 (2002) 1012-1025

[3] S. Deniz, Th. Staubli, Oscillating Rectangular and Octagonal Profiles: Interaction of Leading- and Trailing-Edge Vortex Formation. Journal of Fluids and Structures 11 (1997) 3-31

[4] G. Morgenthal, J.H. Walther, An immersed interface method for the Vortex-In-Cell algorithm, Computers and Structures, No 85, 2007, pp. 712-726, Elsevier Science Ltd, The Netherlands.

[5] M.Astiz, Estudio de las Vibraciones de los Arcos de Alconétar, Hormigón y Acero, 4/2006 (2006) 41-50.

[6] A. S. Corriols. Estudio de las Vibraciones Inducidas por Vórtices en Puentes Arco (Master Thesis), Technical University of Madrid, 2010.

[7] R. C. Battista and M. Pfeil, Reduction of vortex-induced oscillations of Rio-Niterói bridge by dynamic control devices, J. Ind. Aerodyn. 84 (2000) 278-288.

The Seventh International Colloquium on Bluff Body Aerodynamics and Applications (BBAA7)
Shanghai, China; September 2-6, 2012

Unsteady aerodynamic forces on long-span curved roof

Wei Ding [a], Mana Nakamura [b], Satoshi Tanaka [c], Yasushi Uematsu [a]

[a] *Dept. of Architecture & Building Science, Tohoku University, Sendai, Japan*
[b] *Nikken Steel Corporation, Tokyo, Japan*
[c] *Nikken Sekkei Ltd., Tokyo, Japan*

ABSTRACT: The present paper discusses the characteristics of unsteady aerodynamic forces on long-span vaulted roofs, based on a wind tunnel experiment and a CFD simulation. A forced vibration test is carried out in the wind tunnel to investigate the effects of wind speed, vibration amplitude, reduced frequency and rise/span ratio of the roof on the unsteady aerodynamic forces. Furthermore, the influence of the unsteady aerodynamic forces on the dynamic response of practical long-span vaulted roofs is investigated using the results obtained from the wind tunnel experiments. The CFD simulation is used effectively to evaluate the unsteady aerodynamic forces on the vibrating roof in a wider reduced frequency range.

KEYWORDS: Unsteady aerodynamic force, Long-span curved roof, Wind tunnel experiment, Dynamic response, Computational Fluid Dynamics (CFD)

1 INTRODUCTION

Many long-span structures with curved roofs, such as stadiums, auditoriums, airports and railway stations, have been constructed in recent years, because they can provide a large space with no intermediate columns. Being light and flexible, such roofs are vulnerable to dynamic wind actions. Furthermore, the wind-structure interaction may affect the response significantly. The interaction is represented by the unsteady aerodynamic forces, or the motion-induced forces, which may increase or decrease the response of the structure. Many researches have been made of the unsteady aerodynamic forces on long-span bridges and tall buildings (e.g. Taniike et al. [1]). The results indicate that unstable vibration may be induced by the negative aerodynamic damping in some cases. By comparison, the number of researches on long-span roofs is quite limited. Daw and Davenport [2] carried out a forced vibration test on a semi-circular roof to investigate the dependence of unsteady aerodynamic forces on the turbulence intensity, wind speed, vibration amplitude and geometric details of the roof. Ohkuma et al. [3] investigated the mechanism of aeroelastic instability for long-span flat roofs using a forced vibration test in a wind tunnel. They discussed the effects of unsteady aerodynamic forces on the wind-induced responses, based on the wind tunnel experiment as well as on the dynamic response analysis. At present, however, the characteristics of unsteady aerodynamic forces on long-span curved roofs are not understood well. So, it is necessary to investigate this problem further for developing more reasonable methods of response analysis for these roofs.

The objective of the present study is to describe the characteristics of unsteady aerodynamic forces acting on a vaulted roof vibrating in the first anti-symmetric mode. A forced-vibration test is carried out in a turbulent boundary layer. The effects of wind speed, vibration amplitude and frequency on the characteristics of unsteady aerodynamic forces are investigated. However, the range of these parameters involved in the wind tunnel experiments is limited. Therefore, a CFD simulation is carried out to investigate the problem in more detail. In the simulation, the parameters are varied over a wider range.

2 UNSTEADY AERODYNAMIC FORCE

The displacement of structure in the *j*-th mode may be represented by the following equation,

$$z_j(s,t) = \phi_j(s)\, x_j(t) \tag{1}$$

where φ_j and x_j are the mode shape and generalized displacement of the *j*-th mode, respectively; and *s* represents the circumferential coordinate taken along the roof.

Applying a modal analysis to the equation of motion for the roof, we obtain the following equation of motion for the *j*-th generalized displacement:

$$\ddot{x}_j(t) + 2\zeta_j \omega_j \dot{x}_j(t) + \omega_j^2 x_j(t) = F_j(t) / M_j \tag{2}$$

$$F_j(t) = F_{Wj}(t) + F_{Aj}(x_j, \dot{x}_j, \ddot{x}_j, \ldots) \tag{3}$$

where M_j = generalized mass; ω_j = natural circular frequency; ζ_j = critical damping ratio; and F_j = generalized force. F_{Wj} represents the fluctuating wind force due to the oncoming flow and wake instability, while F_{Aj} the unsteady aerodynamic force due to the wind-structure interaction.

In the case of the forced-vibration test, a steady vibration in the first anti-symmetric mode represented by a sine curve is applied to the roof. The unsteady aerodynamic force F_{Aj} (here $j = 1$) may be obtained from Eq. (4) by using the Fourier series at the frequency f_m of the forced vibration:

$$F_{Aj}(t) = F_{Rj} \cos 2\pi f_m t - F_{Ij} \sin 2\pi f_m t \tag{4}$$

$$F_{R_j} = \frac{1}{T}\int_{-T}^{T} F_j(t) \cos 2\pi f_m t\, dt \tag{5}$$

$$F_{I_j} = \frac{1}{T}\int_{-T}^{T} F_j(t) \sin 2\pi f_m t\, dt \tag{6}$$

where F_{Rj} and F_{Ij} are the in-phase and out-of-phase components of the unsteady aerodynamic force, respectively.

The effect of unsteady aerodynamic force may be represented by the aerodynamic stiffness and damping coefficients a_{kj} and a_{cj}, which are given by the following equations [4]:

$$a_{Kj} = \frac{1}{q_H A_s (x_0 / L)} \frac{2}{T} \int_0^T F_j(t) \cos 2\pi f_m t\, dt \tag{7}$$

$$a_{Cj} = \frac{1}{q_H A_s (x_0 / L)} \frac{2}{T} \int_0^T F_j(t) \sin 2\pi f_m t\, dt \tag{8}$$

where q_H = velocity pressure at the mean roof height H; A_s = roof area; x_0 = vibration amplitude; L = span of the roof; f^* = reduced frequency defined by $f_m H / U_H$, with U_H being the mean wind speed at the mean roof height H.

The generalized force F_j may be described in terms of the external and internal pressures p_e and p_i, as shown in Eq. (9):

$$F_j(t) = \int_0^{R_s} \left[p_{e_j}(s,t) - p_{i_j}(s,t) \right] \phi_j(s)\, ds \tag{9}$$

where R_s = total length of the vaulted roof. Internal pressure p_i is ignored in the present study, because the first anti-symmetric mode under consideration causes no change of internal volume.

3 WIND TUNNEL EXPERIMENT

3.1 *Experimental apparatus and procedures*

The experiments were carried out in an Eiffel-type wind tunnel with a working section 6.5m in length and 1.0m×1.4m in cross-section. A turbulent boundary layer with a power-law exponent of α=0.23 was generated on the wind tunnel floor by using a set of turbulence-generating spires installed at the entrance of the working section, and a number of roughness blocks distributed on the floor. The profiles of the mean wind speed and turbulence intensity are shown in Fig. 1. The reference wind speed was measured at a height of Z_G = 500mm. The longitudinal velocity spectrum, not shown here to save space, was found to be generally consistent with the so-called Karman type spectrum.

The wind tunnel model was a vaulted roof made of 0.8mm thick polyester film, as shown in Figs. 2 and 3. A pair of end plates was used to make the flow two-dimensional. Two models with rise/span ratios of 0.15 and 0.20 were tested. Each model had 12 pressure taps of 1mm diameter distributed along the roof's centerline. The pressure taps were connected to pressure transducers in parallel via 80cm lengths of flexible vinyl tubing. The tubing effects were numerically compensated by using the gain and phase-shift characteristics of the pressure measuring system used in the experiment. The signals from the pressure transducers were sampled simultaneously at a rate of 500Hz for a period of approximately 60s. Table 1 summarizes the range of experimental parameters involved in the experiment.

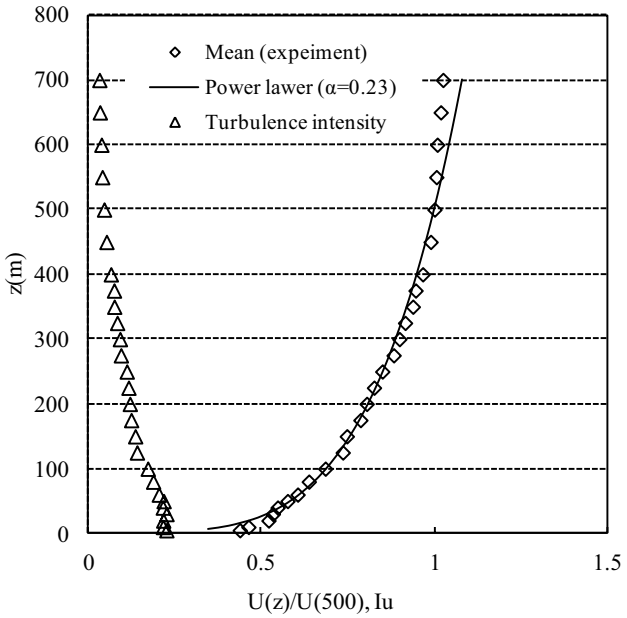

Fig.1 Profiles of the mean wind speed and turbulent intensity

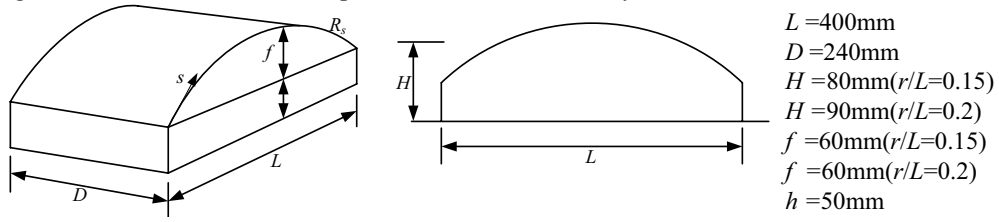

Fig.2 Geometry of the experimental model

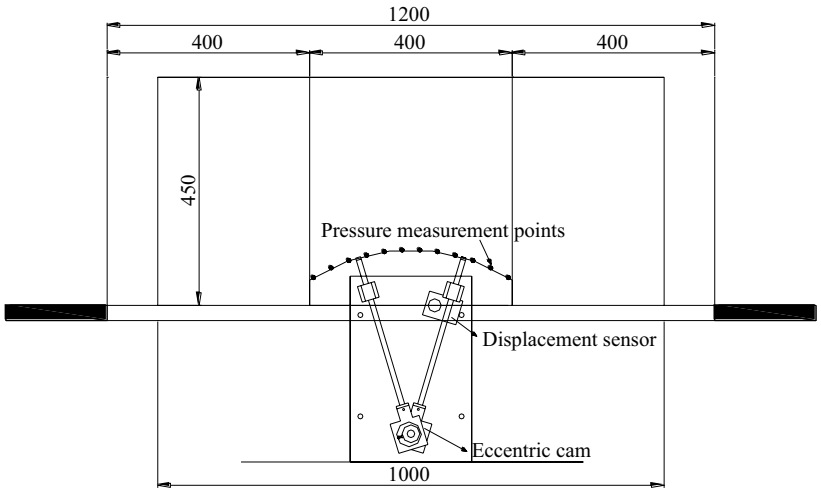

Fig.3 Experimental setup of the forced vibration test

Table 1 Parameters of experiment

Rise/span ratio r/L	0.15, 0.20
Wind speed U_H (m/s)	5.0, 7.0, 10.0
Amplitude of the forced vibration x_0 (mm)	1.0, 2.5, 4.0
Forced vibration frequency f_m (Hz)	5 to 25 at an increment of 1 Hz

3.2 *Results and Discussion*

Fig.4 shows the variation of the aerodynamic stiffness coefficient a_k with the reduced frequency f^* for various wind speeds (Fig. 4(a)) and vibration amplitudes (Fig. 4(b)); the rise/span ratio is 0.15. The value of a_k generally increases with an increase in f^*. As the reduced frequency decreases, the value of a_k approaches the quasi-steady value (dashed line in the figure). Similar results were observed for r/L=0.20. Within the limits of the present experiment, the value of a_k is generally positive, which may reduce the total stiffness of the structural system resulting in a lower natural frequency.

Plotted on Fig.5 are the variations of aerodynamic damping coefficient a_c with the reduced frequency f^* for various wind speeds and vibration amplitudes; the rise/span ratio is again 0.15. The values of a_c are generally negative except for small f^*values, which may result in an increase in the total damping of structural system. The magnitude of a_c increases as the f^* value increases. Similar results were observed for r/L=0.20. It can be seen that the effects of wind speed and vibration amplitude on the aerodynamic stiffness and damping coefficients are not so significant and the values of a_k and a_c are mainly dependent on f^*.

4 PREDICTION OF DYNAMIC RESPONSE

This section outlines a method for predicting the dynamic response of a full-scale vaulted roof to turbulent winds, in which the effects of the unsteady aerodynamic forces are taken into account. As an example, we consider a long-span membrane structure with the same shape as that used in the wind tunnel experiment. In general, the natural frequency of membrane structure with a span of approximately 100m is in a range from 0.5Hz to 1.5Hz and the mass from 2 kg/m^2 to 15 kg/m^2. The dynamic responses of such structures in a turbulent wind are evaluated by using the averaged

curves of aerodynamic stiffness and damping coefficients obtained from the wind tunnel experiments.

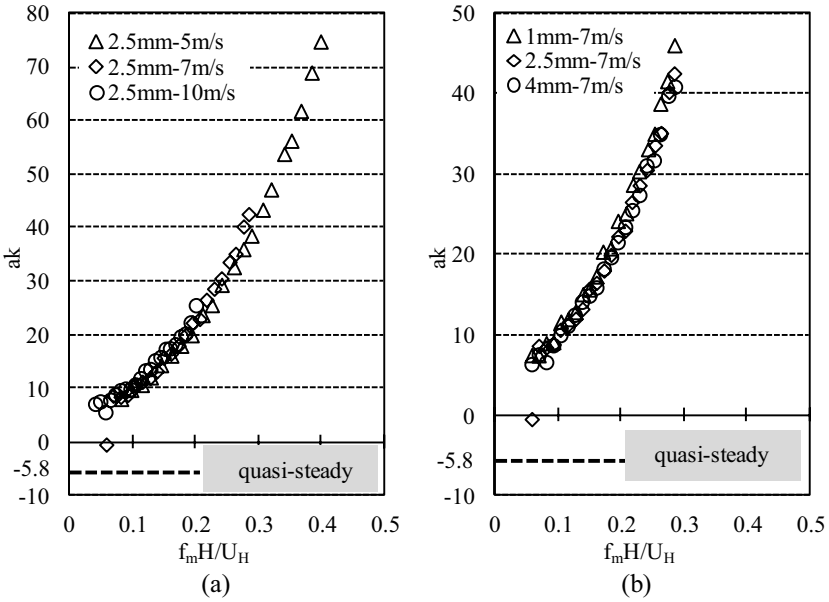

Fig.4 Aerodynamic stiffness coefficient versus f^* (r/L=0.15)

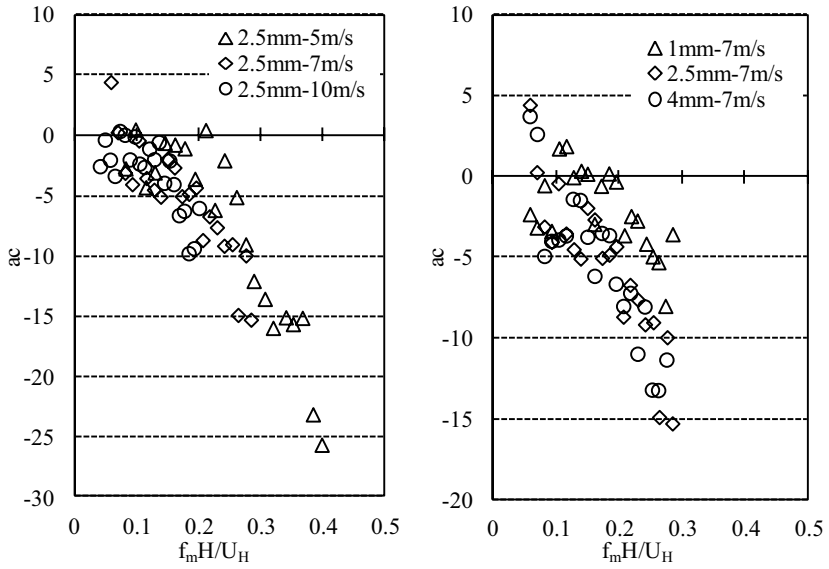

Fig.5 Aerodynamic damping coefficient versus f^* (r/L=0.15)

Aerodynamic stiffness (K_{aj}) and aerodynamic damping ratio (ζ_{aj}) are given by Eqs. (10) and (11). The mechanical admittance including the aerodynamic stiffness and damping is defined by Eq. (12), in which we assume that the structural damping ratio is ζ_s =1% and the natural frequency of the first anti-symmetric mode is f_s=0.5Hz. Only the first vibration mode (j=1) is considered, because the roof response to turbulent wind forces is thought to be dominated by this mode [6].

$$\zeta_{a_j}(f) = -\frac{1}{16\pi^2}\frac{\rho_a}{\rho_{s_j}}\left(\frac{U_H}{f_{s_j}H}\right)^2\frac{H}{L}a_{c_j}(f) \tag{10}$$

$$\frac{K_{a_j}(f)}{K_{s_j}} = -\frac{1}{8\pi^2}\frac{\rho_a}{\rho_{s_j}}\left(\frac{U_H}{f_{s_j}H}\right)^2\frac{H}{L}a_{k_j}(f) \tag{11}$$

$$\left|\chi_j(f)\right|^2 = \frac{1}{\left[1-\left(\frac{f}{f_{s_j}}\right)^2+\frac{K_{a_j}(f)}{K_{s_j}}\right]^2+4\left(\xi_{s_j}+\xi_{a_j}(f)\right)^2\left(\frac{f}{f_{s_j}}\right)^2} \tag{12}$$

Fig.6 illustrates the mechanical admittance functions plotted against frequency f for various wind speeds, where the structural mass is assumed M_s=4kg/m^2. As the wind speed increases, the resonant frequency decreases and the peak value of the mechanical admittance function at the resonant frequency increases. The decrease in the resonant frequency is due to the positive aerodynamic stiffness coefficient.

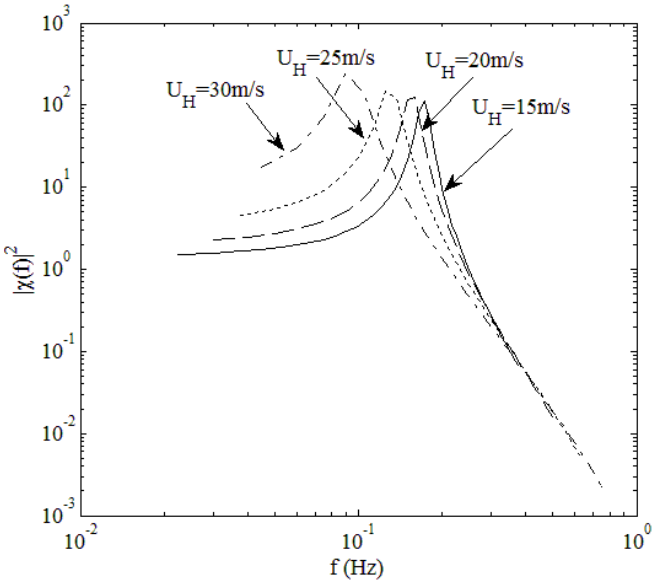

Fig.6 Variation of mechanical admittance function with wind speed

The variation of mechanical admittance function with the roof's mass is illustrated in Fig.7, in which we assume that U_H=20m/s. The resonant frequency increases and the resonant peak value of the mechanical admittance function decreases as roof's mass increases. This feature implies that the increase in mass is quite effective for reducing the aerodynamic excitation of the roof. In other words, the effect of unsteady aerodynamic forces on the response of the roof becomes less significant for heavier roofs.

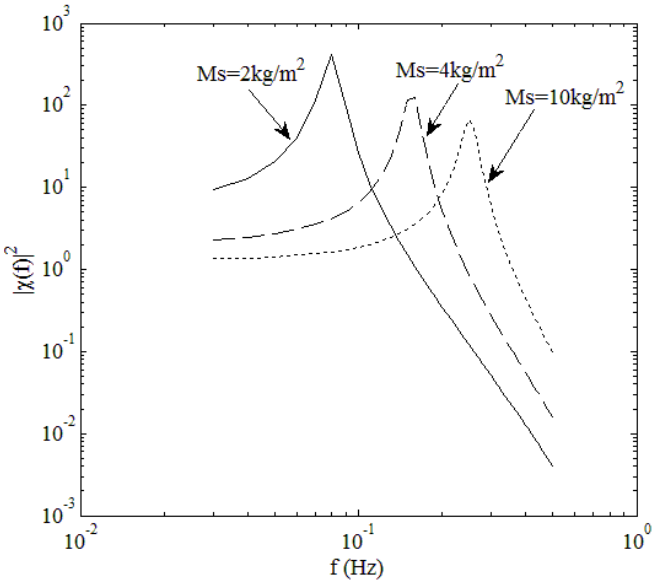

Fig.7 Variation of mechanical admittance function with roof's mass

5 CFD SIMULATION

The unsteady aerodynamic force acting on a vibrating roof in the first anti-symmetric mode is numerically simulated by using a commercial software 'STAR-CD'. As the first step of study, the wind tunnel experiment using a model with r/L=0.15 is reproduced. The amplitude x_0 of vibration is fixed to 4.0mm in this study.

5.1 *Computational conditions*

The large eddy simulation (LES) with the Smagorinsky sub-grid model (C_s=0.12) is used to simulate the flow field around the model. The computational conditions are summarized in Table 2. The computational domain and mesh arrangement are shown in Fig.8. It is important to provide proper inflow condition for predicting the wind loads on structures precisely, particularly for LES. In this study, the inflow turbulence is generated in a preliminary computational domain where roughness blocks are arranged to generate a turbulent boundary layer similar to the wind tunnel flow [7, 8]. The profile of the mean wind speed and turbulent intensity at the inlet of the computational domain are compared with those of the wind tunnel flow in Fig. 9. Although there exists a difference between CFD simulation and wind tunnel experiment for the profile of mean wind speed, the agreement is quite good for the turbulence intensity.

5.2 *Results and discussion*

Fig.10 shows the distributions of the mean wind pressure coefficients along the centerline of the vibrating roof obtained from the CFD simulation and the wind tunnel experiment, in which the results for the frequencies of 10Hz and 20Hz are plotted. A generally good agreement between these two results can be seen. The difference is somewhat larger near the top of the roof; the CFD values are approximately 10% larger in magnitude than the experimental ones. This difference

may be due to a difference in surface roughness of the roof between CFD simulation and wind tunnel experiment.

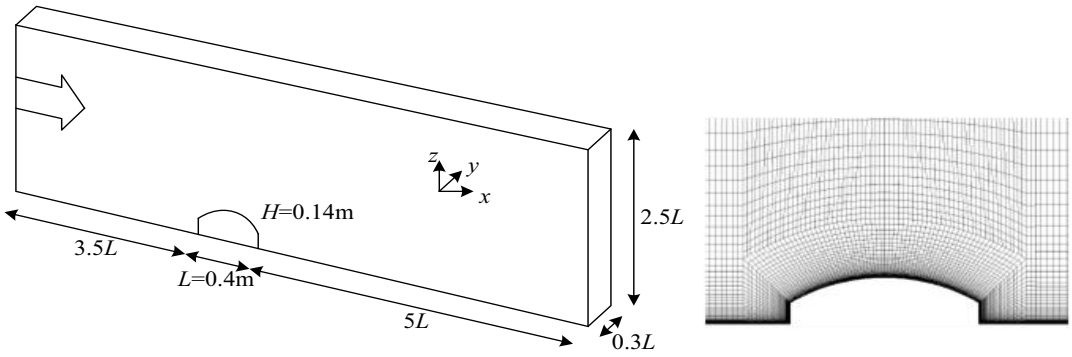

Fig.8 Computational domain and mesh arrangement

Table 2 Computational conditions

Computational domain	$9.5L(x)\times0.3L(y)\times2.5L(z)$
Inlet boundary	Inflow turbulence is generated in preliminary computational domain
Upper boundary	Zero normal velocity and zero normal gradients of other variables
Side boundary	Cyclic boundary conditions
Outlet boundary	Zero normal gradients of all variables
Floor and model surfaces	no-slip condition
Grid discretization	260 (x) ×12 (y) ×64 (z) = (199680)
Convection schemes	Second-order centered difference scheme
Time differential schemes	MARS method
Numerical algorithm	PISO algorithm
Time step	Δt = 2.0E-04 second (Courant Number：9.1E-02)

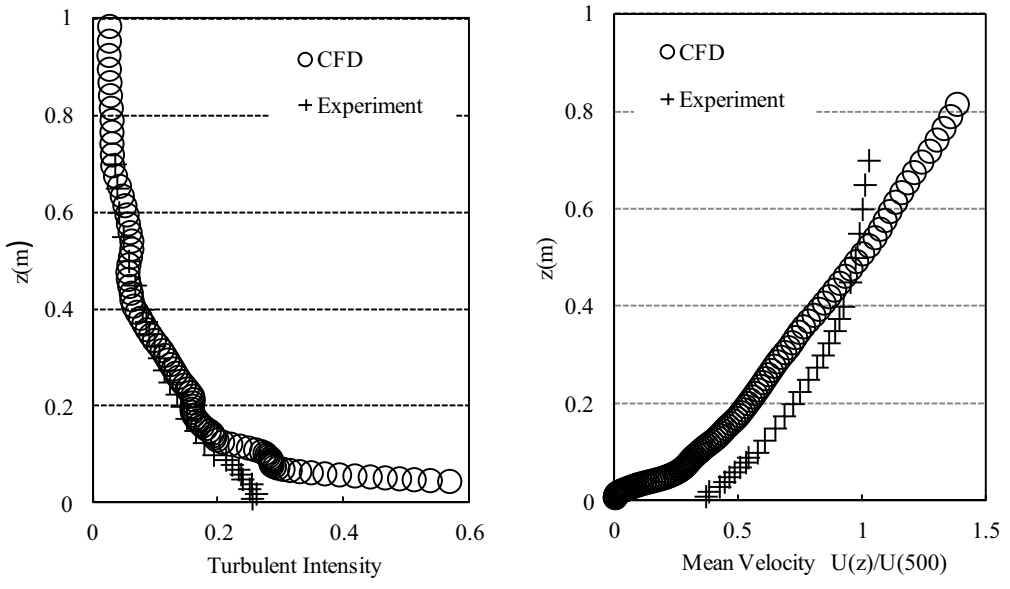

Fig.9 Comparisons of mean wind speed and turbulent intensities of CFD with wind tunnel test

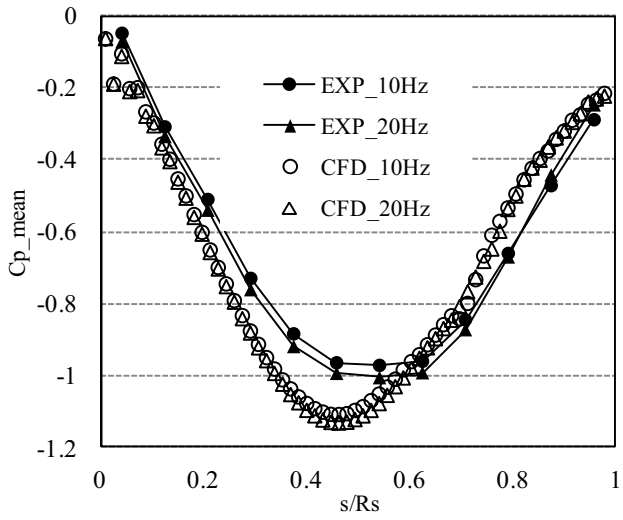

Fig.10 Comparisons between CFD simulation and wind tunnel experiment for the mean wind pressure coefficient

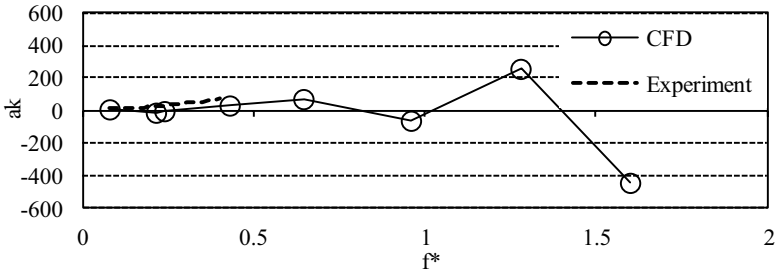

Fig.11 Comparison of aerodynamic stiffness coefficient computed by CFD with wind tunnel test

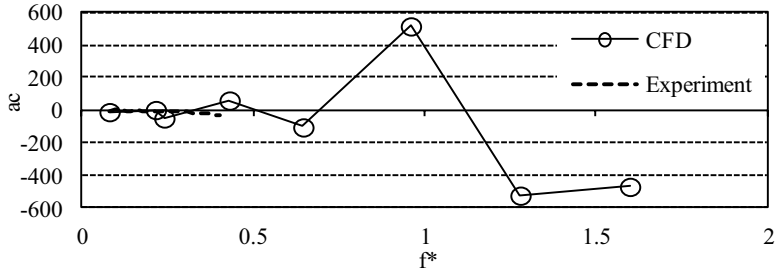

Fig.12 Comparison of aerodynamic damping coefficient computed by CFD with wind tunnel test

Based on the results of the CFD simulation, the aerodynamic stiffness and damping coefficients are calculated by using Eqs. (7) and (8). The aerodynamic stiffness coefficients a_k obtained from the LES and wind tunnel experiment are plotted in Fig. 11 for several reduced frequencies. The both results for the reduced frequency range of 0 to 0.4 are generally consistent with each other. A comparison for the aerodynamic damping coefficients a_c between the LES and wind tunnel experiment is shown in Fig. 12. Although the simulation value of a_c at f^*=0.4 is positive, the general trend of a_c with f^* in the lower f^* range is consistent with the experimental result. In a higher reduced frequency range, such as f^*>0.5 for example, the magnitudes of a_k and a_c obtained from the CFD simulation fluctuate significantly with increasing f^*. It is due to the flow-structure interaction. Such an interaction may be related to the convection velocity of pressure field on the

roof as well as to the roof's vibration speed relative to the wind speed [9]. Future studies will be necessary to discuss this problem in detail.

6 CONCLUSIONS

The unsteady aerodynamic force on a long-span vaulted roof has been investigated based on a wind tunnel experiment as well as on a CFD simulation. The main results obtained in the present study may be summarized as follows:

1) The aerodynamic stiffness and damping coefficients vary with the reduced frequency. The coefficients are influenced by the wind speed, rise/span ratio and vibration amplitude only slightly.
2) Within the limits of the present experiment, the aerodynamic stiffness is generally negative, which decreases the total stiffness of system. However, the aerodynamic damping is positive, which may result in an increase of the total damping of system.
3) As the mass of the roof increases, the effect of the unsteady aerodynamic forces on the roof's response to turbulent winds becomes less significant. And the unsteady aerodynamic forces reduced the resonant frequency and change the resonant peak.
4) The CFD simulation is a useful tool to evaluate the unsteady aerodynamic forces on the vibrating roof in a turbulent flow. The general trends of the aerodynamic stiffness and damping coefficients with the reduced frequency obtained from the CFD simulation are consistent with that from the wind tunnel experiment.

In our future study, we will construct a model of the unsteady aerodynamic force and incorporate it into the wind-resistant design of long-span curved roofs.

REFERENCES

1 Y. Taniike et al., Aerodynamic instability of an oscillation square prism, Architectural Institute of Japan, 306 (1981) 11-20.
2 T. Ohkuma et al., Mechanism of aeroelastically unstable vibration of large span roof, J. Wind Eng. Ind. Aerodyn., 42 (1990) 35-42.
3 D. J. Daw et al., Aerodynamic damping and stiffness of a semi-circular roof in turbulent wind, J. Wind Eng. Ind. Aerodyn., 32 (1989) 83-92.
4 J. Katagiria, et al., Motion-induced wind forces acting on rectangular high-rise buildings with side ratio of 2, J. Wind Eng. Ind. Aerodyn., 89 (2001) 1421-1432.
5 H. Kawai, et al., Wind-induced response of a large cantilevered roof, J. Wind Eng. Ind. Aerodyn., 83 (1999) 263-275.
6 J. Katagiria, et al., Characteristics of motion-induced wind forces during coupled across-wind and torsional vibration, J. Struct. Constr. Eng. AIJ, 543 (2001).15-22.
7 Nozawa, K et al., Large eddy simulation of the flow around a low-rise building immersed in a rough-wall turbulent boundary layer. J. Wind Eng. Ind. Aerodyn., 90 (2002) 1151–1162.
8 K. Nozawa, et al., Large eddy simulation of a turbulent boundary layer over a rough ground surface and evaluation of its fluctuating velocity profile, J. struct. Constr. Eng. AIJ, 541 (2001) 87-94.
9 Y. Uematsu et al., Ovalling oscillations of thin circular cylindrical shells in a cross flow, J. Fluids and Structures, 2 (1988) 285-307.

The Seventh International Colloquium on Bluff Body Aerodynamics and Applications (BBAA7)
Shanghai, China; September 2-6, 2012

Internal stresses in cladding support members of long-span arched roof under wind load

Zhibin Ding [a], Yukio Tamura [a], Akihito Yoshida [a]

[a] *Tokyo Polytechnic University, Iiyama 1583, Atsugi, Kanagawa, Japan*

ABSTRACT: This paper discusses the largest wind load effects on roof cladding support members of a large-span arched roof. The contributions to member stresses due to overall wind effects and local wind effects were investigated using finite element model (FEM) analysis. Wind-induced pressures including mean and fluctuating components were measured on the roof of a 1:400 scale model under a suburban boundary layer wind flow. Measured wind pressures from limited measurement points were expanded to all the structural nodes using the orthonormal coordinate system obtained from the Proper Orthogonal Decomposition (POD) method. The largest load effects (focusing on member stresses) due to overall wind effects were estimated based on the quasi-static method and compared with those estimated by the time-domain analysis of the complete finite element model directly applying the expanded wind load. The contributions due to overall wind effects and local wind effects were compared.

KEYWORDS: Roof cladding-support members; Large-span arched roof; Overall wind effects; Local wind effects; Largest wind load effects; Contributions to largest load effects.

1 INTRODUCTION

Large-span roof structures usually have the characteristics of light mass, high flexibility, slight damping and low natural frequencies. Consequently, their structural systems are more wind sensitive than conventional roofs, and wind load is very important in structural design. Extensive investigations on the characteristics of wind loads and wind-induced responses of conventional roof structures have been conducted in the past [1-4]. Recently, equivalent static wind load methods based on the quasi-steady assumption have been widely used to reproduce largest load effects for structural members [5-7] and adopted in the building codes and laws of many countries, e.g. AIJ-RLB (2004) [8], ASCE/SEI 7-10 (2010) [9], and AS/NZS 1170.2 (2002) [10]. The researches mentioned above focused mostly on estimation of overall wind effects on main structural frames of conventional roof structures.

Large-span roof structures generally consist of main structural frames, roof cladding support members and roofing members. Obviously, stresses in roof cladding support members are affected by local wind pressures and tributary areas. They may also be affected by deformations of main structural frames due to overall wind effects. However, in current wind load codes, both roof cladding support members and roofing members are usually classified as components and cladding, and the wind load effects on such members are determined by local wind pressures and tributary areas only. By ignoring the influence of wind-induced responses of main structural frames, stresses in roof cladding support members are underestimated by current wind load codes.

Arched roofs are widely used for large-span structures such as entertainment or exhibition centers, closed sport buildings, aircraft hangars, etc. The largest wind load effects on roof cladding support members on these roofs are investigated in this paper, focusing on the contributions to member stresses due to overall wind effects and local wind effects. Mean and fluctuating wind pressures were measured simultaneously from the roof of a 1:400 scale model under suburban

boundary layer wind flow. Measured wind pressures were expanded from limited measurement points to all the structural nodes using the orthonormal coordinate system obtained from the Proper Orthogonal Decomposition (POD) method. The largest member stresses due to overall wind effects were estimated based on the quasi-static method. By extracting member stresses due to overall wind effects from those estimated by time-domain analysis of the complete finite element model applying the expanded wind load directly, member stresses due to local wind effects can be obtained. This paper compares the contributions to the largest load effects (maximum and minimum member stresses) due to overall wind effects and local wind effects.

2 MEMBER STRESSES DUE TO OVERALL WIND EFFECTS OR LOCAL WIND EFFECTS

Since the roof cladding support members of large-span roofs support the roofing members, the local wind pressures acting on the tributary areas can cause member stresses, called stresses due to local wind effects. However, roof cladding support members are themselves supported by the main structural frame. The wind-induced responses of the structural frame can also influence roof cladding support member stresses, called stresses due to overall wind effects. The extent of this influence depends on the characteristics of the connections between the roof cladding support members and the main structural frame (e.g., stiffness). The actual member stresses in these members under wind load are the combined stresses due to overall wind effects and local wind effects.

The actual member stresses were calculated by time-history analyses using the Newmark-β method with a completed FE model including a main structural frame and roof cladding support members. The deformations of the main structural frame were also analyzed. Generally, roof cladding support members are much smaller than main structural frame members. The additional stiffness to the main frame due to the roof cladding support members can be neglected, so the deformation of the main structural frame can be assumed to represent the overall wind effect on the entire structure. Since the roof cladding support members were supported by the main frame, the displacements of the supporting points will cause internal stresses in the cladding support members, which were assumed as the stresses due to overall wind effects. Compared with the main structural frame, the natural frequencies and damping of such members were relatively high, and member stresses can be obtained by the quasi-static method. For a static displacement d_i occurring at a support point i, a specific load effect r (e.g. member stress) can be derived as:

$$r = R_i d_i . \tag{1}$$

Here, R_i is the value of the load effect r caused by unit displacement at a support point i. For displacements occurring at all support points i, the load effect r can be indicated as a superposition of Eq. (1). Following the quasi-static assumption, the load effect $r(t)$ can be expressed by:

$$r(t) = \sum_{i=1}^{N} R_i d_i(t) = \{R\}^T \{D(t)\} . \tag{2}$$

The largest load effect $\hat{r}$ can be indicated by:

$$\hat{r} = \{R\}^T \{\hat{D}\} . \tag{3}$$

As mentioned before, the actual member stresses in roof cladding support members under wind load are the combination of stresses due to overall wind effects and to local wind effects. Since the member stresses due to overall wind effects calculated based on the quasi-static method result from the actual member stresses, the components due to local wind effects can be extracted.

3 WIND TUNNEL EXPERIMENTS

3.1 *Experimental arrangements*

The wind tunnel experiment was carried out in a boundary layer wind tunnel at Tokyo Polytechnic University, Japan. The test section was 2.2 m wide and 1.8m high. Suburban terrain characteristics were simulated by spires and roughness elements with the power law exponent of mean wind speed α=0.16. A velocity scale of 1/5 was adopted. The mean wind speed at reference height of the model (average height of the curved roof) was 8.5m/s and the corresponding turbulence intensity was approximately 14%, as shown in Fig. 1. The measured longitudinal spectrum of wind velocity at the reference height is shown in Fig. 2.

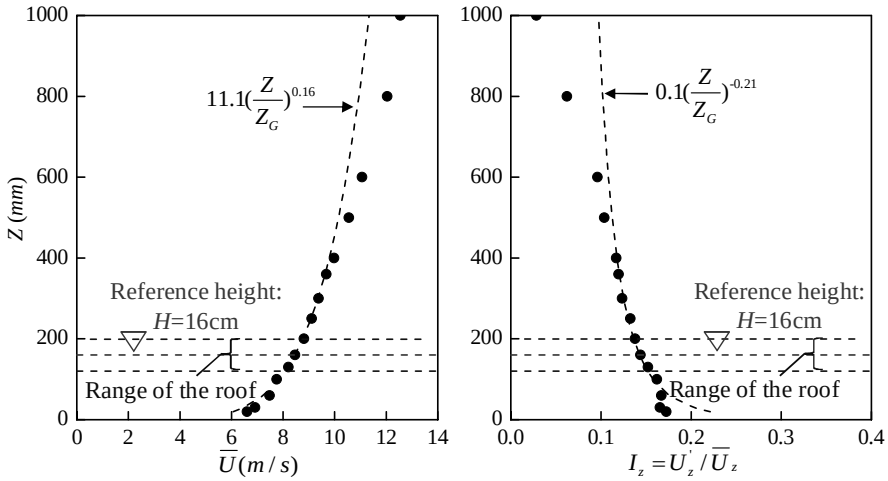

(a) Mean wind speed profile (b) Turbulence intensity profile

Figure 1. Measured longitudinal mean wind velocity and turbulence intensity profiles.

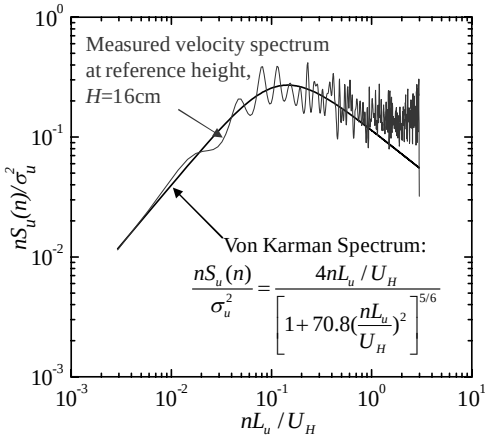

Figure 2. Measured longitudinal spectrums of wind velocity.

The geometric variables relevant to the wind loads on arched-roof buildings were: span, S; length, L; rise, h; and height of walls to eaves level, H. The geometry of the 1:400 scale wind tunnel model is illustrated in Fig. 3(a) together with the coordinate system used in this study. The model has the span S equal to 40cm, corresponding to 160m in full scale. The rise/span ratio h/S was set to 0.2 while the length to span aspect ratio L/S was 1. The wall-height was 12cm. Fig.

3(b) shows a photo of the model mounted on a turning table in the wind tunnel. Pressure taps installed on the roof's upper surface are marked with • and numbers as shown in Fig. 4.

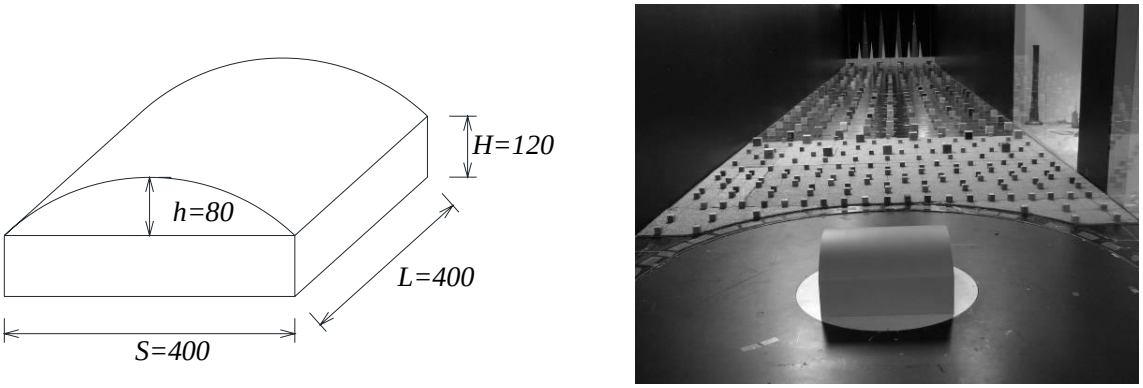

(a) (b)

Figure 3. Experimental model (unit: mm). (a) Geometric variables of arched roof model, (b) photo of model in wind tunnel.

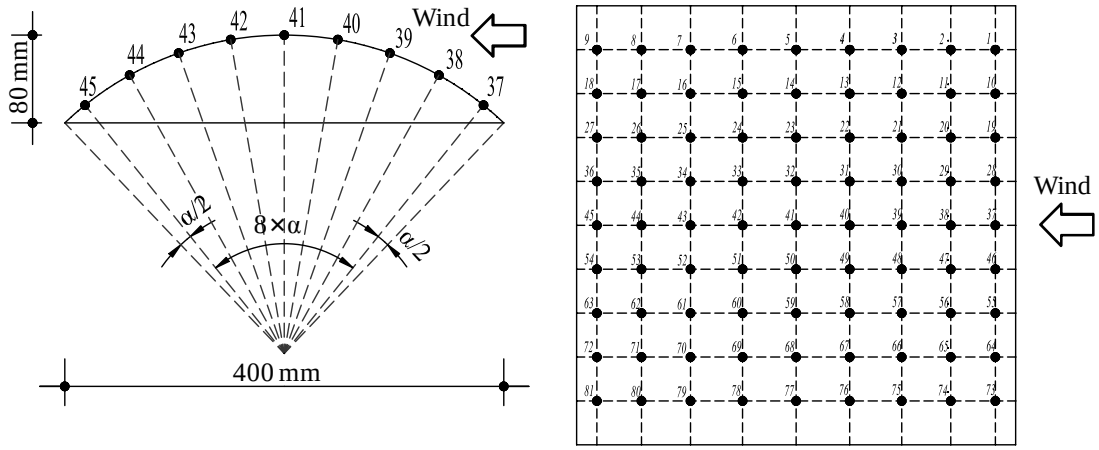

Figure 4. Distribution and numbering of measuring pressure taps for arched model.

Wind pressures were measured with a sampling frequency of 781 Hz using a multi-channel simultaneous fluctuating pressure measurement system. As the time scale of prototype vs. wind tunnel model was 1/80, the sampling frequency of the prototype was equivalent to 10 Hz. The tubing effects were numerically compensated by the gain and phase-shift characteristics of the pressure measuring system [11].

3.2 *Proper orthogonal decomposition*

Since the effect of load distribution is important to the dynamic analysis of an arched roof[12], it is necessary to expand the measured mean or fluctuating wind pressure data at limited measurement points to all the structural nodes on the surface of the roof by applying a proper orthogonal decomposition (POD) method. The eigenvalues λ_k and eigenmodes $\{\Phi\}_k$ were obtained by solving the following equation:

$$[R]\{\Phi\} = \lambda\{\Phi\} \tag{4}$$

where, $[R]$ represents the pressure space correlation matrix. The fluctuating wind pressure field $\{p\}$ can be expressed by:

$$\{p\} = \sum_{k} a_k(t)\{\Phi\}_k \tag{5}$$

where, $a_k(t)$ represents the kth orthonormal coordinate. The eigenvalue λk is the measure of the contribution of each eigenmode to the pressure mean squares, and is normalized as:

$$P_k = \frac{\lambda_k}{\sum_{j=1}^{N} \lambda_j} \tag{6}$$

The normalized eigenvalues P_k are plotted against the mode index k in Fig. 5 for wind directions θ = 0°, 45° and 90°. The accumulated values of P_k up to the 20th eigenmode were approximately 0.9 when the wind direction was 0°. In the following analysis, the wind pressures at the nodes were simulated by the first 20 eigenmodes. The values of $\{\Phi\}_k$ at the nodes of the structural model were interpolated or extrapolated from those at the tap locations given by the POD analysis.

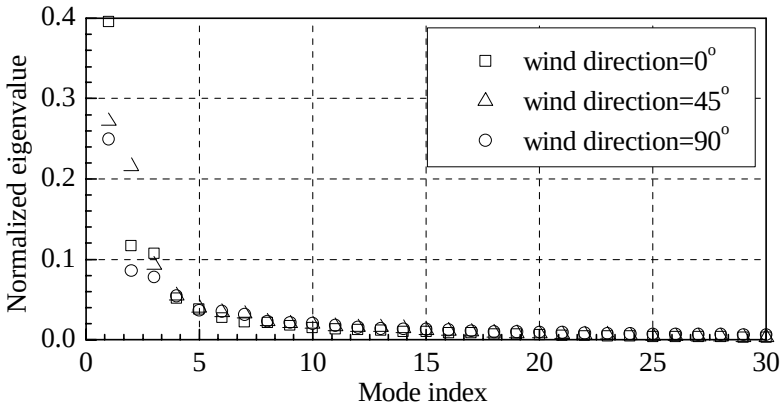

Figure 5. Normalized eigenvalues of fluctuating pressure.

4 ESTIMATION OF LARGEST STRESSES IN ROOF CLADDING SUPPORT MEMBERS

4.1 *Structural model*

As shown in Fig. 3, the wind tunnel test model was an arched roof model including walls, and pressure taps were installed only on the roof's upper surface. The prototype structure was assumed as a closed arched roof structure, in which the roof part was supported by walls or columns. Since the target in this study was the stresses in the roof cladding support members, only the roof structure was modeled by ANSYS software, following the length scale in the wind tunnel of 1:400. The finite element (FE) model of the roof structure was made up of a main structural frame and cladding support members, as shown in Fig. 6(a)-(b). All the joints on the bottom of the roof model were assumed fixed for all six degrees of freedom.

The cladding support members can also be classified as members along the length direction and members along the span direction. The members along the length direction were treated as continuous beams supported by the main structural frame. The support points are marked with ○ in Fig. 6(c). Seventeen beams were arranged at equal intervals of arch length. On the other hand, members along the span direction were connected to adjacent beams and the connection conditions were assumed as rigid.

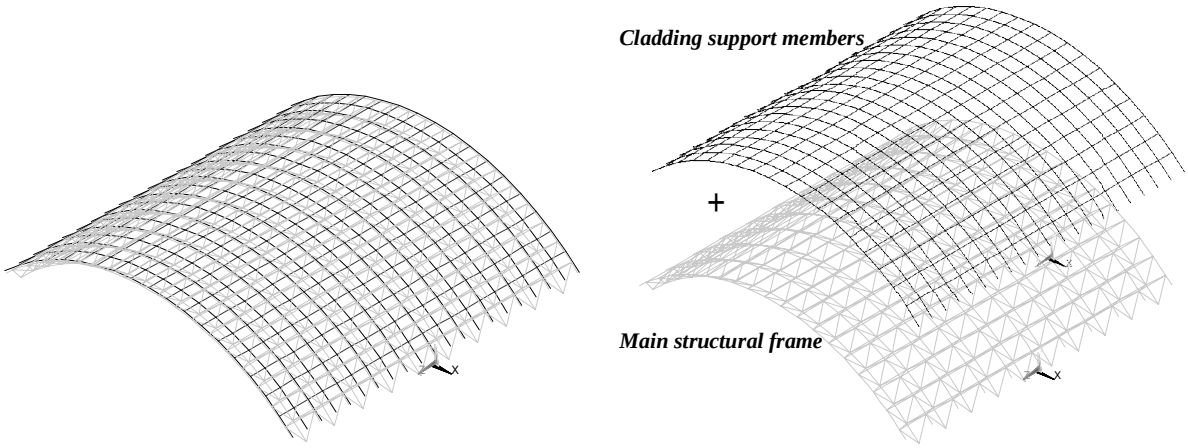

(a) Completed FE model (b) Composition of arched roof FE model

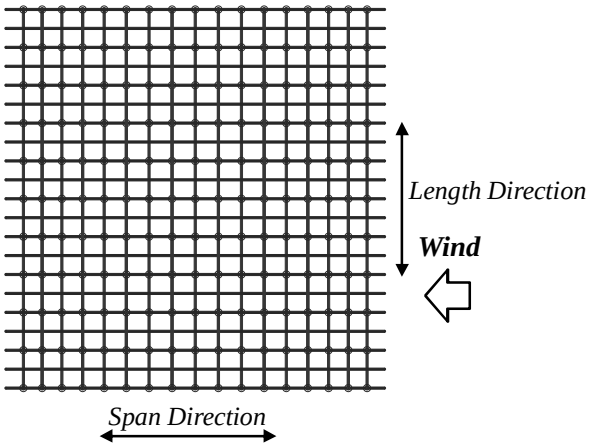

(c) Model of cladding support members

Figure 6. Structural model of arched roof structure: (a) completed FE model; (b) composition of arched roof FE model; (c) model of cladding support members.

4.2 *Computation of largest load effect in time-history analyses*

As mentioned in Sec. 2, the actual member stresses for cladding support members were computed in time-history analyses. The mean wind speed at the reference height (H=64m) was set at 42.5m/s. The critical damping ratios for the first and second modes were set to 1% to determine the two coefficients for the Raleigh damping equation. In the present study, the effects of aerodynamic damping and stiffness were not considered. Member stresses were analyzed for a duration of 11 min and the result for the first 1 min was not used for the statistical analysis because of the non-stationary state.

The loads on the arched roof were transmitted mainly by means of member axial force (hereafter referred to as AF), bending moment (hereafter referred to as BM) and shear force (hereafter referred to as SF). Torsional moment was neglected. Axial stresses in members were evaluated based on the combination of AFs and BMs, while shear stresses in members were evaluated based on SFs. Figure 7 shows the largest AFs, BMs and SFs of the cladding support members obtained from time-history analyses. In the figure, the member number is given in the order of the largest effects. Comparison of Fig. 7(a) and Fig. 7(b) shows that BMs had a more remarkable effect on

the axial stresses for members along the length direction than for members along the span direction. Correspondingly, AFs had a more remarkable effect on the axial stresses for members along span direction than for members along the length direction. Shear stresses due to SFs were more remarkable for members along the length direction.

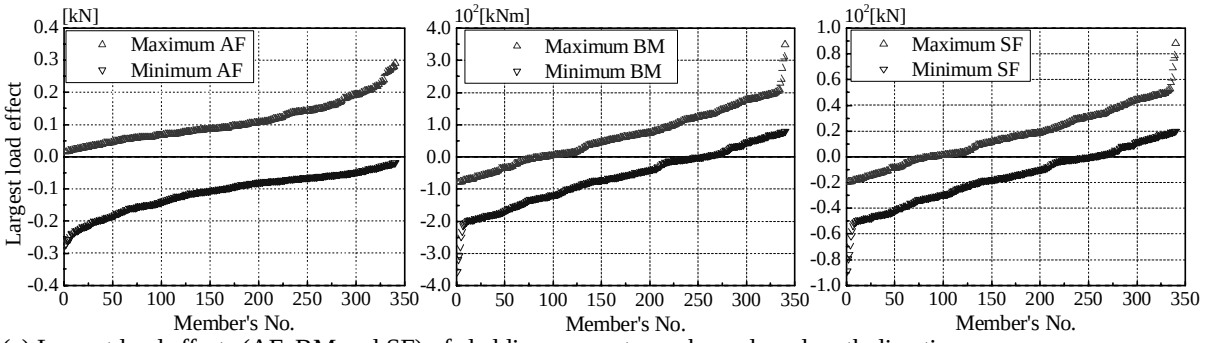

(a) Largest load effects (AF, BM and SF) of cladding support members along length direction

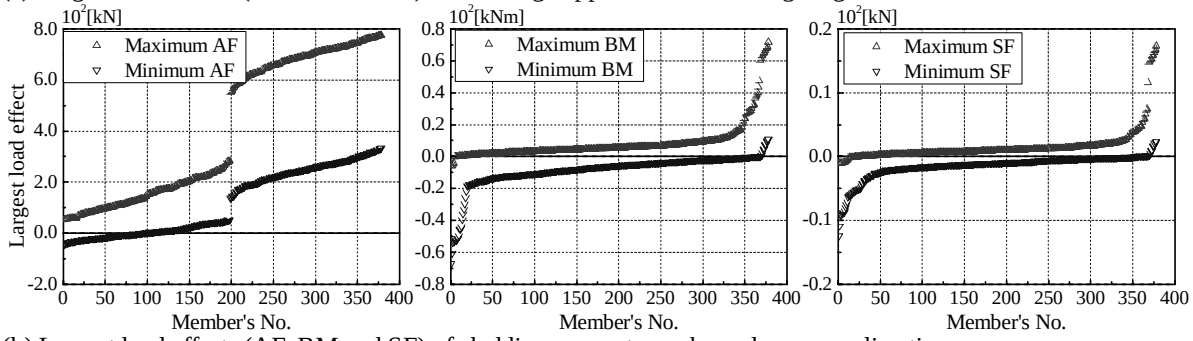

(b) Largest load effects (AF, BM and SF) of cladding support members along span direction

Figure 7. Comparison of largest AFs, BMs and SFs obtained from time-history analyses of cladding support members.

4.3 *Contribution ratios for largest member stresses*

The displacements $\{D(t)\}$ in Eq. (2) of the support points connecting the main structural frame and the cladding support members were also obtained during the time-history analyses of the completed FE model. Only the FE model of cladding support members was used to obtain the $\{R\}$ in Eq. (2), under constraint conditions consistent with those in the completed FE model. The member stresses due to overall wind effects can be obtained with the known $\{R\}$ and $\{D(t)\}$, as mentioned in Sec. 2.

The contribution ratios of overall wind effects and local wind effects for the largest member stresses are defined by:

$$\gamma_o = \frac{\hat{r}_o}{\hat{r}}, \quad \gamma_l = 1-\gamma_o = 1-\frac{\hat{r}_o}{\hat{r}}. \tag{7}$$

Here, γ_o and γ_l are the contribution ratios of overall wind effects and local wind effects respectively. $\hat{r}$, $\hat{r}_o$ represent the actual largest load effect and the largest load effect due to the overall wind effects only, which were focused on the member stresses (maximum and minimum member stresses).

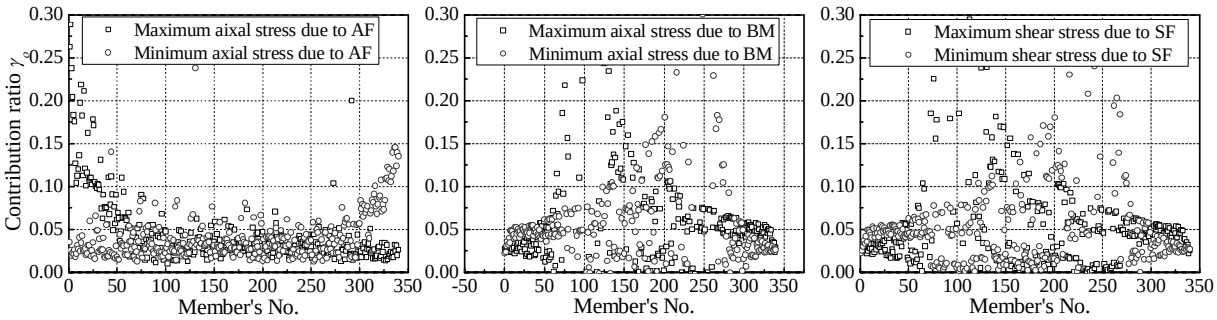

Figure 8. Contribution ratios of overall wind effects for the largest member stresses of members along length direction

Contribution ratios of overall wind effects for the largest member stresses of members along length direction are shown in Fig. 8. As in Fig. 7, the member number is given in the order of the largest effects obtained from the time-history analyses in Fig. 8. The contribution ratios of overall wind effects for the largest member stresses were less than 0.15 for most cladding support members. This means that current wind load codes are not so bad for most cladding support members, which don't take account of the contribution of overall wind effects for largest member stresses. However, the contribution ratio γ_o can be larger than 0.15 for several members and the largest value of γ_o was about 0.3, also shown in Fig. 8. Considering only the contribution of local wind effects for such members would remarkably underestimate the largest member stresses.

5 CONCLUDING REMARKS

Internal stresses in cladding support members of long-span arched roofs under wind load were investigated by time-history analyses of the completed FE model, including main structural frame and cladding support members. Contributions of overall wind effects and local wind effects to the largest member stresses were discussed:

1) The displacements of the supporting points connecting the main structural frame and cladding support members were assumed to represent the overall wind effects of the long-span roof structure.
2) Cladding members stresses due to the overall wind effects were evaluated by a quasi-static method.
3) The contribution ratios of overall wind effects to the largest member stresses were less than 0.15 for most cladding support members. However, there were members for which the contribution ratio can be larger than 0.15 and the largest value was about 0.3. Considering only the contribution of local wind effects to such members would remarkably underestimate the largest member stresses.

6 ACKNOWLEDGEMENTS

This study was funded by the Ministry of Education, Culture, Sports, Science and Technology, Japan, through the Global Center of Excellence Program, 2008-2012, which is gratefully acknowledged.

7 REFERENCES

1 Uematsu, Y., Yamada, M., Inoue, A., Hongo, T., Wind loads and wind-induced dynamic behavior of a single-layer lattice dome, Journal of Wind Engineering and Industrial Aerodynamics 66 (1997), 227-248.
2 Uematsu, Y., Kuribara, O., Yamada, M., Sasaki, A., Hongo, T., Wind-induced dynamic behavior and its load estimation of a single-layer latticed dome with long span, Journal of Wind Engineering and Industrial Aerodynamics 89 (2001), 1671-1687.
3 Nakayama, M., Sasaki, Y., Matsuda, K., Ogawa, T., An efficient method for selection of vibration modes contributory to wind response on dome-like roofs, Journal of Wind Engineering and Industrial Aerodynamics 73 (1998), 31-43.
4 Li, Y.Q., Tamura, Y., Yoshida, A., Katsumura, A., Cho, K., Wind loading and its effects on single-layer reticulated cylindrical shells, Journal of Wind Engineering and Industrial Aerodynamics 94 (2006), 949-973.
5 Zhou, Y., Kareem, A., Gust loading factor: new model. J. Struct. Eng., ASCE 127 (2001), 168-175.
6 Holmes, J.D., Effective static load distributions in wind engineering, Journal of Wind Engineering and Industrial Aerodynamics 90 (2002), 91-109.
7 Katsumura, A., Tamura, Y., Nakamura, O., Universal wind load distribution simultaneously reproducing largest load effects in all subject members on large-span cantilevered roof, Journal of Wind Engineering and Industrial Aerodynamics 95 (2007), 1145-1165.
8 AIJ-RLB, 2004. AIJ Recommendations for Loads on Buildings. Architectural Institute of Japan.
9 American Society of Civil Engineers, 2010. ASCE Standard ASCE/SEI 7-10, Minimum Design Loads for Buildings and Other Structures. Reston, Virginia, USA.
10 Australian/New Zealand Standard, 2002. Structural design actions, Part 2: wind actions, AS/NZS 1170.2.
11 Yoshida, A., Tamura, Y. and Kurita, T., Effects of bends in a tubing system for pressure measurement, Journal of Wind Engineering and Industrial Aerodynamics 89 (2001), 1701-1716.
12 Li, Y.Q., Tamura, Y., Equivalent static wind load estimation in wind-resistant design of single-layer reticulated shells, Wind and Structures , 2005, 8 (6), 443-454.

The Seventh International Colloquium on Bluff Body Aerodynamics and Applications (BBAA7)
Shanghai, China; September 2-6, 2012

Moving downburst effects on long-span roof structure

Chen Yong, Liu Guoguang, Sun Bingnan

College of Civil Engineering and Architecture, Zhejiang University,
No. 388, Yuhangtang Road, Hangzhou, China.

ABSTRACT: Taking the interaction of moving downbursts with buildings into consideration is rather difficult in moving-downbursts-induced structure vibration analysis. By assuming that the jet velocity is proportional to the wind velocity in the fluid field, deterministic-stochastic hybrid model is utilized to generate the fluctuating jet velocity. Consequently, by using the time-varying mean wind pressure coefficients, the wind loading that considers the fluid-structure interaction is attained. Furthermore, the relationship between the mean wind pressure coefficient and the ratio of jet velocity to the translating speed is studied. The comparison of structural dynamics response caused by moving downburst and atmosphere bound layer wind is conducted through a defined downburst factor. It is found that the downburst factor increase with the increment of the structural natural frequency.

KEYWORDS: moving downbursts, CFD simulation, dynamic mesh, wind loading, structural vibration, deterministic-stochastic hybrid model.

1 INTRODUCTION

Thunderstorm downburst is a transient extreme wind, which is a strong downdraft spreading form the center to periphery and occurs during the thunder weather usually. It caused numerous structural destructions worldwide [1]. The studies in recent decades had shown that the thunderstorm downbursts would cause a higher near-surface wind velocity than that in atmosphere bound layer (ABL) winds. And the corresponding wind loading caused has gained many attentions.

The characteristic of wind field of steady thunderstorm has achieved comprehensive understanding. Experimental and numerical results those attained by utilizing the impinging wall jet model rather than vortex mode, showed reasonable agreements with the limited full-scale data [2-4]. For convenience of wind loading studies, many researchers (e.g. Oseguera and Bowles [5], Vicroy[6], Wood[7], etc.), proposed empirical models to describe the wind profiles. With consideration of wind load caused by moving downbursts, vector summation method and deterministic-stochastic hybrid model (DSHM) are mostly used. The former was proposed by Holmes and Oliver to simulate the mean time history of horizontal wind velocity in a travelling downburst [8]. The latter was proposed by Chen and Letchford to simulate the time history of horizontal wind velocity with random fluctuation [9]. So far, the study on the wind field of moving thunderstorm and its effects to structure is scarce. By utilizing a moving wall jet experimental device, Letchford and Chay obtained the transient pressure field on a cube immersed in a moving downburst [10]. Sengupta contributes to computational fluid dynamics (CFD) study on moving down bursts effecting on buildings by using dynamic mesh method [11]. For purpose of using a uniformed equation to consider both gust front wind and conventional wind, Kwon and Kareem presented a new framework of wind loading [12].

In this paper, the dynamics of buildings subjected to moving downbursts are studied. The surface wind pressure of buildings, which is obtained by dynamic-mesh-method-based CFD simulation, is utilized to determine wind loading. By assuming that the quasi-steady assumption is satisfied in moving down burst, the fluctuation component of the wind pressure is simulated ac-

cording to DSHM. The structural dynamics caused by moving downbursts are compared with that by ABL winds, through using a designated downburst factor. In addition, the downburst factor varying with the characteristic of structure dynamics and moving downburst are analyzed.

2 DOWNBURST FACTOR

The conventional gust loading factor (G_{GLF}) is defined as

$$G_{\mathrm{GLF}} = \frac{\hat{x}_{\mathrm{B\text{-}L}}}{\overline{x}_{\mathrm{B\text{-}L}}} \tag{1}$$

where $\hat{x}_{\mathrm{B\text{-}L}}$ and $\overline{x}_{\mathrm{B\text{-}L}}$ represent maximum and mean displacement of a structure subjected to ABL wind. G_{DB} is defined as a ratio of maximum displacements in the moving downbursts to that in ABL winds. Thus

$$G_{\mathrm{DB}} = \frac{\hat{x}_{\mathrm{DB}}(z,t)}{G_{\mathrm{GLF}} \cdot \overline{x}_{\mathrm{B\text{-}L}}(z)} \tag{2}$$

where $\hat{x}_{\mathrm{DB}}(z,t)$ is the maximum displacement of a structure subjected to moving downbursts; z and t are height and time respectively.

In order to comparing the downburst factors those computed using different jet velocities V_{jet}, the displacement of structure under the boundary layer wind load is therefore

$$\overline{x}_{\mathrm{B\text{-}L}}(z) = \left(\frac{V_{\mathrm{jet}}}{V_{\mathrm{jet\_0}}}\right)^2 \overline{x}_{\mathrm{B\text{-}L\_0}}(z) \tag{3}$$

where $\overline{x}_{\mathrm{B\text{-}L\_0}}(z)$ is the displacement of structure subjected to the reference ABL wind; $V_{\mathrm{jet\_0}}$ is the jet velocity when the wind pressure at the height of 10 m is equal to the reference wind pressure in code.

The displacement of structure under downburst can be decomposed into mean displacement $\overline{x}(z,t)$ and fluctuating displacement $\tilde{x}(z,t)$.

$$x_{\mathrm{DB}}(z,t) = \overline{x}_{\mathrm{DB}}(z,t) + \tilde{x}_{\mathrm{DB}}(z,t) \tag{4}$$

Then, the maximum displacements in the downburst can be rewritten as

$$\hat{x}_{\mathrm{DB}}(z,t) \approx \max\left[\overline{x}_{\mathrm{DB}}(z,t)\right] + \max\left[\tilde{x}_{\mathrm{DB}}(z,t)\right] \tag{5}$$

By substitution of Equation 6 into Equation 2, we have

$$G_{\mathrm{DB}} \approx G_{\mathrm{DB\_Sum}} = \overline{G}_{\mathrm{DB}} + \tilde{G}_{\mathrm{DB}}, \quad \overline{G}_{\mathrm{DB}} = \frac{\max\left[\overline{x}_{\mathrm{DB}}(z,t)\right]}{G_{\mathrm{GLF}} \cdot \overline{x}_{\mathrm{B\text{-}L}}(z)}, \text{ and } \quad \tilde{G}_{\mathrm{DB}} = \frac{\max\left[\tilde{x}_{\mathrm{DB}}(z,t)\right]}{G_{\mathrm{GLF}} \cdot \overline{x}_{\mathrm{B\text{-}L}}(z)} \tag{6}$$

where $\overline{G}_{\mathrm{DB}}$ and $\overline{G}_{\mathrm{DB}}$ are designated as mean and fluctuating downburst factors, respectively; the sum of them is the synthesis downburst factor $G_{\mathrm{DB\_Sum}}$.

By using the truncated modes, the displacement has a form of

$$x(z,t)=\phi(z)q(t)=\left[\phi_1(z),\phi_2(z),\cdots,\phi_i(z)\right]\times\left[q_1(t),q_2(t),\cdots,q_i(t)\right]^T \tag{7}$$

Where $\phi_i(z)$ is the *i*th mode; $q_i(t)$ is the corresponding time varying modal displacement. Thus we define the modal-decomposition-based downburst factor $G^{\mathrm{D}}_{\mathrm{DB}\_i}$ as

$$G^{\mathrm{D}}_{\mathrm{DB}\_i}=\frac{\max\left[\phi(z)q_{\mathrm{DB}}(t)\right]}{\phi(z)q_{\mathrm{B\text{-}L}}}=\frac{\max\left[\phi_1(z)q_{\mathrm{DB1}}(t)+\phi_2(z)q_{\mathrm{DB2}}(t)+\cdots+\phi_i(z)q_{\mathrm{DBi}}(t)\right]}{\phi_1(z)q_{\mathrm{B\text{-}L1}}+\phi_2(z)q_{\mathrm{B\text{-}L2}}+\cdots+\phi_i(z)q_{\mathrm{B\text{-}Li}}} \tag{8}$$

3 NUMERICAL SIMULATION

3.1 *Setup and numerical simulation parameters*

We utilized Fluent 6.2, which is commercial CFD software, to achieve a numerical approach. The moving downburst with a jet diameter of 500 m is simulated based on impinging wall jet model, as shown in Figure 1. The jet height is equal to the jet diameter. A long span flat roof whose size is 200×200×20m (length×width×height) is put in the fluid field.

Figure 1 shows the computational model and boundary conditions for downburst simulation. The downburst is modeled as a round jet, impinging onto a flat plate. The size of the three-dimensional computational domain is 18×8×5 D_{jet}, where D_{jet} is the jet diameter. The downburst is simulated to move a distance of 10 D_{jet} in the longitudinal direction.

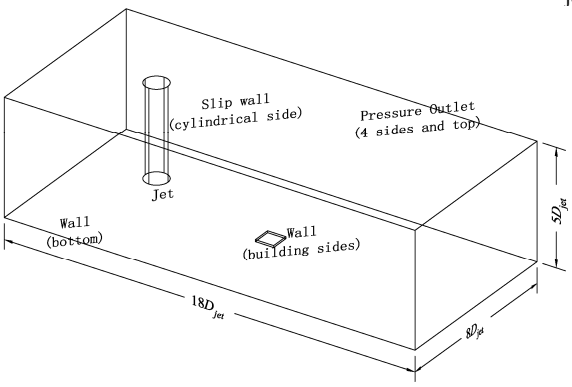

Figure 1. Computational model.

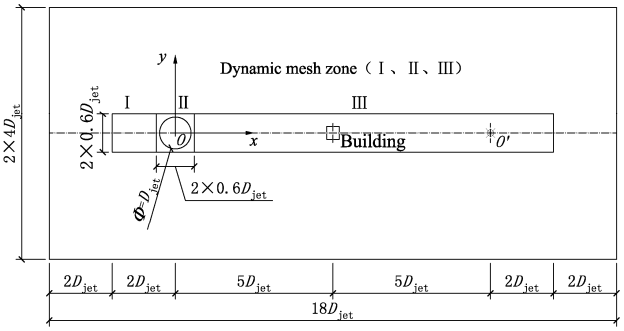

Figure 2. Schematic diagram of dynamic mesh zone.

The dynamic mesh model can be used to simulate the flows where the shape of the domain is changing with the time due to the motion of the boundaries [13]. The motion of the boundary is described by utilizing either boundary profiles, user-defined functions (UDFs), or some specific equations. Based on the motion of boundary, the volume mesh of the domain is automatically updated. Accordingly, the dynamic mesh model is capable of simulating the moving downbursts.

As shown in Figure 2, a dynamic mesh zone is separated from the domain by some non-conformal mesh interface. The dynamic mesh zone is divided into three parts: Ⅰ, Ⅱ and Ⅲ. The part Ⅱ is a rigid body motioning region, and the others are deforming regions. The velocity of the part Ⅱ is specified by UDF. In order to study the wind pressure distribution of the roof, the downburst moves from point *O* to the point *O'*. Due to the motion of part Ⅱ, the cells in part Ⅰ and Ⅲ would be distorted. The layering method is used to update the volume mesh based on predefined split and collapse factors. The split and collapse factors are 0.4 and 0.4, respectively.

The air density is set to be 1.225 kg/m^3 and viscosity 1.7894×10^{-5} kg/ (m·s). The RNG k-ε model is used to simulate the moving downburst. The default model constants in RNG k-ε model are used. For RNG k-ε model, the SIMPLE algorithm is used for solving the pressure-velocity

coupling equations. A standard scheme is employed for pressure discretization, and a 1st order upwind scheme is employed for momentum, TKE and TDR. The residual errors for all the variables are set to be 1×10^{-4}, except for continuity 1×10^{-3}.

All grids are structured grids, except for the meshes in part Ⅱ. Because of the curved boundary in part Ⅱ, the adaptable unstructured grids are used. For the region near the ground and the building faces, enhanced wall treatment is adopted and a fine mesh is used to ensure the $y^+ \le 1$. Figure.3 shows the mesh used in this simulation and the local mesh around wall.

The validity of the numerical simulation is verified by using different domain and grid sizes in the steady-state simulations. For unsteady cases, time steps dependency tests are performed and a non-dimensional time steps are chosen.

$$\Delta t^* = V_t \Delta t / D_{\text{jet}} = 0.008 \tag{9}$$

The jet velocity ratio V_{TJ} is defined as the ratio of the jet translating speed V_{T} to jet velocity V_{jet}. In order to numerically predict the effects of jet velocity ratio of a moving downburst on the roof, two groups of simulations are conducted. In the first group, the jet velocities are kept as 47.5 m/s, and the translating speeds are taken from the followings: 5.0, 10.0, 12.5, 15.0, 17.5, 20.0, 22.5, 23.75, 25.0 m/s. In the other group, the translating speeds are kept as 10.0 m/s, and the jet velocities are varied from the followings: 28.3, 30.0, 40.0, 50.0 m/s.

As shown in the Figure.3, a total of 81 measuring points are uniformly distributed on the roof, and 9 critical measuring points are marked with numbers. The time-varying mean wind pressure coefficient in moving downbursts is defined as

$$\bar{C}_{\text{P}i}(t) = \bar{P}_i(t) / \left(0.5\rho V_{\text{jet}}^2\right) \tag{10}$$

where $\bar{P}_i(t)$ and $\bar{C}_{\text{P}i}(t)$ are mean wind pressure and wind pressure coefficient of the *i*th measuring point, respectively.

The displacement of downburst is non-dimensionalized by the jet diameter.

$$l^* = V_{\text{t}} t / D_{\text{jet}} \tag{11}$$

where V_{t} is the translating speed.

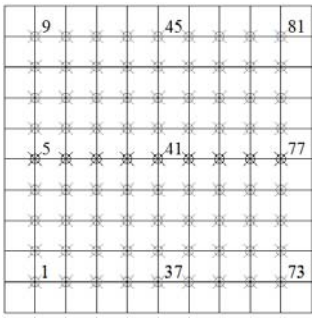

Figure 3. Layout of the measuring points.

3.2 *Results*

At the initial time, the distance ($r_{\text{D-R}}$) from the center of downburst to the center of roof is $5D_{\text{jet}}$. Then, it would be varied with the motion of the downburst. Consequently, and the mean wind pressure distribution on the roof would be time varying. The mean wind pressure distribution on the roof varied with the motion of downburst is shown in Figure.4.

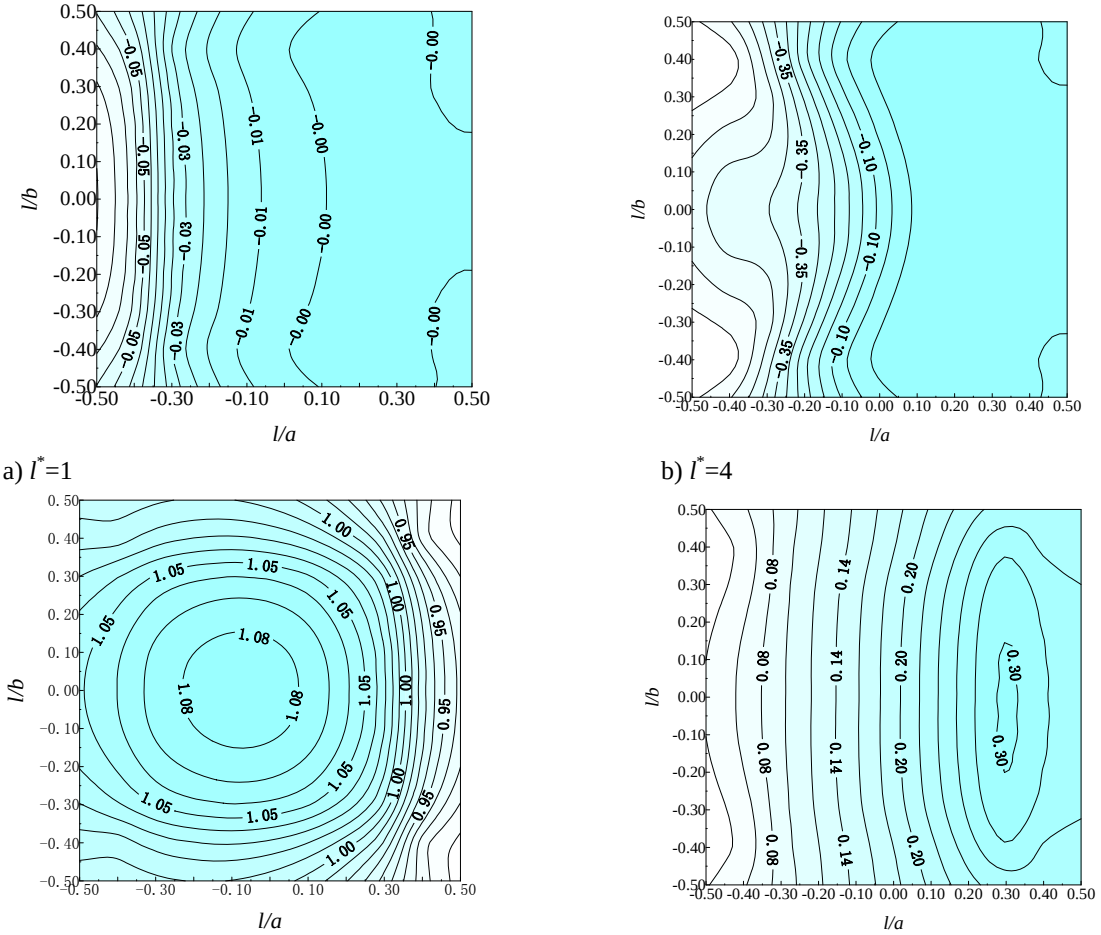

a) l^*=1 b) l^*=4

c) l^*=5 d) l^*=6

Figure. 4 Wind pressure distribution on the roof

While the downburst travels $1D_{jet}$, the roof is still far away from the downburst. The pressure of the most regions on the roof is nearly zero, whereas there is a relatively large negative pressure in the windward area. While the downburst travels $4D_{jet}$, that is say $r_{D\text{-}R}$ is equal to $1D_{jet}$, the pressure distribution is similar to the case of l^*=1, but the negative pressure area get bigger and the minimal negative pressure value become smaller. When the downburst travels $4D_{jet}$, the roof is quite under the center of the downburst, and the pressure distribution is significantly different from others. The whole roof is subjected to positive pressure and the maximum value is about 1.0. When the downburst travels $6D_{jet}$, $r_{D\text{-}R}$ is again equal to $1D_{jet}$, but the distribution is quite different from the case that l^*=1. The values of the pressures in whole roof are positive.

The time histories of mean wind pressures of the measuring points 1, 37, 73 (these three points is on the outmost side line), 5, 41, and 77 (these three points is on the middle line) are chosen to be surveyed. The time histories of mean wind pressure coefficients of all six measuring points for V_{jet}=47.5 m/s and V_t=10.0 m/s are shown in Figure 5. The trend of all six curves are similar, and they all reach their peak values around l^*=5.0.

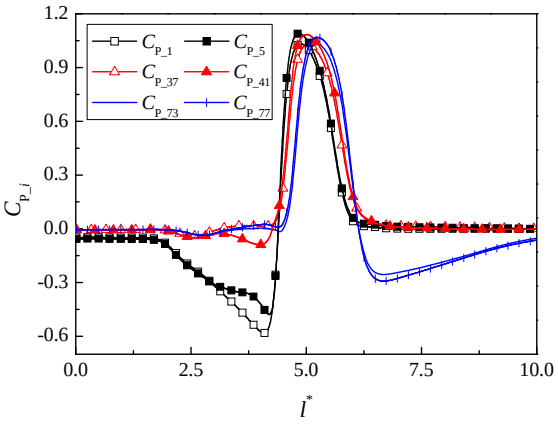

Figure. 5 Time histories of $\overline{C}_{Pi}$.

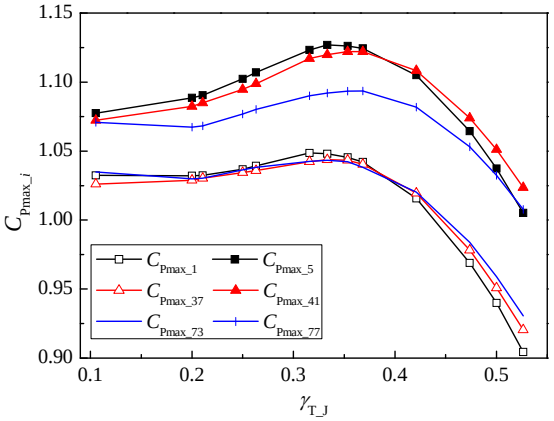

Figure. 6 γ_{T_J} versus the peak value of $\overline{C}_{Pi}$.

The relationship between the jet velocity ratios and the peak value of mean pressure coefficient are shown in Figure 6. It is shown that the peak pressure near middle line is greater than that near the side line. The peak pressure increases with the increment of the jet velocity ratio while the jet velocity ratio is less than 0.316. And it decreases in case of that the jet ratio is greater.

4 DYNAMIC RESPONSE OF THE ROOF

4.1 *Simulation of wind loading*

By using $\overline{C}_{Pi}$, it is easy to achieve the time history of mean wind pressure, according to Equation 10. Nevertheless, in order to conduct structural dynamic analysis, the fluctuation characteristics of wind should be considered. It is assumed that the quasi-steady assumption is still satisfied in a moving downbursts field. Accordingly, the fluctuation component of the wind pressure is proportional to the jet velocity. Thus, we have

$$P_i(t) = 0.5\rho V_J^2 \overline{C}_{Pi}(t) \tag{12}$$

where P_i is the wind pressure of the *i*th surface zone of the building, and V_J is the jet velocity with fluctuation. Note that the jet velocity is proportional to the wind velocity (or horizontal wind velocity) in the fluid field. It is known, DSHM is capable of simulating the horizontal wind velocity in the fluid field of moving downburst. It assumes that the wind speed could be decomposed into a mean wind speed and a fluctuating wind speed. That is to say

$$U(z,t) = \overline{U}(z,t) + \tilde{U}(z,t) \tag{13}$$

where $U(z,t)$ is the wind speed at position *z* and time *t*; $\overline{U}(z,t)$ is a deterministic function and means the mean wind speed; $\tilde{U}(z,t)$ is the fluctuation with zero mean and a stochastic process.

In DSHM, it is also assumed that the fluctuation can be obtained by a stationary random process multiplied by a modulation function. That is to say

$$\tilde{U}(z,t) = a(z,t)\lambda(z,t) \tag{14}$$

where $a(z,t) = 0.10\overline{U}(z,t)$ and is a modulation function; $\lambda(z,t)$ is a stationary Gaussian stochastic process, and could be numerically generated by utilizing the Kaimal spectrum, as shown in Figure 7.

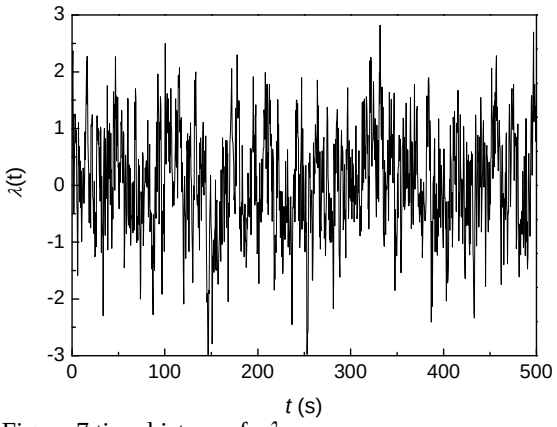

Figure.7 time history of λ.

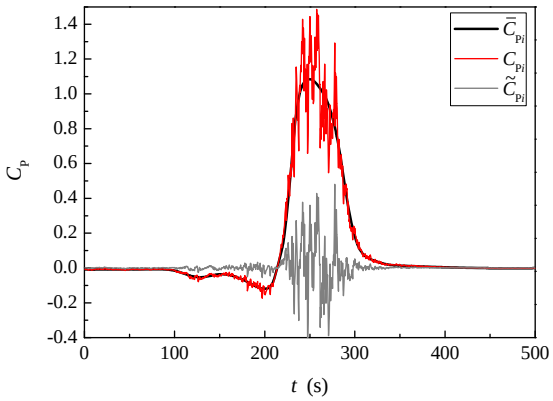

Figure.8 Time histories of wind pressure coefficients.

Note that $U(z,t)$ is proportional to V_J, we have

$$V_J = V_{jet} \cdot [1 + 0.1\lambda(t)] \tag{15}$$

By substituting Equation 15 into Equation 12, the time histories of wind pressure that contains the fluctuation could be attained. Then the wind pressure coefficient would be

$$C_{Pi}(t) = P_i(t) \Big/ \left(0.5\rho V_{jet}^2\right) \tag{16}$$

Figure 8 shows the time histories of three wind pressure coefficient C_{Pi}. And the fluctuation wind pressure coefficient in Figure 8 is defined as

$$\tilde{C}_{Pi} = C_{Pi} - \bar{C}_{Pi}. \tag{17}$$

Finally, the concentrated load on the *i*th node of the roof can be expressed as:

$$F_i(t) = P_i(t) \cdot A_i \tag{18}$$

where A_i is the represented area of the *i*th node.

4.2 *ABL wind load and the finite element model (FEM) of the roof*

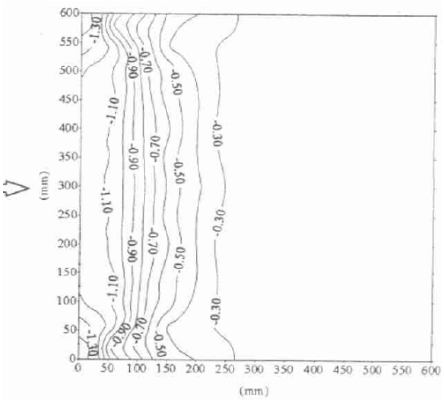

Figure. 9 Wind pressure distribution of the Lu's roof [14].

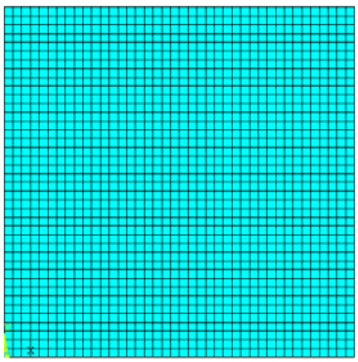

Figure. 10 Element division of the roof.

The result from a rigid model wind tunnel test for a roof, which is conducted by Lu [14], is tread as ABL wind load for the roof. The wind pressure distribution of the Lu's roof is shown in the

Figure9. In addition, Lu proposed an empirical estimation of gust loading factor that is a function of the natural frequency of the structure. It is

$$G_{\mathrm{GLF}} = -0.1348 f^5 + 1.0241 f^4 - 3.1205 f^3 + 4.855 f^2 - 4.046 f + 2.8668 \quad (19)$$

where f is the natural frequency.

The dynamic response of the roof is analyzed in ANSYS 10.0. The roof is simply supported on four sides, and the effects of primary and secondary beam are ignored. The elastic modulus and Poisson's ratio are, respectively, 3.0×10^{10} N/m^2 and 0.31, and the damping ratio of the roof is 0.05. The roof is divided into 1600 element, by using the shell 63.

According to the shell theory, the frequencies of plate are affected by its thickness and surface density. The thickness and density of the roof are changed to get the different natural frequency. Totally, 9 plates are studied and their natural frequency varied from 0.467 Hz to 2.015 Hz.

4.3 *Results and discussion*

With consideration of a moving downburst whose jet velocity and translating speed are 47.5 m/s and 10 m/s respectively, the time histories of displacement and acceleration at the middle of the roof are shown in Figure11 and Figure 12 respectively. In case of moving downbursts, larger displacement and acceleration are observed. The parameters of the moving downburst in following Figures 13-16 are fixed at that V_{jet}=47.5 m/s and V_{t}=10 m/s.

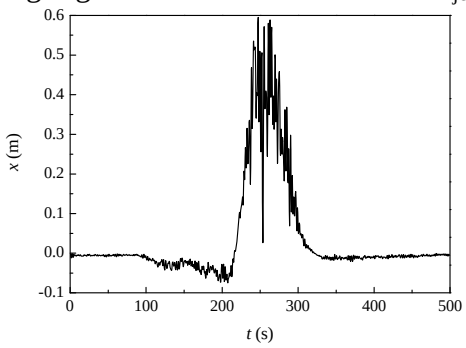

Figure. 11 Time history of the displacement.

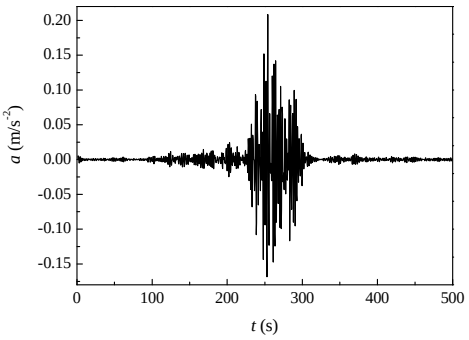

Figure. 12 Time history of the acceleration.

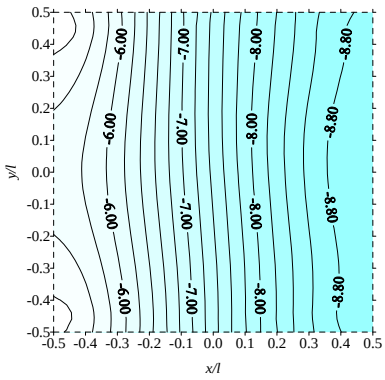

Figure. 13 distribution of G_{DB0} on the roof.

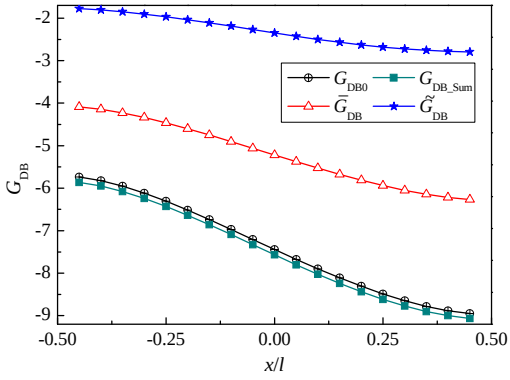

Figure. 14 G_{DB} on the along-wind middle line.

Figure 13 shows the distribution of G_{DB0} on the roof. G_{DB0} is obtained directly according to Equation 2, and is designated as direct downburst factor. Figure 14 shows four kinds of downburst factors of the along-wind middle line. The four downburst factors increase with the in-

crease of x, and the synthesis downburst factor is close to the direct downburst factor. So the dynamic response of downburst on structure could be decomposed into two parts: mean and fluctuation. Additionally, the absolute value of the direct downburst factor are quit larger than 1. It means that the effect of the moving downburst is quit larger than that of ABL wind.

Figure.15 shows the distribution of G_{DB0} and $G_{\mathrm{DB}i}^{D}$ on the along-wind middle line. The G_{DB1}^{D} is a constant at any point. With the increase of the order, the $G_{\mathrm{DB}i}^{D}$ gets closer to the G_{DB0}. The curves of $G_{\mathrm{DB}i}^{D}$ intersect at the middle point of the roof (x/l=0). It means that using the first mode would accurately capture the factor for the center point, whereas first four modes should be taken into consideration for the other locations.

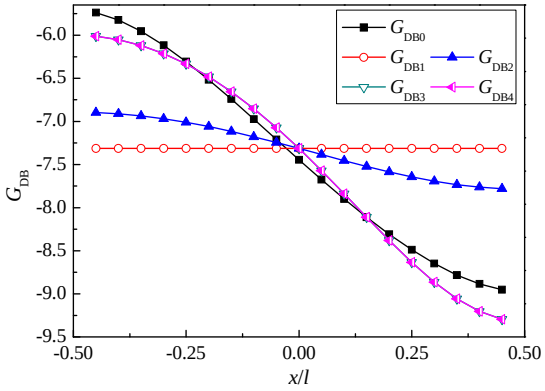

Figure. 15 Comparisons of G_{DB0} and $G_{\mathrm{DB}i}^{D}(z)$.

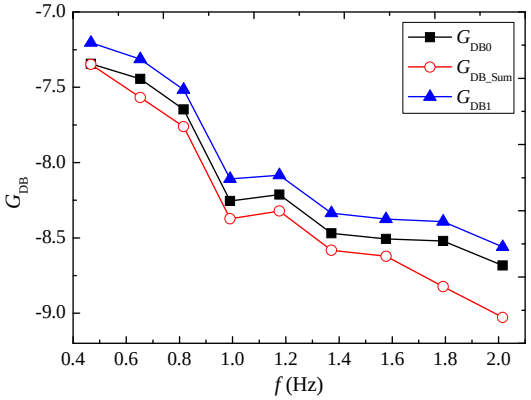

Figure. 16 G_{DB} Varied with natural frequency.

Figure.16 shows the variation of G_{DB0}, $G_{\mathrm{DB\_Sum}}$ and G_{DB1}^{D}, at the middle point of the roof, with the natural frequency of the roof. It is observed all three downburst factors increase with the increasing of natural frequency.

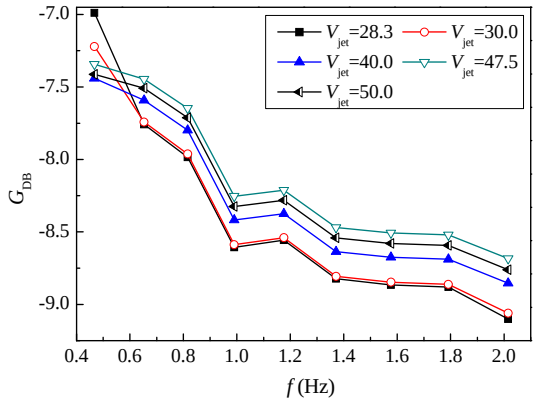

Figure. 17 G_{DB0} varied with jet velocities

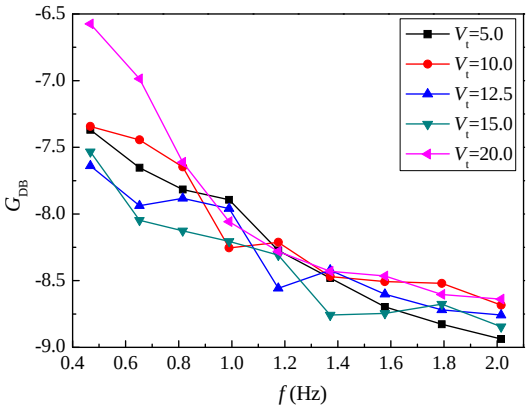

Figure. 18 G_{DB0} varied with translating speeds

Fixing the translating speed at V_{t}=10 m/s, Figure 17 shows the variation of G_{DB0} of the center-point with jet velocities and the natural frequency of the roof. The absolute value of downburst factor increases slightly with the increase of V_{jet} in a range of 28.3 to 50 m/s. Also it increases with the increasing of natural frequency.

Fixing jet velocity at V_{jet}=47.5 m/s, Figure18 shows the varying of G_{DB0} of the center-point with the natural frequency of the roof. The absolute value of downburst factor increases with the increasing of natural frequency, whereas it has little correlation with the translating speed.

5 CONCLUTIONS

In the determination of the wind loading, the wind pressure on the building surface, which is acquired through numerical moving downbursts test, is employed directly. For the purpose of ensuring that the simulated fluctuation component of wind velocity coincides with the field observation, it is assumed that the quasi-steady assumption is satisfied during the simulation of fluctuation component of the wind pressure. Accordingly, the wind pressure simulated would more accurately represent the fluid-structure interaction.

The variation of the wind pressure distribution on the roof with the moving of the downburst is surveyed. It is found that the wind pressure would reach its peak value in case of the center of the roof coinciding with the center of downburst. It is also found that the maximum wind pressure coefficient is merely related to the ratio of jet velocity ratio to translating speed.

In order to compare the results with that obtained from ABL wind, the downburst factor, which is the ratio of the maximum displacement response due to moving downbursts to that due to ABL wind, is introduced. The study revealed that using first four modes would satisfy the accuracy requirement in downburst factor computing, whereas first one mode merely could be utilized to computing the downburst factor of the center-point of the roof. It is found the downburst factor is in a range of 6.5 to 9.0, which means that a moving downburst would cause a serious vertical response. Furthermore, the factor would increase with the increment of the natural frequency of the structure.

6 REFERENCES

1 C.W. Letchford, C. Mans, M.T. Chay. Thunderstorms—their importance in wind engineering (a case for the next generation wind tunnel), J. Ind. Aerodyn., 90 (2002) 1415-1433.

2 M.R. Hjelmfelt. Structure and life cycle of microburst outflows observed in Colorado. Journal of Applied Meteorlogy, 27 (1988) 900-927.

3 F. Caracena, R.L. Holle, F.A. Doswell. Microbursts− a hand book for visual identification. US Dept. of Commerce, NOAA/ERL/ NSSL. 1989.

4 R.P. Selvam, J.D. Holmes. Numerical simulation of thunderstorm downdrafts, J. Ind. Aerodyn., 41-42 (1992) 2817-2825.

5 R.M. Oseguera, R.L. Bowles. A simple, analytic 3-dimensional downburst model based on boundary layer stagnation flow. NASA-TM-100632. Hampton (VA): NASA Langley Research Center, 1988.

6 D.D. Vicroy. Assessment of microburst models for downdraft estimation. J. Aircraft. 29 (1992) 1043-1048.

7 G.S. Wood, K.C. A. Kwok, N.A. Motteram, D.F. Fletcher. Physical and numerical modeling of thunderstorm downbursts. J. Ind. Aerod., 89 (2001) 535–552.

8 J.D. Holmes, S.E. Oliver. An empirical model of a downburst. Eng. Struct., 22 (2000) 1167-1172.

9 L. Chen, C.W. Letchford. A deterministic-stochastic hybrid model of downbursts and its impact on a cantilevered structure. Eng. Struct.. 26 (2004) 619-629.

10 C.W. Letchford, M.T. Chay. Pressure distributions on a cube in a simulated thunderstorm downburst, Part B: moving downburst observations. J. Ind. Aerod., 90 (2002) 733-753.

11 A. Sengupta. Study of micro-induced wind flow and its effects on cube-shaped buildings using numerical and experimental simulations of an impinging jet. Doctor's thesis, Iowa State University, Ames, Iowa, 2007.

12 D.K. Kwon, A. Kareem. Gust-front factor: new framework for wind load effects on structures, J. Struct. Eng., 135:6 (2009) 717-732.

13 FLUENT, 2005, Fluent 6.2 User's guide, Fluent Inc., Lebanon, NH.

14 F. Lu. Study on wind-induced dynamic response and wind load factor for long-span flat roof structures. Doctor's thesis, Zhejiang Universtiy, Hangzhou, China, 2002.

The Seventh International Colloquium on Bluff Body Aerodynamics and Applications (BBAA7)
Shanghai, China; September 2-6, 2012

Database-assisted design for large span roofs

Ying SUN, Yue WU and Shi-Zhao SHEN

School of Civil Engineering, Harbin Institute of Technology, Harbin 150090, China

ABSTRACT: With the almost limitless possibilities of building shapes, the randomness and time-space correlation of wind loading for large span roofs, the characteristics of wind loading will rarely understood or reached by a researcher or a designer. The determination of wind loading becomes key problem during structural design of space structures. This necessitates the development of Database-assisted Design (DAD) method for large span roofs. The DAD approach entails the use of large databases of aerodynamic pressures. In this paper, wind loading models for fluctuating pressure are statistically summed up and sorted into wind loading database system, which can be able picked up by building designers. The program frame and application of wind loading database system are also introduced in this paper.

KEYWORDS: *wind loading database, large span roofs, characteristics of wind pressure, database-assisted design.*

1 INTRODUCTION

Wind loading on large-span roofs is influenced not only by approaching flow, but also by body-induced turbulence. The quasi-steady assumption is not applicable in this condition. The complexity of wind loading on large span roofs stems from its variability of building shape, time/space and spatial characterization of pressure fluctuations. It is blank for wind loading guide for large-span roofs in wind loading standard and codes in China.

In the past, the scientific data used to disseminate in summary form through published papers or reports. Until 1990s, there emerged some expert systems as guideline of design for simple structures, which was only based on logic judge depending on developer's understanding and lack of robust practicability. Recently, with the development of software and hardware, wind loading database technique has great promotion. Database-assisted design for wind loads is in a state of development. Time series of instantaneous pressure distributions for different wind directions are an essential component of the database. Measurements with SM-PSSs have made pressure (aerodynamic) databases accessible for simple low-rise buildings. Exploratory studies of database-assisted design have demonstrated that such designs can be risk-consistent and may be more resistant to damage as well as more economical. Use of BLWT tests with SM-PSS data acquisition for creation of pressure databases is expected to increase for some classes of building geometry. In this paper, wind loading models for fluctuating pressure are statistically summed up and sorted into wind loading database system, which can be picked up by building designers expediently. The program frame and application of wind loading database system are also introduced in this paper.

2 THE DESIGN OF WIND LOADING DATABASE SYSTEM FOR LARGE SPAN ROOFS

The function of Wind Loading Database System (WLDS) is to collect wind loading data of all kinds of structures, summarize and sort these data into reasonable wind loading models, which can become a convenient reference for the wind-resistant design of structures.

The Wind Loading Database System (WLDS) has the following advantages compared with the

traditional method:

(1) Compared with the wind loading design code, WLDS has greater amount of information and more accurate representation of data. Moreover, it facilitated people's queries greatly;

(2) Although the preliminary work to establish the database system is heavy, the WLDS will lead to much lower cost and shorter design cycle in the using process;

(3) The system has flexible modular construction, which make it easy to develop and manage. We will add some artificial intelligence module so that to achieve the forecast of wind load of undocumented shapes;

(4) We can realize the procedural structure of wind-resistant design by combining the WLDS and structural analysis/design software.

The main works of the establishment of WLDS are as follows:

(1) **Data collection**. Mainly from: wind tunnel test data, national load standards, relevant published papers and tests results of CFD simulation;

(2) **Data analysis**. For the data collected in different way is often disorganized and incomplete. The role of the data analysis is to extract the identifiable and useful information such as the probability density distribution of pulse wind pressure, power spectrum information and spatial correlation information, which can greatly reduce data storage space and improve efficiency. The key work of this part is to build a universal wind loading roof model so that we can achieve accurate description of the wind load on roof by identifying several characteristic parameter;

(3) **Data representation**. This part of work like a bridge that connect the database system and user. The designer want to get the most direct and concise form of information while not the complex internal database system. Therefore, it's an important part to improve the availability of the system.

2.1 *The design of function modules*

According to the above ideas, the WLDS should have the following basic functions:

(1) Store and effectively organize data of different basic-shape structures;

(2) Achieve the visualization of data, especially for the wind tunnel test data;

(3) Compare similar structures with different parameters (consult relevant design code and paper) and get the variation trend of wind load according to different parameters, which could help to establish the numerical model of wind load in the future;

(4) Make statistical analysis for the pulse component of the wind load in order to provide a theoretical basis for the structure wind vibration response;

(5) The neural network will be added and wind pressure prediction mechanism will be established.

The wind loading database system should include the following modules based on the above features: data input module, data analysis module, additional modules and output module.

2.2 *Interface design*

In order to make efficient Wind Loading Database System, We use Visual C++ and MySQL compile the analysis module and input module, which achieve inter-invocation of different parts. The data input system was designed in accordance with features such as simple interface, complete content and easy-to-search (see Figure 1). The system is divided into seven menu bars:

standard options, wind information, structure information, design type, result display, system query and help system. In addition, there are some shortcut icons lead to different graphics and data query interface quickly. The relevant site (http://wlds.hit.edu.cn) built up by JSP+MySQL was designed as dynamic web site, which gain the following advantages: small and delicate code, easy maintenance, high efficiency and high adaptability. All of the above make the system easy to deal with the problems such as the data entry, inquiry, editing operation, see Figure 2.

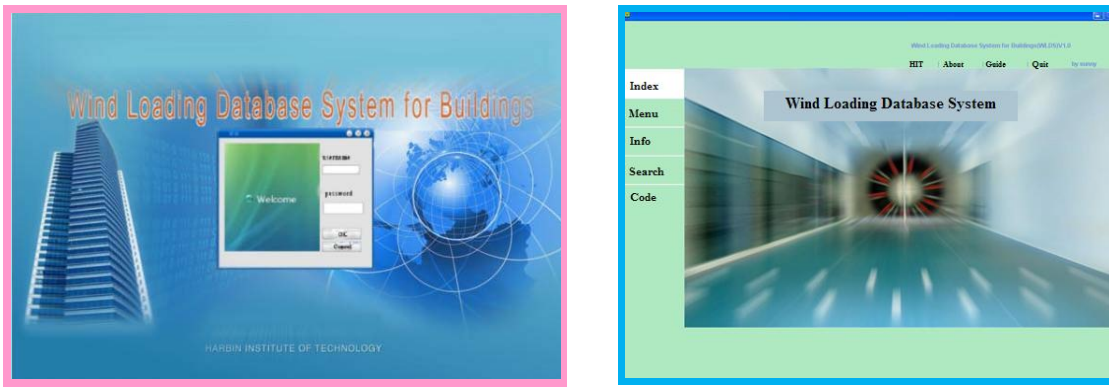

Figure 1 The interface of WLDS

Figure 2 The web page of WLDS for Large-span roof (http://wlds.hit.edu.cn)

3 THE CHARACTERISTICS OF WLDS FOR LARGE-SPAN ROOF

Based on previous research, we can find the flow around large-span roofs has the following features:

(1) Most of wind load on the roof surface is suction. The wind suction is larger near the front of blunt body shape roof and the suction decreases with the increase of distance to the front part. It indicates that the vortex shedding caused before the front of roof is the key factor of the wind load characteristics.

(2) The wind angle has important role in the wind load on roof. The flow separation, vortex shedding phenomena and the position of the maximum wind pressure are different under different wind directions. Therefore, the most adverse wind direction angle of wind load

effect should be took attention in design.

(3) Wind load is sensitive to the change of curvature/slope of the roof.

(4) The flow wind speed, turbulence and rise-to-span ratio is less important to the distribution of overall wind pressure on roof. But these parameters will influence the local wind pressure.

According to the above wind tunnel test results and relevant paper, the large-span roofs can be classified into the following basic shapes: closed straight edge building (Bluff body), closed curved edge building, open buff body building. Body-induced turbulence is the main feature of wind load on the first type of roof. The separation to attach phenomenon is obvious (most are featured as cylinder vortex and conical vortex) in the incoming flow. Flat roof and saddle-shape roof are typical examples. Wind load on the second type of roof will not happen a lot of flow separation effect,. Distribution of wind load is parallel to the shape of roof edge such as spherical shells and round flat roof. The wind load on the third type of roof is complex because of the combined influence of wind pressure on upper and lower surfaces. But most of the open buff body buildings have relevant simple geometry shape, the flow field around them could be simplified into 2D forms. Typical example is cantilevered roof.

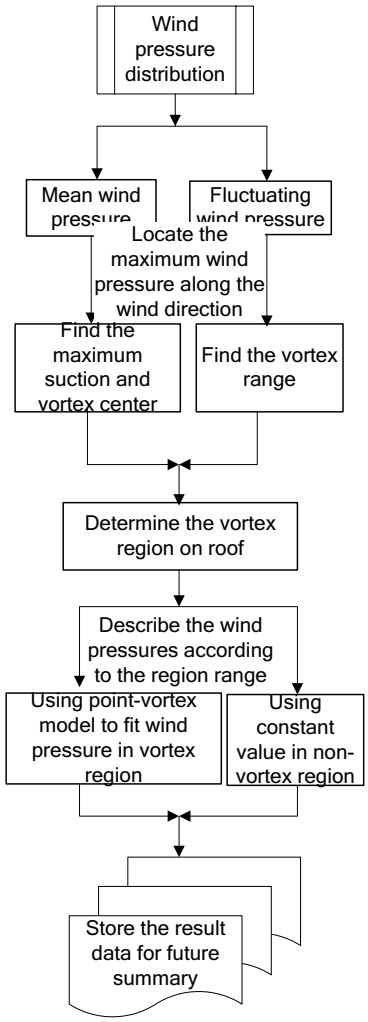

(a) mean wind pressure

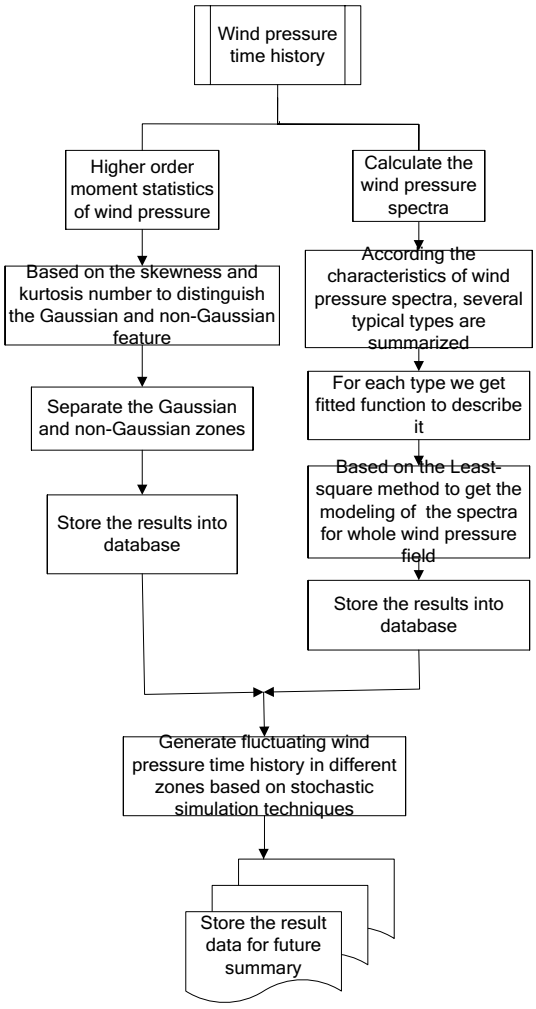

(b) fluctuating wind pressure

Figure 1 The use of WLDS

3.1 *Description of mean wind loading*

First of all, the mean wind pressure and distribution of fluctuating wind pressure on the roof surface are got based on the wind tunnel test data. Secondly, we can get the position of maximum wind suction and the position of maximum wind pressure fluctuation value by slice the pressure profile along the line that perpendicular to the windward roof, which are the centre and edge of the vortex correspondingly. Then we will investigate the trends of maximum wind suction values on the vortex axis and provide basis for the derivation of wind pressure model. Thirdly, we can define the vortex region on roof according to the above research. Fourthly, we can get fitted parameters by using point vortex model to describe the data in the vortex region and use constant value out of the vortex area. Finally, the results are sorted into the database for future comparison and usage. The operation is shown in Figure 3a.

3.2 *Modelling of fluctuating wind load*

The fluctuating characteristics of roof wind pressure are influenced by both approaching turbulence and body-induced turbulence. According to the analysis of wind pressure distribution and wind pressure spectrum, we get the fluctuating feature of different zones on the roofs and make sure the contribution of different turbulences. So we can build up wind pressure spectrum model including influence of approaching turbulence and body-induced turbulence. Since numerical simulations of fluctuating wind pressures are different in Gaussian zone and non-Gaussian zone, the descriptions of wind pressure model should be different based on Gaussian and non-Gaussian zones. Firstly we get high-order statistical moment of wind pressure time series on measure points of roof. The description of the fluctuating wind load need to consider each-order statistical moment of wind pressure time series, Gaussian/non-Gaussian zone partition, wind pressure spectra formula and the accumulation of a large amount of data. For the specific operation procedure, refer to Figure 3b. In addition, because the overall correlation of wind pressure on large-span roof is weak and it's hard to find the law of the correlation, the spatial correlation of the pulse wind pressure model is not list in this paper.

4 CONCLUSIONS

This paper introduce the main flow of WLDS for large-span roof ; make discussion about main function modules, data storage method, data analysis and comparison, process of the usage of system. Make discussion about some technical difficulties of the system. This work will help the development and further supplement of the WLDS for large-span roof.

Reference

1. E. Simiu, J.H. Garrett, K. Reed, Development of computer-based model of standards and attendant knowledge-based and procedural systems, in: Proceedings of the Structure and Engineering in Natural Hazard Mitigation, ASCE, New York, 1993, pp. 841− 846.
2. Rigato, P. Chang, E. Simiu, Database assisted design, standardization, and wind direction effects, J. Struct. Eng. ASCE 127 (8) (2001) 855− 860.
3. P.C. Case, N. Isyumov, Wind loads on low buildings with 4: 12 gable roofs in open country and suburban exposures, J. Wind Eng. Ind. Aerodyn. 77&78 (1998) 107− 118.
4. T. Whalen, E. Simiu, G. Harris, J. Lin, D. Surry, The use of aerodynamic databases for the effective estimation of wind effects in main-force resisting systems: applications to low buildings, J. Wind Eng. Ind. Aerodyn. 77&78 (1998) 685− 693.

The Seventh International Colloquium on Bluff Body Aerodynamics and Applications (BBAA7)
Shanghai, China; September 2-6, 2012

Structural optimization of long span portal-rigid frames under wind action

J. R. Wu [a], C. C. Dong [a], A. Xu[a], J. Y. Fu [a]

[a] *School of Civil Engineering, Guangzhou University, Guangzhou, China*

ABSTRACT: A procedure for wind-resistant optimization design of long-span portal-rigid frame was proposed in this paper by adopting the Optimality Criteria (OC) method and SAP2000 Application Programming Interface (API) for Matlab developing environment. The Equivalent Static Wind Load (ESWL) for the long-span portal–rigid frame was obtained from the measured wind pressure from wind tunnel tests and application of Load Response Correlation (LRC) method. The virtual-work principle was utilized to construct the wind-induced displacement constraint condition. A rigorously derived iteration procedure was proposed to obtain the optimized minimum sections of long-span portal frames while satisfying all the constraint conditions. The optimized results from different types and combinations of ESWL were compared with those corresponding optimization results from wind load by Gust Loading Factor (GLF) method. The effect of connection stiffness of semi-rigid joint and the stiffness of support restraint on the optimization results were also discussed. Only a few iteration numbers for convergence were found in the proposed optimization procedure, and comparison results showed that the OC procedure proposed in this paper was very effective for the wind-resistant optimization design for such long-span portal-rigid steel frames.

KEYWORDS: Equivalent Static Wind Loading; Structural optimization design; Optimality Criteria; portal-rigid frame; SAP2000 API.

1 INTRODUCTION

The low-rise buildings with long-span portal steel frames represent one of the most commonly used structures in commercial and industrial applications. As its long-span, small dimension in cross section and varied height of elements in form of tapered section, the wind loading and wind-induced response are the major factors to be considered for the structural design of such buildings. They have traditionally been designed for wind loads by using simplified code and standard procedures which involve a series of reductive tables and plots that were determined from summary research information or design experiences [1]. It is now practical to incorporate aerodynamic databases and allow the calculation for routine designs of considerably more realistic wind load effects than those based on conventional methods [2].

In the meantime, the design process for such structures is time-consuming. Satisfying strength, stability and flexibility constraints for such structures under wind action is very complex, and is often not done at all or done poorly. For every change in a statically indeterminate structure, a redistribution of internal force occurs which cannot be accurately predicted without reanalyzing the structure. This makes it impossible to determine member sizes in a single step, and iterative methods are required. Even though great advances have been made in automating the design process [3], an effective structural optimization method is not available for such structural systems under dynamic wind action. Structural optimization of structures under seismic load has been ongoing for the past few decades. Truman and Petruska proposed the Optimality Criteria (OC) method for 2D structures using linear elastic time history analysis procedures coupled with actual seismic base excitations [4]. Different earthquake records were considered and

the dynamic responses of structures were monitored at each time step. Compared with structural optimization of structural systems under static load, the wind resistant optimization design of long span portal frame system under dynamic wind loading is much more expensive. As the time variable is typically involved in linear dynamic response optimization, the objective function and the constraints are typically time-dependent functions. Theoretically, the structural optimization process should be conducted at each time instant for dynamic response optimization. Peak values of those functions are usually considered in optimization. Various methods exist to handle the peak values by modifying the conventional methods for linear static response optimization.

On the other hand, optimization methods using Equivalent Static Loads (ESLs) have been proposed to solve various structural optimization disciplines. The disciplines include linear dynamic response optimization [5]. In the equivalent loads method, ESLs are evaluated from the displacement field, the dynamic external loads are transformed to the Equivalent Loads (EL) for linear static analysis, and linear response optimization is carried out based on the EL. The design is updated by the results of linear response optimization.

Most of the modern structural synthesis methods can be classified as being one of two major approaches. One is based on Mathematical Programming (MP) techniques, while the other uses Optimality Criteria (OC). The OC approach has gained tremendous popularity due to its high efficiency. The approach is particularly suitable for large-scale structures since it only has a weak dependence on the size of the structure [6]. Moreover, the convergence of the OC approach does not depend on the starting design and weakly depends on the number of design variables. Chan et al. developed a virtual work formulation approach for wind induced serviceability design of tall buildings [7]. The virtual work expression represents a good approximation of the behavior constraints. Furthermore, the explicit approximate formulation is sufficiently accurate so that this generally leads to smooth and rapid solution convergence. Another advantage of the virtual work formulation approach is that the existing finite analysis software can be directly employed based on internal element forces and moment readily available by common structural analysis programs such as SAP2000 so that the approach can be applied to large scale building structures.

A wind-resistant structural optimization procedure for long-span portal rigid steel frame with tapered section was proposed in this study based on the OC method and the combined SAP2000 Application Programming Interface (API) [8] for Matlab developing enviorment. With the obtained ESWLs, the structural optimization of structures under dynamic wind load was transformed to the integrated process of updating ESWLs and structural optimization under static load. A rigorously derived iteration procedure was selected to obtain the optimized minimum sections of long-span portal frames while satisfying all the constraint conditions. The effect of semi-rigid stiffness of connection joint and the stiffness of support restraint on the optimization results were also discussed.

2 MATHEMATICAL MODEL OF STRUCTURAL OPTIMIZATION IN LONG-SPAN PORTAL RIGID STEEL FRAME WITH TAPERED SECTION

2.1 *Mathematical model of structural optimization*

In order to conduct the wind resistant optimization design of long-span portal steel frame, a mathematical model of structural optimization should be first established, which mainly includes the design variables, constraint conditions and objective functions. For the specified case in this study, the objective function is normally adopted by minimizing the total weight of all the structural elements in the studied structural system, which can be formulated in the following form:

$$W = \rho \sum_{i=1}^{N} L_i (2 w_i^F t_i^F + \frac{t_i^W}{2} \sum_{j=1}^{2} D_{ij}^W) \quad (1)$$

where ρ is the material density, L_i is the length of the *i*-th element, w_i^F, t_i^F, t_i^W are the corresponding width, thickness of flange and the thickness of web for the *i*-th element, D_{i1}^W and D_{i2}^W are height of the web for the ***i***-th element with taped section. *N* is the total number of the design variables.

The constraint conditions were usually selected by limiting the wind-induced displacements as they can reflect the wind effects of studied structure directly. Therefore the wind-induced horizontal displacement (g_1) atop of the column and vertical displacement (g_2) at the mid-span of rafter were set to meet the following constraint conditions:

$$g_k \le g_k^U \quad (k=1, 2) \quad (2)$$

The displacement constraints described in Eq. 2 can be obtained from the following equation by the virtual work principle [7].

$$g_k = \sum_{i=1}^{M} \int_0^{L_i} (\frac{F_{Xk} f_X}{EA} + \frac{F_{Yk} f_Y}{GA_Y} + \frac{F_{Zk} f_Z}{GA_Z} + \frac{M_{Xk} m_X}{GI_X} + \frac{M_{Yk} m_Y}{EI_Y} + \frac{M_{Zk} m_Z}{EI_Z}) dx \quad (k=1,2) \quad (3)$$

where *M* is total structural elements in the optimized structure, *E* and *G* are the elastic and shear modulus of the steel material, A, A_Y, A_Z are the area of cross section, the shear areas about two major axis of cross section respectively. GI_X, EI_Y, EI_Z are torsional stiffness and flexural stiffness for the design section, F_{Xk}, F_{Yk}, F_{Zk}, M_{Xk}, M_{Yk} and M_{Zk} are the internal forces resulted from the applied unit force in the direction at the specified displacement, while f_X, f_Y, f_Z, m_X, m_Y and m_Z are the internal force (axial force, shear force and bending moment in the direction of three major axes) induced from external wind loading.

All the above mentioned internal forces of the elements could be obtained from the finite element analyzed results by SAP2000 API. As the geometry properties could be expressed in the function of a series of design variables, the integration and derivation of the constraint conditions in Eq. (3) with the design variables could be solved easily by the corresponding internal functions in Matlab software system.

For a reasonable optimization design result, the lower and upper bounds of design variables should be defined which are expressed by the following unequal formula:

$$X_i^{\min} \le X_i \le X_i^{\max} \quad (i=1, 2 \ldots N_d) \quad (4)$$

where N_d is the total number of design variables, X_i is the *i*-th design variable, $X_i^{\min}$, $X_i^{\max}$ are its corresponding lower and upper bounds, which is usually obtained from the local, global stability and strength check by the local steel structural design code.

2.2 *Optimality criteria method in structural optimization*

In order to obtain the optimized results, solution for the objective function specified in Eq. (1) should be proposed by the suitable structural optimization method. An effective approach for optimal element sizing design of large-scale structures was adopted in this study, which was based on the Optimality Criteria (OC) method and has been shown to be particularly suited to the design of structural systems with many design variables [6]. A Lagrange function was first con-

structed by combining the objection function and constraint functions with a series of Lagrange multipliers in the following form:

$$L(X_i, \lambda_k) = W(X_i) + \sum_{k=1}^{m} \lambda_k (g_k - g_k^u) \tag{5}$$

where the λ_k is the Lagrange multiplier for the *k*-th constraint function, *m* is the total constraint conditions in the optimization case.

Rather than using an intuitive optimality assumption; the Karush–Kuhn–Tucker (KKT) necessary condition is rigorously derived and employed in the OC method. For KKT condition, Differentiating Eq. (5) with respective to the design variable X_i and rearranging terms to obtain the stationary conditions:

$$(-\sum_{k=1}^{m} \lambda_k \frac{\partial g_k}{\partial X_i}) / \frac{\partial W}{\partial X_i} = 1 \qquad (i=1, 2 \ldots N_d) \tag{6}$$

A recursive algorithm is applied to drive an initial design for satisfying Eq. (6). Multiplying both sides of Eq. (6) by X_i and taking the η-th root, then applying a first-order binominal expansion to obtain the linear recursive relations

$$X_i^{\upsilon+1} = X_i^{\upsilon} \{1 + \frac{1}{\eta}[(-\sum_{k=1}^{m} \lambda_k \frac{\partial g_k}{\partial X_i}) / \frac{\partial W}{\partial X_i} - 1]\}_{\upsilon} \tag{7}$$

where υ+1 and υ indicate the successive iterations, and η is a step-size factor whose value is assumed to 3 in this study. Before the value of design variable $X_i^{\upsilon+1}$ could be found, the unknown Lagrange multipliers λ_k (*k*=1, 2, …, *m*) must first be determined. Considering the change $(g_k^{\upsilon+1} - g_k^{\upsilon})$ in the *k*-th constraint due to the change $(X_i^{\upsilon+1} - X_i^{\upsilon})$ in the design variables, the following expression could be obtained

$$g_k^{\upsilon+1} - g_k^{\upsilon} = \sum_{i=1}^{N} (\frac{\partial g_k}{\partial X_i})(X_i^{\upsilon+1} - X_i^{\upsilon}) \tag{8}$$

Supposing that the *k*-th becomes active after the (υ+1)th iteration so that $g_k^{\nu+1} = g_k^U$, then substituting Eq. (7) into Eq. (8) and rearranging terms to obtain a set of simultaneous equations, it can be expressed in the following

$$\sum_{s=1}^{m} \lambda_s^{\upsilon} (\sum_{i=1}^{N} \frac{\frac{\partial g_k}{\partial X_i} \frac{\partial g_s}{\partial X_i}}{\frac{\partial W}{\partial X_i}}) = -\sum_{i=1}^{N} (\frac{\partial g_k}{\partial X_i})_{\upsilon} X_i^{\upsilon} - \eta (g_k^U - g_k^{\upsilon}) \tag{9}$$

During the evaluation of the OC iterations using Eq. (7), some design variables may be found to exceed their limitations defined in Eq. (4). If these cases occur, they are not allowed to change any further and are deemed to be inactive. Therefore Eq. (9) is modified to include only active design variables in the design optimization in the following form

$$\sum_{s=1}^{m} \lambda_s^{\upsilon} (\sum_{i=1}^{Na} \frac{\frac{\partial g_k}{\partial X_i} \frac{\partial g_s}{\partial X_i}}{\frac{\partial W}{\partial X_i}}) = -\sum_{i=1}^{Na} (\frac{\partial g_k}{\partial X_i})_{\upsilon} X_i^{\upsilon} - \eta (g_k^U - g_k^{\upsilon}) \tag{10}$$

where N_a is the current number of active design variables, the solution of the set of simultaneous equations defined in Eqs. (9) and (10) could be obtained by Gauss-Seidel iteration method. Once $\lambda_k^{\tau+1}$ is found to be less than zero, it indicted that the *k*-th constraint is an inactive con-

straint, then $\lambda_k^{\tau+1}$ is set to be zero during the iteration process. The whole set of recursive formulae for the set of simultaneous equations could ne expressed in the following form:

$$\lambda_k^{\tau+1} = (1/a_{kk})(b_k - \sum_{s=1}^{j-1} a_{ks}\lambda_k^{\tau+1} - \sum_{s=k+1}^{m} a_{ks}\lambda_k^{\tau}) \qquad (k=1, \cdots, m) \tag{11}$$

where k and s are k-th and s-th constraints, $\tau+1$ and τ are two successive iterations of the Gauss-Seidel process and

$$a_{kk} = [\sum_{i=1}^{N} (\frac{\partial g_k}{\partial X_i}\frac{\partial g_k}{\partial X_i} / \frac{\partial W}{\partial X_i})]_\tau \quad a_{ks} = [\sum_{i=1}^{N} (\frac{\partial g_k}{\partial X_i}\frac{\partial g_s}{\partial X_i} / \frac{\partial W}{\partial X_i})]_\tau \quad b_k = -\sum_{k=1}^{N} (\frac{\partial g_k}{\partial X_i})_\upsilon X_i^\upsilon - \eta(g_k^U - g_k^\upsilon) \tag{12}$$

It is noted that the ESWLs for optimized structure are also changed if the design variables are modified in each optimization design cycle. Thus the updating ESWLs must conducted at the first step during each design cycle, which is different from the structural optimization for structures under only static load. Meanwhile the derivation of each constraint could be conducted by utilizing Eq. (3) through SAP2000 API and MATLAB symbolic calculation module in MATLAB developing enviorment.

3 THE PROCESSING OF DYNAMIC WIND LOADING

3.1 *The characteristics of wind loading on long-span portal frame system*

For long-span portal frame system, the wind-induced displacement under dynamic wind loading is mainly contributed from the background response. In this case, the resonant response is negligible, the Load Response Correlation (LRC) method can be used to obtain the ESWLs from the mean and background components.

3.2 *Equivalent Static Wind Loads* (*ESWLs*)

Based on the LRC method of Kasperski and Niemann[9], the ESWLs for long-span portal frame system could be obtained from the following formula

$$[p(z)]_{\hat{r}} = \overline{p}(z) + p_B(z) = \overline{p}(z) + g_B\rho_{pr}(z)\sigma_p(z) \tag{13}$$

where g_B is the peak factor, $\overline{p}(z)$ is the mean wind load, $\sigma_p(z)$ is the standard deviation of the fluctuating wind load, $\rho_{pr}(z)$ is the correlation coefficient between the fluctuating wind load $p'(z)$ and the specified wind-induced response (r), which could be expressed in the following

$$\rho_{pr}(z) = \frac{\sigma_{pr}}{\sigma_p(z)\sigma_{r,B}} = \frac{p'(z,t)\int_0^L p'(z_1,t)I_r(z_1)dz_1}{\sigma_p(z)\sigma_{r,B}} \tag{14a}$$

$$\sigma_{r,B} = \left[\int_0^L\int_0^L \overline{p'(z_1,t)p'(z_2,t)}I_r(z_1)I_r(z_2)dz_1dz_2\right]^{1/2} \tag{14b}$$

where "B" denotes the background response, "L" denotes the length of structural element, $I_r(z)$ is the influence coefficient, i.e. the value of r when a unit load is applied at position z. If the structural system is divided into several discrete elements, Eqs. (14a) and 14(b) can be rewritten as a finite summation:

$$\rho_{pj,r} = \frac{\sum_{j=1}^{N} \overline{p_i'(t)\,p_j'(t)}\beta_i}{\sigma_{pj}\sigma_{r,B}} \tag{15a}$$

$$\sigma_{r,B} = \sum_{i=1}^{N}\sum_{j=1}^{N} \overline{p_i'(t)\,p_j'(t)}\beta_i\beta_j \tag{15b}$$

Then the ESWLs defined in Eq. (13) can also be written as a finite summation:

$$P_{B,j} = g_B \rho_{pj} \sigma_{pj} = \frac{\sum_{i=1}^{N} \overline{p_i'(t) p_j'(t)} \beta_i}{\sigma_{r,B}} = \frac{\sum_{i=1}^{N} \overline{p_i'(t) p_j'(t)} \beta_i}{\sum_{i=1}^{N} \sum_{k=1}^{N} \overline{p_i'(t) p_k'(t)} \beta_i \beta_k} \tag{16}$$

where i and j are element no., N is total number of elements and β_i is the influence coefficient.

4 WIND RESISTANT OPTIMIZED DESIGN OF PORTAL RIGID FRAME UNDER EQUIVALENT STATIC WIND LOAD

4.1 *The source of dynamic wind load and optimized mathematical model description*

The dynamic wind loading was extracted from the aerodynamic database of wind tunnel test on wind pressure of low rise buildings with gable roof type, which was conducted by the Tokyo Polytechnic University [10]. The design mean wind speed is 28*m*/*s* at the height of 10 meter. A long-span portal steel frame building with same scale as the model in the wind tunnel test was selected in this study, whose dimension is 24*m* (length)×16*m* (width)×4*m* (height atop of column), the inclined angle for rafter is β=9.4° , a 2-D long-span portal frame longitudinal direction was selected as the research object for wind resistant structural optimization. The building configuration and the corresponding analyzed model were shown in Figure 1, which indicated the location of wind loading, the dimension size of rafter and column with taped "I" section. For the optimized model in this study, the height of the rafter varied along its span with ratio of d_1:d_2:d_3=0.2:0.6:0.2. For rafter the width, thickness of flange are 0.25*m* and 0.01*m,* the thickness of web is 0.006*m*. The corresponding values for steel column are 0.28*m*, 0.01*m* and 0.008*m* respectively. Two displacement constraints are set during optimization process: the horizontal displacement atop of the column should be less than *H*/60*m* (*H* is the height of the column), the vertical displacement at the mid-span of the rafter should be less than *B*/180*m* (*B* is the span of the rafter). The heights of cross sections 1~5 are set to be optimized design variables. The initial, lower and upper bounds of these design variables were listed in Table 1.

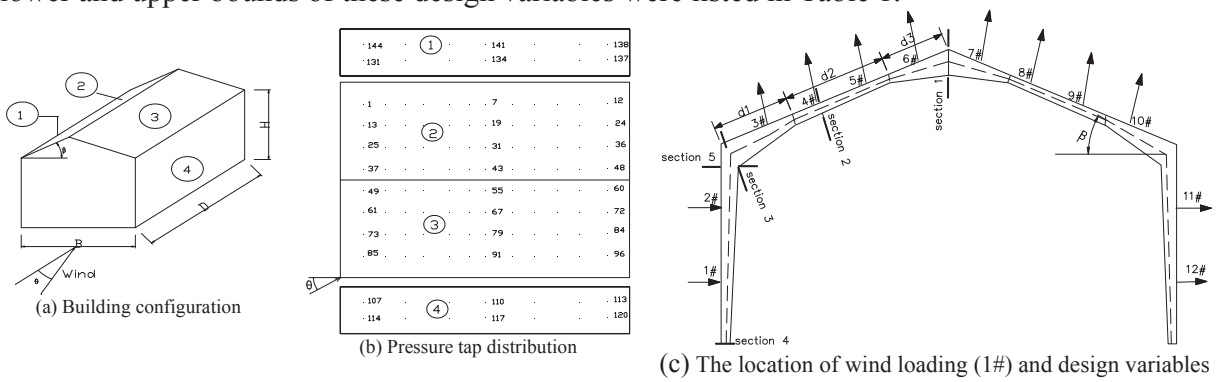

(a) Building configuration

(b) Pressure tap distribution

(c) The location of wind loading (1#) and design variables

Figure 1 The building configuration, pressure taps in wind tunnel test and analyzed model

Table 1 Initial, lower and upper bounds of design variables

Height of web (unit: m)	Section 1	Section 2	Section 3	Section 4	Section 5
Initial values	0.88	0.53	0.83	0.38	0.88
Lower bounds	0.3	0.2	0.3	0.1	0.3
Upper bounds	1.5	1.1	1.4	0.8	1.5

The time history of pressure taps in the middle part of the building (Taps no. 141,134, 7,…,117 in Figure1b) in the wind direction at 45^o were extracted from the aerodynamic database. By multiplying their related tributary areas, the time history of wind loading acting on the nodes (No. 1$^{\#}$~12$^{\#}$ is Figure 1c) can be obtained. With the corresponding mean and standard deviation component of wind loads at these nodes, the equivalent static wind loads can be obtained simply but roughly from the GLF method[11]. The LRC method could be applied to obtain the ESWLs more precisely. The corresponding ESWLs obtained from these two methods were shown in Figure 2, and these ESWLs will be applied as the acting wind loading for the structural optimization process in the following sections. The ESWLs-A indicated the form of equivalent static load distribution that could generate the same maximum horizontal displacement atop of column as dynamic wind load, while ESWLs-B is the corresponding ESWLs for vertical displacement at the mid-span of rafter. It was shown from this figure that there is little difference between ESWLs-A and ESWLs-B, but the absolute values of ESWLs obtained from GLF method are normally larger than those from LRC method.

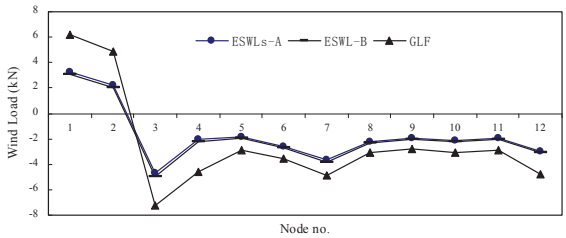

Figure 2 The obtained ESWL series

4.2 *The structural optimization results under single load case from GLF-based or LRC-based ESWLs*

In order to evaluate the effects of different types of ESWLs on the optimized results, these three types of ESWLs were applied on the long-span portal frame separately. The optimized results for the height at cross sections 1~5 were illustrated in Figs. 3(a) ~3(c) respectively.

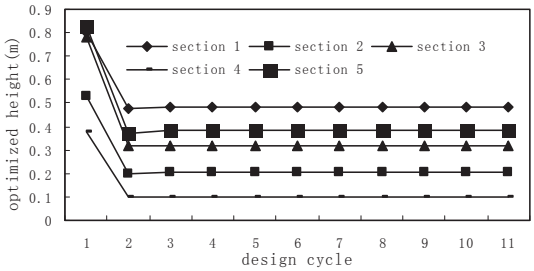

Figure 3a Optimized results for ESWLs-A

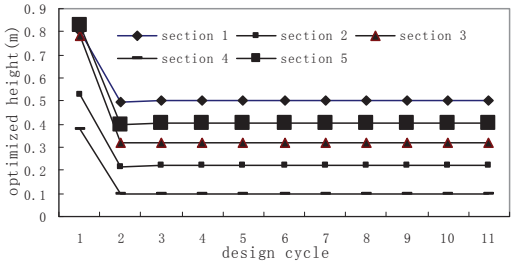

Figure 3b Optimized results for ESWLs-B

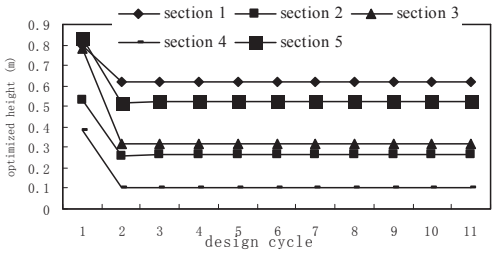

Figure 3c Optimized results for GLF-based EWSL

From the above figures, it was found that there is little difference in the optimized web heights for cross sections 1~5 between the ESWLs-A and ESWLs-B loading cases. However, many differences were shown between the optimized results for ESWLs-A loading case and those optimized results for ESWLs from GLF method. The reason for these differences was that larger values in acting wind loads was applied to the optimized structure by the GLF method. Compared with GLF-based ESWLs, the ESWL obtained from LRC method is defined as the static load that generates the same displacement field by an analysis which is not linear static. It is more possible and suitable static wind load distribution for producing the equivalent wind-induced response from dynamic wind load. Therefore it is more reasonable to conduct the structural optimization of such structures under LRC-based ESWLs.

It was also found from the above figures that all the design variables almost reached their optimized results after only 2 optimized design cycles. Thus it indicated the proposed OC method is very effective for the structural optimization of such long-span portal frames.

4.3 *The structural optimization results under multiple load cases from different forms of LRC-based ESWLs*

As indicated from previous section, the constraints in Eq. (3) and their derivations with the design variables in Eqs. (6)~(11) and (12) could be obtained by the virtual work principle and Matlab symbolic calculus function once the specified ESWLs were applied on the optimized structure. The load distribution with the form of ESWLs-A could generate the exact horizontal displacement atop of column, but it may not produce the same vertical displacement at the mid-span of the rafter as the dynamic wind load. Considering the most unfavorable loading state for the optimized structure, ESWLs-A and ESWLs-B were supposed to be two independent loading cases during the structural optimization process. Thus ESWLs-A was utilized to evaluate the first constraint (horizontal displacement) and its derivation with design variables, while ESWLs-B was used to obtain the second constraint (vertical displacement) and its related derivations simultaneously during the whole optimization process. The optimized heights for cross sections 1~5 under the multiple ESWL cases were shown in Figure 4. Larger values of the optimized height in cross section 2 was found in this wind loading state, while optimized heights for other cross sections were almost the same as those optimized results for ESWLs-A or ESWLs-B. The total weight of the optimized structure was listed in Figure 5 for different ESWL cases in previous sections. It was found that the optimized weight for GLF method is the largest. It was followed by the results for multiple load cases with different forms of LRC-based ESWLs, the related values for ESWLs-A and ESWLs-B are almost the same and least among these wind loading cases.

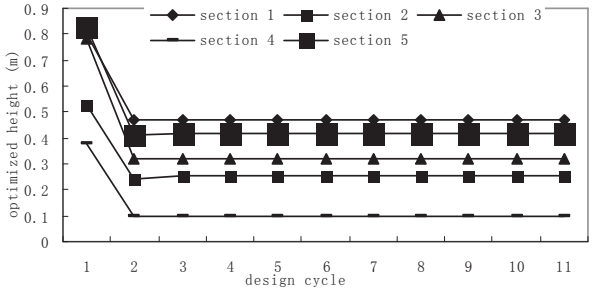

Figure 4 Optimized results for multiple ESWL cases

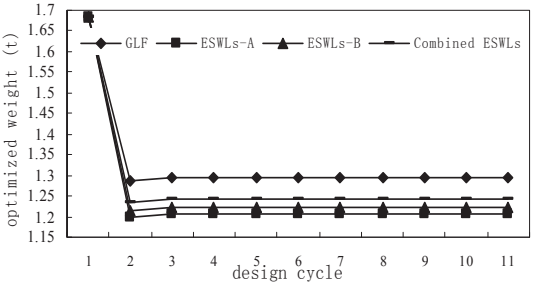

Figure 5 Optimized weights for different ESWLs

4.4 *The effect of support stiffness at column base on optimized results*

The support is normally assumed to be hinged or fixed at column base in numerical finite element analysis on long-span portal frame. However the column base is actually partially-fixed

connection with the ground, its connection stiffness is a certain value between zero and infinite depending on its connecting detail. The internal force distributions of structural elements, especially for the vertical columns, were greatly affected by the support stiffness. Larger values in support stiffness would normally reduce the internal force in some elements but increase the construction cost of the column base. Assuming the support stiffness to be a series of discrete values varied from zero to infinite, the effect of support stiffness at column base on the optimized total weight of the long-span portal steel frame was conducted in this study. The corresponding optimized results were shown in Figure 6. If the construction cost of the column base is excluded in the optimization process, the optimized total weight generally reduce from 1.22*t* to 1.16*t* when the connection stiffness increases from 10 to 2000*kN.m/rad*. Then the optimized total weight of the structure remains unchanged even if the connection stiffness increases to infinite values (i. e. fully-fixed support in SAP2000 analyzed model). Therefore the detailed construction drawing of the column base could be designed according to the optimized results of the studied frame structure.

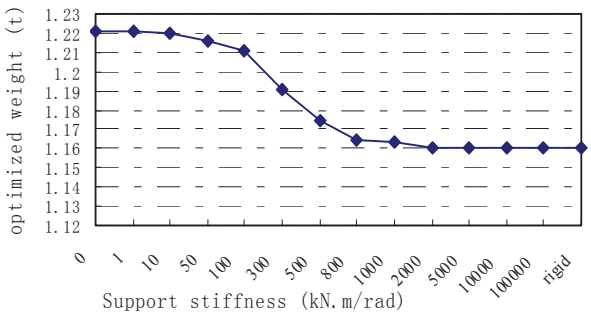

Figure 6 Optimized results with support stiffness

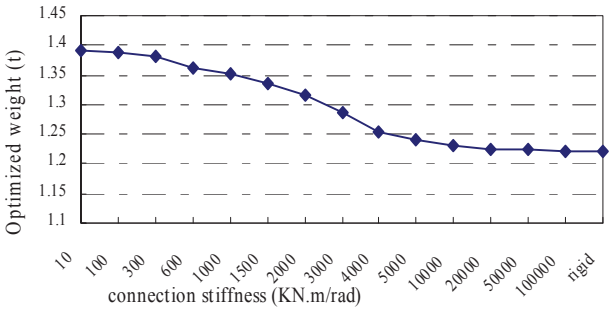

Figure 7 Optimized results with semi-rigid connection stiffness

4.5 *The effect of semi-rigid connection at beam-column joint on optimized results*

Each segments of the rafter, column or beam-column connection joint are regarded to be fully rigid connection for simplicity in numerical finite element analysis on long-span portal frame, but the connection joint between the structural elements are usually partially rigid-connected[12] . The value of connection stiffness for the semi-rigid joint depends on the construction detail of the connection type, the number of connection bolts or the depth of welding. The internal force distributions of structural elements were also greatly affected by the value of connection stiffness. Assuming the connection stiffness of the semi-rigid joint to be a series of discrete values varied from zero to infinite, the effect of semi-rigid connection on the optimized total weight of long-span portal steel frame was also studied. The corresponding optimized results were shown in Figure 7. If the construction cost of the semi-rigid connections is excluded in the optimization process, the optimized total weight sharply reduced from 1.39*t* to 1.226*t* when the connection stiffness of semi-rigid joint increases from 10 to 20000*kN.m/rad*. Then the optimized total weight of the structure reduced very slowly to 1.22*t* until the connection stiffness increases to infinite values (i. e. fully-rigid connection in SAP2000 analyzed model). Based on the empirical formula or information about the relationship between the connection stiffness of semi-rigid connection and the detail of connection type, the semi-rigid connection could be designed according to the optimized results of the studied frame structure.

5 CONCLUSIONS

By utilizing SAP2000 API for Matlab developing environment, a rigorously derived OC method was proposed in this paper to conduct the wind resistant optimization design of a long-

span portal rigid steel frame. The effect of different forms and combination of ESWLs, the stiffness of support restraint and semi-rigid connection on the optimized results were analyzed. The optimized height in cross section for rafters and columns, the optimized total weight of the structural system were obtained, the main conclusions could be summarized in the following:

(1) The proposed OC method was seamlessly integrated with SAP2000 API into wind resistant structural optimization for the long-span portal frame in MATLAB developing environment.

(2) The optimized total weights for the three static wind load cases (ESWLs-A, ESWLs-B and their combination form) are very close; the optimized total weight reduced to its initial values by about 26%~28%. However the distributions in the cross section size were slightly different.

(3) The optimized weight for the static wind load from GLF method reduced by only 23%, which indicated that it was more reasonable to conduct the structural optimization for the portal rigid frame by adopting the ESWLs from LRC method.

(4) The optimized weights generally reduced in a nonlinearity style with the increased support stiffness and the connection stiffness of semi-rigid connection. But the optimized weights almost unchanged when the support or connection stiffness reached above a certain specified value.

6 ACKNOWLEDGEMENTS

The work described in this paper was fully supported by grants from the National Science Foundation of China (51078096 and 50978063), National Science Foundation of Guangdong province (07300081), and the Program for New Century Excellent Talents in Universities of Ministry of Education of China (NCET-09-0082). The financial support is gratefully acknowledged.

7 REFERENCES

[1] American Society of Civil Engineers, Minimum Design Loads for Buildings and Other Structures, ASCE/SEI 7-10, Reston, VA, 2010

[2] T. Whalen, E. Simiu, G. Harris, J. Lin and D. Surry, The use of aerodynamic databases for the effective estimation of wind effects in main wind-force resisting systems: application to low buildings, J. Wind Eng. Ind. Aerodyn., 77&78 (1998) 685-693.

[3] J.A. Main and W.P. Fritz, Database-assisted design for wind: Concepts, software, and examples for rigid and flexible buildings. NIST Building Science Series 180, National Institute of Standards and Technology, Gaithersburg, MD,2006

[4] K.Z. Truman and D.J. Petruska, Optimum design of dynamically excited structural systems using time history analysis, International Conference for Computer Aided Optimum Design of Structures, Boston, 1992, pp. 197-207

[5] G.J. Park, Technical overview of the equivalent static loads method for non-linear static response structural optimization, Struct Multidisc Optim, 43 (2011) 319–337.

[6] M.R. Khan, K.D. Willmert and W.A. Thornton, A new optimality criteria method for large scale structures, Proc. of AIAA 19th Structures, Structural Dynamics and Material Conf., Bethesda, Md., 1978, pp. 47-50.

[7] C.M. Chan, Automatic optimal design of tall steel building frameworks, J. Struct. Eng., 121(1995) 838-847.

[8] Computers and Structures. SAP2000 API Documentation. Computers and Structures Inc. Berkeley, CA, 2008

[9] J.D. Holmes, Effective static load distributions in wind engineering, J. Wind Eng. Ind. Aerodyn., 90(2002), 91-109

[10] Tokyo Polytechnic University. Aerodynamic database of low-rise buildings[EB/OL]. Tokyo, Japan, 2011, http://www.wind.arch.t-kougei.ac.jp/info_center/windpressure/lowrise/mainpage.html

[11] A.G. Davenport, Gust loading factor, J. Struct. Eng., 93(1967), 11-34

[12] C. Faella, V. Piluso and G. Rizzano, Structural Steel Semi-rigid Connections: Theory, Design and Software. CRC Press, 2000

The Seventh International Colloquium on Bluff Body Aerodynamics and Applications (BBAA7)
Shanghai, China; September 2-6, 2012

Cross spectra of wind pressures on domed roofs in boundary layer wind tunnel

Yuan-Lung Lo [a], Jun Kanda [b]

[a] *Tamkang University, Tansui, New Taipei City, Taiwan*
[b] *Nihon University, Chiyoda, Tokyo, Japan*

ABSTRACT: This research intends to investigate the cross spectrum characteristics of wind pressure fluctuations on the surface along the meridian of domed roofs under turbulent wind flows. Wind pressure experiments of domed roofs are conducted considering two roof curvatures and three heights of side walls. From the experimental results, various distribution types of co-coherences are examined and the traditional exponential decaying form is shown insufficient to approximate the general characteristics of co-coherences. By combining the proposed models by Uematsu et al ([1]) and Kanda et al ([2]) and also a phase shift parameter included, the approximation model is then improved to represent the observed coherences generally.

KEYWORDS: Domed roof, Roof curvature, Wind pressure fluctuation, Cross spectrum, Root-coherence, Phase distribution

1 INTRODUCTION

The curved geometric appearance makes the estimation of wind loads a difficult task for wind resistant design of a dome structure. Wind pressure distributions on the roof become more complicated due to the occurrence of separation and the formation of wake. Researches regarding the curved roofs or domed roofs have been investigated for the past two decades, typically the hemispherical domed roofs. Taylor ([3]) measured mean and R.M.S. pressures on the surfaces of domed roofs. Ogawa et al ([4]) investigated mean and R.M.S. wind pressures and spectrum characteristics of domed roofs with three height span ratios in one laminar and two turbulent boundary layer flows. Uematsu et al ([1]) proposed a computer-assisted wind load evaluation system for the design of roof cladding of hemispherical domes. Cheng et al ([5]) conducted a series of wind tunnel tests to investigate the effects of Reynolds number on the aerodynamic characteristics of hemispherical dome in smooth and turbulent boundary layer flows.

However, discussions on cross spectra of wind pressures on domed roofs have not been made sufficiently and usually only one uniform exponential decaying distribution is assumed for all cross spectra on one specific dome roof (Hongo [6]). In this research, wind pressure characteristics and distribution types of cross spectra are examined and the effects of roof curvatures and height-span ratios are investigated. A general approximation model is then proposed to achieve better agreement of approximation, especially for the cross spectra near the separation point.

2 SIMULATED TURBULENT WIND FLOW

2.1 Experimental setting of simulation of turbulent flow and acrylic domed models

The indoor closed-circuit Eiffel type wind tunnel simulator in University of Tokyo is used to generate turbulent boundary layer flow for the wind pressure experiments in this research. The geometric size of the working cross section is 1.8m×1.8m×15.6m. Turbulent wind flow is simu-

lated by the arrangement of spires and roughness blocks to fit the urban terrain (terrain IV, power law index $\alpha = 0.27$) specified in AIJ recommendation ([7]). Wind speed at boundary layer height is 11.00m/sec (U_g). I-type hot wire probe is used for measurements of wind profiles and fluctuating wind speeds. Figure 1 shows the normalized mean wind profile and the turbulence intensity profile compared to the distribution for terrain IV in AIJ model.

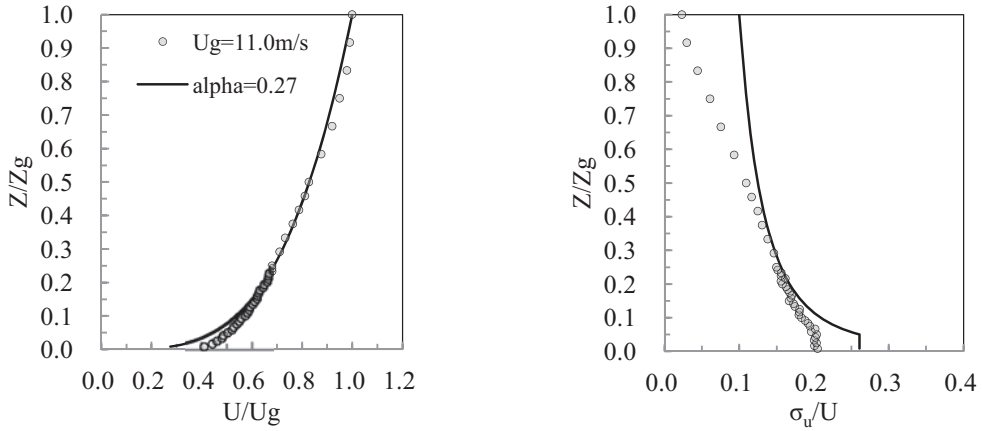

(a) Mean wind speed profile (b) Turbulence intensity profile

Figure 1 Normalized profiles of mean wind speeds and turbulence intensities

Wind pressure measurements in this research are conducted by the micro-pressure measuring system manufactured by Kyowa Electronic Instruments Co., Ltd. Fluctuating pressures on the surface of domed models are simultaneously recorded and then digitalized for saving and further analyses. Each domed model is composed of two acrylic models, a roof model and a cylinder model. The geometric definitions of a testing model are shown in Figure 2. The span of the roof models is fixed to be 300mm. Vinyl tubes for pressure measurements are arranged to taps along the meridian parallel to the wind direction. Two roof curvatures and three side wall heights are selected to understand generally the geometric effect. Table 1 lists the nomenclature of domed models in this research. 1/400 is assumed for the length scale ratio, 1/70 for the time scale and 1/5.7 for the wind speed scale ratio. Figure 3 shows the coordinates inside the wind tunnel.

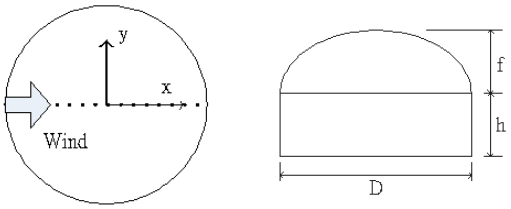

Figure 2 Geometric definitions of a domed model

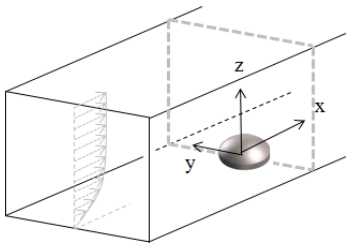

Figure 3 Coordinates inside wind tunnel

Table 1 Nomenclature of domed models

D = 300mm		f/D (roof height to span) 0.2	0.5
h/D (cylinder height to span)	0.0	C0	F0
	0.2	C2	F2
	0.5	C5	F5

Reynolds numbers of domed models are defined as the hemispherical domes by the roof span, mean wind speed at model height, air density, and viscosity constant ([1]). Mean wind speed at the height of the models is varying from 5.1m/sec to 7.5m/sec. The range of Reynolds numbers is 1.1×10^5~1.6×10^5. According to Cheng et al ([5]), when the turbulence intensity of approaching wind is high enough (>18%~20%), the Reynolds number effect is less significant when it is larger than 10^5.

2.2 Basic characteristics of fluctuating wind speeds

Power spectra of fluctuating wind speeds along the vertical profile are examined. Two examples at z=60mm and 150mm are plotted with Karman's model in Figure 4 to show fairly good agreements. σ_u represents standard deviation of fluctuating wind speeds; $S_u(n)$ represents the power spectral density; n represents the frequency; L_{ux} represents the length scale in the along-wind direction; U_z represents the mean wind speed at elevation z.

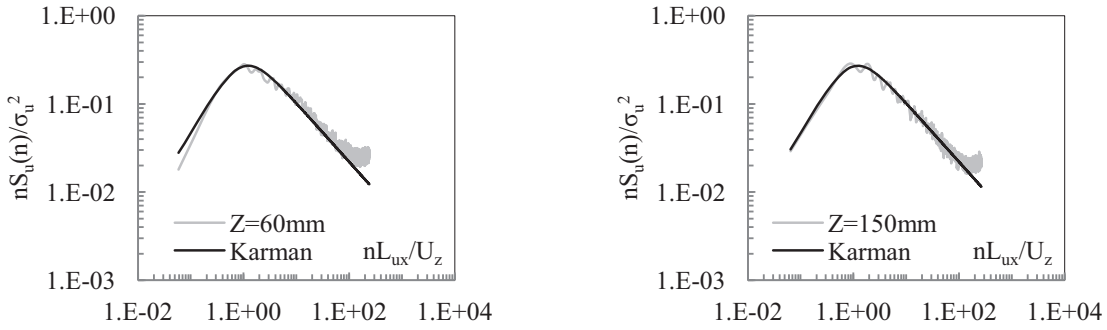

(a) Z = 60mm (b) Z = 150mm

Figure 4 Power spectra of fluctuating wind speeds at elevations

For fluctuating wind speeds at any two points, the cross spectrum of two fluctuating wind speeds or pressures between two points can be defined as follows.

$$S_{12}(r,n) = S_{12}^{C}(r,n) + iS_{12}^{Q}(r,n) \tag{1}$$

where r represents the distance between point 1 and 2; $S_{12}^{C}(r,n)$ represents the real part, co-spectrum; and $S_{12}^{Q}(r,n)$ represents the imaginary part, quadrature-spectrum. Coherence functions can be further defined as the following equations, equation (2) for co-coherence, (3) for root-coherence, and (4) for phase function.

$$C_{12}(r,n) = \frac{S_{12}^{C}(r,n)}{\sqrt{S_1(n)\cdot S_2(n)}} \tag{2}$$

$$R_{12}(r,n) = \frac{\left|S_{12}^{C}(r,n) + iS_{12}^{Q}(r,n)\right|}{\sqrt{S_1(n)\cdot S_2(n)}} \tag{3}$$

$$\theta_{12}(r,n) = \tan^{-1}\left(\frac{S_{12}^{Q}(r,n)}{S_{12}^{C}(r,n)}\right) \tag{4}$$

where $S_1(n)$, $S_2(n)$ represent power spectrum of fluctuating wind speeds at point 1, 2.

Davenport ([8]) proposed a model for root-coherence between two points at different elevations. As the distance increases, the coherence decreases.

$$R_{12}(r_z, n) = \exp\left(-k_z \frac{r_z \cdot n}{\overline{U}_{10}}\right) \tag{5}$$

where k_z is the decay factor around 7.7 and r_z is the vertical distance of two points; U_{10} is the mean wind speed at 10 meter height. Kanda et al ([2]) investigated the variation of coherence near zero frequency and then proposed a modified frequency term for a better modeling. Equation (6) represents the modified co-coherence model.

$$R_{12}(r_y, r_z, n) = \exp\left(-\frac{\sqrt{k_{1y}^2(z_m)\cdot r_y^2 + k_{1z}^2(z_m)\cdot r_z^2}}{\overline{U}_{10}} \cdot n^*\right) \tag{6}$$

$$n^* = \sqrt{\left(\frac{\overline{U}_{10}}{k_2 L(z_m)}\right)^2 + n^2}$$

$$k_{1y}(z_m) = k_y(10)\cdot\left(\frac{z_m}{10}\right)^{-\alpha_{Dy}} = 7.0\left(\frac{10}{z_G}\right)^{-\alpha_{Dy}+\alpha}\left(\frac{z_m}{10}\right)^{-\alpha_{Dy}}$$

$$k_{1z}(z_m) = k_z(10)\cdot\left(\frac{z_m}{10}\right)^{-\alpha_{Dz}} = 6.0\left(\frac{10}{z_G}\right)^{-\alpha_{Dz}+\alpha}\left(\frac{z_m}{10}\right)^{-\alpha_{Dz}}$$

$$\alpha_{Dy} = \alpha_{Dz} = 0.3 + \frac{\alpha}{2}$$

where the subscript, m, represents the geometric average of two points. L(z) is length constant; k_1 and k_2 are the decay factors determining the decaying tendency and the root-coherence value at zero frequency. Co-coherences of two fluctuating wind speeds vertically or horizontally are calculated and compared with root-coherence models of (5) and (6) to verify the consistent characteristics of the simulated turbulent wind flow. Figure 5 and Figure 6 respectively show two cases of vertical co-coherences and two cases of horizontal co-coherences. The coordinates of two points are indicated as Figure 3. It is indicated that Kanda's model provides both better fittings at zero frequency and the whole tendency. It is also known that the decay factor increases with the distance of two points increases since the coherence become weaker. The decay factors are estimated 9.8 and 12.9 in Figure 5(a) and 5(b); 8.8 and 16 in Figure 6(a) and 6(b).

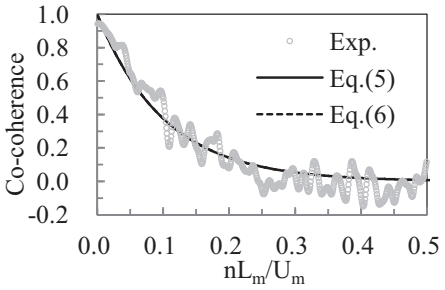

(a) $y_1=y_2=0$; $z_1=60$mm, $z_2=30$mm

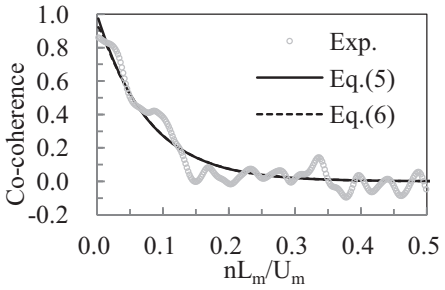

(a) $y_1=y_2=0$; $z_1=150$mm, $z_2=60$mm

Figure 5 Vertical co-coherences compared with equation (5) and (6)

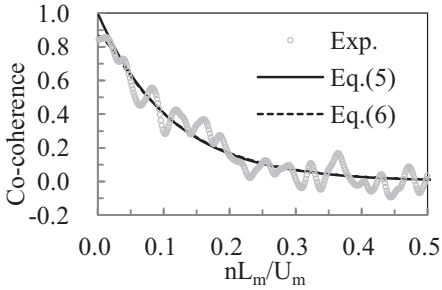

(a) y_1=0, y_2=50mm; z_1=z_2=30mm

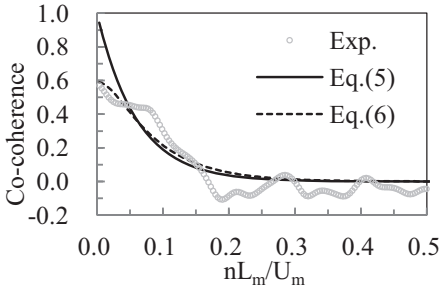

(a) y_1=0, y_2=150mm; z_1=z_2=90mm

Figure 6 Horizontal co-coherences compared with equation (5) and (6)

3 CHARACTERISTICS OF FLUCTUATING WIND PRESSURES

3.1 Distributions of wind pressure coefficients

Wind pressure measurements of domed models are conducted under the simulated turbulent wind flow mentioned in the previous section. The sampling rate is 1000Hz for a 2 minute record. According to the time scale ratio assumed, 14 segments are averaged for the observation results. Moving averaging is also conducted by 1 second average. The definitions of mean and R.M.S. wind pressure coefficients are as follows.

$$C_{p,i} = \frac{p_i - p_s}{q_H} \tag{7}$$

$$C_{p,mean} = \frac{1}{N}\sum_{i=1}^{N} C_{p,i} \tag{8}$$

$$C_{p,rms} = \sqrt{\frac{1}{N}\sum_{i=1}^{N}\left(C_{p,i} - C_{p,mean}\right)^2} \tag{9}$$

$$q_H = \frac{1}{2}\rho\overline{U}_H^2 \tag{10}$$

where p_i and p_s represent instantaneous wind pressure at the i-th point and reference static pressure at model heights. ρ is air density. U_H is the mean wind speed at model heights.

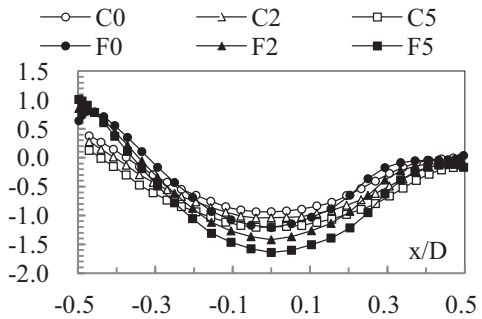

Figure 7 Distributions of mean wind pressure coefficients, $C_{p,mean}$

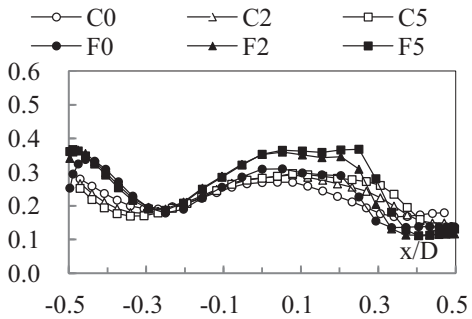

Figure 8 Distributions of R.M.S. wind pressure coefficients, $C_{p,rms}$

Pressure coefficients are plotted in Figure 7 and 8 with respect to f/D and h/D for the mean and RMS respectively to indicate the effects caused by roof curvature and the side wall height. Wind pressures along the meridian can be roughly divided as the windward region, the apex region, and the leeward region. Positive mean wind pressure coefficients can be expected since wind pressure fluctuations in the windward region are mostly affected by the approaching wind. As the flow moves downstream, a thin shear boundary layer forms along the roof surface and negative mean wind pressures are generally distributed in the apex region and leeward region. The apex region and the leeward region are divided by the occurrence of flow separation. Maximum negative pressures can be observed in the apex region. Small mean and R.M.S. coefficients in the leeward region are also indicated. To clarify the wind flow changes on the roof surface, the correlation coefficients between any two neighboring taps are calculated to show the three zones with different patterns as Figure 9.

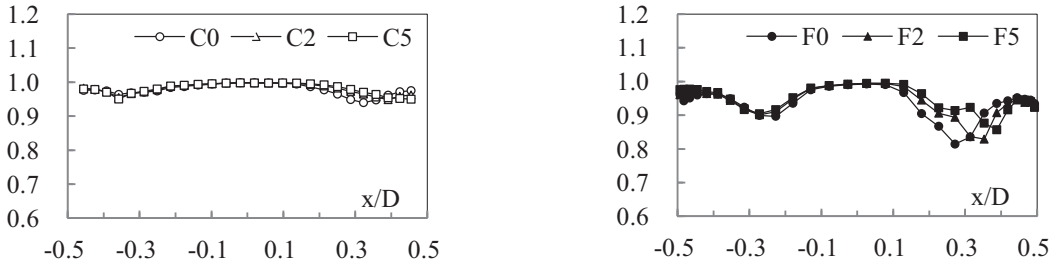

(a) f/D=0.2 models (b) f/D=0.5 models

Figure 9 Distributions of correlation coefficients between two neighboring vinyl tubes

As shown in Figure 9, relatively lower correlation coefficients are observed whenever the wind flow changes. For f/D=0.2 models, the range of the apex region is larger than that for f/D=0.5 models. However, three regions can be more clearly distinguished in those models with higher roof curvatures. It is also indicated that the increase of side wall height slightly pushes the separation point downstream. The three regions can also be named as “windward zone”, “separation zone” and “wake zone” according to the dominant characteristics in each region. Such zoning concept is further used for demonstrating various distribution types of spectrum characteristics in the next two sections. Table 2 lists the channel numbers in each zone/region (zone, hereafter) based on the observations results in this research.

Table 2 Identified channel numbers in three zones based on experimental results

Domed model		Windward zone	Separation zone	Wake zone
f/D=0.2	C0	1~4	5~21	22~27
	C2	1~4	5~24	25~27
	C5	1~4	5~25	26~27
f/D=0.5	F0	1~8	9~20	21~29
	F2	1~8	9~20	21~29
	F5	1~8	9~21	22~29

3.2 Power spectrum characteristics of along the meridian of domed roofs

Power spectrum characteristics of fluctuating wind pressures have been discussed in many publications. Ogawa et al ([4]) proposed fitted parameters for power spectra in three domed models

with different roof curvatures. Qiu et al ([8]) proposed typical power spectra for Gaussian and non-Gaussian zones and weighting factors to approximate power spectra along the meridian. Lo ([9]) then applied the similar idea to find typical power spectra in three zones and provided the fitted parameters of typical power spectra with respect to f/D and h/D for a database work.

Figure 10 shows the power spectra in F0 model to illustrate the dominant characteristics in each zone. The distribution shape of power spectral densities gradually varies from upstream to downstream. Three distinct zones can clearly be identified by several obvious features. For the power spectra in the windward zone, the distribution shape is similar to that of approaching wind speeds. When wind flow moves to the separation zone, a hump at lower frequency appears because of the formation of the thin shear boundary layer. After the occurrence of separation, turbulence energy is dominated by the component resulted from the thin shear boundary and the component resulted from the wake. Two humps are characteristically observed in the wake zone.

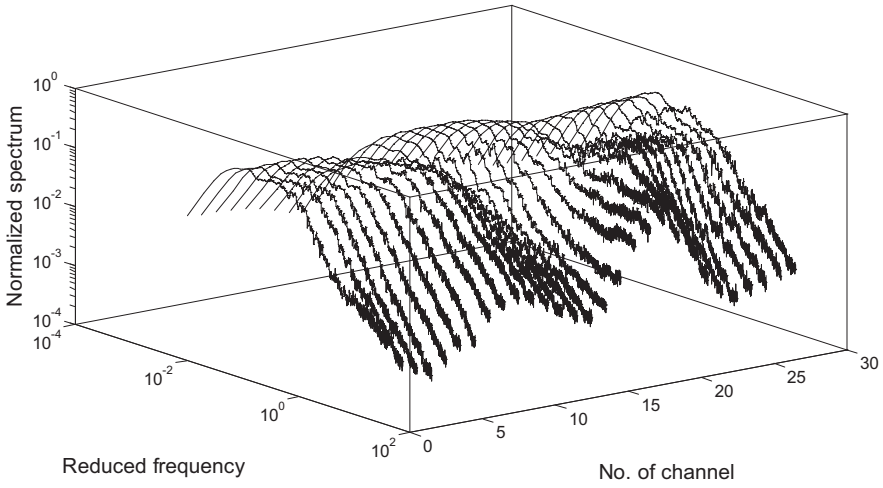

Figure 10 Power spectra along the meridian of F0 model with respect to channel numbers

3.3 Cross spectral characteristics of along the meridian of domed roofs

Cross spectral characteristics of two fluctuating wind pressures can also be examined by co-coherences, root-coherences, and phases, which are defined by equations (2) ~ (4). As discussed in the previous sections, it is clearly noted that each zone contains its specific dominant features in the distributions of wind pressure coefficients and power spectra. Based on the same zoning concept, cross spectra are examined within one zone and across two zones. Typical domed models, C0 model and F0 model, are selected for demonstrating various distribution types of co-coherences in Figure 11.

For co-coherences of two fluctuating wind pressures within the windward zone, a consistent decaying distribution is generally observed. The co-coherence values at zero frequency decrease as the distances between two points increase. It is also indicated that roof curvature results in less significant effect. Within the separation zone, co-coherences are observed to decay quicker with increasing roof curvature and the distance. Within the wake zone, co-coherences remain almost consistent as distance or roof curvature varies. For the co-coherences across the windward zone and separation zone, it is interesting to observe two different patterns when the distance of two points across the apex of the domed model or not. The co-coherence value at zero frequency is negative when the distance across the apex. A clear hump is indicated around reduced frequency

equals 0.1, where a hump can also be pointed out in the distributions of power spectra in the separation zone at lower reduced frequency range. For the co-coherences across the separation zone and wake zone, dramatic decaying is generally observed, especially the cases with larger roof curvature. Low and almost unvaried co-coherences are observed when the distance across the windward zone and the wake zone.

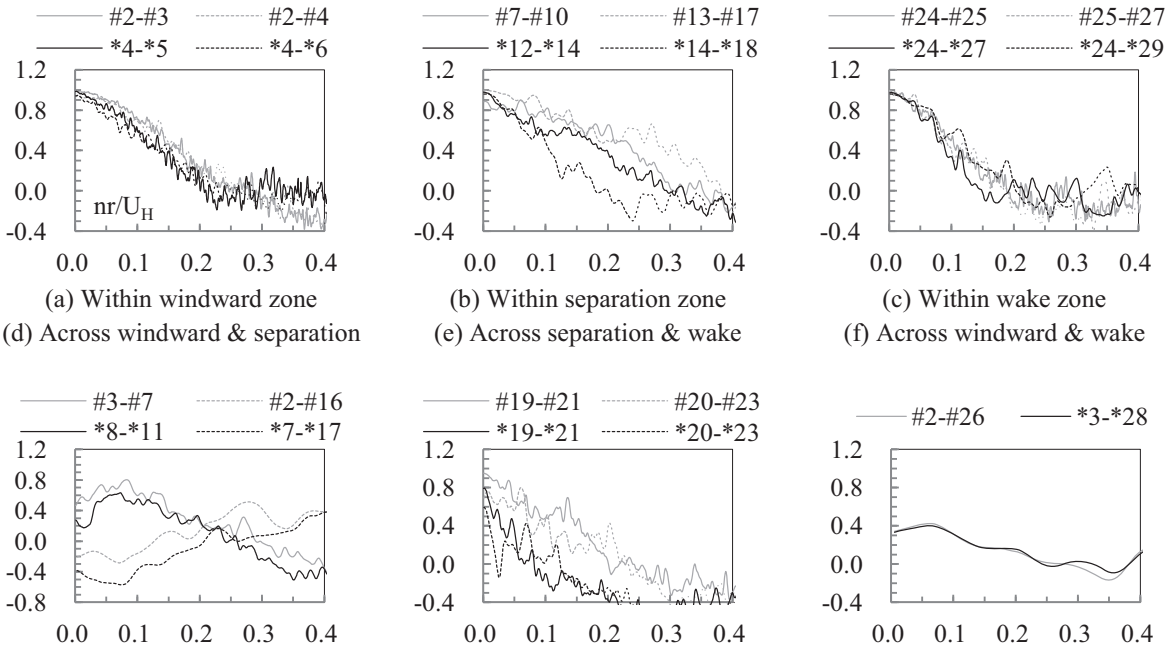

Figure 11 Co-coherences within one zone and across two zones (#: C0 model, *: F0 model)

It is summarized from the aforementioned observations that several features should be focused once the approximation of co-coherence is considered: (1) decaying tendency; (2) co-coherence value at zero frequency; (3) the hump at low reduced frequency corresponding to the dominant power spectrum characteristics in the separation zone; (4) negative co-coherence value when the distance of two points across the windward zone and the separation zone, especially two points are at the upstream side and downstream side of the apex respectively.

4 APPROXIMATION MODELS OF CO-COHERENCES

Different from approximation of fluctuating wind speeds, co-coherences of wind pressures cannot be conveniently replaced by root-coherence and described by Davenport's or Kanda's model. In order to generally approximate the features shown in Figure 11, a formula is proposed by representing first root-coherence and phase separately and then combining by the following equation.

$$C_{p,12}(n) = R_{p,12}(n) \cdot e^{i\theta_{p,12}(n)} \tag{11}$$

where $C_{p,12}(n)$, $R_{p,12}(n)$, and $\theta_{p,12}(n)$ represent co-coherence, root-coherence, and phase of two pressures respectively. Ogawa et al ([4]) and Uematsu et al ([1]) ignore the imaginary part of phase and rewrite (11) as (12):

$$C_{p,12}(n) = R_{p,12}(n) \cdot \cos\left(\theta_{p,12}(n)\right) \tag{12}$$

To satisfy the observations of decaying tendency of co-coherence and the value at zero frequency, Kanda's model is slightly modified and substituted to equation (12) for approximating the root-coherence part. Further, to satisfy the hump observed at lower frequency ranges and two opposite patterns shown in Figure 11(d), two parameters are proposed for better approximation agreement. Equation (12) can then be re-written as follows.

$$\begin{aligned} C_{p,12}(r,n) &= \exp\left(-\frac{\sqrt{k_1{}^2 r^2}}{D}\cdot n^*\right)\cdot\cos\left(2\pi\cdot k_t\cdot\left|\frac{n\cdot r}{\overline{U}_H}-\hat{n}_{cr}\right|-d\theta\right) \\ n^* &= \sqrt{1+\left(\frac{n\cdot D}{k_2\overline{U}_H}\right)^2}-\hat{n}_{st} \end{aligned} \tag{13}$$

where k_1 and k_2 are decay factors determining the decaying tendency and the root-coherence value at zero frequency; k_t is a slope constant of the phase and dθ is a shift constant of phase at zero frequency. $\hat{n}_{cr}$ is the observed dominant reduced frequency of power spectra in the separation zone. $\hat{n}_{cr}$ is around 0.08~0.1 in this research and assumed 0.1 in general. For the co-coherences not across the windward zone and separation zone, $\hat{n}_{cr}$ and dθ can be assumed zero simply.

Approximation of co-coherences of F0 model shown in Figure 11 are conducted and plotted in Figure 12. Fairly good agreement of approximation is achieved by the improved model of equation (13) rather than the exponentially decaying model. Observed features of co-coherences can be satisfied by providing two more parameters, $\hat{n}_{cr}$ and dθ. The fitted parameters in Figure 12 are listed in Table 3 to indicate that only one unique distribution of co-coherence is insufficient for describing the spectrum characteristics, especially integration of wind loads is conducted among certain surface where the separation of wind flow occurs.

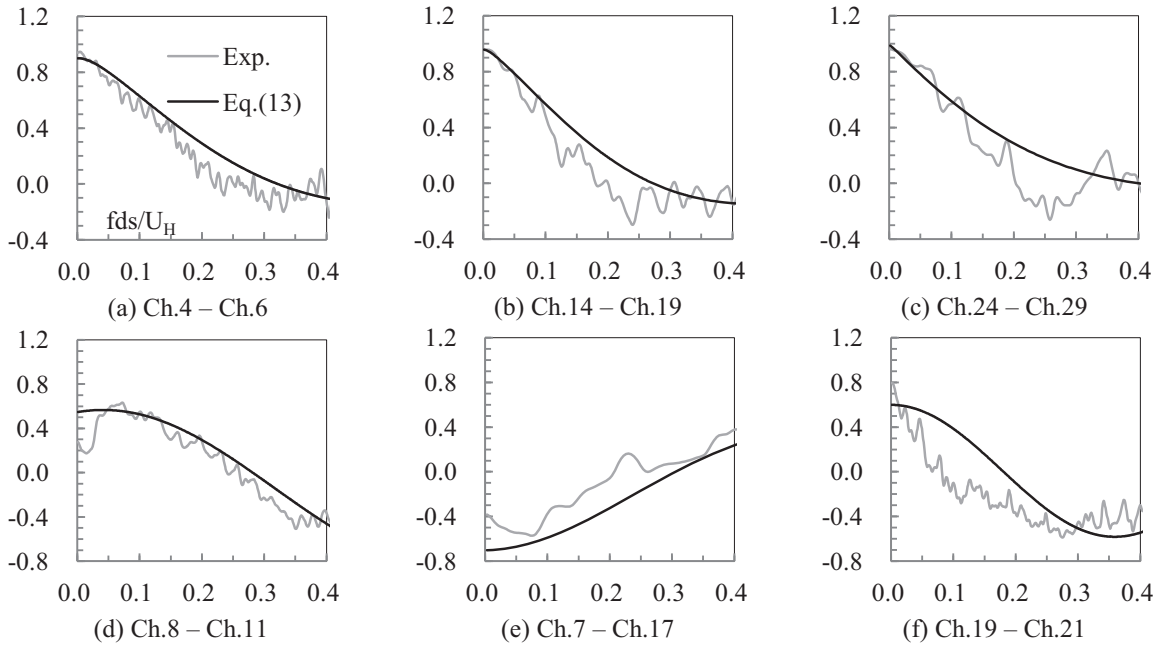

Figure 12 Approximation results of co-coherences in F0 models

Table 3 Fitted parameters of co-coherences in Figure 12 based on equation (13)

	k_1/k_2	k_t	n_{cr}	$d\theta$
Ch.4 – Ch.6	3.24	0.78	0.00	0.00
Ch.14 – Ch.19	3.88	0.92	0.00	0.00
Ch.24 – Ch.29	4.52	0.62	0.00	0.00
Ch.8 – Ch.11	0.56	0.86	0.10	-0.42
Ch.7 – Ch.17	1.48	0.43	0.10	2.61
Ch.19 – Ch.21	0.48	1.39	0.00	0.00

5 CONCLUSIONS

In this research, distribution types of co-coherences were examined and an improved approximation model was proposed by adding two more parameters considering the dominant characteristics of power spectrum and the phase shift when positive pressures convert to significant negative pressures. From the fitted parameters of the proposed model and the approximation results, it is clearly shown that only one unique exponential decaying term is insufficient to represent various coherence features of fluctuating wind pressures on the domed roofs. And it may be considered desirable for integrating wind loads to provide a general co-coherence form based on the zoning concept of wind flow changes.

ACKNOWLEDGEMENTS

Kajima Foundation is acknowledged for its financial support to the wind tunnel experiment in this research. Kyowa Electronic Instruments Co., Ltd. is also acknowledged due to its technological assistance on wind pressure measurement maintenance.

REFERENCES

1 Y. Uematsu, R. Tsuruishi, Wind load evaluation system for the design of roof cladding of spherical domes, J. Ind. Aerodyn., 96 (2008), 2054-2066.

2 J. Kanda, R. Royles, Further consideration of the height dependence of root-coherence in the natural wind, Building and Environment, 13 (1978), 175-184.

3 T. J. Taylor, Wind pressures on a hemispherical dome, J. Ind. Aerodyn., 40 (1991), 199-213.

4 T. Ogawa, M. Nakayama, S. Murayama, Y. Sasaki, Characteristics of wind pressures on basic structures with curved surfaces and their response in turbulent flow, J. Ind. Aerodyn., 38 (1991), 427-438.

5 C. M. Cheng, C. L. Fu, Characteristics of wind loads on a hemispherical dome in smooth flow and turbulent boundary layer flow, J. Ind. Aerodyn., 98 (2010), 328-344.

6 T. Hongo, Experimental studies of fluctuating wind pressures on dome-like roofs, PhD thesis (in Japanese), 1995.

7 Architecture of Institute of Japan, Recommendations for loads on buildings (2004), Maruzen Co., Ltd., 2004.

8 Y. Qiu, Y. Sun, Y. Wu, Power spectra of fluctuating wind pressures on spherical domes, Proceedings of 13th International Conference on Wind Engineering, Amsterdam, 2011.

9 Y. Lo, Characteristics of wind pressure fluctuations on dome-like structures, PhD thesis, 2012.

Wind-induced static performance of cooling tower considering multiple loading effects

X.X. Cheng [a], L. Zhao [a], Y.J. Ge [a]

[a] *State Key Laboratory for Disaster Reduction in Civil Engineering, Tongji University, Shanghai,China*

ABSTRACT: The pressure-measuring tests for certain super large cooling towers are first reported, so the static wind loads on the cooling towers can be easily illustrated with some parameters, such as the surface extreme value pressure distribution, the tower group factor; and the wind-vibration factor. With the help of the finite element method (FEM) numerical simulation, the performance of cooling towers due to the static wind loads, including stress, displacement and local elastic stability are presented. Then, considering material and geometrical non-linearities about the reinforced concrete, the ultimate bearing capacity of the structures under static wind action is also discussed. The analysis process focuses on considerations of some key effects concerning structural design works, i.e., the internal pressure effect, the distribution mode of external surface pressure, the boundary effect, the wind profile index and the group tower interference effect.

KEYWORDS: Cooling tower; Pressure-measuring test; Finite element numerical simulation; Local elastic stability; Material and geometrical non-linearity; Ultimate load bearing capacity

1 INTRODUCTION

Super large hyperbolic cooling towers are extremely sensitive to wind loads, which are usually the control load in structural design and construction. As China stages its fast-growing performance in construction of super large cooling towers and tower groups today, more expectations relating to these huge structures' wind resistance designs are given from engineering circles. However, it seems that the present technical supports can hardly meet current requirements based on the following facts. First, the current Chinese codes (e.g. NDGJ5-88 and GB/T 50102-2003) stipulate that the terms for computation of important design parameters, such as the tower-group factor and the wind-vibration factor, can only be applied to towers under a height of 165-meters. Besides, it is also stipulated in the Chinese codes that group tower interference effects can be ignored for those with bottom center distances above 1.5 times tower diameter, which is different from some other countries' codes (e.g. BTR VGB'Richtlinie Bautechnik bei Kühltürmen and Règles Professionelles applicable à la Construction des Réfrigérants Atmosphériques en Béton Armé) and has been proved to be imperfect by some wind tunnel experimental studies.

Rigid model pressure-measured wind tunnel tests of a 176-meter super large cooling tower and some group towers of different combinations were described briefly in the beginning of this study. Loading the extreme value wind pressure distribution patterns obtained from wind tunnel tests, which are taken as strong wind loads with design wind speed in certain return period, the static structural performances of the cooling towers with different condition combinations based on FEM numerical simulation introducing a bilinear material constitutive model and large deformation geometric nonlinearity considerations are presented. Then, results of the numerical studies including the structural response (internal force and displacement), the tower shell's local elastic stability performance as well as the total structure's ultimate load-carrying capacity are studied. The research process focus on studies of some key effects influencing the structural static performance, i.e. internal pressure effect, considerations for external pressure distribution, boundary effect, wind profile effect and group tower interference effect. The conclusions drawn are of practical significance to relating structural design works.

2 WIND TUNNEL TEST AND DATA PROCESSING

In a practical electric power plant situation in southeast China, a set of designing cooling towers are part of a dense arrangement of large buildings, which are of comparable size with the cooling towers. As a result, the influence of adjacent buildings or towers on cooling towers cannot be ignored, even though the towers' center distances conform to the basic requirements of the Chinese Codes (> 1.5 times the single tower diameter).

Table.1 Building dimensions in the electric power plant

Cooling tower height	177.147m
Tower top diameter	82.260m
Throat diameter	78.216m
Tower base diameter	134.694m
Minimum distance of towers	≥1.5 tower base diameter
Height of half sphericity bunker	80.0m
Chimney height	210.0 m
Hill height	56.5～136.0 m
Other building height	35.0～135.0m

The second stage of the project features two 177-meter super large cooling towers. To the west, there are four 80-meter hemispherical coal bunkers and an 80~140-meter high continuous mountain, and to the south, there is an industrial complex which includes two 210-meter tall chimneys. During the third stage of the project, two new towers, two additional new hemispherical coal bunkers and an industrial complex will also be constructed (see Fig.1 and Table.1 for building dimensions and site plan respectively).

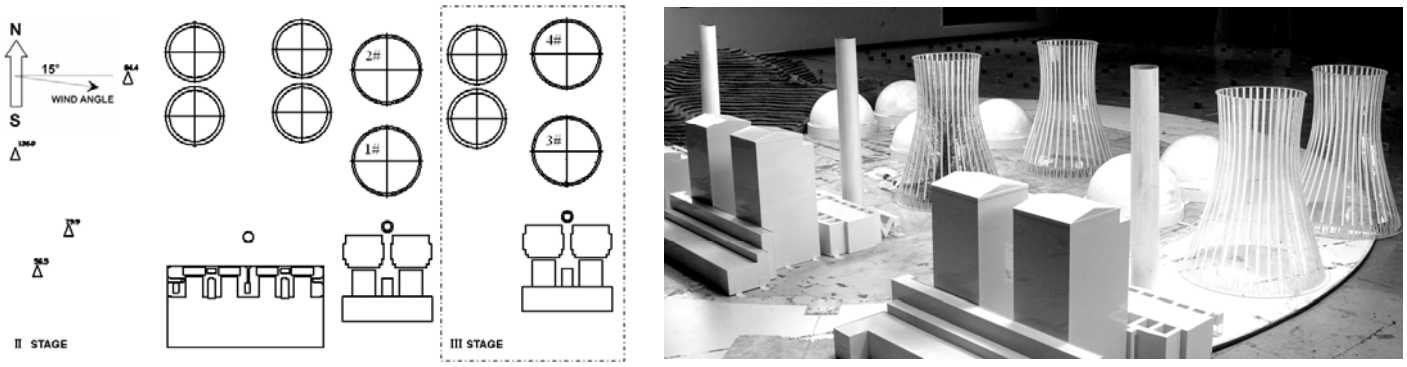

Site plan Site model

Fig.1 Ⅱ and Ⅲ stage cooling tower groups

The test was conducted in the TJ-3 atmospheric boundary layer wind tunnel, which belongs to Tongji University's State Key Laboratory for Disaster Reduction in Civil Engineering. As a closed return-flow wind tunnel with rectangular cross section, the dimensions of its test section are: 15m in the lateral direction, 14m in the longitudinal direction, and it has a height of 2m. Both external and internal pressure-measuring models of the super large cooling tower are 1:200 scale rigid models (see Fig.2), the blockage ratios of the cooling tower and surroundings are less than 7%.

The surrounding landscape of the project is type A according to NDGJ5-88 or GB/T 50102-2003. Measurement of atmospheric boundary layer uses a Streamline hot-wire anemometer of DANTEC Corp. It shows the following: the wind profile exponent a =0.12, the ground surface turbulence intensity is 15%, and the turbulence intensity at the height of the tower top is 10%.

The locations of the taps are shown in Fig.3. For the external pressure measuring tower model, 36 (around the circumferential direction) ×12 (along the meridian direction) taps are arranged. For the internal pressure measuring model, 36 (around the circumferential direction) ×6 (along the meridian direction) taps are arranged. DSM3000 electronic pressure scanners of Scanivalve Corp. are used for mean and fluctuating pressure measurements on model surface. The signal data are acquired at a sampling rate of 312.5Hz, and for each measuring point, the total sampling length is

6000.

Fig.2 a) Model for external pressure

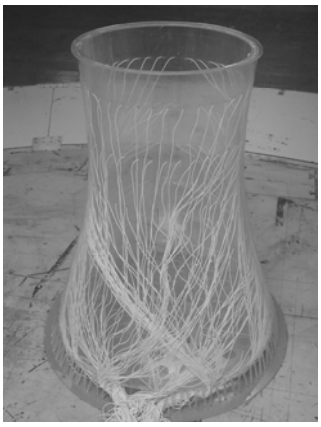

Fig.2 b) Model for internal pressure

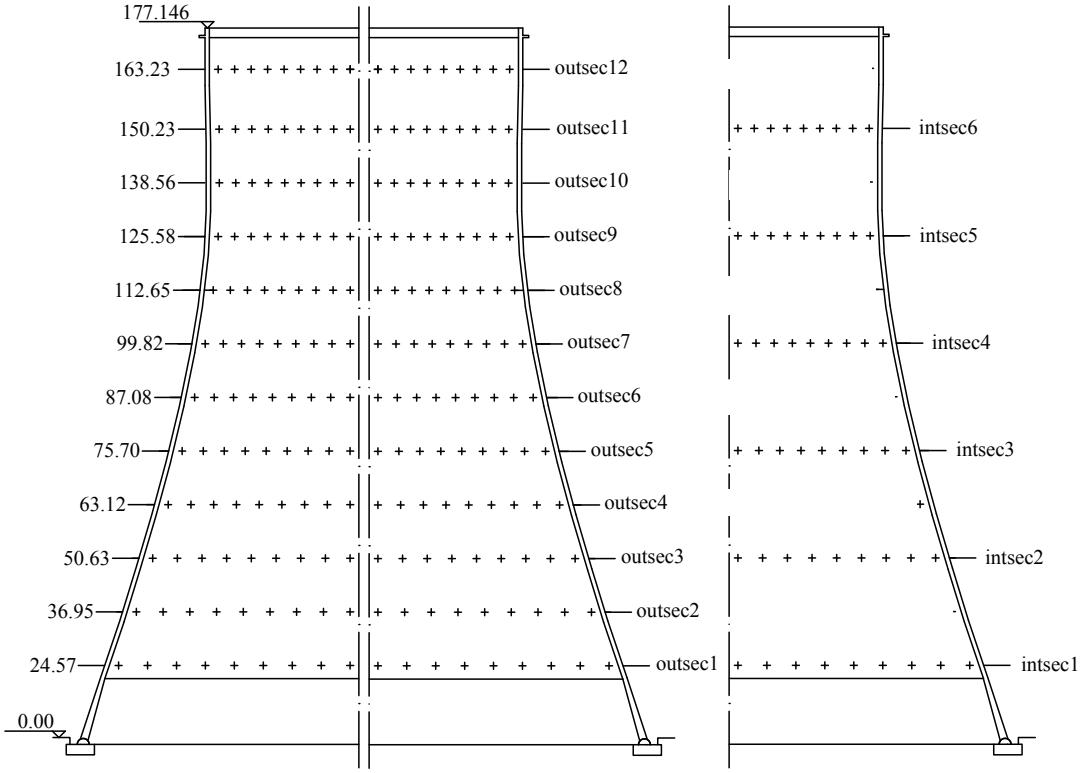

a) Height label (unit: m) b) Taps for external pressure c) Taps for internal pressure

Fig.3 Measured points of outside or inside wind pressure distribution and measured sections of wind-induced vibration response

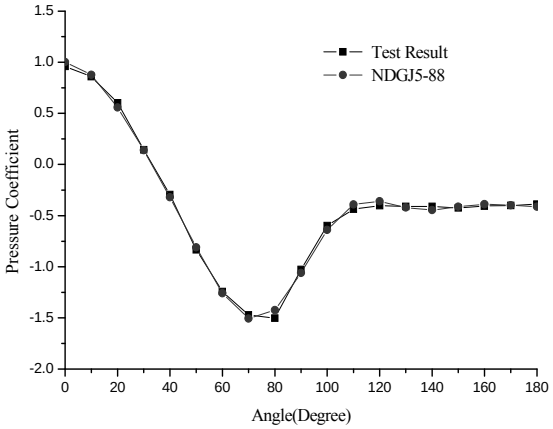

Fig.4 Pressure comparison of test and Codes

The Reynolds number scope ranges from 1.5×10^8 to 3.5×10^8 for the actual super large cooling tower of this project considering design wind speed. However, it is difficult to simulate the actual flow characteristics around the model tower's surface with a super-high Reynolds number by increasing the experimental wind speed and maximizing the models' geometric dimensions for the limitations of wind tunnel technique. The general practice in solving this problem is to adjust the surface roughness of tested cooling tower models to obtain the super-high Reynolds number effects for flow around the surface (see Fig.2), which is successfully done in this study as is shown from a good fitting between two pressure coefficient curves in Fig.4 which are acquired based on tests and code NDGJ 5-88 respectively. In Fig.4, the test results are the mean value of several pressure coefficient distribution patterns around some intermediate pressure-measured cross-sections on the surface of the external pressure measuring model and the data from code NDGJ 5-88 are based on some actual measurement works. The external pressure distribution patterns around a single tower's surface fit a curve in the form of eight-termed trigonometric series according to NDGJ5-88 or GB/T 50102-2003:

$$m_p(q) = \sum_{k=0}^{m} a_k \cos kq \tag{1}$$

in which, fitting parameters a_0=-0.779，a_1=0.313，a_2=1.016，a_3=0.737，a_4=0.044，a_5=-0.1429，a_6=0.074，a_7=0.086.

The definition of a cooling tower's total aerodynamic drag force coefficient (along-wind direction) is as follows:

$$C_D = \frac{\sum_{i=1}^{n} C_{Pi} A_i \cos(q_i)}{A_T} \tag{2}$$

in which, C_D is the structural total drag force coefficient, A_i is the coverage area of the pressure measuring point i, θ_i is the separation angle between the pressure action direction on point i and the wind axis, A_T is the whole structure's projection area along the wind axis.

Considering the time-history correlation between the shape coefficient on the taps and the total structural drag or lift force, the mean results of the pressure extreme value distribution patterns on several intermediate cross-sections are obtained. Fig.5 compares the distribution patterns between the general envelope of test extreme values and codes, which demonstrates that although the pressures in the wake zone and the separation points are the same, there exist certain differences: the maximum and minimum values in the test pressure coefficient extreme value distribution pattern are 1.298 and -2.307 respectively, which equal to 78% and 87% of the code extreme values (1.668 and -2.603, respectively), and the difference of the corresponding angles of maximum negative pressure reaches 10 degrees.

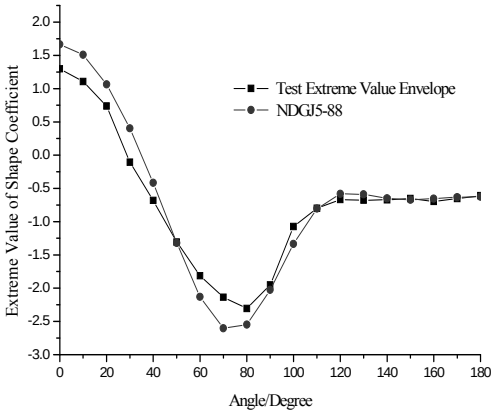

Fig.5 General envelope of test values and codes

According to time domain dynamic analysis based on multipoint fluctuating pressure time history data and aeroelastic model wind tunnel tests (prior works), the wind-vibration factors have been obtained for this project: 1.70 for single tower, 2.22 for two-tower group combination (at the most adverse incoming flow condition), and 2.50 for four-tower group combination (at the most adverse incoming flow condition).

If the tower surface pressure distribution pattern provided by NDGJ5-88 is adopted, the mean value of drag coefficient is 0.437 for uniform flow. For comparison study, the tower group factor is defined as:

$$K_m = \frac{C_{D,\max,single} \cdot P_{ch} \cdot K \cdot M_{if}}{C_{D,mean,single,code} \cdot b_{single,test}} \tag{3}$$

in which, $C_{D,max,single}$ is the extreme value of the drag force coefficient for a single tower in turbulence flow field (0.541); for type A atmospheric flow, P_{ch}=0.541/0.397=1.36 is the ratio of drag force coefficient for a single tower in uniform flow to that in turbulent flow; K is the maximum ratio of the ultimate value of the drag force coefficient of an interfered tower to that of the single tower; M_{if}=1.0+$\beta_{single,test}/\beta_{single,code}$ is the correction term of the tower's wind-induced inertia force, $\beta_{single,test}$ and $\beta_{single,code}$ are the wind-vibration coefficient results based on experimental results (1.70) and code NDGJ5-88 (1.60), respectively; $C_{D,mean,single,code}$ is the mean value of a single tower's drag force coefficient in uniform flow of NDGJ5-88 (0.437). Intrinsically, K_m can be interpreted as the ratio of the experimental value of the total static wind loads for all conditions to total wind load on a single tower based on the codes.

For both the second stage project and the third stage project, the most adverse incoming flow conditions both feature a direction of a clockwise 15° included angle from the east. According to formula (3), tower group factors for a two tower group and a four tower group are 1.226 and 1.385, respectively.

The penetration ratio of the packing layer is modeled using a uniformly pierced organic glass board placed at the bottom of the tower's main body. Experimental results in type A turbulent flow show that the penetration rate has no significant effect on internal pressure distribution patterns, but it is closely related to the internal pressure value. The internal pressure mean value increases when decreasing the draught penetration ratio (see Table.2). For some experimental conditions, the draught penetration ratio is 30%, so the internal pressure distributes uniformly inside the tower shell with the extreme value of -0.656.

Table.2 Internal pressure coefficients of single cooling tower

Draught penetration ratio	100%	55%	30%	15%	3%	0%
Internal pressure mean value*	-0.375 × 1.6	-0.382 × 1.6	-0.410 × 1.6	-0.524 × 1.6	-0.590 × 1.6	-0.761 × 1.6

* Reference wind pressure is wind pressure at the top of tower.

3 FINITE ELEMENT MODEL

The main body of the FEM model is comprised of discrete spatial shell elements, and the top stiffening ring and 48 pairs of herringbone columns connected to a ring foundation with fixed bottom ends are modeled using space beam elements. Two different models using a different number of shell elements (one applies 504 shell elements, the other applies 19008 shell elements) are compared. Results show that none of the relative errors among their corresponding 1st~ 8th modal frequencies is less than 3%, and their corresponding vibration modes are the same. For simplification, the simple model, which applies 504 (36*14) shell elements, is adopted. The main structural characteristics are presented in table.3. Natural frequencies and vibration shapes of the 1st~4th modes are presented in table.4.

Table.3 Main structural characteristics of cooling tower

Component	Height/m	Shell thickness/m	Radius/m	Concrete grade	3D View of cooling tower FE model
Main body	12.216	1.400	67.347	C40	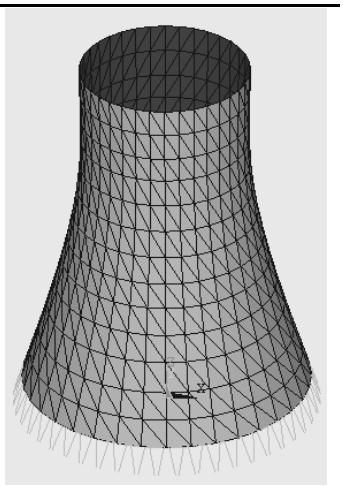
	24.811	0.350	63.334	C40	
	37.405	0.340	59.380	C40	
	50.000	0.330	55.217	C40	
	62.594	0.330	51.656	C40	
	75.189	0.320	48.357	C40	
	87.784	0.320	45.685	C40	
	100.378	0.310	43.123	C40	
	112.973	0.300	41.103	C40	
	125.568	0.271	39.731	C40	
	138.162	0.271	39.132	C40	
	150.757	0.271	39.229	C40	
	163.351	0.271	39.543	C40	
	175.946	0.400	39.860	C40	
Herringbone column	48 pairs, 1300mm diameter			C45	

Table.4 Natural frequency and vibration shape of cooling tower

Mode	Frequency/Hz	Mode shape (number of harmonic waves)	View of mode shape	Mode	Frequency/Hz	Mode shape (number of harmonic waves)	View of mode shape
1st	0.939	circumferential 5; meridian 2	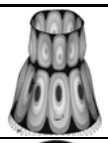	3rd	1.075	circumferential 4; meridian 2	
2nd	1.044	circumferential 5; meridian 2	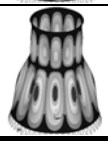	4th	1.125	circumferential 3; meridian 1	

4 SOME KEY EFFECTS ON COOLING TOWERS' WIND-INDUCED STATIC PERFORMANCE USING LINEAR ELASTIC FEM ANALYSES

For this part of the study, the 100 years basic design return period wind speed is 33m/s, the wind profile index is 0.12, and the dead weight is taken into account in load combination.

4.1 Internal pressure effect

Table.5 Response of cooling tower for different internal pressure conditions

Condition		Internal pressure extreme value	Maximum total deformation /m	Maximum primary tensile stress /MPa	Maximum primary compressive stress /MPa
Draught penetration Ratio	100%	-0.637	0.0366	0.733	4.23
	30%	-0.658	0.0366	0.729	4.23
	10%	-0.717	0.0366	0.717	4.23
	0%	-1.082	0.0367	0.644	4.22
No internal pressure		0.0	0.0364	0.868	4.23
General consideration in practical design (NDGJ5-88)		-0.8 (-0.5×1.6)	0.0366	0.701	4.23

The pressure on the external surface of the cooling tower applied for analyses follows the single tower's extreme value distribution pattern obtained in the wind tunnel test mentioned above. Table.5 compares the cooling tower's response under static wind of different internal pressure conditions, demonstrating that with the increase of the draught penetration ratio of the stuffing layer, the absolute value of the negative internal pressure decreases, and the cooling tower's maximum total displacement and the primary compressive stress undergo little change. The maximum primary tensile stress drops smoothly with the increase of the absolute value of the internal pressure as shown in Table.5 (a 12.14% decrease from 100% to 0% draught penetration ratio condition). An analysis based on a representative code (NDGJ5-88) renders results of all structural performances between those of 0% and 10% draught penetration ratio. It is also proved that disregarding the internal pressure is a risky practice in view of the maximum total deformation response.

4.2 Effect of the external pressure extreme value distribution patterns

Through correlation analysis of multipoint fluctuating wind loads on the cooling tower's external surface, the extreme value distribution patterns of the tower's external pressure are obtained (see Fig.5). Compared with the traditional methodology using the mean surface wind pressure distribution pattern from NDGJ5-88 multiplied by a wind-vibration factor, it is found that the method of loading the experimental extreme pressure distribution causes favorable overall structural responses, demonstrating the safe consideration of code NDGJ5-88 (see Table.6). From Table.6, there exists a little disagreement of the occurrence positions of maximum responses between the two methodologies, which is also a major concern in structural design.

Table.6 Response of cooling tower for different external pressure modes

External pressure distribution pattern	Maximum total deformation			Maximum primary tensile stress			Maximum primary compressive stress		
	Response magnitude/m	Occurrence position		Response magnitude/MPa	Occurrence position		Response magnitude/MPa	Occurrence position	
		relative to tower height	Included angle from incoming flow		relative to tower height	Included angle from incoming flow		relative to tower height	Included angle from incoming flow
Experimental result	0.0388	0.746	0°	0.786	0.848	±85°	4.34	0.286	±70°
Traditional consideration (NDGJ5-88)	0.0475	0.783	0°	1.260	0.885	±75°	4.77	0.286	±70°

4.3 Group tower interference effect

Applying the two methodologies mentioned above to consider the external surface pressure distribution, Table.7 shows the cooling towers' responses with different group tower combinations. The responses obtained by loading the pressure distribution pattern obtained from the codes (hereinafter referred to as the traditional methodology) are stronger than the corresponding results obtained by loading pressure distribution patterns based on wind tunnel tests. The occurrence positions of both the maximum total deformation and the primary tensile/compressive stress of the traditional methodology are slightly higher than the computational results using experimental pressure distributions. Difference around 10 to 15 degrees exists between the circumferential occurrence points of the maximum primary tensile stress on the curves calculated using different methodologies considering corresponding group tower combination conditions.

It is notable that by loading the experimental extreme value wind pressure distribution patterns acquired through correlation analysis, the magnitudes of the structural responses of different group tower conditions demonstrate a variation trend different from that of the tower group factors (i.e. the tower group factor for the four tower group condition > that for the two tower group condition > that for the single tower condition, see Section 2). For both the maximum total deformation and the maximum primary compressive stress, the trend is: the responses of the four tower group condition > those of the single tower condition > those of the two tower group condition. The phenomenon can be interpreted that although tower group factors and wind-vibration factors are both increasing when adding tower numbers in the tower group, the lateral load distribution and the load action center of vertical wind loads both change, and the shell thickness at the height of the total load action position changes accordingly, reflected by the descending trends of the heights of the maximum response positions, which is favorable in view of wind effects on the structures.

Table.7 Response of cooling tower with group tower interference effects

External pressure distribution pattern	Condition	Maximum total deformation			Maximum primary tensile stress			Maximum primary compressive stress		
		Response magnitude /m	Occurrence position		Response magnitude /m	Occurrence position		Response magnitude /m	Occurrence position	
			relative to tower height	Included angle from incoming flow		relative to tower height	Included angle from incoming flow		relative to tower height	Included angle from incoming flow
Extreme value (from experiment)	Single tower	0.0388	0.746	0°	0.786	0.848	±85°	4.34	0.286	±70°
	Two towers (second stage)	0.0335	0.746	0°	1.020	0.921	＋90°	4.29	0.247	±70°
	Four towers (third stage)	0.0453	0.709	0°	1.390	0.848	＋90°	4.75	0.247	±70°
Mean value (from NDGJ5-88) ×Km× β	Single tower× 1.70	0.0503	0.782	0°	1.35	0.885	±75°	4.91	0.286	±70°
	Single tower× 2.22	0.0653	0.782	0°	1.80	(0.885, ±75°) or (0.321, 0°)		5.66	0.286	±70°
	Single tower× 2.50	0.0734	0.782	0°	2.11			6.07	0.286	±70°

4.4 Effect studies based on local elastic stability check

As a large thin-walled shell structure, local elastic stability check should be included in a cooling

tower's structural design. According to NDGJ5-88, the following formulae are applied for analyzing of the shell's local elastic stability:

$$0.8K_B(\frac{s_1}{s_{cr1}}+\frac{s_2}{s_{cr2}})+0.2K_B^2[(\frac{s_1}{s_{cr1}})^2+(\frac{s_2}{s_{cr2}})^2]=1 \tag{4}$$

$$s_{cr1}=\frac{0.985E}{\sqrt[4]{(1-n^2)^3}}(\frac{h}{r_0})^{4/3}K_1;\quad s_{cr2}=\frac{0.612E}{\sqrt[4]{(1-n^2)^3}}(\frac{h}{r_0})^{4/3}K_2 \tag{5a,b}$$

in which, σ_{cr1} is circumferential critical pressure; σ_{cr2} is meridian critical pressure; σ_1、σ_2 are circumferential and meridian compressive stresses considering internal suction respectively; E，v are the elastic modulus and the Poisson ratio of shell concrete, respectively; r_0 is the throat radius of the tower body; h is the shell thickness at the tower throat; K_1、K_2 are both determined by the tower body's geometric parameters (in this study, K_1=0.138，K_2=1.267); K_B is the local stability safety factor.

Table.8 compares the cooling tower shell's local stability performances with the effect combinations of different group tower conditions, two kinds of external pressure distribution patterns and different considerations for internal pressure. The minimum K_B on the tower body (the occurrence position is about 0.286 relative to tower height where shell thickness is 0.330 meters) considering different effect combinations are listed in Table.8. For all effect combinations in Table.8, minimum K_B are above 5, meeting the requirements of code NDGJ5-88. Taking into account the internal pressure effects, the circumferential compressive stresses stage an increase of 35.6%, and the meridian compressive stresses are insensitive to the change. As a result, local stability decreases. For consideration of external pressure distribution patterns, the local stability check results based on the traditional methodology is lower than those based on the methodology applying results of prior wind tunnel tests. It is obtained by quantifying the local stability of the cooling tower shell that: single tower's stability >four tower group's stability > two tower group's stability, which is still different from the variation trend of tower group factors (see Section 4.3). The difference should mainly be attributed to changes to the vertical center of total wind action.

Table.8 The local elastic stability due to several effect combinations

Effect combination			Circumferential compressive stress/MPa	Meridian compressive stress/MPa	Angle of minimum K_B position	Minimum K_B
Condition	External pressure distribution pattern	Internal pressure consideration				
Single tower	NDGJ5-88	No	0.382	0.453	±70°	7.153
Single tower	NDGJ5-88	Yes	0.518	0.454	±70°	6.458
Single tower	Experimental result	Yes	0.567	0.382	±60°	6.892
Two towers (second stage)	Experimental result	Yes	0.738	0.355	±70°	6.268
Four towers (third stage)	Experimental result	Yes	0.658	0.384	±80°	6.408

5 SOME KEY EFFECTS ON COOLING TOWERS' ULTIMATE LOAD-CARRYING CAPACITY BASED ON NONLINEAR FEM ANALYSES

Comparison studies of the cooling towers' ultimate load-carrying capacity under wind loads of different working conditions are conducted, which focus on comparisons of the failure shapes of shell and ultimate wind speeds. The static wind stability analysis is based on a general finite

element platform taking into account the dead weight, material and geometric nonlinear effects in analyzing process. The basic failure process of the cooling tower is simulated as follows. First, wind loads of design basic wind speed (set 10m/s on a height of 10 meters as the initial wind speed) are loaded using a step-by-step method (loading step length is around 2.5～10.0m/s). With the increase of wind loads, some local areas on the concrete shell are damaged under tensile stress (for C40 concrete, $f_{tk} \geqslant 2.39$MPa). As a result, the reinforcement bars withstand the whole tensile strength in those failed areas. Then, the shell concrete in the compressive region on the tower body comes to its ultimate compressive condition (for C40 concrete, $f_{ck} \geqslant 26.8$MPa). With the rapid increase of deformation, the structure soon reaches its ultimate condition which can easily be determined from the critical points on wind speed-deformation gradient curves.

5.1 Wind profile effect

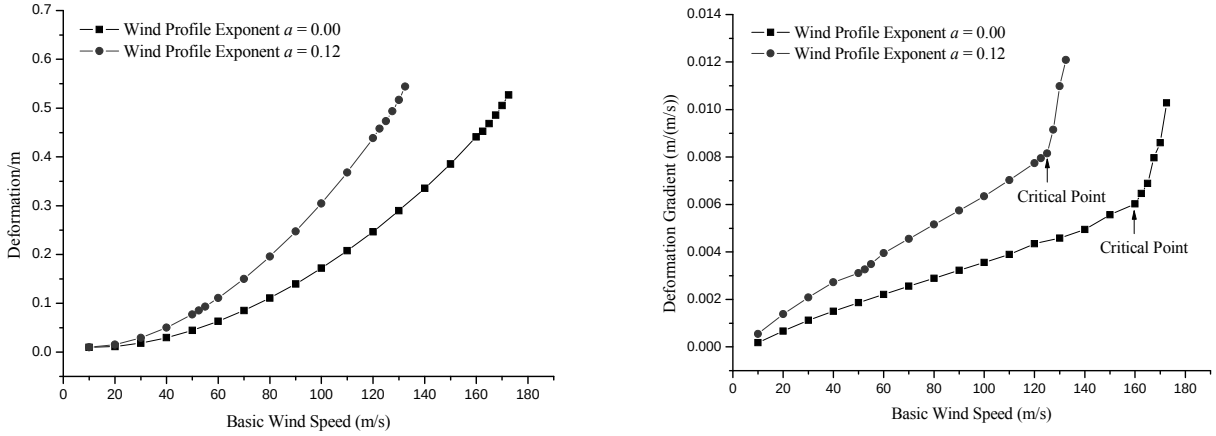

Fig.6 Displacements and their derivatives for different wind profiles

Table.9 Critical states for different wind profiles

Wind profile exponent	Occurrence position of maximum deformation		Critical state in tensile region			Instability critical state (Critical state in compressive region)			
			Occurrence position		Critical wind speed (m/s)	Occurrence position		Critical wind speed (m/s)	Primary compressive stress (MPa)
	Relative to tower height	Included angle from incoming flow	Relative to tower height	Included angle from incoming flow		Relative to tower height	Included angle from incoming flow		
α=0.00	0.782	0°	0.286	0°	72.5	0.209	±70°	160.0	24.2
α=0.12	0.782	0°	0.286	0°	52.5	0.286	±70°	125.0	25.2

Ignoring the internal pressure effect and applying the external wind pressure distribution curve of code NDGJ5-88, a comparison study of the cooling tower's ultimate load-carrying strength based on two different wind profiles (uniform profile and turbulent flow field profile) is conducted (see Fig.6 and Table.9). Results show that there exist noticeable wind profile effects. With the turbulent flow field profile, the vertical action center of the surface aerodynamic loads rises and the center of the maximum compressive stress region rises by 36% compared with that of the uniform flow condition. As the shell thickness at the position of the vertical action center decreases for the turbulent flow condition, the instability critical wind speed drops by 23.4%, causing structural buckling vulnerability.

5.2 Internal pressure effect

The study of the internal pressure effect on the cooling tower's ultimate load-carrying capacity is conducted. Results (Fig.7 and Table.10) show that there is no significant internal pressure effect,

for no notable changes of maximum total static wind-induced deformation have been observed. There is no change of the occurrence position of the maximum deformation, nor is there any change of the occurrence position of tensile stress or compressive stress at critical states according to Table.10. The instability critical wind speed drops by 4.0% after considering the internal pressure effect.

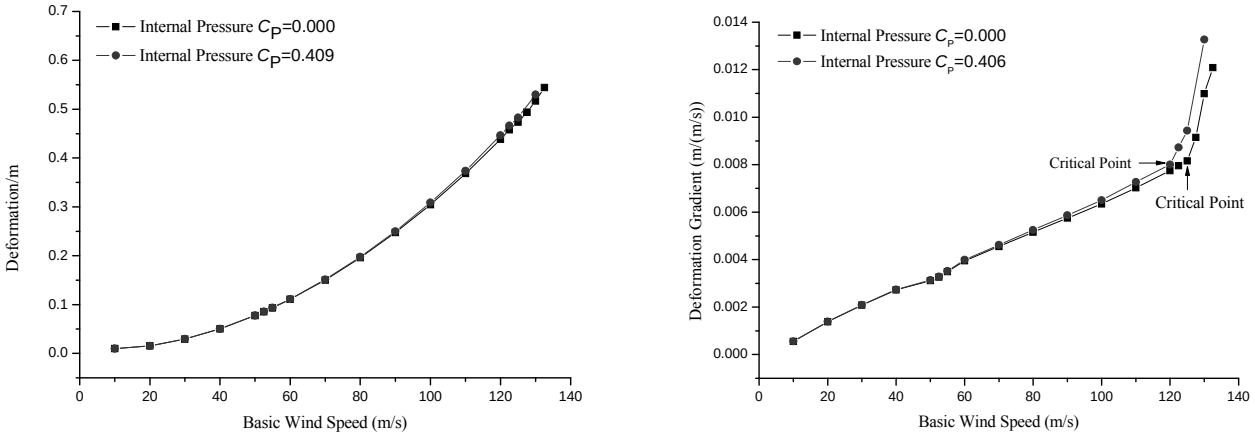

Fig.7 Displacements and its derivatives for different internal pressures

Table.10 Critical states for different internal pressures

Internal pressure	Occurrence positions of maximum deformation		Critical state in tensile region			Instability critical state (Critical state in compressive region)			
			Occurrence position		Critical wind speed (m/s)	Occurrence position		Critical wind speed (m/s)	Primary compressive stress (MPa)
	Relative to tower height	Included angle from incoming flow	Relative to tower height	Included angle from incoming flow		Relative to tower height	Included angle from incoming flow		
C_p=0.000	0.782	0°	0.286	0°	52.5	0.286	±70°	125.0	25.2
C_p=0.409	0.782	0°	0.286	0°	52.5	0.286	±70°	120.0	24.0

5.3 Boundary effect

After the Reynolds number effect modeling, the surface pressure mean value distribution of several intermediate sections coincide with the code results in this study. However, three dimensional effects (or boundary effect) in end regions (the top/bottom areas) of the tower surface can be demonstrated by the notable differences between experimental pressure distribution patterns and the surface pressure curve for sections of all heights given by the code NDGJ5-88, as shown in Fig.8.

Fig.9 and Table.11 both compare the boundary effect on the structural ultimate load-carrying capacity. It is shown that there is no significant boundary effect on the structural ultimate load-carrying capacity by comparison the static wind load deformation-wind speed curves, as well as the occurrence positions of maximum deformation and tensile or compressive stresses (see Fig.9 and Table.11). Since the critical wind speed of the total structural instability drops by 4.2% after considering the boundary effect, the overall boundary effect is mildly adverse.

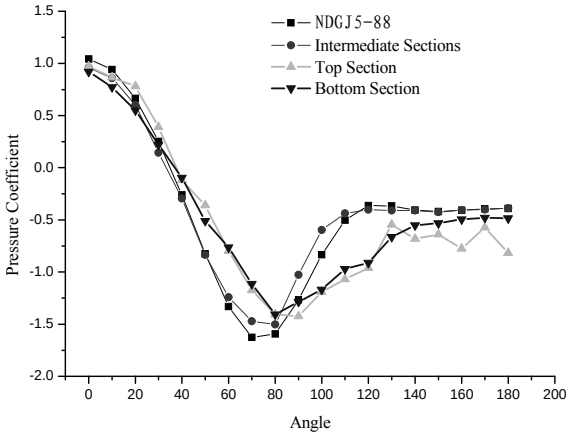

Fig. 8 Surface pressure curves of different heights

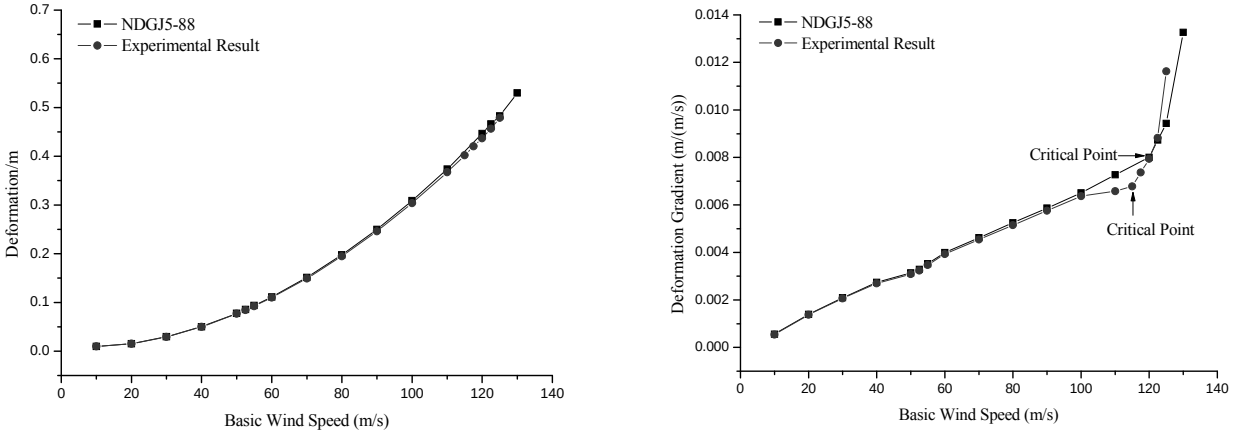

Fig.9 Displacements and its derivatives for different boundary conditions

Table.11 Critical stations for different boundary conditions

Surface pressure	Occurrence positions of maximum deformation		Critical state in tensile region			Instability critical state (Critical state in compressive region)			
			Occurrence position		Critical wind speed (m/s)	Occurrence position		Critical wind speed (m/s)	Primary compressive stress (MPa)
	Relative to tower height	Included angle from incoming flow	Relative to tower height	Included angle from incoming flow		Relative to tower height	Included angle from incoming flow		
NDGJ5-88	0.782	0°	0.286	0°	52.5	0.286	±70°	120.0	24.0
Experimenal results	0.782	0°	0.286	0°	52.5	0.286	±70°	115.0	23.7

5.4 Group tower interference effect

Fig.10 and Table.12 compare the cooling tower's ultimate load-carrying capacity with different group tower interference effects. For different group tower conditions, there is no significant change of the occurrence position of the maximum deformation or the occurrence positions of the maximum tensile/compressive stress at the critical states. Comparing the critical wind speed, it is shown in Fig.10 that: the critical wind speed for single tower > that for four tower group condition > that for two tower group condition. The results coincide with those of the local elastic stability study (see Section 4.4), proving the change of position of the vertical action center.

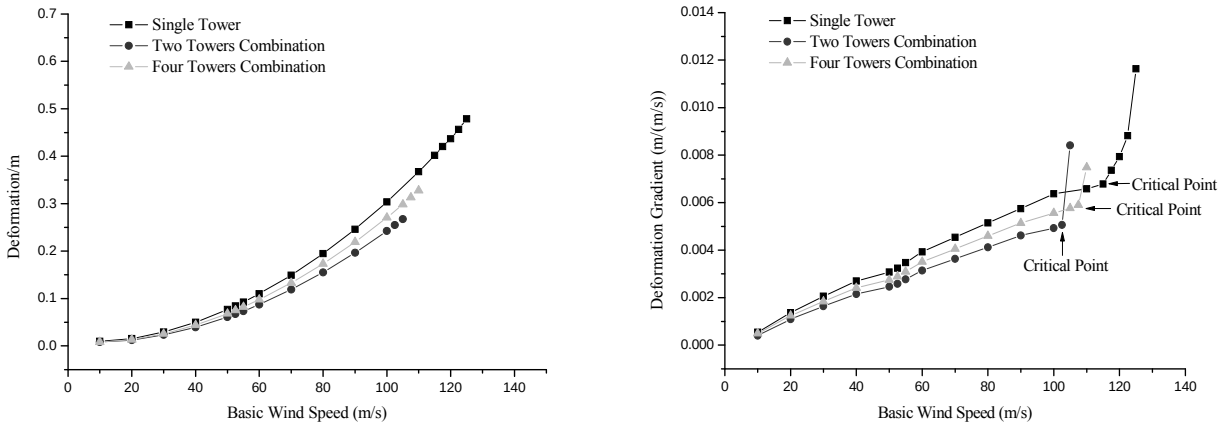

Fig.10 Displacements and its derivatives for different tower group combinations

Table.12 Critical states for different tower group combinations

Group combination	Occurrence position of maximum deformation		Critical state in tensile region			Instability critical state (Critical state in compressive region)			
			Occurrence position		Critical wind speed (m/s)	Occurrence position		Critical wind speed (m/s)	Primary compressive stress (MPa)
	Relative to tower height	Included angle from incoming flow	Relative to tower height	Included angle from incoming flow		Relative to tower height	Included angle from incoming flow		
Single tower	0.782	0°	0.286	0°	52.5	0.286	±70°	115.0	23.7
Two towers	0.782	0°	0.247	0°	50.0	0.286	±70°	102.5	17.5
Four towers	0.782	0°	0.247	0°	52.5	0.286	±70°	107.5	18.5

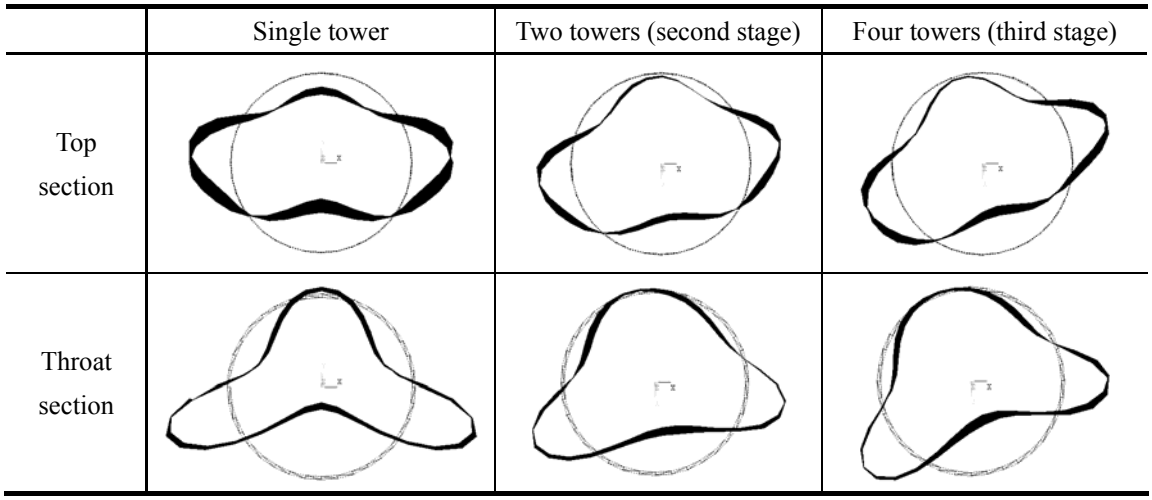

Fig.11 Structural failure shapes for different tower group combinations

Further study of structural failure (or buckling) shapes on both top and throat sections of different tower group combinations conditions are shown in Fig.11. It is demonstrated that the failure shapes of the second stage condition and the third stage condition are similar and there exist some differences in deformation symmetry properties as well as the occurrence position of maximum deformation between the single tower condition and the group tower conditions.

6 CONCLUSIONS

The conclusions drawn in this study are as follows:

(i) Generally, the extreme value wind load action is not taken as the control loading in cooling towers' structural design at present. The internal pressure effect on the tower's local elastic stability and overall structural ultimate load carrying capacity is mildly adverse. According to the

comparison study, the traditional methodology of considering extreme value wind pressure distribution patterns renders adverse structural performance compared with the methodology based on the wind tunnel tests for a single tower.

(ii) There exist notable group tower interference effects on the total extreme value wind loads, the structural responses (deformation and internal force), the local elastic stability, the ultimate load-carrying capacity and the instability shape of the cooling towers situated in the specific engineering site (described in Section 2). The variation trends of the tower group factor, the local elastic stability factor and the critical wind speed with different group tower conditions are different, demonstrating the complexity in considering the group tower interference effect. The methodology in considering group tower interference effect using the external pressure distribution obtained from codes, the tower group interference factor and the wind-vibration factor is conservative compared with the methodology based on the extreme value wind pressure distribution patterns obtained from wind tunnel tests.

(iii) The wind profile effect is obvious. Considering the wind profile of turbulent flow field, the critical wind speed of the instability critical state drops significantly, since the vertical center of the total surface aerodynamic wind action rises.

(iv) The boundary effect causes mildly adverse influence on the cooling tower's total structural stability.

(v) For most conditions referred to in this study, local areas on the concrete shell of cooling tower reach the allowable tensile stress under the action of the wind force with a wind speed of around 50m/s. The total structure's instability critical state generally appears before the crushing of the concrete in the compressive stress region, showing obvious geometric nonlinearity effects.

The FEM numerical simulation in this study applies a simplified way in considering the material nonlinearity effect of concrete. Our further works will lay more emphasis on the structural failure mode analyses applying more precise constitutive model of concrete.

7 REFERENCES

[1] NDGJ5-88. Technical specification for hydraulic design of thermal power plant[S].

[2] GB/T 50102-2003. Code for design of cooling for industrial recirculating water[S].

[3] BTR VGB'Richtlinie Bautechnik bei Kühltürmen[S]. VGB Technische Vereinigung der Großkraftwerksbetreiber e.V., Essen, 1990.

[4] Règles Professionelles applicable à la Construction des Réfrigérants Atmosphériques en Béton Armé[S], Texte Provisoire, SNBATI.

[5] Wolfhard Zahlten, Claudio Borri. Time-domain simulation of the non-linear response of cooling tower shells subjected to stochastic wind loading[J]. Engineering Strutctures, Vol.20 No. 10. pp.881-889,1998.

[6] Goudarzi, Mohammad-Ali, Sabbagh-Yazdi, Saeed-Reza. Modeling wind ribs effects for numerical simulation external pressure load on a cooling tower of KAZERUN power plant-IRAN[J]. Wind and Structures, An International Journal, Vol.11, No. 6, pp. 479-496,2008.

Extreme value distribution of surface aerodynamic pressure of hyperbolic cooling tower

X. P. Liu, L. Zhao, Y. J. Ge

State Key Laboratory for Disaster Reduction in Civil Engineering, Tongji University, Shanghai 200092, China

Abstract

The simultaneous pressure-measuring tests of rigid model for a super large cooling tower were made in TJ-3 wind tunnel of Tongji University. In the process of external wind pressure measurement, by adjusting surface roughness and oncoming wind velocity, the actual aerodynamic characteristics of full-scale cooling towers were illustrated in the scale-reduced testing model with lower Reynolds number. By measuring tail flow of the cooling tower model using high-frequency anemometer, the mean estimating primary vortex shedding frequencies through frequency-spectrum transformation of aerodynamic time history for whole cooling tower was proved to be reasonable and simple. In this paper, the distribution rule about sectional drag force coefficients along the tower height is analyzed based on probability correlation technique, then the Fourier serious fitting curves of wind pressure extreme value distributions along the circumferential direction for each section are also proposed. For internal pressures of the cooling tower, some comparative tests about dependency of internal aerodynamic pressures and various ventilation ratios of stuffing layer located below the cooling tower are firstly carried out, then the internal wind pressure extreme value distributions for commonly-used ventilation ratio are suggested considering the correlation of aerodynamic pressures.

***Key words**:* cooling tower; Reynolds number effect; extreme value distribution

1 Introduction

As a typical high-rise and long-span flexible structure, the wind-induced performance of cooling tower under the dynamic action of wind loads has always been focused with more attention. By simultaneous pressure-measuring tests of cooling tower rigid model in wind tunnel, mean and fluctuating wind pressure distributions over its external and internal surfaces can be obtained. In the process of external wind pressure measurement, by adjusting surface roughness and oncoming wind velocity, the actual aerodynamic characteristics of full-scale cooling towers were illustrated in the scale-reduced testing model with lower Reynolds number. For the sake of simplicity, extreme aerodynamic pressure distribution can be formulated in such expression as below:

$$\mu_p = \mu_m + \sigma_\mu \times g \times \rho \tag{1}$$

in which, μ_p, μ_m and σ_μ are extreme value, mean value and RMS value of pressure shape coefficient, g is peak factor, ρ is correlation coefficient. The statistical estimation algorithm of g and ρ are discussed in details.

For internal pressures of the cooling tower, some comparative tests about dependency of internal aerodynamic pressures and various ventilation ratios of stuffing layer located below the cooling tower are carried out, then the internal pressure extreme value distributions under commonly-used ventilation ratio are suggested basing on the correlation of aerodynamic pressures.

2 Experimental arrangement

The test is carried out in the wind tunnel of TJ-3 atmospheric boundary layer in the State Key Laboratory of Disaster Reduction in Civil Engineering, Tongji University. The wind tunnel is a closed reflux rectangular cross-section wind tunnel, wherein the size of the test section is as follows: the width is 15m, the height is 2m, and the length is 14m. In the test, the engineering site belongs to the landform of Class A, the wind profile index α = 0.12, the surface turbulence intensity is 15%, the turbulence intensity on the top of the cooling tower is 10%. A rigid scale model of cooling tower is made of organic glass according to the scale ratio of 1: 200, in which the external pressure measuring model is a single-layer thin-walled tower drum, the internal pressure measuring model is a double-layer hollow tower drum, the internal and external pressure measuring points are arranged as Figure 1, and the congestion index of the cooling tower and other building models around the same is less than 7%.

The debugging and measurement for the simulated wind field of the atmospheric boundary layer are carried out through the Streamline hotline anemometer produced by DANTEC Company of Denmark, and the measurement for the average inner and outer surface pressure of the cooling tower and the fluctuating pressure is carried out by means of a DSM3000 electronic pressure scanning valve produced by Scanivalve scanning valve company of the United State. The signal sampling frequency is 312.5Hz, and the length for sampled data of a single sample measuring point is 6000 data.

The external pressure measuring model of the cooling tower is provided with 36 × 12 outer surface pressure measuring points along the circular and meridian direction. The internal pressure measuring model is provided with 36 × 6 inner surface pressure measuring points along the circular and meridian direction. The layout for the internal and external pressure measuring points is shown in Figure 2(unit: m).

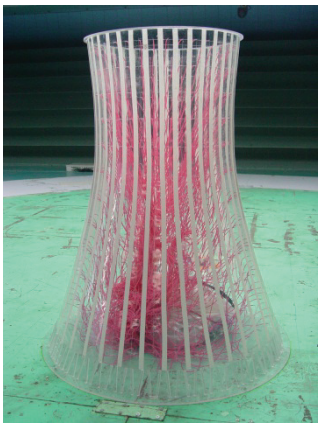

Fig.1a Model for external pressure

Fig.1b Model for internal pressure

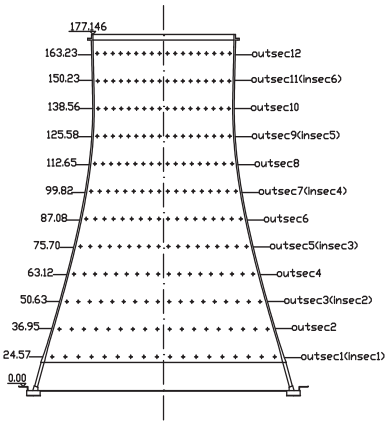

Fig.2 Arrangement for pressure points

The pressure coefficient C_{Pi} in the ith measuring point of surface of the cooling tower is expressed as:

$$C_{Pi} = \frac{P_i - P_\infty}{P_0 - P_\infty} \tag{2}$$

In which, P_i indicates the pressure applied to the ith measuring point, P_0 and P_∞ respectively indicate the total pressure and static pressure in the reference height point while

testing.

The Integral of the overall resistance coefficient (down wind) and the lift coefficient (cross-wind direction) measured in the external surface pressure measuring point of the cooling tower is defined as:

$$C_D = \frac{\sum_{i=1}^{n} C_{Pi} A_i \cos(\theta_i)}{A_T} \qquad C_L = \frac{\sum_{i=1}^{n} C_{Pi} A_i \sin(\theta_i)}{A_T} \tag{3}$$

In the formula, C_D and C_L respectively indicate the overall resistance and lift coefficient of the structure, A_i indicates the pressure of coverage area in the ith measuring point, θ_i indicates the included angle between the pressure and wind axis direction of the ith measuring point, and A_T indicates the projection area of the overall structure along the wind axis direction

The correlation coefficient between the measuring point, and the measuring point and the overall aerodynamic time history is defined as follows:

$$\rho_{xy} = \frac{E[(x - Ex)(y - Ey)]}{\sigma_x \sigma_y} \tag{4}$$

In the formula, Ex, Ey and σ_x, σ_y respectively indicate the expectation and variance for the stochastic sequences $x(t)$ and $y(t)$.

3 Reynolds number effect simulation

3.1Reynolds number effect simulation

The actual aerodynamic characteristics of full-scale cooling towers were well got by adjusting surface roughness for the scale-reduced testing model with lower Reynolds number, including scribed line and paper tape. And When oncoming wind velocity is 8m/s, the test curve of mean surface pressure shape coefficients were fitted well with the suggested curve from China Codes, as shown in Figure 3. In the paper, the range of the Reynolds number Re for the prototype structure of the ultra-large cooling tower under designed wind speed is 1.5×10^8 to 3.5×10^8.

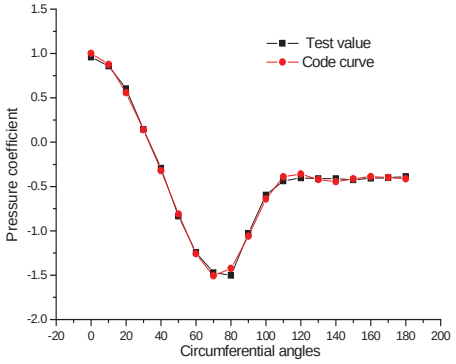

Fig.3 Pressure comparison of test and Codes

Due to the limitation of physical wind tunnel, the form of surface circumferential motion under a high Reynolds number is difficult to be simply reproduced by improving the test wind speed or increasing the geometric dimensions of the structure. The circumferential motion characteristics of the cylinder-like structure are not only related to the Reynolds number, but also closely related to surface roughness and other factors. As experience proves that the circumferential motion characteristics at a high Reynolds number can be approximately simulated by changing the surface roughness of the model. After comparing a variety of proposals of changing the surface roughness, the method for uniformly providing 36 vertical and continuous rough paper tapes (see Figure 1a) of 12mm

wide and 0.1mm thick and regulating test wind speed (4m/s to 12m/s) is finally used for simulating high Reynolds number effects, in which the simulation standard comprises the surface pressure distribution, overall resistance coefficient and value of St number and the like of cooling tower. The average wind pressure distribution coefficient of hyperbolic cooling tower, the simulation standard is a wind pressure distribution eight-item fitting curve measured on the site and recommended in the hydraulic specification, wherein the simulation process is focused on the maximum pressure coefficient, minimum pressure coefficient, wake flow pressure coefficient, zero-pressure coefficient angle, minimum pressure coefficient angle, and separation angle. Compared with Figure 7, it can be found that the average surface pressure distribution for the six middle sections of the cooling tower in case of surface groove + rough paper tape at the test wind speed of 8/s is in good agreement with the standard value, in which the resistance coefficient of the middle section is C_D=0.436, and the integral resistance coefficient of surface pressure specified in China is C_D=0.437.

3.2 *Effect of Weak Flow Vortex Shedding*

Strouhal number is a function of structure geometry and Reynolds number. When the Reynolds number Re is more than 3.5×10^6, the turbulent ingredients in the weak flow vortex shedding of the cylinder-like structure are more prominent; meanwhile, regular vortex shedding phenomenon also will be presented, and the St number at that time is slightly larger than 0.2. The St number is closely related to the dynamic response of the structure, which is also one of the Reynolds number effects to be simulated in the test. Due to the irregularity of turbulent ingredients in the weak flow, the direction measurement for the frequency of vortex shedding is more difficult, and therefore the paper attempts to indirectly determine the outstanding frequency of vortex shedding through the frequency spectrum function for time history of the while lift. In order to verify the validity of the method, the weak flow of the cooling tower is measured in several points by means of a hotline anemometer.

The hotline anemometer is arranged on the protected side of the cooling tower, the height for the probe of the anemometer and the distance to the cooling tower are changed, and a variety of points in the weak flow region of the cooling tower are measured under the condition of a test wind speed of 8m/s. The results show that the weak flow vortex shedding frequencies measured in the point of about 2/3 tower height above the ground and the point part from the protected side surface of the model with about 0.8 times of middle surface radius of the throat part are the most obvious, as shown in Figure 4a). The aerodynamic force time history of the whole cross-wind direction is obtained according to the time history integral of surface pressure coefficient of the cooling tower, and the spectrum function for the time history of lift coefficient is shown in Figure 4b).

The weak flow vortex shedding frequency (2.411Hz) is relatively close to the frequency (2.594Hz) obtained by changing the frequency spectrum of time history of the lift coefficient, in which the relative deviation is 7.5%. The St numbers respectively calculated according to the weak flow vortex shedding frequency and the frequency spectrum change for the time history of lift coefficient are 0.235 and 0.253 (the characteristic size is the diameter of 0.78m for the throat part of the cooling tower model, and the wind speed is

8m/s), both the numbers are greater than 0.2, so that it is further validated that the St number of the cooling tower is completely coincident with the target value simulated in the test.

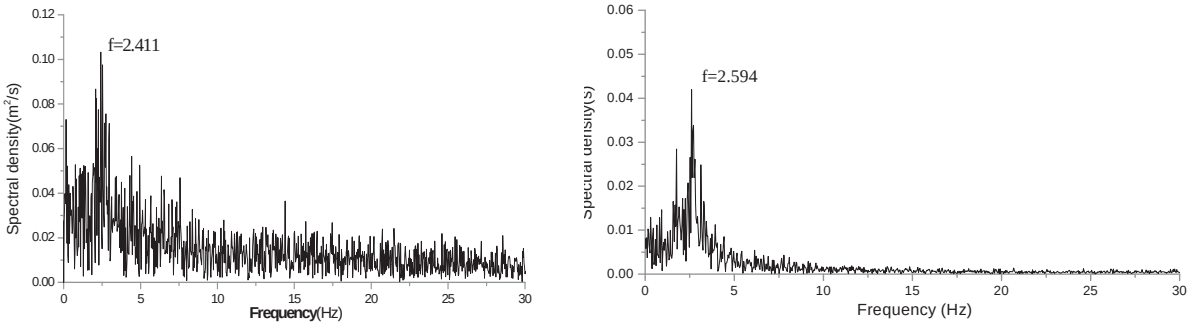

a) Spectrum Function for Time History of Wake Flow

b) Spectrum Function for Time History of Lift Coefficient

Figure 4: Spectrum Function for Fluctuation Vortex Shedding of Wake Flow and Time History of Circular Surface Aerodynamic Force of Tower Drum

4 Extreme pressure of external surface

4.1 *resistance coefficient for Sections*

The average resistance coefficient for the 12 meridian sections of the cooling tower model is arranged along the height and shown in the feature that the value of end part is large and value of middle part is small (as shown in Figure 5), both the resistance coefficients for the section of top and bottom of the cooling tower are significantly greater than the resistance coefficient of middle section, wherein the average

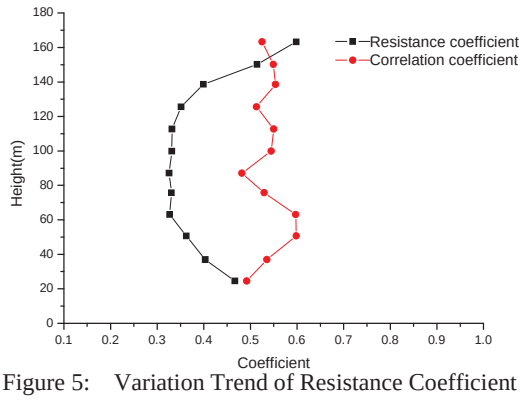

Figure 5: Variation Trend of Resistance Coefficient and Correlation Coefficient along the Height

resistance coefficients for the section of top and bottom of the cooling tower are 0.467 and 0.598, respectively; and the average resistance coefficients are respectively more than the minimum average resistance coefficients of the middle section with (0.326) 43% and 83%. The phenomenon is mainly due to the end effect of circumferential motion on the surface of the cooling tower, the stress of the bottom and top section of the cooling tower is more complicated, the local pressure coefficient is much larger than the designed value in the specification, and the local stability for the end part of the cooling tower shall be paid attention in the design process as the drum wall structure on the top of the cooling tower is relatively thin. In Figure 5, both the correlation coefficients for the time history of resistance coefficient of each section and the time history of resistance coefficient of whole cooling tower structure are about 0.55, which is between 0.48 and 0.60. Due to the impact for end part boundary effect of cooling tower, six representative middle sections (see Figure 2 Outsec4 to Outsec9) are selected as research objects in the simulation of Reynolds number effect and subsequent extreme value analysis for the pressure coefficient of external surface pressure.

4.2 *Extreme Pressure Distribution of External Surface*

4.2.1 *Extreme Pressure of Sections*

During the process for checking the local strength and local stability under the wind load effect of cooling tower, the result for the extreme value of pressure coefficient shall be adopted, but the specification just provides the average pressure coefficient distribution and stipulates the gust effect in the turbulent flow field of Class A is considered with the wind-induced vibration coefficient of 1.6. In order to compare with the extreme value of pressure coefficient specified in the specification, the measured extreme value for the pressure coefficient of each measuring point and the distribution rule thereof are analyzed. See Equation 1 for the definition of extreme value of the pressure coefficient, in which ρ_D and ρ_L are respectively used for the correlation coefficients for the time history of pressure coefficient of each measuring point and the time history of life, and the extreme value for the pressure coefficient related to the structure resistance and lift time history are respectively as follows:

$$\mu_{pD} = \mu_m + \sigma_\mu \times g \times \rho_D \tag{5}$$

$$\mu_{pL} = \mu_m + \sigma_\mu \times g \times \rho_L \tag{6}$$

Firstly, the correlation for the time history of pressure coefficient of each measuring point to the resistance and lift time history of the section is considered only, and it is assumed that all the sections are completely related to the stress time history of the whole cooling tower structure, the correlation coefficients for the average pressure coefficient, root variance and peak factor of each measuring point of the 6 middle sections of the cooling tower, the resistance of the section, and the lift time history in the turbulence flow field of Class A are shown in Figure 6. The distributions for the 6 section extreme values obtained from the Equations (5) and (6) and related to the resistance and lift time history are basically the same (as shown in Figure 7), and the average extreme values of the 6 sections are close to each other after averaging and comparing (as shown in Figure 8).

Taking into account the security of structure design, the envelope value for the two extreme values is compared with the extreme value of the specification (as shown in Figure 9), in which it can be seen that the distribution of pressure coefficient extreme value is slightly different from the result of the specification while considering the correlation of the measuring point to the resistance and lift of the section only, the difference between the corresponding angles of minimum values is about 10 degrees, and the absolute value for the pressure coefficient of the weak flow area of envelope value is greater than the extreme value of Xi'an Thermal Power.

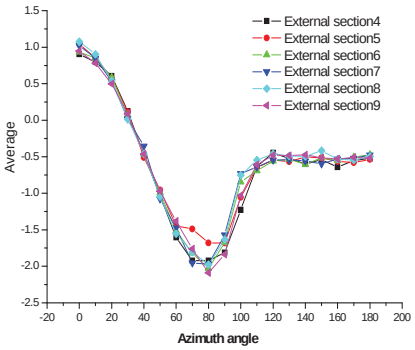

a) Average of Pressure Coefficient

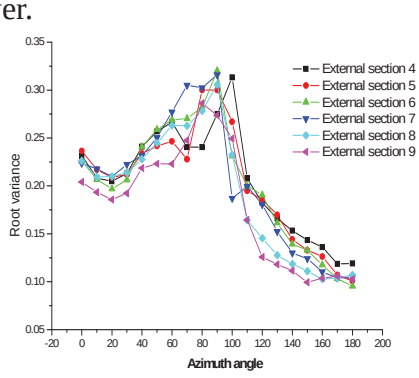

b) Root Variance of Pressure Coefficient

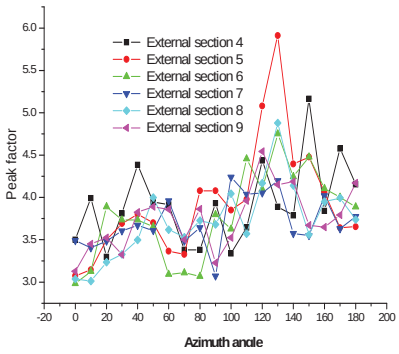

b) Peak Factor of Pressure Coefficient

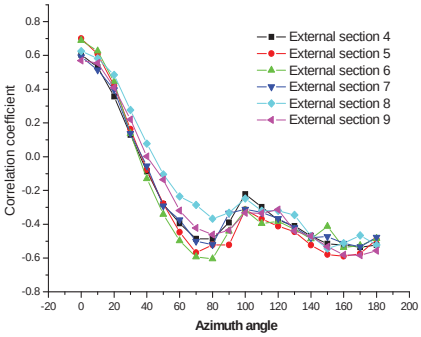

d) Correlation Coefficient between Pressure Coefficient and Section Resistance

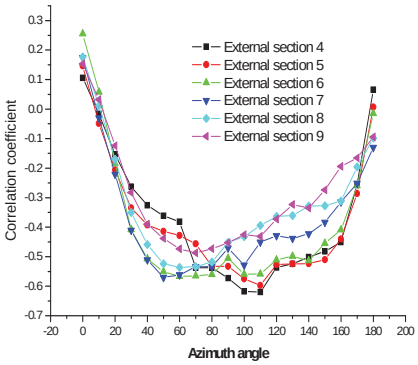

e) Correlation Coefficient between Pressure Coefficient and Section Lift

Figure 6: Distribution Relationship for Characteristic Value of Cooling Tower Outer Surface Pressure Coefficient

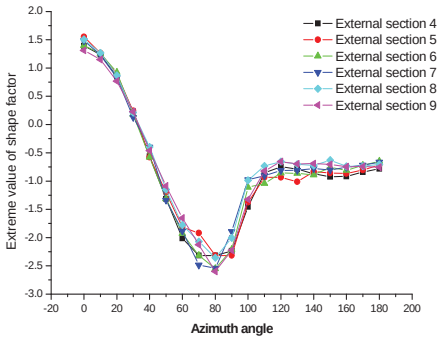

a) Extreme Value of Pressure Coefficient Related to Section Resistance

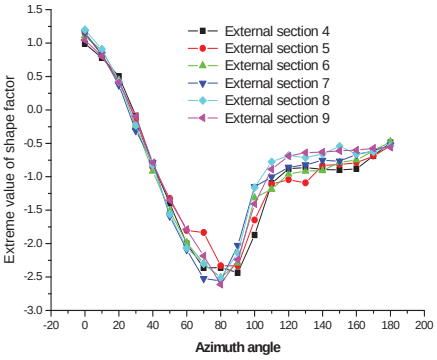

b) Extreme Value of Shape Factor Related to Section Lift

Figure 7 : Circular Distribution for Extreme Value of Pressure Coefficient along Drum Ring

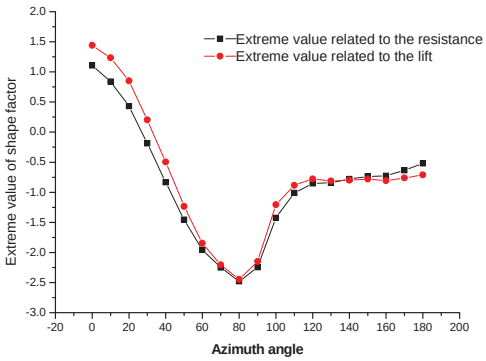

Figure 8: Comparison between Extreme Values of Two Pressure Coefficients

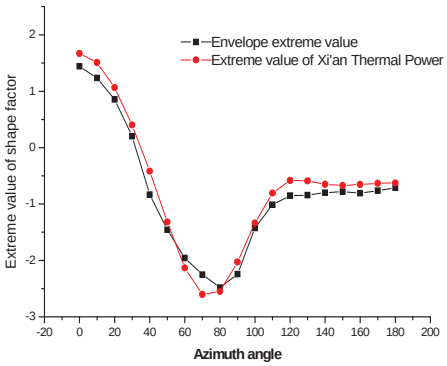

Figure 9 :Comparison between Aerodynamic Extreme Values of Section and Specification

4.2.2 *Extreme Pressure of the whole structure*

The correlation for the pressure coefficient of each measuring point to the resistance and lift time history of the whole structure shall be considered. The through for the calculation and analysis extreme value are the same with that above. Figure 10 and Table 1 compare the distribution of envelope extreme value and specified extreme value. In the process for the consideration of the correlation between the pressure coefficient of each measuring point and the stress time history of the structure, the distribution of pressure coefficient extreme value has a certain difference to the extreme value of the specification, the maximum (1.298) value and minimum (-2.307) value for the extreme value distribution of envelope pressure coefficient are 78% and 87% of the maximum (1.668) value and minimum (-2.603) value of specified extreme value respectively, the difference between the corresponding angles of the maximum negative pressure is 10 degrees, and the differences for the weak flow pressure and separation angle of the two extreme value distributions are small.

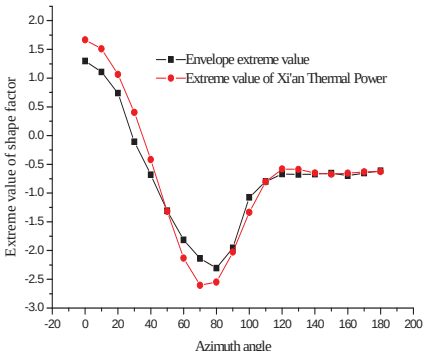

Fig.10 Test general envelope values and codes

Table 1 : Comparison for Characteristic Value of Extreme Value Distribution of Two Pressure Coefficient

Extreme Value Distribution	Maximum Value	Minimum Value	Average of Weak Flow Area	Angle of Minimum Value	Separation Angle
Envelope Extreme Value	1.298	-2.307	-0.661	80°	120°
Specified Extreme Value	1.668	-2.603	-0.629	70°	120°

The extreme value distribution curve of shape coefficient is fitted while considering the correlation to the structure by means of a Fourier series expansion equation $\mu_p(\theta) = \sum_{k=0}^{m} a_k \cos k\theta$ on the basis of least square method. When m is not less than 7, the fitting effect is good, when m is equal to 7, the value of the parameter a_k in the formula is as follows: a0=-0.7789, a1=0.3126, a2=1.0159, a3=0.7366, a4=0.0439, a5=-0.1429, a6=0.0742, and a7=0.0856.

5. Extreme pressure distribution of inner surface

5.1 *Impact of Ventilation Rate*

The ventilation rate of packing layer within the tower is simulated by placing an organic glass plate which is uniformly hollowed in the lower part of the cooling tower. The test results show that the ventilation rate of packing layer within the tower does not have obvious impact on the form of internal pressure distribution curve, closely related to the internal pressure, specifically the ventilation rate is inversely proportional to absolute value of the internal pressure. Table 2 shows the average of inner surface pressure coefficient of different ventilation rates in the turbulence flow field of Class A (taking the wind pressure of tower top as the reference pressure).

Table 2: Inner Surface Pressure Coefficient of Single Cooling Tower

Ventilation Rate	100%	55%	30%	15%	3%	0%
Average Internal Pressure	-0.375	-0.382	-0.410	-0.524	-0.590	-0.761

5.2 *Distribution of Extreme Pressure*

Generally, the ventilation rate of natural draft cooling tower is more than 30%, but the temporary construction facilities will reduce the ventilation rate in the actual operation state, the paper takes the internal pressure with a ventilation rate of 15% as the wind pressure of actual structure due to the consideration of safety. Here, the distribution of extreme internal pressure is analyzed by taking the ventilation rate of 15% for example. The extreme value of pressure coefficient is defined as:

$$C_{pp} = C_{pm} - \sigma_{Cp} \times g \times \rho \tag{7}$$

In the formula, C_{pm} and indicate the average and root variance of pressure coefficient, g indicates a peak factor, and ρ indicates the correlation coefficient for the time history of pressure coefficient of each measuring point to lift time history for the pressure coefficient of each measuring point obtained in the while inner surface integral. Figure 11 shows the average, root variance, peak factor, correlation coefficient and extreme value of internal surface of the six sections. The circular distribution for the average, correlation coefficient and extreme value for the internal pressure coefficient along the inner surface is basically shown in the form of a straight line, and the values thereof are basically the same. The pressure coefficient of each section is average, and the changes for the average pressure coefficient of each section and the extreme value along the height of the cooling tower are compared; according to Figure 12, it can be seen that the pressure coefficient is not obviously changed with the height, but lasso uniformly distributed approximately. Thus, it can be indicated that the internal pressure coefficient of the cooling tower is uniform in the whole inner surface, the extreme internal pressure and average of all the measuring points are average respectively on the basis of the conclusion above, in which the average extreme value (-0.737) is 1.4 times of the mean average (-0.524), less than the wind-induced vibration factor 1.6 of turbulent flow field of Class A

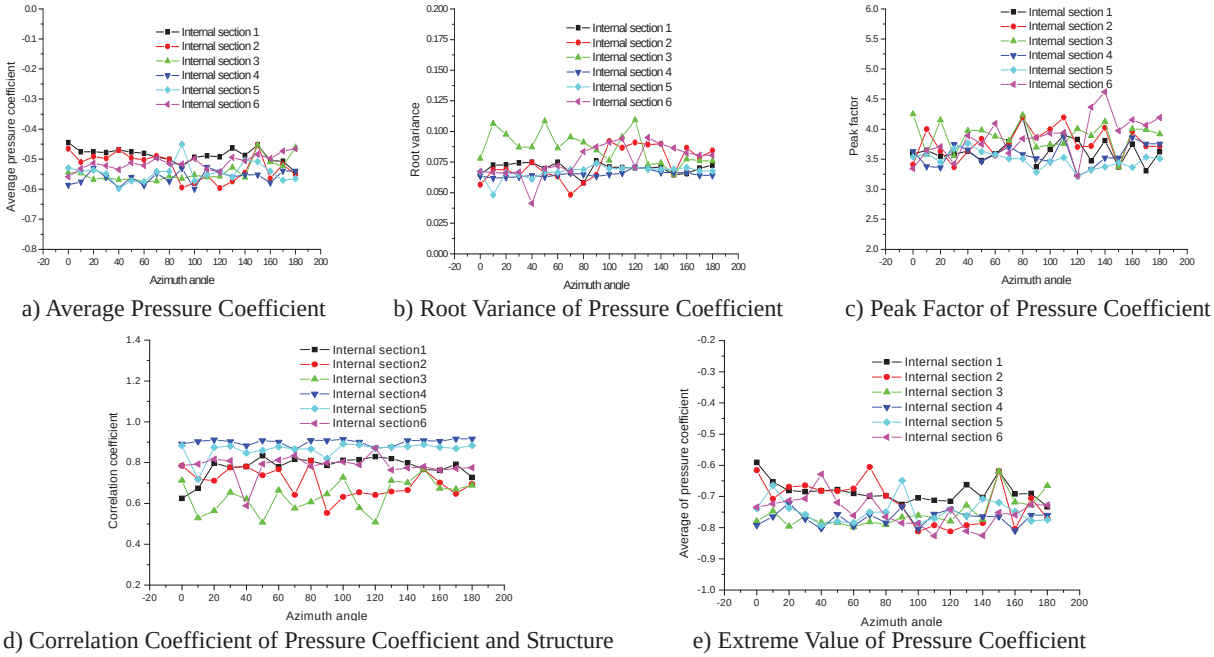

a) Average Pressure Coefficient b) Root Variance of Pressure Coefficient c) Peak Factor of Pressure Coefficient

d) Correlation Coefficient of Pressure Coefficient and Structure e) Extreme Value of Pressure Coefficient

Figure 11: Distribution Relationship for Characteristic Value of Outer Surface Pressure Coefficient of Cooling Tower

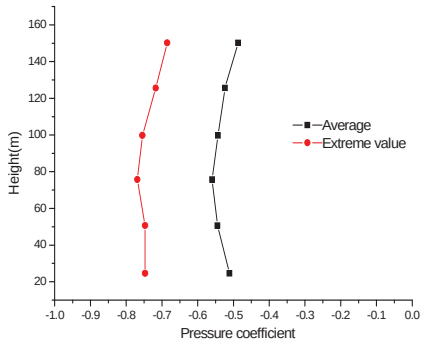

Figure 12: Variation Tend of Pressure Coefficient along the Height

6 conclusion

The study to external and internal pressure distributions of the cooling tower is based on pressure measuring data of the rigid model. And the following summarizes the major findings and conclusions of this study:

1. The actual aerodynamic characteristics of full-scale cooling towers were well got by adjusting oncoming wind velocity and surface roughness for the scale-reduced testing model with lower Reynolds number.
2. In the process for the consideration of the correlation between the pressure coefficient of each measuring point and the stress time history of the structure, the distribution of pressure coefficient extreme value has a certain difference to the extreme value of the China Code which is slightly tends to conservative.
3. The extreme value distribution curve of shape coefficient is fitted while considering the correlation to the structure by means of a Fourier series expansion equation.
4. The ventilation rate is inversely proportional to absolute value of the internal pressure. And the pressure coefficient is not obviously changed with the height, but lasso uniformly distributed approximately.

ACKNOWLEDGEMENTS

The authors would like to gratefully acknowledge the supports of the National Science Foundation of China (51021140005, 50978203 and 51178353), and the supports by Kwang-Hua Fund for College of Civil Engineering, Tongji University.

References

1 H.-J. Niemann, H.-D. Köpper. Influence of adjacent buildings on wind effects on cooling towers[J]. Engineering Structures, Vol. 20. No. 10, pp. 874-880, 1998.

2 M.N. Viladkar, Karisiddappa, P. Bhargava, etc. Static soil–structure interaction response of hyperbolic cooling towers to symmetrical wind loads[J]. Engineering Structures, Vol. 28. pp. 1236-1251, 2006.

3 YAN Wen-cheng，ZHANG Bin-qian，LI Jian-ying. Investigation on characteristics of wind load for super large hyperbolic cooling tower in wind tunnel[J]. Experiments and Measurements in Fluid Mechanics，2003，17(Special issue):85-89.

4 ZHANG Bin-qian，LI Jian-ying，YAN Wen-cheng. Investigation on interrelation of wind load for double super large hyperbolic cooling tower[J]. Experiments and Measurements in Fluid Mechanics，2003，17(Special issue):93-97.

5 NDGJ5-88，Technical specification for hydraulic design of thermal power plant[S].

6 GB/T 50102-2003，Code for design of cooling for industrial recirculating water[S].

7 LIU Tian-cheng，ZHAO Lin，DING Zhi-bin. Test research of flow feature for hyperbolic circular section cooling tower with different superficial roughness[J]. Industrial Construction. 2006，36(396):301-304.

8 WU Ji-ke. Review and expectation of structure analysis for large cooling tower[J]. Mechanics and Practice. 1996，18(6):1-5.

9 LI Pei-hua，ZHOU Liang-mao. Mean wind pressure distribution of full scale hyperbolic cooling tower with natural ventilation[C]. Proceedings of the Fourth China National Conference on Wind Effects[C]. 1989. 222-229

The Seventh International Colloquium on Bluff Body Aerodynamics and Applications (BBAA7)
Shanghai, China; September 2-6, 2012

Ventilation efficiency indices for evaluating ventilation performance of newly-built urban area

Tingting Hu [a], Ryuichiro Yoshie [b]

[a] *Tokyo Polytechnic University, Kanagawa, Japan, tingting@arch.t-kougei.ac.jp*
[b] *Tokyo Polytechnic University, Kanagawa, Japan, yoshie@arch.t-kougei.ac.jp*

ABSTRACT: This paper aims to numerically investigate relationship among ventilation indices which were adopted for estimating ventilation efficiency in newly-built residential areas at pedestrian level. A reference urban block model was designed according to a typical residential area in Shanghai. Urban parameters including building coverage ratio, passage width, building array and building height variation were considered. The ventilation efficiency was evaluated by spatial averaged wind speed ratio (VR_w), volume-averaged normalized concentration (C^*), and visitation frequency (VF). The results showed that, for most cases, a general relationship was found among the three indices: a large value of VR_w and a low value of VF resulted in a low value of C^*. However, a few exceptions were found in the densest case and these were explained by flow rate analysis.

KEYWORDS: urban ventilation; ventilation indices; CFD.

1 INTRODUCTION

Recently, urban ventilation performance is becoming an important concern because of urban heat island effects and air pollution. It is necessary to evaluate urban ventilation performance based on different design parameters in order to improve planning of new-built areas.

Volume-averaged wind speed ratio (VR_w) (Ng, 2009), volume-averaged normalized concentration (C^*), purging flow rate (PFR), residence time (TP) (Kato et al, 2003) and visitation frequency (VF) (Bady et al, 2008), have been successfully applied for evaluating ventilation performance in urban area. The authors have also used the above indices to investigate urban ventilation performance in newly-built area by numerical simulation (Hu and Yoshie, 2011). Based on this previous studies, C^* reflected the integrated effects of other indices such as VR_w and VF, so it can be served as the core index for evaluating ventilation performance. Generally, large VR_w values and small VF values resulted in low C^* values. However, some exceptions were found, for example, low C^* values were found with low VR_w values or large VF values. The reason of such discrepancy needs to be investigated in detail. Therefore, flow rate and mass of pollutant passing through each surface of target control volume were investigated and analyzed. A full-length paper should have a short introduction. This should state the reasons for the work, with brief reference to previous work on the subject.

2 ANALYSIS OUTLINE

2.1 *Analysis model*

A simplified urban block model (Fig. 1a) was designed according to a typical residential area in Shanghai (Fig. 1b). Figure 1c showed an enlarged view of a center block in Figure 1a. The com-

putational domain contained 8 blocks surrounding the central one. All 9 blocks had the same arrangement. Each block comprised a total of 72 residential buildings (48m (L) ×12m (W) ×18m (H)) with 6 stories. The building coverage ratio (BCR), which represents the ratio of ground floor area to lot area, was 40% and the floor area ratio (FAR), which represents the ratio of total floor area to lot area, was 230%.

To compare the ventilation efficiency of different urban patterns, other BCRs and arrays (Layouts 2-18) were considered, as shown in Table 1. The BCR was changed by increasing the building height while keeping the FAR constant. (The sum of building volumes was kept constant). The lengths and widths of buildings were not changed. The passage widths D_1 and D_2 between adjacent buildings (shown in Fig. 1f) changed with BCR and building array. The main road width in these models was 20m for all cases, as shown in Fig. 1a. The minimum distances from buildings to the main road side were designed according to the existing urban planning regulations in Shanghai.

2.2 *Computational condition*

The CFD technique with the standard k-ε model was used. Three wind directions 0°, 45° and 90°, shown in Figure 1a, were analyzed. The computational domain contained 8 blocks surrounding the central one. All 9 blocks had the same arrangement. The domain size was 1378 m (x) × 1378 m (y) × 198 m (z) for the reference case. A structured grid of 2,337,984 meshes was made. Table 2 shows the calculation conditions (AIJ guideline).

Table 1. Parameters for all layouts

Layout	H (m)	BCR (%)	FAR (%)	Array	Layout	H (m)	BCR (%)	FAR (%)	Array
1	18	40	230	A	10	36 & 72	13	230	LH
2	36	20	230	A	11	54 & 90	10	230	LH
3	54	13	230	A	12	12 & 24	40	230	SH
4	72	10	230	A	13	18 & 54	20	230	SH
5	36	20	230	S	14	36 & 72	13	230	SH
6	54	13	230	S	15	54 & 90	10	230	SH
7	72	10	230	S	16	36	20	230	A
8	12 & 24	40	230	LH	17	27	30	230	A
9	18 & 54	20	230	LH	18	27	30	230	A

Note: A: Aligned array; S: Staggered array; LH: Low and High spaced array; SH: Staggered Height array

Table 2. Calculation conditions

Code	Fluent 6.3
Turbulence model	Standard k-ε model
Inlet	$u = U_{ref}\left(z / z_{ref}\right)^{\alpha}, \alpha = 0.27, z_{ref} = 10\text{m}, U_{ref} = 3\text{m/s}$ $k = \left(I(z)u(z)\right)^2, I(z) = 0.1\left(z / z_{\text{G}}\right)^{-\alpha-0.05}, z_{\text{G}} = 550\text{m}$ $\varepsilon = C_{\text{u}}^{1/2} k(z) \dfrac{d(u(z))}{dz}, C_{\text{u}} = 0.09$
Outlet	Outflow
Upper and side surface	Symmetry (for wind direction 0, 90)
Building surface and ground	Wall function

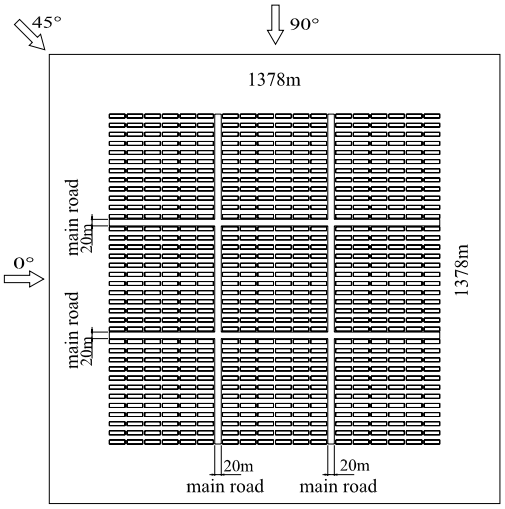

(a) Reference urban block model

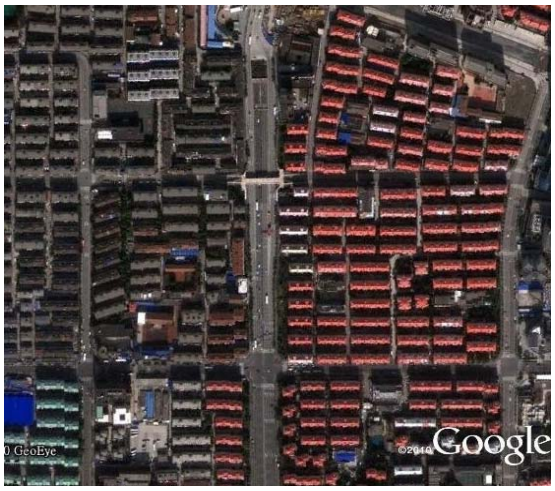

(b) Typical residential area in Shanghai (Google map)

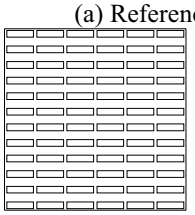

(c) Layout 1 (BCR40%)

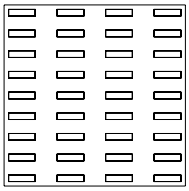

(d) Layout 2 (BCR20%)

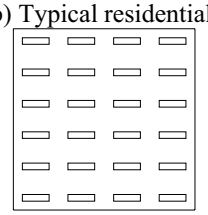

(e) Layout 3 (BCR13%)

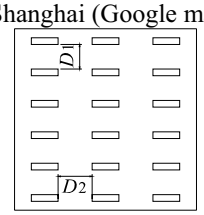

(f) Layout 4 (BCR10%)

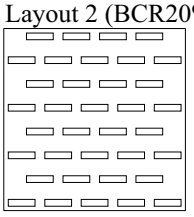

(g) Layout 5 (BCR20%)

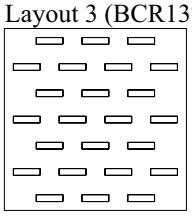

(h) Layout 6 (BCR13%)

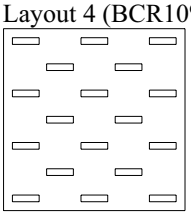

(i) Layout 7 (BCR10%)

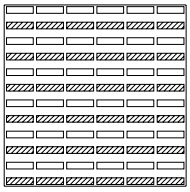

(j) Layout 8 (BCR 40%)

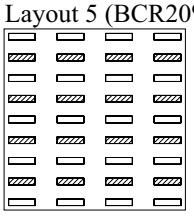

(k) Layout 9 (BCR 20%)

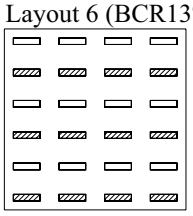

(l) Layout 10 (BCR 13%)

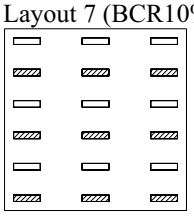

(m) Layout 11 (BCR 10%)

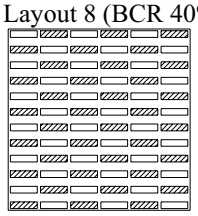

(n) Layout 12 (BCR 40%)

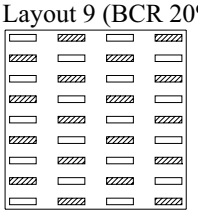

(o) Layout 13 (BCR 20%)

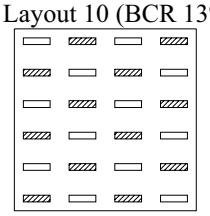

(p) Layout 14 (BCR 13%)

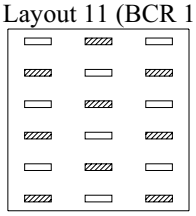

(q) Layout 15 (BCR 10%)

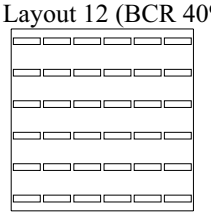

(r)Layout 16 (BCR 20%)

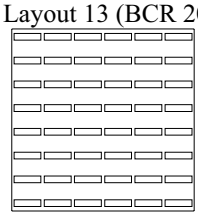

(s)Layout 17 (BCR 30%)

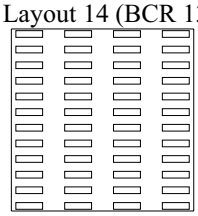

(t) Layout 18 (BCR 30%)

Layout	*H* (m)	
8&12	12m	24m
9&13	18m	54m
10&14	36m	72m
11&15	54m	90m

H of non-uniform layout

Figure 1. Analysis model

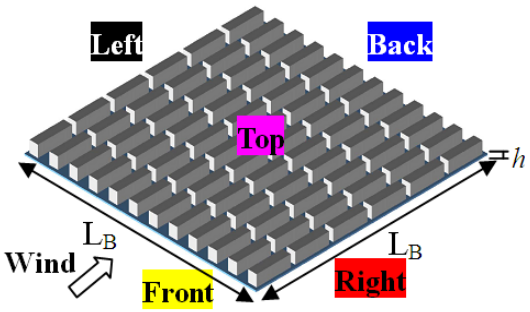

Take layout 1 (BCR=40%, Aligned array) as an example:

Pollutant Source Volume (PSV)

Location:0-2m (z) volume of center block

Size:326m (L_B) 326m (L_B) 2m (h) (Note: except building part)

Five surfaces of PSV

a. Front (Windward surface)

b. Back (Leeward surface)

c. Left, Right (side surfaces)

d. Top (upper surface)

Figure 2. Pollutant Source Volume (PSV)

Wind conditions at pedestrian level in an urban area play an important role in the dispersion of vehicle pollutants, diffusion of heat, and ventilation of buildings, as well as the comfort and safety of pedestrians. Therefore, it is necessary to understand the pedestrian wind environment around buildings 0-2m (z) and to take them into account in urban ventilation design. A uniform pollutant source assumed to be a passive scalar was generated throughout the pollutant source volume (PSV) (0-2m (z) volume of the center block), as shown in Figure 2, to simulate pollution from residence areas and vehicles. Six analysis indices were used to evaluate urban ventilation efficiency for all cases.

2.3 *Analysis indices*

2.3.1 *Spatial Wind Velocity Ratio (*VR_w*)*

Spatial wind velocity ratio (VR_w) is defined as the ratio of average wind velocity at pedestrian level to a reference wind velocity [Ng, 2009], and is calculated as:

$$VR_w = U_p / U_{ref} \quad (1)$$

where U_p is the volume-averaged wind speed in PSV (m/s) and U_{ref} is the inflow wind velocity at 10m height (m/s).

2.3.2 *Volume-averaged Normalized Concentration (*C^**)*

C^* is defined as the volume-averaged normalized concentration, and is calculated as:

$$C^* = (C \times U_{ref} \times W^2)/Q \quad (2)$$

where C is the calculated volume-averaged concentration (kg/kg), Q is the pollution emission rate (m^3/s) and W is the building width (m).

2.3.3 *Inflow rate of air (*$\Delta q_{air,in}$*)*

$\Delta q_{air,in}$ is the inflow rate of air passing through each surface of PSV (kg/s), and is calculated as:

$$\Delta q_{air,in} = \sum_{i=1}^{n} \left(\rho A_i \overline{u_{in,i}} \right) \quad (3)$$

where ρ is the air density (kg/m^3), A_i is the inflow area of cell face i (m^2), $\overline{u_{in,i}}$ is the time-averaged normal inflow wind velocity of cell face i (m/s), and n is the cell number at boundary surface of PSV.

2.3.4 *Inflow rate of pollutants* ($\Delta q_{P,in}$)

$\Delta q_{P,in}$ is the inflow rate of pollutants passing through each surface of PSV (kg/s), and is calculated as:

$$\Delta q_{P,in} = \sum_{i=1}^{n} \left(\rho A_i \overline{c_i} \overline{u_{in,i}} + \rho A_i \overline{c_i' u_{in,i}'} \right) \quad (4)$$

where $\overline{c_i}$ is time-averaged pollutant concentration at the boundary of cell face i (kg/kg), c_i' is the concentration fluctuation (kg/kg), and $u_{in,i}'$ is the inflow velocity fluctuation (m/s).

2.3.5 *Outflow rate of pollutants* ($\Delta q_{P,out}$)

$\Delta q_{P,out}$ is the outflow rate of pollutants passing through each surface of PSV (kg/s), and is calculated as:

$$\Delta q_{P,out} = \sum_{i=1}^{n} \left(\rho A_i \overline{c_i} \overline{u_{out,i}} + \rho A_i \overline{c_i' u_{out,i}'} \right) \quad (5)$$

where $\overline{u_{out,i}}$ is the time averaged normal outflow wind velocity of cell face i (m/s) and $u_{out,i}'$ is the outflow velocity fluctuation (m/s).

2.3.6 *Visitation Frequency (*VF*)*

VF represents the number of times a particle enters the domain and passes through it (Bady et al, 2008). To calculate VF, the following equation was applied:

$$VF = 1 + \Delta q_{P,in} / q_P \quad (6)$$

where q_P is the pollutant generation rate $q_P = PSV \times S$ (kg/s), PSV is the Pollutant Source Volume (m^3), and S is the uniform generation source strength ($kg/m^3 \cdot s$).

3 RESULT AND DISCUSSION

Based on previous studies (Hu and Yoshie, 2011), C^* reflected the integrated effects of other indices such as VR_w and VF, so it can be served as the core index for evaluating ventilation performance. Generally, large VR_w values and small VF values resulted in low C^* values. However, some exceptions were found, for example, low C^* values were found with low VR_w values or large VF values. In order to investigate such discrepancy in detail, flow rate and mass of pollutant which reflected by inflow rate of air ($\Delta q_{air,in}$); inflow rate of pollutants ($\Delta q_{P,in}$) and outflow rate of pollutants ($\Delta q_{P,out}$) passing through each surface of target control volume were studied and analyzed.

3.1 *Relationship between VR_w and C^**

All the cases were classified by three wind directions (Fig. 3a) and four BCRs (Fig. 3b). As expected, VR_w and C^* were negatively correlated for most cases. Several exceptions were indicated by gray dotted circles in both figures.

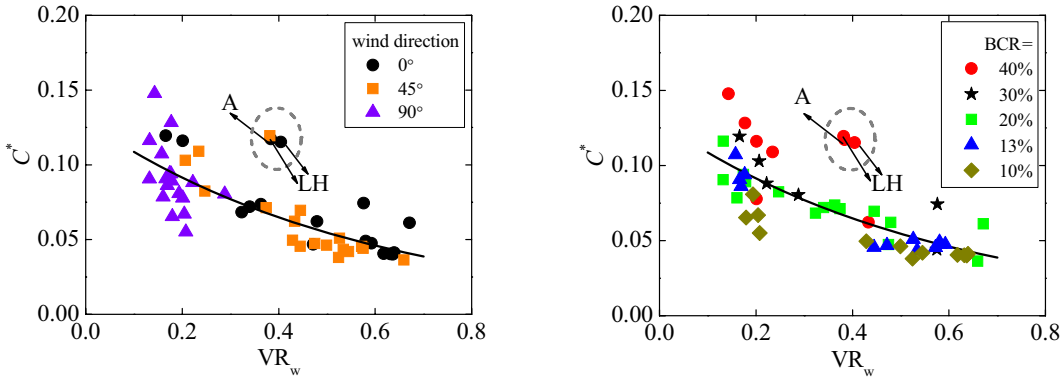

(a) Classified by wind direction θ (b) Classified by BCR

Figure 3. Relationship between VR_w and C^*

For θ=0°, 45°, C^* decreased as VR_w increased except at three points with both high C^* values and VR_w values, which were enclosed by the gray dotted circle. From Figure 3b, the three exceptions share the same BCR (40%) which were the densest situations. The three cases were A and LH arrays. Figures 4a and 4b showed the view of center block of those two arrays and Figure 4c showed that of SH array with BCR (40%) for reference.

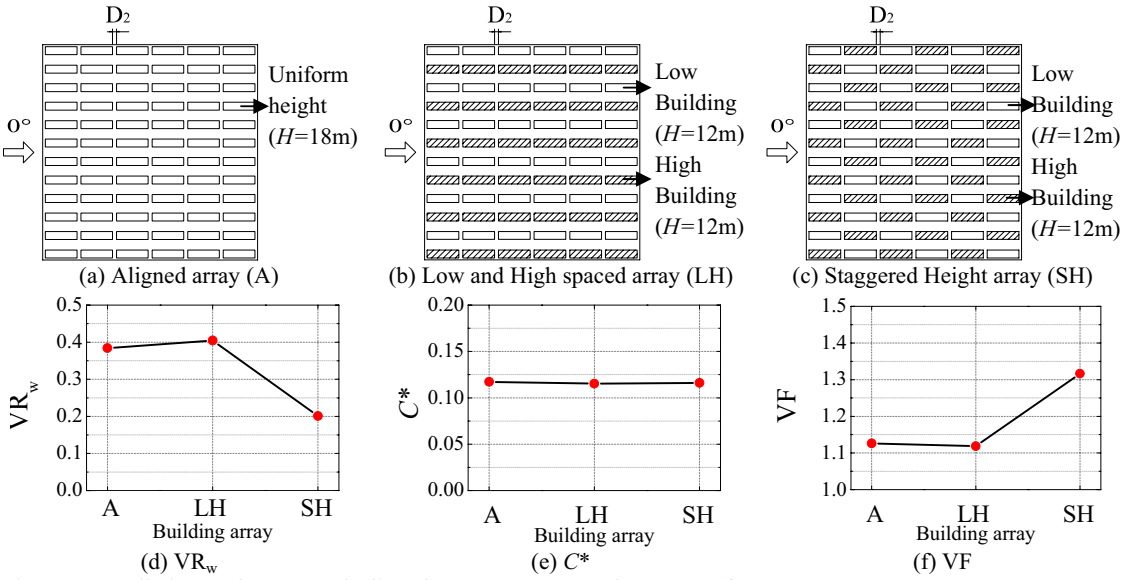

(a) Aligned array (A) (b) Low and High spaced array (LH) (c) Staggered Height array (SH)

(d) VR_w (e) C^* (f) VF

Figure 4. Ventilation performance of Aligned array, LH array and SH array (θ = 0°, BCR = 40%)

As displayed in Figure 4d, VR_w values of A and LH array were higher than that of SH array. It was because in dense area, small passage width D_2 made the passage parallel to the wind direction like a pipe in the A and LH arrays. This pipe-like flow can speed up the wind in stream-wise direction and cause large value of VR_w. Although VR_w values were different between A, LH and SH array, C^* values were almost the same (Fig. 4e). Therefore, the discrepancy that large VR_w values and high C^* values occurred for A and LH arrays. It can be interpreted by flow rate analysis depicted in Figure 5.

According to Figure 5b, on one hand, an even larger amount air entered PSV via the front surface of the A and LH arrays, and much less air entered through the top surface than for the SH array. One the other hand, as displayed in Figure 5c, even larger amount pollutant was ex-

hausted PSV via the back surface of the A and LH arrays, and much less pollutant was exhausted through the top surface than for the SH array. These two reasons resulted in a large value of C^*.It explained the apparent contradictions between the large VR_w and C^* values. It is noted that the contributions of each surface were different in terms of outflow rate of pollutant (Fig. 5c). For A and LH arrays, larger outflows of pollutant discharged from the back surface than for SH array. This was detrimental to downstream regions. Therefore, although C^* was nearly the same in PSV for the three arrays, SH array was more favorable for downstream regions.

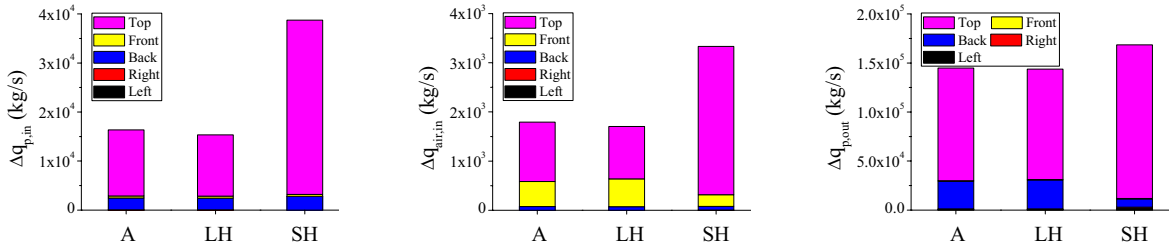

(a) Inflow rate of pollutants (b) Inflow rate of air (c) Outflow rate of pollutants

Figure 5. Flow rate of Aligned array, LH array and SH array (θ = 0°, BCR = 40%)

For θ=90°, the relationship between VR_w and C^* was not clear. VR_w was low and showed little difference while C^* showed large variations for all the cases.

3.2 *Relationship between VF and C^**

The relationship between VF and C^* was classified by BCRs (Fig. 6a) and building arrays (Fig. 6b) respectively. It was shown that C^* generally increased with the increase of VF. However, there were two exceptions.

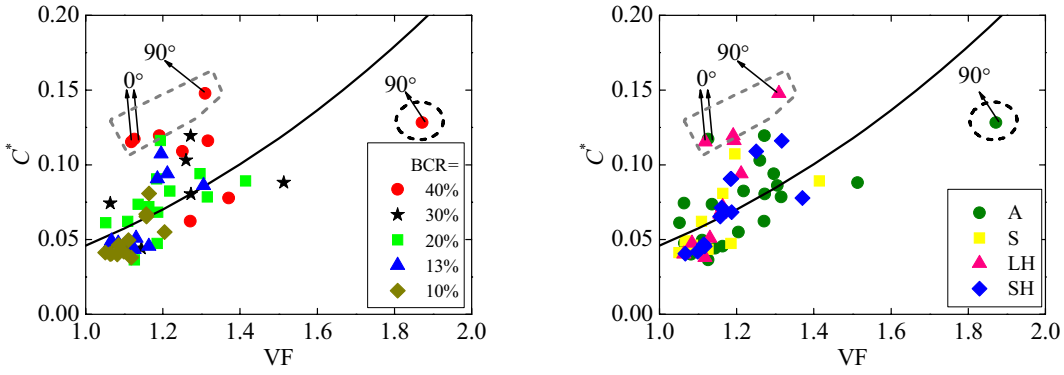

(a) Classified by BCR (b) Classified by building array

Figure 6. Relationship between VF and C^*

One was large values of C^* and small values of VF (pointed out by the gray dotted polygon). It is noted that most of those exceptions were for A and LH arrays with BCR=40% for θ=0°, 90°.

For θ=0°, as displayed in Figures 4e and 4f, for A and LH array, C^* values were high while VF values were small. The explanation was given in Figure 5. According to Figure 5a, a small amount of pollutant re-entered PSV, resulting in a small value of VF for A and LH array. However, the amount of inflow air and outflow of pollutant to PSV were also small for those cases (Figs. 5b and 5c). Therefore, the pollutant couldn't be diluted and removed and led to a high val-

ue of C^*. For LH array in the case of θ=90° (Fig. 7b), C^* values were high (Fig. 7e) while VF values were small (Fig. 7f). The reason was shown in Figure 8. A small amount of pollutant re-entered PSV, lead to small VF value for LH array (Fig. 8a). Meanwhile, the outflow of pollutant (Fig. 8b) and amount of inflow air (Fig. 8c) to PSV were also small and caused large C^* values. This explained the contradiction that small VF value and large C^* value.

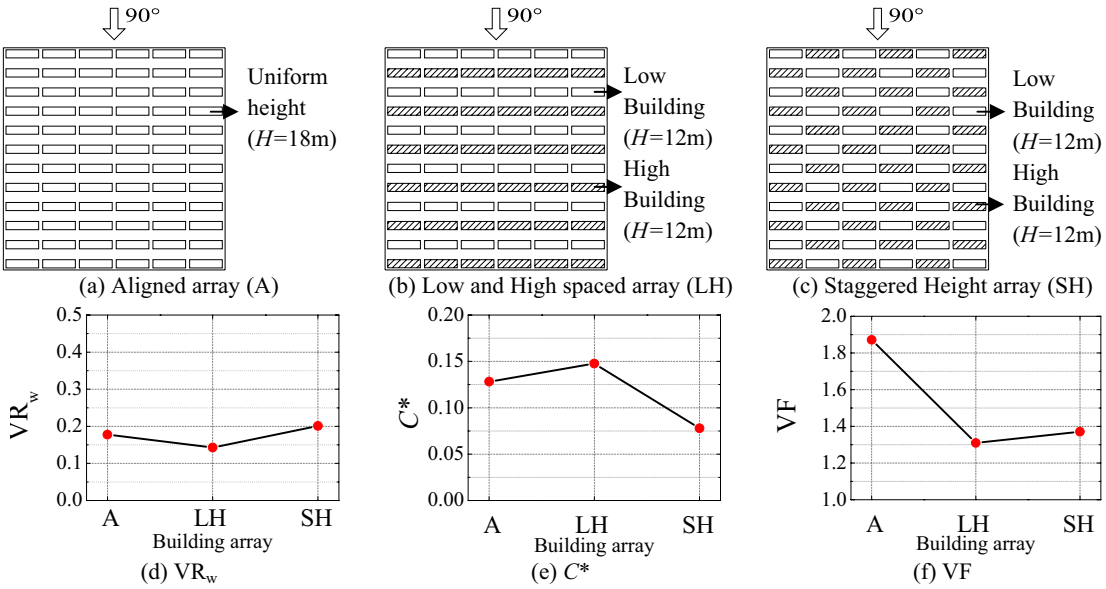

Figure 7. Ventilation performance of Aligned array, LH array and SH array (θ = 90°, BCR = 40%)

Another exception was the A array with BCR=40% for θ=90° (indicated by a black dotted circle in Fig. 6). As depicted in Figures 7e-7f, VF value was very large while the C^* value was not so high. According to Figure 8a, a large amount of inflow pollutant re-entered PSV through the top surface, resulting in a large value of VF. However, the outflow of pollutant and inflow of air were also very large and promoted exhausting and diluting of pollutant (Figs. 8b and 8c). Thus, the value of C^* was not so high.

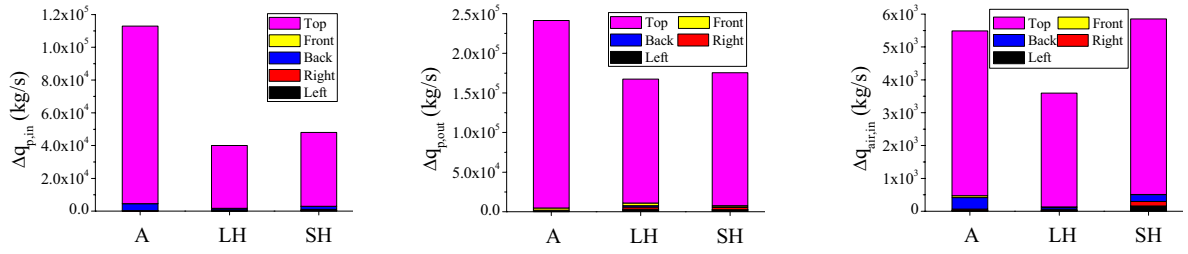

Figure 8. Flow rate of Aligned array, LH array and SH array (θ = 90°, BCR = 40%)

3.3 *Relationship between VR_w and VF*

Figures 9a and 9b showed that VR_w and VF were negatively correlated. As displayed in Figure 9a, for θ=0°, 45°, VF decreased as VR_w increased, and for θ=90°, correlation between VR_w and VF was not clear. VR_w was low and showed few changes while VF showed large differences among all the cases. The A array with BCR=40% for θ=90° showed the largest value of VF. As

discussed in Figure 8a, the largest amount of pollutant re-entered PSV through the top surface, so the value of VF was largest for this case.

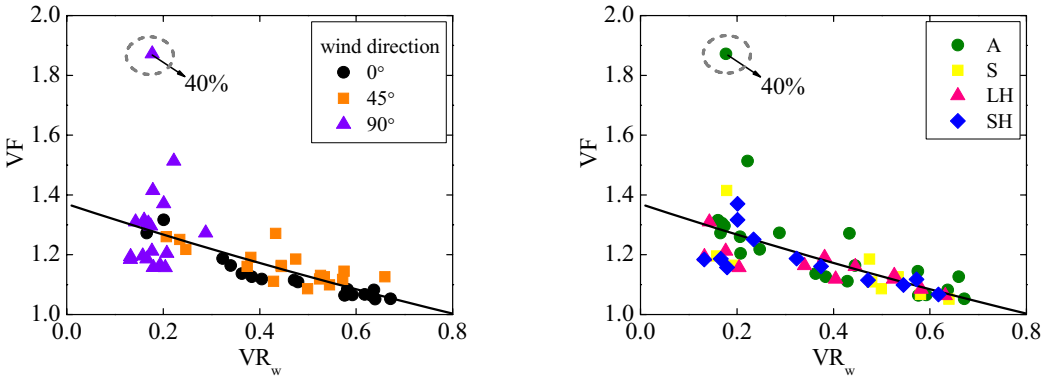

(a) Classified by wind direction θ

(b) Classified by building array

Figure 9. Relationship between VR_w and VF

4 CONCLUDING REMARKS

In order to investigate the ventilation efficiency of newly-planned residential areas, CFD simulations were carried out for various building arrangements. A reference urban model was designed according to a typical existing residential area in Shanghai. Keeping FAR constant, other urban models were designed by changing urban parameters (building coverage ratio, passage width, building array and building height variation).

The ventilation efficiency of the different cases were evaluated by spatially averaged VR_w, C^*, and VF. The detailed ventilation information reflected by inflow rate of pollutants ($\Delta q_{P,in}$), outflow rate of pollutants ($\Delta q_{P,out}$) and inflow rate of air ($\Delta q_{air,in}$) were used to explain the relationship among three indices (VR_w, C^*, and VF).

Relationships among ventilation indices (VR_w, C^*, and VF) were summarized for most cases. In general, large VR_w and small VF resulted in low C^*. However, a few exceptions were found in the dentist cases (BCR=40%). They were explained by flow rate analysis. In detail, with the increase of VR_w value, C^* and VF values decreased respectively for θ=0°, 45° except for A and LH array with BCR=40%. And for θ=90°, relationship between VR_w value and C^*, VF values were not clear, VR_w was low and showed few changes while C^* and VF showed large differences among all the cases. With the increase of VF value, C^* value increased for all wind directions.

5 ACKNOWLEDGEMENTS

This study was funded by the Ministry of Education, Culture, Sports, Science and Technology, Japan, through the Global Center of Excellence Program, 2008-2012, which is gratefully acknowledged.

6 REFERENCES

1 Ng, E.,2009. Air ventilation assessment for high density city – An experience from Hongkong, Proceedings of the seventh International Conference on Urban Climate. Yokohama.

2 Kato,S., Ito,K., Murakami,S., 2003. Analysis of visitation frequency through particle tracking method based on LES and model experiment. Indoor Air 13(2):182–93.

3 Bady,M., Kato,S., Huang,H.,2008.Towards the application of indoor ventilation efficiency indices to evaluate the air quality of urban areas. Building and Environment 43: 1991–2004.

4 Hu, T., Yoshie,R., 2011. Effects of building arrangement on ventilation performance in newly-built urban area. Proceedings of The Thirteenth International conference on Wind Engineering (ICWE13), Amsterdam, The Netherlands.

5 Google Maps 2011. URL: http://maps.google.com/.

6 Tominaga,Y., Mochida,A., Yoshie,R., Kataoka,H., Nozu,T., Yoshikawa, M., Shirasawa,T.,2009. AIJ guidelines for practical applications of CFD to pedestrian wind environment around buildings, Journal of Wind Engineering and Industrial Aerodynamics 96, 1749-1761.

The Seventh International Colloquium on Bluff Body Aerodynamics and Applications (BBAA7)
Shanghai, China; September 2-6, 2012

Characteristics of flow and temperature field along a heated street canyon in the multiple-fan turbulence wind tunnel

Hironori Kikugawa [a], Takanobu Goto [a] , Yuki Yonezawa [a],
Nobumasa Sekishita [b] and Kazuhiko Toshimitsu [a]

[a] *Oita National College of Technology, Oita-city, Oita, Japan*
[b] *Toyohashi University of Technology, Toyohashi, Aichi, Japan*

ABSTRACT: Street canyon phenomenon, in which waste heat and exhaust gases stagnate in the space between multi-story buildings, is contributed for urban air quality deteriorating. The flow field, temperature field, and concentration field of a pollutant in a street canyon are complex. Much research has focused on the flow field, gas concentration field, and their numerical simulations. However, the temperature distribution of the flow field on the street surface has not been investigated experimentally. Therefore, the purpose of this study is to experimentally characterize the effects of building arrangements on the street surface temperature distribution and flow pattern along a heated street canyon. In addition, numerical simulation was used for comparing the experimental results. As a result of this research, contribution factors of cooling effect along the heated street canyon were become clear.

KEYWORDS: Street canyon, wind tunnel, numerical simulation, flow field, temperature field.

1 INTRODUCTION

In recent years, urban air quality has deteriorated due to an increase in the number and density of multi-story buildings. One contributing factor is the street canyon phenomenon, in which waste heat and exhaust gases stagnate in the space which is canopy, above the streets and between high-rise buildings. The flow field, temperature field, and concentration field of a pollutant in a street canyon are complex; highly reliable experimental data is required for the evaluation, prediction and improvement of each field. Much research has focused on the flow field [1], gas concentration field [2-4], and their numerical simulations [3-7]. However, the temperature distribution of the flow field on the street surface has not been investigated experimentally. Therefore, the purpose of this study is to experimentally characterize the effects of building arrangements on the street surface temperature distribution and flow pattern along a heated street canyon. The experiments were performed by actively controlled multiple-fan wind tunnel in our campus; Oita National College of Technology (ONCT). In the ONCT wind tunnel, any kind of turbulent fluctuating flow was generated by actively controlled multiple-fans. This study was carried out under the collaborative work with Toyohashi University of Technology (TUT). TUT wind tunnel has different type of generating turbulence. Compared to our work with different types of turbulent wind properties, it is expected that new knowledge could be obtained. In this paper, as the first step, the effects of building arrangements on street surface temperature and flow patterns with using our multiple-fan wind tunnel are reported. In addition, numerical simulation was used for comparing the experimental results.

2 EXPERIMENTAL SETUP

2.1 *Multiple-fan Wind Tunnel*

The turbulence wind tunnel is an actively controlled multiple-fan-type generator with 66 small, independently computer controlled inlet fans. Each fan duct has separately channels the air from the inlet to the measurement section, at which point the air streams are mixed to create turbulent flow. Any natural turbulent wind condition can be generated by the actively controlled fans. The measurement section has a height of 1015 mm, a width of 1095 mm, and a length of 3600 mm. The wind tunnel apparatus is shown in Figure 1. To generate imitated natural wind in this tunnel, Kármán type spectrum[8-9] was used. This spectrum was shown well the natural wind to set several parameters in the equation (1). To create a time series wind velocity fluctuating data for controlling fans of wind tunnel, inverse FFT method was used.

$$S_u(f) = 4I_u^2 L_u U \frac{1}{\{1+70.8(\frac{fL_u}{U})^2\}^{\frac{5}{6}}} \quad (1)$$

2.2 *Experimental Method*

The street canyon model was built comprising a heated street model and building models. To heat the street model, electrical current was impressed to a thin metal plate directly set in the bottom of the street floor. The building models were made of plastic blocks in three-dimensional configurations. Two normalized sizes were used: 1:1:1 and 2:1:1, where the model size is normalized to the street canyon width. The building models were arranged in several configurations along the heated street, as shown in Table 1. The building models had various combinations of upstream and downstream building heights in both linear and staggered arrangements. Thermography which is infrared imaging camera, was used to observe the temperature distribution of the heated street. In addition, the flow field in the canopy was observed using the smoke-wire method. The wind tunnel was used to test in steady flow and fluctuating turbulent flow.

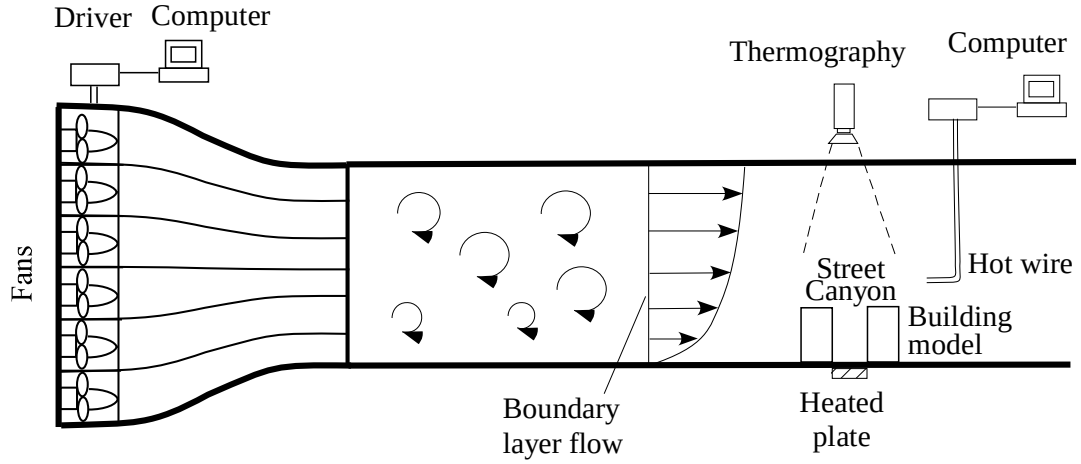

Figure 1. Wind tunnel experimental setup.

Table 1. Configurations of three-dimensional models.

Case	Upstream model	Downstream model	Arrangement
Case 1	1:1:1	1:1:1	Linear
Case 2	2:1:1	2:1:1	Linear
Case 3	1:1:1	2:1:1	Linear
Case 4	2:1:1	1:1:1	Linear
Case 5	Alternating (Symmetrical)		Linear
Case 6	Alternating (Asymmetrical)		Linear
Case 7	1:1:1	1:1:1	Staggered
Case 8	2:1:1	2:1:1	Staggered
Case 9	1:1:1	2:1:1	Staggered
Case 10	2:1:1	1:1:1	Staggered
Case 11	Alternating (Left diagonal)		Staggered
Case 12	Alternating (Right diagonal)		Staggered

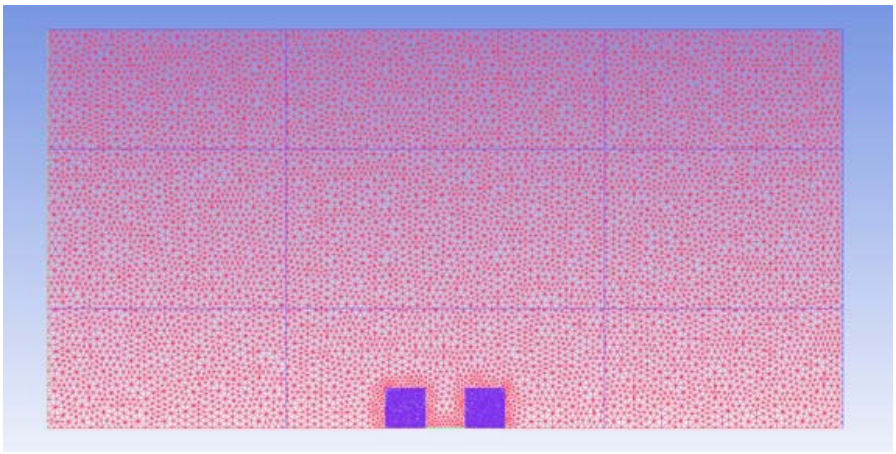

Figure 2. Mesh setup for numerical simulation.

2.3 *Numerical simulation setup*

To comparing the numerical results with the experimental results of temperature field and flow field of wind tunnel experiments, the validity of the numerical analysis methods and results of numerical analysis has been verified. It seems to be able to establish a quantitative approach by creating of numerical calculation of heated street canyon phenomenon. In this study, to investigate for the numerical analysis of temperature field and flow field in the street canyon, general-purpose thermal and fluid analysis software; ANSYS CFX ver.13, was used for steady state flow condition. This software consist of three steps individual software, CFX-Pre which is to set the boundary conditions, CFX-Solver which is to perform the analytical calculations and CFX-Post which is to display the analysis results. Computational domain was set 0.15m for Y-axis, 0.5m for Z-axis, 1m for Z-axis in the direction of the rectangular parallelepiped, which was placed two pitch sizes of imitated buildings toward the street for the original position. Type of mesh was automatically created by Tetra Mixed as shown in Figure 2, which is commonly used in fluid analysis. Mesh points of the analysis model is about 1.6 million. The solver was set by standard k-ε model for turbulent condition.

3 RESULTS AND DISCUSSION

3.1 *Wind tunnel experimental results*

The temperature distributions in low-turbulence steady flow are shown in Figure 3. The Case 1 configuration, per Table 1 (i.e., WS /Hb=1 with 1:1:1 upstream and downstream building models in a linear arrangement), in which the areas in the middle of the street and in front of the downstream buildings were well cooled due to the frontal eddy generated at separation flow reattachment, is shown in Figure 3 (a). The Case 2 configuration, (i.e., 2:1:1 upstream and downstream building models in a linear arrangement), in which the street areas in line with the building gaps were remarkably cooled due to flow acceleration, are shown in Figure 3 (b). However, the areas just behind the upstream buildings were not well cooled due to flow stagnation. Cavity flow was also observed in the street by flow visualization.

The temperature distributions of the Case 3 and Case 4 models are shown in Figure 4. Per Table 1, the Case 3 configuration has taller downstream buildings, whereas the Case 4 configuration has taller upstream buildings. Horseshoe vortices formed in the gaps between the upstream buildings in both configurations. In Case 3, the separation flow from the upstream buildings collided with the downstream buildings and formed a frontal eddy, resulting in effective cooling of the street surface in front of the downstream buildings. Because the upstream buildings in Case 4 are taller, the air flowing between the buildings was accelerated and a lee eddy was formed over the street.

The temperature distributions of the Case 5 and Case 6 model configurations, both of which feature a linear arrangement of alternating building heights, are shown in Figure 5. The Case 5 model is arranged symmetrically, where both upstream and downstream buildings have the same height. The Case 6 model is arranged asymmetrically, where the upstream and downstream buildings have different heights. In Case 5, the street areas in line with the building gaps were well cooled, however, the areas just behind the upstream buildings were not well cooled due to flow stagnation, and the separation flow from the upstream model skimmed over the downstream model. Case 6 exhibited a considerable cooling effect over the street in front of the downstream model, specifically when the air flow collided with the taller downstream buildings and formed a frontal eddy.

The temperature distributions of the Case 4 and Case 10 model configurations are shown in Figure 6. Both configurations feature taller upstream buildings, but Case 4 features a linear arrangement whereas Case 10 features a staggered arrangement. The areas behind the upstream buildings nearest to the gaps were well cooled by the trailing vortices that were generated from the upstream side walls. In Case 10, the trailing vortices collided with the downstream buildings and formed a horizontal frontal eddy. Therefore, the cooling effect of the Case 10 model configuration is slightly higher than that of Case 4. However, if the upstream model were taller than the downstream model, it is clear that the cooling effect would decrease due to flow stagnation behind the upstream model.

The data in Figures 3 through 6 reveal a significant correlation between the formation of an eddy and the cooling effect on the street; how the eddy forms on the street surface determines the cooling effect.

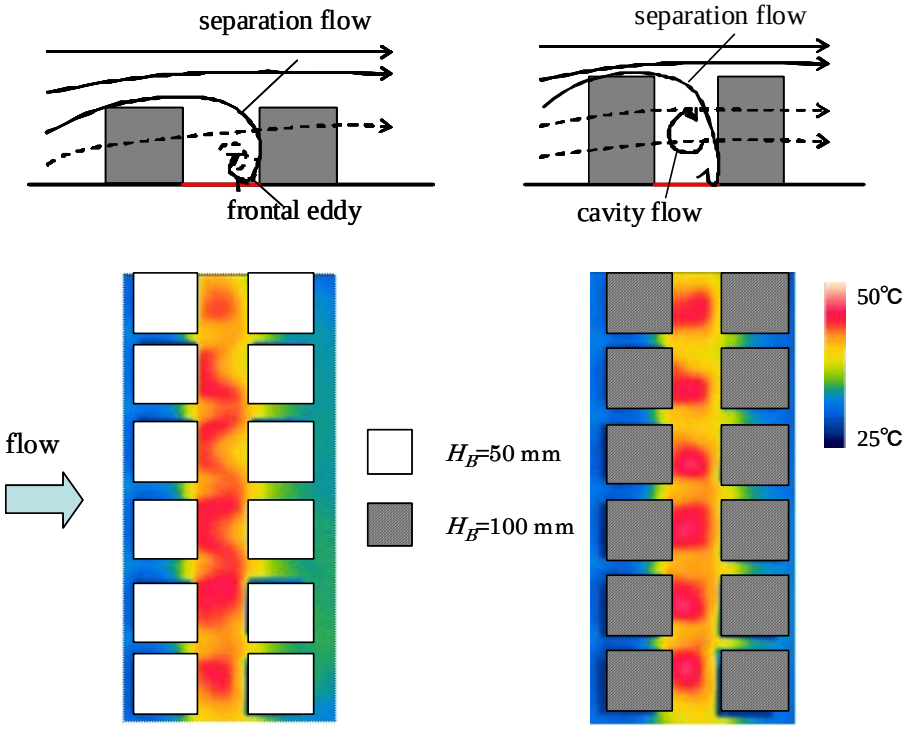

(a) Case 1 (b) Case 2

Figure 3. Temperature distributions of Case 1 and Case 2 models.

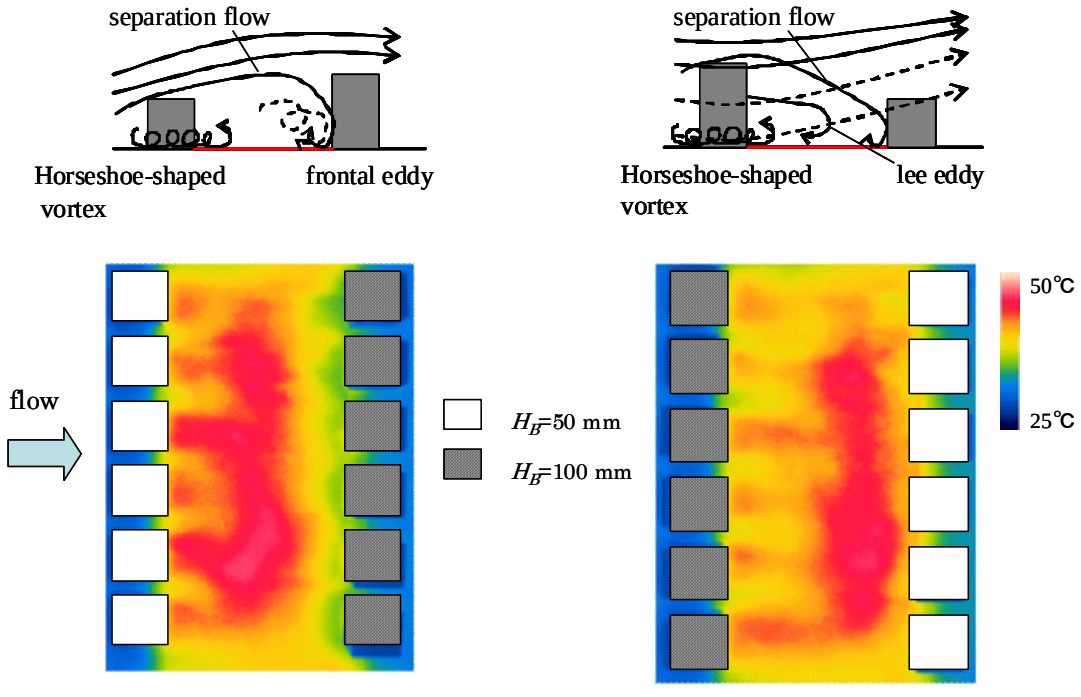

(a) Case 3 (b) Case 4

Figure 4. Temperature distributions of Case 3 and Case 4 models.

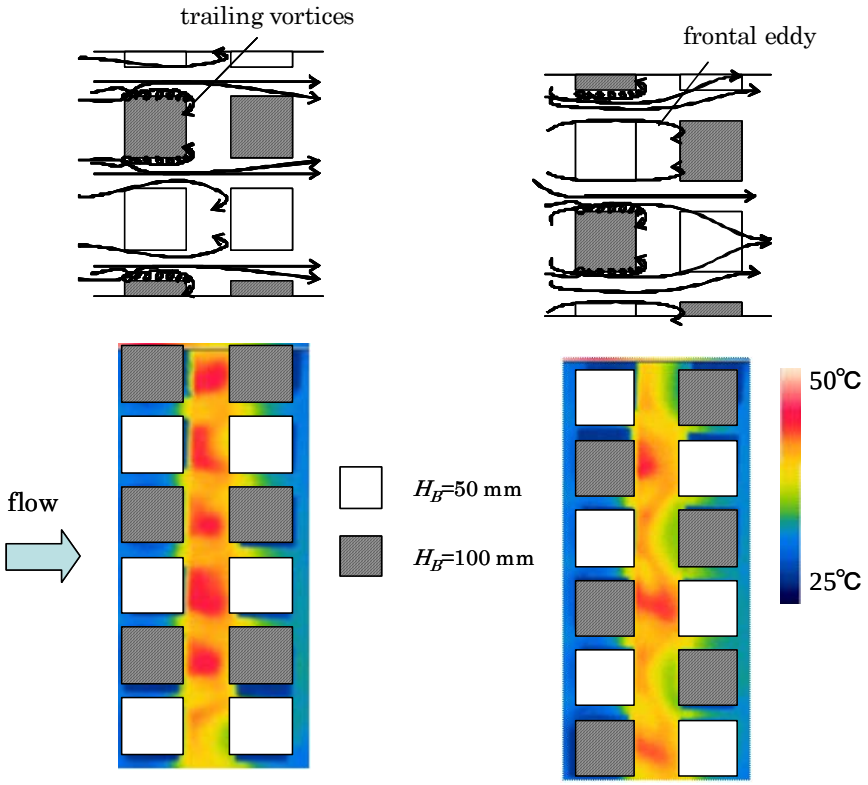

(a) Case 5 (b) Case 6

Figure 5. Temperature distributions of Case 5 and Case 6 models.

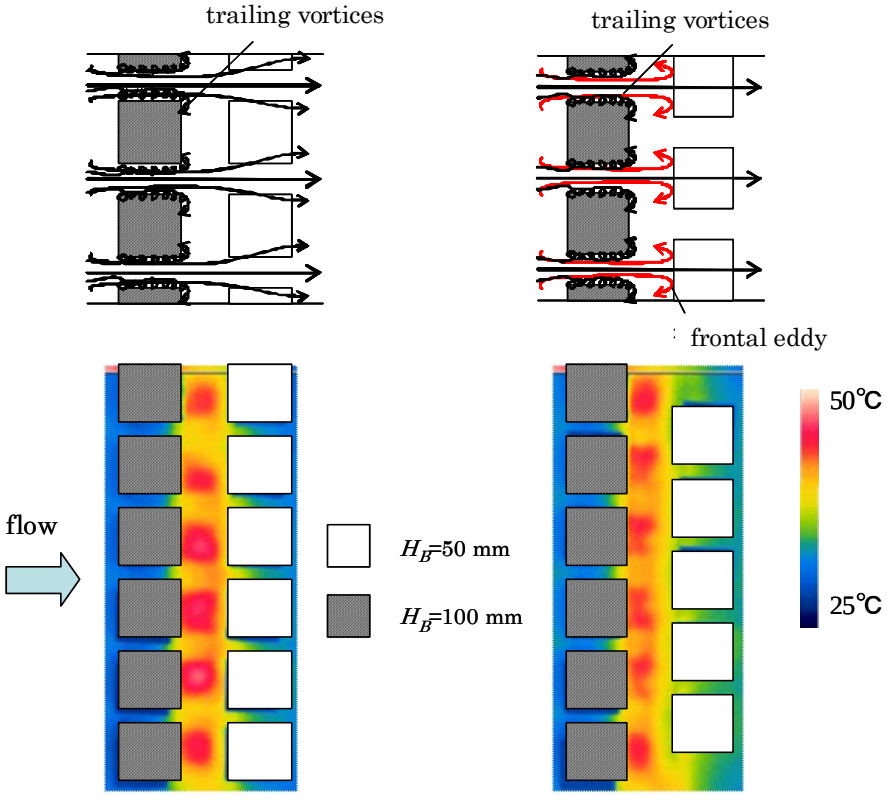

(a) Case 4 (b) Case 10

Figure 6. Temperature distributions of Case 4 and Case 10 models.

3.2 *Numerical simulation results*

Results of numerical analysis are described below in different configurations of building models located in a uniform steady flow as shown in Figure 7. For each case, these figures show the temperature distribution and stream lines.

The temperature distributions and stream lines of the Case 1 model configuration are shown in Figure 7 (a). Some part of airflow at the top of the model which separated the upstream side was reattached to the downstream model on the front surface, and the heated street canyon was cooled by the airflow as the downdraft. In addition, the downdraft would be part of the circulating flow of the entire street, to excite the circulation.

The temperature distributions and stream lines of the Case 2 model configuration are shown in Figure 7 (b). Airflow separated on the leading edge of the front model was increased speed in the gap between the buildings, and the street of the gap between the models surface was cooled well. Circulating flow which was stable in street canyon has been formed, and the separated flow from the upstream model was difficult to approach in the street canyon. It became clear that the cooling range for the backward of the upstream model was narrow compared with the Case 1 configuration.

The temperature distributions and stream lines of the Case 3 model configuration are shown in Figure 7 (c). The most of the separated flow from the upstream side model reattached to the front surface of the downstream side as a downdraft. The downdraft become part of the circulating flow of circulating whole street canyon, and the flow which were passing through above the street made the circulating flow excite furthermore. Therefore, the airflow which reattached to the downstream side model is easy to influx from the top, a large amount of cold air flowed into street, the entire street has been efficiently cooled.

The temperature distributions and stream lines of the Case 4 model configuration are shown in Figure 7 (d). As with Case2, airflow separating on the leading edge of the front model was increased speed in the gap between the buildings, and the street of the gap between the models surface was cooled well. Airflow which separated from the top of the upstream side were passed through downward without reattach on the downstream model, the airflow is difficult to approach from the top to the street surface, stable circulating flow was formed above the street.

Figure 8 shows the temperature distribution and wind velocity vectors of the street surface for the Case1 configuration. Central part of the upstream side behind the model is cooled well by a cold downdraft from the top. Airflow which flows to the rear of the model was reattached to the street surface, high-temperature part formed arched shape. This is because cold air which has flowed into the street from the top, with exchanging heat on the street, spread radially with weakening the cooling capacity. Even though the street surface of the gap between the models were easily cooling, arched shaped high-temperature part were distributed on the street surface. This is because the airflow of the cooling capacity was weakened by heat exchange along the high-temperature part on the street surface.

The data in Figures 7 through 8 reveal a correlation between the temperature distribution and stream structure for the cooling effect on the street; how the downdraft forms in the street for the circulating flow determines the excitation of the cooling.

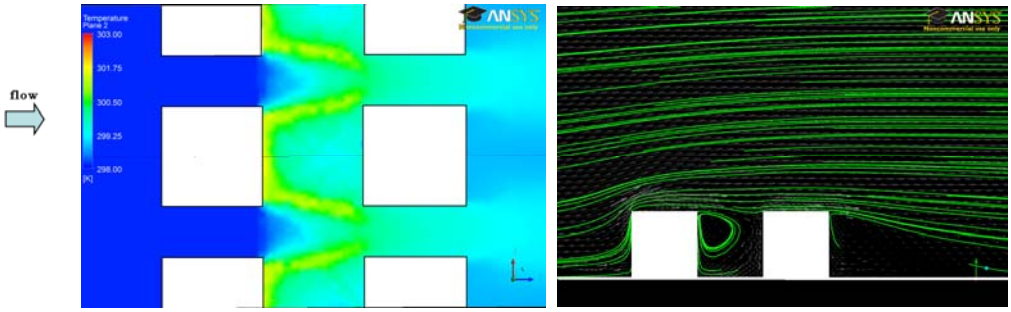

(a) Case 1

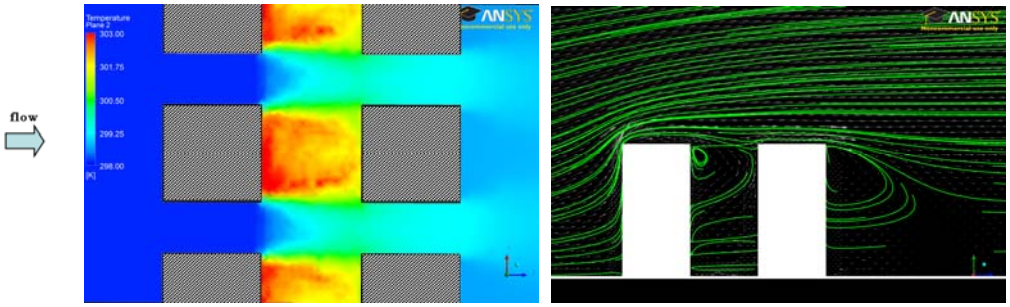

(b) Case 2

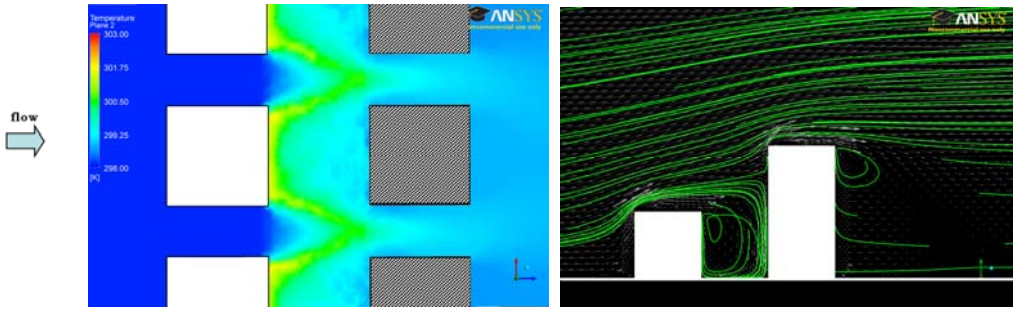

(c) Case 3

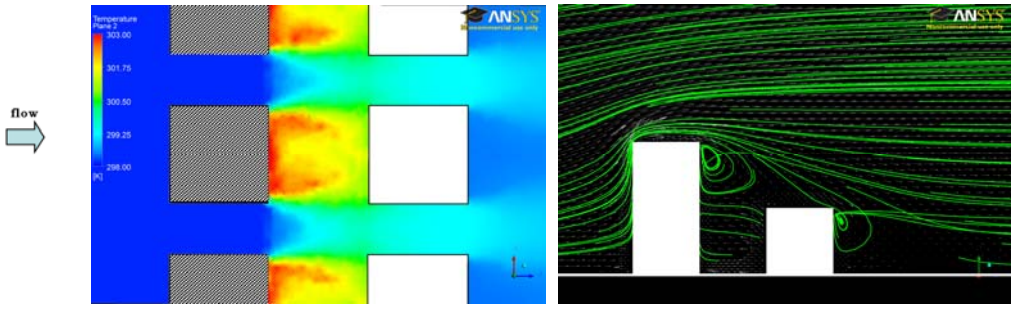

(d) Case 4

Figure 7. Temperature distribution and stream line.

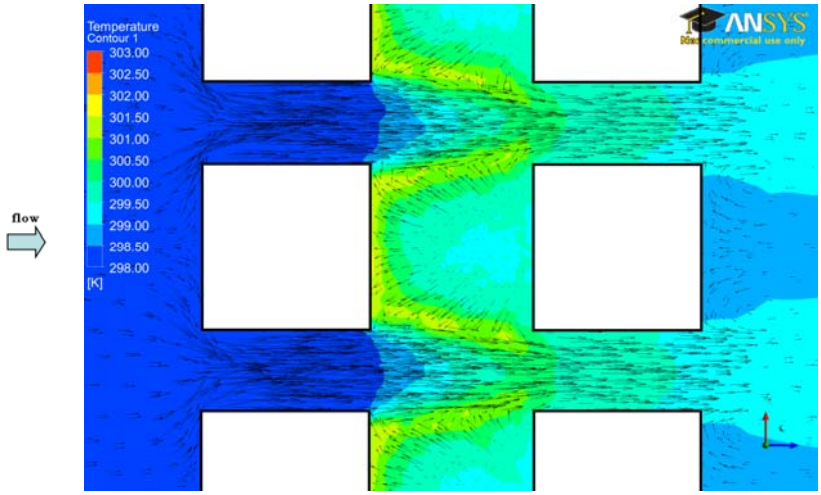

Figure 8. Temperature distribution and flow vector of Case 1.

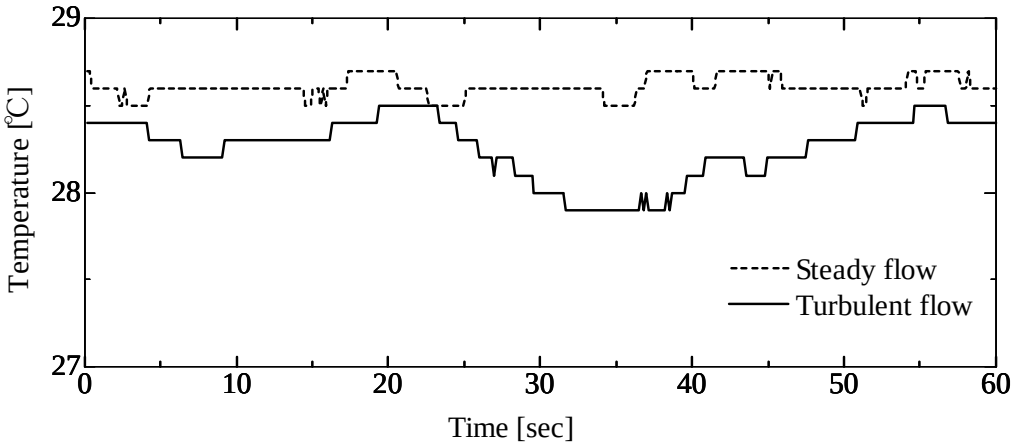

Figure 9. Temperature fluctuation in turbulent flow.

3.3 *Turbulent effects*

The temperature fluctuation in turbulent flow produced by actively controlled multiple-fan is shown in Figure 9. It is clear that the cooling effect of the turbulent flow is greater than steady flow; how well the street is cooled depends on the fluctuation of the turbulence and the downdraft. It is also evident that a turbulent eddy contributes to the cooling of a heated street surface. The average temperature is significantly low in the turbulence flow compared to the steady flow. The maximum and minimum temperature is fluctuating in the turbulent flow depends on the wind velocity. Because a significant velocity fluctuation exists when the actively controlled multiple-fans, the street temperature varies to the steady flow and the temperature distribution never reaches steady-state.

4 CONCLUSIONS

In this research, building models were arranged at the upstream and downstream sides of a heated street canyon, and the temperature distributions of the street were investigated. Several results were observed:

(1) For the wind tunnel experimental results, temperature distribution and flow visualization reveal a significant correlation between the formation of an eddy and the cooling effect on the street; how the eddy forms on the street surface determines the cooling effect.
(2) The numerical simulation results reveal a correlation between the temperature distribution and stream structure for the cooling effect on the street; how the downdraft forms in the street for the circulating flow determines the excitation of cooling.
(3) For the turbulent effects, a significant temperature fluctuation exists when the actively controlled multiple-fans; how the velocity fluctuation varies the street temperature and the temperature distribution never reaches steady-state.

For future work, a database will be created for heated street canyons based on additional experiments in simulated natural wind flow using different types of turbulent wind tunnels.

5 ACKNOWLEDGEMENTS

This work was supported by the cooperation project grant between the University of Technology and the National College of Technology, and was conducted by Toyohashi University of Technology during FY2009 to FY2011.

6 REFERENCES

1 e.g., Oke, T.R., Street design and urban canopy layer climate, Energy and Buildings 11, 1988, pp.103-113.

2 Uehara, K., Yamao, Y., Oikawa S., Mochida, A., Wind-tunnel Experiments on Improving the Natural Ventilation of a Street-Canyon, J. of Jpn. Soc. Atmos. Environ., 42(5), 2007, pp.301-309.[in Japanese]

3 Gromke, C., Ruck, B., Influence of trees on the dispersion of pollutants in an urban street canyon-Experimental investigation of the flow and concentration field, Atmos. Environ. 41, 2007, pp.3278-3302.

4 Khan, I.M., Simons, R.R., Grass, A.J., Upstream Turbulence Effect on Pollution Dispersion, Environ. Fluid Mech. 5, 2005, pp.393-413.

5 Kim, J.J., Baik, J.J., Urban street-canyon flows with bottom heating, Atmos. Environ. 35, 2001, pp.2295-3404.

6 Li, X.X., Liu, C.H., Leung, Y.C., Development of a k-ε model for the determination of air exchange rates for street canyons, Atmos. Environ. 39, 2005, pp.7285-7296.

7 Walton, A., Cheng, A.Y.S., Large-eddy simulation of pollution dispersion in an urban street canyon-Part 2: idealized canyon simulation, Atmos. Environ. 36, 2002, pp.3615-3627.

8 Von Kármán : Progress in the Statictical Theory of Turbulence, Proc. Nat. Acd. Sci., Washington D.C., 1948, pp.530-539.

9 Simiu, E., Scanlan, R.H. : Wind Effects on Structures, Second edition, John Wiley & Sons, 1986, pp.48-65.

The Seventh International Colloquium on Bluff Body Aerodynamics and Applications (BBAA7)
Shanghai, China; September 2-6, 2012

Large-eddy simulation of flow around obstacle arrays using drag force method of gas-solid two-phase flow

Jianying Jiao [a], Ryuichiro Yoshie [b]

[a]*Tokyo Polytechnic University, Kanagawa, Japan*
[b]*Tokyo Polytechnic University, Kanagawa, Japan*

ABSTRACT: The traditional method (body-fitted method) of simulating flows around obstacle arrays is usually used to simulate urban environments. However, with increasing numbers of simulated buildings, a great deal of time and labor are required to generate body-fitted grids. In order to solve this problem, the drag force method using gas-solid two-phase flow was applied to simulate an urban environment. At first, it was important to assess the precision of the drag force method compared with that of the traditional method. Thus, numerical tests were carried out on a high-rise building and building arrays. The results obtained from the traditional method and the drag force method were in good agreement with experimental data. The grids for the drag force method didn't need to be body-fitted, so it required much less time to generate them.

KEYWORDS: Large eddy simulation; subgrid-scale model; drag force.

1 INTRODUCTION

With the increase of urban populations, urban environments have become an important research subject. Increasing numbers of researchers are using CFD to study urban environments. Because of the increase of the computational domain of urban environments and simulated buildings, huge number of grids is needed and a great deal of time and labor are required to generate body-fitted grids. In order to solve this problem, it is not enough to simply improve computer performance. A better method for simulating an urban environment needs be developed.

In the early development stage, restrictions of computer performance enabled flow fields around only simple geometry to be simulated using the traditional method. For example, the flow field around a square cylinder (or other simple geometry building) could be simulated using large eddy simulation. Kelkar and Patankar (1992)[1] predicted vortex shedding behind a square cylinder. Mukhopadhyay et al. (1992)[2] researched wakes behind a square cylinder in a channel. Rodi et al. (1997) [3] simulated the flow field around a square cylinder and a wall-mounted cube flow in a channel. Bouris and Bergeles (1998)[4] predicted vortex shedding from a square cylinder in 2D.

With development of computers, flow fields around building arrays could be simulated by the traditional method. Hanna et al. (2002)[5] used the Smagorinsky model to simulate the flow field around simple obstacle arrays. Tseng (2006)[6] predicted urban dispersion using large eddy simulation. Xie and Castro (2009)[7] applied LES to simulate flow and dispersion in urban streets. Gousseau et al. (2011)[8] adopted RANS and LES to simulate the wind field and pollution dispersion around a group of buildings in a downtown area.

With the increasing numbers of simulated buildings, a great deal of time is required to generate body-fitted grids. To overcome this problem, a drag force method of gas-solid two-phase flow is used to simulate urban environments. This method is introduced in Section 2. Section 3 compares numerical results obtained by this method for wind fields around a high-rise building and building arrays with those obtained by the traditional method and experiment data. Conclusions are given in Section 4.

2 DRAG FORCE METHOD

In our drag force method, the buildings are firstly discretized by a first set of grids, as shown in Fig. 1(a). This first set of grids is a body-fitted one, in which each grid in the building is assumed to be filled with a sphere, as shown in Fig. 1(b). The volume of the sphere is determined such that the air void fraction rate (= $(V_r-V_s)/V_r$) becomes very small (for example 0.001), where V_r=volume of rectangular cell and V_s= volume of sphere.

Secondly, a second set of grids is generated, as shown in Fig. 1(c), in which black and red lines show the second and first set of grids, respectively. The second set of grids is not a body-fitted one and is used for flow calculations. Cells that contain solid parts of a building in the second set of grids are expressed by solid void fractions as:

$$\varepsilon_p = \sum_{k=1}^{N^*} V_k / (\Delta x \Delta y \Delta z) \tag{1}$$

where Δx, Δy, Δz are grid lengths of the second set of grids that contain solid parts of a building, N is the number of spheres in the second set of grids and V_k is the volume of the k^{th} sphere in the second set of grids.

The air void fraction is expressed as:

$$\varepsilon_g = 1-\varepsilon_p \tag{2}$$

The drag force coefficient determined by Ergun/Wen and Yu (1952; 1966)[9, 10] was used, and is expressed as:

$$\beta = \frac{3}{4}\frac{(1-\varepsilon_g)\varepsilon_g}{d_p}\rho_g\left|u_g-u_p\right|C_{D0}\varepsilon_g^{-2.7}, \varepsilon_g > 0.8;\ 150\frac{(1-\varepsilon_g)^2\mu_g}{\varepsilon_g d_p^2}+1.75\frac{(1-\varepsilon_g)\rho_g\left|u_g-u_p\right|}{d_p}, \varepsilon_g \le 0.8 \tag{3}$$

$$C_{D0} = \begin{cases} 24(1+0.15\,\mathrm{Re}^{0.687})/\mathrm{Re}, \mathrm{Re} \le 1000 \\ 0.43, \mathrm{Re} > 1000 \end{cases}, \quad \mathrm{Re} = \rho_g d_p \varepsilon_g \left|u_g-u_p\right|/\mu_g \tag{4}$$

where u_g, u_p, ρ_g and μ_g are gas velocity, solid velocity, gas density and gas viscosity coefficient, respectively. u_p is zero in this method.

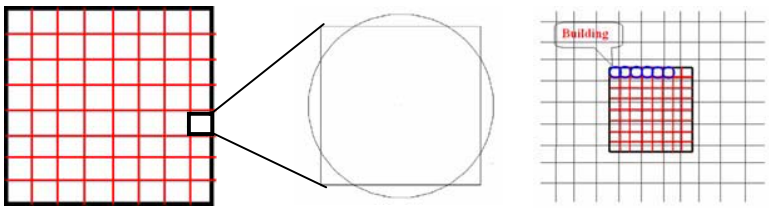

(a) Discretization of building by first set of grids (Body-fitted grids)

(b) A sphere for a grid

(c) First and second sets of grids

Fig.1 Discretization of building for drag force method

The filter (LES) momentum equation is expressed as:

$$\nabla\cdot[(\varepsilon_g)\bar{u}_g] = 0$$
$$\varepsilon_g\left(\frac{\partial\bar{u}_g}{\partial t}+\bar{u}_g\cdot\nabla\bar{u}_g\right) = -\frac{\varepsilon_g\nabla\bar{p}}{\rho_g}+\varepsilon_g\nu_g\nabla\cdot(\nabla\bar{u}_g+\nabla\bar{u}_g^{T})-\frac{\beta\bar{u}_g}{\rho_g} \tag{5}$$

Even if the cells are totally inside the building (even the cells are totally solid), they are treated as fluid cells with very small ε_g (for example, ε_g= 0.001). Thus, it becomes possible to universally apply equations (3) for every cell regardless of its phase (fluid or solid).
With regard to the numerical tests in this paper, the new subgrid-scale model (Gu and Jiao 2011)[11] was used.

3 NUMERICAL TEST

3.1 *HIGH-RISE BUILDING*

Fig. 2 shows a high-rise building with the same geometry as that of the wind-tunnel experiment of Meng and Hibi (1998)[12]. The Reynolds number based on H (building height) and U_H (inflow velocity at $z = H$) was 24,000. H, L and W were 0.16m, 0.08m and 0.08m. The flow field around the high-rise building was simulated by using the traditional method (body-fitted method) and the drag force method. The results by the two methods were compared with experiment data (Meng and Hibi 1998).

The grids and boundary conditions of the numerical test were the same as those of Tominaga et al.[13] (2008). The non-uniform grid and the inflow condition of Kataoka (2002, 2008)[14, 15] were used. The grid numbers using the two methods were almost the same: 60×45×39. The velocity components at the inflow boundary (Kataoka 2008) are given by:

$$\begin{aligned} u_{inlet}(y,z,t) &= < u >_{inlet}(z) + \phi(\theta) \times \{u(y,z,t) - < u > (y,z)\}_{recy} \\ v_{inlet} &= \phi(\theta) \times \{v(y,z,t) - < v > (y,z)\}_{recy} \\ w_{inlet} &= \phi(\theta) \times \{w(y,z,t) - < w > (y,z)\}_{recy} \end{aligned} \tag{6}$$

where subscripts denote the values at the inlet and the downstream (recy) planes and <> is a time-averaged value. $\phi(\theta)$ is the damping function (Kataoka 2008).

Air void fraction in the high-rise building was set to 0.05 in the drag force method.

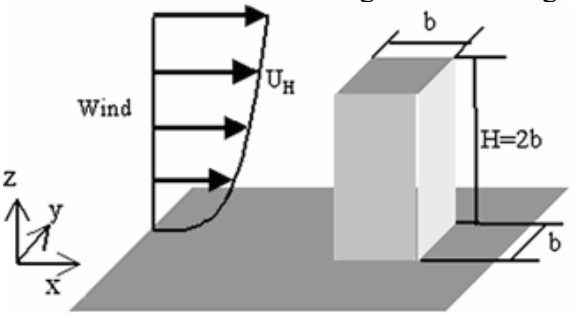

Fig. 2 Geometry of high-rise building

Figs. 3 and 4 show the mean velocity profiles and the r.m.s. value profiles at the y/b = 0 plane. There were nine profiles: at x/b=-0.75, x/b=-0.5, x/b=-0.25, x/b=0, x/b=0.5, x/b=0.75, x/b=1.25, x/b=2 and x/b=3.25. The mean velocities by the drag force method were a little closer to the experiment data than those by the traditional method, as shown in Fig. 3. The r.m.s. values by the traditional method and the drag force method were in agreement with the experiment data, as shown in Fig. 4.

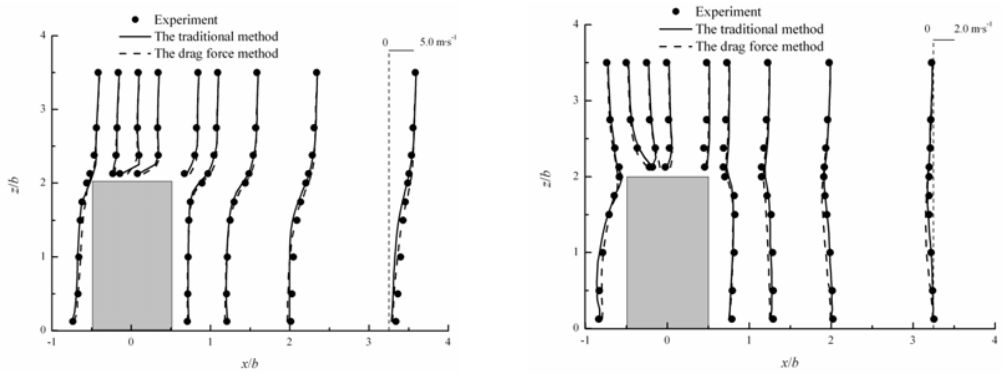

(a) Mean velocity profiles in streamwise direction U ($y/b = 0$)

(b) Mean velocity profiles in normal direction W ($y/b = 0$)

Fig. 3. Mean velocity

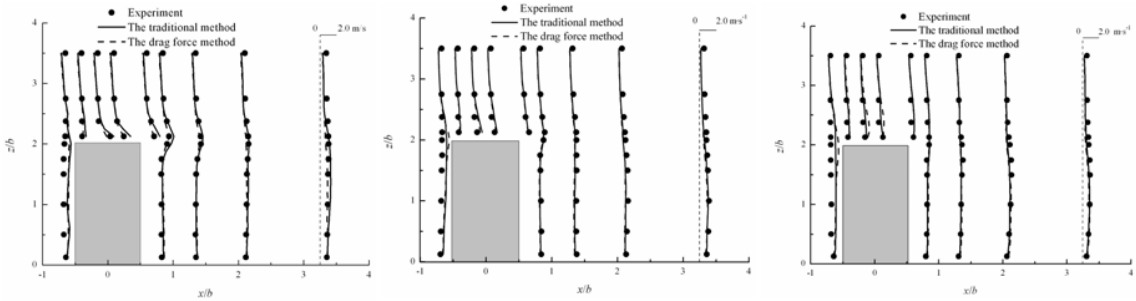

(a) r.m.s. value profiles in stream-wise direction u_{rms} ($y/b = 0$)

(b) r.m.s. value profiles in spanwise direction v_{rms} ($y/b = 0$)

(c) r.m.s. value profiles in normal direction w_{rms} ($y/b = 0$)

Fig.4. r.m.s. value profiles

Figs. 5 and 6 show the mean velocity profiles at $z/b = 0.125$ and 1.25 plane, respectively. The numerical results in Figs. 5 and 6 are in agreement with the experimental data. The results by the drag force method are closer to experimental data than those by the traditional method.

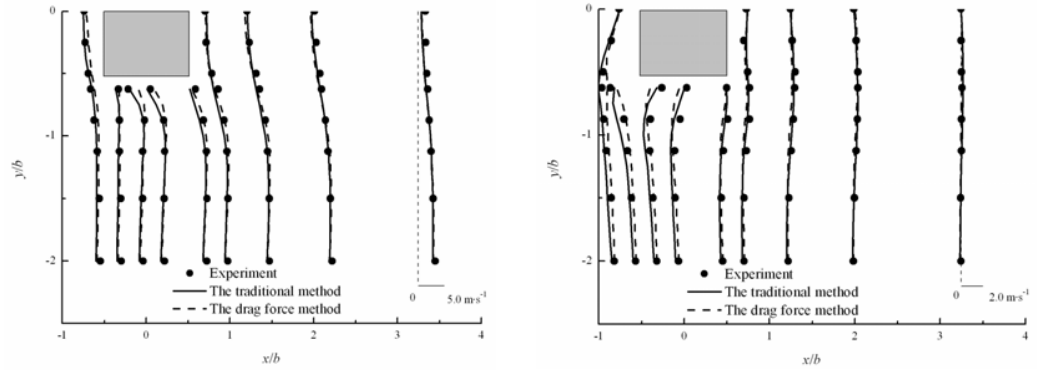

(a) Mean velocity profiles in streamwise direction U ($z/b = 0.125$)

(b) Mean velocity profiles in spanwise direction V ($z/b = 0.125$)

Fig. 5. Mean velocity

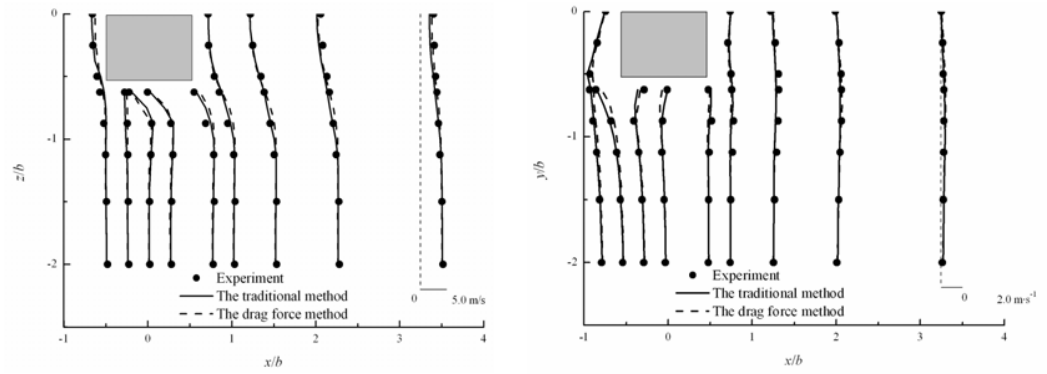

(a) Mean velocity profiles in streamwise direction (b) Mean velocity profiles in spanwise direction V
U (z/b = 1.25) (z/b = 1.25)

Fig. 5. Mean velocity

The major purpose for the numerical simulation of the high-rise building was to validate the precision of the drag force method. It was found that the results by the drag force method were closer to experimental data than those by the traditional method. The numerical results verify that the drag force method can be used to a simulate flow field around a high-rise building.

3.2 *BUILDING ARRAYS*

The flow field around the building arrays was simulated using the traditional method and the drag force method. The geometries of the building arrays, as shown in Fig. 6, were the same as those in the wind-tunnel experiment of Davidson et al. (1996)[16]. The height H, length B and width W were 0.12m. The grid number and boundary conditions were the same those of Gu and Jiao (2011)[17]. The non-uniform grids in the computational domain were used for the simulations of the turbulent flows around staggered and aligned obstacle arrays. The grid numbers of the traditional method and the drag force method were almost the same. The staggered obstacle array had about 816,000 grids and the aligned obstacle array had about 672,000 grids. The velocity formulation at the inflow boundary of Kataoka (2002, 2008) (equation (6)) was used. In the drag force method, the air void fraction in the obstacles was set to 0.05.

Figs. 7 and 8 show the numerical streamwise mean velocity profiles of the staggered obstacle array and the aligned obstacle array, which were compared with experimental data. It was found that the results of the traditional method and the drag force method were in agreement with experimental data.

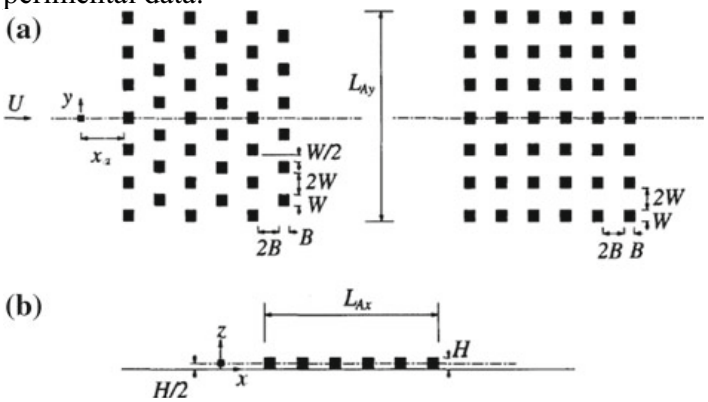

Fig. 6 Geometries of building arrays: (a) Plan view of staggered array configuration (left) and aligned array configuration (right); (b) Side view of aligned array configuration

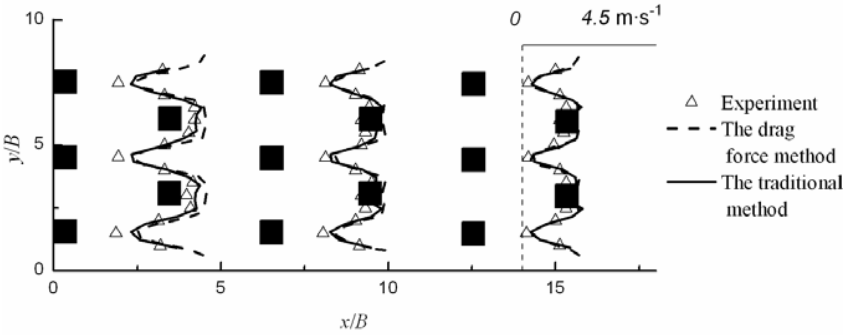

Fig. 7 Lateral profiles of streamwise mean velocity at z = H/2 along x-axis of staggered obstacle array

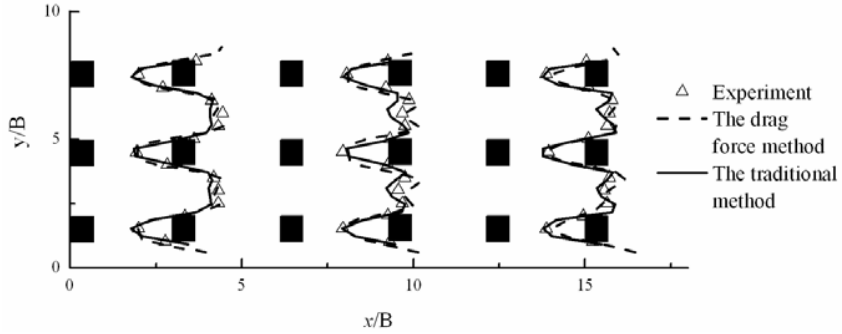

Fig. 8 Lateral profiles of streamwise mean velocity at z = H/2 along x-axis of aligned obstacle array

The numerical simulation results by the drag force method and the traditional method of the staggered obstacle array and the aligned obstacle array were in agreement with experimental data. Thus, the drag force method could be applied to simulate an urban environment. The drag force method doesn't need body-fitted grids and can thus reduce the time required to generate grids.

4 CONCLUSION

With the increasing numbers of simulated buildings required to research urban environments, preprocessing for grids takes a great deal of time and labor, especially when generating hexahedron body-fitted grids. To simplify the generation of grids, a drag force method of gas-solid two-phase flow was proposed. Numerical tests have shown that the results by the traditional method and the drag force method were in agreement with experimental data. The advantages of the drag force method are that it doesn't need body-fitted grids and thus greatly simplifies grid generation, and that it also simplifies simulation of obstacle arrays.

5 ACKNOWLEDGEMENTS

This study was funded by the Ministry of Education, Culture, Sports, Science and Technology, Japan, through the Global Center of Excellence Program, 2008-2012, which is gratefully acknowledged.

6 REFERENCES

1. K. M. Kelkar and S. V. Patankar, Numerical prediction of vortex shedding behind a square cylinder, Int. J. Numer. Meth. Fluids, 14(3) (1992) 327-341
2. A. Mukhopadhyay, G. Biswas and T. Sundararajan, Numerical investigation of confined wakes behind a square cylinder in a channel, Int. J. Numer. Meth. Fluids, 14(12) (1992) 1473-1484
3. W. Rodi, J. H. Ferziger, M. Breuer, and M. Pourquie, Status of large eddy simulation: results of a Workshop, ASME J. Fluids Eng., 119(2) 1997 248–262.
4. D. Bouris, G. Bergeles, 2D LES of vortex shedding from a square cylinder, Journal of Wind Engineering and Industrial Aerodynamics, 80(1-2) (1998) 31-46
5. S. R. Hanna et al, Comparisons of model simulations with observations of mean flow and turbulence within simple obstacle arrays, Atmos Environ 36 (2002) 5067–5079
6. Y. H. Tseng et al, Modeling flow around bluff bodies and predicting urban dispersion using large eddy simulation. Environ Sci Technol 40 (2006) 2653–2662
7. Z. T. Xie, I. P. Castro, 2009. Large-eddy simulation for flow and dispersion in urban streets. Atmospheric Environment 43, 2174-2185.
8. P. Gousseau, B. Blocken, Stathopoulos, T.; van Heijst, G. J. F. CFD simulation of near-field pollutant dispersion on a high-resolution grid: A case study by LES and RANS for a building group in downtown Montreal, Atmospheric Environment, 45(2) (2011) 428-438.
9. C.Y. Wen, Y.H. Yu. (1966) Mechanics of fluidization. Chem. Eng. Prog Symp Ser 62 (62) 100–111.
10. S. Ergun. (1952) Fluid flow through packed columns. Chem. Eng. Prog. 48 89–94.
11. Z. L. Gu, J. Y. Jiao, J. W. Su, Y. W. Zhang, The nature of a universal subgrid eddy viscosity model in a turbulent channel flow. EPL, 94 (2011) 34003; DOI: 10.1209/0295-5075/94/34003.
12. T. Meng, K. Hibi, 1998. Turbulent measurements of the flow field around a high-rise building. J. Wind Eng., Jpn. 76, 55–64
13. Y. Tominaga, A. Mochida, S. Murakami, S. Sawaki, 2008. Comparison of various revised k-ε models and LES applied to flow around a high-rise building model with 1:1:2 shape placed within the surface boundary layer. Journal of Wind Engineering and Industrial Aerodynamics, 96, 389- 411.
14. H. Kataoka, M. Mizuno, 2002. Numerical flow computation around aeroelastic 3D square cylinder using inflow turbulence. Wind and Structures, 5, 379-392.
15. H. Kataoka, 2008. Numerical simulations of a wind-induced vibrating square cylinder within turbulent boundary layer. Journal of Wind Engineering and Industrial Aerodynamics, 96, 1985-1997.
16. M. J. Davidson et al. (1996) Wind tunnel simulations of plume dispersion through groups of obstacles. Atmos Environ 30(22):3715–3731
17. Z. L. Gu, J. Y. Jiao, J. W. Su. Large-eddy simulation of wind field and plume dispersion within different obstacle arrays using dynamic mixing length subgrid-scale model. Boundary-Layer Meteorol, 2010 DOI: 10.1007/s10546-010-9587-8

The Seventh International Colloquium on Bluff Body Aerodynamics and Applications (BBAA7)
Shanghai, China; September 2-6, 2012

Numerical investigation of urban geometry impact on pedestrian wind environment

Azli Abd Razak [a,b*], Naoki Ikegaya [b], Aya Hagishima [b], Jun Tanimoto [b]

[a] *Faculty of Mechanical Engineering, Universiti Teknologi MARA Shah Alam Selangor, Malaysia*
[b] *Interdisciplinary Graduate School of Engineering Science, Kyushu University, Kasuga-shi, Fukuoka, Japan*

ABSTRACT: The main objective of the present study is to assess the influence of urban geometry to the wind environment of pedestrian space based on numerical simulation on airflow over urban-like obstacle. Large-eddy simulation (LES) is use to simulate the airflow over staggered uniform arrays with various plan area density and various aspect ratios. The spatially averaged profiles of mean wind speed and pedestrian wind environment were determine and compared. The result indicates that (1) the spatially-averaged mean wind speed monotonically decreases with the increases of packing density and aspect ratio and (2) the pedestrian mean wind shows the power law relationship to the frontal area ratio of building. In addition simple power law equation presents to explain the relationship.

KEYWORDS: LES, mean wind speed, aspect ratio, plan area ratio, frontal area ratio, pedestrian wind environment

1 INTRODUCTION

The urban wind environment is one of important factors determining the quality of life of urban habitants. Actually, the airflow within urban canopy layer is a driving force of wind-induced ventilation of room air of urban buildings, thus, urban wind condition affects the efficiency of passive control of room air quality. In addition, the transfer phenomena of heat, vapor, and other various types of scalar around urban buildings are deeply related with urban micro-climate and Thermal comfort of pedestrian space [1].

Therefore the physical relation between urban geometry and pedestrian wind environment has been studied aiming for application in urban planning and building design toward more comfort and healthy city. For example, Kubota et al. [2] performed multi-point measurement of mean wind speed using scaled models of real urban districts in a wind tunnel, and revealed that pedestrian mean wind speed decreases linearly with building coverage. Studies focusing on airflow around idealized block arrays have also done [3-4]. Using such idealized block arrays allows them to identify significant and insignificant parameters on urban configuration efficiently. For example, Hang & Li [3] conducted CFD simulation on the effect of geometry on the air exchange rate inside the canyon and revealed that the air exchange rate depends on height of building and λ_p. Next, Zhang et al. [3] concluded that wind environment around the building strongly depends on the building layout and the wind direction.

In general, pedestrian wind environment is associated with the the scalar dispersion which is strongly affected by the process of buoyancy and advection. Li X-X et al. [5] performed Large-Eddy Simulation (LES) on airflow of 2D street canyon with various conditions of building-heights to street-width ratio and reported that the low aspect ratio enhances effectively pollutant

removal. Boppana et al.[6] performed LES of scalar dispersion of 3D block arrays and investigated the influence of heterogeneous block height. They found that tall blocks located in a non-uniform height array generate a larger vertical flux above mean canopy height and weaker streamwise advection.

In the present work, we investigate the relationship between mean wind speed at pedestrian level of uniform urban block arrays and urban geometry parameters, such as plan area ratio (ratio of building roof to ground surface area, λ_p), frontal area ratio (ratio of building frontal area to ground surface area, λ_f) and building aspect ratio (ratio of building roof to frontal area, α_p).Large-Eddy Simulation (LES) with fine Cartesian grid size is done to estimate the spatially distribution of scalar velocity and turbulent statistic within urban canopy layer. The accuracy of the calculated profiles is confirmed by comparing the data with numerical result of Kono et al. [7] and experimental data by Cheng & Castro [8]. Subsequently, mean wind speed at pedestrian derived from the present data of LES is presented under various conditions of urban geometry with a comparison against the experimental result by Kubota [2].

2 NUMERICAL SIMULATON

2.1 *PALM*

Detailed distributions of velocity over idealized urban arrays comprising uniform blocks are simulated using urban version of Parallelized LES Model (PALM) code firstly developed at Institute of Meteorology and Climatology, University of Hannover [9]. PALM can simulate the convective atmospheric boundary layer with explicitly resolved solid obstacles within three-dimensional domain on Cartesian grid. This code solves filtered Navier–Stokes equations with non-hydrostatic incompressible Boussinesq approximation. Finite difference method is used for the discretisation of the differential equation and 3rd order Runge-Kutta scheme is applied for time integration. Massive passing interface (MPI) is use for parallel communication. The further details of urban version of PALM code are described in [10].

Table 1: Geometry of arrays set-up for simulation

Arrays	Case	λ_p (%)	α_p	Block base size	Block height h	Computational domain size $L_x \times L_y \times L_z$
RB1	RB1-4	4.4	1	L	L	$9.5L \times 9.5L \times 4L$
	RB1-8	8.2				$7L \times 7L \times 4L$
	RB1-16	16				$5L \times 5L \times 4L$
	RB1-25	25				$4L \times 4L \times 4L$
	RB1-33	32.7				$3.5L \times 3.5L \times 4L$
	RB1-44	44.4				$3L \times 3L \times 4L$
RB1.5	RB1.5-16	16	1.5	L	$1.5L$	$5L \times 5L \times 6L$
	RB1.5-33	32.7				$3.5L \times 3.5L \times 6L$
	RB1.5-44	44.4				$3L \times 3L \times 6L$
RB0.5	RB0.5-44	44.4	0.5	$2L$	L	$6L \times 6L \times 4L$
RB0.33	RB0.33-44	44.4	0.33	$3L$	L	$9L \times 9L \times 4L$

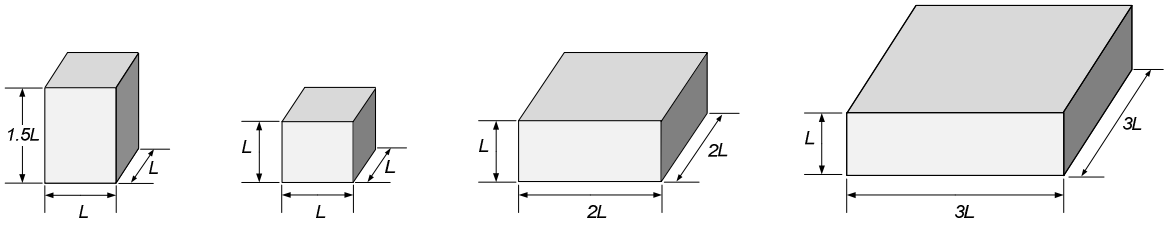

Figure 1. Geometry of the idealized block with different aspect ratio.

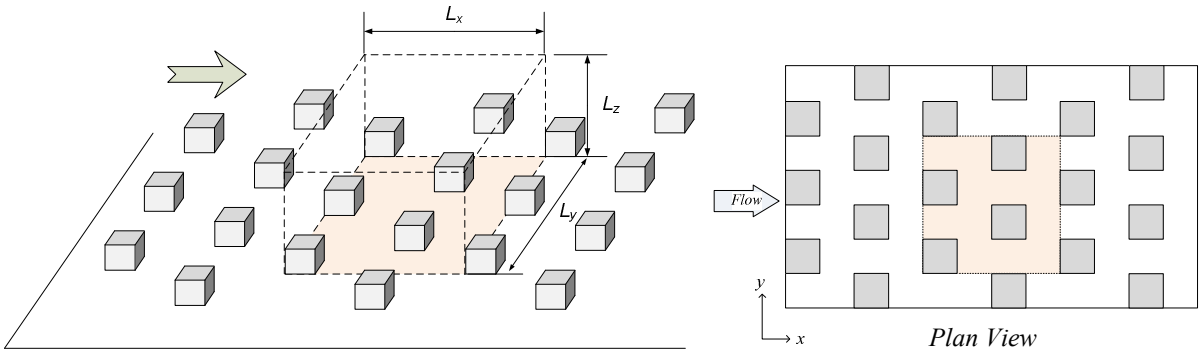

Figure 2. Schematic diagram of computational domain and block arrangement.

2.2 *Simulation set-up*

Table 1 shows the geometry of the arrays analyzed in this study. All arrays consist of uniform rectangular blocks with square base are arranged in staggered layout; the geometry of them were decided based on our previous wind tunnel experiment [11]. A basic length scale of blocks defined as 25m (hereafter L = 25m) in all cases of this simulation which is 1000 times of basic length scale of the wind tunnel experiment [11]. Figure 1 shows the shape of the elements that constitute the arrays.

Periodic boundary conditions are imposed for both spanwise and streamwise boundaries to simulate a horizontal infinite block array. At the bottom of the domain, non-slip condition with Dirichlet type is imposed, and free-slip condition with Neumann type is used at the top of the domain. Because of periodicity, the domain consists of only four unit blocks in staggered arrangement (*see* Figure 2). The computational domain height (L_z) is 4 times of canopy height. The grid size for all cases is fixed to L/64 (0.39m).

The fully developed flow inside computational domain was driven by height-independent constant pressure gradient using the following expression:

$$\frac{\partial P}{\partial x} = -\frac{\rho u_*^2}{L_z} \tag{1}$$

where u_* = friction velocity and L_z = computational domain height.

The u_* is based on the friction velocity calculated by wind tunnel experiment [11]. It refers to the condition of roughness Reynolds number, Re_* ranging from 1.1×10^5 to 4.0×10^5, based on the friction velocity (u_*) and roughness length (z_0) with the assumption that roughness length is about 10% of canopy height. According to Snyder and Castro [12], the fully rough turbulent flow is supposed to develop for condition of Re_* exceeds $O(1)$. In addition, Uehara [13] mentioned that critical Reynolds number for canopy flow to be independent of viscous effect ranging be-

tween 2100 and 15000. Since the current simulation setting satisfies these criteria of Re_*, the viscous effect is supposed to be negligible for all cases. A sequence of $200T$ ($T = h/u_*$, h indicates block height) of the time series calculation data after initial duration about $200T$ is analyzed as data converge statistically to steady state. Although the duration $200T$ is shorter than that proposed by Coceal et al.[14], we confirmed the validity of the duration by comparing mean wind profiles within canopy derived from data of several durations.

2.3 *Validation*

Figure 3 shows vertical profiles of normalized streamwise mean velocity over a cubical array ST1 (λ_p = 0.25) derived from the current simulation, LES result by Kono et al. [7] and a wind tunnel measurement by Cheng & Castro [8] at four locations. The plots for all four measurement points show good agreement with the former data for $z/h < 2$. However the present result underestimates the streamwise mean velocity for $z/h > 2$ as compared to Kono et al.[7]. It is probably due to the different domain height. In their study, the domain height is about $7.5h$ which is greater than that of our simulation. In contrast, the present data qualitatively well agree with the measurement data by Cheng & Castro [8].

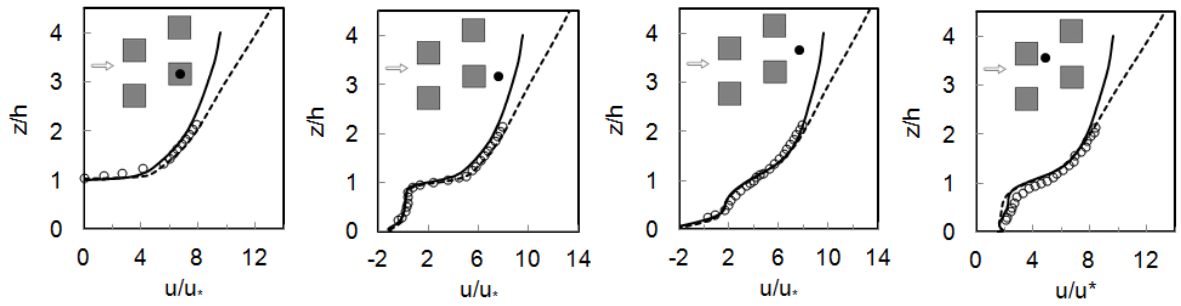

Figure 3. Profile of mean streamwise velocity u, normalize by friction velocity u_* at four different location of a cubical staggered arrays with λp = 25%. (a) above a cube, (b) behind a cube, (c) in front of a cube and (d) in gap. Solid line: RB1-25; dashed line: LES data by Kono et al. [9]; symbol: wind tunnel data from Cheng & Castro [10].

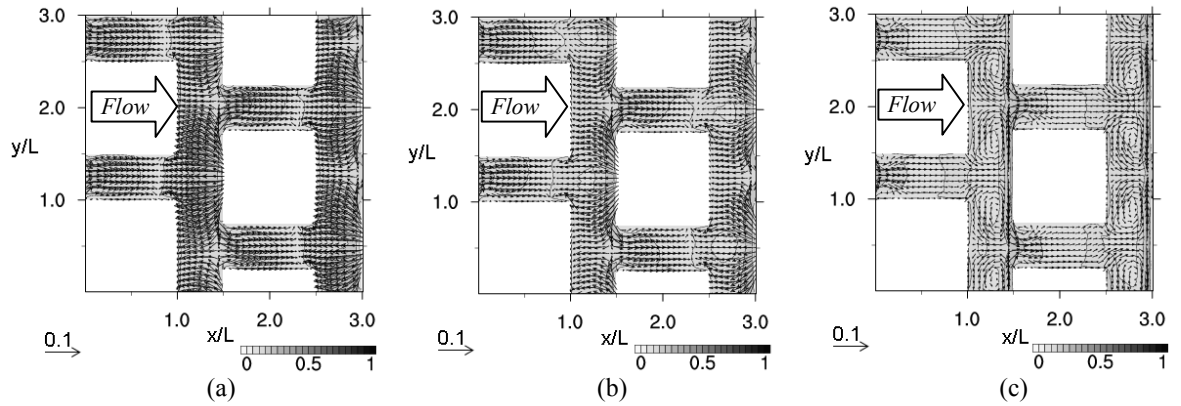

Figure 4. Vector and contour plot of normalized mean wind speed V/V_{ref} of RB1-44 arrays at different horizontal plane height. The data at (a) $z = 0.05h$, (b) $z = 0.1h$, and (c) $z = 0.25h$.

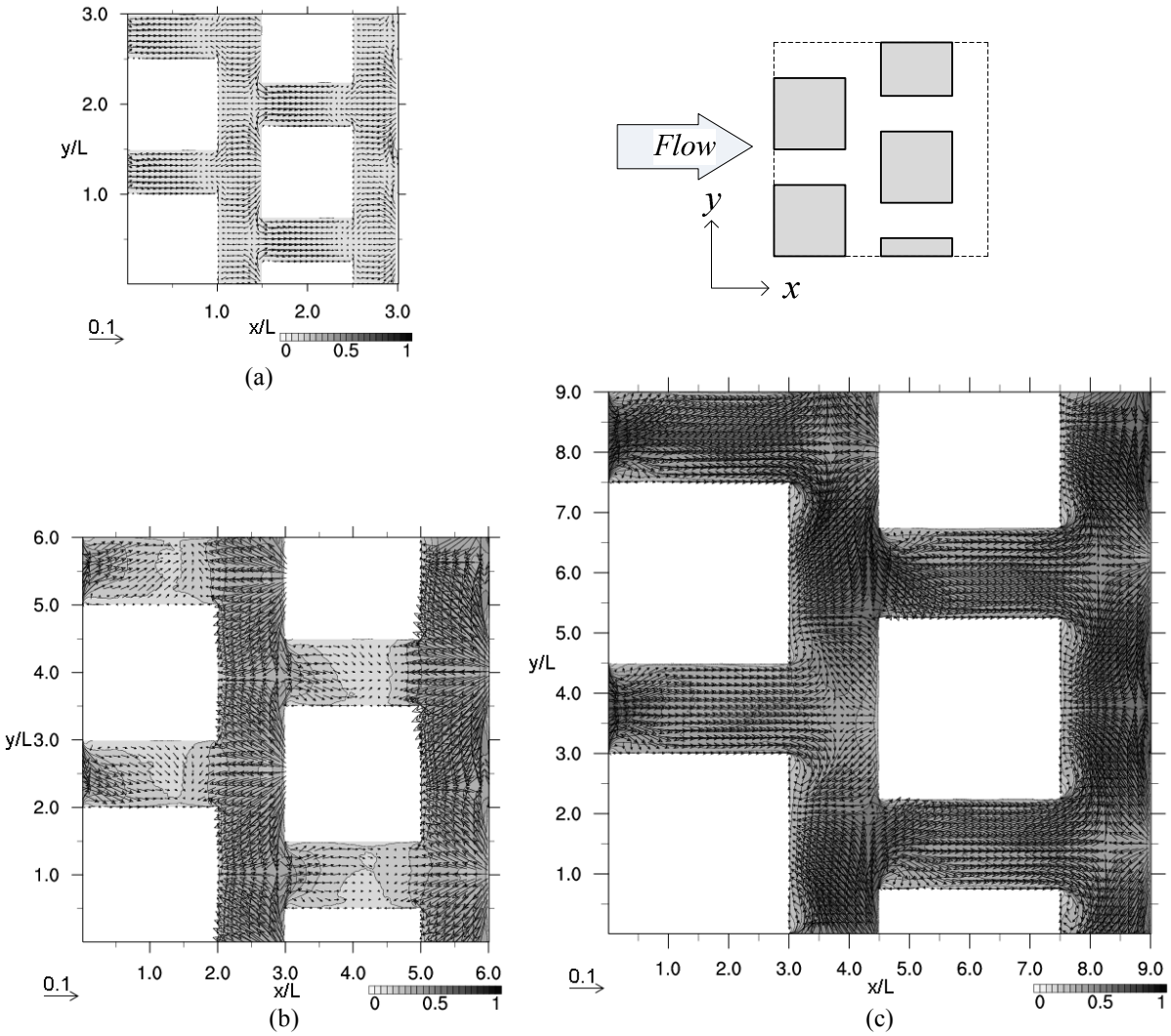

Figure 5. Vector and contour plots of normalized mean wind speed V/V_{ref} at $z = 0.1h$ for $\lambda_p = 44\%$ under various α_p conditions, (a) $\alpha_p = 1.5$, (b) $\alpha_p = 0.5$ and (c) $\alpha_p = 0.33$.

3 RESULT AND DISCUSSION

3.1 *Flow structure*

Mean wind speed within canopy is effective information to assess the thermal comfort of pedestrians. It is consists of mean part ant turbulent part as follows,

$$V = \sqrt{\overline{u}_i^2 + \overline{u_i'^2} + 2\overline{u}_i\overline{u_i'}} \tag{2}$$

where i = indices (1,2, and 3).

A height of 1.5m from the ground surface can be translated into $0.05h$, $0.1h$ and $0.25h$ with the assumption that buildings have 10, 5 and 2 stories respectively and a floor height is 3 m. Since the Reynolds number effect is supposed to be negligible for the current simulation condi-

tion as mention before, the spatio-temporal average of mean wind speed at 0.05*h*, 0.1*h* and 0.25*h* derived from the current simulation can be treated as the pedestrian wind speed in an urban building array with a building storey of 10, 5 and 2, respectively.

We first present the normalized flow pattern of horizontal plane of RB1-44 to show the different trend of pedestrian airflow according to height in Figure 4. The vector plots indicate that reverse flow occurs in front of the block at z = 0.05*h* and 0.1*h* (*see* Figure 4a and b). Figure 4a shows a stronger reverse flow compared to Figure 4b. It might be due to the effects of both shear stress at the ground surface and strong downdraft occurs close to the ground surface. Unlike the similar vector plots for at z = 0.05*h* and z = 0.1*h*, the result of z = 0.25*h* shown in Figure 4c shows different tendency. In this figure, a recirculating vortex pair occurs behind a block has high velocity in front of the block. These three figures indicate that the flow pattern systematically varies depending on the height. In addition, the wind speed decreases with the increase of the height especially at a height z = 0.25*h*.

Next Figure 5 shows the effect of different block aspect ratio α_p on flow pattern under the condition of λ_p = 44%. Comparison between Figures 5a and 5c, both contour and vector plot shows that the normalized wind speed increases especially between adjacent blocks for lower aspect ratio conditions. The reason why the array (RB1.5) shows very low mean wind speed near a street might be caused by the fact that the flow around an array consists of slender blocks is less affected by the longitudinal vortices generated in upward of blocks compared with the flow around a block array with low aspect ratio.

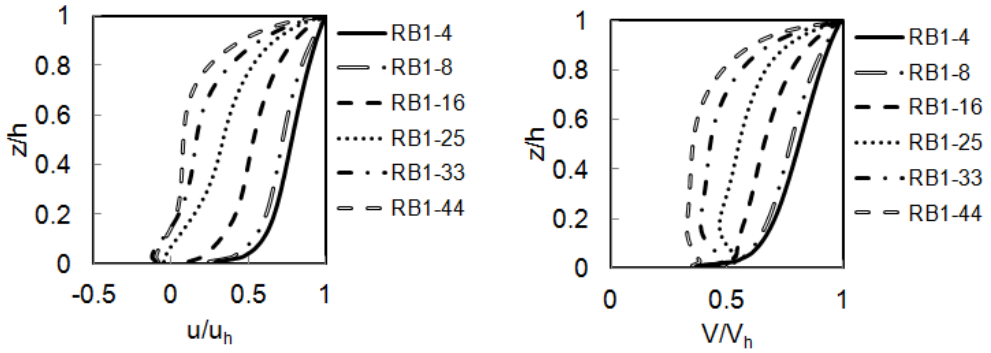

Figure 6. Wind profiles inside canopy normalized by values at canopy height against λ_p. (a) mean streamwise velocity (b) mean wind speed.

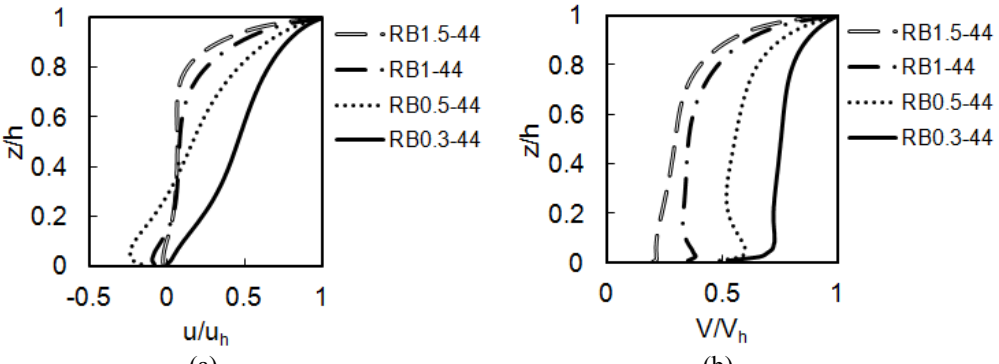

Figure 7. Wind profiles inside canopy normalized by values at canopy height against α_p. (a) mean streamwise velocity (b) mean wind speed.

3.2 *Spatially-average mean flow profile*

Figure 6 indicates the vertical profiles of spatio-temporal average of velocity over cubical arrays (ST1) under various λ_p conditions for streamwise velocity and mean wind speed V. The values are normalized by those at canopy height. The result of normalized streamwise velocity (*see* Figure 6a) indicates that the values of arrays with higher λ_p are approximately lower, but the difference of velocity among arrays varies according to the height. In addition, the spatially averaged velocity of arrays with λ_p over 33% show strong reverse flow below $0.16h$ due to skimming flow regime. As a natural consequence, the mean wind speed profile is dependent with λ_p similar to streamwise velocity, however, the values of arrays with λ_p condition over 25% have an inflection point at a height of around $0.02h$ because of the reverse flow near the street surface as we discussed in section 3.1.

Next, Figure 7 shows the profiles of spatially averaged streamwise velocity and mean wind speed of arrays with different block aspect ratio under the condition of λ_p = 44%. From Figure 7(a), it is clearly found that the streamwise velocity of array RB0.5-44 is significantly negative below $z = 0.35h$, and has the strongest reverse flow within canopy layer among four arrays, despite array block aspect ratio of RB0.5-44 is neither largest nor smallest. In contrast, the streamwise velocity of arrays RB1-44 and RB1.5-44 are nearly constant and zero within lower half of the canopy, and the mean wind speed of the arrays show small compared with the others. Since an array with high block aspect ratio refers to deep street canyon, it is supposed to be reasonable tendency. The mean wind profiles of all arrays are different from the curves of streamwise velocity profiles, and it suggests that the contribution of turbulence part to total kinetic energy is large in pedestrian space. In addition, wind speed profiles of arrays with block aspect ratio below 1.0 have inflection points.

3.3 *Effect of building geometry on pedestrian wind speed*

3.3.1 *Dependencies of plan area ratio and block aspect ratio*

Kubota et al. [2] reported that the plan area ratio strongly affects mean wind speed ratio (the wind speed around the models measure at 5 mm height in the wind tunnel divide by the wind speed at the same height without models) of scaled models of real urban districts consist of various building types. In the present study, mean wind speed ratio was computed by the scalar velocity at pedestrian level normalized by the value at half of computational domain height ($2h_{max}$). Figure 8 shows the relationship between the mean wind speed ratio and the plan area ratio for 3 types of building height, 10, 5, and 2 stories. The wind tunnel data of Kubota et al. [2] are used for comparison. The data of the present experiment shown in Figure 8 (a), (b) and (c) are calculated based on assumption that buildings are 10, 5 and 2 storey respectively.

The mean wind speed of each array monotonically decreases as plan area ratio increases. Such decreasing tendency is consistent with that of the experiment using scaled real urban districts by Kubota. However, the scattering data of mean wind speed due to different block aspect ratio (α_p) at λ_p = 44.4% suggests that plan area ratio is not a parameter to assess universally the pedestrian wind speed. The mean wind speed for arrays with low α_p is higher than that for arrays with high α_p. It is reasonable tendency; because arrays with low α_p refer to shallow street canyon.

3.3.2 *Dependencies of frontal area ratio*

Frontal area ratio λ_f is another important building parameter to evaluate the urban effect on wind environment, because the frontal area of the block is a factor were the pressure drag exerting on the flow [16]. Figure 9 shows the relationship between λ_f. and mean wind speed ratio, in which the data derived based on three different assumptions of building height as mentioned before are illustrated. Figures 9a, b and c indicate that the relationship between λ_f and V/V_{2h} is similar to that between λ_p and V/V_{2h}, but the former one is more universal.

3.4 *Simple estimation of pedestrian wind environment*

A simple mathematical equation can be derived from the present result to estimate the effect of urban geometry on pedestrian wind speed. Based on the non-linear least square method, the mean wind speed velocity ratio can be expressed by simple power law equation as a function of λ_f as below,

$$V/V_{2h} = 2.5\lambda_f^{-4/5} \tag{3}$$

Figures 9a, b and c include the estimates based on equation (3), which agree well with the LES result for all conditions especially in higher frontal area ratio. Thus it is supposed that the equation can be used for assessment of the effect of urban building density on pedestrian wind environment especially in densely packed cities like Tokyo or Hong Kong.

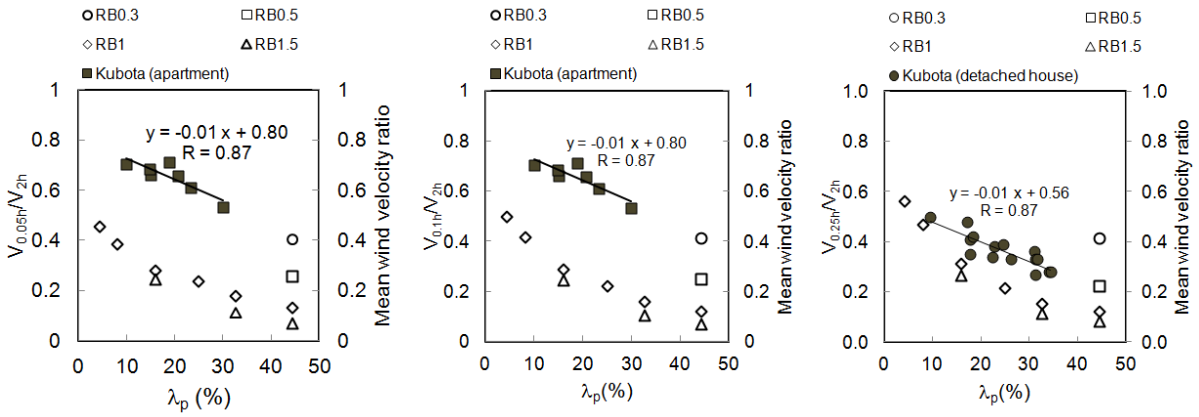

(a) (b) (c)

Figure 8. Relationship between λ_p and mean wind speed ratio of cases. (a) z =0.05h; (b) z =0.1h; (c) z =0.25h.

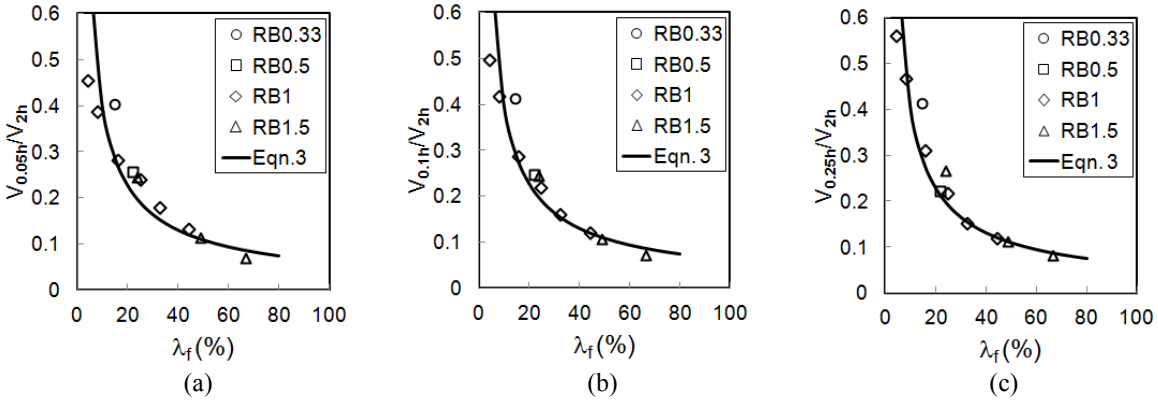

Figure 9. Relationship between λ_f and mean wind speed ratio of cases. (a) z =0.05h; (b) z =0.1h; (c) z =0.25h.

4 CONCLUSION

We have performed Large-eddy simulation of flow over block arrays with various conditions of λ_p and α_p, and the following conclusions are reached. First, the flow patterns clearly indicate the effect of both λ_p and α_p. Different distribution of the wind speed at different horizontal plane height can be translated the pedestrian wind distribution of urban street with different building height. Secondly, the mean wind speed within canopy region is strongly influenced by λ_p and α_p. The mean wind speed increases with decreasing λ_p and α_p within the canopy, and it indicates that the porosity of the building arrays affect the efficiency of ventilation in pedestrian space. Thirdly, the wind speed at pedestrian level show a relatively universal relationship with the frontal area ratio regardless of block aspect ratio and building height, and the tendency can be expressed by a simple power law equation.

5 ACKNOWLEDGEMENTS

The authors wish to express our gratitude to Dr Kono and Professor Kubota, for providing data sets that have been valuable in the validation of our work. This research was financially supported by grant-in aid for scientific research (22360238) from the Ministry of Education, Science and Culture of Japan, and Asahi glass foundation. These simulations were performance on the Kyushu University IBM supercomputing centre.

6 REFERENCES

1 Blocken B, Carmeliet J. Pedestrian wind environment around buildings: Literature review and practical examples. J. Thermal Env. & Bldg. Sci., 28 (2004) 107 – 159.
2 Kubota T, Maiura M, Tominaga Y, Mochida A. Wind tunnel tests on the relationship between building density and pedestrian level wind velocity: Development of guidelines for realizing acceptable wind environment in residential neighborhoods. Building and Environment, 43 (2008) 1699 – 1708.
3 Hang J, Li Y. Ventilation strategy and air change rates in idealized high-rise compact urban areas. Building and Environment, 45 (2010) 2754 – 2767.
4 Zhang A, Gao C, Zhang L. Numerical simulation of the wind field around different building arrangements. J. Wind Eng. Ind. Aerodyn., 93 (2005) 891 – 904.
5 Li X-X, Britter R.E, Norford L.K, Koh T-Y, Entekhabi D. Flow and pollutant transport in urban street canyons of different aspect ratios with ground heating: Large-eddy simulation. Boundary-Layer Meteorol., 142 (2012) 289 – 304.

6 Boppana V.B.L, Xie Z-T, Castro I.P. Large-eddy simulation of flow over random urban like obstacles. Boundary-Layer Meteorol., 135 (2010) 433 – 454.
7 Kono T, Tamura T, Ashie Y. Numerical investigations of mean winds within canopies of regularly arrayed cubical buildings under neutral stability conditions. Boundary-Layer Meteorol., 134 (2010) 131 – 155.
8 Cheng H, Castro I.P. Near wall flow over urban-like roughness. Boundary-Layer Meteorol., 104 (2002) 229 – 259.
9 Raash S, Schrote M. PALM – A large-eddy simulation model performing on massively parallel computers. Meteorologische Zeitschrift, 10 (2001) 363 – 372.
10 Letzel M. High resolution Large-Eddy Simulation of turbulent flow around building. Institute of Meteorology and Climatology, Leibniz University of Hannover, (2007) PhD Thesis.
11 Hagishima A, Tanimoto J, Nagayama K, Meno S. Aerodynamic parameters of regular arrays of rectangular blocks with various geometries. Boundary-Layer Meteorol., 132 (2009) 315 - 337.
12 Snyder W.H, Castro I.P. The critical Reynolds number for rough-wall boundary layers. J. Wind Eng. Ind. Aerodyn., 90 (2002) 41 – 54.
13 Uehara K, Wakamatsu S, Ooka R. Studies on critical Reynolds number indices for wind-tunnel experiments on flow within urban area. Boundary-Layer Meteorol., 107 (2003) 353 – 370.
14 Coceal O, Thomas T.G., Castro I.P. Mean flow and turbulence statistics over groups of urban-like cubical obstacles. Boundary-Layer Meteorol., 121 (2006) 491 – 519.
15 Cheng H, Castro I.P. Near wall flow over urban-like roughness. Boundary-Layer Meteorol., 104 (2002) 229 – 259.
16 Millward-Hopkins J.T, Tomlin A.S, Ma L, Ingham D, Pourkashanian M. Estimation aerodynamic parameter of urban-like surface with heterogeneous building heights. Boundary-Layer Meteorol., 141 (2011) 443 – 465.

The Seventh International Colloquium on Bluff Body Aerodynamics and Applications (BBAA7)
Shanghai, China; September 2-6, 2012

RANS and LES simulations of the interference drag of two cyclists

B. Blocken [a], T. Defraeye [b,c], E. Koninckx [d], J. Carmeliet [e,f], P. Hespel [g]

[a]*Building Physics and Services, Eindhoven University of Technology, P.O. Box 513, 5600 MB Eindhoven, The Netherlands, b.j.e.blocken@tue.nl*
[b]*Division of Building Physics, Katholieke Universiteit Leuven, Kasteelpark Arenberg 40, Leuven, Belgium*
[c]*Division of Mechatronics, Biostatistics and Sensors, Katholieke Universiteit Leuven, Willem de Croylaan 42, Leuven, Belgium*
[d]*Flemish Cycling Federation, Globelaan 49/2, 1190 Brussels, Belgium*
[e]*Chair of Building Physics, Swiss Federal Institute of Technology Zurich (ETHZ), Wolfgang-Pauli-Strasse 15, 8093 Zürich, Switzerland*
[f]*Laboratory for Building Science and Technology, Empa, Überlandstrasse 129, 8600 Dübendorf, Switzerland*
[g]*Research Centre for Exercise and Health, Department of Biomedical Kinesiology, Katholieke Universiteit Leuven, Tervuursevest 101, 3001 Heverlee, Belgium*

ABSTRACT: This paper presents a numerical study of the interference drag of two cyclists in dropped position and in time-trial position. The study is based on 3D laser scanning of the cyclist geometry and on high-resolution grid generation, where the centre of the wall-adjacent cell is at about 15 micrometer from the body surface, resulting in y* values well below 5. The cell size in the wake is about 0.03 m. Both the Reynolds-averaged Navier-Stokes (RANS) approach with closure provided by the standard k-ε model and Large Eddy Simulations (LES) are performed. For LES, the time step is $3x10^{-4}$ s based on the CFL number. The interference drag is evaluated for inter-cyclist spacing varying from d = 0.01 to d = 1 m. Although the RANS and LES approach provided similarly accurate results for pressure coefficients and aerodynamic drag of a single cyclist, the results of both approaches for the interference drag are quite different. Compared to a single cyclist, the drag reduction for the dropped position with d = 0.01 m and with RANS is 2% for the first cyclist and 26% for the second one, while with LES it is 3% and 34%, respectively. For the time-trial position with d = 0.01 m, the reductions with RANS are 3% for the first cyclist and 16% for the second one, while with LES these values are 2% and 36%, respectively. Additional wind tunnel experiments with two cyclists are scheduled for further validation studies. Additional analysis of the CFD results will be performed to analyze the reasons for the large differences between RANS and LES results.

KEYWORDS: Cyclist aerodynamics, drag resistance, Computational Fluid Dynamics.

1. INTRODUCTION

At racing speeds (± 50 km/h in time trails), the aerodynamic resistance experienced by a cyclist, also called drag, is about 90% of his/her total resistance (Grappe et al. 1997, Kyle and Burke 1984). The major part is caused by form drag, related to the position of the cyclist on the bicycle.

Many elite cyclists therefore try to optimise their position for drag by means of field tests or wind tunnel tests. More recently, also Computational Fluid Dynamics (CFD) has been applied in cycling (Hanna 2002, Lukes et al. 2004, Defraeye et al. 2010a, 2010b). Most studies were performed by solving the steady Reynolds-averaged Navier-Stokes (RANS) equations. Most studies have also employed wall-function modelling for the near-wall region. Recent studies however have explicitly resolved the boundary layer by low-Reynolds number modelling (LRNM) (Defraeye et al. 2010a, 2010b). These CFD simulations were validated with detailed wind tunnel measurements on a full-scale (real) cyclist (Defraeye et al. 2010a) and a ½ scale model (Defraeye et al. 2010b). The study by Defraeye et al. (2010a) compared CFD simulations with drag measurements on a full-scale cyclist and indicated that, for the dropped position, Large Eddy Simulation (LES) yields a deviation in the drag area of 3%, while steady RANS with the standard k-ε model yields a deviation of 7% compared to the measurements. However, for the reduced-scale (1:2) model (upright position), steady RANS with the standard k-ε model provided a deviation in the drag area of only 4% compared to 6% with LES (Defraeye et al. 2010b). These results indicate that the RANS and LES results for the aerodynamic drag are very close. Therefore, they might suggest that further studies in cyclist aerodynamics can be conducted with steady RANS and the standard k-ε model, and that more time-consuming and intrinsically more accurate simulations with LES would not be necessary. To analyze the validity of this hypothesis, this paper provides results of a numerical study with both RANS and LES of the interference drag of two cyclists, riding one behind the other, in still air (zero wind speed).

2. CFD SIMULATIONS: COMPUTATIONAL PARAMETERS AND SETTINGS

A digital model of the cyclist was obtained for the dropped position and the time-trial position using a high-resolution 3D laser scanning system (K-Scan, Nikon Metrology, Belgium), capturing the specific body characteristics of the cyclist. For meshing purposes, surface details were smoothed out to some extent and the bicycle was not included in the computational model. Two of these virtual cyclists were placed in a computational domain, one behind the other, with a spacing d varying from d = 0.01 m to 1m, including: 0.01 m, 0.25 m, 0.5 m and 1 m (Figs. 1 and 2).

The size of the computational domain, for the two cyclists with d = 0.01 m, is L x W x H = 21 m x 6 m x 7 m. For the other distances, the length of the domain is increased with the spacing d. The grid is a hybrid grid, consisting of very small prismatic cells in the boundary-layer region near the cyclist's surface, with the first computational cell at only 15 μm from the body surface. This high resolution is needed because low-Reynolds number modelling requires the y^* values of the wall-adjacent cells to be about 1 and certainly lower than 5 (Casey and Wintergerste 2000). Further away from the surface, tetrahedral cells have been used, with an average cell size in the wake region of about 0.03 m. The resulting grids for a single cyclist contain about 7.7×10^6 cells, while the grids for the two cyclists contain about 12.0×10^6 cells. The grids are based on grid-sensitivity analysis according to best practice guidelines in CFD (Casey and Wintergerste 2000, Franke et al. 2007, Tominaga et al. 2008). The grid discretisation error was estimated by means of Richardson extrapolation and was about 3% for the drag force of the single cyclist.

At the inlet, a uniform inlet velocity of 15 m/s is imposed, with zero turbulence intensity, which represents the relative air movement around the cyclists due to the cycling speed in still air

(zero wind speed). For the side and top boundaries, a slip-wall boundary (symmetry) was used. Slip walls assume that the normal velocity component and the normal gradients at the boundary are zero, resulting in flow parallel to the boundary. At the outlet of the computational domain, ambient static pressure was imposed. Two approaches are used: (1) 3D steady RANS with the standard k-ε turbulence model (Launder and Spalding 1972) and with low-Reynolds number modelling (LRNM), for which the one-equation Wolfshtein model (Wolfshtein 1969) is used in this study. Second-order discretisation schemes are used throughout. The SIMPLE algorithm is used for pressure-velocity coupling. Pressure interpolation is second order. (2) 3D LES simulations with the dynamic Smagorinsky subgrid-scale model (Kim 2004) with LRNM. Second-order discretisation schemes are used except for momentum, for which a central differencing scheme is used. Second-order implicit time stepping is used, and 20 iterations per time step were found to be sufficient to have convergence within a time step. The temporal discretisation is related to the spatial discretisation by the CFL (Courant-Friedrichs-Lewy) number: CFL = $u\Delta t/d$, where u is the characteristic velocity in the cell, Δt is the time step and d is the characteristic cell dimension. Time steps resulting in CFL numbers of 1 are suggested in the wake region (Spalart 2001). For the simulations, the choice of the time step and averaging period was also based on a sensitivity analysis. A time step of $3x10^{-4}$ s was chosen, resulting in CFL numbers below about 5 in the majority of the domain, with maximal values that do not exceed 10, and values of about 0.5 in the wake. A dimensionless simulation time of about 2 flow-through-times was found to be sufficient to obtain stationary, i.e. stable averaged, values for drag and surface pressures, where the flow-through-time is defined as: $t_{FT} = UT/L_D$, where U is the free-stream (approach flow) wind speed (15 m/s), T is the averaging period (2.8 s) and L_D is the length of the computational domain (21 m). The simulations were performed with the commercial CFD code Fluent 6.3, which uses the control volume method.

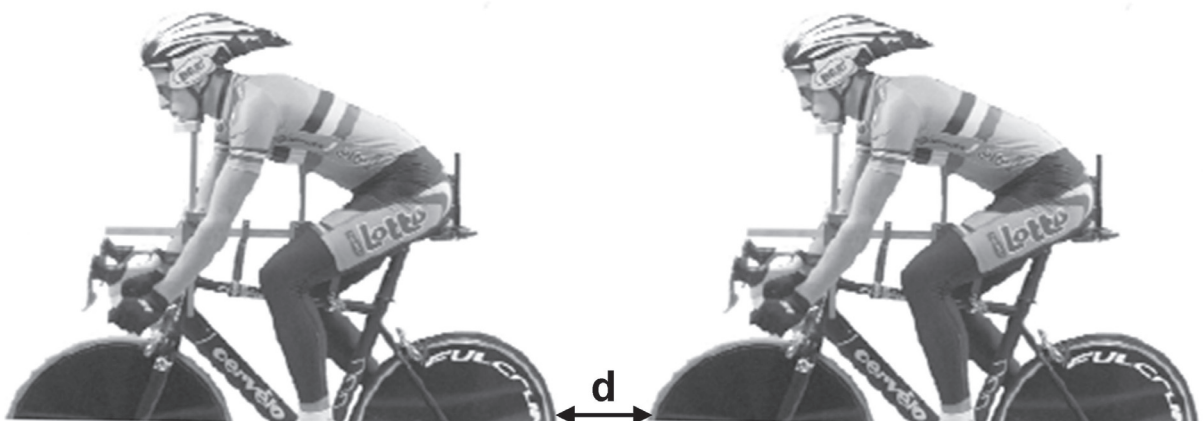

Figure 1. Two cyclists in dropped position at a variable spacing d.

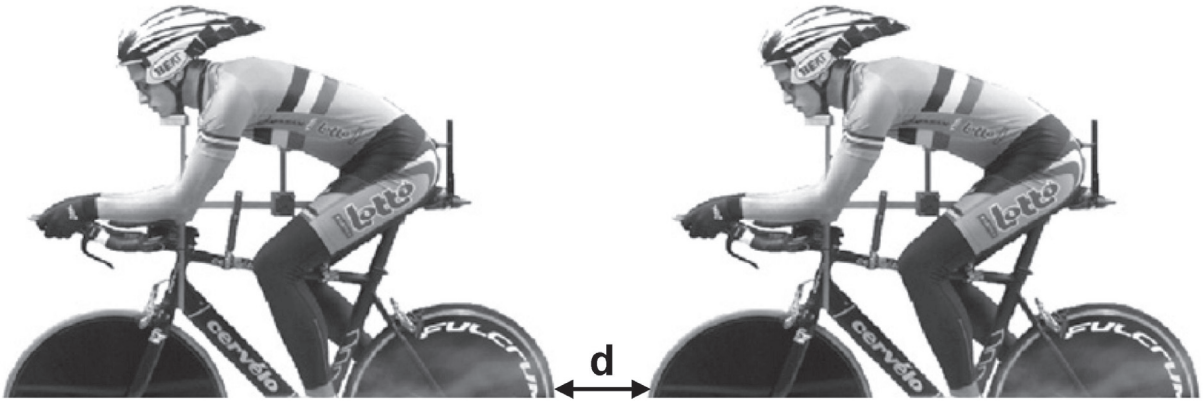

Figure 2. Two cyclists in time-trial position at a variable spacing d.

3. CFD SIMULATIONS: RESULTS

Figure 3 shows an instantaneous image of the velocity contours in a vertical centreplane for the two cyclists in dropped position and with spacing d = 0.01 m. The low-velocity stagnation regions directly upstream of every cyclist can be observed, as well as the turbulent low-velocity wake of the first cyclist that partly engulfs the second cyclist. In this vertical centreplane and in this dropped cyclist position, flow separation is observed at the top of the helmets. The figure also shows the very dense grid resolution on the cyclist bodies and helmets.

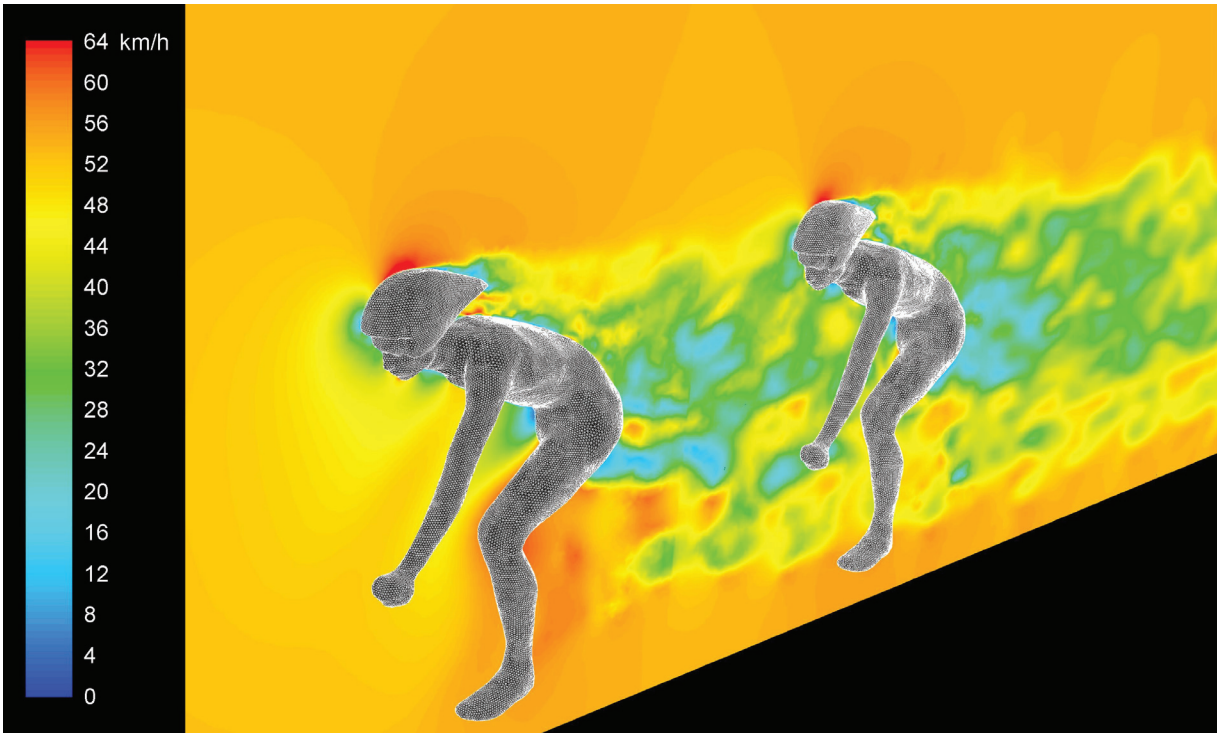

Figure 3. Instantaneous velocity contours in vertical centreplane for two cyclists in dropped position at distance d = 0.01 m.

The results of the simulations are reported in Figures 4 and 5, in terms of drag reduction (DR) for the two cyclists, with respect to a single cyclist, and as a function of the inter-cyclist spacing d. Figure 4 shows the drag reduction for the first and for the second cyclist in dropped position, as obtained with RANS and with LES. It is noteworthy that there is also a drag reduction for the first cyclist due to the proximity of the second cyclist behind him/her, although this drag reduction is limited and it rapidly disappears with increasing inter-cyclist spacing. The intrinsically more accurate LES simulations indicate a larger drag reduction for both cyclists compared to RANS. For d = 0.01 m, LES indicates a reduction of 3% for the first cyclist and 34% for the second cyclist, while RANS indicates 2% for the first cyclist and 26% for the second one. Both approaches indicate a near-linear decrease of the drag reduction with increasing inter-cyclist spacing, although this decrease is more pronounced according to the LES results. At a distance of 1 m, the drag reduction for the second cyclist is still 28% (LES), while that for the first cyclist has become negligible.

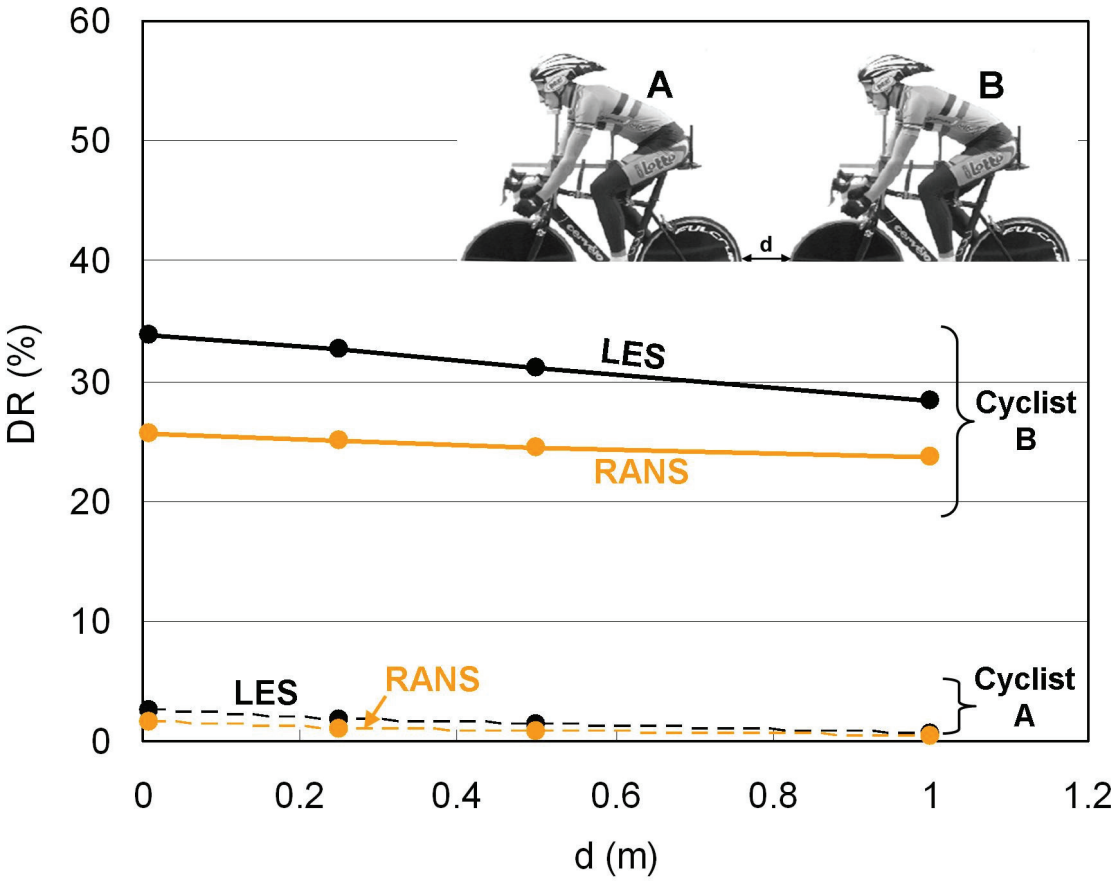

Figure 4. Drag reduction of two cyclists, with respect to a single cyclist, in dropped position at a variable spacing d, as obtained by RANS and LES simulations.

Figure 5 shows the drag reduction for the first and for the second cyclist in time-trial position, as obtained with RANS and with LES. Also here, the drag reduction for the first cyclist due to the proximity of the second cyclist is clearly present. As opposed to the results for the dropped position, the results for the time-trial position show a very large difference between RANS and LES results for the second cyclist, more than a factor 2, while the differences in results for the first cyclist are negligible. For d = 0.01 m, LES indicates a reduction of 2% for the first cyclist and 36% for the second cyclist, while RANS indicates 3% for the first cyclist and 16% for the second one. Both approaches indicate a near-linear decrease of the drag reduction with increasing inter-cyclist spacing, which is most pronounced for the second cyclist with LES. At a distance of 1 m, the drag reduction for the second cyclist is still 30% (LES), while that for the first cyclist has become negligible.

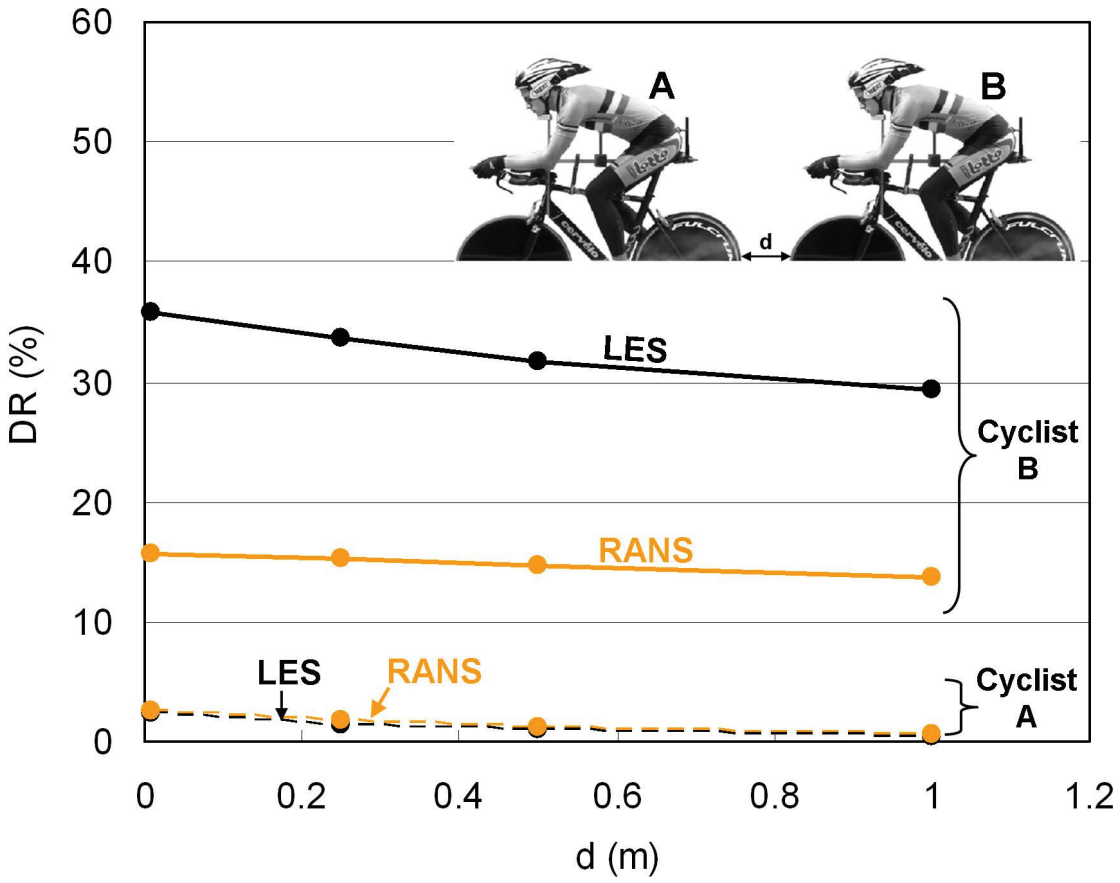

Figure 5. Drag reduction of two cyclists, with respect to a single cyclist, in time-trial position at a variable spacing d, as obtained by RANS and LES simulations.

4. DISCUSSION AND CONCLUSIONS

The interference drag (drag reduction) experienced by a second cyclist due to a cyclist in front of him/her is well-known. The fact that the first cyclist also experiences a drag reduction by the presence of the second one however, is less known, although there are some previous studies that suggest drag reduction of an upstream body by its downstream counterpart (e.g. Iniguez-de-la Torre and Iniguez 2009). The reason for the drag reduction of the first cyclist by the second one is the overpressure region in front of this second cyclist. This overpressure region merges with the underpressure region (wake) behind the first cyclist, thereby reducing the underpressure in this region and reducing the drag force. This effect is more pronounced as the cyclists ride closer behind each other.

Previous numerical studies on the aerodynamics of a single cyclist riding in still air (Defraeye et al. 2010a, 2010b) have shown that the RANS and LES approach provided similarly accurate results for pressure coefficients and aerodynamic drag. In particular, the study by Defraeye et al. (2010a) compared CFD simulations with drag measurements on a full-scale cyclist and indicated that, for the dropped position, Large Eddy Simulation (LES) yields a deviation in the drag area of 3%, while steady RANS with the standard k-ε model yields a deviation of 7%. However, for the reduced-scale (1:2) model (upright position), steady RANS with the standard k-ε model provided a deviation in the drag area of only 4% compared to 6% with LES (Defraeye et al. 2010b). These results might suggest that further studies can be conducted with steady RANS and the standard k-ε model, and that more time-consuming and intrinsically more accurate simulations with LES would not be necessary. However, the comparison of RANS and LES simulations of the interference drag of two cyclists show large to very large differences between both approaches. Compared to a single cyclist, the drag reduction for the dropped position with d = 0.01 m and with RANS is 2% for the first cyclist and 26% for the second one, while with LES it is 3% and 34%, respectively. For the time-trial position with d = 0.01 m, the reductions with RANS are 3% for the first cyclist and 16% for the second one, while with LES these values are 2% and 36%, respectively. Hereby not only the differences between RANS and LES is remarkable, but also the fact that this difference is much larger for the time-trial position than for the dropped position. Additional wind tunnel experiments with two cyclists are scheduled for further validation studies. Also, additional analysis of the CFD results will be performed to analyze the reasons for these large differences between RANS and LES results.

5. REFERENCES

Casey, M., Wintergerste, T., 2000. Best Practice Guidelines. ERCOFTAC Special Interest Group on “Quality and Trust in Industrial CFD”, ERCOFTAC.

Defraeye, T., Blocken, B., Koninckx, E., Hespel, P., Carmeliet J., 2010a. Aerodynamic study of different cyclist positions: CFD analysis and full-scale wind-tunnel tests. Journal of Biomechanics 43(7): 1262-1268.

Defraeye, T., Blocken, B., Koninckx, E., Hespel, P., Carmeliet J., 2010b. Computational Fluid Dynamics analysis of cyclist aerodynamics: Performance of different turbulence-modelling and boundary-layer modelling approaches. Journal of Biomechanics 43(12): 2281-2287.

Franke, J., Hellsten, A., Schlünzen H., Carissimo, B., 2007. Best practice guideline for the CFD simulation of flows in the urban environment, COST Action 732.

Grappe, G., Candau, R., Belli, A., Rouillon, J.D., 1997. Aerodynamic drag in field cycling with special reference to the Obree’s position. Ergonomics 40 (12), 1299-1311.

Hanna, R.K., 2002. Can CFD make a performance difference in sport?. In: Ujihashi, S., Haake, S.J. (Eds.), The Engineering of Sport 4. Blackwell Science, Oxford, pp. 17-30.
Iniguez-de-la Torre, A., Iniguez, J., 2009. Aerodynamics of a cycling team in a time trial: does the cyclist at the front benefit? European Journal of Physics 30, 1365–1369.
Kim, S.-E., 2004. Large eddy simulation using unstructured meshes and dynamic subgrid-scale turbulence models. In: Proceedings of the 34th AIAA Fluid Dynamics Conference and Exhibit, Technical Report AIAA-2004-2548. Port- land, Oregon.
Kyle, C.R., Burke, E.R., 1984. Improving the racing bicycle. Mechanical Engineering 106 (9), 34-45.
Launder, B.E., Spalding, D.B., 1972. Lectures in Mathematical Models of Turbulence, Academic Press, London, England.
Lukes, R.A., Hart, J.H., Chin, S.B., Haake, S.J., 2004. The aerodynamics of mountain bicycles: The role of computational fluid dynamics. In: Hubbard, M., Mehta, R.D., Pallis, J.M. (Eds.), The Engineering of Sport 5. International Sports Engineering Association, Sheffield.
Spalart, P.R., 2001. Young person's guide to Detached-Eddy Simulation grids. NASA Contractor Report CR-2001-211032. NASA, Virginia.
Tominaga, Y., Mochida A., Yoshie, R., Kataoka, H., Nozu, T., Yoshikawa, M., Shirasawa, T., 2008. AIJ guidelines for practical applications of CFD to pedestrian wind environment around buildings, Journal of Wind Engineering and Industrial Aerodynamics 96(10-11), 1749-1761.
Wolfshtein, M., 1969. The velocity and temperature distribution in one-dimensional flow with turbulence augmentation and pressure gradient. International Journal of Heat and Mass Transfer 12 (3), 301-318.

The Seventh International Colloquium on Bluff Body Aerodynamics and Applications (BBAA7)
Shanghai, China; September 2-6, 2012

CFD analysis of wind comfort on high-rise building balconies: validation and application

H. Montazeri [a] , B. Blocken [a], W.D. Janssen [a], T. van Hooff [a,b]

[a]*Building Physics and Services, Eindhoven University of Technology, P.O. Box 513, 5600 MB Eindhoven, The Netherlands, h.montazeri@tue.nl*
[b]*Division of Building Physics, Katholieke Universiteit Leuven, Kasteelpark Arenberg 40, Leuven, Belgium*

ABSTRACT: High-rise buildings can cause wind discomfort on the building balconies, necessitating remedial action. In this paper, a new facade concept is evaluated that is intended to significantly improve wind comfort on the balconies of a 78 m high-rise building. The concept consists of a staggered semi-open second-skin facade that partly shields the balconies from the wind. Evaluation of the concept is performed by steady Reynolds-Averaged Navier-Stokes (RANS) CFD simulations with the realizable k-ε turbulence model in combination with the Dutch wind nuisance standard. First, some results of a CFD validation study for buildings with balconies are briefly presented. Next, similar simulations are used to evaluate the new facade concept by comparing the wind comfort at the balconies with and without application of this concept. It is shown that the new facade concept is quite effective in improving wind comfort at the balconies.

KEYWORDS: Pedestrian wind environment, wind conditions, Computational Fluid Dynamics (CFD), building balconies

1. INTRODUCTION

High-rise buildings can cause high wind speed near ground level and on building balconies, necessitating remedial action. In order to reduce wind discomfort on balconies, different measures can be taken; such as closing the balcony, adding partition walls, etc. Recently a new facade concept was developed by ELD Partnership (ELD 2011). It consists of a staggered semi-open second-skin facade that partly shields the balconies from the wind. It is intended to significantly improve wind comfort on the building balconies. In this paper, the performance of this concept is evaluated by validated CFD simulations and by application of the Dutch wind nuisance standard for a case study with and without application of this new concept.

In the past, several CFD studies have been performed to investigate pedestrian-level wind conditions in complex urban environments (e.g. Stathopoulos and Baskaran 1996, Yoshie et al. 2007, Blocken et al. 2012). The use of CFD for complete wind comfort studies however is still relatively scarce, and this especially holds for studies of wind comfort at building balconies. Indeed, most of the previous CFD studies focused on wind comfort at pedestrian level around buildings. To the best of our knowledge, no CFD study has yet been published with focus on wind comfort on building balconies.

This paper presents the evaluation of the new second-skin facade concept by ELD Partnership to improve wind comfort at building balconies. First, some results of a CFD validation study for buildings with balconies are briefly presented. Next, the new concept is evaluated for the case of

a high-rise (78 m) building in the city of Antwerp. CFD simulations are performed for the building with and without second-skin facade concept implemented. The CFD simulations are performed with the 3D steady Reynolds-Averaged Navier-Stokes (RANS) approach and the realizable k-ε model (Shih et al. 1995). The obtained CFD results are combined with wind speed statistics and a comfort criterion to judge wind comfort on the balconies, according to the Dutch wind nuisance standard.

2. DESCRIPTION OF BUILDING AND URBAN AREA

The new high-rise building of the so-called EPA project is located in the northern part of the city of Antwerp, Belgium. It is north-south oriented and surrounded by other high-rise and low-rise buildings (Fig. 1a). It has dimensions L × B × H = 21.8 × 50.8 × 78.2 m³. The depth of the balconies on the north, east, south and west side of the tower is 1.32 m, 1.3 m, 1.59 m and 1.56 m, respectively. The facade concept is a second-skin concept, with a first and inner skin that acts as traditional facade and a second outer skin that acts as a wind shield for the balconies. The second skin consists of a staggered semi-open glass facade, as indicated in Figure 1b. It has a permanent solid glass balustrade of 1.2 m high, while above this 1.2 m, solid glass facade panels are applied in a staggered configuration. For the comparison study, a reference high-rise building with only the 1.2 m high balustrade will be considered.

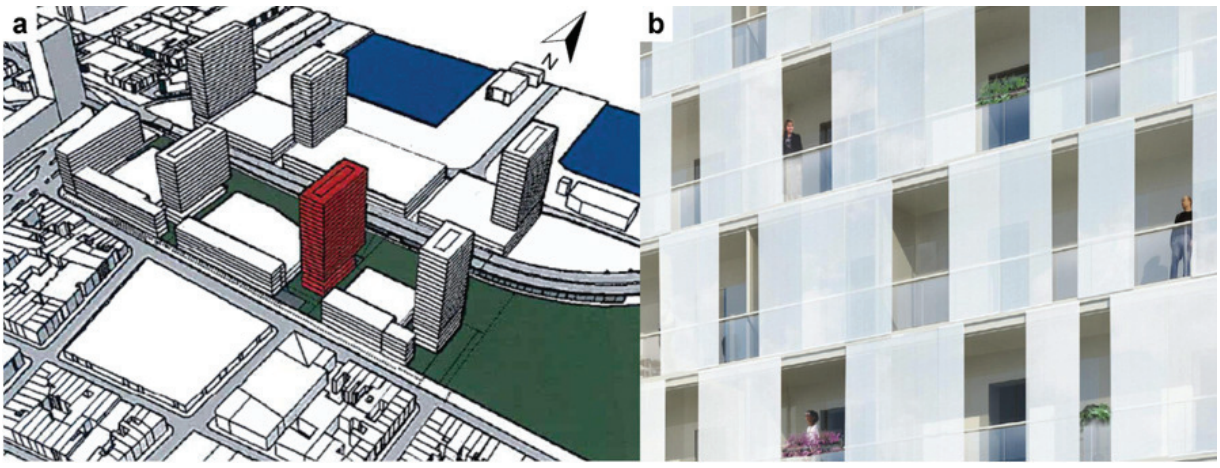

Figure 1. (a) High-rise building under study (red) and nearby urban surroundings. (b) Building facade with second-skin staggered facade concept.

3. CFD VALIDATION

CFD simulations based on the 3D RANS equations in combination with a turbulence model require validation. Validation can be performed by comparison of the CFD results with either full-scale measurements or wind tunnel data. Experimental data of wind conditions for buildings with balconies are very scarce. In this paper, a unique set of wind tunnel measurements of surface pressures on the facade of a building with balconies is used for validation purposes.

3.1. Wind tunnel measurements

Atmospheric boundary layer wind tunnel measurements of wind-induced surface pressure on the facade of a reduced-scale model (1:30) of a medium-rise building were conducted by Chand et al (1998). The incident vertical profile of mean wind speed (i.e. at the location of the test model) can be described by a logarithmic law with aerodynamic roughness length z_0 = 0.008 m and friction velocity u* = 0.72 m/s. Longitudinal turbulence intensity ranged from 13% near ground level to about 3% at gradient height. The building had dimensions $w_m \times d_m \times h_m = 0.25 \times 0.60 \times 0.50$ m^3 (reduced scale, see Fig. 2a) corresponding to full-scale dimensions $W_m \times D_m \times H_m = 7.5 \times 18 \times 15$ m^3. To evaluate the effect of building balconies on mean pressure, the measurements were carried out for an isolated building with and without balconies. Three balconies each with length 0.15 m, width 0.05 m and height 0.03 m were positioned at each floor (Fig. 2a). Surface pressures were measured along three vertical lines on the windward and leeward facade. Each line was in the middle of the balconies and 45 pressure taps were implemented along these lines. Pressure coefficients were related to the incident wind speed at building height (7.1 m/s).

3.2. Comparison of CFD results and wind tunnel measurements

The wind tunnel experiments are reproduced by solving the 3D steady RANS CFD simulations combined with the realizable k-ε model (Shih et al. 1995) and following the best practice guidelines by Franke et al. (2007) and Tominaga et al. (2008a). The computational grid was fully structured and was created using the surface grid extrusion technique presented by van Hooff and Blocken (2010). Figure 2b compares the numerically simulated and measured pressure coefficients at the windward facade of the building with balconies for wind direction 0°. It should be noted that in this validation study, only results for the windward facades are considered. It is important to note that steady RANS CFD is deficient in reproducing the wind flow pattern downstream of windward facades (Murakami 1993, Tominaga et al. 2008b). Nevertheless, this approach is used in this paper, because the accuracy of the wind-flow pattern at side and the leeward facades is less important in wind comfort studies. The reason is that wind comfort studies typically focus on high wind speed positions, i.e. where a certain threshold wind speed is exceeded. Other positions do not contribute to the exceedance probabilities. Figure 2b shows that for the windward facades, the trends are well predicted by the CFD simulations. For the building without balconies, the deviations between the experimental and CFD results are generally less than 10%, while for the building with balconies, they are generally less than 20%.

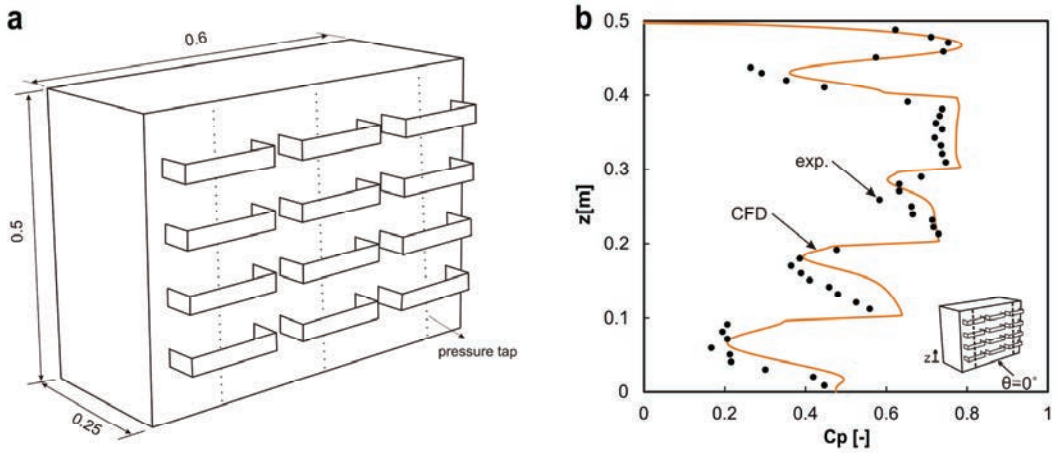

Figure 2. (a) Wind tunnel model of building with balconies and three vertical lines for pressure measurements (reduced-scale dimensions in m); (b) Comparison of wind tunnel and CFD results: pressure coefficient C_p along vertical line near building edge.

4. CASE STUDY: COMPUTATIONAL MODEL AND COMPUTATIONAL PARAMETERS

4.1. Computational geometry and grid

A computational model has been made of the tower and its urban surroundings, which are placed in a computational domain with dimensions of 2080 ×1770 ×400 m^3. The explicitly modeled buildings are the tower itself and the surrounding buildings in a radius of 350 m around the tower. Because of the existing densely built area to the east side of the tower, the buildings placed at that part within a distance of 670 m from the tower are also modeled. The tower is modeled in detail, including staggered facade elements, while the surrounding buildings are included only with their main shape. Special attention was given to the generation of a high-quality and high-resolution grid. The grid was constructed using the surface grid extrusion technique presented by van Hooff and Blocken (2010), which allows a large degree of control over the quality of the grid and its individual cells. It consists of only hexahedral and prismatic cells and does not contain any tetrahedral or pyramid cells. In addition, the grid was constructed following the best practice guidelines by Franke et al. (2007) and Tominaga et al. (2008a). The two grids for building with application of the second-skin facade and the reference building consist of 16,292,495 cells and 15,536,529 cells, respectively (Fig. 3).

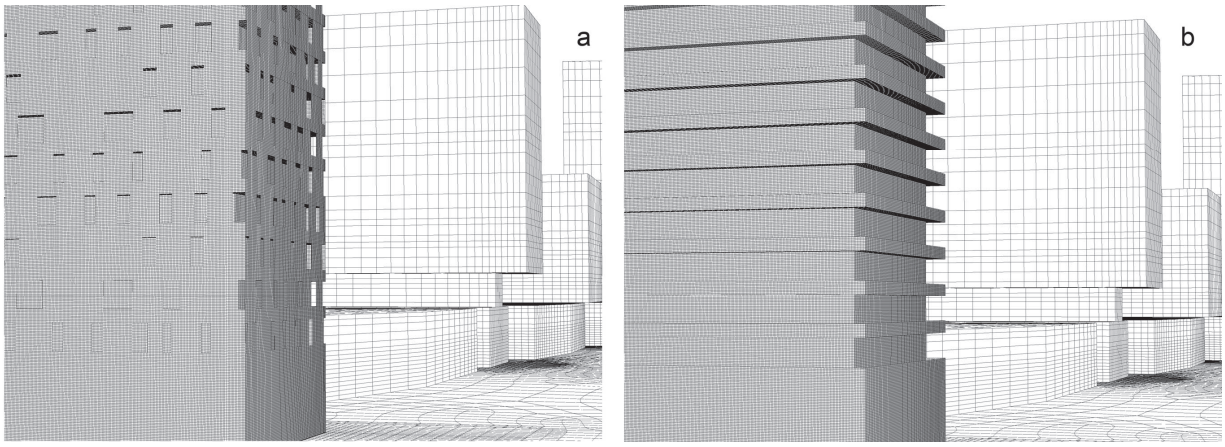

Figure 3. View from north-east at high-resolution computational grid on surfaces of high-rise building tower and surrounding buildings for (a) building with second-skin facade concept (16,292,495) and (b) reference building (15,536,529).

4.2. Boundary conditions

At the inlet of the domain, neutral atmospheric boundary layer inflow profiles of mean wind speed, turbulent kinetic energy and turbulence dissipation rate are imposed. These profiles are based on the aerodynamic roughness length z_0 of the upstream terrain that is not included in the computational domain. At the outlet, zero static pressure is specified. At the sides and the top of the domain, symmetry boundary conditions are imposed (i.e. zero normal velocity and gradients). At the ground surface, the standard wall functions by Launder and Spalding (1974) with the sand-grain roughness modification by Cebeci and Bradshaw (1977). The equivalent sand-grain roughness height k_S and roughness constant C_S are determined based on their relationship with z_0 according to Blocken et al. (2007). At the building surfaces, also standard wall functions are used, with the assumption of smooth walls (k_S = 0 m).

4.3. Solver settings

The CFD simulations are performed using the commercial CFD code Fluent 6.3.26. The 3D steady RANS equations are solved with the realizable k-ε turbulence model (Shih et al. 1995). The choice for this turbulence model is based on the recommendations by Franke et al. (2007) and on earlier successful validation studies for pedestrian-level wind conditions with this turbulence model (Blocken and Persoon 2009, Blocken et al. 2012). Pressure velocity-coupling is taken care of by the SIMPLE algorithm. Pressure interpolation is second order. Second-order discretisation schemes are used for both the convection terms and viscous terms of the governing equations. The simulations are performed for the 12 wind directions θ = 0-330° in 30° intervals.

5. CASE STUDY: CFD SIMULATION RESULTS

Figure 4 shows the local amplification factor U/U_{ref} in a horizontal plane at a height of 1.7 m at the 15th floor of the tower for the two situations and for southwest wind direction. The local amplification factor is defined as the ratio of the local mean wind speed U to the reference wind speed U_{ref} at the same height but in undisturbed (free-stream) conditions. It can be seen that the new concept provides a significantly reduced amplification factor on the balconies two at the windward facades. At the west facade, the amplification factor reduces from a value of about 1.0 to a value of about 0.6.

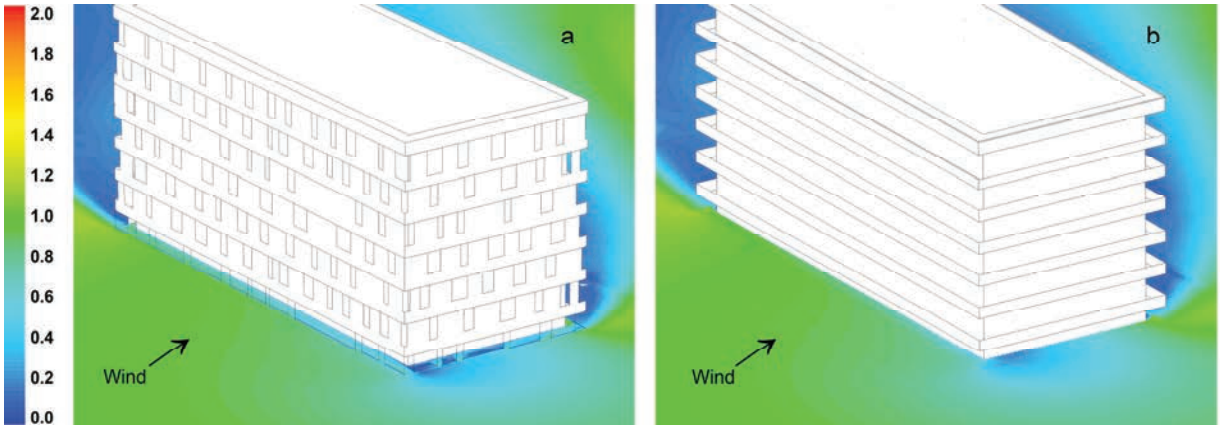

Figure 4. Contours of amplification factor for wind direction 210° in a horizontal plane at a height of 1.7 m above 15th floor for: (a) the building with application of the second-skin facade concept. (b) The reference building.

6. CASE STUDY: WIND COMFORT ASSESSMENT RESULTS

The wind speed amplification factors are used in combination with the Dutch wind nuisance standard for the assessment of wind comfort. For brevity, only some main items of this standard are given here, more details can be found in Willemsen and Wisse (2002, 2007), NEN (2006a, 2006b). The threshold wind speed in the standard is 5 m/s for all activities, while the maximum allowed exceedance probabilities of this threshold vary based on the activity, see Table 1.

Table 1: Criteria for wind nuisance according to NEN 8100 (2006a)

$P(U_{THR} > 5$ m/s (in % hours per year)	Grade	Activity		
		Traversing	Strolling	Sitting
< 2.5	A	Good	Good	Good
2.5 – 5.0	B	Good	Good	Moderate
5.0 – 10	C	Good	Moderate	Poor
10 – 20	D	Moderate	Poor	Poor
> 20	E	Poor	Poor	Poor

For the wind comfort analysis, the wind statistics of the nearby city of Eindhoven are used. Figure 5 illustrates the exceedance probability of the 5 m/s threshold on the 15th floor. Because southwest is the prevailing wind direction, the pattern of exceedance probabilities resembles that of the wind speed amplification factor for southwest wind direction (see Fig. 4). Figure 5 clearly shows that the second-skin facade concept improves wind comfort for a large part of the west facade and also for part of the south facade.

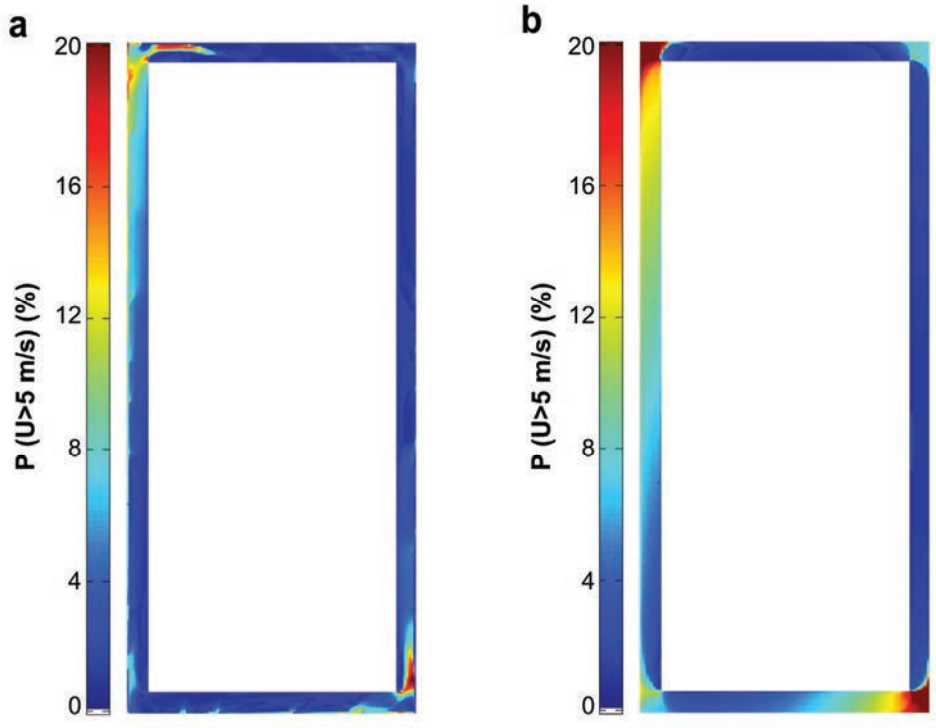

Figure 5. Contours of exceedance probability in a horizontal plane at a height of 1.7 m above 15th floor for: (a) the building with application of the second-skin facade concept. (b) The reference building.

7. DISCUSSION

Some important limitations of this study are mentioned.

- The 3D steady RANS equations have been solved with the realizable k-ε model. It is important to note that steady RANS CFD is generally deficient in reproducing the wind-flow pattern downstream of windward facades (Murakami 1993, Tominaga et al. 2008b).

Nevertheless, this approach is used in this paper, because the accuracy of the wind-flow pattern at side and the leeward facades is less important in wind comfort studies. The reason is that wind comfort studies typically focus on high wind speed positions, i.e. where a certain threshold wind speed is (5 m/s in the present study) is exceeded. Other positions do not contribute significantly or do not contribute at all to the exceedance probabilities.

- No grid-sensitivity analysis was performed. However, the computational grid has been made based on the best practice guidelines by Franke et al. (2007) and Tominaga et al. (2008a) and the grid resolution has been taken either similar or higher than in previous studies for which grid-sensitivity analyses were performed (van Hooff and Blocken 2010, Blocken et al. 2012)..

8. CONCLUSIONS

3D steady RANS CFD simulations have been used in combination with the new Dutch wind nuisance standard to evaluate the performance of a new facade concept. This concept consists of a staggered semi-open second-skin facade that partly shields the balconies from the wind. To achieve this particular purpose, the wind comfort at the balconies with and without application of this concept has been compared. It is shown that the new facade concept is very effective in shielding the balconies and improving the wind comfort.

9. REFERENCES

ELD Partnership, Personal communication, 2011.

B. Blocken, W.D. Janssen, and T. van Hooff, CFD simulation for pedestrian wind comfort and wind safety in urban areas: General decision framework and case study for the Eindhoven University campus, Environmental Modelling & Software, 30 (2012) 15-34.

B. Blocken, T. Stathopoulos, and J. Carmeliet, CFD simulation of the atmospheric boundary layer: wall function problems, Atmospheric Environment, 41 (2007) 238-252.

B. Blocken and J. Persoon, Pedestrian wind comfort around a large football stadium in an urban environment: CFD simulation, validation and application of the new Dutch wind nuisance standard, Journal of Wind Engineering and Industrial Aerodynamics, 97 (2009) 255-270.

T. Cebeci and P. Bradshaw, Momentum Transfer in Boundary Layers, Hemisphere Publishing Corporation, New York, 1977.

I. Chand, P.K. Bhargava, and N.L.V. Krishak, Effect of balconies on ventilation inducing aeromotive force on low-rise buildings, Building and Environment, 33 (1998) 385-396.

J. Franke, H. Schlünzen, B. Carissimo, Best practice guideline for the CFD simulation of flows in the urban environment, (2007).

T. van Hooff and B. Blocken, Coupled urban wind flow and indoor natural ventilation modelling on a high-resolution grid: A case study for the Amsterdam ArenA stadium, Environmental Modelling & Software, 25 (2010) 51-65.

B.E. Launder and D.B. Spalding, The numerical computation of turbulent flows, Computer Methods in Applied Mechanics and Engineering, 3 (1974) 269-289.

NEN, Wind comfort and wind danger in the built environment, NEN8100 (in Dutch) Dutch Standard, 2006a.

NEN, Application of mean hourly wind speed statistics for the Netherlands, NPR 6097:2006 (in Dutch), Dutch Practice Guideline, 2006b.

S. Murakami, Comparison of various turbulence models applied to a bluff body, Journal of Wind Engineering and Industrial Aerodynamics, 46–47 (1993) 21-36.

T.H. Shih, W.W. Liou, A. Shabbir, Z. Yang, and J. Zhu, A new k-ε eddy viscosity model for high Reynolds number turbulent flows, Computers & Fluids, 24 (1995) 227-238.

T. Stathopoulos and B.A. Baskaran, Computer simulation of wind environmental conditions around buildings, Engineering Structures, 18 (1996) 876-885.
Y. Tominaga, A. Mochida, R. Yoshie, H. Kataoka, T. Nozu, M. Yoshikawa, and T. Shirasawa, AIJ guidelines for practical applications of CFD to pedestrian wind environment around buildings, Journal of Wind Engineering and Industrial Aerodynamics, 96 (2008a) 1749-1761.
Y. Tominaga, A. Mochida, S. Murakami, and S. Sawaki, Comparison of various revised k–ε models and LES applied to flow around a high-rise building model with 1:1:2 shape placed within the surface boundary layer, Journal of Wind Engineering and Industrial Aerodynamics, 96 (2008b) 389-411.
E. Willemsen, J.A. Wisse, Accuracy of assessment of wind speed in the built environment, Journal of Wind Engineering and Industrial Aerodynamics, 90 (2002) 1183-1190.
E. Willemsen, J.A. Wisse, Design for wind comfort in The Netherlands: Procedures, criteria and open research issues. Journal of Wind Engineering and Industrial Aerodynamics, 95 (2007) 1541-1550.
R. Yoshie, A. Mochida, Y. Tominaga, H. Kataoka, K. Harimoto, T. Nozu, and T. Shirasawa, Cooperative project for CFD prediction of pedestrian wind environment in the Architectural Institute of Japan, Journal of Wind Engineering and Industrial Aerodynamics, 95 (2007) 1551-1578.

The Seventh International Colloquium on Bluff Body Aerodynamics and Applications (BBAA7)
Shanghai, China; September 2-6, 2012

On validation and solution verification of Large-Eddy Simulation of wind flow around a high-rise building

P. Gousseau [a], B. Blocken [a], G.J.F. van Heijst [b]

[a] *Building Physics and Services, Department of the Built Environment, Eindhoven University of Technology, P.O. Box 513, Eindhoven, The Netherlands*
[b] *Fluid Dynamics Laboratory, Department of Applied Physics, Eindhoven University of Technology, P.O. Box 513, Eindhoven, The Netherlands*

ABSTRACT: Large-Eddy Simulation (LES) of wind flow around a high-rise building is performed with the Smagorinsky subgrid-scale model. Validation of the simulation is performed by comparing the numerical results to wind-tunnel measurements. Very good agreement is found for the mean streamwise velocity. Over-estimation of the turbulent kinetic energy by LES is observed in the wake of the building. Verification of the numerical solution is performed by evaluating the numerical and modeling error contributions with the Systematic Grid and Model Variation technique and by computing the amount of turbulent kinetic energy resolved by the numerical model. It is shown that the numerical and modeling errors are relatively high in magnitude but compensate each other, resulting in a low total error, and explaining the good accuracy of the model. With a computational grid using 20 cells per building side, 80% of the total kinetic energy is resolved on average in the region around the building.

KEYWORDS: Urban wind flow; bluff body aerodynamics; Computational Fluid Dynamics (CFD); validation & verification.

1 INTRODUCTION

In most of the applications of Computational Wind Engineering (CWE) such as pollutant dispersion (e.g. Hanna et al., 2006; Gousseau et al., 2011a; Gousseau et al., 2011b) or pedestrian wind comfort (e.g. Yoshie et al., 2007; Blocken et al., 2012), the accurate simulation of the flow around buildings by the numerical model is needed. In this respect, the good performance of the Large-Eddy Simulation turbulence modeling approach has already been proven (e.g. Murakami, 1993; Shah and Ferziger, 1997; Tominaga et al., 2008a). However, despite the increasing attention given to the quantification of error and uncertainty in Computational Fluid Dynamics (CFD), the techniques that have been developed for general fluid engineering problems to assess the quality of CFD simulations are still marginally used in CWE (Franke, 2010). This is particularly true for LES.

The aim of the present study is to assess the quality of an LES computation of wind flow around an isolated building. The procedure is twofold: on the one hand the validation part and, on the other hand, the solution verification part (Oberkampf and Trucano, 2002).

Validation is defined as "the process of determining the degree to which a model is an accurate representation of the real world from the perspectives of the intended uses of the model" (AIAA, 1998). It will be performed here by comparing the numerical results with the measurements from a reference wind-tunnel experiment.

Verification is defined as "the process of determining that a model implementation accurately represents the developer's conceptual description of the model and the solution to the model"

(AIAA, 1998). The code verification will not be treated here; the solution verification will be performed by (1) evaluating the modeling and numerical error contributions in the LES solution with a multi-grid technique called Systematic Grid and Model Variation (SGMV) (Klein, 2005; Freitag and Klein, 2006; Klein et al., 2008; Celik et al., 2009) and (2) by evaluating the proportion of the total turbulent kinetic energy which is resolved by the LES model with the LES index of quality (*LES_IQ*) (Celik et al., 2005; Celik et al., 2006; Celik et al., 2009).

The reference experiment that will be reproduced with CFD is described in the next section, as well as the numerical model used in the present study. Next, the results are presented and analyzed.

2 NUMERICAL MODEL

2.1 Domain, grid and boundary conditions

The wind-tunnel experiment by Meng and Hibi (1998) has been reproduced with Ansys Fluent 12. It involves a building of dimensions $b \times b \times h$ ($b=h/2=0.08$m) in the streamwise (x), lateral (y) and vertical (z) direction, respectively, placed in the test section of a wind tunnel where an Atmospheric Boundary Layer (ABL) flow is simulated. The Reynolds number based on b and the mean velocity of the incident flow at building height (U_h) is equal to 2.4×10^4. The origin of the coordinate system is the center of the building's ground face.

The computational domain has been created and meshed with the surface-extrusion technique (van Hooff and Blocken, 2010). The domain dimensions are $2.64 \times 0.9 \times 0.9$ m^3 (Fig. 1a). A distance of $4h$ is allocated between the inflow boundary and the windward facade of the building and the outlet face of the domain is located $12.125h$ downstream of the building. In the vertical direction, the height of the wind-tunnel test section is used (0.9m=$5.625h$) and the top wall boundary is modeled. To avoid modeling the side-walls of the wind tunnel (which would require grid refinement and increase the total number of cells significantly), the width of the domain has been chosen slightly smaller than the test-section width (0.9m=$11.25b$ vs. 1.1m). Nevertheless, an empty distance of $5.125b$ is allocated on each side of the building, which ensures low influence of the side boundary conditions on the flow around the building. The resulting blockage ratio is equal to 1.6%, which is below the maximum values recommended by the COST action 732 and AIJ guidelines (Franke et al., 2007; Tominaga et al., 2008b).

The building has been discretized into 20 cells in the x- and y- directions and 40 in the z-direction. Away from the building, the cell dimension has been increased until a maximum of $b/2.2$ with a growth ratio kept around 1.08 to limit commutation error. In total, the grid contains 737,920 hexahedral cells. The grid on the building and ground surfaces can be seen in Figures 1b,c.

Symmetry boundary conditions are set at the sides of the domain (y=±0.45m), imposing zero normal velocity and zero gradients of all variables at these boundaries. At the outlet of the domain, zero static pressure is imposed.

The building and ground surfaces as well as the top boundary of the domain are defined as no-slip walls. The centroids of the wall-adjacent cells are assumed to fall either in the linear sublayer, in the buffer layer or in the logarithmic zone of the boundary layer, depending on the distance to the wall (Ansys Inc., 2009). Note that no special treatment has been applied to the ground surface to take into account its roughness but that the inflow boundary is located close enough to the building to limit the appearance of longitudinal gradients in the ABL profiles (Blocken et al., 2007a; Blocken et al., 2007b).

The time-dependent velocity profile at the inlet is generated by the Vortex Method (VM) (Sergent, 2002; Mathey et al., 2006). The VM consists in generating and transporting randomly in the inlet plane a given number (here: 200) of 2D-vortices whose intensity and size depend on the local value of the turbulent kinetic energy (k) and the turbulence dissipation rate, for which profiles are prescribed based on the experiment. These vortices allow computing the perturbations super-imposed on the mean velocity profile prescribed at the inlet, which corresponds to the one measured in the empty test section of the wind tunnel. Note that the VM showed good performance when applied to pollutant dispersion studies by the authors (Gousseau et al., 2011a; Gousseau et al., 2011b; Gousseau et al., 2012).

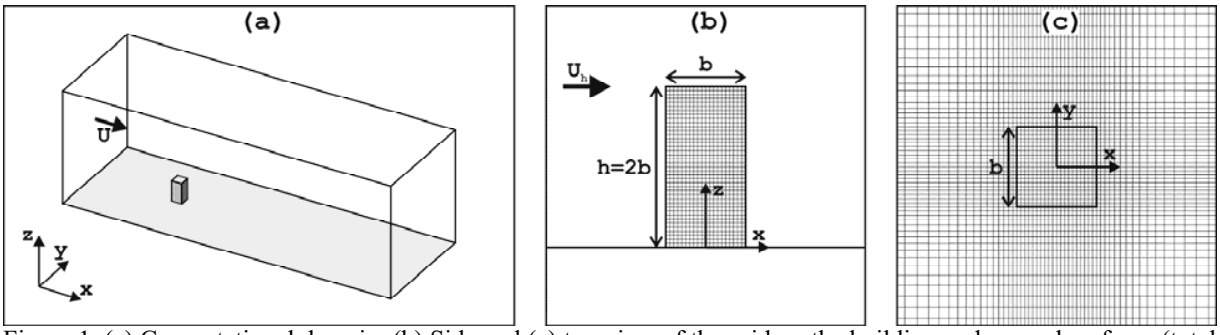

Figure 1. (a) Computational domain. (b) Side and (c) top view of the grid on the building and ground surfaces (total number of cells: 737,920).

2.2 LES modeling

Large-Eddy Simulation has been used with the standard Smagorinsky subgrid-scale (SGS) model. The filter width is directly related to the cell size (implicit filtering): it is equal to the cubic root of the cell volume. The Smagorinsky constant C_s, which allows computing the SGS turbulent viscosity, has been set to 0.1, which appears to be an appropriate value for flow around bluff bodies (Rodi et al., 1997; Thomas and Williams, 1997; Xie and Castro, 2009). Note that another simulation with a different C_s value (C_s=0.15) has also been run in order to estimate the modeling error (Section 4) but no plots of the results are shown here.

The bounded central-differencing scheme is used to discretize the convection term in the filtered momentum equation. From the pressure values at the cell centers, the face values are computed with a second-order scheme. Pressure-velocity coupling is performed with the fractional-step method (Kim and Moin, 1985; Bell et al., 1989).

Time discretization is second-order implicit. The non-iterative scheme is used for time advancement, which decreases the computational time significantly without affecting the overall accuracy of the simulation (Ansys Inc., 2009). The time-step value (Δt) has been set to 8×10^{-4}s, corresponding to 0.045 time units ($t_u=b/U_h$). Each simulation is initialized with the solution of a preceding RANS simulation on which random noise is super-imposed. After an initialization period T_{init}=3.2s corresponding to 5.4 flow-through times ($T_{ft}=L_x/U_h$, where L_x is the length of the computational domain), the statistics are sampled for T_{avg}=12.8s=21.8T_{ft}=718t_u. It has been verified that at the end of this averaging period the mean values of velocity are converged.

3 VALIDATION: COMPARISON BETWEEN EXPERIMENTAL AND NUMERICAL RESULTS

Figure 2 shows the experimental and numerical profiles of non-dimensional mean streamwise velocity (U/U_h) in the vertical mid-plane V0 (Fig. 2a) and in the horizontal plane H10 at 10 cm from the ground (Fig. 2b). The plotting lines are located at x/b=-0.75; -0.25; 0.5; 1.25; and 3.25. One can notice the very good agreement between the LES results and the measurements, along all lines, including in the wake recirculation zone of the building – a zone where the flow is known to be especially challenging to predict.

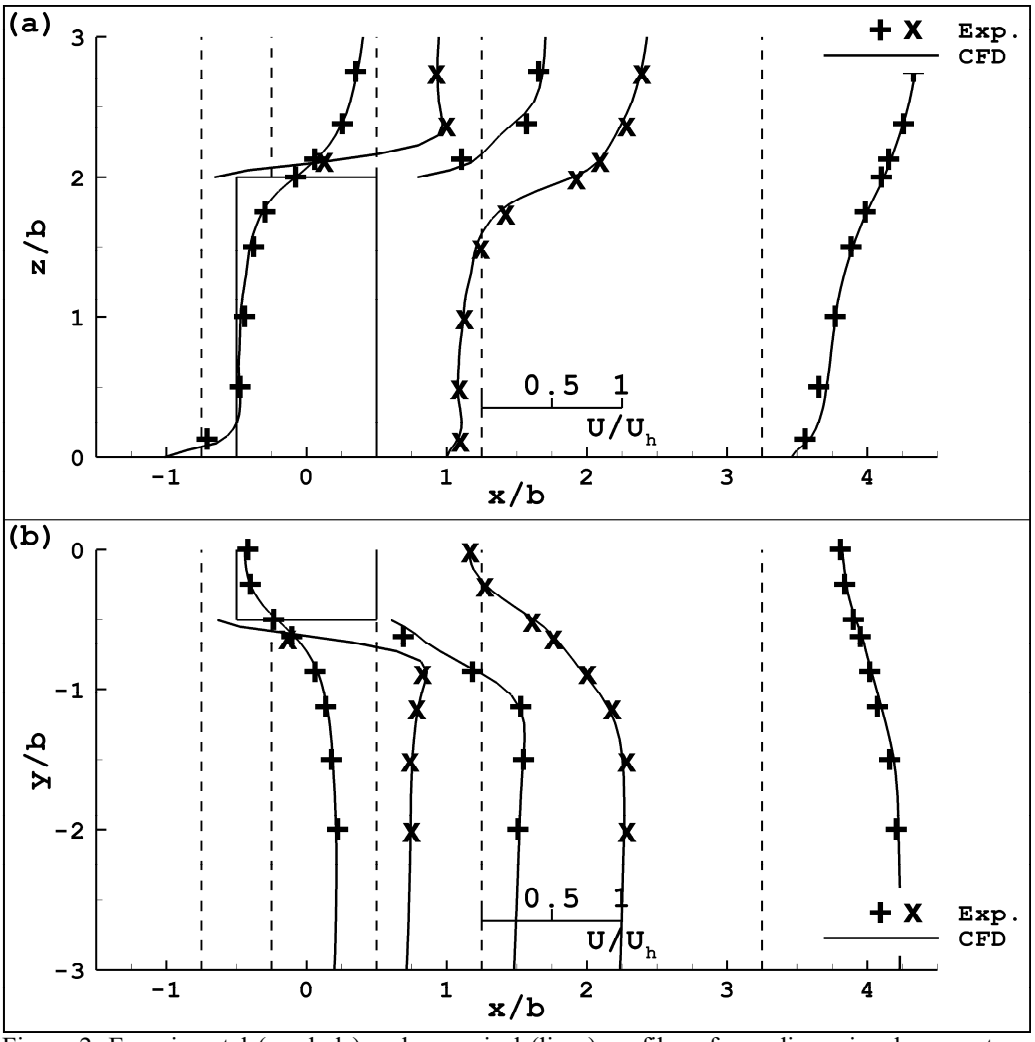

Figure 2. Experimental (symbols) and numerical (lines) profiles of non-dimensional mean streamwise velocity in the planes (a) V0 and (b) H10.

The profiles of non-dimensional turbulent kinetic energy (k/U_h^2) in the planes V0 and H10 are shown in Figure 3. Good agreement is found between experiments and LES, except in the wake of the building where the LES model over-estimates the measured turbulent kinetic energy values. Nevertheless, these results demonstrate the good performance of the vortex method to generate inflow turbulence in the case of ABL flow.

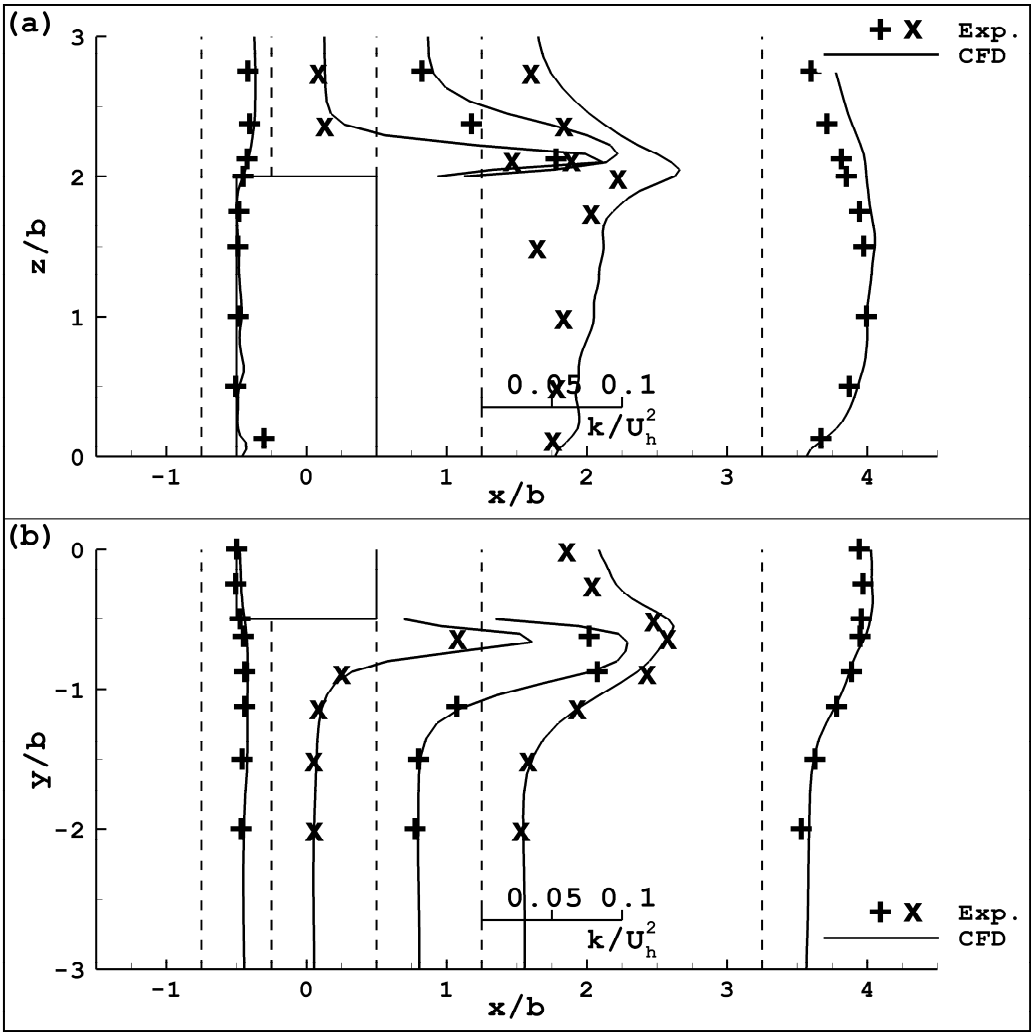

Figure 3. Experimental (symbols) and numerical (lines) profiles of non-dimensional turbulent kinetic energy in the planes (a) V0 and (b) H10.

4 ESTIMATION OF THE NUMERICAL AND MODELING ERROR

In the context of LES with implicit filtering, the modeling (ε_m) and numerical (ε_n) errors interact and cannot be evaluated separately. The Systematic Grid and Model Variation (Klein, 2005) is therefore used here to provide an estimation of these two types of error, based on Richardson extrapolation. The difference between the exact solution of the flow equations (u_e) and the numerical solution (u_1) is equal to the sum of these two error contributions which are assumed to scale with the filter width:

$$u_e - u_1 = \varepsilon_m + \varepsilon_n = c_m \Delta^m + c_n \Delta^n \tag{1}$$

where c_m and c_n are coefficients to be determined, Δ is the filter width, n=2 is the order of accuracy of the numerical scheme and m is taken equal to its theoretical value 2/3 as suggested in (Freitag and Klein, 2006). The LES simulation has been performed on the same grid with a modified model coefficient C_s=0.15 (solution u_2) and with C_s=0.1 on a finer grid with 30 cells per building side (solution u_3). Applying the same procedure to these two numerical solutions yields:

$$u_e - u_2 = \beta c_m \Delta^m + c_n \Delta^n \tag{2}$$

$$u_e - u_3 = c_m (\alpha\Delta)^m + c_n (\alpha\Delta)^n \tag{3}$$

where β=0.15²/0.1²=2.25 is the model variation factor equal to the ratio of the square of the C_s values and α=2/3 is the refinement factor equal to the ratio of the filter width/grid size on the fine grid to the one on the coarse grid. The combination of Equations 1, 2 and 3 allows determining the unknowns of the problem (u_e, c_m and c_n) and estimating ε_m and ε_n. The SGMV technique has been applied here for the mean velocity.

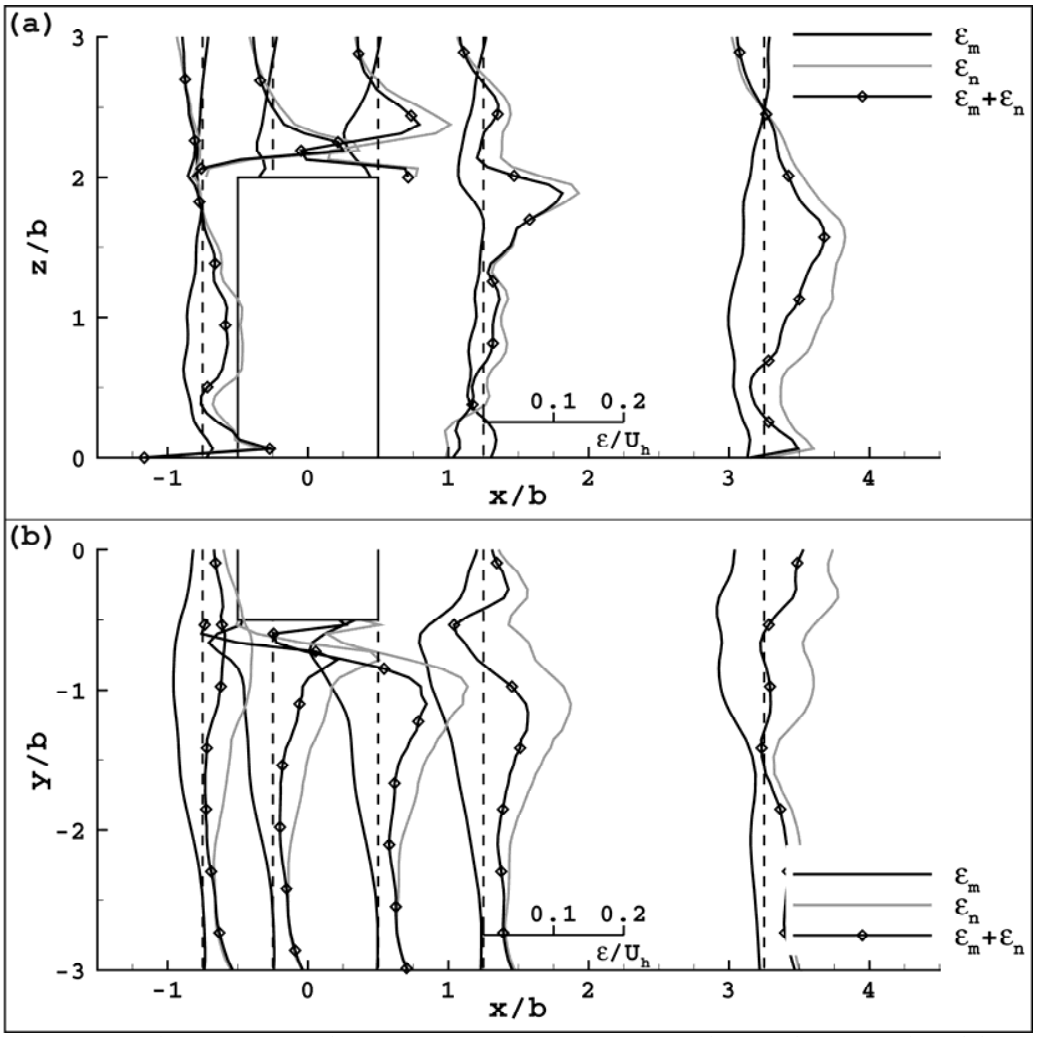

Figure 4. Results of SGMV technique for LES20-1: Estimation of the non-dimensional modeling, numerical and total error on mean streamwise velocity prediction in the planes (a) V0 and (b) H10.

Figure 4 shows the resulting estimation of ε_m and ε_n (normalized by U_h) for the "reference" simulation (i.e. the one presented in Section 3, on the coarse grid with C_s=0.1). The sum of these two error contributions is also shown. Note that it is advised to use the sum of the magnitudes $|\varepsilon_m|+|\varepsilon_n|$ to get an estimation of the uncertainty of the computation (Freitag and Klein, 2006). The numerical error is relatively high, especially above roof level and in the wake of the building (Fig. 4a) as well as in the side shear layer (Fig. 4b) where it can reach up to 15% of the reference

velocity. Noticeably, the SGS modeling error is generally of opposite sign than the one of ε_n, with similar order of magnitude, which significantly decreases the total error on mean velocity. This error compensation is an explanation for the good agreement between measurements and the LES results presented in Section 3. The uncertainty $|\varepsilon_m|+|\varepsilon_n|$, however, is rather high on this computational grid.

5 LES INDEX OF QUALITY

Since a grid-independent solution cannot be achieved with LES and implicit filtering, a way to determine whether a given grid is suitable is to evaluate the amount of turbulent kinetic energy that it allows resolving. This is the purpose of the LES index of quality (*LES_IQ*) (Celik et al., 2005): to evaluate the proportion of total kinetic energy (k_{tot}) resolved by LES on a particular grid. k_{tot} can be decomposed into the resolved part (k_{res} which was symbolized by k in the validation part), the contribution of the SGS model (k_{SGS}), and the contribution of the numerical dissipation (k_{num}):

$$LES\_IQ = \frac{k}{k_{tot}} = \frac{k}{k + k_{SGS} + k_{num}} = 1 - \frac{k_{tot} - k}{k_{tot}} \tag{4}$$

As suggested by Pope (Pope, 2000), an LES computation can be judged to be well-resolved when 80% of the turbulent kinetic energy is resolved. In some cases, k is found to be higher on a coarser grid than on a finer one (Celik et al., 2005). This was observed in the present computations (above roof level and in regions of very low k) so the generalized formula has been used to keep *LES_IQ* below the ideal value of 1:

$$LES\_IQ = 1 - \frac{|k_{tot} - k|}{k_{tot}} \tag{5}$$

Based on Richardson extrapolation, the combined contribution of SGS model and numerical diffusion is assumed to scale with the grid size/filter length (Celik et al., 2005):

$$k_{tot} - k = a_k \Delta^n \tag{6}$$

where n=2 is the order of accuracy of the numerical scheme and a_k is a coefficient that can be determined by running the simulation on two grids with different resolution. Here, the same fine grid as the one used in Section 4 (with 30 cells per building side) is used.

Figure 5 shows the profiles of *LES_IQ* along the same lines that were used in the validation part, as well as the averaged values of *LES_IQ* on each line for $z/b<3$ (plane V0) and $-3<y/b<0$ (plane H10). On the nine measurement lines in the plane V0 for $z/b<3$, on average 76% of k_{tot} is resolved by the LES computation with 20 cells per building side (Fig. 5a). The flow regions where the least energy is resolved are the upstream part of the roof ($-0.5<x/b<0$) and the far-wake ($x/b\approx3.25$). On the measurement lines in H1 and H10, for $-3<y/b<0$, on average 80% and 84% of the total turbulent kinetic energy are resolved. The profiles of *LES_IQ* for several lines in the plane H10 are shown in Figure 5b. On average over all the measurement lines, the LES modeling used here allows resolving 80% of k_{tot}. Thus, if the threshold of 80% is used to define a well-resolved LES (Pope, 2000), our simulation can be classified in this category.

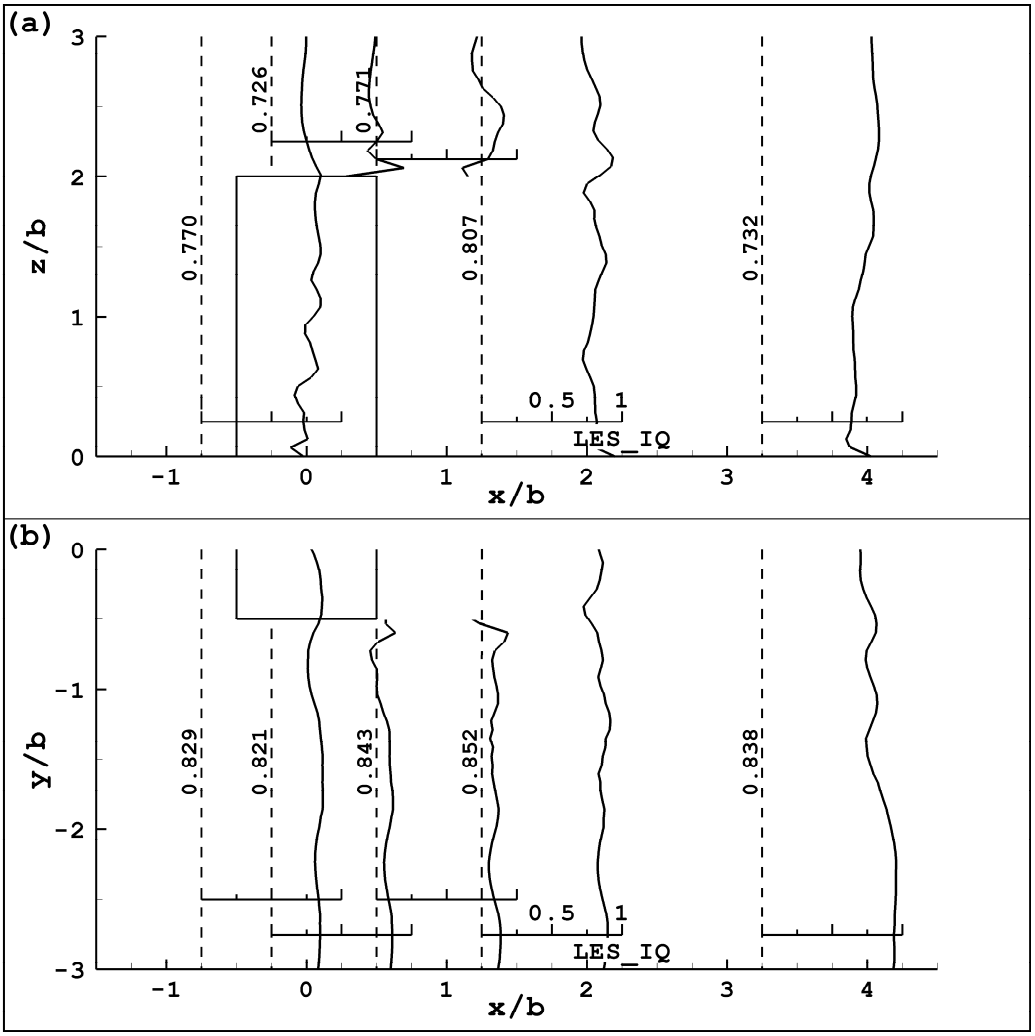

Figure 5. Profiles of *LES_IQ* in the planes (a) V0 and (b) H10. The values averaged on (a) $0<z/b<3$ and (b) $-3<y/b<0$ are indicated on each line.

6 DISCUSSION AND CONCLUSIONS

Large-Eddy Simulation of wind flow around a high-rise building with aspect ratio 1:1:2 has been performed. The standard Smagorinsky subgrid-scale model has been used, with C_s=0.1. A structured computational grid with 20 cells per cube side has been used.

Validation of the simulation has been performed in the first part of the study: the numerical results have been compared to the wind-tunnel measurements in terms of non-dimensional mean streamwise velocity and turbulent kinetic energy. Very good agreement between numerical and experimental values of U/U_h was found. Concerning k/U_h^2, a slight over-estimation of the experimental values by LES was observed in the wake of the building but the agreement remained fairly good in the other regions of the flowfield. These results demonstrate the good performance of the vortex method to generate inflow turbulence in the case of ABL flow.

The second part of the study presented some elements of solution verification. An estimation of the modeling and numerical error has been provided with the Systematic Grid and Model Variation technique. Both error contributions have been shown to be relatively high in magnitude

(which creates a high uncertainty on the results) but because they are of opposite sign, they compensate each other. Consequently, the resulting total error is low, which explains the good accuracy of the present LES modeling in mean velocity prediction.

The LES index of quality (*LES_IQ*) has been used to evaluate the proportion of total turbulent kinetic energy which is resolved by the present LES modeling. On average, in the zone around the building, 80% of the total turbulent kinetic energy is resolved which qualifies the present numerical modeling as "well-resolved LES". The regions of the flow field where the least energy is resolved are the far-wake and roof detachment region.

The procedure applied here to the case of an isolated building will be repeated on other configurations representative of urban geometry in future research.

7 REFERENCES

AIAA, Guide for the verification and validation of Computational Fluid Dynamics simulations, American Institute of Aeronautics and Astronautics, AIAA-G-077-1998, 1998.

Ansys Inc., Ansys Fluent 12.0 - Theory Guide, 2009.

J.B. Bell, P. Colella and H.M. Glaz, A second-order projection method for the incompressible Navier-Stokes equations, Journal of Computational Physics, 85 (1989) 257-283.

B. Blocken, J. Carmeliet and T. Stathopoulos, CFD evaluation of wind speed conditions in passages between parallel buildings–effect of wall-function roughness modifications for the atmospheric boundary layer flow, Journal of Wind Engineering and Industrial Aerodynamics, 95 (2007a) 941-962.

B. Blocken, T. Stathopoulos and J. Carmeliet, CFD simulation of the atmospheric boundary layer: wall function problems, Atmospheric Environment, 41 (2007b) 238-252.

B. Blocken, W.D. Janssen and T. van Hooff, CFD simulation for pedestrian wind comfort and wind safety in urban areas: General decision framework and case study for the Eindhoven University campus, Environmental Modelling & Software, 30 (2012) 15-34.

I. Celik, Z.N. Cehreli and I. Yavuz, Index of resolution quality for Large Eddy Simulation, Journal of Fluids Engineering, 127 (2005) 949-958.

I. Celik, M. Klein, M. Freitag and J. Janicka, Assessment measures for URANS/DES/LES: an overview with applications, Journal of Turbulence, 7 (2006) 1-27.

I. Celik, M. Klein and J. Janicka, Assessment measures for engineering LES applications, Journal of Fluids Engineering, 131 (2009) 10 pages.

J. Franke, A. Hellsten, H. Schlünzen and B. Carissimo, Best practice guideline for the CFD simulation of flows in the urban environment, COST Action 732, 2007.

J. Franke, A review of verification and validation in relation to CWE, The Fifth International Symposium on Computational Wind Engineering, May 23-27.

M. Freitag and M. Klein, An improved method to assess the quality of large eddy simulations in the context of implicit filtering, Journal of Turbulence, 7 (2006) 1-11.

P. Gousseau, B. Blocken, T. Stathopoulos and G.J.F. van Heijst, CFD simulation of near-field pollutant dispersion on a high-resolution grid: a case study by LES and RANS for a building group in downtown Montreal, Atmospheric Environment, 45 (2011a) 428-438.

P. Gousseau, B. Blocken and G.J.F. van Heijst, CFD simulation of pollutant dispersion around isolated buildings: On the role of convective and turbulent mass fluxes in the prediction accuracy, Journal of Hazardous Materials, 194 (2011b) 422-434.

P. Gousseau, B. Blocken and G.J.F. van Heijst, Large-Eddy Simulation of pollutant dispersion around a cubical building: Analysis of the turbulent mass transport mechanism by unsteady concentration and velocity statistics, Environmental Pollution (2012), doi: 10.1016/j.envpol.2012.03.021.

S.R. Hanna, M.J. Brown, F.E. Camelli, S.T. Chan, W.J. Coirier, O.R. Hansen, A.H. Huber, S. Kim and R.M. Reynolds, Detailed simulations of atmospheric flow and dispersion in downtown Manhattan. An application of five computational fluid dynamics models, Bulletin of the American Meteorological Society, 87 (2006) 1713-1726.

J. Kim and P. Moin, Application of a fractional step method to incompressible Navier-Stokes equations, Journal of Computational Physics, 59 (1985) 308-323.

M. Klein, An attempt to assess the quality of large eddy simulations in the context of implicit filtering, Flow, Turbulence and Combustion, 75 (2005) 131-147.

M. Klein, J. Meyers and B.J. Geurts, Assessment of LES quality measures using the error landscape approach, Quality and reliability of Large-Eddy Simulations, .

F. Mathey, D. Cokljat, J.P. Bertoglio and E. Sergent, Assessment of the vortex method for large eddy simulation inlet conditions, Progress in Computational Fluid Dynamics, 6 (2006) 58-67.

Y. Meng and K. Hibi, Turbulent measurements of the flow field around a high-rise building, Journal of Wind Engineering, 76 (1998) 55-64.

S. Murakami, Comparison of various turbulence models applied to a bluff body, Journal of Wind Engineering and Industrial Aerodynamics, 46 & 47 (1993) 21-36.

W.L. Oberkampf and T.G. Trucano, Verification and validation in computational fluid dynamics, Progress in Aerospace Sciences, 38 (2002) 209-272.

S.B. Pope, Turbulent flows, Cambridge University Press, 2000.

W. Rodi, J.H. Ferziger, M. Breuer and M. Pourquié, Status of Large Eddy Simulation: Results of a workshop, Journal of Fluid Engineering, 119 (1997) 248-262.

E. Sergent, Vers une méthode de couplage entre la simulation des grandes échelles et les modèles statistiques, Ecole Centrale de Lyon, 2002.

K.B. Shah and J.B. Ferziger, A fluid mechanicians view of wind engineering: Large eddy simulation of flow past a cubic obstacle, Journal of Wind Engineering and Industrial Aerodynamics, 67-68 (1997) 211-224.

T.G. Thomas and J.J.R. Williams, Development of a parallel code to simulate skewed flow over a bluff body, Journal of Wind Engineering and Industrial Aerodynamics, 67 & 68 (1997) 155-167.

Y. Tominaga, A. Mochida, S. Murakami and S. Sawaki, Comparison of various revised k-ε models and LES applied to flow around a high-rise building model with 1:1:2 shape placed within the surface boundary layer, Journal of Wind Engineering and Industrial Aerodynamics, 96 (2008a) 389-411.

Y. Tominaga, A. Mochida, R. Yoshie, H. Kataoka, T. Nozu, M. Yoshikawa and T. Shirasawa, AIJ guidelines for practical applications of CFD to pedestrian wind environment around buildings, Journal of Wind Engineering and Industrial Aerodynamics, 96 (2008b) 1749-1761.

T. van Hooff and B. Blocken, Coupled urban wind flow and indoor natural ventilation modelling on a high-resolution grid: A case study for the Amsterdam ArenA stadium, Environmental Modelling & Software, 25 (2010) 51-65.

Z.T. Xie and I.P. Castro, Large-eddy simulation for flow and dispersion in urban streets, Atmospheric Environment, 43 (2009) 2174-2185.

R. Yoshie, A. Mochida, Y. Tominaga, H. Kataoka, K. Harimoto, T. Nozu and T. Shirasawa, Cooperative project for CFD prediction of pedestrian wind environment in the Architectural Institute of Japan, Journal of Wind Engineering and Industrial Aerodynamics, 95 (2007) 1551-1578.

The Seventh International Colloquium on Bluff Body Aerodynamics and Applications (BBAA7)
Shanghai, China; September 2-6, 2012

Study on characteristics of ore storage-pile fugitive-dust based on wind tunnel experiments

Yonghua Xue [a]

[a]*Tianjin Research Institute for Water Transport Engineering of Ministry of Transport, 2618#, Xingang Road No.2, Tanggu, Binhai New Area, Tianjin, China*

ABSTRACT: Dust is the main pollution issue of the bulk port. This paper investigated characteristics of ore storage-pile fugitive-dust by means of wind tunnel experiments. Three typical ore, including Australia, Indian and Brazil ore, were selected, since these ore are common in ports. The proportion of model and corresponding boundary conditions was determined under wind tunnel parameters. Relationship between amount of dust and ore particle size distribution, startup wind velocity and mean wind velocity were investigated by regression analysis. Furthermore, difference on amount of dust between single-pile and multi-piles was also examined. The paper presents a mathematical model of ore dust and a new practical method for calculation of ore fugitive dust.

KEYWORDS: Ore dust, Wind tunnel, Windblown particles, Regression analysis

1 INTRODUCTION

Wind erosion is a major cause of particulate pollution in the yard of ports [1]. Recently, atmospheric dispersion of wind-blown dust particles from coal piles in the open storage yards has brought about severe air pollution and environmental problems due to fugitive dust emission. Therefore, it is of great importance to analyze the motion of wind-blown particles in order to develop effective means for controlling the particulate pollution.

Studies have been carried out to investigate the mechanisms of wind-blown particles. Bagnold (1941) investigated the wind-induced sand movement in a Libyan desert [2]. Finney (1934) used wind tunnel simulations to investigate snowdrift phenomena [3]. Zingg (1952) investigated the movement of sedimentary materials and particle saltation by means of a wind tunnel test [4].

Coal pile has been the research focus of windblown particles regularity, while few model established for ore pile. There is considerable throughout of ore in most ports, which continued to grow rapidly. Since coal and ore are very different in particle size distribution, density and moisture content, the research on ore windblown particle regularity and the associated coefficient is very urgent.

Wind-induced movement of small particles has been classified into three transport processes: saltation, suspension and surface creep [1]. Saltation is the primary wind erosion mechanism, referring to a bouncing motion of particles. In general, particles with diameters ranging from about 100 to 1000 μm are involved in the saltation process. These particles lift off the surface and travel in curved trajectories under the influence of wind and gravity. The particles engaged in saltation are sufficiently massive that air turbulence has little influence on their motion. The ballistice trajectory of particles undergoing this kind of motion is 5-10 times longer than the maximum height. Most mass transportation occurring near the ground surface is due to saltation [5].

The study carried out s series of wind tunnel experiments and the data collected were analyzed by mathematical methods. Particle size distribution, startup wind velocity, mean velocity and stacked pattern were discussed separately.

2 EXPERIMENTAL APPARATUS AND METHODS

Experiments were performed in a opened blow-out boundary wind tunnel with a test section size of 4.4m (W) × 2.5m (H) × 15.0m (L). Wind tunnel fan speed is controlled in direct mode and the maximum wind speed is 30 m/s. Wind tunnel turbulence intensity is less than 1% and axial static pressure gradient (d*p*/d*x*) is less than 0.01m. Spires and roughness elements were installed along the span wise direction to creat a neutrally buoyant atmospheric boundary layer.

2.1 *Similarity criteria*

Geometry similarity

Geometry similarity is the basic condition of flow similarity. For the wind tunnel test, model scale is the ratio of corresponding length of several similar objects. According to the yard of the actual situation and the wind tunnel size, the model scale of experiment is 1:100.

A schematic diagram of the wind tunnel test section is shown in figure 1(a) and size description of standard ore pile tested in experiments is shown in figure 1(b).

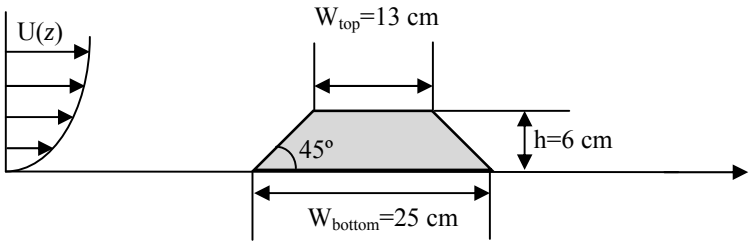

Figure 1(a). Schematic diagram of ore pile settings in the test section of wind tunnel

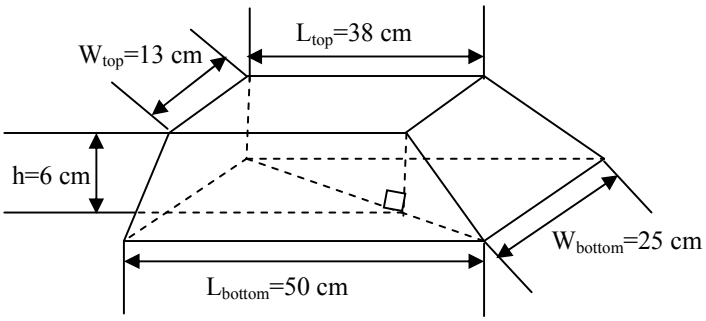

Figure 1(b). Schematic diagram of standard single ore pile size.

Long side of ore pile was set facing the wind stream in the wind tunnel test section in the single pile experiment. On the other hand, settings of ore piles in multi-pile experiments were similar to single pile, but in the 2×2 pattern.

One or four Ore-pile were placed in the middle of test section of the wind tunnel.

Atmospheric boundary layer similarity

Artificial boundary layer was simulated by spires and roughness elements. Expression of the power functions of wind velocity profile deduced by near the ground and neutral stratification and underlying surface conditions as follows:

$u/u_1=(z/z_1)^m$

where u is the mean wind velocity (m/s), u_1 is the wind velocity (m/s) of height z_1 and m is a function of surface roughness and temperature stratification, which values depending on different regions and atmosphere stability.

Renault similarity

In addition to similarity of geometry and atmospheric boundary layer, Renault similarity is also an important prerequisite for the wind tunnel experiments. This study experimental wind velocity range of 4.5~12 m/s meets the Renault similarity requirements.

2.2 *Experimental apparatus*

Ore size distributions were measured by sonic vibration of semi-automatic screening particle size analyzer. ESJ200-4A and YP 200K-1 electronic balance were employed to weight measurement.

2.3 *Materials*

Three typical ore, including Australia ore, Indian ore and Brazil ore, were collected in port of Xiamen. All of ore samples were flattened and natural dried for 20 days in laboratory. Australia ore nature moisture content was 3.8%, while Brazil and Indian ores were 3.5% and 2.9%. Data of size distribution were acquired by particle size analyzer referred above. The size distribution of three ore type is illustrated in Figure 2.

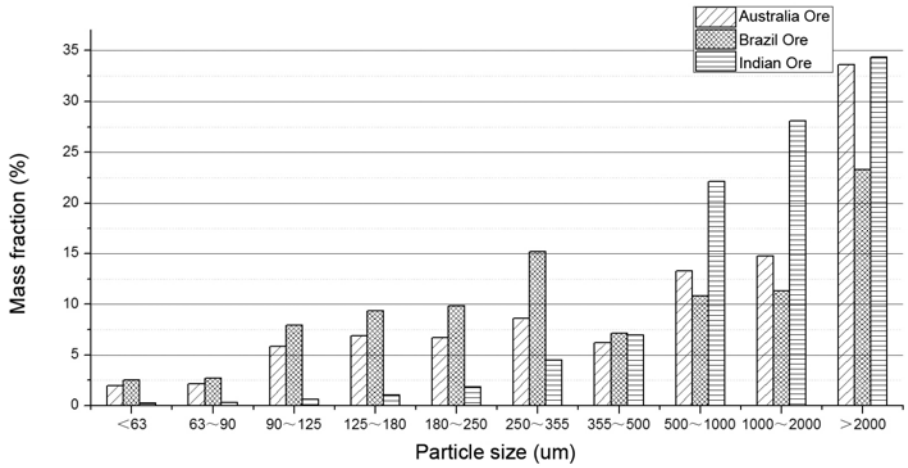

Figure 2. Size distributions of three typical ore

Smaller size was observed in Australia and Brazil ore, while Indian ore dust particle size is larger. This may lead to different dust characteristic, including startup wind velocity and amount of windblown dust. Furthermore, finer particles were observed in Brazil ore samples than Australia ore.

2.4 *Particle startup wind velocity experiments*

Method for the determination of the startup wind velocity as follows:
Ore powder with natural moisture was spread evenly on a sheet as much as possible to avoid surface wrinkles. Digital camera was mounted above the tested ore pile to monitor particle status. Start the wind tunnel, gradually increasing wind velocity and observe the movement of particles at the same time.

The wind velocity was recorded when obvious particles movement was observed. Repeat this test process 5 times to acquire the mean startup velocity for each type of ore. The results of startup velocity are list in table 1.

Table 1. Startup wind velocity for tested ore.

Ore type	Startup wind velocity (m/s)
Australia	4.0
Brazil	4.6
Indian	4.9

2.5 *Windblown experiments*

Each of ore pile put in the wind tunnel for experiment was placed on a thin enough sheet, which weighted together with the ore pile both before and after test. Each test lasted 15 minutes. The test wind velocity (U) includes 4.5, 6, 8, 10 and 12 m/s. weight of ore blown off could be calculated by weight difference.

3 RESULTS AND DISCUSSION

Figure2 shows the relationship between quantity of windblown dust and mean wind velocity, which obtained by regression analysis. With wind velocity increases, the quantity of windblown dust increases rapidly and then slowly.

According to data collected in the wind tunnel experiments of three ores, quantity of windblown dust was deduced as follows:

$Q=A\times(U-U_0)^3$

Where Q is the quantity of windblown dust, A is species coefficient, U is mean wind velocity during an experiment and U_0 is the startup wind velocity of corresponding species. The detailed values are shown in table 2 and the regression curves are illustrated in the figure 3.

Table 2. Coefficient of quantity of windblown dust on mean velocity

Coefficient	Australia Ore	Brazil Ore	Indian Ore
A	0.0206	0.0263	0.0284
U_0	4.0	4.6	4.9

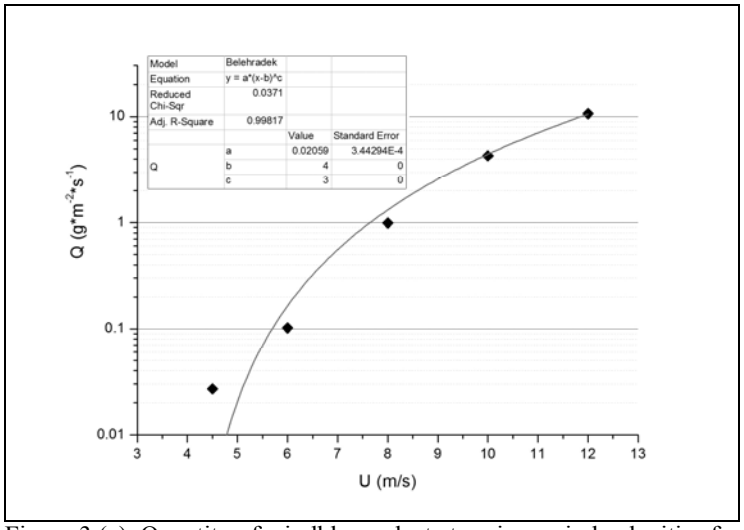

Figure 3 (a). Quantity of windblown dust at various wind velocities for Australia ore.

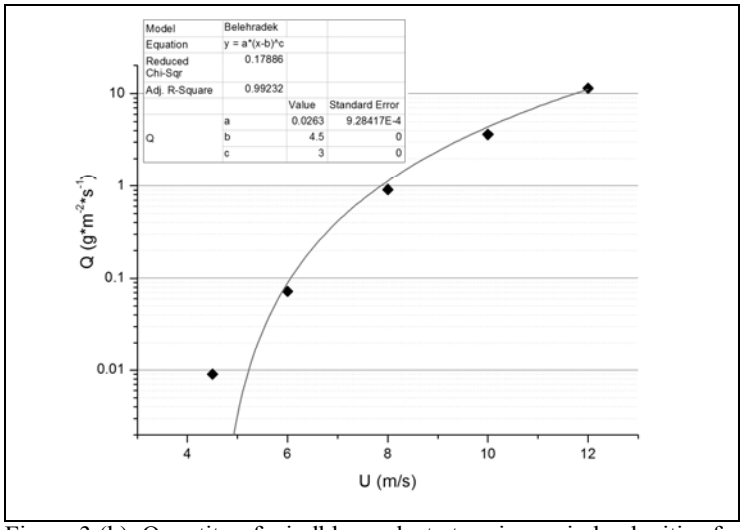

Figure 3 (b). Quantity of windblown dust at various wind velocities for Brazil ore.

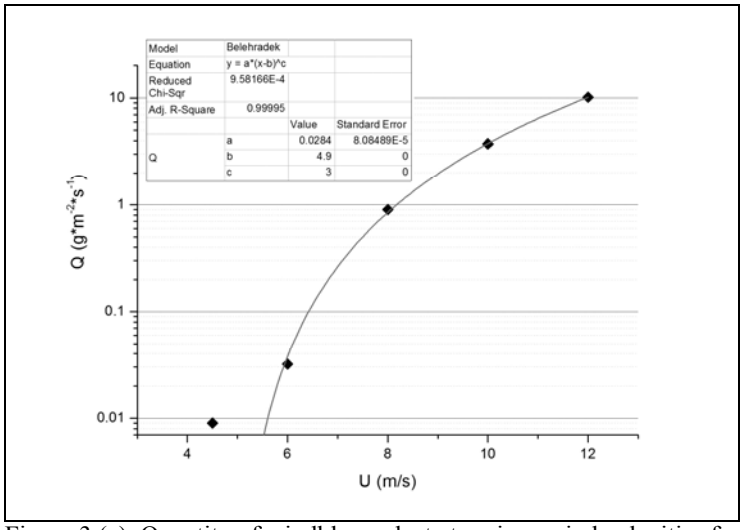

Figure 3 (c). Quantity of windblown dust at various wind velocities for Indian ore.

In the case of ore natural moisture content, similar regularity of windblown dust was observed between Australia and Brazil ore. However, less dust blown off was observed in Indian ore experiment at lower velocity (< 8 m/s). This phenomenon may relate to greater particles than the other two ores.

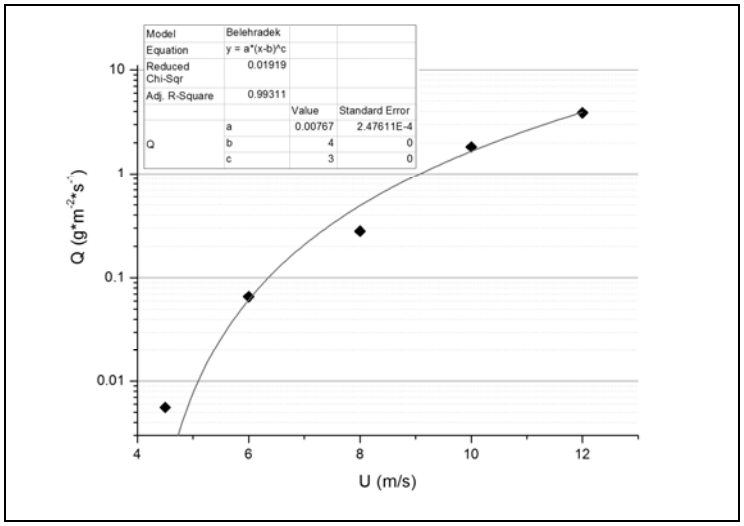

Figure 4. Quantity of windblown dust at various wind velocities for Australia ore.

Figure 4 shows the curve regressed of multi-pile experiment. In this case, the coefficient A value is 0.00767. Contrast to single pile result, only 30% dust was blown off under the same conditions. The result indicated that less dust be blown off in the multi-pile pattern, which may be due to mutual shelter effect of the piles and then reduced wind velocity.

4 CONCLUSION

In this paper, a preliminary study on windblown dust law of different ore was carried out by wind tunnel simulation. Quantity of windblown ore increases with increasing wind velocity, especially when the wind speed is greater than 8 m/s. Expressions were regressed by mathematical

method, which could be used to estimate windblown dust. Because of shelter effect of piles between each other, the quantity of windblown dust of multi-pile is far less than single pile.

REFERENCES

1 S.J. Lee, K.C. Park and C.W. Park, Wind tunnel observations about the shelter effect of porous fences on the sand particle movements, Atmospheric Environment, 36(2002), p.1453-1463.
2 R.A. Bagnold, The physics of blown sand and desert dunes. Mathuen, London, 1941.
3 E.A. Finney, Snow control on the highway, Michigan Engineering Experiment Station (East Lansing), Bulletin No. 57, pp.62.
4 A.W. Zingg, Wind tunnel studies of the movement of sedimentary material. Proceedings of the Fifth Hydraulics Conferences, Vol.34, University of Iowa, pp.111-135.
5 R.J. Kind, Mechanics of Aeolian transport of snow and sand. Journal of Wind Engineering and Industrial Aerodynamics 36, 855-866.

The Seventh International Colloquium on Bluff Body Aerodynamics and Applications (BBAA7)
Shanghai, China; September 2-6, 2012

Aerodynamic stability of road vehicles in dynamic motion

S.Y. Cheng [a], M. Tsubokura [a], T. Nakashima [b], Y. Okada [a,c], T. Nouzawa [c]

[a] *Graduate School of Engineering, Hokkaido University, Japan*
[b] *Graduate School of Engineering, Hiroshima University, Japan*
[c] *Vehicle Testing & Research Department, Mazda Motor Corporation, Japan*

ABSTRACT: A method for dynamic coupling simulation of flow and vehicle motion was developed based on large eddy simulation technique with moving boundary methods. The method was applied to investigate the aerodynamic stability of vehicle under a transient driving situation. A coefficient to quantify the aerodynamic damping was defined. For the sedan-type, simple body models investigated, the underbody provides the highest proportion of aerodynamic damping. However, it is the trunk deck contribution that causes the different damping magnitudes in the models with distinct A- and C-pillar geometrical configurations.

KEYWORDS: Aerodynamics, transient, LES, vehicle, stability, damping, pitching.

1 INTRODUCTION

In principle, automotive aerodynamics comprises the drag, lift, and side force coefficients, in conjunction with the rolling, yawing, and pitching moment coefficients. In real-world situation, the aerodynamic forces and moments which act on a vehicle are of transient nature. However, development of vehicle aerodynamics to date has mainly been focused on the steady-state components, particularly the drag coefficient, C_d. This coefficient can only be used to evaluate performances related to fuel efficiency and top speed, and provides no indication in regard to the vehicle's performance in terms of stability.

To consider the stability factors under the effect of transient aerodynamics, several assessment methods have been proposed in the literature. These methods rely on either drive test (e.g. Howell and Le Good, 1999; Okada et al, 2009) or wind tunnel measurement (e.g. Aschwanden et al, 2006). The former can only be performed after a development mule is produced, while the latter requires a complex test rig to manipulate the vehicle motion for a dynamic assessment. In addition, due to limited numbers of probe that can be attached to the test vehicle without altering the surrounding flow, drive test and wind tunnel measurement provide very limited flow information about the test. The lack of flow information could impede detailed flow analysis which is needed for identifying the underlying mechanism.

To overcome these limitations, thus the main objective of the present study is to develop a numerical method for the assessment of vehicle aerodynamic stability performance under a transient driving situation. The method allows manipulation of vehicle body motion during flow simulation, and quantification of vehicle stability performance on the basis of the aerodynamic damping generated by the vehicle, which is depending on the vehicle's body shape configuration.

2 SIMPLE BODY MODELS

Okada et al (2009) reports that the main differences between the upper body geometry of vehicles with different pitching stability characteristics lie in the A- and C-pillar shapes; the lower stability vehicle has a more angular A-pillar and rounder C-pillar configurations. Hence, to emphasis these differences, the present study creates two simple body models with opposite A- and

C-pillar geometrical configurations. In particular, the model that represents the lower-stability sedan adopts an angular A-pillar and rounded C-pillar configurations. Whilst, the model represents the higher-stability sedan adopts the opposite configurations. For convenience of discussion, the model represents the sedan of lower stability is designated "model A", and the one represents the higher stability sedan is "model B", respectively, hereafter (see Figure 1(a)).
In general, both models are the 1:20-scale, simple bluff-bodies with same height h, width w, and length l measurements of 65, 80, and 210 mm, respectively. The models have A- and C-pillars with the same slant angles of 30° and 25°, respectively, which are based on the configurations of real vehicle.

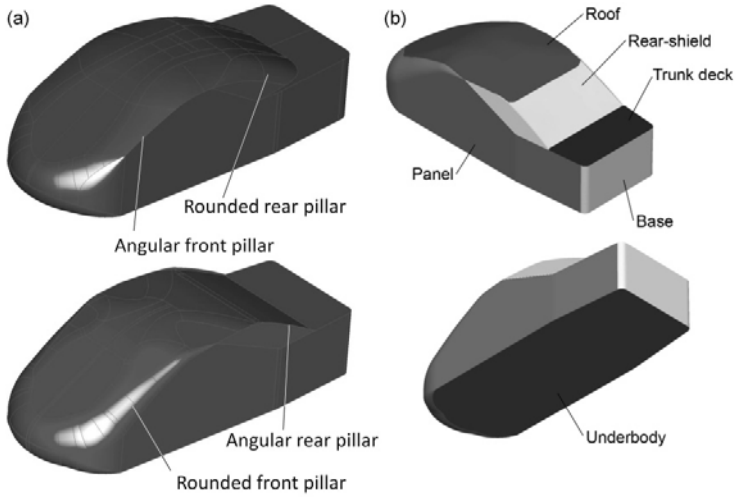

Figure 1. Simple body models: (a) model A (Top) and model B (Bottom); (b) Designations of body part.

3 NUMERICAL METHODS

3.1 *Governing equations*

The LES solves the following spatially filtered continuity and Navier-Stokes equations:

$$\frac{\partial \bar{u}_i}{\partial x_i} = 0 \tag{1}$$

$$\frac{\partial \bar{u}_i}{\partial t} + \frac{\partial}{\partial x_j}\bar{u}_i\bar{u}_j = -\frac{\partial \bar{P}}{\partial x_i} + 2\frac{\partial}{\partial x_j}\left(\nu + \nu_{\mathrm{SGS}}\right)\bar{S}_{ij} \tag{2}$$

$$\bar{P} = p/\rho + \left(\overline{u_i u_j} - \bar{u}_i\bar{u}_j\right)/3 \tag{3}$$

where u_i, p, ρ, ν and S_{ij} are the i-th velocity component, pressure, density, kinematic viscosity and strain rate tensor. The over-bar denotes a spatially filtered quantity. Meanwhile, the standard Smagorinsky model is adopted to model the subgrid-scale (SGS) eddy viscosity ν_{SGS} of Eq. (2).
The simulation software is an in-house CFD code, namely, the "FrontFlow/red-Aero". Originally, the researchers develop the code for the "Frontier Simulation Software for Industrial Science" project. Then, Tsubokura et al. (2009a) optimizes it for vehicle-aerodynamics simulation. Tsubokura et al. (2009b) has validated the code on the basis that the results obtained with the code compared favorably with the wind-tunnel measurements on the pressure distribution along

the centerline of ASMO model and the flow field around a full-scale production car (including a complicated engine room and under-body geometry).

3.2 *Discretization*

The governing equations were discretized by using the vertex-centered unstructured finite-volume method. We adopted the second-order central differencing scheme for spatial derivatives, and exploited the blending of 5% first-order upwind scheme for the convection term for numerical stability reason. Meanwhile, pressure-velocity coupling was preserved by the SMAC (simplified marker and cell) algorithm.
For time advancement, the LES adopts the Euler implicit method. This is because an implicit scheme can accommodate larger time difference than an explicit one without causing numerical instability, especially in the case of a vehicle simulation in which the velocity and mesh size vary strongly. With larger permissible time difference (Δt = 1×10-5 s), the scheme needs lesser time steps (hence, shorter simulation time) to obtain a reliable time- and phase-averaging statistic. Such feature is important in dynamic LES cases, because they normally need over hundred thousand of time steps to obtain an adequate phase-averaging statistic. In the present study, the computations took about 50,000 simulation steps (over five pitching cycle) to reach a stable periodic condition and the subsequent 150,000 steps to covers 15 cycles of pitching oscillation for obtaining an adequate phase-averaging statistic.

3.3 *Computational domain and boundary conditions*

The computational domain resembles a rectangular wind-tunnel test section. Its cross section covers 1.52*l* on both sides of the model and height of 2.23*l*. This set-up produces a small blockage ratio of 1.53%, which is well within the typically accepted range of 5% in automotive aerodynamic testing (Hucho and Sovran, 1993). The model was situated near the domain floor at a ground clearance of 0.071*l*. The inlet boundary was located 3.14*l* upstream, while the outlet boundary was 6.86l downstream.
At the inlet boundary, the air flow approaches at a constant velocity of 16.9 m/s, corresponding to Re of 2.3×10^5 (based on vehicle length *l*). Meanwhile, a zero-gradient condition is imposed at the outlet boundary. The ceiling and side boundaries of the domain were treated with free-slip wall-boundary condition. The ground surface is divided into two zones. The upstream zone (which covers 3*l* from the inlet boundary) is defined as a free-slip wall condition to avoid boundary-layer formation. This setting simulates the wind-tunnel experimental condition, thus ensure the consistency of flow condition between the LES and wind tunnel test so that direct comparison between their results is allowed during validation. The remaining ground and vehicle surface are treated with the logarithmic-law ($y^+ > 11.63$) or linear law functions ($y^+ < 11.63$) depending on the obtained y^+ values. We have found that the very fine spatial resolution adopted produces the $y^+ < 4$ around the vehicle surface, thus the estimation is by the linear law function, which corresponds to the no-slip wall condition.

错误！未找到引用源。FORMULATION OF AERODYNAMIC DAMPING COEFFICIENT

4.1 *Periodic-pitching-oscillation condition*

By employing the ALE technique, we imposed a periodic pitching oscillation on the models during flow simulation to probe their dynamic response. The axis of rotation is located at the lower part of the front section of model at 0.821*l* from the rear end, corresponding to the front-wheel axle of a real vehicle. This setting is in accordance with the road-test results of Okada et al.

(2009), in which the notchbacks experienced more significant ride-height fluctuation at the back than the front. Hence, the models were rotated in a manner that simulates the rear-ride height fluctuation of the real vehicles. The pitch angle θ of the models is defined as:

$$\theta = \theta_0 + \theta_1 \sin\varphi(t) \quad , \quad \varphi(t) = 2\pi f_p t \tag{4}$$

By setting θ_0 and θ_1 equal to 2°, the vehicle models were forced to oscillate at amplitude of 2°. Although this value is larger than the range a vehicle would encounter under normal driving conditions, it has the advantage of producing more distinct aerodynamic damping effect in vehicles of different stability characteristics. Thus make it easier to interpret the underlying physical mechanism. Frequency f_p was 10 Hz, which corresponds to a Strouhal number (St) of 0.13, normalized by l and U_{inlet}. This value was chosen in consideration of the St of 0.15 obtained by road test by Okada et al. (2009). Figure 2 shows the sign convention for aerodynamic pitching moment M and angle θ.

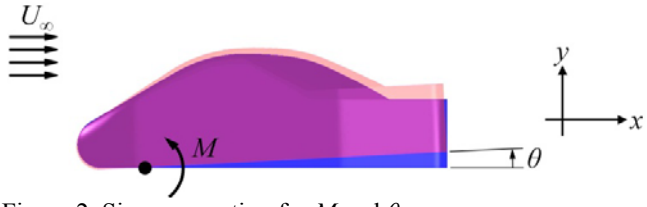

Figure 2. Sign convention for M and θ.

4.2 *Periodic-pitching-oscillation condition*

The estimated phase-averaged pitching moment $<M>_p$ can be decomposed into steady and unsteady components. The equation for phase-averaged pitching moment $<M>_p$ in terms of pitch angle θ is given as the following expansion:

$$< M >_p = C_0 + C_1\theta + C_2\dot{\theta} + C_3\ddot{\theta} \tag{5}$$

where, respectively, the single dot and double dots in the third and fourth terms indicate the first and second derivatives with respect to time t. Both C_0 and C_1 are static components; the former denotes the pitching moment M at zero pitch, while the latter describes the quasi-static behavior by taking into account the pitch-angle variation in a static manner. C_2 is associated with aerodynamic damping, and C_3 is an added moment of inertia that is proportional to angular acceleration.

Substituting Eq. (4) into (5) and rearranging gives:

$$< M >_p = \left(C_0 + C_1\theta_0\right) + \left[C_1 - \left(2\pi f_p\right)^2 C_3\right]\theta_1 \sin\varphi(t) + 2\pi f_p \theta_1 C_2 \cos\varphi(t) \tag{6}$$

The above equation can then be rewritten by using new parameters, namely, M_{stat}, M_{dis} and M_{ang} as

$$< M > p = M_{\text{stat}} + M_{\sin}\sin\phi(t) + M_{\cos}\cos\phi(t) \tag{7}$$

where, M_{stat} is a constant, which set the baseline for the $<M>_p$. M_{dis} is the amplitude of the term which in-phase with the imposed pitching displacement, and M_{ang} is the amplitude of the term in-phase with the angular velocity.

4.3 *Definition of aerodynamic damping coefficient*

During one pitching cycle, time t varies from 0 to $2\pi/\omega$. Hence, the work done by the aerodynamic pitching moment M on the vehicle model during one pitching cycle is:

$$W = \frac{1}{\omega}\int_0^{2\pi} M \ \frac{\mathrm{d}\theta}{\mathrm{d}t}\mathrm{d}(\omega t) \tag{8}$$

Substituting Eq. (7) and (10) into eq. (11), the work done during one pitching cycle becomes

$$\begin{aligned} W = {} & M_{\mathrm{stat}}\theta_1 \int_0^{2\pi} \cos\omega t \ \mathrm{d}(\omega t) \\ & + M_{\mathrm{dis}}\theta_1 \int_0^{2\pi} \sin\omega t \cos\omega t \ \mathrm{d}(\omega t) \\ & + M_{\mathrm{ang}}\theta_1 \int_0^{2\pi} \cos\omega t \cos\omega t \ \mathrm{d}(\omega t) \end{aligned} \tag{9}$$

The first and second integrals yield the value zero, and that the third one is π. Hence, the net work per pitching cycle is:

$$W = M_{ang}\theta_1\pi \tag{10}$$

The result of the integration reveals that the net work done on the vehicle by aerodynamic pitching moment M over a pitching cycle is depends on the component in-phase with the angular velocity M_{ang}. In Eq. (10), θ_1 and π are given. Hence, the parameter M_{ang} reflects the dynamic response of the vehicle. This parameter can be presented in a non-dimensional form. If normalized in a similar manner to the pitching-moment coefficient, it becomes:

$$C_{\mathrm{AD}} = \frac{M_{\mathrm{ang}}}{\frac{1}{2}\rho U_\infty^2 A l_w} \tag{11}$$

where ρ, U □ , A, and l_w are fluid density, mainstream velocity, vehicle frontal area, and wheelbase. It depends on the sign of C_{AD}, a negative value implies a tendency for aerodynamics to damp the pitching oscillation, whereas a positive value enhances the vehicle motion (i.e. negative damping). The coefficient thus enables quantitative evaluation of vehicle stability; therefore, it is termed "aerodynamic-damping coefficient."

5 RESULTS AND DISCUSSIONS

5.1 *Aerodynamic damping coefficient of simple body models*

Figure 3 shows the $<M>_p$ as a function of phase angle φ for models A and B. The coefficients in Eq. (7) are obtained by fitting the equation to the $<M>_p$ data set by nonlinear least squares regression. Solid lines in Figure 3 are the fitted functions for the two models. Table 1 summarizes the corresponding C_{AD} for comparison. As shown in the table, the aerodynamic damping coefficient C_{AD} for the two models are negative, implying a tendency to resist the pitching motion. Between them, however, model B has a higher aerodynamic-damping coefficient C_{AD}, by about 37%. This finding is consistent with the fact that model B was created on the basis of the pillar-shape configurations of real vehicle with higher stability.

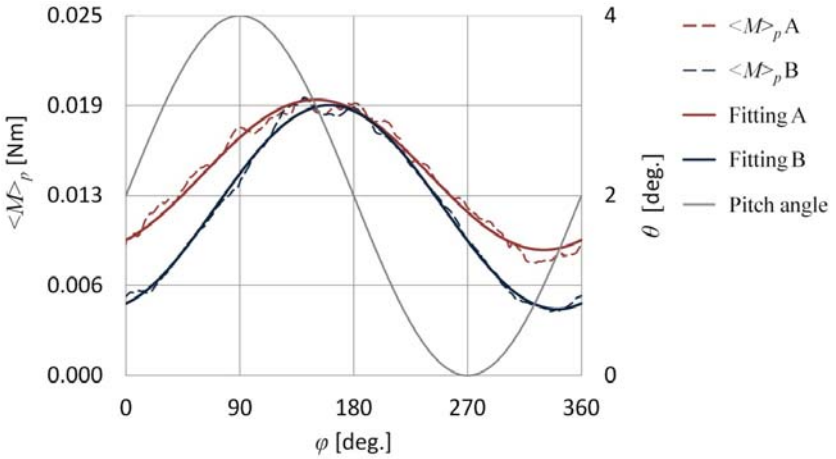

Figure 3. Phase-averaged M and fitted functions.

Table 1. Aerodynamic damping coefficient C_{AD}

Body part resignations	Model A	%	Model B	%	diff	%
Underbody	-0.0309	78.6	-0.0347	60.6	-0.00376	21.0
Trunk deck	-0.00205	5.2	-0.0100	17.5	-0.00795	44.4
Rear-shield	-0.000350	0.9	-0.00709	12.4	-0.00674	37.7
Roof	-0.00658	16.7	-0.00607	10.6	0.000513	-2.9
Base	0.000162	-0.4	0.000128	-0.2	-0.0000342	0.2
Panel	0.000376	-1.0	0.000453	-0.8	0.0000769	-0.4
Overall	-0.0394	100.0	-0.0573	100.0	-0.0179	100.0

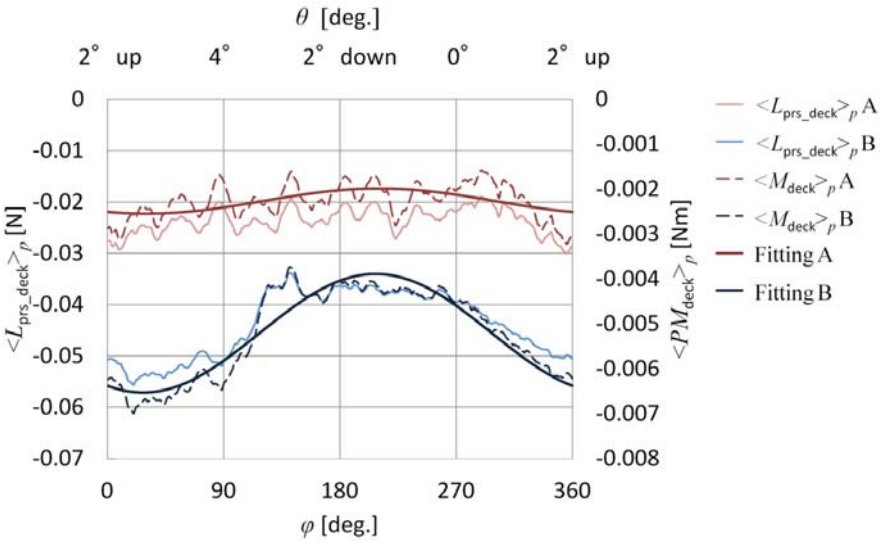

Figure 4. Phase-averaged M and fitted functions.

In general, as shown in Table 1, the main contribution in model A, which was created based on the characteristic aerodynamic features of lower stability sedan, is from the underbody and roof. Whilst, the main contribution in model B is from the underbody, upper rear section (i.e. trunk deck and rear shield) and roof. The reason for the models to have a different damping magnitude is because of the relatively high damping contribution from the upper rear section of model B,

particularly the trunk deck. Figure 4 shows that the curves of trunk deck fitted function of the two models have very similar phase shift. However, the relatively low trunk deck contribution in model A is caused by the smaller fluctuation amplitude.

5.2 *Aerodynamic damping mechanism*

5.2.1 *Main aerodynamic damping contribution*

The underbody has the highest damping contribution due to two reasons: First, the dynamic effect, i.e. vehicle motion, has caused the phase of phase-averaged underbody pitching moment $<M_{underbody}>_p$ curve to shift (by about 128° and 134° in model A and model B, respectively) at the pitching oscillation frequency (see Figure 5), thus produces a negative M_{ang}; Second, its relatively large surface area and moment arm produce a significantly larger M_{ang} magnitude then other body parts.

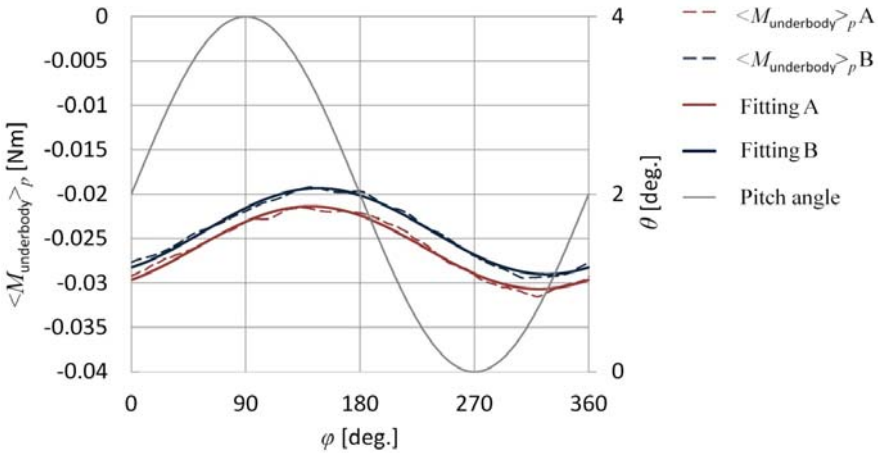

Figure 5. $<M_{underbody}>_p$ and fitted functions of underbody: (a) Model A; (b) Model B.

The behavior of $<M_{underbody}>_p$ curve can be explained by first considering the quasi-steady flow conditions with the model fixed at a range of pitch angle θ. As the underfloor clearance downstream of the pitch axis increases with θ, the flow decelerates and causes the static pressure to rise. The increase of static pressure with increasing θ causes a corresponding increase in underbody pitching moment. Hence, in the quasi-steady conditions, the maximum and minimum peaks would lie at 4° and 0° pitch, respectively. However, due to the pitching motion of models, there is an additional dynamic effect which causes the curve to overshoot. Figure 6 shows the properties of airflow in the underfloor clearance of model B at four pitching stages (similar trend is obtained in model A, thus only the results of model B is used for the discussion). As the underbody moves downwards from 4° pitch, the decreasing underfloor clearance is accompanies by flow acceleration, which may be evident by the relatively high streamwise velocity component during the 2° tail-down pitching cycle. However, the static pressure of underbody increases despite the acceleration of streamwise velocity component. In addition, for the same underfloor clearance at 2° tail-up and tail-down pitching cycles, the former exhibits a relatively strong cross flow velocity. Hence, it may be deduced that the increment of static pressure during a tail-down pitching cycle is caused by the conversion of cross flow kinetic energy into the dynamic pressure at the underbody. Meanwhile, the further decrement in static pressure during the tail-up pitching cycle is associated with "suction" effect (i.e. surrounding fluid is being "pull" away) the leeward side of a bluff body immersed in a flowing fluid would normally experienced, as the underbody surface is now at the leeward side.

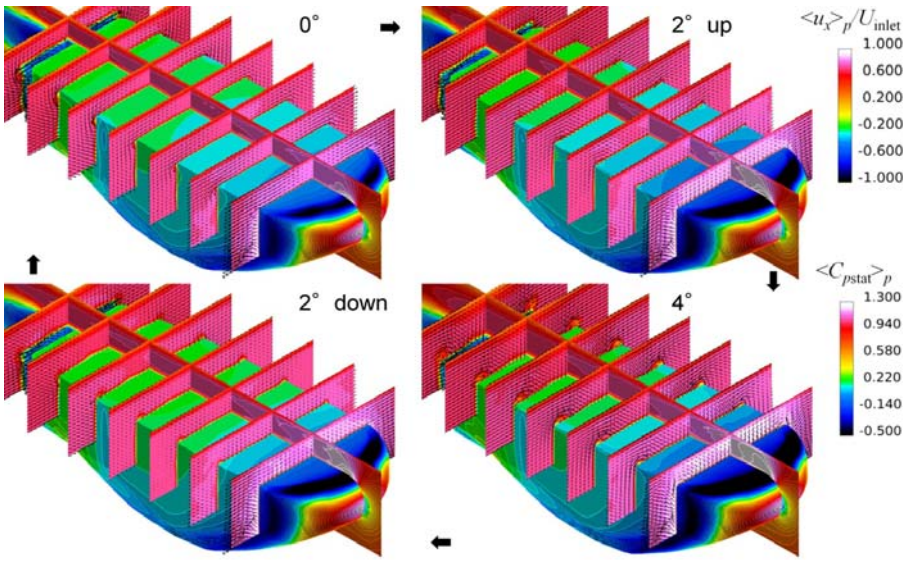

Figure 6. Phase-averaged velocity distribution at underfloor clearance and static pressure of underbody; model B.

5.2.2 *Comparison between two aerodynamic configurations*

Figure 4 shows that the phase-averaged trunk deck pressure lift $\langle L_{prs\_deck} \rangle_p$ and phase-averaged trunk deck pitching moement $\langle M_{deck} \rangle_p$ curves of the two models are matching well, implies that the $\langle M_{deck} \rangle_p$ is mainly caused by the trunk deck surface static pressure. Ideally, the pressure force should be in-phased with the angular velocity of pitching to produce a maximum damping. That is, the $\langle L_{prs\_deck} \rangle_p$ peaks at φ = 180°, and reaches the minimum at φ = 0 or 360°. The $\langle L_{prs\_deck} \rangle_p$ curves for the two models nearly meet this criterion, with only a slight phase shift. Hence, the C_{AD} obtained from the two models are having the same sign. However, the relatively large fluctuation range in model B has resulted in a higher damping magnitude.

Next, we discuss the reasons that cause the trends observed in Figure 4. As shown, model B has a relatively low attainable $\langle L_{prs\_deck} \rangle_p$, which is caused by its concentrated C-pillar vortices (marked "B" in Figure 7). The concentrated vortices induced a narrow, low-static-pressure region at the sides of its trunk deck (marked "A" in Figure 7). In contrast, the C-pillar vortices in model A were weaker and less concentrated (marked "D" in Figure 7). As a result, the vortices induced a wider low static pressure region (marked "C" in Figure 7), which results in the higher attainable $\langle L_{prs\_deck} \rangle_p$ in model A.

At φ = 0 or 360°, $\langle L_{prs\_deck} \rangle_p$ in the two models were at the lower range, which was due to the increase of static pressure at the sides of trunk deck (i.e. the low pressure region narrows down). This tendency is caused by the decrease in the slant angle of C-pillar during tail-up pitching cycle. Hence, the models generate the weaker C-pillar vortices which diminish the drop in static pressure.

At φ = 90°, the C-pillar vortices in model A were elevated by the trunk deck surface, thus its distance from A-pillar vortices (marked "E" in Figure 7) decreases (see Figure 7). These two pillar vortices, which rotate in directions opposite one another, interact with each other and generate a strong cross flow which passing through them and rolled upwards at the centerline, forming an upwash inducing, circulatory structure (marked "F" in Figure 7). Due to the strong cross flow and the upwash inducing circulatory structure, the static pressure in the central region drops and causes the $\langle L_{prs\_deck} \rangle_p$ in model A to rise.

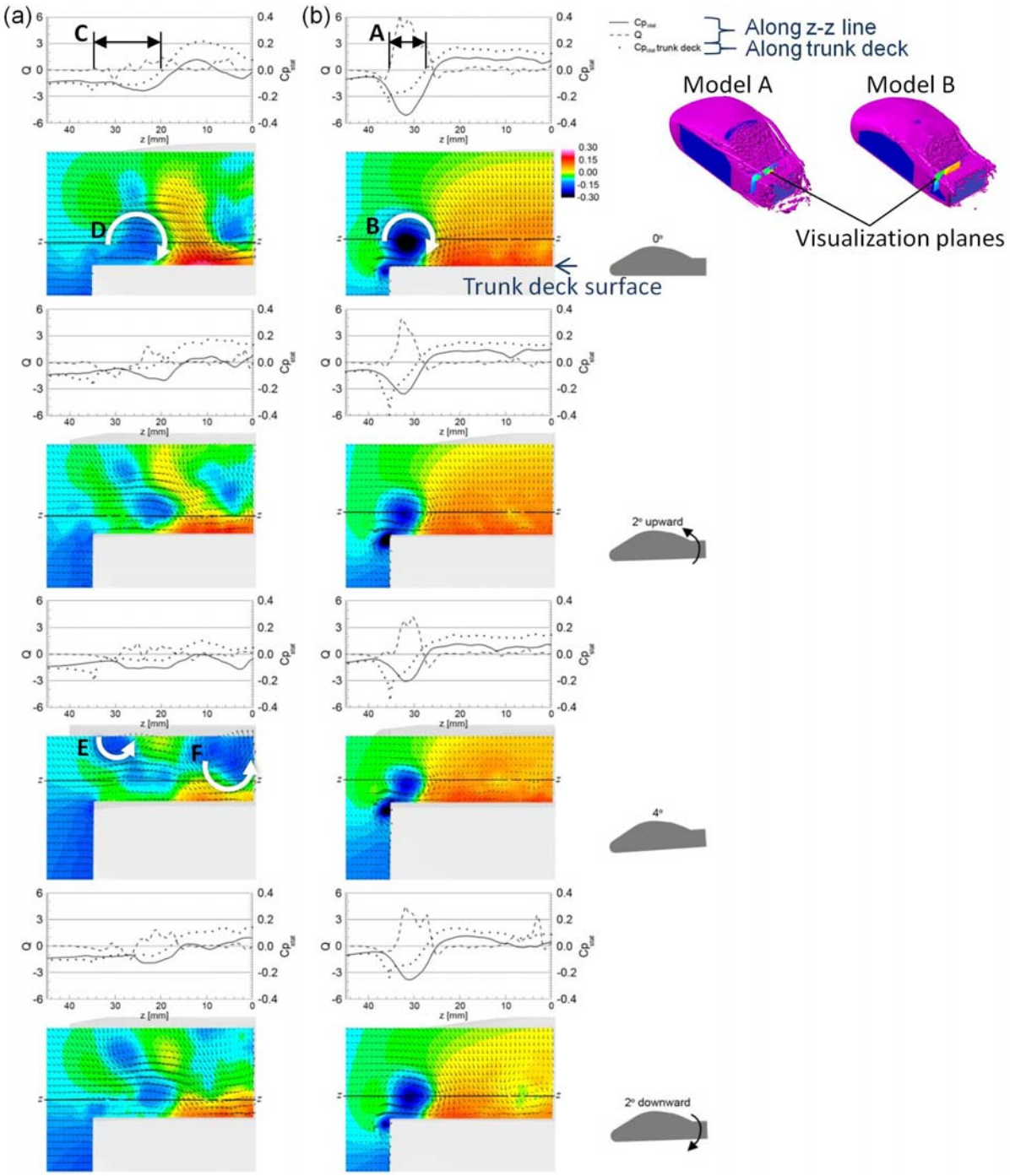

Figure 7. Distribution of cross flow velocity and static pressure above trunk deck at four different pitching stages: (a) Model A; Model B.

At φ = 180 and 270°, $<L_{prs\_deck}>_p$ in the two models are at the higher range. The higher $<L_{prs\_deck}>_p$ in these instances was mainly caused by the decrease of static pressure at the sides of trunk deck. The slant angle of C-pillar increases with decreasing pitch angle. Hence, during the tail-down pitching cycle, the models generate the stronger C-pillar vortices which result in larger pressure drop on the trunk deck surface.

Although the models share the same tendency in how the C-pillar vortices affect the surface pressure at the side of trunk deck, but the distinct flow topology in the central region has caused the $<L_{prs\_deck}>_p$ curves to behave differently at $\varphi = 180°$. In model A, despite the larger pressure drop at the side, the $<L_{prs\_deck}>_p$ failed to reach a much higher value because of the increased of static pressure in the central region. This increment is caused by the attenuation of cross flow velocity and circulatory structure with decreasing pitch angle. As has been discussed earlier, with decreasing pitch angle, the gap between the A- and C-pillar vortices becomes larger, and thus their interaction which promotes the cross flow, becomes weaker. In model B, however, the drop in static pressure in the central region is due to the formation of the circulatory structure, and the dynamic effect (i.e. low static pressure at the leeward side) has caused the $<L_{prs\_deck}>_p$ to further increase. This produces the relatively large M_{ang}, and hence, a higher damping coefficient.

6 CONCLUSIONS

The present study has shown the potential use of LES as a tool to assess the aerodynamic stability of vehicle which takes into account the effect of transient aerodynamics. The proposed aerodynamic damping coefficient enables direct comparison of aerodynamic stability performance between two vehicle. For the simple body models investigated, the underbody provides the highest proportion of aerodynamic damping. However, it is the trunk deck contribution that causes the different damping magnitudes in the models with distinct A- and C-pillar geometrical configurations.

7 ACKNOWLEDGEMENTS

This work was supported by the 2007 Industrial Technology Research Grant program from the New Energy and Industrial Technology Development Organization (NEDO) of Japan. Development of the base software FFR was supported by the FSIS and “Revolutionary Simulation Software (RSS21)” projects sponsored by MEXT, Japan. The first author’s Ph.D. program is sponsored by Ministry of Higher Education and Universiti Teknikal Malaysia Melaka, Malaysia.

8 REFERENCES

1 J. Howell and G. Le Good, The influence of aerodynamic lift on high speed stability, SAE Paper No 1999-01-0651.
2 Y. Okada, T. Nouzawa, T. Nakamura and S. Okamoto, S., Flow structure above the trunk deck of sedan-type vehicles and their influence on high-speed vehicle stability 1st report: On-Road and Wind-Tunnel Studies on Unsteady Flow Characteristics that Stabilize Vehicle Behavior, SAE Paper No. 2009-01-0004.
3 P. Aschwanden, J. Müller, and U. Knörnschild, Experimental study on the influence of model motion on the aerodynamic performance of a race car, SAE Paper 2006-01-0803.
4 M. Tsubokura, T. Nakashima, K. Kitoh, Y. Sasaki, N. Oshima, and T. Kobayashi, Development of an Unsteady Aerodynamic Simulator Using Large-Eddy Simulation Based on High-Performance Computing Technique, SAE International Journal of Passenger Cars; Mechanical Systems, 2-1 (2009a) 168-178.
5 M. Tsubokura, T. Kobayashi, T. Nakashima, T. Nouzawa, T. Nakamura, H. Zhang, K. Onishi, N. Oshima, Computational visualization of unsteady flow around vehicles using high performance computing, Computers & Fluids, 38 (2009b) 981-990.
6 W-H. Hucho, G. Sovran, Aerodynamics of road vehicles. Annual Review of Fluid Mechanics, 25 (1998) 485-537.

The Seventh International Colloquium on Bluff Body Aerodynamics and Applications (BBAA7)
Shanghai, China; September 2-6, 2012

Large Eddy Simulation of the flow around a train passing a stationary freight wagon

Yebo Liu [a], Hassan Hemida [b], Zhiming Liu [a]

[a] *School of Mechanical, Electronic and Control Engineering, Beijing Jiaotong University, Beijing, China*
[b] *School of Civil Engineering, University of Birmingham, Birmingham , UK*

ABSTRACT: The aerodynamic performance of a stationary double-stacked freight wagon passed by a high speed passenger train was investigated using Large-Eddy Simulation (LES). The passenger train was a 1/20 scaled model of the ICE2-like shape high speed train, consisted of nose, two coaches, inter-carriage gap and tail. The simulation was performed at Reynolds number of 2×10^5 based on the speed and height of the passenger train. To isolate the effect of the mesh resolution on the LES results, three different LES computations were performed using three different meshes: course, medium and fine, consisted of 3.2 million, 6.9 million, and 9.0 million nodes, respectively. The aerodynamic loads on the freight containers and passenger train were obtained during the passing process. High side force coefficient was observed on the containers when the passenger train approaches the freight wagon followed with a sudden reduction. The near wake flow of the passenger train generated suction side forces, which is followed by a significant increase in side force in the far wake flow. Similar behavior was noticed in the lift and drag coefficients. The effect of track spacing was investigated by performing simulations at two different track spacings: 3.5m and 4m. The results showed that reduction in track spacing generally increased the aerodynamic forces on both the freight wagon and passenger train.

KEYWORDS: LES, Train aerodynamics, Sliding mesh, Aerodynamic coefficients, Train pressure pulses, Train passing

1 INTRODUCTION

Freight trains with double-stacked containers are used worldwide (such as North America, China and Australia) for their high loading capacity compared to single-stacked freight trains. However, high loading capacity also means a relatively large volume and a correspondingly large exposed surface area and hence side forces when exposed to cross winds [1]. Apart from larger drag force than that of passenger trains, the increase side force in the cross wind induces more critical aerodynamic problems, such as overturning or derailment, especially when the containers are empty. A recent example is the derailment of freight train 3DA2K near Tarcoola, SA, in 2006 [2]. Although the train was travelling at a relatively low speed of 67km/h, two double stacked wagons derailed, primarily because of a strong wind gust. As a consequence, 15 of the 31 wagons subsequently detached. Another example of these accidents was in 2008, when two empty single-stacked containers were blown off the freight train 4E90 by aerodynamic force [3].

To assess the aerodynamic performance of freight trains, various researches have been carried out. Li and Tian [4] and Watkins et al [5] have found out that there is a significant effect of the inter-car gaps in the aerodynamic performance of freight trains. Smaller inter-car gaps or reducing the inter-car gaps by placing smaller containers in between can reduce the drag force effectively. Xiong and Liang [6] have conducted an experiment on a full scale double-stacked con-

tainer trains passing through the tunnel and found that the drag force of the freight train significantly increases at the entrance of the tunnel and continuously drops thereafter. They have also concluded that the drag force is proportional to the square of the train speed. Another issue is the aerodynamic response of the freight train when subjected to crosswinds. Hemida and Baker [7] investigated the flow around a freight wagon subjected to a side wind of 90° yaw angle using Large Eddy Simulation (LES) and they showed that the flow topology in the wake of the wagon is much more complex than that around passenger trains. Alam and Watkins [8] came to the conclusion that crosswinds have significant effect on the lateral stability of double-stacked wagons. Baker et al [9] have integrated the aerodynamic forces into train modeling to study the critical wind speed for both passenger and freight trains in regard to derailment. However, strong winds are not the only cause of side wind problems, as the passing of high speed trains produces strong winds and pressure pulses generated in the slipstream. These winds and pressure can add additional challenge to the stability of double stacked containers.

Mancini and Malfatti [12] conducted a full scale study of a high-speed ETR 500 train, passing another ETR 500 train and a freight train in open air. The results showed that the magnitude of pressure pulses are dramatically reduced on the roof and the side not facing the passing train compared to the active side. Johnson and Dalley [13] conducted a physical experiment using a 1/25 scale model on a moving model rig. Their results were consistent with the ones gained from the full scale experiments of Mancini and Malfatti [12]. By performing over 60 firings, it was confirmed that the pressures varied linearly with the square of the train speed and that, increasing track spacing led to a decrease in pressures regardless of the nose shape. Li and Liu [14] gained the formulae for calculating the amplitude of the air pressure pulse according to the track spacing and train velocity, by simulating about 100 operating cases for CRH3 high speed train, including 6 track spacings (from 4.26 m to 5.26 m) and 38 speeds of train passage (from zero to 500 km/h). Other formulae are in the literature [15-16]. These formulae differed from one author to another, but they all came to the same conclusion, that a higher speed and a closer track spacing cause higher pressures. The risk of derailment of double-stacked container trains passed by high speed trains has been assessed by combining CFD simulation with a vehicle dynamic model by Holmes and Schroeder [17] but they haven't considered track spacing effect. Full scale measurements of a high speed train passing a stationary double-stacked container wagon were also carried out by MacNeill et al [18], in which pressures at different positions of the wagon were measured at different speeds. They have showed that the surface pressure increases with increasing the train speed. There is however limited information on the effect of track spacing on the aerodynamics of freight trains passed by high speed passenger trains and thus these is a necessity for research into this area to improve operational safety of the rail network as a whole.

The work detailed in this paper, thus, studies the aerodynamic performance of a stationary double-stacked freight wagon passed by a high speed passenger train using LES. Two track spacings of 3.5m and 4m were considered. The accuracy of LES was investigated through performing three different computations using three different meshes and by comparing the results with available experimental work. The computational package CFX5 is utilized to simulate the passing train using the sliding mesh technique.

2 TRAIN MODELS

The models used in this work are a 1/20 scale of a high speed ICE2-shape passenger train and a double-stacked freight wagon. The high speed passenger train is shown in Figure 2(a). The model is simplified by omitting the bogies and protruding equipment (such as the pantograph), while the inter-carriage gap, nose and tail are kept. The ICE2-like shape train consists of a lead-

ing car and an end car with height of h = 0.179m, width of 0.84h and total combined length of 14.81h. The leading car is separated geometrically as two parts, the head and car 1. Accordingly, the end car is also separated as two parts, the tail and car 2. The clearance between the train and the floor is 0.24h. The double-stacked wagon, shown in Figure 2(b), has top and bottom containers, both with the same width of 0.70h. The length and height of the top container are 5.0h and 0.73h, respectively, while the corresponding dimensions for the bottom container are 3.35h and 0.36h, respectively. The clearance between the wagon and the floor is 0.16h.

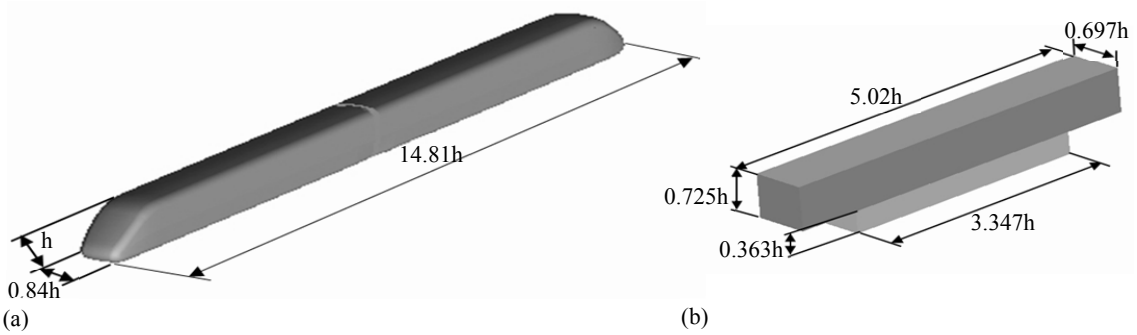

(a) (b)

Figure 2. (a) ICE2-like shape train model. (b)Double stacked wagon mode

3 COMPUTATIONAL DOMAIN AND BOUNDARY CONDITIONS

The computational configuration consists of two domains: stationary and rotating. The coordinate system is shown in Figure 3, where X points to stream-wise direction, Y points to span-wise direction and Z points to the upward direction. The length and width of the domain is 83.678h and 6.35h respectively, with the rotating domain having a downstream length of 22h from the tail of the high speed train. The distance between the freight wagon and the passenger train in the stream-wise direction is 23.44h while two different track spacings are modeled (3.5m and 4m) in the span-wise direction. There is an extension of approximately 3h for the stationary domain in the span-wise direction while it is 5.26h for the rotating domain (see Figure 3(b)). To simulate a train passing event, the rotating domain follows the path of a curve with radius of 5587howards the stationary domain (see Figure 4). A radius of 5587h is chosen here so that the passing event approximates a straight line. The angular velocity is defined equivalently to the moving train speed of 20m/s, which corresponds to a Re of $2x10^5$ based on the height and speed of the moving train.

No-slip boundary conditions are applied on the surfaces of both the train and the wagon, as well as on the floor of the stationary domain. Symmetrical boundary conditions are employed on the roof and sides (normal to the span-wise direction) of the computational domain while translational periodicity is used at inlets and outlets. A counter rotating wall boundary condition is applied on the floor of the rotating domain to suppress the early build-up of the upstream boundary layer. The transient general grid interface (GGI) is employed between the two domains for exchanging information at each time step. Both stationary and moving domains are initialized by zero velocity at the start of the simulation. Considering the length of the computational domain and the train speed, a time step of 0.0001s is applied, which allows the model to capture more details of the air flow for the simulation time of 0.5s. This covers the complete procedure of high speed train approaching, passing and leaving the freight wagon. The viscous diffusion and subgrid fluxes are approximated by a second order accurate central difference scheme for better accuracy in boundary layers.

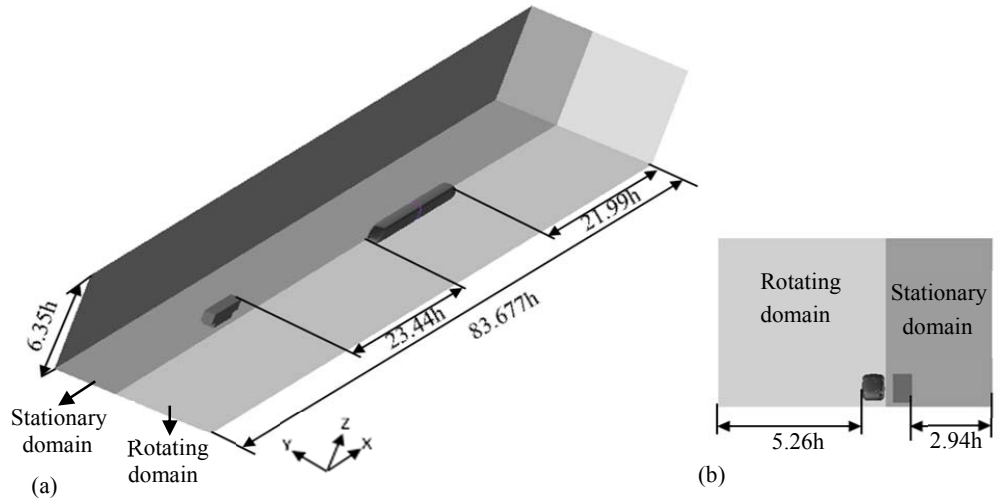

Figure 3. Computational domain showing dimensions of the rotating and stationary domains

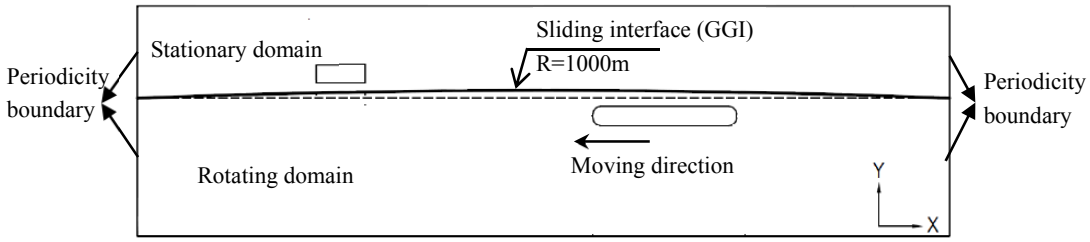

Figure 4. Realization of the train passing event

4 RESULTS

This section reports the LES results for the aerodynamic performance of the freight wagon passed by the ICE2-like shaped train. The passing speed is 20m/s, which corresponds to a Re of 2×10^5 based on the height and speed of the train. The flow can therefore be considered turbulent with the aerodynamic coefficients being independent of Reynolds number. Aerodynamic coefficients are analyzed for three scenarios with two different track spaceings: 3.5m and 4m, for both the wagon and the passenger train.

5.1 *Assessment of the numerical accuracy*

To simulate the train passing event, GGI frame change connections are used in the simulation. There are three types of GGI frame change connection models available in CFX: Frozen Rotor, Stage and Transient Rotor-Stator. Since the transient interaction effects at the sliding interface are of interest to this research, the Transient Rotor-Stator model is applied, which predicts the true transient interaction of the flow between the stationary and rotating domains. This is also the reason for choosing the curved sliding interface (See Figure 4).

To assess numerical accuracy, three computations were carried out for the track spacing of 3.5m based on different meshes: coarse, medium and fine, which contain 3.2 million, 6.9 million, and 9.0 million nodes, respectively. The ICEM-CFD package is employed to generate the hexahedral type meshes. The two domains (rotational and stationary) are meshed separately since a

sliding mesh technique is adapted to simulate the passing event. An O-type grid is deployed around the ICE2-shape train to generate a smooth mesh in all directions, as shown in Figure 5 (a), whilst the H-type grid is adapted everywhere else in the model. To reduce computational cost the hyperbolic stretching meshing law was applied in the upward direction to make the mesh coarser in the regions further away from the model area of interest (see Fig. 5 (b)). The same logic is applied in the span-wise direction. The stretching ratio in both directions is kept within 2.0. A uniform meshing law is applied in the stream-wise direction. To ensure both sides of the interface have similar mesh revolutions, the maximum ratio between the largest and the smallest cell in this direction was about 1.6 in both domains. This increases the accuracy of information transferred through the interface. A constant time step of 1×10^{-4} s is used throughout the entire simulation.

The aerodynamic coefficients: drag coefficient (C_D), side force coefficient (C_S) and lift coefficient (C_L), are defined as:

$C_D = \frac{\int p_s dA_x}{0.5\,\rho\,A\,V^2}$, $C_S = \frac{\int p_s dA_y}{0.5\,\rho\,A\,V^2}$ and $C_L = \frac{\int p_s dA_z}{0.5\,\rho\,A\,V^2}$, respectively, where p_s is the surface pressure, A_x, A_y and A_z are projected surface areas in the X, Y and Z directions, respectively. A is the reference area, chosen as 10 m^2 for the full scale dimensions. ρ is the air density.

Figure 6 shows C_S values of the top container using three different meshes against the distance between the freight wagon and the passenger train. The distance of 0 m corresponds to arrival of the passenger train at the wagon whilst the distance of around 3.56 m refers to when the high speed train just leaves the wagon. With the approach of the high speed train to the freight wagon, the Cs of the top container increases, with the first positive peak occurring just after the high speed train arrives. Following this, the gradient falls sharply to a trough which is of similar magnitude to the first peak, but of negative value. This all occurs within the relatively short time of 0.05s. The next positive peak displayed in Figure 6, follows on the heel of another negative through when the tail of the train leaves the wagon. Both the latter peaks are of smaller magnitude than the former two, indicating that the influence of the head of the train on C_S is stronger than the tail of the train. These results are consistent with both experiments and numerical simulations [12-14]. Figure 6 also shows that the Cs values gained from the fine mesh are in good agreement with the ones gained from the medium mesh, meaning that no mesh refinement is needed. To reduce the computational cost, a medium mesh is used to perform the LES for the track spacing of 4m.

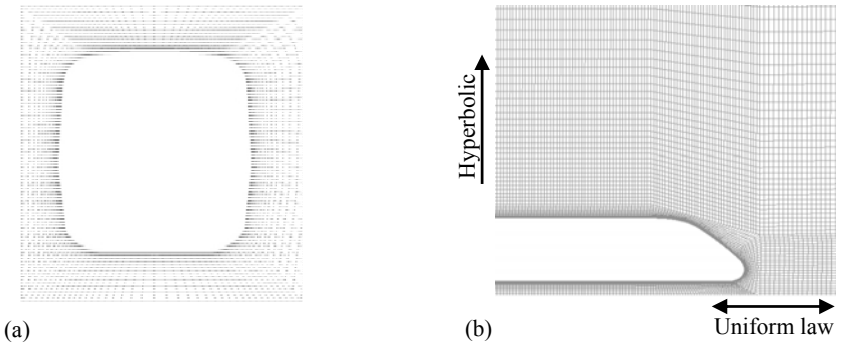

Figure 5. The fine mesh around the ICE2-like shape train (a) The O-type grid around the train (b) Hyperbolic law in the upward direction and uniform law in the stream wise direction

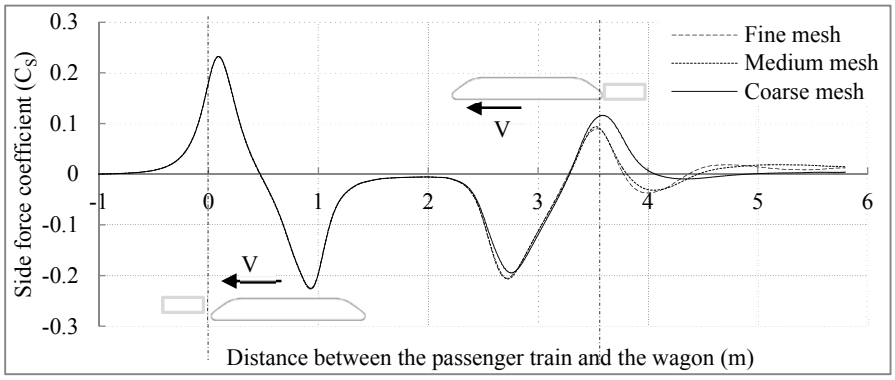

Figure 6. Side force coefficients of the above container from three different meshes

5.2 *Passing phenomena and the effect of track spacing on the wagon*

To assess the influence of different track spacings on the wagon, the aerodynamic coefficients, C_S, C_D and C_L, were obtained for track spacings of 3.5m and 4m.

Figure 7 (a) and (b) show the side force coefficient on the top and bottom containers, respectively, for different track spacings (TS) against the distance between the passenger train and the freight wagon. For the top container, both track spacings show a similar trend in Cs, with the first pulse caused by the approaching of the head of the train while the leaving of the tail of train causes the second pulse, but of smaller amplitude than the preceding one. The positive peak presents a lateral push force to the container whereas the negative one means a lateral pull force. These push-pull forces reduce the lateral stability of the wagon and could potentially lead to derailment. Generally, larger track spacing induces smaller C_S values, and this effect is highlighted in the peaks and troughs of the data, with a 20% decrease in amplitude evident at these points, while the differences are negligible between the two pulses. Similar information is displayed in Figure 7 (b) for the bottom container. However, the peak values of Cs are considerably smaller than the corresponding ones for the top container. In according with Equation (8), this variation is due to the difference in the pressure distribution p_s, and the fact that, the top container has larger area (A_y) than the bottom container. Figure 8 shows the pressure distribution on the side surfaces of the containers when the train arrives. The dark color represents areas of high pressure, most of which is located at the front part of the top container and is the reason for the high side force coefficients in Figure 7 (a).

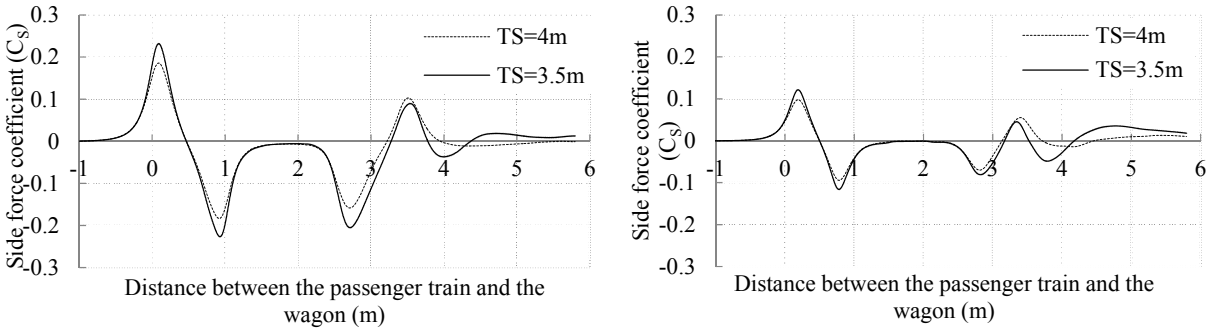

Figure 7. Side force coefficients of the containers (a) C_S of the top container (b) C_S of the bottom container

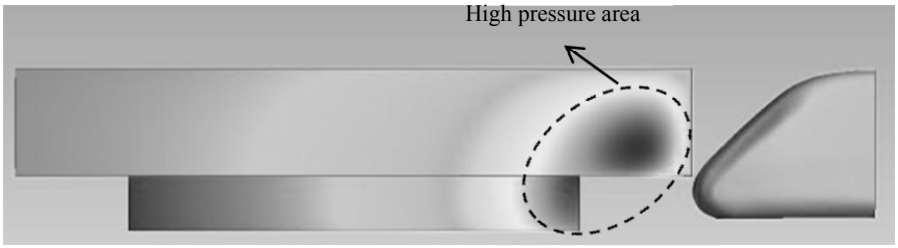

Figure 8. Pressure distribution on the side surfaces of the containers

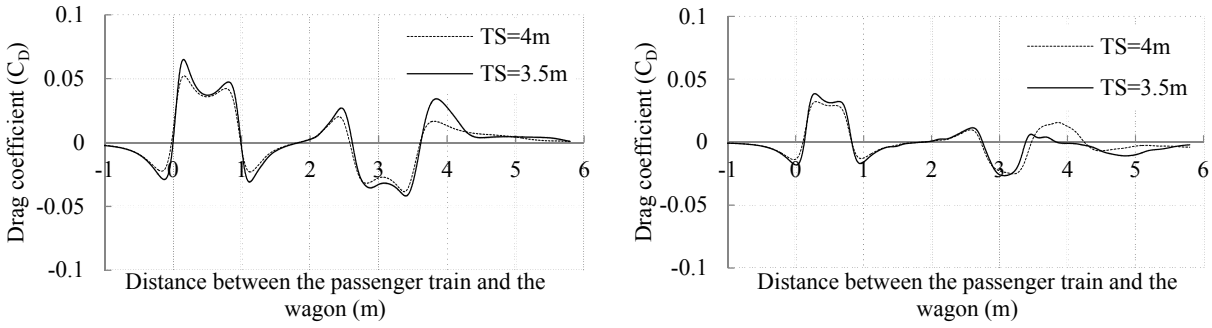

Figure 9. Drag coefficients of the containers (a) C_D of the top container (b) C_D of the bottom container

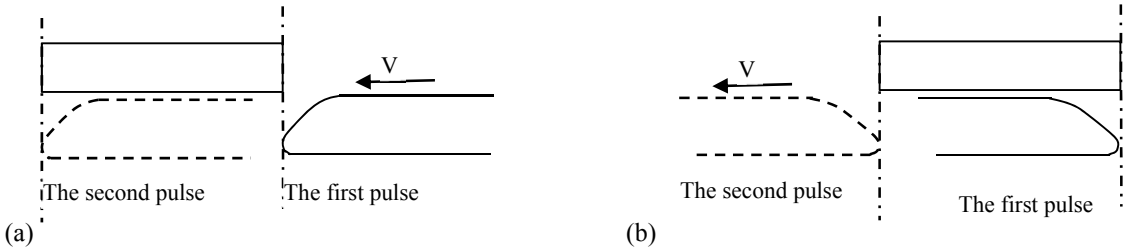

Figure 10. (a) Positions of the head of the train for the pulses (b) Positions of the tail of the train for the pulses

Figure 9 (a) shows C_D variation with the two different track spacings for the top container. With the head of the train approaching, the drag coefficient begins to fall the first negative peak and then increases sharply to the first positive peak. The C_D then drops a little but begins to increase after the head of the train reaches the middle of the wagon, to produce a second positive peak. There is then a subsequent sharp decline to the second negative trough when the head of the train leaves the tail of the wagon. It's noticed that the second pulse at the end of the train passing has smaller amplitude than the first one occurring when the passenger train approaches the freight wagon. Two pulses are also observed when the tail of the train arrives at the front of the wagon and when it leaves the tail of the wagon. Similar to the side force coefficient, the pulses in C_D caused by the tail of the train are weaker than the ones caused by the head of the train. Figure 10 (a) portrays the positions where the peaks occur. C_D values from the track spacing of 3.5 m are generally slightly larger than the one from the track spacing of 4m. During the head and the tail of the train passing, this difference is distinct with approximate 19% decrease when

considering the track spacing of 4m. A similar phenomenon occurs to the bottom container with smaller peak values of C_D than for the top container, as shown in Figure 9 (b).

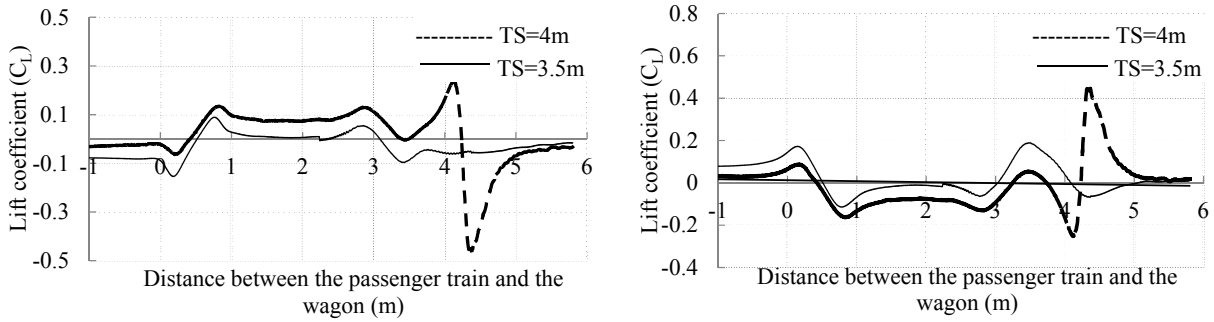

Figure 11. Lift coefficient of the containers (a) C_L of the top container (b) C_L of the bottom container

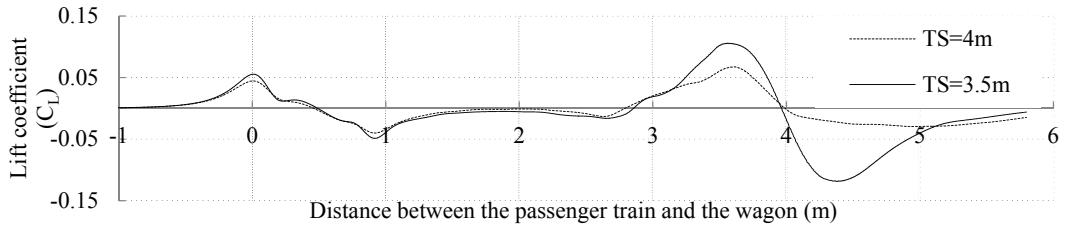

Figure 12. Combined lift coefficient from both containers

A comparison of the lift coefficients is shown in Figure 11. It can be seen from Figure 11 (a) that, when the train approaches the freight wagon, the top container is first exposed to a negative lift force, which means a force is acting vertically downwards on the container. After the head of the train arrives at the middle of the wagon, this force changes to being positive and a peak is observed in C_L just before the head of the train leaves the tail of the wagon. Then during the train passing, the force keeps almost steady until the tail of the train arrives at the front of the wagon, causing another peak and then another drop when leaving the wagon. It's remarkable that larger track spacing causes higher lift force on the top container. Figure 11 (b) shows the lift coefficient observed on the bottom container, of larger amplitude than on the top container. Different from the top container, increasing track spacing causes significant decrease in C_L on the bottom container. For the majority of the passing event, the top and bottom containers have alternative results of lift coefficient--one has positive value at the same time as the other has negative, and vice versa. Figure 12 shows the combined lift coefficient from the top and bottom containers to allow for analysis of the wagon as a whole. It is clearly showed that the maximum value occurs when the tail of the train passes the wagon. This means that the tail of the train passing has a stronger influence on the lift coefficient than the head of the train. Last, larger track spacing finally decreases the C_L for the whole wagon although increases C_L of the top container.

Table 1. The peak values decrease of aerodynamic coefficients of the wagon from track spacing 3.5m to 4m

Track spacing (m)	Side force coefficient (CS)	Drag coefficient (C_D)	Lift coefficient (C_L)
3.5m	-0.276	0.036	0.0992
4m	-0.220	0.026	0.0576
Percentage drop (%)	20	27	42

From the analysis above, it's known that increasing the track spacing generally decreases the peak value of the coefficients for the whole wagon. The maximum percentage decrease of the peak values from TS=3.5m to TS=4m are listed in Table 1.

5.3 *Passing phenomena and the effect of track spacing on the passenger train.*

In this section only the side force and lift coefficients of the head of the passenger train are investigated, limited to the space of the paper. As shown in Figure 13 (a), when approaching the wagon, the side force coefficient of the head of the passenger train drops to the first trough which means the maximum push force occurs here. Right after this, the side force coefficient increases to the first positive peak, of much smaller amplitude, when the head of the train leaves the wagon. This means when passing the wagon, the head of the train is exposed to a first push force and then a pull force, which potentially worsens the lateral stability. Figure 13 (b) shows the lift coefficient of the head of the train. When the head of the train approaches and leaves the wagon, a pulse occurs in the lift coefficient. It is noticeable that C_L stays negative, which means that the head of the train is loaded under a downward lift force throughout the passing event. Typically, the coefficients are smaller in the results from the track spacing of 4m than for the track spacing of 3.5m. However, this difference is most prominent for the lift coefficient results (as shown in Figure 13 (b)), where a track spacing increase from 3.5m to 4m results in roughly a 10% decrease in C_L for the majority of the passing procedure.

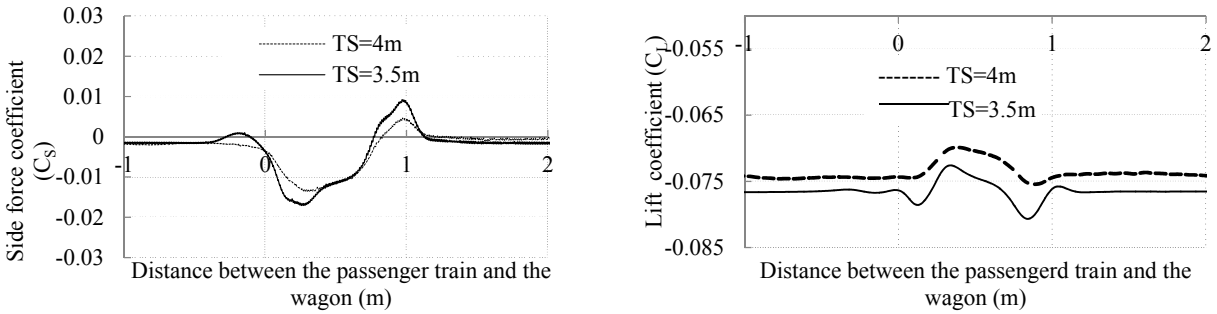

(a) (b)

Figure 13. Coefficients of the head of the train (a) C_S of the head of the train (b) C_L of the head of the train

CONCLUSIONS

This work has investigated the aerodynamic performance of a double-decker stationary freight wagon being passed by a high speed train using LES. The influence of two different track spacings, 3.5m and 4m were assessed in terms of three aerodynamic coefficients: side force coefficient, drag coefficient and lift coefficient. Principal conclusions from the simulations are:

1. Increasing the track spacing from 3.5 m to 4m results in a larger decrease in the lift coefficients in comparison to the side and drag coefficients for both the freight wagon and passenger train. The peak C_L of the wagon decreases up to 40% in value when the track spacing increases from 3.5m to 4m, which occurs when the tail of the train leaves the wagon. The passing event has almost negligible effect on the lift coefficient of the passenger train, which reduces by a small amount during the passing procedure.
2. When the track spacing increases the lift coefficient of the top container increases, whilst the values of the bottom container decrease. It is noticeable that while the top container is

exposed to a positive lift force, the bottom container is simultaneously exposed to a negative lift force, and vice versa. However, the combined coefficient of the two containers still shows the tendency of increasing coefficients with decreasing track spacing.

3. The reduction in the track spacing also generally increases the side and the drag coefficients for both the wagon and the passenger train, especially at the moment when the passenger train approaches or leaves the wagon. The top container is on the whole subjected to larger side forces than the bottom one.

REFERENCES

1 F. Alam, & S. Watkins, Crosswinds Effects on High Cube Freight Trains. Proceedings of the 3rd BSME-ASME Thermal Engineering Conference, Bangladesh, 2006, Paper AU-002, pp. 7-12.

2 The Australian Transport Safety Bureau, Derailment of train 3DA2K – Tarcoola, SA. Report 2006/012: 2008.

3 RAIB, Detachment of containers from freight wagons near Cheddington and Hardendale, Report 12/2009; 2009.

4 Y-f. Li, H-q. Tian & M-z. Yang, Aerodynamic drag analysis of double-deck container vehicles with different structures. Journal of Central South University of Technology. 2011, 18, pp. 1311−1315.

5 S. Watkins, J.W. Saunders & H. Kumar, Aerodynamic drag reduction of goods trains. Journal of Wind Engineering and Industrial Aerodynamics, 1992, Vol. 40, No.2, pp. 147-178.

6 X-h. Xiong & X-f. Liang, Experimental research on pressure drag of the double container car passing through tunnel. Journal of Experiments in Fluid Mechanics, 2006, Vol. 20, No. 3, pp. 18−22.

7 H. Hemida & C. Baker, Large-eddy simulation of the flow around a freight wagon subjected to a crosswind. Computers & Fluids, 2010, Vol. 39, pp. 1944 – 1956.

8 F. Alam & S. Watkins, Lateral stability of a double stacked container wagon under crosswinds. Proceedings of the International Conference on Mechanical Engineering, Dhaka, Bangladesh, 2007.

9 C. Baker & H. Hemida, Integration of crosswind forces into train dynamic modeling. Proceedings of the Institution of Mechanical Engineers, Part F: Journal of Rail and Rapid Transit, 2011, Vol. 225, pp. 154-164.

10 Federal Railroad Administration of USA, Assessment potential of aerodynamics effects on personnel and equipment in proximity to high-speed train operations. Report DOT/FRA/ORD-99/11, 1999.

11 R. S. Raghunathan, H.D. Kim and T. Setoguchi, Aerodynamics of high-speed railway trains, Review Article. Progress in Aerospace Sciences, 2002, Vol. 38, No. 6–7 , pp. 469-514

12 G. Mancini & A. Malfatti, Full scale measurements on high speed train Etr 500 passing in open air and in tunnels of Italian high speed line, 2002, Transaero, Vol. 79, pp. 101-122.

13 T. Johnson & S. Dalley, 1/25th scale moving model tests for the TRANSAERO project", Notes on Numerical Fluid Mechanics, 2002, Vol. 79, pp. 123-135.

14 R. Li, J. Liu, Z. Qi & W. Zhang, Air pressure pulse developing regularity of high-speed trains crossing in open air. Journal of Mechanical Engineering, 2011, Vol. 47, No.4, pp. 125-130.

15 H. Tian, Research and application of air pressure pulse from trains passing each other. Journal of Railway Science and Engineering, 2004, Vol. 1, No.1, pp. 83-89.

16 J. Steinbuer, Calculation of unsteady pressures during passing and tunnel entrance of trains. ASME Aerodynamics of Transportation, 1979, Vol. 6, pp.77-119.

17 S. Holmes & M. Schroeder, High speed passenger and intercity train aerodynamic computer modeling. The International Mechanical Engineering Congress & Exposition, Orlando, Florida, 2000, pp. 1-8.

18 R. MacNeill, S. Holmes & H. Lee, Measurement of the aerodynamic pressures produced by passing trains. ASME/IEEE Joint Rail Conference. Washington, 2000, pp. 1-8.

19 H. Hemida, H. Krajnovic & S.L. Davidson, Large-eddy simulations of the flow around a simplified high speed train under the influence of a cross-wind. AIAA paper, 2005, No. AIAA-2005-5354.

20 H. Krajnovic, S. Davidson,L.,Flow around a simplified car, part1:large-eddy simulation. ASME: Journal of Fluids Engineering, 2005, Vol. 127, pp. 907–918.

21 H. Hemida, N. Gil & C. Baker, LES of the slipstream of a rotating train. Journal of Fluids Engineering (ASME), 2010, Vol. 132, pp. 1-9.

22 J. Smagorinsky, General circulation experimental with the primitive equations. Mon. Weather Rev., 1963, Vol. 91, pp. 99-164.

The Seventh International Colloquium on Bluff Body Aerodynamics and Applications (BBAA7)
Shanghai, China; September 2-6, 2012

Determination of aerodynamic characteristics of a vehicle immerged in the wake of bridge tower using computational fluid dynamics

Bin Wang[a], You-Lin Xu[a], Le-Dong Zhu[b], Yong-Le Li[c]

[a]*Department of Civil and Structural Engineering, The Hong Kong Polytechnic University, Hong Kong, China*
[b]*Department of Bridge Engineering, Tongji University, Shanghai, China*
[c]*Department of Bridge Engineering, Southwest Jiaotong University, Chengdu, China*

ABSTRACT: The running safety analysis of a vehicle subjected to crosswinds is one of the issues concerned in wind engineering. Particularly as a vehicle moves passing by a bridge tower, the shielding effect of the tower on wind forces of the vehicle occurs, which leads to a sharp change of aerodynamic forces on the vehicle in danger. To explore the aerodynamic forces acting on the vehicle passing by the bridge tower, the flows around the vehicle immerged in different positions to the bridge tower are simulated using the computational fluid dynamics (CFD) technique in this study. The aerodynamic forces measured in the wind tunnel are used to confirm the simulation results. Meanwhile, the aerodynamic characteristics of the vehicle immerged in the wake of the bridge tower and the flow field features are explored in detail.

KEYWORDS: vehicle, bridge tower, crosswinds, aerodynamics, computational fluid dynamics

1 INTRODUCTION

Vehicle behavior under crosswinds is one of the issues concerned in wind engineering. The running safety analysis of a vehicle subjected to crosswinds probably started from the Baker's work in 1986 (Baker[1]). Since then, several studies on the safety of a vehicle subjected to crosswinds have been carried out. Particularly as a vehicle moves passing by a bridge tower, the shielding effect of the tower on wind forces of the vehicle occurs, which leads to a sharp change of aerodynamic forces on the vehicle in danger. The safety of a vehicle running through a tower region is therefore concerned. The aerodynamic forces of a vehicle in the wake of a bridge tower should be studied to make sure the running safety of the vehicle. Wind tunnel tests are a common method to obtain the aerodynamic forces on a vehicle. Charuvisit et al.[2] tested the transient aerodynamic side force and yawing moment on a vehicle when it passed by a bridge tower subjected to crosswinds. Argentini et al.[3] carried out wind tunnel tests to measure the aerodynamic forces and the surface pressure distributions of the stationary vehicle model. With the rapid development of computer hardware, computational fluid dynamics (CFD) can be employed as an alternative tool, practically in the flow visualization which cannot be achieved easily by wind tunnel tests. In this study, the flows around a bridge tower and a vehicle in different positions behind the bridge tower are simulated using the CFD technique. The aerodynamic forces measured in a wind tunnel are used to confirm the simulation results. Then, the aerodynamic characteristics of the vehicle immerged in the wake of the bridge tower and the flow field features are explored in detail.

2 MODELS

A typical high-sided articulated lorry, which was investigated extensively by Baker and his colleagues in wind tunnels and later used in the dynamic analysis of wind-vehicle-bridge systems (Xu & Guo[4], Cai & Chen[5], Chen & Wu[6]), is selected as the reference vehicle. The geometric scales of the vehicle are shown in Fig.1. A long span highway bridge is also selected. It is a cable-stayed bridge of double towers with a main span of 688m (see Fig.3). The tower composes of a pair of side by side legs and a transverse beam to support and restrain the deck (see Fig.2). The tower legs are inclined from the height of deck to both the ends with a chamfered rectangle section. The transverse beam connected the two legs with a rectangle cross section. A flat box girder with side fairing is selected as the bridge deck, as seen in Fig.4. The cross section of the deck was 34.0m wide and 3.5m high carrying a dual two-lane highway on the upper surface. Two lines of handrail, four lines of protection rail and two lines of I-shape maintenance trace are mounted on the bridge deck. Both the vehicle and bridge models are scaled with a length ratio of 1:25. Under the crosswinds, the vehicle running on the upwind first lane is impacted by the bridge tower more seriously than the one running on the other lanes. Therefore the vehicle is arranged on the upwind first lane in this study. Because of the complex flow field around the tower, the vehicle in different locations with reference to the tower may suffer distinct wind flow. To reflect the influence of distance from the tower, three different positions of the vehicle in the wake of bridge tower are considered. They are (1) the vehicle immerged behind the tower entirely (position Xd1 in Fig.5), (2) half-length of the vehicle immerged behind the tower (position Xd3 in Fig.5), and (3) the vehicle just getting rid of the tower (position Xd5 in Fig.5). Aerodynamic forces of the same vehicle model were tested in the TJ-3 wind tunnel of the State Key Laboratory for Disaster Reduction in Civil Engineering at Tongji University in Mainland China. The models mounted in the wind tunnel are shown in Fig.6.

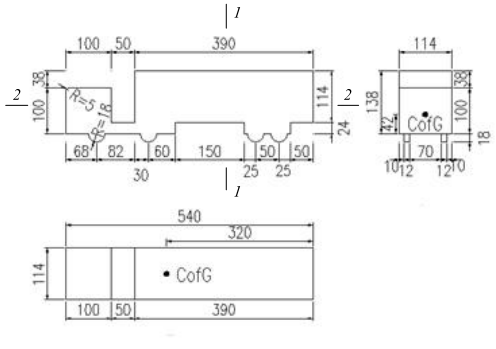

Figure 1. Dimensions of vehicle model (unit: mm)

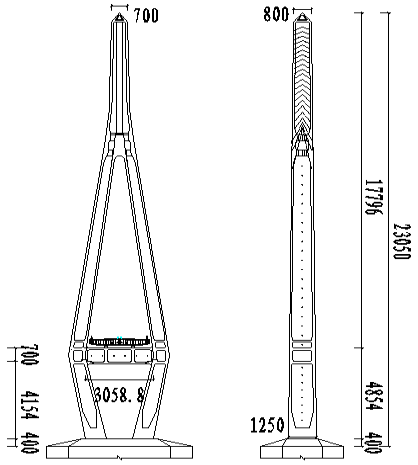

Figure 2. Dimensions of bridge tower (unit: cm)

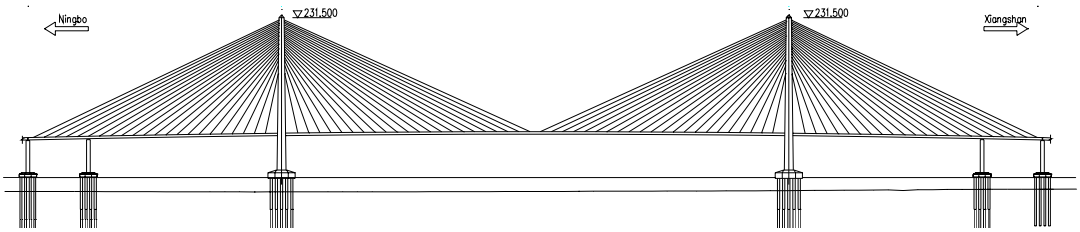

Figure 3. Elevation of the selected bridge (unit: cm)

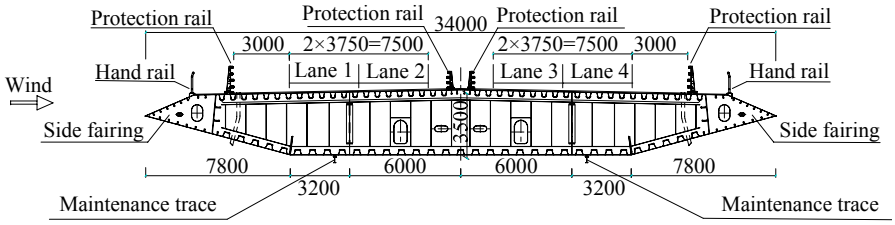

Figure 4. Cross section of bridge deck (unit: mm)

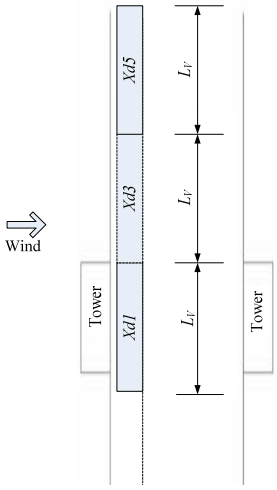

Figure 5. Vehicle locations

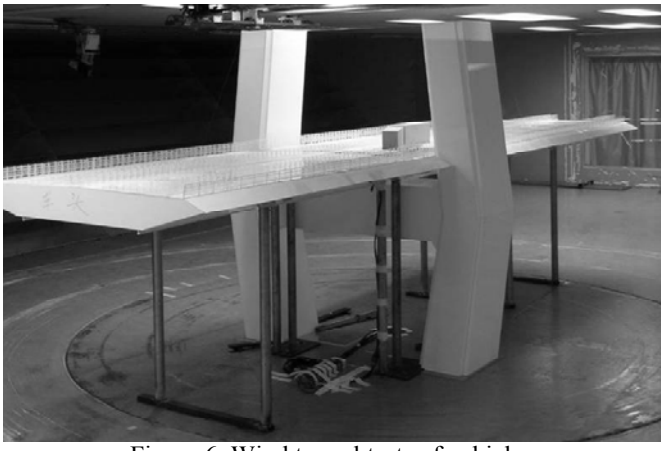

Figure 6. Wind tunnel tests of vehicle

3 NUMERICAL METHOD

3.1 Governing equations

In order to explore the flow characteristics around and the aerodynamic forces on the vehicle-bridge system, the large eddy simulation (LES) method is adopted for this study. In LES, turbulent flows are decomposed into large and small scales of turbulence by means of a high-pass filter in space. The large-scale turbulence flows can then be computed accurately by using the LES governing equations while the effect of the small-scale turbulence can be estimated through the subgrid-scale (SGS) model with the understanding that the small scales of turbulence tend to more homogeneous and universal, and less affected by the boundary conditions than the

large-scale ones. A box filter expressed by Eq. (1) is used for performing the spatial scale separation and a filtered variable is expressed by Eq.(2).

$$G(x,x') = \begin{cases} 1/V, x' \in v \\ 0, x' \notin v \end{cases} \tag{1}$$

$$\overline{\varphi}(x) = \int_v G(x,x')\varphi(x')dx' \tag{2}$$

where G is the filter function; φ is the variable before filtering; $\overline{\varphi}$ is the variable after filtering; v denotes the computational cell; and V is the computational volume. By applying the filtering operation to the momentum and continuity equations, the LES governing equations can be derived as

$$\rho\frac{\partial \overline{u_i}}{\partial t} + \rho\frac{\partial}{\partial x_j}\left(\overline{u_i}\,\overline{u_j}\right) = -\frac{\partial \overline{p}}{\partial x_i} + \mu\frac{\partial^2 \overline{u_i}}{\partial x_j \partial x_j} - \frac{\partial \tau_{ij}}{\partial x_j} \tag{3}$$

$$\frac{\partial \overline{u_i}}{\partial x_i} = 0 \tag{4}$$

where μ_i (i=1, 2, 3) is the filtered velocity component in the Cartesian coordinates; p is the filtered pressure; ρ is the fluid density; μ is the dynamic viscosity coefficient; and τ_{ij} is the subgrid-scale stress expressed by

$$\tau_{ij} = \rho\overline{u_i u_j} - \rho\overline{u_i}\,\overline{u_j} \tag{5}$$

The subgrid-scale stress must be modeled, and the subgrid-scale turbulent model employed in this study is based on the Boussinesq hypothesis.

$$\tau_{ij} = -2\mu_t\overline{S_{ij}} + \frac{1}{3}\tau_{kk}\delta_{ij} \tag{6}$$

$$\overline{S_{ij}} = \frac{1}{2}\left(\frac{\partial \overline{u_i}}{\partial x_j} + \frac{\partial \overline{u_j}}{\partial x_i}\right) \tag{7}$$

where μ_t is the subgrid-scale turbulence viscosity; τ_{kk} is the isotropic part of the subgrid-scale stress. The subgrid-scale turbulence viscosity can be determined by using the Smagorinsky-Lilly model. The Smagorinsky constant equal to 0.1.

3.2 Numerical models

In the simulation, only one wind direction (wind perpendicular to the bridge deck) is considered. Fig.7 shows the computational flow domain when the vehicle is located at Xd3. The entire computational domain is a box shape enclosed by six boundary faces. B, BV and BT represent the width of the deck, the length of the vehicle and the width of tower, respectively. The height of the computational domain is 7m which leads a blockage ratio at the level of the wind tunnel

tests. All those sizes determining the computational flow domain are optimized through parameter studies.

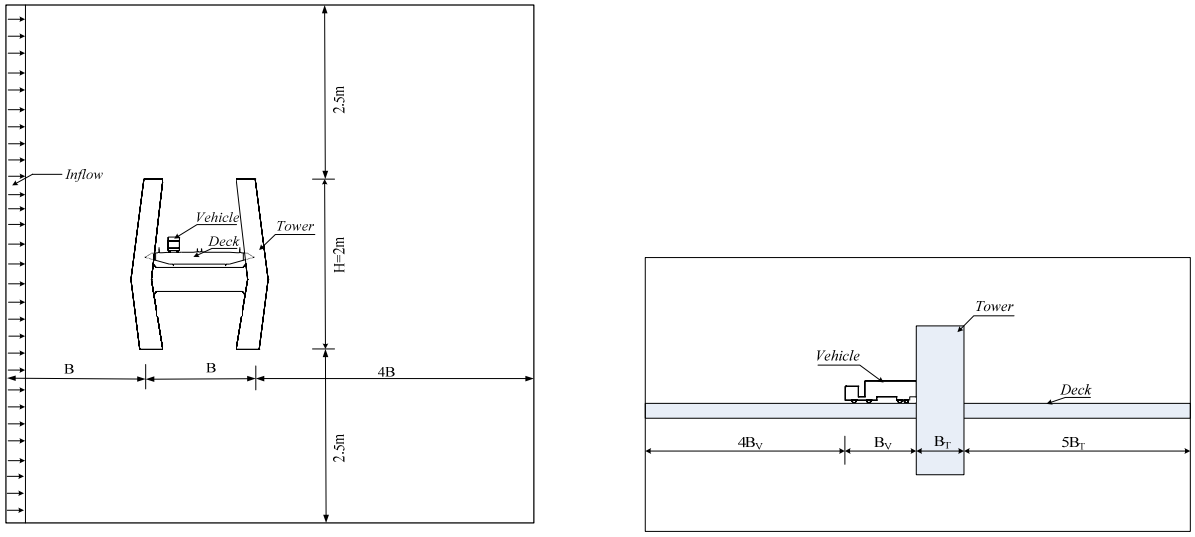

(a) (b)

Figure 7. Computational domain sketch: vehicle-bridge system

3.3 Boundary conditions

The input boundary face is set as flow inlet with a uniform velocity of 10m/s, which leads to a Reynolds number of 1.13×10^5 in terms of the height of the vehicle. The output boundary face is specified as flow outlet with zero pressure. The other boundaries are all defined in such a way that the gradients of flow variables (including velocity and pressure) normal to those boundary faces are zero. The surfaces of the vehicle and the bridge are all modeled as nonslip wall boundaries.

3.4 Meshing

The characteristic sizes of components of the vehicle-deck-tower system vary from the size of rails to the size of tower greatly. The complex geometric shape and the large variation of characteristic size lead to a complicated flow field around the system in space. In order to obtain a relative adequate spatial discretization grid system corresponding to the ability of the current using PC, the grid optimization is achieved. Since the simulation with the LES method is time-consuming for the flow around three-dimensional complex geometric body, steady RANS equations enclosed with SST two-equation turbulence model are solved during the process of grid optimization.

3.5 Computational scheme

The LES governing equations are discretized using a three-dimensional finite volume method. The convective and diffusive terms are approximated by the bounded central differences of second-order accuracy and central difference respectively. The time integration is performed using the second-order implicit method. Pressure and velocity are solved with the SIMPLEC algorithm.

4 SIMULATION RESULTS

4.1 Aerodynamic forces and coefficients

The numerical simulation provides the pressure distribution over the surfaces of the vehicle. The aerodynamic forces acting on the vehicle can then be acquired by integrating the pressures over the surface. The aerodynamic forces and coefficients discussed below refer to the mean values. There are six aerodynamic force components on the vehicle in the Cartesian coordinate system: lift force FL, drag force FD, side force FS, pitching moment MP, yawing moment MY and rolling moment MR, as shown in Fig.8. The non-dimensional aerodynamic coefficients are defined by

$$C_L = \frac{F_L}{qA}; \; C_D = \frac{F_D}{qA}; \; C_S = \frac{F_S}{qA} \tag{8}$$

$$C_P = \frac{M_P}{qAL}; C_Y = \frac{M_Y}{qAL}; C_R = \frac{M_R}{qAL} \tag{9}$$

$$q = 0.5\rho U^2 \tag{10}$$

where ρ is the air density; U represents the mean wind speed at the inlet boundary of the computational domain; A is the frontal project area of the vehicle without wheels and it refers to the project area in the X-Y plane in this study as shown in Fig.8; and L represents the maximum length of the vehicle in the Z-Y plane as shown in Fig.8. The aerodynamic force coefficients of the vehicle at different positions are listed in Table 1 for wind perpendicular to the length of the vehicle. From the comparative results of aerodynamic forces between the simulation and the wind tunnel texts, it can be seen that the simulated aerodynamic coefficients agree well with the experiment in general. The simulated coefficients demonstrate the same trend with the change of the vehicle location as the wind tunnel tests. The lift force coefficients are sensitive to the experimental conditions (Coleman & Baker[7]) and the calculated lift force coefficients are a slightly larger than the test values for all three locations. Compared with the test results, the calculated side force coefficients are a slightly larger while the calculated pitching moment coefficients are lower than the test results. When the vehicle moves out of the shielding area of the tower (from Xd1, Xd3 to Xd5), its side force, drag force, pitching and rolling moment all increase while its lift force decreases. The yawing moment decreases first and increases late.

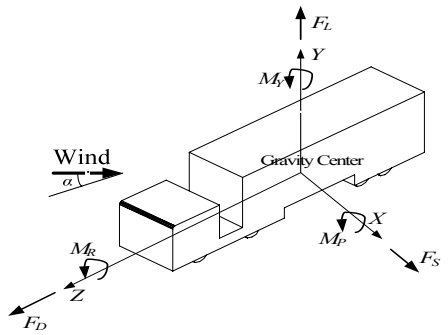

Figure 8. Definitions of aerodynamic forces

Table 1. Aerodynamic Coefficients of Vehicle

	Xd1		Xd3		Xd5	
	Experiment	LES	Experiment	LES	Experiment	LES
C_S	1.145	1.840	4.120	4.857	4.494	5.260
C_L	0.112	0.650	-0.939	-0.360	-0.837	-0.334
C_D	-0.136	-0.369	0.499	0.409	0.490	0.327
C_P	-0.062	0.039	-0.225	-0.217	-0.248	-0.262
C_Y	-0.670	-0.799	-0.371	-0.655	-0.473	-0.781
C_R	-0.129	-0.105	-0.251	-0.236	-0.236	-0.247

4.2 Flow fields

The visualization ability of CFD simulation is used here to analyze the flow fields around the vehicle. The instantaneous flow structures in terms of vorticity magnitude and the averaging flow structures in terms of projected streamlines and velocity contours are included. Sections shown as 1-1 and 2-2 in Fig.1 are selected to present the characteristic flow structures around the vehicle. The instantaneous contours of vorticity magnitude around the vehicle at different locations from the tower in the selected sections are shown in Fig.9, Fig.10 and Fig.11. Influenced by the tower, the flow environment becomes more and more complex from Xd5 to Xd1. At Xd5, the vortex street in the wake of vehicle-deck is disturbed slightly by the tower. At Xd3, the vortex street in the wake of vehicle-deck is interfered by the flow around the tower obviously. At Xd1, the selected vehicle section is immerged into the flow region of tower totally.

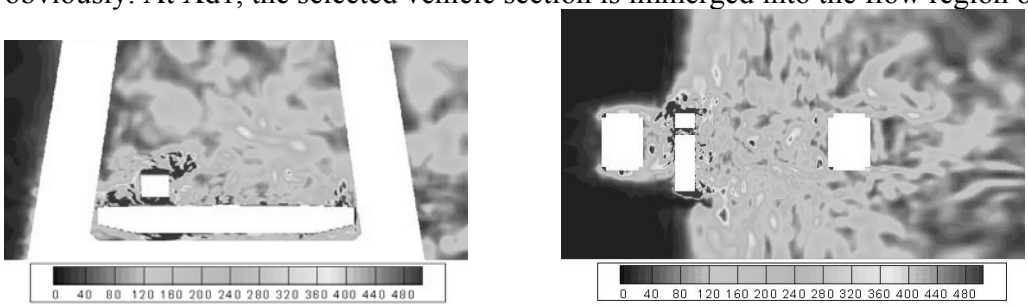

(a) section 1-1 (b) section 2-2

Figure 9. Contours of instantaneous vorticity magnitude for vehicle at Xd1 (unit: s-1)

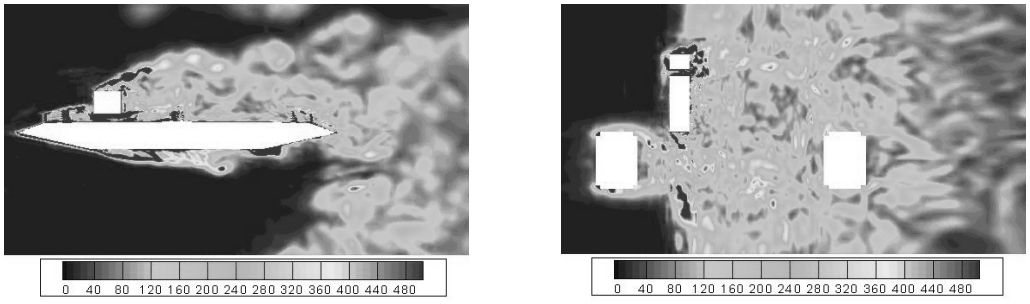

(a) section 1-1 (b) section 2-2

Figure 10. Contours of instantaneous vorticity magnitude for vehicle at Xd3 (unit: s-1)

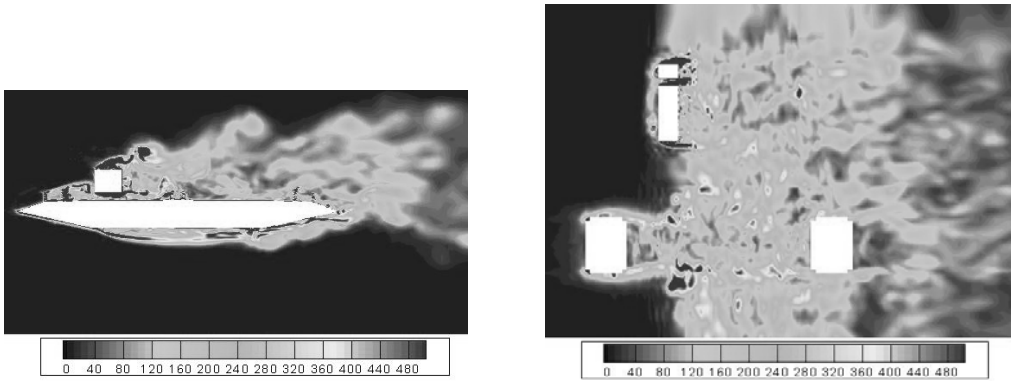

(a) section 1-1 (b) section 2-2

Figure 11. Contours of instantaneous vorticity magnitude for vehicle at Xd5 (unit: s-1)

The averaging projected streamlines and velocity contours of the vehicle at different locations are displayed in Fig.13, Fig.14 and Fig.15. Different flow structures are formed. Flow separates at the upwind tower leg. At Xd1, the vehicle is almost totally immerged in the separating wake of the upwind tower leg while the separated flow from the tower pushes on the tail part of the vehicle. The symmetric flow feature around the tower is disturbed slightly by the vehicle. At Xd3, the accelerated flow around the upwind tower leg pushes to the vehicle. The separated flow around the vehicle in Section 1-1 reattaches to the bridge deck again. At Xd5, the vehicle nearly gets rid of the impact of the wake of the tower. The separated flow around the vehicle in Section 1-1 does not reattach to the bridge deck.

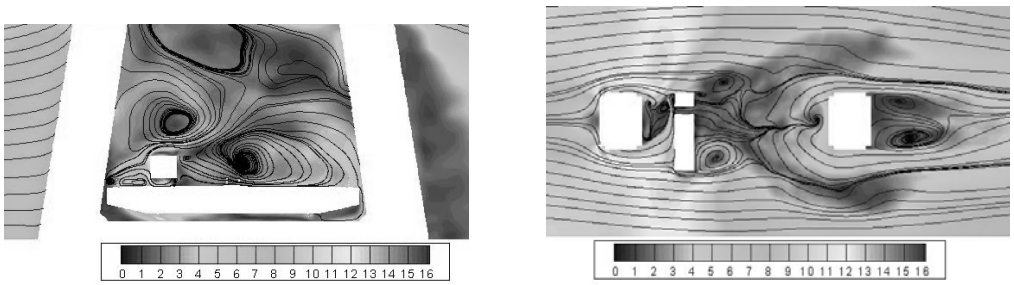

(a) section 1-1 (b) section 2-2

Figure 12. Projected streamlines and velocity contours for vehicle atXd1 (unit: m/s)

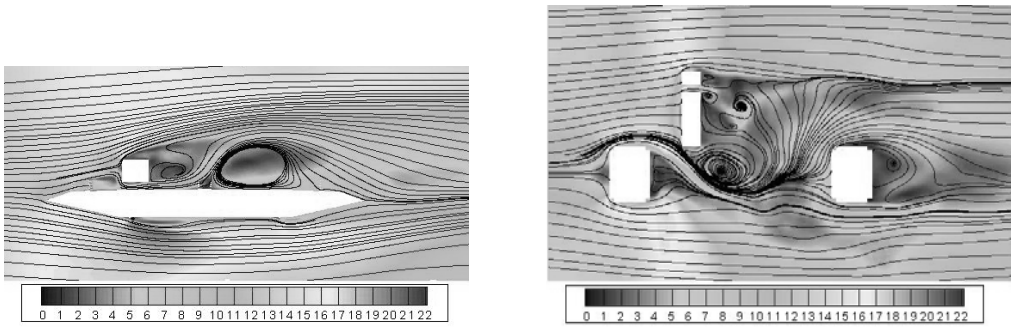

(a) section 1-1 (b) section 2-2

Figure 13. Projected streamlines and velocity contours for vehicle at Xd3 (unit: m/s)

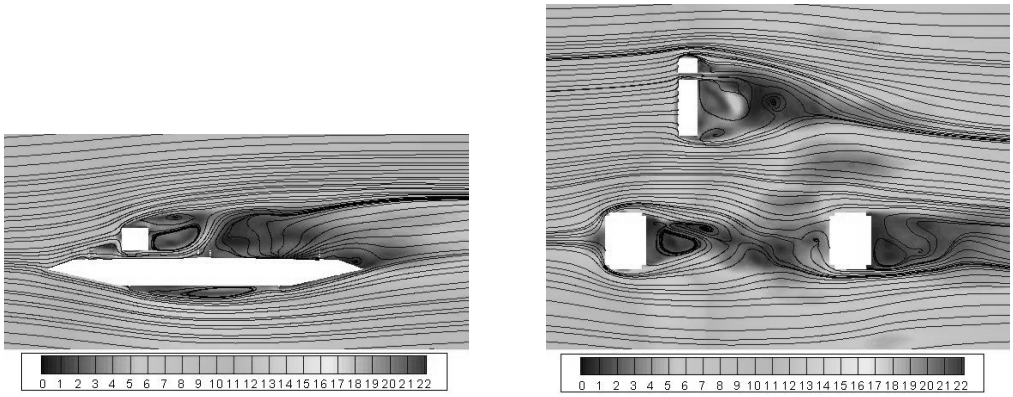

(a) section 1-1 (b) section 2-2

Figure 14. Projected streamlines and velocity contours for vehicle at Xd5 (unit: m/s)

4.3 Surface pressure distributions on vehicle

The mean pressure distributions over the surfaces of the vehicle under the three conditions are computed and displayed in Fig.16 for the case of wind perpendicular to the vehicle. The flow acts on the upwind side surface of the vehicle directly and some stagnation areas are formed. All the surfaces except the upwind one are in the flow separate region of the vehicle with negative pressure due to the flow separations around these surfaces. Compared with Xd5, the stagnation area for Xd3 moves to the head part while the area for Xd1 focuses on the tail part of the vehicle.

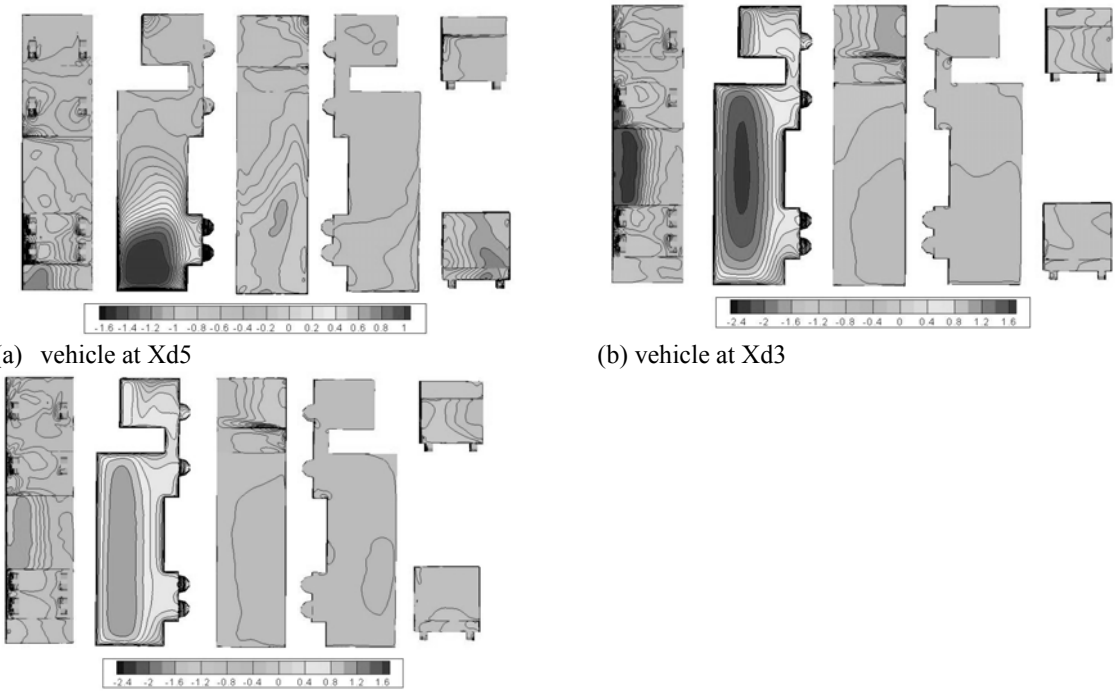

(a) vehicle at Xd5 (b) vehicle at Xd3

(c) vehicle at Xd1

Figure 15. Mean pressure distribution on vehicle (unit: Pa)

5 CONCLUSIONS

By using large eddy simulation method, the aerodynamic characteristics of a vehicle across a bridge tower have been investigated. The simulated aerodynamic coefficients agreewith the experimental results in general. The simulated coefficients demonstrate the same trend with the change of the vehicle location as the wind tunnel tests. When the vehicle moves out of the shielding area of the tower, its side force, drag force, pitching and rolling moment increase while its lift force decreases. The yawing moment decreases first and increases later. The instantaneous contours of vorticity magnitude show a complex flow environment around the vehicle due to the tower. The averaging projected streamlines and velocity contours show different flow separation phenomena around the vehicle at different locations. The flow acts on the upwind side surface of the vehicle directly and some stagnation areas are formed. All the surfaces except the upwind one are in the flow separate region of the vehicle with negative pressures.

6 ACKNOWLEDGEMENTS

The authors wish to acknowledge the financial supports from the Research Grants Council of the Hong Kong (PolyU 5311/07E), The Hong Kong Polytechnic University through a PhD studentship, and the State Key Laboratory for Disaster Reduction in Civil Engineering of China (2006-A-01).

7 REFERENCES

1 C. J. Baker, A simplified analysis of various types of wind-induced road vehicle accidents, J. Wind Eng. Ind. Aerodyn, 22(1986)69-85.
2 S. Charuvisit, K. Kimura, Y. Fujino, Experimental and semi-analytical studies on the aerodynamic forces acting on a vehicle passing through the wake of a bridge tower in cross wind, J. Wind Eng. Ind. Aerodyn, 92(2004) 749-780.
3 T.Argentini et al., Cross-wind effects on a vehicle crossing the wake of a bridge pylon, J. Wind Eng. Ind. Aerodyn, 99(2011) 734-740.
4 Y. L. Xu, W. H. Guo, Dynamic analysis of coupled road vehicle and cable-stayed bridge systems under turbulent wind, Eng. Struct, 25(2003)473-486.
5 C. S. Cai, S. R. Chen, Framework of vehicle–bridge–wind dynamic analysis, J. Wind Eng. Ind. Aerodyn, 92(2004)579-607.
6 S. R. Chen, J. Wu, Performance enhancement of bridge infrastructure systems: Long-span bridge, moving trucks and wind with tuned mass dampers, Eng. Struct, 30(2008)3316-3324.
7 S. Coleman, C. Baker, An experimental study of the aerodynamic behaviour of high sided lorries in cross winds, J. Wind Eng. Ind. Aerodyn, 53(1994) 401-429.

The Seventh International Colloquium on Bluff Body Aerodynamics and Applications (BBAA7)
Shanghai, China; September 2-6, 2012

On the characterization of wind profiles generated by road traffic

Salvadori S. [a], Morbiato T. [b], Mattana A. [a], Fusto E. [b]

[a] *CRIACIV, University of Firenze, via di S. Marta, 3 – Florence, Italy*
[b] *ICEA Dept., University of Padova, via Marzolo, 3 – Padova, Italy*

ABSTRACT: This paper analyses the flow field and the power wasted by a heavy-duty truck of modified GTS standard shape (equivalent to GCM class 8). Computational fluid dynamics has been used to analyze truck models at cruise conditions. The selected test matrix includes the study of an isolated truck and of a train of two and three trucks to evidence interaction effects. For each case three different velocities have been considered. The numerical campaign is able to quantify the drag coefficient distribution, the losses generated on the roof by viscous phenomena and the changes in velocity distributions. An in-situ experimental campaign is also settled in the truck lane of Venice highway using ultrasonic anemometers and video cameras set on the same measurement frame. Non-dimensional velocity distributions along the vehicle confirm that the height of the separation bubble is dependent on the number of trucks.

KEYWORDS: Truck, Drag Coefficient, Power Losses, CFD, Ultrasonic Anemometer

1 ACKNOWLEDGEMENTS

The *TrEo* group would like to acknowledge the funding institution “Progetti di Eccellenza - Fondazione Cassa di Risparmio di Padova e Rovigo” for supporting the proposed research. The Scientific Board, composed of Prof. R. Vitaliani of the University of Padova and Prof. C. Borri of the University of Firenze, is also acknowledged.

2 INTRODUCTION

The effects induced by the transit of heavy-duty trucks have been widely addressed in the open literature. Experimental results mainly derive from works on road sign resistance, some insights being captured with accuracy and wealth of details. From a numerical point of view, much information are provided on the turbulence modeling effects, ranging from simple Reynolds Averaged Navier-Stokes (RANS) calculations to Large Eddy Simulation (LES), and on the unsteady flow field occurring in the rear part of the vehicles. Research on the premature failure of the USA type cantilevered traffic signal structures and deficiencies in the UK design standards on road signs gave the opportunity to obtain details about what happens in the proximity of a passing truck. A review of the work done in the field of induced gust loads on cantilevered structures can be found in the work of Albert [1]. The works by Cali and Covert [2] and Quinn et al. [3] are of interest for the reliability and size of their experimental databases. Cali and Covert [2] performed experimental measurements of the loads on a 1:30 scale model of an overhead highway sign with varying sign height and truck length, speed and shape. They described in detail the interaction between a road sign and a passing truck through the force coefficient evaluated on the sign itself. Vehicle passing was divided into four phases that always occur, the last one depending on the dimension of the truck only. Quinn et al. [3] studied the phenomena responsible for the vehicle-

induced loads. Their experimental apparatus was used to evaluate longitudinal loads on real signs of different size and shape placed at the side of the carriageways of two different roads. They demonstrated that the load induced by the truck passing is due to the pressure field related to the potential flow region of the vehicle slipstream, rather than a significant vehicle induced gust effect. Considering the evaluation of the drag coefficient of moving trucks, the works of Ougburn et al. [4], Storms et al. [5], Wood and Bauer [6] and Diebler and Smith [7] provide detailed information on the power wasted for aerodynamic effects. From a numerical point of view, Salari et al. [8], Roy et al. [9] and Veluri et al. [10] demonstrated that the RANS approach is able to predict pressure fields on trucks surfaces except for the base region. It is also concluded that although in the latter zone pressure field and flow structure predictions do not match with experimental data, an accurate prediction of the vehicle drag depends on the turbulence model only. Veluri et al. [10] quantified that error in around 5% when using k-ε or k-ω models, while higher discrepancies have been individuated when using Spalart-Allmaras or SST. The latter results have also been confirmed by the RANS simulations performed by Pointer [11], with an improved performance of SST model. Hyams et al. [12] presented a detailed study using RANS and Unsteady RANS (URANS) approaches. There are no relevant differences between the steady and the time-averaged data, neither in terms of pressure distributions along surfaces nor in terms of drag coefficient evaluation. There is also a good agreement with experimental data, except for the base region where an improved approach seems to be necessary. The work of Maddox et al. [13] deals with the comparison between purely RANS prediction and Detached Eddy Simulation (DES), both working with the Spalart-Allmaras turbulence model. They demonstrated that the a RANS approach is equivalent to DES except for the evaluation of the base region, where the recirculation flow is well captured by the resolution of large eddies. A detailed description of the flow field occurring in the base region has been proposed by Krajnović and Davidson [14] using LES on a simplified geometry. A more realistic vehicle is investigated with LES by Östh [15]. Although the accuracy of LES is very high, the computational load is unacceptable while the discrepancy between the experimental and the numerical drag coefficients is of the same order of magnitude found for a simple RANS calculation with a k-ε closure. Although there is a wide literature on the selected topic, information on the energy transfer due to the skin-friction on the roof of trucks as well as a detailed description of the flow field generated by the truck movement is missing. The present paper studies this topic both from an experimental and a numerical point of view. Results are discussed also considering the literature data and an insight on the separated boundary layer occurring on the trailer roof is presented.

3 DESCRIPTION OF THE PROPOSED APPROACH

The power wasting related to the skin-friction effect occurring on the roof of a truck has been estimated by means of a mono-dimensional approach based on the data available in the open literature for a scaled GTS. Once that activity has been concluded, the analysis of the induced pressure and velocity fields generated by trucks has been performed considering both an experimental and a numerical approach. The latter has been used to study a controlled environment where the truck passing effect could be isolated and the truck-truck interaction studied for typical cruise conditions. Furthermore, the numerical results have been used to quantify the amount of power that is transferred to the turbulent boundary layer, thus validating the simplified approach. The experimental approach demonstrated the accuracy of the numerical analysis and provided further information on the realistic situation, including the individuation of velocity peaks as well as the presence of long lines of trucks over the investigated area.

3.1 *The numerical approach*

Computational Fluid Dynamics (CFD) allows for detailed analysis of complex geometries. Incompressible, steady simulations have been performed on a specific vehicle model, which is defined to represent the typical European truck. The inherent complexity of the research demands for simplified approaches, and then a 2D numerical campaign has been completed using the commercial code ANSYS Fluent®. Calculations have been performed in the relative frame of reference and are second order accurate in space. Turbulence is modeled using the two equations k-ε model with standard wall functions. Simulations have been performed considering up to three trucks to study the aerodynamic effects. A total amount of 18 simulations have been performed, as reported in Table 1.

Table 1. Test matrix

Section	Vehicles	Distance (m)	Domain H x L (m2)	Number of elements	Speed (km/h)
W,NW	1 truck	0	100 x 120	~250,000	90 ,100 ,110
	2 truck	10	100 x 148	~300,000	90 ,100 ,110
	3 truck	10, 10	100 x 176	~360,000	90 ,100 ,110

A vehicle with a shape like that of the GTS has been considered, including the tractor-trailer gap. The computational domains represent both a section at the centerline of the truck (called No-Wheels, NW) and a section that includes the wheels (identified by W, Wheels). Minor details are neglected since the main contribution to the wasted power and air displacement comes from the bulk of the vehicle. Computational domains are discretized with an unstructured mesh where both triangular and quadrilateral elements are used (Figure 1a). Special attention has been paid to the discretization of the gap between the trucks and the lower region of the domain, where the re-circulating phenomena should occur (Figure 1b). The top of the domain has been modeled using a far-field condition where the total pressure is uniform and the flow is undisturbed. Those dimensions provide a vertical blockage of approximately 5% that will introduce an overshoot of velocity in the near-truck region. That effect will be considered while discussing the obtained results. For each investigated case, the last truck has been maintained at a constant distance from the outlet section to keep unchanged the reference pressure value for the pressure coefficient calculation.

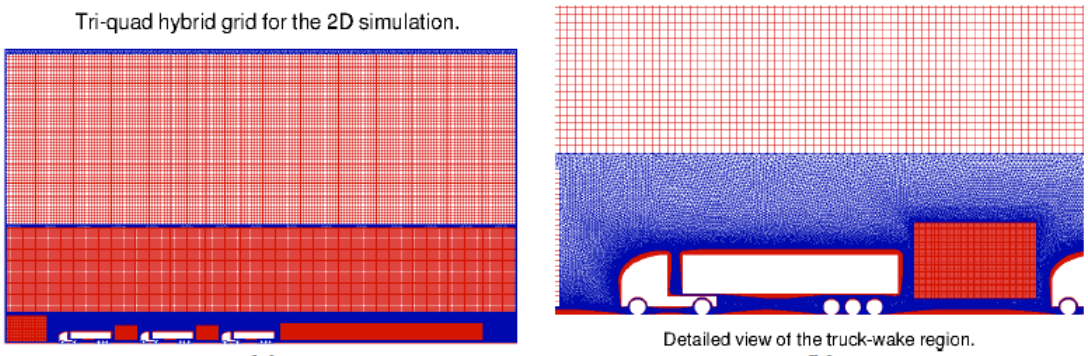

Figure 1. Computational grid of the three-trucks case: full domain (a) and wake region (b)

3.2 *The experimental apparatus*

The aim of the experimental campaign is to reconstruct the wind velocity profile on the top of truck in the lane axis, with an approach taking into account three-dimensional components attributed both to viscous fluid transportation properties and to interaction between pressure wave, rear wake, and vehicles gap in high traffic density. To this aim, the Venice link highway offers steel bridge frames of 200mm squared hollow sections bearing the traffic messages led panels and pictograms. To prevent interferences in wind measurements, at the chosen frame the 2.5m high panel in the instruments approaching direction has been removed, and substituted by a low solidity 50x50mm net handrail only 2mm thick. Each lane is instrumented with 3 ultrasonic tri-axial anemometers (USA) 40 Hz hi-freq. sampling, cantilevered > 2m from frame and placed at 5.50 m minimum headroom from road, at 6.50 m and at 7.50 m. The vertical alignment is avoided for two adjacent instruments in order to maximize mutual distance, and achieve not-interfering condition according to the ILAC MRA certified instrument. Another tri-axial USA is placed at 12 m height, sampled 8 Hz and interpolated to 40 Hz in order to get an ambient wind survey to calibrate traffic wind from aerodynamic losses. To correctly estimate interactions in high traffic density, an image tracking system is integrated with synchronous wind speed sampling. A couple of video cameras are set on the top of the measurement frame bridging the roadways. While the USA network is acquiring the environmental wind speed and the vehicle induced wind gusts, the cameras extract the size and speed of those vehicles, which generated the perturbations exciting the measurement system. Once truck geometry, speed and trajectory are estimated with a stereo tracking algorithm, a statistics is made on the collected data and estimates. A typical anemometry set for a single lane 3.5m wide is illustrated in Figure 2.

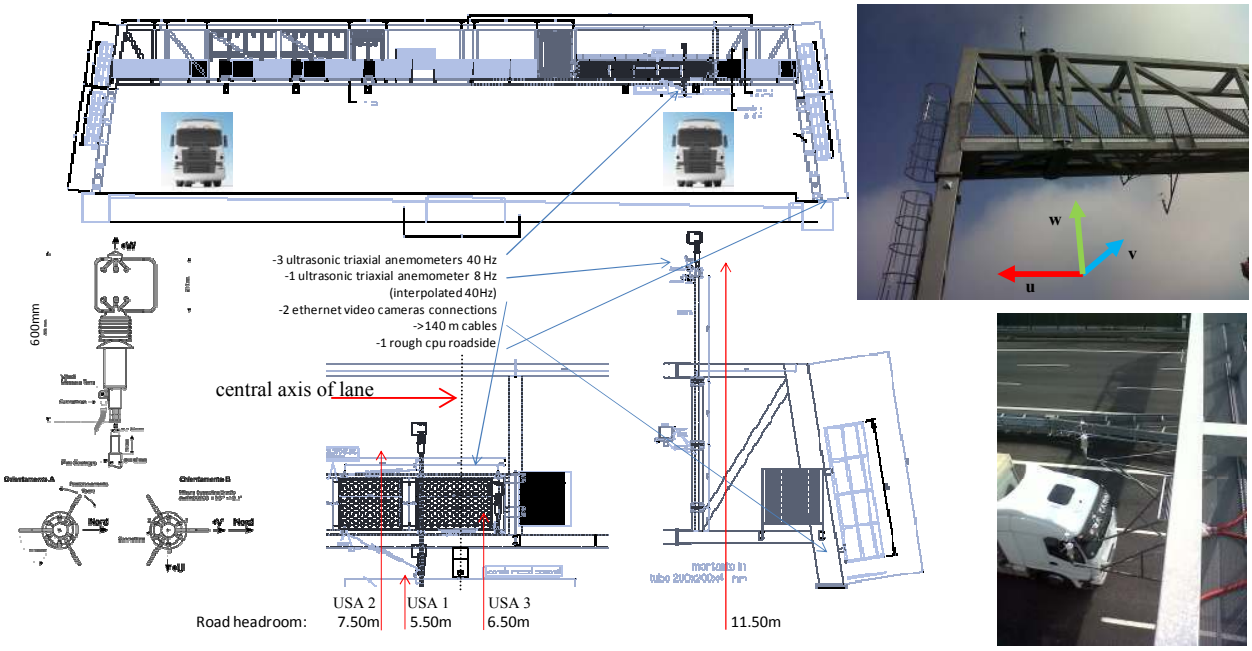

Figure 2. Experimental apparatus on the highway for a typical single-lane one directional set-up: the wind speed co-ordinates system and the USA numbering conventions are indicated. Note that USAs are placed symmetrically respect to central axis of the lane (1,2 one side, 3 other side)

4 NUMERICAL ANALYSIS OF LOSSES AND OF THE PRESSURE/VELOCITY PROFILES

The aim of the numerical activity is to investigate the pressure and velocity profiles generated by a moving truck and to quantify the amount of power lost by skin-friction on the roof of the truck itself. For the latter analysis the data available in the open literature for a Class-8 tractor-trailer are used. According to Ougburn et al. [4], the engine of a truck moving at 100km/h provides an amount of power of approximately 132kW. The 48% of that amount, around 63kW, is wasted for aerodynamic effects that are accounted for when the drag coefficient (Cd) is evaluated. The use of CFD will provide detailed information on the Cd distribution and then on the distribution of losses.

4.1 *Evaluation of the power losses related to the trailer roof skin-friction*

A preliminary analysis based on the assumption that the trailer roof can be treated as a flat plate will provide an estimation of the energetic content of the developing turbulent boundary layer. The skin-friction values for the full-scale GTS case can be estimated considering the drag coefficient values proposed by Storms et al. [5] for a 1/8-scaled model. Dynamic similarity is considered to scale the truck velocity and maintain the same Reynolds numbers. Being the flow incompressible and maintaining the flow viscosity unaltered, the ratio between the model and the full-scale truck velocities is 8. As a consequence, for a truck moving at 100km/h a Re of 4.8E+06 must be considered. According to Storms et al. [5] the total drag coefficient is almost constant for Re number higher than 1E+06, and then a constant value can be assumed. A C_d value of 0.249 is calculated integrating on the trailer the experimental skin friction distribution for the GTS model as found in Storms et al. [5] and depicted in Figure 3 with red squares (the leading edge starting at x/w = 2), together with its interpolation curve (in blue) and the theoretical turbulent flat plate prediction for a Reynolds number of 2.E+06 (dashed black).

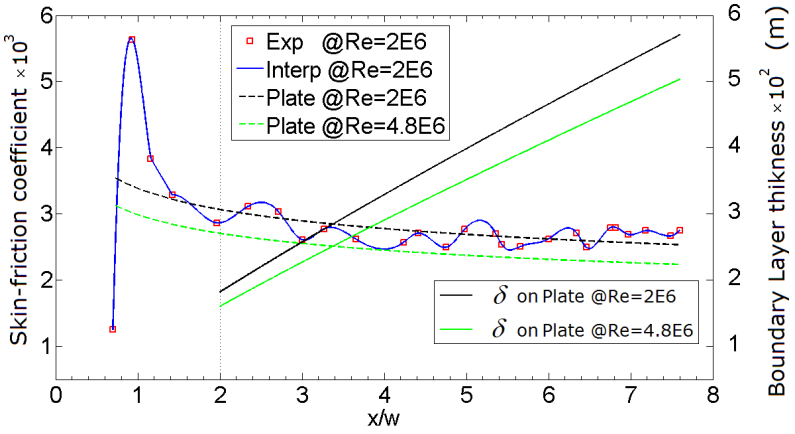

Figure 3. Skin friction and boundary layer thickness distribution for the GTS model at 2.E+06 and 4.8E+06 Reynolds numbers

The evaluation of the skin-friction drag can be performed considering a flat plate subject to the selected conditions. The skin-friction distribution at the needed Reynolds number of 4.8E+06 can be evaluated using Equation 1 (dashed-green curve in Figure 5).

$$c_f = \frac{0.034}{\mathrm{Re}_x^{1/7}} \tag{1}$$

The experimental results obtained on the 1/8-scaled model are compared with the data obtained for a full-scale flat plate at 100km/h in Table 1. Subscript $_c$ stands for "corrected", the latter being used to indicate the GTS total drag coefficient accounting also for the wheels (+0.1, Wood and Bauer [6]), the tractor-trailer gap (+0.1, Wood and Bauer [6]) and the under-body (+0.07, deduced from Diebler and Smith [7]) contributions. It can be evidenced that the $C_{df,roof}$ value obtained for a full-scale truck leads to an underestimated value of total drag contribution (around -13.8%) with respect to the experimental data.

Table 2. Comparison between GTS drag values for different Re numbers

Case	Re	C_d	$C_{d,c}$	$C_{df,roof}$	$C_{df,roof}/C_{d,c}$ (%)
Experimental	2.E+06	0.249	0.519	0.0101	1.95
Flat-plate (full scale)	4.8E+06	0.249	0.519	0.0087	1.68

As suggested by White [16], it is possible to calculate the boundary layer thickness on the roof of the GTS at full-scale. Assuming for simplicity that the boundary layer can be modeled using a power law as suggested by Prandtl, its growth is reported in Figure 5 for Re = 2.E+06 (black curve) and for Re = 4.8E+06 (green curve). Similar evaluations could be performed starting from the data obtained by Storms et al. [5] and varying the Reynolds number to mimic different truck velocities. Values of the boundary layer thickness with varying speed at the leading edge (LE), at the middle point (MP) and at the trailing edge (TE) of the trailer for the full scale GTS are shown in Table 3.

Table 3. Boundary layer thickness at the trailer's roof and skin-friction power losses computed using an approximate approach based on the full-scale flat-plate assumption for a GTS model

Speed	δ (cm)			$P_{f,roof}$
(km/h)	LE	MP	TE	(kW)
90	13.0	27.6	40.9	0.91
100	12.8	27.2	40.3	1.23
110	12.7	26.8	39.7	1.61

Once the value of the skin-friction drag is available it is also possible to evaluate the power transferred to the boundary layers using Equation 2:

$$P_{f,roof} = \frac{1}{2}\rho_r U_r^3 A_r C_{df,roof} \tag{2}$$

In that equation U_r is the vehicle's speed, ρ_r is the air density at ambient conditions and A_r is the projected area of the truck as seen from the main-flow. Although skin-friction coefficients are made non-dimensional basing on the wetted area, the truck frontal area is now used for homogeneity with the drag coefficient definition. The truck power transferred to the roof boundary layer is reported in Table 2. As can be seen, at 100 km/h the power losses generated by the skin-friction on the roof of the trailer amounts to 1.23kW, which is around 1% of the total power produced by the engine and around 2% of the aerodynamic losses. The obtained results demonstrate that the skin-friction on the trailer roof provides a negligible contribution to the net aerodynamic

losses. It is worth noting that these flat-plate predictions assume implicitly that the boundary layer transition locates at the same point of the experimental case, while increasing the Reynolds number implies that transition occurs somewhere before and that boundary layer becomes thinner. Therefore, numerical simulations are necessary to focus into the flow field around the truck, where the prevailing losses are spent to displace the fluid from the vehicle way.

4.2 *CFD of the selected cases*

As already pointed out, the RANS approach is used to study a truck moving in a leveled and windless highway. Several simulations have been performed to gain general rules for the phenomena involved, also considering the effects of trailing trucks.

4.2.1 *2D results*

Since one of the objectives of the activity is to evaluate the height of the recirculating boundary layer over the trucks, comparisons are always performed considering the last truck of the row. Only the results obtained for 100km/h will be shown, being negligible the differences between the non-dimensional profiles obtained for the other cases. Furthermore, there are no relevant differences between the case with wheels and the case that mimic the central section of a real truck, and then only the case with wheels will be shown. The data obtained for the no-wheels case will be used in the evaluation of the total drag coefficient. The non-dimensional absolute axial velocity profiles are shown in Figure 4 and Figure 5-a for the case with wheels. Velocity profiles are depicted for three axial positions: the leading edge (LE) and trailing edge (TE) of the trailer and its mid-point (MP). The absolute axial component of the velocity is divided by the truck velocity U_0; the distance from the road is divided by the height of the truck. Dashed lines indicate the minimum height where obstacles position is allowed in European countries. For each profile, the Y/H position that corresponds to the $V_x/U_0 = 0$ value can be considered as the height where the separation bubble ends. As can be observed, the highest value of the separation bubble height, reached near the TE, is almost negligible when considering a single truck moving along the lane, being Y/H around 1.1 at the TE for $V_x = 0$. A different behavior can be observed looking at the last truck of a row of two or three, being the Y/H value correspondent to the bubble closure always equal to or higher than 1.2. In fact, at the LE the Y/H value reaches values of 1.3 for a row of three (Figure 4-a) and maintained over 1.25 also at MP (Figure 4-b) and TE (Figure 5-a). The latter result indicates that the separation bubble never reattach on the third truck when considering a row of three, which is a conditions that often occurs.

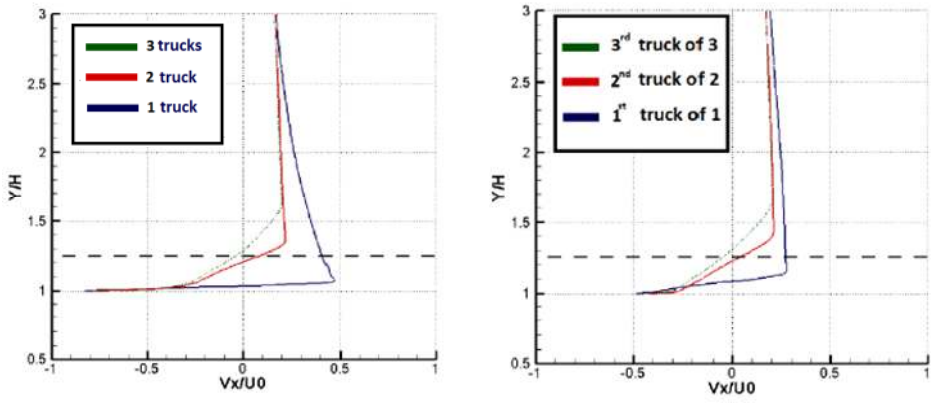

(a) 100km/h @LE, W (b) 100km/h @MP, W

Figure 4. Leading edge and mid-point profiles for wheel (W) case at 100km/h

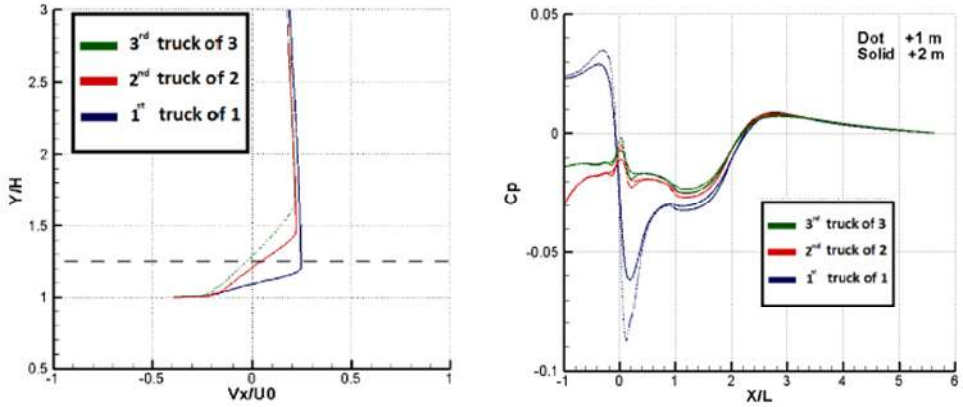

(a) 100km/h @TE, W (b) 100km/h, W

Figure 5. Trailing edge profiles for wheel (W) case and pressure coefficient distribution at 100km/h

That differences between the flow fields are also evidenced by the absolute velocity field near LE and TE for the cited cases, as shown using the same velocity scales in Figure 6 and Figure 7. The flow separation is depicted with a red line (that indicates $V_x = 0$) in Figure 6-a near the LE and in Figure 7-a near the TE of the first truck. As can be seen, the effect induced by the skin-friction on the shear layer is limited and the flow velocity turns to 0 not far from the trailer roof. Looking at the velocity field generated by the third truck (Figure 6-b and Figure 7-b), it is clearly visible that the flow is almost constant and moves in the direction of the truck, which means that the flow is completely separated. It can be supposed that the longest the truck row will be, the higher will be the separated region. It is worth mentioning that the Y/H value where an undisturbed flow can be individuated is at least 1.15 for the first truck at MP (Figure 5-a). Considering a value of 4m for H, which is the value chosen in this study as representative of European trucks, the height of the boundary layer is at least 60cm instead of the 40cm predicted for 100km/h by the flat plate approach (Table 3). The latter neglect the presence of flow separation, which is the driving phenomenon when studying trucks aerodynamics. It must be observed that in a 2D simulation, the blockage effect of the truck height is a crucial parameter and that the velocity modules are slightly overestimated. Nevertheless, the observed trends will not change in a realistic environment, as demonstrated by the experimental campaign described below.

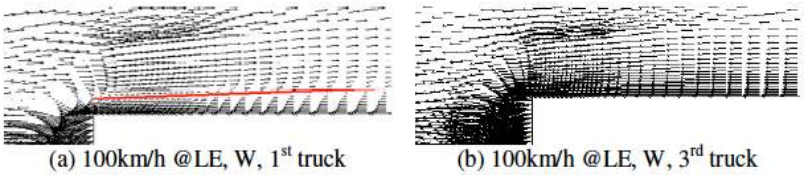

(a) 100km/h @LE, W, 1st truck (b) 100km/h @LE, W, 3rd truck

Figure 6 Leading edge profiles for wheel case at 100km/h

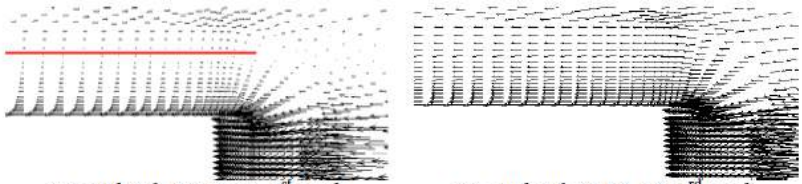

(a) 100km/h @TE, W, 1st truck (a) 100km/h @TE, W, 3rd truck

Figure 7 Trailing edge profiles for wheel case at 100km/h

A final comment can be done on the pressure fields associated to the already discussed velocity profiles. In Figure 5-b the pressure coefficient C_p is reported for two different heights above the truck roof. As expected, the pressure fluctuation associated with the first truck is quite high (from +0.35 to -0.9) and the overall C_p trend is coherent with the description provided by Cali and Covert [2]. The subsequent trucks are subject to a smaller pressure drop that results in a smaller drag coefficient associated to the truck progress.

4.3 *C_d distribution*

The drag coefficients calculated using the data obtained from the numerical simulation of a single truck are shown in Table 4 for three different velocities. The C_d value is evaluated considering both the pressure (C_{dp}) and the skin-friction (C_{df}) effects. The relative contribution of the roof skin-friction to the total C_d can be compared with the data found in the open literature and from the flat plate approach (Table 2). It can be observed that the $C_{df,roof}/C_d$ value obtained for 100km/h is very similar to the experimental one (1.95%). That means that a 2D analysis is able to predict with reasonable accuracy the viscous drag effects also with a steady assumption, and that such kind of approach could be considered as a preliminary step in the truck shape optimization, prior to the use of accurate but demanding approaches as URANS or LES.

Table 4. Drag values calculated using both NW and W data

Speed (km/h)	C_{dp}	C_{df}	C_d	C_{df}/C_d (%)	$C_{df,roof}/C_d$ (%)
90	0.466	0.0172	0.483	3.50	1.79
100	0.464	0.0173	0.481	3.16	1.81
110	0.463	0.0168	0.432	3.47	1.80

5 EXPERIMENTAL TESTS ON A HIGHWAY

Vehicle-induced turbulence, hence the mark of the wind flow generated by road traffic, is highlighted via TKE turbulent kinetic energy:

$$e_i = \frac{1}{2}\left(\overline{u'^2_i} + \overline{v'^2_i} + \overline{w'^2_i}\right) \tag{3}$$

In particular, according to Kalthoff et al. [17], TKE difference between anemometer position lee and windward, normalized to wind speed u directed across highway, shows a strong correlation (R=0.77) with hourly traffic density of heavy duty vehicles circulating at a mean speed V=120 km/h. This is globally a sign of non-negligible energy along a non-ambient wind direction, due to highway traffic. Stemming from these global findings, the experimental campaign illustrated in Figure 2 goes further into the reconstruction of the wind profile due to heavy-duty traffic. A first signal processing gives the time domain results as presented in Figure 8. Mean ambient wind speed is evaluated each 10' and subtracted to obtain turbulent components (blue to green lines in Figure 8). The issue of filtering possible turbulent ambient wind speeds is addressed considering that atmospheric wind spectrum is generally characterized by a macro meteorological peak, followed by a spectral gap (10' to 60') and a micro meteorological peak (45"-50"). While single vehicle passages occur at sub 1" periods (gray bands in Figure 8), columns of trucks are also encountered collectively giving non negligible TKE during up to 50" periods: applying a multi-band filter to exclude both macro and micro atmospheric peaks is therefore not advisable, preferring a base band (random noise) Parks-McClellan FIR linear phase filter at 0.05 Hz cut-off (red line in Figure 8). It is worth noting from wind speed sign in Figure 8 that the flow moves in the direc-

tion of the truck and not opposite, as previously discussed and obtained via CFD. Finally, the peak detector fed with such a filtered signal, could detect the correct local maxima by looking for downward zero-crossings in the smoothed first derivative that exceeded a certain pre-determined minimum "slope threshold" at those points where signal exceeded a certain minimum "amplitude threshold", determining the coordinates (time instant and height), and approximate width of each peak by least-squares curve-fitting the top part of the peak (Oppenheim et al. [18]).

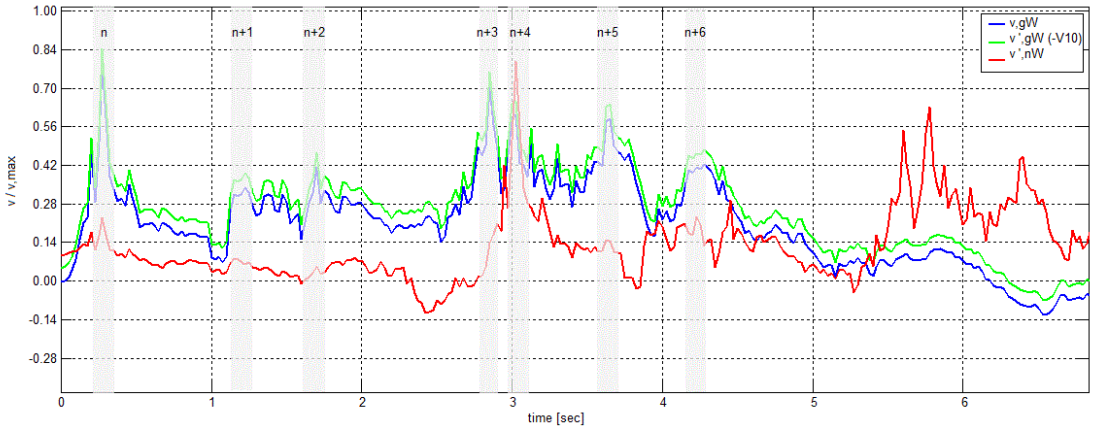

Figure 8 Sub-process n°6/12: 12h00 to 14h00: Time series of the normalized wind speed component directed along highway at 5.50m high USA: gross wind (blue), turbulent wind (green), turbulent filtered wind (red). Leading edge passages are also highlighted in gray bands.

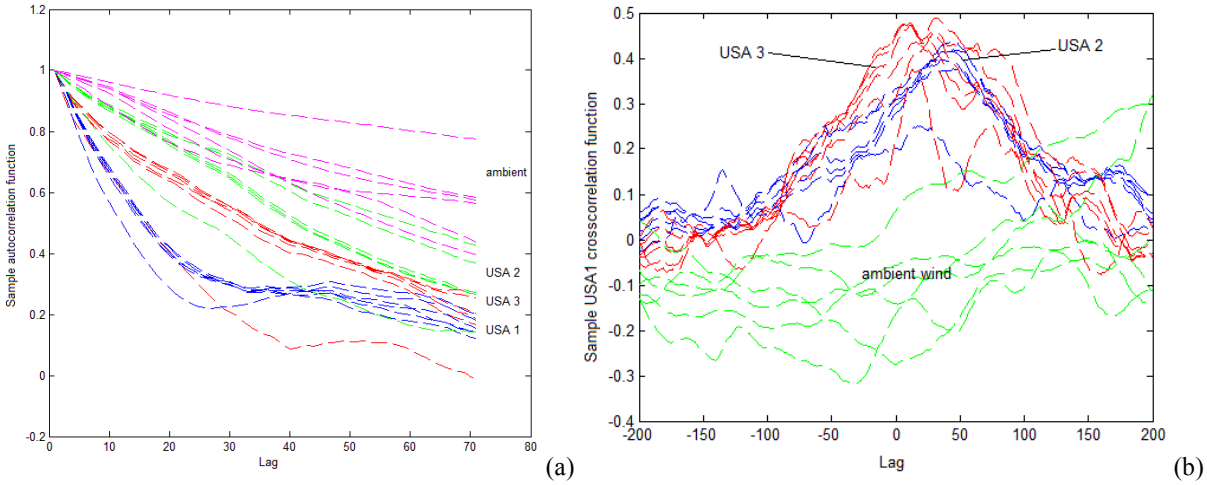

(a) (b)

Figure 9. Sub-process n°6/12: 12h00 to 14h00: (a) Sample autocorrelation functions of the single lane USA for multiple days realizations: USA 1 blue, USA 2 green, USA 3 red, ambient wind magenta; (b) Sample cross-correlation functions of USA 1 with USA 2 (blue), USA 3 (red) and ambient wind (green) for multiple days realizations. Refer to Figure 3 for USA numbering convention and geometry.

Frequency domain signal analysis is aimed at extracting the PSD of the daily traffic process, which is conveniently divided into 12 homogeneous sub-processes of 2 hours slice. Such hypothesis of circadian rhythm can be verified by a look at Figure 9-a, where multiple samples of different days (Monday to Friday population) show autocorrelation functions of the single lane USAs (see Figure 2 for numbering) that are generally less scattered than ambient wind USA. Furthermore USA 1, closest to top of truck, shows the narrowest band autocorrelation. Figure 9-b shows sample cross-correlation functions of the closest USA 1 to top of truck with other instruments of

the single-lane set: low coherence of the traffic induced turbulence with ambient wind results self-evident, while peaks and phase shifts in vertical upper USA 2 and lateral intermediate USA 3 positions (please refer to Figure 2 for USA numbering convention) tell us something about the three-dimensional structure of the separated wave induced by traffic. In fact, a high correlation and a minor shift with lateral intermediate position indicates possibly a proof for the experimental set-up assumption of the flow acting similarly in the 3.5m lane width as a whole; note also that symmetrical truck side edges vorticities can be considered in USA 1-USA 3 cross-correlation measurements, as the anemometers are placed symmetrically respect to central axis of truck (assumed to coincide with central axis of the lane, see Figure 2). Similarly, coherence of the three-dimensional structure of the wave can be assessed from the fact that in Figure 9-b cross-correlation peak with upper USA 2 is delayed from the peak of lower USA 3, closer to the wave source.

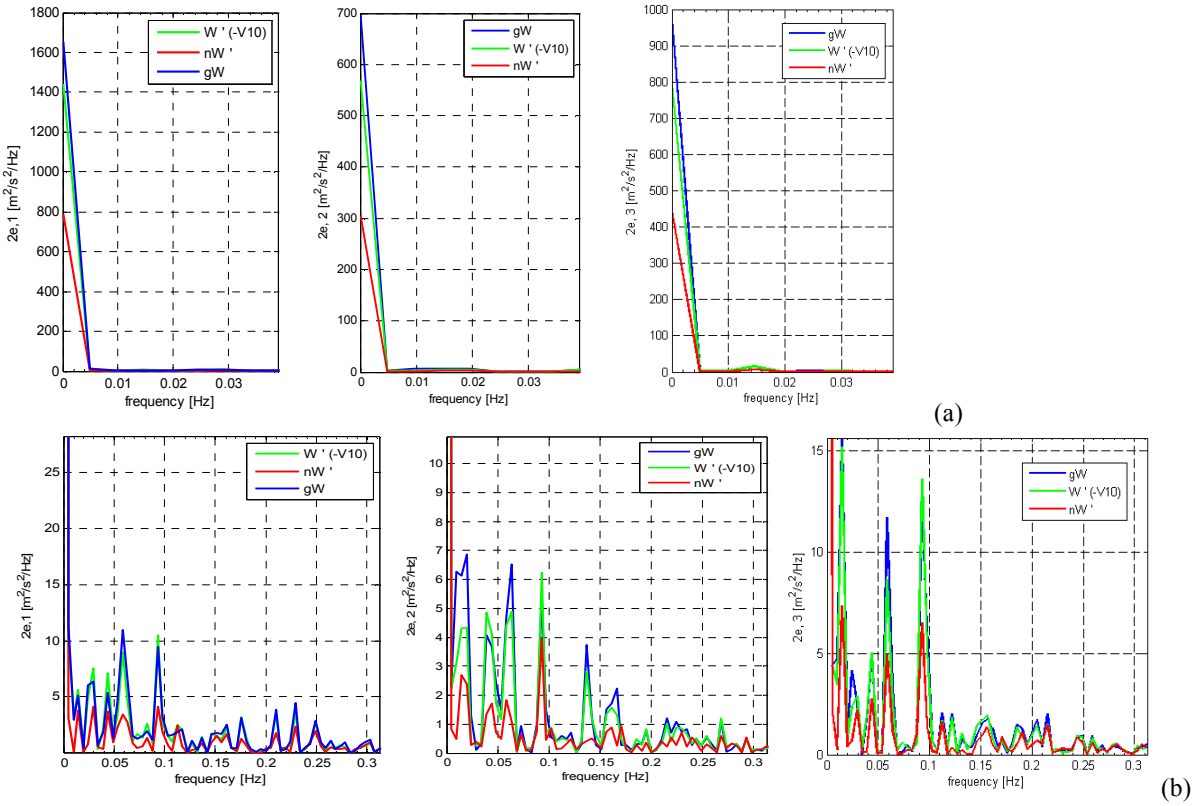

Figure 10. Sub-process n°6/12: 12h00 to 14h00: (a) PSD or 2e of USA 1, 2 and 3: detail of 0 Hz region of spectra; (b) PSD or 2e of USA 1, 2, and 3: detail of sub-Hertzian region of spectra. Each PSD contains three different signals transforms: gross wind (blue), turbulent wind (green), turbulent filtered wind (red).

Ergodicity assumption is also used to derive the PSD of the 12 sub-processes as the limit of the statistic mean:

$$\lim_{T\to\infty} E[\widetilde{PSD}_{\mathbf{gW-V_m}}(f)_T] = PSD_{\mathbf{gW-V_m}}(f) \tag{4}$$

where $\mathbf{gW - V_m}$ indicates the turbulent filtered signal. In fact, under the verified cyclostationary process assumption, one can take N days samples as N realizations, thus feeding equation (4) with:

$$\widetilde{PSD}_{\mathbf{gW}-\mathbf{V_m}}(f) = \frac{1}{N}\sum_{n=0}^{N-1}\frac{1}{T}\left|FFT\left(\mathbf{gW}-\mathbf{V_m}\right)_N\right|^2 \quad (5)$$

Pseudo spectral density of the absolute value of the turbulent wind vector can be seen as twice the relative TKE (see Equation 3). In Figure 10 are therefore presented the PSD or TKE of the single-lane anemometers set: detail is given to show both the 0 Hz and sub-Hertzian regions of the spectra containing energy. As the single vehicle passage has a main frequency widely above the sub-Hertzian region, the peak frequencies highlighted in Figure 10 can be typical of a certain regularity in the transit process, or to better say the slow separated wave of a column of trucks may be credited with.

6 CONCLUSIONS

It has been demonstrated that a 2D numerical approach is sufficiently accurate for a preliminary study of the drag coefficient and of the flow field related to the truck passing. Furthermore, flow structures above the truck have been successfully described. A direct link between the height of the separation bubble and the number of trucks has also been individuated both using CFD and experimental analysis.
In fact, results obtained from the motorway campaign have demonstrated good agreement with CFD simulations in reconstructing the wind velocity profiles for truck aerodynamic losses. In particular the contribute due to interaction between pressure wave, rear wake, and vehicles gap has proven to distinguish flow in high traffic density, and can be characterized by the proposed experimental set-up.

7 REFERENCES

[1] M.N. Albert. Field Testing of Cantilevered Traffic Signal Structures under Truck-Induced Gust Loads. MSc Thesis, University of Austin, Texas, May 2006.

[2] P.M. Cali and E.E. Covert. Experimental Measurements of the Loads Induced on an Overhead Highway Sign Structure by Vehicle-Induced Gusts. Journal of Wind Engineering and Industrial Aerodynamics, 84:87–100, April 2000.

[3] A.D. Quinn, C.J. Backer and N.G. Wright. Wind and Vehicle Induced Forces on Flat Plates - Part 2: Vehicle Induced Force. Journal of Wind Engineering and Industrial Aerodynamics, 89(9):831–847, April 2001.

[4] M. Ougburn, L. Ramroth and A.B. Lovins. Transformational Trucks: Determining the Energy Efficiency Limits of a Class-8 Tractor-Trailer. Rocky Mountain Institute Report, T08-08, July 2008.

[5] B.L. Storms, J.C. Ross, J.T. Heineck, S.M. Walker, D.M. Driver and G.G. Zilliac. An Experimental Study of the Ground Transportation System (GTS) Model in the NASA-Ames 7- by 10-ft Wind Tunnel. NASA Technical Memorandum, TM-2001-209621, February 2001.

[6] R.M. Wood and S.X.S. Bauer. Simple and Low-Cost Aerodynamic Drag Reduction Devices for Tractor-Trailer Trucks. SAE Technical Paper, 2003-01-3377, November 2003.

[7] C. Diebler and M. Smith. A Ground-Based Research Vehicle for Base Studies at Subsonic Speeds. NASA Technical Memorandum, TM-2002-210737 ,April 2002.

[8] K. Salari, J.M. Ortega and P.J. Castellucci. Computational Prediction of Aerodynamic Forces for a Simplified Integrated Tractor-Trailer Geometry. AIAA Fluid Dynamics Meeting, Portland, OR, United States, UCRL-CONF-204887, June 2004.

[9] C.J. Roy, J. Payne and M. McWherter-Payne. RANS Simulations of a Simplified Tractor/Trailer Geometry. ASME J. Fluids Eng., 128(5):1083 (7 pages), September 2006.

[10] S.P. Veluri, C.J. Roy, A. Ahmed, R. Rifki, J.C. Worley and B. Recktenwald. Joint Computational/Experimental Aerodynamic Study of a Simplified Tractor/Trailer Geometry. ASME J. Fluids Eng., 131(8):081201 (9 pages), August 2009.

[11] W.D. Pointer. Commercial CFD Code Validation for External Aerodynamics Simulations of Realistic Heavy-Vehicle Configurations. In "DOE Project on Heavy Vehicle Aerodynamic Drag FY 2005 Annual Report", UCRL-TR-217193, November 2005.
[12] D.G. Hyams, K. Sreenivas, R. Pankajakshan, D.S. Nichols, W.R. Briley and D.L. Whitfield. Computational Simulation of Model and Full Scale Class 8 Trucks with Drag Reduction Devices. Computers and Fluids, 41(1):27-40, February 2011.
[13] S. Maddox, K.D. Squires, K.E. Wurtzler and J.R. Forsythe. Detached- Eddy Simulation of the Ground Transportation System. In "The Aerodynamics of Heavy Vehicles: Trucks, Buses, and Trains." Lecture Notes in Applied and Computational Mechanics, Book 19. October 2004.
[14] S. Krajnović and L. Davidson. Development of Large-Eddy Simulation for Vehicle Aerodynamics. In: Proc. of IMECE2002, New Orleans, Louisiana, USA, IMECE2002-32833, November 2002.
[15] J. Östh. A LES Study of a Simplified Tractor-Trailer Model. Master's Thesis in Solid and Fluid Mechanics, Chalmers University Of Technology, 2010:34, 2010.
[16] F.M. White. Fluid Mechanics. McGraw-Hill, Fourth Edition, November 2002.
[17] N. Kalthoff, D. Baumer, U. Cosmeier, M. Kohler and B. Vogel, Vehicle Induced Turbulence near a Motorway, Atmospheric Environment, 39:5737-5749, 2005.
[18] A. V. Oppenheim, R. W. Schafer, J. R. Buck, Discrete-Time Signal Processing (2nd Edition) (Prentice-Hall Signal Processing Series), June 2011

The Seventh International Colloquium on Bluff Body Aerodynamics and Applications (BBAA7)
Shanghai, China; September 2-6, 2012

Wind tunnel measurements of aerodynamic forces on vehicles and bridges under crosswinds

Yan Han[a], Steve C. S. Cai[b,a], Zhengqing Chen[c], Jiexuan Hu[a], Chunguang Li[a]
[a]*School of Civil Engineering and Architecture, Changsha University of Science & Technology, Changsha, Hunan, China, 410004*
[b]*Department of Civil and Environmental Engineering, Louisiana State University, Baton Rouge, USA, LA 70803*
[c]*Wind Engineering Research Center, College of Civil Engineering, Hunan University, Changsha, Hunan, China, 410082*

ABSTRACT: An accurate identification of the aerodynamic characteristics of vehicles and the corresponding bridge is the premise for the coupling vibration analysis of the wind-vehicle-bridge system. At present, the interaction of aerodynamic forces between the road vehicles and bridge is ignored in most researches. In the present study, an experimental setup was made to measure the aerodynamic characteristics of vehicles and the bridge for different cases in a wind tunnel considering the aerodynamic interference. The influence of the wind turbulence, the wind speed, the vehicle interference, and the distance of vehicle from the windward edge of the deck on the aerodynamic coefficients of vehicles, and the influence of vehicles on the static coefficients of the bridge were investigated based on the experimental results. The change reasons of the aerodynamic characteristics of vehicles and the bridge were attempted to be researched and the reliability of the measured results was validated according to the results of surface pressure of the vehicle and the bridge. The measured results showed that the wind turbulence, the vehicle interference, and the vehicle distance from the windward edge significantly affected the aerodynamic coefficients of vehicles. However, the influence of the wind speed on the aerodynamic coefficients of the studied vehicle is small. The static coefficients of the bridge were also significantly influenced by the presence of vehicles.

KEYWORDS: wind-vehicle-bridge system; cross winds; aerodynamic characteristics; aerodynamic interference; wind tunnel tests; numerical simulation.

1 INTRODUCTION

Economic and social developments increase tremendously the traffic volume over bridges and roads. Heavy road vehicles on bridges may significantly change the local dynamic behavior and affect the fatigue life of the bridge. On the other hand, the vibrations of the bridge under cross winds also in turn affect the safety of the road vehicles. These inevitably increase the potential risk of road vehicles moving on a bridge and subjected to strong winds. Thus, it is important to study the dynamic interaction between the bridge, road vehicles, and wind loads for ensuring the safety and normal working performance of both the road vehicles and bridge. Most existent research works focus on either wind action on vehicles running on roadway (Baker, 1986; 1987; 1988; 1991a,b), wind effect on the bridge without considering vehicles (Scanlan, 1990), or vehicle-bridge interaction analysis without considering wind effect (Yang, 1997; Pan, 2002).

For exactly estimating the response of a bridge and the safety of the vehicles moving on the bridge under cross winds, it is necessary to establish an analytical framework of vehicle-bridge-wind interaction. This problem has been noticed and studied by researchers in China and abroad. Xu et al. (2003) have investigated the coupled dynamic analysis of road vehicle and cable-stayed bridge system under turbulent wind. Cai et al. (2004) have built a framework for the vehicle-

bridge-wind aerodynamic analysis, which lays a very important foundation for road vehicle accident analysis based on dynamic analysis results and facilitates the aerodynamic analysis of bridges considering vehicle-bridge-wind interaction. Han and Chen (2007) also presented a state of the art three-dimensional dynamic model of the wind-vehicle-bridge coupling vibration. However, the aerodynamic forces on vehicles in previous studies were either built on the work undertaken by Baker [1991a,b] or obtained from wind tunnel tests, which did not consider the interaction of aerodynamic forces between the road vehicles and the bridge.

The aerodynamic force coefficients of vehicles under wind loads depend on not only the shapes of vehicles but also those of infrastructures, such as the bridge. On the other hand, the aerodynamic parameters of the bridge will be influenced by the vehicles on it. Therefore, in order to predict the performance of vehicle-bridge system under wind loads rationally, it is necessary to study the aerodynamic properties of road vehicles and bridges considering the interaction of aerodynamic forces between the road vehicles and the corresponding bridges. There is a wealth of data pertaining to the wind load coefficients for vehicles on standard 'open ground' scenario (Baker, 1991a; Quinn et al., 2007). However, the corresponding data for bridge decks with vehicles is sparse. Coleman and Baker (1990; 1994) measured the load coefficients of an articulated lorry positioned on the bridge deck model. Minoru Suzuki et al. (2003) carried out three kinds of wind tunnel tests to evaluate the aerodynamic characteristics of typical configurations of vehicles on typical configurations of infrastructures such as bridges and embankments. But the load coefficients of the bridge deck model were not presented. Li et al. (2004) developed a separation device, called the Cross Slot System, to measure the aerodynamic characteristics of the rail vehicle-bridge system taking aerodynamic interaction between the rail vehicle and the bridge into account. Diana and co-workers (Diana, 2004; 2006) undertaken much work on the aerodynamic effects of rail vehicles. Though these researches (Li, 2004; Diana, 2004; 2006) aimed at rail vehicles, the method is worth learning for road vehicles. Han et al. (2011) calculated the load coefficients for a car container running on the bridge and the load coefficients for the bridge were also investigated by numerical simulations (CFD).

This paper developed an experiment technique and carried out a series of wind tunnel experiments to examine the aerodynamic characteristics of vehicles and bridge in the HD-2 wind tunnel at Hunan University. All the measurements were undertaken in static conditions (i.e., with no vehicle movement) over a range of yaw angles from 0^o~90^o. The tests were carried out in both smooth flow and high turbulence flow simulated by a turbulence producing grid.

The experimental set-up adopted for the wind tunnel tests is outlined in Section 2, which illustrates the bridge deck and vehicle geometries and the instrumentation, test conditions and testing procedure, and the characteristics of the simulated wind. Section 3 reports and examines the values of the aerodynamic force/moment coefficients of the vehicle and the bridge corresponding to a variety of configurations tests. More specifically, the six studied cases are presented and compared. Finally, some conclusions are drawn in Section 4. It is found that the wind turbulence, the vehicle interference, and the vehicle distance from the windward edge significantly affected the aerodynamic coefficients of vehicles. However, the influence of the wind speed on the aerodynamic coefficients of the studied vehicle is small. The static coefficients of the bridge were also significantly influenced by vehicles.

2 WIND TUNNEL EXPERIMENTS

The experiment is carried out in the HD-2 wind tunnel of Hunan University that is a low-speed, one-close-circuit medium-sized boundary layer wind tunnel with two parallel test sections.

2.1 *Bridge deck and vehicle geometries*

The models are made with polymethylmethacrylate and the scale is 1:32. The bridge section model is divided into three parts. The intermediate part is the testing model with a length of 1.04 m. The two terminal parts are the compensation models with a length of 0.5 m, the role of which is to avoid the flow around the end and to improve the test precision. The distance between the intermediate part and the terminal part is 0.005 m. The details and dimensions of the bridge deck section and the vehicle are given in Figs. 1a and 1b. The distance between the bottom of the vehicle and the top surface of the bridge deck is 0.015 m. The distance of the vehicle from the bridge deck windward edge is defined by *d* with the values of 0.166 m and 0.547 m corresponding to the two different transverse positions of the vehicle on the bridge deck, windward and leeward, as shown in Fig. 1c. Three vehicles are made to investigate the aerodynamic interference between vehicles, which are laid on the bridge deck with an equal distance of 0.156 m between vehicles along the longitudinal direction, as shown in Fig. 1c. The middle vehicle model is the test vehicle and the terminal vehicle models are the interference vehicles.

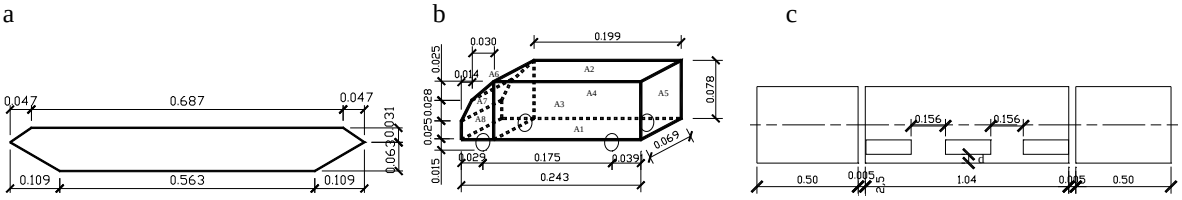

Fig.1 Model geometry and overall dimensions (Unit: m) (a: Bridge cross section model; b: Vehicle model; c: Layout plan of the model)

2.2 *Experimental set-up*

The experimental set-up is composed of three test frames, the middle test frame and the two end compensation frames, as shown in Fig. 2, each of which is composed of three parts, the upper, the middle, and lower parts. The upper part fixes the model to the test frame by using bolts. The middle part is the circular steel tube with a litter smaller diameter, of which the top is connected with the upper part by using bolts and the end is inserted into the circular steel tube of the lower part and fixed with the lantern ring. The lower part is the composite structure of the circular steel tube with a greater diameter and steel bar, which is connected with the rotating table in the wind tunnel by using bolts. In the experimental process, the test frames and the models are rotating with the table together to vary the wind yaw angle.

2.3 *Turbulence wind field simulation*

A passive turbulence generator was developed for generating homogeneous turbulence wind field, as shown in Fig. 3. The characteristics of the generated flow in the wind tunnel were measured by a TFI Series 100 cobra probes (Turbulent Flow Instrumentation). The turbulence intensity at the deck height was approximately 10% in the flow direction. The longitudinal integral scale for the streamwise velocity was 0.5 m which is well above the vehicle height (or length or width); thus ensuring that the turbulent structures are well correlated over the vehicles.

Fig. 4 indicates the power spectral density of the approaching streamwise velocity. To facilitate a comparison between the wind tunnel simulation and the target spectrum at full scale (i.e., the Von Karman Spectrum) both the axes in Fig. 4 have been non-dimensionalized. The horizontal axis represents the reduced frequency ($\overline{f} = f.L_u / U$) defined by the product of the frequency (*f*) and the turbulence length scale (L_u), divided by the reference mean wind speed. On the vertical axis the spectrum is multiplied by the frequency and divided by the mean velocity variance. The experimental and target spectra agree qualitatively well over a large proportion of the reduced frequency range, which suggests that the turbulence simulation is sufficient for the current purposes.

2.4 *Force measurements*

The forces on the bridge and the vehicle were determined by integrating the pressure of the pressure taps measured using electronically scanning pressure measurement system. The bridge model was installed with 329 pressure-taps, mounted flush with the surfaces of the bridge model and connected to the pressure transducers via flexible tubing. Seven pressure-tapped strips were located along the span of the bridge deck, as shown in Fig. 5a, to take into account the span-wise correlation of the aerodynamic forces. Each pressure-tapped strip has 47 pressure-taps representing the surface pressure distributions, as shown in Fig. 5b. The vehicle model was installed with 200 pressure-taps, as shown in Fig. 6. Figs. 7 and 8 outline the sign conventions for aerodynamic forces of the bridge and the vehicle, respectively.

Fig.2 Experimental setup

Fig. 3 Passive grid device

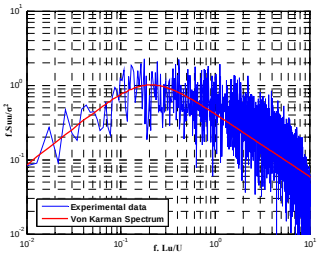

Fig. 4 Power spectral density of wind field

a b

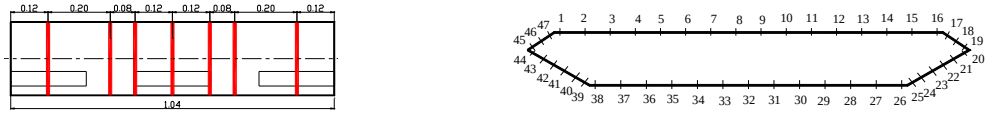

Fig. 5 The sketch map of pressure taps of the bridge cross section: (a) The positions of seven pressure-tapped strips (dimensions in meters); (b) The positions and notions of pressure-taps for each pressure-tapped strip

a b c d e f

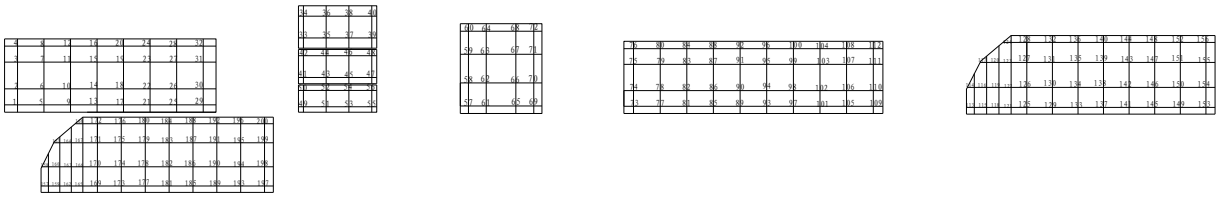

Fig. 6 The positions and notions of pressure-taps for each surface of the vehicle: (a) Top surface; (b) Frontal surface; (c) Back surface; (d) Bottom surface; (e) Left side surface; (f) Right side surface

The instantaneous fluctuating surface pressure at time t in a particular strip (j=1-7) were integrated independently over each of the seven pressure-tapped strips. The lift force $F_{Vj}(t)$, drag force $F_{Hj}(t)$ and the pitching moment $M_j(t)$ per unit span length of the bridge deck were calculated according to Equations (1a), (1b) and (1c), respectively, as:

$$F_{Vj}(t)=\sum_{i=1}^{47} p_{ij}(t)\Delta A_{ij}\cos(\alpha_{ij}) \qquad (1a)$$

$$F_{Hj}(t)=\sum_{i=1}^{47} p_{ij}(t)\Delta A_{ij}\sin(\alpha_{ij}) \qquad (1b)$$

$$M_j(t)=\sum_{i=1}^{47} p_{ij}(t)\Delta A_{ij}d_{Hij}\sin(\alpha_{ij})+\sum_{i=1}^{47} p_{ij}(t)\Delta A_{ij}d_{Vij}\cos(\alpha_{ij}) \qquad (1c)$$

where $p_{ij}(t)$ = the instantaneous fluctuating surface pressure of the bridge at time t; ΔA_{ij} = the tributary area of a pressure-tap of the bridge; α_{ij} = angle between the local (pressure-tap) and vertical axis; and d_{Hij}, d_{Vij} = pitching moment arms about the centre of the bridge deck.

The instantaneous fluctuating surface pressures at time t were integrated independently over each surface of the vehicle. The side force $F_S(t)$, lift force $F_L(t)$, drag force $F_D(t)$, pitching moment $F_P(t)$, yawing moment $F_R(t)$, and rolling moment $F_R(t)$ of the vehicle were calculated according to Equations (2a), (2b) and (2c), respectively, as:

$$F_S(t)=\sum_{i=1}^{200} p_i(t)\Delta A_i\Theta_{Si} \quad (2a) \qquad F_L(t)=\sum_{i=1}^{200} p_i(t)\Delta A_i\Theta_{Li} \quad (2b) \qquad F_D(t)=\sum_{i=1}^{200} p_i(t)\Delta A_i\Theta_{Di} \quad (2c)$$

$$F_P(t)=\sum_{i=1}^{200} p_i(t)\Delta A_i\Theta_{Li}d_{(L\text{-}S)i}+\sum_{i=1}^{200} p_i(t)\Delta A_i\Theta_{Di}d_{(D\text{-}S)i} \quad (2d)$$

$$F_Y(t)=\sum_{i=1}^{200} p_i(t)\Delta A_i\Theta_{Si}d_{(S\text{-}L)i}+\sum_{i=1}^{200} p_i(t)\Delta A_i\Theta_{Di}d_{(D\text{-}L)i} \quad (2e)$$

$$F_R(t)=\sum_{i=1}^{200} p_i(t)\Delta A_i\Theta_{Li}d_{(L\text{-}D)i}+\sum_{i=1}^{200} p_i(t)\Delta A_i\Theta_{Si}d_{(S\text{-}D)i} \quad (2f)$$

where $p_i(t)$ =the instantaneous fluctuating surface pressure of the vehicle at time t; $\Delta A_i(t)$ the tributary area of a pressure-tap of the vehicle; Θ_{Fi} ($F=S, L, D$)= the decomposition coefficients of surface pressure along the direction of side, lift, or drag force; $d_{(L\text{-}S)i}$ and $d_{(D\text{-}S)i}$ =horizontal moment arms of lift force and vertical moment arm of drag force contributing to the pitching moment, respectively; $d_{(S\text{-}L)i}$ and $d_{(D\text{-}L)i}$ = horizontal moment arms of side force and horizontal moment arm of drag force contributing to the yawing moment, respectively; $d_{(S\text{-}D)i}$ and $d_{(L\text{-}D)i}$.= vertical moment arm of side force and horizontal moment arms of lift force contributing to the rolling moment, respectively.

Based on the integrated lift force, drag force, and pitching moment, the corresponding force and moment coefficients of the bridge were determined according to Equations (3a), (3b) and (3c), respectively, as:

$$C_{F_H}=\frac{1}{7}\sum_{j=1}^{7}\frac{\bar{F}_{Hj}}{0.5\rho U^2B} \quad (3a) \qquad C_{F_V}=\frac{1}{7}\sum_{j=1}^{7}\frac{\bar{F}_{Vj}}{0.5\rho U^2B} \quad (3b) \qquad C_M=\frac{1}{7}\sum_{j=1}^{7}\frac{\bar{M}_j}{0.5\rho U^2B^2} \quad (3c)$$

where ρ = the air density; U = the mean wind speed on the elevation of the bridge; $\bar{F}_{Hj}$, $\bar{F}_{Vj}$ and $\bar{M}_j$ = the time averaged values of the lift force, drag force, and pitching moment in equations (1a), (1b) and (1c) over the required time period for Strip j; and B= the width of the bridge deck.

Based on the integrated side force, lift force, drag force, pitching moment, yawing moment, and rolling moment, the corresponding force and moment coefficients of the vehicle were determined according to Equations (4a)-(4f), respectively, as:

$$C_S(\psi)=\frac{\bar{F}_S}{0.5\rho V^2A} \quad (4a) \qquad C_L(\psi)=\frac{\bar{F}_L}{0.5\rho V^2A} \quad (4b) \qquad C_D(\psi)=\frac{\bar{F}_D}{0.5\rho V^2A} \quad (4c)$$

$$C_P(\psi)=\frac{\bar{F}_P}{0.5\rho V^2Ah} \quad (4d) \qquad C_Y(\psi)=\frac{\bar{F}_Y}{0.5\rho V^2Ah} \quad (4e) \qquad C_R(\psi)=\frac{\bar{F}_R}{0.5\rho V^2Ah} \quad (4f)$$

where $\bar{F}_S$, $\bar{F}_L$, $\bar{F}_D$, $\bar{F}_P$, $\bar{F}_Y$ and $\bar{F}_R$ = the time averaged values of the side force, lift force, drag force, pitching moment, yawing moment, and rolling moment in equations (2a)-(2f) over the required time period; A= frontal area of the vehicle; h is the distance from the gravity center of the vehicle to the road surface; and V is the relative wind speed to the vehicle, of which the specification is shown in Fig. 9.

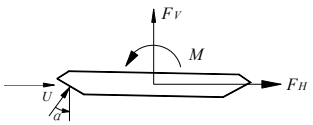

Fig. 7 Sign convention for aerodynamic forces of the bridge

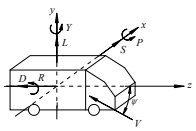

Fig. 8 Sign convention for aerodynamic forces of the bridge

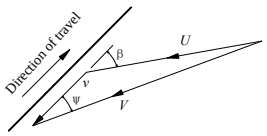

Fig. 9 Velocities and directions

In Fig. 9, v is the vehicle speed; ψ is the relative wind yaw angle to the vehicle; β is the angle between the wind direction and the vehicle direction of travel, and $\psi=\beta$ in this paper.

2.5 *Test configurations and experimental procedure*

Table 1 outlines the experimental configurations examined in the current work. In order to vary the yaw angle for the vehicle, the bridge and vehicle were simply rotated with respect to the oncoming wind together with the test frame and the rotating table in the wind tunnel. Seven yaw angles of 0^o, 15^o, 30^o, 45^o, 60^o, 75^o and 90^o were investigated. To investigate the influence of wind velocity, two velocities of 10 m/s and 20 m/s were adopted. Three vehicles were laid on the bridge deck with an equal distance of 0.156 m between the vehicles along the longitudinal direction to investigate the aerodynamic interference between the vehicles. The tests were carried out in smooth flow and turbulent flow with approximately 10% turbulence intensity described in Section 2.3. The local wind field of the surface of the bridge deck is expected to be modified as a result of the vehicle. Also, the local wind field of the vehicle is expected to be modified as a result of the bridge. Then, the vehicle model was positioned at two different locations corresponding to windward and leeward lanes.

Table 1 Measured cases in wind tunnel

Cases	Testing objects	Wind Velocity (m/s)	Wind field	Distance (d) of vehicle from the wind ward edge of the deck (m)	Wind yaw angle (^{o})
1	Bridge with one vehicle	10	Smooth	0.166	0, 15, 30, 45, 60, 75, 90
2	Bridge with one vehicle	20	Smooth	0.166	0, 15, 30, 45, 60, 75, 90
3	Bridge with one vehicle	10	Smooth	0.547	0, 15, 30, 45, 60, 75, 90
4	Bridge with one vehicle	10	Turbulent	0.166	0, 15, 30, 45, 60, 75, 90
5	Bridge with three vehicles	10	Smooth	0.166	0, 15, 30, 45, 60, 75, 90
6	Bridge with no vehicle	10	Smooth	0	0, 15, 30, 45, 60, 75, 90

3 EXPERIMENTAL RESULTS AND DISCUSSION

3.1 *Aerodynamic force coefficients*

Figure 10 illustrates the variation of force and moment coefficients of the vehicle with respect to the yaw angle ψ for cases 1and 5. It can be seen that for case 1, the side force coefficient C_S increases with the increase of the yaw angle ψ and reaches a maximum value at around 90^o yaw angle. But the increment between the yaw angles of 60-90 degrees is less significant. Such a trend is similar to that shown in the literature (Baker, 1991a; Coleman, 1990), although it is noted that the maximum values typically occur between yaw angles of 60-90 degrees. The lift force coefficient C_L increases and then decreases with the increase of the yaw angle ψ, and reaches a maximum value at around 30^o yaw angle, which is positive for $15^o<\psi<60^o$, and negative for other yaw angles. The positive values (sign convention shown in Fig. 8) of C_L are not good for traffic safety. The magnitude of the drag force coefficient C_D increases to a maximum at $\psi=30^o$ and then decreases to near zero for $\psi=90^o$, i.e. pure cross wind conditions, which seems reasonable. The aerodynamic moments reflect the trends of the aerodynamic forces. The yawing moment coefficient, determined mainly by the horizontal moment arm of the drag force, and to a lesser extent of that of the side force, shows similar variations to those observed in the drag force coefficient. The pitching moment and rolling moment results, relatively small, are changing irregularly, and are probably affected by some unknown experimental error.

In addition, from the comparison of the results for cases 1 and 5 (one vs. three vehicles in Fig. 10), it can be seen that the change trend of the aerodynamic coefficients is similar for the two cases, except for the pitching moment coefficient. The side force coefficient C_S in case 5

with three vehicles is obviously less than that in case 1 with one vehicle for $\psi<45^o$ because of the blocking effect of the frontal vehicle on the middle vehicle, i.e. the test vehicle. When the blocking effect is not obvious for $\psi>45^o$, the side force coefficient C_S for case 5 is slightly larger than that in case 1 due to the effect of the frontal and posterior vehicles on the surrounding flow field. There is a obvious difference in the lift force coefficient C_L between cases 1 and 5, especially for 30^o yaw angle, at which the lift force coefficient C_L for case 5 is obviously less than that in case 1, which means the effect of frontal and posterior vehicles is good for traffic safety. The frontal vehicle affects the drag force coefficient C_D greatly, which reduces the magnitude of the drag force coefficient C_D, especially for $\psi<60^o$. The magnitudes of the pitching moment coefficient C_P and the yawing moment coefficient C_Y for case 5 are less than those in case 1, while the rolling moment coefficient C_R is generally larger (in absolute values) due to the interference of frontal and posterior vehicles.

Figure 11 illustrates the variation of the aerodynamic force coefficients of the vehicle with respect to yaw angle ψ for cases 1and 4 (smooth vs. turbulent flow). It can be seen that the side force coefficient C_S for turbulent flow is smaller than that in the smooth flow and the difference increases with the increase of the yaw angle. The turbulence effects on the lift force coefficient C_L is not obviously for low yaw angles. For $\psi>40^o$, the lift force coefficient C_L in turbulent flow is significantly greater than that in the smooth flow case. The magnitude of the drag force coefficient C_D for the turbulent flow is smaller than that in the smooth flow for $\psi<45^o$, and slightly greater for $\psi>45^o$. The turbulence reduces the yawing moment basically and affects the pitching and rolling moment irregularly.

A further investigation on the influence of the distance of the vehicle from the windward edge of the deck on the aerodynamic force coefficients is illustrated in Figure 12 which shows the evolution of the aerodynamic coefficients with respect to the two distances (i.e., d=0.166 m and 0.547 m corresponding to cases 1 and 3). For $\psi<30^o$, there is a good agreement between the results of the side force coefficient C_S in the two cases. But the increase of the distance reduces C_S greatly for $\psi>30^o$. At zero degree yaw angle, the lift force coefficient C_S is not affected by the distance. But it decreases with the increase of distance d for $\psi<40^o$, and increases for $\psi>40^o$. The increase of the distance increases the magnitude of the rolling moment coefficient C_R for all yaw angles, except for 30 degree. The changing of the distance affects the drag force, pitching moment, and yawing moment coefficients insignificantly.

Figure 13 shows the variation of the aerodynamic force coefficients of the vehicle with respect to the yaw angle ψ for cases 1 and 2 (10 vs. 20 m/s wind velocity) to investigate the effect of the wind speed on the coefficients. It can be seen that three is very little difference between the results for all the aerodynamic force coefficients, which is perhaps not surprising since the vehicle model has sharp windward edges. As a result, the coefficients will be little affected by the Reynolds number (i.e. the wind velocity here).

Table 2 gives the static aerodynamic force coefficients of the bridge for cases 6, 1, 5 and 3 at the 90^o yaw angle. The results show that the aerodynamic force coefficients of the bridge are affected by the vehicles greatly, especially for lift force coefficient C_V, which increases significantly with the increase of the vehicle number. The drag force coefficient C_H with one vehicle is obviously greater than that with no vehicle, but little smaller than that with three vehicles, which indicates the drag force coefficient C_H is independent of the number of vehicles. The magnitude of the pitching moment coefficient C_M with three vehicles is significantly greater than that with one vehicle or with no vehicle, but there is little difference between the results with one vehicle and with no vehicle. The distance of the vehicle from the windward edge of the bridge deck affects the aerodynamic force coefficients of the bridge greatly. It not only affects the magnitude but also the direction.

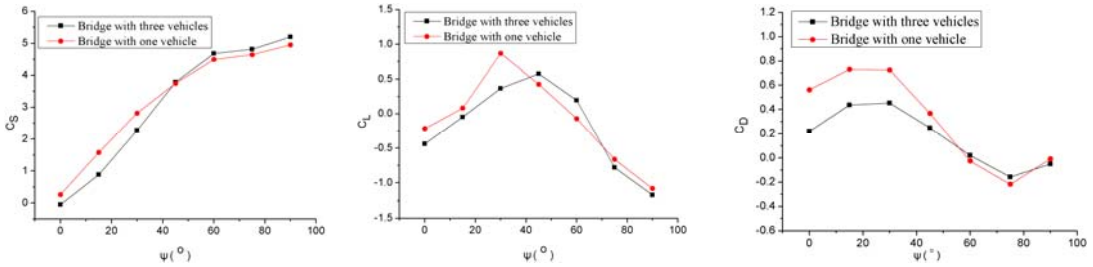

(a) Side force coefficient (b) Lift force coefficient (c) Drag force coefficient

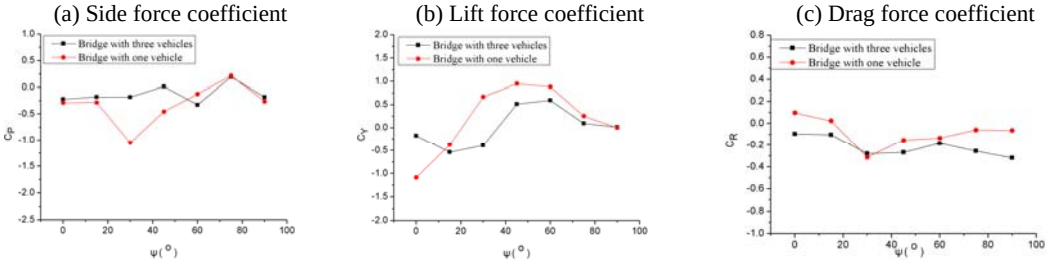

(d) Pitching moment coefficient (e) Yawing moment coefficient (f) Rolling moment coefficient

Fig.10 Aerodynamic force coefficients of the vehicle vs yaw angle ψ for cases 1 and 5

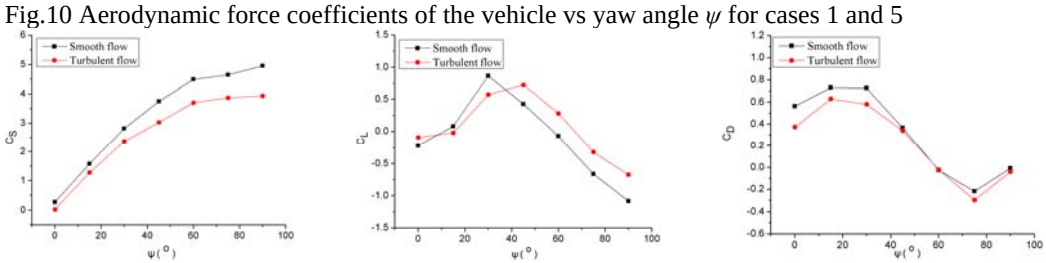

(a) Side force coefficient (b) Lift force coefficient (c) Drag force coefficient

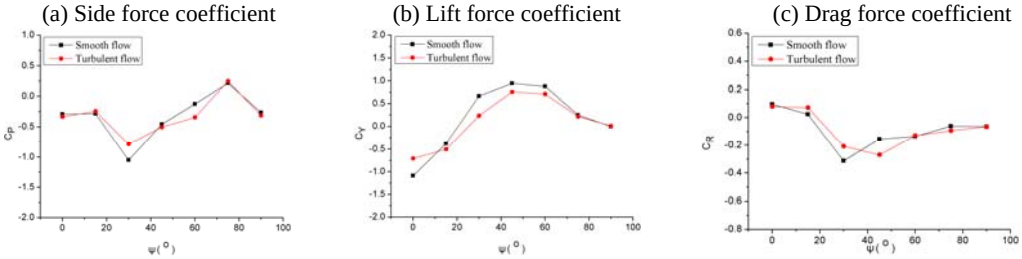

(d) Pitching moment coefficient (e) Yawing moment coefficient (f) Rolling moment coefficient

Fig.11 Aerodynamic force coefficients of the vehicle vs yaw angle ψ for cases 1 and 4

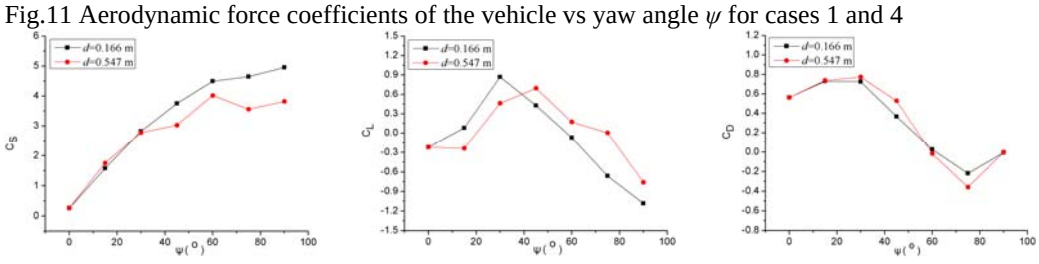

(a) Side force coefficient (b) Lift force coefficient (c) Drag force coefficient

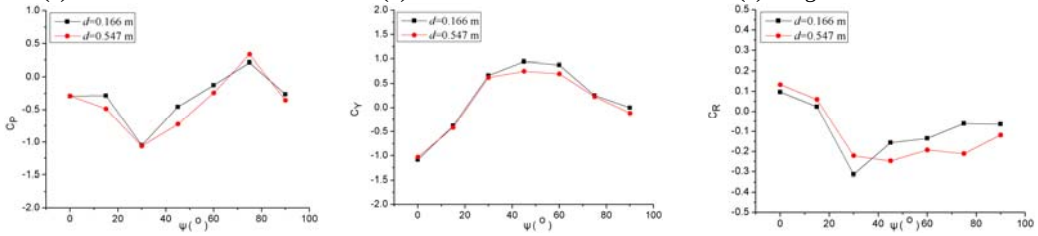

(d) Pitching moment coefficient (e) Yawing moment coefficient (f) Rolling moment coefficient

Fig.12 Aerodynamic force coefficients of the vehicle vs yaw angle ψ for cases 1 and 3

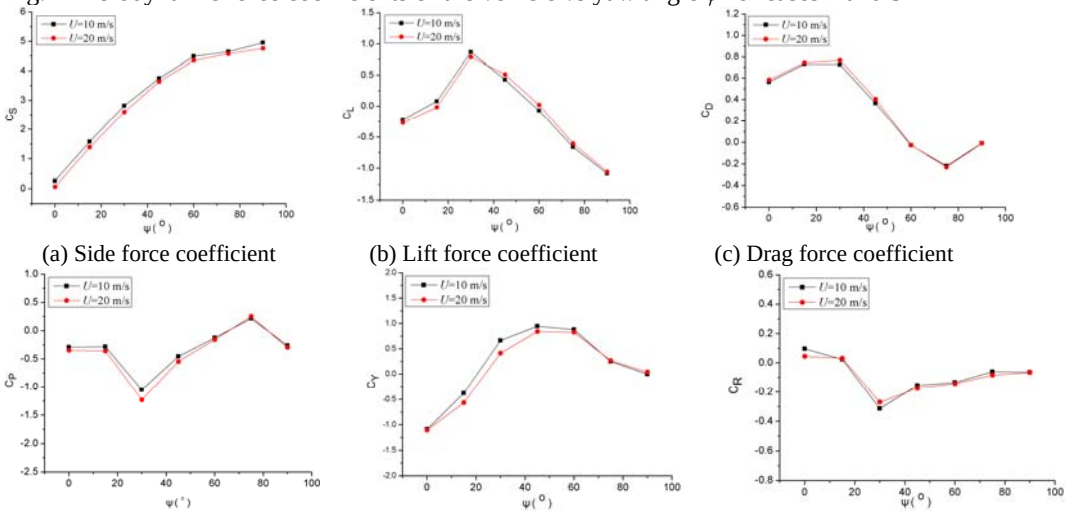

(a) Side force coefficient (b) Lift force coefficient (c) Drag force coefficient

(d) Pitching moment coefficient (e) Yawing moment coefficient (f) Rolling moment coefficient

Fig.13 Aerodynamic force coefficients of the vehicle vs yaw angle ψ for cases 1 and 5

Table 2 Static coefficients of the bridge

Coefficients	With no vehicle	With one vehicle (d=0.166 m)	With three vehicle (d=0.166 m)	With one vehicle (d=0.547m)
C_V	0.1486	0.2602	0.3287	-0.0983
C_H	0.0583	0.0669	0.0672	-0.0830
C_M	-0.0175	-0.0141	-0.0341	0.0445

3.2 *Pressure distribution*

A further investigation on the change reasons of the aerodynamic forces for the vehicle and the bridge is illustrated in the following figures, showing the surface pressure distribution of the vehicle and the bridge. Figure14 gives the pressure contour maps of the windward side surface of the vehicle at the 90^o yaw angle for cases 1, 4, 5 and 3. Figure 15 gives the pressure contour maps of the frontal surface of the vehicle at the 0^o yaw angle for cases 1 and 5. Figure 16 shows the pressure distribution of the top pressure taps of the middle strip of the bridge deck at the 90^o yaw angle for cases 1, 3, 5 and 6. It can be seen from these figures that there are no abnormal values for all pressure taps, demonstrating the accuracy and reliability of the experimental results.

From Figures 14(a) and 14(c), it can be seen that there is a good agreement between the pressure contour maps, which verifies that the effect of the frontal and posterior vehicles on the side force coefficient C_S is not obvious, just as shown in Figure 10(a). By comparing Figure 14(a) with Figure 14(b), it can be seen that the pressure for case 4 is obviously smaller than that in case 1, which explains the decrease of the side force coefficient C_S in turbulence flow at the 90^o yaw angle, as shown in Figure 11(a). Though the pressure in case 3 is not smaller than that in case 1, as illustrated in Figures 14(a) and 14(d), the high pressure area becomes small, which decreases the side force coefficient C_S at the 90^o yaw angle obviously, as shown in Figure 12(a).

As illustrated in Figures 15(a) and 15(b), the pressure in case 5 is obviously smaller that in case 1 for the blocking effect of the frontal vehicle, which is the main reason for the obvious decrease of the drag force coefficient C_D at the 0^o yaw angle, as shown in Figure 10(c).

From Figure 16, it is observed that for case 6 (with no vehicle), the pressure is negative, that is, the measured point is subjected to a tensile force with an upward direction (i.e. the positive direction of life force). The pressure increases (the absolute value decreases) with the increase of the distance from the windward edge and then basically remains unchanged after the

distance is up to a certain value. For case 1 (one vehicle with d=0.166m), the pressure of the measured point located in front of the vehicle on the windward side increases sharply with the increase of the distance due to the blockage effect of the vehicle, changing from negative to positive. The pressure turns to be negative when the measured point is located under the vehicle and approaches to the value like that in case 6. The magnitude of the pressure for case 1 is larger than that in case 6 with the direction upward, which leads to the lift force coefficient C_V to change correspondingly. For case 5 (with three vehicles), the variation of the pressure is similar to that in case 1, except for the pressure taps in front of the windward side of the vehicle. Since there are three strips of the bridge deck (as shown in Figure 3(a)) affected by the vehicles, the lift force coefficient C_V in case 5 is obviously higher than that in case 1. For case 3 (one vehicle with d=0.547m), the pressure increases with the increasing of the distance, turns from negative to positive, but decreases sharply near the vehicle and becomes negative. There are half measured points that have positive pressure values with a downward direction. As a result, the lift force coefficient C_V in case 3 is negative and is lower than that in case 6. From the above analysis, it is not hard to understand the change reason of the lift force coefficients presented in table 2.

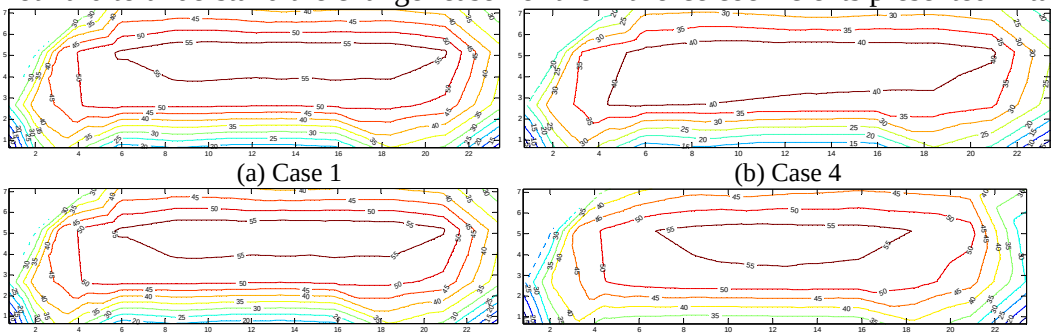

(a) Case 1 (b) Case 4

(c) Case 5 (d) Case 3

Fig.14 Pressure contour map of the windward side surface of the vehicle at 90° yaw angle

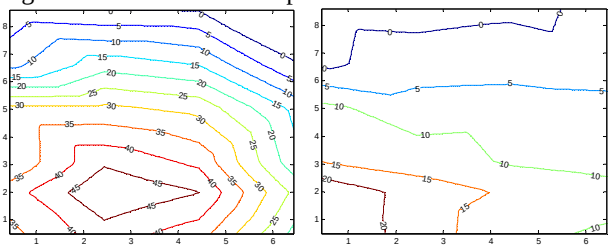

(a) Case 1 (b) Case 5

Fig.15 Pressure contour map of the frontal surface of the vehicle at 0° yaw angle

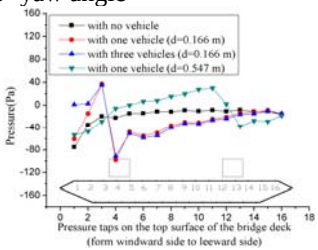

Fig.16 The pressure of top pressure taps of the middle strip

4 CONCLUSIONS

The present work has investigated the aerodynamic force coefficients of the vehicle and the bridge by carrying out six experimental tests in wind tunnel. Based on the experimental results, the following conclusions can be drawn:

(1) The analysis of surface pressure distributions of the vehicle and bridge proves that experimental results in this paper are accurate and reliable.

(2) The aerodynamic coefficient is obviously a function of the yaw angle. The side force coefficient C_S increases with the increase of the yaw angle ψ, the lift force coefficient C_L increases and then decreases with the increase of the yaw angle ψ, the drag force coefficient C_D increases and then decreases with the increase of the yaw angle ψ, the yawing moment coefficient shows similar variations to those observed in the drag force coefficient, and the pitching moment and rolling moment results are relatively small.

(3) The interference of vehicles, the flow turbulence, and the cross position of vehicles largely affect the aerodynamic force coefficients of vehicles, but the wind velocity basically has no influence on these coefficients. The effects of the number of vehicles and the distance of vehicles from the windward edge on the aerodynamic force coefficients of bridges are strong. When there is a vehicle or no vehicle on the bridge, the aerodynamic force coefficients of the bridge is largely affected, just as do the number of vehicles and the distance of vehicles from the windward edge.

(4) There are still many factors that may affect the aerodynamic force coefficients of the vehicle, such as the configuration of the bridge cross section, the vehicle type, and the running environment (on bridge, embankment, or ground). These factors should be studied to develop empirical formulas to calculate the aerodynamic forces for typical vehicles.

(5) It is known that vehicles on bridges have significant effect on the static aerodynamic forces of the bridge. How much effect of the vehicle on other aerodynamic forces of the bridge, such as the self-excited force and buffeting force, and on the wind-induced vibrations of the bridge is worth a further study.

5 ACKNOWLEDGEMENTS

The authors would like to gratefully acknowledge the supports from the National Science Foundation of China (Project No. 50908025; 51108045; 51178066), from the School of Civil Engineering and Architecture, Changsha University of Science and Technology and the Wind Engineering Research Center of Hunan University in China.The second author also appreciates the support from the National Science Foundation of USA (Project CMMI-0927824).

6 REFERENCES

[1] Baker, C.J., 1986. A simplified analysis of various types of wind-induced road vehicle accidents. Journal of Wind Engineering and Industrial Aerodynamics, 22, 69-85.
[2] Baker, C.J., 1987. Measures to control vehicle movement at exposed sites during windy periods. Journal of Wind Engineering and Industrial Aerodynamics, 25, 151-161.
[3] Baker, C.J., 1988. High sided articulated road vehicles in strong cross winds. Journal of Wind Engineering and Industrial Aerodynamics, 31, 67-85.
[4] Baker, C. J., 1991a. Ground vehicles in high cross winds .1. Steady aerodynamic forces, Journal of Fluids and Structures, 5, 69-90.
[5] Baker, C. J., 1991b. Ground vehicles in high cross winds .2. Unsteady aerodynamic forces, Journal of Fluids and Structures, 5, 91-111.
[6] Scanlan, R. H. and Jones, N. P., 1990. Aeroelastic analysis of cable-stayed bridges, Journal of Structural Engineering, ASCE, 116(2), 279-297.
[7] Yang, Y. B. and Yau, J. D., 1997. Vehicle-bridge interaction element for dynamic analysis, Journal of Structural Engineering, ASCE, 123, 1512-1518.
[8] Pan, T. C. and Li, J., 2002. Dynamic vehicle element method for transient response of coupled vehicle-structure systems, Journal of Structural Engineering, ASCE, 128(2), 214-223.
[9] Xu, Y. L. and Guo, W. H., 2003. Dynamic analysis of coupled road vehicle and cable-stayed bridge system under turbulent wind, Engineering Structures, 25, 473-486.
[10] Cai C. S. and Chen S. R., 2004. Framework of vehicle-bridge-wind dynamic analysis, Journal of Wind Engineering and Industrial Aerodynamics, 92, 579-607.
[11] Han W. S. and Chen A. R., 2007. Three-dimensional coupling vibration of wind-vehicle-bridge systems, China civil engineering journal, 40(9), 53-58 (In Chinese).
[12] Quinn, A.D., Sterling, M., Robertson, A.P., Baker, C.J., 2007. An investigation of the wind-induced rolling moment on a commercial vehicle in the atmospheric boundary layer. Proceedings of the Institution of Mechanical Engineers Part D-Journal of Automobile Engineering, 221, 1367-1379.
[13] Coleman S. A. and Baker C. J., 1990. High side road vehicles in cross winds, Journal of Wind Engineering and Industrial Aerodynamics, 36, 1383-1392.

[14] Coleman, S.A. and Baker, C.J., 1994. An experimental study of the aerodynamic behaviour of high sided lorries in cross winds. Journal of Wind Engineering and Industrial Aerodynamics, 53, 401-429.
[15] Minoru Suzuki, Katsuji Tanemoto and Tatsuo Maeda, 2003. Aerodynamic characteristics of train/vehicles under cross winds, Journal of Wind Engineering and Industrial Aerodynamics, 91, 209-218.
[16] Li Y. L., Liao H. L. and Qiang S. Z., 2004. Study on Aerodynamic Characteristics of the Vehicle-bridge System by the Section Model Wind Tunnel Test. Journal of the China Railway society, 26(3), 71-75.
[17] Cheli F., Corradi R., Diana G., Tomasini G. A numerical experimental approach to evaluate the aerodynamic effects on rail vehicle dynamics supplement to vehicle system dynamics, The Dynamics of Vehicles on Roads and on Tracks, Vol. 41, 2004,pp:707-716.
[18] Cheli F., Desideri R., Diana G., Mancini G., Roberti R., Tomasini G. Cross wind effects on tilting trains, Proceedings of WCRR 2006 7th World Congress on Railway Research, Montreal, Canada, June 4-8, 2006, pp. 1-8.
[19] Han Y., Cai C. S., Chen Z. Q. and Hu J. X., 2011. Aerodynamic characteristics of road vehicles and bridges under cross winds, Proceedings of the 13th International Conference on Wind Engineering, Amsterdam, the Netherlands.

The Seventh International Colloquium on Bluff Body Aerodynamics and Applications (BBAA7)
Shanghai, China; September 2-6, 2012

Control of the aerodynamic drag of Ahmed model with slot jet

Wang Hanfeng [a], Xu Mengxia [a]

[a]*National engineering laboratory for high-speed railway construction, Central South University, Changsha, China*

ABSTRACT: The effects of a slot jet on the aerodynamic drag of an Ahmed model with the slant angle of 25º is investigated using LES technique. Three jet directions are considered, i.e. along slant surface (case 1), backwards horizontally (case 2) and 30º inclined upward (case 3). There is a pair of symmetrical streamwise tail vortices, which accounts for a major part of the aerodynamic drag. The slot jet has significant effects on the near wake and aerodynamic drag. For case 1, the tail vortices are enhanced and the drag is increased by about 0.91%. While for cases 2 and 3, the application of slot jet extends the reverse flow zone and suppresses the tail vortices. The total aerodynamic drag reduces by 7.88% and 3.64% for these two cases, respectively.

KEYWORDS: Ahmed model, Tail vortex, Flow control, Drag reduction, LES.

1 INTRODUCTION

Control of the aerodynamic drag of a road vehicle is one of the most important research problems about vehicle aerodynamics, which is directly related to the fuel efficiency. Generally, the drag of a vehicle is proportion to the square of its speed. The aerodynamic drag on a road vehicle typically accounts for about 70% of its total resistance when its speed reaches 90 Km/h. The control of aerodynamic drag becomes widely concerned because of the skyrocketing fuel cost and increasing environmental burden from fossil fuels.

The geometrical figure of road vehicle is usually a three-dimensional (3D) bluff body. The aerodynamic drag on a bluff body is largely determined by the pressure difference between its front and rear end[1, 2], and closely related to the flow separation near the rear end[1]. The flow in the near wake of this 3D bluff body is highly complex, unsteady. To facilitate the comparative aerodynamic studies, Ahmed[3] proposed a generic vehicle configuration, named "Ahmed model". Despite that the Ahmed model has been proposed for nearly three decades, it is still frequently used for the investigation of the 3D wake flow and aerodynamic performance for road vehicles[4-7]. The near wake structure and consequently the aerodynamic drag of Ahmed model strongly depend on the rear slant angle[2, 3]. For the slant angle of approximately 25º to 30º, large longitudinal vortex structures occur in the near wake, which lead to a considerable increase in aerodynamic drag.

Recently, the flow control techniques have been more and more studied for drag reduction, with the Ahmed model as a benchmark[7]. Some passive control methods, such as: tail clapboards[8], flaps near the flow separation point[9] and deflector[10] etc., have been successfully used for drag reduction. However, most of these passive control techniques introduce quite unsightly appendages on the body, which is in contradiction with design constraints[7]. This fact makes active control by jet and/or suction very attractive. For Ahmed model with the slant angle of 25º, Roumeas *et al.*[11] used steady aspiration on the top edge of the slant and obtained about 17% drag reduction. Krajnovic *et al.*[12] made numerical simulations of the same case and obtained a little bit more than 7% reduction using steady blowing and suction at the slant top edge.

In the present paper, the flow around and the aerodynamic drag on an Ahmed model with a slant angle of 25º are investigated using large eddy simulation (LES) technique. A slot jet at

slant top edge is employed to control the flow. Three jet directions are presently studied to examine the effects of jet direction on the near wake flow structure and aerodynamic drag.

2 LES & CONTROL CASES

2.1 *LES method*

The governing equations of LES are the incompressible Navier-Stokes and the continuity equations filtered with the implicit spatial filter of characteristic width Δ, which is the grid resolution. The goal of this filtering is to decompose the fluid motion into a large-scale component that is resolved directly, and the small subgrid scale (SGS) which is modeled using SGS model. The filtered LES equations are shown in Eqs. (1 & 2), where the overbar denotes the filtered variable, ρ and ν are the density and kinematics viscosity of fluid, respectively.

$$\frac{\partial \overline{u}_i}{\partial x_i} = 0 \tag{1}$$

$$\frac{\partial \overline{u}_i}{\partial t} + \frac{\partial \overline{u}_i \overline{u}_j}{\partial x_j} = -\frac{1}{\rho}\frac{\partial p}{\partial x_i} + \nu \frac{\partial^2 \overline{u}_i}{\partial x_i \partial x_j} - \frac{\partial \tau_{ij}}{\partial x_j} \tag{2}$$

The influence of the small scale turbulence on the large energy carrying scales in Eq. (2) appears in the SGS tensor, $\tau_{ij} = \overline{u_i u_j} - \overline{u}_i \overline{u}_j$ [4]. The algebraic eddy viscosity model proposed by Smagorinsky[13], shown in Eq. (3), is presently used for its simplicity and low computational cost, where the SGS viscosity $\nu_t = (C_s \Delta)^2 \left|\overline{S}\right|$. $\left|\overline{S}\right|$ is the resolved rate-of-strain tensor, and $\left|\overline{S}\right| = (2\overline{S}_{ij}\overline{S}_{ij})^{0.5}$, where $S_{ij} = \frac{1}{2}(\frac{\partial \overline{u}_i}{\partial x_j} + \frac{\partial \overline{u}_j}{\partial x_i})$. The filter width Δ is defined as $\Delta = (\Delta_x \Delta_y \Delta_z)^{1/3}$, where Δ_i are the computational cell sizes in three coordination directions. Readers may refer to Krajnovic & Davidson[4] for detailed description of the LES method presently used.

$$\tau_{ij} = \overline{u_i u_j} - \overline{u}_i \overline{u}_j = -2\nu_t \overline{S}_{ij} + \frac{\tau_{kk}\delta_{ij}}{3} \tag{3}$$

2.2 *Generic vehicle mode and numerical details*

An Ahmed model with the slant angle of 25º is presently investigated. The dimensions are shown in figure 1(a), the length (l), width (w) and height (h) are 1044 mm, 389 mm and 288 mm, respectively. The computational domain is 8l in length, 10w in width and 5h in height. The model is 2l from the inlet and 50mm above the bottom wall. The blockage ratio is 2%. Definition of the coordinate system is shown in figure 1(b).

The computational domain is meshed into hexahedrons. The grid size reduces gradually with the wall approached, so that most of the grids concentrate around the Ahmed model. The total number of grid is about 180 million. The y^+ on the model surface ranges from 0.7 to 33, which is considered enough to capture the larger scale flow structure.

A uniform velocity U_∞ of 25m/s is used as the inlet boundary layer condition in present LES. Corresponding Reynolds number, based on U_∞ and l, is 1.75×10^6. Pressure boundary condition is used at the exit of computation domain. The lateral and ceiling surfaces of the computa-

tional domain are treated as slip surfaces using symmetry condition. No slip boundary layer conditions are used on the surfaces of Ahmed model and ground wall.

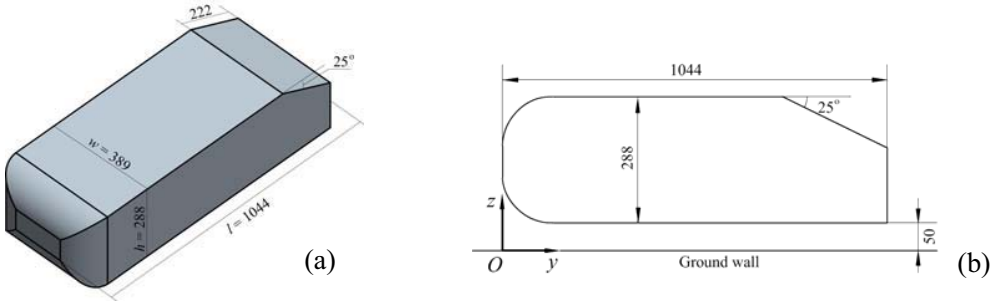

Figure 1. Generic vehicle model and control cases: (a) dimension of Ahmed model, (b) definition of the coordinate system. All dimensions are in mm.

2.3 *Control cases*

To manipulate the near wake flow and subsequently the aerodynamic drag on the Ahmed model, a slot jet at the top edge of the slant surface was used. Three different jet directions were tested. For case 1, the direction of the slot jet is along the slant surface, for case 2, the jet is horizontally backwards, while for case 3, the jet direction is inclined upwards with an angle of 30º, as shown in figure 2. To provide a benchmark, the case without control was taken as case 0. The length of the slot was equal to the width of the model, and the width of slot is 11 mm, 5% of the slant length. The slot jet velocity (U_J) is 9 m/s for the three cases, corresponding to a jet intensity c_μ = 5×10^{-3}. c_μ is defined by Eq. (4)[14], in which A_J and A_B are the projected area of the slot jet and the Ahmed body in flow direction, respectively.

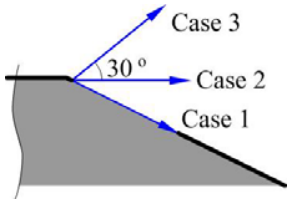

Figure 2. Configuration of control cases.

$$c_\mu = \frac{A_J}{A_B} \cdot \frac{U_j^{\,2}}{U_\infty^{\,2}} \tag{4}$$

3 RESULTS & DISCUSSIONS

3.1 *The new wake flow structures*

Figure 3 presents the isosurfaces of instantaneous streamwise vorticity, i.e., ω_y^*. In present paper, the superscript asterisk represents the normalization with U_∞ and/or l. Obviously, the near wake is highly complex and 3D. A pair of streamwise tail vortices occurs near the side edges of slant face (as shown in figure 3), similar to that observed by Vino *et al.*[15] with smoke visualization technique. The time-averaged near wake structure is shown in figure 4, together with the schematic near wake structure proposed by Ahmed *et al.*[3] for comparison. The shear layers from the ceiling and bottom surfaces form a recirculation zone downstream the body. A pair of symmetrical tail vortices dominates the near wake, which is responsible for a significant part of

the lift and drag[16]. The time averaged flow structure of present LES, as shown in figure 4(b), corresponds well with the proposed flow model, which validates the present results. For an Ahmed model with the slant angle of 25º, the reported drag coefficient (C_D) was scattered for different techniques, e.g. 0.30 by Ahmed et al.[3] and 0.32 by Vino et al.[15] The present C_D for case 0 is 0.33, which will be used as a benchmark to evaluate the effectiveness of the slot jet on drag reduction.

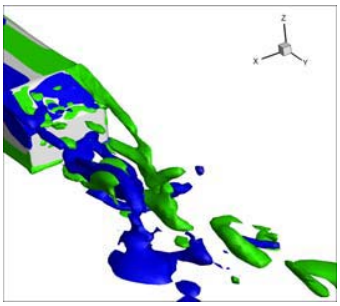

Figure 3. Isosurfaces of instantaneous streamwise vorticity, $\left|\omega_y^*\right| = \pm 6$.

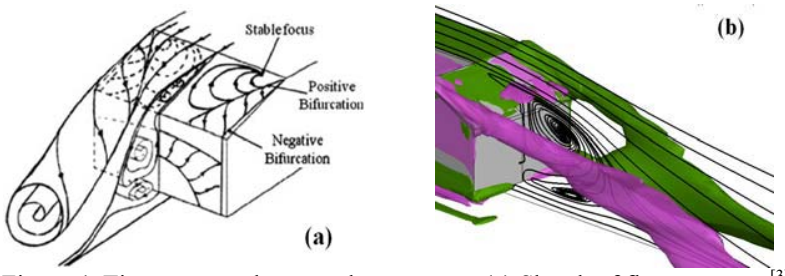

Figure 4. Time-averaged near wake structure: (a) Sketch of flow structure[3], (b) Present LES result.

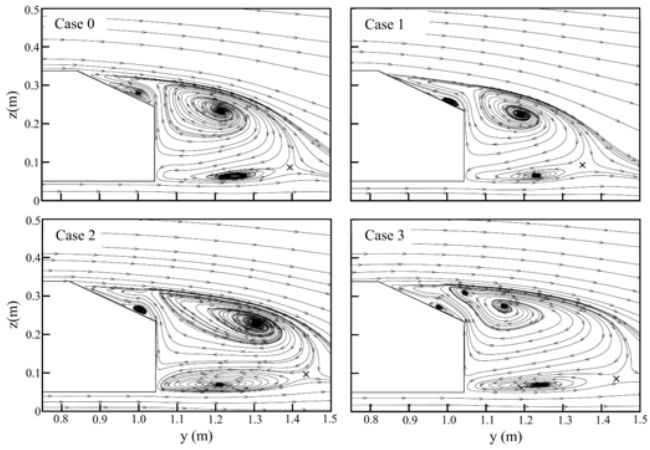

Figure 5. Time-averaged sectional streamlines in the central symmetry plane for different cases.

The time-averaged sectional streamlines in the central symmetry plan are shown in figure 5 for the four cases. The shear layers from the top and bottom surfaces of the model form a reverse flow zone. Under the effects of the negative pressure on slant and rear end, the upper shear layer exhibits a strong downwash and forms a saddle point, denoted by "×", with the lower shear layer. The streamwise position of this saddle point can represent the length of the reverse flow zone. For case 1, the downwash becomes more remarkable and the saddle point shifts upstream to the model, which suggests that the reverse flow zone shrinks in case 1. Contrarily, the down-

wash flow becomes weaker and the streamwise extent of reverse flow zone enlarges in cases 2 and 3. For a 2D bluff body, the length of reverse flow zone is in contrast with the aerodynamic drag[17]. In view of the extended reverse flow zone in cases 2 and 3, the corresponding aerodynamic drag may reduces, which will be discussed in detail later.

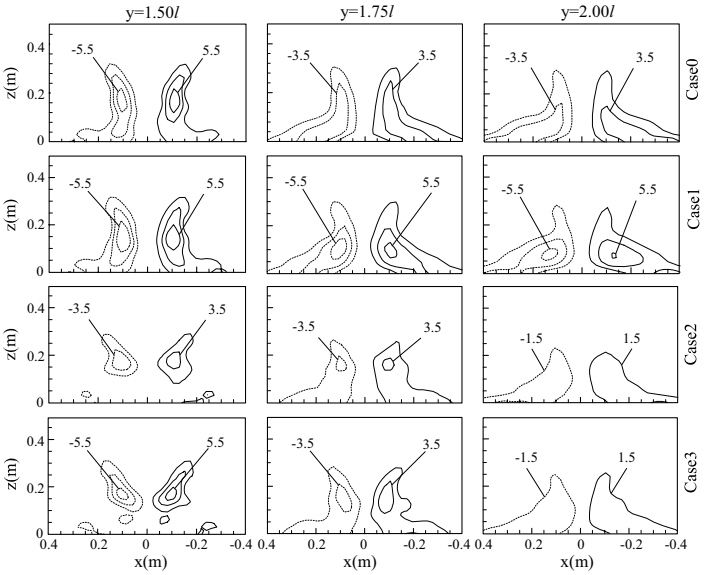

Figure 6. Time-averaged normalized streamwise vorticity ω_y^* for different cases (contour interval=2.0).

Figure 6 presents the time-averaged ω_y^* contours at different downstream positions for the four cases. For case 0, i.e. without control, there is a pair of symmetrical streamwise vortices, which decays monotonously as moving downstream for the three y positions as shown in figure 6. Obviously, this pair of tail vortices is associated with the downwash flow from the slant, as shown in figure 4. Although, the intensity of tail vortices is the same for case 0 and case 1 at y = 1.5l, the size of these vortices is slightly larger for the later. For case 1, the vortex intensity does not diminish with increasing y. This observation may be ascribed to the effects of the slot jet along slant surface. The slot jet in case 1 enhances the downwash flow (as shown in figure 5) and subsequently the associated tail vortices. For cases 2 and 3, the application of slot jet noticeably suppresses the tail vortices, especially for the former. For example, at y = 1.5l, the maximum of ω_y^* is 3.5, about 64% of that for case 0. The application of slot jet in cases 2 and 3 increases the decaying rate of tail vortices. At y = 2.0l, the maximum of ω_y^* is 1.5, about 43% of that for case 0. Since the tail vortices are responsible for a significant part of the aerodynamic drag[16], the variation of tail vortices as shown in figure 6 suggests that the slot jet has significant effects on the aerodynamic drag.

3.2 *Pressure distribution and aerodynamic drag*

Pressure coefficients (C_p) on the slant and rear end are presented in figure 7 for the four cases, which is defined as $C_p = 2(p - p_\infty)/\rho U_\infty^2$, where p_∞ is the static pressure of oncoming flow, ρ is the density of air. For case 0, the pressure gradient is remarkable near the top and side edges of the slant surface, suggesting strong flow separation there which forms the tail vortices. For case 1, the slot jet is along the slant, which reinforces the momentum of shear flow and may postpone the flow separation. Consequently, the absolute value of C_p on the slant is slightly smaller for

case 1 than for case 0. However, the absolute value of C_p on rear end for case 1 is larger than that for case 0. That is, the slot jet at the top edge of slant changes not only the pressure distribution on the slant surface, but also alters the whole wake flow. For cases 2 and 3, the extremum of C_p on the slant is -0.25, slightly higher than -0.3 for case 0. On the rear end, although the extremum of C_p for case 2 is the same with case 0, the range of the contour of -0.2 is obviously larger for the former. For case 3, the extremum of C_p is -0.2 one the rear end, slightly smaller than the corresponding value of -0.15 for case 0.

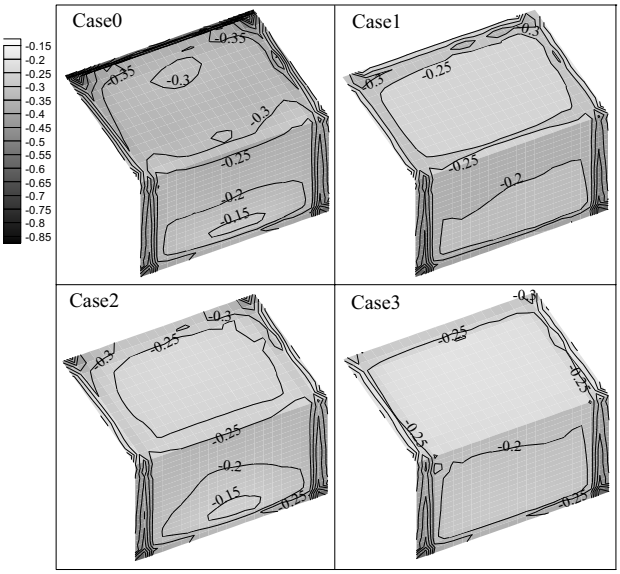

Figure 7. Pressure coefficient on the slant and rear end (contour interval=0.05).

Table 1. Drag coefficients of the model and its different parts.

	Case0	Case1	Case2	Case3
Drag from the front end, C_{D_front}	0.020	0.020	0.020	0.022
Drag from the side walls, $C_{D\_sidewall}$	0.043	0.043	0.042	0.042
Drag from the slant, C_{D_slant}	0.103	0.099	0.084	0.091
Drag from the rear end, C_{D_back}	0.164	0.171	0.158	0.163
C_D	0.330	0.333	0.304	0.318
Drag reduction efficiency	---	-0.91%	7.88%	3.64%

To highlight the effects of slot jet on the aerodynamic drag, table 1 lists the overall drag coefficients C_D and its components from different parts of the Ahmed model. For all cases, the drag from the front end of the model is almost unchanged, suggesting that the application of slot jet does not noticeably change the flow near the head. The drag from side walls is largely dominated by the turbulence friction on side walls, which is related to the Reynolds number, wall roughness etc. The present slot jet does not change $C_{D\_sidewall}$, similar to that observed for C_{D_front}. Both C_{D_front} and $C_{D\_sidewall}$ account for a small portion of total aerodynamic drag. As listed in table 1, most C_D results from the negative pressure distribution on the slant and rear end, consistent with that proposed by Drouin *et al.*[16]. For case 1, although the application of slot jet reduces slightly the drag on slant, C_{D_back} is increased by about 4.3%, which is consistent with the pressure distribution shown in figure 7. The total drag reduction for case 1 is -0.91%, i.e., C_D for case 1 is slightly bigger than that for case 0. Cases 2 and 3 reduce C_D by 7.88% and 3.64%, respectively.

Considering the effects of slot jet on the near wake structure, following observations can be made. Firstly, C_D is inversely correlated with the length of reverse flow zone, i.e. a smaller

length corresponds to a larger C_D. Secondly, C_D is inversely correlated with the strength of tail vortices. A horizontal slot jet, i.e. case 2, suppresses the tail vortices significantly and results in the smallest C_D for present invested cases. While for case 1, the tail vortices are enhanced and the corresponding C_D is slightly bigger than that without control. Finally, the application of slot jet at the top edge of slant modifies not only the pressure distribution on the slant, but also changes that on the rear end. The total C_D largely comes from the slant and rear end. To evaluate the over all drag reduction efficiency, the combined effects on both slant and rear end should be considered.

4 CONCLUSIONS

A steady slot jet at the top edge of the slant of an Ahmed model is used to control the aerodynamic drag. The slant angle is 25º. Three slot jet directions are investigated using LES technique. For case 1, the slot jet is along the slant surface; for case 2, it is horizontally backwards; and for case 3, it is inclined upwards by 30º relative to the horizontal direction. Based on the simulation results, the following conclusions can be drawn:

(1) There is a pair of symmetrical streamwise tail vortices in the near wake, which is responsible for the negative pressure distribution on the slant and rear end. This negative pressure on slant and rear end accounts for about 80% of the total aerodynamic drag.

(2) The aerodynamic drag is inversely correlated with the length of reverse flow zone and the strength of tail vortices.

(3) The slot jet has strong effects on the near wake and subsequently the aerodynamic drag. For case 1, the length of reverse flow zone shrinks significantly and the tail vortices are enhanced, the corresponding C_D is about 0.91% larger than that without control. While, for cases 2 and 3, the application of slot jet enlarges the reverse flow zone and suppress the tail vortices. The corresponding drag reduction is about 7.88% and 3.64%, respectively.

5 ACKNOWLEDGEMENTS

The authors wish to acknowledge support given to them from the National Natural Science Foundation of China through grants 51108468.

6 REFERENCES

1 W. Hucho and G. Sovran, Aerodynamics of road vehicles, Ann. rev. fluid mech., 1993(25) 485-537.
2 D. Krentel, R. Muminovic, A. Brunn, W. Nitche and R. King, Application of active flow control on generic 3D car models. In R. King (Ed.), Active Flow Control II, Springer-Verlag, Berlin Heidelberg, 2010, pp. 223-239.
3 S.R. Ahmed, G. Ramm and G. Faltin, Some salient features of the times-averaged ground vehicle wake, SAE Society of Automotive Eng., 1984, 1(840300): 1-31.
4 S. Krajnovic and L. Davidson, Flow around a simplified car, Part 1: Large eddy simulation, J. Fluids Eng., 2005(127) 907-918.
5 S. Krajnovic and L. Davidson, Flow around a simplified car, Part 1: Understanding the flow, J. Fluids Eng., 2005(127) 919-928.
6 P. Gillieron and A. Kourta, Aerodynamic drag reduction by vertical splitter plates, Exp. Fluids, 2010(48) 1-16.
7 P. Joseph, X. Amandolese and J.L. Aider, Drag reduction on the 25º slant angle Ahmed reference body using pulsed jets, Exp. Fluids, 2011 DOI 10.1007/s00348-011-1245-5.
8 R. Verzicco, M. Fatica, G. Iaccarino, P. Moin and B. Khalighi, Large Eddy simulation of a road vehicle with drag-reduction devices, AIAA J. 2002(40) 2447-2455.
9 J.F. Beaudoin and J.L. Aider, Drag and lift reduction of a 3D bluff body using flaps, Exp. Fluids, 2008(44) 491-501.
10 G. Fourrie, L. Keirsbulck, L. Labraga and P. Gillieron, Bluff-body drag reduction using a deflector, Exp. Fluids, 2011(50) 385-395.

11 M. Roumeas, P. Gillieron and A. Kourta, Separated flows around the rear window of a simplified car geometry, J Fluid Eng., 2008(6) 1229-1139.
12 S. Krajnovic, J. Östh and B. Basara, LES of active flow control around an Ahmed body with active flow control, In: Conference on modeling fluid flow (CMFF'09), 2009, Budapest.
13 J. Smagorinsky, General circulation experiments with the primitive equations, Mon. Weather Rev., 1963(91) 99-165.
14. A. Brunn, E. Wassen, D. Sperber, W. Nitsche and F. Thiele, Active drag control for a generic car model, In R. King (Ed.), Active Flow Control, Springer-Verlag, Berlin Heidelberg, 2007, 247-259.
15 G. Vino, S. Watkins, P. Mousley, J. Watmuff and S. Prasad, Flow structures in the near-wake of the Ahmed model, J. Fluids. Struc., 2005(20) 673-695.
16 V. Drouin, A. Giovannini and P. Gillieron, Topology and characterization of the vertical near-wake flow over a simplified car model. In Proceedings of the Bluff body wakes and vortex induced vibrations (BBVIV 3) conference, 2002, Port-Douglas, Australia.
17 S. Balachandar, R. Mittal and F.M. Najjar, Properties of the mean recirculation region in wakes of two-dimensional bluff bodies, J. Fluid Mech., 1997(351), 167–199.

The Seventh International Colloquium on Bluff Body Aerodynamics and Applications (BBAA7)
Shanghai, China; September 2-6, 2012

Flow measurement of vortex-induced vibration of parallel bridge girders by PIV

Jin Park [a], Ho-Kyung Kim [a], Sun-Joong Kim [a]

[a] *Seoul National University, 599 Gwanak-ro, Gwanak-gu, Seoul, Korea*

ABSTRACT: A vortex-induced vibration has been observed in a parallel cable-stayed bridge. In order to understand the aerodynamic behavior of the bridge, a series of wind tunnel tests was performed. The flow around the decks is investigated with the help of a Particle Image Velocimetry.

KEYWORDS: parallel bridge, vortex-induced vibration (VIV), particle image velocimetry (PIV), wind tunnel test, flow measurement

1 INTRODUCTION

A vortex-induced vibration (VIV) has been observed in a parallel cable-stayed bridge. The maximum single amplitude was found to be almost 20 cm at the center of the main span. The bridge is composed of a streamlined steel box deck with 344 m in span length. Both the decks are equipped with guide vanes to mitigate the VIV. The performance of the guide vanes were satisfied with the design allowance for the case of single location. However, the parallel disposition seems to promote the VIV currently observed. The two bridges are very closely disposed, and the clear distance between each deck is shorter than a deck width (see Fig. 1). The center to center gap distance X is 22.25 m and the deck widths of investigated and proximate bridges are, respectively, 12.69 m and 11.86 m, then the ratio X / B is 1.75 ~ 1.88.

This kind of aerodynamic interference has been reported between closely spaced two decks (Honda et al., 1993; Larsen et al., 2000; Kimura et al., 2008). If the two bridge decks are close to each other, the behavior of VIV of one bridge deck will be affected by another deck. This parallel effect is sensitive to the ratio X / B, and it is even serious with the ratio as much as 8 (Kimura et al., 2008).

Most of the previous researches concentrated on the aerodynamic performances of the parallel decks, and introduced interesting results. However it did not derive any general conclusion for parallel bridge behaviors. In order to confirm that the vibration of investigated bridge is originated from the parallel disposition of the decks, the flow field is observed in 2D wind tunnel with Particle Image Velocimetry (PIV).

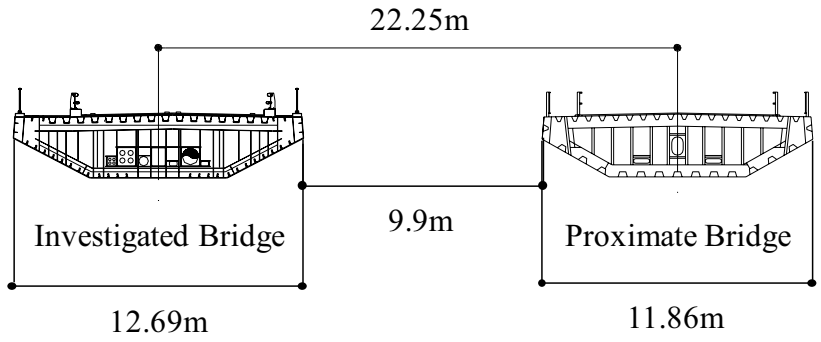

Figure 1. Girder section configuration (Guide vanes are not included)

2 VIV OF PARALLEL BRIDGE DECKS

A series of 2D wind tunnel tests was performed with 1/36 scaled section models. The dimensions including the gap distance and dynamic properties of the real bridges were reflected in section model by the law of similitude. Table 1 shows dynamic parameters for the model setup.

The tests are mainly performed for 3 cases. In Case 1, the investigated bridge is tested alone. In Case 2, the investigated bridge is placed at windward while the proximate bridge is located at leeward. This case has the same wind direction as the VIV occurred for the actual bridge. In Case 3, the test is performed for the opposite wind direction. Thus the investigated and proximate bridges are set at the leeward and windward, respectively. All cases are performed in smooth flow. The test section of the wind tunnel is 1.0 m in width and 1.5 m in height.

Tests results are shown in Figure 2 with a prototype scale. The damping ratios are under-tuned in the experiments in order to emphasize the vibrations of decks. In Cases 2 and 3, the maximum amplitudes of the investigated bridge are respectively 4.7~6.2 times larger than Case 1 in the vertical VIV. In Case 2, especially, VIV occurs at wind velocity of 12~14 m/s and that is similar to wind velocity for VIV of real bridge, 13~15 m/s. For the torsional VIV, parallel effect increases the displacement for Case 3, while decreases for Case 2.

Table 1. Dynamic parameters of the investigated and proximate bridges

Parameters	Investigated brdige			Proximate bridge		
	Proto	Model design	Model measured	Proto	Model design	Model measured
Length (m)	32.4	0.9	0.9	32.4	0.9	0.9
Width (m)	12.69	0.353	0.353	11.86	0.329	0.329
Mass (kg/m)	8978	6.927	6.697	6950	5.363	5.304
Mass moment of inertia (kg·m^2/m)	152836	0.091	0.090	84030	0.050	0.052
Vertical natural frequency (Hz)	0.436	2.180	2.180	0.513	2.561	2.550
Torsional natural frequency (Hz)	1.834	9.165	8.867	1.490	7.444	7.533
Vertical damping ratio (%)	-	-	0.100	-	-	0.090
Torsional damping ratio (%)	-	-	0.100	-	-	0.060

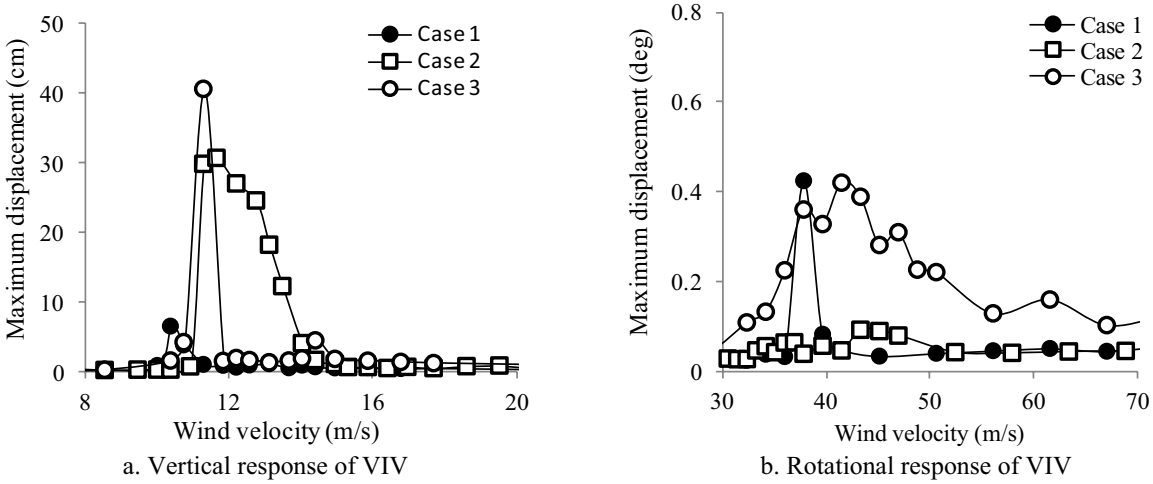

a. Vertical response of VIV

b. Rotational response of VIV

Figure 2. Wind velocity and amplitude of VIV

3 FLOW MEASUREMENT BY PIV

There is no doubt that the aerodynamic characterastics of the bridge decks are influenced by aerodynamic interference due to parallel disposition of two bridge decks. In order to interpret the VIV mechanism observed in the wind tunnel tests, flow visualization is required.

There was an attempt to show the flow patterns around the decks with CFD analysis (Meng et al., 2011). The research compares the flow patterns of two types of single deck which are, respectively, semi-closed box deck and single full-closed box deck with that of double semi-closed box decks. It says that the flow around double decks is significantly different from that of single deck. According to the CFD results, the paper anticipates that the VIV resonances of bridges, especially for leeward one, would be magnified if the both bridges have same aerodynamic configuration and natural frequencies, but if not, in contrast, the VIV resonances would be non-synchronous and weakened. The investigated bridge and proximate bridge have similar shapes and frequencies and, as a result, the VIV is anticipated as was observed.

The PIV images could cover sufficient area for analysis at one time as long as the system is consisted of a laser with light intensity of 135 mJ at 15 Hz and a digital CCD camera with 2M pixel resolution at 15 fps (a maximum frame rate of 32). The sampling rate is not high enough to get the very clear procedure of VIV formation. This problem may be enhanced in further study with a triggering technique for a series of divided target phases.

Figure 3 shows the flow around the single bridge deck. The contour represents the magnitude of velocity vector and the white lines denote the streamlines. It can be seen that the flow separation occurs alternately from the top and bottom of the deck, and then moves to leeward for a certain distance, converging into one flow. For this reason, a triangular area is obviously observed right behind the deck where the flow velocity is nearly zero.

Figure 4 shows the flow around the double decks with the contour and streamlines. It can be seen that the flows suddenly converge right behind the windward deck, and stirs up the gap space then moves to leeward side. In this situation, additional large eddies are generated in the gap space. The rotational direction of eddies keep changing periodically, and accordingly, the direction of flow streams changes up and down alternately. This will be the source of VIV excitation.

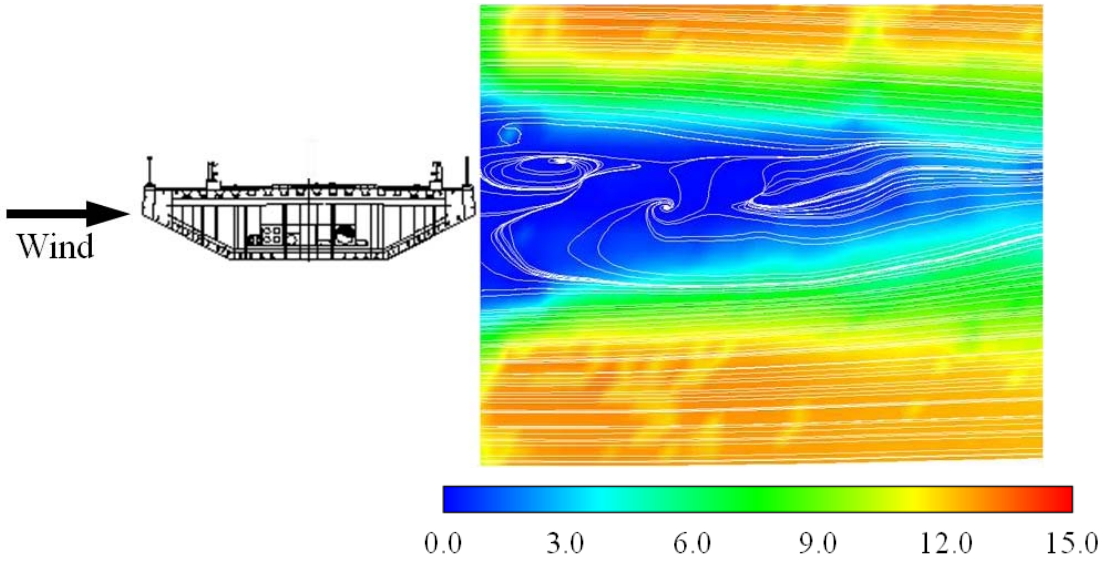

Figure 3. Flow around the investigated deck

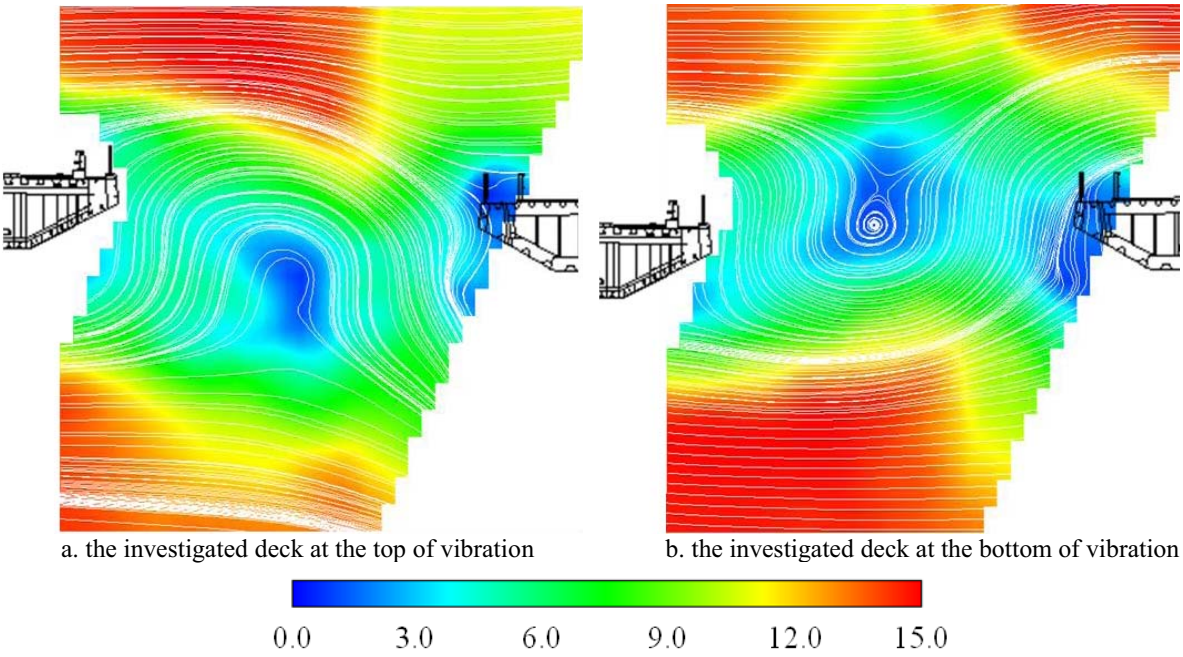

Figure 4. Flow around parallel decks

4 CONCLUSION

The VIV for a parallel cable-stayed bridge is realized in a wind tunnel test. In order to confirm the resource of the VIV, three cases of comparative tests were performed. The simulated tests successfully demonstrated the VIV characteristices for the parallel bridges. The flow field is traced with a PIV test. The large eddies is confirmed at the gap between two bridge decks. This alternating vortex maybe the source of the VIV observed in the field monitoring.

5 ACKNOWLEDGEMENTS

This research was supported by grant (09CCTI-A052531-05-000000) from the Ministry of Land, Transport and Maritime (MLTM) of Korean government through the Core Research Institute at Seoul National University for Core Engineering Technology Development of Super Long Span Bridge R&D Center.

6 REFERENCES

1 Honda, A., Shiraishi, N., Matsumoto, M., Fuse, Y., Sumi, K., Sasaki, N., Aerodynamic stability of Kansai International Airport access bridge, J. Wind Eng. Ind. Aerodyn., 49 (1993) 533-542.

2 Larsen, S.V., Astiz, M.A., Larose, G.L., Aerodynamic interference between two closely spaced cable supported bridges, In: Proc. 4th Int. Colloquium on Bluff Body Aerodynamics and Applications, Bochum, 2000, pp. 147-154.

3 Kimura, K., Shima, K., Sano, K., Kubo, Y., Kato K., Ukon H., Effects of separation distance on wind-induced response of parallel box girders. J. Wind Eng. Ind. Aerodyn., 96 (2008) 954-962.

4 Meng, X., Zhu, L., Guo, Z., Aerodynamic interference effects and mitigation measures on vortex-induced vibrations of two adjacent cable-stayed bridges. Frontiers of Architecture and Civil Engineering in China 5 (2011) 510-517.

The Seventh International Colloquium on Bluff Body Aerodynamics and Applications (BBAA7)
Shanghai, China; September 2-6, 2012

Simultaneous PIV/pressure measurements of the flow around elongated bluff bodies

Zachary J. Taylor [a], Roi Gurka [a, b], Gregory A. Kopp [a]

[a]*Boundary Layer Wind Tunnel Laboratory, Faculty of Engineering, University of Western Ontario, London, Canada*
[b]*Department of Chemical Engineering, Ben-Gurion University, Beer-Sheva, Israel*

ABSTRACT: Synchronized pressure and Particle Image Velocimetry (PIV) data are presented from experiments on 6 elongated bluff bodies of varying leading edge geometry and constant chord-to-thickness ratio of 7. The experiments spanned a range of Reynolds numbers of order 10^4, and the results show marked differences from previous results at lower Reynolds numbers. The surface pressure data show a gradual transition between two extremes. One extreme shows characteristics of being dominated by the separating-reattaching flow at the leading edge while the other shows that the trailing edge is dominant. The transition between these two extremes is observed to be continuous. The PIV data have been phase averaged, and a relationship is proposed to account for the observed shedding frequency variation which suggests that the leading edge geometry is a form of passive flow control.

KEYWORDS: Elongated bluff bodies, shedding frequency, vortex shedding, separation, reattachment, flow control

1 INTRODUCTION

Elongated bluff bodies contrast with shorter vortex shedding bluff bodies by the addition of leading edge separation-reattachment. The most common engineering application for these bodies is the case of suspension bridges. The geometry of the deck of a suspension bridge causes the flow to separate at the leading edge and reattach along the body before separating at the trailing edge, which initiates the vortex shedding process. Vortex shedding induced resonance is an issue for long-span suspension bridges whose design and construction makes them relatively flexible. A recent high profile example of vortex-induced vibrations on a full scale bridge structure was the Great East Belt Bridge in Denmark (Larsen et al., 2000).

Previous studies on elongated bluff bodies are few and typically limited to lower Reynolds numbers ($Re < 2000$); however, these works place the studies at higher Reynolds numbers in better context. The first indication that elongated bluff bodies are distinct from shorter bluff bodies was found in the splitter plate experiments of Nakamura and Nakashima (1986). In these experiments, a vortex street-like arrangement of vortices was observed even with the presence of a splitter plate in the wake. This result was surprising because the splitter plate negated the reliance on shear layer interaction in the recirculation region suggested by Gerrard (1966) to be crucial to the development of the vortex street for a circular cylinder. Nakamura and Nakashima (1986) realized that the vortex street-like arrangement was the result of an instability of the leading edge flow. Naudascher and Wang (1993) referred to this instability as the Impinging Leading Edge Vortex (ILEV) instability realizing that it was the leading edge vortices passing the trailing edge corner which completed the feedback loop to the leading edge vortex shedding. Thus, the vortex street-like arrangement of Nakamura and Nakashima (1986) was the observation of staggered leading edge vortices not trailing edge vortices observed in the wake

of circular cylinders. Hourigan et al. (2001) have discussed the relative importance between leading edge vortex shedding and trailing edge vortex shedding for elongated bluff bodies at low Reynolds numbers. They show that the preferred shedding frequency of leading edge vortices is determined by the natural trailing edge vortex shedding. Likewise, Mills et al. (2002) use external forcing at higher Reynolds numbers, and they show that the strongest shedding occurs when the external forcing is close to the trailing edge vortex shedding frequency. Similarly, the majority of the previous studies at higher Reynolds numbers are focused on external forcing (e.g., Stokes and Welsh, 1986; Parker and Welsh, 1983).

One of the most important studies of elongated bluff bodies at higher Reynolds numbers is that of Parker and Welsh (1983). Although the focus of their study was on acoustic forcing of the wake, they performed experiments over an extensive range of elongation, or chord-to-thickness, ratios up to $c/t = 52$. Within the range of elongation ratios there was a broad range ($7.6 < c/t < 25$) where the hot-wire anemometer in the wake did not detect any periodicity. This result suggests that periodic vortex shedding in the wake is suppressed over this elongation ratio range – a surprising result due to the persistence of vortex shedding for shorter bluff bodies. Roshko (1993) has shown that vortex shedding occurs for Reynolds numbers over at least 6 orders of magnitude even though its nature changes substantially. Others (e.g., Pastoor et al., 2008) have attempted to destroy vortex shedding as a form of drag reduction. However, vortex shedding has proven to be a persistent aerodynamic phenomenon, which is why its suppression over a wide range of elongation ratios for rectangular cylinders demonstrates the distinction between shorter bluff bodies and elongated bluff bodies at higher Reynolds numbers.

Recently, in Taylor et al., (2011), we showed that several key trends related to shorter bluff bodies do not hold for elongated bluff bodies. The trends to which we refer were established primarily by Roshko (1954) who related base pressure, the scale of the recirculation region and the shedding frequency to each other. One of the reasons, which we offered in Taylor et al. (2011), to explain the departure from these established trends was a noticeable change in the dynamics of the formation process in the recirculation region using a force balance on the time-averaged recirculation region of three elongated bluff bodies of differing geometries. The force balance method allows for an assessment of three key forces in closing the recirculation region. These three forces are the surface integrals of the Reynolds shear stress, the streamwise Reynolds normal stress and the pressure, along the boundary of the recirculation region. As the scale of the leading edge separation-reattachment zone grew, it was observed that the dominance of the force due to the pressure decreased while the scale of the near wake recirculation region remained largely unaffected. Thus, it was suggested that the leading edge plays a critical role in the formation process of the near wake. However, it remains unclear the extent to which the leading edge geometry affects the wake shedding frequency at higher Reynolds numbers.

2 EXPERIMENTAL SETUP

2.1 *Wind tunnel tests*

The experiments were performed in Boundary Layer Wind Tunnel II at the University of Western Ontario. This wind tunnel is of closed circuit design consisting of a high-speed test section with a cross-section 3.35 m wide by 1.83 m high. In this case, we have utilized the smooth flow at the upstream end of the 39 m long test section which is measured to be uniform to within 1% away from the walls and to have turbulence intensity less than 1%.

2.2 *Model details*

The wind tunnel model was designed to accommodate different forebodies (i.e., attachments to the leading edge). The basic model was of rectangular cross-section with a chord (defined as the streamwise dimension) of 533.4 mm and a thickness of 76.2 mm giving an elongation ratio, or chord-to-thickness ratio, of $c/t = 7$. In this study, we used a combination of the base model and five forebodies which are shown in Figure 1. The leading edge separation angles are marked in Figure 1 and referred to in the text by θ. The leading edge separation angles have not been measured but are assumed to be tangent to the leading edge forebody at the fixed separation points. The validity of this assumption was confirmed in our previous study on elongated bluff bodies (Taylor et al., 2011). The shapes used in the current study allow us to capture both extremes at the leading edge: the case of no separation ($\theta = 0°$), a blunt leading edge ($\theta = 90°$), and a range in between.

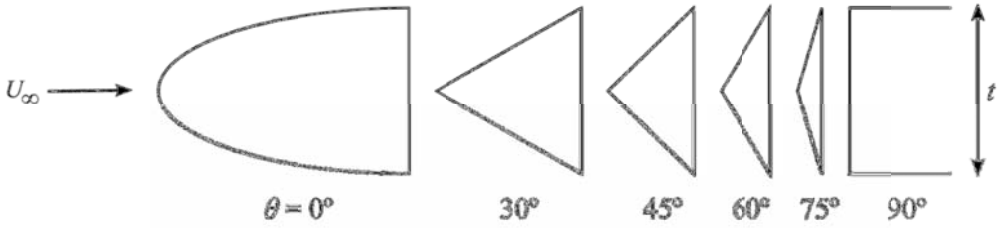

Figure 1. The five different forebodies and the leading edge of the base model (far right) are shown. Angles refer to the assumed leading edge separation angle, t is the thickness of the model and U_∞ the free stream speed.

2.3 *Pressure measurements*

Surface pressure measurements have been performed at 512 tap locations around the body (see Figure 2). The location of the taps yields three rings of sectional data in addition to five rows of spanwise data. The combination of tube length and restrictor size is one of the standard ones used at the BLWTL which has been repeatedly tested to ensure the frequency response is flat until approximately 200 Hz. We have sampled data from all 512 pressure taps near-simultaneously at a sampling frequency of 500 Hz and the data have been low pass filtered at 180 Hz to remove any effects of tube resonance. Multiplexed pressure scanners are used to sequentially scan up to 16 taps at each 0.002 s (corresponding to the 500 Hz sampling frequency). These measurements are interpolated in time to yield data which are essentially sampled simultaneously at all 512 pressure taps at 500 Hz. Phase lag tests have been performed to ensure that there are no errors from this procedure. The reader is referred to Ho et al. (1999) for more details on the pressure scanning system used in the current study.

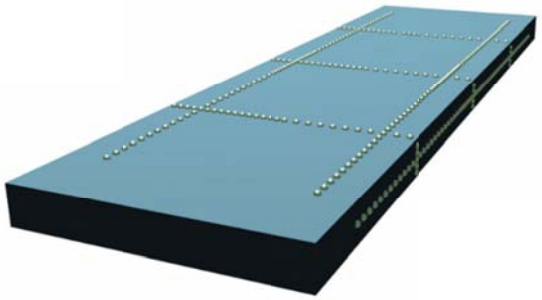

Figure 2. Gray markers represent the location of the surface pressure taps around the body. The camera in this figure is pointed at the trailing edge and top surfaces of the model.

2.4 *Particle Image Velocimetry measurements*

The Particle Image Velocimetry data were obtained using a custom long-duration time-resolved system developed at the University of Western Ontario. Development of the system is described in detail in Taylor et al. (2010). The camera has a 1024x1024 pixels^2 CMOS sensor with a 10-bit dynamic range. The innovation in the system comes from the streaming capability provided by IO Industries where the full resolution data can be streamed from the camera at 1000 frames per second for more than 20 minutes. In these experiments, the data are sampled simultaneously with the pressure data for 64 sec.

The large scale flow facility is seeded with atomized olive oil with a mean particle size of 1 μm (Echols and Young, 1963). Illumination is provided by the Quantronix Darwin Duo laser which is a double-head Nd:YLF laser operating with a wavelength of 527 nm. Due to the repetition rate required by the cameras, the laser has to have substantial power and this laser can produce 80W of light power. Operating at 1000 Hz, the laser provides 22 mJ of light in each half of a PIV interrogation pair.

To limit the reflection that makes measurements near the body difficult, the camera was placed so that the center of the field of view coincided with the lower trailing edge corner of the body (Figure 3). Using this technique, the amount of reflected light from surface reflections entering the camera is significantly reduced without the use of expensive coatings. Because of the large scale nature of the wind tunnel, getting a sufficient combination of seeding and illumination proved to be the most challenging experimental aspect of the work. However, by focusing the available illumination power on the near wake, suitable signal-to-noise ratios were obtained over a region 1.6*t* x 1.2*t* and velocity data were sampled encompassing the entire recirculation region (Figure 3).

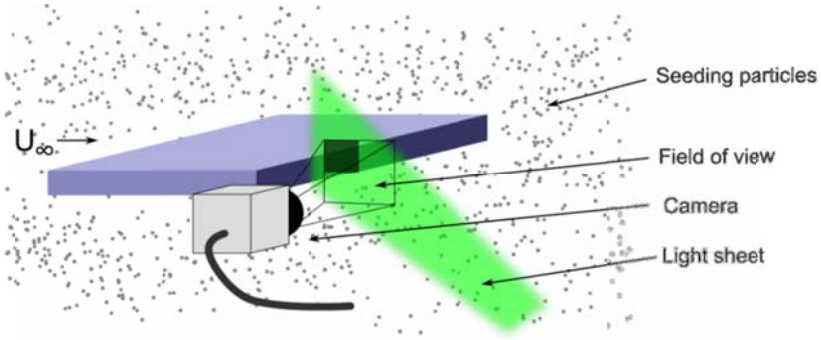

Figure 3. Schematic of the PIV setup.

2.5 *Phase averaging procedure*

All of the data have been phase averaged based on the time signal of a pressure tap in the recirculation region. Two examples of the pressure time series at this location are shown in Figure 4. Figure 4(a) shows the data for $\theta = 0°$ where the signal is distinctly periodic even though the amplitude of the signal changes continuously in time. In contrast, Figure 4(b) shows the data for $\theta = 90°$ where the signal is noticeably noisier, yet a distinct periodicity is still observed. The fitted data in Figure 4 is computed using the coefficients of the dominant frequencies from a FFT performed on 2 sec. long windows. The fitted data were used to perform the phase average.

Phase averaging of the data is performed following the approach of Reynolds and Hussain (1972). In this approach the data are decomposed as follows (note that in our example we decompose the pressure, but the same is done for each component of velocity as well),

$$p = \langle p \rangle + \tilde{p} + p' \tag{1}$$

In Eq. 1, p is the instantaneous value of pressure, $\langle p \rangle$ is the global time averaged pressure, $\tilde{p}$ is the periodic component and p' is the fluctuation from the global time average and the periodic component. This fluctuating term is often referred to as the 'incoherent' part of the flow associated with turbulent motion whereas the periodic component is responsible for fluctuations from the global time average, but is a 'coherent', or organized, fluctuation.

Taking the reconstructed time signal, as described above, and dividing each cycle into 16 bins we obtain an expression for each bin n,

$$\tilde{p}_n = \frac{1}{N_n}\sum_{i=1}^{N_n} p(\tau_i) \times M \qquad \text{where, } M = \begin{cases} 1, & \text{for } \dfrac{(n-1)}{16 f_s} \le \tau_i < \dfrac{n}{16 f_s} \\ 0, & \text{otherwise} \end{cases} \tag{2}$$

where τ_i is the time (starting from $\tau = 0$) of a discrete sample and f_s is the vortex shedding frequency of the wake for each body.

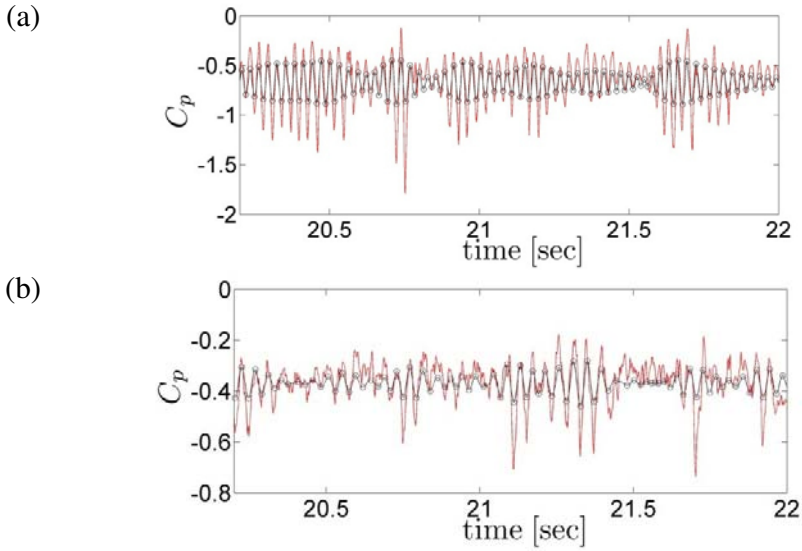

Figure 4. Example of the time signals from which the phase averages are constructed. (a) θ = 0°, (b) θ = 90°.

3 RESULTS

3.1 *Shedding frequency*

The most important aerodynamic feature in application to bridge structures is the shedding frequency since it is the shedding frequency which dictates when vortex-induced resonance will begin. We have measured the shedding frequency by calculating the time series of the sectional lift force, which is computed at each time step by integrating the surface pressures around each streamwise loop of pressure taps. The shedding frequency is normalized using the Strouhal number based on the model thickness as $St = ft/U_\infty$, where f is the shedding frequency in Hz, t is the model thickness and U_∞ the free stream speed.

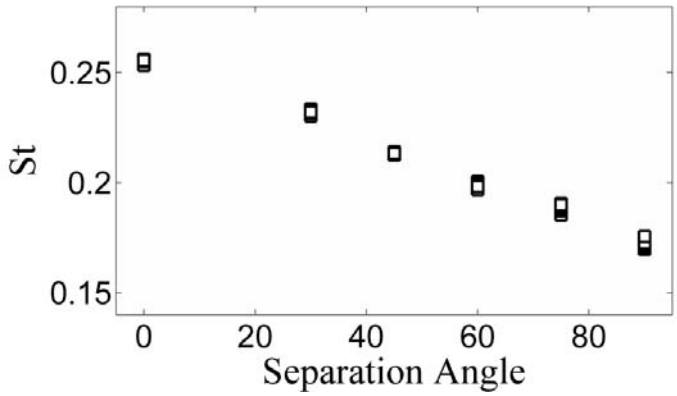

Figure 5. Thickness-based Strouhal number variation with leading edge separation angle. Each square marker represents a separate Reynolds number between 4-7.5x10^4.

3.2 *Leading edge separation bubble*

The size of the mean leading edge separation bubble is x_r and is estimated by the fluctuating pressures along the surface. Roshko and Lau (1965) showed that the mean pressures underneath separation bubbles collapse when the streamwise dimension is scaled by x_r. Their observation was true for a wide variety of leading edge geometries. Additionally, Ram and Arakeri (1990) observed that the maximum fluctuating pressures occur at the same streamwise location when scaled by x_r and that these maxima occur at approximately $0.95x_r$. Thus, we define the leading edge reattachment length by $x_r = x|_{max(Cp')}/0.95$ and mark the potential errors due to the spatial resolution of the pressure taps in Figure 6.

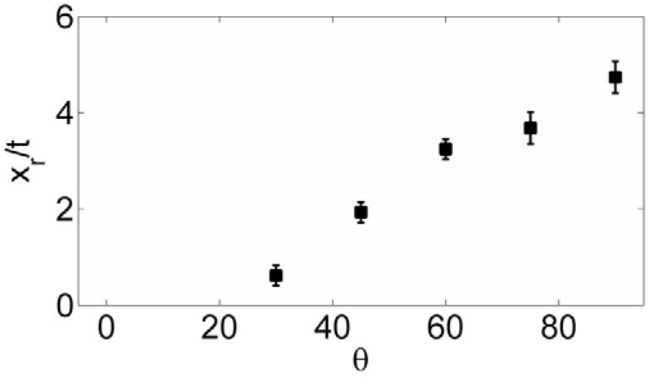

Figure 6. Leading edge mean reattachment length x_r is normalized by the thickness, t, and plotted against the leading edge separation angle, θ. Error bars mark uncertainty in the estimate arising from the spatial resolution of the pressure taps.

Another method to quantify the leading edge separation bubble is to study the vortices which are shed from this location. It should be noted that there is no periodicity to the shedding of vortices from the leading edge at the Reynolds numbers of the present study. This result is anticipated from Cherry et al. (1984) who also characterize leading edge vortices shed from a blunt-nosed semi-infinite plate using autocorrelations. In Figure 7, we present contours of the autocorrelation coefficient defined as,

$$R(\Delta x, \mathrm{T}) = \frac{\langle p_1'(x_0,\tau) p_2'(x_0+\Delta \mathrm{x},\tau+\mathrm{T})\rangle}{\sigma_{p_1}\sigma_{p_2}} \tag{3}$$

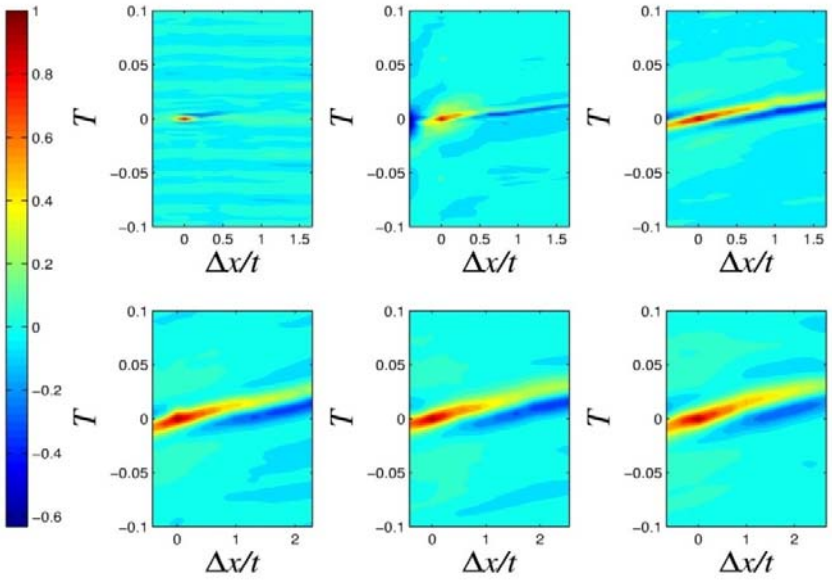

Figure 7. Contours of the correlation coefficient defined by Eq. 3 with $x_0 = x|_{max(Cp')}$. From top left to bottom right: θ = 0°, 30°, 45°, 60°, 75°, 90°. Color map applies to all θ.

where x_0 is a reference streamwise location; τ is time; Δx and T are the spatial and time lags, respectively; a prime marks a fluctuation from the mean; angle brackets represent the time-average of the entire time series; and, σ is the standard deviation. In Figure 7, we define the reference streamwise location, x_0, as $x_0 = x|_{max(Cp')}$ which is just upstream of the mean reattachment length.

The ridge of high correlation observed in Figure 7 was suggested by Cherry et al. (1984) to correspond to a 'footprint' of a leading edge vortex, and by calculating the slope of this ridge one obtains an approximation to the convection speed of a vortex traveling along the surface. For all cases with leading edge separation (i.e., all but θ = 0°) the range of estimated convection speeds is 0.5-0.55U_∞.

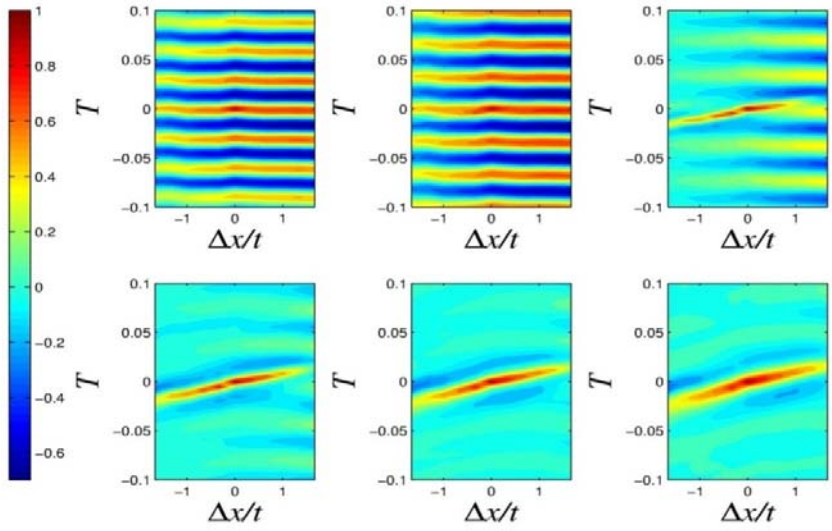

Figure 8. Contours of the correlation coefficient defined by Eq. 3 with $x_0 = 5.5t$. From top left to bottom right: θ = 0°, 30°, 45°, 60°, 75°, 90°. Color map applies to all θ.

Having used the autocorrelation in space and time to characterize the leading edge vortices, we perform a similar analysis near the trailing edge. This type of analysis allows us to explore the state of the leading edge vortices when they approach the trailing edge. In Figure 8 we once again show contours of the correlation coefficient defined by Eq. 3, but the reference streamwise value has changed to $x_0 = 5.5t$. It is observed from Figure 8 that for $\theta = 75°$ and 90° little has changed between the autocorrelation map at this location and that shown near the leading edge in Figure 7. However, this is in contrast to the case of $\theta = 0°$ and 30° where the autocorrelation map is dominated by a strong periodic feature in time whose wavelength matches that of the wake vortex shedding. Therefore, we have cases which can be labeled as 'trailing edge dominated' ($\theta = 0°$ and 30°) and cases which can be labeled as 'leading edge dominated' ($\theta = 75°$ and 90°), yet the most striking feature of Figure 8 is the apparent continual transition between these two extremes. The transition is apparent from the autocorrelation maps of $\theta = 45°$ and 60° because characteristics of both leading and trailing edge features are observed.

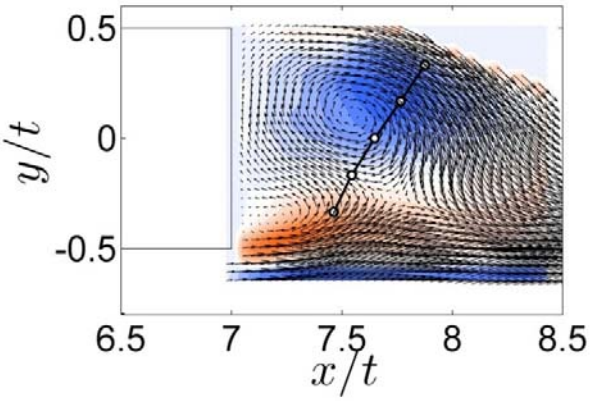

Figure 9. Phase averaged velocity vectors and vorticity contours (red: positive, blue: negative). Line is phase averaged pressure where distance from the surface is representative of suction at that location.

3.3 *Results of the phase average*

The phase averaging procedure is discussed in detail in §2.5 and an example of the result is shown in Figure 9. From Figure 9 it is observed that we can estimate features of the vortices in the near wake region with data that are spatially well resolved.

Although various features of the vortices in the near wake region can be computed, we focus on the convection speed. We suggest that the convection speed during the growth process and the shedding frequency are closely related. This notion is somewhat intuitive because if a vortex leaves the recirculation faster, then the next vortex can form sooner. Gerrard (1966) used a similar argument in his hypothesis regarding the effects of free stream turbulence on the shedding frequency of a circular cylinder. Using the phase averaged data in the recirculation region, we estimate the convection speed of a clockwise vortex (i.e., $y < 0$) through the vortex shedding cycle; these data are plotted in Figure 10. Agreeing with our hypothesis, it is observed that when the shedding frequency is higher the vortices have greater convection speeds through the recirculation region.

4 DISCUSSION & CONCLUSIONS

Based on the data presented, it is apparent that there is a gradual transition between bodies which are dominated by the leading edge flow and those which are dominated by the near wake. No-

where is this transition more evident than in Figure 8. As we have previously discussed, from this figure there are clear cases (θ = 75° and 90°) that are 'leading edge dominated' and other cases (θ = 0° and 30°) that are 'trailing edge dominated'. The transition between these two extremes appears to be gradual suggesting a continuous, rather than discontinuous, influence of the leading edge separating-reattaching flow on the near wake vortex shedding.

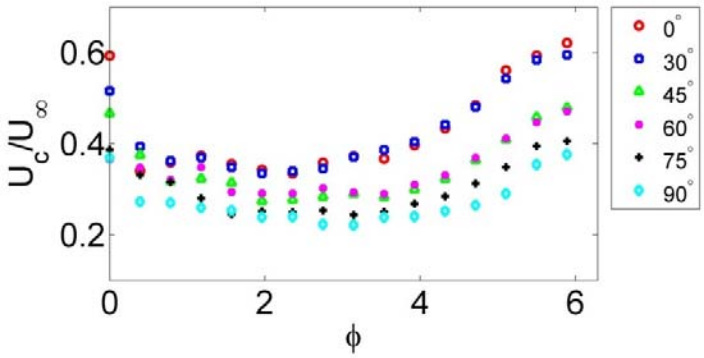

Figure 10. Phase averaged convection speed of a vortex ($y < 0$) through all phases $\phi \in [0,2\pi]$. Values in the legend correspond to the leading edge separation angle, θ.

We have not shown the frequency content of the leading edge separation bubble, but we could not detect any peaks in the spectra of the surface pressure data near the leading edge which confirms the suppression of the ILEV instability for all of these bodies at Reynolds number $O(10^4)$. Therefore, the determination of the shedding frequency at these Reynolds numbers must be a different mechanism than the feedback instability at lower Reynolds numbers.

A larger leading edge reattachment length corresponds to stronger separation, and it is expected that turbulence of larger scale is also produced. Therefore, we suggest that the leading edge flow is still significant in the determination of the shedding frequency; however, at higher Reynolds numbers it is no longer through a feedback mechanism. Returning to the hypothesis that faster moving vortices in the recirculation region (Figure 10) accompany higher shedding frequency, the turbulence created at the leading edge is suggested to slow down the growing vortices, which lowers the shedding frequency.

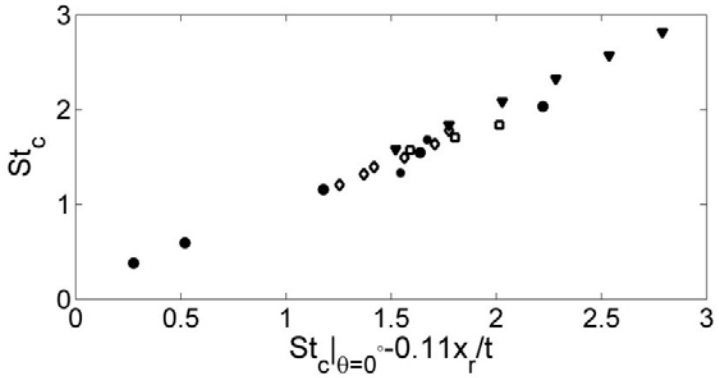

Figure 11. Plot of the modified chord-based Strouhal. Legend: Naudascher & Wang (1993): □ – Rectangular cylinder, ● – Semi-circular leading edge; ▼ - Elliptical leading edge from Mills et al. (2005); * – from Taylor et al. (2011); ◊ – Present data.

Extending this hypothesis to other elongated bluff bodies, we propose that the chord-based Strouhal number be modified by,

$$St_c = St_c|_{\theta=0} - g(x_r) \quad (4)$$

where, $g(x_r)$ is some function based on the reattachment length. Combining the data from Figure 5 and Figure 6 we obtain,

$$St_c|_{c/t=7} = St_c|_{c/t=7,\theta=0^\circ} - 0.11x_r \ . \quad (5)$$

We extend this relationship established for *c/t* = 7 to other bodies using data available in the literature (Figure 11). From Figure 11 it appears that this relationship yields a reasonable collapse of the data. Therefore, it appears that the leading edge offers a type of flow control through the level of turbulence rather than synchronization through feedback as it does at lower Reynolds numbers. Further studies are underway to examine how the turbulence created at the leading edge is connected to the vortex convection speed in the recirculation region.

REFERENCES

Cherry, N., Hillier, R. and Latour, M., Unsteady measurements in a separated and reattaching flow, Journal of Fluid Mechanics, 144 (1984) 13-46.

Echols, W. and Young, J., Studies of portable air-operated aerosol generators, Naval Research Laboratory, Technical report 5929 (1963).

Gerrard, J. H., The mechanics of the formation region of vortices behind bluff bodies, Journal of Fluid Mechanics, 25 (1966) 401-413.

Ho, T.C.E., Lythe, G.R., and Isyumov, N., Structural loads and responses from the integration of simultaneous pressures, Proc. 10th International Conference on Wind Engingeering, Copenhagen, Denmark (1999) 1505-1510.

Hourigan, K., Thompson, M. C. and Tan, B. T., Self-sustained oscillations in flows around long blunt plates, Journal of Fluids and Structures, 15 (2001) 387-398.

Larsen, A., Esdahl, S., Anderson, J. E. and Vejrum, T., Storebaelt suspension bridge - vortex shedding excitation and mitigation by guide vanes, Journal of Wind Engineering and Industrial Aerodynamics, 88 (2000) 283-296.

Mills, R., Sheridan, J. and Hourigan, K., Wake of forced flow around elliptical leading edge plates, Journal of Fluids and Structures, 20 (2005) 157-176.

Mills, R., Sheridan, J. and Hourigan, K., Response of base suction and vortex shedding from rectangular prisms to transverse forcing, Journal of Fluid Mechanics, 461 (2002) 25-49.

Nakamura, Y. and Nakashima, M., Vortex excitation of prisms with elongated rectangular, H and T cross-sections, Journal of Fluid Mechanics, 163 (1986) 149-169.

Naudascher, E. and Wang, Y., Flow-induced vibrations of prismatic bodies and grids of prisms, Journal of Fluids and Structures, 7 (1993) 341-373.

Parker, R. and Welsh, M., Effects of sound on flow separation from blunt plates, International Journal of Heat and Fluid Flow, 4 (1983) 113-127.

Pastoor, M., Henning, L., Noack, B. R., King, R. and Tadmor, G., Feedback shear layer control for bluff body drag reduction, Journal of Fluid Mechanics, 608 (2008) 161-196.

Ram, H. G. and Arakeri, V., Studies on unsteady pressure fields in the region of separating and reattaching flows, Journal of Fluids Engineering, 112 (1990) 402-408.

Reynolds, W. and Hussain, A., The mechanics of an organized wake in turbulent shear flow. Part 3. Theoretical models and comparisons with experiments, Journal of Fluid Mechanics, 54 (1972) 263-288.

Roshko, A., On the drag and shedding frequency of two-dimensional bluff bodies, NACA Technical Note 3169 (1954).

Roshko, A., Perspectives on bluff body aerodynamics, Journal of Wind Engineering and Industrial Aerodynamics, 49 (1993) 79-100.

Roshko, A. and Lau, J., Some observations on transition and reattachment of a free shear layer in incompressible flow, Proceedings of the Heat Transfer and Fluid Mechanics Institute, 18 (1965) 157-167.

Stokes, A. and Welsh, M., Flow-resonant sound interaction in a duct containing a plate, II: Square leading edge, Journal of Sound and Vibration, 104 (1986) 55-73.

Taylor, Z. J., Gurka, R., Kopp, G. A. and Liberzon, A., Long-duration time-resolved PIV to study unsteady aerodynamics, IEEE Transactions on Instrumentation and Measurement, 59 (2010) 3262 - 3269.

Taylor, Z. J., Palombi, E., Gurka, R. and Kopp, G. A., Features of the turbulent flow around symmetric elongated bluff bodies, Journal of Fluids and Structures, 27 (2011) 250-265.

The Seventh International Colloquium on Bluff Body Aerodynamics and Applications (BBAA7)
Shanghai, China; September 2-6, 2012

PIV and pressure measurements on two high-rise models in tandem arrangement

Arjen de Jong [a], Alexander Bronkhorst [a,b], Chris Geurts [a,b] and Carine van Bentum [a]

[a] *TNO, Delft, the Netherlands*
[b] *Eindhoven University of Technology, Department of the Built Environment, Eindhoven, the Netherlands*

ABSTRACT: Particle Image Velocimetry (PIV) and pressure measurements were performed on a high-rise model with a height (H) of 0.48 m and a width (B) of 0.12 m in a turbulent atmospheric boundary layer. Experiments were carried out for an isolated model and four tandem configurations with varying separation distance (S) between the models. Mean and standard deviation were determined for the PIV and the pressure dataset. Both velocity fields and pressure coefficient distributions show an increase in mean and fluctuating components near the entrance of the passage with decreasing separation distance. Proper Orthogonal Decomposition (POD) was performed on the PIV data to determine the most energetic modes. These modes were compared with observations from literature for tandem configurations in a laminar boundary layer. Similar modes were found (single, gap and coupled mode). In the current study it was found that the modes can occur simultaneously. Also the dominant mode differs from previous results described in literature for the investigated setup ranges.

KEYWORDS: High-rise buildings, wind interference, tandem arrangement, Particle Image Velocimetry

1 INTRODUCTION

Wind flow around a single isolated building has been studied extensively. Typical flow phenomena, such as the separation bubble and vortex shedding are quite well understood. There is less understanding on the changes of existing phenomena or the emergence of new phenomena when two or more high-rise buildings are in close proximity. A typical case is the tandem configuration, in which the wind approaches the buildings parallel to the intermediate passage. This configuration is known for particularly large mean velocities in the passage (e.g. Blocken et al, 2007) and large negative mean (Bronkhorst et al, 2011) and peak (Kim et al, 2010) pressures on the passage facades.

Yen and Liu (2010) performed pressure and visualization measurements using the smoke-streak technique on two square cylinders in side-by-side arrangement in quasi two-dimensional laminar flow. They found a change in flow patterns and vortex shedding frequency with increasing separation distance and classified three vortex shedding modes: the single mode ($S/B < 0.1$), the gap-flow mode ($0.1 < S/B < 5.5$) and the coupled vortex-shedding mode ($S/B > 5.5$). The gap-flow mode exhibits anti-phase vortex shedding; the vortex streets behind both models are symmetric with respect to the gap centre line. The coupled vortex-shedding mode has in-phase vortex shedding: the vortex streets behind both models are the same as the vortex street behind a single building, the interaction is observed in the in-phase rhythm of the vortex shedding. These flow characteristics of the tandem configuration defined by Yen and Liu (2010) for laminar flow were, to the author's knowledge, never investigated in an atmospheric turbulent boundary layer.

The goal of this paper is to obtain a better understanding of the flow phenomena and related pressure effects encountered in a tandem configuration of high-rise models in an atmospheric boundary layer. Particle Image Velocimetry (PIV) measurements were performed to obtain ve-

locity vector fields in the horizontal plane around the models. Separate pressure measurements in the same plane gave data on the local pressure distribution. This work describes the set up of the experiments and discusses results and findings.

2 MATERIALS AND METHODS

Wind tunnel experiments were carried out in the open circuit atmospheric boundary layer (ABL) wind tunnel of TNO in the Netherlands. It has a working section of approximately 13.5 m in length; the test section has a 3 m width and 2 m height. The boundary layer applied in this study had an aerodynamic roughness length z_0 = 3.2 mm. A detailed description of the flow field is given in Bronkhorst et al (2011).

2.1 *Pressure measurements*

The reference model is a wooden square cylinder with a height of H = 0.48 m and width B = 0.12 m. The pressure tap distribution on the faces is illustrated in Figure 1(a). The interfering model has the same dimensions as the reference model. Measurements were performed on the isolated configuration and four tandem configurations [as illustrated in Figure 1(b)]. The reference model was instrumented with pressure taps at 38 locations on each face. The current study only uses the data obtained at 0.32 m height (row i = 4), which is 2/3H. The pressures were measured with a sampling rate of 400 Hz for a period of approximately 20.5 seconds. During pressure measurements the undisturbed static and dynamic pressure were measured with a pitot-static tube positioned at model roof height (H = 0.48 m). The mean velocity at this height, U_H = 14.2 m/s, corresponds with a width-based Reynolds number of $Re = U_H B/\nu \approx 1.1 \times 10^5$.

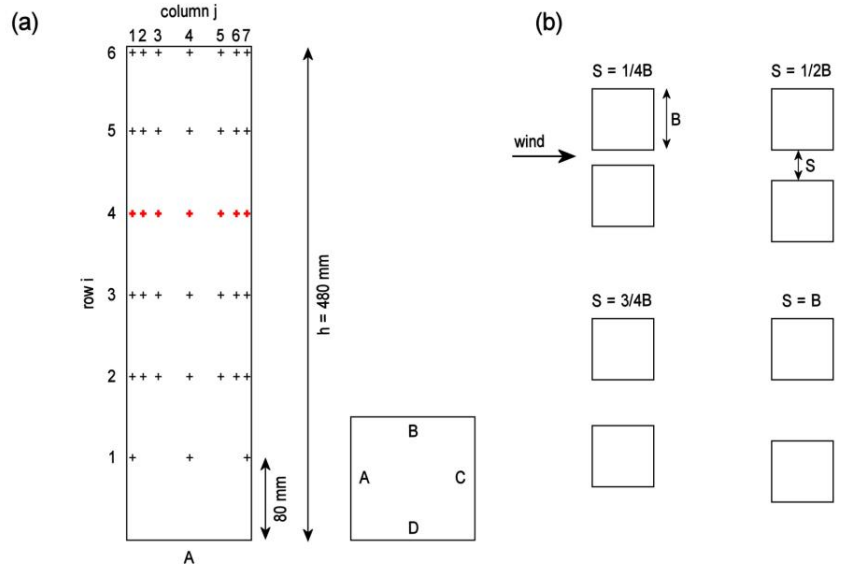

Figure 1. (a) pressure tap distribution on face A, the same distribution is found on face B, C and D, this study only uses the data obtained in row i = 4; (b) investigated tandem configurations.

2.2 *PIV measurements*

The tandem configuration consists of two wooden square cylinders with a height H = 0.48 m and width B = 0.12 m. Measurements were performed with a mean velocity at model height,

U_H = 14.2 m/s. The isolated configuration and four tandem configurations, illustrated in Figure 1(b), were investigated.

In order to evaluate the flow around the tandem square cylinders, two-component particle image velocimetry (PIV) is employed. The PIV measurements provide a velocity vector field with 2 velocity components in horizontal streamwise and spanwise x- and y-direction (u_x and u_y) at a height of z = 0.32 m from the ground. The PIV field of view (FOV) of approximately 600 by 460 mm is indicated in Figure 2(a), and is chosen to encompass the flow around both cylinders, the intermediate passage and a large portion of the cylinder wakes.

The illumination over the field of view is provided by a Quantel Evergreen 200 Nd:YAG double puls laser with 200 mJ maximum puls energy. The light sheet is generated downstream of the object of investigation. A LaVision Imager Intense CCD camera is placed above at a 90° angle with respect to the illumination sheet, and captures 1376 x 1040 pixel images, illustrated in Figure 2(b). The illumination and recording devices were synchronized and controlled by a LaVision Programmable timing unit controlled by Davis (Version 8, 64 bit) Software. Each test consisted of 200 image pairs at a recording frequency of 10 Hz. The double pulse interval was 250 microseconds. The chosen magnification yields a typical digital resolution of 2.3 pixels/mm. The images were analyzed with the Davis software; reflections in the raw images were corrected for through subtraction of the minimum pixel values over the 200 images, resulting in images as illustrated in Figure 2(c). Velocity vector fields were obtained through a multi-stereo cross-correlation with a final interrogation window of 16 x 16 pixels with 75% overlap.

The instantaneous velocity magnitudes are computed using $u(t) = [u_x(t)^2 + u_y(t)^2]^{1/2}$. The time-averaged mean and standard deviation velocity magnitudes, U and u_{std} respectively, were computed from the velocity magnitude time series. The results are presented non-dimensionally, referenced to the mean velocity at model height, U_H.

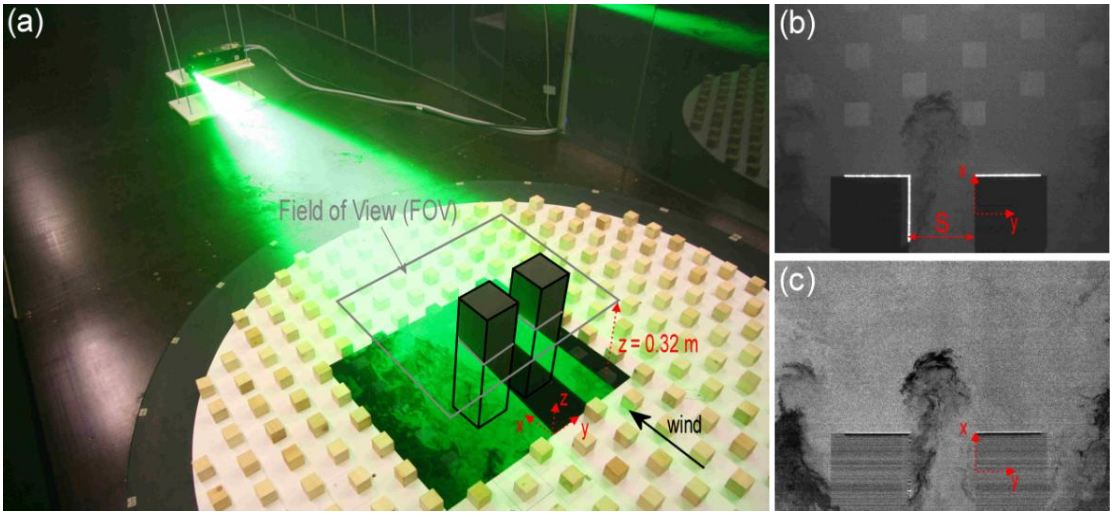

Figure 2. PIV measurements: (a) experimental set up, (b) raw image, (c) image after manipulation to correct for reflections.

3 RESULTS AND DISCUSSION

3.1 *Mean and standard deviation velocity field and pressure coefficient distribution*

The mean velocity field around the single isolated building at $z = 2/3H$ is illustrated in Figure 3(a). Flow phenomena such as the separation on the side face and the counter rotating mean wake structure behind the model are visible in the vector field. These flow features change significantly when two models are placed in tandem arrangement. First of all, for the studied configurations, the vector fields indicate that mean separation and recirculation are not present in the passage. Instead an increase is observed in the passage and low forward velocity around the side walls. Secondly, the strength of the jet at the exit of the passage has a large influence on the mean wake structure behind the models.

Blocken et al (2007) performed a tandem configuration study on building models with full scale dimensions B x D x H = 40 m x 20 m x 20 m. They determined an increase in mean velocity at pedestrian level (2 m). However, at larger heights (approximately $\frac{1}{2}H$) they found a decrease in mean longitudinal velocity of 10-25%. Blocken et al related this effect to an upward flux through the top of the passage caused by the overpressure region in front of the buildings near the ground. This effect reduced the longitudinal velocity through the passage at larger heights. The current study shows that the height of the buildings has a large influence on the flux through the passage, as there is a large velocity increase in the passage. In case of high-rise buildings, the high pressure region is not near the ground, resulting in a downward flux below approximately $2/3H$ (i.e. the stagnation point of buildings is in the region of $2/3H$) and an upward flux above $2/3H$.

Figure 3(b) shows the mean pressure coefficient distribution. On face A, the mean pressure coefficient increases with decreasing separation distance. This increase is particularly large near the passage entrance, where an increase is observed from $C_{p,mean} = 0.3$ (isolated case) to $C_{p,mean} = 0.6$ ($S/B = \frac{1}{4}$). This increase indicates the merging of the overpressure regions in front of the two buildings. The mean pressure distribution on face B is severely influenced by the neighbouring model. Near the entrance, the mean pressure coefficient increases with decreasing separation distance, from $C_{p,mean} = -0.7$ in the isolated case to $C_{p,mean} = -1.6$ for $S/B = \frac{1}{4}$. Near the passage exit, the mean pressure coefficients decrease towards the coefficients observed on face C. The influence of the adjacent model on the mean pressure coefficient distribution on face C and D is small.

Figure 4(a) shows the standard deviation velocity fields with decreasing separation distance. The high velocities near the sides are characteristic for the shear layer. In the tandem configuration, an increase is observed in the shear layers near the faces on the outside. In the passage, large values are found closer to the building face than on the outside faces. With decreasing separation distance, the large standard deviation velocities are concentrated near the entrance of the passage.

Figure 4(b) illustrates the standard deviation pressure coefficient distribution. On face A, a small increase is found which is largest at a separation distance of $S/B = \frac{1}{2}$. Large effects are observed on the distribution of face B in the passage. In the isolated case, the largest coefficients are observed near the trailing edge. This increase is a well-known effect caused by reattachment (e.g. Surry and Djakovich, 1995). The movement of the zone of reattachment results in a change in inclination with which the fluid approaches the surface which is responsible for an increased variation in pressure. Because the velocity magnitude varies little, no large standard deviation values are observed in this region.

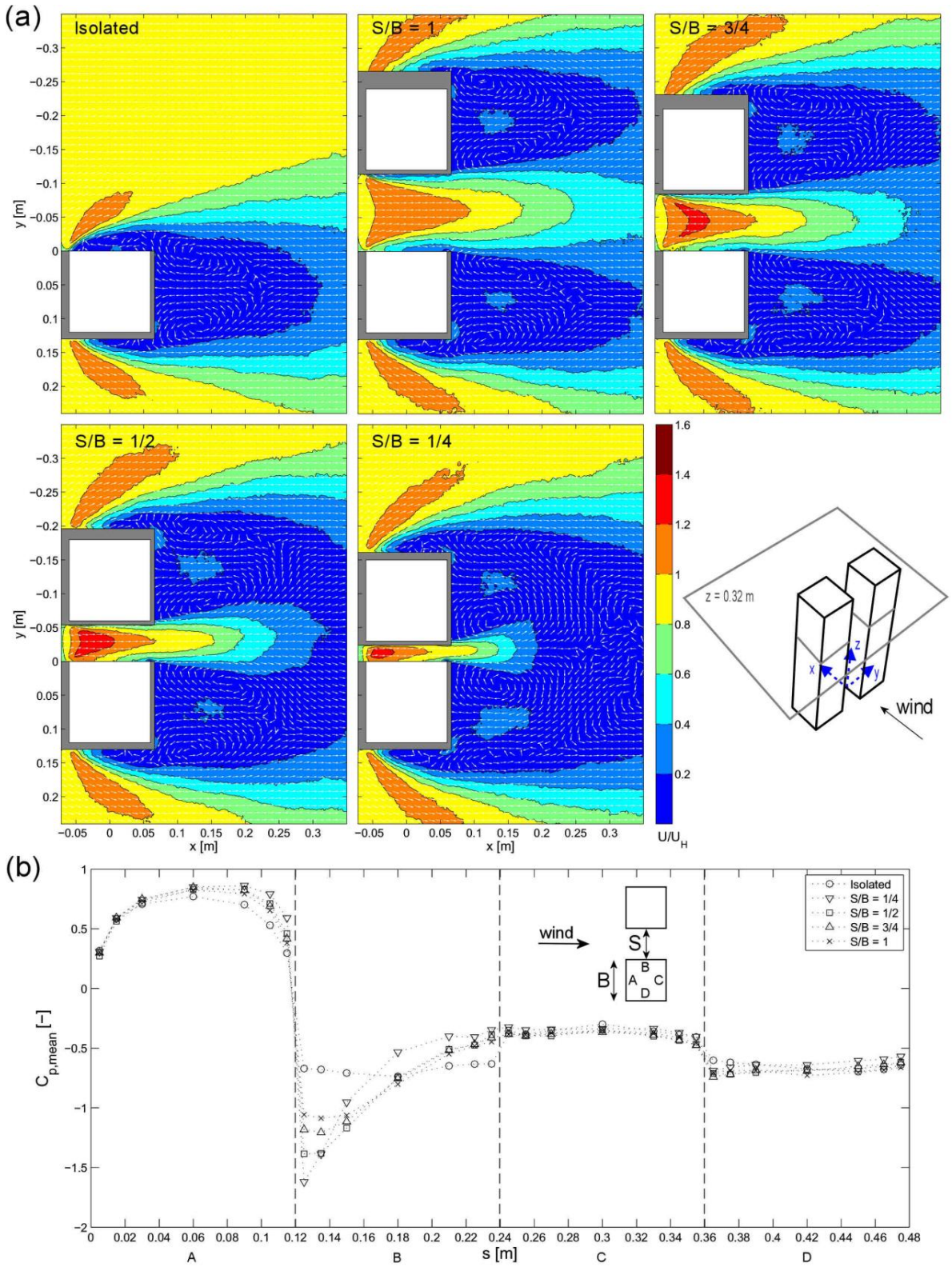

Figure 3. (a) Variation of the mean velocity field with increasing separation distance between the buildings at 2/3*H*: isolated building; *S/B* = 1; *S/B* = ¾; *S/B* = ½; *S/B* = ¼. (b) Influence of the separation distance on the mean pressure coefficient distribution at 2/3*H*.

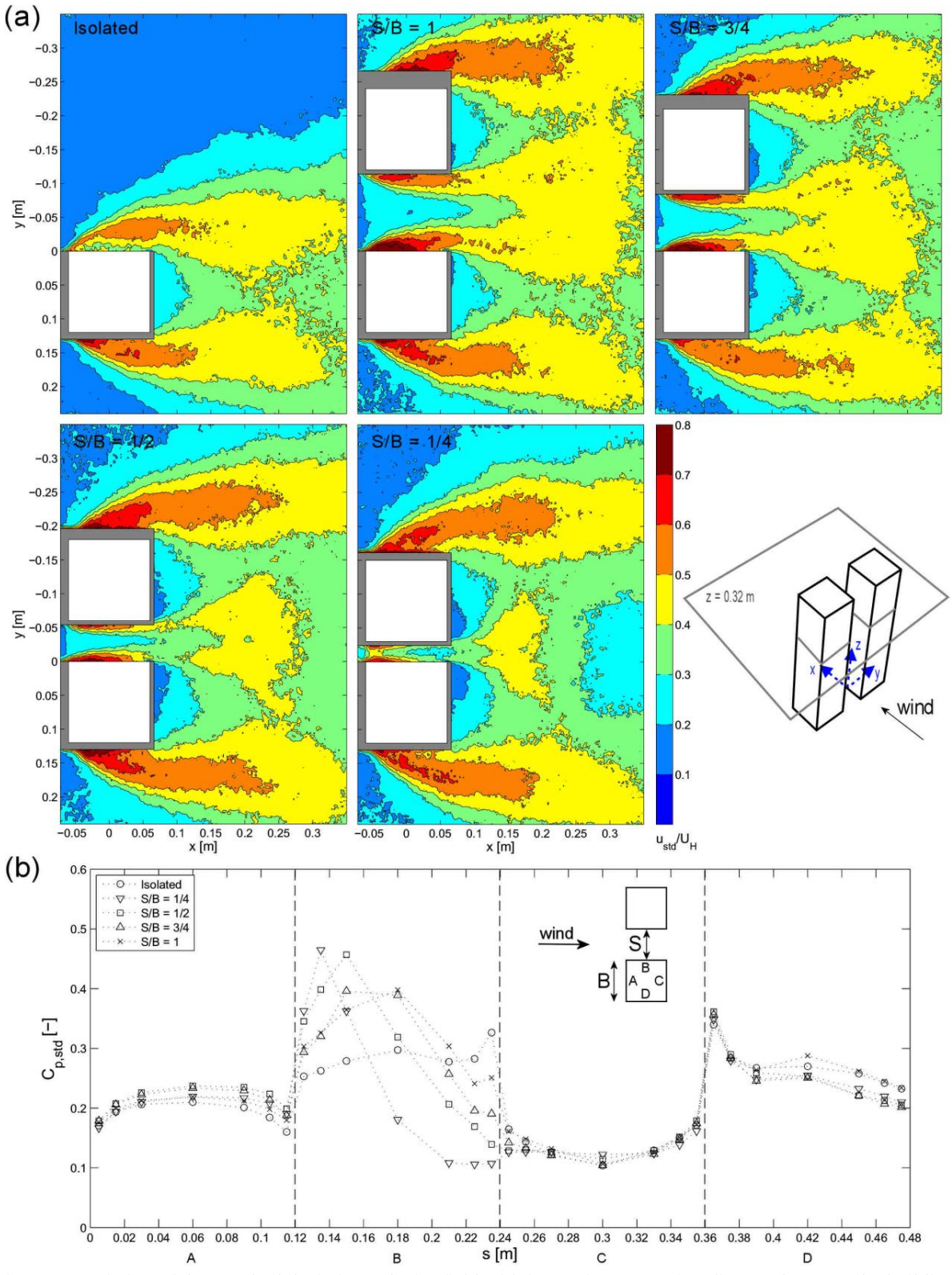

Figure 4. Variation of the standard deviation velocity field with increasing separation distance between the buildings at 2/3*H*: isolated building; *S*/*B* = 1; *S*/*B* = ¾; *S*/*B* = ½; *S*/*B* = ¼. (b) Influence of the separation distance on the standard deviation pressure coefficient distribution at 2/3*H*.

The standard deviation pressure coefficients near the entrance of the passage increase with decreasing separation distance. This is in agreement with the increase in velocity fluctuations in this region. Near the exit of the passage, there is a reduction in standard deviation pressure coefficient. The standard deviation velocities also show a decrease in this region. Small effects are observed on face C and D.

3.2 *Instantaneous and POD analysis of the velocity field*

Figure 4 shows three sequential snapshots of the *S/B* = ¾ configuration. Large differences compared to the mean flow results of figure 2 can be observed. Where the mean velocity field of figure 2 indicated no separated flow in the inner passage, the instantaneous velocity fields show separation does occur, either on left or right side or simultaneously on both sides. These observations are in agreement with the standard deviation visualizations observed in Figure 4.

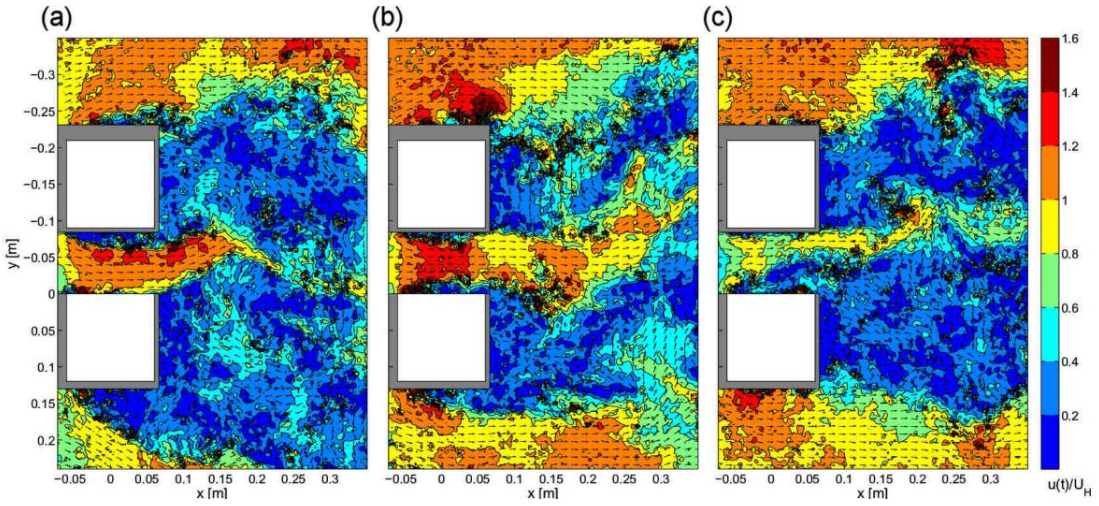

Figure 5. Instantaneous velocity fields illustrating the alternating behavior of the separation zones in the passage: (a) separated zone on right side, (b) separated zone on both sides, (c) separated zone on left side.

In order to obtain a better understanding of the underlying patterns in the turbulent flow, proper orthogonal decomposition (POD) was employed on each dataset of 200 vector fields. POD is a mathematical procedure that uses an orthogonal transformation to convert a set of observations of possibly correlated variables into a set of values of linearly uncorrelated variables. The transformation is defined in such a way that the first principal component has the largest possible variance and each succeeding component in turn has the highest variance possible under the constraint that it be orthogonal to (i.e., uncorrelated with) the preceding components. For velocity fields, the largest variance corresponds to the highest fluctuation kinetic energy. The two most energetic modes for *S/B* = ¾ and the most energetic mode for *S/B* = ¼ are depicted in Figure 6. On the left of the figure, the modified fluctuation velocity magnitude $\mathrm{sgn}(u_y) \bullet U_i$ for the 1st and 2nd mode is depicted. The $\mathrm{sgn}(u_y)$ term is added to indicate the relative direction in the mode shape. On the right of the figure, the mode velocity field is added to and subtracted from the mean velocity field to show the influence of the mode on the velocity field.

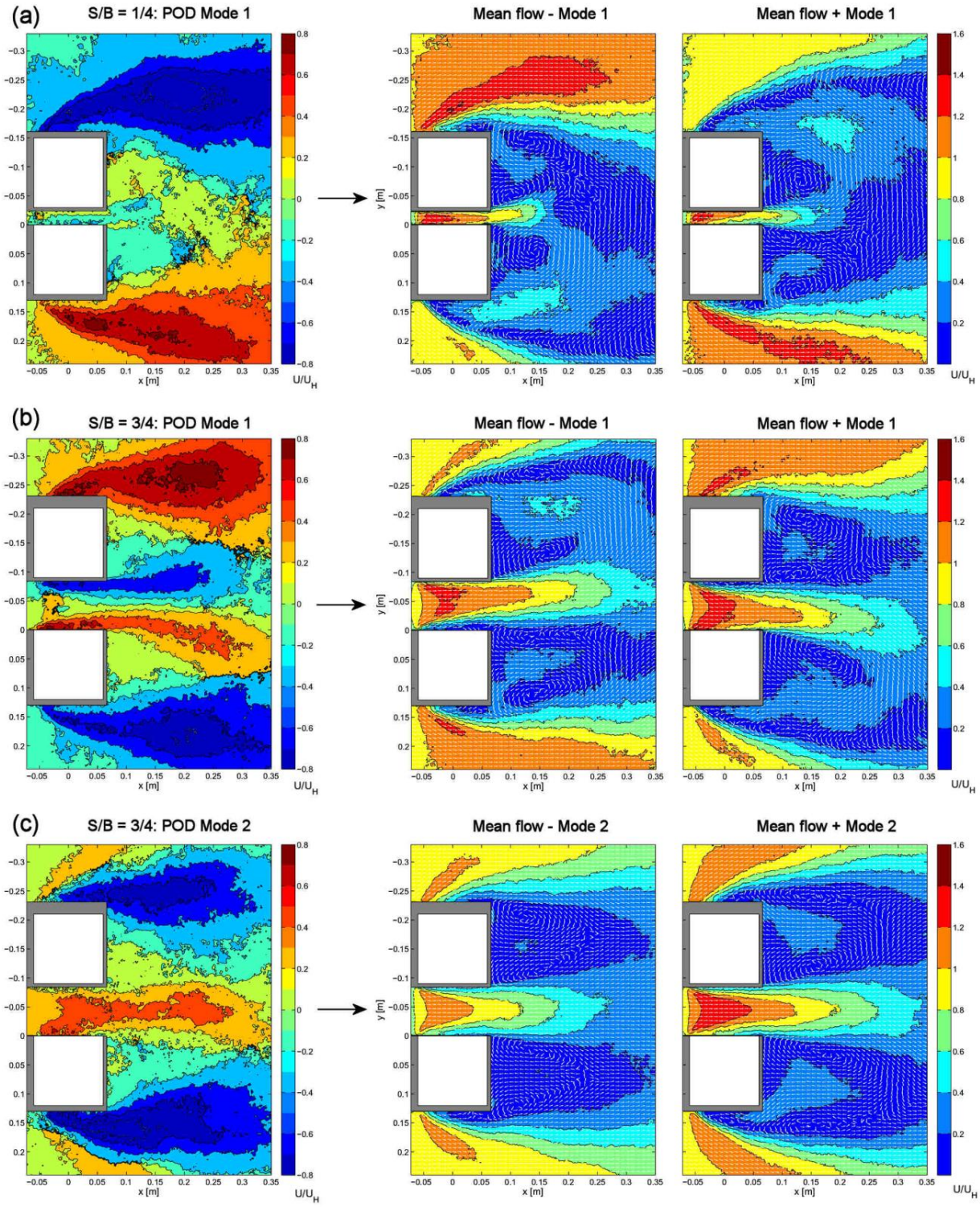

Figure 6. POD modes and effect in the flow field for: (a) Mode 2 (S/B = ¼), (b) Mode 1 (S/B = ¾) and (c) Mode 2 (S/B = ¾).

The 1st POD mode obtained for *S/B* = ¼ is illustrated in Figure 6(a). Most of the energy of this mode is observed in the flow outside of the tandem configuration, little energy is observed in the passage. This energy distribution is similar to the single model case, which is why this mode is defined as a single mode in Table 1. The 1st POD mode determined for *S/B* = ¾ is shown in Figure 6(b). For this separation distance, an increase in energy is observed both on the outside as well as in the passage. This mode is responsible for in-phase vortex shedding behavior of the vortex streets behind both models, in Table 1 this mode is specified as the coupled mode. This mode also is characterized by alternating separation from either sidewall in the passage, something observed in the snapshots of figure 5 as well. Figure 6(c) shows the 2nd POD mode determined for *S/B* = ¾, this mode is responsible for large velocity fluctuations in the gap between the models. In Table 1 this mode is defined as the gap flow mode. For some S/B values, the mode is characterized by combined separation from both sidewalls simultaneously in the passage, something observed in the snapshots of figure 5 as well. .

The modes illustrated in Figure 6 and provided in Table 1 are similar with the flow patterns described by Yen and Liu (2010). They performed smoke visualizations on similar models in a laminar boundary layer ($2262 < Re < 12560$) for opening ratios of $S/B = 0$ to 12, and observed a number of distinct flow patterns:

1. the single mode ($S/B < 0.1$);
2. the gap-flow mode ($0.1 < S/B < 6$);
3. the coupled vortex shedding mode ($S/B > 6$).

The specific ranges defined by Yen and Liu for the three observed modes, suggests that these modes do not exist simultaneously in laminar boundary layer flow. The energy fractions specified in Table 1 shows that these modes can coexist and that the gap-flow mode, for the studied cases, is an energy-wise secondary flow mode with respect to the single and coupled mode. The gap-flow mode coexists with the coupled mode. The difference in oncoming turbulence levels between both studies could be responsible for the different observations between the current work and the study performed by Yen and Liu (2010). Although the spectral characteristics of the pressure measurements performed by Yen and Liu (2010) suggest less stringent ranges for the different flow modes in a laminar flow as well.

Table 1. Energy fractions of flow modes obtained with POD and comparison with Yen and Liu (2010).

Separation Distance	Energy fractions per flow mode			Flow mode Yen and Liu
	Single	Coupled	Gap-flow	(2010)
Isolated	20%	-	-	Single
S/B = 1/4	16%	-	-	Gap-flow
S/B = 1/2	-	16%	6%	Gap-flow
S/B = 3/4	-	16%	6%	Gap-flow
S/B = 1	-	15%	7%	Gap-flow

4 CONCLUSIONS

Particle Image Velocimetry (PIV) and pressure measurements were performed to obtain a better understanding of the flow phenomena and related pressure effects encountered in a tandem

configuration of high-rise models in an atmospheric boundary layer. The mean and standard deviation values of the velocity field and the model pressure coefficient distribution were determined. Increases in mean and standard deviation velocity were observed in the passage with decreasing normalized separation distance (*S/B*).The regions of high standard deviation velocity fluctuations can be related to wall pressures in the passage region. Although the mean flow shows no backflow in the passage, intermittent separation from the sides of the passage occurs. POD is implemented to determine the most energetic modes. Three modes can be observed, single, coupled and gap-flow. For the isolated building and S/B=1/4 case, the single mode is dominant. For the other separation distances, both gap-flow and coupled mode coexist, with the coupled mode being dominant energy-wise. This is in contract with literature on laminar boundary layer flows, where only isolated modes are observed, and only the gap-flow mode is present in the currently investigated S/B ranges. The differences should be caused by the turbulence in the oncoming boundary layer. The currently observed coupled and gap–flow mode can be linked to separation of one or both inner walls in the passage respectively. An investigation into a more direct link between observed flow modes, velocity fluctuations and peak façade pressures is intended in future research.

5 REFERENCES

A.J. Bronkhorst, C.P.W. Geurts, B. Blocken, C.A. van Bentum, 2011, Pressure effects due to wind interference between mid-rise and high-rise buildings, 13th International Conference on Wind Engineering, Amsterdam, the Netherlands.

B. Blocken, J. Carmeliet, T. Stathopoulos, 2007, CFD evaluation of wind speed conditions in passages between parallel buildings – effect of wall-function roughness modifications for the atmospheric boundary layer flow, J. Wind Eng. and Ind. Aerodyn. 95, 941-962.

D. Surry, D. Djakovich, 1995, Fluctuating pressures on models of tall buildings, J. Wind Eng. and Ind. Aerodyn., 58, 81-112.

S.C. Yen, J.H. Liu, 2010, Wake flow behind two side-by-side square cylinders, International Journal of Heat and Fluid Flow,

W. Kim, Y. Tamura, A. Yoshida, 2011, Interference effects on local peak pressures between two buildings, J. Wind Eng. Ind. Aerodyn., 99, 584-600.

The Seventh International Colloquium on Bluff Body Aerodynamics and Applications (BBAA7)
Shanghai, China; September 2-6, 2012

Local flow field of a surface-mounted finite square prism

N. Rostamy, J.F. McClean, D. Sumner, D.J. Bergstrom, J.D. Bugg

Department of Mechanical Engineering, University of Saskatchewan
57 Campus Drive, Saskatoon, Saskatchewan, Canada

ABSTRACT: The local flow field of a surface-mounted finite-height square prism was studied experimentally in a low-speed wind tunnel using particle image velocimetry (PIV). The prism was mounted normal to a ground plane and was partially immersed in a flat-plate turbulent boundary layer. Four finite square prisms of aspect ratios AR = 9, 7, 5 and 3 were tested at a Reynolds number of Re = 4.2×10^4. PIV velocity field measurements were made in a vertical plane parallel to the mean flow direction on the flow centreline, within two diameters upstream and five diameters downstream of the prism, and also above the free end. In the near-wake region, the large recirculation zone contains a vortex immediately behind and below the free end; the size and strength of this vortex increases as the aspect ratio of the prism decreases. A second vortex is found behind the prism near the prism-wall junction; this vortex was not observed for the prisms of AR = 5 and 3, indicating a distinct wake structure for these prisms compared to those of AR = 9 and 7.

KEYWORDS: Bluff body, finite square prism, near wake, recirculation zone, vortex structures, particle image velocimetry

1. INTRODUCTION

The flow around surface-mounted circular cylinders of finite height is more complex than the familiar case of a two-dimensional or "infinite" circular cylinder [1]. Surface-mounted cylinder-like or prismatic structures are found in many engineering applications, such as the flow past high-rise buildings, oil storage tanks, chimneys and cooling towers. For these bluff bodies, the flow field is strongly influenced by the flow around the free end and the flow around the junction between the cylinder and the surface.

The flow around a finite square prism of side length, D, and height, H, mounted normal to a ground plane (Fig. 1) is influenced by the aspect ratio, AR (= H/D), the Reynolds number, Re (= DU_∞/ν, where U_∞ is the freestream velocity and ν is the kinematic viscosity), and the relative thickness of the boundary layer on the ground plane, δ/D (where δ is the boundary layer thickness at the location of the prism). The flow around the prism-wall junction (at the ground plane) and over the free end cause the local flow field to become strongly three-dimensional. Some of the most extensive insight into the wake vortex dynamics (vortex shedding, streamwise vortex structures) of the finite square prism comes from recent experimental studies by Wang et al. [2, 3], Wang and Zhou [4], and Bourgeois et al. [5]. These studies used a variety of experimental techniques, including flow visualization, thermal anemometry, laser Doppler velocimetry (LDV), and particle image velocimetry (PIV).

Because of the complexity of the flow field around the surface-mounted finite-height square prism, and the many influencing parameters, further study is needed to obtain a complete physical understanding of the wake behavior, especially very close to the prism, i.e., the local

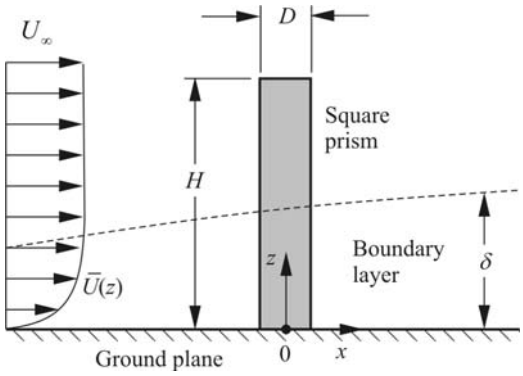

Figure 1. Schematic representation of the flow past a finite-height square prism mounted normal to a ground plane and partially immersed in a flat-plate boundary layer.

flow field. In the present study, the local flow fields of surface-mounted finite-height square prisms were investigated in a low-speed wind tunnel using the PIV technique. Of particular interest in the present study were the flow in the near-wake region and the effect of aspect ratio.

2. EXPERIMENTAL APPARATUS

The experiments were conducted in a low-speed closed-return wind tunnel with a test section of 1.96 m (length) × 0.91 m (height) × 1.13 m (width). The streamwise freestream turbulence intensity was less than 0.6% and the mean velocity non-uniformity outside the test section's wall boundary layers was less than 0.5%. An aluminum ground plane was installed on the floor of the wind tunnel test section and a fully developed turbulent boundary layer was produced on the ground plane at the location of the finite square prism.

Four different, smooth, aluminum square prism models, all of the same width, D = 31.5 mm, were tested. The free end of each prism was a flat surface with sharp perimeter edge. Each prism had a different height, giving prisms with AR = 9, 7, 5, and 3, similar to the earlier experiments of [1,6]. The prisms were anodized flat black to minimize unwanted reflections from the laser light sheet used for the PIV measurements. Each prism was partially immersed in the turbulent boundary layer on the ground plane. The experiments were conducted at a freestream velocity of U_∞ = 20 m/s, giving a Reynolds number, based on prism width, of Re = 4.2×10^4.

The wind tunnel data were acquired using a computer with a 1.8-GHz Intel Pentium 4 processor, a National Instruments PCIe-6259 16-bit data acquisition board, and LabVIEW software. The freestream conditions were obtained with a Pitot-static probe, Datametrics Barocell absolute and differential pressure transducers, and an Analog Devices AD590 integrated circuit temperature transducer. To characterize the boundary layer on the ground plane, a boundary layer Pitot tube and an X-wire boundary layer probe were used to measure its mean velocity profile. At the location of the prism (with the prism removed), the boundary layer thickness was δ = 54 mm providing a thickness-to-width ratio of δ/D = 1.7 and a thickness-to-height ratio ranging from δ/H = 0.2 (for AR = 9) to δ/H = 0.6 (for AR = 3).

Velocity field measurements in the vicinity of the finite square prism were made with a PIV system. The laser light (532 nm) was supplied by a 200-mJ/pulse dual Nd:YAG Gemini PIV 15 laser from New Wave Research, which had a maximum pulse frequency of 15 Hz. A TSI

light arm was used to deliver the laser beam from the laser to the light sheet optics. The light sheet optics included either a −50-mm or −25-mm cylindrical lenses and 500-mm, 750-mm, or 1000-mm spherical lenses, depending on the location of the field of view. Images were acquired with a CCD camera (MegaPlus ES4020, double frames, 2048 × 2048 pixels) and captured by a 64-bit EDT PCI DV C-Link frame grabber on a computer workstation. The timing of the laser, camera, and frame grabber was controlled by a Berkeley Nucleonics 505-8C digital delay generator synchronizer. The flow was seeded by atomized propylene glycol droplets produced by a theatrical fog machine.

PIV measurements were made in vertical (*x*-*z*) planes located on the centreline of the test section ($y = 0$). The light sheet optics were located above the wind tunnel test section and the laser light was directed through a small aperture in the test section roof and towards the ground plane. The field of view was 61 mm × 61 mm (1.9*D* × 1.9*D*) yielding an image resolution of about 30 μm/pixel. For the tallest prism (of AR = 9), more than 25 fields of view were used to build a composite picture of the flow field upstream and downstream of the prism. For each field of view, an ensemble of 1,000 sample images was acquired from which the mean velocity vector field was determined. Image pairs were processed with a half-padded FFT cross-correlation algorithm, a relative maxima peak detection algorithm, and a Gaussian sub-pixel interpolation algorithm. A Hart correlation-based (CBC) validation method [7] with 50% overlap was used for reducing the sub-pixel errors and eliminating spurious vectors from the PIV results. The cellular neural network (CNN) method [8] together with dynamic threshold outlier identification was used as a post-interrogation algorithm to detect spurious vectors in PIV measurements. Most fields of view were analyzed with initial interrogation areas of 32×32 pixels. Owing to large pixel displacements in some limited regions of the flow, initial interrogation sizes of 64×64 pixels were used in the remaining fields of view. In all cases a two-level analysis technique was used that halved the interrogation area size during the second pass. In addition, a 50% interrogation area overlap was used in all cases. The resulting velocity vector fields contained approximately 127 × 127 and 63 × 63 velocity vectors with a vector spacing (spatial resolution) of approximately 0.015*D* and 0.03*D*, respectively. This spatial resolution is significantly greater than the seven-hole probe experiments of Sumner et al. [1], the X-probe measurements of Adaramola et al. [6], and the PIV studies of Wang and Zhou [4] and Park and Lee [9] in the literature. The uncertainty in the mean velocity measurements was estimated to be about 2%.

3. RESULTS AND DISCUSSION

Figure 2 shows the local mean velocity vector field on the wake centerline ($y/D = 0$) for each of the four prisms (of AR = 9, 7, 5, and 3); the corresponding mean flow streamlines are shown in Figure 3. In Figure 2, the in-plane mean velocity components are made dimensionless with the freestream velocity ($\overline{U}/U_\infty$, $\overline{W}/U_\infty$). The mean fields are calculated from an ensemble of 1,000 instantaneous PIV velocity fields.

Upstream of the prism, for all four aspect ratios, part of the approach flow moves up and over the tip and separates from the leading edge of the free end. No flow reattachment occurs on the free end (Figs. 2 and 3). The other part of the approach flow, closer to the ground plane, moves downwards as it nears the prism and recirculates upstream of the prism-wall junction. It is in this region where the familiar horseshoe vortex is located (although it cannot be discerned in Figs. 2 and 3). In the near-wake region, a strong downwash flow (downward-directed velocity vectors in Fig. 2) is observed immediately downstream of the free end in the near wake of the

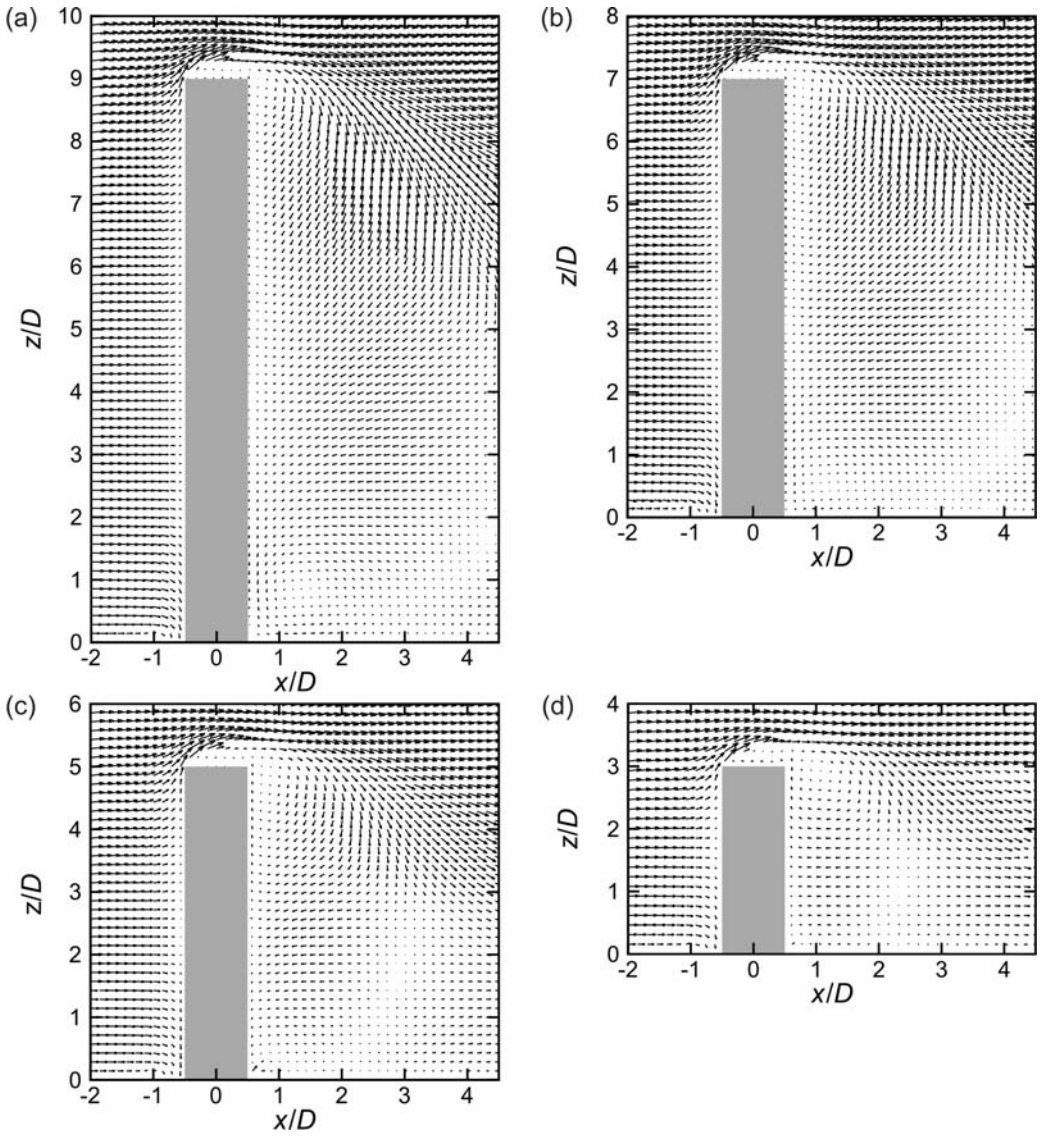

Figure 2. Mean velocity vector field ($\overline{U}/U_\infty$, $\overline{W}/U_\infty$ components) in a vertical plane on the wake centerline (y/D = 0, the symmetry plane): (a) AR = 9; (b) AR = 7; (c) AR = 5; (d) AR = 3.

prism (Fig. 2). The downwash originates downstream of the free-end recirculation zone, persists in the streamwise direction and descends into the central portion of the wake.

In the mean streamlines shown in Figure 3, part of the downwash flow is directed towards the ground plane and returns upstream to stagnate onto the rear surface of the prism; a large recirculation zone forms behind the prism. The rest of the downwash flow moves away from the prism into the far wake. As seen in Figure 3, a small vortex forms immediately downstream of the trailing edge of the free end. The size of the vortex is a function of the prism aspect ratio, such that the largest vortex occurs for the smallest aspect ratio (AR = 3, Fig. 3d). According to Figures 3a,b,c, for AR = 9, 7 and 5, respectively, some of the downwash flow is directed along the prism wall toward the ground plane, whereas for AR = 3 (Fig. 4d), flow moves upwards along the prism wall toward the free end, resulting in a larger vortex just below the free end.

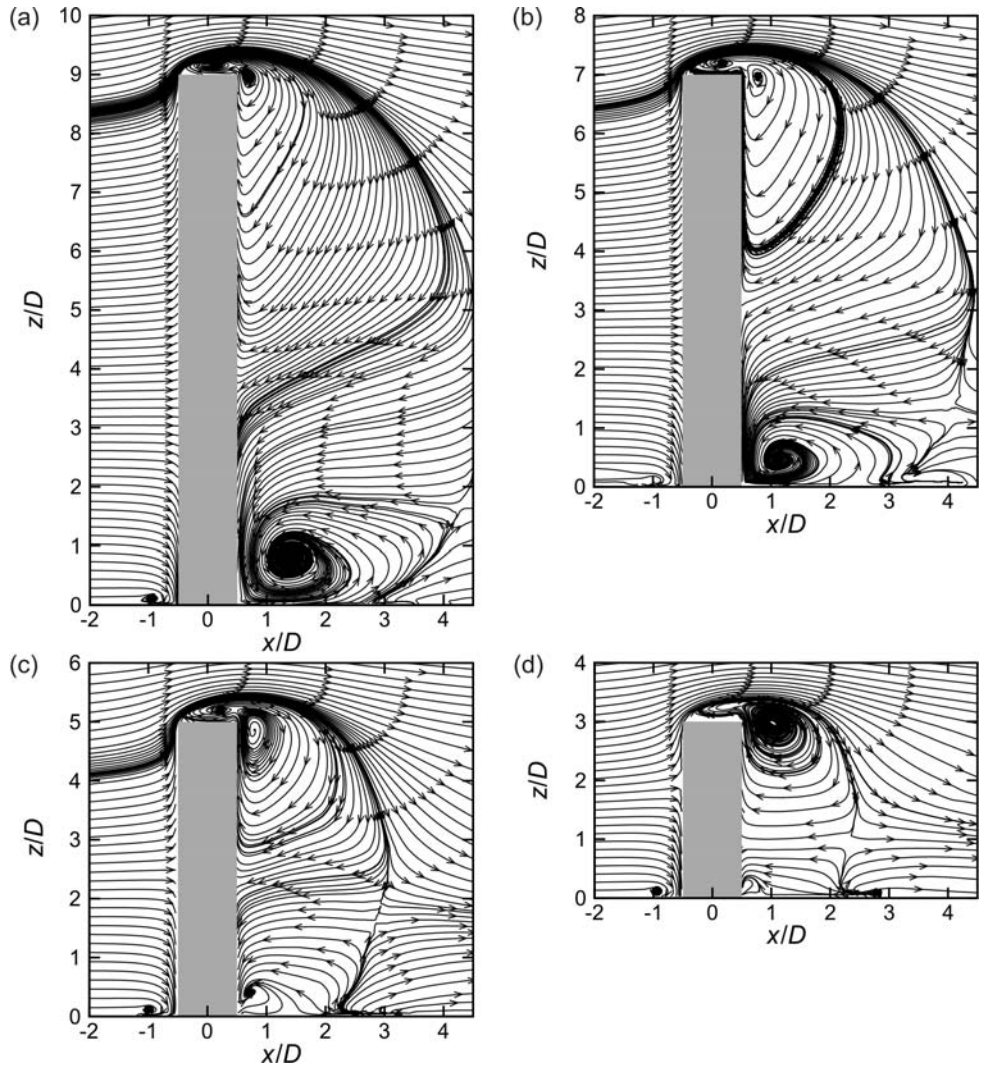

Figure 3. Mean streamlines in a vertical plane on the wake centerline (y/D = 0, the symmetry plane), corresponding to the mean velocity fields in Figure 2: (a) AR = 9; (b) AR = 7; (c) AR = 5; (d) AR = 3.

According to Figures 2 and 3, another vortex, with CCW sense of rotation, can be found immediately behind the prism, near the prism-wall junction, for AR = 9 and 7 (Fig. 3a,b); enlargements of these vortices are shown in Figure 4. This vortex is much weaker and nearly absent for the prisms of AR = 5 and 3 (Figs. 3c,d and 4c,d). The distinct near-wake structure for AR = 3, and to some extent for AR = 5, suggest the critical aspect ratio for these prisms is between AR = 5 and AR = 3.

Figure 5 shows how the maximum length of the recirculation zone is dependent on the square prism's aspect ratio. According to this figure, the maximum length of the recirculation zone increases from L_{max}/D = 2.3 for AR = 3 to L_{max}/D = 4.2 for AR = 9. In Figure 5, the present data are compared to the square prism data of Wang and Zhou [4] and Bourgeois et al. [5]. Good agreement can be seen between the present data and the other studies for prisms of AR = 3, 5, and 7.

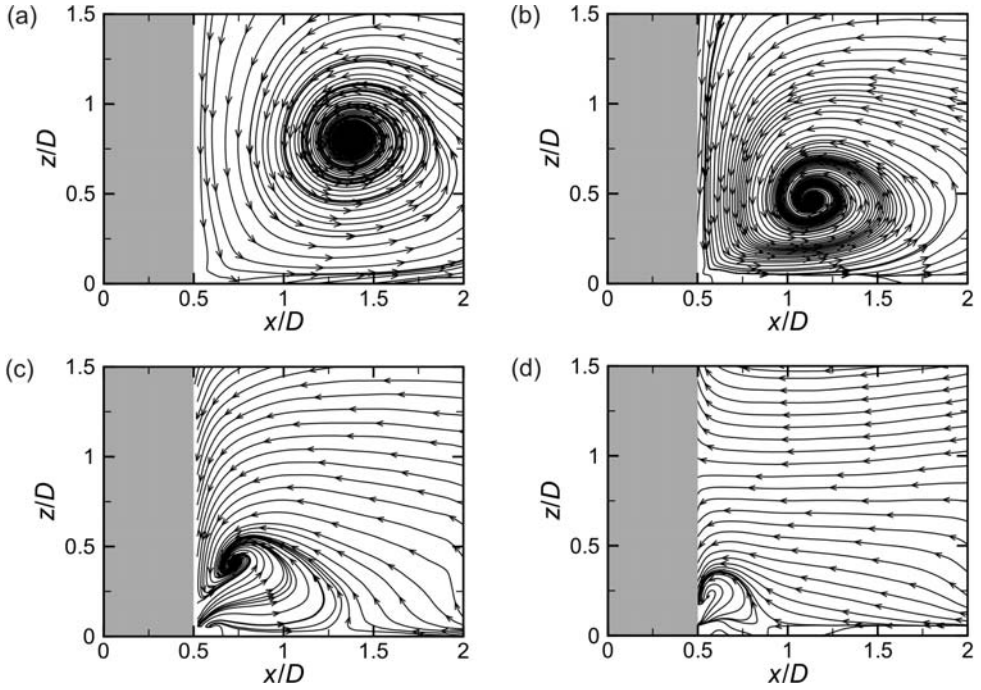

Figure 4. Mean streamlines immediately behind the prism at the junction with the ground plane: (a) AR = 9; (b) AR = 7; (c) AR = 5; (d) AR = 3.

A contour plot of the streamwise turbulence intensity (u'/U_∞), on the wake centreline, is shown in Figure 6. The highest values of streamwise turbulence intensity are encountered above the free end of the prisms of AR = 9, 7, and 5 (Figs. 6a,b,c), while the highest value of u'/U_∞ for AR = 3 (Fig. 6d) occurs farther downstream, showing a distinct turbulence structure for AR = 3. For all four prisms, the highest values of wall-normal turbulence intensity (w'/U_∞, not shown) are encountered within the recirculation zones of the prisms. The location of highest wall-normal turbulence intensity in the near-wake region tends to move downward and towards the prism as the aspect ratio of the prism decreases.

The Reynolds shear stress field on the wake centreline for AR = 3 (Fig. 7d) is distinct from those for AR = 9, 7, and 5 (Fig. 7a,b,c). For the three most slender prisms, the near-wake region is characterized by two regions of elevated Reynolds shear stress: a region of negative shear stress at the top of the wake and a region of positive shear stress closer to the ground plane. For AR = 3 (Fig. 7d), however, the region of positive shear stress below the free end is almost absent, showing a distinct wake structure for this prism. Furthermore, the positive Reynolds shear stress just below the prism free end decreases in size and level as the aspect ratio of the prism decreases; it disappears for AR = 3.

The mean cross-stream vorticity ($\overline{\omega_y} D/U_\infty$) fields for the four finite square prisms are shown in Figure 8. Upstream of the prism, the negative (CW) vorticity near the ground plane reveals the presence of the boundary layer and horseshoe vortex. For all four aspect ratios, negative vorticity is generated as the flow moves around the free end and downward into the near-wake of the prism. It is apparent that as the square prism aspect ratio decreases, the region of mean cross-stream vorticity behind the prism becomes larger in area and extends farther downstream. Close to the prism-wall junction, and immediately behind the prism, a small region of positive (CCW) vorticity is found for the prisms of AR = 9, 7 and 5 (Figs. 8a,b,c). This corresponds to the small recirculation shown earlier (Figs. 3a,b,c and 4a,b,c). Compared to AR =

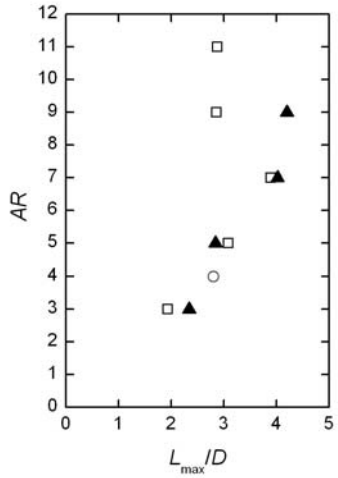

Figure 5. Maximum streamwise length of the mean recirculation zone for different aspect ratios. ▲, Present study, square prism, Re = 4.2×10^4; □, Wang and Zhou [4], square prism, Re = 9.3×10^3; ○, Bourgeois et al. [5], square prism, Re = 1.2×10^4.

9, 7, and 5, no region of positive vorticity is found in the region immediately behind the prism at its junction with the wall for the prism of AR = 3 (Fig. 8d).

4. CONCLUSIONS

In the present study, the local flow field and near wake of a surface-mounted finite square prism were investigated in a low-speed wind tunnel at Re = 4.2×10^4 using PIV. The prism was mounted normal to a ground plane and was partially immersed in a flat-plate turbulent boundary layer with δ/D = 1.7 at the location of the prism. Four prism aspect ratios were considered, AR = 9, 7, 5, and 3. PIV velocity measurements were made in a vertical plane on the flow centreline, upstream and downstream of the prism, with a special focus on the near-wake recirculation zone. The results of the present study have improved the limited state of information on the local flow field of a surface-mounted finite square prism and the influence of aspect ratio.

In the near-wake region, a large recirculation region forms behind the prism. Downwash flow enters the central portion of the wake where some flow from the free end reverses and moves toward the rear surface of the prism. A small vortex is located just downstream of the free end behind the prism and below the main downwash flow. This vortex is found for all four aspect ratios. Near the ground plane and close to the prism-wall junction, a second vortex forms; this vortex is weak or nearly absent for the prisms of AR = 5 and 3. The maximum length of the recirculation zone (L_{max}/D) increases with the prism aspect ratio from 2.3D for AR = 3 to 4.2D for AR = 9. Elevated levels of wall-normal turbulence intensity and Reynolds shear stress also occur above the free end of the square prism. Cross-stream vorticity production also occurs around the free end and into the downwash region behind the prism. This region of mean vorticity extends farther downstream as the aspect ratio decreases.

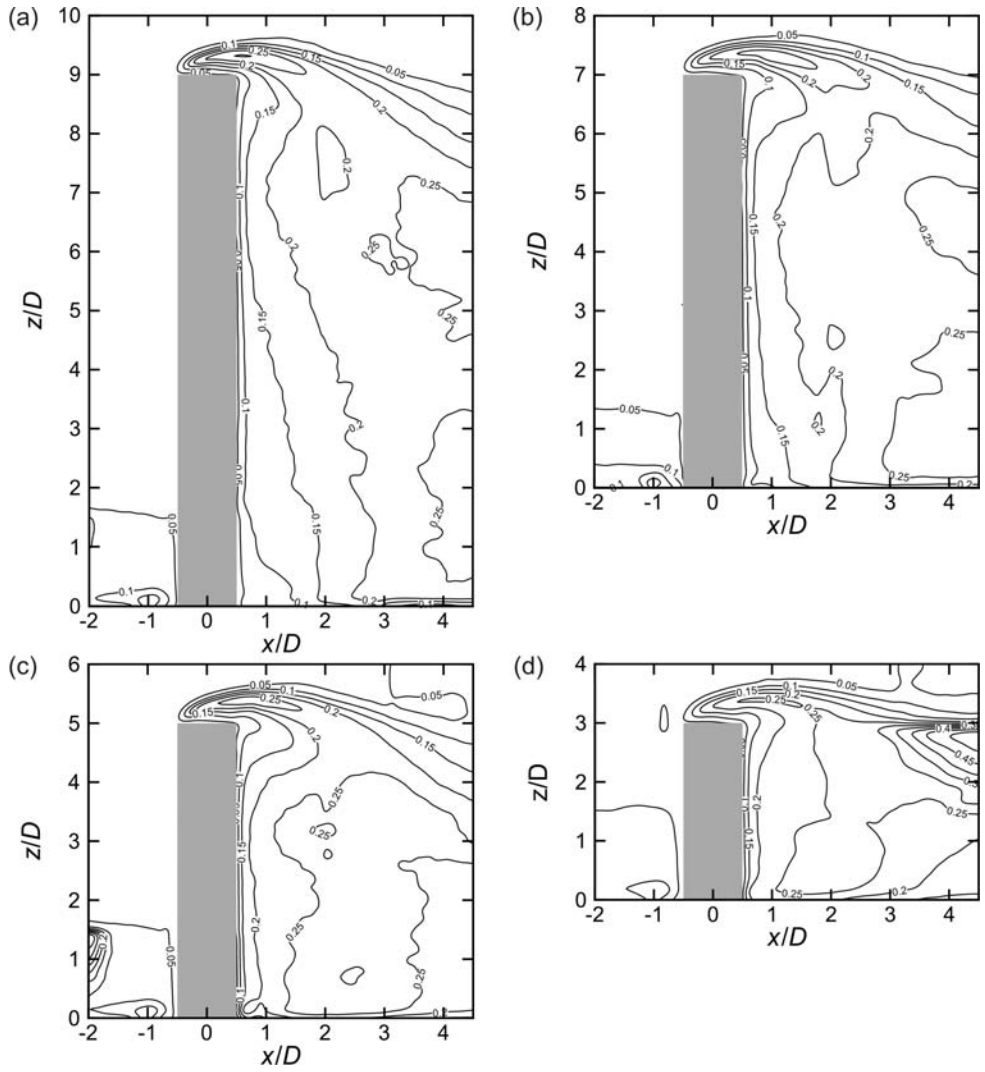

Figure 6. Streamwise turbulence intensity contours in a vertical plane on the wake centerline (y/D = 0, the symmetry plane): (a) AR = 9; (b) AR = 7; (c) AR = 5; (d) AR = 3.

ACKNOWLEDGMENTS

The authors acknowledge the support of the Natural Sciences and Engineering Research Council of Canada (NSERC). The assistance of D.M. Deutscher and Engineering Shops is gratefully acknowledged.

REFERENCES

1 D. Sumner, J.L. Heseltine, O.J.P. Dansereau, Wake structure of a finite circular cylinder of small aspect ratio, Exp. Fluids, 37 (2004) 720-730.
2 H.F. Wang, Y. Zhou, C. Chan, K.S. Lam, Effect of initial conditions on interaction between a boundary layer and a wall-mounted finite-length-cylinder wake, Phys. Fluids, 18 (2006) 065106.

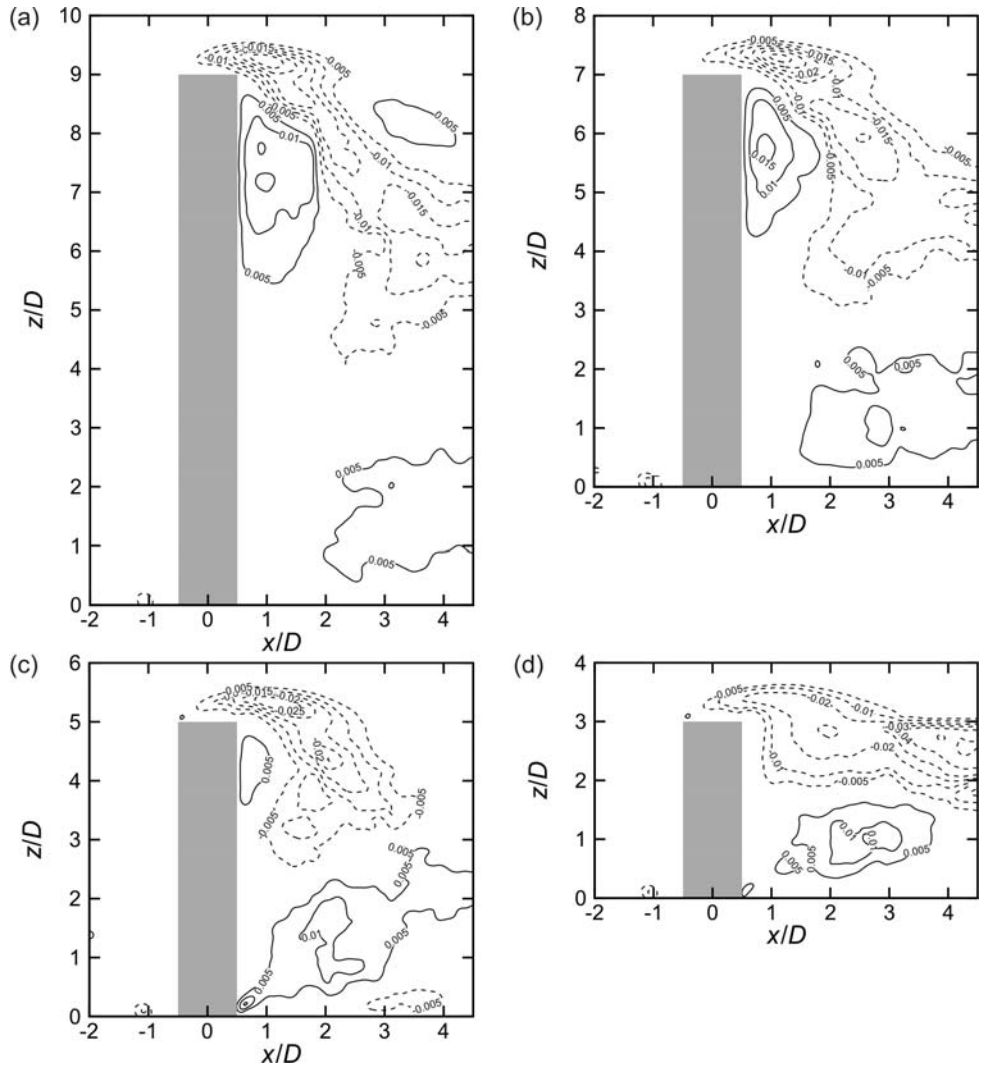

Figure 7. Reynolds shear stress contours in a vertical plane on the wake centerline (y/D = 0, the symmetry plane): (a) AR = 9; (b) AR = 7; (c) AR = 5; (d) AR = 3. Solid contour lines represent positive Reynolds shear stress, dashed contour lines represent negative Reynolds shear stress.

3 H.F. Wang, Y. Zhou, C. Chan, T. Zhou, Momentum and heat transport in a finite-length cylinder wake, Exp. Fluids, 46 (2009) 1173-1185.
4 H.F. Wang, Y. Zhou, The finite-length square cylinder near wake, J. Fluid Mech., 683 (2009) 453-490.
5 J.A. Bourgeois, P. Sattari, R.J. Martinuzzi, Alternating half-loop shedding in the turbulent wake of a finite surface-mounted square cylinder with a thin boundary layer, Phys. Fluids, 23 (2011) 095101.
6 M.S. Adaramola, O.J. Akinlade, D. Sumner, D.J. Bergstrom, A.J. Schenstead, Turbulent wake of a finite circular cylinder of small aspect ratio, J. Fluid Struct., 22 (2006) 919-928.
7 D. Hart, PIV error correction, Exp. Fluids, 29 (2000) 13-22.
8 A.M. Shinneeb, J.D. Bugg, R. Balachandar, Variable threshold outlier identification in PIV data, Meas. Sci. Technol., 15 (2004) 1722-1732.
9 C.W. Park, S.J. Lee, Effects of free-end corner shape on flow structure around a finite cylinder, J. Fluid Struct., 19 (2004) 141-158.

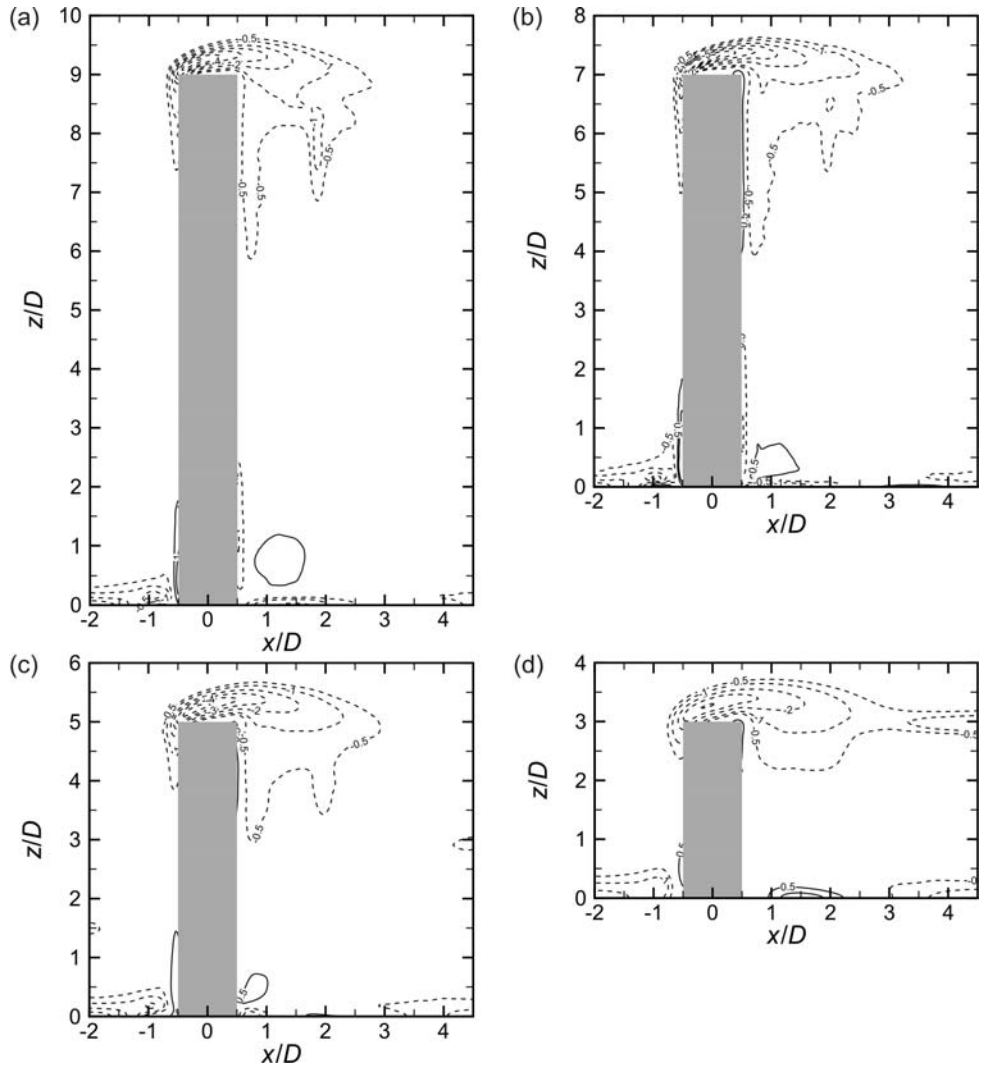

Figure 8. Mean in-plane dimensionless vorticity contours in a vertical plane on the wake centerline (y/D = 0, the symmetry plane): (a) AR = 9; (b) AR = 7; (c) AR = 5; (d) AR = 3. Solid contour lines represent positive (CCW) vorticity, dashed contour lines represent negative (CW) vorticity.

The Seventh International Colloquium on Bluff Body Aerodynamics and Applications (BBAA7)
Shanghai, China; September 2-6, 2012

Unsteady features of bluff body wake with application to building wake length

L. Cheng, K. M. Lam*

Department of Civil Engineering, University of Hong Kong, Pokfulam, Hong Kong

ABSTRACT: This study is targeted at obtaining fluctuating characteristics of building wakes through measurement of unsteady velocity fields with time-resolved particle image velocimetry (PIV). Proper orthogonal decomposition is applied to the PIV data to identify low-dimensional substructures of the building wake. This leads to a more reliable estimation of the fluctuating ground-level length of the building wake from an instantaneous PIV snapshot. The statistics of unsteady wake lengths is important in the probability-based risk assessment of critical events of wind environment around buildings such as dispersion of hazardous pollutants, pedestrian danger and risks to aircraft landings on airport runways.

KEYWORDS: Building wake, particle-image velocimetry, proper orthogonal decomposition

1 INTRODUCTION

Wind environment around buildings has received increasing attention from researchers for a number of applications. Building wakes are known to affect dispersion of pollutants by wind. Environmental wind conditions on the pedestrian level are modified by the presence of buildings. A recent review can be found in Blocken and Carmeliet [1]. In high-rise urban areas, massive tall building developments are often accused of reducing the available wind flow to the downwind low-rise part of a city for ventilation and pollutant dispersion [2,3]. Tsang et al. [2] conducted parametric wind tunnel studies to investigate the wind environment around a group of buildings and concluded that the air movement behind the buildings is governed by the backflow created by vertical recirculation and flow passing through building separations. The relationship between these two kinds of flow determines the existence of low wind speed zones, which may impair air ventilation, and high wind speed zones, which may cause pedestrian discomfort. Yim et al. [3] studied the adverse impacts of this "wall effect" with computational fluid dynamics. The numerical results suggest that alignment of high-rise buildings leads to "wall effect" not only on air ventilation but also on pollutant dispersion rate.

Another undesirable effect of building wakes is the possible risks to aircraft landings on airport runways [4]. The objective of this study is triggered by a number of assessments of building-induced disturbance to wind flow field near runways of the Hong Kong Airport. There exist concerns about the spatial extent of building wakes causing sudden changes in wind speeds on the runways.

There have been numerous wind-tunnel and numerical investigations of wake characteristics and pollutant dispersion behaviors behind buildings of different sizes and geometries [1] but the experimental and numerical results are mostly limited to time-averaged mean wind speeds and statistical properties such as turbulence intensities. While these mean flow properties are generally useful in applications such as assessment of wind environmental conditions around tall buildings for pedestrian comforts or pollutant dispersion efficiency in downwind regions, unsteady and fluctuating flow quantities are equally important in critical situations such as dispersion of

hazardous matters and building-induced wind shear events on runways. These latter applications call for a probability approach for appropriate risk assessment and data on the fluctuating characteristics of building wakes are required. As a basic feature, it is desirable to know the maximum and minimum spatial extents of the building wake over time.

This paper reports an attempt to obtain some characteristics of fluctuating building wake through laboratory measurement. Unsteady velocities in the wake of a surface mounted bluff body are measured with time-resolved particle image velocimetry (PIV) and proper orthogonal decomposition is employed to interpolate PIV database and identify low-dimensional substructures of the building wake.

2 EXPERIMENTAL TECHNIQUES

In this study, turbulent flow behind a tall building model was measured with PIV. Fig.1 shows the schematic of the experimental arrangement. The first set of experiments was carried out in a water channel with width of 0.3 m. The target geometrical scale of the testing was 1:1000. The building model was a square-section tall building of height H = 75 mm and breadth B = 30 mm. For optical access, the building model was made of plexiglass. To simulate wind profiles over a suburban terrain, three triangular spires and 750 mm fetch of roughness elements were placed on the ground level plate upstream of the building model. Experiments were performed with the water depth 0.375 m above the ground level plate and flow velocity $U_H \approx 0.13$ m/s at the roof height of the building model. The Reynolds number was $\mathrm{Re} \approx U_H B/\nu = 4{,}350$.

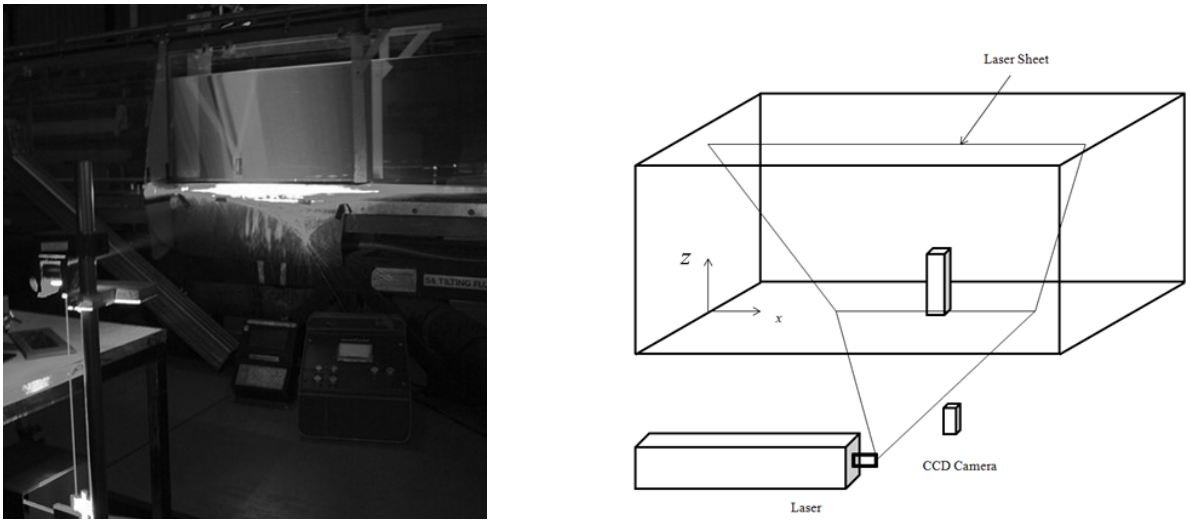

Figure 1. Experimental setup for PIV measurement.

A continuous-wave Argon-ion laser was used to generate a laser sheet to illuminate a two-dimensional plane of the flow. For flow on the central stream-wise vertical plane (x-z) of the building wake, the laser sheet was shone from below the transparent ground level plate. Neutrally buoyant polyamid particles of 35 μm nominal diameter were used to seed the water. Flow images were captured with a high speed camera (model PCO 1200hs) viewing through the transparent side window of the water channel. The camera had a resolution of 1280×1024 pixels and was set at a speed of 100 image/s to capture a time sequence of particle images of 1000-image length.

Particle images recorded on two consecutive images were analyzed for an instantaneous PIV snapshot using a PIV analysis software. The analysis was based on the spatial cross-correlation algorithm [5] but with adaptive and multi-pass interrogation windows. In the final iteration, PIV vectors were obtained on interrogation areas of size 32×32 pixels and with a 50% overlap. Thus, the two-dimensional velocity field at each time instant was consisted of 79×63 vectors of U and V.

3 POD ANALYSIS

Proper orthogonal decomposition (POD) is an efficient and elegant method of identifying lower order substructures by projecting the high-dimensional data onto a lower-dimensional space and capturing the dominant features (coherent structures) of the spatial-temporal fields with POD modes. POD is widely used in many disciplines such as image processing, signal analysis and data compression, with applications to turbulent flows starting from Lumley [6]. Kostas et al. [7] applied the snapshot POD analysis on both velocity data and vorticity data to investigate flow behind a backward-facing step at Reynolds numbers 580 and 4660. Adrian et al. [8] studied a fully developed channel flow at Reynolds number 5387 with POD analysis of PIV velocities and suggested that POD is effective at identifying the inhomogeneous spatial distribution of various eddy scales.

This study adopts the snapshot POD method [9] which solves the eigenvalue problem necessary for POD analysis in an efficient way. The implementation of POD analysis is as follows. From PIV measurement, a set of velocity components (u, v) sampled over N time steps for a period of T are obtained. First, the time-average velocity field is calculated and removed from each member of the ensemble, such as:

$$\overline{u}(x,y)=\frac{1}{N}\sum_{n=1}^{N}u(x,y,t_n)$$

The fluctuating velocity field is then given by:

$$u'(x,y,t_n)=u(x,y,t_n)-\overline{u}(x,y)$$

The two-point averaged spatial correlation function is then computed by:

$$R(x_i,x_j;y_i,y_j)=\frac{1}{N}\sum_{n=1}^{N}u'(x_i,y_i,t_n)u'(x_j,y_j,t_n)$$

The eigenvalue problem can be solved as:

$$R\Phi=\lambda\Phi$$

The N POD modes are obtained as the columns (φ) of the eigenfunctions Φ. The corresponding element of the eigenvalue vector λ defines the relative contribution of each mode to the fluctuating velocity field. Thus, the cumulative energy contribution from the first k modes is given by:

$$E_k=\sum_{i=1}^{k}\lambda_i\Big/\sum_{i=1}^{N}\lambda_i$$

After obtaining the POD modes, reconstruction of any of the original PIV snapshots can be performed using all or some of the modes as:

$$u_i(x,y,t) = a_i(t)\varphi_i$$

The coefficients $a_i(t)$ are obtained from the projection of the original data onto the POD modes:

$$\mathbf{A} = \left\langle \Phi^T, C \right\rangle$$

4 RESULTS AND DISCUSSION

The first target flow information is the fluctuating ground-level length of the building wake on the x-z plane. Figure 2 shows an example of instantaneous velocity field in the building wake from one PIV snapshot. Due to the low density of seeding particles in the wake, valid PIV velocity vectors cannot be obtained at some points. Ideally, the velocity vector map can show how wind flow over the building roof subsequently curves downwards towards the ground and the ground-level wake length can be determined by the point of reattachment. In the practical situation, the flow is highly turbulent and three-dimensional. It is difficult to trace the instantaneous streamlines and determine the wake length.

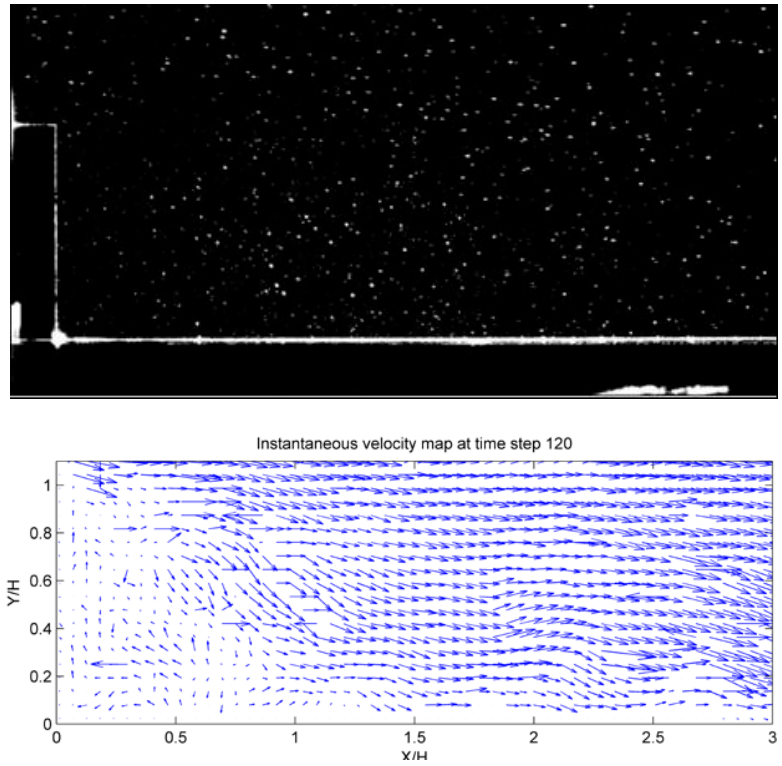

Figure 2. Example of PIV snapshot: single flow image; instantaneous velocity filed in the building wake.

The mean velocity vectors on the *x*-*z* plane averaged over all 1,000 PIV snapshots were shown in Fig. 3. The time-averaged mean flow paths and the recirculating flow behind the building are clearly revealed. However, it should be noted that this mean flow pattern will not occur at any instant along the time-axis. Figure 4 shows the axial distributions of the mean velocity component

U and the axial turbulence intensity near the ground level. The data are taken from the PIV interrogation windows closest to the ground. The mean axial velocities change from negative values inside the building wake to positive values downstream of the mean wake length. The mean building wake length is found for the change of sign at $L_w/H = 0.69$. At or very near to this location, the turbulence intensity reaches its peak value.

Figure 5 shows the velocity profiles of mean horizontal velocity components as a function of height above ground at locations upstream and downstream of the mean building wake length. Upstream of the mean building wake length, at $x/H < 0.69$, there always are some velocities having negative values. Downstream of the mean building wake length, velocities are all positive with magnitudes gradually increasing with increasing downstream distance. In other words, the mean building wake length is the location where the separation streamline from the building roof reattaches to the ground or the location where the ground-level velocities returns to the downstream direction from the reverse flow direction within the building wake.

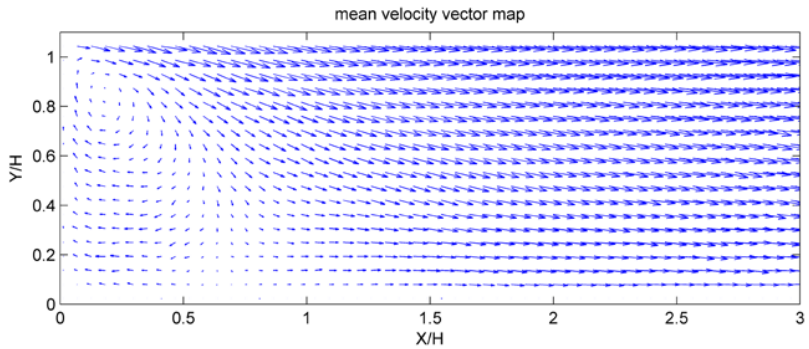

Figure 3. Mean velocity vectors on *x*-*z* plane averaged over 1,000 PIV snapshots.

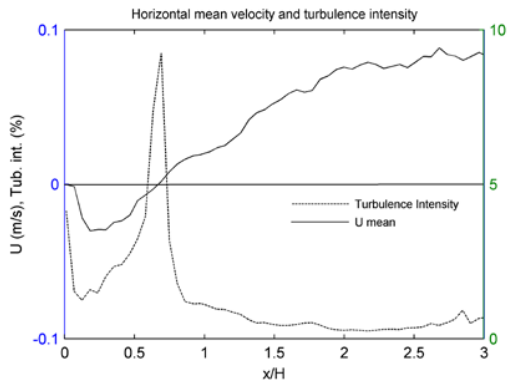

Figure 4. Mean horizontal velocity component and turbulence intensity near ground.

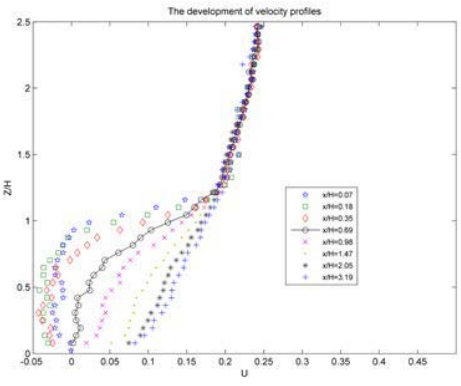

Figure 5. Profiles of mean horizontal velocities.

Attempt is made to apply the above feature to estimate the instantaneous building wake length from a PIV snapshot such as that in Fig. 2. From the instantaneous velocity vectors at any instant, the variation of horizontal velocity components along the lowest measurement points near the ground level is examined. The building wake length at that instant is determined as the length from the rear face of the building model to the location beyond which the instantaneous horizon-

tal velocities at the ground level become always positive. This is the location where the separation streamline from the building roof reattaches to the ground or the location where the ground-level velocity returns to the downstream direction from the reverse flow direction with in the building wake.

This method of wake length estimation is applied to the ensemble of 1,000 PIV snapshots. Figure 6 shows the probability density function (pdf) of the ensemble of unsteady building wake lengths. It is found that near a half of ensemble have the building wake lengths distributed over a wide range between $L_w = 0.2H$ and $1.2H$. The other half have very short wake lengths at $L_w < 0.2H$. This pdf distribution is not consistent with the feature of the mean flow pattern in Figs. 3-4. It appears that the instantaneous flow pattern consists of a number of flow structures of scales much smaller than the mean recirculating vortex. Wind flow separates on the roof leading to an unsteady shear layer behind the building model. Along the shear layer, a series of small-scale vortices are generated and this may contribute to the very small building wake lengths at some instants.

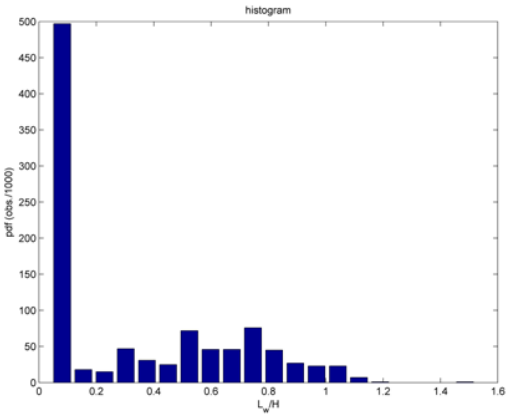

Figure 6. Histogram of building wake length of original data.

The result of Fig. 6 shows that it is not satisfactory by conducting probabilistic analysis directly with the raw velocity data. Thus, POD analysis is attempted as a potential approach in solving this problem. The two plots in Fig. 7 show the mean contours and the first five POD modes of the horizontal and vertical velocities. From the mean contour of horizontal velocity U, it can be discovered that the streamline from the top of the building reaches the ground level at the point around $x/H \approx 0.7$ and there exist some small scale turbulence before the reattachment point. In the first two U-POD modes, there exist a lot of small scale fluctuations throughout the building wake, while for modes 4 and 5 the scales of turbulent eddies become larger. In the V-POD modes, the turbulence scales are relatively larger than those in U-POD modes. Figure 8 shows that the cumulative energy of the first 50 POD modes. It is surprising to find only around 22% of the total energy is contained with these modes. The poor energy convergence may be attributed to the large variety of scales present throughout the flow. The increased level of flow complexity near the reattachment region may result in a less efficient decomposition.

Using the first 10 POD modes, the 1000 instantaneous velocity fields are reconstructed. In using only the lower modes, turbulent eddies of smaller scales are removed and only the more coherent flow eddies are retained. The unsteady building wake lengths are then estimated from these reconstructed velocity fields with the same method of ground-level horizontal velocities. Figure 9 shows the resulting pdf of the building wake lengths. The unrealistic peak at very smaller values is very much reduced and the distribution is now over a narrow range between $L_w =$

0.4H and 0.9H and with a peak at $L_w \approx 0.75H$. This peak value coincides with the mean flow patterns in Fig. 4. The original flow structure behind a building on the two-dimensional plane is complicated and upstream of the reattachment point, there exist many small-scale flow eddies behind the building. But with the reconstructed data, the small-scale structures are filtered and the reattachment point can be more easily determined. The probability distribution of L_w in Fig. 9 is valuable in the probability assessment of building wake effects such as ventilation efficiency and runway operation.

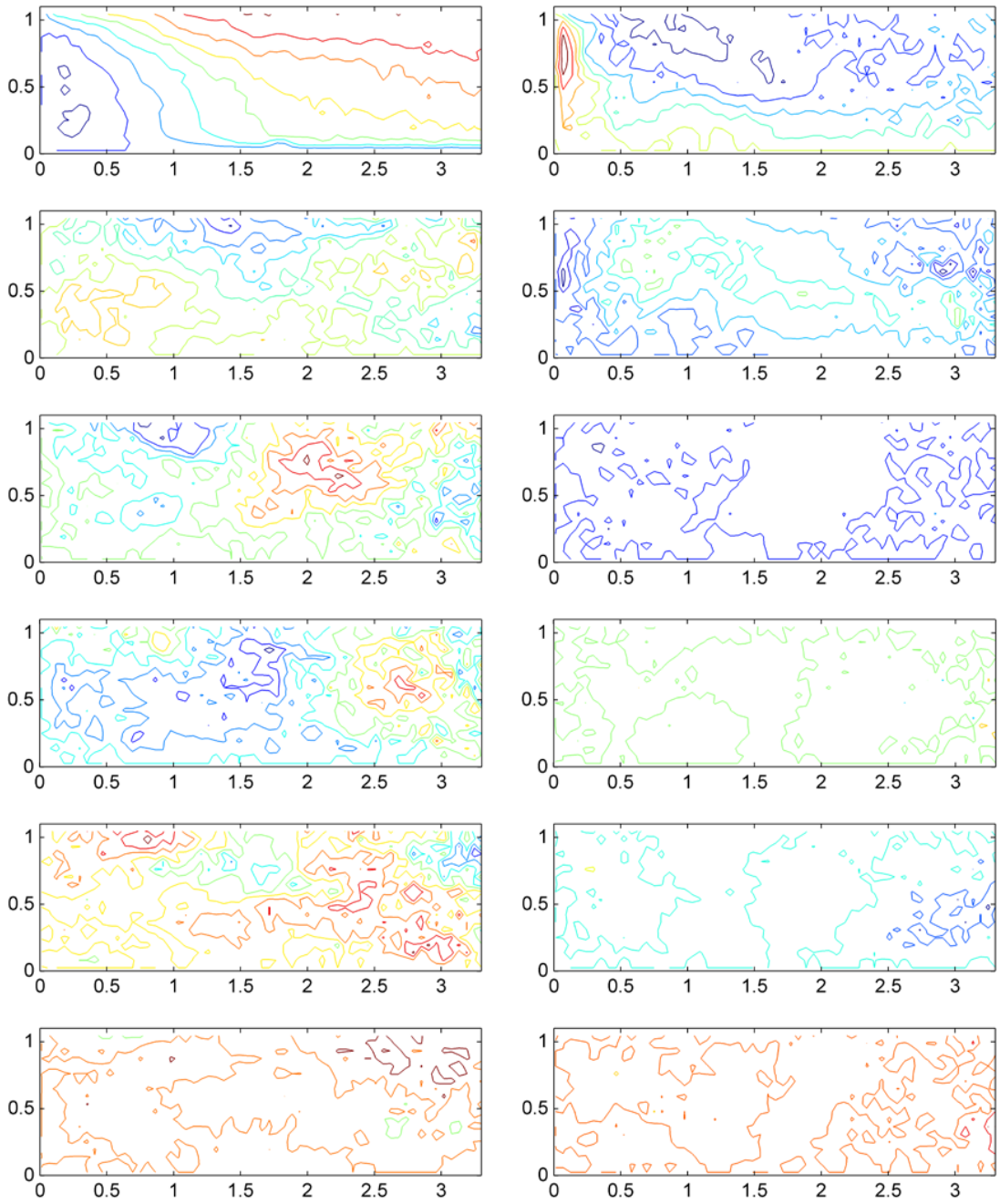

Figure 7. Mean flow and first five POD modes of horizontal (U) and vertical (V) velocities.

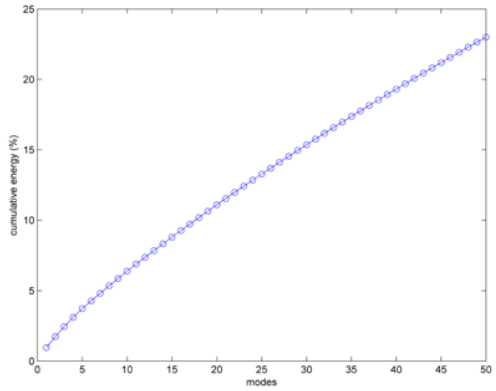

Figure 8. Cumulative energy of first 50 POD modes.

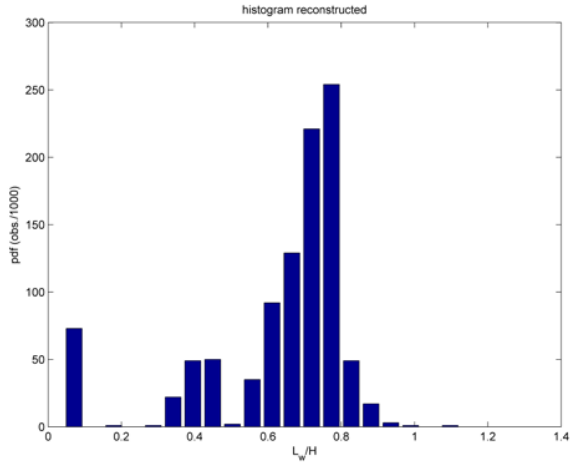

Figure 9. Histogram of building wake lengths from reconstructed data using first 10 modes.

5 CONCLUDING REMARKS

Unsteady velocity fields on the central vertical plane of a building wake are measured with time-resolved PIV in an attempt to determine some statistics of the fluctuating building wake length on the ground level. It is found that presence of small scale turbulent eddies and three-dimensionality of the flow renders estimation of the wake length from an instantaneous PIV snapshot difficult. The use of POD analysis allows filtering of small-scale flow eddies in the reconstructed velocity fields, leading to a more reliable estimation of the building wake lengths. The statistics of fluctuating characteristics of the building wake are useful in the probability-based risk assessment of critical events such as dispersion of hazardous matters and building-induced wind shear events on runways.

The Reynolds number in the reported experiments is not sufficiently high to model full-scale wind flow past a real building. More refined experiments are being carried out on building models of a larger geometric scale in a boundary layer wind tunnel. Time-resolved PIV measurements will be made to measure the unsteady flow fields on both horizontal and vertical planes in the building wake.

6 REFERENCES

[1] B. Blocken and J. Carmeliet , Pedestrian wind Environment around buildings: Literature Review and Practical Examples, J. Thermal Envelope Build. Sci. 28 (2004) 107-159.
[2] C.W. Tsang, K.C.S. Kwok and P.A. Hitchcock, Effects of building separation and podium on pedestrian-level wind environment. Proc. 7th Asia-Pacific Conf. Wind Engineering, Taipei, 2009, Paper M1B-3, 1-8.
[3] S.H.L. Yim, J.C.H. Fung, A.K.H. Lau and S.C Kot, Air ventilation impacts of the 'wall effect' resulting from the alignment of high-rise buildings. Atmos. Environ. 43 (2009)4982-4994.
[4] H.W. Krus, J.O. Haanstra, R. van der Ham and B. Wichers Schreur, Numerical simulations of wind measurements at Amsterdam Airport Schipol. J. Wind. Eng. Ind. Aerodyn. 91 (2003) 1215-1223.
[5] C.E. Willert and M. Gharib, Digital particle image velocimetry. Exp. Fluids 10 (1991) 181-193.
[6] J.L. Lumley, The structure of inhomogeneous turbulent flows. In: Atmospheric Turbulence and Radio Wave Propagation (eds. A.M. Yaglom, V.I. Tatarsky), Nauka, Moscow, 1967, 166-178.
[7] J. Kostas, J. Soria and M. S. Chong, A comparison between snapshot POD analysis of PIV velocity and vorticity data. Exp Fluids 38 (2005) 146-160.
[8] R. Adrian, K. Christensen and Z.C. Liu, Analysis and interpretation of instantaneous turbulent velocity fields. Exp Fluids 29 (2000) 275-290.
[9] L. Sirovich, Turbulence and the dynamics of coherent structures. Part 1: Coherent structures, Quart. Appl. Math. 45 (1987) 561-571.

The Seventh International Colloquium on Bluff Body Aerodynamics and Applications (BBAA7)
Shanghai, China; September 2-6, 2012

Structure of conical vortex on and behind a cube in smooth and turbulent flows

Hiromasa Kawai[a], Yasuo Okuda[b] and Masamiki Ohashi[b]

[a] *Faculty of Science and Engineering, Tokyo Denki University, Ishizaka, Hatoyama, Hiki, Saitama 350-0394, Japan,*
[b] *National Institute for Land and Infrastructure Management, 1, Tsukuba, Ibaraki, 305-0802, Japan*

ABSTRACT: The structure of the conical vortices on and behind the cube in uniform smooth flow and turbulent boundary layer flow when flow attacks normal to the diagonal line is investigated by synchronous measurements of 3D-SPIV and multi pressure sensor systems. The conical vortex at one side is always stronger than that at the other side. The conical vortices at the both sides sway in a body on the cube, and the strength of vortices changes all the time. The side at the stronger vortex changes occasionally in relatively long interval An arch-type vortex is formed behind the cube in any times of which shape is reentrant at the center and inclines to the side of the stronger conical vortex. When the conical vortex at one side is stronger, the vortex at the other side is drawn into the one side of the arch-type vortex.

KEYWORDS: Cube, 3D-SPIV, Conical vortex, Arch-type vortex, Switching phenomenon, Flow interaction

1 INTRODUCTION

When flow attacks to a flat roof from an oblique angle, a pair of conical vortices is formed on the roof. The vortices induce strong suction on the roof along the windward edges. Roof tiles are often scattered by the local strong peak negative pressure induced by the conical vortices [1],[2],[3],[4],[5],[6].

The vortex at one side of the roof is always stronger than that at the other side. The stronger vortex switches side by side occasionally in smooth flow. This phenomenon is known as the switching of flow pattern [6],[7]. On the other hands, a very strong conical vortex is formed on one side in turbulent flow when a strong gust attacks to the eave in a particular angle of attack of around 25 degree, and the pulse like extremely large negative pressure is induced [6].

In order to investigate how the switching is induced and what causes the switching, Nishimura et al. measured pressure on the flat roof in smooth flow with and without a splitter plate in the wake [8]. According to the experimental results, they have mentioned that the switching is induced by flow instability related with an interaction between the conical vortex and the separated shear layer from the side of the model in the wake. This remark is deduced from the simultaneous measurement of pressure fluctuations on the roof and the base floor.

This research has been planned to make clear the mechanism of the switching and the interaction between the conical vortices and the separated shear layer in the wake.

2 EXPERIMENTAL DESCRIPTION

In order to achieve the objectives of the research, the three dimensional stereoscopic PIV system (3D-SPIV) is used to measure three components of velocity vector on and behind a cube synchronized with pressure measurement on the cube. The experiments were carried out at the boundary layer wind tunnel of Building Research Institute in Japan with the test section of 3m x

2.5m. In order to avoid the effect of naturally developing boundary layer on the tunnel floor, a horizontal flat plate was set at 30cm above the tunnel floor shown in Figure 1. In the experiments, two kinds of approaching flow are used. One is a nearly smooth uniform flow (USF) and the other is turbulent boundary layer flow (TBL). Figure 2 shows profiles of mean wind speed and turbulence intensity in stream wise direction in the both flow at the position of the cube. According to the profile of USF shown as red circles, the flow is influenced by boundary layer developed on a flat plate up to 40mm from the plate and blue circles show TBL. The flow is uniform and the turbulence intensity is below 1% beyond 40mm. TBL was produced by roughness blocks and spires. The turbulence intensity is 13% to 20% up to 100mm in TBL.

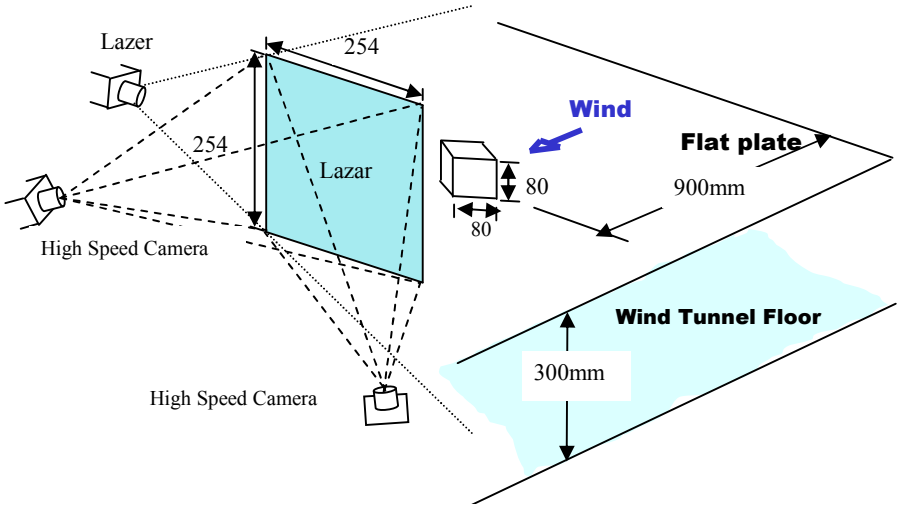

Figure 1 Experimental set up for 3D-SPIV in USF

A cube of which side is 80mm is used for the experiment in USF, and a cube of which side is 50mm is used for the experiment in TBL. The cube was set at 957mm downstream from the windward edge of the flat plate to the center of the cube normal to the diagonal line in USF. In TBL, the cube was set at 825mm. The reference wind speed, U, was set at 5m/sec at 100mm above the plate. The coordinate is defined as x in stream wise direction, y in cross flow direction and z in vertical direction. The characteristic length is the length of diagonal line of the cube, which is defined as D, so the Reynolds number based on D and U are 24960 and 15600 respectively in USF and TBL.

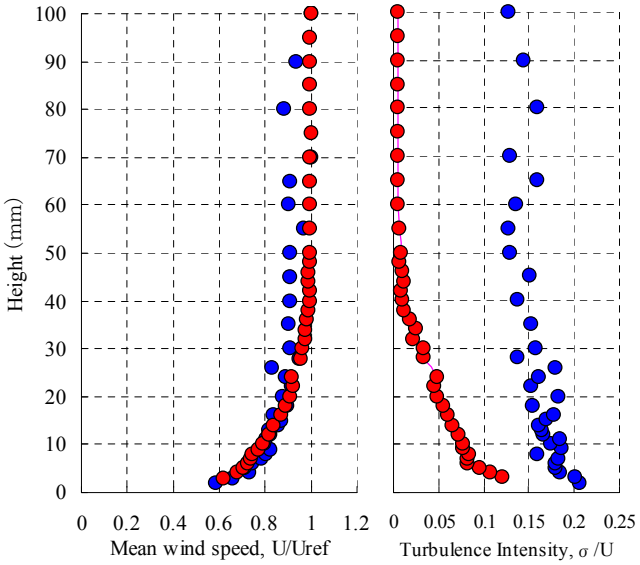

Figure 2 Profiles of mean velocity and turbulence intensity

Figure 1 shows the experimental set up for 3D-SPIV in USF which can measure three components of velocity vector on a plane based on two pairs of shots taken by two high speed cameras. The measurements in USF were carried out in 7 perpendicular planes (y-z plane) on the cube and in the wake behind the cube at x/D=-0.5, -0.25, 0, 0.25, 0.5, 1.0, 1.5. In the measurements, instantaneous velocity vectors at 77 x 63 points on each plane of which resolution is 4.26mm, were calculated from a pair of shots, which are taken by high-speed video cameras with intervals of 0.05msec. In each run 2727 pairs of the shot were taken at 250Hz rate. On the other hands, the measurements in TBL were carried out in 16 perpendicular planes from x/D=-0.25 to

3.0 with intervals of 0.25D. In the measurements, instantaneous velocity vectors at 63 x 63 points on each plane of which resolution is 4.11mm, were calculated from a pair of shots, which are taken by high-speed video cameras with intervals of 0.05msec. In each run 2727 pairs of the shot were taken at 500Hz rate. See the detail of the 3D-SPIV in Kawai et al. [9].

3 EXPERIMENTAL RESULTS AND DISCUSSIONS

3.1 *Flow structure on and behind the cube in USF*

Figure 3 shows the velocity vectors and the stream-wise component of the vorticity as the isogram in the five perpendicular planes (y-z plane). Red zone shows anti-clockwise vorticity and blue zone shows clockwise vorticity. The large vorticity zone produced by the conical vortex enlarges towards the downstream until x=1D. The zone is almost disappear at x=1.5D, which means the conical vortices are drawn into an arch type vortex in the wake as discussed later in detail. Figure 4 shows the velocity vectors and the stream-wise component of the vorticity at x=1D. It is shown in Figure 4 that strong downwash is induced by the conical vortices and the vortex at the left hand side is drawn towards the right hand side.

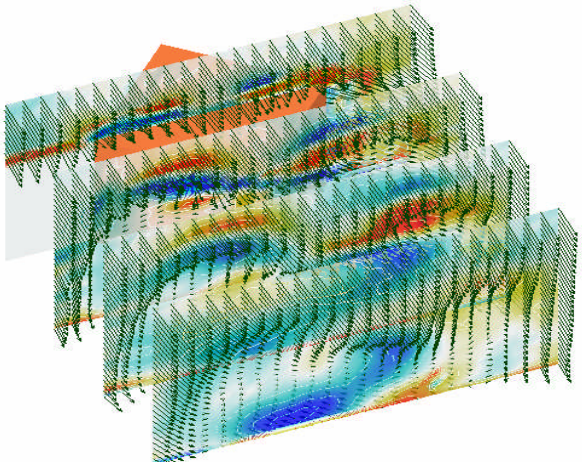

Figure 3 Velocity vectors and stream-wise vorticity on and behind the cube in USF

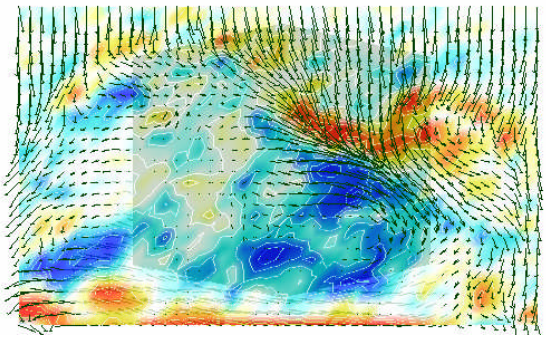

Figure 4 Velocity vectors and stream-wise vorticity at x=1.0D in USF

3.2 *POD analysis of velocity fluctuation behind the cube in USF*

In order to make clear the structure of the wake behind the cube and the draw of the conical vortex, POD analysis is carried out for the velocity fluctuations. Figure 5 shows the first modes for the three components at x=1D together with the velocity vector in the first mode. (a), the stream wise component of the velocity fluctuation, shows that an center of the separated shear layer is depressed and the layer moves and inclines to the right side. (b), the lateral component of the velocity fluctuation, shows that the draw of the left side conical vortex to the right side is shown as

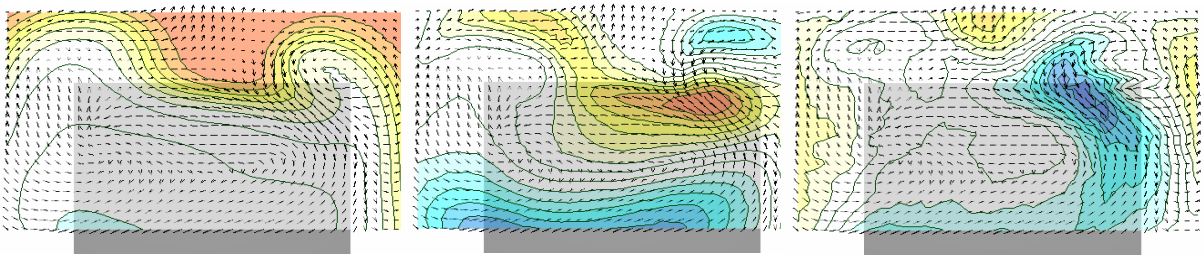

(a) Stream-wise component (b) Lateral component (c) Vertical component

Figure 5 First mode of POD of three components of velocity fluctuation in USF

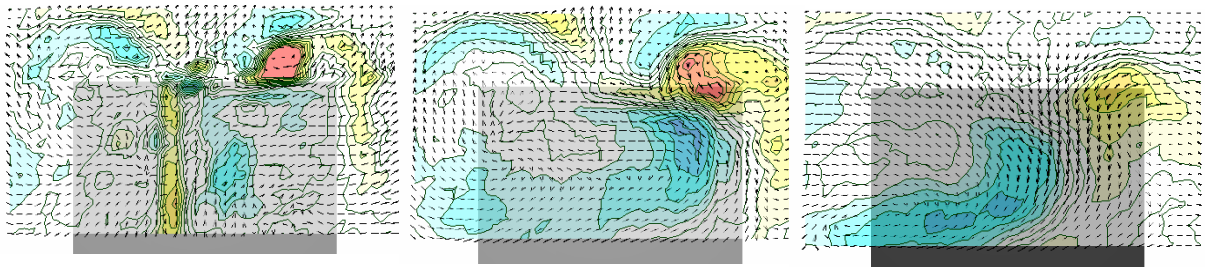

(a) x=0.5D (b) x=1.0D (c) 1.5D

Figure 6 First mode of POD of stream-wise vorticity fluctuation in USF.

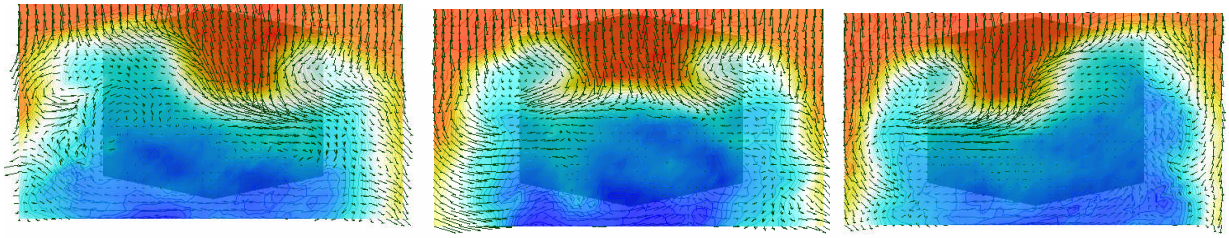

(a) x=0.5D (b) x=1.0D (c) 1.5D

Figure 7 Sway of the conical vortex and switching phenomenon of the flow in USF.

wake at x=1.5D. On the other hands the conical vortex at the right hand side stays at the same position at x=0.5D, 1D and 1.5D though its vorticity becomes weaker as x increase.

3.3 *Sway of the conical vortex and switching phenomenon of the flow in USF*

As discussed in the former section, the flow is unsymmetrical and the conical vortex at one side is always stronger than that at the other side. However, the stronger vortex side changes occasionally in relatively long interval. This phenomenon is known as the switching of the flow pattern. The phenomenon is discussed in this section.

Figure 7 shows the velocity vectors and the stream-wise component of the velocity at x=1D when the switching phenomenon occurs. Red zone shows positive and blue zone shows negative. White zone shows when the velocity is 0, and it corresponds with the center of the shear layer. (a) shows that the vortex at the left hand side is stronger, (b) shows that the vortex at the right hand side is stronger and (c) is the instant of the switching from (a) to (b).

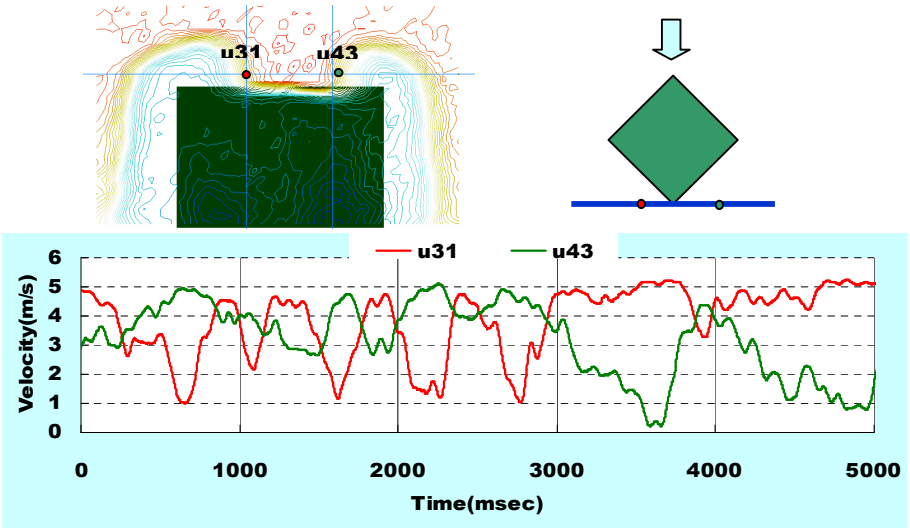

Figure 8 Velocity fluctuations at the edge of the shear layer.

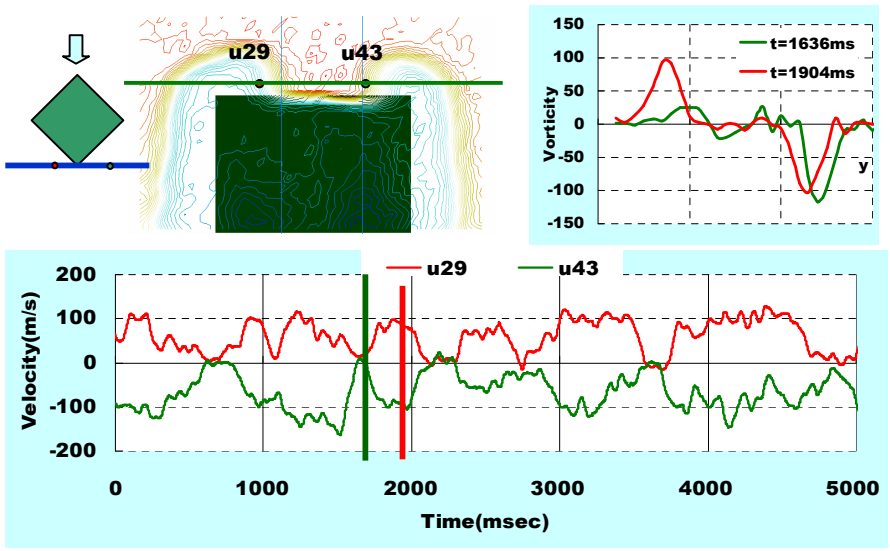

The conical vortex sways all the time even when the vortex at one side is stronger Figure 8 shows time history of stream wise velocity component just out side of the shear layer behind a cube in USF when the vortex at the right hand side is stronger than that at the left hand side. The green line shows the velocity fluctuation at the right hand side, u43 and the red line shows that at the left hand side, u31. The velocities both at u43 and u31 fluctuate nearly regularly in the period of 0.4sec to 0.6sec until 3 second, and then the velocity at u43 decreases after the switching of the flow pattern occurs. The velocities at the both sides fluctuate out of phase. This means that the conical vortices sway quasi-periodically in a body suggested by Kawai el. [4]. The moment of switching corresponds when the pair of the vortices moves to the left.

Figure 9 shows time history of stream wise component of vorticity at u29 and u43 in USF when the vortex at the right hand side is stronger than that at the left hand side. The vorticity fluctuates in the same period of the velocity fluctuation shown in Figure 8. Figure .9b shows the profiles of the vorticity along the green line at the instant of 1636msec and 1904msec. When the vorticity at u43 is nearly 0 at 1636msec, the velocity at u43 reaches the peak and the peak value of the vorticity at the right hand side reaches the maximum. This corresponds that the conical vortex reaches to the most right side. In this instant, the vortex at the left hand side becomes weak as shown by a green line in Figure 9b. When the vortex moves to the left, the vorticity at u43 increases and then takes the peak at 1904msec. In this instant, the strength of the vortices at both sides is almost same as shown by a red line in Figure 9b. The switching occurs when the vortex at the left hand side is stronger a little than that at the right hand side at the instant of 3000msec.

3.4 *Structure of flow in the wake and pressure on the cube in TBL*

The general feature of the flow on and behind the cube does not so change from USF to TBL except that the sway of the conical vortex is not so regular but random and the switching is affected by the approaching turbulence.

In order to investigate the interaction between the conical vortex and the separated shear layer from the side, the three components of the vorticity are calculated at x=0.75D and shown in Figure 10 with the velocity vector. (a) is the stream wise component, (b) the lateral component and (c) is the vertical component of the vorticity. The large positive stream wise vorticity zone (clock-wise vorticity) shown as blue region in Figure 10a spreads under the negative vorticity zone (anti-clock-wise vorticity) at the right hand side. The pattern of the isogram is similar to that

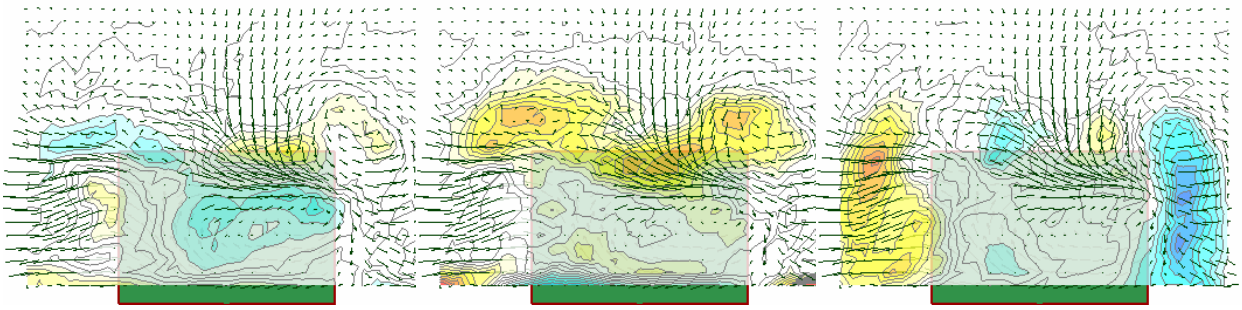

(a) Stream-wise component (b) Lateral component (c) Vertical component

Figure 10 Three components of vorticity in TBL

of Figure 6b in USF. The lateral component of the vorticity shown in Figure 10b shows again the draw of the vortex from the left to the right. The large positive and negative zones of the vertical component of the vorticity locate at the outside of the cube which is induced by the separated shear layer from the side. Moreover, the small zones of negative and the positive vertical vorticity are seen near the center of the cube which is induced by the reentrant arch-type vortex behind the cube.

Figure 11 shows the pressure distribution on the cube when the strength to the conical vortex at the right hand side becomes the maximum. Blue zone shows negative and red zone shows positive. When the conical vortex at the right hand side becomes much stronger that that at the left hand side, the negative pressure on the upper surface at the right hand side becomes larger and the large negative peak pressure is induced near the windward corner. The negative pressure on the right leeward side increases at the same time. Particularly, the large negative peak pressure acts on the leeward corner at the right hand side.

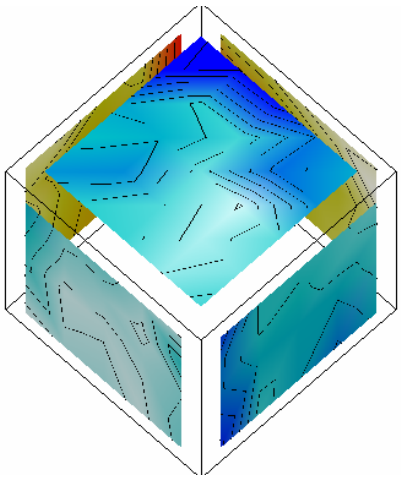

Figure 11 Pressure distribution the cube in TBL when the strength of the conical vortex at the right hand side reaches to peak.

3.5 *Structure of vortex behind the cube*

Figure 12 shows the three dimensional stream lines behind the cube in TBL. The stream lines are drawn from x=0.75D. According to Figure 12, the roll up of the separated shear layer from the side seems to connect to the roll up of the shear layer over the cube and to form an arch-type vortex. When the conical vortex at the right hand side is stronger than that at the left hand side, the conical vortex at left hand side is drawn into the wake to bring the large clockwise circulation in the wake. The arch-type vortex inclines greatly to the right side by the interaction between the conical vortex and the separated shear layer. When the strength of the pair of vortices is same, the very clear arch-type vortex can be seen in the move.

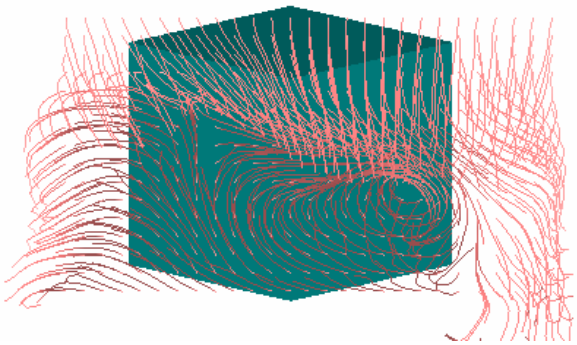

Figure 12 3D stream lines behind the cube in TBL Starting points are on the perpendicular plane (y-z plane) at x=0.75D.

According to the above results, the schematic picture of the vortex in the wake behind the cube is shown in Figure 13 when the conical vortex at the right hand side is stronger than that at the left side. The shape of the arch-type vortex is reentrant at the center by the down wash induced by the pair of the conical vortices and inclines to the right. When the conical vortex at the left hand side is drawn to the right, the sign of the vorticity of the conical vortex and the arch-type vortex is opposite each other and the conical vortex is drawn into the wake over the arch-type vortex. On the other hand, the vorticity of the conical vortex at the right hand side has the same sign of that of the arch-type vortex, so the conical vortex makes to increase the vorticity of the arch-type vortex.

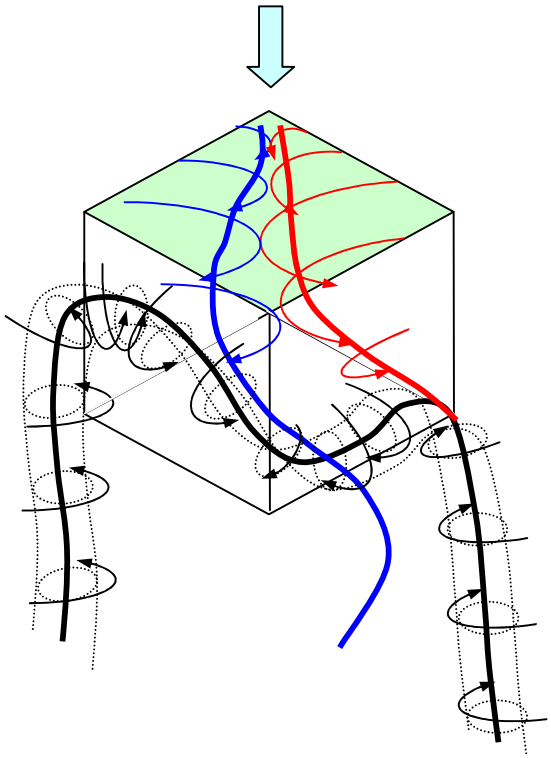

Figure 13 Schematic model of the interaction between the conical vortices and arch-type vortex behind the cube.

4 SUMMARY AND CONCLUSIONS

The structure of the conical vortices on and behind the cube in USF and TBL when flow attacks normal to the diagonal line is investigated by synchronous measurements of 3D-SPIV and multi pressure sensor systems. According to the measurement, the following results are found.

(1) The conical vortex at one side is always stronger than that at the other side. The side at the stronger vortex changes occasionally in relatively long interval. By this change the flow pattern switches to the reflected pattern.
(2) The conical vortices at the both sides sway quasi-periodically in a body on the cube in USF, and the strength of vortices changes all the time. When the strength of the vortex at one side increases, the strength at the other side decreases.
(3) The trigger of the switching is brought by the sway of the conical vortex. When the order of the strength of the conical vortices changes at both sides by the sway, the flow pattern is switched to the reflected pattern.
(4) An arch-type vortex is formed behind the cube in any times of which shape is reentrant at the center and inclines to the side of the stronger conical vortex. When the conical vortex at one side is stronger, the vortex at the other side is drawn into the one side of the arch-type vortex.

The structure of the flow in TBL is similar generally to that in USF.

5 REFERENCES

1 K.C.Mehta, M.L.Levintan, R.E.Iverson and J.R.McDonald, Roof corner pressures measured in field on a low building, J. Wind Eng. Aerodyn., 1992, Vol.41-44, 181-192
2 F.Wu, P.P.Sarkar and K.C.Metha, Full-scale study of conical vortices and roof corner pressures, J. Wind and Structures, 1999, Vol.4, No.2, 131-146
3 Banks, D, R.N.Meroney,P.P.Sarkar, Z.Zhao & F.Wu, Flow visualization of conical vortices on flat roofs with simultaneous surface pressure measurement, J. Wind Eng. Ind. Aerodyn., 2000, Vol.84(1) ,65-85

4 H.Kawai and G.Nishimura : Characteristics of fluctuating suction and conical vortices on a flat roof in oblique flow, Journal of Wind Engineering and Industrial Aerodynamics, 1996, Vol.60, pp.211-225.
5 H.Kawai, Structure of conical vortices related with suction fluctuation on a flat roof in oblique smooth and turbulent flows, J. Wind Eng. Ind. Aerodyn., 1997, Vol.71, 579-588
6 H.Kawai, “Local peak pressure and conical vortex on building”, J. Wind Eng. Aerodyn. , 2002, Vol.92, 251-263, 2002
7 Y.Taniike and T.Taniguchi, Switching phenomenon of conical vortices on various flat roofs, Proc. 10th Int. Conf. Wind Eingineering, 1999, 1203-1208
8 H.Nishimura and H.Kawai, Switching phenomenon of conical vortices on the flat roof of a low-rise building, J. Wind Eng.(Japan), 2010, Vol.4, No125, 99-106.
9 H.Kawai, Y.Okuda and M.Ohashi, Near wake structure behind a 3D square prism with an aspect ratio of 2.7 in a shallow boundary layer flow, J. Wind Eng. Ind. Aerodyn., 2012, (in press)

The Seventh International Colloquium on Bluff Body Aerodynamics and Applications (BBAA7)
Shanghai, China; September 2-6, 2012

Assessment of design wind speeds for metro cities of India

K. Suresh Kumar [a], C. Cini [b], Valerie Sifton [c]

[a,b]*RWDI (India), T5, Thejaswini, Technopark, Trivandrum, India*
[c]*RWDI Inc., 650 Woodlawn Road West, Guelph, Ontario, Canada*

ABSTRACT: Prediction of site specific wind speed plays a key role in the determination of wind-induced response of structures. The wind speed value is typically taken from the local code of practice, which is IS:875 - Part 3 [1] in India. Considering that this code hasn't been updated for the last 25 years, a revisit of the wind speed including the last three decades of data is warranted. In this paper, the design wind speeds for the metro cities of India have been assessed based on the local airport data.

KEYWORDS: Design wind speed, India.

1 INTRODUCTION

India is witnessing an unprecedented amount of construction in the tall building area to meet up with the ever increasing demand for housing in the Indian metros (Mumbai, Delhi, Kolkata, and Chennai – see Figure 1). Significant growth in tall building sector is connected to the growing economy, and this is expected to persist for long time.

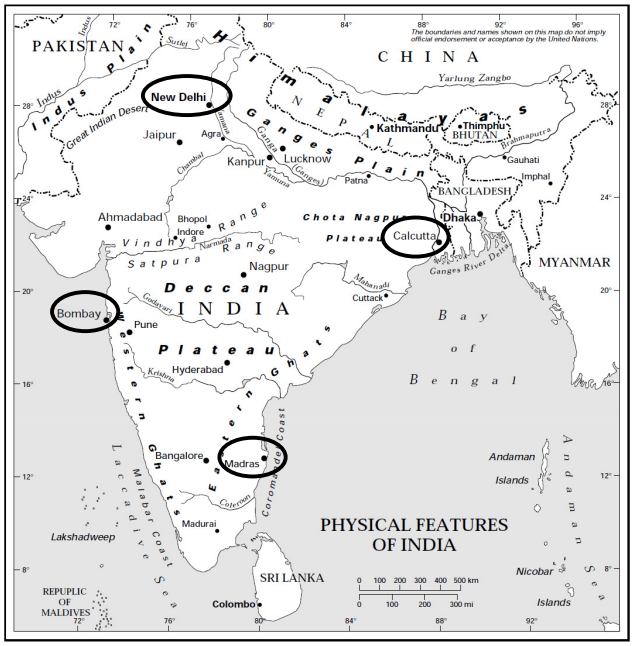

Figure 1. Map of India showing metros.

In connection with this growth, tall building construction requirements are changing frequently. Tall building committee is set up in Mumbai to review all the design and regulate the tall building construction in Mumbai. Also, many tall building designs are nowadays confirmed through wind tunnel tests determining wind loads and accelerations precisely. Challenges behind the wind design of tall buildings are emerging as well in the form of complex geometries, surroundings and structural forms.

One another important parameter for wind design is the wind climate itself. Indian wind loading standard [1] provides the basic wind speed (3-sec gust) for all the locations in India with the help of a wind map. This has been widely used for design by most of the practitioners. Note that 10% change in speed can alter the subjected load at least by 20% and also this has significant impact on acceleration prediction as well. In view of this there exists a dire need to assess the wind speed accurately across the subcontinent based on authentic data. Note that the wind map of India in the IS:875 – Part 3 [1] is based on the measured wind speed data at the airports up to early 1980's. In addition to this data, another 30 years of data spanning between 1980 and 2010 were included in this study.

2 WIND CLIMATE OF INDIA

India is situated roughly between 8^{o}N and 37^{o}N latitude, where there are four climatic zones namely alpine, sub-tropical, tropical and arid. In India, synoptic climate drivers cause pressure system winds. The synoptic climate drivers are (1) North-east monsoon (Winter monsoon) and (2) South-west monsoon (Summer monsoon). In case of north-east monsoon, the cold dry air over North Asia during October and March creates high-pressure areas blowing winds from north-east to south-west. Though winds lost their moisture while crossing central Asia, gets humidity from Bay of Bengal while crossing and resulting into showers in south India. In case of south-west monsoon, the hot air that rises over south Asia during April and May creates low-pressure areas into which the cooler, moisture-bearing winds from the south ocean flow. These climate drivers are pictorially shown in Figure 2.

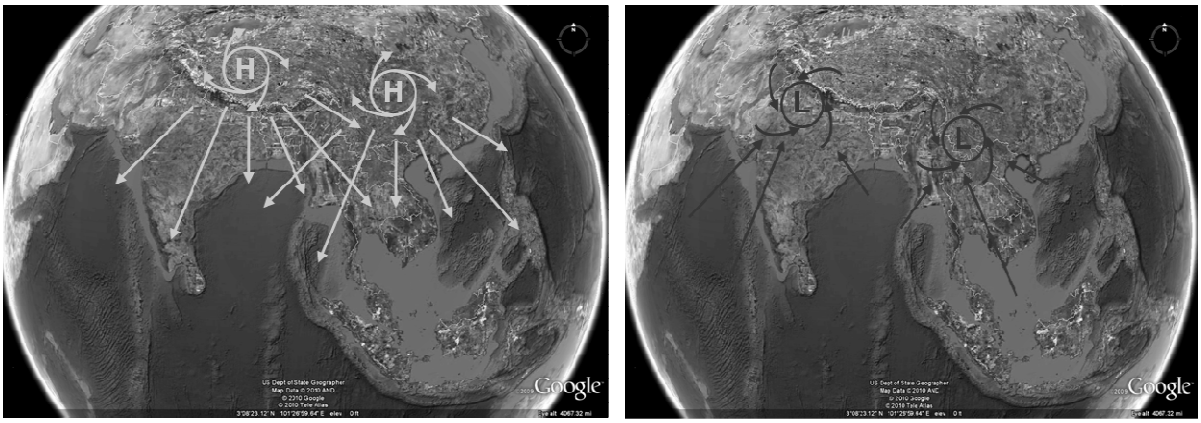

Figure 2. North-east monsoon, South-west monsoon.

In addition, thunderstorm winds are common in India. Thunderstorm winds are localized phenomenon caused by temperature gradient in cloud resulting in vertical convective motions. Tropical cyclones (rotating type wind) are also common in India especially in the east coastal regions.

Mumbai is located in the west coast (Lat 19° 04'N, Lon 72°52' E) and the wind climate is influenced by synoptic system monsoons and thunderstorms. In the past, cyclonic systems never made a landfall in Mumbai. Most of these cyclonic systems made landfall further north of Mumbai and Mumbai is only affected by the very outer bands of the cyclonic systems. The frequency of occurrence of cyclones over Arabian Sea is lower than that over the Bay of Bengal on the east coast of India due to the colder water currents in Arabian Sea.

Delhi is located in the interior of north India (Lat 28° 38'N, Lon 77°13' E). Delhi wind climate is influenced by monsoons and thunderstorms. Kolkata is located in the north east coast (Lat 22° 34'N, Lon 88°21' E). Kolkata wind climate is influenced by monsoons, thunderstorms and cyclones. Chennai is located in the south east coast (Lat 13° 04'N, Lon 80°15' E). Similar to Kolkata, Chennai wind climate is also influenced by monsoons, thunderstorms and cyclones.

Synoptic system monsoons and cyclonic systems cover a vast area and prolong for several hours/days and therefore, anemometer measurements from airports likely can capture the wind characteristics of these systems at least at lower levels. However, in the case of thunderstorms, considering its local nature and short duration, airport measurements alone may not be sufficient to capture its strength in case when this happens on another part of the same city away from airport. Therefore, other means of measurements such as wind profiler, radiosonde, doppler radars, GPS receivers, aircraft reconnaissance, and meso-scale regional numerical prediction should be explored. The design wind speed predictions based on airport data shall be checked against other measured data to confirm the inclusion of the severity of the thunderstorm activity in the region.

3 DESIGN WIND SPEED FOR MUMBAI

Traditional methods for assessing the wind climate for wind engineering purposes are based on analysis of long term surface records from a nearby meteorological station, typically measured at a height of 10 m above ground. For this assessment, hourly surface wind data from the following stations were used: (1) Chhatrapati Shivaji International Airport (CSI, Station Index: 43003, before known as SantaCruz Airport) for a period of 1969 – 1999 provided by India Meteorological Department (IMD) at Pune, (2) Chhatrapati Shivaji International Airport (CSI) data for a period of 2000 – 2007 provided by NCDC (National Climatic Data Center of USA), and (3) Colaba Observatory (Station Index: 43057) data for a period of 1969 – 2007 provided by IMD at Pune. Provided hourly surface wind data were carefully reviewed and subsequently filtered to avoid the contamination of reliable data with the potentially erroneous readings.

Measured wind speeds are adjusted by direction to compensate for the effects of upwind terrain and surface characteristics using ESDU [2] methods. This correction for site-specific terrain effects generates winds corresponding to standard open terrain condition. Extreme value analyses are then performed for the determination of wind speeds with respect to return period. Site-specific Weibull climate models are also developed to assess the relationship between wind speed and return period, as well as to establish the directional distribution of strong winds.

Monthly peak mean hourly wind speeds were analyzed using the standard Gumbel method by fitting Fisher-Tippet Type I distributions to the data. Various fitting methods were used which included fitting velocity squared (V^2) instead of velocity (V), and using a least-squares fitting versus the method of moments. A comparison of the various fitting methods was used to evaluate the best fit to the data. The V least-squares fitting method as shown in Figure 3 provides the closest fit to the data.

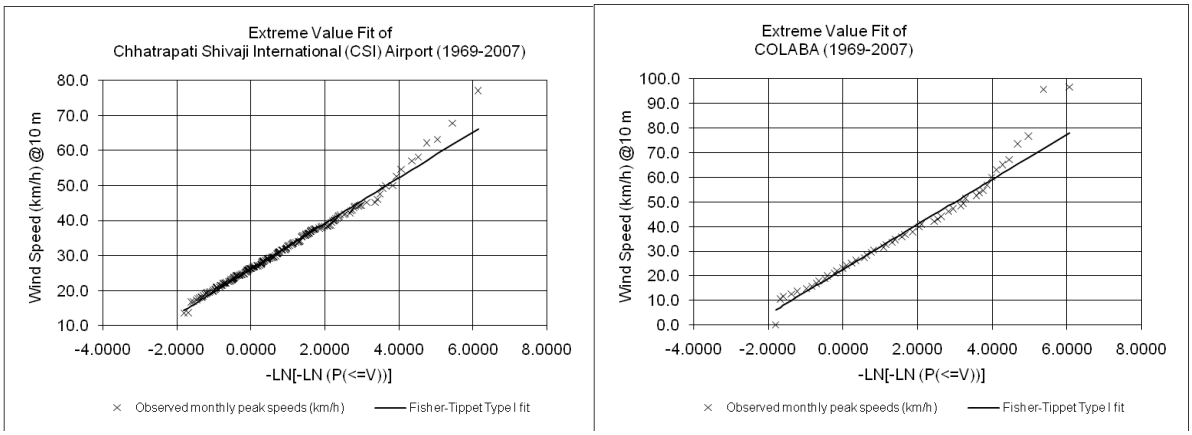

Figure 3. Extreme value fit of wind speed – Mumbai.

Based on this analysis, it is found that the estimated 50-year return period mean-hourly wind speed is 18.9 m/s and 22.5 m/s corresponding to CSI and Colaba data respectively. Recognizing the fact that the current structural design practice of India IS:875 - Part3 (1987) [1] is widely adopted as a reference document, the relationship between gust and mean-hourly speeds must be defined. Based on the ASCE 7-05 Standard [3] conversion factor of 1.52, the equivalent 3-seconds gust speeds are 28.7 m/s and 34.2 m/s corresponding to the CSI and Colaba data respectively. Further, the factor of 1.52 is confirmed by checking the gust/mean ratio obtained from the measurements as shown in Figure 4. These predicted speeds are similar to the recent predictions made by Lakshmanan et al. [4] for Mumbai based on the uncorrected gust data. However, note that these speeds are significantly lower than the IS code [1] recommended speed of 44 m/s for Mumbai. The hand book published by Standards Australia on the design wind speeds for the Asia-Pacific region [5] suggests a 3-sec gust wind speed of 39 m/s for Mumbai, which is about 11% lower than the suggested speed in the IS code. Recently, Aurelius and Cammelli [6] predicted considerably lower speed for Mumbai than those stipulated in the IS code. As per the current study, the best estimate 50-year return period Basic Wind Speed (3-seconds gust) for Mumbai is 39 m/s. This best estimate speed is higher than the predicted speed based on airport data and this is to account for uncertainties in the data. Similar wind speed values have also been obtained by analyzing the measured gust data.

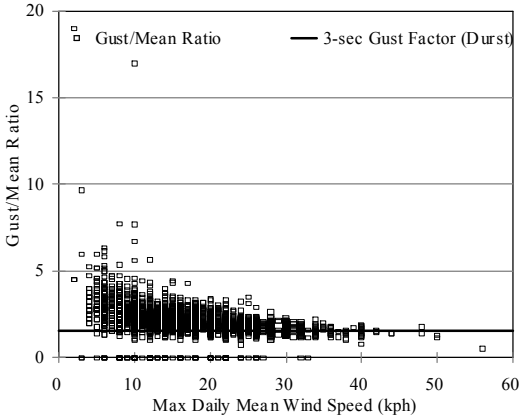

Figure 4. Gust to Mean Ratio – Mumbai.

4 DESIGN WIND SPEED FOR DELHI

For the assessment of wind speed for Delhi, hourly surface wind measurement data from the following stations were used: (1) Indira Gandhi International Airport data (IGI, Station Index: 42181, before known as PALAM Airport) for a period of 1969 – 1996 provided by IMD at Pune, (2) Indira Gandhi International Airport (IGI) data for a period of 1996 – 2009 provided by NCDC USA, and (3) Safdurjung Airport (Station Index: 42182) data for a period of 1969 – 2006 provided by IMD at Pune. Similar analysis as previously discussed was carried out, and the V least-squares fitting method as shown in Figure 5 provides the closest fit to the data.

Based on this analysis, it is found that the estimated 50-year return period mean-hourly wind speed is 27.1 m/s and 29.1 m/s corresponding to IGI and Safdurjung data respectively. The equivalent 3-seconds gust speeds are 41.3 m/s and 44.3 m/s corresponding to the IGI and Safdurjung data respectively. These predicted speeds are closer to the recent predictions made by Lakshmanan et al. [4] for Delhi based on the uncorrected gust data. RWDI also performed extreme value analysis on the uncorrected peak daily gust data for 38 years. The IGI gust data yields a 50-year gust value of 46 m/s at 10 m height, while the Safdurjung data yields a 50-year gust value of 44 m/s. These gust speeds are in the same range as the earlier predictions based on mean-hourly data. Also, note that these speeds are closer to the IS code [1] recommended speed of 47 m/s for Delhi. The hand book published by Standards Australia on the design wind speeds for the Asia-Pacific region [5] suggests a 3-sec gust wind speed of 44 m/s for Delhi, which is about 6% lower than the suggested speed in the IS code. As per RWDI's analysis, the best estimate 50-year return period Basic Wind Speed (3-seconds gust) for Delhi is 44 m/s.

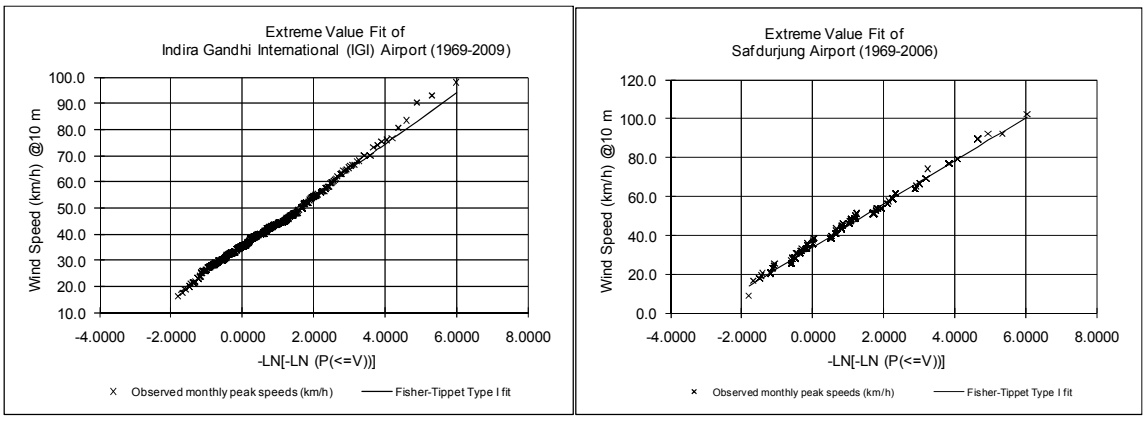

Figure 5. Extreme value fit of wind speed – Delhi.

5 DESIGN WIND SPEED FOR KOLKATA

For the purpose of this assessment, 3-hourly/1-hourly surface wind measurement data from the following stations were used: (1) Netaji Subhash Chandra Bose International Airport data (Station Index: 42809, before known as DUM DUM Airport) for a period of 1969 – 1987 provided by IMD at Pune and (2) Netaji Subhash Chandra Bose International Airport data for a period of 1987 – 2010 provided by NCDC USA. Similar analysis as previously discussed was carried out, and the V least-squares fitting method as shown in Figure 6 provides the closest fit to the data.

Based on this analysis, it is found that the estimated 50-year return period mean-hourly wind speed is 30.5 m/s. The equivalent 3-seconds gust speed is 46.4 m/s. This predicted speed is matching the recent predictions made by Lakshmanan et al. [4] for the Kolkata Dum Dum station based on the uncorrected gust data. Note that these speeds are about 5% lower than the IS code [1] recommended speed of 50 m/s for Kolkata. The hand book published by Standards Australia on the design wind speeds for the Asia-Pacific region [5] suggests a 3-sec gust wind speed of 44 m/s for Kolkata, which is 12% lower than the suggested speed in the IS code. As per RWDI's analysis, the best estimate 50-year return period Basic Wind Speed (3-seconds gust) for Kolkata is 47 m/s.

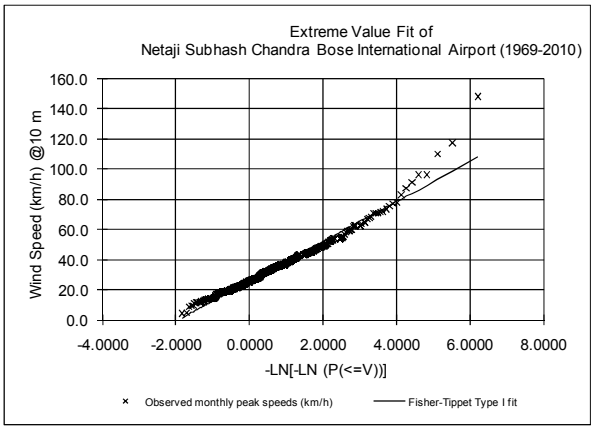

Figure 6. Extreme value fit of wind speed – Kolkata.

6 DESIGN WIND SPEED FOR CHENNAI

For the purpose of this assessment, 3-hourly/1-hourly surface wind measurement data from Minambakkam International Airport (MIA) for a period of 1973 – 2010 provided by NCDC USA were used. Similar analysis as previously discussed was carried out, and the V least-squares fitting method as shown in Figure 7 provides the closest fit to the data.

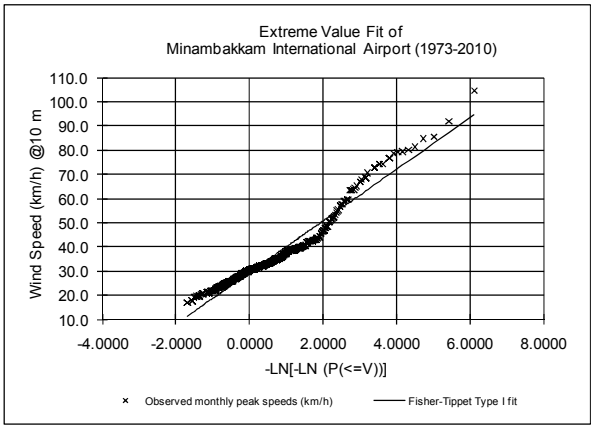

Figure 7. Extreme value fit of wind speed – Chennai.

Based on this analysis, it is found that the estimated 50-year return period mean-hourly wind speed is 27.1 m/s. The equivalent 3-seconds gust speed is 41.2 m/s. This predicted speed is in between the recent predictions made by Lakshmanan et al. [4] for two stations (MIA and Harbour) in Chennai based on the uncorrected gust data. However, note that these speeds are significantly lower than the IS code [1] recommended speed of 50 m/s for Chennai. The hand book published by Standards Australia on the design wind speeds for the Asia-Pacific region [5] suggests a 3-sec gust wind speed of 44 m/s for Chennai, which is 12% lower than the suggested speed in the IS code. As per the current study, the best estimate 50-year return period Basic Wind Speed (3-seconds gust) for Chennai is 44 m/s.

7 DISCUSSION

The summary of the findings are shown in Table 1. In general, the wind speeds in the IS code map seem higher than reality. Mumbai and Chennai basic wind speed values in the code appear conservative. Based on all the evidence that we have provided in this paper, the basic wind speed for Mumbai and Chennai can be at least 10% lower than the current value in the code. In

Table 1. 50-yr Return Period Basic Wind Speed Data

Location	Based on	Basic Wind Speed (m/s)
Mumbai	IS: 875	44.0
	HB 212	39.0
	Lakshmanan et al. (CSI Airport)	35.0
	Lakshmanan et al. (Colaba)	28.0
	RWDI (CSI Airport)	28.7
	RWDI (Colaba)	34.2
	RWDI - Best Estimate	39.0
Delhi	IS: 875	47.0
	HB 212	44.0
	Lakshmanan et al. (Safdurjung)	39.0
	Lakshmanan et al. (IGI Airport)	45.0
	RWDI (Safdurjung)	44.3
	RWDI (IGI Airport)	41.3
	RWDI - Best Estimate	44.0
Kolkata	IS: 875	50.0
	HB 212	44.0
	Lakshmanan et al. (Calcutta)	41.0
	Lakshmanan et al. (Dum Dum)	46.0
	RWDI (Nataji Subhash Chandra Bose)	46.4
	RWDI - Best Estimate	47.0
Chennai	IS: 875	50.0
	HB 212	44.0
	Lakshmanan et al. (Minambakkam)	39.0
	Lakshmanan et al. (Harbour)	45.0
	RWDI (Minambakkam)	41.2
	RWDI - Best Estimate	44.0

RWDI's opinion, further studies utilizing upper air data and meso-scale modelling [7] would be helpful in reinforcing the current findings and recommend appropriate speed for strength design of structures. In addition, a special dispensation from local building authorities of the corresponding cities to use the lower speed is warranted. Until then for strength design, we recommend IS code specified speed for all the cities.

The data reported in Table 1 corresponding to Lakshmanan et al. [4] is based on uncorrected gust data. In their work, it was assumed the peak wind data as the speed sustained over 1- minute duration and subsequently converted to 3-seconds format by multiplying all the peak data by a factor of 1.16. So, their prediction based on corrected data is the value reported in Table 1 factored by 1.16. On the other hand, based on discussions with IMD, it is our understanding that the data has been measured at the end of every hour for a two minute period and subsequently, two minute average has been reported on every hour and also a maximum gust speed is recorded for a day. Although the gust data doesn't specify an averaging time, the trend of the ratio of the peak gust to the maximum mean hourly speed is towards approximately 1.5 which indicates it is likely close to a 3-seconds gust. So it is of our opinion that the gust speeds reported by IMD need not undergo any correction as done by Lakshmanan et al. [4].

Recently, government of India initiated STORM programme [8] for better understanding of the structure and characteristics of the severe local thunderstorms in the eastern and north-eastern India covering West Bengal, Jharkhand, Orissa, Assam and parts of Bihar. These areas were affected by severe thunderstorms during the pre-monsoon months (in particular April & May). These thunderstorms are locally named as "Kalbaishakhi" meaning calamities in the month of Baishakh. These storms are also called "Nor'wester" meaning travelling from north-west to south-east. These severe thunderstorms bring thunder, squall lines, lightening and hail cause extensive losses in agricultural, damage to structure and also loss of life. The STORM programme includes both observations and numerical predictions. These data can be explored in the future. The squalls associated with Nor'wester are mostly from a northwesterly direction. The highest winds in these squalls are reported to be 140-150 kph [8]. Note that Kolkata is prone to Nor'wester storm where the code suggested speed is 50 m/s (180 kph). Note that the highest reported speed must be associated with a higher return period than 50-year return period used in the code. Further, Sutapa Chaudhuri and Anirban Middey [9] reported the peak gust speed during thunderstorm activity in Kolkata based on radiosonde and rawinsonde data. They reported peak gust speeds ranging between 40 to 120 kph. This is based on 140 thunderstorm activity over Kolkata during pre-monsoon season (April-May) for the years 1997-2009.

In contrary to the current results of this study, Prem Krishna [10] and Subhash and Tamura [11] reported the occurrence of high wind speed cyclonic storms in the eastern coast of India than the recommended basic wind speed for the region specified in IS:875 – Part 3 [1]. Though the risk associated with the occurrence of these extreme storms is not completely understood, they are of the opinion that the applicability of the IS: 875 – Part 3 wind speed map especially at the east coast needs to be investigated further.

With regard to Cyclonic storms on the east coast (between Thoothukudi and Kolkata) and west coast (between Trivandrum and Daman Diu), the best track data of tropical cyclone disturbances over the north Indian ocean published at the web site of IMD has been investigated. The published data is for the duration from 1990 till 2010. The landfall of cyclonic disturbances has been categorized based on the coast and the speed. The maximum sustained surface speed has been converted to 3-sec gust speed and the frequency of occurrence of different intensity storms has been determined and plotted in Figure 8.

Note that very few low intensity storms made landfall on the west coast in comparison to the east coast. The maximum 3-sec gust wind speed resulted out of these storms are much lower than the maximum IS:875 speed of 44 m/s for the west coast below Daman and Diu. Many significant cyclonic activities were originated in Arabian Sea but majority of those storms were swept away

by the prevailing easterly winds expected in latitudes below 30^o. As a result, many of these storms originated in Arabian Sea made landfall in Yemen, Oman and east of Africa.

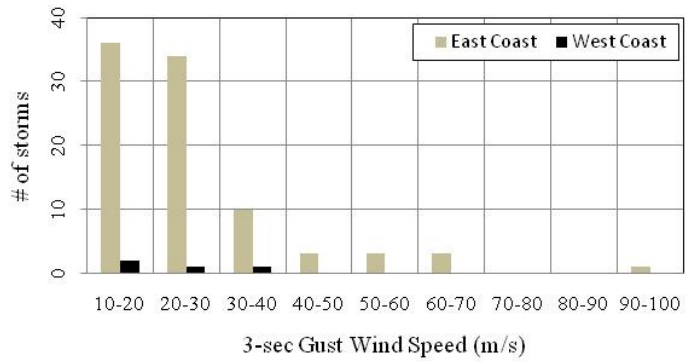

Figure 8. Frequency of cyclonic disturbances on Indian coast between 1990 and 2010.

On the other hand, significant number of cyclonic activities originated in Bay of Bengal, travelled with the prevailing easterly wind and made landfall on the east coast of India. Figure 8 depicts that occasional severe storms made landfall on the east coast of India. The speed corresponding to some of these storms are indeed higher than the IS code speed of 50 m/s for these regions. However, the return period associated with these storms are unknown. Further investigations in this regard using simulations are essential.

8 CONCLUDING REMARKS

The design wind speed for four metro cities of India (Mumbai, New Delhi, Kolkata and Chennai) has been investigated based on data measured at the airports. In summary, the design wind speeds for metro cities of India have been found to be about 5-10% lower than the wind speed provided in Indian standard. This can have significant impact on the prediction of wind-induced loads/motions of structures.

In general, the quality of the data prior to couple of decades is poor. This restricts the duration of years of good data to 10-20 years. Further, there is little dialogue between the community who uses the data and the community who measures them. For instance, three hourly wind direction measurements are still ongoing which is basically not useful for knowing the wind directionality with certainty. Considering the numerous uncertainty in measured data, further study of wind climate is recommended using upper air data and meso-scale modelling. This study will be extremely beneficial for all the future developments in metros and nearby regions. Further, this will provide adequate confidence to lower the speed than what is in the code currently and also help to change the wind speed map in the code.

9 REFERENCES

1 IS:875 – Part 3, Code of Practice for Design Loads for Buildings and Structures – Part 3 Wind Loads, Bureau of Indian Standards, New Delhi, 1987.

2 ESDU, Strong Winds in the Atmospheric Boundary Layer, Part 1 & 2: Mean Hourly Speeds & Discrete Gust Speeds, Items 82026 & 83045, Engineering Sciences Data Unit, ESDU International, 27 Corsham Street, London N16UA, 1982 & 1983.
3 ASCE 7-05 Standard, Minimum design loads for buildings and other structures, Published by the American Society of Civil Engineers, 1801 Alexander Bell Drive, Reston, Virginia, USA, 2005.
4 Lakshmanan et al., Basic wind speed map of India with long-term hourly wind data, Current Science, 96-7 (2009) 911-922.
5 HB 212, Design Wind Speeds for the Asia-Pacific Region, Standards Australia, Sydney, 2002.
6 L. Aurelius, and S. Cammelli, A detailed assessment of design wind speeds for Mumbai, 13th Int. Conf. of Wind Engineering (13 ICWE), Amsterdam, The Netherlands, 2011.
7 M. Lepage, X. Qui, and V. Sifton, What's the latest tool in wind engineering: A new role for weather simulations to assist wind engineering projects, RWDI Publications, Technote #28, 2006.
8 Expert Committee, Severe Thunderstorms – Observations & Regional Modelling (STORM) Programme, Department of Science & Technology, Government of India, New Delhi, December 2005.
9 Sutapa Chaudhuri and Anirban Middey, Adaptive neuro-fuzzy inference system to forecast peak gust speed during thunderstorms, Meteorology and Atmospheric Physics, 114-3/4 (2011), 139-149.
10 Prem Krishna, The Indian wind loading standard: A case for review, Proc. 3rd Nat. Conf. on Wind Engineering, Kolkata, India, 2006.
11 C.Y. Subhash and Y. Tamura, Some issues concerning to the Indian wind loading standard [IS:875 (Part 3) – 1987], Proc. 12th Int. Conf. on wind Engineering, Cairns, Australia, 2007, pp. 2679-2686.

The Seventh International Colloquium on Bluff Body Aerodynamics and Applications (BBAA7)
Shanghai, China; September 2-6, 2012

Statistical spectrum model of wind velocity at Beijing Meteorological Tower

Yang Qingshan,Tian Yuji, Li Bo and Chen Bo

School of Civil Engineering, Beijing Jiaotong University, Beijing 100044, China

Abstract: The wind velocity spectra at Beijing Meteorological Tower are calculated using Hilbert-Huang transform and Fourier transform, respectively. A innovative model of wind velocity spectrum, which is accordant with the characteristics in both the inertial subrange and the large eddies range, is presented in this paper. The method of least squares is adopted to obtain the parameters in the model. Then the differences between the FFT spectrum and the HHT spectrum are compared. It is indicated that the values of the HHT spectrum in the energy containing range are slightly larger than those of the FFT spectrum while the values of the HHT spectrum in both inertial subrange and dissipation subrange are very close to that of Fourier spectrum. It is concluded that the HHT spectrum describes elaborately and accurately the spectrum values in the low frequencies and the fitted wind velocity model provides a reference for reconstructing the near-ground wind field of Beijing city in wind tunnel test and for numerical simulation.

Keywords: turbulent spectrum, wind velocity spectrum, inertial subrange, HHT, FFT

1 Turbulent spectrum theory

The theory of the turbulent spectrum originated from Richardson's view of the energy cascade [1], that is to say, the turbulence is composed of eddies of different sizes. When the energy enters into the atmosphere, the kinetic energy of the molecules increases and then the large eddies flow, break up and transfer their energy to somewhat smaller eddies. These smaller eddies undergo a similar break-up process, and transfer their energy to the smallest eddies. This is called energy cascade, in which energy is transferred to successively smaller and smaller eddies until the kinetic energy is dissipated by the molecular viscosity.

In turbulent flow at sufficiently high Reynolds number, the energy of the small-scale motions is determined by the kinematic viscosity and the energy transfer rate. This is called Kolmogorov's first hypothesis. In the region of small eddies, the energy of the relatively larger eddies is uniquely determined by the energy transfer rate, independent of the kinematic viscosity. This is called Kolmogorov's second hypothesis [2]. According to the two hypotheses, the atmospheric molecules absorb energy and flow in the form of the large eddies; the energy containing range is composed of these large-scale eddies. The turbulent motions of the small-scale eddies are statistically isotropic and form a universal equilibrium range, in which the energy transfer range is named the inertial subrange while the region of the smallest-scale eddies is designated as the dissipation subrange. From the second hypothesis it follows that the turbulent spectrum in the inertial subrange is deduced from the dimensional analysis and is expressed as

$$E(k) = C\varepsilon^{2/3}k^{-5/3} \tag{1}$$

where k is the wavenumber, ε is the energy transfer rate, and C is a universal constant. In Equation (1), the turbulent spectrum is nominated as the Kolmogorov $-5/3$ law.

Since 1940s', many researchers have devoted their attention to studying the turbulent spectrum and many spectrum models have been established. It is assumed that the turbulent energy is transferred from large to small eddies in terms of an "eddy viscosity" [3]. This logical assumption indicates that the transfer term in the turbulent spectrum dynamic equation is represented by the same form of the viscous dissipation term. Kolmogorov's $-5/3$ law in the inertial subrange is confirmed after some other assumptions are introduced while the spectrum decay quite rapidly with the -7th power of the wave number in the region of the smallest eddies. The same conclusions were drawn by some other predecessors [4, 5].

The decay of the spectrum of isotropic turbulence was investigated when the external forces causing the turbulent motion were removed [6]. The approximate solution of the spectrum dynamic equation gives that the spectrum is pro-

portional to the wavenumber in the region of the larger eddies while the spectrum drops off much faster for the largest eddies. Furthermore, some experimental results show that the spectrum values of the largest eddies are not the maximum and that the spectrum of the largest eddies decays with the -4th power of the wave number [7].

Traditionally, the energy spectrum of the homogeneous and isotropic turbulent flow is the Fourier transform of its auto-correlation function, i.e.,

$$E_j(k) = \frac{1}{\pi}\int_{-\infty}^{+\infty} Q_j(\xi)\exp(-ik\xi)d\xi \tag{2}$$

where k is the wavenumber, $E_j(k)$ is designated as the one-side spectrum of jth ($j = u, v, w$) turbulent component, where u, v, w are the symbols of longitudinal, horizontal and vertical components, respectively, and $Q_j(\xi)$ is the spatial correlation function of jth component. Considering the even function $Q_j(\xi)$ in homogeneous turbulence, Equation (2) can take the form of the correlation coefficient $q_j(\xi)$ and it follows that

$$E_j(k) = \frac{2\sigma_j^2}{\pi}\int_0^{+\infty} q_j(\xi)\exp(-ik\xi)d\xi \tag{3}$$

where σ_j^2 is the variance of the jth turbulent component, and $q_j(\xi)$ is the spatial correlation coefficient, $q_j(\xi) = Q_j(\xi)/\sigma_j^2$. When the wavenumber k tends to zero at the two sides of Equation (3), it is obtained that

$$E_j(0) = 2\sigma_j^2 L_j/\pi \tag{4}$$

where L_j is the integral length scale of jth component ($L_j = \int_0^{+\infty} q_j(\xi)d\xi$). It is indicated that the spectrum value of zero wavenumber is dependant on the integral length scale and the standard deviation of the fluctuating wind. Under the condition of roughness terrain, the integral length scale increases with the increase of height while the standard deviation decreases with the increase of height; hence, the turbulent spectrum varies with the increase of height. When the wavenumber k is equal to zero, the derivative of $E_j(k)$ is zero, i.e.,

$$dE_j(k)/dk\big|_{k=0} = 0 \tag{5}$$

The aforementioned research results of turbulent spectrum are illustrated in Figure 1, in which the energy spectrum curve varies with the wavenumber.

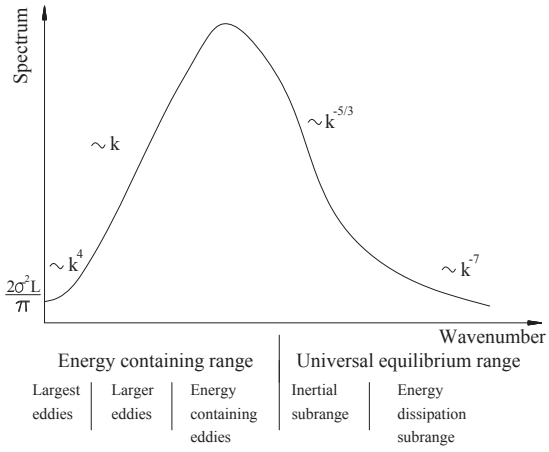

Figure 1 Illustration of turbulent spectrum and wavenumber

2 Wind velocity spectrum model

From Taylor's hypothesis or the frozen-turbulence approximation, the wavenumber can be expressed as the frequency, $k = 2\pi n/U$, where n is the frequency and U is the mean wind velocity, and the wavenumber spectrum of turbulence is represented by the frequency spectrum, $E_j(k) = US_j(n)/2\pi$, where $S_j(n)$ is the one-side power spectrum of jth turbulent component in the frequency domain. Considering Equations (4) and (5), the power spectrum $S_j(n)$ must satisfy the following two conditions, i.e.,

$$S_j(0) = 4\sigma_j^2 L_j/U \tag{6}$$

$$dS_j(n)/dn\big|_{n=0} = 0 \tag{7}$$

Based on the Kolmogorov's second hypothesis, the power spectrum in inertial subrange was presented by Batchelor in 1953 [8], which is given by

$$\frac{nS_j(n)}{u_*^2} = \alpha_j f^{-2/3} \tag{8}$$

where u_* is the friction velocity, α_j is a constant, and f is the Monin similarity coordinate, $f = nz/U$ and $f > 0.2$. Simiu and Scanlan [9] deduced the constant in Equation (8) of longitudinal velocity uctuation of wind turbulence and $\alpha_u = 0.26$ while Tieleman [10] gave the constants of the three components and $\alpha_u = 0.27$, $\alpha_v = 0.36$ and $\alpha_w = 0.36$.

In 1946, Von Karman [11] presented an empirical power spectrum model of the longitudinal turbulent flow observed in grid generated turbulence in a wind tunnel as

$$\frac{nS_u(n)}{u_*^2}=\frac{4f\beta_u L_u/z}{\left(1+70.8f^2L_u^2/z^2\right)^{5/6}} \tag{9}$$

where β_u is the turbulence intensity coefficient, $\beta_u=\sigma_u^2/u_*^2$, and z is the height. It is obvious that Karman spectrum $S_u(n)$ in Equation (9) satisfies the two conditions shown in Equations (6) and (7); meanwhile, it satisfies other three requirements, as presented by Simiu [9], for wind velocity spectrum; the third requirement is that the Karman spectrum $S_u(n)$ in Equation (9) is consistent with Equation (8) in the inertial subrange if $L_u\approx 0.3\beta_u^{3/2}z$; the fourth requirement is that $S_u(n)$ is a monotonically descending function; the fifth requirement is that the integral of $S_u(n)$ is the variance. In fact, the Karman spectrum is an interpolated expression of the spectrum in the inertial subrange and the spectrum value at zero frequency.

Karman spectrum was fitted statistically from the data of the homogenous and isotropic turbulence, therefore it is unsuitable for the wind spectrum of the roughness terrain in the near-ground range [9]. It is evident that Karman spectrum agrees well with Equation (8) in free stream conditions while it deviates slightly from the spectrum curve at the energy containing range and the dissipation subrange. In the energy containing range, Karman spectrum curve is an approximately horizontal line; it is implied that the large eddies with different frequencies contain the similar or identical amounts of kinetic energy. This overestimates the spectrum values at the energy containing range. Therefore, the wind-resistant design of lower frequency structures, such as an oil platform or a cable-stayed bridge, assures more safety when Karman spectrum is used.

The foundation of studying the wind velocity spectrum in wind engineering is established on the basis of Equations (8) and (9). As stated by Solari [12], the spectral formulas in engineering practice are actually deduced from three procedures. The first procedure is the direct use of Equation (9) in practice, in which parameters L_u and β_u are determined by the actual turbulence observed at the rough sites[13-15]. The second procedure consists of the polynomial spectral equations valid in the energy containing range and linked smoothly to Equation (8) to represent the spectrum at the inertial subrange. The third procedure is to define a single expression, such as Karman spectrum, to describe the spectrum at zero frequency and in the inertial subrange. A universal spectrum formula for homogenous and isotropic turbulence was presented by Fichtl [18], which has the form

$$\frac{nS_j(n)}{u_*^2}=\frac{A_j f}{\left(1+B_j f^{\gamma_j}\right)^{5/(3\gamma_j)}} \tag{10}$$

where A_j, B_j and γ_j are the three parameters to be determined. It is clear that the requirement of Equation (6) is satisfied if $A_j=4\beta_j L_j/z$ and the other four requirements are satisfied. Based on different observations, some expressions of spectrum like the form of Equation (10) have been presented [16, 19-25] since 1960s', in which parameter γ_j is usually specified as 1, 2 or $5/3$.

To avoid the determination of the friction velocity u_* and the coefficient β_u during the statistical process for the actual wind flow, Karman spectrum in Equation (9) is rewritten as

$$\frac{nS_u(n)}{\sigma_u^2}=\frac{4f_u}{\left(1+70.8f_u^2\right)^{5/6}} \tag{11}$$

where f_u is a dimensionless coordinate, and $f_u=nL_u/U$. After the three parameters U, L_u and σ_u^2 are specified by their empirical formulas on any height, Karman spectrum on this height can be expressed definitely. Equation (11) is directly used by Japanese Wind Code (AIJ-RLB-2004) and Australian Code (AS/NZS 1170.2-2002). An empirical spectrum model presented by Solari [19] is adopted by American Wind Code (ANSI/ASCE 7-10), i.e.,

$$\frac{nS_u(n)}{\sigma_u^2}=\frac{6.868f_u}{\left(1+10.302f_u\right)^{5/3}} \tag{12}$$

The spectrum expression in European Wind Code (BS EN 1991-1-4:2005) is similar to Equation (12) and it is

$$\frac{nS_u(n)}{\sigma_u^2}=\frac{6.8f_u}{\left(1+10.2f_u\right)^{5/3}} \tag{13}$$

Both Chinese Wind Code (GB50009-2006) and Canadian Code (NBCC-2005) directly use Davenport spectrum [26], that is,

$$\frac{nS_u(n)}{\sigma_u^2}=\frac{2x^2/3}{\left(1+x^2\right)^{4/3}} \tag{14}$$

where $x=1200n/U_{10}$ and U_{10} is denoted as the 10-minute mean wind speed over a flat, open terrain at a height of 10m. Davenport spectrum was fitted on the basis of different data observed in different countries, at different terrains and different heights. It cannot reflect the variation of the spectrum at different heights. The value of Davenport spectrum at zero frequency is zero, and less than the theoretical value shown in Equation (6). Compared with the three spectra models presented respectively by Karman [11], Simiu [17] and Solari [19], the values of Davenport spec-

trum are much smaller in the low frequency range and larger in the high frequency range.

3 HHT and Hilbert energy spectrum

In the history of wind engineering, Fourier transform is the efficient tool for transforming the time histories of wind velocity and pressure into the spectra in the frequency domain. In fact, a time history is represented by the summation of many sine and cosine complex functions via Fourier transform. These trigonometric functions are symmetrical and stationary, therefore a crucial restriction of the Fourier transform is that the measured signals must be strictly periodic or stationary. In the process of Fourier spectrum analysis, the transient characteristics of a time history are lost since Fourier transform is the integral with respect to time; on the other hand, Fourier transform needs many high-frequency harmonic waves to fit non-stationary data. These spurious harmonics might make mathematical sense, but do not really make physical sense at all and can disorder the energy spectrum distribution. Consequently, the values of energy spectrum at the low-frequency range are usually underestimated in engineering practice [27]. The other signal processing methods based on Fourier transform, such as short-term Fourier transform, Wigner-Ville distribution, suffer all the limitations of the Fourier analysis.

As the measured time histories of wind flow manifest strong nonlinear and nonstationary features, it is necessary to select the relatively stationary records of wind velocity as the samples of Fourier transform. The advent of wavelet transform in 1980s' provided an attractive method to analyze nonstationary process. Some researchers in wind engineering tried to use wavelet transform to analyze the measured signals of wind velocity [28-30]. Wavelet transform, whose basis function is also priori as it is for Fourier transform, decomposes a time history into a series of wavelet components, which have the nonlinear and nonstationary characteristics. However, wavelet transform is a regional presentation of the data in time-frequency plane and is useful for characterizing gradual frequency changes, but does not provide the instantaneous frequencies.

In 1998, Hilbert-Huang transform (HHT) [31] was presented to serve as an innovative signal processing method to analyze adaptively nonlinear and nonstationary data. HHT is based on the empirical mode decomposition (EMD) method, which generates a collection of intrinsic mode functions (IMFs). Expressed as IMFs, the data have well-behaved Hilbert transform, from which the instantaneous frequencies can be estimated at a proper time. Thus, any event on the time as well as the frequency axis can be localized. The IMFs can serve as the basis of an expansion of the data which can be linear or nonlinear, stationary or nonstationary, and they are complete, nearly orthogonal and adaptive.

In the traditional statistical analysis of turbulence, the power spectrum density resulted from Fourier transform of correlation function describes the fluctuating wind energy distribution in the frequency domain. Similarly, this concept can be extended to the definition of the fluctuating wind energy spectrum via HHT, i.e., the Hilbert energy spectrum, which describes detailedly the fluctuating wind energy distribution in the time-frequency plane. Assuming $u(t)$ is the fluctuating wind velocity of longitudinal component, the analytical signal of $u(t)$ is as follows

$$\begin{aligned} u_a(t) &= u(t) + i\cdot\tilde{u}(t) = \sum_k \left[c_k(t) + i\cdot\tilde{c}_k(t)\right] \\ &= \sum_k A_k(t,n) e^{i\cdot\theta_k(t)} \end{aligned} \tag{15}$$

where $c_k(t)$ is the kth IMF of $u(t)$; $\tilde{c}_k(t)$ is denoted as the Hilbert transform of $c_k(t)$; $A_k(t,n)$ is the amplitude of kth analytical component in time-frequency plane and $A_k(t,n) = \sqrt{c_k^2(t) + \tilde{c}_k^2(t)}$; $\theta_k(t)$ is the instantaneous phase; n is the instantaneous frequency, and $n = d\theta_k(t)/(2\pi dt)$.

It is recognized that the energy contained in analytical signal $u_a(t)$ is two times as much as that of the original signal $u(t)$, i.e., $\sum_k A_k^2(t,n) = 2u^2(\mathrm{t})$. The duration T of the fluctuating wind history is divided into N_1 intervals and the time step is Δt while the frequency range $f_{\max}/2$, where $f_{\max}$ is the sampling frequency, is divided into N_2 intervals and the frequency step is Δn. Then the Hilbert energy spectrum of $u(t)$ can be defined as the energy density distribution in a time-frequency space divided into equal size bins of $\Delta t \times \Delta n$ with the value in each bin designated as $\sum A_k^2(t,n)/(2N_1N_2)$ at the proper time and the corresponding instantaneous frequency, that is,

$$S_u(t,n) = \frac{\sum_k A_k^2(t,n)}{2N_1N_2\Delta t\Delta n} \tag{16}$$

It is clear that the double integrals of Hilbert energy spectrum $S_u(t,n)$ with respect to time and frequency result in the variance of the fluctuating wind history. If integrating the Hilbert energy spectrum $S_u(t,n)$ with respect to time only, the Hilbert marginal spectrum with respect to frequency is defined simply as

$$S_u(n) = \int_0^T \frac{\sum_k A_k^2(t,n)}{2N_1N_2\Delta t\Delta n} dt \tag{17}$$

The definition of the Hilbert marginal spectrum in Equation (17) would facilitate comparison with the Fourier power spectrum. The marginal spectrum reflects the wind energy

distribution at each instantaneous frequency whereas the Fourier power spectrum represents the wind energy distributed in the global frequency.

4 Wind spectrum at Beijing Meteorological Tower

The Beijing Meteorological Tower (Figure 2), which is situated inbetween the Northern 3rd Ring Road and the Northern 4th Ring Road of Beijing city, was set up in 1978 by the Institute of Atmospheric Physics (IAP), Chinese Academy of Sciences (CAS). Before 1990, there was no any high structure near the tower, thus the tower was the best station to observe meteorology and measure the suburb boundary layer of Beijing city. Since 1990s', the scale of Beijing city has largely expanded with the tremendous urbanization. MuDan Yuan and GuanCheng Yuan residential buildings with height less than 60m were built in 1990s' in the north and south of the tower. GuanCheng Yuan residential buildings, located closely to the tower, are the primary rough elements influencing the near-ground wind flow. The tower is now surrounded by residential buildings of 30m to 60m in height and is located in a prosperous city zone completely. Hence, the meteorological tower becomes the best observation station to study the urban boundary layer (UBL) of Beijing city.

In 2000, three supersonic anemometers named UAT_1, whose sampling frequency is 10Hz, were installed at the 47m, 120m and 280m above ground level, respectively to record the turbulence flow. Since then, more and more measured records of turbulence flow have been accumulated. The wind velocity spectrum is investigated in this paper using the measured turbulent records by the tower from 2005 to 2007, plus partial records of 2002. All of the records were provided by IAP, CAS.

(a) 1980s' (b) 2010s'

Figure 2 Beijing Meteorological Tower

According to the previous research, the northwest wind dominates in the spring, autumn and winter. Thus all the 10-minute, northwest wind records of the three seasons in 2002, 2005, 2006 and 2007 were classified by the mean speeds at 47m. The number of samples in each speed block is listed in Table 1.

It is known from Equations (6), (8)~(14) that the turbulent spectrum values are dependant on the integral length scale and the mean speed. Therefore, both the integral length and the mean speed varying with the height must be determined before the wind spectrum is fitted.

The integral length scales of the wind samples in each block are calculated. It is indicated that the mean integral length scales increase with the increase of the wind speeds while the slope of the integral length scale curve becomes smaller and smaller. The varied integral length scales exhibit a stable value when the wind speed is larger than 8m/s at 47m. Then the integral length scales of the 378 samples of the last four blocks in Table 1 are reanalyzed. It is shown that the probability distribution of the integral length scales of the 378 samples scatters in a very large range, in which the probabilities of occurrence of the largest or the larger integral length scales are very small. After the singular samples in the last four blocks shown in Table 1 are discarded, the integral length scales and the mean speeds are calculated and listed in Table 2. The fitted profiles of the integral length scales using the available samples are as follows:

$$L_u = \begin{cases} 90\left(Z/30\right)^{0.55}, & 30\text{m} < Z \le 450\text{m} \\ 90, & Z \le 30\text{m} \end{cases} \tag{18}$$

$$L_v = \begin{cases} 45\left(Z/30\right)^{0.70}, & 30\text{m} < Z \le 450\text{m} \\ 45, & Z \le 30\text{m} \end{cases} \tag{19}$$

$$L_w = \begin{cases} 15\left(Z/30\right)^{0.85}, & 30\text{m} < Z \le 450\text{m} \\ 15, & Z \le 30\text{m} \end{cases} \tag{20}$$

After Hilbert-Huang transform is conducted, the analytical signals of the available samples are obtained. Then the Hilbert energy spectra defined in Equation (16) and the marginal spectra defined in Equation (17) are calculated. Figures 3~5 give the dimensionless marginal spectra and their mean spectra (the thick solid line) of the longitudinal components for the wind speed blocks.

It can be seen from the spectra curves in double logarithm coordinate system that the nine mean spectra are nearly straight lines if the dimensionless frequency nL_u/U is larger than 0.2. Therefore it is reasonable to regard the point of $nL_u/U = 0.2$, where the corresponding frequency n is about 0.016Hz, as the lower bound of the inertial subrange. After the nine mean spectra curves in the inertial subrange ($n = 0.016 \sim 0.5\text{Hz}$) are fitted with linear model, the slope of the fitted line varies from -0.507 to -0.664 with 95% confidence and the mean slope is -0.588, which is less than the theoretical value -2/3 (shown in Equation (8)) of the homogenous and isotropic turbulence because the wind flow at

Beijing Meteorological Tower is influenced by the rough surface. Considering this phenomenon, it is assumed approximately that the dimensionless spectrum $nS_u(n)/\sigma_u^2$ of the longitudinal component is proportional to the dimensionless frequency $f_u^{-3/5}$ ($f_u = nL_u/U$) in the inertial subrange and the counterparts of the horizontal and vertical components take the same forms.

Table 1 Number of 10-minute, northwest samples in each block

Mean speed at 47m	2-3m/s	3-4m/s	4-5m/s	5-6m/s	6-7m/s	7-8m/s	8-9m/s	9-10m/s	10-11m/s	11-12m/s
Number of samples	1778	1574	1241	925	698	499	274	76	24	5

Table 2 Integral length scales and mean speeds of available samples

Mean speed at 47m		47m			120m			280m		
		u	v	w	u	v	w	u	v	w
8-9m/s	Number of samples	228	243	259	222	240	248	213	238	230
	Integral length scale (m)	115.2	61.6	22.0	192.9	118.8	48.7	307.4	214.9	100.1
	Mean speed (m/s)	8.4	8.4	8.4	11.6	11.6	11.6	14.4	14.3	14.4
9-10m/s	Number of samples	64	69	72	62	70	69	58	67	64
	Integral length scale (m)	115.2	61.6	22.0	192.9	118.8	48.7	307.4	214.9	100.1
	Mean speed (m/s)	9.4	9.4	9.4	12.9	12.8	12.9	15.6	15.7	15.5
10-12m/s	Number of samples	24	29	28	23	28	28	18	29	29
	Integral length scale (m)	115.2	61.6	22.0	192.9	118.8	48.7	307.4	214.9	100.1
	Mean speed (m/s)	10.5	10.6	10.5	14.5	14.6	14.7	18.1	17.8	17.8

According to the universal formula of the empirical wind velocity spectrum in Equation (10), the following expression is presented to fit the fluctuating wind velocity spectrum at Beijing Meteorological Tower, that is,

$$\frac{nS_j(n)}{\sigma_j^2} = \frac{a_j f_j}{\left(1 + b_j f_j^{\gamma_j}\right)^{8/(5\gamma_j)}} \tag{21}$$

where σ_j^2 is the variance of the jth component and a_j, b_j and γ_j are three parameters to be estimated. Equation (21) is an interpolation function of the spectrum in the inertial subrange and the theoretical spectrum value at zero frequency if a_j=4, and it mainly describes the shape of spectrum in the inertial subrange, in which $S_j(n)$ is proportional to $f_j^{-8/5}$, and does not represent well the shape of the spectrum in energy containing range and the dissipation subrange.

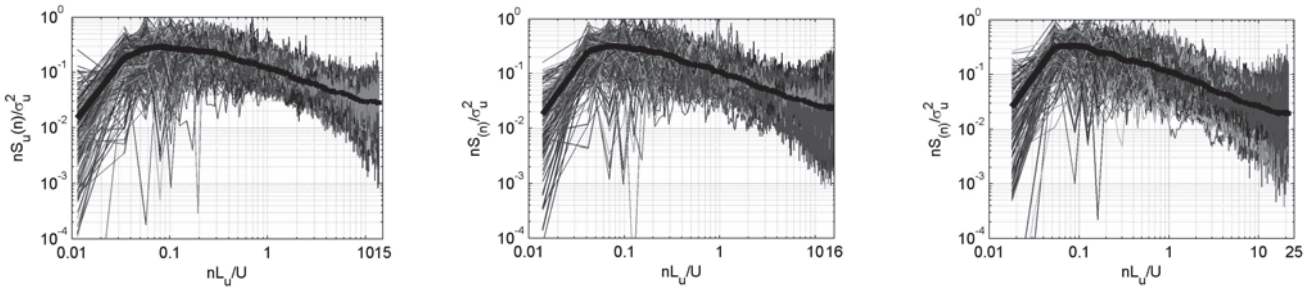

(a) At the height of 47m (b) At the height of 120m (c) At the height of 280m

Figure 3 Longitudinal spetra and mean spectra for wind speed at 8-9m/s

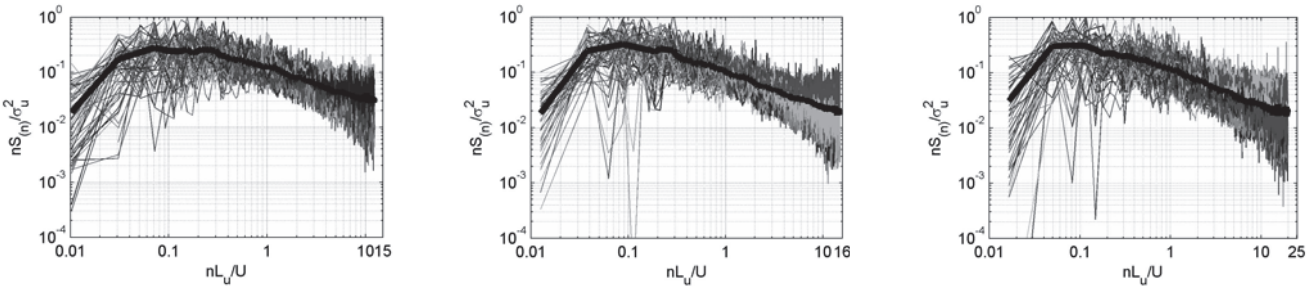

(a) At the height of 47m (b) At the height of 120m (c) At the height of 280m

Figure 4 Longitudinal spetra and mean spectra for wind speed at 9-10m/s

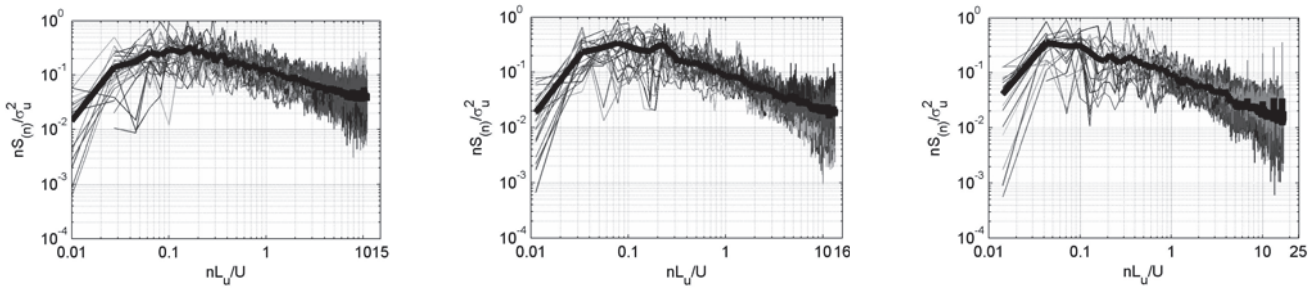

(a) At the height of 47m (b) At the height of 120m (c) At the height of 280m

Figure 5 Longitudinal spetra and mean spectra for wind speed at 10-12m/s

To fit better in the energy containing range, another expression of the fluctuating wind velocity spectrum is presented in this paper, i.e.,

$$\frac{nS_j(n)}{\sigma_j^2}=\frac{4f_j\left(1+a_jf_j\right)}{\left(1+b_jf_j^{\gamma_j}\right)^{13/(5\gamma_j)}} \tag{22}$$

It is evident that the requirement of Equation (6), $S_j(0)=4\sigma_j^2L_j/U$, is satisfied at zero frequency while the derivative at zero frequency is a constant, $dS_j(n)/dn=4\sigma_j^2L_j^2a_j/U^2$, which means that the $S_j(n)$ is a linear function with the slope of $4\sigma_j^2L_j^2a_j/U^2$, agreeing with the conclusion of Heisenberg [6] in the region of the larger eddies. In the inertial subrange, the dimensionless spectrum $nS_j(n)/\sigma_j^2$ is approximately proportional to $f_j^{-3/5}$ if f_j is larger than 0.2. This agrees with the mean spectra shapes, shown in Figures 3~5, in the inertial subrange. In a word, Equation (22) is consistent with the characteristics of spectrum shape in large eddies range and the inertial subrange.

With the increase of the mean wind speed, the number of the available samples decreases. If the total samples of the speed bocks in Table 2 are collected to fit the spectrum, the contributions of the high speed samples can not be reflected because the number of high speed samples is much less than the number of the low speed samples. To overcome this drawback, the nine mean spectra curves shown in Figures 3~5 are collected and considered as the fitted target. The fitted results using Equations (21) and (22) are plotted in Figures 6~8. By using the fast Fourier transform (FFT), the same process is conducted and the fitted spectra are indicated in Figures 9~11.

Compared with the calculated spectra using HHT, the deviatability of the FFT spectra in the high frequency range is much larger in the universal equilibrium range. Figures 12~14 show the comparison of the fitted spectra using HHT and FFT. It is apparent that the fitted spectrum value using HHT is larger than the counterpart using FFT in the energy containing range, and the peak frequency of the HHT spectrum is less than that of the FFT spectrum. This phenomenon can be explained by FFT itself: Because many high frequency harmonic waves in FFT are introduced to fit the peak of a time history, the high frequency spectrum becomes larger and correspondingly the low frequency spectrum becomes smaller. It is known that the HHT spectrum behaves better than the FFT spectrum in the energy containing range.

In the inertial subrange, the measured turbulent spectra at Beijing Meteorological Tower vary approximately with the -8/5 power of the frequency and agree closely with the Kolmogorov $-5/3$ law of the homogenous and isotropic turbulence. Hence, the fitted spectra can be compared with Karman spectrum (Figure 12). The FFT spectrum is very close to Karman spectrum both in the universal equilibrium range and in the large or largest eddies range while the Karman spectrum is slightly larger in the region of energy

containing eddies than the FFT spectrum. The HHT spectrum is larger than Karman spectrum in the energy containing range while it is approximately identical to Karman spectrum in the universal equilibrium range. Since Karman spectrum is based on FFT, its value in the energy containing range may be less than the accurate value.

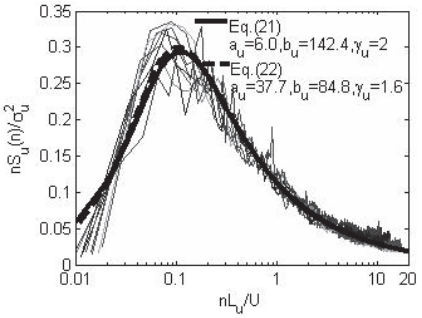

Figure 6 Longitudinal spectra using HHT

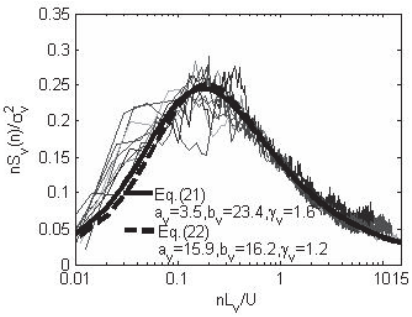

Figure 7 Horizontal spectra using HHT

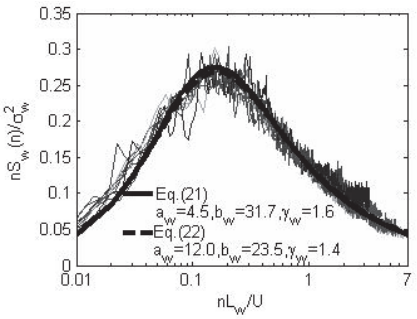

Figure 8 Vertical spectra using HHT

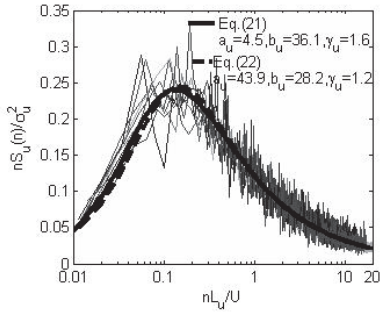

Figure 9 Longitudinal spectra using FFT

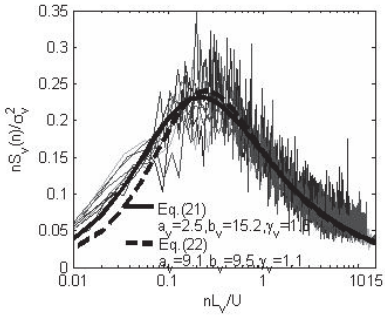

Figure 10 Horizontal spectra using FFT

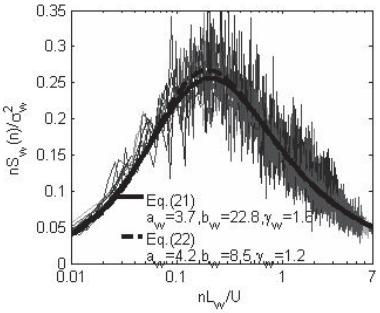

Figure 11 Vertical spectra using FFT

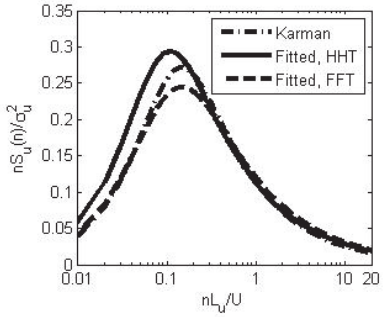

Figure 12 Comparison of longitudinal spectra

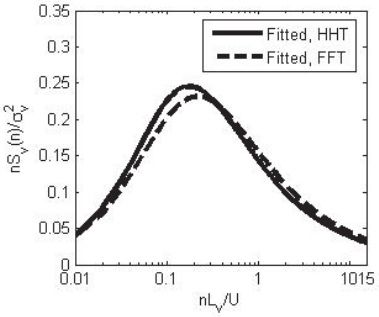

Figure 13 Comparison of horizontal spectra

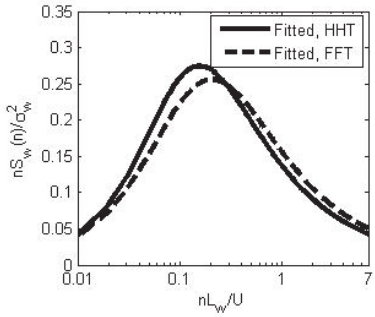

Figure 14 Comparison of vertical spectra

5 Conclusions

The research history of the turbulent spectrum and the practical spectra models in the wind engineering is summarized briefly in this paper. Then an innovative wind spectrum model is presented to reflect additionally the characteristic of wind spectrum in the region of the large eddies. The wind velocity spectra of the measured turbulence at Beijing Meteorological Tower are calculated using HHT and FFT, respectively, and are fitted using the method of least squares to estimate the parameters in the empirical models. The fitted results show that the presented model can fit the measured spectra well as the universal spectrum model does while the spectrum values of the presented model in the region of the large eddies are more accurate and the theoretical value at zero frequency is satisfied.

During the process of calculating the wind velocity spectra of the measured turbulence using FFT, many high-frequency harmonic waves are introduced to fit the peaks of a nonstationary history. This confuses the energy distribution in the frequency domain and leads to the low values of the low-frequency spectrum. The wind velocity spectra resulted from HHT can reflect the wind spectra at the proper time and the corresponding instantaneous frequency, and can obtain the accurate spectra values in the region of the large eddies. Hence, the fitted spectrum using HHT is slightly larger than the FFT spectrum while the spectrum in the universal equilibrium range is very close to the FFT spectrum.

This work was supported by the National Natural Science Foundation of China (Grant Nos.90815021, 51021140005, 50978025 and 50938008).

1 Richardson L F. Weather prediction by numerical process. Cambridge University Press, Cambridge, England, 1922
2 Kolmogorov A N. The local structure of turbulence in incompressible viscous fluid for very large Reynolds numbers. Dokl. Akad. Nauk SSSR, 1941, 30: 299-303 (in Russian)
3 Heisenberg W. Zur statistischen theorie der turbulenz. Max Plank Institute fur Physik, Gottingen, 1946
4 Weiszacker C F. Von. Das spectrum der turbulenz, Max Plank Institute fur Physik, Gottingen, 1946
5 Pao Y H. Structure of turbulent velocity and scalar fields at large wave-numbers. Phys. Fluids, 1965, 8: 1063-1075
6 Heisenberg W. On the theory of statistical and isotropic turbulence. Proc. R. Soc. London Ser. A, 1948, 195: 402-406
7 Batchelor G K. Kolmogoroff's theory of locally isotropic turbulence. Mathematical Proceedings of the Cambridge Philosophical Society, 1947, 43(4): 533-559
8 Batchelor G K. The theory of homogeneous turbulence. Cambridge University Press, Cambridge, England, 1953
9 Simiu E, Scanlan R H. Wind Effects on Structures: Fundamentals and Applications to Design. third edition, Wiley, New York, USA, 1996
10 Tieleman H W. Wind characteristics in the surface layer over heterogeneous terrain. Journal of Wind Engineering and Industrial Aerodynamics, 1992, 41(1-3): 329-340
11 Karman T Von. Progress in the statistical theory of turbulence. Proc. Nat. Acad. Sci. USA, 1948, 34(11): 530-539
12 Solari G. Turbulence modeling for gust loading. J. Struct. Engrg., ASCE, 1987, 113(7): 1550-1569
13 Wyngaard J C, Cote O R., Rao K S. Modeling the atmospheric boundary layer. Advances in Geophysics, Academic Press, 1974, 18A: 193-211
14 Deaves D M, Harris R I. A mathematical model of the structure of strong winds. CIRIA Report 76, Construction Industry Research and Information Association, London, U.K, 1978
15 Engineering Sciences Data Unit . Characteristics of atmospheric turbulence near the ground. Part II: Single point data for strong winds (neutral atmosphere). ESDU 85020, ESDU, London, U.K., 1985
16 Simiu E. Wind spectra and dynamic alongwind response. Struct. Div., ASCE, 1974, 100(9): 1897-1910
17 Simiu E, Leigh S D. Turbulent wind and tension leg platform surge. Struct. Eng., ASCE, 1984, 110(4): 785-802
18 Fichtl G E, McVehil G E. Longitudinal and lateral spectra of turbulence in the atmospheric boundary layer at the Kennedy Space Center. Appl. Meteorol., 1970, 9: 51-63
19 Solari G. Gust buffeting. I: peak wind velocity and equivalent pressure. Journal of structural engineering, 1993, 119(2): 365-382
20 Lumley J L, Panofsky H A. The Structure of Atmospheric Turbulence. Wiley, New York, 1962
21 Kaimal J C, Wyngaard J C, Izumi Y, Cote O R. Spectral characteristics of surface layer turbulence. Quart J Roy. Meteorol Soc., 1972, 98:563-589
22 Hino M. Spectrum of gusty wind, Proceedings of the 3rd International Conference on Wind Effects on Buildings and Structures, Tokyo, Japan, 1971: 69-77
23 Harris R I. The nature of the wind. Proceedings of the Seminar on the Modern Design of Wind Sensitive Structures, Institution of Civil Engineers, London, 1970: 29-55
24 Kareem A. Wind induced response analysis of tension leg platforms. J Struct Engng, ASCE 1985, 111(1): 37-55
25 Tieleman H W. Universality of velocity spectra. J Wind Engng Ind Aerodynam, 1995, 56:55-69
26 Davenport A G. The spectrum of horizontal gustiness near the ground in high winds. Quarterly Journal of the Royal Meteorological Society, 1961, 87(372): 194-211
27 Huang N E, Chern C C, Huang K, et al. A new spectral representation of earthquake data: Hilbert spectral analysis of station TCU129, Chi-Chi, Taiwan, 21 September 1999. Bull. Seismol. Soc. Am., 2001, 91: 1310-1338
28 Kareem A, Kijewski T. Time-frequency analysis of wind effects on structures. Journal of Wind Engineering and Industrial Aerodynamics, 2002, 90: 1435-1452
29 Xu Y L, Chen J. Characterizing nonstationary wind speed using empirical mode decomposition. J. Struct. Eng., 2004, 130: 912-920
30 Li Q S, Wu J R. Time–frequency analysis of typhoon effects on a 79-storey tall building. Journal of Wind Engineering and Industrial Aerodynamics, 2007, 95: 1648-1666
31 Huang N, Shen Z, Long S, et al. The empirical mode decomposition and the Hilbert spectrum for nonlinear and non-stationary time series analysis. Proc. Roy. Soc. Lond., 1998, 454A: 903-993

The Seventh International Colloquium on Bluff Body Aerodynamics and Applications (BBAA7)
Shanghai, China; September 2-6, 2012

Amplification effect of rough underlying surface on the strong wind parameters at typhoon eye wall

wenchao Chen [a], lili Song [b,c], Liu Aijun [a], shiqun Zhi [a]

a Guangdong Climate Center, No.6 Fujin Road, Guangzhou, China
b Public Meteorological Service Center, CMA, No46 Southstreet, Zhongguancun, Beijing, China
c Guangzhou Institute of Tropical and Marine Meteorology, CMA, No.6 Fujin Road, Guangzhou, China

ABSTRACT: Based on nearly one year normal wind data and the wind data of typhoon Hagupit and Nesat observed by the meteorological towers located at South China Sea and the coast, the underlying surfaces of the meteorological towers were classified to two exposures, the characteristics of the power-law exponents of the wind profiles, turbulence intensities over different underlying surfaces were analyzed. It were found that when the roughness length of underlying surface was larger than 6cm, the power-law exponent at typhoon condition was 1.5-2 times compared with the power-law exponents of exposure D and C (0.3 and 0.22) given in Chinese code. The near surface wind speed decayed more significantly, the power-law exponent and the turbulence intensities were larger in typhoon condition than in normal wind condition, especially over the rough underlying surface. Rough underlying surface has significant amplification effect on the wind parameters in typhoon condition. The amplification factors were calculated and the mathematical relationship between the amplification factors and the underlying surface roughness lengths were established. Based on these mathematical relationships, the wind parameters at the place attacked by typhoon eye wall can be estimated by the roughness length of the underlying surface and the wind parameters in normal wind condition which were more easily to measure.

KEYWORDS: landing typhoon, power-law exponent of wind profile, turbulence intensity, roughness length, amplification factor.

1 INTRODUCTION

Typhoon has control impact on the urban planning and construction, design of major engineering structure. The impact of strong wind on building and structure can be divided into static load induced by mean wind and dynamic load induced by turbulent wind. The vertical distribution of the surface wind (wind profile for short) is often used to reflect the impact of the mean wind speed and is mainly described by the power-law in the code of wind resistance engineering. The power-law exponent can present the changing rate of the wind speed with height. The power exponents of the wind profiles corresponding to four kinds of exposures which are type A, B, C and D with different roughness in the code [1] are 0.12, 0.16, 0.22 and 0.3. The turbulence intensity is an index to assess the fluctuation of the wind field which is often used in the study of turbulent wind. Some observation facts showed that the characteristics of the wind profile and turbulent wind in typhoon process has significant difference with that in normal wind system. At present, most of the investigations of typhoon wind profiles were based on the wind data at typhoon periphery at which the wind speeds are not so strong. Tamura et al. [2] analyzed the power-law exponent of the wind profiles based on the typhoon periphery wind data observed at Seashore and two inland residential areas by Doppler sodar. The study showed that the power-law exponents are small at Seashore and apt to grow larger as the wind blows over a longer fetch with inland

roughness. Based on the data obtain from 52m observation tower, Shanmugasundaram et al. [3] found the power-law exponent of tropical cyclone was larger than that in normal wind condition and the power-law exponent would decrease with the wind speed. Song et al. [4] analyzed the gradient wind data observed at a complex terrain and found the wind profile over complex terrain didn't satisfied with the power-law even in neutral atmospheric condition. Chen [5] found that the gust factor has positive relationship with the roughness length of underlying surface and established an equation to describe the relationship according to the gust factors over different underlying surface. It seems that the typhoon wind parameters would increase to a certain extent by the influence of the special vortex structure and the rough underlying surface. In order to further investigate this amplification effect of power-law exponent of typhoon wind profile over rough underlying surface, the observation wind data of typhoon Hagupit and Nesat and the wind data obtained at the same towers in normal wind condition are compared and analyzed. It is hoped that some results which is meaningful in the engineering apply can be achieved.

2 BASIC DATA SOURCE AND PROCESSING

In order to analyze the variation characteristics of the typhoon wind profiles over different underlying surfaces, the observation data of two typhoon cases which can represent the whole typhoon processes and the observation site had obvious different the underlying surfaces were chosen and analyzed. The data in this paper included the measurement at three gradient observation towers near the passage of strong typhoon Hagupit made landfall in Guangdong, China in 2008 and one gradient observation tower near the passage of typhoon Nesat made landfall in Hainan, China in 2011.

2.1 *Description of landing typhoon Hagupit and the instrument setting*

Strong typhoon Hagupit landed to the coastal region of Chencun Town, Dianbai County, Maoming, Guangdong Province at 06:45 am (Beijing time, the same below) on 24th Sep. 2008 (Fig. 1). The maximum 3sec average gust wind speed recorded at the coastal meteorological station at the center of typhoon landfall was 58m/s while the maximum 10min mean wind speed was 48m/s.

There are three meteorological mast towers located near the passage of strong typhoon Hagupit which were Zhizai Island tower, Qinba tower, Wuyang tower and the shortest distances between these three towers and the center of typhoon Hagupit were 8.5km, 12km, 18.3km, respectively (Fig.1). The shortest distance between Zhizai Island and the coast was 4.5km. The 100m high gradient tower was located at the top of the island 10m above sea level.The anemometers were equipped at the heights of 10, 20, 40, 60, 80, 100m and wind vanes were set at the heights of 10, 60, 100m. But the wind vane at the heights of 10m and 100m were destroyed during the typhoon Hagupit center passed and the wind direction data were missing. Both of the 80m high Qinba tower and 70m high Wuyang tower were located at the coast with altitude of 19m and 7m high. The anemometers equipped at Qinba tower were at the heights of 10, 30, 50, 70, 80m while the anemometers equipped at Wuyang tower were at the heights of 10, 30, 50, 70m. The wind vanes were installed at 10m and 75m at Qinba tower and the wind vanes are installed at 10m and 70m at Wuyang tower. During the passage of typhoon Hagupit, the maximum 10min mean wind speed at 100m high of Zhizai Island tower, at 70m high of Qinba tower and Wuyang tower were 48.5m/s, 33.9m/s and 31.3m/s when the gust (3sec) wind speed were 59.8m/s, 43.6m/s and 44m/s respectively.

2.2 *Description of landing typhoon Nesat and the instrument setting*

Strong typhoon Nesat landed to the coastal area of Wengtian County, Wencchang, Hainan Province at 14:30 on 14th Oct. 2011 (Fig. 1) with the minimum air pressure of 960 hPa and the central wind force of 14 grads which had reach 42m/s. Xiuying tower located at the northeast of typhoon track. The shortest distances between these three towers and the center of typhoon Hagupit was 8km.

Xiuying tower was located at the coast with the coastline runs northeast-southwest. There were sparse houses at the southeast of the tower. The underlying surface of the tower is near surface sward. The anemometers and wind vanes were equipped at the heights of 10, 20, 40, 60, 80, 100m.The observed maximum 10min mean wind speed and gust wind speed were 34.2m/s and 41.3m/s at the height of 100m at Xiuying tower which appeared before the typhoon center passed. The NRG-Symphonie type #40 anemometer and type #200p wind vane were used at four observation towers.

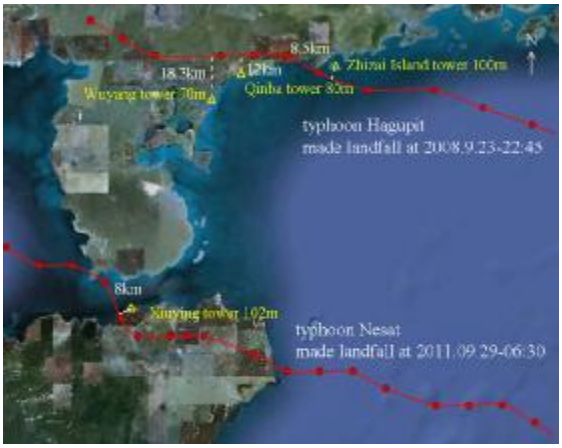

Figure 1. Path of typhoon Hagupit, Nesat and the location of the observation tower relative to the typhoon center

2.3 *Typhoon strong wind representative assessment*

Due to the eddy structure of typhoon system, the wind field structure and wind turbulence characteristics are obviously different in different locations relative to typhoon such as typhoon center, typhoon strong wind region and the periphery [6]. Since wind resistance engineering is mainly concerned with the characteristics of strong wind, the selected basic data must represent the whole observation process which included typhoon eye, typhoon strong wind and the periphery wind. According to the eddy structure of typhoon and the Beaufort scale of strong typhoon wind, two criteria should be fulfilled at the same time to prove whether the typhoon center has passed over the observation site [7]: (1) The wind direction with wind speed exceeding 8th grade Beaufort scale (10 min mean wind speed of 8th grade is 17.2 m/s) successively alters over 120°. (2) The variation of wind speed with time shows an “M” shape during the passage of typhoon and if a low wind speed less than 11 m/s (5th grade) occurs between two peak values, it can be judged as the typhoon eye area [8].

According to two criteria mention above, it can be claimed that the wind data obtained from these four meteorological towers were able to represent the specific wind characteristics of strong typhoon Hagupit and Nesat.

3 CLASSIFICATION OF THE UNDERLYING SURFACE

3.1 *Wind type classification base on the characteristics of the underlying surface*

Considering that the roughness of the underlying surface has direct impact on the characteristics of near surface wind, it is necessary to classify the observed wind according to the characteristics of the underlying surfaces so as to quantitatively investigate the differences between the winds over different underlying surfaces. The wind types were classified by the method recommended in the WMO technical document [9].According to the characteristics of the surrounding surfaces of four observation towers, the wind can be divided into two types:

The wind obtained by Zhizai island tower can be seen as inshore sea surface wind: wind came from 67.5°–247.5° (clockwise, similarly hereinafter) underlying surface can be seen as onshore wind at inshore sea surface. The wind from other orientation was defined as offshore wind at inshore sea surface (Fig. 2a). Qinba, Wuyang and Xiuying tower can be seen as coastal tower: wind respetively came from 90°–247.5°, 45°–202.5° and 225°–67.5° underlying surface were onshore wind at the coast and the wind from other orientation was defined as offshore wind at the coast (Fig. 2b-3d).

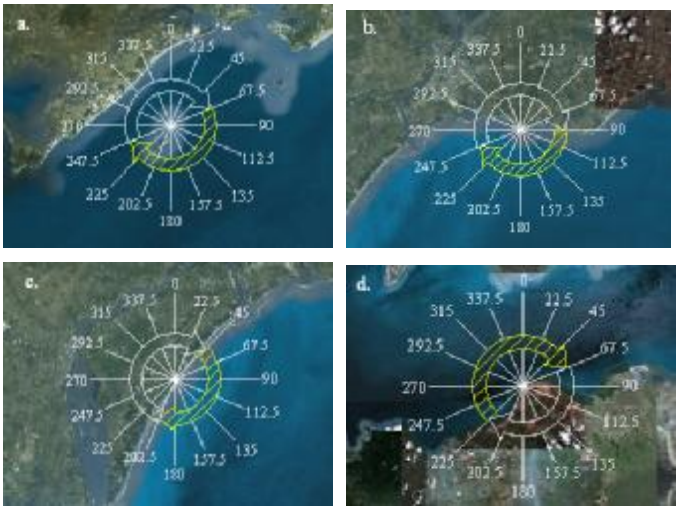

Figure 2. Wind type classification over different underlying surface.
(a: Zhizai Island tower; b: Qinba tower; c: Wuyang tower; d: Xiuying tower; shaded arrow: onshore wind orientation; hollow arrow: offshore wind orientation)

3.2 *Calculation of the underlying surface roughness length*

Aerodynamic roughness length is defined as the height at which the wind speed decreases to zero and this is an important parameter to indicate the roughness of the surface. For the purpose of examining that whether the classification of the near surface wind was reasonable. The roughness lengths of different underlying surfaces were calculated based on nearly one year of normal wind data (no influence by typhoon) in neutral atmospheric condition at each gradient tower and the logarithmic wind profile fitting method.

According to the wind profile equation given by Monin and Obukhov [10]:

$$\mathrm{U}(z) = u_* \left[\ln\left(z / z_0\right) - y\ (z / L) \right] / k \tag{1}$$

where κ=Karman constant, u*=friction velocity, z0=roughness length, ψ=Monin-Obukhov function, L=Monin-Obukhov length. Most strong wind happens in the neutral stability atmosphere and in the neutral stability condition, L=∞ and ψ=0. Eq.(1) can be simplified as below:

$$U(z) = u_* \ln(z / z_0) / k \quad (2)$$

where u* and z_0 are considered as the fitting parameters. By the method of the least square fitting, the height at which the wind speed becomes zero can be seen as roughness length z_0. The calculation result of the roughness lengths is given in Table 1.

Table 1 also gave the detailed description of the underlying surface at the orientation of land and sea. Compared with the roughness length and the description of the underlying surfaces, the roughness length calculated by logarithmic-law fitting can even describe the slight variations of different underlying surfaces.

Table 1. Roughness length of different underlying surface in normal wind condition

Observation tower	Wind type	Orientation (clockwise)	Description of the underlying surface	Roughness length (cm)
Zhizai Island tower	Offshore wind at inshore sea surface	247.5°-67.5°	Sea surface nearby and there is 4.5km wide sea area between the tower and the land northwest.	0.0682
	Onshore wind at inshore sea surface	67.5°-247.5°	Open sea area, an island of 3.5 km2 lies on 180–210° to the tower and about 1 km from the tower	0.0204
Qinba tower	Offshore wind at the coast	247.5°-90°	Dense forest at the coast with residential area nearby	12.6567
	Onshore wind at the coast	90°-247.5°	Open sea area and the underlying surface of 211°–247.5° to the tower is bay	0.2732
Wuyang tower	Offshore wind at the coast	202.5°-45°	coast with cultivated land and sparse forest and residential area	6.0773
	Onshore wind at the coast	45°-202.5°	Complete open sea surface	0.0123
Xiuying tower	Offshore wind at the coast	67.5°-225°	There are sparse houses at the southeast of the tower. The underlying surface of the tower is near surface sward.	8.6109
	Onshore wind at the coast	225°-67.5°	Sea surface, there is 21km wide sea area between the tower and the land at the north.	0.6248

4 CHARACTERISTICS OF THE TURBULENCE PARAMETERS OVER DIFFERENT UNDERLYING SURFACES

4.1 *Selection of the wind data samples*

In consideration of the wind resistance engineering mainly focused on the strong wind characteristics, here we only chose the wind data with the wind speed exceeding 8th grade Beaufort scale to analyze. Due to the typhoon wind speed varied significantly with height so in this paper, it was specified that the selection of the 8th grade strong wind at Zhizai Island tower, Qinba tower, Wuyang tower and Xiuying tower were respectively based on the wind speed at the height of 60m, 70m, 70m and 60m.

When the strong typhoon occurred, the atmosphere was in neutral stability condition. In order to make a comparison with the typhoon wind, the normal wind data were also selected in neutral atmosphere.

4.2 *The parameter used to describe the characteristics of the wind profile*

Due to the lack of a universal mathematical model which can describe the complex wind profiles accurately. The power-law fitting (eq.3) is widely recommended to estimate the wind speed at different height in engineering design. The wind profile obtained by the least square fitting which is closest to the real wind is called best power-law fitting (best fitting for short hereafter). But under the consideration of the safety for engineering wind resistance, except for the best fitting, the envelope curve power-law fitting (envelope fitting for short hereafter, the fitting wind speeds obtained by the envelope fitting are larger or equal to the observed wind speed at all the observation heights) are also applied in order to assess and choose the most suitable power-law exponent.

$$u = u_1 \left(z / z_1 \right)^{a} \tag{3}$$

Where the u = the wind speed at the height of z, u_1 = the wind speed at the height of z_1, α = power-law exponent which can indicate the variation of the wind speed with height.

4.3 *The characteristics of the wind profiles over different underlying surface*

Figure 3 showed the mean wind profiles observed at four meteorological tower in typhoon and normal condition. All of the normal wind profiles basically accorded with the power-law. But the wind profiles observed at Zhizai Island tower which was the nearest observation site to the center of typhoon Hagupit appeared significant variation. The onshore wind profile showed an "S" shape and negative wind shear appeared at the height of 40m to 60m. And the wind profiles observed at other three towers were basically satisfied with the power-law.

In view of the normal wind profiles, the differences between the offshore wind profile and onshore wind profile were very small at Zhizai Island tower, Wuyang tower and Xiuying tower while that difference was very large for the case of Qinba tower. The offshore wind lower than 30m decayed more significantly than onshore wind at Qinba tower which maybe induced by the large roughness length difference between two exposures which was 12.38cm. And the roughness length differences between two exposures were 0.05cm, 6.07cm and 7.99cm at Zhizai Island tower, Wuyang tower and Xiuying tower respectively.

Whether for normal wind or typhoon wind, the near surface wind speed came from rough underlying surface decayed more significantly than that from smooth underlying surface, especially for typhoon wind. Comparison of the wind profiles from the same underlying surface showed that the typhoon wind decayed more significantly than that in normal wind condition, especially for offshore wind. The differences value between the wind speeds at the lowest two level at Qinba tower, Wuyang tower and Xiuying tower in typhoon wind condition were 2.4times, 5.3 times and 4.8 times compared with that in normal wind condition.

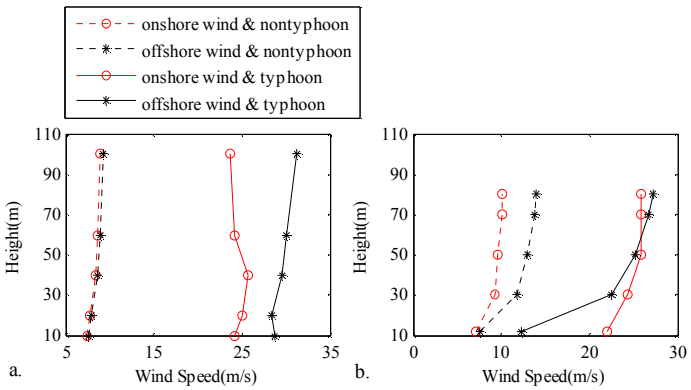

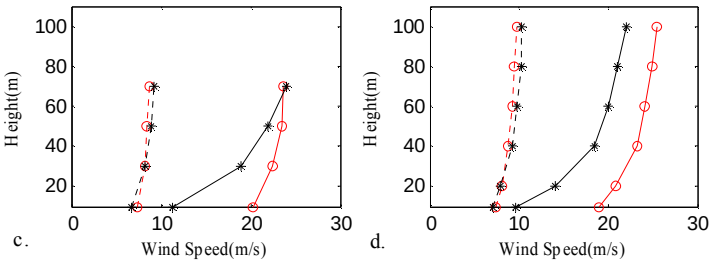

Figure 3. Wind profiles over different underlying surface.
(a: Zhizai Island tower; b: Qinba tower; c: Wuyang tower; d: Xiuying tower)

4.4 *The amplification effect of different underlying surfaces on power-law exponents of typhoon wind profiles*

Table 2 listed the power exponents of the best fitting and envelope fitting. The roughness lengths of offshore wind exposure at Qinba tower, Wuyang tower and Xiuying tower were 12.6567cm, 6.0773cm and 8.6109cm which were close to the class D or C exposures given in Chinese code. And the power exponents of the best fitting observed at the eyewall were 0.453, 0.404 and 0.382 while the power exponents of the envelope fitting were 0.661, 0.474 and 0.538 which were 1.5-2 times compared with the power exponent of class D, C exposures (0.3, 0.22) recommended by the code. The power exponents of the best fitting in normal wind condition were 0.342, 0.170 and 0.174 while that of the envelope fitting were 0.478, 0.180 and 0.188. The power-law exponent at Qinba tower was slightly larger than the value given in code while it were opposite for Wuyang and Xiuying tower. The wind profile exponent of the onshore strong wind which came from smooth sea surface (as the class A exposure in Chinese code) was less than the recommended value (0.12).

Table 2. Power-law exponents of typhoon wind profiles and normal wind profiles

Observation tower	Wind type	Roughness length (cm)	Normal wind		Typhoon wind		Amplification factor	
			α1	α2	α3	α4	α3/α1	α4/α2
Zhizai Island tower	Offshore wind	0.0682	0.086	0.088	0.028	0.036	0.327	0.414
	Onshore wind	0.0204	0.076	0.079	0.004	0.050	0.057	0.637
Qinba tower	Offshore wind	12.6567	0.342	0.478	0.453	0.661	1.326	1.382
	Onshore wind	0.2732	0.198	0.274	0.092	0.109	0.466	0.399
Wuyang tower	Offshore wind	6.0773	0.170	0.180	0.404	0.474	2.379	2.643
	Onshore wind	0.0123	0.083	0.089	0.084	0.092	1.011	1.033
Xiuying tower	Offshore wind	8.6109	0.174	0.188	0.382	0.538	2.201	2.864
	Onshore wind	0.6248	0.121	0.132	0.132	0.147	1.092	1.116

To calculate the ratio between the power-law exponents of typhoon wind profile and normal wind profile which is called amplification factors and figure 4 showed the variation of the amplification factors with roughness length. When the roughness length was small, the typhoon power-law exponents were generally less then that of normal wind. When the roughness lengths were larger than 0.6cm, the amplification factor became larger than 1. The amplification factor for best fitting and envelope fitting were 1.3-2.4 and 1.4-2.9 when the roughness length increased to nearly 10cm. It can be suggested that the rough underlying surface have significant amplification effect on the power-law exponent of strong typhoon wind profile.

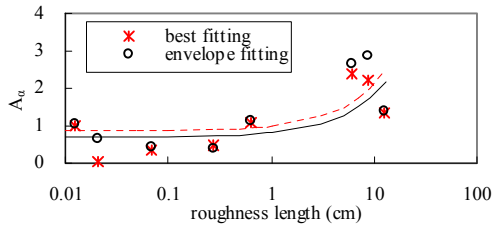

Figure 4. Relationship between the amplification factors of power-law exponent and the roughness length.

In order to quantitatively assess the amplification effect, the linear fittings were done according to equation 4.

$$A_a = A \cdot z_0 + B \tag{4}$$

where z0 = roughness length, Aα = amplification factor of power-law exponent, A and B were fitting parameters. The result shows that for best fitting: $A_a = 0.115 z_0 + 0.702$ and for envelope fitting: $A_a = 0.128 z_0 + 0.858$.

4.5 *Characteristics of turbulence intensity profile*

Turbulence intensity can reflect the wind fluctuant characteristics and the definition showed in equation 5.

$$I_i = s_i / U \tag{5}$$

where σ_i = standard deviation of turbulent wind u(t), v(t) and w(t) with 0.1s time period for i=1,2,3. U = 10min mean wind speed.

Figure 5 showed the turbulence intensity profiles. The turbulence intensity decreased with height and the turbulence intensity observed at inshore sea tower and the onshore wind observed at coastal tower were obviously less than that of the offshore wind at coastal tower. The typhoon turbulence intensity were generally larger than that in normal wind condition, especially under the influence of the rough exposure. The turbulence intensities at the lowest level at Zhizai Island tower, Qinba tower, Wuyang tower and Xiuying tower were 0.111、0.313、0.338 and 0.307 in typhoon condition which were 1.691, 1.123, 1.419 and 1.823 times compared with the turbulence intensities in normal wind.

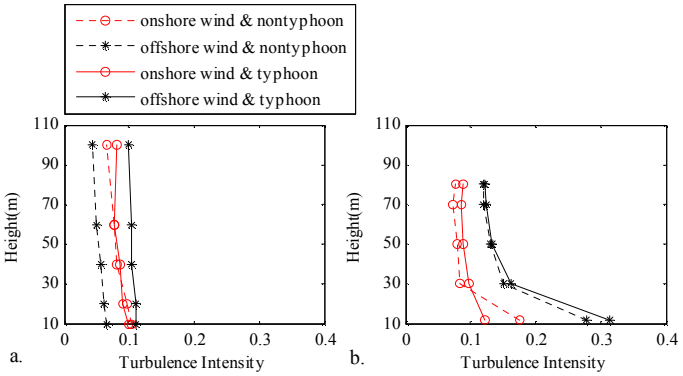

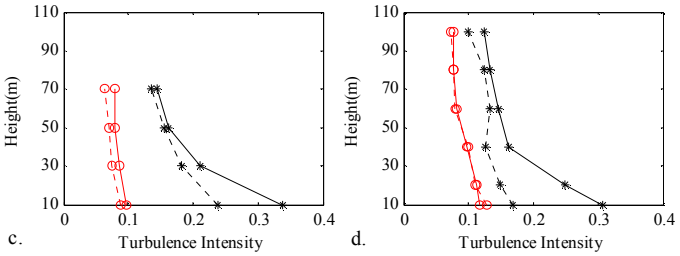

Figure 5. Turbulence intensity profiles over different underlying surface.
(a: Zhizai Island tower; b: Qinba tower; c: Wuyang tower; d: Xiuying tower)

4.6 *The amplification effect of different underlying surfaces on turbulence intensity*

Ratio between the turbulence intensity of typhoon wind and normal wind were calculated and the results showed the amplification factor were mostly larger than 1 except for some onshore wind samples and this suggested that the typhoon turbulence intensities were basically larger than that of normal wind.

Figure 6 showed the relationship between the amplification factor and the roughness length. The amplification factors increased with the roughness length of the underlying surface. The amplification factor can reach 1.832 when the roughness length increased to about 10cm. Linear fitting was applied according to equation 6 in order to quantitatively analyzing the amplification effect of the underlying surface on typhoon turbulence intensity.

$$A_{ti}=C\cdot z_0+D \tag{6}$$

where z_0 = roughness length, A_{ti} = amplification factor of turbulence intensity, C and D were fitting parameters. The result showed $A_{ti}=0.029z_0+1.112$.

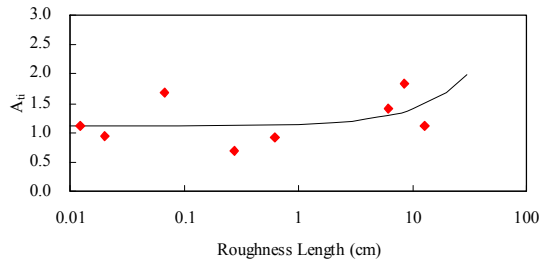

Figure 6. Variation of amplification factors of turbulence intensity and the roughness length.

These equations can applied to estimate the wind parameters at strong typhoon eye wall in the area influenced by typhoon frequently which means only the precise roughness length and the normal wind parameters were needed but not the wind data at typhoon eye wall. In fact, the opportunity to measure the strong typhoon passed over a given gradient tower face to face is rare.

5 SUMMARY AND DISCUSSION

Based on the normal wind data and the wind data of typhoon Hagupit and Nesat observed by the meteorological towers located at South China Sea and the coast, the power-law exponent and turbulence intensity over different exposure were analyzed. The results were found as follows.

(1) The wind profile in the near surface decayed more significantly than that in normal wind condition, especially for the wind came form rough underlying surface. When the roughness lengths

were larger than 6cm, the power-law exponent of typhoon wind profiles were 1.5-2 times compared with the power exponent of class D, C exposures (0.3, 0.22) recommended by the code.
(2) The amplification factor of best fitting and envelope fitting were 1.3-2.4 and 1.4-2.9 and the amplification factor of turbulence intensity can reach 1.832 when the roughness length increased to nearly 10cm. It can be seen that the rough underlying surface have significant amplification effect on the wind parameters of strong typhoon wind.
(3)The amplification factors of power-law exponent and turbulence intensity had positive relationship with roughness length. And these relationships can be precise described by linear equations. In the design of wind resistance engineering, the wind parameters at strong typhoon eye wall in the area influenced by typhoon frequently can be estimated based on the roughness length of the underlying surface and the wind parameters observed in normal wind condition.

The measured facts and change regulations achieved based on the data analysis of typical wind typhoon Hagupit and Nesat three observation towers were representative to some extent. But due to the complex structure of typhoon, the special area, size of typhoon eye, the thickness of typhoon eye wall and so on varied significantly in different typhoon case and the wind parameters were also influenced by the terrain, horizontal pressure difference, the distance between typhoon center and measuring site and so on. more observation cases are needed to examine the relationship between other influence factors and the wind parameter and find out more universal and regulations and conclusion.

6 ACKNOWLEDGEMENTS

The work described in this paper is fully supported by Major Program of National Natural Science Foundation of China (90715031), General Program of National Natural Science Foundation of China (40775071) and National Ministry of Science and Technology Public Benefit Specific Research Foundation (GYHY200806012)

7 REFERENCES

1 Ministry of Construction People's Republic of China, Load code for the design of building structures, China Architecture & Building Press, (2002) 49-49.
2 Y. Tamuraa, Y. Iwatani, K. Hibi, K. Suda, O. Nakamura, T. Maruyama and R. Ishibashi, Profiles of mean wind speeds and vertical turbulence intensities measured at seashore and two inland sites using Doppler sodars, J. Ind. Aerodyn., 95 (2007) 411-427.
3 J.Shanmugasundaram, P. Harikrishna, S. Gomathinayagam, N. Lakshmanan, Wind, terrain and structural damping characteristics under tropical cyclone conditions. Engineering Structures, 21 (1999) 1006-1014.
4 Song L.L., Wu Z.P., Qin P., Huang H.H, Liu A.J., Zhi S.Q., An analysis of the characteristics of strong winds in the surface layer over a complex terrain. Acta Meteorologica Sinica, 67(3) (2009) 452-460.
5 Chen W.C., Song L.L., Zhi S.Q., et al, Analysis on gust factor of tropical cyclone strong wind over different underlying surfaces, Science China Technological Sciences, 54(10) (2011) 2576-2586.
6 Song L.L, Pang J.B., Jiang C.L., Huang H.H. and Qin P., Field measurement and analysis of turbulence coherence for Typhoon Nuri at Macao Friendship Bridge. Science China Technological Sciences, 53(10) (2010) 2647-2657.
7 Song L.L., Li Q.S., Chen W.C, et al., 2012. Wind characteristics of a strong typhoon in marine surface boundary layer. Wind and Structures, 15(1), pp 1-16.
8 Chen R.S., Typhoon. Fujian Science & Technology Press, (2002) 414-417.
9 B.A.Harper, J.D.Kepert, J.D.Ginger. Guidelines for converting between various wind averaging periods in tropical cyclone conditions. sixth tropical cyclone RSMCs/TCWCs technical coordination meeting technical document, Brisbane, (2009) 4-4.
10 Simiu, E., Scanlan, R.H, 1996. Wind effects on structures: An introduction to wind engineering, version 2. Shanghai. Tongji University Press, (1992) 27-29.

The Seventh International Colloquium on Bluff Body Aerodynamics and Applications (BBAA7)
Shanghai, China; September 2-6, 2012

Wind profiles from a Sodar system under hilly terrain

Y.C. HE [a], P.W. CHAN [b], Q.S. LI [a]

[a]*Dept. of Civil and Architectural Engineering, City University of Hong Kong, Hong Kong*
[b]*Hong Kong Observatory, Hong Kong*

ABSTRACT: This paper focuses on an investigation of hilly effects on vertical distributions of both mean wind speed and turbulence components within the surface layer. Profiles of wind speed and turbulence intensity under conditions with both upwind hills and downwind hills are presented and discussed. Phenomena of forced convection due to hill obstructions are observed and discussed through comparison with the log law models which correspond to the case with open flat terrain. Relationships between the vertical wind speed and longitudinal wind speed are highlighted. A stability parameter is introduced to help depict wind speed profiles using the log-linear model. Specific estimating operators for a number of key parameters involved in the log-linear model are proposed.

KEYWORDS: hill, wind profile, forced convection, wind speed, turbulence intensity, Sodar.

1 INTRODUCTION

Hilly terrain may bring in different wind characteristics from those under open flat terrain conditions. For example, speed-up effect near mountain crest has been recognized long time ago, and has been stipulated in wind load code of several countries and regions [1-4]. It has been reported that geometry and coverage (or roughness) of hills, as well as spatial distances away from hill crests have significant effects on the distributions of both mean wind speed and fluctuation components [5,6]. According to reference [7], studies on wind characteristics under hilly conditions began from the 1930s with simply phenomenological observations. Theoretical analysis of non-viscous flows over hills came out in the 1950s, and developed into a more matured research topic since the 1970s [8]. As the fast development of CFD techniques and wind tunnel tests in recent years, more specific studies on air motions under complicated hilly terrains have been conducted by numerical and wind tunnel investigations[9-11]. More detailed reviews on this topic are summarized by References [7, 12].

Hong Kong is sited on the southeast coastal line of mainland China, and is featured by complicated hilly/mountainous terrains. It is one of the most typhoon-prone areas in the world. The potential danger for aircrafts and dense distributions of high-rise buildings against strong winds makes it of great importance to clarify the hilly effects on near surface boundary layer wind characteristics. Up to now, Hong Kong Observatory (HKO) has established about 50 surface weather stations which are equipped with traditional meteorological instruments and 6 stations with remote sensing devices to serve for weather forecast for both daily life and civil aviation of Hong Kong International Airport (HKIA). Most of these stations are located among hills or mountains terrains and have been put into use for decades or years. This paper focuses on an investigation of wind profiles based on the wind data recorded from a Sodar profiler system during windstorms at a weather station around HKIA.

2 WEATHER STATION AND DATA QUALTITY CONTROL

2.1 *Local terrain of the weather station*

Sui Ho Wan (SHW) meteorological station is located at the foot of hills on the northeast coast of Lantau Island, and is in front of the runway of HKIA. Except for the north-west azimuth range where there is a stretch of open water, this station is basically surrounded by hills or mountains whose body heights extend from ~100m (east) to several hundred meters, as shown in Figure 1.

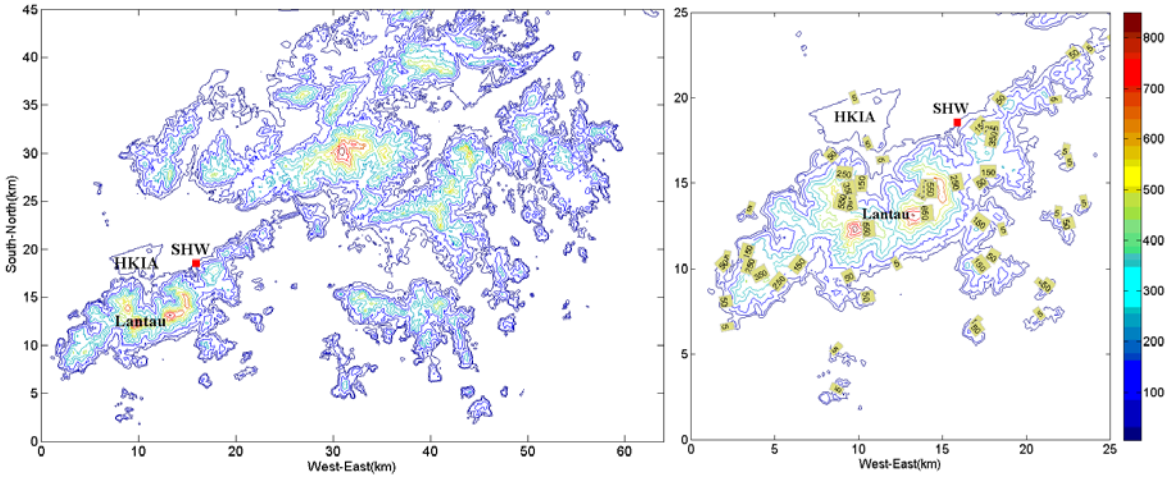

Figure 1. Location of the SHW meteorological station and surrounding terrain conditions.

2.2 *Data quality control*

SHW has been equipped with a Sodar profiler system by HKO for years. The profiler system can provide 5min-to-5min updated non-overlapping average wind profile records. The detecting range extends from 5m to 100m above the local ground (4.7m above the mean sea level) with a height resolution of 5m. But due to nearby obstructions, records below 25m (i.e., levels at 5, 10, 15, and 20m) are found to be contaminated severely by surrounding clutter interferences, and are discarded in this study. Consequently, there are totally 16 height levels where the recorded data are considered herein. For each of these levels, the recorded wind information includes the mean horizontal wind speeds and directions in a pair of orthogonal directions, a couple of standard deviation values of the corresponding horizontal wind speeds within the average duration, the vertical wind speed and corresponding standard deviation value, as well as the index numbers of signal-to-noise-ratio (SNR) in these 3 directions for data quality control. In this study, records with SNR index number no smaller than 8 are regarded as credible, and a profile with at least 13 credible records (totally 16) is regarded as acceptable. All the following analysis is based on the acceptable profiles during strong windstorms including tropical cyclones and severe monsoons from 2008 to 2010 (http://www.weather.gov.hk/cis/warndb_e.htm).

It is noteworthy that the Sodar profiler system may lose efficiency in case of heavy rains. Data collected under these conditions may be unaccepted through the quality control process. However, since strong winds are usually accompanied with heavy rains, a considerable amount of dataset recorded during high wind speeds is probably excluded. Another point to be noted is that the Sodar system can only detect components of wind velocity vector along the vertical direction (w), and a couple of horizontal directions (x, y) which are orthogonally distributed with each other and have been fixed during the installation of the Sodar system. The longitudinal mean wind speed U and the effective standard deviation σ_U, as well as the effective turbulence intensity (the effective value is adopted to distinguish it from the traditional form) are calculated:

$$U=\sqrt{U_x^2+U_y^2};\ \sigma_U=\sqrt{\sigma_x^2+\sigma_y^2};TI_i=\sigma_i/U,i=U,W. \quad (1)$$

3 RESULTS OF THE MEASUREMENTS

3.1 *Reference wind speed and direction*

Under thermally neutral stratification conditions, wind characteristics are generally dominated by wind strength and upwind terrain setups. Thus, it is necessary to categorize the records into different groups according to the reference wind speed and direction. We use the mean boundary layer (MBL) values which are defined as the arithmetic average wind speed V and the vector average direction θ of all height level records within 25-100m. Wind direction is defined as positive along clockwise from north, which is in consistence with the meteorological convention.

In consideration of both the local upwind terrains and the amount of selected datasets, the upwind azimuth of the weather station is uniformly divided into 6 sections sequentially from the north (or 0°) along clockwise, which are denoted as θi (i=1, 2, 3, 4, 5, 6). This study only considers θ2 (60-120°) and θ6 (300-360°) sections which correspond to the upwind hilly terrain and downwind hilly terrain, respectively. The reference wind speeds are divided into groups starting from 0 with an incremental step of 3m/s, which are denoted as Vi (i=1, 2, 3…).

3.2 *Results with upwind hills*

Wind flows from the θ2 azimuth section blow through the hilly obstruction before arriving to the SHW station. Figure 2 shows the profiles of the normalized longitudinal wind speed (U_{Norm}), the effective turbulence intensity (TI) and the vertical wind speed (W). It is found that both the longitudinal and vertical mean wind speed profiles demonstrate evidently different features from those under open flat terrain conditions. The ensemble mean longitudinal speed deviates gradually from the log-law predictions with height. The ensemble mean vertical wind speed increases in absolute value with height consistently, while the negative values of the vertical wind speed denote downward direction. On the other hand, the profiles of the horizontal TI show an exponentially decreasing trend with height.

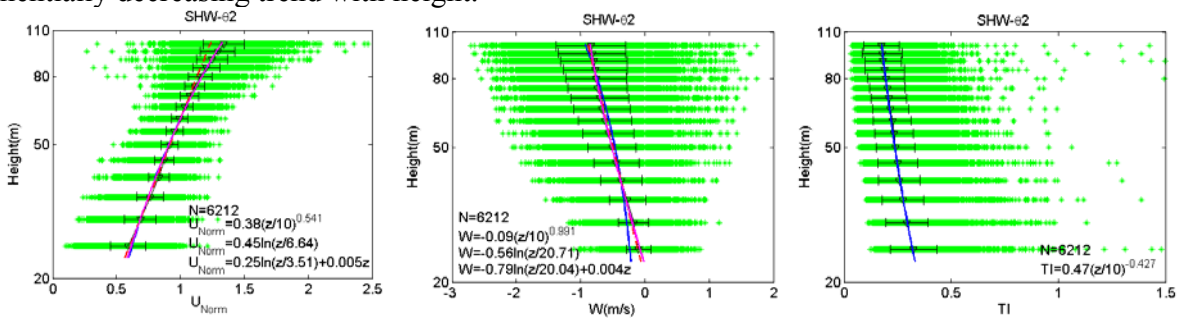

Figure 2. Profiles of normalized longitudinal speed (left), vertical speed (middle) and effective horizontal turbulence intensity (right), fitted by the power law (green line), log law (red dash line), and log-linear law (magenta line), with upwind hills (datasets with V>5m/s).

The log-law is generally used to model the vertical distributions of mean wind speed in the surface layer. Here and throughout this paper, a form of the log-law with no zero-displacement term is adopted due to the reasons: (1) by comparison, an introduction of a zero-displacement parameter is not very helpful to improve final fitting results; (2) according to ESDU-82026[13], zero-displacement for rugged hilly terrain (roughness length scale is 3-5m) is about $d=12z_0$, or 36-60m. This value is too large compared to the detecting range of 25-100m in this study.

Figure 3 shows the results in consideration of the wind strength effect. Profiles of the longitudinal mean wind speed follow both the power law and log-law quite well below certain heights. Beyond these heights, wind speed begins to speed up and sways to the right side of the log-law predictions. But, the power-law is still able to provide acceptable estimations. It is observed that the height where the log-law begins to depart from the ensemble measurement profiles decreases with wind strength. This is quite similar to the case of vertical speed profiles. The profiles of σ_U and σ_W have the same tendency with each other. The values basically increase with the reference speed. But, as wind speed strengthens, the profiles ascend monotonously along height first, then level off, and finally decrease vertically. The effective TI basically decreases with the increase of both the reference wind speed and height. But, in case of weak winds, thermal effect may dominate air motion, and TI shows much more fluctuations with distinctly large values.

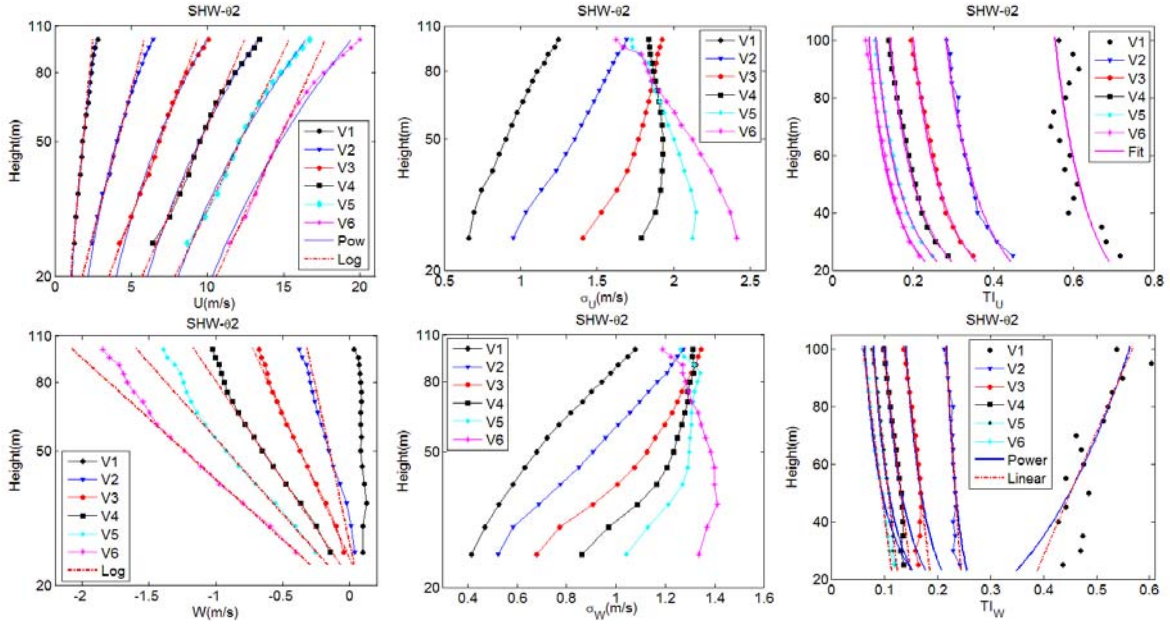

Figure 3. Profiles of ensemble mean wind speed (left) fitted by the log law and/or the power law, effective standard deviation of wind speed (middle), and effective turbulence intensity (right) fitted by the power law and/or the linear law in the θ6 azimuth section with upwind hills (Except for the case of TI_W fitted by 5^{th}-16^{th} height levels, all other fitting lines are based on the lowest 8 levels within the range of 25-60m); the y-axis with range of 20-110m is in a log format, while the one with a range of 20-100 is in the linear format, hereafters.

It is evident that there are correlations between the longitudinal wind speed and vertical wind speed components. Air flows overcoming the upwind hill obstructions go downwards as they move ahead. This forced downward convection process accompanies with energy transmission from the upper upwind flows to the beneath atmosphere. The larger the downward speed is, the stronger the longitudinal wind speed becomes. But more energy is expected to join air flows at the upper part of the beneath atmosphere during this superincumbent process, which leads to the deviation of the observed profiles from the log-law predictions. Similarly, more turbulent downward flows also correspond to more fluctuating longitudinal wind speeds.

Hence, the longitudinal mean wind speed values are dependent upon both local terrain setups and upwind flows. Analogue to the Monin-Obukhov (M-O) similarity theory[14], this study assumes that turbulence characteristic quantities within the forced convection surface layer can be described by using a stability parameter ξ. $\xi=0$,$\xi>0$, and $\xi<0$ correspond to conditions of the unforced convection, downward forced convection and upward forced convection, respectively.

Using the log-linear model, wind speed profile under thermally neutral conditions with the forced convection can be expressed as:

$$U(z) = (u_{*0} / k)\ln(z / z_0) + \xi z. \quad (2)$$

where k≈0.4 is the von Karman constant, u_{*0} is the surface friction velocity, z_0 is the roughness length scale and z is the height.

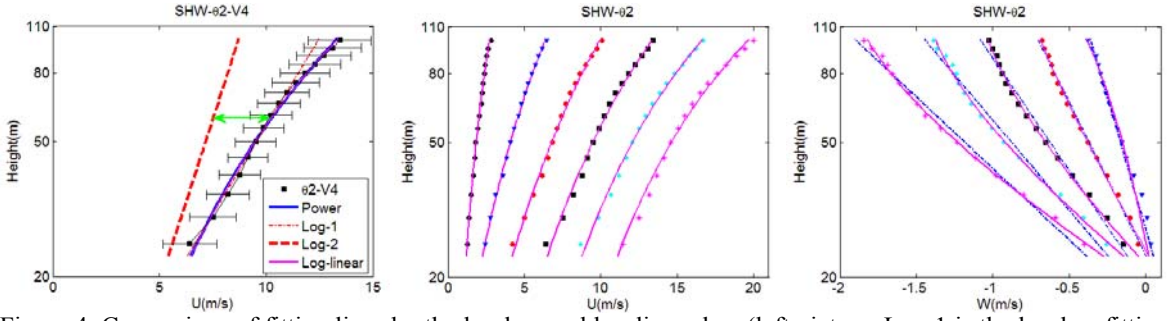

Figure 4. Comparison of fitting lines by the log law and log-linear law (left picture: Log-1 is the log-law fitting line using the lowest 10 levels data. Log-linear is the log-linear law fitting line. Log-2 is drawn from the log-linear line by setting ξ=0. Green line with arrows is the difference between the measurements and Log-2 line), profiles of longitudinal speed (middle) fitted by the log-linear model (in magenta), and profiles of vertical speed (right) fitted by both the log law (in blue) and log-linear model (in magenta) for the θ2 section.

The left picture in Figure 4 presents a comparison between the log-law model (Log-1) and the log-linear model (Log-linear) for the case of θ2 & V4. Another log-power line, denoted as Log-2, is also plotted, which is deduced from Equation 2 by setting ξ=0. As discussed above, Log-2 is governed by the local terrain roughness. It forms the asymptotic line that the mean wind profile should approach to downward the height. The deviation between the profile and the asymptotic line, indicated by the green arrowed line, stands for the wind component related to the downward flows. It is evident that a direct fitting of the longitudinal mean wind speed using the log-law (Log-1) would overestimate both the dynamic roughness length scale and the friction velocity.

Table 1. Fitting parameters for profiles of longitudinal wind speed for θ2 section with respect to different reference speeds (N: specimen number; R^2: fitting goodness).

				Power Law			Log Law		Log-linear Law			
Vi	*N*	U_{MBL}	σ_{MBL}	U_{10}	α	R^2	$2.5u_*$	z_0	$2.5u_*$	z_0	ξ	R^2
*V*2	2752	4.61	1.41	1.39	.665	.997	2.54	9.85	1.48	7.35	.025	.998
*V*3	2573	7.50	1.78	2.72	.564	.993	3.61	7.50	2.16	4.66	.033	.994
*V*4	1944	10.4	1.88	4.32	.488	.993	4.17	5.07	2.23	2.02	.046	.994
*V*5	633	13.1	1.93	5.96	.442	.993	4.65	3.68	2.17	0.77	.060	.995
*V*6	90	15.9	2.01	7.84	.394	.984	4.45	1.86	2.02	0.22	.072	.991

The other two pictures in Figure 4 show the ensemble mean profiles fitted by the log-linear model for both longitudinal (the middle picture) and vertical (the right picture) wind speeds. Table 1 and Table 2 list the key parameters involved in the fitting models. It can be seen that both the power law and log-linear law are able to provide favorite estimations for the longitudinal mean wind speed. But, the performance of the log-linear model is a little better. The power exponent decreases with the reference wind speed; while the stability parameter increases with it. For the vertical speed profiles, since both the log law and log-linear law agree with the measurements (nearly all R^2>0.995) well, the log-law with the simpler form is adopted. The results

for the V1 group are excluded herein, as which show remarkable deviations from those for other groups. This may be attributed to thermal effects under weak wind conditions.

Table 2. Fitting parameters for profiles of vertical speed for θ2 section with respect to different mean boundary layer speeds.

				Log Law			Log-linear Law			
Vi	N	W_{MBL}	σ_{MBL}	$2.5u_*'$	z_0'	R^2	$2.5u_*'$	z_0'	ξ	R^2
$V2$	2752	-0.198	0.981	-0.237	26.50	0.9154	-0.119	48.44	-0.0029	0.9769
$V3$	2573	-0.436	1.141	-0.502	23.85	0.9960	-0.585	22.28	0.0019	0.9966
$V4$	1944	-0.718	1.215	-0.743	20.98	0.9983	-1.008	19.00	0.0065	0.9976
$V5$	633	-0.992	1.268	-0.968	19.41	0.9964	-1.323	17.62	0.0093	0.9973
$V6$	90	-1.328	1.322	-1.206	18.03	0.9954	-1.594	16.74	0.0103	0.9984

3.3 *Results with downwind hills*

Results for the section θ6 with downwind hills are shown in Figure 5. Compared to the case of section θ2 with upwind hill obstructions, the longitudinal speed profiles for this section deviate from the log-law predictions to the left-hand-side. The vertical ensemble mean wind speed is positive and increases logarithmically along height. The effective turbulence intensity does not decrease monotonously with altitude. But, its variation follows three consecutive parts: the decreasing part, the leveling off part, and the increasing part. This is attributed to the less increase of U and a relatively faster increase of σ_U along height, which will be shown in Figure 6.

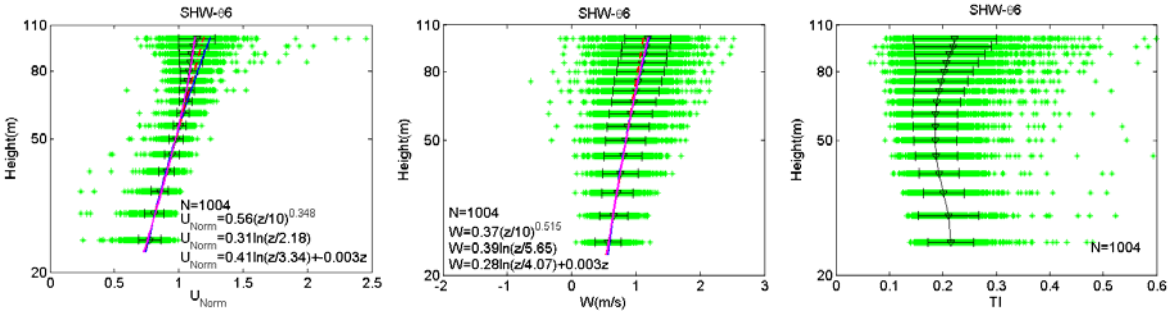

Figure 5. Profiles of normalized longitudinal speed (left), vertical speed (middle) and horizontal effective turbulence intensity (right), fitted by the power law (green line), log law (red dash line), and log-linear law (magenta line), for the θ6 azimuth section with downwind hills (datasets with V>5m/s).

Figure 6 shows the profiles of mean and standard deviation of wind speed as well as the effective turbulence intensity, with respect to different reference speeds. As the reference speed increases, the longitudinal speed deviates from the log-law predictions more evidently and the height where the log-law begins to fail to predict the measurements decreases consistently. Standard deviations, σ_U and σ_W, of wind speed increase with both the reference speed and height. σ_W is distributed in a linear form along height, compared to a more complicated nonlinear form of σ_U.

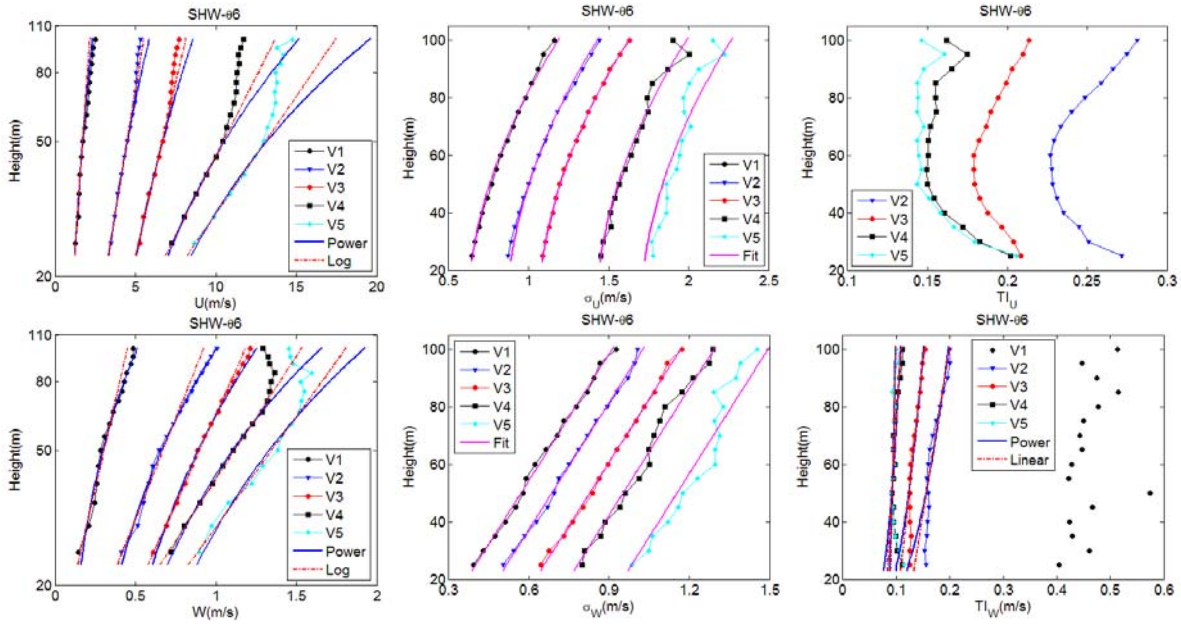

Figure 6. Profiles of mean (left) and standard deviation (middle) of wind speed, and effective turbulence intensity (right) in both longitudinal and vertical directions, for θ6 azimuth section with down-hills (fitting lines for U profiles are based on the lowest 6 levels data, W profiles are based on the lowest 10 levels data, TI_w profiles are determined by the top 12 levels data, others are based on the total 16 levels data).

Following the analysis method for the θ2 section, the log-linear law is adopted to model both the longitudinal and vertical wind speed profiles. Selected results are shown in Figure 7 and Tables 3-4. All of the fitting results agree well with the measurements, with the minimum R^2 of 0.968 for the vertical speed profile for the case of V5 where there are only 10 specimens. Opposite to the results of the θ2 section, direct usage of the log-law herein would underestimate both the roughness scales and the surface friction velocities. Meanwhile, the calculated z_0 increases with the reference speed, compared to the decreasing trend for the θ2 section. This may lie in that stronger wind, while disturbed by the downwind hills, will generate more turbulent air flows. This may also account for the continuous increase of σ_u and σ_w along altitude with respect to different reference wind speeds, compared to the situations of increasing first, then leveling off and finally decreasing along height with respect to different reference speeds for the θ2 section.

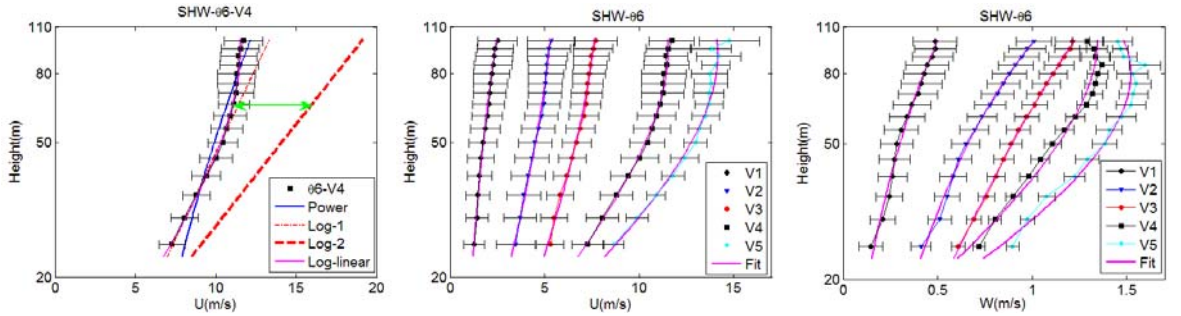

Figure 7. Comparison of fitting lines by the log law and log-linear law (left picture: Log-1 is the log-law fitting line using the lowest 10 levels data. Log-linear is the log-linear law fitting line. Log-2 is drawn from the log-linear line by setting ξ=0. Green line with arrows is the difference between the measurements and Log-2 line). Profiles of longitudinal speed (middle) fitted by the log-linear model (in magenta), and profiles of vertical speed (right) fitted by the log-linear model (in magenta) for the θ6 section.

Table 3. Parameters of the log-linear models for profiles of longitudinal speed in θ6 section with downwind hills.

				Power Law		Log Law		Log-linear Law			
Vi	N	U_{MBL}	σ_{MBL}	U_{10}	α	$2.5u_*$	z_0	$2.5u_*$	z_0	ξ	R^2
$V1$	396	1.934	0.867	0.800	0.495	0.811	5.474	0.415	1.941	0.0084	0.994
$V2$	1164	4.652	1.112	2.474	0.369	1.570	2.829	2.110	4.252	-0.014	0.993
$V3$	491	6.815	1.308	3.918	0.325	2.053	1.973	2.900	3.515	-0.021	0.992
$V4$	46	10.41	1.670	5.238	0.409	3.977	3.854	7.218	7.091	-0.076	0.996
$V5$	10	12.81	1.949	6.405	0.414	5.008	4.062	9.460	7.536	-0.103	0.982

Table 4. Parameters for profiles of vertical speed using the power, log and log-linear laws in θ6 section

				Power Law		Log Law		Log-linear Law			
Vi	N	W_{MBL}	σ_{MBL}	W_{10}	α	$2.5u'_*$	z'_0	$2.5u'_*$	z'_0	ξ	R^2
$V1$	396	1.934	0.655	0.084	0.785	0.211	11.84	0.104	9.485	0.0026	0.988
$V2$	1164	4.652	0.771	0.251	0.601	0.364	7.935	0.160	3.330	0.0048	0.996
$V3$	491	6.815	0.912	0.401	0.494	0.412	5.646	0.327	4.401	0.0020	0.999
$V4$	46	10.41	1.037	0.430	0.584	0.596	7.690	1.040	10.24	-0.010	0.978
$V5$	10	12.81	1.239	0.567	0.530	0.664	6.601	1.114	10.33	-0.018	0.968

3.4 *Empirical models of key parameters*

From the above analysis, all the parameters involved in the fitting models are of wind speed dependence. This part will model these key parameters as a function of the reference wind speed, based on the fitting results as listed in Tables 1-4. The following criteria are adopted herein: (1) predictions should make sense under limiting conditions (e.g., $z_0>0$ for $U\rightarrow\infty$, 0); (2) predictions are able to reflect the varying trend of modeled parameters; (3) models should be robust.

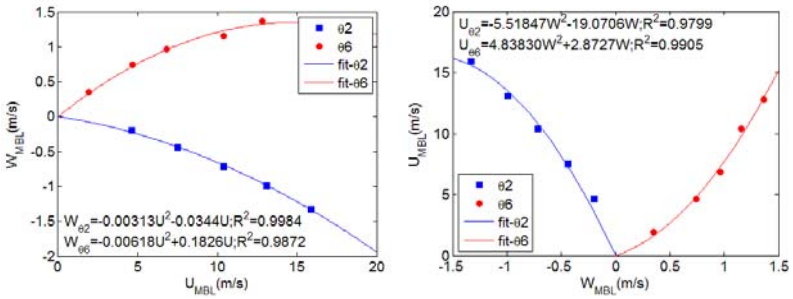

Figure 8. Correlations between the ensemble-mean boundary layer (MBL) values of longitudinal speed and vertical speed in both θ2 andθ6 sections using quadratic models.

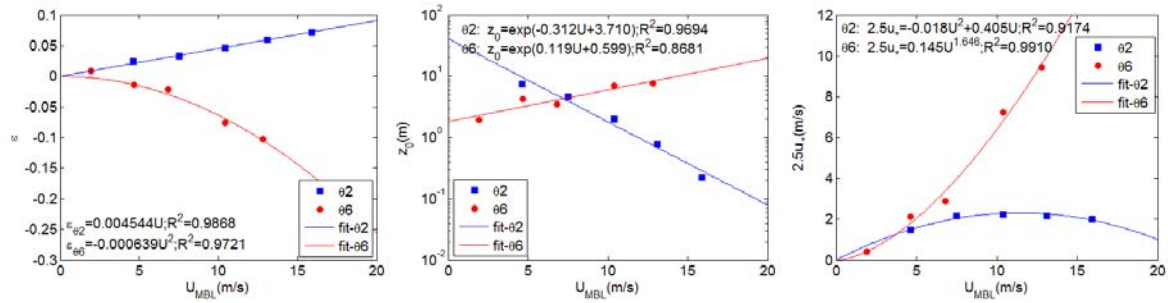

Figure 9. Correlations between the mean boundary layer (MBL) value of longitudinal speed and the stability parameter (ξ), effective dynamic roughness length scale (z_0), and the friction velocity (u_*).

Figure 8 shows the correlations between the mean boundary layer values (MBL) of the ensemble-mean longitudinal speed profile and the ensemble-mean vertical speed profile for both θ2

and θ6 sections, using quadratic models. In the left picture, U_{MBL} is the independent variable, while in the right picture, the independent variable is W_{MBL}. It can be seen that the modeled W_{MBL} for the θ6 section with respect to U_{MBL} in the left picture and the modeled U_{MBL} for the θ2 section with respect to W_{MBL} in the right picture are capped with peak values. But, there is no evidence for the existence of these upper limits. Therefore, the following two un-capped fitting equations are adopted, through which, U_{MBL} and W_{MBL} can be estimated from each other.

$$W_{MBL} = -3.13\times10^{-3}U_{MBL}^2 - 3.44\times10^{-2}U_{MBL}, \quad for\ \theta2; \tag{3}$$

$$U_{MBL} = 4.84W_{MBL}^2 + 2.87W_{MBL}, \quad for\ \theta6. \tag{4}$$

Figure 9 shows the results for the three parameters involved in the log-linear law (see Equation 2). The empirical fitting equations are given by:

$$\xi = 4.54\times10^{-3}U_{MBL}, \quad for\ \theta2; \tag{5}$$

$$\xi = -6.39\times10^{-4}U_{MBL}^2, \quad for\ \theta6. \tag{6}$$

$$z_0 = \exp(-0.312U_{MBL} + 3.71), \quad for\ \theta2; \tag{7}$$

$$z_0 = \exp(0.119U_{MBL} + 0.599), \quad for\ \theta6. \tag{8}$$

$$2.5u_* = -0.018U_{MBL}^2 + 0.405U_{MBL}, \quad for\ \theta2; \tag{9}$$

$$2.5u_* = 0.145U_{MBL}^{1.646}, \quad for\ \theta6. \tag{10}$$

Using Equations 2-10, the longitudinal mean wind profiles within the considered height range (25-100m) can be predicted, in case of giving the value of either U_{MBL} or W_{MBL}.

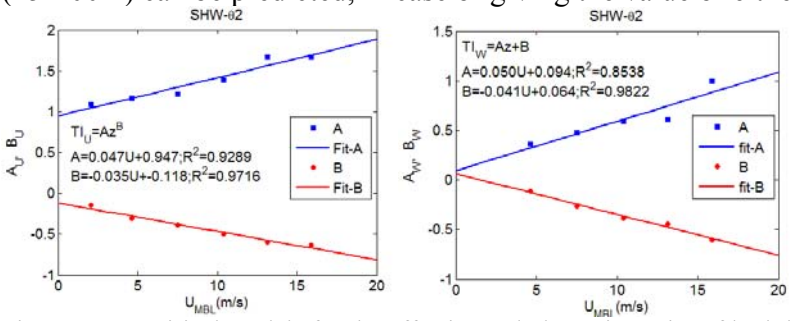

Figure 10. Empirical models for the effective turbulence intensity of both horizontal speed (left) and vertical speed (right) for the θ2 azimuth section.

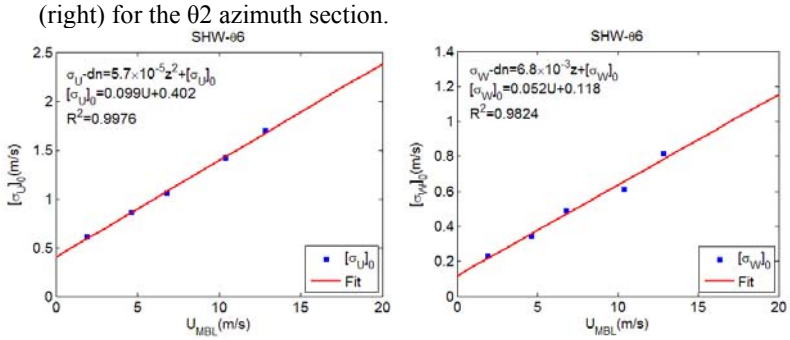

Figure 11. Empirical models for the effective standard deviation of both horizontal speed (left) and vertical speed (right) for the θ6 azimuth section.

The standard deviation of wind speed and the turbulence intensity (TI) can be inferred from each other through Equation 1. From Figure 3 and Figure 6, for the θ2 section, it is more feasible to model the effective TI first, and then formulate σ. But, for the θ6 section, the procedure is op-

posite, i.e., determining σ first and then computing the effective TI is more appropriate. The associated results are shown in Figure 10 (for θ2) and Figure 11 (for θ6):

$$TI_U = (0.047U_{MBL} + 0.947)z^{(-0.035U_{MBL} - 0.118)},\ for\ \theta 2; \tag{11}$$

$$TI_W = (1.97\times10^{-3}/U_{MBL} - 8.24\times10^{-4})z + 0.568U_{MBL}^{-0.533}\quad (U_{MBL} < 40),\ for\ \ \theta 2; \tag{12}$$

$$\sigma_U = 5.7\times10^{-5}z^2 + (0.099U_{MBL} + 0.402),\ \ for\ \theta 6; \tag{13}$$

$$\sigma_W = 6.8\times10^{-3}z + (0.052U_{MBL} + 0.118),\ \ for\ \theta 6. \tag{14}$$

Using Equation 1 and Equations 11-14, the effective standard deviation and the effective turbulence intensity of both horizontal speed and vertical speed can be determined.

From the previous analysis it can be seen that the effective standard deviation of horizontal wind speed and the vertical speed for both θ2 (Figure 3) and θ6 (Figure 6) sections are positively correlated with each other. Under open flat neutral conditions, the relationship between σ_W and σ_U can be depicted by the following equation as recommended in ESDU[15]:

$$\sigma_W / \sigma_U = 1 - 0.45\cos^4[\pi z/(2h)],\ h = u_*/(6f). \tag{15}$$

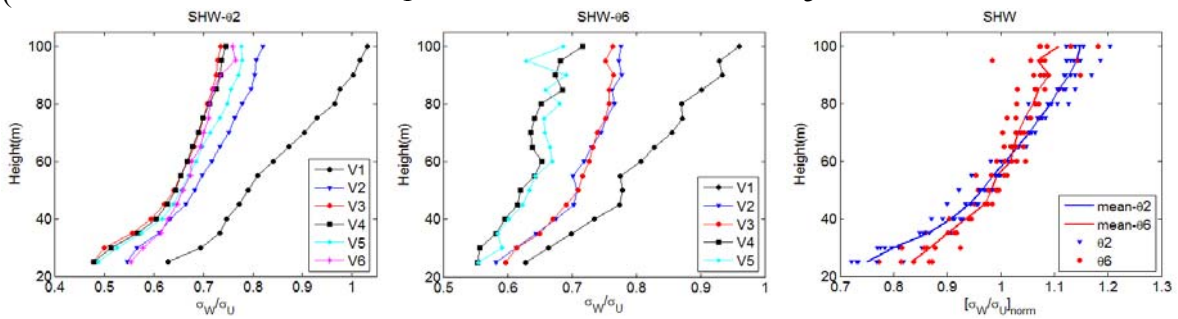

Figure 12. Correlations between the standard deviations of both vertical speed and horizontal speed with respect to different reference speeds in both θ2 (left) and θ6 sections (middle), and the correlations regardless of wind strength (right, the values are normalized by the MBL values).

In the above equation, h is the depth of the atmospheric boundary layer with the order of 1000m. But, the results under hilly terrains obtained in this study show significant differences. Figure 12 shows the variations of the ratio of σ_W/σ_U with respect to both height and reference wind speed. A best fit for the measurements using Equation 15 (other coefficients are still kept, and z and h are regarded as variables) finds the estimated h≈100m which is in the order of the characteristic height of upstream hills. Another point is that, according to ESDU[15], under neutral conditions all open flat terrains correspond to almost the same ratio of σ_W/σ_U irrespective of the nature of the terrain surfaces. But under hilly terrains, it is clear from the right picture in Figure 12 that the topographic effect can not be neglected. This is a feature of wind characteristics under hilly terrains as distinguished from those with open flat terrains.

4 CONCLUSIONS

This paper has analyzed the hill effects on near surface wind characteristics based on the field measurements from a Sodar profiler system. The longitudinal wind speed is found to be closely correlated to the forced convective flows. The θ2 azimuth section with upwind hills corresponds to downward flows (or negative vertical speed). The longitudinal mean wind speed in this section speeds up at higher altitudes and gradually departs from the log-law predictions. The θ6 section with downwind hills corresponds to upward flows. The longitudinal mean wind speed in this section also deviates from the log-law predictions and levels off along height at the upper alti-

tude range. The height where the log-law begins to fail to model the mean wind speed in both the sections decreases as the reference speed increases. The log-linear law is adopted to model the mean wind speed profiles. Results from the model agree well with the measurements. The effective standard deviations of wind speed in horizontal and vertical directions are also found to be closely correlated with each other in both sections. But the profiles in one section vary remarkably to those in the other section. The ratios of σ_w/σ_u in these two sections are different from those stipulated in the ESDU model for open flat terrains. A number of empirical estimators for both the mean wind speed profiles and the standard deviation of wind speed profiles are presented. The findings of this study can be used as reference for the determination of wind profiles under hilly terrain conditions.

5 ACKNOWLEDGEMENTS

The authors would like to express their gratitude to HKO for the provision of the wind data records and the permission of using the data for this study. The work described in this paper was supported by research grants from the Research Committee of City University of Hong Kong (Project No. 7002661 and 9667046).

6 REFERENCES

1 AS/NZS 1170.2:2002, Australian/New Zealand Standard Structural design actions Part 2: Wind actions.
2 Code of Practice on Wind Effects in Hong Kong, Buildings Department of Hong Kong, Hong Kong, 2004.
3 China Academy of Building Research, National standards of the People's Republic of China, Construction structure load standard (GB50009-2001, 2006), Beijing: Chinese Architecture Industry Press, 2006.
4 Architectural Institute of Japan, AIJ Recommendation for Loads on Building, Japan, 2004.
5 Lemelin, D.R., Surry, D., and Davenport, A.G., Simple approximations for wind speed-up over hills, *Journal of Wind Engineering and Industrial Aerodynamics* **28**: 117-127, 1988.
6 Cao, S., and Tamura, T., Experimental study on roughness effects on turbulent boundary layer flow over a two-dimensional steep hill. *Journal of Wind Engineering and Industrial Aerodynamics* **94**: 1–19, 2006.
7 Wood, N., Wind flow over complex terrain: a historical perspective and the prospect for large-eddy modeling, *Boundary-Layer Meteorology* **96**: 11-32, 2000.
8 Jackson, P.S., and Hunt, J.C.R., Turbulent wind flow over a low hill, *Quarterly Journal of the Royal Meteorological Society* **101**: 929-955, 1975.
9 Tamura, T., Cao, S., and Okuno, A., LES study of turbulent boundary layer over a smooth and a rough 2D hill model, *Flow, Turbulence and Combustion* **79**, 405–432, 2007.
10 Takahashi, T., Ohtsu, T., Yassin, M.F., and Kato, S., Turbulence characteristics of wind over a hill with a rough surface, *Journal of Wind Engineering and Industrial Aerodynamics* **90**: 1697-1706, 2002.
11 Keith, W.A., and Dale, E.H., Observations of boundary-layer wind-tunnel flow over isolated ridges of varying steepness and roughness, *Boundary-Layer Meteorology* **112**: 525-556, 2004.
12 Taylor, P.A., Mason, P.J., & Bradley, E.F., Boundary-layer flow over low hills, *Boundary-Layer Meteorology* **39**: 107-132, 1987.
13 ESDU Strong winds in the atmospheric boundary layer. Part 1: mean-hourly wind speeds. Item No. 82026, ESDU International, London, 1982.
14 Garratt, J.R., The atmospheric boundary layer, Cambridge atmospheric and space science series, Cambridge University Press, 49-59, 1992.
15 ESDU Characteristics of atmospheric turbulence near the ground. Part 2: single point data for strong winds (neutral atmosphere). Item No. 85020, ESDU International, London, 1985.

The Seventh International Colloquium on Bluff Body Aerodynamics and Applications (BBAA7)
Shanghai, China; September 2-6, 2012

A conditional analysis of roller vortices within the atmospheric log layer

G. A. Rosi, R. J. Martinuzzi, D. E. Rival

Department of Mechanical Engineering, University of Calgary, 2500 University Dr. NW, Calgary, Alberta, Canada

ABSTRACT: The scope of this work is a characterization of the fluctuations and near-ground roller vortices within the turbulent atmospheric boundary layer (ABL) at heights of approximately 5% of the ABL thickness. This height is comparable to a y+ value of approximately 100. To evaluate the roller vortices, a conditional-analysis technique is applied on a data set acquired on January 5th, 2012. This study begins with an evaluation of the ABL stability and thickness (δ). Subsequently statistical descriptors of the turbulent fluctuations are compared to those measured by Klebanoff [1] over a flat plate. The ABL data set is demonstrated to be neutral with a thickness of approximately 1000m. The statistical descriptors of the turbulent fluctuations of the data are found to qualitatively agree with values measured over a flat plate. From the conditional analysis, it is found that the centre heights of the roller vortices follow a Rayleigh distribution with a mean and standard deviation of 0.056δ and 0.027δ, respectively. However, the roller vortices concentrated around 0.05δ tend to have near-zero strength, while vortices above or below increase in strength. The concentration of near-zero strength vortices at 0.05δ is believed to be caused by the omission of the viscous core in the theoretical model.

KEYWORDS: Atmospheric turbulence, coherent structures, conditional analysis.

1 INTRODUCTION

Understanding turbulent fluctuations and coherent structures in the lower log layer of the atmosphere is valuable for several applications such as wind-turbine control, managing gusts during the takeoff and landing of aircraft, as well as wind loadings on large civil structures. Earlier research into atmospheric turbulence has generally focused on the time-averaged characteristics of the velocity fluctuations. For example, as demonstrated in Kaimal [2], the power spectra of the velocity fluctuations and their cross-correlations follow normalized curves that are functions of the Richardson number. Similar relations involving the fluctuation spectra have been determined and are well documented in various texts such as Lumley and Panofsky [3] and Kaimal and Finnigan [4].

The drawback of quantifying events in this manner is that no information regarding short-term coherent structures within the wind field is obtained. For this reason, methods such as Conditional Analysis and Proper Orthogonal Decomposition (POD) have recently been used to

investigate coherent structures directly. In meteorological studies, POD has provided significant results; see Wilson [5] and Lin et al. [6]. However, meteorological studies focus primarily on heights beyond 0.2δ. Furthermore, the coherent structures that are studied are on the order of δ, which are not of interest in the current study. In contrast, studies on canonical turbulent boundary layers (TBL) have investigated turbulent coherent structures on orders much smaller then the TBL thickness. For example, the properties of hairpin and horseshoe vortices are well documented [7] and have been measured experimentally by Schroeder et al. [8] and Adrian [9]. It has been shown that at 5% of the TBL thickness, i.e. the lower log layer, canonical TBLs are populated by both streak vortices and hairpin vortices; see Robinson [7] and Smith and Walker [10].

Given the breadth of research performed on canonical TBLs, demonstrating that ABLs share similarities with canonical TBLs would be extremely valuable for future wind-tunnel modelling. Scarabino et al. [11] attempted to demonstrate the similarities between ABLs and canonical TBLs by showing that both share similar coherent structures. Using data collected by Sterling et al. [12], velocity fluctuations of extreme gust events were classified into three groups and were then ensemble averaged. One of the ensemble groups exhibited vortex-like flow, which led Scarabino et al. [11] to fit a hairpin vortex model onto the ensemble average. In this regard the study had limited success: Although the hairpin-vortex model accounted for sharp changes in streamwise velocity, it failed to capture the simultaneous vertical fluctuations properly.

It is believed that the shortcomings of the hairpin-vortex model in Scarabino et al. [11] were due to an oversimplification since it was assumed that a gust event could be represented by a simple hairpin vortex. In reality, there are a wide range of structures within TBLs, thus resulting in much more complicated flow fields. It is argued that these coherent structures must be studied first in terms of their strength and orientation prior to investigating how they contribute to gust events. Thus, the current study takes a different approach than that in Scarabino et al. [11]. Rather than identifying gust events within the data and attempting to fit a certain coherent structure to each, events that meet specific criteria suggestive of a hairpin vortex are identified instead. Velocity fields are then determined for each specific event and compared to experimental data. In this way the height and strength of hairpin vortices within the lower log region of the ABL can be determined, statistically analysed and compared to those within canonical TBLs.

Since the structure of hairpin vortices is complex, it is assumed that such vortices can be simplified as two-dimensional rollers instead. This assumption is based on the following observations: (1) It is noted in Robinson [7] that the lifespan of transverse vortices is much longer than the lifespan of streamwise vortices; and (2) through experiments performed by Head and Bandyopadhyay [13] at $0 \leq Re_\theta \leq 10000$, it was found that the legs of hairpin vortices are around 100 wall units (y+) apart, which in the ABL translates to approximately 50m.

The current study compares properties of ABLs to those of canonical TBLs. First various statistical descriptors of turbulent fluctuations measured by a wind mast are compared to measurements taken over a flat plate. Subsequently a conditional analysis is used to identify hairpin-vortex events. The occurrence-frequency distributions of normalized circulation ($\Gamma/U_0\delta$) and normalized vortex-centre height (a/δ) are discussed, as well as the correlation between normalized circulation and normalized height. By assaying the reasonableness of the aforementioned results, the robustness of the model is then evaluated.

2 EXPERIMENTAL METHODS

For this investigation, a 2-hour long data set was acquired on January 5th, 2012 from a 50m wind mast erected on university land. The area is primarily rural. It is generally flat with a shallow depression of 5m depth upwind of the mast. A schematic of the wind mast, with the approximate positioning of its sensors, is provided in Figure 1a. A photograph depicting the mast and the surrounding terrain is shown in Figure 1b. The five cupped anemometers (CA) and wind vanes (WV), as well as the two-component ultrasonic anemometer, are all used to determine the mean wind speed and direction. Coherent structures are determined using the measurements taken by the two three-component ultrasonic anemometers (3CUS). The 3CUS sensors are located at 40m and 50m heights.

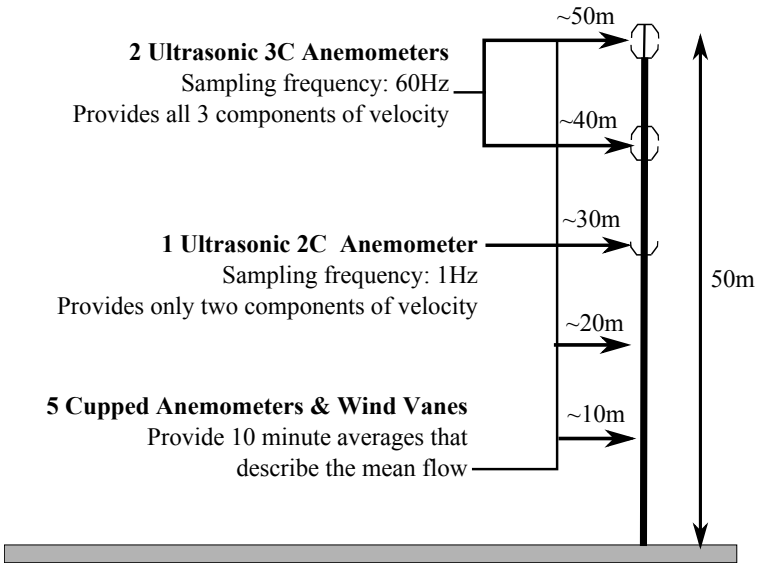

(a)

(b)

Figure 1: (a) A schematic of the wind mast with the approximate positioning of sensors indicated. (b) A photograph of the mast and surrounding terrain.

During the experiment the mean wind velocity profile varied considerably. The data was therefore split into 10-minute long sets during which the mean velocity remained fairly constant. The reference frames of the two 3CUSs were rotated so that the x-, y-, and z-axes were respectively oriented into the streamwise, vertical and lateral wind directions as determined by the WVs. This was performed independently for each 10-minute data set. Upon performing this rotation, the x-axis mean velocities measured by the 3CUS sensors were nearly equal to the velocity measured by the CA of corresponding height (mean discrepancy of $\pm$0.7m/s). The other two components measured essentially zero mean velocities (mean discrepancy of $\pm$0.5m/s). The mean values of all three components of the 3CUS sensors were subtracted from the respective component for each 10-minute data set. This modified data now represented the wind fluctuations in the longitudinal, vertical and lateral directions.

A condition suggestive of hairpin vortex impingement will now be presented. It is argued that a hairpin vortex be represented as an infinitely long potential vortex being convected towards the mast, as shown in Figure 2. The circulation of the vortex is Γ and the vortex centre sits at an arbitrary height $y = a$. Also the vortex is convected by the mean local velocity U_a

at the vortex-centre height. To account for ground effect, two counter-rotating vortices are positioned at heights $+a$ and $-a$. Figure 2 also shows the mast with the heights of the top and bottom ultrasonic sensors labelled as h_T and h_B, respectively. If Taylor's hypothesis is assumed to hold, then the vortex's shape should not change as it convects. This allows b to be set equal to $-U_a(t - t_R)$, where t_R is the instant the vortex centre has passed the mast.

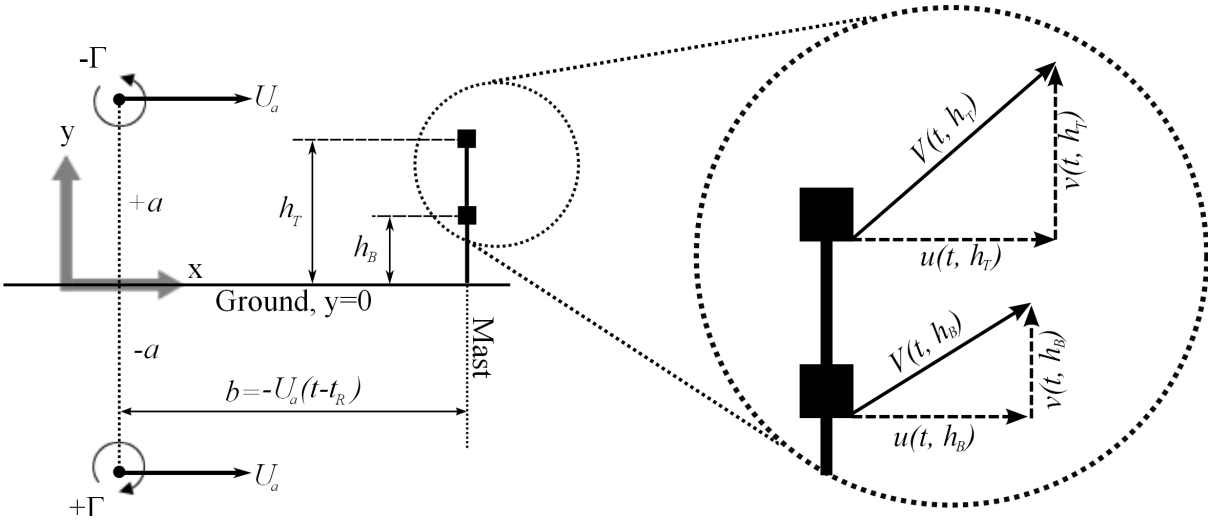

Figure 2: A potential line vortex of circulation Γ at an arbitrary height a being convected towards the mast at U_a (the mean wind velocity at height a). The vortex induces a fluctuation field V, comprised of a streamwise component u and vertical component v. Fluctuations from the mean velocity are measured by the two 3CUS sensors at heights h_T and h_B. A counter rotating vortex at $-a$ has been included to account for ground effect.

The fluctuation field generated by this vortex is given by u and v, which are the longitudinal and vertical fluctuations induced by the vortex, respectively. At the top and bottom 3CUS sensors, the vortex induces fluctuations of:

$$\vec{V}(t, h_T) = u(t, h_T)\hat{\imath} + v(t, h_T)\hat{\jmath} \tag{1}$$

$$\vec{V}(t, h_B) = u(t, h_B)\hat{\imath} + v(t, h_B)\hat{\jmath}. \tag{2}$$

If the current vortex is far from other vortices, then the fluctuation field is given by:

$$u(t, y) = +\frac{\Gamma(y-a)}{\pi((U_a(t-t_R))^2 + (y-a)^2)} - \frac{\Gamma(y+a)}{\pi((U_a(t-t_R))^2 + (y+a)^2)} \tag{3}$$

$$v(t, y) = +\frac{\Gamma U(t-t_R)}{\pi((U_a(t-t_R))^2 + (y-a)^2)} - \frac{\Gamma U(t-t_R)}{\pi((U_a(t-t_R))^2 + (y+a)^2)}. \tag{4}$$

The vortex-induced fluctuations at the sensors can be determined by replacing y with h_T and h_B in equations (3) and (4). If corresponding components are divided by one another, followed by setting t to t_R, equations (5) and (6) are determined:

$$\frac{u(0, h_T)}{u(0, h_B)} = \frac{a^2 - h_B^2}{a^2 - h_T^2} = F \tag{5}$$

$$\frac{v(0, h_T)}{v(0, h_B)} = \frac{h_T}{h_B}\left(\frac{a^2 - h_B^2}{a^2 - h_T^2}\right)^2 = \frac{h_T}{h_B}F^2, \tag{6}$$

where F is only dependent on the heights of the two 3CUS sensors and the vortex-centre height.

It is interesting to note that F is only negative when $h_B < a < h_T$. Also note that regardless of vortex-centre height, equation (6) is never negative, meaning that vertical fluctuations always occur in the same direction.

Equations (5) and (6) define a condition for identifying roller vortices. If a vortex centre passes the mast at time t_R, then the following must hold true at that instance as well:

$$\frac{v(t_R, h_T)}{v(t_R, h_B)} = \frac{h_T}{h_B}\left(\frac{u(t_R, h_T)}{u(t_R, h_B)}\right)^2. \tag{7}$$

By locating a time instance where (7) is satisfied, F is effectively known. From F, the values of a and Γ can be determined, thereby defining equations (3) and (4) completely. Finally equations (3) and (4) can be tested against the data time series in the immediate vicinity of t_R. If a roller in fact passes at t_R, then equations (8) and (9) must be true during the immediate time series:

$$\sigma_T = \overline{|u(t, h_T) - u(t, h_T)_D|} = 0 \quad \sigma_B = \overline{|u(t, h_B) - u(t, h_B)_D|} = 0 \tag{8}$$

$$\nu_T = \overline{|v(t, h_T) - v(t, h_T)_D|} = 0 \quad \nu_B = \overline{|v(t, h_B) - v(t, h_B)_D|} = 0, \tag{9}$$

where subscript D indicates fluctuations measured in the data set. Equations (8) and (9) will be evaluated over approximately $t_R \pm \frac{1}{2}T$, where T is the integral time scale of the fluctuations as determined from the data set. T is determined by integrating the autocorrelation functions of the turbulent fluctuations. It was determined that T for this data set is on the order of 1s. The details of how this was determined are not included in the current study. If equations (8) and (9) are nearly equal to 0, then the roller model predicts fluctuations of similar value to those in the data. Rollers must track fluctuation trends as well. For this reason, all roller events are manually checked to ensure that the immediate fluctuation trends are captured.

3 RESULTS & DISCUSSION

This section describes the ABL data set by evaluating important descriptors such as the stability, the thickness and the Reynolds number. Afterwards, the results of the conditional analysis are evaluated.

3.1 *Description of the ABL Data Set*

The stability of the ABL may be determined by analysing the mean velocity profile. In a neutral ABL, the mean velocity profile fits well onto the curve given by Kaimal and Finnigan [4]:

$$U(y) = \frac{u_*}{k}\ln\frac{y}{y_0}, \tag{10}$$

where y is the vertical distance from the ground, u_* is the friction velocity, k is the von Karman constant (approximately 0.4) and y_0 is the friction length. Both u_* and y_0 are determined from the curve fit. Figure 3a shows the mean velocity measurements taken by the cupped anemometers for the first 10-minute data set. The solid curve represents equation (10) fitted onto the mean velocity measurements. The friction velocities and roughness lengths for all 11 sets are provided in Figure 3b. The R^2 values are provided also, which are a measure of the quality of the fit. All the R^2 values for the 10-minute time sets exceed 0.97, indicating that equation (10) is a good descriptor of the mean velocity. Thus the ABL is presumably neutral. Also, the fact that the wind-velocity profiles are well described by a logarithmic fit indicates that the mast sits within the log region of the ABL.

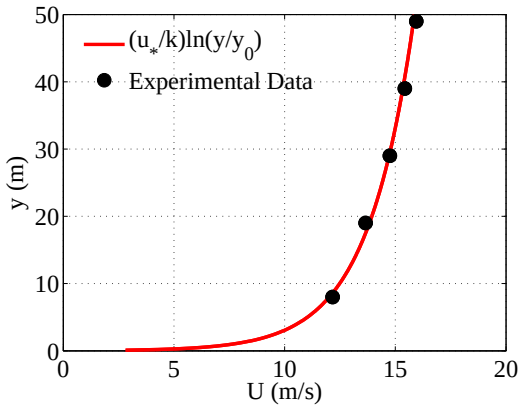

(a)

Time Set	y_0 (cm)	u_* (m/s)	R^2
1	2.62	0.84	0.992
2	3.99	0.87	0.979
3	3.49	0.89	0.986
4	5.51	0.96	0.988
5	2.93	0.96	0.989
6	3.72	0.88	0.987
7	4.21	0.89	0.971
8	5.99	0.86	0.982
9	5.06	0.83	0.995
10	10.24	0.84	0.947
11	10.28	0.77	0.989

(b)

Figure 3: (a) The mean velocity profile for the first 10-minute set (14:50 to 15:00). (b) Roughness lengths, friction velocities and R^2 values for each 10-minute set as approximated by fitting the data to (10).

There are various methods to approximate the ABL thickness. For example, Blackadar and Tennekes [14] provides an approximation for δ of neutral ABLs based on friction velocity and Coriolis effects. The current study determines δ by comparing the ABL data to data collected from canonical TBLs over a flat plate. Cheng [15] states that the velocity profiles of TBL flow over a flat plate is classically represented as:

$$\frac{U}{U_0} = \left(\frac{y}{\delta}\right)^{\frac{1}{m}} \text{ where } m \approx \ln \frac{y_0}{0.2\delta}. \tag{11}$$

This provides an iterative method for determining the value of δ: Its value is first assumed; then the profile provided by equation (11) is compared to the experimentally measured profile normalized by U_0. A value of 1000m for δ provides reasonable agreement between equation (11) and the experimental data, as shown in Figure 4. The error bars in Figure 4 represent a single standard deviation in the observed results.

Figure 4 also shows various statistical descriptors of the turbulent fluctuations as measured by the 3CUS sensors (observed flow), as well as those measured in a canonical TBL over a flat plate by Klebanoff [1]. The statistical descriptors of the fluctuations for the observed flow and TBL flow share the same order of magnitude. However, the statistical descriptors for the observed flow and TBL flow often differ by approximately one standard deviation. The discrepancy between the observed flow and TBL flow may be due to the difference in Reynolds number. The TBL-flow data was collected at a Reynolds number $Re_x = 4.2. \times 10^6$ while the Reynolds number for this ABL data is approximately $Re_x = 4.3. \times 10^{15}$.

3.2 *Results of the Conditional Analysis*

The conditional analysis was performed on all eleven 10-minute data sets. 774 events were identified in which the roller model accurately tracked the fluctuations within an acceptable degree of precision. It was often found, however, that precision had to be compromised for the sake of accuracy. Table 1 quantifies the precision error of the roller model by providing the mean values of σ_T, σ_B, ν_T and ν_B. On average, the 50m 3CUS sensor was less precise then its 40m counterpart. This is likely because the turbulent intensities at 50m are greater then those at 40m.

Figure 5 shows the occurrence-frequency distribution of vortex-centre height a and circu-

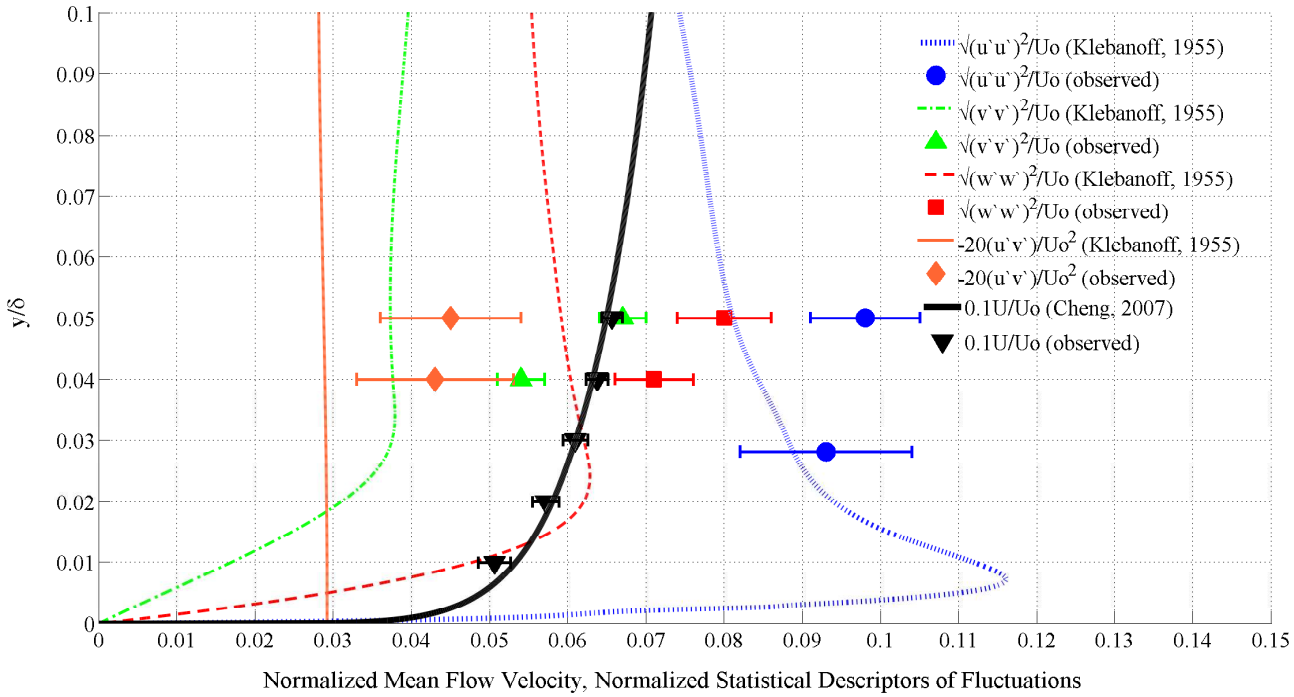

Figure 4: Theoretical and observed values for the velocity profile and its respective turbulent fluctuations.

σ_T (m/s)	σ_B (m/s)	ν_T (m/s)	ν_B (m/s)
0.772	0.561	1.093	0.610

Table 1: The mean precision error of the roller model in tracking the measured fluctuations. The precision error is evaluated for all eleven 10-minute sets. σ and ν refer to precision errors of the streamwise and vertical fluctuation components, respectively. Subscripts T and B refer to the top and bottom 3CUS sensors, respectively.

lation Γ normalized by δ and $U_0\delta$, respectively. The distribution of a resembles a Rayleigh probability distribution. The mean of a is 0.056δ, while the standard deviation of a is 0.027δ. In contrast, Γ appears normally distributed; its mean is $0.000U_0\delta$ while its standard deviation is $0.010U_0\delta$.

It is possible that the near-ground roller vortices have vortex-centre heights that follow the distribution shown in Figure 5a. Various studies performed on canonical TBLs have found similar distributions. From data of a numerical simulation of a canonical boundary layer ($Re_\theta = 670$) by Spalart [16], Robinson [17] found that spanwise vortices also follow a Rayleigh distribution with an average height of approximately 0.2δ. From experiments run at $Re_\theta = 1120$ Smith and Lu [18] also found that the vortex-centre heights follow a Rayleigh distribution with an average height of 0.06δ. Finally, from experiments Wu and Christensen [19] found that over a large Reynolds-number range ($4000 \leq Re_\theta \leq 11000$) the centre height of the spanwise vortices followed a Rayleigh distribution with a mean of approximately 0.06δ.

It seems unlikely that the circulation is normally distributed about 0. Wu and Christensen [19] found that the circulation of spanwise vortices followed a bimodal distribution about 0 ($Re_\theta = 8830$), while in Robinson [17] the circulation distribution was slightly skewed towards prograde vortices. Furthermore results from Wu and Christensen [19] demonstrate that pro-

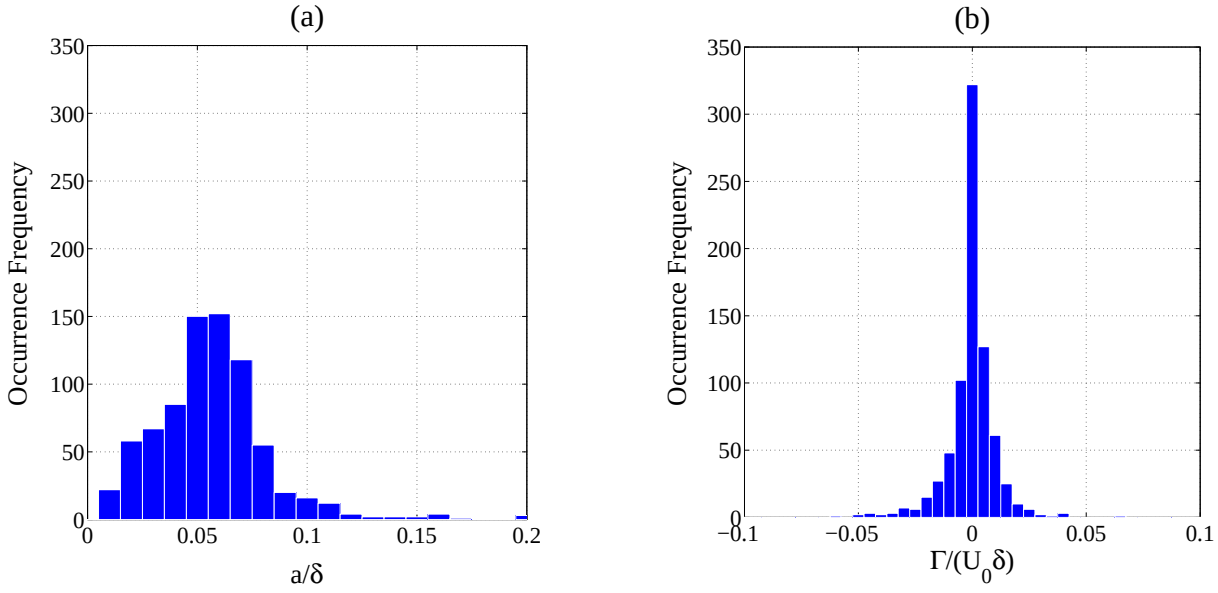

Figure 5: Occurrence-frequency distributions of (a) vortex-centre height a and; (b) circulation Γ for all eleven 10-minute data sets. Γ is normalized by $U_o\delta$, while a is normalized by δ. δ is assumed to equal 1000m, while U_0 is determined by evaluating equation (10) at 1000m.

grade vortices are more common near the shearing surface, while retrograde vortices are more common higher up in the boundary layer. Note that a prograde vortex causes a negative streamwise fluctuation below its centre while a retrograde vortex causes a positive fluctuation below its centre. Thus it would be expected for the circulation distribution in Figure 5b to be shifted to the right.

The zero mean in circulation is likely caused by shortcomings in the conditional model. One significant limitation in the model is the absence of a viscous core for the roller vortices. This may have caused the model to underestimate the circulation magnitude for the roller vortices concentrated at 0.05δ, the height at which the two 3CUS sensors are located. If a vortex-centre is at a similar height as the 3CUS sensors, then the sensors would possibly be within the viscous core. Being inside the viscous core would cause the conditional model to substantially underestimate the circulation. This is because the model does not account for the decrease in velocity inside the viscous core. Figure 6 shows normalized circulation plotted against normalized vortex-centre height, which in fact demonstrates that circulation tends to 0 as the vortex-centre height approaches 0.05δ. This supports the argument that neglecting the viscous core may have skewed the results. However, the circulation distribution determined by the current study may in fact be correct. Results from Wu and Christensen [19] demonstrate that as the Reynolds number is increased the ratio of prograde to retrograde vortices approaches unity.

4 CONCLUSIONS & RECOMMENDATIONS

The current study characterised the fluctuations and coherent structures within the atmospheric log layer. Hairpin-vortex structures were identified using a conditional analysis that modelled hairpin-vortices as infinitely long roller vortices convected towards the mast. For simplicity the roller vortices were assumed to be irrotational. It was found that the ABL data set qual-

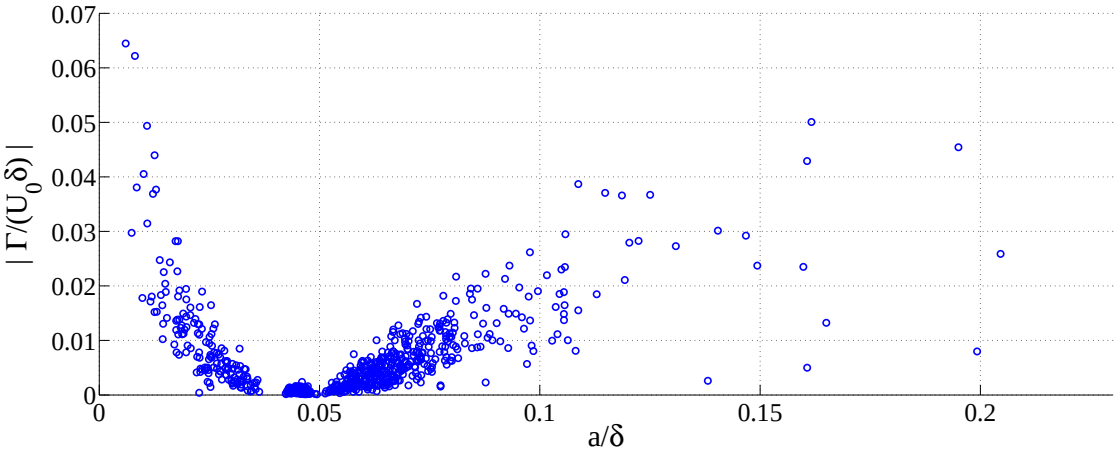

Figure 6: The magnitude of circulation Γ plotted against vortex-centre height a for all eleven 10-minute data sets. Γ and a are normalized as they were in Figure 5.

itatively agreed with statistical descriptors of TBL flow. The conditional analysis found that the occurrence frequency of vortex height followed a Rayleigh distribution, with a mean and standard distribution of 0.056δ and 0.027δ, respectively. The circulation followed a normal distribution with a mean and standard deviation of $0.000U_0\delta$ and $0.010U_0\delta$, respectively, with the bulk of the rollers measured around 0.05δ having circulations near zero. Despite the mean circulation of zero, the height distribution determined by the conditional analysis agreed with previous studies. The conditional model should be updated to account for the viscous core so as to accurately evaluate the vortex rollers when in proximity to the sensors.

5 ACKNOWLEDGEMENTS

The authors wish to thank the generous financial and technical support of Genivar Wind in the development and operation of the wind mast. Thanks also go to the Canadian School of Energy and Environment for their financial backing.

REFERENCES

[1] P. Klebanoff, "Characteristics of turbulence in a boundary layer with zero pressure gradient," *NACA Rep.*, 1955.

[2] J. C. Kaimal, "Turbulence spectra, length scales and structure parameters in the stable surface layer," *Boundary-Layer Meteorology*, vol. 4, pp. 289–309, 1972.

[3] J. L. Lumley and H. A. Panofsky, *The Structure of Atmospheric Turbulence*. Rochester, NY: John Wiley & Sons, 1964.

[4] J. C. Kaimal and J. J. Finnigan, *Atmospheric Boundary Layer Flows–Their Structure and Measurement*. New York, NY: Oxford University Press, 1994.

[5] K. D. Wilson, "Empirical orthogonal function analysis of the weakly convective atmospheric boundary layer. part i: Eddy structures," *Journal of Atmospheric Sciences*, vol. 53, no. 6, pp. 801–823, 1995.

[6] C. Lin, Q. Xia, and R. Calhoun, "Retrieval of urban boundary layer structures from doppler lidar data. part ii: Proper orthogonal decomposition," *Journal of Atmospheric Sciences*, vol. 65, pp. 21–42, 2008.

[7] S. K. Robinson, "Coherent motions in the turbulent boundary layer," *Annual Review of Fluid Mechanics*, vol. 23, 601-639 1991.

[8] A. Schroeder, R. Geisler, K. Staack, G. E. Elsinga, F. Scarano, B. Wieneke, A. Henning, C. Poelma, and

J. Westerweel, "Eulerian and langrangian views of a turbulent boundary layer flow using time-resolved tomographic piv," *Experiments in Fluids*, 2011.
[9] R. J. Adrian, "Hairpin vortex organization in wall turbulence," *Physics of Fluids*, 2007.
[10] C. R. Smith and D. A. Walker, *Fluid Vortices*. Norwell, MA: Kluwer Academic Publishers, 1995, ch. Turbulent Wall-Layer Vortices, pp. 235–290.
[11] A. Scarabino, P. J. Sterling, M.and Richards, and R. P. Baker, C. J.and Hoxey, "An investigation of the structure of ensemble averaged extreme wind events," *Wind and Structures*, pp. 135–151, 2007.
[12] M. Sterling, C. J. Baker, P. J. Richards, R. P. Hoxey, and A. D. Quinn, "An investigation of the wind statistics and extreme gust effects at a rural site," *Wind and Structures*, vol. 9, pp. 193–215, 2006.
[13] M. R. Head and P. R. Bandyopadhyay, "New aspects of turbulent boundary-layer structure," *Journal of Fluid Mechanics*, vol. 107, 1981.
[14] A. K. Blackadar and H. Tennekes, "Asymptotic similarity in neutral barotropic planetary boundary layers," *Journal of Atmospheric Sciences*, vol. 25, pp. 1015–1020, 1968.
[15] N.-S. Cheng, "Power-law index for velocity profiles in open channel flows," *Advances in Water Resources*, 2007.
[16] P. R. Spalart, "Direct simulation of a turbulent boundary layer up to $r_\theta = 1410$," *Journal of Fluid Mechanics*, pp. 61–98, 1986.
[17] S. K. Robinson, "A review of vortex structures and associated coherent motions in turbulent boundary layers," in *IUTAM Symposium on Structure of Turbulence and Drag Reduction*, 1989, pp. 23–50.
[18] C. R. Smith and J. Lu, "The use of a template-matching technique to identify hairpin vortex flow structures in turbulent boundary layers," *Near Wall Turbulence*, pp. 248–267, 1990.
[19] Y. Wu and K. T. Christensen, "Population trends of spanwise vortices in wall turbulence," *Journal of Fluid Mechanics*, vol. 568, pp. 55–76, 2006.

The Seventh International Colloquium on Bluff Body Aerodynamics and Applications (BBAA7)
Shanghai, China; September 2-6, 2012

Regeneration of occurrence frequencies and vertical profiles of wind velocity by WRF calculation

Ryuichiro Yoshie [a] , Masanori Mochizuki [b]

[a] *Tokyo Polytechnic University, Atsugi, Kanagawa, Japan, yoshie@arch.t-kougei.ac.jp*
[b] *Tokyo Polytechnic University, Atsugi, Kanagawa, Japan, m1064010@st.t-kougei.ac.jp*

ABSTRACT: We intend to use the WRF (The Weather Research and Forecasting Model） to prepare standard wind data at high altitude for the assessment of pedestrian wind environment, and also to investigate urban heat island phenomena. Before doing these investigations, it is necessary to confirm the prediction accuracy of WRF. In this study, the measured occurrence frequencies and vertical wind velocity profiles obtained by Doppler Soda at Minami-senju (inland area in Tokyo) were compared with those calculated by the WRF model. In order to well regenerate the vertical profile of wind velocity by WRF, appropriate surface roughness should be given to the WRF calculation. Thus, we used GIS data to appropriately classify land-use categories and to give a roughness length to the WRF calculation. The WRF calculation results using GIS data were compared with those of WRF using default values. The occurrence frequency and the vertical profiles of wind velocity calculated by WRF using GIS data agreed very well with those of the observation data. The calculated results of WRF using GIS were much better than those of WRF using default values.

KEYWORDS: WRF, vertical profile of wind velocity, occurrence frequency of wind velocity

1 INTRODUCTION

To assess the pedestrian wind environment around tall buildings based on occurrence frequencies of wind velocities we need reliable statistical wind observation data from near their construction sites. However, wind observatories are not always located near construction sites. Even if they do, the observation height is sometimes not high enough and the wind data are affected by surrounding buildings. Meso-scale simulation can be an alternative to direct observation. The authors intended to use the WRF (The Weather Research and Forecasting Model), a meso-scale simulation model, in order to prepare standard wind data at high-altitude for the assessment of the pedestrian wind environment. We also plan to use WRF for research on urban heat island phenomena, which is becoming serious in large cities in Japan. One of the effective countermeasures against heat island phenomena is to lead cool air of sea breeze into urban canopies. This strategy strongly depends on the vertical profile of wind velocity and the temperature of the sea breeze. Before doing these investigations using WRF, it is necessary to confirm how WRF can correctly regenerate the occurrence frequencies and vertical profiles of wind velocities. For this validation, observation data measured by Doppler Sodar in the Minami Senju district in Tokyo (Miyashita et al. 2002) were used. In order to well regenerate the vertical profile of wind velocity by WRF, it is considered that an appropriate surface roughness should be given to the WRF calculation. However, the default setting of WRF based on USGS (United States Geological Survey) expresses urban areas as only by one category and gives a uniform roughness length regard-

less of building densities and heights. Thus, we used GIS (Geographic Information System) data to appropriately classify urban land-use categories and to give roughness lengths to the WRF calculation. We conducted two cases of WRF calculations using a default setting and using GIS data, and the results were compared with the observation data.

2 OUTLINE OF CALCULATIONS

2.1 *Calculation Period, Initial and Boundary Conditions, Physics Scheme*

Calculations were carried out for a period of one month from May 1 to May 31, 2000. To set initial and boundary conditions we used FNL (Final) Operational Global Analysis data from the NCEP (National Center for Environmental Prediction). Table 1 gives an overview of the Physics Schemes used for these calculations.

Table 1: Physics Schemes

Physics scheme	microphysics	WRF 6 graupel class
	Longwave	Rapid Radiative Transfer Model
	Shortwave	Gudhia showtwave
	Surface layer	Monin-Obukhov (Janjic Eta) scheme
	Land surface	Noah land surface model
	Planetary boundary layer	Mellor-Yamada-Janjic scheme (2.5 level closure model)
	Cumulus	no
	Urban canopy	no

2.2 *Calculation Domains and Grid Intervals*

The calculations were conducted using three-stage, two-way nesting grids. The calculation domains and grid resolution are shown in Table 2 and Figure 1. The Minami Senju district, used for the comparison between observation and WRF calculations, is included in Domain 3.

Table 2: Computational Domain and Grid Resolution

	Domain (km) X×Y×Z	Grid Size X×Y×Z	Horizontal grid intervals (km)
Domain 1	450×450×20	50×50×60	9
Domain 2	180×180×20	60×60×60	3
Domain 3	60×60×20	60×60×60	1

※We used unequal intervals for the vertical grid and small intervals for areas near the ground surface.

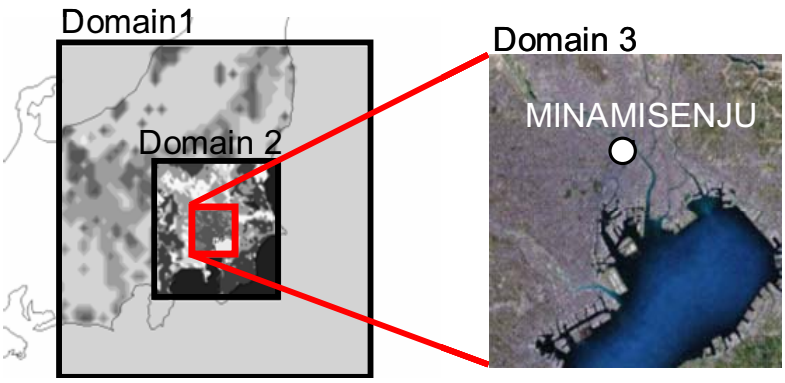

Figure 1: Computational Domain

2.3 *Setting Land-Use Categories and Ground-Surface Parameters*

Default setting of WRF employs the USGS's (United States Geological Survey) 24 categories of land use and their corresponding ground-surface parameters such as roughness length, albedo, and so forth. However, in the USGS, urban area is expressed by only one category and its roughness length is uniformly 0.8m regardless of building density and building height. Moreover, some areas that would be considered "urban" in reality are classified as pasture, grassland, and other categories in the USGS. Thus, the USGS does not sufficiently express the actual circumstances of Tokyo. For these reasons, we used the Digital Map 5000 and National Land Numerical Information Report (both referred to as "GIS" hereafter) published by the Ministry of Land, Infrastructure, Transport, and Tourism to appropriately classify land-use categories. Furthermore, we classified the urban area into three categories, "Low", "High", and "Commercial". We mainly used the Digital Map 5000, adding supplementary data from the National Land Numerical Information Report for places not covered by the former. The procedures for classifying land-use and determining ground-surface parameters are as follows.

Firstly, we netted the GIS in a 1km × 1km mesh, which is the same size as the grid in Domain 3 of the WRF calculation. Then, the area for each land-use category in each 1km×1km grid was calculated, and the land-use category occupying the largest area within each grid was determined to be a representative land-use category in the grid.

Secondly, we classified urban area into three categories to reflect the diverse urban configurations of Tokyo. (As described above, in the default setting of WRF with USGS, the urban area is expressed by only one category regardless of building density and building height.). We used land-use categories from the Digital Map 5000 and assigned them to three different urban categories: "Low," "High," and "Commercial". "General Low-Rise Residential area," "High-Density Residential area," and "Others" (including "Land for Public Facilities") in the Digital Map 5000 were assigned to the "Low" urban category; "Medium- and High-Rise Residential area" to the "High" urban category; and "Area for Commercial and Business Use" to the "Commercial" urban category. We totaled the areas occupied, respectively, by the Low, High, and Commercial category in each grid square, and the urban category with the largest area was determined to be a representative urban category for that grid square.

Finally, GIS land-use categories were corresponded to the USGS land-use categories, and surface parameters were determined as shown in Table 3. The USGS uses a uniform roughness length of 80cm for the urban area, but for this study we used 70cm, 100cm, and 150cm for Low urban area, High urban area, and Commercial urban area, respectively. We adopted these values

by referring to Grimmond and Oke (1999). Figure 2 shows land-use categories based on the USGS (Figure 2a) and the GIS (Figure 2b), which shows large differences between them.

Table 3: Land-use Categories and Surface Parameters

No.	USGS/SIB Land-Use Category	GIS Land-Use Category	Urban Category	Surface Z0 [cm]	Albedo [%]	Soil Moisture [%]	Surface Emmisivity [%]
1	Urban Land	House and Pablic Building	Low	70	15	10	88
			High	100			
			Commercial	150			
2	Dryland Cropland and Pasture	Farm	-	15	17	30	98.5
3	Irrigated Cropland and Pasture	Paddy Field	-	10	18	50	98.5
7	Grassland	Park and Grass	-	12	19	15	96
15	Mixed Forest	Forest	-	50	13	30	97
16	Water	Lake and Sea	-	0.01	8	100	98
19	Barren or Sparsely Vegetated	Soil Surface	-	1	25	2	90

2a) USGS

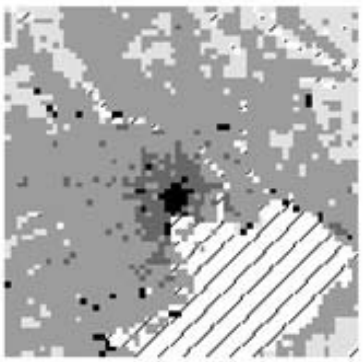

2b) GIS

Figure 2: Land-use Categories in Domain 3

2.4 *Calculation Cases*

We carried out two kinds of calculations: one using the default setting of WRF with USGS (Case 1), and the other using the land-use categories and surface parameters based on GIS data as described in 2.3 (Case 2).

3 COMPARISON OF WRF-CALCULATED RESULTS WITH OBSERVATION DATA

3.1 *Occurrence Frequencies of Wind Velocities at High Altitude*

Figure 2 compares the probabilities of exceedance of mean wind velocity (10 minutes averaging 300m high) between the results of WRF and observation data. Case 1 and case 2 indicate WRF calculations using the default value and GIS data, respectively. The probability of exceedance of wind velocity calculated by Case 2 agreed very well with the observation data. The probability of exceedance calculated by Case 1 was higher than that of Case 2. However, the difference was not so large at this high altitude.

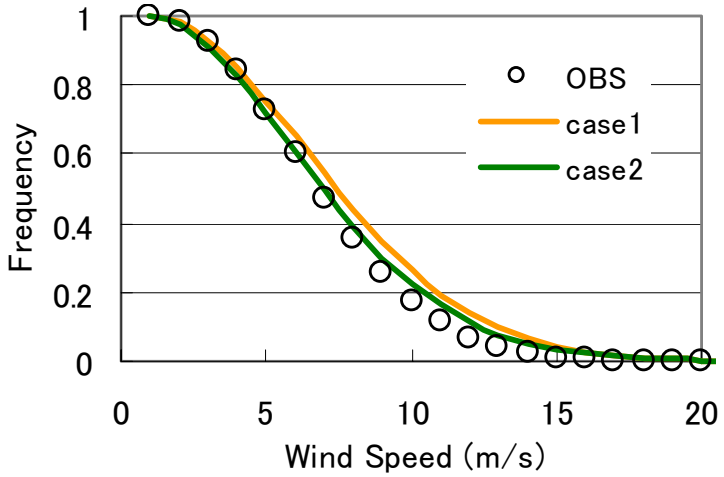

Figure 3: Probability of Exceedance for Mean Wind Speed

3.2 *Vertical Profiles for Mean Wind Velocities*

For this comparison, we firstly extracted southerly wind (wind direction=180° ±33° at 200m high) for both observation and calculation. Then the vertical profiles of wind velocity of the observation data were classified into eight clusters by cluster analysis. Corresponding clusters of calculated results were made so that each cluster at the same time of the observation data became the same cluster.

Figure 4 shows vertical profiles of wind velocities in the eight clusters. Averaged values ±1 σ (standard deviation) at each height in each cluster are plotted in the figures. The value shown in the caption for each cluster is the occurrence frequency for that cluster. Except for Figure 4f (Cluster 6), there is a pretty good match between observation and calculated results. In particular, Case 2 using GIS is remarkably close to the observation values. Case 1 using the default setting of USGS generally show higher values than the observation data. The calculated wind velocities for Case 6 do not correspond with observation data because Cluster 6 includes many data obtained during rainy weather. In both Case 1 and Case 2, during rainy weather the WRF calculation tends to produce a higher wind velocity than the observations.

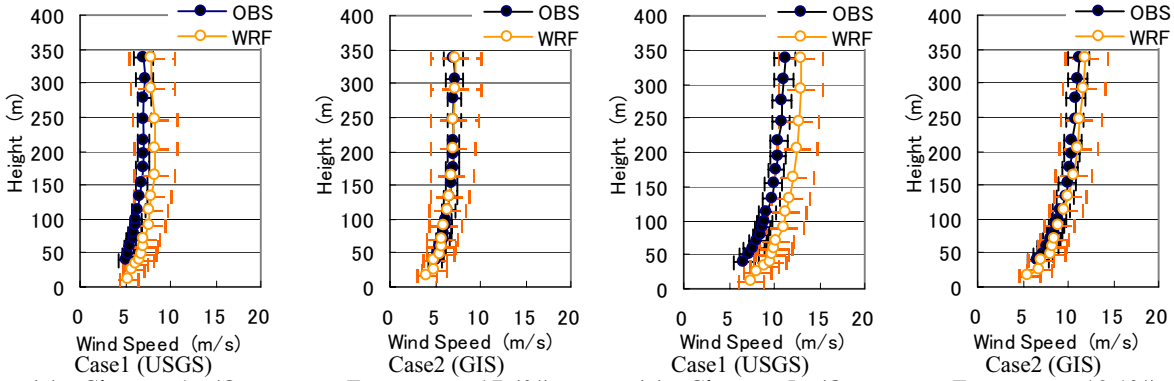

4a) Cluster 1 (Occurrence Frequency 17.4%) 4e) Cluster 5 (Occurrence Frequency 19.1%)

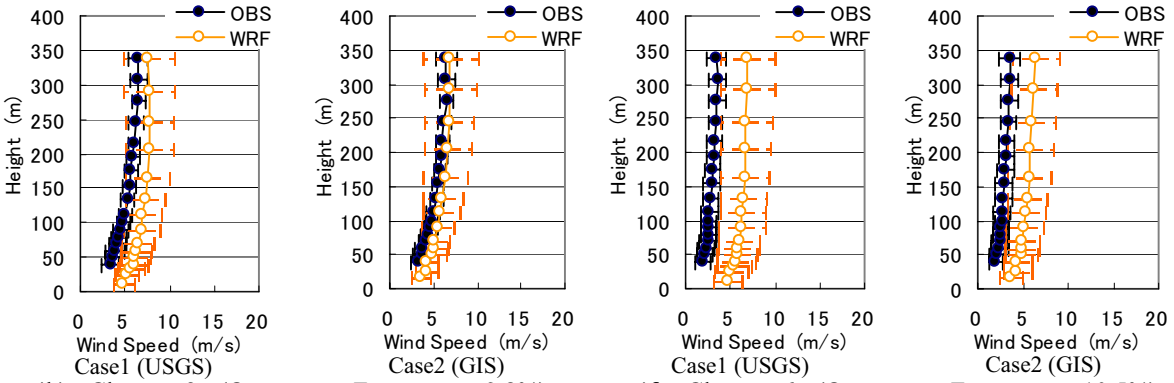

4b) Cluster 2 (Occurrence Frequency 9.8%) 4f) Cluster 6 (Occurrence Frequency 10.5%)

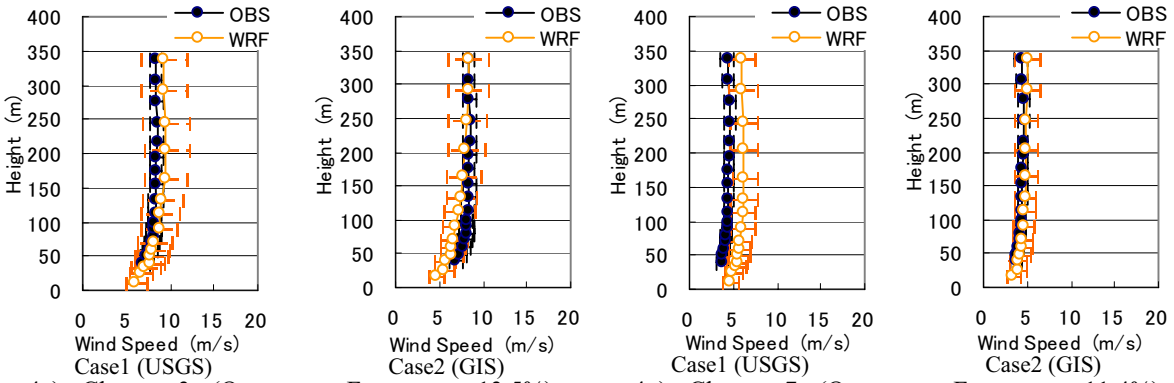

4c) Cluster 3 (Occurrence Frequency 13.5%) 4g) Cluster 7 (Occurrence Frequency 11.4%)

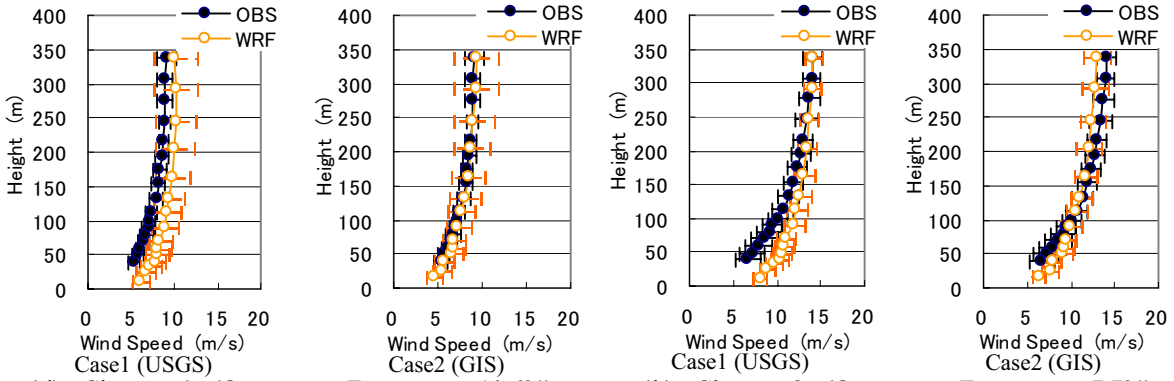

4d) Cluster 4 (Occurrence Frequency 10.6%) 4h) Cluster 8 (Occurrence Frequency 7.7%)

Figure 4: Vertical Profile of Mean Wind Speed

4 CONCLUSION

Two cases of WRF calculations were conducted using the default setting (Case1) and based on GIS-derived land-use categories and surface roughness lengths (Case2). The calculated results were compared with the observation data measured by Doppler Soda at Minami Senju. The calculated probabilities of exceedance of wind velocity at high altitude (especially Case2) corresponded very well with that of the observation. In addition, it was apparent that calculated vertical profiles of mean wind velocity of Case 2 were very close to those of the observation.

5 ACKNOWLEDGEMENTS

This study was partially supported by the Ministry of Education, Culture, Sports, Science and Technology, Japan, through the Global Center of Excellence Program of Tokyo Polytechnic University. We would also like to express our gratitude to the Japan Society for the Promotion of Science (JSPS) for Grant-in-Aid for Scientific Research (B), (No. 21360283).

6 REFERENCE

Chung and Yoshie, 2010, Classification of vertical profiles of wind velocity and temperature in sea breeze using cluster analysis, Summaries of technical papers of Annual Meeting Architectural Institute of Japan ,D-1,975-976

Grimmond, C. S. B. and T. R. Oke , 1999,Aerodynamic Properties of Urban Areas Derived from Analysis of surface Form, J. Applied Met., 38, 1262-1292

Miyashita, K.,Suda, K., Iwatani, Y., Hibi, K., Ishibashi. S., and Tamura, Y., 2002,Observations of wind speed profiles over various surface roughness sites using Doppler sodars : Part 19 Characteristics of natural winds in Tokyo city area, Summaries of technical papers of Annual Meeting Architectural Institute of Japan ,B-1,103-104

The Seventh International Colloquium on Bluff Body Aerodynamics and Applications (BBAA7)
Shanghai, China; September 2-6, 2012

CFD Prediction of gusty winds corresponding to observed values around mountainous terrain

Eriko Tomokiyo [a], Kazuhiro Otsubo [b], Junji Maeda [a], Yasuyuki Shuto[c]

[a]*Faculty of Human-Environment Studies, Kyushu University, Fukuoka, Japan*
[b]*Graduate School of Human-Environment Studies, Kyushu University, Fukuoka, Japan*
[c]*Kyushu Electric Power Co., Inc., Fukuoka, Japan*

ABSTRACT: Structural damage resulting from strong winds associated with Typhoon Tokage (No. 23, 2004) was concentrated in Ogi City in Saga Prefecture located in northern Kyushu, Japan, even though Ogi City was more than 300 km from the typhoon's path. It may be because the winds that blow from mountains became stronger through the effect of downslope winds in stable conditions of the atmospheric layer. Here, we discuss our LES results of wind simulation in view of the effects of inflow wind profiles and grid resolutions. It was found that the simulated wind speeds became higher using the inflow winds experienced during the passing of Typhoon Tokage and the intensities of turbulence were larger using a fine domain resolution. It was confirmed that the results of the simulation help to explain how the convergence of wind speeds was affected by the local terrain and the weather conditions in Ogi City.

KEYWORDS: Computational fluid dynamics, Typhoon Tokage, Local terrain, Wind disaster

1 INTRODUCTION

Ten typhoons hit Japan in 2004. Figure 1 shows the paths of these typhoons and a close-up image of the routes of four typhoons that directly caused structural damage to the Kyushu area. Typhoon Tokage was unique because the associated damage was concentrated in Ogi City, which is located in Saga Prefecture in northern Kyushu, despite the fact that the city was more than 300 km away from the typhoon's path [1]. Residents in this region are familiar with the strong northwesterly winds that blow down from northern mountainous terrain every winter. The mountain-

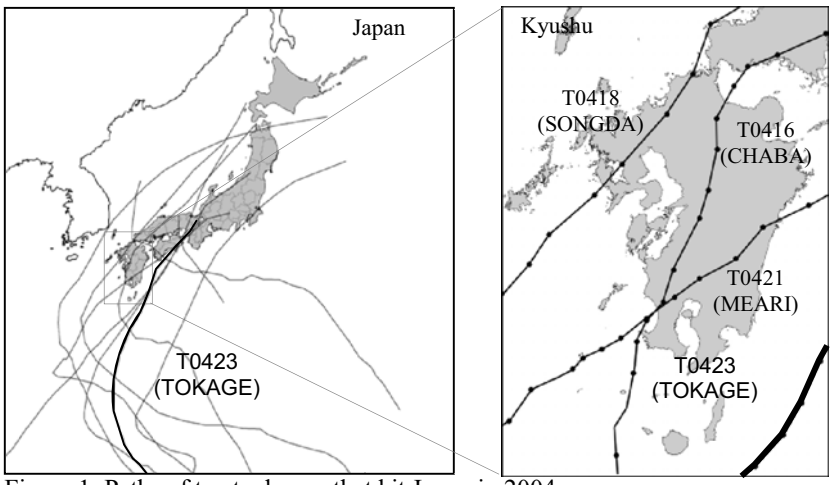

Figure 1. Paths of ten typhoons that hit Japan in 2004.

ous terrain of the area may have contributed to the strength of the northeasterly winds that were associated with Tokage. The authors focused on the effect of the mountainous terrain on the northerly winds blowing around Ogi City and examined the outbreak of strong winds during Typhoon Tokage using computational simulation. It is said that the atmospheric layer is in a neutral condition, when strong winds continue. However, the winds that blow from mountainous terrain may become stronger due to the effect of downslope winds in the stable conditions of the atmospheric layer. The effect of the upper atmosphere on strong downslope winds has been examined [2]. We have previously discussed the wind conditions in a neutral or stable condition of the atmospheric layer [3] and examined the effect of inflow wind profiles [4,5].

We are familiar with several CFD programs useful for carrying out local terrain analyses and wind assessment in and nearby urban areas. Although some attempts to predict hazardous strong winds over a wide area have been made in the past, few of them made use of records of observed strong winds.

In this paper, we discuss the effect of inflow wind profiles and grid resolutions on wind enhancement around Ogi City, where structural damage due to Typhoon Tokage was concentrated, using LES software [6] and refer to several sets of observed wind data gathered at NeWMeK sites [7].

2 FEATURES OF STRUCTURAL DAMAGE INFLICTED BY TYPHOON TOKAGE

Figure 2 shows the peak gust distributions found during Typhoon Tokage. Strong winds were measured around Ogi City in Saga Prefecture, which was located more than 300 km away from the typhoon's path. Figure 3 indicates the time evolutions of wind speed and direction measured

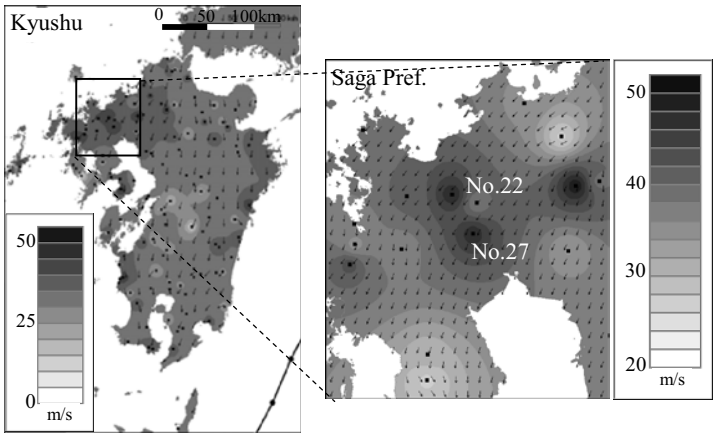

Figure 2. Peak gust distributions in Saga, Kyushu during Typhoon Tokage.

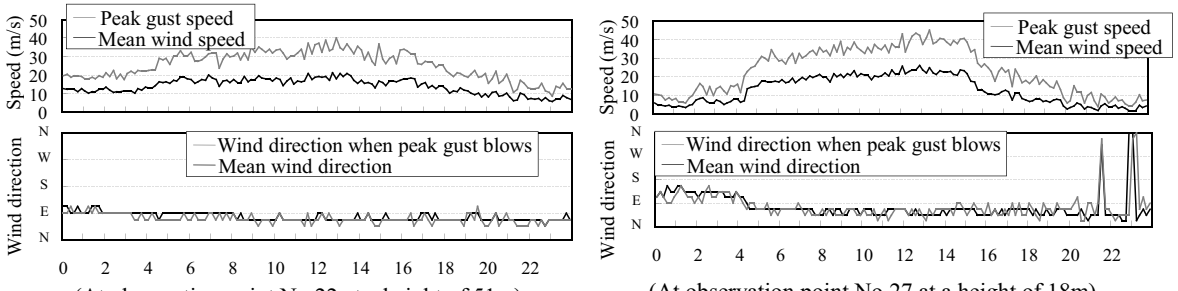

(At observation point No.22 at a height of 51m) (At observation point No.27 at a height of 18m)

Figure 3. Time evolution of winds in Saga, Kyushu during Typhoon Tokage.

on October 20, 2004. The winds measured at NeWMeK observation point No. 27, located at the foot of the mountainous terrain, were stronger than those found at observation point No. 22.

Figure 4a illustrates the rate of residential damage experienced in Kyushu and in Saga Prefecture. As shown in the figure, structural damage was concentrated in Ogi City in Saga Prefecture. As indicated in Figure 4b, there is a shallow valley near the southward-facing slope of the mountains on the windward side of Ogi City. The concentration of structural damage found in this area may have resulted from the enhancement of strong winds by the mountainous terrain.

3 COMPUTATIONAL SIMULATION OF WIND FLOW USING LES SOFTWARE

We simulated the wind flows observed around Ogi City using LES software and NeWMeK data. In order to consider the significant details of complex terrain, the software employs a body-fitted coordinate grid system. The turbulence model uses large eddy simulation, and its governing equations are incompressible continuity equations and Navier-Stokes equations. The standard Smagorinsky model is applied to the sub-grid scale model.

The focal area was 18 km x 18 km x 5km, including the area of Ogi City, and is illustrated in Figure 5. Two computational domains using different grid resolutions were installed to compare simulated results. As shown in Figure 6a, the number of grid points in the x, y and z-directions for one domain was 91, 91 and 51 respectively. The other domain was divided into 161, 161 and 51 in the x, y and z-directions respectively, as indicated in Figure 6b. The buffer

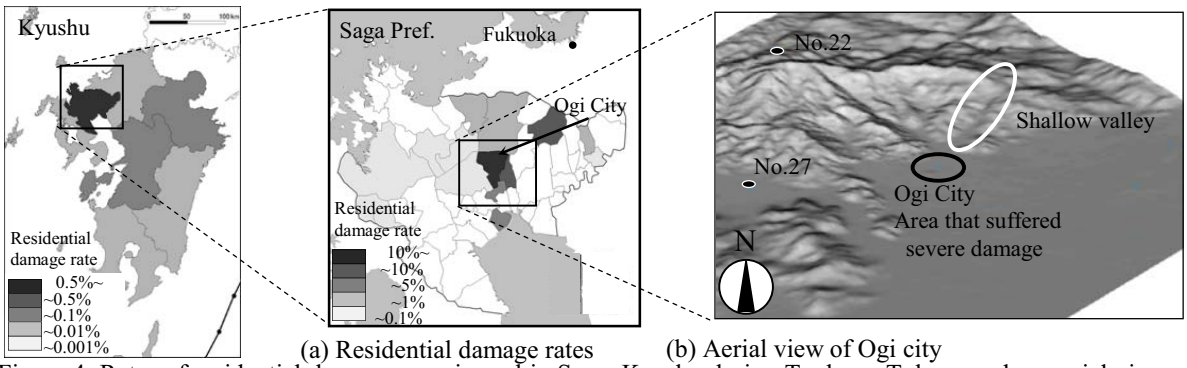

(a) Residential damage rates (b) Aerial view of Ogi city

Figure 4. Rates of residential damage experienced in Saga, Kyushu during Typhoon Tokage and an aerial view of Ogi City.

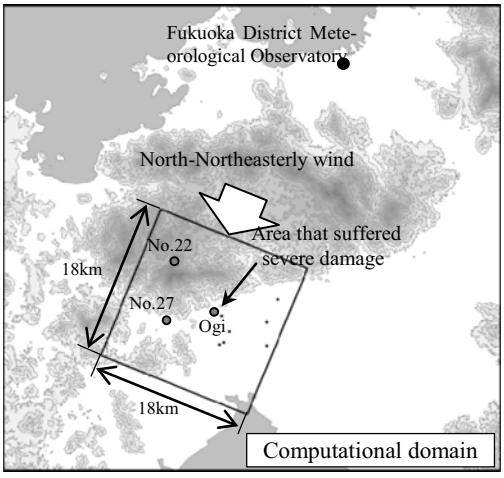

Figure 5. Focal area of simulation.

domain located in front of the inflow boundary was divided into 20, and the domain located behind the outflow boundary was divided into 10 for the purpose of making calculations under stable conditions. The minimum distance between grid points in the z-direction was approximately 3 m. The altitudes of the terrain were calculated based on a digital 50m-grid map provided by the Geographical Survey Institute. It was estimated that the wind blew from the north-northeast during the typhoon. The boundary conditions were as follows: an outflow based on the convection boundary condition, the free-slip condition for top and side boundaries, and the non-slip condition for ground and an inflow wind corresponding with the wind profile. No roughness was specified at ground level.

Two inflow wind profiles were used in this study. One of the inflow wind profiles was defined by the power law, using a power index of 1/7. The other was based on information gathered through upper-air observations carried out at the Fukuoka District Meteorological Observatory when Typhoon Tokage hit Kyushu. Figure 7 shows information about wind direction and wind speed that was gathered during the upper-air observations. The profiles of inflow wind in the following simulations were modified as shown in Figure 8. The Reynolds number was set at 10^4. The Froude number was set at 1000 to suit a neutral condition. The computation time unit was 0.002 seconds and the number of calculations was 20,000. The results of the second half of the calculations are discussed in the following section.

The results of the simulation were converted to actual scale using the maximum mean wind speed of 21.5 m/s, which was measured at observation point No. 22. We compared the simulated results under four different conditions as listed in Table 1.

Table 1. Simulation parameters.

Case No.	Resolution	Inflow wind profile
Case 1	91x 91x51	Based on Power law (Power index 1/7)
Case 2	91x 91x51	Based on Typhoon Tokage data
Case 3	161x161x51	Based on Power law (Power index 1/7)
Case 4	161x161x51	Based on Typhoon Tokage data

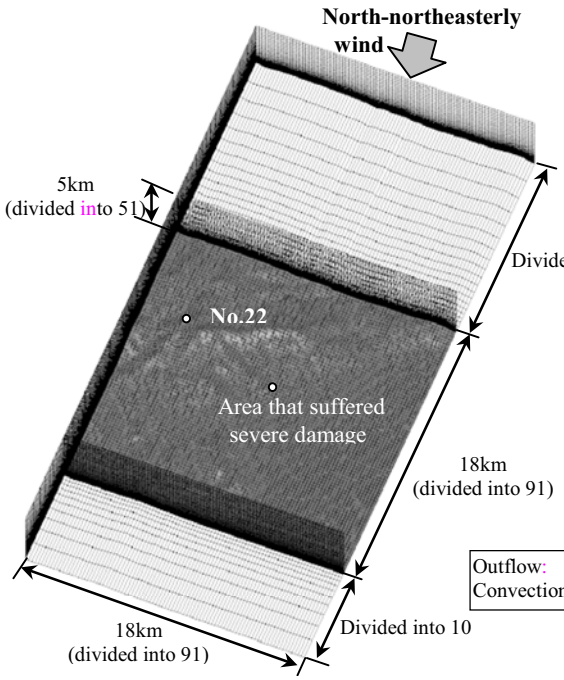

(a) Fine computational domain

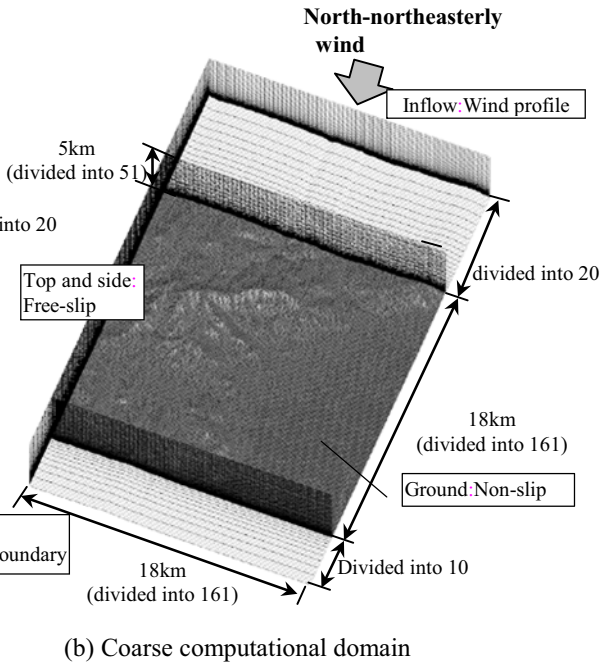

(b) Coarse computational domain

Figure 6. Two different computational domains.

4 RESULTS AND DISCUSSIONS

4.1 *Flow patterns for simulated winds*

Figure 9 shows the flow patterns for the simulated mean wind speeds at a height of about 10 m; charts a, b, c, and d illustrate the flows corresponding to the respective cases of Table 1. Each arrow in the figure indicates the vector of wind found at each focal point. The shallow valley was located to the windward side of the Ogi area which experienced severe damage. We found that winds converged here due to the mountainous terrain. The distributions of mean wind speeds at the foot of the mountainous terrain varied due to each condition resulting from the numerical resolutions and the wind profiles used in these simulations. As we compared Figures 9a and 9b using the coarse grid of 91 x 91, the wind speeds that were calculated based on inflow wind profiles during Typhoon Tokage were higher than those simulated using only the power index of 1/7, particularly in a plain to the east of the focal point, Ogi. The wind speeds resulting from the fine grid as shown in Figure 9c were higher than those using the coarse grid as indicated in Figure 9a using the same inflow based on the power index of 1/7. As shown in Figure 9d, the winds which were calculated based on inflow wind profiles during Typhoon Tokage using the fine grid of 161 x 161 converged markedly due to the shallow valley near the southward-facing slope of the mountainous terrain and a strong wind area was produced in the southeast of the focal point, Ogi.

Figures 10, 11 and 12 show the flow patterns of simulated mean wind speeds at the vertical section including observation points No. 22 and No. 27, and the focal point, Ogi. The locations of each section are shown in Figure 9a. As shown in Figure 10, the wind speed distributions on the leeward side of the mountainous terrain differ considerably depending on domain resolutions and inflow profiles. However, wind speeds at No. 22 located on the windward side of the moun-

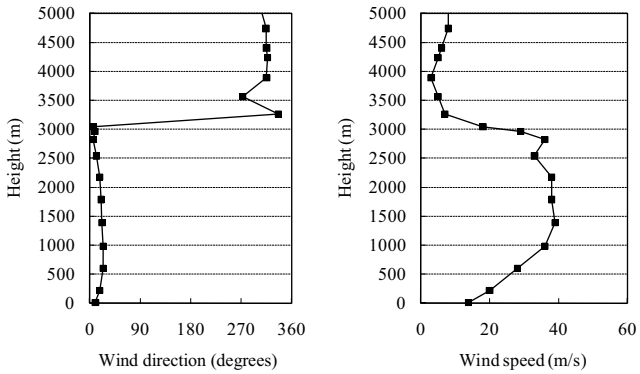

(a) Wind direction (b) Wind speed

Figure 7. Information gathered during upper-air observations by Fukuoka District Meteorological Observatory.

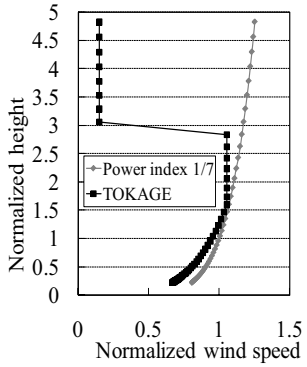

Figure 8. Profiles of inflow winds used in the simulation.

tainous terrain are almost the same. Figures 11a and 12a indicate that the mean wind speeds were small at the foot of the mountainous terrain when inflow winds based on the power law were used in the coarse grid. Figures 11c and 12c illustrate that wind speeds become larger when using finer divisions. On the other hand, the mean wind speeds shown in Figures 11b and 12b were larger at observation point No. 27 and the focal point, Ogi, when we used the profiles of inflow winds based on upper-air information associated with Typhoon Tokage in the coarse grid of 91 x 91. As shown in Figures 11c and 12c, wind speeds became larger near observation point No. 27 and the Ogi area when using the finer division. Figures 11d and 12d illustrate that when inflow winds resulting from the typhoon were used, the simulated wind speeds became much larger at the foot of the mountainous terrain. As indicated in Figures 11b and 11d, it was found that the simulated winds flowed along the surface of the mountainous terrain at observation point No. 27 using the inflow winds during the typhoon. Similarly, as illustrated in Figures 10b and 10d, the simulated winds flowed along the surface of the ground around Ogi. As a result, the mean wind speeds at the foot of the mountainous terrain were significantly larger when inflow winds based on Typhoon Tokage were used.

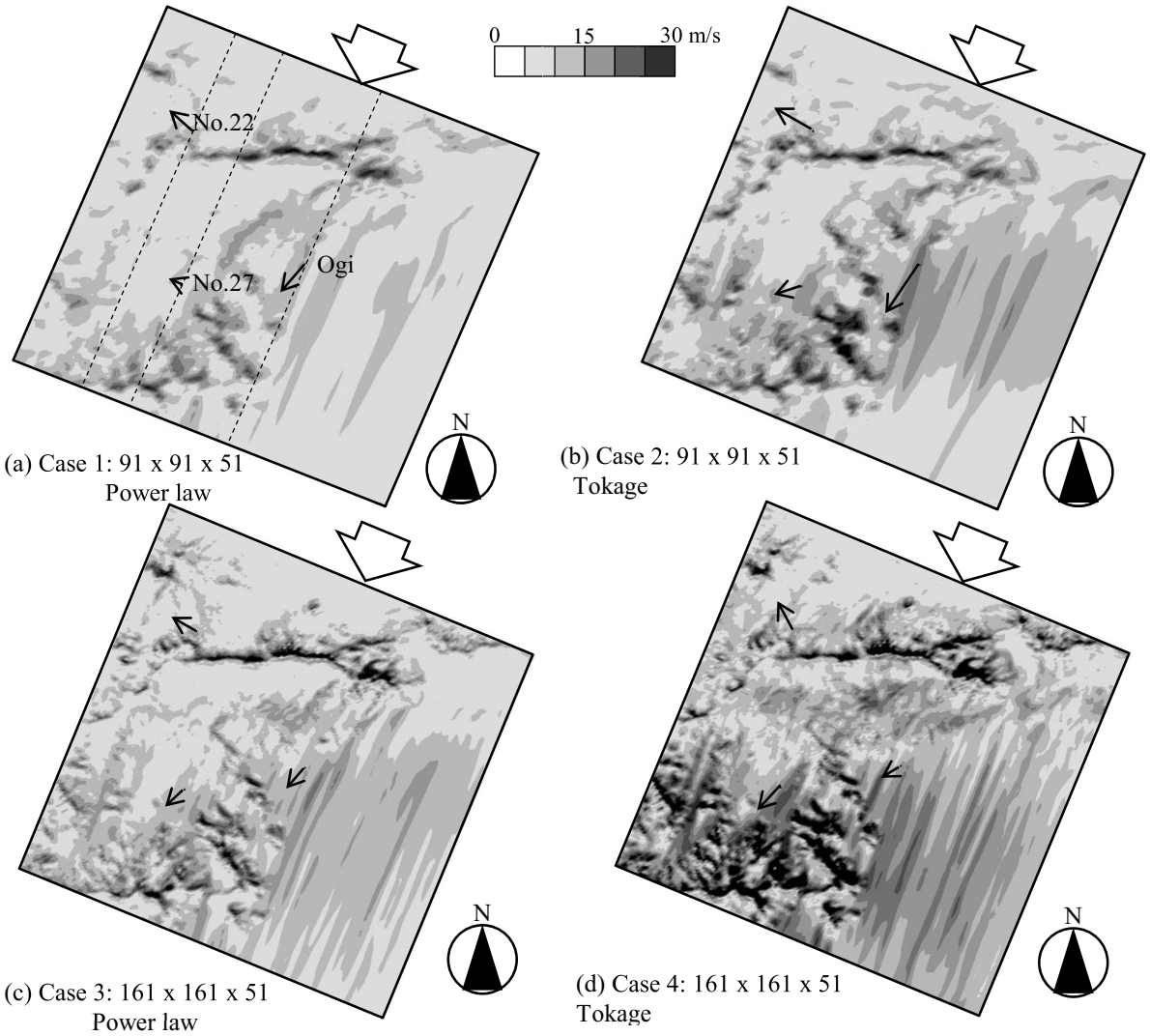

Figure 9. Flow patterns of simulated mean wind speed at a height of about 10m in square area of Figure 5.

4.2 *Simulated winds at observation points*

Table 2 describes mean wind speeds and directions, intensities of turbulence, and simulated peak gust speeds found at each focal point. The simulated wind speeds at the levels of 51m and 18m are shown in the table. These levels are the heights at which anemometers were installed. The intensities of turbulence are larger in the finer grid at both observation points. In particular, intensity of turbulence became large at No. 22 located at the summit of the mountainous terrain, using the profiles of inflow winds associated with Typhoon Tokage in the fine resolution.

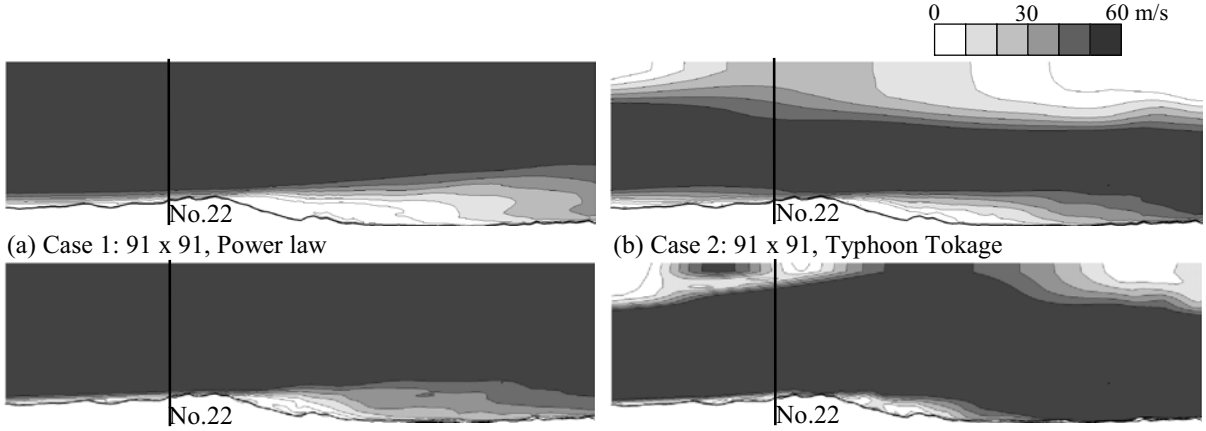

(a) Case 1: 91 x 91, Power law (b) Case 2: 91 x 91, Typhoon Tokage

(c) Case 3: 161 x 161, Power law (d) Case 4: 161 x 161, Typhoon Tokage

Figure 10. Flow patterns of simulated mean wind speed at No.22.

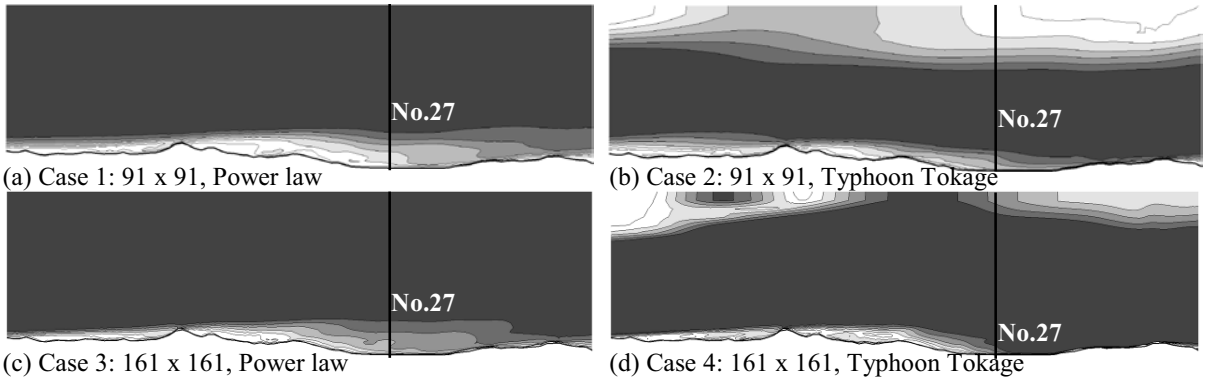

(a) Case 1: 91 x 91, Power law (b) Case 2: 91 x 91, Typhoon Tokage

(c) Case 3: 161 x 161, Power law (d) Case 4: 161 x 161, Typhoon Tokage

Figure 11. Flow patterns of simulated mean wind speed at No.27.

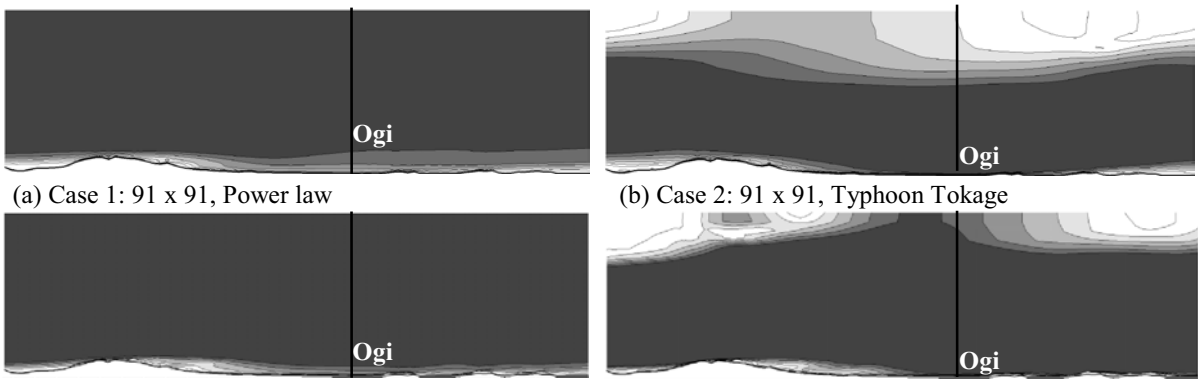

(a) Case 1: 91 x 91, Power law (b) Case 2: 91 x 91, Typhoon Tokage

(c) Case 3: 161 x 161, Power law (d) Case 4: 161 x 161, Typhoon Tokage

Figure 12. Flow patterns of simulated mean wind speed at Ogi.

Table 2. Simulated mean wind speeds and directions, intensities of turbulence, peak gust speeds based on power law.

Profile of inflow wind			Power law		
Numerical Resolution (X x Y x Z)	Focal Point (Remarkable height)	Mean wind Speed (m/s)	Mean direction (degrees)	Intensity of turbulence	Simulated peak gust speed (m/s)
	No.22 (about 51m)	21.5	109.5 (ESE)	0.15	27.7
91 x 91 x 51	No.27 (about 18m)	5.4	113.6 (ESE)	0.54	31.9
	No.22 (about 51m)	21.5	93.5 (E)	0.18	28.9
161 x 161 x 51	No.27 (about 18m)	8.1	47.3 (NE)	0.67	42.3

Profile of inflow wind			Tokage (0423)		
Numerical Resolution (X x Y x Z)	Focal Point (Remarkable height)	Mean wind speed (m/s)	Mean direction (degrees)	Intensity of turbulence	Simulated peak gust speed (m/s)
	No.22 (about 51m)	21.5	80.1 (E)	0.30	30.4
91 x 91 x 51	No.27 (about 18m)	9.4	71.6 (ENE)	0.47	15.9
	No.22 (about 51m)	21.5	113.4 (ESE)	0.35	38.2
161 x 161 x 51	No.27 (about 18m)	11.1	42.5 (NE)	0.52	29.3

Table 3. Observed wind record at No. 22 and No. 27 at 12:50 on Oct. 20, 2004.

Observation point			No.22		
Mean wind speed (m/s)	Direction	Peak gust speed (m/s)	Direction	Intensity of turbulence	Gust factor
. 21.5	NE	34.2	NE	0.27	1.6

Observation point			No.27		
Mean wind speed (m/s)	Direction	Peak gust speed (m/s)	Direction	Intensity of turbulence	Gust factor
. 23.8	NNE	43.5	NE	0.24	1.8

Figure 13 indicates the recorded measurements and the numerical results at observation point No. 22. Charts a, b and c in Figure 13 include mean wind speed and direction profiles, and time evolutions of wind speeds and directions. The time scale of numerical computation was changed using the following formula.

$$t^* = \frac{\bar{t}}{H/U}$$

Here, the reference height H is 1,024m, the height of the mountain where observation point No. 22 was located, and the representative wind speed, U is 21.5 m/s recorded at observation point No. 22. The simulated time unit t* = 0.002 seconds, represents real time of approximately 1 second. Although the observed mean wind direction of wind during Tokage was northeast at observation point No. 22, the simulated winds blew from the east-northeast. Even though we expected that the simulated mean wind directions would correspond with the measured wind direction, the simulated directions disagreed with the measured value at No. 22. As shown in Figure 13c, although wind speed changed gradually in the simulation, high-frequency waves were not generated. Simulated maximum wind speed was 27.7 m/s in the coarse grid when inflow winds were based on the power law, and simulated speed was 28.9 m/s using the fine grid. Calculated maximum value was 30.4 m/s in the grid divided into 91 x 91, using inflow winds based on Typhoon Tokage, and speed was 38.2m/s in the grid divided into 161 x 161. Mean wind speeds, peak gust speeds, and intensities of turbulence recorded in the 10 minutes after 12:50 on Oct. 20 2004 are listed in Table 3. Peak gust speed of 34.2m/s at No.22 was observed during the period.

Figures 14a, b and c indicate mean wind speed and direction profiles, and time evolutions of wind speeds and directions at No. 27. Table 3 shows that mean wind speed was 23.8 m/s and

the mean wind direction at that time was north-northeast at No. 27 at the foot of the mountainous terrain. As shown in Figure 14a, mean wind speeds became larger in the case of the fine grid than the coarse grid. And mean wind speeds using inflow profiles during Typhoon Tokage were larger than using inflow winds based on the power law. Figure 14b shows that winds blew from the northeast and simulated wind directions corresponded with observed values. As indicated in Figure 14c, calculated wind speeds and directions were not able to generate fluctuations as large as those observed. But wind speed fluctuations were larger in the fine grid than in the coarse grid. Intensities of turbulence using the fine resolution are shown in Table 2. Simulated maximum wind speed when inflow winds were based on the power law was 31.9 m/s in the coarse grid, and 42.3 m/s in the fine grid. Calculated maximum value using inflow winds based on Typhoon Tokage was 15.9 m/s in the coarse grid, and 29.3m/s in the fine grid. Observed maximum value was 43.5 m/s at No. 27.

As a result, wind speeds in the simulation fluctuated greatly, using inflow winds based on upper-air information associated with Typhoon Tokage when compared with using inflow winds based on the power law. Based on these results, it seems that calculated wind speeds in the case based on the inflows associated with Typhoon Tokage corresponded to the observed values. Moreover, although high-frequency winds like those observed could not be generated in this calculation, intensities of turbulence became much larger using the fine calculation domain. Consequently, it seems that calculated peak gust speeds using the fine resolution corresponded more closely to actual observed values.

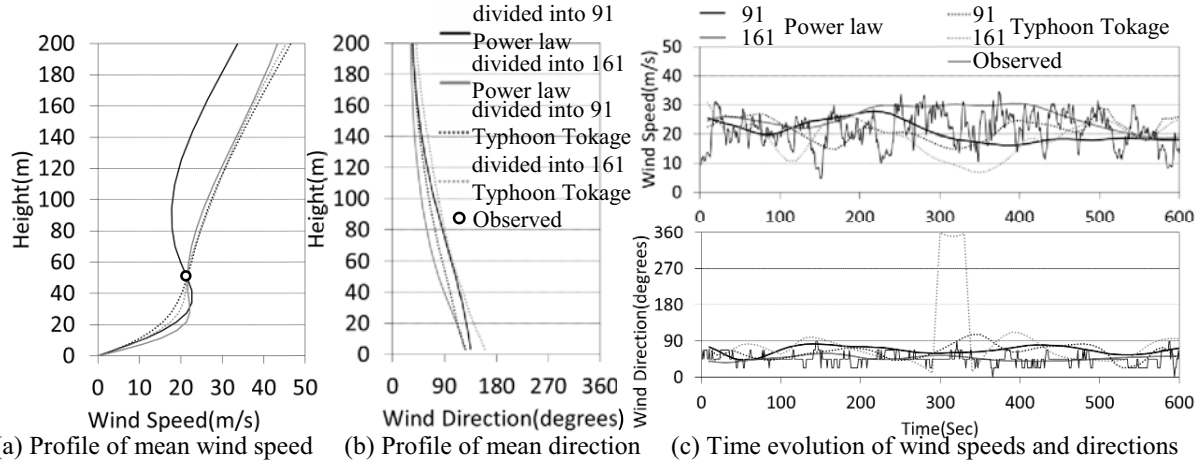

(a) Profile of mean wind speed (b) Profile of mean direction (c) Time evolution of wind speeds and directions

Figure 13. Profile of simulated mean wind speed and direction, time evolution of winds at No.22.

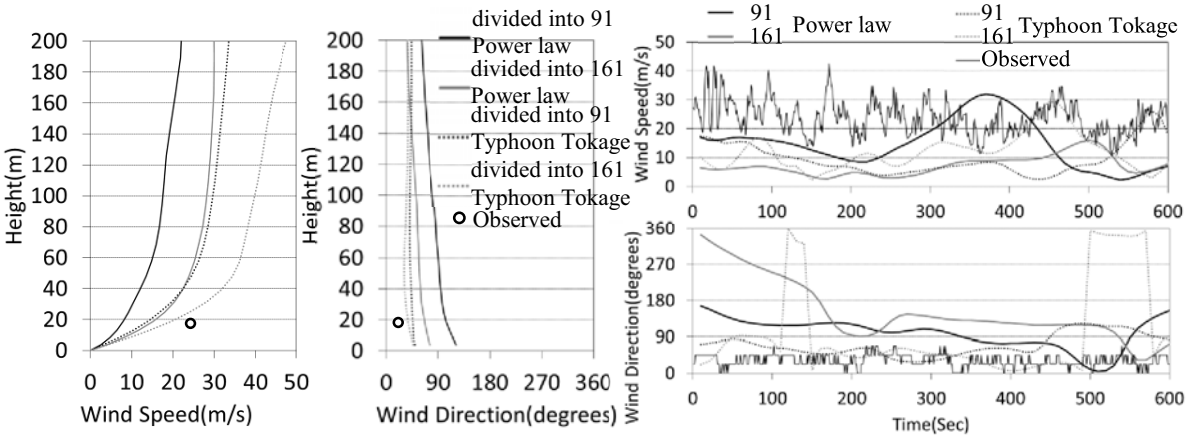

(a) Profile of mean wind speed (b) Profile of mean direction (c) Time evolution of wind speeds and directions

Figure 14. Profile of simulated mean wind speed and direction, time evolution of winds at No.27.

5 CONCLUSIONS

Residential damage due to strong winds associated with Typhoon Tokage (T0423) was concentrated in a specific small area around Ogi City, Saga Prefecture, which has mountainous terrain on the windward side. The flow patterns of wind speed around Ogi City were numerically simulated under two profiles of inflow winds. One of the profiles was defined by the power law and the other was based on upper-air observations measured by a nearby meteorological station. We compared CFD analytical results with coarse and fine grid resolutions in the target area using LES model simulation software. The following features were found:

1 The winds ran along the surface of the mountainous terrain and much stronger winds hit Ogi City when the measured inflow wind profile during Typhoon Tokage was used.
2 A strong wind area was produced in the southeast of the Ogi area based on the inflow winds associated with Typhoon Tokage.
3 Although fluctuating winds corresponding to the observed winds could not be generated using the LES computational technique in this study, the intensity of turbulence became larger using the fine resolution grid.
4 It seems that the calculated peak gust speeds using the fine resolution and the observed wind profile corresponded more closely to actual observed values.
5 The upper-air conditions resulting from the typhoon may also have played a role in causing the outbreak of much stronger winds.

6 ACKNOWLEDGEMENTS

This research was supported by the Ministry of Education, Culture, Sports, Science and Technology, Grant-in-Aid for Scientific Research (C), 2010～2012, 23510227.

7 REFERENCES

1 E. Tomokiyo, J. Maeda, N. Tsuru, Wind Disaster in Kyushu due to Typhoons in 2004-Residential Damage in Kyushu, Japan, in: Proceedings of the 6th Asia-Pacific Conference on Wind Engineering, Seoul, Korea, 2005, pp.2862-2873.
2 M. Aihara, M. Hirosawa, On severe downslope wind due to the mountain wave-induced critical level, Papers in Meteorology and Geophysics, 39(2), (1988) 59-77.
3 E. Tomokiyo, J. Maeda, et al., Structural damage caused by local winds associated with Typhoon Tokage (0423) passing, in: Proceedings of the 4th International Symposium on Computational Wind Engineering, Yokohama, Japan, 2006, pp.361-364.
4 E. Tomokiyo, J. Maeda, T. Uchida, CFD prediction of wind distribution around Ogi City in Saga Prefecture, Japan, in: Proceedings of 12th International Conference on Wind Engineering, Cairns, Australia, 2007, pp.607-614.
5 E. Tomokiyo and J. Maeda, CFD prediction of local winds associated with Typhoon Tokage (2004) -Effects of atmospheric stability on the increase of strong winds-, The Fifth International Symposium on Computational Wind Engineering (CWE2010), North Carolina, USA, 2010, USB.
6 T. Uchida and Y. Ohya, Numerical study of stably stratified flows over a two-dimensional hill in a channel of finite depth, Fluid Dynamics Research 29, (2001) 227-250.
7 E. Tomokiyo, J. Maeda, et al., Typhoon damage analysis of transmission towers in mountainous regions of Kyushu, Japan, Wind & Structures, An International Journal, 7(5), (2004) 345-357.

The Seventh International Colloquium on Bluff Body Aerodynamics and Applications (BBAA7)
Shanghai, China; September 2-6, 2012

Effects of the swirl ratio on the turbulent flow fields of tornado-like vortices by using LES turbulent model

Zhenqing Liu [a], Takeshi Ishihara[b]

[a]*Department of Civil Engineering , School of Engineering, The University of Tokyo, 7-3-1, Hongo, Bunkyo-ku, Tokyo, Japan*
[b]*Department of Civil Engineering , School of Engineering, The University of Tokyo, 7-3-1, Hongo, Bunkyo-ku, Tokyo, Japan*

ABSTRACT: Tornado-like vortices have been investigated by using LES turbulence model. The flow fields are visualized by virtual water vapor injected from the ground of the numerical model and the evolution from a single-celled vortex into a multi-vortex configuration is successfully reproduced. The flow fields as well as the force balance of four typical tornado configurations, weak vortex, vortex breakdown, vortex touch-down and multi-vortex are investigated. The definitions for the swirl ratio are summarized and the local corner swirl ratio is found to be robust and proposed to universalize the researches.

KEYWORDS: Tornado-like vortex, Swirl ratio, Flow fields, LES, CFD simulation.

1 INTRODUCTION

Tornadoes are one of the severe natural phenomenons and considered as the most violent storm on earth, which makes it important to take proper consideration of tornado-induced wind loads and tornado-borne missiles for wind resistant design of structures. Therefore, detailed information of the three-dimensional flow fields is necessary. Many researchers are motivated to observe the wind dynamics and collect the data in real tornadoes by using velocity and pressure instrumentation. However, due to the extreme danger faced by the observers, data collection for tornado's internal flow fields is still not much of a success. Reproducing tornadoes experimentally or numerically is therefore an alternative.

Laboratory simulations provide a safe, reproducible and controllable approach for the tornado-related researches. Mitsuta and Monji (1984) modified the simulator to provide the circulation by four small fans installed in the circulation chamber. Transition of a vortex from a one-cell to two-cell structure occurred throughout the whole convergence layer in their simulator. Haan et al. (2008) developed a large laboratory simulator with guide-vanes at the top to make the translation of the tornadoes reproducible. Most recently, Tari, P.H. et al. (2010) quantified both the mean and turbulent flow fields for a range of swirl ratios spanning from F0 to F2 scale by using the Particle Image Velocimetry (PIV) method. However, in view of the limitation of observation methods and the extremely complicated flow fields near the ground, it is difficult to make detailed three-dimensional measurements in the boundary layer which has been universally believed to be the most important region in the tornado-like vortices.

Recently, with the advancement in the computer technology, many numerical studies have been conducted. Nolan and Farrell (1999) explored the dynamics of axisymmetric tornado-like vortices. The internal swirl ratio as well as the vortex Reynolds number was defined. D.C

Lewellen et al. (2000) explored some tornado structures being expected to occur in nature. They defined the local corner swirl ratio and proposed the existence of a critical swirl ratio, at which the largest swirl velocity occurs very close to the ground. Ishihara et al. (2011) used LES turbulent model to simulate the flow fields of two types of tornado-like vortices and validated the model by comparing with laboratory simulators. The formation of one-cell and two-cell type vortices were investigated by examining axisymetric time averaged Navier-Stokes equations. However, among all the simulators the definition for the swirl ratio is not uniform and varies from one to another.

In this study, a numerical model representing the Ward-type tornado simulator is built and four typical types of tornado vortices are examined. The details of this model and the case settings are introduced in section 2 including its dimension, grid distribution and boundary conditions. In section 3 the three-dimensional flow fields as well as the force balance is provided. Section 4 proposes a universal definition of swirl ratio to unify the researches.

2 NUMERICAL MODEL

2.1 *Governing equations*

The governing equations employed in LES model are obtained by filtering the time-dependent Navier-Stokes equations as follows:

$$\frac{\partial \rho \tilde{u}_i}{\partial x_i} = 0 \tag{1}$$

$$\frac{\partial}{\partial t}(\rho \tilde{u}_i) + \frac{\partial}{\partial x_j}(\rho \tilde{u}_i \tilde{u}_j) = \frac{\partial}{\partial x_j}\left(\mu \frac{\partial \tilde{u}_i}{\partial x_j}\right) - \frac{\partial \tilde{P}}{\partial x_i} - \frac{\partial \tau_{ij}}{\partial x_j} \tag{2}$$

where $\tilde{u}_i$ and $\tilde{p}$ are filtered mean velocity and filtered pressure respectively. ρ is density, τ_{ij} is subgrid- scale stress and is modeled as follows:

$$\tau_{ij} = -2\mu_t \tilde{S}_{ij} + \frac{1}{3}\tau_{kk}\delta_{ij}, \quad \tilde{S}_{ij} \equiv \frac{1}{2}\left(\frac{\partial \tilde{u}_i}{\partial x_j} + \frac{\partial \tilde{u}_j}{\partial x_i}\right) \tag{3}$$

where μ_t is subgrid-scale turbulent viscosity, and $\tilde{S}_{ij}$ is the rate-of-strain tensor for the resolved scale.

Smagorinsky-Lilly model is used for the subgrid-scale turbulent viscosity,

$$\mu_t = \rho L_s^2 \left|\tilde{S}\right| = \rho L_s \sqrt{2\tilde{S}_{ij}\tilde{S}_{ij}}, \quad L_s = \min\left(\kappa\delta, C_s V^{1/3}\right) \tag{4}$$

where L_s is the mixing length for subgrid-scales, κ is the von Karman constant, 0.42, C_s is Smagorinsky constant, δ is the distance to the closest wall and V is the volume of a computational cell. In this study, C_s is determined as 0.032 based on Oka and Ishihara (2009).

When a wall-adjacent cell is in the laminar sublayer, the wall shear stress is obtained from the laminar stress-strain relationship as follows:

$$\frac{\bar{u}}{u_\tau} = \frac{\rho u_\tau y}{\mu} \tag{5}$$

If the mesh cannot resolve the laminar sublayer, it is assumed that the centroid of the wall-adjacent cells fall within the logarithmic region of the boundary layer, and the law-of-the-wall is employed:

$$\frac{\bar{u}}{u\tau_{\tau}} = \frac{1}{k}\ln E\left(\frac{\rho u_{\tau} y}{\mu}\right) \tag{6}$$

where $\bar{u}$ is the filtered velocity tangential to wall, u_{τ} is the friction velocity and the constant E is 9.793.

2.2 *Configurations and solution scheme*

In this study, a Ward-type simulator (Ward et al. 1972) is chosen and numerically simulated. The configurations of the numerical model are shown in Figure 1(a). Two significant geometry parameters are the height of the inlet layer, h, and the radius of the updraft hole, r_o, which are 200mm and 150mm respectively. The velocity profiles at the inlet are specified as below:

$$\begin{cases} U_{rs} = U_1\left(\dfrac{z}{z_1}\right)^{\frac{1}{n}} \\ V_{rs} = -U_{rs}\tan(\theta) \end{cases} \tag{7}$$

where, U_{rs} and V_{rs} are radial velocity and the tangential velocity at $r=r_s$, n equals to 7, the reference velocity U_1 and the reference height z_1 are set to 0.24m/s and 0.01m respectively through matching the velocity profile in the previous study by Ishihara et al. (2011), and θ is the degree of the inflow angle.

Considering the axisymmetry of tornado-like vortex, an axisymmetric topology method is adopted, see Figure 1(b). With an intent to investigate the turbulent features quantitatively in the vicinity of the center and the region near the ground, very fine mesh is considered in the convergence region. The total mesh number is about 7.8×10^6. Table 1 summarizes the parameters for the mesh and the system of the PC cluster used in this study.

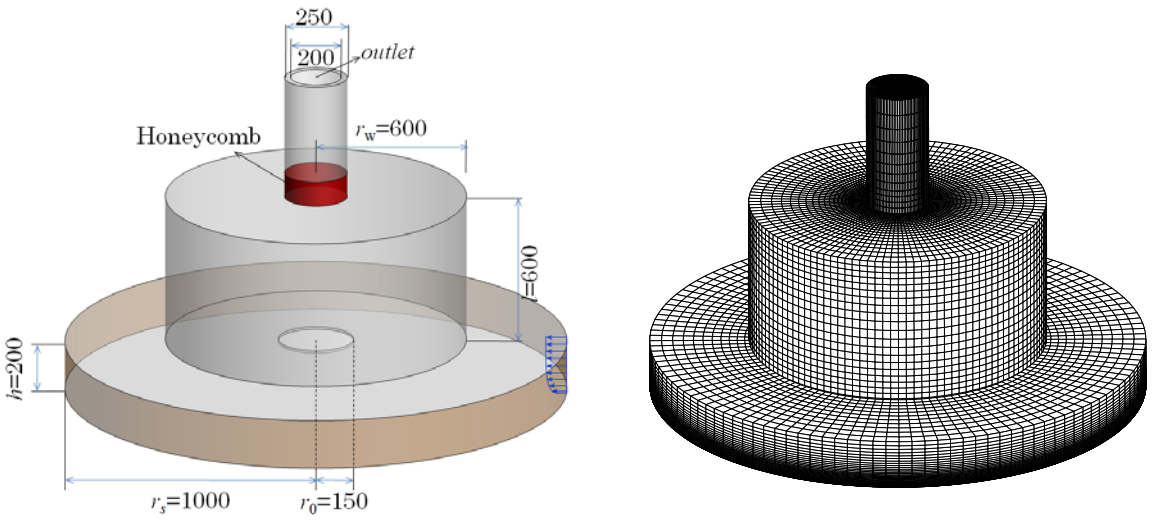

Figure 1. Geometry(a) and mesh(b) of the model.

Table 1. Parameters for the mesh and the system of PC cluster

Mesh size in the radial direction	1.0～25.0mm
Mesh size in the vertical direction	0.1～5.0mm
Mesh number	784200
CPU	Athlon 64 Processor3200, 2.01GHz
Number of nodes	8
CPU time for the case of S=2.44	150h

Finite volume method is used for the present simulations. SIMPLE (semi-implicit pressure linked equations) algorithm is employed for solving the discritized equations (Ferziger and Peric, 2002). The pressure at inlet of the convergence region is set to zero, and velocity at the outlet (0, 0, W_0) is given as (0, 0, 9.55m/s) to generate upward flow in the tornado. Three velocity components and the pressure are set as zero for the initial conditions.

2.3 *Swirl ratio definitions and Case settings*

In both the laboratory and the numerical simulators, a correlation has been found between the vortex structure and the swirl ratio. Various definitions for the swirl ratio have been proposed in the previous studies.

The swirl ratio has historically been defined as the ratio of angular momentum to radial momentum in the vortex, and expressed in the following forms:

$$S_{out}=\frac{\Gamma_\infty r_0}{2Qh},\ S_{out}=\frac{\Gamma_\infty}{2Qa}\ \text{and}\ S_{out}=\frac{\tan\theta}{2a} \tag{8}$$

where, $\Gamma_\infty$is the circulation at the outer edge of the convergence region, $\Gamma_\infty=2\pi r_s h V_\infty$, and a is the aspect ratio, $a=h/r_0$. In case the circulation is imposed by using guide vanes instead of rotating screen, the ratio of the circulation rate to the volume flow rate can easily be replaced by tanθ, where θ is the angle of the guide vanes.

In ISU tornado simulator by F. L. Haan Jr.(2008) the swirl ratio is specifically modified as:

$$S=\frac{r_c\Gamma_c}{2Qh}=\frac{r_c(2\pi r_c V_c)}{2Q}=\frac{\pi r_c^2 V_c}{Q} \tag{9}$$

in which, the circulation, Γ_c, is estimated using the multiplication of the maximum tangential velocity, V_c, and r_c, $\Gamma_c=2\pi r_c h V_c$, r_c is radius of maximum tangential velocity, V_c, in the quasi-cylindrical region.

D.C. Lewellen(2000) proposed a local corner flow swirl ratio, S_c. The specific form of the local corner flow swirl ratio is:

$$S_c=\frac{r_c^*\Gamma_\infty^{*2}}{\Upsilon} \tag{10-a}$$

in which, r_c^* is the characteristic length scale, calculated as $r_c^*\equiv\Gamma_\infty^*/V_c$, $2\pi\Gamma_\infty^*$ is the circulation per unit height in the outer region expressed as $2\pi\Gamma_\infty^*=2\pi V_\infty r_\infty$, Υ is the total depleted circulation flux flowing through the corner flow region, expressed as:

$$\Upsilon\approx 2\pi\int_0^{r_2} W(r,z_2)\,\Gamma_d(r,z_2)\,r\,dr \tag{10-b}$$

where, Γ_d is the depleted angular momentum and defined as $\Gamma_d=\Gamma_\infty-Vr$, r_2 is the radius safely outside of the upper-core region, z_2 is the height just above the corner flow.

Table 2. Case settings and accompany tornado vortex parameters.

Case	θ (°)	S_{out}	S	S_c	Re	Q(m^3/s)	V_c (m/s)	r_c (m)
Case1	46.8	0.4	0.02	0.71	1.6×10^5	0.30	10.72	0.014
Case2	58.0	0.6	0.06	1.59	1.6×10^5	0.30	9.84	0.024
Case3	64.9	0.8	0.12	2.36	1.6×10^5	0.30	9.11	0.035
Case4	69.4	1	0.23	2.93	1.6×10^5	0.30	9.62	0.047
Case5	76.0	1.5	0.34	4.16	1.6×10^5	0.30	10.99	0.054
Case6	79.4	2	0.69	5.39	1.6×10^5	0.30	12.35	0.073
Case7	82.1	2.7	1.06	6.74	1.6×10^5	0.30	14.26	0.084
Case8	83.5	3.3	1.58	7.96	1.6×10^5	0.30	15.98	0.105
Case9	84.4	3.8	2.44	8.89	1.6×10^5	0.30	18.62	0.112
Previous	60.0	0.65	0.08	3.05	1.6×10^5	0.30	8.33	0.030

Notes:

- Case1, Case2, Case4 and Case9 are four typical types of tornado configuration and are chosen for detailed flow field analysis.
- Previous case is the simulation carried out by Ishihara (2011).

In this study, the swirl ratio is increased through increasing the inflow angle. Nine cases are calculated systematically. The case settings as well as tornado vortex parameters for each case are illustrated in Table 2, in which Re is the Reynolds number defined as $Re=W_0D/\upsilon$, $D=2r_0$. It can be found the swirl ratio S_{out} tends to have a larger value compared with S. On the other hand, the local corner swirl ratio S_c shows the maximum value for the same corner flow pattern.

3 FLOW FIELDS CHARACTERISTICS

It is necessary to make the air flow visible and evaluate the vortex in a qualitative manner. For this purpose virtual water vapor is selected as the visualizing substance injected from the bottom of the model. The particles are not released until the flow fields are in the quasi-steady stage to eliminate the effect of the transit field solution.

As the value of the swirl ratio is increased, the vortex goes through various stages, as depicted in Figure 2. When S=0.02, we find the central core to have a smooth, laminar appearance. The core extends upward from the surface to the high elevation spreading radially slightly with height, shown in Figure 2(a). For S=0.06, a "vortex breakdown" occurs where the flow transitions from a tight, laminar vortex to a broader, turbulent state, see Figure 2(b). At S=0.23, the radius of the vortex core increases and the altitude of the breakdown decreases, as shown in Figure 2(c). The vortex breakdown is just above the boundary layer. A still further increase in swirl ratio to S=2.44 results in the breakdown being forced further toward the surface layer, see Figure 2(d). The core of the vortex expands substantially, leaving a relatively calm inner subcore. Concurrent with the expansion of the core the inner downflow penetrates to the lower surface, and in this particular snapshot, a family of several secondary vortices rotating about the main vortex is evident.

3.1 *Mean flow fields*

Quantitative analysis can be achieved by examining the distributions of the mean velocity components. In the following discussion, the maximum tangential velocity in the cyclostrophic balance region, V_c, will be used to normalize the flow fields. The radial distance is normalized by the core radius of the tornado vortex in cyclostrophic balance region, r_c.

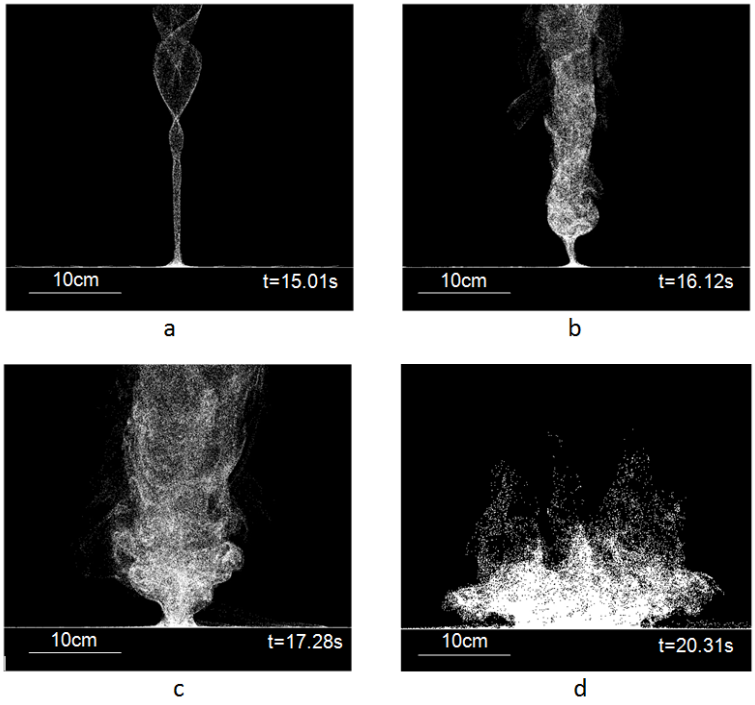

Figure 2. Flow visualization by injecting water vapor from the ground for four typical types of tornado-like vortices, (a) weak vortex, S=0.02, (b) vortex breakdown, S=0.06, (c) vortex touch-down, S=0.23, (d) multi-vortex, S=2.44.

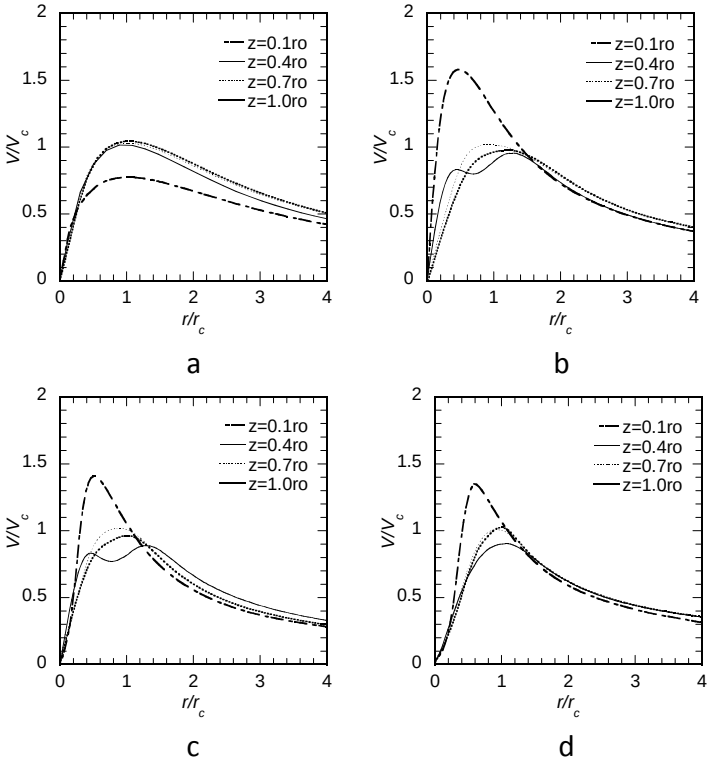

Figure 3. Radial profiles of the normalized tangential velocity for four typical types of tornado-like vortices, (a) weak vortex, S=0.02, (b) vortex breakdown, S=0.06, (c) vortex touch-down, S=0.23, (d) multi-vortex, S=2.44.

The radial profiles of the mean tangential velocity, V, versus nondimensional radial distance are shown in Figure 3(a). For the very low swirl ratio case, S=0.02, the mean tangential velocity field is apparently one dimensional except the layer very near the ground. The core radius, R, defined based on the location of the maximum tangential velocity at each elevation, is almost consistent. For S=0.06, the swirl overshoot appears at the surface layer with maximum tangential velocity being 1.6 times of V_c, and the core radius increases from $0.5r_c$ to $1.0r_c$ with height forming a funnel shape. Further increasing the swirl ratio to the stages of touch-down and multi-vortex, the ratio of maximum swirl velocity, V_{max}, to V_c is nearly a constant, varying in between 1.3 to 1.5, and the radial location of V_{max} changes very slightly, holding about $0.5r_c$.

3.2 *Force balances analysis*

The contributions from each term in Navier-Stokes equation can be calculated by force balances analysis. Ishihara, T. (2011) investigated the force balances of two typical stages by using the time-averaged axisymmetric Navier-Stokes equations. However, a systematic cross comparison for the force balances in various types of vortices is limited and deserved to be studied.

The time-averaged radial Navier-Stokes equation can be expressed as:

$$U\frac{\partial U}{\partial r}+W\frac{\partial U}{\partial z}-\frac{V^2}{r}=-\frac{1}{\rho}\frac{\partial P}{\partial r}-\left(\frac{\partial u^2}{\partial r}+\frac{\partial uw}{\partial z}-\frac{v^2}{r}+\frac{u^2}{r}\right)+D_u \tag{11}$$

The left hand side consists of the radial advection term, A_{ru}, the vertical advection term, A_{zu}, as well as the centrifugal force term, C_r. The right hand side of the equation is the radial pressure

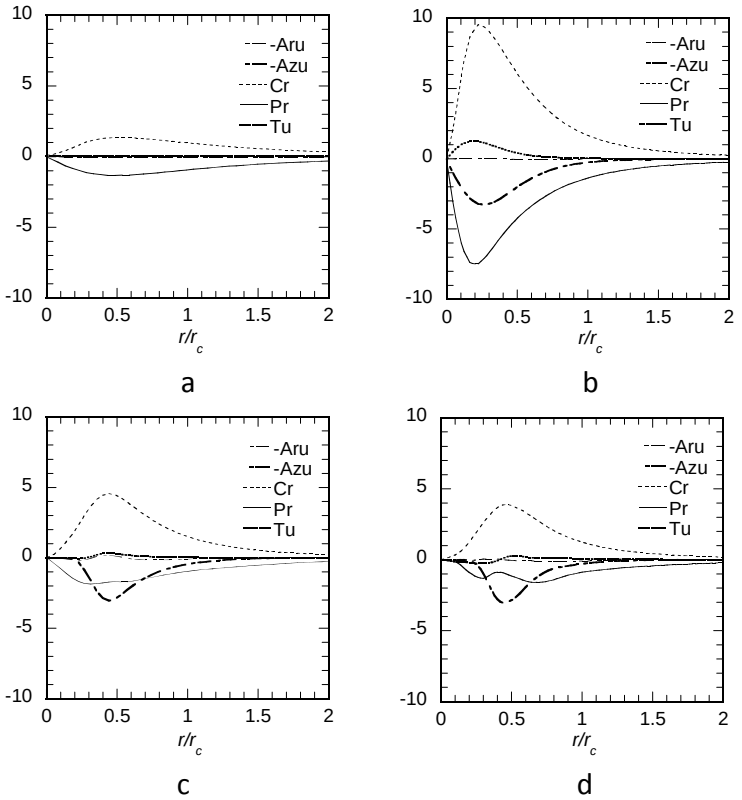

Figure 4. Radial force for four typical types of tornado-like vortices, (a) weak vortex, S=0.02, (b) vortex breakdown, S=0.06, (c) vortex touch-down, S=0.23, (d) multi-vortex, S=2.44.

gradient term, P_r, turbulent force term, T_u, and the diffusion term, D_u. The diffusion term, D_u, in the equation is small enough to be ignored compared with the other terms. u,v,w are root mean squares of the radial, tangential and vertical velocities.

Due to the slight change for the height of maximum tangential velocity, the terms in the radial momentum equations are computed at z=0.1r_o as a function of r/r_c for all the four stages, as shown in Figure 4. Examination of Figure 4(a) reveals that turbulence plays little role for weak vortex stage in the radial momentum balance. The centrifugal term and pressure gradient term are the significant portion of the total balance. Increasing the swirl to S=0.06, the flow evolves from laminar vortex to a turbulent state, followed by a significant change of the radial balance, as shown in Figure 4(b). The principle balance is in between the centrifugal term, pressure gradient term, turbulent term and vertical advective term. The emergence of the turbulent term is the manifestation of the unsteadiness of the flow fields. Figure 4(c) displays the terms in the radial balance for the case of vortex touch-down. The centrifugal term is mainly balanced by the pressure gradient term as well as the vertical advective term. However, different with the state of vortex breakdown, in some region the vertical advection term becomes more important than the pressure gradient term. Radial force balance for multi-vortex is presented in Figure 4(d), which is almost coincident with that for vortex touch-down.

4 PERFORMANCE OF LOCAL CORNER SWIRL RATIO

A pictorial approach is adopted to show how the surface intensification and the shape of the vortices change with the swirl ratio S_c, as illustrated in Figure 5, where U_{min} is the minimum averaged radial velocity, V_{max} is the maximum averaged tangential velocity, W_{max} is the maximum vertical velocity, r_{vmax} and h_{vmax} are the radius and height of the location of the maximum tangential velocity respectively. The parameters V_{max}/V_c, $-U_{min}/V_{max}$, W_{max}/V_{max} and the ratio of r_{vmax} to h_{vmax} are examined. The results of this study will be compared with the previous laboratory-scale numerical study by Ishihara et al. (2011) and the full scale numerical study by Lewellen et al. (2000). It is worth to be mentioned that the methods to obtain the angular momentum are different from one to another. In the previous study by Ishihara et al. (2011), the azimuthal momentum of the inflow is imposed by guide vanes, while in the present 8 cases the circulation is obtained directly from the velocity profile at the inlet boundary. For the full scale numerical model by Lewellen et al. (2000), the boundary condition is obtained from an inner nest of a thunderstorm simulation.

The ratio of the maximum averaged swirl velocity, V_{max}, to the maximum averaged swirl velocity in the upper cyclostrophic region, V_c, as a function of the local corner swirl ratio is demonstrated in Figure 5(a). Examining the set of present cases, the ratio increases sharply from the very low swirl ratio until S_c equals to around 1.6 where the pattern of vortex breakdown occurs and the distinct peak ratio reaches to about 1.7. For increasing the swirl ratio, the ratio of V_{max} to V_c decreases moderately and at last becomes almost a constant varying the values in between 1.3 and 1.5.

Figure 5(b) shows the ratio $-U_{min}/V_{max}$ as a function of the local corner swirl ratio. This ratio increases suddenly from the state of weak vortex, however, it is obvious that, except the very low swirl cases, $-U_{min}/V_{max}$ is insensitive to the swirl ratio and all the data are scattered about a central value 0.65. This near consistency is the indication of the dependency between the low-level radial overshoot and the swirl overshoot.

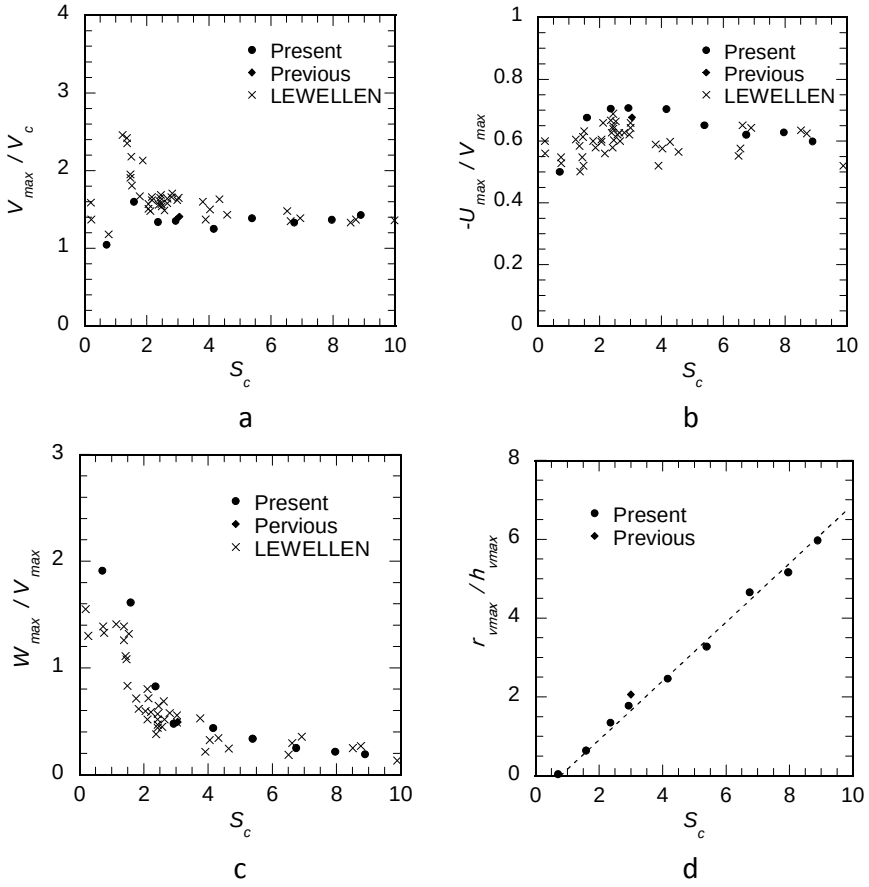

Figure 5. Summery surface intensification and the geometry of tornado vortices as a function of local corner swirl ratio, (a) the ratio of V_{max}/V_c, (b) the ratio of $-U_{min}/V_{max}$, (c) the ratio of W_{max}/V_{max} and (d) the aspect ratio of r_{vmax}/h_{vmax}.

The ratio W_{max}/V_{max} shows the maximum value, about 1.9, at the stages with very low swirl ratios, and decreases with increasing the swirl ratio, as demonstrated in Figure 5(c). The maximum vertical velocity is larger than the maximum tangential velocity until the vortex reaches to the touch-down state, after which the near consistency for the ratio W_{max}/V_{max} is observed with a central value of about 0.4.

A vortex aspect ratio defined as the ratio of r_{vmax} to h_{max} is applied to evaluate the structure of the flow in the vortex corner. As observed in Figure 5(d), the vortex aspect ratio increases linearly with S_c having a slope of about 0.7.

The values of V_{max}/V_c, $-U_{min}/V_{max}$ and W_{max}/V_{max} as a function of local corner swirl ratio obtained in Lewellen et al. (2000) and Ishihara et al. (2011) are also shown for comparison. Even though the present, previous and Lewellen's cases use different numerical models to generate the vortices, it is obvious that the results from different models exhibit the universally same tendencies. Therefore it can be argued that it is reasonable to universalize the researches by using the local corner swirl ratio.

5 CONCLUSIONS

The flow fields as well as the force balances of tornado-like vortices have been investigated by using the LES turbulent model in this study. Following summarizes the conclusions.

1. The visualized flow fields by the injected water fog from the ground successfully show the evolution from a single-celled vortex into a two-cell vortex configuration containing multiple subsidiary vortices.

2. The maximum normalized tangential velocity occurs at the stage of vortex breakdown, after which the maximum tangential velocity almost holds as a constant and the normalized radial location of V_{max} changes very slightly. Turbulence plays little role for weak vortex stage in the radial momentum balance. From the stage of vortex breakdown the force balance changes dramatically and the effects of turbulence emerge.

3. The values of V_{max}/V_c, $-U_{min}/V_{max}$ and W_{max}/V_{max} obtained from different simulators are plotted as a function of local corner swirl ratio and show good comparison. The vortex aspect ratio r_{vmax}/h_{rvmax} shows linear relationship with the local corner swirl ratio having a slope of about 0.7. Based on the consistency provided by the local corner swirl ratio, it is proposed to universalize the researches.

REFERENCES

1 Ferziger, J. and Peric, M., Computational method for fluid dynamics, 3rd Edition, , 2002, Springer.
2 Haan, F.L., Sarkar, P.P., Gallus, W.A., Design, construction and performance of a large tornado simulator for wind engineering applications, Engineering Structures, 2008, Vol.30, pp.1146-1159.
3 Ishihara, T., Oh, S., and Tokuyama, Y., Numerical study on flow fields of tornado-like vortices using the LES turbulence model, Journal of Wind Engineering and Industrial Aerodynamics, 2011, Vol.99, pp.239-248.
4 Lewellen, D.C., Lewellen, W.S., and Sykes, R.I., Large-eddy simulation of a tornado's interaction with the surface, Journal of the Atmospheric Sciences, 1997, Vol.54, pp.581-605.
5 Lewellen, D.C., Lewellen, W.S., and Xia. J., The influence of a local swirl ratio on tornado intensification near the surface, Journal of the Atmospheric Sciences, 2000, Vol.57, pp.527-544.
6 Mitsuta,Y. and Monji, N., Development of a laboratory simulator for small scale atmospheric vortices, Natural Disaster Science, 1984, Vol.6, pp.43-54.
7 Nolan, D.S. and Farrell, B.F., The structure and dynamics of tornado-like vortices, Journal of the Atmospheric Sciences, 1999, Vol.56, pp.2908-2936.
8 Oka,S. and Ishihara,T., Numerical study of aerodynamic characteristics of a square prism in a uniform flow. Journal of Wind Engineering and Industrial Aerodynamics, 2009, Vol.97, pp.548–559.
9 Tari, P.H., Gurka, R., Hangan, H.. Experimental investigation of tornado-like vortex dynamics with swirl ratio: The mean and turbulent flow fields, Journal of Wind Engineering and Industrial Aerodynamics, 2010, Vol.98, pp.936-944.
10 Ward, N.B., The Exploration of Certain Features of Tornado Dynamics Using a Laboratory Model, Journal of the Atmospheric Sciences, 1972, Vol.29, pp.1194-1204.

The Seventh International Colloquium on Bluff Body Aerodynamics and Applications (BBAA7)
Shanghai, China; September 2-6, 2012

Generation of inflow turbulence using the local differential quadrature method

Tong WANG, Shu-yang CAO, Yao-jun GE

State Key Laboratory for Disaster Reduction in Civil Engineering, Tongji University, Shanghai 200092, China

ABSTRACT: Inflow turbulence plays an important role in the field of computational wind engineering. Whereas, generation of inflow turbulence through preliminary numerical simulation of a turbulent boundary layer using traditional low-order numerical algorithms usually can not yield satisfied results corresponding with the prescribed statistics, especially as the power spectral density for lack of high-frequency energy. This paper extends the traditional differential quadrature method (DQM) to the direct numerical simulation (DNS) of inflow turbulence based on the idea of localization with a common staggered mesh. This local DQM can be viewed, to some extent, as a generalized finite difference method whose weighting coefficients can be obtained from different interpolation base functions. It is found that the polynomial interpolation base functions and the Fourier expansion both perform well for the local DQM in modeling turbulence. This method is successfully applied to generate inflow turbulence and good results obtained. Comparisons show that the mean property and turbulence intensity can be well preserved and the high-frequency energy is efficiently improved with increasing the number of locally referenced points of the local DQM.

KEYWORDS: generation of inflow turbulence; the local differential quadrature method; high-frequency energy; turbulent boundary layer; interpolation base functions; DNS.

1 INTRODUCTION

The advent of high-speed computer and the development of accurate numerical algorithms have provided an important third approach — Computational Wind Engineering (CWE), in addition to theory analysis and experiment, for researchers to study the effects of air flow on structures which are usually located at the bottom of the turbulent atmospheric boundary layer (ABL). It is well known that the characteristics of the turbulent ABL vary with the land surface roughness, and that the wind-induced responses of structures are determined mainly by the interaction of the atmospheric turbulence and the released vortex of structures. So the imposed inflow turbulence at the inlet boundary has to satisfy the prescribed requirements, and also the turbulence statistics should not change a lot in the empty wind tunnel (Blocken, *et al.* 2007; Murakami 1998). Besides, in practice, estimating time history of dynamic wind load on structures by performing an unsteady LES heavily depends on the accurate inflow condition at every time step. Therefore, a crucial precondition to the above research activities using CWE is to generate appropriate inflow boundary conditions in accordance with characteristics of the turbulent ABL, i.e. generation of inflow turbulence, which has been a hot research topic in the field of CWE for the past two decades (Nozawa and Tumura 2002).

At present, several methods have been developed to generate inflow turbulence and can generally be classified into two types. The first one is to artificially generate time series of velocity fluctuations by performing an inverse Fourier transformation for the prescribed spectral densities, i.e. the so called “synthetic method” (Kondo, *et al.* 1997, Murayama, *et al*. 1999, Mathey, *at al.* 2006, Huang, *at al.* 2010). The other is to directly conduct preliminary simulation of a turbu-

lent boundary layer using computational fluid dynamics (CFD) (Lund, *at al.* 1998, Nozawa and Tumura 2002, Kataoka and Mizuno 2002, Tabor and Baba-Ahmadi 2009), simply denoted here as "direct method". A more comprehensive review of various methods commonly used for generation of inflow turbulence was given by Tabor and Baba-Ahmadi (2009) and Huang, *et al.* (2007) in which these methods were classified into three types, i.e. precursor database, synthetic method and recycling method. Here the precursor database and the recycling method are combined as the direct method because they are both based on CFD simulation. The synthetic method is relatively convenient and timesaving. And more importantly, the stochastic of its generated inflow turbulence can be guaranteed to satisfy the prescribed target characteristics. Kondo, *et al.* (1997) presented a method to deal with the divergence-free operation to ensure the continuity condition. Huang, *at al.* (2010) proposed a new inflow turbulence generator not only rigorously satisfying the divergence-free condition but also suitable for parallel computation. However, application of this method is limited by the fatal deficiency that its generated turbulent inflow data do not satisfy the Navier-Stokes equations. So the characteristics of the imposed inflow turbulence at the inlet can not be well preserved in the computational domain. In contrast, the direct method avoids this severe defect of the synthetic method, while requires a large computational load. Although the direct method has achieved great success in practice, it still has some defects, for example, it is relatively hard for the direct method to obtain satisfied results corresponding with the prescribed power spectral density for lack of high-frequency energy which is of great importance for analyzing the buffeting response of wind-sensitivity structures and for estimating wind energy utilization. This paper just focuses on the direct method as well as on the improvement to the high-frequency energy.

Generally, there are two approaches to enhance the high-frequency energy in CFD simulation of inflow turbulence. One is to use a fine grid, and the other using a high–precision algorithm which has been adopted in the present paper. The traditional high-order methods used in direct numerical simulation (DNS) of turbulence are compact finite difference, spectral and spectral elements methods. These methods are more accurate while not practical in CWE for their complexity and non-universality. This paper focuses on another high-order algorithm, the differential quadrature method (DQM) proposed by Bellman and Casti (1971). This method is highly accurate and conceptually simple, and has been reported to solve various problems of fluid mechanics. Nevertheless owing to the limitation of its quadrature rules, the traditional DQM has so far been used only for regular domain and laminar flows with a collocated mesh which commonly can not guarantee the continuity condition on boundaries and is prone to bring pressure oscillation. Sun and Zhu (2000) proposed an upwind local DQM to overcome some of the above difficulties. Shu, *et al*. (2003) developed a Local radial basis function-based differential quadrature (RBF-DQ) method, which is essentially a mesh-free approach, to expand its application. However, this method has never been used to turbulent flows and with a staggered mesh.

This paper extends the traditional DQM to turbulence simulation based on the idea of localization analogous to that of Sun and Zhu (2000), but with a common staggered mesh. An upstream grid number n_u and a downstream grid number n_d are introduced into the formulae of the present local DQM. By changing n_u and n_d, different upwind/central schemes of the local DQM can be obtained. Besides, the weighting coefficients can be calculated using different interpolation base functions. Two kinds of interpolation base functions, polynomial and Fourier, will be used and studied for turbulence simulation. Influences of several upwind schemes of the local DQM on high-frequency energy will also be investigated. In the next section, fundamentals of the traditional DQM and the local DQM are shown. Section 3 presents verification of this local DQM for turbulence modeling based on the channel flow. Then a recycling approach for generation of inflow turbulence used in this paper is introduced in Section 4. And Section 5 presents

and analyzes the numerical results of inflow turbulence generated using the present local DQM. Finally, some conclusions are summarized in Section 6.

2 THE LOCAL DIFFERENTIAL QUADRATURE METHOD

To roundly understand the local DQM, the traditional DQM is introduced. The idea of the traditional DQM is essentially an extension of the integral quadrature. It approximates an ordinary/partial derivative of a function with respect to a coordinate direction at a mesh point as the weighted linear sum of all the functional values in the whole domain along that direction. Details can be found in Shu (2000). Without losing generality, consider a one-dimensional function $f(x)$ defined in $[a, b]$. Using the DQM, the nth-order derivative of $f(x)$ with respect to x at a point x_i can be expressed as

$$f^{(n)}\left(x_i\right)=\sum_{k=1}^{N} w^{(n)}\left(i,k\right) f\left(x_k\right), \quad i=1,2,\ldots,N \text{ and } n=1,2,\ldots,N-1 \tag{1}$$

where $a=x_1<x_2<\ldots<x_{N-1}<x_N=b$ are the discrete grid coordinates which can be arbitrarily distributed in space, N the total grid number in x direction, and $w^{(n)}(i,k)$ the corresponding weighting coefficient which can be calculated from various interpolation base functions. For example, weighting coefficients of the first-order derivative can be calculated using the polynomial interpolation base functions, the so-called PDQ by Shu (2000), as

$$\begin{cases} w^{(1)}\left(i,k\right)=\prod\limits_{\substack{k=1\\k\neq i,j}}^{N}\left(x_i-x_k\right)\Big/\prod\limits_{\substack{k=1\\k\neq j}}^{N}\left(x_j-x_k\right), & \text{for } i\neq j \\ w^{(1)}\left(i,i\right)=-\sum\limits_{j=1,j\neq i}^{N} w_{i,j}^{(1)}, & \text{for } i=j \end{cases} \tag{2}$$

or using the Fourier series expansion, the so-called FDQ by Shu (2000), as

$$\begin{cases} w^{(1)}\left(i,k\right)=\dfrac{\pi}{2\left(b-a\right)}\prod\limits_{\substack{k=1\\k\neq i,j}}^{N}\sin\left[\dfrac{\pi\left(x_i-x_k\right)}{2\left(b-a\right)}\right]\Big/\prod\limits_{\substack{k=1\\k\neq j}}^{N}\sin\left[\dfrac{\pi\left(x_i-x_k\right)}{2\left(b-a\right)}\right], & \text{for } i\neq j \\ w^{(1)}\left(i,i\right)=-\sum\limits_{j=1,j\neq i}^{N} w_{i,j}^{(1)}, & \text{for } i=j \end{cases} \tag{3}$$

Weighting coefficients for higher order derivatives can be directly obtained by using the matrix multiplication approach,

$$\left[w^{(n)}\right]=\left[w^{(1)}\right]^{n} \tag{4}$$

It can be seen from the above statement that the traditional DQM is, in fact, a global method because it connects the derivative of a function with respect to a coordinate direction at a given point with all the functional values along that direction in the computational domain. Just as stated in the first section, the traditional DQM is limited to regular domain and laminar flows on a collocated mesh because of its global quadrature rule. In order to extend its application, Sun and Zhu (2000) introduced the idea of localization combined with the upwind mechanism. Next, we will show a local DQM analogous to but different from that of Sun and Zhu (2000).

Unlike the traditional DQM, derivative of a function with respect to a coordinate at an internal point is expressed as a weighted linear sum of the function values at partial grid points rather

than at all the grid points along that coordinate direction. In details, consider an internal point x_i, the derivative of $f(x)$ with respect to x at this point can be expressed as a weighted linear sum of the function values at q grid points near x_i along the x direction, that is to say

$$f^{(n)}(x_i) = \sum_{k=1}^{q} w^{(n)}(r,k) f(x_{i-r+k}) \tag{5}$$

where $q=n_u+n_d+1$; n_u and n_d are the upstream grid number and the downstream grid number, respectively, and they should satisfy $n_u \geq 1$, $n_d \geq 0$ and $n_u \geq n_d$; The number r can be determined in terms of velocity $u(x_i)$ as follows

$$r = \begin{cases} n_u + 1 & u(x_i) \geq 0 \\ n_d + 1 & u(x_i) < 0 \end{cases} \tag{6}$$

It is clear that if $n_u > n_d$, an upwind scheme is obtained, and $n_u = n_d$ corresponds to a central scheme. Fig. 1 illustrates the grid distribution of the local DQM as $n_u=3$ and $n_d=2$.

Figure 1. Grid points used in the local DQM as $n_u=3$ and $n_d=2$

The difference of the present local DQM from that of Sun and Zhu (2000) just lies in the formula of r. In Sun and Zhu (2000), r is determined by

$$r = \begin{cases} q/2+1 & q \text{ is even, } u(x_i) \geq 0 \\ q/2 & q \text{ is even, } u(x_i) < 0 \\ (q+1)/2+1 & q \text{ is odd, } u(x_i) \geq 0 \\ (q+1)/2-1 & q \text{ is odd, } u(x_i) < 0 \end{cases} \tag{7}$$

Evidently, the local DQM of Sun and Zhu (2000) just has upwind schemes, besides the upwind grid number is larger than the downstream grid number by only one or two corresponding to the even or odd q, respectively. So the present local DQM is relatively more general.

It has to be indicated here that the weighting coefficient $w^{(n)}(r,k)$ in Eq. (5) should be calculated from the referenced q grid coordinates x_j ($j=i-r+1,\ldots,i-r+q$) rather than from the N grid coordinates x_j ($j=1,\ldots,N$) using Eq. (2) or Eq. (3). Besides, when an internal point x_i locates its position near the boundary, there may not be enough grid points to introduce upwind or central mechanisms. Then one should adjust n_u and n_d to guarantee that the referenced points are not outside the computational domain, and this treatment will inevitably compromise the accuracy near the boundary. However, this problem will not be considered in the present paper.

The formula (5) is just the present local DQM which imposes the differential quadrature rule on a local domain rather than on the whole domain. Actually this method can be considered, to some extent, as a generalized high-order finite difference method for the weighting coefficients can be obtained by using various interpolation base functions. For example, if the polynomial interpolation base functions are used, the local DQM is identical with the highest-order, i.e. (q-1)th, finite difference scheme according to the demonstration of Shu (2000). And if the Fourier expansion is used, the local DQM is similar, to some extent, to the spectral element method. In

addition, because the differential quadrature rule is used locally, the staggered mesh can also be introduced. From this point, the local DQM is similar to the FDM and FVM except the values of weighting coefficients and the approach to calculate them.

3 VERIFICATION OF THE LOCAL DQM

In this section, the above local DQM is applied to model the channel flow at Re_τ=180 to check its validation for turbulence simulation. Two kinds of interpolation base functions, polynomial and Fourier expansion, are used to calculate the weighting coefficients to study the effects of different base functions on numerical results. For convenient, the above two cases are denoted as "local PDQ" and "local FDQ", respectively, for short. The governing equations used here, and also hereafter for generation of inflow turbulence, are the three-dimensional unsteady incompressible Navier-Stokes equations in Cartesian coordinate,

$$\begin{cases} \nabla \cdot \mathbf{V} = 0 \\ \mathbf{V}_t + (\mathbf{V} \cdot \nabla)\mathbf{V} + \nabla p/\rho = \nu \nabla^2 \mathbf{V} \end{cases} \tag{8}$$

where $\mathbf{V}=\{u,v,w\}^{\mathrm{T}}$ is the velocity vector, p the pressure, ρ the density and v the kinematic viscosity coefficient. A common staggered mesh is introduced: the pressure p is defined in the center of the cell, and the velocities u, v and w are defined on the surface center of the cell normal to x, y and z axis, respectively.

The traditional fractional step method is applied to solve the above equations. And the local DQM shown ahead is only used to discretize the convection terms in space while calculating the intermediate velocities, and the viscous terms are spatially discretized by the three-point second-order central difference scheme. In time, the first-order explicit Euler scheme is used for the unsteady terms, the second-order Adams-Bashforth scheme for the convection terms and Crank-Nicolson for the viscous terms.

The computational domain is $2\pi\times2\times\pi$ in longitudinal (streamwise), vertical (wall-normal) and spanwise direction, respectively, with a coarse mesh, 65×65×65. Uniform grid is used in the streamwise and spanwise direction, and unequal in vertical direction. The vertical grid size varies gradually from 0.005 (y^+=0.9) near the wall to 0.064 (y^+=11.5) at the center of the channel. Boundary conditions here are: a periodic condition for the streamwise and spanwise directions, a non-slip boundary condition for the upper and bottom floors.

Fig. 2 and Fig. 3 show the calculated mean velocity profiles and *root-mean-square* (*rms*) of velocity fluctuations using the local PDQ and the local FDQ, respectively, compared with numerical data of Del Alamo and Jimenez (2003).

Three central schemes, CS3(n_u = n_d =1), CS5(n_u = n_d =2) and CS7(n_u = n_d =3), and three upwind schemes, US4(n_u =2, n_d =1), US6(n_u =3, n_d =2) and US8(n_u =4, n_d =3), are considered for the local DQM. Because the Reynolds number here is not very large, there is no distinct unphysical oscillation while using central schemes. The time step, Δt, for the local PDQ is specified as 0.0001 and 0.00005 respectively for the upwind and central schemes. For the local FDQ, Δt is fixed as 0.00005 for all schemes, and it is hard to obtain convergent results using a larger time step as that of PDQ.

As shown in Figs. 2 and 3, the results of the present local DQM have a good agreement with those of Del Alamo and Jimenez (2003) obtained by using the spectral method, though the present grid mesh is much coarse. It should be indicated here that CS3 and US4 of the local PDQ are identical with the traditional three-point second-order central difference and the four-point third-order upwind difference, respectively. It is clear that the present results are improved efficiently with increasing the number of referenced points, and the central schemes are more accu-

rate than the upwind schemes for possessing the least numerical diffusion. Comparisons between Fig. 2 and 3 indicate that the local PDQ and the local FDQ yield almost the same mean-velocity profiles, while some discrepancy for *rms* of velocity fluctuations. So it can be concluded that the local DQM is applicable for the turbulence simulation.

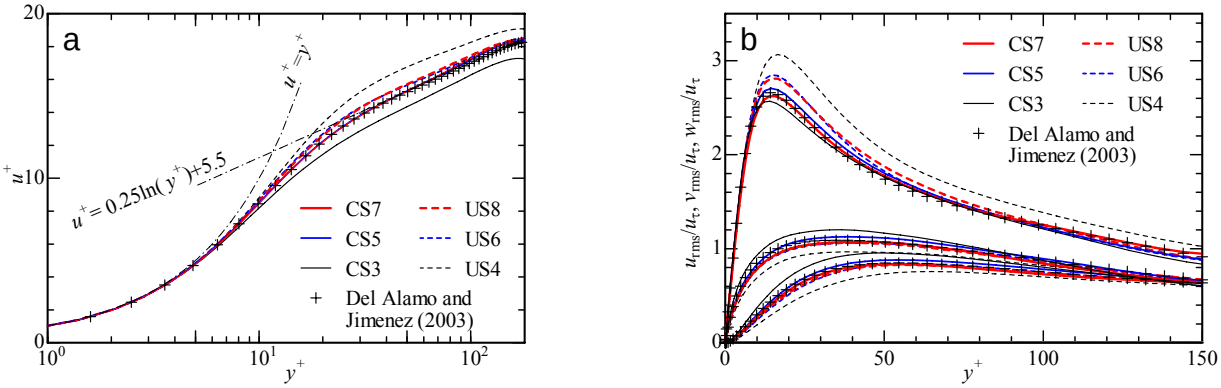

Figure 2. Numerical results of the local PDQ for the channel flow at Re_τ=180: (a) Mean-velocity profiles; (b) *rms* of velocity fluctuations

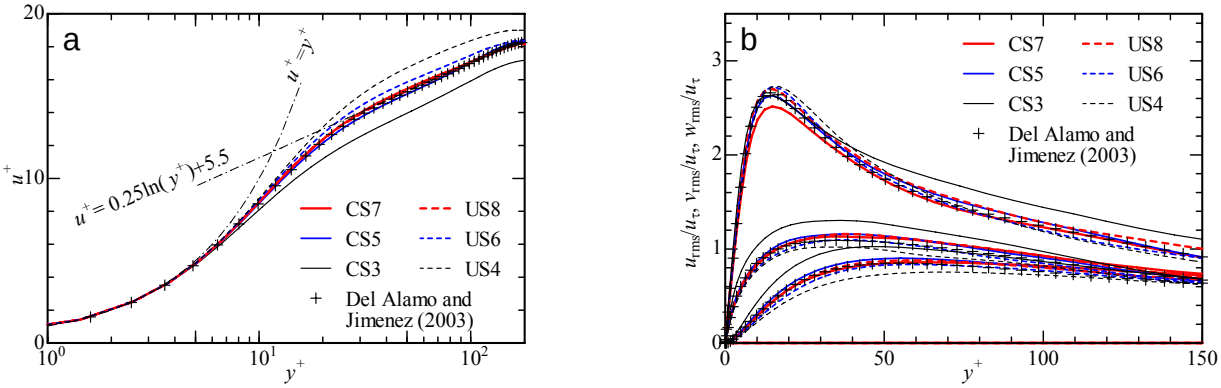

Figure 3. Numerical results of the local FDQ for the channel flow at Re_τ=180: (a) Mean-velocity profiles; (b) *rms* of velocity fluctuations

4 APPROACH FOR GENERATING INFLOW TURBULENCE

The most widely used direct method for generation of inflow turbulence is the recycling method in which the velocity in a downstream plane is extracted and rescaled for the inflow boundary. In this method, the region used to generate turbulence is usually referred to as ‘‘driver region’’, and the second region that we are interested in is usually referred to as ‘‘main region’’. Lund, *et al.* (1998) first proposed this rescaling recycling method to generate developing turbulent inflow data for LES. Kataoka and Mizuno (2002) simplified Lund’s method by assuming that the boundary layer thickness is constant within the driver section. Nozawa and Tumura (2002) extended Lund’s method to a rough-wall boundary layer flow using a roughness block arrangement. For simplicity, the simplified recycling method proposed by Kataoka and Mizuno (2002) is adopted in this paper to generate inflow turbulence, and its detailed process is shown in Fig. 4.

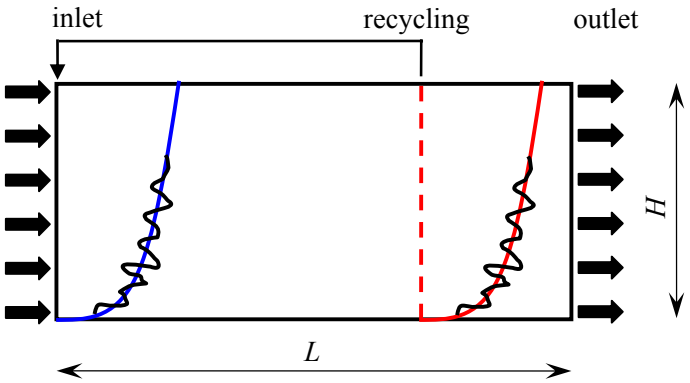

Figure 4. Sketch map of Kataoka's recycling method

A mean velocity profile is prescribed at the inlet, and only the fluctuating part is directly extracted from the recycling station to the inlet boundary without rescaling. The velocity components at the inlet are given as follows,

$$\begin{cases} u_{\text{inlt}}(y,z,t) = \langle u \rangle_{\text{inlt}}(z) + \phi(\eta) \times \{ u(y,z,t) - \langle u \rangle(y,z) \}_{\text{recy}} \\ v_{\text{inlt}}(y,z,t) = \phi(\eta) \times \{ v(y,z,t) - \langle v \rangle(y,z) \}_{\text{recy}} \\ w_{\text{inlt}}(y,z,t) = \phi(\eta) \times \{ w(y,z,t) - \langle w \rangle(y,z) \}_{\text{recy}} \end{cases} \tag{9}$$

where the subscripts denote the values at the inlet (inlt) and the recycling (recy) station, and $\langle \bullet \rangle$ represents a time-averaged value. $\langle u \rangle_{\text{inlt}}$ is set as the prescribed velocity profile. The added damping function $\phi(\eta)$ blocks the velocity fluctuation from developing in the free stream. Kataoka (2008) gave the damping function as

$$\begin{cases} \phi(\eta) = \dfrac{1}{2}\left\{ 1 - \tanh\left[\dfrac{8.0(\eta - 1)}{0.82 - 0.4\eta} \right] \Big/ \tanh(8.0) \right\} \\ \eta = y/\delta \quad (\delta : \text{boundary layer thickness}) \end{cases} \tag{10}$$

Other boundary conditions are: a convection outflow boundary condition for the outlet, a free-slip boundary condition for the ceiling, a non-slip boundary condition for the bottom and a periodic condition for the spanwise boundary.

5 GENERATION OF INLFOW TURBULENCE USING THE LOCAL DQM

Generation of inflow turbulence using traditional low-order numerical algorithms usually suffers the difficulty of bad statistics, especially as the power spectral density for lack of high-frequency energy. An efficient approach to solve this defect is to use a finer mesh which consequently results in a large computational load. Another efficient way is to use high-order methods. In this section, the local DQM will be used to generate inflow turbulence at two relatively high Reynolds numbers, $Re_\theta \approx 1120$ and 1460, based on the recycling approach presented in Section 4. At these high Reynolds numbers, it is hard for the central schemes of the local DQM to obtain convergent results because of large numerical oscillation. In addition, the local PDQ and the local FDQ have almost the same behavior in turbulence simulation just as shown in Section 3. So, only upwind schemes of the local PDQ are used here, which undoubtedly introduce some nu-

merical diffusion. However, our focus will mainly be put on preservation and the high-frequency energy.

5.1 *Details for the calculation*

It is assumed that the boundary layer thickness is constant in the recycling section from the inlet to the recycling station (Kataoka and Mizuno 2002), so the streamwise length of the recycling section can not be very large. Referring to the work of Kataoka and Mizuno (2002) and Kataoka (2008), the streamwise length of the recycling section is specified here as δ, and the whole computational domain is L=1.5δ in flow direction, H=1.6δ in vertical direction and 1.2δ in spanwise direction. A relatively coarse mesh, 50×90×40 in streamwise, vertical and spanwise direction, is generated. Uniform grid is used in the streamwise and spanwise direction, and unequal in vertical direction. The vertical grid size varies from 0.0012δ near the wall to 0.078δ at the ceiling. The discretization schemes are the same as those of Section 3 and the same staggered mesh is used. The damping function of Eq. (10) is applied.

Two different mean-velocity profiles of power law are prescribed at the inlet boundary with exponent α=0.21 and 0.17 for Re_θ≈1120 and 1460, respectively.

5.2 *Results and comparisons*

Fig. 5 shows the calculated mean-velocity profiles at several positions, x/δ=0.25, 0.75 and 1.25, in streamwise direction compared with target ones, numerical data of Jimenez, *et al.* (2009) at Re_θ≈1100 and experimental data of DeGraaff and Eaton (2000) at Re_θ≈1430.

Only three upwind schemes, US4(n_u =2, n_d =1), US6(n_u =3, n_d =2) and US8(n_u =4, n_d =3), are considered here . As shown in Fig. 5, the calculated mean-velocity profiles of the above three schemes all have a good agreement with the target one while the discrepancy becomes a little larger at downstream. As a whole, the mean-velocity profile is well preserved in the computational domain.

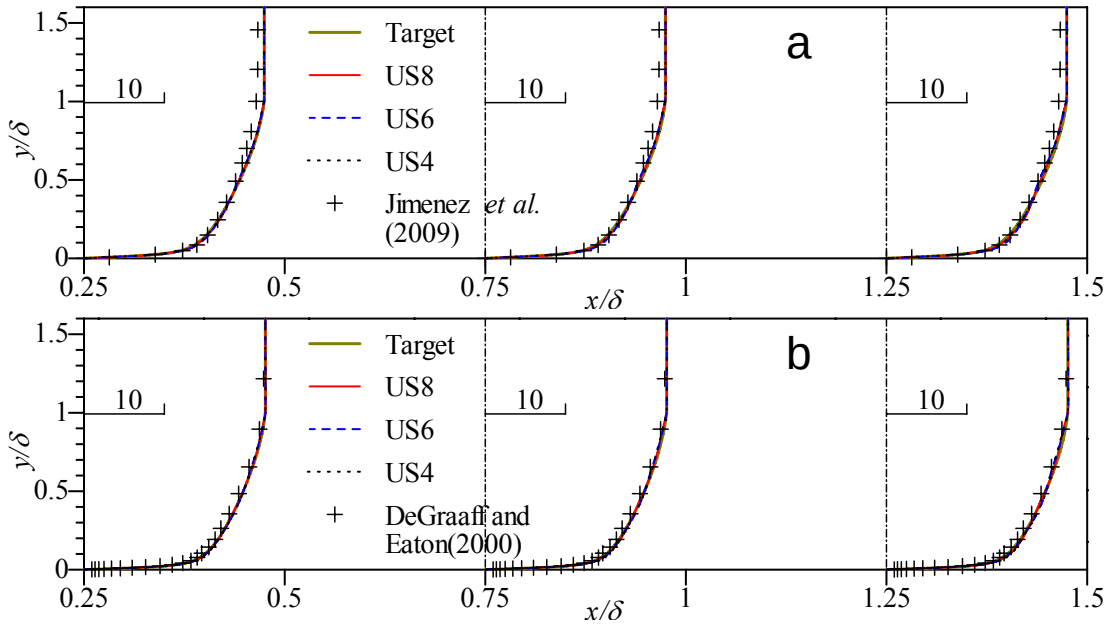

Figure 5. Calculated *rms* profiles: (a) α=0.21 and Re_θ≈1120; (b) α=0.17 and Re_θ≈1460

Fig. 6 shows the calculated *rms* of the streamwise velocity fluctuation in wall unit, u_{rms}/u_τ, compared with the numerical results of Jimenez *et al.* (2009) at $Re_\theta \approx 1100$ and experimental data of DeGraaff and Eaton (2000) at $Re_\theta \approx 1430$. Like the mean velocity, the profile of *rms* can also be well preserved in the computational domain. However, all the three upwind schemes overestimate *rms* within the height of δ and underestimate it above this height. Good agreement is shown for the higher order scheme, US8, although there is a large discrepancy in the outer region. This may attribute to the selection of the damping function. In our trial calculations, it is found that the *rms*, especially in the outer region, heavily depends on the selection the damping function. However, we are not going to discuss this problem, because our focus is not here.

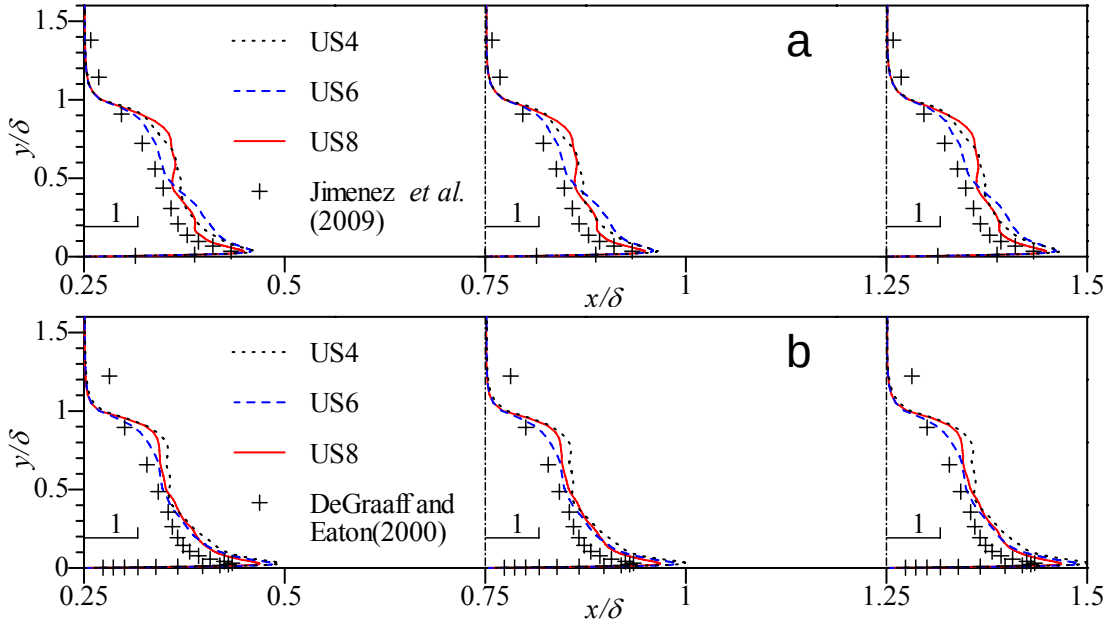

Figure 6. Calculated *rms* profiles: (a) α=0.21 and $Re_\theta \approx 1120$; (b) α=0.17 and $Re_\theta \approx 1460$

From the above results and comparisons, it can be concluded that the recycling method based on the local DQM can generate relatively satisfied mean and *rms* results. Besides, this method has a good preservation which may mainly attribute to the short streamwise length of the computational domain.

Fig. 7 shows the power spectral densities of the along-wind velocity fluctuation at x/δ=0.75, y=0.075δ ($y^+ \approx 32$) and z/δ=0.6 for Re_θ=1120 and at x/δ=0.75, y=0.075δ ($y^+ \approx 43$) and z/δ=0.6 for Re_θ=1460, compared with the Karman spectrum. The data of US4 follows the Karman spectrum until $n\delta/U$=2.3, US6 until $n\delta/U$=3.5 and US8 until $n\delta/U$=4.3 for $Re_\theta \approx 1120$. The improvement of high-order schemes to the high-frequency energy is remarkable. And similar conclusions can be obtained for $Re_\theta \approx 1460$. This can also be obtained from the corresponding time histories of the along-wind velocity as shown in Fig. 8.

Only one second, from 6 to 7, of the time history is presented in Fig. 8 for a clear show. Mean velocities of the three time histories are almost the same. It can be seen clearly from Fig. 8 that the curves become smoother and smoother with decreasing the order of the local PDQ from US8 to US4. It means that smaller vortex can be represented using higher-order schemes of the local DQM at the same mesh.

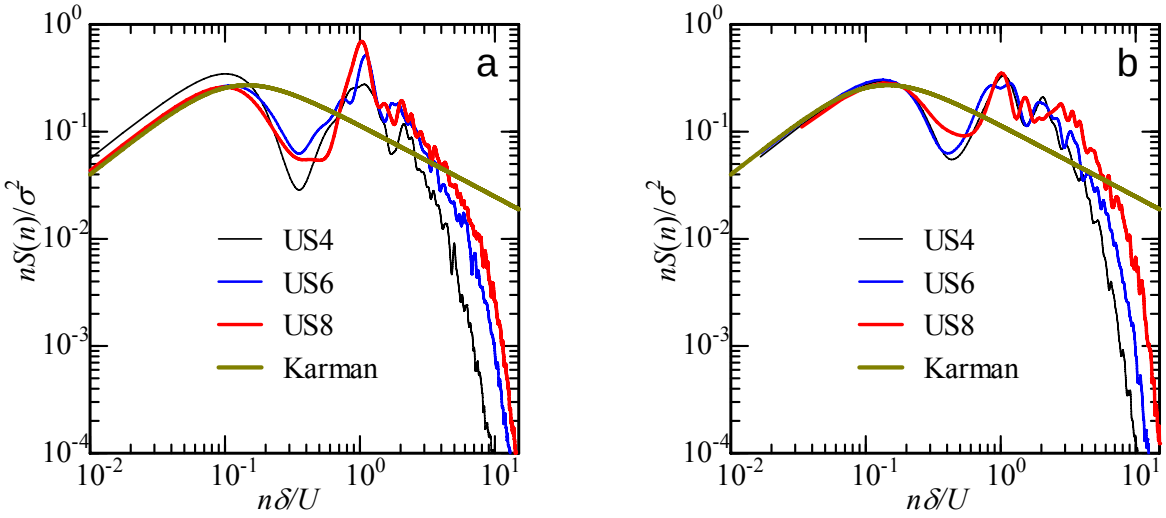

Figure 7. Calculated power spectral densities: (a) α=0.21 and Re_θ≈1120; (b) α=0.16 and Re_θ≈1460

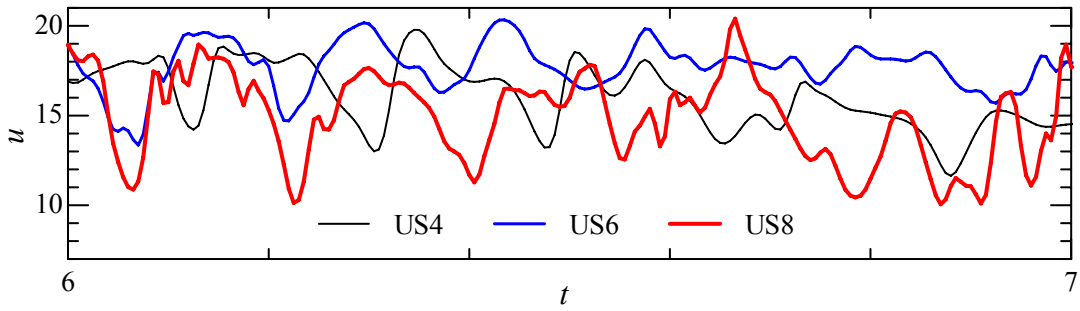

Figure 8. Time histories of the along-wind velocity for Re_θ≈1120 at x/δ=0.75, y/δ=0.056, and z/δ=0.6

6 CONCLUSIONS

In this paper, a local DQM is developed from the traditional global DQM based on the idea of localization combined with a common staggered mesh, different from existing ones. This method can be viewed as a generalized finite difference method. An upwind grid number and a down-stream grid number are introduced into the formulae of this local DQM. Different upwind/central schemes of the local DQM can be obtained by changing these two numbers. The local PDQ whose weighting coefficients are obtained by polynomials and the local FDQ whose weighting coefficients calculated by the Fourier expansion are both applied to the channel flow with several upwind/central schemes. Results indicate that the local PDQ and the local FDQ both perform well, and the central schemes are more accurate than the upwind ones for possessing the least numerical diffusion. Finally, the local PDQ is successfully applied to generate inflow turbulence with several upwind schemes. The mean properties and turbulence intensities can be well pre-served in the computational domain. With increasing the referenced grid number, the high-frequency energy is efficiently enhanced.

7 ACKNOWLEDGEMENTS

This work is supported by the National Natural Science Foundation of China (No. 50978202) and the NSFC-JST Cooperative Research Project (No. 51021140005).

8 REFERENCES

1 R. Bellman and J. Casti, Differential quadrature and long-term integration, *J. Math. Anal. Appl.*, **34** (1971) 235-238.

2 B. Blocken, T. Stathopoulos and J. Carmeliet, CFD simulation of the atmospheric boundary layer: wall function problems, *Atmos. Environ.*, **41** (2007) 238-252.

3 D.B. DeGraaff and J.K. Eaton, Reynolds-number scaling of the flat-plate turbulent boundary layer, *J. Fluid Mech.*, **422** (2000) 319-346.

4 J.C. Del Alamo and J. Jimenez, Spectra of the very large anisotropic scales in turbulent channels, *Phys. Fluids*, **15** (2003) 41-44.

5 S.H. Huang, Q.S. Li and J.R. Wu, A general inflow turbulence generator for large eddy simulation, *J. Wind Eng. Ind. Aerod.*, **98** (2010) 600-617.

6 S.H. Huang, Q.S. Li and S. Xu, Numerical evaluation of wind effects on a tall steel building by CFD, *J. Constr. Steel Res.*, **63** (2007) 612-627.

7 J. Jimenez, S. Hoyas, M.P. Simens and Y. Mizuno, Comparison of turbulent boundary layers and channels from direct numerical simulation, *Sixth International Symposium on Turbulence and Shear Flow Phenomena*, Seoul, Korea, 2009, pp. 289-294.

8 H. Kataoka, Numerical simulations of a wind-induced vibrating square cylinder within turbulent boundary layer, *J. Wind Eng. Ind. Aerod.*, **96** (2002) 1985-1997.

9 H. Kataoka and M. Mizuno, Numerical flow computation around aeroelastic 3D square cylinder using inflow turbulence, *Wind Struct.*, **5** (2002) 379-392.

10 K. Kondo, S. Murakami and A. Mochida, Generation of velocity fluctuations for inflow boundary condition of LES, *J. Wind Eng. Ind. Aerod.*, **67/&68** (1997) 51–64.

11 T.S. Lund, X.H. Wu and K.D. Squires, Generation of turbulent inflow data for spatially-developing boundary layer simulations, *J. Comput. Phys.*, **140** (1998) 233-258.

12 F. Mathey, D. Cokljat, J.P. Bertoglio and E. Sergent, Assessment of the vortex method for large eddy simulation inlet conditions. *Progress in Computational Fluid Dynamics, An International Journal*, **6** (2006) 58–67.

13 S. Murakami, Overview of turbulence models applied in CWE-1997, *J. Wind Eng. Ind. Aerod.*, **74-76** (1998) 1-24.

14 T. Maruyama, W. Rodi, Y. Maruyama and H. Hiraoka, Large eddy simulation of the turbulent boundary layer behind roughness elements using an artificially generated inflow, *J. Wind Eng. Ind. Aerod.*, **83** (1999) 381–392.

15 K. Nozawa and T. Tamura, Large eddy simulation of the flow around a low-rise building immersed in a rough-wall turbulent boundary layer, *J. Wind Eng. Ind. Aerod.*, **90** (2002) 1151-1162.

16 C. Shu, Differential Quadrature and Its Applications in Engineering, Springer, London, 2000.

17 C. Shu, H. Ding and K.S. Yeo, Local radial basis function-based differential quadrature method and its application to solve two-dimensional incompressible Navier‐ Stokes equations, *Comput. Methods Appl. Mech. Engrg.*, **192** (2003) 941-954.

18 J.A. Sun and Z.Y. Zhu, Upwind local differential quadrature method for solving *incompressible* viscous flow, *Comput. Methods Appl. Mech. Engrg.*, **188** (2000) 495-504.

19 G.R. Tabor and M.H. Baha-Ahmadi, Inlet conditions for large eddy simulation: a review, *Comput. Fluids*, **39** (2010) 553–567.

The Seventh International Colloquium on Bluff Body Aerodynamics and Applications (BBAA7)
Shanghai, China; September 2-6, 2012

3-D LES numerical simulation researches on wind flows interfered by rough waves

Fuyou Xu[1*], Xuyong Ying[2], Zhe Zhang [3], Wenjuan Lou[4]

[1,2,3]School of Civil Engineering, Dalian University of Technology, Dalian China 116024
[4]School of Architecture Engineering, Zhejiang University, Hangzhou China 310012
Corresponding author E-mail: fuyouxu@hotmail.com

ABSTRACT: Under the actions strong wind over the sea, rough waves may roar and interfere wind flows. The flows may become extreme complicated and fluctuated and incur unusual response for structures in this region. The strong interfered performances of wind flows near sea surface by rough waves are investigated by using the 3-D LES (Large-Eddy-Simulation) numerical simulation technique. The research results indicate that the numerical simulation results are basically consistent with those by wind tunnel experiments. The difference can not be avoided and the major causes are presented. With the interference of wave, the wind flows fluctuated intensely, and the unsteady characteristics is very significant, which largely dependent upon the wave shapes. The apparent influential region by wave ranges from the wave crest to 15 times of wave height downwind horizontally and 4 times of wave height upward vertically.

KEYWORDS: 3-D LES; sea wave; aerodynamic interference; numerical simulation

1. INTRODUCTION

On the extreme (such as once every hundred years) climatic conditions, under the actions of strong wind, wild sea waves (crest may be higher than 8m, or even more) may appear. The combined effects from wind, waves and currents will have an extremely negative impact on bridges and/or offshore platforms. Wave velocity is generally lower than the wind speed, thus the wave can be regarded as an obstacle, and it will influence the downwind flow field characteristics, especially for the roaring wave, its impact is very significant, may lead to very complex wind flow field. The turbulence intensity and wind angle of attack, etc. may be completely different with the normal wind field. Therefore, unusual impact from the interfered wind flows may construct the terrible threat to the artificial structures. However, only a few researches have been carried out in references and/or documents [1-4]. Exhaustive investigations on this issue should be further conducted

In order to study the influence of wind interfered by rough waves on bridge and/or offshore platform, it is necessary to investigate the characteristics of wind flow downwind of the wave beforehand. Wind tunnel test and numerical simulation are both applicable, and the latter one is expounded and the results are compared with by the former one in this study. The properties are analyzed and summarized, and some conclusions are drawn.

2. WAVE SHAPE

For actual sea waves, enormous forms can be observed and it is impossible to investigate all of them. In this study, only the extreme cases are concerned. The waves with 8m height are considered as the examples. For such fairly rough waves, the shape is relatively simple and the distance between two wave peaks is very long (maybe longer than 500m). So for the high waves, it is rarely to observe several accompanied peaks, and one single wave may usually emerge. For the sea waves, two simplified shapes are selected and quantified with scale of 1:40. Certainly, the influence of more types of wave shapes and even groups of waves on wind flows can be studied with similar methods.

Wave shape type 1: certain function curve, x=exp(0.25*z), y=(normpdf(0,4,x), plot(x,y) ($3 \le x \le 9.9$). The shape can be achieved through stretching or panning the curve in both horizontal and vertical coordinates, and the width and height are 30cm and 20cm, respectively.

$$y = \frac{689.6552}{(0.3255x+4)\sqrt{2\pi}} e^{\frac{-8}{(0.3255x+4)^2}} - 21.7241 \quad (5.7849 \le x \le 24.2151)$$

Wave shape type 2: The probabilistic density function of standard normal distribution, and the interval of X axis is[-2.5, 2.5]. The shape can be realized through the curve, and the width and height are 60cm and 20cm, respectively.

$$y = 50\frac{1}{\sqrt{2\pi}} e^{\frac{-x^2}{288}} \quad (-30 \le x \le 30)$$

The graphs of two wave shapes are plotted in Fig.1.

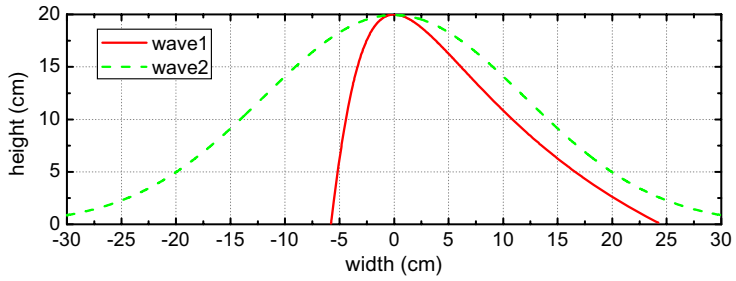

Fig.1 Wave shape graphs

3. NUMERICAL SIMULATION MODEL

3.1 *Geometric modeling and meshing*

The geometric ratio is 1:40 for numerical modeling, and the three-dimensional computational domain is taken as 26m (length) × 2.5m (height) × 1m (Width). The horizontal distance between wave crest and inlet is 8m, and the outlet is 18m apart from the crest. The model is 0.2m high. The computational domain for Wave 1 meshes is shown in Fig. 2, and the triangle unstructured mesh is adopted. Boundary layer mesh is used for Near-wall region meshing to ensure the requirements of stable numerical solving on the wall boundary layer. The boundary layer height of the first grid is 0.0002m. Owing to the fact of two-dimensional segmental rigid computational model, the statistical average of the flow maybe assumed in the spanwise direction, and it is divided into 30 grids. The total volume mesh number is about 1,230,750. The sketch maps of 2-D and 3-D local computational domain and meshgrids are shown in Fig.2 For Wave 2, it is similar to that of wave 1 using the same modeling approaches, and the total volume mesh number is about 1,619,430.

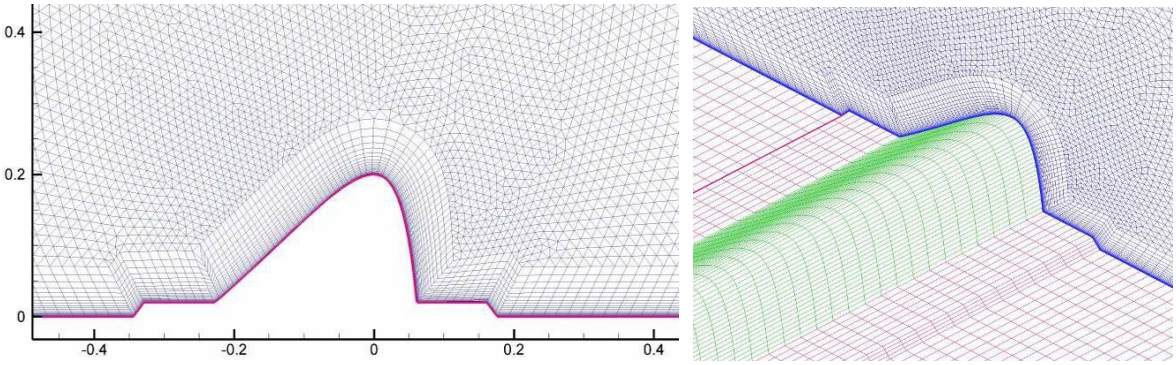

(a)2-D local grids sketch (b)3-D local grids sketch

Fig.2 Computational domain and meshgrids

3.2 *Computational parameters*

The3-dimensional Large Eddy Simulation model is utilized for numerical analysis. The spatial discretization can be realized using central difference, and the velocity pressure coupling maybe solved using the SIMPLE (Semi-Implicit Method for Pressure-Linked Equations) algorithm based on decoupling idea. The convergence criterion for Iterative calculation is set to be the non-dimensional root mean square residual decays below 10^{-4}.

The boundary conditions for the numerical model are respectively set as follows: the inlet flow velocity is smoothly 10m/s (It need to be mentioned that the Reynolds number effect may exist, which is not considered for limitation of the context length); the outlet flows are completely developed; the top surface is free boundary; the side surface is symmetric boundary; the model surface and sea level is no-slipping wall boundary, and the standard wall function is adopted; the time interval of calculation step is 0.005s; when the flow field become stable, the calculation time is 15s, and the steps are 3000.

4 RESULTS AND ANALYSIS

The contours of different parameters are plotted in Fig.4-Fig.7, respectively.

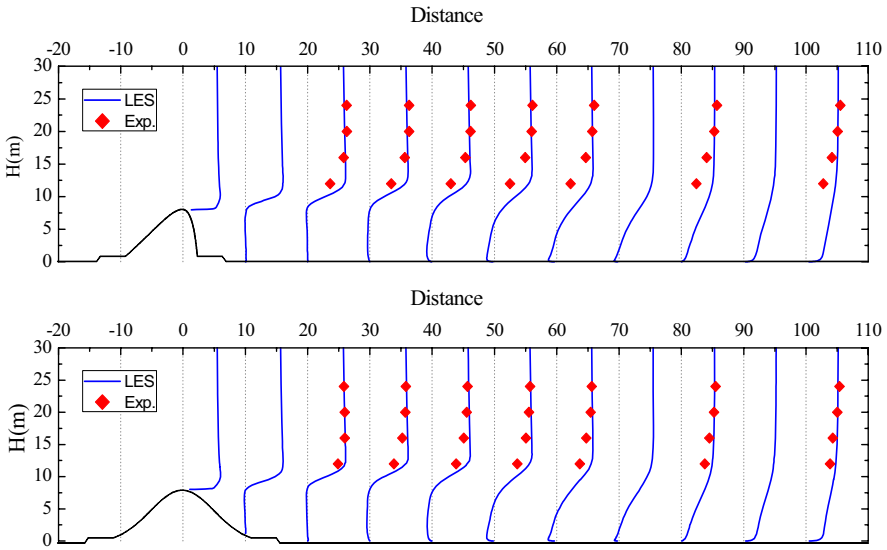

Fig.3 Horizontal mean velocity profiles

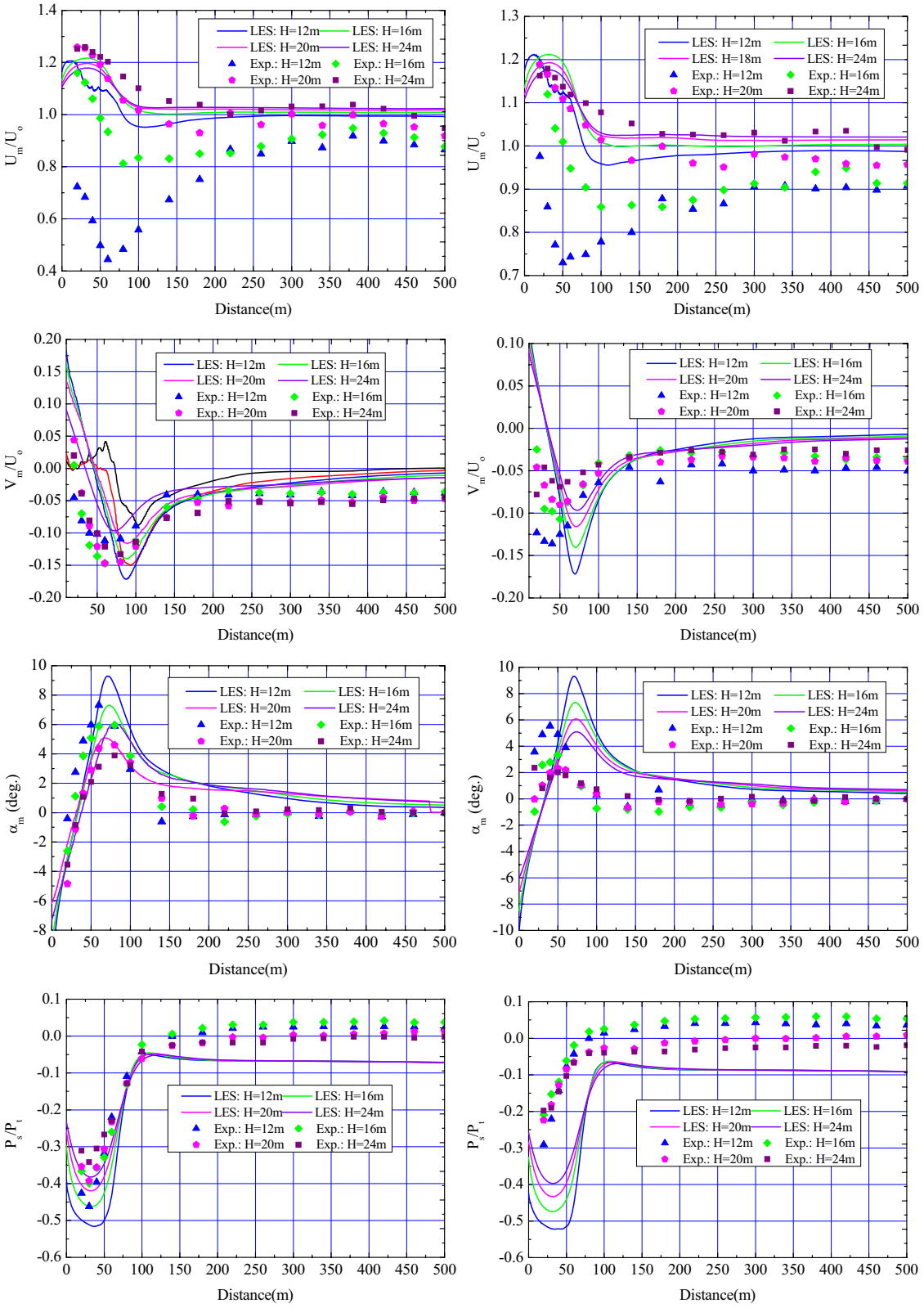

(a) Mean values

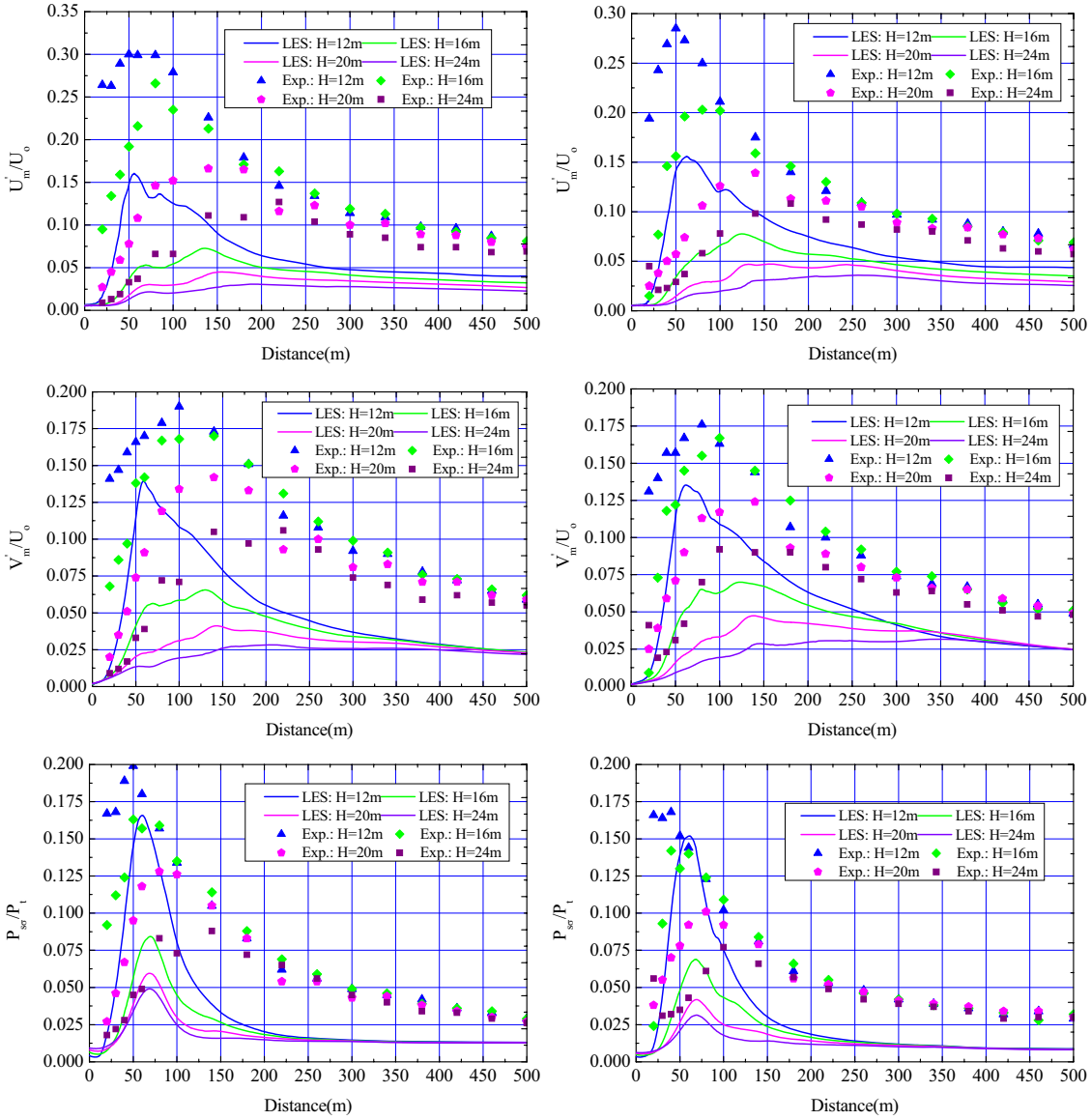

(b) Std values

Wave 1 Wave 2

Fig.4 Comparisons of computational and experimental results

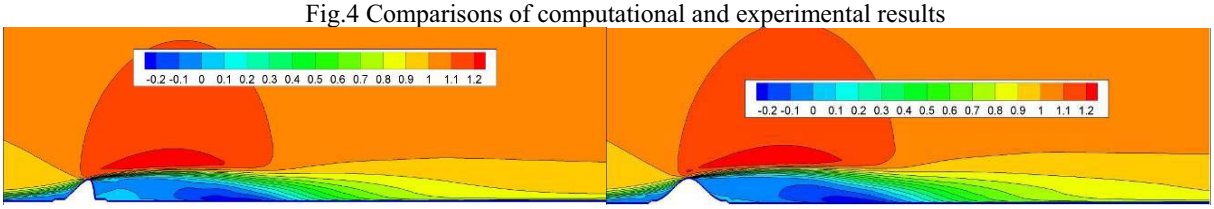

(a) Horizontal mean velocity contour

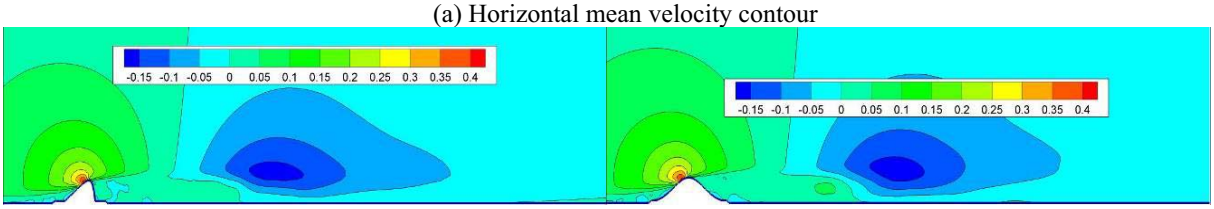

(b) Vertical mean velocity contour

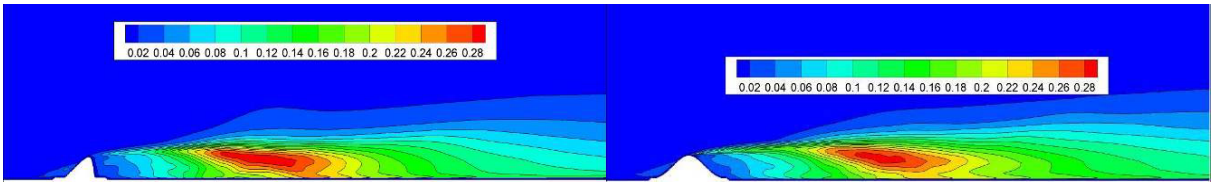

(c) Horizontal fluctuated velocity contour

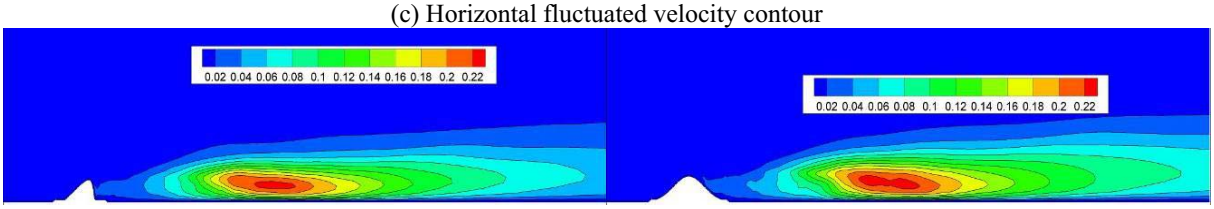

(d) Vertical fluctuated velocity contour

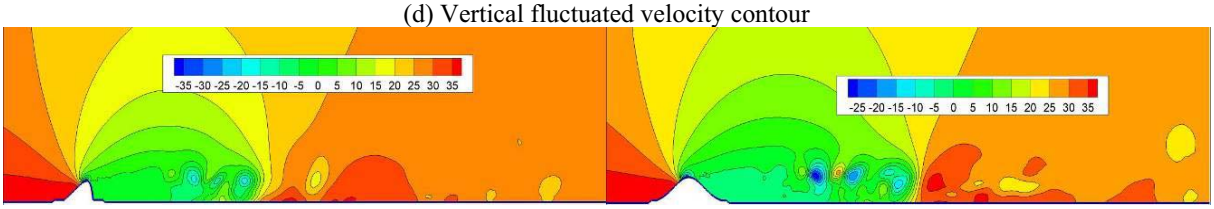

(e) Instantaneous pressure contour

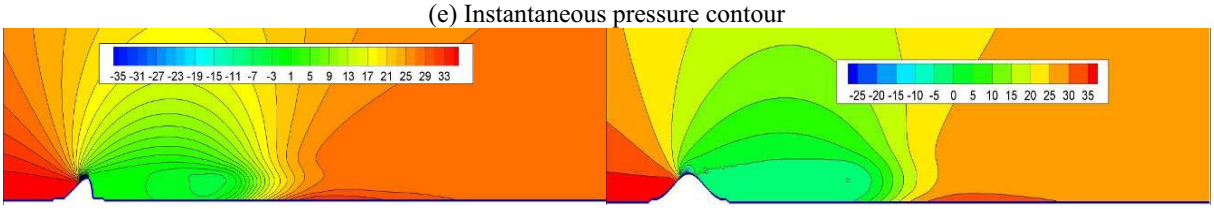

(f) Mean pressure contour

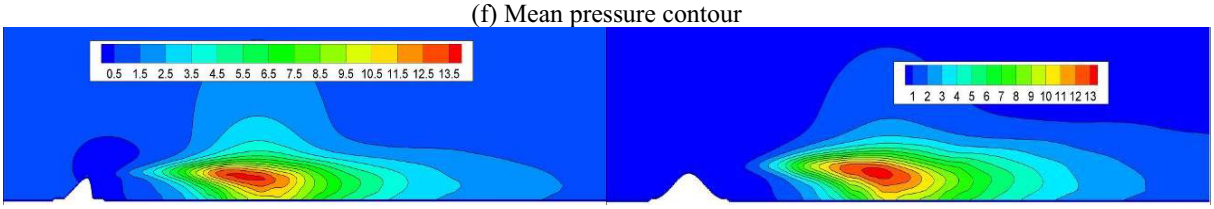

(g) Fluctuated pressure contour

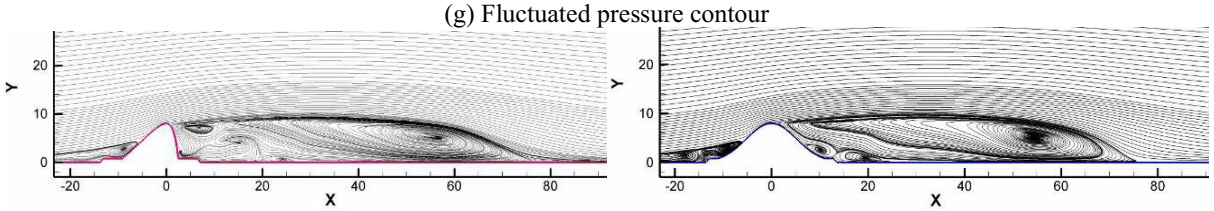

(h) Mean flow traces

Fig.5 2-D flow contours and flow traces

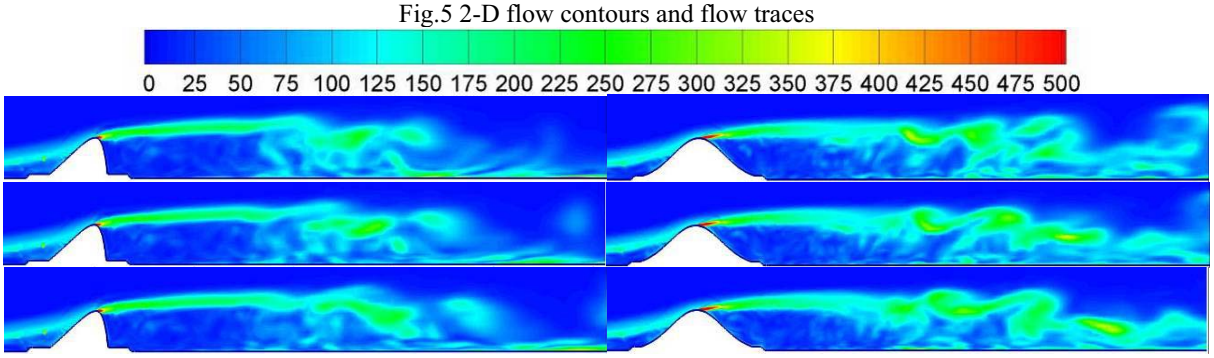

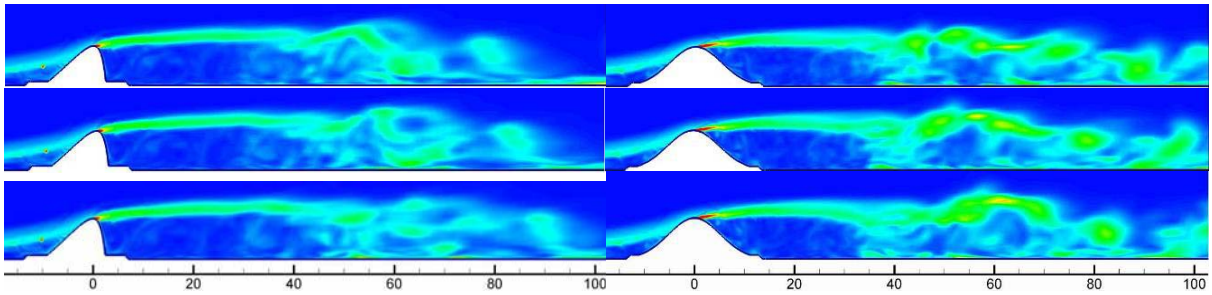

Fig. 6 Instantaneous 2-D vorticity maps at different time (Time interval: 0.025s)

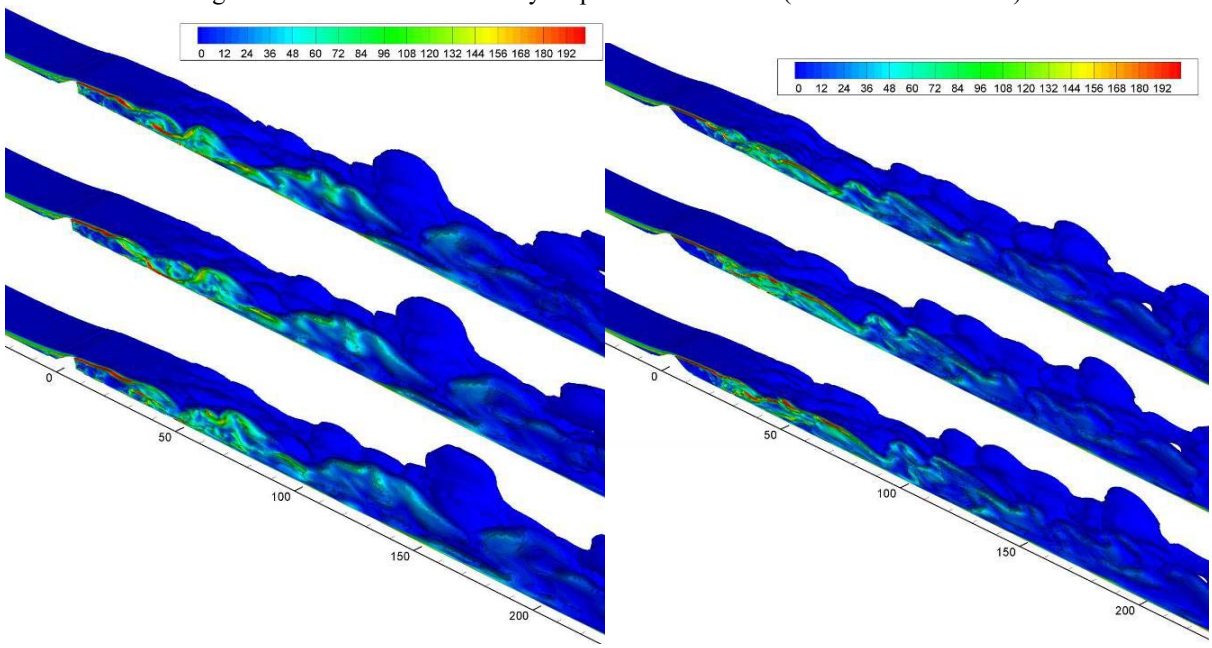

Fig. 7 Instantaneous 3-D vorticity maps at different time (Time interval: 0.05s)

From Fig.3, it can be seen that:

(1) In front of sea wave, in the region of 3-4m upside of sea surface level, the wind velocity behaves obvious difference, and the major causes may include two aspects: on one hand, air is viscous and one boundary layer is inevitable in which the velocity increase from zero to be 10m/s; on the other hand, owing to the obstacle effect from wave, the velocity near the sea surface is relatively lower. For the influence extent from the above two aspects, it can be analyzed by means of the following two techniques: no wave, i.e. remove the wave; the wave is set at the entrance of flows. In the region outside of 40m in front of wave, the wave effect is negligible, and the gradient flows property is similar, which may be mainly caused by the first reason. For the region behind wave and the distance maybe about 30m, the mean velocity is almost zero when the height is lower than wave crest. It may be considered as a "stagnant water area". When the mean velocity is negative, it may be regarded as a "backwater area". Such backwater area can be detected in the region from 35-70m behind the wave. Behind this area, the boundary layer thickness increase owing to the obstacle effect of wave.

(2) For the two heights of 30cm and 40cm, the numerical results are higher than those of experimental ones. For the two heights of 50cm and 60cm, the numerical and experimental results are almost identical. The reasons maybe provided as follows. The wind tunnel laboratory walls are not absolutely smooth, and the testing points are apart from the flow inlet entrance. Therefore, thicker boundary layer appears. Whereas, the smooth wall modeling is utilized for CFD numerical simulation. Thus, the results difference near the wall region is comparatively

apparent. In addition, differences between the wind tunnel test model and numerical simulation model can not be avoided. The testing model may be relatively rough than the computational ones. Such influence may become weaker with the distance farther from the wave, and the results tend to be more close to each other.

From Fig.4, it can be observed that:

(1) For the mean wind velocity of horizontal flow, the numerical simulation results are higher than those of wind tunnel test ones. The closer to wave and the closer to sea surface, the apparent difference. In such regions, the flow fields are more complicated, and the result accuracy is relatively unsatisfactory for both wind tunnel test and numerical simulation.

(2) For the mean wind velocity of vertical flow, in a very wide region behind the wave, the value is negative. The results difference between the numerical computation and wind tunnel test is very obvious in the region that near the wave. The vertical velocity is almost negligible when the distance is 150m far from the wave. The numerical results trend of two types of waves is almost similar.

(3) For the mean angle of incidence, the results from numerical computation and wind tunnel test are relatively close for wave 2. The numerical simulation results are comparatively higher. For wave 3, the results from two methods are distinct. The major cause is the complex flow fields and extreme fluctuation near the wave, and the accuracy is difficult to be ensured for both wind tunnel test and numerical simulation.

(4) For the mean static pressure, the numerical simulation results are lower than those of experimental ones, and the difference is more obvious for wave 3. The systematic error may happen for testing apparatus and/or numerical calculation.

(5) For the standard deviation of all parameters, the numerical simulation results are lower than those of experimental ones. The major cause may include the following two aspects. The experimental instruments and signals are inevitably interfered and contaminated by a large variety of noises. The testing conditions (eg. roughness, turbulence, and so on) can not be so realistic as the numerical simulation. In addition, the wind tunnel width is 3m, while the wave model length is 2.5m, and the more obvious 3-D around flow effect may be incurred.

From Fig.5-Fig.7, it can be detected that:

Except the region that close to wave, the interfered wind flows by two waves are fundamentally similar in other regions. All calculation conditions are basically identical. Although the wave shape is different, the wave height is the same and the configurations are smooth and a bit similar. Two complicated flow fields can be detected: one is the “stagnant water area” that locates in the interval from wave crest to 30m downwind; the other is the “backwater area” that locates in the interval from 30 to 80m downwind of the crest, and the height is within 1.5 times of the wave height. For bridge deck, the height may be higher than this area. With the interference effects of wave, the angle of incidence may deviate from zero to the formidable values, which may bring a challenging threat to the safety of bridge.

5 CONCLUDING REMARKS

The strong interfered performances of wind flows near sea surface by rough waves are investigated by using the 3-D LES numerical simulation technique. The research results indicate that the numerical simulation results are basically consistent with those by wind tunnel experiments. The difference can not be avoided and the major causes are presented. With the interference of wave, the wind flows fluctuated intensely, and the unsteady characteristics is very significant, which largely dependent upon the wave shapes. The apparent influential region by wave ranges from the wave crest to 15 times of wave height downwind horizontally and 4 times

of wave height upward vertically. So if the bridge deck and/or offshore platform are located such a region, adverse wind effects may incur and more comprehensive researches on wind-resistant performance of bridge and/or offshore platform are strongly recommended to be conducted.

REFERENCES

1 Sun Luzhong,Yin Hongbo, Li Xia,et al., Analysis of wind flowing around trestle bridge deck based on large eddy simulation method. Port Engineering Technology, 6(2008) 5-9.
2 LI Xia, SUN Lu-zhong, YIN Hong-bo, et al., Displacement response of flexible overhead trestle bridge subjected to coupling of wind and wave, Journal of Vibration and Shock, 30(2011) 117-121.
3 LI Xia, SUN Lu-zhong, YIN Hong-bo, et al., Influence of wind speed and wave height on displacement response of single span overhead trestle bridge, Journal of PLA University of Science and Technology(Natural Science Edition), 12(2011) 172-177.
4 XIE Xing-kun, YIN Hong-bo, SUN Lu-zhong, et al.. Detached eddy simulation of wind flow around trestle bridge deck, Journal of PLA University of Science and Technology(Natural Science Edition), 12(2011) 273-278.

Appropriate shape of boundary transition section of terrain model for mountains-gorge bridge site

Peng Hu*, Yongle Li, Haili Liao

Department of Bridge Engineering, Southwest Jiaotong University, Chengdu, China

ABSTRACT: To study the appropriate boundary transition section shape of terrain model for mountains-gorge bridge site, a kind of transition curves was derived based on the theory of flow around cylinder with ideal fluid, took an ideal 2D platform terrain as an analysis model to comparatively analyze the flow separation behavior and distribution characteristics of average wind field after airflow flowed along the transition section between curve transition section with equivalent angle of 30° and ramp transition section with included angle of 30° by CFD commercial software FLUENT 6.3, and the total flow transition length of different curve transition sections was also compared. The result shows that when air flows along the curve transition section with equivalent angle of 30°, the distribution characteristics of wind velocity field after airflow flowed along the transition section are much closer to the distribution characteristics of reference wind velocity field than that when airflow flows along the ramp transition section with included angle of 30°, and its total flow transition length is also the relative shortest. The research conclusions could provide some references for the terrain model studies of wind characteristics over the mountains-gorge bridge site.

KEYWORDS: mountains-gorge; terrain model; transition section; bridge site; wind characteristics; CFD

1 INTRODUCTION

When air flow over the mountains-gorge terrain, the air will subject to the blocking, uplifting and separating effects by the mountains, and the air will also subject to the channeling effect and blocking effect by the gorges. For long span bridge in the mountains-gorge terrain, wind characteristics over these bridge sites are very complex, which have a great difference compared with the bridges in the sea or river. There will be a large error if study the wind characteristic of these bridge sites according to the conventional regulation and stipulation (2004). In addition, it is difficult to have experience references from others because the complex of bridge sites terrain and every bridge sites has its own inherent characteristics. With development of the west regions of China, more bridges located in mountains-gorge terrain will be built due to the complex terrain in these regions and the limits of the transport line grade. Therefore, the study on the wind characteristic over bridge site in complex terrain is very urgent and necessary.

The calculation of complex flow over mountains-gorge terrain in practical applications is a difficult task to complete. Theoretical studies are limited by the inherent difficulties to treat real hill or mountains-gorge geometries and boundary conditions and it is also limited by the complexity of the model equations that try to mimic the most important physical phenomena present in the atmospheric boundary layer. Whereas field experimental campaigns are extremely expensive to be carried out and easily affected by environment condition which become a real urgent problem to be solved. A more feasible procedure to analyze the problem is the wind tunnel test method and numerical simulation method, but there is a specific problem in modeling a mountains-gorge terrain model in the wind tunnel test method and numerical simulation method: for the mountains-gorge terrain, it usually has a large elevation

difference everywhere, naturally, there will exist a distance (Δh, as shown in Fig.1) between the terrain model boundary and the wind tunnel floor (or the bottom of the computational domain in numerical simulation method) for the limited terrain area considered in one test, and the air would be separated from the model boundary if the there was no transition section from the wind tunnel floor to the terrain model boundary. In order to let the air flow over the terrain "smoothly", Hu et al. (2006) studied the wind characteristic parameters of a bridge across the V shape valley by terrain model wind tunnel test, and adopted a transitional additional terrain to let the air flow over the terrain model; Chen (2008) also adopted this method in another long span bridge in mountains-gorge terrain. Maurizi (1998) discussed the wind flow over a mountainous area at an altitude of 1000m above sea level, and used a ramp additional terrain with a maximum slope of 10% to let the air flow over the mountainous terrain. Although the transitional additional terrain and the ramp additional terrain have a simple form, the problem is that whether they are valid as a boundary transition section shape to let the air flow over the terrain smoothly.

The undisturbed wind field is usually taken as the reference wind field in wind tunnel tests. In an objective manner, when the inlet air flow over the appropriate boundary transition section, the air should keep the same characteristics as the reference wind field, so the undisturbed wind field will show more representative to act as the reference wind field in further studies. Comprehensive consideration of the boundary transition section in the wind tunnel and the numerical simulation methods, two principles that the appropriate boundary transition section should be satisfied: a) the air should keep the same characteristics as the reference wind field when the air flow over the transition section, and air separation could not occur at the end of the transition section; b)the length of the air flow from the starting point of the transition section to the point that the air get stable is fully short, because a longer transition section will further reduce the model scale factor as the test section of a wind tunnel is limited; besides, for the numerical simulation method a longer transition section also increase calculation region size and computational cost.

To study the appropriate boundary transition section shape of terrain model for mountains-gorge bridge site in wind tunnel test and numerical simulation test, in this paper, a kind of transition section curves was derived based on the theory of flow around cylinder with ideal fluid, took an 2D platform terrain as an analysis model to comparative analyze the flow separation behavior and distribution characteristics of wind velocity field after air flowed along the transition section between curve transition section and the ramp transition section by CFD commercial software FLUENT 6.3, and the total flow transition length of different curve transition section shapes were also compared. The research conclusions could provide some references for the terrain model studies of wind characteristics over the mountains-gorge bridge site.

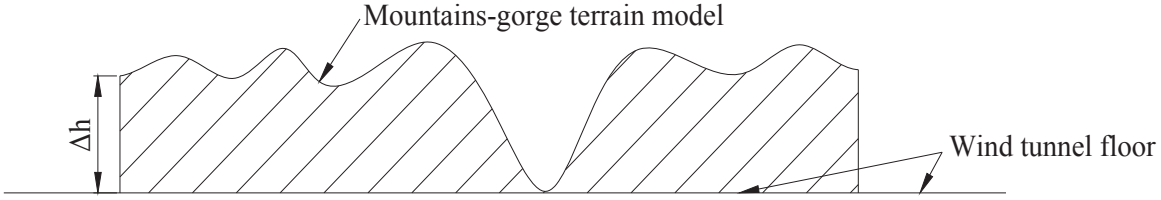

Fig.1 Distance between the terrain model boundary and the wind tunnel floor

2 TRANSITION SECTION CURVES BASED ON IDEAL FLUID AROUND CYLINDER THEORY

The undisturbed reference inlet air can be regarded as a uniform rectilinear flow, and its vertical wind velocity is zero. Therefore, the vertical wind velocity of the flow at the starting and end points of the transition section should also be equal to zero. When the air flow over

the transition section, except for the flow near the wall is subjected to the influence of air viscosity, the airflow could be taken as the potential flow in other large regions. Based on the theory of flow around cylinder with ideal fluid, the stream function and the wind velocities are given as follows:

$$\psi = U_\infty y\left(1-\frac{a^2}{x^2+y^2}\right) \tag{1}$$

$$u = \frac{\partial \psi}{\partial y} = U_\infty\left[1+a^2\frac{y^2-x^2}{\left(x^2+y^2\right)^2}\right] \tag{2}$$

$$v = -\frac{\partial \psi}{\partial x} = -U_\infty a^2\frac{2xy}{\left(x^2+y^2\right)^2} \tag{3}$$

where ψ is the stream function; U_∞ is the inference wind velocity, a is the radius of the cylinder; u、v are the longitudinal velocity and vertical velocity, respectively; x、y are the corresponding coordinate of the flow, as shown in Fig.2.

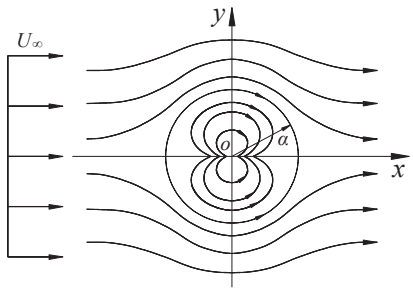

Fig.2 Flow around cylinder with ideal fluid

It can be seen from Eq. (3) that, when $x=0$ or $x=\pm\infty$, the vertical wind velocity v is equal to zero. According to the nature of stream function, each streamline can be regarded as a wall without influence the initial flow field. Therefore, the streamline can be taken as the shape of transition section, and its starting and end points are just the coordinate points of which vertical wind velocity is zero in Fig.2. Note that, the transition section may have an indefinite length if take the coordinate point $x=\pm\infty$ at the end point of the transition section. Therefore, to satisfy the length requirements of transition section, the Eq. (1) can be rewritten as:

$$\begin{aligned}\psi &= U_\infty y\left[1-\frac{a^2}{y^2}\cdot\frac{1}{1+(x/y)^2}\right]\\ &= U_\infty y\left[1-\frac{a^2}{y^2}\cdot\sum_{n=0}^{\infty}(-1)^n\left(\frac{x}{y}\right)^{2n}\right]\\ &= U_\infty y\left\{1-\frac{a^2}{y^2}\left[1-\left(\frac{x}{y}\right)^2+\left(\frac{x}{y}\right)^4-\left(\frac{x}{y}\right)^6+\left(\frac{x}{y}\right)^8-\left(\frac{x}{y}\right)^{10}+\cdots\right]\right\}\end{aligned} \tag{4}$$

From the perspectives of practical applications and further researches, retaining only the first five terms in Eq.(4), and the corresponding stream function and the vertical wind velocities as given as:

$$\psi_5 = U_\infty y - a^2 U_\infty \frac{1}{y} + a^2 U_\infty \frac{x^2}{y^3} - a^2 U_\infty \frac{x^4}{y^5} + a^2 U_\infty \frac{x^6}{y^7} - a^2 U_\infty \frac{x^8}{y^9} \tag{5}$$

$$v_5 = -\frac{\partial \psi_5}{\partial x} = -2a^2 U_\infty \frac{x}{y^3} + 4a^2 U_\infty \frac{x^3}{y^5} - 6a^2 U_\infty \frac{x^5}{y^7} + 8a^2 U_\infty \frac{x^7}{y^9} \tag{6}$$

Let the vertical wind velocity in Eq. (6) equal to be zero, and then it leads to:

$$\begin{cases} x_1 = 0.778y \\ x_2 = 0 \end{cases} \tag{7}$$

where x_1、x_2 can be taken as the x-coordinate value of starting and end points of the transition section, respectively. Substituting Eq. (7) into Eq. (5) yields:

$$\begin{cases} y_1 - \dfrac{0.673a^2}{y_1} = \dfrac{\psi_5}{U_\infty} \\ y_2 - \dfrac{a^2}{y_2} = \dfrac{\psi_5}{U_\infty} \end{cases} \tag{8}$$

where y_1、y_2 are the corresponding y-coordinate value of starting and end points of the transition section, respectively, and the value of y_1、y_2 can be obtained from Eq.(8):

$$\begin{cases} y_1 = \dfrac{m + \sqrt{m^2 + 2.692a^2}}{2} \\ y_2 = \dfrac{m + \sqrt{m^2 + 4a^2}}{2} \end{cases} \tag{9}$$

where $m=\psi_5 / U_\infty$.

Hence, the starting coordinate point (x_1, y_1) and end coordinate point (x_2, y_2) are all determined via Eqs. (7) and (9). Since the length of the air flow from the starting point of the transition section to the point that the air get stable must be fully short. Therefore, the length of transition section also should be fully short. For the shortest transition section (refer to the projected length), in other words, its equivalent slope k_0 (shown in Fig.3), which can be expressed as Eq. (10), must be maximum.

$$k_0 = \frac{y_2 - y_1}{x_2 - x_1} = \frac{y_2 - y_1}{0.778y_1} \tag{10}$$

Substituting Eq. (9) into Eq. (10) yields:

$$k_0 = 1.285\left(\frac{\sqrt{m^2 + 4a^2} - \sqrt{m^2 + 2.692a^2}}{m + \sqrt{m^2 + 2.692a^2}} \right) \tag{11}$$

And when $m \to -\infty$, the maximum k_0, denoting by k_{0max}= 0.624, which is independent of the value of a. Usually, the height of transition section is approximately equal to the height of the terrain model boundary, denoted by h_0, thus, $h_0 = y_2 - y_1$, according to the Eqs. (9) and (11), the relation between a and m can be obtained as follows:

$$\begin{cases} \dfrac{m+\sqrt{m^2+4a^2}}{2}-\dfrac{m+\sqrt{m^2+2.692a^2}}{2}=h_0 \\ 1.285\left(\dfrac{\sqrt{m^2+4a^2}-\sqrt{m^2+2.692a^2}}{m+\sqrt{m^2+2.692a^2}}\right)=k_0 \end{cases} \tag{12}$$

It should be noted that, the above equations are all derived based on the potential flow theory, therefore, in the actual viscous fluid, the value of k_0 need to adjusted, but the value of k_0 must smaller than $k_{0\max}$= 0.624. When the values of h_0 and k_0 are determined, then the values of a and m can be obtained by solving the Eq.(12), next substituting h_0 and k_0 into the Eq. (5) yields the following form of transition section curve:

$$y-\frac{a^2}{y}+\frac{a^2x^2}{y^3}-\frac{a^2x^4}{y^5}+\frac{a^2x^6}{y^7}-\frac{a^2x^8}{y^9}-m=0 \tag{13}$$

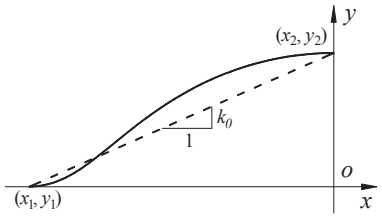

Fig.3 Equivalent slope of curve transition

3 WIND CHARACTERISTICS BETWEEN CURVE TRANSITION SECTION AND RAMP TRANSITION SHAPES

The references (Hu et al. 2006; Chen et al. 2008) both adopted the ramp transition section, but the applicability of the ramp transition section to the boundary transition section for the mountains-gorge bridge site terrain model needs to be validated. Therefore, the flow separation behavior and distribution characteristics of wind velocity field between the curve transition section and the ramp transition section are compared in the next.

3.1 *Numerical model*

In order to focus on the flow characteristics of different transition sections, the terrain model was simplified to a 2D platform terrain with the height of 0.385m, and the same two transition sections are ser at the two ends of the platform terrain. The total length of transition sections and the platform terrain is 18.0m. Since the ramp transition section with a angle of 30° could satisfy the practical engineering (Hu et al. 2006), so the curve transition section with the equivalent slope of 0.58 (corresponding equivalent angle is 30°) are chosen to be compared. Using the parameters of h_0 =0.385m and k_0 =0.58, the specific form of curve transition section can be obtained by Eqs.(12) and (13), and it is given as Eq.(14). Besides, an empty domain model with no transition sections is also presented to serve as a basic reference model, it could judge which transition section is better when the air flow over the transition section. The 2D platform terrain model and different transition sections are shown in Fig.4.

$$y-\frac{21.298}{y}+\frac{21.298x^2}{y^3}-\frac{21.298x^4}{y^5}+\frac{21.298x^6}{y^7}-\frac{21.298x^8}{y^9}+15.968=0,\quad (0.664\le x\le 0) \tag{14}$$

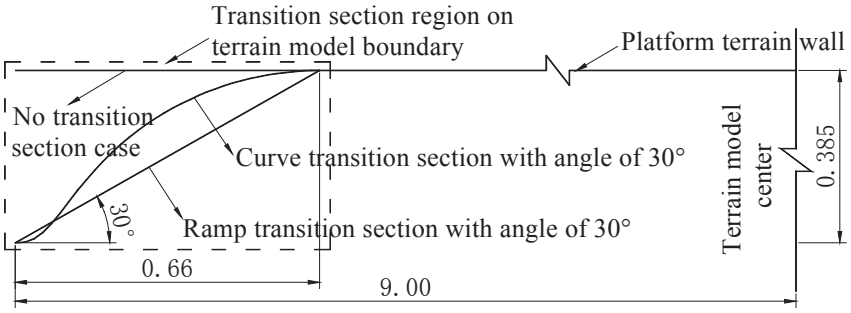

Fig.4 Terrain model and different transition section shapes (dimensions are given in m)

3.2 *Boundary conditions and analysis parameters*

The length from the center of terrain model to the inlet and outlet boundaries are 35.0m and 55.0m, and the height of the domain is 15.0m, satisfying the requirement of blocking ration smaller than 3% (Bekele and Hangan 2002). The domain is discretized by structured meshes and the height from the center of the wall-adjacent cell to the bottom wall is 0.0005m. As a result, the total number of meshes is 700,000. The boundaries are shown in Fig.5, in which the inlet velocity is 10.0/s and the turbulence intensity is 0.5%. In this investigation, the CFD commercial software FLUENT 6.3 is employed, and the flow is supposed to be incompressible and steady. When choosing the discretization schemes for the governing equations, the SIMPLEC algorithm is applied to the pressure-velocity coupling, the second order interpolation scheme is used for pressure, and the second order upwind scheme is adopted for moment and turbulence properties. The values set for the inlet boundary are used to initialize the flow field, and the scaled residuals for all variables are set to be 10^{-6}. For the no transition section case, the height of the domain is 14.615m (=15m-0.385m), and the corresponding inlet velocity is set to 10.263m/s (=10×15/14.615m/s).

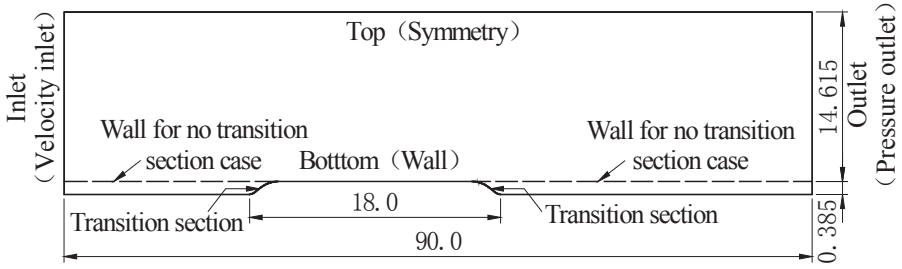

Fig.5 Schematic diagram of computational domain and boundary conditions (unit: m)

3.3 *Comparison of flow separation behavior*

Flow separation can lead to a thicker boundary layer or a more unstable flow; therefore, an appropriate boundary transition section should avoid the flow separation. Fig.6 compares the wall shear stress between the curve transition section with equivalent angle of 30° and the ramp transition section with an angle of 30°. It can be seen from the figure that the wall shear stress of curve transition section and the ramp transition section are all smaller than zero at the starting point (x=-9.0m), which indicates that the flow separation is occurred. Furthermore, at the end point (x=-8.34m) of the transition section, only the wall shear stress of the ramp transition section is also smaller than zero, so flow separation is also occurred at this position for the ramp transition section. Fig.6 also shows the wall shear stress of no transition section case, the wall shear stresses of curve transition section are closer to those of

no transition section case, which implies that the flow characteristics near the wall for the curve transition section are more close to those of no transition section.

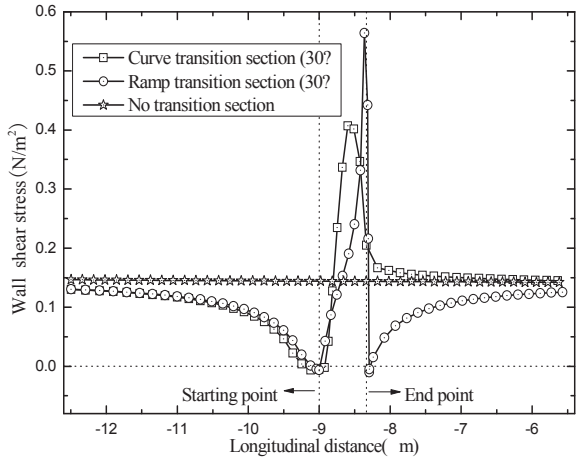

Fig.6 Distributions of wall shear stress

3.4 *Distribution characteristics of wind field after air flowed over the transition section*

When air flows over the transition section, the characteristics of the air, such as the velocity and wind attack angle, will inevitably change. For different transition sections, the distribution characteristics of wind field will have great differences. A reasonable treatment is to adopt the normalization value. The normalized wind velocity profiles at the end point of the two transition sections and the middle of the platform terrain are shown in Figs.7 and 8, the wind velocity at the end point of the ramp transition section accelerate greatly, which has a great difference from that of no transition section case. However, the wind profile of the curve transition section is more close to that of the no transition section case. In Fig.8, the wind profile of the curve transition section is also more close to that of the no transition section case than the ramp transition section, which indicates that the distribution characteristics of wind field after the air flowed over the transition section is more similar to those of the no transition section case.

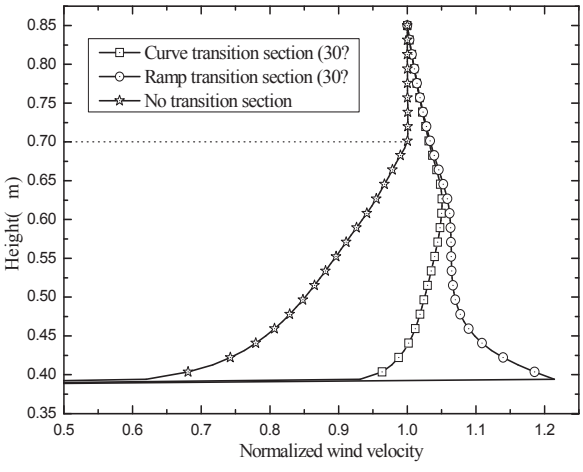

Fig.7 Normalized wind velocity profiles at the end of transition section

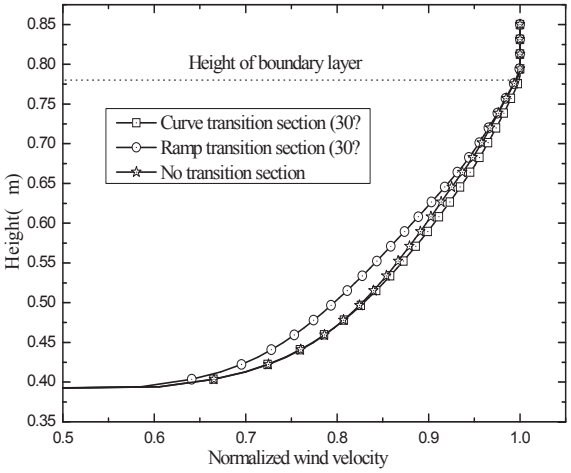

Fig.8 Normalized wind velocity profiles at the middle of terrain model

In order to investigate the normalized wind velocity from the end point of the transition section to the middle of the platform terrain, a term of "relative normalized wind velocity difference (denoted by γ)" is introduced:

$$\gamma = \sum_{h>0.385}^{h=H} \frac{\left| v_h / v_H - v_{0h} / v_{0H} \right|}{v_{0h} / v_{0H} \cdot N} \tag{15}$$

where H is the height of the boundary layer; v_h is the velocity at the height of h from the wall; v_{0h} is the velocity at the height of h from the wall for the no transition section case, v_H is the velocity at the boundary layer, v_{0H} is the velocity at the boundary layer for the no transition section case, and N is the numbers of the points from the wall to the boundary layer. Therefore, the relative normalized wind velocity difference γ along the terrain with different transition sections are shown in Fig.9, with the position near the middle of the platform, the value of γ are all close to that of no transition section case, however, the curve transition section is more closer to the no transition section case than the ramp transition section in the value of γ.

In order to investigate the wind attack angle from the end point of the transition section to the middle of the platform terrain, similarly, the wind attack angle at different transition sections are shown in Fig.10. It can be seen from the figure that the change law of wind attack angle is similar to the relative normalized wind velocity difference γ. Furthermore, the normalized wind velocity difference and the wind attack angle of curve transition section in Figs. (9) and (10) are faster to be stable as the no transition case. Therefore, the total flow transition length of the curve transition section is shorter than that of the ramp transition sections.

As discussed above, the normalized wind velocity difference and the wind attack angle of curve transition section is closer to the no transition section case than those of the ramp transition section, which indicates that the curve transition section is more suitable to be a boundary transition section in the complex terrain.

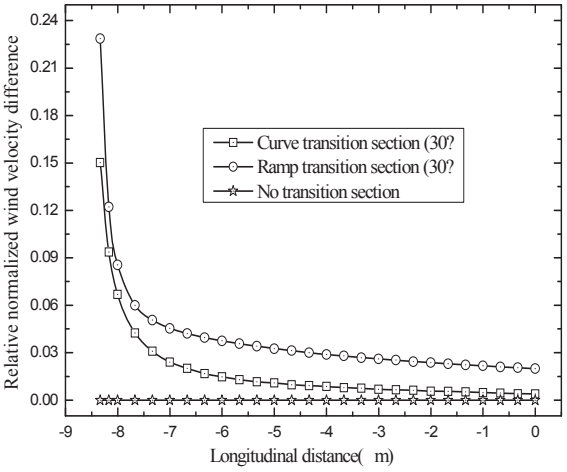

Fig.9 Distributions of average relative normalized wind velocity difference after airflow flowed along the transition section

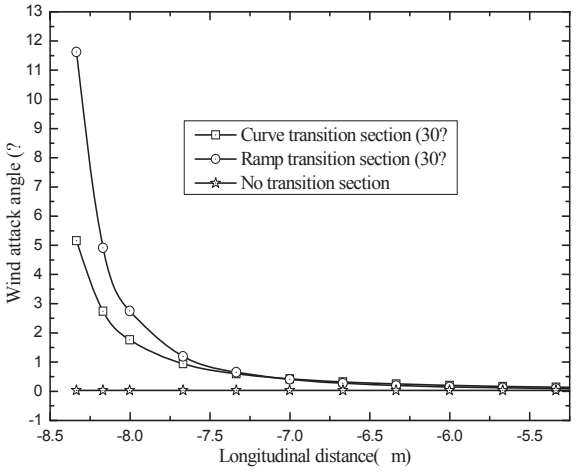

Fig.10 Distributions of average wind attack

4 WIND CHARACTERISTICS AMONG DIFFERENT CURVE TRANSITION SECTION SHAPES

In order to consider the different curve transition section shapes, the two other curve transition sections with equivalent angle of 20°and 10° are added in this study case, the different curve transition sections are shown in Fig.11.

Fig.12 shows the wind velocity profiles at the middle of the terrain for different curve transition sections, the different wind velocity profiles all have high concordance with each other. Since the wind velocity along the vertical direction for different curve transition

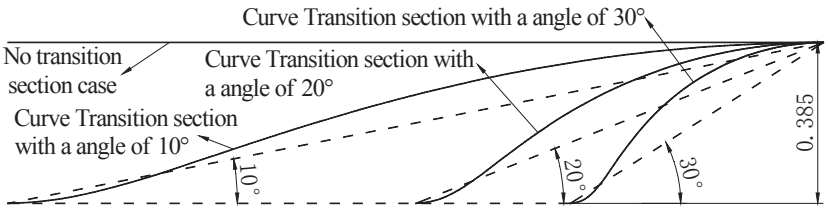

Fig.11 Different curve transition section shapes (dimensions are given in m)

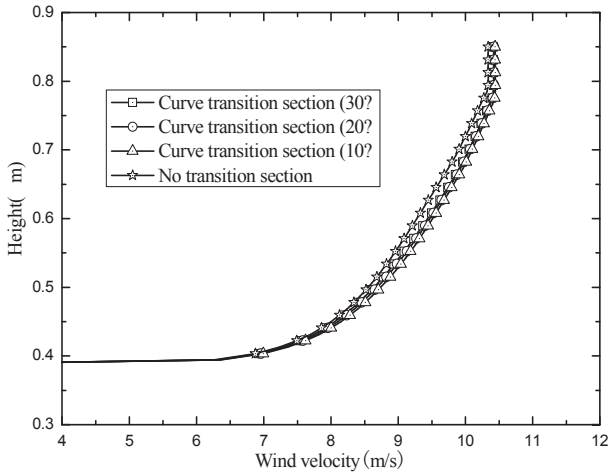

Fig.12 Wind velocity profiles at the middle of terrain model

sections can be probably different. Therefore, a term of "relative wind velocity difference (denoted by α)" is introduced:

$$\alpha = \frac{|v_h - \eta v_{0h}|}{\eta v_{0h}}, \quad \eta = \frac{14.615}{15 - y} \tag{16}$$

where y is the height from the bottom of the domain, η is the velocity ration factor, which is introduced to consider the different domain height between the model with transition sections and the model with no transition section (shown in Fig.5). The relative wind velocity difference α and the wind attack angle along the transition section and the platform terrain at the height h=0.05m are shown in Fig.13 and 14. It can be seen from the figures that the values of relative wind velocity difference α for different curve transition sections are all decrease first, then increase and then decrease again, but with the position near the middle of the platform, these values are all consistent with the no transition section case. However, it should be noted that the curve transition section with equivalent angle of 30° is faster to be stable as the no transition case. Similarly, the change law of wind attack angle is similar to that of the relative wind velocity difference, as shown in Fig.14. Through the analysis of change laws of relative wind velocity difference and the wind attack angle, it could be concluded that the total flow transition length of curve transition section with equivalent angle of 30° is shorter than those of the other curve transition sections with equivalent angle of 20°and 10°.

5 CONCLUSIONS

To study the appropriate boundary transition section shape of terrain model for mountains-gorge bridge site, a kind of transition section curves were derived based on the theory of flow around cylinder with ideal fluid. Through the analysis of different transition

sections including the curve transition sections and ramp transition section, some main conclusions are given as follows:

(1) Air separation occurs when the air flow along the ramp transition section, while it does not occur when the air flow along the curve transition section.

(2) The relatively normalized velocity profile and the wind attack angle of air flow along curve transition section are closer to those of no transition section case than air flow along the ramp transition section.

(3) The total flow transition length of the curve transition section with equivalent angle of 30° is shorter than the other curve transition sections with equivalent angle of 20°and 10°.

(4) The curve transition section with equivalent angle of 30°could be applied to the boundary transition section shape of the mountains-gorge terrain model in wind tunnel test and numerical simulation test.

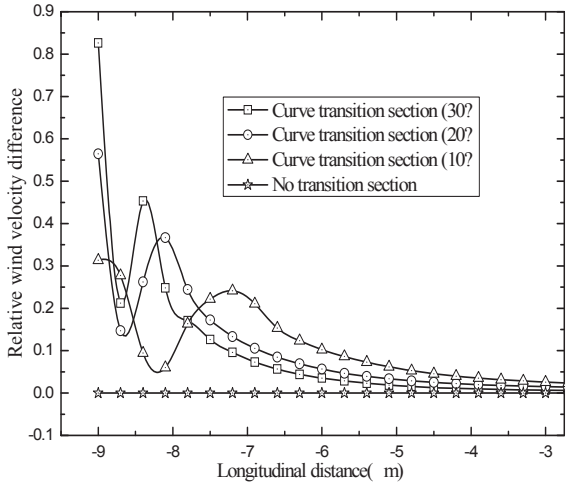

Fig.13 Distributions of relative wind velocity difference with 0.05m high above the wall

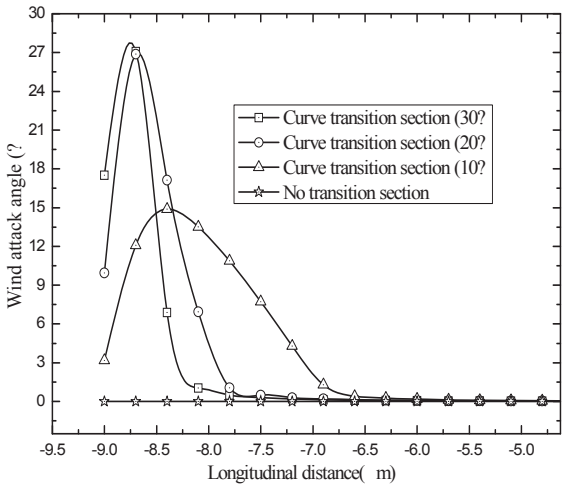

Fig.14 Distributions of wind attack angle with 0.05m high above the wall

6 ACKNOWLEDGEMENTS

The writers are grateful for the financial supports from the National Natural Science Foundation of China under Grant NNSF-90915006, New Century Excellent Talents in University of China under Grant NCET-06-0802, Outstanding Young Academic Leaders Program of Sichuan Province under Grant 2009-15-406 and Fundamental Research Funds for the Central Universities under Grant 2010XS02.

7 REFERENCES

1 Wind-resistent Design Specification for Highway Bridges, China Communications Press, Beijing, 2004.
2 F. Q. Hu, A. R. Chen and D. L. Wang. Experimental study of wind field in bridge site located in mountainous area, Journal of Tongji University: Natural Science, 2006, 34(6): 721-725.
3 Z. Q. Chen, C. G. Li, Z. T. Zhang and J. H. Liao. Model test of wind field characteristics of long-span bridge site in mountainous valley terrain, Journal of Experiments in Fluid Mechanics, 2008, 22(3): 54-59.
4 A. Maurizi, J. M. L. M. Palma and F. A. Castro. Numerical simulation of the atmospheric flow in a mountainous region of the North of Portugal, Journal of Wind Engineering and Industrial Aerodynamics, 1998, 74-76: 219-228.
5 S. A. Bekele and H. Hangan. A comparative investigation of the TTU pressure envelop. Numerical versus laboratory and full scale results, Wind and Structures, 2002, 5(2-4): 337-346.

*Corresponding author. E-mail: hupengmail@126.com (P. Hu)

The Seventh International Colloquium on Bluff Body Aerodynamics and Applications (BBAA7)
Shanghai, China; September 2-6, 2012

Inflow turbulence generation for LES of wind flow around bluff body

B.W. Yan[a], Q.S. Li[a]

[a] *Department of Civil and Architectural Engineering, City University of Hong Kong, Hong Kong*

ABSTRACT: Large eddy simulation (LES) has been widely applied in wind-related problems. A key issue to ensure obtaining accurate results by LES is to generate an appropriate inflow field satisfying the physical wind characteristics in the atmospheric boundary layer (ABL). The methods adopted in this study for inflow field generation include two statistical methods (the random flow generation method (RFG) and the synchronizing random flow generation method (DSRFG) and a numerical method (the recycling method). These inflow generation methods are used to predict the wind effects on the Commonwealth Advisory Aeronautical Council (CAARC) standard tall building. The computational results show that all the three methods can reproduce the time-averaged velocity and turbulence intensity profiles quite well at the building position. However, the RFG method is incapable of generating fluctuating velocity satisfying the prescribed von Karman spectrum, and the DSRFG method yields random flow field satisfying the target spectrum at the inlet, while the recycling method generates the streamwise velocity fluctuation quite well at the inlet. The mean pressure coefficients on the front surface of the building are accurately predicted by all the inflow turbulence generators (the three methods), and the pressure coefficients distribution patterns on the side and back surfaces are well predicated, while some discrepancies still exit between the numerical results and wind tunnel measurements. All the RMS pressure coefficients obtained by the inflow turbulence generation methods fall in the range of wind tunnel data, illustrating that the effects of turbulence characteristics on the wind-induced pressures on the tall building are reproduced to some extent.

KEYWORDS: inflow turbulence generation; CFD, LES; bluff body; wind effect

1 INTRODUCTION

Large eddy simulation (LES) has been developed since the 1960s. But, its application to industrially relevant problems has only recently become available as LES requires sufficiently powerful computing resources. With developments of computational fluid dynamics (CFD) techniques, LES has been widely applied to simulate turbulent flows of engineering interest. In computational wind engineering (CWE), LES has become a powerful tool which has been applied in the predication of wind effects on buildings and structures, wind flow characteristics and topographical effects, wind fields in densely-arranged cities and atmospheric environments [1]. For the application of LES in atmospheric boundary layer, a very important issue to enable the LES techniques to obtain accurate results is to generate a physically appropriate flow field as an inflow boundary condition (inflow turbulence) satisfying prescribed spatial and temporal wind characteristics, since inaccurate generations of inflow turbulence can result in inaccurate simulation results of wind effects on buildings and structures. Several inflow turbulence generation techniques have been proposed in the past decade. They can be classified into three categories: synthetic method, precursor simulation, and recycling method.

The simplest method is to superimpose the random noise with proper turbulence intensity on the measured mean velocity distribution. But, such a method requires sufficient field measurement information from ground to the gradient height, which is usually not available, and this method ignores the cross-correlations between velocity components, namely Reynolds stresses

and spatial relations in turbulence structures. And the Lack of the spatial information can be solved by taking considerable settling distance to simulate the entire upstream region before the mean flow reaches the equilibrium boundary layer. Instead of using the problem-dependent settling distance, the recycling method was introduced by Spalart [2] using the periodic boundaries to reduce the settling distance. This method was further developed by Lund et al. [3] who introduced the rescaling idea to specify a precise inlet profile satisfying the prescribed shear stress and momentum thickness. Kataoka and Mizuno [4] simplified Lund's rescaling method using the constant boundary layer thickness in place of the similarity laws of the boundary law. Nozawa and Tamura [5] further developed Lund's method for generation of boundary layer conditions. Their method is similar to the method employed in wind tunnel tests to simulate boundary layer conditions. Liu and Pletcher [6] indicated that the position of the recycling and rescaled plane could cause a difficulty resulting from the coupling of the initial and inflow condition which will influence the computational cost, and they proposed a modification to Lund's method by using dynamically positioned recycling plane according to instantaneous flow properties. All the above mentioned methods demand an auxiliary LES computation with streamwise periodic boundaries to specify a fully developed inlet profile for the flow around complex geometries as the starting point. For the synthetic methods, one common way is to obtain the velocity fluctuations from an inverse Fourier transform of prescribed spectrum which follows the prescribed power spectrum density and spatial correlations. This method was initiated by Hoshiya [7], then developed by Iwatani [8], and Kondo et al. [9]. Another synthetic approach is based on proper orthogonal decomposition (POD) and linear stochastic estimation (LSE) in combination with the simultaneously measured fluctuating velocity obtained by hot wire probes or stereoscopic particle image velocimetry (SPIV) conducted by Perret et al.[10]. The methods based on the variant of spectral method for generation of an isotropic continuous flow field were further developed by several researchers including Smirnov et al. [11], Klein et al. [12], Batten et al. [13] and Huang et al. [14]. Smirnov et al. [11] superimposed turbulence length scale and time scale into the basic model proposed by Kraichnan [15] to generate an isotropic divergence-free fluctuating velocity field with the target length scale and time scale, and they realized the inhomogeneous and anisotropic turbulence characteristics through a scaling and orthogonal transformation of the resulted flow field with a given anisotropic velocity correlation tensor. Huang et al. [14] further developed the Kraichnan's approach to establish a general inflow turbulence generation method capable of generating a spatially correlated turbulent flow field satisfying any target spectrum including the von Karman spectrum through the discretizing and synthesizing procedures. Another method, the precursor simulation, was conducted to run a separate precursor calculation of an equilibrium flow to generate a library of turbulent database that can be reintroduced into the main simulation. Although the method demands extra computational efforts and cost to establish the database, the inflow field should possess the main characteristics of turbulence structures including temporal and spatial fluctuations and a reasonable energy spectrum.

2 INFLOW TURBULENCE GENERATION METHODS

The methods adopted in this study are the random flow generation method by Smirnov et al. [10] and the discretizing and synthesizing random flow generation method by Huang et al. [14], and the recycling and rescaling method based on Kataoka's research works [4].

2.1 *Random flow generation method (RFG)*

The spectral synthesizer in the Fluent code is based on the RFG method modified by Smirnov et al. [11]. The method can be used to generate fluctuating velocities which are computed by synthesizing a divergence-free velocity vector field from the summation of Fourier harmonics on the basis of the input turbulence boundary conditions. In the implementation of the Fluent code, the number of the Fourier harmonics is fixed to 100 [16].

2.2 *Discretizing and synthesizing random flow generation (DSRFG)*

Another approach employed in the study is DSRFG, which is based on Kraichnan's method to establish a general inflow turbulence generator capable of generating a spatially correlated turbulent flow field satisfying any target spectrum including the von Karman spectrum. A brief formulation of the method is presented below [14].

$$u(x,t)=\sum_{m=k_0}^{k_{\max}} u_m(x,t)=\sum_{m=k_0}^{k_{\max}}\sum_{n=1}^{N}\left[\, p^{m,n}\cos(\tilde{k}^{m,n}\cdot\tilde{x}+\omega_{m,n}t)+q^{m,n}\sin(\tilde{k}^{m,n}\cdot\tilde{x}+\omega_{m,n}t)\right] \tag{1}$$

where $p^{m,n}=\dfrac{\varsigma\times k^{m,n}}{\left|\varsigma\times k^{m,n}\right|}\sqrt{a\dfrac{4E(k_m)}{N}}$, $q^{m,n}=\dfrac{\xi\times k^{m,n}}{\left|\xi\times k^{m,n}\right|}\sqrt{(1-a)\dfrac{4E(k_m)}{N}}$, $\tilde{x}=\dfrac{x}{L_s}$, $\tilde{k}^{m,n}=\dfrac{k^{m,n}}{k_0}$, $\left|k^{m,n}\right|=k_m$,

$\omega_{m,n}\in N(0,2\pi f_m)$, $f_m=k_m\times U_{avg}$, ς and ξ are the vector form of ς_i^n and ξ_i^n. L_s is the turbulence integral length scale which denotes the two-point spatial correlation. a is a random number uniformly distributed between 0 and 1. U_{avg} is the average velocity at the reference height. N =100 (sampling number for each wave number k_m).

The artificial velocity fluctuations generated by the turbulence generation method will be resolved by the grid which is commonly chosen to be the spatial filter in LES. This means that the artificial velocity will be transformed into velocities and SGS viscosities through the chosen SGS model. For this reason, the grid scale between the main building and the inlet of the computational domain should be fine enough to enable most of the artificial velocity fluctuations generated at the inlet can be resolved and then acting on buildings.

2.3 *Recycling method*

The recycling and rescaling method is based on the approach proposed by Kataoka and Mizuno [4], which is a simplified version of Lund's method. In the modified method, the development of the boundary layer thickness is neglected and treated as constant and the mean velocity profile is fixed at inflow. As shown in Figure.1, the approach is to extract instantaneous velocity fluctuations from the recycled station and reintroduce the rescaled fluctuations at the inlet in an auxiliary simulation of a zero pressure gradient boundary layer, which is denoted as driver section. The auxiliary simulation is spatially developing through the rough wall surface, and generates its own inflow conditions which make the approach convenient for an existing inflow–outflow computational domain that can be converted to the inflow turbulence generator after a sequence of simple operations. The coupled inlet and recycling plane are defined as "pseudo-periodic condition", and the periodic boundary conditions in the streamwise direction are appropriate for fully developed flow without a need for a development section. In this study, the inflow generation calculation in the driver region is synchronized with the main simulation in the main domain (shown in Figure.2). The velocity fluctuation was generated based on Kataoka's method [4], and the rough wall surface is realized with the cubic roughness elements arranged in the streamwise direction.

L is the width of the cubic roughness element while G is the center distance between the neighboring roughness elements. In this case, G is chosen as $5L$, and such an arrangement gave a roughness density λ=8.0%. In addition, the generation of the Gaussian random perturbations is superimposed in the top region at the inlet for the recycling method in the auxiliary computation since the lower turbulence intensity generated by the recycling method was observed in recent study. The velocity components prescribed at the inlet following Kataoka's method [4] are given as follows:

$$
\begin{aligned}
u_{inlt(y,z,t)} &= \langle u \rangle_{inlt}(z) + \phi(\theta) \times \{u(y,z,t) - \langle u \rangle(y,z)\}_{recy} \\
v_{inlt(y,z,t)} &= \phi(\theta) \times \{v(y,z,t) - \langle v \rangle(y,z)\}_{recy} \\
w_{inlt(y,z,t)} &= \phi(\theta) \times \{w(y,z,t) - \langle w \rangle(y,z)\}_{recy}
\end{aligned} \tag{2}
$$

The following damping function [16] was adopted to restrict the velocity fluctuations from developing for the unstable conditions.

$$
\phi(\theta) = 0.5 \left\{ 1 - \frac{\tanh\left[\dfrac{8.0(\theta - 1.0)}{-4.0(\theta - 0.3) + 0.7} \right]}{\tanh(8.0)} \right\} \tag{3}
$$

where $\theta = z / \delta$, δ is the boundary layer thickness.

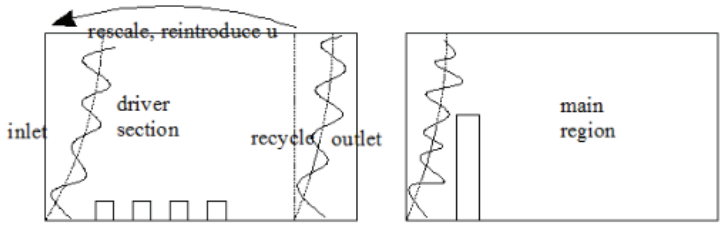

Figure.1 Schemetic view of the recycleing method

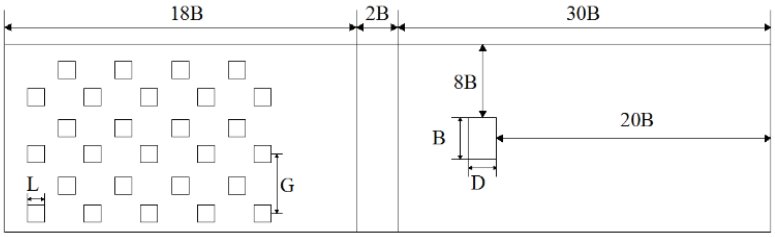

Figure.2 Roughness arrangement and dimensions of the compuational domain

3 BUILDING MODEL, COMPUTATIONAL DOMAIN, MESH ARRANGEMENT AND BOUNDARY CONDITIONS

3.1 *Building model*

In this study, the selected building is the Commonwealth Advisory Aeronautical Council (CAARC) standard tall building. The building shape is rectangular prismatic and its full-scale dimensions are: sides 30.8 m by 45.72 m and height 183.88 m with density 160 kg/m^3 and natural frequency 0.2 Hz. As introduced by Melbourne [18], the building is flat-topped, without parapets, and the external surfaces are flat without mullions or other geometric disturbances. Since

the 1970s, the building model has been intensively investigated in various wind tunnels as a standard model to study the wind effects on tall buildings and several wind tunnel measurements about this building model were reported [19,20].

3.2 *Computational domain*

A 1:250 scale rigid model of the CAARC building is considered in this study. The main computational domain is shown in Fig.2. The Reynolds numbers involved in the simulations is the same as that in the wind tunnel experiment conducted by Obasaju [19] in British Maritime Technology (BMT) Environmental Wind Tunnel. As shown in Fig.2, the computational domain covers 30*B* (*B* is the breadth of the building model) in the streamwise direction, 17*B* in the spanwise direction and 2*H* (*H* is the height of the building model) in the vertical direction. The blockage ratio of the computational domain is nearly 3% which is regarded as acceptable in CWE community. In consideration of the periodic boundary in the spanwise direction, the size of the across-wind dimension is chosen to be at least twice the size of the largest eddy.

3.3 *Mesh arrangement*

For the auxiliary driver section using the recycling method, structured mesh arrangement is applied to discretize driver section, and for the need of capturing the turbulence generated by the roughness elements, the grid points are clustered near the cubic element surfaces and the ground neighborhood. About 1.2×10^6 mesh elements are used in discretizing driver section.

For the mesh arrangements in the main region, the structured mesh is used in the domain far from the building model and the unstructured mesh is adopted near the building model surfaces, since the Fluent code [16] is capable of dealing with both structured and unstructured grids. The advantages of this kind of mesh arrangement are capable of refining the grid distribution in the building surface neighborhood and avoiding excessive grid-stretching and reduce the total grid number in the main region. On the surfaces of the building model, a boundary layer with 20 grids is adopted and the first grid height next to the building surface is chosen as *B*/1000 and a growth factor 1.05 so that the near-wall grid y^+ ($y^+=\rho uy/\mu$) is in the order of unit. Finally, the total grid number in the main region is almost 1.5×10^6.

3.4 *Boundary conditions*

In order to obtain better agreement between wind tunnel experiment and numerical results, the inflow boundary conditions adopted in this study is identical as that in the wind tunnel experiment of Obasaju [19]. The log law wind speed profile of the atmospheric boundary layer simulated in the wind tunnel study of Obasaju [19] is given as follows:

$$\frac{U}{U_\tau}=2.5\ln(\frac{Z-D}{Z_0}) \tag{4}$$

where U_τ is friction velocity, D is the zero plane above ground, and Z_0 is the surface roughness length parameter. The parameters chosen in the present numerical simulation are U_τ=14.5m/s, D=10 mm, Z_0=1.3 mm. The inlet wind speed corresponding to the building height is U_H=14.5 m/s.

As discussed by Tominaga et al. [21], the influence of inflow turbulence for the LES was extremely important. Hence the turbulence intensity profile should be properly reproduced for the accurate simulation of the wind effects on the tall building. The profiles of the mean wind speed and turbulence intensity are shown in Fig.3.

For the case using the inflow turbulence generated by the recycling method, pseudo-periodic boundary conditions are used in the streamwise directions, and the velocity inlet is used for the cases using other inflow generation methods. For all the cases, the periodic boundary conditions are used in the spanwise direction, with all properties being equal at equivalent points on pairs of periodic boundaries which means the distance between the two periodic boundaries

must be such that two-point correlations are zero for all points on a pair of periodic boundaries. This denotes that the distance should be chosen to be at least twice the size of the largest eddies so that the effect of one boundary on the other is minimal. A symmetry condition (vanishing vertical derivatives of the streamwise and spanwise velocity components, as well as vanishing vertical velocity) at the top boundary of the computational domain is adopted. For the LES simulation, outflow boundary conditions are less troublesome, and the familiar zero gradient boundary condition is used for all the variables normal to the outflow boundary. For all the surfaces of the cubic roughness elements, the building model and the ground, the boundary conditions are set to be no-slip wall boundary (u=v=0) which is appropriate for the velocity components at solid walls.

4 IMPLEMENTING AND NUMERICAL SETUP

4.1 *Subgrid-scale turbulence model*

The subgrid-scale (SGS) turbulence models in Fluent code employ the Boussinesq hypothesis as in the RANS models. The simple model was firstly built on Prandtl's mixing length model and it is assumed that we can define a SGS viscosity μ_{SGS} in terms of one length scale and one velocity scale, as suggested by Smagorinsky [22]. However, the Smagorinsky model is purely dissipative which is not particularly appropriate for the high Reynolds number bluff body flows. Germano et al. [23] conceived a procedure in which the Smagorinsky model constant, C_S, is dynamically computed based on the information provided by the resolved scales of motion. The dynamic procedure thus obviates the need for users to specify the model constant C_S in advance. In this study, the dynamic Smagorinsky-Lily model is adopted as the default subgrid-scale turbulence model, and the C_S obtained by the dynamic Smagorinsky-Lilly model varies in time and space over a fairly wide range. In Fluent code, C_S is clipped between zero and 0.23 by default to avoid numerical instability [16].

4.2 *Solution strategy*

The solver for incompressible flow in Fluent code employs an algorithm which belongs to a general class of methods called the projection method [24]. In the projection method, the governing equations are solved sequentially. The pressure velocity coupling method chosen for the present simulation is SIMPLC (Semi-Implicit Method for Pressure-Linked Equations Consistent) algorithm [25], which is one of variants of the basic SIMPLE algorithm. For LES, second-order or higher-order discretisation techniques are needed, because upwind differencing, which was standard practice in early CFD computations with RANS turbulence modelling, is far too diffusive and generates large truncation errors. The bounded central difference, a default convection scheme for LES in Fluent code, is used to discretize the convective terms of momentum equations for its relative low diffusivity. The central differencing is also applied to discretize the diffusion term. The time derivative is discretized using the second order backward differences and the spatial discretization is treated implicitly. The non-linear terms produced by fully-implicit discretization of the convection term is solved by an iterative process. The Green-Gauss cell based method is used for numerical approximation of pressure gradients. In order to obtain numerical solutions that are statistically converged quickly, steady RANS model had been used before the LES was performed. In other words, the results of the RANS simulation were adopted to be the initial solutions of the LES.

A 12CPUs workstation was used in parallel for the LES. With consideration of the accuracy of the LES and computational expenses, it was decided to adopt 0.025 seconds per time step for the computations and the convergence criterion for the scaled residuals within one time step is less than 1×10^{-4}.

5 RESULTS AND DISCUSSIONS

5.1 *Wind characteristics*

Velocity values are taken at the building model position for all the inflow generation methods to validate the characteristics of the generated velocity field when the main domain is computed with the building model filled with additional computing grid points.

In this section, the time-averaged longitudinal velocity and turbulence intensity profiles at the building model position are compared with the target profiles. As demonstrated in Figure.3, the time-averaged velocity and turbulence intensity profiles are reproduced quite well. For the mean velocity profile, all the methods reproduce the variations of velocity in vertical direction quite well, while that generated by DSRFG is slightly higher in the ground neighborhood and lower at the top in comparison with those by the other methods and the target profile. For the turbulence intensity profile, all the three methods generate reasonable results, although there are some discrepancies between the target values and the predictions generated by the RFG and the recycling method which reproduce lower turbulence intensity at higher elevations. Particularly, the turbulence intensity reproduced by the recycling method can impose the random perturbation at the top inlet in the auxiliary driver section for the inflow turbulence generation.

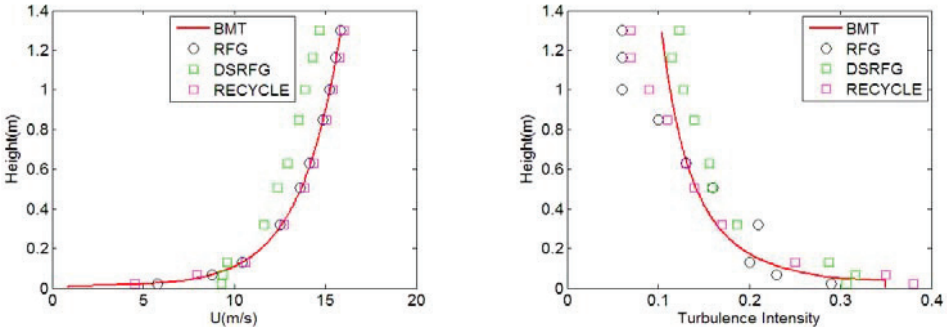

Figure.3 Mean velocity profile and turbulence intensity profile at the building position

The velocity values reproduced by DSRFG at the inlet of the main region are considered herein. In Fig.4, the wind velocity spectral curves at the inlet and the building model position are displayed, which were obtained by two power spectral density estimators: Welch estimator and Yuler-Walker estimator. The spectra of u, v and w velocity fluctuations at the inlet demonstrated in Figs.4(a)~(c) are found to be predicted well in comparison with the target Karman spectrum, while the spectra of three velocity component fluctuations at the building model position (shown in Figs.4(d)~(f)) illustate relatively large discrepancies in the frequency range larger than 1 Hz. Such a decay of the power spectral density in the relatively higher frequency range was reported to be caused by the grid resoluation [4]. Therefore, it is necessary to refine the grids distributed between the building surfaces and the inlet to minimize the decay of the ernergy contained in the high frequency range.

As discussed in [14] and shown in Figs.5(a)~(c), the velocity component fluctuations generated by RFG are incapable of simulating wind velocities satisfying the von kaman spectrum. Actually, there are obvious discrepancies between the simulated spectra and the target spectra. In particular, the energy contained in the high frequency range is neglected by RFG and such a spectrum is called Gaussian spectrum. For the longitudinal velocity fluctuating component, the spectrum simulated by the recycling method is found to follow the target von Karman spectrum until the frequency reaches to 0.2 Hz, while the energy contained in the higher frequency range shows some discrepancies compared with the von Karman spectrum. Such a decay in the high frequency range may be attributed to the restriction of the grid resolution.

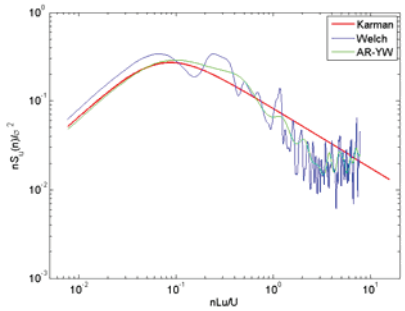

Figure.4 (a) u by DSRFG at inlet

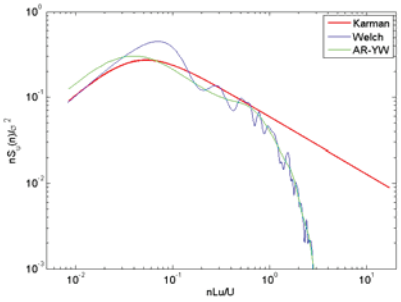

Figure.4 (d) u by DSRFG at building position

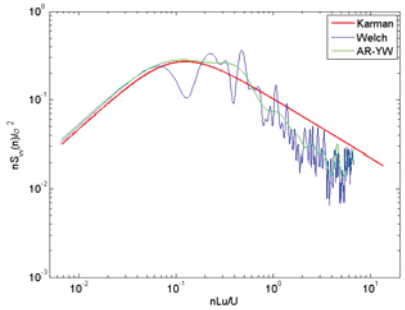

Figure.4 (b) v by DSRFG at inlet

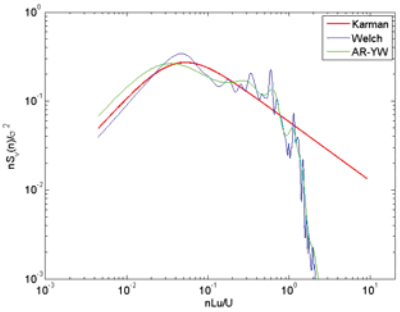

Figure.4 (e) v by DSRFG at building position

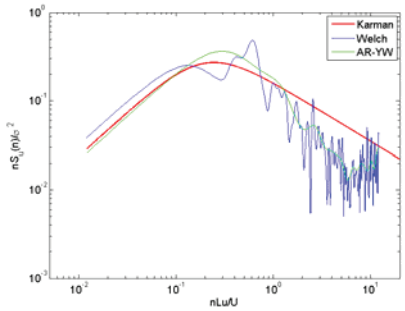

Figure.4(c) w by DSRFG at inlet

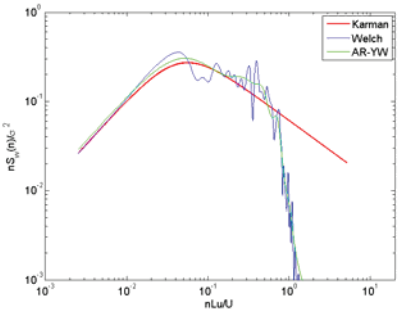

Figure.4 (f) w by DSRFG at building position

Figure.4 Spectra of u, v and w by DSRFG at inlet and building position

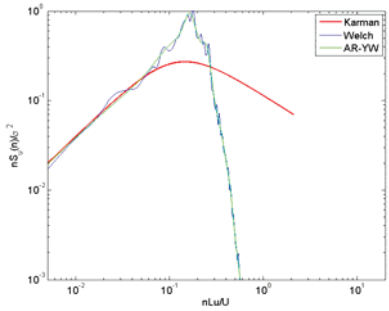

Figure.5(a) u by RFG at building position

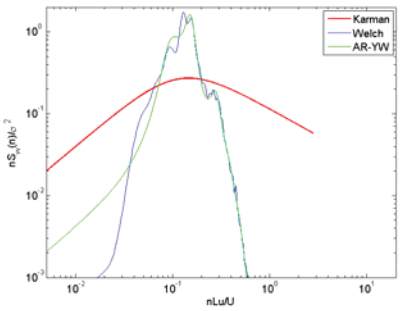

Figure.5(b) v by RFG at building position

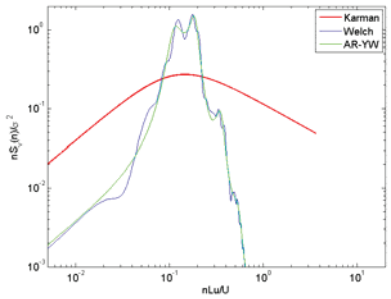

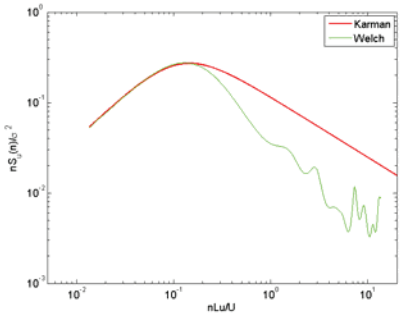

Fgiure(c) w by RFG at building position Figure.5(d) u by the recycling method at inlet

Figure.5 Spectra of u, v and w by RFG at building model position and u by the recycling method at inlet

5.2 *Wind loading on the building model*

The incident wind flow considered in this study is normal to a side of the building model surface. Fig.6 shows the mean and RMS pressure coefficients at the 2/3 height of the building model, as demonstrated in Fig.6, which were obtained by the present LES and wind tunnel tests. It can been seen that the mean pressure coefficients on the windward face calculated by the three inflow generation methods are nearly the same as those of differet wind tunnel experiments. For the side and back faces, the mean wind pressure distribution patterns predicted by different inflow turbulence generation methods are consistent with those of various wind tunnel experiments. For RMS pressure coefficients shown in Fig.6, not only obvious discrepancies exit between the numerical predictions and the wind tunnel test data, but also among the model experimental results. As discussed by Li and Melbourne [26, 27], the reasons for the discrepancies of RMS pressure coefficients among different wind tunnel experiments can be attributed to the different turbulence intensity and turbulence integral length scale values or profiles of approaching wind flows as well as blockage ratio encountered in the model tests.

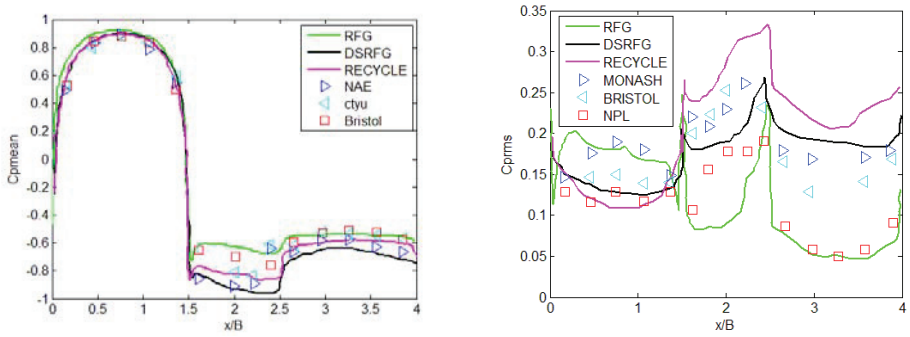

Figure.6 Mean and RMS pressure coefficients at 2/3 height of the building model

As shown in Fig.6, the fluctuating pressure coefficient distribution shapes calculated by the three inflow turbulence generation methods are similar while the distribution predicted by DSRFG is enveloped by the wind tunnel experimental measurements. This illustrates that DSRFG can provide more accuarte predictions of the wind loading on the tall building than the other two methods.

6 CONCLUSIONS

In this study, we focused on examining the performance of three methods (DSRFG, RFG and the recycling method) for inflow turbulence generation. The computational results showed that all

the three methods can reproduce the time-averaged velocity and turbulence intensity profiles at the building position quite well. The spectra of random wind velocities reproduced by DSRFG showed good agreement with the target spectrum at the inlet and that of the longitudinal velocity simulated by the recycling method is similar to the von-Karman spectrum. However, RFG is incapable of generating fluctuating velocity satisfying the prescribed von Karman spectrum. The velocity spectra at the building position simulated by DSRFG and the recycling method are affected by the grid resolution between the windward surface of the building and the inlet. The lower grid resolution may result in fast decay of wind velocity spectra in the high frequency range. In order to verify the accuracy of the wind loading predication by the three methods, the time-averaged and RMS pressure coefficients distributed at the 2/3 height of the CAARC building were compared with available wind tunnel test data obtained by several labs. It was found that the mean pressure coefficients on the front surface of the building were accurately predicted by all the three inflow generation methods and the pressure coefficient distribution pattern on the side and back surfaces were also well predicated. All the RMS pressure coefficients obtained by the three inflow turbulence generation methods fall in the range of the model test data by various wind tunnel experiments, verifying that the effects of turbulence characteristics of approaching wind flows on the building surface pressures were reproduced to some extent. It was shown through the comparison that DSRFG can provide more accuarte predictions of the wind loading on the tall building than the other two methods.

7 ACKNOWLEDGEMENT

The work described in this paper was fully supported by a grant from the Research Grants Council of Hong Kong Special Administrative Region, China (Project No: CityU 117709) and a grant from City University of Hong Kong (Project No. 7002615). The authors would like to thank Dr. Shenghong Huang of the University of Science and Technology of China for helpful discussions.

8 REFERRENCE

1 Tamura T. Towards practical use of LES in wind engineering. J Wind Eng Ind Aerodyn 2008;96:1451-71.
2 Spalart PR, Leonard A. Direct numerical simulation of equilibrium turbulent boundary layers. 5th Symposium on Turbulent Shear Flows 1985;1:9.
3 Lund S, Wu X, Squires KD. Generation of Turbulent Inflow Data for Spatially-Developing Boundary Layer Simulations. Journal of Computational Physics 1998;140:233-58.
4 Kataoka H, Mizuno M. Numerical flow computation around aeroelastic 3 D square cylinder using inflow turbulence. WIND STRUCT INT J 2002;5:379-92.
5 Nozawa K, Tamura T. LES of the flow around a low-rise building immersed in a rough-wall turbulent boundary layer. J Wind Eng Ind Aerodyn 2002;90:1151-62.
6 Liu K, Pletcher RH. Inflow conditions for the LES of turbulent boundary layers: a dynamic recycling procedure. Journal of Computational Physics 2006;219:1-6.
7 Hoshiya M. Simulation of multi-correlated random processes and application to structural vibration problems. Proceedings of JSCE 1972;204:121-8.
8 Iwatani Y. Simulation of multi-dimensional wind fluctuations having any arbitrary power spectra and cross spectra. Journal of Wind Engineering 1982;11:5-18.
9 Kondo K, Murakami S, Mochida A. Generation of velocity fluctuations for inflow boundary condition of LES. J Wind Eng Ind Aerodyn 1997;67:51-64.
10 Perret L, Delville J, Manceau R, Bonnet J P. Generation of turbulent inflow conditions for LES from stereoscopic PIV measurements. Int J Heat Fluid Flow 2006;27:576-84.

11 Smirnov A, Shi S, Celik I. Random flow generation technique for LESs and particle-dynamics modeling. Journal of Fluids Engineering 2001;123:359.
12 Klein M, Sadiki A, Janicka J. A digital filter based generation of inflow data for spatially developing direct numerical or LESs. Journal of Computational Physics 2003;186:652-65.
13 Batten P, Goldberg U, Chakravarthy S. Interfacing statistical turbulence closures with large-eddy simulation: Boundary conditions for LES. AIAA J 2004;42:485-92.
14 Huang S H, Li Q S, Wu J R. A general inflow turbulence generator for LES. J Wind Eng Ind Aerodyn 2010;98:600-17.
15 Kraichnan R H. Diffusion by a random velocity field. Phys Fluids 1970;13:22.
16 Fluent 6.3 user's guide. Fluent Inc 2006.
17 Kataoka H. Numerical simulations of a wind-induced vibrating square cylinder within turbulent boundary layer. J Wind Eng Ind Aerodyn 2008;96:1985-97.
18 Melbourne W.H. Comparison of measurements on the CAARC standard tall building model in simulated model wind flows. J Wind Eng Ind Aerodyn 1980;6:73-88.
19 Obasaju E. Measurement of forces and base overturning moments on the CAARC tall building model in a simulated atmospheric boundary layer. J Wind Eng Ind Aerodyn 1992;40:103-26.
20 Goliger A, Milford R. Sensitivity of the CAARC standard building model to geometric scale and turbulence. J Wind Eng Ind Aerodyn 1988;31:105-23.
21 Tominaga Y, Mochida A, Murakami S, Sawaki S. Comparison of various revised k-ε models and LES applied to flow around a high-rise building model with 1: 1: 2 shape placed within the surface boundary layer. J Wind Eng Ind Aerodyn 2008;96:389-411.
22 Smagorinsky J. General circulation experiments with the primitive equations. Mon Weather Rev 1963;91:99-164.
23 Germano M, Piomelli U, Moin P, Cabot WH. A dynamic subgrid−scale eddy viscosity model. Physics of Fluids A: Fluid Dynamics 1991;3:1760.
24 Chorin A J. Numerical solution of the Navier-Stokes equations. Math.Comp 1968;22:745-62.
25 Van Doormaal J, Raithby G. Enhancements of the SIMPLE method for predicting incompressible fluid flows. Numerical Heat Transfer 1984;7:147-63.
26 Li Q S, Melbourne W.H. The effect of large-scale turbulence on pressure fluctuations in separated and reattaching flows. J Wind Eng Ind Aerodyn 1999;83:159-69.
27 Li Q S, Melbourne W.H. An experimental investigation of the effects of free-stream turbulence on streamwise surface pressures in separated and reattaching flows. J Wind Eng Ind Aerodyn 1995;54:313-23.

The Seventh International Colloquium on Bluff Body Aerodynamics and Applications (BBAA7)
Shanghai, China; September 2-6, 2012

Turbulence simulation in wavelet domain based on Log-Poisson model: univariate and multivariate wind processes

Chao Yin[a], Teng Wu [a], Ahsan Kareem [a]

[a]*Nathaz Modeling Laboratory, University of Notre Dame, Notre Dame, IN, USA*

ABSTRACT: The wind in atmospheric boundary layer is characterized as turbulent flow at a high Reynolds number. The complexity in turbulence is mainly from its nonlinear and multi-scale structure. This paper simulates the wind process utilizing the wavelet domain based on the Log-Poisson model where both multi-scale structure and the intermittency could be properly represented. Following simulating a univariate process, a methodology for simulating multivariate processes is also established, where a correction technique based on the coherence of the wavelet coefficients at each scale is utilized. The resulting simulation follows the characteristic features of the sample record and offers a more realistic simulation than the spectral representation based methods.

KEYWORDS: Turbulence; non-Gaussian; wavelet; Log-Poisson model; multivariate processes

1 INTRODUCTION

The wind process in atmospheric boundary layer is characterized as turbulent flow at a high Reynolds number. A physical origin of the complexity in turbulence is due to the nonlinearity controlled by the Navier-Stokes equations. As a result, turbulent flows are naturally described based on the statistics theory. Typically, turbulent fluctuations are assumed to be Gaussian. Conventional wind process simulation, such as spectral representation, is based on this assumption. Another physical origin of the complexity in turbulence is due to the multi-scale property resulting from nonlinear interactions, where the turbulence are better described utilizing the statistics of velocity difference at two locations compared with that of velocity fluctuations at a single location. As a strong discontinuous nature of turbulence, internal intermittency seems only changing the velocity statistics slightly (a broad banded probability density distribution (PDF) compared to Gaussian distribution), while it has significant effects on the statistics of the velocity difference (a considerably larger tail PDF compared with Gaussian distribution).

In order to take into account the effects of intermittency, several phenomenological models have been introduced in the literature, such as Log-normal and other multifractal models. Obviously, the conventional wind process simulation cannot take intermittency into account. On the other hand, these random cascade models are convenient to be incorporated in the wavelet based simulation[1,2]. Specifically, the recently developed Log-Poisson model[3], which is claimed to be able to reveal the physical mechanism of the intermittency phenomenon, is utilized in this study. As a result, the intermittency will be preserved in the simulated turbulence utilizing wavelet domain. The boundary condition effects on the energy containing (EC) range and the non-local relationship between the scales in the multiplicative cascade process of the inertial subrange are included in the simulation. In addition, the wavelet domain also facilitates to include non-stationary feature in the simulation often observed in atmospheric turbulence. Based on this developed framework, univariate and multivariate wind process simulation schemes are proposed and their efficacy is demonstrated by examples.

2 ANALYSIS OF WIND PROCESS

Conventional strategies of simulating wind processes are usually restricted to the second-order statistics with implied Gaussian assumption. These strategies can be generalized by Karhunen-Loeve (K-L) expansion and numerically realized with the Galerkin Scheme [4]. The generalized Gaussian process simulation scheme is given as[5]

$$V(\theta,t) \approx \sum_{k=1}^{N} \lambda_k \xi_k(\theta) \phi_k(t) \approx \sum_{k=1}^{N} \lambda_k \xi_k(\theta) \left[\sum_{m=1}^{N} d_m^{(k)} \psi_m(t) \right] \tag{1}$$

where θ is the original random variable; $V(\theta,t)$ is the target random process with respect to time *t*; $\{\lambda_k\}$ are the eigenvalues of K-L expansion; $\{\xi_k(\theta)\}$ is the identical independent distribution (*i.i.d*) standard Gaussian sequence; $\{\phi_k(t)\}$ are the eigenfunctions corresponding to $\{\lambda_k\}$; $\{d_m^{(k)}\}$ are the coefficients corresponding to the prescribed truncated orthogonal basis $\{\psi_m(t), m=1,2,\cdots N\}$. Suppose Fourier basis is selected, the simulation is equivalent to the spectral representation. On the other hand, the simulation can be extended to the nonstationary Gaussian process if wavelet basis is selected[5].

A typical turbulent flow field is not necessarily Gaussian as demonstrated by some experimental data[e.g.,6]. Specifically, the PDFs of velocity differences at the inertial scale exhibit a significant longer tail than Gaussian distribution, which is related to the intermittency in turbulence. Conventional schemes based on the second-order statistics are insufficient to describe such a non-Gaussian process. On the other hand, since typical dynamical information in turbulence is contained in the scaling quantities, based on which the wavelet coefficients are generated, wavelet expansion utilizing higher-order statistics is an appropriate tool to analyze and simulate such a multi-scale process with non-Gaussian PDF.

2.1 *Scaling properties of turbulence*

There are two significant scaling quantities describing the multi-scale structure of turbulence: the energy dissipation rate ε and the velocity difference δv. In this study, the characteristics of δv are utilized. For a turbulence flow, within the inertial range, the p^{th} order moment of δv_l at scale l has a power-law dependence on l [3],

$$\left\langle \delta v_l^p \right\rangle \sim l^{\tau_p} \tag{2}$$

where ⟨ ⟩ denotes the expectation of the random variable; τ_p represents the exponent at the p^{th} order moment. Within the EC range, δv is related to the boundary condition and may exhibit nonstationary features as it reflects the external mechanism.

2.2 *Statistical property of the Log-Poisson random cascade model*

The universal scaling law can be realized via a Log-Poisson process, which is a random multiplicative cascade process[1]. Within the inertial range, for the case of p=1, the velocity difference δv_{l_1} at scale l_1 and the velocity difference δv_{l_2} at scale l_2 has the following relation [1,3]

$$\delta v_{l_1} = W_{l_1,l_2} \delta v_{l_2} = \left[\left(\frac{l_2}{l_1} \right)^{\gamma-1} \beta^{n_{l_1,l_2}} \right]^{\frac{1}{3}} \delta v_{l_2} \tag{3}$$

where W_{l_1,l_2} is the multiplicative factor between δv_{l_1} and δv_{l_2}; γ and β are the scale-related parameters and need to be estimated based on the real turbulence flow, however, refer-

ence [3] suggests that $\gamma = 2/3, \beta = 2/3$; n_{l_1,l_2} is the independent Poisson random variable with mean λ_{l_1,l_2}, satisfying the following relation[1,2,3]

$$\lambda_{l_1,l_2} = -\frac{\gamma}{\beta - 1} \ln \frac{l_2}{l_1} \tag{4}$$

It should be noted that the above relation from l_2 directly to l_1 is identical to l_2 via l_3 to l_1.

3 SIMULATION OF WIND PROCESS

The wavelet technique is utilized here to simulate the multi-scale structure of the turbulence flow. Suppose only δv_l in the EC range depends on the external mechanism, it is reasonable to attribute the nonstationary part in the turbulence flow to δv_l within this range. Therefore, it is necessary to determine the critical scale l_c, which pinpoints the EC range and the inertial range. Usually, l_c is assumed corresponding to the frequency f_c which makes $f\tilde{S}_{VV}(f)$ maximum, where $\tilde{S}_{VV}(f)$ is the power spectrum of the wind velocity $V(t)$ with zero mean value. The frequency f_c is a function of mean wind velocity an integral scale as Karman spectrum is utilized.

Haar wavelet function is chosen here since it represents a clear physical meaning of velocity difference. Correspondingly, the relation between the wavelet scale order j and the dominant frequency f_j of *j*th Haar wavelet function can be determined[Appendix A]. Particularly, the relation between j_c and f_c is shown as

$$j_c = n + \mathrm{int}\left\{\log_2\left(\frac{f_c}{0.742}\right)\right\} \tag{5}$$

where *n* is the highest wavelet scale order used in the simulation.

3.1 *Simulation of univariate wind process*

Use $m_V(b_k, a_j)$ to denote the wavelet coefficient at the a_j scale and b_k time position, associated with the normalized form $\zeta(b_k, a_j)$. With Haar wavelet transform, $m_V(b_k, a_j)$ is closely related to δv at l_j scale[Appendix B].

3.1.1 *Simulation scheme*

The simulation scheme of univariate wind process in wavelet domain is presented in Fig. 1, which is described as follows:

(1) Determine j_c using Eq. (5);

(2) Within the EC range, $\{\delta v_{l_{j,i}}\}$ $(j = 1,\cdots,j_c;\ i = 1,\cdots,2^{n-1})$ are produced from *i.i.d* standard Gaussian sequence and transformed to $\{\zeta(b_k, a_j)\}$ $(j = 1,\cdots,j_c;\ k = 1,\cdots,2^{j-1})$;

(3) Within the inertial range, $\{\delta v_{l_{j,i}}\}$ $(j = j_c + 1,\cdots,n;\ i = 1,\cdots,2^{n-1})$ are produced independently from $\{\delta v_{l_{j-1,i}}\}$ or $\{\delta v_{l_{j_c,i}}\}$ base on

$$\delta v_{l_{j,i}} = W_{j,j-1}\delta v_{l_{j-1,i}} \quad \text{or} \quad \delta v_{l_{j,i}} = W_{j,j_c}\delta v_{l_{j_c,i}} \tag{6}$$

where

$$W_{j,j-1} = \left(\frac{l_{j-1}}{l_j}\right)^{\gamma} \beta^{n_{j,j-1}},\quad W_{j,j_c} = \left(\frac{l_{j_c}}{l_j}\right)^{\gamma} \beta^{n_{j,j_c}} \tag{7}$$

and then transform the generated $\{\delta v_{l_{j,i}}\}$ to $\{\zeta(b_k, a_j)\}$ $(j = j_c + 1,\cdots,n;\ k = 1,\cdots,2^{j-1})$;

(4) $m_V\left(b_k,a_j\right)$ is adjusted from $\zeta\left(b_k,a_j\right)$ according to the wavelet coefficients correlation at the same scale, which shares the following relation with conventional spectral density for stationary process[Appendix C]

$$m_V\left(b_k,a_j\right)=\zeta\left(b_k,a_j\right)\times\sqrt{\left\langle\left|m_V\left(b_k,a_j\right)\right|^2\right\rangle}=\zeta\left(b_k,a_j\right)\times\sqrt{2^{a_j}\int_{-\infty}^{\infty}\left|\tilde{\psi}_{a_j,b}\left(f\right)\right|^2 S_{VV}\left(f\right)df} \tag{8}$$

where $\tilde{\psi}_{a_j,b}\left(f\right)$ is the Fourier spectrum of wavelet function $\psi_{a_j,b}\left(t\right)$ at scale a_j; $S_{VV}\left(f\right)$ is the conventional spectral density with mean velocity. For a non-stationary process, the above equation is only approximately satisfied, while the exact energy distribution of wavelet coefficients should refer to the technique as Eq.(1). In essence, the eddies could be treated as scale-dependent stationary within the inertial range as they depend mainly on the internal mechanism of the turbulence rather than the external condition;

(5) Sythesize the wind process v from the generated $m_V\left(b_k,a_j\right)$.

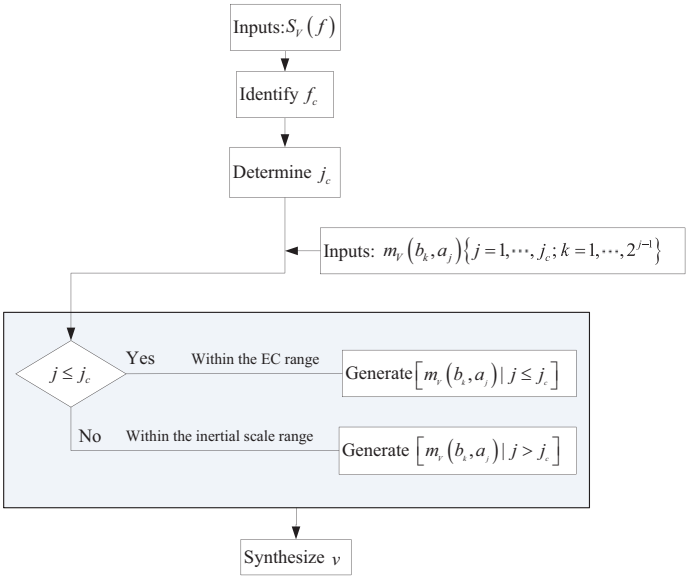

Figure 1 Simulation of univariate wind process.

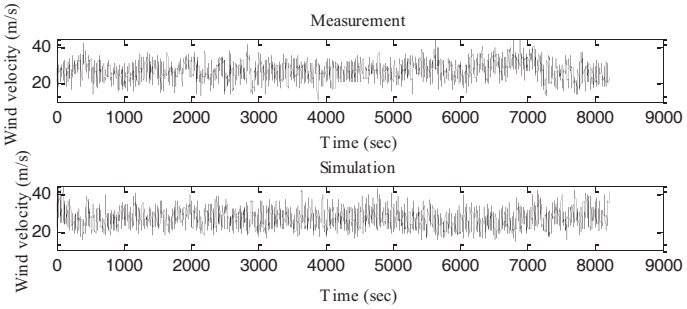

Figure 2 The measurement and simulation result of a univariate wind process.

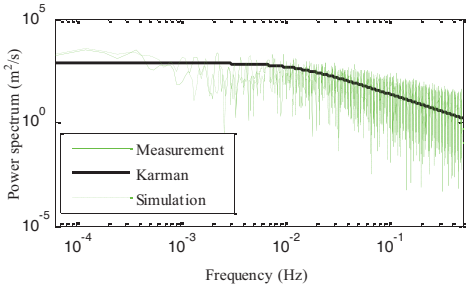

Figure 3 Power spectrum

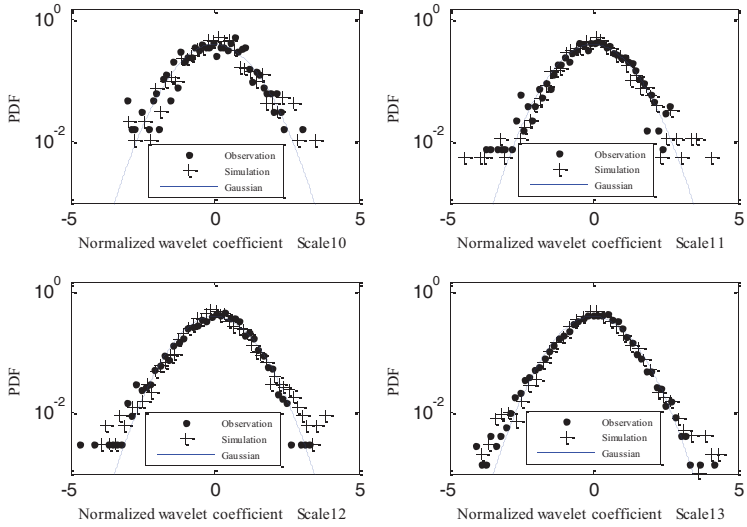

Figure 4 PDF of wavelet coefficients at some typical inertial scales.

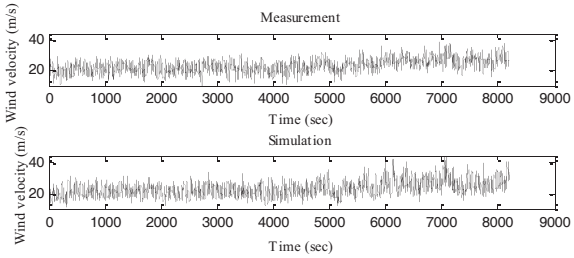

Figure 5 The measurement and simulation result of univariate nonstationary wind process.

3.1.2 *Case study*

Hurricane Katrina is utilized in this study to demonstrate the effectiveness of the proposed simulation framework. The measured data and the simulation result are shown in Fig. 2. ℓ_u is estimated as 247m and $j_c = 7$. The power spectra based on the measured and simulated data are presented in Fig. 3 together with Karman spectrum. PDFs of the wavelet coefficients at some typical inertial scales are given in Fig. 4. There is 4.59% error between the variances of the simulated process and of the measurement. A nonstationary case is shown as Fig. 5.

3.1.3 *Discussion*

It is interesting to notice that reference [1] has used a similar approach to simulate a univariate stationary wind process. This study offers a reasonable strategy for simulating nonstationary

wind. More importantly, there is a major distinction in the treatment of the Log-Poisson model between this study and reference [1]:

(1) Within the inertial range, it is known that the universal scaling law is obtained from the ergodicity assumption which implies stationarity, however, the algorithm for generating the wavelet coefficients in reference [1] distorts the ergodicity in three aspects. First, the odd wavelet coefficients are generated by involving an algebraic average of the wavelet coefficients at larger scale, while the even wavelet coefficients are not, which are given here[1],

$$\tilde{\zeta}\left(b_{k=2i+1},a_j\right)=s\times\left(2/3\right)^{m/3}2^{-1/9}\frac{\sqrt{2}\left[\tilde{\zeta}\left(b_{k=i},a_{j-1}\right)+\tilde{\zeta}\left(b_{k=i+1},a_{j-1}\right)\right]}{2} \tag{9}$$

$$\tilde{\zeta}\left(b_{k=2i},a_j\right)=s\times\left(2/3\right)^{m/3}2^{-1/9}\tilde{\zeta}\left(b_{k=i},a_{j-1}\right) \tag{10}$$

where s is a binomial random variable taking the value +1 or -1; m is equivalent to $n_{j,j-1}$ in this study. The ergodicity assumption indicates that $\zeta\left(b_k,a_j\right)$ should have identical property at each scale while reference [1] obtains the odd and even terms using different schemes; second, both $\tilde{\zeta}\left(b_{k=2i},a_j\right)$ and $\tilde{\zeta}\left(b_{k=2i+1},a_j\right)$ deviate from the actual random variables $\zeta\left(b_k,a_j\right)$ since another random variable s is involved in the expression. The case of $\tilde{\zeta}\left(b_{k=2i+1},a_j\right)$ is worse due to the average operation previously discussed; third, there should be 2^{j_n-1} basic *i.i.d* Gaussian random variables to generate the wavelet coefficients at each scale instead of 2^{j_c-1}.

(2) Reference [1] simply regards the wavelet coefficient $\tilde{\zeta}\left(b_k,a_j\right)$ equivalent to the velocity difference δv_{l_j} and supposes they have the same statistical property. Actually, inferred by the wavelet decomposition algorithm, $\tilde{\zeta}\left(b_k,a_j\right)$ should be determined based on the contribution from all the $\delta v_{l_{j,i}}$ s. The weighting of the contribution from each $\delta v_{l_{j,i}}$ depends on the selected wavelet function. For example, for Haar wavelet basis, which is utilized in this study, the relation between the velocity difference and the wavelet coefficients is presented in Appendix A.

(3) In reference [1], it is stated *"when the large fluctuations occurred at a certain scale j, the coefficient fluctuations become large around the same time at the other j: the local self-similarity was realized with the algorithm in this study."* Actually, this local strong fluctuation is a false appearance caused by the manipulation in the algorithm: all the samples of $\tilde{\zeta}\left(b_k,a_j\right)$ in the inertial range are generated from the same series of samples $\tilde{\zeta}\left(b_k,a_{j_c}\right)$. In this regard, the difference between the samples of $\tilde{\zeta}\left(b_k,a_{j_c}\right)$ will be passed down which causes similar corresponding difference between $\tilde{\zeta}\left(b_k,a_j\right)$ at all smaller scales. Actually, the universal scaling law holds true only in the statistical meaning rather than the sample meaning, therefore, the samples of $\tilde{\zeta}\left(b_k,a_j\right)$ should be generated independently from the samples of $\tilde{\zeta}\left(b_k,a_{j_c}\right)$, instead of reusing at each time.

3.2 *Simulation of multivariate wind processes*

The available information in simulating multivariate wind processes is the cross power spectrum $S_{XY}\left(f\right)$ and the trends represented by $\bar{m}_X\left(b_k,a_j\right)$ and $\bar{m}_Y\left(b_k,a_j\right)\left(j=1,\cdots,j_c;\ k=1,\cdots,2^{j-1}\right)$ at the target locations X and Y. The main object is to generate $\bar{m}_X\left(b_k,a_j\right)$ and $\bar{m}_Y\left(b_k,a_j\right)$ $\left(j=j_c+1,\cdots,n;\ k=1,\cdots 2^{j-1}\right)$ from the wavelet coefficient cross spectral density at the same scale between X and Y. The relation is shown as follows for stationary processes[Appendix C]

$$\tilde{C}_{m_Xm_Y}\left(f,a_j\right)=\int_{-\infty}^{\infty}C_{m_Xm_Y}\left(\tau,a_j\right)e^{-i\tau\omega}d\tau=2^a\left|\psi_{a_j,b}\left(f\right)\right|^2S_{XY}\left(f\right)e^{i\tau f} \tag{11}$$

where $\tilde{C}_{m_Xm_Y}\left(\omega,a_j\right)$ is the wavelet coefficient cross spectral density (CPD) at the same scale. Similar to the univariate case, for non-stationary processes, the above equations are approximately satisfied.

3.2.1 *Simulation scheme*

The simulation scheme of multivariate wind processes in wavelet domain is presented in Fig. 6, which is described as follows:

(1) Generate respectively the initial wavelet coefficients $m_X^0\left(b_k,a_j\right)$ and $m_Y^0\left(b_k,a_j\right)$ using the univariate simulation strategy described in section 3.1;

(2) Within the EC range, produce the final wavelet coefficients $m_X\left(b_k,a_j\right)$ and $m_Y\left(b_k,a_j\right)$ using conventional multivariate Gaussian simulation strategy at each scale;

(3) Within the inertial range, estimate the first four moments $d_{X,i,j}^T$ and $d_{Y,i,j}^T$ $\left(j=j_c+1,\cdots,n;\ i=1,\cdots,4\right)$ at each scale from the produced $m_X^0\left(b_k,a_j\right)$ and $m_Y^0\left(b_k,a_j\right)$. Calculate the target $\tilde{C}_{m_Xm_Y}^T\left(f\right)$ from $S_{XY}\left(f\right)$ and set the initial coherence value $\gamma_{m_Xm_Y}^D=\gamma_{m_Xm_Y}^T$, the iteration number *it*=1, where

$$\gamma_{m_Xm_Y}^2\left(f\right)=\frac{\left|\tilde{C}_{m_Xm_Y}\left(f\right)\right|^2}{\tilde{C}_{m_Xm_X}\left(f\right)\tilde{C}_{m_Ym_Y}\left(f\right)} \tag{12}$$

(4) A set of Gaussian correlated processes $m_X^G\left(b_k,a_j\right)$ and $m_Y^G\left(b_k,a_j\right)\left(j=j_c+1,\cdots,n\right)$ are generated using a standard multivariate Gaussian simulation algorithm[8];

(5) Transform respectively the obtained m_X^G and m_Y^G through forward Modified Hermite Transformation and spectral correction[9,10] to the non-Gaussian m_X^{NG} and m_Y^{NG} which matches their target $\tilde{C}_{m_Xm_X}^T\left(f\right),\tilde{C}_{m_Ym_Y}^T\left(f\right)$ and target moments $d_{X,i,j}^T$, $d_{Y,i,j}^T$;

(6) Measure the coherence $\gamma_{m_Xm_Y}^{NG}$ from the generated m_X^{NG} and m_Y^{NG} and compare it with the target coherence $\gamma_{m_Xm_Y}^T$ to determine the error as

$$err=\left\|\gamma_{m_Xm_Y}^{NG}-\gamma_{m_Xm_Y}^T\right\| \tag{13}$$

(7) If the error is below the acceptance level, the iteration ends. If not, update $\tilde{C}_{m_Xm_Y}^D$ by

$$\tilde{C}_{m_Xm_Y}^D\left(it+1\right)=\tilde{C}_{m_Xm_Y}^D\left(it\right)+\tilde{C}_{m_Xm_Y}^D\left(it\right)\left(\tilde{C}_{m_Xm_Y}^T-\tilde{C}_{m_Xm_Y}^{NG}\right) \tag{14}$$

until the error is accepted;

(8) Generate the wind processes v_X and v_Y from $m_X\left(b_k,a_j\right)$ $\left(j=1,\cdots,j_c\right)$, m_X^{NG} and $m_Y\left(b_k,a_j\right)$ $\left(j=1,\cdots,j_c\right)$, m_Y^{NG} respectively .

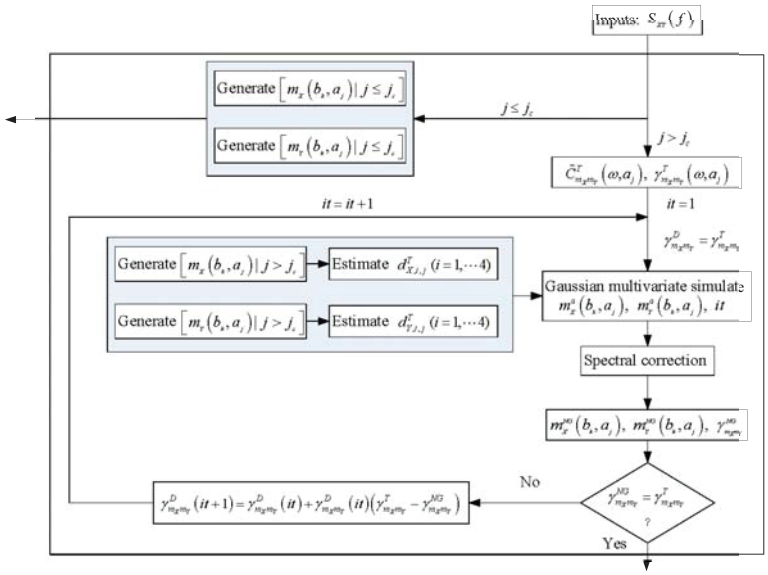

Figure 6 Simulation of multivariate wind processes.

3.2.2 *Case study*

Two measurements drawn from different passages of Hurricane Katrina are employed to simulate the multivariate wind processes. The generated time histories are show in Fig. 7. The cross correlation coefficients of the measurement and simulation exhibit good agreement (Fig. 8).

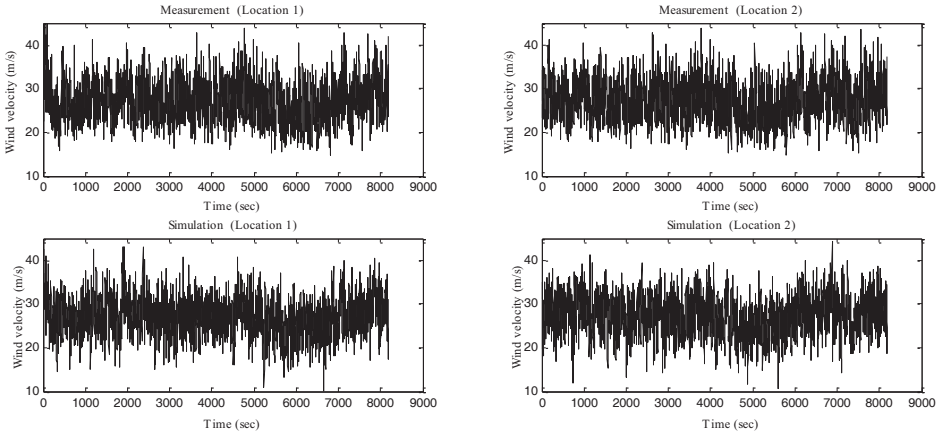

Figure 7 The measurements and simulation results of multivariate wind processes.

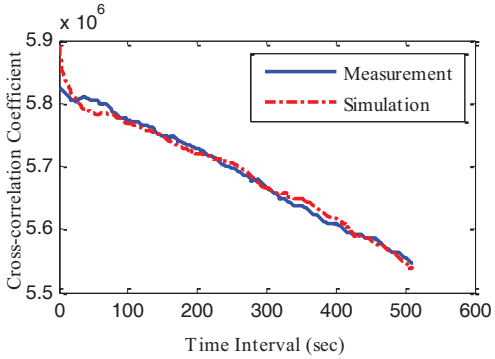

Figure 8 Coefficients of cross-correlation function.

4 CONCLUSION

A methodology of simulating univariate and multivariate turbulence flows in wavelet domain is proposed. This method, utilizing the Log-Poisson random cascade model, emphasizes the internal intermittency effect of the turbulence fluctuations in this simulation. The simulation results agree with both the power spectrum and the statistical information presented by the scaling law, thus present a better representation of the natural wind process than the conventional methods which only considers the second-order moments. Furthermore, in the simulation of the multivariate processes, the wavelet coefficients are iteratively updated to match the wavelet coefficients coherence at the same scale, thereby guaranteeing the consistence of the cross correlation function between the measurement and the simulation results.

5 ACKNOWLEDGEMENTS

The support for this project provided by the NSF Grant # CMMI 09-28282 which is gratefully acknowledged. We also thank Dr. Kurtis R. Gurley for the assistance in programming the multi-variate non-Gaussian simulation and providing the data set.

6 APPENDIX

A. When time interval is 1sec, the Fourier spectrum of Haar wavelet function is shown as

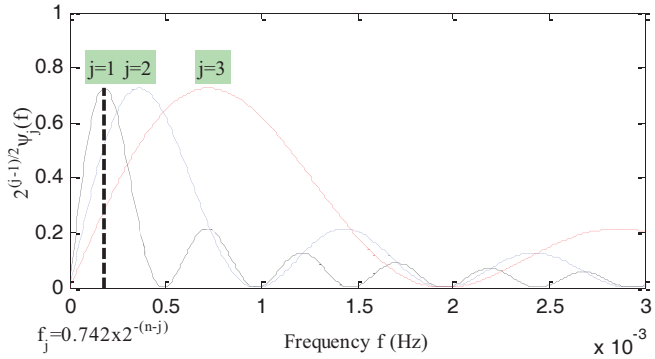

Figure 9 Absolute Fourier spectrum of Haar wavelet

B. The Discrete Haar wavelet reconstruction algorithm is shown as follows:

$$m_V\left(b_k,a_j\right)\sim\frac{1}{2^{n-j}}\sum_{i=2^{n-j}\times(k-1)+1}^{2^{n-j}\times k}\delta v_{l_{j,i}},\ \left(k=1,\cdots,2^{j-1}\right) \tag{15}$$

In order to explain clearly the relation between velocity difference δv_{l_j} and wavelet coefficient $m_V\left(b_k,a_j\right)$, the above algorithm is expressed in unnormalized form. Specifically, suppose a wind process $v(t)$ including 8 discrete points, there are

$$\begin{aligned}
&m_V\left(b_1,a_3\right)\sim\delta v_{l_{3,1}}=v_1-v_2,\ m_V\left(b_2,a_3\right)\sim\delta v_{l_{3,2}}=v_3-v_4,\cdots,m_V\left(b_4,a_3\right)\sim\delta v_{l_{3,4}}=v_7-v_8\\
&m_V\left(b_1,a_2\right)\sim\frac{1}{2}\sum_{i=1}^{2}\delta v_{l_{2,i}}=\frac{1}{2}\left[\left(v_1-v_3\right)+\left(v_2-v_4\right)\right],\ m_V\left(b_2,a_2\right)\sim\frac{1}{2}\sum_{i=3}^{4}\delta v_{l_{2,i}}=\frac{1}{2}\left[\left(v_5-v_7\right)+\left(v_6-v_8\right)\right]\\
&m_V\left(b_1,a_1\right)\sim\frac{1}{4}\sum_{i=1}^{4}\delta v_{l_{1,i}}=\frac{1}{4}\left[\left(v_1-v_5\right)+\left(v_2-v_6\right)+\left(v_3-v_7\right)+\left(v_4-v_8\right)\right]
\end{aligned} \tag{16}$$

When applied in the reconstruction like the simulation in this study, $\left\{\delta v_{l_{j,i}}\right\}$ represent a *i.i.d* sequence. Therefore, $m\left(b_k,a_j\right)$ is another random variable different from δv_{l_j}, furthermore, indicated by Central Limit Theorem, $m\left(b_k,a_j\right)$ approaches Gaussian distribution closer than δv_{l_j}.

C. The relation between the wavelet coefficients cross-correlation at the same scale and the conventional cross-correlation is shown as[11]

$$\begin{aligned}
C_{m_X m_Y}\left(b_1,b_2,a_1,a_2\right)&=\left\langle\int_{-\infty}^{\infty}m\left(b_1,a_1\right)m^*\left(b_2,a_2\right)\right\rangle\\
&=\left\langle\int_{-\infty}^{\infty}\int_{-\infty}^{\infty}\psi\left(t_1-b_1,a_1\right)\psi^*\left(t_2-b_2,a_2\right)x\left(t_1\right)y^*\left(t_2\right)dt_1dt_2\right\rangle\\
&=\int_{-\infty}^{\infty}\int_{-\infty}^{\infty}\psi\left(t_1-b_1,a_1\right)\psi^*\left(t_2-b_2,a_2\right)\left\langle x\left(t_1\right)y^*\left(t_2\right)\right\rangle dt_1dt_2\\
&=\sqrt{2^{a_1+a_2}}\int_{-\infty}^{\infty}\int_{-\infty}^{\infty}\psi\left(2^{a_1}t_1-b_1\right)e^{-it_1f}\psi^*\left(2^{a_2}t_2-b_2\right)e^{it_2f}R_{XY}\left(t_1,t_2\right)e^{i(t_2-t_1)f}dt_1dt_2
\end{aligned} \tag{17}$$

If X and Y are both stationary, the above equation can be written further as

$$C_{m_X m_Y}(b_1,b_2,a_1,a_2)=\sqrt{2^{a_1+a_2}}\int_{-\infty}^{\infty}\int_{-\infty}^{\infty}\psi\left(2^{a_1}t_1-b_1\right)e^{-it_1 f}\psi^*\left(2^{a_2}t_2-b_2\right)e^{it_2 f}\int_{-\infty}^{\infty}S_{XY}(f)\,df\,dt_1 dt_2$$
$$=\sqrt{2^{a_1+a_2}}\int_{-\infty}^{\infty}\tilde{\psi}_{a_1,b_1}(f)\tilde{\psi}^*_{a_2,b_2}(f)S_{XY}(f)\,df \tag{18}$$

Then it can derive the following expressions

$$C_{m_X m_Y}(\tau,a_j)=2^{a_j}\int_{-\infty}^{\infty}\left|\tilde{\psi}_{a_j,b}(f)\right|^2 S_{XY}(f)\,df \tag{19}$$

$$\tilde{C}_{m_X m_Y}(f,a_j)=2^{a_j}\left|\tilde{\psi}_{a_j,b}(f)\right|^2 S_{XY}(f) \tag{20}$$

$$C_{m_V m_V}(\tau,a_j)=2^{a_j}\int_{-\infty}^{\infty}\left|\tilde{\psi}_{a_j,b}(f)\right|^2 S_{VV}(f)\,df \tag{21}$$

$$\tilde{C}_{m_V m_V}(f,a_j)=2^{a_j}\left|\tilde{\psi}_{a_j,b}(f)\right|^2 S_{VV}(f) \tag{22}$$

Obviously, a stationary process implies a scale-dependent stationary process.

7 REFERENCES

1 Gurley, K. and Kareem, A., Applications of Wavelet Transforms in Wind, Earthquake and Ocean Engineering, Engineering Structures, 21(2) (1999): 149-167.

2 Kitagawa, T. and T. Nomura, A wavelet-based method to generate artificial wind fluctuation data, Journal of Wind Engineering and Industrial Aerodynamics, 91(7)(2003): 943-964.

3 She, Z.-S. and E. C. Waymire, Quantized Energy Cascade and Log-Poisson Statistics in Fully Developed Turbulence, Physical Review Letters, 74(2) (1995): 262-265.

4 R.G. Ghanem, P.D. Spanos, Stochastic finite elements: a spectral approach, Springer-Verlag, New York, 1991.

5 K.K. Phoon, H.W. Huang, et al., Comparison between Karhunen-Loeve and wavelet expansions for simulation of Gaussian processes, Computers & Structures, 82 (13-14) (2004): 985-991.

6 C.W. Van Atta and W.Y. Chen, Statistical self-similarity and inertial subrange turbulence, Statistical models and turbulence, Lecture Notes in Physics 12, edited by M. Rosenblatt and C.W. Van Atta, Springer-Verlag, Berlin, (1972), pp. 402-426.

7 Z.-S. She and S. A. Orszag, Physical model of intermittency in turbulence: Inertial-range non-Gaussian statistics, Physical Review Letters., 13(1991): 1701-1704.

8 Shinozuka, M. and G. Deodatis, Simulation of Stochastic Processes by Spectral Representation, Applied Mechanics Reviews, 44(4) (1991): 191-204.

9 Gurley, K. R. and A. Kareem, A conditional simulation of non-normal velocity/pressure fields, Journal of Wind Engineering and Industrial Aerodynamics, 77–78 (1998): 39-51.

10 Gurley K. R., Modelling and simulation of non-Gaussian processes, PhD Thesis, University of Notre Dame, (1997).

11 Zeldin, B. A., Representation and synthesis of random fields: ARMA, Galerkin, and wavelet procedures, PhD thesis, Rice University, Houston, (1996).

The Seventh International Colloquium on Bluff Body Aerodynamics and Applications (BBAA7)
Shanghai, China; September 2-6, 2012

Coupling method of WRF-LES and LES based on scale similarity model

Kojiro Nozawa [a], Tetsuro Tamura [b]

[a]*Institute of Technology, Shimizu Corporation, Tokyo, Japan*
[b]*Tokyo Institute of Technology, Yokohama, Japan*

ABSTRACT: The one-way coupling method is applied to connect meso-scale model WRF and micro-scale LES using the scale similarity model to get rid of numerical errors at the interface between coarse grid and fine grid. The coupling between coarse-grid WRF-LES and fine-grid LES is studied on a free convective boundary layer flow with no heat flux from the ground. We found that the connection between the coarse grid WRF-LES and the fine grid LES works well without large interpolation errors.

KEYWORDS: Large-Eddy-Simulation, WRF, scale similarity model, one-way coupling, immersed boundary method.

1 INTRODUCTION

The connection between a meso-scale model and a micro-scale LES is significant to simulate the micro-scale meteorological problem such as strong wind events due to the typhoon using LES. In these problems the mean velocity profiles and the mean wind directions change with time according to the movement of the typhoons. The inflow turbulence generating technique for LES which uses turbulent boundary layer driver can't support such mean velocity transition because this technique assumes that the simulating turbulent boundary layer flow is in equilibrium. Although, a fine grid micro-scale LES could not be connected to a coarse grid meso-scale WRF directly.

In LES when the grid is suddenly refined at the interface of nested grids which is normal to the mean advection the resolved shear stresses decrease due to the interpolation errors and the delay of the generation of smaller scale turbulence that can be resolved on the finer mesh [1]. The adjustment region is required to regenerate the high wavenumber part in the energy spectrum of the fluctuating velocity. In the grid nesting approach for LES the commutation errors are thought to be very significant near the nest inflow interfaces.

Nozawa and Tamura [2] proposed the method which could get rid of these numerical errors at the interface between coarse grid and fine grid by applying the one-way coupling method using the scale similarity model [3]. In the method the mean velocity component of the fine grid is equal to the velocity of the coarse grid and the averaged fluctuating velocity component of the fine grid is zero. Meanwhile the high wavenumber fluctuating velocity component of the fine grid which is implicitly estimated as subgrid-scale turbulence in the coarse grid is reproduced explicitly in the fine grid near the nest inflow interface. The fluctuating components of the fine grid velocity could be estimated solving the momentum equations which could be derived by subtracting coarse grid filtered Navier-Stokes equations from fine grid filtered Navier-Stokes equations. In order to validate the approach an apriori test was carried out. The LES of a turbulent boundary layer flow over rough surface was conducted using the fine grid and the fluctuating component of the fine grid velocity was reproduced introducing the low-pass filtered finely resolved velocity data into the momentum equations. The reproduced fluctuating velocity component agreed well with the true value which was derived by subtracting the generated low-pass

filtered velocity data from the finely resolved LES velocity data (Figure 1). The kinetic energy spectrum of total velocity by summing up the reproduced fluctuating velocity component and low-pass filtered velocity fitted well to the -5/3 power law for the inertial subrange (Figure 2).

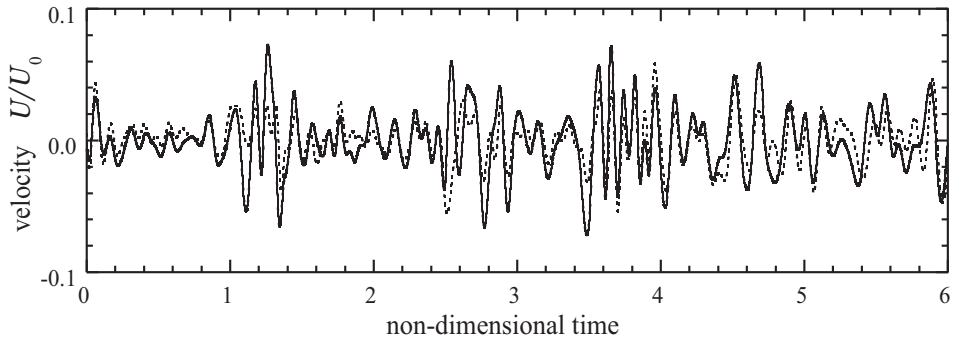

Fgure 1. Time history of streamwise fluctuating velocity component for the apriori test conducted by Nozawa and Tamura [2], solid line: reproduced fluctuating component, dashed line: true value.

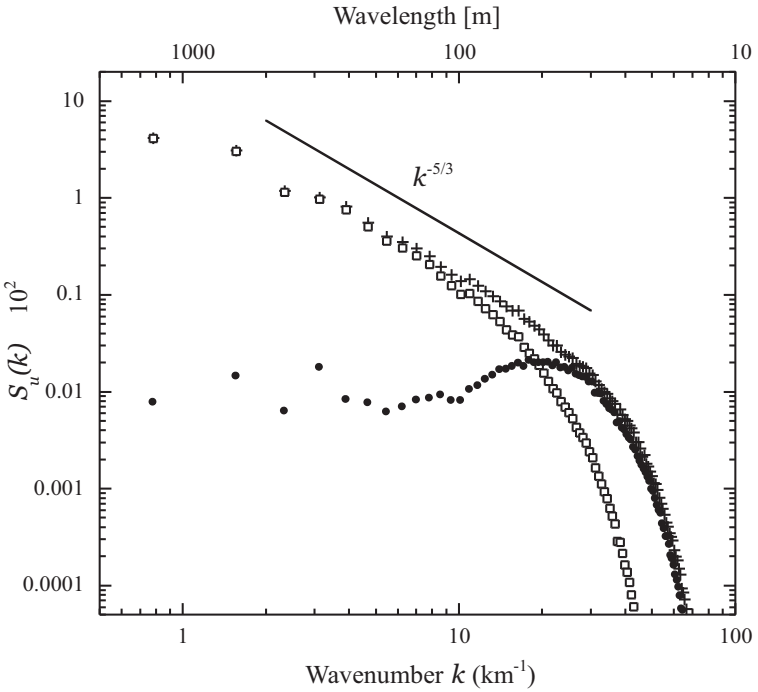

Fgure 2. Streamwise kinetic energy spectra for the apriori test conducted by Nozawa and Tamura [2], •: reproduced fluctuating component, □: low-pass filtered velocity, +: true value.

In this paper the method is introduced to nest meso-scale WRF [4] and micro-scale LES. The low-pass filtered velocity component of the micro-scale LES should be equal to the velocity of the meso-scale WRF and the averaged fluctuating velocity component of the micro-scale LES must be almost zero. Meanwhile the fluctuating velocity component of the micro-scale LES is implicitly estimated as subgrid-scale turbulence in the meso-scale WRF. So the grid-scale turbu-

lence in the micro-scale LES must be reproduced explicitly at the connection with the meso-scale WRF flow. This grid-scale turbulence in the micro-scale LES could be estimated using the scale similarity model when the filter width of the meso-scale WRF is in the range of inertial subrange of an energy spectrum. So in this study we carry out an idealized free convective boundary layer flow using WRF-LES mode [4-6]. The velocity data simulated in the WRF-LES is imposed to a fine-grid LES and the grid-scale fluctuating velocity of the fine-grid LES would be reproduced using the proposed one-way coupling method.

2 ONE-WAY COUPLING METHOD

The Navier-Stokes equations which are filtered with the LES grid filter width ($\overline{\Delta}$) are written as below:

$$\frac{\partial \overline{U}_i}{\partial t} + \frac{\partial \overline{U}_i \overline{U}_j}{\partial x_j} = -\frac{\partial \overline{P}}{\partial x_i} - \frac{\partial \overline{\tau}_{ij}}{\partial x_j} \tag{1}$$

where $\overline{U}_i$= velocity in *i*th-direction filtered with LES grid filter; $\overline{P}$=filtered pressure; and $\overline{\tau}_{ij}$=subgrid scale Reynolds stresses. In this filtered Navier-Stokes equations, the diffusion terms is neglected because of high Reynolds number. The filtered Navier-Stokes equations for coarser grid system which are filtered with filter width $\widetilde{\Delta}$ are written as below:

$$\frac{\partial \widetilde{U}_i}{\partial t} + \frac{\partial \widetilde{U}_i \widetilde{U}_j}{\partial x_j} = -\frac{\partial \widetilde{P}}{\partial x_i} - \frac{\partial \widetilde{\tau}_{ij}}{\partial x_j} \tag{2}$$

where $\widetilde{U}_i$=filtered velocity in *i*th-direction; $\widetilde{P}$=filtered pressure; and $\widetilde{\tau}_{ij}$=subgrid scale Reynolds stresses. We assume the filter width $\widetilde{\Delta}$ is much larger than that of the LES grid filter $\overline{\Delta}$. The filtered velocity $\overline{U}_i$ can be decomposed into $\overline{\widetilde{U}}_i$ and u_i as below:

$$\overline{U}_i = \overline{\widetilde{U}}_i + u_i . \tag{3}$$

The velocity $\overline{\widetilde{U}}$ is fluctuating very slowly due to the filter width, $\overline{\widetilde{\Delta}}\left(=\sqrt{\widetilde{\Delta}^2+\overline{\Delta}^2}\right)$. The velocity u_i is a fluctuation component which consists with subgrid scale turbulence of the coarser grid system. If the difference between the two filter widths is large enough we can obtain the equation:

$$u_i \approx \overline{U}_i - \widetilde{U}_i . \tag{4}$$

By using this relation, we can extract the equations of motion for fluctuation velocity components u_i by subtracting equation (2) from equation (1).

$$\frac{\partial u_i}{\partial t} + \frac{\partial}{\partial x_j}\left(\overline{U}_i \overline{U}_j - \widetilde{U}_i \widetilde{U}_j\right) = -\frac{\partial}{\partial x_i}\left(\overline{P} - \widetilde{P}\right) - \frac{\partial}{\partial x_j}\left(\overline{\tau}_{ij} - \widetilde{\tau}_{ij}\right) \tag{5}$$

Figure 3 indicates that we only have to obtain the difference between the finer grid grid-scale (GS) turbulence and the coarser grid GS turbulence to reproduce the fluctuation velocity components u_i of the equations (5). In the equations there two subgrid-scale stress terms, $\overline{\tau}_{ij}$ is for energy cascade from finer grid GS turbulence to SGS turbulence, and $\widetilde{\tau}_{ij}$ is the production term which cascade turbulence energy form coarser grid to finer grid.

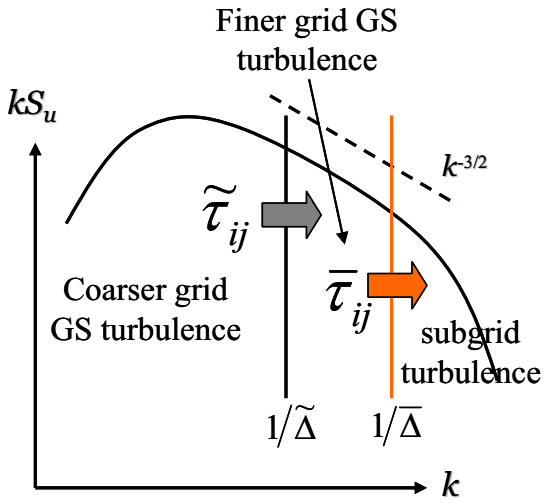

Figure 3. Schematic representation of the energy spectrum of turbulence.

These equations could be solved in the same manner to solve the Navier-Stokes equations by adding an equation of continuity for the fluctuation velocity. Additional restriction that time-space average of fluctuation velocity components u_i is zero will make averaged $\overline{U}_i$ follow the mean value of $\widetilde{U}_i$. The technique for the immersed boundary method proposed by Goldstein et al [7] is applied to force the averaged fluctuating velocity component to zero. Goldstein et al proposed the method to determine the velocity at particular point to the desired value in an unsteady viscous flow. The body force f_i which is controlled by the feedback system is imposed to the equation (5):

$$f_i(t,x_i) = \alpha \int_0^t err(\tau,x_i)d\tau + \beta \cdot err(t,x_i). \tag{6}$$

The quantities α and β are negative constants and $err(t, x_i)$ is a residual error between the simulated velocity and the determined velocity. The error being feed back is the velocity integral and the velocity itself. In this study we applied this feedback system to control u_i to zero. The quantities are α=-2000 and β=-30 in this study.

The subgrid scale Reynolds stresses implemented in coarser grid Navier-Stokes equation (2) is the production term in equation (5). In this method the scale similarity model [3] is applied to the subgrid scale stresses: $\widetilde{\tau}_{ij}$ and the Smagorinsky model is applied to the subgrid scale stresses: $\overline{\tau}_{ij}$. The filter width of the coarse grid has to be in the inertial subrange of energy spectrum to predict the production terms in equation (5) properly.

3 NUMERICAL METHOD

3.1 *WRF-LES*

The advanced research WRF[4] is widely used mesoscale meteorological model and in this study we carry out a single domain idealized free convective boundary layer flow using WRF-LES mode with the periodic boundary condition in horizontal plane. WRF-LES eddy viscosity is predicted using 1.5-order, level 2.5 Mellor-Yamada-Janjic (MYJ), TKE (turbulence kinetic energy) equation with local kinetic energy vertical mixing. The MYJ planet boundary layer scheme predicts the generation and redistribution of TKE in the boundary layer, uses the value of TKE to

compute a spatially varying eddy viscosity, and then diffuses simulated quantities vertically in the boundary layer. In this study the heat flux from the ground is zero. The geostropic wind speed is 10m/s in east-west direction. The Coriolis parameter is 10^{-4}/s.

In this study, the computational region of the WRF-LES is 13km in east-west direction, 6.5km in north-west direction and 2km in vertical direction. The horizontal grid space is 50m. The size of stretched vertical grid is from 40m to 60m (figure 4).

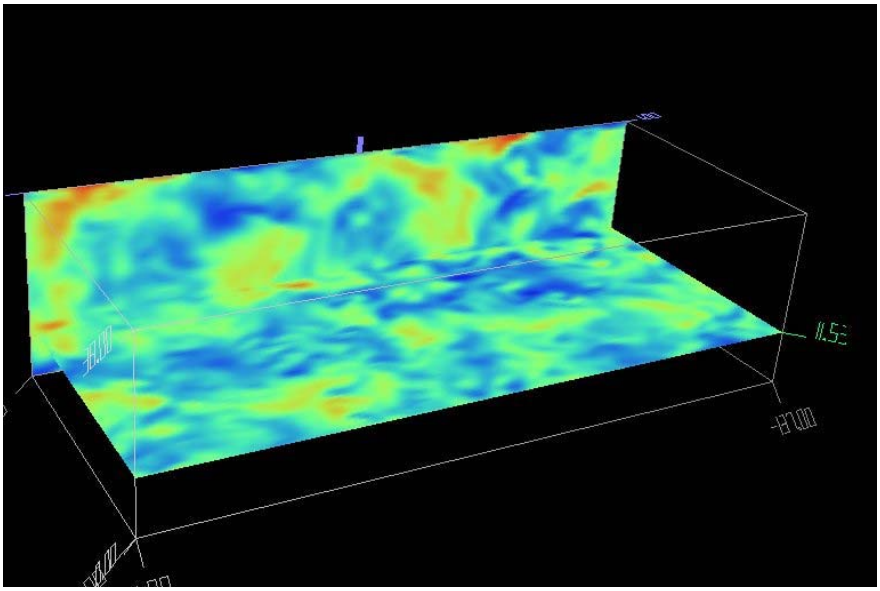

Figure 4. Distribution of east-west wind velocity using WRF-LES (red: high speed, blue: low speed).

3.2 *Micro scale LES*

The micro scale incompressible LES is simulated using the equation (5). Fourth-order central differencing scheme is used as spatial discretization and second-order time accurate explicit Adams-Bashforth differencing scheme is used for the convective terms and SGS turbulent diffusion terms. There is no thermal effect to the fine-grid LES. The WRF-LES velocity data is interpolated to the filtered ($\widetilde{\Delta}$) variables in equation (5).

The LES horizontal grid space is 25m. The LES computational region is 6.5km in east-west direction, 2.7km in north-west direction and 1km in vertical direction.

In this method the scale similarity model which parameterizes the subgrid-scale stress terms requires the grid scale filter ($\widetilde{\Delta}$) of the WRF-LES in the fine-grid LES. Although the grid size ratio ($\widetilde{\Delta}/\overline{\Delta}$) is 2 in this study, high wavenumber turbulence has decline due to the numerical filter (damping) in WRF-LES. The numerical filter width ($\widetilde{\Delta}^*$) is estimated about 8.5 times as large as the grid size ($\overline{\Delta}$) in fine-grid LES. So in this study the explicit filter width ($\widetilde{\Delta}^*$) of the scale similarity model is set to $8.5\overline{\Delta}$.

4 RESULTS

The WRF-LES was run for 10 hours and statistical data were estimated with averaging over the horizontal plain. Figure 5 shows the time history of east-west direction velocities at height 740m.

The mean velocity of the WRF-LES simulation is 10m/s and its standard deviation is 1.3m/s. While the time averaged velocity of the fine-grid LES is 0.005m/s and its standard deviation is 0.71m/s. This meant that technique for the immersed boundary method worked well to force the averaged fluctuating velocity component to zero. The high frequency oscillation still occured in the fluctuating component of the fine-grid LES while the WRF-LES velocity has only lower frequency oscillation compared to that in the fluctuating component of the fine-grid LES. The high frequency turbulence is reproduced rapidly as soon as the coupling method is applied. The streamwise velocity contours at the horizontal section at z=800m are shown in figure 6. We could find the large scale turbulence structures in the WRF-LES contour, while the large scale turbulence is not generated in the fluctuating component of the fine-grid LES contour.

Figure 7 shows the kinetic energy spectra for east-west velocity fluctuations at height 740m. The inertial subrange of the kinetic energy spectrum of the coarse grid WRF-LES is limited up to wavenumber $2km^{-1}$. We could find the fluctuating component of the fine-grid LES has extended the high wavenumber region of the inertial subrange. The results indicate that the coarse-grid WRF-LES and the fine-grid LES could be smoothly connected by using the proposed method.

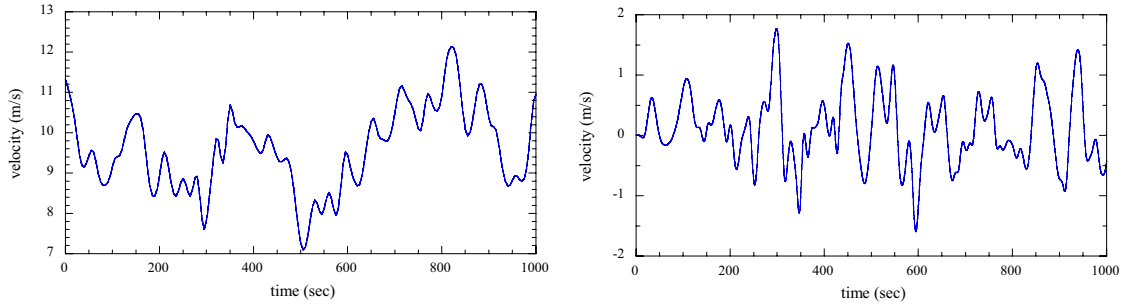

Figure 5. Time history of east-west velocity at z=740m. Left: WRF-LES, Right: fluctuating component of the fine-grid LES.

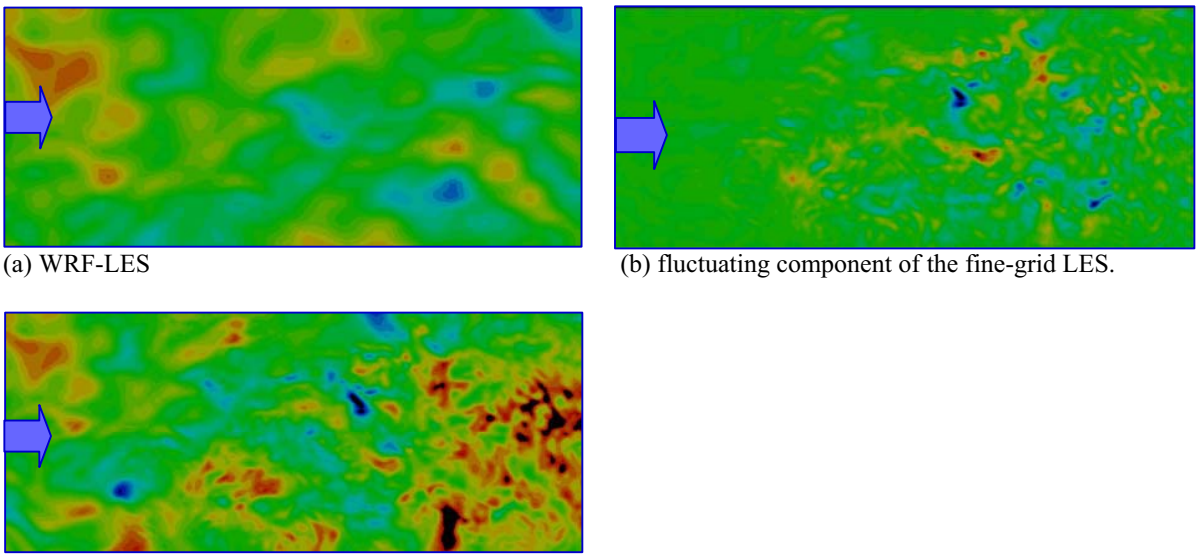

(a) WRF-LES

(b) fluctuating component of the fine-grid LES.

(c) WRF-LES + fluctuating component of the fine grid LES.

Figure 6. East-west velocity contours at horizontal section at z=800m.

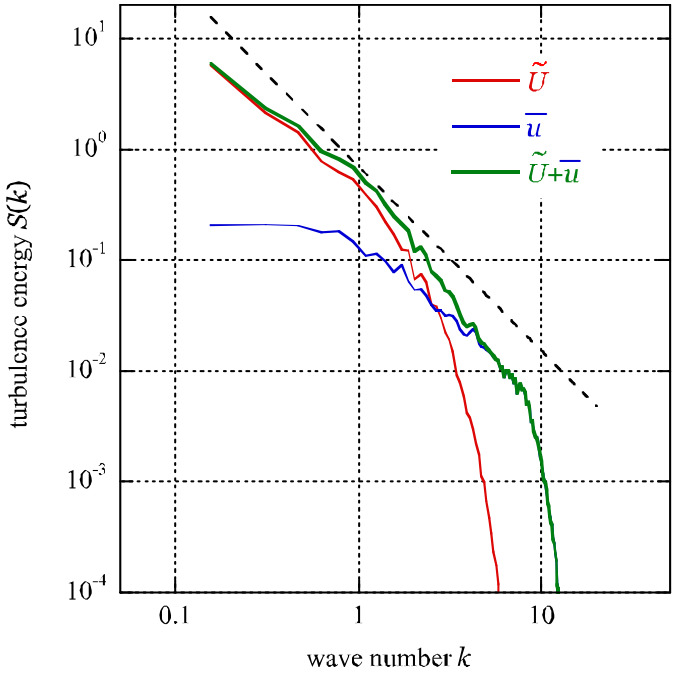

Figure 7. Kinetic energy spectra of the fluctuating velocities at z=740m. ($\widetilde{U}$: WRF-LES, $\overline{u}$: fluctuating component of fine-grid LES)

5 CONCLUSIONS

The one-way coupling method is applied to connect meso-scale model WRF and micro-scale LES using the scale similarity model. The coupling between WRF and LES is studied on a free convective boundary layer flow with no heat flux from the ground nesting coarse grid WRF-LES and fine grid LES.

The time history and the instantaneous contours of the east-west direction velocity showed that the high frequency oscillation was generated in the fluctuating component of the fine-grid LES while the WRF-LES velocity had only lower frequency oscillation compared to that in the fluctuating component of the fine-grid LES. The kinetic energy spectra for the east-west velocity fluctuations of the fine-grid LES had power in the high wavenumber region where energy by WRF-LES turbulence decreased due to the artificial damping. The results indicate that the coarse mesh and the fine mesh could be smoothly connected by using the proposed method.

In this study the time series of WRF-LES velocity data were interpolated to a whole domain of the fine-grid LES and the time-averaged velocity distribution coincide with the distribution of coarse-grid WRF-LES velocity. So to connect WRF-LES and LES against the flow over complex terrain the coupling method should be modified that time-averaged velocity distribution near the surface is determined by the local effect of the terrain.

6 REFERENCES

1 Piomelli, U., Kang, S., Ham, F. and Iaccarion, G., Effect of discontinuous filter width in large-eddy simulations of plane channel flow, Proc. Center for Turbulence Research Summer Program 2006, Stanford University (2006).

2 Nozawa, K. and Tamura, T., Coupling method of meso-scale model and LES based on scale similarity model, Proc. of the Fifth International Symposium on Computational Wind Engineering, (2010).

3 Bardina, J., Ferziger, J. H. and Reynolds, W. C., Improved subgrid scale models for large eddy simulation, AIAA Paper, No.80-1357 (1980).
4 Moeng, C.-H., Dudhia, J. Klemp, J., and Sullivan, P., Examining two-way grid nesting for large eddy simulation of the PBL using the WRF model, Monthly Weather Review 135, (2007), pp.2295-2311.
5 Hattori, Y., Moeng, C.-H., Hirakuchi, H., Ishihara, S., Sugimoto, S. and Suto, H., Numerical simulation of turbulence structures in the neutral-atmospherice surface layer with a mesoscale meteorological model, WRF, Proc. of the Fifth International Symposium on Computational Wind Engineering, (2010).
6 Mirocha, J. and Kirkil, G., Nested high-resolution mesoscale/large eddy simulations in WRF: challenges and opportunities, Proc. of the Fifth International Symposium on Computational Wind Engineering, (2010).
7 Goldstein, D., Handler, R. and Sirovich, L., Modeling a No-slip Flow Boundary with an External Force Field, J. of Computational Physics, 105, (1993), pp.354-366.

The Seventh International Colloquium on Bluff Body Aerodynamics and Applications (BBAA7)
Shanghai, China; September 2-6, 2012

LES of local severe suction on side face of a three-dimensional square cylinder

Yoshiyuki ONO[a], Tetsuro Tamura[b]

[a] *Technical Research Institute, Obayashi Corporation4-640 Simokiyoto, Kiyose, Tokyo, Japan*
[b] *Department of Environmental Science and Technology, Tokyo Institute of Technology 4259 Nagatsuta, Midori-ku, Yokohama, Japan*

ABSTRACT: The purpose of this paper is to investigate turbulence effects on characteristics of local severe suction on side face of a three-dimensional square cylinder by LES. The behavior of conical vortices associated with local suctions at the angle of the attack $\theta=0^o$, and glancing angle are focused on. First, the computed results for distribution of the pressure coefficients are validated through comparison with the experimental data. Next, using the computed results, the effects of inflow turbulence on the high peak suctions and flow characteristics are examined. As a result, high peak suctions occur associated with wake characteristics and flow reattachment characteristics affected by the large scale fluctuation of oncoming turbulence.

KEYWORDS: *LES, local severe suction, conical vortex, three-dimensional square cylinder*

1 INTRODUCTION

Recent advancements of computational techniques have made it possible to easily simulate the flow around a bluff body, and many investigations have been reported regarding as applicability of computational models. Recently, in AIJ (Architectural Institute of Japan) CFD working group, around 10 members computes the flow around a three-dimensional square cylinder (breadth(B):depth(D):height(H)=1:1:3,1:1:4) in boundary-layer turbulence by use of LES codes, such as commercial software, open source software and self-development software, and discusses adequate computational conditions and numerical formulations through the comparison with experimental data for the aerodynamic forces and the pressure coefficients.

On the other hand, the flow around a square cylinder is sensitively changed depending on angle of the attack. It is well known that local severe suctions occur in the flow separation regions of a three-dimensional square cylinder. Okuda et al. [(1)] showed from the results of wind tunnel experiments (wind pressure measurements and flow visualization) that the local severe suctions near the leading edge were mainly caused by two types of conical vortices. One was an inverted conical vortex on the middle or lower side of the cylinder in the case where the wind perpendicularly attacked the front of the cylinder ($\theta=0^o$). This inverted conical vortex was nearly periodically formed associated with vortex shedding and causes a large fluctuation of the pressure near the bottom of the leading edge. The other was a standing conical vortex near the upper corner of the leading edge at the glancing angle ($\theta=13\sim15^o$) which leads to large level of the negative pressure. This vortex is hardly affected by vortex shedding in the wake. If the wind velocity did not change, the fluctuating suction was zero [(1)].

These experimental results by Okuda et al. [1] clarified the flow mechanism of local negative suctions on the surfaces of a three-dimensional square cylinder. However, the boundary-layer thickness is much lower than a cylinder height, so the oncoming flow is nearly smooth flow except the lower region of a square cylinder.

On the other hand, Surry et al. [2] investigated relationships of high peak suctions with the characteristics of oncoming turbulence using the wind tunnel experiments. The results of pressure measurements on the side of the cylinder at angle of the attack $\theta=0^o$ reveal distinct periodicity associated with vortex shedding, as reported by Okuda et al [1]. Furthermore, the occurrence of peak event always coincides with the fluctuation induced by vortex shedding, an increase in turbulence intensity obscures the periodicity of vortex shedding, but peak relationship with remaining randomized vortex shedding appears to be maintained.

Okuda et al. [3] investigate characteristics of local negative suctions from the results of the outdoor measurements. Above two types of the local severe suctions are also recognized even in natural wind condition. However, the peak of the negative pressure becomes a sharp and peak values are much larger in natural wind condition compared with those of the wind tunnel experiments [1].

Above studies [1], [2], [3] on characteristics of local suctions near the leading edge have been investigated by utilizing the wind tunnel experiment. So, the data of pressure are easily obtained, but the information of flow structure could not be easily obtained. Namely, the flow mechanism causing local suctions especially in boundary-layer turbulence has not reached completely understanding.

The authors of this paper computed the flow around of a low-rise structure (B: D: H=1:1:0.5) by utilizing the LES method [4]. We used an over set grid in curvilinear coordinate system in order to sufficient grid resolution near the leading edge of the roof of the cylinder, and then showed that the computed results showed very good agreement with the experimental data. Also, based on the computed results, the flow mechanism causing the local suctions on the roof in uniform and boundary-layer turbulence flows is clarified [5].

In this research, the LES method [4] using sufficient grid resolution is applied to the flow around a square cylinder (B: D: H=1:1:4) in boundary-layer turbulence at angles $\theta=0^o$, $15^o$of the attack, and unsteady characteristics of conical vortex are investigated. First the present LES model is validated for prediction of the pressure characteristics on a square cylinder through comparison with the experimental data [6]. Next, the relationships between high peak suctions and unsteady motions of two types of conical vortices such as an inverted conical vortex and a standing conical vortex in boundary layer turbulence are investigated by computed data.

2 PROBLEM FORMULATION

The governing equations are given by the incompressible Navier-Stokes and the continuity equations. To advance the solutions of velocities and pressure in time, a fractional step method is employed. The time integral of the momentum equation is hybrid, that is to say, the Crank-Nicolson scheme is applied to the viscous terms and the explicit third-order Runge-Kutta method is used for convective terms. Spatial derivatives of variables are treated as second-order central difference. Convective terms are approximated using the higher-order interpolation method. We use the dynamic-mixed model. To avoid the numerical instability, the very small numerical dissipation is added to the convective terms. The details of the present numerical formulation can be referred in (Ono&Tamura, 2002[4]).

3 COMPUTATIONAL MODEL

As a computational model, we deal with a three-dimensional square cylinder (Breadth: Depth: Height=1:1:4). An overset grid is used to get sufficient resolution near the cylinder. Figure 1 shows computational grid system which consists of three grids (Grid1; 155X160X80, Grid2; 201X66X100, Grid3; 40X40X65). Wind angles of the attack are set to 0 and 15ºas shown in Figure 2. The convective condition is imposed at downstream boundary. No-slip condition is used at the cylinder surface. Smallest grid size is 0.1/ $(Re)^{0.5}$ ($Re=U_H B/\nu$,:$U_{H:}$ is oncoming velocity at the height of the cylinder, ν is the kinematic viscosity).The Reynolds number (Re) is equal to 36,000.

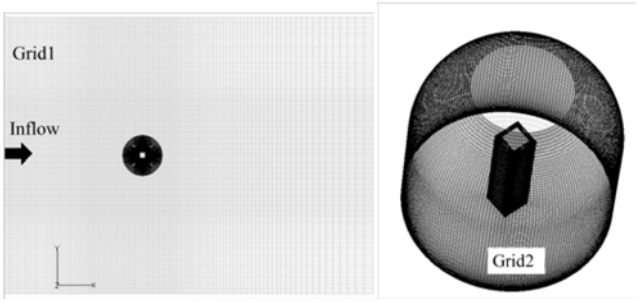

Figure 1 Computational grid system

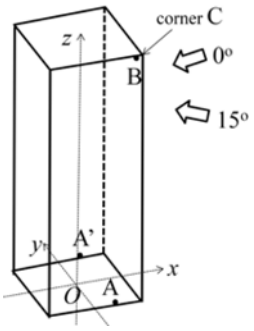

Figure 2 Angle of the attack

Inflow turbulence is generated using the simplified method of the quasi-periodic condition proposed by Kataoka et al. [7], and then developed over the upwind fetch with the surface roughness. Figure 2(a), (b) show the comparison of computed results for profiles of time-averaged velocity and turbulent intensity with the experimental data. The present computations show good agreement with the experimental results. The computed power spectrum distribution is also presented in Figure 2(c). It can be confirmed that the computed result agrees with the experimental data and the Karman-type spectrum. The computed turbulent scale by fitting to the Karman-type spectrum (Figure 3 (3)) is 4.5 B.

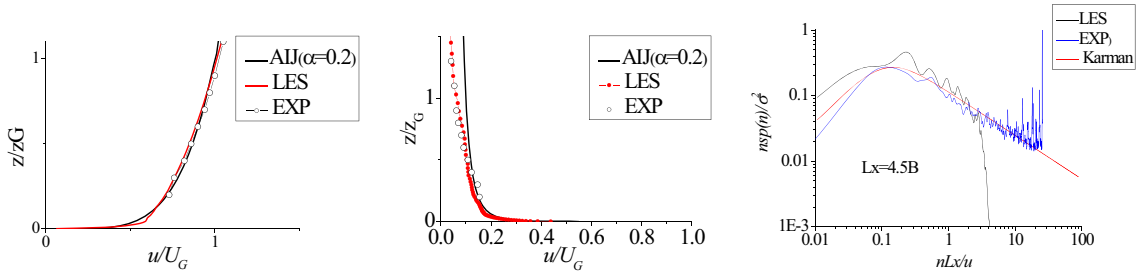

(1) Profile of mean velocity (2) Profile of fluctuating velocity (3) Power spectrum distribution

Figure 3 Comparison of computed inflow turbulence with experimental data

4 VALIDATION OF COMPUTATIONAL MODEL

Figure 4 (1), (2) show the comparison of the computed results with the experiments for the mean pressure distributions and the RMS value of the fluctuating pressure coefficients on a square cylinder. Concerning the mean pressure distributions, the present computations show good agreement with the experiments [6], though the computed stagnation points tend to be located upper than those in the experiments. This discrepancy must be due to the difference of vertical resolutions of the sampling points used for the visualization.

In the cases of $\theta=0^o$, large values of the fluctuating pressure coefficients are recognized near the bottom of the leading edges (A, A'). Furthermore, concerning the mean pressure distributions at the glancing angle, the local suction occurs near the upper corner of leading edge (B). Namely, local suctions at $\theta=0^o$ and the glancing angle which are observed in the experiments in smooth flow [1] are recognized even in boundary-layer turbulence.

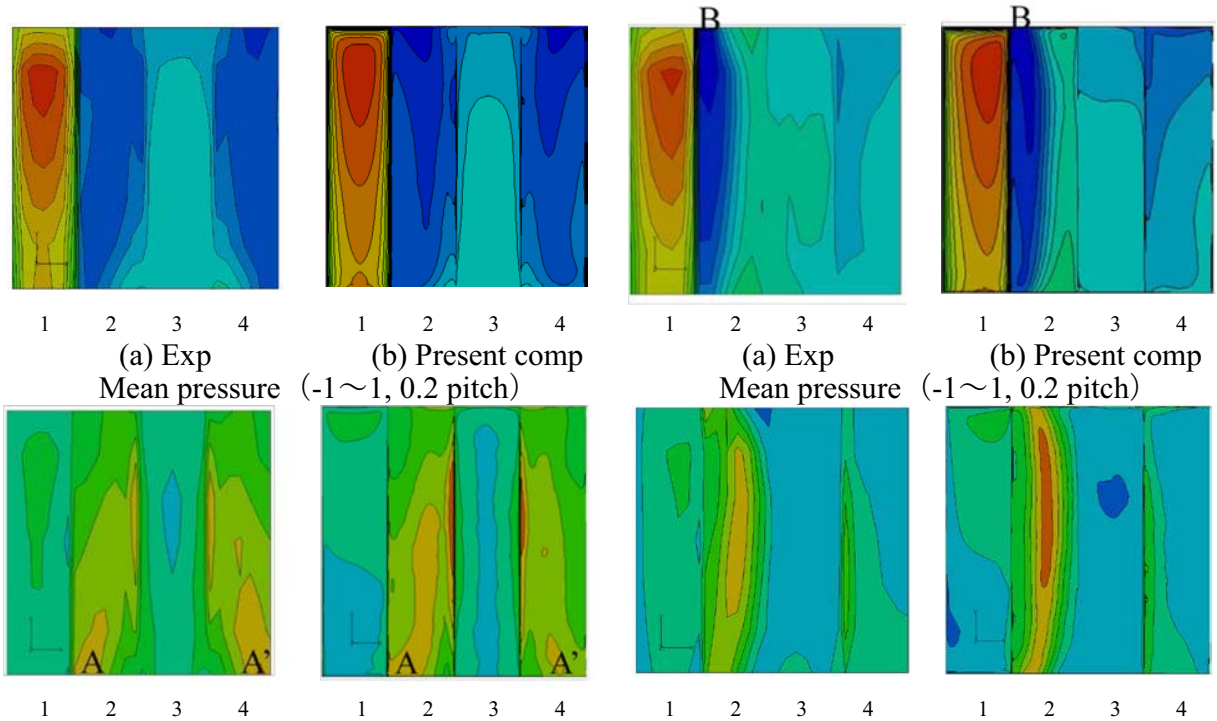

(a) Exp (b) Present comp (a) Exp (b) Present comp

Mean pressure (-1～1, 0.2 pitch) Mean pressure (-1～1, 0.2 pitch)

(a) Exp (b) Present comp (a) Exp (b) Present comp

Fluctuating pressure (0～0.4,0.04 pitch) Fluctuating pressure (0～0.4,0.04 pitch)

(1) Angle of the attack 0^o (2) Angle of the attack 15^o

Figure 4 Distributions of mean and fluctuating pressure coefficients on square cylinder

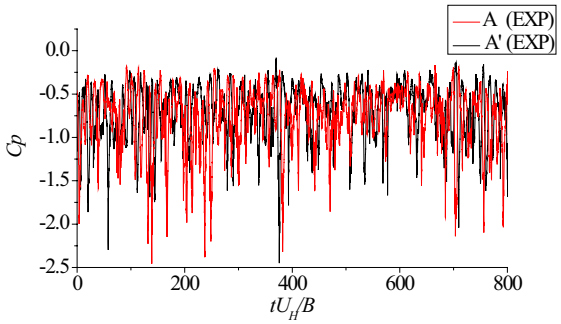

(1) Experimental data (800 dimensionless times)

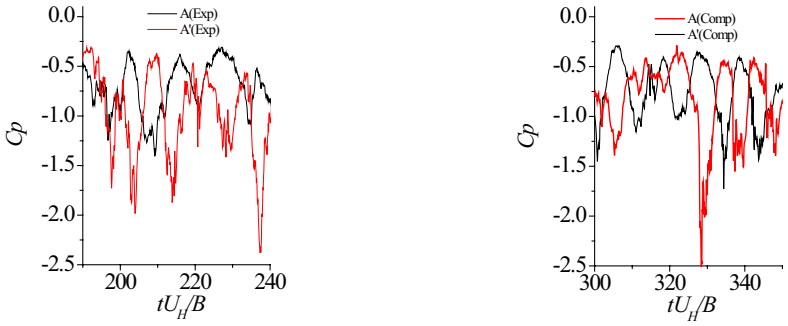

Exp Comp

(2) 50 dimensionless times

Figure 5 Time histories of the pressure coefficients of A and A'($\theta=0^o$)

5 STUDY OF RELATIONSHIP OF FLOW STRUCTURE AND LARGE SUCTION

5.1 *Large suction near the bottom of leading edge at angle of the attack $\theta=0^o$*

Figure 5 (1),(2) show experimental results[6] for time histories of pressure coefficients at the points A, A' (shown in Figure 2)near lower corner of the leading edge at $\theta=0^o$. In Figure 5(1), pulse-like peaks are randomly observed in the pressure fluctuations. On the other hand, looking at time histories in about 50 dimensionless time in details (Figure 5(2)), the levels of the negative pressures of A, A' change in turn periodically, though the peak values are randomly changed. These characteristics of peak suctions show the same tendencies as the experiments by Surry et al. [2].

Figure6 (1)-(4) show the iso-surface (p= -1.45) of pressure and the contours of the vorticities at the section of z/B=2, 0.01 before and after the high peak suction occurs at the point A. In (1) tU_H/B=326.3, the vortex begins to be formed in the wake region of the cylinder. After that, the separated shear layer approaches closely to the side surfaces of the cylinder and the negative pressure region is recognized in wide range near side face (2). In (3) where the high peak suction occurs, the shear layer reattaches to the side surface and the separatio bubble is formed near the bottom of the leading edge. In (4), wake vortex sheds downstream, the level of the negative pressure is recovered. Therefore, based on instantaneous flow characteristics, it can be presumed that the behavior of the wake vortices result in the reattachment of the separated shear layer near the bottom of the leading edge, and the strong curvature of the separation bubble leads to the high peak suction.

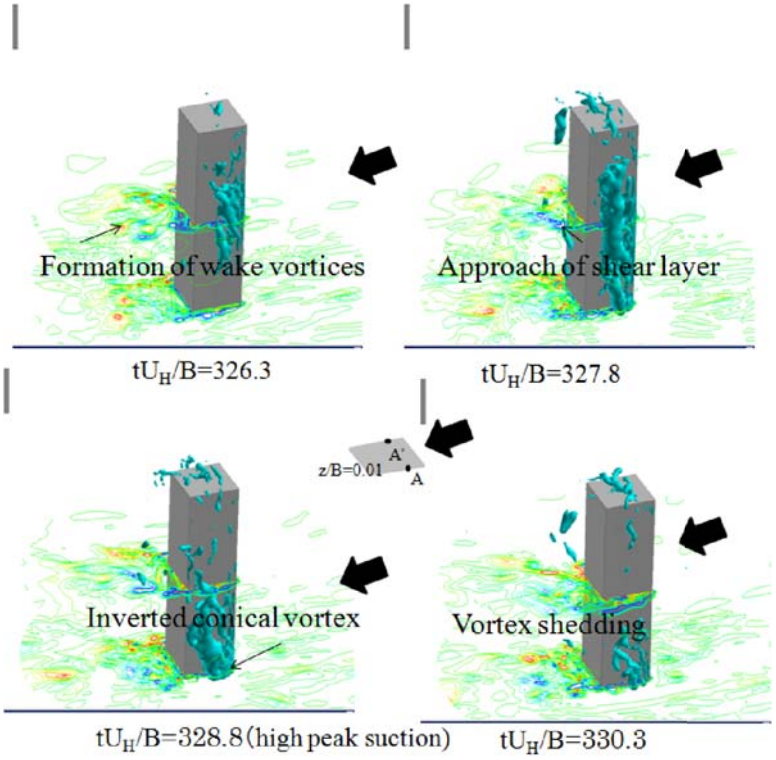

Figure 6 Iso-surface of instantaneous pressure and vorticities contours
(p=1.45, $\theta=0^{o}$)

Figure 7 (1),(2) show the iso-surface (p=-0.75) of the conditional pressure. Conditional sampling manner indicates two types of averaged data. One is the averaged data when the peak values (Cp_{peak}) of the pressure coefficients of point A are large than -1.5 and smaller than -1.0. The other is averaged data when Cp_{peak} are smaller than -2.3.

In the case (1) ($-1.5<Cp_{peak}<-1.0$), the iso-surface is depicted near the side of the cylinder. However, it is not recognized in wake region because the levels of the negative pressure are not so high. On the other hand, in case (2) ($Cp_{peak}<-2.3$), the iso-surface is depicted not only near the side surface but also near the base of the cylinder. Figure 8 (1), (2) show the contours of conditional vorticities at the section of z/B=0.01. The strong circulation of the separation bubble is recognized in the case (2)($Cp_{peak}<-2.3$).

Therefore, high peak suction occurs, when periodic vortices are strongly formed near the base of the cylinder and the early reattachment of the separated shear layer near the bottom of the leading edge is caused.

Figure 9 shows the time histories of the pressure coefficient at the point A and the fluctuating velocities at the three points (T0, T1, T2) in the upwind region. It can be seen that the velocities at all points largely increase and its state continues before the high peak suctions occur. It can be presumed that this process of change in velocities causes the wake vortices to be strongly formed, and then results in the large peak suction near the bottom corner of the leading edge of the cylinder.

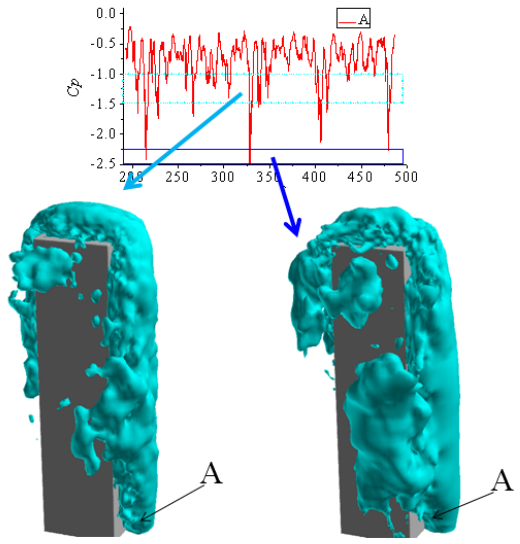

(1) -1.5<$Cp_{\_peak}$<-1.0 (2) $Cp_{\_peak}$ <-2.3

Figure 7 Iso-surface of conditional pressure (θ=0°)
($Cp_{\_peak}$ is the peak values of negative pressure)

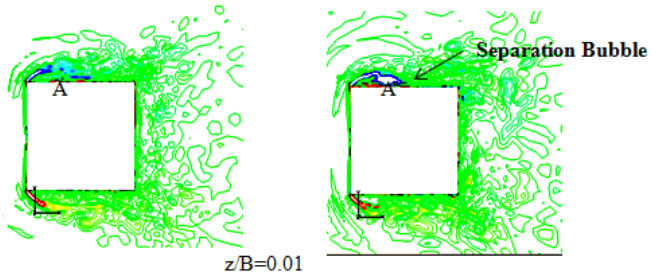

(1) -1.5<$Cp_{\_peak}$<-1.0 (2) $Cp_{\_peak}$ <-2.3

Figure 8 Conditional vortices contours (θ=0°)

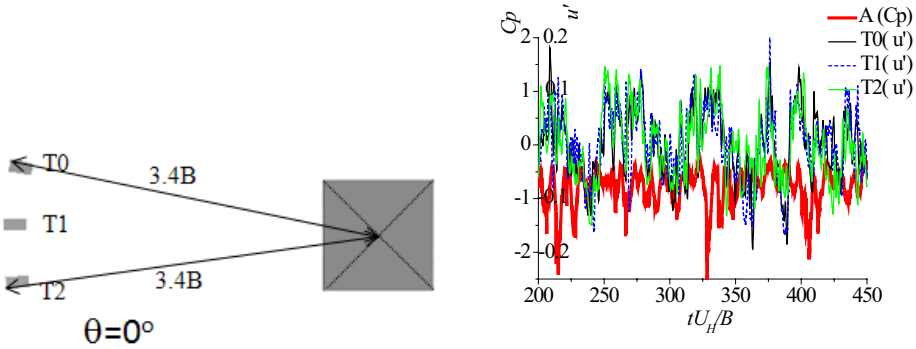

Location of reference points

Figure 9 Time histories of the pressure coefficients at A
and velocity at T0,T1,T2 (θ=0°)

5.2 *Large suction near the upper corner of leading edge at glancing angle*

Figure 10 (1), (2) show the time histories of the pressure coefficients at the point B (shown in Figure 2) near the upper corner of the leading edge at the glancing angle (θ=15^o). The pulse-like peaks are intermittently recognized in the temporally sequential data for both of the present computation and the experiments [6]. These kinds of peaks had not been observed in the experiments in smooth flow [1]. In the case of smooth flow [1], a standing vortex is formed near the upper corner of the leading edge and leads to stationary local suction.

In order to investigate relationship between the occurrence of high peak suctions and the behavior of a standing vortex in boundary-layer turbulence, the iso-surface (p=-1.2) of the pressure around the cylinder before and after the high peak suction occurs are shown in Figure 11 (1)-(4). In (1) tU_H/B=168.8, the flow separates from the leading edge of the cylinder and the regions of negative pressure are recognized near the side of the cylinder. On the other hand, in (2) tU_H/B =170.2, the conical vortex begins to be formed near the upper leading corner. In (3) tU_H/B 171.3 where high peak suction occurs, the conical vortex is clearly recognized. After that, negative pressure is recovered when the conical vortex becomes unclear.

This conical vortex is similar to a standing vortex in smooth flow [1]. However, this vortex does not always exist in boundary-layer turbulence. The conical vortex is intermittently recognized at the moment high peak suction occurs. Also, the level of peak suctions induced by the conical vortex is much larger than that by a standing vortex [1].

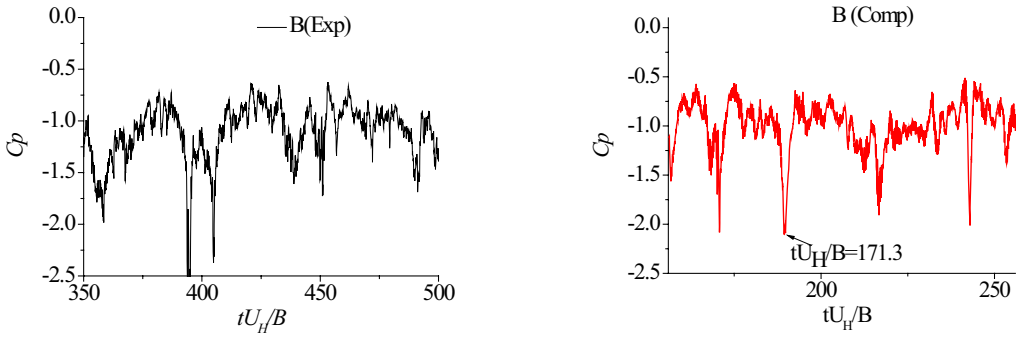

(1) Exp[6] (2) Comp

Figure 10 Time histories of the pressure coefficients of B (θ=15^o)

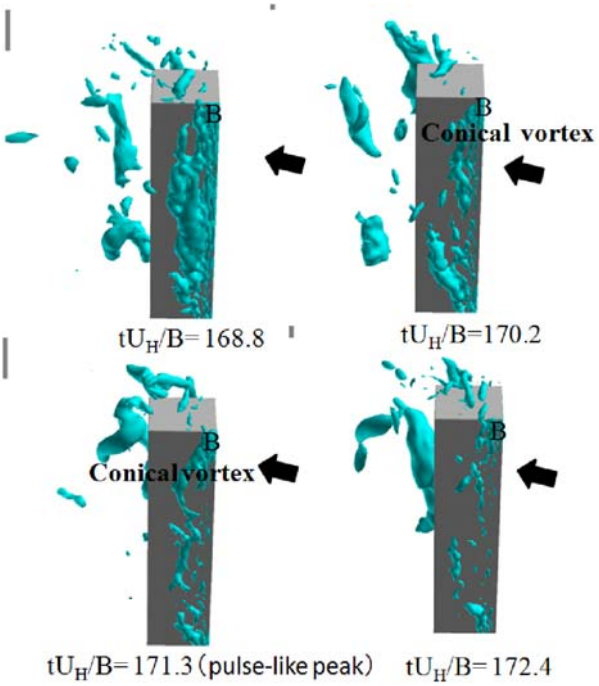

Figure 11 Iso-surface of instantaneous pressure (p=1.2)

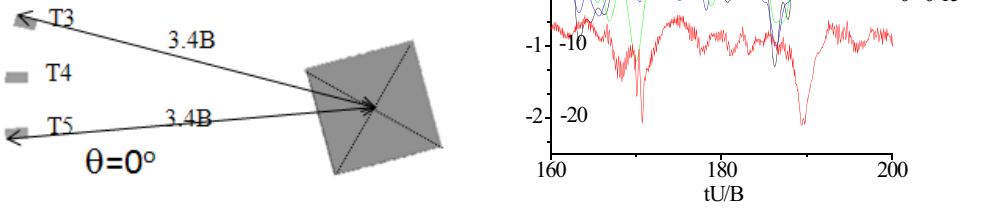

Location of reference points

Figure 12 Time histories of the pressure coefficients at A

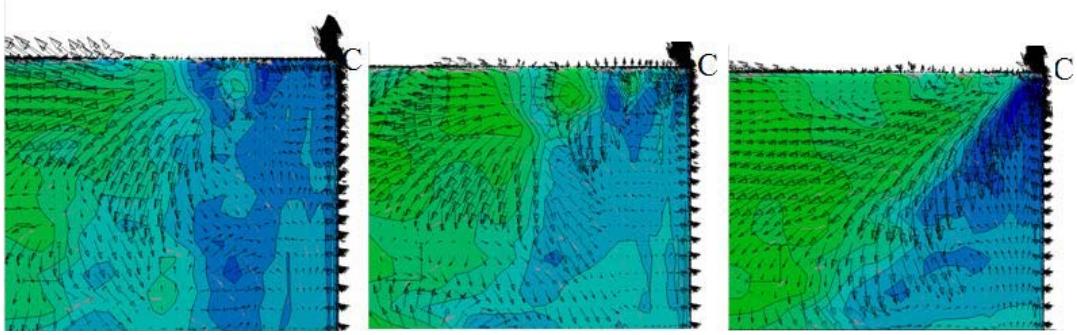

(1) tU_H/B= 169.2 (2) tU_H/B= 170.2 (3) tU_H/B= 171.3

Figure 13 Time series of velocity vectors and pressure distributions

Figure 12 shows the time histories of pressure coefficients at the point B and the fluctuating angle of the attack at the three points (T3, T4, T5) in the upwind region. It can be found that the angles of the attack of all points show a decrease (the angles of the attack changes in anticlockwise direction) before peak suctions occur. After that, peak suction is recognized when the angle of the attack gradually increases.

Figure 13 shows the time series of the velocity vectors and the pressure distributions on the plane close to the side surface. A decrease of the angle of the attack causes the reattachment points to move downstream (the green domain showing a pressure recovery region moves downstream). On the other hand, reattachment points tend to approach closely to the upper corner (C) (the green domain approaches C), as angle of the attack begins to increase. The occurrence of the strong circulation of the conical vortex associated with this change in angle of the attack leads to high peak suction near the upper corner of the leading edge.

6 CONCLUSION

Unsteady characteristics of the conical vortices near the bottom of leading edge at $\theta=0^o$ and near the upper corner of the leading edge at the glancing angle are studied by LES analysis. It is made sure that the present LES model can simulate the pressure characteristics on the square cylinder through comparison with the experimental data. As a result of study of computed flow structure, it can be presumed that the large scale fluctuation of oncoming flow plays an essential role for vortex structures close to a square cylinder. It introduces a conical vortex generation and its concentration near the leading edge, and results in high peak suctions

7 REFERENCES

1 Y. Okuda, Y. Taniike, Conical vortices over side face of a three dimensional square prism, J. Ind. Aerodyn., Vol. 50, 1993, pp 163-172.

2. Surry D. Surry: D. Djakovich, Fluctuating pressures on models of tall buildings, J. Ind. Aerodyn., Vol.58, Issues 1–2, 1995, pp 81–112

3. Y.Okuda, J. Katsura, S. Kawamura, Local severe suctions on the side of a prism model on a field, J. Ind. Aerodyn., Vol.72, 1997, pp 23-32.

4. Y. Ono, T. Tamura：Large eddy simulation using a curvilinear coordinate system for the flow around a square cylinder, Wind& Structure,Vol5, No2, 2002, pp369-378.

5. Y. Ono, T. Tamura and H. Kataoka: LES analysis of unsteady characteristics of conical vortex on a flat roof ,, J. Ind. Aerodyn, Vol. 96, 10-11, 2008, pp 2007-2018.3.

6. Y. Ono, T. Tamura: LES prediction and its validation for wind pressure on a square cylinder with angle of attack, Annual Meeting, Japan Society of Fluid Mechanics,2011,pp,318 (In Japanese)

7. H. Kataoka, M. Mizuno.: Numerical flow computation around aero-elastic 3D square cylinder using inflow turbulence, Wind& Structure, vol5, No2, 2002,379-392.

The Seventh International Colloquium on Bluff Body Aerodynamics and Applications (BBAA7)
Shanghai, China; September 2-6, 2012

LES for wind load estimation by unstructured grid system

Masaru YOSHIKAWA [a], Tetsuro TAMURA [b]

[a]*Taisei Corporation, 344-1 Nase-cho, Totsuka-ku, Yokohama, Japan*
[b]*Tokyo Institute of Technology, G5-7, 4259 Nagatsuda, Midori-ku, Yokohama, Japan*

ABSTRACT: Recent development of high-performance computers and techniques on computational fluid engineering has enabled us to simulate the complicated flow such as the wind in urban area. Large Eddy Simulation (LES) is expected to be adopted as an effective technique to evaluate wind load on buildings for wind-resistant design. In this research, the accuracy of LES to evaluate surface pressures on the 3D square cylinder model is examined. Especially, the availability of LES using unstructured grid system is studied to estimate fluctuating as well as mean component of pressures by comparison with experimental results. The computed results correlate highly with the experiments, including the case of a square cylinder with angle of attack for wind direction which introduces a local negative pressure on the side.

KEYWORDS: LES, Unstructured grid system, Fluctuating pressure, Square cylinder.

1 INTRODUCTION

As a result of wide spread of commercial or open source CFD software on the research as well as its practical usage, very large scale computations of complicated flow such as wind around a building and urban flows in cities have been often performed. Recent development of parallel computing technique based on the unstructured grid systems makes it possible to deal with the actual flow phenomena. While, it remains still important to investigate the accuracy of time variation of the physical quantities under the unsteady numerical simulation, such as Large Eddy Simulation (LES). So, using a fundamental object, many researchers have tried to predict the aerodynamic forces and pressures under the unsteady situations. Kataoka and Tamura [1] carried out the numerical prediction of the peak pressures on three-dimensional square cylinder by the overset structured grid system based on the generalized coordinate system. They suffered from the reproducibility of the minimum local negative peak pressure, because of the insufficient power of turbulence structures.

Unstructured grid systems are superior to conventional structured grid system in terms of not only the adaptability to configuration but also flexibility to element size density at each location in the computational region. Therefore the unstructured grid with local refinement can meet the sensitivity of aerodynamic forces on the square cylinder with a glancing angle [2]. This paper examines the accuracy of LES based on the unstructured grid system. Especially, focusing on the local pressure fluctuation, which is required to estimate the wind loads for claddings, the validity of LES is examined by comparison with experimental data.

2 BUILDING MODEL

A square cylinder model is chosen as an objective building and its width (B), depth (D) and height (H) are 30m,30m and 90m respectively. Namely, the aspect ratio H/B is equal to 3. The design wind speed is set as U_H=41.9m/s at the building's top.

3 WIND TUNNEL EXPERIMENT

The wind-tunnel experiment is carried out for obtaining reference data of fluctuating wind pressures. A 1/300 scaled model is used and wind pressures are measured at 308 points on the walls (figure 1 and 2). The experimental wind velocity is set as U_H=11.6m/s and the experimental Reynolds number is 77,000. The time- histories of wall surface pressures are recorded at 1kHz sampling frequency. Then they are converted into the time- histories of 1-second mean pressures with real scale by taking moving average over consecutive 12 data. The 4 parts of 10-minute (real scale) time- histories are taken and the pressure coefficients (mean value, fluctuating value, maximum value and minimum value) are determined by taking ensemble averaging over 4 values obtained from each 10-minute time- histories.

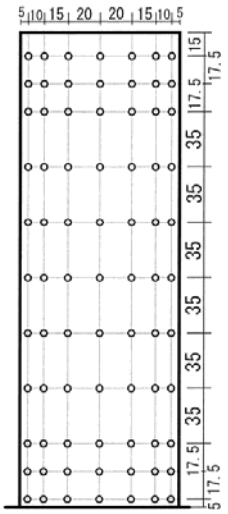

Figure 1. Measurement points

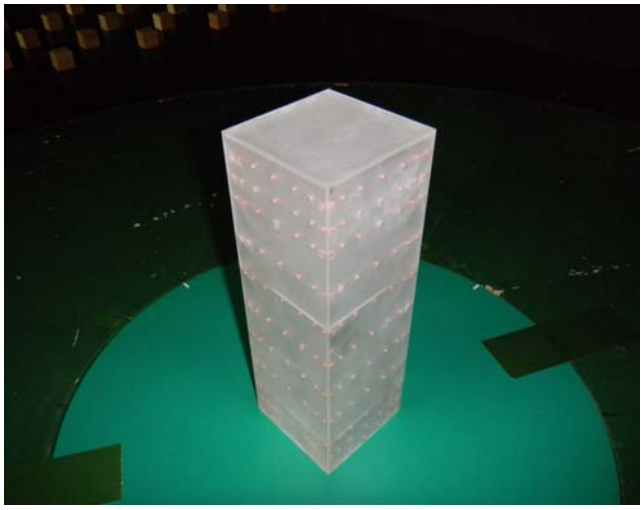

Figure 2. Experimental model

4 NUMERICAL METHOD

Three-dimensional incompressible Navier-Stokes equations are used as governing equations. The Reynolds number is set to 72,000. Equations are transformed into the discretized form by the finite volume method (FVM) and computational domain is divided using the tetrahedral and prismatic cells. As the flow velocities and the pressures are defined on the vertexes of cells, the configuration of control volume is polyhedral. The second-order central difference scheme is applied to the convective term and diffusion term. The time derivative term adopts the second-order implicit scheme. The physical time step is set as $\Delta t U_H/B$=0.03.

For subgrid scale model of LES, the standard Smagorinsky model is employed. The universal constant is equal to 0.15 and the filter size is automatically determined by a volume *V* of the con-

trol volume through $V^{1/3}$. Van Driest type of wall-damping function is applied for eddy viscosity of subgrid scale.

5 INFLOW TURBULENCE GENERATION

Inflow turbulence is numerically generated using the wind tunnel model shown in figure 3. Spires and roughness blocks are appropriately placed inside the wind tunnel model. Uniform flow is set on the inlet boundary and boundary-layer turbulence is developed in the model as is the case in the wind tunnel experiment. Time- histories of wind velocity are accumulated at each point on the section adjacent to the outlet boundary (shown in figure 3). The time- histories are saved in a file and applied to the inlet boundary of another model with a square cylinder described below as the inflow turbulence. Generated velocity profiles are shown in figure 4 with the reference wind tunnel data. The profiles of time averaged windward velocity <*u*> and turbulence intensity *I* are reproduced quite well. The power spectral density of windward velocity fluctuation is shown in figure 5 with the Karman-type spectrum. The computed spectrum power decreases rapidly at the non-dimensionalized frequencies nLx/U higher than 1.0.

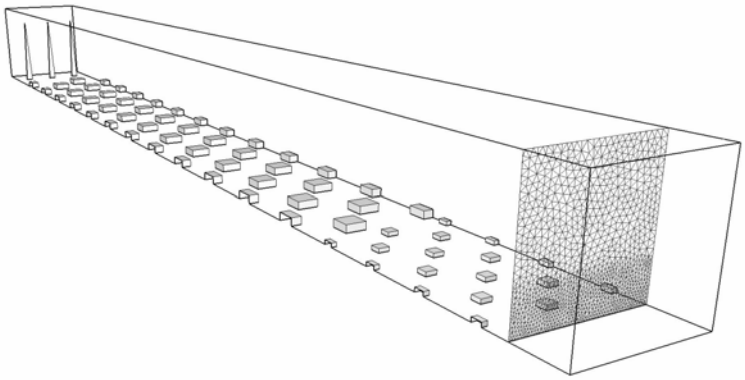

Figure 3. Computational model for inflow turbulence

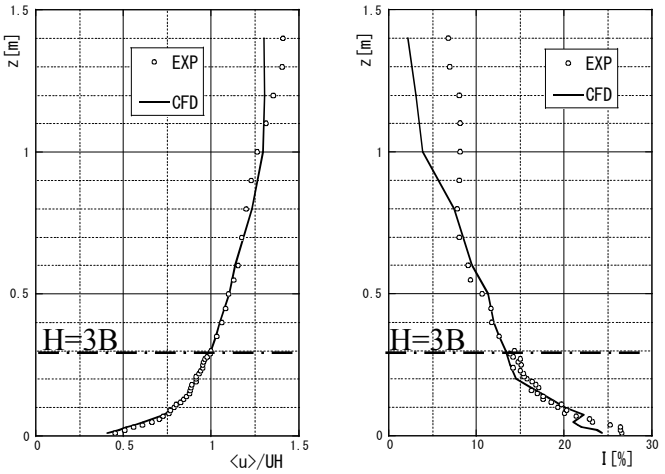

Figure 4. Generated velocity profiles

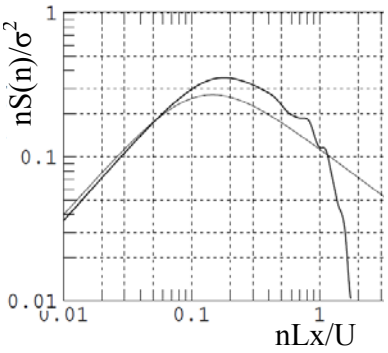

Figure 5. Power spectral density

6 GRID SYSTEM FOR 3D SQUARE CYLINDER

Figure 6 shows the unstructured grid system of whole domain for the 3D square cylinder model. The whole domain size is 20B×30B×15B. The distance between inlet boundary and the center of square cylinder is 8B. For the unstructured meshes the advancing front method is used to create the tetrahedral in the domain based on the volume mesh density at each location determined preliminarily. Then prismatic cells are inserted on the walls and the ground based on a triangular surface mesh. Figure 7 shows the grid systems near the square cylinder for wind directions of 0 and 15 degrees. These two grid systems are independently generated for the wind direction and possess the highest spatial resolution (approximately B/64) around the corner edges of the square cylinder. The number of cells is approximately 3,300,000 and the number of vertexes is approximately 660,000. The inflow turbulence, which is recorded as described in the last chapter, is imposed time-sequentially on the inlet boundary.

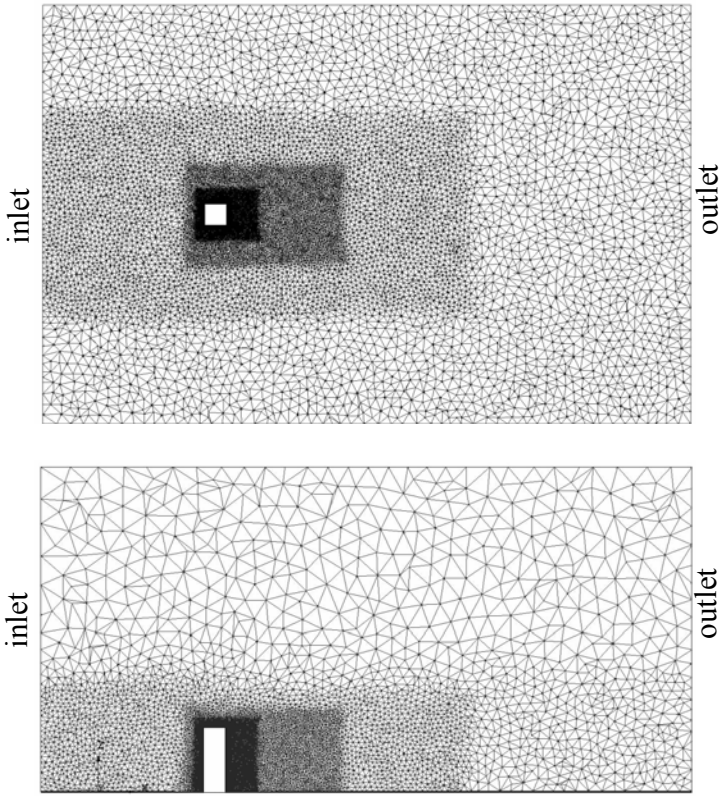

Figure 6. Unstructured grid system (whole domain)

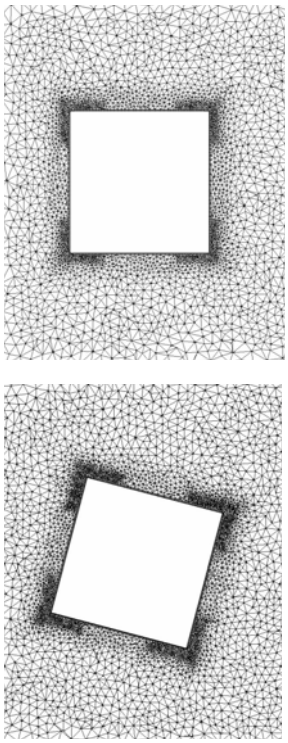

Figure 7. Unstructured grid system (near the square cylinder)

7 COMPUTED RESULTS

7.1 *Distributions of surface pressure coefficients*

Figure 8 and 9 show the distributions of surface pressure coefficients obtained by LES. The mean pressure coefficients Cpm and the fluctuating pressure coefficients Cps are shown for wind directions of 0 and 15 degrees. For the case of 15-degree wind direction, surface pressure coefficients show asymmetrical distributions. The position of maximum Cpm value moves toward windward side of surface A and local negative pressure value, which is definitely lower than that of 0 degree, appear on the windward edge of surface B.

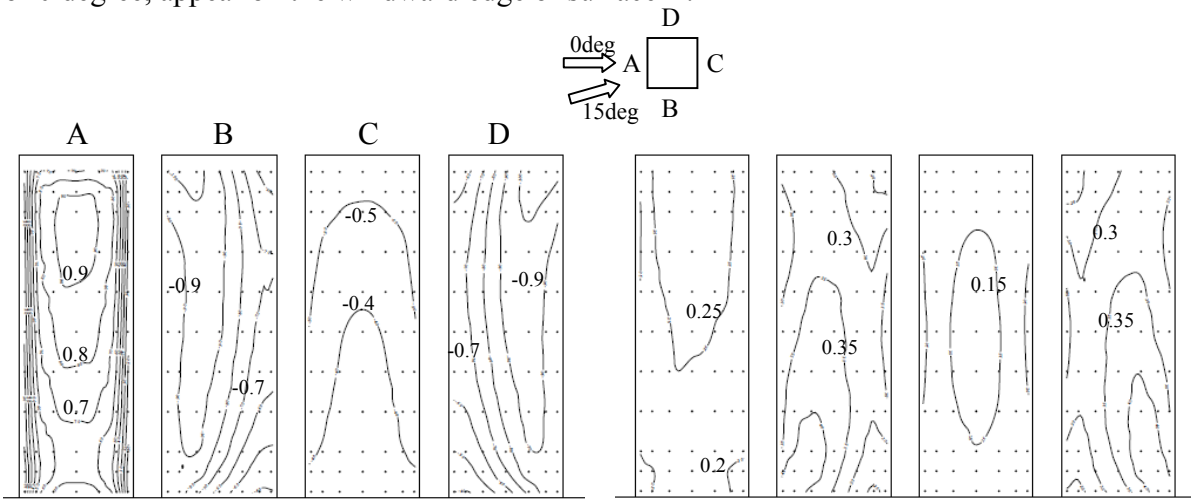

Mean pressure coefficients Cpm Fluctuating pressure coefficients Cps

Figure 8. Distributions of surface pressure coefficients (wind direction 0 deg.)

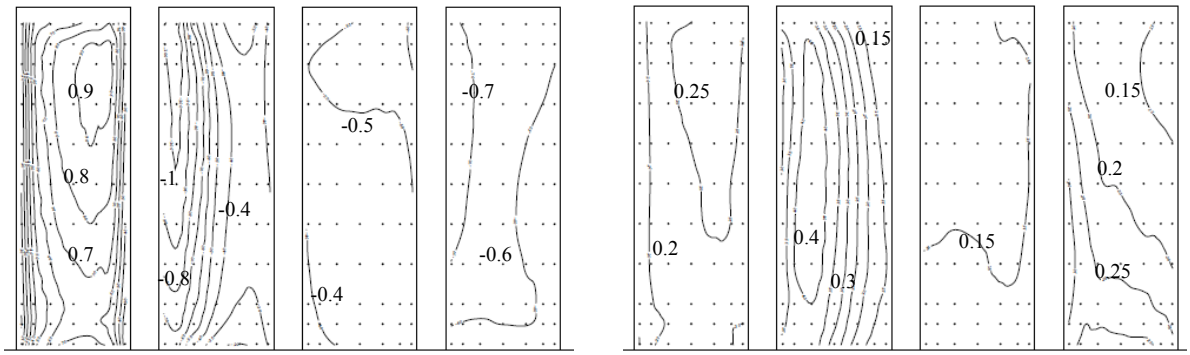

Mean pressure coefficients Cpm Fluctuating pressure coefficients Cps

Figure 9. Distributions of surface pressure coefficients (wind direction 15 deg.)

7.2 *Correlations of surface pressure coefficients with experimental results*

Figure 10 and figure 11 show correlations of the computed surface pressure coefficients with the experimental results for wind directions of 0 and 15 degrees. The mean pressure coefficients Cpm, the fluctuating pressure coefficients Cps, the maximum peak pressure coefficients Cpmax, and the minimum peak pressure coefficients Cpmin are shown. Each symbol represents the com-

puted and the experimentally-measured values at a corresponding sampling point. The computed mean pressure coefficients Cpm quite coincide well with the experimental data, including the case of 15-degree wind direction. The fluctuating and peak pressure coefficients Cps,Cpmax and Cpmin also maintain high correlations although they show relatively disperse distributions compared with Cpm. The computed results slightly tend to overestimate the peak pressure coefficients. But we need to take care of an essentially-contained variability of experimental data and discuss the effects on the correlations.

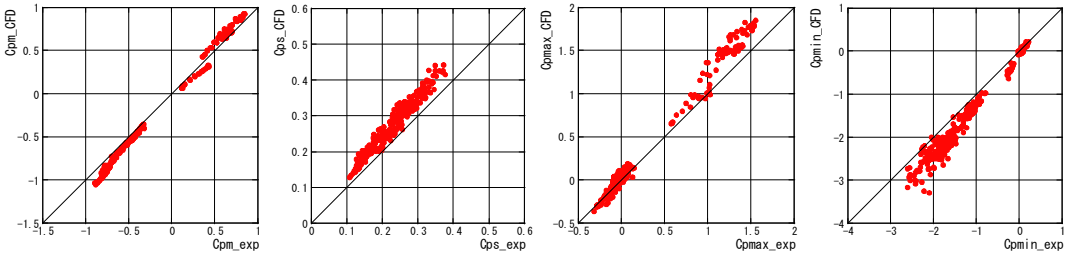

Figure 10. Correlations of pressure coefficients (0 deg)

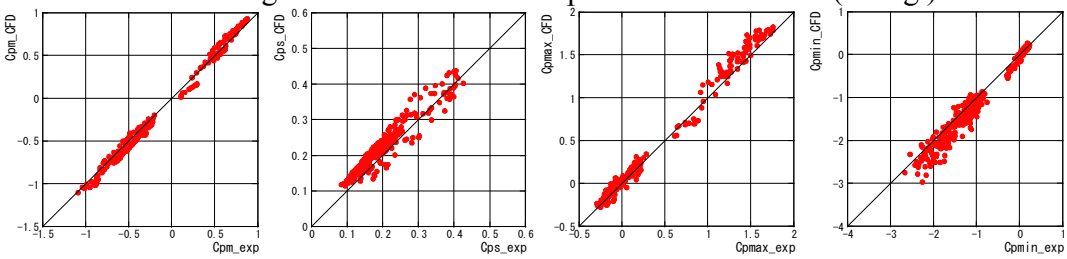

Figure 11. Correlations of pressure coefficients (15 deg)

8 CONCLUSIONS

The fluctuating as well as mean pressures on the square cylinder were computed by LES using unstructured grid system and compared with the wind tunnel experiments. On the whole, the computed results correlated highly with experiments though the computations slightly tended to overestimate the peak pressure coefficients. The reproducibility of inflow turbulence and appropriate spatial resolution at each location are required even in the case of unstructured grid system. It can be concluded that LES using unstructured grid system is effective to evaluate even the fluctuating component of the pressures on buildings for wind-resistant design.

9 REFERENCES

1 H.Kataoka and T.Tamura, Numerical prediction of the peak pressure distributions on square cylinder by LES, 2012, Proc. 13th International Conference of Wind Engineering, Netherlands.

2 M.Yoshikawa, Evaluation of wind pressure using LES with unstructured mesh system, 2010, Summaries of Thchnical Papers of Annual Meeting, Architectural Institute of Japan B-1 (in Japanesse).

The Seventh International Colloquium on Bluff Body Aerodynamics and Applications (BBAA7)
Shanghai, China; September 2-6, 2012

LES of fluctuating wind pressure on a 3D square cylinder for PIV-based inflow turbulence

Yusuke Maruyama [a], Tetsuro Tamura [b], Yasuo Okuda [c], Masamiki Ohashi [c]

[a] *Maeda Corp., Tokyo, Japan*
[b] *Tokyo Institute of Technology, Yokohama, Japan*
[c] *NILIM, Tsukuba, Japan*

ABSTRACT: We carried out LES of fluctuating wind pressure on a three-dimensional square cylinder for PIV-based inflow turbulence which is generated by using stereo PIV measurement data for inflow condition. PIV experiment was executed at low Reynolds number, so we try to produce the higher Reynolds number inflow turbulence using the low Reynolds number turbulence which was obtained on the basis of PIV measurement results. Also, using the obtained data at higher Reynolds number, we discuss the accuracy of prediction of wind loads on the cladding by comparison with wind tunnel experimental results.

KEYWORDS: LES, Wind Pressure, 3D Square Cylinder, Inflow Turbulence, PIV, Reynolds Number

1 INTRODUCTION

Wind loads acting on buildings immersed within a turbulent boundary layer are sensitively characterized by the approaching flow. In view of fluid dynamics, inflow wind fluctuations tend to affect the computed aerodynamic characteristics based on wake structures of an object, then their set-up should be concerned for CFD applications, since CFD has much flexibility for inflow generation. So, we proposed a new method for generating inflow turbulence where stereo PIV measurement results are directly used to impose the inflow boundary condition of LES (1). Namely we carried out LES of a turbulent boundary layer developed on a flat floor using stereo PIV measurement results at inflow and the generated PIV-based inflow turbulence was saved as the database after a full development. Also, this paper presents the computed results of the fluctuating wind pressure acting on rectangular cylinder obtained by LES under the condition of oncoming turbulence. But PIV experiment was executed at very low Reynolds number, so we try to make higher Reynolds number inflow turbulence modifying low-Reynolds-number turbulence provided by PIV measurement. It can be expected that this turbulent structures result in the accurate fluctuating components of physical quantities. Hence we aim at discussing the accuracy of prediction of wind loads on the cladding by comparison with wind tunnel experimental results.

2 LES FOR INFLOW GENERATION USING STEREO PIV MEASUREMENT DATA

PIV wind tunnel experiments were executed for a turbulent boundary layer developing on a flat plate using the wind tunnel of Building Research Institute. We measured the three-dimensional wind velocity of the turbulent boundary layer using a stereo PIV system assembled by SEIKA Corporation (Photo1 & Figure 1). The sampling frequency of the flow velocity images for the digital high-speed video camera was set to 1000Hz, and non-dimensionalized Nyquist frequency was equivalent to 3.57, and the Reynolds number Re_δ was equal to 8,400.
We used the image deformation correlation algorithm (sub-pixel image shifting) repeatedly five times for PIV images analysis to reduce noise elements in high frequency region. But a few noise

elements remain in high frequency region and sometimes very large spike-shaped peaks appear. So we corrected the PIV time histories by peak cutting and moving average. Figure 2 shows statistics of inflow velocity corrected PIV measurement data.

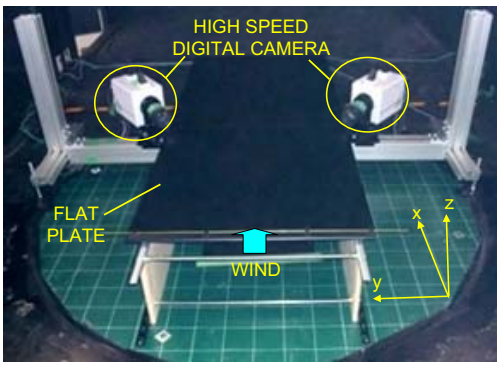

Photo 1 PIV measurement setup

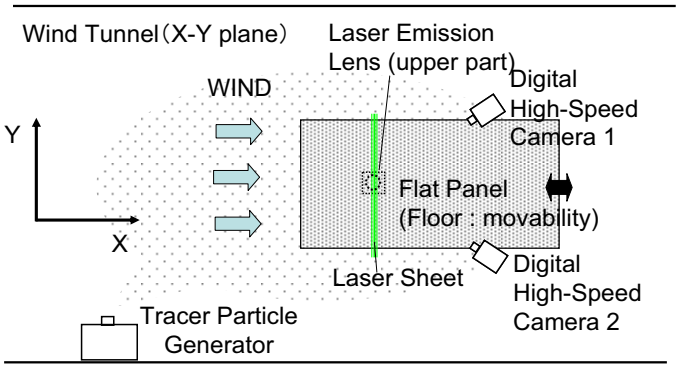

Figure 1 Outline of stereo PIV measurement

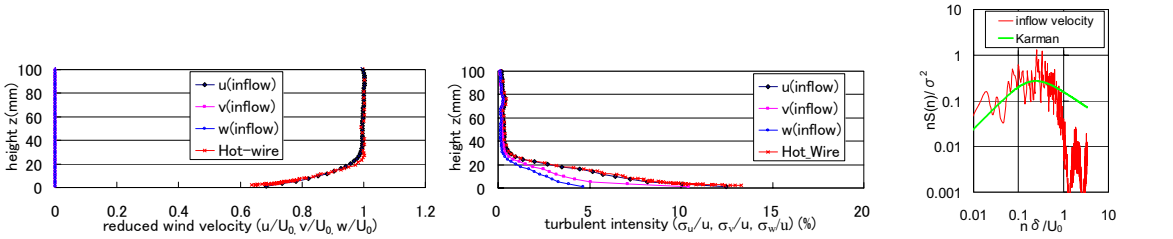

(a) profile of mean velocity (b) profile of turbulent intensity (c) power spectral density

Figure 2 Statistics of inflow velocity based on PIV measurement data

LES computation using PIV-based inflow turbulence for inflow generation was carried out by OpenFOAM which has been widely circulated as an open-source code. The governing equations are given by the continuity and the incompressible Navier-Stokes (N-S) equations. This code uses the unstructured-grid based concept and the finite volume method for discretization of the governing equations. For the turbulence model of LES the standard Smagorinsky model is employed. The no-slip condition is used for the bottom boundary to this LES. This means the sufficiently fine mesh is required for near-wall region. The Reynolds number Re_δ (=U0δ/ν, U0: wind velocity above turbulent boundary layer, δ: turbulent boundary layer thickness, ν: kinematic viscosity) is 8,400 and Re_τ(=u_τ δ / ν, u_τ: friction velocity on floor) is about 360.

Fig.3 depicts the instantaneous velocity field as a result of LES computation. The wind velocity distribution has striped patterns with a long streamwise length near the floor. It can be thought that streak structures are surely formed immediately above the bottom surface. According to wind velocity contours in the vertical section, it is confirmed that velocity fluctuations given as inflow condition have convected smoothly downstream with drag effects by a bottom wall, and the turbulent boundary layer is appropriately developed with coherent structures such as bursting phenomena.

Fig.4 shows vertical profiles of mean wind velocity and turbulent intensity for *u*-component reduced by friction velocity u_τ. Both LES results correspond closely to experimental results by Degraaff and Eaton. Figure 5 shows the power spectral density of wind velocity of inflow data and the LES result with fully developed state near the wall (z+=11) and at the log-law region (z+=130). It is confirmed that turbulence structures near the wall are generated by appropriate

numerical method which can handle the grid size and the numerical dissipation. At the log-law region, spectral shapes of LES fit to the Karman type spectrum sufficiently.

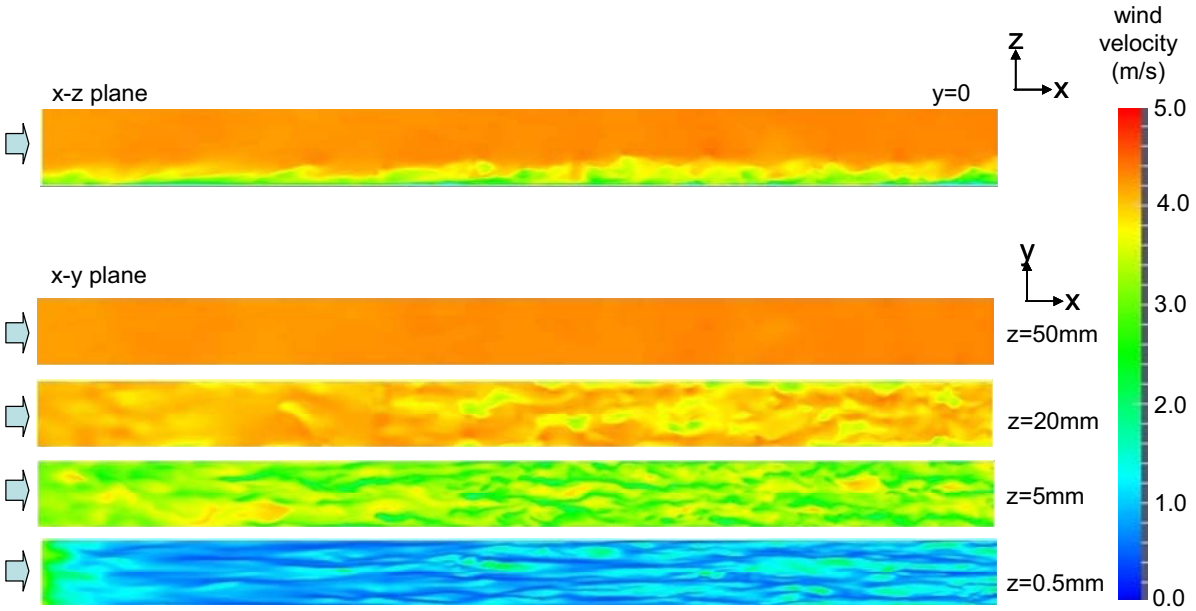

Figure 3 Instantaneous wind velocity distributions by LES for inflow generation

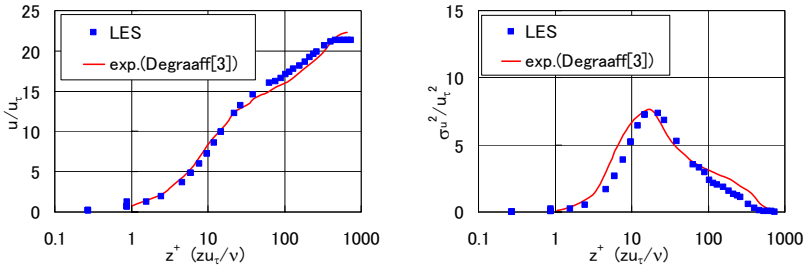

(a) mean wind velocity (b) turbulent intensity

Figure4 Profiles of mean wind velocity and turbulent intensity reduced by friction velocity u_τ

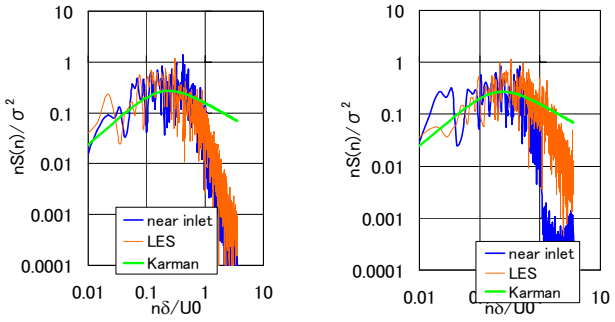

(a) near wall (z^+=10.8) (b) log-law region (z^+=130)

Figure5 Power spectral density of LES result

Inflow data for turbulent boundary layer simulation provided by the stereo PIV measurement has low-frequency fluctuations but no high-frequency fluctuations, and the accuracy level of PIV data near the wall is low by reflection of laser beam. In LES low-frequency fluctuations given by

PIV measurement data are maintained in whole computational domain. While, high-frequency fluctuations are generated by the energy cascade. Turbulence structures near the wall can be reproduced by high resolution in near-wall region under the usage of no-slip condition. Accordingly, the present proposed models using LES, the turbulent boundary layer can be reproduced by relatively short fetch.

3 GENERATION METHOD OF HIGH-REYNOLDS INFLOW TURBULENCE

It is expected to acquire wind loads on structures by calculating flow field around bluff bodies with inflow turbulence which simulates the boundary-layer type of flow structures in wind engineering. We aim at creating the database of inflow turbulence for LES calculation based on the PIV measurement data. However, the Reynolds number and the boundary layer thickness obtained in PIV wind tunnel experiment are restrictive, so some problems occur in similarity to calculation for actual wind loads evaluation. Here, we propose a method generating inflow turbulence at higher Reynolds number. We have verified the validity of this method by LES using the inflow turbulence with the low Reynolds number developed on the flat plate shown in chapter 2, and discuss the enhanced applicability of inflow turbulence database based on PIV measurement results.

The Reynolds number Re_δ (defined by boundary layer thickness δ) of the PIV based inflow turbulence presented in the preceding chapter is about 8400, while the Reynolds number Re (defined by the width of 3D-cylinder) is about 2000. Here, in realizing the computation of the flow field around a three dimensional square cylinder at the same order of Re as the wind tunnel experiment, we try to set about 5 times Re as the order exceeding 10000. For this, the kinematic molecular viscosity is changed to 1/5 on calculation.

In the process of the rescaling by Lund et al.(2), a boundary layer is generally divided into two domains, one is an inner region where the law of the wall can be realized, the other is outer region where the velocity defect law can be realized. Basically using this concept, the conversion from low to higher Reynolds number flow for inflow turbulence is also enforced to each region.

In the inner region the law of the wall can be realized, and the mean velocity profile collapses the logarithmic distribution to z+ non-dimensionalized by the friction velocity u_τ and the kinematic viscosity ν shown in Fig.4. Since Re is converted into 5 times higher by 1/5 ν , also as a result of larger u_τ, the vertical size of the inner region estimated on the basis of z+ is reduced to less than 1/5 on dimensionalized scale (Fig. 6). In the outer region, the boundary layer thickness is the same for both the Reynolds number flows, inflow turbulence fluctuations are corresponding to each other at same height. However, since the wind velocity at the top of the inner region is specified, the velocity at upper location in outer region should be shifted following the inner value, so that this method assumes to have an average wind velocity profile according to the power law on the flat plate with α=0.15. The outline of the procedure of changing the Reynolds number of the inflow turbulence is shown in Fig. 6. The profile of mean wind velocity with z+ is shown in Fig. 7.

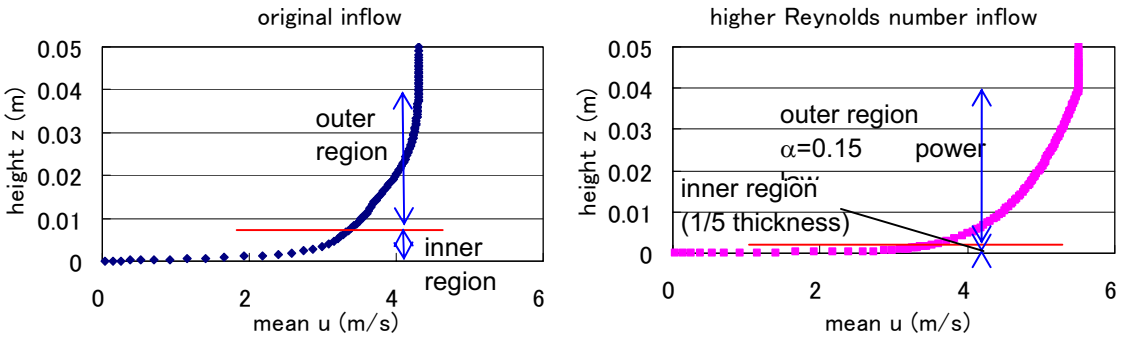

Figure 6 Outline of the procedure of changing the Reynolds number of the inflow turbulence

In order to confirm that this inflow turbulence generated for higher Reynolds number flow is adapted to the whole computational domain, we executed LES of turbulent boundary layer using this inflow turbulence for inflow condition. Computation outline is the same as that of the preceding chapter, the mesh resolution in the vertical direction is made for the first mesh point to be set to $z^+<1$ near the wall and the mesh resolution in the spanwise direction is twice finer than the former case.

Figure8 shows the profiles of mean wind velocity and the standard deviation reduced by friction velocity u_τ. In buffer layer, The computed wind velocity shows smaller values. It is considered that this phenomenon is caused by the discontinuity of fluctuation component of inflow at the connecting point between the inner and the outer regions, in spite of connecting mean component of inflow smoothly. Figure9 shows the instantaneous flow field of LES at the higher Reynolds number. In inner region, the distribution of 1/5 height of higher Reynolds number flow (fig.9 z=0.1mm) is similar to that of low Reynolds number flow (Fig.3 z=0.5mm). In outer region, the distribution of each flow at the same height (Fig.3 and Fig.9 z=20mm) is well alike. This means that it is rational to divide into two regions at inner and outer sides to generate the higher Reynolds number inflow turbulence.

Since it is mostly in agreement to inflow above log-law region, we carry out LES of flow field around a 3 dimensional square cylinder using this computed result as inflow turbulence.

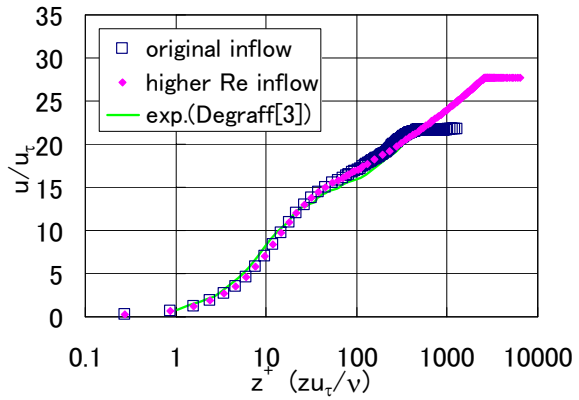

Figure 7 Profiles of mean wind velocity with high Reynolds number reduced by friction velocity u_τ

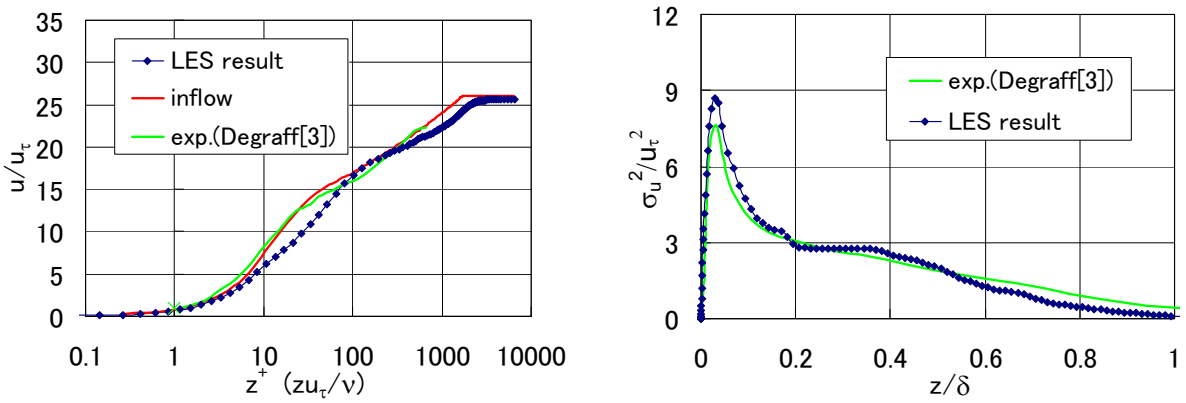

(a) mean wind velocity (b) fluctuating wind velocity

Figure 8 Profiles of mean wind velocity and turbulence of LES result with high Reynolds number

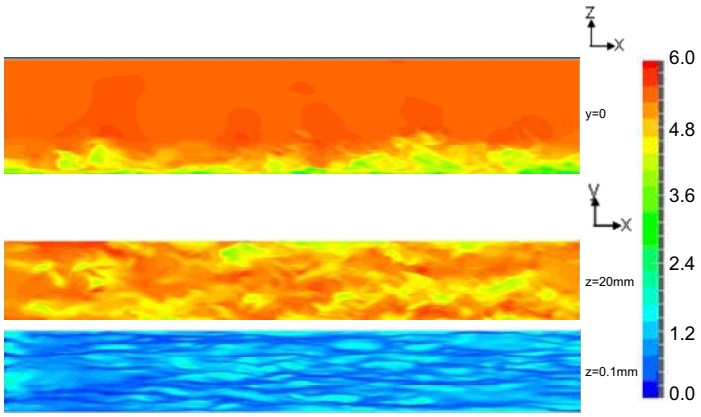

Figure 9 Instantaneous wind velocity distribution by LES for higher Reynolds number flow

4 LES AROUND 3D SQUARE CYLINDER FOR PIV-BASED INFLOW

LES of flow field around a 3-dimensional square cylinder is carried out using inflow turbulence generated in the preceding chapter. Figure10 shows the outline of mesh generation for this computation. The resolution around the square cylinder is raised using refinement mesh function equipped in OpenFOAM four times. Whenever it uses refinement function, the mesh resolution in the three directions becomes twice respectively. Therefore, the resolution of domain 5 is 16 times that of the outer domain 1. One side of the square cylinder is divided into 120 meshes.

Figure 11 shows the instantaneous flow field of the computed result. Figure 12 shows the mean and fluctuating pressure coefficients compared with the experimental result at several heights.

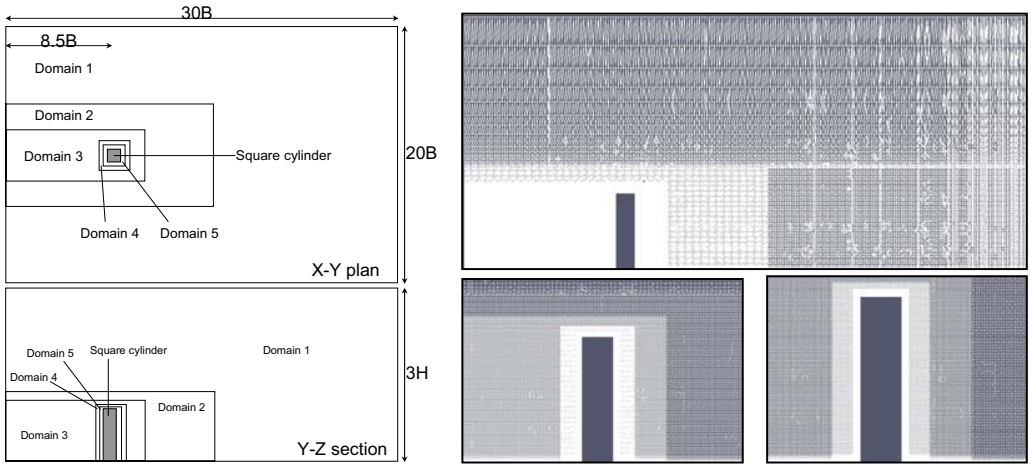

Figure 10 Outline of mesh generation by refinement function and meshes around a square cylinder

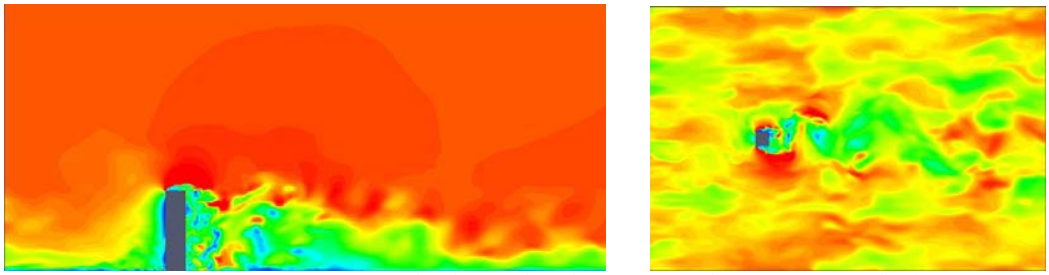

Figure 11 Instantaneous wind velocity distribution around a 3D square cylinder

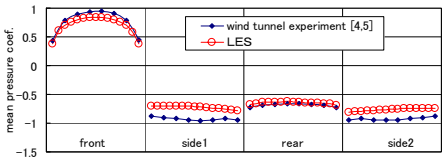

(a) mean pressure coefficient (z=3/4H)

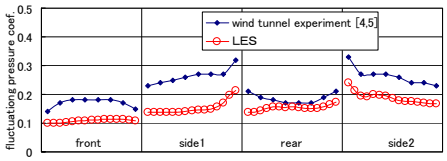

(b) fluctuating pressure coefficient (z=3/4H)

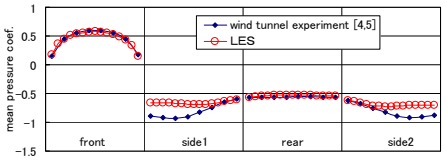

(c) mean pressure coefficient (z=1/20H)

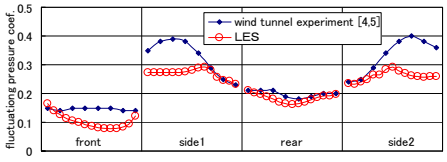

(d) fluctuating pressure coefficient (z=1/20H)

Figure 12 Pressure coefficients on a 3D square cylinder

Height at z=3/4H is located near the stagnation point, and height of z=1/20H is near the floor. Mean pressures of front and rear surfaces correspond with those of experiment. Mean pressure on side wall is different from that of experiment. Especially, it differs near the frontal location. Fluctuating pressure coefficient of front surface is different from the experimental result. At side surface, although fluctuating pressure coefficient value is different from the experimental result, it is qualitatively similar. At rear surface, fluctuating pressure coefficient is corresponding with experimental result. In this LES, since the height of the square cylinder to boundary layer thickness is higher as compared with the experiment, it can be considered that turbulent intensity in the upper part of a square cylinder is small. As a result, the fluctuating pressure coefficients are not in agreement with experimental data.

5 CONCLUSIONS

We executed LES of flow filed around a 3-dimentional square cylinder to estimate pressures on the surfaces using PIV based inflow turbulence for inflow condition. To compare LES results with experiment results, we tried to reproduce higher Reynolds number inflow turbulence modifying low-Reynolds-number turbulence provided by PIV measurement. In this paper, we proposed the method of generating inflow turbulence at higher Reynolds number, using the concept that the boundary-layer type of turbulent structures are divided into an inner and outer regions. In order to use this method, it is a future problem to maintain a continuity of turbulent structures at the connecting position. The LES results for wind pressure on the square cylinder using PIV based inflow turbulence was qualitatively in agreement with experimental data.

6 REFERENCES

Journals

1 Maruyama Y., Tamura T., Okuda Y., Ohashi M., 2012. LES of turbulent boundary layer for inflow generation using stereo PIV measurement data, Journal of Wind Engineering and Industrial Aerodynamics, In Press, Available online

2 Lund, T. S., Wu, X., Squires, K. D., 1998. Generation of turbulent inflow data for spatially developing boundary layer simulation, Journal of Computational Physics, 140, 233-258.

3 Degraaff, David B., Eaton John K., 2000. Reynolds-number scaling of the flat-plate turbulent boundary layer , Journal of Fluid Mechanics, vol.422, pp. 319-346.

Proceeding

4 Tamura T., Nozu T., Kishida T., Katsumura A., Okuda Y., 2011. Higher–accurate prediction of wind pressure on high-rise building , Proceeding of the 25th Symposium on Computational Fluid Dynamics, JSFM, pp1-3, in Japanese

Personl comunication

5 Katsumura A., Wind tunnel experiment results of pressure coefficients on a square cylinder

The Seventh International Colloquium on Bluff Body Aerodynamics and Applications (BBAA7)
Shanghai, China; September 2-6, 2012

Introduction of unstructured-grid system on LES for wind pressure estimation on a building in cities

Tetsuro Tamura [a], Tsuyoshi Nozu [b]

[a]*Tokyo Institute of Technology, G5-7 4259, Nagatsuta, Yokohama, JAPAN*
[b]*Shimizu Corporation, 3-4-17, Etchujima, Koto-ku, Tokyo, JAPAN*

ABSTRACT: This paper discusses the availability of LES on the wind-resistant design of buildings in cities. In order to predict the wind pressures on actual complicated-shaped buildings with good accuracy, we introduce the unstructured-grid system which is formulated on the open source CFD code. Especially the hybrid method is employed consisting of the Cartesian grid for the accurate turbulence structures in the urban canopy, and the unstructured-grid for the accurate wake flows around the specified building inside the densely arrayed buildings in the center of cities. The obtained results of pressure distributions, focusing on the corner of buildings, are estimated in comparison with the previous experimental data.

KEYWORDS: LES, unstructured grid, wind pressure, city

1 INTRODUCTION

This paper discusses the higher-accurate LES (Large eddy simulation) for the wind loading estimation on a specified building in cities. Thus far Urban winds have been often simulated by RANS model from an environmental point of view, where the wind velocity prediction is essential. This case showed good performance of RANS model [1]. On the LES of the urban wind, the Cartesian grid system with equal increment was often used and its accuracy was generally enough for the wind velocity prediction [2], [3]. However with regard to the wind pressure and force predictions, we have encountered a different story. This paper introduces the overset grid with finer mesh for the near region of the specified building by employing the unstructured grid system and realizes the accurate aerodynamic prediction by LES. In order to simulate numerically the turbulent flows around buildings in cities, we have to take care of the following issues:

- The approaching flow is a turbulent boundary layer over a rough wall.
- The other buildings exist neighboring to the specified building
- A pack of buildings cover a region with a relatively large area which forms a canopy locally.

Accordingly for constructing the numerical model we have to set up unsteady turbulent flow field at the inflow condition and impose the bottom boundary condition representing directly the surface shape of buildings and trees. The authors showed, on the preceding paper [3], the numerical model for urban flows in Fig. 1. This model consists of two driver regions for the approaching turbulent flow. One is for generating the turbulent boundary layer over rough surface by the rescaling technique [4] and the other is for arranging the boundary layer to develop along the fetch under the boundary condition imposed to the urban area. Also, the model has the domain which is used for LES of the flow over an actual urban area. Using the uniform grids with 2.5m in the horizontal direction and the stretching grid upward with sufficiently fine grid near the ground, the building are represented by using several tens meshes for the building

breadth. It is not fine enough for mesh to represent the building shape but the previous LES examples showed the success of the LES prediction for the flow field. Accordingly the Cartesian-grid based method can simulate the gap flows among the buildings and transportation problems of mass and gas in cities. However the predictive accuracy of the above method is ambiguous for the estimation of the wind pressures and forces on the specified building which is focused on in the city.

This study examines advantages and disadvantages for the LES model applied to the wind-resistant design of buildings under high wind and proposes the higher-accurate predictive method appropriate to practical usage.

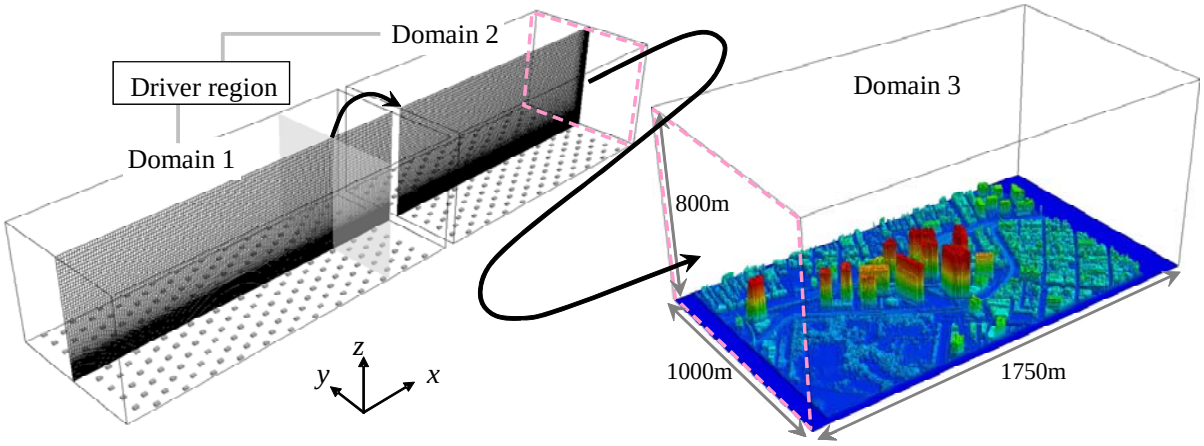

Figure 1. Numerical model of urban wind (Cartesian grid).

2 PROBLEM FORMULATIONS

2.1 *Hybrid method*

For the LES analysis for the specified building in the city center, it is important to set up how to resolve the flow around the building and its near region or the urban area consisting of many other buildings. As far as the prediction of wind velocity, it is not so significant to reproduce the shape of the building. The Cartesian grid method has been applied to this problem (see Figure 1). However in order to predict the wind pressures and forces, the overlaid method is sometimes employed, introducing the generalized coordinate system. When taking into consideration the building aspect in city, complexity level is very high due to the cladding, wall texture, window sash and balcony. Their representation requires multiple superposition of the overlaid area. These parts are so small that their influence on the wind pressure and force is weak, so they are possibly neglected. For checking it, this study introduces the numerical model which can estimate the effect of cladding, such as an unstructured grid system. Here we pick up OpenFOAM which is widely used as an open source code. Figure 2 illustrates the numerical model where the area including the specified building and its circumstances are clipped for the unstructured grid area obtained by the mesh generation software (SnappyHexa).

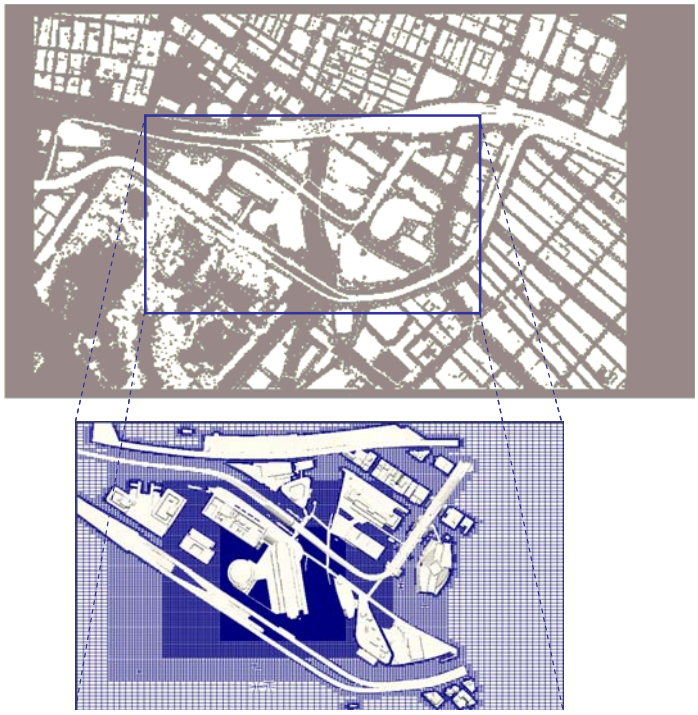

Figure 2. Unstructured grid for near-region of the building.

2.2 *Turbulent simulation*

The governing equations for LES are the filtered forms for the continuity and the incompressible Navier-Stokes equations as follows:

$$\frac{\partial \overline{u}_i}{\partial x_i} = 0 \tag{1}$$

$$\frac{\partial \overline{u}_i}{\partial t} + \overline{u}_j \frac{\partial \overline{u}_i}{\partial x_j} = -\frac{\partial \overline{p}}{\partial x_i} + \frac{\partial}{\partial x_j} \frac{1}{\mathrm{Re}} \left(\frac{\partial \overline{u}_i}{\partial x_j} + \frac{\partial \overline{u}_j}{\partial x_i} \right) - \frac{\partial}{\partial x_j} \tau_{ij} \tag{2}$$

where u_i, p, Re *and* τ_{ij} stand for velocity, pressure, the Reynolds number and the sub-grid scale (SGS) Reynolds stress ($\overline{u_i u_j} - \overline{u}_i \overline{u}_j$). Concerning the sub-grid scale modeling, the Smagorinsky type of dynamic procedure [5], [6] was employed for representing the eddy viscosity concept.

$$\tau_{ij} - \frac{1}{3}\delta_{ij}\tau_{kk} = -2\nu_e \overline{S}_{ij} = -2C\overline{\Delta}^2 \left|\overline{S}\right| \overline{S}_{ij} \tag{3}$$

where C denotes the model coefficient for SGS modeling of velocity, S_{ij} the strain rate tensor, and $\overline{\Delta} = \left(\overline{\Delta}_x \overline{\Delta}_y \overline{\Delta}_z\right)^{1/3}$ grid-filter width, respectively. The model coefficients C are evaluated dynamically using the Germano identity.

$$C = -\frac{\langle L_{ij} M_{ij} \rangle}{\langle M_{ij} M_{ij} \rangle}, \quad L_{ij} = \widetilde{\overline{u}_i \overline{u}_j} - \widetilde{\overline{u}}_i \widetilde{\overline{u}}_j, \quad M_{ij} = 2\left(\widetilde{\overline{\Delta}^2 \left| \overline{S} \right| \overline{S}_{ij}} - \overline{\Delta}^2 \widetilde{\left| \overline{S} \right| \overline{S}_{ij}} \right) \tag{4}$$

2.3 *Unstructured grid embedded in the near region of the specified building*

According to Figure 3, the curved surface of the building can be represented smoothly. On the inflow boundary of the unstructured grid area, turbulent flow is given by one-way method, which is obtained using LES on the Cartesian coordinate grid system. Appropriate resolution to the near region of the building, neighboring area and the surrounding buildings area is selected making use of the property of the unstructured grid such as the variability of the resolution on each area. Numerical method of OpenFOAM is summarized as follows [7]. This code uses the finite volume method to solve the systems of partial differential equations ascribed on any three dimensional unstructured grid of tetra, prism, hexa and polyhedral cells. The temporal term of the governing equations is treated by using the Crank-Nicolson scheme, which is the second-order difference in time. Other terms of the governing equations are discretized using the second-order limited central difference. The governing equations are solved sequentially using the resulting PISO (*P*ressure-*I*mplicit *S*plitting *O*peration) algorithm. The solution is performed implicitly by matrix inversion using the incomplete Cholesky conjugate gradient method. The code is parallelized using the message-passing interface (MPI).

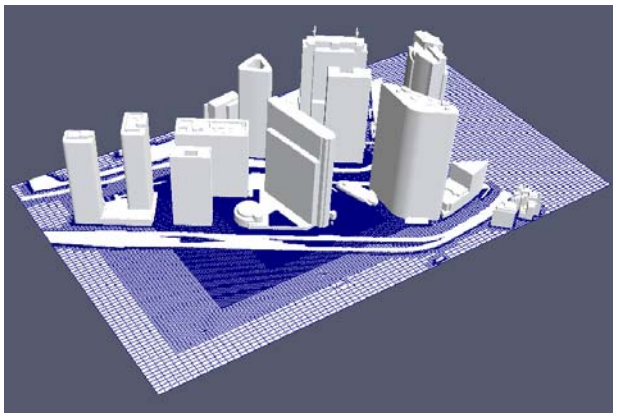

Figure 3. Unstructured grid system around buildings with smoothly curved surfaces.

3 LES RESULTS BY THE OPEN FOAM

This session shows the numerical results for turbulent flows around the buildings obtained by LES using Open FOAM as an open source code.

Figure 4 depicts the LES results for the wind velocity distributions among the densely arrayed tall buildings. It can be recognized that the flow with fully developed turbulence comes from the inflow boundary into the computational region. Also, the separated flow from a plate-shaped building at the center acts directly on the wing-type building behind and rolls into the wake formed between these two buildings. This rolling up is stronger at lower level. Also, it generates the high wind region in front of the wing-type building.

Figure 5 illustrates the turbulence structures developed behind a pack of the tall buildings. We can see that the wind velocity decreases in the wake, as increasing the fluctuation with small vortices generated there. These vortices exist in the higher altitude as well and influence widely the mechanism of unsteady flow patterns around the top edge of urban canopy.

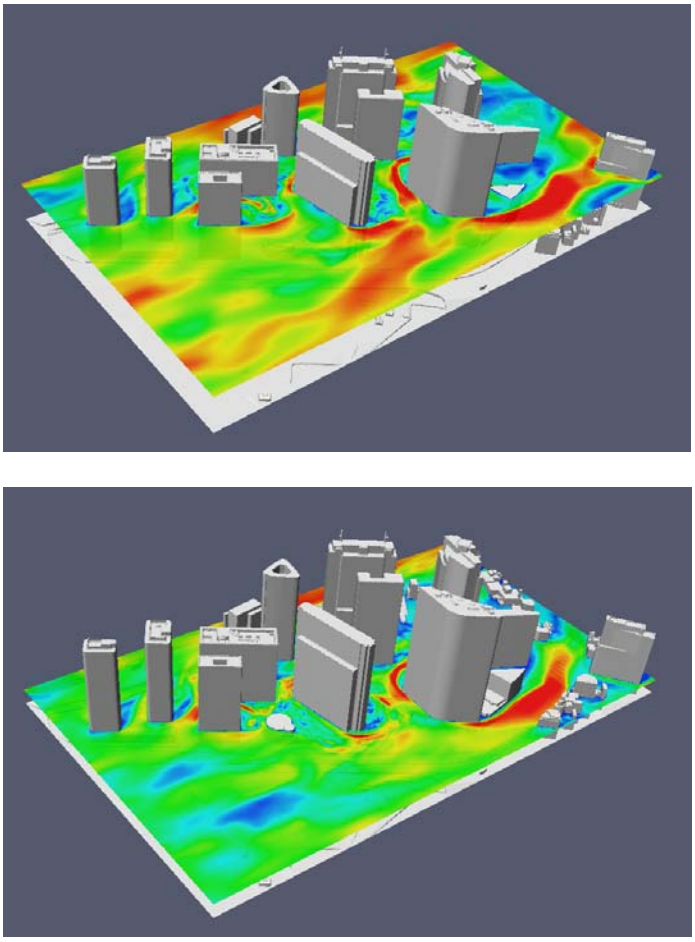

Figure 4. LES results of wind velocity around the densely arrayed buildings in cities (top: at 65m high, bottom: at 25m high).

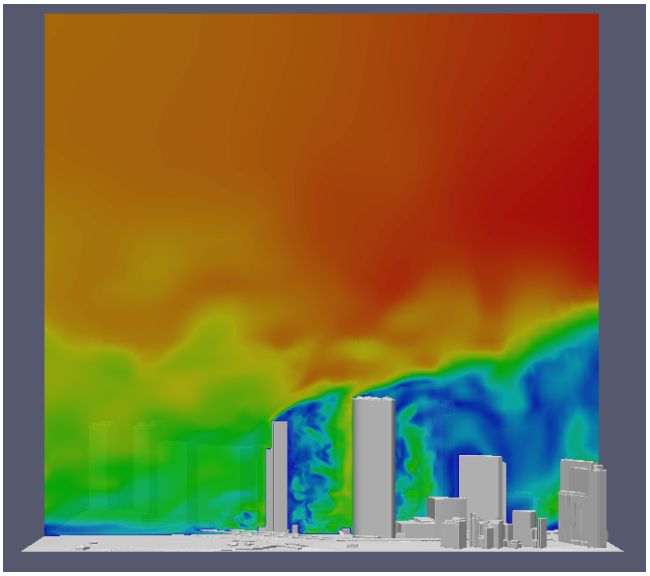

Figure 5. Computed wind velocity field on vertical section.

Figure 6 illustrates the pressure distributions on the surface of tall buildings existing densely in the triangular-shaped area. It is clearly recognized that there exist a positive pressure area at stagnation point in front of the plate-shaped tall building. Also, we can see partly high positive pressure zone at front surface of the wing-shaped building behind, where the shear flow separated from the frontal tall building acts straightly. On the tall building which locates further downstream inside a pack of tall buildings, the flow is rolling up behind the plate-shaped building and attacks with increasing its velocity. On the attacked area at the side of further downstream building, the high positive pressure occurs locally.

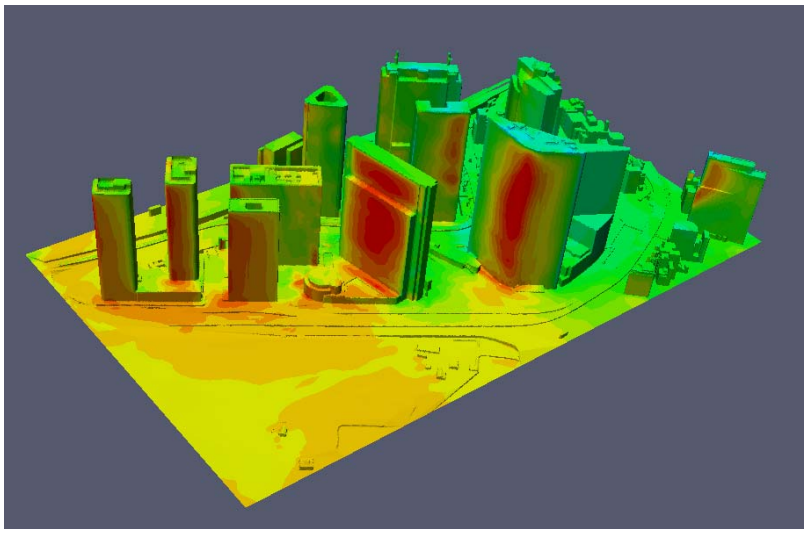

Figure 6. Computed instantaneous pressure contours on the tall buildings.

Figure 7 depicts the instantaneous streamlines added to the pressure distributions on various tall buildings in Fig.6. The flow, after attacking to the plate-shaped building, separated at its side. Subsequently the flow acted on the wing-shaped building at the rear. At the frontal stagnation of the wing building the flow is divided to right and left. One is going straight along the main street and the other is rolling inside between the plate- and the wind-shaped buildings and is followed by going into the closed-space area. Furthermore the flow attacks locally on the part of the frontal surface and forms the stagnation area biasedly. Accordingly in the packed area of tall buildings the flow is going inside with affected respectively by the surrounding building where the specific pressure distribution is attributed to each flow pattern formed.

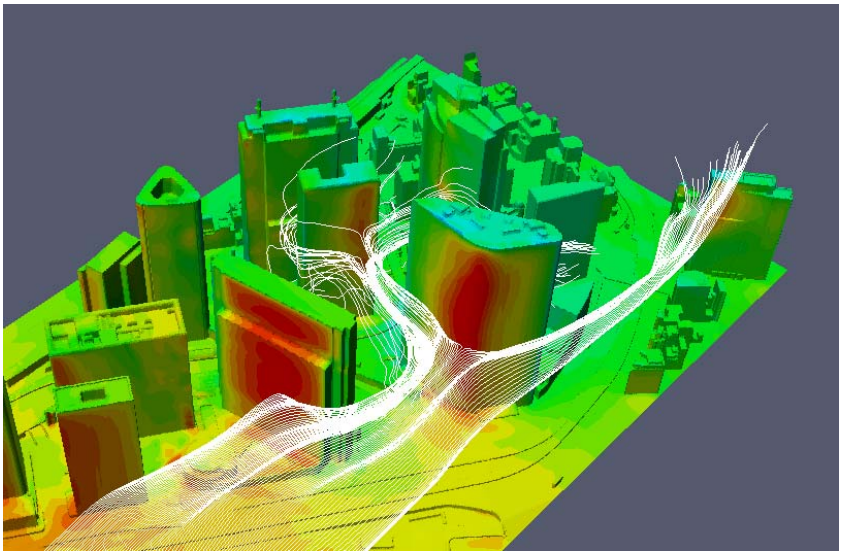

Figure 7. Computed instantaneous stream lines with pressure contours on the tall buildings.

4 PRESSURE DISTRIBUTIONS ON THE TALL BUILDING -COMPARISON WITH EXPERIMENTAL DATA

Figures 8 and 9 indicate details of the pressure distributions on the plate-shaped building. The pressures at higher level, since the section becomes smaller, are different from that of the lower level. The higher zone has another stagnation point separately and generates the very local negative pressures on both the upstream corners. Its magnitude is larger at the side of inside the pack where the separated shear layer is bending due to the surrounding buildings and approaching to the side of the plate-shape of building. Figure 9 shows the comparison of LES and experimental data for mean pressure coefficients at each height indicated by the dashed lines in Fig. 8. Correspondence of LES results (lines) and experimental data (symbols) is definitely good in quantitative sense at almost area, so guarantees the practical usage of LES technique. But the locality of the pressures on the upstream corner is so intensive that grid resolution at this area should be set with careful insight.

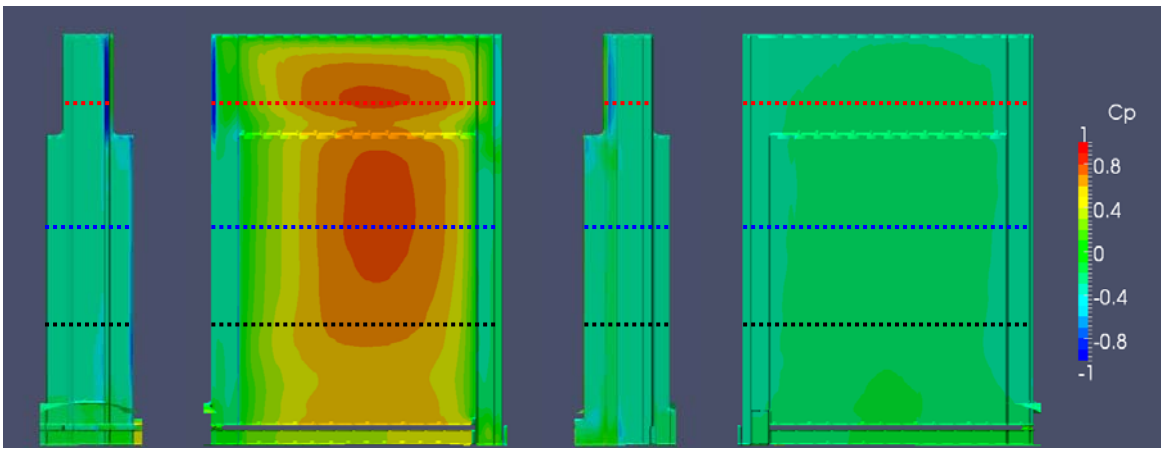

Figure 8. Computed time-averaged pressure contours on the tall building.

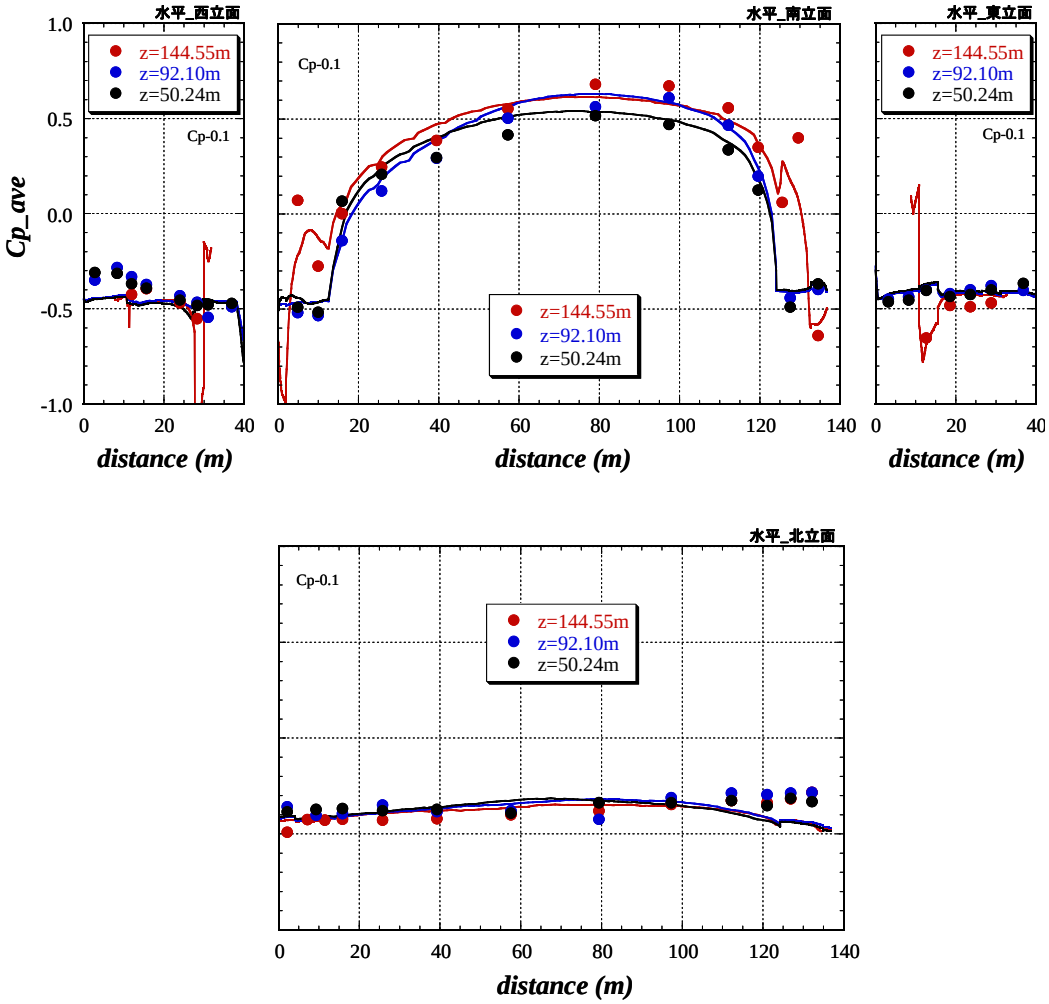

Figure 9. Computed and experimental time-averaged pressure contours at each height on the tall building(top: front and sides, bottom: back).

5 PRESSURE DISTRIBUTIONS ON THE TALL BUILDING -COMPARISON WITH EXPERIMENTAL DATA

Figure 10 shows comparison of the LES results obtained by using the conventional Cartesian grid and by using the unstructured grid system embedded in the near-region of the specified building. The unstructured grid used here is formulated at the Open FOAM and has a tendency to give solutions affected sensitively by the grid size. In the present case, very fine mesh is used near the plate-shaped building at center but the mesh behind it becomes rough rapidly. As a result, the solution there shows the vortex structures become smoother compared with the flow by the Cartesian grid and tend to lose their fine structures. But taking into consideration the same resolution at rear for Cartesian and unstructured grids, the numerical scheme of present unstructured grid has a tendency to generate the dissipative solution. This means it an expected issue that the high-accuracy of discretization for unstructured grid should be developed. However it can be considered that the finer mesh of unstructured grid in the limited area around the specified

building can generate the better results for the pressure distributions due to reproduction of the sufficiently fine turbulence structures comparable to the results by the Cartesian grid as well as the shape of the complicated building (refer to Session 4). The present overset grid method proposed is much expecting for the practical use since the unsteady structures of turbulence can be reproduced in almost area by the Cartesian grid and the higher compatibility to configuration of the object can be realized by the unstructured grid for the near area.

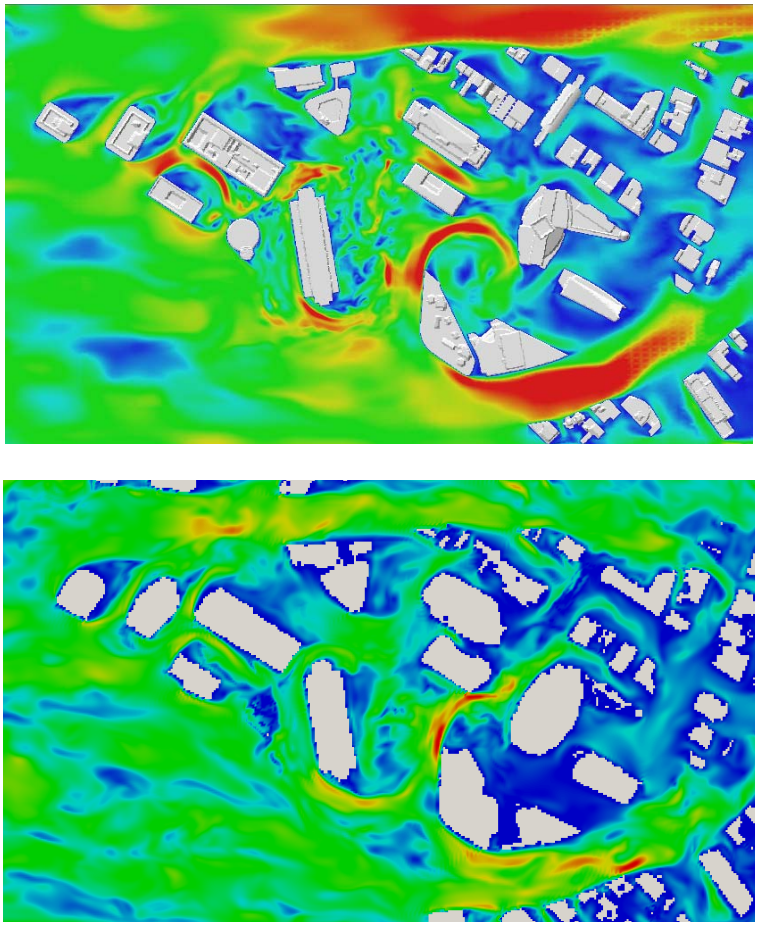

Figure 10. Comparison of wind velocity field (top: unstructured grid, bottom: Cartesian grid).

6 CONCLUSIONS

The conclusions of this study can be shown as follows:

- Using the LES model of the method overlaid by the unstructured grid system, the appropriate turbulence structures at inflow and among a pack of tall buildings can be simulated.
- The pressure distribution on the specified building obtained by the present LES is appropriate in order to realize the practical use of CFD technique for wind-resistant design of the buildings.

7 REFERENCES

1 B. Blocken, S. Roels, J. Charmeliet, Modification of pedestrian wind comfort in the Silvertop Tower passages by an automatic control system. J. Wind Eng. Ind. Aerodyn., 92, (2004) 849-873.

2 T. Tamura, Y. Okuda, T. Kishida, O. Nakamura, K. Miyashita, A. Katsumura, M. Tamari, LES for aerodynamic characteristics of a tall building inside a dense city district, CWE2010, 2010.

3 T. Nozu, T. Tamura, LES of turbulent wind and gas dispersion in a city, J. Wind Eng. Ind. Aerodyn.

4 K. Nozawa, T.Tamura, Large eddy simulation of the flow around a low-rise building in a rough-wall turbulent boundary layer, J. Wind Eng. Ind. Aerodyn., 90, (2002) 1151-1162.

5 M. Germano, U. Piomelli, P. Moin, W.H. Cabot, A dynamic subgrid-scale eddy viscosity model, Physics of Fluids, A, vol. 3, No. 7, (1991) 1760-1765.

6 D.K. Lilly, A proposed modification of the Germano subgrid-scale closure method, Phys. Fluids, Vol. A4, No. 3, (1992) 633-635.

7 OpenFOAM, http://www.openfoam.com/

Author Index

Author Name		First page				
Freda	A.	**793**	**939**	**1162**		
Fu	J. Y.	**1584**				
Fusto	E.	**1729**				
Galal	K.	**1209**				
Garber	J.	**151**				
Ge	Y. J.	**161**	**170**	**344**	**399**	**410**
		441	**480**	**765**	**1048**	**1359**
		1365	**1604**	**1618**	**1891**	
Georgakis	C. T.	**689**	**699**			
Geurts	C.	**531**	**1314**	**1776**		
Giappino	S.	**327**				
Gilbert	T.	**1457**				
Gioffrè	M.	**825**				
Goto	T.	**1639**				
Gousseau	P.	**1028**	**1682**			
Gromke	C.	**1421**				
Gu	D.	**244**				
Gu	M.	**510**	**813**	**959**	**1197**	**1238**
		1429				
Guan	Q. H.	**1078**				
Guha	T. K.	**1228**				
Gui	X. L.	**546**				
Guo	C. P.	**1078**				
Guo	Z. S.	**429**				
Guo	Z. W.	**480**				
Gurka	R.	**1766**				
Hagishima	A.	**1656**				
Haines	M.	**1276**				
Han	N.	**510**				
Han	W. S.	**774**				
Han	Y.	**1742**				
Han	Z. L.	**546**				
Hasegawa	K.	**180**				
He	T.	**601**				
He	Y.	**877**				
He	Y. C.	**1842**				
Heijst	G. J. F.	**1028**	**1682**			
Hemida	H.	**1709**				
Hemmatti	A.	**1124**				
Hernández	S.	**112**	**1038**	**1490**		
Hespel	P.	**1666**				

Author Name		First page				
Li	H.	**664**	**1086**			
Li	J. W.	**755**	**774**	**1078**	**1096**	
Li	K. M.	**1334**				
Li	L. Y.	**1359**				
Li	M. S.	**1058**				
Li	Q. S.	**214**	**835**	**1187**	**1842**	**1921**
Li	S. Y.	**654**				
Li	Y. C.	**1447**				
Li	Y. L.	**1467**	**1474**	**1719**	**1911**	
Li	Y. G.	**1183**				
Li	Y. Q.	**200**	**1220**			
Li	B.	**1823**				
Li	Q. X.	**521**				
Liang	C. C.	**1447**				
Liang	S. G.	**565**				
Liao	H. L.	**419**	**889**	**1058**	**1371**	**1474**
		1911				
Lim	H. C.	**244**				
Lin	G. C.	**1020**				
Lipecki	T.	**282**	**573**	**1142**	**1152**	
Liu	A. J.	**1832**				
Liu	G. G.	**1569**				
Liu	J. X.	**774**	**1078**	**1096**		
Liu	M. G.	**141**				
Liu	Q. K.	**671**				
Liu	S. Y.	**441**				
Liu	X. B.	**1528**				
Liu	X. P.	**1618**				
Liu	Y. B.	**1709**				
Liu	Z. M.	**1709**				
Liu	Z. Q.	**1881**				
Liu	Z. W.	**1500**	**1528**			
Lo	Y. L.	**1594**	**919**			
Lou	W. J.	**1902**				
Lu	A. P.	**344**				
Ma	T. T.	**161**				
Ma	W. Y.	**671**				
Maeda	J.	**621**	**1871**			
Makihara	K.	**1381**				
Marrè-Brunenghi	M.	**793**				
Martinuzzi	R. J.	**929**	**1854**			

Author Name		First page		
Maruyama	Y.	**1966**		
Matsui	M.	**356**	**1248**	
Matsukawa	S.	**555**		
Matsumiya	H.	**715**		
Matsumoto	M.	**23**		
Mattana	A.	**1729**		
Matteoni	G.	**689**		
McCarthy	J. M.	**1401**		
McClean	J. F.	**899**	**1786**	
Mehta	K. C.	**1114**		
Meng	X. L.	**429**		
Mochizuki	M.	**1864**		
Montazeri	H.	**1674**		
Moonen	P.	**1000**		
Morbiato	T.	**1729**		
Morgenthal	G.	**490**	**1536**	
Muggiasca	S.	**327**		
Nagao	F.	**555**		
Nakamura	M.	**1550**		
Nakamura	O.	**393**		
Nakashima	T.	**1699**		
Nguyen	C. H.	**1162**		
Nieto	F.	**112**	**1038**	**1490**
Nishihara	T.	**715**		
Nishijima	K.	**364**		
Noda	M.	**555**		
Norris	S. E.	**1411**		
Nouzawa	T.	**1699**		
Nozawa	K.	**206**	**1942**	
Nozu	T.	**206**	**1974**	
Ohashi	M.	**1805**	**1966**	
Ohkuma	T.	**356**	**1324**	
Okada	R.	**1304**		
Okada	Y.	**1699**		
Okuda	Y.	**1805**	**1966**	
Ono	Y.	**1950**		
Ooka	R.	**969**		
Ortiz	X.	**1124**		
Otsubo	K.	**621**	**1871**	
Ou	J. P.	**1266**		
Pagani	A.	**725**		

Author Name		First page				
Stathopoulos	T.	**978**	**1209**			
Sterling	M.	**1457**	**1480**			
Sterling	S.	**1276**				
Stoyanoff	S.	**151**	**725**			
Sumner	D.	**899**	**1786**			
Sun	B. N.	**1569**				
Sun	X. Y.	**234**				
Sun	H. X.	**1183**				
Sun	Y.	**1579**				
Sun	Y. G.	**1058**				
Suo	Q. F.	**419**				
Suzuki	K.	**640**				
Szabó	G.	**1349**				
Szecsányi	L.	**1349**				
Takeda	F.	**1294**				
Takeuchi	T.	**621**				
Tamura	T.	**1942**	**1950**	**1960**	**1966**	**1974**
Tamura	Y.	**200**	**356**	**383**	**393**	**500**
		705	**849**	**1248**	**1256**	**1304**
		1437	**1560**			
Tanaka	S.	**1550**				
Tang	H. Q.	**565**				
Tang	S. R.	**664**				
Tang	Y.	**541**	**803**			
Tanimoto	J.	**1656**				
Tatewaki	Y.	**919**				
Taylor	Z. J.	**1766**				
Thompson	M. C.	**13**				
Tian	Y. J.	**1823**				
Tominaga	Y.	**1020**				
Tomokiyo	E.	**1871**				
Toshimitsu	K.	**1639**				
Tse	T. K. T.	**1429**				
Tsubokura	M.	**1699**				
Tsurumi	T.	**1324**				
Tu	J. H.	**591**				
Tu	N. K.	**959**				
Tubino	F.	**1162**				
Tun	Y.	**254**				
Uematsu	Y.	**1294**	**1550**			
Vullo	E.	**151**	**725**			

Author Name		First page				
Wang	B.	**1719**				
Wang	C. Y.	**1508**				
Wang	D. Y.	**521**				
Wang	F.	**1304**				
Wang	H. F.	**949**	**1754**			
Wang	L.	**565**				
Wang	Q.	**419**	**1371**			
Wang	T.	**1891**				
Wang	X.	**1197**				
Wang	X.J	**1183**				
Wang	Y.	**671**				
Wang	Y. P.	**1334**				
Watkins	S.	**1401**				
Weng	X. Y.	**1048**				
Wevers	C.	**1010**				
Wong	J.	**631**				
Wood	D.	**1124**				
Wu	D.	**813**				
Wu	J. R.	**1584**				
Wu	M. X.	**1467**				
Wu	T.	**56**	**453**	**470**	**654**	**1932**
Wu	T. R.	**1508**				
Wu	Y.	**234**	**1579**			
Xiang	H. F.	**1365**				
Xiang	H. Y.	**1467**	**1474**			
Xie	J. M.	**104**				
Xing	X. J.	**1078**				
Xiong	Y.	**959**				
Xu	A.	**1584**				
Xu	F. Y.	**272**	**1902**			
Xu	K.	**170**				
Xu	M. X.	**1754**				
Xu	Y. L.	**889**	**1719**			
Xue	Y.H.	**1692**				
Yamada	H.	**180**	**264**			
Yan	B. W.	**1921**				
Yan	X.G.	**1183**				
Yan	Y. L.	**803**				
Yang	D. C.	**1365**				
Yang	L. G.	**541**	**1429**			
Yang	Q.	**849**				